



## Impedance of Silver Oxide-Zinc Cells

H. A. Frank,\* W. L. Long, and A. A. Uchiyama\*

Jet Propulsion Laboratory, Pasadena, California 91103

### ABSTRACT

Over 100 sealed AgO-Zn cells were subjected to prolonged periods of storage over a range of temperatures and storage modes including open circuit, trickle charge, and float charge. Impedances of these cells were monitored throughout and to the end of the storage period at which point their transient voltage characteristics were observed at the onset of discharge. Results revealed that the impedances of these cells tended to increase with time on stand and that the magnitude of the impedance rise was dependent primarily on temperature and to a lesser degree on storage mode. Typical values for 50 A-hr cells were usually less than 100 mohm at time zero (immediately after activation) and from 1 to 30 ohm after 6-10 months of storage. Transient voltages of these cells were noted to drop sharply during the first msec of discharge and then to rise and reach a stabilized value during the following few seconds. Magnitude of the initial drop as well as the stabilized voltage values were found to be related to impedance but not in a linear manner. Magnitude and duration of the low transient voltages may be unacceptable in some applications of these cells. Cause for the impedance variations is attributed to changes that occur at the positive electrode. Results provide new and useful information for designers and users of AgO-Zn-based power systems.

During the course of test and evaluation of AgO-Zn cells and batteries for Mariner spacecraft (1), it was deemed advisable to measure, among other characteristics, internal cell impedance in that these impedance measurements were known to be nondestructive and to provide additional back-up data along with weight, voltage, capacity, etc., to insure uniformity and functionality of the flight cells.

Periodic review of the tabulated data revealed what was believed to be a trend towards increased impedance with increased time on stand. This observation was deemed significant for two reasons. First, the trend had not heretofore been reported in the literature. There was in fact found to be a relative scarcity of information on impedances of AgO-Zn cells (2). Secondly, the trend could conceivably cause voltage regulation problems on the Mariner power system or any other AgO-Zn-based power system which was to be subjected to long periods of stand before use.

As a result of these considerations, it was deemed advisable to initiate a separate and detailed study on the impedance characteristics of AgO-Zn cells. First, it was desired to obtain data on the impedance variations of these cells during the course of stand over a range of temperatures and storage modes including open circuit, trickle charge, and float charge. Next, it was desired to examine the transient voltage characteristics of these cells at the onset of discharge after the stand period. Finally, as a supplemental objective, it was desired to examine any possible correlation between impedance and state of charge of AgO-Zn cells.

\* Electrochemical Society Active Member.

Key words: AgO-Zn cells, impedance of electrochemical cells, storage modes, transient discharge voltages.

### Experimental

The cells which were employed in this study were the same as those which were flown on the Mariner VI and VII spacecraft. These were manufactured by the Electric Storage Battery Company and were designated as Model 257. The cells were packaged in plastic (ABS) cases as three-cell monoblocks as shown in Fig. 1. Rated capacity of each was 50 A-hr. Each cell contained 12 positive and 13 negative plates and its electrolyte consisted of 153g of 45% KOH. Each of the 12 positive plates contained 13.8g of active material with width, height, and thickness of 6.45 cm, 7.82 cm, and 0.65 cm, respectively. Eleven of the 13 negative plates were located in the center of the cell stack.

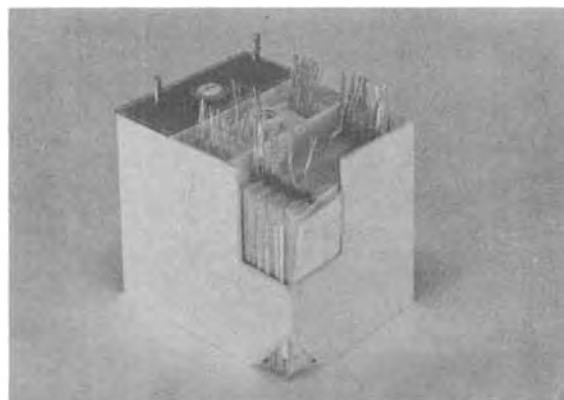


Fig. 1. AgO-Zn monoblock (3 cells, 50 A-hr each)

These were identical and each contained 11.7g of active material, had the same width and height as above, and thickness of 0.11 cm. The other two negative plates were the end plates in the stack. These contained 5.7g of active material, the same width and height as above, and thickness of 0.07 cm. Absorber material on the positive plates consisted of one turn of polypropylene with thickness of 0.015 cm. Retainer material on the negative plates consisted of one fold of a cellulose material (Viscon Type RD.35) with thickness of 0.008-0.013 cm. Separation consisted of six turns of 0.025 cm cellophane on each positive plate. The positive plates were prepared by first milling sheets of silver powder dispersed in a plastic pore former which was later burned off in a sintering process. Two sheets were then pressed on either side of a silver grid and the assembly was then sintered to form a plate. The negative plates were prepared by pressing a mixture of ZnO, HgO, and Teflon on both sides of a silver grid. The cell was assembled by installing the unformed plates (Ag and ZnO), adding electrolyte, and then forming the plates by charging at 1.85A. Excess electrolyte was then drained from the cell and the cell was finally sealed and ready for use. Over-all cell weight was 660g.

All impedance measurements were made with a commercial milliohmeter (Keithley Instruments Model 503) modified by placing a 12,000 mF electrolytic capacitor in series with its constant current leads and voltage sensing leads. The instrument operated by delivering 40 Hz square wave current (0.033-0.0001A rms) in the current leads and measuring voltage drop across the voltage sensing leads with a synchronous vacuum tube voltmeter. The meter contained several ranges from 1 mohm to 100 ohm. Calibration checks with precision shunts were performed periodically and accuracy of all ranges was always found to be within  $\pm 2\%$  of full scale.

Test procedures, unless otherwise noted, were the same for each cell and consisted of the following. First, the impedance and open circuit voltage of the cells were measured in the "as-received" condition from the manufacturer. Next, the cells were given a "top-off" charge to insure that they were fully charged at the beginning of the test period. This "top-off" charge was carried out at constant current of 0.6A to a cutoff voltage of 1.97V. At this point, the cells were divided into several groups, each of which was placed on a different mode of stand. One group was left in the open circuit, fully charged condition and placed in an environmental chamber at 4°C. Two other groups were similarly left in the open circuit, fully charged condition and placed in other environmental chambers at temperatures of 21° and 38°C. One group was discharged 50% and then placed on open circuit stand at room temperature, 21°C. Another group was discharged 100% and then placed on open circuit stand again at room temperature. Three other groups were placed on stand under the condition of constant current trickle charge at room temperature and at currents of 2, 5, and 10 mA. Finally, one group was placed on stand under the condition of constant potential "float" charge at 1.87 V/cell and at room temperature. Voltages and impedances of all cells were measured periodically at intervals of at least once per week.

The transient discharge voltage measurements were carried out on three-cell monoblocks rather than on single cells. The monoblocks were wired with heavy duty cable across 4.5 ohm loads (to give a nominal current of 10A) and discharge was triggered with a heavy duty mercury switch. Monoblock voltages were measured with both an oscilloscope (Tektronix, Model 535 A, equipped with a Polaroid camera) and an oscillograph (Sanborn, Model 297).

## Results

Impedance and voltage variations of the cells during the various modes of stand are given in Fig. 2 through 10. In each of these figures the shaded areas cover the

range in values of impedance and voltage for the indicated number of cells. Figures 2, 3, and 4 give the characteristics of cells on stand in the open circuit and fully charged condition at temperatures of 4°, 21°, and 38°C, respectively. Figure 5 gives the characteristics of cells on stand in the open circuit and 50% discharged condition at 21°C. Figure 6 gives the characteristics of cells on stand in the open circuit and 100% discharged condition at 21°C. Figures 7, 8, and 9 give the characteristics of cells on stand at 21°C, with application of constant current trickle charge currents of 2 mA, 5 mA, and 10 mA, respectively. Figure 10 gives the characteristics of cells on stand at 21°C with application of a constant potential "float" charge of 1.87 V/cell.

Figures 11 and 12 give typical variations in impedance and voltage of these cells during the course of charge and discharge.

Table I gives the impedance values of a cell before and 1.0 sec after a discharge period at 10A.

Figures 13, 14, and 15 give the voltage characteristics of three typical monoblocks during the onset of discharge. Table II summarizes the pertinent data from these figures and also gives additional monoblocks and cell data. The first two columns in Table II designate the monoblock numbers and their respective cell numbers. The next two columns give the individual cell and monoblock open circuit voltages, respectively, after they had equilibrated at room temperature and before discharge. The next two columns give the individual cell and monoblock impedances before the discharge period. The next column gives the minimum monoblock voltage during the first millisecond of discharge as per the oscilloscope trace. The last column gives the "stabilized" monoblock voltage after the first few seconds of discharge as per the oscillograph trace.

Figures 16 and 17 give the relationship between a cell's impedance and its transient voltages at the onset of discharge. These curves were obtained by normalizing the data in Table II.

Figures 18 through 21 give the impedance and voltage histories of cells which exhibited short circuit failure modes. Finally, Fig. 21 gives the effect of ambient temperature on the impedance of three typical cells, and Table III gives the resistivity of silver and its oxides.

## Discussion

Falk and Salkind state that the impedance of sealed silver batteries is usually quite low and that typical values for partially discharged cells range from 0.07/C to 0.40/C ohm, where C is the cell capacity in A-hr (3). On this basis, the impedances of the 50 A-hr cells employed herein would be expected to range from 1.4 to 8 mohm. Inspection of Fig. 5 and Table I reveals that the initial impedances of partially discharged 50 A-hr cells ranged from 5 to 11 mohm. Therefore, there appears to be good agreement between the observed and literature values of Ag-Zn cell impedance.

Examination of Fig. 2, 3, and 4 reveals a gradual increase in impedance with time for cells on open circuit stand in the fully charged condition. The change in impedance with time was noted to increase somewhat with ambient temperature. For example, the impedances of cells stored for 8 months were noted to be in the range of 1.3 to 3.3 ohm at 4°C, 2.5 to 3.5 ohm at 21°C, and 9.0 to 16.0 ohm at 38°C. Open circuit voltages of the cells stored at 4° and 21°C were noted to remain relatively constant near 1.86V throughout the entire test period. Open circuit voltages of the cells stored at 38°C were however, noted to decline slightly during this period with a

Table I. Impedance values of cell No. 766 before and 1.0 sec after discharge at 10A. Cell voltage was 1.845V before discharge and 1.390V near end of discharge period.

Impedance before discharge	3.400 ohm
Impedance after 1.0 sec discharge at 10A	0.015 ohm



Table II. Impedances and transient voltages of monoblocks at the onset of a 10A discharge

Monoblock No.	Cell No.	Cell OCV (V)	Monoblock OCV (V)	Cell impedance (ohm)	Monoblock impedance (ohm)	Minimum transient monoblock voltage (V)*	Stabilized monoblock voltage (V)**
1	1639	1.86	5.58	0.080	0.24	4.73	4.80
	1640	1.86		0.075			
	1641	1.86		0.082			
2	1642	1.86	5.58	0.085	0.27	4.6	4.75
	1643	1.86		0.106			
	1644	1.86		0.082			
3	1726	1.86	5.58	0.062	0.21	4.83	4.85
	1727	1.86		0.074			
	1728	1.86		0.071			
4	1741	1.86	5.58	0.071	0.30	4.63	4.75
	1742	1.86		0.146			
	1743	1.86		0.080			
5	1645	1.86	5.58	0.420	1.31	3.63	4.40
	1646	1.86		0.440			
	1647	1.86		0.450			
6	1648	1.86	5.58	0.360	1.18	3.73	4.40
	1649	1.86		0.410			
	1650	1.86		0.410			
7	1729	1.86	5.58	0.330	1.19	3.78	4.50
	1730	1.86		0.400			
	1731	1.86		0.460			
8	1744	1.86	5.58	0.290	1.01	3.88	4.56
	1745	1.86		0.360			
	1746	1.86		0.360			
9	1651	1.85	5.55	2.330	11.73	3.00	4.36
	1652	1.85		5.200			
	1653	1.85		4.200			
10	1654	1.85	5.55	5.700	12.10	2.95	4.30
	1655	1.85		4.200			
	1656	1.85		2.200			
11	1732	1.85	5.55	3.100	10.80	3.00	4.38
	1733	1.85		4.000			
	1734	1.85		3.700			
12	1747	1.85	5.55	3.600	11.40	3.00	4.44
	1748	1.85		4.200			
	1749	1.85		3.600			

\* From oscilloscope trace during first msec.

\*\* From oscillograph trace during first 10 sec.

minimum value of 1.847V for one cell. Examination of Fig. 5 reveals a somewhat lower rate of increase in impedance with time for cells which were stored in the 50% discharged condition. Impedances of a few such cells given in Fig. 5 were found to remain in the range of 0 to 10 mohm throughout the entire test period. Open circuit voltages of these cells remained in the range of 1.59 to 1.62V throughout the test. Examination of Fig. 6 reveals that cells which were stored in the fully (100%) discharged condition exhibit a constant and low impedance in the range of 2 to 3 mohm throughout the entire test. Open circuit voltages of these cells remained in the range of 1.58 to 1.60V during this time.

Examination of Fig. 7, 8, and 9 reveals an unusual but yet consistent shape of the impedance-time curves for cells which were stored with application of a constant current trickle charge. Impedance is noted to first pass through a maximum, then a minimum, and finally to continue a gradual increase with increase in stand time. A rigorous explanation of the shape of these curves is not available at the present time. It is noted, however, that the transition from the maximum to the minimum in the impedance curves occurs at a point in time when the cell voltages rise from the 1.9V level to the 2.0V level. Since gassing ( $O_2$  evolution) is known to occur at the higher voltages, it is quite likely then that the unique shape of the impedance-time curves is associated with gassing and pressure rise. Aside from this point, however, there is noted to be good correspondence, at least in the early stages of stand, between the shape and slope of the impedance vs. time curves for cells stored in this mode and those stored on open circuit. In addition, it

is noted that those cells which were stored at the higher current levels of 5 and 10 mA (not necessarily recommended by the manufacturer) developed leaks after periods of 6 to 2 months, respectively. These current levels are therefore excessive for long-term

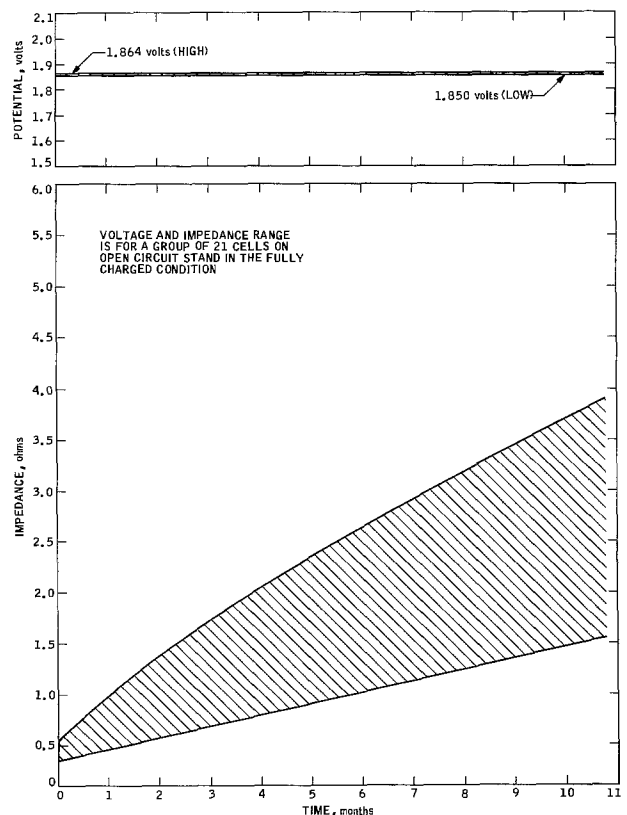


Fig. 2. Voltage and impedance of cells on open circuit stand in the fully charged condition at 4°C.

Table III. Resistivity of silver and its oxides (10)

Component	Resistivity (ohm-cm)
Ag	$1.6 \times 10^{-6}$
Ag <sub>2</sub> O	$10^8$
AgO	10

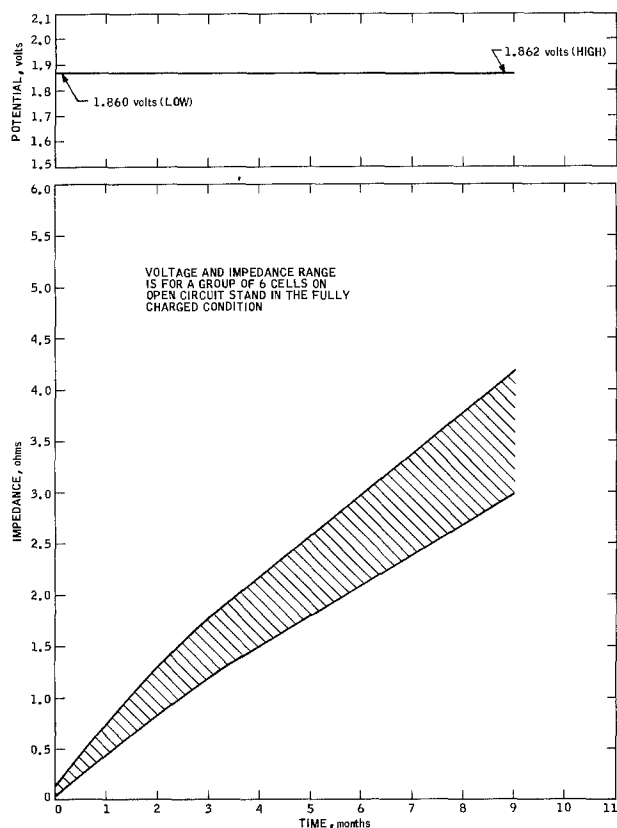


Fig. 3. Voltage and impedance of cells on open circuit stand in the fully charged condition at 21°C.

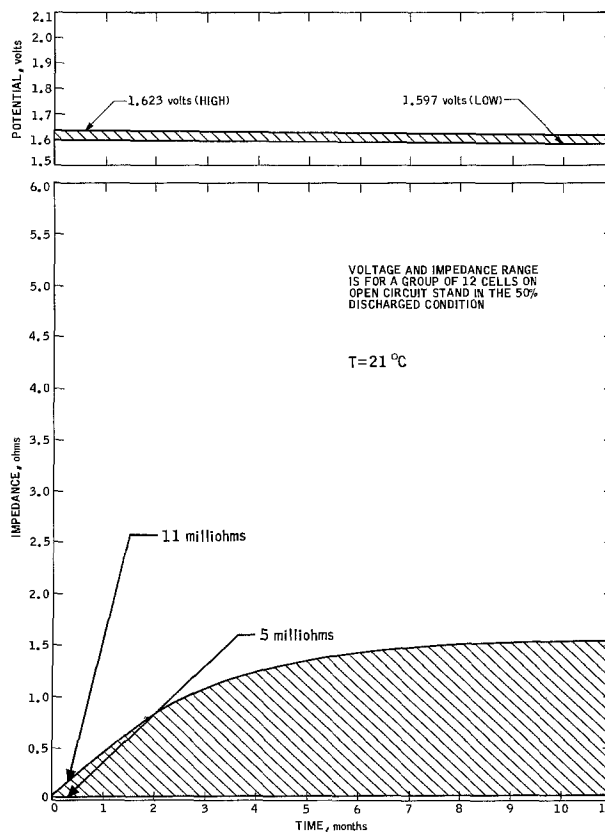


Fig. 5. Voltage and impedance of cells on open circuit stand in the 50% discharged condition at 21°C.

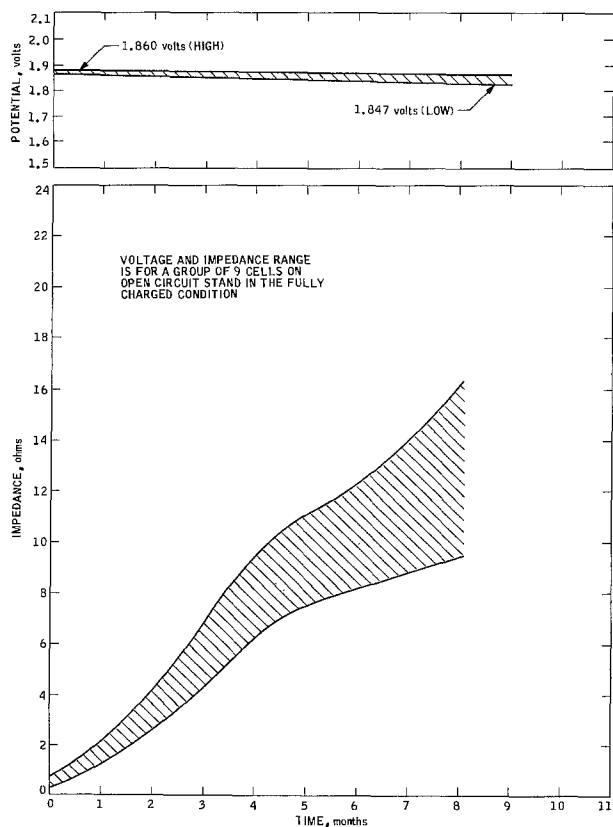


Fig. 4. Voltage and impedance of cells on open circuit stand in the fully charged condition at 38°C.

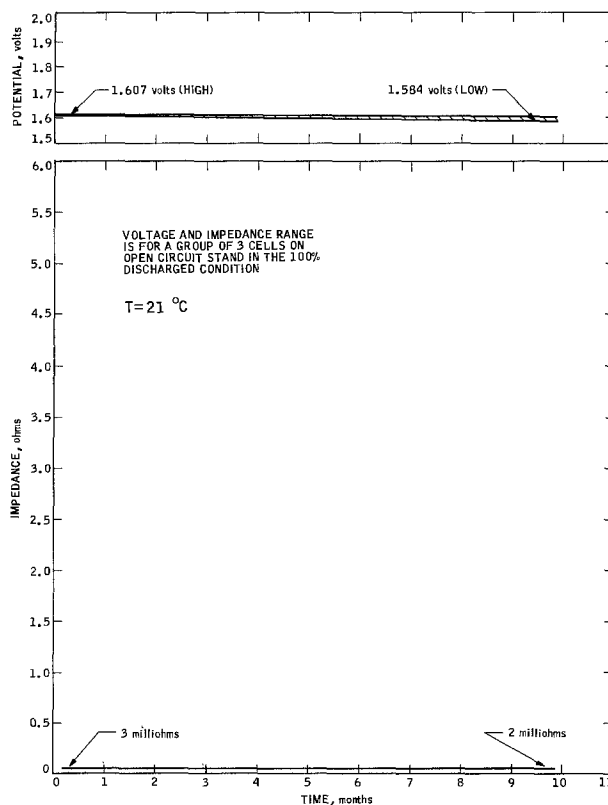


Fig. 6. Voltage and impedance of cells on open circuit stand in the 100% discharged condition at 21°C.

storage of this size cell and the maximum level for safe storage is estimated to be near 2 mA.

The variation of cell impedance with time on stand is attributed to chemical changes that occur within the positive silver electrodes. At any given time the species

which are present in this electrode are the higher oxide,  $\text{AgO}$ , the lower oxide,  $\text{Ag}_2\text{O}$ , and silver metal,  $\text{Ag}$ . In a freshly and fully charged cell, the predominant species is the higher oxide  $\text{AgO}$  which, as indicated in Table III, has a relatively low resistivity. Hence, the impedance of a freshly charged cell should

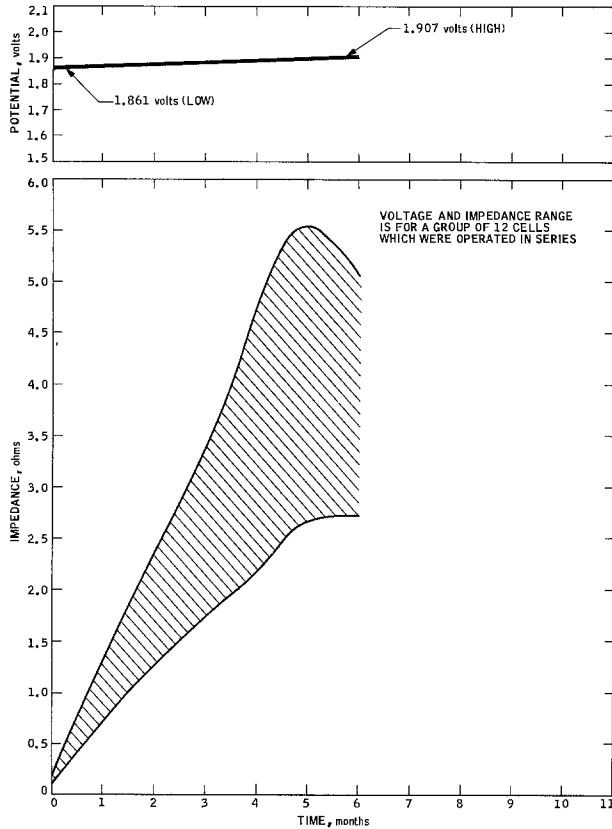


Fig. 7. Voltage and impedance of cells on 2.0 mA constant current trickle charge at 21°C.

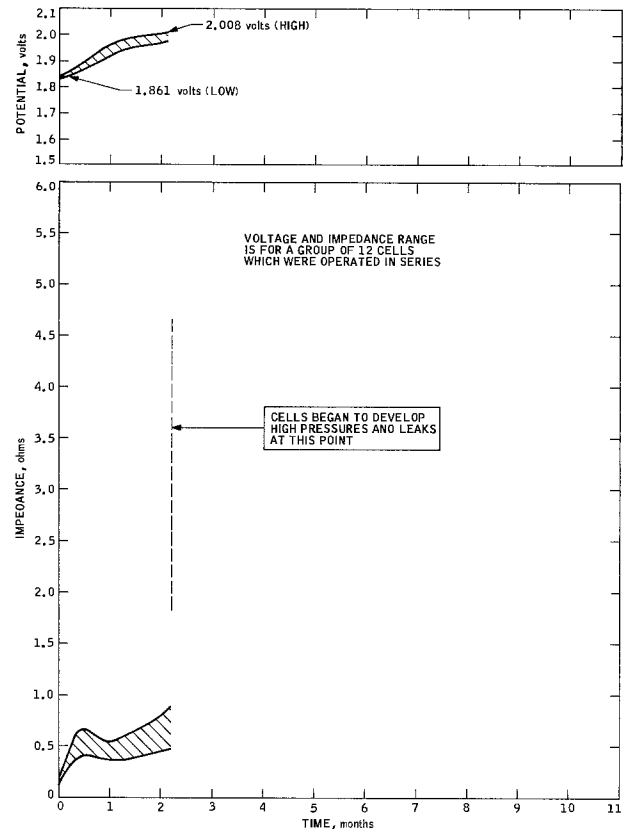


Fig. 9. Voltage and impedance of cells on 10.0 mA constant current trickle charge at 21°C.

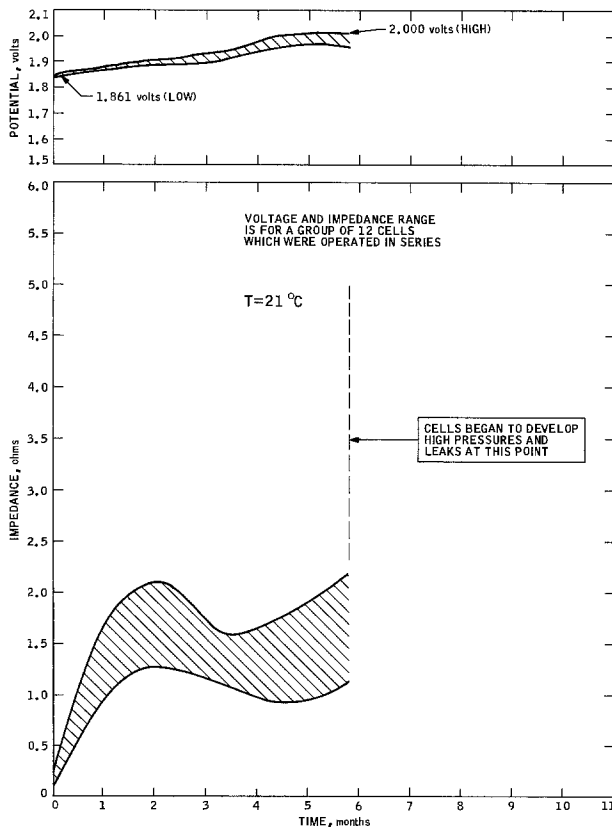


Fig. 8. Voltage and impedance of cells on 5.0 mA constant current trickle charge at 21°C.

and has been found to exhibit relatively low impedance as evidenced by the above results. During the course of extended periods of stand, the higher oxide, AgO, is slowly converted to the lower oxide, Ag<sub>2</sub>O, via two possible chemical reactions. The first of these

involves decomposition of the higher oxide to form the lower oxide and oxygen ( $2\text{AgO} \rightarrow \text{Ag}_2\text{O} + \frac{1}{2}\text{O}_2$ ) (4). The second involves reaction of the higher oxide with metallic silver particles and the silver grid to form the lower oxide ( $\text{Ag} + \text{AgO} \rightarrow \text{Ag}_2\text{O}$ ) (5). The net result of these reactions is believed to be the formation of a layer of Ag<sub>2</sub>O which completely surrounds the electrode. As noted in Table III, the resistivity of the Ag<sub>2</sub>O material is exceptionally high so that the growth of the layer of this material is the most likely explanation of the observed trend towards increased impedance with time on stand. Support for this explanation is given in a prior study of Ag electrodes by Cahan *et al.* (6). The observed trend toward increased rate of change of impedance at elevated temperatures is compatible with the above in that the above reactions proceed faster at the elevated temperatures and proceed to form the layer at a faster rate. The fact that the partially and completely discharged cells did not exhibit as large a rise in impedance as the fully charged cells is also compatible with the above in that these cells contain appreciable amounts of highly conductive silver particles (see Table III) that provide low resistance electrical paths. The fact that the cells on both constant current and float charge (Fig. 7-10) also exhibited increased impedance with time on stand would at first glance appear to be contradictory to the above explanation regarding a buildup of a layer of Ag<sub>2</sub>O. The basis for this contradiction would be that the application of a charge current would tend to reconvert the high resistance layer of Ag<sub>2</sub>O back to the lower resistance AgO material. The only explanation for the observed results in these cases is, then, that the rate of formation of the Ag<sub>2</sub>O layer (by the above reactions) is greater than the rate of conversion of the Ag<sub>2</sub>O layer to AgO material (by electrochemical reaction). Some basis for this explanation can be established by comparing known rates of formation of Ag<sub>2</sub>O *via* decomposition of AgO with the rates at which Ag<sub>2</sub>O would be electrochemically reconverted to AgO by the currents employed in these tests. Ruetschi, for example, shows that at 45°C the decomposition rate of AgO in

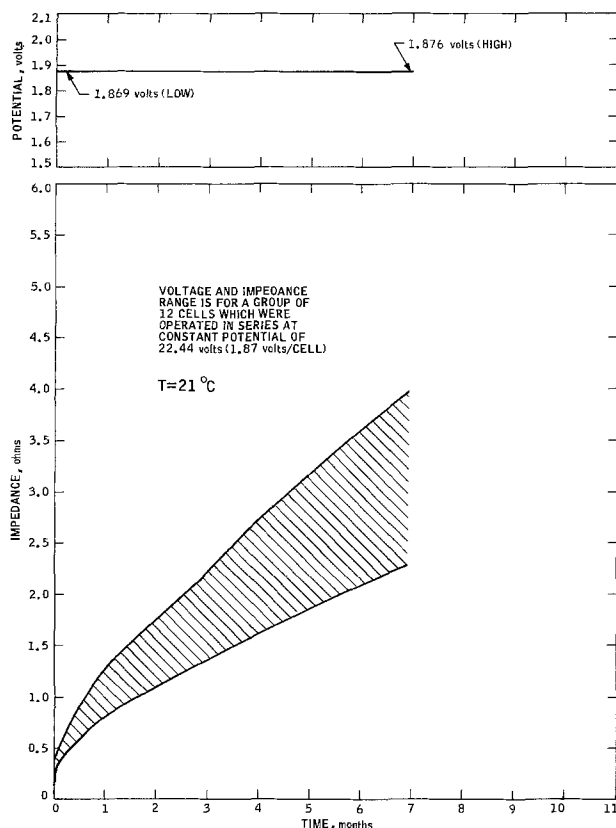


Fig. 10. Voltage and impedance of cells on constant potential float charge at 1.87 V/cell at 21°C.

45% KOH is, in terms of the reaction product, equivalent to approximately  $0.1 \text{ cm}^3 \text{ O}_2/\text{hr-g AgO}$  (7). Since these cells contained 166g of active positive material, the maximum rate, assuming all the material is  $\text{AgO}$ , would be  $16.6 \text{ cm}^3 \text{ O}_2 \text{ hr}$ . Under these conditions, then, the cell would be forming  $\text{Ag}_2\text{O}$  at a current equivalent rate near 80 mA. The current equivalent rate at which  $\text{Ag}_2\text{O}$  is simultaneously being reconverted to  $\text{AgO}$  is equal to the charge currents which varied from 2 to 10 mA for the constant current tests and near 2 mA for the constant potential tests. Comparison of these currents, therefore, reveals that the rates of formation of  $\text{Ag}_2\text{O}$  are, at least in these examples, appreciably greater than the rates at which this material is reconverted to  $\text{AgO}$ . Therefore, there is some basis to believe that high resistance layer of  $\text{Ag}_2\text{O}$  can be formed for the condition of stand with application of small currents by constant current or constant potential charge.

Inspection of Fig. 11 reveals a sharp maximum or peak in voltage during the early portion of a constant

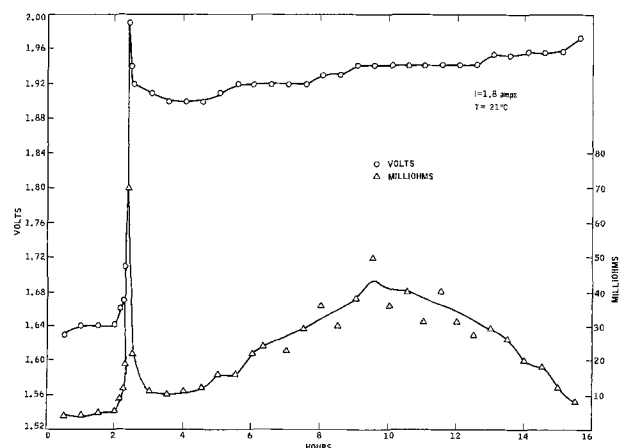


Fig. 11. Voltage and impedance during charge

current charge of this type cell. Cell impedance was also noted to exhibit a maximum or peak during this same time period. This phenomena has been previously reported in the literature (8, 9), and may again be associated with the formation of a high resistance layer of  $\text{Ag}_2\text{O}$  which completely surrounds the electrode. The sharp rise would correspond to the time during charge when the layer of high resistance  $\text{Ag}_2\text{O}$  is completely formed and decline would correspond to the onset of production of lower resistance  $\text{AgO}$  material.

Inspection of Fig. 12 reveals that cell impedance is quite low and in the range of 0 to 10 mohm during discharge. The gradual decline in impedance and slight rise in voltage during discharge is attributed to the formation of increasing amounts of highly conductive metallic silver particles. The frequency of performing measurements during this test was quite long (approximately once each 15 min), so that it was not possible to examine the initial transient voltage and impedance characteristics during the early (0-10 sec) portion of discharge. These characteristics were, however, observed in subsequent tests as described below.

Typical voltage traces of three monoblocks during the onset of discharge at 10A are given in Fig. 13, 14, and 15. The upper curve in each case gives the high-

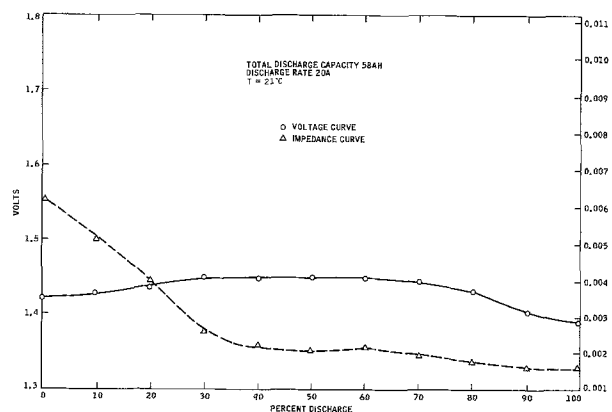


Fig. 12. Voltage and impedance during discharge

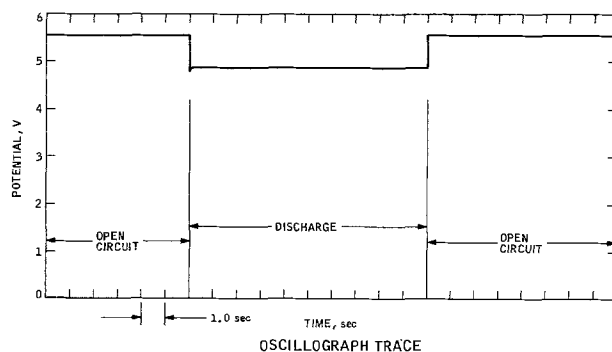
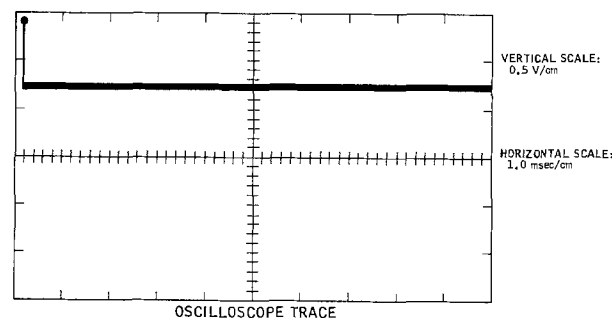


Fig. 13. Transient voltage characteristics of a monoblock with relatively low impedance at the onset of discharge at 10A at 21°C (monoblock No. 3).

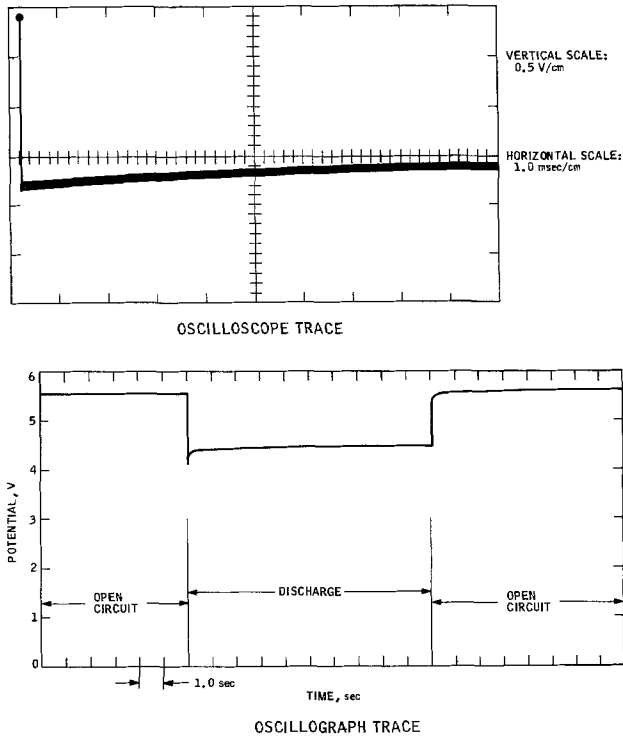


Fig. 14. Transient voltage characteristics of a monoblock with relatively high impedance at the onset of discharge at 10A at 21°C (monoblock No. 8).

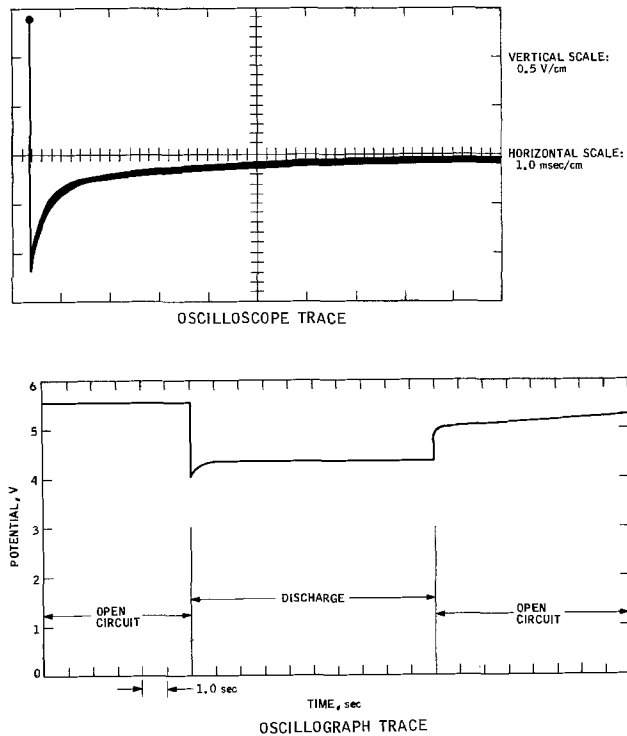


Fig. 15. Transient voltage characteristics of a monoblock with very high impedance at the onset of discharge at 10A at 21°C (monoblock No. 10).

speed oscilloscope trace and the lower curve gives the somewhat lower speed oscillograph trace. Table II summarizes the pertinent data from the traces of these and nine other monoblocks and also gives additional monoblock and unit cell data. Monoblocks 1 through 4 may be classified as "low resistance" units in that their over-all impedances range from 0.21 to 0.30 ohm (0.07-0.10 ohm/cell). These exhibit minimum voltages of 4.60-4.83V (1.52-1.61 V/cell) during the first msec of discharge and stabilized voltages of 4.75-4.85V (1.57-1.61 V/cell) almost immedi-

ately thereafter. Monoblocks 5 through 8 may be classified as medium resistance units in that their over-all impedances range from 1.01 to 1.31 ohm (0.34-0.44 ohm/cell). These exhibit minimum voltages of 3.63-3.88V (1.21-1.29 V/cell) during the first msec of discharge and stabilized voltages of 4.40-4.56V (1.47-1.52 V/cell) within a few seconds thereafter. Monoblocks 9 through 12 may be classified as high resistance units in that their over-all impedances range from 10.80 to 12.10 ohm (3.60-4.03 ohm/cell). These exhibit minimum voltages of 2.95 to 3.00V (0.98-1.00 V/cell) during the first msec of discharge and stabilized voltages of 4.30-4.44V (1.43-1.48 V/cell) within several seconds thereafter. These results indicate a trend of increased time for cell voltage to reach a stabilized value at the beginning of discharge with increased cell impedance. The results also indicate a trend of lower cell voltages with increased cell impedance as discussed in detail below.

The above monoblock data were normalized on a unit cell basis and are given in Fig. 16 and 17 in terms of unit cell voltage vs. corresponding unit cell impedance. Figure 16 pertains to the minimum voltages which were consistently attained during the first msec of discharge at 10A. Figure 17 pertains to the stabilized voltages which were consistently attained after several seconds of discharge at 10A. Also included in these figures, for design purposes, is the

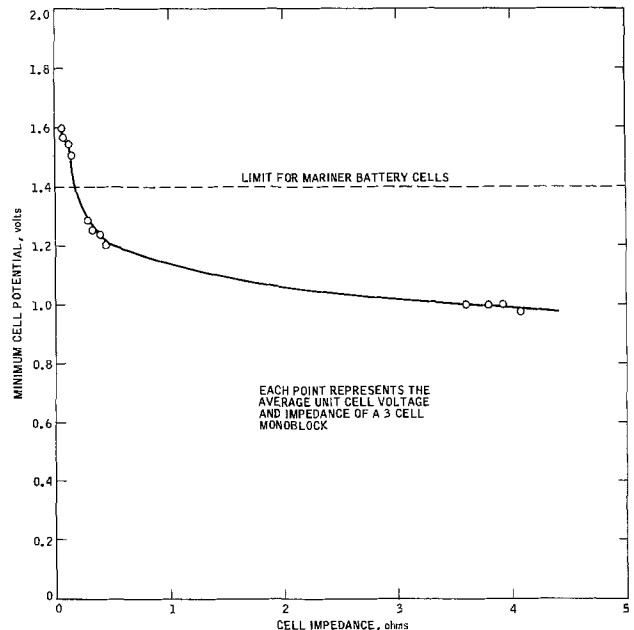


Fig. 16. Minimum cell voltage during first msec of discharge at 10A and at 21°C.

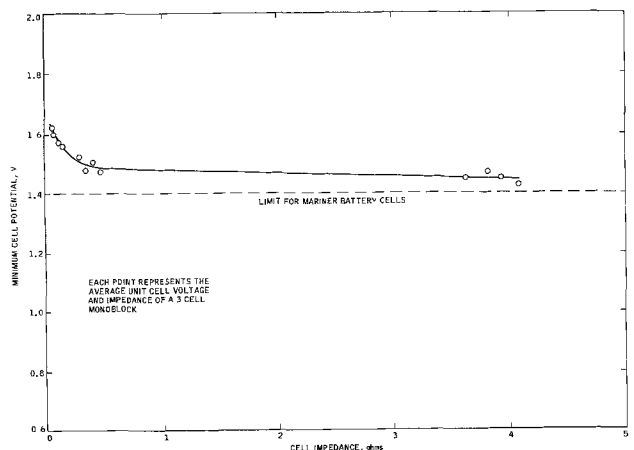


Fig. 17. Stabilized voltages after first few seconds of discharge at 10A and at 21°C.

minimum voltage specification limit for the Mariner cells. From a simplified "Ohm's law" point of view (where voltage is a linear function of impedance at constant current), one might at first predict that these curves should be approximately linear and have a slope of 10 V/ohm. This prediction would at least be thought to be applicable to the curve in Fig. 16 wherein the voltage measurements should not be influenced to any large degree by polarization phenomena in that the measurements were taken at very short periods of time after the start of discharge. Detailed examination of Fig. 16 reveals that only a portion of the curve is in accord with the above relation. This portion is for cells with impedances less than about 0.3 ohm. The curve reveals appreciably higher voltages than would be predicted from the Ohm's law relation for cell with impedances in excess of 0.3 ohm. Detailed examination of Fig. 17 reveals that essentially the whole curve is in disagreement with the above relation. In this case the discrepancy is even larger than the above, i.e., voltages are even higher than in Fig. 16 for corresponding impedance values.

Explanation for the above phenomena is twofold in nature. First, it is quite likely that polarization effects are present and that these effects account for a portion of the above-noted discrepancies. Secondly it is quite likely that there is a decline in cell impedance shortly after the start of discharge. Evidence to this effect was obtained in a special test wherein the impedance of one cell was measured before and 1.0 sec after a discharge at 10.0A. Results given in Table I revealed that the impedance dropped sharply during this period from 3.400 to 0.015 ohm. Based on results of the oscilloscope and oscillograph tracers, it appears that most of this decline in impedance occurs within the first msec of discharge. Although a rigorous explanation for this phenomena cannot be offered at the present time, it is quite likely that it is associated with the electrochemical reduction of the highly resistive layer of  $Ag_2O$ . Regardless of the explanation, however, the result establishes a very practical and significant point in that it suggests a method for avoiding the large transient voltage drops of high impedance cells, i.e., by merely subjecting them to a short "conditioning" discharge before employing them for their primary discharge application. The "conditioning" discharge may be carried out at the  $C/5$  rate for 1.0 sec.

During the course of this investigation there were noted to be several cells, especially those at elevated temperatures, which exhibited sudden voltage declines and subsequent failure. Since logs had been maintained on the voltages and impedances of these cells, it was decided to examine these data in detail in order to establish if these cells exhibited any unusual variations in impedance. In this manner it might be possible to employ the impedance measurement as a means of identifying faulty or deteriorated cells. Figures 18 through 21 give plots of the voltages and impedances of four such cells. Examination of these plots reveals

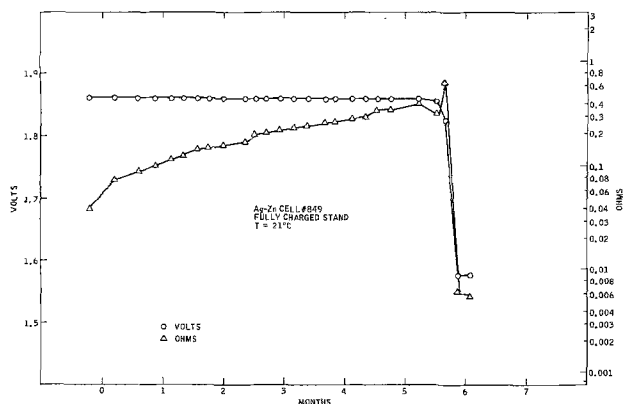


Fig. 18. Deterioration of AgZn cell No. 849

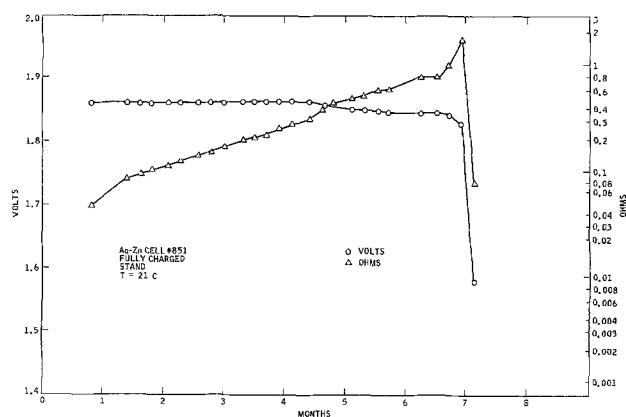


Fig. 19. Deterioration of AgZn cell No. 1069

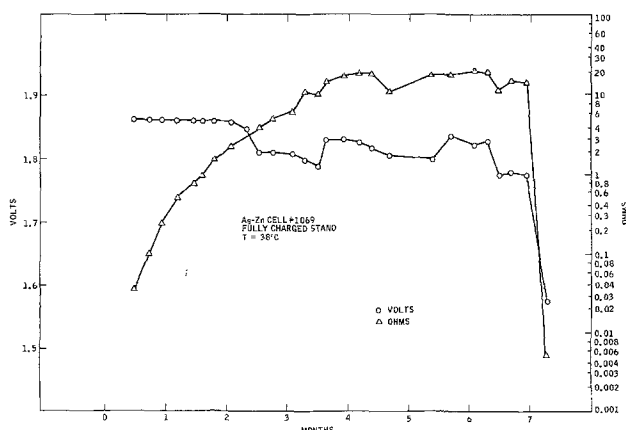


Fig. 20. Deterioration of AgZn cell No. 1071

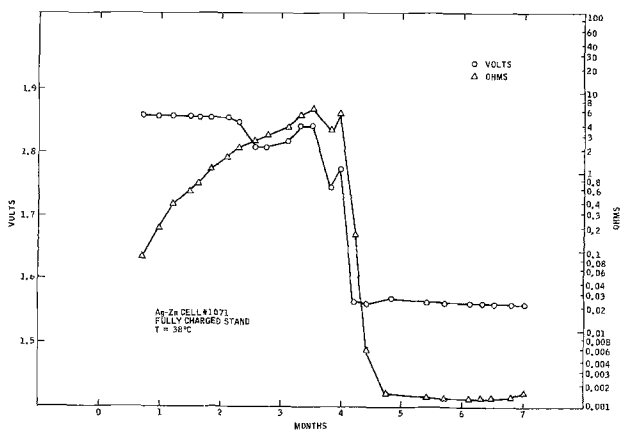


Fig. 21. Deterioration of AgZn cell No. 851

no unusual variations in the impedances of these particular cells up to the point of failure. During this time these cells exhibit a gradual rise in impedance in a similar manner to other cells which did not exhibit failure. At the time of failure, however, these cells exhibit a sharp decline in impedance and also cell voltage. On this basis, then, there does not appear to be any convincing evidence that these impedance measurements may be used to predict the condition or state of charge of Ag-Zn cells in their early stages of life. The feasibility of employing impedance measurements for this purpose cannot, however, be ruled out altogether with the information obtained to date.

The effect of temperature on impedance of these cells is given in Fig. 22. The upper curves give the variation for two typically high resistance cells which had been in storage for almost three years in the fully charged condition at 4°C. The lower curve gives the variation for a typically low resistance cell which had

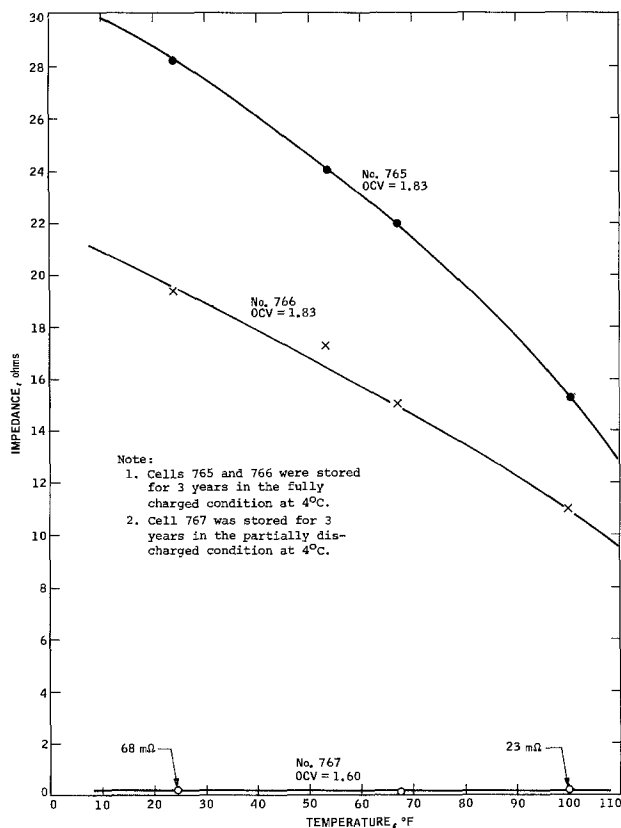


Fig. 22. Effect of temperature on impedance of AgZn cells

been in storage under the same conditions as above but had been partially (about 10%) discharged at room temperature before these impedance measurements. Results indicate that the impedances of all of these cells decline with temperature and in an essentially linear manner in the range of 4° to 38°C.

Finally, it is well to mention that there is some, but not conclusive, experimental data to confirm the belief that the positive electrode, and in particular the Ag<sub>2</sub>O film, is responsible for all the above-observed variations in impedance and voltage. It is conceivable that changes in the negative electrode, the separator, and electrolyte may also occur and may account for some of the observed phenomena. Additional and more fundamental studies involving the use of reference electrodes and microscopic examinations would be required to resolve this issue. Such studies have been outlined and will be carried out at a later date. Results obtained to date do, however, stand by themselves in that they provide the designers of AgO-Zn-based power systems with a great deal of practical and heretofore unpublicized data on the impedance characteristics of these cells.

### Conclusions

Significant findings of this study are summarized below.

1. Impedances of AgZn cells have been found to increase during prolonged periods of storage. The rate of change of impedance with time has been found to increase at elevated temperatures and to be influenced to some degree by the mode of storage.

2. In accordance with prior literature, there has been found to be a peak in the voltage-time curve of Ag-Zn cells during the early portion of constant current charge.

3. Impedances of Ag-Zn cells decrease appreciably and rapidly within the first msec of discharge.

4. The instantaneous voltage drop during the first msec of discharge has been found to increase with initial cell impedance, but not in a linear manner.

5. Cell voltages exhibit a partial recovery after the instantaneous voltage drop. The level of recovery and recovery times vary with initial cell impedance. Recovery times for the cells employed here were in the range of essentially zero to several seconds.

6. In order to satisfy demanding voltage regulation requirements, it would be well to subject aged cells to a short preliminary discharge prior to subjecting them to their primary discharge.

### Acknowledgments

This paper presents the results of one phase of research carried out at the Jet Propulsion Laboratory, California Institute of Technology under Contract No. NAS 71000, sponsored by the National Aeronautics and Space Administration.

Manuscript submitted April 25, 1975; revised manuscript received Sept. 8, 1975.

Any discussion of this paper will appear in a Discussion Section to be published in the December 1976 JOURNAL. All discussions for the December 1976 Discussion Section should be submitted by Aug. 1, 1975.

Publication costs of this article were partially assisted by the Jet Propulsion Laboratory.

### REFERENCES

1. "Mariner Mars 1969 Final Project Report," JPL Technical Report 321460 Vol. 1, Development, Design, and Test, pp. 85-89, (Nov. 1, 1970).
2. P. Bauer, "Batteries For Space Power Systems," NASA SP-172, p. 174, National Aeronautics and Space Administration, Washington, D.C. (1968).
3. S. U. Falk and A. J. Salkind, "Alkaline Storage Batteries," p. 424, John Wiley & Sons, Inc., New York (1969).
4. A. Fleischer and J. Lander, "Zinc-Silver Oxide Batteries," p. 123, John Wiley & Sons, Inc., New York (1971).
5. *Ibid.*, p. 149.
6. B. D. Cahan, J. B. Ockerman, R. F. Amlie, and P. Rüetschi, *This Journal*, **107**, 725 (1960).
7. A. Fleischer and J. Lander, "Zinc-Silver Oxide Batteries," p. 125, John Wiley & Sons, Inc., New York (1971).
8. *Ibid.*, p. 134.
9. E. A. Butler, "Studies of Reaction Geometry in Oxidation and Reduction of The Alkaline Silver Electrode," Final Report, JPL Contract 951157, Brigham Young University, Provo, Utah (April 1966).
10. A. Tvarusko, *This Journal*, **115**, 1106 (1968).



# Thin-Film Galvanic Cell Pb/PbF<sub>2</sub>/PbF<sub>2</sub>,CuF<sub>2</sub>/Cu

John H. Kennedy\* and James C. Hunter\*\*

Department of Chemistry, University of California, Santa Barbara, California 93106

## ABSTRACT

Thin-film solid-state galvanic cells were fabricated using Pb metal as anode, PbF<sub>2</sub> as electrolyte, and CuF<sub>2</sub> as cathode. Because of the high resistivity of CuF<sub>2</sub>, it was codeposited with PbF<sub>2</sub> to form a more conductive mixed cathode layer. Such cells developed open-circuit voltages from 0.61 to 0.70V, compared to 0.70V theoretical. Cells were discharged at room temperature with current densities of >10 μA/cm<sup>2</sup>. At elevated temperatures the current densities attainable were considerably higher. Cells discharged under constant load exhibited relatively constant voltage during discharge and a sudden drop-off at the end of discharge. Cathode utilization for the cathode-limited cells was typically 30-40%. Attempts to recharge these cells were unsuccessful.

Thin-film solid-state galvanic cells have been a subject of considerable recent interest. The combination of solid electrolyte materials with thin-film techniques holds promise of yielding miniaturized batteries with high energy density, wide operating temperature range, and long shelf life. Such batteries could complement other miniaturized electronic devices, such as integrated circuits, thin-film resistors, and thin-film capacitors.

Masters, Vouros, and Clune (1, 2) have developed vacuum-evaporated thin-film galvanic cells using silver as anode; silver chloride, bromide, or iodide as electrolyte; and platinum as cathode. This was a concentration cell with rather low power. Goldberg (3) patented improved methods of forming the electrolyte layer in this cell.

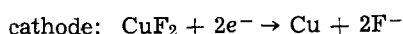
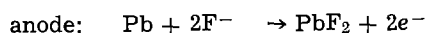
Ervin (4) patented a sprayed-in-place cell using a silver anode, silver rubidium iodide electrolyte, and tellurium tetraiodide cathode.

Sator and Perrot (5, 6) constructed thin-film cells of the type Pb/PbCl<sub>2</sub>/AgCl/Ag. These were developed further by Moulton *et al.* (7), and by Swindells and Lanier (8). Swindells and Lanier also developed an improved cell of the type Mg/MgCl<sub>2</sub>, LiCl/AgCl/Ag. In this cell the MgCl<sub>2</sub> electrolyte was doped with up to 50% LiCl by weight to increase its conductivity.

Liang, Epstein, and Boyle (9) constructed thin-film cells of the type Li/LiI/AgI/Ag. These cells developed over 2V, and could provide current densities of over 100 μA/cm<sup>2</sup>.

In a previous paper we reported the solid electrolyte properties of PbF<sub>2</sub> (10). For thin films,  $\sigma$  values of  $>1 \times 10^{-6}$  (ohm-cm)<sup>-1</sup> were obtained. This conductivity is sufficient that PbF<sub>2</sub> might be of use as electrolyte in thin-film galvanic cells.

CuF<sub>2</sub> is a possible choice for a cathode material. The following reaction



$$\Delta G = \Delta G_f(\text{PbF}_2) - \Delta G_f(\text{CuF}_2) = -32.1 \text{ kcal/mole}$$

leads to a cell voltage of 0.7V. In fact, CuF<sub>2</sub> has already found use as a cathode material in nonaqueous liquid electrolyte batteries (11, 12).

Several problems had to be overcome in order to use CuF<sub>2</sub> as a cathode material in these liquid electrolyte batteries. CuF<sub>2</sub> is a highly resistive material;  $\rho > 10^{10}$  ohm-cm at 25°C (13). In order to use it as a cathode material it was necessary to increase its conductivity. Mixing the CuF<sub>2</sub> with graphite has been tried with

some success (14). This only increases the electronic conductivity which may be sufficient with a liquid electrolyte. In a solid-state system, however, it would also be helpful to increase the ionic conductivity of the cathode. Recharging of liquid electrolyte cells with CuF<sub>2</sub> cathodes has also proven difficult (15), and there is indication of large overvoltage effects in these cells. The high resistivity of CuF<sub>2</sub> was expected to be a problem in solid-state thin-film cells, but it was not clear whether overvoltage effects would be comparable to those in the liquid electrolyte cells.

The presence of water can have large effects on the performance of CuF<sub>2</sub> cathodes for the liquid electrolyte systems. It is desirable to have completely anhydrous CuF<sub>2</sub>, as even small amounts of water react with the Li anodes used in such cells. Water in the cells also increases the solubility of CuF<sub>2</sub> in the electrolyte, leading to dissolution of the cathode and discharge of the cell. Therefore, high purity anhydrous CuF<sub>2</sub> has been used in these cells. Care must also be taken to insure that CuF<sub>2</sub> remains anhydrous, as it tends to absorb water to form the dihydrate



The presence of water would also be expected to cause problems in the formation of thin-film cells with CuF<sub>2</sub> cathodes. Heating CuF<sub>2</sub> in the presence of water leads to decomposition, with the formation of CuO, HF, and H<sub>2</sub>O (16, 17). Even if only small amounts of water were present, the outgassing and resultant spattering could make deposition of good films impossible. In addition, films of CuF<sub>2</sub> may have to be coated to protect them from being attacked by moisture in the air.

Some other fluoride materials are even less stable than CuF<sub>2</sub> and would yield correspondingly higher voltages. Thus a cell with AgF cathode would have a theoretical OCV of 1.3V, while a PbF<sub>4</sub> cathode would lead to an OCV of 2.56V. However, these latter materials are so unstable that it is questionable whether such materials could be vacuum evaporated.

In addition, electronic conductivity of PbF<sub>2</sub> becomes appreciable above 1.3V (10) and, thus, the use of high voltage cells could lead to self-discharge.

Even CuF<sub>2</sub> would be expected to cause difficulties in conventional vacuum evaporation. Evaporation from the typical evaporation sources such as tungsten, molybdenum, carbon, or aluminum oxide boats is thermodynamically unfavorable. However, whether or not successful evaporations can be carried out from any of these sources will depend on the rates of reaction, and even on the degree of wetting of the source by the CuF<sub>2</sub>. We report here the results of fabricating thin-film galvanic cells with PbF<sub>2</sub> electrolyte and CuF<sub>2</sub> cathodes.

## Experimental

*Thin-film deposition.*—Thin films were prepared by vacuum evaporation in a Fairchild custom evaporator

\* Electrochemical Society Active Member.

\*\* Electrochemical Society Student Member.

Key words: copper fluoride, galvanic cell, lead fluoride, solid electrolyte, thin-film cell.

using resistance sources. A Sloan Omni-IIa deposition control unit with quartz crystal oscillator sensor was used to monitor deposition rate and film thickness.

Cells were made with two different geometries. One type of cell (Fig. 1) had twelve small 0.1 cm<sup>2</sup> area cells, while the other type contained four larger 2 cm<sup>2</sup> cells per slide (Fig. 2). Conductivity cells were made by depositing a bottom layer of metal, followed by a layer of the material being studied, and by an upper metal electrode layer. Galvanic cells were made by depositing a bottom layer of anode metal, a middle layer of electrolyte, and two upper layers containing cathode material and cathode current collector. In some cells a layer of Kodak Microneg Photoresist (an organic polymer sensitive to u.v. light) was applied to protect the underlying films from moisture.

**X-ray diffraction analysis.**—A Philips Electronics x-ray diffraction unit with scintillation counter was used with CuK $\alpha$  x-rays. Powder x-ray spectra were made using the conventional holder. X-ray studies could also be made on thin films by breaking the glass microscope slide substrate in half and inserting the half-substrate in the sample holder. A Philips Electronics x-ray fluorescence instrument was also used, with Mo target and LiF crystal, for elemental analysis.

**Electrical measurements.**—OCV measurements were made using a Keithley Model 610c electrometer, with input impedance greater than 10<sup>14</sup> ohm.

A Keithley Model 260 picoampere source was used for constant-current charge and discharge of cells. A Hewlett-Packard Mosely chart recorder Model 7100b was used to record cell voltages during discharge.

Resistivity measurements (standard two-electrode technique) were made using a GRC 1650A bridge at 1 kHz.

### Results and Discussion

**Selection of deposition source.**—Attempts to deposit CuF<sub>2</sub> were made from tungsten and molybdenum boats without success. The resulting films were reddish in color and smooth initially, but upon contact with air they rapidly crinkled and lost adhesion to the substrate. X-ray studies showed only a few very tiny peaks, and these could not be assigned. The films probably contained some hygroscopic tungsten or molybdenum fluorides caused by reaction of CuF<sub>2</sub> with the boats.

Deposits from alumina-lined molybdenum boats were also unsuccessful. Resulting films were yellow

in color and exhibited very poor adhesion. Decomposition again probably occurred. X-ray studies, hampered by the poor adhesion, showed only some tiny peaks which could not be assigned.

Deposition from a carbon source gave films which were identified by x-ray diffraction as anhydrous CuF<sub>2</sub>. The adhesion of these films depended on the substrate temperature; films deposited on unheated substrates had poor adhesion, while those deposited on substrates at 220°C adhered extremely well. It was also found that films deposited with considerable spattering had poor adhesion, while films evaporated without spattering exhibited good adhesion. In all of these cases, even for films with poor adhesion, the CuF<sub>2</sub> structure was seen in x-ray studies. Fresh films showed no peaks for any of the hydrated forms of CuF<sub>2</sub> or for any other materials. However, the films were rather dark in color, while pure CuF<sub>2</sub> powder was white. This dark color could be due to the presence of impurities in the film, possibly from partial decomposition to copper metal, or perhaps to the incorporation of some fluorinated carbon compounds from reaction with the evaporation source. This could actually be beneficial for the cathode layer because it might lead to higher electronic conductivity.

**Film sensitivity to moisture in air.**—CuF<sub>2</sub> films deposited on glass substrates from carbon sources seemed only moderately sensitive to moisture in air. The smoother the film the less sensitive it appeared to be, probably because of the reduced true surface area. A study was made in which both CuF<sub>2</sub> powder and a CuF<sub>2</sub> film were exposed to air, and studied at intervals by x-ray. The fresh CuF<sub>2</sub> powder showed only peaks due to CuF<sub>2</sub>, but after exposure to air (>24 hr) a peak assigned to the dihydrate was seen. Another peak due to CuOHF also appeared after longer exposure (>10 days).

The fresh CuF<sub>2</sub> film showed a tiny broad peak due to the dihydrate and/or the oxyfluoride. After 168 days of exposure to air the film's appearance had hardly changed, and an x-ray study at this time showed almost the same features: only a small peak due to the dihydrate and/or the oxyfluoride of about the same height as for the fresh film. However, such a film would react with excess moisture rapidly; for example, holding the slide in one's hand caused crazing and blistering of the film in seconds. Therefore it was concluded that films of anhydrous CuF<sub>2</sub> could be obtained, and with moderate care they could be kept essentially anhydrous. However, for extended use in cells which might be handled frequently it would be necessary to cover the CuF<sub>2</sub> with a protective coating.

**Conductivity of CuF<sub>2</sub> thin films.**—Conductivity measurements were made on Cu/CuF<sub>2</sub>/Cu cells fabricated using the masking geometry described in a previous paper (10). A conductivity value of  $1.6 \times 10^{-9}$  (ohm-cm)<sup>-1</sup> was found at 25°C. This is somewhat higher than the values of  $10^{-10}$ - $10^{-11}$  (ohm-cm)<sup>-1</sup> reported for pure chemically formed thin films (13). This difference in conductivity could be due to the presence of impurities in the film as proposed above, or to some grain boundary effects. It should be noted that the increase in conductivity was comparable to the increase in conductivity of PbF<sub>2</sub> films compared to pressed pellet or single crystal PbF<sub>2</sub> noted in our earlier paper. A temperature study was performed, and an Arrhenius plot resulted in a value for  $\Delta H$  of 0.345 eV, somewhat below  $\Delta H$  values for ionic conduction in fluorides. It was not determined whether the observed conductivity was primarily ionic or electronic, but, in any case, the film conductivity was quite low. It was clear that improved CuF<sub>2</sub> cathode conductivity would be necessary for use in thin-film galvanic cells.

**Deposition of mixed PbF<sub>2</sub>-CuF<sub>2</sub> films.**—PbF<sub>2</sub> and CuF<sub>2</sub> were codeposited from the same boat to achieve mixed films with improved ionic conductivity. This was similar to the practice of mixing cathode and elec-

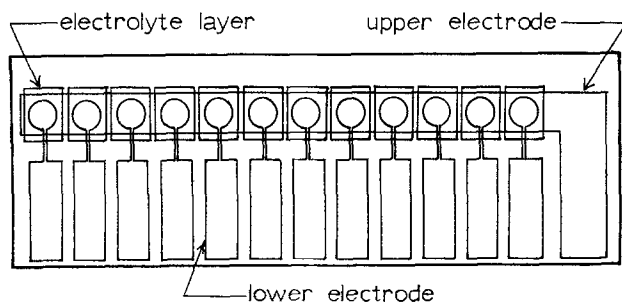


Fig. 1. Thin-film cell configuration of 0.1 cm<sup>2</sup> cells

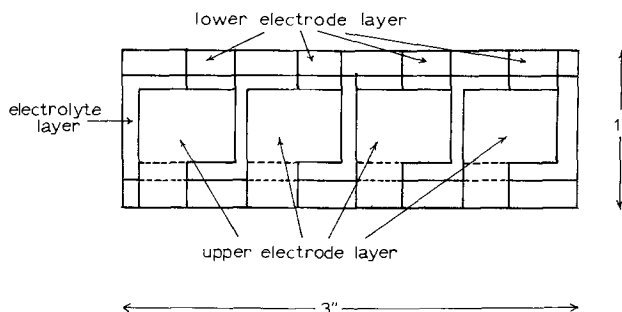


Fig. 2. Thin-film cell configuration of 2 cm<sup>2</sup> cells

trolyte as used in pressed-pellet cells. The  $\text{PbF}_2$  has a lower melting point than  $\text{CuF}_2$  ( $822^\circ\text{C}$  vs.  $950^\circ\text{C}$ ) and was observed to evaporate at lower temperatures. However, it was found that a mixture of the two could be codeposited. One would expect that the initial composition of the evaporant would be relatively rich in  $\text{PbF}_2$  while later in the deposit it would be relatively rich in  $\text{CuF}_2$ . If one deposits a cell in the sequence Pb layer,  $\text{PbF}_2$  layer,  $\text{CuF}_2$ - $\text{PbF}_2$  mixture layer, Cu layer, then one would have the favorable situation of a gradation from  $\text{PbF}_2$ -rich to  $\text{CuF}_2$ -rich through the cathode film, with a very high effective contact area between electrolyte and cathode. The actual composition of the cathode film would depend on the initial composition of the mixture in the evaporation source and to what extent the evaporation proceeded. With initial composition of approximately 70 mole per cent (m/o)  $\text{CuF}_2$ , and evaporating a large part, but not all, of the mixture, one might estimate over-all composition of about 50 m/o  $\text{CuF}_2$ .

X-ray studies were made on the codeposited mixed films. Some structure was seen in early films (Fig. 3a), with peaks attributable to both  $\text{PbF}_2$  and  $\text{CuF}_2$ . However, as care was taken to avoid spattering of the mixture in the boat, and to avoid both the earliest and latest fractions of the deposit by using a shutter in front of the substrate, films were obtained which showed little or no structure under x-ray diffraction (Fig. 3b). Only one very broad peak around  $27^\circ$  could be seen, possibly due to  $\text{CuF}_2$ . Thus it appeared that the mixed films had a very fine-grained or amorphous nature. Studies of such films with scanning electron microscopy showed no visible grains.

**Conductivity of mixed films.**—Conductivity measurements were made on mixed films with copper electrodes. Values for  $\sigma$  were in the range  $10^{-6}$ – $10^{-8}$  ( $\text{ohm-cm}$ ) $^{-1}$ , depending on the extent of the deposit. Longer deposit times with larger amounts of  $\text{CuF}_2$  gave the lower conductivity values. Even so, a marked improvement was achieved compared to the pure  $\text{CuF}_2$  films. Another benefit of the mixed films was the ease of deposition. The  $\text{CuF}_2$ - $\text{PbF}_2$  mixture melted at a lower temperature than the pure  $\text{CuF}_2$ , leading to improved outgassing characteristics and less spattering during deposition. In addition it was found that smooth adherent films could be obtained without substrate heating.

**Galvanic cells.**—Cells of the type  $\text{Pb}/\text{PbF}_2/\text{PbF}_2$ ,  $\text{CuF}_2/\text{Cu}$  were deposited using the  $0.1\text{ cm}^2$  area masks.

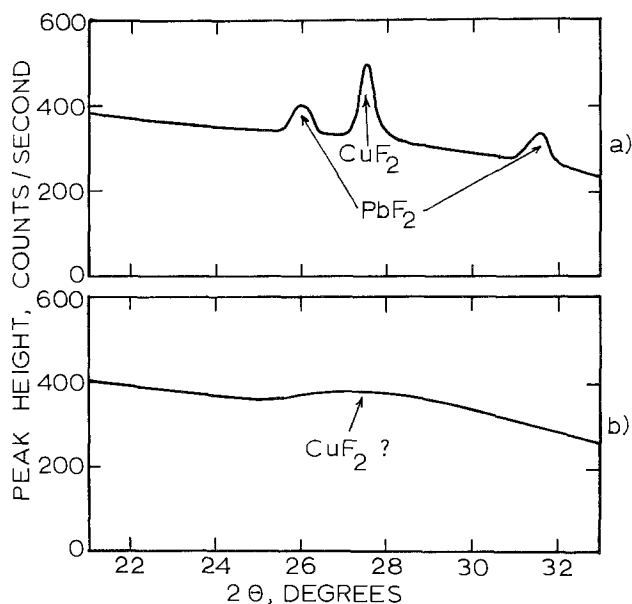
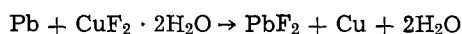


Fig. 3. X-ray spectra of mixed  $\text{PbF}_2/\text{CuF}_2$  films: (a) early film, with  $\text{PbF}_2$  and  $\text{CuF}_2$  peaks, (b) later film, with almost no structure apparent.

In addition, some cells were made with  $2\text{ cm}^2$  area. The best cells were made without any substrate heating. Substrate heating for the cathode layer led to better adhesion of that layer, but caused the lifting of the underlying layers. Heating the substrate for all the layers led to increased numbers of shorted cells, probably due to increased Pb and  $\text{PbF}_2$  grain size and correspondingly increased numbers of pinholes. The yields of nonshorted  $2\text{ cm}^2$  cells were smaller than for the  $0.1\text{ cm}^2$  cells, but with care to avoid spattering of deposits moderate yields of the larger cells could be obtained. Some cells that were found to be initially shorted eventually "healed," but with lower than normal capacity. Finished cells were coated with Kodak Microneg photoresist to protect the  $\text{CuF}_2$  from moisture. Some cells were left uncoated for comparison, and within days these films crazed and blistered. The sealed cells did not show any deterioration after weeks of exposure to air.

The OCV's of cells ranged from 0.56 to 0.70V. However, the lower OCV's were obtained for cells deposited from early fractions of the deposition mixture, and these cells had poor performance. Although no appreciable  $\text{CuF}_2 \cdot 2\text{H}_2\text{O}$  was detected by x-ray, it is interesting to note that the following cell reaction



has a theoretical OCV of 0.57V. This value agrees with the lowest cell values observed and may represent cells which had inadvertently been exposed to water vapor.

The cells with good performance had OCV's of 0.61–0.70V. The occurrence of lower than theoretical OCV in some cells could also indicate the presence of electronic leakage in the cells. However, the electronic conductivity of pure  $\text{PbF}_2$  has been found to be quite low (10), so this was probably not the reason for lower OCV's. Figure 4 shows the OCV of a cell as a function of time. Initial voltage was 0.63V and subsequently rose to 0.66V. Even after several weeks the OCV was the same, and the cell was subsequently discharged with no apparent loss of capacity on storage. Therefore it appeared that the lower OCV's were not due to electronic leakage.

Another possible explanation of OCV lower than theoretical is that a solid solution of  $\text{CuF}_2$  and  $\text{PbF}_2$  was present, and the OCV would then indicate the  $\text{CuF}_2$  activity at the active site. The x-ray data indicated an amorphous phase (Fig. 3b) supporting this possibility.

Cells were discharged under various loads and at different temperatures, and the cell voltages measured vs. time. Figure 5 shows a typical discharge curve for a small  $0.1\text{ cm}^2$  area cell at  $25^\circ\text{C}$  with a 3.3 megohm load. Upon first application of the load the cell voltage dropped to 0.22V, but as the cell started to discharge, the cell voltage rose gradually to 0.46V. This "activa-

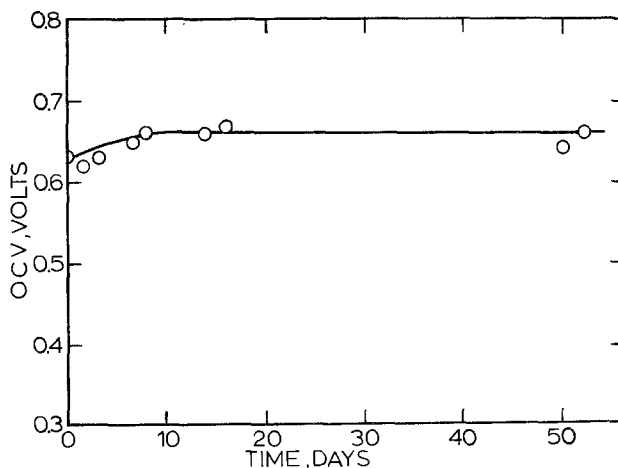


Fig. 4. OCV as a function of time for  $\text{Pb}/\text{PbF}_2/\text{PbF}_2$ ,  $\text{CuF}_2/\text{Cu}$  cell.

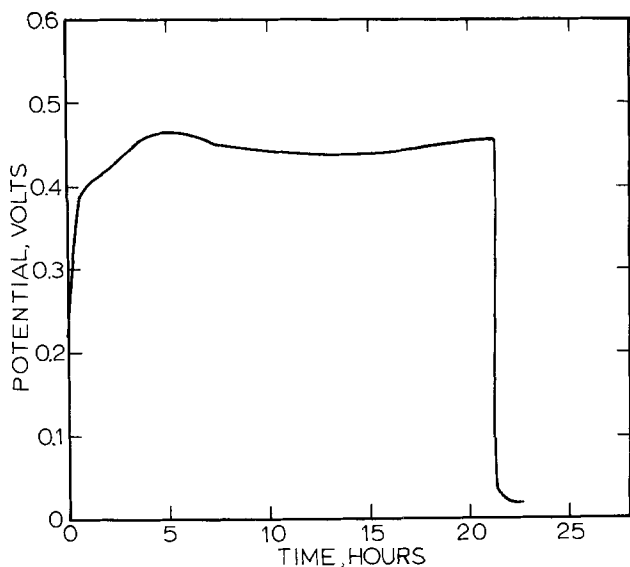


Fig. 5. Discharge curve at 25°C through 3.3 megohm load

tion effect" has been present for other solid-state batteries (18). The voltage then remained nearly constant during the rest of the discharge. Finally, the cell voltage dropped rapidly to 20-50 mV. The open-circuit voltage of such cells measured with an electrometer was still over 0.5V, although it was no longer possible to draw appreciable current from them. This is understandable if we consider the geometry of the cells. With the small 0.1 cm<sup>2</sup> cells, the cathode mixture and the upper copper electrode were deposited in the form of a long strip common to all the cells. But only the CuF<sub>2</sub> located directly above the smaller Pb electrodes could react easily. Once this CuF<sub>2</sub> was consumed there was still sufficient CuF<sub>2</sub> not directly above the Pb electrodes to establish the OCV, but only very low currents could be maintained with the extremely high resistance through the longer electrolyte path.

Figure 6 shows discharge curves for 0.1 cm<sup>2</sup> cells under various constant loads at 25°C, and Fig. 7 shows discharge curves with 300,000 ohm loads at 25°C and at 75°C. From the maximum current densities observed in Fig. 7 and assuming an OCV of 0.7V, one can use an Arrhenius relationship to obtain a  $\Delta H$  value of 0.33 eV. This is quite close to the value obtained from a conductivity cell of pure CuF<sub>2</sub> mentioned earlier, and is smaller than the value of 0.54 eV found for conductivity cells of PbF<sub>2</sub>. This supports the contention that the rate-determining step in the cell reaction involves the CuF<sub>2</sub> cathode material.

Table I summarizes the data for discharge of several cells of both 0.1 and 2 cm<sup>2</sup> area. The actual capacity of the cells is listed, both in terms of coulombs of charge and in terms of equivalents of CuF<sub>2</sub>. These cells were all constructed with an excess of the anode material. Therefore, if the amount of CuF<sub>2</sub> present in the cathode film were known, the actual per cent utilization of cathode material could be calculated. However, the fact

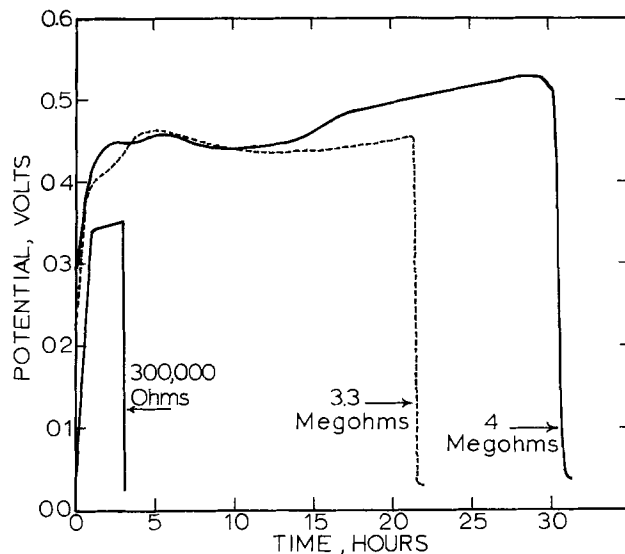


Fig. 6. Discharge curves at 25°C through various loads

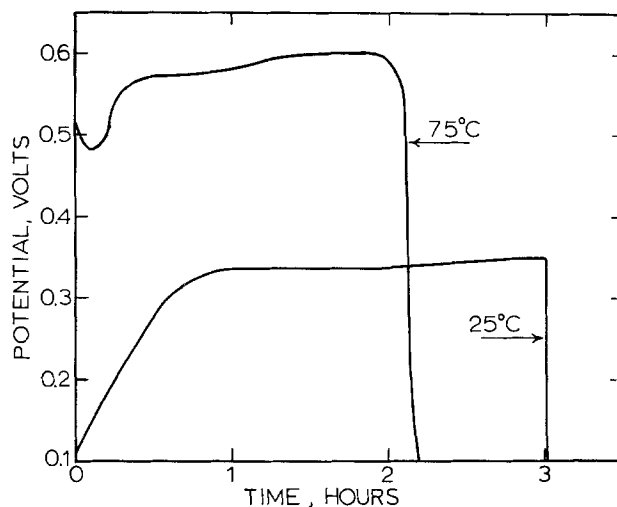


Fig. 7. Discharge curves at 25° and 75°C through 300,000 ohm loads.

that a mixed film was used for the cathode, and that the x-ray diffraction studies gave no peaks prevented calculations based on these methods. The cells were estimated to be about 50 m/o CuF<sub>2</sub> from the evaporation conditions and a check on this assumption was made by studying some of the CuF<sub>2</sub>-PbF<sub>2</sub> films using x-ray fluorescence analysis. Results showed 52-56 m/o CuF<sub>2</sub> in the films. The percentage utilization for the cells listed in Table I was calculated using this information. For the small cells it can be seen that the maximum utilization was 40% with most of the discharges in the range of 30-40%. Therefore, it appears that only a fraction of the available capacity of the cells could be used. A possible explanation is that much

Table I. Performance of Pb/PbF<sub>2</sub>/PbF<sub>2</sub>,CuF<sub>2</sub>/Cu thin-film galvanic cells

Cell	Cell area, cm <sup>2</sup>	Temperature, °C	Load, ohm	Capacity, coulombs*	Capacity, equiv of CuF <sub>2</sub> *	% utilization**
A-78-B4	2.0	25	100,000	$4.9 \times 10^{-2}$	$5.1 \times 10^{-7}$	6.7
A-78-B3	2.0	25	300,000	$1.3 \times 10^{-1}$	$1.4 \times 10^{-6}$	17.9
A-78-S7	0.1	25	300,000	$1.1 \times 10^{-2}$	$1.2 \times 10^{-7}$	30.8
A-78-S10	0.1	25	$3.3 \times 10^6$	$1.0 \times 10^{-2}$	$1.1 \times 10^{-7}$	29.0
A-78-S9	0.1	25	$4 \times 10^6$	$1.3 \times 10^{-2}$	$1.4 \times 10^{-7}$	35.6
A-78-S12	0.1	50	300,000	$0.6 \times 10^{-2}$	$0.6 \times 10^{-7}$	16.3
A-78-S6	0.1	50	$4 \times 10^6$	$1.4 \times 10^{-2}$	$1.4 \times 10^{-7}$	36.8
A-78-S3	0.1	75	300,000	$1.5 \times 10^{-2}$	$1.5 \times 10^{-7}$	40.0
A-78-S8	0.1	75	$4 \times 10^6$	$0.3 \times 10^{-2}$	$0.3 \times 10^{-7}$	8.7

\* Measured capacity from discharge of cells.

\*\* Calculated utilization of cathode, assuming 54 m/o CuF<sub>2</sub> in 10,000Å thick cathode film, or  $3.8 \times 10^{-7}$  equivalent of CuF<sub>2</sub> in each 0.1 cm<sup>2</sup> cell.

of the  $\text{CuF}_2$  was isolated in the  $\text{PbF}_2$ -rich part of the cathode film, without electronic contact to the Cu electrode, or became isolated during discharge. A lack of complete utilization of cell capacity has also been reported by Liang *et al.* (9) for the  $\text{Li/LiI/AgI/Ag}$  system.

The  $\text{Pb/CuF}_2$  cells with high OCV showed no evidence of self-discharge with storage. One particular cell was stored for over six weeks to measure OCV. The cell was subsequently discharged with no loss of capacity. This is in contrast to the thin-film cells of Liang which self-discharged *via* migration of silver ion in the cell (9).

**Recharging of cells.**—Cell A-78-S1 was discharged for one hour at  $1 \mu\text{A}$  current at  $75^\circ\text{C}$ . This was only a partial ( $\sim 33\%$ ) discharge. Figure 8 shows that the cell voltage leveled off at about 0.6V, 0.1V below the theoretical OCV. Then the cell was charged at  $1 \mu\text{A}$ . There appeared to be a slight plateau area around 1.1-1.2V, but the voltage then climbed more steeply again. It is clear from Fig. 8 that the cell reaction was not reversible, and that charging this cell was not feasible at  $75^\circ\text{C}$ .

All attempts to recharge cells after they had been completely discharged met with failure; only extremely low currents would flow through the cells at reasonable charging voltages. Although these currents led to

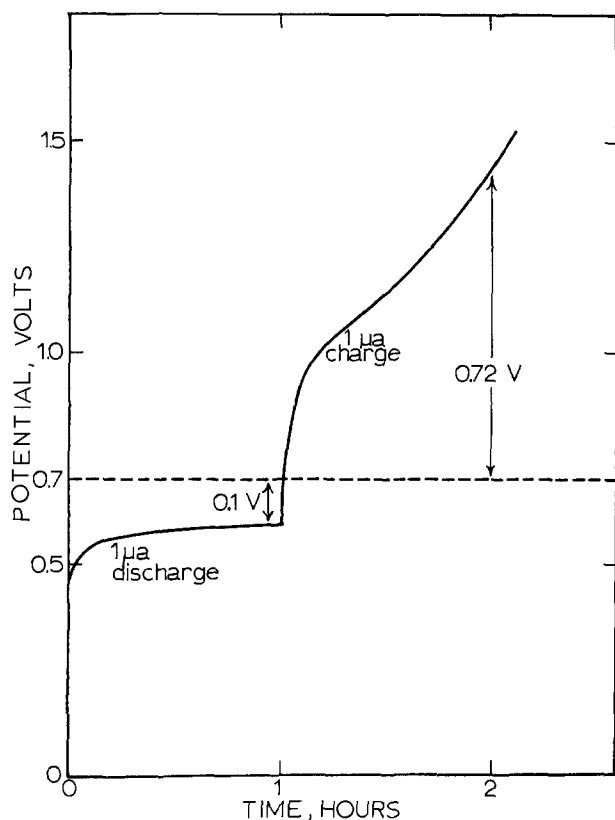


Fig. 8. Attempt to recharge thin-film cell, potential vs. time for  $1 \mu\text{A}$  discharge and  $1 \mu\text{A}$  charge cycles.

the proper QCV, the capacity of recharged cells was small. This discouraging result is consistent with the results of similar recharging attempts for  $\text{CuF}_2$  in non-aqueous liquid electrolyte batteries.

### Summary

Thin-film galvanic cells using  $\text{PbF}_2$  electrolyte, an anion conductor, have been successfully fabricated and discharged electrochemically. It was necessary, however, to codeposit  $\text{PbF}_2$  with the  $\text{CuF}_2$  cathode material to increase its ionic conductivity. The technique of codeposition is analogous to the conventional technique of mixing electrolyte and electrode material in pressed-powder cells. The  $\text{Pb/PbF}_2/\text{PbF}_2/\text{CuF}_2/\text{Cu}$  cells exhibited discharge characteristics similar to other thin-film cells reported in the literature, but they were not rechargeable.

### Acknowledgments

The authors acknowledge financial support of this project by the National Science Foundation, Grant No. GH-37144. This paper was taken in part from the Ph.D. dissertation of James C. Hunter, University of California, Santa Barbara, 1974.

Manuscript received July 14, 1975; revised manuscript received Aug. 4, 1975.

Any discussion of this paper will appear in a Discussion Section to be published in the December 1976 JOURNAL. All discussions for the December 1976 Discussion Section should be submitted by Aug. 1, 1976.

Publication costs of this article were partially assisted by the University of California, Santa Barbara.

### REFERENCES

1. J. I. Masters, P. Vouros, and J. P. Clune, U.S. Pat. 3,575,715 (1971).
2. J. I. Masters and P. Vouros, *This Journal*, **116**, 880 (1969).
3. G. M. Goldberg, U.S. Pat. 3,554,795 (1971).
4. G. Ervin, U.S. Pat. 3,701,685 (1972).
5. A. Sator, *Compt. Rend.*, **234**, 2283 (1952).
6. M. Perrot and A. Sator, *ibid.*, **234**, 1883 (1952).
7. C. W. Moulton, M. Hacskaylo, and C. Feldman, Paper 62 presented at the Electrochemical Society Meeting, Toronto, Canada, May 3-7, 1964.
8. F. E. Swindells and W. R. Lanier, U.S. Pat. 3,547,700 (1970).
9. C. C. Liang, J. Epstein, and G. H. Boyle, *This Journal*, **116**, 1322 (1969).
10. J. H. Kennedy, R. Miles, and J. Hunter, *ibid.*, **120**, 1441 (1973).
11. J. J. Auburn, K. W. French, S. I. Lieberman, V. K. Shah, and A. Heller, *ibid.*, **120**, 1613 (1973).
12. K. H. M. Braeuer and J. A. Harvey, "Status Report on Organic Electrolyte High Energy Batteries," DA Task 1CO 14501 A 34A-00-01 (1967).
13. S. S. Flaschen and P. D. Garn, *J. Am. Ceram. Soc.*, **42**, 641 (1959).
14. B. Burrows, *This Journal*, **118**, 1130 (1971).
15. P. Bauer, "Batteries for Space Power Systems," p. 199, U.S. Government Printing Office, Washington, D.C. (1968).
16. C. M. Wheeler, Jr. and H. M. Haendler, *J. Am. Ceram. Soc.*, **76**, 263 (1954).
17. L. V. My, G. Perinet, and P. Bianco, *J. Chem. Phys.*, **63**, 719 (1966).
18. C. C. Liang, *Appl. Solid State Sci.*, **4**, 95 (1974).

# The Electrodeposition of Aluminum from Aromatic Hydrocarbon

## I. Composition of Baths and the Effect of Additives

E. Peled\* and E. Gileadi\*

*Institute of Chemistry, Tel-Aviv University, Ramat-Aviv, Israel*

### ABSTRACT

Electroplating of aluminium on copper and steel substrates was conducted at room temperature. The bath consisted basically of  $\text{AlBr}_3$  and an alkali metal bromide such as  $\text{KBr}$  dissolved in a suitable mixture of aromatic hydrocarbons. The bath was operated under conditions resembling industrial operation. Oxygen and humidity were removed by bubbling nitrogen through the bath. The effect of bath composition on the quality of the plated product is discussed in detail. Transference numbers were measured. The aluminium is shown to be present in the form of a negative ion ( $\text{Al}_2\text{Br}_7^-$ ), the transference number of which is larger than that of the solvated positive ion. The reactions taking place during deposition and dissolution of aluminium in this system are discussed in detail.

Aluminium cannot be electrodeposited from aqueous or other protic solvents because decomposition of the solvent, accompanied by copious hydrogen evolution, occurs at the potential required to deposit the metal, and the current efficiency is essentially zero. Attempts to employ aprotic, polar solvents such as acetonitrile, DMF, pyridine, propylene carbonate, etc., failed,<sup>1</sup> probably since the small, highly charged  $\text{Al}^{+3}$  ion is very heavily solvated and decomposition of the solvent requires less energy than desolvation of the ion and electrodeposition of the metal. This is particularly so for the solvent molecules in the inner solvation shell which are highly polarized by the central ion.

Aluminium was successfully electrodeposited by Brenner *et al.* (1) from a bath consisting of  $\text{AlCl}_3$  and  $\text{LiAlH}_4$  dissolved in diethyl ether. This bath has not been adopted on a wide industrial scale because of its hazardous nature and the high cost of the bath components. Two other baths, one based on  $\text{LiAlH}_4$  and  $\text{AlCl}_3$  in tetrahydrofuran (3, 4), the other on molten alkyl aluminium compounds (5), are presently under investigation on pilot plant scale.

Aromatic hydrocarbons represent a unique class of solvents of great interest for electrochemical research and technology. Simple ionic salts, *e.g.*, alkali halides, are insoluble in them because of their low dielectric constant, while covalent salts such as  $\text{AlX}_3$ , where X is a halide ion other than  $\text{F}^-$ , are very soluble. Rigorously dried  $\text{AlBr}_3$  dissolved in an aromatic hydrocarbon yields clear solutions having a pale yellow to orange tint, depending on the hydrocarbon employed. The electrical conductivity is very low (*ca.*  $10^{-9}$  mho  $\cdot$   $\text{cm}^{-1}$ ) (6). However, alkali halides can be dissolved in these systems, yielding an electrolytic solution of medium conductivity (up to 6 mmho  $\text{cm}^{-1}$ ) (7-12), which is sufficient both for electrochemical measurements and for electroplating applications. A maximum in conductivity is reached when the molar ratio of, say,  $\text{AlBr}_3$  to  $\text{MBr}$  (where M is an alkali metal or the ammonium ion) is 2:1, indicating that  $\text{Al}_2\text{Br}_7^-$  and  $\text{M}^+$  ions are probably formed. There is evidence in the literature showing that the solvation number of these ions (when  $\text{M} = \text{H}$ ) is different in different hydrocarbons (13). The stability of the solvated  $\text{Al}_2\text{Br}_7^-$  ions (and possibly of some  $\text{AlBr}_4^-$  ions which may also be present when the amount of  $\text{MBr}$  added is increased) depends on the hydrocarbon used. In the presence of  $\text{HBr}$ <sup>2</sup> it is found to increase in the order benzene < toluene < xylene < mesitylene (14). Cryoscopic mea-

surements indicated that in the presence of alkali halides, larger aggregates having the general formula  $(\text{Al}_2\text{Br}_7^- \text{M}^+)_n$ , where *n* may be as large as four, may also be formed (10, 12, 15).

Plotnikov and co-workers studied these systems about forty years ago and showed that it was possible to electrodeposit aluminium on platinum or copper from solutions of  $\text{AlBr}_3/\text{MBr}$  in benzene, toluene, and xylene (7, 16-20). However, the deposits obtained were in most cases of poor quality, the cathodic current efficiencies were low, and the solvents were decomposed in the course of electrolysis (10). Pospikhov, who reviewed the field in 1937, concluded that these systems were not suitable as plating baths for industrial applications (19). Recently, the system of  $\text{AlBr}_3$  dissolved in xylene with  $\text{HBr}$  added was investigated in detail (21, 22). Aluminium was electrodeposited with high current efficiencies of *ca.* 90%. Two side reactions were also observed, *viz.*, reduction of the solvent and hydrogen evolution. Capuano and Davenport published recently a patent (23) and two papers (24, 25) in which the electroplating of aluminium from solutions of  $\text{AlBr}_3$  in mixed aromatic hydrocarbons was reported. The quality of plating was found by these authors to depend on the hydrocarbons used. Thus, for example, benzene mixed with durene gave very poor results, while toluene mixed with ethyl benzene yielded excellent deposits. A main feature of the work of Capuano and Davenport is that all experiments were performed in the presence of small amounts of water (introduced by partial saturation of the hydrocarbon used as solvent with water before addition of  $\text{AlBr}_3$ ), or with  $\text{HBr}$  continuously added (23-25). Water or  $\text{HBr}$  were considered by these authors to be indispensable components of the plating bath, without which aluminium could not be electrodeposited.

In the present work a systematic study of the effect of the composition of the baths on the quality of aluminium electrodeposited on copper or steel substrate, is presented. Special emphasis is placed on the effects of: (i) different aromatic hydrocarbons, (ii) organic and inorganic salts, and (iii) hydrobromic acid on the performance of the plating baths.

### Experimental

Solutions were made up of AR-grade chemicals without further purification. All experiments were performed in airtight cells under an atmosphere of dry nitrogen. The inert gas flow was maintained continuously from the time a solution was made up until it was finally discarded (in many cases this lasted several months). The cell, electrodes, plating procedure, and preparation of metal surfaces were described in an earlier publication (26). Most experiments were

\* Electrochemical Society Active Member.

Key words: aluminium, electrodeposition, nonaqueous plating bath, aromatic hydrocarbons, aluminium bromide.

<sup>1</sup> Reviews of previous work are given in Ref. (1, 2).

<sup>2</sup>  $\text{AlBr}_3$  is very hygroscopic and any moisture absorbed immediately causes the formation of  $\text{HBr}$  and aluminium hydroxide or hydroxybromide.

conducted at cathodic current densities of 5-10 mA · cm<sup>-2</sup>, but in some cases a wider range of 0.5 to 40 mA · cm<sup>-2</sup> was employed. Cathodic and anodic current efficiencies were determined by weighing the samples before and after electrolysis at a constant current. Since the main purpose of the present study was to evaluate the influence of various bath components and additives on the quality of electrodeposits and on the cathodic and anodic current efficiency under conditions resembling industrial operation, the cells were opened for changing samples in the regular laboratory atmosphere and the highly hygroscopic AlBr<sub>3</sub> was used as purchased without further drying.<sup>3</sup> Thus, it may be assumed that varying small amounts of humidity entered the bath and HBr was present in small quantities in all experiments.

The purity of electrodeposited aluminium was determined in the following manner: The sample was rinsed in a warm (60°C) 1M NaOH solution for a few seconds to remove the outermost oxide layer. It was subsequently washed in water, dried in acetone, and weighed. All the aluminium was then dissolved in warm 1M NaOH, the substrate was dried and weighed again. The total amount of aluminium in solution was determined gravimetrically with 8-hydroxy quinoline and this was compared to the weight-loss observed above.

Transference numbers were measured in a conventional Hittorf cell. Copper wires (1 mm diam) were used in the form of a helix for both electrodes. Electrolysis was conducted for 1.5-2 hr at a constant current of 20 mA. The volume of both anode and cathode compartments was 5 cm<sup>3</sup>. The solution, prepared under anhydrous conditions, consisted of 0.7M KBr and 2.0M AlBr<sub>3</sub> in toluene. The concentrations of potassium and aluminium in the anolyte were determined by atomic absorption spectroscopy. Electrolysis time was calculated to give only a small concentration change (ca. 10%). In this way errors due to dissolution of copper and conduction of current by copper ions were minimized. The use of a copper anode insures that changes of concentration of potassium and aluminium in the anolyte are only caused by migration. Use of an aluminium anode would require a knowledge of the current efficiency of anodic dissolution, which has not been measured under the experimental conditions prevailing in this experiment.

## Results

*The basic system.*—The basic system consists of a solution of AlBr<sub>3</sub> in toluene (or benzene) in roughly equal weights. If prepared under rigorously dry conditions, this would have very low conductivity and electrodeposition would not be possible. However, under the conditions maintained in all experiments reported here, some moisture, and hence some HBr, was always present, giving sufficient conductivity to allow electroplating. The basic system and the same system with either an alkali bromide (or iodide) or a Lewis base added were tested.

*Aluminium bromide in toluene or benzene.*—Aluminium bromide is very soluble in aromatic hydrocarbons. Two or three molar solutions of AlBr<sub>3</sub> in benzene or toluene were prepared and tested. A tarlike organic deposit containing little or no aluminium was formed if benzene was the solvent. In toluene a gray to black deposit was produced and the current efficiency for aluminium deposition was less than 50%. Results were generally irreproducible and satisfactory electrodeposits could not be obtained in these systems.

*The effect of addition of hydrocarbons and amines.*—Aromatic hydrocarbons such as ethylbenzene, mesitylene, and naphthalene were added in quantities ranging from 3 to 15 weight per cent (w/o) to the basic system of AlBr<sub>3</sub> in toluene. White gray electrodeposits

having a metallic appearance were observed. A similar improvement in the quality of the electrodeposits resulted from the addition of dimethyl aniline or triethyl amine in comparable concentrations. The cathodic current efficiency was still highly irreproducible and ranged from 20% to nearly 100% in different experiments. Heavy dendrite formation was observed. The conductivity of the solutions varied with time and typically decreased from an initial value of 1-2 mmho · cm<sup>-1</sup> to ca. 0.1 mmho · cm<sup>-1</sup> within a few days.<sup>4</sup>

*The effect of addition of alkali halides.*—Alkali bromides or iodides were added to solutions of AlBr<sub>3</sub> in toluene. The concentrations were about 0.1-1.0M. The conductivity of the baths was increased and stabilized in the range of 0.5-6 mmho · cm<sup>-1</sup>, depending on concentration. Dendrite formation was significantly reduced and the cathodic current efficiency was higher in most experiments. Deposits obtained in freshly prepared solutions were generally poor, but after a few days, and after several samples had been plated, the quality of electrodeposits was greatly improved and was comparable to those described above. Better results were generally observed in the presence of iodides than with bromides.<sup>5</sup> The baths tended to be unstable and were found to deteriorate after a few weeks of operation.

*The complete plating bath.*—The experiments described above have shown that the basic system of AlBr<sub>3</sub> in benzene or toluene with either a Lewis base or an alkali bromide did not yield satisfactory results. A suitable bath should contain both an alkali bromide (or iodide) and a Lewis base such as a large aromatic hydrocarbon or an amine. The effect of the addition of different compounds from these classes is discussed below.

*The effect of alkali halides.*—A solution of AlBr<sub>3</sub> (2-3M) in toluene, with ethylbenzene or naphthalene in concentrations ranging from 3-30 w/o was employed in these experiments. Bromides or iodides of Li<sup>+</sup>, Na<sup>+</sup>, K<sup>+</sup>, and NH<sub>4</sub><sup>+</sup> were added in concentrations of 0.1-1.0M. Excellent electrodeposits were obtained. The current efficiency increased with the concentration of the salt, and the tendency to form dendrites decreased. The purity of the electrodeposited aluminium was 99.5%, equal to the purity of the aluminium anodes used in these experiments.

When the concentration of the alkali salt was higher than 1M, codeposition of the salt and possibly of organic matter occurred. In some cases, when only ca. 70% of the electrodeposit consisted of aluminium, this was immediately apparent upon inspection of the sample. In other cases, when the purity was as high as 95%, apparently smooth and uniform electrodeposits were obtained, but these exhibited very poor corrosion resistance. Codeposition of salt appeared to be more severe in the presence of iodides than with bromides at comparable concentration.

Addition of alkali chlorides caused a decrease in current efficiency and gave rise to electrodeposits of poor quality. In the presence of alkali fluorides a white powder was formed in the bath and the current efficiency for aluminium deposition decreased.

*The effect of cations on bath performance.*—Addition of bromides of Li<sup>+</sup>, Na<sup>+</sup>, K<sup>+</sup>, and NH<sub>4</sub><sup>+</sup> gave indistinguishable results. A few attempts were made to electrodeposit a Mg/Al alloy by adding MgBr<sub>2</sub> in 0.1M concentration. (The solubility of this salt is much lower than that of alkali bromides or iodides.) In these experiments only aluminium was electrodeposited.

Several quaternary ammonium bromides (tetramethyl and tetraethyl ammonium bromide, ethyl pyri-

<sup>4</sup> The initial conductivity depends on the amount of moisture present in the AlBr<sub>3</sub> used or that entering the cell accidentally during preparation of the solution. This may depend on a number of factors such as the temperature and relative humidity, the skill of the experimenter, etc.

<sup>5</sup> It is very likely that part of the AlBr<sub>3</sub> could be replaced by AlI<sub>3</sub> in all plating experiments, yielding similar or even better results. In view of the higher cost and lower stability of AlI<sub>3</sub>, this would be of little industrial interest, however.

<sup>3</sup> Studies in rigorously dried systems are under way and will be reported elsewhere (27, 28).



dinium bromide, and pyridinium hydrobromide) were tested in a bath containing  $\text{AlBr}_3$  in a mixture of, say, toluene and ethylbenzene. These cations caused an apparent improvement in the results. Very smooth deposits were obtained and dendrite formation was completely suppressed. The current efficiency was close to 100% (except in the case of pyridinium hydrobromide where it was only 60–80%). However, the coatings offered poor corrosion protection. Chemical analysis showed that the concentration of aluminium in the electrodeposit was ca. 95% or less, and incorporation of salt took place.

In order to minimize the incorporation of these salts in the electrodeposit and yet make use of their beneficial effects, another series of experiments was conducted. In these, the bath contained an alkali bromide in the usual concentration range (ca. 0.5M) and a small amount (0.01–0.1M) of quaternary ammonium bromide. An improvement in bath performance was observed. Thick and smooth deposits could be formed with few or no dendrites. However, some salt was still incorporated in the electrodeposit; its purity was only 98% and its resistance to corrosion was poor.

The organic cations had a distinct effect on plating from a solution containing only one hydrocarbon. It was already pointed out that a solution of  $\text{AlBr}_3$  and  $\text{MBr}$  in benzene gave tarlike deposits, while in toluene it gave grayish dark aluminium deposits with low cathodic current efficiency. The addition of 0.01 w/o ethyl pyridinium bromide made it possible to electrodeposit aluminium from a solution of  $\text{AlBr}_3$  in benzene at low current efficiencies (although the quality of the electrodeposit was poor). The addition of 0.02 w/o of the same material to the toluene based solution yielded smooth deposits at high current efficiencies, although some salt was still incorporated in the deposited film.

*The effect of Lewis bases.*—Two classes of compounds were tested in these experiments: (i) derivatives of benzene having one or several side chains or naphthalene and its derivatives, and (ii) aromatic and aliphatic amines and some ethers.

In the first group the compounds tested were: ethyl benzene, diethyl benzene, ethyl-methyl benzene, triethyl benzene, mesitylene, durene, hexamethylbenzene, ter-butyl benzene, naphthalene and its ethyl and methyl derivatives, and anthracene and its methyl derivatives. These compounds are known to be stronger Lewis bases than toluene or benzene. They were added in concentrations of 0.1M up to several molar to baths consisting of  $\text{AlBr}_3$  (2–3M) and  $\text{MBr}$  (0.1–1M) in toluene. Greatly improved results were observed upon the addition of derivatives of benzene and naphthalene (and of naphthalene itself). The cathodic current efficiency was close to 100% at current densities of 5–10  $\text{mA} \cdot \text{cm}^{-2}$ , and high-quality, pure electrodeposits were obtained.<sup>6</sup> At higher current densities the cathodic current efficiency was found to decrease significantly (at 30  $\text{mA} \cdot \text{cm}^{-2}$  it was down to 40%). The anodic current efficiency was close to 100% when current densities of 1–10  $\text{mA} \cdot \text{cm}^{-2}$  were used for several hours. However, the decrease of weight of anodes after several weeks of operation was higher than that calculated from the total charge passed. This is probably caused by mechanical disintegration of the anodes and to a lesser degree by chemical dissolution which takes place in solutions which have not been rigorously purified and dried (27–29). Addition of anthracene and its derivatives also improved the performance of the baths, but to a lesser extent. These baths tended to deteriorate rather rapidly. In certain baths containing a high concentration of naphthalene (ca. 2M and comparable to the concentration of  $\text{AlBr}_3$ ), codeposition of salt was observed. No such effect was observed when the concentration of naphthalene was below 1M.

In the second group the compounds tested were: pyridine, tri-ethyl-amine, and N,N dimethyl aniline.

<sup>6</sup> Further details on tests of the quality of electrodeposits are given elsewhere (26).

These compounds are even stronger Lewis bases. Their presence in solution in concentration of a few tenth molar improved the properties of the plating bath in a manner similar to the effect of the hydrocarbons in the first group above. Chemical dissolution of the copper cathodes was observed in freshly prepared solutions containing any one of the above-mentioned amines. Electrolysis of such solutions yielded a highly decorative gold colored deposit of a copper/aluminium alloy which, however, had very poor corrosion resistance. After aging the bath for a few days, chemical dissolution stopped and pure aluminium electrodeposits were obtained.

A higher concentration of N,N dimethyl-aniline of ca. 0.7M prevented electrodeposition of aluminium.

In an additional series of experiments, tetrahydrofuran in molar concentration equal to that of  $\text{AlBr}_3$  was added instead of an amine. A tarlike deposit containing some aluminium was formed.

*The effect of HBr.*—A solution of  $\text{AlBr}_3$  and naphthalene in toluene was saturated with HBr. The conductivity of the resulting solution was 13  $\text{mmho} \cdot \text{cm}^{-1}$ . The copper cathode (surface area 10  $\text{cm}^2$ ) dissolved rapidly in this solution (weight loss was 0.08 g/hr) and aluminium could not be electrodeposited. Hydrobromic acid was removed from solution by bubbling dry nitrogen. The decrease in concentration can be followed in this system (where no alkali bromide was added) by the decrease in conductivity. Aluminium could be deposited only when the conductivity was less than 8  $\text{mmho} \cdot \text{cm}^{-1}$ . At 5  $\text{mmho} \cdot \text{cm}^{-1}$  the current efficiency was 35% and at 1  $\text{mmho} \cdot \text{cm}^{-1}$  or less it was close to 100%. In the last solution the rate of corrosion of the copper cathode on open circuit was only 5 mg in 24 hr, more than two orders of magnitude slower than in a solution saturated with HBr.

*The effect of oxygen.*—Oxygen does not react chemically with the components of the bath at a significant rate. Thus, it may be allowed to saturate the bath and can subsequently be removed by bubbling an inert gas without adversely affecting its performance. However, during electroplating oxygen must be absent since its reaction at the electrodes prevents deposition of aluminium and causes rapid deterioration of the bath. In an experiment conducted in a solution saturated with oxygen, the voltage between a copper cathode and an aluminium reference electrode rose within minutes from a few millivolts to many volts. At the end of electrolysis the copper cathode was coated with a black tar which did not contain aluminium.

*The effect of ions of heavy metals.*—Ions of heavy metals, such as copper and iron, interfere with the electrodeposition of aluminium. Alloys of various composition are electrodeposited, the adhesion to the substrate metal is usually poor, and the deposits are gray and have poor corrosion resistance. Heavy ions can be removed by preelectrolyzing on a dummy cathode.

*Transference numbers.*—Preliminary experiments were performed to determine approximately the transference numbers of potassium and aluminium, by the Hittorf method. A solution of 0.7M KBr and 2M  $\text{AlBr}_3$  in toluene was employed. Two copper electrodes were used in the cell and chemical analysis of the solution in the anode compartment was carried out. The concentration of potassium was found to decrease while that of aluminium was found to increase. The transference numbers were:  $t_{\text{K}^+} = 0.3 \pm 0.1$  and  $t_{\text{Al}_2\text{Br}_7^-} = 0.7 \pm 0.1$ . If one were to assume that aluminium was present mainly in the form of the smaller ion  $\text{AlBr}_4^-$ , its calculated transference number would be  $t_{\text{AlBr}_4^-} = 1.4 \pm 0.2$  which is clearly unacceptable.

*The solubility of  $\text{AlBr}_3$  and KBr in cyclohexane.*—Aluminium bromide was dissolved in 70  $\text{cm}^3$  cyclohexane in an atmosphere of dry nitrogen, giving a clear, colorless solution which was 0.7M in  $\text{AlBr}_3$ . Dry KBr (2.1g) was added and the solution was stirred for

24 hr. Most of the KBr did not dissolve and the concentration of potassium in solution was  $4 \times 10^{-4}M$ . The conductivity was below  $10^{-7}$  mho  $\cdot$  cm $^{-1}$ . No attempt was made to electrodeposit aluminium from this system.

### Discussion

*The structure of the electrolyte.*—Aluminium bromide, which has predominantly covalent bonds, is soluble in aromatic hydrocarbons and in cyclohexane. The resulting solution is nonconducting. Simple ionic salts, such as KBr, are not soluble in hydrocarbons, but are readily soluble in an aromatic hydrocarbon containing  $AlBr_3$ . The solubility of KBr (and other alkali bromides or iodides) is dependent on the concentration of aluminium bromide. In solutions that have not been dried rigorously, it does not exceed the molar ratio of  $KBr:AlBr_3$  (1:2), corresponding to the formation of  $Al_2Br_7^-K^+$ . When a higher proportion of alkali bromide is dissolved, some  $AlBr_4^-K^+$  is probably formed, but the above ratio never exceeds 1:1.

The fact that KBr cannot be dissolved to any significant extent in a solution of  $AlBr_3$  in cyclohexane is rather interesting in view of the fact that the dielectric constants of cyclohexane and, say, toluene are nearly the same. It would appear that the difference is due to the great difference in polarizability of the two types of solvents, which allows stabilization of the ions in the aromatic but not in the alicyclic system. It is interesting to note in this context that the dielectric constant of a solution of toluene containing 50 w/o  $AlBr_3$  was found to be 2.75 (30) while that of pure toluene is 2.28.

The transference numbers reported here, which indicate that aluminium appears in solution as negative ions, are in agreement with the earlier interpretation of Plotnikov *et al.* (7, 10, 11). The fact that  $t_+ < t_-$  indicates that the potassium ion is more heavily solvated.

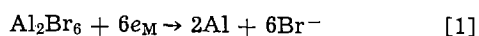
The conductivity observed in these solutions is much lower than for aqueous solutions of comparable concentration. Thus, a solution of 1M  $Al_2Br_7^-K^+$  in toluene has a conductivity of ca. 5 mmho  $\cdot$  cm $^{-1}$ , while the conductivity of an aqueous 1M KCl solution is ca. 100 mmho  $\cdot$  cm $^{-1}$ . This difference can be ascribed to several factors: (i) the viscosity of the organic solution is about four times higher (31), (ii) the radius of the solvated ions is larger, and (iii) partial association of the positive and negative ions may occur.

Double layer capacity measurements, to be reported elsewhere (29), as well as earlier work on solvation, indicate that the solvated radius of ions in this system is larger than in water. This, together with the difference in viscosity, could explain a major part of the difference in conductivity, indicating that ion pair formation is not predominant in this system. This would appear unusual, in view of the low dielectric constant, but can be understood as resulting from the large solvated radii of the ions, which keeps them far apart and reduces the electrostatic attraction forces between them.

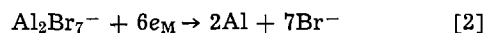
Vapor pressure measurements have shown that in toluene one molecule of the solvent is attached strongly to each  $Al_2Br_6$  molecule forming a  $\pi$  complex (32). When HBr was also present, complexes of the type  $ArH_2^+Al_2Br_7^-$  (14) or  $3Ar \cdot Al_2Br_6 \cdot HBr$  were found (13). The solvation number in this case varies for different aromatic hydrocarbons.

*Reactions at the cathode and the anode.*—The alkali halides added to the solution of  $AlBr_3$  in a mixture of aromatic hydrocarbons serve two purposes: (i) to increase and stabilize the conductivity, and (ii) to convert most of the aluminium present in solution to the negative ion  $Al_2Br_7^-$  (or to  $AlBr_4^-$  in the presence of a high concentration of MBr), as indicated by transference number measurements.

The primary cathode reaction could be either



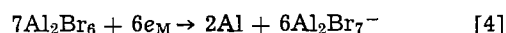
or



When the ratio of molar concentrations of  $MBr:AlBr_3$  is much lower than 0.5, both reactions may occur. As this ratio approaches 0.5, Eq. [2] probably becomes predominant. Since the simple  $Br^-$  ion is apparently not stabilized in this system,<sup>7</sup> Eq. [1] must be followed by a chemical reaction of the type

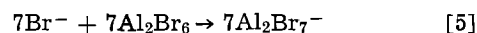


giving the over-all reaction



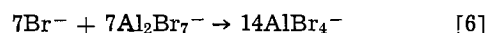
Thus, less than one electron is passed in the over-all reaction for each  $Al_2Br_6$  molecule reaching the surface.<sup>8</sup> This can be put differently by stating that for each molecule of  $Al_2Br_6$  discharged at the electrode, six molecules of  $Al_2Br_6$  are required to complex the free  $Br^-$  ions left behind. Thus, if the current density is too high and/or stirring insufficient, a deficiency of  $Al_2Br_6$  molecules may develop in the diffusion layer causing codeposition of the alkali bromide.

Equation [2] will be followed, for the same reasons, by the chemical step

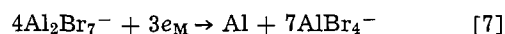


Combining Eq. [2] and [5] gives the same over-all reaction, represented by Eq. [4].

As the ratio of  $MBr:AlBr_3$  approaches or even exceeds 0.5, the primary electrode reaction becomes predominantly that shown in Eq. [2], but this could now be followed by a reaction such as



which leads to the over-all reaction



Here again poor mixing or a high current density could cause a deficiency of  $Al_2Br_7^-$  at the electrode and result in codeposition of the salt. In this situation the number of electrons passed in the over-all reaction per molecule of  $AlBr_3$  (calculated) reaching the surface is  $n = \frac{3}{8}$ .

At the anode the situation is obviously reversed. The over-all reaction given in Eq. [4] is likely to predominate, since this requires only three ions of  $Al_2Br_7^-$  for each atom of aluminium dissolved, while in Eq. [7] one would require seven ions of  $AlBr_4^-$ , the concentration of which is very low in most situations.

If the supply of  $Al_2Br_7^-$  ions to the anode is insufficient due to their low concentration in solution (when the ratio of  $MBr$  to  $AlBr_3$  is small compared to 0.5), insufficient stirring, too high current density, or a combination of these factors, anodic dissolution cannot occur at the desired rate, the potential will rise, and side reactions (probably decomposition of the solvent or bromine evolution) will occur which shorten the lifetime of the plating bath.

From the above discussion it may be concluded that the concentration of  $MBr$  in solution should be chosen so that it is sufficiently high to provide good conductivity, good throwing power, and efficient anodic dissolution, yet sufficiently low to avoid codeposition of the salt. The importance of proper stirring and of limiting the current density employed becomes evident for both cathodic and anodic reactions.

If oxygen is present in the solution during electrolysis, the anode is covered with an oxide layer and anodic dissolution is diminished. Bromine evolution occurs (10) and this reacts with the solvent to form a

<sup>7</sup> This may be inferred from the fact that  $MBr$  is soluble in an aromatic hydrocarbon only in presence of  $AlBr_3$ .

<sup>8</sup> This is an interesting point for the calculation of the diffusion limited current to be expected in, say, a potentiostatic transient. If the concentration of aluminium is expressed formally as the molar concentration of  $AlBr_3$ , the number of electrons passed in the over-all reaction, according to Eq. [4] will be  $n = 3/7$ , rather than 3, as one might be led to assume.

variety of high molecular weight compounds, causing rapid deterioration of the bath. At the cathode oxygen is apparently reduced instead of aluminium and an oxide layer is also formed, as evidenced by the rapid increase in measured voltage drop between the cathode and an aluminium wire reference electrode.

The effect of quaternary ammonium salts in small concentrations is probably due to strong adsorption of the ion at the electrode surface. This also accounts for the tendency of incorporation of salts into the electrodeposits, causing poor corrosion resistance, as described above.

*The effect of HBr and of Lewis bases.*—All the experiments described in this paper were performed under conditions which may resemble industrial operation. Thus, all solutions contained a small amount of HBr, formed as a result of interaction of  $\text{AlBr}_3$  with moisture entering the cell during changing of the samples. It is known (13, 14) that the reaction of HBr with  $\text{AlBr}_3$  and the aromatic hydrocarbon  $\text{ArH}$  gives rise to a complex of the form  $\text{ArH}_2^+ \text{Al}_2\text{Br}_7^-$  which can be reduced at the cathode. The stability of this complex increases in the order benzene < toluene < m-xylene < mesitylene. Reduction of the protonated hydrocarbon competes with electrodeposition of aluminium, and hence the cathodic current efficiency decreases with increasing concentration of HBr until a point is reached where it becomes negligible. This can account for the fact that in the work of Capuano and Davenport (23-25), where moisture or HBr were added on purpose, the cathodic current efficiency was never found to exceed 85%. In the present work, where the level of HBr was kept low, current efficiencies approaching 100% were observed in solutions containing a mixture of hydrocarbons and an alkali halide.

Benzene is a weak Lewis base and hence even a small amount of HBr prevents electrodeposition of aluminium. Toluene is a stronger base and electrodeposition does occur under the same conditions, but at low current efficiencies. When mesitylene is used as the main solvent, or when it is added to toluene in substantial quantities, a higher level of moisture can be tolerated in the system (up to a few tenths per cent  $\text{H}_2\text{O}$ ), still yielding good electrodeposits at high cathodic current efficiencies. The same is true for naphthalene and for derivatives of benzene with highly branched side chains. It would appear that in all these cases the proton is stabilized by the aromatic hydrocarbon, which is a strong Lewis base compared to benzene or toluene, and reduction of the  $\text{ArH}_2^+$  complex occurs at a much slower and often negligible rate. Aliphatic and aromatic amines, which are even stronger Lewis bases, can serve the same purpose.

#### Acknowledgments

The authors wish to thank Mr. Meron, Head, Department of Materials Engineering, Israel Aviation Industries, and Mr. Tillis of the same department for their encouragement in the course of this work. Thanks are also due to Mrs. I. Armel and Mr. Y. Canfi for their technical assistance in performing the experiments described in this paper.

Manuscript submitted June 24, 1975; revised manuscript received Sept. 8, 1975.

Any discussion of this paper will appear in a Discussion Section to be published in the December 1976

JOURNAL. All discussions for the December 1976 Discussion Section should be submitted by Aug. 1, 1976.

#### REFERENCES

1. A. Brenner, in "Advances in Electrochemistry and Electrochemical Engineering," Vol. 5, C. W. Tobias, Editor, p. 217, Interscience, New York (1967); D. I. Couch and A. Brenner, *This Journal*, **99**, 234 (1952).
2. E. J. Smith and L. D. McGraw, in "Modern Electroplating," F. A. Lowenheim, Editor, John Wiley & Sons, New York (1963).
3. M. Yoshio and N. Ishibashi, *J. Appl. Electrochem.*, **3**, 321 (1973).
4. M. Koike and K. Sekimoto, *Kinzoku*, No. 4, 77 (1972).
5. R. Dotzer, *Chem. Ingr. Tech.*, **45**, 653 (1973); G. Iwantschiff and R. Dötzer, *Werkstofftechnik*, **3**, 9/34 U. 10/22 (1972).
6. D. D. Eley and P. J. King, *J. Chem. Soc.*, **1952**, 2517.
7. V. A. Plotnikov and S. I. Yakubson, *J. Gen. Chem. USSR*, **6**, 1690 (1936).
8. V. A. Plotnikov and E. Ya. Gorenbein, *ibid.*, **7**, 372 (1937).
9. E. Ya. Gorenbein, *Univ. Etat. Kiev, Bull. Sci. Rec. Chim.*, **1**, 101 (1935).
10. V. A. Plotnikov, I. A. Sheka, and V. A. Yankelevich, *J. Gen. Chem. USSR*, **3**, 481 (1933).
11. V. A. Plotnikov, I. B. Barmashenko, and E. B. Gitman, *Mem. Inst. Chem. Acad. Sci. Ukr. SSR*, **5**, 3 (1938).
12. E. Ya. Gorenbein, *J. Gen. Chem. USSR*, **9**, 2041 (1939).
13. F. Norris and J. N. Ingraham, *J. Am. Chem. Soc.*, **62**, 1298 (1940).
14. H. C. Brown and W. J. Wallace, *ibid.*, **75**, 6268 (1953).
15. V. A. Plotnikov and S. Yakubson, *Z. Physik. Chem.*, **138**, 251 (1928).
16. V. A. Plotnikov and E. Ya. Gorenbein, *Mem. Inst. Chem. Acad. Sci. Ukr. SSR*, **3**, 471 (1936).
17. V. A. Yankelevich and I. A. Sheka, *ibid.*, **5**, 59 (1938).
18. V. A. Plotnikov and S. I. Yakubson, *Z. Physik. Chem. Alit.*, **A147**, 227 (1930).
19. D. A. Pospekhov, *Usp. Khim.*, **6**, 515 (1937).
20. V. A. Plotnikov and A. T. Dibrova, *Zapiski Inst. Khim. Acad. Sci. USSR*, **7**, 337 (1940).
21. L. Simanavicius and A. Karpavichyus, *Lietuvos TSR Mokslu Akad. Darbai, Ser. B*, **83**, 1 (1971).
22. L. Simanavicius, A. Karpavichyus, and P. Dobrovol'skis, in "Electrodeposition of Metals," Proceedings of the 10th Lithuanian Conference of Electrochemistry, Israel Program for Scientific Translations (1970).
23. G. A. Capuano and W. G. Davenport, *Can. Pat.* 945, 935 (1974), *U.S. Pat.* 3,775,260 (1973).
24. G. A. Capuano and W. G. Davenport, *This Journal*, **118**, 1688 (1971).
25. G. A. Capuano and W. G. Davenport, *Plating*, **60**, 251 (1973).
26. E. Peled and E. Gileadi, *ibid.*, **62**, 342 (1975).
27. E. Peled, A. Meitavski, and E. Gileadi, *Z. Physik. Chem. (N.F.)*, In press.
28. A. Reger, E. Peled, and E. Gileadi, *This Journal*, In press.
29. E. Peled, S. Ziegel, and E. Gileadi, In preparation.
30. J. Timmermans, "Physico Chemical Constants of Binary Systems in Concentrated Solutions," p. 1038, Interscience, New York (1959).
31. I. Gorenbein and G. A. Redlar, *J. Gen. Chem. USSR*, **11**, 1069 (1941).
32. H. C. Brown and W. J. Wallace, *J. Am. Chem. Soc.*, **75**, 6265 (1953).



## The Electrode Potential of the Chromate (VI)-Lithium Chromate (V) System in Molten Lithium Chloride-Potassium Chloride Eutectic

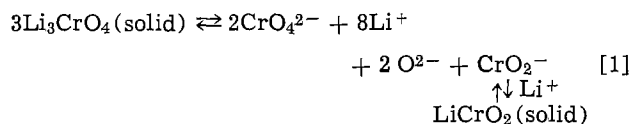
Katsumi Niki\*

Department of Electrochemistry, Yokohama National University, Minami-ku, Yokohama 233, Japan

and Isamu Uchida\* and Herbert A. Laitinen\*

Department of Chemistry, University of Florida, Gainesville, Florida 32611

The electrochemical reduction of chromate ion,  $\text{CrO}_4^{2-}$ , in lithium chloride-potassium chloride eutectic melt (1), and the effect of various divalent metal ions (2-5) and water (6), have been studied extensively. Laitinen and Bankert (1) observed that the reduction of chromate ion was a single, irreversible and diffusion controlled three-electron process, yielding an unstable initial product believed to be  $\text{Li}_3\text{CrO}_4$ . Recently Uchida and Laitinen (6) isolated  $\text{LiCrO}_2$  as the reduction product from moist melts. On the other hand, Niki and Laitinen (7) found that  $\text{Li}_3\text{CrO}_4$ , which is assumed to be one of the intermediate compounds in the reduction of  $\text{CrO}_4^{2-}$  in  $\text{LiCl-KCl}$  melt, is relatively stable in  $\text{LiCl-KCl}$  melt. Because of the limited solubility of  $\text{Li}_3\text{CrO}_4$  there is an equilibrium in the disproportionation reaction; namely



In the present work, the electrode potential of  $\text{CrO}_4^{2-}/\text{Li}_3\text{CrO}_4$  and the equilibrium of the disproportionation reaction of  $\text{Li}_3\text{CrO}_4$  were investigated to correlate these values to the electrochemical behavior of chromate ion.

### Experimental

**Reagent.**— $\text{Li}_3\text{CrO}_4$  was prepared by neutralizing  $\text{CrO}_3$  by  $\text{Li}_2\text{CO}_3$ , and then it was recrystallized and dried at  $200^\circ\text{C}$  under vacuum for about 8 hr. All chemicals used in the present work were either the AR or the primary standard grade. The  $\text{LiCl-KCl}$  eutectic melt was supplied by Anderson Physics Laboratories, Incorporated, Champaign, Illinois.

**$\text{Li}_3\text{CrO}_4$  electrode.**—A mixture of the stoichiometric amount of  $\text{Li}_2\text{CrO}_4$  and  $\text{Li}_2\text{CO}_3$  was maintained at  $450^\circ\text{C}$  in a platinum crucible for 5 hr under vacuum. Then the temperature of the mixture was increased gradually. When a liquid phase formed at about  $550^\circ\text{C}$ , a platinum flag 0.06 mm thick and 6.37 mm in diameter with 36 gauge platinum wire as an electrical lead, was immersed in the melt. After the platinum surface was wetted by the viscous melt, it was pulled out from the melt. Then the temperature of a furnace was increased up to  $750^\circ\text{C}$ . The viscous melt solidified and black crystals covered the surface of the platinum flag. The platinum flags covered by  $\text{Li}_3\text{CrO}_4$  were stored

in a vacuum desiccator and used as indicator electrodes. Fine  $\text{Li}_3\text{CrO}_4$  crystals formed in the crucible were also stored in a vacuum desiccator and used for the disproportionation reaction measurement. The purity of  $\text{Li}_3\text{CrO}_4$  was better than 99% as determined from the close agreement between the observed ratio of  $\text{Cr(VI)}:\text{Cr(III)}$  in a 6N  $\text{HCl}$  solution with the theoretical ratio of 2:1 and the agreement between the weight of  $\text{Li}_3\text{CrO}_4$  taken and calculated from the total Cr recovered.  $\text{Li}_3\text{CrO}_4$  was handled under nitrogen atmosphere.

**Electrochemical measurement.**—The electrochemical cell assembly has been described in detail (8). A known amount of  $\text{Li}_2\text{CrO}_4$  was added to each compartment containing 3 ml of the melt in the cell, and the exact concentration of chromate ion in the melt was determined by coulometric titration after the potential measurement (2). The electrode potentials of the  $\text{Li}_3\text{CrO}_4$  electrode in the chromate solutions were measured with a Leeds and Northrup Student Type 8687 volt potentiometer against the  $\text{Pt(II)}/\text{Pt}$  electrode. The preparation and construction of  $\text{Pt(II)}/\text{Pt}$  electrode have been described (8-9).

All potentials shown in this work are given with respect to the 1M  $\text{Pt(II)}/\text{Pt}$  electrode, and all experiments were carried out at  $450^\circ \pm 1^\circ\text{C}$ .

**Disproportionation of  $\text{Li}_3\text{CrO}_4$ .**—About 200 mg of  $\text{Li}_3\text{CrO}_4$  was added to each 3 ml compartment in the cell. These compartments were of Pyrex glass with a fritted glass bottom which acted as a salt bridge. The melt was stirred occasionally with a glass rod and maintained for about 30 min. After equilibrium has been attained, the electrode potential of the  $\text{Li}_3\text{CrO}_4$  electrode in these melts was measured and then a sample of the melt containing chromate ion was taken by the sampling tube for the determination of chromium (7).

**Analysis of chromates.**—Analytical procedures for the chromium compounds were the same as in the previous work (7).

### Results and Discussion

**Equilibrium potential of  $\text{CrO}_4^{2-}/\text{Li}_3\text{CrO}_4$  system.**—The electrochemical cell used for the equilibrium potential measurement of the  $\text{CrO}_4^{2-}/\text{Li}_3\text{CrO}_4$  system was

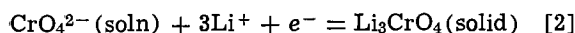
$\text{Pt}/\text{Li}_3\text{CrO}_4/\text{CrO}_4^{2-}$  (in Li, KCl) //

$\text{Pt(II)} (1.0\text{M in Li, KCl})/\text{Pt}$

\* Electrochemical Society Active Member.

Key words: chromium (V), lithium chromate (V), electrode potential, molten salt, disproportionation.

The half-cell reaction on the left-hand side of the cell is given by



If the cell reaction is reversible, the equilibrium potential of the  $\text{CrO}_4^{2-}/\text{Li}_3\text{CrO}_4$  system is given by

$$E = E^\circ + \frac{RT}{F} \ln \frac{a_{\text{CrO}_4^{2-}}}{a_{\text{Li}_3\text{CrO}_4}} \quad [3]$$

Since  $\text{Li}_3\text{CrO}_4$  is solid and the activity coefficient of  $\text{CrO}_4^{2-}$  is assumed to be unity, Eq. [3] leads to

$$E = E^\circ + 0.1435 \log C_{\text{CrO}_4^{2-}} \quad (\text{at } 450^\circ\text{C}) \quad [4]$$

The equilibrium potential of the  $\text{Li}_3\text{CrO}_4$  electrode with various concentrations of chromate ion is shown in Fig. 1. The electrode attained an equilibrium potential within 10 min and gave a stable value for more than 1 hr when the concentration of  $\text{CrO}_4^{2-}$  was greater than 0.02M in the melt. At lower concentrations of  $\text{CrO}_4^{2-}$  ( $<0.015\text{M}$ ),  $\text{Li}_3\text{CrO}_4$  on the platinum electrode was probably oxidized to  $\text{CrO}_4^{2-}$  by PtO on the platinum surface and the concentration of chromate ion became higher in the vicinity of the electrode. Accordingly, the electrode potential of the  $\text{Li}_3\text{CrO}_4$  electrode became more positive than that expected from the Nernst equation (4).

The equilibrium potential (V vs. Pt(II), 1M/Pt) of the  $\text{CrO}_4^{2-}/\text{Li}_3\text{CrO}_4$  system at  $450^\circ\text{C}$  is given empirically by

$$E = -(0.761 \pm 0.004) + 0.141 \log C_{\text{CrO}_4^{2-}} \quad [5]$$

The slope of the Nernst equation agreed well with a one-electron process corresponding to Eq. [2].

**Disproportionation of  $\text{Li}_3\text{CrO}_4$  in LiCl-KCl melt.**—In our previous work (7), it was shown that  $\text{Li}_3\text{CrO}_4$  disproportionates to  $\text{CrO}_4^{2-}$  and  $\text{LiCrO}_2$  in the LiCl-KCl melt. If the disproportionation reaction of  $\text{Li}_3\text{CrO}_4$  takes place in the melt according to Eq. [1], when the LiCl-KCl melt is saturated by both  $\text{Li}_3\text{CrO}_4$  and  $\text{LiCrO}_2$ , then the equilibrium constant for this disproportionation reaction is given by

$$K = [\text{CrO}_4^{2-}][\text{O}^{2-}] \quad [6]$$

The concentration of  $\text{CrO}_4^{2-}$  ion in the melt in the

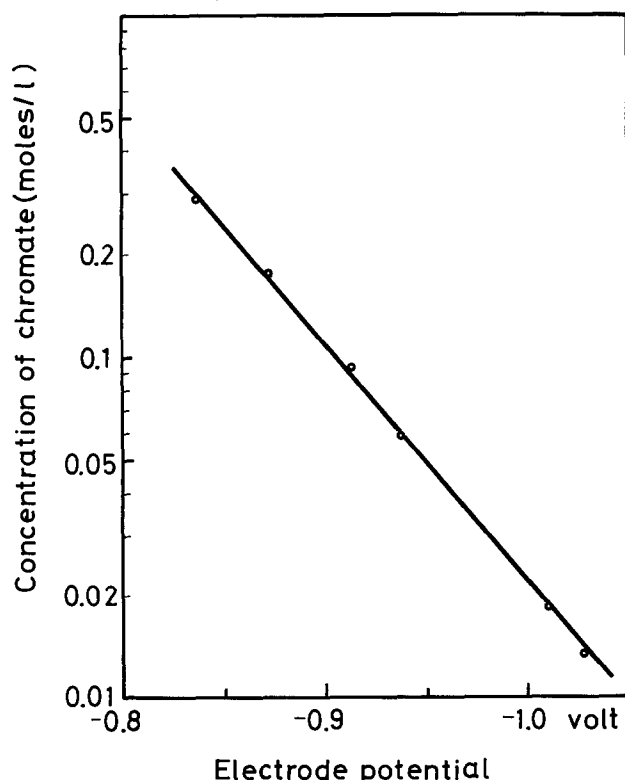


Fig. 1. Equilibrium potential of  $\text{CrO}_4^{2-}/\text{Li}_3\text{CrO}_4$  system in LiCl-KCl eutectic melt at  $450^\circ\text{C}$ .

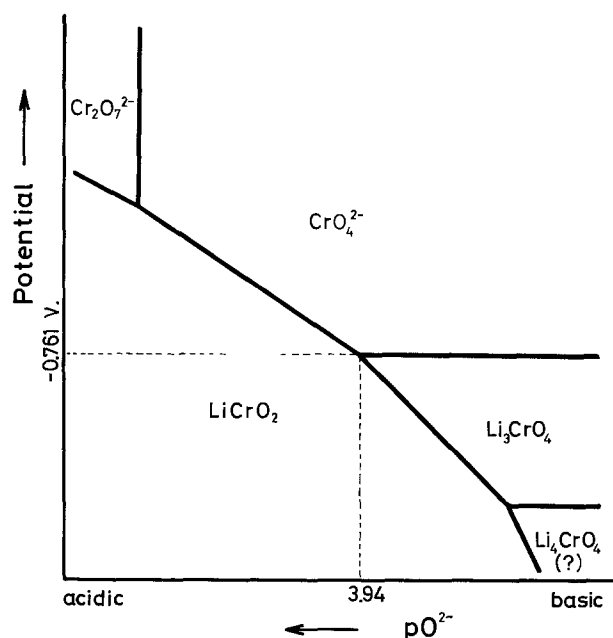


Fig. 2. Potential- $p\text{O}^{2-}$  diagram of chromates in LiCl-KCl eutectic melt at  $450^\circ\text{C}$ .

presence of excess amounts of  $\text{Li}_3\text{CrO}_4$  was  $(0.0107 \pm 0.0002)\text{M}$  and the equilibrium constant for the reaction [1] is given by

$$K = [(1.07 \pm 0.002) \times 10^{-2}]^2 = (1.15 \pm 0.04) \times 10^{-4} \text{ mol}^2 \text{ l}^{-2} \quad (\text{at } 450^\circ\text{C})$$

When the concentration of  $\text{CrO}_4^{2-}$  was 1.0M in the melt in the presence of excess amounts of  $\text{Li}_3\text{CrO}_4$ , the electrode potential of the  $\text{CrO}_4^{2-}/\text{Li}_3\text{CrO}_4$  is  $-0.761\text{V}$  (vs. 1.0M Pt(II)/Pt) and the concentration of  $\text{O}^{2-}$  in the melt can be calculated to be  $1.145 \times 10^{-4}\text{M}$ . Figure 2 shows the semiquantitative  $p\text{O}^{2-}$ -potential diagram of chromium, which we have described qualitatively in a previous paper (7).

#### Acknowledgment

Part of this research was supported by the Japan Society for the Promotion of Science under the Japan-U.S. Cooperative Science Program, and part by the Army Research Office (Durham) (I. U. and H. A. L.).

Manuscript submitted Feb. 19, 1975; revised manuscript received Sept. 2, 1975.

Any discussion of this paper will appear in a Discussion Section to be published in the December 1976 JOURNAL. All discussions for the December 1976 Discussion Section should be submitted by Aug. 1, 1976.

Publication costs of this article were partially assisted by the University of Florida.

#### REFERENCES

- H. A. Laitinen and R. D. Bankert, *Anal. Chem.*, **39**, 1790 (1967).
- J. H. Propp and H. A. Laitinen, *ibid.*, **41**, 644 (1969).
- B. Popov and H. A. Laitinen, *This Journal*, **117**, 482 (1970).
- K. W. Hanck and H. A. Laitinen, *ibid.*, **118**, 1123 (1971).
- H. A. Laitinen and L. R. Lieto, *Croat. Chem. Acta*, **44**, 275 (1972).
- I. Uchida and H. A. Laitinen, To be published.
- K. Niki and H. A. Laitinen, *J. Inorg. Nucl. Chem.*, In press.
- H. A. Laitinen and C. H. Liu, *J. Am. Chem. Soc.*, **80**, 1015 (1958).
- H. A. Laitinen and J. W. Pankey, *ibid.*, **81**, 1053 (1959).

# The Rotating Cone Electrode

E. Kirowa-Eisner and E. Gileadi\*

*Institute of Chemistry, Tel-Aviv University, Ramat-Aviv, Israel*

The rotating disk electrode and rotating ring-disk electrodes have long become standard tools in the study of electrode reactions. Other configurations such as the rotating hemisphere (1) and rotating ring (2) or ring-ring electrodes (3) have also been tested experimentally and the relevant equations derived. In all these cases, the rate of mass transport, and hence the limiting current density, was always found to be proportional to the square root of the angular velocity,  $\omega$ , as derived by Levich for the rotating disk electrode (4). Recently it was shown (5) that a substantial degree of eccentricity of the rotating disk electrode could be allowed (up to ca. 64% of the radius of the disk) without affecting the limiting current at all.

One of the experimental problems often occurring when a rotating disk electrode is employed is a tendency for a gas bubble to be trapped at the center of the disk where the radial forces are balanced. This occurs particularly when vigorous gas evolution takes place.

Use of a rotating ring instead of a disk has been suggested to overcome this difficulty (2, 3). This may solve the problem partially since, if the bubble trapped at the center of rotation is not too large it will leave the electrode itself unshielded. However, the existence of a bubble at the center of the disk will alter the conditions of flow and, hence, introduce an error in the measurement of the limiting current density.

Recently it has been suggested (6) that a rotating cone electrode could be used instead of a rotating disk. In this configuration, a bubble at the tip of the cone would not be stable, and smooth flow past the electrode surface may be expected even in reactions in which vigorous gas evolution occurs. Preliminary experiments showed that the linear relationship between  $i_L$  and  $\omega^{1/2}$  was maintained for this configuration.

Mass transport to a conical electrode has been considered by several authors (7-10). In all these studies the electrode was stationary and the fluid was forced past it. The boundary layer problem for a rotating cone has been treated by a number of authors (11-13) for heat and mass transport situations not related to electrochemical systems. The equations for a rotating cone electrode have been derived recently by Newman and Mohr (14) in a form commonly used by electrochemists. The result for the local mass transfer rate at the limiting current is

$$j = 0.62C_b\sqrt{\nu\omega \sin \theta} Sc^{-2/3} \quad [1]$$

The over-all mass transfer rate for a conical electrode of base radius  $r$  is

$$J_{\text{tot}} = 0.62\pi C_b r^2 \sqrt{\frac{\nu\omega}{\sin \theta}} Sc^{-2/3} \quad [2]$$

where the Schmidt number  $Sc$  is a dimensionless quantity given by  $Sc = \nu/D$ .

These equations may be rewritten in simple form to relate the limiting current density  $i_L$  and the limiting current  $I_L$  on a rotating disk (4) and rotating cone having the same base radius. Thus

$$i_L(\text{cone}) = i_L(\text{disk}) \sin^{1/2} \theta \quad [3]$$

$$I_L(\text{cone}) = I_L(\text{disk}) \sin^{-1/2} \theta \quad [4]$$

## Experimental

The equations given above show that the rotating cone electrode can be a useful tool in electrode kinetic

studies just as the rotating disk, and the very same equations can be used to separate the activation-controlled current from the total current measured under conditions of mixed mass transport and activation control. In this work the validity of the above equations was tested experimentally, care being taken to achieve the highest possible experimental accuracy. Equations [3] and [4] were tested in a solution of 4.00 mM hydroquinone in 2.0M KCl.

*The electrodes, solution, and experimental setup.*—As shown in Fig. 1, a platinum cylinder of 4.80 mm diameter and 11 mm length was press fitted into a Teflon holder (outer diameter 12 mm). The same electrode was machined to different angles ( $\theta = 60^\circ$ - $25^\circ$ ) on an accurate lathe. The electrode assembly was centered carefully to within 0.02 mm to minimize wobble. The accuracy of the angles machined was  $\pm 1/4^\circ$ .

A flat platinum electrode about 2 cm<sup>2</sup> area, situated at a distance of about 2 cm from the rotating electrode served as the counterelectrode. A commercial mercury/mercurous sulfate electrode (Radiometer Type K601) served as the reference.

All chemicals were analytical grade and were used without further purification. Hydroquinone was dried at 80°C. All solutions were prepared in triple-distilled water.

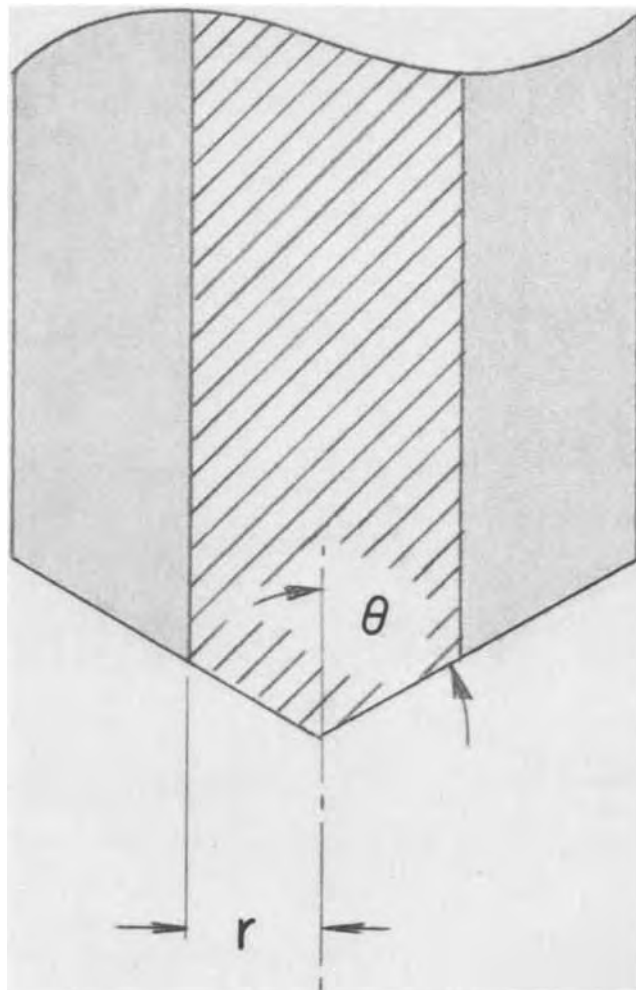


Fig. 1. Structure of cone electrode, defining the cone angle  $\theta$  and radius  $r$ . Shaded area is Teflon holder.

\* Electrochemical Society Active Member.  
Key words: rotating electrodes, mass transport.

Measurements were performed potentiostatically, with an Elron Model CHP-1 potentiostat. No IR correction was necessary, since measurements were taken in the limiting current region. A Pine Instrument rotator and a Metrohm Type EA 870-20 thermostated cell were used. Currents were recorded on a Yokogawa Type 3077 X-Y recorder.

**Procedure.**—Each new electrode was degreased with acetone, cleaned in nitric acid (1:1), and washed with tripe-distilled water, all in an ultrasonic cleaner. Before each run the electrode was pretreated electrochemically in 0.5M H<sub>2</sub>SO<sub>4</sub> in a procedure similar to that proposed by Gilman (15,16). This consisted of the following sequence of potential (vs. NHE) and time: 1.85V (10 sec); 1.20V (25 sec); 0.10V (25 sec). The sequence was repeated several times, after which a cyclic voltammogram was taken to verify the cleanliness of the surface.

The pretreated electrode was washed with triple-distilled water and transferred to the cell containing about 80 cm<sup>3</sup> of 4.00 mM hydroquinone solution in 2M KCl, which had been deaerated with purified nitrogen. The conical electrode was immersed about 2 cm below solution level. No bubbles were formed even at the highest rotation velocity of 10<sup>4</sup> rpm employed.<sup>1</sup>

The potential was set to a value of 1.02V vs. NHE, in the region of limiting current, and the current was measured. Each measurement was restricted to 5 sec to minimize changes in concentration of hydroquinone during the whole run. At least five runs in freshly prepared solutions were made for each angle of the cone, and the limiting current was measured at nine rotation velocities, between 4 × 10<sup>2</sup> and 1 × 10<sup>4</sup> rpm.

### Results

The dependence of the limiting current  $I_L$  on the square root of the rotation velocity  $\omega$  is shown in Fig. 2 for different values of the angle  $\theta$ . The correlation factor for a single line was very high, in the range of 0.99995-0.99999. The standard deviation of the slope was 0.5% for the rotating cone (based on seven measurements) and 0.2% for the rotating disk (based on six measurements).

In Table I the experimental slopes of  $\partial i_L(\text{cone})/\partial \omega^{1/2}$  are compared with the values calculated according to

<sup>1</sup> In an early experiment, where a thicker Teflon sleeve was employed, bubbles were formed at intermediate rotation velocities.

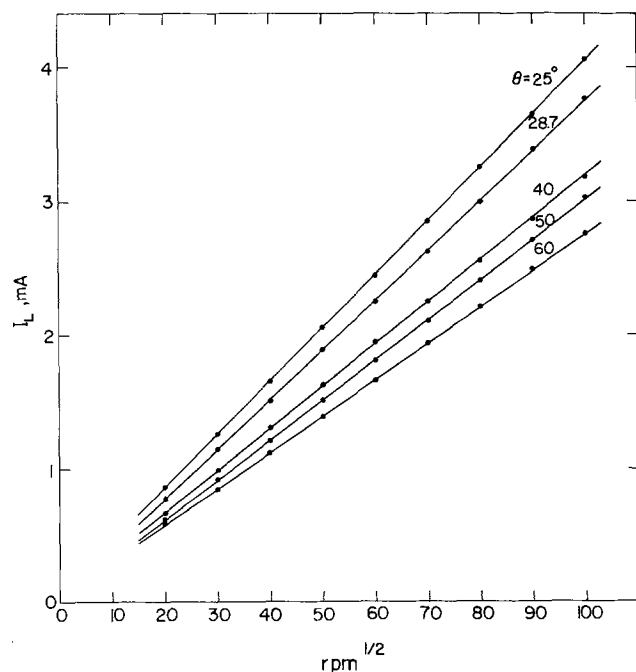


Fig. 2. Limiting current/angular velocity relationship at different cone angles,  $\theta$ . 4 mM hydroquinone, 2M KCl, 25°C. Radius of cone base: 2.4 mm.

Table I. Comparison of experimental and calculated limiting current densities on rotating cone electrode for 4.00 mM hydroquinone in 2M KCl.

Cone angle (°)	Experimental for $400 \leq \omega \leq 10^4$ rpm	Calculated after Eq. [3]	Difference between experimental and calculated values, per cent	
			For $400 \leq \omega \leq 10^4$ rpm	For $400 \leq \omega \leq 3.6 \times 10^3$ rpm
25	93.0	91.4	+1.8	+1.3
28.7	98.6	97.4	+1.2	+0.5
40	111.2	112.7	-1.3	+0.2
45	118.3	118.2	+0.1	+0.1
50	125.9	123.0	+2.4	+0.2
60	131.4	130.8	+0.5	+0.5

Eq. [3]. A slight positive deviation occurs, which is probably due to imperfections of the surface of the cone electrode causing turbulence, particularly at higher rotation velocities. If the above slopes are recalculated on the basis of the same data but restricted to the range of  $4 \times 10^2 \leq \omega \leq 3.6 \times 10^3$  rpm, agreement between theory and experiment is improved as shown in the last column of Table I. It can be concluded that the current at the rotating cone electrode behaves according to the theoretical equations given above.

### Acknowledgments

The authors wish to acknowledge the help of Professor J. Newman and Dr. C. M. Mohr, Department of Chemical Engineering, University of California at Berkeley, in discussion of the theoretical equations of the rotating cone electrodes.

Thanks are also due to Mrs. G. Costica for technical assistance and Mr. N. Lavie and Mr. Y. Dreilinger for construction of the conical electrodes.

Manuscript submitted June 19, 1975; revised manuscript received Sept. 11, 1975.

Any discussion of this paper will appear in a Discussion Section to be published in the December 1976 JOURNAL. All discussions for the December 1976 Discussion Section should be submitted by Aug. 1, 1976.

Publication costs of this article were partially assisted by Tel-Aviv University.

### LIST OF SYMBOLS

$C_b$	bulk concentration of active species (mole/cm <sup>3</sup> )
$D$	diffusion coefficients (cm <sup>2</sup> /sec)
$i_L$	limiting current density (A/cm <sup>2</sup> )
$I_L$	limiting current (A)
$j$	local mass-transfer rate (mole/cm <sup>2</sup> sec)
$J_{tot}$	total mass-transfer rate (mole/sec)
$r$	radius of base of cone electrode*
$\nu$	kinematic viscosity (cm <sup>2</sup> /sec)
$\theta$	cone angle (half the opening angle of the cone) *
$\omega$	angular velocity (radian/sec)
$Sc$	Schmidt number of solution (dimensionless)

\* See Fig. 1 for definition of  $r$  and  $\theta$ .

### REFERENCES

- D. T. Chin, *This Journal*, **118**, 1434 (1971).
- I. V. Kadija and V. M. Nakic, *J. Electroanal. Chem.*, **34**, 15 (1972).
- I. V. Kadija and V. M. Nakic, *ibid.*, **35**, 177 (1973).
- B. Levich, *Acta Physicochimica U.R.S.S.*, **17**, 257 (1942); B. Levich, "Physicochemical Hydrodynamics," Prentice-Hall, Englewood Cliffs, New Jersey (1962).
- C. M. Mohr, Jr. and J. Newman, *This Journal*, **122**, 928 (1975).
- E. Gileadi, E. Kirowa-Eisner, and J. Penciner, "Interfacial Electrochemistry—An Experimental Approach," Experiment No. 5, Addison-Wesley Publishing Co., Inc., Reading, Massachusetts (1975).
- H. Matsuda, *J. Electroanal. Chem.*, **15**, 109 (1967); *ibid.*, **21**, 433 (1969); *ibid.*, **22**, 413 (1969).
- Khr. Iv. Noninski, *Khim. Ind.*, **44**, 359 (1972); *ibid.*, **45**, 80 (1973).
- J. C. Bazan and C. L. Rosenberg, *Anales Asoc.*



- Quim. Arg.*, **60**, 447 (1972).  
 10. J. Jordan, R. A. Javick, and W. E. Ranz, *J. Am. Chem. Soc.*, **80**, 3846 (1958).  
 11. C. S. Wu, *Appl. Sci. Res., Sect. A*, **8**, 140 (1959).  
 12. C. L. Tien, *J. Heat Transfer*, **82**, 252 (1960).  
 13. C. L. Tien and D. T. Campbell, *J. Fluid Mech.*, **17**, 105 (1963).  
 14. J. Newman and C. M. Mohr, Private communication.  
 15. S. Gilman, *Electrochim. Acta*, **9**, 1025 (1964).  
 16. E. Gileadi, E. Kirova-Eisner, and J. Penciner, "Interfacial Electrochemistry—An Experimental Approach," p. 311, Addison-Wesley Publishing Co., Inc., Reading, Massachusetts (1975).

# Brief Communication



## A Calculation of the Entropy Maximum for the Double Layer in Terms of the Water Molecule Structure

J. O'M. Bockris\* and M. A. Habib

School of Physical Sciences, The Flinders University of South Australia, Bedford Park, S. A., 5042, Australia

Oriented dipoles of water at interfaces were first introduced into electrochemical concepts by Lange and Mischenko (1). [See also Bockris and Potter's (2) initial numerical use of the concept.] Recognition of the effects of their presence lacked wide acceptance. Watts-Tobin and Mott (3, 4) and others (5) attributed the anodic capacitance hump to water orientation as a function of potential, thereby signifying that the most random orientation of water dipoles should be at a potential positive to the pzc. This is not consistent with the experimental fact that the dependence of the surface-excess entropy of the electrode-solution interface measured by Hills and Payne (6) and by Harrison *et al.* (7) on electrode charge is near parabolic with a maximum at  $q = -4$  to  $-6 \mu\text{C cm}^{-2}$ . Reeves (8) separated out the contribution to surface-excess entropy by water dipoles. This solvent-excess entropy also shows a maximum at  $q \approx -4 \mu\text{C cm}^{-2}$ . Levine, Bell, and Smith (9) considered the orientation of water molecules in the double layer, but did not calculate the corresponding entropy charge relation. Conway and Gordon (10) considered the entropy change due to water molecule displacement during the adsorption of organic molecules in terms of the original model of water molecule in the double layer due to Bockris, Devanathan, and Müller (11). The conclusion was that the entropy associated with the water molecules would pass through a maximum at the pzc, and this is at variance with the new experimental data (8). Nevertheless, we have found the solvent entropy-electrode charge relation can indeed be quantitatively interpreted in terms of an oriented water layer (3, 4, 11) at the interface.

Let there be  $N$  unassociated solvent dipoles present on the metal surface among which  $N_{\uparrow}$  are with their oxygen end towards the surface (up dipoles) and  $N_{\downarrow}$  are in the reverse position (down dipoles) so that  $N = N_{\uparrow} + N_{\downarrow}$ . The orientational entropy is then given by

$$S = k \ln \frac{N!}{N_{\uparrow}! N_{\downarrow}!} \quad [1]$$

or

$$S = \frac{1}{2} kN [2 \ln 2 - \{(1+R) \ln(1+R) + (1-R) \ln(1-R)\}] \quad [2]$$

where

$$R = (N_{\uparrow} - N_{\downarrow})/N \quad [3]$$

Considering the interaction of a dipole with the double-layer field and the surrounding dipoles,  $N_{\uparrow}$  is given by (22)

$$N_{\uparrow} = N_{\square} \exp \left[ \frac{1}{kT} (-\Delta G_{\uparrow}^c + \bar{\mu}X - U\bar{c}R) \right] \quad [4]$$

where  $N_{\square}$  = number of vacant sites available to unassociated water molecules,  $\bar{\mu}$  = the effective dipole moment of the water molecule adsorbed on the electrode,  $X$  = the double-layer field,  $\bar{c}$  = number of nearest neighbors which interact with the central water,  $U$  = interaction energy of a dipole with its nearest neighbor, and  $\Delta G_{\uparrow}^c$  = the nonelectrostatic part of the chemical term in the free-energy adsorption. Similarly

$$N_{\downarrow} = N_{\square} \exp \left[ \frac{1}{kT} (-\Delta G_{\downarrow}^c - \bar{\mu}X + U\bar{c}R) \right] \quad [5]$$

With  $X = 4\pi q/\epsilon$  and

$$-[(\Delta G_{\uparrow}^c - \Delta G_{\downarrow}^c)/kT] = -[\Delta \Delta G^c/kT] = b \quad [6]$$

one gets

$$R = \frac{\exp \left[ \frac{8\pi\bar{\mu}q}{\epsilon kT} - \frac{2U\bar{c}R}{kT} + b \right] - 1}{\exp \left[ \frac{8\pi\bar{\mu}q}{\epsilon kT} - \frac{2U\bar{c}R}{kT} + b \right] + 1} \quad [7]$$

The position of the maximum in orientational entropy may be obtained by differentiating Eq. [2] with respect to  $q$  and equating  $dS/dq = 0$ , i.e., at the maximum

$$\frac{1}{2} kN \left[ \ln \frac{1-R}{1+R} \right] \frac{dR}{dq} = 0 \quad [8]$$

Since  $1/2 kN \neq 0$ , either  $\ln[(1-R)/(1+R)] = 0$  or  $dR/dq = 0$ . From Eq. [7]

$$\frac{dR}{dq} = \frac{2Ae^y}{(e^y + 1)^2 + 2Be^y} \quad [9]$$

where

$$A = \frac{8\pi\bar{\mu}}{\epsilon kT}; \quad B = \frac{2U\bar{c}}{kT}; \quad \text{and} \quad y = Aq - BR + b \quad [10]$$

\* Equations [2] and [8] were published by Hills and Hsieh (21) after these authors had been given an early version of the present paper for review by the present authors. The origin of the equations was acknowledged in their paper.

From Eq. [9] and [10] it is evident that  $dR/dq \neq 0$ . Hence Eq. [8] is satisfied only when  $\ln[(1 - R)/(1 + R)] = 0$ . Thus, the solution of Eq. [8] is  $R = 0$ . Hence from Eq. [7]

$$(q)_{S=S_{\max}} = -\frac{b\epsilon kT}{8\pi\bar{\mu}} \quad [11]$$

The water molecules are preferentially adsorbed at the pzc (13-15) which means  $|\Delta G^c_{\uparrow}| > |\Delta G^c_{\downarrow}|$ , i.e.,  $b$  is positive (Eq. [6]). According to Bockris, Devanathan and Müller (11),  $\Delta\Delta G^c$  may be due to a difference in the image interaction in the two orientations favoring the case in which the oxygen atom is towards the metal, since the dipole is then about  $0.05 \times 10^{-8}$  cm closer to the metal (11, 16). Then (11),  $\Delta U_{\text{image}} = -3/2 \bar{\mu}^2 d / r_w^4$ , where  $d$  is the difference in distances between the metal surface and the centers of "up" and "down" dipoles. With  $\bar{\mu} = \mu/\sqrt{3}$  (3),  $d = 0.05\text{\AA}$ ,  $r_w = 1.38\text{\AA}$ , and  $\mu = 1.84D$ , we obtain  $\Delta U_{\text{image}} = -1.42 \text{ kJ mole}^{-1}$ . Due to the difference in positions of the centers of "up" and "down" dipoles, there will be a difference in the dispersion interaction energies of each of these two types of dipoles with the metal surface. The difference from two orientations is then (16),  $\Delta U_{\text{disp}} = C[\{1/(\bar{R} - d)^3\} - \{1/(\bar{R} + d)^3\}]$ , where  $\bar{R}$  is the distance between the centers of the adsorbent atom Hg and adsorbate water dipole, and  $C$  is given by (16-18)

$$C = \frac{\pi n m c^2 \alpha_1 \alpha_2}{\alpha_1 / \chi_1 + \alpha_2 / \chi_2}$$

where  $m$  is the electronic mass;  $c$  the velocity of light;  $\alpha_1, \alpha_2$  are the polarizabilities;  $\chi_1$  and  $\chi_2$  are diamagnetic susceptibilities of the metal and adsorbate atom or molecule, respectively; and  $n$  is the number of adsorbent atoms per  $\text{cm}^3$ . Now (16),  $\alpha_{\text{water}} = 1.44 \times 10^{-24} \text{ cm}^3$ ,  $\alpha_{\text{Hg}} = 5.05 \times 10^{-24} \text{ cm}^3$ ;  $\chi_{\text{water}} = -2.16 \times 10^{-29} \text{ cm}^3$ ,  $\chi_{\text{Hg}} = -5.61 \times 10^{-29} \text{ cm}^3$ ; and  $n = 4.26 \times 10^{22}$  (19). With these values and taking  $d = 0.05 \times 10^{-8}$  cm and  $\bar{R} = r_w + r_{\text{Hg}} = (1.5 + 1.38) \times 10^{-8}$ , one gets  $\Delta U_{\text{disp}} = -1.3 \text{ kJ mole}^{-1}$ . The total energy difference  $\Delta\Delta G^c$  is then  $\Delta\Delta G^c = \Delta U_{\text{image}} + \Delta U_{\text{disp}} = -1.42 - 1.3 = -2.72 \text{ kJ mole}^{-1}$ . Thus,  $b = -\Delta\Delta G^c/kT = 1.1$ . With this value of  $b$  and  $\epsilon = 6$  (20), the position of maximum orientational entropy is found from Eq. [11] to occur at  $q = -3.5 \mu\text{C cm}^{-2}$  at  $25^\circ\text{C}$  [experiment,  $-4 \mu\text{C cm}^{-2}$  (8)]. The position of the entropy maximum is independent of  $U, C$  and  $N$  (Eq. [11]). The orientational entropy as a function of  $q$  as calculated from Eq. [2] is shown in Fig. 1. If, instead of  $0.05\text{\AA}$ , the electrical center of "up" dipole is taken as  $0.1 \times 10^{-8}$  cm closer to the metal than that of "down" dipole, then  $\Delta U_{\text{image}} = -2.80 \text{ kJ mole}^{-1}$ , and  $\Delta U_{\text{disp}} = -2.6 \text{ kJ mole}^{-1}$ . With this value of  $\Delta\Delta G^c = -2.8 - 2.6 = -5.4 \text{ kJ mole}^{-1}$ , the orientational entropy maximum is found to occur at  $q = -6.9 \mu\text{C cm}^{-2}$  (experiment,  $-4 \mu\text{C cm}^{-2}$ ). It follows that the two-state ("up" and "down") water dipole layer is consistent with the experimental findings (6-8) that the position of the maximum of the water component of the entropy of the double layer occurs on the negative side of the pzc, and that the mean of the range of the theoretical calculations of the  $q_{\max}$  is about  $1 \mu\text{C cm}^{-2}$  negative to that observed.

On this basis, interfacial water molecules have zero orientation (i.e., are most loosely bound) at a potential cathodic to the pzc. This is inconsistent with the attribution of a capacitance hump to dielectric saturation, as has been the view of a number of workers (3, 5, 9), because such a hump occurs only at charges positive to the pzc. The alternative model of the anodic capacitance hump, i.e., the anion repulsion model (11, 12) is consistent with the entropy results.

Manuscript submitted May 14, 1975; revised manuscript received Aug. 29, 1975.

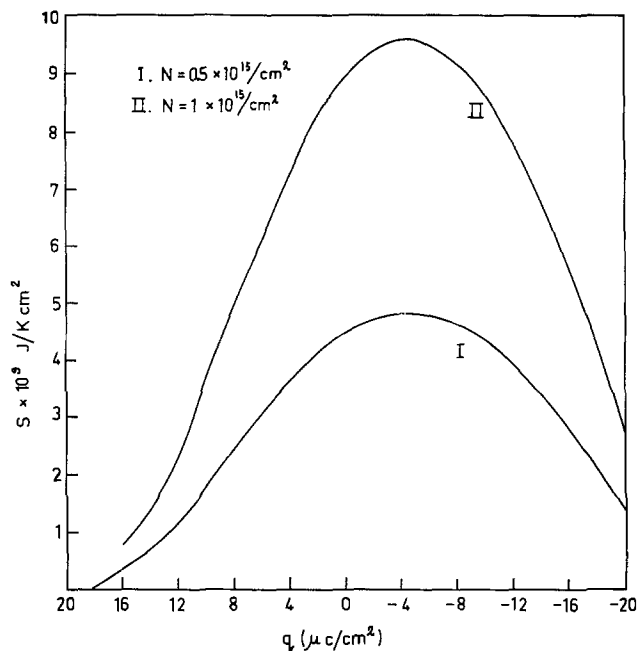


Fig. 1. The orientational entropy of interfacial water as a function of electrode charge.  $\Delta\Delta G^c = -4.2 \text{ kJ mole}^{-1}$  and  $(Uc/kT) = 2$ .

Any discussion of this paper will appear in a Discussion Section to be published in the December 1976 JOURNAL. All discussions for the December 1976 Discussion Section should be submitted by Aug. 1, 1976.

Publication costs of this article were partially assisted by the Flinders University of South Australia.

#### REFERENCES

- E. Lange and K. P. Miscenko, *Z. Phys. Chem.*, **A149**, 1 (1930).
- J. O'M. Bockris and E. C. Potter, *J. Chem. Phys.*, **20**, 614 (1952).
- R. J. Watts-Tobin, *Phil. Mag.*, **6**, 133 (1961).
- N. F. Mott and R. J. Watts-Tobin, *Electrochim. Acta.*, **4**, 79 (1961).
- J. R. MacDonald and C. A. Barlow, *J. Chem. Phys.*, **36**, 3062 (1962).
- G. J. Hills and R. Payne, *Trans. Faraday Soc.*, **61**, 37 (1965); G. J. Hills, *J. Phys. Chem.*, **73**, 3591 (1969).
- J. A. Harrison, J. E. B. Randles, and D. J. Schiffrin, *J. Electroanal. Chem.*, **48**, 359 (1973).
- R. M. Reeves, in "Modern Electrochemistry," Vol. 9, B. E. Conway and J. O'M. Bockris, Editors, Plenum Press, New York (1974).
- S. Levine, G. M. Bell, and A. L. Smith, *J. Phys. Chem.*, **73**, 3534 (1969).
- B. E. Conway and G. M. Gordon, *ibid.*, **73**, 3609 (1969).
- J. O'M. Bockris, M. A. V. Devanathan, and K. Müller, *Proc. Roy. Soc.*, **A274**, 55 (1963).
- J. O'M. Bockris and M. A. Habib, *J. Res. Inst. Catalysis, Hokkaido Univ.*, **23**, No. 1 (1975).
- A. N. Frumkin, Z. A. Iofa, and M. A. Gerovich, *J. Phys. Chem. USSR*, **30**, 1445 (1956).
- J. E. B. Randles and K. S. Whitely, *Trans. Faraday Soc.*, **52**, 1509 (1956).
- S. Trasatti, *J. Electroanal. Chem.*, **33**, 351 (1971).
- J. O'M. Bockris, M. Green, and D. A. J. Swinkles, *This Journal*, **111**, 743 (1964).
- A. Muller, *Proc. Roy. Soc.*, **A154**, 624 (1936); J. G. Kirkwood, *Z. Physik.*, **33**, 57 (1932).
- M. Polanyi, *Trans. Faraday Soc.*, **28**, 316 (1936).
- C. Kittel, "Introduction to Solid State Physics," 4th ed., John Wiley & Sons, Inc., New York (1971).
- K. Müller, *J. Res. Inst. Catalysis, Hokkaido Univ.*, **14**, 224 (1966).
- G. J. Hills and S. Hsieh, *J. Electroanal. Chem.*, **58**, 289 (1975).
- J. O'M. Bockris and A. K. N. Reddy, "Modern Electrochemistry," Vol. 2, Roseta ed., Plenum Press, New York (1973).



## Low Temperature Oxidation of Silicon Studied by Photosensitive ESR and Auger Electron Spectroscopy

Jerzy Ruzykto,<sup>1</sup> Ikuo Shiota, Nobuo Miyamoto, and Jun-ichi Nishizawa\*

*Tohoku University, Research Institute of Electrical Communication, Sendai, Japan*

### ABSTRACT

The effect of hydration of silicon oxide surfaces on the thermal oxidation process has been investigated, and the following three-step model for the thermal oxidation of silicon has been proposed: (i) In the temperature range of oxidation up to 600°C the number of Si-OH groups on the surface increases very rapidly with increasing temperature of oxidation, mainly due to the oxidation of Si-H groups from the etched surface; (ii) at 600°-800°C there is a gradual dehydration of the oxide surface due to the transformation of Si-OH into Si-O; and (iii) above 800°C, the oxidation process is little affected by surface hydration but there exists an anomaly in hydration around 800°C.

Electron spin resonance (ESR) absorption studies on the Si-SiO<sub>2</sub> system are known (1, 2) to be very useful for obtaining valuable information on the electronic properties of its interface defects. These investigations have usually been performed on samples with relatively thick oxide layers grown at temperatures above 1000°C. In this work, however, the surfaces of thin silicon oxide layers grown at the low temperature (200°-900°C) are investigated by means of a photosensitive ESR method which is based on a new detection mechanism.

The nature of the ESR centers reported here is not essentially different from that reported previously (3, 4) for the etched silicon surface where the ESR centers were described to be related to adsorbed water on structural surface hydroxyl groups. Nevertheless, the characteristic dependence of photoinduced ESR lines on the oxidation temperature, as referred to in earlier work (3), has to be given a detailed explanation of the mechanism of oxidation of silicon at low temperature. In addition, recent interest in silicon MIOS memory devices and MOS tunnel diodes with a structural feature of having a thin oxide layer grown at low temperature has made this subject of research more important.

The oxide layer was also investigated by Auger electron spectroscopy in order to analyze the oxide composition. This procedure allowed us to establish the relation between the oxide hydration and oxide layer composition and consequently to propose a new model for the thermal oxidation of silicon by taking into account the change of oxide hydration. The rate of this hydration is a critical factor for the determination of oxidation steps.

### Experimental

N-type, (111) oriented, single crystal silicon wafers with high resistivity (250 and 500 ohm-cm) were

\* Electrochemical Society Active Member.

<sup>1</sup> On leave from Instytut Technologii Elektonowej, Politechnika Warszawska, 00-662 Warsaw, Poland, sponsored by Ministry of Education of Japan.

Key words: low temperature oxidation, surface hydration and dehydration, photoinduced ESR, Auger.

used, together with some of the high-resistivity (100) oriented samples. Before oxidation, samples were etched in a 4HNO<sub>3</sub>:2HF:1CH<sub>3</sub>COOH solution and then rinsed in deionized water. Dimensions of the samples after etching were about 1 × 0.3 × 0.02 cm.

The samples were oxidized in an atmosphere of either dry or wet O<sub>2</sub> in the temperature range 200°-900°C and then quenched in air to room temperature within a few minutes after oxidation.

The light with a higher energy than the energy gap of Si was illuminated at right angles to the sample surface which was dipped in liquid nitrogen and located at the center of the TE<sub>102</sub> rectangular resonant cavity. Photostimulated ESR measurements have been made by a Varian Model 4502-15 X-band spectrometer with a sensitivity of 2 × 10<sup>11</sup> spins/gauss.

The appearance of photoinduced ESR lines is based on a mechanism different from the ordinary ESR absorption in which the paramagnetic absorption losses at the resonance are detected as the change in quality factor *Q* of the resonant cavity. In the present case, however, the change in quality factor *Q* is directly related to the phenomenon of spin dependent photoconductivity (5) where the photogenerated free carriers in bulk silicon undergo an enhanced surface recombination through the saturated paramagnetic surface states. Therefore, the reduction of dielectric loss caused by the resonant decrease of free carriers substantially overcomes the ordinary paramagnetic absorption loss. The resulting large photoinduced ESR lines always have an inverted phase of the ordinary ESR absorption lines. This mechanism will be discussed in detail elsewhere (6), but it should be noted that the tunneling of the photogenerated carriers from silicon to paramagnetic surface states distributed both on the oxide surface and inside its layer is essential for the present detection method.

In consequence, the application of this method is limited to the systems where the ESR centers are located within the tunneling distance of carriers photo-generated in silicon. The estimation of the *g*-value has been made by a comparison of obtained ESR lines

with those from the standard samples ( $Mn^{2+}$  in  $MgO$ ) with known parameters.

Analysis of the oxide composition and measurements of the oxide thickness have been performed by means of Auger electron spectroscopy combined with argon sputter etching. Auger spectra were taken in the vacuum range of  $10^{-9}$  Torr immediately after the primary electron beam was collimated on the sample surface in order to avoid the accumulation of the beam-induced effects.

### Results

The detected ESR lines have been found to be the superposition of the two lines with  $g$ -values of 2.007 and 2.004. The most characteristic feature of the observed over-all photoinduced ESR line was the strong dependence of its height on the oxidation temperature (the line height means a peak-to-peak value of the first derivative curve of the absorption type). This dependence is shown in Fig. 1 for both dry and wet oxidation. In Fig. 2 the change in the shape of the over-all ESR line is shown. The results shown in Fig. 1 and 2 reflect that the observed photoinduced ESR lines are sensitive to the content of water in the oxidizing ambient. On the other hand, no influence has been observed by changing the substrate orientation from (111) to (100).

The measurements of Auger electrons from the oxidized surfaces were performed in order to clarify the change in ESR line height with increasing temperature of oxidation. The results revealed that the changes in the Auger peaks of silicon and oxygen are related to the observed behavior of ESR lines. The 91 and 1618 eV Auger peaks which correspond to the  $L_{2,3}VV$  and the  $KLL$  Auger transition for elemental silicon, respectively, decrease with increasing temperature of oxidation, while the 1606 eV  $KLL$  transition peak for silicon in silicon oxide and the 512 eV oxygen  $KLL$  transition peak increase with increasing temperature of oxidation. This relationship is shown in Fig. 3. There is an abrupt increase in the amount of oxygen when the oxidation temperature exceeds  $600^\circ C$ . This phenomenon is accompanied by the increased rate of oxide growth (Fig. 4).

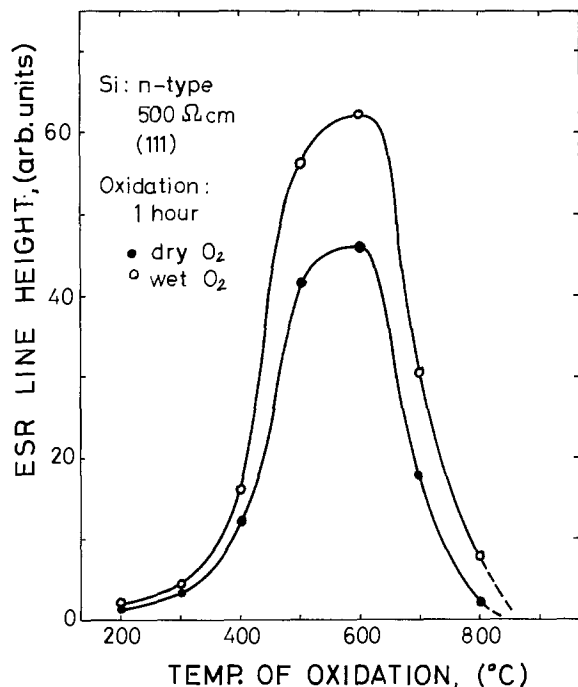


Fig. 1. Change in over-all photoinduced ESR line height with oxidation temperature of silicon in wet and dry  $O_2$  for 1 hr. The curves represent average values from several experimental runs. No ESR signals were observed in the samples oxidized at  $900^\circ C$ .

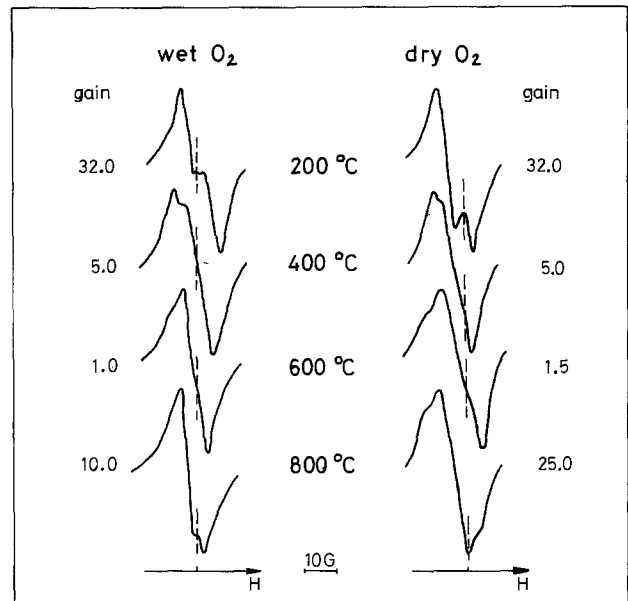


Fig. 2. Changes in line shape of over-all photoinduced ESR lines with oxidation for 1 hr.

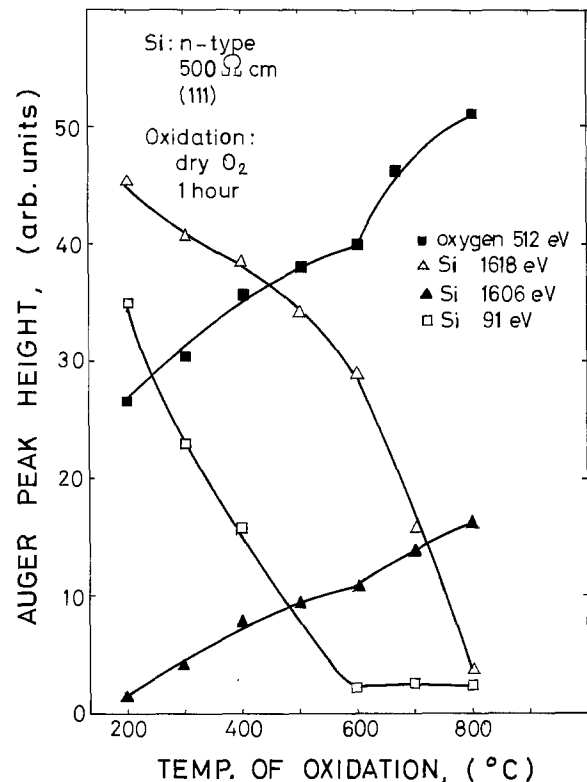


Fig. 3. Relative change in the Auger peak height with oxidation temperature.

The dependence of the ESR line height on the oxidation time at  $600^\circ C$  is presented in Fig. 5, and that at  $800^\circ$  and  $900^\circ C$  in dry  $O_2$  is given in Fig. 6. It can be seen from Fig. 6 that during the oxidation at  $800^\circ C$  the ESR line height remains almost unchanged compared with the case of  $600^\circ$  and  $900^\circ C$  oxidation, although the oxide layer is increased in thickness with increasing oxidation time as shown in Fig. 7. Also, silicon 1606 eV and oxygen Auger peaks are characterized by a smooth and slight increase (10%) with oxidation time at  $800^\circ C$  (from 10 to 60 min). Further information about the investigated centers was obtained by vacuum baking before and after oxidation. In this case, oxidation was 1 hr at  $600^\circ C$  and vacuum baking 1 hr at  $350^\circ C$  in  $10^{-5}$  Torr. ESR measurements

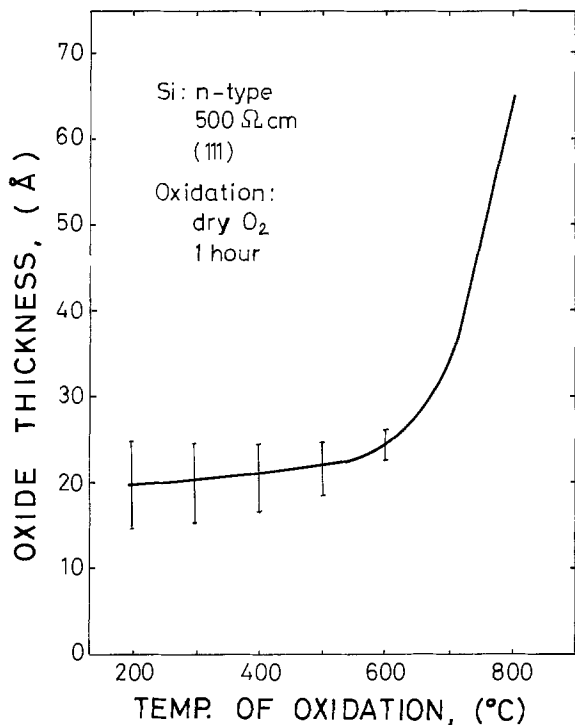


Fig. 4. Silicon oxide thickness vs. oxidation temperature in dry  $O_2$ . The curve is a plot of averaged data points and several experimental runs.

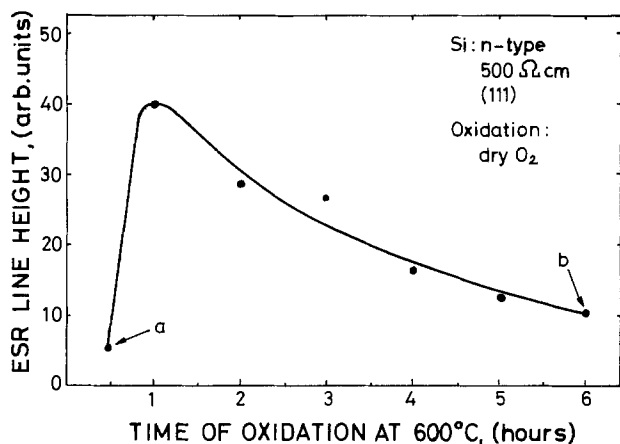


Fig. 5. Change in over-all photoinduced ESR line height with oxidation time at  $600^\circ C$ . At point a and b, the oxide thickness was about 20 and  $40\text{\AA}$ , respectively.

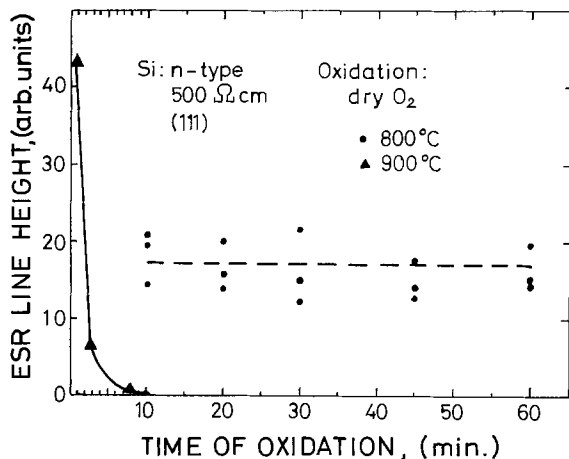


Fig. 6. Change in over-all photosensitive ESR line height with oxidation time at  $800^\circ C$  (broken line shows scattering of data in this case) and  $900^\circ C$ .

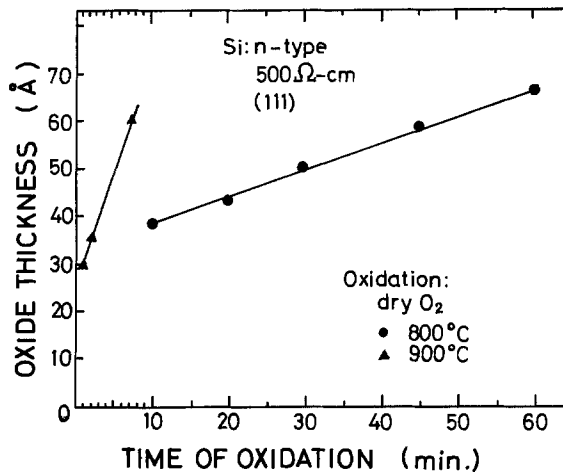


Fig. 7. Silicon oxide thickness vs. oxidation time at  $800^\circ$  and  $900^\circ C$ .

were made after cooling to room temperature, while retaining the samples in vacuum, and no ESR lines were then detected. However, the ESR line appeared again after introducing air into the vacuum system at room temperature, although its intensity was considerably weaker. The effect of the prevacuum baking on the ESR lines is shown in Fig. 8. The gradual decrease of the ESR line height in the oxidized samples after vacuum baking (curve 1) can be attributed to the same effect as in the case of the merely vacuum-baked samples (curve 2) (3, 4). The difference in height of ESR lines between the two cases clearly shows an influence of the oxidation process. It should be noted that no ESR lines are observed from the samples prevacuum baked above  $900^\circ C$ .

#### Discussion

The over-all photoinduced ESR line height may be an adequate measure for the surface hydration, i.e., the number of Si-OH groups on the oxide surface. The reason for the appearance of the two component ESR lines is difficult to clearly establish. In previous work (4), a tentative model was proposed in which the two ESR lines originate from two different structures resulting from the interaction of Si-OH groups with a water molecule adsorbed on the surface. It is well known that Si-OH groups on the surface take the form either isolated from each other or connected through hydrogen bonding (7). Correlating two types of Si-OH groups to the two-component ESR lines may present another possible model.

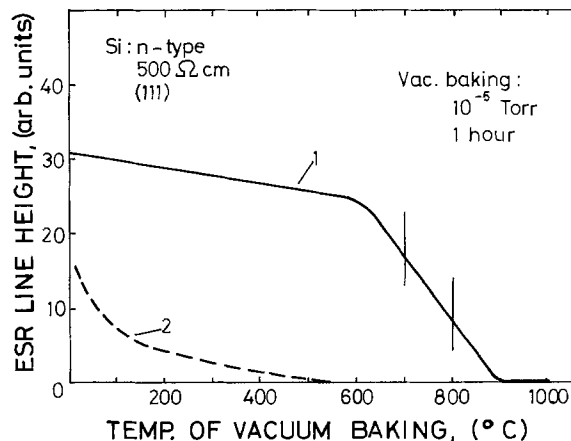


Fig. 8. Effect of vacuum baking; curve 1, vacuum baked and then oxidized at  $600^\circ C$  for 1 hr in dry  $O_2$ ; curve 2, vacuum baked only (3).

It is obvious from Fig. 8 that the oxidation process produces an additional amount of Si-OH groups to those originally existing on the etched surface. One of the mechanisms of Si-OH formation is considered to be related to the oxidation of Si-H groups on the etched silicon surface. This reaction does not depend on the water content in the oxidizing atmosphere and occurs at the same rate whether the atmosphere is dry or wet O<sub>2</sub>. In addition, Si-OH groups can also be formed due to the reaction of water with the weakly bonded Si-O-Si which can exist on the etched silicon surface. This phenomenon occurs more preferably in the wet oxidizing atmosphere, which is responsible for the higher ESR line intensity in the samples oxidized in wet O<sub>2</sub> (Fig. 1).

Let us consider the behavior of KLL Auger peaks for silicon and oxygen in the oxide layer with regard to the change in ESR line height with oxidation temperature. In the temperature range of oxidation from 200° to 600°C, the amounts of silicon (1606 eV) and oxygen increase with increasing temperature (Fig. 3). This increase, however, is not accompanied by the rapid growth of the oxide layer (Fig. 4). Therefore, the additional amount of oxygen that appears in the oxide layer is used for both the oxidation of Si-H groups at the oxide surface and the oxidation of unoxidized silicon within the oxide layer. The former is reflected in the increase of ESR line height (Fig. 1), and the latter in the decrease of silicon shown by the 91 and 1618 eV Auger peaks in Fig. 3.

From the above discussion the transformation of Si-H to Si-OH through oxidation appears to be the origin for the rapid increase of ESR line height in the temperature range up to 600°C.

It is known that Si-H bonds, with three oxygens bonded to one silicon, are stable up to about 600°C. This effect might be one of the reasons why the increase of the ESR line height is virtually stopped when the oxidation temperature reaches 600°C (Fig. 1) but a prolonged oxidation at 600°C causes Si-OH bonds to reduce as seen from Fig. 5. The same effect was also observed in the case of the 900°C oxidation, but in this case the destruction of Si-OH bonds proceeds very rapidly and no ESR lines were detected after 10 min oxidation (Fig. 6). At this oxidation temperature an initial increase of the ESR line height (as is in the case of oxidation at 600°C) was not observed, probably because of the immediate destruction of Si-H bonds after oxidation. With regard to these results, an anomalous behavior of the ESR line on isothermal oxidation at 800°C should be emphasized. As can be seen from Fig. 6, the ESR line height remains unchanged up to the 1 hr oxidation, although some scattering of the experimental data is observed. It should be noted that the oxide thickness was about the same in both the 800° and 900°C oxidation (Fig. 7), so that such a different behavior cannot be attributed to the photosensitive ESR method used in this work. Therefore, some peculiar effects are expected to occur at the oxidation temperature of 800°C in terms of surface hydration.

The same approach in terms of surface hydration should be fundamentally made to explain the change in ESR line height above 600°C as shown in Fig. 1, since the tendency of decreasing ESR line height was also recognized in the samples with the same oxide thickness formed at different temperatures above 600°C. In the case of wet oxidation, however, Si-OH groups may exist up to a higher temperature. This might be a reason for the higher ESR line height of the wet oxidized samples. In the case of oxidation for

1 hr, the critical temperature at which the ESR lines completely vanish, is probably close to 900°C (Fig. 1), but this temperature cannot be directly considered as a temperature of complete dehydration of the oxide surface, because of the excessively thick oxide layers of these samples which are beyond the thickness limit for the ESR detection method applied in the present work (6).

### Conclusions

The process of thermal oxidation of silicon below 800°C has been found to be affected by the hydration of the oxide surface and it has been proposed to divide the process into three steps corresponding to each stage of surface hydration, i.e., the temperature ranges of oxidation,  $T \leq 600^\circ\text{C}$ ,  $600^\circ < T < 800^\circ\text{C}$ , and  $T \geq 800^\circ\text{C}$ . In the first temperature range, the number of Si-OH groups on the surface increases very rapidly mainly due to the oxidation of Si-H groups, and reaches the highest value for samples oxidized at 600°C. Simultaneously, the oxidation of the unoxidized silicon in oxide layers on etched surfaces occurs, but very slow oxide growth is observed. The process of oxide surface dehydration, resulting from the destruction of Si-OH bonds, begins in the second range of oxidation, and proceeds through the change of Si-OH into Si-O. The rate of dehydration is lower in the case of wet oxidation. For  $T \geq 800^\circ\text{C}$ , the effect of surface hydration has little influence on the oxidation process but there exists an anomaly around 800°C in terms of surface hydration.

It is suggested that the results presented in this work can be of interest in the fabrication of MNOS memory devices on silicon where the oxide layer is usually formed under conditions similar to those of these experiments. Also the properties of oxide-nitride interfaces are of great importance for the characteristics of the devices. In addition, these results give valuable information on the mechanism of low temperature passivation (8) of silicon surfaces.

### Acknowledgment

The authors wish to thank the staff of Laboratory for Crystal Structure and Lattice Defects, Research Institute of Electrical Communication, Tohoku University, for their assistance during ESR measurements.

Manuscript submitted April 29, 1975; revised manuscript received Aug. 14, 1975.

Any discussion of this paper will appear in a Discussion Section to be published in the December 1976 JOURNAL. All discussions for the December 1976 Discussion Section should be submitted by Aug. 1, 1976.

Publication costs of this article were partially assisted by Tohoku University.

### REFERENCES

1. A. G. Revesz and B. Goldstein, *Surface Sci.*, **14**, 361 (1969).
2. Y. Nishi, *Japan. J. Appl. Phys.*, **10**, 52 (1971); Y. Nishi, K. Tanaka, and A. Ohwada, *ibid.*, **11**, 85 (1972).
3. I. Shiota, N. Miyamoto, and J. Nishizawa, *Surface Sci.*, **36**, 414 (1973).
4. I. Shiota, N. Miyamoto, and J. Nishizawa, Proc. 2nd International Conf. on Solid Surfaces, Kyoto, March 1974, *Japan. J. Appl. Phys. Supplement 2*, Part 2, 417 (1974).
5. D. J. Lepine, *Phys. Rev.*, **B6**, 436 (1972).
6. I. Shiota, N. Miyamoto, and J. Nishizawa, To be published.
7. L. H. Little, "Infrared Spectra of Adsorbed Species," Academic Press, London (1966).
8. H. Iizuka and J. Nishizawa, *JIEE Japan*, **89**, 59 (1969).

# High Quality RF-Sputtered Silicon Dioxide Layers

H.-U. Schreiber<sup>1</sup> and E. Fröschle

Institut für Halbleitertechnik, RWTH Aachen, D-5100 Aachen, Germany

## ABSTRACT

Very homogeneous SiO<sub>2</sub> layers were prepared by rf sputtering of SiO<sub>2</sub> in Ar or Si in O<sub>2</sub> with Ar on Si substrates which had been cleaned *in situ* by sputter etching. After a short anneal in N<sub>2</sub> (20 min at 1050°C and a 10 min postmetallization anneal at 500°C), surface charge, surface-state density, and stability were similar to those reported for good, thermally grown oxides. Best results were obtained with reactively sputtered SiO<sub>2</sub>.

Insulating layers of rf-sputtered silicon dioxide are often used in integrated circuit technology for multi-layer wiring and passivation (1). However, their homogeneity, electrical breakdown strength, and interface quality were, up to the present time, inferior to those of thermally grown oxide films. Some improvement in breakdown strength could be made by bias sputtering, as proposed by Maissel *et al.* (2, 3). In this method sputter etching takes place during deposition. The purpose of the work described here was to investigate whether sputter etching before depositing the SiO<sub>2</sub> also gives improved breakdown characteristics, and to find methods for preparing sputtered oxide layers on Si substrates with an interface quality comparable to that for thermally grown oxide.

## Sputtering Apparatus

For our rf-sputtering experiments we used a commercial MRC apparatus which was somewhat modified to suit our particular requirements. It has a shielded substrate carrier to which the rf power can be switched. This allows sputter etching of the silicon substrate before sputtering SiO<sub>2</sub> onto it. The rf generator with matching network had a maximum output of 1 kW at 13.56 MHz. The diameter of the targets and the substrate electrode was 12.5 cm, their separation 5 cm. The most important differences from the standard design were the following: First, we used a turbomolecular high-vacuum pump instead of the usual oil-diffusion pump. This gives a vacuum free of oil vapor. Next, we added an apparatus for loading and unloading under dust-free conditions. It consisted of a blower with 0.3 μm filter, a plastic hose, and a Plexiglas cylinder with air lock surrounding the sputtering chamber. Third, we inserted a tunable L-C network between substrate and ground for bias sputtering as was also done by Logan (4). The reason for this will become clear from the schematic drawing of the sputtering module and its equivalent circuit shown in Fig. 1. The dark space before the electrodes is represented by a capacitor shunted with a diode.

If the substrate electrode is connected, as usual, directly to ground in the same way as all the metallic parts of the sputtering module, the rf current is distributed through all these surfaces. The current through the substrate electrode is therefore so small that not much bias appears there and sputtering of this surface does not take place. By tuning out the capacitive part of the dark space impedance in front of the substrate electrode, most of the rf current will flow this way, giving it nearly the same bias as the target electrode.

## Experimental

Most of our experiments were done with MOS capacitors having evaporated Al electrodes of 0.3-1.5 mm diameter on SiO<sub>2</sub> films of 0.16 μm thickness which were sputtered onto {111}-orientated n-type silicon wafers

with donor concentrations of  $5 \cdot 10^{15} \text{ cm}^{-3}$ . High quality capacitors were mostly fabricated as follows:

(i) Before sputtering the Si wafers were thoroughly cleaned with standard chemical methods. Rubbing with a cotton pad soaked with detergents before the chemical cleaning and spinning off the quartz-distilled water after the last step reduced the pinhole density significantly.

(ii) Best results were obtained if the wafers were laid onto a SiO<sub>2</sub> disk of 3 mm thickness and 12.5 cm diameter, covering the substrate electrode totally, but lying on it loosely.

(iii) For *in situ* cleaning, 1 μm of the Si wafer was sputter etched away in Ar. At  $3 \times 10^{-3}$  mm Hg the etch rate with 400W of rf power was approximately  $5 \times 10^{-6}$  cm/min. To minimize radiation damage the rf power was decreased toward the end in steps of 6 min at 50, 40, 15, and 10W.

(iv) SiO<sub>2</sub> was then sputtered either from a SiO<sub>2</sub> target (impurities  $\ll 0.3\%$ , VP grade of MRC) in Ar of  $5 \times 10^{-3}$  mm Hg pressure or reactively from a Si target (impurities  $\ll 0.001\%$ , VP grade of MRC) in a mixture of O<sub>2</sub> ( $1.5 \times 10^{-3}$  mm Hg) and Ar ( $0.8 \times 10^{-3}$  mm Hg). With 300W of rf power the deposition rates were  $1.8 \times 10^{-6}$  and  $5 \times 10^{-7}$  cm/min, respectively.

(v) To reduce the radiation damage further, the wafers were annealed 20 min at 1050°C in N<sub>2</sub>. The outermost 0.015 μm SiO<sub>2</sub> was etched away afterwards in buffered HF giving better electrical stability.

(vi) The Al contacts of the MOS diodes were fabricated by high-vacuum evaporation of 0.3 μm Al out of a Na-free tungsten coil using a metal mask with 64 holes.

(vii) As often done with thermally grown oxides, a post-Al annealing of 20 min in N<sub>2</sub> at 500°C followed as the last step.

**Breakdown characteristics.**—For measurement of the current-voltage characteristics we used MOS capacitors of the dimensions shown in Fig. 2. They were probed with whiskers, the Al usually being positive. However, reversing the polarity had little effect on the data. As shown in Fig. 2 the current-voltage characteristics of

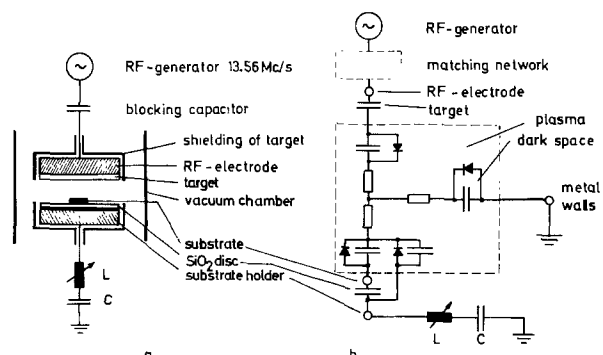


Fig. 1. Schematic (a) and equivalent circuit (b) of the rf sputtering system with L-C tuning network for bias sputtering.

<sup>1</sup> Present address: IV. Ruhr-Universität Bochum, Institut für Elektronische Bauelemente, D-4630 Bochum, Germany.

Key words: MOS diodes, breakdown, flatband voltage.



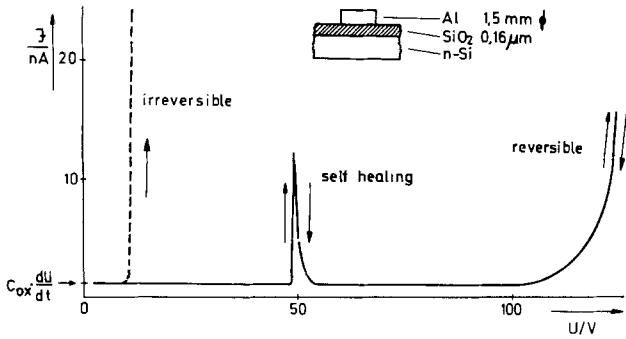


Fig. 2. MOS diode and typical breakdown characteristics

good MOS capacitors, measured by applying a ramp voltage with constant slope, are composed of constant charging currents at small voltages and sharply rising currents at higher ones. The latter are probably caused by the onset of Poole-Frenkel conductance (5) and are reversible, if limited by a high resistance.

Large defects presumably give permanent breakdowns; small pinholes, however, only temporary shorts. Figure 3 shows a scanning electron micrograph of an area where self-healing breakdown has taken place. The breakdown occurred in the middle of the round crater where the Si and the SiO<sub>2</sub> were melted. The heat arising from the breakdown also caused melting of the aluminum in the neighborhood. The metal receded by surface tension, thereby removing the short between Si and Al. The best results were achieved with silicon wafers, cleaned with the procedure described and sputter etched 1 μm before the SiO<sub>2</sub> deposition. The small spread in the characteristics of the 64 MOS diodes on a wafer and their high freedom from defects is apparent from Fig. 4. Less than 3% of them broke down at electric field strengths below 6 MV/cm.

For evaluating the influence of the different treatments, the percentage of diodes showing their first



Fig. 3. Scanning electron micrograph of area in an Al-SiO<sub>2</sub>-Si capacitor where self-healing breakdown took place.

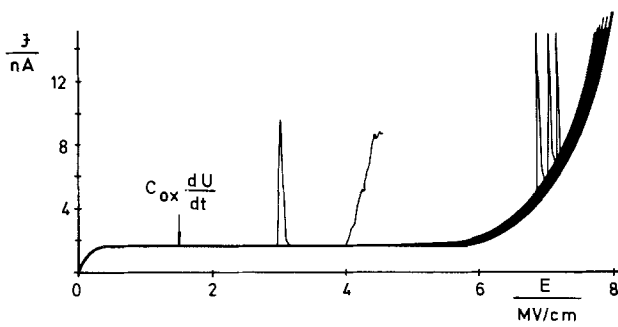


Fig. 4. Measured characteristics of 64 MOS diodes (1.5 mm diam) on a typical wafer after 1 μm sputter etching.

breakdown in a given field interval was plotted as a function of the electric field at breakdown. "First breakdown" was taken to be the first self-healing event which was detected by a very sensitive measuring circuit or a rise of current to more than 10<sup>-8</sup>A. With standard chemical cleaning nearly all MOS diodes broke down at fields below 2 MV/cm, as was also found in Ref. (3), without bias sputtering. By rubbing off the wafers with a cotton pad soaked with detergent before the final chemical cleaning with boiling HNO<sub>3</sub> and by spinning off the quartz-distilled rinsing water as a last step, the breakdown strength could be greatly improved (Fig. 5a).

Very high homogeneity was achieved by removing through sputter etching at least 1 μm of the Si wafer before depositing the SiO<sub>2</sub> (see Fig. 5b, 5c, and 9a). Continued etching did not give further improvement, if the wafers had been cleaned as described before. With standard cleaning a sputter etch of 5 μm was required to obtain the same result (6, 7). The etching was done mostly *in situ*, but no difference was found if the wafer were removed from the apparatus and stored in dust-free air for some minutes before depositing SiO<sub>2</sub>.

*Influence of bias sputtering.*—To test whether these results may also be obtained by etching the substrate during and not before deposition, some experiments with bias sputtering were made. By tuning the inductance as described above, the substrate bias was varied giving a variation of the coefficient of re-emission, K<sub>R</sub>, from 0.3 to 0.9. K<sub>R</sub> was measured by a similar technique as used in Ref. (3). As done by Logan (4) and Maissel (3), we too measured the voltage, U<sub>B</sub>, between the substrate holder and ground (see Fig. 1) and used it as an indicator of bias conditions. U<sub>B</sub>, however, is not identical with the true bias between substrate surface and plasma.

As shown in Fig. 6 the mean field for first breakdown decreased rapidly with increasing bias. Scanning electron micrographs of SiO<sub>2</sub> layers sputtered onto Si with high bias showed partially refilled scratches and craters (Fig. 7). They appear to be caused by breakdown during sputtering because no such structures were observed without bias. Similar effects were found also by McCaughan (11). The difference between our measurements and the results of Maissel *et al.* (3) who reported a distinct improvement by bias sputtering in the range of K<sub>R</sub> = 0.3-0.6 could not be resolved. Perhaps it may be contributed to by the absence of oil and grease vapors in our system which gives reasonably good breakdown characteristics even without sputter etching.

*Interface properties of Ar-sputtered SiO<sub>2</sub> on Si.*—In order to test the usefulness of sputtered SiO<sub>2</sub> for MOS devices oxide charge, interface-state density and stability were measured under various sputtering and

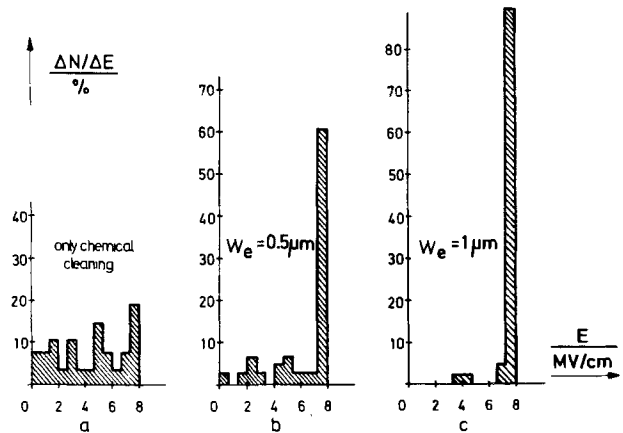


Fig. 5. Breakdown distributions (percentage  $\Delta N/\Delta E$  of first breakdown at fields between  $E$  and  $E + \Delta E$ ) for different thicknesses  $w_e$  of Si removed by sputter etching.

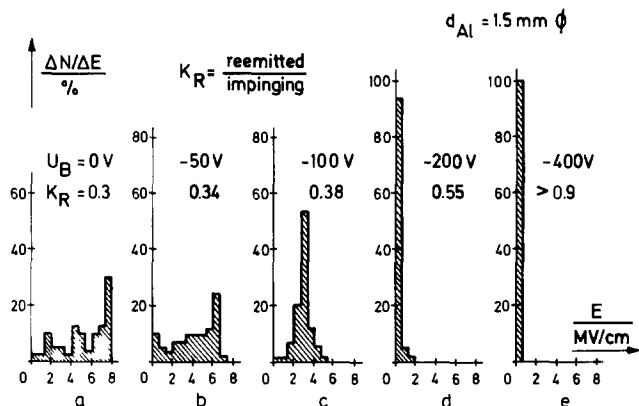


Fig. 6. Dependence of breakdown distributions on substrate holder voltage  $U_B$  during sputtering.

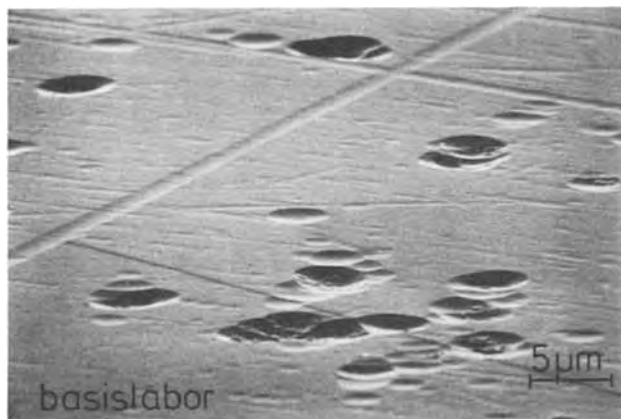


Fig. 7. Scanning electron micrograph of a  $\text{SiO}_2$  layer prepared by bias sputtering at  $U_B = -400\text{V}$ ,  $K_R > 0.9$ .

annealing conditions on MOS diodes with Al electrodes of 0.3 mm diameter. These measurements were made using the conventional high-frequency (3 MHz) capacitance-voltage method. Flatband voltage,  $V_{FB}$ , and oxide-charge density,  $N_{ox}$ , were determined by comparison of experimental with theoretical curves (8). The determination of  $V_{FB}$  of sputtered  $\text{SiO}_2$  films is considerably more accurate than with thermally grown ones because much less impurity redistribution should take place. The interface-state density,  $N_{ss}$ , near the conduction band was estimated after Ref. (9) from C-V measurements at 300°K and 77°K. Stability was measured by the standard temperature-bias test in which the MOS diodes were stressed for 20 min at 200°C with +30V (2 MV/cm) on the Al electrode and subsequently cooled down with the voltage on. The resulting shift of the flatband voltage should be less than 0.1V on good gate oxides for MOS devices.

Without annealing, the densities of surface charge and especially of surface states were very high for sputtered  $\text{SiO}_2$ . Therefore, we used an annealing procedure, which is also often used on thermal oxides. First, we used a high-temperature treatment of 20 min at 1050°C in  $\text{N}_2$ . This was followed by a short etch in buffered HF to remove the outermost 0.015  $\mu\text{m}$  of the  $\text{SiO}_2$  before Al deposition and a 10 min anneal at 500°C in  $\text{N}_2$  after metallization. After this procedure, dry thermal oxides on {111} Si give flatband voltages of 1-2V, shifting less than 0.1V in the stress test if clean, Na-free tungsten filaments are used for evaporating the Al. Their surface-state densities are negligible.

For sputtered  $\text{SiO}_2$  on sputter-etched Si this anneal was not able to reduce the surface-state density below  $10^{11} \text{ cm}^{-2} \text{ eV}^{-1}$  if the rf power was not decreased toward the end of the etching. We usually did this in steps of approximately 6 min at 50, 40, 15, and 10W. The main etching was done at 400W ( $3.2 \text{ W/cm}^2$ ) in

Ar at a pressure of  $3 \times 10^{-3} \text{ mm Hg}$ , giving an etch rate of  $5 \times 10^{-6} \text{ cm/min}$ . Using this process, flatband voltages of 8V corresponding to  $10^{12} \text{ oxide charges/cm}^2$ , a shift of 0.5V during the stress test and surface-state densities less than  $3 \times 10^{10} \text{ cm}^{-2} \text{ eV}^{-1}$  were achieved. For obtaining this stability it was necessary to separate the Si wafer from the substrate holder by a  $\text{SiO}_2$  disk which allowed some heating up during sputtering and prevented contamination of the wafer by material etched away from the substrate holder. If the disk was cemented with epoxy to the water-cooled substrate holder, relatively large flatband shifts were observed, even after an anneal at 1050°C.

The effect of the annealing temperature on  $N_{ox}$  and  $N_{ss}$  is shown in Fig. 8. From it can be concluded that an annealing step at a temperature of at least 1050°C is essential for obtaining usable films. The annealing and etching caused some deterioration of the breakdown strength as may be seen from Fig. 9. This effect could possibly be reduced by using cleaner annealing conditions.

**Sputtering in  $\text{O}_2$ -Ar mixtures.**—The relatively high flatband voltage could be reduced by adding a small amount of  $\text{O}_2$  to the sputtering ambient (see Fig. 10). For more than 3 volume per cent (v/o)  $\text{O}_2$  the flatband voltage on {111} Si was less than 1V. The same effect could be achieved by bias sputtering if the bias was higher than 50V (see Fig. 11), but in this case the stability was not as good as without bias.  $\text{O}_2$  addition without bias did not cause the stability to deteriorate. However, the observed shift of 0.5V is too high for good MOS devices. It was probably caused by the Na content of the  $\text{SiO}_2$  target which was only 99.7% pure.

Because targets of very pure silicon are easily available, reactively sputtering of Si in an Ar- $\text{O}_2$  mixture

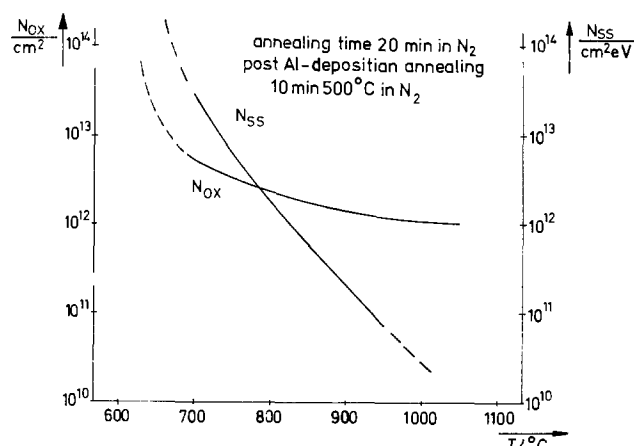


Fig. 8. Influence of annealing temperature on surface-charge density,  $N_{ox}$ , and surface-state density,  $N_{ss}$ , for Ar-sputtered  $\text{SiO}_2$  films.

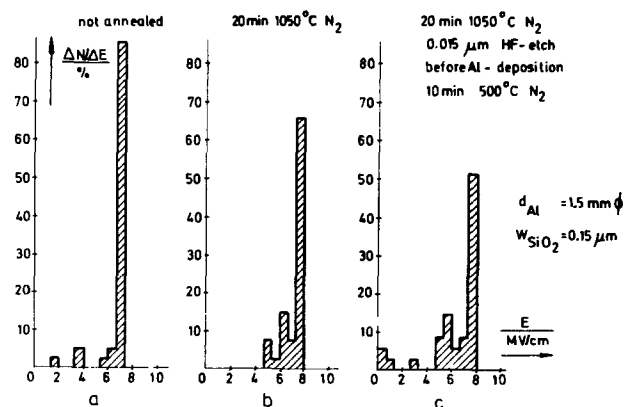


Fig. 9. Effect of annealing and etching on the breakdown distribution.

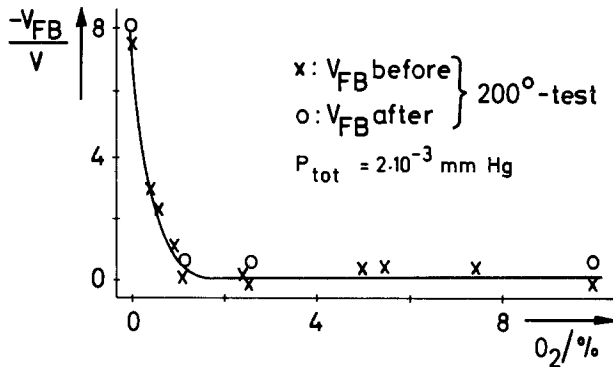


Fig. 10. Lowering of flatband voltage by addition of  $O_2$  during sputtering of  $SiO_2$ .

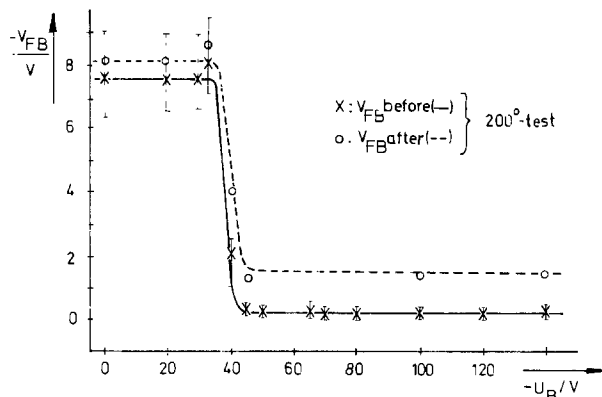


Fig. 11. Lowering of flatband voltage by bias sputtering of  $SiO_2$

was also tried. As may be seen from Fig. 12, very stable  $SiO_2$  layers with low flatband voltage could be made in a range of 40-80%  $O_2$ . The flatband voltage shifted less than 0.1V during the usual 200°C-2 MV/cm temperature-voltage stress tests. Regarding breakdown strength and surface-state density  $N_{ss}$ , we found no difference in layers made by sputtering  $SiO_2$  in Ar.

### Conclusions

The present study has shown that it is possible to deposit, by means of sputtering,  $SiO_2$  layers on Si, which after suitable annealing have the same quality as the best  $SiO_2$  layers prepared by thermal oxidation. The high intrinsic prebreakdown strength, shown in Fig. 4 (7.5 MV/cm at  $10^{-6}$  A  $cm^{-2}$ ), compared with the usual sputtered  $SiO_2$  layers (1) may probably be

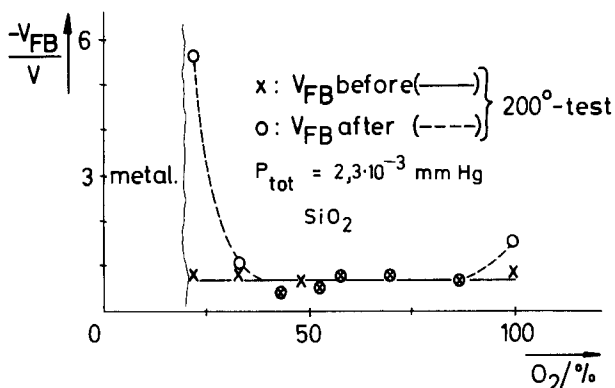


Fig. 12. Flatband voltage of MOS diodes prepared by reactively sputtering Si in an  $O_2$ -Ar mixture.

attributed to the freedom from oil and grease vapors of the sputtering ambient. Very high homogeneity and low densities of weak spots could be achieved by sputter etching approximately  $1 \mu m$  of Si before the deposition, thus removing all dirt and foreign particles from the wafer.

Sputter etching, however, leaves a damaged layer near the surface of the Si and, also, Ar ions are implanted. As shown by Yamamoto (10), with back scattering analysis 20 min annealing in  $N_2$  is sufficient to remove the Ar but does not heal out the damage of the Si completely. This agrees with our results. The rf power had to be reduced toward the end of the etching to keep the damage of the Si so low that it could be removed by the same annealing procedure which is also customarily used on thermal  $SiO_2$ . It is also sufficient to remove enclosed Ar (12) and defects in the sputtered  $SiO_2$  (13). Upon such annealing in  $N_2$  at 1050°C before and at 500°C after Al deposition, MOS diodes of very good quality could be made, especially by reactively sputtering Si in an  $O_2$ -Ar mixture. Their flatband voltage was below 1V and shifted less than 0.1V during a 20 min temperature-voltage stress test with 2 MV/cm at 200°C. The interface-state density was below  $3 \times 10^{10} cm^{-2} eV^{-1}$ .

Rf sputtering from a  $SiO_2$  target in pure Ar resulted in higher surface-charge densities than with reactively sputtered  $SiO_2$ , probably because of oxygen vacancies (14). They could be avoided by adding 3%  $O_2$  to the Ar. Stability during the bias-temperature stress test, however, was not as good as with reactively sputtered  $SiO_2$ , probably because of lower purity of the target.

### Acknowledgments

The authors are indebted to Prof. E. Kubalek and the Basislabor of RWTH for providing the electron micrographs. They would like to acknowledge the support of the Deutsche Forschungsgemeinschaft which enabled these investigations through the Sonderforschungsbereich 56 "Festkörperelektronik."

Manuscript submitted Dec. 27, 1974; revised manuscript received Sept. 8, 1975. This was Paper 116 presented at the Boston, Massachusetts, Meeting of the Society, Oct. 7-11, 1973.

Any discussion of this paper will appear in a Discussion Section to be published in the December 1976 JOURNAL. All discussions for the December 1976 Discussion Section should be submitted by Aug. 1, 1976.

### REFERENCES

1. D. L. Tolliver, Paper 120 presented at The Electrochemical Society Meeting, Boston, Mass. Oct. 7-11, 1973.
2. L. I. Maissel and P. M. Schaible, *J. Appl. Phys.*, **36**, 237 (1965).
3. L. I. Maissel, R. E. Jones, and C. L. Standley, *IBM J. Res. Develop.*, **14**, 176 (1970).
4. J. S. Logan, *ibid.*, **14**, 172 (1970).
5. J. Frenkel, *Phys. Rev.*, **54**, 647 (1938).
6. H.-U. Schreiber and E. Fröschle, 2. Deutsche Sputtering Schule, Rottach-Egern, 30 (1971).
7. H.-U. Schreiber, Thesis, RWTH Aachen, Aachen, Germany (1973).
8. A. Goetzberger, *Bell System Tech. J.*, **45**, 1097 (1966).
9. D. M. Brown and P. V. Gray, *This Journal*, **115**, 760 (1968).
10. Y. Yamamoto, K. Shinada, T. Itoh, and K. Yada, *Jap. J. Appl. Phys.*, **13**, 551 (1974).
11. D. V. McCaughan and R. A. Kushner, *Proc. IEEE*, **62**, 1236 (1974).
12. G. C. Schwartz and R. E. Jones, *IBM J. Res. Develop.*, **14**, 52 (1970).
13. D. V. McCaughan and V. T. Murphy, *J. Appl. Phys.*, **44**, 3182 (1973).
14. J. L. Vossen, *J. Vacuum Sci. Technol.*, **8**, 12 (1972).

# Anodic Processing for Multilevel LSI

G. C. Schwartz\* and V. Platter

IBM System Products Division, East Fishkill Facility, Hopewell Junction, New York 12533

## ABSTRACT

Anodic processing for multilevel LSI is attractive because planar structures can be made. For complete flexibility of design, it is advantageous that portions of the first level of interconnection metallization be isolated initially from silicon, and that the required contact to silicon be made using overpasses on a subsequent level. Anodic processes previously described required that there be a direct contact to silicon for each land to be defined. This restriction can be circumvented by depositing a thin conductive layer before deposition of the interconnection metallurgy and eventually converting it to an insulator. The requirements for a suitable underlay are given, and the choice of hafnium for this purpose is explained. The details of the anodic processing are described and discussed. Conversion of the underlay to an insulator requires both anodization until barrier layer growth ceases and oxidation at elevated temperature; 450°C in steam for 30 min yields excellent results. The leakage current between closely spaced conductors is decreased substantially by the use of this underlay process as compared to the previously described anodic processes.

For multilevel aluminum or aluminum alloy land systems in LSI, anodic processing has two main advantages over conventional subtractive etching. First, planar structures can be fabricated. This eliminates the reliability hazards associated with covering large and often steep metal edges with an insulator. Also photolithography difficulties are reduced. Second, there is substantially less loss in cross-sectional area. Therefore the current-carrying capability of a conductor formed anodically is greater than that formed conventionally using the same mask.

Anodic processing substitutes conversion of the unwanted metal to an insulating film for the removal of unwanted metal. Because relatively thick (10,000Å) metal films are required for the circuitry, the unwanted metal is converted to porous anodic oxide as barrier layer growth is limited. Oxalic acid is used as the electrolyte in the completely planar process (1) since it is compatible with photoresist, it can be decomposed at the completion of anodic processing, and, at the appropriate current densities, the voltages are suitable for semiconductor device fabrication.

All previously described anodic processes (1, 2, 3) had required that there be a direct contact to silicon for every land to be defined. This requirement arises from the need to supply current to the lands after the anodization is apparently complete, so that the residual aluminum which clings to the edges of the lands forming bridges between closely spaced conductors can be converted to insulating anodic oxide. But for complete flexibility of design of integrated circuits with multilevel metallization, it is often desirable to isolate from silicon, initially, portions of the first-level metallization and use "overpasses" on a subsequent level. To be able to isolate, anodically, such electrically "floating" conductors, we have adopted a scheme developed by Romankiw (4) for anodic processing, making the changes necessary to achieve the very low leakage levels required for integrated circuits, but not for the applications for which Romankiw designed his procedure.

Before deposition of the aluminum or aluminum alloy film used for the interconnection pattern, Romankiw proposed that a thin metal film be deposited to carry current to the lands which are not connected to silicon. This film must subsequently be converted to an insulator. We have concluded that the metal used as an underlay must meet certain requirements: (i) it

must be able to be converted to an insulator under conditions compatible with semiconductor device processing and with the presence of the overlying anodic oxide; (ii) it must not react chemically with the electrolyte used to form the porous anodic oxide; (iii) if it can be anodized, it must anodize at or very close to 100% efficiency to avoid oxygen evolution which may cause lifting of the overlying anodic oxide; (iv) it must adhere well to the substrate and the overlying anodic oxide must adhere well to it; and (v) it must not degrade device performance.

The most suitable underlay we have found is hafnium. It forms a barrier layer upon anodization in oxalic acid with no perceptible oxygen evolution. Moreover, the anodization ratio of hafnium is high (11.6Å Hf/V) which means that the final voltage to which the formed structures will be subjected at the completion of anodic processing will be relatively low since underlay films 150-200Å thick are suitable. Hafnium can be oxidized thermally at low temperature. A discrete hafnium layer is maintained when the metals hafnium and aluminum (or aluminum alloy) are deposited sequentially at elevated substrate temperature to insure good adhesion, yet adequate interdiffusion occurs during the final anneal at the completion of the anodic processing. The interdiffusion has been demonstrated by the use of helium ion backscattering. In Fig. 1 is shown the backscattering spectrum for aluminum in a film consisting of 2μ of aluminum with a hafnium layer 1000Å thick on its surface, both before and after heat-treatment in helium at 400°C for 1 hr. It can be seen that after the anneal, aluminum has reached the surface of the film. Adequate interdiffusion occurs even when the hafnium is exposed to air before deposition of the interconnection metallurgy. Individual test transistors made with and without a hafnium underlay have identical electrical characteristics.

The resistivity changes in an aluminum (17,000Å)-hafnium (240Å) film during anneal at 400°C in an inert atmosphere are shown in Fig. 2. When an evaporated aluminum film is annealed at a temperature above its deposition temperature, an initial decrease in resistivity is always observed. This is probably due to a decrease in defects in the grain boundaries. The subsequent small increase in resistivity can be attributed to dissolution of the hafnium and to intermetallic compound formation. However, this increase is very small and would not affect the performance of the interconnection metallization.

Anodic processing is performed as described in a previous paper (1); this method uses a two-current mode

\* Electrochemical Society Active Member.

Key words: multilevel metallization, planar metallization, large-scale integrated circuits, anodic oxidation, aluminum alloy metallurgy.

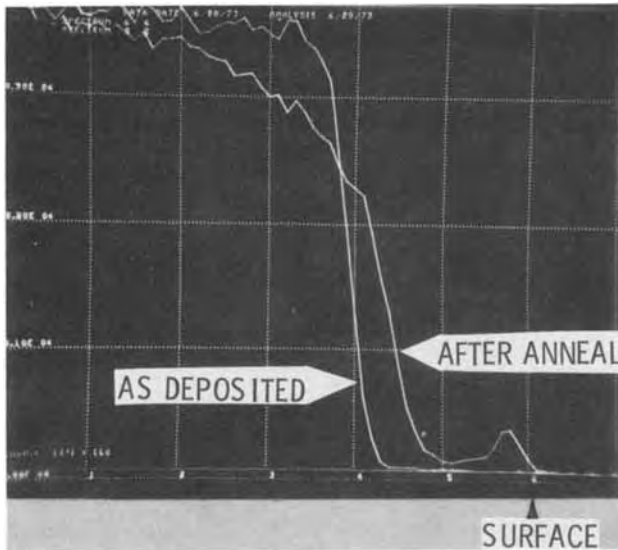


Fig. 1. Energy spectrum obtained by means of helium ion back-scattering of aluminum in a film consisting of  $2\mu$  of aluminum with  $1000\text{\AA}$  of hafnium on its surface before and after anneal in helium at  $400^\circ\text{C}$  for 1 hr.

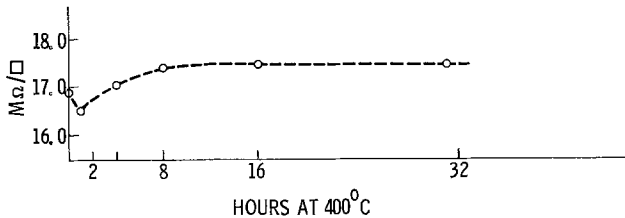


Fig. 2. Resistivity changes in an aluminum-hafnium film during anneal at  $400^\circ\text{C}$  in an inert atmosphere. The film:  $17,000\text{\AA}$  Al/ $240\text{\AA}$  Hf-insulated substrate.

for the isolation anodization of the Al/AlCu film since this had resulted in the best line profile. A typical curve for the isolation anodization in 8% oxalic acid of the metal film Al/AlCu/Hf is shown in Fig. 3.

A current density of  $3.5\text{ mA/cm}^2$  is used at the start of the anodization. At point A in Fig. 3 the aluminum cap has been anodized completely and there is an upward inflection in the voltage curve indicating the beginning of the AlCu layer (5). A control circuit automatically reduces the current (to  $1\text{ mA/cm}^2$ ) when a time which corresponds to the anodization of about two-thirds of the film is reached; i.e., at point B. At point C the anodization is apparently complete because the voltage starts to rise (to a preset limit), and the current starts to decay. Thus, point C is also the beginning of the "decay period." The time it takes to

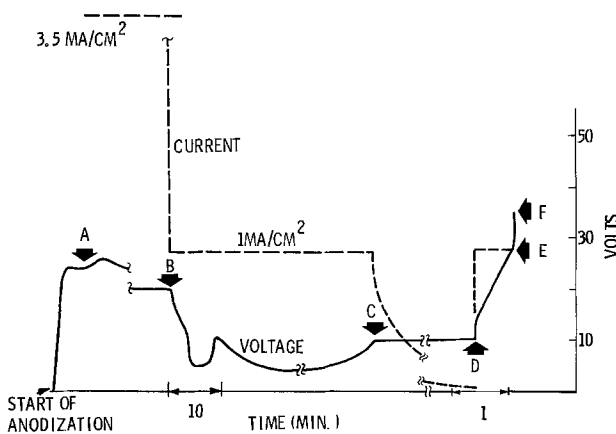


Fig. 3. Constant current anodization in 8% oxalic acid of the film: Al/AlCu/Hf-insulated substrate.

reach point C depends upon the thickness of the film and the copper concentration in the AlCu film. At  $3.5\text{ mA/cm}^2$  aluminum anodizes at about  $750\text{ \AA/min}$ ; an AlCu (4%) film anodizes at about  $450\text{ \AA/min}$  at the same current density.

Point C is also the beginning of the "decay period." In Fig. 4, are shown scanning electron micrographs of three pairs of conductors, separated by  $3, 6, \text{ and } 15\mu$ ,<sup>1</sup> as they appear after a relatively short "decay period." The anodic aluminum oxide has been removed in phosphochromic acid to reveal any metal particles. It can be seen that the isolated aluminum particles (the "cosmetic defects") are completely converted to anodic aluminum oxide, but that closely spaced lines are bridged. In Fig. 5 the final isolation after suitable "decay" is shown; this would correspond to point D in Fig. 3. From Fig. 4 it is quite clear that the more widely spaced lines are isolated more rapidly, but Fig. 5 shows that the final line width is independent of the spacing. The "decay" time required in any given application will depend on the thickness of the interconnection metallization and the smallest spacing in the pattern being formed. For  $1.5\mu$  metal, 45 min are required to isolate the  $3\mu$  space.

The time interval C-D is preset and, when point D is reached, the voltage is allowed to rise automatically

<sup>1</sup> For the  $15\mu$  spacing, one of the conductors is not shown in the photograph because the spacing was too wide for the second of the pair to be included in the field of view of the SEM at that magnification.

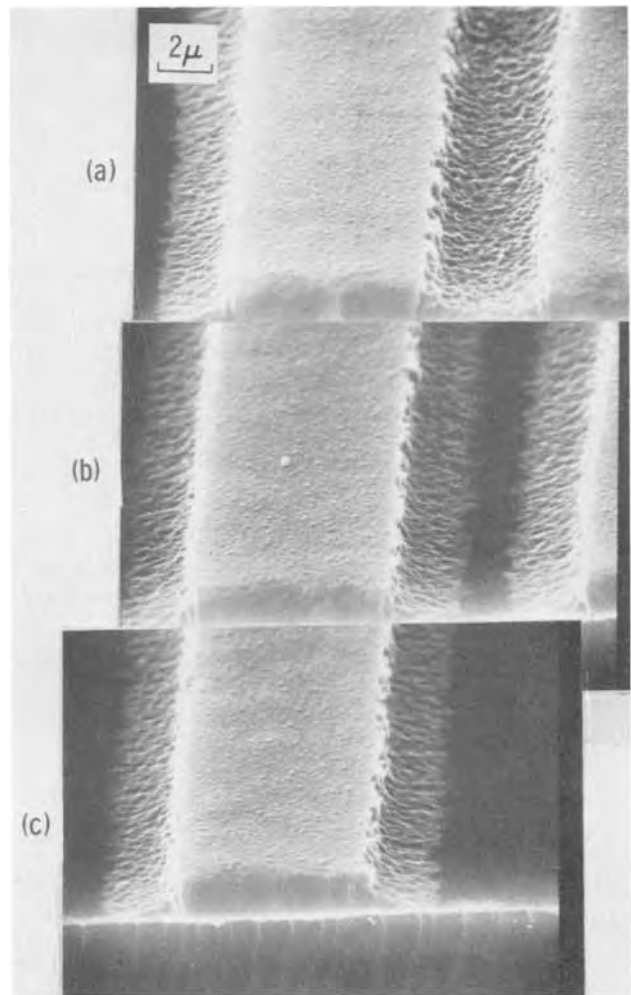


Fig. 4. Scanning electron micrographs showing the effect of a short current decay on the isolation of adjacent conductors. The anodic aluminum oxide has been removed in phosphochromic acid. Three pairs of lines are shown: (a) Space between conductors  $\sim 3\mu$ , (b) Space between conductors  $\sim 6\mu$ , and (c) Space between conductors  $\sim 15\mu$  (second conductor not shown).

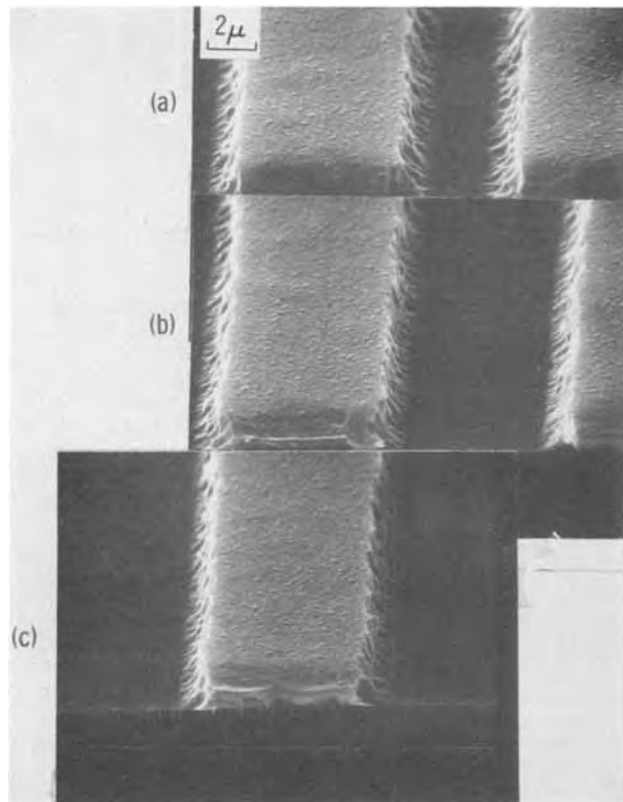


Fig. 5. Scanning electron micrographs showing the effect of adequate current decay on the isolation of adjacent conductors. The anodic aluminum oxide has been removed in phosphochromic acid. Three pairs of lines are shown: (a) Space between conductors  $\sim 3\mu$ , (b) Space between conductors  $\sim 6\mu$ , and (c) Space between conductors  $\sim 15\mu$  (second conductor not shown).

and the hafnium is anodized to form a barrier layer as shown by the linear increase in voltage at constant current ( $1 \text{ mA/cm}^2$ ). At point E, the voltage rises abruptly; when it reaches a preset limit, F, the circuit is opened automatically. Because barrier layer growth ceases at voltage E, it is said that the hafnium is "completely" anodized. The anodizing ratio,  $11.6 \text{ \AA Hf/V}$  was determined by anodizing, at  $1 \text{ mA/cm}^2$  in oxalic acid, a series of hafnium films of known thickness and determining the voltage at which the abrupt rise occurred. The voltage E is, within a few volts, the value expected from the known thickness of the hafnium underlay. It should be emphasized that during the "decay period" the voltage should be well below E to insure current flow to the otherwise isolated residual metal.

However, even after the apparent complete anodization of the underlay, adjacent conductors are still electrically shorted, no matter how long the "decay period." Therefore the residue of the underlay metal must be oxidized thermally. The conditions for oxidation of this residual thin layer are much more severe

Table I. Leakage current at 10V (after sufficient decay)  
 $3\mu$  space between conductors  $9 \times 10^{-2} \text{ cm}$  long

Sample	Leakage current
Conductor connected to silicon during processing	$10\text{-}20 \times 10^{-12} \text{ A}$
"Floating" lines, no underlay	Short
"Floating" lines, hafnium underlay	Short
Hf anodized to completion only	Short
Hf not anodized: $450^\circ\text{C}$ in $\text{O}_2$ , 1 hr	$2\text{-}18 \text{ \AA}$
Hf anodized to completion: $450^\circ\text{C}$ in $\text{O}_2$ , 30 min	$40 \times 10^{-9} \text{ A}$
Hf anodized to completion: $400^\circ\text{C}$ in steam, 30 min	$50 \times 10^{-9} \text{ A}$
Hf anodized to completion: $450^\circ\text{C}$ in steam, 30 min	$0.1 \times 10^{-12} \text{ A}$
Hf anodized to completion; $450^\circ\text{C}$ in forming gas, 30 min	Short

than might be predicted from the published data on the low temperature oxidation of such metals (6). The presence of the overlying layer of porous anodic oxide greatly inhibits the oxidation, even though the barrier layer at the base of the pores is quite thin (the anodization is finished at a low voltage) and probably does not have the integrity usually associated with the barrier layer formed on pure aluminum because the copper dissolves in the electrolyte. The residual layer can be oxidized in dry oxygen at  $450^\circ\text{C}$  for 30 min, but using steam as the oxidation medium causes a substantial reduction in leakage current between adjacent conductors. Typical leakage values for a variety of pro-

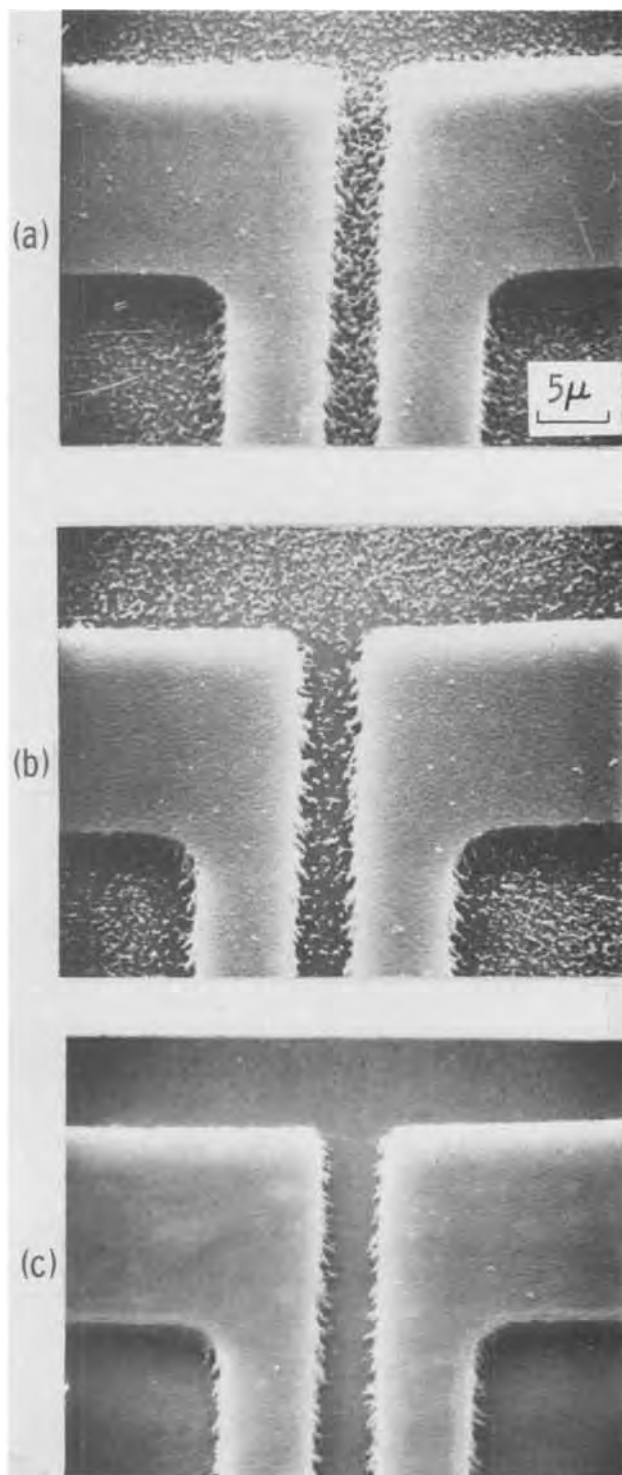


Fig. 6. Scanning electron micrographs of a pattern formed by anodic processing. (a) Floating lines; (b) lines connected to silicon, after decay; and (c) floating lines, hafnium underlay process.



cessing conditions are given in Table I. It can be seen that using the underlay process with steam oxidation results in leakage current about 100 times smaller than that obtained by standard processing, *i.e.*, no underlay, but every conductor connected directly to silicon. During the steam oxidation of the residual underlay, the porous anodic oxide is sealed, making it less vulnerable to attack by the reagents used to form the interlevel via holes.

However, unless the underlay is anodized until barrier layer growth ceases, it is not possible to oxidize it (to achieve suitable leakage values) at a temperature and for a time reasonable for semiconductor devices. We have also shown that the underlay does not react, to any significant extent, with either an SiO<sub>2</sub> underlay or a porous anodic aluminum oxide overlay, since a 450°C anneal in a nonoxidizing atmosphere for the same length of time does not produce any detectable reduction in the leakage current between adjacent conductors.

In Fig. 6 are shown scanning electron micrographs of our standard test structure in which the porous anodic oxide has been removed in phosphochromic acid to reveal the residual aluminum particles. In (a) are anodically processed "floating" lines; in (b) are lines anodically processed in the "standard" way; *i.e.*, no underlay, but every line connected directly to silicon; and (c) are anodically processed "floating lines" when the hafnium underlay process is used.

### Conclusions

We have described a method of anodic planarization for LSI which eliminates the necessity of direct contact to silicon for every conductor formed. The method consists of using a hafnium underlay beneath the aluminum or aluminum alloy interconnection metallization and anodizing the hafnium underlay to "completion" after isolation and decay, then oxidizing the

residue of the underlay in steam at 450°C for 30 min. Semiconductor devices with electrical characteristics identical to those made by conventional processing have been made using this technique.

### Acknowledgments

The authors would like to thank R. Lever for performing the helium ion backscattering experiments, and F. Ordonez for the excellent scanning electron micrographs. We are grateful for J. Van Steenburgh's assistance with the evaporations.

Manuscript submitted June 30, 1975; revised manuscript received Sept. 16, 1975. This was Paper 78 presented at the Toronto, Canada, Meeting of the Society, May 11-16, 1975.

Any discussion of this paper will appear in a Discussion Section to be published in the December 1976 JOURNAL. All discussions for the December 1976 Discussion Section should be submitted by Aug. 1, 1976.

*Publication costs of this article were partially assisted by IBM Corporation.*

### REFERENCES

1. G. C. Schwartz, Abstract 3, p. 13, The Electrochemical Society Extended Abstracts, Spring Meeting, San Francisco, California, May 12-17, 1974; G. C. Schwartz and V. Platter, *This Journal*, **122**, 1508 (1975).
2. H. Tsunemitsu and H. Shiba, Abstract 18.4, IEEE International Electron Device Meeting, October 1969; *NEC Research and Development*, **74**, April 1972.
3. W. R. McMahon, Abstract 7.1, IEEE International Electron Devices Meeting, October 1970.
4. L. Romankiw, Private communication.
5. G. C. Schwartz, Abstract 80, p. 182, The Electrochemical Society Extended Abstracts, Spring Meeting, Toronto, Canada, May 11-16, 1975.
6. E. A. Guibransen and K. F. Andrews, *This Journal*, **96**, 364 (1949).

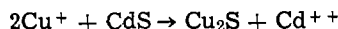
## Ion Backscattering Study of Cu<sub>2</sub>S Formation on Single Crystal CdS

J. A. Borders\*

*Sandia Laboratories, Albuquerque, New Mexico 87115*

### ABSTRACT

Ion backscattering has been used to study the formation of Cu<sub>2</sub>S layers on single crystal CdS due to the chemical ion exchange reaction



The reaction is found to proceed most rapidly on the A (Cd) face, slower on the B (S) face, with the reaction proceeding slowest on faces perpendicular to the  $\langle 11\bar{2}0 \rangle$  axis. Reactions on the A and B faces are characterized by a very nonuniform Cu<sub>2</sub>S-CdS interface, whereas the interface for reactions along the  $\langle 11\bar{2}0 \rangle$  is much more uniform. The reaction in the latter case may be controlled by surface nucleation, and layer formation subsequent to formation of a 300-500 Å thick layer is much slower. The formation of Cu<sub>2</sub>S on the A and B faces has an activation energy of 0.9-1.5 eV. Preparation of the surface by polishing leads to a larger rate of Cu<sub>2</sub>S formation and Cu<sub>2</sub>S-CdS interfaces which are more uniform as a function of depth than those in etched samples.

Energetic ion backscattering is a relatively recent tool for the study of the near-surface layers in solids. It is the only nondestructive technique for measuring the depth distribution of atomic composition over

micron-thick layers with significant depth resolution (100-200 Å). So far, ion backscattering has been applied mainly to studies of thin-film interdiffusion and interfacial reactions, particularly in the area of semiconductor device technology (1), but there have been few applications to studies of surface chemical reactions.

\* Electrochemical Society Active Member.  
Key words: cadmium sulfide, copper sulfide, thin film solar cells, ion backscattering analysis.

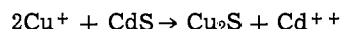
A technologically important system where a surface chemical reaction plays an important role is the CdS-Cu<sub>2</sub>S system. This system is one of the most frequently mentioned candidates for thin-film solar cells and extensive phenomenological information is available. In this paper we report the results of an investigation of the formation of Cu<sub>2</sub>S layers on the surfaces of single crystal CdS using 2.0 MeV He ion backscattering. The ion backscattering provides a direct measure of the depth distribution of atomic composition in the first few thousand angstroms of the sample. Temperature dependences of the depth distributions enable the reaction energetics to be determined over a limited temperature region. The important effects of crystallographic orientation of the CdS substrates have been measured and the effect of surface preparation of the CdS was briefly investigated.

### Experimental

Samples of single crystal CdS were obtained from Eagle-Pitcher and Cleveite Corporation in the form of thin platelets of thickness  $\sim 0.5$  mm. These specimens included both platelets with the C axis in the plane of the platelet and samples with the C axis perpendicular to the platelet. The platelets were cut to the appropriate sample dimensions ( $6.5 \times 6.5$  mm) for the backscattering experiments. The A (0001) and B (000 $\bar{1}$ ) faces of the samples with the C axis perpendicular to the plane of the sample were identified by a 1 min etch in a 50% by volume mixture of HCl and H<sub>2</sub>O. Optical microscope observations indicate that small hexagonal structures begin to form on one of the surfaces. By comparison with known preferential etching (2) behavior in a solution of HNO<sub>3</sub>, CH<sub>3</sub>COOH, and H<sub>2</sub>O in the volume ratios 6:6:1, the surface showing the hexagonal structures was identified as the A (Cd) face. Samples with the C axis in the plane of the platelet were etched for 30 sec in 30% by volume HCl in H<sub>2</sub>O. The crystallographic orientation of these samples was determined by x-ray diffraction to be  $\langle 11\bar{2}0 \rangle$ .

Two samples, an A-face sample and a sample with the C axis in the plane of the surface, were polished to an optically clear finish on a polishing wheel using 0.25  $\mu$ m diamond paste as an abrasive. These samples were then gently swabbed with 30% HCl for 5 min to remove surface damage yet retain the optically smooth surface finish.

The Cu<sub>2</sub>S layers were formed by dipping in a copper chloride solution developed by Fahrenbruck (3). This dipping treatment forms Cu<sub>2</sub>S by the reaction



with the excess cadmium going into solution. Distilled H<sub>2</sub>O was boiled in a flask while argon was bubbled through the H<sub>2</sub>O. After 20 min, 19.8 g/liter CuCl, 37.3 g/liter KCl, and 13.9 g/liter NH<sub>2</sub>OHHCl were added without disturbing the argon atmosphere in the flask. The solution temperature was then stabilized at the desired dipping temperature and the samples immersed for the desired time while attached to a stainless steel paddle. After dipping, the samples were immediately rinsed with distilled H<sub>2</sub>O, dried, and inserted in the sample holder for the backscattering analysis.

In order to verify that samples reached thermal equilibrium quickly at the shortest dipping times (15 sec), samples of all orientations which had been subjected to two successive 15 sec dips were compared to samples dipped once for 30 sec. For samples of the same orientation there was no difference in the amount or depth distribution of Cu<sub>2</sub>S formed by the two procedures.

All analyses were accomplished with 2.0 MeV He<sup>+</sup> ions at a nominal beam current of 3.0 nA and a beam spot size of  $1.0 \times 1.0$  mm. Scattered ions were de-

tected at a laboratory angle of 160° in a silicon surface barrier detector. Further amplification and analysis was done using standard nuclear spectroscopy electronics, pulse pile-up rejection circuitry, and a PDP-11-based pulse height analysis system (4).

### Data Analysis

A typical ion backscattering spectrum from a CdS sample with a thin layer of Cu<sub>x</sub>S, where  $x \approx 2.0$  as will be discussed, is shown in Fig. 1 (top). These data are for (0001) CdS dipped for 2 min at a solution temperature of 65°C. In Fig. 1 (bottom) is a spectrum taken of an untreated sample of CdS. The formation of the Cu<sub>2</sub>S surface layer is manifested in two ways: (i) the Cd edge is shifted to lower energies due to passage of the ions through and energy loss in the Cu<sub>2</sub>S and (ii) the appearance of scattering due to the Cu atoms themselves. Since the Cu scattering at a given depth occurs at a lower energy than Cd scattering from the same depth, the analysis of the data is more complex than for a heavier atom layer on a lighter atom substrate. It is assumed that the reader is familiar with measurements of the depth dependence of atomic composition by ion backscattering. For a detailed discussion of the principle of the technique and how the information is obtained see Ref. (1). Brice has developed a technique for the extraction of the scattering yields of each component of a binary target (5) and has written a computer code which performs this function. The code as written requires a rather large computer, but by making some restrictions in the capabilities and generality of the code, we have been able to implement this program in a PDP-11 with 28K core. The program is written in an interpretive language and thus requires about five hours to analyze 100 channels.

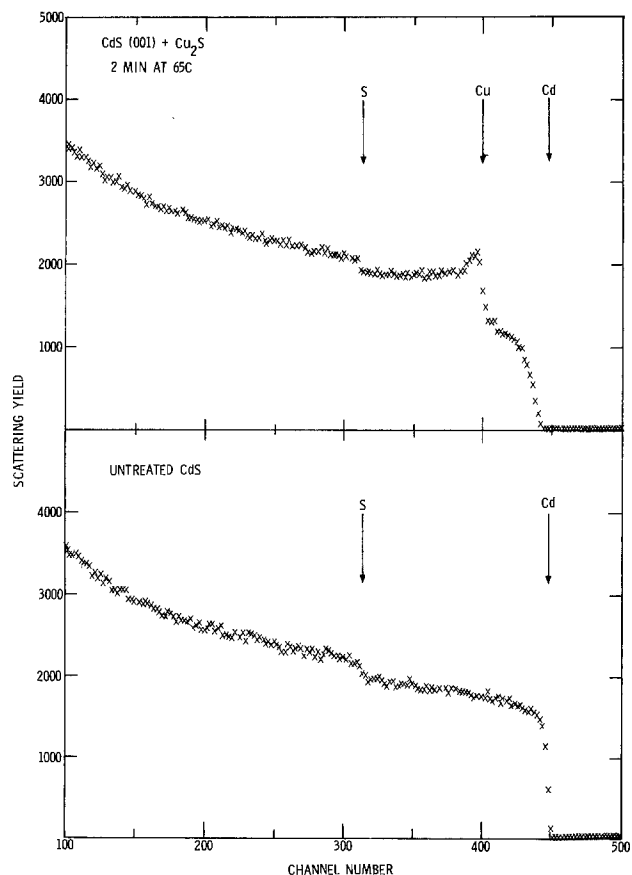


Fig. 1. Backscattering spectra from a sample of CdS (A face) dipped for 2 min at 65°C (top) and an untreated sample of CdS (bottom). The labeled arrows represent the channel where surface scattering from the three constituents will occur.



Several assumptions must be made in order to interpret the data. Since the Brice program is only applicable to binary targets, we have assumed that all the Cd is in the form CdS and all the Cu in the form CuS<sub>0.5</sub>. CdS is the only known compound in the CdS binary system and CdCl<sub>2</sub>, which would be the reaction product in the dipping reaction, is water soluble. The reasons for the assumption that all the Cu is in the form CuS<sub>0.5</sub> or equivalently Cu<sub>2</sub>S are not so obvious. The CuS<sub>0.5</sub> form is used rather than Cu<sub>2</sub>S to normalize both molecules to one metallic atom apiece, since we are measuring the helium ion scattering from Cd and Cu and not from S. The solubility of Cu in CdS has been measured by Sullivan (6) and can be expressed as

$$[\text{Cu}] = 6.6 \times 10^{22} \text{ atom/cm}^3 \times \exp[-0.505 \text{ eV}/kT] \quad [1]$$

At the temperatures we are concerned with in this work, 65°–85°C, the solubilities calculated from Eq. [1] vary from  $2\text{--}5 \times 10^{15} \text{ atom/cm}^3$ . However, the scattering of Cu at the surface in general is superimposed on Cd scattering from deeper in the sample, and the scattering from one atom of Cd is greater than the scattering from one atom of Cu by a factor  $(Z_{\text{Cd}}/Z_{\text{Cu}})^2 = (48/29)^2 = 2.74$ . Because of these problems, we are limited to measuring copper atomic concentrations  $\geq 1/100$  of the Cd atomic concentration. This works out to a practical limit of about  $2 \times 10^{20} \text{ Cu atom/cm}^3$ . Thus any copper which we detect must be tied up in a compound, since the maximum solubility of copper in CdS is below our practical detection limits for this system by a factor of  $10^5$ .

It is well documented that the Cu-S phase diagram is complicated (7). A large number of Cu<sub>x</sub>S compounds exist near a value of  $x = 2.0$ . Ion backscattering cannot measure microstructure. At best it measures atomic ratios averaged over the beam area (typically  $\sim 1 \text{ mm}^2$  as a function of depth. Other workers have shown by x-ray diffraction techniques (7) that the Cu<sub>x</sub>S compound which forms on single crystal CdS during the dipping reactions is predominantly Cu<sub>2</sub>S. For our purpose, however, the exact stoichiometry of the Cu-S compound makes little difference. Thus as we refer to Cu<sub>x</sub>S, we have assumed  $x = 2.0$  for calculations. It is possible that ternary Cd-Cu-S compounds are formed, which would change some of the conclusions presented here. However, x-ray diffraction measurements (7) by other workers did not show evidence for such compounds.

Stopping power data for He ions in CdS are limited (8) and none exist for He in Cu<sub>2</sub>S, so values for Cd, Cu, and S were used (9) to generate values of the stopping power of CdS and CuS<sub>0.5</sub> for He ions as a function of energy by assuming Bragg's Rule for additivity of atomic stopping powers applied to CdS and CuS<sub>0.5</sub>. These values were then fit to the Brice formula (10) to give an analytic expression for the electronic stopping power,  $\epsilon$ . The values of  $\epsilon$  used, along with the resultant Brice parameters, are listed in Table I.

Since the Brice techniques depend on comparing the scattering from the heaviest component of a two-

component sample to the scattering from a reference sample composed of the pure heaviest component, the amount of the lighter component required to produce the observed reduction in scattering from the heavier component is calculated and its scattering yield is subtracted from the total scattering spectrum at the appropriate energy. The exact choice of this energy is critical. If the energy is slightly too high or too low, a dip or bump will be produced in the calculated scattering yield from the heavier component with a corresponding bump or dip in the calculated scattering yield from this lighter component at a greater depth. Fortunately, if the chosen energy is close to the appropriate energy, these inaccuracies are limited in magnitude and depth and can easily be removed manually. The contribution of the sulfur to the scattering spectrum has been completely neglected in using the Brice extraction technique. This is not a serious error as long as we confine ourselves to analyses of spectra at energies above that expected for scattering from sulfur atoms at the surface.

Figure 2 shows the results of the extraction process for the data of Fig. 1. The upper part of the figure shows the CdS scattering after subtraction of the CuS<sub>0.5</sub> scattering which is shown in the middle section. The lower part of the figure shows the depth distribution of CuS<sub>0.5</sub>.

### Results and Discussion

The effect of crystallographic orientation of the CdS substrate on the rate and nature of Cu<sub>2</sub>S formation was rather large. Figure 3 shows backscattering spectra for samples of the three orientations after dipping treatment at 85°C for 45 sec. The A-face and B-face samples show similar behavior with more Cu<sub>2</sub>S being formed on the A face than on the B face. Both of these samples have a well-defined surface layer of pure Cu<sub>2</sub>S. Behind the surface layer the ratio of  $[\text{Cu}_2\text{S}]/[\text{CdS}]$  as a function of depth decreases mono-

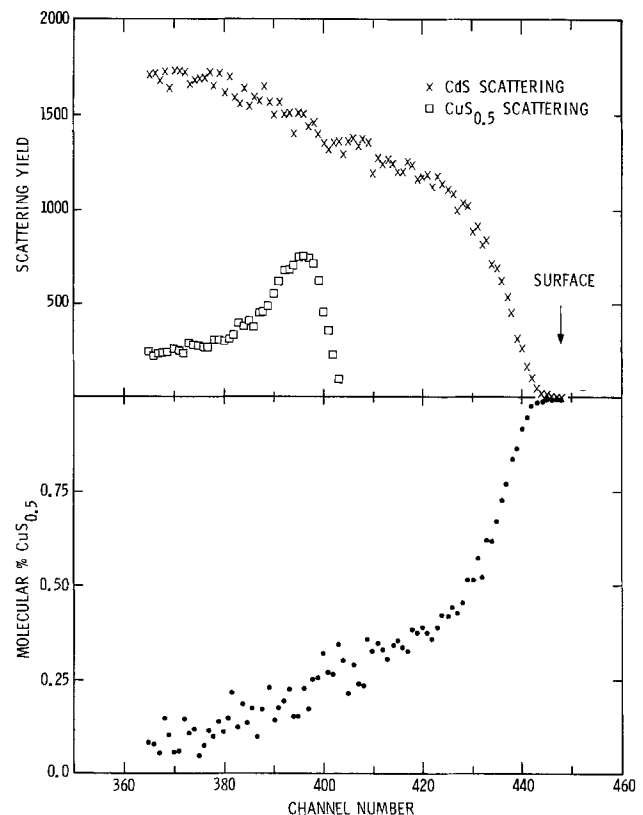


Fig. 2. The top of this figure shows the scattering from Cd (X) and Cu (□) assuming that they are always present in the forms CdS and CuS<sub>0.5</sub>, respectively. The original data is that from the top of Fig. 1. In the bottom of Fig. 2 the molecular concentration of CuS<sub>0.5</sub> is calculated from the separated spectra shown above it.

Table I.  $\epsilon \times 10^{-15} \text{ eV cm}^2/\text{atom}$

Energy (keV)	Cd	Cu	S	Brice parameters	
				CdS	CuS <sub>0.5</sub>
400	96.33	62.41	62.12		
600	107.0	68.20	68.61		
800	112.0	71.77	69.72		
1000	113.0	73.58	67.75		
1200	111.4	74.05	64.72	Z <sub>2</sub>	64
1400	108.1	73.50	61.48	Z	2.077
1600	103.8	72.24	58.37	a	0.3504
2000	94.71	68.48	52.89	n	3.249
2800	84.81	62.0	43.88		
4000	72.53	54.72	35.83		

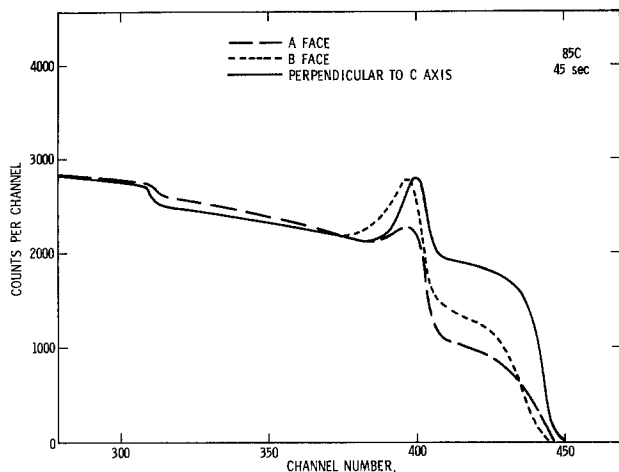


Fig. 3. Backscattering spectra from samples of the three different orientations studied for a dipping treatment of 45 sec at 85°C. The lines were drawn through the actual data points for clarity.

tonically with increasing depth as can be seen from the Cd scattering yield in the energy region between channels 410 and 450. In contrast, the  $\langle 11\bar{2}0 \rangle$  sample shows a surface layer of  $\text{Cu}_2\text{S}$  with no significant Cu scattering at depths beyond the surface layer. This can also be seen in the sharpness of the Cd scattering edge for the  $\langle 11\bar{2}0 \rangle$  sample indicating a  $\text{Cu}_2\text{S}$ -CdS interface at very well-defined depth.

The behavior on the  $\langle 11\bar{2}0 \rangle$  sample can be analyzed without recourse to the Brice subtraction technique. By simply integrating the counts under the copper scattering peak, a measure of the  $\text{Cu}_2\text{S}$  formation is obtained. Data of the formation of  $\text{Cu}_2\text{S}$  on the face perpendicular to the  $\langle 11\bar{2}0 \rangle$  axis are shown in Fig. 4 as a function of dipping time at various temperatures and for both polished and etched samples dipped at 75°C. The general behavior of the curves shows a rapid formation of  $\text{Cu}_2\text{S}$  followed by a period of slower growth. In all cases investigated, the growth slowed at thicknesses between  $1.5$  and  $2 \times 10^{17}$   $\text{CuS}_{0.5}$  molecules  $\text{cm}^{-2}$ . If we assume that this layer is  $\text{Cu}_2\text{S}$  with a bulk density of  $5.6 \text{ g/cm}^3$  (11), the thickness range is 350-500Å. The rapid increase in the amount of  $\text{Cu}_2\text{S}$  observed, followed by a slower growth is most probably related to nucleation of the  $\text{Cu}_2\text{S}$  layer on the surface of the CdS. Such effects have previously been suggested by Fahrenbuck (3). In the spectra which showed very small amounts of  $\text{Cu}_2\text{S}$ , the Cu scattering peak is not energy-resolution limited, but is wide

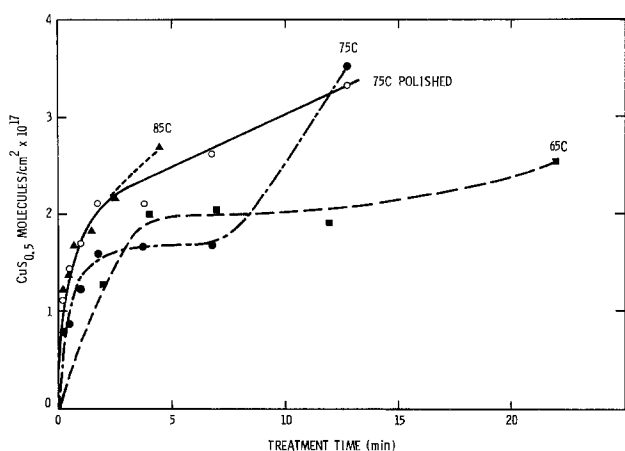


Fig. 4. Total amount of  $\text{CuS}_{0.5}$  formed on  $\langle 11\bar{2}0 \rangle$  samples as a function of time at different dipping temperatures 65°C (■), 75°C (●), 85°C (▲). Also shown are data for a polished sample treated at 75°C (○).

enough to correspond to  $\sim 300\text{Å}$  of  $\text{Cu}_2\text{S}$ . As the treatment time is lengthened, the peak increases in height without appreciable widening, suggesting that  $\text{Cu}_2\text{S}$  nucleates at favorable spots on the surface and the nuclei are about 300Å thick. After a layer of  $\text{Cu}_2\text{S}$  has been formed over the entire surface, the process is no longer controlled by nucleation, but either by the reaction rate for the conversion of CdS to  $\text{Cu}_2\text{S}$  or by diffusion of Cu through the already formed layer of  $\text{Cu}_2\text{S}$ .

As discussed in the previous section, the Brice technique has been applied to the A-face spectra to generate data on the depth distribution of  $\text{Cu}_2\text{S}$  on samples of that orientation. Figure 5 shows data on the depth distribution of  $\text{Cu}_2\text{S}$  subject to the assumptions explained in the previous section. The solid lines are drawn through the actual data points which resemble the data points shown in the bottom half of Fig. 2.

These depth distributions resemble diffusion profiles, but it is important to realize that they cannot be diffusion profiles. The amounts of Cu measured in these experiments are many orders of magnitude above the amounts which can be dissolved in CdS as explained in the previous section. This result suggests that there is lateral variation in  $\text{Cu}_2\text{S}$  formation across the area of the analyzing beam. At any given depth there are regions of  $\text{Cu}_2\text{S}$  and regions of CdS. Since the amount of  $\text{Cu}_2\text{S}$  decreases monotonically with increasing depth in the CdS, a model of cone-shaped regions of  $\text{Cu}_2\text{S}$  growing into the CdS is suggested. Such behavior could easily arise if growth took place preferentially at defects such as dislocations. But whatever the course,  $\text{Cu}_2\text{S}$  growth parallel to the C axis appears to take place with a very non-uniform interface, whereas the interface is much more uniform for growth perpendicular to the C axis.

If the growth of the  $\text{Cu}_2\text{S}$  is limited by the ion-exchange reaction rate, the concentration vs. depth should be linear beyond the initial surface layer. If the limitation is diffusion of Cu through the  $\text{Cu}_2\text{S}$  layer which has already formed, a plot of the logarithm of concentration vs. depth squared should be a straight line. Unfortunately, our data are not sufficiently accurate to distinguish these two forms of kinetic behavior. This does not, however, prevent us from obtaining data on the energetics of the reaction. As has been previously observed (12), by plotting the time-to-equivalent backscattering spectra on an Arrhenius-type diagram, the slope of the line connecting equivalent spectra gives the activation energy

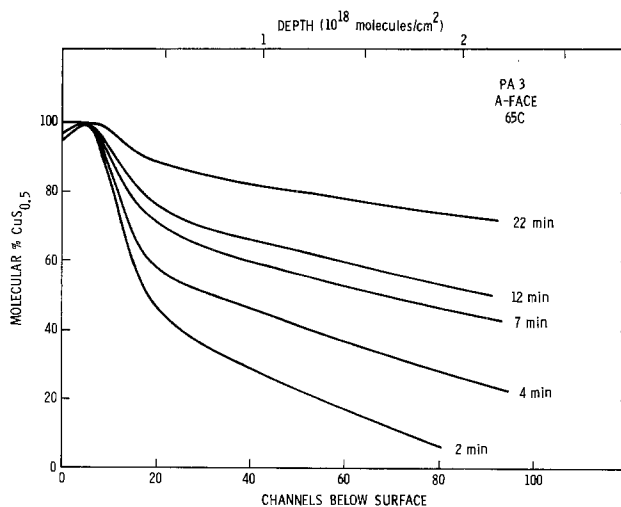


Fig. 5. Depth distributions of  $\text{CuS}_{0.5}$  as a function of energy (lower horizontal axis) and equivalently depth (upper horizontal axis). These concentrations are the average over a 1 mm beam-spot area.

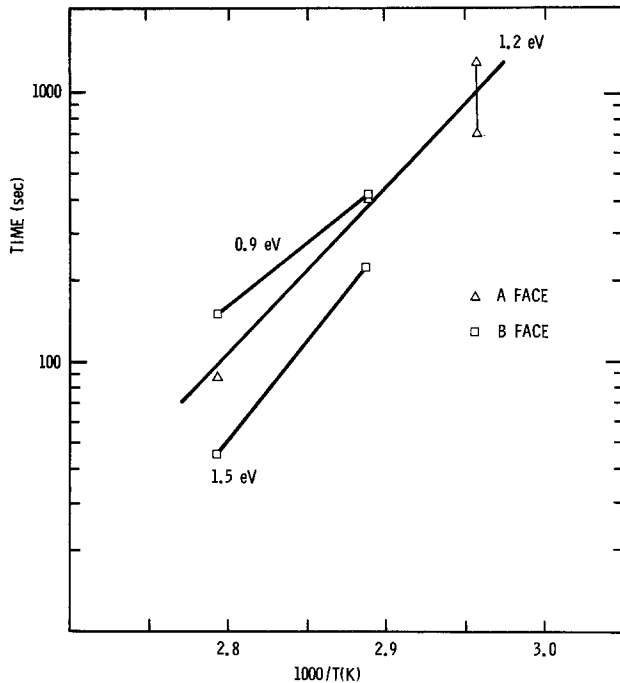


Fig. 6. Arrhenius plot of time to equivalent spectra for A-face ( $\Delta$ ) and B-face ( $\square$ ) samples. The heavy lines connect the equivalent points. The two points at  $65^\circ\text{C}$  connected by a vertical line indicate that the equivalent spectrum fell somewhere between the two points.

of the process. Data for the A and B faces are shown in Fig. 6. There is some scattering in the slope, most probably due to difficulties in picking exactly equivalent spectra, but the data are fairly consistent with an activation energy of 0.9-1.5 eV. It must be cautioned that if more than one process is active during the time taken to produce the spectra, the activation energy derived from Fig. 6 will not be simply related to either individual process, but this is the case in other methods of determining activation energies as well.

Some preliminary results on the effect of surface preparation were obtained on samples which had been polished to an optical finish using  $0.25\ \mu\text{m}$  diamond paste. Figure 4 shows the growth of  $\text{Cu}_2\text{S}$  vs. dipping time for a polished and a normal-etched  $\langle 11\bar{2}0 \rangle$  sample dipped in a  $75^\circ\text{C}$  solution. The short time behavior of the polished sample shows much faster growth than the etched sample, but the curves then cross at high values of  $\text{Cu}_2\text{S}$  layer thickness.

For A-face samples which had been polished, the difference between polished and etched samples is the most apparent. As can be seen in the spectra shown in Fig. 7, the Cu scattering for polished samples shows a less rapid change in  $\text{Cu}_2\text{S}$  concentration vs. depth than for the etched sample. Indeed, the polished sample almost has a uniform layer of  $\text{Cu}_2\text{S}$  which grows linearly in time, but as can be noticed from the Cd scattering remaining in the region between channels 410-450, the layer is not uniform.

We suggest that these results indicate the  $\text{Cu}_2\text{S}$  formation on CdS is very dependent on surface damage and on the crystalline perfection of the near-surface layers of the host CdS crystal.

### Conclusions

The results contained in this paper represent the first application of energetic ion backscattering to the study of an aqueous chemical reaction. While mostly phenomenological, information has been obtained on  $\text{Cu}_2\text{S}$  formation on single crystal CdS in a thickness region of technological importance (0-5000Å). There exist no other data in this region of interest. We

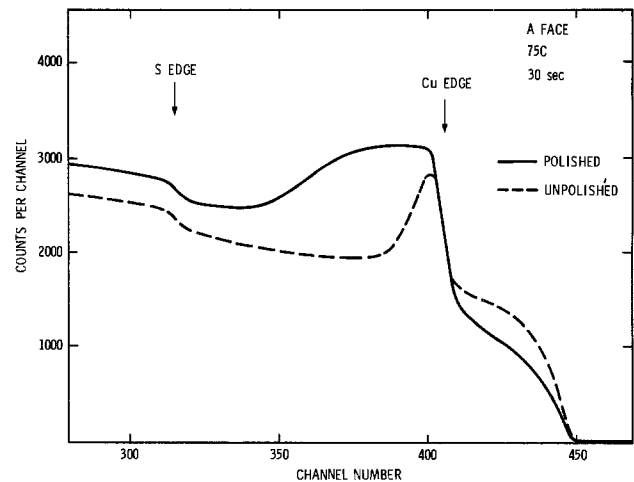


Fig. 7. Backscattering spectra from a polished and an unpolished A-face sample. Both samples were dipped for 30 sec at  $75^\circ\text{C}$ . The lines were drawn through the individual data points.

have demonstrated that the reaction is faster on the A face than the B face, and faster along the C axis than perpendicular to it. Estimates of the energetics of the reaction along the C axis have been obtained. We have shown that the  $\text{Cu}_2\text{S}$  layer formed on single crystal CdS is not uniform in depth, but is propagated into the crystal with great lateral nonuniformity. It is suggested that dislocations may enhance  $\text{Cu}_2\text{S}$  formation due to the local lattice strain. Also, the effects of surface preparation of  $\text{Cu}_2\text{S}$  layer formation have been shown to be quite large.

CdS is a complicated material and samples from different suppliers or samples from the same supplier, but cut from different boules, behaved very differently. However, if we are to ever understand the mechanisms of  $\text{Cu}_2\text{S}$  formation on thin-film CdS where the effects of polycrystallinity and grain morphology may very well be large, we must first attempt to understand what happens in the simpler system of  $\text{Cu}_2\text{S}$  on single crystal CdS.

### Acknowledgments

The author would like to thank J. H. Smalley for his skilled assistance with the experimental work and R. Berg for his valuable comments on the CdS- $\text{Cu}_2\text{S}$  system.

This work was supported by the United States Energy Research and Development Administration (ERDA).

Manuscript submitted July 18, 1975; revised manuscript received Sept. 3, 1975. This was Paper 121 presented at the Toronto, Canada, Meeting of the Society, May 11-16, 1975.

Any discussion of this paper will appear in a Discussion Section to be published in the December 1976 JOURNAL. All discussions for the December 1976 Discussion Section should be submitted by Aug. 1, 1976.

Publication costs of this article were partially assisted by Sandia Laboratories.

### REFERENCES

1. J. A. Borders and S. T. Picraux, *Proc. IEEE*, **62**, 1224 (1974).
2. E. P. Warekios, M. C. Lavine, A. N. Mariano, and H. C. Gatos, *J. Appl. Phys.*, **33**, 690 (1962); see also *ibid.*, **37**, 2203 (1966).
3. A. L. Fahrenbruck, Ph.D. Thesis, Stanford University (1973).
4. Tennecomp Systems, Model TP-5000.
5. D. K. Brice, *Thin Solid Films*, **19**, 121 (1973).
6. G. A. Sullivan, *Phys. Rev.*, **184**, 796 (1969).
7. L. R. Shiozawa *et al.*, "Research on the Mechanism of the Photovoltaic Effect in High Efficiency CdS Thin-Film Solar Cells," Aerospace Research-Laboratories Final Report, Contract AF33(615)-5224 (July 1969).

8. P. F. Engel, J. A. Borders, and F. Chernow, *J. Appl. Phys.*, **45**, 38 (1974).  
 9. J. F. Ziegler and W. K. Chu, *Thin Solid Films*, **19**, 281 (1973).  
 10. D. K. Brice, *Phys. Rev.*, **A6**, 1791 (1972).  
 11. Handbook of Chemistry and Physics, 47th ed., The Chemical Rubber Co., Cleveland, Ohio (1966).  
 12. J. A. Borders, *Thin Solid Films*, **19**, 359 (1973).

## The Effects of Processing on Hot Electron Trapping in SiO<sub>2</sub>

R. A. Gdula

IBM System Products Division, East Fishkill Facility, Hopewell Junction, New York 12533

### ABSTRACT

Avalanche injection of hot electrons into the insulator of an MOS capacitor has been used to study electron trapping in SiO<sub>2</sub>. Oxides formed by thermal oxidation in dry O<sub>2</sub>, O<sub>2</sub> + HCl, O<sub>2</sub> + H<sub>2</sub>O, steam, and chemical vapor-deposited (CVD) SiO<sub>2</sub> were subjected to avalanche charging. Pure, dry thermal SiO<sub>2</sub> was found to trap up to  $2.6 \times 10^{12}$  e/cm<sup>2</sup>. The trapping efficiency of SiO<sub>2</sub> varied by three orders of magnitude, depending on forming and annealing conditions.

Goetzberger and Nicollian (1) reported the occurrence of avalanche-produced hot carriers as early as 1966. Subsequently, the conditions under which hot carriers can be produced in MOS structures were outlined (2), and hot carrier injection was used to study high current densities and trapping in SiO<sub>2</sub> (3, 4). At about the same time, it was discovered that hot carrier injection could degrade the performance of silicon planar transistors (5, 6) and produce instabilities in MOSFET's (7). A practical use for the phenomenon was found with the introduction of the FAMOS<sup>1</sup> device (8). These problems induced further studies (9-13).

Avalanche injection of hot carriers into SiO<sub>2</sub> can be conveniently produced using a simple MOS capacitor. A high frequency (> 1 kHz) a-c signal of sufficient amplitude is impressed across the capacitor. Once each cycle the silicon beneath the field plate becomes depleted because the inversion layer cannot form quickly enough. When the field in the silicon becomes strong, large quantities of minority carriers are created by ionization multiplication, and the Si is said to avalanche. These minority carriers are accelerated toward the Si-SiO<sub>2</sub> interface by the field across the depletion region. Some achieve sufficient energy to overcome the potential barrier (~3.25 eV) at the interface and enter the SiO<sub>2</sub>. Most drift through the SiO<sub>2</sub> and are collected on the metal field plate, but some become trapped in the SiO<sub>2</sub>. The details of this trapping and how it is affected by processing are the subject of this paper.

### Experimental Procedures

**Sample preparation.**—Silicon wafers (5.7 cm diameter, boron-doped, p-type, <100> orientation of various resistivities) were quartered, stripped in concentrated HF, and given an inorganic cleaning in hot aqueous solutions of NH<sub>4</sub>OH + H<sub>2</sub>O<sub>2</sub> and HCl + H<sub>2</sub>O<sub>2</sub> finished by copious rinsing in deionized water. SiO<sub>2</sub> films were formed by thermal oxidation at 1000°C in various ambients, or provided by CVD. When required, annealing in N<sub>2</sub> or Ar was performed at 1050°C for various lengths of time. Pure aluminum was evaporated from an e-gun source through metal masks to form  $5.32 \times 10^{-3}$  cm<sup>2</sup> capacitors. Aluminum was also deposited on the wafer back sides and annealed in N<sub>2</sub> at 400°C for 20 min to provide ohmic contacts to the silicon. Mobile charge levels were checked by the I-V loop technique (14, 15) after biasing the capacitors at  $+2 \times 10^6$  V/cm, 200°C, for 10 min. Mobile charge levels in all cases were found to be  $< 3 \times 10^{10}$  charges/cm<sup>2</sup>. SiO<sub>2</sub> film thickness was measured with an ellipsometer.

**Measurement techniques.**—Starting with a virgin (unprobed) capacitor, the high frequency (1 MHz) C-V characteristic was determined. Then the capacitor was avalanched for specified time periods ranging from 1 sec to several thousand seconds using the circuit of Ref. (4). The average d-c current flowing through the sample was monitored by a Keithley Model 615 electrometer operating in the normal mode. The sample was then reconnected to the C-V measuring apparatus through a switch box and the C-V characteristic redetermined. The number of hot electrons injected into and passed through the SiO<sub>2</sub> per unit area and collected on the Al field plate ( $N_{\text{collected}}$ ) was calculated from the area of the field plate and the integrated area under the I vs. time curve. A measure of the number of electron charges trapped per unit area ( $\Delta N_{\text{eff}}$ ) was calculated from the shift between the C-V traces using the equation

$$\Delta N_{\text{eff}} = \frac{\Delta V_{\text{FB}} \epsilon_0 K_{\text{SiO}_2}}{q D_{\text{SiO}_2}} \quad [1]$$

where  $\Delta V_{\text{FB}}$  is the lateral displacement of the C-V traces at the flatband condition in volts,  $\epsilon_0$  is the permittivity of free space (farad/cm),  $K_{\text{SiO}_2}$  is the SiO<sub>2</sub> dielectric constant (taken to be 4),  $q$  is the electronic charge in coulombs, and  $D_{\text{SiO}_2}$  is the SiO<sub>2</sub> thickness (cm). Although Eq. [1] assumes all the trapped charge is located in a uniform sheet at the Si-SiO<sub>2</sub> interface which may not be strictly correct,  $\Delta N_{\text{eff}}$  is useful in predicting the behavior of actual MOSFET devices. For most of the work it was found convenient to keep the current through the oxide constant by continuously adjusting the applied voltage. All measurements were made with the sample in darkness.

### Results and Discussion

**Operating conditions.**—It quickly became apparent that the silicon substrate doping level had a profound effect on sample behavior. The applied voltage necessary to sustain avalanche currents (at  $J_{\text{dc}} = 2 \times 10^{-6}$  A/cm<sup>2</sup>) varied drastically as a function of  $N_A$  as seen in Fig. 1. ( $J$  represents the particle current through the device.) This is in agreement with the work of Goetzberger and Nicollian (2) who considered the edge of the depletion region to be a step junction. According to their data, uniform avalanche behavior can be expected in the  $10^{16}$ - $10^{18}$  atom/cm<sup>3</sup> doping range. At lighter doping levels edge breakdown dominates, and at higher doping levels direct tunneling occurs. For the purposes of this investigation, it was found convenient to use the  $7 \times 10^{15}$  to about  $1 \times 10^{17}$  range; accordingly, most of the samples investigated were constructed on 0.4 or 2 ohm-cm material.

Key words: avalanche injection, hot minority carriers, annealing.  
<sup>1</sup> Floating gate avalanche injection metal oxide semiconductor.

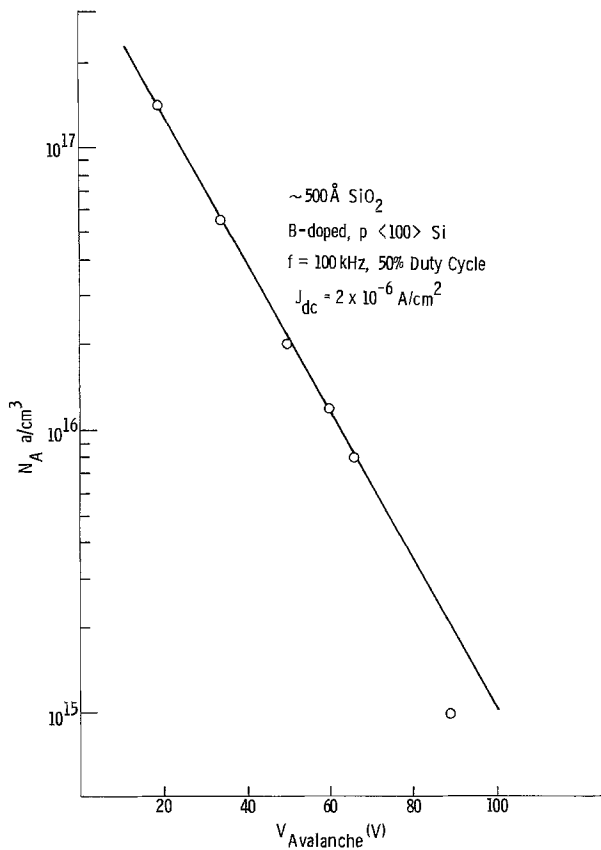


Fig. 1. Applied voltage necessary to sustain an avalanche current of  $2 \times 10^{-6} \text{ A/cm}^2$  as a function of Si doping level.

It was also quite apparent that the avalanching conditions affected behavior. For example,  $J_{dc} < 10^{-7} \text{ A/cm}^2$  did not cause C-V shifts  $> 10 \text{ mV}$  (the accuracy of the measurements) in reasonable experimental times ( $\sim 100 \text{ sec}$ ), while  $J_{dc} > 10^{-3} \text{ A/cm}^2$  caused insulator dielectric breakdown or a peculiar damage change in the silicon that shows up as an abnormal C-V trace and gives zero C-V shifts even for passage of very large numbers of electrons. Frequency, duty cycle, and pulse shape also affected  $J_{dc}$ . For the results described here, the apparatus was operated within the following conditions:  $J_{dc} = 2 \times 10^{-7}$  to  $2 \times 10^{-5} \text{ A/cm}^2$ ,  $f = 100 \text{ kHz}$ , duty cycle = 50%, pulse rise time =  $0.8 \mu\text{sec}$ , and pulse fall time =  $0.16 \mu\text{sec}$ .

*Typical data and conditions.*—Typical data on a virgin MOS capacitor whose oxide was thermally grown in dry O<sub>2</sub> at 1000°C and subsequently N<sub>2</sub> annealed is shown in Fig. 2. From such a plot the important parameter, instantaneous effective trapping efficiency TE, defined as

$$TE \equiv \frac{dN_{\text{eff}}}{dN_{\text{collected}}} \quad [2]$$

may be calculated. It is instructive to note that initially TE is quite high, trapping 2 electrons for every 100 electrons passing through the oxide, but TE gradually falls off to very low values. When very large numbers of electrons have passed through the structure, the trapping appears to saturate and then relax as shown in Fig. 3, which shows more extensive data from the identical sample discussed in Fig. 2. This maximum trapping is another important parameter, as it puts an upper bound on the threshold shifts of MOSFET devices and in principle allows a calculation of trapping density in the dielectric film. However, assumptions as to the spatial distribution of the charges are required. Moreover, we expected a saturation of the C-V shift but not a reversal of it. Reversal implies a reduction in the net moment of charge which could be caused

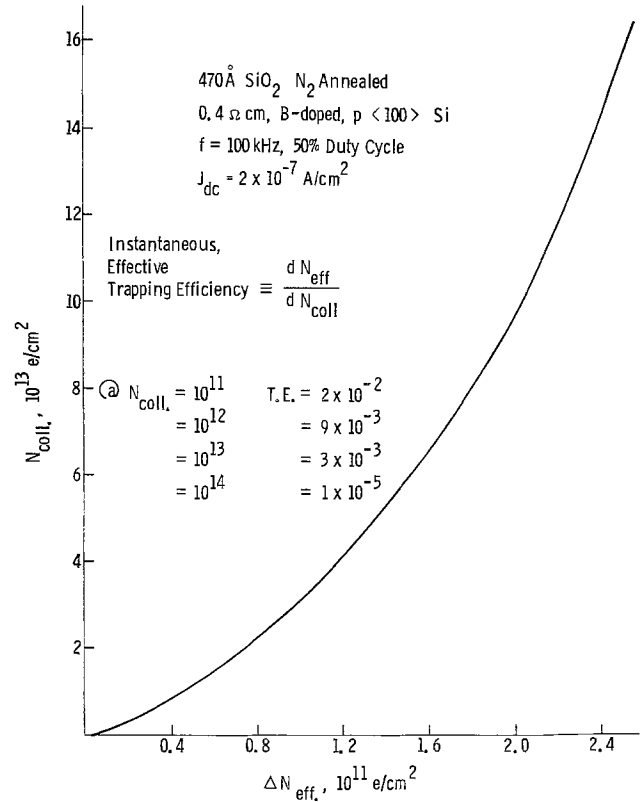


Fig. 2. Typical linear plot of MOS capacitor data

either by detrapping of electrons or compensation by positive charges.

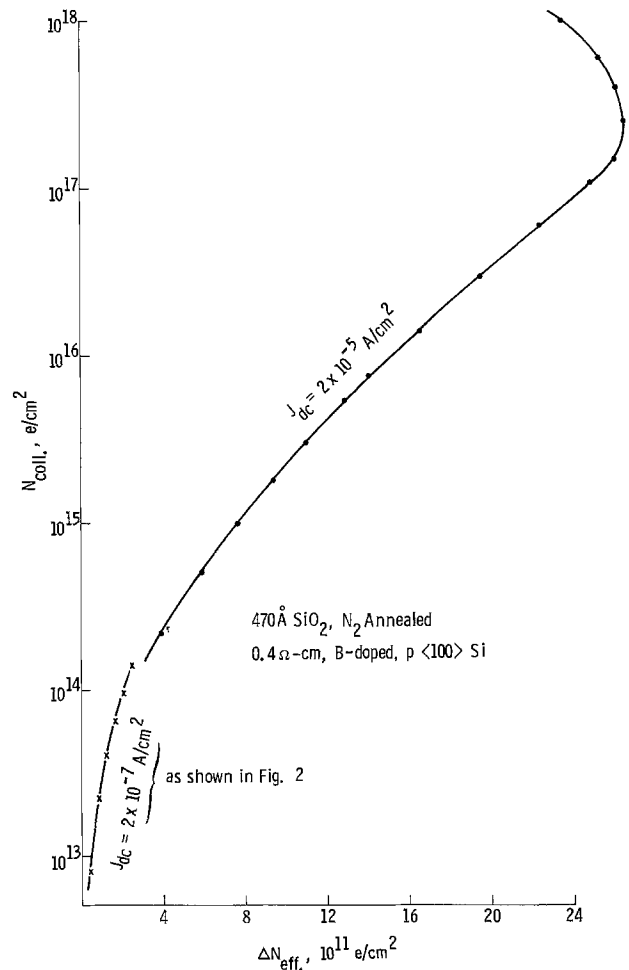


Fig. 3. Typical log-normal plot of MOS capacitor data

A simple experiment was performed to determine the stability of these trapped hot electrons in  $\text{SiO}_2$ . A typical sample of  $\text{N}_2$  annealed, dry thermal oxide  $\sim 570\text{\AA}$  thick had an initial  $N_{\text{eff}} = 0.78 \times 10^{11}$  positive charge/cm<sup>2</sup>. It was avalanche charged at  $J_{\text{dc}} = 2 \times 10^{-5}$  A/cm<sup>2</sup> for 1000 sec. As quickly as possible (in about 10 sec) the C-V characteristic was retraced and  $N_{\text{eff}}$  was found to be  $11.24 \times 10^{11}$  negative charges/cm<sup>2</sup>. Thereafter the C-V trace was redetermined at specified intervals with the capacitor allowed to float in between. The results are given in Fig. 4. Less than 10% of the charge was lost in 270,000 sec and 11 C-V trace sweeps ( $-5$  to  $+5\text{V}$ ) over that time. This sample was also subjected to  $\pm 5 \times 10^6$  V/cm fields for 100 sec with no significant detrapping. This is in agreement with Nicollian *et al.* (9) who also found their trapped electrons to be quite stable.

To assess the magnitude of the oxide field during avalanche charging, a series of samples with  $\text{N}_2$  annealed, dry thermal oxide was made with  $D_{\text{SiO}_2}$  varying from 250 to 1200 $\text{\AA}$ . Under standard conditions ( $f = 100$  kHz, 50% duty cycle) the applied voltage was determined to sustain avalanche in each sample at  $J_{\text{dc}} = 2 \times 10^{-6}$  A/cm<sup>2</sup>. These are shown in Fig. 5. By extrapolating the line to zero oxide thickness, the silicon is found to avalanche at 25.7V. Since the field in the silicon cannot exceed the avalanche field, any voltage above  $V_{\text{avalanche}}$  must be dropped in the oxide. The slope of the line yields  $E_{\text{ox}} = 1.7 \times 10^6$  V/cm at the start of avalanche. During long-term avalanching,  $E_{\text{ox}}$  would increase to only about  $3 \times 10^6$  V/cm because  $V_{\text{applied}}$  was continuously increased to keep  $J_{\text{dc}}$  constant. Therefore, detrapping of electrons is unlikely.

For some isolated samples fast surface-state densities were measured by the quasistatic C-V technique (16). Fast state density at  $V_{\text{FB}}$  was found to change little, sometimes decreasing, sometimes increasing for

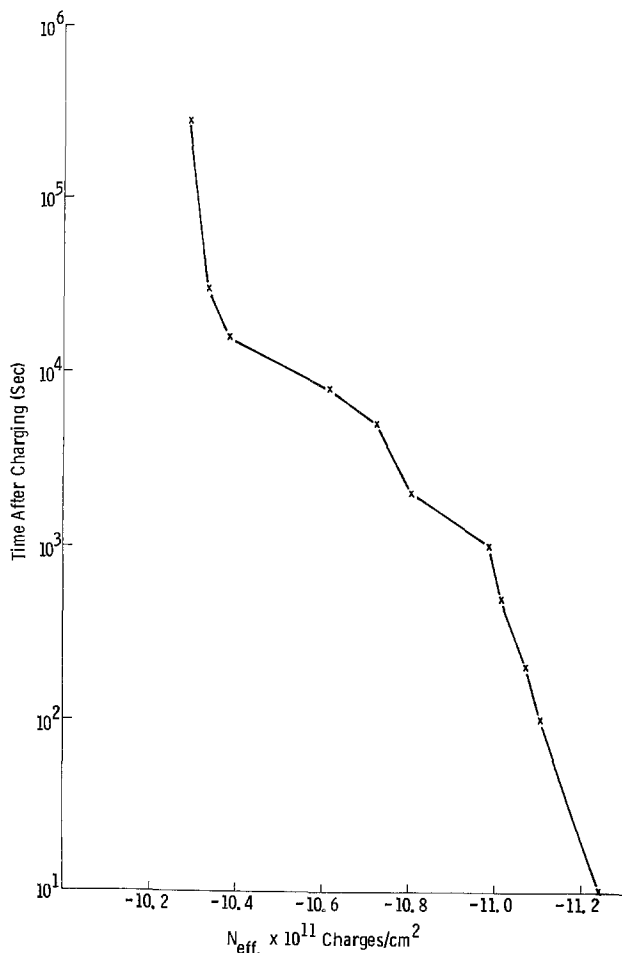


Fig. 4. Detrapping of charge-dry thermal  $\text{SiO}_2$ , floating

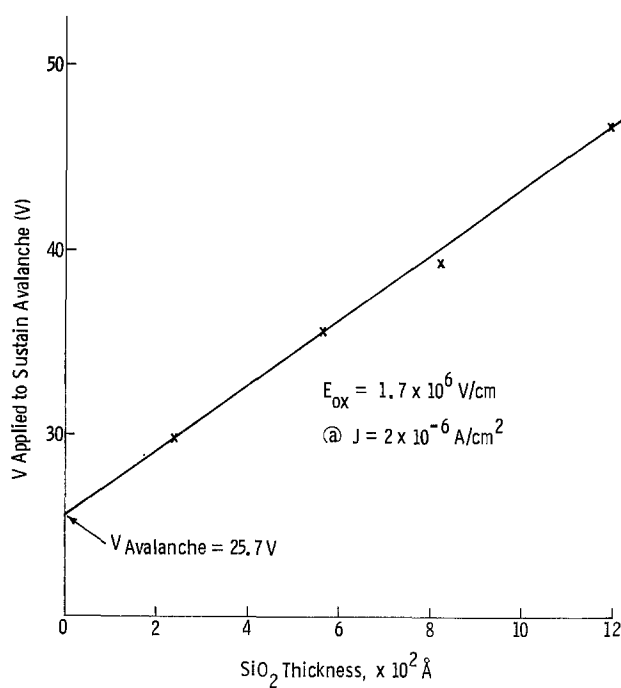


Fig. 5.  $V_{\text{applied}}$  required to sustain avalanche at  $J_{\text{dc}} = 2 \times 10^{-6}$  A/cm<sup>2</sup> as a function of oxide thickness.

$N_{\text{collected}} < 10^{16}$  e/cm<sup>2</sup>, but increased dramatically in the region where the C-V shifts slowed down and reversed direction. It is likely then that the reversal of  $N_{\text{eff}}$  is due to fast surface-state generation. This severely complicates the task of determining the true number of electrons trapped, and hence the use of  $\Delta N_{\text{eff}}$  for comparative purposes.

**Effects of oxide processing.**—To compare trapping in  $\text{SiO}_2$  formed by various typical processes, a series of samples was made having  $D_{\text{SiO}_2} \approx 500\text{\AA}$ , with no high-temperature annealing. Thermal  $\text{SiO}_2$  films were grown in dry  $\text{O}_2$ , dry  $\text{O}_2 + 3\%$  HCl, dry  $\text{O}_2 + 3\%$   $\text{H}_2\text{O}$ , and steam. CVD oxide films were deposited using the  $\text{SiH}_4 + \text{O}_2$  reaction at 800°C. BSG films containing  $\sim 5$  weight per cent (w/o)  $\text{B}_2\text{O}_3$  were deposited using the same reaction with diborane as the dopant source, also at 800°C. These samples were avalanche-charged at  $J_{\text{dc}} = 2 \times 10^{-5}$  A until the trapping saturated. Their behavior is compared in both Fig. 6 and Table I; the results are quite amazing.  $\text{SiO}_2$  was made to accumulate  $> 5 \times 10^{12}$  negative charges/cm<sup>2</sup>. Also there is a three order of magnitude difference in the rate of trapping between dry thermal oxide and B-doped CVD oxide. The data suggest that the degree of trapping depends somehow on the OH concentration incorporated in the oxide during forming. The hydroxyl content of the samples listed in Table I was determined from the 2.73  $\mu\text{m}$  absorption peak in the ir spectrum following

Table I. Trapping parameters of  $\text{SiO}_2$  formed by different processes on 0.4 ohm-cm, B-doped,  $p < 100 >$  Si

Oxide type	Initial $V_{\text{FB}}$ (V)	Effective saturated trapping density ( $\times 10^{11}$ /cm <sup>2</sup> )	Effective trapping efficiency ( $\times 10^{-8}$ ) <sup>(a)</sup>	Hydroxyl concentration (w/o)
Dry $\text{O}_2$	-1.28	17	5.7	Not detected
Dry $\text{O}_2 + 3\%$ HCl	-1.28	18	16	Not detected
Dry $\text{O}_2 + 3\%$ $\text{H}_2\text{O}$	-1.24	23	58	—
Steam	-1.51	39	180	0.10
CVD	-1.20	56	520	0.44
B-doped CVD	-0.80	57	5000	0.45

(a) When  $1 \times 10^{12}$  electrons/cm<sup>2</sup> have been trapped.

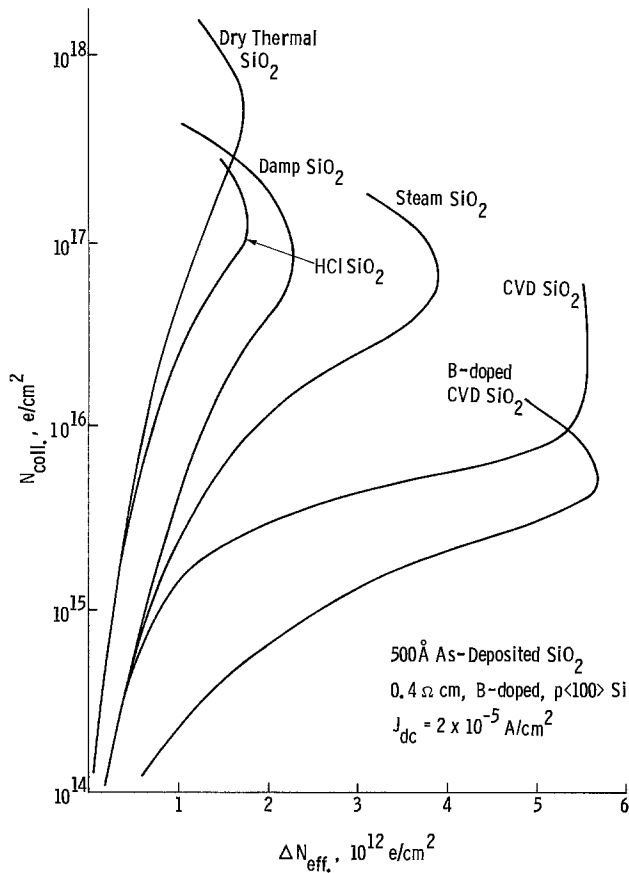
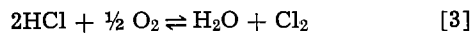


Fig. 6. Trapping behavior of SiO<sub>2</sub> formed by different processes; no high-temperature anneal.

the method of Hetherington and Jack (17). The values for the CVD oxides are well within the levels that can be expected (18). The 0.1 w/o OH measured for the steam oxide is slightly less than that reported by Burkhardt using radio tracer techniques (19). The hydroxyl concentration of the dry O<sub>2</sub> + 3% H<sub>2</sub>O sample was not measured. No OH in the dry O<sub>2</sub> + 3% HCl sample could be detected by our measurements although, by inference, some should be present in the oxide due to the fact that about 15% of HCl dissociates at 1000°C, according to the equilibrium reaction



so the oxidizing ambient contained about 0.5% H<sub>2</sub>O by calculation. There should be no detectable OH concentration in thermal SiO<sub>2</sub> grown in dry O<sub>2</sub> (18). The OH group has been reported (3, 4, 9) to be associated with an electron-capturing center in SiO<sub>2</sub>. It also appears from our current data that boron incorporated in SiO<sub>2</sub> is associated with a strong trapping center. This has been observed by Young for the case of B implanted in SiO<sub>2</sub> (20). If B in SiO<sub>2</sub> is associated with an electron trapping center, this may explain why dry thermal SiO<sub>2</sub> grown on heavily B-doped silicon traps more than SiO<sub>2</sub> grown on lightly B-doped silicon. Figure 7 shows comparisons for two samples processed under identical conditions (oxide grown in dry O<sub>2</sub> at 1000°C, annealed in dry N<sub>2</sub> at 1050°C for 15 min). Because of the favorable segregation coefficient, B is incorporated into the growing SiO<sub>2</sub> film. It is expected that a greater boron concentration in the oxide will result from growth on a more heavily B-doped substrate. The data shows that thermal oxide on 0.4 ohm-cm B-doped silicon traps more efficiently than thermal oxide on 2 ohm-cm, B-doped silicon.

Since the OH group in SiO<sub>2</sub> has been associated with an electron trapping center, and since OH can be expelled from SiO<sub>2</sub> by heating, it is instructive to determine the effects of high-temperature annealing. Ac-

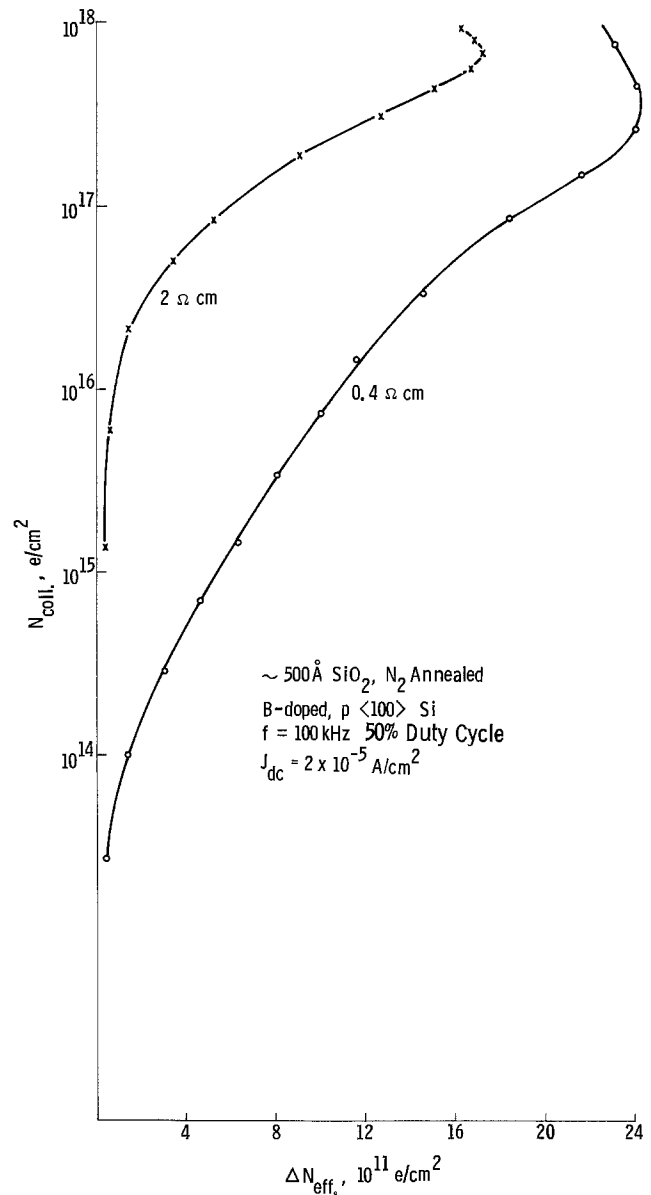


Fig. 7. Trapping in dry, thermal SiO<sub>2</sub> grown on Si of different B-doping levels.

cordingly, oxide samples from the same experiment as those reported in Fig. 6 and Table I were annealed in dry N<sub>2</sub> at 1050°C for 15 min. The results are reported in Table II. As divergent as the results were before annealing, after N<sub>2</sub> annealing all the SiO<sub>2</sub> films behaved quite similarly. The effect due to OH appears to have been leveled. Trapping decreased in the most efficient films, but increased in the least efficient films. This adverse effect of annealing on the least efficient films may be due to additional boron incorporation into the oxide during annealing. The BSG sample was not tested

Table II. Trapping parameters of SiO<sub>2</sub> after high-temperature N<sub>2</sub> annealing

Oxide type	Initial V <sub>FB</sub> (V)	Effective saturated trapping density (× 10 <sup>11</sup> /cm <sup>2</sup> )	Effective trapping efficiency (× 10 <sup>-6</sup> ) <sup>(a)</sup>
Dry O <sub>2</sub>	-0.91	25	59
Dry O <sub>2</sub> + 3% HCl	-0.85	22	24
Dry O <sub>2</sub> + 3% H <sub>2</sub> O	-0.86	22	29
Steam	-0.77	26	66
CVD	-0.65	24	29

<sup>(a)</sup> When 1 × 10<sup>12</sup> electrons/cm<sup>2</sup> have been trapped.

because boron diffusion occurred during annealing, and no C-V trace could be obtained.

Additional annealing experiments were done with 500Å oxide films grown in dry  $O_2 + 5\%$  HCl. These samples were annealed for up to 300 min in  $N_2$  and 960 min in Ar at 1050°C. These were then avalanche-charged and the results are shown in Fig. 8 and 9. Clearly annealing reduced trapping; after very long anneals these HCl-SiO<sub>2</sub> samples approached the behavior of dry  $O_2$  SiO<sub>2</sub>.

### Conclusions

1. Hot electron avalanche injection is an effective method to study how processing affects trapping in SiO<sub>2</sub> films on silicon.
2. Pure, dry, thermal SiO<sub>2</sub> was found to trap as many as  $2.6 \times 10^{12}$  electrons/cm<sup>2</sup>.
3. The trapping efficiency of SiO<sub>2</sub> films can vary by three orders of magnitude, depending on the formation method.
4. The trapping ability of SiO<sub>2</sub> varies with its OH concentration, which in turn is affected by the forming process. OH groups in SiO<sub>2</sub> are associated with electron trapping centers.
5. Boron in SiO<sub>2</sub> may also be associated with an electron trapping center.
6. High-temperature annealing in a moisture-free ambient can reduce trapping in SiO<sub>2</sub> due to OH groups.

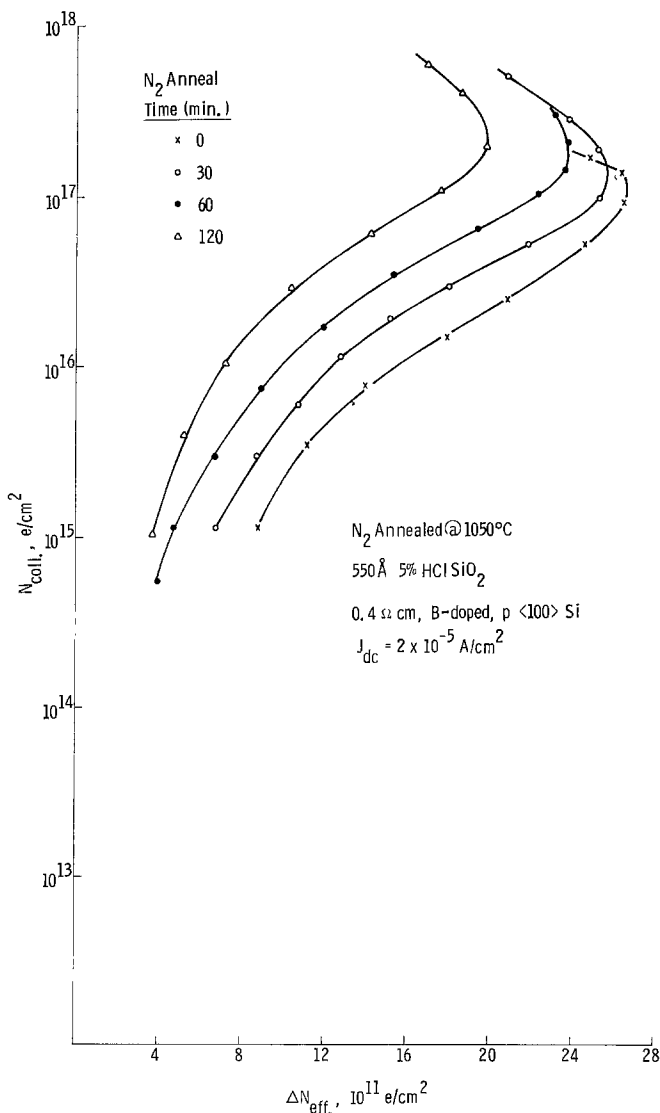


Fig. 8. Trapping in HCl oxide as a function of  $N_2$  anneal time at 1050°C.

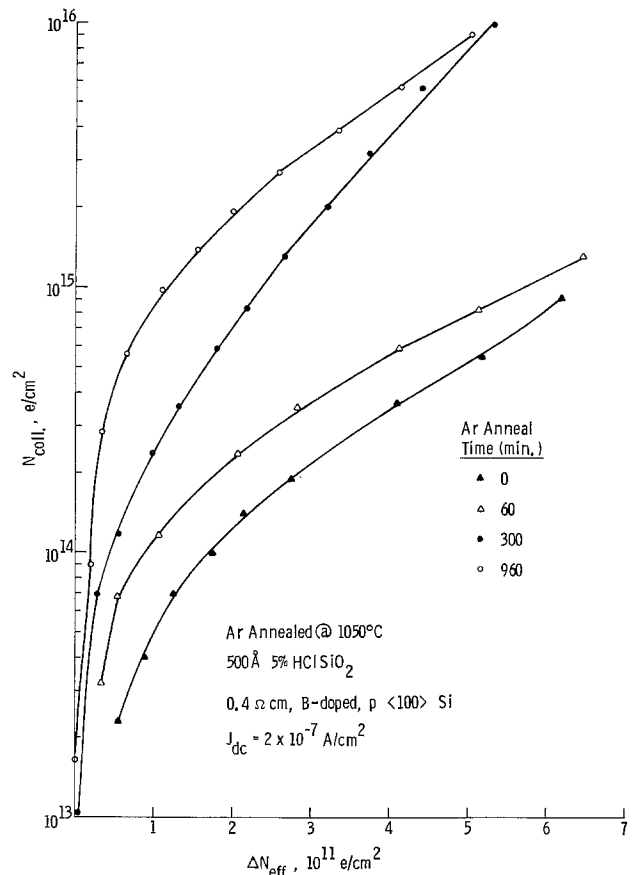


Fig. 9. Trapping in HCl oxide as a function of Ar anneal time at 1050°C.

### Acknowledgments

The author wishes to thank J. C. Hollis, F. J. Hoey, and E. J. Vishnesky for their assistance in sample preparation and electrical measurements, and W. A. Pliskin for ir measurements. Also thanks are due to E. L. Boyd, W. A. Pliskin, M. Shatzkes, and D. Young for many helpful discussions.

Manuscript submitted March 6, 1975; revised manuscript received Aug. 21, 1975.

Any discussion of this paper will appear in a Discussion Section to be published in the December 1976 JOURNAL. All discussions for the December 1976 Discussion Section should be submitted by Aug. 1, 1976.

Publication costs of this article were partially assisted by IBM Corporation.

### REFERENCES

1. A. Goetzberger and E. H. Nicollian, *Appl. Phys. Letters*, **9**, 444 (1966).
2. A. Goetzberger and E. H. Nicollian, *J. Appl. Phys.*, **38**, 4582 (1967).
3. E. H. Nicollian, A. Goetzberger, and C. N. Berglund, *Appl. Phys. Letters*, **15**, 174 (1969).
4. E. H. Nicollian and C. N. Berglund, *J. Appl. Phys.*, **41**, 3052 (1970).
5. J. F. Verwey, *Appl. Phys. Letters*, **15**, 270 (1969).
6. B. A. McDonald, *IEEE Trans. Electron Devices*, **ED-17**, 871 (1970).
7. H. Hara, Y. Okamoto and H. Ohnuma, *Japan. J. Appl. Phys.*, **9**, 1103 (1970).
8. D. Frohman-Bentchkowsky, "Digest of Technical Papers," IEEE Intern. Solid State Circuits Conf., p. 80, Lewis Winner, New York (1971).
9. E. H. Nicollian and C. N. Berglund, *J. Appl. Phys.*, **42**, 5654 (1971).
10. C. A. Neugebauer, J. F. Burgess, R. E. Joynson, and J. L. Mundy, *Thin Solid Films*, **13**, 5 (1972).
11. C. A. Neugebauer, J. F. Burgess, R. E. Joynson, and J. L. Mundy, *J. Appl. Phys.*, **43**, 5041 (1972).



12. J. Bonnet and L. Lassabatere, *Thin Solid Films*, **22**, 177 (1974).
13. R. Verkuil, Unpublished work.
14. N. J. Chou, *This Journal*, **118**, 601 (1971).
15. M. Kuhn and D. J. Silversmith, *ibid.*, **118**, 966 (1971).
16. M. Kuhn, *Solid State Electron.*, **13**, 863 (1970).
17. G. Hetherington and K. H. Jack, *Phys. Chem. Glasses*, **3**, 129 (1962).
18. W. A. Pliskin and H. S. Lehman, *This Journal*, **112**, 1013 (1965).
19. P. J. Burkhardt, *ibid.*, **114**, 196 (1967).
20. D. Young, Unpublished work.

## Ionic Conductivity of Doped Beta-Lead Fluoride

John H. Kennedy\* and Ronald C. Miles\*

*University of California, Department of Chemistry, Santa Barbara, California 93106*

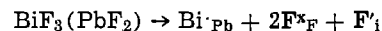
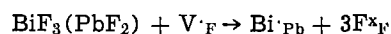
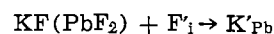
### ABSTRACT

The electrical conductivity of  $\beta$ -PbF<sub>2</sub> in single crystal and pressed pellets was measured by a-c bridge techniques. Aliovalent cation fluoride doping was used to elucidate the conductivity mechanism in the extrinsic region, 25°-180°C. Conduction was shown to be via fluoride ion vacancies. Potassium fluoride dopant increased the ionic conductivity of  $\beta$ -PbF<sub>2</sub> from  $5 \times 10^{-7}$  to  $1 \times 10^{-3}$  ohm<sup>-1</sup>-cm<sup>-1</sup> at room temperature. However, galvanic cells utilizing the higher conductivity of the doped material failed due to formation of a passivation layer of pure  $\alpha$ -PbF<sub>2</sub> at the anode/electrolyte interface.

Some of the properties of lead fluoride have been known since Tubandt studied the transport number in 1921 (1). However, the solid-state ionic defect formation and conduction mechanisms have only been recently investigated. Lead fluoride occurs in two phases which exist at room temperature. The  $\alpha$ -phase has an orthorhombic unit cell structure and is similar to the lead halides, PbCl<sub>2</sub> and PbBr<sub>2</sub>. Beta-lead fluoride is cubic like CdF<sub>2</sub> and CaF<sub>2</sub>, as are all transition metal fluorides whose cation-to-anion radius ratio is greater than or equal to 0.73. In a previously published part of our study of polycrystalline material we verified Tubandt's finding that at least the  $\beta$ -PbF<sub>2</sub> fluorite structure conducted by anionic migration, and that the  $\alpha$ -PbF<sub>2</sub> structure probably exhibited a similar mechanism (2). We also confirmed Sauka's findings that the  $\alpha$ -phase was metastable at room temperature and atmospheric pressure, while the  $\beta$ -phase is apparently stable up to the melting point. The conductivity of lead fluoride at high temperature near the melting point (322°C) was investigated by Derrington and O'Keeffe (3). They found unusually high values which they attributed to "dynamic ion disorder" of the fluoride sublattice. At lower temperatures, Schoonman *et al.* found two Arrhenius slopes and a knee where they met at about 200°C in single crystals of  $\beta$ -PbF<sub>2</sub> (4). Both Derrington and O'Keeffe (3) and Schoonman *et al.* (4) ascribed the high temperature conductivity of  $\beta$ -PbF<sub>2</sub> to fluoride interstitial ions which were formed by a Frenkel mechanism. The other cubic fluorides are also known to form interstitial defects in that manner (5-7). However, Schoonman stated that the knee he observed at 200°C was most likely a shift from interstitial movement to vacancy movement at lower temperatures, rather than being the usual transition from an intrinsic to extrinsic region. This was based on the fact that the upper slope was too low to be a heat of formation, and the trace impurities present should have generated fluoride vacancies.

In order to understand the low temperature conduction mechanism of  $\beta$ -PbF<sub>2</sub>, aliovalent impurities were doped into the  $\beta$ -PbF<sub>2</sub> lattice. The concentration of defects will change with doping in order to maintain charge neutrality. As the following equations show, each KF introduced into  $\beta$ -PbF<sub>2</sub> may create a

fluoride ion vacancy or consume an existing interstitial, while each trivalent cation fluoride such as BiF<sub>3</sub> can consume an existing vacancy or create an interstitial



A change in the conductivity of  $\beta$ -PbF<sub>2</sub> upon doping with known impurities will determine whether the material is conducting via vacancies or interstitial ions.

### Experimental

*Aliovalent doping.*—Orthorhombic  $\alpha$ -PbF<sub>2</sub> (ROC/RIC 99.999% pure) was used without further purification. Aliovalent cation fluorides were doped into  $\beta$ -PbF<sub>2</sub> by diffusion and by making use of the  $\alpha$ - to  $\beta$ -phase transition. A melt of the mixtures was not used in this study since decomposition of lead fluoride was noted after melting. Also, melting alone does not insure that the dopant has moved into the lead fluoride lattice. Instead, mixtures were heated beyond the phase transition temperature of about 350°C. It was anticipated that during the phase transition the impurities would be incorporated into the new crystal lattice.

The mixtures were made by successive dilution and mixed overnight on a ball mill. They were then loaded into vials and sealed either under nitrogen or vacuum. Each vial was heated to about 500°C. When x-ray analysis showed that the lead fluoride had been converted to the cubic form, pellets were pressed at about 50,000 psi in a Perkin-Elmer evacuable KBr die. This caused some reconversion to the orthorhombic form so that the pellets had to be reheated in sealed vials with PbF<sub>2</sub> packing. No impurity lines or movement of peaks which would indicate a change in lattice spacing were observed in the x-ray spectra.

*Conductivity measurements.*—The experimental procedures used have been reported previously (2). It has since been found that the electrodes which gave the least a-c frequency dependence were those applied by vacuum deposition of lead metal onto surfaces precleaned by glow-discharge followed by an application of graphite (Aquadag) to protect the thin

\* Electrochemical Society Active Member.

Key words: aliovalent doping, fluoride ion conductivity, galvanic cells, lead fluoride, solid electrolyte.

film of lead. Single crystals were measured with the Aquadag alone as the electrode material due to their sensitivity to thermal shock. Also the GRC-1650A impedance bridge previously used was modified by addition of an external, parallel variable capacitor which greatly improved the detector nulls. The series equivalent of the cell resistance could be found by (8, 9)

$$R_s = R_B / [1 + (\omega R_B C_B)^2]$$

where  $R_s$  = cell series resistance,  $R_B$  = bridge resistance,  $C_B$  = bridge capacitance, and  $\omega$  = angular velocity.

Only in the case of the single crystals where painted graphite alone formed the electrodes was the  $\omega R_B C_B$  term significant. As previously described, the frequency-dependent terms were separated by use of empirical functions.

**Single crystals.**—Single crystals of pure and doped  $\beta$ -PbF<sub>2</sub> were grown by Stockbarger's technique of pulling from the melt as described by Jones (10). It was necessary to premelt the starting material under a flow of HF to eliminate impurities which would have otherwise caused decomposition. Two single crystals were grown, one of undoped PbF<sub>2</sub> and the other of 1 mole per cent (m/o) KF-doped PbF<sub>2</sub>. Both crystals were extremely brittle and for this reason temperature studies were somewhat limited.

### Results

**Total conductivity.**—NaF, KF, and BiF<sub>3</sub> were used to dope impurity cations into  $\beta$ -PbF<sub>2</sub>. The resulting changes in electrical conductivity determined by the a-c bridge can be seen in Fig. 1. Both NaF and KF increased the conductivity while BiF<sub>3</sub> decreased the conductivity. The slopes of the Arrhenius plots are listed in Table I in terms of a heat of activation. The conductivities and Arrhenius slopes of the NaF-

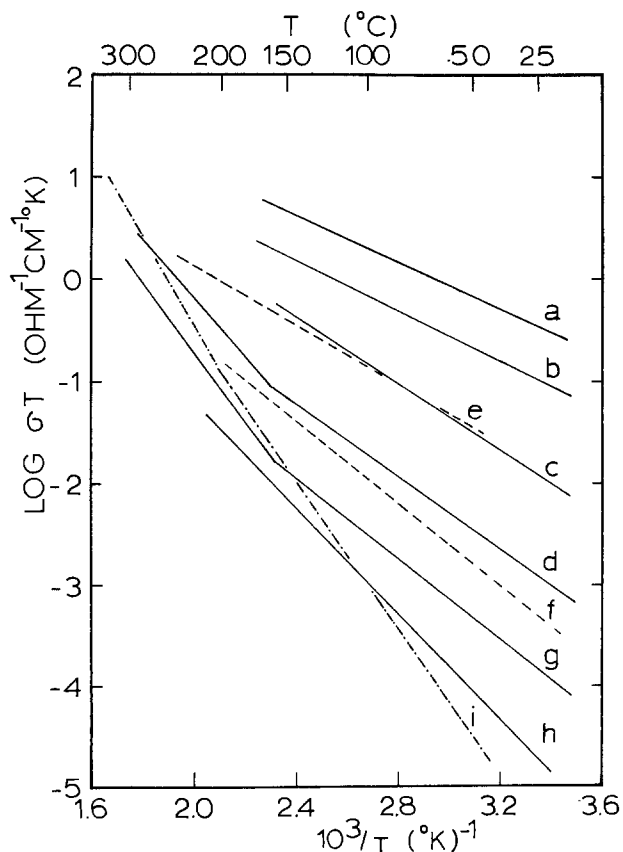


Fig. 1. Ionic conductivity of doped and undoped  $\beta$ -PbF<sub>2</sub>. KF doping: (a) 2 m/o, (b) 1 m/o, (c) 0.5 m/o, (d) 0.1 m/o. NaF doping: (e) 1.5 m/o, (f) 0.5 m/o. Undoped  $\beta$ -PbF<sub>2</sub>: (g) 99.999%  $\beta$ -PbF<sub>2</sub>, (i) results from Ref. (4). BiF<sub>3</sub> doping: (h) 1 m/o.

doped samples were lower and steeper, respectively, than those of the KF-doped samples of the same doping concentration. However both appeared to have activation energies that approached 0.21 eV as the doping was increased.

**Electronic conductivity.**—Wagner polarization cells were made from samples of pure as well as NaF- and BiF<sub>3</sub>-doped samples of  $\beta$ -PbF<sub>2</sub>. The cells were constructed by vacuum deposition of a thin film of lead on one side of a pressed pellet of  $\beta$ -PbF<sub>2</sub> followed by painting the other side with colloidal graphite (Aquadag). Polarization curves were taken at room temperature and under vacuum. An equation relating the observed current to the electronic conductivity and some results for undoped lead fluoride at 150°C were given previously (2). The NaF-doped samples gave currents which were below the detection limit of the apparatus which was about  $1 \times 10^{-10}$  ohm<sup>-1</sup> cm<sup>-1</sup>. New data for undoped cubic lead fluoride at 25°C are shown in Fig. 2 and were ambiguous as to whether the current was carried by electrons or holes. However these new lower conduction values for purer lead fluoride than used previously are in reasonable agreement with those observed by Schoonman (11). The electronic conductivity for BiF<sub>3</sub>-doped  $\beta$ -PbF<sub>2</sub> is shown in Fig. 3 and indicates electron carriers. Except for the BiF<sub>3</sub>-doped material, the electronic conductivity measured was far below the total electrical conductivity observed. At room temperature, the conductivity of 1 m/o BiF<sub>3</sub> in  $\beta$ -PbF<sub>2</sub> was  $6.4 \times 10^{-8}$  ohm<sup>-1</sup> cm<sup>-1</sup>, while the electronic conductivity was  $4.0 \times 10^{-8}$  ohm<sup>-1</sup> cm<sup>-1</sup>. Since the electronic

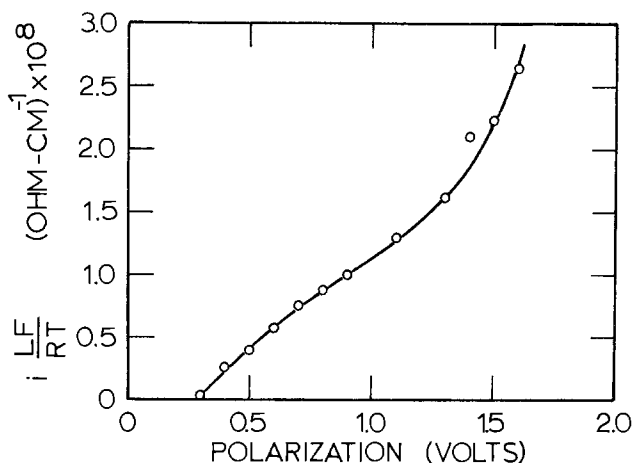


Fig. 2. Electronic current of  $\beta$ -PbF<sub>2</sub> pressed pellet cell vs. applied voltage at 25°C.

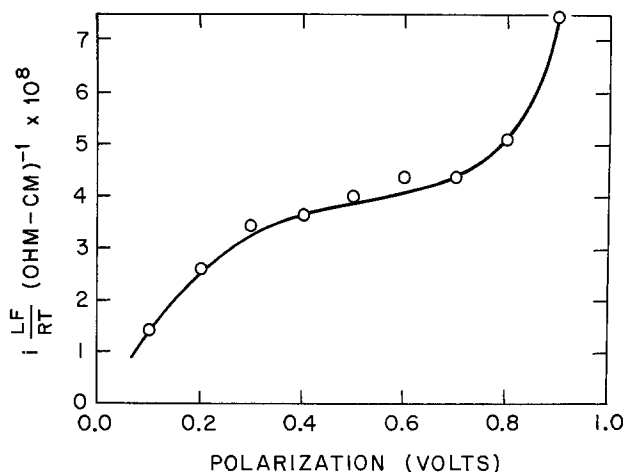


Fig. 3. Electronic current of 1 m/o BiF<sub>3</sub>-doped  $\beta$ -PbF<sub>2</sub> pressed pellet cell vs. applied voltage at 25°C.

contribution to the total conductivity was so large, the Arrhenius plot for the BiF<sub>3</sub>-doped  $\beta$ -PbF<sub>2</sub> was not considered in the elucidation of the ionic conduction mechanism.

### Discussion

The increased conductivity observed when  $\beta$ -PbF<sub>2</sub> was doped with monovalent cation fluorides was due to an increase in ionic conductivity since the electronic conductivity was observed to decline. The extrinsic semiconductor nature of  $\beta$ -PbF<sub>2</sub> which was apparent when BiF<sub>3</sub> was doped into the lattice has been observed before by Chan and Shields (12) and also by Arkhangel'skaya *et al.* (13).

The fact that the ionic conductivity of  $\beta$ -PbF<sub>2</sub> increased upon doping with KF and NaF, while it decreased when BiF<sub>3</sub> was introduced, indicated that the ionic current was carried by mobile, fluoride ion vacancies when the temperature was below about 180°C. Above this transition point the steeper slope may represent an intrinsic region where the conducting defects ( $V_F$ ) are being formed in significant number by thermal generation, or it may represent a shift to a new conduction mechanism, *i.e.*, fluoride interstitials as suggested by Schoonman *et al.* and Derrington and O'Keefe. If both slopes are extrinsic, however, one must assume nonequilibrium between vacancies and interstitials.

If the knee in the Arrhenius slope represented a transition from an extrinsic to an intrinsic region as the temperature increased, then the activation energy of the extrinsic lower slope was  $\Delta H_m$ , the heat of movement, while the intrinsic upper slope was  $\Delta H_m + \Delta H_f/p$ , the sum of the heat of movement and of formation. The constant,  $p$ , represents the number of defects formed, and would be 2 for a Frenkel or 3 for a Schottky mechanism. The values for these two slopes were

$$\text{lowest slope} = \Delta H_m = 0.21 \text{ eV}$$

$$\text{highest slope} = \Delta H_m + \Delta H_f/p = 0.66 \text{ eV}$$

The value for  $\Delta H_f$  would be 0.90 eV (Frenkel) or 1.35 eV (Schottky). Both of these values are rather low and cast doubt on the extrinsic-intrinsic regions hypothesis. Based on the melting point of PbF<sub>2</sub> (822°C) an estimate for  $\Delta H_f$  (Frenkel) is 2.72 eV (4).

Our doping studies show that fluoride ion vacancies are the conductive species, and vacancies can be formed by either a Schottky or Frenkel mechanism. However, studies at higher temperatures (3, 4) have indicated that fluoride ion interstitials are the predominant conductive species. Since interstitials are formed by a Frenkel mechanism and not the normal Schottky mechanism (anti-Schottky defect requires the formation of lead interstitials in addition), it is logical to assume that a Frenkel mechanism prevails at all temperatures with vacancies being the predominant conductive species at low temperature (<200°C) and with interstitials becoming predominant at high temperatures because their heat of movement is higher. However, the possibility of both Schottky and Frenkel mechanisms existing in PbF<sub>2</sub> cannot be ruled out.

It should be noted that a transition from vacancy to interstitial conduction would allow Arrhenius plots of doped samples to cross the undoped line. Potassium fluoride doping would increase the concentration of vacancies and enhance vacancy conduction at low temperature but would decrease the concentration of interstitials and therefore decrease conductivity at high temperature. A transition from extrinsic to intrinsic would not predict such a crossing. Figure 1 shows that the doped lines may cross the undoped lines in the 200°-300°C region. For more data concerning crossing see Ref. (15).

It is dangerous to try and fit results for polycrystalline materials into mathematical models designed for purely bulk effects. Therefore, the doping results were

checked by growing a single crystal of 1 m/o KF-doped  $\beta$ -PbF<sub>2</sub>. It was possible that there might be several pathways by which the conducting species,  $V_F$  and possibly  $F_i$  ions, were moving which would complicate the heats of movement. This effect had been described by Mizuta and Yanagida (14) in the case of CaF<sub>2</sub>, which also conducts by fluoride ion vacancies. They found that the Arrhenius activation energy depended on the history or degree of sintering of the polycrystalline material, and that there were three extrinsic heats of movement: bulk, grain boundary, and grain surface. However, the single crystal of doped PbF<sub>2</sub> gave essentially the same values of conductivity and Arrhenius slope as the polycrystalline material (Table I). Therefore, in this case, the ionic transport mechanism was not dependent on the polycrystalline nature of the material.

A method for calculating the concentration of defects in the undoped material assuming it is extrinsic in nature can be developed from doping studies using the conventional equation

$$\sigma = ne\mu$$

For the undoped material containing an extrinsic concentration of defects,  $n_0$

$$\sigma_0 = n_0e\mu$$

and for the doped material

$$\sigma = (n_0 + n_d)e\mu$$

Since extrinsic conductivity is assumed, the addition of defects by doping ( $n_d$ ) will not affect those present in the undoped material ( $n_0$ ). If we assume for the moment that mobility does not change with doping level then

$$\frac{\sigma}{\sigma_0} = 1 + \frac{n_d}{n_0}$$

A plot of  $\sigma/\sigma_0$  vs.  $n_d$  should be a straight line with a slope of  $1/n_0$ . This plot is shown in Fig. 4. Straight lines were not obtained, and the upward curvature indicated higher conductivities than predicted at high doping levels. If one reviews the activation energies given in Table I it can be seen that the activation energy decreased as alkali metal concentration increased. Thus, the basic assumption which is made in most doping studies that the mobility does not change with doping level was not true in this case. If we take a more general approach, namely

$$\sigma T = \sigma^0 e^{-\Delta H_m/kT}$$

where the preexponential term,  $\sigma^0$ , is directly proportional to the concentration of conductive species, then

$$\sigma^0_0 = kn_0$$

and

$$\sigma^0 = k(n_0 + n_d)$$

Again a ratio of conductivities can be used to give

Table I. Experimental heats of activation

Material	$\Delta H$ (eV)
$\beta$ -PbF <sub>2</sub> , undoped	0.39-0.50, 0.66 <sup>(a)</sup>
$\beta$ -PbF <sub>2</sub> , undoped single crystal	0.60 (25°-150°C)
1 m/o BiF <sub>3</sub>	0.53
0.5 m/o NaF	0.39
1.5 m/o NaF	0.22
0.1 m/o KF	0.33, 0.51 <sup>(a)</sup>
0.5 m/o KF	0.31
1.0 m/o KF	0.22
1.0 m/o KF, single crystal	~0.2 <sup>(b)</sup> (25°-90°C)
2.0 m/o KF	0.21

<sup>(a)</sup> Upper slope at high temperature (>180°C).

<sup>(b)</sup> Slope was frequency dependent.

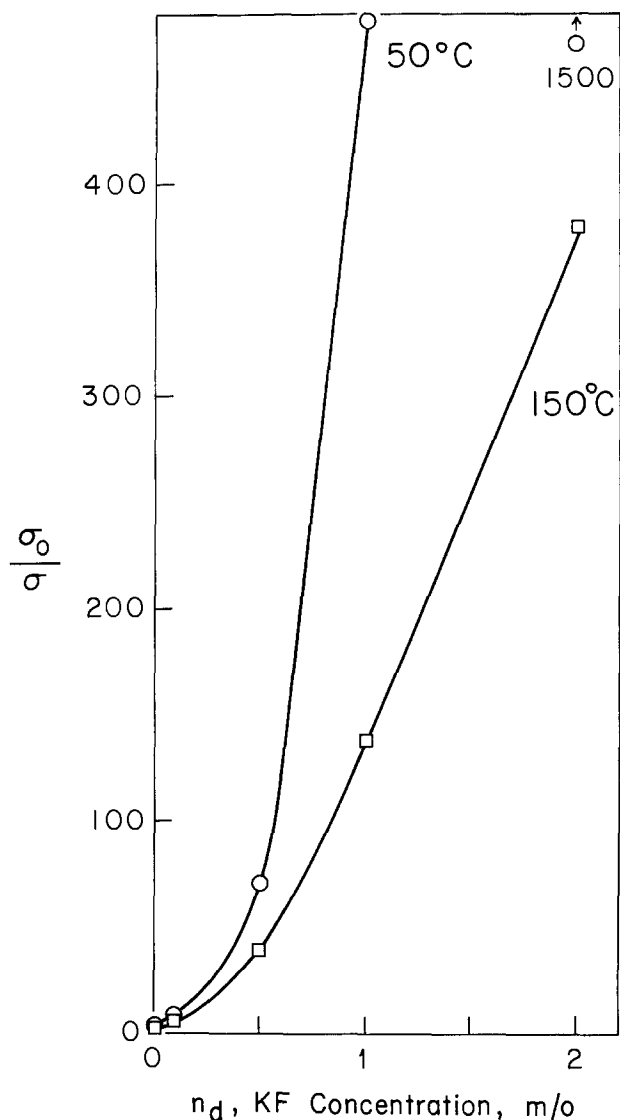


Fig. 4. Conductivity as a function of KF doping level.  $\circ$  50°C,  $\square$  150°C.

$$\frac{\sigma^{\circ}}{\sigma_0} = 1 + \frac{n_d}{n_0}$$

In this case the extrapolated infinite temperature values are used and a plot is shown in Fig. 5. A value of 0.5 m/o for the concentration of extrinsic defects in undoped lead fluoride was obtained from the slope. However, the conductivity was considerably lower than with 0.5 m/o KF doping because the heat of movement was higher for undoped  $\text{PbF}_2$  than for KF-doped  $\text{PbF}_2$ .

A plot of  $\Delta H_m$  as a function of doping level is shown in Fig. 6. It appears that the heat of movement for vacancies can vary from above 0.5 eV in nominally pure  $\text{PbF}_2$  to 0.21 eV in highly doped  $\text{PbF}_2$ . The sensitivity of the activation energy to impurity level explains why several different values have been observed by various investigators for nominally pure  $\beta\text{-PbF}_2$  from below 0.5 eV (2) to 0.7 eV (4).

A change in the extrinsic heat of movement has not been previously reported for analogous solid electrolytes. This may be the result of the high doping levels used in this study or may be specific to  $\text{PbF}_2$ . A concentration of 1 m/o KF is large enough to place a potassium ion within several cell lattice constants of any other ion in the lattice. The difference then between the KF and NaF doping experiments may be the result of different charge densities between sodium and potassium which would affect the energy

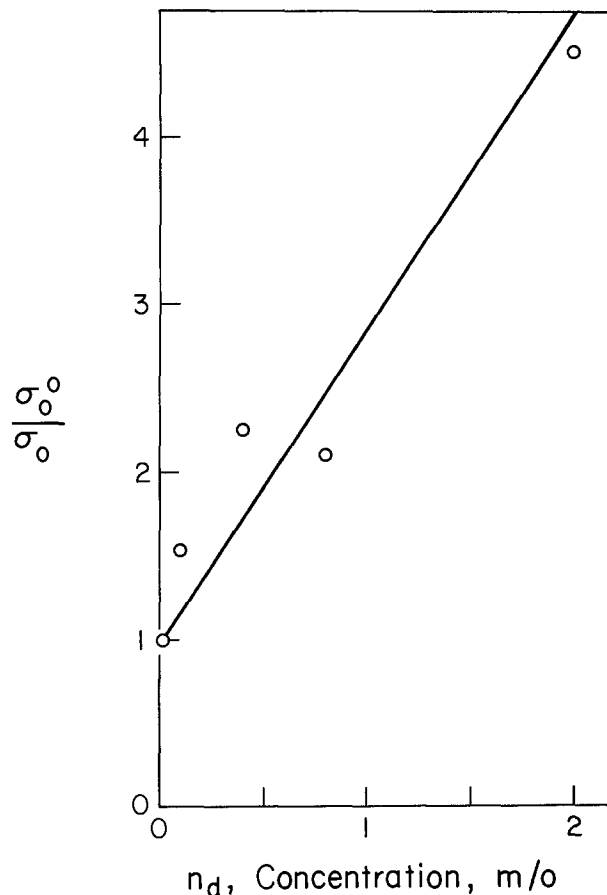


Fig. 5. Preexponential factor as a function of KF doping level

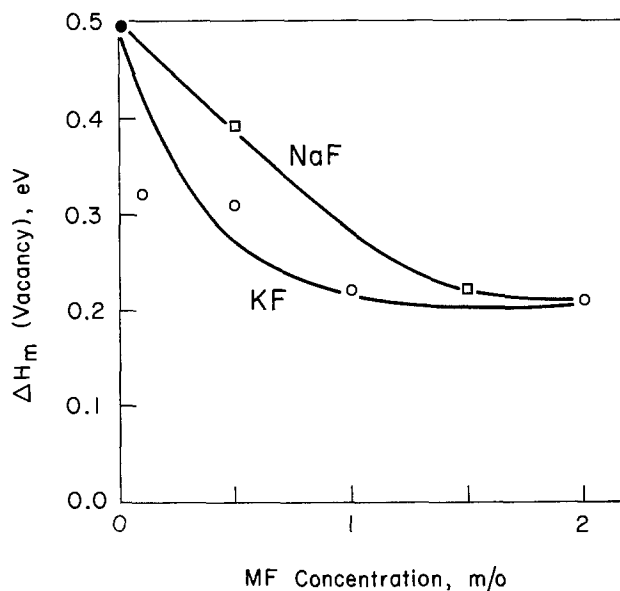


Fig. 6. Heat of motion of vacancy as a function of doping level.  $\circ$  KF,  $\square$  NaF,  $\bullet$  undoped  $\text{PbF}_2$ .

barriers the fluoride ion vacancy experiences at these high doping levels as it migrates.

Recently a paper was published describing similar experiments with lead fluoride (15). Most of the results are in general agreement with those presented here, however some differences were observed. Doping with  $\text{YF}_3$  increased conductivity while our results with  $\text{BiF}_3$  showed a decrease in conductivity. This difference between the  $\text{MF}_3$  compounds should be studied in more detail. Liang and Joshi also described a linear increase in conductivity with doping up to 1 m/o. We have observed more curvature especially

at the higher doping levels (as high as 2 m/o). Finally, we have observed a gradual decrease in activation with increased doping level while Liang and Joshi observed only the high slope for undoped samples and the low slope for doped samples. We agree on both the high and low slope limiting values, but interpretation depends somewhat on whether or not intermediate values are observed. Additional studies should be undertaken to examine these differences and to design experiments which will discriminate between various conductivity mechanisms which have been postulated.

**Galvanic cells.**—Potassium fluoride-doped  $\beta$ -PbF<sub>2</sub> was used as an electrolyte in galvanic cells to test its high conductivity. Solid-state cells were constructed with CuF<sub>2</sub> and AgF as cathode materials. The anticipated open-circuit voltages of 0.70 and 1.30V were achieved, but the cell potentials fell rapidly when placed under load and current drawn.

In order to examine the electrolytic properties exclusive of the galvanic cell configuration, a Pb/PbF<sub>2</sub>/Pb cell was constructed by applying a thin film of lead to serve as a cathode on a pressed pellet (2 m/o KF doped-PbF<sub>2</sub>), and pressing a plate of lead metal against the opposite side of the pellet. In this cell, lead metal would be deposited at the cathode and lead fluoride would be formed at the anode. However, the lead fluoride formed would be pure and would not show the high conductivity of the doped material unless KF were able to diffuse into the newly formed layer. The formation of pure PbF<sub>2</sub> would be similar to the formation of a passivation layer and explain the poor performance of the galvanic cells.

Two Pb/PbF<sub>2</sub>/Pb cells were run, one at 100°C and the other at 250°C. They yielded currents of several hundred microamperes and about 1 mA, respectively, at an applied voltage of one volt. After one day, the current of the cell at 250°C was essentially zero. The cell at 100°C took several more days until the current decayed to near zero. About 9 coulombs of charge passed through the higher temperature cell while about 2 coulombs passed through the lower temperature cell.

Inspection of both lead plate anodes under a microscope revealed deposits, roughly circular in shape. In some places, the deposits had coalesced, but nowhere were they any higher than 40 $\mu$ . There were no corresponding pits in the adjacent pellet surfaces. X-ray analysis of the deposits showed the presence of  $\alpha$ -PbF<sub>2</sub> and Pb<sub>2</sub>O<sub>2</sub> but no  $\beta$ -PbF<sub>2</sub> (Table II). Apparently deposition occurred at a number of preferred active sites and ceased when they were consumed. Possibly these sites were merely high pressure contact points between the lead plate and the pressed pellet of doped electrolyte. It has been shown previously that  $\beta$ -PbF<sub>2</sub> converts to  $\alpha$ -PbF<sub>2</sub> when under pressure (2). This could explain why the lead fluoride was formed in the  $\alpha$ - rather than  $\beta$ -form. Thus, even though doped  $\beta$ -PbF<sub>2</sub> has quite high ionic conductivity its use may not be possible in lead anode galvanic cells because the anode product will be low conductivity pure  $\alpha$ -PbF<sub>2</sub>.

### Conclusion

It has been shown that  $\beta$ -PbF<sub>2</sub> conducts by fluoride ion vacancy movement when at temperatures below 180°C. Furthermore, the conductivity can be considerably enhanced by doping with monovalent cation fluorides. The presence of monovalent cations also appears to decrease the heat of movement for the

Table II. X-ray data of lead anode surface

$2\theta$ , degrees	$d$ , A	$I$	$I/I_0$ (Pb)	$I/I_0$ ( $\alpha$ -PbF <sub>2</sub> )	$I/I_0$ (Pb <sub>2</sub> O <sub>2</sub> )	Assignment
26.83	3.320	56			100	Pb <sub>2</sub> O <sub>2</sub> (3.33)
27.10	3.288	10		100		$\alpha$ -PbF <sub>2</sub> (3.290)
27.70	3.218	3		30		$\alpha$ -PbF <sub>2</sub> (3.222)
29.12	3.064	7			13	Pb <sub>2</sub> O <sub>2</sub> (3.07)
29.20	3.056	7		70		$\alpha$ -PbF <sub>2</sub> (3.058)
31.00	2.882	43			78	Pb <sub>2</sub> O <sub>2</sub> (2.88)
31.26	2.859	58	100			Pb (2.855)
36.28	2.474	20	35			Pb (2.475)
38.15	2.357	8		80		$\alpha$ -PbF <sub>2</sub> (2.364)
42.31	2.134	6		60		$\alpha$ -PbF <sub>2</sub> (2.135)
44.40	2.039	16			29	Pb <sub>2</sub> O <sub>2</sub> (2.03,2.04)

Comments: Two peaks from Pb<sub>2</sub>O<sub>2</sub> were missing,  $d = 2.86$  ( $I/I_0 = 60$ ) and  $d = 2.70$  ( $I/I_0 = 70$ ). The first was probably masked by the lead at  $d = 2.855$ .  $\alpha$ -PbF<sub>2</sub> was also missing one peak,  $d = 2.475$  ( $I/I_0 = 26$ ). Undoubtedly it was masked by the lead peak at  $d = 2.475$ . Only one x-ray out of three taken showed a very small peak at  $d = 3.425$  which could be attributed to  $\beta$ -PbF<sub>2</sub> at  $d = 3.428$ . X-ray diffraction of a lead plate after being heated at 250°C for several days showed that none of the lead oxide peaks from this spectrum corresponded to the x-ray diffraction pattern shown above.

vacancies. Its usefulness in a solid-state cell, however, is possibly limited due to the formation of an anode passivation layer consisting of low conductivity pure  $\alpha$ -PbF<sub>2</sub>.

### Acknowledgment

This paper was taken in part from the Ph.D. dissertation of RCM, University of California, Santa Barbara, 1974. The authors acknowledge financial support of this project by the National Science Foundation, Grant No. GH-37144. The authors also thank Mr. Neil Nighman for his help in growing single crystals of lead fluoride. One of the authors (JHK) thanks the Japan Society for the Promotion of Science for a visiting professorship grant and Professors T. Takahashi and O. Yamamoto for helpful discussion.

Manuscript submitted March 4, 1975; revised manuscript received July 14, 1975.

Any discussion of this paper will appear in a Discussion Section to be published in the December 1976 JOURNAL. All discussions for the December 1976 Discussion Section should be submitted by Aug. 1, 1976.

Publication costs of this article were partially assisted by the University of California.

### REFERENCES

1. C. Tubandt, *Z. Anorg. Chem.*, **115**, 105 (1921).
2. J. H. Kennedy, R. Miles, and J. Hunter, *This Journal*, **120**, 1441 (1973).
3. C. E. Derrington and M. O'Keeffe, *Nature, Phys. Sci.*, **246**, 44 (1973).
4. J. Schoonman, G. J. Dirksen, and G. Blasse, *J. Solid State Chem.*, **7**, 245 (1973).
5. R. W. Ure, *J. Chem. Phys.*, **26**, 1363 (1957).
6. E. Barsis and A. Taylor, *ibid.*, **45**, 1154 (1963).
7. Y. T. Tau and D. Kramp, *ibid.*, **53**, 3691 (1970).
8. D. O. Raleigh, *J. Phys. Chem. Solids*, **29**, 261 (1968).
9. J. Braunstein and G. D. Robbins, *J. Chem. Ed.*, **48**, 52 (1971).
10. D. A. Jones, *Proc. Phys. Soc.*, **65B**, 165 (1955).
11. J. Schoonman, Private communication.
12. K. K. Chan and L. Shields, *J. Phys. C. (Solid State Phys.)*, **2**, 1978 (1969).
13. V. A. Arkhangel'skaya, V. G. Erofeichev, and M. N. Kiseleva, *Soviet Physics, Solid State*, **14**, 2953 (1973).
14. S. Mizuta and H. Yanagida, *Denki Kagaku*, **40**, 787 (1972).
15. C. C. Liang and A. V. Joshi, *This Journal*, **122**, 466 (1975).

# The Preparation and Properties of (111)Si Films Grown on Sapphire by the SiH<sub>4</sub>-H<sub>2</sub> Process

H. M. Manasevit,\* F. M. Erdmann, and A. C. Thorsen<sup>1</sup>

Rockwell International, Electronics Research Division, Anaheim, California 92803

## ABSTRACT

An experimental study of the effects of various parameters on the properties of (111) and (100)Si films grown on sapphire ( $\alpha$ -Al<sub>2</sub>O<sub>3</sub>) by the SiH<sub>4</sub> pyrolysis CVD method has been carried out. The following were examined: autodoping, growth temperature and growth rate, As-doped n-type films, p-type films doped with B, properties as a function of film thickness, and the effect of reactor configuration. It was determined that at growth rates of  $\sim 2$ -6  $\mu\text{m}/\text{min}$  in a vertical reactor n-type (111)Si films grown at temperatures of 1050°-1100°C on Al<sub>2</sub>O<sub>3</sub> substrates oriented near the (11 $\bar{2}$ 0) plane are electrically superior to those grown on (01 $\bar{1}$ 2)Al<sub>2</sub>O<sub>3</sub> and (10 $\bar{1}$ 4)Al<sub>2</sub>O<sub>3</sub> over the temperature range 950°-1100°C. Films with electron mobilities as high as 600-700 cm<sup>2</sup>/V-sec for carrier concentrations of 10<sup>16</sup>-10<sup>17</sup> cm<sup>-3</sup> were obtained. P-type Si films grown using B<sub>2</sub>H<sub>6</sub> as the dopant source were also electrically better on  $\sim(11\bar{2}0)$ Al<sub>2</sub>O<sub>3</sub> [(111)Si-growth] than on (01 $\bar{1}$ 2)Al<sub>2</sub>O<sub>3</sub> [(100)Si growth], Hall mobilities being  $\sim 2$ -3 times larger for hole concentrations 10<sup>16</sup>-10<sup>17</sup> cm<sup>-3</sup>. A comparison of film properties of n-type films as a function of thickness indicated both the (100) and (111)Si films behave essentially the same way, i.e., the average mobilities show a steady decrease with decreasing film thickness. These studies revealed the strong interrelationships that exist among the various parameters involved in optimizing Si growth on insulators and indicated that growth conditions (i) must be optimized for the particular substrate orientation chosen; (ii) differ for those substrate orientations which lead to the same Si orientation; (iii) are dependent on reactor geometry; and (iv) should be optimized for the particular film thickness desired.

Silicon-on-sapphire (SOS) is now over a decade old, having been first announced by our laboratory in 1963 (1). However, only in the last few years has a pronounced interest in SOS been demonstrated.

A major emphasis has been placed on the use of (01 $\bar{1}$ 2)Al<sub>2</sub>O<sub>3</sub> as the substrate orientation since it controls the growth of (100)-oriented Si, which is preferred for MOS structures in bulk Si because surface states are minimized; however, better electrical properties have been reported for (111)Si/(0001)Al<sub>2</sub>O<sub>3</sub> films grown by chemical vapor deposition (2). The best films were grown at the relatively high temperature of  $\sim 1200^\circ\text{C}$  (2). Two other principal orientations that were identified during our early studies (3) as influencing the growth of (111)Si are (10 $\bar{1}$ 4)Al<sub>2</sub>O<sub>3</sub> and  $\sim(11\bar{2}0)$ Al<sub>2</sub>O<sub>3</sub>. This paper reports the results of a study to compare the properties of (111)Si films grown on these orientations with (100)Si films grown on (01 $\bar{1}$ 2)Al<sub>2</sub>O<sub>3</sub>. Some studies were also performed on (11 $\bar{2}$ 3)Al<sub>2</sub>O<sub>3</sub>, which induces Si growth about 7.5° off the (111)Si plane. Substrates cut  $\sim 5^\circ$  off the (11 $\bar{2}$ 0) plane of Al<sub>2</sub>O<sub>3</sub> toward the [10 $\bar{1}$ 0] direction were used to ensure that the growth was single crystal with the (111) plane of Si parallel to the (11 $\bar{2}$ 0) plane of Al<sub>2</sub>O<sub>3</sub> (3).

## Experimental

Except as noted, the Si growth studies involved the formation of films by the pyrolysis of SiH<sub>4</sub>-H<sub>2</sub> mixtures in the apparatus depicted in Fig. 1. It consists of a vertical 60 mm OD quartz tube 38 cm long, containing a SiC-covered carbon pedestal ("Ti-Kote," Texas Instruments) which could be rotated and inductively heated; a manifold made from 1/4 in. stainless steel (Type 316) tubing; appropriate flow meters (Brooks Instruments) for monitoring the gas flows; Teflon con-

nectors (Beckman Instruments) to facilitate reactor exchange; and provision for separate evacuation of the flow lines and the reactor. During the working day, a continual flow was maintained in the gas lines; only the reactor portion and connections were evacuated between experiments.

The H<sub>2</sub> carrier gas was Pd-purified, and the He was grade 6<sup>TM</sup> from Airco. The dopant sources used contained 200 ppm AsH<sub>3</sub> in H<sub>2</sub> (Airco) and 195 ppm B<sub>2</sub>H<sub>6</sub> in H<sub>2</sub> carrier gas (Scientific Gas). Temperatures of the SiC-coated carbon pedestal were measured with an optical pyrometer and were not corrected for any apparent emissivity changes caused by the intervening quartz chamber wall. Total gas flows of 6 lpm were used in the experiments described.

The substrates, which in most cases possessed an oval shape, were fabricated from 0.5 in. diameter Verneuil and Czochralski rods obtained from Union Carbide (San Diego, California), and Crystal Optics (Ann Ar-

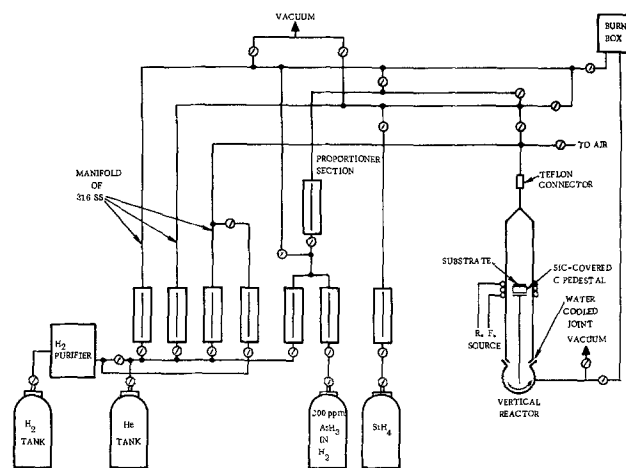


Fig. 1. Schematic diagram of chemical vapor deposition apparatus

\*Electrochemical Society Active Member.

<sup>1</sup> Present address: Rockwell International Science Center, Thousand Oaks, California 91360.

Key words: silicon-on-sapphire, (111)Si films, heteroepitaxy, chemical vapor deposition, anisotropy.

bor, Michigan). They were oriented at Rockwell and cut and polished at Insaco (Quakertown, Pennsylvania), and at Rockwell. Measurements of film conductivity type, resistivity, carrier concentration, and carrier mobility were made utilizing either the van der Pauw method (4) or the more accurate and conventional Hall-effect bridge method. The Hall-effect bridges etched in Si on a given substrate orientation fortunately were, in most cases, placed in the same direction with respect to the crystallographic axes in the plane of the substrates. The importance of this point is discussed later.

### Results and Discussion

**Study of autodoping in (100) and (111)SOS films.**—Autodoping from the  $\text{Al}_2\text{O}_3$  substrates has been shown to cause appreciable doping of epitaxial Si films grown in  $\text{H}_2$  (5, 6). In order to determine more precisely the extent of this doping in our reactor, a number of intentionally undoped (100)- and (111)-oriented,  $\sim 2 \mu\text{m}$  thick films were grown in  $\text{H}_2$  as a function of temperature from 1050° to 1150°C at a growth rate of  $\sim 2 \mu\text{m}/\text{min}$ . The carrier concentration data are shown in Fig. 2 for the unannealed films. Each data point represents an average value for data obtained from 1 to 3 samples. Slight changes in growth temperature appreciably altered the extent of autodoping, since the acceptor concentration varied by over two orders of magnitude for growth temperature changes of just 100°C, i.e.,  $2\text{--}3 \times 10^{15}/\text{cm}^3$  at 1050°C to  $\sim 3\text{--}5 \times 10^{17}/\text{cm}^3$  at 1150°C. Autodoping appeared to be slightly less in (111)Si on  $\sim(11\bar{2}0)\text{Al}_2\text{O}_3$  than for (100)Si on  $(01\bar{1}2)\text{Al}_2\text{O}_3$  for a given growth temperature. Further studies on the effect of  $\text{Al}_2\text{O}_3$  in a system containing Si are presented as an Appendix to this paper.

**Effect of growth temperature on film properties.**—The electrical properties of As-doped films grown at a rate of  $\sim 2 \mu\text{m}/\text{min}$  in our reactor indicated equivalent quality (111)Si on  $(10\bar{1}4)\text{Al}_2\text{O}_3$  and (100)Si on  $(01\bar{1}2)\text{Al}_2\text{O}_3$  at growth temperatures from 950°–1050°C for donor concentration from  $10^{16}$  to  $10^{18} \text{cm}^{-3}$ . When  $\sim(11\bar{2}0)\text{Al}_2\text{O}_3$  was examined as a substrate for (111)Si

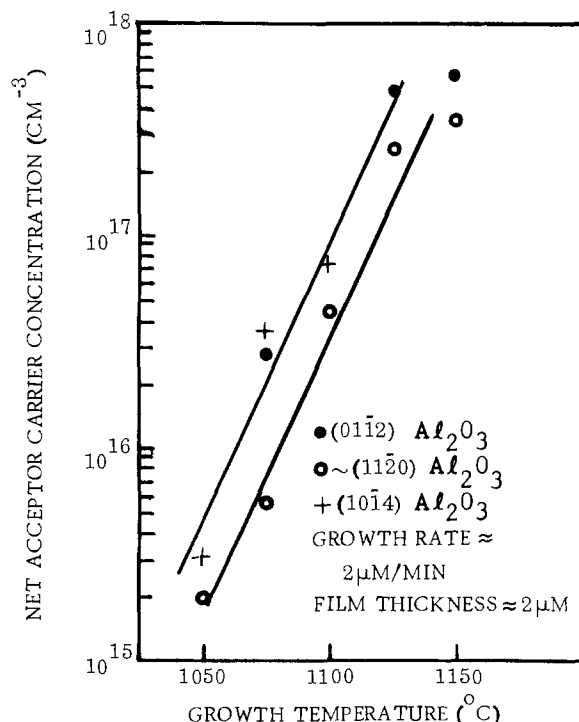


Fig. 2. Variation of net acceptor carrier concentration due to Al autodoping as function of growth temperature for intentionally undoped and unannealed Si/ $\text{Al}_2\text{O}_3$  films. (Data points are averaged values.)

growth, it was found necessary to use temperatures in excess of 1050°C to obtain reflective n-type films. Determination of the correct carrier concentration for films grown at these temperatures was of course complicated by an autodoping species from the  $\text{Al}_2\text{O}_3$  substrate, which served to compensate the As added and had to be removed before the net donor concentration could be established. For this reason, an 1100°C anneal first in  $\text{O}_2$  and then in  $\text{N}_2$  was employed for all films grown at or above 1050°C before measurement in order to render the contaminant electrically inactive.

In Fig. 3, the mobilities of films grown on  $(01\bar{1}2)$  and  $\sim(11\bar{2}0)\text{Al}_2\text{O}_3$  substrates are plotted as a function of growth temperature. At each temperature data for a number of films with net donor concentrations between  $1$  and  $5 \times 10^{16} \text{cm}^{-3}$  are averaged; the bars indicate the range of mobilities over which the points are averaged, and the number next to the point indicates how many samples contributed to the average value plotted. It was found that for a growth rate of  $\sim 2 \mu\text{m}/\text{min}$  the electron mobility in (100)Si (values of  $\sim 500\text{--}550 \text{cm}^2/\text{V}\text{-sec}$ ) was nearly independent of growth temperature ( $T_g$ ) for  $1040^\circ\text{C} \leq T_g \leq 1100^\circ\text{C}$ . For (111)Si growth on the  $\text{Al}_2\text{O}_3$  orientation near the  $(11\bar{2}0)$  plane, film mobilities appeared to improve with increasing growth temperature and exceeded those obtained for (100)Si by about 25% (values of  $650\text{--}700 \text{cm}^2/\text{V}\text{-sec}$ ) at the higher growth temperatures.

Growth of Si on various other  $\text{Al}_2\text{O}_3$  orientations at high growth temperature was also examined. The  $(10\bar{1}4)$  and  $(11\bar{2}3)\text{Al}_2\text{O}_3$  orientations were used as substrates for Si growth at temperatures from 1075° to 1150°C. For film thicknesses of  $1.5\text{--}1.9 \mu\text{m}$  and donor concentrations of  $1\text{--}2 \times 10^{16} \text{cm}^{-3}$ , the  $(10\bar{1}4)$  and  $(11\bar{2}3)$  orientations yielded films with mobilities of  $400\text{--}500 \text{cm}^2/\text{V}\text{-sec}$  over the whole temperature range, values inferior to those measured in the better (111)-oriented films grown on  $\sim(11\bar{2}0)\text{Al}_2\text{O}_3$ .

**Effect of growth rate on film properties.**—Growth rate-mobility data for  $2 \mu\text{m}$ -thick films grown at 1075°C on  $(01\bar{1}2)\text{Al}_2\text{O}_3$  and also on  $\sim(11\bar{2}0)\text{Al}_2\text{O}_3$  are plotted in Fig. 4. The data suggest an improvement in film properties at growth rates exceeding  $1 \mu\text{m}/\text{min}$ ; the mobility maxima occur in films grown at a rate of about  $4 \mu\text{m}/\text{min}$  for  $(01\bar{1}2)\text{Al}_2\text{O}_3$  and about  $2 \mu\text{m}/\text{min}$  for films grown on substrates with an orientation near  $(11\bar{2}0)\text{Al}_2\text{O}_3$ . These films were grown under conditions of constant dopant gas flow. However, as shown in Fig. 5, an exponential relationship exists between growth rate and carrier concentration. Such a relationship is not expected since the growth rate is a linear function of  $\text{SiH}_4$  flow rate. That is, a simple dilution of the

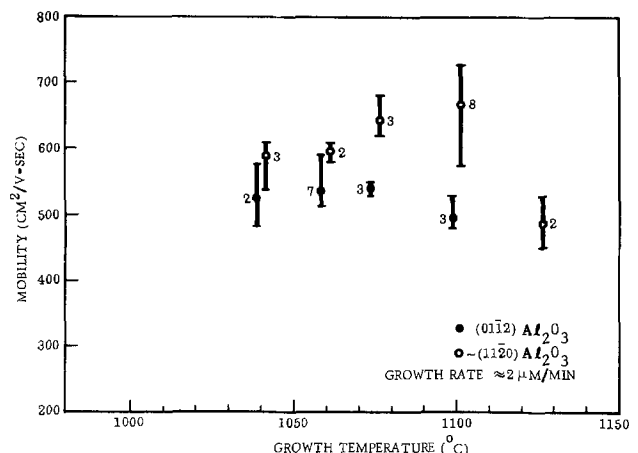


Fig. 3. Variation of Hall mobility with growth temperature for Si/ $\text{Al}_2\text{O}_3$  films having net donor carrier concentration of  $1.5 \times 10^{16} \text{cm}^{-3}$ . (Films were annealed before electrical measurement.)

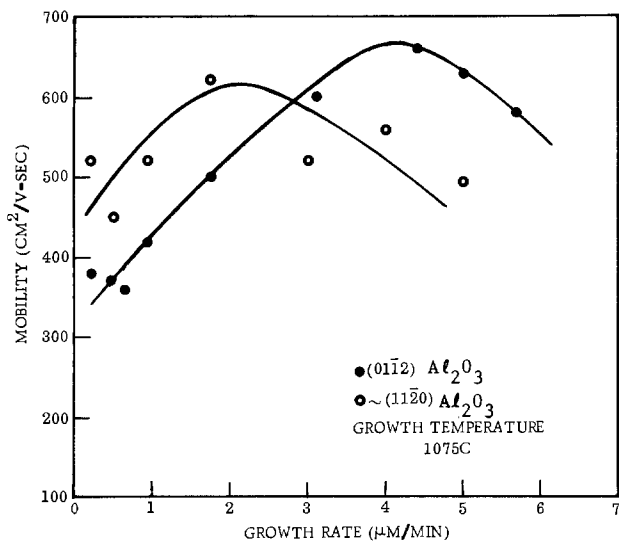


Fig. 4. Variation of Hall mobility with growth rate for n-type Si/Al<sub>2</sub>O<sub>3</sub> films grown at 1075°C. (Annealed at 1100°C in O<sub>2</sub> and N<sub>2</sub>.)

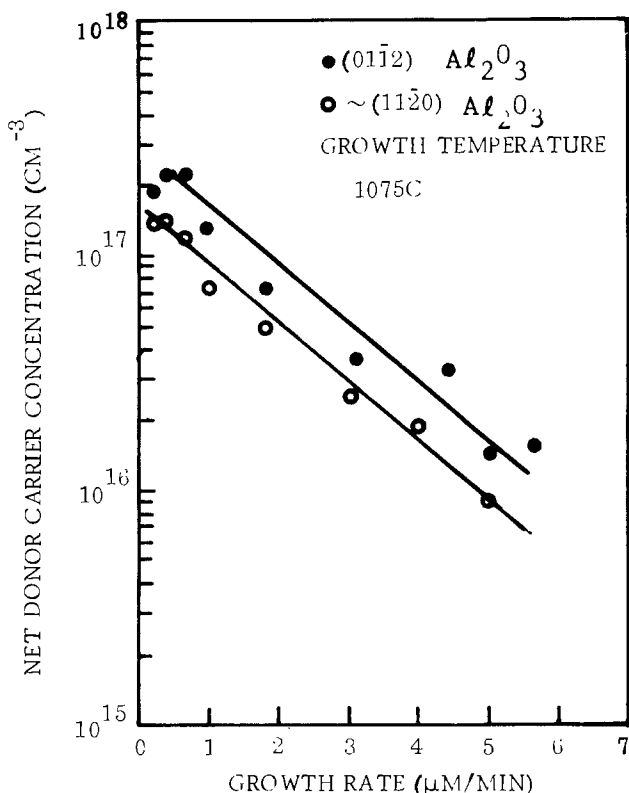


Fig. 5. Variation of net donor carrier concentration with growth rate for Si/Al<sub>2</sub>O<sub>3</sub> films grown at 1075°C with constant dopant-gas flow rate. (Annealed at 1100°C in O<sub>2</sub> and N<sub>2</sub>.)

dopant gas by the increasing silane flow rate would be expected to lead to a linear variation of carrier concentration with growth rate. In any case, a substantial part of the mobility decrease at the low rate is a consequence of an increasing carrier concentration. Unfortunately, studies relating growth rate to mobility at constant donor concentrations and different temperatures were not made in our reactor. The data, however, do indicate the importance of making gas-phase doping concentrations consistent with growth rate when one attempts to grow a homogeneously doped film by a dual-rate growth process (7).

One can also note from Fig. 5 that the donor concentration measured in films on  $\sim(11\bar{2}0)\text{Al}_2\text{O}_3$  are consistently lower than those grown simultaneously on

$(01\bar{1}2)\text{Al}_2\text{O}_3$ . This is consistent with the results on autodoping shown in Fig. 2 and suggests that both donor and acceptor dopants are incorporated less easily into the (111)-oriented Si lattice.

**Properties of p-type, B-doped Si/Al<sub>2</sub>O<sub>3</sub> films.**—Doping experiments with Si films on Al<sub>2</sub>O<sub>3</sub> for the purpose of achieving p-type films were undertaken with diborane (B<sub>2</sub>H<sub>6</sub>) as the source of B. Calibration data for a range of carrier concentrations from  $\sim 3 \times 10^{16}$  to  $\sim 2 \times 10^{20}$  cm<sup>-3</sup> were established for  $\sim 2$  μm thick, p-type Si films grown at  $\sim 2$  μm/min on  $(01\bar{1}2)\text{Al}_2\text{O}_3$  at 1025°C (unannealed) and on  $(01\bar{1}2)$ ,  $\sim(11\bar{2}0)$ , and  $(10\bar{1}4)\text{Al}_2\text{O}_3$  at 1075°C (annealed); the data are shown in Fig. 6.

Since the data points essentially define a single straight line for both the unannealed and annealed films, the annealing was effective in removing the p-type autodoping species without disturbing the B-species in the film. Hall mobility as a function of hole concentration for the films is shown graphically in Fig. 7. The electrical properties of the B-doped (100)Si are similar to those previously reported in the literature

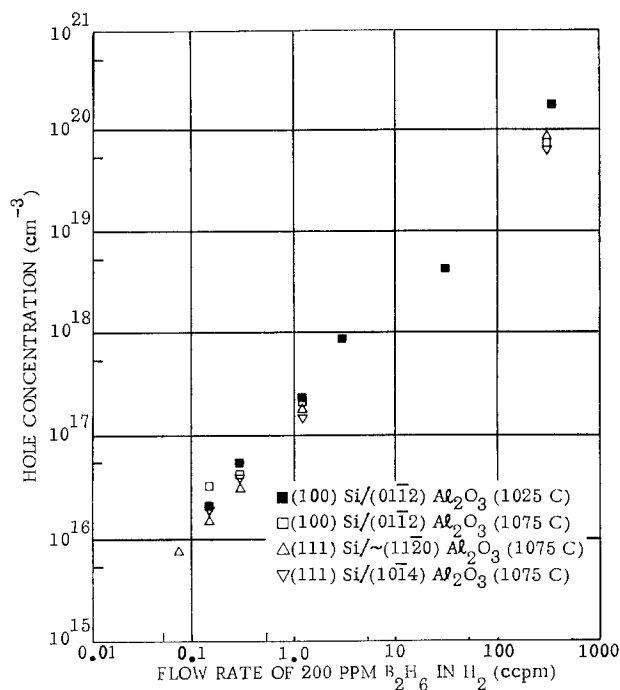


Fig. 6. Calibration curve for growth of p-type Si/Al<sub>2</sub>O<sub>3</sub> films using B<sub>2</sub>H<sub>6</sub> dopant source. The films were annealed at 1100°C in O<sub>2</sub> and N<sub>2</sub>.

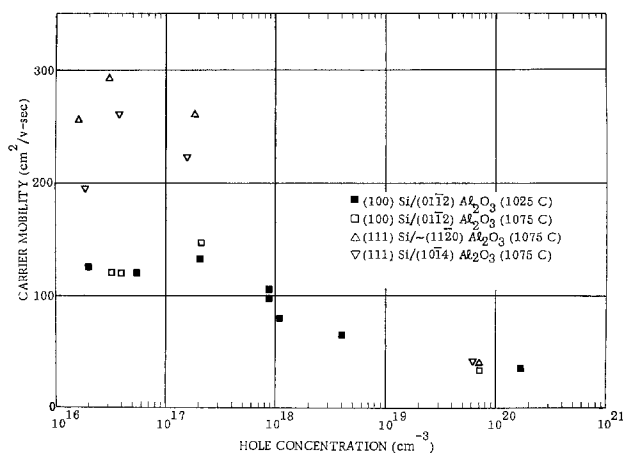


Fig. 7. Electrical properties of p-type Si/Al<sub>2</sub>O<sub>3</sub> films doped with boron.



(8) and are equivalent for films of the same carrier concentration grown at 1025° and 1075°C; therefore, either growth temperature appears to be adequate for p-type (100)Si growth.

The electrical data for the p-type films grown on  $\sim(11\bar{2}0)$  and  $(10\bar{1}4)$   $\text{Al}_2\text{O}_3$  were most encouraging, with mobilities exceeding those measured on  $(01\bar{1}2)$   $\text{Al}_2\text{O}_3$  twofold or more for hole concentrations in the  $10^{16}$ - $10^{17}$   $\text{cm}^{-3}$  range. The results are close to those values for bulk Si and appear to be the largest yet recorded for Si films only 2  $\mu\text{m}$  thick on  $\text{Al}_2\text{O}_3$ . Almost equivalent properties were obtained for p-type (111) films grown on  $(10\bar{1}4)$  and  $\sim(11\bar{2}0)$   $\text{Al}_2\text{O}_3$ . This was surprising since, as previously noted, n-type films grown in  $\text{H}_2$  on  $\sim(11\bar{2}0)$   $\text{Al}_2\text{O}_3$  were superior to those grown on  $(10\bar{1}4)$  substrates. Very high mobilities have also been reported for (111)-oriented p-type films grown on (111)spinel (9). These have been explained by a piezoresistance effect due to the compressive stress in the films.

**Variations in Si film properties with thickness.**—It has been reported on many occasions that the electrical properties of heteroepitaxial semiconductor films tend to be inferior close to the substrate on which growth occurs (10, 11). A comparison was therefore made of the variation of electrical properties with film thickness for relatively thin, annealed, n-type (100) and (111)Si films grown at 1100°C.

From Fig. 8, it can be observed that the carrier concentration remained relatively constant, decreasing only slightly for thinner films, but the average mobilities showed a more pronounced decrease with decreasing film thickness for both orientations. Films that were reduced stepwise in thickness by polishing and then remeasured electrically also showed the same general thickness dependence on average mobility and carrier concentration. The average mobilities for (111)Si films  $\sim 0.5$ - $1.0$   $\mu\text{m}$  thick grown on  $\sim(11\bar{2}0)$   $\text{Al}_2\text{O}_3$  also appear

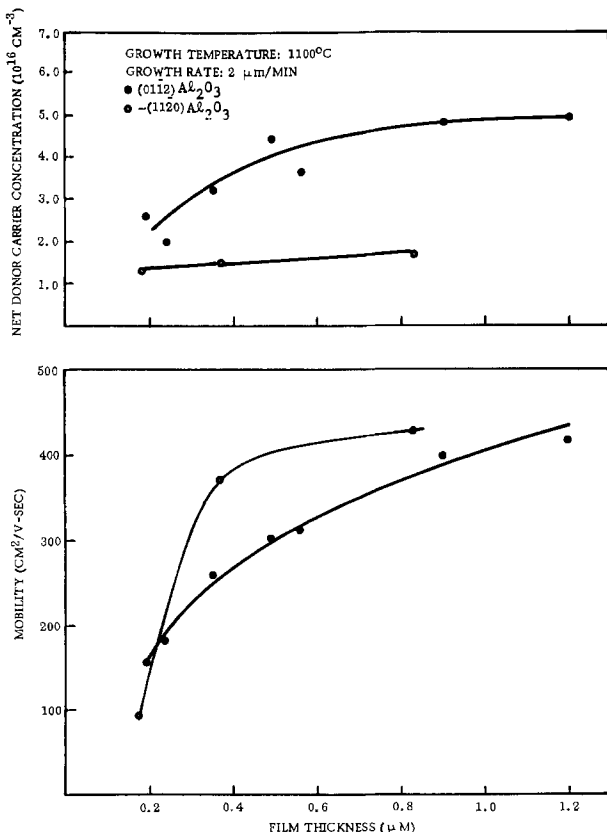


Fig. 8. Variation of film properties with film thickness for thin n-type  $\text{Si}/\text{Al}_2\text{O}_3$  films. (All films annealed after growth for 1 hr in  $\text{O}_2$  at 1100°C.)

to be slightly superior to those found in (100)Si films grown in our vertical apparatus. However, they are essentially the same as those reported by Cullen and Corboy (12) for (100)Si-on-sapphire grown in their reactor at 1000°C. (See next section.)

**Effects of reactor configuration on film properties.**—Because of differences in growth reactors found in various laboratories, several experiments were conducted to investigate the effects that different reactor geometry may have on film properties. Experiments were performed on  $(01\bar{1}2)$   $\text{Al}_2\text{O}_3$  and  $\sim(11\bar{2}0)$   $\text{Al}_2\text{O}_3$  in a horizontal reactor system which normally would accommodate up to four 2 in. diameter wafers per run. Even though the typical growth rate used in this reactor ( $\sim 1$   $\mu\text{m}/\text{min}$ ) was not the same as that used most often in the vertical reactor, and the  $\text{H}_2$  carrier-gas flows ( $\sim 40$  lpm) were substantially greater than those used in the vertical system (6 lpm), the limited data obtained are considered meaningful because they supported the purpose for which the experiments were performed.

The growth temperature was varied from 960° to 1100°C. The visual appearance of those films grown at 1075° and 1100°C indicated a deterioration of film quality; therefore, only those films grown in the range 960°-1075°C were evaluated electrically.

The electrical data shown in Fig. 9 indicate a uniform increase in electron mobility with decreasing growth temperature for 1.0-1.4  $\mu\text{m}$  thick films grown on  $(01\bar{1}2)$   $\text{Al}_2\text{O}_3$ , i.e., from a value of about 325  $\text{cm}^2/\text{V}\text{-sec}$  at 1075°C to approximately 600  $\text{cm}^2/\text{V}\text{-sec}$  at 960°C for carrier concentrations in the range  $\sim 2$ - $6 \times 10^{16}$   $\text{cm}^{-3}$ .

The mobilities of films grown simultaneously on  $\sim(11\bar{2}0)$   $\text{Al}_2\text{O}_3$ , on the other hand, showed a maximum of over 600  $\text{cm}^2/\text{V}\text{-sec}$  at  $\sim 1050^\circ\text{C}$ , with only a slight decrease at 1030° and 1075°C. The results are different from the data obtained on films grown in the vertical reactor system, for in this set of experiments, (100)-oriented Si films were produced with properties essentially as good as those measured in (111)-oriented Si. It is apparent that the determination of optimum film growth parameters relate to the growth apparatus being employed, and a comparison of results from different laboratories must always be made with this fact in mind.

**Anisotropy considerations.**—During the latter part of the studies just described, it was established that the electrical properties of SOS are not isotropic in the plane of the film (13, 14). Using a specifically designed double Hall-bridge pattern etched in the Si film so that independent measurements of Hall mobility were made every 18° in the plane of the films, Hughes and Thorsen determined the amount of anisotropy as described by a parameter  $A$  [ $A \equiv (\mu_{\text{max}} - \mu_{\text{min}})/\mu_A$ , where  $\mu_A = (1/2)(\mu_{\text{max}} + \mu_{\text{min}})$ ] of 9% for (100)Si/ $(01\bar{1}2)$   $\text{Al}_2\text{O}_3$  (13) and about 40% for (221)Si/ $(1\bar{1}\bar{2}2)$   $\text{Al}_2\text{O}_3$  (14). Preliminary data indicate anisotropy in mobility for (111)Si films also, averaging 16% for

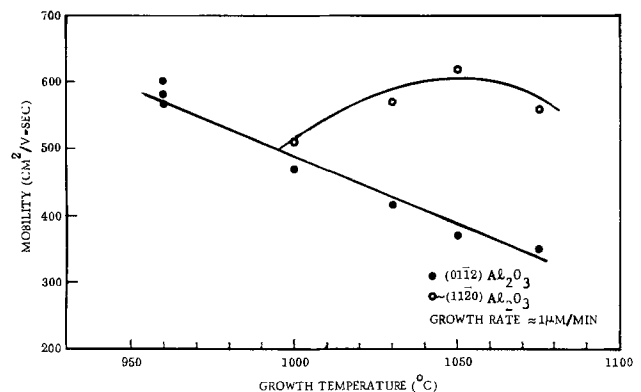


Fig. 9. Variation of Hall mobility with growth temperature for n-type  $\text{Si}/\text{Al}_2\text{O}_3$  films grown in a horizontal reactor.

(111)Si growth on  $\sim(1\bar{1}20)\text{Al}_2\text{O}_3$  and 30% for (111)Si growth on  $(10\bar{1}4)\text{Al}_2\text{O}_3$  (15).

These variations in mobility could have led to considerable scatter in the electrical data if circular substrate wafers had been used in these studies prior to the discovery of anisotropy in these films. But, because of the oval shape of the substrate and the operator's tendency to place a square-shaped Hall-effect bridge in approximately the same direction in the Si film relative to the sides of the substrate (and hence to the crystallographic axes of the substrate), it is believed that most of the data obtained can be correlated with the parameter changes made. Since the average anisotropy in mobility for (111)Si on  $\sim(1\bar{1}20)\text{Al}_2\text{O}_3$  is only slightly greater (7%) than that found for (100)Si on  $(01\bar{1}2)\text{Al}_2\text{O}_3$ , we feel that the higher mobilities measured in 2  $\mu\text{m}$  thick (111)Si films on  $\sim(1\bar{1}20)\text{Al}_2\text{O}_3$  grown in the vertical reactor are in fact real and consistent with an improved film quality. A correlation between electrical data and device data is now required to determine if  $\sim(1\bar{1}20)\text{Al}_2\text{O}_3$  is a superior substrate orientation for devices made in silicon-on-sapphire.

### Summary and Conclusions

An experimental study of the effects of various parameters on the properties of (111) and (100)Si films grown on  $\text{Al}_2\text{O}_3$  by the  $\text{SiH}_4\text{-H}_2$  pyrolysis CVD method was carried out in a vertical growth system. It was established that significant autodoping occurs in Si on  $\text{Al}_2\text{O}_3$  at temperatures greater than about 1050°C.

Essentially equivalent (100)- and (111)-oriented, n-type Si films grew on  $(01\bar{1}2)$  and  $(10\bar{1}4)\text{Al}_2\text{O}_3$  substrates at deposition temperatures of 950°-1050°C (below autodoping range) and at growth rates of  $\sim 2 \mu\text{m}/\text{min}$ .

$\text{Al}_2\text{O}_3$  substrates having orientations near the  $(1\bar{1}20)$  plane, which were not previously used in heteroepitaxy growth parameter studies, were also utilized for (111)Si heteroepitaxy, but required temperatures  $> 1050^\circ\text{C}$  for the growth of films with good electrical properties. For growth rates of  $\sim 2 \mu\text{m}/\text{min}$ , films were obtained with electron mobilities of 600-700  $\text{cm}^2/\text{V}\text{-sec}$  for net carrier concentrations of  $10^{16}\text{-}10^{17} \text{ cm}^{-3}$ , which exceeded the mobilities we obtained on either  $(01\bar{1}2)\text{Al}_2\text{O}_3$  or  $(10\bar{1}4)\text{Al}_2\text{O}_3$ . At higher Si growth rates (up to  $\sim 6 \mu\text{m}/\text{min}$ ) and deposition temperatures  $T_g$ , good quality films ( $\mu \sim 500\text{-}600 \text{ cm}^2/\text{V}\text{-sec}$ ) were also formed on  $(01\bar{1}2)\text{Al}_2\text{O}_3$  ( $1040^\circ\text{C} \leq T_g \leq 1100^\circ\text{C}$ ).

At the high growth temperatures it was found necessary to "homogenize" the electrical properties of the films by an  $\text{O}_2$ ,  $\text{N}_2$  anneal in order to deactivate the autodoping species.

P-type Si films were also grown using  $\text{B}_2\text{H}_6$  as the dopant source. As in the case of the n-type films, better films were obtained on  $\sim(1\bar{1}20)\text{Al}_2\text{O}_3$  [(111)Si growth] than on  $(01\bar{1}2)\text{Al}_2\text{O}_3$  [(100)Si growth]; Hall mobilities were  $\sim 2\text{-}3$  times larger for films with net hole concentrations  $10^{16}\text{-}10^{17} \text{ cm}^{-3}$ .

A comparison of film properties of n-type films as a function of thickness indicated both the (100) and (111)Si films behave the same way, i.e., the average mobilities show a steady decrease with decreasing film thickness. The average mobilities were slightly superior for  $\sim 0.5\text{-}1.0 \mu\text{m}$  films grown  $\sim(1\bar{1}20)\text{Al}_2\text{O}_3$ .

These studies revealed the strong interrelationships that exist among the various parameters involved in optimizing Si growth on insulators. Evaluation of the electrical properties of Si films on those orientations that produce the best Si overgrowths demonstrated that growth conditions (i) must be optimized for the particular substrate orientation chosen; (ii) differ for those substrate orientations which lead to the same Si orientation; (iii) are dependent on reactor geometry; and (iv) probably should be optimized for the particular film thickness desired. In addition, care must be

exercised in measurement techniques when using mobility as a figure of merit because of the differences caused by anisotropy considerations.

### Acknowledgments

The authors wish to thank J. P. Wendt for carrying out the electrical measurements, R. E. Johnson for performing the photolithographic processing, angle-lapping, and staining, Fred Forrest for developing special techniques for producing scratch-free  $(10\bar{1}4)$ -oriented substrates, L. A. Moudy and A. J. Hughes for helpful discussions regarding orientation-relationship data and anisotropy, R. Harada for growth experiments in the horizontal reactor, and R. P. Ruth for a review of the manuscript. The work reported in this paper was supported in part by the Advanced Research Projects Agency under Order No. 1585, and monitored by the U.S. Army Missile Command, Redstone Arsenal, Alabama, under contract No. DAAH01-70-C-1311.

Manuscript submitted Dec. 10, 1974; revised manuscript received Sept. 3, 1975. This was Paper 140 presented at the New York, New York, Meeting of the Society, Oct. 13-17, 1974.

Any discussion of this paper will appear in a Discussion Section to be published in the December 1976 JOURNAL. All discussions for the December 1976 Discussion Section should be submitted by Aug. 1, 1976.

Publication costs of this article were partially assisted by Rockwell International.

### APPENDIX

In order to examine further the effect of the presence of  $\text{Al}_2\text{O}_3$  in a system containing Si, two experiments were performed, one in  $\text{H}_2$ , the other in He. An oval  $\text{Al}_2\text{O}_3$  wafer ( $13 \times 16 \text{ mm}$ ) was placed on a  $\sim 60 \text{ ohm-cm}$  n-type HF-dipped mechanically polished Czochralski-grown Si wafer. The composite was heated in the CVD reactor at a pedestal temperature of  $1100^\circ\text{C}$  for 1 hr in  $\text{H}_2$  or in He, with these carrier gases flowing at a rate of 5 lpm. For the  $\text{H}_2$  case, after the  $\text{Al}_2\text{O}_3$  was removed, a mesa about  $1 \mu\text{m}$  high which profiled the oval wafer was in evidence, and the Si which had been exposed to the  $\text{H}_2$  was eroded considerably. The Si mesa and surrounding area were p-type and etched. Angle-lapping and staining revealed a relatively uniform p-type layer  $\sim 2.4 \mu\text{m}$  thick at the mesa and a somewhat irregularly shaped layer  $\sim 1.7 \mu\text{m}$  thick in the etched area where the wafer was positioned. A van der Pauw measurement of the mesa, which was cut from the rest of the wafer, gave the following properties:  $\rho = 3.5 \text{ ohm-cm}$ ;  $p = 6.3 \times 10^{15} \text{ cm}^{-3}$ ;  $\mu = 284 \text{ cm}^2/\text{V}\text{-sec}$ .

A subsequent anneal for 1/2 hr in  $\text{O}_2$  plus 2 hr in  $\text{N}_2$ , a process which has usually been found sufficient to deactivate the Al-containing impurity species in thin SOS films, diffused the p-type impurity further into the substrate and at the same time converted the top of the p-type layer to n-type. An additional 18 hr of anneal (1/2 hr  $\text{O}_2 + 17\frac{1}{2} \text{ hr N}_2$ ) almost converted the whole layer to n-type, as evidenced by only a residual stain of the layer at its deepest penetration.

Without  $\text{Al}_2\text{O}_3$  present in the reactor, another unused piece of the same Si wafer used in the above experiment remained n-type and relatively high resistivity after treatment in  $\text{H}_2$  for 1 hr at  $1100^\circ\text{C}$ .

Some attack of the Si by  $\text{Al}_2\text{O}_3$  was also in evidence when He was used as the carrier gas, but the etching was much less severe; essentially no mesa was formed. The Si surface just below the  $\text{Al}_2\text{O}_3$  was converted to p-type, however, as in the  $\text{H}_2$  experiment.

These results demonstrate the need for minimizing the reactions between Si,  $\text{Al}_2\text{O}_3$ , and  $\text{H}_2$ . They also suggest that some reaction products may be generated during the early stages of Si growth which could affect the mode of nuclei formation, be incorporated into the growing film, and affect the crystallinity of the films at the Si- $\text{Al}_2\text{O}_3$  interface. Such impurities may constitute an additional factor in determining the defect structure in SOS films, in addition to that attributed to lattice mismatch and strains at the Si- $\text{Al}_2\text{O}_3$  interface. Autodoping can presumably be minimized by the use of an inert atmosphere, lower growth temperatures, and high growth rates to seal the  $\text{Al}_2\text{O}_3$  surface as fast as possible.

## REFERENCES

1. H. M. Manasevit and W. I. Simpson, *Proc. Am. Phys. Soc.*, Edmonton, Alberta, Canada, Late News Item (1963).
2. D. J. Dumin, *J. Appl. Phys.*, **38**, 1909 (1967).
3. H. M. Manasevit, R. L. Nolder, and L. A. Moudy, *Trans. Met. Soc. AIME*, **242**, 465 (1968).
4. L. J. van der Pauw, *Philips Res. Rept.*, **13**, 1 (1958).
5. D. J. Dumin and P. H. Robinson, *This Journal*, **113**, 469 (1966).
6. J. Mercier, *ibid.*, **117**, 812 (1970).
7. G. E. Gottlieb and J. F. Corboy, Jr., *J. Cryst. Growth*, **17**, 261 (1972).
8. D. J. Dumin and P. H. Robinson, *J. Appl. Phys.*, **39**, 2759 (1968).
9. H. Schlotterer, *Solid State Electron*, **11**, 947 (1968).
10. D. J. Dumin and P. H. Robinson, *J. Cryst. Growth*, **3/4**, 214 (1968).
11. A. C. Ipri, *J. Appl. Phys.*, **43**, 2770 (1972); *Appl. Phys. Letters*, **20**, 1 (1972).
12. C. W. Cullen and J. F. Corboy, *This Journal*, **121**, 1345 (1974).
13. A. J. Hughes and A. C. Thorsen, *J. Appl. Phys.*, **44**, 2304 (1973).
14. A. C. Thorsen and A. J. Hughes, *Appl. Phys. Letters*, **21**, 579 (1972).
15. A. J. Hughes and A. C. Thorsen, Unpublished data.

## Amorphous CVD Al<sub>2</sub>O<sub>3</sub> Films by Ta-Doping and Their Physicochemical Properties

Paul J. Tsang,\* Ronald M. Anderson, and Serge Cvikevich

IBM System Products Division, East Fishkill Facility, Hopewell Junction, New York 12533

### ABSTRACT

Tantalum-doped alumina films were deposited by the pyrolysis of a vapor mixture of TaCl<sub>5</sub> and AlCl<sub>3</sub> in the presence of hydrogen and carbon dioxide in the temperature range of 800°-950°C. The Ta content seems limited to 5.5 mole per cent of Ta<sub>2</sub>O<sub>5</sub>. The films, with only a minute amount of Ta, are crystalline, having the properties of pure alumina films. When the Ta content exceeds a certain level, the films become amorphous. Amorphous films have an optical index of refraction of 1.68 and a dielectric constant ranging from 9.5 to 12.0. Amorphous films are etchable in the diluted, buffered HF solution and show a d-c conduction governed by the Poole-Frenkel effect.

Chemical vapor deposited (CVD) alumina (Al<sub>2</sub>O<sub>3</sub>) films, because of their negative dielectric charges (1), have found applications as gate insulators for the conventional, insulator-gated, field-effect transistors (IGFET) (2-4) and as the field insulators for n-channel MOSFET IC's (5). In addition, it has been shown that electrically alterable read-only memory FET's can be fabricated using layered Al<sub>2</sub>O<sub>3</sub>-SiO<sub>2</sub> gate insulators (6). The capability of alumina to resist radiation damage (7) also makes it attractive for devices used in space applications.

The chemical vapor deposition of alumina films can be achieved by either thermal decomposition of Al organometallic compounds (8) at temperatures below 600°C, or by the pyrolysis of aluminum halides (9, 10) at temperatures higher than 700°C. The alumina films formed at lower temperatures are mostly amorphous, whereas the high temperature films formed by the pyrolysis of Al halides are crystalline.

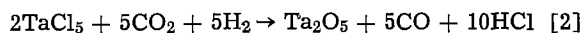
Generally, films used for device fabrication are deposited above 800°C because they are relatively stable during device processing and possess good dielectric strength. Unfortunately, the grain boundaries of the high temperature crystalline films are potential, long-term failure sites. In addition, the high temperature crystalline films are not etchable by the buffered HF solution, the photolithographic etchant most commonly used in microelectronics fabrication. Extra processing steps are required if these films are used. To provide ease of device fabrication and film integrity, amorphous Al<sub>2</sub>O<sub>3</sub> films formed at high temperatures are therefore desired.

Many elements present as impurities are capable of retarding the transformation of the metastable  $\gamma$ -Al<sub>2</sub>O<sub>3</sub> phase into the stable  $\alpha$ -phase, due to their preference in occupying the tetrahedral sites in the oxygen lattice

(11). In addition, the introduction of impurity during film formation may also favor the growth of amorphous films due to an increase in configurational entropy (12), and/or due to the impurity-induced change of film nucleation and growth behavior (13). It may therefore be possible to form amorphous CVD Al<sub>2</sub>O<sub>3</sub> films at relatively high temperatures by impurity doping. This paper describes the deposition and physicochemical properties of amorphous Al<sub>2</sub>O<sub>3</sub> films doped with Ta and formed in the temperature range that is normally used for forming crystalline pure alumina films.

### Experimental

*Film deposition.*—It is well known that at temperatures above 700°C, CVD Al<sub>2</sub>O<sub>3</sub> films and Ta<sub>2</sub>O<sub>5</sub> films can be formed by the pyrolysis of AlCl<sub>3</sub> (9) and TaCl<sub>5</sub> (14), respectively, in the presence of H<sub>2</sub> and CO<sub>2</sub> through the following probable reactions



In this work, the formation of Ta-doped alumina was achieved by the pyrolysis of a vapor mixture of AlCl<sub>3</sub> and TaCl<sub>5</sub>. The AlCl<sub>3</sub> and TaCl<sub>5</sub> vapors were generated by heating AlCl<sub>3</sub> and TaCl<sub>5</sub> powders.<sup>1</sup>

The film deposition system is shown in Fig. 1. It consists of a reaction chamber, a TaCl<sub>5</sub> vapor saturator, an AlCl<sub>3</sub> vapor saturator, and feed lines which interconnect the halide vapor saturators through precision flow meters and control valves to allow close control of the AlCl<sub>3</sub> and TaCl<sub>5</sub> mixture flow to the reaction chamber for film deposition. All the feed lines and valves that connect the saturators to the reaction chamber were heated to 145°-160°C to prevent any halide condensation. A rf heated, silicon carbide-coated

\* Electrochemical Society Active Member.  
Key words: thin films, dielectric amorphous alumina, Ta-doping, Poole-Frenkel electrical conduction.

<sup>1</sup> AlCl<sub>3</sub> powder of 99.999% pure was purchased from Apache Chemical Company and the high purity resublimed TaCl<sub>5</sub> powder was purchased from Alpha Inorganics (Ventron).

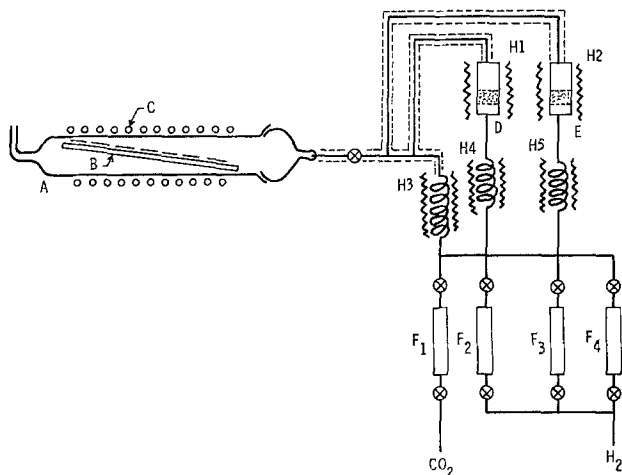


Fig. 1. Film deposition system. A, reactor; B, substrate susceptor; C, rf heating coil; D and E,  $\text{AlCl}_3$  and  $\text{TaCl}_5$  saturators; H1 to H5, heaters; F1 to F4, flow meters.

graphite susceptor was used as a film substrate holder and heater. The temperatures of the substrates were measured by a Leeds and Northrup optical pyrometer and are reported in this paper uncorrected. The "true" substrate temperatures are, in general,  $15^\circ$  higher.

The  $\text{AlCl}_3$  and  $\text{TaCl}_5$  powders in their vapor saturators were heated to  $115^\circ$  and  $130^\circ\text{C}$ , respectively. At these temperatures,  $\text{AlCl}_3$  and  $\text{TaCl}_5$  vapors of approximately the same pressure of 4.3 mm Hg were generated (15, 16), and the vapors were then carried out of the saturators by hydrogen gas, which itself was preheated to the saturator temperatures through separate lines and heaters. The saturation levels of the halide vapors in  $\text{H}_2$  carrier gas were not measured, but the consistencies of their saturation were checked before and after the Ta-doped alumina film deposition by measuring the growth rate of  $\text{Al}_2\text{O}_3$  and  $\text{Ta}_2\text{O}_5$  control films. Hydrogen was also used as a main diluent. It was first mixed with  $\text{CO}_2$  and was then heated to about  $400^\circ\text{C}$ . The preheated  $\text{H}_2$  and  $\text{CO}_2$  mixture, after picking up the halide-carrying  $\text{H}_2$  flows that come out of the saturators, was fed into the reaction chamber for film deposition.

By varying the flow ratio of  $\text{AlCl}_3$  and  $\text{TaCl}_5$  the present system can deposit either pure  $\text{Al}_2\text{O}_3$  or  $\text{Ta}_2\text{O}_5$  films or Ta-doped alumina films in the temperature range of  $800^\circ$ - $950^\circ\text{C}$ . The films were deposited on either bare or slightly oxidized Si substrates (usually p-type  $\langle 100 \rangle$ ). In the former case, the as-received substrates were chemically cleaned before film deposition, whereas in the latter case, the substrates were chemically cleaned and then oxidized to form 50-60 Å of  $\text{SiO}_2$  before film deposition. The pure alumina films deposited in this system are polycrystalline and have physicochemical properties similar to those reported by Doo and Tsang (17) and others (18). The pure  $\text{Ta}_2\text{O}_5$  films deposited in this system at  $900^\circ\text{C}$  have an averaged, ellipsoidally measured, index of refraction of  $2.30 \pm 0.10$  and a dielectric constant (measured at 1 MHz) larger than 43. These are in good agreement with the findings reported by Knausenberger and Tauber (14). Transmission electron microscope (TEM) examinations of these  $\text{Ta}_2\text{O}_5$  films show that they are  $\beta$ - $\text{Ta}_2\text{O}_5$  and have a microstructure similar to that observed by Spyridelis *et al.* (19). The Ta-doped alumina [henceforth called  $(\text{Ta})\text{Al}_2\text{O}_3$ ] films are smooth and shiny in appearance but show an orange-peel surface texture when examined by a high-power phase-contrast microscope.

The conditions for film deposition were studied. As in the case of pure alumina films, the most important factor affecting film deposition and film quality was the mole (or volume) ratio of  $\text{CO}_2$  to the halides. It was observed that a  $\text{CO}_2$  to total halide mole ratio of larger than 500 to 1 is required in order to deposit

films with good insulating properties. All the films studied in this experiment were deposited with the  $\text{CO}_2$  to total halide mole ratio equal to or larger than 800 to 1. In order to obtain homogeneous, single modal films with uniform thickness, the total halide content in the feed gas was kept to less than 0.1% by properly adjusting the flow rate ratio of the main  $\text{H}_2$  diluent and the halide-carrying  $\text{H}_2$  gas. With this halide concentration in the gas phase and with the  $\text{TaCl}_5$  to  $\text{AlCl}_3$  mole ratio being kept at less than 1.8 to 1, the  $(\text{Ta})\text{Al}_2\text{O}_3$  film deposition was similar to that of pure alumina films, i.e., the film growth was predominated by the surface reactions. The growth rate of the films was primarily determined by and slightly varied by the  $\text{AlCl}_3$  concentration in the gas flow, and was increased exponentially with the decreasing reciprocals of the deposition temperatures in the range of  $800^\circ$ - $900^\circ\text{C}$  studied, with an apparent activation energy similar to that of pure alumina films as shown in Fig. 2. The addition of  $\text{TaCl}_5$  to the gas flow has an effect of reducing the over-all growth rate of the film. As can be seen in Fig. 3, the film growth rate was decreased monotonically with increasing  $\text{TaCl}_5/\text{AlCl}_3$  mole ratio up to 1.8 to 1. When this halide ratio was increased beyond 1.8 to 1, a drastic increase in film growth rate and a change of film morphology from single modal to bimodal were observed. The study of the film deposition was not pursued beyond the halide ratio of 1.8.

The Ta content of the films was determined by the electron microprobe method, using the pure CVD  $\text{Al}_2\text{O}_3$  and  $\text{Ta}_2\text{O}_5$  films obtained in the present system as standards. The Ta content of the film increases with the increasing volume (or mole) ratio of  $\text{TaCl}_5$  to  $\text{AlCl}_3$  in the feed gas. By assuming full saturation of the halides in the  $\text{H}_2$  carrier gas (i.e., each cubic centimeter of  $\text{H}_2$  passing through the saturator carries out  $4.3/760 \text{ cm}^3$

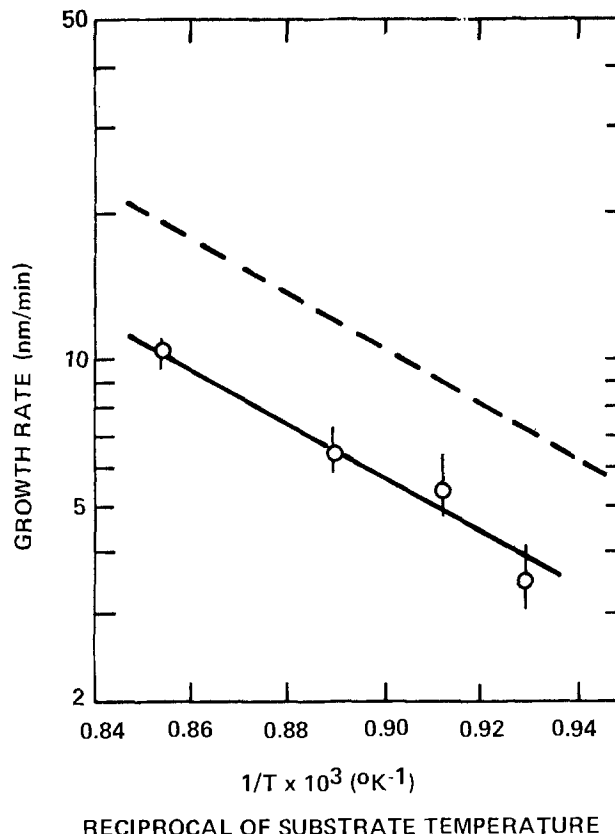


Fig. 2. Arrhenius plot of the growth rate of the  $(\text{Ta})\text{Al}_2\text{O}_3$  films in the temperature range of  $800^\circ$ - $900^\circ\text{C}$  (solid curve). The total halide concentration in the gas phase was  $2.5 \times 10^{-4}$  and the  $\text{TaCl}_5/\text{AlCl}_3$  ratio was kept at 1.3 to 1. The dotted curve in the figure shows the growth rate of pure alumina films in the same temperature range.

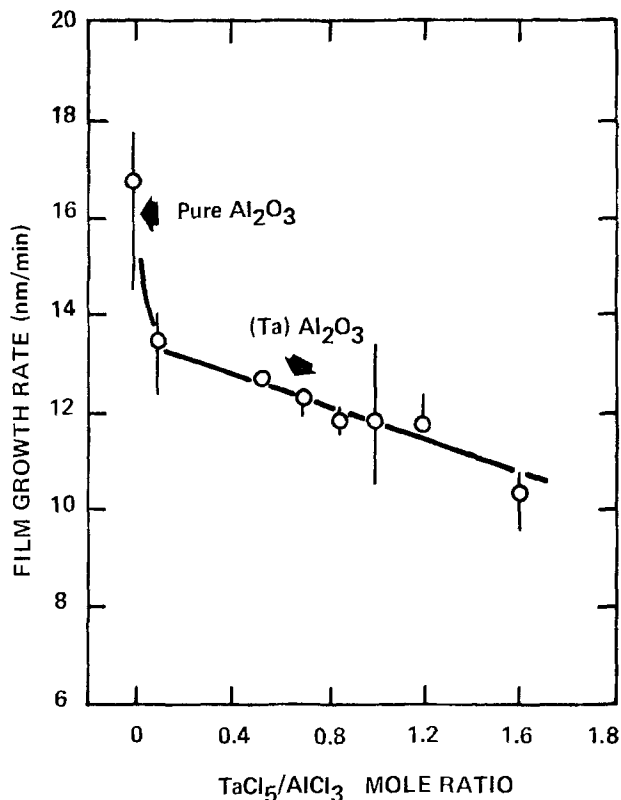


Fig. 3. The growth rate of the  $(\text{Ta})\text{Al}_2\text{O}_3$  film at  $900^\circ\text{C}$  as a function of the  $\text{TaCl}_5/\text{AlCl}_3$  mole ratio in the gas phase. The total halide concentration in the gas phase was varied from  $1.8\text{--}3.0 \times 10^{-4}$ , with the  $\text{AlCl}_3$  concentration in the gas phase kept constant at  $1.8 \times 10^{-4}$ .

halide vapor), we were able to relate the Ta content of the film [in mole per cent (m/o) of  $\text{Ta}_2\text{O}_5$  in the film] with the volume ratio of  $\text{TaCl}_5$  to  $\text{AlCl}_3$  in the feed gas, as shown in Fig. 4.<sup>2</sup> The Ta content of the film rises rather rapidly with the  $\text{TaCl}_5$  to  $\text{AlCl}_3$  ratio and levels off at about 5.5 m/o of  $\text{Ta}_2\text{O}_5$ . The saturation of Ta in the film shown in Fig. 4 may be attributed to system limitations. However, since a drastic increase in film growth rate and a change of film morphology from single modal to bimodal were observed as the  $\text{TaCl}_5/\text{AlCl}_3$  ratio was increased beyond 1.8 to 1, the saturation level in Fig. 4 may also suggest the limitation of incorporating  $\text{Ta}_2\text{O}_5$  into the CVD  $(\text{Ta})\text{Al}_2\text{O}_3$  films. A limited Ta solubility in the amorphous  $(\text{Ta})\text{Al}_2\text{O}_3$  films formed by the pyrolysis of Ta-pentaethoxide [ $\text{Ta}(\text{OC}_2\text{H}_5)_5$ ] and  $\text{AlCl}_3$  was also reported by Matsuo (20).

**Measurements of film properties.—Crystal structure.**—X-ray diffractometry and the transmission electron microscope (TEM) were used to study the crystallinity and structure of the films. For the x-ray diffraction study, the as-received films were used. The samples for TEM studies were prepared by back etching the silicon substrate with a mixture of  $\text{HF} + 2\text{HNO}_3 + 3\text{CH}_3\text{COOH}$  through a wax mask. This leaves a 1 mm circle of unsupported film stretched over the etched hole in the silicon wafer which is suitable for TEM examination.

**Film properties.**—The etchability of the film in various chemicals was measured at room temperature by observing thickness change with immersion time in the chemical. The film thickness, before and after etching, and the film optical index of refraction were measured by ellipsometry.

<sup>2</sup> Since good consistency of the halide saturation levels in the  $\text{H}_2$  carrier gas was seen, the effect of less than full halide saturation in Fig. 2 would be the multiplication of a factor of less than unity to the  $\text{TaCl}_5$  to  $\text{AlCl}_3$  ratio. However, the general characteristics of the Ta content vs.  $\text{TaCl}_5$  to  $\text{AlCl}_3$  ratio would still prevail.

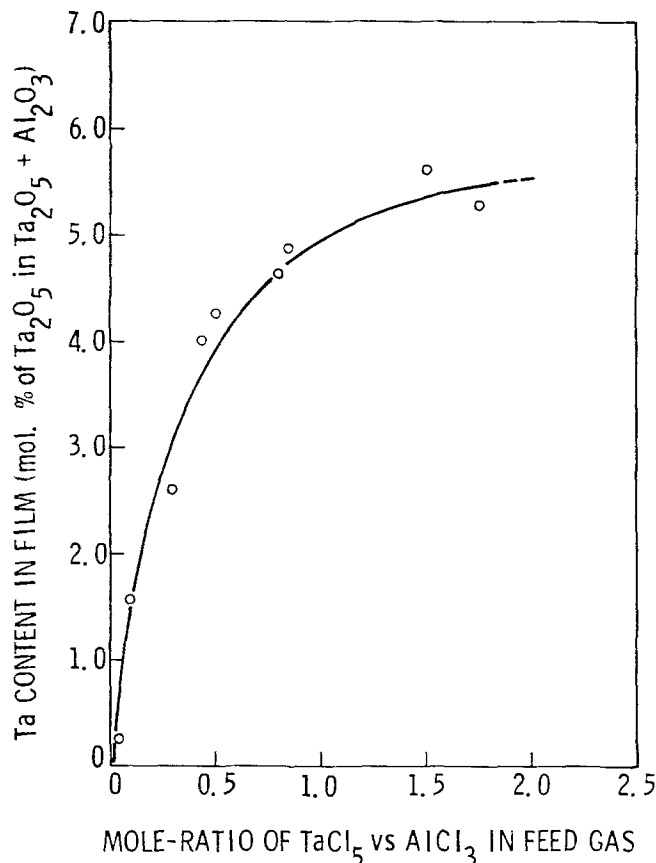


Fig. 4. Ta-content of the  $(\text{Ta})\text{Al}_2\text{O}_3$  film deposited at  $900^\circ\text{C}$  as a function of mole ratio of  $\text{TaCl}_5/\text{AlCl}_3$  in feed gas.

**Electrical characteristics.**—The conventional MIS (metal insulator semiconductor) type samples were fabricated for electrical measurements. In general, pure aluminum was used as the top electrode; however, in the case of d-c conduction measurements, gold top electrodes were used in some samples to study the effect of injecting electrode material on the film's conduction. To provide ohmic contact to the Si substrate, a layer of Al was evaporated onto its back side and the sample was subsequently annealed at  $420^\circ\text{C}$  for 20 min in forming gas. This postmetal anneal also served to reduce surface-state charge of the sample. The capacitance of the MIS samples was measured by a Boonton 710A capacitance meter at 1.0 MHz, while the breakdown strength of the films was measured by the linear I-V ramping technique.

In the film d-c conduction measurements, current transients were observed at lower applied voltages which decay to a quasi steady state in 3-4 min. Therefore, in order to eliminate the transient currents, the I-V characteristics of the films were obtained by applying an incremental stepwise voltage to the sample and measuring the film current 10 min after the voltage application at each voltage step.

### Results and Discussion

**Structure and crystallinity of the films.**—Films deposited at  $900^\circ\text{C}$  with only a minute quantity of Ta doping ( $\text{Ta}_2\text{O}_5 \leq 0.1$  m/o) are crystalline and have the same crystal structure as that of the pure  $\text{Al}_2\text{O}_3$  films examined. X-ray diffractometry performed on these low Ta content films, and the pure alumina films, produced patterns consisting of the few strongest lines of  $\kappa\text{-Al}_2\text{O}_3$ . However, the transmission electron diffraction (TED) pattern of the same films contained a very large number of diffraction lines. The list of interplanar spacings generated from the electron diffraction pattern does not completely match those of any of the alumina phases found in the literature although most of the  $\kappa$ -alumina reflections are accounted for. It is

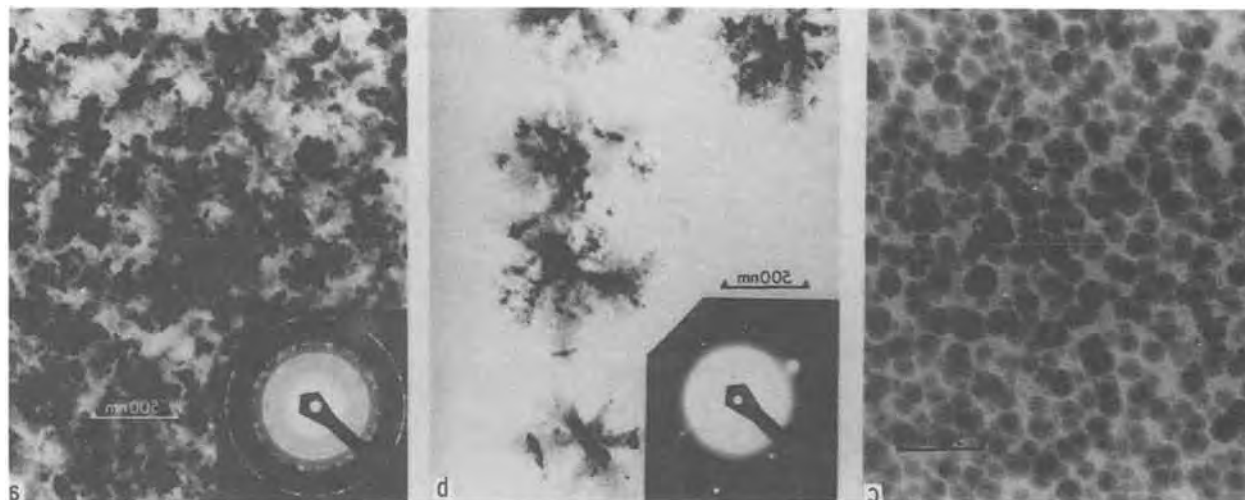


Fig. 5. TEM microstructures of the  $(\text{Ta})\text{Al}_2\text{O}_3$  films deposited on bare silicon: (a) film deposited at  $900^\circ\text{C}$  containing  $\sim 4.1$  m/o  $\text{Ta}_2\text{O}_5$  showing amorphous materials appeared at the film's grain boundaries; (b) film deposited at  $900^\circ\text{C}$  containing  $\sim 5.5$  m/o  $\text{Ta}_2\text{O}_5$ , showing amorphous matrix with  $\kappa'$ -crystallites; and (c) film deposited at  $825^\circ\text{C}$  containing  $\sim 4.8$  m/o  $\text{Ta}_2\text{O}_5$ . No TED pattern was obtainable from this film; the dark dots in the photo, indicated by arrow, are believed to be  $\kappa'$ -embryos.

possible that the extra diffraction lines seen in these CVD alumina films resulted from the occupation by Al atoms of the abnormal octahedral sites of the distorted spinel lattice of the  $\kappa$ -alumina giving rise to  $\kappa$ -alumina structure factor forbidden reflections. Since a complete crystallographical determination of the film is out of the scope of the present experiment, detailed structure analysis was not pursued. However, we were able to obtain the lattice parameters of an orthorhombic unit cell which accounts for the majority of the observed reflections. Calculated interplanar spacings are compared with observed reflections in Table I. We will designate the crystal structure of the films as  $\kappa'$ - $\text{Al}_2\text{O}_3$ , as a variation of  $\kappa$ - $\text{Al}_2\text{O}_3$ , for the convenience of later discussion. These lightly doped films had grain size of the order of 100 nm.

Table I. Crystallographic data

TED measured interplanar spacings	Calculated <sup>(a)</sup> interplanar spacings	Indices	$\kappa$ -alumina interplanar spacings
4.72	6.16	110	6.2
	4.75	101	
	4.53	200	4.5
4.20	4.20	020	4.2
3.14	3.15	121	
	3.02	300	3.04
2.81	2.80	030	2.79
2.76	2.79	002	
	2.70	221	2.70
2.55	2.54	112	2.57
2.42	2.41	131	2.41
2.39	2.38	230	
2.33	2.33	022	2.32
2.28	2.29	212	2.26
	2.18	410	2.16
2.11	2.10	040	
2.08	2.07	222	2.06
2.05	2.05	330	
2.03	2.03	411	
1.99	1.99	420 +	1.99
1.97	1.97	041 +	1.95
1.94	1.93	132 +	
1.87	1.86	003 +	1.87
	1.82	103 +	1.82
	1.75	402 +	1.74
1.64	1.64	341 +	1.64
1.57	1.54	440 +	1.54
1.49	1.49	512 +	1.49
1.45	1.44	052 +	1.44
	1.43	522 +	1.43
1.40	1.40	060 +	
1.395 (100%) <sup>(b)</sup>	1.395	004	1.395 (100%)

<sup>(a)</sup> Interplanar spacings calculated using an orthorhombic unit cell with lattice constants  $a_0 = 9.06$ ,  $b_0 = 8.41$ ,  $c_0 = 5.58\text{\AA}$ .

<sup>(b)</sup> The 1.395 line is the 100% intensity line in the TED pattern and for  $\kappa$ -alumina. In general, the TED intensities differed from the  $\kappa$ -alumina intensities. This is expected, as electron diffraction intensities usually do not track x-ray intensities and the TED pattern shows preferred orientation effect.

A decrease in film crystallinity with increasing Ta content was seen. TEM examination of films deposited at  $900^\circ\text{C}$  showed that diffuse grain boundaries were first formed in the film when a small amount of Ta was added. As the Ta content of the films was increased, the diffuse grain boundaries were replaced by amorphous material, Fig. 5a. At about this point, the film ceased to produce coherent x-ray diffraction patterns, although the  $\kappa'$ -alumina pattern was still obtainable via electron diffraction. The amorphous grain boundary width expanded at the expense of the crystalline grains, as the Ta content of the film was increased. The entire film became amorphous when the  $\text{Ta}_2\text{O}_5$  content of the film reached about 5.5 m/o.

The effects of Ta on the alumina film deposition are, apparently, to inhibit crystal nucleation and to retard grain growth. The effect was more prominent when the films were deposited on oxidized, rather than bare, Si substrates. When the films were deposited directly on bare silicon substrates, there were always some discrete  $\kappa'$ -crystallites included in the film, as shown in Fig. 5b, which, from TEM examination, were nucleated from sites on the silicon surface. The nucleation of the  $\kappa'$ -crystallites was greatly suppressed when the films were deposited on oxidized silicon wafers.

The same crystalline to amorphous structural transition was seen in films deposited at lower temperatures. It was found that by lowering the film deposition temperature the minimum amount of Ta required to produce amorphous films was reduced. At  $800^\circ\text{C}$ , complete amorphous films can be found with  $\text{Ta}_2\text{O}_5$  content as low as 4.5 m/o. Figure 5c shows a near amorphous film deposited at  $825^\circ\text{C}$ , with  $\text{Ta}_2\text{O}_5$  of 4.8 m/o. The film did not show a TED pattern, although TEM revealed bimodal morphology of the film. The dark dots in Fig. 5c are believed to be embryos of  $\kappa'$ -crystallites which were brought out by the silicon etching during TEM sample preparation. Films with the same Ta content would be partly crystalline if deposited at  $900^\circ\text{C}$ . On the other hand, it would be completely amorphous if it were deposited at  $800^\circ\text{C}$ .

Throughout the entire film structure studies, the  $\beta$ -Ta and/or  $\beta$ - $\text{Ta}_2\text{O}_5$  diffraction lines were never observed. Table II summarizes the structural change of the film with its Ta content and the deposition temperature.

*Physicochemical properties of the films.*—As in the case of the pure alumina films, the etchability of the  $(\text{Ta})\text{Al}_2\text{O}_3$  films in concentrated HF and  $\text{NH}_4\text{F}$  buffered HF (BHF) solutions depends on the crystallinity of the film. A highly crystallized film (film with well-defined

Table II. Variation of film crystallinity with Ta content

Sample	$T_{\text{dep}}$ (°C)	Ta content (m/o $\text{Ta}_2\text{O}_5$ )	Crystallinity of film		
			X-ray	TED	TEM
1101	900	0.00	$\kappa'$	$\kappa'$	Crystalline
1089	900	0.15	$\kappa'$	$\kappa'$	Crystalline
1067	900	4.09	Amor.	$\kappa'$	Xtal. d. gb. <sup>(a)</sup>
1134	900	4.62	Amor.	$\kappa'$	Xtal. + amor. gb. <sup>(b)</sup>
1176	900	4.88	Amor.	$\kappa'$	Xtal. + amor. gb. <sup>(b)</sup>
1154	900	5.61	Amor.	$\kappa'$	Amor. + xtal. <sup>(c)</sup>
1158	900	5.27	Amor.	( $\kappa'$ )	Amor. (xtal.) <sup>(d)</sup>
1198	825	4.80	Amor.	Amor.	( $\kappa'$ ) embryos
1205	800	4.50	Amor.	Amor.	Amorphous

(a) Crystalline with diffuse grain boundary.

(b) Crystalline with amorphous grain boundary.

(c) Mixture of crystalline and amorphous phases.

(d) Amorphous film matrix with a small number of  $\kappa'$  crystallites.

x-ray and TED patterns) will not be etched by concentrated HF. On the other hand, a completely amorphous film (film structureless under TED examination) can be readily etched by a diluted BHF solution. The etch rate of the amorphous film in a 10:1 BHF solution is about 240 Å/min and seems to be independent of Ta content. The partly crystalline films with a mixture of amorphous and  $\kappa'$ - $\text{Al}_2\text{O}_3$  phases can also be etched with diluted BHF but the differences in etch rates of the two phases yields a rough surface. At room temperature, none of the common acids, such as  $\text{HNO}_3$ ,  $\text{HCl}$ , and  $\text{H}_2\text{SO}_4$ , were found to etch the  $(\text{Ta})\text{Al}_2\text{O}_3$  films, whether crystalline or amorphous. In hot (185°C)  $\text{H}_3\text{PO}_4$ , uniform etchings of all the  $(\text{Ta})\text{Al}_2\text{O}_3$  films were observed. The partly crystalline films had an etch rate of approximately 240 Å/min while the etch rate of the amorphous films exceeded 500 Å/min.

The measured values of the index of refraction,  $n$ , of the crystalline and partly crystalline films were scattered; they fell in the range of 1.70–1.80. On the other hand, the index of refraction of the amorphous films remained a consistent value of between 1.66 to 1.68 without regard to the Ta content of the film.

**Dielectric characteristics of the films.**—The dielectric constants of the films were calculated from the capacitance and the thickness of the films. The dielectric constant  $K$  of the crystalline and partly crystalline films ranged from 8.0 to 10.0. No correlation between  $K$  and the Ta content of the film could be found. The dielectric constants of the amorphous films were found to range from 9.5 to 12.0, and seemed to increase slightly with Ta content of the film.

The dielectric breakdown strength  $E_b$  of the films, measured from the Al-(Ta) $\text{Al}_2\text{O}_3$ -Si (MAS) structures, was found to be 5–7 MV/cm.  $E_b$ 's measured on the Al-(Ta) $\text{Al}_2\text{O}_3$ -SiO<sub>2</sub>-Si (MAOS) structures (with 55Å underlying SiO<sub>2</sub>) were, in general, larger than 7.0 MV/cm. Table III summarizes the physicochemical properties of the film.

The C-V characteristics of the Al-(Ta) $\text{Al}_2\text{O}_3$ -Si (MAS) diodes are shown in Fig. 6. Curve (a) shows a typical C-V plot of a MAS diode with a highly crystallized, low Ta content (Ta) $\text{Al}_2\text{O}_3$  film. Except for the "sense" of the C-V hysteresis, it is very similar to that of a MAS diode with a pure  $\text{Al}_2\text{O}_3$  film. From the C-V

Table III. Physicochemical properties of film

	Partly crystalline	Amorphous
$n^{(a)}$	1.70–1.80	1.68 ± 0.01
$K^{(b)}$	8.00–10.0	9.5–12.0
BVD <sup>(c)</sup>	60 mV/cm	5.0–7.0 mV/cm
Etch rate BHF	Slow and uneven	Fast and even (~4 Å/sec)
Hot $\text{H}_3\text{PO}_4$	Normal to fast	Fast (~10 Å/sec)

(a)  $n$  = Index of refraction.(b)  $K$  = Dielectric constant measured at 1 MHz.

(c) BVD = Dielectric breakdown strength.

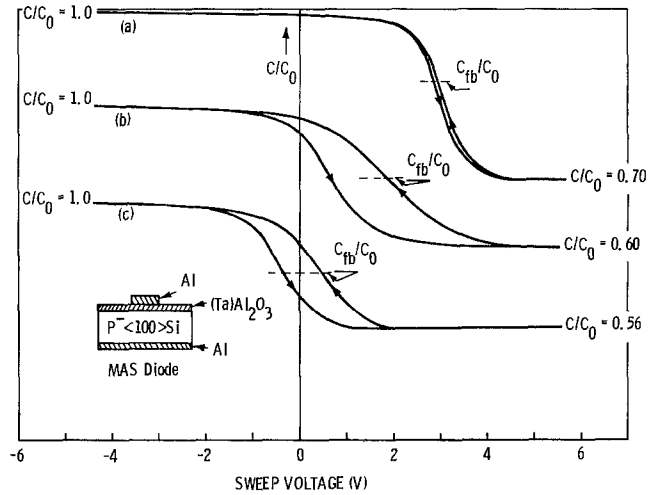


Fig. 6. C-V characteristics of MAS capacitors: (a) with crystalline film; (b) with partly crystalline film; and (c) with amorphous film.

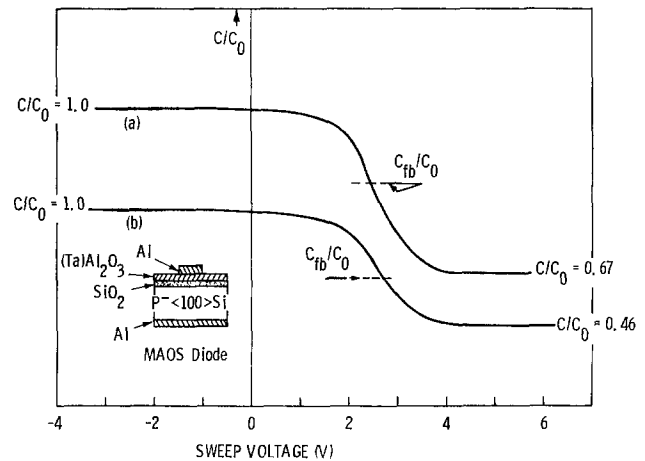


Fig. 7. C-V characteristics of MAOS capacitors: (a) with partly crystalline film; (b) with amorphous film.

hysteresis sense, it appears that acceptor-type, slow surface states exist at the Si-(Ta) $\text{Al}_2\text{O}_3$  interface. The density of these surface states appears to increase with the decreasing crystallinity of the film. This is seen in the extremely large C-V hysteresis in the MAS diodes with the partly crystalline film [Fig. 6, curve (b)] and with the amorphous film [Fig. 6, curve (c)]. The assumption of the existence of surface states at the Si-(Ta) $\text{Al}_2\text{O}_3$  interface is further confirmed by the absence of C-V hysteresis in the MAOS diodes (Fig. 7).

From the positive flatband voltage of the MAS and MAOS diodes examined, it was found that negative charges of the order of  $10^{12}$  q/cm<sup>2</sup> exist in the (Ta) $\text{Al}_2\text{O}_3$  film and/or at the SiO<sub>2</sub>-(Ta) $\text{Al}_2\text{O}_3$  interface. In the MAS diodes, the dielectric charge seems to decrease with the crystallinity of the films. In the MAOS diodes, the crystallinity of the film has little effect on the dielectric charge level, Table IV.

**D-C conduction of the films.**—Figure 8 shows the d-c conduction of an amorphous film deposited at 800°C. The  $\ln(J/E)$ 's, where  $J$  is the current density and  $E$  is the applied field, were plotted against the square

Table IV. Dielectric charge and crystallinity of films

Sample	Diode	$V_{\text{fb}} - \phi_{\text{ms}}$ (V)	$Q_{\text{eff}}$ (q/cm <sup>2</sup> )	Crystallinity of (Ta) $\text{Al}_2\text{O}_3$ film
1053-1	MAS	+2.90	$1.4 \times 10^{12}$	Crystalline
1160-1	MAS	+1.85	$1.05 \times 10^{12}$	Partly crystalline
1206-1	MAS	+0.05	$3.3 \times 10^{11}$	Amorphous
1077-2	MAOS	+1.10	$1.2 \times 10^{12}$	Crystalline
1160-2	MAOS	+2.45	$1.18 \times 10^{12}$	Partly crystalline
1206-2	MAOS	+2.70	$1.10 \times 10^{12}$	Amorphous



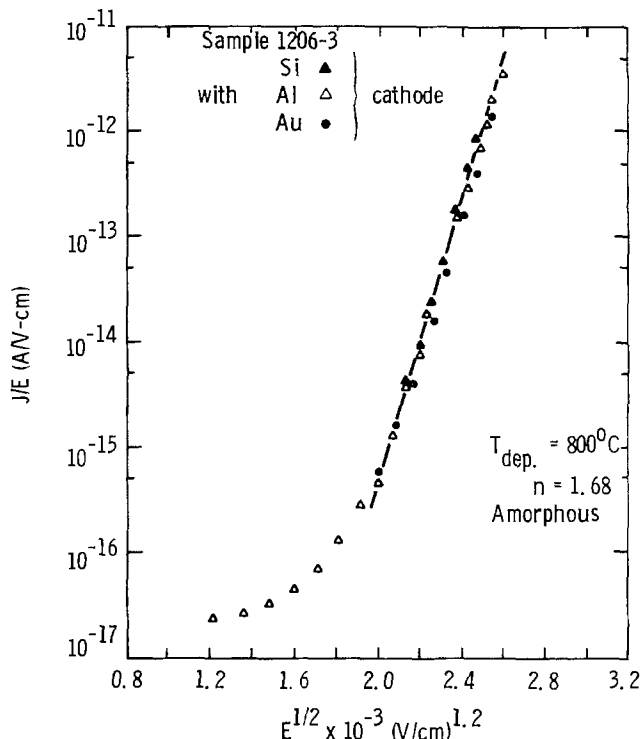


Fig. 8.  $J$ - $E$  characteristics of an amorphous film deposited at  $800^{\circ}\text{C}$ .

root of the applied field. It can be seen that (i) a linear relationship between  $\ln(J/E)$  and  $E^{1/2}$  exists at fields higher than  $3.5 \times 10^6$  V/cm; and (ii)  $J$  is independent of the injecting electrode material. The exponential dependency of film current density on  $E^{1/2}$  and the insensitivity of  $J$  on the electrode material indicate that the conduction is controlled by the Poole-Frenkel (PF) effect (21). The slope  $\mathcal{S}_{PF}$  of the  $\ln(J/E)$  vs.  $E^{1/2}$  plots shown in Fig. 6 yields a value of  $1.6 \times 10^{-2}$ .

It is known that the PF effect (21) arises from the field-assisted thermionic emission of electrons (or holes) from the coulombic traps in the films. The PF conduction of a film that contains only coulombic traps takes the form of Eq. [3] (22), which has a slope  $\mathcal{S}_{PF}$  of the  $\ln(J/E)$  vs.  $E^{1/2}$  plot equals to  $\beta_{PF}/2kT$ , where  $\beta_{PF} = (e^3/\pi\epsilon_0\epsilon_f)^{1/2}$  is the Poole-Frenkel constant

$$J = e\mu E(N_c N_d)^{1/2} \exp -(\psi_d - \beta_{PF} E^{1/2})/2kT \quad [3]$$

where  $e$  = electric charge,  $\mu$  = charge (electron) mobility,  $N_c$  = density of states of the film's conduction band,  $N_d$  = density of the film's coulombic traps,  $\beta_{PF}$  = Poole-Frenkel constant, and  $\psi_d$  = energy of the film's coulombic trap.

The PF constant and the slope of the  $\ln(J/E)$  vs.  $E^{1/2}$  plot, can be calculated by knowing the dynamic dielectric constant  $\epsilon_f$  of the film, or the films' optical index of refraction,  $n$ , since to the first approximation, the dynamic dielectric constant of the film equals the square of the film's optical index of refraction (23). Using the measured value  $n(=1.68)$  of the  $800^{\circ}\text{C}$  film, a theoretical  $\mathcal{S}_{PF}$  of  $0.785 \times 10^{-2}$  is calculated, which is only half of the experimental value. The large experimental  $\mathcal{S}_{PF}$  seen in the film can be explained if, besides the coulombic traps, the existence of neutral traps in the films is assumed (24). In this case, the Poole-Frenkel conduction of the film takes a different form due to the change of the Fermi energy caused by the presence of neutral traps. With the coulomb traps, of density  $N_d$ , and neutral traps, of density  $N_t$ , coexisting in the film, the Poole-Frenkel current density  $J$  takes the form of Eq. [4]

$$J = e\mu N_c(N_d/N_t)^{1/2} \exp -(\psi_d - \beta_{PF} E^{1/2})/kT \quad [4]$$

where  $N_t$  is the density of film's neutral traps, which has a slope of the  $\ln(J/E)$  vs.  $E^{1/2}$  plot equal to  $\beta_{PF}/kT$ , and yields a value of  $1.57 \times 10^{-2}$  if  $n = 1.68$  for the  $800^{\circ}\text{C}$  films is used for calculation. This is in very good agreement with experimentally obtained values.

The current-temperature measurement of the films at constant fields shows an exponential dependency of the conduction current with the reciprocal of the measuring temperature. From the  $\ln(J/E)$  vs.  $1/T$  plots, the apparent activation energy of the film conduction,  $\phi$ , was found to vary linearly with  $E^{1/2}$ , as expected from Eq. [4]. Extrapolating the  $\phi$  vs.  $E^{1/2}$  curve to zero field yields the coulombic trap energy of 1.80 eV below the conduction band of the film.

Similar  $I$ - $V$  characteristics were seen in the films deposited at higher temperatures. However, the slope of their  $\ln(J/E)$  vs.  $E^{1/2}$  plots were smaller, ranging from  $1.14 \times 10^{-2}$  to  $1.3 \times 10^{-2}$ . In addition, a small dependency of  $J$  on the injecting electrode material was also seen. In the films deposited at higher temperatures, some  $\kappa'$ -(Ta)Al<sub>2</sub>O<sub>3</sub> crystallites were always present in the amorphous film matrix. It is possible then that these crystallites increase either the relative neutral trap density or the dynamic dielectric constant, or both. Both of these effects would result in a reduction of the slope of the Poole-Frenkel plot of the film (24, 25).

### Summary

Present work has shown that Ta-doped Al<sub>2</sub>O<sub>3</sub> films can be formed by the pyrolysis of a vapor mixture of TaCl<sub>5</sub> and AlCl<sub>3</sub> in the presence of hydrogen and carbon dioxide in the temperature range of  $800^{\circ}$ - $950^{\circ}\text{C}$ . The maximum Ta doping level of the  $900^{\circ}\text{C}$  films appears to be limited to 5.5 m/o of Ta<sub>2</sub>O<sub>5</sub>. With only a minute amount of Ta, the films are crystalline, having the properties of pure alumina films. When the Ta content exceeds a certain level, the film becomes amorphous. The amorphous films have a smaller optical index of refraction and a slightly larger dielectric constant, as compared with pure alumina films. Amorphous films are etchable in diluted, buffered HF solution at room temperature.

Probably due to the smaller energy bandgap (20), the d-c conduction of the amorphous films was found to be governed by the Poole-Frenkel effect. The energy level of the coulombic traps was found to be 1.80 eV from the conduction band of the film.

The films have negative dielectric charge and good dielectric properties in general. The amorphous film's etchability, in buffered HF solution, makes its use more attractive for microelectronic applications.

### Acknowledgment

The authors are indebted to Mr. William N. Patterson for his assistance in film deposition and to Dr. William A. Pliskin and Dr. Morris Shatzkes for their critical review of the manuscript. Mr. J. F. Shepard's suggestion to do this work and his encouragement are also acknowledged.

Manuscript submitted March 21, 1975; revised manuscript received Aug. 4, 1975. This was Paper 18 presented at the San Francisco, California, Meeting of the Society, May 12-17, 1974.

Any discussion of this paper will appear in a Discussion Section to be published in the December 1976 JOURNAL. All discussions for the December 1976 Discussion Section should be submitted by Aug. 1, 1976.

Publication costs of this article were partially assisted by IBM Corporation.

### REFERENCES

- H. E. Nigh *et al.*, *IEEE Trans. Electron Devices*, **ED-14**, 631 (1967).
- P. B. Hart and P. S. Walsh, Paper 113 presented at The Electrochemical Society Meeting, Los Angeles, California, May 10-15, 1970.
- P. J. Tsang, V. Y. Doo, and C. Johnson, Jr., Paper 170 presented at The Electrochemical Society



- Meeting, Atlantic City, New Jersey, Oct. 4-8, 1970.
4. Shigern Nishimatsu and Takashi Takuyama, *Suppl. J. Japan. Soc. Appl. Phys.*, **39**, 125 (1970).
  5. P. J. Tsang and J. F. Shepard, Paper 168 presented at The Electrochemical Society Meeting, Miami Beach, Florida, Oct. 8-13, 1972.
  6. N. J. Chou and P. J. Tsang, *Met. Trans.*, **2**, 659 (1971).
  7. K. H. Zaininger and A. S. Waxman, *IEEE Trans. Electron Devices*, **ED-16**, 333 (1969).
  8. J. Aboaf, *This Journal*, **115**, 948 (1967).
  9. S. K. Tung and R. E. Caffrey, *ibid.*, **117**, 91 (1970).
  10. P. Balk and F. Stephany, *ibid.*, **118**, 1634 (1971).
  11. G. C. Bye and G. T. Simpkin, *J. Am. Ceram. Soc.*, **57**, 367 (1974).
  12. E. O. Jones, "Glass," John Wiley & Sons, Inc., New York (1956); W. H. Zachariassen, *J. Am. Chem. Soc.*, **54**, 38 (1932).
  13. F. C. Eversteyn and B. H. Put, *This Journal*, **120**, 106 (1973).
  14. W. H. Knausenberger and R. N. Tauber, *ibid.*, **120**, 927 (1973).
  15. "Handbook of Chemistry and Physics," R. C. Weast *et al.*, Editors, 45th edition The Chemical Rubber Co. (1964).
  16. H. Schafer and S. Kahleldurg, *Z. Anorg. Allgem. Chem.*, **305**, 184 (1960).
  17. V. Y. Doo and P. J. Tsang, Paper 6 presented at The Electrochemical Society Meeting, New York, New York, May 4-9, 1969.
  18. P. Tsujide, S. Nakanuma, and Y. Ikushima, *This Journal*, **117**, 703 (1970).
  19. J. Spyridelis *et al.*, *Phys. Status Solidi*, **19**, 683 (1967).
  20. Takeshi Matsuo, *Japan. J. Appl. Phys.*, **12**, 1862 (1973).
  21. D. R. Lamb, "Electrical Conduction Mechanisms in Thin Insulating Films," pp. 74, 87, Methuen and Co. Ltd. (1967).
  22. J. R. Yeagan and H. L. Taylor, *J. Appl. Phys.*, **39**, 5600 (1968).
  23. N. F. Mott and R. W. Gurney, "Electronic Process in Ionic Crystals," 2nd edition, Chap. V, Oxford University Press, Fair Lawn, New York (1948).
  24. J. G. Simmons, *Phys. Rev.*, **155**, 657 (1967).
  25. S. M. Hu, D. R. Kerr, and L. V. Gregor, *Appl. Phys. Letters*, **10**, 97 (1967).

## Flame Fusion Growth of Spinel and Sapphire Crystals for ESFI SOS Technology

R. Falckenberg

Siemens AG, Forschungslaboratorium, München, Germany

### ABSTRACT

A modified flame fusion process has been developed to grow crystals at low cost for use as substrate for the ESFI® SOS technology. Mg-Al spinel and sapphire single crystals with diameters up to 50 mm have been grown. Differences between both kinds of crystals are described concerning the behavior during the widening phase and the cooling phase of the growth process. Crystalline perfection was investigated in both crystals by the x-ray topography.

Mg-Al spinel as well as sapphire crystals are used as an insulating substrate material for the ESFI® SOS technology (1). For the synthesis of these crystals we investigated the flame fusion process, because it is a technique requiring no crucibles. Therefore it offers a possibility of lower costs compared to the Czochralski method, especially if iridium crucibles have to be used. As compared with crucible-grown crystals, the perfection of Verneuil crystals is worse; the electrical properties, however, of silicon films deposited on both kinds of substrates (2-4) do not show a significant difference. Verneuil sapphire (5) and spinel are produced on a large scale for jewels and bearings; severe limitations, however, exist especially as far as crystals of large diameter and suitable orientation are concerned. The diameter required for substrate wafers is between 50 and 75 mm; the orientation is  $\langle 100 \rangle$  and  $\langle \bar{1}012 \rangle$  for Mg-Al spinel and sapphire, respectively.

Two phenomena can be observed, if such crystals are grown by the flame fusion process: (i) cracking of the crystals during the cooling down phase and (ii) melt runover during the widening phase of the growth process.

With spinel crystals, it could be shown that cracking can be avoided by modifying the technique (6). The idea of the modification is to essentially exclude the temperature shock a crystal suffers at the end of the growth process when the flame is quenched. This is done by a ceramic furnace insert which deflects the flame gases immediately below the growth front of the growing crystal; from the beginning of the growth process, the bulk of the crystal is in thermal equilib-

rium with this insert. During the cooling down, the cooling rate is determined by the heat capacity of the insert. By this method, even the stoichiometric variation of Mg-Al spinel could be grown (Fig. 1).

The phenomena of melt runover can be understood by considering a model which explains the mechanism of crystal widening (9). According to this model an increase in flame power leads to remelting of a thin layer of already crystallized matter immediately below the growth front. The excess melt runs down at the crystal rim and forms a protrusion along the solid-liquid transition line. This line goes around the top of the crystal. The lower part of the protrusion solidifies. This model conception requires the radial temperature gradient at the solid-liquid transition line to stay below a certain critical magnitude, if the formation of a protrusion that is widening of the crystal is to occur.

Now alone the fact that a large crystal diameter requires a large growth chamber leads to low wall temperatures inside the growth chamber and consequently to an increase of the temperature gradient in question. Device parameters affecting the gradient are furnace insulation, multiple burners (10-12), displaceable heat shields and additional heating of the side walls of the growth chamber. An example of a displaceable insert device and additional heating for the modified flame fusion technique is shown schematically in Fig. 2. In contrast to afterheaters (13-16), which are thought for an *in situ* annealing of a crystal after the growth process, additional heating during crystal growth has to be confined to side walls of the growth chamber situated at (and above) the level of the solid-liquid transition line of the crystal. Additional heating below this level

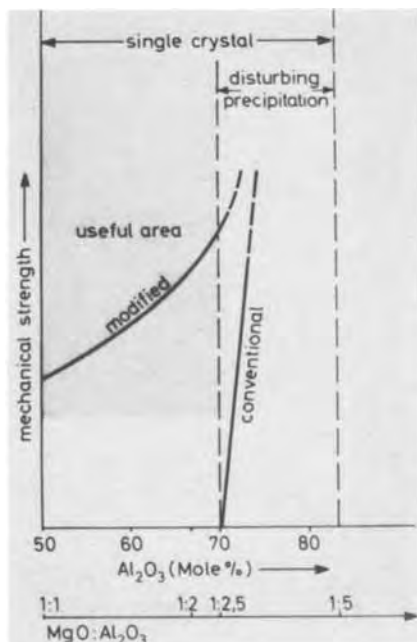


Fig. 1. Spinel substrate growth by flame fusion. The useful area is limited by too low mechanical strength (7) and by precipitations (8) arising during thermal treatment which disturb the epitaxial growth of silicon films.

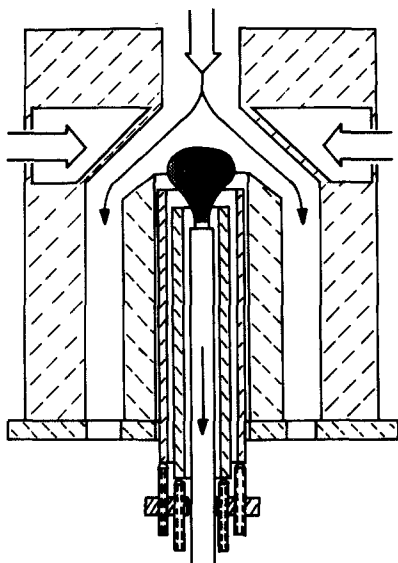


Fig. 2. Furnace with telescopic insert and additional heating of the side walls of the growth chamber for the growth of large diameter crystals.

would, at the high temperatures required, lead to an unstable growth situation due to the decrease of the axial temperature gradient along the crystal.

In Table I the results are shown which were obtained with spinel of a molar composition  $\text{MgO}:\text{Al}_2\text{O}_3 = 1:2$  and with sapphire. All the changes of the device parameters shown are acting in a direction as to keep the radial temperature gradient at the level of the solid-liquid transition line below a critical value. Above this value widening of the crystal would not be possible without melt runover. In a displaceable heat shield device as depicted in Fig. 2 but without additional heating, spinel crystals could be grown up to a diameter of 50 mm (Fig. 3). In the identical device, sapphire crystals could be grown only up to a diameter of 38 mm; trying to enlarge the diameter further led to melt runover. According to the model of crystal widening, the radial temperature gradient had to be further decreased. With the device shown in Fig. 2 we

Table I. Influence of device parameters on the diameter of Mg-Al spinel and sapphire crystals

Device parameters	Maximum crystal diameter [mm]	
	spinel	sapphire
poor furnace insulation, 2-tube burner	20	—
furnace insulation reinforced, 2-tube burner	35	—
furnace insulation reinforced, 3-tube burner	40	—
furnace insulation reinforced, 3-tube burner, telescopic insert	50	38
additional heating of side walls	—	53

used additional oxyhydrogen burners heating the side walls of the growth chamber. In this way sapphire crystals with a diameter up to about 50 mm could be grown (Fig. 3). A further enlargement was not possible in this device because of the inner diameter of the growth chamber being only 60 mm.

At the end of the growth process the flame was quenched. The spinel crystals obtained were mechanically stable; annealing before machining was not necessary. Sapphire crystals of  $\langle\bar{1}012\rangle$  orientation cracked if the diameter was larger than  $\sim 45$  mm; strength and diameter could be increased further by choosing a different orientation, e.g.,  $\langle\bar{1}010\rangle$ .

For x-ray topography spinel and sapphire crystals were cut into wafers perpendicular to the growth axis. The spinel samples were lapped with SiC, polished with  $\text{Al}_2\text{O}_3$ , thoroughly cleaned with Ultrasonics, etched with hot phosphoric acid, treated with sulfuric acid, and rinsed with distilled water. The final thickness of the samples was  $300 \mu\text{m}$ . With the sapphire slices, lapping as well as polishing was done with diamond paste. Figure 4 shows the x-ray topographies demonstrating the crystal quality. The spinel crystal shows a number of subgrains with deviations in orientation from the growth axis  $\langle 100 \rangle$  of up to  $2^\circ$ . The sapphire crystal essentially shows only tensions with a deviation from the growth axis not exceeding  $1^\circ$ .

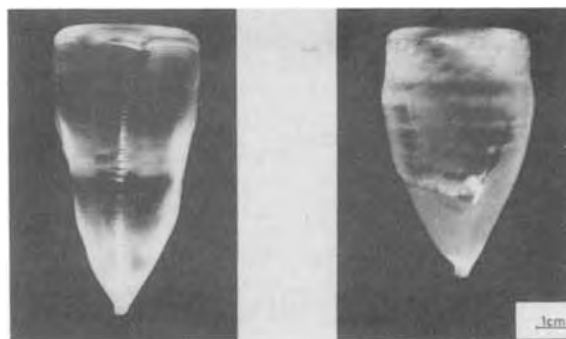


Fig. 3. Mg-Al spinel single crystal (molar composition  $\text{MgO}:\text{Al}_2\text{O}_3 = 1:2$ ) and sapphire crystal, grown by the modified flame fusion process. Orientation  $\langle 100 \rangle$  and  $\langle\bar{1}012\rangle$ , respectively.

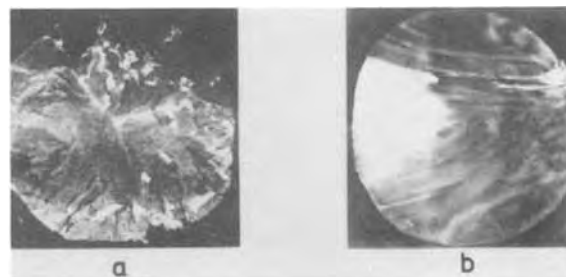


Fig. 4. X-ray topographies (Lang mode) of Mg-Al spinel (a) and sapphire (b), the reflecting planes being  $\{400\}$  and  $\{012\}$  respectively. Radiation  $\text{Mo K } \alpha_1$ .

Growing spinel and sapphire distinct differences have been found in the way the crystals behaved during the widening phase as well as during the cooling down phase of the growth process. Different behavior in the diameter increasing may be due to differences in the thermal conductivities, emissivities, and IR absorptions; values which apply at high temperatures are known only for the IR absorption which indeed is lower for sapphire than for spinel. About the sensitivity of cracking measurements with polycrystalline  $\text{Al}_2\text{O}_3$  material have been conducted by Schwartz (17), there are however no investigations of Mg-Al spinel, which could be compared with these results.

#### Acknowledgments

The author wishes to acknowledge the work of J. v. Ivanits who assisted in crystal growth and of H. Grienauer who did the x-ray topography. For valuable discussions the author would like to thank Dr. E. Preuß.

Manuscript submitted July 24, 1975; revised manuscript received Sept. 18, 1975. This was Paper 223 presented at the Toronto, Canada, Meeting of the Society, May 11-16, 1975.

Any discussion of this paper will appear in a Discussion Section to be published in the December 1976 JOURNAL. All discussions for the December 1976 Discussion Section should be submitted by Aug. 1, 1976.

Publication costs of this article were partially assisted by Siemens AG.

#### REFERENCES

1. H. Schlötterer, *Electronics*, **42**, 113 (1969).
2. M. Druminski and Ch. Kühn, Paper presented at the GdCh-meeting "Grundlagen der Epitaxie," Erlangen, Germany, Sept. 1974.
3. M. Druminski, Ch. Kühn, E. Preuß, H. Splittgerber, D. Takacs, and J. Tihanyi, Paper presented at ESSDERC, Nottingham, Sept. 74.
4. G. W. Cullen and F. C. Dougherty, *J. Cryst. Growth*, **17**, 230 (1972).
5. J. Ricard and A. Cioccolani, *ibid.*, **13/14**, 718 (1972).
6. R. Falckenberg, *ibid.*, **13/14**, 723 (1972).
7. J. G. Grabmaier and R. Falckenberg, *J. Am. Ceram. Soc.*, **52**, 648 (1969).
8. R. Falckenberg, *Mater. Res. Bull.*, **8**, 171 (1973).
9. R. Falckenberg, *J. Cryst. Growth*, **29**, 195 (1975).
10. J. A. Adamski, *J. Appl. Phys.*, **36**, 1784 (1965).
11. R. A. Lefevew, *Rev. Sci. Instr.*, **33**, 769 (1962).
12. Ch. H. Moore, *Trans. Am. Inst. Mining Met. Eng.*, **184**, 194 (1949).
13. W. Seifert, *J. Cryst. Growth*, **12**, 17 (1972).
14. R. S. Mitchell, *Rev. Sci. Instr.*, **36**, 1667 (1965).
15. R. H. Arlett and M. Robbins, *J. Am. Ceram. Soc.*, **50**, 273 (1967).
16. L. Merker, *ibid.*, **45**, 366 (1962).
17. B. Schwartz, *ibid.*, **35**, 325 (1952).

## MOS (Si-Gate) Compatibility of RF Diode and Triode Sputtering Processes

A. K. Sinha

Bell Laboratories, Murray Hill, New Jersey 07974

#### ABSTRACT

Using a Si-gate CMOS tester the MOS compatibility has been demonstrated of a metallization process involving triode sputter etch cleaning of Si prior to PtSi contact formation, triode sputter deposition of Ti/TiN/Pt layers, and rf diode sputter etching of the Pt using Ni as a sputter etch mask. The radiation damage induced in the gate regions of CMOS capacitors by each step of this metallization process has been evaluated, and the surface states and oxide charge resulting from the damage have been shown to be completely annealable using hydrogen. Triode sputter etch cleaning of the Si prior to PtSi formation was found to introduce considerable radiation damage. All of this damage could be removed after sintering and stripping the unreacted Pt by a hydrogen anneal at a temperature in the range of 375°-400°C and for times in the range of ½ to 1 hr. Subsequent triode sputter deposition of Ti/TiN/Pt leads to the generation of only a small peak ( $\sim 1-2 \times 10^{10} \text{ cm}^{-2} \text{ eV}^{-1}$ ) in the  $N_{ss}$  distribution in the lower half of the bandgap. Sputter etching of Au and Pt in an rf-diode system at rf power levels of 2 W  $\text{cm}^{-2}$  (sputter etch rate  $\sim 900 \text{ \AA/min}$  for Au) also leads to considerable radiation damage. However, for a lower rf power of  $\sim 1.2 \text{ Wcm}^{-2}$ , which is practical if Pt only is sputter etched, little additional damage is observed over and above that induced during triode sputter deposition of Ti/TiN/Pt. Our results indicate that if a hydrogen anneal is performed prior to the final metal deposition (i.e., prior to the structure being sealed if a  $\text{Si}_3\text{N}_4$  layer is used), then excess hydrogen can be trapped in the  $\text{SiO}_2$  and poly-Si layers. A low temperature inert ambient anneal (e.g., 325°C, 1 hr, vacuum) can then be used subsequent to final metal deposition, during which hydrogen is redistributed, neutralizing any surface states at the Si/SiO<sub>2</sub> interface.

A recent technology for  $\text{Si}_3\text{N}_4$ -sealed MOS-LSI devices utilizes chemical vapor deposited (CVD) poly-Si for the first level conductor (gates) separated from the second level metallization (contacts and interconnections) by an intermediate dielectric layer consisting of CVD  $\text{SiO}_2$  followed by  $\text{Si}_3\text{N}_4$  (1). The second level metallization processing involves the use of filament evaporation to form  $\text{Pd}_2\text{Si/Ti/Pd}$ . Evaporation was

Key words: heat-treatment, LSI processing, metallization, uniform gold process.

chosen over sputtering because (i) sputtering as opposed to filament evaporation can cause radiation-induced damage (2), leading to unwanted interface states and trapped charge in the MOS structures, and (ii) it was considered very difficult to anneal out any radiation damage since the combination of metal contacts and  $\text{Si}_3\text{N}_4$  in the intermediate dielectric layer seals the device from the hydrogen required for low temperature (< 450°C) annealing of the interface states (3, 4). Sputter deposition has certain obvious advan-

tages though, an important one being that the step coverage is better than that usually obtained by evaporation (5). Poor step coverage by second level metallization is especially undesirable in the contact areas, since it can provide paths for migration of impurities such as Na and Au.

The objective of the present work was (i) to characterize any radiation-induced damage in Si-gate MOS structures due to triode sputter deposition and etching, and rf diode sputter etching, and (ii) to devise annealing schemes that would eliminate such damage in Si-gate devices sealed with  $\text{Si}_3\text{N}_4$ . For this purpose, a realistic test vehicle was used in which most of the thin gate oxide areas are covered by layers of poly-Si and intermediate level dielectrics.<sup>1</sup> The uniform gold process (7) was utilized for metal pattern generation for second level metallization. This process has been successfully used for metal gate MOS and bipolar devices. For bipolar devices, the metallization scheme consists of PtSi/Ti/TiN/Pt/Au which is metallurgically more reliable than the  $\text{Pd}_2\text{Si}/\text{Ti}/\text{Pd}/\text{Au}$  system. The uniform gold process is LSI compatible, since only one critical photoresist step is required as opposed to two for the standard Pd or Pt etch processes. The process studied involves triode sputter etch cleaning prior to PtSi contact formation, triode sputter deposition of Pt for PtSi, triode sputter deposition of Ti, TiN, and Pt layers, and electroplating of Au and Ni. The Au and Pt layers are removed by sputter etching in an rf diode system using selectively plated Ni as the mask. Each of the steps and combinations, thereof, have been evaluated with regard to the radiation-induced damage they produce in the above-mentioned MOS structure. An effective annealing scheme has been devised which utilizes intentionally trapped hydrogen to anneal out interface states in sealed MOS structures.

### MOS Test Structure and Processing

Figure 1(a) shows a photomicrograph of a completed chip of the CMOS tester; the upper left corner shows the MOS capacitors on n-Si substrates and on the p-tub. Details of the MOS capacitors including metal contacts (rectangular-shaped pads,  $4 \times 10$  mil, over square window,  $3 \times 3$  mil) to the poly-Si electrodes

<sup>1</sup> Extensive studies were recently carried out by McCaughan *et al.* (2) on apparently "unannealable-degradation" of thin oxide films and interfaces due to various sputter deposition and back-sputtering processes; however, their test structures involved direct exposure of the gate oxide to various plasmas, following which the gate electrodes were evaporated.

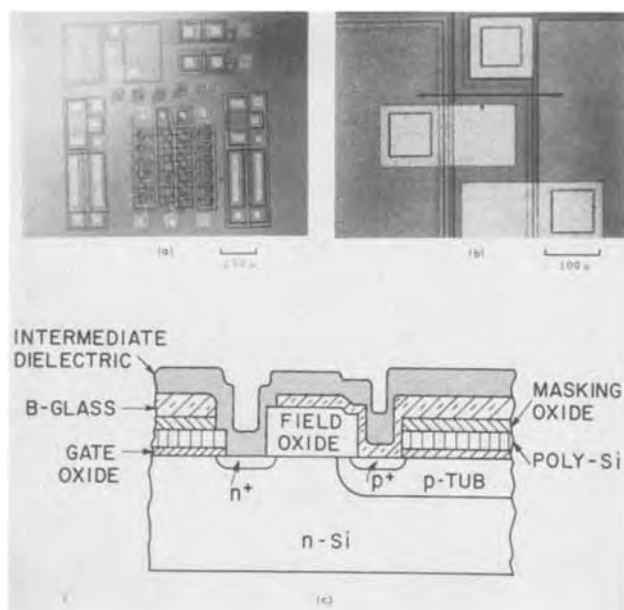


Fig. 1. (a) Photomicrograph of the CMOS tester. (b) Details of the p- and n-channel MOS capacitors. (c) Schematic cross section through the unmetallized portion of (b).

(area =  $10^{-3}$  cm<sup>2</sup>) and that (square-shaped pad,  $4 \times 4$  mil over window,  $3 \times 3$  mil) to the p-tub are shown in Fig. 1(b), whereas Fig. 1(c) shows schematically a cross section through the unmetallized portion of the two capacitors, including the n<sup>+</sup> and p<sup>+</sup> guard rings. The Si substrates consisted of  $\langle 100 \rangle$  n-type material doped with As to  $N_D \approx 1.5 \times 10^{15}$  cm<sup>-3</sup> whereas the p-tubs were doped with B to  $N_A \approx 1.5 \times 10^{16}$  cm<sup>-3</sup>. The gate oxide (1000Å thick) was grown on a freshly exposed Si surface prepared by stripping 1μ thick steam-oxide off the gate areas. The oxidation was done in HCl-cleaned quartz tube furnaces in a dry O<sub>2</sub> ambient at 1100°C (40 min) following which the oxidized Si wafers were annealed in Ar, also at 1100°C (30 min) using the same furnace. The first level (gate) metallization consisted of poly-Si doped with P to a sheet resistance of  $\sim 10$  ohm/□. The poly-Si electrodes were defined using steam-grown oxide (2500Å) as a mask. The p<sup>+</sup> areas ( $N_A \sim 2 \times 10^{19}$  cm<sup>-3</sup>) were formed using 1000Å of B-doped "Silox" oxide (followed by 2000Å of undoped SiO<sub>2</sub>, both made by reacting SiH<sub>4</sub> and O<sub>2</sub> at 480°C) as a diffusion source, with a drive-in at 1100°C (2 hr, N<sub>2</sub>). Next, n<sup>+</sup> areas ( $N_D \sim 10^{20}$  cm<sup>-3</sup>) were doped using PBr<sub>3</sub> (1100°C, 30 min). The intermediate dielectric layer separating the first level poly-Si metallization from the second level metallization normally consists of a composite layer of 1μ SiO<sub>2</sub> and 1-2000Å Si<sub>3</sub>N<sub>4</sub> through which windows are opened down to the diffused Si areas as well as to the poly-Si. In the present experiments, the Si<sub>3</sub>N<sub>4</sub> layer was omitted. However, the annealing schemes were devised keeping this Si<sub>3</sub>N<sub>4</sub>-sealing layer in mind.

The second level (contact and interconnection) metallization consists of PtSi ohmic contacts to n<sup>+</sup> and p<sup>+</sup> Si areas and to poly-Si, Ti/TiN/Pt/Au interconnections up to the termination areas, where a third level of metallization (beam leads) is built up by selectively electroplating thick Au beams ( $\sim 12\mu$ ). The characteristics of the sputtering stations (8) used in our experiments are given in Table I.

Finally, the back side of the Si wafers was cleaned and metallized with evaporated Al to form a large area ohmic contact to the n-Si substrate. Contacts to the p-tub were provided on front side of the wafer, along side each n-channel capacitor as shown in Fig. 1(b).

### MOS Measurement Technique

For MOS measurements, the test facility consisted of an Electroglas 910 prober equipped with a Temptronix TP35 thermochuck; the whole apparatus was completely enclosed in a dry N<sub>2</sub> glove box containing air interlocks. High frequency (1 MHz) C-V measurements were made at sweep rates of 100 mV/sec and quasi-static measurements were made at sweep rates of 20 mV/sec using the slow-ramp technique described by Kuhn (9). On a limited number of samples, mea-

Table I. Characteristics of the triode and rf diode machines/processes used in the present work

- |     |   |
|-----|---|
| (A) | Triode machine  |
|     | Plasma in the Ti confinement tube: 80V, d.c., 10A                                   |
|     | Ta filament (cathode of confinement tube): 54A, a.c.                                |
|     | Ar pressure: 2μ   |
| (a) | Sputter etch cleaning mode  |
|     | Substrate table (Al coated with Pt): 500V peak-to-peak, rf ( $\sim 250$ W rf power) |
|     | Catch plate (stainless steel) grounded  |
|     | Si sputter etch rate $\approx 400$ Å/min  |
| (b) | Sputter deposition mode   |
|     | Target (Ti or Pt, 12 in. diam): $-500$ V, d.c.                                      |
|     | Substrate table: grounded through the rf power supply                               |
|     | pN <sub>2</sub> for TiN: $7 \times 10^{-5}$ Torr                                    |
|     | Deposition times: 1 min for 500Å Pt   |
|     | 3½ min for 1000Å Ti   |
|     | 2 min for 100Å TiN  |
|     | 3 min for 1500Å Pt  |
| (B) | Rf diode sputter etching machine  |
|     | Rf power: 2 Wcm <sup>-2</sup> at 13.7 MHz (14 in. diam cathode)                     |
|     | Cathode self-bias: 1800V peak-to-peak, $-900$ V, d.c.                               |
|     | Pressure: 20μ (80% Ar, 20% air)   |
|     | Cathode/anode spacing: 2 in.  |
|     | Au sputter etch rate: 900 Å/min   |

measurements were also made of the minority carrier storage time, oxide breakdown voltage, and the mobile charge density. The storage times were determined by pulsing the MOS capacitors into deep depletion and then plotting the recovery of inversion capacitance as a function of time.

The high frequency and quasi-static C-V data were analyzed in the manner described, *e.g.*, by Wagner and Berglund (10). The Si-doping level  $N_{D,A}$  was estimated from the measured inversion capacitance,  $C_{inv}$  ( $Fcm^{-2}$ ) and the flatband voltage,  $V_{FB}$ , was estimated from the calculated flatband capacitance  $C_{FB}$ . For nonideal C-V curves, the net oxide charge,  $Q_t$  ( $cm^{-2}$ ) at flatband can be calculated using the relationship (11)

$$Q_t = (\phi_{MS} - V_{FB}) \cdot \frac{C_{ox}}{q} \quad [1]$$

where  $\phi_{MS}$  is the work function difference between the metal gate and the Si-substrate (for  $n^+$  poly-Si, its Fermi level was assumed to coincide with the Si-conduction band edge),  $C_{ox}$  is the oxide capacitance ( $Fcm^{-2}$ ), and  $q$  is the electronic charge. This simple equation does not allow one to separate the true fixed charge,  $Q_{ss}$  (always positive) from charges ( $N_{st}$ , positive or negative) trapped in the surface states. The latter are responsible for distortions in the high frequency C-V curves. The interface states density,  $N_{SS}$  ( $cm^{-2} eV^{-1}$ ) was calculated from the dispersion in the quasi-static and high frequency curves, in accordance with the relationship (12)

$$N_{SS} = \frac{C_{ox}}{q} \cdot \left[ \frac{1}{1/C_{qs} - 1} - \frac{1}{1/C_{hf} - 1} \right] \quad [2]$$

where  $C_{qs}$  and  $C_{hf}$  are normalized values (on a scale of 1.0, which represents the accumulation capacitance) of the quasi-static and the high frequency capacitances, respectively, at a given gate bias. The  $N_{SS}$  results from Eq. [2] are truly valid only in the potential range extending from about flatband point to the midgap. In a number of cases, the quasi-static C-V curves were analyzed in detail to give  $N_{SS}$  as a function of the relative surface potential,  $\psi_s$ , which was calculated from the area under the quasi-static curve (12)

$$\psi_s = \int_{V_0}^V [1 - C_{qs}] \cdot dV \quad [3]$$

The  $N_{SS}$  vs.  $\psi_s$  results for p- and n-channel capacitors were plotted on the same graph labeling  $\psi_s = 0$  at midgap, so that  $\psi_s(FB) \approx +|\phi_F|$  for the p-channel and  $-|\phi_F|$  for the n-channel capacitor. Positive values of  $\psi_s$  then signify the upper half of the bandgap and the negative values represent the lower half of the bandgap.

### The Over-all Metallization Process

Figure 2 shows typical high frequency C-V curves (solid lines) for p- and n-channel capacitors subjected to the over-all metallization process outlined in Table I. Also shown for comparison are the dashed C-V curves (high frequency and quasi-static), which correspond to well-annealed CMOS capacitors. The solid C-V curves reflect certain obvious effects of radiation damage; they are greatly distorted indicating a high density of surface states,  $N_{SS}$ . The negative shift of both C-V curves is taken as an indication of a large positive charge  $Q_{ss}$ . One consequence of the large  $Q_{ss}$  and high  $N_{SS}$  is to significantly decrease the apparent threshold voltage for the corresponding MOS transistor from the intended values of approximately  $\mp 1.5V$  (for p- and n-channel, respectively) to about  $-5.0$  and  $-1.0V$ , respectively, as indicated in Fig. 2.

For an understanding of the MOS damage shown in Fig. 2, the effects were studied of each of the three radiation-damage inducing steps in the metallization process, namely, sputter etch cleaning of Si, sputter deposition, and sputter etching of the deposited metallization. These results are considered below.

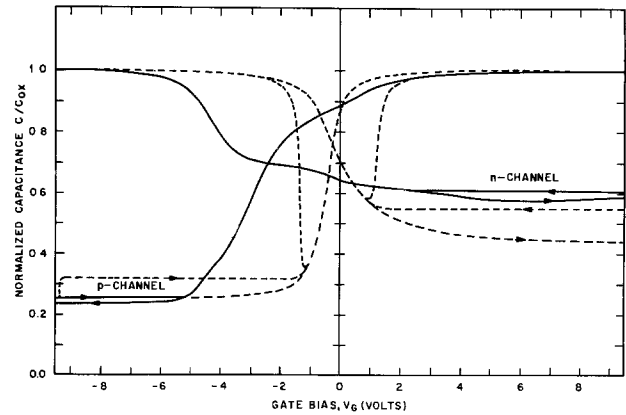


Fig. 2. High frequency C-V curves for CMOS capacitors subjected to the standard metallization process (solid lines). The dashed lines show C-V curves (high frequency and quasi-static) for well-annealed capacitors, with no radiation damage.

*Sputter etch cleaning.*—The preferred practice of forming PtSi ohmic contacts to Si (13) involves *in situ* rf-sputter etch cleaning of the exposed Si areas (*e.g.*, source, drain, and guard rings in the Si substrate, and contact areas of the  $n^+$  poly-Si gate); this is followed by sputter deposition of Pt and sintering of the Pt layer to form PtSi ohmic contacts. For sputter etching, an rf potential is applied to the substrates, and the substrates achieve a negative self-bias equal to approximately one-half the peak-to-peak rf potential. As a result of this potential, the substrates are subjected to bombardment by energetic  $Ar^+$  ions extracted from the plasma. With no metal barriers present yet, direct damage can occur, in the case of IG-FET's (insulated gate field effect transistors), at the edge of the gate oxide/Si interface which gets exposed when windows are formed in the source and drain areas. In the case of test capacitors, a similar situation arises at the  $p^+$  contacts to the p-tub. Moreover, indirect damage can result from  $Ar^+$ -ion bombardment of the poly-Si layer over the Si/SiO<sub>2</sub> interface. Although the exact mechanisms are not apparent, sputter etch cleaning was found to be the most severe radiation-damage inducing step of the metallization process.

The radiation damage induced by sputter etching is expected to be cumulative, *i.e.*, it will depend upon the product of the intensity of radiation and time of exposure. The effect of the duration of sputter etch cleaning is shown in Fig. 3 and 4 which show complete C-V curves (high frequency and quasi-static, p- and n-channel) for samples sputter etch cleaned for 3 min and 1 min, respectively. Subsequent to sputter etching but prior to C-V measurements both of these samples were coated with 500Å of sputtered Pt, sintered at 650°C (20 min) in Ar/10% air ambient and the unre-

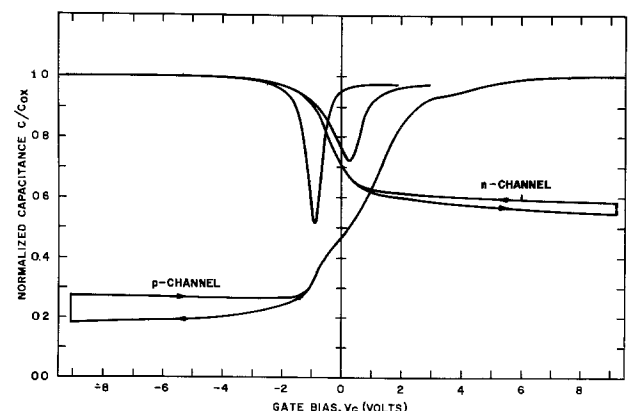


Fig. 3. C-V curves for CMOS capacitors processed through 3 min of sputter etch cleaning and PtSi formation in the contact windows.

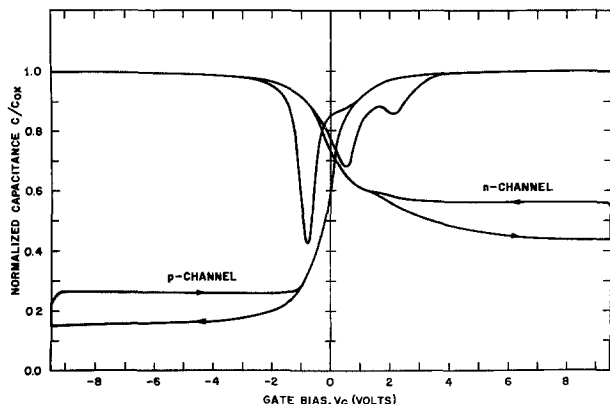


Fig. 4. C-V curves for CMOS capacitors processed through 1 min of sputter etch cleaning and PtSi formation in the contact windows.

acted Pt was etched away using hot *aqua regia*. The high frequency C-V curve for the p-channel capacitor of Fig. 3 is severely distorted and shifted in the positive direction. The positive shift of the p-channel C-V curve is also seen for the sample of Fig. 4 which was sputter cleaned for 1 min, but it is considerably less in extent. These positive shifts (apparent negative  $Q_t$ ) appear to be the result of a large  $N_{SS}$  effect.

The data in Fig. 3 and 4 were analyzed to give a distribution of surface states density  $N_{SS}$  with the relative surface potential  $\psi_s$  (Fig. 5). In both cases, i.e., for 3 and 1 min backsputter cleaning, the  $N_{SS}$  vs.  $\psi_s$  distributions are similar; they show a shallow minimum near the mid-gap and a well-defined peak near the p-channel flatband point in the upper half of the forbidden band. The area under the peak of Fig. 5(a) was used to estimate  $N_{st}$ , the (negative) charge ( $-6.5 \times 10^{11} \text{ cm}^{-2}$ ) associated with the interface traps which, in the present case, act as acceptor states. Moreover, the shift in high frequency C-V curves for p-channel capacitors gives  $Q_t$  ( $= Q_{SS} + N_{st}$ ) as  $-3.4 \times 10^{11} \text{ cm}^{-2}$ , so that the radiation-induced  $Q_{SS}$  appears to be  $\sim 3 \times 10^{11} \text{ cm}^{-2}$ . A similar calculation for the case of Fig. 5(b) gives the trapped charge  $N_{st}$  as  $-10^{11} \text{ cm}^{-2}$  and the radiation-induced  $Q_{SS}$  as  $\sim 2 \times 10^{10} \text{ cm}^{-2}$ . In both cases, negative  $N_{st}$  dominates  $Q_{SS}$ , but only for p-channel capacitors presumably because the portion of the forbidden gap available for occu-

pancy by negative charges increases on going from midgap to flatband of p-channel capacitors; a reverse situation holds for n-channel capacitors.

Nearly ideal MOS characteristics are restored, i.e., the surface states are completely neutralized upon hydrogen annealing either of the above two samples at, e.g.,  $380^\circ\text{C}$  for  $\frac{1}{2}$  hr. This is evident from the data shown in Fig. 6 according to which both p- and n-channel capacitors have a  $Q_{SS} \sim 0$  (i.e.,  $< 10^{10} \text{ cm}^{-2}$ ) and midgap  $N_{SS} < 10^{10} \text{ cm}^{-2} \text{ eV}^{-1}$ . In the case where the intermediate oxide is covered with  $\text{Si}_3\text{N}_4$ , the  $\text{H}_2$  annealing would primarily occur by lateral migration of the H atoms across the wall of the contact windows, i.e., in the region between the top  $\text{Si}_3\text{N}_4$  layer and the PtSi layer present at the bottom of the contact apertures. The device is not fully sealed (against  $\text{H}_2$ ) until the contact windows are covered with Ti/TiN/Pt metallization upon subsequent sputter deposition.

*Ti/TiN/Pt triode sputter deposition.*—Triode sputter deposition of Ti/TiN/Pt was carried out on wafers which contained sintered PtSi ohmic contacts and were  $\text{H}_2$ -annealed for times in excess of those required to neutralize the previously present interface states. Metal pads were then defined over the contact areas by chemical etching in conjunction with usual photolithographic techniques. During the sputter deposition step, most of the particle bombardment is due to low energy neutrals, however, during the early stages of deposition, until a continuous layer (1000-2000Å) of metal film is formed, the Si-gate areas ( $\sim 5000\text{Å}$  thick) are exposed to the u.v. radiation and voltages of the plasma, which can produce radiation damage (14).

The effect of triode sputter deposition is shown in Fig. 7 in the form of high frequency and quasi-static C-V plots. It may be seen that sputter deposition after PtSi formation and  $\text{H}_2$  anneal does not appreciably distort the high frequency C-V curves, but the quasi-static C-V curves show evidence of interface states, whose distribution is shown in Fig. 8. This  $N_{SS}$  distribution has a peak in the lower half of the bandgap; however, the  $N_{SS}$  values are relatively low (in the range of  $1-7 \times 10^{10} \text{ cm}^{-2} \text{ eV}^{-1}$ ) so that the effects of any charge trapping are not reflected by appreciable distortion of the high frequency C-V curves.

*Sputter etching for metal pattern generation.*—The radiation damage induced in MOS Si-gate structures by rf diode sputter etching for metal pattern genera-

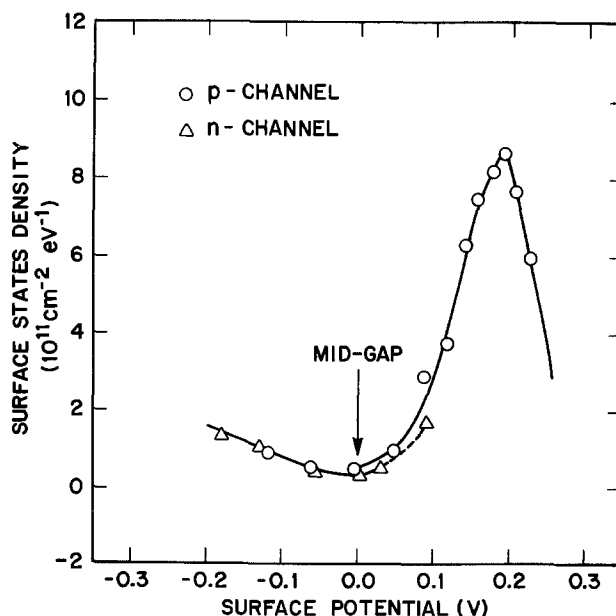
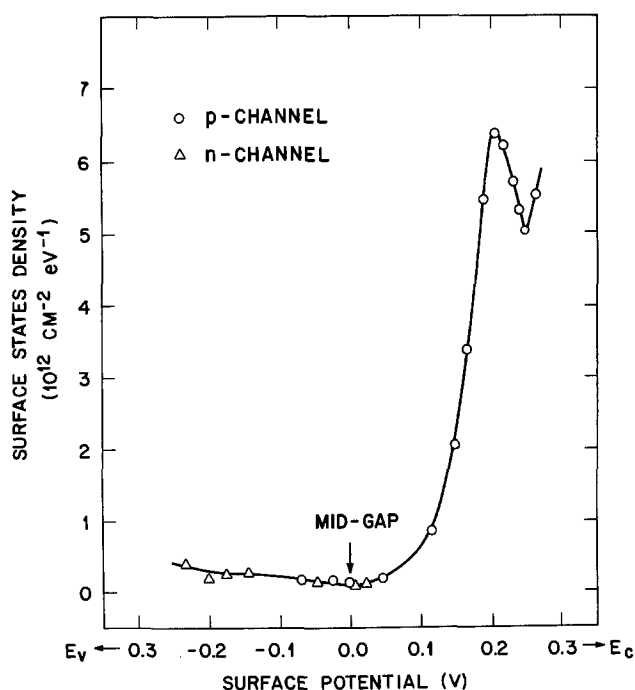


Fig. 5(a) and (b). Interface states density vs. surface potential curve for CMOS capacitors of Fig. 3 and 4, respectively

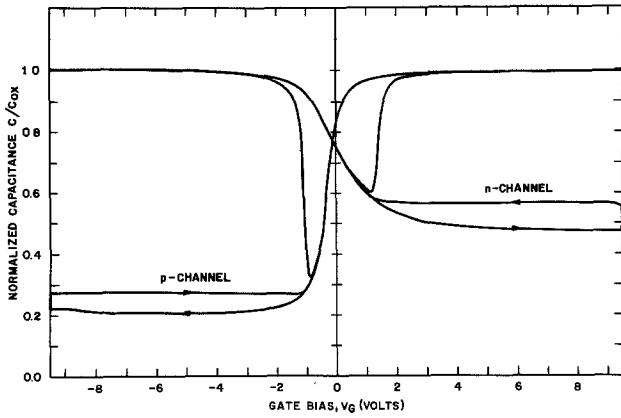


Fig. 6. Effect of H<sub>2</sub> anneal (380°C, 1/2 hr) on the CMOS capacitors of Fig. 3 or 4.

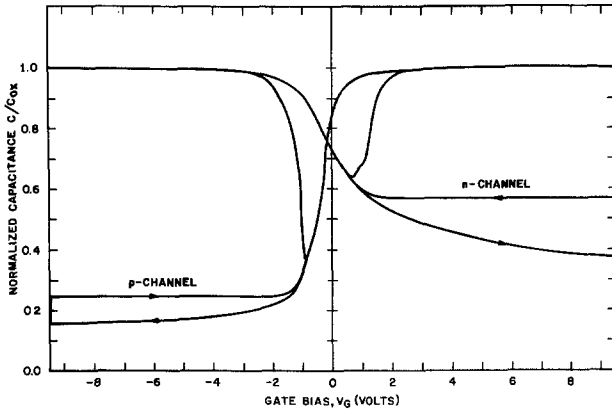


Fig. 7. Effect of Ti/TiN/Pt triode sputter deposition on the CMOS capacitors containing PtSi contacts and H<sub>2</sub> annealed prior to triode sputter deposition.

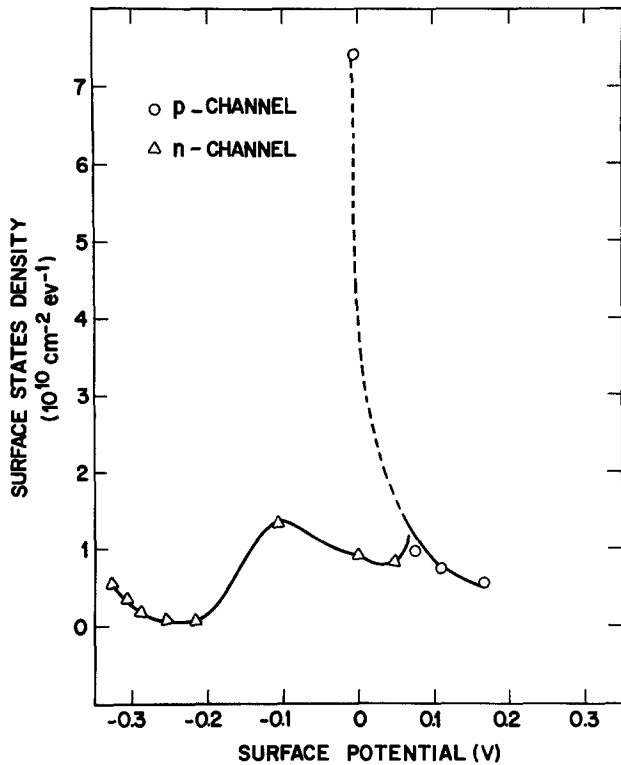


Fig. 8. Surface states density vs. surface potential for the CMOS capacitor of Fig. 7.

tion (uniform gold process) has been recently investigated (15). It was concluded that the damage is primarily due to x-rays (bremmstrahlung and character-

istic) generated by secondary electrons accelerated from the cathode which strike the anode. Since many types of MOS SIC's may require gold only on the beam leads and not on the intrachip metallization, sputter etch processes for metal patterning with and without gold (i.e., those utilizing high and low rf power levels, see below) on the intrachip metallization were compared. Two sets of conditions were evaluated. First, samples containing PtSi/Ti/TiN/Pt and H<sub>2</sub>-annealed after PtSi formation were uniformly plated with gold (1μ) and selectively plated with a Ni mask. The Au and Pt layers were removed by sputter etching for 30 min at an incident rf power to the cathode of 2 Wcm<sup>-2</sup>. This condition corresponds to a cathode d-c self-bias of -900V, an rf peak-to-peak voltage of 1800V, and a gold sputter etch rate of ~900 Å/min. Second, samples, containing PtSi/Ti/TiN/Pt were selectively plated directly with Ni and the Pt removed by sputter etching for 20 min at an incident rf power to the cathode of 1.2 Wcm<sup>-2</sup>. This corresponds to a cathode self-bias of -500V, d.c., and an rf peak-to-peak voltage of 1000V. Elimination of Au on the intrachip metallization makes it practical to consider sputter etching at lower power levels which should be milder conditions as far as MOS damage is concerned.

The C-V data for the sample sputter etched at a power of 2 Wcm<sup>-2</sup> are shown in Fig. 9. Considerable damage has occurred to the CMOS capacitors as reflected in the large positive Q<sub>t</sub> (4-5 × 10<sup>11</sup> cm<sup>-2</sup> eV<sup>-1</sup>) and N<sub>SS</sub> values. The distribution of N<sub>SS</sub> vs. ψ<sub>s</sub> is shown in Fig. 10. The N<sub>SS</sub> shows a peak in the upper half of the bandgap near the flatband point for the p-channel capacitor. From the area under this peak, the charge N<sub>st</sub> trapped in the surface states is estimated as ~10<sup>11</sup> cm<sup>-2</sup>. This is relatively small compared to Q<sub>t</sub> (= Q<sub>SS</sub> + N<sub>st</sub>) so that irrespective of the sign of N<sub>st</sub>, Q<sub>SS</sub> will be a large positive number (3-6 × 10<sup>11</sup> cm<sup>-2</sup>). Thus, in contrast with the case of sputter etch cleaning, here the radiation-induced positive Q<sub>SS</sub> dominates N<sub>st</sub>. At this stage, it is not possible to determine whether the N<sub>st</sub> is associated with acceptor states (i.e., N<sub>st</sub> ~ -10<sup>11</sup>, Q<sub>SS</sub> ~ 5-6 × 10<sup>11</sup> cm<sup>-2</sup>) or with donor states (i.e., N<sub>st</sub> ~ 10<sup>11</sup>, Q<sub>SS</sub> ~ 3-4 × 10<sup>11</sup> cm<sup>-2</sup>).

The effect of sputter etching at the lower power of 1.2 Wcm<sup>-2</sup> is shown in Fig. 11. Although this sample shows only a slight increase in Q<sub>t</sub>, the MOS degradation is manifested by an order of magnitude increase in N<sub>SS</sub> over that characteristic of well-annealed samples (see, e.g., results given below). The resulting distribution of N<sub>SS</sub> with ψ<sub>s</sub> is shown in Fig. 12. It is characterized by a minimum near the midgap. These N<sub>SS</sub> values are comparable to those induced by sputter deposition of Ti/TiN/Pt layers (Fig. 8) so that it appears that the simple expedient of reducing the rf power used for sputter etching was effective in mini-

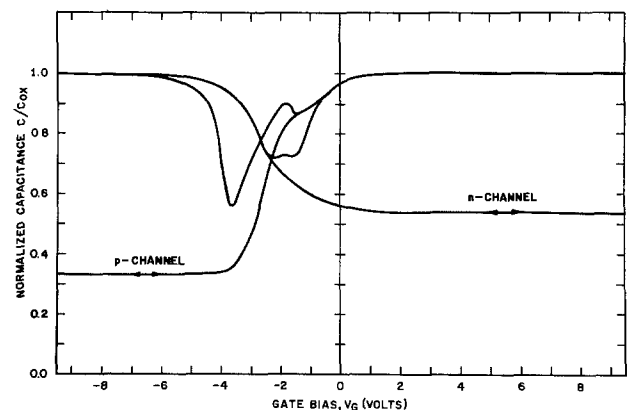


Fig. 9. C-V curves for CMOS capacitors processed through PtSi contacts, H<sub>2</sub> anneal, Ti/TiN/Pt sputtering, Au electroplating, and sputter etching at high powers (2 Wcm<sup>-2</sup>).

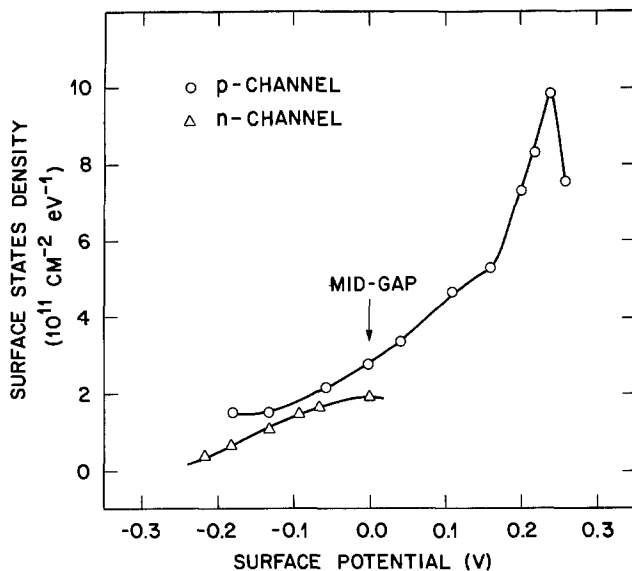


Fig. 10. Surface states density distribution curve for the CMOS capacitor of Fig. 9.

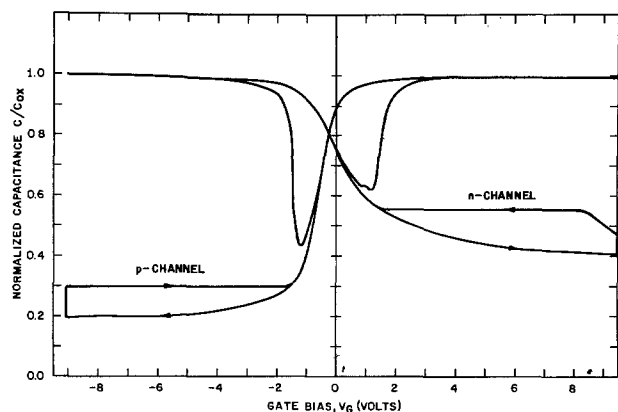


Fig. 11. C-V curves for CMOS capacitors processed through PtSi contact formation,  $H_2$  anneal, Ti/TiN/Pt sputtering, and sputter etch through Pt at low powers ( $1.2 \text{ Wcm}^{-2}$ ).

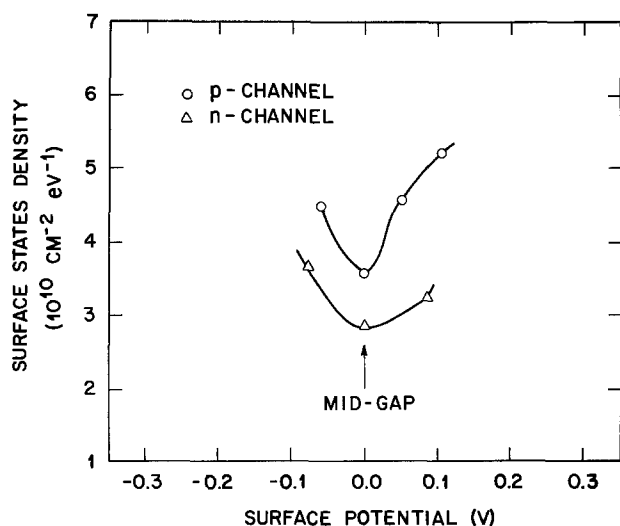


Fig. 12. Surface states density distribution curve for the CMOS capacitor of Fig. 11.

mizing additional damage during the sputter etch step. Furthermore, a partial annealing<sup>2</sup> of the  $N_{SS}$  due to trapped  $H_2$  (see below) might have also occurred dur-

<sup>2</sup> Although the Si wafers are clamped to a water-cooled cathode plate for efficient cooling during sputter etching, surface temperatures in the range  $100^\circ\text{--}200^\circ\text{C}$  are attained.

ing sputter etching to give the appearance of only a small net increase in  $N_{SS}$ .

### Use of Trapped Hydrogen for Annealing Interface States

The combination of a  $Si_3N_4$  seal and sputtered Ti/TiN/Pt metallization in the contact windows would render devices impervious (at practical postmetallization processing temperatures) to hydrogen which is required to neutralize the surface states associated with dangling bands at the Si/SiO<sub>2</sub> interface (16). Although the upper limit of postmetallization  $H_2$ -annealing temperature can be set by a variety of reasons, for systems containing Au, it will definitely be below the Au-Si eutectic point ( $370^\circ\text{C}$ ), and in the case of Al thin films it will be  $\leq 450^\circ\text{C}$  because of excessive hillock formation and grain growth. Our results indicate that part of the hydrogen previously introduced (during  $380^\circ\text{C}$ , 1/2 hr  $H_2$  anneal) in the devices after PtSi formation in the contacts gets trapped into the SiO<sub>2</sub> and poly-Si layers of the device. A subsequent anneal in an inert ambient such as *vacuo*<sup>3</sup> causes this trapped hydrogen to redistribute and anneal out the additional interface states produced by Ti/TiN/Pt sputter deposition and Pt sputter etching steps. The results of a vacuum anneal at  $325^\circ\text{C}$  (1 hr) are shown in Fig. 13 for a sample that received triode Ti/TiN/Pt sputter deposition and Pt removal by diode sputter etching. Nearly ideal MOS characteristics have been restored after the  $325^\circ\text{C}$  "redistribution anneal." The midgap surface states density is reduced by about an order of magnitude  $\sim 4 \times 10^9 \text{ cm}^{-2} \text{ eV}^{-1}$  for the p-channel device and to  $\sim 9 \times 10^9 \text{ cm}^{-2} \text{ eV}^{-1}$  for the n-channel device. The resulting  $Q_{SS}$  is nearly zero (*i.e.*,  $< 10^{10} \text{ cm}^{-2}$ ) for both cases and the calculated threshold voltages are found to be approximately  $\mp 1.5\text{V}$ , respectively, for the p- and n-channel devices, as expected.

Additional measurements of storage time, oxide breakdown voltage, and mobile charge were made on a limited number of MOS capacitors subjected to the hydrogen-redistribution anneals. Figure 14 shows typical plots of the normalized MOS capacitance as a function of time after the capacitors were driven into deep depletion by a pulse voltage of  $-10\text{V}$  or  $+10\text{V}$  for the p- and n-channel devices, respectively. The capacitors gradually recovered to the equilibrium state of inversion. The resulting transients were analyzed by the procedure suggested by Heiman (17). For the p-channel capacitors, the  $\tau$  was estimated at midpoint of the transient as 0.1 and 0.23 msec whereas for the n-channel capacitor on diffused p-tubs,  $\tau$  was found to be

<sup>3</sup> Vacuum annealing was initially tried to ensure moisture-free samples. Equally good results have been obtained by annealing in  $N_2$  or forming gas but only provided the samples had earlier received a  $H_2$ -annealing treatment prior to sputter deposition.

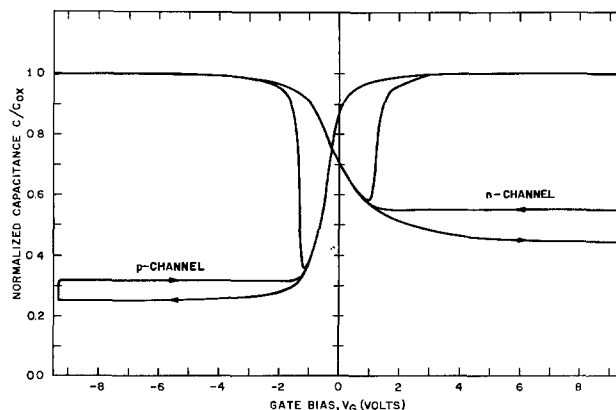


Fig. 13. Nearly ideal C-V curves of CMOS capacitors processed through PtSi contacts,  $H_2$  anneal, Ti/TiN/Pt sputtering, Pt sputter etch, and a final vacuum anneal ( $324^\circ\text{C}$ , 1 hr) to redistribute the previously trapped  $H_2$ .



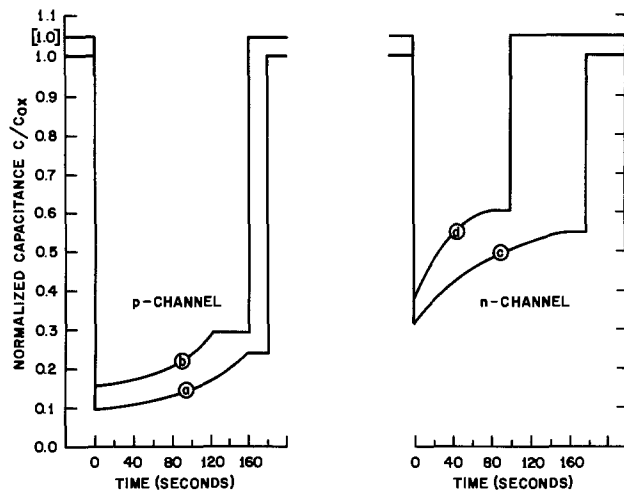


Fig. 14. Normalized MOS capacitance vs. time for capacitors of Fig. 13 driven into deep depletion: (a) and (b) p-channel; (c) and (d) n-channel.

much shorter at 9 and 5  $\mu\text{sec}$ . These values are generally representative of those expected for well-annealed MOS samples.

Gate-oxide breakdown voltages were also measured for a limited number of capacitors after the H-redistribution anneal. These ranged from 30 to 65V (for 1000Å thick gate oxide) with a median of about 50V.

Bias-stress aging experiments were carried out ( $\pm 10\text{V}$  on gate oxide, 250°C, 30 min) on the annealed samples with a view to determine any mobile charge ( $\text{Na}^+$ ) in the gate oxide. The total flatband shifts were always less than 0.1V indicating that the present CMOS device processing (which included a 1000°C  $\text{PBr}_3$  getter step) was effective in keeping the mobile charge density acceptably below  $10^{10}$  atom  $\text{cm}^{-2}$ , and that mobile charges were not activated in the gate oxide as a result of the above processing steps.

Long-term negative bias-temperature aging studies (4) were not carried out, but they would be required to verify the permanence of the anneal. In view of the low values of  $N_{\text{SS}}$  that were achieved, there is reason to believe that significant charge trapping and consequent shifts in threshold voltage should not occur.

### Conclusions

Using a Si-gate CMOS structure, the MOS compatibility has been demonstrated of a process involving (i) triode sputter etch cleaning of contact areas, triode sputter deposition of Pt (for PtSi) and Ti, TiN, Pt layers, and rf diode sputter etching of the Pt layer and (ii) use of trapped hydrogen for annealing interface states in sealed MOS structures. The conclusions reached should be of general validity to Si-gate MOS devices, even though details of the radiation damage may depend critically on the specific structure employed.

1. The dominant modes of damage were found to be generation of surface states, radiation-induced  $Q_{\text{SS}}$ , and lifetime degradation, all of which are annealable using hydrogen.

2. The triode sputter etch cleaning step introduces surface states whose distribution shows a peak in the upper half of the bandgap. A large negative charge in the surface traps appears to dominate the (positive) radiation-induced  $Q_{\text{SS}}$ .

3. The triode sputter deposition process (following PtSi contact formation and  $\text{H}_2$  annealing) of Ti/TiN/Pt layers leads to a small peak in  $N_{\text{SS}}$  in the lower half of the bandgap.

4. Rf diode sputter etching (of Au and/or Pt) at high powers ( $2 \text{ Wcm}^{-2}$ ) produced a peak in  $N_{\text{SS}}$ , also in the upper half of the bandgap. In this case a large positive radiation-induced  $Q_{\text{SS}}$  dominates any charges associated with surface traps. For low power sputter etching ( $1.2 \text{ Wcm}^{-2}$ ), the  $N_{\text{SS}}$  distribution contains no peaks, only a shallow minimum is present near the midgap and no charge trapping is observed.

5. In sealed MOS structures which are impervious to hydrogen during postdamage annealing, hydrogen can be introduced and trapped in the oxide layer prior to the deposition of the final metallic layer seal. A low temperature, inert ambient anneal (e.g., 325°C, 1 hr vac) can then be employed, subsequent to sputter deposition of the metallic layer, whereby the hydrogen redistributes by migration to the Si/SiO<sub>2</sub> interface and repairs the MOS damage.

6. MOS structures subjected to the above H-redistribution anneal have midgap  $N_{\text{SS}}$  in the  $10^9 \text{ cm}^{-2} \text{ eV}^{-1}$  range, nearly zero  $Q_{\text{SS}}$  (i.e.,  $< 10^{10} \text{ cm}^{-2}$ ), and lifetime of 10-100  $\mu\text{sec}$ . With careful processing, no mobile charges are introduced or activated by the above processes.

### Acknowledgments

The author is indebted to E. F. Labuda for many helpful suggestions in the course of this work, and for reviewing the manuscript. Appreciation is also extended to L. B. Fritzing for his generous assistance with metallization processing, to T. E. Smith for technical assistance with the MOS measurements, and to E. H. Nicollian, H. J. Levinstein, and R. S. Wagner for their suggestions.

Manuscript submitted July 16, 1975; revised manuscript received Sept. 22, 1975.

Any discussion of this paper will appear in a Discussion Section to be published in the December 1976 JOURNAL. All discussions for the December 1976 Discussion Section should be submitted by Aug. 1, 1976.

Publication costs of this article were partially assisted by Bell Laboratories.

### REFERENCES

1. J. T. Clemens, Unpublished.
2. D. V. McCaughan and R. A. Kushner, *Proc. IEEE*, **62**, 1236 (1974).
3. B. E. Deal, E. L. MacKenna, and P. L. Castro, *This Journal*, **116**, 997 (1969).
4. E. H. Nicollian, 12th Annual IEEE Proc. Rel. Physics, p. 267, 1974.
5. A. K. Sinha, Proc. 6th Int. Vac. Congress, *Japan. J. Appl. Phys., Suppl.* **2**, 487 (1974).
6. W. T. Lynch and W. J. Bertram, Unpublished.
7. E. F. Labuda, G. K. Herb, W. D. Ryden, L. B. Fritzing, and J. M. Szabo, Jr., Abstract 78, p. 195, The Electrochemical Society Extended Abstracts, Spring Meeting, San Francisco, California, May 12-17, 1974.
8. L. B. Fritzing, To be published.
9. M. Kuhn, *Solid-State Electron.*, **13**, 873 (1970).
10. S. Wagner and C. N. Berglund, *Rev. Sci. Instr.*, **43**, 1775 (1972).
11. A. S. Grove, B. E. Deal, E. H. Snow and C. T. Sah, *Solid-State Electron.*, **8**, 145 (1965).
12. C. N. Berglund, *IEEE Trans. Electron. Devices*, **ED-13**, 701 (1966).
13. A. K. Sinha, *This Journal*, **120**, 1767 (1973).
14. A. S. Grove, "Physics and Technology of Semiconductor Devices," John Wiley & Sons, Inc., New York (1967).
15. W. D. Ryden, E. F. Labuda, and J. T. Clemens, To be published.
16. E. Kooi, *Philips Res. Rept.*, **21**, 477 (1966).
17. F. P. Heiman, *IEEE Trans. Electron. Devices*, **ED-14**, 781 (1967).

# Characterization of Thin Anodized Films on Aluminum with Soft X-ray Spectroscopy

W. L. Baun

Air Force Materials Laboratory (MBM), Wright-Patterson AFB, Ohio 45433

and T. J. Wild and J. S. Solomon

University of Dayton Research Institute, Dayton, Ohio 45469

## ABSTRACT

Two methods utilizing x-ray spectra from the electron microbeam probe for the determination of aluminum oxide film thickness for a broad range of thicknesses are described. One method uses the direct measurement of oxygen K emission while the other uses the changes in fine features of the x-ray spectra with changes in oxide film thickness. For oxides formed by barrier anodization technique, films as thin as 20-30Å and as thick as several thousand angstroms could be measured by these methods.

The thickness of thin films is usually determined by optical methods such as ellipsometry or interferometry or by an indirect method such as calculation from the evaporation of a known weight of material in a vacuum evaporator. Depth profiling techniques in which an inert gas ion beam sputters away surface layers while the surface is sampled are being used increasingly. Such depth profiling is done with ion scattering spectroscopy (ISS), secondary ion mass spectroscopy (SIMS), Auger electron spectroscopy (AES), and electron spectroscopy for chemical analysis (ESCA). Both the optical methods and techniques depending on sputter etching give good results in selected cases. However, the optical methods suffer greatly when the film is not uniform and the substrate is not flat (macroscopic) and smooth (microscopic). Other factors such as the film being a color which absorbs the probing radiation also can interfere with optical measurements such as ellipsometry. The accuracy of methods using sputter etching depends on a knowledge of the film sputtering rate, which even for pure materials varies greatly (depending on experimental conditions, especially ion beam voltage). There are also problems due to ion beam crater shape (sampling from the sides as well as the bottom of the crater), redeposition of sputtered material back into the crater, surface roughness, and other factors.

Each of the aforementioned techniques gave good results on idealized aluminum oxide films on aluminum. Such samples were prepared by vacuum evaporating aluminum on glass microscope slides and anodizing under barrier conditions at low voltages. When real samples which had been cut by shear techniques from bulk sheet stock subjected to surface oxidizing etches or to standard surface preparation prior to anodization were investigated, very poor results were often obtained probably due to surface roughness. X-ray emission technique similar to that used by Sewell *et al.* (1, 2) for thin films of Ta<sub>2</sub>O<sub>5</sub> on Ta by means of oxygen K measurement looked attractive for determining thickness of aluminum oxide on aluminum. In addition, the striking changes in the fine features of aluminum K spectra with changes in chemical combination (3, 4) showed promise for characterizing these films, both from the standpoints of thickness and structure.

## Experimental

The Hitachi XMAS electron microbeam probe analyzer equipped with a dispersing KAP crystal and an

Key words: films, x-ray, Al<sub>2</sub>O<sub>3</sub>, spectroscopy, anodization.

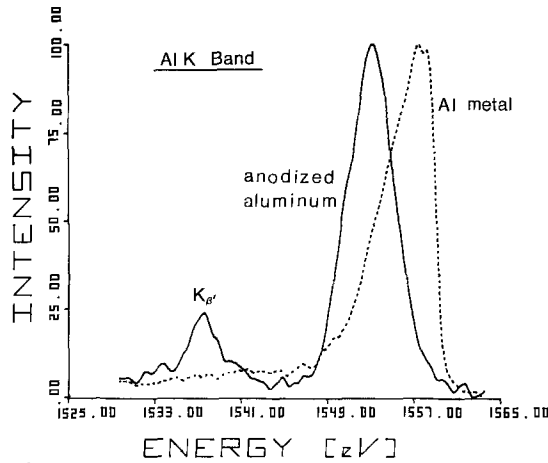
ultrathin polypropylene-windowed flow proportional detector was used for results on oxygen K radiation shown here. For aluminum K spectra high resolution was provided by use of an ADP dispersing crystal. The electron beam potential was 10 kV with  $1 \times 10^{-6}$ A electron beam current using approximately 5  $\mu\text{m}^2$  beam. X-ray data was collected by step-scan techniques on paper tape and inputted to a time-share computer, X and Y intercepts for each point were calculated, and plots were prepared by a digital plotter. Samples were prepared in a stirred bath of 1% ammonium borate in ethylene glycol. Except as discussed later, anodizing voltages were maintained (constant voltage) in a range which gave a barrier anodized film.

## Background on X-ray Spectra

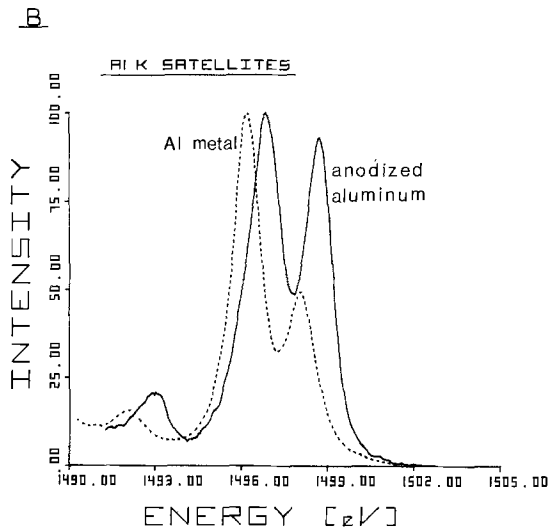
The fine features of x-ray emission spectra may be used to determine chemical bonding. By operation at low voltages and other techniques the method can provide near-surface characterization on areas as small as 1  $\mu\text{m}^2$ . Aluminum K spectra are especially sensitive to changes in chemical bonding. Figure 1 shows the K band ( $K_{\beta}$ ) from aluminum metal and an anodized film. The large shift in the band as well as the appearance of  $K_{\beta}'$  in the oxide due to a molecular orbital transition forms the basis of using these fine features. Also shown in Fig. 1 is the K satellite group, the principal lines of which are stronger than  $K_{\beta}$  and are thus usually easier to use. The use of these features assumes that the oxide is on the surface and that a uniform change from "metal" to "oxide" spectra will take place when going from no film on the surface to a point where all x-ray emission emanates from the oxide film. This upper limit was about 4000Å in this work where 10 keV electrons were used but could be increased by an increase in operating voltage.

## Results

The most obvious method of using x-rays to determine oxide thickness is that of direct measurement of oxygen K intensities similar to the method of Sewell *et al.* (1, 2, 5). Such results are shown in Fig. 2 where the OK intensities obtained from anodized films on aluminum are plotted vs. the anodizing voltage. The anodization constant was determined to be 14 Å/V using ellipsometric techniques on vacuum-evaporated Al films anodized under the same conditions as the samples described earlier. Note that the intercept is not at zero, probably due to oxygen in solution in the bulk and to the natural oxide film which immediately covers an aluminum surface. The linear



A



B

Fig. 1. Changes in fine features of x-ray emission spectra with changes in chemical combination; spectra from Al metal and aluminum oxide (anodized aluminum). A. the Al K band, B. the Al K satellites  $K\alpha_3$  and  $K\alpha_4$ .

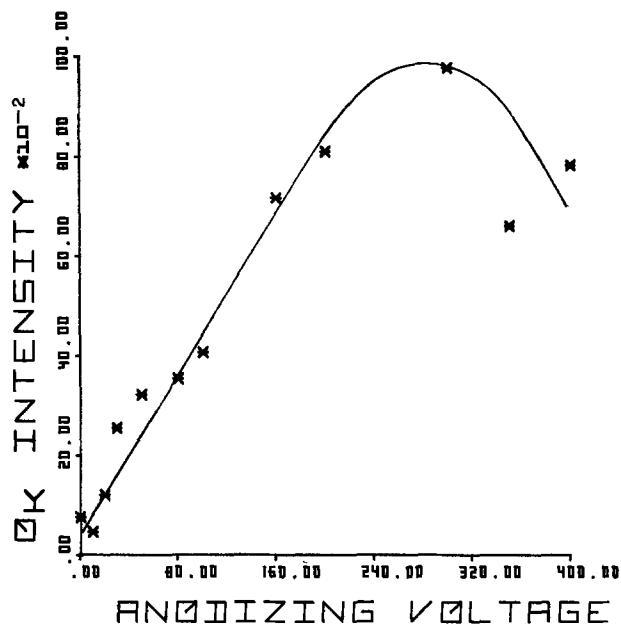


Fig. 2. Oxygen K x-ray intensities vs. anodizing voltage for aluminum (1% ammonium borate in ethylene glycol).

portion of the curve may be more nearly exponential if more points were added and better precision were achieved. Such a shape would be in keeping with elec-

tron and x-ray attenuation in the films, and would be in better agreement with the data of Mitchell and Sewell (5) on aluminum. However, data shown here, because of the use of a higher take-off angle and higher electron energies, would be less susceptible to absorption effects compared with the results of Mitchell and Sewell.

The changes in Al K x-ray spectra provide another method of determining oxide film thickness. Figure 3 shows the orderly change in the K band which involves valence electrons in going from Al metal to a thick 400V film. For reference, a spectrum is also shown for sapphire. Sapphire, the corundum structure, exhibits two maxima on the main K band, while anodized films show only one, indicating that the anodized film is not corundum structure and that x-ray fine features are sensitive not only to nearest neighbors, but also to the way in which they are arranged in the compound.  $K\beta'$  originates only from the oxide due to a molecular orbital transition, and therefore becomes stronger with increasing oxide thickness in relation to the K band as seen in Fig. 4. Work is continuing to determine if the observed scatter is due to statistical measurement problems such as surface

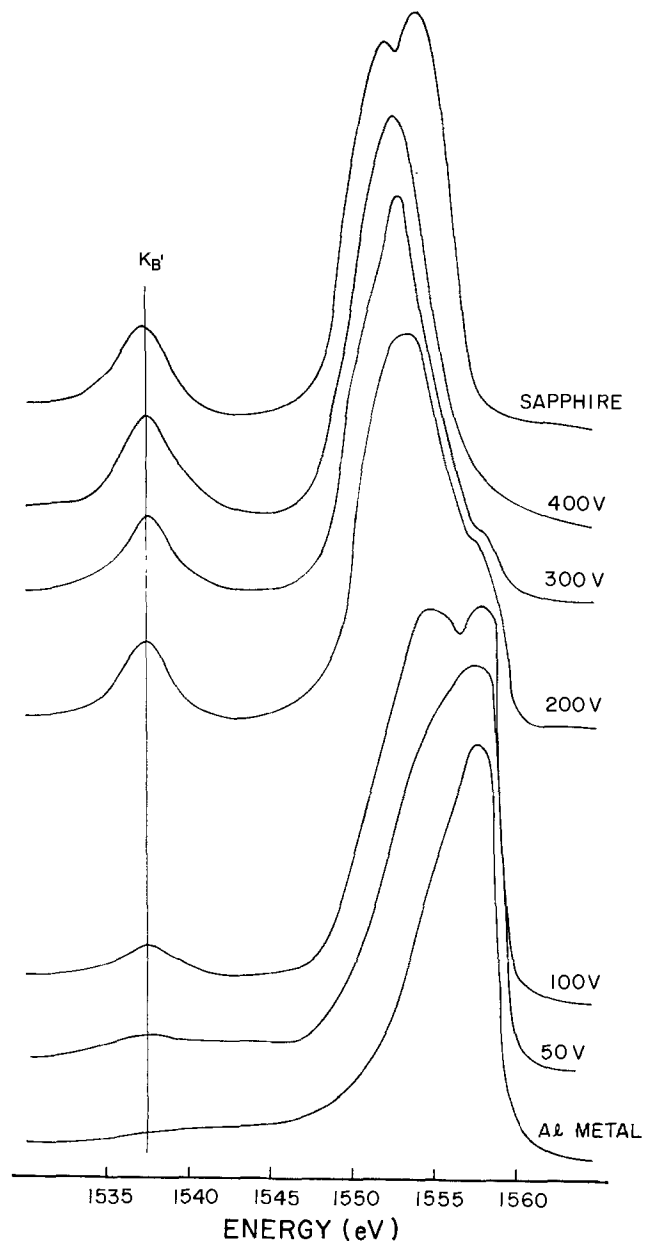


Fig. 3. The Al K band for samples anodized at various voltages compared to  $Al_2O_3$ , sapphire.

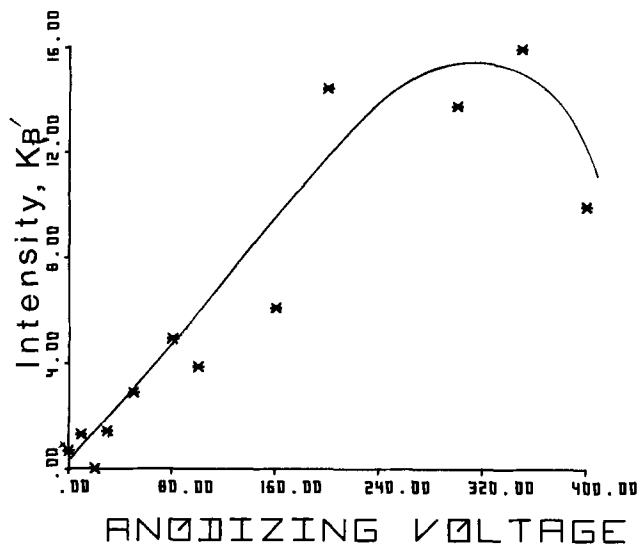


Fig. 4. The relationship of Al  $K_{\beta'}/K_{\beta}$  to anodizing voltage for aluminum.

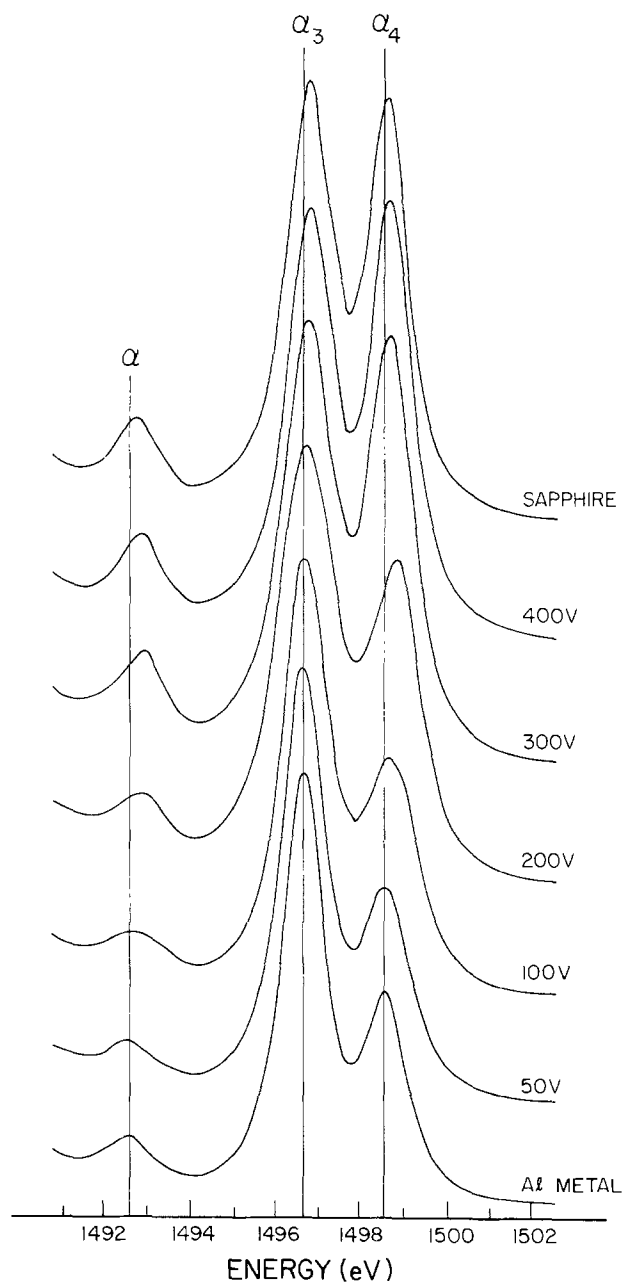


Fig. 5. Al K satellites for samples anodized at various voltages compared to  $Al_2O_3$ , sapphire.

charging or whether changes in anodization conditions or inhomogeneities in the film are responsible.

The strong satellites  $K_{\alpha_3}$  and  $K_{\alpha_4}$  which originate from multiply ionized states, provide another method of measuring film thickness as seen by the continuous change in the spectra in going from pure metal to a thick 400V film as seen in Fig. 5. The spectrum from sapphire in this case is virtually identical to the spectrum from the thick anodized film indicating that the satellite lines are not sensitive to structural changes. The ratio  $K_{\alpha_4}/K_{\alpha_3}$  is shown in Fig. 6. Notice in this plot the curve comes to a maximum and remains constant once the ratio has attained a value of approximately unity representing emission from only oxide. In measurements of OK intensities a similar effect was seen except that a maximum was reached followed by a decline giving the appearance that the film was becoming thinner with increasing anodizing voltage. It was suspected that a change in mechanism of anodization was responsible for the curve shape and current *vs.* time recordings were made at constant voltage for both high and low voltages. It was found for this electrolyte concentration that barrier oxide films are formed up to 250V; above this voltage a combination of barrier and porous film exists. Hoar and Yahalom (6) have shown detailed results of current density *vs.* time for aluminum anodization in which the curves may be analyzed as having one component which is due to barrier film forming and a superimposed component due to pore formation. Figure 7 illustrates this phenomenon for the electrolyte used here where A is current-time relationship for 50V and shows a typical curve for a barrier film while B is obtained at 300V and shows first barrier formation during the early sharp surge followed by a break in the curve indicating porous oxide formation. Electron micrographs of replicas at high magnification show the increase of the pore structure in the higher voltage oxide. Therefore, apparently the bend in the OK intensities represents a change in oxide bulk density rather than the oxide becoming thinner at higher voltages. That is, because of the pores, there are fewer oxygen sites per unit area. In addition it is possible that in the porous oxide the stoichiometric ratio between oxygen and aluminum is different from the barrier oxide. How-

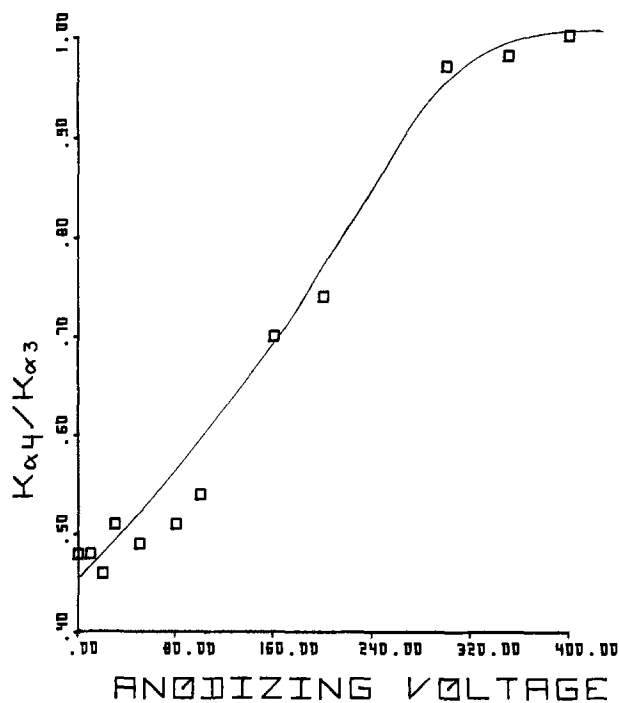


Fig. 6. The relationship of Al  $K_{\alpha_4}/K_{\alpha_3}$  to anodizing voltage for aluminum.

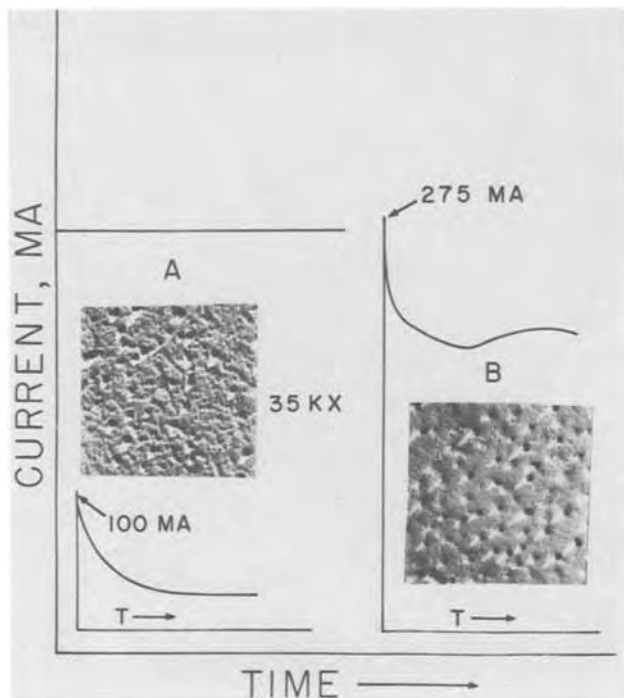


Fig. 7. Current vs. time curves and electron micrographs (35,000 $\times$ ) for aluminum anodized at voltages of 50V (A) and 300V (B) in 1% ammonium borate in ethylene glycol.

ever, in a nonaqueous system such as used here, this is unlikely.

### Conclusions

The x-ray emission method, either the direct measurement of oxygen K intensities, or the measurement of changes in the fine features of x-ray spectra, gives thickness information on aluminum oxide on aluminum over a wide range of thickness from about 20 $\text{\AA}$  to several thousand  $\text{\AA}$ . The technique lends itself to practical samples which are not amenable to measurement by methods enumerated earlier. The range of thickness could be increased compared to the results shown here. That is, much thicker films could be measured by using higher electron beam voltage.

### Acknowledgments

The ellipsometry measurement of film thickness of oxides on vacuum-evaporated films by Neil T. McDevitt is appreciated by the authors.

Manuscript submitted Feb. 25, 1975; revised manuscript received Aug. 16, 1975.

Any discussion of this paper will appear in a Discussion Section to be published in the December 1976 JOURNAL. All discussions for the December 1976 Discussion Section should be submitted by Aug. 1, 1976.

Publication costs of this article were partially assisted by The Air Force Materials Laboratory.

### REFERENCES

1. P. B. Sewell, D. F. Mitchell, and M. Cohen, *Surface Sci.*, **29**, 173 (1972).
2. P. B. Sewell and D. F. Mitchell, *J. Appl. Phys.*, **42**, 5879 (1971).
3. D. W. Fischer and W. L. Baun, *ibid.*, **36**, 534 (1965).
4. W. L. Baun, *ibid.*, **40**, 4210 (1969).
5. D. F. Mitchell and P. B. Sewell, *Thin Solid Films*, **23**, 109 (1974).
6. T. P. Hoar and J. Yahalom, *This Journal*, **110**, 614 (1963).

## Synthesis and Luminescence Properties of Europium-Activated Yttrium Oxysulfide Phosphors

Markus Koskenlinna, Markku Leskelä, and Lauri Niinistö

Department of Chemistry, Helsinki University of Technology, SF-02150 Otaniemi, Finland

### ABSTRACT

A new method of preparing brightly emitting Eu:Y<sub>2</sub>O<sub>2</sub>S phosphors is described. Yttrium sulfite doped with Eu is used as starting material and the Eu-activated oxysulfide is obtained from it either directly by reducing the sulfite with carbon monoxide, or by first oxidizing sulfite and then reducing the obtained oxysulfate. The properties of the phosphors and the effect of impurities on their luminescence spectra are briefly discussed.

Due to its bright luminescence under cathode ray excitation, europium-activated yttrium oxysulfide is a widely used red-emitting phosphor in color television picture tubes (1). Several methods have been reported for the synthesis of rare earth (RE) oxysulfides; they include reaction of RE oxides with various sulfur-containing reagents (e.g., H<sub>2</sub>S, CS<sub>2</sub>, NH<sub>4</sub>SCN) (2-4), reduction of RE sulfates by hydrogen (5, 6) and by carbon monoxide (7), reaction between RE oxides and sulfides (8), and methods employing sulfurizing fluxes (9, 10).

Key words: luminescence, phosphors, yttrium oxysulfide, europium oxysulfide.

In our previous study concerning the thermal decomposition of RE sulfites it was found that under certain conditions they form oxysulfides in reducing atmospheres (11). Based on that reaction, this report describes a new method for the preparation of brightly emitting europium-activated yttrium oxysulfide phosphors. Their properties are also briefly discussed, with special emphasis on the effect of impurities on the luminescence brightness.

### Experimental

*Materials and analytical methods.*—Three different grades of yttrium oxide (99.9, 99.99, and 99.999% with

respect to RE impurities) were used in the experiments. The purity of europium oxide was 99.9%. Both oxides were produced by Kemira Oy, Oulu, Finland.

The purity of the starting materials as well as that of the phosphors was analyzed with an AEI MS702 mass spectrometer, using spark-source excitation and electrical detection. The amount of europium present in the sulfites and phosphors was analyzed by atomic absorption spectrometry with a Perkin-Elmer 303 instrument. The purities of deionized water, ethanol, ether, and acetic acid used for washing the phosphors were also checked by AAS.

**X-ray diffraction.**—The homogeneity and crystallinity of the sulfites and oxysulfides were checked by x-ray diffraction using a Philips powder diffractometer with Ni-filtered  $\text{CuK}\alpha$  radiation. The accurate unit cell parameters of the synthesized oxysulfides were calculated by a least-squares procedure from x-ray diffraction photographs taken with a Guinier camera (Enraf-Nonius FR 552). Potassium chloride was used as internal standard, and the films were measured with a microdensitometer.

**Thermal analysis.**—The formation of  $\text{Eu: Y}_2\text{O}_2\text{S}$  from the sulfite was investigated in a Mettler Thermoanalyzer by simultaneously recording the TG, DTG, and DTA curves. The flow rate of CO was  $90 \text{ cm}^3/\text{min}$ . The sample holder was an aluminum oxide crucible (diam-8 mm, depth 20 mm). The stability of the activated phosphor in vacuum ( $4 \cdot 10^{-5} \text{ atm}$ ) was checked in another experiment where it was heated from  $25^\circ$  to  $1000^\circ\text{C}$ . The heating rate in both experiments was  $6^\circ/\text{min}$ .

**Luminescence measurements.**—Luminescence spectra of the phosphors were measured with a Hitachi Perkin-Elmer fluorescence spectrometer, Type MPF-3A. In relative intensity measurements the instrumental parameters were as follows: sensitivity: 2; slit:  $2 \mu\text{m}$ ; filter: UV-D25 (excitation), UV-39 (emission); wave length: 324 nm (excitation), 500-700 nm (emission).

**Scanning electron microscopy.**—SEM pictures were taken with a JEOL scanning electron microscope, Type JSM-U3.

**Synthesis of the oxysulfide phosphors.**— $\text{Y}_2\text{O}_3$  containing the desired amount of  $\text{Eu}_2\text{O}_3$  was suspended in water. A slow stream of sulfur dioxide was led into this suspension until the RE oxides dissolved. Complete precipitation of RE ions as sulfites was achieved by boiling the solution and simultaneously leading nitrogen gas through to remove excess sulfur dioxide. Due to the small difference in solubilities of yttrium and europium sulfites, the crystalline precipitate contained europium sulfite homogeneously dispersed in yttrium sulfite. It was washed with deionized water and dried with ethanol and ether. As an example of the amounts of reagents and the time required the following values can be given:  $\text{Y}_2\text{O}_3$  1.5g,  $\text{Eu}_2\text{O}_3$  0.149g [6 mole percent (m/o)],  $\text{H}_2\text{O}$   $150 \text{ cm}^3$ ,  $\text{SO}_2$   $100 \text{ cm}^3/\text{min}$  for 1.5 hr, and boiling time 1 hr.

The sulfites obtained can be reduced to oxysulfides by the action of carbon monoxide at  $600^\circ\text{--}900^\circ\text{C}$ . In a typical experiment, 0.5g of sulfite was reduced in a quartz reaction vessel (volume  $80 \text{ cm}^3$ ) by leading in carbon monoxide ( $100 \text{ cm}^3/\text{min}$ ) for 60 min at  $750^\circ\text{C}$ .

An alternative route, requiring slightly higher reduction temperatures, consists of the oxidation of sulfites in air to oxysulfates and then their reduction by carbon monoxide to oxysulfides. For example, 0.5g of sulfite was fired in air at  $950^\circ\text{C}$  for 1 hr and the oxysulfate thus obtained was reduced by CO ( $100 \text{ cm}^3/\text{min}$ ) at  $830^\circ\text{C}$  during 1 hr.

Finally, in order to improve the crystallinity and luminescence properties of the oxysulfide, it was fired in nitrogen for 1 hr at a temperature  $50^\circ\text{--}100^\circ\text{C}$  higher

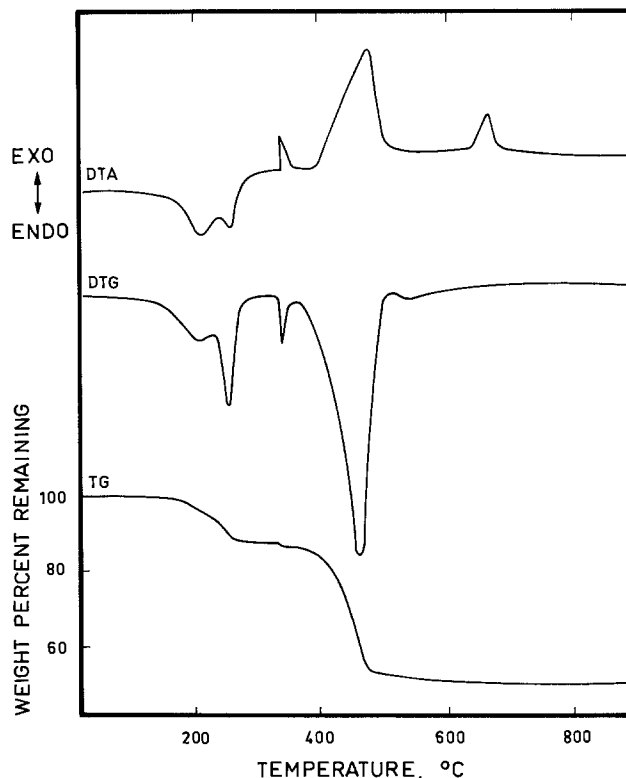


Fig. 1. Results of thermal analysis showing the formation of oxysulfide by carbon monoxide reduction of yttrium sulfite trihydrate containing 6 m/o Eu.

than the reduction temperature. Cooling was also carried out under nitrogen in order to avoid the formation of oxysulfate by oxidation.

## Results and Discussion

**Preparation of phosphors.**—Results of thermal analysis indicated that first an endothermic dehydration reaction takes place in the temperature range  $150^\circ\text{--}270^\circ\text{C}$  (Fig. 1). The observed weight loss corresponds to three molecules of water. The anhydrous sulfite is then reduced to oxysulfide in a two-stage exothermic process. The first step, at  $330^\circ\text{--}340^\circ\text{C}$ , clearly visible in both DTA and TG curves, is due to the reduction of europium sulfite; yttrium sulfite is reduced at the higher temperature range of  $360^\circ\text{--}490^\circ\text{C}$ . The exothermic peak not involving a weight change at  $640^\circ\text{C}$  is probably due to recrystallization of the phosphor.

The over-all weight loss (46.60%) calculated from the TG curve is smaller than the theoretical value (47.90%), indicating the formation of other sulfides besides the desired oxysulfide. The sulfides may be washed from the product by dilute acetic acid in which they are readily soluble (12). This lowers the yield, however, because oxysulfide is slightly soluble in acetic acid.

In this work the reaction temperature was optimized with respect to luminescence intensity and yield. Figure 2 shows the amount of material soluble in 2.5M acetic acid (mainly sulfides) and the luminescence intensity of the remaining oxysulfide phosphor. Temperatures around  $700^\circ\text{C}$  seem to be best for oxysulfide formation, but the optimum temperature with respect to both yield and intensity is somewhat higher, around  $750^\circ\text{C}$ . If an alternative preparative route employing the reduction of oxysulfate is used, the amount of material soluble in acetic acid remains fairly constant (approx. 5%), but the optimum intensity is obtained with reaction temperatures of  $800^\circ\text{--}850^\circ\text{C}$  and a post-synthesis  $\text{N}_2$  anneal at  $900^\circ\text{--}950^\circ\text{C}$ . There seem to be no significant differences in luminescence properties of phosphors prepared by the two alternative methods.

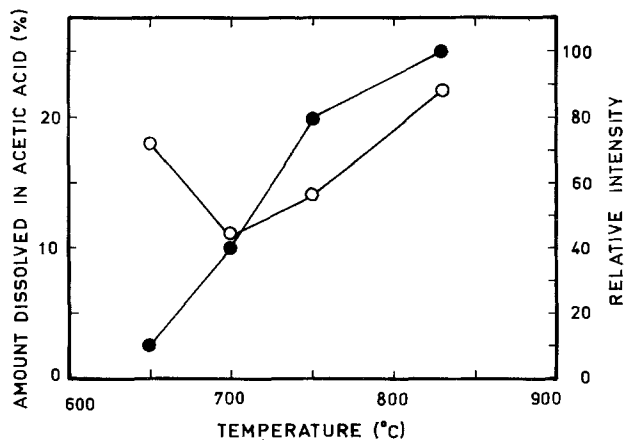


Fig. 2. The amount of material soluble in acetic acid (2.5M) in phosphors prepared by direct reduction of sulfites (open circles) and their relative brightnesses (filled circles) as functions of the reducing temperature.

*Properties of the phosphors.*—The phosphors prepared were pale brown. Their thermal stability in the absence of oxygen was good; heating in vacuum ( $4 \cdot 10^{-5}$  atm) up to 1000°C caused the weight to drop only 0.8%.

According to x-ray diffraction patterns the phosphors were well crystallized. The unit cell parameters for Eu: Y<sub>2</sub>O<sub>2</sub>S with different Eu contents are given in Table I; they show a slight increase with increasing europium concentration.

Firing in nitrogen improves the luminescence properties significantly by increasing the crystallite size of the phosphor. This was visible in the line widths of the powder patterns taken before and after firing in nitrogen. The increase of particle size was also observed in SEM pictures. The intensity obtained after 1 hr firing may be as high as 5-10 times the original.

*Effect of impurities on the luminescence spectra.*—In the present study yttrium oxides of three different purities were employed in order to study the effect of impurities in the starting materials on the luminescence properties. Table II lists results of a mass spectrometric analysis of these starting materials, numbered I to III in order of increasing purity. Oxysulfide phosphors prepared under similar conditions from these oxides showed a relative luminescence intensity of 40, 50, and 100 for samples I/a, II/a, and III/a, respectively.

Much higher impurity levels, however, may be introduced during the preparation and subsequent handling. Table II also lists the results of mass spectrometric analyses for Eu: Y<sub>2</sub>O<sub>2</sub>S phosphors prepared from these starting materials by (a) direct reduction of yttrium sulfite by carbon monoxide, (b) reduction after oxysulfate conversion and, for comparison, by (c) sulfurization of Eu: Y<sub>2</sub>O<sub>3</sub> in a sulfur-sodium carbonate-potassium carbonate flux (10), or (d) by method same as (c) but with mechanical dispersion (13). When comparing the analytical results for different phosphors it should be kept in mind that although spark source mass spectrometry is a very sensitive method of analysis, its precision with the logarithmic

Table I. Unit cell parameters of europium-activated yttrium oxysulfides. Estimated standard deviations are given in parentheses.

Europium content (m/o)	a (Å)	c (Å)
0	3.7910(7)	6.5959(19)
3	3.7936(7)	6.5977(16)
6	3.7947(7)	6.5995(14)
9	3.7967(7)	6.6029(22)

Table II. Mass spectrometric analyses (in ppm) of three yttrium oxides and phosphors prepared therefrom

Element	Sample*									
	I	II	III	I/a	II/a	III/a	III/b	I/b	III/c	II/d
Yb	5			10				10		
Ho	6	4	4	6		5	4	7	4	4
Dy	10	40	5	20	50	20	20	15	20	30
Tb	5	25		3	40	1	2	5	2	25
Gd	25	10	6	40	30	20	10	30	20	20
Sm	40	15	15	50	20	25	15	60	20	20
Nd	20	3	4	20	10	4	8	10	10	10
Pr	8			7	5	2	4	6	5	5
Ce	25	1	4	25	15	6	10	20	10	15
La	20	8	5	35	20	10	35	30	20	15
Mo								600	200	200
Zn	35	10	5	50	40	20	20	20	200	200
Cu	20	10	10	100	50	50	50	100	200	200
Ni	2	1		30	20	20	30	30	300	100
Fe	20	20	10	100	100	40	70	400	>1000	1000
Mn	10	10	10	10	10	10	10	200	1000	>500
Cr	30	30	20	30	30	30	30	200	100	1000
Ca	15	15	15	40	40	30	30	40	300	>300
K	15	15	15	100	100	50	100	200	>1000	>1000
Si	100	50	30	800	1000	200	600	600	>3000	1000
Al	10	10	10	30	50	30	10	30	>100	70
Na	100	10	10	100	200	50	100	200	>2000	>4000

\* Roman numbers I, II, and III refer to Y<sub>2</sub>O<sub>3</sub> of 99.9, 99.99, and 99.999% purity, respectively. Small letters after the solidus indicate the method of preparation: (a) reduction of sulfite, (b) reduction after conversion to oxysulfate, (c) use of sulfurizing flux with dispersion of Eu in Y<sub>2</sub>O<sub>3</sub> by oxalate precipitation, and (d) use of sulfurizing flux with mechanical dispersion of Eu in Y<sub>2</sub>O<sub>3</sub>. In the preparation of the three last phosphors, a quartz boat inside a steel reactor was employed; in other preparations apparatuses made entirely of quartz were used. The impurities originating from the activator (6 m/o Eu in all phosphors) have been taken into account in the values for the yttrium oxides.

scanning method can be estimated to be at best only  $\pm 20\%$ .

The results show clearly that the use of a quartz boat significantly increases the silicon content. Nevertheless, the impurity levels for the present method are generally lower than those associated with the flux method, where in spite of careful washings, high contents of alkali and alkaline earth metals originating from the flux are introduced into the phosphor in addition to the high content of silicon from the quartz vessel. The presence of steel, even though not in direct contact with the sample, causes the Fe and Mn contents to rise significantly, as can be seen in the values for the last three phosphors prepared in the quartz vessel inside a steel reactor (Table II).

It is well known that minute amounts of other rare earths influence the luminescence properties of Eu: Y<sub>2</sub>O<sub>2</sub>S phosphors. Only Tb and Pr have been reported to increase the luminescence intensity (14), all other RE's reduce the brightness and/or lead to other undesired effects; e.g., dysprosium increases the decay time (15).

Much less information is available on the effect of ions other than RE's on the luminescence properties of europium-activated yttrium oxysulfide phosphors. Mathers (15) reports that alkali metals are not usually considered detrimental to the spectra in amounts less than 100 ppm. At higher amounts they have been found to increase the brightness somewhat; the upper limit of alkali concentration has been reported to be 3000 ppm (16). Conversely, too high calcium and iron concentrations lower the brightness (15); no reports seem to be available on the effect of silicon on the spectra.

Table III lists the luminescence spectra with line identification of the same samples for which mass spectrometric analyses were performed (17). The effect of other rare earths on the spectra of Eu: Y<sub>2</sub>O<sub>2</sub>S phosphors is noticeable in a few cases. For instance, the <sup>5</sup>D<sub>2</sub> → <sup>7</sup>F<sub>4</sub> transition, which is the strongest line due to terbium (18), is only present in the spectra of phosphors prepared from the 99.99% yttrium oxide, which contained 25 ppm terbium (Tables II and III).

The most striking feature of the spectra is, however, the differences in the relative line intensities of the

Table III. Relative intensities for different emission fluorescent wavelengths in samples of Eu: Y<sub>2</sub>O<sub>2</sub>S. Excitation wavelength 312.0 nm.

Wave-length (nm)	Sample*							Corresponding transition (7)
	I/a	II/a	III/a	I/b	III/b	III/c	II/d	
626.9	100	100	100	100	100	100	74.5	<sup>5</sup> D <sub>0</sub> → <sup>7</sup> F <sub>2</sub>
617.0	48.2	50.0	42.3	48.0	44.1	50.5	36.7	<sup>5</sup> D <sub>0</sub> → <sup>7</sup> F <sub>2</sub>
596.0	67.2	56.7	43.3	55.2	53.7	71.0	50.2	<sup>5</sup> D <sub>0</sub> → <sup>7</sup> F <sub>1</sub>
587.8	14.8	12.6	12.4	13.7	12.1	14.4	42.7	<sup>5</sup> D <sub>0</sub> → <sup>7</sup> F <sub>3</sub>
583.7	24.6	27.5	22.5	23.7	24.3	26.5	21.0	<sup>5</sup> D <sub>1</sub> → <sup>7</sup> F <sub>0</sub>
571.0	0.5	0.2	0.1	0.2	0.1	0.4	1.6	<sup>5</sup> D <sub>2</sub> → <sup>7</sup> F <sub>5</sub>
565.6	1.7	0.6	0.2	0.5	0.2	1.1	3.9	<sup>5</sup> D <sub>1</sub> → <sup>7</sup> F <sub>2</sub>
556.3	10.6	5.3	5.5	6.9	3.4	6.9	26.0	<sup>5</sup> D <sub>1</sub> → <sup>7</sup> F <sub>2</sub>
545.0	—	2.3	—	—	—	—	15.6	<sup>5</sup> D <sub>2</sub> → <sup>7</sup> F <sub>4</sub>
540.0	39.1	23.2	22.8	29.1	14.5	26.9	100	<sup>5</sup> D <sub>1</sub> → <sup>7</sup> F <sub>1</sub>
529.6	—	0.5	0.3	0.6	0.3	0.8	3.3	<sup>5</sup> D <sub>3</sub> → <sup>7</sup> F <sub>6</sub>
513.7	12.0	6.3	4.3	8.9	4.1	9.8	49.8	<sup>5</sup> D <sub>2</sub> → <sup>7</sup> F <sub>3</sub>
497.0	9.1	5.5	5.2	8.5	4.3	7.5	39.4	<sup>5</sup> D <sub>3</sub> → <sup>7</sup> F <sub>5</sub>
491.0	4.7	4.1	5.5	7.2	3.9	4.2	20.5	<sup>5</sup> D <sub>2</sub> → <sup>7</sup> F <sub>2</sub>
483.0	1.2	2.2	5.2	5.5	3.4	1.3	4.7	**
476.0	3.3	3.4	6.7	7.1	4.5	3.0	14.5	<sup>5</sup> D <sub>2</sub> → <sup>7</sup> F <sub>1</sub>
470.0	10.1	9.2	16.0	19.7	11.4	8.9	52.9***	<sup>5</sup> D <sub>3</sub> → <sup>7</sup> F <sub>4</sub>
465.0	2.3	4.6	10.8	12.1	7.2	2.5	2.5	<sup>5</sup> D <sub>2</sub> → <sup>7</sup> F <sub>0</sub>
452.0	1.2	2.6	6.7	6.7	4.3	1.5	4.9	**
446.5	1.1	2.1	5.6	5.1	3.3	1.4	4.1	<sup>5</sup> D <sub>3</sub> → <sup>7</sup> F <sub>3</sub>
440.0	—	—	—	—	—	—	2.6	**
429.9	0.9	1.6	4.3	—	2.7	1.2	3.2	<sup>5</sup> D <sub>3</sub> → <sup>7</sup> F <sub>2</sub>
423.1	0.9	1.7	4.3	4.0	2.8	1.2	3.6	**
417.1	1.6	3.2	8.1	9.2	6.4	2.0	7.3	<sup>5</sup> D <sub>3</sub> → <sup>7</sup> F <sub>1</sub>
414.0	—	—	—	—	—	0.7	2.1	**
409.9	—	—	—	—	1.6	—	—	**

\* The sample numbering is explained in Table II. In each sample the strongest line has been given the value of 100. The relative intensity values for different samples determined with instrumental parameters described in the text, were as follows (sample III/a 100): I/a 40, II/a 50, III/a 100, I/b 48, III/b 90, III/c 90, and II/d 2.

\*\* Unassigned.  
\*\*\* Unresolved.

sample containing most impurities (II/d) as compared with the other spectra. This sample also had the lowest relative brightness, a value of only 2, whereas III/a had the highest value of 100, and III/c had a value of 90. The difference between the samples III/c and II/d is certainly due not only to impurities in the starting materials but also to different dispersion methods of the activator. In sample II/d Eu<sub>2</sub>O<sub>3</sub> was mechanically dispersed in Y<sub>2</sub>O<sub>3</sub> (13); in the other sample (III/c), oxalate precipitation and subsequent firing were employed in obtaining the oxide (10).

The iron concentrations introduced in the phosphors by the steel reactor seem not to be so high as to have a distinct effect on the over-all brightness. This can be seen by comparing, for instance, the samples I/a (relative brightness 40) and I/b (relative brightness 48) prepared in quartz and steel reactors, respectively (Tables II and III). However, the effect of an individual element other than a RE on the spectra is difficult to evaluate on the basis of present material and it would require a further study.

### Summary

The reduction of Eu-doped yttrium sulfite hydrate by carbon monoxide offers a new possibility for the

preparation of Eu: Y<sub>2</sub>O<sub>2</sub>S phosphors. The reaction and annealing temperatures required are not significantly lower than in the case of sulfate reduction. However, an advantage of the present method over the sulfate route lies in the ease and completeness of precipitating homogenous starting materials for the synthesis.

The rare earth impurities in the starting materials as well as other impurities mainly introduced during processing can seriously degrade the luminescent properties of the phosphors.

### Acknowledgments

The authors are indebted to Dr. I. Yliruokanen and Mr. L. Hiltunen, M.Sc. for valuable aid in mass spectrometric analyses. Kemira Oy has supported this work by providing the rare earth oxides.

Manuscript submitted June 3, 1975; revised manuscript received Aug. 25, 1975.

Any discussion of this paper will appear in a Discussion Section to be published in the December 1976 JOURNAL. All discussions for the December 1976 Discussion Section should be submitted by Aug. 1, 1976.

### REFERENCES

1. M. R. Royce, U.S. Pat. 3,418,246 (1968).
2. P. N. Yocom, U.S. Pat. 3,418,247 (1968).
3. H. A. Eick, *J. Am. Chem. Soc.*, **80**, 43 (1958).
4. E. J. Yarembash, E. S. Vigileva, A. A. Reshchikova, A. I. Zachatskaya, G. N. Novikova, and E. J. Boev, *Izv. Akad. Nauk. SSSR, Neorg. Mater.*, **7**, 1551 (1971).
5. J. W. Haynes and J. J. Brown, *This Journal*, **115**, 1060 (1968).
6. J. J. Pitha, A. L. Smith, and R. Ward, *J. Am. Chem. Soc.*, **69**, 1870 (1947).
7. V. P. Surgutskii and V. V. Serebrennikov, *Russ. J. Inorg. Chem.*, **9**, 435 (1964).
8. P. Khodadad, T. Tek, J. Flahaut, and L. Domange, *C. R. H. Acad. Sci.*, **260**, 2235 (1965).
9. L. Ozawa and M. Jaffe, *This Journal*, **117**, 1297 (1970).
10. M. R. Royce, S. M. Thomsen, and P. N. Yocom, U.S. Pat. 3,502,590 (1970).
11. M. Koskenlinna and L. Niinistö, *Suomen Kemistilehti*, **B46**, 326 (1973).
12. J. Flahaut, M. Guittard, and M. Patrie, *Bull. Soc. Chim. France*, **1958**, 990.
13. L. G. van Uitert, U.S. Pat. 3,243,723 (1966).
14. H. Yamamoto, T. Kano, Y. Otomo, and K. Urabe, "Proceedings of the Ninth Rare Earth Research Conference," Blacksburg, Virginia, p. 503 (1971).
15. J. E. Mathers, in "Analysis and Applications of Rare Earth Materials," O. B. Michelson, Editor, p. 241, Universitetsforlaget, Oslo (1973).
16. W. H. Byler, J. J. Mattis, S. A. Ring, L. E. Sobon, K. A. Wickersheim, and M. Tecotzky, U.S. Pat. 3,515,675 (1970).
17. C. W. Struck and W. H. Fonger, *J. Luminescence*, **1**, 456 (1970).
18. M. R. Royce and A. L. Smith, Abstract 34, p. 94, Electrochemical Society Extended Abstracts, Spring Meeting, Boston, Massachusetts, May 5-9, 1968.



# On the Kinetics of the X-Ray Irradiation-Caused Degradation of Photoluminescence of Some Phosphors

George T. Bauer\*

Webster Research Center, Xerox Corporation, Rochester, New York 14644

## ABSTRACT

The growth of absorption and the degradation of photoluminescence of calcium tungstate and zinc silicate phosphors have been studied as functions of x-ray exposure. The characteristics of the growth curves are observed to be very similar to those reported for F centers in alkali halides. Based on the theoretical analysis of the kinetics, the fast initial growth of the absorption is interpreted as arising from the imperfections present in the phosphors prior to irradiation, while the following slow linear rise is attributed to the effect of new radiation-induced imperfections. From the two stages of growth curves, the two periods of degradation of photoluminescence observed could be quantitatively explained. These results indicate that the u.v. and visible absorption of radiation-produced color centers is the major cause of degradation of the phosphors studies. The observed dark recovery of absorption and of luminous efficiency after ceasing the irradiation of the phosphors was also found to be a correlated effect.

The degradation of phosphors as the effect of exciting irradiation is known to be a limiting factor in many applications. The degradation of the luminescence of some x-ray or u.v.-irradiated single crystals and phosphors has been attributed to the absorption of the irradiation-produced color centers (1, 2). In a previous publication, we reported results on the effects of x-ray and ultraviolet irradiation on different types of phosphors (3). We found that a decrease of luminous efficiency of the irradiated phosphors was always accompanied by increased absorption. In most cases, the absorption coefficient increased in the absorption band as well as in the emission band. The absorption bands could be partially or completely bleached out by a one-hour heat-treatment at 400°C. The reflectance data and glow curves of x-ray-irradiated phosphors were very similar to the ones obtained after long-term u.v. irradiation. These results indicate that the formation of color centers by irradiation in phosphors is a quite common phenomenon and is not restricted to those few basic types that had been studied in this respect by other authors (1, 2).

Our work also resulted in some increased insight into the various processes which are going on in the phosphors when irradiated. In certain phosphors, such as calcium tungstate and zinc silicate, the irradiation-caused degradation could be completely interpreted in terms of the absorption of irradiation-produced absorbing centers. Some part of the exciting energy in this phosphor is absorbed in radiation-produced color centers instead of being absorbed in the luminescent centers. A part of the emitted luminescent light is also absorbed by color centers. According to the experiments, the light emitted by color centers—if any—did not contribute to the luminous efficiency of these phosphors. In some other materials (for example, phosphate-type phosphors) glow curve measurements indicated an additional loss (3) which seemed to be connected with an energy transfer process between activator and color centers. In these cases, the induced traps should give rise to radiationless transitions or to emission outside the visible range.

In our previous measurements (3), the irradiation times did not vary over a wide range, and, consequently, did not yield enough information concerning the time dependence of the degradation of the phosphors. It appeared that for those particular phosphors

in which the absorption of radiation-produced color centers is the only cause of degradation, the time dependence of this process should be described by the time-dependent change of their absorption coefficient. Thus, the problem can be reduced to interpreting the growth of absorption of these phosphors.

The growth of absorption of x-ray-irradiated alkali halides, a classical problem of color center research, has been studied by a number of authors (4, 5). In general, the physical processes which result in the growth of absorption were found to be rather complicated. However, in several cases, good agreement between theory and experiments (6, 7) was reported. Such detailed studies, although they might provide a better understanding of the degradation process, were not conducted for irradiated phosphors. The reason for the lack of such efforts should be attributed not only to the well-known complexity of the problem, but also to the difficulties encountered in measuring the absorption coefficient of powder phosphors. However, the absorption coefficient can be determined accurately enough for such purposes from measurements of diffuse optical properties of phosphor layers (8, 9). The problem can be simplified further because, as has been shown previously (3), only the relative values of the absorption coefficients of phosphors as a function of exposure are needed to interpret quantitatively the effect of color centers in the degradation process.

In this work, we study the time-dependent degradation of x-ray-irradiated  $\text{CaWO}_4:\text{Pb}$  and  $\text{Zn}_2\text{SiO}_4:\text{Mn,Pb,As}$ . The phosphors were made available to us by Westinghouse Corporation. The main effect of irradiation in these phosphors seems to be that it changes the visible and ultraviolet absorption of the phosphors. Long-term x-ray exposure induces only barely detectable new glow peaks over room temperature. Therefore, those other effects of x-rays which are related to energy transfer processes are neglected.

The choice of x-rays for irradiation was based on practical considerations. The irradiation time needed with x-rays is relatively short and the penetration depth is large, making it possible to use known techniques for the measurement of optical properties of powder phosphors.

However, based on the similarity of the effects of x-rays and u.v. on optical characteristics of phosphors, we may expect the results obtained here to hold also for degradation produced by other forms of excitation.

The theory and the experimental work can be divided into two major parts: the first is concerned with

\* Electrochemical Society Active Member.  
Key words: luminescence, phosphor degradation kinetics, color centers.

the growth of absorption; the second is the basic problem, the time-dependent degradation of the selected phosphors. Some efforts have also been concentrated on the study of dark recovery of the absorption and luminescence.

### Theory

*Calculation of the growth of the absorption.*—We suppose that the growth of absorption of the irradiated phosphors can be attributed to the increase in concentration of the irradiation-produced color centers. As it is known from the extensive literature (4), the presence of imperfections in the crystal (*e.g.*, vacancies, interstitials, impurities) gives rise to color center formation. In the two sample phosphors, the concentrations of the activator and the color centers before and after the irradiation are small; that is, the absorption is in the "weak" region. Also, as indicated by relatively high quantum efficiency of the photoluminescence of the phosphors (10), absorption by impurities is negligible. The phosphor prior to irradiation already contains electron or hole-type imperfections of concentration  $N_0$ , and the irradiation produces new imperfections. The concentration of the new imperfections is proportional to  $I_0$ , the intensity of the x-rays, and to the elapsed time,  $\tau$ , of irradiation. The total imperfection concentration,  $N$ , can be expressed by Eq [1]

$$N = N_0 + a_2 I_0 \tau \quad [1]$$

The growth of  $C_1(\tau)$ , the color center concentration, can be described by Eq. [2]

$$\frac{dC_1(\tau)}{d\tau} = a_1 I_0 [N_0 + a_2 I_0 \tau - C_1(\tau)] - a_3 I_0 C_1(\tau) - a_4 C_1(\tau) \quad [2]$$

According to the first term in Eq. [2], the irradiation produces new color centers and the rate of the concentration growth is proportional to the intensity of irradiation,  $I_0$ , and to the concentration of the available unfilled imperfections. The second term indicates that the radiation destroys color centers and that the rate of destruction is proportional to their instantaneous concentration,  $C_1(\tau)$ , and to  $I_0$ . The third term on the right of the equation expresses the fact that spontaneous recovery which does not depend on the intensity of the radiation may also occur,  $a_1$ ,  $a_2$ ,  $a_3$ , and  $a_4$  are rate constants in Eq. [1] and [2].

The integral of Eq. [2], taking into account the boundary condition, is

$$C_1(\tau) = f_0(1 - e^{-g_0\tau}) + h_0\tau \quad [3]$$

where

$$f_0 = \frac{I_0^2 (a_1^2 N_0 + a_1 a_3 N_0 - a_1 a_2) + a_1 a_4 I_0 N_0}{[I_0 (a_1 + a_3) + a_4]^2} \quad [4]$$

$$g_0 = I_0 (a_1 + a_3) + a_4 \quad [5]$$

$$h_0 = \frac{I_0^2 a_1 a_2}{I_0 (a_1 + a_3) + a_4} \quad [6]$$

From the  $C_1(\tau)$  concentration and  $\sigma_i(\lambda)$ , the capture cross section of the color centers for absorption, the induced absorption coefficient can be expressed (3) as  $C_1(\tau)\sigma_i(\lambda)$ . Adding the induced absorption to the value of the initial absorption of the phosphor prior to the irradiation,  $a(\lambda, \tau = 0)$ , the whole absorption is

$$a_i(\lambda, \tau) = a(\lambda, \tau = 0) + C_1(\tau)\sigma_i(\lambda) \\ \equiv a(\lambda, \tau = 0) + f_0\sigma_i(\lambda)(1 - e^{-g_0\tau}) + h_0\sigma_i(\lambda)\tau \quad [7]$$

Based on the experimental fact that no reciprocity failure was found within the applied exposure range, we introduce the exposure,  $E = i\tau$ , instead of  $\tau$ , where  $i$  is the anode current in the x-ray tube. The relative absorption coefficient [ $a_{ir}(\lambda, \tau)$ ] expressed with  $E$  from Eq. [7] is

$$a_{ir}(\lambda, E) = a_r(\lambda, E = 0) + f(1 - e^{-gE}) + hE \quad [8]$$

The coefficients  $f$ ,  $h$ , and  $g$  differ from  $f_0\sigma_i$ ,  $h_0\sigma_i$ , and  $g_0$ , respectively, only by numerical factors.

*The decrease of the luminous efficiency.*—As shown previously (3), the luminous efficiency,  $L_i$ , of an x-ray-irradiated phosphor can be expressed in terms of the unirradiated one,  $L$ , by the initial absorption coefficient  $a_r(\lambda, E = 0)$  and by the absorption coefficient of the irradiated phosphor  $a_{ir}(\lambda, E)$  both measured at the wavelength of excitation

$$\frac{L_i}{L} = m_v(E) \frac{a_r(\lambda, E = 0)}{a_{ir}(\lambda, E)} \quad [9]$$

where  $m_v(E)$  is that part of the loss which is caused by self-absorption of the emitted light by the irradiation-produced color centers. An approximate expression for  $m_v(E)$  is given in Ref. (3). The exposure-dependent change of the  $L_i/L$  relative efficiency with respect to  $\lambda$  wavelength excitation is from Eq. [8] and [9]

$$\frac{L_i}{L} = m_v(E) \frac{a_r(\lambda, E = 0)}{a_r(\lambda, E = 0) + f(1 - e^{-gE}) + hE} \quad [10]$$

*Spontaneous recovery of the absorption coefficient and of the luminous efficiency.*—In Eq. [2], the rate constant,  $a_4$ , is related to the spontaneous bleaching of the phosphor at room temperature. In phosphors in which such a phenomenon actually occurs, both the absorption and the luminous efficiency might recover partially or return to their original values after the irradiation has stopped. Based on Eq. [2], the change in the concentration of the color centers at a time  $\tau^*$  elapsed after ceasing the irradiation at time  $\tau_0$  is

$$\frac{dC_1(\tau^*)}{d\tau} = -a_4 C_1(\tau^*) \quad [11]$$

The integral of Eq. [11] is

$$C_1(\tau) = C_1(\tau_1) e^{-a_4\tau^*} \quad [12]$$

Let  $a_{ir}(\lambda, \tau^*)$  be the relative absorption coefficient of the phosphor after  $\tau^*$  elapsed time of dark recovery. Multiplying Eq. [12] by the capture cross section of the color center related to  $\lambda$ , the wavelength of excitation, and adding the initial absorption of the phosphor prior to the irradiation  $a_r(\lambda, E = 0)$  to the induced absorption, we obtain for the time dependence of the relative absorption coefficient

$$a_{ir}(\lambda, \tau^*) = a_r(\lambda, E = 0) + \sigma_i(\lambda) C(\tau_1) e^{-a_4\tau^*} \\ \equiv a_r(\lambda, E = 0) + a_{ir}(\lambda, E = i\tau_1) e^{-a_4\tau^*} \quad [13]$$

Let us consider that the visible absorption does not change during the recovery. That is

$$m_v(\tau_1) = m_v(\tau_1 + \tau^*) \quad [14]$$

Then, based on Eq. [9] from Eq. [13] and [14], we obtain for the recovery of the luminous efficiency

$$\frac{L_i}{L} = \frac{a_r(\lambda, E = 0)}{a_{ir}(\lambda, \tau^*)} \\ = \frac{a_r(\lambda, E = 0)}{a_r(\lambda, E = 0) + a_{ir}(\lambda, E = i\tau_1) e^{-a_4\tau^*}} \quad [15]$$

### Experimental

*Irradiation and optical measurements.*—The phosphors were irradiated by 50 kV unfiltered tungsten x-rays. The measurements of the relative absorption coefficient and of the luminous efficiency of the phosphors were based on diffuse reflectance measurements made on 2 mm-thick powder layers. The apparatus used for the irradiation, excitation, and optical measurements of the phosphors was described previously

(3). An important aspect of the optical measurements is that they were carried out on two characteristic wavelengths: one of these wavelengths is in the tail of the absorption band of the phosphors, the other is within the emission band. The absorption of the irradiation-induced color centers in a wavelength which corresponds to the tail of the absorption band can be quite high compared to the absorption of the phosphor prior to irradiation. The decrease of luminous efficiency related to excitation occurs in the peak of the absorption band, and it is easier to measure this change (3). Some measurements have been also made near the peak of the excitation band.

The absorption coefficients of the irradiated phosphors used in this study, as measured by diffuse reflectance,  $R(\lambda)$ , were small enough to use the weak absorption limit of the expression (9) for the relative absorption coefficient

$$a_r(\lambda) = \frac{(1 - R(\lambda))^2}{R(\lambda)} \quad [16]$$

The relative luminous efficiency of the irradiated phosphor in terms of the unirradiated one,  $L_i/L$ , can be expressed using the relative brightness  $I$  and  $I_i$ , and reflectances,  $R(\lambda)$  and  $R_i(\lambda)$ , of the phosphor before and after irradiation, respectively (10)

$$\frac{L_i}{L} = \frac{I_i}{I} \frac{1 - R(\lambda)}{1 - R_i(\lambda)} \quad [17]$$

**Results**

*The growth of absorption.*—The change of the relative absorption coefficient of calcium tungstate was measured at three different wavelengths. One of these wavelengths (2537Å) is well within the absorption band of the phosphor while another one (3120Å) falls in the tail of the absorption band. Measurements were also carried out at 4358Å, a wavelength inside the emission band. Two series of measurements with different irradiation times were made; the first using 50 kV, 40 mA, and the second using 50 kV, 4 mA tungsten x-rays. Figures 1 through 4 show  $a_{ir}(\lambda, E)$ , the measured relative absorption vs. the relative exposure,  $E = i\tau$ , where  $i$  is the anode current in mA and  $\tau$  is the elapsed time of irradiation in minutes. Figure 1 shows the growth of the relative absorption coefficient measured at 3120Å in the exposure range 0-40 mA·min. Some measurements were made by irradiation with 50 kV, 40 mA tungsten x-rays (solid points) while others were made with 50 kV, 4 mA tungsten x-rays (open points). The geometrical configurations of the samples were the same for both exposures. As this and following figures indicate, the relative absorption co-

efficients can be considered as a function of the product,  $i\tau$ . That is, within the anode current range applied in this work, the reciprocity failure is negligible. Therefore, in the following figures, the absorption as well as the luminous efficiency of the phosphors is plotted vs. the relative exposure,  $E$ .

The absorption coefficient of calcium tungstate measured at this wavelength suddenly increases right after beginning the irradiation. Figure 2 shows that this part of the fast growth of absorption is followed by a very slow linear rise. This initial sudden rise of the growth curve is characteristic for both phosphors studied at every measured wavelength.

Figures 3 and 4 show the exposure dependence of absorption of the calcium tungstate measured at 4358Å. The curve has the same characteristic as the one measured at 3120Å. However, the absorption of the phosphor prior to the irradiation is near zero at this wavelength. The growth of absorption is also smaller than on the curve measured at 3120Å. According to our model, this means that the capture cross section for absorption of the radiation-induced color centers is smaller in the visible than well inside the absorption band. Here, too, the sudden rise of the absorption at low exposures is followed by a slow linear rise (Fig. 4). The value of reflectance of the calcium tungstate was found to be very small ( $R \approx 0.07$ ) at 2537Å and did not show any change within the applied range of exposure. Obviously, the capture cross section and concentration of the activators are much higher than

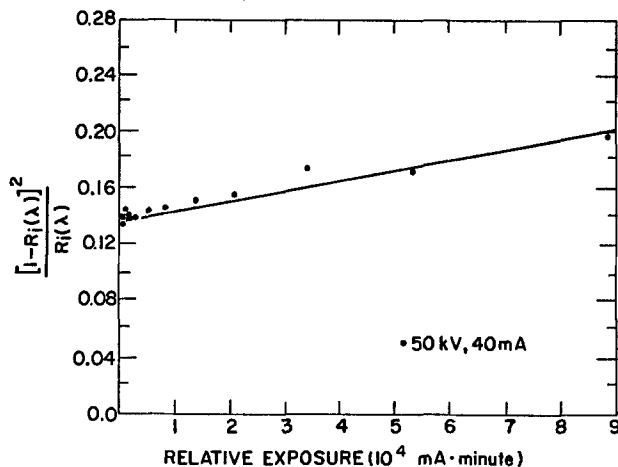


Fig. 2. X-ray-exposure dependence of the relative absorption coefficient of calcium tungstate at 3120Å (long-term exposures). Dots measured; line calculated.

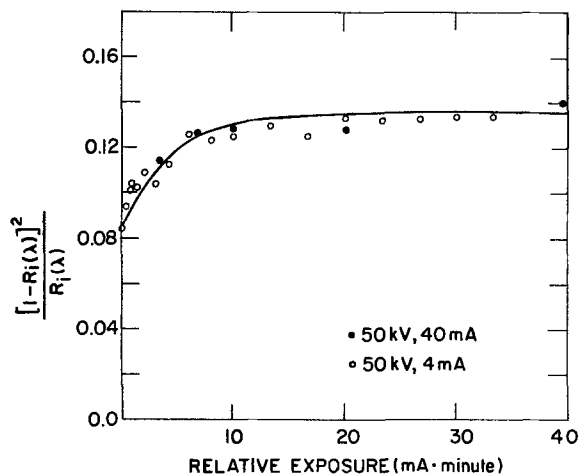


Fig. 1. X-ray-exposure dependence of the relative absorption coefficient of calcium tungstate at 3120Å (short-term exposures). Dots measured; line calculated.

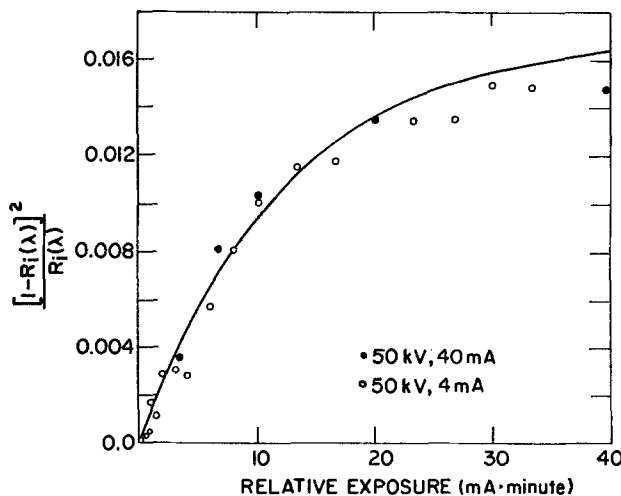


Fig. 3. X-ray-exposure dependence of the relative absorption coefficient of calcium tungstate at 4358Å (short-term exposures). Dots measured; line calculated.

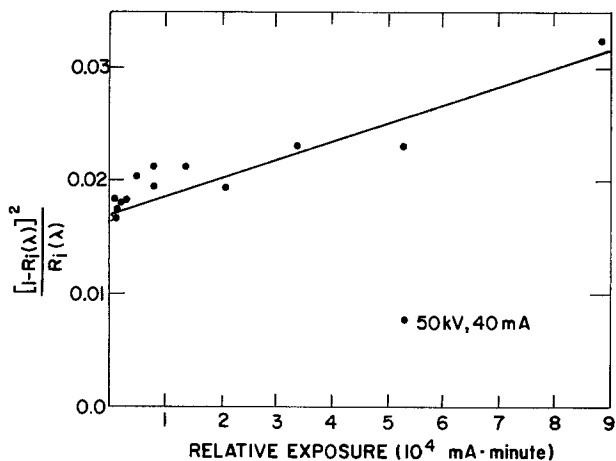


Fig. 4. X-ray-exposure dependence of the relative absorption coefficient of calcium tungstate at 4358Å (long-term exposures). Dots measured; line calculated.

those of the induced color centers and the latter cannot significantly contribute to the whole absorption.

The exposure dependency of the change of the relative absorption coefficient of zinc silicate samples has been measured at 3650Å (Fig. 5) and 4358Å (Fig. 6). The growth of absorption of the zinc silicate is similar to that of the calcium tungstate. Again, a sudden rise is followed by a slower, more gradual growth. If we

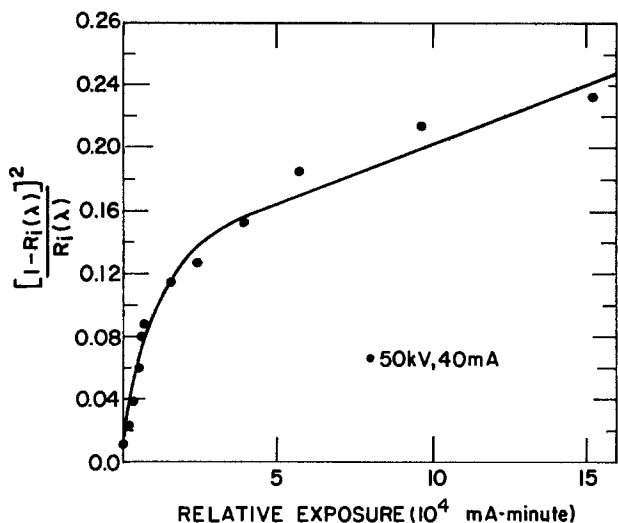


Fig. 5. X-ray-exposure dependence of the relative absorption coefficient of zinc silicate at 3650Å. Dots measured; line calculated.

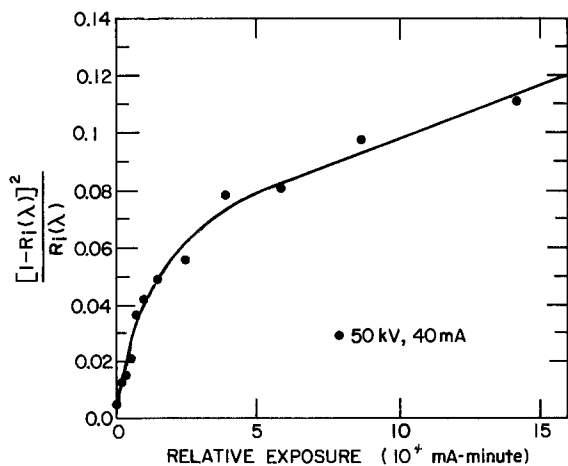


Fig. 6. X-ray-exposure dependence of the relative absorption coefficient of zinc silicate at 4358Å. Dots measured; line calculated.

compare Fig. 5 to Fig. 6, we can see that if the same exposure is applied, the increase of the absorption coefficient is smaller at 4358Å than at 3650Å. 40 mA for 63 hr x-ray exposure causes only a very slight change (from  $R \approx 0.08$  to  $R \approx 0.07$ ) in the reflectance of zinc silicate measured at 2537Å.

*The degradation of the luminous efficiency.*—The brightness of the irradiated samples was measured while exciting the phosphors at the same wavelength at which the reflectance measurements were completed. The changes of the luminous efficiency of calcium tungstate related to excitation at 2537 and 3120Å are shown in Fig. 7 and 8. The luminous efficiency is again a function of the exposure only, that is, the reciprocity failure is negligible, as was also found for the absorption.

Comparing the absorption and luminous efficiency results, Fig. 1 and 7 and Fig. 2 and 8, respectively, it

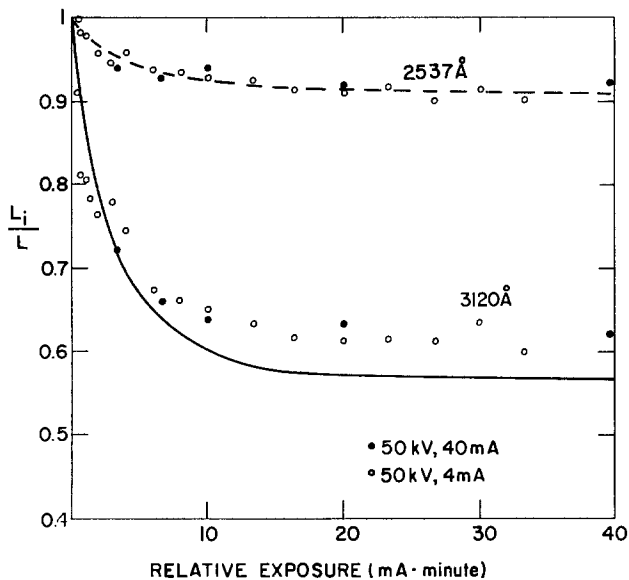


Fig. 7. X-ray-exposure dependence of the relative luminous efficiency of calcium tungstate related to excitation at 2537 and 3120Å (short-term exposures). Dots measured; continuous line calculated.

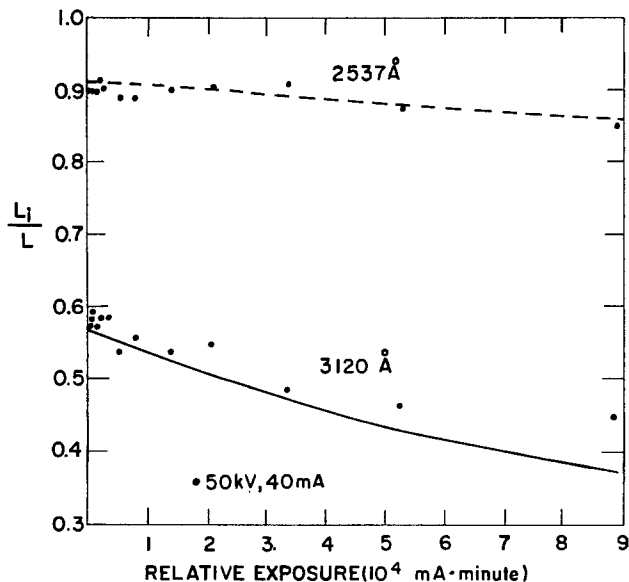


Fig. 8. X-ray-exposure dependence of the relative luminous efficiency of calcium tungstate related to excitation at 2537 and 3120Å (long-term exposures). Dots measured; continuous line calculated.

is noticeable that the sudden increase of the absorption measured at 3120Å (within the exposure range 0-10 mA·min) coincides with a sudden decrease of the luminous efficiency. After 10 mA·min of exposure, the decrease of luminous deficiency slows down, which corresponds to the slower rise of absorption which also occurs at longer exposures. The decrease of the luminous efficiency is significantly smaller at 2537Å than at 3120Å.

The degradation of zinc silicate is more extensive and the close correlation between the radiation-induced change of absorption and luminous efficiency can also be seen in this case. After several minutes of irradiation, the luminous efficiency of zinc silicate related to 3650Å excitation drops below 10% of its initial value (Fig. 9). This is obviously connected with the change of the absorption which increases after the same exposure to about ten times its initial value (Fig. 5).

*Spontaneous bleaching.*—The stability of color centers is known to be dependent on the temperature of their environment. The observed connection between degradation and color center formation of irradiated phosphors suggested a study of the dark recovery of irradiated calcium tungstate at room temperature. In order to avoid the possible bleaching effect of the sources used for excitation, each sample was used for only one measurement. The samples studied were irradiated by 50 kV, 40 mA x-rays for 10 min and kept in the dark until the time of measurement. As Fig. 10 shows, the absorption of the sample measured at 3120Å suddenly decreases after the irradiation ceases. Later, the change slows down. The same character of recovery was observed when the relative absorption of the samples was measured at 4358Å (Fig. 11). The dark recoveries of the measured luminous efficiencies related to 2537 and 3120Å excitation are shown in Fig. 12. The decrease of the absorption after the interruption of irradiation is accompanied by an increase of luminous efficiency of the phosphor. The extent of the recovery related to 3120Å excitation is greater than that related to excitation at 2537Å.

*Comparison of the experiments with theory.*—The exposure dependence of the relative absorption coefficient,  $a_{ir}(\lambda, E)$  was calculated for the studied phosphors at the wavelength of the measurements from Eq. [8]. Applying the least squares method, the best fits for calcium tungstate could be achieved with constants

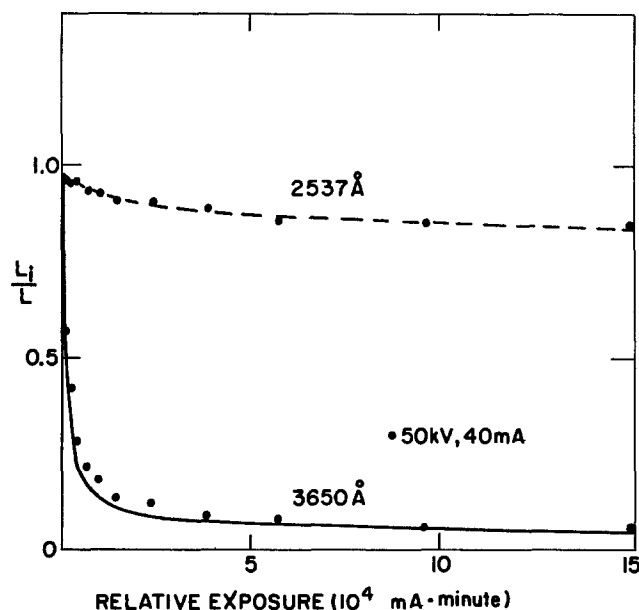


Fig. 9. X-ray-exposure dependence of the relative luminous efficiency of zinc silicate related to excitation at 2537 and 3650Å. Dots measured; continuous line calculated.

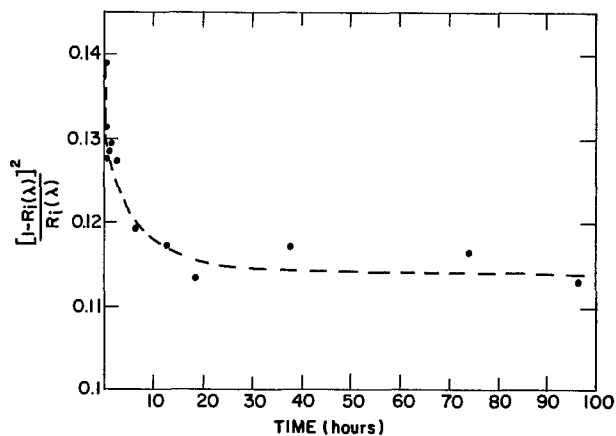


Fig. 10. Spontaneous recovery of the relative absorption coefficient of calcium tungstate at 3120Å after an exposure of 40 mA, 10 min by 50 kV x-rays.

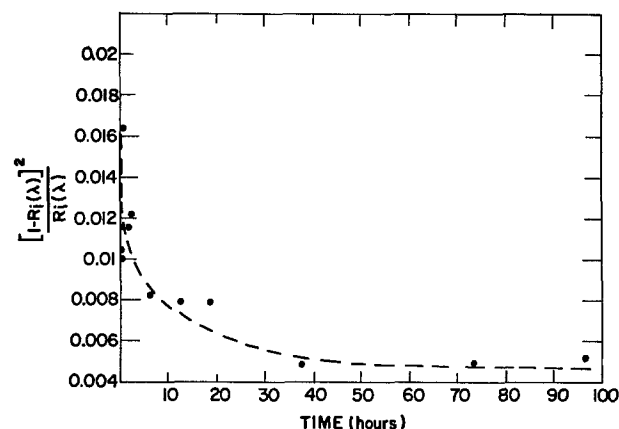


Fig. 11. Spontaneous recovery of the relative absorption coefficient of calcium tungstate at 4358Å after an exposure of 40 mA, 10 min by 50 kV x-rays.

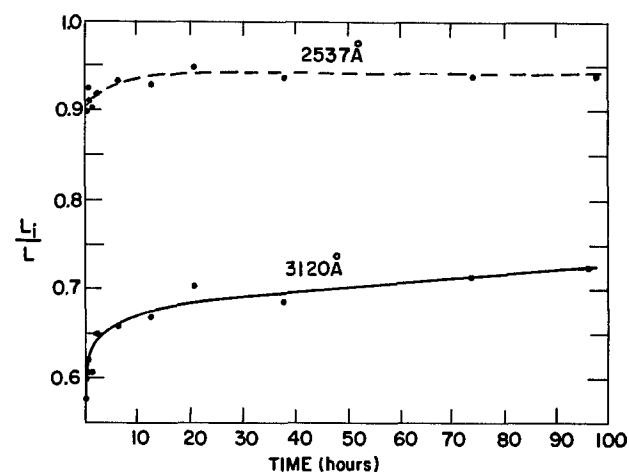


Fig. 12. Spontaneous recovery of the relative luminous efficiency related to excitations at 2537 and 3120Å, respectively, after an exposure of 40 mA, 10 min by 50 kV x-rays. Dots measured; continuous line calculated from absorption data.

shown in Table I. The calculated curves together with the measured points are shown in Fig. 1-4. The curves calculated for zinc silicate with the constants shown in Table II are plotted in Fig. 5 and 6. The calculation of the exposure-dependent change of the luminous efficiencies of calcium tungstate (Fig. 7 and 8) and zinc silicate phosphors (Fig. 9) were based on Eq. [10]. The values of  $m_v(E)$  in Eq. [10] were calculated from the measurements (3). Within the range of exposures, the variation of  $m_v(E)$  was found to be very small com-

Table I. Calcium tungstate

	$\lambda = 3120\text{\AA}$	$\lambda = 4358\text{\AA}$
$f$	$5.18 \cdot 10^{-2}$	$1.69 \cdot 10^{-2}$
$g$ (in mA · min)	$2.33 \cdot 10^{-1}$	$8.03 \cdot 10^{-2}$
$h$ (in mA · min)	$7.68 \cdot 10^{-7}$	$1.64 \cdot 10^{-7}$

Table II. Zinc silicate

	$\lambda = 3650\text{\AA}$	$\lambda = 4358\text{\AA}$
$f$	$1.14 \cdot 10^{-1}$	$5.7 \cdot 10^{-2}$
$g$ (in mA · min)	$1 \cdot 10^{-4}$	$8 \cdot 10^{-5}$
$h$ (in mA · min)	$7.53 \cdot 10^{-7}$	$3.3 \cdot 10^{-7}$

pared to the change of the relative absorption  $a_{ir}(\lambda, E)$ . The other parameters that appear in Eq. [10] were taken from the absorption data shown on Table I or II.

Except for the initial region, the recovery of the absorption of calcium tungstate after 10 min of irradiation by 50 kV, 40 mA x-rays cannot be fitted by Eq. [13]. However, as Fig. 12 shows, the recovery of  $L_i/L$  luminous efficiency can be fitted well applying Eq. [15], using the measured values of the relative absorption coefficients  $a_{ir}(\lambda, \tau^*)$  and  $a_r(\lambda, E = 0)$ .

### Discussion

Theoretical interpretation of the experimental results gives a more complete understanding of the degradation kinetics of the model phosphors studied. Let us discuss first the growth of absorption. The initial fast period and the slow linear rise of the growth curves which follows can be correlated with the imperfections originally present in the phosphors and the ones formed by the radiation, respectively. If  $a_2$  in Eq. [2] is equal to 0, then, from Eq. [4], [5], [6], and [7],  $h$  in Eq. [8] is also equal to 0, but  $f$  and  $g$  do not vanish. The second linear section,  $hE$ , of the growth of absorption curves (Fig. 2, 4, 5, 6) is connected with the new imperfections because, in Eq. [1],  $a_2$  is the rate constant of the generation of new imperfections by the radiation. The first fast rise of the curves (Fig. 1, 3, 5, 6) that corresponds to the second term,  $f(1 - e^{-gE})$ , in Eq. [8] is connected mainly with the imperfections already present in the phosphors prior to the irradiation. This second term approaches the value of  $f$  to within 1% after an exposure of  $E > 60$  mA·min for calcium tungstate and  $E > 4.6 \cdot 10^4$  mA·min for zinc silicate.

These results are very similar to those obtained for the growth of F centers in KCl by other authors (5, 6, 7). The accuracy of our measurements was not enough for a definite identification of an inflection point on the growth curves (6) which would indicate that the initial and the radiation-induced vacancies behave differently (7). In Ref. (5-7), the optical density measurements were made near the peak of the characteristic band of the F centers in the alkali halide crystals studied. The concentration of the F centers could be determined from absorption measurements (11). In our case, the types of centers are not yet identified; the reflectance measurements (3) indicate that several different types could have formed in the phosphors by irradiation, and their absorption bands might overlap. There is another indication from this work that in calcium tungstate at least two different color centers are produced by the irradiation. Comparing Eq. [7] and [8] if only one type of color centers was formed,  $g$  in Eq. [8] would not be a function of the wavelength-dependent, capture cross section of the color centers, but would be related only to their concentration. In calcium tungstate,  $g$  was found to be a function of the wavelength of measurement (Table I) while in zinc silicate, within the error of measurement,  $g$  had the same value at both measured wavelengths.

The calculated curves of degradation which are based on the calculated growth of absorption curves

fit the measured values for zinc silicate reasonably well (Fig. 9), while there is some deviation from the measured values in the case of calcium tungstate (Fig. 7 and 8). We attribute these deviations to the error of the measurement rather than to other unknown effects. We can rather safely say that the u.v. and visible absorption of irradiation-produced color centers is the major cause of the degradation of the photoluminescence of these phosphors. Other effects of the irradiation, if any, are negligible in this respect. Comparing the results obtained for the degradation to the analysis (above) of the growth of absorption curves, it is quite obvious that according to our model the initial fast degradation is connected with the imperfections prior to the irradiation of the phosphors while the following slow change can be attributed to new imperfections formed by the irradiation. A closer model of the absorption (12) and the energy levels involved could not be determined from our measurements which are related to the time-dependent change of the absorption and of the luminescence only.

We do not completely understand why the recovery of absorption follows the calculated values, Eq. [13], only during the initial period of recovery. In order to explain the experimental findings that the absorption (Fig. 10 and 11) and luminous efficiency (Fig. 12) do not completely regain the original value after irradiation stops, further study is needed. However, calculating the recovery of the luminescence from Eq. [15] with the experimentally measured absorption values during the recovery, good agreement with the experiments could be obtained (Fig. 12). The recovery phenomenon in general and this result in particular are additional proof that degradation is strictly connected with the absorption of color centers produced in the phosphors.

A reasonable approach to slowing down the initial fast degradation of phosphors should be the elimination of the imperfections originally present by annealing, by charge compensation, or by other methods. The rate and extent of the dark recovery should also be important in most applications, although it is not yet known how it can be influenced. Enhancing the absorption of the luminescent centers by increasing the activator concentration also seems feasible. However, it is restricted by the phenomenon of concentration quenching.

### Acknowledgments

The author wishes to thank Drs. Esther Conwell, Gustav Pfister, and Richard Zallen for their comments on the manuscript.

Manuscript submitted Aug. 7, 1974; revised manuscript received Sept. 5, 1975. This was Paper 46 presented at the Washington, D.C., Meeting of the Society, May 9-13, 1971.

Any discussion of this paper will appear in a Discussion Section to be published in the December 1976 JOURNAL. All discussions for the December 1976 Discussion Section should be submitted by Aug. 1, 1976.

Publication costs of this article were partially assisted by the Xerox Corporation.

### REFERENCES

- H. N. Hersch, *J. Chem. Phys.*, **30**, 790 (1959); L. Suchow, *This Journal*, **108**, 847 (1961); J. H. Singleton and L. Suchow, *ibid.*, **110**, 36 (1963); E. F. Apple, *ibid.*, **110**, 374 (1963); L. E. Vrenken, T. H. DeVette, and R. W. Van der Wolf, *Illumin. Engr.*, **59** (1964).
- B. Segall, G. W. Ludwig, H. H. Woodbury, and P. D. Johnson, *Phys. Rev.*, **128**, 76 (1962); R. K. Swank, *ibid.*, **135A**, 266 (1964); W. W. Piper, L. C. Kravitz, and R. K. Swank, *ibid.*, **138A**, 1802 (1965).
- G. T. Bauer, *This Journal*, **115**, 1176 (1968).
- K. Przibram, "Irradiation Colors and Luminescence," Pergamon Press, London (1956).
- I. L. Mador, R. F. Wallis, M. C. Williams, and R. C.

- Herman, *Phys. Rev.*, **96**, 617 (1954); R. B. Gordon and A. S. Nowick, *ibid.*, **101**, 977 (1956); A. S. Nowick, *ibid.*, **111**, 16 (1958).
6. H. W. Etzel and J. G. Allard, *Phys. Rev. Letters*, **2**, 452 (1959).
  7. P. V. Mitchell, D. A. Wiegand, and R. Smoluchowski, *Phys. Rev.*, **121**, 484 (1961).
  8. P. D. Johnson and F. J. Studer, *J. Opt. Soc. Am.*, **40**, 121 (1950); Z. Bodo, *Acta Phys. Hung.*, **1**, 135 (1951); P. D. Johnson, *J. Opt. Soc. Am.*, **42**, 978 (1952); O. P. Girin and B. J. Stepanov, *Zh. Eksperim. i Teor. Fiz.*, **27**, 281 (1954); G. T. Bauer, G. Gergely, and J. Adam, "Festkörperphysik," Akademie Verlag, Berlin (1961); G. T. Bauer, *Acta Phys. Hung.*, **14**, 311 (1962); N. T. Melamed, *J. Appl. Phys.*, **34**, 560 (1963); G. Körtum, "Reflectance Spectroscopy," Springer-Verlag, New York (1969).
  9. V. V. Antonov-Romanovskii, *Zh. Eksperim. i Teor. Fiz.*, **26**, 459 (1954); I. Masuda, *J. Phys. Soc. Japan*, **16**, 105 (1961); I. Masuda, *Oyo Butsuri*, **28**, 147 (1959).
  10. G. T. Bauer, *Acta Phys. Hung.*, **11**, 225 (1960); A. Brill, in "Luminescence of Organic and Inorganic Materials," H. P. Kallman and G. M. Spruch, Editors, p. 479, John Wiley & Sons, Inc., New York (1962).
  11. A. Smakula, *Z. Physik.*, **59**, 603 (1930); D. L. Dexter, *Phys. Rev.*, **101**, 48 (1956).
  12. P. D. Townsend and F. C. Kelly, "Colour Centres and Imperfections," Crane, Russak and Company, Inc., New York (1973).

## Low Energy Ion-Electron Luminescence: A New Technique for the Excitation of Inorganic Phosphors

Jerry Kramer

*GTE Laboratories Incorporated, Waltham, Massachusetts 02154*

### ABSTRACT

A new technique for the excitation of inorganic phosphors by low kinetic energy ions (<40 eV) and low kinetic energy electrons (<20 eV) has been demonstrated and characterized. The characteristic light output of the phosphor has been used as a probe of the excitation mechanism. An empirical relationship between the light output and the ion and electron currents has been determined and used to ascertain the change in light output as a function of ion and electron kinetic energy and ionization potential. The excitation mechanism starts with the formation of holes by the ion beam. Although the holes are mobile in the lattice, some of the holes get trapped. In a second step electrons interact with these trapped holes to create an excited state(s) of the phosphor. Energy is transferred to the luminescent centers resulting in the characteristic emission of the phosphor. The slow or rate-limiting step in the production of light by low energy ions and electrons is the emission of light. Of the ten phosphors examined for low energy ion-electron excitation, six showed detectable levels of light output and, hence, we conclude that this excitation technique is quite general. The efficiency of light production observed for  $\text{Y}_2\text{O}_3\text{-Eu}$  is  $\sim 1$  photon per 40  $\text{N}_2^+$  ions and no effort has been made to increase this efficiency. We refer to the light produced by this excitation technique as low energy ion-electron luminescence (LEIEL).

This paper presents a new technique for the excitation and subsequent characteristic emission of an inorganic phosphor. This new technique is based upon the interaction of low kinetic energy ions (<40 eV kinetic energy) and electrons (< 20 eV kinetic energy) with a phosphor.

Two schemes which are widely employed today for phosphor excitation involve electromagnetic radiation or charged particles with high kinetic energy, usually in excess of 1 keV (1). In the case of electromagnetic radiation, the exciting species are generally u.v. photons or higher energy x-rays. For charged particles, the exciting species are either negatively charged electrons (cathodoluminescence) or positively charged ions (ionoluminescence). For both electrons and ions the luminous output is kinetic energy dependent, increasing with kinetic energy.

A third excitation scheme is radical recombination luminescence (RRL), a phenomenon often referred to in the early literature as candoluminescence (2). RRL was initially observed when flames, a rich source of radicals, were "played upon" phosphor surfaces. More recent work has utilized microwave discharges as radical sources and confirmed the validity of radical excitation. RRL involves the recombination of two neutral species (which may be the same) on a phosphor surface. The energy of excitation can be thought of,

naively, as equal to the recombination energy of the two radicals, or, equivalently, to the bond energy of the molecular bond formed in the recombination. As an example, in the case of two hydrogen atoms, the excitation energy would be 4.5 eV. For the sake of comparison, a 4.5 eV photon would have a wavelength of  $\sim 2750\text{\AA}$ . The efficiency of RRL is quite low. Typical efficiencies for RRL of about 1 photon/ $10^5$  radicals are found experimentally. These low efficiencies relate, in part, to an excitation mechanism involving many steps, only one of which involves the formation of a bond between the two radicals.

An interesting extension of these ideas involves the use of oppositely charged species to excite luminescent materials. The available recombination energy of low kinetic energy ions and electrons can be thought of as approximately equal to the ionization potential of the neutral atom or molecule formed in the recombination. The ionization potentials of most neutrals range from about 10 to 25 eV. The corresponding wavelengths of photons of that energy span the range from about 1250 to 500 $\text{\AA}$ . Conceptually, the excitation of phosphors by ions and electrons can be thought of as primarily a potential energy phenomenon, rather than a kinetic energy process.

The idea that ions and electrons could excite a phosphor has been speculated upon in the literature of flame-excited luminescence (2). However, controlled

experiments to test this hypothesis have not been reported to date.

We present the first experiments on the excitation of luminescence in inorganic phosphors by low kinetic energy ions and electrons. The phenomenon is found to be complex, being very much dependent upon the interaction of the ions and electrons with the phosphor. The phosphor does not act as a simple third body which accepts the recombination energy of the ions and electrons. In contrast to RRL, the efficiency of light production by low kinetic energy ions and electrons is quite high.

### Experimental

The low energy ion-electron luminescence (LEIEL) apparatus is shown schematically in Fig. 1. The glass outer envelope of the system is connected to glass-to-metal seals and copper-gasketed stainless steel flanges which are used for supports and feedthroughs. The use of flanges permitted independent removal of the following four main components: (i) the ion source, (ii) the electron source, (iii) the phosphor support, and (iv) the vacuum system. Positive ions, generated in the ion source, and electrons from the electron source interacted with a phosphor sample. The light produced was spectrally analyzed by a monochromator and detected by a photomultiplier tube. Modulation of the charged beam(s) discriminated against the background d-c light signal as well as metastables and allowed measurement of the phase shift of the modulated light signal relative to the modulated charged beam.

The ion source and ion optics are from a Process Analyzers, Incorporated Quad 1200 RGA ionizer with electronic circuitry from a Quad 250B ionizer controller. The ion source potential was positive with respect to ground and determined the ion kinetic energy (maximum 40 eV). The first and third grids of the Einzel lens were at ground potential and the second grid at  $-90\text{V}$  to discriminate against electrons. The ion beam was modulated by applying a square wave potential (positive with respect to the ion source) to the first grid of the Einzel lens. Ions left the third grid and drifted  $\sim 5\text{ cm}$  to a phosphor plate oriented at a  $45^\circ$  angle to the axis of the ion beam. The only modification of the ion source consisted of replacing the tungsten filament with a directly heated oxide filament. This change significantly reduced background light. With an oxide filament emission current of  $150\ \mu\text{A}$ , 50 eV ionizing energy, and a source pressure of  $6 \times 10^{-4}$  Torr of  $\text{N}_2$ , an ion current of  $\sim 6 \times 10^{-8}\text{A}$  was detected at the phosphor plate. The detected ion current was not significantly altered when a phosphor was on the plate. A baffle, attached to the third grid, served to reduce the pressure in the phosphor region, relative to the source region, by a factor of  $\sim 20$ .

Since mass discrimination has not been incorporated into the apparatus, ion beams derived from diatomic neutrals will contain some monatomic ions. All experiments, however, were run with an ion source ionizing energy of 50 eV and were reproducible. For simplicity, we shall refer to an ion beam, derived from  $\text{N}_2$  neutrals, as  $\text{N}_2^+$  ions with the understanding that  $\text{N}^+$  ions are also present.

The electron source consisted of the heater, Ba/SrO cathode, and the first two grids from a Sylvania ST 4716 A CRT electron gun. The indirectly heated cathode was at a negative potential with respect to ground (normally  $-3\text{V}$ ). The first grid was negative with respect to the cathode and was used to control the electron current. The second grid was positive with respect to the cathode and a square wave potential on grid two produced a modulated electron beam. The electron beam, which is normal to the phosphor plate and elevated  $45^\circ$ , originated  $\sim 3\text{ cm}$  from the phosphor plate.

At the low electron source cathode to phosphor potentials used in these experiments, the electron kinetic energy is dependent upon the contact potential of the phosphor and the oxide cathode as well as the cathode bias. These contact potentials are, in general, not known and we report the cathode bias which, within an additive constant, equals the electron kinetic energy. Since our results are correlated with a change in electron kinetic energy, knowledge of the actual electron kinetic energy is not necessary. We also note that surface charging will change the electron kinetic energy at a given cathode bias.

All phosphors, except one, have been obtained from GTE Sylvania. The exception,  $\text{SrAl}_2\text{O}_4\text{-Eu}$ , has been synthesized and characterized previously (3-5). Phosphors are settled from acetone onto a stainless steel flat and baked at  $\sim 400^\circ\text{-}500^\circ\text{C}$  for 15 min. Typical calculated phosphor thicknesses were about  $10\ \mu$ . The stainless steel flat was attached to an insulating ceramic block and a lead from the flat connected to an electrometer to ground.

The apparatus was evacuated by a 4 in. oil diffusion pump filled with Convalex 10 pump oil. A Freon-cooled baffle above the pump reduced backstreaming and a gate valve isolated the system from the pump. Pressures below  $1 \times 10^{-7}$  Torr, as measured by an ionization gauge in the ion source region, were obtained routinely and provision existed for baking the apparatus to  $400^\circ\text{C}$ .

The detection scheme is shown schematically in Fig. 2. A modulated electron beam plus an unmodulated ion beam produced a modulated light signal from the phosphor. The light was passed through a  $\frac{1}{4}$  meter Jarrell-Ash monochromator and detected by a 1P28 PMT. The photomultiplier tube current generated a voltage across a  $10^4$  ohm resistor to ground and the a-c voltage was detected by a PAR HR-8 lock-in amplifier.

The phase of the modulated light was determined relative to an external reference from the Tektronix 161. The phase of the modulated current signal was also determined relative to the same external reference and the difference between these two phases was taken as the phase shift.

Modulation techniques, in addition to providing phase shift data which can be correlated with radiative lifetimes for first order processes, discriminate against background d-c light from filaments and possible effects from metastables. Modulation of both beams with continuously variable phase provides mechanistic information about the interaction of the ions and electrons with the phosphor.

In general, the charging of phosphor surfaces by low energy electrons necessitated the following experimental sequence. The ion source was turned on and an initial ion current  $I_T^\circ$ , was detected by the electrometer. (It is assumed that the ion current detected at the electrometer is proportional to the ion current which strikes the phosphor surface.) Electrons were then added in incremental amounts and the decrease in  $I_T^\circ$  was taken equal to the electron current,  $I_e$ , an indirectly measured quantity. At each new value of  $I_e$ , the light output was measured and the phase shift could be determined.

As arbitrary standard conditions, we have studied the interaction of a beam of electrons modulated at 100 Hz with the electron source cathode biased 3V nega-

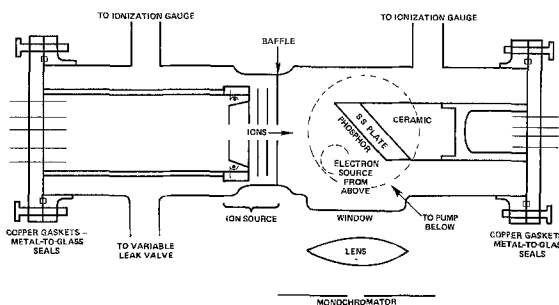


Fig. 1. Schematic diagram of the low energy ion-electron luminescence apparatus (viewed from above).



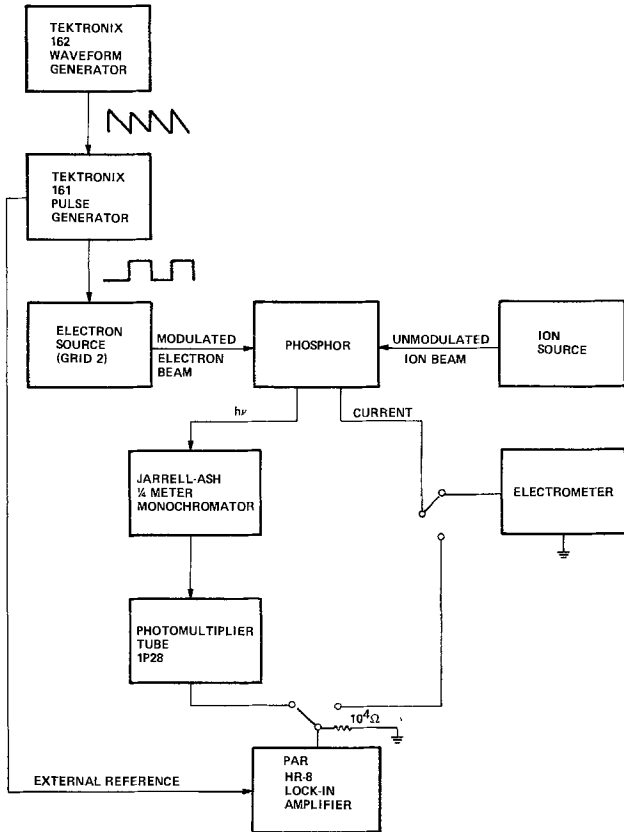


Fig. 2. Schematic diagram of the detection schemes. Modulation of the ion beam instead of the electron beam requires that the square wave go to grid 1 of the ion source rather than grid 2 of the electron source. Incorporation of a second Tektronix 161, triggered by the same 162, generates a modulated ion beam as well, with continuously variable phase with respect to the modulated electron beam.

tive with respect to the phosphor plate, and an unmodulated beam of 40 eV kinetic energy  $N_2^+$  ions. Typical ion currents,  $I_T^\circ$ , were in the range of  $1-10 \times 10^{-8}$  A and almost all data was determined for  $|I_T^\circ| > |I_e|$ .

**Results**

We find that the interaction of a beam of low kinetic energy electrons and ions with a phosphor leads to the production of visible light characteristic of that phosphor. This light output has been used as a probe of the excitation mechanism: to probe the mechanism we measured the change in light output as a function of the external variables of the experiment. Initially, the quantitative relationship between light output and ion and electron currents was determined. This relationship provided a basis of comparison for the effect of variables such as electron and ion kinetic energy and ionization potential on the light output. Most of the experiments involved the interaction of ions and electrons with a  $Zn_2SiO_4$ -Mn phosphor. However, nine other phosphors were also studied in order to determine: (i) the generality of the phenomenon, which we shall refer to as low energy ion-electron excitation (LEIEE), (ii) the relative efficiencies of the different phosphors, and (iii) whether the quantitative relationships observed for  $Zn_2SiO_4$ -Mn held for the other phosphors.

The LEIEL spectrum of  $Zn_2SiO_4$ -Mn was the same as the emission spectrum observed by the more conventional excitation schemes of photoexcitation or cathode-ray excitation of the same phosphor. In the quantitative results which follow, the light output for  $Zn_2SiO_4$ -Mn was measured without slits on the monochromator ( $\sim 300\text{\AA}$  bandpass) and centered at  $5280\text{\AA}$ .  $Zn_2SiO_4$ -Mn has a broad emission, peaking at  $5280\text{\AA}$ , and a bandwidth at half-height of  $410\text{\AA}$  (6).

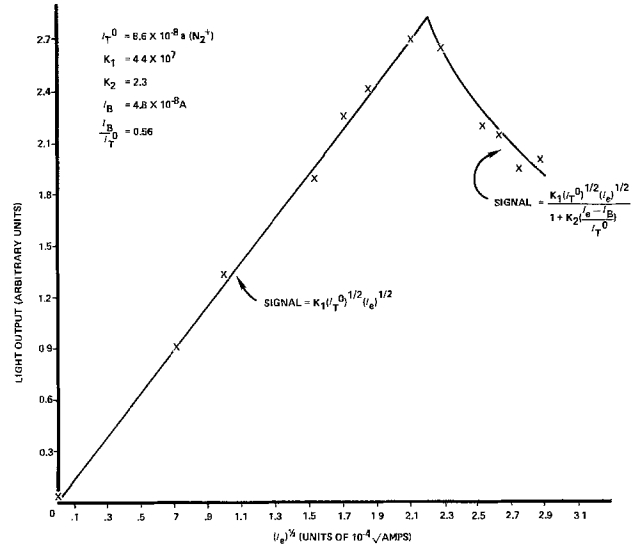


Fig. 3. Light output vs.  $(I_e)^{1/2}$ . Experimental conditions:  $Zn_2SiO_4$ -Mn; 40 eV  $N_2^+$  ions, unmodulated; electrons modulated at 100 Hz, cathode biased 3V negative. Crosses refer to the experimental points and the solid line to the empirical equation.

The light output of  $Zn_2SiO_4$ -Mn vs.  $(I_e)^{1/2}$  is shown in Fig. 3 for our arbitrary standard conditions. Qualitatively, the light output increased with increasing  $I_e$  and then started to fall off. This falloff was not associated with a change in the emission spectrum. The electron current at which falloff began was arbitrarily called  $I_B$ . The dependence of light output on  $I_T^\circ$  was determined by running experiments at different initial ion currents. The initial ion current could be varied by changing the neutral gas pressure or the emission current of the filament in the ion source and equivalent results were obtained with each method.

The relationships observed for ions at 40 eV were

$$S = \text{light output} = K_1(I_T^\circ)^{1/2}(I_e)^{1/2} \text{ for } (I_e < I_B) \quad [1a]$$

and

$$S = \frac{K_1(I_T^\circ)^{1/2}(I_e)^{1/2}}{1 + K_2 \frac{(I_e - I_B)}{I_T^\circ}} \text{ for } (I_e > I_B) \quad [1b]$$

$K_1$  is the scaling factor for output at values of  $I_e < I_B$ , the constant  $K_2$  determines the magnitude of the falloff, and  $I_B/I_T^\circ$  relates to when the falloff begins.

In Table I we tabulate the constants  $K_1$ ,  $K_2$ , and  $I_B/I_T^\circ$  (95% confidence levels) determined for our arbitrary standard conditions at a large number of different initial ion currents and also the constants determined at an ion kinetic energy of 20 eV. For our standard conditions we found that the falloff began when 55% of the initial ion current had been neutralized. Halving the ion kinetic energy to 20 eV resulted in a marked

Table I. Light output equation constants

$$S = \text{light output} = K_1(I_T^\circ)^{1/2}(I_e)^{1/2} \text{ for } (I_e < I_B)$$

$$S = \frac{K_1(I_T^\circ)^{1/2}(I_e)^{1/2}}{1 + K_2 \frac{(I_e - I_B)}{I_T^\circ}} \text{ for } (I_e > I_B)$$

	$K_1^{a,b}$	$K_2^{a,c}$	$I_B/I_T^{a*}$
$N_2^+$ (KE = 40 eV) Modulate electrons—100 Hz	$4.2 \pm 0.2 \times 10^7$	$2.9 \pm 0.5$	$0.55 \pm 0.02$
$N_2^+$ (KE = 20 eV) Modulate electrons—100 Hz	$1.9 \pm 0.2 \times 10^7$	—	—

<sup>a</sup> 95% confidence levels.  
<sup>b</sup> Units of  $(A)^{-1/2}$ .  
<sup>c</sup> Dimensionless.

decrease ( $\sim$  half) in the light output ( $K_1$ ) at  $I_e < I_B$  and, in addition, the falloff was not observed in four out of five runs. Hence, at 20 eV ion kinetic energy,  $I_B/I_T^\circ$  approaches unity.

In Fig. 4 we plot the light output vs.  $(I_e)^{1/2}$  for ion kinetic energies of 20 eV, 30 eV, and 40 eV. We see that whereas no falloff is observed at 20 eV and the 40 eV curve follows the relationships of Eq. [1], the results at 30 eV indicate that the light output has saturated.

More negative values of electron source cathode bias led to increased electron kinetic energy and, as shown in Fig. 5, increasing electron kinetic energy led to a linear increase in the light output ( $K_1$ ) at  $I_e < I_B$ . Also, increasing electron kinetic energy resulted in larger values of  $I_B/I_T^\circ$ . In comparing the effect of increasing electron and ion kinetic energy, we found that both led to an increase in light output. However, the behavior observed for  $I_B/I_T^\circ$  was opposite: increasing electron kinetic energy increased  $I_B/I_T^\circ$  while increasing ion kinetic energy decreased  $I_B/I_T^\circ$ .

Ions, derived from  $N_2$  neutrals, were used in most of our experiments. In order to explore the effect of ionization potential on the light output we examined

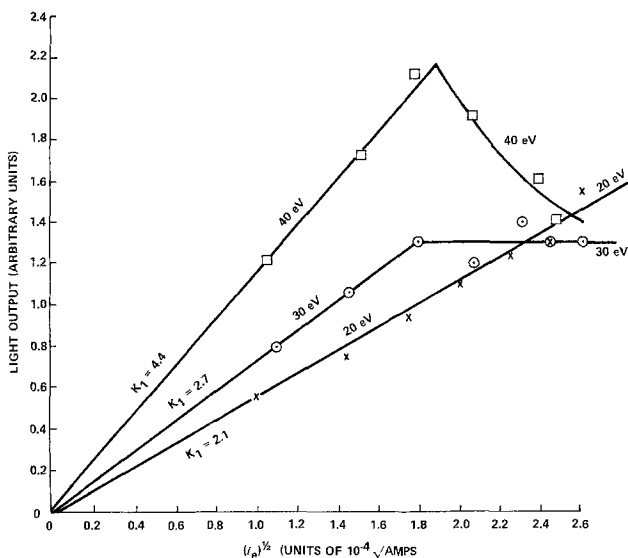


Fig. 4. Light output vs.  $(I_e)^{1/2}$  for different ion kinetic energies. Experimental conditions:  $Zn_2SiO_4$ -Mn; electrons modulated at 100 Hz, cathode biased 3V negative;  $N_2^+$  ions unmodulated, 40 eV ( $\square$ ),  $I_T^\circ = 7.0 \times 10^{-8}A$ , 30 eV ( $\odot$ ),  $I_T^\circ = 6.9 \times 10^{-8}A$ , and 20 eV ( $\times$ ),  $I_T^\circ = 7.2 \times 10^{-8}A$ .

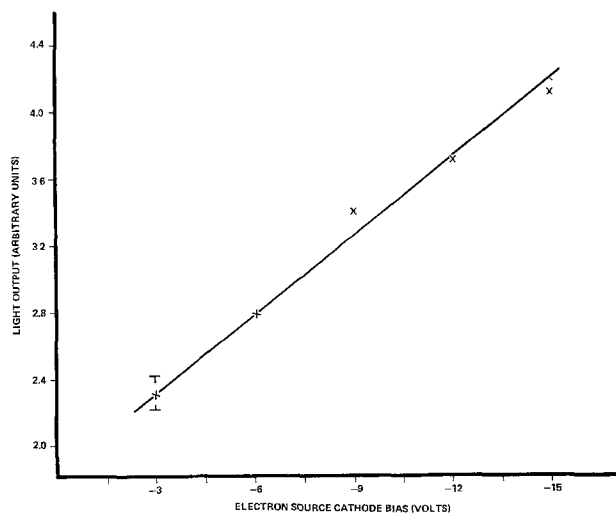


Fig. 5. Light output vs. electron kinetic energy. Experimental conditions;  $Zn_2SiO_4$ -Mn; 40 eV  $N_2^+$  ions, unmodulated; electrons modulated at 100 Hz.

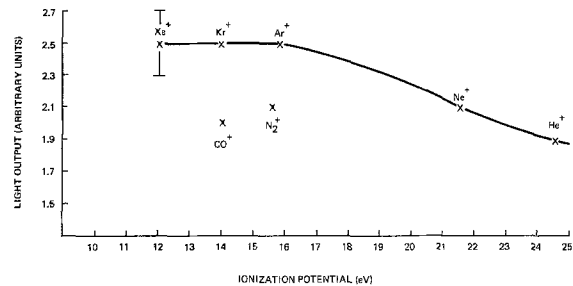


Fig. 6. Light output vs. ionization potential. Experimental conditions:  $Zn_2SiO_4$ -Mn; 40 eV ions, unmodulated; electrons modulated at 100 Hz, cathode biased 3V negative.

the light output for all the inert gas ions and  $CO^+$ . Polyatomic neutral sources could not be used because mass separation was lacking and  $O_2$  was excluded because of potential damage to the oxide filaments. The light output for the various ions used showed the same dependence on  $I_T^\circ$  and  $I_e$  (including falloff) as observed with  $N_2^+$ . In Fig. 6 the light output,  $K_1$ , for  $I_e < I_B$  is shown vs. the ionization potential of the neutrals (7). A gradual increase in light output ongoing from  $He^+$  to  $Ne^+$  to  $Ar^+$  (decreasing IP) was observed and then the signal remained constant through  $Xe^+$ . The ions derived from diatomic neutrals,  $N_2^+$  and  $CO^+$ , showed lower light outputs than the monatomic ions,  $Ar^+$  and  $Kr^+$ , respectively, with comparable ionization potentials.

The interaction of two charged beams with a phosphor allowed each beam to be modulated separately or to modulate both beams with continuously variable phase between them. We have shown the results of four different modulation schemes in Table II. As our basis of comparison, we considered the constants  $K_1$ ,  $K_2$ , and  $I_B/I_T^\circ$  for unmodulated 40 eV  $N_2^+$  ions and electrons modulated at 100 Hz. We observed that modulating both beams, in phase and out of phase, did not have a large effect on the constants in the light output equation. A small decrease in  $K_1$  for the case of both beams modulated out of phase was most apparent. In addition, note that the falloff was observed for both of these modulation schemes. In contrast, modulating the ion beam with an unmodulated electron beam resulted in very weak light output, too weak to be quantitatively measured. Finally, it was noted that modulating both beams out of phase at 20 Hz still produced a strong signal relative to both beams modulated in phase at 20 Hz.

Modulation of the electron beam plus an unmodulated ion beam produced a modulated light output.

Table II. Light output equation constants for different modulation schemes

$$S = \text{light output} = K_1(I_T^\circ)^{1/2}(I_e)^{1/2} \text{ for } (I_e < I_B)$$

$$S = \frac{K_1(I_T^\circ)^{1/2}(I_e)^{1/2}}{1 + K_2 \frac{(I_e - I_B)}{I_T^\circ}} \text{ for } (I_e > I_B)$$

	$K_1^{a,b}$	$K_2^{a,c}$	$I_B/I_T^\circ^a$
$N_2^+$ (KE = 40 eV) Modulate electrons—100 Hz	$4.2 \pm 0.2 \times 10^7$	$2.9 \pm 0.5$	$0.55 \pm 0.02$
$N_2^+$ (KE = 40 eV) Modulate electrons and $N_2^+$ 100 Hz—in phase	$4.0 \pm 0.6 \times 10^7$	$2.8 \pm 0.9$	$0.53 \pm 0.05$
$N_2^+$ (KE = 40 eV) Modulate electrons and $N_2^+$ 100 Hz—out of phase	$3.7 \pm 0.6 \times 10^7$	$2.7 \pm 0.9$	$0.50 \pm 0.06$
$N_2^+$ (KE = 40 eV) Modulate ions—100 Hz	—	—	—

<sup>a</sup> 95% confidence levels.  
<sup>b</sup> Units of  $(A)^{-1}$ .  
<sup>c</sup> Dimensionless.

This light output was phase shifted with respect to the current beams and the magnitude of the phase shift was dependent upon the modulation frequency. The phase shift could be determined for each incremental addition of electron current to the initial ion current,  $I_T^\circ$ . The magnitude of the phase shift was also dependent upon whether  $I_e$  was less than  $I_B$  or greater than  $I_B$ .

Before the falloff,  $I_e < I_B$ , the phase shift was approximately constant for each incremental addition of  $I_e$ . The quantitative relationship between phase shift,  $\theta$ , and the modulation frequency,  $f = \omega/2\pi$ , was

$$\frac{\omega}{\tan \theta} = \frac{1}{\tau} = \frac{1}{\tau_0} + c\omega \quad [2]$$

where  $c$  is a constant and  $\tau$  is a first-order decay time. In the limit of zero frequency,  $\tau_0$  equals  $2.6 \times 10^{-3}$  sec. Rearrangement of Eq. [2] yields

$$\tan \theta = \frac{\omega\tau_0}{1 + c\omega\tau_0} \quad [3]$$

These results are shown in Fig. 7.

After the falloff, the phase shift gradually decreased. Associated with this change was a change in the phase of the current beam and the light as well as the difference between them. Phase shifts determined near  $|I_T^\circ| \approx |I_e|$  did not show the same dependence upon frequency as shown in Eq. [2]. Near  $|I_T^\circ| \approx |I_e|$  the phase shift data could be fit to the equation

$$\frac{\omega}{\tan \theta} = \frac{1}{\tau} \quad [4]$$

and  $\tau \approx 1.5 \times 10^{-3}$  sec.

When both beams were modulated, the phase shift of the light correlated with the modulated electron beam, rather than the modulated ion beam. The magnitude of the phase shift was the same for modulation of both beams or the electron beam alone.

Nine other phosphors were examined for their LEIEL properties (8). A list of the phosphors studied and their relative efficiencies are shown in Table III. The luminescence observed showed no deviation from the normal emission spectrum. All phosphors, with sufficient emission to be quantitatively examined, showed the same dependence on  $I_T^\circ$  and  $I_e$ , including falloff, as  $Zn_2SiO_4$ -Mn. This relationship, (Eq. [1a]), with corrections for phosphor bandpass, PMT spectral response, and phosphor decay time, was used to determine the relative efficiencies. Selected checks of the effect of ion and electron kinetic energy and ionization potential on the light output revealed the same behavior as ob-

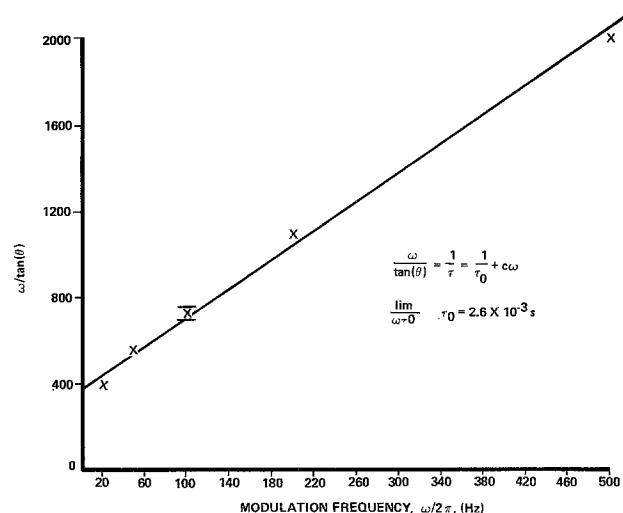


Fig. 7. Relationship between phase shift and modulation frequency ( $I_e < I_B$ ). Experimental conditions:  $Zn_2SiO_4$ -Mn; 40 eV  $N_2^+$  ions, unmodulated; electrons modulated, cathode biased 3V negative.

Table III. The relative LEIEL efficiency of different phosphors

Phosphor	Efficiency <sup>a,b</sup>
$Y_2O_3$ -Eu	10
$YVO_4$ -Eu	5
$Zn_2SiO_4$ -Mn	5
$Ba_2P_2O_7$ -Ti	3
$MgWO_4$	2
$SrAl_2O_4$ -Eu	1
$ZnCdS$ -Cu <sup>c</sup>	Very weak (?)
$Ca_3F(PO_4)_3$ -Sb,Mn	Very weak (?)
$CaSiO_3$ -Mn-Pb	Not observed
$ZnS$ -Ag <sup>c</sup>	Not observed

<sup>a</sup> Light output corrected for emission bandpass, PMT spectral response, and lifetime. Experimental conditions: 40 eV  $N_2^+$  ions, unmodulated,  $I_T^\circ = 8 \times 10^{-8}$ A; electrons modulated, cathode biased 3V negative.

<sup>b</sup> Arbitrary units.

<sup>c</sup> These samples were not baked in air to prevent formation of an oxide coating on the surface.

served with  $Zn_2SiO_4$ -Mn. The only deviation from the results observed with  $Zn_2SiO_4$ -Mn related to phase shifts. Neither  $Y_2O_3$ -Eu nor  $YVO_4$ -Eu showed the linear frequency dependence on lifetime of Eq. [2] observed with  $Zn_2SiO_4$ -Mn at  $I_e < I_B$ .

When both beams were modulated at 20 Hz out of phase, the first six phosphors in Table III showed significant light outputs relative to in-phase modulation at 20 Hz. This was true even for  $SrAl_2O_4$ -Eu with a decay time of  $\sim 10$   $\mu$ sec to 10% initial brightness (3). By way of comparison, LEIEL in  $SrAl_2O_4$ -Eu was also observed at an electron beam modulation frequency of 10 kHz, the limit of the square wave generator.

$SrAl_2O_4$ -Eu and  $Y_2O_3$ -Eu both had sufficient conductivity to conduct a modulated low kinetic energy electron beam (cathode = -15V) without significantly charging the phosphor surface. In both cases, no evidence of light was observed at the normal sensitivity used for LEIEL, even though the electron current was  $\sim 5$ -10 times the initial ion current normally used in an experiment.

In order to obtain a rough measure of the absolute quantum efficiency of the LEIEL process we have utilized ZnO. ZnO is excited by very low kinetic energy electrons and the quantum efficiency for 10 eV electrons is about 1 photon per 200 electrons (9). The ZnO light output, which is proportional to  $I_e$ , was measured at a modulated current of  $8 \times 10^{-8}$ A and 10 eV kinetic energy (cathode-phosphor bias) and corrected for PMT response, bandpass, and phosphor decay time. We have compared the light output of ZnO with the light outputs of the various phosphors in Table II at the experimental conditions given. The light output of ZnO was approximately equal to the light output for  $MgWO_4$ . Hence, we conclude that at an initial ion current,  $I_T^\circ$ , of  $8 \times 10^{-8}$ A  $MgWO_4$  has a maximum light output upon the addition of electrons corresponding to about 1 photon per 200  $N_2^+$  ions. No effort has been made to increase the yields for any phosphor.

## Discussion

We begin our discussion by considering the effect of electrons and ions alone on the phosphor, followed by the development of a model and subsequent refinements derived from quantitative data.

**Electron-phosphor interactions.**—When electrons interact with a phosphor, secondary electrons are emitted from the phosphor (10). The secondary electron emission coefficient, defined as the ratio of secondary electrons to primary electrons, is dependent upon the electron kinetic energy. At low kinetic energy the secondary electron emission coefficient of the phosphor is less than unity and in time the phosphor charges to the negative bias of the electron source cathode. For many phosphors, at approximately 50-200 eV, the secondary emission coefficient rises above unity and no negative charging is observed (11). Finally, at still higher kinetic energies ( $\sim 1$ -60 keV) the secondary electron

emission coefficient falls below unity again (11). In addition to producing secondary electrons, primary electrons also interact with a phosphor to produce visible light *via* cathode ray excitation (1). The kinetic energy threshold for the production of light is typically several hundred electron volts, however, notable exceptions such as ZnO have thresholds below 3 eV (9). For the continuous production of light, the phosphor must not charge negatively. In two phosphors used for the LEIEL experiments, charging did not occur at the typical electron kinetic energies of our experiments. It is significant that no light was detected in these two phosphors.

**Ion-phosphor interactions.**—The interpretation of ion-phosphor interactions is more complicated than electron-phosphor interactions. The complications arise because an ion has potential as well as kinetic energy by virtue of its ability to recombine with an electron. At high-ion kinetic energies (for example  $>1000$  eV), the ion bombards the phosphor and the interaction is dominated by the kinetic energy. As with the primary electrons, one observes secondary electron emission (12) and the production of light (ionoluminescence) (1). At low ion kinetic energies, the ion spends a much greater time near the surface of the phosphor and, hence, the potential energy of the ion can play a more dominant role. When low kinetic energy ions, with sufficient potential energy, approach within a few angstroms of a phosphor surface, neutralization of the ion can occur before the ion strikes the phosphor surface in a process involving the phosphor, the ion, and an electron from the valence band of the phosphor. Ion neutralization and the subsequent effect on the phosphor are best considered by reviewing some of the elementary theory of ion neutralization spectroscopy (12-14).

In Fig. 8 we see a diagram of the interaction of an ion with a phosphor surface (15).  $E = 0$  represents the vacuum level of the phosphor as well as a free electron and ion separated to infinity. The incoming ion approaches the phosphor surface and at some critical distance,  $s$ , dependent upon the ion kinetic energy, an electron from the valence band tunnels through the potential barrier to neutralize the incoming ion. The neutralized ion retains much of its kinetic energy (velocity) and continues toward the phosphor, striking the surface as a neutral. For neutralization to occur, the recombination energy of the ion, which in first order neglects the interaction with the phosphor and can be taken as the ionization potential (IP), must be greater than the energy from the top of the valence band to free space ( $\phi^*$ ). The valence electron, upon tunneling from the valence band, creates a hole and generally this hole is formed very close to the surface. If the  $IP > \phi^*$ , excess energy must be dissipated and if  $IP > \phi^* + \Delta E_g$  (the bandgap), a second electron from the valence band can be excited into the conduction band in an Auger-type process creating an electron-hole pair. Finally, if the  $IP > 2\phi^*$ , secondary electrons can be emitted.

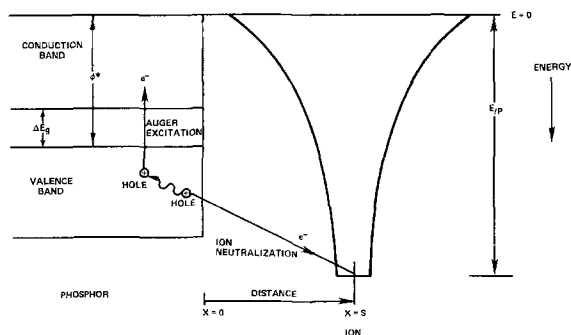


Fig. 8. Schematic energy diagram of low kinetic energy ion-phosphor interaction.

In semiconductors the secondary electron emission coefficient is only very weakly dependent upon ion kinetic energy, but the secondary electron yield increases dramatically for ions with increasing ionization potentials (16). Because of the high conductivity of the semiconductors, no surface charging was observed. For an insulator such as amorphous selenium, surface charging is most apparent (14). In the case of  $\text{SiO}_2$  films, ion neutralization processes lead to degradation of the MOS quality  $\text{SiO}_2$  films (17) and impurity migration from the surface to the Si substrate (18).

In our experiments on phosphors, surface charging, if present, was not pronounced enough to repel the incoming unmodulated ion beam. Compared to an unmodulated ion beam, square wave modulation halved the detected ion current with the phosphor present. For identical settings of the ion source, nearly the same ion current was detected by the electrometer with and without a phosphor present. From these observations we conclude that most of the holes formed upon neutralization have sufficient mobility to reach the electrometer and prevent charge buildup.

**Formation of a trapped hole.**—In the LEIEL experiments luminescence was only observed when ions as well as electrons interacted with the phosphor. By modulating both beams out of phase it was determined that the two charged species did not have to be coincident for light to be produced. This result suggested two possible roles for the ions. The first was that the electrons excited the phosphor *via* a conventional cathodoluminescent type excitation and that ions passively provided charge neutrality. A second mechanism assumes a more active role for the ion in the excitation process. Our results suggest that the active role for the ions is dominant.

Low energy ions ( $>100$  eV) interacting with metal surfaces show almost a 100% neutralization efficiency:  $\sim 0.1\%$  reflected ions and metastable atoms are observed (19). At the opposite end of the conductivity scale, the insulator, amorphous Se, shows a 100% charging efficiency in the region of low surface charge, and no difference was observed in charging behavior among any of the ions at any energy ( $<200$  eV) in the limit of zero surface charge (14). If we make the logical assumption that all the different ions are neutralized with 100% efficiency at the phosphor surface, then the observed differences in light output as a function of ionization potential indicate an active role for the ions. The square root dependence on the ion current in the light output equation is also suggestive of an active ion role. For two phosphors, electron charging did not occur at low electron kinetic energy and no luminescence was observed when the positive ion current was zero. Thus, for these two phosphors, the ions must play an active role and this strongly suggests that the ions take an active role in all the other phosphors.

One could argue that the decreased light output observed when only the ions are modulated is indicative of a passive role for the ions. The ions could preserve charge neutrality and the electrons produce a d-c light signal undetected by the lock-in amplifier. A more likely explanation, which preserves the active role, involves the formation of a trapped hole by the ion. If the ion beam creates a trapped hole whose lifetime is long with respect to the modulation frequency, then modulation of the ion beam at that frequency will lead to a decreased a-c light signal (20). This explanation requires that the ion beam creates an intermediate excited state of the phosphor which cannot luminesce. When both beams are modulated out of phase, the phase of the light output correlates with the electron beam rather than with the ion beam. Hence, we conclude that the electron beam interacts with the trapped hole of the phosphor to create an excited state(s) that leads to luminescence.

In the case of phosphors, temporary trapping of holes has been shown to lead to luminescence in  $\text{SrAl}_2\text{O}_4\text{-Eu}$  (5). Although the  $\text{Eu}^{+2}$  emission in  $\text{SrAl}_2\text{O}_4\text{-Eu}$  has a

fast (10  $\mu$ sec) decay to 10% of initial brightness, a long-lasting persistence of many seconds is observed (3). This luminescence has been shown to be associated with trapped holes that are thermally deactivated. We note that LEIEL was observed in  $\text{SrAl}_2\text{O}_4\text{-Eu}$ . In  $\text{SrAl}_2\text{O}_4\text{-Eu}$  the hole trapping levels are associated with defects in the lattice. In general, a second possibility for a hole trap is the activator ion itself. For example,  $\text{Mn}^{+2}$  could act as a hole trap by forming  $\text{Mn}^{+3}$ . Upon deactivation of the  $\text{Mn}^{+3}$  to  $\text{Mn}^{+2}$  with an electron, the  $\text{Mn}^{+2}$  could be left in an excited state and hence, might luminesce. A third possibility is that two mobile holes will dimerize and be trapped. This concept has been postulated with regard to  $\text{CaF}_2$  and will be amplified later (21).

All our results point to the formation of a trapped hole by the ion beam. The correlation between the electron beam and the light output, determined from the phase shift, and the ability to produce light with the beams out of phase supports the idea that electrons interact with the trapped holes in a second step to produce an excited state(s) of the phosphor. The light emission from LEIEL agrees with the other conventional excitation schemes and, hence, the same emitting state is most probably involved in the different excitation schemes. This is entirely reasonable, in that most phosphor excitation schemes with widely varying energy inputs lead to the same emission spectrum of the phosphor. Finally, the phase shift in  $\text{Zn}_2\text{SiO}_4\text{-Mn}$  extrapolated to zero modulation frequency yields a first order decay time of  $2.6 \times 10^{-3}$  sec which is similar to the value of  $2.5 \times 10^{-3}$  sec at  $15^\circ\text{C}$  determined by photo-excitation of the same sample (22).

*Possible mechanisms and kinetic energy dependence.*—The light output equations for ions at 40 eV are

$$S = \text{light output} = K_1(I_T^\circ)^{1/2}(I_e)^{1/2} \text{ for } (I_e < I_B) \quad [1a]$$

and

$$S = \frac{K_1(I_T^\circ)^{1/2}(I_e)^{1/2}}{1 + K_2 \frac{(I_e - I_B)}{I_T^\circ}} \text{ for } (I_e > I_B) \quad [1b]$$

We note that the falloff does not begin when electrons are first added to the phosphor, but only after a significant fraction of the initial ion current has been neutralized. As seen in Fig. 4, the falloff at 30 eV is different, being better represented by a term in the denominator of the light output equation which reflects saturation, and that at 20 eV no falloff is observed. Common to the results at these three kinetic energies, however, is the light output equation,  $K_1(I_T^\circ)^{1/2}(I_e)^{1/2}$ , for  $I_e < I_B$ . We start by discussing a possible mechanism which might give rise to the square root behavior of the ion and electron currents.

Ions interact with the phosphor at low kinetic energy and are neutralized when they approach within a few angstroms of the phosphor surface. The neutralized ion continues its path toward the phosphor and strikes the phosphor surface as a neutral with some kinetic energy. Results on low energy ions (25-600 eV) interacting with a tungsten wire indicate that at the energies used in those experiments approximately 50% of the kinetic energy of the ion is transferred to the tungsten lattice by the neutralized ion (23). The incoming ion is neutralized when an electron from the valence band of the phosphor tunnels to the approaching ion leaving a hole at the surface of the phosphor. In the case of metals or semiconductors, the mobility of the holes formed (or electrons) is high enough to prevent charge buildup at the surface, while in the case of insulators such as amorphous selenium, rapid charge buildup with an initial 100% efficiency is observed at the surface. For phosphors with conductivities between insulators such as amorphous selenium and semiconductors, we postulate that positive charge buildup at the surface is kept down because the kinetic energy of the neutralized ion frees the hole from the surface of the

phosphor and creates a mobile hole. Recent experiments in low energy ion bombardment effects in  $\text{SiO}_2$  have also postulated this "knock-on" effect with regard to impurity migration (17). The increasing ability to free holes from the surface of the phosphor may explain the increase in light output before falloff observed with increasing ion kinetic energy.

Holes, once freed from the surface region, are mobile and can migrate to the phosphor substrate and be collected by the electrometer or they may be trapped along the way. The square root dependence on the ion current in the light output equation mechanistically suggests that two mobile holes combine to form a trapped hole. The rate of production of trapped holes,  $dp_t/dt$ , is proportional to the rate of creation of holes,  $I_T^\circ$ , minus the rate at which trapped holes are formed in a process dependent upon the square of the hole concentration,  $p$ . Thus

$$\frac{dp_t}{dt} = \beta I_T^\circ - kp^2 \quad [5]$$

and at steady state  $dp_t/dt = 0$  and

$$[p]_\alpha (I_T^\circ)^{1/2} \quad [6]$$

The dimerization of holes has been postulated previously in work done on  $\text{CaF}_2$  (21). X-irradiation of  $\text{CaF}_2$  doped with  $\text{Tm}^{+3}$  produces self-trapped ( $V_K$ ) centers at liquid  $\text{N}_2$  temperatures.  $\text{Tm}^{+3}$  ions enhance  $V_K$  production by trapping electrons and hence, are converted to  $\text{Tm}^{+2}$  ions. Upon warming the crystal to room temperature, about 90% of the  $V_K$  centers are changed to nonparamagnetic hole centers (24). The nonparamagnetic nature and complex decay kinetics of these room temperature hole centers are compatible with the formation of hole pairs as the stable hole centers.

In analogous fashion, the dependence of the light output on the square root of the electron current suggests that two electrons may be involved in the production of light. The light output would be expected to increase with increasing electron kinetic energy if the excitation of a valence electron were involved in initiating the luminescence. This may explain the results of Fig. 5 which shows the light output vs. electron kinetic energy. Two other factors which might be relevant are that increasing electron kinetic energy will lead to less negative surface charging of the phosphor because of the increasing secondary electron emission coefficient, and that different electron kinetic energies will lead to different penetration depths of the electrons into the phosphor. Also at very low electron kinetic energy, cathodoluminescent processes show a "dead layer" effect which has been attributed to surface recombination (25). Our understanding of LEIEL, however, is not sufficiently developed to examine these three effects in any detail.

In order that the light output be proportional to the square roots of the two currents the light output must also be proportional to the first power of the hole concentration and the first power of the electron concentration. From the analysis above, however, the light output should be proportional to the square of the hole and electron concentrations. At this time we cannot resolve this discrepancy, nor can we suggest an alternative mechanism which might fit the data better. We might also add that the influence of the hole concentration gradient from surface to substrate on the light output is not known, nor is the effect of the diffusion of the holes and electrons.

*Falloff.*—The falloff in light output is shown in Fig. 4 for a number of different ion kinetic energies. The falloff represents a competition between radiative and nonradiative processes. Interestingly, this competition does not begin at the start when electrons are added, but only after a finite percentage of the ion current has been neutralized. This suggests that the falloff in light output must be triggered by some state of the system.

Secondly, the functional form of the falloff changes dramatically with ion kinetic energy and does not even occur at an ion kinetic energy of 20 eV.

The triggering of the falloff is kinetic energy dependent. For electrons, increasing the kinetic energy increases the percentage of the ion current which is neutralized before falloff occurs. In contrast, increasing the ion kinetic energy from 20 to 30 eV decreases the percentage of the ion current which is neutralized before falloff occurs. This opposite behavior for oppositely charged species suggests that an electrostatic phenomenon may be responsible for the falloff. We also note that when the falloff occurs, the phase of the ion and electron beams change with respect to a reference. Charging of the phosphor surface would lead to distortion of the square wave ion plus electron signal and, hence, produce a phase shift.

*Effect of ionization potential.*—Our results show that the kinetic energy of the ion beam has a much greater effect on the light output than the chemical identity of the ion, *i.e.*, the ionization potential. However, when the ionization potential is less than  $\phi^*$  (Fig. 8), insufficient energy is available for neutralization by an electron tunneling from the valence band, and, hence, the light should be very low or nonexistent. In contrast to our results, the secondary electron emission observed in ion neutralization spectroscopy is strongly dependent upon the ionization potential, increasing with increasing ionization potential, and very weakly dependent upon the ion kinetic energy (16). This suggests that for LEIEL the ability of an ion with high ionization potential to form an electron-hole pair in a secondary Auger process either does not lead to luminescence, or that any luminescence obtained from the Auger process is swamped by a different luminescent process which has a weak inverse dependence on the ionization potential.

The hole produced by the incoming ion, once freed from the surface of the phosphor, can either migrate to the substrate and be neutralized or be trapped in the bulk. A competition exists between these possibilities. One factor which may influence this competition is the energy of the hole initially formed, relative to the top of the valence band. Those holes formed closer to the top of the valence band may have a higher probability of being trapped. For a given ion current, ions with smaller ionization potentials capable of being neutralized by valence electrons will produce a greater percentage of holes closer to the top of the valence band, and hence more light will be produced per unit ion current.

The decreased light output of  $N_2^+$  relative to  $Ar^+$ , and  $CO^+$  relative to  $Kr^+$ , may relate to the ability of diatomic species to vibrate and rotate (26). Excitation of vibrational and rotational modes of  $N_2$  and  $CO$  at the time of neutralization may decrease the percentage of the ion kinetic energy which is transferred to the phosphor relative to monatomic species. In general, some of the effect of ionization potential on light output may also relate to the inherent efficiency of kinetic energy transfer by the neutral to the lattice.

Although holes may be trapped either at the surface or in the bulk, our results suggest that the trapped holes responsible for luminescence are in the bulk. If a surface phenomenon were involved, one would expect that vacuum conditions, sample preparation, and time would play a major role in the light output obtained. Reproducible results were obtained, however, over periods of months without changing samples or baking the apparatus. In addition, fresh samples could be inserted into the system and, with no other preparation than evacuating the system, luminescence could be observed. Surely, by the modern standards of surface science, our phosphor surfaces were not clean.

Mass sputtering by ion beams with kinetic energies in excess of 500 eV is commonly used to clean surfaces. Low energy ion-surface collisions have produced optical radiation which arises from sputtered material

(27). Some samples showed thresholds as low as  $\sim 50$  eV (27). Although sputtering could be occurring in our experiments during ion irradiation, the low ion currents and low kinetic energies argue against significant amounts of sputtering.

*Phase shifts.*—The phase shift of the light output in  $Zn_2SiO_4$ -Mn vs.  $\omega$  before the falloff is shown in Fig 7. We will only consider the region before falloff because of possible electrostatic complications that arise after falloff.

The relationship between the phase shift and  $\omega$  in  $Zn_2SiO_4$ -Mn before falloff (assuming that  $\tau$  is a constant independent of  $\omega$ ) is

$$\theta = \tan^{-1} \frac{\omega\tau_0}{1 + c\omega\tau_0} \quad [7]$$

where  $c$  is a constant. This differs from the normal equation for a first-order decay process by the  $1 + c\omega\tau_0$  term in the denominator. Extrapolation of the phase shift to zero frequency to eliminate frequency dependent effects yields a first-order decay time,  $\tau_0$ , of 2.6 msec.  $Zn_2SiO_4$ -Mn shows a first-order decay to below 10% of initial brightness and photoluminescent decay data from this laboratory on the same sample yields a first-order decay time of 2.5 msec at 15°C (22). The excellent agreement between these two values implies that the slow step in the production of light by LEIEL is the emission of light. In support of this conclusion, the first-order decay times for  $YVO_4$ -Eu and  $Y_2O_3$ -Eu were in reasonable agreement with the values obtained by other methods. Also the transit time of the ions to the phosphor is much faster than the luminescent decay times.

The  $1 + c\omega\tau_0$  term in the denominator of the phase shift, although unusual, is reproducible. It may, however, be unique for  $Zn_2SiO_4$ -Mn in that it was not observed with  $Y_2O_3$ -Eu or  $YVO_4$ -Eu. The fact that the  $1 + c\omega\tau_0$  term was not observed with  $Y_2O_3$ -Eu or  $YVO_4$ -Eu also tends to rule out experimental artifacts as the origin of the  $1 + c\omega\tau_0$  term. A mechanism which might explain the physical origin of the  $1 + c\omega\tau_0$  term is not apparent.

An alternative interpretation of the experimental data is that the phase angle,  $\theta$ , is equal to  $\tan^{-1}(\omega\tau)$  as expected for a first-order process, but that  $\tau$  changes with frequency. This interpretation, however, requires that increasing frequency leads to apparent radiative lifetimes which are increasingly shorter than the natural lifetime obtained by photoluminescence. It is unreasonable that the lifetime could decrease by a factor of 5 ongoing from a modulation frequency of 20 to 500 Hz, especially with no indication that the lifetime was reaching a steady value.

*Other phosphors.*—Of the ten phosphors studied, six showed detectable levels of light by the LEIEL excitation technique. From this result we conclude that LEIEL is a reasonably general phenomenon and that the technique should be capable of exciting a large number of phosphors. The fact that all six phosphors showed the same functional dependence on  $I_T^\circ$ ,  $I_e$ , and  $I_B$  in the light output equations as well as the same qualitative effect of electron and ion kinetic energies and ionization potential on light output indicates that the same general excitation mechanism leading to light production is operative in all of these phosphors. The linear frequency dependence of the emitting state lifetime observed in  $Zn_2SiO_4$ -Mn may be peculiar to that material.

Calibration of the light output with a ZnO standard shows that the LEIEL process is quite efficient.  $Y_2O_3$ -Eu has a maximum light output (just before falloff begins) with 40 eV  $N_2^+$  ions and cathode bias of  $-3V$  which corresponds to about 1 photon per 40  $N_2^+$  ions. No effort was made to maximize the light output of these phosphors by altering the phosphor itself. There seems no reason to believe that a phosphor optimized for u.v. or electron excitation will be optimized for LEIEL excitation.

### Acknowledgments

The author wishes to thank Drs. Adam Heller and Joseph Lester for their many helpful discussions. This work was sponsored in part by the Office of Naval Research.

Manuscript submitted June 11, 1975; revised manuscript received Sept. 2, 1975.

Any discussion of this paper will appear in a Discussion Section to be published in the December 1976 JOURNAL. All discussions for the December 1976 Discussion Section should be submitted by Aug. 1, 1976.

Publication costs of this article were partially assisted by GTE Laboratories Incorporated.

### LIST OF SYMBOLS

LEIEL	low energy ion-electron luminescence
LEIEE	low energy ion-electron excitation
$I_T^\circ$	the initial ion current passing through the phosphor and detected by an electrometer
$I_e$	the electron current determined from the decrease in $I_T^\circ$ upon the addition of electrons
$I_B$	the electron current at which the light output starts to deviate from a $K_1(I_T^\circ)^{1/2}(I_e)^{1/2}$ dependence
$f$	the frequency at which the ion or electron beams, or both, are modulated
$\omega$	the modulation frequency, $f$ , divided by $2\pi$
$\theta$	the phase shift of the light output signal relative to the modulated current signal
$\tau$	the first-order decay time to $1/e$ of initial value
$\phi^*$	the energy difference from the top of the valence band to free space
$\Delta E_g$	the bandgap

### REFERENCES

- For a general discussion on phosphors the reader is referred to H. W. Leverenz, "An Introduction to Luminescence of Solids," John Wiley & Sons, Inc., New York (1950).
- For a recent review see H. F. Ivey, *J. Luminescence*, **8**, 271 (1974).
- F. C. Palilla, A. K. Levine, and M. R. Tomkus, *This Journal*, **115**, 642 (1968).
- G. Blasse and A. Bril, *Philips Res. Rept.*, **23**, 201 (1968).
- V. Abbruscato, *This Journal*, **118**, 930 (1971).
- "Zinc Orthosilicate: Mn, Type 2282," Sylvania Phosphors, Technical Information Bulletin.
- J. L. Franklin *et al.*, "Ionization Potentials, Appearance Potentials, and Heats of Formation of Gaseous Positive Ions," National Standard Reference Data System, NBS-26, 1969.
- A tenth phosphor, ZnO, showed the usual property of being excitable by a low energy ion beam by itself. The results for this phosphor will be reported on elsewhere.
- P. Wachter, *Z. Physik.*, **161**, 62 (1961).
- For a discussion of secondary electron emission see A. Van der Ziel, "Solid State Physical Electronics," Chapter 10, Prentice Hall, Inc., Englewood Cliffs, N.J. (1957).
- H. W. Leverenz, "An Introduction to Luminescence of Solids," p. 435, John Wiley & Sons, Inc., New York (1950).
- See, for example: I. A. Abroyan, M. A. Eremeev, and N. N. Petrov, *Soviet Phys. Usp.*, **10**, 332 (1967).
- H. D. Hagstrum, *Phys. Rev.*, **122**, 83 (1961).
- D. W. Vance, *J. Appl. Phys.*, **42**, 5430 (1971).
- We consider the phosphor as a semiconductor or insulator, depending upon its conductivity, with special radiative properties which do not affect the ion neutralization results observed in semiconductors and insulators.
- See, for example: Y. Takeishi and H. D. Hagstrum, *Surface Sci.*, **3**, 175 (1965).
- D. V. McCaughan and V. T. Murphy, *I.E.E.E. Trans. Nucl. Sci.*, **19**, 249 (1972).
- D. V. McCaughan, R. A. Kushner, and V. T. Murphy, *Phys. Rev. Letters*, **30**, 614 (1973).
- H. D. Hagstrum, *Phys. Rev.*, **96**, 325 (1954).
- The relationship among modulation frequency, first-order decay time, and signal intensity is discussed in J. Perel, R. H. Vernon, and H. L. Daley, *J. Appl. Phys.*, **36**, 2157 (1965).
- Z. J. Kiss and D. L. Staebler, *Phys. Rev. Letters*, **14**, 691 (1965).
- R. Pappalardo and J. Moore, Private communication.
- H. F. Winters and D. Horne, *Phys. Rev.*, **B-10**, 55 (1974).
- J. H. Beaumont, W. Hayes, D. L. Kirk, and G. P. Summers, *Proc. Roy. Soc. (London)*, **Ser. A 315**, 69 (1970).
- G. Gergely, *J. Phys. Chem. Solids*, **17**, 112 (1960).
- Decreased secondary electron emission yields for diatomic ions vs. monatomic ions with the same ionization potential have been observed in the ion neutralization spectroscopy of metals. Calculations have shown that the decreased yield is consistent with the ability of the diatomic ion to vibrate and rotate. See J. B. French and R. H. Prince, in "The Structure and Chemistry of Solid Surfaces," G. Somorjai, Editor, Chapter 48, John Wiley & Sons, Inc., New York (1969).
- C. W. White and N. H. Tolk, *Phys. Rev. Letters*, **26**, 486 (1971).



# Structures and Optical Properties of Rf-Sputtered $\text{Bi}_{12}\text{GeO}_{20}$ Films

Tsuneo Mitsuyu, Kiyotaka Wasa, and Shigeru Hayakawa

Wireless Research Laboratory, Matsushita Electric Industrial Company, Limited, Kadoma, Osaka, Japan

## ABSTRACT

Thin films of  $\text{Bi}_{12}\text{GeO}_{20}$  were prepared on glass and silicon substrates by rf-sputtering with the growth rate of 0.04-1.5  $\mu\text{m/hr}$ . The crystalline structure of the films varied mainly with the substrate temperature: the amorphous state was obtained below 150°C of the substrate temperature; polycrystalline with fcc form between 150° and 350°C; and polycrystalline with bcc form above 400°C. The (111)-oriented aluminum films deposited on glass substrates were found to enhance the preferred orientation of the bcc films in the  $\langle 321 \rangle$  direction. These sputtered films exhibited the near ultraviolet optical absorption edges at 460-620  $\text{m}\mu$ , and a broad absorption at about 20  $\mu\text{m}$  in the infrared region.

$\text{Bi}_{12}\text{GeO}_{20}$  (BGO) in the body-centered cubic (bcc) system is strongly piezoelectric, optically active, photoconductive, and exhibits an electro-optic effect. Large single crystals of BGO are made by the Czochralski method (1) and are studied for fabricating ultrasonic devices (2).

Thin films of BGO are usable for the fabrication of thin-film surface acoustic wave devices. The BGO films reduce the dimension of the acoustic devices owing to their low sound velocities (3) and also have a potential in the fabrication of thin-film optical devices such as light modulators, deflectors, and switches (4). Several processes are used to make the BGO film: chemical vapor deposition (CVD), liquid phase epitaxial growth, and cathodic sputtering. The CVD method was examined to deposit the single crystal BGO films on a surface of monocrystalline substrates by Silvestri *et al.* (5). In addition, several workers have succeeded in fabricating highly oriented or single crystalline films of multicomponent oxides such as ferroelectric  $\text{Bi}_4\text{Ti}_3\text{O}_{12}$  and  $\text{LiNbO}_3$  by cathodic sputtering (6-8). The cathodic sputtering process has the advantage that a wide variety of materials can be deposited on various substrates with little cross contamination.

Recently we have fabricated thin films of BGO on heterogeneous substrates by rf sputtering. This paper describes the structure and some optical properties of rf-sputtered BGO films.

## Experimental Procedures

An rf diode sputtering apparatus of a hemispherical electrode system was used for depositing the BGO films. The electrode configuration of the sputtering apparatus is schematically shown in Fig. 1. A polycrystalline BGO hemispherical target 25 mm in diameter was used as cathode. The target was prepared as follows: First, powder of  $\text{Bi}_2\text{O}_3$  (purity, 99.8%) and  $\text{GeO}_2$  (purity, 99.9999%) mixed at the mole ratio of 6:1 was pressed into a column and the column was prebaked in air for about 4 hr at 800°C in order to synthesize BGO grains. Then, the grains were pressed into a column again and were sintered in air at the same firing condition to the prebaking process. Finally, the sintered column was formed into a hemispherical shape. The x-ray diffraction pattern and the corresponding lattice constant of the target well agreed with the ASTM data (card No. 23-71) for the bcc phase of the BGO. Borosilicate glass and (111)-oriented single crystal wafers of Si were used as substrates. These substrates were placed on a holder

Key words: bismuth germanium oxide, rf sputtering, piezoelectric film, optical absorption.

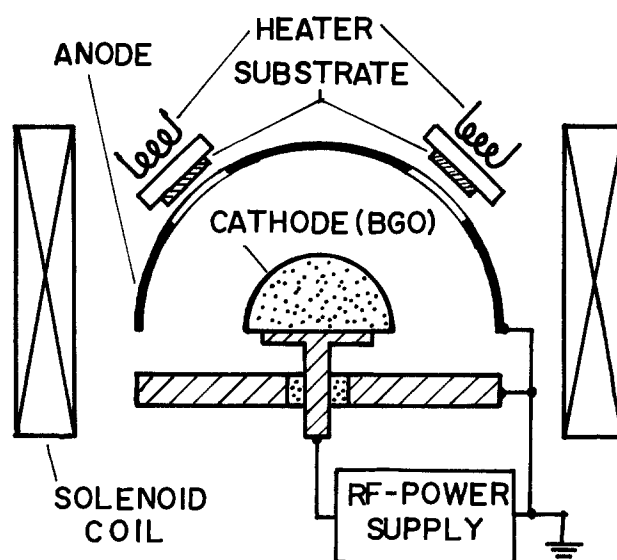


Fig. 1. Electrode configuration of rf-sputtering system

located behind the anode. Table I shows typical sputtering conditions for the film preparation. Under these conditions the BGO films were prepared with a growth rate of 0.04-1.5  $\mu\text{m/hr}$ . The sputtered films were 0.15-3.0  $\mu\text{m}$  thick.

Crystalline structures of the films sputtered on the glass and Si substrates were determined by x-ray diffraction and reflection electron diffraction (RED). Optical transmission spectra were examined at room temperature. The glass substrates were used in the visible region and the Si substrates, in the infrared region.

## Results and Discussion

It was observed that the crystalline structure of the sputtered films scarcely depended on the substrate material or the growth rate, but strongly depended on the substrate temperature during the sputtering process. At the substrate temperature below 150°C

Table I. Sputtering conditions for the film preparation

Target area	9 $\text{cm}^2$
Target-substrate spacing	2-3 cm
Sputtering gas	Ar(50%) + $\text{O}_2$ (50%)
Gas pressure	$5 \times 10^{-3}$ Torr
Background pressure	$2 \times 10^{-6}$ Torr
Rf power	5-20W
Magnetic field	100G
Substrate temperature	100°-500°C



(not deliberately heated) the sputtered films were amorphous. These films were yellow and transparent. At the substrate temperature between 150° and 350°C, the sputtered films were dark brown and showed a different x-ray diffraction pattern with that of the bcc phase. From the x-ray analyses, this phase is found to be the impure phase of  $\text{Bi}_2\text{O}_3$  with a face-centered cubic (fcc) form which has been designated as  $\delta^*$ - $\text{Bi}_2\text{O}_3$  by Gattow and Schröder (9). A comparison of the x-ray diffraction data for the film obtained in our experiment with the data for  $\delta^*$ - $\text{Bi}_2\text{O}_3$  prepared from a composition  $6\text{Bi}_2\text{O}_3 \cdot \text{GeO}_2$  by Gattow and Fricke (10) (listed as  $\text{Bi}_{12}\text{GeO}_{20}$  in ASTM card No. 17-812) is given in Table II. The lattice constant  $a = 5.55\text{Å}$  for the former is slightly smaller than  $a = 5.57\text{Å}$  for the latter. This fcc phase is considered to be a metastable state since it has transformed easily into the bcc phase by annealing at 400°C for 1 hr. This consideration is confirmed by the fact that the bcc phase is found to be stable at any temperature below the melting point of 935°C (11). In the bulk BGO, the fcc phase can be obtained only by quenching a melt (10). It is noted that in the sputtering film growth process, the metastable fcc phase can be easily grown without any additional quenching process.

Films of the bcc phase were obtained at the substrate temperature above 400°C. The films of the bcc phase were pale yellow and semitransparent. X-ray data for these films and the ASTM data for the pulled single crystal BGO are also given in Table II. The lattice constant for the film is  $a = 10.16\text{Å}$  which is slightly greater than the ASTM data,  $a = 10.146\text{Å}$ . At the substrate temperature of 350°-400°C, sputtered films were mixtures of the fcc and bcc phases.

Figure 2 shows typical RED patterns and electron micrographs for the BGO films of the amorphous, fcc, and bcc phases on the glass substrates. It is observed that the crystallites of the bcc phase are much larger than that of the fcc phase. The RED patterns indicate that all these films are polycrystalline and scarcely exhibit a preferred orientation. Similar results were obtained for the films on Si substrates. But a slight tendency of the (321) orientation was observed for the bcc films as shown in Fig. 3 when the glass substrate was coated with a thin (111)-oriented Al layer (vacuum deposited), the growth rate was very low (0.04  $\mu\text{m/hr}$ ), and the sputtered film was very thin (0.15  $\mu\text{m}$ ).

The crystalline structures of the BGO films sputtered on glass or Si substrates are summarized in Table III.

Table II. X-ray diffraction data for  $\text{Bi}_{12}\text{GeO}_{20}$ 

fcc $\text{Bi}_{12}\text{GeO}_{20}$ ( $\delta^* - \text{Bi}_2\text{O}_3$ )					bcc $\text{Bi}_{12}\text{GeO}_{20}$				
Films		ASTM 17-812			Films		ASTM 23-71		
d(Å)	I	d(Å)	I	hkl	d(Å)	I	d(Å)	I	hkl
3.204	100	3.21	100	111	3.591	19	3.57	30	220
2.776	19	2.78	45	200	3.211	100	3.20	100	310
1.960	31	1.965	65	220	2.930	26	2.922	40	222
1.674	19	1.681	70	311	2.718	64	2.702	90	321
1.600	8	1.605	18	222	2.540	3	2.569	5	400
1.386	1	1.393	10	400	2.395	5	2.384	10	330+
1.272	7	1.278	25	331	2.272	8	2.265	10	420
1.240	4	1.244	20	420	2.167	13	2.158	20	332
					2.074	8	2.066	20	422
					1.992	12	1.986	40	510+
					1.855	5	1.852	30	521
					1.742	22	1.738	80	530+
					1.693	13	1.690	50	600+
					1.647	15	1.644	70	611+
					—	—	1.564	10	541
					1.531	3	1.529	10	622
					1.498	12	1.495	70	631
					—	—	1.464	10	444
					1.437	4	1.434	60	543+
					—	—	1.416	10	640
					1.385	3	1.379	60	721+
					—	—	1.355	20	642
					—	—	1.332	50	730
					1.289	1	1.288	40	651+
					—	—	1.267	5	800
					—	—	1.249	40	811+
					—	—	1.231	30	820+
					1.215	3	1.212	100	653

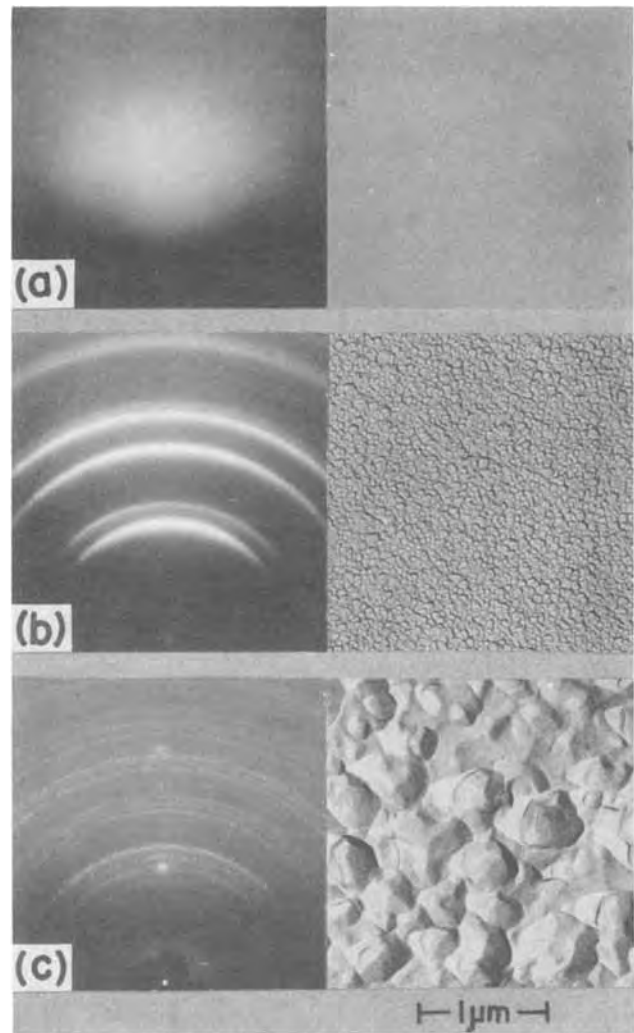


Fig. 2. Typical reflection electron diffraction patterns and electron micrographs of  $\text{Bi}_{12}\text{GeO}_{20}$  films sputtered onto glass substrates: (a) film sputtered at about 100°C with growth rate of 0.25  $\mu\text{m/hr}$ , amorphous state; (b) film sputtered at 200°C, 0.20  $\mu\text{m/hr}$ , fcc form; (c) film sputtered at 400°C, 0.15  $\mu\text{m/hr}$ , bcc form.

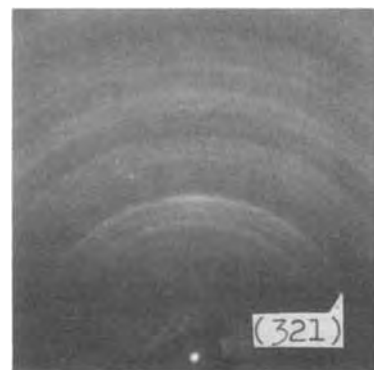


Fig. 3. Reflection electron diffraction pattern of bcc  $\text{Bi}_{12}\text{GeO}_{20}$  film about 0.15  $\mu\text{m}$  thick sputtered onto thin (111)-oriented Al layer on glass substrate with growth rate of 0.04  $\mu\text{m/hr}$  and substrate temperature of 400°C.

Optical absorption spectra in the visible and infrared region were measured for the three types of film. The results are shown in Fig. 4 and 5. In the visible region, although absorption edges of the films are not sharp, the absorption edges can be approximately estimated at 510, 620, and 460  $m\mu$  for the amorphous, fcc, and bcc phases, respectively. The absorption edge at 450  $m\mu$  was reported for single crystal BGO (bcc phase)

Table III. Crystalline structures of  $\text{Bi}_{12}\text{GeO}_{20}$  films sputtered on glass or Si substrates under various conditions

Sample No.	Substrate material	Substrate temperature ( $^{\circ}\text{C}$ )	Growth rate ( $\mu\text{m/hr}$ )	Film thickness ( $\mu\text{m}$ )	Crystalline structure
M5G-M	Glass	100	1.0	3.0	amorphous
M7G-M	Glass	100	0.25	1.8	amorphous
M27S	Si	100	0.64	2.1	amorphous
M7G	Glass	200	0.20	1.5	fcc
M5G	Glass	275	0.60	1.8	fcc
M5S	Si	300	0.60	1.8	fcc
M25G-B	Glass	350	1.2	1.2	fcc
M26G-B	Glass	350	0.17	0.6	fcc
M23G-B	Glass	375	1.2	1.2	fcc + bcc
M26G-A	Glass	375	0.17	0.6	fcc + bcc
M24G-A	Glass	400	0.44	1.2	bcc
M14G	Glass	400	0.15	0.6	bcc
M15S	Si	400	0.30	1.2	bcc
M20A	Al*	400	0.04	0.15	bcc**
M24S	Si	500	0.44	1.2	bcc

\* Thin (111)-oriented Al layer vacuum deposited on a glass substrate.

\*\* A slight tendency of the (321) orientation was observed.

(1), which well agreed with our results for films of the bcc phase. In the infrared region, a broad absorption at a wavelength of about  $20\ \mu\text{m}$  was observed for all the three types of film. In the films of the bcc phase, several remarkable peaks were superposed on the absorption band. These peaks may correspond to vibration modes peculiar to the bcc structure of BGO.

The refractive index  $n$  was determined from the number of optical interference fringes in the visible transmission spectrum by using the well-known relation  $n = m\lambda_1\lambda_2/2t(\lambda_1 - \lambda_2)$ , where  $m$  denotes the number of fringes between optical wavelength  $\lambda_1$  and  $\lambda_2$ , and  $t$  is the film thickness. Taking  $m = 5$  for  $\lambda_1 = 720\ \text{m}\mu$ ,  $\lambda_2 = 583\ \text{m}\mu$ , and  $t = 3.0\ \mu\text{m}$  for the sputtered amorphous BGO films, we have  $n = 2.6$ , which is nearly equal to the single crystal value of 2.55 (1). The values for the crystalline BGO films, however, cannot be determined due to their high optical absorption in the visible region.

### Summary

We attempted to grow thin films of  $\text{Bi}_{12}\text{GeO}_{20}$  on glass and silicon substrates by rf sputtering with the growth rates of  $0.04$ – $1.5\ \mu\text{m/hr}$ . The structure of the sputtered films varied mainly with the substrate temperature  $T_s$  as follows: for  $T_s \lesssim 150^{\circ}\text{C}$  films were

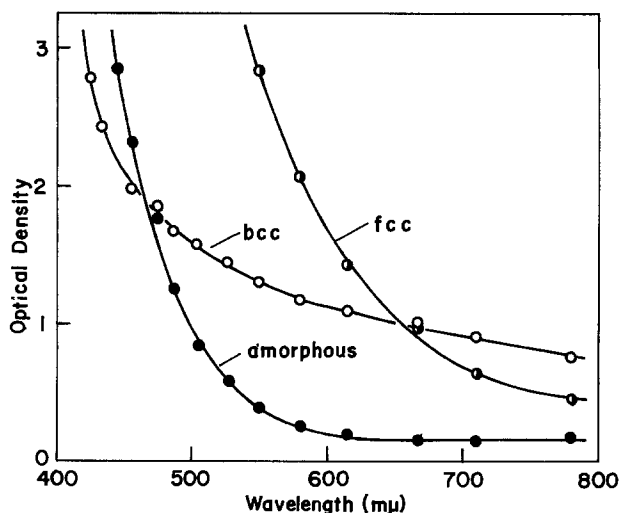


Fig. 4. Optical absorption spectra in the visible region for three types of sputtered  $\text{Bi}_{12}\text{GeO}_{20}$  films.

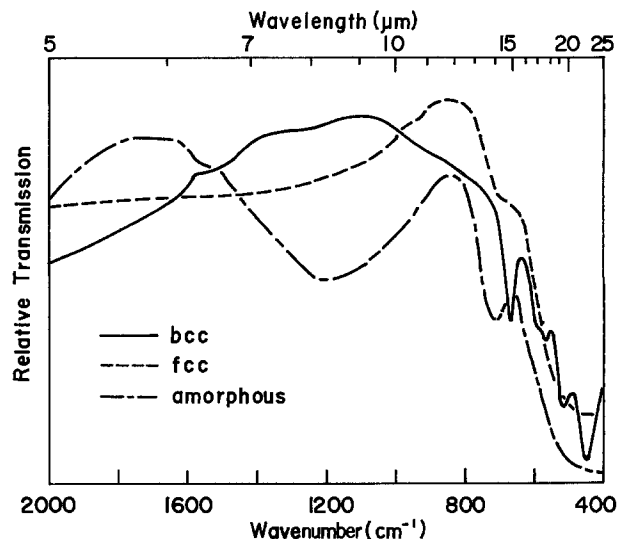


Fig. 5. Infrared transmission spectra for three types of sputtered  $\text{Bi}_{12}\text{GeO}_{20}$  films.

amorphous; for  $150^{\circ}\text{C} \lesssim T_s \lesssim 350^{\circ}\text{C}$  films were polycrystalline with the fcc structure which was the metastable impurity form of  $\text{Bi}_2\text{O}_3$  designated as  $\delta^*$ - $\text{Bi}_2\text{O}_3$ ; for  $T_s \gtrsim 400^{\circ}\text{C}$  films were polycrystalline with the bcc structure which was the normal phase of BGO; for  $350^{\circ}\text{C} \lesssim T_s \lesssim 400^{\circ}\text{C}$  the films were a mixed phase of the fcc and bcc structures. Optical transmission study indicated that the ultraviolet absorption edges were located at  $510$ ,  $620$ , and  $460\ \text{m}\mu$  for the amorphous, fcc, and bcc phases, respectively, and a broad absorption, at about  $20\ \mu\text{m}$  for all films. Although highly oriented BGO films of the bcc phase could not be obtained on glass or silicon substrates, (111)-oriented aluminum films deposited on the glass substrates were found to enhance the preferred orientation of the BGO films.

### Acknowledgments

The authors wish to thank Dr. S. Mori and Mr. H. Yamao for their electron microscopic analyses.

Manuscript submitted June 30, 1975; revised manuscript received Sept. 17, 1975.

Any discussion of this paper will appear in a Discussion Section to be published in the December 1976 JOURNAL. All discussions for the December 1976 Discussion Section should be submitted by Aug. 1, 1976.

Publication costs of this article were partially assisted by the Matsushita Electric Industrial Company, Limited.

### REFERENCES

1. A. A. Ballman, *J. Cryst. Growth*, **1**, 37 (1967).
2. E. G. Spencer, P. V. Lenzo, and A. A. Ballman, *Proc. IEEE*, **55**, 2074 (1967).
3. M. Onoe, A. W. Warner, and A. A. Ballman, *IEEE Trans. Sonics Ultrasonics*, **SU-14**, 165 (1967).
4. S. E. Miller, *IEEE J. Quantum Electron.*, **QE-8**, 199 (1972).
5. V. J. Silvestri, T. O. Sedgwick, and J. B. Lander-mann, *J. Cryst. Growth*, **20**, 165 (1973).
6. W. J. Takei, N. P. Formigoni, and M. H. Fran-combe, *J. Vacuum Sci. Technol.*, **7**, 442 (1969).
7. S. Takada, M. Ohnishi, H. Hayakawa, and N. Miko-shiba, *Appl. Phys. Letters*, **24**, 490 (1974).
8. S. Fukunishi, A. Kawana, N. Uchida, and J. Noda, *Japan. J. Appl. Phys. Suppl.*, **2**, 749 (1974).
9. G. Gattow and H. Schröder, *Z. Anorg. Allgem. Chem.*, **318**, 176 (1962).
10. G. Gattow and H. Fricke, *ibid.*, **324**, 287 (1963).
11. E. M. Levin and R. S. Roth, *J. Res. Nat. Bur. Std.*, **A68**, 197 (1964).

# An Optically Effective Intermediate Layer Between Epitaxial Silicon and Spinel or Sapphire

Ch. Kühl, H. Schlötterer,\* and F. Schwidofsky

Siemens AG, Forschungslaboratorien, München, Germany

## ABSTRACT

The existence of an optically effective intermediate layer between epitaxial silicon and spinel or sapphire has been proved. By measuring the optical and geometric thickness of the films as a function of film thickness a difference in the thickness values was found which could be interpreted as the thickness of an intermediate layer. This layer was also measured directly with a stylus tracer yielding a thickness of about 40 nm. Reflection electron diffraction and secondary ion mass spectroscopy were performed. A growth model for the silicon films is proposed which assumes that aluminum silicates will be formed due to reactions with the substrate as long as the substrate surface is uncovered. Despite or possibly because of this existing intermediate layer good epitaxial silicon films are obtained.

The fact that strong orientation relationships can be found in the case of epitaxial silicon films on insulating substrate crystals has already been discussed in numerous papers (1, 2). A one-to-one coordination of the atoms of the two corresponding net planes of film and substrate, respectively, is in most cases given as an explanation (3, 4), and the substitution of atoms of the substrate surface by silicon atoms resulting in a Si-O bonding is discussed in literature. To overcome the relatively great mismatch or misfit of the lattice constants and distances which is frequently encountered, multiple fits had been used to match these differences (2, 4), a practice often adopted for epitaxy (5). Especially in the case of silicon-on-sapphire, some disagreement between different investigators was found (4) concerning the exact orientation relationships. Considering all these and similar aspects, one gains the impression that the existence of symmetry elements, especially symmetry axes like three- or fourfold rotation axes perpendicular to the surface plane, is more relevant to achieving good epitaxy than an exact atom-to-atom matching. This impression is confirmed by the fact that transition or intermediate layers are often discovered in connection with the epitaxy of vapor-deposited films (6).

Mercier (7) has used infrared spectroscopy to confirm the presence of Si-Al and Si-O bonds in silicon, films, but it was not possible to determine whether these were situated near the interface or in the silicon film itself. In the case of silicon on Mg-Al spinel and sapphire, we had experimental findings that suggest the existence of an intermediate layer which is in any case optically effective. We therefore studied this system in more detail in order to prove this hypothesis.

## Experimental Methods and Results

The epitaxial silicon films on spinel or sapphire studied were produced by chemical vapor deposition in the  $\text{SiH}_4/\text{H}_2$  system in a water-cooled horizontal reactor at substrate temperatures of 1080° and 1000°C and at growth rates of 1.5 and 2.5  $\mu\text{m}/\text{min}$ , respectively. The substrates were single crystals of magnesium-aluminum spinel (Verneuil) with (100) surfaces and single crystals of sapphire (Czochralski) with (1012) surfaces.

**Thickness measurements.**—A simple experimental procedure was adopted, which is shown schematically in Fig. 1. After the epitaxial deposition a mask is applied and the unmasked part of the silicon film has been etched away by an acid etch of 95 ml 65%  $\text{HNO}_3$ , 5 ml 40% HF, and 1g  $\text{NaNO}_2$  (8) resulting in a step.

The step height, i.e., the geometric film thickness  $d_G$ , is measured with a Perthen stylus tracer, Model ECW-L. The measured value may be a little less than the real distance of the silicon surface from the substrate since the acid may not remove all of the film also at the unmasked parts. The optically determined average film thickness,  $d_O$ , is calculated by evaluating the extrema of the interference fringes caused by reflection at the assumed optically effective interfaces air/film and film/substrate (9). The refractive index of the silicon films has been assumed to be that of bulk silicon. This assumption is suggested by earlier results and will be justified by the results discussed later on. The reflectance measurements were carried out in the wavelength range 1-2.5  $\mu\text{m}$  with a Zeiss two-beam spectrophotometer, Model DMR 21, which was adapted by the construction of a reflection attachment.

Comparing the film thicknesses obtained with the different methods one observes that in all cases the optical thickness was less than the geometric thickness. We therefore assumed the existence of an intermediate layer giving rise to the difference in height between the substrate surface and the optically effective film boundary. To prove this hypothesis, we thinned several films with an initial thickness of about 1-2  $\mu\text{m}$  in steps of about 0.2  $\mu\text{m}$  by means of an alkaline etch of 30% KOH, 15 ml isopropanol at 84°C (8). After each step thickness measurements were performed with both methods.

In order to avoid falsifications caused by surface roughness, the surface of the film was carefully polished and cleaned after each thinning step.

Figure 2 shows the difference between both types of thickness values as a function of the optical thickness. Though there is a large spread of the values due to experimental error, a systematic positive difference is evident, which we interpret as the thickness of an intermediate layer between film and substrate; the thickness of this layer varies between 40 and 70 nm for different silicon-on-spinel samples. With silicon-on-sapphire, values were found (20-40 nm), which

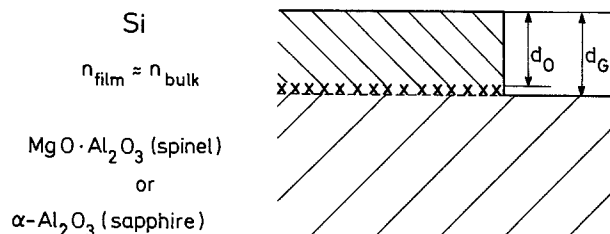


Fig. 1. Optical and geometrical thickness of an epitaxial silicon film on spinel or sapphire (xxx intermediate layer).

\* Electrochemical Society Active Member.  
Key words: optical interferences, thickness measurement, absorption, electron diffraction, SIMS.

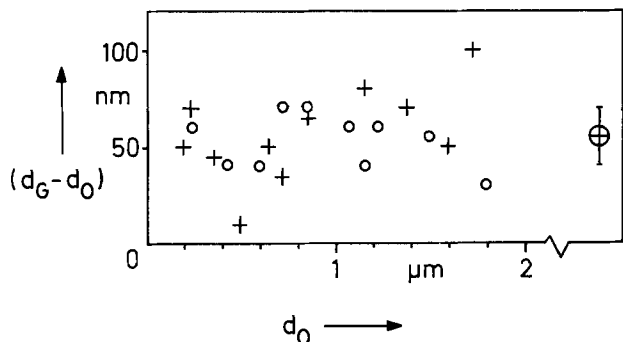


Fig. 2. Thickness of the intermediate layer on spinel vs. optical silicon thickness (+ sample 1, O sample 2, ⊕ mean value).

were systematically lower than those of spinel but which also showed some scatter.

Since the difference between geometric and optical thickness turns out to be independent of the film thickness, the refractive index of the film which had been assumed to be that of bulk silicon can be regarded as constant in all parts of the film. In principle, at a given film thickness, one could equalize the results of both measurements by assuming a refractive index  $n'$  smaller than that of bulk silicon. But in an earlier paper (10) it had already been shown that this should only be possible if a relatively high oxygen content is present, which is not the case with our films being produced in a reducing hydrogen atmosphere. On the other hand, if the geometric thickness is used for evaluation,  $n'$  should decrease strongly with decreasing thickness, but no signs of such a decrease have been found.

But the existence of the intermediate layer could also be proved directly: after the last etching step a scarcely visible layer remained showing a remarkably reduced etch rate compared to the silicon etch rate. In one case it was possible to measure this residual layer employing the step method, as described above. The result was a geometric thickness of about 40 nm. The spectral reflectance of this layer showed no difference compared to the substrate. Therefore, we assume that the optical constants of the intermediate layer scarcely differ from those of the substrate (sapphire:  $n = 1.76$ ,  $k = 0$ ; spinel:  $n = 1.71$ ,  $k = 0$  at  $\lambda = 1 \mu\text{m}$ ).

**Absorption measurements.**—We also calculated the average absorption constant  $\alpha$  at the different steps of film thickness according to a method described in a previous paper (11). The results are shown in Fig. 3. We observed a distinct increase in the absorption constant as we approached the substrate/silicon interface ( $d_0 = 0$ ). Other measurements, e.g., lifetime and mobility measurements in the silicon films, also indicate a poor crystal quality near the interface (12).

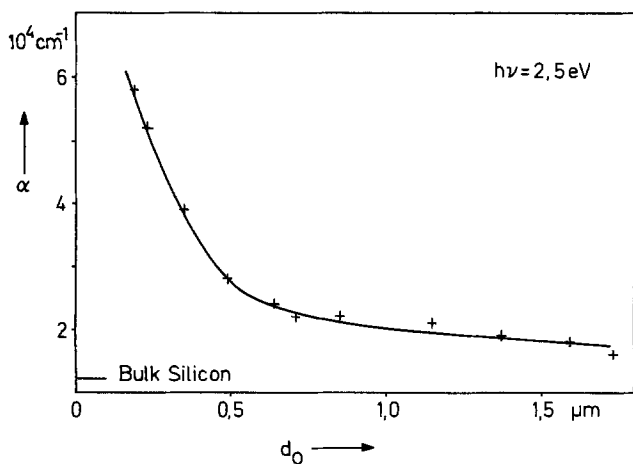


Fig. 3. Absorption constant vs. optical film thickness for a successively thinned epitaxial silicon film on spinel.

These results lead us to assume that a disordered region exists near the bottom of the silicon film, which can be correlated with the intermediate layer.

**Analysis of the intermediate layer.**—**Secondary ion mass spectroscopy.**—In order to analyze the composition of the intermediate layer, secondary ion mass spectroscopy (SIMS) was performed (13) using Balzers equipment. The primary beam consisted of  $\text{Ar}^+$  ions with an energy of 450 eV and a current density of  $10^{-8} \text{ A cm}^{-2}$ . The target area was  $0.1 \text{ cm}^2$ . The surface of three samples was investigated, i.e., a thin silicon film of about 100 nm, an intermediate layer with a thickness of about 40 nm, and a spinel surface as it appears after the acid etch. The most important results are shown in Fig. 4. With decreasing film thickness the magnesium and aluminum signals increase, whereas those of silicon and silicon compounds decrease. It is also seen that the spinel surface is giving signals of silicon and silicon oxides after the removal of the silicon film by the acid etch. This shows that on top of the substrate a thin film has remained containing those materials besides the components of the substrate. So even  $d_G$  does not correspond to the real distance between the silicon film surface and the true substrate crystal. That can be understood by the

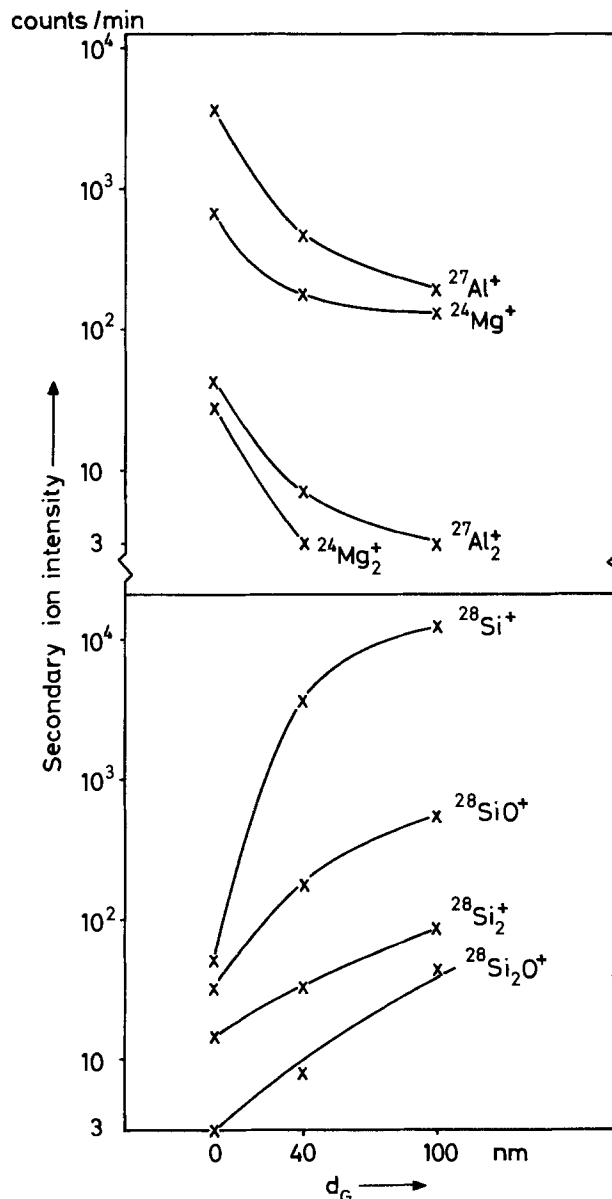


Fig. 4. SIMS analysis of the intermediate layer: intensity of characteristic signals vs. geometric thickness. Upper (lower) part: complex ions originating from the spinel substrate (silicon film).

experimental fact that highly doped silicon has a very small etch rate, even with the acid etch.

At a first glance the SIMS result obtained with the silicon compounds is not in agreement with the decrease of the oxygen content expected with increasing distance from the oxide-substrate interface. But here we have to remember that we do not have a true profile measurement, but only the surface investigation of three samples. We therefore assume that the oxygen has not been incorporated during the epitaxial growth, but that the silicon near the surface has been oxidized during and after the etching process. Consequently the concentration of the silicon oxides decreases in the same way as the concentration of silicon itself. Similar results are obtained with silicon films on sapphire.

**Electron diffraction.**—In order to see a possible structural difference between the substrate and the intermediate layer, reflection electron diffraction was performed with a Siemens Elmiskop (electron energy 80 keV). Figure 5 (a) shows the diffraction pattern of the intermediate layer, whereas for the purpose of comparison, Figure 5 (b) shows the pattern of a spinel substrate, and Figure 5 (c) the pattern of an epitaxial

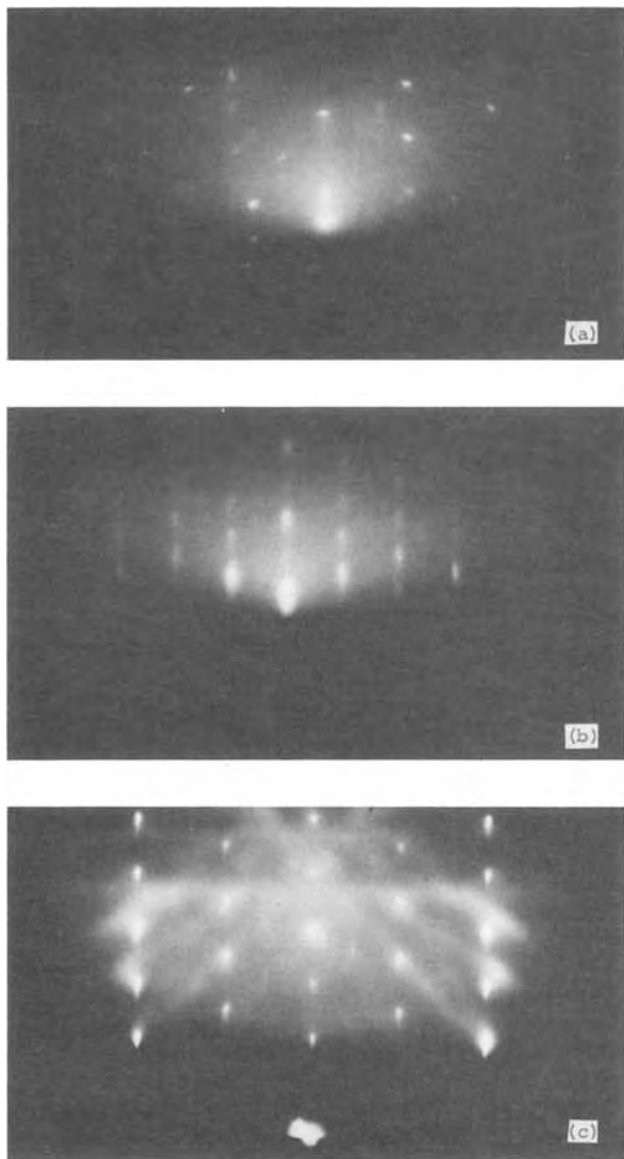


Fig. 5. (a) Electron diffraction pattern of the intermediate layer, (b) electron diffraction pattern of the spinel substrate, (c) electron diffraction pattern of the epitaxial silicon film on spinel. All obtained with (100) surfaces, the incident beam being parallel to [011].

silicon film. In the latter case, besides the Bragg reflection spots, we also see rather distinct Kikuchi lines, indicating the good quality of the film.

Only part of the reflection spots in Fig. 5 (a) can be identified either as spinel [Fig. 5 (b)] or silicon [Fig. 5 (c)], whereas the other spots are probably due to some crystalline Al-Mg silicates. Unfortunately these spots could not easily be related to the generally known silicates. Nevertheless, the electron diffraction results, together with the SIMS data, suggest that the intermediate layer contains crystalline compounds differing both from the spinel substrate and the silicon film. More exhaustive experiments will have to be conducted to investigate the properties of the intermediate layer.

### Discussion

The present investigations have shown that there is a gradual transition from the  $\text{Al}_2\text{O}_3$  and  $\text{MgO}$  of the substrates to the pure silicon of the final film, the thickness of the transition layer in the case of sapphire being somewhat smaller than with spinel. The formation of the transition layer obviously is in connection with the well-known chemical reactions during the nucleation phase in the epitaxial growth (14).

For explanation we therefore make use of the following growth model: during the first phase of growth volatile reaction products like  $\text{SiO}$  and  $\text{Al}_2\text{O}$  are produced and partly included into the growing film (15). The amount of these reaction products will be proportional to the uncovered surface of the substrate since the reaction cannot take place below the silicon nuclei and islands. Therefore this amount decreases with increasing silicon coverage of the surface and, consequently, the concentration of the included compounds will also decrease. At the moment at which the surface is completely covered with silicon, the situation drastically changes as no more oxygen will be included in the silicon film. The consequence is a change of the composition due to the lack of oxygen. As long as oxygen is present, we will have some kind of aluminum silicates, which all indeed have optical constants (16) similar to those of the substrates ( $\text{Al}_2\text{O}_3$ ,  $\text{MgO-Al}_2\text{O}_3$ ). Therefore the optically effective interface will be located at a thickness containing so much silicon and so little magnesium, aluminum, and oxygen that it is rather the optical behavior of probably highly doped silicon than that of oxide compounds.

The different etch behavior of the alkaline and acid etch is in agreement with the differences in the ratio of etch rates for silicon and silicon oxide films (8). The alkaline etch rate is much more reduced by oxygen than that of the acid etch.

Using the expression "intermediate layer" rather than "transition layer" is, therefore, really appropriate because from the optical point of view it is a layer of definite thickness between substrate and silicon film (15). The experimental observation that this thickness is somewhat less with sapphire than with spinel can be explained by the different nucleation behavior of the two materials. The average thickness which is necessary to cover the substrate completely is smaller in the case of sapphire (15, 17), so that the thickness of the intermediate layer is also smaller. It seems that the intermediate layer matches the differences between substrate and silicon lattice. On the other hand, Distler *et al.* (18) found that the orienting influence of a single crystal substrate can be transmitted even through an amorphous intermediate layer. They studied, among other things, the oriented growth of PbS on top of amorphous carbon on NaCl. The authors give as an explanation of their observation the existence of long-range active centers on the substrate surface which induce epitaxial growth at a remarkable distance. However, Chopra (19) supports the hypothesis that epitaxial growth is an interfacial phenomenon and that the orienting influence of a substrate is confined to its surface plane only and the atoms located in it. Despite Chopra's argument we get good epitaxial silicon films on spinel or sapphire, as can be seen in Fig. 5 (c)

(Kikuchi lines) although an intermediate crystalline layer does exist. We could even assume that the intermediate layer is responsible for the achieved good epitaxial relation since the rather great mismatch between the lattice parameters of film and substrate will be reduced by such a layer.

### Acknowledgments

The authors wish to express their thanks to Dr. R. Falckenberg for providing the spinel substrates and to Dr. M. Druminski and Mrs. S. Rheinboldt for providing the epitaxial silicon films. We also wish to thank Dr. R. Buhl, Balzers AG, for SIMS measurements and helpful discussions.

This work has been supported by the technological program of the Federal Department of Research and Technology of the FRG. The authors alone are responsible for the contents.

Manuscript submitted June 9, 1975; revised manuscript received Sept. 22, 1975. This was Paper 27 RNP presented at the San Francisco, California, Meeting of the Society, May 12-17, 1974.

Any discussion of this paper will appear in a Discussion Section to be published in the December 1976 JOURNAL. All discussions for the December 1976 Discussion Section should be submitted by Aug. 1, 1976.

Publication costs of this article were partially assisted by Siemens AG.

### REFERENCES

1. H. M. Manasevit and W. I. Simpson, *J. Appl. Phys.*, **35**, 1349 (1964).
2. J. D. Filby and S. Nielsen, *Brit. J. Appl. Phys.*, **18**, 1357 (1967).
3. R. Nolder and I. Cadoff, *Trans. Met. Soc. AIME*, **233**, 549 (1965).
4. H. Seiter and C. Zaminer, *Z. Angew. Phys.*, **20**, 158 (1965).
5. D. Pashley, *Phil. Mag. Suppl.*, **5**, 174 (1956).
6. H. Mayer, in "Advances in Epitaxy and Endotaxy," H. G. Schneider and V. Ruth, Editors, p. 63, VEB Deutscher Verlag für Grundstoffindustrie, Leipzig (1971).
7. J. Mercier, *This Journal*, **117**, 666 (1970).
8. Ch. Raetzel, S. Schild, and H. Schlötterer, Paper 142 presented at the Electrochemical Society Meeting, New York, New York, Oct. 13-17, 1974.
9. J. F. Hall and W. F. C. Ferguson, *J. Opt. Soc. Am.*, **45**, 714 (1955).
10. R. Hezel and F. Schwidefsky, *Siemens Forsch.-Entw.-Ber.*, **1**, 297 (1972).
11. Ch. Köhl, H. Schlötterer, and F. Schwidefsky, *This Journal*, **121**, 1496 (1974).
12. M. Druminski, Ch. Köhl, E. Preuss, F. Schwidefsky, J. Tihanyi, and K. Schmid, Paper 139 presented at the Electrochemical Society Meeting, New York, New York, Oct. 13-17, 1974.
13. A. Benninghoven, in "Ergebnisse der Hochvakuumtechnik und der Physik Dünner Schichten," M. Auwärter, Editor, p. 81, Wissenschaftl. Verlagsges. mbH, Stuttgart (1971).
14. H. M. Manasevit, A. Miller, F. L. Morritz, and R. Nolder, *Trans. Met. Soc. AIME*, **233**, 540 (1965).
15. H. Schlötterer, *J. Vacuum Sci. Technol.*, To be published.
16. Powder Diffraction File of the JCPDS.
17. G. W. Cullen and J. F. Corboy, *This Journal*, **121**, 1345 (1974).
18. G. I. Distler, S. A. Kobzareva, and Y. M. Gerasimov, *J. Cryst. Growth*, **2**, 45 (1968).
19. K. L. Chopra, *J. Appl. Phys.*, **40**, 906 (1969).

## A New Fast Technique for Large-Scale Measurements of Generation Lifetime in Semiconductors

Wolfgang R. Fahrner<sup>1</sup> and Christian P. Schneider

IBM System Products Division, East Fishkill Facility, Hopewell Junction, New York 12533

### ABSTRACT

This paper describes a technique that permits measurements of generation lifetime in the range of  $\geq 1$  msec to  $\ll 0.1$  nsec. For the measurements, a metal oxide semiconductor (MOS) capacitor is biased into strong inversion and subsequently switched into deep depletion. An appropriate experimental setup prints out or displays a typical recovery time, which is introduced into a computer fed by the theoretical generation model and the wafer data. The technique is suitable for process characterization.

The determination of lifetime in silicon (Si) is of great technological importance. Since the basic paper by Zerbst (1), important contributions to the literature have been made by others (2-4). Large-scale measurements of minority carrier lifetime have become desirable for many applications. The usual technique, described by Zerbst, is too cumbersome for large-scale measurements. Faster techniques (5) very often do not give the same results as a Zerbst plot. This paper describes a technique capable of rapid measurements of generation lifetime with good precision. Three, slightly modified, measurement setups using this technique allow coverage in silicon of the wide spectrum of lifetimes which are of practical interest. The measurements are carried out on metal

oxide semiconductor (MOS) capacitors. [We used thermally grown oxides 1000 to 5000Å thick. The  $\langle 100 \rangle$  oriented substrates (mostly p-type) had resistivities of 1-20 ohm-cm. The p-type samples were selected so that no lateral currents occurred due to channel injection. Aluminum dots were evaporated onto the oxide to form MOS capacitors.] A voltage,  $V_a$ , is applied to a metal dot, and a steady-state inversion regime is established. Then a voltage step or pulse,  $\Delta V_a$ , is added. This creates a depletion layer underneath the dot, thus reducing the value of the total measured capacitance and increasing the (absolute) value of the voltage drop across the interface. The time difference,  $t$ , between switching ( $t = 0$ ) and reaching a preselected percentage of the equilibrium value is printed or displayed on a counter. This value is fitted to the thermal generation model by computer.

<sup>1</sup> Present address: Institute for Applied Solid-State Physics, D-78 Freiburg i. Br., Eckerstrasse 4, West Germany.

Key words: lifetime, MOS process control, silicon characterization.

### Theoretical

This technique is not bound to a specific model of relaxation. For the sake of simplicity, we use the well-known equations given by Zerst (1) and re-write them in a convenient form. The applied voltage is the sum of the voltage drop,  $V_{ox}$ , across the oxide and the surface potential,  $\phi_s$

$$V_a + \Delta V_a = V_{ox} + \phi_s \quad [1]$$

Differentiation with respect to time and the use of equations

$$\phi_s = q \cdot N_A \cdot \epsilon_{Si} / (2C_D^2) \quad [2]$$

$$V_{ox} = (Q_D + Q_I) / C_{ox} \quad [3]$$

and

$$dQ_D/dt = C_D \cdot d\phi_s/dt \quad [4]$$

yields

$$(q \cdot \epsilon_{Si} \cdot N_A / 2) d(1/C_D^2) / dt + (C_D \cdot q \cdot N_A \epsilon_{Si} / 2 \cdot C_{ox}) \cdot d(1/C_D^2) / dt + (1/C_{ox}) dQ_I/dt = 0 \quad [5]$$

The integration of Eq. [5] requires knowledge of the generation current,  $I_{Gen} = dQ_I/dt$ . Most commonly, the thermal generation model

$$dQ_I/dt = qn_i(x_D - x_{Df}) / 2\tau = I_{th} \quad [6]$$

is adopted. This model is not always valid. Discrepancies are found, especially for long-lifetime silicon at the end of the  $C$ - $t$  return curve, where a faster generation mechanism might exceed the decreasing thermal generation. The origins for these deviations may be channel injection, enhanced generation due to inhomogeneities, or defects in both the oxide and the silicon.

In the case of channel injection or injection due to inhomogeneities, a simple model for  $dQ_I/dt$  can be assumed, namely

$$dQ_I/dt = I_{Gen} = I_{th} + aI_1$$

where

$$I_1 = \begin{cases} I_0 = \text{const for } C < C_f \\ 0 \text{ otherwise} \end{cases}$$

measures the contribution of the injection to the total current.

Note that Eq. [6] does not contain any surface contribution  $I_s = n_i \cdot q \cdot s_0$  for the following reason: In a comparison of  $I_s$  and  $I_{th}$ ,  $s_0$  values in the order of 10-700 cm/sec were reported (6). These data are obtained from techniques based on switching the MOS structure from accumulation to deep depletion. By switching from inversion to deep depletion, as done in this technique, one obtains  $s_0$  values in the order of  $10^{-2}$  cm/sec. The reason for the reduction is the screening of the surface by an inversion layer. The lifetimes are found to be in the range of 1 nsec-1 msec. The space-charge width,  $x_D$ , depends on the doping concentration,  $N_A$ , and the applied voltage. Assuming typical values  $x_D = 10^{-4}$  cm  $\gg x_{Df}$ ,  $s_0 = 10$  cm/sec, and  $\tau = 50$   $\mu$ sec, one obtains  $I_s/I_{th} = 10$ , whereas, with the "inversion screened"  $s_0$  value of  $10^{-2}$  cm/sec,  $I_s$  is small compared with  $I_{th}$ , even for very long lifetimes and small space-charge widths.

In this paper, we adopt the thermal generation model. The reason is shown below, where Eq. [5] is solved for different models for the generation current  $dQ_I/dt$ . Combining Eq. [5] and [6], we obtain

$$\frac{C_{ox} + C_D}{C_{Df} - C_D} \cdot \frac{1}{C_D^2} dC_D = \frac{n_i}{2\tau N_A} \frac{1}{C_{Df}} dt \quad [7]$$

This equation can easily be solved by normalization (replacing  $C_D$  by  $C_D/C_{Df} = C_{DR}$ ,  $C_{ox}$  by  $C_{ox}/C_{Df}$ , and  $C_{Df}$  by 1) and by changing twice the variable  $C_{DR} = 1/x_R = 1/\sqrt{\phi_R}$ , where  $x_R = x_D/x_{Df}$  and  $\phi_R = \phi_s/\phi_{sf}$ . The final result is

$$\sqrt{\phi_R} + (C_{Df}/C_{ox} + 1) \ln(\sqrt{\phi_R} - 1) = -t'_R \quad [8]$$

where

$$t'_R = \frac{n_i}{2N_A\tau} \cdot \frac{C_{Df}}{C_{ox}} (t - t_0)$$

This is the basic equation for the measurement of the short lifetimes (low-frequency measurement).

When the MOS capacitance is measured with a high-frequency signal, the total capacitance is  $C = C_{ox}C_D/(C_{ox} + C_D)$ . In this case, Eq. [7] can be rewritten

$$\frac{1}{C_R^2(1 - C_R)} \frac{dC_R}{dt} = \frac{C_f}{C_{ox}} \frac{n_i}{2\tau N_A} \quad [9]$$

and its solution is

$$\left[ \ln \frac{C_R}{1 - C_R} \right] - \frac{1}{C_R} = t''_R \quad [10]$$

where  $C_R$  is the normalized capacitance,  $C_R = C/C_f$ . Equation [10] is essentially the same as Heiman's result (5). Heiman, however, did not use this result, but its differential form (Eq. [9]). Furthermore, he switched from accumulation to inversion. For silicon with lifetimes  $\tau \geq 10$   $\mu$ sec, a Heiman plot gives satisfactory results only during a very short range of the measuring time, as shown below. Equation [10] is used here to measure longer lifetimes (high-frequency measurement). Both Eq. [8] and [10] are plotted in Fig. 1 and 2. In Fig. 1, we reverse the  $\phi_R$  axis because we do the same in the measurement (cf. Eq. [12a], below). Equation [5] has been integrated for

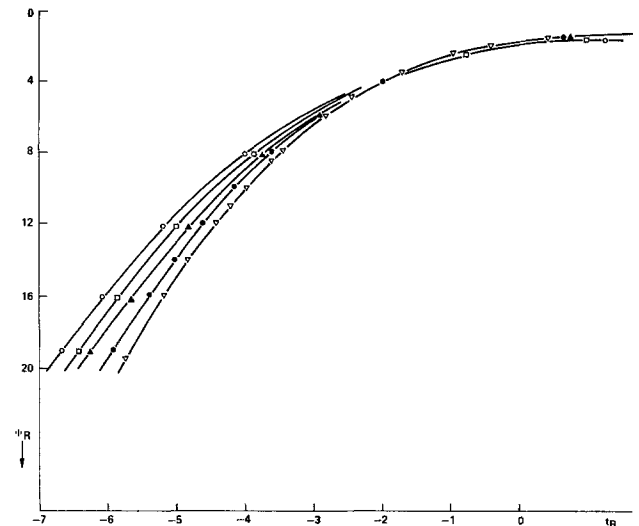


Fig. 1. Relaxation of the surface potential  $\phi_R$  for different values of  $C_{Df}/C_{ox}$ .  $\nabla$ ,  $C_{Df}/C_{ox} = 0.1$ ;  $\bullet$ ,  $C_{Df}/C_{ox} = 0.3$ ;  $\blacktriangle$ ,  $C_{Df}/C_{ox} = 0.5$ ;  $\square$ ,  $C_{Df}/C_{ox} = 0.7$ ;  $\circ$ ,  $C_{Df}/C_{ox} = 0.9$ .

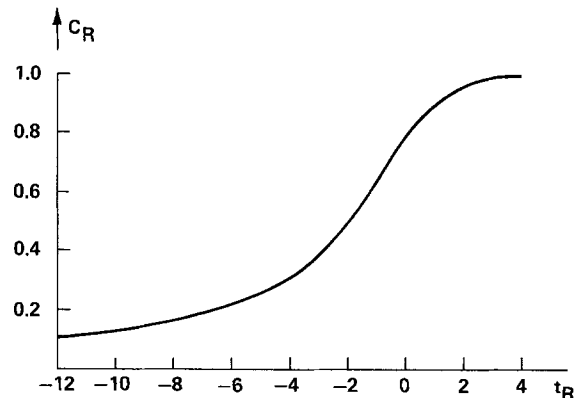


Fig. 2. Relaxation of an MOS capacitance already in inversion to which a voltage step is applied.

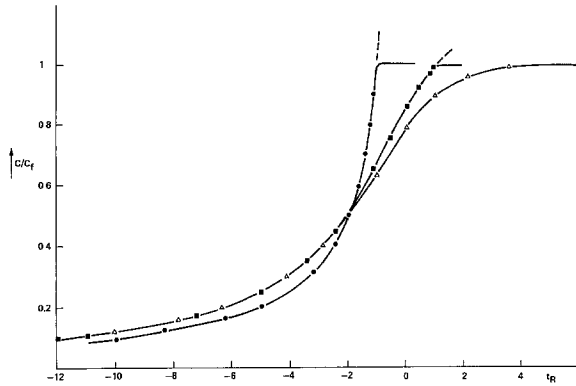


Fig. 3. Relaxation of the capacitance for  $I_{Gen} = I_{th} + \alpha I_0$ .  $\Delta$ ,  $\alpha = 0$ ;  $\blacksquare$ ,  $\alpha = 0.1$ ;  $\bullet$ ,  $\alpha = 1$ .

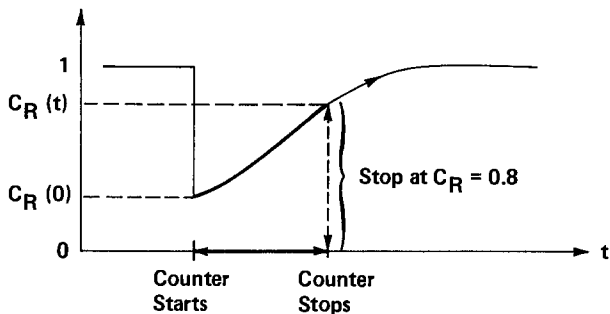


Fig. 4. Representative C-t plot.  $t_0 = 0$ ;  $C_R = C/C_f$

several other modes of relaxation. Of these, we present one example (Fig. 3), where we add a constant current to the thermal current. The parameter,  $\alpha$ , is a measure for the contribution of these additional currents;  $\alpha = 0$  means a pure thermal generation. It can be seen that for  $C_R \leq 0.9$ , if the  $t_r$  axis is expanded or compressed, the curves will be similar. On the other hand, a variation of  $\tau$  has the same effect. Thus, an additional generation current is equivalent to a reduction of the lifetime in the thermal generation model. This observation is valid for any reasonable generation current that decreases toward zero when the capacitance approaches  $C_f$ .

We use Eq. [10] (high-frequency measurement) to demonstrate this technique. When we measure two capacitance values  $C_R(t)$  and  $C_R(t_0)$  at the corres-

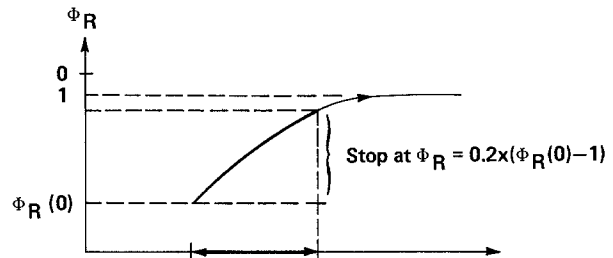


Fig. 5. Representative  $\phi$ -t plot.  $t_0 = 0$

ponding times  $t$  and  $t_0$ , we can calculate  $\tau$ , because the other parameters involved are easily available.  $C_{ox}$  and  $C_f$  can be obtained by standard C-V measurements. From these values,  $N_A$  can be calculated. The room temperature value of  $n_i$  is  $1.4 \times 10^{10} \text{ cm}^{-3}$ . For  $t_0$  we choose the onset of the step or pulse ( $t_0 = 0$ ). Rather than measure the capacitance after a fixed time  $t$ , we select a fixed capacitance value, e.g.,  $C_R = 0.8$ , and measure the time,  $t$ , between switching and reaching the selected capacitance level. Figure 4 shows a schematic C-t plot and the measured time interval.

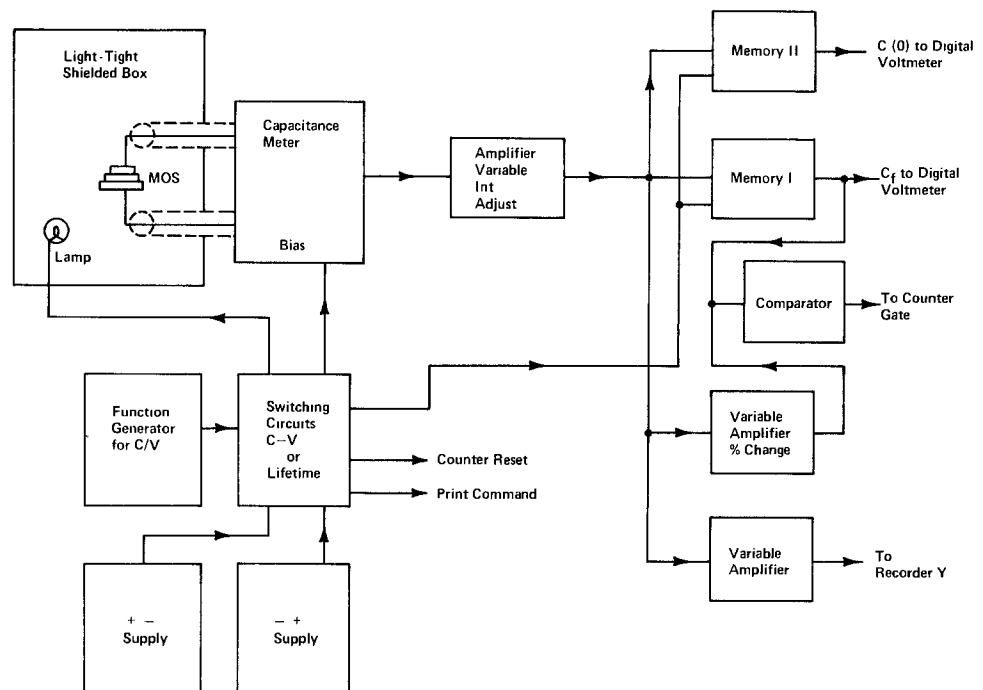
An analog technique is used in the low-frequency case. Instead of  $C_R$ , a specific change of  $\phi_R$  (and its time duration) is measured. Only the counting of the time is slightly different; for example, we count now between  $t = 0$  and the time when  $\phi_R = 0.2 \times (\phi_R(0) - 1)$  (Fig. 5). This alteration is caused by the experimental conditions (see below).

**Experimental and Results**

As shown in Fig. 6a and b, the first, high-frequency, measurement setup essentially consists of a 1 MHz capacitance meter, two power supplies, two memories, a voltage comparator, a plotter, and a printer. Care must be taken that one does not switch the voltage through zero, because the majority carrier response is much faster than any switching time. This setup can be used for relaxation times  $T = 2\tau N_A/n_i \geq 100$  msec. This lower limit is caused by the transient time of the bridge.

A similar setup is used for  $T$  values  $> 1$  msec (Fig. 7). The block diagram of this setup has been published by Princeton Applied Research, Princeton, New Jersey (7). In this case, the output of a lock-in is proportional to  $C_R$ . For  $T \lesssim 1$  sec, the plotter must be replaced by an oscilloscope. We use a Tektronix sam-

Fig. 6a. Block diagram of the long-lifetime case.





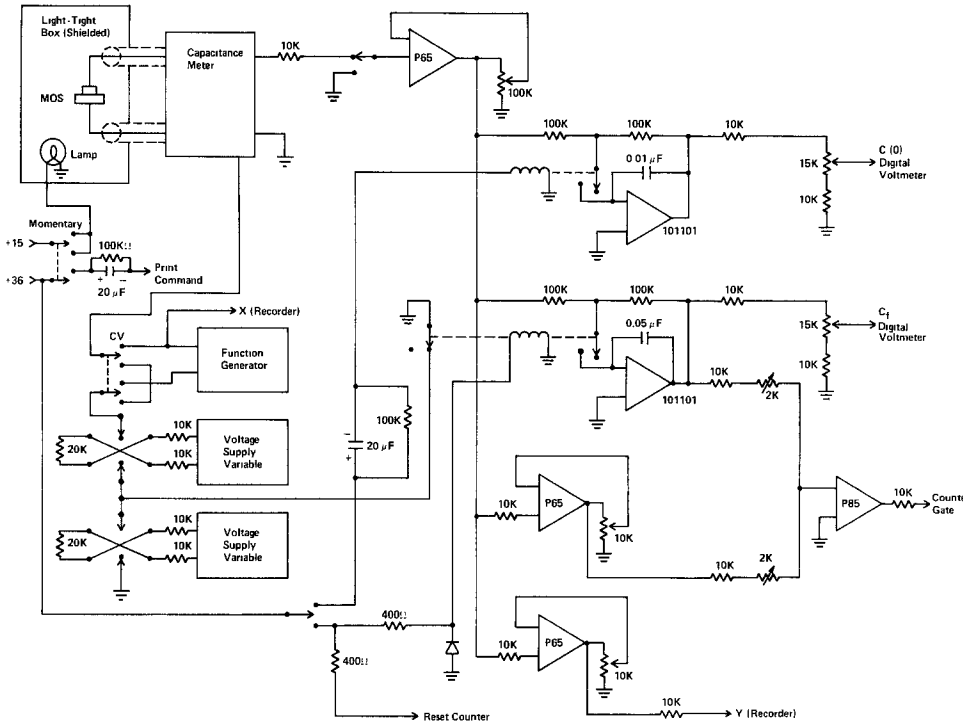


Fig. 6b. Schematic of the long-lifetime case.

pling oscilloscope, which can be connected to a digital counter. We count the time between  $t = 0$  and the instant  $C_R = 0.8 \times (1 - C_R(0))$  (as an example).

The third setup is used for the "short" lifetime case  $T < 4$  sec. As shown in Fig. 8, it consists of a series combination of the MOS capacitor,  $C$ , and a standard capacitor,  $C_{st} \gg C$ . The voltage drop,  $V_{st}$ , across  $C_{st}$  is measured with an operational amplifier. The large parallel resistor,  $R$ , defines the d-c potential for the amplifier. The condition  $R \gg 1/\omega C_{st}$  yields the upper limit for the measurable  $T$  values:  $T \ll R \cdot C_{st} \cdot 2\pi$ . It is favorable to choose a large value of  $R$  rather than of  $C_{st}$ , because an increase in  $C_{st}$  implies a loss in resolution. We can write

$$V_{st} = V_a(1/C_{st}) / (1/C + 1/C_{st})$$

$$V_{st} \approx V_a \cdot C/C_{st} \tag{11}$$

However,  $C$  is a mixture of the high- and low-fre-

quency capacitance and relaxes finally to  $C_{ox}$ . Though it might be possible to calculate  $C(t)$  analytically, we prefer a different, more convenient interpretation. We write the voltage drop,  $V_{MOS}$ , across  $C$  as

$$V_{MOS} = V_{ox} + \phi_s$$

Thus

$$V_a = V_{st} + V_{ox} + \phi_s$$

Because  $C_{st}$  and  $C_{ox}$  are linear capacitors

$$V_{st} \cdot C_{st} = V_{ox} \cdot C_{ox}$$

$$V_a = V_{st}(1 + C_{st}/C_{ox}) + \phi_s$$

and, finally

$$V_{st} = (V_a - \phi_s) / (1 + C_{st}/C_{ox}) \tag{12a}$$

$$\phi_s = V_a - V_{st}(1 + C_{st}/C_{ox}) \tag{12b}$$

By measuring  $V_{st}$ , we know  $\phi_s$  and can use Eq. [8]. Note that, in Eq. [11] and [12],  $V_a$  assumes two different values. For this reason, we do not obtain the same final values before and during the pulse as in Fig. 4, but two values as shown in Fig. 9. The time measurement is again performed with a digital counter connected to a sampling scope. The advantage

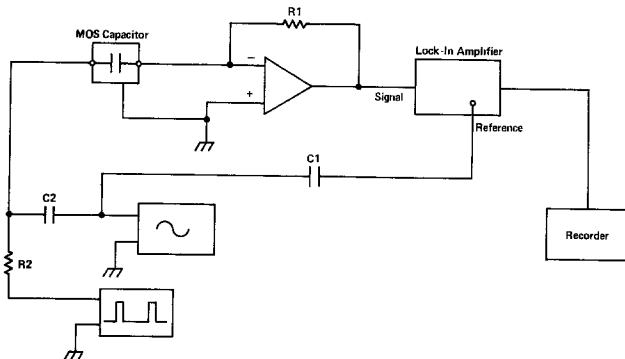


Fig. 7. Block diagram of the medium-lifetime case

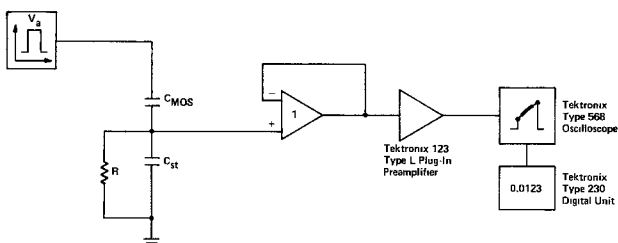


Fig. 8. Block diagram of the short-lifetime case

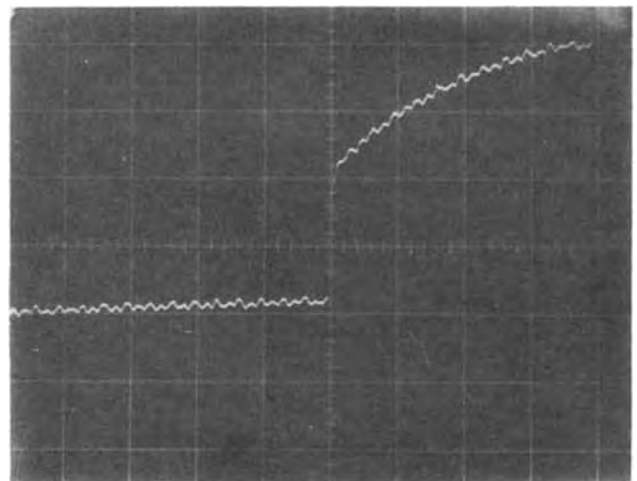


Fig. 9. Photograph of a  $C$ - $t$  trace of a low-frequency measurement. Note that the scale factor  $V_a$  changes when the pulse is switched on (50 msec/horizontal division).

in using the scope and counter is the speed and accuracy of the reading. The error in reading without the counter can be larger than 100%, especially for small  $\Delta V_a$  signals. Figure 10 shows how the time marks of the counter are set. The left time mark is set at the onset of the pulse and indicates the start of the counting (left arrow). The stop time mark can be seen at the end of the pulse (right arrow). The time of an 80% vertical transition between the zones is measured as indicated by the heavy line. Note that we are within the upper limit for the  $RC_{st}$  ( $10^7 \text{ ohm} \times 10^{-7} \text{F}$ ) combination, as shown by the slight tilt of the last horizontal line.

In Fig. 11 and 12, the results of two measurements are fitted to the thermal relaxation curve described by Eq. [10]. Good agreement is obtained in Fig. 11, whereas, for the long-lifetime silicon in Fig. 12, the agreement is merely satisfactory. This is in accord with the general observation that in this range ( $\tau \approx 1 \text{ msec}$ ) the error becomes 100%. A Zerbst plot (Fig. 13) taken from Fig. 11 gives  $\tau = 2.5 \times 10^{-3} \text{ sec}$  and  $s_0 = 3.7 \times 10^{-2} \text{ cm/sec}$ . This technique yields  $\tau = 1.3 \cdot 10^{-3} \text{ sec}$  with  $C_{ox} = 130 \text{ pf}$ ,  $C_f = 75 \text{ pf}$ ,  $C_R(0) = 0.339$ , and  $t = 1060 \text{ sec}$  for a selected level  $C_R(t) = 0.8$ .

These experiments were repeated with different samples. Following are typical results obtained

$\tau$  (Zerbst) = 420  $\mu\text{sec}$  -  $\tau$  (this technique) = 252  $\mu\text{sec}$   
 $\tau$  (Zerbst) = 144  $\mu\text{sec}$  -  $\tau$  (this technique) = 108  $\mu\text{sec}$   
 $\tau$  (Zerbst) = 5.6  $\mu\text{sec}$  -  $\tau$  (this technique) = 4.6  $\mu\text{sec}$   
 $\tau$  (Zerbst) = 1 msec -  $\tau$  (this technique) = 850  $\mu\text{sec}$

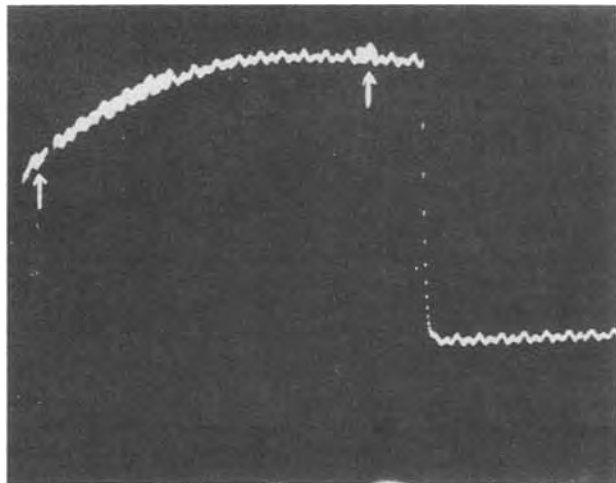


Fig. 10. Photograph of the same sample as in Fig. 9. The time marks and the portion of the curve during which the counter operates are intensified. The sequence of the pulse is reversed compared with Fig. 9.

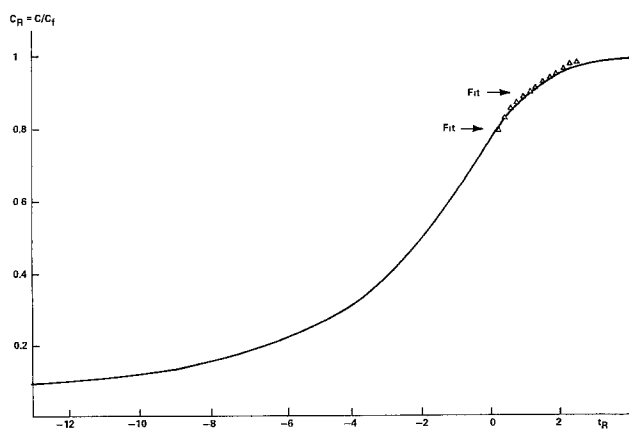


Fig. 11. C-t plot of a sample fitted to the thermal relaxation curve.

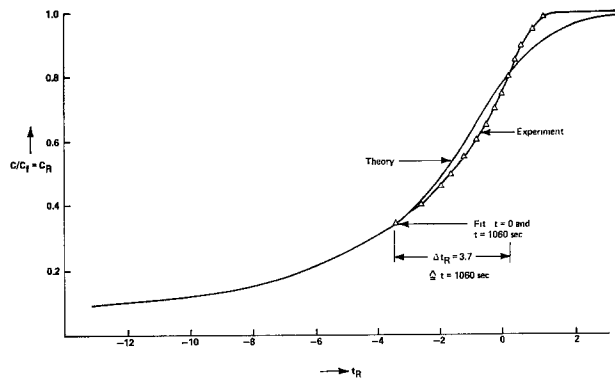


Fig. 12. Same curve as in Fig. 11, taken from another sample

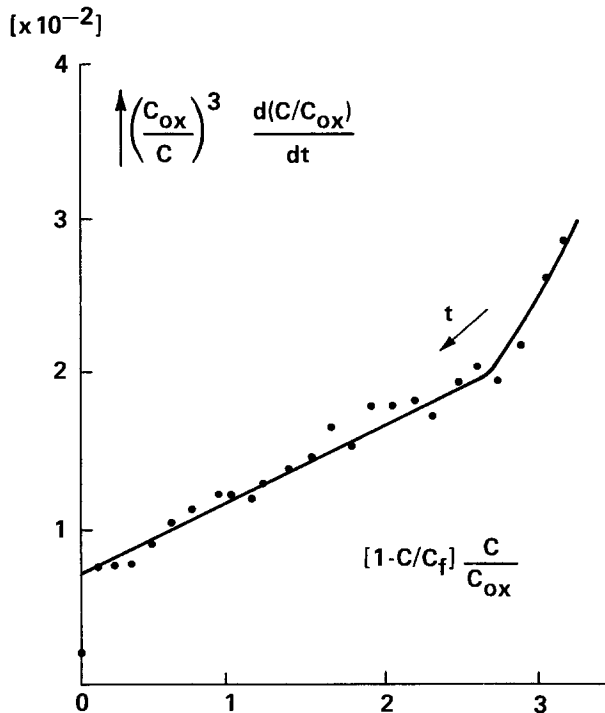


Fig. 13. Zerbst plot for the sample of Fig. 12

Furthermore, we examine how a nonthermal generation mechanism affects the reliability of this technique. This is done by shining controlled intensities of light on the sample or by using mechanically or chemically stressed substrates for the MOS fabrication. The general result is as follows: Whenever a reasonable Zerbst plot is obtained, a lifetime results which agrees with the value of our technique. However, when the Zerbst plot fails, our technique still reports at least an "effective" lifetime, which can be used for process monitoring.

In Fig. 14, we show an example of a Heiman plot. (We define a Heiman plot as the  $\tau$  vs.  $t$  curve, where  $\tau$  has been obtained from a C-t plot with the procedure proposed by Heiman (5); cf. Eq. [9].) The data are taken from the sample used in Fig. 12. It can be seen that the agreement is poor.

It is possible to make the measurements and the data evaluation even more expedient by calculating, rather than measuring,  $C_R(0)$ . For this purpose, we use the following model: A fast-increase  $dV_a$  of the applied voltage displaces a charge  $dQ = C(V_a) \cdot dV_a$  across the capacitor,  $C$ . Only the majority carriers can follow, and a space charge  $q \cdot N_A \cdot dx_{D1}$  matches  $dQ$ . Thus,  $C$  consists of the series combination  $C_{ox}$  and  $\epsilon_{Si}/x_{D1}$  with the initial condition  $x_{D1} = x_{D0}$  or  $C = C_f$  for  $t = 0$ . (Because of this initial condition, we cannot assume  $\epsilon_{Si}/x_D \gg C_{ox}$  as done by others (8) in solving Eq. [7].) The solution of the differential

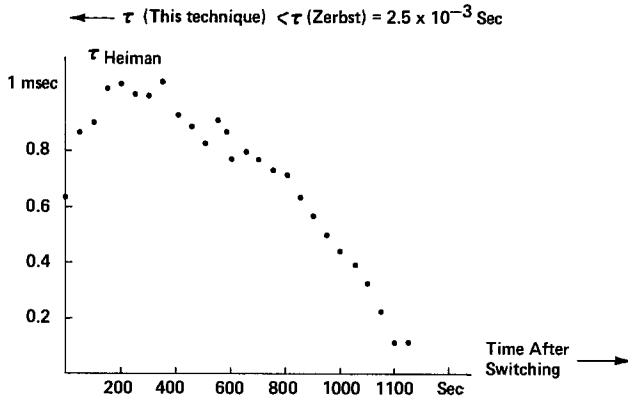


Fig. 14. Heiman plot for the sample of Fig. 12

equation

$$N_A \cdot q \cdot dx_{D1} = (1/C_{ox} + x_{D1}/\epsilon_{Si})^{-1} \cdot dV_a$$

is

$$N_A \cdot q x_{D1}^2 / (2 \cdot \epsilon_{Si}) + N_A q x_{D1} / C_{ox} = \Delta V_a + N_A q x_{D0}^2 / (2 \epsilon_{Si}) + N_A \cdot q \cdot x_{D0} / C_{ox}$$

or

$$x_{D1} = (-\epsilon_{Si} / C_{ox}) + \sqrt{2 \Delta V_a \cdot \epsilon_{Si} / (N_A \cdot q) + ((\epsilon_{Si} / C_{ox}) + x_{D0})^2} \quad [13]$$

We obtain a depletion capacitance

$$C_D(0) = \epsilon_{Si} / x_{D1}$$

and

$$C_R(0) = (C_{ox} \cdot C_D(0) / (C_{ox} + C_D(0))) / C_f \quad [14]$$

We check this model by switching an MOS capacitance with  $\Delta V_a$  values = 1, 2, 3 . . . 10V. The bias  $V_a$  is 20 and 40V. The results and the comparison with the theoretical values according to Eq. [14] can be seen in Fig. 15. As expected, there is no measurable difference between the 20 and 40V measurements. The systematic discrepancy between the experimental and theoretical values can be explained by the error in determining the doping concentration. Different measurements give a value between  $8 \cdot 10^{14}$  and  $1.3 \cdot 10^{15} / \text{cm}^3$ . The same model can be used to calculate  $\phi_R(0)$ . It must be emphasized that this model ignores some effects that might reduce the value of  $C_R(0)$ . Among these, the lateral current paths and the finite thickness of the inversion layer, probably, are most important.

### Summary

A new fast technique for large-scale measurements of silicon lifetimes is described. The error limit, compared with a Zerbst plot, is less than 20% for  $\tau \leq 10$

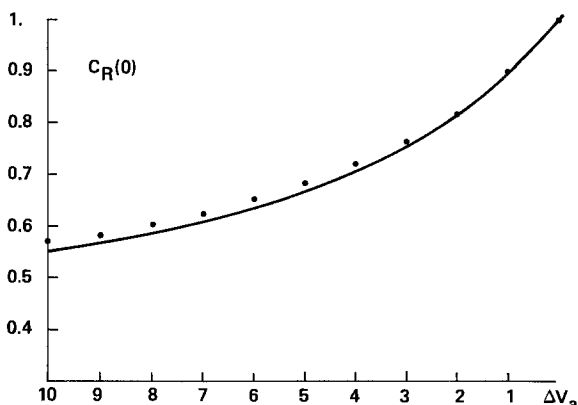


Fig. 15.  $C_R(0)$  vs.  $\Delta V_a$  experiment. Theory: solid line.  $C_{ox} = 123 \text{ pf}$ ;  $A = 1.765 \cdot 10^{-2} \text{ cm}^2$ ;  $N_A = 9 \cdot 10^{14} \text{ cm}^{-3}$ .

$\mu\text{sec}$  and increases to  $\approx 100\%$  for  $\tau \approx 1 \text{ msec}$ . This error limit can be reduced by choosing a smaller stopping level  $C_R(t)$ . For the long-lifetime case, the measurement time is determined by the setting of the selected level and by the  $\tau$  value of the silicon itself. For the short-lifetime case, it is determined by the time required to find the optimum pulse frequency. The computer time can be disregarded.

### Acknowledgments

The authors are grateful to Dr. G. H. Schwuttke for his continuous encouragement and support of this work. A setup similar to our low-frequency setup has been developed independently by K. Ziegler and E. Klausmann for the measurement of equilibrium surface potentials. We are obliged to them for communicating their results in advance of publication.

This research was supported, in part, by the Advanced Research Projects Agency of the Department of Defense under contract DAHC-15-72-0274. The views and conclusions contained in this document are those of the authors and should not be interpreted as necessarily representing the official policies, either expressed or implied, of the Advanced Research Projects Agency or the U.S. Government.

Manuscript submitted Dec. 16, 1974; revised manuscript received Aug. 27, 1975.

Any discussion of this paper will appear in a Discussion Section to be published in the December 1976 JOURNAL. All discussions for the December 1976 Discussion Section should be submitted by Aug. 1, 1976.

Publication costs of this article were partially assisted by IBM Corporation.

### LIST OF SYMBOLS

C	measured capacitance
$C_f$	minimum capacitance of high-frequency C-V curve
$C_D$	depletion capacitance
$C_{ox}$	oxide capacitance
$C_I$	inversion capacitance
$C_{st}$	standard capacitance
$\phi_s$	surface potential
$V_a$	applied voltage
$V_{ox}$	voltage drop across the oxide
$Q_I$	inversion charge
$Q_D$	depletion charge
$N_A$	doping density
$\epsilon_{Si}$	dielectric constant of silicon
q	elementary charge
$x_D$	depletion width
$\tau$	lifetime
t	time
$s_0$	surface generation velocity
$n_i$	intrinsic carrier density

### Subscripts

a	applied
ox	oxide
f	final, in equilibrium
th	thermal
Gen	generation
s	surface
R	in reduced units
D	depletion

### REFERENCES

1. M. Zerbst, *Z. Angew. Phys.*, **22**, 1, 30 (1966).
2. P. Tomanek, *Solid-State Electron.*, **12**, 301 (1969).
3. S. R. Hofstein, *IEEE Trans. Electron Devices*, **ED-14**, 785 (1967).
4. D. K. Schroder and H. C. Nathanson, *Solid-State Electron.*, **13**, 577 (1970).
5. F. P. Heiman, *IEEE Trans. Electron Devices*, **ED-14**, 11, 781 (1967).
6. Y. Kano and A. Shibata, *Japan. J. Appl. Phys.*, **11**, 8, 1161 (1972).
7. Princeton Applied Research, Tech. Note TN102.
8. J. S. T. Huang, *Proc. IEEE*, **58**, 11, 1489 (1970).

# Deposition and Properties of Silicon on Graphite Substrates

T. L. Chu,\* H. C. Mollenkopf, and Shirley S. C. Chu

Southern Methodist University, Dallas, Texas 75275

## ABSTRACT

Polycrystalline silicon has been deposited on low-cost graphite substrates by the thermal decomposition of silane and thermal reduction of trichlorosilane with hydrogen in a gas flow system. The microstructures and crystallographic properties of deposited silicon were studied over a wide range of deposition conditions by metallographic and x-ray techniques, respectively. The observed differences in the properties of silicon layers deposited by silane and trichlorosilane processes were attributed to the difference in the chemical reversibility of the reactions. The microstructure of silicon deposited by the trichlorosilane process was improved by the addition of hydrogen chloride to the reactant mixture. Solar cells were prepared from silicon layers deposited on graphite substrates by a one-step process using silane or trichlorosilane and appropriate dopants, and AMO efficiencies of up to 1.5% were obtained.

The current interest in the terrestrial utilization of solar energy by photovoltaic converters has stimulated considerable research and development efforts in low-cost solar cells. Silicon solar cells which have been used reliably in spacecrafts for many years are manufactured from semiconductor-grade silicon and are far too expensive for terrestrial applications. The use of polycrystalline silicon layers on suitable substrates is considered as a promising approach for the fabrication of low-cost solar cells (1). In this approach, the selection of the substrate is an important consideration. Steel is the most economical choice for a large area substrate; however, polycrystalline silicon solar cells deposited on steel substrates were found to have low conversion efficiencies because of the incompatibility of the properties of iron and silicon (2). Graphite is more compatible with silicon in properties than steel. Several types of low-cost graphite have a thermal expansion coefficient similar to that of silicon. Graphite is relatively inert toward silicon at temperatures used for the deposition of silicon. Also, graphite has high thermal and electrical conductivities and may be used as an ohmic contact to the solar cell. Thus, graphite appears to be the most promising substrate for low-cost silicon solar cells at present.

In this work, the thermal decomposition of silane and the thermal reduction of trichlorosilane with hydrogen have been used for the deposition of silicon on graphite substrates. The microstructure and crystallographic properties of silicon deposited under a wide range of conditions were studied. Using appropriate dopants during the deposition process, p-n junction solar cell structures were prepared and characterized. The experimental procedures used for the deposition process and the properties of deposited silicon and solar cells are discussed in this paper.

## Deposition of Silicon on Graphite Substrates

The thermal decomposition of silane and the thermal reduction of trichlorosilane have been used extensively for the deposition of silicon. The relative merits of these two processes are fairly well established (3). The decomposition of silane is thermochemically and kinetically more favorable than the reduction of trichlorosilane. Silane is thermochemically unstable at room temperature and higher, and decomposes rapidly at temperatures above 700°C, thus enabling the deposition of silicon at lower temperatures (4). However, the thermal instability of silane tends to promote nucleation by pyrolysis in the gas phase, and the gas-phase nucleation must be suppressed by optimizing the experimental conditions, such as the use of water-cooled reaction tube, low partial pressure of silane in the reactant mixture, etc (3). Furthermore, the reduction of

trichlorosilane with hydrogen is chemically reversible while the decomposition of silane is essentially irreversible. Because of these differences, the properties of silicon are sometimes dependent on the chemical reaction used. The thermal reduction of trichlorosilane was emphasized in this work because of its economic advantages.

The deposition of silicon was carried out by using the apparatus shown schematically in Fig. 1. The flow of various gases was directed by appropriate valves and measured by flowmeters. Hydrogen purified by diffusion through a palladium-silver alloy was used as a carrier gas to introduce trichlorosilane into the reaction tube and as a diluent in all deposition reactions. Trichlorosilane was kept in a double-wall stainless steel cylinder with gas inlet and outlet tubes, and a constant temperature fluid was circulated through the jacket of the container to maintain the temperature of trichlorosilane at  $15.5^\circ \pm 0.5^\circ\text{C}$ . The reactant mixture of the desired composition was introduced into a fused silica reaction tube of 55 mm ID. In the reaction tube, the graphite substrates (PLC graphite supplied by POCO Graphite, Incorporated and CMB graphite supplied by Union Carbide Corporation) were supported on a susceptor, and the susceptor was heated externally by an rf generator. The chemical reaction takes place on the substrate surface, depositing silicon.

The substrate temperature was in the range of 950°-1250°C. In all experiments, the flow rate of hydrogen was maintained at 20 liter/min, and the concentration of the silicon compound in the reactant mixture was adjusted to yield deposition rates in the range of 0.2-3  $\mu\text{m}/\text{min}$ . In the silane process, for example, the average deposition rate of silicon at 1050°C was about 0.3 and 1.3  $\mu\text{m}/\text{min}$  when the reactant mixture contained 0.03 and 0.13% silane respectively. At silane concentrations below about 0.2%, the deposition rate was essentially a linear function of the concentration of silane in the reactant mixture. The average deposition rate of silicon

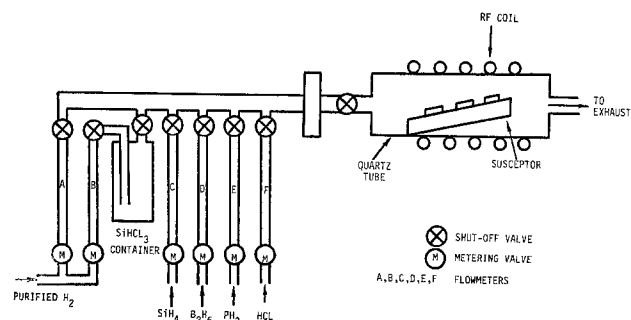


Fig. 1. Schematic diagram of the apparatus for the deposition of silicon.

\* Electrochemical Society Active Member.

Key words: graphite, silane, silicon, solar cells, trichlorosilane.

was essentially independent of temperatures in the range of 1050°-1150°C. At higher temperatures, 1200°C for example, the contribution of gas-phase nucleation becomes noticeable. The deposition of silicon by the trichlorosilane process can be carried out at higher temperatures, 1250°C for example, and at higher rates, 3  $\mu\text{m}/\text{min}$  for example, with negligible contribution of gas-phase nucleation. The average deposition rate of silicon at 1250°C can be increased from about 0.25 to 2  $\mu\text{m}/\text{min}$  by increasing the concentration of trichlorosilane in the reactant mixture from 0.1 to 1%.

### Microstructure of Silicon

Silicon deposited on graphite substrates by silane and trichlorosilane processes was all polycrystalline, and its microstructure was found to depend strongly on the substrate temperature and deposition rate. In general, silicon deposited at low temperatures and high rates consisted of micrometer-size crystallites, and the size of crystallites increased with increasing deposition temperature or decreasing deposition rate.

Silicon layers deposited on graphite substrates at 1000°C or above by the silane process usually consisted of crystallites with well-developed faces, particularly when low deposition rates were used. An example is shown in Fig. 2 where the scanning electron micrograph of the as-deposited surface of a silicon layer deposited on a graphite substrate at 1100°C at a rate of 1  $\mu\text{m}/\text{min}$  is reproduced. The grown surface of most crystallites is hexagonal and has been shown to be of a {110} orientation by x-ray diffraction. The six side faces of the crystallites are therefore of (111), ( $\bar{1}\bar{1}\bar{1}$ ), ( $\bar{1}\bar{1}\bar{1}$ ), ( $\bar{1}\bar{1}\bar{1}$ ), ( $\bar{1}\bar{1}\bar{1}$ ), and ( $\bar{1}\bar{1}\bar{1}$ ) orientations. The edges of the hexagons are along  $[\bar{1}\bar{1}0]$ ,  $[\bar{1}\bar{1}2]$ , and  $[\bar{1}\bar{1}2]$  directions, and the angle between  $[\bar{1}\bar{1}0]$  and  $[\bar{1}\bar{1}2]$  is 54.74°, and that between  $[\bar{1}\bar{1}2]$  and  $[\bar{1}\bar{1}2]$  is 70.53°. These relations have also been verified. The vertical cross section of silicon/graphite specimens was studied by conventional metallographic techniques. Figure 3 shows the mechanically polished and chemically etched surface of the vertical cross section of a silicon/graphite specimen deposited at 1100°C. The etching process has revealed the grain boundaries, and it is seen that the structural perfection of the silicon layer improved with increasing thickness.

The microstructure of silicon deposited by the thermal reduction of trichlorosilane with hydrogen was studied in more detail. At 950°C and below, the silicon deposit was found to consist of very small crystallites, less than 1  $\mu\text{m}$  in diameter. As the substrate temperature was increased, the size of silicon

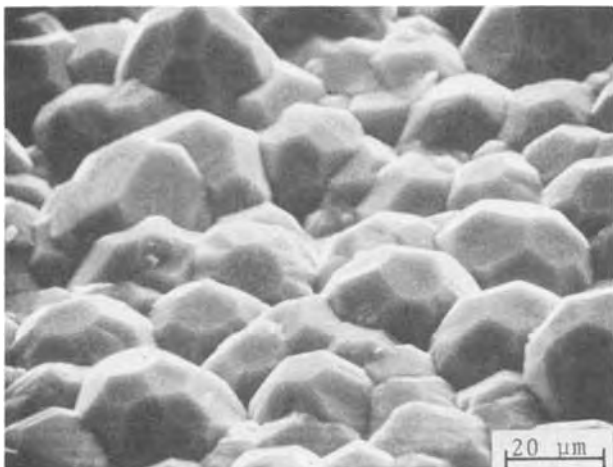


Fig. 2. Scanning electron micrograph of the as-grown surface of a silicon layer deposited on graphite substrates at 1100°C by the pyrolysis of silane at a rate of 1  $\mu\text{m}/\text{min}$ .

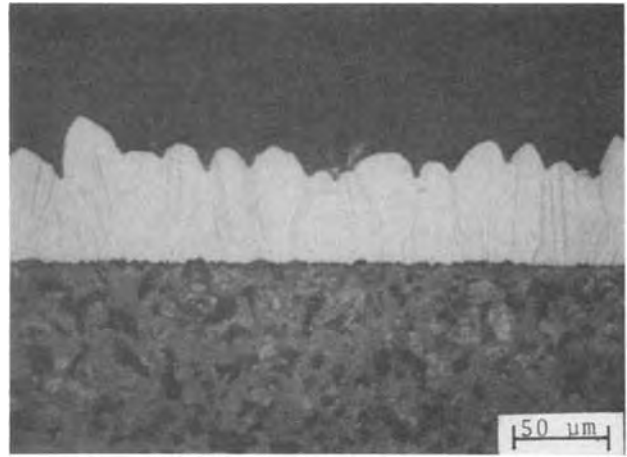
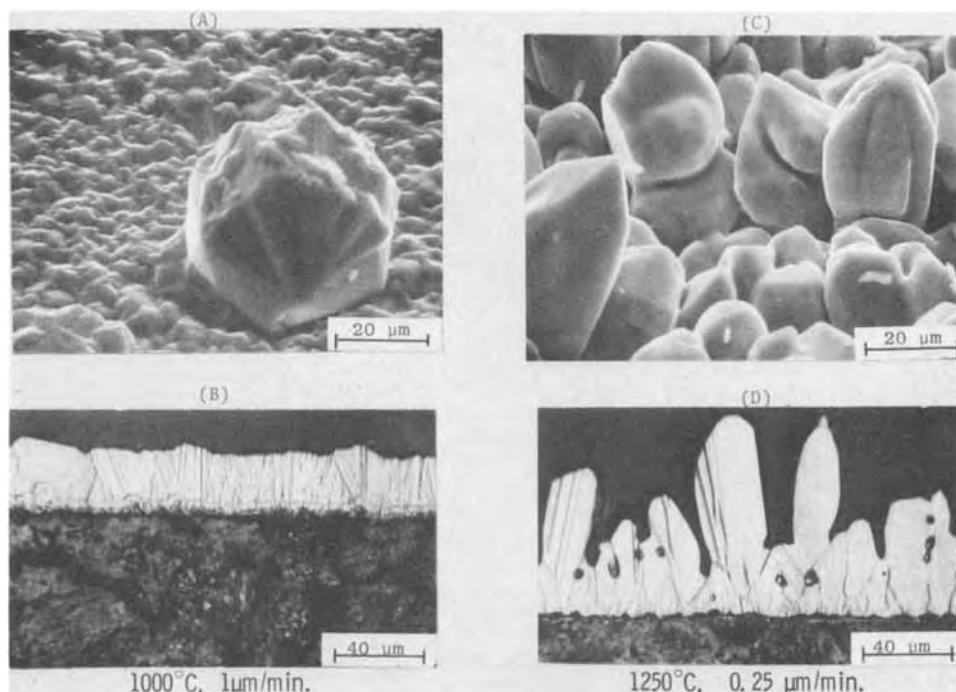


Fig. 3. Mechanically polished and chemically etched surface of the vertical cross section of a silicon/graphite specimen prepared by the pyrolysis of silane at 1100°C.

crystallites increased, and the deposition rate was found to have a very pronounced effect on the microstructure of silicon, particularly at high substrate temperatures. Figure 4 (A and B, respectively) shows the scanning electron micrograph of the as-deposited surface and the mechanically polished and chemically etched surface of the vertical cross section of a silicon sample deposited on graphite at 1000°C at about 1  $\mu\text{m}/\text{min}$ . The average size of the crystallites is 3-5  $\mu\text{m}$ , smaller than those obtained by the thermal decomposition of silane. Furthermore, the crystallites in silicon layers from the trichlorosilane process were less uniform in size; considerably larger crystallites were sometimes intermingled with the smaller ones. The presence of crystallites of widely differing sizes could be due to (i) the inhomogeneities on the substrate surface affecting the nucleation and growth of silicon or (ii) the chemical transport of silicon between neighboring crystallites due to the difference in surface energy or temperature. The transport of silicon does not occur in the silane process since the thermal decomposition of silane is essentially irreversible. When silicon was deposited at 1250°C at about 1  $\mu\text{m}/\text{min}$ , the microstructure of the silicon was very similar to that shown in Fig. 4B, except that the average size of crystallites was increased to 8-10  $\mu\text{m}$ . By reducing the deposition rate to 0.25-0.3  $\mu\text{m}/\text{min}$ , crystallites as large as 30  $\mu\text{m}$  were frequently obtained. Examples of the as-deposited and cross-sectioned surfaces are shown in Fig. 4C and D, respectively. However, the as-deposited surface became very irregular due presumably to the nucleation and transport processes discussed earlier. The transport process becomes more pronounced at low deposition rates. In extreme cases, the silicon layer was not continuous with gaps between crystallites even when the average thickness of the layer was greater than 50  $\mu\text{m}$  (Fig. 5).

Since large crystallites in silicon layers are preferred for solar cell purposes, high substrate temperatures and low deposition rates must be used. However, silicon layers deposited by the trichlorosilane process under these conditions exhibited such surface roughness that the formation of large-area, uniform, shallow p-n junctions becomes extremely difficult. To modify the nucleation and growth of silicon on graphite substrates, hydrogen chloride was added to the reactant mixture. It has been shown that at low Si/Cl ratios in the reactant mixture, preferential deposition into surface depressions can be achieved (6, 7). This is due presumably to the thermochemical nature of the reaction that at low Si/Cl ratios, the transport of silicon takes place from a low temperature region to a higher temperature zone, opposite to the direction of transport at high Si/Cl ratios (8). Since silicon at the surface of tall crystallites is at a lower temperature than that

Fig. 4. Scanning electron micrographs of the as-deposited surface (A and C) and optical micrographs of the polished and etched cross-sectioned surface (B and D) of silicon deposited on graphite by the trichlorosilane process under different conditions.



of shorter ones, the transport process will reduce the surface irregularity of the deposited silicon layer.

A number of silicon layers were deposited on graphite substrates by the thermal reduction of trichlorosilane containing various concentrations of hydrogen chloride. High substrate temperatures and low deposition rates were used in order to obtain large crystallites. As expected, the addition of hydrogen chloride to the reactant mixture was found to decrease the deposition rate of silicon. For example, the average deposition rate of silicon at 1250°C using a reactant mixture containing 0.13% trichlorosilane and 0.4% hydrogen chloride was about 0.2  $\mu\text{m}/\text{min}$ , as compared with an average deposition rate of 0.3-0.35  $\mu\text{m}/\text{min}$  without using hydrogen chloride. However, the addition of hydrogen chloride to the reactant mixture has reduced considerably the surface roughness of the deposited silicon. Figure 6 shows the mechanically polished and chemically etched surface of the vertical cross section of such a specimen. A comparison of Fig. 6 and 4D or 5 indicates clearly the advantage of using hydrogen chloride in the deposition process. Once a reasonably uniform silicon layer is formed on the graphite substrate, higher deposition rates may be used without degrading the microstructure of the deposited silicon.

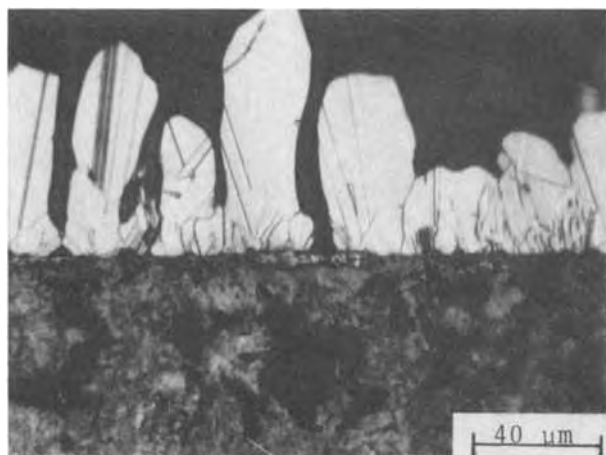


Fig. 5. Mechanically polished and chemically etched surface of the vertical cross section of a silicon layer deposited on a graphite substrate 1250°C at a rate of 0.2  $\mu\text{m}/\text{min}$ .

#### Crystallographic Properties of Silicon

The crystallographic properties of a number of silicon layers deposited on graphite substrates by the silane and trichlorosilane processes under a wide range of substrate temperatures, deposition rates, and dopant concentrations were examined by the x-ray diffraction technique using a General Electric Model XRD-6 diffractometer with  $\text{CuK}\alpha$  radiation. Polycrystalline silicon powder of random orientations is known to show three strong diffraction peaks associated with  $\{111\}$ ,  $\{220\}$ , and  $\{311\}$  reflections with  $2\theta$  values of 28.4°, 47.3°, and 56.1° and relative intensities of 100, 60, and 35, respectively (9). The diffraction spectra of the silicon layers were obtained by scanning  $2\theta$  in the range of 20°-60°. When the thermal decomposition of silane was used for the deposition of silicon, the  $\{220\}/\{111\}$  intensity ratio was found to depend strongly on the substrate temperature, deposition rate, and the extent of doping. In general, unintentionally doped silicon layers deposited at low temperatures and high rates exhibited very large  $\{220\}/\{111\}$  intensity ratios, up to about 1000 indicating that the silicon crystallites show a very strong  $\{110\}$  preferred orientation. This ratio was found to decrease with increasing substrate temperature, decreasing deposition rate, or the introduction of a high concentration of dopants. The crystallographic properties of silicon on graphite substrates are very similar to those on borosilicate/steel substrates (10). However, when the thermal reduction of trichlorosilane was used for the deposition of silicon of various doping levels on graphite at 1000°-1250°C and at 0.2-2  $\mu\text{m}/\text{min}$ , the  $\{220\}/\{111\}$  intensity ratio was found to be in the range of 0.4-5, indicating

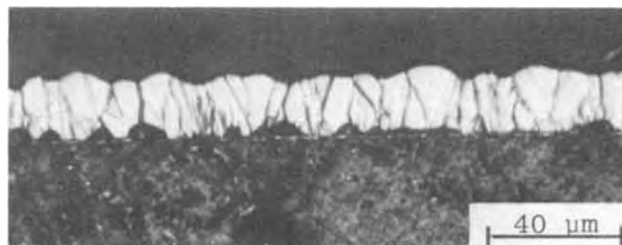


Fig. 6. Mechanically polished and chemically etched surface of the vertical cross section of a silicon/graphite specimen deposited at 1250°C by using a reactant mixture containing 0.13% trichlorosilane and 0.4% hydrogen chloride.



no significant preferred orientation in the crystallites of the silicon deposit. In some silicon layers deposited at 1250°C, crystallites exhibited a slight preferred {111} orientation, as indicated by the {220}/{111} intensity ratios. Figure 7 shows typical diffraction spectra of silicon layers deposited by the silane and trichlorosilane processes. Figure 7A shows the diffraction spectrum of a boron-doped silicon layer deposited on a graphite substrate at 1100°C by the thermal decomposition of silane, where the {220}/{111} intensity ratio is about 150 (the {111} reflection was measured at a considerably magnified scale). Figure 7B shows the diffraction spectrum of an unintentionally doped silicon layer deposited on a graphite substrate at 1000°C and at 0.25  $\mu\text{m}/\text{min}$  by the thermal reduction of trichlorosilane, where the {220}/{111} intensity ratio is about 2.8. The difference in the crystallographic properties of silicon deposited by the silane and trichlorosilane processes is presumably also related to the difference in the reversibility of the chemical reactions.

### Preparation and Characterization of Solar Cells

Silicon deposited on graphite substrates at temperatures of 1150°C or lower by the silane and trichlorosilane processes without intentional doping was always of high electrical resistivity, due at least in part to the grain boundary effects. When the trichlorosilane process was used for the deposition of silicon at higher temperatures, the deposit was always p-type with an electrical resistivity dependent on substrate temperature and deposition rates. For example, silicon deposited at 1250°C at a rate of 1  $\mu\text{m}/\text{min}$  had a resistivity of 5-10 ohm-cm, and the resistivity was decreased to 1 ohm-cm or less when the deposition rate was reduced to about 0.25  $\mu\text{m}/\text{min}$ . These results strongly suggest the diffusion of impurities from the graphite substrate into the silicon deposit at high temperatures.

The electrical resistivity of silicon deposited on graphite substrates by both silane and trichlorosilane

processes was controlled by using phosphine and diborane as dopants. Polycrystalline silicon p-n junction solar cell structures were prepared on graphite substrates, 3 cm  $\times$  3 cm in area, by depositing successively 10-40  $\mu\text{m}$  of 0.002-0.003 ohm-cm p-type silicon, 8-10  $\mu\text{m}$  of 0.2-2 ohm-cm p-type silicon, and 0.2-0.4  $\mu\text{m}$  of 0.001-0.002 ohm-cm n-type silicon. The use of a relatively thick, boron-doped layer at the initial stage of silicon deposition was to improve the microstructure of silicon in the junction region without contributing appreciatively to the series resistance of the device. The thickness and resistivity of the p<sup>+</sup> and p-silicon layers were obtained by measuring the resistivity profile along the angle-lapped surface of the specimen using a spreading resistance probe. During the angle-lapping process, however, the n<sup>+</sup>-silicon layer was always removed due to its small thickness and rough surface. The thickness of the n<sup>+</sup>-silicon layer was deduced from the duration of deposition under conditions established for a low deposition rate, and its resistivity was determined by the four-point probe technique.

The electrical resistivity of silicon layers deposited by the silane process was readily controlled by introducing an appropriate amount of the desired dopant into the reactant mixture. When the thermal reduction of trichlorosilane was used for the deposition of silicon, the resistivity of the p-layer was found to be less uniform. Furthermore, the addition of hydrogen chloride to the reactant mixture severely interfered with the control of dopant distribution in the p-silicon layer. This is again due to the chemical transport associated with the reversibility of the trichlorosilane process. During the deposition of the p<sup>+</sup>-silicon layer, low resistivity boron-doped silicon was also deposited on the susceptor. Since the susceptor was at a higher temperature than the substrates, silicon and boron were transported from the susceptor onto the substrate by hydrogen chloride during the subsequent deposition, and this transport process resulted in the low and non-uniform resistivity in the p-silicon layer. Therefore, hydrogen chloride was added to the reactant mixture only during the initial deposition of the p<sup>+</sup>-silicon layer. Figure 8 shows the mechanically polished and chemically etched surface of the vertical cross section of a solar cell structure on a graphite substrate deposited by using a hydrogen-trichlorosilane-hydrogen chloride mixture and appropriate dopants. The etching process has delineated the p-p<sup>+</sup> junction due to their difference in chemical potentials (11); however, the n<sup>+</sup>-silicon layer, about 2000Å in thickness, was removed by etching.

Mesa diodes were isolated from the above structures by evaporating titanium-silver dots of 0.75 mm diameter on the silicon surface followed by masking and etching. Typical current-voltage characteristics of these diodes deposited by the silane process are shown in Fig. 9. The "n" value in the diode equation, cal-

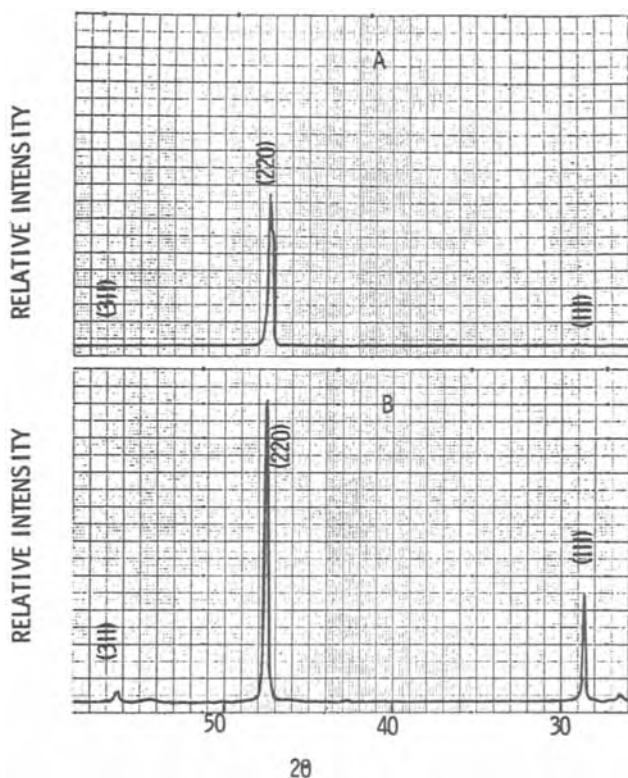


Fig. 7. X-ray diffraction spectra of (A) a boron-doped silicon layer deposited on a graphite substrate at 1100°C by the thermal decomposition of silane, and (B) an undoped silicon layer deposited on a graphite substrate at 1000°C by the thermal reduction of trichlorosilane.



Fig. 8. Mechanically polished and chemically etched surface of the vertical cross section of a polycrystalline silicon solar cell deposited on a graphite substrate by using a hydrogen-trichlorosilane-hydrogen chloride mixture (the n<sup>+</sup>-layer was removed by etching).

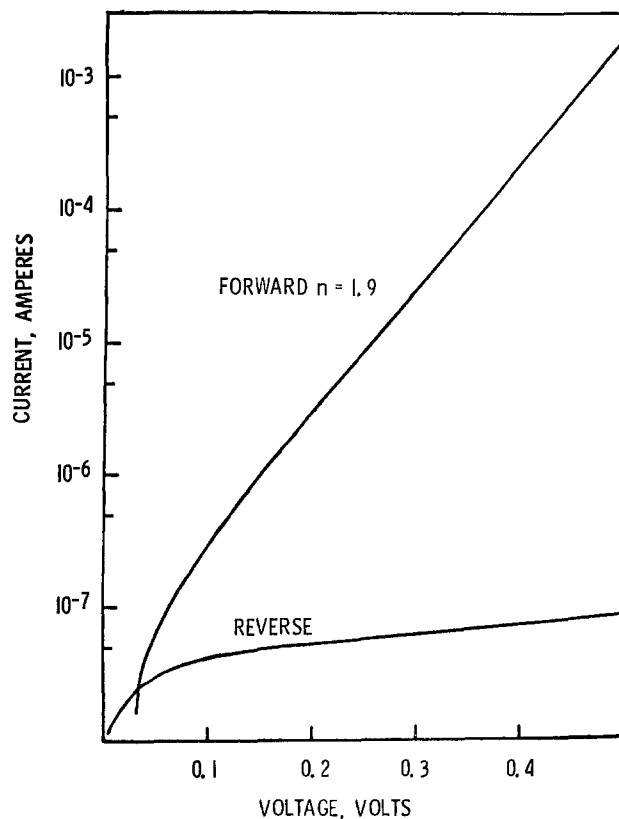


Fig. 9. Current-voltage characteristics of a polycrystalline silicon p-n junction of 0.75 mm diameter deposited on a graphite substrate by the silane process.

culated from the forward characteristics, is 1.9, very similar to that for single crystalline silicon p-n junctions, indicating that the grain boundaries in polycrystalline silicon on graphite substrates do not play a significant role in current conduction. The reverse current density, however, is considerably higher than that in single crystalline silicon p-n junctions.

A number of solar cells were fabricated from n<sup>+</sup>-silicon/p-silicon/p<sup>+</sup>-silicon/graphite structures deposited by both silane and trichlorosilane processes. A grid contact of about 1500Å titanium and 5 μm silver was evaporated onto the n<sup>+</sup>-silicon surface, and the graphite substrate served as the other ohmic contact to the solar cell. The four sides were cut off to remove the silicon deposit on the periphery. The current-voltage characteristics of resulting solar cells, 2.5 cm × 2.5 cm in area, were measured under illumination with an AMO solar simulator at room temperature. The conversion efficiencies of cells prepared by the silane and trichlorosilane processes were similar and were in the range of 1.0-1.5%. An example of the current-voltage characteristics of a polycrystalline silicon solar cell on a graphite substrate prepared by the trichlorosilane process is shown in Fig. 10. The open-circuit voltage, short-circuit current density, and fill factor are 0.33V, 13 mA/cm<sup>2</sup>, and 0.47, respectively, corresponding to a conversion efficiency of 1.5%.

### Summary and Conclusions

Polycrystalline silicon layers have been deposited on graphite substrates by the thermal decomposition of silane and the thermal reduction of trichlorosilane under a wide range of conditions. Because of the difference in the chemical reversibility of these two reactions, silicon layers deposited by silane and trichlorosilane processes had different microstructures and crystallographic properties. The microstructure of silicon deposited by the trichlorosilane process may be improved by adding hydrogen chloride to the reactant mixture. Silicon layers containing crystallites with an average size of 20-30 μm can thus be obtained by

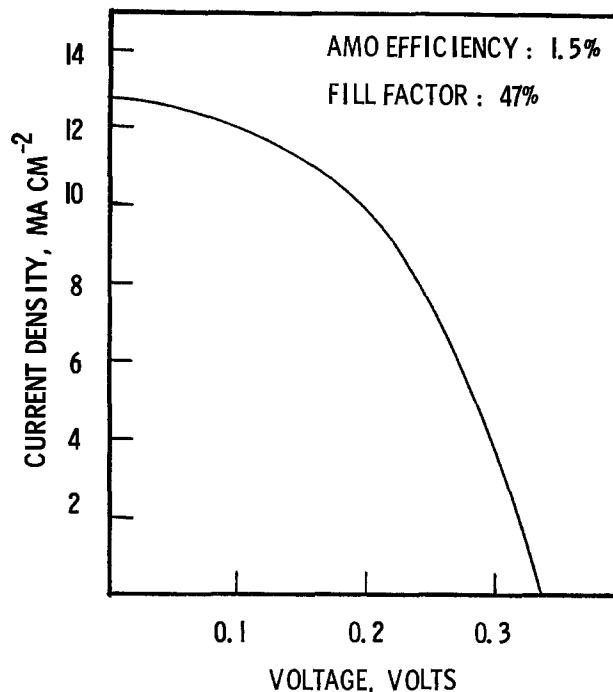


Fig. 10. Current-voltage characteristics of a polycrystalline silicon solar cell on a graphite substrate, deposited by the trichlorosilane process, under illumination with an AMO simulator.

either process. Solar cells with AMO efficiencies of up to 1.5% were obtained by controlling the dopant distribution in deposited silicon in a one-step deposition process. No appreciable differences in the characteristics of solar cells prepared by the two processes were observed.

### Acknowledgments

The authors wish to thank Mr. Bill Parker for most of the photomicrographs reported in this paper.

This work was supported by the National Science Foundation, Research Applied to National Needs (RANN), under Grant AER 73-07843 (GI-38981).

Manuscript submitted June 16, 1975; revised manuscript received Sept. 15, 1975.

Any discussion of this paper will appear in a Discussion Section to be published in the December 1976 JOURNAL. All discussions for the December 1976 Discussion Section should be submitted by Aug. 1, 1976.

Publication costs of this article were partially assisted by Southern Methodist University.

### REFERENCES

1. T. L. Chu, in "Workshop Proceedings—Photovoltaic Conversion of Solar Energy for Terrestrial Applications, Cherry Hill, N. J., Oct. 23-25, 1973," Vol. I, p. 17, NTIS PB-1213.
2. T. L. Chu, J. C. Lien, H. C. Mollenkopf, S. C. Chu, K. W. Heizer, F. W. Voltmer, and G. F. Wakefield, *Solar Energy*, **17**, 229 (1975).
3. T. L. Chu and G. A. Gruber, *This Journal*, **114**, 522 (1967).
4. C. H. Lewis, H. C. Kelly, M. B. Giusto, and S. Johnson, *ibid.*, **108**, 1114 (1961).
5. E. Sirtl and A. Adler, *Z. Metallk.*, **52**, 529 (1961).
6. W. R. Runyan, E. G. Alexander, and S. E. Craig, *This Journal*, **114**, 1154 (1967).
7. R. K. Smeltzer, Abstract 224, p. 555, The Electrochemical Society Extended Abstracts, Fall Meeting, New York, New York, Oct. 13-17, 1974.
8. L. P. Hunt and E. Sirtl, *This Journal*, **119**, 1941 (1972).
9. H. E. Swanson and R. K. Fuyat, NBS Circular 539, p. 8, 1953.
10. T. L. Chu, H. C. Mollenkopf, and Shirley S. Chu, *This Journal*, **122**, 1681 (1975).
11. T. L. Chu and J. R. Gavalier, *Electrochim. Acta*, **10**, 1141 (1965).



# Preparation and Properties of SiO<sub>2</sub> Films from SiH<sub>4</sub>-CO<sub>2</sub>-H<sub>2</sub>

A. K. Gaid,\* G. K. Ackermann,<sup>1</sup> V. J. Lucarini,\* and R. L. Bratter

IBM System Products Division, East Fishkill Facility, Hopewell Junction, New York 12533

## ABSTRACT

This paper presents the results of chemical vapor deposited (CVD) silicon dioxide films on silicon from an SiH<sub>4</sub> + CO<sub>2</sub> + H<sub>2</sub> system. The kinetics of this reaction have been studied with a barrel reactor. The activation energy ( $\Delta E$ ) of the SiH<sub>4</sub>, CO<sub>2</sub> reaction in hydrogen is 106.7 J/g mol (25.4 kcal/g mol) in the temperature range 800°-1050°C. The SiH<sub>4</sub> and CO<sub>2</sub> reaction in hydrogen is shown to be a first-order reaction with respect to SiH<sub>4</sub> (CO<sub>2</sub>:SiH<sub>4</sub>  $\geq$  20). The deposition rates of SiO<sub>2</sub> are dependent only on deposition temperature and on SiH<sub>4</sub> mole fraction. They are independent of the CO<sub>2</sub>:SiH<sub>4</sub> ratio in the experimental range of 7:1-120:1. Electrical characterization was carried out on MOS capacitors of  $\sim$ 1300Å dielectric thickness. The breakdown field was found to be  $(7.8 \pm 0.1 \times 10^6 \text{ V/cm})$ . Measurements of oxide charges, of mobile charges, and of fast surface-state density show that these oxides are stable under positive and negative bias, with maximum shifts of 250 mV after 50 hr stress at 200°C and  $\pm 2 \times 10^6 \text{ V/cm}$  electrical field. Postdeposition high-temperature anneal deteriorates the V<sub>FB</sub> stability under negative-bias temperature stress. The index of refraction depends on the CO<sub>2</sub>:SiH<sub>4</sub> ratio, going above 1.46 at a ratio  $<10$ . Ratios of CO<sub>2</sub>:SiH<sub>4</sub>  $\geq$  50 give reproducible results at an average index of  $1.454 \pm 0.001$ . Etch rates in "P-etch" for 1000°C deposited samples are  $\sim$ 50% faster than thermal oxides grown at the same temperature.

Chemical vapor deposited (CVD) SiO<sub>2</sub> films have several advantages in planar semiconductor device processing over the oxidation of silicon. Since no silicon of the substrate is consumed, the junction movement, pileup, or depletion of dopants at SiO<sub>2</sub>-Si interfaces is minimized. Thick films of SiO<sub>2</sub>, which may be used in the field region of integrated FET circuits, can be deposited with greater ease than thermal oxidation because the deposition rates are not diffusion-limited in the solid. One application of CVD oxides where the thermal oxide does not compete is the use of CVD oxides as photolithographic masks for films not etched in fluorides, such as silicon nitride. Finally, CVD oxides lend themselves to *in situ* processing where two or more films are required and one of these films is SiO<sub>2</sub>.

Silica films have been deposited by a variety of chemical systems, at both high and low temperatures (1-10). It was desirable in this case to select a process that would produce SiO<sub>2</sub> films with etch rates close to those of thermal SiO<sub>2</sub>, so as to avoid excessive undercutting during etching. Since etch rate is inversely proportional to deposition temperature, the process had to be carried out at a high temperature (1000°C). SiH<sub>4</sub> was preferred over other silicon-bearing compounds (e.g., SiCl<sub>4</sub> or SiBr<sub>4</sub>) because of its gaseous nature and resulting ease of metering control. *In situ* processing also favors SiH<sub>4</sub> because one has only to replace the oxidant with NH<sub>3</sub> to deposit silicon nitride or discontinue the oxidant flow to deposit polysilicon. It was also desirable to use an oxidant that would have a minimal gas-phase reaction with SiH<sub>4</sub> so as to keep the reactor down time to a minimum. This led to the investigation of the SiH<sub>4</sub> and CO<sub>2</sub> reaction. Swann and Payne (4) and Kroll *et al.* (5) reported on the SiH<sub>4</sub>-CO<sub>2</sub> system. Our purpose is to investigate further the deposition kinetics, to obtain an empirical rate expression, and to examine the physical and electrical properties of the resulting SiO<sub>2</sub> films.

## Experimental

**Equipment.**—The equipment used for the entire experimental investigation was a vertical, cold-wall, barrel-type, induction-heated reactor (11). The silicon "wafers" were placed on an SiC-coated graphite susceptor. Figure 1 gives a schematic cross-sectional view of the reactor. The fused-quartz chamber is 18 in.

( $\sim$  45 cm) long, with an internal diameter of 9 in. ( $\sim$  23 cm). The susceptor is placed in the chamber so that its leading edge is  $\sim$  5 in. (12.7 cm) from the molybdenum distributor. The susceptor is hexagonal and is divided into three tiers, or "rings." Each of the six faces of the susceptor makes an angle of  $\sim$ 3° with the central vertical axis. The susceptor is placed on a fused-quartz pedestal, which in turn is supported by a fused-quartz pedestal. The susceptor, approximately 8.25 in. (21 cm) long, was rotated at about 8 rpm throughout this experimental work. The volume of the annulus between the susceptor and the chamber (i.e., the volume of the deposition zone) is  $\sim$ 5 liters.

The temperature was measured with an optical pyrometer.<sup>2</sup> All temperatures reported were corrected for system transmission losses and for emissivity (12). The reacting and the carrier gases were introduced from the top of the reactor after each had been metered through a separate rotometer. Each rotometer was calibrated. The silane used was a 5% mixture in nitrogen or hydrogen. The SiH<sub>4</sub>, CO<sub>2</sub>, and the carrier gas (either H<sub>2</sub> or N<sub>2</sub>) were filtered (submicron filters) before they passed through their respective rotometers.

**Typical deposition conditions and measurement technique.**—Three, 2¼ in. (5.7 cm) Si, 11-25 ohm-cm, p-type,  $<100>$  wafers were processed in each experimental run, unless otherwise indicated. One wafer each

<sup>2</sup> The temperature along the susceptor length is  $\pm 10^\circ\text{C}$  of any reported value.

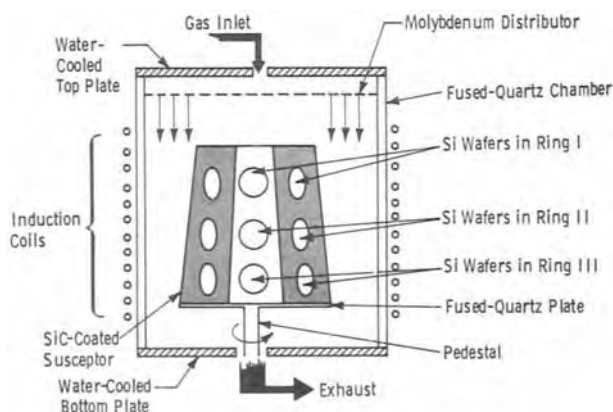


Fig. 1. Schematic cross-sectional view of barrel reactor

\* Electrochemical Society Active Member.

<sup>1</sup> Present address: IBM Deutschland Boeblingen (Lab) 0711 Boeblingen, Germany.

Key words: silicon dioxide, dielectric films, MOS, CVD, thin films.

was placed in rings 1, 2, and 3, at a predetermined fixed position. The remaining positions on the susceptor were filled with dummy wafers. Before loading in the reactor, wafers were cleaned ultrasonically in hot (85°C) deionized water (for 5 min), followed by H<sub>2</sub>SO<sub>4</sub>/HNO<sub>3</sub> (3:1, at 120°C) cleaning (for 10 min), followed by 10:1 dilute HF dip (10 sec). The wafers were then rinsed in running deionized water (for 5 min) and subsequently spin-dried. The wafer surface was hydrophobic after this cleaning.

During the experimental work, the carrier gas flow rate (H<sub>2</sub> in most cases) was varied between 60 and 120 liters/min and the SiH<sub>4</sub> flow rate (5% in H<sub>2</sub> or N<sub>2</sub>) between 60 and 1000 cm<sup>3</sup>/min. The SiH<sub>4</sub>:CO<sub>2</sub> ratio was changed between 7:1 and 120:1. The deposition temperature range was 800°-1050°C; the deposition time was never less than 5 min or greater than 25 min.

The resulting SiO<sub>2</sub> film thicknesses were measured by CARIS<sup>3</sup> (>1500Å) and by ellipsometry (≤1500Å). The index of refraction was always measured by ellipsometry. Five thickness measurements were taken per wafer; these five readings cover ~80% of the total wafer area. Peripheral readings were taken 0.125 in. (3.18 mm) away from the edge of the wafer. The typical within-a-run deposition uniformity was ≤±5% at 1000°C and at a total flow rate of ~110 liters/min; the worst case within-a-run uniformity at any temperature and flow (within the experimental range) was ~±15%. The deposition rates used in this report are therefore average deposition rates over three rings (i.e., 15 measurements); thus, as a first approximation, we neglected the silane concentration variations along the susceptor length.

### Experimental Results

**Preliminary experiments.**—Preliminary experiments were performed using an H<sub>2</sub> and N<sub>2</sub> mixture as a carrier gas at a deposition temperature of 1000°C. The H<sub>2</sub>/N<sub>2</sub> ratio was varied from 0.03:1 to 1.5:1, with similar results. The films deposited were dendritic in appearance. When these films were etched in 5:1 diluted HF, a brown film was left on the silicon surface. Swann and Payne (4) reported similar observations when they used argon as a carrier gas. The brown film on the silicon surface was etchable only in I-etch,<sup>4</sup> suggesting that the brown film is a silicon-rich film (mostly polysilicon).

The use of pure H<sub>2</sub> as a carrier gas prevented the formation of either "dendritics" or the silicon-rich brown film. The SiO<sub>2</sub> films thus deposited were etchable in diluted HF (5:1) and left the silicon surface clean (hydrophobic). The remaining investigations used H<sub>2</sub> as a carrier gas.

**Deposition rates (SiH<sub>4</sub>-CO<sub>2</sub>-H<sub>2</sub> system).**—The parameters whose effect on deposition rate of SiO<sub>2</sub> has been investigated are SiH<sub>4</sub> mole fraction, SiH<sub>4</sub>:CO<sub>2</sub> ratio, deposition temperature, and H<sub>2</sub> flow rate.

**Deposition rate vs. SiH<sub>4</sub> mole fraction.**—Figure 2 shows the log of SiO<sub>2</sub> deposition rate as a function of silane mole fraction ( $X_{\text{SiH}_4}^0$ ), as determined by the entering gas composition. The slope of the graph is very nearly 1, which shows that the SiH<sub>4</sub>-CO<sub>2</sub> reaction in H<sub>2</sub> is a first-order reaction with respect to SiH<sub>4</sub>. For Fig. 2, the deposition temperature and the H<sub>2</sub> and CO<sub>2</sub> flow rates were kept constant. Note that the CO<sub>2</sub>:SiH<sub>4</sub> ratio varied from ~20 to 200 during this experiment; however, it is important to point out that only the SiH<sub>4</sub> concentration is a variable for Fig. 2. Hence, Fig. 2 is the result of a classical experiment to isolate the order of the reaction with respect to SiH<sub>4</sub> (13).

**Deposition rate vs. SiH<sub>4</sub>:CO<sub>2</sub> ratio.**—Figure 3 graphs the deposition rate as a function of CO<sub>2</sub>/SiH<sub>4</sub> ratio for the two SiH<sub>4</sub> mole fractions. The deposition tempera-

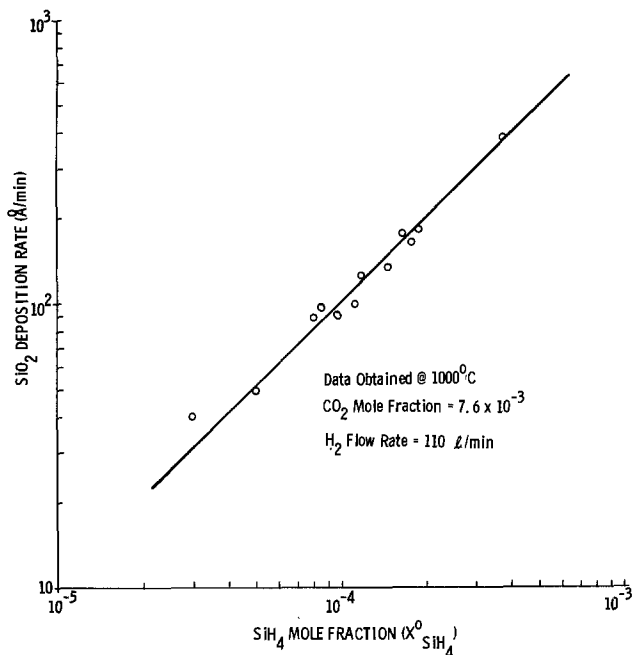


Fig. 2. Deposition rate as a function of SiH<sub>4</sub> mole fraction in the feed. Deposition temperature, H<sub>2</sub> flow, and CO<sub>2</sub> flow kept constant.

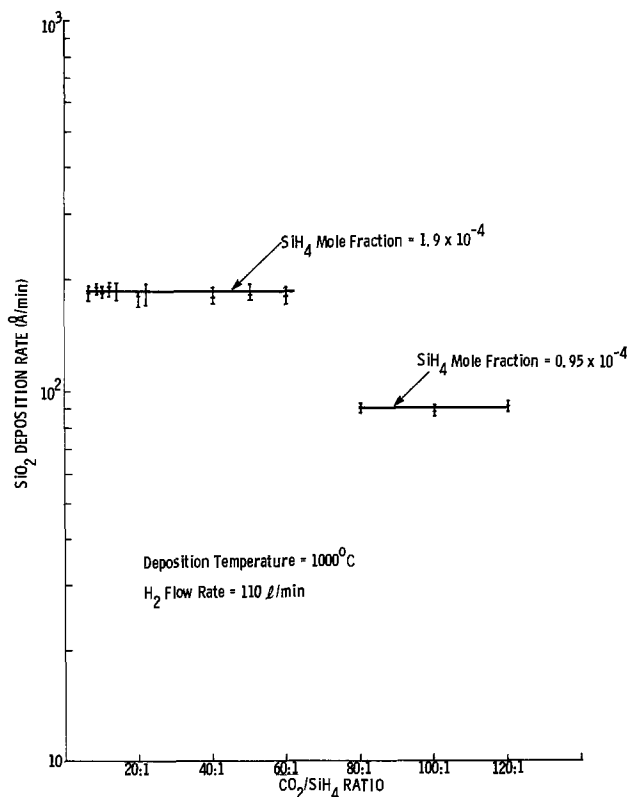


Fig. 3. Deposition rate as a function of CO<sub>2</sub>:SiH<sub>4</sub> ratio at two silane mole fractions, at 1000°C and at constant H<sub>2</sub> flow rate.

ture and the H<sub>2</sub> flow rate were kept constant. The deposition rate is independent of the CO<sub>2</sub>:SiH<sub>4</sub> ratio in the experimental range of 7:1-120:1. Note that, for a fixed SiH<sub>4</sub> mole fraction (e.g.,  $1.9 \times 10^{-4}$ ), the deposition rate is independent of the CO<sub>2</sub> concentration.

These results are consistent with the classical "method of excesses" or "isolation technique" (14); i.e., when a large excess of one reaction chemical is used as compared with another, the reaction rate is independent of the concentration of the chemical being used in large excess. The lack of dependence of deposition rate on CO<sub>2</sub> concentration, however, is in total disagreement with

<sup>3</sup> Constant angle reflection interference spectroscopy.

<sup>4</sup> I-etch is a mixture of stock solution and HNO<sub>3</sub> in the ratio of 1:5. The stock solution is a mixture of CH<sub>3</sub>COOH, HF, HNO<sub>3</sub> in a 1:2:5 ratio, saturated with iodine and allowed to settle overnight (14 hr).

the results reported by Swann and Payne (4) and by Kroll *et al.* (5). Both papers reported an increase in deposition rate with increasing CO<sub>2</sub>:SiH<sub>4</sub> ratio. The likely reason for this discrepancy is the difference in reactor design. In both papers, a pedestal or pancake-type reactor was used where the flow of gas is at right angles to the wafer surface. In our reactor, the flow of gases is nearly parallel to the wafer surface. These two very different flow patterns will have a markedly different mass and energy transfer and, hence, possibly, different results.

**Deposition rate vs. deposition temperature.**—Figure 4 shows the deposition rate as a function of reciprocal temperature at a constant injected SiH<sub>4</sub> mole fraction of  $1.9 \times 10^{-4}$ . Two CO<sub>2</sub>:SiH<sub>4</sub> ratios were used, 12 and 40, and the H<sub>2</sub> flow rate was kept constant at 110 liters/min. The activation energy obtained from Fig. 4 is 25.4 kcal/g mol (106.7 J/g mol).

**Deposition rate vs. flow rate.**—To determine whether the deposition rate of SiO<sub>2</sub> is limited by the surface chemical reaction rate or controlled by mass transfer, an experiment was performed in which the H<sub>2</sub> flow rate was varied from 60 to 115 liters/min. The deposition temperature was kept constant at 1000°C. The SiH<sub>4</sub> and CO<sub>2</sub> mole fractions were also constant at  $1.9 \times 10^{-4}$  and  $1.14 \times 10^{-2}$ , respectively. Figure 5 shows the results, with the deposition rate plotted against the square root of the flow rate.

For all practical purposes, the deposition rate is independent of the flow rate, and, hence, the SiH<sub>4</sub>-CO<sub>2</sub> reaction in H<sub>2</sub> is limited by the surface-chemical-reaction rate, with the experimental flow range 60-115 liters/min.

**Rate expression (empirical).**—Following the standard procedure for obtaining an empirical rate expression for any heterogeneous reaction (13), and knowing that the reaction is (i) independent of CO<sub>2</sub> concentration (Fig. 3), (ii) first order with respect to SiH<sub>4</sub>

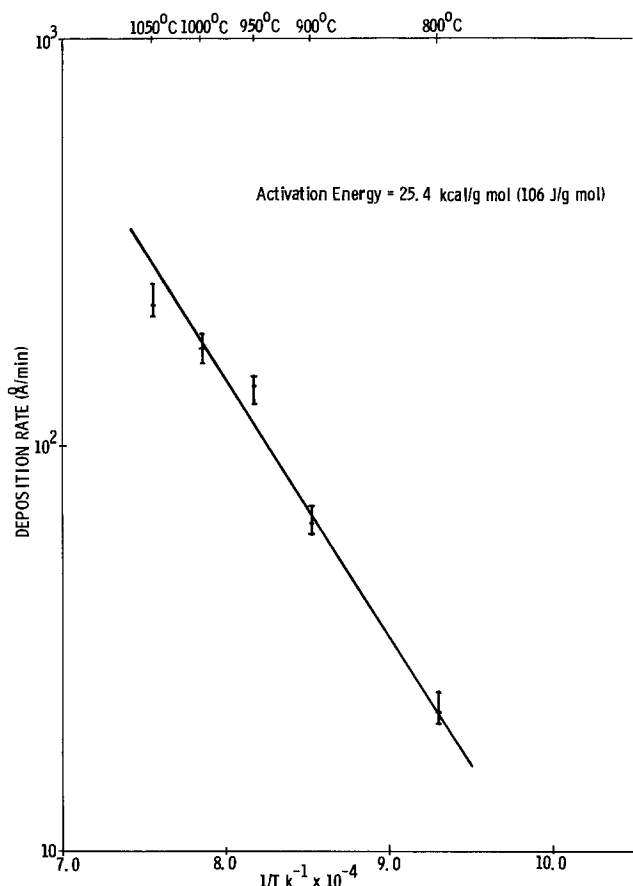


Fig. 4. Deposition rate as a function of  $1/T$ , at constant H<sub>2</sub> flow rate and SiH<sub>4</sub> mole fraction. Two CO<sub>2</sub>:SiH<sub>4</sub> ratios, 12 and 40.

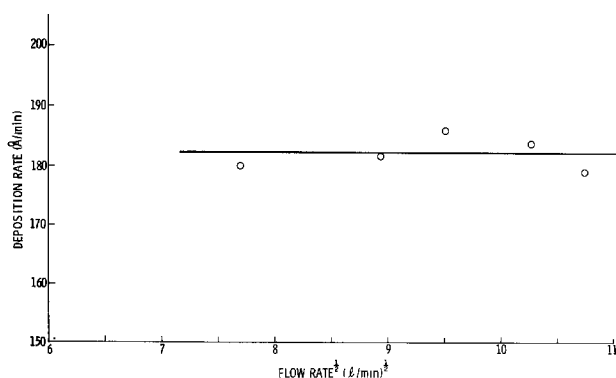


Fig. 5. Deposition rate as a function of square root of flow rate at 1000°C. SiH<sub>4</sub> mole fraction constant at  $1.9 \times 10^{-4}$ . Constant CO<sub>2</sub>:SiH<sub>4</sub> ratio of 60.

(Fig. 2), and (iii) surface-chemical-reaction-limited (Fig. 5), we can arrive at the following rate expression

$$r_{\text{SiO}_2} = K_s C_{\text{SiH}_4}^0 [1 - Y_{\text{SiH}_4}] \quad [1]$$

where  $r_{\text{SiO}_2}$  = deposition rate of SiO<sub>2</sub> (moles/min),  $C_{\text{SiH}_4}^0$  = silane concentration in the feed (moles/liter),  $K_s$  = the rate constant for surface chemical reaction (liters/min), and  $Y_{\text{SiH}_4}$  = fraction of silane converted to deposit.

The fraction of SiH<sub>4</sub> converted to SiO<sub>2</sub> can be calculated by mass-balance, and its value is small, *i.e.*, 0.02-0.15, depending on the deposition temperature. Thus, neglecting  $Y_{\text{SiH}_4}$  and expressing deposition rate in Å/min and concentration as mole fraction, we can rewrite Eq. [1] as

$$d_{\text{SiO}_2} = K'_s X_{\text{SiH}_4}^0 \quad [2]$$

where  $d_{\text{SiO}_2}$  is the deposition rate in Å/min,  $X_{\text{SiH}_4}^0$  is the mole fraction of silane in the feed, and  $K'_s$  is the rate constant in Å/min. The value of  $K'_s$  has been calculated from the data of Fig. 2, at 1000°C, to be approximately equal to  $10^6$  Å/min.

Now

$$K'_s = K'_0 \exp [-\Delta E/RT] \quad [3]$$

where  $K'_0$  is the frequency factor in Å/min and  $\Delta E$  the activation energy. The activation energy is 25.4 kcal/mole (Fig. 4), and the calculated value of  $K'_0$  is  $2 \times 10^{10}$  Å/min.

Thus, the empirical rate expression for SiO<sub>2</sub> deposition is

$$d_{\text{SiO}_2} = 2 \times 10^{10} \cdot \exp [-25400/RT] \cdot X_{\text{SiH}_4}^0 \quad [4]$$

where  $R$  is the gas constant (1.98 cal/g mole °K) and  $T$  is temperature in °K.

**Physical properties.**—Table I lists the physical properties of SiO<sub>2</sub> grown from the SiH<sub>4</sub>-CO<sub>2</sub>-H<sub>2</sub> system as a function of deposition parameters and anneal conditions.

**Refractive index.**—The refractive index was measured by ellipsometry at 5460 Å (mercury-light wavelength). The refractive index of deposited SiO<sub>2</sub> is very close to that of the thermal SiO<sub>2</sub> (1.462) (15). Owing to densification, the annealing treatment increases the refractive index of as-deposited samples. There also appears to be some effect due to the CO<sub>2</sub>:SiH<sub>4</sub> ratio. However, although CO<sub>2</sub>:SiH<sub>4</sub> ratios greater than 20:1 do not seem to affect the refractive index within measurement accuracy, for a deposition temperature of 1050°C and a low CO<sub>2</sub>:SiH<sub>4</sub> ratio of 12, the refractive index goes up, indicating that the film may be silicon-rich. As Table I shows, only the third-place decimal in the refractive index was affected by the CO<sub>2</sub>:SiH<sub>4</sub> ratio from 20:1 to 120:1. Ratios of SiH<sub>4</sub>:CO<sub>2</sub>  $\geq$  50:1 are preferred because the run-to-run refractive index reproducibility is considerably improved (*i.e.*,  $\pm 0.001$  run-to-run).

Table I. Physical properties of SiO<sub>2</sub> grown from SiH<sub>4</sub>-CO<sub>2</sub>-H<sub>2</sub>

Deposition temperature (°C)	CO <sub>2</sub> /SiH <sub>4</sub>	Densification in N <sub>2</sub> ambient		Refractive index (5460Å)	Etch rate in P-etch at 25°C (Å/sec)	Etch rate in 5:1 HF at 25°C (Å/sec)	Density* (g/cm <sup>3</sup> )	Sample thickness (μm)
		Temp (°C)	Time (min)					
950	12	—	—	1.460	3.21	9.5	2.19	0.36
950	12	1100	30	1.462	2.1	7.2	2.28	0.38
1000	12	—	—	1.458	2.97	7.9	2.25	0.33
1000	12	1100	30	1.462	2.07	7.2	2.30	0.33
1050	12	—	—	1.469	—	8.2	2.10	0.21
1050	20	—	—	1.458	2.92	8.5	2.20	0.40
1050	20	1100	30	1.462	2.06	7.2	2.24	0.40
1000	20	—	—	1.458	—	8.8	—	0.10
1000	50	—	—	1.455	—	8.5	—	0.12
1000	60	—	—	1.454	—	9.1	—	0.12
1000	120	—	—	1.453	—	9.1	—	0.10

\* By weight loss method.

Infrared absorption spectra of a limited number of as-deposited samples were taken. All samples were deposited at 1000°C. First absorption maxima lay at ~1070 cm<sup>-1</sup> for all samples.

**Etch rate.**—Etch rate was determined by etching the samples in P-etch (15) [15 parts HF (49%), 10 parts HNO<sub>3</sub> (70%), and 100 parts H<sub>2</sub>O]. Typically, SiO<sub>2</sub> deposited at 1000°C etched ~50% faster than thermal oxide. In P-etch, the etch rate appears to be a function of deposition temperature (Table I). Sample-to-sample variations in etch rate decreased as the deposition temperature was increased. All samples when annealed in N<sub>2</sub> at 1100°C for a half-hour had an etch rate of between 2.1 and 2.06 Å/sec. The etch rate in 5:1 diluted HF also showed a drop upon annealing; however, this etchant did not delineate the etch rate as a function of deposition temperature.

**Density.**—Film density was measured by the weight-loss method; i.e., deposited wafers were weighed and then stripped and reweighed. The density of as-deposited samples appears consistently lower than that of annealed samples. The density of all samples varied between 2.1 and 2.3 g/cm<sup>3</sup>. The density of the annealed sample approached that of thermal oxide (2.27 g/cm<sup>3</sup>) within measurement accuracy.

**Electrical properties.**—Several samples were prepared from the SiH<sub>4</sub>-CO<sub>2</sub>-H<sub>2</sub> system at 1000°C, with the CO<sub>2</sub>:SiH<sub>4</sub> ratio varying from 40:1 to 60:1. All wafers were n-type Si, <100>, 8.5-20 ohm-cm, 5.72 cm (2¼ in.) diameter. The total SiO<sub>2</sub> thickness deposited was ~1350Å. Most wafers were split in half after the SiO<sub>2</sub> deposition. One portion of each wafer was then annealed at 1050°C for 15 min in N<sub>2</sub> (standard anneal for thermal SiO<sub>2</sub>). Then, clean 20-mil aluminum dots were evaporated on both halves of the wafers. The metallized wafers were annealed at 400°C for a half-hour in N<sub>2</sub>.

Following are the results of measurements on MOS capacitors.

**Dielectric strength.**—Twenty MOS capacitor dots in each sample were biased in accumulation, and the bias voltage was ramped at a rate of approximately 1 V/sec. The capacitor leakage current was monitored with a picoammeter. The dielectric breakdown was considered to have occurred when the leakage was greater than or equal to 2 nA. All samples exhibited the same dielectric breakdown field (*E<sub>B</sub>*). There was no dependence on CO<sub>2</sub>:SiH<sub>4</sub> ratio or the postdeposition anneal. The *E<sub>B</sub>* value obtained was 7.8 × 10<sup>6</sup> V/cm, and the breakdown distribution obtained was very tight in every case, with a standard deviation  $\sigma_{E_B} \leq 0.1 \times 10^6$  V/cm.

**Dielectric constant.**—The thickness measured by ellipsometry and C-V measurements agreed within 50Å in all cases. This leads to the conclusion that the dielectric constant lies between 3.8 and 4.0. Annealed halves of wafers were thinner by ~30Å than the nonannealed halves. This means that there is densification of the order of 2-3% upon annealing.

**Oxide fixed charges (*Q<sub>ox</sub>*).**—The fixed oxide charges were measured by means of the C-V technique. There was no influence of CO<sub>2</sub>:SiH<sub>4</sub> ratio on the fixed charges; however, annealing showed the expected reduction in fixed charges. The *Q<sub>ox</sub>* for nonannealed wafers was 2.8 (±0.2) × 10<sup>11</sup> cm<sup>-2</sup>, and the *Q<sub>ox</sub>* for annealed wafers was 1.3 (±0.5) × 10<sup>11</sup> cm<sup>-2</sup>.

**Mobile charges (*Q<sub>m</sub>*).**—Mobile charges were measured by applying ±2 × 10<sup>6</sup> V/cm for 10 min at 200°C. This technique is similar to the one used by Kriegler *et al.* (16). The shift in flatband under positive bias was converted into mobile charge. In no case was the shift in the flatband under negative bias taken into account, for two reasons:

1. In most cases, the shift in the flatband under negative bias was negligible (i.e., ≤25 mV). This also means that the mobile charges were present at the metal/SiO<sub>2</sub> interface.

2. In some cases, the flatband shift was significant under negative bias (i.e., ≥50 mV), but the direction of the shift was wrong, i.e., as if more positive charges were being accumulated at the SiO<sub>2</sub>/Si interface. This effect (discussed in greater detail under Stability) is due to fast surface-state generation at the SiO<sub>2</sub>/Si interface (17).

There was no measured effect of CO<sub>2</sub>:SiH<sub>4</sub> ratio on mobile charge. The annealed wafers had a mobile charge of <1 × 10<sup>10</sup>, whereas the nonannealed wafers showed a mobile charge of 2.7 (±0.5) × 10<sup>10</sup> cm<sup>-2</sup>. The apparent higher mobile charges in nonannealed wafers are most likely due to run-to-run variations of the Al evaporator. The nonannealed halves of wafers were metallized first. Thermal oxide monitor wafers in the above two metallization runs were checked and showed the same general trend as the CVD oxide wafers.

**Fast surface states (*N<sub>FS</sub>*).**—Fast surface states were determined by the quasistatic technique of Kuhn (18). This technique was modified after Castange (19) and Kerr (20). The modification involved the use of a high-frequency C-V trace in place of the ideal. The *N<sub>FS</sub>* was obtained from accumulation to onset of inversion by comparison of the high- and low-frequency C-V traces.

$$N_{FS} = \frac{C_{FS}}{q} = \left[ \frac{C_{LF} \cdot C_{OX}}{C_{OX} - C_{LF}} - \frac{C_{HF} \cdot C_{OX}}{C_{OX} - C_{HF}} \right] \frac{1}{q} \quad [5]$$

where *C<sub>FS</sub>* = capacitance due to fast surface states, *C<sub>OX</sub>* = oxide capacitance, *C<sub>LF</sub>* = low-frequency capacitance at a given voltage on the metal electrode, *C<sub>HF</sub>* = high-frequency capacitance at a given voltage on the metal electrode, and *q* = electronic charge 1.6 × 10<sup>19</sup>.

Equation [5], in which all capacitances are per unit area, determines *N<sub>FS</sub>* as a function of applied electrode voltage. This voltage can be readily converted into surface potential [e.g., Kuhn (18)], so *N<sub>FS</sub>*, as a function of surface potential, is given in this investigation.

The fast surface-state densities are generally small in all samples. Annealed samples show somewhat higher *N<sub>FS</sub>* than nonannealed samples. The difference in the two cases, however, is not considered significant,

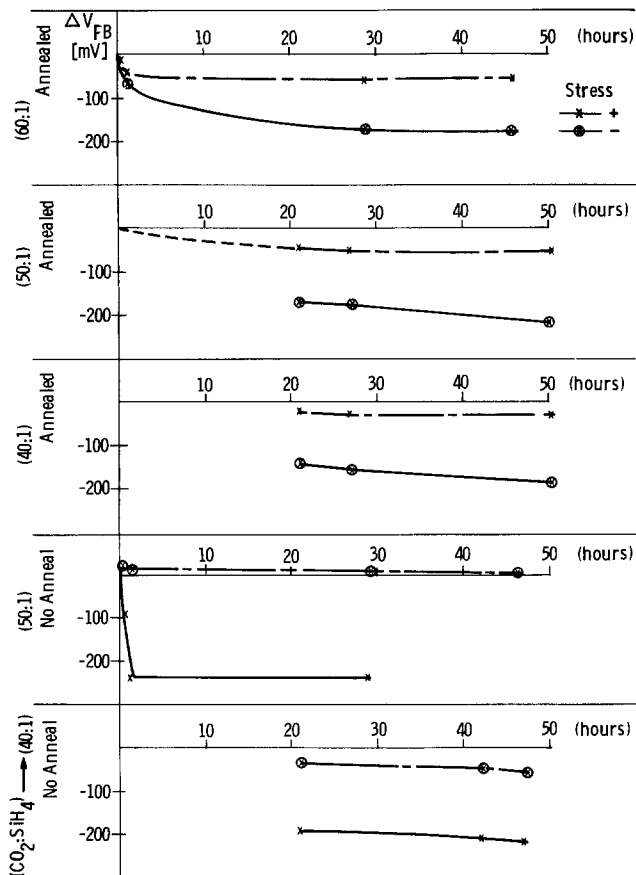


Fig. 6. Change of flatband voltage under the influence of temperature-bias stressing.

and all samples measured can be adequately represented by an  $N_{FS}$  value of  $1.5 (\pm 0.5) \times 10^{10} \text{ cm}^{-2} \cdot \text{eV}^{-1}$  (at mid-bandgap).

**Stability**—As shown in Fig. 6, 50-hr stress data on some samples were accumulated at 200°C and  $2 \times 10^6$  V/cm with both polarities on the metal of the MOS capacitor. The positive-bias data confirm the short-term stress data. There is a shift in the flatband voltage within the first hour and then a fast leveling off. This can be explained by the movement of mobile ions. Under negative bias, there is again a negative shift, the final value of which is larger for the annealed wafers than for the nonannealed wafers. There was no discernible dependency of  $V_{FB}$  shift on the CO<sub>2</sub>:SiH<sub>4</sub> ratio. Negative shifts under negative bias are commonly attributed to an increase of fast surface-state density (17). It was not expected that the nonannealed wafers would display fewer fast surface states after temperature bias stressing.

To check the above expectation, several MOS capacitors on both annealed and nonannealed wafers were stressed for 20 hr at  $\pm 2 \times 10^6$  V/cm and 200°C. Most of the observed shift in  $V_{FB}$  occurs within this time span (Fig. 6). Table II presents the initial and final values of the  $N_{FS}$  at mid-bandgap. Note that there is a significant difference between annealed and non-

Table II. Fast surface states as a function of temperature-bias stress and postdeposition high temperature (1050°C, 15 min, N<sub>2</sub>) anneal

Sample	$N_{FS} \text{ cm}^{-2} \text{ eV}^{-1}$ (at mid-bandgap) $\times 10^{10}$		
	Initial	After 20 hr of $+2 \times 10^6$ V/cm and 200°C	After 20 hr of $-2 \times 10^6$ V/cm and 200°C
As deposited	1.1 ( $\pm 0.3$ )	1.2 ( $\pm 0.3$ )	2.5 ( $\pm 0.3$ )
Annealed	1.8 ( $\pm 0.2$ )	3.1 ( $\pm 0.5$ )	6.6 ( $\pm 0.7$ )

\* Note: Values in parentheses are twice the standard deviation.

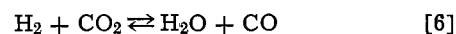
nealed samples and, contrary to the above expectation, the annealed samples show higher, fast surface-state density after temperature- and negative-bias stressing. The behavior of the annealed samples is much like the dry, O<sub>2</sub>-grown thermal oxides (17), whereas the nonannealed wafers appear to characterize the CVD oxides.

The behavior of the CVD oxides investigated is not believed to be limited to oxides deposited in SiH<sub>4</sub>-CO<sub>2</sub>-H<sub>2</sub>. This effect is most likely due to the deposition temperature used in this case (i.e., 1000°C). Thus, the high-temperature postdeposition anneal deteriorates the stability of the CVD oxides under temperature- and negative-bias stressing.

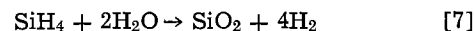
### Discussion

It has been shown that the SiH<sub>4</sub>-CO<sub>2</sub> reaction is first order with respect to SiH<sub>4</sub>. This was determined by using the "method of excesses," or "isolation," technique (14); i.e., CO<sub>2</sub> had considerably larger concentration than SiH<sub>4</sub>. Therefore, as expected, the reaction rate was independent of the CO<sub>2</sub> concentration. The same technique (i.e., excess SiH<sub>4</sub> compared with CO<sub>2</sub>) or the use of molar ratios of SiH<sub>4</sub> and CO<sub>2</sub> cannot isolate the reaction order with respect to CO<sub>2</sub>, because, in both cases, silicon-rich films are deposited (i.e., no longer SiO<sub>2</sub>). There is no other known technique that would isolate reaction order with respect to CO<sub>2</sub>. Thus, the experimental data cannot firmly support a reaction mechanism, and none will be postulated here. However, we shall discuss our results in the light of the mechanism previously postulated.

Tung and Caffrey (1), Steinmaier and Bloem (21), and Rand and Ashworth (8) proposed a two-step kinetic mechanism for SiO<sub>2</sub> deposition from SiCl<sub>4</sub>-CO<sub>2</sub>-H<sub>2</sub> and SiBr<sub>4</sub>-CO<sub>2</sub>-H<sub>2</sub>. The first step involves so-called "water-gas" reaction



The second step involves oxidation (hydrolysis) of silicon halides with H<sub>2</sub>O. Similar two-step kinetics may also be written for SiH<sub>4</sub>, the second step being



These authors realized that intermediate-reaction steps must exist, e.g., that reactions [6] and [7] may proceed via a free-radical chain mechanism or any other equally probable path. It is also generally accepted that the water-gas reaction is the slower and, hence, the rate-controlling step.

Then, Tingey (22) experimentally determined the forward rate expression of reaction [6] in the temperature range of 800°-1050°C. The experimentally determined activation energy for H<sub>2</sub>O formation from H<sub>2</sub> and CO<sub>2</sub> is 78 kcal/g mole (22). Therefore, if the water-gas reaction is rate controlling for SiO<sub>2</sub> deposition from SiH<sub>4</sub>-CO<sub>2</sub> reaction in H<sub>2</sub>, the observed activation energy should be of the order of 78 kcal/g mole. We have obtained an activation energy of 25.4 kcal/g mole for SiO<sub>2</sub> deposition. These results are inconsistent with the water-gas mechanism. Only the Steinmaier and Bloem (21) results are consistent with water-gas reaction. These authors obtained an activation energy of 82 kcal/g mole for SiCl<sub>4</sub>-CO<sub>2</sub>-H<sub>2</sub>. However, Tung and Caffrey (1), who also studied the SiCl<sub>4</sub>-CO<sub>2</sub>-H<sub>2</sub> system, reported an activation energy of 51.6 kcal/g mole. Similarly, Rand and Ashworth (8) reported an activation energy of 30 kcal/g mole for the SiBr<sub>4</sub>-CO<sub>2</sub>-H<sub>2</sub> system in the temperature range of 800°-950°C. Thus, hardly any of the activation energy data involving CO<sub>2</sub> and H<sub>2</sub> support the so-called water-gas mechanism.

The inconsistency of the activation energy data led us to perform several experiments, with hopes of answering a two-part question: (i) Does H<sub>2</sub>O form in our reactor under the experimental conditions of flow? (ii) What physical evidence would be produced if H<sub>2</sub>O were to form in the reactor? It was assumed that, if H<sub>2</sub>O were formed, the thermal oxidation of silicon would occur in the absence of SiH<sub>4</sub>. In the presence of SiH<sub>4</sub>,

we expected some homogeneous reaction (manifested by reaction-chamber clouding) besides the usual heterogeneous reaction. Several experiments, with results, are presented below.

Cleaned Si wafers were exposed to an  $H_2$  and  $CO_2$  ambient ( $\leq 1.2\%$   $CO_2$ ) at  $1000^\circ C$  for 1 hr. The wafers were hydrophobic before and after exposure to the  $H_2$  and  $CO_2$  ambient. Ellipsometric measurements showed that the wafers had  $\leq 15\text{\AA}$  of  $SiO_2$  before and after. Now the question arose whether other oxidants produced similar results. This led us to repeat the above experiment with  $N_2O$  which resulted in the growth of  $\cong 600\text{\AA}$   $SiO_2$  on the silicon wafers (23). To check whether the formation of  $SiO_2$  from the  $N_2O$  and  $H_2$  reaction was due to the  $H_2O$  formation or to the decomposition of  $N_2O$  and subsequent oxidation of silicon by oxygen, we repeated the experiment with  $N_2O$  and  $N_2$ . The resulting film was only  $\sim 150\text{\AA}$  thick (23). Clearly,  $H_2O$  is formed when wafers are heated in  $N_2O$  and  $H_2$ , whereas  $H_2O$  is not likely to form from  $CO_2$  and  $H_2$  under the flow conditions of the reactor. This conclusion is consistent with, and supported by, two facts: (i) when the  $SiH_4$ - $N_2O$ - $H_2$  system is used for  $SiO_2$  deposition ( $850^\circ$ - $1000^\circ C$ ), the reaction chamber clouds very rapidly (23), whereas when the  $SiH_4$ - $CO_2$ - $H_2$  system is used there is no evidence of reaction-chamber clouding; (ii) the deposition rate of  $SiO_2$  from the  $SiH_4$ - $N_2O$ - $H_2$  system is  $\sim 2$ -10 times higher than the  $SiH_4$ - $CO_2$ - $H_2$  system, depending on deposition temperature ( $850^\circ$ - $1000^\circ C$ ) for identical  $SiH_4$  and oxidant mole fraction (23).

Experiments with mixtures of  $H_2$  and  $O_2$  and of  $N_2$  and  $O_2$  showed results similar to those of  $H_2$  and  $N_2O$  and of  $N_2$  and  $N_2O$ ; i.e., a higher thickness of thermal  $SiO$  was grown with the  $H_2$  and  $O_2$  mixture. Clearly,  $H_2O$  was being produced by the reaction of hydrogen and oxygen. We then attempted to study the rate of reaction of  $SiH_4$  with  $H_2O$  using the  $SiH_4$ - $O_2$ - $H_2$  system. The task, however, was nearly impossible because of the chamber clouding which necessitated reactor cleaning after every run. We were able to obtain deposition-rate data at  $800^\circ$ - $850^\circ C$ , however, before abandoning the effort. The deposition rate of  $SiO_2$  from the  $SiH_4$ - $O_2$ - $H_2$  system was nearly an order of magnitude greater than that obtained from the  $SiH_4$ - $CO_2$ - $H_2$  system for identical temperature,  $SiH_4$ , and oxidant mole fractions (24). The results of the experiments with  $SiH_4$ - $O_2$ - $H_2$  and  $SiH_4$ - $N_2O$ - $H_2$  are at variance with the water-gas mechanism for the  $SiH_4$ - $CO_2$ - $H_2$  system because, if  $H_2O$  is produced from  $CO_2 + H_2$ , which subsequently reacts with  $SiH_4$  to produce  $SiO_2$ , then the deposition rate of  $SiO_2$  should not significantly change, irrespective of the source of  $H_2O$ .

Finally, Tingey (22) experimentally showed that the water-gas reaction is homogeneous, i.e., that  $H_2O$  is produced in the gas phase. This should result in the homogeneous reaction of  $SiH_4$  and  $H_2O$ ; yet the  $SiH_4$ - $CO_2$ - $H_2$  reaction is singularly characterized by the lack of homogeneous reaction, i.e., no clouding of the reaction chamber by gas-phase reaction. The above experimental and activation energy data neither support nor are consistent with the water-gas reaction mechanism for  $SiH_4$ - $CO_2$ - $H_2$ . It is therefore probable that the  $SiH_4$ - $CO_2$  reaction could proceed via direct oxidation of silane, as suggested by Swann and Payne (4), some complex free-radical chain mechanism, as alluded to by Rand and Ashworth (8), or any other mechanism that does not include water-gas reaction as a step.

### Summary and Conclusion

We have presented the results of  $SiH_4$ - $CO_2$  reaction in  $H_2$  in the temperature range  $850^\circ$ - $1050^\circ C$ . We have used a multiple-wafer reactor in sharp contrast to Swann and Payne's single-wafer reactor. Our results should find more application in CVD practice because the flow of gases is nearly parallel to the wafer surface. Unlike Swann and Payne, we have been able to isolate the order of the  $SiH_4$ - $CO_2$  reaction with respect to  $SiH_4$

and the activation energy and frequency factor of the reaction. However, care should be exercised in extrapolating and using these results to predict the  $SiO_2$  deposition rate for  $SiH_4$  concentrations larger than 0.06-0.07% because, at higher concentrations than these, the  $SiO_2$  films become silicon-rich; i.e., codeposition of Si and  $SiO_2$  occurs.

We have shown that the physical and electrical properties of  $SiO_2$  deposited at  $1000^\circ C$  are comparable to those of steam-grown oxide. In fact, the fast surface-state densities are considerably lower in these CVD oxides than in steam-grown oxides. The low level of fast surface-state density may be attributed to the use of  $H_2$  during deposition. The stability of these oxides under temperature ( $200^\circ C$ ) and bias  $\pm 2 \times 10^6$  V/cm has been demonstrated. The negative effects of post-deposition anneal in  $N_2$  at a temperature higher than the deposition temperature have also been shown.

The use of  $CO_2$  does not result in a homogeneous reaction, especially at higher temperatures, i.e., of the order of  $1000^\circ C$ . This is a significant advantage, since it keeps the reactor down time to a minimum. However, the use of  $CO_2$  has often raised the possibility of carbon inclusion. Though we do not have any direct evidence of the presence or absence of carbon in  $SiO_2$  films deposited from  $SiH_4$ - $CO_2$ - $H_2$ , trace quantities of carbon may well be incorporated in these films. None of the measured physical and electrical properties, however, show any unusual or detrimental effects of these trace impurities, if present.

Finally, the CVD  $SiO_2$  film from  $SiH_4$ - $CO_2$ - $H_2$  could be readily used as a photolithographic mask for films like  $Si_3N_4$  and in the field or the gate region of an integrated FET circuit.

### Acknowledgments

The authors are indebted to A. A. Kozul and T. O. Williams for preparing the samples.

Manuscript submitted April 10, 1974; revised manuscript received July 16, 1975. This was Paper 50 presented at the San Francisco, California, Meeting of the Society, May 12-17, 1974.

Any discussion of this paper will appear in a Discussion Section to be published in the December 1976 JOURNAL. All discussions for the December 1976 Discussion Section should be submitted by Aug. 1, 1976.

Publication costs of this article were partially assisted by IBM Corporation.

### REFERENCES

1. S. K. Tung and R. E. Caffrey, *Trans. Met. Soc. AIME*, **233**, 572 (1965).
2. M. J. Rand, *This Journal*, **114**, 274 (1967).
3. T. L. Chu, J. R. Szidon, and G. A. Gruber, *Trans. Met. Soc. AIME*, **242**, 532 (1968).
4. R. C. G. Swann and A. E. Payne, *This Journal*, **116**, 1014 (1969).
5. W. J. Kroll, R. L. Titus, and J. B. Wagner, Abstract 13, p. 31, The Electrochemical Society Extended Abstracts, Spring Meeting, Houston, Texas, May 7-11, 1972.
6. M. L. Barry, in "Chemical Vapor Deposition, 2nd International Conference," John M. Blocher, Jr. and James C. Withers, Editors, The Electrochemical Society Softbound Symposium Series, New York (1970).
7. T. Miyazaki, I. Yoshida, M. Horiuchi, and T. Tokuyama, *ibid.*, p. 571.
8. M. J. Rand and J. L. Ashworth, *This Journal*, **113**, 48 (1966).
9. L. V. Gregor, in "Physics of Thin Films," Vol. 3, p. 133, Georg Hass and R. E. Thun, Editors, Academic Press, Inc., New York (1966).
10. V. Y. Doo, D. W. Boss, R. Valletta, and W. A. Pliskin, Paper 42, presented at Electrochemical Society New York, New York, Meeting, May 4-9, 1969.
11. E. O. Ernst, D. J. Hurd, and G. Seeley, U. S. Pat. 3, 424,629, Assigned IBM Corporation.
12. F. G. Allen, *J. Appl. Phys.*, **28**, 1510 (1957).
13. O. Levenspiel, "Chemical Reaction Engineering," John Wiley & Sons, Inc., New York (1967).

14. G. W. Castellan, "Physical Chemistry," p. 607, Addison-Wesley Publishing Co., Inc., Reading, Mass. (1964).
15. W. A. Pliskin and H. S. Lehman, *This Journal*, **112**, 1013 (1965).
16. R. J. Kriegler, Y. C. Cheng, and D. R. Colton, *ibid.*, **119**, 388 (1972).
17. A. Goetzberger, A. D. Lopez, and R. J. Strain, *ibid.*, **120**, 90 (1973).
18. M. Kuhn, *Solid-State Electron.*, **13**, 873 (1970).
19. R. Castange, C. Y. Lebd. Se'anc, *Acad. Sci. (Paris)*, **267**, 866 (1968).
20. D. R. Kerr, Private communication.
21. W. Steinmaier and J. Bloem, *This Journal*, **111**, 206 (1964).
22. G. L. Tingey, *J. Phys. Chem.*, **70**, 1406 (1966).
23. R. L. Bratter and A. K. Gaind, Unpublished work.
24. R. L. Bratter, Unpublished work.

## Fabrication of P-Channel Silicon Gate LSI Devices with Si<sub>3</sub>N<sub>4</sub>/SiO<sub>2</sub> Gate Dielectric

Alfred P. Turley,\* R. M. McLouski,\* P. R. Reid, and D. H. McCann

*Westinghouse Advanced Technology Laboratory, Baltimore, Maryland 21203*

### ABSTRACT

Processing of p-channel silicon gate devices with a Si<sub>3</sub>N<sub>4</sub>/SiO<sub>2</sub> gate dielectric is described in detail. Some attractive features of this particular process include polysilicon to silicon contacts, improved metal step coverage obtained with a glass flow anneal, low fast surface-state density for good 1/f noise performance, and high parasitic field threshold voltages obtained by ion implantation of arsenic.

Because of the work function difference between p-type polycrystalline silicon gate electrodes and lightly doped n-type silicon substrates, most p-channel silicon gate devices have been fabricated on <111> oriented silicon substrates. This avoids the possibility of very low threshold or depletion mode devices which can result if <100> oriented substrates are used. This result is a direct consequence of the lower fixed positive charge density at the SiO<sub>2</sub>-Si interface of <100> oriented silicon substrates. However, for devices used in analog signal processing, the use of <111> material will degrade the 1/f noise performance of such IGFET'S because of the high fast surface-state density associated with this orientation. To take advantage of the better 1/f noise performance obtained on <100> material and still maintain a reasonable threshold voltage (-1.3V), silicon gate devices can be fabricated with a Si<sub>3</sub>N<sub>4</sub>/SiO<sub>2</sub> gate dielectric. The desired threshold voltage can be obtained by controlling the amount of fixed positive charge at the nitride-oxide interface formed during the nitride deposition. Other advantages of the dual dielectric structure are: (i) Si<sub>3</sub>N<sub>4</sub> is superior to SiO<sub>2</sub> as a boron diffusion barrier (2), (ii) the composite structure has better integrity than a SiO<sub>2</sub> gate, and (iii) higher transconductance FET's result from the higher dielectric constant of Si<sub>3</sub>N<sub>4</sub>.

Other attractive features of this particular process are polysilicon-silicon contacts which allow very high packing densities because they take up less area than metal-silicon contacts, improved metal step coverage obtained with a glass flow anneal (4), and high parasitic field threshold voltages obtained by ion implantation of the surface (except active regions) with arsenic.

### Process Sequence

An outline of the process is given in the flow chart in Table I. The starting wafer material is 4-8 ohm-cm, <100>, n-type. The first step is the formation of the gate oxide. This is thermally grown in an atmosphere of 10% HCl + 90% O<sub>2</sub> for 13 min at 1000°C. The resulting oxide thickness is about 300Å. This is followed by the deposition of the gate nitride. About 800Å of

silicon nitride is deposited at 750°C with an ammonia to silane ratio of 250:1. In the next step, the first photoengraving operation is performed. A mask is applied to define islands of nitride which will ultimately become the active devices. A photoresist mask is used and the silicon nitride is plasma etched (5). The 300Å of oxide under the nitride stops the plasma etching process. With the photoresist still on the wafer, an arsenic implant is next performed at an energy of 80 keV and a dose of  $5 \times 10^{11}$  cm<sup>-2</sup>. The photoresist acts as a mask which prevents penetration of the arsenic into active device regions. After photoresist removal, a cross section of a transistor structure appears as in Fig. 1. The transistor gate, source, and drain will be formed in the region defined by the island of silicon nitride. The arsenic implant in the surrounding regions will prevent parasitic transistor action by keeping the surface from inverting at voltages less than -35V. The next processing step forms the field oxide region by steam oxidation at 1100°C.

About 10 kÅ of SiO<sub>2</sub> is grown in 2.5 hr in the regions surrounding the nitride islands. Only about 300Å of the nitride is oxidized. This is removed by dip etching for 30 sec in a 10:1 HF solution. At this point in the process, the structure is annealed in dry O<sub>2</sub> for 30 min at

Table I. Process flow chart

1. Starting material: 4-8 ohm-cm, <100>, n-type
2. Gate oxidation: 300Å (10% HCl + 90% O<sub>2</sub>, 13 min at 1000°C)
3. Gate nitride: 800Å (NH<sub>3</sub>/SiH<sub>4</sub> = 250 at 750°C)
4. Device window mask (plasma etch Si<sub>3</sub>N<sub>4</sub>)
5. Ion implant arsenic (E = 80 keV, dose =  $5 \times 10^{11}$  cm<sup>-2</sup>)
6. Steam oxidation: 10 kÅ (H<sub>2</sub> + O<sub>2</sub>, 150 min at 1100°C)
7. Etch oxidized nitride (~300Å)
8. O<sub>2</sub> anneal (30 min at 1050°C)
9. Polysilicon-silicon contact window mask
10. Polysilicon deposition (4 kÅ at 700°C)
11. Polysilicon gate and interconnect mask (plasma etch poly and nitride, chem. etch gate oxide to define self-aligned gate)
12. Boron diffusion (diborane source)
  - a. Deposition: 18 min at 980°C
  - b. Drive: 60 min, O<sub>2</sub> at 1000°C
13. Phosphorus-doped oxide deposition (~5% phosphorus, 15 kÅ)
14. Via and contact window mask
15. Glass flow anneal (O<sub>2</sub>, 20 min at 1050°C)
16. Hydrogen anneal (30 min H<sub>2</sub> at 800°C)
17. Dip etch 30 sec in 10:1 HF (removes oxide from windows in doped glass)
18. Metallization (10 kÅ of Al-Si)
19. Metal interconnect mask
20. Sinter metal (30 min, N<sub>2</sub> at 500°C)

\* Electrochemical Society Active Member.  
Key words: polysilicon, insulator, MOSFET, noise.



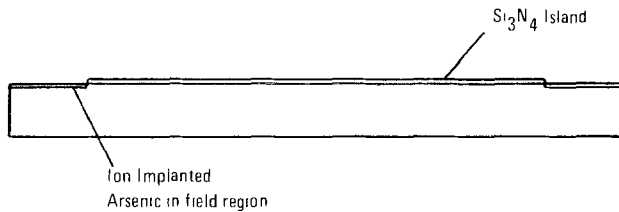


Fig. 1. Device cross section after ion implantation of arsenic in field regions. Step 5 in process flow chart.

1050°C. This anneal converts about 50Å of the nitride surface to oxide and has the effect of stabilizing the structure (6). Figure 2 shows the transistor structure cross section at this point of the process. The device is now ready for opening contact windows for the polysilicon-silicon contacts. Again, a photoresist mask is used and the silicon nitride is plasma etched followed by an oxide etch. Figure 3 shows the device cross section at this point. Polysilicon is now deposited to a thickness of 4000Å with a deposition temperature of 700°C. A mask to define the polysilicon interconnect pattern and the self-aligned gate structure is next applied. A photoresist mask is used and the polysilicon is plasma etched. The plasma etching continues through the polysilicon and the silicon nitride around the gate electrode. A short oxide etch (~300Å) then completes the self-aligning gate definition. The transistor cross section at this point is shown in Fig. 4. A boron diffusion now forms the source and drain and also dopes the polysilicon conductor lines. Reoxidation in dry O<sub>2</sub> for 60 min at 1000°C during the boron drive forms about 700Å of SiO<sub>2</sub> over the polysilicon and source-drain regions. This oxide prevents counterdoping of the p-type regions by the phosphorus-doped oxide deposited in the next step.

This doped oxide is about 15 kÅ thick and contains about 5-6% phosphorus. The structure at this point is shown in Fig. 5. Contact windows and vias are opened in the doped oxide. An anneal is performed on the phosphorus-doped oxide under the following conditions: (i) 20 min, O<sub>2</sub> at 1050°C; (ii) 30 min, H<sub>2</sub> at 800°C. This high temperature anneal causes the viscosity of the doped oxide to decrease to the point where it begins to flow, giving rise to smooth oxide

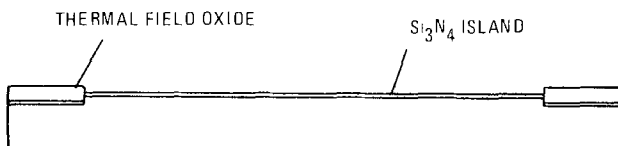


Fig. 2. Device cross section after formation of field oxide and anneal. Step 8 in process flow chart.

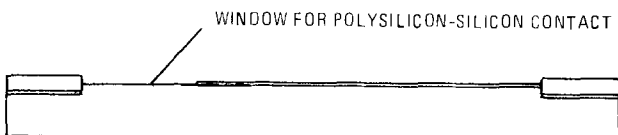


Fig. 3. Device cross section after etching of contact windows for polysilicon-silicon contacts. Step 9 in process flow chart.

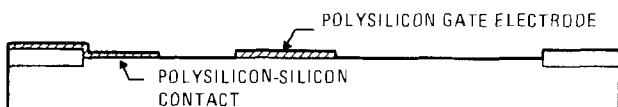


Fig. 4. Device cross section after definition of polysilicon conductor lines. Step 11 in process flow chart.

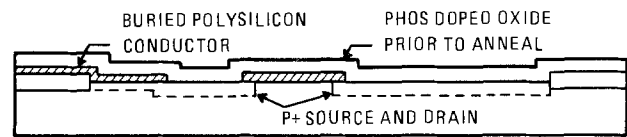


Fig. 5. Device cross section after source-drain diffusion and deposition of phosphorus-doped oxide insulator. Step 13 in process flow chart.

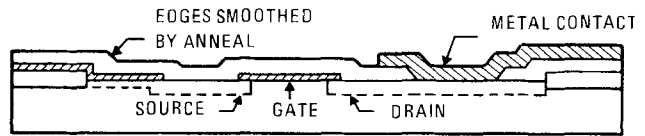


Fig. 6. Device cross section at completion of process

edges over polysilicon steps and via and contact windows. A small amount of oxide is formed in the open windows during the anneal. This can be removed by a short dip etch before metallization. The hydrogen part of the anneal is the last high temperature step before metallization greatly reduces the number of fast surface states at the Si-SiO<sub>2</sub> interface in the gate regions, which in turn produces devices with excellent 1/f noise characteristics. The effects of the glass flow anneal are shown in the SEM photograph of Fig. 7. Note the excellent metal coverage of oxide steps.

The processing is completed with a metal deposition (10 kÅ of Al-Si), interconnect photoengraving, and sintering. The completed cross-section transistor structure is shown in Fig. 6. A photograph of a section of a completed device is shown in Fig. 8.

### Device Characteristics

The threshold voltage of transistors fabricated by this process is greatly influenced by fixed positive charge formed at the silicon nitride-silicon dioxide interface in the gate dielectric. The magnitude of this charge is strongly influenced by the silicon nitride deposition parameters. Our nitride is deposited at 750°C with an ammonia/silane ratio of 250:1. The parameters that influence charge magnitude are deposition rate and deposition temperature. Temperature has by far the strongest effect with deposition rate being a second-order effect. Figure 9 shows the deposition temperature effect by comparing the C-V characteristics of MOS capacitors formed at deposition temperatures of 750° and 800°C. The negative shift of the 800°C curve indicates a larger fixed positive inter-

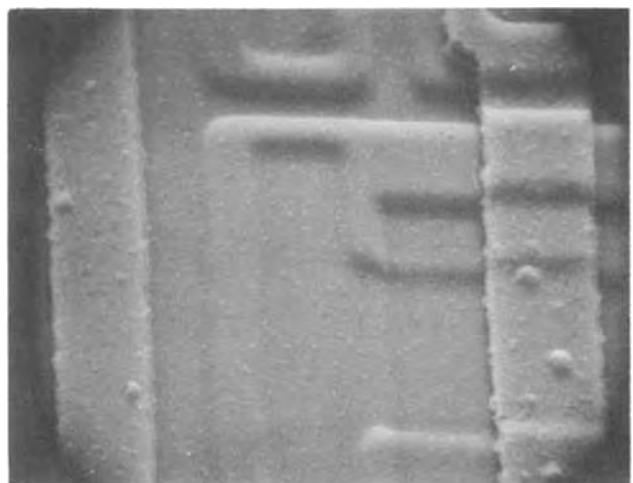


Fig. 7. SEM photograph showing the effects of the glass flow anneal on smoothing oxide edges and sloping oxide steps.



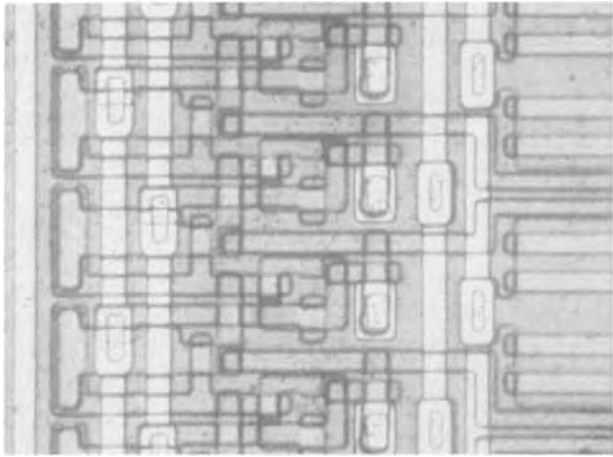


Fig. 8. Photograph of a portion of a completed LSI device. Shown are several stages of a dynamic shift register.

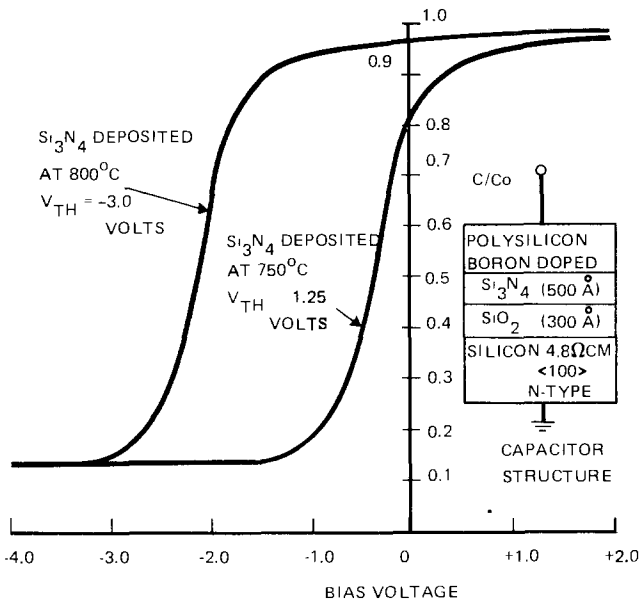


Fig. 9. MOS C-V curves showing the effect of nitride deposition temperature on the magnitude of the fixed charge formed at the nitride-oxide interface.

face charge. This data indicates a nitride charge of  $2 \times 10^{12}$  charges/cm<sup>2</sup> at the 800°C deposition temperature and  $7 \times 10^{11}$  charges/cm<sup>2</sup> at the 750°C deposition temperature. The charge at the nitride-oxide interface is transformed to a charge at the silicon surface ( $Q_{eff}$ ) by the following equation

$$Q_{eff} = \frac{\frac{\epsilon_{ox}}{\epsilon_n} t_n}{t_{ox} + \frac{\epsilon_{ox}}{\epsilon_n} t_n} Q_n \quad [1]$$

In this equation, one can think of the term  $(\epsilon_{ox}/\epsilon_n) t_n$  as an effective oxide thickness of the nitride as far as its dielectric properties are concerned. Since  $\epsilon_{ox}/\epsilon_n \sim 0.6$ , one sees that 500Å of nitride is equivalent to 300Å of oxide for capacitance calculations.

The threshold voltage is given by the equation

$$V_{th} = \phi_{GS} - \frac{1}{C_i} (Q_{eff} + Q_{ss} + \sqrt{2\epsilon_s q N_d (2\phi_F)}) \quad [2]$$

Thus one concludes that increasing  $Q_{eff}$  will make the threshold voltage more negative. The threshold voltage of 24 devices from different wafers in different runs was measured. The mean and standard deviation were

-1.31 and 0.17V, respectively. The transconductance at VGS = -5V was also measured and normalized to unity width to length ratio. The mean and standard deviation were 32 and 3.84 μ-mhos, respectively.

The stability of the threshold voltage was examined by making temperature-bias stressed C-V measurements. Figure 10 shows the flatband voltage shift vs. time for a +15V bias at 200°C. The instabilities noted are not caused by ionic contamination but by the difference in the resistivity of the nitride and oxide (6). The resistivity of the silicon nitride is less than the oxide resistivity; hence, when bias is applied, the nitride oxide layers form a resistive divider and charge slowly accumulates at the nitride oxide interface. One can increase the nitride resistivity by oxidizing its surface. This small amount of oxide on the nitride surface effectively increases the nitride resistivity and improves stability. This effect is shown in Fig. 10 where

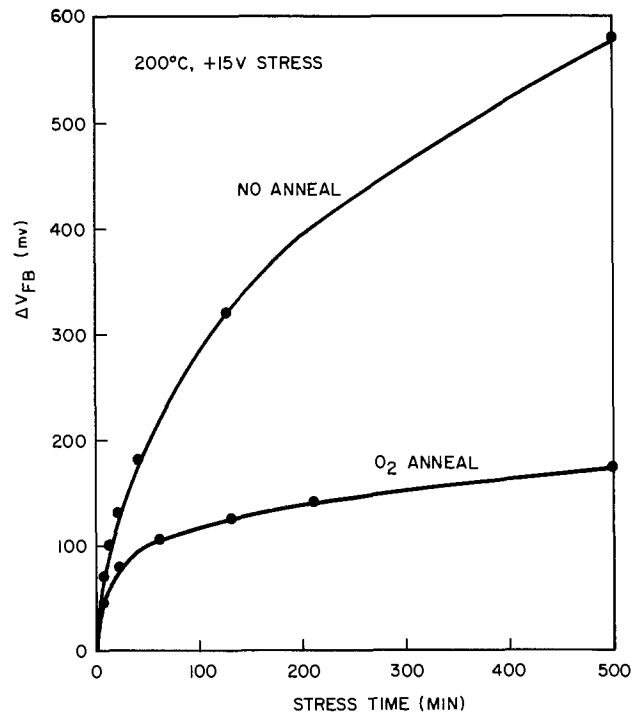


Fig. 10. Flatband voltage shift under temperature-bias stress

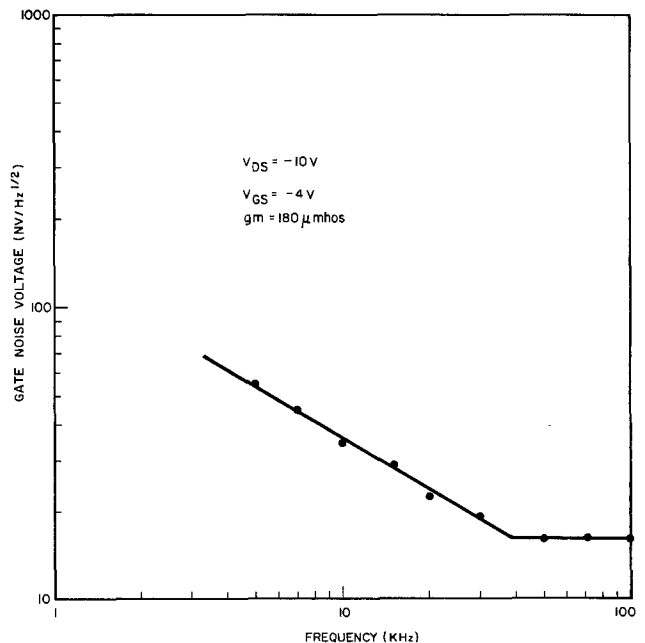


Fig. 11. Noise spectra of typical transistor

oxidized and nonoxidized samples are compared. This is the reasoning behind the oxygen anneal in step 8 of the process as indicated in Table I. Under a negative bias stress of  $-15\text{V}$  at  $200^\circ\text{C}$ , the oxidized samples shifted only 20 MV and saturated to this value after 5 min of stress. The nonoxidized sample shifted 40 MV under the same conditions.

The noise performance achieved with these devices is shown in Fig. 11. Here is plotted the noise voltage referred to the gate *vs.* frequency. The  $1/f$  portion of the noise spectra shows about a 12% improvement over the performance attained with an equivalent device made with a metal gate and an oxide insulator.

### Conclusion

We have devised and demonstrated a process for fabrication of p-channel silicon gate MOS devices with a silicon nitride/silicon dioxide gate dielectric for both digital and analog LSI applications. The process features include small area polysilicon-silicon contacts; smoothed, sloped oxide steps for excellent metal coverage; low fast surface-state density with a  $\text{H}_2$  anneal; good threshold stability with an  $\text{O}_2$  anneal; high parasitic field threshold voltages from ion implantation of arsenic in the field oxide regions.

### Acknowledgments

The authors wish to acknowledge the help in process development given by D. A. Tremere, P. D. Blais, P. L.

Hower, P. Rai-Choudhury, and R. N. Ghostagore of the Westinghouse Research and Development Center, Pittsburgh, Pennsylvania. The authors also wish to thank Dr. M. Lonky for the noise measurements.

Manuscript submitted April 16, 1975; revised manuscript received Aug. 21, 1975. This was Paper 189 presented at the New York, New York, Meeting of the Society, Oct. 13-17, 1975.

Any discussion of this paper will appear in a Discussion Section to be published in the December 1976 JOURNAL. All discussions for the December 1976 Discussion Section should be submitted by Aug. 1, 1976.

Publication costs of this article were partially assisted by Westinghouse Electric Corporation.

### REFERENCES

1. H. C. Lin, J. L. Halsor, and P. J. Hayes, *IEEE Trans. Electron Devices*, **ED-19**, 1199 (1972).
2. V. Doo, *ibid.*, **ED-13**, 561 (1966).
3. S. Abbas, A. Nagarajan, and P. Stern, Paper 171 presented at The Electrochemical Society Meeting, Miami Beach, Florida, Oct. 8-13, 1972.
4. W. E. Armstrong and D. L. Tolliver, *This Journal*, **121**, 307 (1974).
5. L. L. Fritz, *Solid State Technol.*, **14**, No. 12, 43 (1971).
6. R. C. Dockerty, C. A. Barile, A. Nagarajan, and S. M. Zalar, *Rel. Phys. Symp.*, 159 (1973).
7. R. C. Dockerty and M. D. Cowan, Paper 51 presented at The Electrochemical Society Meeting, San Francisco, California, May 12-17, 1974.

## Studies of the Ti-W Metallization System on Si

J. M. Harris,\* S. S. Lau, and M.-A. Nicolet

California Institute of Technology, Pasadena, California 91125

and R. S. Nowicki\*<sup>1</sup>

Fairchild Camera and Instrument Corporation, Research and Development Laboratory,  
Palo Alto, California 94304

### ABSTRACT

MeV backscattering spectrometry and x-ray diffraction are used to investigate the behavior of sputter-deposited Ti-W mixed films on Si substrates. During vacuum anneals at temperatures of  $700^\circ\text{C}$  for several hours, the metallization layer reacts with the substrate. Backscattering analysis shows that the resulting compound layer is uniform in composition and contains Ti, W, and Si. The Ti:W ratio in the compound corresponds to that of the deposited metal film. X-ray analyses with Reed and Guinier cameras reveal the presence of the ternary  $\text{Ti}_x\text{W}_{(1-x)}\text{Si}_2$  compound. Its composition is unaffected by oxygen contamination during anneal, but the reaction rate is affected. The rate measured on samples with about 15% oxygen contamination is linear, of the order of  $0.5 \text{ \AA}/\text{sec}$  at  $725^\circ\text{C}$ , and depends on the crystallographic orientation of the substrate and the d-c bias during sputter deposition of the Ti-W film.

Titanium and tungsten have both been used for many years as materials for metallizing integrated circuits (1). Tungsten is used because its coefficient of expansion closely matches that of silicon, and titanium is used because of its strong adherence to oxides. A metallization scheme has also been developed which uses a mixture of titanium and tungsten (2). Like many of the transition materials, Ti and W both form silicides. The formation of  $\text{WSi}_2$  from thin tungsten films on Si has been studied by several authors (3, 4). The formation of  $\text{TiSi}_2$  by thin films on Si has also been studied (5), though not to as great an extent as  $\text{WSi}_2$ . To our knowledge, the present investigation is the first to con-

sider the interaction of a mixed thin film with silicon. This study shows that, like Ti and W individually, a thin composite layer of Ti and W deposited on Si by sputtering and annealed in vacuum forms a disilicide. This ternary disilicide is studied using the techniques of x-ray diffraction,  $^4\text{He}$  backscattering spectrometry (BS), and Auger electron spectrometry (AES).

### Sample Preparation

Films of 1000-1500Å were deposited by RF sputtering from an arc-melted  $\text{Ti}_{0.3}\text{W}_{0.7}$  target onto silicon and carbon substrates. The silicon substrates were n- or p-type, 1-10 ohm-cm single crystal wafers of  $\langle 111 \rangle$ ,  $\langle 110 \rangle$ , or  $\langle 100 \rangle$  orientations which had been mechanically polished and chemically etched. The polycrystalline carbon substrates were 0.5 in. squares and were polished and cleaned prior to sputter deposition.

\* Electrochemical Society Active Member.

<sup>1</sup> Present address: Hewlett-Packard Advanced Product Division, Cupertino, California 95014.

Key words: thin-film reactions, silicide formation, Ti-W metallization,  $^4\text{He}$  backscattering.

During deposition, the substrates rested on a water-cooled pallet and the deposition temperature was monitored by a shielded iron-constantan thermocouple placed on the substrate surface. Substrates were loaded through a side loader which was evacuated by a cryogenic pumping station so as to prevent contamination of the target during loading.

Prior to loading, the silicon substrates were dipped in HF, rinsed in deionized water, and dried with high purity isopropanol. After loading, the sputtering chamber was evacuated to a background pressure of  $1 \times 10^{-6}$  Torr. Argon of 5N purity which had passed through a titanium purifier was used to backfill the chamber. The Ti-W target was given a short presputter to insure a clean surface, and the substrates were sputter cleaned immediately before deposition. During deposition the substrates were held at a negative bias ranging from 0 to 50V with respect to ground. The maximum temperature measured during deposition was about 300°C. The Ti-W films deposited on Si have a resistivity of about 80  $\mu\text{ohm-cm}$ , irrespective of the substrates or bias voltage. The films deposited on carbon were analyzed by BS to check for possible contaminants. Carbon substrates rather than Si were used for these measurements so that the BS signal from the substrate would not interfere with signals from possible nitrogen or oxygen impurities. No oxygen or nitrogen could be detected. The samples deposited with -50V bias showed the largest amount of contamination, which consisted of Ar and was less than 2 atomic per cent (a/o). Examination of the films on silicon substrates by SEM at 30K magnification revealed a featureless surface.

Anneals were performed in an evacuated quartz-tube furnace. The furnace was pumped from one end by a  $\text{LN}_2$  trapped oil diffusion pump and from the other end by a water-cooled titanium sublimation pump. The vacuum during anneals was typically  $7 \times 10^{-7}$  Torr. The temperature in the center of the furnace was measured by a Chromel-Alumel thermocouple which had been calibrated to an accuracy of  $\pm 1^\circ\text{C}$  against a mercury thermometer to a temperature of 350°C. The thermometer was calibrated against the freezing point and the boiling point (corrected for barometric pressure) of  $\text{H}_2\text{O}$ . The temperature stability of the furnace was measured to be  $\pm 2^\circ\text{C}$  over a period of 20 hr. The furnace was constructed so that many samples could be loaded and annealed sequentially during a single pump-down, and samples were always placed at the position within the furnace where it had been calibrated. Samples could be grouped and annealed simultaneously in the furnace.

### Analytical Techniques

**Backscattering spectrometry (BS).**—The experimental setup and analytical method for BS have been reviewed elsewhere (6). In brief, the technique consists of placing a sample in a beam of monoenergetic  $^4\text{He}^+$  ions and energy analyzing those He atoms which are scattered from the sample. BS with MeV  $^4\text{He}^+$  ions provides information on concentration profiles in depth with a resolution of about 200Å and to depths of about 3000-5000Å. In thicker films, the depth resolution degrades due to energy straggling within the target. The beam spot is typically 1-2  $\text{mm}^2$  and hence backscattering analysis required samples whose lateral composition is uniform over at least such a dimension.

**X-ray analysis.**—Two types of x-ray diffraction analyses were performed. The first type uses the Reed Camera (7) geometry which is basically a glancing angle x-ray diffraction setup with a fixed angle of incidence. The structure of the thin-film samples is identified in a manner similar to that employed with the Debye-Scherrer camera. Because of the glancing angle of incidence of the x-rays (8-14° with respect to the specimen surface), a relatively large volume is examined although the samples are thin. For example, at an incident angle of 10° the x-ray path length is 6

times the film thickness. The incident x-ray beam used for the exposure was  $\text{CuK}_\alpha$  radiation collimated through two pinholes. The diffraction pattern is recorded on film placed along a 5 cm radius from the sample center.

The second type of x-ray diffraction analysis performed used a Guinier camera (8). This is a transmission x-ray diffraction apparatus in which the sample rotates with respect to the beam during exposure.  $\text{CuK}_\alpha$  radiation was used in conjunction with x-ray film to record the diffraction patterns. The Guinier camera requires thin samples so as to not substantially attenuate the diffracted x-rays. To this end, the rear side of a reacted sample was lapped until the sample thickness was reduced to between 50-60 $\mu$ . The sample was then ultrasonically cleaned and rinsed in diluted HF. A similar sample of the bare silicon substrate was also prepared in this way. By comparing the x-ray diffraction patterns from both samples, the diffraction lines due to the silicide could be identified.

Given the camera constant and an accurate measurement of the silicide diffraction line spacing, determination of the cell parameters can be made. The camera constant was determined by measurement of the camera radius and verified using the diffraction lines from a strain-free sample of polycrystalline silicon powder. The silicide diffraction line spacing was measured with an optical comparator to  $\pm 0.01$  mm, which gave an uncertainty of  $\pm 0.01\text{Å}$  in the unit constants. The advantage of the Guinier technique is to enable an accurate determination of the cell constants, whereas the Reed camera can detect the presence of phases without special preparation of the specimens.

**Auger electron spectroscopy (AES).**—AES has been reviewed recently in the literature (9). This technique uses the decay by electron emission of sample atoms which experience inner shell ionization by an energetic electron beam. Energy analysis of these emitted Auger electrons allows one to perform an elemental analysis of the sample surface. Typically, sensitivities of about 1 a/o can be obtained.

Auger electrons originate only from atoms excited in the outermost atomic layers. Hence, elemental depth profiling requires a sequential removal of thin layers between measurements. This can be accomplished by sputtering. To obtain the depth profile of a sample requires knowledge of the sample's sputtering rate and the sputtering time. BS can be used conveniently to determine the film thickness and thereby calibrate the sputtering rate.

AES and BS nicely complement each other. AES is more sensitive than BS for profiling light elements in heavy matrixes, and BS can be used to measure the thickness and composition of the film quantitatively in a relatively short time ( $\sim 10$ -20 min).

### Results

**Characterization of ternary silicide.**—Films of Ti-W having about 30 a/o Ti (10% by weight) prepared as described above were vacuum annealed at 800°C for 20 min. The surface changed from the smooth metallic luster of Ti-W to a deep silver-gray. Examination by SEM at 4500 $\times$  magnification revealed a uniform and gently undulating surface. The undulations were typically 2.5  $\mu\text{m}$  across and  $< 0.05$   $\mu\text{m}$  in height (as determined by measurement with a Sloan Dektak).

X-ray diffraction analysis by Reed camera revealed the presence of only one compound (Fig. 1). The diffraction pattern corresponds to that described by the ASTM powder diffraction compilation No. 6-0599. This compound has a chemical formula of  $\text{Ti}_x\text{W}_y\text{Si}_2$ , where  $x + y = 1$ , with a hexagonal  $\text{CrSi}_2$ -type (C-40) structure. X-ray analysis by the Guinier camera supported the Reed camera results in that no crystal structures other than the C-40 type were detectable. The line spacings from the Guinier photographs gave cell parameters of  $a_0 = 4.61 \pm 0.01\text{Å}$  and  $c_0 = 6.48 \pm 0.01\text{Å}$ .

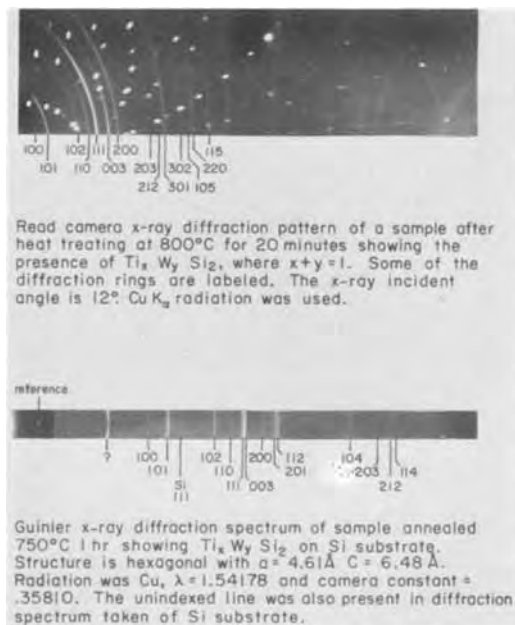


Fig. 1. X-ray diffraction pattern taken with Reed camera (top) and Guinier camera (bottom) of reacted samples.

2 MeV  $^4\text{He}^+$  BS analysis of films reacted at 725°C for 40 min revealed that the atomic concentration ratio of the films is  $\text{Ti}:\text{W}:\text{Si} = 0.3:0.7:2.0$  (Fig. 2). The compound maintains this composition at temperatures ranging from 675° to 900°C. Additional experiments established that the compound formed was independent of substrate orientation, doping type, substrate bias during sputter deposition, and the sample contamination by oxygen during annealing.

Once formed, the compound adheres strongly to the silicon substrate. The compound seems unaffected by hot  $\text{H}_2\text{O}_2$ , HF, or CP-4, and dissolves only slowly in aqua regia. Indium solder would not adhere to the compound.

**Kinetics of silicide formation.**—The reaction rate of the compound formation was investigated by BS on samples annealed in vacuum for increasing periods of time. To translate the energy scale of a BS spectrum into a depth scale, we assumed a density of  $7.54 \times 10^{22}$  atom/cm<sup>3</sup> for the compound, as calculated from the measured unit cell parameters. Using this density, 10 keV in a BS spectrum corresponds to about 106 Å of compound.

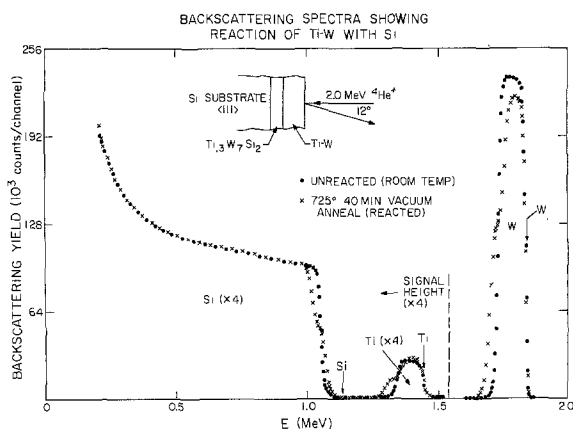


Fig. 2. Backscattering spectra showing a virgin (room temperature) and a covered, annealed (725°C, 40 min,  $7 \times 10^{-7}$  Torr) sample of Ti-W on Si. The Si substrate is  $\langle 111 \rangle$  single crystal n-type with resistivity of 10 ohm-cm. The Ti-W film was deposited with  $-50\text{V}$  bias. Arrows indicated the position of signals from Si, Ti, and W on the sample surface.

Films deposited on  $\langle 111 \rangle$  silicon at  $-50\text{V}$  bias and annealed at  $5 \times 10^{-6}$  Torr and 725°C were found to have reaction rates of about 9.7 Å/min. Improving the vacuum to  $7 \times 10^{-7}$  Torr and covering the metallized side of the sample with a clean Si wafer during anneal increased the reaction rate by approximately a factor of 2 (Fig. 5). Figure 3 shows a  $\langle 111 \rangle$  silicon sample of which half of the metallized side was covered with a Si wafer during an anneal at  $7 \times 10^{-7}$  Torr and 725°C for 45 min. The uncovered side (top) shows little reaction whereas the covered side (bottom) is almost completely reacted. A subsequent AES analysis of this sample (Fig. 4) reveals that the uncovered half of the sample has a larger concentration of oxygen than does the covered half.

In Fig. 2 the ratio of the signal height of the remaining unreacted tungsten to that of the unreacted silicon substrate is smaller than that same ratio measured on the virgin sample. This was true for partially reacted samples which had been covered and annealed in the highest vacuum attainable. If this difference is attributed to oxygen contamination, then the samples annealed in the cleanest vacuum still contained up to 15 a/o oxygen. Since oxygen has been shown to influence rates, the kinetics studies performed here are to be interpreted with caution and the results should be regarded as preliminary.

Reaction rate studies at 750°, 725°, and 700°C were performed on covered samples annealed at  $7 \times 10^{-7}$  Torr. Samples annealed at each temperature were all cut from the same wafer and loaded simultaneously. The samples were then annealed sequentially. When precautions to reproduce the vacuum were taken, the results were reproducible. The analysis of the backscattering yields established that after anneal all the samples were contaminated 15-20%, presumably by

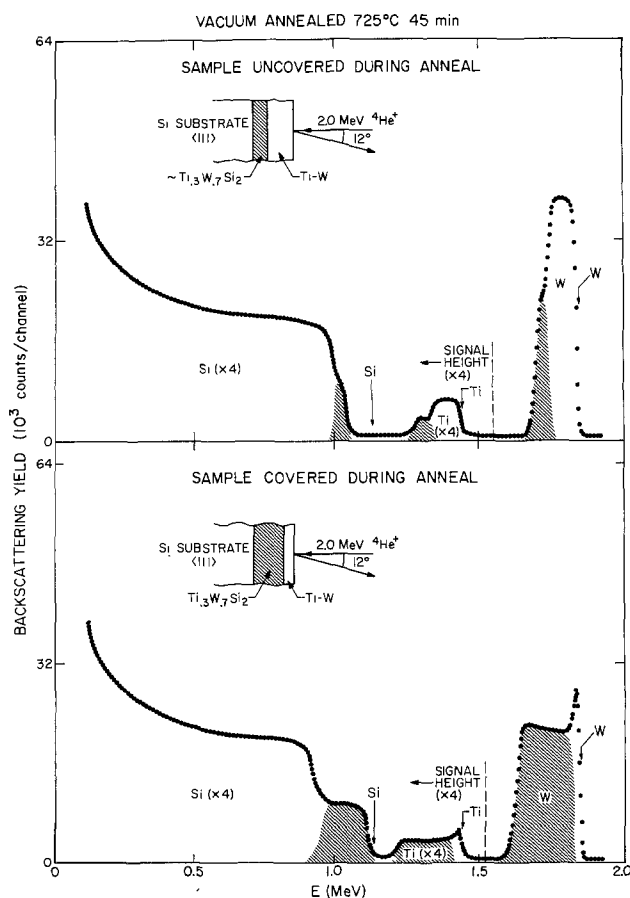


Fig. 3. Backscattering spectra of a partially covered sample annealed at 725°C for 45 min. Top shows portion of sample which was uncovered during anneal and bottom shows covered part. Arrows indicate the position of signals from Si, Ti, and W on the sample surface.

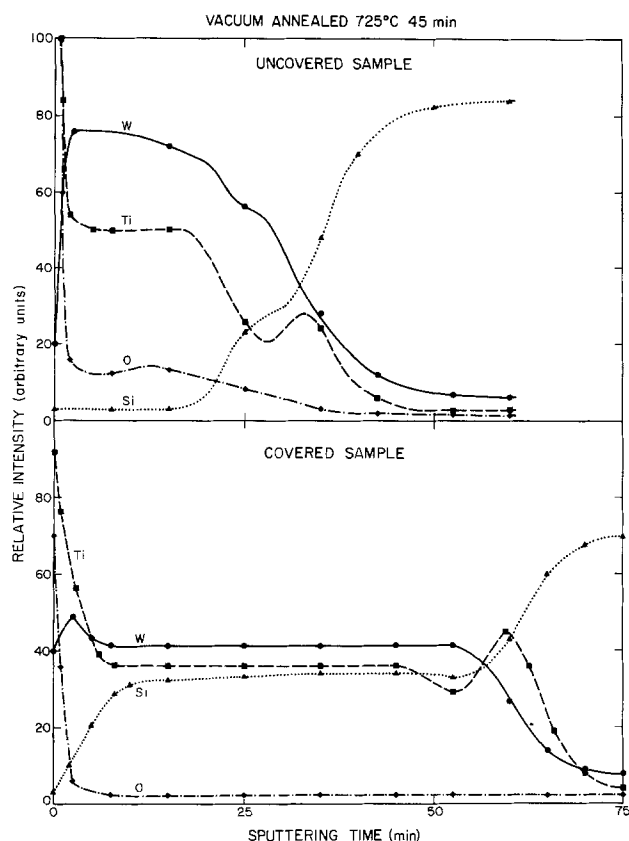


Fig. 4. AES depth profile of W, Ti, Si, and O in the uncovered (top) and covered (bottom) parts of the sample in Fig. 3.

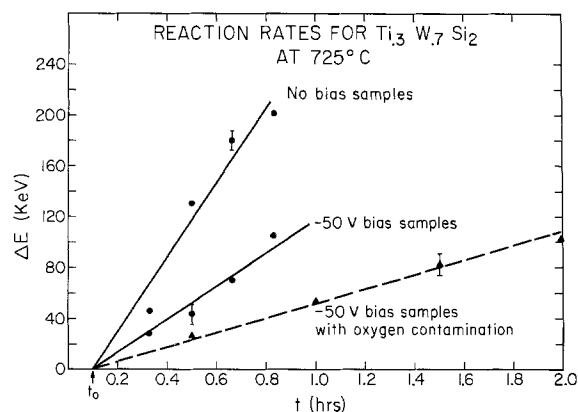


Fig. 5. A plot of compound thickness (expressed in terms of backscattering energy loss) vs. anneal time. The warm-up time for a sample placed in the vacuum furnace is denoted by  $t_0$ . Lines marked "No bias samples" and "-50 V bias samples" were annealed covered at a vacuum of  $7 \times 10^{-7}$  Torr. Line marked "-50V bias samples with oxygen contamination" refers to samples annealed uncovered at a vacuum of  $5 \times 10^{-6}$  Torr. (10 keV corresponds to about  $106\text{\AA}$  of compound).

oxygen. The reaction has a linear time dependence at all temperatures and over the entire range of oxygen contamination. An apparent activation energy of 4.5 eV is determined from the reaction rate vs. temperature (Fig. 6).

The rate of reaction is influenced by several parameters. This fact was established by comparing two samples which differed only in the parameter of interest. These sample pairs were sandwiched together with the metallized sides face to face and annealed in a vacuum similar to that used in the rate vs. temperature studies. This procedure also gave reproducible results. From such comparison, it was established that the reaction rate is influenced by the bias applied during sputter deposition (Fig. 5). Samples deposited on

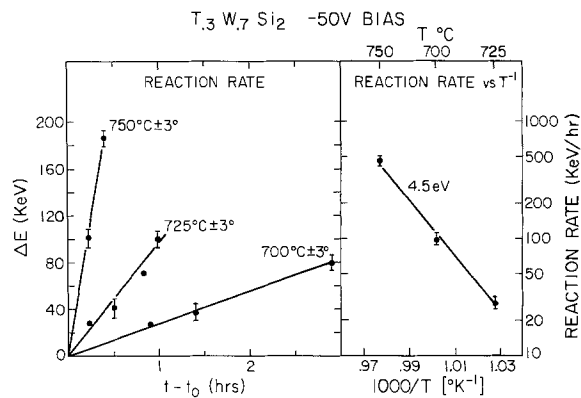


Fig. 6. (Left) plot of compound thickness (expressed in terms of backscattering energy loss for 2.0 MeV  $^4\text{He}^+$  ions, 10 keV corresponds to about  $106\text{\AA}$  of compound) vs. anneal time,  $t$ , minus warm-up time  $t_0$ . (Right) plot of log of reaction rate vs. reciprocal anneal temperature (yields activation energy of 4.5 eV).

$\langle 111 \rangle$  silicon substrates react slower than those deposited on  $\langle 110 \rangle$ , and samples prepared on  $\langle 100 \rangle$  react the fastest. On the other hand, the dopant type of the Si substrate had no measurable effect on the reaction rate, nor did changes of the doping level from 2 to 10 ohm-cm.

### Discussion and Conclusion

Transition metal silicides typically form complete solid solutions when the two constituting binary silicides are isomorphous. A partial solid solution or ternary compound forms when the two binary silicides are nonisomorphous (10).  $\text{TiSi}_2$  has an orthorhombic (C-54) structure with a packing sequence ABCD, but  $\text{WSi}_2$  has a tetragonal (C-11b) structure with a packing sequence ABAB. Hence one expects that a ternary compound will form with Ti, W, and Si. Formation of ternary compounds has also been reported in both the Ti-Mo-Si system and the Ti-Re-Si system (10).

The Ti-W-Si system has been studied by Nowotny (11). He reports a ternary disilicide of composition  $\text{Ti}_2\text{W}_{1-x}\text{Si}_2$  for  $x > 0.6$  but a mixture of  $\text{TiSi}_2$  and  $\text{WSi}_2$  for  $x < 0.6$ . In the present case,  $x = 0.3$ ; compound formation is observed nevertheless. This discrepancy between Nowotny and the present work could possibly be due to the fact that Nowotny investigated bulk samples prepared by high pressure sintering at  $1300^\circ\text{C}$  while we consider thin-film samples prepared near  $750^\circ\text{C}$ .

We attribute the surface distortion after compound formation to the volume expansion the film experiences as a result of Si inclusion. This expansion is substantial since the film undergoes only a small atomic density change (approximately  $6.14 \times 10^{22}$  atom/cm<sup>2</sup> for the initial Ti-W layer, as calculated from the weighted sum of the elemental densities; approximately  $7.54 \times 10^{22}$  atom/cm<sup>3</sup> for  $\text{Ti}_{0.3}\text{W}_{0.7}\text{Si}_2$  calculated for the compound from the x-ray data).

A reduction of reaction rates by oxygen contamination has been observed by Kräutle (12) in the formation of  $\text{VSi}_2$  by thin films of V on Si. It is remarkable that the rate of reaction is closely linear in spite of considerable oxygen contamination (Fig. 5). The observations that the rate remains linear at reduced oxygen contamination and that the substrate crystal orientation also influences the rate, is consistent with a reaction-limited mechanism. This hypothesis is further supported by the fact that Borders (4) reports linear rates for the  $\text{WSi}_2$  formation. No published data exist for reaction rates of Ti films on Si substrates.

The observed activation energy of 4.5 eV is high. Sinha (13) also reported a high activation energy of 4.4 eV for  $\text{WSi}_2$  growing at the expense of PtSi. On the other hand, the activation energies quoted for the formation of  $\text{WSi}_2$  films on Si range from 2 to 3 eV (4). Our value of 4.5 eV may thus be the result of

Ti<sub>0.3</sub>W<sub>0.7</sub>Si<sub>2</sub> growing at the expense of an oxide of titanium and/or tungsten. An argument against this hypothesis is the fact that no oxides of Ti or W were detected in the x-ray photographs. The x-ray analysis, however, is not very sensitive to small oxide concentrations over narrow regions such as the reaction interface. At present, the high value of the activation energy is not understood.

The influence of deposition bias on the reaction rate may also be a contamination effect. The samples with -50V deposition bias had both lower reaction rates and higher argon contamination levels than the sample deposited at zero bias. However, certain parameters of the films such as stress or crystal grain size which could influence the reaction rate, were not well characterized. Differences in these parameters could also contribute to variations in reaction rates between samples prepared at different biases.

Since we were unable to perform anneals without introducing detectable amounts of contamination, the kinetics data presented here are to be considered preliminary. It would also be worthwhile to extend this study to Ti-W films with various initial compositions, or to other disilicide-forming bimetal combinations. The results would be of value to the subject of ternary silicides in general, and to their possible application in silicon device technology in particular.

#### Acknowledgments

We wish to thank Paul Turner for allowing the use of his sputtering system. We also thank Dr. C. A. Evans, Jr., University of Illinois, Urbana, for his Auger analysis, and Dr. Sten Samson for the use of his Guinier camera and for his help in the x-ray analysis. We express our appreciation to the Kellogg Radiation Laboratory for the use of their 3 MeV accelerator and to Dr. C. A. Barnes for his continuous assistance.

This work was supported in part by the National Aeronautics and Space Administration (J. Maserjian and J. Boreham, Jet Propulsion Laboratory) and by

the Air Force Cambridge Research Laboratories (D. E. Davies).

Manuscript submitted June 11, 1975; revised manuscript received Aug. 13, 1975. This was Paper 108 presented at the Toronto, Canada, Meeting of the Society, May 11-16, 1975.

Any discussion of this paper will appear in a Discussion Section to be published in the December 1976 JOURNAL. All discussions for the December 1976 Discussion Section should be submitted by Aug. 1, 1976.

Publication costs of this article were partially assisted by the California Institute of Technology.

#### REFERENCES

1. J. L. Vossen, *J. Vacuum Sci. Technol.*, **11**, 60 (1974).
2. J. A. Cunningham, *IEEE Trans. on Reliability*, **R19**, 182 (1970).
3. L. D. Locker and C. D. Capio, *J. Appl. Phys.*, **44**, 4366 (1973); A. K. Sinha, M. H. Reed, and T. E. Smith, *This Journal*, **120**, 1775 (1973).
4. J. A. Borders and J. N. Sweet, in "Proceedings of the International Conference on Applications of Ion Beams to Metals," S. T. Picraux, E. P. Eer-Nisse, and F. L. Vook, Editors, p. 179, Plenum Press, New York (1974).
5. H. Kräutle, M.-A. Nicolet, and J. W. Mayer, *ibid.*, p. 193. See also, *Phys. Status Solidi*, (a)**10**, k33 (1973).
6. W. K. Chu, J. W. Mayer, M.-A. Nicolet, T. M. Buck, G. Amsel, and F. Eisen, *Thin Solid Films*, **17**, 1 (1973).
7. S. S. Lau, W. K. Chu, J. W. Mayer, and K. N. Tu, *ibid.*, **23**, 205 (1974).
8. A. Guinier, "X-ray Crystallographic Technology," Hilgar and Watts, Limited, London (1952).
9. C. C. Chang, in "Characterization of Solid Surfaces," Kane and Larrabee, Editors, p. 509, Plenum Press, New York (1974).
10. H. J. Goldschmidt, "Interstitial Alloys," p. 323, Plenum Press, New York (1967).
11. H. Nowotny, R. Kieffer, and H. Schachner, *M. L. Chem.*, **83**, 1243 (1952).
12. H. Kräutle, M.-A. Nicolet, and J. W. Mayer, *J. Appl. Phys.*, **45**, 3304 (1974).
13. A. K. Sinha and T. E. Smith, *ibid.*, **44**, 3465 (1973).

## Isochronal Annealing of Silicon-Phosphorus Solid Solutions

P. Ostojca, D. Nobili, A. Armigliato, and R. Angelucci

C.N.R. Laboratorio Lamel, 40126 Bologna, Italy

#### ABSTRACT

Isochronal annealings of 500 hr per pulse, in steps of 25°C, have been performed in the range 400°-800°C on silicon single crystals of well-known composition bulk-doped with phosphorus. Dopant concentrations were 1.7, 3.3, 3.7 5, 5.8, and  $7.5 \times 10^{19}$  at/cm<sup>3</sup>. The annealing curves, determined by electrical resistivity measurements, are reported and discussed. A resistivity increase, attributed to phosphide precipitation, takes place above 400°C in the dopant richest alloy. It is noticed that a high density of dislocations (about  $10^8$  cm<sup>-2</sup>) does not alter the kinetics of this process. At 550°C coherent precipitates of interstitial character have been observed by TEM; their density and mean size are consistent with a SiP composition. The features of the defects associated with the dissolution process are also reported. Phosphorus diffusivity for precipitation, calculated at 550°C, turns out to be about five orders of magnitude higher than expected from extrapolation of well-known high temperature values. The solubility of phosphorus in silicon, determined by the kinetics of recovery of resistivity, results as about  $7 \times 10^{19}$  at/cm<sup>3</sup> at 650°C.

Phase equilibria and the related kinetics in the binary systems of silicon and its substitutional dopants are important for basic knowledge. Further, this information presents a relevant interest for the technology and failure physics of silicon devices. Our laboratory is involved in a research program concerning

**Key words:** silicon, phosphorus-doped, annealing, precipitation, solubility.

the Si-B and the Si-P systems (1, 2). The present study deals with the precipitation of phosphorus by isochronal annealing of bulk-doped silicon single crystals. The formation of phosphide precipitates in silicon has been observed by several authors, mainly by TEM examinations (3-10). This technique has also been used, together with x-ray topography, in our laboratory (11, 12). All the above studies were carried out

on specimens doped by diffusion which, therefore, presented concentration gradients. As a consequence, the kinetics of the process have never been analyzed.

Isochronal kinetics constitute an obvious step in determining the temperature above which precipitation takes place at a measurable rate. They can give information on the diffusivity, as well as on the influence of lattice defects on the nucleation of the new phase. The purpose of our work was also the determination of reliable values of phosphorus solubility at low temperature. The status of knowledge in the whole range below the eutectic temperature is lacking: values at 900°C and above are widely scattered (a single research has reported data below this temperature) and no data are available below 700°C (13).

The annealing and quenching method is widely used in phase diagram determinations; its precision can be improved by increasing the annealing time and comparing precipitation and dissolution results. The experimental procedures of this method unambiguously satisfy the condition that both the primary solid solution and its conjugate phase must be competing for equilibrium. It is open to question if this basic thermodynamic condition has been fulfilled in solubility determinations based on measurements of surface concentration of the dopant after predeposition in an oxidizing atmosphere (14).

In the silicon-phosphorus system below the eutectic temperature, the conjugate phase is Si-P, base-centered orthorhombic (14, 15). This structure has recently been confirmed on small phosphide precipitates by electron diffraction studies carried out in our laboratory (12).

### Experimental

Our experiments were carried out on (111)-oriented, bulk-doped silicon single crystals. Six compositions were studied. The corresponding phosphorus concentrations are reported in Table I. Slices were nominally dislocation free, with an actual density  $< 10^8 \text{ cm}^{-2}$ . These alloys have been the subject of previous investigations concerning the dependence on phosphorus concentration of electrical resistivity and mobility (16, 17), as well as of lattice parameter (18). The concentration of dopant has been determined by neutron activation analysis; by this technique and gamma-scintillation spectrometry we also performed the analysis of about forty metallic impurities. The results of these analyses are reported in a previous paper (16). Oxygen, as well as carbon and nitrogen content, was determined by ion activation analysis. The content of carbon was about  $4 \times 10^{17}$  and that of nitrogen about  $1.5 \times 10^{17}$  at/cm<sup>3</sup>. Oxygen concentration was found to range between  $6 \times 10^{15}$  and  $3.7 \times 10^{17}$  at/cm<sup>3</sup>; the figures for each composition are reported in Table I. Precise lattice parameter determinations were carried out along the diameter of some representative wafers. Lattice parameter oscillations, although increasing with dopant concentration, turned out to be small, and a homogeneity of 10<sup>-3</sup>% was ensured near the wafer center from where we obtained our samples. The techniques of chemical analysis and of structural examinations have been described in detail in the above-mentioned papers (16, 18).

Isochronal annealings were performed in the temperature range 400°-800°C in steps of 25°C. by using a vacuum furnace (10<sup>-6</sup> Torr) for shorter times (21 hr

per pulse), and quartz tubes sealed under the same vacuum for longer treatments (500 hr per pulse). The temperature stability was kept better than  $\pm 0.5^\circ\text{C}$  even for the longer times by using a CAT control system. The heating and cooling times of our specimens were of the order of some minutes. To follow the annealing behavior, we performed room temperature electrical resistivity measurements after each heating pulse. Our previous work (16) allowed us to obtain a reliable relationship between resistivity and the concentration of electrically active phosphorus in the heavy doping range. Repeatability of our resistivity determinations turned out to be  $\pm 0.5\%$ ; this was confirmed by measuring in each run unannealed reference dummy samples of composition similar to that of the specimens. Moreover, the experiments were carried out on several samples, at least ten, of each composition. Half of the most heavily doped specimens were deformed by a four-point bending technique (19) in order to observe the influence of the high density of dislocations introduced (about  $10^8 \text{ cm}^{-2}$ ). At the end of selected annealing steps, samples were thinned with the jet-etching technique and observed by TEM in order to follow the structural modifications induced by the annealing process. Our instrument was a Siemens Elmiskop 101 equipped with a  $\pm 45^\circ$  double tilting cartridge.

### Results

*Electrical measurements.*—The resistivity curves after isochronal annealing of 500 hr per pulse of the samples with phosphorus concentrations 1.7, 3.3, 3.7, 5, and  $5.8 \times 10^{19}$  at/cm<sup>3</sup> are reported in Fig. 1. The resistivity values of the unannealed reference dummy sample, also reported in this plot, refer to electrical measurements performed in the same run as the corresponding annealed specimens. The most diluted compositions clearly exhibit a negative resistivity variation in the temperature range 450°-575°C, with two minima centered at 500° and 550°C, respectively. The

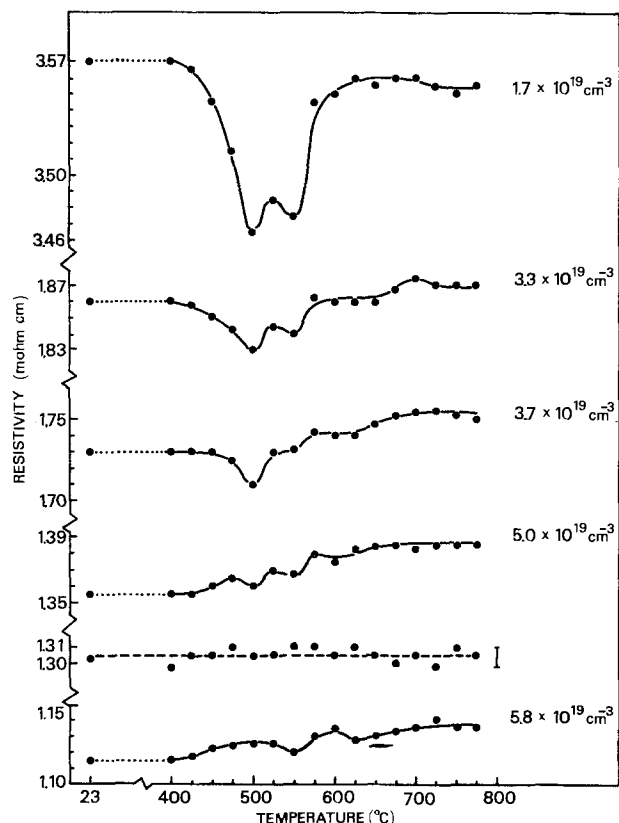


Fig. 1. Electrical resistivity vs. temperature for 500 hr per pulse annealing of Si samples bulk-doped with increasing P concentrations (solid lines). The behavior of the unannealed reference dummy sample is also reported (broken line).

Table I.

Samples	Resistivity (ohm · cm)	Phosphorus conc (at/cm <sup>3</sup> )	Oxygen conc (at/cm <sup>3</sup> )
W/na	$3.5 \times 10^{-3}$	$1.7 \times 10^{19}$	$6.1 \times 10^{15}$
A/na	$1.9 \times 10^{-3}$	$3.3 \times 10^{19}$	$7.9 \times 10^{15}$
M/n4	$1.7 \times 10^{-3}$	$3.7 \times 10^{19}$	$3.7 \times 10^{17}$
M/n3	$1.3 \times 10^{-3}$	$5.0 \times 10^{19}$	$3.7 \times 10^{17}$
M/n2	$1.1 \times 10^{-3}$	$5.8 \times 10^{19}$	$3.7 \times 10^{17}$
M/n1	$8.5 \times 10^{-4}$	$8.5 \times 10^{19}$	$3.7 \times 10^{17}$



amplitude of this effect decreases with increasing phosphorus, and the minimum at 500°C is not observed in the alloys with dopant concentration exceeding  $5 \times 10^{19}$  at/cm<sup>3</sup>. A third slight inflection, centered at about 625°C, is also noticed and is significant considering the reproducibility that we observed between the specimens with the same composition as well as the behavior of the different alloys.

The isochronal annealing kinetics for the P-richest composition ( $7.5 \times 10^{19}$  at/cm<sup>3</sup>) are reported in Fig. 2. A resistivity increase can be clearly seen above 400°C. The amplitude of this effect is higher as the annealing time is longer, and is of about 11% in curve (a), which corresponds to 500 hr of annealing per pulse. Two small resistivity minima, superimposed on the main peak, are in any case noticed. In curve (a) they are centered at 550° and 625°C, that is, corresponding to the minima observed in Fig. 1. In curve (b), which corresponds to 21 hr annealing per pulse, they are shifted to about 575° and 675°C, respectively. After high temperature annealing the resistivity recovers approximately its original value. At the end of the heat-treatment of 21 hr per pulse [curve (b)], the samples were isochronally annealed for the same time per pulse, at decreasing temperatures. A resistivity increase has been obtained also in this case, thus indicating that the phenomenon is reversible. As will be discussed later, the resistivity peak in Fig. 2 is attributed to a decrease of the concentration of the charge carriers due to precipitation of phosphorus in a supersaturated solid solution. Finally, it is worthwhile to remark that the behavior of the deformed specimens, which contain a high density of dislocations, is indistinguishable from that of the undeformed ones.

**TEM examinations.**—Due to the destructive character of electron microscopy, a limited number of situations have been studied by TEM in bright and dark field two-beam conditions, as well as by using the weak beam dark field technique (20). Our observations on the most heavily doped specimens, isochronally heated 500 hr per pulse, were carried out after annealing up to 500°, 550°, and 775°C, respectively. Prior to annealing the specimens did not exhibit the presence of any crystallographic defect.

(i) *Specimens annealed up to 500°C.*—Images taken in different areas of these specimens did not reveal any defect, either in bright or dark field two-beam conditions. Images taken with the weak beam dark field technique clearly displayed, as shown in Fig. 3, a large density of small defects, typically about 50Å in diameter. It was, in any case, difficult to decide from con-

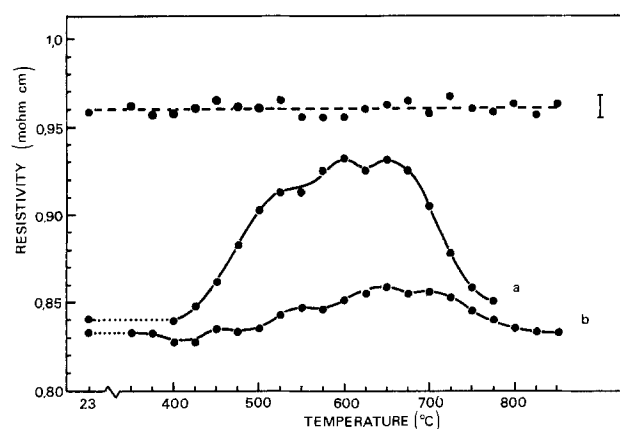


Fig. 2. Electrical resistivity vs. temperature for 500 hr per pulse, curve (a), and 21 hr per pulse, curve (b), annealing of Si samples bulk-doped with P ( $7.5 \times 10^{19}$  at/cm<sup>3</sup>). The same curves hold also for specimens containing a high density ( $\sim 10^8$  cm<sup>-2</sup>) of dislocations. The broken line refers to the unannealed reference dummy sample.

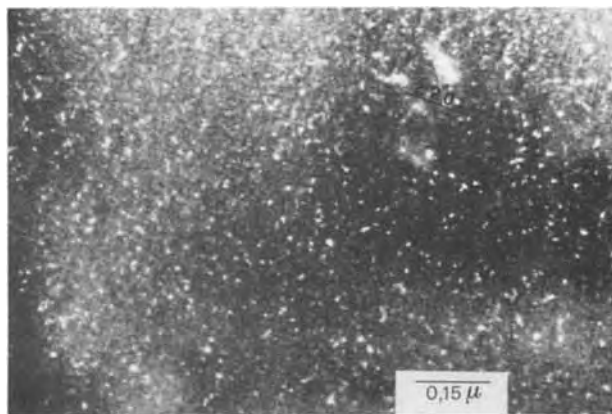


Fig. 3. Small defects in one of the most heavily doped samples annealed up to 500°C. Weak beam ( $-g, g$ ) image.

trast experiments whether such defects were precipitates or dislocation loops.

(ii) *Specimens annealed up to 550°C.*—As reported in previous papers (1, 2), the observations carried out on these samples revealed the presence of a high density (about  $6 \times 10^{13}$  cm<sup>-3</sup>) of coherent precipitates which, from dark field images, were found to be interstitial in character, with strain parameter  $\epsilon = 2.5 \times 10^{-2}$ . A typical bright field image of these particles is shown in Fig. 4. From the Ashby and Brown theory it was possible to compute their average radius which came out at about 130Å. These figures, compared with the amount of electrically inactive phosphorus deduced from resistivity data, are consistent with the hypothesis that the particles are SiP precipitates. Weak beam images taken in the same areas revealed again, as shown in Fig. 5, the presence of the small defects already observed in the samples annealed up to 500°C.

(iii) *Specimens annealed up to 775°C.*—Images taken both from deformed and undeformed specimens exhibited a large amount of dislocation loops. A typical micrograph is reported in Fig. 6, which also evidences one of the dislocations introduced by bending the unannealed specimen. The loops displayed in this picture are of interstitial type, and the same holds for the loops in Fig. 7. Loops like the ones marked B and D in Fig. 6 and M in Fig. 7 are perfect loops with Burgers vectors of the type  $a/2 \langle 110 \rangle$ . Those marked A and C in Fig. 6 and L in Fig. 7 are stacking fault loops with Burgers vectors of the type  $a/3 \langle 111 \rangle$ . This latter statement becomes apparent if one looks at the weak beam micrograph of Fig. 8, taken in the ( $-g, g$ ) orientation. The fringes observed in this figure are spaced by 36Å, which is in very good agreement with the

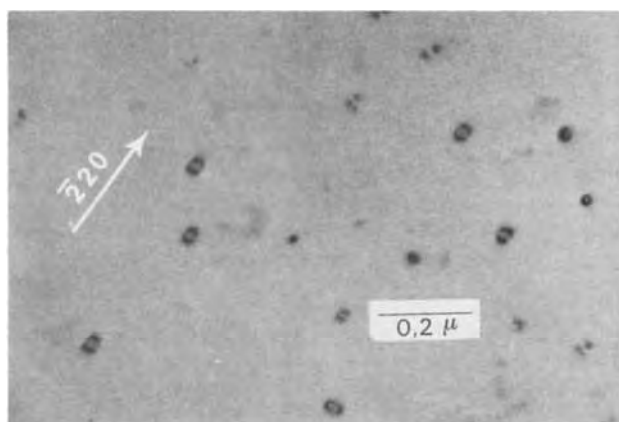


Fig. 4. Coherent precipitates in one of the most heavily doped samples annealed up to 550°C. Bright field image.



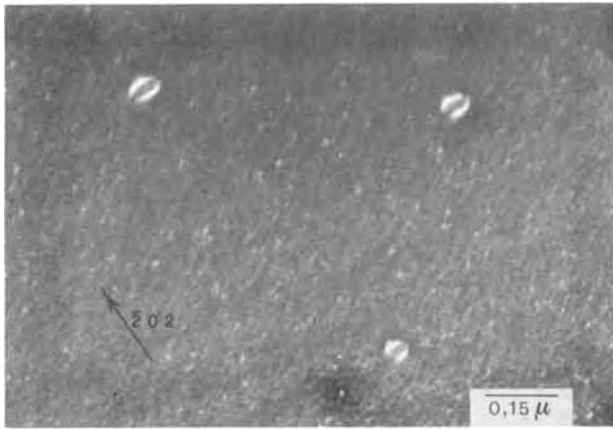


Fig. 5. Coherent precipitates and small defects in the same sample as Fig. 4. Weak beam ( $-g, g$ ) image.

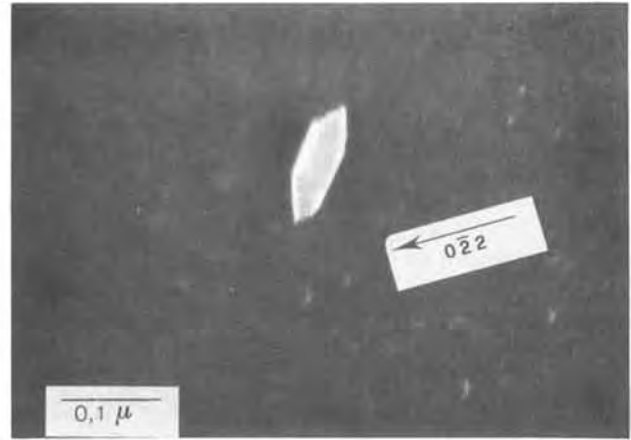


Fig. 8. Weak beam ( $-g, g$ ) image of the stacking fault loop (L) of Fig. 7, showing the  $36\text{\AA}$  spaced fringes given by the  $0\bar{2}2$  reflection.

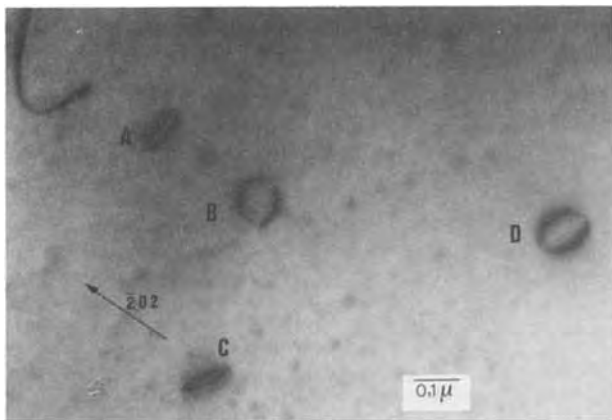


Fig. 6. Perfect dislocation loops (B and D) and stacking fault loops (A and C) in one of the most heavily doped samples annealed up to  $775^\circ\text{C}$ . One of the dislocations introduced by bending is also visible. Bright field image.

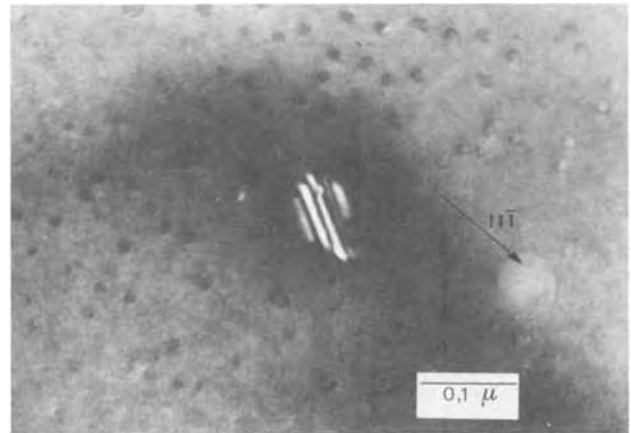


Fig. 9. Weak beam ( $-g, g$ ) image of the stacking fault loop (L) showing the  $144\text{\AA}$  spaced fringes, given by the  $1\bar{1}\bar{1}$  reflection.

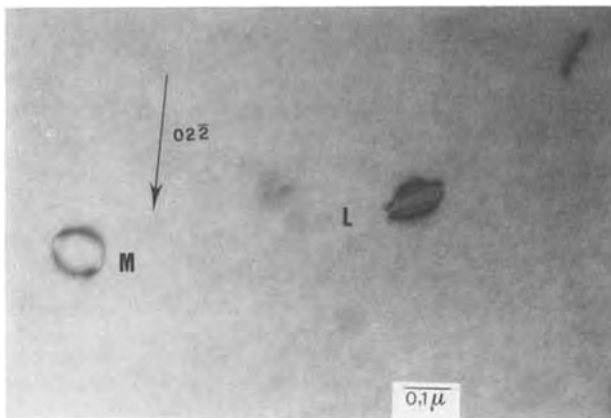


Fig. 7. Perfect dislocation loop (M) and stacking fault loop (L) in the same sample as Fig. 6. Bright field image.

theoretical fringe spacing  $d$  obtained from the formula  $d = \frac{1}{S'} \cot \alpha$ , where  $S'$  is the deviation of the  $0\bar{2}2$  reciprocal lattice point from the sphere of reflection, and is given by  $1/S' = 1/\lambda g^2$ .  $\lambda$  is the electron wavelength that, in our case, corresponds to  $369 \times 10^{-4}\text{\AA}$ , and  $\alpha$  is the angle between the surface of the specimen and the  $(1\bar{1}\bar{1})$ -inclined plane of the fault ( $\alpha = 70.5^\circ$ ) (21). A further check is given by the calculation of the spacing of the fringes observed in Fig. 9, taken with  $g =$

$1\bar{1}\bar{1}$ , still in weak beam orientation. One gets  $d = 144\text{\AA}$ , in good agreement with the theoretical value of  $142\text{\AA}$ . A certain number of vacancy loops were also observed, like the ones labeled A and C in Fig. 10, found near the loop G which is of interstitial type. Finally, we notice that the small defects like those shown in Fig. 3 are rare at this stage of annealing; nevertheless they are actually present, although with lower concentration.

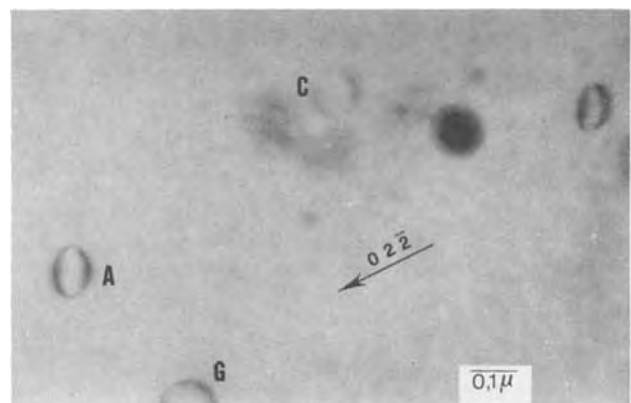


Fig. 10. Vacancy dislocation loops (A and C) together with an interstitial one (G) in the same sample as Fig. 6-9. Bright field image.

### Discussion and Conclusion

We consider, first, the resistivity peaks in Fig. 1. The influence of the concentration of phosphorus in the range from  $1.7$  to  $3.8 \times 10^{19}$  at/cm<sup>3</sup>, as well as that of the content of carbon and oxygen, has been studied in a previous work based on isochronal annealing of 21 hr per pulse. It was observed that the amplitude of the peaks does not depend on the concentration of carbon and oxygen (22). Further, these previous results are in agreement with the observation that the amplitude of the main negative peaks, centered at 500° and 550°C, respectively, in Fig. 1, decreases with the increasing phosphorus concentration. Moreover, it can be seen that by increasing the annealing time per pulse the amplitude of the peaks increases, and they result in being more clearly resolved and slightly shifted toward lower temperatures.

These observations suggest that the resistivity peaks in Fig. 1 are probably due to rearrangements of point defects, giving rise to complexes which are dissolved again with increasing temperature, as can be seen from the resistivity recovery at the end of each peak. In fact, if one computes from our experimental data the contribution to the conductivity due to the donors involved in such complexes, one gets a value which remains nearly constant, at least within the experimental errors, throughout the range of concentrations of phosphorus. This consideration allows us to conclude that these donor complexes should not depend on the P content, although the relative amplitude of the dips in Fig. 1 is lower as the resistivity decrement due to the increasing P concentration is higher. Further information on the nature of these phenomena should be obtained by comparing the annealing behavior of n- and p-doped crystals. We shall report in a further work the results of a research in progress on silicon doped with boron.

The resistivity peak in Fig. 2 can be attributed to phosphide precipitation followed by redissolution at high temperature. In fact it is observed only in the most heavily doped alloy; the compositions with a comparable amount of impurities, but less rich in phosphorus, do not show this phenomenon. These conclusions are in agreement with the formation of coherent precipitates of the type shown in Fig. 4. The mean size and density of these precipitates are in keeping with a SiP composition. In addition they are dissolved after annealing up to 775°C, when the resistivity has recovered its original value.

It is unlikely that the small defects shown in Fig. 3 are phosphide precipitates; if so, they should be unstable with respect to the larger ones. On the contrary, a considerable fraction of these defects is still present after annealing up to 775°C. The dislocation and stacking fault loops previously analyzed show the formation of excess point defects, mainly interstitials. They are associated with the dissolution of phosphide precipitates; in fact, these defects are absent in less-doped alloys annealed in the same way. The formation of dislocation loops takes place also in specimens undergoing isothermal precipitation of phosphorus, as evidenced by TEM observations which are at present in progress. The amount of inactive phosphorus resulting from the 500 hr per pulse annealing [Fig. 2, curve (a)] and the onset of the redissolution process at 650°C allows determination of the solid solubility of phosphorus in silicon at this temperature, which is about  $7 \times 10^{19}$  at/cm<sup>3</sup>. This figure should be practically unaffected by the interface effects, which can greatly increase the solubility of very fine particles. In fact, the 500 hr per pulse annealing gives rise, as shown in Fig. 4, to a high density of precipitates with radius larger than 100Å. The above solubility is in good agreement with the value of  $7 \times 10^{19}$  at/cm<sup>3</sup> at 700°C reported by Abrikosov *et al.* (23).

All experiments on the heavily doped alloy have shown that the kinetics of precipitation and redissolution are unaffected by the presence of dislocations. This result is interesting also in the aging of electronic devices. A reasonable hypothesis is that the available point defects provide more suitable centers competing for the formation of critical nuclei.

To account for these precipitation phenomena, the diffusivity of phosphorus has to be much higher than that expected. In fact, the diffusion length  $\sqrt{Dt}$  calculated at 550°C using diffusivity values determined in our laboratory (24) or well-known data found in literature (13, 25) and taking  $t = 1000$  hr turns out to be only a few angstroms. A calculation, albeit crude, of the diffusivity involved in our experiments can be performed using the model of Ham (26), considering the spherical symmetry and the radius ( $\sim 130$ Å) of our coherent precipitates, admitting that the composition is SiP, and assuming, from extrapolation of our experimental data on the isochronal curve (a) in Fig. 2, a solubility of  $6 \times 10^{19}$  at/cm<sup>3</sup> at 550°C. This calculation gives  $D \simeq 5 \times 10^{-17}$  cm<sup>2</sup>sec<sup>-1</sup>, that is, five orders of magnitude higher than the diffusivity value at 550°C calculated by extrapolation of our high temperature data, as well as of the above-cited data found in literature.

Actually, preliminary results of the data analysis on the isochronal curve, combined with those of isothermal annealing in progress, suggest that the activation energy for diffusion is substantially reduced. The discrepancy could be explained either by a completely different diffusion mechanism, active at low temperature, or by an excess of point defects associated with the precipitation process. Further research is in progress on isothermal annealing followed by TEM observations and lattice parameter determinations with the aim of contributing to the clarification of the precipitation process.

### Acknowledgments

Thanks are due to Dr. J. W. Steeds of the H. H. Wills Physics Laboratory, Bristol University, and Drs. P. G. Merli and M. Servidori for useful suggestions and discussion on the electron microscopy results. The skillful technical assistance of Mr. L. Dori and Mr. G. Ruffini is also acknowledged.

Manuscript submitted July 23, 1975; revised manuscript received Sept. 12, 1975. This was Paper 222 presented at the New York, New York, Meeting of the Society, Oct. 13-17, 1974.

Any discussion of this paper will appear in a Discussion Section to be published in the December 1976 JOURNAL. All discussions for the December 1976 Discussion Section should be submitted by Aug. 1, 1976.

Publication costs of this article were partially assisted by C.N.R.-Lamel.

### REFERENCES

1. R. Angelucci, A. Armigliato, D. Nobili, and P. Ostojica, Abstract 222, p. 548, The Electrochemical Society Extended Abstracts, Fall Meeting, New York, New York, Oct. 13-17, 1974.
2. A. Armigliato, D. Nobili, and P. Ostojica, Proceedings of the 8th International Congress on Electron Microscopy, Vol. I, p. 668, Canberra, 1974.
3. R. Stickler and P. F. Schmidt, *This Journal*, **111**, 1188 (1964).
4. M. L. Joshi, *ibid.*, **112**, 912 (1965).
5. T. W. O'Keefe, P. F. Schmidt, and R. Stickler, *ibid.*, **112**, 878 (1965).
6. M. L. Joshi, *ibid.*, **113**, 45 (1966).
7. C. G. Beck and R. Stickler, *J. Appl. Phys.*, **37**, 4683 (1966).
8. M. L. Joshi and S. Dash, *IBM J. Res. Dev.*, **11**, 271 (1967).
9. E. Levine, J. Washburn, and G. Thomas, *J. Appl. Phys.*, **38**, 87 (1967).
10. R. J. Jaccodine, *ibid.*, **39**, 3105 (1968).
11. C. Ghezzi and M. Servidori, *J. Mater. Sci.*, **9**, 1797 (1974).

12. M. Servidori and A. Armigliato, *ibid.*, **10**, 306 (1975).
13. V. M. Glazov and V. S. Zemskov, "Physico-Chemical Principles of Semiconductor Doping," p. 141, JPST Press, Jerusalem (1968).
14. R. P. Elliott, "Constitution of Binary Alloys," p. 716, McGraw-Hill Book Co., New York (1965).
15. T. Wadsten, *Univ. Stockholm Chem. Communic.*, **7**, 1 (1973).
16. F. Mousty, P. Ostoja, and L. Passari, *J. Appl. Phys.*, **45**, 4576 (1974).
17. G. Baccarani and P. Ostoja, *Solid-State Electron.*, **18**, 579 (1975).
18. G. Celotti, D. Nobili, and P. Ostoja, *J. Mater. Sci.*, **9**, 821 (1974).
19. E. Susi, L. Dori, and M. Servidori, *Met. Ital.*, **65**, 147 (1973).
20. D. J. H. Cockayne, I. L. F. Ray, and M. J. Whelan, *Phil. Mag.*, **20**, 1265 (1969).
21. R. Bicknell, *J. Microsc.*, **98**, 165 (1973).
22. P. Ostoja, D. Nobili, and A. Armigliato, *Met. Ital.*, **65**, 65 (1973).
23. N. Kh. Abrikosov, V. M. Glazov, and C.-Y. Liu, *Russ. J. Inorg. Chem.*, **7**, 429 (1962).
24. G. Masetti, S. Solmi, and G. Soncini, *Solid-State Electron.*, **16**, 1419 (1973).
25. D. L. Kendall and D. B. De Vries, in "Semiconductor Silicon," B. R. Haberecht and E. L. Kern, Editors, p. 358, The Electrochemical Society Softbound Symposium Series, New York (1969).
26. F. S. Ham, *J. Phys. Chem. Solids*, **6**, 335 (1958).

## Solid-State Ionics—High-Conductivity Solid Copper Ion Conductors

### Organic Ammonium Halide-Copper (I) Halide Double Salts

Takehiko Takahashi,\* Noboru Wakabayashi, and Osamu Yamamoto

*Department of Applied Chemistry, Faculty of Engineering, Nagoya University, Nagoya 464, Japan*

#### ABSTRACT

The copper ion conductivities of the system organic substituted ammonium halide-copper(I) halide have been measured in the solid state, and the relation between the formation of high conductivity compounds and the conformation of organic substituted ammonium halides was examined. No high copper ion conductivity was found in the system unsaturated azacyclic substituted ammonium halide-copper(I) halide, while high copper ion conductivity was found in the saturated azacyclic substituted ammonium halide-copper(I) halide system. For example, the system 1-methylpiperidinium bromide-copper(I) bromide at the composition of 84 mole per cent CuBr gave the conductivity of  $8.2 \times 10^{-3}$  (ohm-cm)<sup>-1</sup> at room temperature.

Ionic conduction in the system substituted ammonium iodide-silver iodide was studied extensively by Owens (1), Owens, Christie, and Tiedeman (2), and Beradelli *et al.* (3), and many compounds were reported to have the ionic conductivities in the range of  $8 \times 10^{-4}$  to  $6 \times 10^{-2}$  (ohm-cm)<sup>-1</sup> at 25°C. From the conductivity measurements of a large number of the systems, Owens *et al.* (2) concluded that the formation of ion conductive compounds was related to the size of organic ammonium ions. Recently, double salts formed by the combination of copper(I) halide with N-alkyl-hexamethylenetetramine halide (4), and N,N'-dialkyl-triethylenediamine dihalide (5) have been found to exhibit high ionic conductivity at room temperature. In order to extend the area of high copper ion conductivity solid electrolytes, the electrical conductivities of the products formed by the reaction between copper(I) halides and organic ammonium halides have been measured (6, 7). The relations between the formation of copper ion conductive compounds and the size and conformation of the organic substituted ammonium ion are discussed.

#### Experimental

**Materials.**—Copper(I) halides were purified by recrystallizing in the corresponding hydrohalogenic acid. The substituted ammonium halide salts were prepared by the method A used generally, except for ethane-1, 2-bis-piperidinium bromide, and pentane-1,5-bis-morpholinium bromide which were prepared by the method B (8). The typical examples of synthesis are as follows:

**Method A:** To a solution containing 10 mliters (0.10 mole) of piperidine in 50 mliters of ethyl alcohol were slowly added 14g (0.098 mole) of a methyl iodide solution in 10 mliters of ethyl alcohol and the mixture was refluxed for 1 hr. After being filtered, the precipitate was dried in vacuo on P<sub>2</sub>O<sub>5</sub>. A yield of 1.5g of product (about 10% yield) was obtained.

**Method B:** To 3.8g (0.44 mole) of morpholine a solution containing 15g (0.065 mole) of 1,5-dibromopentane in benzene were added slowly at 0°C and the mixture was allowed to stand at room temperature for 2 days. After being filtered, the precipitate was dried in vacuo on P<sub>2</sub>O<sub>5</sub>. A yield of 22g of product (80% yield) was obtained.

The electrolytes were prepared by combining copper(I) halides (CuX) with substituted ammonium halides (QX). The appropriate quantities of CuX and QX were thoroughly ground together before being pressed to form a pellet under a pressure of 4000 kg/cm<sup>2</sup>, and then heated in a sealed, evacuated Pyrex vessel. The reactions were carried out below the decomposition temperatures of the starting materials, which were determined by thermogravimetric analysis.

**Electrical conductivity.**—The conductivity was measured with a 1000 Hz conductance bridge. The frequency dependence of the resistance was not observed in the frequency range of 1000-10,000 Hz. The conductivity measurement cell was as follows

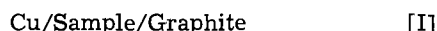
Cu, Sample (2:1 weight ratio) / Sample /  
Cu, Sample (2:1 weight ratio)

The sample of about 0.8g was stacked between two

\* Electrochemical Society Active Member.  
Key words: solid electrolyte, copper ion conductor, copper(I) halide, organic ammonium halide.

electrodes and pressed into a pellet of 13 mm diameter under a pressure of 4000 kg/cm<sup>2</sup>. The conductivity was measured in nitrogen gas flow.

**Electronic conductivity.**—The electronic conductivities of some of the samples have been measured by the Wagner polarization method (9). To cell [I] with a copper anode and a graphite cathode, d.c. was applied at a voltage less than the decomposition voltage of the samples



The sample was pressed in the shape of pellet, 13 mm in diameter and 3 mm thick. A constant current supplier was used and the resulting voltage was measured with a high impedance digital voltmeter.

**Thermogravimetric analysis (TGA).**—The decomposition temperatures of the samples were determined by thermogravimetric analysis, the heating rate of which was 3.3°C/min.

### Results and Discussion

The electrical conductivities at room temperature for the organic ammonium iodide-copper(I) iodide systems, viz., tetramethyl ammonium iodide ((CH<sub>3</sub>)<sub>4</sub>NI), 1-methyl pyridinium iodide (C<sub>5</sub>H<sub>5</sub>NCH<sub>3</sub>I), 1-methyl pyrrolidinium iodide (C<sub>4</sub>H<sub>9</sub>NCH<sub>3</sub>I), 1-methyl piperidinium iodide (C<sub>5</sub>H<sub>11</sub>NCH<sub>3</sub>I), and 1-methyl morpholinium iodide (C<sub>4</sub>H<sub>9</sub>ONCH<sub>3</sub>I)-copper(I) iodide systems, are shown in Table I, where  $\sigma_e$  and  $\sigma_i$  are the electronic and ionic conductivity, respectively. The ionic conductivities of the silver iodide-organic ammonium iodide systems shown in this table were measured by Owens *et al.* (1, 2). In the silver iodide-organic ammonium iodide and copper(I) halide-organic ammonium halide systems as the high silver and copper ion conductivities (1, 2, 4, 5) were found at the composition between 80 and 90 mole per cent (m/o) silver iodide and copper halide, it may be assumed in the present investigation that if high conductivity materials could be formed, they would contain almost the same percentage of copper(I) iodide. So the thermal reaction products containing about 84 m/o copper iodide were examined. Table I shows that the C<sub>5</sub>H<sub>11</sub>NCH<sub>3</sub>I-CuI and C<sub>4</sub>H<sub>9</sub>ONCH<sub>3</sub>I-CuI systems give relatively high conductivities of  $8.6 \times 10^{-4}$  (ohm-cm)<sup>-1</sup> and  $5.8 \times 10^{-4}$  (ohm-cm)<sup>-1</sup> at room temperature, respectively. According to x-ray investigation, these systems did not give the diffraction patterns of the starting materials but gave the new phase diffraction patterns, which showed that the new conductive double salts were obtained in these systems at the composition of about 84 m/o CuI. In the (CH<sub>3</sub>)<sub>4</sub>NI-CuI, C<sub>5</sub>H<sub>5</sub>NCH<sub>3</sub>I-CuI, and C<sub>4</sub>H<sub>9</sub>NCH<sub>3</sub>I-CuI systems, however, no conductive

double salts were formed, and the conductivities of these systems were the same order of magnitude as that of CuI and the conduction was mainly due to electrons. The x-ray diffraction patterns of these systems were the same as those of the starting materials. In other unsaturated azacyclic substituted ammonium iodide (the derivatives of the 1-methyl pyridinium iodide)-copper(I) iodide systems, no high conductive material was found in all the systems investigated: 1-hydro pyridinium iodide, 1,4-dimethyl pyridinium iodide, 1,3-dimethyl pyridinium iodide, 1,2,6-trimethyl pyridinium iodide, 1-hydro-3,5-dimethyl pyridinium iodide, 1,3,5-trimethyl pyridinium iodide, 1-methyl quinolinium iodide, and 1-ethyl quinolinium iodide-copper(I) iodide systems, and 1-hydro-2-methyl quinolinium bromide-copper(I) bromide system.

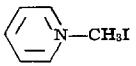
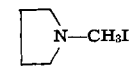
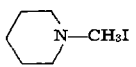
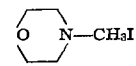
It is of interest to define by what parameters the existence of the conductive compounds were determined. It was suggested by Owens *et al.* (2) that in the silver iodide-organic ammonium iodide systems, the formation of high ionic conductivity compounds was related to the size of the organic ammonium ions. Table I indicates that in the copper(I) iodide-organic ammonium iodide systems, though C<sub>5</sub>H<sub>5</sub>NCH<sub>3</sub><sup>+</sup> and C<sub>5</sub>H<sub>11</sub>NCH<sub>3</sub><sup>+</sup> have almost the same size, only the latter gave high conductive materials. Therefore, the parameters other than the size of organic ammonium ions may be important to obtain high copper ion conductivity materials. One of these parameters may be the flexibility of organic ammonium ions; 1-methyl pyridinium ion has a plane structure, while 1-methyl piperidinium ion and 1-methyl morpholinium ion have flexible structures. Further, 1-methyl pyrrolidinium ion has a plane structure and tetramethyl ammonium ion has a rigid tetrahedral structure. That is, the flexible organic ammonium ions give a high ionic conductivity compound when they combine with copper(I) iodide. The other alkyl piperidinium halide, alkyl morpholinium halide, and alkyl piperadanium halide-copper(I) halide systems were examined also and the results of the electrical conductivity obtained are shown in Table II. Of these systems, the highest conductivity of  $8.2 \times 10^{-3}$  (ohm-cm)<sup>-1</sup> at 20°C is found in 1-methyl piperidinium bromide-copper(I) bromide, the conductivity value of which is comparable to that of N-alkyl hexamethylene-tetramine halide-copper(I) halide double salts reported previously (4) and one order of magnitude higher than that of the copper(I) iodide-1-methyl piperidinium iodide system. Gamma-copper(I) iodide and  $\gamma$ -copper(I) bromide have zinc blende structures, and the structure of copper(I) bromide is more open than that of copper(I) iodide. These results suggest that in the high ionic conductivity compounds, the structure of metal halide may play an important role.

In the 1,2- and 1,4-dimethyl piperidinium bromide-copper(I) bromide systems, the reaction products which gave the x-ray diffraction patterns of new compounds have lower conductivities than the compound in 1-methyl piperidinium bromide-copper(I) bromide system at room temperature, which suggested that the steric effect of substituted groups in the 1,2- and 1,4-dimethyl piperidinium bromide-copper(I) bromide systems may interrupt the diffusion of copper(I) ions.

**Conductivity.**—The composition dependence of the electrical conductivity was determined for three systems, viz., the 1-methyl piperidinium bromide-copper(I) bromide, 1-methyl piperidinium iodide-copper(I) iodide, and 1-methyl morpholinium iodide-copper(I) iodide systems. Figure 1 shows the conductivity as a function of mole per cent of copper(I) halide. The highest values of conductivity are  $8.2 \times 10^{-3}$ ,  $8.6 \times 10^{-4}$ , and  $5.8 \times 10^{-4}$  (ohm-cm)<sup>-1</sup> for the C<sub>5</sub>H<sub>11</sub>NCH<sub>3</sub>Br-CuBr, C<sub>5</sub>H<sub>11</sub>NCH<sub>3</sub>I-CuI, and C<sub>4</sub>H<sub>9</sub>ONCH<sub>3</sub>I-CuI systems, respectively, at the composition of about 84 m/o CuX.

The conductivities of C<sub>5</sub>H<sub>11</sub>NCH<sub>3</sub>Br 16 m/o-CuBr 84 m/o and C<sub>5</sub>H<sub>11</sub>NCH<sub>3</sub>I 16 m/o-CuI 84 m/o were mea-

Table I. Electrical conductivity of the copper(I) iodide-organic ammonium iodide systems and silver iodide-organic ammonium iodide systems at room temperature

	CuI	AgI
Tetramethyl ammonium iodide (CH <sub>3</sub> ) <sub>4</sub> NI	$\sigma_e \gg \sigma_i$	$4 \times 10^{-2}$
1-Methyl pyridinium iodide 	$\sigma_e \gg \sigma_i$	$1 \times 10^{-2}$
1-Methyl pyrrolidinium iodide 	$\sigma_e \gg \sigma_i$	$8 \times 10^{-3}$
1-Methyl piperidinium iodide 	$8.6 \times 10^{-4}$	
1-Methyl morpholinium iodide 	$5.8 \times 10^{-4}$	

**Table II. Electrical conductivity of the copper(I) halide-derivatives of 1-methyl piperidinium iodide systems at room temperature**

		(ohm-cm) <sup>-1</sup>
1-Methyl piperidinium iodide		$8.61 \times 10^{-4}$
1-Ethyl piperidinium iodide		$2.70 \times 10^{-7}$
Piperidinium bromide		$2.18 \times 10^{-7}$
1-Methyl piperidinium bromide		$8.24 \times 10^{-8}$
1-Ethyl piperidinium bromide		$4.24 \times 10^{-6}$
1,2-Dimethyl piperidinium bromide		$9.25 \times 10^{-5}$
1,4-Dimethyl piperidinium bromide		$1.15 \times 10^{-5}$
Ethane-1,2-bis-piperidinium bromide		$1.2 \times 10^{-7}$
Morpholinium iodide		$\sigma_e \gg \sigma_i$
1-Methyl morpholinium iodide		$5.80 \times 10^{-4}$
1-Ethyl morpholinium iodide		$7.62 \times 10^{-5}$
Morpholinium bromide		$\sigma_e \gg \sigma_i$
1-Ethyl morpholinium bromide		$2.66 \times 10^{-7}$
Pentane-1,5-bis-morpholinium bromide		$<10^{-9}$
Piperadinium iodide		$\sigma_e \gg \sigma_i$
1,4-Dimethyl piperadinium iodide		$3.22 \times 10^{-5}$

sured at different temperatures. These samples were not decomposed up to 110°C in nitrogen atmosphere. The logarithmic conductivity *vs.* the reciprocal of the absolute temperature curves for these samples are shown in Fig. 2. These curves give straight lines in the range of temperature studied. The activation energies for conduction calculated from these curves are 3.7 kcal/mole for C<sub>5</sub>H<sub>11</sub>NCH<sub>3</sub>Br 16 m/o-CuBr 84 m/o and 5.1 kcal/mole for C<sub>5</sub>H<sub>11</sub>NCH<sub>3</sub>I 16 m/o-CuI 84 m/o; these values are almost the same as those of previously reported high copper ion conductivity solid electrolytes (4).

**Electronic conductivity.**—Electronic conductivity for some systems has been measured by Wagner's polarization method. According to Wagner's theoretical analysis (9) the current density *J* in cell [I] is given by

$$J = I/A = (RT/LF) [\sigma_e \{1 - \exp(-EF/RT)\} + \sigma_h \{\exp(EF/RT) - 1\}] \quad [1]$$

where *I* is the current, *A* the cross-sectional area, *L* the thickness of the sample, *E* the applied voltage, and *F* the Faraday constant, and  $\sigma_e$  and  $\sigma_h$  are the excess electron and hole conductivities of the sample which is in equilibrium with metallic copper. The plots of  $\log I$  *vs.* *E* give virtually straight lines whose slopes are close to the value of  $F/2.30RT$  at each temperature. Since the excess electron conduction is negligible, Eq. [1] may be written as

$$\log I = \log \sigma_h ART/LF + EF/2.30RT \quad [2]$$

if  $EF/RT \gg 1$ . The values of  $\sigma_h$  were then calculated

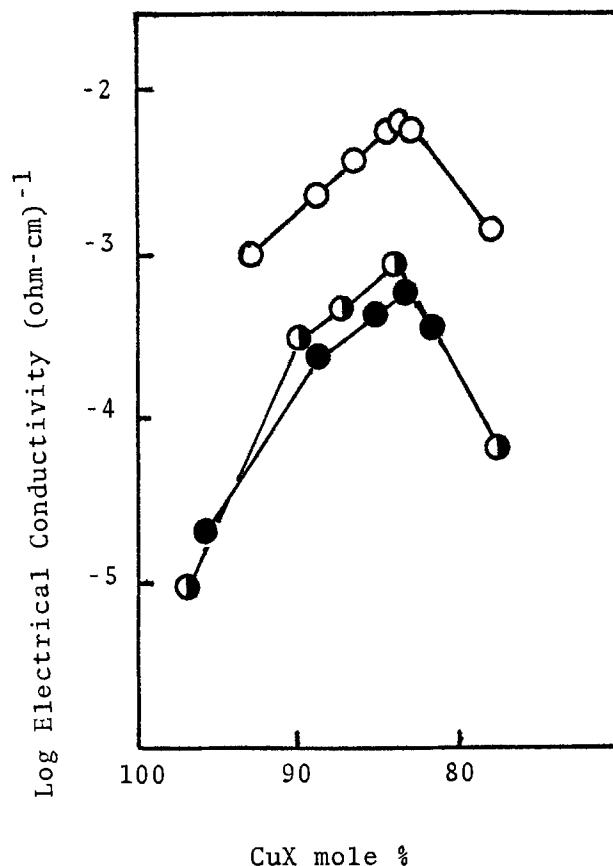


Fig. 1. Composition dependence of electrical conductivity of the binary solid electrolyte systems C<sub>5</sub>H<sub>11</sub>NCH<sub>3</sub>Br-CuBr (○), C<sub>5</sub>H<sub>11</sub>NCH<sub>3</sub>I-CuI (◐), and C<sub>4</sub>H<sub>9</sub>ONCH<sub>3</sub>I-CuI (●) at 25°C.

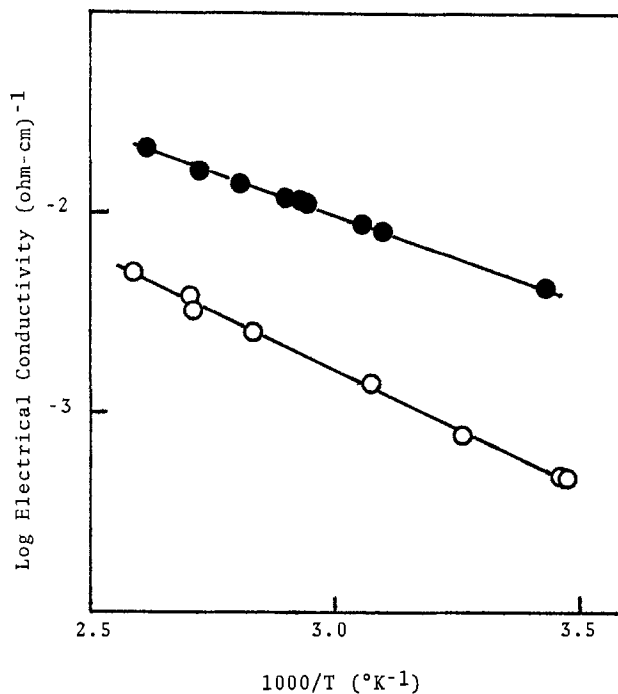


Fig. 2. Temperature dependence of the electrical conductivity of 6CuBrC<sub>5</sub>H<sub>11</sub>NCH<sub>3</sub>Br (●) and 6CuIC<sub>5</sub>H<sub>11</sub>NCH<sub>3</sub>I (○).

from Eq. [2]. Figure 3 shows the values of  $\sigma_h$  for the C<sub>5</sub>H<sub>11</sub>NCH<sub>3</sub>Br-CuBr, C<sub>5</sub>H<sub>11</sub>NCH<sub>3</sub>I-CuI, and C<sub>4</sub>H<sub>9</sub>ONCH<sub>3</sub>I-CuI systems as a function of the composition of CuX at 110°C. The electronic conductivity for these systems decreases with decreasing copper(I) halide content. The conductivity of C<sub>5</sub>H<sub>11</sub>NCH<sub>3</sub>Br 16 m/o-CuBr 84 m/o is lower than  $3.2 \times 10^{-12}$  (ohm-cm)<sup>-1</sup> at 110°C. The temperature dependence of the

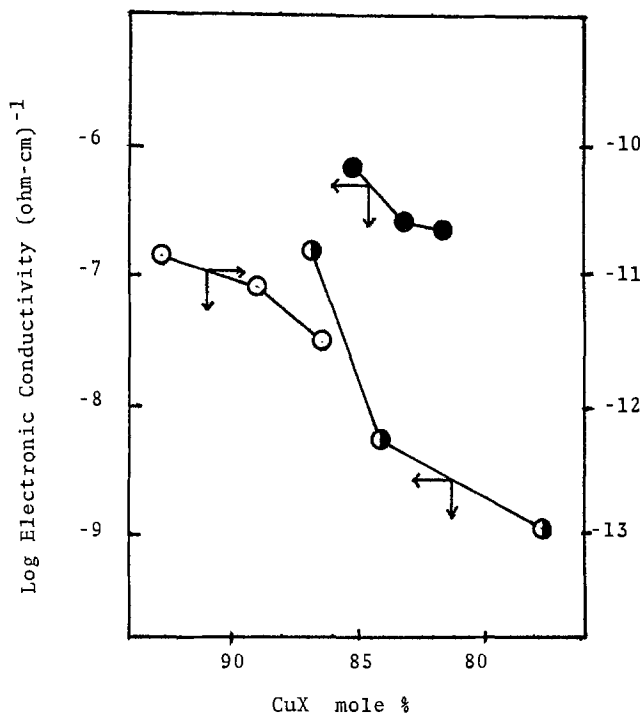


Fig. 3. Composition dependence of the electronic conductivity of the binary solid electrolyte systems  $C_5H_{11}NCH_3Br-CuBr$  ( $\circ$ ),  $C_5H_{11}NCH_3I-CuI$  ( $\bullet$ ), and  $C_4H_9ONCH_3I-CuI$  ( $\bullet$ ).

electronic conductivity of the  $C_5H_{11}NCH_3Br-CuBr$  system is shown in Fig. 4. Thus, it is concluded that the conduction in the systems  $C_5H_{11}NCH_3Br-CuBr$ ,  $C_5H_{11}NCH_3I-CuI$ , and  $C_4H_9ONCH_3I-CuI$  is essentially ionic.

### Conclusion

It is concluded from the experimental results that the formation of high copper ion conductivity solids in the organic ammonium halide-copper(I) halide system is related to not only the size of ammonium ion, but also to its flexibility.

Manuscript submitted June 2, 1975; revised manuscript received Aug. 16, 1975.

Any discussion of this paper will appear in a Discussion Section to be published in the December 1976 JOURNAL. All discussions for the December 1976 Discussion Section should be submitted Aug. 1, 1976.

Publication costs of this article were partially assisted by the authors.

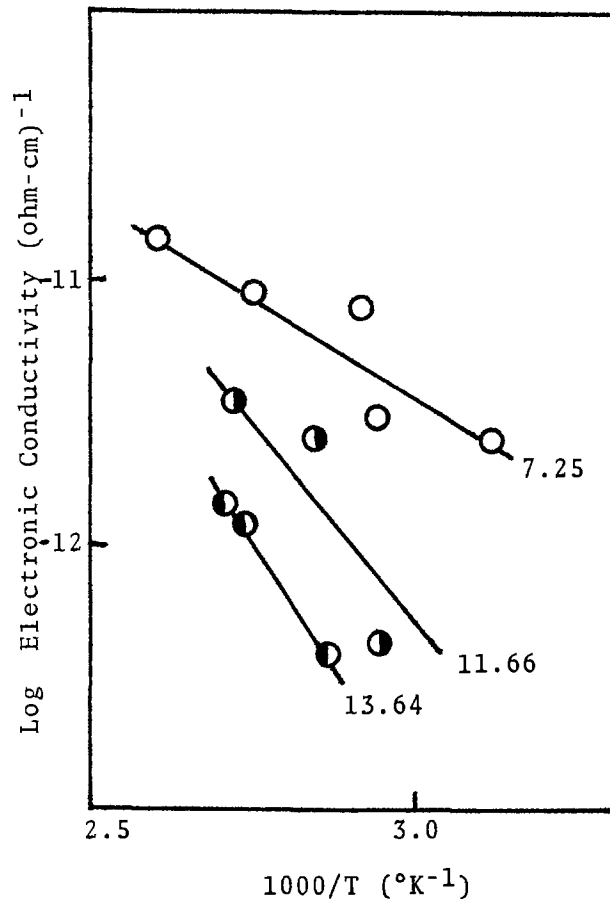


Fig. 4. Temperature dependence of the electronic conductivity of  $C_5H_{11}NCH_3Br-CuBr$ .  $C_5H_{11}NCH_3Br$  (m/o): ( $\circ$ ) 7.25, ( $\bullet$ ) 11.66, ( $\bullet$ ) 13.64.

### REFERENCES

1. B. B. Owens, *This Journal*, **117**, 1536 (1970).
2. B. B. Owens, J. H. Christie, and G. T. Tiedeman, *ibid.*, **118**, 1144 (1971).
3. M. L. Berardelli, C. Biondi, M. De Rossi, G. Fonseca, and M. Giomini, *ibid.*, **119**, 114 (1972).
4. T. Takahashi, O. Yamamoto, and S. Ikeda, *ibid.*, **120**, 1431 (1973).
5. T. Takahashi and O. Yamamoto, *ibid.*, **122**, 83 (1975).
6. T. Takahashi, N. Wakabayashi, O. Yamamoto, and S. Ikeda, Abstracts, 40th Meeting Electrochem. Soc. Japan, Satsuporo, August 1973.
7. A. F. Sammells, Ext. Abst. Fall Meeting Electrochem. Soc., Oct. (1974) New York.
8. K. Sanada, A. Iwasawa, E. Tsuchida, and I. Shinohara, Abstracts, vol. I, p. 1, 27th Fall Meeting of the Chemical Society of Japan, Nagoya, October 1972.
9. C. Wagner, Proc. 7th Meeting C.I.T.C.E., Lindau, 1955, p. 361, Butterworths, London (1957).

# Mass Spectrometric Investigation of the Reaction Velocities of $\text{BCl}_3$ and $\text{BBr}_3$ with Oxygen and Water Vapor in a Diffusion Furnace

V. Geiss<sup>1</sup> and E. Fröschle

Institut für Halbleitertechnik, RWTH Aachen, D-51 Aachen, Germany

## ABSTRACT

The velocities of the reactions of  $\text{BCl}_3$  and  $\text{BBr}_3$  with  $\text{O}_2$  and  $\text{H}_2\text{O}$  were measured in a diffusion tube. The conditions (gas composition, gas velocity, temperature) were those commonly used in the open tube diffusion process. For the analysis the gaseous reaction products were sampled with a quadrupole mass spectrometer at different locations in the tube. The measurements indicate that with  $\text{H}_2\text{O}$  the reaction proceeds rapidly, but with  $\text{O}_2$  very slowly. Therefore, with  $\text{O}_2$  present in the gas mixture, large variations of the gas composition occur along the length of the tube. The time behavior of this reaction is described by its half-life and its dependence on temperature and  $\text{O}_2$  partial pressure.

A commonly employed method for the diffusion of boron into silicon is the "open tube" technique, using nitrogen with a small percentage of oxygen as a carrier gas and boron halides such as boron trichloride ( $\text{BCl}_3$ ) (2) or boron tribromide ( $\text{BBr}_3$ ) (3-6). If surface concentrations below saturation are desired, the diffusion process is performed in two steps, a boron deposition step at temperature below  $1000^\circ\text{C}$  and a drive-in step above  $1000^\circ\text{C}$ . The reproducibility of the results depends mainly on the boron deposition step. The oxygen reacts with the boron halides and the silicon to produce  $\text{B}_2\text{O}_3$  and  $\text{SiO}_2$ .  $\text{B}_2\text{O}_3$  and  $\text{SiO}_2$  form a borosilicate glass (BSG), which functions as a secondary dopant source during deposition and drive-in.

When using the process in the fabrication of semiconductor devices, a relatively long (typically 10 in.) zone of constant  $\text{B}_2\text{O}_3$  supply is mandatory in order to obtain uniform deposition on the many silicon substrates in the same run. The quality of BSG which is formed on the silicon wafers at each position in the diffusion tube is strongly dependent on the temperature, gas composition, and gas velocity. In fact, for an arbitrarily chosen set of conditions, the zone where appreciable deposition occurs may even fall entirely upstream or downstream of the position of the sample support. This suggests that the time necessary for carrying the  $\text{B}_2\text{O}_3$  formation reaction to completion is comparable to that required for the flow of the gas through the tube of the diffusion furnace (6). Thus it appears that the kinetics of  $\text{B}_2\text{O}_3$  formation play a decisive role in the boron diffusion process. Therefore, we have studied the kinetics by analyzing the gas composition in a diffusion tube using a mass spectrometer. It will be shown that the data obtained lead to a clearer understanding of the system and facilitate optimization of the diffusion process.

## Reactions and Equilibrium States

The compositions of the gas phases in thermodynamic equilibrium at  $973^\circ\text{C}$  and  $1053^\circ\text{C}$  were calculated for the diffusion systems  $\text{BCl}_3\text{-O}_2$  and  $\text{BBr}_3\text{-O}_2$  using the JANAF Tables (1). The results of these calculations are shown in Tables I and II. Here the partial pressure of the main reaction products which result from reactions of the doping gases with the oxygen are listed. The initial pressures of the doping gases and oxygen correspond to the values which were used in the gas analysis experiments.

<sup>1</sup> Present address: Institut für Werkstoffe der Elektrotechnik, Ruhr-Universität Bochum, D-463 Bochum, Germany.

Key words: gas analysis, doping gases, boron, silicon.

At the temperature used,  $\text{Cl}_2$  is dissociated partially and  $\text{Br}_2$  largely according to



and



At equilibrium the gas phase consists entirely of the reaction products and residual oxygen. The partial pressure of all boron containing gaseous species is small compared to the boron content of the input gas. From this one can conclude that the main part of the

Table I. Initial and equilibrium partial pressures of the system  $\text{BCl}_3\text{-O}_2$  (1)

Initial partial pressures							
	$P_{\text{BCl}_3(\text{g})}/\text{atm}$						$P_{\text{O}_2(\text{g})}/\text{atm}$
$T = 973^\circ\text{C}$	$1.6 \cdot 10^{-4}$						$1 \cdot 10^{-2}$
$T = 1053^\circ\text{C}$	$6.5 \cdot 10^{-5}$						$1 \cdot 10^{-2}$
Equilibrium partial pressures							
Substance	Cl	Cl <sub>2</sub>	BO <sub>2</sub>	B <sub>2</sub> O <sub>3</sub>	BClO	BCl <sub>3</sub>	$\Sigma \text{ Bor}/\%$ as B <sub>2</sub> O <sub>3</sub> liquid
$P/\text{atm at } T$	1	1.9	2.9	3.9	3.4	8.4	99.8
$= 973^\circ\text{C}$	$10^{-4}$	$10^{-4}$	$10^{-7}$	$10^{-8}$	$10^{-8}$	$10^{-11}$	
$P/\text{atm at } T$	1	4.6	1.5	3.8	8.6	3.1	96.4
$= 1053^\circ\text{C}$	$10^{-4}$	$10^{-5}$	$10^{-6}$	$10^{-7}$	$10^{-8}$	$10^{-11}$	

Table II. Initial and equilibrium partial pressures of the system  $\text{BBr}_3\text{-O}_2$  (1)

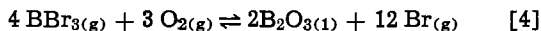
Initial partial pressures							
	$P_{\text{BBr}_3(\text{g})}/\text{atm}$						$P_{\text{O}_2(\text{g})}/\text{atm}$
$T = 973^\circ\text{C}$	$3.5 \cdot 10^{-5}$						$1 \cdot 10^{-2}$
$T = 1053^\circ\text{C}$	$3.4 \cdot 10^{-5}$						$1 \cdot 10^{-2}$
Equilibrium partial pressures							
Substance	Br	Br <sub>2</sub>	BO <sub>2</sub>	B <sub>2</sub> O <sub>3</sub>	BBrO	BBr <sub>3</sub>	$\Sigma \text{ Bor}/\%$ as B <sub>2</sub> O <sub>3</sub> liquid
$P/\text{atm at } T$	1	2.8	1.9	3.9	8.0	5.2	99.2
$= 973^\circ\text{C}$	$10^{-4}$	$10^{-6}$	$10^{-7}$	$10^{-8}$	$10^{-11}$	$10^{-10}$	
$P/\text{atm at } T$	1	9.5	1.1	3.8	3.2	7.7	94.6
$= 1053^\circ\text{C}$	$10^{-4}$	$10^{-7}$	$10^{-6}$	$10^{-7}$	$10^{-10}$	$10^{-10}$	

boron injected into the diffusion system is deposited as a condensed phase, probably as liquid  $B_2O_3$ .

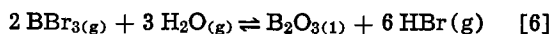
Therefore, good approximations of the over-all reactions are



and



Calculations of the equilibrium pressures in the systems  $BCl_3$ - $H_2O$  and  $BBr_3$ - $H_2O$  are given in Tables III and IV. For a very small surplus of water vapor ( $P_{H_2O} < 10^{-6}$  atm), as a good approximation the following over-all reactions are valid



A larger surplus of water vapor would reduce the amount of the  $B_2O_3$  in favor of  $HBO_2$ .

### Experimental

For the experiments a three-zone resistance-heated diffusion furnace was used. The nitrogen carrier gas passed through the full length of the tube and could be mixed with oxygen and water vapor (Fig. 1). A smaller part of nitrogen carried the doping gases  $BCl_3$  or  $BBr_3$  through an extra tube to the beginning of the constant temperature zone, where the gases were mixed. Both gases were preheated while flowing through the heated front part of the furnace. Thus the chemical reactions would start at a well-defined position. The temperature was kept uniform, within  $2^\circ C$  over the range of  $5 < L < 60$  cm. The velocity of the  $N_2$  carrier gas was mostly  $v = 1$  cm/sec. All gases except water vapor were dried to the extent that the residual partial pressure of water vapor was less than  $10^{-6}$  atm. In this way, unwanted reactions of the doping gases already in the supply tubes could be pre-

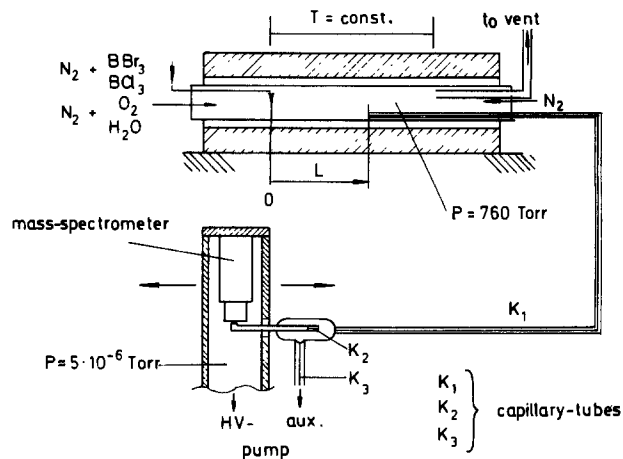


Fig. 1. Diffusion furnace and gas sampling system

vented. To avoid contamination of the colder end zone of the quartz tube by condensation, the reaction products were exhausted from the hot zone and dry nitrogen was blown in from the downstream side to provide a gas buffer.

For the analysis of the gas composition in the tube, a small part of the gas was pumped through a quartz capillary tube into a quadrupole mass spectrometer. The gas transport through the capillary tube to the spectrometer took about 0.2 sec. It cannot be excluded that during this time the reaction could reverse itself due to cooling. In fact although the stable form of bromine at the temperatures and concentrations in the reaction tube is  $Br$ , it was always measured as  $Br_2$ , the stable form at room temperature. The calibration of the mass spectrometer was done by controlled dilution of  $Cl_2$ ,  $Br_2$ ,  $BCl_3$ , and  $BBr_3$  with an error of less than  $\pm 10\%$ . The reproducibility of the concentration measurements in the  $10^{-4}$  atm range was about  $\pm 3\%$ . The amount of condensed material could be determined from the differences between the partial pressures of the gaseous species at input and their measured value after reaction. The vacuum system together with the capillary tube could be moved in such a way that sampling of the gas was possible in the range  $-10 < L < 60$  cm. Changes of the gas composition along the tube could thus be measured as a function of the distance from the doping gas inlet or as a function of time, since the gas velocity was known.

### Results

An example of such a mass spectrometric measurement of the reaction of  $BCl_3$  with  $O_2$  at  $1057^\circ C$  is shown in Fig. 2. The decrease of the  $BCl_3$  partial pressure and the increase of the  $Cl_2$  partial pressure are

Table III. Initial and equilibrium partial pressures of the system  $BCl_3$ - $H_2O$  (1)

Initial partial pressures							
	$P_{BCl_3(0)}/atm$						$P_{H_2O(0)}/atm$
$T = 973^\circ C$	$3.3 \cdot 10^{-5}$						$5.1 \cdot 10^{-5}$
$T = 1053^\circ C$	$3.3 \cdot 10^{-5}$						$5.2 \cdot 10^{-5}$
Equilibrium partial pressures							
Substance	HCl	$H_2O$	$BHO_2$	$B_2O_3$	$BCl_3$	$B(OH)_3$	$\Sigma Bor/\%$ as $B_2O_3$ liquid
$P/atm$ at $T = 973^\circ C$	1	1	2.7	3.9	2.6	1.2	93.3
$P/atm$ at $T = 1053^\circ C$	$10^{-4}$	$10^{-9}$	$10^{-9}$	$10^{-9}$	$10^{-11}$	$10^{-11}$	83.5

Table IV. Initial and equilibrium partial pressures of the system  $BBr_3$ - $H_2O$  (1)

Initial partial pressures							
	$P_{BBr_3(0)}/atm$						$P_{H_2O(0)}/atm$
$T = 973^\circ C$	$3.3 \cdot 10^{-5}$						$5.1 \cdot 10^{-5}$
$T = 1053^\circ C$	$3.3 \cdot 10^{-5}$						$5.2 \cdot 10^{-5}$
Equilibrium partial pressures							
Substance	HBr	$H_2O$	$BHO_2$	$B_2O_3$	$B(OH)_3$	$BBr_3$	$\Sigma Bor/\%$ as $B_2O_3$ liquid
$P/atm$ at $T = 973^\circ C$	1	1	1.8	3.9	1.5	1.5	94.4
$P/atm$ at $T = 1053^\circ C$	$10^{-4}$	$10^{-9}$	$10^{-9}$	$10^{-9}$	$10^{-11}$	$10^{-12}$	83.7

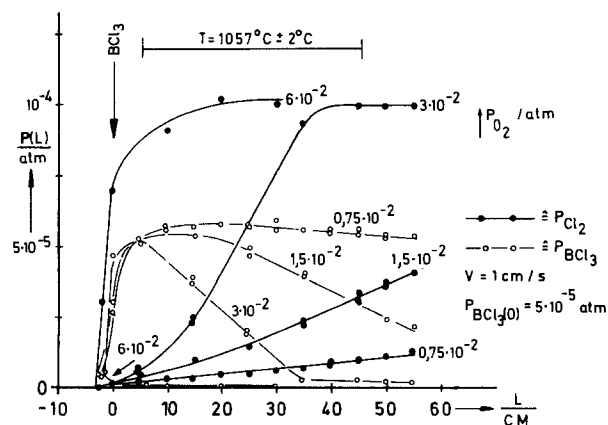


Fig. 2. Reaction of  $BCl_3$  with  $O_2$  as a function of the location in the tube at  $1057^\circ C$  for different  $O_2$  partial pressures.



represented as a function of the distance  $L$  from the doping gas inlet with the  $\text{O}_2$  pressure as a parameter. The input pressures of  $\text{BCl}_3$  and the gas velocity were kept constant for these series of measurements. Increasing the  $\text{O}_2$  partial pressure caused an increase of the reaction velocity.

In spite of a considerable surplus of oxygen and the fact that at equilibrium the gas phase contains only the oxidation products, the reaction velocity is remarkably low. The decrease in the partial pressure of  $\text{BCl}_3$  is balanced by the increase in that of  $\text{Cl}_2$ . Other chlorine containing gaseous compounds could not be measured. This appears to confirm Eq. [3] as the correct expression for the over-all reaction. It must be remarked that only the gaseous compounds  $\text{BCl}_3$ ,  $\text{O}_2$ , and  $\text{Cl}_2$  can be analyzed with the mass spectrometer.  $\text{Cl}$  reacts during sampling to  $\text{Cl}_2$ .  $\text{B}_2\text{O}_3$  could not be detected because at the temperatures used it is a liquid and condensed at the tube walls. Figure 3 shows data for the reaction of  $\text{BCl}_3$  with  $\text{O}_2$  at the lower temperature of  $973^\circ\text{C}$ . As expected, lower temperatures cause smaller reaction velocity.

Similar measurements were done with  $\text{BBr}_3$  as a dopant (Fig. 4). They agree with the assumption that Eq. [4] represents the over-all reaction. Comparing the  $\text{BBr}_3$  and  $\text{BCl}_3$  data, it may be seen that for the same  $\text{O}_2$  partial pressure and temperature the reaction velocity is very much higher with  $\text{BBr}_3$ .

In order to characterize the reaction velocity we used the half-life  $\tau_h$ , i.e., the time in which the initial concentration of the doping gas has been reduced by 50%. The values of  $\tau_h$  were read or extrapolated from Fig. 2-4 and plotted as a function of the initial  $\text{O}_2$  partial pressure (Fig. 5). Similar experiments were done for other initial partial pressures of the doping gases in the region  $2 \cdot 10^{-5} < P < 2 \cdot 10^{-4}$  atm. They showed that in this region  $\tau_h$  is independent of the initial doping gas pressure. This indicates that the reaction is first order in the doping gas. Assuming the

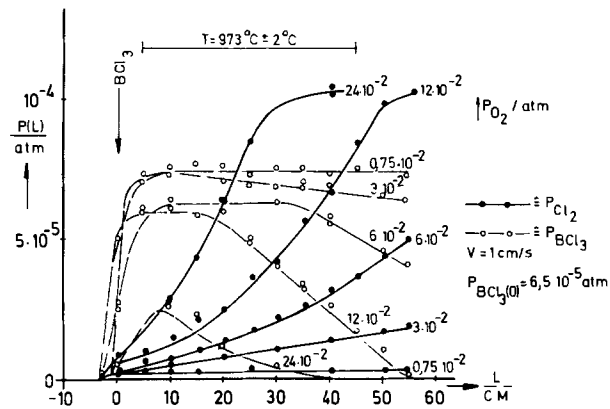


Fig. 3. Reaction of  $\text{BCl}_3$  with  $\text{O}_2$  as a function of the location in the tube at  $973^\circ\text{C}$  for different  $\text{O}_2$  partial pressures.

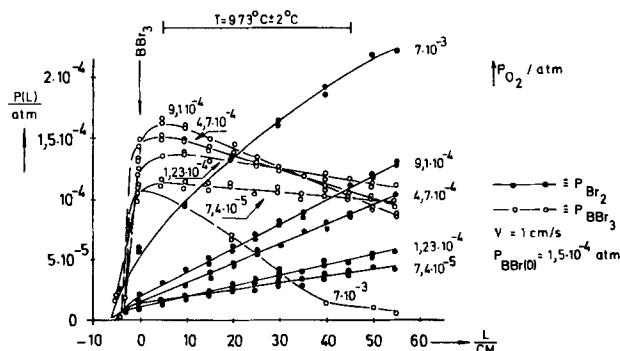


Fig. 4. Reaction of  $\text{BBr}_3$  with  $\text{O}_2$  as a function of the location in the tube at  $973^\circ\text{C}$  for different  $\text{O}_2$  partial pressures.

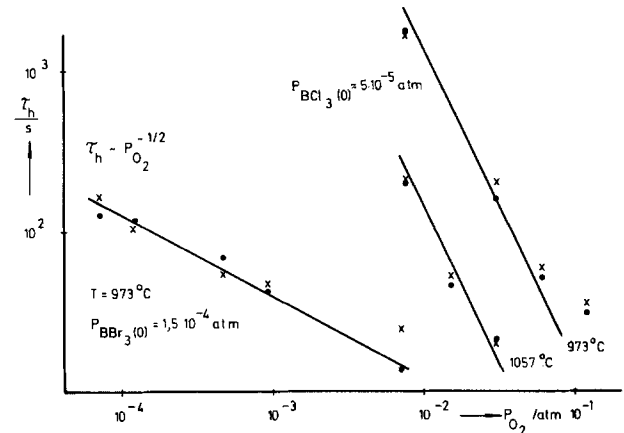


Fig. 5. Half-life  $\tau_h$  of  $\text{BBr}_3$  and  $\text{BCl}_3$  as a function of the  $\text{O}_2$  partial pressure; left-hand side:  $\text{BBr}_3$ , right-hand side:  $\text{BCl}_3$ ; ● calculated from  $\text{BCl}_3$ ,  $\text{BBr}_3$ ; × calculated from  $\text{Cl}_2$ ,  $\text{Br}_2$  partial pressures.

commonly observed exponential temperature dependence, the following expression can be obtained from Fig. 5 for the half-life of  $\text{BCl}_3$  reacting with  $\text{O}_2$

$$\tau_h/\text{sec} = 2.2 \cdot 10^{-17} (P_{\text{O}_2}/\text{atm})^{-2} \exp(3.9 \text{ eV}/kT) \quad [7]$$

The dependence of the time constant on the oxygen partial pressure is that of a third order reaction in  $\text{O}_2$ .

The reaction rate of  $\text{BBr}_3$  with oxygen was determined only at the lower temperature of  $973^\circ\text{C}$ . The dependence of the half-life of  $\text{BBr}_3$  on  $\text{O}_2$  partial pressure may be expressed as

$$\tau_h/\text{sec} = 1.3 \times (P_{\text{O}_2}/\text{atm})^{-1/2} \quad [8]$$

It is somewhat surprising that the pressure dependence of this reaction is very different from the  $\text{BCl}_3$  reaction and corresponds to a reaction order between the first and second. At higher temperatures ( $T > 1000^\circ\text{C}$ ), the reaction of  $\text{BBr}_3$  with nitrogen starts, which makes the measurement of the oxygen reaction rate impossible.

In order to determine if the walls of the tube had any effect on the reaction rate, some measurements were made after the diffusion tube had been partially filled (up to 20 cm) with quartz wool. No difference in the reaction profiles could be noticed, which proves that the reactions are volume processes.

Using water vapor instead of oxygen, the reaction with both doping gases was found to go to completion near  $L = 0$  for all gas velocities investigated even at  $973^\circ\text{C}$ . The time constants  $\tau_h$  were too small to be measured.

## Discussion

The foregoing data show that under the commonly used conditions for boron deposition the doping gases  $\text{BCl}_3$  and  $\text{BBr}_3$  react rather slowly with oxygen, though at equilibrium only the oxidation products are left in the system. Figure 5 shows that at  $973^\circ\text{C}$  and with an oxygen pressure of  $5 \cdot 10^{-2}$  atm the half-life  $\tau_h$  for the reaction of  $\text{BCl}_3$  with oxygen is about 100 sec. This means that for a gas velocity of 1 cm/sec the reaction cannot be completed within the length of a typical diffusion tube. With  $\text{BBr}_3$  more favorable results can be expected since for the above-mentioned conditions the time  $\tau_h$  is about 6 sec.  $\text{BBr}_3$  does not dissociate thermally into boron and bromine at temperatures as low as  $200^\circ\text{C}$ , as was hypothesized in Ref. (5). Such a dissociation could not even be noticed at  $973^\circ\text{C}$ .

A quantitative comparison between the mass spectrometric measurements and published diffusion measurements is not possible, since in the literature generally no information is given concerning the distance between the doping gas inlet and the first silicon wafer, the linear gas velocity and the temperature pro-

file of the tube. Nevertheless a qualitative comparison can be made.

Parekh and Goldstein (6) describe diffusion investigations in an oxidizing atmosphere using  $\text{BBr}_3$  as dopant. In the direction of flow of the gas, they first observed in the diffusion tube an area with decreasing sheet resistance, then one with constant sheet resistance, and finally an area with rising sheet resistance. They showed that the interesting area of constant sheet resistance moves toward the doping gas inlet for rising temperatures and oxygen partial pressures and decreasing gas velocities.

The same behavior was observed in our mass spectrometric investigations for the reaction zone with decreasing dopant pressures and increasing pressures of the reaction products (Fig. 3). Taking our results and those of Parekh and Goldstein together, it follows that constant sheet resistances can be expected when a major part of the doping gas has reacted to form  $\text{B}_2\text{O}_3$ . The  $\text{B}_2\text{O}_3$  is carried by the gas stream and will condense at the same time on the quartz walls and the silicon wafers. As long as the BSG layer formed in this way has an adequate thickness, constant sheet resistances are obtained upon the drive-in. Since the reaction proceeds very slowly, the amount of the  $\text{B}_2\text{O}_3$  formed is insufficient in the part of the tube near the inlet. In the third zone the supply of  $\text{B}_2\text{O}_3$  is depleted because of the continuous condensation of this compound.

Using water vapor instead of oxygen, the doping gases react immediately. When a small surplus of water is used mainly  $\text{B}_2\text{O}_3$  will be formed. This reaction proceeds even in low temperatures. Therefore all carrier

gases must be dried thoroughly to prevent unwanted reactions in the supply tubes.

### Acknowledgments

The authors are indebted to Professors P. Balk and E. Kubalek for helpful discussions. They would like to acknowledge the support of the Deutsche Forschungsgemeinschaft, which enabled these investigations in the Sonderforschungsbereich 56 "Festkörperelektronik."

Manuscript submitted Dec. 27, 1974; revised manuscript received Sept. 8, 1975.

Any discussion of this paper will appear in a Discussion Section to be published in the December 1976 JOURNAL. All discussions for the December 1976 Discussion Section should be submitted by Aug. 1, 1976.

### REFERENCES

1. JANAF Thermochemical Tables, Dow Chemical Co., Midland Michigan (1965).
2. K. D. Kang, R. R. Burgess, and Y. D. Kwon, Paper 520 presented at The Electrochemical Society Meeting, Montreal, Canada, Oct. 6-11, 1968.
3. J. F. Shephard, R. J. Dendall, and P. Balk, Paper 196 presented at The Electrochemical Society Meeting, Philadelphia, Pennsylvania, Oct. 9-14, 1966.
4. H. D. Pawlowski and J. C. Brixey, Paper 173 presented at The Electrochemical Society Meeting, Chicago, Illinois Oct. 15-19, 1967.
5. G. M. Oleszek and W. M. Whittemore, Paper 303 presented at The Electrochemical Society Meeting, New York, New York, May 4-9, 1969.
6. P. C. Parekh and D. R. Goldstein, *Proc. IEEE*, **57**, 9 (1969).

## Thermodynamic Domains of the Various Solid Deposits in the B-C-H-Cl Vapor System

M. Ducarroi

Laboratoire des Ultra-Réfractaires, C.N.R.S., Odeillo, 66120 Font-Romeu, France

and C. Bernard

Centre d'Information de Thermodynamique Chimique Minérale, E.N.S.E.E.G., 38401 Saint Martin d'Heres, France

### ABSTRACT

Calculations have been made of the equilibrium conditions under which chemical deposition of  $\text{B}_4\text{C}$  from  $\text{BCl}_3$ - $\text{CH}_4$ - $\text{H}_2$  mixtures takes place. Pure  $\text{B}_4\text{C}$  is mainly obtained for gas-phase mixtures in which  $\text{BCl}_3/\text{CH}_4 > 1$  and  $\text{H}_2/\text{BCl}_3 > 1$ . The maximum yield is obtained in the range 1675°-2075°K for the initial composition  $\text{BCl}_3 = 0.1$ ,  $\text{CH}_4 = 0.02$ ,  $\text{H}_2 = 0.88$ . The dependence of the hydrogen partial pressure on the equilibrium composition is discussed. At high temperatures with a large excess of hydrogen, the tendency is to form gaseous  $\text{BH}_2$  and  $\text{BH}_3$  instead of condensed species. With decreasing the amount of hydrogen, graphite begins to deposit under  $\text{CH}_4/\text{BCl}_3 \ll 1/4$  ratios. At lower temperatures the equilibrium content of  $\text{BCl}_2\text{H}$  increases as the  $\text{H}_2/\text{BCl}_3$  ratio falls. The results of the calculations are confirmed by experimental data.

Chemical vapor deposition is a complex process in which many factors affect the deposition, and thus the process is difficult to optimize. Nevertheless it can be analyzed in terms of thermodynamic, transport, and kinetic factors to find a set of deposition conditions which will produce the desired goal.

The thermodynamic system evaluation is the first step of a complete analysis. The equilibrium composition is obtained by such calculations and sometimes

Key words: boron carbide, vapor deposition, efficiency, boron trichloride, methane.

unsuspected reactions may be deduced from atomic balances equations. The thermodynamic analysis has been used by many authors in order to predict the preparation conditions of doped layers, solid solutions, binary or ternary compounds (1-9).

The conclusions obtained from the thermodynamic evaluation may be useful to describe a reaction mechanism. Using a thermodynamic approach, the presence of  $\text{BCl}_2\text{H}$  in the B-Cl-H system was demonstrated at equilibrium, this fact has been used by Carlton (10) to postulate a kinetic model taking into account this

species. The present paper is concerned with a thermodynamic analysis of the B-C-H-Cl vapor system in order to define optimum conditions for deposition of  $B_4C$  from  $BCl_3$ - $CH_4$ - $H_2$  gas mixtures. This compound has interesting properties (light weight, extreme hardness, resistance to abrasion, resistance to chemical attack) and is employed in the nuclear, metallurgical, and watch industries.

A number of investigators have attempted to prepare it as coatings, but in most cases the chemical vapor deposition of  $B_4C$  seems to be difficult. According to different authors, deposits may be either boron rich or carbon rich depending on the composition of the initial gas phase. Deposits of pyrolytic carbon +  $B_4C$  or pyrolytic carbon only may be produced (11-16). Furthermore, there exists no thermodynamic study which gives the solid deposit domains in this system.

### Procedure

The computation procedure employed for the determination of the equilibrium in a system taking into account several condensed species is based on the minimization of the free energy and is detailed in a previous paper (18). It is a time-sharing program. The necessary starting data are the free-energy function and the standard heats of formation of the chemical species considered. In calculations of the equilibrium of the system B-C-H-Cl, the following species were chosen:  $BCl_3$ ,  $CH_4$ ,  $H_2$ ,  $BCl_2H$ ,  $BH$ ,  $BH_2$ ,  $BH_3$ ,  $B_2H_6$ ,  $B_5H_9$ ,  $B_2Cl_4$ ,  $Cl_2$ ,  $HCl$ ,  $C_2H_2$  in the gas phase, and  $B_4C$ , C(graphite), B( $\alpha$ ) in the condensed phase. In addition, we define the total pressure, the temperature, and the initial gas-phase composition (number of moles of species), that is, in our case, for the total pressure  $P = 1$  atm

$$BCl_3 : a \text{ moles} \equiv P_0 BCl_3$$

$$CH_4 : b \text{ moles} \equiv P_0 CH_4$$

$$H_2 : 1-a-b \text{ moles} \equiv P_0 H_2$$

Most of our results are presented in terms of efficiency  $\eta$ .  $\eta$  is defined with respect to the content of  $BCl_3$  for all components of boron

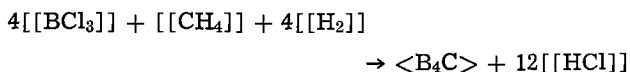
$$\eta_{BCl_3} = \frac{BxCyClzHw}{a} = \frac{x Q_{eq}}{a} 100$$

For C,  $CH_4$ , and  $C_2H_2$  the coefficient of conversion is defined with respect to the initial methane

$$\eta_{CH_4} = \frac{CyHw}{b} = \frac{y Q_{eq}}{b} 100$$

### Results and Discussion

The general behavior of the equilibrium is shown in Fig. 1-9. The variation of the boundaries of the deposition ranges as a function of the initial partial pressures is shown in Fig. 1-3 for three temperatures ( $1400^\circ$ ,  $1800^\circ$ ,  $2200^\circ K$ ). The calculation precision is of  $10^{-8}$  molecule and in this case it follows a same order precision for the individual boundary line evaluations. The dotted line, for the case of B and C atomic balances, represents the stoichiometry of the following reaction



So the diagram is divided in two regions: the upper part which represents all the input values of composition with an excess of boron (with respect to the above-mentioned reaction); the lower part in which are the reactant concentrations with an excess of carbon.

The  $B_4C$  deposit domain is very narrow but it extends into a wide range of initial compositions: into

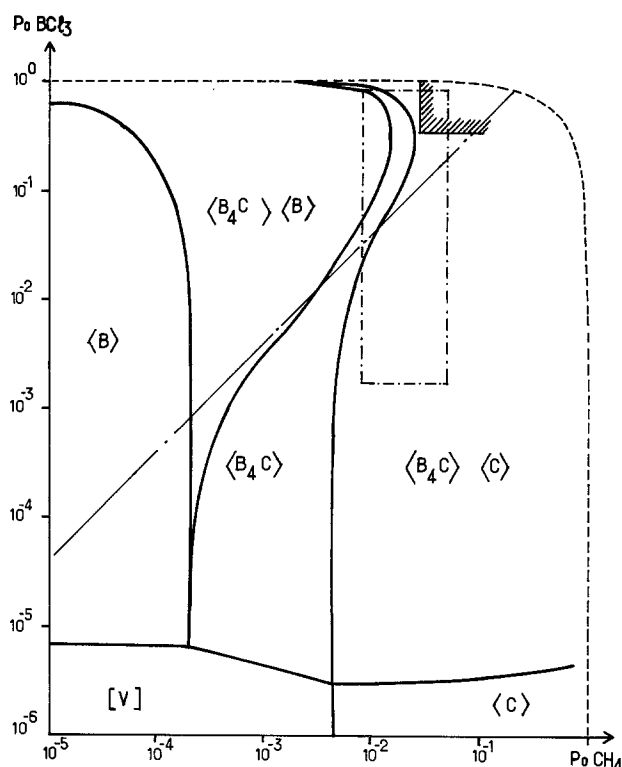


Fig. 1. Deposition domains of the solid species at  $T = 1400^\circ K$ ,  $P = 1$  atm. // = composition range of Fitzer and Röhlm (16), - - - = composition range of Moore and Volk (15).

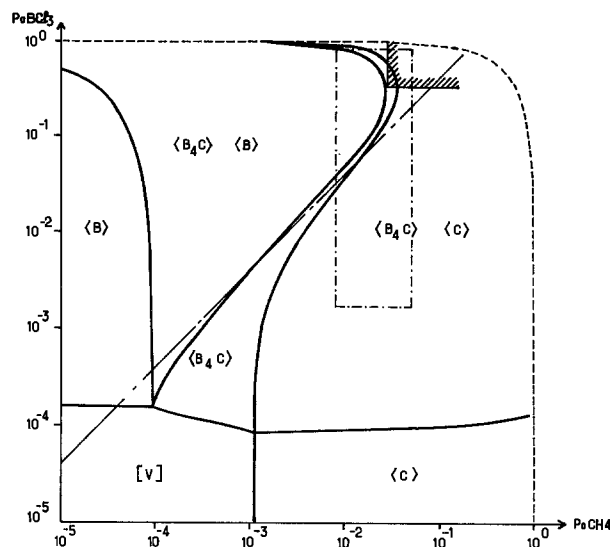


Fig. 2. Deposition domains of the solid species at  $T = 1800^\circ K$ ,  $P = 1$  atm. // = composition range of Fitzer and Röhlm (16), - - - = composition range of Moore and Volk (15).

the carbon-excess side for the low partial pressures of  $BCl_3$  and  $CH_4$ , that is a large excess of hydrogen; into the boron-excess side for initial mixtures with a moderate dilution with  $H_2$ . The domain of pure  $B_4C$  is neighbored by the two-phase domains  $B_4C$ -C and  $B_4C$ -B, it is limited at the lowest part by the gas phase and at its limits by the pure solid-phases B and C.

An increase in the temperature greatly favors the stability of the gas phase and the pure carbon domain. At  $2200^\circ K$  these two phases appear in the upper part of the diagram for high partial pressures of  $BCl_3$  ( $BCl_3 > 0.7$ ). Figure 4 shows the details of this zone. At lower temperature the results of the calculations indicate the same phenomenon. According to Table I we can see the phase boundaries at  $1400^\circ$ - $1800^\circ K$  for different initial concentrations of  $CH_4$ . This table shows

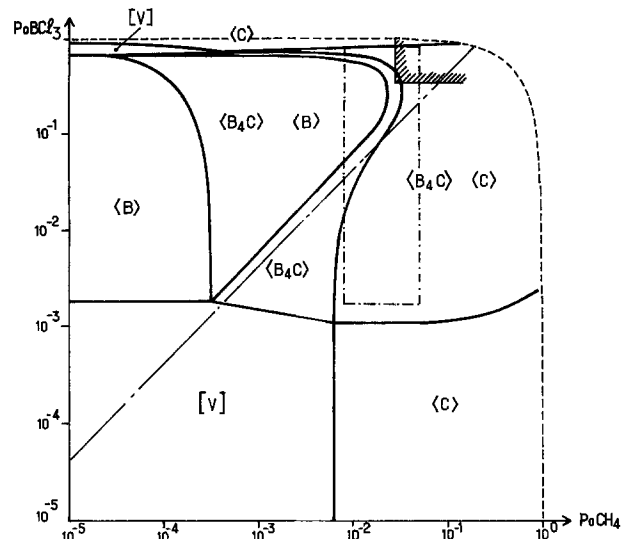


Fig. 3. Deposition domains of the solid species at  $T = 2200^\circ\text{K}$ ,  $P = 1$  atm.  $////$  = composition range of Fitzner and Röhm (16),  $-\cdot-$  = composition range of Moore and Volk. (15).

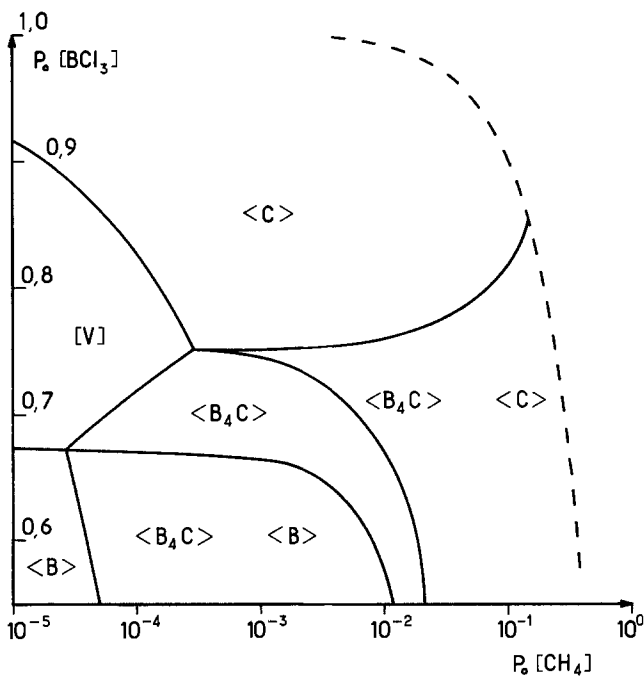


Fig. 4. Details of the deposition domains at  $2200^\circ\text{K}$ ; [V] = vapor phase.

us the precision that the method provides. As a result of the thermodynamic calculation we obtained the gas-phase equilibrium composition. The equilibrium values depend markedly both on the temperature and the excess of hydrogen (that is the ratio  $\text{H}_2/\text{BCl}_3$ ).

In the low temperatures side, the predominant species in the gas phase are  $\text{H}_2$ ,  $\text{HCl}$ ,  $\text{CH}_4$ ,  $\text{BCl}_3$ , and  $\text{BCl}_2\text{H}$ . Dilution with a large excess of  $\text{H}_2$  insures the complete reduction of  $\text{BCl}_3$  producing free boron; the decomposition of  $\text{CH}_4$  is inhibited. As  $\text{H}_2/\text{BCl}_3$  decreases, the formation of  $\text{BCl}_2\text{H}$  increases. When the value of this ratio is unity,  $\text{BCl}_3$  is still present but  $\text{CH}_4$  completely disappears to give free carbon and boron carbide.

In the high temperatures side,  $\text{H}_2$ ,  $\text{HCl}$ ,  $\text{C}_2\text{H}_2$ ,  $\text{CH}_4$ ,  $\text{BH}_2$ ,  $\text{BH}_3$ ,  $\text{BCl}$ ,  $\text{BCl}_2$ , and  $\text{BCl}_3$  are the major species with a trend to the formation of molecules with B-H or C-H bonds as the excess of hydrogen increases. Then the condensed phases completely disappear. If there is no excess of hydrogen, the molecules with B-Cl bonds are mainly formed in the vapor state and solid

Table I. Examples of phase boundaries at  $T = 1400^\circ$  and  $1800^\circ\text{K}$ , vs. initial concentrations\*

$\text{BCl}_3$	$T = 1400^\circ\text{K}$			$T = 1800^\circ\text{K}$	
	$\text{CH}_4$ $1 \cdot 10^{-5}$	$\text{CH}_4$ $1 \cdot 10^{-4}$	$\text{CH}_4$ $2 \cdot 10^{-3}$	$\text{CH}_4$ $1 \cdot 10^{-5}$	$\text{CH}_4$ $1 \cdot 10^{-3}$
0.6	x				
0.65	•				
0.8	"				
0.95	"	•	•	•	•
0.96	"	"	•	•	•
0.97	"	"	○	○	○
0.9755	"	"	"	○	○
0.9757	"	"	"	○	○
0.976	"	"	"	○	○
0.99	•	•	■	■	■
0.995	"	•	"	"	△
0.997	•	○	"	"	"
0.9977	○	○	"	"	"
0.997999	"	■	■	"	"
0.998	"	"	"	"	△
0.9985	○	"	////	"	△
0.99865	■	"	////	"	"
0.9989	△	"	////	"	"
0.999	△	△	////	"	△
0.9991	"	"	////	"	////
0.9999	"	•	////	"	////
0.99999	△	////	////	△	////

\* x = <B>, • = <B<sub>4</sub>C><B>, ○ = <B<sub>4</sub>C>, ■ = <B<sub>4</sub>C><C>, △ = <C>, \* [V] //// = end of calculation.

$\text{B}_4\text{C}$  and  $\text{C}$  tend to deposit. Figure 5 details the phenomenon shown in Fig. 4. If the input partial pressure of  $\text{BCl}_3$  is 0.8 atm, deposition of pure  $\text{B}_4\text{C}$  is impossible for a partial pressure of  $\text{CH}_4$  ranging from  $1 \times 10^{-5}$  to  $7 \times 10^{-2}$ . The homogeneous equilibrium is due to the pressure of  $\text{C}_2\text{H}_2$ ,  $\text{BCl}_2$ ,  $\text{BCl}$ , and  $\text{BCl}_2\text{H}$  and to the high content of  $\text{BCl}_3$  in the equilibrium vapor. The carbon is easily obtained as soon as the amount of  $\text{CH}_4$  in the initial gas is very low (e.g.,  $\text{CH}_4/\text{BCl}_3 = 2.5 \cdot 10^{-4}$ ).

Consequently, it is intended to optimize the input composition of the reactants for a given constant partial pressure of  $\text{CH}_4$  ( $P_0\text{CH}_4 = 2 \cdot 10^{-2}$ ) and a range of  $P_0\text{BCl}_3$  ( $0.1 < P_0\text{BCl}_3 < 0.75$ ), that is, in the widest part of the region in which the deposition of pure  $\text{B}_4\text{C}$  occurs. Variation of the equilibrium yield of each vapor species and condensed phases is shown in Fig. 6-8 for

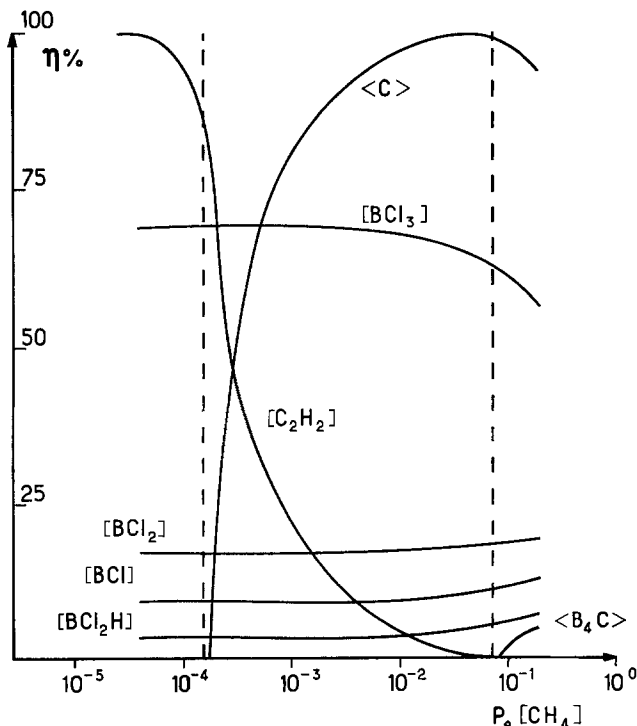


Fig. 5. Variation of the equilibrium yields with  $P_0\text{CH}_4$ ;  $P_0\text{BCl}_3 = 0.8$  atm,  $T = 2200^\circ\text{K}$ .

1400°, 1800°, and 2200°K. The plots illustrate the evolution of the gas phase reactions as a function of temperature. At 1400°K the pure B<sub>4</sub>C is expected to deposit inside a wide concentration range of boron trichloride (from 0.17 to 0.55). At 1800°-2200°K, this range is becoming narrower and is divided in two parts (0.08 <

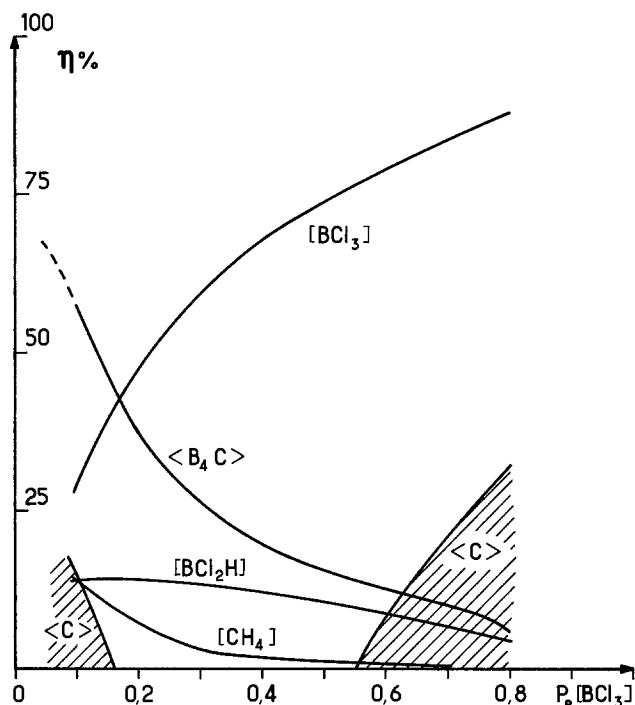


Fig. 6. Variation of the equilibrium yields with  $P_0\text{BCl}_3$ ;  $P_0\text{CH}_4 = 0.02 \text{ atm}$ ,  $T = 1400^\circ\text{K}$ .

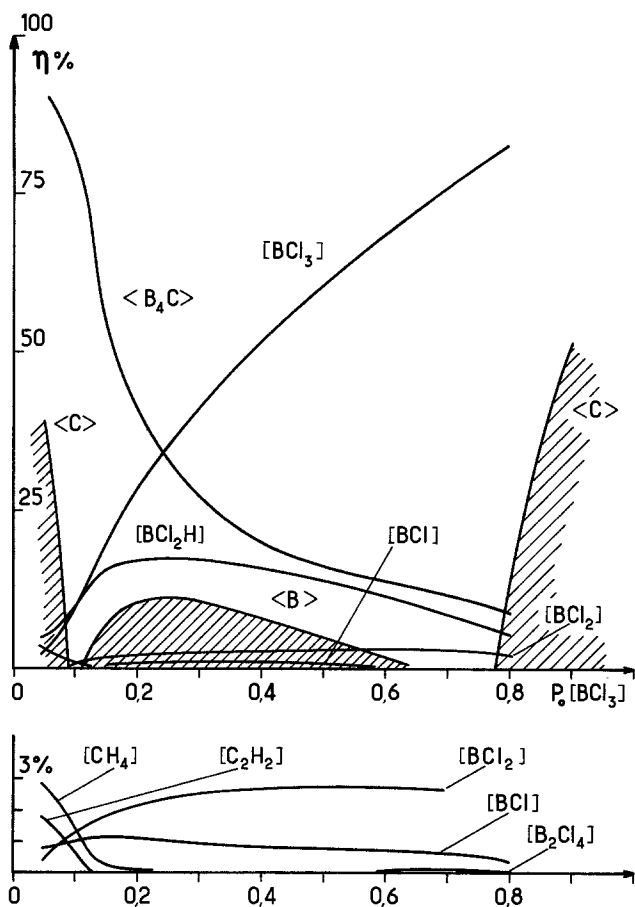


Fig. 7. Variation of the equilibrium yields with  $P_0\text{BCl}_3$ ;  $P_0\text{CH}_4 = 0.02 \text{ atm}$ ,  $T = 1800^\circ\text{K}$ .

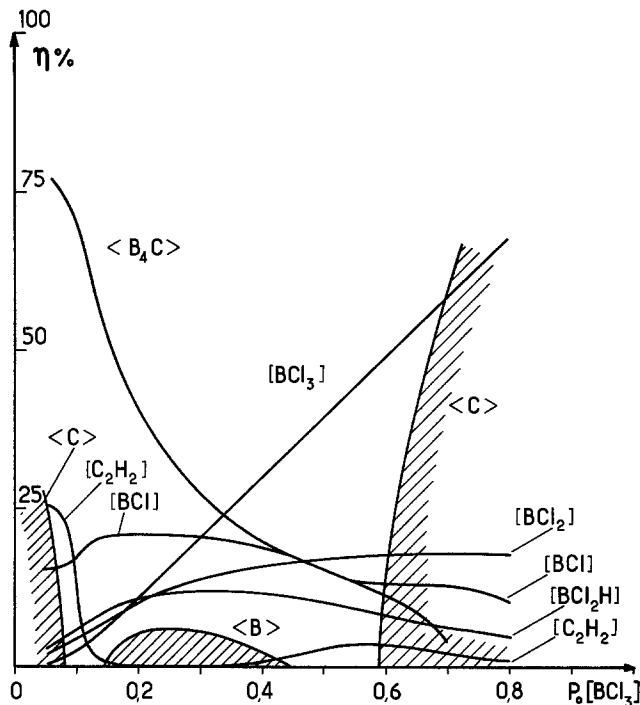


Fig. 8. Variation of the equilibrium yields with  $P_0\text{BCl}_3$ ;  $P_0\text{CH}_4 = 0.02 \text{ atm}$ ,  $T = 2200^\circ\text{K}$ .

$P_0\text{BCl}_3 < 0.12$ ;  $0.64 < P_0\text{BCl}_3 < 0.78$ ) due to the presence of a boron deposit. As shown in Fig. 6-8, the equilibrium amount of boron carbide depends markedly on the initial  $\text{BCl}_3$ ; there is a significant trend toward increasing the solid yield with decreasing the inlet  $\text{BCl}_3$  partial pressure. Therefore we choose  $P_0\text{BCl}_3 = 0.1 \text{ atm}$  to study the amount of thermodynamically available  $\text{B}_4\text{C}$  in relation to the temperature of deposition. The maximum is found at 1900°K for the input partial pressures,  $P_0\text{BCl}_3 = 0.1$ ,  $P_0\text{CH}_4 = 0.02$ ,  $P_0\text{H}_2 = 0.88$  (Fig. 9). In the temperature range 1675°-2075°K, the solid yield is around 75-80%. One must remember that high efficiencies and quality of the deposit may not occur together. Therefore, if a continuous layer is desired, it would be necessary to lower the temperature under 1225°K to be out of a two solid deposit domain.

It is interesting to check the results of the theoretical analysis with experimental data. The work of Moore and Volk concerning the chemical vapor deposition of  $\text{B}_4\text{C}$  from  $\text{BCl}_3$ ,  $\text{CH}_4$ ,  $\text{H}_2$  with various concentrations  $a, b, c \geq 0$  has been employed for comparison. Three types of experiments were performed by these authors. The deposition without hydrogen in the temperature range 1823°-2373°K at low pressures lead to  $\text{B}_4\text{C}$ -C deposits. At 2473°K, under precise experimental conditions, C (graphite) is obtained. With moderate dilu-

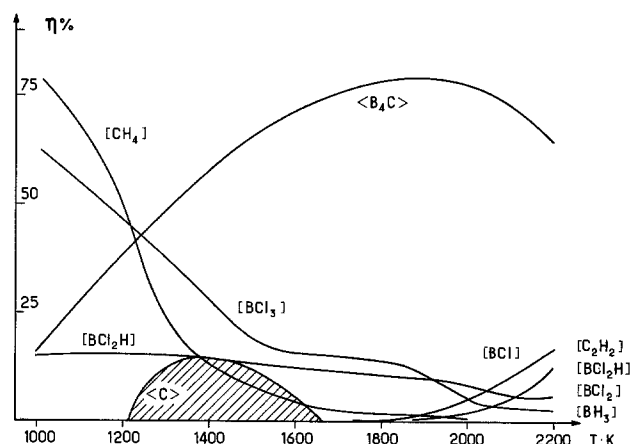


Fig. 9. Temperature dependence of the equilibrium yields;  $P_0\text{CH}_4 = 0.02 \text{ atm}$ ,  $P_0\text{BCl}_3 = 0.1 \text{ atm}$ .

Table II. Comparison of some experimental results (15) and calculations

BCl <sub>3</sub>	CH <sub>4</sub>	H <sub>2</sub>	Moore and Volk			T <sub>K</sub>	Calculations	
			T <sub>K</sub>	P <sub>Torr</sub>	Phases		P <sub>Torr</sub>	Phases
0.604	0.396	0	1823	1	B <sub>4</sub> C-C	1800	1	B <sub>4</sub> C-C
0.2	0.8	0	2473	3.5	C	2200	3.5	C
0.211	0.789	0	2223	4	B <sub>4</sub> C-C	2200	15	B <sub>4</sub> C-C
0.251	0.749	0	2223	4	B <sub>4</sub> C-C	2200	10	C
							15	B <sub>4</sub> C-C
0.604	0.396	0	2223	2.5	B <sub>4</sub> C-C	2200	10	C
							65	B <sub>4</sub> C-C
0.248	0.152	0.6	2223	0.5	B <sub>4</sub> C-C	2200	60	C
							20	B <sub>4</sub> C-C
0.284	0.146	0.570	2223	0.83	B <sub>4</sub> C-C	2200	15	C
							25	B <sub>4</sub> C-C
							20	C

tion of reactants with H<sub>2</sub>, B<sub>4</sub>C-C deposits are formed. Deposition with a large excess of H<sub>2</sub> above 1300°K at low pressures can produce massive B<sub>4</sub>C and boron- or carbon-rich structures depending on the value of CH<sub>4</sub>/BCl<sub>3</sub>.

The comparison of some experimental and calculated results for initial compositions without H<sub>2</sub> and with a moderate dilution is presented in Table II. Agreement is good for the first two cases though the conditions of calculation are slightly different. In Fig. 1-3 a temperature rise produces a wide enlargement of the range of pure carbon, in addition this boundary shift is favored with a decrease in pressure; subsequently, a pure C deposit would be obtained for BCl<sub>3</sub> = 0.2, CH<sub>4</sub> = 0.8, and T > 2200°K. In the other cases the computer results are a bit different. The general trend is to find B<sub>4</sub>C-C deposition for higher values of total pressure than in the experiments of Moore and Volk, but nevertheless of the same order of magnitude. When large excesses of hydrogen are used, the nature of the deposit in relation to the experimental conditions is not sufficiently specified by these authors to allow a valid comparison with calculations. Nevertheless, the deposition of B<sub>4</sub>C-B, B<sub>4</sub>C, and B<sub>4</sub>C-C above 1300°K, for 0.0098 < a < 0.785, 0.0079 < b < 0.049, and 0.166 < c < 0.9823, as a function of the BCl<sub>3</sub>/CH<sub>4</sub> ratio must be compared with Fig. 1-3. They show, in the zone defined by the previous values a, b, and c, the possibility of depositing the different condensed phases. In addition, in this zone, it has been checked that a large reduction of total pressure does not much affect the deposition range of B<sub>4</sub>C; that is, Fig. 1-3 can probably be used for lower pressures.

Moreover, in a recent work, Fitzer and Röhm mention that deposit structures consisting alternatively of boron and boron carbide can be obtained due to an oscillating chemical reaction influenced by mass transport phenomena. Though the deposition conditions are imprecisely defined (BCl<sub>3</sub> 35%, BCl<sub>3</sub>/CH<sub>4</sub> ratios between 10:1 and 1:2, H<sub>2</sub>, 1473° < T < 1973°K, P = 1 atm) this experimental observation can be compared with the fact that the range of input compositions used by these authors extend from the B<sub>4</sub>C single-phase region to the B<sub>4</sub>C-C two-phase region (Fig. 2-3). Thus the different solid phases would be generated by small fluctuations in the initial partial pressures.

## Conclusions

This paper has shown the narrowness of the thermodynamic range of deposition of pure boron carbide and has defined the variation of that range with temperature. The solid phases obtained from the system depend strongly on the initial concentration, in contrast to the phenomenon shown in the previous study of the Ti-C-H-Cl vapor system in which the deposition range of TiC was very wide. The thermodynamic approach is very useful for forecasting the best conditions for deposition, and for determining the influence or different parameters on the gas and solid phases. The maximum yield of B<sub>4</sub>C (75-80%) is obtained between 1675° and 2075°K for the following partial pressures: P<sub>0</sub>BCl<sub>3</sub> = 0.1; P<sub>0</sub>CH<sub>4</sub> = 0.02; P<sub>0</sub>H<sub>2</sub> = 0.88. In addition, the thermodynamic results agree with some previous experiments. Thus, it seems that a real deposition system would be near an equilibrium system.

Manuscript received May 20, 1975; revised manuscript submitted Sept. 16, 1975.

Any discussion of this paper will appear in a Discussion Section to be published in the December 1976 JOURNAL. All discussions for the December 1976 Discussion Section should be submitted by Aug. 1, 1976.

Publication costs of this article were partially assisted by C.N.R.S.

## REFERENCES

1. F. A. Kuznetsov, *Thin Solid Films*, **13**, 303 (1972).
2. H. Nagai, T. Shibata, and H. Okamoto, *Japan J. Appl. Phys.*, **10**, 1337 (1971).
3. S. Minagawa, H. Seki, and H. Eguchi, *ibid.*, **11**, 855 (1972).
4. M. E. Weiner, *This Journal*, **119**, 496 (1972).
5. R. F. Lever, *IBM J. Res. Develop.*, **8**, 460 (1964).
6. L. P. Hunt and E. Stirl, *This Journal*, **120**, 806 (1973).
7. V. S. Kilin, A. I. Evstyukhin, and V. S. Dergunova, *Russ. J. Phys. Chem.*, **42**, 410 (1968).
8. S. Minagawa and H. C. Gatos, *Japan J. Appl. Phys.*, **19**, 844 (1971).
9. D. W. Shaw, Second International Spring School on Crystal Growth, L 11-12, Tokyo, March 31-April 7, 1974.
10. H. E. Carlton, J. H. Oxley, E. H. Hall, and J. M. Blocker, in "Chemical Vapor Deposition: Second International Conference," J. M. Blocher, Jr. and J. C. Withers, Editors, p. 209, The Electrochemical Society Softbound Symposium Series, New York (1970).
11. K. Ploog, *J. Cryst. Growth*, **24**, 197 (1974).
12. S. Mierzejewska and T. Niemyski, *J. Less-Common Metals*, **8**, 368 (1965).
13. A. A. Cochran, J. B. Stephenson, and J. G. Donaldson, *J. Metals*, **22**, 37 (1970).
14. R. G. Bourdeau, U.S. Pat. 3,334,967 (1967).
15. A. W. Moore and H. F. Volk, U.S. Clearinghouse Fed. Sci. Tech. Inform., AD-693882 (1969).
16. E. Fitzer and M. Röhm, in "Chemical Vapor Deposition: Fourth International Conference," G. F. Wakefield and J. M. Blocher, Jr., Editors, p. 133, The Electrochemical Society Softbound Symposium Series, Princeton, N. J. (1973).
17. P. Vay, Ph.D. Thesis, Grenoble (1971).
18. C. Bernard, Y. Deniel, A. Jacquot, P. Vay, and M. Ducarroir, *J. Less-Common Metals*, **40**, 165 (1975).



## Flux Growth of the Gallium Analog of Beta-Al<sub>2</sub>O<sub>3</sub>

L. M. Foster\* and J. E. Scardefield

IBM Thomas J. Watson Research Center, Yorktown Heights, New York 10598

The importance of the alkali aluminate,  $\beta$ -Al<sub>2</sub>O<sub>3</sub>, as a solid electrolyte in secondary batteries and other electrochemical applications is well known (10). The gross features of the  $\beta$ -Al<sub>2</sub>O<sub>3</sub> structure that allow the high mobility of the alkali ions are clearly recognized, and detailed mechanisms of the conduction process have been proposed (2-7). It is recognized that neither Na<sup>+</sup>, Al<sup>+++</sup>, nor perhaps even oxygen itself is specifically required for the high conduction in this structure, but rather an open, highly defective layer in the lattice is necessary through which an ion species can move with a low activation energy *via* a vacancy mechanism. In beta-alumina the requisite structure must result in part from charge compensation by Na<sup>+</sup> and vacancies when the Mg<sup>++</sup> of spinel (MgAl<sub>2</sub>O<sub>4</sub>) is replaced by Al<sup>+++</sup>, but the process is complex and not completely understood.

There is a very large number of other crystals with the spinel structure, and the process of fast ion conduction should be common to many of them if the same charge compensating substitutions can be made. In 1951, Foster and Stumpf (8) described the extensive isomorphism between the alumina and gallia systems and, in particular, prepared the gallium analogs of sodium and potassium beta-alumina.<sup>1</sup> Fast ion conduction has recently been demonstrated in this material (9-11), and it is apparent that it has the same highly defective structure as  $\beta$ -Al<sub>2</sub>O<sub>3</sub>.

In spite of the similarities between  $\beta$ -Al<sub>2</sub>O<sub>3</sub> and its gallium analog, subtle differences are expected which can be exploited to increase our understanding of this interesting class of materials. For example, because Ga<sup>+++</sup> is slightly larger than Al<sup>+++</sup>, the slot width—the distance across the conducting plane—is slightly greater in the gallium analog. This should result in higher conductivity for the gallium compound, especially for the larger alkali ions. The uptake of water in the conduction plane, which has a profound effect on the stability and conductivity of the beta-aluminas (12), is also likely to be quantitatively and perhaps qualitatively different in the gallium analogs. Finally, subtle differences between the Al<sub>2</sub>O<sub>3</sub>-Na<sub>2</sub>O and Ga<sub>2</sub>O<sub>3</sub>-Na<sub>2</sub>O systems should make it possible to elucidate features of these complex phase diagrams by providing an alternative system to study.

It is desirable to employ high quality monocrystals in a study of the properties of a new material. The present paper describes progress toward producing such crystals of the gallium analog of  $\beta$ -Al<sub>2</sub>O<sub>3</sub> by a flux growth method. With growth parameters thus determined, it should also be possible to prepare monocrystalline layers by a liquid-phase epitaxial technique if a suitable substrate can be found.

\* Electrochemical Society Active Member.

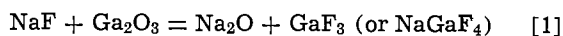
Key words: solid electrolytes, crystal growth, flux growth.

<sup>1</sup> The unfortunate nomenclature error that gave rise to  $\beta$ -Al<sub>2</sub>O<sub>3</sub> is compounded in the gallia system. The metastable phase, alpha-gallia, was named to show the isomorphism with  $\alpha$ -Al<sub>2</sub>O<sub>3</sub>. If this pattern were continued, the high-temperature-stable phase of Ga<sub>2</sub>O<sub>3</sub> would have been called theta to show the analogy to  $\theta$ -Al<sub>2</sub>O<sub>3</sub>. This was not done, however, and, instead, stable Ga<sub>2</sub>O<sub>3</sub> was designated  $\beta$ -Ga<sub>2</sub>O<sub>3</sub> throughout the literature. The gallium isomorphs of  $\beta$ -Al<sub>2</sub>O<sub>3</sub> thus remain nameless and will be referred to herein simply as alkali gallates.

### Experimental

It is known that foreign ions substitute readily in the  $\beta$ -Al<sub>2</sub>O<sub>3</sub> structure, both in the conduction plane and in the spinel body (13, 14). We wished to avoid that complication in the present study and so were restricted to the use of a sodium salt for the flux. However, the use of pure sodium carbonate was known to produce solids far to the Na<sub>2</sub>O side of Ga<sub>2</sub>O<sub>3</sub>-Na<sub>2</sub>O phase diagram, and sodium borate produces a series of complex borates. NaCl exhibits very low solubility for oxides and is not suitable for that reason. NaF emerged, therefore, as the most logical choice.

Early experiments had shown that Na<sub>2</sub>O·*x*Ga<sub>2</sub>O<sub>3</sub> with the  $\beta$ -Al<sub>2</sub>O<sub>3</sub> structure was formed to varying degrees depending on conditions from Ga<sub>2</sub>O<sub>3</sub>-NaF melts (8). Since some Na<sub>2</sub>O was required to produce the gallate, it obviously resulted from partial reaction of the Ga<sub>2</sub>O<sub>3</sub> with the flux, thus



The details of the complex ternary or quaternary system that results are not known. However, it was established empirically that 7.5 weight per cent (w/o) of Ga<sub>2</sub>O<sub>3</sub> will completely dissolve in NaF at 1350°C, and that the liquidus at that composition is about 1300°C. When the Ga<sub>2</sub>O<sub>3</sub> content was higher than about 8%, primary bar-shaped crystals of  $\beta$ -Ga<sub>2</sub>O<sub>3</sub> were found admixed with the Na<sub>2</sub>O·*x*Ga<sub>2</sub>O<sub>3</sub> product. When it was appreciably lower, small needlelike crystals appeared. Their composition was approximately Na<sub>2</sub>O·2.5Ga<sub>2</sub>O<sub>3</sub>, and not the 3Na<sub>2</sub>O·5Ga<sub>2</sub>O<sub>3</sub> phase reported by Boilot *et al.* (9).

Contrary to most solvents that are employed for flux growth of oxides, the NaF in the present case is not the most volatile species. Consequently, one of the preferred growth practices, isothermal vaporization of the flux, is not possible. The most volatile species is GaF<sub>3</sub>, or possibly NaGaF<sub>4</sub>, the gallium analog of aluminum atmolite, NaAlF<sub>4</sub>. Loss of this material by vaporization forces reaction [1] to the right with the formation of more Na<sub>2</sub>O, and changes the composition of the Na<sub>2</sub>O·*x*Ga<sub>2</sub>O<sub>3</sub> product to lower values of *x*. In fact, control of the GaF<sub>3</sub> activity was absolutely essential for reproducibility in the present experiments. This could be accomplished by employing a controlled "leak," such as a hole of predetermined size in an otherwise sealed container. However, we found it more satisfactory to try to assure zero leak rate by use of tightly pressed-in crucible covers or, in some cases, welded closures.

**Growth procedure.**—A suitable charge composition was 78.0 NaF, 6.3 Ga<sub>2</sub>O<sub>3</sub>, and 15.7 NaCl w/o. The NaCl was an inert diluent that was added to facilitate the removal of the flux from the product through formation of the NaF-NaCl eutectic (mp 674°C), and by increasing the solubility of the flux in water.

The dried components were placed into a standard 110 ml conical platinum crucible, and an inverted lid pressed in. If a leak was suspected, the lid was autogeneously welded in. Total charge weights of both 80 and 160g were employed. The charge was held at

1350°C for about 2 hr, then the temperature was lowered at approximately 4°C/hr to 1200°C. The crucible was then inverted so that most of the flux drained away from the crystal product, which generally adhered to the crucible bottom.

When cold, the flux was broken out of the top and the crucible was filled with granular NaCl which was melted and held at approximately 900°C for an additional 2 hr. This further removed residual flux that adhered to the crystals.

Some  $\text{Na}_2\text{O} \cdot x\text{Ga}_2\text{O}_3$  product could be removed at this stage, but generally the crystals adhered tightly to the platinum and, since they are very friable, it was difficult to remove them without damage. Generally it was necessary to boil water in the crucible for an hour or two in order to free them.

**Description of product.**—Typical flux-grown crystals are shown in Fig. 1. The figure illustrates one of the remaining problems with the method: recovery of the product without damage. Although a profusion of small (1-5 mm), free crystals could be recovered that were excellent for x-ray and optical studies, etc., larger ones generally cracked during cooldown because of differential contraction between the platinum or adhering flux and the crystals. This is a common problem of flux growth of most materials and presumably can be alleviated by further manipulation of the heat flow pattern during growth.

The crystals had the  $\beta\text{-Al}_2\text{O}_3$  structure. A comparison of their properties with those of a "standard"  $\beta\text{-Al}_2\text{O}_3$  sample obtained from the Carborundum Company is given in Table I. No fluorine was detectable in the crystals by electron microprobe analysis

### Discussion and Summary

It has been demonstrated that the gallium analog of  $\beta\text{-Al}_2\text{O}_3$  can be grown from a NaF flux. The problems common to most flux growth processes, uncontrolled nucleation and difficulty of recovery of the product, are thought to be solvable with design changes so that larger perfect crystals can be grown. The growth parameters have been sufficiently well established for liquid phase epitaxy to be undertaken as an alternative procedure if a suitable substrate can be found.

The practice of boiling the crystals in water to free them from the crucible, although undesirable, appears not to alter them. An electron microprobe analysis of

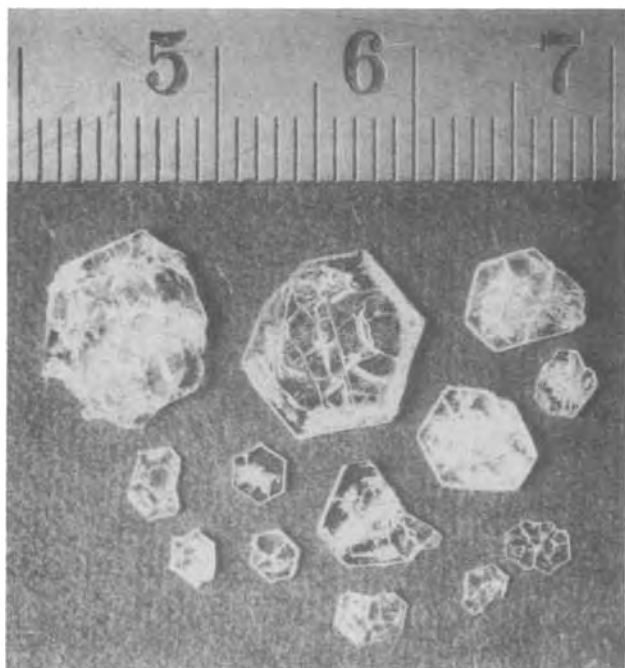


Fig. 1. Crystals of  $\text{Na}_2\text{O} \cdot 7.43\text{Ga}_2\text{O}_3$  grown from a NaF flux

Table I.

	$\text{Na}_2\text{O} \cdot x\text{Ga}_2\text{O}_3$	$\text{Na}_2\text{O} \cdot 8\text{Al}_2\text{O}_3$
Composition*	$x = 7.43 \pm 0.37$	—
Space group	$P6_3/mmc$	$P6_3/mmc$
a	5.81Å	5.61Å
c	23.13Å	22.41Å
Slot width	4.87Å	4.76Å
Index of refraction ( $\eta_0$ )	1.85	1.66

\* By electron probe analysis.

a water-treated surface gave the same sodium content as an analysis of an internal surface exposed by cleaving. It is possible, of course, that sodium might have been extracted from the very outer atomic layers of the crystal and not be detected by this technique.

The Ga analog of the three-block  $\beta''\text{-Al}_2\text{O}_3$  structure was never observed in our experiments, even though the growth temperature was below that where  $\beta''$  transforms irreversibly to  $\beta$  (approximately 1380°C). The reason cannot be insufficient soda content, as is sometimes stated with respect to the alumina system, since when large volatile losses were permitted, the soda-rich phase of composition approximately  $\text{Na}_2\text{O} \cdot 2.5\text{Ga}_2\text{O}_3$  appeared, still without any evidence of a  $\beta''$  phase. As in the aluminum system, the conditions for stability of the three-block phase are unclear, and this is further evidence that the  $\beta''$  phase is metastable, although stabilization of the  $\beta$  phase by traces of fluoride cannot be excluded.

Manuscript submitted June 17, 1975; revised manuscript received Sept. 17, 1975. This was Paper 4 presented at the Toronto, Canada, Meeting of the Society, May 11-16, 1975.

Any discussion of this paper will appear in a Discussion Section to be published in the December 1976 JOURNAL. All discussions for the December 1976 Discussion Section should be submitted by Aug. 1, 1976.

Publication costs of this article were partially assisted by IBM Corporation.

### REFERENCES

1. See, for example: J. T. Kummer, in "Progress in Solid State Chemistry," Vol. 7, Reiss and McCaldin, Editors, Chap. 5, Pergamon Press, Inc., New York (1972); "Fast Ion Transport in Solids—Solid State Batteries and Devices," W. van Gool, Editor, American Elsevier, New York (1973); M. S. Whittingham and R. A. Huggins, in "Solid State Chemistry, Proceedings of 5th Materials Research Symposium," Special Publication No. 364, p. 139, National Bureau of Standards, Washington, D.C. (1972).
2. M. J. Rice and W. L. Roth, *J. Solid State Chem.*, **4**, 294 (1972).
3. H. Sato, *J. Chem. Phys.*, **55**, 677 (1971).
4. W. van Gool, *Ann. Rev. Phys. Chem.*, **25**, 311 (1974).
5. R. D. Armstrong, R. S. Bulmer, and T. Dickinson, "Fast Ion Transport in Solids—Solid State Batteries and Devices," W. van Gool, Editor, p. 269, American Elsevier, New York (1973).
6. R. Kikuchi, *ibid.*, p. 249.
7. H. Rickert, *ibid.*, p. 3.
8. L. M. Foster and H. C. Stumpf, *J. Am. Chem. Soc.*, **73**, 1590 (1951).
9. J. P. Boilot, J. Thery, and R. Collongues, *Mater. Res. Bull.*, **8**, 1143 (1973).
10. H. C. Brinkhoff, *J. Phys. Chem. Solids*, **35**, 1225 (1974).
11. R. J. Chicotka, Abstract 5, p. 16, The Electrochemical Society Extended Abstracts, Spring Meeting, Toronto, Canada, May 11-16, 1975.
12. Ford Motor Company Contract Report No. NSF-C805(AER-73-07199) for period June 30, 1974 to Dec. 31, 1974, p. 106.
13. Y. Y. Yao and J. T. Kummer, *J. Inorg. and Nucl. Chem.*, **29**, 2453 (1967).
14. J. T. Kummer, in "Progress in Solid State Chemistry," Vol. 7, Reiss and McCaldin, Editors Chap. 5, Pergamon Press, Inc., New York (1972).



# The Cathodic Corrosion of Aluminum

E.P.G.T. van de Ven and H. Koelmans

Philips Elcoma H.O.C. Laboratory and Philips Research Laboratories, Eindhoven, The Netherlands

When hydrogen is cathodically evolved at a metal in an electrolyte, an increase of the hydroxyl ion concentration at the electrode surface results. This alcalization effect (1) is responsible for the cathodic corrosion of an amphoteric metal like Al (2). Though this phenomenon has been known for decades, detailed information about how the cathodic corrosion depends on current density, ionic composition of the electrolyte, and especially on temperature is still lacking. The present work, in which we consider the influence of these parameters, is part of an effort aimed at a better understanding of the electrolytic corrosion of the Al metalization tracks on integrated circuits during temperature-humidity-bias tests. The corrosion observed after these tests is often mainly cathodic (3, 4).

## Experimental

The experiments were done with thin disks of 99.99% Al which formed the end faces of a cylindrical cell of polymethylmethacrylate. The Al disks had a diameter of 2 cm and a thickness of 100  $\mu\text{m}$ . The design of the cell is sketched in Fig 1. During the experiments the current was kept constant. The amount of corrosion produced at both the cathode and the anode was determined from weight-loss measurements. The corrosion products were removed with an aqueous solution of  $\text{H}_3\text{PO}_4$  and  $\text{CrO}_3$ .

## Results and Discussion

Figure 2 shows, in an Arrhenius plot, how the rate of electrolytic corrosion at both the cathode and anode depends on temperature. The experiments were done in  $5 \times 10^{-4}\text{N}$  NaCl at a number of constant currents. The rate of corrosion at the anode is independent of temperature at all current densities used. In agreement with others(5) we found that for every three electrons flowing in the external circuit slightly more than one Al atom is oxidized. In our experiments we found 3e equivalent to 1.16 Al.

Corrosion at the cathode is more complicated. In the range of low temperatures the lines for the cathodic attack run parallel to the line found for chemical dis-

Key words: integrated circuits, aluminum metalization, temperature-humidity-bias tests.

solution of the same Al disks in NaOH (see Fig. 2), which suggests that in this temperature range cathodic corrosion is similar to dissolution in an NaOH solution of constant concentration. At higher temperatures the lines for the cathodic corrosion level off to a constant value corresponding to a situation where for every three electrons flowing three atoms of Al pass into solution. Our interpretation is that at higher temperatures all the hydroxyl ions formed by the electrochemical reaction  $\text{H}_2\text{O} + e \rightarrow \text{OH}^- + 1/2\text{H}_2$  are used up in the ensuing chemical dissolution reaction  $\text{OH}^- + \text{Al} + \text{H}_2\text{O} \rightarrow \text{AlO}_2^- + 3/2\text{H}_2$ . In the high-temperature range the rate of cathodic corrosion is limited by the electrochemical production of  $\text{OH}^-$ , i.e., by the current density, independent of temperature. At these high temperatures the over-all reaction is  $\text{Al} + 2\text{H}_2\text{O} + e \rightarrow \text{AlO}_2^- + 2\text{H}_2$ , hence, for every electron one Al atom dissolves, as observed. At lower temperatures the rate of corrosion is limited by the chemical dissolution reaction, part of the  $\text{OH}^-$  ions produced are carried away from the cathode into the bulk of the electrolyte by diffusion and electrical migration. The simple dissolution of Al in NaOH is also limited by the chemical surface reaction  $\text{OH}^- + \text{Al} + \text{H}_2\text{O} \rightarrow \text{AlO}_2^- + 3/2\text{H}_2$ . Therefore, in the low temperature range, the temperature dependenc of cathodic corrosion is described by an activation energy (0.47 eV/at = 10.8 kcal/mole) equal to that observed for the chemical dissolution of Al in NaOH.

The results of Fig. 2 also show that in the lower temperature range the influence of current density is rather weak, an increase in current density by a factor of ten produces an increase in the rate of cathodic corrosion by a factor of only about two. Apparently in the range of the steady-state  $\text{OH}^-$  concentrations produced at the current densities used in our experiments, the influence of  $\text{OH}^-$  concentrations on the chemical dissolution reaction is not very pronounced. The results of Caldwell and Albano (2) also indicate that at low  $\text{OH}^-$  concentration the influence of concentration is rather small.

We next investigated the influence of ionic composition of the electrolyte on cathodic corrosion. The results for a number of electrolytes, all in a concentra-

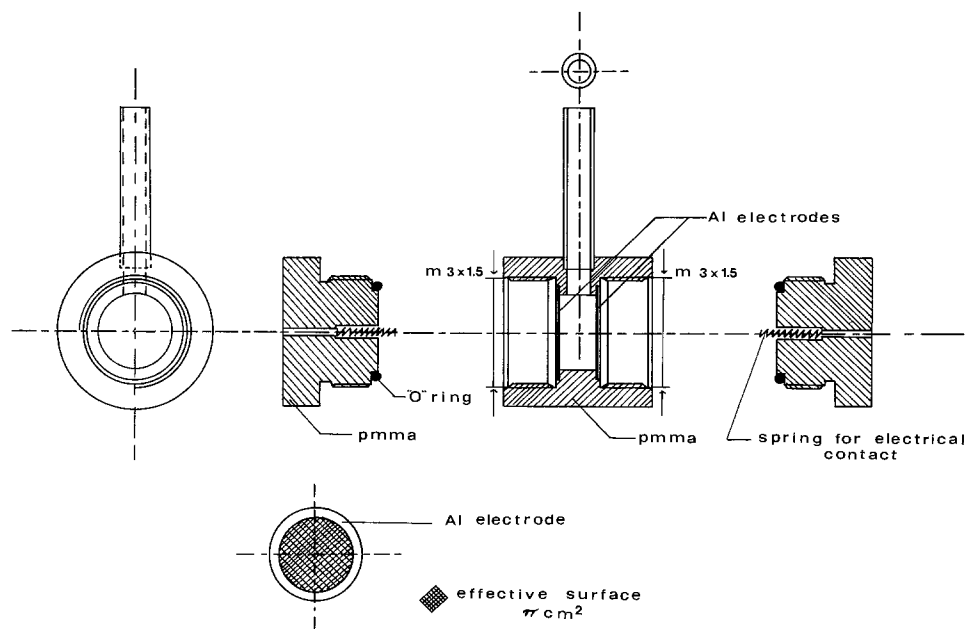
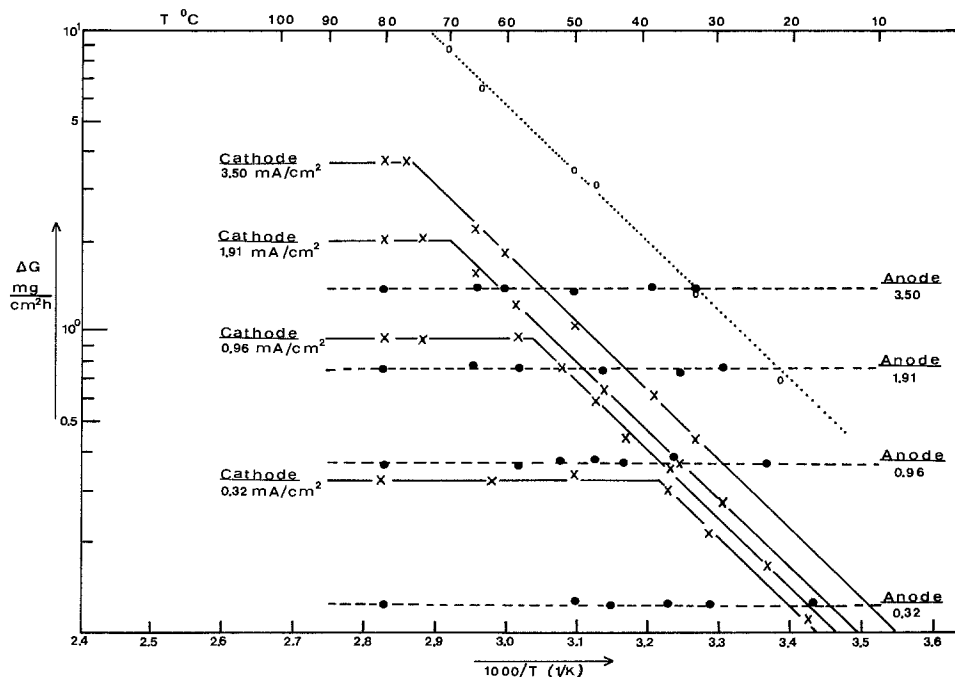


Fig. 1. Design of the cell used in the cathodic corrosion experiments. Cell volume  $\pi \text{ cm}^3$ .

Fig. 2. Arrhenius plot of the rate of cathodic (—) and anodic (----) corrosion of Al at various current densities in NaCl  $5 \times 10^{-4}N$ . Also shown is the line for dissolution of Al in  $2.5 \times 10^{-2}N$  NaOH (.....).



tion of  $5 \times 10^{-4}M$  are summarized in Table I. The results of Table I show that the rate of cathodic Al corrosion does not depend on the nature of the anion used and remains unchanged in an acid medium down to a pH of at least 3.3. In both the neutral and the acid solutions the addition of a drop of phenolphthalein gave a red color at the cathode when the current was switched on. This means that for the current density used ( $1.91 \text{ mA/cm}^2$ ), even in the acid solutions the pH at the surface of the cathode rises to at least 8.5.

### Conclusions

In summary we conclude:

1. The influence of temperature, current density, and ionic composition of the electrolyte on the cathodic corrosion of Al can be interpreted on the basis of the alcalization theory.
2. With regard to the influence of temperature two regions were found: (i) a low-temperature region where the increase in cathodic corrosion with rising temperature is governed by an activation energy equal

to that observed for the chemical dissolution of Al in NaOH, and (ii) a high-temperature region where cathodic corrosion is independent of temperature.

3. In the high-temperature region the cathodic corrosion of Al is proportional to the current density, whereas in the low-temperature region the influence of current density is rather weak.

4. Our experiments show that the cathodic corrosion of Al does not depend on the type of anion used and does not require the presence of large amounts of cations capable of forming a strong base.

Manuscript submitted April 24, 1975; revised manuscript received Aug. 17, 1975.

Any discussion of this paper will appear in a Discussion Section to be published in the December 1976 JOURNAL. All discussions for the December 1976 Discussion Section should be submitted by Aug. 1, 1976.

Publication costs of this article were partially assisted by Philips Research Laboratories.

### REFERENCES

1. K. J. Vetter, "Electrochemical Kinetics," p. 183, Academic Press, New York (1967).
2. B. P. Caldwell and V. J. Albano, *Trans. Electrochem. Soc.*, **76**, 271 (1939).
3. W. M. Paulson and R. W. Kirk, 12th Annual IEEE Reliability Physics Symposium, Las Vegas, Nevada, April 1974, pp. 172-179.
4. H. Koelmans, 12th Annual IEEE Reliability Physics Symposium, Las Vegas, Nevada, April 1974, pp. 168-171.
5. M. E. Straumanis and K. Poush, *This Journal*, **112**, 1185 (1965).

Table I. Cathodic corrosion of Al in various electrolytes, current density  $1.91 \text{ mA/cm}^2$ ;  $T = 25^\circ\text{C}$

Electrolyte $5 \times 10^{-4}M$	Cathodic corrosion ( $\text{mg/cm}^2 \text{ hr}$ )	Electrolyte $5 \times 10^{-4}M$	Cathodic corrosion ( $\text{mg/cm}^2 \text{ hr}$ )
NaCl	$0.19 \pm 0.015$	HCl	0.19
NaNO <sub>3</sub>	0.19	HNO <sub>3</sub>	0.19
Na <sub>2</sub> PO <sub>4</sub>	0.19	H <sub>2</sub> PO <sub>4</sub>	0.18

# Impurity Striations during Faceted Crystal Growth

W. Bardsley and D. T. J. Hurle

Royal Radar Establishment, Great Malvern, Worcestershire, England

The occurrence of impurity striations in melt-grown crystals due to crystal rotation and/or nonsteady convective motion in the melt is now well established. [See, for example, reviews by Hurle (1) and by Gatos and Witt (2).] Recent elegant work by Witt and co-workers (3,4) has shown that while striations occur on both faceted and nonfaceted portions of the growth surface, the operative mechanisms are different. Specifically, in nonfaceted regions striations result from modulation of the microscopic growth rate (3) and are particularly pronounced if "melt-back" occurs during part of the periodic growth cycle. Clearly, the striations arise from modulation of the height of the impurity boundary layer by the varying growth rate. In contrast, on faceted growth surfaces the microscopic growth rate appears to be sensibly constant (4) despite the presence of temperature fluctuations or oscillations in the bulk of the melt and the occurrence of striations is ascribed to modulation of the thickness of the impurity boundary layer by the nonsteady convective motion.

In recent experiments under conditions of near-zero gravity aboard Skylabs III and IV where gravity-induced convection was suppressed, Witt *et al.* (5) demonstrated that striations were eliminated in melt-grown Te-doped InSb except that they observed irregularly spaced striations remaining on peripheral facets [Fig. 17 and 18 of Ref. (5)]. The authors ascribed these anomalous striations to the occurrence of nucleation at the exterior edge of the facet where its rate would be sensitive to vibration or to the arrival of a foreign particle.

The purpose of this note is to report the occurrence of similar striations on an earth-grown single crystal of Ga-doped Ge grown some years ago by the authors during a study of the effects of constitutional supercooling (6-8). However, these striations occurred on microfaceted regions of the crystal growth surface well away from its free surface and had a relatively regular periodicity (Fig. 1). The crystals were grown on a  $\langle 110 \rangle$  axis by pulling from the melt without rotation of either the crystal or the crucible. The pull rate was

Key words: crystal growth, growth striations, germanium, semiconductor single crystal.

9 cm/hr and the concentration of Ga was adjusted so as to produce a cellular structure over the whole of the growth surface. This cellular structure consisted of a corrugated array composed of  $\{111\}$  microfacets. The section shown in Fig. 1 contains the growth axis and is orthogonal to the axis of the corrugations. Some of the cells exhibit bands of striations. The distribution of the bands and their extent are apparently quite random. They start and stop quite abruptly. The etchant used was 1.3 HF:HNO<sub>3</sub> at 70°C; it is of course possible that other etchants might have revealed additional striae, but in any event it is clear that two different modes of growth can occur in any given cell. The fact that the striations start and stop at the same time on each of the pair of facets which make up the cell suggests that nucleation of layer growth on both faces is occurring at the line of intersection, i.e. at the apex of the cell. These observations suggest that the process is a fundamental one involving some form of oscillatory coupling between the nucleation event and the solute and thermal fields rather than due simply to foreign particles. The temporal spacing of the striae is of the order of 1 sec. The fact that neighboring cells do not show the same effect at the same time implies that the process must be very sensitive to the longer range solute field. It seems likely that the explanation must involve a mechanism for the periodic growth of the cell apex which modulates the rate of supply of layer sources; an explanation involving step bunching [see, for example, Parker's review (9) on the kinematic theory of layer growth] seems less probable.

Manuscript submitted Aug. 18, 1975; revised manuscript received Sept. 22, 1975.

Any discussion of this paper will appear in a Discussion Section to be published in the December 1976 JOURNAL. All discussions for the December 1976 Discussion Section should be submitted by Aug. 1, 1976.

## REFERENCES

1. D. T. J. Hurle, *J. Cryst. Growth*, **13/14**, 39 (1972).
2. H. C. Gatos and A. F. Witt, in "Recent Advances in Science and Technology of Materials," Vol. I,

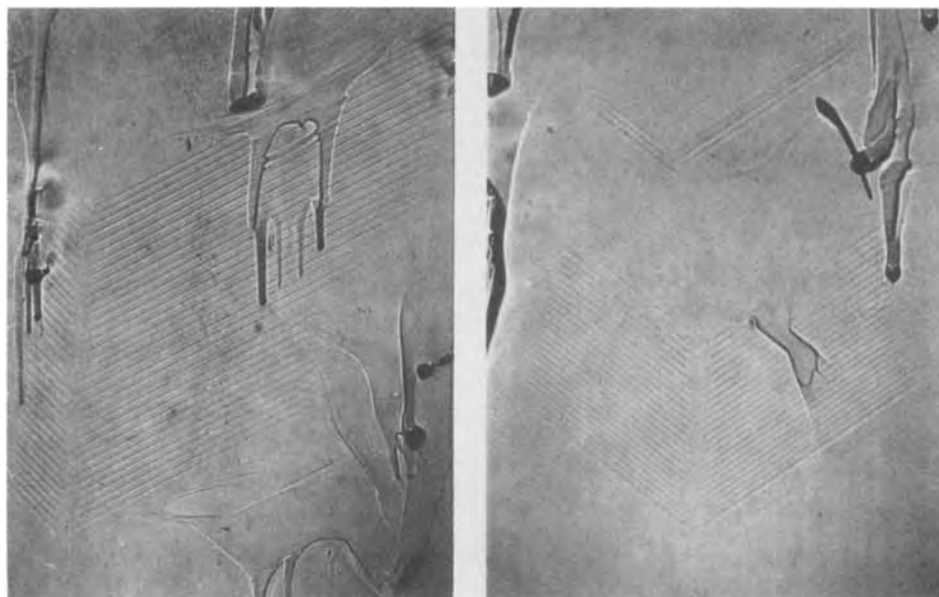


Fig. 1. Two nonadjacent regions of  $\langle 110 \rangle$  Ga-doped Ge single crystal showing striations on the  $\{111\}$  microfaceted cells (the growth axis is vertically downward). The "paint tears" effect is the result of the migration of trapped liquid gallium droplets (8). Magnification: X70.

- A. Bishay, Editor, p. 59, Plenum Publishing Co., New York (1974).
3. A. F. Witt, M. Lichtensteiger, and H. C. Gatos, *This Journal*, **120**, 1119 (1974).
  4. *Ibid.*, **112**, 787 (1974).
  5. A. F. Witt, H. C. Gatos, M. Lichtensteiger, M. C. Lavine, and C. J. Herman, *ibid.*, **122**, 276 (1975).
  6. D. T. J. Hurle, *Solid-State Electron.*, **3**, 37 (1961).
  7. W. Bardsley, J. M. Callan, H. A. Chedzey, and D. T. J. Hurle, *ibid.*, **3**, 142 (1961).
  8. W. Bardsley, J. S. Boulton, and D. T. J. Hurle, *ibid.*, **5**, 395 (1962).
  9. R. L. Parker, in "Solid State Physics: Advances in Research and Applications," Vol. 25. H. Ehrenreich, F. Sietz, and D. Turnbull, Editors, p. 151, Academic Press, Inc., New York (1970).
  10. D. T. J. Hurle, J. B. Mullin, and E. R. Pike, *Phil. Mag.*, **9**, 423 (1964).

## Brief Communications



### The Effect of a Prior Sirtl Etch on Subsequent Thermally Induced Processing Damage in Silicon Wafers

W. A. Porter, D. L. Parker, and L. G. Reed

*Institute for Solid State Electronics, Texas A&M University, College Station, Texas*

Sirtl etch (1) has traditionally been used to identify the presence and density of dislocations in silicon. The relationship between the levels of stress in silicon, and the formation of dislocations by thermal cycling has previously been established (2). Furthermore, it has been shown that residual impurities such as chromium left by Sirtl etching can be removed (3), reducing dangers of contamination. This note reports that prior Sirtl etching of silicon wafers results in reduced dislocation densities after subsequent thermal cycling.

#### Experimental

The photographs in Fig. 1, 2, and 3 are x-ray topographs of the same 2 in. silicon wafer. A modified Berg-Barrett type camera was used with copper radiation and the (440) reflection. The topograph in Fig. 1

Key words: defects, damage, processing, silicon.

was made after diamond scribing a line across the front (polished) side of the wafer, two triangles on the front side, two triangles on the backside (unpolished), and the S-3 nomenclature on the front side. (The two fainter triangles in the topograph are on the back side of the wafer.) The topograph in Fig. 2 was made after the right half of the wafer was given a 5 min Sirtl etch. Note that the scribe marks in the Sirtl etched half are now barely visible. This illustrates the well-known ability of the etch to relieve stress due to lattice damage.

The topograph shown in Fig. 3 was made after an 8200Å oxide was grown in steam at 1100°C. The wafer was processed horizontally on a flat quartz boat with the edges of the wafer near the ends of the scribed line overhanging the edges of the carrier about ¼ in. on each side. Of course, the maximum thermal

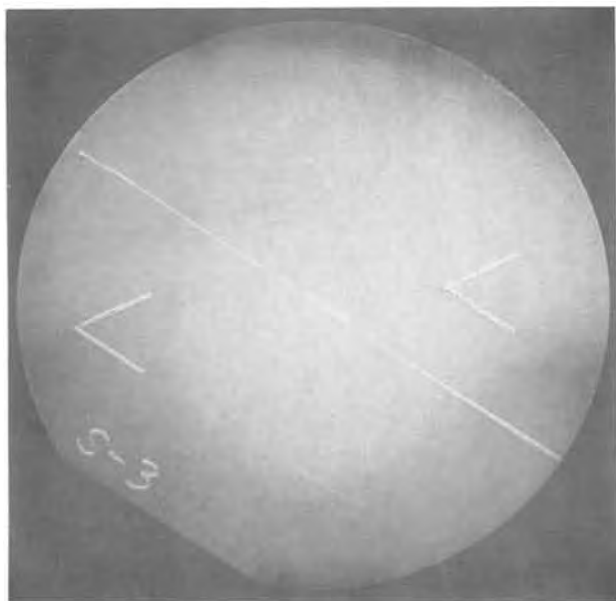


Fig. 1. An x-ray topograph of the 2 in. silicon wafer after scribing.

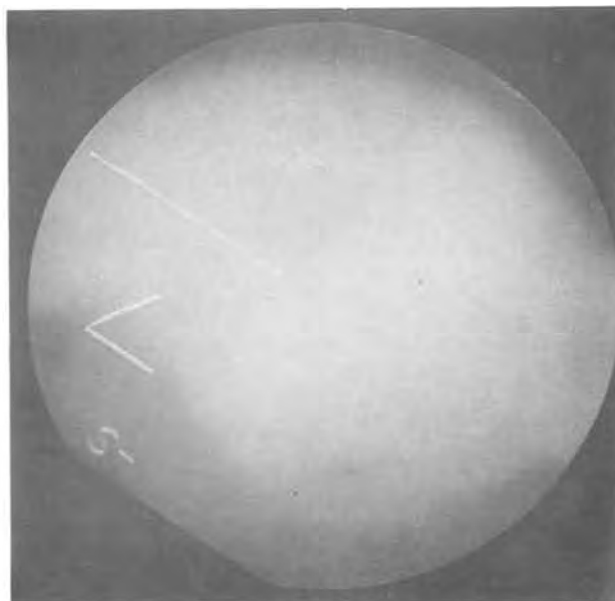


Fig. 2. An x-ray topograph of the same wafer after the right half was given a 5 min Sirtl etch.

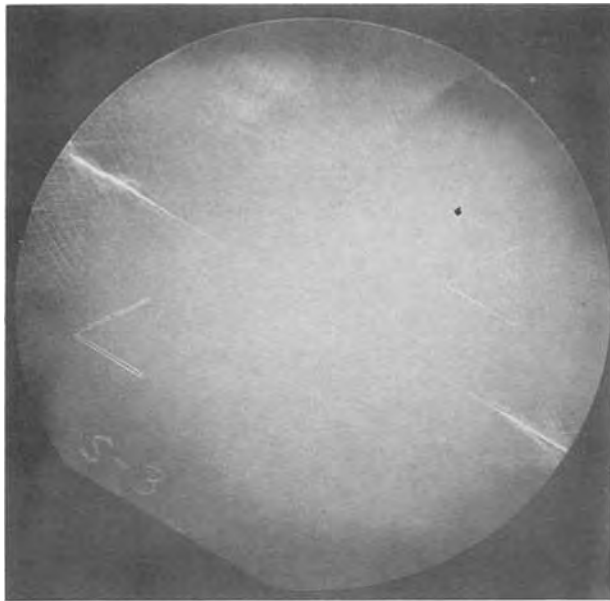


Fig. 3. An x-ray topograph of the wafer after a thermal oxidation step. Note the relative abundance of processing damage on the half of the wafer that was not stress relieved.

stress during insertion and withdrawal from the furnace is produced in the overhanging area of the wafer. Note that there is considerably less process-induced slip damage in the etched half of the wafer. Careful examination of this topograph will reveal the location

of the meniscus produced in the etch solution. It is seen at the wafer's edge between the S and the 3 and extends to the opposite edge of the wafer.

### Conclusion

Visual demonstration using x-ray topography has been given to demonstrate the reduction in thermally generated defects in silicon when a stress relief Sirtl etch is used prior to thermal processing. The potential influence and application of this technique to silicon devices is presently being studied and is the objective of a masters thesis, where preliminary results indicate that a Sirtl etch as short as 30 sec provides significant reduction in subsequent process-induced damage.

### Acknowledgments

This research was supported by NASA and the Air Force under NASA contract NAS8-26379.

Manuscript received July 17, 1975.

Any discussion of this paper will appear in a Discussion Section to be published in the December 1976 JOURNAL. All discussions for the December 1976 Discussion Section should be submitted by Aug. 1, 1976.

Publication costs of this article were partially assisted by Texas A&M University.

### REFERENCES

1. V. E. Sirtl and A. M. Adler, *Z. Metallk.*, **52H**, 529 (1961).
2. W. A. Porter, D. D. Drew, and J. S. Linder, *J. Appl. Phys.*, 1477 (1972).
3. W. A. Porter, A. Gupta, and D. L. Swindle, *This Journal*, **120**, 589 (1973).

## Vapor-Phase Growth of Thin GaAs Multilayer Structures

K.-H. Bachem and M. Heyen

*Institute of Semiconductor Electronics/Sonderforschungsbereich 56, Technical University, Aachen, Germany*

The ability to deposit multilayer epitaxial structures has become an essential requirement for the fabrication of properly functioning GaAs devices. As an example, conventionally constructed MESFET's using a single epitaxial layer grown directly on a semi-insulating substrate exhibit loops and poor saturation behavior in their I-V characteristics. It has been found recently, in this laboratory as well as by other workers (1-3), that these undesirable effects are greatly reduced by depositing an undoped buffer layer between substrate and active film. In the present report we will describe the special technique which we have successfully employed to obtain sequences of differently doped epitaxial layers in one run under well-defined conditions.

A schematic diagram of the apparatus for deposition of epitaxial layers from the  $\text{AsCl}_3\text{-H}_2\text{-Ga}$  system, as used in this work, is shown in Fig. 1. The reactor is distinguished from conventional systems by the design of the substrate holder (4), as will become clear in the description of a typical loading and deposition sequence. After chemically etching in an aqueous  $\text{H}_2\text{SO}_4\text{-H}_2\text{O}_2$  solution and cleaning in organic solvents, the GaAs substrate is subsequently inserted into the depression of the base plate. It is covered by the quartz plate and  $\text{H}_2$ -flushed cap and introduced into the apparatus. The entire reactor is flushed with  $\text{H}_2$  and heated up. The Ga source is saturated with As at  $880^\circ\text{C}$  under formation of a GaAs crust. As a next step the source temperature is slowly decreased during which

time the reactor is being etched using the upper gas inlet. When the deposition conditions (substrate temperature  $750^\circ\text{C}$ , source temperature  $850^\circ\text{C}$ ) have been reached, the etching is terminated and the deposition flow switched on. The gas phase is allowed to reach a stable composition. At this point, cap and plate are removed to the position shown by the dashed lines, thereby initiating the deposition process. After the desired growth has been effected, the cover is put back in place, thus terminating the deposition. New deposition conditions are now established in the system and the

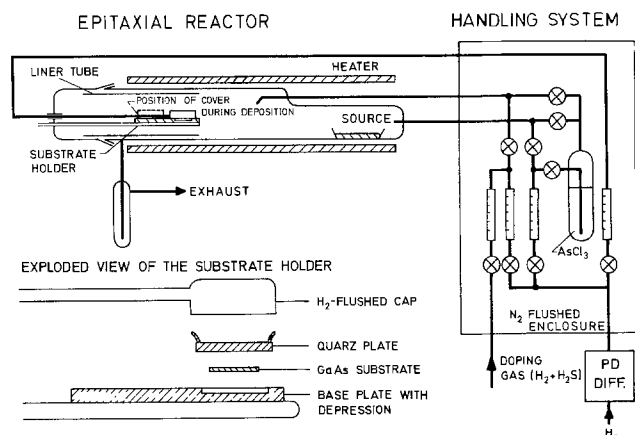


Fig. 1. Schematic diagram of the epitaxial deposition system

\* Electrochemical Society Active Member.  
Key words: gallium arsenide submicron multilayer, gallium arsenide MESFET, gallium arsenide steady-state growth and doping.

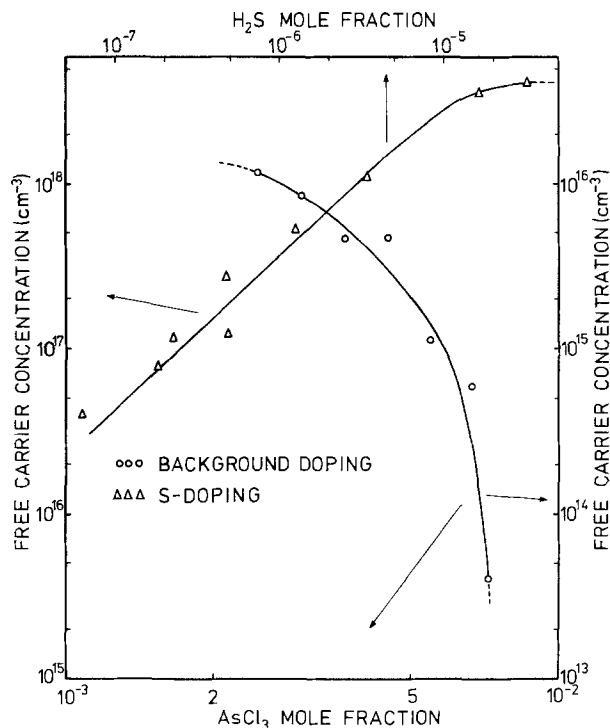


Fig. 2. Variation of the free carrier concentration  $n$  ( $\text{cm}^{-3}$ ) with  $\text{AsCl}_3$  mole fraction (background doping) and  $\text{H}_2\text{S}$  mole fraction at  $\text{AsCl}_3$  mole fraction of  $6.67 \cdot 10^{-3}$  (S-doping).

apparatus is ready for growth of a next layer for a preset gas-phase composition.

Because the growth rates in the  $\text{AsCl}_3$ - $\text{H}_2$ -Ga system are relatively high, the growth of submicron layers requires the ability to select well-defined, very short deposition times. The ability to remove and close the cover in approximately 2 sec means that this second condition is also fulfilled in our apparatus.

In the apparatus, doping levels from the  $10^{13}$  to the  $10^{18} \text{ cm}^{-3}$  range have been reproducibly obtained, and one can grow a low-doped layer immediately after a high-doped layer without contamination of the former by the latter. The range below  $1 \cdot 10^{16} \text{ cm}^{-3}$  is controlled by the well-known  $\text{AsCl}_3$  mole fraction dependence of the background doping (2, 6, 7). The larger values are realized by injecting a  $\text{H}_2\text{S}$ - $\text{H}_2$  mixture into the gas stream (Fig. 2). For each run the doping gas was premixed in a stainless steel container from  $\text{H}_2$  and a 1000 ppm  $\text{H}_2\text{S}$ -in- $\text{H}_2$  source. It was injected into the reactor at a constant flow rate in all experiments. The concentration in the container was determined photometrically using the methylene blue method (8) after extracting the  $\text{H}_2\text{S}$  from a predetermined volume of doping gas with an aqueous zinc acetate solution.

A typical example of the structures prepared by this method is the following double layer epitaxial film for MESFET application. At the before-mentioned system temperatures, an  $\text{AsCl}_3$  mole fraction of  $7.1 \cdot 10^{-3}$ , and a flow rate of 950 ml/min (tube diameter: 60 mm), the film growth rate of  $0.3 \mu \text{ min}^{-1}$  is obtained. Since the structure consists of a  $1.5 \mu$  thick buffer layer ( $n = 4 \cdot 10^{13} \text{ cm}^{-3}$ ) and a  $0.1 \mu$  active layer ( $n = 2 \cdot 10^{17} \text{ cm}^{-3}$ ), a deposition time of only 20 sec is required for the second film. The doping profile obtained from C-V measurements shows a steep transition between the layers; it drops from  $1 \cdot 10^{17}$  to  $1 \cdot 10^{16}$  in  $0.054 \mu$ , which is very close to the value calculated by Johnson and Panousis (5) for an idealized steplike doping profile. For the transition between active layer and substrate in the conventional structure, the considerably larger distance of  $0.12 \mu$  was found for the same drop. This observation is indicative of the boxlike impurity profile attainable with the present apparatus in the case of the double layer structure.

Results on these and other device applications of the described deposition technique will be published elsewhere.

Manuscript submitted Jan. 23, 1975; revised manuscript received Aug. 15, 1975. This was Paper 264RNP presented at the New York, New York, Meeting of the Society, Oct. 13-17, 1974.

Any discussion of this paper will appear in a Discussion Section to be published in the December 1976 JOURNAL. All discussions for the December 1976 Discussion Section should be submitted by Aug. 1, 1976.

Publication costs of this article were partially assisted by the Technical University, Aachen.

#### REFERENCES

1. L. Hollan, "GaAs 1974 Symposium Proceedings," Institute of Physics and the Physical Society, p. 22 (1975).
2. T. Nozaki, M. Ogawa, H. Terao, and H. Watanabe, *ibid.*, p. 46.
3. M. J. Cardwell, I. Goddridge, and J. A. Turner, Paper presented at ESSDERC 1974, Nottingham, England (1974).
4. K.-H. Bachem, G. Erlaki, and W. Markert, "Chemical Vapor Deposition, Fourth International Conference," G. F. Wakefield and J. M. Blocher, Jr., Editors, p. 296, The Electrochemical Society Soft-bound Symposium Series, New York (1973).
5. W. C. Johnson and P. T. Panousis, *IEEE Trans. Electron. Devices*, **ED-18**, 965 (1971).
6. J. V. Dilorenzo, *J. Cryst. Growth*, **17**, 189 (1972).
7. D. J. Ashen, P. J. Dean, D. T. J. Hurle, J. J. Mullin, A. Royle, and A. M. White, "1974 GaAs Symposium Proceedings," Institute of Physics and the Physical Society, p. 229 (1975).
8. M. S. Budd and H. A. Bewick, *Anal. Chem.*, **24**, 1536 (1952).



## Ni-Cd Cell Simulation: A New Model for Satellite Power Systems Application

A. R. Durando

*Chevron Oil Field Research Company, La Habra, California 90631*

and C. T. Leondes

*School of Engineering and Applied Science, University of California, Los Angeles, California 90024*

### ABSTRACT

A new mathematical model has been developed for a nickel-cadmium electrochemical cell for simulation of a satellite solar array-battery power system. Since temperature variations in the system are caused primarily by the thermodynamics of the charge-discharge process and by the coupling between the electrical and chemical phenomena, the new model is intended to stress these characteristics. A mixed theoretical and empirical approach is followed, using fundamental relationships to describe the mechanisms underlying the process and empirical equations to describe those phenomena which are not clearly understood theoretically but are well documented experimentally. The resulting model consists of three nonlinear, time variant, ordinary differential equations with five unknown parameters to be identified to match an experimental trajectory. The three states of the system are the cell reversible potential, temperature, and concentration. The model is applicable to other types of cells with minor modifications.

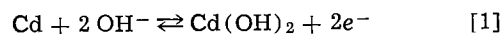
Many battery power system models in present use rely on table-look-up techniques and describe static conditions, such as capacity and charge-discharge efficiency at standard constant rates (1, 2). The behavior of electrochemical cells is usually represented by purely electrical relationships, where all effects which are not electrical in nature are neglected. Graphic techniques based on battery test data, formerly developed for use in hand calculations (3), have been extended through digital computer applications to handle complete electrical power systems (1). The Power Subsystem Orbital Performance Analysis Program (4) combines the electrical analysis with a transient thermal analysis of that portion of the spacecraft whose thermal characteristics interact with the electric power system. The transient thermal analysis is accomplished by performing successive electrical solutions at relative short time intervals, calculating the heat dissipation and temperature of each of the components of interest, and summing the temperature increments algebraically over the total time period. While the temperature variations are accounted for, they are not described by mathematical relationships based on fundamental mechanisms regulating the thermodynamic processes involved with the cell operation. Other investigators (2) have used a complete set of mathematical relationships for each of the black boxes within the power system. They consider all functional relationships concerning voltage, current, and temperature from the point of view of an equivalent electrical cir-

cuit. No chemical and thermodynamical phenomena are described in the model.

The present model is an attempt to describe the basic phenomena occurring during the charge-discharge operation of an electrochemical cell. All relationships are derived from fundamental equations that are well known in the respective disciplines from which they are taken and are combined to obtain differential equations that represent the transient behavior of the variables of interest. Some empirical equations are used to describe processes for which no better relationships are known, but they do not enter into the dynamics of the system.

### The Nickel-Cadmium Cell

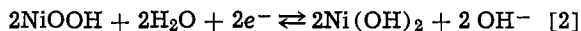
The reactions of the nickel-cadmium cell have been the subject of extensive investigation (5-8). A complete description of the chemical process must account for various secondary reactions which may occur depending on the state of charge and the operating conditions. The basic charge-discharge reactions are usually recognized to occur as indicated below. At the negative electrode (anode during discharge) the main reaction may be written



so that on discharge the cadmium metal is emitting bivalent ions, immediately reacting with the hydroxyl ions of the electrolyte (normally KOH) to form cadmium hydroxide (5).

The reactions of the positive electrode are still in

some doubt, but the one most commonly reported is (1, 5)



where it can be assumed that trivalent nickel ions are formed by dissolution and dissociation of NiOOH. On discharge they are transformed into bivalent nickel ions, which react almost instantaneously with the hydroxyl ions of the electrolyte, forming nickel (II)-hydroxide.

Among the most significant secondary reactions are those that involve evolution of gases from the electrodes. Of these, only overcharge is considered in this model.

### Electrical Model

The framework on which the model is based lies in the electrical analog of the electrochemical cell. The electrical circuit corresponding to the charging phase of the cell operation is shown in Fig. 1. The charging control,  $U$ , a voltage applied at the cell terminals, may be a constant, a step function, or a continuous function of time, depending on what charge control policy has been adopted. The counterelectromotive force within the cell is given by the sum of the cell's reversible potential,  $E_r$ , and the counterelectromotive force of polarization,  $E_a$ . These potentials are described in detail in the sequel. The various impedances in the diagram refer to processes that are well simulated by resistors because of their physical characteristics.  $R_t$  corresponds to the cell terminal impedance, assumed constant within the range of application of the model.  $R_i$  is the internal impedance, a variable function of various parameters.  $R_l$  is a constant impedance corresponding to the cell leakage path.  $R_o$  is an impedance corresponding to the overcharge process.

Network analysis of the model in Fig. 1 yields a set of equations which constitute the electrical constraints on the system. Since the circuit as represented contains no energy storage elements (capacitors, inductors), the resulting equations do not contain any dynamic term and correspond to steady-state relationships.

Mesh equations can be established and solved (9) for the currents through each branch of the network, as functions of the state of the system. The solution yields the following equations

$$I_{\text{tot}} = \frac{U(R_i R_l + R_l R_o + R_l R_o) - (R_o R_l) E_a + E_r}{R_t(R_i R_l + R_l R_o + R_l R_o) + R_l R_l R_o} \quad [3]$$

$$I_r = \frac{R_o}{R_o + R_l} \left[ \frac{I_{\text{tot}}(R_l R_o + R_l R_l) - R_o(E_r + E_a)}{R_l(R_l + R_o) + R_l R_o} \right]$$

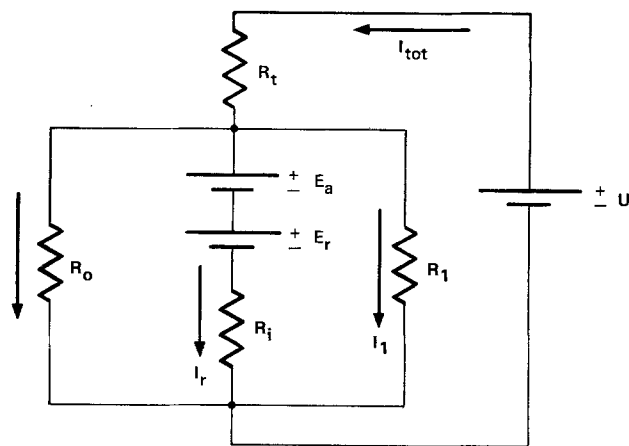


Fig. 1. Electrical model.  $U$ , applied voltage, control;  $E_a$ , polarization potential;  $E_r$ , cell reversible potential;  $R_t$ , cell terminals impedance;  $R_l$ , leakage path impedance;  $R_o$ , overcharge path impedance;  $R_i$ , cell internal impedance;  $I_{\text{tot}}$ , total current through cell;  $I_l$ , leakage current;  $I_o$ , overcharge current;  $I_r$ , reversible reaction current.

$$I_1 = I_{\text{tot}} \left[ 1 - \frac{R_l R_o + R_l R_l}{R_l(R_l + R_o) + R_l R_o} \right] + \frac{R_l R_o + R_l R_l}{R_l(R_l + R_o) + R_l R_o} \quad [5]$$

$$I_o = \frac{I_{\text{tot}} R_l (R_l R_o + R_l R_l) + (E_r + E_a) (R_l R_l + R_l R_o)}{(R_o + R_l) (R_l R_l + R_l R_o + R_l R_o)} \quad [6]$$

where  $R_t$  and  $R_l$  are constants;  $R_o$ ,  $R_i$ ,  $E_a$ ,  $E_r$ , and  $U$  are functions of time. These equations describe the electrical state of the cell and must be satisfied at every instant time during the dynamic evolution of the system. Thus, Eq. [3] through [6] represent a set of algebraic constraints on the dynamic system whose differential equations are derived in the sequel.

Various types of overpotential are exhibited by the nickel-cadmium cell. The ohmic overpotential, because of its nature, behaves like a resistance and it can be incorporated with the terminal impedance,  $R_t$ , which affects the same current path. The concentration overpotential, caused by the concentration gradient of  $\text{OH}^-$  ions in solution, is relatively small during normal operation and is neglected here. The activation overpotential, defined as the sum of the discharge and reaction overpotentials (10) (principally caused by hydrogen and oxygen evolution at the electrodes), is accounted for in the model as a counterelectromotive force,  $E_a$ , which opposes the flow of current through the reversible path (see Fig. 1). The activation overpotential is electrically in series with the cell reversible potential,  $E_r$ , and it changes polarity between charge and discharge, so that it always opposes the direction of flow of the current through the reversible path.

The activation overpotential of a cell depends greatly on its electrical characteristics and on the operating conditions. Most noticeably,  $E_a$  depends on the system's state of charge, current, and temperature. The dependence of overpotential upon current density is well represented by the Tafel equations, written as

$$E_a = k_1 T + k_2 T \log I_r, \quad E_a > 0.05 V \quad [7]$$

$$E_a = k_3 T I_r, \quad E_a \leq 0.05 V \quad [8]$$

where  $k_1$ ,  $k_2$ , and  $k_3$  are empirical constants. Equations [7] and [8] can be fitted to any given galvanic cell in terms of polarization *vs.* current data, with temperature as a parameter.

Because of the multiplicity of phenomena affecting the overcharge current, no simple theoretical equation describing the process is found in the literature. An empirical description is adopted here which attempts to represent the behavior of the system with respect to the controlling variables. Experimental tests show that the overcharge current for the nickel-cadmium cell is linearly proportional to the system's temperature for a given applied voltage (11). Furthermore, the cell potential increases very rapidly after the overcharge current sets in, so that a fair approximation is given by the relation

$$I_o = \alpha_1 T e^{\alpha_2 (E_r - E_{r,\text{min}})} \quad [9]$$

where  $\alpha_1$  and  $\alpha_2$  are constant parameters, and  $E_{r,\text{min}}$  is the minimum value of reversible potential at which the overcharge process becomes significant (usually the value corresponding to the fully charged state). Modeling the overcharge path as a variable impedance, it follows that such impedance may be represented by

$$R_o = \frac{k_4 e^{-k_5 (E_r - E_{r,\text{min}})}}{T}, \quad E_r \geq E_{r,\text{min}} \quad [10]$$

where  $k_4$ ,  $k_5$ , and  $E_{r,\text{min}}$  are empirical parameters to be fitted from experimental data for values of the reversible potential greater than  $E_{r,\text{min}}$ .



Since the overcharge current is practically negligible for lower values of the cell reversible potential, the corresponding model impedance may be represented by a very large constant value,  $M$ , and the model equation then becomes

$$R_o = M, \quad E_r < E_{r,\min}. \quad [11]$$

Thus, Eq. [10] and [11] are used in the model and in the solution of the circuit described in Fig. 1.

The internal resistance of the nickel-cadmium cell is found to increase with the reversible potential. At the same time, the internal resistance is inversely proportional to the temperature of the system, as a higher temperature increases the mobility of ions and therefore enhances the transport of electricity through the electrolyte. The following empirical equation is used to represent this behavior

$$R_i = \frac{\beta_1 + \beta_2 E_r^h}{T^3} \quad [12]$$

where  $\beta_1$  and  $\beta_2$  are constant parameters, and  $h$  and  $j$  are exponential values to be found experimentally. Since the resistance dependence on the reversible potential is nearly linear for small potential variations, its description may be simplified by using two straight lines for two ranges of operation (for a given value of  $T$ ). Similarly, since the temperature dependence is only grossly determinable experimentally, the assumption of inverse linearity seems to be justified for the sake of simplicity. Accordingly, the cell internal impedance is described by the following two equations

$$R_i = \frac{k_6 + k_7 E_r}{T}, \quad E_r \geq E_{r,\min}. \quad [13]$$

$$R_i = \frac{k_8}{T}, \quad E_r < E_{r,\min}. \quad [14]$$

where  $k_6$ ,  $k_7$ , and  $k_8$  are constant parameters to be fitted experimentally by standard regression techniques.

#### Dynamic Equation for Reversible Potential

The dynamic equation for the reversible potential of the nickel-cadmium cell is derived from the Nernst equation for the potential of a galvanic cell. Expressed in terms of activities of the reacting species, the equation may be simplified to

$$E_r = E_r^\circ + \frac{RT}{F} \ln [a_{H_2O}] \quad [15]$$

where  $E_r^\circ$  is the standard electromotive force for the cell,  $R$  is the universal gas constant,  $F$  is Faraday's constant, and  $a_{H_2O}$  is the activity of water in the cell. Under the assumption of ideality the activity of a component may be substituted with its mole fraction, which is easily observable and measurable in practice. Equation [15] then becomes

$$E_r = E_r^\circ + \frac{RT}{F} \ln X_{H_2O} \quad [16]$$

Differentiating with respect to  $X_{H_2O}$ , expanding the total differential  $dX_{H_2O}$ , and substituting it into Eq. [16] yields

$$\frac{dE_r}{dn_{H_2O}} = \frac{RT}{Fn_{H_2O}} [e^{(-F/RT)(E_r - E_r^\circ)} - 1] \quad [17]$$

This equation represents the functional relationship between  $E_r$  and the chemical composition of the solution in the cell during charge or discharge. Since these processes are accompanied by current flow, Faraday's law may be used to express Eq. [17] in terms of the electrical charge flowing through the cell,  $dq$ . The term  $dn_{H_2O}$  corresponds to the number of water moles being formed or consumed during the reaction (which corresponds, in turn, to a change in potential  $dE_r$ ). The

mole/equivalent ratio for this reaction is one to one, so that, in applying Faraday's law  $N = dn_{tot} = 1$ , and the current through the system is

$$I_r = \frac{dq}{dt} = \frac{dn_{H_2O} F}{dt} \quad [18]$$

Notice that the subscript  $r$  here refers to the reversible path of the model, that is,  $I_r$  is the current associated with the reversible reactions in the cell only, and no other phenomena. Substituting Eq. [18] into [17] yields

$$\frac{dE_r}{dt} = \frac{RTI_r}{F^2 n_{H_2O}} [e^{(-F/RT)(E_r - E_r^\circ)} - 1] \quad [19]$$

which is the theoretical dynamic equation for the reversible potential,  $E_r$ . Substituting the groups  $R/F^2$  and  $F/R$  with  $p_1$  and  $p_2$ , respectively, yields the model equation

$$\frac{dE_r}{dt} = \frac{p_1 T I_r}{n_{H_2O}} [e^{(-p_2/T)(E_r - E_r^\circ)} - 1] \quad [20]$$

where  $p_1$  and  $p_2$  are constant parameters to be identified by data matching,  $E_r^\circ$  is the standard electromotive force for the cell,  $T$  and  $n_{H_2O}$  are the cell temperature and water concentration, respectively.

Notice that, according to Eq. [20], a positive  $I_r$  corresponds to a positive gradient of  $E_r$ , as expected for the charging process indicated in the model of Fig. 1. Also, the gradient is directly proportional to the current,  $I_r$ , and the temperature,  $T$ , and inversely proportional to the water concentration,  $n_{H_2O}$ .

Equation [20] contains four variables that are functions of time:  $E_r$ ,  $T$ ,  $n_{H_2O}$ , and  $I_r$ . Of these, only the first three can be expressed by independent differential equations based on physical properties of the system. The fourth variable,  $I_r$ , is simply a variable parameter of the model, completely determined by the other variables. Since the equivalent circuit does not contain any capacitors or inductors, the current does not possess any transient characteristics of its own and its value depends only on the circuit equations.

#### Dynamic Equation for Cell Temperature

Internal heat generation occurs when current flows through the system and electrical work is dissipated by the resistances in the circuit. At the same time, the chemical processes during the charge and discharge phases display very strong exothermic and endothermic characteristics at different stages of the reactions. Temperature phenomena can be accounted for by using fundamental relationships for the electrical work dissipated and the heat of reaction in a heat balance around the cell. Treating the cell in lumped form, the heat balance yields

$$\rho C_p V \frac{dT}{dt} = q_{gen} + q_{in} - q_{out} \quad [21]$$

where  $\rho$ ,  $C_p$ ,  $V$ , and  $T$  are the cell equivalent density, heat capacity, volume, and temperature;  $q_{gen}$  is the rate of heat generated within the cell, and  $q_{in}$  and  $q_{out}$  are rates of heat input and output.

The rate of heat evolution in the nickel-cadmium cell is estimated by analyzing two separate sections of the circuit independently. The first section is the so-called reversible path, according to Fig. 1; the second one corresponds to the rest of the circuit, that is, the overcharge and the leakage paths. Reversible here refers to the chemical characteristics of the reactions, not to the conditions under which they take place. In fact, whenever  $U > E_r$ , the process occurs under conditions that do not involve maximum electrical work and that are, therefore, thermodynamically irreversible. The current through the path is  $I_r$ , that is, that fraction of  $I_{tot}$  that contributes to the charging reactions. The heat generated by this process can be estimated if the reversible potential of the cell and the entropy of the reaction are

known. The enthalpy change resulting from the addition of heat and electrical work to the system,  $\Delta H$ , is given by the first law of thermodynamics

$$\Delta H = Q_{\text{gen}} + W \quad [22]$$

Defining  $W$  in terms of electrical work, and adding and subtracting the reversible work expressed both in terms of electrical work and free energy, Eq. [22] becomes

$$\begin{aligned} Q_{\text{gen}} &= \Delta H - \int UI_r dt + W_{\text{rev}} - W_{\text{rev}} \\ &= \Delta H - \int UI_r dt + \int E_r I_r dt - \Delta G \end{aligned} \quad [23]$$

But the system's free energy change may be expressed in terms of enthalpy at a given temperature,  $\Delta G = \Delta H - T\Delta S$ , so that Eq. [23], after simplification, becomes

$$Q_{\text{gen}} = \int (E_r - U) I_r dt + T\Delta S \quad [24]$$

Differentiating with respect to time, an equation is obtained for the heat rate of generation in the reversible path,  $q_{\text{gen},1}$  which can be further simplified if the temperature of the system changes slowly, i.e., if  $dT/dt \cong 0$ , to yield

$$q_{\text{gen},1} = (E_r - U) I_r + T \frac{dS}{dt} \quad [25]$$

Since the change in entropy is linearly proportional to the quantity of materials reacted,  $(dS/dt)I_r = (\Delta S/\Delta t)I_r = KI_r$ , where  $K$  is a proportionality constant equal to  $\Delta S/F$ . The final equation then becomes

$$q_{\text{gen},1} = (E_r - U) I_r + KI_r T \quad [26]$$

Turning to the heat generated in the other parts of the electrical model, it is apparent that it is well approximated by that fraction of the total power to the system that was not utilized in the reversible path. Since the total power to the system is given by  $UI_{\text{tot}}$ , defining the charging efficiency as the fraction of total current that contributes to the charging reaction,  $\eta = I_r/I_{\text{tot}}$ , it follows that

$$q_{\text{gen},2} = (1 - \eta) UI_{\text{tot}} \quad [27]$$

where  $q_{\text{gen},2}$  is the heat generated in the remainder of the circuit.

Combining Eq. [26] and [27], and expressing the reversible current in terms of the charging efficiency, the final equation for the total heat rate of generation is obtained

$$q_{\text{gen}} = [I_{\text{tot}}(E_r - U) + I_{\text{tot}}TK]\eta + I_{\text{tot}}U(1 - \eta) \quad [28]$$

where, according to the model in Fig. 1,  $I_{\text{tot}}$  is the total current through the cell for a given applied terminal potential,  $U$ ;  $K$  is a constant for the process which accounts for the entropy change during the reaction. Substituting this equation into the heat balance, rearranging, and letting  $q = q_{\text{in}} - q_{\text{out}}$  be the net heat transfer through the boundary of the system, gives

$$pC_p V \frac{dT}{dt} = [I_r(E_r - 2U + TK) + I_{\text{tot}}U] + q \quad [29]$$

Solving for  $dT/dt$  and substituting  $K$  and  $pC_p V$  with the parameters  $p_3$  and  $p_4$  to be fitted from real data, the dynamic equation for the temperature of the cell is obtained

$$\frac{dT}{dt} = \frac{I_r(E_r - 2U + Tp_3) + I_{\text{tot}}U + q}{p_4} \quad [30]$$

Equation [30] shows that the temperature variations during the charge phase are the net result of competing effects. A positive contribution to the temperature slope derives from the total power supplied to the system, as indicated by the term  $I_{\text{tot}}U$ . The thermodynamic effect, represented by  $I_r Tp_3$  varies according to the over-all entropy change during the reaction. During the charge

process, for instance, the entropy change is negative so that the term  $I_r Tp_3$  contributes negatively to the slope of the temperature equation. Similarly, the net heat flow rate through the boundary,  $q$ , is directly proportional to the temperature derivative, so that the temperature of the cell increases when heat is absorbed through the boundary and decreases when heat is lost to the surroundings. All other terms in Eq. [30] are the result of the particular electrical configuration of the model and of the assumptions made in its derivation.

### Dynamic Equation for Cell Concentration

The composition of the electrolyte solution in the nickel-cadmium cell varies only because of the water consumption or formation during the process. Thus, the variation of the number of water moles,  $n_{\text{H}_2\text{O}}$ , during the reaction is directly related to the charge flowing through the solution,  $dq$

$$dn_{\text{H}_2\text{O}} = \frac{dq}{F} \quad [31]$$

Since the current contributing to the reaction is  $I_r = dq/dt$ , converting  $F$  to an identifiable parameter,  $p_4$ , this equation becomes

$$\frac{dn_{\text{H}_2\text{O}}}{dt} = \frac{I_r}{p_4} \quad [32]$$

which represents the dynamic equation for the total number of moles in the electrolyte solution. Since  $I_r$  is positive during charge and negative during discharge, the number of water moles increases and decreases during the respective operations. This conforms with the expected result, as indicated by the reaction equation, where water is formed during charge and consumed during discharge.

### Model Test

For the purpose of testing the behavior of the model, the equations presented here were fitted to typical nickel-cadmium cell data. Specifically, all data used refer to a Gulston 20A-h, sealed, sintered plate cell. The parameters in the dynamic equations were identified according to a procedure based on sensitivity functions (12) and a charge cycle was simulated and compared to experimental data. The results are reported in Fig. 2, 3, and 4.

The model showed the ability to fit the dynamic behavior of a typical nickel-cadmium cell and appears to be a viable tool for studying power systems. The parameters can be identified to match a specific real system, and the resulting equations are manageable from the standpoint of numerical computation. The dynamic description of the temperature in the system, the reversible potential, and the water concentration within the galvanic cell, as well as the electrical variables of interest, such as current through the terminals, over-

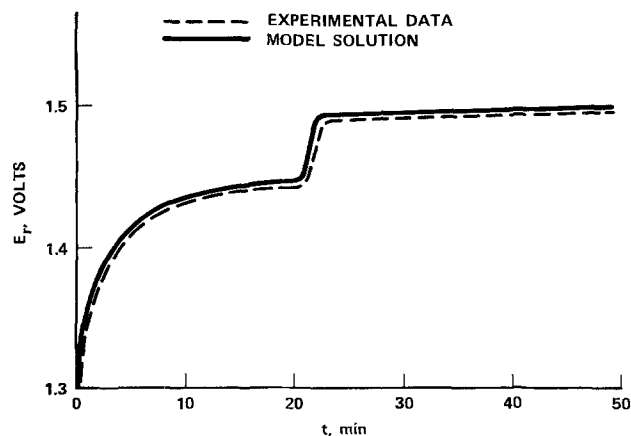


Fig. 2. Reversible potential trajectory

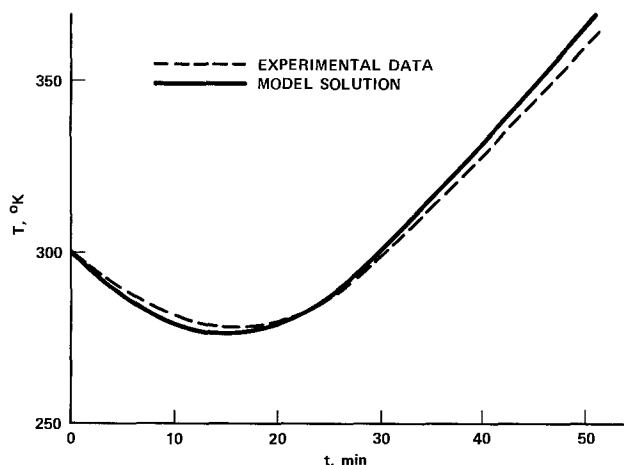


Fig. 3. Temperature trajectory.

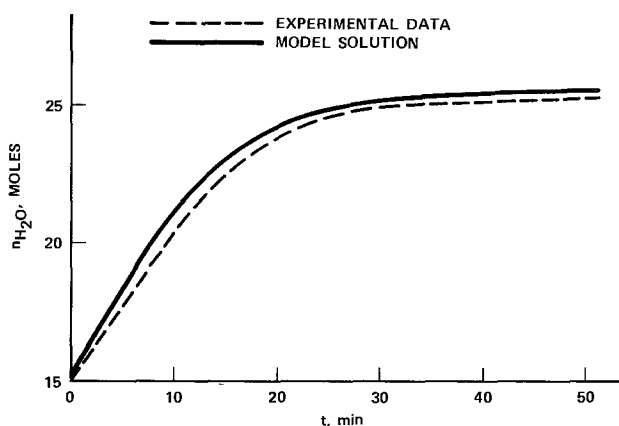


Fig. 4. Concentration trajectory

charge current, and charging efficiency, are available at every time as a result of the transient computations.

### Practical Considerations

From the foregoing, the present model consists of three differential equations for the reversible potential, temperature, and concentration, with five parameters to be identified experimentally, and of a set of algebraic constraints derived from the electrical characteristics of the system. Not all the significant phenomena occurring during the operation of the nickel-cadmium cell are purported to be represented in the model. The pressure buildup within the sealed cell, and its effect on the temperature of the system, for instance, are completely neglected. So are the capacity of the cell, its state of charge, and any memory effect which might affect the parameters of the equations. These simplifications are tolerated for the sake of simplicity of the model, which would otherwise become too complicated and possibly intractable for computation. Furthermore, these processes are not well understood and are difficult to describe quantitatively, so that the practical usefulness of a more complicated model is questionable.

The equations derived here correspond to the model shown in Fig. 1, which is a charge model. But the re-

sults obtained during the derivation are valid for the discharge phase as well, with the appropriate modifications. Notably, a load must be substituted for the charging potential,  $U$ , and the polarity of the activation overpotential,  $E_a$ , must be reversed. Furthermore, since the opposite reaction would be taking place on discharge, the value of  $K$  in Eq. [29] must be reversed in sign.

The equations, derived for an electrochemical cell, are equally applicable to a battery of cells, as long as no qualitative difference between the various elements is present. Of course, different data would apply, and the model parameters would correspondingly have different values.

Finally, notice that the equations derived are valid with slight modifications for any electrochemical cell. Once the chemical reaction involved is established, and the significant products and reactants are known, the dynamic equation for the reversible potential can be modified accordingly. The different thermodynamic properties of the new system must be taken into account in the heat and concentration equations. In general, then the same set of equations may be fitted to the operating characteristics of a given cell or battery.

### Acknowledgment

The research in this paper was supported in part under AFOSR Grant 72-2166.

Manuscript submitted Dec. 19, 1974; revised manuscript received Sept. 10, 1975.

Any discussion of this paper will appear in a Discussion Section to be published in the December 1976 JOURNAL. All discussions for the December 1976 Discussion Section should be submitted by Aug. 1, 1976.

Publication costs of this article were partially assisted by the University of California.

### REFERENCES

1. P. Bauer, NASA SP-172, Washington, D. C. (1968).
2. H. G. Zimmerman and R. G. Peterson, "An Electrochemical Cell Equivalent Circuit for Storage Battery/Power System Calculations by Digital Computer," Lockheed Missiles and Space Company, Sunnyvale, California (1971).
3. N. B. Worth, *IEEE Trans. Aerospace*, **AS-2**, (2), 780 (1964).
4. P. Bauer, *IEEE Trans. Aerospace and Electronic Systems*, **AES-5**, (6), 934 (1969).
5. S. U. Falk, *This Journal*, **107**, 661 (1960).
6. F. P. Kober, *ibid.*, **112**, 1064 (1965).
7. W. N. Carson, *et al.*, "Characterization of Nickel-Cadmium Electrodes. Final Report," Goddard Space Flight Center, General Electric Co. Advanced Technology Laboratories, Schenectady, New York, 1963-1964 (NASA CR-63916, N65-29148).
8. "Testing and Evaluation of Nickel-Cadmium Spacecraft Type Cells. Final Report," Cook Electric Co., Dayton, Ohio, 1965 (NASA CR-63181, N65-25404).
9. H. K. Messerle, "Dynamic Circuit Theory," Pergamon Press, New York (1965).
10. G. Kortum, "Treatise on Electrochemistry," p. 443, Elsevier Publishing Co., Amsterdam (1965).
11. R. C. Shair and H. N. Seiger, in "Batteries," Pergamon Press, New York (1958).
12. A. R. Durando, Ph.D. Dissertation, UCLA (1973).

# Discharge Behavior of Redox Thermogalvanic Cells

Brian Burrows\*

Battelle, Geneva Research Centre, 1227 Carouge-Geneva, Switzerland

## ABSTRACT

The discharge behavior of thermogalvanic cells based on a dissolved redox couple, namely ferro-ferricyanide, was investigated as a function of redox couple concentration, temperature difference, electrode placement and configuration, and forced convection. The principal source of cell polarization was found to be the rate of mass transfer of electroactive species to the electrode surfaces. This concentration polarization is instrumental in limiting the power output of aqueous redox thermogalvanic cells to values  $<0.1 \text{ mW cm}^{-2}$ . A practical feature of such cells, however, is that a continuous power output can be maintained indefinitely provided that the half-cell temperature difference remains constant.

Thermogalvanic cells are the electrochemical equivalent of thermoelectric devices and can directly convert thermal to electrical energy (1). Conceptually and operationally, however, thermogalvanic cells are considerably more complex since ionic as well as electronic conduction is involved. Thus under discharge conditions the transport and discharge of ions will cause, in general, permanent changes to occur at the electrodes. This is a considerable inconvenience in a practical device.

Despite the inconvenience of mass transfer, a certain amount of interest was shown in thermogalvanic cells for power generation during the early 1960's. In particular, attention was directed to analyzing the properties of cells having molten salt or solid-state electrolytes to take advantage of the large temperature differentials and hence relatively large cell voltages obtainable (2-6).

In these studies it was shown that the material properties of thermogalvanic and thermoelectric cells, as measured by the figure of merit, were comparable. The figure of merit,  $Z$ , is defined as

$$Z = \frac{s^2}{\rho k} \text{ K}^{-1} \quad [1]$$

where  $s$  is the Seebeck coefficient in  $\text{V K}^{-1}$ ,  $\rho$  is the specific resistivity in  $\text{ohm-cm}$ , and  $k$  is the specific thermal conductivity in  $\text{W cm}^{-1} \text{ K}^{-1}$ . Ionic conductors were found to have figures of merit of  $\sim 10^{-3} \text{ K}^{-1}$ , i.e., similar to  $Z$  values of semiconducting materials such as PbTe and BiTe used in thermoelectric devices (7). Apart from having similar  $Z$  values, both thermogalvanic cells and thermoelectrics have conversion efficiencies which are Carnot limited (7, 8). This was another reason why thermogalvanic cells based on high temperature electrolytes were initially of interest. In fact, though, only two experimental investigations of the power generating or discharge behavior of thermogalvanic cells have been reported (9, 11). In both cases solid electrolytes were used.

Weininger (9) investigated the  $\text{Ag}/\alpha\text{-AgI}/\text{Ag}$  and the  $(\text{Pt})\text{I}_2/\alpha\text{-AgI}/\text{I}_2(\text{Pt})$  cells at temperatures of  $150^\circ\text{--}500^\circ\text{C}$ . The latter was also the subject of a patent (10). The polarization behavior of the  $\text{Na}/\beta\text{-Al}_2\text{O}_3/\text{Na}$  thermocell was reported by Weber (11) over the temperature range of  $200^\circ\text{C}$  at the cold electrode and up to  $800^\circ\text{C}$  at the hot electrode. This cell has also been patented (12).

In both of the patented cells it should be noted that the problem of mass transport under current-drain conditions, which was alluded to earlier, was overcome by using a gaseous ( $\text{I}_2$ ) electrode in one case and a liquid (Na) electrode in the other. External connec-

tions between the hot and cold electrode allowed mass transfer while ionic transport occurred through the composition-invariant solid electrolyte. Two other versions of high temperature thermogalvanic cells having gas electrodes have also been described in the patent literature (13, 14).

Although the use of gaseous or liquid electrodes circumvents the mass transfer problem it is at the expense of extra complexity in the cell design. As the low d-c voltages obtainable with direct energy conversion devices necessitate the use of large numbers of cells to obtain practically useful voltages, it is imperative that cells be simple, durable, and cheap. Therefore, it was thought that a simpler means of avoiding the mass transfer problem in a thermogalvanic cell would be to use cells based on dissolved redox couples with inert solid electrodes. The liquid electrolyte could be either aqueous or molten salt.

The discharge behavior of redox thermogalvanic cells based on the  $\text{Fe}^{2+}/\text{Fe}^{3+}$  couple in aqueous electrolyte has been recently reported (15). It was shown that continuous power outputs could be obtained from such cells with no change in electrolyte composition or activity of the electrodes. In this paper the results of a more detailed investigation of the discharge behavior of a cell based on the  $\text{Fe}(\text{CN})_6^{4-}/\text{Fe}(\text{CN})_6^{3-}$  couple in aqueous electrolyte is reported. An aqueous electrolyte was chosen for simplicity since the aim of the study was to evaluate the factors which limit the power output.

## Experimental

Most of the experiments were carried out in a U-shaped test cell. The arms of this cell were jacketed and the temperatures in each half-cell were controlled to  $\pm 0.1^\circ\text{C}$  by a continuous flow of water from two thermostated water baths. A linear cell was also used for some experiments; this was essentially a straightened U-cell. The temperature of the colder half-cell was always maintained at  $30^\circ\text{C}$  while that of the hotter half-cell was varied between  $50^\circ$  and  $80^\circ\text{C}$ .

Platinum electrodes were used as the working or current-carrying electrodes. These were of the platinum inlay type (No. 39272) supplied by Beckman Instruments Incorporated. The planar surface of these electrodes was  $0.196 \text{ cm}^2$  and they were placed centrally in each vertical arm of the U-cell with a distance of about 25 cm separating the electrode surfaces. A length of Pt wire was wrapped around each working electrode with one end of the wire terminating just in front of the electrode face. The Pt wires served as reference electrodes and allowed the individual measurement of the working electrode polarization.

A rotating electrode was fabricated from a Pt-inlay electrode and was used for investigating the influence of forced convection on the polarization in each half-cell. A procedure similar to that described by Marcoux

\* Electrochemical Society Active Member.

Key words: direct energy conversion, device, power output, concentration polarization, ferro-ferricyanide couple.

and Adams (16) was followed in making the rotating electrode which was coupled to a d-c motor using a chuck constructed in these laboratories.

The influence of electrode area on cell polarization was investigated using platinized Pt-inlay electrodes. The platinization was carried out in the usual way in a solution of chloroplatinic acid and lead acetate. Pt-foil electrodes were also used in some experiments. These had a total area of 4 cm<sup>2</sup> and were spot welded to thin Pt wires which acted as both support and current collector.

Solutions of Fe(CN)<sub>6</sub><sup>3-</sup> and Fe(CN)<sub>6</sub><sup>4-</sup> ions in 0.5M K<sub>2</sub>SO<sub>4</sub> were prepared from K<sub>3</sub>Fe(CN)<sub>6</sub> and K<sub>4</sub>Fe(CN)<sub>6</sub>·3H<sub>2</sub>O. These salts were supplied by Fluka AG and were > 99% pure. The K<sub>2</sub>SO<sub>4</sub> used for making up the supporting electrolyte was > 99% pure. For each experiment a fresh solution of the dissolved redox couple was prepared and deoxygenated for 10 min by bubbling nitrogen through the solution.

The discharge behavior of the redox thermogalvanic cells was investigated by applying constant current between the two working electrodes and recording the cell voltage when steady state had been attained. For each discharge current, the polarization at each working electrode with respect to the Pt wire reference electrodes was also recorded. A digital voltmeter was used to monitor the potentials to ± 0.1 mV.

The resistance of the electrolyte between the two working electrodes was measured with a conductivity bridge (Philips Model PW 9501) at 2000 Hz. For a given electrolyte concentration and temperature difference the same value was obtained using either smooth or platinized Pt electrodes. As a check on the accuracy of the a-c resistance measurements, a current interruptor technique was also used to measure the IR drop between the electrodes. Agreement to within ± 5% was found using the two methods for measuring electrolyte resistance.

## Results

A typical set of experimental polarization measurements obtained for the redox thermogalvanic cell

(30°C) Pt/Fe(CN)<sub>6</sub><sup>3-</sup> (M<sub>1</sub>),

Fe(CN)<sub>6</sub><sup>4-</sup> (M<sub>2</sub>)/Pt (30°C + ΔT) [A]

is presented in Table I where *i* is the discharge current density, *V*<sub>cell</sub> is the cell voltage as measured by the potential of the working electrode in the hot half-cell with respect to that of the working electrode in the 30°C half-cell, η<sub>30</sub> and η<sub>80</sub> are electrode overpotentials measured with respect to a Pt-wire reference electrode, *V*<sub>IR-free</sub> is the cell voltage after correction for the ohmic voltage drop, η<sub>IR-free</sub> is the cell overvoltage due to charge-transfer and mass-transfer polarization calculated from the difference *V*<sub>cell</sub> (at *i* = 0) - *V*<sub>IR-free</sub> (at *i* = *i*), and *P* is the power density given by the product *i* · *V*<sub>IR-free</sub>.

In Table I the effect of temperature on polarization of the individual electrodes is evident as η<sub>30</sub> is greater

Table I. *V-i* characteristics of the redox thermogalvanic cell (30°C) Pt/Fe(CN)<sub>6</sub><sup>3-</sup> (0.1M), Fe(CN)<sub>6</sub><sup>4-</sup> (0.1M)/Pt (30 + ΔT°C) in 0.5M K<sub>2</sub>SO<sub>4</sub>\*

<i>i</i> mA cm <sup>-2</sup>	<i>V</i> <sub>cell</sub>	η <sub>30</sub>	η <sub>80</sub>	<i>V</i> <sub>IR-free</sub>	η <sub>IR-free</sub>	<i>P</i> μW cm <sup>-2</sup>
0	-73.9					
0.05	-71.2	-1.9	+0.4	-71.8	2.1	3.6
0.10	-68.4	-3.1	+1.0	-69.6	4.3	7.0
0.15	-67.3	-3.7	+1.2	-69.2	4.7	10.4
0.26	-62.6	-6.2	+2.1	-65.7	8.2	17.1
0.51	-53.5	-10.6	+5.0	-59.7	14.2	30.5
1.02	-35.5	-18.3	+10.6	-47.9	26.0	48.9
1.53	-14.0	-26.4	+20.3	-32.6	41.3	49.9
2.56	+23.5	-42.3	+27.8	-8.5	65.4	21.8

\* Area of Pt-inlay electrodes = 0.196 cm<sup>2</sup>, ΔT = 50°C, R<sub>cell</sub> = 62 ohm. All voltages and potentials are in mV.

than η<sub>80</sub>. It can also be seen that the sum of the absolute electrode overpotentials (η<sub>30</sub> + η<sub>80</sub>) at low current densities corresponds closely to the cell overvoltage (η<sub>IR-free</sub>). These overvoltages should, of course, correspond as the electrode overpotentials contain only a small ohmic component but this component will become significant at high current densities as was observed.

When a constant current was being drawn from a redox thermogalvanic cell [A] with ΔT = 50°C, a steady-state voltage was rapidly attained. This voltage was observed, however, to fluctuate in a more or less cyclic manner with an amplitude which increased with increase in discharge current density. Experiments showed that these fluctuations decreased to insignificant levels when the bulky Pt-in-glass electrodes were replaced by Pt-foil electrodes having a thin Pt wire spot welded to the foil as current collector. This suggests that the oscillations in cell voltage can be largely attributed to convective effects caused by the Pt-inlay electrodes acting as heat sinks.

## Discussion

*Influence of concentration.*—The cell overvoltage-current characteristics for [Fe(CN)<sub>6</sub><sup>3-</sup>] = [Fe(CN)<sub>6</sub><sup>4-</sup>] = 0.2, 0.1, 0.05, and 0.02 mole liter<sup>-1</sup> with a ΔT of 50°C in each case are plotted in Fig. 1. It should be noted that the cell overvoltage has been corrected for the ohmic drop between the two working electrodes and so only includes contributions from mass-transfer and charge-transfer polarization at the electrode/electrolyte interfaces.

The form of the η-log *i* curves in Fig. 1 is typical of mass transfer-controlled electrode processes. Thus, a limiting current is evident which is proportional to

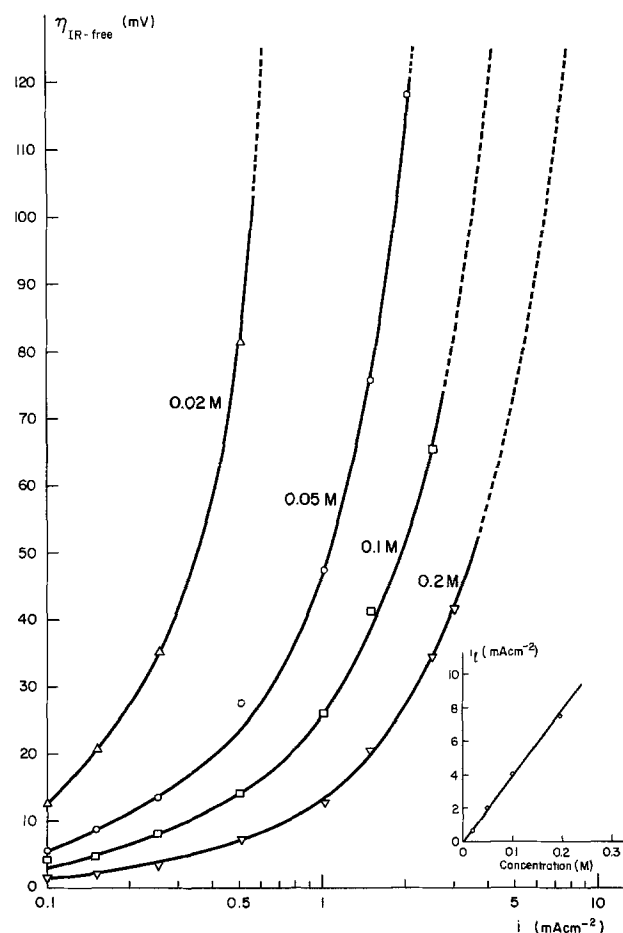


Fig. 1. Cell overvoltage (η<sub>IR-free</sub>) vs. log *i* for thermogalvanic cells (ΔT = 50°C) based on the Fe(CN)<sub>6</sub><sup>3-</sup>/Fe(CN)<sub>6</sub><sup>4-</sup> couple as a function of concentration. Inset: Limiting current (*i*<sub>l</sub>) vs. concentration.

concentration (see inset to Fig. 1). This is in accordance with the equation relating limiting current ( $i_l$ ) to concentration of electroactive species for a mass transfer-limited electrode process. This well-known equation (17) is

$$i_l = 10^3 \frac{nFD C}{\delta} \quad [2]$$

where  $i_l$  is in mA cm<sup>-2</sup>;  $n$ ,  $F$ , and  $D$  have their usual meanings;  $C$  is the concentration in mole cm<sup>-3</sup>; and  $\delta$  is the thickness of the Nernst diffusion layer in cm. As a quantitative check on the numerical values obtained for the limiting current we can calculate  $i_l$  from Eq. [2].

The diffusion coefficients for the Fe(CN)<sub>6</sub><sup>3-</sup> and Fe(CN)<sub>6</sub><sup>4-</sup> ions in 0.5M K<sub>2</sub>SO<sub>4</sub> are  $8.9 \times 10^{-6}$  and  $8.0 \times 10^{-6}$  cm<sup>2</sup> sec<sup>-1</sup>, respectively (18). Taking a mean value for  $D$  of  $8.5 \times 10^{-6}$  cm<sup>2</sup> sec<sup>-1</sup> and  $\delta = 3 \times 10^{-2}$  (17), the calculated value of  $i_l$  for a 0.1M solution is 2.7 mA cm<sup>-2</sup>. This value is in excellent agreement with the extrapolated value of  $i_l$  for the 0.1M solution in Fig. 1 of 4 mA cm<sup>-2</sup>. Similarly, it can be shown that the limiting currents for the other concentrations are also in good agreement.

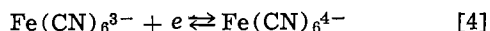
In general, it is the relative values of  $i$ ,  $i_l$ , and  $i_0$  which determine the degree of potential loss at an electrode (19). In the cells under investigation it appears that the polarization losses arise from mass-transport limitations which implies that for a given concentration  $i_l \ll i_0$ . To check that, in fact, this is the situation, we can estimate  $i_0$  for, say, a 0.1M solution of Fe(CN)<sub>6</sub><sup>3-</sup> and Fe(CN)<sub>6</sub><sup>4-</sup> ions from the available kinetic data.

The equation relating  $i_0$  to concentration and the standard rate constant ( $k_s$ ) is

$$i_0 = nF k_s a_o^{1-\alpha} a_R^\alpha \quad [3]$$

where  $i_0$  is in A cm<sup>-2</sup>,  $k_s$  is in cm sec<sup>-1</sup>;  $a_o$  is the activity of oxidant in mole cm<sup>-3</sup>,  $a_R$  is the activity of reductant in mole cm<sup>-3</sup>,  $\alpha$  is the transfer coefficient, and  $n$  and  $F$  have their usual significance.

For the redox reaction



the standard rate constant has been measured as  $2 \times 10^{-2}$  cm sec<sup>-1</sup> with a transfer coefficient of 0.5 (18). Using Eq. [3] it can then be calculated that for a solution 0.1M in both Fe(CN)<sub>6</sub><sup>3-</sup> and Fe(CN)<sub>6</sub><sup>4-</sup> ions the exchange current density will be 0.19 A cm<sup>-2</sup>. This value is an unrealistic maximum since we have assumed that the activities of Fe(CN)<sub>6</sub><sup>3-</sup> and Fe(CN)<sub>6</sub><sup>4-</sup> ions are identical to their concentrations. If, in the absence of activity coefficient data, we assume that the activities are only 10% of the concentrations, then  $i_0$  would be 19 mA cm<sup>-2</sup>. This value of  $i_0$  is still an order of magnitude greater than the maximum current drawn from the thermogalvanic cells (see Fig. 1) which further confirms that mass-transfer polarization is the primary cause of the cell polarization observed in Fig. 1.

The influence of concentration on power output can be seen in Fig. 2 where  $P$  is plotted vs. discharge current for [Fe(CN)<sub>6</sub><sup>3-</sup>] = [Fe(CN)<sub>6</sub><sup>4-</sup>] = 0.2, 0.1, and 0.05M. The power output for each concentration has a maximum value which increases with both current density and concentration. The relationship between  $P_{\text{max}}$  and concentration is shown in the inset. Since the solubility limit of the ferro-ferricyanide couple is 0.2M in 0.5M K<sub>2</sub>SO<sub>4</sub>, the maximum observed power output was limited to 93 μW cm<sup>-2</sup>. The proportionality between maximum power output and concentration of electroactive species is not unexpected in view of the fact that the IR-free cell voltage increases in proportion to the increase in concentration for a given applied current density (see Fig. 1).

*Influence of temperature difference.*—The influence of  $\Delta T$  on the  $V$ - $i$  characteristics of thermogalvanic

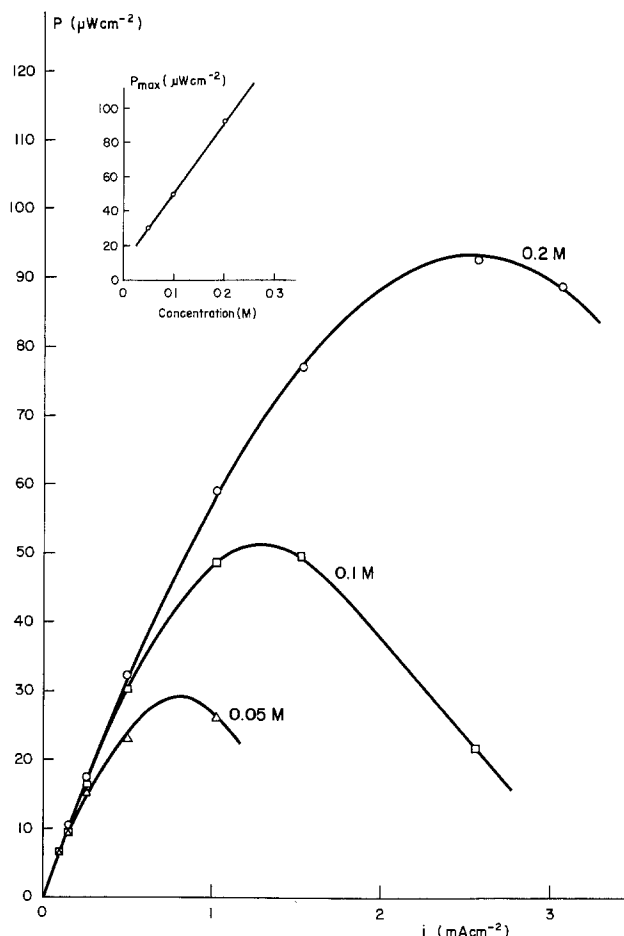


Fig. 2. Power output vs. discharge current for thermogalvanic cells ( $\Delta T = 50^\circ\text{C}$ ) based on the Fe(CN)<sub>6</sub><sup>3-</sup>/Fe(CN)<sub>6</sub><sup>4-</sup> couple as a function of concentration. Inset: Maximum power output vs. concentration.

cells [A] with [Fe(CN)<sub>6</sub><sup>4-</sup>] = [Fe(CN)<sub>6</sub><sup>3-</sup>] = 0.1M was investigated for  $\Delta T$  of 50°, 40°, 30°, and 20°C. The variation of initial cell voltage ( $V_{\text{cell}}$  at  $i = 0$ ) with  $\Delta T$  is linear (see Fig. 3) and the slope of 1.4 mV °C<sup>-1</sup> is the average value of the Seebeck coefficient.

The cell overvoltage ( $\eta_{\text{IR-free}}$ ) vs.  $\log i$  curves were independent of  $\Delta T$ , i.e., decreasing  $\Delta T$  from 50° to 20°C did not alter the overvoltage characteristics. This insensitivity of  $\eta$  to  $\Delta T$  is surprising in view of the observation that  $\eta_{30} > \eta_{30} + \Delta T$ . One would have expected, for a mass-transfer controlled process, that with decrease in  $\Delta T$  the cell overvoltage would have increased. Perhaps this effect is counteracted by an equivalent decrease in  $\eta$  due to the decrease in thermal diffusion (Soret effect) at lower  $\Delta T$ . The temperature differential did, however, influence the power output as shown in Fig. 4 where  $P$  is plotted vs.  $i$  for  $\Delta T$  of 50°, 40°, 30°, and 20°C. It is evident that  $P$  goes through a maximum for each  $\Delta T$  and in the inset to Fig. 4 the increase of  $P_{\text{max}}$  with increase in  $\Delta T$  is shown.

*Influence of electrode placement.*—The  $V$ - $i$  characteristics of cell [A] were also investigated in a linear cell in which the 80°C half-cell was vertically above the 30°C half-cell. Comparison of the cell overvoltage with that measured under identical conditions in a U-cell showed that the polarization behavior was the same. This indicates that any convective effects are localized in the half-cells and do not affect the cell as a whole.

Direct measurements of the temperature gradient at the bottom of the hot (80°C) compartment showed that 2 cm away from the bottom of the compartment the temperature was only 35°C and 3.5 cm into the connecting arm of the U-cell the temperature was 30°C; the same as that in the cold electrode compartment.

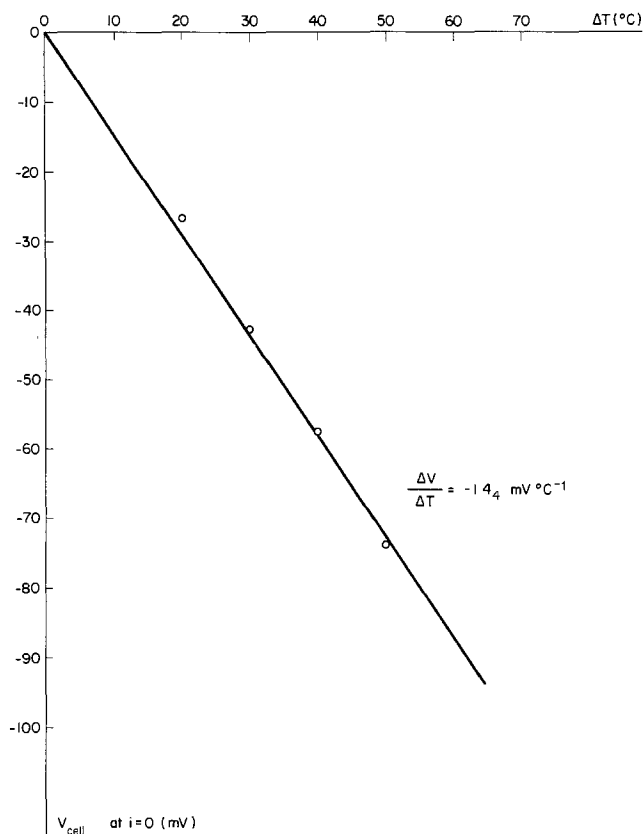


Fig. 3. Initial cell voltage ( $V_{80/30}$  at  $i = 0$ ) vs.  $\Delta T$  for thermogalvanic cells based on the  $\text{Fe}(\text{CN})_6^{3-}/\text{Fe}(\text{CN})_6^{4-}$  couple (0.1M).

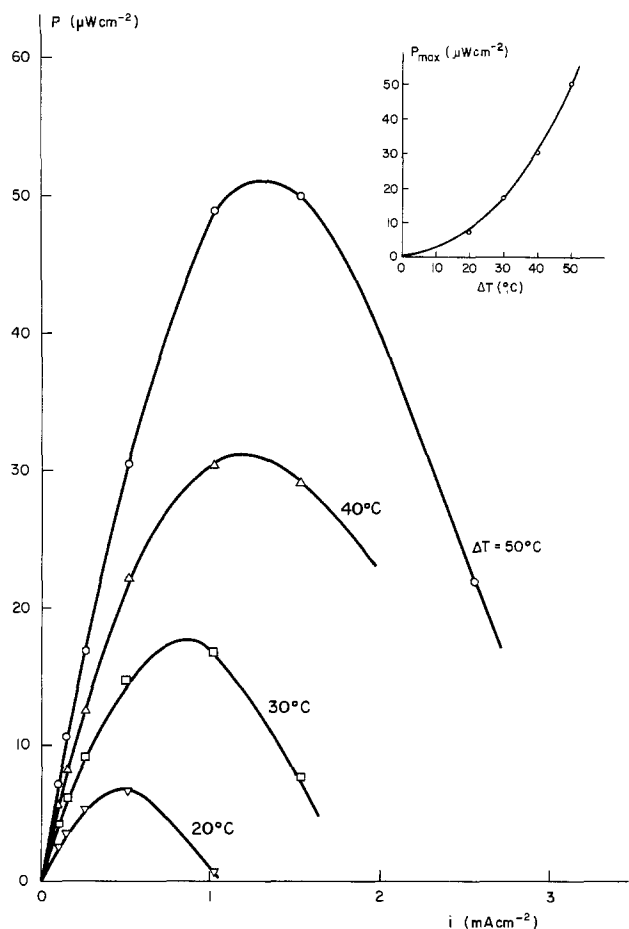


Fig. 4. Power output vs. discharge current for thermogalvanic cells based on the  $\text{Fe}(\text{CN})_6^{3-}/\text{Fe}(\text{CN})_6^{4-}$  couple (0.1M) as a function of  $\Delta T$ . Inset: Maximum power output vs.  $\Delta T$ .

The minimum distance which could, therefore, be maintained between the two electrodes, while still preserving a  $\Delta T$  of 50 $^{\circ}\text{C}$ , is 3.5 cm. Now the values of  $P$  used in Fig. 2 and 4 are calculated from IR-free cell voltages and so are ideal values. Correcting the maximum measured power output of 93  $\mu\text{W cm}^{-2}$  (see Fig. 2) to take into account the internal resistance of 6 ohm when the electrode separation is 3.5 cm results in a reduction of  $P_{\text{max}}$  by 5% to 88  $\mu\text{W cm}^{-2}$ . Thus the influence of electrolyte resistance on maximum power output is relatively minor primarily, of course, because the current is small being only 0.5 mA in the above case.

A second modification of electrode placement was investigated in a U-cell using Pt-foil rather than Pt-inlay working electrodes. Again there was no significant difference between the results obtained with the two electrode configurations but the degree of cycling of the cell voltage was much less in the case of the Pt-foil electrodes indicating reduced convective effects (see Results).

*Influence of electrode roughness.*—The roughness factor (ratio of real to geometric area) of a platinum electrode can be readily increased by platinizing. The minimum increase which can be obtained is of the order of 100 (20). If, as the results indicate, the polarization in thermogalvanic cells based on the ferri-ferricyanide couple is mass-transfer controlled, then increasing the roughness factor should have no effect on the polarization behavior of the cell (21).

The polarization results obtained for cell [A] with an equimolar 0.1M  $\text{Fe}(\text{CN})_6^{3-}/\text{Fe}(\text{CN})_6^{4-}$  solution at  $\Delta T = 50^{\circ}\text{C}$  using platinized Pt-inlay electrodes were, as expected, identical to the results obtained with smooth electrodes.

*Influence of forced convection.*—Since the power output of redox thermogalvanic cells is constrained by the rate of mass transfer of the electroactive species in solution, it was of interest to determine to what extent forced convection could improve the cell performance. Experiments were again carried out in a cell [A] containing an equimolar 0.1M solution of ferri-ferricyanide. The results are summarized in Fig. 5. It should be noted that the distance of 25 cm between the two electrodes was such that electrode rotation did not influence the thermal gradient between the two half-cells.

It can be seen that forced convection in either of the two compartments leads to a considerable reduction in overvoltage. Adding together the effects of stirring in both compartments, one can derive a curve for the cell overvoltage in which both electrodes are rotating. Thus, at a discharge current density of 3.5  $\text{mA cm}^{-2}$ , forced convection leads to a substantial fourfold reduction in the cell overvoltage which produces in turn a fourfold increase in the power output over the maximum of 52  $\mu\text{W cm}^{-2}$  obtained with stationary electrodes at a current density of 1.3  $\text{mA cm}^{-2}$ . For a 0.2M (saturated) solution, which was found to give the maximum power output of almost 0.1  $\text{mW cm}^{-2}$ , we could therefore expect an output of about 0.4  $\text{mW cm}^{-2}$  under forced convection conditions.

Unfortunately this fourfold increase in power output to a maximum of about 0.4  $\text{mW cm}^{-2}$  is still an order of magnitude less than what is obtained using solid-state photovoltaic or thermoelectric devices for direct energy conversion.

In view of the fact that the rate of mass transfer of the ions of the redox couple to the electrodes is the principal cause of cell polarization (which in turn limits the maximum power output) one could, in principle, obtain higher power outputs with redox couples which are more soluble than the ferri-ferricyanide system. Experiments with a thermogalvanic cell based on the ferrous-ferric chloride (2 mole liter $^{-1}$ ) system gave, however, a maximum power output of only 42  $\mu\text{W cm}^{-2}$  (15) which illustrates the limitations of going in this direction.

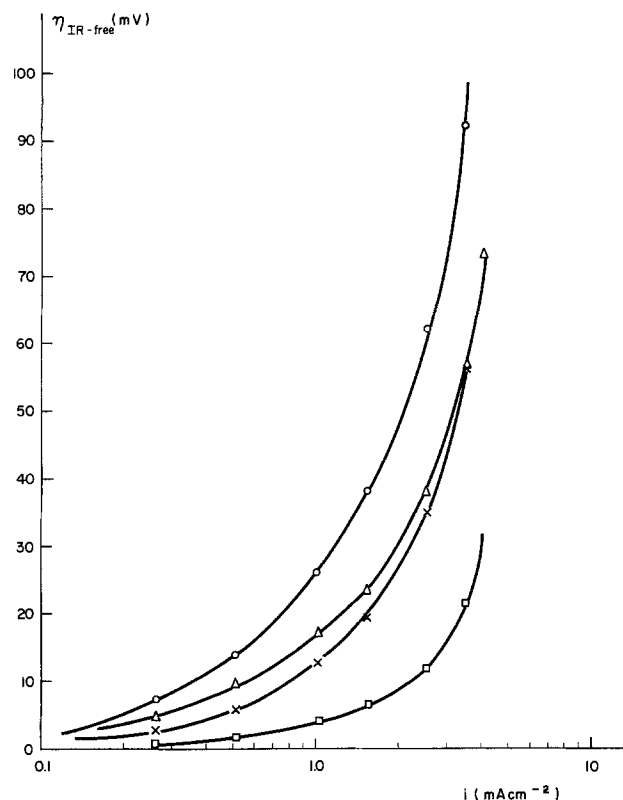


Fig. 5. Cell overvoltage ( $\eta_{IR-free}$ ) vs.  $\log i$  for thermogalvanic cells based on the  $\text{Fe}(\text{CN})_6^{3-}/\text{Fe}(\text{CN})_6^{4-}$  couple (0.1M):  $\odot$  both electrodes stationary;  $\triangle$  rotating electrode in 80°C half-cell; X rotating electrode in 30°C half-cell;  $\square$  rotating electrodes in both half-cells (derived curve). OCV: 73.8 mV. Rotation speed: 880 rpm.

This low power output resulted from the fact that the  $\text{Fe}^{2+}/\text{Fe}^{3+}$  couple in HCl had a Seebeck coefficient of only  $0.6 \text{ mV } ^\circ\text{C}^{-1}$ , which is only one-third as large as that of the  $\text{Fe}(\text{CN})_6^{3-}/\text{Fe}(\text{CN})_6^{4-}$  couple in  $\text{K}_2\text{SO}_4$ . (The  $i_0$  values for the two values are of similar magnitude.) Hence, for two cells with the same  $\Delta T$ , mass-transfer polarization is a larger proportion of the initial cell voltage for the ferrous-ferric system than it is for the ferro-ferricyanide system.

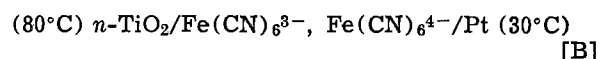
Thus, in general, it is more advantageous to have a redox couple with a higher Seebeck coefficient than with a higher solubility. Seebeck coefficients are, however, limited to values in the region of  $0.5\text{--}1.5 \text{ mV } ^\circ\text{C}^{-1}$  (22) and solubilities are limited to  $1\text{--}2 \text{ mole liter}^{-1}$  in aqueous solution so there would seem to be little possibility of obtaining an order of magnitude improvement in the power outputs of aqueous redox cells.

One could, of course, use molten salts as electrolyte media for dissolved redox couples to take advantage of the larger available  $\Delta T$  and the higher solubilities, and it is conceivable that one could obtain power outputs of up to  $15 \text{ mW cm}^{-2}$  (15) which would make redox thermogalvanic cells comparable in power density to solid-state thermoelectric and photovoltaic cells (23). The problem with high temperature systems, however, is that materials problems are considerable and an economically viable device is unlikely to be based on molten electrolytes.

A means of augmenting the power outputs of the otherwise attractive redox thermogalvanic cells (continuous steady-state power outputs, invariant electrodes and electrolytes) without recourse to high temperature systems could be through a judicious combination of the photogalvanic effect (24) with the thermogalvanic effect in the one cell. The photogalvanic effect would be primarily used to induce a substantial change in the potential of one (illuminated) electrode with respect to the other (dark) electrode. That is, the high energy photons of the u.v. and visible

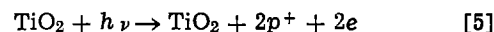
regions of the solar spectrum would be used for activating a suitable semiconductor or dye-sensitized electrode, thereby changing its normal (unilluminated) rest potential. At the same time, the thermal energy in the IR region would be used to heat the electrolyte in the vicinity of the illuminated electrode.

A possible photo/thermogalvanic cell is the following



illuminated (anode)                      dark (cathode)

The operation of this cell is shown schematically in Fig. 6. The photogalvanic properties of semiconducting  $\text{TiO}_2$  have recently been reported (25, 26) and in cell [B] this electrode would function as an anode, *viz.*



complementing the anodic reaction of the redox couple in the thermogalvanic cell *via* the reaction



The cell voltage in the absence of illumination would be some tens of millivolts (due to the thermogalvanic effect) but with the  $\text{TiO}_2$  electrode illuminated it could be several hundreds of millivolts (due to the photogalvanic effect being superimposed on the thermogalvanic effect). Such photo/thermogalvanic cells are currently under investigation.

### Acknowledgments

Manuscript submitted June 30, 1975; revised manuscript received Oct. 3, 1975.

Any discussion of this paper will appear in a Discussion Section to be published in the December 1976 JOURNAL. All discussions for the December 1976 Discussion Section should be submitted by Aug. 1, 1976.

Publication costs of this article were partially assisted by Battelle.

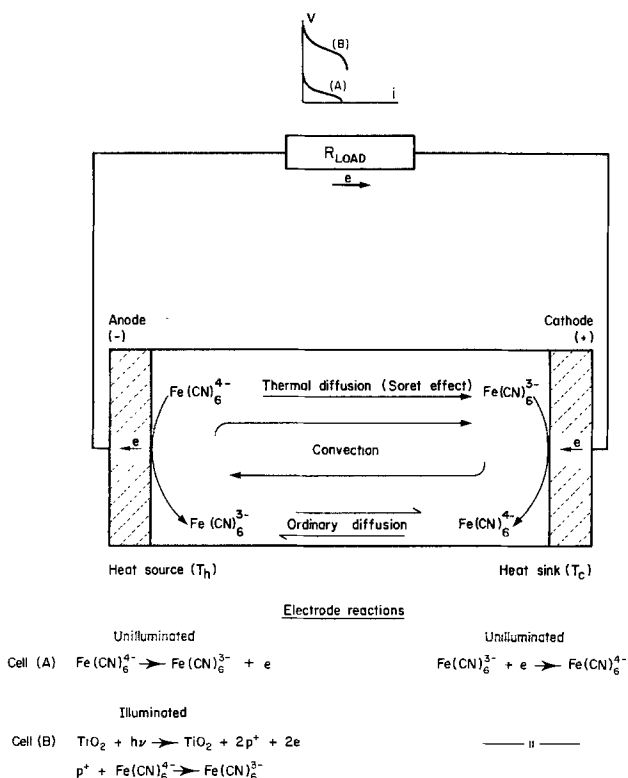


Fig. 6. Schematic diagram of the operation of a redox thermogalvanic cell [A] and photothermogalvanic cell [B] showing the electrode reactions which can occur.



## REFERENCES

1. W. Vielstich, "Fuel Cells," pp. 345-361, Wiley-Interscience, New York (1960).
2. B. R. Sundheim, in "Thermoelectric Materials and Devices," I. B. Cadoff and E. Miller, Editors, Chap. 14, Van Nostrand Reinhold Co., New York (1960).
3. R. W. Christy, *ibid.*, Chap. 12.
4. R. Zito, *AIAA J.*, **1**, 2133 (1963).
5. T. Warrantowicz, *Adv. Energy Conv.*, **4**, 149 (1964).
6. H. P. Meissner *et al.*, *ibid.*, **5**, 205 (1965).
7. S. L. Soo, "Direct Energy Conversion," Chap. 5, Prentice-Hall, Englewood Cliffs, N. J. (1968).
8. M. Telkes, *J. Appl. Phys.*, **25**, 765 (1954).
9. J. L. Weininger, *This Journal*, **111**, 769 (1964).
10. U.S. Pat. 2,890,259 (1959).
11. N. Weber, *Adv. Energy Conv.*, **14**, 1 (1974).
12. U.S. Pat. 3,458,356 (1969).
13. U.S. Pat. 3,311,506 (1967).
14. U.S. Pat. 3,293,079 (1966).
15. B. W. Burrows, Proc. 10th Intersociety Energy Conversion Engineering Conference, p. 821 (1975).
16. L. Marcoux and R. Adams, *Anal. Chem.*, **39**, 1828 (1967).
17. T. N. Anderson and H. Eyring, in "Physical Chemistry: An Advanced Treatise, Vol. IXA Electrochemistry," H. Eyring, Editor, pp. 268-269, Academic Press, New York (1970).
18. D. H. Angell and T. Dickinson, *J. Electroanal. Chem.*, **35**, 55 (1972).
19. B. W. Burrows, *J. Chem. Educ.*, **48**, 732 (1971).
20. A. M. Feltham and M. Spiro, *J. Electroanal. Chem.*, **35**, 181 (1972).
21. R. de Levie, in "Advances in Electrochemistry and Electrochemical Engineering," Vol. 6, P. Delahay, Editor, Wiley-Interscience, New York (1967).
22. A. J. de Bethune, T. S. Licht, and N. Swendeman, *This Journal*, **106**, 617 (1959).
23. N. Fuschillo *et al.*, *Adv. Energy Conv.*, **6**, 103 (1966).
24. M. D. Archer, *J. Appl. Electrochem.*, **5**, 17 (1975).
25. A. Fujishima and K. Honda, *Nature*, **238**, 37 (1972).
26. J. Keeney *et al.*, *ibid.*, **253**, 719 (1975).

## Electrophoretic Mobilities of Cadmium Hydroxide, Nickel Hydroxide, and Silver Oxide in Ni-Cd and Ag-Zn Battery Electrolytes

S. W. Mayer

*Chemistry and Physics Laboratory, Laboratories Operations,  
The Aerospace Corporation, El Segundo, California 90245*

### ABSTRACT

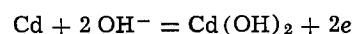
Since cadmium migration damage of separators is a major cause of Ni-Cd battery failures or performance degradation, a series of electrophoretic mobility measurements has been made for cadmium hydroxide suspensions in concentrated KOH battery electrolyte at several concentrations of  $K_2CO_3$  to investigate whether electrophoresis of cadmium hydroxide could be the mechanism for migration to separators. It was found that the mobility of the cadmium hydroxide suspension in an applied electrical field is adequate to account for the observed migration of cadmium hydroxide to separators. The view that high carbonate concentrations in Ni-Cd battery electrolyte may increase cadmium migration damage of separators is consistent with these electrophoretic measurements since it was demonstrated that increasing  $K_2CO_3$  concentration from 0.8 to 6.2% increased cadmium hydroxide migration by a factor of 3. Zeta potentials have been calculated from the data. Similar measurements have been made for nickel hydroxide suspensions in Ni-Cd battery electrolyte at several  $K_2CO_3$  concentrations. The results are consistent with ion probe analyses for nickel in nylon separators exhibiting considerable cadmium migration. Silver oxide mobility reached a maximum at 5.1%  $K_2CO_3$  and declined at 15.8%  $K_2CO_3$ .

A major cause of premature failure in modern Ni-Cd spacecraft batteries (1, 2) is short-circuiting through separators damaged by cadmium hydroxide or cadmium that has migrated into the separator (3). The migrating material is apparent in the separator as a black or dark gray, nonuniform deposit. When the amount of migrated material is so large that extensive penetration into and through the separator occurs, the battery fails, or its performance degrades very severely because of internal short circuits through the separator and consequent rapid self-discharge (2, 3).

The cause of this damaging migration, however, is not well understood. There is some belief that the source of the migrated material is cadmium dissolved in the KOH electrolyte, since the solubility of cadmium ions in this electrolyte is finite, although admittedly very small (1). Tests of cation and anion exchange ca-

capacity of the nylon separators, however, show almost no ion exchange capacity, both for separators exhibiting considerable cadmium migration and for new separators (3). Furthermore, the surfaces of the separators nearest the Cd-Cd(OH)<sub>2</sub> electrode are always much more contaminated with cadmium than the surfaces furthest from the cadmium electrode. This suggests that the source of the cadmium deposited in the separator is not cadmium ions dissolved in the solution since the solution would penetrate the porous separator uniformly rather than favoring the surface nearest the Cd-Cd(OH)<sub>2</sub> electrode. It seemed possible that the deposit on the separator could be particles of insoluble Cd(OH)<sub>2</sub> from the negative plate although this source has not previously been mentioned (1, 2). On the cadmium plate, particulate Cd(OH)<sub>2</sub> is formed during discharge

**Key words:** electrophoresis, cadmium migration, silver oxide mobility.



[1]

If the  $\text{Cd}(\text{OH})_2$  particles have a net negative charge in the KOH electrolyte (possibly arising from preferential absorption of  $\text{OH}^-$  ions as compared to absorption of  $\text{K}^+$  ions), they would tend to be repelled by the negative field when the cadmium electrode is being charged and migrate electrophoretically toward the positive field of the nickel hydroxide electrode (4). Migrating negative particles of  $\text{Cd}(\text{OH})_2$  would first be stopped on the surface of the separator nearest the cadmium electrode. The particles would tend, during subsequent charging, to migrate further towards the positive electrodes through those pores of the separator that are large enough to permit their passage. This mechanism for migration would be consistent with the observed preferential deposition on the surface of the separator nearest the cadmium electrode, followed by penetration into the separator as the number of cycles increases (2).

In order to determine whether this particulate electrophoresis explanation of migration in Ni-Cd cells might be possible, the electrophoretic measurements for  $\text{Cd}(\text{OH})_2$  described in this report have been made in the 34% KOH electrolyte used in Ni-Cd cells. The electrophoretic mobility and zeta potential measurements for  $\text{Cd}(\text{OH})_2$  were also conducted in the presence of added  $\text{K}_2\text{CO}_3$  since it is thought possible that the presence of  $\text{K}_2\text{CO}_3$  in Ni-Cd batteries increases migration damage (2, 5). After the electrophoresis measurements showed that particulate  $\text{Cd}(\text{OH})_2$  does migrate towards the positive electrode in KOH, similar sets of measurements were made on nickel hydroxide and silver oxide because of their relevance to Ni-Cd and Ag-Zn spacecraft batteries. Reduction potential measurements were also made to determine whether, during charging of Ni-Cd batteries, potentials were reached near the separators that were sufficient to convert migrated  $\text{Cd}(\text{OH})_2$  to metallic cadmium particles.

### Experimental

Electrophoretic mobility and zeta potential determinations for cadmium hydroxide, nickel hydroxide, and silver oxide were made by the method of Sennett and Olivier (6) as modified by Long and Ross (7). Through the use of a cylindrical sample chamber rotating at 30 rpm, suspensions containing up to 40% of the hydroxide can be investigated. In this variation of the Hittorf technique, a constant potential gradient is applied by means of stainless steel electrodes to the rotating suspension of metal hydroxide particles in KOH electrolyte, and the weight of metal hydroxide migrating in 360 sec to the 2.0 cm diam electrode in a collection cell is determined. The electrophoretic mobility and zeta potential can then be calculated (6).

The samples of metal hydroxide suspension were prepared by adding a solution of the reagent-grade nitrate salt drop by drop, with stirring, to analyzed reagent-grade KOH solutions that had, according to the analysis, only 0.01%  $\text{CO}_2$  contamination. The cadmium hydroxide suspension contained 13.9%  $\text{Cd}(\text{OH})_2$  in 34% KOH. The nickel hydroxide suspension consisted of 5.2%  $\text{Ni}(\text{OH})_2$  in 34% KOH. To prepare the silver oxide suspension, 70g of  $\text{AgNO}_3$  were dissolved in 35 ml of water. The solution was stirred drop by drop into 800 ml of 45% KOH.

In order to test the effect of  $\text{K}_2\text{CO}_3$  on the electrophoretic mobility, the desired weight of anhydrous reagent-grade  $\text{K}_2\text{CO}_3$  was dissolved in the appropriate suspension. The temperature of the samples was 21°C during the electrophoretic mobility measurements.

### Results and Discussion

The electrophoretic mobility  $m$  of cadmium hydroxide and nickel hydroxide suspensions in 34% KOH was calculated (6) on the basis of Eq. [2] after the weight had been measured of each hydroxide (in separate experiments) that collected at the positive electrode in 360 sec

$$m(\text{cm/sec per V/cm}) = \frac{WK}{tRifd} \quad [2]$$

where  $W$  denotes the grams of particulate migrating to the electrode in  $t$  sec,  $K$  is the cell conductivity constant (0.8905),  $i$  is the current (set at 5 mA),  $f$  is the product of the volume fraction of the particulate with the volume fraction of the electrolyte,  $d$  is the density difference between the particulate and the electrolyte, and  $R$  is the resistance of the electrolyte suspension of the particulate in the sample chamber as measured with a Wheatstone bridge. The density data used for  $\text{Cd}(\text{OH})_2$ ,  $\text{Ni}(\text{OH})_2$ , and  $\text{Ag}_2\text{O}$  were their handbook values of 6.4, 4.1, and 7.4 g/cm<sup>3</sup>, respectively. The density of KOH electrolyte has been reported (1). The particle sizes of the suspensions were large enough so that they settled out when allowed to stand 15 min, leaving a clear supernatant electrolyte which showed almost no colloidal Tyndall effect in the beam of a helium-neon laser. Although cadmium is known (1, 5) to have a low solubility in concentrated KOH solutions as a negative ion, the rate of cadmium deposition on the positive electrode was considered to be too small to have a significant effect because the low concentration of the cadmium ion would produce a correspondingly low rate of cadmium deposition.

The zeta potential  $p$  (in volts) was calculated (6) by

$$p = 1.3 \times 10^6 \eta m/D \quad [3]$$

where  $\eta$  is the electrolyte viscosity in poises,  $D$  is its dielectric constant, and  $m$  is the mobility calculated from Eq. [2].

The cadmium and nickel hydroxides migrated to the positive electrode because the particulates in the suspension apparently had acquired a negative charge by adsorbing hydroxyl and carbonate anions preferentially compared to their adsorption of potassium cations from the electrolyte. Table I presents the data for the weight of cadmium hydroxide particulate collected in the positive electrode cell in 360 sec for the suspension originally containing 13.9%  $\text{Cd}(\text{OH})_2$  in 34% KOH. Battery electrolyte generally contains  $\text{K}_2\text{CO}_3$  in addition to KOH as a result of  $\text{CO}_2$  absorbed from the atmosphere or of  $\text{CO}_2$  produced by separator degradation (1, 2), and it is believed that cadmium migration damage of separators may become more severe as the concentration of carbonate in the electrolyte increases (5, 8). The electrophoretic mobility was consequently measured at three higher concentrations of  $\text{K}_2\text{CO}_3$ , using other portions of the stock suspension of 13.9%  $\text{Cd}(\text{OH})_2$  in KOH electrolyte. The results, shown in Table I, are consistent with the view that higher levels of carbonate contamination do tend to increase cadmium migration, since the quantity of  $\text{Cd}(\text{OH})_2$  collected at the electrode increased from 31.0 mg with 0.8%  $\text{K}_2\text{CO}_3$  present to 181.4 mg at the 9.0%  $\text{K}_2\text{CO}_3$  level. The 9.0%  $\text{K}_2\text{CO}_3$  concentration is characteristic of high levels of carbonate contamination occasionally observed (8), and the 0.8%  $\text{K}_2\text{CO}_3$  concentration is within the normal range for electrolyte in new Ni-Cd batteries (1).

Table I also contains the calculated electrophoretic mobilities and zeta potentials corresponding to each concentration of  $\text{K}_2\text{CO}_3$ . The mobilities do not increase with  $\text{K}_2\text{CO}_3$  levels as rapidly as the weight of  $\text{Cd}(\text{OH})_2$  collected at the positive electrode, inasmuch as the re-

Table I. Migration of cadmium hydroxide suspensions in Ni-Cd battery electrolyte

$\text{K}_2\text{CO}_3$ concentration, w/o	Suspension collected at anode, mg	Mobility, $10^{-3}$ cm/sec per V/cm	Zeta potential, mV
0.8	31.0	0.08	46
3.1	60.9	0.11	63
6.2	98.8	0.14	81
9.0	181.4	0.18	104

sistance of the suspension increases with added  $K_2CO_3$ . The lowest mobility in Table I is, however, easily sufficient to allow particles of  $Cd(OH)_2$  to migrate into the separator and toward the positive plate during the Ni-Cd cell-charging process which would take 10 hr at the C/10 rate. An applied charging voltage of 1.5 between plates separated by 2 mm would provide a potential gradient of 7.5 V/cm. The lowest mobility in Table I would then produce a  $Cd(OH)_2$  particle velocity of 20 mm/hr. As the separator is closer to the  $Cd(OH)_2$  plate than 0.3 mm, it is evident that even higher charging rates than C/10 provide ample time for  $Cd(OH)_2$  to migrate electrophoretically to the separator. The increase in mobility as the carbonate concentration is raised suggests that the  $Cd(OH)_2$  particles acquire a higher negative charge because of stronger preferential adsorption for the doubly charged carbonate anion than for the singly charged hydroxyl anion. The observed trend towards increased zeta potentials at higher carbonate concentrations is consistent with higher charge density, because of increased carbonate adsorption, on the cadmium hydroxide particles.

As shown by the data in Table II, higher concentrations of  $K_2CO_3$  did not increase the quantity of  $Ni(OH)_2$  suspension that migrated towards the positive electrode. Nickel hydroxide, nevertheless, does have a relatively strong tendency to migrate towards the positive electrode at lower  $K_2CO_3$  levels. During 360 sec in 2.7%  $K_2CO_3$ , 132 mg of  $Ni(OH)_2$  migrated to the anode, compared to 61 mg of  $Cd(OH)_2$  in 3.1%  $K_2CO_3$ . It should be noted, however, that the direction of the electrophoretic mobility of the  $Ni(OH)_2$  suspension in the Ni-Cd battery would cause the suspension to move toward the  $Ni(OH)_2$  positive plate during charging. Consequently, unlike cadmium hydroxide, it would not tend to migrate away from the plate where it should remain for better battery performance and lifetime. The electrophoretic mobility measurements are consistent with the results of separator chemical analyses by ion probe (3), which show that virtually no migration of nickel to separators occurs even when the cadmium migration damage is severe.

The electrophoretic measurements for suspensions of silver oxide in 43% KOH electrolyte of Ag-Zn spacecraft batteries demonstrate that the sign of the charge on  $Ag_2O$  suspensions is opposite to that on the cadmium hydroxide or nickel hydroxide suspensions. The quantity of  $Ag_2O$  migrating to the cathode in 360 sec increased sharply (Table III) when the  $K_2CO_3$  concentration was raised to 5.1 from 2.0%, but declined at higher concentrations of carbonate. The lowest rate of migration was obtained at the lowest concentration of carbonate. Accordingly, it is not recommended that carbonates should be added to Ag-Zn battery electrolyte to suppress silver migration. Since zinc oxide is soluble in KOH electrolyte, no electrophoretic measurements were needed for zinc oxide in this study.

Table II. Electrophoretic mobility of nickel hydroxide suspensions in Ni-Cd battery electrolyte

$K_2CO_3$ concentration, w/o	Suspension collected at anode, mg	Mobility, $10^{-3}$ cm/sec per V/cm	Zeta potential, mV
1.6	143.3	0.74	430
2.7	132.4	0.67	390
3.6	126.6	0.64	370
6.5	43.4	0.21	120

Table III. Migration of silver oxide suspensions in Ag-Zn battery electrolyte

$K_2CO_3$ concentration, w/o	Suspension collected at cathode, mg	Mobility, $10^{-3}$ cm/sec per V/cm	Zeta potential, mV
2.0	51.5	0.29	300
5.1	380.1	1.68	1700
8.3	259.1	1.14	1200
15.8	92.2	0.41	420

The electrophoretic mobility data (Table I) for cadmium hydroxide in Ni-Cd battery electrolyte show that the mobility of  $Cd(OH)_2$  is sufficient to allow it to reach and penetrate the separator. Such deposits in the separator will be more damaging to battery performance by producing internal shorting between the plates if they are converted from  $Cd(OH)_2$ , which has a high resistance to electron flow, to cadmium metal which has a low resistance. The mechanisms whereby  $Cd(OH)_2$  in the separator can be reduced to Cd metal during battery charging will require extensive investigation before their relative contributions can be evaluated. One mechanism could consist of electron tunneling (9) from the cadmium electrode to  $Cd(OH)_2$  deposited on the surface of the separator. Tunneling is very dependent on the distance from the electrode source, and it is uncertain that enough of the separator in a typical Ni-Cd cell is sufficiently close to the cadmium electrode to permit significant tunneling of electrons to the separator. Other mechanisms could depend on the reduction of soluble impurities in the electrolyte at the cadmium electrode during battery charging, followed by diffusion of these reduced impurities to the separator where they would reduce the migrated  $Cd(OH)_2$  to Cd metal if their reduction potentials were adequate. These mechanisms are analogous to the nitrate-nitrite shuttle for producing Ni-Cd battery self-discharge (2, 5).

Nitrite, however, is not a sufficiently strong reducing agent to be efficient for the reduction of  $Cd(OH)_2$  to Cd metal. The following experimental test was, therefore, made with a 12 A-hr Ni-Cd spacecraft cell to investigate whether sufficiently strong reducing potentials occurred in the electrolyte adjacent to separator surfaces during the cell-charging process. The Ni-Cd cell had been subjected to 100 charge-discharge cycles during preflight testing. Cell state-of-charge at the beginning of the test was 90%. The cell was cut open and the pack of plates was raised from the casing so that about 75% of the plate height remained in the casing. The cell was then immersed in 34% KOH electrolyte (at 25°C) so that electrolyte contact was established with the plates. An Hg-HgO reference electrode, with a bridge containing 31% KOH, was placed in the electrolyte. The reference electrode was connected with a 1.2-cm<sup>2</sup> platinum foil electrode, which was inserted diagonally into the immersed portion of the plate pack, between the sixth cadmium electrode and its adjacent nylon separator. The objective of the platinum foil was to act as a potential-indicating electrode for the Ni-Cd cell electrolyte near the surface of the separator, as the cell was being charged. The cell was charged at 1.4V and 0.50A, and the emf of the platinum foil-HgO reference electrode pair was monitored with a high-impedance digital voltmeter. After 30 min, the observed emf of the electrode pair stabilized near  $-0.93V$  and remained at  $-0.93 \pm 0.01V$  during the 3 hr of cell charging.

This potential is sufficient to reduce much of the  $Cd(OH)_2$  in a separator to Cd metal, and indicates that the electrolyte near the surface of the separator does contain reduced compounds or ions capable of converting some of the migrated  $Cd(OH)_2$  to Cd in the separator. The reduced compounds in the electrolyte could be impurities, or hydrogen could be formed in solution at the observed voltage of the platinum-foil indicator electrode. One possible impurity that would attain suitable reducing potentials (10) in KOH electrolyte is the stannite ion; another possibility is sulfite ion. Aldehydes formed at the cadmium electrode (during charging) from carboxylic acid produced by degradation of the nylon separator could also act as a soluble reducing agent to convert  $Cd(OH)_2$  to Cd metal in the separator. Another possibility is that a combination of several such soluble reducing agents could form the Cd metal that causes internal shorting and consequent battery failure.

### Acknowledgments

This work reflects research supported by the U.S. Air Force Space and Missiles Systems Organization (SAMSO) Contract No. AF04701-73-C-0074.

Manuscript submitted April 25, 1975; revised manuscript received Oct. 27, 1975. This was Paper 47 presented at the New York, New York, Meeting of the Society, Oct. 13-17, 1974.

Any discussion of this paper will appear in a Discussion Section to be published in the December 1976 JOURNAL. All discussions for the December 1976 Discussion Section should be submitted by Aug. 1, 1976.

Publication costs of this article were partially assisted by The Aerospace Corporation.

### REFERENCES

1. S. U. Falk and A. J. Salkind, "Alkaline Storage Batteries," John Wiley and Sons, Inc., New York (1969).
2. P. Bauer, "Batteries for Space Power Systems," NASA SP-172 (1968).
3. S. W. Mayer and D. Taylor, TR-0074(4270-10)-3, The Aerospace Corp., El Segundo, Calif. (1974).
4. M. Bier, Editor, "Electrophoresis," Academic Press, Inc., New York (1959).
5. E. J. Casey, A. R. Dubois, P. E. Lake, and W. J. Morez, *This Journal*, **112**, 371 (1965).
6. P. Sennett and J. P. Olivier, *Ind. Eng. Chem.*, **57**, 3250 (1965).
7. R. P. Long and S. Ross, *J. Colloid Sci.*, **20**, 438 (1965).
8. D. L. Barney *et al.*, in "Power Sources 3," D. H. Collins, Editor, pp. 119-133, Oriel Press Ltd., New castle-upon-Tyne, England (1971).
9. J. O. Bockris and A. K. N. Reddy, "Modern Electrochemistry," pp. 959-974, Plenum Press, New York (1970).
10. W. M. Latimer, "Oxidation Potentials," Prentice-Hall, Inc., Englewood Cliffs, N. J. (1959).

# Anodic Dissolution of Titanium in Acidic Sulfate Solutions

## II. Effects of Ti(III) and Ti(IV) Ions

Eugene J. Kelly\*

Chemistry Division, Oak Ridge National Laboratory, Oak Ridge, Tennessee 37830

### ABSTRACT

At an active-state titanium electrode, Ti(IV) ions are reduced to Ti(III), and the reduction reaction is first order with respect to the concentration of Ti(IV) ions. The current density corresponding to the reduction reaction adds algebraically to the current densities corresponding to the active-state dissolution of the metal to form Ti(III) ions in solution and to the hydrogen evolution reaction. At constant potential, the rates of the latter two reactions are not affected by Ti(III) or Ti(IV) ions. However, the reduction of Ti(IV) ions is accompanied by a displacement of the open-circuit (corrosion) potential in the noble direction and, consequently, by an increase in the open-circuit corrosion rate. When the concentration of Ti(IV) exceeds a certain critical value, the active-state titanium passivates. At a passive-state titanium electrode, Ti(III) ions are oxidized to Ti(IV), and the oxidation reaction is first order with respect to the concentration of Ti(III). The current density corresponding to the oxidation of Ti(III) ions simply adds to the current density corresponding to the dissolution of the passive metal. The rate of the latter reaction is not affected by Ti(III) or Ti(IV) ions. Electrolyte-coupled active-passive titanium systems, *i.e.*, systems in which active-state and passive-state electrodes are collocated in the same body of electrolyte, are capable of generating the critical concentration of Ti(IV) ions required to passivate the active surface, a "self-healing" phenomenon relevant to localized (pitting, crevice, etc.) corrosion. Also, under appropriate conditions, dissolution rates of titanium in the active state (open-circuit or polarized) may be accurately determined by monitoring the current at the passive sensor electrode in an electrolyte-coupled system.

The first paper in this series (1) described the results of a study of the electrochemical behavior of zone-refined titanium in hydrogen-saturated acidic sulfate solutions ( $\text{pH} < \sim 2.5$ ). Although the primary objective of the earlier investigation was the determination of the mechanism of titanium dissolution in the active state and in the active-passive transition (passivation) potential region, the kinetics of oxidation of Ti(III) ions in solution to Ti(IV) at a passive titanium surface, and the effect of this reaction on the current-density/potential curve in the passive state were also examined. It was shown that, at constant potential and pH, the oxidation of Ti(III) ions to Ti(IV) is first order in the Ti(III) concentration, and that the current density corresponding to this reaction simply adds to the current density corresponding to the passive-state dissolution of the substrate metal. The Ti(III) ion had no

discernible effect on the dissolution rate of the passive metal. Many authors have noted the increased current density observed at a passive titanium electrode in the presence of Ti(III) ions, and have attributed the effect to the electrodeposition of a thick oxide film (2, 3), or to a peculiar "depassivating effect" in which the Ti(III) ions bring about an increase in the dissolution rate of the passive metal (4, 5). On the other hand, Kuznetsova *et al.* (6) concluded that the dissolution rate of passive titanium is reduced by the presence of Ti(III) ions. Consequently, depending upon the particular author, Ti(III) ions increase, decrease, or have no significant effect upon the dissolution rate of passive titanium.

Weiman (7), Andreeva and Yakovleva (8), and Sinigaglia *et al.* (9), among others, have all observed that, above a certain critical concentration, Ti(IV) ions in solution passivate an active titanium surface. In addition to this observation, Thomas and Nobe (5) con-

\* Electrochemical Society Active Member.

Key words: titanium, corrosion, active state, passive state, self-healing.

cluded that at concentrations below the critical concentration required for passivation, Ti(IV) ions inhibit the anodic dissolution of titanium in the active state. All investigators agree that Ti(IV) ions are electrochemically inert at a passive titanium surface and have no effect on the passive-state dissolution rate of the metal.

In the initial portion of this paper, the kinetics of reduction of Ti(IV) ions to Ti(III) at an active titanium surface, and of oxidation of Ti(III) ions to Ti(IV) at a passive titanium surface are examined in detail. An analysis of the effects of these reactions on the current/potential behavior of titanium in the active and passive states is presented, and the effects of Ti(III) and Ti(IV) ions on the dissolution rate of titanium in the active and passive states are determined. The latter portion of the paper is devoted to a study of electrolyte-coupled active-passive titanium systems, *i.e.*, systems in which active and passive electrodes are collocated in the same body of electrolyte. The oxidation of Ti(III) ions at a passive titanium sensor electrode serves as the basis for a very sensitive method for monitoring active-state dissolution rates. In addition, electrolyte-coupled active and passive metal/electrolyte reaction systems are encountered in localized attack of metals (pitting corrosion, crevice corrosion, etc.) (10), and the results of this study add to our understanding of the mechanism involved in localized corrosion.

### Experimental

The experimental apparatus and techniques have been described elsewhere (11) and, therefore, only a brief resume is given here. The three-compartment cell assembly (test, reference, and counterelectrode compartments) was made of Pyrex glass and Teflon, and was so designed that solutions could be added to or removed from the cell without exposure to the atmosphere. All compartments were jacketed and maintained at a constant temperature ( $\pm 0.02^\circ\text{C}$ ) which, except where noted, was  $30^\circ\text{C}$ . A stream of hydrogen was passed through all compartments at all times. The hydrogen source was a Matheson generator which produces ultra pure gas via diffusion of electrolytically generated hydrogen through a palladium membrane. Additional stirring in the test compartment was achieved with a Teflon-coated magnetic stirrer.

The titanium electrodes employed in this study were made from zone-refined, polycrystalline titanium (Materials Research Corporation). The cylindrical electrodes were mounted on Teflon electrode holders which exposed either one planar surface or the cylindrical surface or both. All solutions were prepared from reagent grade materials and triply distilled water. Stock solutions of Ti(IV) in 1N  $\text{H}_2\text{SO}_4$  were prepared by dissolving approximately 2g of zone-refined titanium in a sulfuric acid solution (55.6 ml conc  $\text{H}_2\text{SO}_4$  + 200 ml  $\text{H}_2\text{O}$ ) at  $\sim 70^\circ\text{C}$  under a helium atmosphere. The resulting deep purple solution was cooled to room temperature, and filtered through a medium porosity glass filter directly into a two-liter volumetric flask. A small amount of the solution was held back. Hydrogen peroxide (30% solution) was added to the volumetric flask until the purple Ti(III) solution just became colorless. The next drop of  $\text{H}_2\text{O}_2$  produced an orange color which was eliminated by addition of some of the Ti(III) solution that was held back. The addition of increasingly dilute  $\text{H}_2\text{O}_2$  and Ti(III) solutions was repeated several times, with the final solution in the volumetric flask containing a negligible excess of Ti(III). The solution was then diluted with  $\text{H}_2\text{O}$  to the two-liter mark. Except where noted otherwise, Ti(III) solutions were prepared by anodic oxidation of titanium at  $E_m$  (see text) in acidic sulfate solutions having the desired pH.

In those instances where test solutions were analyzed for Ti(III) via permanganate titration, the  $\text{KMnO}_4$  solutions were 0.5M in  $\text{H}_2\text{SO}_4$ , and were presaturated with  $\text{H}_2$ . Solution transfer and titration were conducted under a hydrogen atmosphere. A standard peroxide

colorimetric method was employed in the determination of Ti(IV) in test solutions (12). A 2 ml sample of test solution was transferred to a 10 ml volumetric flask, 0.2 ml of  $\text{H}_2\text{O}_2$  (30% solution) was added, and the solution was diluted to the 10 ml mark with 0.5M  $\text{H}_2\text{SO}_4$ . The absorbance was measured at a wavelength of  $410\text{ m}\mu$ , using a Beckman Model DU Quartz Spectrophotometer with a  $\text{H}_2$  lamp and a 1 cm cell.

In experiments involving only one test electrode, a Wenking potentiostat (Model 61 RH) was used in conjunction with a Wenking precision potentiometer (Model PPT-67), and a Hewlett-Packard/Moseley recorder (Model 7100B, Model 17501A plug-ins). In experiments involving two test electrodes (electrolyte-coupled active and passive titanium electrodes), an ORNL potentiostat (Model Q-2003) was used with a potentiostat derived from a Philbrick Model Q3-A2P differential amplifier to form a dual potentiostat. A common reference and counterelectrode completed the four-electrode systems.

All electrode potentials ( $E$ ) were measured against a saturated calomel electrode and, unless stated otherwise, all  $E$  values are given with reference to SCE.

### Results and Discussion

In order to acquaint the reader with various aspects of the titanium system, typical steady-state polarization curves are shown in Fig. 1. In 1N  $\text{H}_2\text{SO}_4$ , titanium undergoes spontaneous active-state dissolution accompanied by the hydrogen-evolution reaction. As the potential of the titanium is made increasingly positive (noble) relative to the corrosion potential ( $E_c = -735 \pm 5\text{ mV vs. SCE}$ ), the anodic current density increases to a maximum ( $i_m$ ) at the critical potential ( $E_m$ ), and then decreases as the metal is transformed from the active to the passive state. In a previous study (1), coulometric-weight loss measurements at  $E_m$  and  $E_m + 160\text{ mV}$  demonstrated that, in the active and active-passive transition potential regions (*i.e.*, in the potential regions where curves A and D coincide), titanium is oxidized to form Ti(III) ions in solution. In the passive state, the metal is oxidized to form the passive

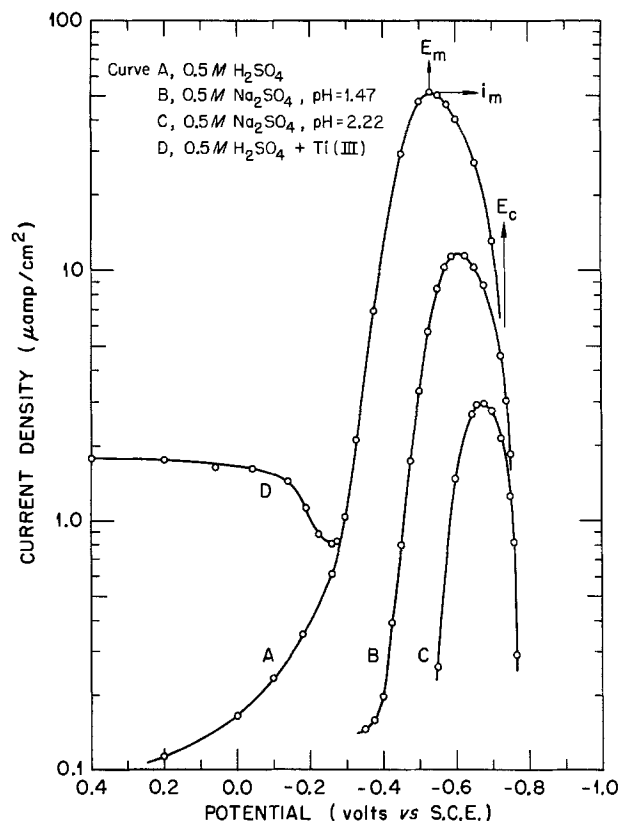


Fig. 1. Effects of Ti(III) concentration and pH on the steady-state anodic polarization of titanium.

film ( $\text{TiO}_2$ ) and  $\text{Ti(IV)}$  ions in solution. Curves A, B, and C illustrate the effect of pH on the polarization behavior of titanium. If the effect of the hydrogen evolution reaction is taken into account, it may be shown (1) that  $d \log i_m/d\text{pH} = -2/3$ ,  $d \ln i_m/dE_m = F/2RT$ , and  $dE_m/d\text{pH} = -(4/3) 2.303 RT/F$ . These diagnostic criteria are satisfied by the mechanism of titanium dissolution presented earlier (1). Here, our interest is focused on the difference between curves A and D, a difference which results from the presence of  $\text{Ti(III)}$  ions in the electrolyte phase.

**Oxidation of  $\text{Ti(III)}$  ions in solution to  $\text{Ti(IV)}$  at a passive titanium surface.**—In order to examine the oxidation of  $\text{Ti(III)}$  ions at a passive titanium surface, a titanium electrode was maintained in a steady state at 0 mV vs. SCE (curve A), and a solution of known concentration of  $\text{Ti(III)}$  ions in  $\text{H}_2$ -saturated 1N  $\text{H}_2\text{SO}_4$  was added in measured volume increments to the test cell containing a known volume of 1N  $\text{H}_2\text{SO}_4$ . After each addition, the current density increased, moving from its initial value on curve A toward curve D. Let  $i_p^*$  represent the current density corresponding to the passive-state dissolution of titanium in the absence of  $\text{Ti(III)}$  ions (curve A), and  $i_p$  the current density observed when the concentration of  $\text{Ti(III)}$  is  $C_3$ . If the oxidation of  $\text{Ti(III)}$  ions at the passive surface has an order ( $n$ ) with respect to the  $\text{Ti(III)}$  concentration, then

$$i_3 = k_3 C_3^n \quad [1]$$

where  $i_3$  is the current density corresponding to the  $\text{Ti(III)}$  oxidation reaction, and  $k_3$  is a constant (at constant potential and pH). If  $i_3$  simply adds to  $i_p^*$ , and  $i_p^*$  is not affected by the presence of  $\text{Ti(III)}$  ions, then

$$i_p = i_p^* + i_3 \quad [2]$$

and, in view of Eq. [1]

$$i_p = i_p^* + k_3 C_3^n \quad [3]$$

According to Eq. [3], a plot of  $\log(i_p - i_p^*)$  vs.  $\log C_3$  should result in a straight line having a slope equal to  $n$ . The experimental data shown in Fig. 2 are in complete agreement with Eq. [3], and prove that  $n = 1$  i.e.

$$i_p = i_p^* + k_3 C_3 \quad [4]$$

The measurement of  $i_p$  at constant potential and pH provides a method for determining the concentration of  $\text{Ti(III)}$  ions in a solution containing both  $\text{Ti(III)}$  and  $\text{Ti(IV)}$  ions.

The preceding analysis requires that, under potentiostatic conditions

$$\partial C_3/\partial t = -A_p i_3/Fv \quad [5]$$

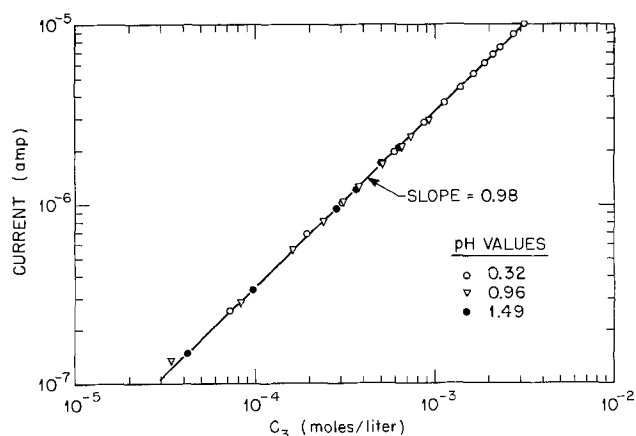


Fig. 2. Oxidation of  $\text{Ti(III)}$  to  $\text{Ti(IV)}$  at a passive-state titanium electrode ( $E = 0$  mV vs. SCE). Determination of order ( $n$ ) with respect to  $\text{Ti(III)}$  concentration (Eq. [3]). Plot of  $\log(i_p - i_p^*)$  vs.  $\log C_3$ . Data for higher pH values normalized to curve for pH = 0.32 at  $1 \times 10^{-6}\text{A}$ .

and

$$\partial C_3/\partial t = (A_p i_3/Fv) + (A_p i_p^*/4Fv) \quad [6]$$

where  $A_p$  is the area of the passive electrode,  $v$  is the volume of electrolyte, and  $F$  is the Faraday constant. In the section of this paper dealing with the behavior of electrolyte-coupled active and passive electrodes, it will be shown that Eq. [5] and [6] are obeyed, thereby proving the validity of the analysis presented above in the derivation of Eq. [4]. If the increased current density observed at a passive titanium electrode in the presence of  $\text{Ti(III)}$  ions resulted from a "depassivating" effect (4, 5), Eq. [4] would require the effect to be such that the passive-state dissolution rate of the metal itself be a linear function of  $C_3$ . No evidence has been presented to support such a hypothesis. Moreover, Eq. [5] and [6] would not be applicable. The same considerations also lead to the rejection of the hypothesis that  $\text{Ti(III)}$  ions retard the passive-state dissolution of titanium.

The potential independence of the  $\text{Ti(III)}$  oxidation reaction at more positive potentials (see curve D) can be attributed to the fact that the reaction rate depends only on the oxide-solution interfacial potential difference,  $\Delta\phi_s$ . If  $d\Delta\phi_{ox}/dE$  is virtually equal to unity, where  $\Delta\phi_{ox}$  is the potential difference between the metal and the oxide-solution interface, and  $E$  is the electrode potential relative to the reference electrode, then, since  $d\Delta\phi_s/dE = 1 - d\Delta\phi_{ox}/dE$ ,  $\Delta\phi_s$  remains essentially independent of  $E$ .

If at some point along curve D (Fig. 1), the pH is increased by the addition of concentrated  $\text{NaOH}$ , the rate of oxidation of  $\text{Ti(III)}$  ions in solution increases and becomes dependent upon the stirring rate as the reaction passes from activation to mass transport control. A corresponding buildup in film thickness is evidenced by an interference-color sequence in which the initially metallic gray electrode ultimately becomes dark blue. During this process a white precipitate ( $\text{TiO}_2$ ) accumulates in the cell. As the  $\text{Ti(III)}$  is depleted, the color sequence reverses, and eventually, the electrode returns to its original gray color, and the current density returns to the value given by curve A (Fig. 1). These results are consistent with a pH dependent hydrolysis of  $\text{Ti(III)}$ , with the hydrolysis product being the electrochemically active species. According to Pescok and Fletcher (13),  $\text{Ti(III)}$  hydrolyzes at low pH ( $< 3$ ) to form  $(\text{TiOH})^{+2}$ . If the oxidation of  $(\text{TiOH})^{+2}$  to  $\text{Ti(IV)}$  is the rate-determining step, the corresponding current density may be approximated by  $i_3 = F(D/\delta)k\gamma C_3/[k\gamma + (D/\delta)(1 + a_{\text{H}^+}/K_h)]$ , where  $k$  is the rate constant for the rate-determining step,  $K_h$  is the hydrolysis constant,  $\gamma$  and  $D$  are the activity and diffusion coefficients for  $\text{Ti(III)}$ , and  $\delta$  is the diffusion layer thickness. Although the hydrolysis of  $\text{Ti(III)}$  ions in sulfate media has not been examined, the preceding expression is qualitatively consistent with the observed pH effects.

**Reduction of  $\text{Ti(IV)}$  ions in solution to  $\text{Ti(III)}$  at an active titanium surface.**—The upper curve in Fig. 3 is a typical anodic polarization curve for titanium in deoxygenated 1N  $\text{H}_2\text{SO}_4$ . At any point along this curve, the net anodic current density ( $i_a$ ) is given by the algebraic sum of the partial anodic current density corresponding to the oxidation of titanium to  $\text{Ti(III)}$  ions in solution ( $i_d$ ), and the partial cathodic current density corresponding to the hydrogen evolution reaction ( $i_H$ ), i.e.,  $i_a = i_d + i_H$ . It should be noted that, by convention, net and partial anodic (oxidation) current densities are positive, while net and partial cathodic (reduction) current densities are negative. At the open-circuit corrosion potential,  $E_{\text{corr}}$ ,  $i_a = 0$  and, consequently,  $i_d = |i_H|$ . As the potential become increasingly positive relative to  $E_{\text{corr}}$ ,  $i_d$  increases and  $|i_H|$  decreases. Coulometric-weight loss experiments have shown that at potentials as negative as  $E_m$ ,  $|i_H|$  is negligible compared to  $i_d$  ( $|i_H| < 0.02 i_d$  at  $E_m$ ). The lower curve in Fig. 3 is the anodic polarization curve in 1N  $\text{H}_2\text{SO}_4$  containing

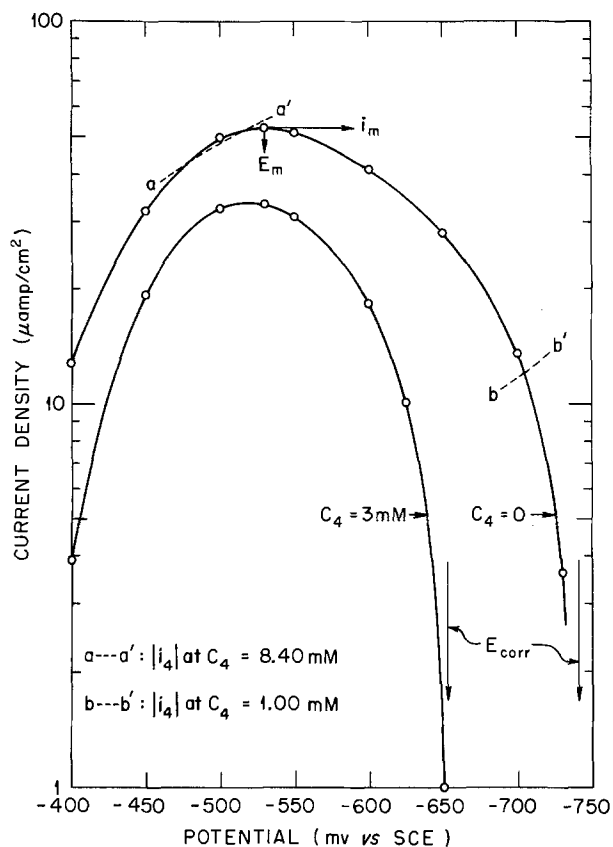


Fig. 3. Effect of Ti(IV) ions on the steady-state anodic polarization of titanium in 1N H<sub>2</sub>SO<sub>4</sub>. See text for explanation of dashed lines, a--a' and b--b'.

Ti(IV) ions at a concentration  $C_4 = 3$  mM. At first glance, it is easy to see how one might erroneously conclude that Ti(IV) ions inhibit the dissolution of titanium, since the entire anodic polarization curve is lowered by Ti(IV) ions. For example, in a coulometric-weight loss experiment conducted at  $E_m$  ( $-530$  mV vs. SCE) one might anticipate on the basis of Fig. 3 that, for  $C_4 = 3$  mM, the current density calculated from the weight loss data would be  $33.3 \mu\text{A}/\text{cm}^2$ , just as the current density of  $52.8 \mu\text{A}/\text{cm}^2$  ( $i_m$ ) was calculated from the weight loss data when  $C_4 = 0$ . Actually, in either case, the experimentally observed weight loss corresponds to  $52.8 \mu\text{A}/\text{cm}^2$  (i.e., to  $i_m$ ).

The effects of Ti(IV) ions on the polarization, dissolution, and open-circuit corrosion behavior of titanium can be explained and completely quantified if one assumes the following: (i) Ti(IV) ions are reduced to Ti(III) in the potential region under consideration; (ii) Ti(IV) ions have no effect other than to contribute a cathodic current density corresponding to their reduction ( $i_4$ ), i.e., neither  $i_d$  nor  $i_H$  are affected by the presence of Ti(IV) ions; (iii) it is assumed that Ti(III) ions have no effect on the active-state system (in contrast to their reduction at a passive surface). Then, the net anodic current density is given by Eq. [7]

$$i_a = (i_d + i_H) + i_4 \quad [7]$$

which, in accordance with the second assumption above, becomes

$$i_a = i_a^* + i_4 \quad [8]$$

where  $i_a^* = (i_d + i_H)_{C_4=0}$  is given by the upper curve in Fig. 3. The experiments described below prove the validity of the aforementioned assumptions.

A titanium electrode was maintained at  $E_m$  in 1N H<sub>2</sub>SO<sub>4</sub>. The steady-state value of  $i_a$  was  $54.2 \mu\text{A}/\text{cm}^2$ . Then, known volumes of a standard solution of Ti(IV) in 1N H<sub>2</sub>SO<sub>4</sub> were added to the cell solution and  $i_a$  was measured as a function of  $C_4$ . The results are shown in Fig. 4. According to Eq. [8],  $(\partial i_a / \partial C_4)_E = (\partial i_4 / \partial C_4)_E$ ,

and it therefore follows from the results shown in Fig. 4 that

$$i_4 = -k_4 C_4 \quad [9]$$

In other words, the reduction of Ti(IV) to Ti(III) is first order in  $C_4$ . It should be noted that, unlike the oxidation of Ti(III) in 1N H<sub>2</sub>SO<sub>4</sub>, the reduction of Ti(IV) ions in 1N H<sub>2</sub>SO<sub>4</sub> is, in the absence of stirring, under partial mass-transport control. The partial transport control was totally eliminated in these experiments by use of the magnetic stirrer. Substituting  $i_4$  from Eq. [9] into Eq. [8], one obtains Eq. [10]

$$i_a = i_a^* - k_4 C_4 \quad [10]$$

The measurement of  $i_a$  at constant potential and pH enables one to determine  $C_4$  in a mixture of Ti(III) and Ti(IV) ions. The addition of Ti(IV) required 2.73 hr. Upon completion of the addition, the electrode was maintained at  $E_m$  for another 218.47 hr, during which time samples were periodically removed from the cell and analyzed for Ti(III) via permanganate titration and for total Ti(III + IV) via the hydrogen peroxide spectrophotometric method. The concentration of Ti(IV) was calculated as the difference,  $C_4 = C_{\text{Total Ti}} - C_3$ . In Fig. 5,  $-i_4$  (calculated by use of Eq. [8]) is plotted against the concentration of Ti(IV) determined by the chemical analyses. The value of  $k_4$  is identical to that determined by the addition experiment (cf. Fig. 4). During the 221.2 hr in which Ti(IV) was present, the titanium electrode exhibited a weight loss of 19.25 mg; this corresponds to a constant dissolution current density ( $i_d$ ) of  $53.24 \mu\text{A}/\text{cm}^2$ . In the absence of Ti(IV), the dissolution current density values were  $54.2 \mu\text{A}/\text{cm}^2$  (cf. Fig. 4),  $52.8 \mu\text{A}/\text{cm}^2$  (cf. Fig. 3,  $i_m$ ), and  $51.6 \mu\text{A}/\text{cm}^2$  (used in Fig. 5).

As a consequence of the reduction of Ti(IV) ions to Ti(III) at an active surface,  $C_4$  decreases with time, and  $C_3$  increases. The increase in  $C_3$  is augmented by the dissolution of the metal. In accordance with the

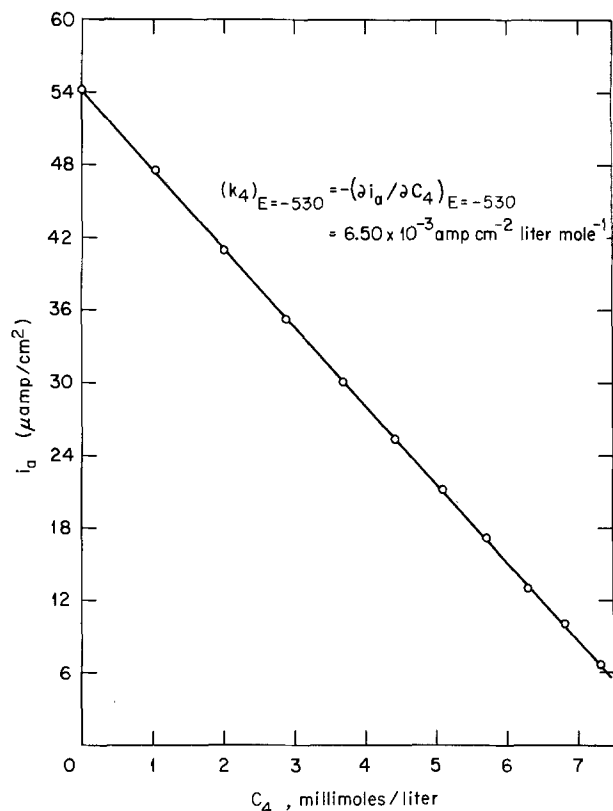


Fig. 4. Effect of Ti(IV) concentration on current density at an active-state titanium electrode ( $E = -530$  mV vs. SCE) in 1N H<sub>2</sub>SO<sub>4</sub>. Direct addition of Ti(IV) ions.



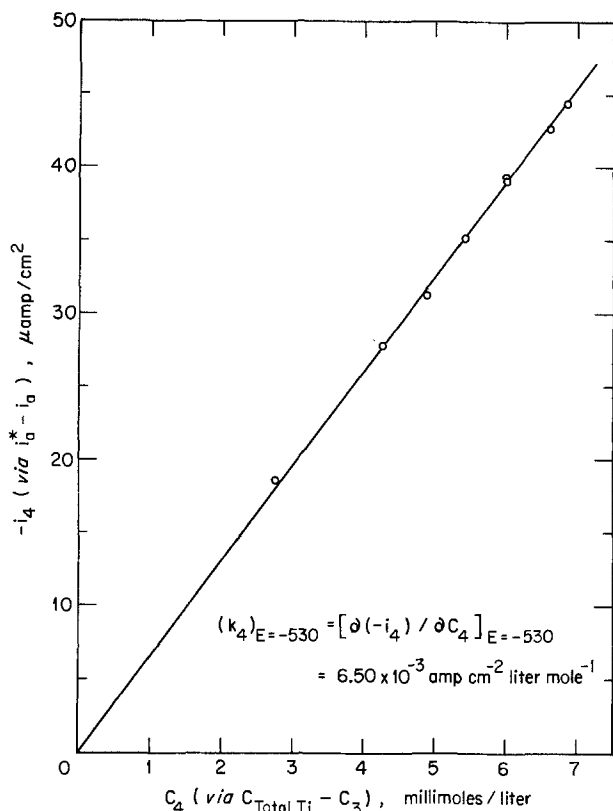


Fig. 5. Reduction of Ti(IV) to Ti(III) at an active-state titanium electrode ( $E = -530$  mV vs. SCE) in  $1N$   $H_2SO_4$ . Effect of Ti(IV) concentration on reduction current density (Eq. [9]).

assumptions made at the beginning of this section, one may write

$$dC_4/dt = -A_a |i_4| / Fv \quad [11]$$

where  $A_a$  is the area of the active-state electrode. At constant potential,  $k_4$  is constant, and substitution of  $|i_4|$  from Eq. [9] into Eq. [11], followed by integration, leads to Eq. [12]

$$C_4 = C_4^0 \exp(-A_a k_4 t / Fv) \quad [12]$$

If  $C_4$  from Eq. [12] is substituted into Eq. [10], one obtains the equation describing a potentiostatic current/time transient at an active-state titanium electrode in the presence of Ti(IV)

$$i_a = i_a^* - k_4 C_4^0 \exp(-A_a k_4 t / Fv) \quad [13]$$

In a typical test of Eq. [13], an electrode ( $A_a = 30 \text{ cm}^2$ ) was maintained at a constant potential ( $E_m$ ) in  $1N$   $H_2SO_4$  until a steady-state value of  $i_a^*$  was well established. Then, at time zero, the solution was replaced with  $200 \text{ ml}$  of  $1N$   $H_2SO_4$  containing Ti(IV) ions at a concentration of  $1.69 \times 10^{-2}$  moles/liter. The observed value of  $i_a$  immediately changed from the net anodic ( $i_a^* = 57.8 \mu\text{A}/\text{cm}^2$ ) to a net cathodic value of  $50.3 \mu\text{A}/\text{cm}^2$ . Substituting those values in Eq. [13], with  $t = 0$ , gives  $k_4 C_4^0 = |i_4^0| = 108.1 \mu\text{A}/\text{cm}^2$ , and, therefore,  $k_4 = 6.40 \times 10^{-3} \text{ A cm}^{-2} \text{ liter mole}^{-1}$ . As Ti(IV) is consumed, the observed current density returns to  $i_a^*$ . The potentiostatic current density/time transient is shown in Fig. 6. According to Eq. [13], a plot of  $\log(i_a^* - i_a)$  vs.  $t$  should result in a straight line having an intercept at  $t = 0$  equal to  $\log k_4 C_4^0$ , i.e.,  $\log |i_4^0|$ , and a slope  $[\partial \log(i_a^* - i_a) / \partial t]_E = -A_a k_4 / 2.303 Fv$ . The results are shown in Fig. 7. The value of  $k_4$  calculated from the slope is  $6.41 \times 10^{-3} \text{ A cm}^{-2} \text{ liter mole}^{-1}$ , and, from the intercept at  $t = 0$ ,  $|i_4^0| = 108 \mu\text{A}/\text{cm}^2$ . The concentration of Ti(III) during the transient is given by Eq. [14]

$$C_3 = (C_4^0 - C_4) + i_a^* t / 3Fv \quad [14]$$

where use has been made of the fact that, at  $E_m(-530$

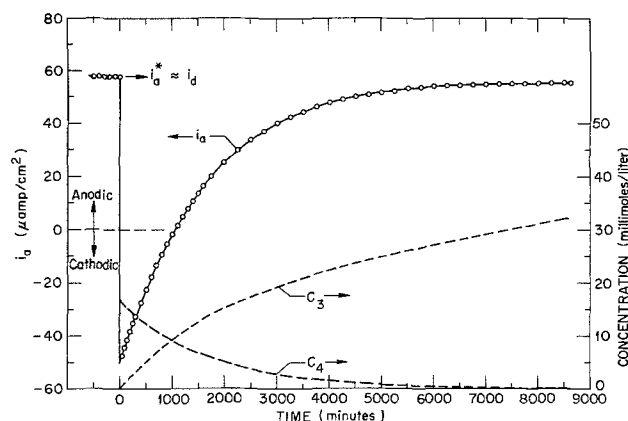


Fig. 6. Potentiostatic current density/time transient at an active-state titanium electrode ( $E = -530$  mV vs. SCE) in  $1N$   $H_2SO_4$ . Concentration/time curves calculated via Eq. [12] and [14].

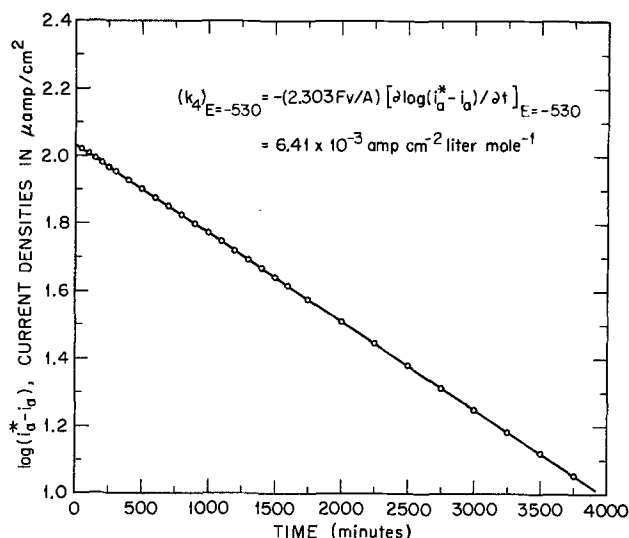


Fig. 7. Test of Eq. [13] using the potentiostatic current density/time transient shown in Fig. 6.

mV vs. SCE),  $i_d \approx i_a^*$ . Equations [12] and [14] were used to calculate  $C_4$  and  $C_3$ , respectively, and the results are shown in Fig. 6. The applicability of Eq. [13] over the Ti(III) and Ti(IV) concentration ranges shown in Fig. 6, ranges which embrace those for which  $i_d$  has been reported (5) to be a function of both  $C_3$  and  $C_4$ , together with the results presented in Fig. 4 and 5, clearly demonstrates that neither ion has any effect on  $i_d$ , and confirms the validity of the assumptions listed at the beginning of this section.

It is important to distinguish between the dissolution rate of the metal at a specified potential and the open-circuit dissolution rate (corrosion rate). The former, as shown above, is independent of  $C_4$ , but the latter is not. According to Eq. [8], at a specified potential, the difference in the  $i_a$  values shown by the upper and lower curves in Fig. 3 is equal to  $|i_4|$  and, consequently, the corresponding value of  $k_4$  may be determined by inserting  $i_4$  and the specified concentration of Ti(IV) into Eq. [9]. Then, having thus determined the potential dependence of  $k_4$ , Eq. [9] may be used to construct  $|i_4|$ /potential curves (for example, a-a' and b-b' in Fig. 3) for any value of  $C_4$ . At the open-circuit corrosion potential,  $i_a = 0$  and, according to Eq. [8],  $|i_4| = i_a^*$ , i.e., the open-circuit corrosion potential in the presence of Ti(IV) is given by the intersection of the corresponding  $|i_4|$ /potential curve with the upper curve in Fig. 3. The corrosion potential/ $C_4$  curve calculated in this manner is shown by the dashed curve in Fig. 8. The solid curve (open circles) in Fig. 8 shows the experimentally observed corrosion potential as a



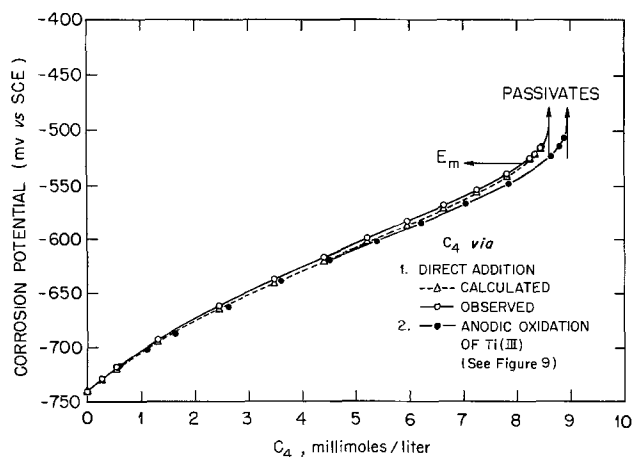


Fig. 8. Effect of Ti(IV) concentration on the open-circuit (corrosion) potential of titanium in 1N H<sub>2</sub>SO<sub>4</sub>.

function of  $C_4$ . The data for the solid curve were obtained by an addition experiment in which known volumes of a standard Ti(IV) solution [Ti(IV) in 1N H<sub>2</sub>SO<sub>4</sub>] were added to the cell which initially contained a known volume of 1N H<sub>2</sub>SO<sub>4</sub>. It is important to note that when  $C_4$  reaches the level at which the  $|i_4|$ /potential curve is tangent to the upper curve in Fig. 3, the titanium should passivate. This was observed to occur at  $C_{Ti(IV)} = 8.6$  mM. If  $k_4$  were independent of potential, passivation would have occurred at the concentration for which  $|i_4| = i_m$ , i.e., at approximately 8.0 mM.

The open-circuit corrosion rate is given by the value of  $i_a$  existing at the intersection of the upper curve in Fig. 3 and the  $|i_4|$ /potential curve. With increasing  $C_4$ , the corrosion potential becomes increasingly positive (cf. Fig. 8) and, consequently the corrosion rate increases. Thus, although the dissolution rate of titanium at a specified potential is independent of  $C_4$ , the open-circuit dissolution rate (corrosion rate) increases with increasing  $C_4$  to a maximum of  $i_m$ , decreases slightly as  $C_4$  increases further to the critical concentration, and, finally, drops sharply as  $C_4$  exceeds the critical concentration and the metal passivates.

**Electrolyte-coupled active and passive titanium systems.**—The experiments described above involved either an active or a passive titanium electrode. Attention is now directed toward systems in which active and passive electrodes exist simultaneously in the same volume of electrolyte, i.e., toward electrolyte-coupled systems. At the active-state electrode, the metal is oxidized to form Ti(III) ions in solution. At the passive-state electrode, the metal is oxidized to form Ti(IV) ions in solution. In the coupled system, coupling of the active and passive systems is a consequence of the oxidation of Ti(III) ions to Ti(IV) at the passive surface, and the reduction of Ti(IV) ions to Ti(III) at the active surface.

It has been shown (cf. Fig. 8) that the direct addition of Ti(IV) ions can lead to the passivation of an active titanium surface. If Ti(III) ions are oxidized to Ti(IV) at a passive titanium surface (cf. Fig. 2), and if the product of the oxidation reaction is Ti(IV) in solution rather than an electrodeposited TiO<sub>2</sub> oxide, then it should be possible to passivate an active electrode by oxidizing Ti(III) ions to Ti(IV) at a passive electrode sharing the electrolyte with the active electrode. In order to test this conclusion, one electrode ( $A_p = 30$  cm<sup>2</sup>) was maintained in the passive state ( $E = 0.0$  mV vs. SCE) in 1N H<sub>2</sub>SO<sub>4</sub>, while a second electrode, the identical electrode employed in Fig. 3, 4, and 5 ( $A_a = 1.58$  cm<sup>2</sup>), was left in the active state at open circuit in the same solution. At  $t = 0$ , the solution was replaced by 200 ml of 1N H<sub>2</sub>SO<sub>4</sub> containing Ti(III) ions at an initial concentration of 34.9 mM. The solution was prepared by the method shown in Fig. 6 and, consequently, also contained a small amount of Ti(IV),

$C_4^0 = 0.55$  mM. The open-circuit potential of the active electrode was recorded as a function of time, and the result is shown in Fig. 9. The potential of the active electrode became increasingly noble, demonstrating that the oxidation of Ti(III) ions at the passive electrode results in Ti(IV) ions in solution. At a potential slightly more noble than  $E_m$  (for reasons explained in the preceding section), the active electrode suddenly passivated ( $t = 4514$  min), i.e., the critical concentration of Ti(IV) ions was exceeded. The concentration of Ti(IV) ions in solution was calculated by means of Eq. [15]

$$C_4 = C_4^0 + (A_p/4Fv) \int_0^t i_p^* dt + (A_p/Fv) \int_0^t i_3 dt - (A_a/Fv) \int_0^t |i_4| dt \quad [15]$$

The current at the passive electrode ( $I_p$ ) was monitored during the experiment, and used to evaluate the first two integrals on the right side of Eq. [15]. The last integral in Eq. [15] arises as a result of the reduction of Ti(IV) ions to Ti(III) at the small active surface. Since  $I_p \gg |I_4|$ , the contribution of the last integral is small, i.e., the last term increases from 0 at  $t = 0$  to only  $0.833 \times 10^{-3}$  moles/liter at 4514 min. The evaluation of this integral was accomplished by determining the area under the  $|i_4|/t$  curve, the values of  $|i_4|$  being read from the upper curve of Fig. 3 for the corresponding potential values shown in Fig. 9. In Fig. 8, the active electrode potentials shown in Fig. 9 are plotted (solid circles) against the corresponding values of  $C_4$ . The results obtained in this experiment are in excellent agreement with those obtained by the direct addition of Ti(IV) ions. The critical concentration of Ti(IV) required to passivate the active electrode,  $C_4 = 8.94$  mM, compared to  $C_4 = 8.6$  mM via direct addition, confirms again the assumptions implicit in Eq. [15]. In particular, the results demonstrate that the current efficiency for the formation of an electrodeposited oxide (TiO<sub>2</sub>) via the oxidation of Ti(III) ions

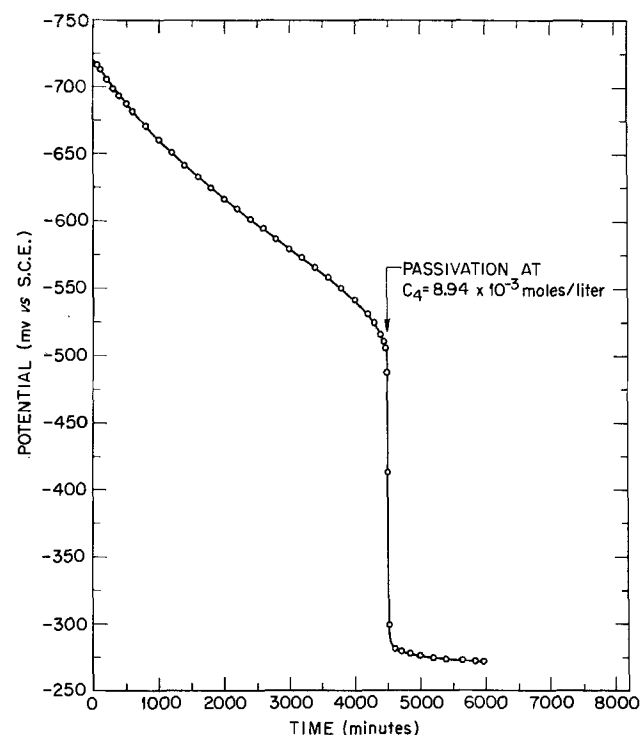


Fig. 9. Ennobling and passivation of an active-state titanium electrode by Ti(IV) ions generated via the oxidation of Ti(III) ions at a passive ( $E = 0$  mV vs. SCE) titanium electrode collocated in 1N H<sub>2</sub>SO<sub>4</sub>.  $C_3^0 = 34.9$  mM,  $C_4^0 = 0.55$  mM,  $A_p = 30$  cm<sup>2</sup>,  $A_a = 1.58$  cm<sup>2</sup>. (Also see Fig. 8.)

at the passive surface is negligible compared to the current efficiency for the formation of Ti(IV) ions in solution. In Fig. 9, the potential of the electrode upon passivation (i.e.,  $t > 4514$ ) increases to approximately  $-275$  mV vs. SCE, and continues to increase slightly with time. According to Schmets *et al.* (14), the standard potential for the  $\text{Ti}^{3+}/\text{TiO}^{+2}$  couple is approximately  $0.10\text{V}$  vs. SHE. Using this value, together with the values of  $C_3$  and  $C_4$  existing at  $t = 4514$  min, 26.35 and 8.94 mM, respectively, one would conclude that if the potential of the titanium electrode upon passivation were determined solely by this couple, the potential would be  $-208$  mV vs. SCE. Since the current due to the metal dissolution reaction must be added to that due to the  $\text{Ti(III)}$  oxidation reaction, the  $\text{Ti}^{3+}/\text{TiO}^{+2}$  couple is not solely responsible for the open-circuit potential, and as observed ( $-275$  mV vs. SCE), one should expect a slightly more negative value than  $-208$  mV vs. SCE.

In the experiment just described, a potentiostat was used to maintain the passive electrode at a constant potential while the active electrode was left at open circuit. In the experiments which follow, a dual potentiostat was employed to maintain one electrode at a constant potential in the active state and a second electrode at a constant potential in the passive state. The time derivatives of the  $\text{Ti(III)}$  and  $\text{Ti(IV)}$  concentrations are given by Eq. [16] and [17]

$$dC_3/dt = (A_a i_d / 3Fv) - (A_a i_4 / Fv) - (A_p i_3 / Fv) \quad [16]$$

$$dC_4/dt = (A_a i_4 / Fv) + (A_p i_3 / Fv) + (A_p i_p^* / 4Fv) \quad [17]$$

If  $i_3$  and  $i_4$  are expressed in terms of  $C_3$  and  $C_4$  via Eq. [1] and [9], respectively, Eq. [16] and [17] may be rewritten as follows

$$dC_3/dt = (A_a i_d / 3Fv) + (A_a k_4 C_4 / Fv) - (A_p k_3 C_3 / Fv) \quad [18]$$

$$dC_4/dt = (A_p i_p^* / 4Fv) - (A_a k_4 C_4 / Fv) + (A_p k_3 C_3 / Fv) \quad [19]$$

Letting  $C_T = (C_3 + C_4)$ , and adding Eq. [18] and [19], one obtains Eq. [20]

$$dC_T/dt = (1/Fv) (A_a i_d / 3 + A_p i_p^* / 4) \quad [20]$$

Under the prescribed potentiostatic conditions,  $i_d$ ,  $i_p^*$ ,  $k_3$ , and  $k_4$  are all constant, and, consequently, Eq. [18]-[20] may be solved to obtain  $C_3$ ,  $C_4$ , and  $C_T$  as functions of time

$$C_3 = C_3^0 + \alpha [1 - \exp(-Kt/Fv)] + A_a k_4 \beta t \quad [21]$$

$$C_4 = C_4^0 - \alpha [1 - \exp(-Kt/Fv)] + A_p k_3 \beta t \quad [22]$$

$$C_T = C_T^0 + K\beta t \quad [23]$$

where, in order to simplify writing,  $\alpha$ ,  $\beta$ , and  $K$  represent the following

$$\alpha = (1/K) [(A_p k_3 A_a i_d / 3K) + (A_a k_4 C_4^0) - (A_p k_3 C_3^0) - (A_a k_4 A_p i_p^* / 4K)] \quad [24]$$

$$\beta = (1/KFv) [(A_a i_d / 3) + (A_p i_p^* / 4)] \quad [25]$$

$$K = (A_p k_3 + A_a k_4) \quad [26]$$

If  $C_3$  and  $C_4$  given by Eq. [21] and [22] are substituted into Eq. [4] and [10], respectively, one obtains equations describing the current density-time transients at the passive and active electrodes

$$i_p = i_p^* + k_3 C_3^0 + k_3 \alpha [1 - \exp(-Kt/Fv)] + k_3 A_a k_4 \beta t \quad [27]$$

$$i_a = i_d - k_4 C_4^0 + k_4 \alpha [1 - \exp(-Kt/Fv)] - A_p k_3 k_4 \beta t \quad [28]$$

If  $1 \gg Kt/Fv$ , the exponential term in Eq. [27] may be expanded to yield a limiting expression for  $i_p$

$$(i_p)_{t \rightarrow 0} \rightarrow i_p^0 + (k_3 / Fv) [A_a k_4 C_4^0 - A_p k_3 C_3^0 + (A_a i_d / 3)] t \quad [29]$$

i.e., for small values of  $t$ ,  $i_p$  is a linear function of time. Moreover, if  $C_4^0 = C_3^0 = 0$  or, more generally, if  $(A_a i_d / 3) \gg (A_a k_4 C_4^0 - A_p k_3 C_3^0)$ , the slope of the straight line obtained from a plot of  $i_p$  vs.  $t$  is simply  $A_a k_3 i_d / 3Fv$ , i.e., from the measured value of the slope, one may calculate the dissolution rate of the active-state titanium electrode. Since the slope is proportional to  $i_d$ , a change in  $i_d$  produced by a change in the potential of the active-state electrode results in an immediate change in the slope  $(\partial i_p / \partial t)_E$ . Typical experimental results are shown in Fig. 10. The passive electrode was maintained at  $0$  mV vs. SCE in  $250$  ml of  $1N$   $\text{H}_2\text{SO}_4$ . From  $0$  to  $1600$  min, the active electrode was set at  $E_m$  ( $-530$  mV vs. SCE). Utilizing the fact that at  $E_m$ ,  $i_a = 5.38 \times 10^{-5}$  A/cm $^2 \approx i_d$ ,  $k_3$  may be calculated from the slope of the straight line and the measured value of  $i_a$ , i.e.,  $k_3 = 3Fv(\partial i_p / \partial t) / A_a i_a = 1.17 \times 10^{-3}$  A cm $^{-2}$  liter mole $^{-1}$ . At  $t = 1600$  min, the potential of the active-state electrode was changed from  $E_m$  to  $-730$  mV vs. SCE (approximately equal to the open-circuit corrosion potential), and maintained constant from  $1600$  to  $3500$  min. If  $S_1$  is the slope of the initial linear segment ( $t = 0$  to  $t = 1600$ ), and  $S_2$  is the slope of the second linear segment ( $t = 1600$  to  $t = 3500$ ), then  $(i_d)_{E=-730} = (i_d)_{E=-530} (S_2 / S_1) = (i_d)_{E=-530} 2.53$ , i.e.,  $i_d$  at  $E = -730$  mV vs. SCE =  $2.13 \times 10^{-5}$  A/cm $^2$ . In addition to confirming the validity of Eq. [29], the results shown in Fig. 10 demonstrate a novel, and very sensitive method for measuring or continuously monitoring dissolution or corrosion rates. It should be noted that in this experiment, the dissolution rate of the active specimen at  $-730$  mV vs. SCE, for example, amounted to only  $32.1$   $\mu\text{g/hr}$ , and only a few hours are needed to determine the slope with sufficient accuracy.

A general test of Eq. [27] and [28] is provided by the data shown in Fig. 11. According to Eq. [27] and [28],

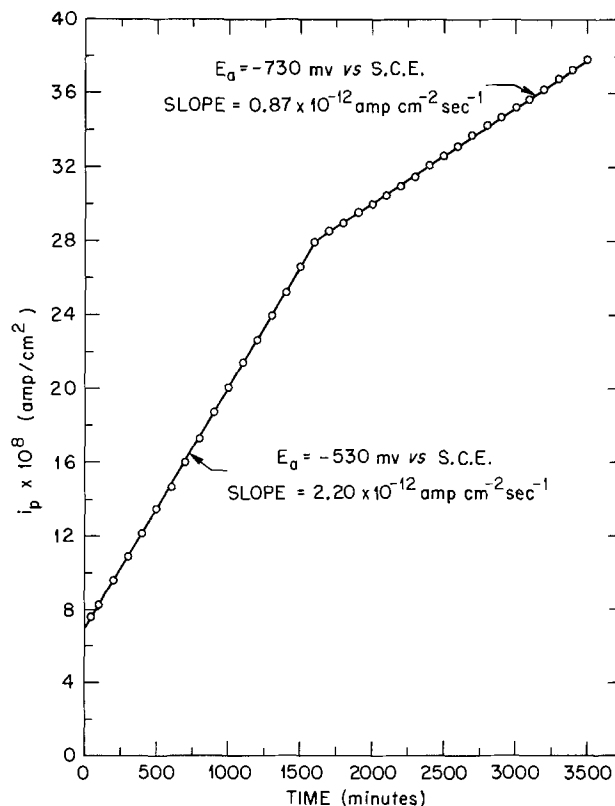


Fig. 10. Determination of dissolution rates of active-state titanium via monitoring the current density at a passive titanium electrode ( $E = 0$  mV vs. SCE) collocated in  $1N$   $\text{H}_2\text{SO}_4$ .  $C_3^0 = C_4^0 = 0$ ,  $A_a = A_p = 2.53$  cm $^2$ . Application of Eq. [29].

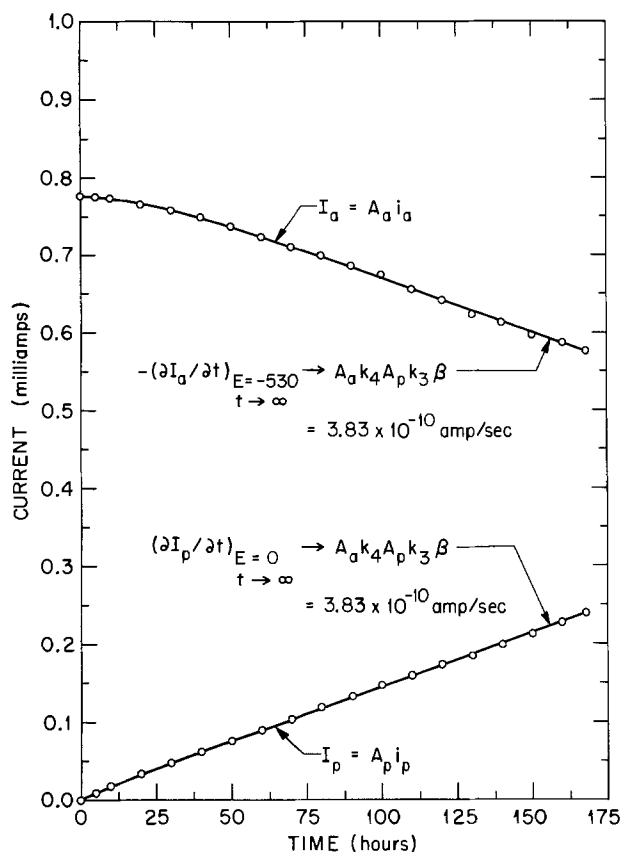


Fig. 11. Current/time transients at electrolyte (1N H<sub>2</sub>SO<sub>4</sub>)-coupled active ( $E = -530$  mV vs. SCE) and passive ( $E = 0$  mV vs. SCE) titanium electrodes.  $C_3^0 = C_4^0 = 0$ .  $A_p = A_a = 15$  cm<sup>2</sup>,  $v = 100$  ml. Test of Eq. [27] and [28].

if currents ( $i_a = A_a i_a$  and  $I_p = A_p i_p$ ) rather than current densities are plotted against time, the slopes,  $-(\partial I_a/\partial t)_{E=-530}$  and  $(\partial I_p/\partial t)_{E=0}$ , should approach the same value,  $A_a k_4 A_p k_3 \beta$ , as  $t \rightarrow \infty$ . This is confirmed by the results shown in Fig. 11. In this particular experiment, the measured values of  $A_p i_p$  and  $A_a i_a$  (recalling that, at  $E_m$ ,  $i_a \approx i_d$ ) were  $1.53 \times 10^{-6}$  A and  $7.76 \times 10^{-4}$  A, respectively. Also,  $C_3^0 = C_4^0 = 0$ ,  $A_p = A_a = 15$  cm<sup>2</sup>, and  $v = 100$  ml. The preceding data permits  $\beta$  to be evaluated via Eq. [25]. From  $(\partial i_p/\partial t)_{E=0}$  as  $t \rightarrow 0$ ,  $k_3$  may be evaluated as discussed in connection with Fig. 10. Then, having evaluated  $\beta$  and  $k_3$ , one may evaluate  $k_4$  from the aforementioned slope,  $A_a k_4 A_p k_3 \beta$ . The values found for  $k_3$  and  $k_4$  were  $1.12 \times 10^{-3}$  and  $6.31 \times 10^{-3}$  A cm<sup>-2</sup> liter mole<sup>-1</sup>, respectively.

The continuous decrease in  $i_a$  shown in Fig. 11 is a consequence of the increase in  $C_4$ . Given sufficient time, the critical concentration required to passivate an active-state titanium surface would be attained. In other words, even with  $C_3^0 = C_4^0 = 0$ , an electrolyte-coupled active and passive titanium system can generate a concentration of Ti(IV) ions in the electrolyte phase sufficient to bring about the passivation of the active surface. Using reasonable values for the quantities appearing in Eq. [22], [24], [25], and [26], one may easily show that, for very small volumes of electrolytes the time required to passivate an active surface may be reduced to a few minutes. With regard to localized corrosion (crevice, pitting, etc.), these observations suggest the following situation. As Ti(III) ions egress from the active-state base of a pit or crevice (10, 15-17), they encounter condition under which they are known to be oxidized to Ti(IV) ions in solution (i.e., a passive surface). The resultant Ti(IV) ions are transported back to the base of the pit where they encounter conditions under which they are known to be reduced to Ti(III) ions (i.e., an active surface), and to accelerate the open-circuit dissolution rate of the active-state

base. Thus, Ti(IV) ions would have a deleterious effect on pitting or crevice corrosion, but only if the concentration of Ti(IV) remained below the critical concentration required to passivate the active surface. If the critical concentration is attained, the metal passivates and pitting ceases. This phenomenon of spontaneous self-healing has long been recognized in pitting and crevice corrosion (10). Although one normally associates localized corrosion phenomena with solutions other than the 1N H<sub>2</sub>SO<sub>4</sub> (for example, with halide solutions), and such systems involve nonuniform concentrations within the constrained geometry, the electrochemical factors described above remain operative, and the basic rationale provided for the mechanism of self-healing should remain applicable.

### Summary

In the active state, titanium is oxidized to form Ti(III) ions in solution. At an active titanium surface, Ti(IV) ions are reduced to Ti(III), and the reduction reaction is first order with respect to the concentration of Ti(IV) ions. At a constant potential, neither the active-state dissolution rate of the metal nor the rate of the hydrogen evolution reaction are affected by Ti(III) or Ti(IV) ions. However, the current density corresponding to the reduction of Ti(IV) ions adds algebraically to the current densities of the metal dissolution and hydrogen evolution reactions and, as a consequence, the open-circuit (corrosion) potential of the active-state titanium becomes increasingly positive (noble) as the concentration of Ti(IV) increases. When the concentration of Ti(IV) exceeds a certain critical value, the active-state metal passivates.

In the passive state, titanium is oxidized to form the passive film (TiO<sub>2</sub>) and Ti(IV) ions in solution. At a passive titanium surface, Ti(III) ions are oxidized to Ti(IV), and the oxidation reaction is first order with respect to the concentration of Ti(III) ions. The current density corresponding to the oxidation of Ti(III) ions simply adds to the current density corresponding to the dissolution of the passive metal. The latter is not affected by the presence of Ti(III) or Ti(IV) ions.

When active and passive titanium surfaces are collocated in the same body of electrolyte, coupling of the active and passive systems occurs as a result of the oxidation of Ti(III) ions at the passive surface and the reduction of Ti(IV) ions at the active surface. Such electrolyte-coupled active-passive systems are capable of generating the critical concentration of Ti(IV) ions required to passivate the active surface. This "self-healing" phenomenon is of interest in relation to localized corrosion. In addition, under the appropriate conditions, dissolution rates of titanium in the active-state (open-circuit or polarized) may be determined by monitoring the current at the passive sensor electrode in an electrolyte-coupled active-passive system.

### Acknowledgments

This research was sponsored by the Energy Research and Development Administration under contract with the Union Carbide Corporation.

Manuscript submitted Aug. 18, 1975; revised manuscript received Oct. 23, 1975.

Any discussion of this paper will appear in a Discussion Section to be published in the December 1976 JOURNAL. All discussions for the December 1976 Discussion Section should be submitted by Aug. 1, 1976.

Publication costs of this article were partially assisted by Oak Ridge National Laboratory.

### REFERENCES

1. E. J. Kelly, "Proceedings International Congress on Metallic Corrosion, 5th, Tokyo, 1972," p. 137, NACE, Houston (1974).
2. M. Stern and H. Wissenberg, *This Journal*, **106**, 755 (1959).
3. J. A. Petit and F. Dabosi, *Corrosion Sci.*, **14**, 123 (1974).

4. R. V. Tsvetnova and A. I. Krasil'shchikov, *Russ. J. Phys. Chem., (English)*, **39**, 109 (1965).
5. N. T. Thomas and Ken Nobe, *This Journal*, **119**, 1450 (1972).
6. E. G. Kuznetsova, A. A. Sokolov, V. M. Novakovskii, and Ya' M. Kolotyrgan, *Zaschita Metallov*, **8**, 409 (1972); *Protection of Metals*, **8**, 364 (1972).
7. S. H. Weiman, *Corrosion*, **22**, 98 (1966).
8. V. V. Andreeva and E. A. Yakovleva, *Z. Physik. Chem.*, **226**, 232 (1964).
9. D. Sinigaglia, G. Taccani, and B. Vicentini, *Werkstoffe u. Korrosion*, **24**, 1027 (1973).
10. I. L. Rosenfeld, "Proceedings International Congress on Metallic Corrosion, 5th, Tokyo, 1972," p. 53, NACE, Houston (1974).
11. E. J. Kelly, *This Journal*, **115**, 1111 (1968).
12. M. Codell, "Analytical Chemistry of Titanium Metals and Compounds," p. 87, Interscience Publishers, Inc., New York (1959).
13. R. L. Pescok and A. N. Fletcher, *Inorg. Chem.*, **1**, 155 (1962).
14. J. Schmets, J. Van Muylder, and M. Pourbaix, "Atlas of Electrochemical Equilibria in Aqueous Solutions," p. 213, Pergamon Press, Inc., New York (1966).
15. J. C. Griess, *Corrosion*, **24**, 96 (1968).
16. B. Vicentini, *Werkstoffe u. Korrosion*, **25**, 593 (1974).
17. D. Sinigaglia, B. Vicentini, and G. Taccani, *ibid.*, **25**, 25 (1974).

## On the Initiation of Crevice Corrosion on Stainless Steel

Göran S. Eklund\*

Swedish Institute for Metal Research, Stockholm, Sweden

### ABSTRACT

The site of crevice corrosion initiation on stainless steels has been investigated. It has been found that the initiation takes place at sulfide inclusions situated at the junction between a covering layer and the free metal surface with a portion of the inclusion covered and the rest exposed to the solution. A mechanism is suggested based on electrochemical dissolution of the sulfide inclusions.

Crevice corrosion is one of the most common, severe, and difficult to control forms of corrosion experienced with stainless steels. Numerous investigations have been carried out on the subject and a number of crevice corrosion mechanisms have been proposed (1-4, 6). The theoretical interpretation has usually been based on some sort of concentration cell and the explanation of the initiation is in most cases deduced from results obtained on specimens where the attack is already established and in which a low pH, low oxygen concentration in the crevice, etc. have been observed (1, 5, 6). Very few investigations deal with the initiation process itself and the possible sites for initiation.

Several methods for testing crevice corrosion are described in the literature (1, 7-10), but the majority of these can only provide qualitative data. Some workers have used special experimental arrangements in order to obtain more precise data on the corrosion rate and the electrochemical behavior (1, 11). Apparently none of the methods described are suitable for detailed visual studies of the initiating sites at high magnifications.

In this work, crevice corrosion has been studied by interrupting the process at an early stage of development and the corroded areas have been observed by scanning electron microscope (SEM) and analyzed *in situ*. Based on these observations a crevice corrosion initiation mechanism is suggested.

### Experimental

The cell used for the experiments was made of transparent perspex and is shown in Fig. 1. The samples were 2 mm thick disks, 25 mm in diameter. After polishing to 1  $\mu$ m diamond, they were covered with edge protecting lacquer around the circumference. Special care was taken to avoid crevice development at the junction between the lacquer and the free metal surface. A suitable seal around the lacquered edge was effected via an O-ring and clamping arrangement; around 2 cm<sup>2</sup> of free surface was exposed to the corrosion solution (Fig. 1). On the free metal surface perpendicular to the milling direction, streaks of

"Lacomit" were applied; this is known to have poor adherence and the aim was that crevice corrosion attack took place preferentially under this lacquer. The solution used in all experiments was 0.1M NaCl. The initial attack was developed by a galvanostatic technique using current densities of 1, 0.1, and 0.01 mA/cm<sup>2</sup> giving charge densities of 10, 20, and 40 mAs/cm<sup>2</sup> over the surface.

After the test the samples were washed with water and alcohol, and then dried in a warm airstream. The washing was carried out carefully to avoid loss of corrosion products. A thin layer of gold was vaporized

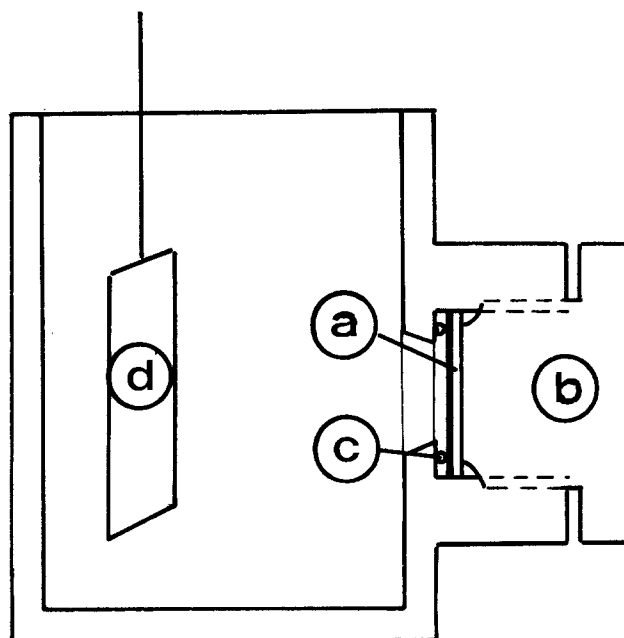


Fig. 1. Corrosion cell of transparent perspex. The sample (a) is held tight against the cell wall with a brass screw (b) also serving as a lead. A seal is effected by the o-ring (c), (d) denotes the counter-electrode.

\* Electrochemical Society Active Member.

Key words: crevice corrosion, stainless steel, sulfide inclusions.

Table I. Alloy composition

Alloy Nr	C %	Si %	Mn %	P %	S %	Cr %	Ni %	Mo %	N %
1	0.048	0.53	1.26	0.009	0.003	18.1	9.3	0.01	0.052
2	0.047	0.44	1.48	0.011	0.03	18.5	9.3	0.01	0.057
3	0.040	0.54	1.42	0.010	0.3	17.9	9.3	0.02	0.108

onto the surface before observations in the microscope. In order to examine the attack under the Lacomit more closely, the lacquer was removed by acetone on some of the samples.

The materials used were hot-rolled and annealed 18-8 steels with three different levels of sulfur. The three different alloys were made from the same melt via separate additions of sulfur. Disks were punched out from the as-received strips, and the disks were annealed at 1000°C for 1 hr and quenched in water. The metallurgical structure was fully austenitic after this heat-treatment.

The compositions of the materials are given in Table I.

### Results

In the optical micrograph, Fig. 2, where the Lacomit is still covering the metal surface, the crevice attack has started at a single point and then spread under the lacquer in a butterfly fashion. In the vicinity of the initiation point the lacquer has become detached from the metal surface and bent upward, thus widening the crevice and giving rise to bend contours. This behavior was typical for the crevice corrosion attack observed on all the materials investigated irrespective of whether the mouth of the crevice was facing up or down.

A closer examination of the mouth of a crevice, Fig. 3, reveals that products in the form of rods and spheres have been formed and these are probably inclusions or corrosion products transported to the mouth by a flow of liquid from the interior. By careful removal of the lacquer with acetone, wiping the surface lightly with cotton wool, and then examining the same area, it was possible to establish that the light rods and spheres were in fact corrosion products covering inclusions embedded in the metal matrix. Compare Fig. 3 and 4 showing the same area before and after the removal of the lacquer. X-ray analysis (EDAX) of the inclusions showed that they were manganese sulfides with iron and chromium in solid solution.

In all the alloys investigated, crevice corrosion seems to have started at sulfide inclusions at the junction between the lacquer and the free metal surface, with a portion of each inclusion covered by the lacquer and the rest exposed to the solution. Figure 5 is an example of such an inclusion partly covered with the

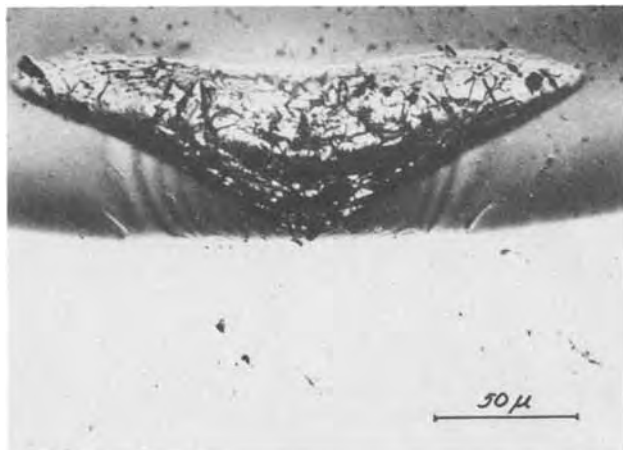


Fig. 2. Crevice corrosion attack under the lacquer covering upper half of picture; lower, brighter part is exposed metal. Notice bend contours on the lacquer around the initiation point.



Fig. 3. Corrosion products around the initiation point; the light rods and spheres are manganese sulfides covered with reaction products.

lacquer. The inclusion has started to dissolve preferentially along the sulfide-metal interface giving rise to a small groove. The dissolution and formation of corrosion products proceeds underneath the lacquer bending it upward as shown in Fig. 6 where the reaction products still remain on the sulfide surface. The frequency of attack increases with the current density, but, on the other hand, the amount of charge influences only the severity of the attacks and results in a lace-like pattern at the mouth of the crevices at the highest values, Fig. 7.

### Discussion

As mentioned above, many initiation mechanisms have been suggested but most, however, are based on differences in metal ion or oxygen concentration between the crevice and its surroundings. Consequently the term concentration cell corrosion has been used to describe this form of attack.

Studies by Schafer *et al.* (3) have shown that metal ion and oxygen concentration differences do indeed exist in a crevice, but according to Fontana and Greene (4) this is not the basic reason for the attack. They formulated a mechanism in which metal dissolution as well as oxygen reduction takes place all over the surface including the crevice. The solution in the crevice will soon become impoverished in oxygen and the potential difference thus established between the crevice and the outer surface effects a migration of the chloride ions into the former so as to conserve the charge balance. This explains the high chloride and metal ion concentration and the low oxygen concentration observed in the crevice. The metal chlorides formed in the crevice can now hydrolyze giving a low pH and making it possible for the reaction to proceed.

The results of this investigation however suggest another mechanism. It is shown that the crevice at-



Fig. 4. Same area as in Fig. 3 after removal of the lacquer and wiping the surface with cotton wool. The dark areas represent manganese sulfides free from reaction products.

tacks have started at certain points on the boundary between the lacquer and the free metal surface and then spread underneath the lacquer. Careful examination has proven that the starting points in all cases were sulfide inclusions. It can therefore be assumed that the inclusions take an active part in the initial crevice corrosion reaction.

It is known that sulfide inclusions are to a limited extent electronic conductors and can be polarized to the potential of a passive steel surface (16). At this potential the sulfides are not thermodynamically stable and tend to dissolve. The comparatively low electronic conductivity causing the dissolution to take place preferentially along the metal-sulfide interface, hence resulting in small grooves, is shown in Fig. 5.

Because the sulfides are formed in the melt when the steel solidifies, no oxide layer will exist at the interface between sulfides and metal. Hence, when the sulfides dissolve, a fresh metal surface is exposed to the environment. The solution around this microarea so exposed will be different from that of the bulk and contain hydrogen sulfide and its protolysed products as well as metal ions emanating from the sulfide. Apart from Mn, the metal ions comprise iron and chromium which undergo both complex reactions and hydrolysis with residual oxygen, water, and migrating chloride ions thus creating a low pH locally (12).

Eventually, the solution about the microarea will reach a composition such that a passivation of the continuously uncovered metal surface can no longer take place. Metal ions from the matrix enter the solution and the potential drops drastically staying at this low level as long as the metal dissolves.

Now, if the geometrical conditions around the microarea make replenishment of the solution difficult, the hydrolysis of the metal ions from the matrix can



Fig. 5. Inclusion situated at the junction between the lacquer and the free metal surface. Part of the inclusion faintly visible under the lacquer. The inclusion is preferentially dissolved along the sulfide-metal interface.

maintain the attack. On the other hand, if the solution is diluted, the concentration of hydrogen sulfide and hydrogen ions will decrease and the metal passivates.

The initiation and passivation take place quite a number of times on the metal surface. The sudden potential drops observed during galvanostatic tests at low current densities (17) and the current peaks appearing in potentiostatic tests near the pitting potential (18) can be interpreted as attempts of pitting or crevice corrosion at sulfide inclusions.

An obvious question is why do all inclusions not behave in the above manner? The answer lies in the local differences in sulfide composition resulting in different electronic conductivities which is turn influence the dissolution properties and the ability to generate acid solutions.

Since the composition of the inclusion determines the current density or potential at which its dissolution begins, it is obvious that the higher the applied potential or current, the greater the number of inclusions that are activated and, consequently, the frequency of attack can be increased.

Because dilution of the solution is difficult in narrow crevices, e.g., under debris etc. it is clear that corrosion takes place more easily at partly covered inclusions, than on the free metal surface.

It is well known that the pitting and crevice corrosion potential decreases with increasing sulfur content in the steel (19). There is, however, no reason to believe that the composition and the reactivity of the passive layer should change as a result of small variations in the sulfur content. The mechanism proposed by Fontana and Greene (4) whereby the passive layer dissolves and reduces oxygen in the crevices, hence initiating crevice corrosion, thus seems unlikely.

On the other hand, the composition of the sulfide inclusions should change with the sulfur content of the steel because they are formed from residual liquid in the ingot with different degrees of segregation. Now,



Fig. 6. Sulfide covered with reaction products. The reaction has proceeded under the lacquer causing detachment from the metal surface.

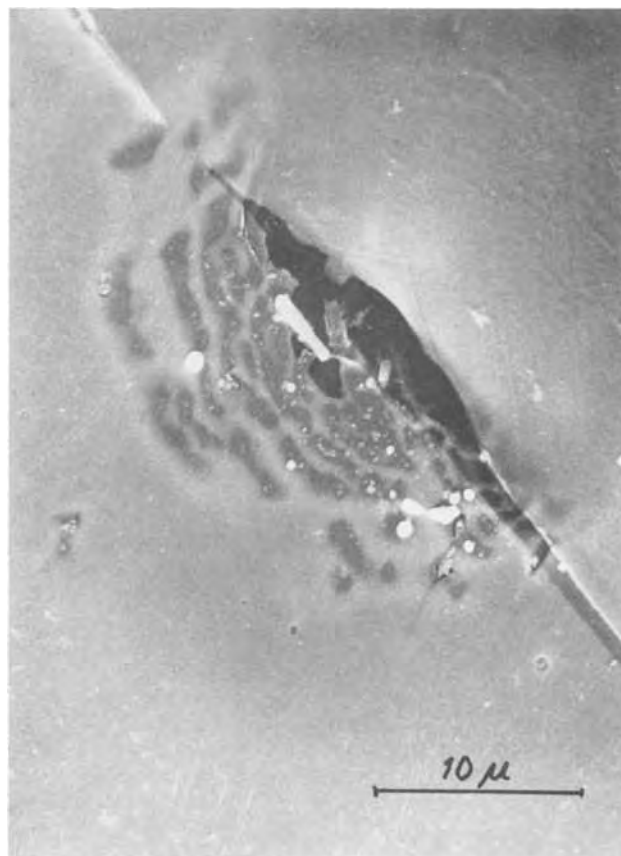


Fig. 7. Mouth of crevice corrosion attack. The reaction is well developed and a characteristic lacelike pattern of corrosion attack is evident.

the kinetics of sulfide dissolution depends on their composition and so, therefore, will the time available for dilution of the solution by diffusion into the region immediately surrounding the microarea; hence, as the rate of dissolution increases, the probability that the uncovered metal surface will become passivated is reduced.

In summary, the above reasoning indicates that the prime cause of crevice corrosion is an electrochemical dissolution of the sulfide inclusions with the formation of an acid solution and an uncovering of virgin metal surface. Dilution of this acid solution is more difficult in crevices and so the attack can propagate in these regions. It must, however, be borne in mind that the proposed mechanism is not limited to sulfides only but can also be applied to other inclusions provided they are capable of being polarized and releasing metal ions which can hydrolyze.

#### Acknowledgments

Manuscript submitted June 17, 1975; revised manuscript received Sept. 1, 1975.

Any discussion of this paper will appear in a Discussion Section to be published in the December 1976 JOURNAL. All discussions for the December 1976 Discussion Section should be submitted by Aug. 1, 1976.

Publication costs of this article were partially assisted by the Swedish Institute for Metal Research.

#### REFERENCES

1. I. L. Rosenfeld and I. K. Marshakow, *Corrosion*, **20**, 115t (1964).
2. H. H. Uhlig, "Corrosion Handbook," John Wiley & Sons, Inc., New York (1948).
3. G. J. Schafer, J. R. Gabriel, and P. K. Foster, *This Journal*, **107**, 1002 (1960).
4. M. G. Fontana and N. D. Greene, "Corrosion Engineering," McGraw-Hill Book Co., New York (1967).
5. I. B. Ulanowskii and I. M. Korovin, *J. Appl. Chem. USSR*, **31**, 1352 (1958).
6. G. Karlberg and G. Wranglén, *Corrosion Sci.*, **11**, 499 (1971).
7. J. K. Rice and C. M. Loucks, *Materials Protection*, **4**, 14 (1965).
8. H. P. Godard, *ibid.*, **2**, 38 (1963).
9. W. A. Mueller, *Corrosion*, **25**, 473 (1969).
10. D. A. Jones and N. D. Greene, *ibid.*, **25**, 367 (1969).
11. W. D. France and N. D. Greene, Jr., *ibid.*, **24**, 247 (1968).
12. G. S. Eklund, *This Journal*, **121**, 467 (1974).
13. K. Sano and M. Inoye, *J. Iron Steel Inst. (Japan)*, **45**, 9 (1959).
14. I. S. Brammar and R. W. K. Honeycombe, *J. Iron Steel Inst. (London)*, **202**, 335 (1964).
15. R. Kiessling and N. Lange, *ibid.*, **202**, 761 (1963).
16. G. S. Eklund, *Scand. J. Metals*, **1**, 331 (1972).
17. G. S. Eklund, *Jernkont. Ann.*, **154**, 321 (1970).
18. E. Brauns and W. Schwenk, *Werkstoffe Korrosion*, **12**, 73 (1961).
19. B. Rondot, B. M. Da Cunha, and J. Montriell, *Mem. Sci. Rev. Met.*, **69**, 807 (1972).



# A Study of the Anodic Oxide of Vanadium under Anodic and Cathodic Conditions

J. C. Clayton and D. J. De Smet\*

Department of Physics and Astronomy, The University of Alabama, University, Alabama 35486

## ABSTRACT

The anodic oxide film formed on vanadium in an electrolyte of acetic acid, sodium borate, and a small quantity of water has been studied using ellipsometric and electrical measurements. These studies indicate that when a cathodic current is applied to a vanadium electrode upon which an anodic oxide film has been grown conversion of the anodic oxide occurs, and a new species or complex is formed on the electrode surface. Re-application of an anodic current converts the film back to its original state. Both the refractive index and the solubility of the cathodically converted film differ from the anodic film. In particular, the cathodically converted film is much less soluble in water than is the anodic film. Ellipsometric data are consistent with a model in which the conversion of the film begins at the oxide/electrolyte interface and proceeds toward the metal. Other possible models are given for comparison purposes.

Several studies of the anodic oxidation of vanadium have appeared in the literature (1-4) subsequent to the first work on this material by Keil and Salomon (5). These authors were able to oxidize vanadium anodically by employing an almost totally nonaqueous electrolyte consisting of acetic acid, sodium borate, and a small amount of water. This electrolyte makes manageable the problem of dissolution of the anodic oxide of vanadium in water and in electrolytes containing large quantities of water.

In the course of our experimental work on the anodic oxidation of vanadium, for some reason that we cannot now recall, we applied a cathodic current to a sample covered with an anodic film. When this was done, we noticed that the film changed its interference color slightly and then gas evolution occurred. Upon removing the sample from the electrolyte and attempting to rinse the film off of the vanadium surface with water, our standard operating procedure, we found this film to be insoluble. This led us to the hypothesis that a cathodic current caused the film to convert to a different form. The purpose of this paper is to examine this hypothesis in some detail and to present a model for the conversion process that accounts for the experimental data.

Ellipsometry has become one of the standard techniques for the study of thin films. This is due in part to the fact that, provided certain assumptions are met, ellipsometry allows the determination of both the thickness and index of refraction of a thin film. Employing an automatic nulling ellipsometer also allows us to monitor, *in situ*, changes which are occurring on the electrode surface. Others have employed ellipsometry to monitor changes in the structure of thin films as these films convert from one form to another; most notably Hopper and Ord (6) concerning the conversion of nickel hydroxide films and Dell'Oca (7) on the conversion of silicon nitride to silicon dioxide.

## Experimental

The samples used in our experiments were made from 99.98% pure vanadium rods,  $\frac{1}{4}$  in. in diameter, obtained from Materials Research Corporation. The samples were cut to a length of 0.7 cm and drilled along the axis of the cylinder. A small flat area was ground on the side of the cylindrical surface for ellipsometric measurements. The flat area was hand polished using a stainless steel block and various grades of lapping compound. The final mechanical polish was done with jeweler's rouge. The sample was then

mounted between Teflon washers in a sample holder similar to that described by Feller and Osterwald (8) and electropolished for approximately 2 min at a potential of 16V in a mixture of 75% ethanol and 25% sulfuric acid at room temperature (9). This electropolish gave good specular reflection from the flat surface of the sample.

Before each experiment the sample was washed in distilled water, dried, anodically oxidized to a potential of 50V, and rinsed again in water to remove the oxide that was formed. This procedure was repeated several times to insure reproducibility. The sample was then transferred to the ellipsometer cell, and an oxide was formed galvanostatically to a preset potential. The sample was held potentiostatically at this potential for some time to measure the combined leakage and dissolution current. If after 30 min this current was less than  $120 \mu\text{A}/\text{cm}^2$ , the oxide was dissolved in distilled water, the sample replaced in the ellipsometer cell, and an experiment was begun.

The cell used was a hollow equilateral triangular prism with windows mounted so that ellipsometer measurements could be taken at an angle of incidence of  $60^\circ$ . This cell was fitted with standard taper joints for the sample, a coiled platinum wire cathode, a platinum wire reference electrode, and a gas dispersion tube. All experiments were done at room temperature.

The electrolyte used was similar to that first reported by Keil and Salomon (5) and appears to be the only electrolyte that will sustain the formation of a vanadium oxide film. Since the anodic oxide of vanadium dissolves in water and also, more slowly, in this electrolyte which contains a small amount of water, we chose to modify the recipe of Keil and Salomon by reducing the water content of the solution. The solution used contained 19g of  $\text{Na}_2\text{B}_4\text{O}_7 \cdot 10 \text{H}_2\text{O}$ , 10.6 ml of water, and enough acetic acid to make 1.0 liter of solution. This electrolyte has a higher resistivity than the usual electrolyte used for the anodic oxidation of vanadium, but it reduces the effects of oxide dissolution. The resistivity of the solution was not high enough to influence the uniformity of thickness of the oxide over the electrode surface for the current densities used here. The solution was bubbled with argon both prior to and during the experiments. The index of refraction of this solution is 1.3707 at a wavelength of  $6328\text{\AA}$ .

The electrical circuitry used is identical to that described by De Smet and Hopper (10). Voltage vs. time curves were recorded using a Hewlett-Packard Model 7004 x-ray recorder. All potentials are mea-

\* Electrochemical Society Active Member.

Key words: ellipsometry, conversion, film, refractive index.



sured relative to the platinum wire reference electrode and are uncorrected for factors such as  $IR$  drop across the electrolyte. Current densities were calculated by dividing the applied current by the macroscopic surface area of the sample.

The automatic ellipsometer used in these experiments was constructed in this laboratory based on a design described by Ord (11-12). The instrument operates by alternately locating the null settings of the polarizer and analyzer with typical nulling times of about 4 sec for the experiments presented here. The polarizer and analyzer are Glan-Thompson prisms driven in  $0.01^\circ$  steps by stepping motors. The compensator is a quarter-wave plate with its fast axis fixed at  $-45^\circ$  situated between the polarizer and the sample. The light source is a low-powered HeNe laser which operates at a wavelength of 6328Å. A 1P21 photomultiplier tube is used as the detector. Polarizer and analyzer settings and the potential of the electrode were recorded on a digital printer at the end of each nulling sequence. The ellipsometric data are reported in this work directly as the polarizer and analyzer settings at null.

### Results

We begin by recalling the behavior of a vanadium electrode under constant-current conditions. Vanadium differs in some respects from most of the other valve metals in that there is a transition region which occurs prior to the commencement of oxide film growth, and in this transition region vanadium ions go into solution (4). In fact, growth of the anodic oxide could not be initiated using the current densities we were interested in, consequently a current density of  $1.5 \text{ mA/cm}^2$  was used to initiate growth. Upon attaining steady-state growth conditions, the current density was lowered to  $275 \mu\text{A/cm}^2$ .

Figure 1 shows the ellipsometric data for steady-state growth with an applied current density of  $275 \mu\text{A/cm}^2$ . Before the current was applied the ellipsometer null settings give the starting point. As the film grew, the ellipsometric data traced out a curve in a clockwise direction. The null settings of the ellipsometer for the first loop of data are shown in this figure as open circles. Since during the experiment our ellipsometer recorded more than 1200 data points for this loop, only representative data points are plotted. The gap between the clean surface point and the next data point represents the transition region where oxide growth was initiated; we did not attempt to record data in this region.

As growth proceeds, this first loop closes upon itself, approximately, and a second loop, represented by a few squares, is traced out. The second loop does not exactly coincide with the first loop because during growth the vanadium oxide film exhibits a small amount of field-induced optical anisotropy similar to that reported for the anodic oxides of tantalum and

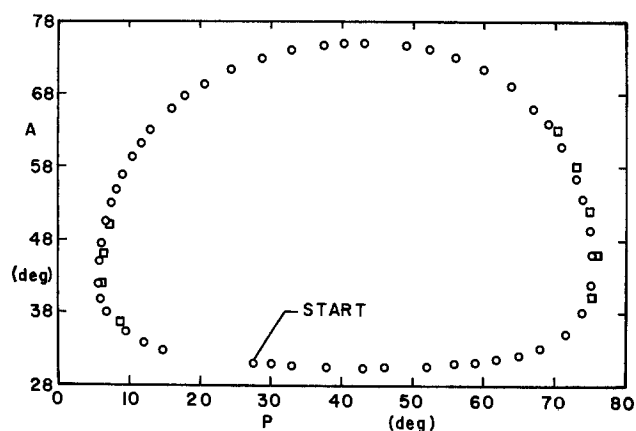


Fig. 1. Ellipsometer null settings for the growth of an anodic oxide film on vanadium at a current density of  $275 \mu\text{A/cm}^2$ . Open circles, first loop; open squares, second loop.

niobium (13-15). This effect will be treated in more detail in another study and is small enough that it can be ignored here.

The data in Fig. 1 can be fitted by a curve representing the growth of a uniform film of index 2.392 on a substrate of index 4.346 - 3.744i, and the film thickness at each point of the  $P$ - $A$  curve can be calculated. Figure 2 shows a plot of the calculated film thickness vs. the electrode potential during film growth. The slope of this line gives a value for the electric field in the film of  $2.63 \times 10^6 \text{ V/cm}$  for a current density of  $275 \mu\text{A/cm}^2$ .

Let us now turn our attention to what occurs when an anodically grown film is subjected to an applied cathodic current. Figure 3 shows a typical potential vs. time curve for a portion of the anodic growth, the cathodic conversion, and subsequent anodic reconversion of a film formed on a vanadium electrode. The portion of the curve labeled A-B represents anodic oxidation. At point B the current was reversed so that the current density was  $-275 \mu\text{A/cm}^2$ . For this applied cathodic current the potential-time curve traced out the section of the curve labeled C-D-E; the length of time necessary to reach point D depended on the thickness of the oxide at point B. At point E the current was switched back to the anodic direction. We have assumed that at point E the conversion was complete. With an anodic current again flowing the potential traced out F-G-H, with steady-state growth condi-

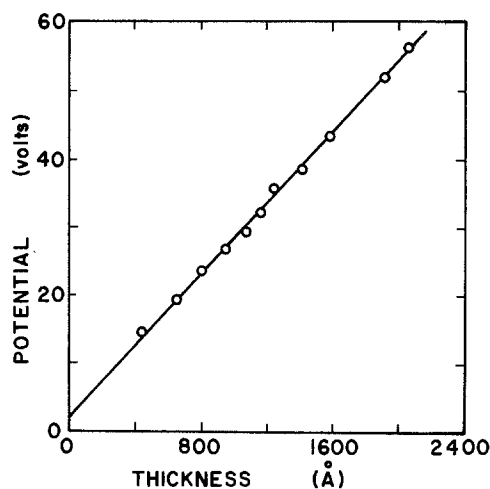


Fig. 2. Potential vs. thickness for the anodic oxidation of vanadium at a current density of  $275 \mu\text{A/cm}^2$ . Thicknesses were calculated from the data in Fig. 1.

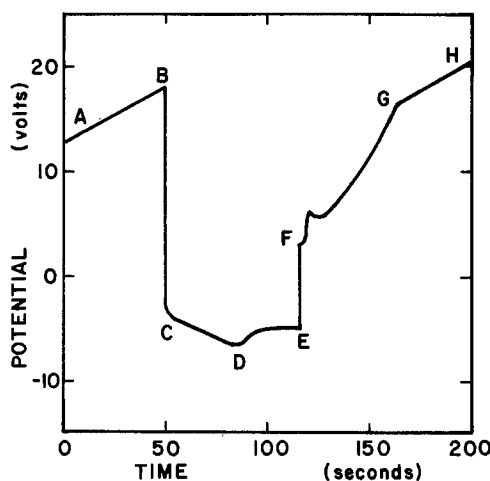


Fig. 3. Potential vs. time for a portion of the anodic oxidation (A-B), the cathodic conversion (B-C-D-E), and anodic reconversion (E-F-G) of the film formed on vanadium. At point B the current density was changed from  $+275 \mu\text{A/cm}^2$  to  $-275 \mu\text{A/cm}^2$ . At point E the current density was changed back to  $+275 \mu\text{A/cm}^2$ .

tions being reattained at point G and anodic oxidation recommencing along G-H. This process of conversion and reconversion can be repeated any number of times using different values of the starting anodic potential (point B in Fig. 3) and consequently different values of the thickness of the anodic oxide when the conversion process was initiated.

The automatic ellipsometer was used to monitor optical changes of the electrode which occurred during a conversion process. We first present ellipsometric data for the points at which the conversion process was initiated and the points at which the conversion process was completed for conversions started at several different thicknesses. Note that the point where the conversion was complete is not well determined by electrical data; we determined the point where the conversion is complete in terms of the ellipsometer settings. When the changes in null settings of the ellipsometer became small (a few hundredths of a degree per null), conversion was considered to be completed and the applied current was switched back to the anodic direction.

Figure 4 shows the *P* and *A* null settings for the anodically formed film and for the film after cathodic conversion is completed. The open symbols are the data points for the anodic film and are the *P*-*A* settings measured at points similar to B in the voltage-time curve in Fig. 3. The closed symbols are the data points for the cathodically converted film; they are the *P*-*A* settings that are obtained for the film at points similar to E in Fig. 3. Open circles on the anodic *P*-*A* curve correspond to closed circles on the cathodic curve, etc. The points are numbered in order of increasing film thickness; the conversion process begins on a particular unprimed numbered point and ends at the point with the same primed number. The entire collection of *P*-*A* points represent ellipsometric data obtained for a sequence of successive voltage-time curves similar to those shown in Fig. 3. These were acquired during a single experiment without removing the sample from the cell.

The solid line through the open symbols in Fig. 4 is a theoretical curve for the growth of a film with refractive index 2.392 on a substrate of refractive index 4.346 - 3.743i, and the solid line through the closed symbols is a curve representing a film with a constant refractive index 2.013 - 0.046i and increasing thickness on the same substrate. The starting point is also indicated. These two lines fit the two sets of data points quite well. Thus we conclude that the application of a cathodic current to a vanadium electrode covered by an anodic oxide film converts this film in some manner from a film of refractive index 2.392 to a film of refractive index 2.013 - 0.046i.

We can also determine the thickness of the film for each of the data points in Fig. 3 using these refractive

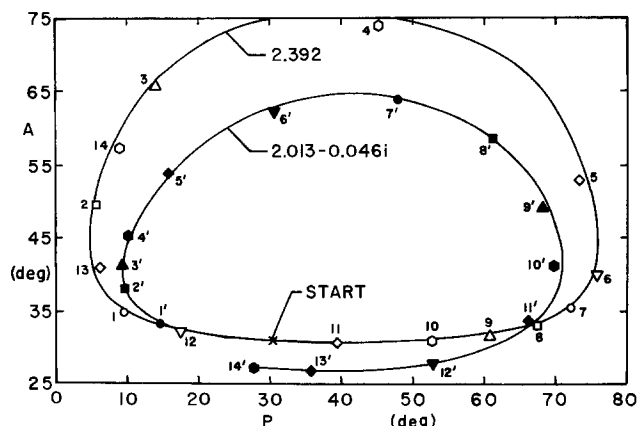


Fig. 4. Ellipsometer null settings for points at which the cathodic conversion process was initiated (open symbols) and points at which the conversion process was complete (closed symbols). The solid lines represent calculated null settings for films of refractive index 2.392 and 2.013 - 0.046i.

Table I. Calculated thicknesses for the points where the conversion process was initiated,  $D_a$ , and the points where the conversion process was complete,  $D_c$ . The conversion numbers correspond to the numbers in Fig. 4.

Conversion number	Anodic thickness, $D_a$ (Å)	Cathodic thickness, $D_c$ (Å)	Conversion ratio, $D_c/D_a$
1	303	295	0.973
2	498	483	0.970
3	582	560	0.962
4	646	622	0.963
5	757	724	0.956
6	869	826	0.950
7	957	900	0.940
8	1040	973	0.936
9	1138	1067	0.938
10	1246	1175	0.943
11	1412	1358	0.962
12	1684	1614	0.958
13	1938	1866	0.963
14	2068	1991	0.963
		Average	0.956
		Standard deviation	0.012

indices. The thickness at each point was determined by finding the thickness for the point on the theoretical *P*-*A* curve that was closest to the actual experimental point. For the anodic points the index of the film used was 2.392 and for the cathodic points the index of the film was 2.013 - 0.046i. The values of the thicknesses obtained in this manner are given in Table I. As can be seen from the numbers in the table, the conversion ratio, defined as  $D_c/D_a$ , is approximately constant and independent of the thickness of the anodic oxide prior to conversion. The average value of  $D_c/D_a$  is 0.956 with a standard deviation of 0.012.

We have thus far determined that a conversion of the anodic film takes place, but we have not said anything about how it takes place. We mentioned earlier that the entire conversion process was monitored using the ellipsometer. In order to answer the question of how the conversion process occurs, we must propose possible models for the process, examine the ellipsometric curves predicted by these models, and compare these predicted curves with the actual experimental data.

Figure 5 shows, schematically, three possible models for the conversion process. We have selected these models because we believe that they are the three simplest hypotheses that might describe the manner in which the film changes. In each of the models an initial film of refractive index  $n_i$  and thickness  $D_i$  is replaced by a film of refractive index  $n_f$  and thickness  $D_f$ . For the conversion process we use  $n_i = 2.392$ ,  $n_f = 2.013 - 0.046i$ , and the appropriate thicknesses are listed in Table I.

In the first model, labeled I in Fig. 5, we assume that the conversion process begins at the oxide/electrolyte interface and proceeds inward toward the metal. At any intermediate point during the conver-

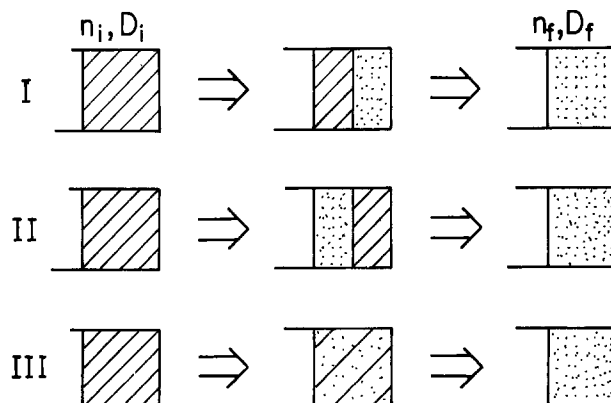


Fig. 5. Schematic of three possible models that can describe the conversion of a film with an initial refractive index  $n_i$  and initial thickness  $D_i$  to a film with a final refractive index  $n_f$  and final thickness  $D_f$ .

sion process there are two layers on the electrode, an inner layer of refractive index  $n_i$  and an outer layer of refractive index  $n_f$ . The boundary between the two layers is assumed to be sharp. The second model, labeled II, is similar to model I except that here we assume that the conversion process begins at the metal/oxide interface and proceeds outward. At an intermediate point during conversion the film will consist of two layers, an inner layer of refractive index  $n_f$  and an outer layer of refractive index  $n_i$ . In model III we assume that the conversion occurs uniformly throughout the film and that the film remains homogeneous at any instant. In addition, we assume that all changes in the film proceed in a linear manner; that is, the fractional change in the real and imaginary parts of the refractive index and the fractional change in the thickness at any instant are the same.

It should be emphasized that the predicted ellipsometric curve for each model depends only on the thickness and index of refraction of the initial film and the thickness and refractive index of the converted film. These values have already been determined using the data in Fig. 4. There are no additional adjustable parameters included in any of the models so we are not curve fitting here; we only seek to determine if any of the models predict the experimental data adequately.

Figure 6 shows the experimental data, plotted as open circles for the conversion of an anodic oxide film with an initial thickness of 757Å. This particular conversion begins at point number 5 on the anodic curve and ends at point number 5' on the curve for the converted film. The letters in Fig. 6 label the  $P$ - $A$  data points that correspond to similarly lettered points in the potential vs. time curve in Fig. 3. The conversion begins at point B and is complete at point E. Not all data points obtained during the conversion process are shown, in particular the density of the experimental points near the point E is much greater than illustrated. Also shown in the figure are the predicted curves for the three proposed models; the number under each curve corresponds to the number of the model shown in Fig. 5.

It is evident from this figure that model I seems to describe the experimental data best. There is some deviation of the data points from curve I in the upper right-hand corner of the figure, but in this region the experimental null settings were changing rapidly and the amount of time required to determine a null becomes important. If we were to correct for the nulling time of our instrument these points would more closely approximate curve I.

In order to demonstrate that Fig. 6 does not represent an unusual set of circumstances that only accidentally show agreement between the experiment and

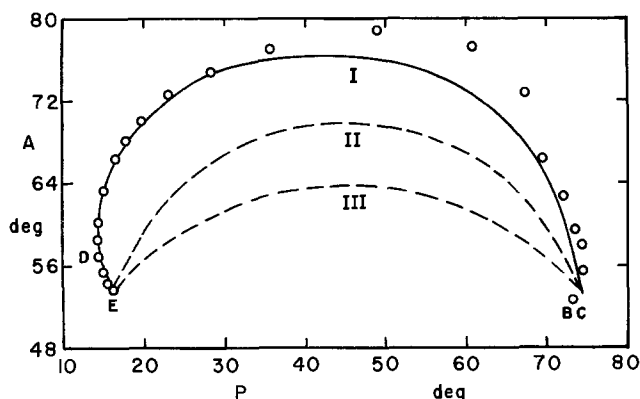


Fig. 6. Ellipsometer null settings, represented by open circles, recorded for the conversion of an anodic film with an initial thickness of 757Å to a cathodic film with a thickness of 724Å. Points B, C, D, and E correspond to similarly labeled points in Fig. 3. The lines represent calculated curves based on the three models presented in Fig. 5.

model I, we present two additional conversion curves in Fig. 7 and 8. Again the experimental points are represented by open circles and again the  $P$ - $A$  curves for the three models are shown for comparison. These are conversion numbers 12 and 13 of Fig. 4. We see that in these cases model I also best accounts for the experimental data. The agreement is surprisingly good considering that the curves for the model are calculated using only the parameters found for the starting point and the end point for the conversion process. The agreement of model I with the data over a wide range of initial thicknesses indicates that this is the correct model to describe the process.

Thus far we have said little about the reconversion of the film in region F-G-H of Fig. 3. We have mentioned that in this region a reconversion of the cathodic back to the original anodic film occurs, at least to the extent that in region G-H the film is indistinguishable from an anodically formed oxide. The ellipsometric data for a typical reconversion are shown in Fig. 9, along with calculated curves for the three models presented previously. The solid line through the data points is not a calculated curve, but has been added as an aid in following the sequence of data points. The curves based on the three models, represented by dashed curves, are labeled with the appropriate model numbers. The models for reconversion differ from the conversion models in that here we assume that the initial film has a refractive index of 2.013 - 0.046i and the final film has a refractive index of 2.392. The initial thickness for the reconversion models was taken to be the thickness of the appropriate cathodic layer in Table I. The final thickness for the reconverted layer was computed using the  $P$ - $A$  point at which the reconversion curve returned to the curve

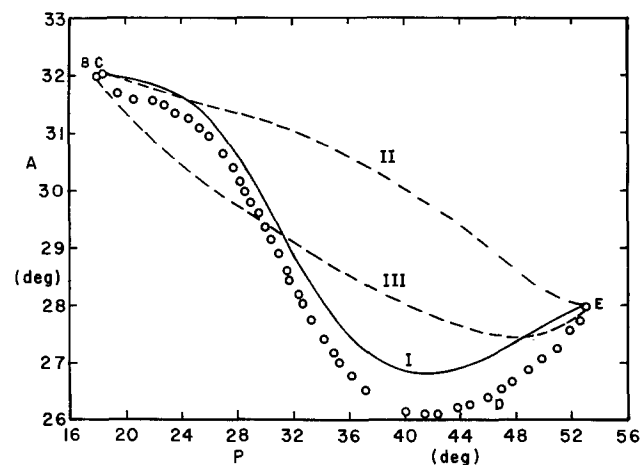


Fig. 7. Ellipsometric null settings for the conversion of an anodic film with an initial thickness of 1684Å to a cathodic film with a thickness of 1614Å. Other features are the same as in Fig. 6.

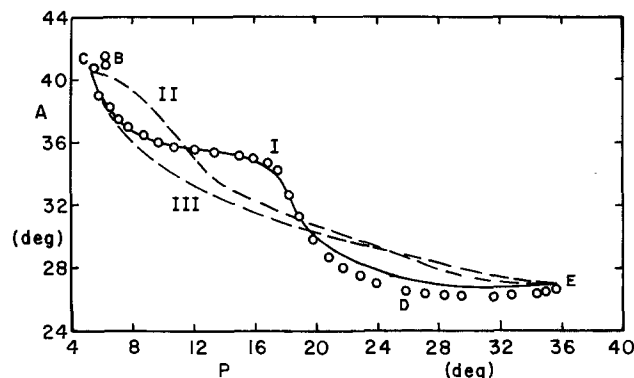


Fig. 8. Ellipsometric null settings for the conversion of an anodic film with an initial thickness of 1938Å to a cathodic film with a thickness of 1866Å. Other features are the same as in Fig. 6.

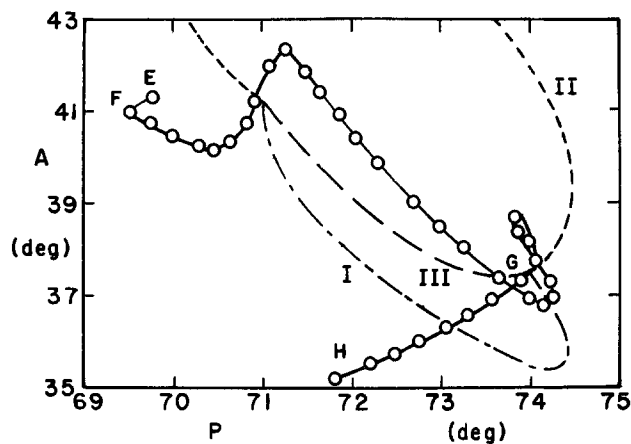


Fig. 9. Ellipsometric null settings, represented by open circles, for the reconversion of a cathodic film with an initial thickness of 1175 Å. Points, E, F, G, and H correspond to similarly labeled points in Fig. 3. The dashed lines represent calculated curves based on the three models presented in Fig. 6.

for anodic growth. This thickness was always found to be smaller than the thickness at which the process was initiated; i.e., in Fig. 3 the thickness of the oxide at point G is always less than at point B.

Figure 10 shows another reconversion beginning at a different initial thickness. As can be seen from Fig. 9 and 10, none of the models fits the experimental data particularly well. Therefore, the process of reconversion must differ in some way from the processes assumed in the models. Nevertheless, if we must select one of these models as a first approximation to the actual process, we would choose model I. While model I does not always give the best fit to the experimental data, it does always approximate the shape of the data. In Fig. 10, it is the only model that gives the same direction of curvature as the experimental points. Choosing model I as a reasonable first approximation to the actual process is not completely meaningless. As was stated above, the thickness of the anodic oxide after a complete conversion-reconversion cycle was less than at the beginning of such a cycle. Using model I, we can account for this by proposing that as the anodic layer is reestablished at the film/electrolyte interface it also slowly dissolves.

### Discussion

By using an automatic ellipsometer to follow the changes in optical properties of a vanadium electrode, we have found that an anodically formed film on the electrode undergoes a change in refractive index and thickness when a cathodic current is applied. The

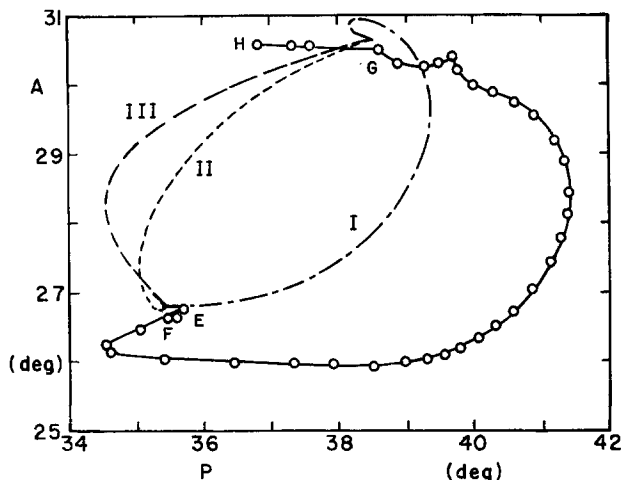


Fig. 10. Ellipsometric null settings for the reconversion of a cathodic film with an initial thickness of 1866 Å. Other features are the same as in Fig. 9.

anodic oxide on vanadium was found to have a refractive index of 2.392, whereas the cathodically converted film had a refractive index of 2.013 — 0.046i. The ratio of the thickness of the anodic oxide to the thickness of the cathodic film was found to be almost constant, independent of the thickness of the anodic oxide when the conversion process was initiated. Further, the conversion can be accounted for by a model in which the conversion begins at the oxide/electrolyte interface and proceeds inward.

We propose that the reconversion of the film can be approximated by a similar model. While the predicted ellipsometer null settings for such a model do not fit the experimental data particularly well, they at least show approximately the same shape as the experimental data. In fact we are not entirely surprised at this lack of fit. The model assumes that a sharp interface exists between the two films present on the electrode during reconversion, whereas there is no obvious physical reason to make this happen.

The fact that the anodic film is much more soluble in water than the cathodically converted film provides another method of distinguishing between the two types of film. We can examine the results of a few simple experiments in which the solubility is tested by noting how rapidly the interference color of the film changes, thus indicating how quickly the film is being dissolved.

Using Fig. 3 as a guide, if we open the circuit in the region A-B, remove the sample from the cell, and place it in water, the oxide is found to completely dissolve in a matter of seconds. If, on the other hand, we form a cathodic film in the region D-E, remove the sample from the cell, and place it in water, there is no apparent color change in the interference color of the film over a period of a few minutes. This merely demonstrates the degree of difference in the solubilities of the two types of film.

We can also perform slightly more complicated experiments. For example, if an anodic film is formed and then a cathodic current is applied for only a short time, the film does not change its interference color when placed in water. This is exactly what we would expect using our proposed model for the conversion process. The cathodic current has caused the outer portion of the film to convert, and this outer film prevents the dissolution of the inner anodic oxide that has yet been converted.

Furthermore, if a film which has been cathodically converted is subjected to an anodic current for a short time and then placed in water, we find that the interference color changes rapidly for a few seconds and then stops changing, leaving some film on the surface. This is consistent with a model in which the reconverted anodic oxide is formed on the outside and the portion which is formed is dissolved away, leaving only the cathodic film. In fact, the film can be removed from the surface in a controlled manner by carefully controlling the amount of time that the anodic current is applied to a cathodically converted film.

Finally, we believe that by applying a carefully controlled series of anodic and cathodic currents to an anodically oxidized vanadium electrode, a series of layers can be produced within the film. For example, if we partially convert an anodic oxide by applying a cathodic current for a short time and then reconvert part of the converted layer, we would produce a film that consisted of three layers: an anodic oxide next to the metal, a cathodically converted layer on top of this, and another anodic oxide layer on the outer surface of the film.

We do not choose here to propose a detailed mechanism for the conversion process. We do not believe that we have sufficient information to present a meaningful picture at the present time. In particular, the chemical composition of the films was not measured in this work. This information is probably essential to a detailed description of this process. Even less can be said with certainty concerning the reconversion of a

cathodically treated layer. The reconversion process cannot be simply the reverse of the conversion process; if it were it would have to proceed from the metal/film interface outward. Despite the lack of close agreement between the data and the models for reconversion, we can definitely tell from our data that the cathodically treated film is not simply reconverted to an anodic film beginning at the metal/film interface proceeding outward. Any detailed explanation of the conversion and reconversion would have to account for this general behavior.

#### Acknowledgment

One of us (J.C.C.) would like to thank the Graduate School of The University of Alabama for financial support for portions of this work.

Manuscript submitted July 3, 1975; revised manuscript received Sept. 26, 1975. This was Paper 94 presented at the Toronto, Canada, Meeting of the Society, May 11-16, 1975.

Any discussion of this paper will appear in a Discussion Section to be published in the December 1976 JOURNAL. All discussions for the December 1976 Discussion Section should be submitted by Aug. 1, 1976.

Publication costs of this article were partially assisted by The University of Alabama.

#### REFERENCES

1. B. H. Ellis, M. A. Hopper, and D. J. De Smet, *This Journal*, **118**, 860 (1971).
2. R. G. Keil and K. Ludwig, *ibid.*, **118**, 864 (1971).
3. M. A. Arora and R. Kelley, *ibid.*, **120**, 128 (1973).
4. R. G. Keil and R. E. Salomon, *ibid.*, **115**, 628 (1968).
5. R. G. Keil and R. E. Salomon, *ibid.*, **112**, 643 (1965).
6. M. A. Hopper and J. L. Ord, *ibid.*, **120**, 183 (1973).
7. C. J. Dell'Oca, *ibid.*, **120**, 1225 (1973).
8. H. G. Feller and J. Osterwald, *ibid.*, **111**, 119 (1964).
9. J. H. Richardson, "Optical Microscopy for the Materials Sciences," pp. 406-407, Marcel Dekker, Inc., New York (1971).
10. D. J. De Smet and M. A. Hopper, *This Journal*, **116**, 1184 (1969).
11. J. L. Ord and B. L. Wills, *Appl. Opt.*, **6**, 1673 (1967).
12. J. L. Ord, *Surface Sci.*, **16**, 155 (1969).
13. W. D. Cornish and L. Young, *Proc. Roy. Soc. London, A*, **335**, 39 (1973).
14. K. K. Yee and L. Young, *Appl. Opt.*, **14**, 1316 (1975).
15. W. P. Wang and J. L. Ord, Paper 89 presented at the Electrochemical Society Meeting, Toronto, Canada, May 11-16, 1975.

## Polarization Resistance Study of the Effect of Alpha-Amino Acids on Copper Corrosion Kinetics

A. G. Keenan, Charles A. Webb, and David A. Kramer\*

Department of Chemistry, University of Miami, Coral Gables, Florida 33124

and Kenneth G. Compton

Rosenstiel School of Marine and Atmospheric Science, Division of Ocean Engineering, Virginia Key, Miami, Florida 33149

#### ABSTRACT

In connection with studies of the greater corrosion rates of metals in natural sea water as compared to equivalent saline solutions, a study of the influence of organic constituents has been initiated. This paper describes polarization resistance measurements, at low overvoltages, of copper corrosion in aerated aqueous solutions containing a series of ten  $\alpha$ -amino acids. The data were analyzed by a novel computer program called CORFIT. The solutions were brought to a constant ionic strength of 0.7M with  $\text{KNO}_3$  and maintained at pH 7. The amino acids were all found to accelerate the corrosion by a mechanism in which their anionic forms adsorb on the surface and form complex ions of lower than normal stoichiometry with  $\text{Cu(II)}$ . The corrosion reactions were under anionic control and involved oxidation of copper to  $\text{Cu}^{2+}$ . Use of constant ionic strength eliminated changes in transfer coefficient due to changing ligand concentration and simplified the kinetic analysis of the corrosion data. The results open up a new procedure for studying the role of organic constituents of natural water systems in electrode adsorption and corrosion processes. A novel parameter to characterize quantitatively corrosion accelerators of this type is suggested.

Numerous publications have appeared dealing with corrosion of copper under a wide variety of conditions, mostly in acidic or basic solutions containing copper ion initially and excluding dissolved oxygen (1). Few authors have carried out fundamental electrochemical studies in solutions free of copper initially (2) or related to natural water systems (3). It has been reported (4, 5) that the corrosion of copper in natural sea water is greater than in synthetic sea water or in sodium chloride solution. It seems reasonable to attribute this increase in corrosion to the organic constituents which are known to be present in natural sea

water. Results are reported herein for a number of  $\alpha$ -amino acids which occur in natural sea water at concentrations of the order of  $10^{-7}\text{M}$  (6) and which form stable complexes with  $\text{Cu(II)}$  ion (7).

A polarization resistance method (8) was used at low overvoltages and in solutions of pH 7-9 whose ionic strength was kept constant at the sea-water value of 0.7M by addition of the indifferent electrolyte  $\text{KNO}_3$ . The data were analyzed by means of a novel computer program called CORFIT, kindly furnished to us prior to its publication by Mansfeld (9).

The results were analyzed by means of the well-known equation employing standard symbols (10)

$$i = i_{\text{CORR}}[\exp(2.3\eta/b_a) - \exp(-2.3\eta/b_c)] \quad [1]$$

\* Electrochemical Society Student Member.

Key words: copper, corrosion, amino acids, polarization resistance, cupric complexes.

where the anodic and cathodic Tafel slopes are defined as

$$b_a = 2.3RT/\alpha nF \text{ and } b_c = 2.3RT/\alpha nF$$

and  $\alpha_a$ ,  $\alpha_c$  are the anodic and cathodic transfer coefficients, respectively.

The derivation of this equation requires the assumption that the corrosion reactions are activation controlled.

The present research uses polarization resistance measurements at low overvoltages and currents. This technique has been described by Wagner and Traud (11) and by Stern *et al.* (12, 13). From Eq. [1]

$$(di/d\phi)_{\eta=0} = 2.3 i_{\text{corr}} [(b_a + b_c)/b_a b_c] \quad [2]$$

or

$$i_{\text{corr}} = (1/2.3 R_p) [b_a b_c / (b_a + b_c)] \quad [3]$$

where  $R_p = (d\phi/di)_{\eta=0}$  is the polarization resistance.

The polarization resistance technique utilizes the  $i$  vs.  $\eta$  data which are taken at small values of  $\eta$  where the net measured current is comprised of both the partial anodic and partial cathodic currents. This offers the advantage that the observed currents are so low that the surface of the corroding electrode has not been altered. In the past the method has suffered from the fact that the measurements have only given values for  $R_p$  at much greater current densities. However, an analysis using the CORFIT program (8, 9, 14) allows values for  $R_p$ ,  $b_a$ ,  $b_c$ , and  $i_{\text{corr}}$  using Eq. [3], to be calculated from a single set of  $i$  vs.  $\eta$  data. The Tafel slopes are thus obtained from the mixed current region where  $\eta < RT/nF$  and no Tafel lines are observed.

### Experimental

A tubular internal flow electrode was used (15). This was constructed from a 2.5 cm length of 0.635 cm ID commercial copper tubing. Emission spectrographic analysis showed 99.95% copper with the major impurities silver, nickel, zinc, and iron each present at less than 0.01%. Various methods of electroplating and electropolishing (16) the internal surface of the copper tube were tried. Scanning electron microscope study at 5000 $\times$  showed that the following procedure gave the best surface, uniformly smooth and relatively free of pits and extrusion lines. The electrode was placed into a line of plastic tubing and 85%  $\text{H}_3\text{PO}_4$  pumped through it at 600  $\text{cm}^3/\text{min}$ . A constant anodic current of 45  $\text{mA}/\text{cm}^2$  was passed using an axial copper wire for the cathode. The polishing was continued for several minutes after the potential had stabilized at  $2.7 \pm 0.2\text{V}$ . The electrode was then rinsed with water and methanol to remove the last traces of phosphate (17) and transferred immediately into the corrosion apparatus.

This apparatus was based on the 1 liter Greene six-neck polarization cell (18). The working electrode was mounted in a line of polyethylene tubing in such a manner that solution in the cell could be circulated through it with a noncontaminating Varistaltic pump. Surge tanks made from polyethylene bottles smoothed out the flow whose rate was measured with a calibrated rotameter. The auxiliary electrode was a platinum wire sealed through a T-shaped polyethylene tube and held axially in the working electrode by means of polyethylene spacers. The reference electrode was an Orion 90-02 double junction electrode which was calibrated before each run with a Beckman SCE. The reference electrode and a Corning Model 500 pH electrode entered the polarization cell through side necks. The cell also contained a thermometer and a sintered glass diffuser for purging with gas. The three-electrode system was connected to a Wenking 70-TS-1 potentiostat.

All runs were made with solutions which were brought to the sea water ionic strength of 0.7M by addition of  $\text{KNO}_3$ . The pH was controlled to  $\pm 0.1$

units by addition of  $\text{NaOH}$  or  $\text{HNO}_3$ . The solutions were saturated and continually purged with a slow stream of air. No difference was observed between air from a cylinder or from an aeration pump. Temperature was constant at the ambient laboratory value of  $24.5^\circ \pm 0.5^\circ\text{C}$ . After equilibration for about 10 min (with the solution circulating) until a stable rest potential was attained, the working electrode potential was incremented in steps of 4 mV and the current read after 30 sec. The potential sweep was from an initial cathodic overpotential of  $-20$  to  $+20$  mV. The overvoltage-current data were then read into the CORFIT computer program.

All the polarization data were obtained at a flow rate which gave a linear velocity of 26  $\text{cm}/\text{sec}$  for solution passing the inner surface of the TIFE. This velocity is well into the region of turbulent flow, the turbulence parameter (10) exceeding the critical value of 1 by a factor of 1830. Most data were collected with polarization current densities not exceeding 10  $\mu\text{A}/\text{cm}^2$ . In a few cases, the maximum was 20  $\mu\text{A}/\text{cm}^2$ .

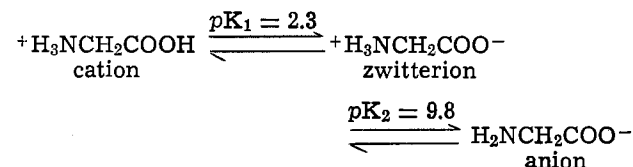
About 10 independent runs were made at each concentration. The Tafel slopes were found to be independent of the concentration. The best values for  $i_{\text{corr}}$  were obtained by using in Eq. [3] a value for each Tafel slope averaged over all of the runs with amino acids, irrespective of the concentration.  $\phi_{\text{corr}}$  was obtained from the  $i$  vs.  $\eta$  data (9).

### Results and Discussion

The values of  $i_{\text{corr}}$  and of  $\phi_{\text{corr}}$  determined in the low current linear polarization region were found to be independent of flow velocities ranging from 10 to 50  $\text{cm}/\text{sec}$ . Thus, the electrode processes in the range studied were under activation control (19, 20).

Glycine was used as a prototype for the  $\alpha$ -amino acids and was studied in some detail. Table I presents the results obtained for the corrosion parameters for glycine solutions. It is seen that with increasing amino acid concentration at constant pH, the corrosion rate increases, while the corrosion potential becomes more negative. Both  $b_a$  and  $b_c$  remain constant at 50 and 60 mV, respectively. Reference to a standard Evans diagram shows that the copper is corroding under anodic control (10), that is, the amino acid is influencing the rate of the anodic dissolution of the copper metal.

Glycine exists predominantly in three forms in aqueous solution, the concentrations being determined by the pH.



The relative concentrations of these ions are given by the relation

$$pH_{\text{soln}} - pK = \log[(\text{basic form})/(\text{acidic form})]$$

The values for  $pK$  were taken from the literature for zero ionic strength (20, 21). The values at 0.7M are not available, but for the amino acids where  $pK$  is reported as a function of ionic strength the differences are of the same order as variations between the different authors. The concentrations of the forms can thus be calculated for various values of pH and total glycine concentration.

A study of  $i_{\text{corr}}$  values as a function of glycine concentration and pH makes it possible to determine that only the anion participates in the anodic dissolution of copper. It is seen that for constant total glycine, the corrosion rate increases significantly with pH and so does the concentration of the anion. Concentration of the cation decreases by orders of magnitude and of the zwitterion remains essentially constant. For entries where the concentration of the anion is

Table I. Effect of pH on corrosion rate with glycine

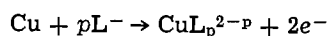
Total glycine (M)	pH	$\phi_{\text{corr}}$ (mV vs. SCE)	$i_{\text{corr}}$ ( $\mu\text{A}/\text{cm}^2$ )	Cation (M)	Zwitterion (M)	Anion (M)
0.0010	7.0	-101 $\pm$ 8	0.40	$2.0 \times 10^{-8}$	$9.98 \times 10^{-4}$	$1.6 \times 10^{-5}$
0.0100	7.0	-168 $\pm$ 7	1.18	$2.0 \times 10^{-7}$	$9.98 \times 10^{-3}$	$1.6 \times 10^{-5}$
0.1000	7.0	-218 $\pm$ 10	2.44	$2.0 \times 10^{-6}$	$9.98 \times 10^{-2}$	$1.6 \times 10^{-4}$
0.0010	8.0	-102 $\pm$ 2	1.51	$2.0 \times 10^{-9}$	$9.84 \times 10^{-4}$	$1.6 \times 10^{-5}$
0.0100	8.0	-187 $\pm$ 3	2.64	$2.0 \times 10^{-8}$	$9.84 \times 10^{-3}$	$1.6 \times 10^{-4}$
0.0001	9.0	-151 $\pm$ 4	1.39	$1.7 \times 10^{-11}$	$8.62 \times 10^{-5}$	$1.4 \times 10^{-5}$
0.0010	9.0	-161 $\pm$ 1	2.57	$1.7 \times 10^{-10}$	$8.62 \times 10^{-4}$	$1.4 \times 10^{-4}$

essentially constant at  $1.4\text{--}1.6 \times 10^{-5}\text{M}$ , the corrosion current is also constant within experimental error within the range  $1.18\text{--}1.51 \mu\text{A}/\text{cm}^2$ . Similarly, when the anion concentration is constant in the range  $1.4\text{--}1.6 \times 10^{-4}\text{M}$ , the current is constant at  $2.44\text{--}2.64 \mu\text{A}/\text{cm}^2$ . For the two constant corrosion current ranges just mentioned, the concentrations of cation and zwitterion change by four and two orders of magnitude, respectively.

The corrosion parameters for copper with a series of  $\alpha$ -amino acids in solutions whose ionic strength was brought to 0.7M by adding  $\text{KNO}_3$  were next measured at pH 7.0. The acids are listed in Table II with their structure,  $pK_2$  values, and Tafel constants which were independent of concentration. By analogy with glycine it was assumed that the anionic form was corrosion active and the concentrations of this species were calculated as before. The corrosion currents and potentials are given in Table III.

The amino acids all accelerate the corrosion of copper and it has been shown that the reactions are all under anodic control. Table II shows that the anodic Tafel slopes lie in the range  $35 \leq b_a \leq 61$  mV. If the reasonable assumption is made that the anodic reaction mechanism involves the same number of electrons for the oxidation of copper in the presence of each of the amino acids, then this value must equal 2. This follows because  $b_a = 2.3 RT/\alpha nF = 59.2/\alpha n$  at  $25^\circ$  and in principle  $\alpha$  must be bounded by  $0 \leq \alpha \leq 1$ . The range of observed  $b_a$  values can therefore only be accommodated with a common integral  $n$  by the values  $n = 2$  and  $0.49 \leq \alpha \leq 0.85$ .

The conclusion that  $n = 2$  is of course reinforced by the known fact that amino acids stabilize  $\text{Cu}^{2+}$  ion in aqueous solution and form soluble complexes with it (7). The proposed anodic reaction for corrosion of copper in the presence of amino acids at pH 7 is therefore



where  $\text{L}^-$  is the amino acid anion and the copper in the complex ion product is  $\text{Cu(II)}$ . Evaluation of the electrochemical reaction order  $p$  is discussed later.

When the corrosion current is plotted against the logarithm of the amino acid concentration, as in Fig. 1, very interesting results are obtained. The amino acids fall on three distinctly grouped lines. The groups correlate beautifully with the expected adsorption properties of the acids. Referring to the structures of the acids given in Table III, it is seen that in Fig. 1

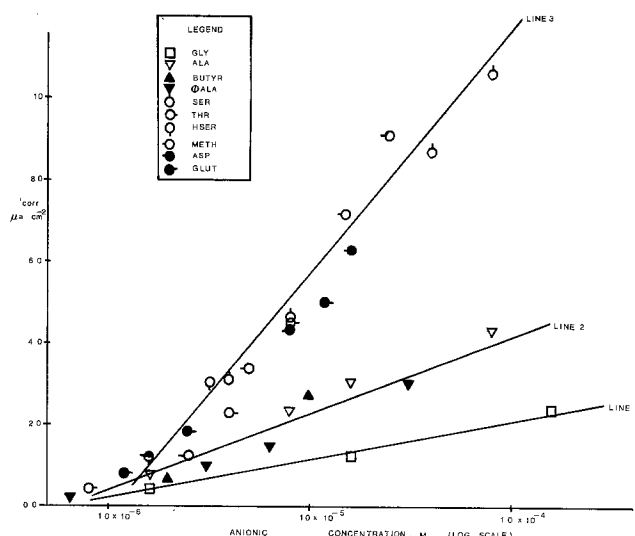
Table II.  $\alpha$ -amino acids  $\text{H}_2\text{N}-\overset{\text{R}}{\text{C}}-\text{COO}^-$

Amino acid	-R	$pK_2$	$b_a$ (mV)	$b_c$ (mV)
Glycine	-H	9.8	50 $\pm$ 9	60 $\pm$ 8
Alanine	- $\text{CH}_3$	9.8	45 $\pm$ 7	59 $\pm$ 6
Phenylalanine	- $\text{CH}_2\phi$	9.2	35 $\pm$ 3	56 $\pm$ 7
Butyryne	- $\text{CH}_2\text{CH}_2\text{CH}_3$	9.7	42 $\pm$ 8	56 $\pm$ 9
Serine	- $\text{CH}_2\text{OH}$	9.1	61 $\pm$ 9	68 $\pm$ 7
Homoserine	- $\text{CH}_2\text{CH}_2\text{OH}$	9.5	58 $\pm$ 8	59 $\pm$ 8
Threonine	- $\text{CH}(\text{OH})\text{CH}_3$	9.1	54 $\pm$ 5	59 $\pm$ 8
Methionine	- $\text{CH}_2\text{SCH}_2\text{CH}_3$	9.3	50 $\pm$ 2	59 $\pm$ 4
Aspartic acid	- $\text{CH}_2\text{COO}^-$	9.8	57 $\pm$ 7	61 $\pm$ 7
Glutamic acid	- $\text{CH}_2\text{CH}_2\text{COO}^-$	9.6	50 $\pm$ 6	57 $\pm$ 4

Table III. Corrosion currents and potentials for  $\alpha$ -amino acid anions at pH 7.0

Amino acid	Total conc (M)	Anion conc (M)	$i_{\text{corr}}$ ( $\mu\text{A}/\text{cm}^2$ )	$\phi_{\text{corr}}$ (mV vs. SCE)
Glycine	0.0010	$1.6 \times 10^{-6}$	0.40	-101 $\pm$ 8
	0.0100	$1.6 \times 10^{-5}$	1.18	-168 $\pm$ 7
	0.1000	$1.6 \times 10^{-4}$	2.44	-218 $\pm$ 10
Alanine	0.0010	$1.6 \times 10^{-6}$	0.82	-88 $\pm$ 5
	0.0050	$8.0 \times 10^{-6}$	2.45	-107 $\pm$ 2
	0.0100	$1.6 \times 10^{-5}$	3.10	-118 $\pm$ 2
Phenylalanine	0.0500	$8.0 \times 10^{-5}$	4.31	-142 $\pm$ 7
	0.0001	$6.3 \times 10^{-7}$	0.12	-39 $\pm$ 2
	0.0005	$3.1 \times 10^{-6}$	1.02	-74 $\pm$ 2
Butyryne	0.0010	$6.3 \times 10^{-6}$	1.45	-77 $\pm$ 3
	0.0050	$3.1 \times 10^{-5}$	3.04	-91 $\pm$ 4
	0.0010	$2.0 \times 10^{-6}$	0.70	-71 $\pm$ 2
Serine	0.0050	$1.0 \times 10^{-5}$	2.76	-100 $\pm$ 2
	0.0005	$4.0 \times 10^{-6}$	3.09	-72 $\pm$ 2
	0.0010	$7.9 \times 10^{-6}$	4.53	-92 $\pm$ 2
Homoserine	0.0050	$4.0 \times 10^{-5}$	8.73	-131 $\pm$ 3
	0.0100	$7.9 \times 10^{-5}$	10.60	-142 $\pm$ 3
	0.0005	$1.6 \times 10^{-6}$	1.19	-88 $\pm$ 4
Threonine	0.0010	$3.2 \times 10^{-6}$	3.04	-101 $\pm$ 2
	0.0001	$7.9 \times 10^{-7}$	0.41	-44 $\pm$ 2
	0.0005	$4.0 \times 10^{-6}$	2.37	-78 $\pm$ 2
Methionine	0.0010	$7.9 \times 10^{-6}$	4.67	-86 $\pm$ 2
	0.0005	$2.5 \times 10^{-6}$	1.20	-79 $\pm$ 2
	0.0010	$5.0 \times 10^{-6}$	3.38	-89 $\pm$ 2
Aspartic acid	0.0030	$1.5 \times 10^{-5}$	7.20	-111 $\pm$ 2
	0.0050	$2.5 \times 10^{-5}$	9.10	-128 $\pm$ 3
	0.0010	$1.6 \times 10^{-6}$	1.22	-84 $\pm$ 2
Glutamic acid	0.0050	$8.0 \times 10^{-6}$	4.38	-88 $\pm$ 7
	0.0100	$1.6 \times 10^{-5}$	6.30	-90 $\pm$ 2
	0.0005	$1.2 \times 10^{-6}$	0.75	-70 $\pm$ 3
	0.0010	$2.5 \times 10^{-6}$	1.80	-73 $\pm$ 2
	0.0050	$1.2 \times 10^{-5}$	4.94	-78 $\pm$ 5

glycine which has only a hydrogen atom as a substituent on the basic  $\alpha$ -amino acid structure, is by itself on line 1. The corrosion current shows the least concentration dependence on this weakly adsorbed species. On line 2 in a second group are alanine, phenylalanine, and butyryne. These three have aliphatic and aromatic substituents which can be expected to increase the van der Waals surface adsorption. Members of this group increase the corrosion current appreciably. The remaining acids belong to a third group and increase the corrosion current strikingly as shown by line 3. The substituents on these acids

Fig. 1. Corrosion current density as a function of  $\alpha$ -amino acid anion concentration.



contain the polar groups OH, COO<sup>-</sup>, and SH which involve electronegative Group VI elements. These would be expected to enhance adsorption since the corroding electrode is positive to the point of zero charge (10).

Convenient corrosion acceleration parameters may be developed by fitting least square analytical expressions of the form

$$i_{\text{corr}} = a + b \log(L^-)$$

to the lines in Fig. 1. Table IV gives the results. The intercept  $a$  may be termed the standard-state corrosion current density since it refers to the state where  $(L^-) = 1$ . It should serve as a useful quantitative parameter to characterize corrosion accelerators.

The electrochemical kinetic order of this corrosion reaction (10) is defined as

$$p = (d \log i_a / d \log C_{AA})_{\phi} \quad [4]$$

where  $C_{AA}$  is the amino acid concentration.

This quantity may be obtained from data of Table I at various arbitrarily chosen constant values of  $\phi$  by graphing  $i_a$  against  $\phi$  using the known Tafel slope

$b_a$  and the fact that  $i_a = i_{\text{corr}}$  at  $\phi = \phi_{\text{corr}}$ . Alternatively, using Eq. [1] to [3], it can be shown that the reaction order is also equal to

$$(d \log i_{\text{corr}} / d \log C_{AA})_{\eta=0} - (1/b_a) (d \phi_{\text{corr}} / d \log C_{AA}) \quad [5]$$

The initial results indicated that all the bidentate ligands (the first 8 in Table II) gave an order of  $1.5 \pm 0.3$  while the tridentate ligands (aspartic and glutamic acids) gave a value near 1.0. Since the data in the present paper indicate unequivocally that complex ion formation involving amino acid ligands plays a part in anodic copper corrosion in these systems, it is tempting to speculate that the above reaction orders give information about the composition of the transition state complexes involved in the rate-determining anodic step. Thus the apparent order of 1.5 for the bidentate ligands might be taken to indicate that a complex involving three ligands bound to every two copper atoms plays a role. One of the ligands might bridge the copper atoms in a bidentate manner while each of the other two was chelated entirely to one of these atoms. The apparent order of one for the tridentate ligands would indicate a completely chelated complex involving one ligand per copper atom.

The above view is further enhanced by the observation that the product of the apparent reaction order times the number of chelating groups on the ligand for both bidentate and tridentate species is equal to the same value three. Thus the activated complex in both cases would have the same characteristic in the respect that three bonds between organic ligand and each copper ion are required. The normal stoichiometry of Cu(II)-amino acid complexes in solution is  $\text{CuL}_2$  (7) involving four bonds per Cu. The distorted version is required by the steric hindrance of the surface and

by the surface adsorption forces which undoubtedly play a role in the process as shown by the correlations in Fig. 1 and the attendant discussion above. If the activated complex energy barrier lies close to the metal surface, as it would for a charge-transfer reaction involving complexation, then the normal solution stoichiometry would not be expected due to the steric impossibility of formation of the square planar cupric-amino acid anion chelate where the octahedral cupric species has Jahn Teller stretched axial positions that are occupied by solvent molecules in the normal solution configuration. After the activation barrier to the corrosion process has been surmounted, the complex would of course disproportionate to its normal stoichiometry on passage into solution.

### Acknowledgments

This research was made possible by support from the Alcoa Foundation and the Sea Grant Program. The authors also wish to thank Dr. Florian Mansfeld for valuable comments, and Dr. H. L. Craig for assistance with the scanning electron microscope.

Manuscript submitted Feb. 24, 1975; revised manuscript received Sept. 17, 1975.

Any discussion of this paper will appear in a Discussion Section to be published in the December 1976 JOURNAL. All discussions for the December 1976 Discussion Section should be submitted by Aug. 1, 1976.

Publication costs of this article were partially assisted by the University of Miami.

### REFERENCES

1. A. J. Read, *J. Phys. Chem.*, **76**, 3656 (1972).
2. C. P. Kim and K. Nobe, *Corrosion*, **27**, 382 (1971).
3. L. Guiliiana, A. Tamba, and C. Modena, *Corrosion Sci.*, **11**, 485 (1971).
4. F. L. LaQue, *Corrosion*, **13**, 330t (1957).
5. K. G. Compton, NACE Corrosion/73 National Meeting, Anaheim, Calif., p. 9/1, March (1973).
6. F. S. Wagner, *Marine Sci.*, **14**, 114 (1969).
7. L. G. Sillén and A. E. Martell, Special Publication No. 25, The Chemical Society, London (1970).
8. K. B. Oldham and F. Mansfeld, *Corrosion Sci.*, **13**, 813 (1973).
9. F. Mansfeld, *Corrosion*, **29**, 397 (1973).
10. J. O'M. Bockris and A. K. N. Reddy, "Modern Electrochemistry," Plenum Press, New York (1970).
11. C. Wagner and W. Traud, *Z. Elektrochim.*, **44**, 391 (1938).
12. M. Stern and A. L. Geary, *This Journal*, **104**, 56 (1957).
13. M. Stern and E. D. Weisert, *Proc. A.S.T.M.*, **59**, 1280 (1959).
14. F. Mansfeld, *This Journal*, **120**, 515 (1973).
15. L. G. Austin, P. Palassi, and R. R. Klimpel, *Adv. Chem. Ser.*, **47**, 35 (1965).
16. K. Niki, F. M. Delnick, and N. Hackerman, *This Journal*, **122**, 855 (1975).
17. J. A. S. Green, H. D. Mendenberg, and H. T. Yolken, *ibid.*, **117**, 433 (1970).
18. S. B. Greene and N. D. Greene, *Electrochem. Technol.*, **1**, 276 (1963).
19. K. J. Vetter, "Electrochemical Kinetics: Theoretical and Experimental Aspects," Academic Press, New York (1967).
20. A. L. Bacarella and J. C. Griess, Jr., *This Journal*, **120**, 459 (1973).
21. R. M. C. Dawson, D. C. Elliott, W. H. Elliott, and K. M. Jones, Editors, "Data for Biochemical Research," 2nd ed., Clarendon Press, Oxford (1969).
22. E. J. Cohn and J. T. Edsall, "Proteins, Amino Acids, and Peptides as Ions and Dipolar Ions," A.C.S. Monograph Series, Hafner Publishing Co., New York (1965).

Table IV. Corrosion acceleration parameters

Amino acid group	Intercept $a$ ( $\mu\text{A}$ )	Slope $b$ ( $\mu\text{A}/\text{cm}^2$ )	Standard deviation $\sigma$
I	6.1	1.0	0.11
II	12.7	2.0	0.30
III	33.1	5.5	0.63



# Some Aspects of the Electrochemical Behavior of Zinc in the Presence of Acrylate and Methacrylate Anions

P. F. Hutchison and J. Turner

Timex Corporation, Washington NE37 3HW, Tyne and Wear, England

## ABSTRACT

The influence of acrylate and methacrylate anions on the anodic behavior of zinc in concentrated sodium hydroxide solution at ambient temperature and under quiescent conditions has been studied using cyclic linear sweep voltammetry. The effect that these additives have on the corrosion rate of the zinc electrode, and on hydrogen evolution in particular, is examined. Experiments show that although the organic species exhibit a marked over-all catalytic effect on both zinc dissolution and hydrogen evolution, the corrosion rate is little affected. Despite an apparent deleterious effect on passivation, results suggest that the additives improve the solubility of the anodic product in the electrolyte. A mechanism is tentatively suggested for the catalytic evolution of hydrogen.

It has been shown (1) that acrylate and methacrylate ions, present in solution to the extent of 0.1% by weight, lower the double layer capacitance (Cdl) of the Zn-KOH interphase. This effect, seemingly limited to high KOH concentrations ( $\geq 30\%$  by weight), probably reflects adsorption of the organic anions at the electrode surface.

In view of the possible use of such additives in zinc-alkali cells it was decided to examine any influence they might have on the passivation and corrosion behavior of the zinc electrode. Zinc deposition was not considered since we were primarily interested in the application of the organic additives to primary cells, following information (2) of experimental evidence to suggest that such anions might improve the efficiency of the zinc anode on discharge.

## Experimental

A diagram of the three electrode Pyrex cell is given in Fig. 1. Zinc foil, thickness 0.15 mm, purity 99.995+%, Goodfellow Metals Limited, was blanked into 2.54 cm diam disks which were given a 1 sec dip in 3N nitric acid, followed by thorough rinsing in triply distilled water prior to incorporation into the cell. The working electrode was positioned horizontally facing upwards so as to eliminate all but local convection at the zinc surface.

Key words: zinc, corrosion, passivation, acrylic anions.

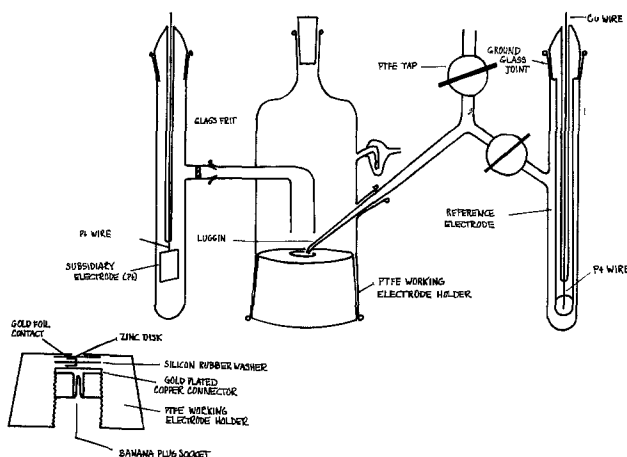


Fig. 1. Cell diagram

Experiments were performed using electrolyte deoxygenated by passage of nitrogen (BOC, white spot grade) for 1 hr, and the cell was assembled under a nitrogen atmosphere in a glove box. 10N solutions were made up from BDH 'AnalaR' sodium hydroxide pellets using triply distilled water, and the organic anions were added in the form of the acids, *viz.*

acrylic acid	} Koch-light, puriss.	{ 0.1 volume per cent (v/o) (0.015M)
methacrylic acid		

A cyclic linear potential sweep was applied to the zinc electrode *via* a Chemical Electronics TR40/3A potentiostat in conjunction with a linear sweep unit; cyclic voltammograms were recorded on a Bryans X-Y plotter Type 26000A4, and the potential of the working electrode, with respect to the Hg-HgO reference electrode, was also measured on a Solartron LM1620 D.V.M. The cathodic excursion always preceded the anodic excursion.

The corrosion rate of the zinc was also determined volumetrically by monitoring the volume of hydrogen evolved when one gram of granular zinc (particle size 125-250  $\mu\text{m}$ , Berk Limited) was exposed to 20 ml of 10N NaOH in the apparatus shown in Fig. 2. The 100 ml volumetric flask was immersed in an oil bath maintained at 50°C. After addition of the alkali to the zinc, the mixture in the flask was evacuated in a desiccator

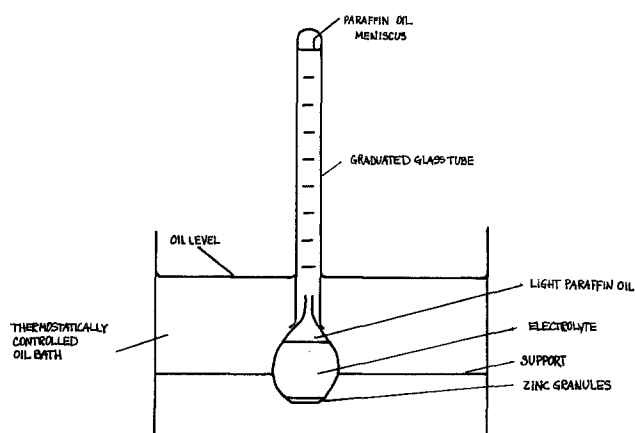


Fig. 2. Gassing test apparatus.

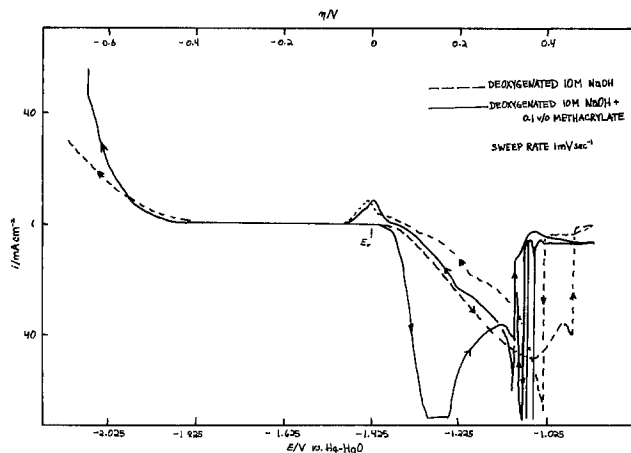


Fig. 3. Cyclic voltammograms. - - - 10M NaOH, ——— 10M NaOH/0.1 v/o methacrylic acid, ····· 10M NaOH/0.1 v/o acrylic acid, Y-axis:  $i/mA\ cm^{-2}$ , X-axis: upper  $\eta/V$ , lower  $E/V$  vs. Hg-HgO.

for 1 hr to remove any entrapped air prior to commencement of the experiment.

### Results and Discussion

The form of the anodic portion of the voltammogram obtained under quiescent conditions in the absence of additives can be seen from Fig. 3. It seems fairly certain (3-6) that the first peak in the anodic sweep corresponds to the formation of a porous film of ZnO by a dissolution-precipitation mechanism and the active-passive transition to a low porosity film forming directly on the metal surface, the sharp peak obtained on the return sweep corresponding to reduction of the latter film.

The influence of the various additives on the corrosion parameters and passivation behavior of the zinc is summarized in Tables I and II, respectively. Their effect on the corrosion rate is only slight, as confirmed by the gassing test results presented in Fig. 4. Conversely, the anions appear to have a marked effect on anodic behavior; a typical voltammogram for methacrylate is presented in Fig. 3. Similar results were obtained for acrylate.

It can be seen that adsorbed anions have a pronounced over-all kinetic effect, both zinc dissolution, and hydrogen evolution at overpotentials  $> -550$  mV, occurring more readily; conversely, inhibition appears to occur in the case of  $H_2$  evolution for the overpotential range  $-400\ mV < \eta < -550\ mV$ .

Representative Tafel plots for zinc dissolution and hydrogen evolution are presented in the form of an Evans diagram, constructed from the experimentally obtained voltammograms, in Fig. 5. Although hydrogen evolution is suppressed in the vicinity of the corrosion

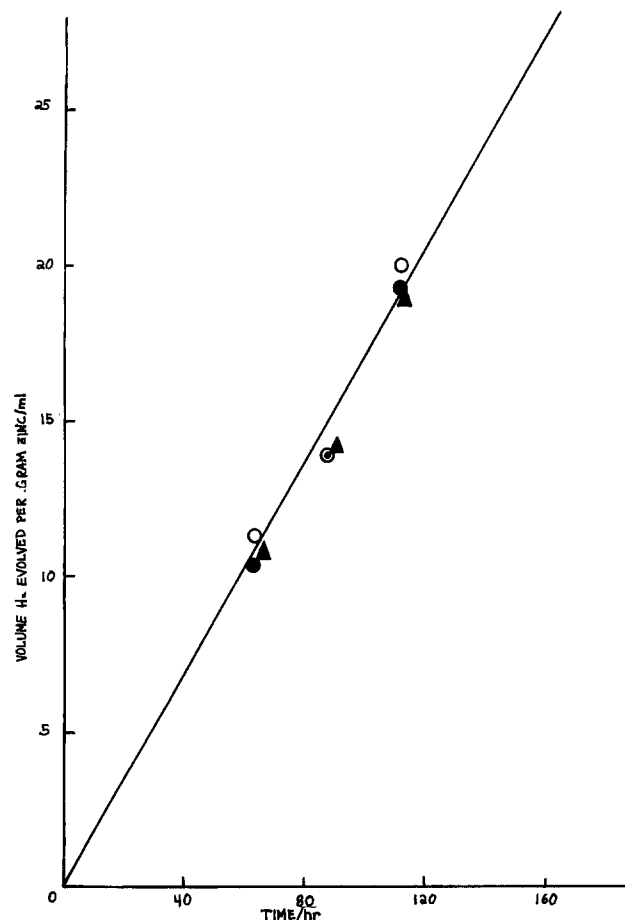


Fig. 4. Gassing test results. ○ = 10M NaOH, ● = 10M NaOH/0.1 v/o acrylic acid, △ = 10M NaOH/0.1 v/o methacrylic acid, Y-axis: volume  $H_2$  evolved per gram zinc/ml, X-axis: time/hr.

potential, the increase in the zinc dissolution rate results in a slight increase in the corrosion current with a corresponding displacement of the corrosion potential towards the equilibrium potential of Zn/Zn<sup>II</sup> electrode.

Since the  $H_2-H^+$  exchange reaction involves the adsorption of reactive species, anionic adsorption would be expected to have at least three kinetic effects: (i) variation of  $\phi_2$  the potential at the outer Helmholtz plane (OHP), (ii) variation of  $\Delta G^\circ$  for hydrogen adsorption, and (iii) decrease of area available for hydrogen adsorption. The influence of anionic adsorption on the overvoltage in the absence of adsorption of reactants and products follows from the Butler-Volmer relationship which implies that, at constant current, the change of overvoltage ( $\Delta\eta$ ) resulting from a vari-

Table I\*

Electrolyte 10M NaOH + anion	$i_{corr}/mA\ cm^{-2}$	$E_{corr}/V$ vs. Hg-HgO	$i_0(H_2)/mA\ cm^{-2}$	Tafel slope ( $H_2$ ) $mV\ decade^{-1}$
0.1 v/o acrylate	$2.03 \pm 0.25$	$-1.456 \pm 0.001$	$0.067 \pm 0.017$	$63 \pm 6$
0.1 v/o methacrylate	$1.85 \pm 0.20$	$-1.459 \pm 0.002$	0.064	$56 \pm 7$
Pure 10M NaOH	$1.69 \pm 0.14$	$-1.481$	$0.14 \pm 0.006$	$76 \pm 4$

\* All data obtained from Evans diagrams such as that depicted in Fig. 5.

Table II.

Conditions	Peak I	Peak II (active-passive)	Max/ $mA\ cm^{-2}$ peak I	Sweep rate
10M NaOH	$380 \pm 13$	$500 \pm 2$	$46.4 \pm 1.6$	1 mV sec <sup>-1</sup>
10M NaOH + 0.1 v/o acrylate	$140 \pm 8$	$325 \pm 4$	$70.8 \pm 1.0$	1 mV sec <sup>-1</sup>
10M NaOH + 0.1 v/o methacrylate	$150 \pm 9$	$325 \pm 3$	$76 \pm 0.5$	1 mV sec <sup>-1</sup>

\* All potentials quoted in mV with respect to Zn-Zn<sup>2+</sup>.

ation  $\Delta\phi_2$  is given by

$$\Delta\eta = \left(1 - \frac{z}{\alpha n}\right) \Delta\phi_2 \quad [1]$$

The quantities  $\Delta\eta$  and  $\Delta\phi_2$  have the same sign for  $z/\alpha n < 1$  and opposite signs for  $z/\alpha n > 1$ , and thus  $\Delta\eta$  has the same sign in the reduction of anions and the opposite sign to  $\Delta\phi_2$  in the reduction of cations ( $z \cong n$ ) and  $0 < \alpha < 1$ ). The specific adsorption of anions makes  $\phi_2$  more negative (7), and therefore  $\Delta\eta$  more positive for the reduction of  $H^+$ ; hence (i) would be expected to exert a catalytic influence on the  $H_2$  evolution reaction. (ii) and (iii) would have the opposite effect, and it would therefore appear that (ii) and (iii) dominate at low overpotential; this situation, however, would probably pertain over the entire potential range for which the organic adsorbed, and the very marked catalysis at overpotentials  $> -550$  mV must consequently arise from factors not mentioned in the foregoing discussion. The above equation and considerations apply strictly only to the case of mercury and dilute amalgams and it is not suggested that they afford a formal description of the situation at a solid electrode where the double layer structure is less well known. However, it is suggested that the treatment will have some qualitative significance and give some insight into the situation prevailing at the electrode surface, particularly since it can be supposed that the rate determining step of the over-all process is still hydrogen ion discharge resulting in the formation of an adsorbed hydrogen atom [(cf. mercury and dilute amalgams (8))].

As the potential of the zinc is made more negative during the cathodic excursion the pH of the electrolyte in the vicinity of the cathode decreases, in the following fashion: the variation of  $[H_3O^+]$  and  $[OH^-]$  close to the electrode surface obeys the Boltzmann distribution

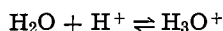
$$[H_3O^+]_s = [H_3O^+]_b \exp(-\phi_2 F/RT) \quad [2]$$

$$[OH^-]_s = [OH^-]_b \exp(-\phi_2 F/RT) \quad [3]$$

where the indices  $s$  and  $b$  define concentrations close to the electrode surface (interphasial region up to and including the OHP) and in the bulk of the solution, respectively. For an acid-base system



or

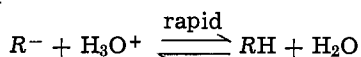


Thus

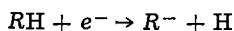
$$\begin{aligned} \left(\frac{[H_2O]}{[OH^-]}\right)_s : \left(\frac{[H_2O]}{[OH^-]}\right)_b &= \left(\frac{[H_3O^+]}{[H_2O]}\right)_s : \left(\frac{[H_3O^+]}{[H_2O]}\right)_b \\ &= \frac{[H^+]_s}{[H^+]_b} \\ &= \exp(-\phi_2 F/RT) \end{aligned}$$

where it has been assumed that the surface and bulk concentrations of water are equal; this will only be approximately true for the polar water molecules but will suffice for the present analysis. Thus as the electrode potential becomes more negative, the pH will decrease. The ratio  $[H^+]_s/[H^+]_b$  can amount to several orders of magnitude (9).

It is conceivable that the following equilibrium may be established between the specifically adsorbed organic anions (at the IHP) and the protonic species populating the OHP



followed by electron transfer thus



with subsequent hydrogen evolution

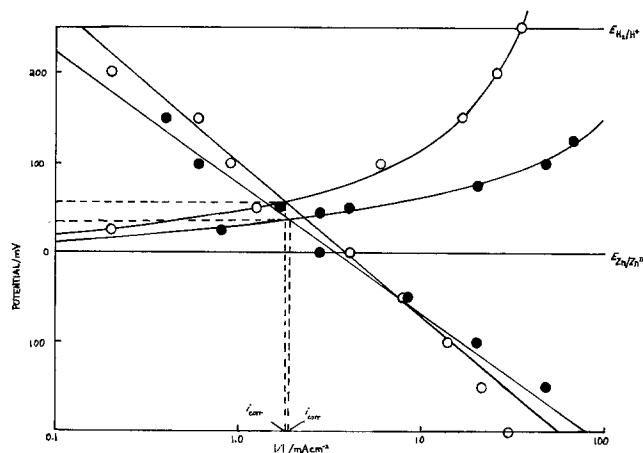


Fig. 5. Evans diagram.  $\circ$  = 10M NaOH,  $\bullet$  = 10M NaOH/0.1 v/o methacrylic acid, Y-axis: potential/mV, X-axis:  $|i|/mA\ cm^{-2}$ .

It follows from the above that the equilibrium between  $R^-$  and  $H_3O^+$  would be extremely potential dependent; the over-all process would correspond to the catalytic action of certain organics on hydrogen evolution cited in the literature (9) and could be an explanation for the observed pronounced increase in the rate of hydrogen evolution with increase in potential.

The anions appear also to catalyze the dissolution of zinc, a direct consequence of which is the earlier saturation of the diffusion layer in the anodic potential scan with the resulting marked cathodic displacement of peak I. The similar displacement in the active-passive transition presumably arises from a variation in the texture and composition of the film formed in the presence of the adsorbed species to that formed in pure electrolyte (4). It is possible that the anions serve as impurity centers for film nucleation. The multiple-peak effect observed probably arises from the organic anions adsorbing onto certain preferred sites on the zinc surface, as a result of which the film formed might be expected to vary in composition and thickness over the surface area of the electrode. Similar experimental work on the influence of  $SiO_3^-$  (4) where optical photomicroscopy was employed has shown that the film formed in the presence of the anion does in fact reduce in stages, giving rise to several reduction peaks on the cathodic going sweep of the anodic excursion. It is suggested that a similar effect is being observed in the case of the organic species. In contrast to  $SiO_3^-$ , the current maximum of peak I in the presence of the acrylic anions is much greater than in the pure electrolyte, suggesting that in the latter case the solubility of the zinc oxide-zinc hydroxide is substantially improved in the presence of these additives. It is possible that the anions stabilize micelles of  $ZnO-Zn(OH)_2$  by provision of a better-developed hydration sheath. Such a mechanism has been proposed (10-12) for the stabilization of electrolytically generated zincate solutions.

## Conclusions

Although the acrylic type anions have been shown to have a detrimental effect on the passivation of zinc in alkaline solution, results suggest that they could act as extenders for the zinc electrode at very low current drain. The influence of such additives on the corrosion rate of the zinc is only minimal.

The addition of these organics to the electrolyte of secondary zinc-silver oxide cells has been correlated (1) with an increase in cycle life, a phenomenon possibly related to a change in morphology of the electrodeposited zinc resulting from adsorption of the anions at the zinc-alkali interphase. In respect of rechargeable systems, the apparent catalytic influence which the ions have on hydrogen evolution is of interest, since such an effect could be a distinct disadvantage in high rate secondary cell applications.

Manuscript submitted July 9, 1975; revised manuscript received Sept. 26, 1975.

Any discussion of this paper will appear in a Discussion Section to be published in the December 1976 JOURNAL. All discussions for the December 1976 Discussion Section should be submitted by Aug. 1, 1976.

Publication costs of this article were partially assisted by the Timez Corporation.

#### REFERENCES

1. T. P. Dirkse, *This Journal*, **115**, 1169 (1968).
2. A. G. Palmer, Private communications.
3. R. W. Powers and M. W. Breiter, *This Journal*, **116**, 719 (1969).
4. R. W. Lewis and J. Turner, *J. Appl. Electrochem.*, To be published.
5. R. W. Powers, *This Journal*, **116**, 1652 (1969).
6. Z. Nagy and J. O'M. Bockris, *ibid.*, **119**, 1129 (1972).
7. P. Delahay, "Double Layer and Electrode Kinetics," John Wiley & Sons, Inc., New York (1966).
8. A. N. Frumkin, in "Advanced Electrochemistry," Vol. III, P. Delahay and C. W. Tobias, Editors, Interscience, New York (1963).
9. S. G. Mairanovskii, *J. Electroanal. Chem.*, **4**, 166 (1962).
10. V. N. Flerov, *Zh. Prikl. Khim.*, **30**, 1326 (1957).
11. V. N. Flerov, *ibid.*, **31**, 49 (1957).
12. V. V. Bakaev, V. N. Shirokov, and V. N. Flerov, *Electrokhimiya*, **7**, 376 (1971).

## Analysis of the Air-Formed Oxide Film on a Series of Iron-Chromium Alloys by Ion-Scattering Spectrometry

R. P. Frankenthal\* and D. L. Malm

Bell Laboratories, Murray Hill, New Jersey 07974

#### ABSTRACT

Low energy ion-scattering spectrometry has been used to obtain the composition-depth profiles of air-formed oxide films on a series of iron-chromium alloys. By using iron, chromium,  $\text{Fe}_2\text{O}_3$ ,  $\text{Cr}_2\text{O}_3$ , and  $\text{Fe}_{1.5}\text{Cr}_{0.5}\text{O}_3$  as standards, the atom composition ratios Cr/Fe and O/M ( $M = \text{Fe} + \text{Cr}$ ) have been obtained quantitatively as a function of sputtering time. The air/oxide interface appears to be oxygen-rich or metal-deficient. The Cr/Fe ratio is low at this interface but increases and peaks a few angstroms inside it. This ratio then diminishes continuously to its value in the alloy at the oxide/metal interface. The O/M ratio diminishes continuously from the air/oxide to the oxide/metal interface and appears to be independent of alloy composition. There is no region of constant concentration of any of the components. The average Cr content of the oxide varies linearly with alloy composition but exceeds the Cr content of the alloy. This may be associated with the method of surface preparation. Based on differences in the shape of the composition profiles, it is speculated that the distribution and bonding of cations in the oxide phase, not their concentration, differentiate the stainless from the nonstainless alloys.

There have been numerous studies of the composition of oxide films on austenitic stainless steels, e.g., Ref. (1-6). There have been relatively few studies on ferritic stainless steels or on the Fe-Cr binary system, and in particular of the effect of chromium content of the alloy on the composition of the oxide film. Yearian *et al.* (7) measured the lattice parameters of iron-chromium spinels. McBee and Kruger (8) measured the lattice parameters of the anodically formed passivating film on a series of iron-chromium alloys by transmission electron diffraction. The oxides on the alloys with relatively low chromium content are spinel-like, while the oxide on an Fe24Cr [Fe-24 weight per cent (w/o) Cr] alloy gave no diffraction pattern. They concluded that the films tend to become amorphous as the chromium content of the alloy is increased. Holliday and Frankenthal (9) characterized by soft x-ray spectrometry the anodically formed passivating film on the same alloys examined by McBee and Kruger (8) and interpreted their data to indicate that substantial changes occurred in film thickness and composition (Cr/Fe ratio) at an alloy Cr content of about 12%, the composition that separates the stainless from the nonstainless steels; this technique averages the composition across the film. Neither the atomic composition of the oxide film nor its variation with position from the air/oxide to the oxide/metal interface has been established.

Surface analysis techniques, such as photoelectron, Auger-electron, ion-scattering, and secondary-ion mass spectrometry, when combined with inert gas ion sputtering, are well suited for depth profiling thin oxide films. To make these techniques quantitative, however, it is necessary to have suitable calibration standards, to establish the variation of the sensitivities of the different elements with changes in the composition of the matrix, and to show that preferential enrichment of an element does not occur in any of the phases during sputtering.

In the present study, low energy ion-scattering spectrometry was used to obtain in a quantitative manner the composition profiles as a function of depth of the oxide film formed in air at room temperature on the same series of iron-chromium alloys used previously (8, 9), as well as on iron and on chromium. Low energy ion-scattering spectrometry (ISS), introduced by Smith (10, 11), has recently been reviewed by Buck and Poate (12). ISS is unique among the family of surface analysis techniques that have been introduced in recent years in that it examines only the outermost atomic layer of the surface. For surface analysis, a low energy (1-3 keV) monoenergetic beam of inert gas ions, e.g.,  $\text{He}^+$  or  $\text{Ne}^+$ , of mass  $M_1$  and energy  $E_0$  is directed at the surface atoms of mass  $M_2$ . A fraction of the incident ions will experience an elastic binary collision with the surface atoms; of these, another fraction will be reflected through a laboratory angle of  $90^\circ$  and have a reduced energy  $E_1$ . Providing the mass of the surface

\* Electrochemical Society Active Member.

Key words: chromium, ion-scattering spectrometry, iron, oxide, passivity, stainless steel.

Table I. Composition of alloys (a/o)

Nominal Cr content	Fe5Cr 5.1	Fe10Cr 10.2	Fe12Cr 12.7	Fe14Cr 15.1	Fe24Cr 25.0
--------------------	--------------	----------------	----------------	----------------	----------------

atom ( $M_2$ ) is greater than that of the incident ion ( $M_1$ ), the following relation is obeyed for these ions

$$\frac{E_1}{E_0} = \frac{M_2 - M_1}{M_2 + M_1} \quad [1]$$

Thus, for a well-collimated, monoenergetic, incident ion beam, the ion energy distribution of the scattered fraction collected at  $90^\circ$  will consist of a peak or series of peaks corresponding to each element on the surface, the height of which is proportional to the surface concentration of the element. The incident ion beam also sputters the surface, so that a series of spectra obtained as a function of sputtering time give a depth profile through the surface layer.

In addition to determining the composition profiles of the oxide films, the merits and limitations of ISS and of the spectrometer used in these studies are discussed in the context of the present study.

### Experimental

The materials studied were iron, chromium, and a series of iron-chromium alloys, the compositions [atom per cent (a/o)] of which are given in Table I. The oxide films on most of these alloys have been studied previously (8, 9).<sup>1</sup>

Each specimen was mechanically polished with a suspension of  $1 \mu\text{m}$  alumina particles in water, rinsed in distilled water, in methanol, dried in a stream of nitrogen, and stored in a plastic box at room temperature and humidity for at least 24 hr before analysis.

Films of  $\alpha\text{-Fe}_2\text{O}_3$  and  $\text{Cr}_2\text{O}_3$  several hundred angstroms thick were grown by the oxidation of iron and of chromium at  $417^\circ\text{C}$  (13) and  $700^\circ\text{C}$  (14), respectively. Their identity was confirmed by low angle reflection electron diffraction. The oxide  $\text{Fe}_{1.5}\text{Cr}_{0.5}\text{O}_3$  was prepared by heating measured quantities of  $\text{Fe}(\text{NH}_4)_2(\text{SO}_4)_2 \cdot 6\text{H}_2\text{O}$  and  $\text{CrNH}_4(\text{SO}_4)_2 \cdot 12\text{H}_2\text{O}$  in a porcelain crucible with a gas burner until the  $\text{H}_2\text{O}$  and  $\text{NH}_3$  had been expelled and then firing the residue at  $1000^\circ\text{C}$  for several hours. Chemical analysis indicated Fe-53.1 w/o, and Cr-16.2 w/o, giving an atom ratio Fe/Cr = 3.05. The balance, 3.07 w/o, is close to the desired O content of 30.4 w/o.

All spectra were obtained with a 3M Company Model 520 ion-scattering spectrometer. This instrument measures the scattered ion energy distribution only at  $90^\circ$  to the incident ion beam. Spectra were obtained both with  $^{20}\text{Ne}$  and with  $^3\text{He}$  as incident ions. In the  $^{20}\text{Ne}$  spectra, the peaks for Fe and Cr are well resolved; however, an O peak is not measured since it is lighter than the incident ion (Eq. [1]). When  $^3\text{He}$  is used as the incident ion, the O peak and the metal (M) peak are observed, but the Fe and Cr peaks are not resolved. All spectra were obtained with a noble ion gas pressure of  $2 \times 10^{-5}$  Torr, an incident ion energy of 2.5 keV, an ion beam current density of  $1 \mu\text{A}/\text{cm}^2$ , and an ion beam diameter of 0.32 cm at half-maximum intensity. The best vacuum obtained with this spectrometer before introduction of the inert gas was in the low  $10^{-8}$  Torr range, even after bake-out. A major fraction of the residual gas is  $\text{H}_2\text{O}$ , as determined with a quadrupole mass spectrometer.

### Results and Discussion

For iron, chromium, and each alloy a series of  $^{20}\text{Ne}$  spectra and a series of  $^3\text{He}$  spectra were recorded for different sputtering times (Fig. 1-3). In the initial spectra the desired peaks were generally masked by adsorbed surface impurities; however, after sputter etching approximately a monolayer, well-defined peaks

<sup>1</sup> The analyses given for these alloys in Ref. (8) and (9) are in weight per cent.

were obtained. Corrections were made for the overlapping of the spectra (Fig. 1) by calculating the fractional contribution of the overlapping spectrum to the sum of the spectra at the energy corresponding to the peak and weighting this for the relative concentrations of Fe and Cr. Correction for the background was made by drawing base lines as shown (Fig. 2 and 3). All results are expressed as peak height ratios, which are relatively insensitive to the manner in which the base lines are drawn.

From each  $^{20}\text{Ne}$  spectrum the Cr/Fe peak height ratio was calculated and plotted as a function of sputtering time (Fig. 4). The bell-shaped part of the curve represents the composition profile through the oxide from the air/oxide interface ( $t = 0$ ) to the oxide/alloy interface. The horizontal segment represents sputtering through the alloy. From each  $^3\text{He}$  spectrum the O/M ( $M = \text{Fe} + \text{Cr}$ ) peak height ratio was calculated and plotted as a function of sputtering time (Fig. 5). The oxygen peak does not vanish, hence the O/M ratio never approaches zero even after hours of sputtering. This is due to the continuous partial reoxidation of the active metal surface by the residual water vapor in the vacuum system when sputtering with  $^3\text{He}$ .

To interpret the data quantitatively, the relative sensitivity of each atomic species and its variation from metal to alloy must be determined, and the absence of preferential sputtering of any element from

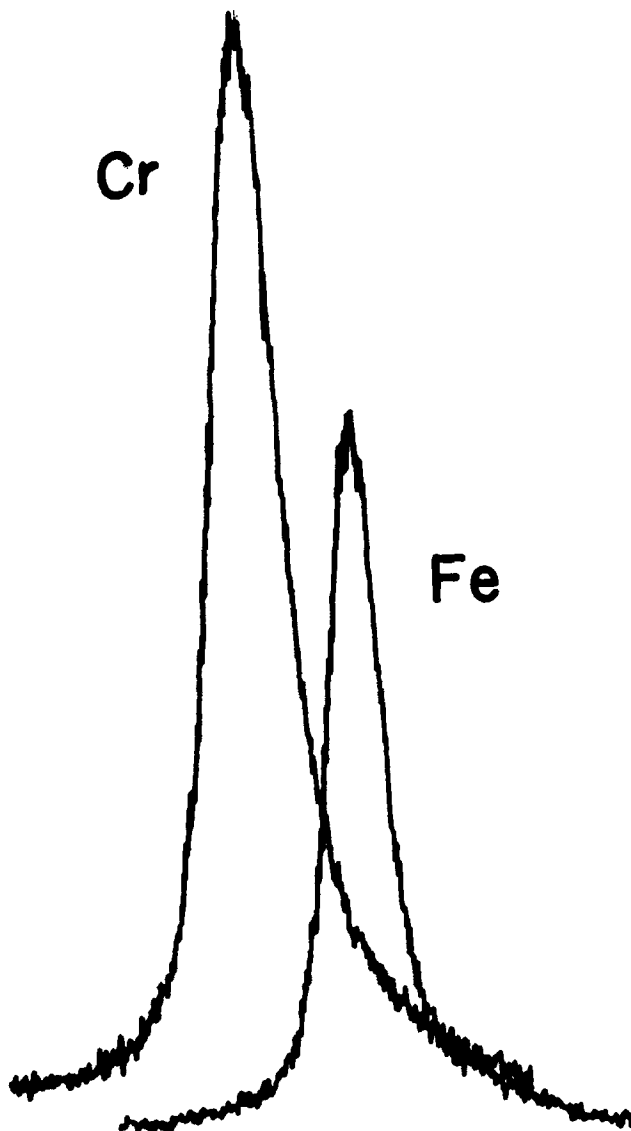


Fig. 1.  $^{20}\text{Ne}$  spectra of iron and of chromium metal after sputter etching the oxide films. Spectrum of each metal recorded on same graph to show relative position and overlap. Chromium sensitivity is 1.5 times that of iron.

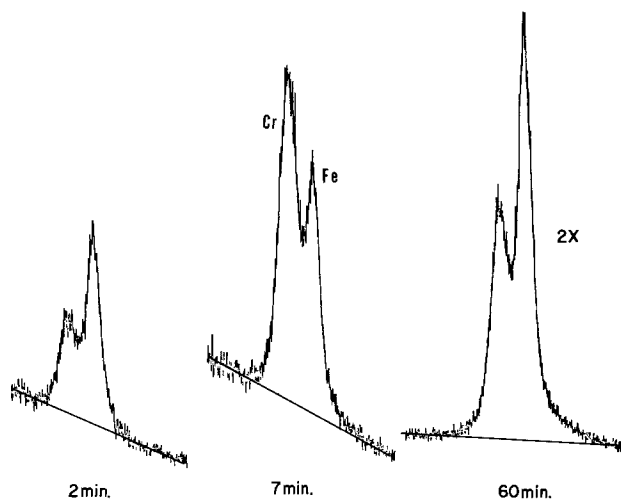


Fig. 2.  $^{20}\text{Ne}$  spectra of an Fe24Cr alloy at different sputtering times. Cr peak is at left and Fe peak is at right in each spectrum. Note change in relative peak heights of Fe and Cr with sputtering time. First two spectra are within the oxide; last is from the alloy.

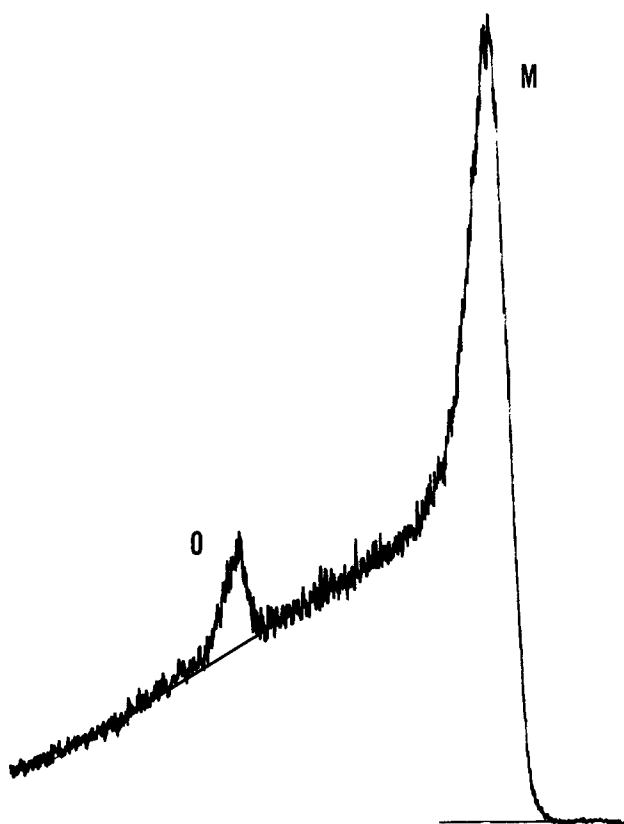


Fig. 3.  $^3\text{He}$  spectrum of an Fe24Cr alloy after sputtering for 5 min. Note low sensitivity of O peak (left) relative to M peak (right). Fe and Cr cannot be resolved with  $^3\text{He}$ .

the alloy or from the oxide surface must be established. From the  $^{20}\text{Ne}$  spectra of iron and of chromium (Fig. 1), obtained after the oxides had been sputter etched, the relative sensitivity of the two metals, i.e., the peak height ratio Cr/Fe, was  $1.5 \pm 0.1$ ; the limits represent the extremes from many measurements taken after various sputtering times and on different days. When the experimental Cr/Fe peak height ratio for each alloy is corrected for the relative sensitivity of the two metals, good agreement is observed between the corrected ratio and that obtained from chemical analysis of the alloy (Fig. 6). In  $^{20}\text{Ne}$  spectra obtained from a pellet of the oxide  $\text{Fe}_{1.5}\text{Cr}_{0.5}\text{O}_3$ , the average peak height ratio Cr/Fe was 0.52 in 15 measurements over a sputtering period of 180 min; the average devia-

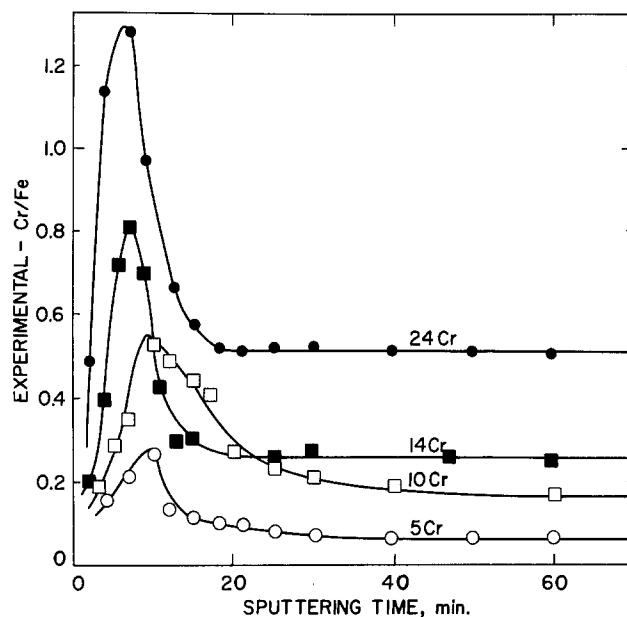


Fig. 4. Experimentally measured Cr/Fe peak height ratio as function of sputtering time with  $^{20}\text{Ne}$  for four iron-chromium alloys. Cr content of alloy is shown on each curve. Bell-shaped part of curve is composition profile through oxide, horizontal part is the bulk alloy.

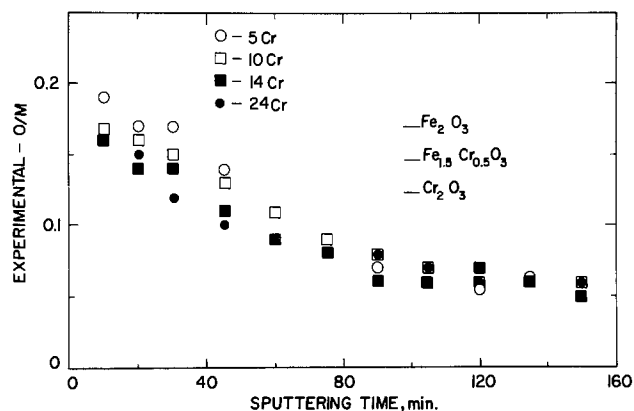


Fig. 5. Experimentally measured O/M peak height ratio as function of sputtering time with  $^3\text{He}$  for different alloys. Ratios for three oxide standards are also shown.

tion was 0.02 and the maximum deviation was 0.03. Correcting this peak height ratio for the relative concentration of Fe and Cr in the oxide gives a relative sensitivity Cr/Fe of 1.58, in agreement with that obtained from the metals.

From the  $^3\text{He}$  spectra of the oxides  $\text{Fe}_2\text{O}_3$  and  $\text{Cr}_2\text{O}_3$ , the peak height ratios  $\text{O}/\text{Fe} = 0.17$  and  $\text{O}/\text{Cr} = 0.12$  were obtained. Dividing the former by the latter gives a relative sensitivity Cr/Fe of 1.4, again in agreement with that found for the metals and the mixed oxide. The low sensitivity of oxygen, evidenced by the O/Fe and the O/Cr ratios, clearly limits the accuracy and precision of this result, as well as others calculated from O/M peak height ratios. The O/Fe and O/Cr sensitivities are obtained by dividing the above ratios by 3/2 to correct for the atomic composition of the oxides; this gives relative sensitivities of  $\text{O}/\text{Fe} = 0.11$  and  $\text{O}/\text{Cr} = 0.08$ .

All the above results are explicable if (a) the relative sensitivity  $\text{Cr}/\text{Fe} = 1.5 \pm 0.1$  is the same for the metals, the alloys, and the oxides, (b) the sensitivity of O is independent of the oxide composition, and (c) preferential sputtering does not occur, within the detection limits of the spectrometer. While other explanations of the results may be postulated, they require compensating effects that appear to be unreasonable. For example, the agreement between the ISS data and

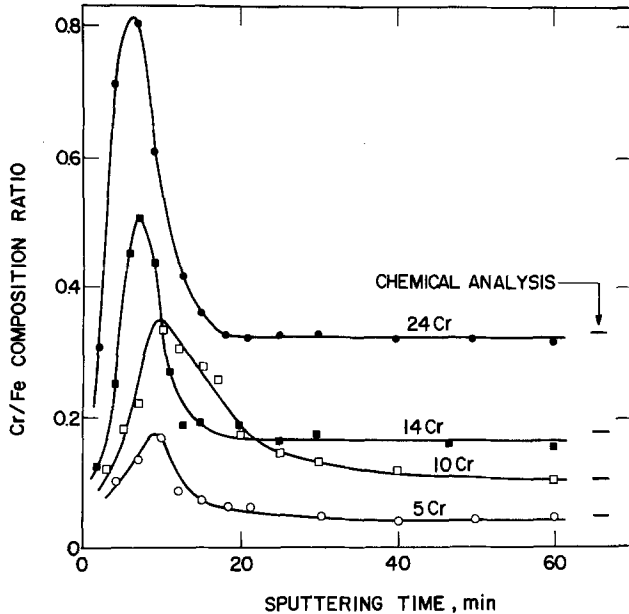


Fig. 6. Cr/Fe atom composition ratio as function of sputtering time for four iron-chromium alloys. Curves obtained after correcting experimental data for relative sensitivities of Fe and Cr in the oxides and in the alloys. Ratio for each alloy determined by chemical analysis is shown to right of each curve.

chemical analysis of the alloys (Fig. 6) could result from the preferential sputtering of one component compensating for changes in the relative sensitivities of Cr and Fe with changes in alloy composition; alternatively, the O sensitivity could be dependent on oxide composition but changes in a manner that is compensated for by changes in the sensitivity of Cr or Fe and/or by preferential sputtering of one of the elements. Since there is no evidence for any of these effects, the simpler explanation given above is preferred.

Having established that the relative sensitivity Cr/Fe is independent of phase, the data of Fig. 4 were corrected for the relative sensitivity to give the atomic composition ratios through the oxides and into the alloys (Fig. 6). The curve for the Fe12Cr alloy (not shown) lies between those for the Fe10Cr and Fe14Cr alloys.

The atom composition ratio O/M is now calculated. The data of Wehner and co-workers (15, 16) and of Oechsner (17) indicate that the sputtering rates for helium and neon are approximately proportional to their masses, all other conditions being the same. Assuming then that the sputtering rate for  $^{20}\text{Ne}$  is 20/3 times that for  $^3\text{He}$ , the abscissas in Fig. 5 and 6, i.e., the sputtering times, can be related. Thus one obtains from Fig. 6 the Cr/Fe atom composition ratio corresponding to the O/M ratio at any given time in Fig. 5. From this and from the relative sensitivities of the elements, the atom composition ratio O/M was calculated as a function of sputtering time (Fig. 7). The data include all the alloys and iron. The error bars indicate extremes and are within experimental error, which is  $\pm 0.1$ . The data for chromium fall on the initial part of the curve, but at later times the points lie slightly above those shown. This may be due to the greater affinity of chromium for oxygen,<sup>2</sup> which makes it a better getter for the residual water vapor in the vacuum system. The lack of dependence of the O/M ratio on alloy composition, unless accidental, confirms the assumption that the sputtering rates are proportional to the masses of the sputtering ions.

The sputtering rates were not measured. They may be estimated from (19)

$$S = 0.2Y\bar{V}I_p + d^{-2} (\text{Å/hr}) \quad [2]$$

<sup>2</sup> Standard free energies of formation for  $\text{Cr}_2\text{O}_3$ ,  $\text{Fe}_2\text{O}_3$ , and  $\text{Fe}_3\text{O}_4$  are -167, -118, and -121 kcal/mol O<sub>2</sub>, respectively (18).

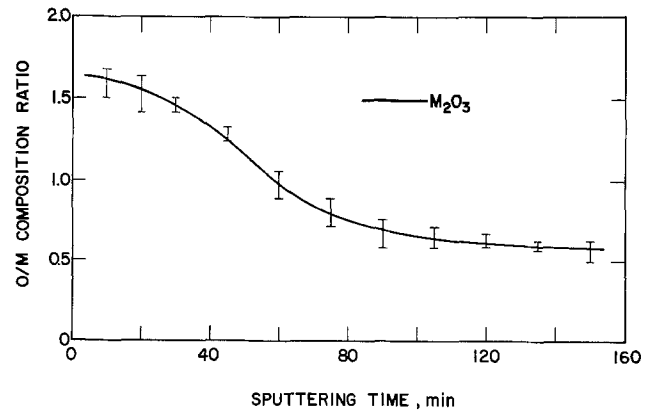


Fig. 7. O/M atom composition ratio as a function of sputtering time for five alloys and iron after correcting for relative sensitivities and relative sputtering rates with  $^3\text{He}$  and  $^{20}\text{Ne}$ . Ratio corresponding to  $\text{M}_2\text{O}_3$  is also shown.

in which  $S$  is the rate,  $Y$  is the sputtering yield,  $\bar{V}$  is the average atomic volume in  $\text{Å}^3$ ,  $I_p$  is the ion beam current in nA, and  $d$  is the ion beam width at half-maximum intensity in mm. The yield of iron sputtered with 2.5 keV Ne ions is estimated to be 2 atoms/ion by extrapolating the data of Wehner and co-workers (15, 16). The other factors in the above equation are known, so that a sputtering rate of approximately 300-400 Å/hr is calculated for iron. The rate for chromium is similar. It has been estimated (20) that chromium is sputtered 5 to 10 times faster than  $\text{Cr}_2\text{O}_3$ . Assuming that iron and the alloys also sputter 5 to 10 times faster than their oxides, we estimate the sputtering rate of the oxides to be  $60 \pm 20$  Å/hr with  $^{20}\text{Ne}$ . The sputtering rate of the oxides with  $^3\text{He}$  is of the order of 10 Å/hr. From Fig. 6 and assuming a sputtering rate of 60 Å/hr with  $^{20}\text{Ne}$ , the oxide thicknesses are estimated to be 20 Å for the high-Cr alloys (Cr > 12%) and 30-40 Å for the low-Cr ones (Cr < 12%), in agreement with previous results (9). These differences in thickness are masked during sputtering with  $^3\text{He}$  (Fig. 7) by the continuous reoxidation of the surface by the residual water vapor.

Each point on the composition profiles is an average over all crystallographic planes, grain boundaries, and surface defects. Nonuniform sputtering and mixing due to knock-on effects have not been considered. These would smear out compositional variations. Thus sharp changes in composition over a distance of a few angstroms may be lost, and the true peak in the Cr/Fe composition ratio in the oxides may be somewhat greater.

From the composition profiles (Fig. 6 and 7) it appears that the composition of the oxide film changes continuously with depth. At the air/oxide interface the film appears to be an oxygen-rich or metal-deficient  $\text{M}_2\text{O}_3$  with a low Cr content for all the alloys. Immediately beneath the surface layer the Cr content rises sharply, peaks, and then decays to its level in the bulk alloy. At its maximum the Cr content is two to three times that in the alloy. However, even for the Fe24Cr alloy the maximum observed Cr/Fe ratio is only about 0.8. The interface between the oxide and the alloy appears quite sharp, although less so for the low-Cr alloys. This is evident in Fig. 6 but not in Fig. 7, probably because of the inability to attain an oxygen-free surface. There is no region of constant O/M composition ratio, indicating that there is no layer of finite thickness in which an oxide of constant composition exists.

The average Cr/Fe composition ratio in the oxide film is given by

$$\left(\frac{\text{Cr}}{\text{Fe}}\right)_{\text{avg}} = \frac{1}{t_{0/a}} \int_0^{t_{0/a}} \left(\frac{\text{Cr}}{\text{Fe}}\right) dt \quad [3]$$

in which  $t$  is the sputtering time and  $t_{0/a}$  is the time

to sputter to the oxide/alloy interface.  $(\text{Cr}/\text{Fe})_{\text{avg}}$  may be obtained by integrating the area under each curve in Fig. 6. Then the average fraction of metal or cations in the film that is Cr is given by

$$\left(\frac{\text{Cr}}{\text{Cr} + \text{Fe}}\right)_{\text{avg}} = \frac{(\text{Cr}/\text{Fe})_{\text{avg}}}{1 + (\text{Cr}/\text{Fe})_{\text{avg}}} \quad [4]$$

This is plotted as a function of alloy composition in Fig. 8. The dashed line in this figure shows the result that would be obtained if these were equal. It is seen that there is an excess of Cr in the oxide over that in the alloy. The excess increases with increasing alloy Cr content. The slope of the plot is 1.35. No change in slope is observed around the alloy composition of 12Cr, as had previously been suggested (9). The reason for this difference between the two studies may be associated with the different means of surface and oxide film preparation or with the different analytical techniques. In the earlier x-ray study, the films were produced by anodic oxidation; also, this technique measures a signal that emanates from the bulk of the oxide, not only from the surface as with ISS. This latter point will be further discussed below.

The excess chromium in the film indicates a loss of iron. Since the profiles do not show an excess of iron at the oxide/alloy interface, it must have been lost during the mechanical polishing operation. This may be due to one of the following: (i) The rate of chromium metal dissolution under the polishing conditions is slower than that of iron, (ii) chromium passivates more readily than iron under these conditions, or (iii) the iron oxides or hydroxides formed are more soluble than the chromium ones. Since this result appears to have been affected by the technique of surface preparation, it is not clear whether the result is relevant to our understanding of the mechanism of passivation. However, it may be relevant technologically since similar techniques are in common use.

Despite these considerations, it is well known that the corrosion resistance of steels in most environments is governed more by the Cr content of the steel than by the means of surface preparation. The effect of alloy Cr content on the electrochemical and corrosion properties of steels is greatest around 12% (21, 22), leading to the hypothesis that a major change in film composition may occur at this alloy composition. This is not evident from Fig. 8 or from the variation of the peak Cr/Fe ratio in Fig. 6 as a function of alloy composition. An examination of the data in Fig. 6 does show some differences between the low-Cr and the high-Cr

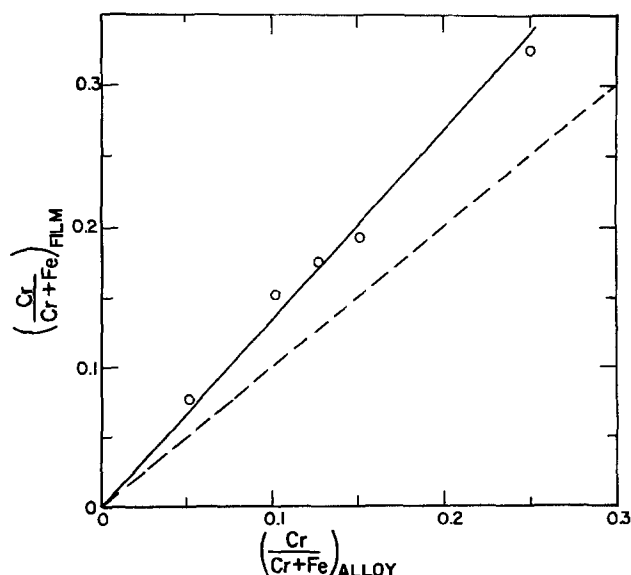


Fig. 8. Average oxide film Cr content vs. alloy Cr content, showing a linear relation from 0 to 25% Cr in the alloy. Dashed line represents equal concentrations in the oxide and alloy.

steels. First, the high-Cr alloys have a thinner oxide than the low-Cr ones. Second, the distribution of Cr in the low-Cr alloys is more skewed than in the high-Cr ones. Third, the maximum in the Cr/Fe composition ratio appears at a sputtering time of  $6 \pm 1$  min for the high-Cr alloys and at  $10 \pm 1$  min for the low-Cr ones. The corresponding times on the curve of Fig. 7, i.e., the times to sputter to the same depth with  $^3\text{He}$ , are 40 and 70 min; the O/M atom composition ratios for these times are 1.3 and 0.8, respectively.

From this we speculate that the "stainless" behavior may not be associated with the quantity of chromium in the film but with the distribution, the defect structure, and the bonding of the cations. For the stainless alloys, the Cr content of the oxide is greatest when the O/M atom composition ratio is in a range corresponding to  $\text{M}_2\text{O}_3$  or  $\text{M}_3\text{O}_4$ . But for the nonstainless alloys, the maximum Cr content of the oxide occurs in a region which is highly oxygen deficient,  $\text{O}/\text{M} < 1$  or  $\text{MO}_{1-x}$ . Thus the shift in the position of the maximum in the Cr/Fe composition ratio between the stainless and the nonstainless alloys is accompanied by a change in the proportions in which the oxygen is bonded to Cr and Fe and hence in the valence states of the cations. Unfortunately, ISS gives no information on the valence state. However, since the free energy of formation of  $\text{Cr}_2\text{O}_3$  is about 50 kcal/mol more negative than that of  $\text{Fe}_2\text{O}_3$  or  $\text{Fe}_3\text{O}_4$  (18), it appears likely that the average valence state of Fe decreases more rapidly with distance into the oxide than that of Cr.

*Comparison of ISS and soft x-ray spectrometry data.*—Both techniques have shown that the oxide film on the low-Cr alloys is thicker than that on the high-Cr ones. However, the data from the soft x-ray study (9) suggested that the Cr content of the oxide increased more sharply between the 10Cr and the 14Cr alloys than is expected on the basis of the change in alloy composition. This was not found in the ISS study. This discrepancy probably results from the different resolving powers of the two techniques. ISS resolves each atomic layer, while soft x-ray spectrometry obtains its signal from throughout the oxide. For the latter technique, the signal from beneath the surface is attenuated exponentially with depth according to Beer's law. The maximum in the Cr/Fe composition ratio occurs at 6 min for the high-Cr alloys and at 10 min for the low-Cr ones (Fig. 6). Thus the Cr x-ray signal from the oxide on the low-Cr alloys is attenuated more than that from the high-Cr ones, resulting in a greater difference in the signal intensity than dictated by the average Cr content of the oxide.

### Summary

Composition-depth profiles have been obtained for the oxides on a series of iron-chromium alloys ranging in composition from 0 to 25 a/o Cr. From the spectra of a series of standards, it was determined that the relative sensitivities of the oxide components are independent of alloy or oxide composition and phase. No preferential sputtering of any component is observed, within the resolution of the spectrometer. The profiles show there is no region of constant concentration of any component within the oxide. The O content diminishes continuously from the air/oxide to the oxide/alloy interface. The Cr content is low at the air/oxide interface but then rises sharply and peaks a few angstroms inside that interface; it then decreases continuously to its value in the alloy at the oxide/alloy interface. The average Cr content of the oxide varies linearly with alloy composition and exceeds the Cr content of the alloy. This may be associated with the method of surface preparation. It is speculated that differences in distribution and bonding of the cations within the oxide phase distinguish the stainless from the nonstainless alloys.

### Acknowledgments

We wish to thank Mrs. I. D. Payne for recording many of the ISS spectra, G. W. Kammlott for the elec-



tron diffraction data, and M. Robbins for help in preparing the iron-chromium oxide standard.

Manuscript submitted July 22, 1975; revised manuscript received Sept. 23, 1975. This was Paper 90 presented at the Dallas, Texas, Meeting of the Society, Oct. 5-10, 1975.

Any discussion of this paper will appear in a Discussion Section to be published in the December 1976 JOURNAL. All discussions for the December 1976 Discussion Section should be submitted by Aug. 1, 1976.

Publication costs of this article were partially assisted by Bell Laboratories.

#### REFERENCES

1. N. A. Nielsen and T. N. Rhodin, Jr., *Z. Elektrochem.*, **62**, 707 (1958).
2. C. T. H. Stoddart and E. D. Hondros, *Nature Phys. Sci.*, **237**, 90 (1972).
3. J. B. Lumsden and R. W. Staehle, *Scripta Met.*, **6**, 1205 (1972).
4. N. Takahashi and K. Okada, *Japan. J. Appl. Phys.*, **11**, 1580 (1972).
5. J. P. Coad and J. G. Cunningham, *J. Electron Spectr.*, **3**, 435 (1974).
6. R. Schubert, *J. Vacuum Sci. Technol.*, **11**, 903 (1974).
7. H. J. Yearian, J. M. Kortright, and R. H. Langenheim, *J. Chem. Phys.*, **22**, 1196 (1954).
8. C. L. McBee and J. Kruger, *Electrochim. Acta*, **17**, 1337 (1972).
9. J. E. Holliday and R. P. Frankenthal, *This Journal*, **119**, 1190 (1972).
10. D. P. Smith, *J. Appl. Phys.*, **38**, 340 (1967).
11. D. P. Smith, *Surface Sci.*, **25**, 171 (1971).
12. T. M. Buck and J. M. Poate, *J. Vacuum Sci. Technol.*, **11**, 289 (1974).
13. E. J. Caule, K. H. Buob, and M. Cohen, *This Journal*, **108**, 829 (1961).
14. E. A. Gulbransen and K. Andrew, *ibid.*, **99**, 402 (1952).
15. N. Laegreid and G. K. Wehner, *J. Appl. Phys.*, **32**, 365 (1961).
16. D. Rosenberg and G. K. Wehner, *ibid.*, **33**, 1842 (1962).
17. H. Oechsner, *Z. Physik*, **261**, 37 (1973).
18. "Selected Values of Chemical Thermodynamic Properties," NBS Circular 500. National Bureau of Standards, Department of Commerce, Washington, D. C. (1952).
19. R. E. Honig, in "Advances in Mass Spectrometry," Vol. 6, A. R. West, Editor, Elsevier Publishing Co., Barking, England (1974).
20. R. N. Yasko and L. J. Fried, *Rev. Sci. Instr.*, **43**, 335 (1972).
21. H. H. Uhlig, "Corrosion and Corrosion Control," 2nd ed., chap. 5 and 6, John Wiley & Sons, Inc., New York (1971).
22. H. Kaesche, "Die Korrosion der Metalle," chap. 7, Springer Verlag, Berlin and New York (1966).

## Anodic Oxide Films on Nickel in Acid Solutions

B. MacDougall\* and M. Cohen\*

National Research Council of Canada, Division of Chemistry, Ottawa, Ontario, Canada K1A 0R9

#### ABSTRACT

The formation and removal of steady-state oxide films on nickel electrodes anodized in  $\text{Na}_2\text{SO}_4$  solutions of pH 8.4-2.0 have been examined. Surface activity measurements showed that complete removal of all of these oxide films was possible in solutions of pH  $\leq 2.8$  with moderate cathodic treatments. Instability of the pH in the vicinity of the electrode was the probable cause of oxide nonreducibility at pH  $> 2.8$ . The oxide was removed cathodically by a galvanostatic charging technique in pH 2.8 and a relative measure of the amount of oxide remaining at any time during the cathodic pulse could be obtained by subsequent application of an anodic potential step. No significant chemical dissolution of the oxide occurred during cathodic charging, in contrast to the situation on open circuit. However, the quantity of oxide on anodized nickel could not be determined from the total cathodic charge passed in its removal because of simultaneous massive hydrogen evolution. This was not the case with the oxide on electropolished nickel where galvanostatic charging techniques could be used to accurately determine the oxide thickness.

In a previous paper (1), electropolished nickel was shown to have a thin (6-8Å) film of NiO of somewhat expanded lattice parameter (by ca. 2%) which could be reduced with sufficient cathodic polarization in pH 8.4  $\text{Na}_2\text{SO}_4$ . In contrast, the steady-state oxide on nickel electrodes anodized in pH 8.4  $\text{Na}_2\text{SO}_4$  was a 9-12Å film of NiO, with normal lattice parameter, which could not be cathodically reduced in the neutral solution. Consequently, cathodic coulometry in neutral solution could not be used to determine film thickness of the anodically formed oxide. While x-ray emission and anodic potential step techniques provided alternative methods for measuring steady-state nickel oxide coverages in neutral solution, they could not be used for accurate determination of very small oxide coverages (e.g., less than a monolayer). A sensitive *in situ* cathodic treatment in an electrolyte where oxide reduction is possible, e.g., a more acid solution, should provide a method for accurately determining small oxide coverages and also for characterizing and comparing the steady-state oxides formed at different potentials.

\* Electrochemical Society Active Member.

Key words: passivity, nickel oxide, cathodic reduction, chemical dissolution.

There have been suggestions in the literature (2-7) that the oxide film formed on anodized nickel in acid solutions is also susceptible to cathodic removal in these acid solutions. However, little quantitative work has been done in either determining the extent of oxide removal at various pH's or in characterizing the nickel oxides formed. The present work involves an investigation in the pH range 8.4-2.0 of the cathodic reduction behavior of the steady-state oxide film on anodized nickel electrodes. The oxides formed at different pH's are compared with regard to both electrochemical and electron-optical properties. At the lower pH values investigated, the usefulness of the cathodic galvanostatic charging technique for determining oxide thicknesses on both anodized and electropolished nickel is examined. While mainly steady-state films are discussed here, the investigation provides a basis for further work dealing with the early and intermediate stages of nickel oxidation in solution.

#### Experimental

*Specimen preparation.*—Polycrystalline specimens,  $1 \times 2.5$  cm, were prepared from zone-refined nickel

sheet of 99.996% purity as described elsewhere (1). They were degreased with benzene, chemically polished (1), electropolished for 2 min at 23°C in a 57% sulfuric acid solution at ca. 0.5 A-cm<sup>-2</sup> and then annealed at 800°C in a vacuum of 10<sup>-8</sup> Torr. The specimens were electropolished again immediately before use in an experiment. A (111) nickel single crystal was used to obtain information regarding the lattice parameters of nickel oxides.

**Reference electrode.**—Potentials quoted in this paper are referred to the Hg<sub>2</sub>SO<sub>4</sub> electrode in 0.15N Na<sub>2</sub>SO<sub>4</sub> (+0.665V<sup>1</sup> with respect to the standard reversible hydrogen electrode).

**Solution.**—Deaerated solutions of 0.15N Na<sub>2</sub>SO<sub>4</sub> had their pH's adjusted to various values in the range 8.4-2.0. Experiments were conducted at 25°C.

**Apparatus.**—A Princeton Applied Research Model 175 universal programmer was used in conjunction with a Wenking fast-rise potentiostat to obtain the potentiodynamic sweep profiles. These profiles and the galvanostatic cathodic charging curves were recorded on a Hewlett-Packard Model 7004B X-Y recorder. A high-speed Brush recorder was used to follow the initial rapid decrease of current after an anodic potential step treatment. Two types of electrochemical cell were used, one having the counter and recording electrodes in the same compartment and the other having them in different compartments separated by a glass frit and stopcock. The former cell was used for potential step experiments since large, initial current surges were involved. Both cells contained 50 ml of electrolyte and gave similar potentiodynamic sweep and galvanostatic charging results.

**Electrochemical procedure.**—After electropolishing, the electrodes were immersed in deaerated Na<sub>2</sub>SO<sub>4</sub> solutions of various pH's under cathodic polarization sufficient to remove the prior 6-8Å film of NiO. The oxide-free electrodes were then anodized using either the potentiodynamic sweep or potential step methods, the latter being most frequently used. Unless specified otherwise, it is to be assumed that the potential step method was employed. An anodization time of 1 hr was used to establish the steady-state condition of oxide coverage (1). The effect of various cathodic treatments on the anodized electrodes was analyzed in terms of the charge under the anodic peak on a subsequent anodic sweep. Electrochemical transfer experiments were carried out by anodizing for 1 hr at one pH, then immediately transferring through the air to a fresh, deaerated solution of another pH where the anodized specimen was given a cathodic reduction. The effect of this air exposure on the steady-state oxide films was investigated by comparing, in pH 2.8 solutions, the open-circuit potential-time curves for anodized nickel with and without the air exposure. The similarity of results indicated that the brief air exposure did not significantly alter the steady-state oxide on anodized nickel.

Cathodic charging curves were obtained on both electropolished and anodized nickel electrodes in pH 2.8 Na<sub>2</sub>SO<sub>4</sub>, the electropolished specimens being immersed in the solution under cathodic polarization. At any time during this reduction, the relative degree of activity of the electrode could be obtained by interrupting the cathodic charging with an anodic potential step and measuring the anodic charge passed. The anodic potential step technique was also used to study chemical dissolution of the steady-state oxide in the more acid solutions. In this case, the relative activity of anodized nickel electrodes was determined after various times on open circuit. If the solution was to be analyzed for nickel, after either the open-circuit or

cathodic charging experiments, the nickel electrodes were transferred to a fresh electrolyte after anodization.

## Results

**Reduction of nickel oxide in acid solutions.**—Figure 1 shows anodic potentiodynamic *i*-*V* profiles obtained on nickel electrodes at pH of 4.0 and 2.8 with a sweep rate of 10 mV-sec<sup>-1</sup>. The cathodic currents have been omitted for simplicity and the sweep limits have been adjusted to take account of the 60 mV shift of the nickel oxide formation potential with unit pH change. Profiles 1 and 3 were obtained on electropolished nickel electrodes, after a prior cathodic treatment of 2 min at -1.2 and -1.27V at pH 2.8 and 4.0, respectively. At both pH values, cathodic treatment of electropolished nickel at more negative potentials and/or for longer periods of time did not lead to any increase in the charge under the anodic peaks, i.e., the quantity of nickel dissolved remained the same.<sup>2</sup> Profiles 2 and 4 are the second anodic sweeps after anodic cycling to 0 and -0.07V and cathodic cycling to -1.0 and -1.07V in pH 2.8 and 4.0, respectively. The very small difference in anodic peak charges at pH 2.8 (profiles 1 and 2) disappeared and the sweeps became identical with a slightly more vigorous cathodic treatment of the anodized nickel. At pH 4.0 the difference between the first and successive sweeps remained large even after a vigorous cathodic treatment of the anodized nickel electrode. This is shown by profile 5 which is the anodic sweep on the anodized electrode after a prior cathodic treatment of 10 min at -1.37V. It should be noted that the anodic treatments specified in Fig. 1 probably did

<sup>2</sup> Cf. Ref. (1, 8) where solution analysis by atomic absorption spectroscopy showed that almost all the charge under the anodic peak is accounted for by Ni<sup>2+</sup> in solution.

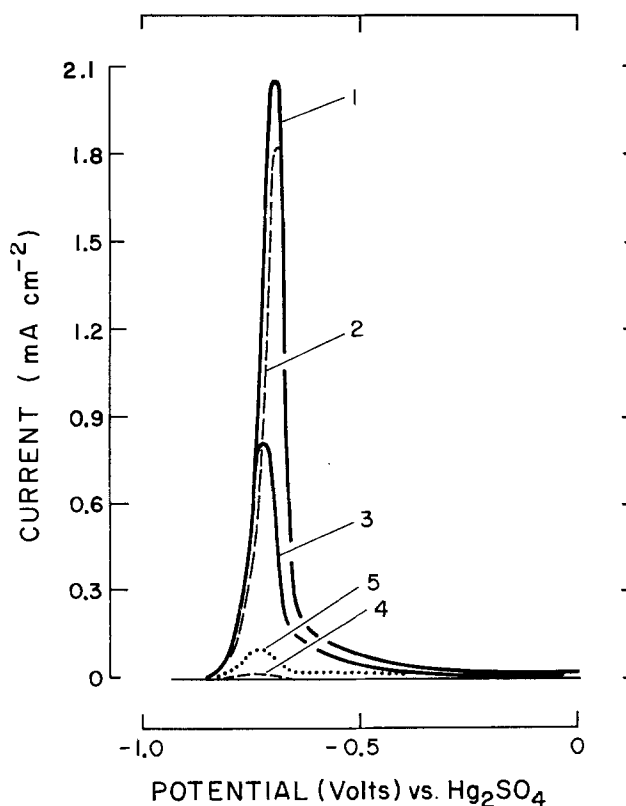


Fig. 1. Anodic potentiodynamic current-potential profiles for nickel electrodes at 10 mV-sec<sup>-1</sup> at pH 2.8 (profiles 1 and 2) and pH 4.0 (profiles 3 to 5) under various electrode conditions: (profiles 1 and 3) after a cathodic reduction of electropolished nickel sufficient for removal of the prior oxide (see text); (profiles 2 and 4) second anodic sweep after initially cycling to 0 and -0.07V at 10 mV-sec<sup>-1</sup> and then cathodic cycling -1.0 and -1.07V, respectively; profile 5 anodic sweep on anodized nickel in pH 4.0 after cathodic reduction at -1.37V for 10 min.

<sup>1</sup> This potential was measured against both a saturated calomel electrode and hydrogen reference electrode. The hydrogen reference was used with a 0.15N Na<sub>2</sub>SO<sub>4</sub> solution acidified to pH 2.8 with H<sub>2</sub>SO<sub>4</sub>, and there was thus no liquid junction potential.

not give steady-state oxide films on nickel because of the transient nature of the sweep technique. However, the same principles apply in the situation where anodic holding is used to produce an equilibrium oxide film.

The surface activity of a nickel electrode at any pH will be defined here as the ratio of the anodic peak charge during a potentiodynamic sweep on that electrode to the charge obtained on an oxide-free nickel surface with a similar sweep (e.g., curve 1, Fig. 1). Figure 2 shows the dependence of electrode surface activity on solution pH after a standard anodic and cathodic treatment. Since this work was concerned with the steady-state oxide on anodized nickel, the anodic treatment employed in Fig. 2 was 1 hr at  $V_a = \{0.17V - (0.06V)(pH)\}$ , i.e.,  $V_a = 0V$  at pH = 2.8. This anodization potential was well within the passive region (Fig. 1) and the 1 hr anodization time allowed the current to fall to  $<2 \times 10^{-7} \text{ A-cm}^{-2}$  with little further decrease of current with time. A standard cathodic treatment of 3 min at  $V_c = \{-1.03V - (0.06V)(pH)\}$ , i.e.,  $V_c = -1.2V$  at pH = 2.8, completely removed the oxide on anodized nickel only in solution of pH  $\leq 2.8$ . At pH  $> 2.8$ , the amount of surface activity which could be recovered was highly dependent on solution stirring by bubbling  $N_2$  through the cell during the cathodic treatment; this was not the case at pH  $\leq 2.8$ . Also shown in Fig. 2 is the effect of a more severe cathodic treatment, i.e., 10 min at  $V_c = \{-1.33V - (0.06V)(pH)\}$ , i.e.,  $V_c = -1.5V$  at pH 2.8, on nickel surfaces given the same anodic treatment as described above. Even with this more intense cathodic polarization, little surface reactivation was observed above a pH of ca. 4.0. Measurement of the solution pH showed that the variation during a run was less than 0.1 pH unit over the range examined (2.0-5.0).

Figure 3 shows the effect of cathodic reduction potential at pH 2.8 on surface activity of a nickel electrode previously anodized for 1 hr at 0V in the same solution. Using a 3 min polarization time, the minimum cathodic potential required for complete activation of the anodized nickel electrode in pH 2.8 is seen to be close to  $-1.05V$ .

*Oxide characterization as a function of pH.*—The oxide thickness was determined by x-ray emission spectroscopy at solution pH values of 8.4, 4.5, and 2.8. The anodic treatment was that used in Fig. 2, i.e., 1 hr for all pH's at an equivalent NiO formation potential. The

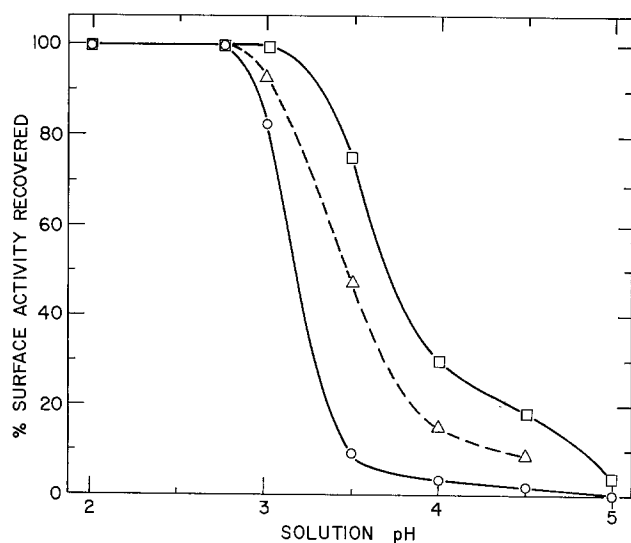


Fig. 2. Variation of surface activity with pH of solution in which standard anodic and cathodic treatment is applied. The prior anodization is for 1 hr at  $V_a = \{0.17V - (0.06V)(pH)\}$  with the subsequent cathodic treatment being:  $\Delta$ , 3 min at  $V_c = \{-1.03V - (0.06V)(pH)\}$  with  $N_2$  bubbling during treatment;  $\circ$ , as in  $\Delta$  but without  $N_2$  bubbling;  $\square$ , 10 min at  $V_c = \{-1.33V - (0.06V)(pH)\}$  with  $N_2$  bubbling during treatment.

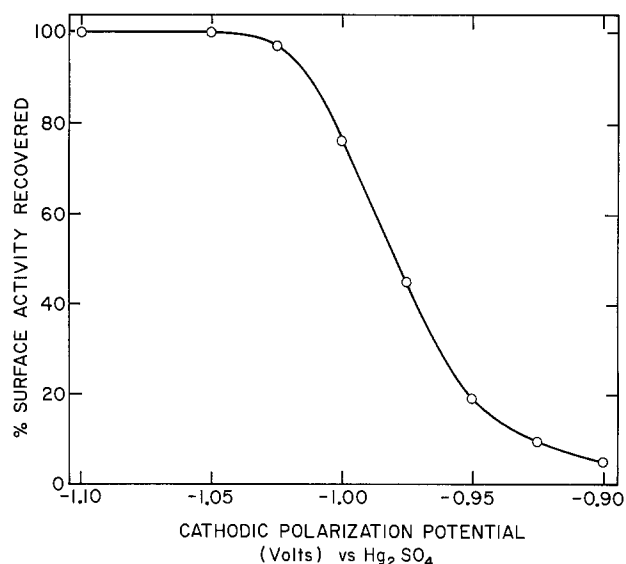


Fig. 3. Dependence of surface activity of a nickel electrode previously anodized for 1 hr at 0V in pH 2.8 on the cathodic potential at which the electrode is polarized for 3 min in the same solution.

oxide thickness was the same within experimental error, i.e., 9-12Å, at each pH investigated. At pH 2.8, this oxide thickness was independent of anodization potential over the range  $-0.4$  to  $+0.3V$ , similar to results in pH 8.4 (1). Reflection electron diffraction patterns were taken of a (111) nickel crystal surface given the above anodic treatment at pH = 8.4, 4.5, and 2.8. All patterns were those of NiO and were similar with regard to (i) measured lattice parameter (which was closer to stoichiometric NiO than that on electropolished nickel), (ii) oxide epitaxy, and (iii) grain size (1).

To check on the electrochemical properties of oxides formed at different pH values, a nickel electrode was anodized at  $-0.34V$  for 1 hr in pH 8.4  $Na_2SO_4$  and then transferred to a cell with a pH 2.8 solution. The anodized electrode was given a cathodic treatment in the pH 2.8 solution which is just sufficient for removal of the oxide formed at 0V for 1 hr in the same solution, i.e., 3 min at  $-1.05V$  (see Fig. 3). This treatment gave a total reactivation of the surface toward nickel dissolution on a subsequent anodic sweep indicating complete removal of the oxide formed in neutral solution. The same experiment was also performed in the reverse direction, i.e., the steady-state anodization was done in pH 2.8 at 0V for 1 hr with the cathodic reduction in pH 8.4 (for 10 min at  $-1.45V$ ). The surface activity on the following anodic sweep in the same pH 8.4 solution was very low, the oxide formed in pH 2.8 being as nonreducible in pH 8.4 as the oxide formed in pH 8.4 itself.

*Determination of oxide coverage.*—Figure 4a shows the cathodic galvanostatic charging curves at  $20 \mu\text{A-cm}^{-2}$  in pH 2.8 for nickel electrodes which had been given a prior anodization at 0V for 15 sec, 1 min, and 1 hr in the same solution. Also shown is the charging curve obtained upon immersion of a freshly electropolished nickel electrode into a pH 2.8  $Na_2SO_4$  solution. Figure 4b shows the charging curves for electropolished and anodized nickel electrodes with a more sensitive time base. The eventual, steady cathodic potential at  $20 \mu\text{A-cm}^{-2}$  (Fig. 4a) was the same in all cases except for an anodization of 1 hr at 0V. In this case, the potential was still positive by 0.12V to that expected for an oxide-free surface after 1 hr of cathodic polarization. This situation persisted even after an intervening potentiostatic cathodic reduction of 10 min at  $-1.3V$ , a treatment which should have removed any remaining oxide (Fig. 3). No detectable roughening of the surfaces was observed by either electron diffraction or

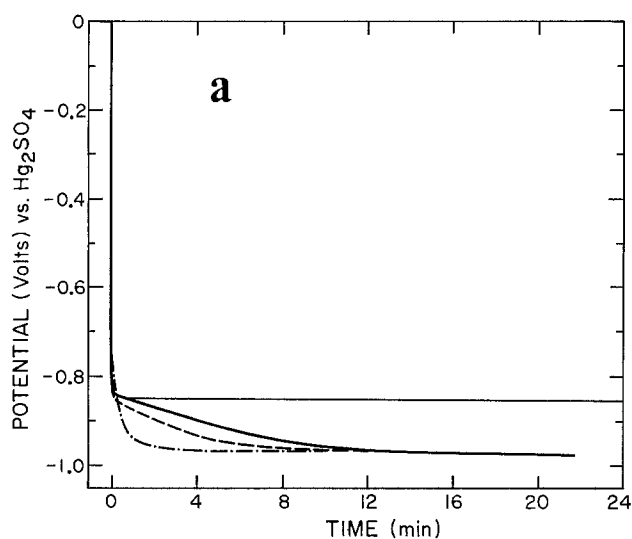


Fig. 4a. Cathodic galvanostatic charging curves, at  $20 \mu\text{A-cm}^{-2}$ , of nickel electrodes in various electrochemical states in pH 2.8  $\text{Na}_2\text{SO}_4$ : —●—●, electropolished nickel; ---, anodized at 0V for 15 sec; ■, anodized at 0V for 1 min; —, anodized at 0V for 1 hr.

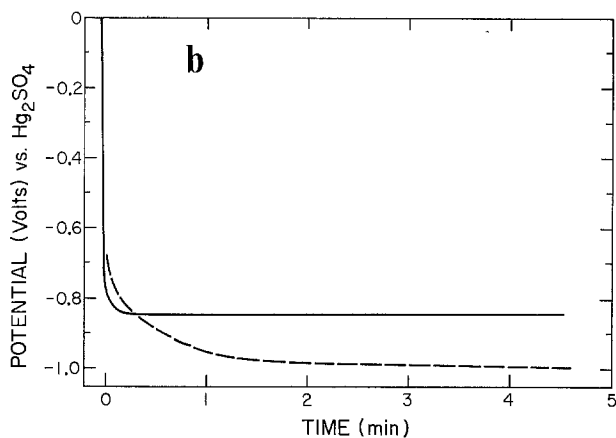


Fig. 4b. As in (a) but with a more sensitive time base: ---, electropolished nickel; —, anodized at 0V for 1 hr.

replica electron microscopy after any of the electrochemical treatments referred to in Fig. 4a, eliminating this as a possible explanation.

The surface activity of the electrode can be determined at any time during the cathodic charging by stepping the potential back to 0V and comparing the anodic charge passed with that obtained from a known oxide-free surface (i.e., cathodically reduced electropolished nickel). Figure 5 shows the results obtained when this technique was applied to electrodes which had been anodized at 0V for either 1 min or 1 hr and then cathodically charged at  $20 \mu\text{A-cm}^{-2}$ . As expected, the rate of surface reactivation was more rapid after the 1 min anodization than the 1 hr anodization. It is also seen that the steady potential at a cathodic current of  $20 \mu\text{A-cm}^{-2}$  can vary with the prior anodization treatment of the electrode even if the surface becomes oxide free.

To determine whether possible changes in the electrolyte composition are responsible for this potential shift, two experiments were carried out. First, a freshly electropolished nickel electrode was immersed with cathodic polarization into the "used"  $\text{Na}_2\text{SO}_4$  solution which had given the charging curve in Fig. 4a after 1 hr at 0V. The potential rapidly adjusted itself to the correct value expected for an oxide-free surface (i.e., ca. -1.0V). Second, an electrode which had been anodized for 1 hr at 0V was transferred to a fresh pH 2.8

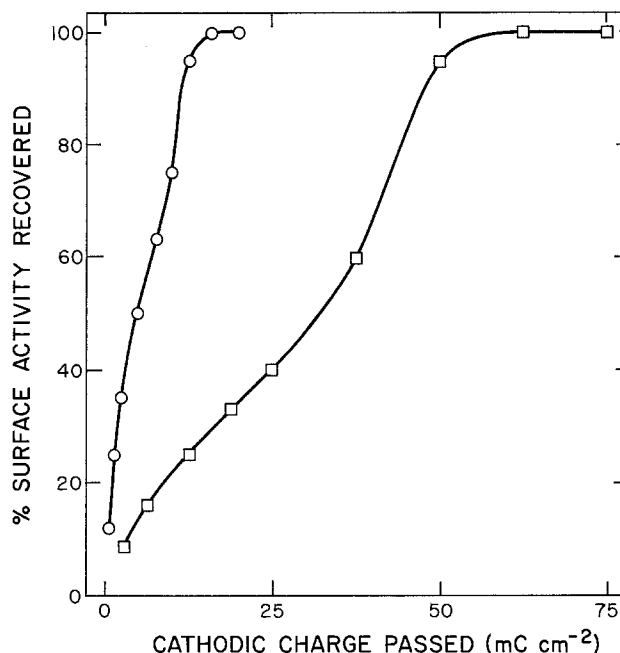


Fig. 5. Dependence of percentage of surface activity recovered on the charge passed during cathodic galvanostatic charging at  $20 \mu\text{A-cm}^{-2}$  of nickel electrodes anodized at 0V for either 1 min (○) or 1 hr (□). pH of anodization and reduction was 2.8.  $0.47 \text{ mC-cm}^{-2}$  corresponds to one oxygen atom per surface nickel;  $1 \text{ mC-cm}^{-2} = 6.9\text{\AA} \text{ NiO}$ .

solution and cathodically polarized at  $20 \mu\text{A-cm}^{-2}$ . The resulting steady potential was still 0.12V positive to that expected for the oxide-free surface. These results indicate that possible changes in the electrolyte during the 1 hr anodization at 0V were not responsible for the 0.12V anodic shift in the steady potential for hydrogen evolution at  $20 \mu\text{A-cm}^{-2}$ .

The anodic potential step technique was thus used in conjunction with cathodic charging curves to determine the time (and charge) required for complete removal of the oxide formed after either 1 min or 1 hr at 0V. From Fig. 4 and 5 the charges are seen to be ca.  $15 \text{ mC-cm}^{-2}$  for the 1 min film and  $65 \text{ mC-cm}^{-2}$  for the 1 hr film formed at 0V. These charges correspond to 85 and  $370\text{\AA}$  of NiO. In comparison with the x-ray emission data which indicates a steady-state film thickness of 9-12 $\text{\AA}$ , these values are much too high and indicate that cathodic side reactions were playing a major role during oxide reduction of anodized nickel.

To investigate the possibility of  $\text{Ni}^{2+}$  reduction contributing to the cathodic charges given in Fig. 5, solutions were analyzed for  $\text{Ni}^{2+}$  at times of 1 min and 1 hr after stepping the potential of an initially oxide-free electrode to 0V. The quantities of  $\text{Ni}^{2+}$  removed from the electrode surface were 1.8 and  $2.4 \mu\text{g-cm}^{-2}$ , respectively. Galvanostatic cathodic charging curves were obtained after prior anodizations at 0V for 1 min and 1 hr in solutions containing 9 and  $12 \mu\text{g-cm}^{-2}$  of dissolved  $\text{Ni}^{2+}$ , i.e., concentrations five times more than are found after a single anodization. The results were not altered by the increased concentrations of  $\text{Ni}^{2+}$ . Further experiments were conducted to check the influence of solution agitation during the anodization at 0V on the cathodic charges consumed in the subsequent galvanostatic reactivation of the surface. No effect was observed with the anodization times employed, these being 1 sec, 1 min, and 1 hr at 0V.

The cathodic charging curve obtained after 1 hr anodization at 0V did not show the arrest structure expected for oxide reduction. With a more sensitive potential scale (not shown here), a slight increase of voltage with time was observed during the first 50 min of polarization. It was, however, insignificant when compared with the definite arrest structures evident on electrodes given a short anodization at 0V (15 sec and

1 min) and on electropolished nickel (Fig. 4a and b). The structure within the charging curve of electropolished nickel was only resolved when the sensitivity of the time base was increased considerably (Fig. 4). The arrest charge indicates an NiO thickness of ca. 7Å on electropolished nickel, in excellent agreement with the x-ray emission results.

**Role of chemical dissolution in oxide removal.**—In order to determine the stability of the steady-state oxide on anodized nickel toward chemical dissolution in the pH 2.8 solution, previously anodized electrodes were left in the solution on open circuit for various times. The effect of this treatment on the NiO coverage could be determined by subsequent initiation of an anodic potential step back to the anodization potential. Figure 6 shows the effect of time on open circuit on the potential and surface activity of a nickel electrode which was previously anodized at 0V for 1 hr in the same solution. Identical results were obtained with anodized nickel electrodes which were transferred to a fresh pH 2.8 solution with brief exposure to air during the transfer. For times on open circuit of less than ca. 50 min, very little surface reactivation was observed. However, at longer times the activity increased very rapidly with complete surface reactivation occurring within 110 min. The beginning of the significant increase in surface activity is seen to correspond with the abrupt change in the open-circuit potential to ca. -0.75V. Table I gives the corresponding quantities of nickel in solution for various times on open circuit in a fresh pH 2.8 solution. Also given is the amount of nickel in solution after surface reactivation has been achieved by cathodic charging, i.e., after 50 min at  $-20 \mu\text{A}\cdot\text{cm}^{-2}$  (see Fig. 5).

### Discussion

In a previous paper (1) it was shown that the steady-state oxide on anodized nickel electrodes could not be cathodically reduced in the pH 8.4  $\text{Na}_2\text{SO}_4$  solution. Cathodic characterization of the oxide was thus impossible and electropolishing in sulfuric acid before cathodic reduction was required for reactivation of the nickel surface after anodization. The present investigation was undertaken to determine whether the oxide film on anodized nickel electrodes is susceptible to complete cathodic removal at pH more acidic than 8.4. The results were positive and an "optimum" pH was established at which to investigate the anodization of nickel electrodes by cathodic reduction techniques.

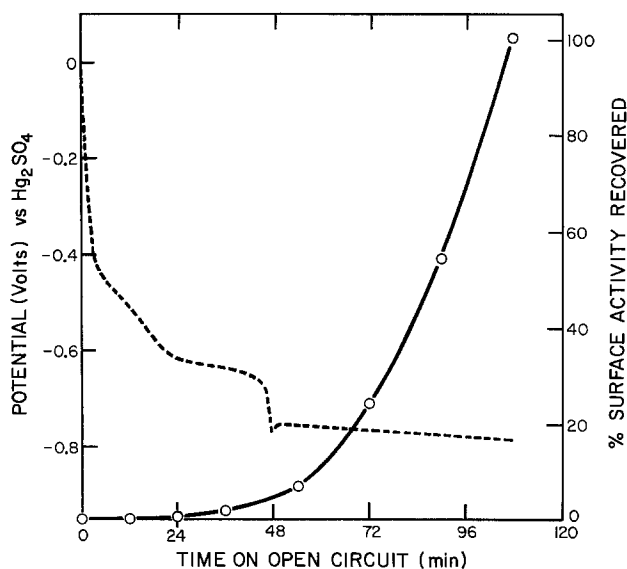


Fig. 6. Dependence of percentage of surface activity recovered on the time at open circuit in pH 2.8 after a previous anodization for 1 hr at 0V in pH 2.8 (○). Also shown is the corresponding variation of open-circuit potential with time (---).

Table I. Quantity of  $\text{Ni}^{2+}$  dissolved in pH 2.8 solutions after various treatments of nickel electrodes which have been previously anodized at 0V for 1 hr in a separate pH 2.8 solution

Treatment of anodized nickel	$\text{Ni}^{2+}$ dissolved* ( $\mu\text{g}\cdot\text{cm}^{-2}$ of electrode)
30 min on open circuit	<0.5
60 min on open circuit	1.3
75 min on open circuit	2.0
110 min on open circuit	3.5
50 min at $-20 \mu\text{A}\cdot\text{cm}^{-2}$	<0.5

\* The amount of  $\text{Ni}^{2+}$  in 12A of NiO is  $0.6 \mu\text{g}\cdot\text{cm}^{-2}$ .

The first part of the present work consisted of producing and characterizing an oxide-free surface as a reference. From the work in neutral solution (1), it is known that the oxide film on a freshly electropolished nickel electrode can be reduced with a moderate cathodic treatment and the same approach was adopted here (Fig. 1). When the charge under the current peak on a subsequent anodic sweep is a maximum, i.e., not increased by further cathodic treatment of the electropolished nickel, the surface is defined as being free of oxide and having a surface activity of 100%. Conversely, any diminution of this maximum charge is taken to indicate the presence of oxide on the surface. Development of detailed relationships between surface activity and oxide coverage will be discussed in a later paper. However, the present results indicate that the steady-state oxide formed on nickel electrodes anodized in the passive (potential) region can be completely removed at  $\text{pH} \leq 2.8$  with a moderate cathodic treatment. At  $\text{pH} > 2.8$ , oxide removal became more difficult with increasing pH and at pH 5.0 even vigorous cathodic treatments (Fig. 2) did not lead to any substantial surface reactivation. For further experimental work, a pH of 2.8 was chosen rather than a lower pH because of the smaller amount of anodic nickel dissolution and correspondingly lower degree of surface roughening at the higher pH.

The difference in cathodic reduction behavior of anodized nickel at different pH's may be due to a combination of two factors: (i) The oxide formed at lower pH (2.8) is different from that formed at higher pH (4.5 or 8.4), i.e., the former is more easily reducible; and/or (ii) the cathodic reduction reaction is possible at lower pH but not at higher pH. There were several important results which indicate that the oxide formed in the steady state at pH 2.8 was similar to that formed under the same conditions at pH 4.5 or 8.4. First, the oxide thickness as determined by x-ray emission spectroscopy (1) was the same at pH = 8.4, 4.5, and 2.8, i.e., 9-12Å, a thickness which has been shown to be independent of anodization potential within experimental error at pH 2.8 and 8.4. Second, the electron diffraction patterns of a (111) nickel crystal surface anodized at pH 8.4, 4.5, or 2.8 were similar with regard to measured lattice parameters, epitaxy, and grain size of the oxide. Third, the electrochemical transfer experiments indicated that the oxide formed at pH 2.8 was nonreducible in pH 8.4 electrolyte, exactly like the oxide formed at pH 8.4; they also showed that in the pH 2.8 solution, the oxide formed at pH 8.4 was as easily removed as that formed at pH 2.8. These various results indicate that in the pH range 8.4-2.8 the characteristics of the oxide formed on anodized nickel in the steady state are not a function of the pH of anodic formation. The variation of extent of oxide removal with pH must therefore be associated with the cathodic reduction reaction. The pH dependence of this reaction ( $\text{NiO} + 2\text{H}^+ + 2e = \text{Ni} + \text{H}_2\text{O}$ ) is the most probable cause of the present results even though the bulk solution pH did not change significantly over the range examined. The pH instability in the vicinity of the electrode during the cathodic treatment as a result of accompanying molecular hydrogen evolution is indi-

cated by the increased extent of surface reactivation with  $N_2$  bubbling at  $pH \cong 3.0$  (Fig. 2).

In neutral solution, cathodic coulometry could not be used to determine oxide thickness because of the stability of the oxide in  $pH$  8.4. Alternatively, the anodic potential step technique, with the total anodic charge corrected for that portion associated with  $Ni^{2+}$  dissolution, provided an accurate method of evaluating the oxide thickness. In the more acidic solutions (e.g.,  $pH$  2.8) the portion of the anodic charge associated with oxide formation was smaller in comparison with that due to nickel dissolution and accurate thickness determinations by the potential step technique were not possible. Since cathodic reduction in the  $pH$  2.8  $Na_2SO_4$  solution resulted in complete removal of the steady-state oxide on anodized nickel, the possibility of making accurate *in situ* oxide thickness measurements seemed to exist. There were, however, two potential sources of error associated with: (i) chemical dissolution of the oxide in the  $pH$  2.8 solution, and (ii) parallel cathodic side reactions. Chemical dissolution of the oxide during its galvanostatic removal would, in the absence of cathodic side reactions, lead to the estimated oxide coverage being less than the true value. In fact, the estimated coverage was much larger than the true oxide coverage, indicating that (ii) must play a major role but still saying nothing about (i). To obtain information on the possible role of (i), the open-circuit experiments must be correlated with the cathodic charging result.

The open-circuit experiments showed (Fig. 6) that the rate of recovery of surface activity was slow for times corresponding to those required for cathodic galvanostatic removal of the oxide at  $20 \mu A\text{-cm}^{-2}$  (i.e., 50 min). After the 50 min induction period the rate of recovery of surface activity was very rapid. These results can be explained in terms of a nonuniform chemical attack of the oxide film [e.g., see Ref. (9-14)] with subsequent exposure of localized areas of the nickel surface. This could explain the abrupt change in open-circuit potential after ca. 40 min exposure (Fig. 6). Nickel dissolution can occur by a corrosion mechanism from those oxide-free areas on open-circuit and cause undermining of the remaining oxide on the surface. The 40 min induction period would thus be the time required for localized chemical attack to bare enough nickel surface for oxide undermining and subsequent rapid surface reactivation to occur. When the anodized nickel electrode is given a cathodic galvanostatic polarization, the rate of surface reactivation does not change abruptly after a certain percentage of activity is recovered (Fig. 5). This is due to the absence of oxide undermining in this latter situation since the electrode is being cathodically protected, with respect to nickel dissolution, by the applied cathodic current. These conclusions are supported by the observation that while considerable nickel is found in solutions after surface reactivation has been achieved by open-circuit dissolution, very little dissolved nickel is found in solution after surface reactivation by cathodic charging (Table I). The results thus indicate that chemical dissolution of the oxide did not play a significant role during cathodic galvanostatic charging, eliminating the first potential source of error associated with oxide thickness measurements.

From the number of coulombs passed during cathodic charging, the thickness of the steady-state oxide on anodized nickel was calculated to be ca. 45 times greater than that determined by the x-ray method. Hence, cathodic side reactions played a major role during cathodic galvanostatic removal of the oxide on anodized nickel. The most probable cathodic side reactions are hydrogen evolution and  $Ni^{2+}$  deposition from solution. Parallel  $Ni^{2+}$  deposition did not appear to play a significant role since the galvanostatic cathodic charges, which were highly dependent on the time of prior anodization at 0V, were independent of  $[Ni^{2+}]$  in solution. The diffusion-limited current can be

calculated for  $Ni^{2+}$  deposition from the solution containing  $0.24 \mu g\text{-ml}^{-1}$  (i.e.,  $4 \times 10^{-6} M Ni^{2+}$ ) dissolved during 1 hr anodization at 0V with solution agitation to give a uniform concentration. The corresponding maximum charge for  $Ni^{2+} + 2e \rightarrow Ni$  during a 50 min cathodic reduction in a static solution is  $0.7 mC\text{-cm}^{-2}$ . This charge is insignificant when compared with the  $65 mC\text{-cm}^{-2}$  actually passed (Fig. 5). Another confirmatory observation was that the cathodic charges passed in galvanostatic reactivation of the surface (Fig. 4a and 5) were independent of solution agitation during the 1 sec, 1 min, and 1 hr anodizations at 0V. This last result can be due to either of the following: (i) The  $Ni^{2+}$  concentration near the electrode does not affect the measured cathodic charge, since it is probable that this concentration will be lower with solution agitation (this should be especially true after only 1 sec at 0V because of the short time available for diffusion of  $Ni^{2+}$  to the bulk of the solution), or (ii) these times at 0V were sufficient for establishment of a more uniform concentration distribution even in the static solutions. This second possibility was the assumption made when calculating the diffusion-limited current; hence the same conclusions concerning the role of  $Ni^{2+}$  apply. The above observations thus eliminate the possibility of both  $Ni^{2+}$  near the electrode and in the bulk of the solution contributing to the measured cathodic charge. In a paper to be published, it will be shown that the  $Ni^{2+}$  deposition only plays a significant role at much more cathodic potentials (ca.  $-1.3V$ ), giving rise to a diffusion-controlled current peak on a cathodic potentiodynamic sweep.

The above conclusions leave hydrogen evolution as the cathodic side reaction responsible for the low current efficiency of  $NiO$  reduction. Indeed, it was shown earlier (1) that the rate of hydrogen evolution is 250% higher on anodized nickel than oxide-free nickel in  $pH$  8.4, i.e., the oxide on anodized nickel (almost stoichiometric  $NiO$ ) is an excellent catalyst for hydrogen evolution. With the exception of the 1 hr anodization at 0V, the results in Fig. 4a can be interpreted in relation to an increase in the overpotential for hydrogen evolution as the oxide is slowly removed by cathodic reduction at  $20 \mu A\text{-cm}^{-2}$ . The cathodic potential reaches a maximum when the nickel surface becomes oxide free. After a 1 hr anodization at 0V, the situation is more complex with the cathodic potential appearing to reach its steady value very rapidly after initiation of the cathodic polarization (Fig. 4a and b). With a more sensitive potential axis, a very small potential arrest can be observed during the 50 min reactivation of the surface. However, the steady cathodic potential on the oxide-free surface at  $20 \mu A\text{-cm}^{-2}$  is ca. 0.12V more anodic after the 1 hr at 0V than after either the shorter anodizations or the electropolishing. This anomalous result was not due to changes in either composition of the electrolyte or roughness of the nickel surface during the 1 hr at 0V. The possible explanations remaining are: (i) Some other property of the nickel surface, e.g., distribution of active sites or hydride formation, is influenced by the 1 hr at 0V and subsequent cathodic reduction; (ii) the nickel surface was not completely free of oxide after the 50 min of cathodic charging. With regard to (ii), the anodic potential step, used to determine surface activity, may have: (a) been insensitive to the remaining oxide; or (b) helped to remove it physically by undermining. If remaining oxide on the surface is the explanation, then it is a very difficult species to reduce since more severe cathodic polarization at  $-1.3V$  after 1 hr anodization at 0V did not lead to any change in the 0.12V shift. Such an oxide species (or coverage) would be able to lower significantly the overpotential for hydrogen evolution and also not have a detectable influence on the extent of nickel dissolution with subsequent anodization. The present investigation does not allow a resolution of these various possibilities.

As a consequence of the results presented in this paper, it appears that the x-ray emission technique must be used to determine equilibrium oxide thicknesses (i.e., 9-12Å) on anodized nickel in the pH 2.8 solutions. On the other hand, the oxide on electro-polished nickel (of somewhat expanded NiO lattice) is removed readily with a high current efficiency, the determined oxide coverage value being in agreement with that from x-ray analysis.

### Summary

1. The oxide formed by steady-state oxidation of nickel at pH 8.4 had the same electrochemical and electron-optical characteristics as that formed under similar conditions at pH 4.5 or 2.8.

2. While this oxide was not susceptible to cathodic reduction at pH 8.4, it could be removed at pH 2.8 with the appropriate cathodic treatment.

3. The oxide films formed by the steady-state oxidation at pH 2.8 were 9-12Å in thickness. In this thickness range, *in situ* cathodic reduction could not be used to measure the thickness due to the very large charge contribution from parallel hydrogen evolution.

4. The oxide films are removed only slowly on open circuit and dissolve by a combination of local attack and undermining.

### Acknowledgment

The authors thank Dr. D. Mitchell for the x-ray determination of oxygen content on nickel.

Manuscript submitted Aug. 14, 1975; revised manuscript received Oct. 1, 1975.

Any discussion of this paper will appear in a Discussion Section to be published in the December 1976 JOURNAL. All discussions for the December 1976 Discussion Section should be submitted by Aug. 1, 1976.

Publication costs of this article were partially assisted by the National Research Council of Canada.

### REFERENCES

1. B. MacDougall and M. Cohen, *This Journal*, **121**, 1152 (1974).
2. A. B. Ijzermans, *Corrosion Sci.*, **10**, 113 (1970).
3. N. Sato and G. Okamoto, *This Journal*, **111**, 897 (1964).
4. I. A. Ammar and S. Darwish, *Electrochim. Acta*, **11**, 1541 (1966).
5. J. Osterwald and H. H. Uhlig, *This Journal*, **108**, 515 (1961).
6. G. T. Burstein and G. A. Wright, *Electrochim. Acta*, **20**, 95 (1975).
7. J. O'M. Bockris, A.K.N. Reddy, and B. Rao, *This Journal*, **113**, 1133 (1966).
8. B. MacDougall and M. Cohen, *ibid.*, **122**, 383 (1975).
9. M. J. Pryor and U. R. Evans, *J. Chem. Soc.*, **1949**, 3330.
10. M. J. Pryor and U. R. Evans, *ibid.*, **1950**, 1259, 1266.
11. M. J. Pryor, *ibid.*, **1950**, 1274.
12. K. Nii, *Corrosion Sci.*, **18**, 181 (1969).
13. J. W. Diggle, in "Oxides and Oxide Films," J. W. Diggle, Editor, Vol. 2, p. 281, Marcel Dekker, New York (1973).
14. D. Yoke, A. Riga, R. Greef, and E. Yeager, *Electrochim. Acta*, **13**, 1351 (1968).

## The Theory of Rate Limitation

M. A. Fullenwider\*

RKP Industries, Incorporated, Allentown, Pennsylvania 18103

### ABSTRACT

The theory of rate limitation is reviewed, and two possible cases are further distinguished. Mathematical expressions are developed for one case where gaussian behavior is simulated. Recent experimental results are taken to be evidence in favor of a strong interstitial-phonon interaction at the surface. Situations are discussed where rate limitation may be misinterpreted as concentration-dependent diffusion.

The theory of rate limitation in diffused systems was treated by Miller and Smits (1) in the 1950's. Since then, experimental results with the hydrogen-palladium system (2) have pointed to a type of rate limitation not treated by these authors. It is the purpose of this paper: (i) to further distinguish the two cases, (ii) to propose a mechanism for the second case, (iii) to develop mathematical expressions for the second case that pertain to the situation where it simulates the gaussian profile, and (iv) to bring out some points concerning the implications of rate limitation in the physical theory of diffused systems.

### Physical Rate Limitation

As brought out previously (3), in the formation of semiconductor junctions by solid-state diffusion there is the possibility of two types of rate limitation. The type discussed by Miller and Smits (1) and corresponding to the radiation boundary condition of Carslaw and Jaeger (4) we will call here "physical rate limitation." The reason for this terminology is that the radiation boundary condition in the theory of heat transfer (in the absence of convection) corresponds to the passage of heat into a substrate covered with a thin "skin" of

a poorly conducting substance. In the theory of diffusion the skin must then be composed of a material with a smaller diffusion coefficient than that of the substrate, e.g., an oxide coating of some sort. Figure 1 illustrates the potential energy profile for such a situation. In Fig. 1 the skin is between  $- \delta$  and  $x = 0$ . Here the potential

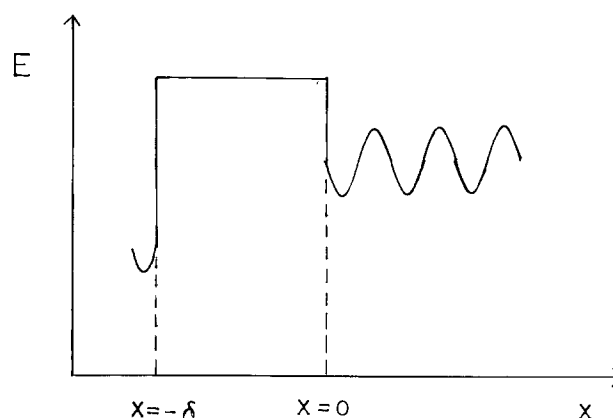


Fig. 1. Potential energy profile corresponding to the radiation boundary condition.

\* Electrochemical Society Active Member.

Key words: semiconductor diffusion, rate limitation, concentration-dependent diffusion, hydrogen in metals.



hump at the surface has a square configuration because the skin must be supposed to have some finite thickness larger than the interatomic distance of the substrate.

Physical rate limitation derives from the boundary condition at the surface ( $x = 0$ )

$$[c_e - c(0, t)]K = -D[\partial c(x, t)/\partial x]_{x=0} \quad [1]$$

where  $x$  is distance into the semi-infinite substrate,  $c_e$  is the final equilibrium concentration at  $x = 0$  as time becomes infinite,  $D$  is the diffusion coefficient, and  $K$  is a constant analogous to an electrical conductance in that a region of small size and small diffusivity may be the equal of a large region of larger diffusivity. If a more detailed knowledge for a particular system, *i.e.*, of the thickness and diffusivity of the skin, were available, then, of course, it would be possible to construct a better model, but this information is not usually known. In the mathematical treatment of the physical case the boundary condition, Eq. [1], remains the same for the two cases corresponding to (a) the error function complement profile and (b) the gaussian profile. In case (b) the quantity  $c_e$  is simply set equal to zero (5), since the final equilibrium concentration of a unit instantaneous point source must be zero at large times. The mathematical expressions are, case (a)

$$c(x, t) = c_e \left\{ \operatorname{erfc} [x/2(Dt)^{1/2}] - \exp [(Kx - K^2t)/D] \operatorname{erfc} \left[ \frac{x}{2(Dt)^{1/2}} + K(t/D)^{1/2} \right] \right\} \quad [2]$$

and case (b)

$$c(x, t) = [a/(\pi Dt)^{1/2}] \exp(-x^2/4Dt) \times \left\{ 1 - K(\pi t/D)^{1/2} \exp \left[ \frac{x}{2(Dt)^{1/2}} + K(t/D)^{1/2} \right]^2 \right\} \times \operatorname{erfc} \left[ \frac{x}{2(Dt)^{1/2}} + K(t/D)^{1/2} \right] \quad [3]$$

where  $a$  is the quantity of substance at the surface initially in moles-cm<sup>-2</sup>.

### Chemical Rate Limitation

An endothermic potential energy profile representing the situation for what we will call here "chemical rate limitation" is shown in Fig. 2. Here the potential step at the surface has the usual chemical shape, and its thickness is roughly the same as the interstitial spacings of the substrate. The expression corresponding to the error function complement profile, representing a strong interstitial-phonon interaction at the surface (to be discussed), derives from the constant flux boundary condition

$$j = -D[\partial c(x, t)/\partial x]_{x=0} \quad [4]$$

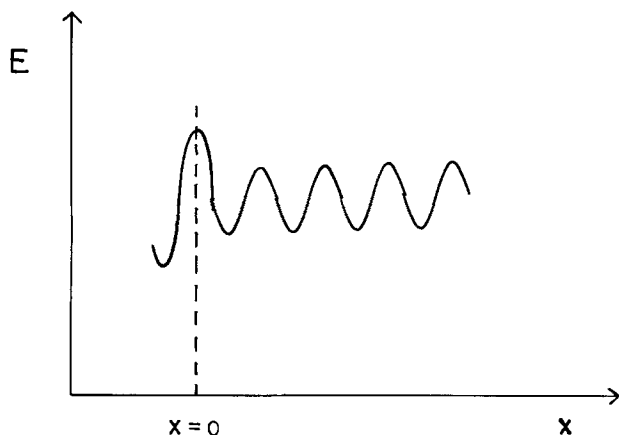


Fig. 2. Potential energy profile for chemical rate limitation

where both sides of the equation are taken, in this particular case, to be constant, since, in the absence of mechanical deformation or temperature change of the substrate, the phonon flux to and from the surface can be assumed to be constant and the interaction to proceed by a process of apertures slightly larger than available otherwise being created in the surface structure adjacent to the adsorbed interstitials as the phonons arrive at the surface and the interstitials then "falling" into these openings. Once inside the substrate the interstitials may then be imagined to go on about the usual random diffusional process.

The expression is (3)

$$c(x, t) = 2j(t/D)^{1/2} \operatorname{erfc}[x/2(Dt)^{1/2}] \quad [5]$$

or

$$c(x, t)/c_0 = \exp(-x^2/4Dt) - x(\pi/4Dt)^{1/2} \operatorname{erfc}[x/2(Dt)^{1/2}] \quad [6]$$

where  $c_0$  now varies as a function of time. Equations [5] and [6] correspond to Eq. [2] in that they both have the possibility of applying in the infinite surface source situation, *i.e.*, where the error function complement profile might reasonably be expected to apply in the absence of rate limitation.

Now moving on to the case corresponding to the gaussian profile we are led to consider the general expression for a chemical process

$$\text{Rate} = k \prod_{n=1}^n c_n^{x_n} \quad [7]$$

where  $k$  is a rate constant, the remainder of the expression is a product of powers and concentrations, and the sum of the  $x_n$  is the order of the reaction. Taking the interstitial-phonon interaction to be strong and assuming: (a) the interaction is nonspecific, *i.e.*, that a single, isolated, adsorbed solute atom has no more chance of interaction than one closely oriented with respect to other adsorbed atoms, and (b) the interaction is of first order in the concentration of the adsorbed species at the surface, then we have for the rate

$$dc_T/dt = k_1(a - c_T) \quad [8]$$

where  $c_T$  is the total amount of adsorbed species which has interacted at time  $t$  and crossed the surface potential into the bulk substrate in moles-cm<sup>-2</sup>,  $k_1$  is the first-order rate constant, and  $a$  has the same meaning as in Eq. [3]. Integrating Eq. [8], with the condition  $c_T = 0$  at  $t = 0$ , we get

$$c_T = a[1 - \exp(-k_1t)] \quad [9]$$

and since  $c_T$  is the total amount of solute atoms present in the substrate at time  $t$ , we can write the following boundary conditions to be solved in conjunction with the diffusion equation

$$c(x, t) = 0, \quad x \rightarrow \infty \quad [10]$$

$$c(x, t) = 0, \quad t = 0 \quad [11]$$

and from Eq. [9]

$$\int_0^\infty c(x, t) dx = a[1 - \exp(-k_1t)] \quad [12]$$

Using the Laplace transformation method, we have for  $c(x, t)$

$$c(x, t) = [a/(\pi Dt)^{1/2}] \left[ \exp(-x^2/4Dt) + 4(D^3t/\pi)^{1/2} \int_0^\infty \frac{4v^2 \exp(-4Dv^2t)}{k_1 - 4Dv^2} \cos(2vx) dv \right] \quad [13]$$

Equation [13] has the following limits

$$\lim_{k_1 \rightarrow \infty} c(x, t) = [a/(\pi Dt)^{1/2}] \exp(-x^2/4Dt) \quad [14]$$



the regular gaussian profile, and

$$\lim_{k_1 \rightarrow 0} c(x, t) = 0 \quad [15]$$

Thus when  $k_1$  is large, gaussian behavior will result, and when small, there will be no diffusion.

Also, just inside the surface (neglecting a small term, higher by a degree in  $k_1$ )

$$c(0, t) = c_0 = [a/(\pi Dt)^{1/2}] \operatorname{erf}(k_1 t)^{1/2} \quad [16]$$

and

$$\lim_{t \rightarrow 0} c_0 = 0 \quad [17]$$

Equation [16] is plotted for various values of  $k_1$  in Fig. 3. It can be seen that in the limit as  $t$  becomes large,  $c_0$  will always approach the gaussian values for even small  $k_1$ . However, the profile can be expected to deviate more from the gaussian shape as  $k_1$  becomes smaller, see the Discussion section.

From Eq. [3] we get the following relation for  $c_0$  to be compared with Eq. [16]

$$c_0 = [a/(\pi Dt)^{1/2}] \times [1 - K(\pi t/D)^{1/2} \exp(K^2 t/D)] \times \operatorname{erfc}[K(t/D)^{1/2}] \quad [18]$$

### Discussion

There has long been something lacking in thoughts about diffused systems. The usual boundary condition, corresponding to an infinite surface source, partially superseded by Miller and Smit's Eq. [1], was the simple

$$c(0, t) = c_0 = \text{const}, \quad t > 0 \quad [19]$$

Now Eq. [19] implies a certain passivity to the nature of the effect of the surface on the diffusion process occurring.

At the same time diffusion has been experimentally observed many times in substrates that are strongly endothermic absorbers of the diffusing species, e.g., hydrogen in iron, nickel, and platinum. In fact enough hydrogen goes into the bulk of these metals that it causes embrittlement. For these systems one might well ask the question, "How does the hydrogen ever get in there at all, if it is so difficult energetically?" At one time it was thought that hydrogen entered these metals only under circumstances of high equivalent pressure (6, 7). Recently, however, it was shown experimentally that at atmospheric pressure enough hydrogen penetrates, at least iron, to cause embrittlement (8). The exact mechanism of this process is still not clear (9, 10). In any case, the passive type of surface depicted by Eq. [19] would seem unlikely, and it would appear that the strong interstitial-phonon interaction referred to earlier in the text and previously considered as a

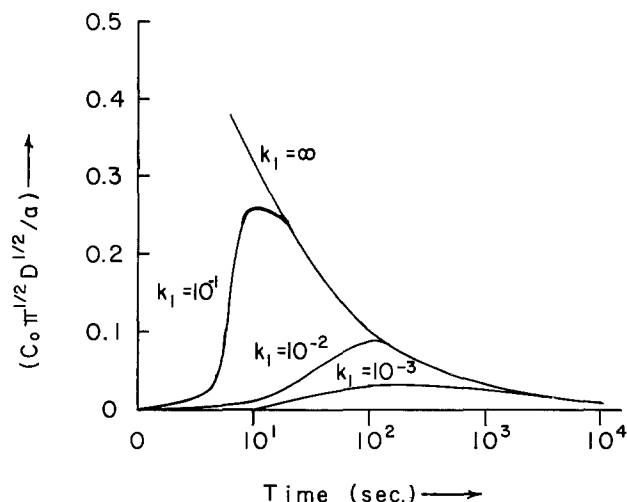


Fig. 3.  $c_0$  for various values of  $k_1$  as a function of time

possibility (11) is more probable. In this context the surface can be thought of as having the positive influence of acting as an interstitial "pump."

Both types of rate limitation have been observed experimentally. Ghoshtagore (12) has reported the physical case in the diffusion of boron and phosphorus into silicon. The previously referred to experiments with the hydrogen-palladium system (2) exhibited rate limitation of the chemical type. It might be argued that since the hydrogen was introduced electrochemically in the experiments the constant flux might have been simulated by some chemical process outside the surface. However, in contrast to most other work done with the bi-electrode technique where hydrogen is generated at the input side galvanostatically and in the overvoltage region, these experiments were performed in the underpotential region and utilized the potentiostatic technique in introducing the hydrogen, and there is no doubt that the infinite surface source situation would obtain under these circumstances.

Possibly a more important topic involves the possibility of rate limitation being misinterpreted as concentration-dependent diffusion. The physical case is rather specialized, and here there seems to be no chance of error. In the chemical case the whole matter hinges upon the rate of attainment of the equilibrium concentration just beneath the input surface, and unfortunately some of the solutions of the diffusion equation, involving the use of Eq. [6] and [13] as initial conditions, are not easily accessible analytically. If equilibrium is attained rapidly with respect to the total diffusion time, then the classical cases of gaussian and error function complement profiles will result. However, if this time is finite, then, in general, the diffusion coefficient will appear to increase with time after equilibrium is reached if one tries to fit data with the classical profiles.

As mentioned in a previous note (3) in the case of slow equilibrium, infinite surface source type situations can be approximated by an equation of the type

$$c(x, t) = c_0 \operatorname{erfc} \{x/2[D(t + t_1)]^{1/2}\} \quad [20]$$

after equilibrium has been established, where  $c_0$  is now a constant,  $t$  is the time after equilibrium,  $t_1$  is a fitting parameter such that Eq. [20] fits Eq. [5] at  $t = 0$  [the shape of the curves are very similar (3)], and Eq. [20], of course, is not a true solution to the diffusion equation.

In the case of a finite surface source there two non-gaussian possibilities: (i) slow time to equilibrium and saturation not being reached, and (ii) the same except that saturation is reached before the maxima in Fig. 3, causing the curve to have a flat portion. In the first case Eq. [13] gives an exact solution, and the second is more complicated. Both cases will exhibit the same apparent increase in diffusion coefficient after equilibrium (or saturation) if attempts are made to fit them to the gaussian profile.

In summary, it would appear reasonable that a strong interstitial-phonon interaction at least initiates most diffusion processes. The classical gaussian and error function complement profiles hold true only if the time to equilibrium is short, and if this time is not short more complicated behavior will result which in many cases may be misinterpreted as concentration-dependent diffusion.

Manuscript submitted June 13, 1975; revised manuscript received ca. Oct. 13, 1975.

Any discussion of this paper will appear in a Discussion Section to be published in the December 1976 JOURNAL. All discussions for the December 1976 Discussion Section should be submitted by Aug. 1, 1976.

### REFERENCES

1. R. C. Miller and F. M. Smits, *Phys. Rev.*, **107**, 65 (1957).
2. M. A. Fullenwider, *This Journal*, **122**, 648 (1975).
3. M. A. Fullenwider, *ibid.*, **121**, 314 (1974).

4. H. S. Carslaw and J. C. Jaeger, "Conduction of Heat in Solids," p. 18, Oxford (1959).
5. F. M. Smits, *Proc. I.R.E.*, **46**, 1049 (1958).
6. W. Beck, J. O'M. Bockris, J. McBreen, and L. Nanis, *Proc. Roy. Soc.*, **A290**, 220 (1966).
7. J. O'M. Bockris and P. K. Subramanian, *Electrochim. Acta*, **16**, 2169 (1971).
8. H. H. Johnson, "Proceedings of Conference, Fundamental Aspects of Stress Corrosion Cracking, Columbus, 1967," p. 446, National Assn. Corrosion Engineers (1969).
9. R. A. Oriani, *Ber. Bunsen-Gesellschaft*, **76**, 848 (1972).
10. M. A. Fullenwider, *This Journal*, **121**, 1589 (1974).
11. P. Gosar, *Il Nuovo Cimento*, **31**, 781 (1964).
12. R. N. Ghoshtagore, *Solid-State Electron.*, **15**, 1113 (1972).

## Behavior of Pure and Platinum-Doped Sodium Tungsten Bronze Electrodes in Oxygen-Saturated Phosphoric Acid

A. J. Appleby<sup>\*1</sup> and C. Van Druen

*Institute of Gas Technology, Chicago, Illinois 60616*

### ABSTRACT

Platinum-doped tungsten bronze electrodes of composition  $\text{Na}_{0.7}\text{WO}_3$  have been examined for the reduction of oxygen in 0.1N  $\text{H}_2\text{SO}_4$  and  $\text{HClO}_4$ , together with orthophosphoric acid at various concentrations up to 14.5N (85 weight per cent). Whereas good activities of aged electrodes were shown in  $\text{H}_2\text{SO}_4$  and  $\text{HClO}_4$ , those in  $\text{H}_3\text{PO}_4$  were poor. This is attributed to the formation of phosphotungstate. It is concluded that such compounds are unsuitable for use as catalysts in phosphoric acid fuel cells.

Tungsten bronzes have been shown to possess catalytic activity for a number of reactions, in particular for certain organic processes (1, 2). Sodium bronzes were examined by Sepa *et al.* (3) for electrocatalytic oxygen reduction. They concluded that these materials were about as active as platinum in dilute sulfuric acid. As a result of this work, the tungsten bronzes were examined by a number of workers for electrocatalytic hydrogen and CO oxidation (4-6) and oxygen reduction (5-8). The oxygen-reduction activity was shown by Fishman *et al.* (7, 9) to be due to the presence of traces of noble metals, in particular platinum. This result has been more recently confirmed by Bockris and McHardy (10), who have examined the synergistic effect of the bronze on platinum for oxygen reduction.

More recent work has tended to examine more specific aspects of the electrochemistry of tungsten bronzes. For example, the electrochemistry of bronze formation (11) has been studied, together with the effects of bronze structure on hydrogen evolution (12, 13). The effect of anodization bronzes in sulfuric acid solution has also been investigated (14).

In the present paper, work on oxygen electrode processes on undoped and platinum-doped sodium tungsten bronzes is reported.

### Experimental

*Preparation of tungsten bronze single crystals.*—Large single crystals (about 1 cm cubes) of tungsten bronze of composition approximating to  $\text{Na}_{0.7}\text{WO}_3$  were prepared by the electrolytic technique from a fused 2:1  $\text{Na}_2\text{WO}_4:\text{WO}_3$  mixture by the method described by Lovrecek, McHardy, and Bockris (15). Specimens were grown around seed crystals tied by fine gold wires. A current density of 20 mA/cm<sup>2</sup> was used. The undoped samples described in this work were prepared at the Institute of Gas Technology, whereas the doped crystals (0.05% Pt) were prepared at the University of Pennsylvania. The electrolytic cell in the latter case used a two-electrode technique with a potential divider and a

subsidiary platinum anode (15). The total (apparent) geometrical area of the electrode was calculated from the crystal dimensions and was used for current-density determinations.

### Results and Discussion

*Oxygen electrode reactions on Pt-doped tungsten bronze: dilute  $\text{H}_2\text{SO}_4$  and  $\text{HClO}_4$ .*—Initial experiments were conducted at room temperature in dilute (0.1N) sulfuric acid to check the reproducibility of data with that reported by previous workers (10). A three-compartment cell with hydrogen reference electrode was used for all experiments. The sulfuric acid solutions (together with all the solutions reported below) were made up from triple-distilled water (all-silica still) and analytical reagent grade acid. They were preelectrolyzed for at least 15 hr at a total current of 50 mA, using platinum black fuel-cell electrodes (Allis-Chalmers) before experiments were started. Electrodes were hung in the solutions on their gold suspension wires, and were previously placed above the solution during preelectrolysis. Initial open-circuit potentials noted for the bronze crystals in oxygen-saturated electrolyte were high: about 850 mV/HRE.

Galvanostatic plots for the anodic process under steady-state conditions were first obtained after a preliminary anodization of the bronze crystal. The object of this anodization was to produce a reproducible surface for oxygen evolution. Anodic plots from high to low current densities were first carried out. At current densities above about  $10^{-6}$  A/cm<sup>2</sup> these initial plots were similar to those shown as plot 2 on Fig. 1. At lower current densities, potential values recorded were lower than those shown above, and in addition a time dependence of potential was noted. For example, at a current density of  $2 \times 10^{-8}$  A/cm<sup>2</sup>, the potential fell from an initial value of 1340 mV to a value of 1200 mV vs.  $\text{H}_2$  after 1.5 hr, after which the series of plots given in Fig. 1 was obtained.

At low current densities, the potential values recorded were essentially time independent (i.e., in the potential range up to 1500-1600 mV). At higher potentials, results became time dependent: Points shown on

<sup>\*</sup> Electrochemical Society Active Member.

<sup>1</sup> Present address: Laboratoires de Marcoussis, 91-Marcoussis, France.

Key words: oxygen reduction, fuel cells, electrocatalysis.

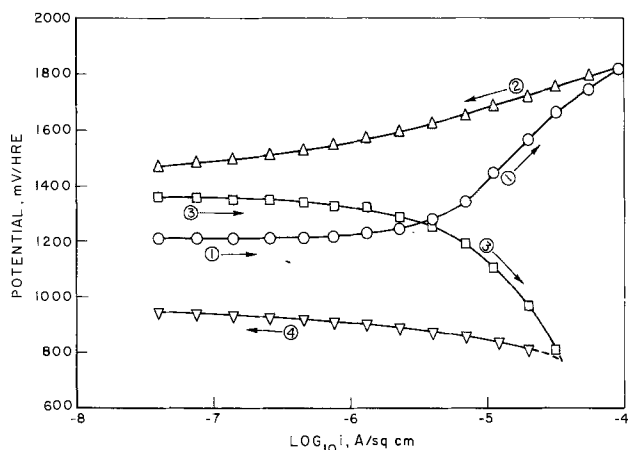


Fig. 1.  $V\text{-}\log_{10} i$  plots on preanodized Pt-doped tungsten bronze: oxygen-saturated  $0.1N H_2SO_4$ ,  $25^\circ C$ . Arrows show plotting direction.

Fig. 1, curve 1 were taken after 2 min polarization. The hysteresis effect even after preliminary anodization is very marked. This implies a reanodization of the electrode surface after the decay of the original anodized state [cf. Ref. (14)].

After such treatment, cathodic behavior shown on plot 3, Fig. 1, was typically obtained. Most of the cathodic current in such plots is evidently used in restoring the bronze surface to its original condition, rather than for oxygen reduction. A typical return plot after this treatment is shown as plot 4, Fig. 1. If we conclude that the electrode surface is in a stable state after this treatment (as in the anodic case), then the activity of the electrode for the only other possible cathodic process (reduction of oxygen) is on the same order as that for platinum under these conditions, as observed by Bockris and McHardy (10) for "aged" electrodes (*i.e.*, electrodes that had either been anodized or exposed to lower positive potentials for long periods).

A different series of experiments, using the same steady-state technique, was conducted on nonanodized electrodes (fresh electrodes, or those that had had previous cathodic pretreatment of the types shown as curves 3 and 4 in Fig. 1). Results obtained in  $0.1N H_2SO_4$  and  $0.1N HClO_4$  were essentially superposable, showing that the anion had little or no effect in these cases. Results obtained in the latter solution are shown in Fig. 2. Hysteresis is very much less marked than in Fig. 1, and the anodic plots occur at much lower potentials than on preanodized electrodes. The cathodic plots are at lower potentials than the final plot on Fig. 1 (plot 4) and probably correspond to the plots observed by Bockris and McHardy (10) on fresh electrodes. In all cases, the points observed were unstable, and the values shown on Fig. 2 correspond to a time interval of 2 min between current densities.

**Oxygen electrode reactions in 85% orthophosphoric acid (Pt-doped tungsten bronze).—Solution.**—The acid was purified by hydrogen peroxide treatment as in previous work (16).

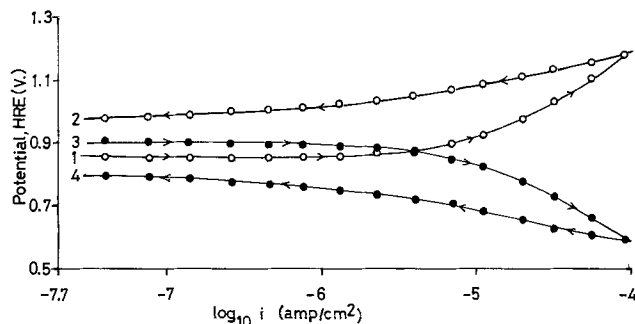


Fig. 2.  $V\text{-}\log_{10} i$  plots as Fig. 1,  $0.1N HClO_4$ . Nonpreanodized crystal.

Table I. Extrapolated rates at the reversible oxygen potential,  $1/\alpha$  values, and Tafel slopes for anodic and cathodic processes as a function of temperature in oxygen-saturated 85% orthophosphoric acid; Pt-doped tungsten bronze crystals

	Temperature, $^\circ C$	Extrapolated rate ( $A/cm^2$ )	$1/\alpha$	Tafel slope (mV/decade)
Anodic process	51.0	$9.0 \times 10^{-7}$	4.07	263
	68.0	$2.3 \times 10^{-6}$	3.77	255
	100.0	$2.4 \times 10^{-5}$	3.58	265
	118.0	$5.8 \times 10^{-5}$	3.87	300
Cathodic process	53.0	$2.1 \times 10^{-14}$	1.66	107
	68.0	$7.5 \times 10^{-13}$	1.82	123
	81.0	$2.9 \times 10^{-12}$	1.78	125
	100.0	$9.5 \times 10^{-12}$	1.72	127
	118.0	$10^{-11}$	1.48	120

**Anodic processes.**—Anodic Tafel plots on 0.05% Pt-doped  $Na_{0.7}WO_3$  single crystal electrodes were obtained, starting at the rest potential in oxygen-saturated solution. This was consistently about 100 mV lower than in dilute sulfuric or perchloric acids for fresh electrodes.

The points in Fig. 3 were obtained on preanodized electrodes (cf. Fig. 1 for dilute sulfuric acid) and correspond to the steady-state condition for oxygen evolution (less than 1 mV change in 2 min). Tafel behavior was obtained at each temperature, but the slopes were extremely high ( $\sim 4RT/F$ ), and the apparent  $\alpha$ -values were temperature dependent (see Table I).

**Cycling data.**—A plot of the same type as in Fig. 2 (for fresh electrodes, 2 min between points) was obtained in oxygen-saturated orthophosphoric acid at  $25^\circ C$  (Fig. 4). Hysteresis was much greater than in sulfuric or perchloric acid, and the level of activity indicated in the final plot (Fig. 1, plot 4) for oxygen reduction was very low. No Tafel slope as such was observed: The final cathodic plot (descending current densities) was almost horizontal. Overpotentials increased slowly with time (see below). The electrode was extremely sluggish on changing the current density compared with the corresponding case in  $H_2SO_4$ .

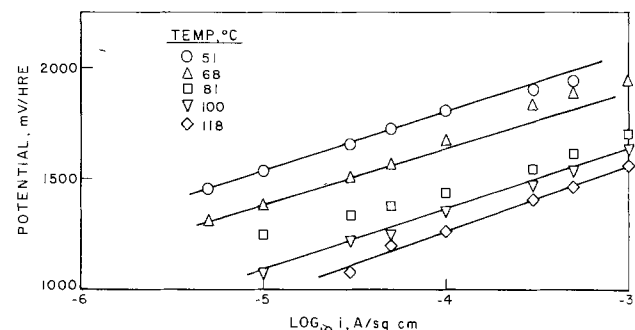


Fig. 3. Anodic Tafel plots in oxygen-saturated 85%  $H_3PO_4$  as a function of temperature, Pt-doped tungsten bronze (steady-state data).

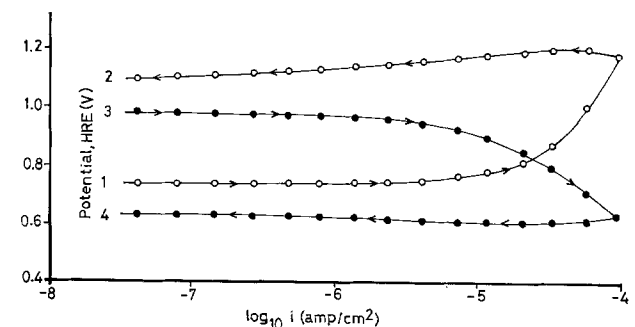


Fig. 4.  $V\text{-}\log_{10} i$  plots as Fig. 1 and 2: 85%  $H_3PO_4$ . Nonpreanodized crystal.

**Cathodic reduction of oxygen.**—Descending galvanostatic plots, taken after the electrode had reached its rest potential in oxygen-saturated solution, are shown in Fig. 5 as a function of temperature. Again, great sluggishness was observed on changing current density, and several hours were required between points at low current densities. In each case, a Tafel slope was observed. However,  $\alpha$  was strongly temperature dependent: The observed Tafel slopes were almost independent of temperature.

Values of the Tafel slope and  $\alpha$ -values are given as a function of temperature in Table I. The Tafel plots were extrapolated back to the theoretical reversible oxygen potentials in each case. Values of the apparent  $i_0$  value for oxygen reduction, assuming this to be the major process involved, are also given in Table I. It is clear that the values obtained are several orders of magnitude less than the values for the initial anodic process extrapolated from the data given in Fig. 3 to the reversible oxygen potentials. This argues that the anodic process observed is attributable to anodization of the surface rather than to oxygen evolution.

**Effect of phosphoric acid concentration on cathodic plots.**—Crystals were examined in solutions of different  $H_3PO_4$  concentration in the range 0.1–5M at 25°C. Solutions were in each case preelectrolyzed for 15 hr before testing was conducted, electrodes being hung above the solution during preparation in the manner described above. Open-circuit potentials were found not to depend significantly on the acid concentration; they were far below ( $\sim 200$  mV) those registered in dilute sulfuric (or perchloric) acids for fresh electrodes. Descending galvanostatic Tafel plots were obtained at each acid concentration, allowing sufficient time to reach equilibrium in each case. Results are shown in Fig. 6. In every case the Tafel slope was close to 100 mV/decade, and the overpotential was essentially independent of the acid concentration: A variation in overpotential of only about 15 mV was observed in the concentration range studied.

The results obtained suggest that the phosphate ion inhibits the crystal surface for the oxygen-reduction reaction.

**Studies on Pt-doped tungsten bronzes previously aged in orthophosphoric acid.**—In view of the reduced

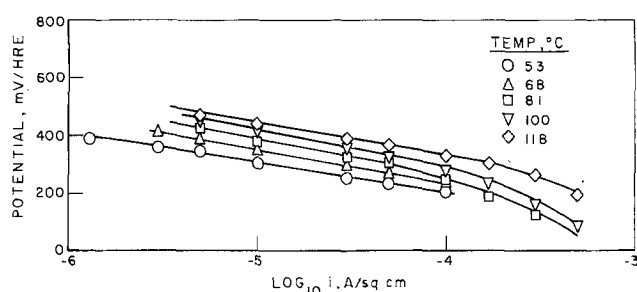


Fig. 5. Cathodic Tafel plots in oxygen-saturated 85%  $H_3PO_4$  as a function of temperature, Pt-doped tungsten bronze (steady-state data).

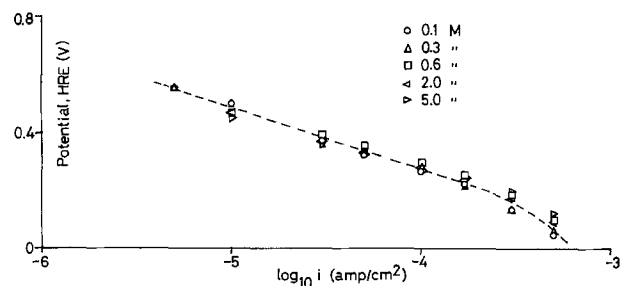


Fig. 6. Cathodic Tafel data in oxygen-saturated  $H_3PO_4$  solutions at 25°C as a function of concentration, Pt-doped tungsten bronze (steady-state data).

activity of crystals in orthophosphoric acid (Fig. 4-6) for the cathodic process compared with that in dilute sulfuric acid (aged electrodes, Fig. 1) a test was effected to determine the state of the surface after exposure to orthophosphoric acid.

Figures 7 and 8 show the effect of anodic and cathodic polarization, respectively, in 0.1N sulfuric acid after crystals had been used to obtain cathodic data in 85% orthophosphoric acid (Fig. 5). After the tests in orthophosphoric acid, the crystals were simply rinsed with distilled water and placed in oxygen-saturated preelectrolyzed sulfuric acid solution. The anodic and cathodic galvanostatic plots were then conducted.

Figure 7 (anodic data) shows that the orthophosphoric acid treatment appears to be equivalent to the anodizing treatment illustrated in Fig. 1. The curve on Fig. 7 represents the descending current density plot under the same conditions as Fig. 2 (ascending and descending current densities from the open-circuit potential, 2 min between points). No prolonged anodization was conducted, yet results were very similar to those shown in Fig. 1.

In Fig. 8 cathodic data is shown, taken at ascending current densities from the open-circuit potential on a new crystal directly after phosphoric acid treatment. Data for aged electrodes in dilute sulfuric acid (curve 4, Fig. 1) are also shown for comparison. A marked increase in activity after phosphoric acid treatment occurs.

There is thus no evidence of permanent deactivation of the surface of the Pt-doped bronze crystal by exposure to 85% orthophosphoric acid: On the contrary, this material has appeared to have activated its surface. The treatment perhaps corresponds to the marked aging phenomenon described by Bockris and McHardy (10) after continued polarization.

**Oxygen electrode reactions on undoped tungsten bronzes in orthophosphoric acid solutions.**—Data similar to those shown in Fig. 2 and 4 were obtained in 85% orthophosphoric acid using undoped bronze crystals of composition  $Na_{0.7}WO_3$ . The experimental method was the same as previously described; the temperature of the measurements shown in Fig. 9 was 55°C, but results

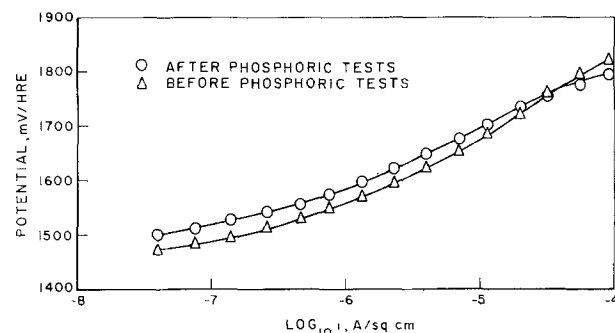


Fig. 7. Anodic  $V-\log_{10} i$  plots on Pt-doped tungsten bronze in oxygen-saturated 0.1N  $H_2SO_4$ , 25°C, after exposure to cathodic polarization in 85%  $H_3PO_4$ .

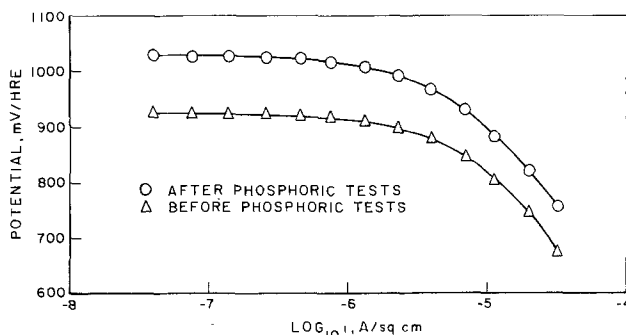


Fig. 8. Cathodic  $V-\log_{10} i$  plots, conditions as Fig. 7

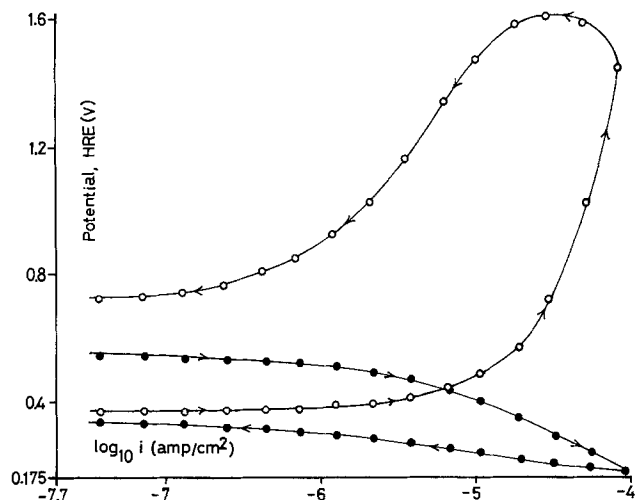


Fig. 9.  $V\text{-}\log_{10} i$  plots as Fig. 4: 85%  $\text{H}_3\text{PO}_4$ , 55°C, undoped tungsten bronze crystals.

were similar at lower temperatures (25°C). The most noteworthy differences between the results obtained on undoped and doped crystals are as follows:

(a) Open-circuit potentials were very much lower. A value close to 340 mV was registered at 55°C on undoped crystals. At 25°C, the values were  $\sim 150$  mV lower.

(b) On anodic polarization, potential remains essentially steady for current densities up to  $5 \cdot 10^{-6}$  A/cm<sup>2</sup>, then rises extremely rapidly, to give values that are comparable with those registered on Pt-doped crystals at current densities of about  $8 \cdot 10^{-5}$  A/cm<sup>2</sup> (Fig. 4). On reversing the anodic plotting direction, the current density falls rapidly, giving a final rest potential of about 700 mV. This decays after an interval of 2-3 hr by about 100 mV. The final curve of the cathodic cycle indicates much lower activity than that in the case of the doped crystal. This confirms that the first (ascending current density) anodic cycles in Fig. 1 and 2 are due to anodization of the surface rather than to oxygen evolution.

To investigate the effect of the concentration of orthophosphoric acid, a similar plot was conducted in 2M  $\text{H}_3\text{PO}_4$  at 25°C (Fig. 10). Under these conditions, higher current densities are required to anodize the bronze surface, and much less hysteresis is observed.

### Conclusions

The present results confirm those obtained by Bockris and McHardy (10) on Pt-doped tungsten bronzes for the oxygen electrode reaction in sulfuric acid medium. In general, fresh crystals, or those subjected to cathode treatment after anodizing or aging, show poor activity for oxygen reduction. Initial anodic treatment of fresh crystal surfaces involves a change of the condition of the surface, probably due to sodium ion loss. After this treatment (aged condition) the crystals appear to show activity for oxygen reduction comparable to that for platinum. Behavior is dominated by the state of the surface and the history of pretreatment.

In phosphoric acid these effects are much more exaggerated, and cathodic activity is very much less than in sulfuric or perchloric acid at all phosphoric acid

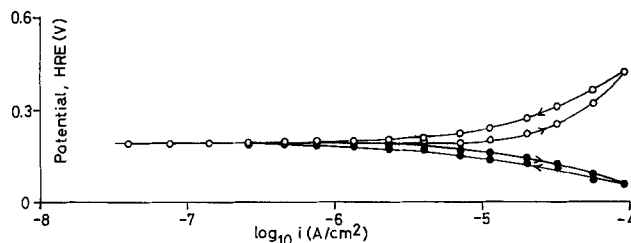


Fig. 10.  $V\text{-}\log_{10} i$  plots as Fig. 9: 2M  $\text{H}_3\text{PO}_4$ , 25°C, undoped tungsten bronze crystals.

concentrations studied. This deactivation is not permanent: After washing, crystals show activity in sulfuric acid similar to that of aged crystals, and much less hysteresis. We suggest that the deactivation is due to the formation of phosphotungstates at the bronze surface. We conclude that tungsten bronzes of the composition used here, whether undoped or doped with platinum, are unusable as oxygen-electrode catalysts in conventional phosphoric acid fuel cells.

### Acknowledgments

We thank the sponsors of the TARGET program and Pratt & Whitney Division of United Aircraft Corporation for permission to publish this paper.

Manuscript submitted Dec. 2, 1974; revised manuscript received Aug. 8, 1975.

Any discussion of this paper will appear in a Discussion Section to be published in the December 1976 JOURNAL. All discussions for the December 1976 Discussion Section should be submitted by Aug. 1, 1976.

### REFERENCES

1. E. O. Brimm, J. C. Brantley, J. H. Lorenz, and M. H. Jellinek, *J. Am. Chem. Soc.*, **73**, 5427 (1951).
2. A. A. Balandin and N. P. Sokolova, "Problems in Kinetics and Catalysis," Vol. 10, p. 363, Akad. Nauk SSSR, Moscow (1960).
3. D. B. Sepa, A. Damjanovic, and J. O'M. Bockris, *Electrochim. Acta*, **12**, 746 (1967).
4. L. W. Niedrach and H. I. Zeligler, *This Journal*, **116**, 152 (1969).
5. B. Brody, *J. Catalysis*, **10**, 13 (1968).
6. R. D. Armstrong, A. F. Douglas, and D. E. Williams, *Energy Conversion*, **11**, 7 (1971).
7. J. H. Fishman, J. F. Henry, and S. Tessore, *Electrochim. Acta*, **14**, 1314 (1969).
8. A. Damjanovic, D. Sepa, and J. O'M. Bockris, *J. Res. Inst. Catalysis, Hokkaido Univ.*, **16**, 1 (1968).
9. J. H. Fishman, Private communication, March 1968, transmitted to J. McHardy, January 1969.
10. J. O'M. Bockris and J. McHardy, *This Journal*, **120**, 53, 61 (1973).
11. J.-P. Randin, *ibid.*, **120**, 1325 (1973).
12. J. O'M. Bockris, A. Damjanovic, and R. J. Mannan, *J. Electroanal. Chem.*, **18**, 349 (1968).
13. D. B. Sepa, D. S. Ovcin, and M. V. Vojonovic, *This Journal*, **119**, 1285 (1972).
14. J.-P. Randin, A. K. Vijh, and A. B. Chughtai, *ibid.*, **120**, 1174 (1973).
15. B. Lovrecek, J. McHardy, and J. O'M. Bockris, Rept. No. 2, Contract DA 44-009-AMC 469 (T), Ft. Belvoir, Va., U.S. Army Mobility Res. and Devel. Center.
16. A. J. Appleby, *J. Electroanal. Chem.*, **24**, 97 (1970).

# Electrochemical Semipermeability and the Electrode Microsystem in Solid Oxide Electrolyte Cells

J. Fouletier, P. Fabry, and M. Kleitz\*

*E.N.S. d'Electrochimie et d'Electrometallurgie de Grenoble,  
Domaine Universitaire, 38401 Saint Martin d'Hères, France*

## ABSTRACT

New evidence is put forward within the framework of a recently introduced model. The electrodes are viewed as measuring the oxygen chemical potential in a "microsystem" which exchanges oxygen at a finite rate with the surrounding gas being analyzed. In high temperature oxygen gauges, the oxygen flux resulting from the electrochemical oxygen semipermeability of the electrolyte can have two effects other than reducing the theoretical emf by the factor  $(1 - \bar{t}_e)$  which appears to induce error of second order only. The oxygen semipermeability can obviously modify the oxygen content of the gas analyzed and also can disturb the equilibrium between the electrode microsystem and the analyzed gas. A special experimental setup was assembled to study both phenomena. The results showed that the second is generally far from being negligible and may lead to noticeable measurement error. A new arrangement with a zirconia point electrode is proposed to eliminate this source of error in oxygen gauges working at very high temperatures. The new arrangement was utilized to measure accurately the oxygen semipermeability of a  $ZrO_2$ - $Y_2O_3$  [9 mole per cent (m/o)] electrolyte at temperatures up to  $1650^\circ\text{C}$ . The semipermeability was found to be proportional to  $(P_3^{1/4} - P_2^{1/4})$ , where  $P_3$  and  $P_2$  are the equivalent oxygen pressures in the layers of oxygen adsorbed on both bases of the pellet. The activation energy of the electronic conductivity equaled 2.02 eV.

In several papers dealing with different phenomena such as the oxygen electrode overpotential (1), the time lag of the oxygen gauge electrode (2), and the kinetics of point-electrode oxidation (3), it was established that a solid electrode on stabilized zirconia does not directly measure the oxygen pressure in the surrounding atmosphere. The proposed phenomenological description of the over-all oxygen electrode process is sketched in Fig. 1. The electrode formed by the contact between the metal and the solid electrolyte is viewed as measuring the oxygen activity in a microsystem which more or less easily exchanges oxygen with the surrounding gas. It was first suggested that the microsystem was formed by a layer of adsorbed oxygen on zirconia (4). Mogab (5) also admitted the existence of an intermediary step of oxygen adsorption on zirconia in oxygen gauges. A recent systematic study (6) of the influence of the metal and the electrolyte seemed to indicate that they both contribute to determining the oxygen capacity of the microsystem.

In an oxygen gauge, the oxygen pressure over the reference electrode is generally different from that of the measuring electrode, resulting in an oxygen semipermeability flow through the electrolyte. (The characteristics of this phenomenon are recalled later on.) The relevant local oxygen flux must be taken into account in the oxygen balance of the microsystem. If the oxygen exchange rate with the surrounding gas is slow, as is the case under low oxygen pressure, this flux can make the microsystem deviate from its equilibrium with the gas. The importance of the induced error was recently investigated with a special differential assemblage of two gauges (7). The error can be significant even if the oxygen semipermeability flux is not high enough to alter the oxygen pressure in the gas being measured. Quantitatively, with the commonly used zirconia tubes and with air as a reference gas, the oxygen semipermeability flux is high enough above  $1150^\circ\text{K}$  to induce changes greater than 1 ppm in the oxygen content of the analyzed gas. Between  $900^\circ$  and  $1050^\circ\text{K}$  the tubes can be sufficiently impervious so that no change is noticed on a 0.1 ppm scale, but the

oxygen semipermeability flux is still high enough to significantly disturb the equilibrium between the microsystem and the gas. We will report here on a more detailed investigation of these phenomena.

## Experimental Setup

The measurements were carried out with the cell and the gas circuit schematically depicted in Fig. 2 and 3.

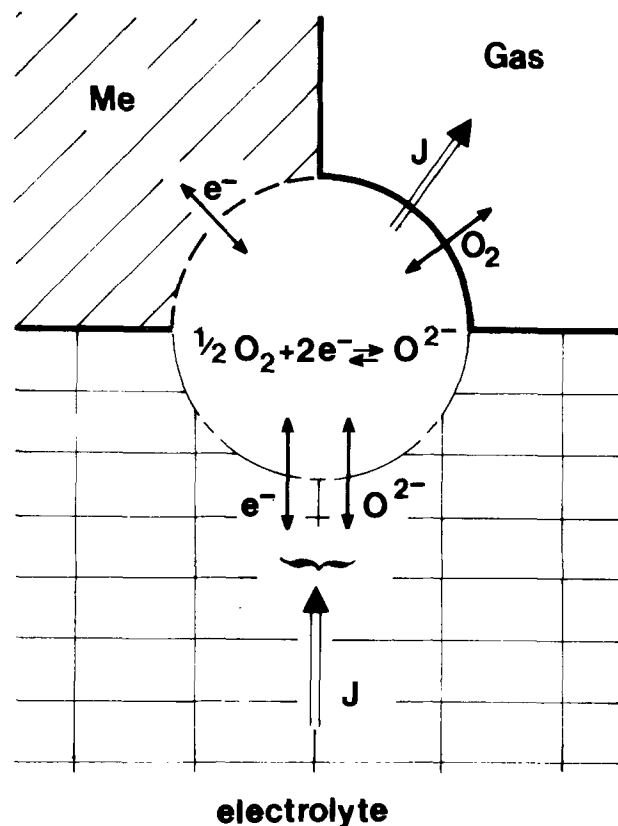


Fig. 1. Oxygen electrode microsystem; Me: inert metal, J: local oxygen semipermeability flux.

\* Electrochemical Society Active Member.  
Key words: oxygen gauge, electrode potential, zirconia, electronic conductivity, oxygen permeation.

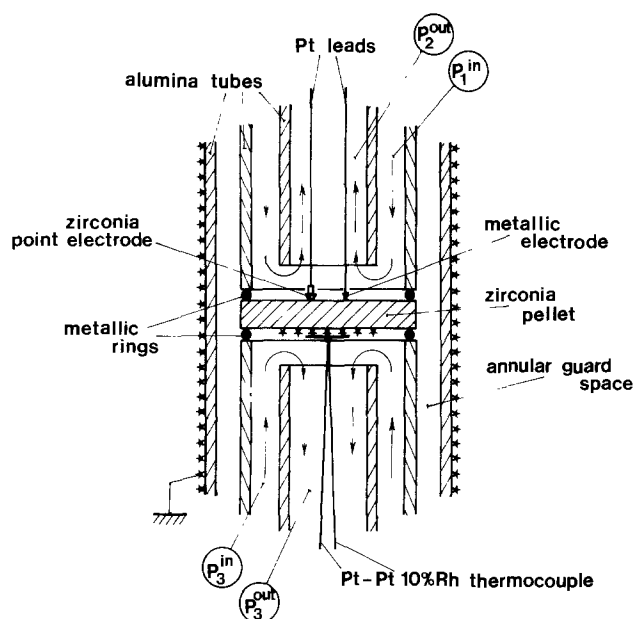


Fig. 2. Experimental cell

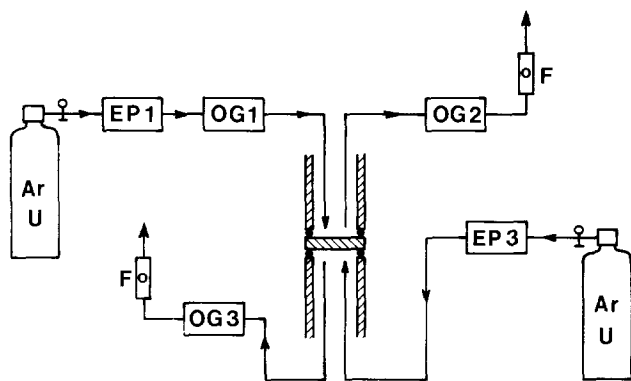


Fig. 3. Gas circuit; EP: electrochemical oxygen pump, OG: differential oxygen gauge, F: accurate displacement flowmeter.

The essential part of the cell which has already been described in other papers (3, 8) comprised a pellet of stabilized zirconia pressed between two alumina tubes and two metallic rings of gold or platinum. Such metallic seals were studied in detail by de Bruin *et al.* (9-11). They were also used by Takahashi *et al.* (12) and more recently by Zador *et al.* (13), Jakes (14), and Guillot *et al.* (15). The gas tightness thus ensured can be very good up to 1900°K. A vacuum of about  $10^{-2}$  Torr is furthermore maintained in the annular guard space (Fig. 2). Among other advantages, this is the best way to minimize the effects of the local cell action by the local electrodes formed on both sides of the metallic ring. Under such conditions, variations of the order of a tenth of a ppm in the oxygen content of the gas streaming in the upper part of the cell could be measured as a function of the oxygen content in the gas in the lower part.

When the oxygen semipermeability of a solid electrolyte is studied, such a cell has the great advantage of yielding data relevant to an isothermal sample which is not the case with the more commonly used tubular cells.

The reference electrode of the electrochemical cell was formed by a layer of porous painted platinum (Degussa No. 308 A). The measuring electrode was a simple point electrode. At least as far as potentiometric measurements are concerned, such electrodes respond as large-surface porous electrodes (16).

Two samples of  $ZrO_2-Y_2O_3$  9 m/o electrolyte were studied. The starting materials were the pure oxides [ $ZrO_2$  (Nobel Bozel, and Merck) and  $Y_2O_3$  (Pechiney)] which were ground to diameters less than  $40 \mu m$  in a Linatex mill with zirconia balls. The samples were prepared by dry mixing the oxide powders, pressing under  $1 \text{ tcm}^{-2}$ , and firing at 2300°K for 1 hr [for more details see Ref. (17)]. Their measured lattice parameters were 5.139 and 5.140Å, respectively, and their densities equaled 91% of the theoretical value. Up to 1300°K, they appeared perfectly impervious in our experiments; on varying the oxygen pressure in the lower part of the cell, no change was detected within 0.1 ppm in the oxygen content of the gas streaming on the other side of the pellet. Their analyses and sizes are given in Table I.

The metals used for preparing the point electrodes were nominally pure metals purchased from Caplain St. Andre.

As first proposed by Moebius (18), the working gas circuit (Fig. 3) was based on the utilization of solid oxide electrolyte cells. It was formed of an argon cylinder (Argon U Air Liquide), a pressure expansion valve and an accurate needle valve which maintained the gas flux strictly constant, an electrochemical pump EP1, an oxygen gauge OG1, the cell proper, a second oxygen gauge OG2, and an accurate flowmeter. The apparatus was connected by stainless steel tubes and Viton O-ring seals. The gauges were differential assemblages (7) working at about 900°K. Such gauges can accurately measure oxygen content higher than a few  $10^{-2}$  ppm. When no contamination occurred in the cell, the agreement between the oxygen measurements by the two gauges OG1 and OG2 was always better than 10% of the measured values over the  $1-10^6$  ppm range. Furthermore, the stability of the gauge voltages was such that for any given experiment, variation of the order of 1% in oxygen content could be measured for any oxygen content greater than a few ppm.

The accurate displacement flowmeter connected at the end of the gas circuit allowed us to use the Faraday law test (7). The verification of this law with the help of an oxygen pump and an accurate flowmeter was shown to be the best test to verify the good performances of an oxygen gauge.

As shown in Fig. 3, the reference gas circuit was very similar. Sometimes air was also used as a reference gas. A typical gas flow rate in both circuits was 10 liter/hr.

When working with oxygen contents of the order of a few ppm or less, about half a day was required for the surfaces of the whole circuit to be in equilibrium with the gas. The measurements were always performed when equilibrium was reached. This point was

Table I. Analysis and sizes of the two samples studied

Sample	Main impurities which could influence the electronic conductivity			Main impurities which could form segregated phases at the grain boundaries			Size	
	Cu (ppm)	Fe (ppm)	Mn (ppm)	Si (ppm)	Mg (ppm)	Al (ppm)	Effective permeation area (cm <sup>2</sup> )	l (mm)
A ZrO <sub>2</sub> -Nobel Bozel Y <sub>2</sub> O <sub>3</sub> -Pechiney	3	270	~10	100-500	50-100	200	2.27	3.3
B ZrO <sub>2</sub> -Merck Y <sub>2</sub> O <sub>3</sub> -Pechiney	5	250	~10	100-500	50-100	250	2.27	3.8

checked by verifying that the voltages were stable to 1 mV over several hours.

The oxygen pressures measured by the gauges OG1, OG2, and OG3 will be called  $P_1$ ,  $P_2$ , and  $P_3$ , respectively. The pressure  $P_3$  was the reference oxygen pressure in the cell (cf. Fig. 2). The pressure  $P_1$  was the oxygen pressure in the working gas arriving in the cell, and  $P_2$  after passing in the cell. The difference

$$\Delta P = P_2 - P_1 \quad [1]$$

resulted from the oxygen semipermeability flow through the sample and its measurement was used to determine the corresponding flux.

#### An Oxygen Gauge with a Zirconia Point Electrode

The first set of measurements was devoted to verifying an assumption which derives from the model proposed in Fig. 1. Within the framework of this model, the departure of an electrode from its equilibrium potential results from the oxygen semipermeability flow arriving at its triple contact. If the cell geometry is designed in such a way that the oxygen flow does not reach the electrode, the measured potential must equal the theoretically expected value, which takes into account the usual  $(1 - \bar{t}_e)$  factor.

The cell geometry which was investigated is sketched in Fig. 4. The electrochemical cell is formed by the reference electrode deposited on the pellet; the electrolyte composed of the pellet and a small point "electrode" of the same composition as the pellet and simply put in contact with it; and the measuring electrode coated on the top of the probe.

In another work (44) it has been shown that two blocks of stabilized zirconia simply put in contact, behave as a massive sintered pellet as regards the ohmic resistance.

The whole zirconia point electrode, apart from the small contact area, is surrounded by the same atmosphere. Thus, there is no oxygen activity gradient through the material. Should the oxygen activity on the contact surface be very different, it would be reasonable to assume that the resulting oxygen flow would be directed toward the closest free surface, as shown in the magnified part of Fig. 4. For these reasons, no oxygen flow emerges in the area of the measuring electrode which therefore must remain in equilibrium with the surrounding gas. Under these conditions the oxygen gauge sketched in Fig. 4 must correctly measure the oxygen pressure in the gas streaming over the zirconia point electrode whatever the oxygen semipermeability flow through the pellet.

This point was first verified by using the Faraday law test. This was done with air as a reference gas.

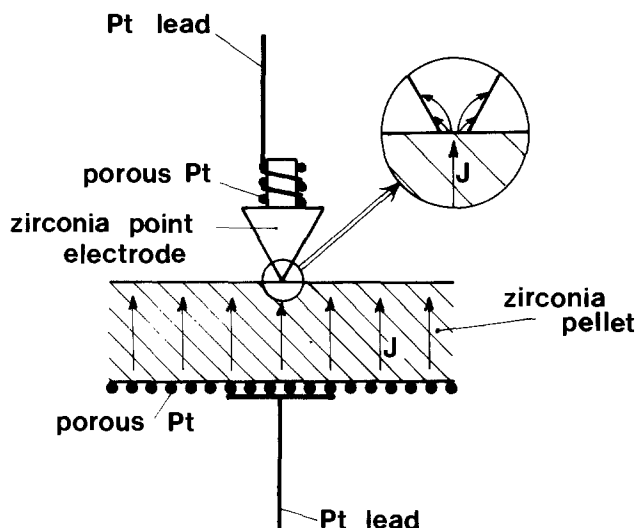


Fig. 4. Oxygen gauge with a zirconia point electrode;  $J$ : oxygen semipermeability flux.

Under these conditions, the reference electrode remained in equilibrium with the gas (see Fig. 7-9). Figure 5 gives a typical result. The current shown in abscissa is that which passed in the pump EP1, and the oxygen pressure is that deduced from the voltage of the gauge with the zirconia point electrode. The theoretical slope indicated was calculated according to the Faraday law [cf. Ref. (7)] by using an accurate measurement of the gas flow rate.

This point was again verified by comparing the zirconia point electrode gauge voltage to the theoretical value,  $E_{th}$

$$E_{th} = \frac{RT}{4F} \ln \frac{P_2}{P_3} \quad [2]$$

This comparison was made several times at temperatures up to 1800°K. Each time the oxygen pressure in the reference gas was sufficiently high so that the reference electrode was in equilibrium, the agreement was within the experimental scatter: the oxygen pressure deduced from the zirconia point electrode potential was always equal to  $P_2$  ( $1 \cdot 10^6$  ppm) to within 10%.

From a practical standpoint the arrangement with a zirconia point electrode is therefore an easy way to avoid the disturbing effect of the oxygen semipermeability on the measuring electrode. This could be particularly useful in gauges working at very high temperatures. A small difficulty in using such an arrangement has, however, been noted. It seems that sometimes a small spurious emf of a few millivolts is added to the gauge voltage. No obvious explanation was found for this phenomenon. This point should be investigated. It appeared in contradiction with the paper by Yushina *et al.* (19) where it was reported that no voltage drop was observed at a contact between two zirconia-based electrolytes.

Obviously such an arrangement can only eliminate the errors due to the disturbing effect on the electrode equilibrium but not the bulk effect which is usually

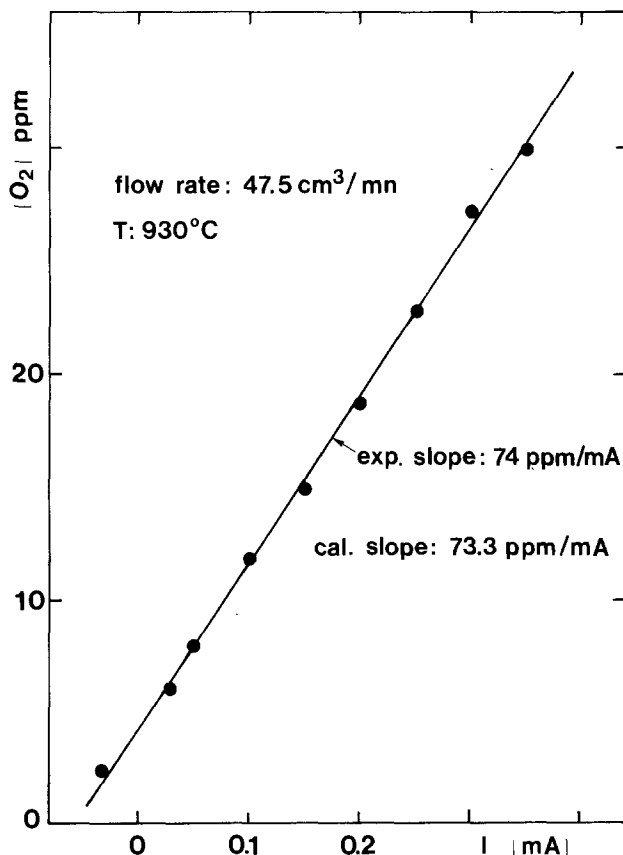


Fig. 5. Verification of the Faraday law with a zirconia point electrode;  $I$ : current passing through the upstream oxygen pump.



expressed by the factor  $(1 - \bar{t}_e)$  in the relation

$$E = (1 - \bar{t}_e)E_{th} \quad [3]$$

Using an average value of the published data for the ionic conductivity of the  $ZrO_2$ - $Y_2O_3$  9 m/o electrolyte and the results presented later on, the semipermeability parameters and the relevant electronic conductivity,  $\bar{t}_e$ , could be calculated and was found to be  $6.10 \cdot 10^{-4}$  at  $1250^\circ K$  and  $2.10 \cdot 10^{-3}$  at  $1725^\circ K$  under air. The error expressed by the factor  $(1 - \bar{t}_e)$  is very small when compared to the other effects and will be neglected hereafter.

### Measurements

The zirconia point electrode previously described was included in our cell. It provided a second "reference" electrode. Figure 6 is a sketch of the electrochemical cell which was investigated. We have represented adsorbed oxygen layers as definite phases. We furthermore formally characterize the oxygen activity in the adsorbed layers by their equivalent oxygen pressures  $P'$  which are equal to that in the gas which would be in equilibrium with the considered adsorbed layer. The change in the adsorbed oxygen level in the vicinity of the metals (Fig. 6) is a schematic way of representing the contribution of the metal to the modification of the amount of oxygen locally retained. This will represent the microsystem of the corresponding electrode.

The potentials of the metal and the zirconia probe as compared to the reference electrode will be called  $E_{Me}$  and  $E_z$ , respectively. We can write

$$E_{Me} = \frac{RT}{4F} \ln \frac{P'_2}{P'_3} \quad [4]$$

$$E_z = \frac{RT}{4F} \ln \frac{P_2}{P_3} \quad [5]$$

According to our analysis, the error of measurement made with regular gauges working at high temperature results mostly from:

(i) the alteration of the pressure  $P_1$  in the gas being analyzed to a pressure  $P_2$ . This alteration will be characterized by the parameter

$$\Delta P = P_2 - P_1 \quad [6]$$

(ii) the difference between the measured voltage  $E_{Me}$  (Eq. [4]) and the theoretical value  $E_{th}$  (Eq. [2]). This difference may result from a disturbance of the equilibrium of the measuring and the reference elec-

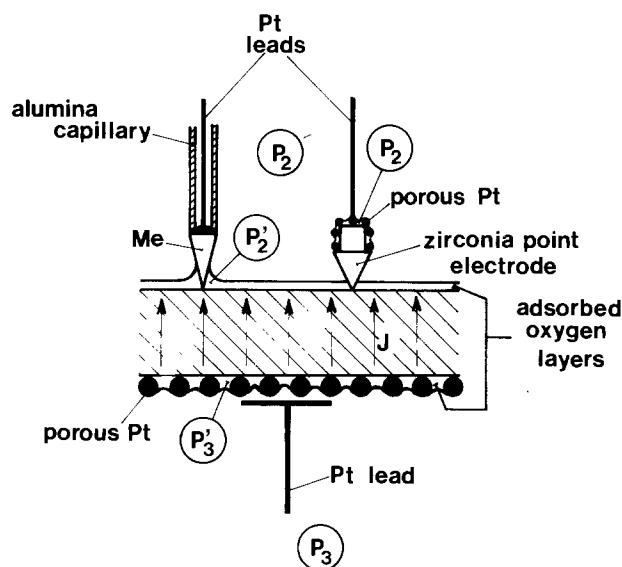


Fig. 6. Schematic representation of the investigated electrochemical cell showing oxygen adsorbed layers on the zirconia surfaces of interest.

trode, i.e.  $P'_2$  being different from  $P_2$ , and  $P'_3$  from  $P_3$ . These two possible contributions can be characterized by the parameters

$$\Delta E = \frac{RT}{4F} \ln \frac{P'_2}{P_2} \quad [7]$$

$$\Delta E_{Ref} = \frac{RT}{4F} \ln \frac{P'_3}{P_3} \quad [8]$$

which can be simply measured or calculated according to the formulae

$$\Delta E = E_{Me} - E_z \quad [9]$$

$$\Delta E_{Ref} = E_z - E_{th} \quad [10]$$

Figures 7-9 show typical measurements of the parameters  $\Delta P$ ,  $\Delta E$ , and  $\Delta E_{Ref}$  as functions of the oxygen reference pressure  $P_3$ . Before analyzing these results, several qualitative observations must be mentioned:

(i) At  $1410^\circ K$ , the alteration  $\Delta P$  of the oxygen content was always smaller than 1 ppm. Below this temperature no alteration of the utilized gas was observed; in spite of this, a large departure from the theoretical voltage  $E_{th}$  was measured. This confirmed the results previously recalled: the error made with the gauges does not solely result from the alteration of the oxygen content in the analyzed gas. Further, the variation  $\Delta E$  does not arise merely from a diffusion profile in the gas phase. The effect of a gaseous diffusion was observed (16) to be noticeable only with high oxygen flux through the electrolyte. Such effects were also reported (25) in the case of gauges working at very high temperature where the electrochemical semipermeability was very large.

In our experiments the deviations  $\Delta E$  were smaller the higher the temperature. This does not mean that  $\Delta E$  is inherently a decreasing function of the temperature. It results mostly from an increase in  $P_2$  through  $\Delta P$  due to an enhancement of the electrolyte semipermeability, the error  $\Delta E$  being a decreasing function of  $P_2$ .

(ii) The measurements reported in Fig. 10 were carried out with the electrolyte sample B and a zirconia point electrode from the same bath as sample A. As shown in Fig. 10, a spurious increment of about 5 mV is measured for the zirconia point electrode (see above).

(iii) The great difference between the results obtained with samples A and B with a platinum electrode (compare Fig. 10 and 11) indicates that the error made by a zirconia gauge may vary greatly from one electrolyte to the other. We were unable to put forward a determinant parameter. The analysis showed no significant impurity-content differences which could account for the observed results. With regard to this point, with regular commercial tubes the alteration of the oxygen pressure in the analyzed gas is usually observed, on a 1 ppm scale, above  $1100^\circ K$ ; with our sample this only occurs above  $1400^\circ K$ .

(iv) Figure 11 shows that the error can be noticeable for oxygen content much higher than 1 ppm.

(v) The existence of a noticeable error  $\Delta E_{Ref}$  for the reference electrode confirms, at least qualitatively, that the errors reported here are not a specific property of the metallic point electrode.

(vi) The results reported in Fig. 10 confirm that the nature of the metal contributes to determining the characteristics of the electrode microsystem. From a practical viewpoint, silver should be a better electrode in a gauge working at medium temperature. Another work (2) has shown, furthermore, that the electrode time lag is much shorter with silver than with platinum, especially at a temperature around  $900^\circ K$ .

(vii) Silver and gold electrodes seem to behave quite similarly in spite of the very different properties of the corresponding metal-oxygen systems. The large devia-

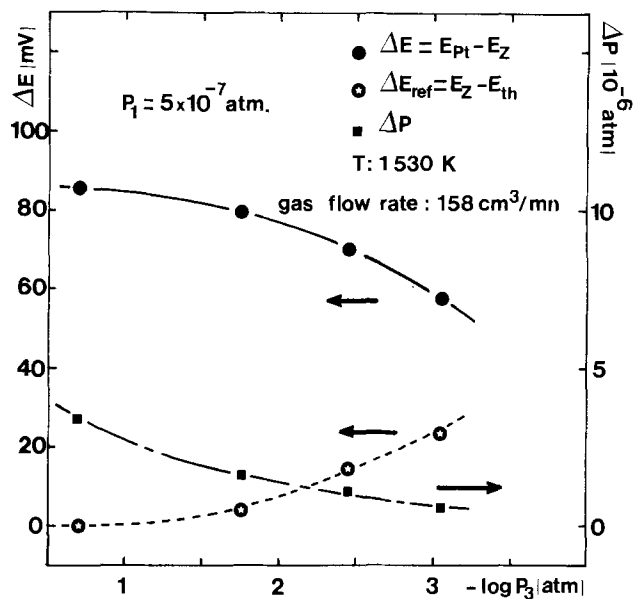


Fig. 7

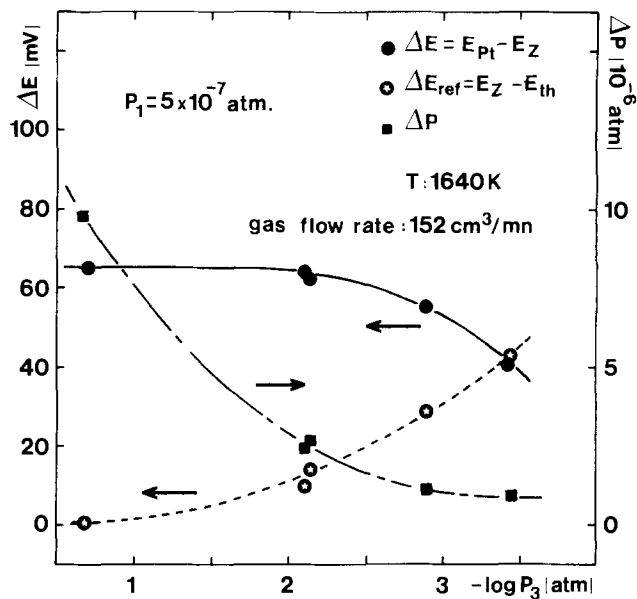


Fig. 8

Fig. 7, 8, 9. Variations of the different types of error in an electrochemical oxygen gauge as a function of the reference oxygen pressure  $P_3$ .  $\Delta P$ : error due to the oxygen contamination of the analyzed gas;  $\Delta E$ : error due to the departure from the equilibrium of the measuring electrode with the gas analyzed;  $\Delta E_{Ref}$ : error due to the departure from the equilibrium of the reference electrode with the reference gas.

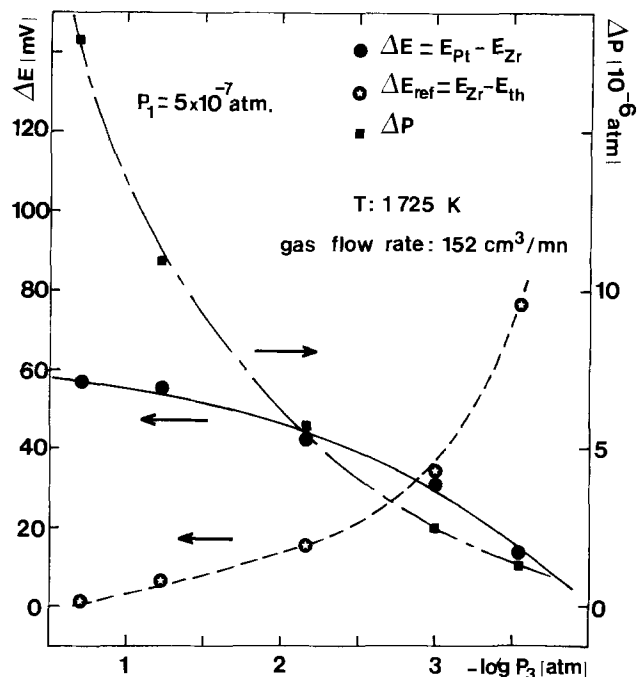
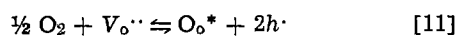


Fig. 9

tion when rhodium is used as an electrode could indicate that the formation of surface oxides, which is well known for platinum and rhodium, might play a part in the errors we have measured.

**Oxygen Semipermeability**

The primary cause of all the observed deviations  $\Delta P$ ,  $\Delta E$ , and  $\Delta E_{Ref}$  is the oxygen semipermeability of the electrolyte which has been frequently observed and studied (5, 7, 18, 20-36). The papers dealing with this phenomenon agree on its interpretation: under high or medium oxygen pressure, it results from a diffusion of holes,  $h^\cdot$ , electrically compensated by a diffusion of oxide ions  $O^{2-}$ . The flux of the former species is rate limiting. The hole concentration depends on the oxygen pressure in equilibrium with the material according to the reaction



and the resulting relation

$$[h^\cdot] = \frac{a \cdot [V_{O^\cdot}]^{1/2} \cdot P_{O_2}^{1/4}}{[O_{O^\cdot}]^{1/2}} \quad [12]$$

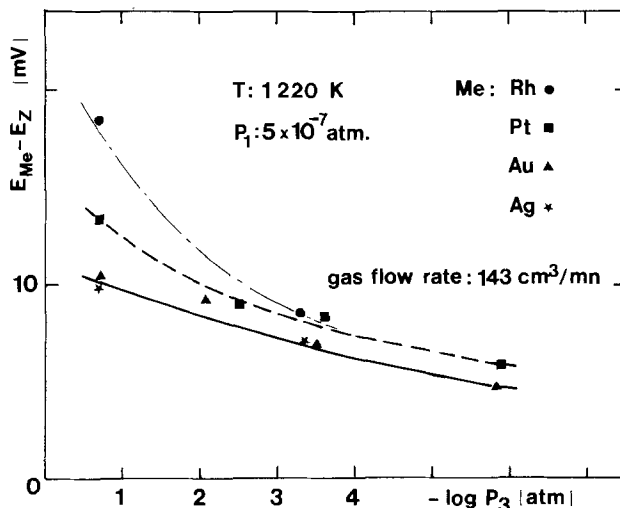


Fig. 10. Influence of the nature of the metal (Me) forming the metallic point electrode on the error  $\Delta E$ .

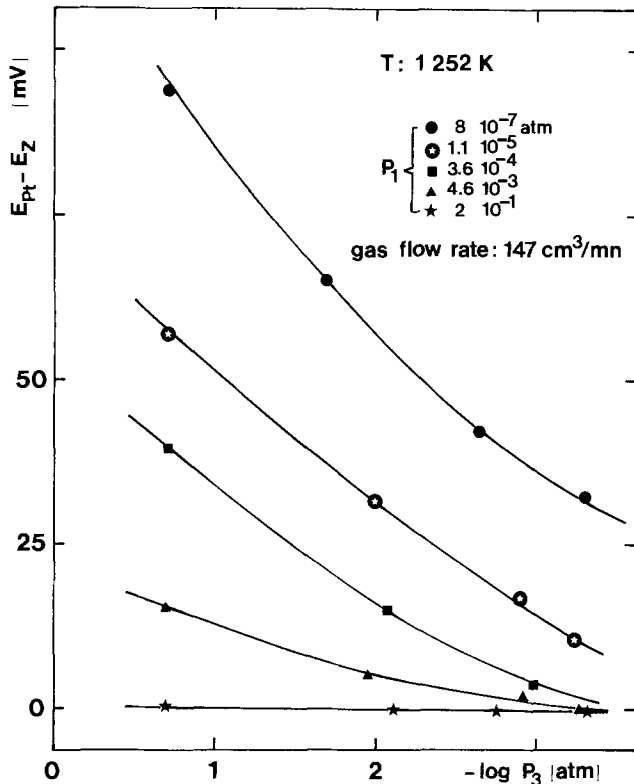


Fig. 11. Variations of the error  $\Delta E$  in ranges where the oxygen semipermeability flux is negligible as far as alteration of the oxygen content of the analyzed gas is concerned.

or more simply

$$[h\cdot] = A \cdot P_{O_2}^{1/4} \quad [13]$$

the oxide-ion and oxide-ion-vacancy concentrations being essentially constant.

Under these conditions the hole flux through a square centimeter of a zirconia pellet can be calculated within the framework of the Wagner theory (20, 22, 28, 38) or, more simply, as follows. Under high or medium oxygen pressures the  $V_{O\cdot}$  concentration is essentially constant, there is no chemical potential gradient for this species and the current density carried by the  $O^{2-}$  ions (or the corresponding vacancies) is simply given by the relation

$$I_{ion} = \frac{\sigma_{ion}}{l} \Delta V \quad [14]$$

where  $\sigma_{ion}$  is the ionic conductivity of the material,  $l$  the length of the conduction path, and  $\Delta V$  the variation in electrostatic potential. The current carried by the holes can be expressed as

$$I_h = \frac{\bar{\sigma}_h}{l \cdot F} \cdot \tilde{\Delta\mu}_h \quad [15]$$

where  $\bar{\sigma}_h$  is the average hole conductivity and  $\tilde{\Delta\mu}_h$  the variation of the hole electrochemical potential.

Under stationary conditions at open circuit there is no net current passing through the electrolyte and  $I_{ion}$  is equal to  $I_h$ . Then, combining Eq. [14] and [15] gives

$$\Delta V = \frac{\bar{\sigma}_h}{\sigma_{ion}} \cdot \frac{\tilde{\Delta\mu}_h}{F} \quad [16]$$

The conductivity ratio is roughly of the order of  $10^{-2}$ , and  $\tilde{\Delta\mu}_h \cdot F^{-1}$  which is equal to the cell voltage is smaller than 400 mV; therefore  $\Delta V$  is smaller than a few millivolts and can be considered in a first approximation as zero.

Under these conditions, the hole flux  $J$  is due only to a chemical diffusion and can be expressed as

$$J = -U_h [h\cdot] \text{grad } \mu_h \quad [17]$$

where  $U_h$  is the mobility of the holes,  $[h\cdot]$  their local concentration, and  $\mu_h$  their chemical potential. If  $\mu_h$  can be expressed as

$$\mu_h = RT \ln [h\cdot] \quad [18]$$

the flux, in a one-dimension geometry, is simply

$$J = -RTU_h \frac{d[h\cdot]}{dx} \quad [19]$$

Under steady-state conditions, there is no local accumulation of holes (no change in the stoichiometry) and  $J$  is a constant through the material. Therefore the derivative of  $[h\cdot]$  is a constant,  $[h\cdot]$  is a linear function of  $x$ , and  $J$  is equal to

$$J = RTU_h \left\{ \frac{[h\cdot]_3 - [h\cdot]_2}{l} \right\} \quad [20]$$

where  $[h\cdot]_3$  and  $[h\cdot]_2$  are the local hole concentrations on the surfaces of the pellet.

According to formula [13],  $J$  can be expressed as a function of the oxygen pressures surrounding these surfaces as

$$J = \frac{A \cdot RTU_h}{l} (P_3^{1/4} - P_2^{1/4}) \quad [21]$$

or more simply

$$J = \frac{\rho}{l} \cdot (P_3^{1/4} - P_2^{1/4}) \quad [22]$$

In the literature, this flux is frequently written as

$$J = \frac{\pi^*}{l} \quad [23]$$

The parameters are related by the expression

$$\pi^* = \rho (P_3^{1/4} - P_2^{1/4}) \quad [24]$$

If we take the model of Fig. 6 into account, the oxygen activity in the adsorbed phases, i.e., the equivalent pressures  $P'_3$  and  $P'_2$ , must be substituted for the gas pressures  $P_3$  and  $P_2$

$$J = \frac{\rho}{l} (P'_3{}^{1/4} - P'_2{}^{1/4}) \quad [25]$$

We will neglect here the local modifications of these equivalent oxygen pressures due to the influence of the metal. Insofar as the semipermeability is concerned, they appeared as a second order cause of error.

In Fig. 12 we have compared the measured values of  $J$  as functions of the measured pressures according to formulae [22] and [25]. The flux  $J$  was simply deduced from  $\Delta P$  using the measured values of the working gas flow rate and the sample surface. The comparison seems to indicate that formula [25] better fits the experimental results. The experimental results obtained at the other working temperatures yield similar plots.

In order to have a good determination of the parameter  $\rho$  for sample A, we carried out measurements over a wide temperature range, up to 1900°K. This was done with air as a reference gas and a working gas containing 0.5 ppm of oxygen initially. The pressure change  $\Delta P$ , the voltages  $E_Z$ ,  $E_{Pt}$ , and the gauge voltages were measured at various temperatures. The parameter  $\rho$  was calculated according to formula [25].

The results are reported in Fig. 13 together with the values representing the slope of the straight lines obeying relation [25] (cf. Fig. 12). The data fit well an Arrhenius law with an activation energy of 2.02 eV. This value is compared with the published data together with other parameters in Table II.

The scatter observed in the low temperature range results from the uncertainty of the measurements; in this range, the fluxes were determined by variations in oxygen content of the gas lower than 1 ppm. Taking into account the good fit in the range where the measurements were accurate enough, we have assumed that

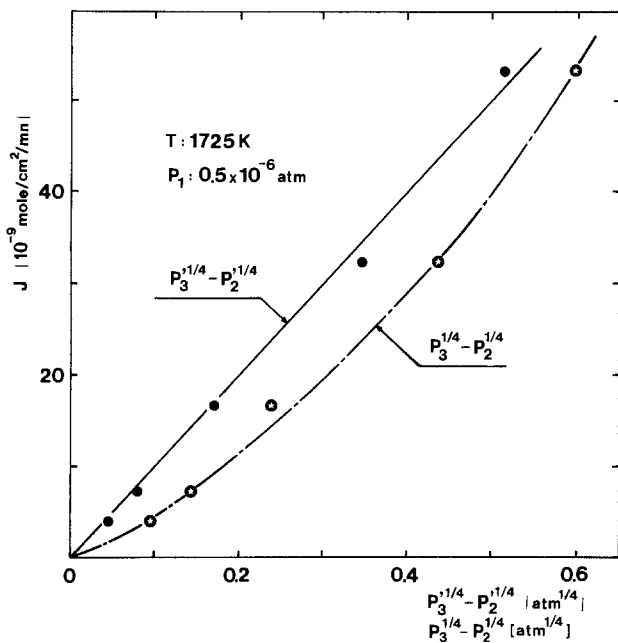


Fig. 12. Oxygen electrochemical semipermeability flux expressed as a function of the oxygen pressures  $P_2$  and  $P_3$  in the gases and the equivalent oxygen pressures  $P'_2$  and  $P'_3$  in the adsorbed layers.

the Arrhenius law represented by the straight line in Fig. 13 and Eq. [25] accurately determines the parameter  $\rho/l$  over the whole investigated range. In what follows, we will sometimes refer to these data and calculate the oxygen fluxes according to the relevant equations when the measurements were not accurate or sensitive enough.

#### Departure from Equilibrium Between the Electrode and the Gas

The oxygen semipermeability flux is determined by the electronic current through the electrolyte. The oxide ion flux, which is the oxygen semipermeability flux, simply compensates this current electrically. If the electronic current should pass in an external circuit, the oxide ion flux would be the same. This latter situation corresponds to electrode overpotential measurements. The "error"  $\Delta E$  is then called the overpotential

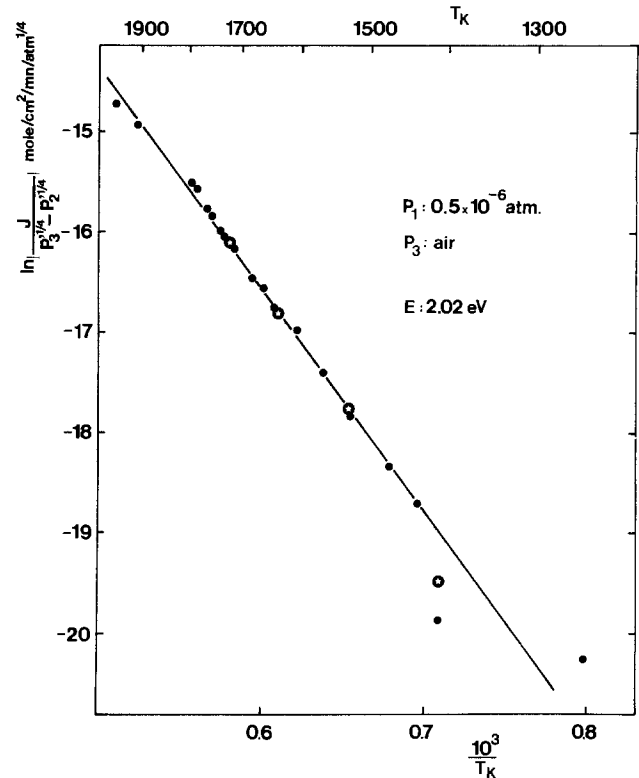


Fig. 13. Variation of the electrochemical semipermeability coefficient as a function of temperature. Stars: points representing the slope of the straight lines obeying relation [25].

$\eta$  and the oxide ion flux is simply the current  $I$ . From the similarity of these two situations it can be inferred that the relation between the error  $\Delta E$  and the semipermeability flux  $J$  must be similar to that between the overpotential  $\eta$  and the current  $I$ . The influence of the nature of the metal is qualitatively the same in both cases. It was shown (16) that the overpotential of a platinum electrode is higher than that of a silver electrode and that rhodium enhances the overpotential even more. The results just reported (cf. Fig. 10) are the same.

The overpotential  $\eta$  was found (4, 6, 16) to be related to the current  $I$  by the equation

Table II. Values of the oxygen semipermeability flux  $\pi^*$  and the activation energy  $E$  of the electronic conductivity calculated from published data

Electrolyte $ZrO_2$	Authors	$\pi^*$ at 1200°C (mole · cm <sup>-1</sup> · sec <sup>-1</sup> )	Oxygen pressure conditions		$E$ (eV)	Temp range (°C)	Pressure law
			$P_1$	$P_3$			
Oxygen Semipermeability Flux Measurements							
+ 11 m/o MgO	H. H. Moebius <i>et al.</i> (18)	$4 \times 10^{-7}$	N <sub>2</sub>	air	( $T > 1200^\circ\text{C}$ ) 1.81	800-1600	—
+ 8 m/o CaO	A. W. Smith <i>et al.</i> (27)	$1.4 \times 10^{-11}$	CO	25 Torr	2.41	1100-2050	$P_3^{1/4}$
+ 15 m/o Y <sub>2</sub> O <sub>3</sub>	R. Fabre (28)	$6.9 \times 10^{-10}$	N <sub>2</sub>	1 atm	0.39	1100-1300	—
+ 15 m/o CaO	R. Fabre (28)	$2.1 \times 10^{-9}$	N <sub>2</sub>	1 atm	0.53	1100-1300	—
+ 9 m/o Y <sub>2</sub> O <sub>3</sub>	R. Fabre (28)	$1.9 \times 10^{-10}$	N <sub>2</sub>	1 atm	2.3	1100-1300	—
+ 5 w/o (CaO + MgO)	H. Ullmann (29)	$1.8 \times 10^{-7}$	N <sub>2</sub>	air	( $T > 1200^\circ\text{C}$ ) 1.89 ( $T < 1200^\circ\text{C}$ ) 2.40	800-1400	—
+ 11 m/o CaO	R. Hartung <i>et al.</i> (30)	$2.5 \times 10^{-11}$	N <sub>2</sub>	air	2.25	800-1400	—
+ 14 m/o MgO	R. Hartung <i>et al.</i> (30)	$5.4 \times 10^{-11}$	N <sub>2</sub>	air	1.87	800-1400	—
+ 4.7 w/o CaO + 1.45 w/o MgO	B. Koroušić (31)	$2.7 \times 10^{-7}$	Ar	air	( $T < 1500^\circ\text{C}$ ) 1.89 ( $T > 1000^\circ\text{C}$ ) 2.17	1100-1600	$(P_3 - P_2)^{1/4}$
+ 7.5 w/o CaO	L. Heyne <i>et al.</i> (32)	$4 \times 10^{-11}$	vacuum	30 Torr	1.9	600-1000	$P_3^{1/3}$
+ CaO	W. A. Fischer (26)	$3 \times 10^{-10}$	$10^{-4}$ atm	1 atm	2.4	1342-1627	$1 - P_2^{1/4}$
+ Y <sub>2</sub> O <sub>3</sub> (zircoa)	C. B. Alcock <i>et al.</i> (33)	$3.3 \times 10^{-11}$	Ar, N <sub>2</sub> -O <sub>2</sub> , CO/CO <sub>2</sub>	25 Torr	2.48	1000-1600	$P_3^{1/2}$
+ 15 m/o CaO	V. V. Samokhval <i>et al.</i> (34)	$1.1 \times 10^{-10}$	$2.1 \times 10^{-3}$ atm	air	2.44	1000-1400	—
+ 7.5 w/o CaO	K. Kitazawa <i>et al.</i> (35)	$2.3 \times 10^{-10}$	$10^{-3.5}$ - $10^{-1.5}$ atm	air	( $T > 900^\circ\text{C}$ ) 2.73	640-1200	$P_3^m$ , ( $1/4 < m < 1/2$ )
+ 15 m/o CaO	R. A. Giddings <i>et al.</i> (39)	$1.8 \times 10^{-10}$	Fe/FeO	air	2.18	960-1222	—
+ 9 m/o Y <sub>2</sub> O <sub>3</sub>	This study	$4.1 \times 10^{-11}$	$5 \times 10^{-7}$ atm	air	2.02	950-1650	$P_3^{1/4} - P_2^{1/4}$
+ 15 m/o CaO	S. F. Palguez <i>et al.</i> (45)	$4.3 \times 10^{-11}$			1.61		
+ 10 m/o Y <sub>2</sub> O <sub>3</sub>	S. F. Palguez <i>et al.</i> (45)	$3 \times 10^{-11}$	0.01-1 atm	1 atm	1.87	900-1250	$P_3^{1/4}$
+ 10 m/o Sc <sub>2</sub> O <sub>3</sub>	S. F. Palguez <i>et al.</i> (45)	$2 \times 10^{-11}$			1.69		
Electronic Conductivity Measurements							
+ 15 m/o CaO	J. W. Patterson <i>et al.</i> (40)	$6.5 \times 10^{-10}$	Blocking electrode	air	2.2	800-1000	$P_3^{1/4}$
+ 15 m/o CaO	R. A. Giddings <i>et al.</i> (39)	$4 \times 10^{-10}$	Blocking electrode	air	2.27	932-1155	—

$$\eta = \frac{RT}{zF} \ln \frac{I_1 - I}{I_1} \quad [26]$$

With platinum,  $z$  was found (4, 16) to equal 2, and  $I_1$  is a parameter which appeared (6) to be proportional to the square root of the oxygen pressure  $P_{O_2}$  in the surrounding gas under oxygen pressures higher than about  $10^{-4}$  atm and to  $P_{O_2}^{2/3}$  under lower pressures.

According to the similarity previously mentioned, the error  $\Delta E$  should therefore be related to the oxygen semipermeability flux  $J$  by the equation

$$\Delta E = \frac{RT}{2F} \ln \frac{I_1 - J \cdot F}{I_1} \quad [27]$$

or after transformation

$$J \cdot F = -I_1 \left( \exp \frac{2F\Delta E}{RT} - 1 \right) \quad [28]$$

To check the validity of this equation we plotted  $J$  as a function of  $(\exp 2F\Delta E/RT - 1)$  under such conditions that  $I_1$  could be considered as constant, that is to say, under a constant oxygen pressure. Under these conditions we could obviously not measure experimentally the flux  $J$  which is determined by the variations of the oxygen pressure. We used instead a calculation based on Eq. [25] and on the Arrhenius law shown in Fig. 13. Figure 14 and 15 give two examples of such plots obtained with the point electrode.

We also studied the variations of  $I_1 \cdot F^{-1}$  which is equal to  $J(\exp 2F\Delta E/RT - 1)^{-1}$  as a function of the oxygen pressure in the surrounding gas. Figures 16 and 17 show two plots of these variations which confirm

that the  $P_{O_2}^{1/2}$  and  $P_{O_2}^{2/3}$  laws are approximately obeyed in the medium and low oxygen pressure ranges. In fact, some of our experimental results do not fit these laws so well, the exponent in the observed  $P_{O_2}^m$  ranging from 0.5 to 0.75.

It was also shown (6) that the proportionality coefficients  $B_{1/2}$  and  $B_{2/3}$  between  $I_1$  and  $P_{O_2}^{1/2}$  or  $P_{O_2}^{2/3}$

$$I_1 = B_{1/2} P_{O_2}^{1/2} \quad [29]$$

$$I_1 = B_{2/3} P_{O_2}^{2/3} \quad [30]$$

are activated with activation energies of 1.15 eV for  $B_{1/2}$  and 1.10 for  $B_{2/3}$ . The results obtained with the large surface electrode and under medium oxygen pressures give an activation energy of approximately 1.0 eV which is in rather good agreement with that just recalled. The results obtained with the point electrode and under low oxygen pressure are unfortunately totally different; the activation energy is equal to 1.9 eV. No obvious explanation was found for this difference. Several suggestions could be made: (i) the investigated temperature ranges are different: 1050°-1480°K for the overpotential measurements, 1250°-1900°K for the measurements reported here; (ii) the similarity on which our derivation is based holds only for a macroscopic approach. On a microscopic scale the dominant elementary step of the over-all phenomenon would be different. In the semipermeability experiments the gradients of chemical potential are regularly directed from one surface of the electrolyte to the other. In the overpotential experiments, in the close vicinity of the electrode, the electrochemical potential gradients are certainly directed toward the

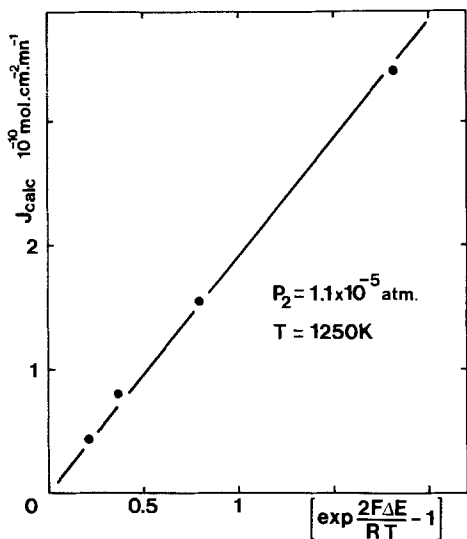


Fig. 14

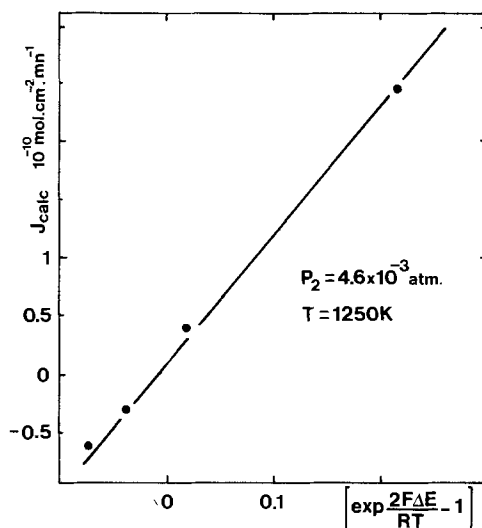


Fig. 15

Fig. 14, 15. Verification of Eq. [28] expressing the similarity between the error  $\Delta E$  and a conventional overpotential.

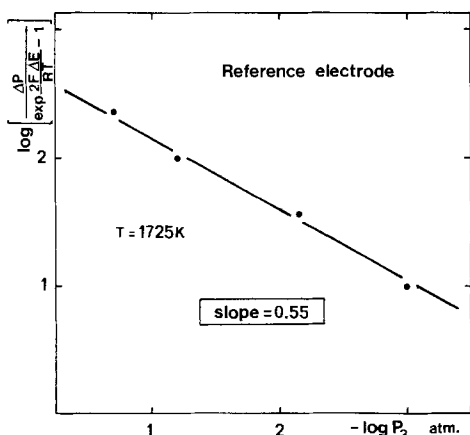


Fig. 16

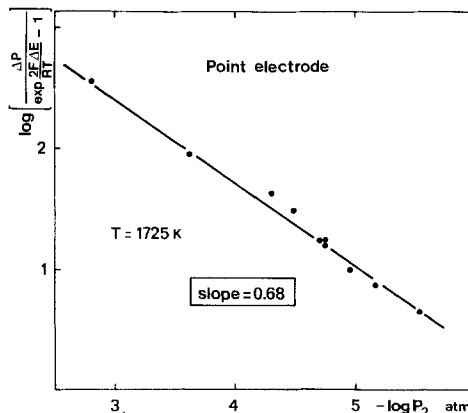


Fig. 17

Fig. 16, 17. Variation of the parameter  $I_1$  as a function of the oxygen pressure.

triple contact of the electrode. This could cause diffusion on the surface of the sample, for example.

### Conclusions

Whatever the physical description of the microsystem, it seems well established that it constitutes a necessary intermediate stage between the electrode and the gas. Furthermore, the oxygen exchange rate between the microsystem and the gas has a finite value which is not always sufficient to maintain the equilibrium. From this simple statement several practical conclusions must be drawn. When making a gauge, it is of interest to select not only the electrolyte having the smallest semipermeability coefficient  $\rho$ , but also the electrode materials leading to the smallest overpotential of the electrode.

A gauge voltage  $E$  can be written

$$E = \frac{RT}{4F} \ln P - \frac{RT}{4F} \ln P_{\text{Ref}} \quad [31]$$

As previously shown, the error made in ascribing the first term to the oxygen pressure being measured can be decomposed into two components,  $\Delta P$  and  $\Delta E$ . Although not recognized so far, the error  $\Delta E$  may have been very frequent. For instance, the experimental results recently reported by Cherkasov *et al.* (25) and Alcock *et al.* (33) where the departures from the theoretical emf were much larger than that predicted by the  $(1 - \bar{t}_e)$  coefficient, were likely to result from a noticeable value for the error  $\Delta E$ .

Increasing the gas flow rate, as it is frequently suggested (37), until the gauge voltage no longer depends on it only reduces the error  $\Delta P$  to a very negligible value but not necessarily  $\Delta E$ . (In fact, in such an experiment  $\Delta E$  increases as  $\Delta P$  decreases.) The results reported here have shown that  $\Delta E$  can be very large even when  $\Delta P$  is zero. In fact, all the experiments we have done so far indicate that, with oxygen contents smaller than roughly 50 ppm and air as a reference gas, it is necessary to operate the gauge at a temperature at least 200° lower than that where the semipermeability flux becomes noticeable on a 1 ppm scale to have any chance of observing a negligible  $\Delta E$  value.

The properties previously described are not specific to oxygen; they were also observed with CO-CO<sub>2</sub> mixtures and are likely to hold with the H<sub>2</sub>-H<sub>2</sub>O system. In any cell where the electrode potentials are fixed by gaseous systems, the errors previously described may be found. That means, in particular, that we may make errors in measuring an electronic transport number by the emf method using gaseous systems. The errors are especially likely when the oxygen flux through the sample, that is to say its electronic conductivity, is large and also when the buffer effect of the gases is weak (argon with low oxygen content, CO-CO<sub>2</sub> mixtures with small content of either CO or CO<sub>2</sub>, etc.). This point was verified experimentally (3) by comparing the results obtained under these conditions on a ZrO<sub>2</sub>-Y<sub>2</sub>O<sub>3</sub>-CeO<sub>2</sub> sample to those obtained with metal-metal oxide electrodes. They have shown that the error may be very large.

In transient phenomena like those described by Heyne (32), for instance, the electrode microsystems are likely to play an important part in the measurement of the time lag of the oxygen permeation.

Referring to the results obtained with the zirconia point electrode, another remark can be made regarding the solid bielectrolyte cells which were used for instance by Tretyakov *et al.* (36), Fender *et al.* (41), and Salzano *et al.* (42), and which were criticized by Shores and Rapp (43). According to the arguments raised in the last paper and our results, the only positive way of using such cells is to insure the contact between the two electrolytes by coarse grains of a conveniently selected electrolyte surrounded by a gas having an oxygen activity close to that surrounding the less reversible electrode of the cell. This has the advantage of stopping the semipermeability flux in the

intermediate space and then preventing this flux from reaching the considered electrode and disturbing its equilibrium. This obviously does not in principle reduce the errors which are usually described by the  $(1 - \bar{t}_e)$  factor. On the other hand, insuring the contact between the two electrolytes by a metal such as platinum doubles the sources of error by doubling the number of electrode microsystems which can be disturbed. This point is well substantiated by the results which were obtained with the differential gauges (7).

### Acknowledgments

The authors are greatly indebted to Mr. Hénault and Mr. Dessart for the preparation of the samples.

Manuscript submitted March 27, 1975; revised manuscript received Oct. 27, 1975.

Any discussion of this paper will appear in a Discussion Section to be published in the December 1976 JOURNAL. All discussions for the December 1976 Discussion Section should be submitted by Aug. 1, 1976.

Publication costs of this article were partially assisted by Equipe Associée au CNRS, ERA 384.

### REFERENCES

1. M. Kleitz, P. Fabry, and E. Schouler, in "Fast Ion Transport in Solids," W. Van Gool, Editor, p. 439, North-Holland Publishing Co., Amsterdam (1973).
2. J. Fouletier, H. Seiner, and M. Kleitz, *J. Appl. Electrochem.*, **4**, 305 (1974).
3. P. Fabry, M. Kleitz, and C. Déportes, *J. Solid State Chem.*, **5**, 1 (1972).
4. M. Kleitz, C. Déportes, and J. Besson, Proceedings of the Deuxième Journées Internationales d'Etudes des Piles à Combustible, p. 354, COMASI, Bruxelles (1967).
5. C. J. Mogab, *J. Vacuum Sci. Technol.*, **10**, 852 (1973).
6. P. Fabry and M. Kleitz, *J. Electroanal. Chem.*, **57**, 165 (1974).
7. J. Fouletier, H. Seiner, and M. Kleitz, *J. Appl. Electrochem.*, **5**, 177 (1975).
8. P. Fabry, Diplôme d'Etudes Approfondies, Grenoble (1968).
9. H. J. de Bruin, A. F. Moodie, and C. E. Warble, *J. Austr. Ceram. Soc.*, **7**, 57 (1971).
10. H. J. de Bruin, A. F. Moodie, and C. E. Warble, *Gold Bull.*, **5**, 62 (1972).
11. H. J. de Bruin, A. F. Moodie, and C. E. Warble, *J. Mater. Sci.*, **7**, 909 (1972).
12. T. Takahashi, K. Ito, and H. Iwahara, Proceedings of the Deuxième Journées Internationales d'Etudes des Piles à Combustible, p. 42, Bruxelles (1967).
13. S. Zador and C. B. Alcock, *J. Chem. Thermodyn.*, **2**, 9 (1970).
14. D. Jakes, *Collection Czech. Chem. Commun.*, **38**, 1 (1973).
15. A. Guillot, P. Canale, and A. M. Anthony, *Rev. Int. Hautes Temp. Refract.*, **11**, 93 (1974).
16. M. Kleitz, Thesis, Grenoble (1968).
17. E. Schouler, M. Kleitz, and C. Déportes, *J. Chim. Phys.*, **9**, 1309 (1973).
18. H. H. Moebius and R. Hartung, *Silikat. Tech.*, **16**, 276 (1965).
19. L. D. Yushina and S. V. Karpachev, *Tr. Inst. Elektrokhim., Akad. Nauk SSSR, Ural'sk. Filial*, **14**, 122 (1970).
20. J. Weissbart and L. S. Rowley, Paper 31 presented at The Electrochemical Society Meeting, Washington, D. C., October 11-15, 1964.
21. Y. M. Ovchinnikov, S. V. Karpachev, A. D. Neumin, and S. F. Palguyev, *Ogneupory*, **30**, 40 (1965).
22. A. A. Vecher and D. V. Vecher, *Dokl. Akad. Nauk Belorussk. SSR*, **11**, 610 (1967).
23. A. A. Vecher and D. V. Vecher, *Russ. J. Phys. Chem.*, **42**, 48 (1968).
24. W. A. Fischer and D. Janke, *Z. Physik. Chem. (Frankfurt)*, **69**, 11 (1970); *Arch. Eisenhuettenw.*, **41**, 1027 (1970).
25. P. A. Cherkasov, W. A. Fischer, and C. Pieper, *ibid.*, **42**, 873 (1971).
26. W. A. Fischer, in "Fast Ion Transport in Solids," W. Van Gool, Editor, p. 503, North-Holland Publishing Co., Amsterdam (1973).

27. A. W. Smith, F. W. Meszaros, and C. D. Amata, *J. Am. Ceram. Soc.*, **49**, 240 (1966).  
 28. R. Fabre, Thesis, Grenoble, (1967).  
 29. H. Ullmann, *Z. Physik. Chem.*, (Leipzig), **237**, 71 (1968).  
 30. R. Hartung and H. H. Moebius, *ibid.*, **243**, 133 (1970).  
 31. B. Koroušić, *Rudarsko-Met. Zbornik*, **2-3**, 275 (1971).  
 32. L. Heyne and N. M. Beekmans, *Proc. Brit. Ceram. Soc.*, **19**, 229 (1971).  
 33. C. B. Alcock and J. C. Chan, *Can. Met. Quart.*, **11**, 559 (1972).  
 34. V. V. Samokhval, G. I. Loiko, and A. A. Vecher, *Russ. J. Phys. Chem.*, **47**, 1283 (1973).  
 35. K. Kitazawa and R. L. Coble, *J. Am. Ceram. Soc.*, **57**, 360 (1974).  
 36. J. D. Tretyakov and A. Muan, *This Journal*, **116**, 331 (1969).  
 37. H. Ullmann, *Z. Physik. Chem. (Leipzig)*, **250**, 195 (1972).  
 38. C. Wagner, *Proc. Intern. Comm. Electrochem. Thermodyn. Kinet.*, 7th Meeting, London, 1955, p. 361, Butterworths, London (1957).  
 39. R. A. Giddings and R. S. Gordon, *This Journal*, **121**, 793 (1974).  
 40. J. W. Patterson, E. C. Bogren, and R. A. Rapp, *ibid.*, **114**, 752 (1967).  
 41. B. E. F. Fender and F. D. Riley, in "Chemically Extended Defects in Non-Metal," L. Eyring, Editor, p. 54, North-Holland Publishing Co., Amsterdam (1970).  
 42. F. J. Salzano, H. S. Isaacs, and B. Minushkin, *This Journal*, **118**, 412 (1971).  
 43. D. A. Shores and R. A. Rapp, *ibid.*, **118**, 1107 (1971).  
 44. P. Fabry, Thesis, To be published.  
 45. S. F. Palguez, V. K. Gilderman, and A. D. Neujmin, *This Journal*, **122**, 745 (1975).

## Energy Curves for the Hydrogen Evolution Reaction: Case of the Discharge Step

C. M. Marschoff\* and P. J. Aragón\*<sup>1</sup>

*Departamento de Química, Universidad de los Andes, Mérida, Venezuela*

### ABSTRACT

Using the Gomer-Swanson approximation and the results from Smith *et al.* (46), the potential energy curves for the discharge step of the hydrogen evolution reaction (HER) on several metals are obtained as a function of bond order. Using a modified BEBO method the classical activation energy is calculated in each case considered. "True" activation energies and enthalpy changes are estimated. Previous work is reviewed.

Although they are of undisputable importance in the study of rate processes, the calculation and experimental determination of activation energies have been only seldomly performed in the case of electrode processes. Even less have they been used in theoretical interpretation or prediction of reaction mechanisms. There are, indeed, powerful reasons for this being so: (i) in the experimental determination of activation energies there exists a thermal effect on the potential measurements that cannot be avoided (1) and that is due to the arbitrariness of the zero definition in the potential scale; (ii) the theoretical calculations of potential energy curves as a function of distance to the electrode must include image interactions, whose values are not well known for points located at very short distances from the metallic surface (2-4).

Nevertheless, any effort directed to the development of a theoretical approach to electrode processes must be recognized as worthwhile, and this should include, in a natural way, use and interpretation of activation energies. Up to now this has been approached by two main routes, namely, the so-called electrostatic theories and the model and methods based on the absolute rate theory.

The electrostatic approach, developed chiefly by Marcus (5-10) and Levich, Dogonadze, and co-workers (11-16) has been recently reviewed by Lamy (17). However, application of these models to real cases is difficult, and accord with experiment is far from good (18) due to oversimplifying assumptions of the theory; particularly, the dielectric continuum hypothesis (19) and the lack of specific consideration of the metallic surface (20) must be pointed out.

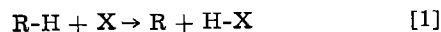
On the other hand, typical transition state theories (21,22) are known to be unreliable (23), and the modifications proposed to account for electrode processes (24-27) have shown inconsistencies, specially regarding vibrational characteristics and bond orders during the activation process (28). Besides, these models, as those based on the electrostatic approach, also dismiss the influence of the metallic surface through image effects.

As the exact solution of the many-body problem corresponding to the situation at an electrode-solution interface is far beyond actual computer facilities, it seems reasonable to look for empirical or semiempirical methods in order to attack some of the questions already unsolved in electrode processes. Considering the simplest electrode process, *i.e.*, the hydrogen evolution reaction when discharge is rate determining, Salomon, Enke, and Conway (3) have proposed that the bond energy-bond order (BEBO) method developed by Johnston and co-workers (29-31) for proton transfer might be used. Calculations based on the BEBO method have not been further pursued and even the attempt by Salomon *et al.* is only rarely mentioned in the literature (18, 28).

In this paper, some considerations on the use of the BEBO method for electrode processes are given, and a new way of calculating activation energies for the discharge step in HER is presented.

### The BEBO Method in Electrode Processes

The BEBO method was developed as an empirical tool for calculating activation energies of proton transfer reactions that proceed in the gas phase. The basic assumption of the method is that, since bonds involving a hydrogen atom have energies of about 100 kcal/mole or more, and activation energies for processes of the type



\* Electrochemical Society Active Member.

<sup>1</sup> Present address: COMINCO Research Centre, Sheridan Park, Ontario L6K 1B4, Canada.

Key words: proton transfer, image forces, BEBO method, "jellium" model for surfaces, Gomer-Swanson approximation.

are always below 20 kcal/mole, the activation step of such reactions should proceed through gradual destruction of the R-H bond and simultaneous gradual building up of the H-X bond. Considering bond order as a measure of bond existence the above argument is resumed in the postulate of total bond order conservation (31)

$$n + m = 1 \quad [2]$$

where, referring to reaction [1],  $n$  is the bond order for the R-H molecule and  $m$  is the H-X bond order. Bond order is defined as a function of bond length through the following equation, due to Pauling (32)

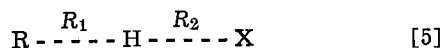
$$R = R_s - 0.26 \ln n \quad [3]$$

where  $R$  is the bond length at bond order  $n$  and  $R_s$  is the nonperturbed bond length, *i.e.*, bond length when  $n$  is 1. Besides, bond energy and bond order are linked through the following equation (31)

$$D = D_s n^p \quad [4]$$

where  $D$  is the bond energy at bond order  $n$ ,  $D_s$  is the bond energy for the nonperturbed bond and  $p$  is a characteristic index that depends on the row of the Periodic Table in which the atoms forming the bond are located.

Considering the activated complex corresponding to reaction [1] as



Eq. [4], together with condition [2], permits the calculation of  $D_1$  and  $D_2$ , the bond energies for R-H and H-X bonds respectively, as a function of bond order. Nevertheless, in order to obtain the total energy for the whole system, the triplet repulsion between R and X must be taken into account. The expression proposed by Johnston and Parr (31), based on an anti-Morse function is

$$V = \frac{D_{3s} \exp(-a\Delta R_s) \cdot (nm)^{0.26a}}{2} \cdot \frac{1 + \exp(-a\Delta R_s) (nm)^{0.26a}}{2} \quad [6]$$

where  $V$  is the triplet energy,  $D_{3s}$  is the bond energy for the R-X molecule,  $a$  is the Morse constant for the same bond and  $\Delta R_s$  is

$$\Delta R_s = R_{1s} + R_{2s} - R_{3s} \quad [7]$$

the  $R_{1s}$  being the equilibrium distances for the corresponding bonds.

The total energy for the system is obtained, defining the energy zero for the configuration consisting of the R-H molecule at infinite distance from X, as

$$E = D_{1s}(1 - n^p) - D_{2s}(1 - n)^q + V \quad [8]$$

where  $q$  is the analog of  $p$  for the H-X bond. The maximum of this function should give the classical activation energy; so, differentiating Eq. 8 with respect to  $n$  and equating to zero, the bond orders at the activated complex configuration are obtained. Using these values in Eq. [8], one may calculate the activation energy.

As it has been said, the value thus obtained corresponds to the classical activation energy,  $E_c$ . If the "true" activation energy,  $E_o$  is wanted, the vibrational frequencies of the activated state should be known. Johnston and Parr suggest a way of calculating these frequencies through the determination of the force constants along the reaction coordinate and along the direction perpendicular to the reaction coordinate. The first of these force constants,  $F_\rho$ , is obtained by twice differentiating Eq. [8] with respect to  $\rho$ , the reaction coordinate. The second,  $F_\sigma$ , is calculated assuming that it follows a Badger-like rule (30, 33)

$$F_\sigma = \frac{F_{1s}n^3 + F_{2s}m^3 + F_{3s}(nm)^{0.26a} \exp(-a\Delta R_s)}{n^2 + m^2} \quad [9]$$

From the knowledge of  $F_\rho$  and  $F_\sigma$  it is possible to obtain the force constants along the internal coordinates  $F_{11}$ ,  $F_{22}$ , and  $F_{12}$ . Then, using Wilson's method, the frequencies in the activated state are calculated.

Considering that the HER on Hg has the discharge step as rate determining (34, 35) and accepting Conway and Salomon's suggestion that the rate-determining event in this case is the adiabatic transfer of a proton followed by nonadiabatic electron neutralization (36-38), Salomon *et al.* (3) used the BEBO method for the calculation of some fundamental parameters (activation energy, absolute electrode potential) of this electrode reaction. It will prove convenient for this presentation to describe, at least roughly, this calculation. According to the absolute rate theory (39), the exchange current may be expressed as a function of the classical activation energy, the vibrational frequencies of the activated complex, the absolute electrode potential corresponding to the electron reaction under study and a set of experimentally available data such as the electrochemical transfer coefficient for the particular reaction, the potential at the outer Helmholtz plane [obtainable for Hg from Grahame's data (40, 41)], partition functions for the hydroxonium ion, etc. Using these values and the experimentally determined exchange current, the following equations were obtained for a 0.1N HCl solution (3)

$$\exp(\beta\phi_r F/RT) = 1.31 \times 10^{22} \pi^3 (2 \sinh u\#)^{-1} \exp(-E_c/RT) \quad [10]$$

at 25°C and

$$\exp(\beta\phi_r F/RT) = 4.45 \times 10^{19} \pi^3 (2 \sinh u\#)^{-1} \exp(-E_c/RT) \quad [11]$$

for 85°C. In these expressions  $\beta$  is the transfer coefficient,  $\phi_r$  is the absolute electrode potential,  $E_c$  is the classical activation energy, and  $u$  is defined as  $hc\omega/2kT$  being  $\omega$  the frequency in  $\text{cm}^{-1}$ . The vibrational frequencies at the activated state may be obtained through the BEBO method if the necessary data are known. However,  $D_{2s}$ , the bond energy for the proton-metal bond is not experimentally accessible; hence, in Salomon *et al.*'s calculation this quantity is taken as an adjustable parameter. The corresponding absolute electrode potential is obtained for each  $D_{2s}$  value, both at 25°C and at 85°C. Then, using the Gibbs-Helmholtz equation,  $\Delta S$  and  $\Delta H$  are calculated for the electrode reaction. Once  $\Delta H$  is known, the experimentally accessible activation energy may be calculated through the relation

$$E_{\text{exp}} = E_o + RT - \beta\Delta H \quad [12]$$

where  $E_o$  is obtained through the well-known equation

$$E_o = E_c - \frac{1}{2} hc \sum (\omega_{H+} - \omega\#) \quad [13]$$

The value of  $D_{2s}$  that makes the calculated  $E_{\text{exp}}$  fit the observed value is considered to be the correct energy for the proton-metal bond.

Although the present authors think that electrode processes involving proton transfer may be reasonably considered within the basic ideas underlying the BEBO method, there are several observations that must be made on the calculation carried out by Salomon *et al.* In the first place, it must be said that, although the electrostatic energy arising as a consequence of image effects is somehow considered when the energy of the metal-proton bond is fitted to the observed value of the activation energy, image effects are absolutely dismissed in the initial state. In this case, the total energy of the system is considered to be simply that of the nonperturbed hydrogen oxygen bond,  $D_{1s}$ . Now, the image interaction will exist not only when the proton-



metal bond is formed, but also in the initial state, since the hydroxonium ion carries an electric charge and is in close vicinity to the metallic surface. In consequence, the bare use of  $D_{1s}$  should not be acceptable. On the other hand, the way in which image effects are taken into account when the system is in the final state is also not correct. This is so because being due to long range forces, image interactions will depend on the metal-proton distance in a different way than that proposed by Johnston and Parr for chemical bonds; hence, the energy contribution due to electrostatic image effects should be included as a separate term in the expression that relates the total energy of the system with distances between atoms or, considering Pauling's relation, with bond orders.

Second, a word must be said with respect to the use of the equation linking bond length and bond order. Pauling's original relation, Eq. [3], was obtained for simple bonds between atoms or groups in cases in which no external fields were acting on the system. The situation when a proton approaches a metallic surface is very different: electric fields (due to image effects) appear, and the bond is not a bond between two free atoms or groups of atoms but between a free ion (the proton) and a metal atom that, being part of a lattice, has lost its translational freedom degrees and is subject to strong interactions with its neighbors. In consequence, it seems reasonable to assume that the original equation relating bond length and bond order should be modified to take into account the presence of the surface and the different nature of the bond established.

Third, it should be pointed out that the expression used by Salomon *et al.* for the triplet repulsion energy is not correct. They consider

$$V = D_{3s} \exp(-a\Delta R_s) nm^{0.26a} (1 + nm^{0.26a})/2 \quad [14]$$

instead of the correct expression, Eq. [6]. The omission of the brackets in the latter equation is due to a misprint in the original paper by Johnston and Parr [cf. Eq. (22) and (23) in Ref. (31)]. This mistake has little consequence on the absolute value of the total energy of the system since triplet terms are very small (20); however, since bond orders at the activated state are obtained by differentiation of the total energy with respect to  $n$ , the omission becomes significant, as is shown in Table I, where the bond order values that maximize both the correct form of the total energy and that used by Salomon *et al.* are listed, as well as the activation energies and absolute electrode potentials that result in each case if the calculation proposed by these authors is carried out.

Finally, there remains the question of the accuracy of the method. In reference to this, there are two facts that should be considered: (i) Two differentiations must be made on expressions that are ultimately empirical or semiempirical. The first one is performed in order to obtain the bond orders at the activated complex; the second differentiation is made when the Gibbs-Helmholtz equation is employed in order to determine the  $\Delta H$  value for the electrode reaction. Differentiating an empirical expression will introduce a larger error than that contained in the original equation, and this will be particularly true in the case of the Gibbs-Helmholtz equation since it is performed assuming linear behavior between 25° and 85°C. (ii) The vibrational characteristics of the activated complex are not reliable, since the value of the force constant on the direction perpendicular to the reaction

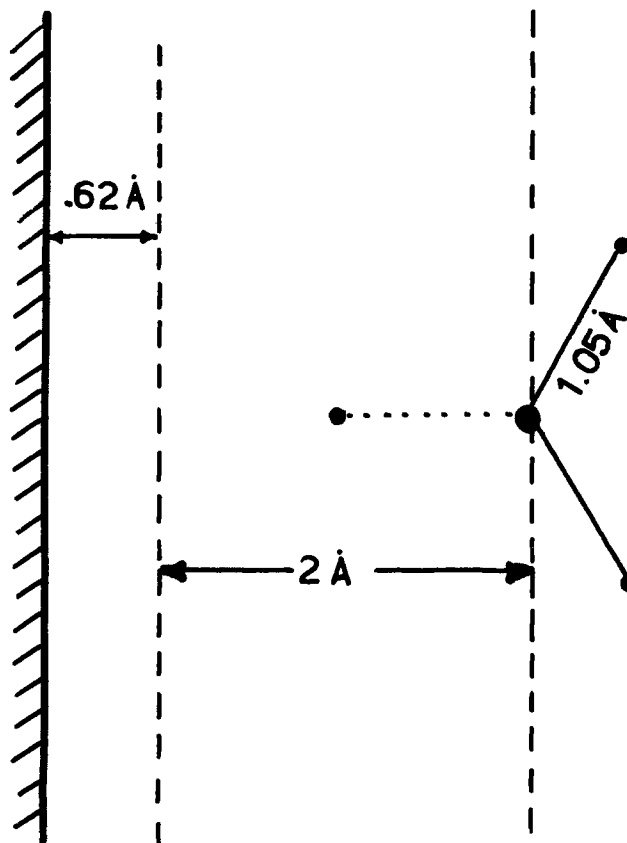


Fig. 1. Model for the system at the initial state. The screening length is that of Hg.

coordinate,  $F_{\sigma}$ , is of dubious validity because this force constant is obtained through an expression proposed by similarity with an empirical rule for diatomic molecules, due to Badger (30, 33). The use of this definition, as one of the present authors has shown (20, 42) leads to some contradictions in the bond order values at the activated complex.

In consequence, if the BEBO method or its basic ideas are to be applied to the HER, these points should be kept in mind. As we shall see, when they are considered it will be necessary to restate some of Johnston's considerations in order to deal with electrode processes.

### Model for the Activation Event

In view of Conway and Salomon's arguments (36-38) and considering that the binding energy of a proton to a water molecule is about 180 kcal/mole (43, 44), compared to a total ionic hydration energy of about 245 kcal/mole (45), the hypothesis of an adiabatic proton transfer as rate-determining event will be accepted. Also, the description given in Ref. (3) of the activated complex will be retained with a few extra considerations. The initial situation will be depicted as a planar hydroxonium ion located at the inner Helmholtz plane (accessible for instance by a Grotthuss mechanism) with its oxygen atom at about 2 Å from the metallic surface (considered as a plane) as shown in Fig. 1. As in Ref. (3), the nonreacting O-H bonds will be considered to remain unmodified during the activation process carrying the system from the initial to the

Table I. Obtained values for bond order of the O-H bond in the activated state ( $n\#$ ) and for energetic parameters using the method proposed by Salomon *et al.* (3) with Eq. [13] for the triplet repulsion (first row) and using the correct form, Eq. [6] (second row).

$D_{2s}$ , kcal/mole	$n\#$	$E_c$ , kcal/mole	$E_o$ , kcal/mole	$\phi_{25}$ , mV	$\phi_{85}$ , mV	$\Delta H$ , kcal/mole	$E_{exp}$ , kcal/mole
155	0.20	29.1	25.5	-225	-185	10.9	20.1
155	0.15	30.6	28.3	-386	-208	-11.4	34.6

activated state. The final state will be considered as a proton adsorbed onto the metallic surface.

It is convenient here to point out that the configuration assumed for the final state does not consider the fact of electron transfer from the metal to the proton. In consequence, this state need not have actual existence and in the case of HER is, almost surely, hypothetical. This may be considered so, if the activation energy is going to be obtained through the drawing of potential energy curves for the initial and "final" states, because the rate-determining event takes place before the electron is transferred.

The adopted model for the activation process and the activation complex allows treating the problem as if it were a three "particle" system composed of the OH<sub>2</sub> group (assumed to be invariant during the activation process), the proton, and the metallic surface. The zero point energy will be defined for the configuration in which all the three entities lie infinitely apart from each other. The bond length for the non-reacting O-H groups will be considered to be 1.05Å (43) and the equilibrium proton-metal distance will be taken to be 0.6Å according to calculations made by Smith, Ying, and Kohn (46).

### Image Effects and Energy Calculations for Two Specific Configurations

As pointed out previously electrostatic effects due to image interactions should be included at every stage of the process as a different term than those corresponding to bond energies. Of course, the electrostatic energy resulting from image interactions between atoms and the metal should not be considered as a modification to the bond energy of a particular bond but, rather, as a contribution to the total energy of the system that may be written, for any configuration, as

$$E = U_{\text{elect}} + U_{\text{nonel}} \quad [15]$$

where  $U_{\text{elect}}$  represents the contribution of the coulombic interactions and  $U_{\text{nonel}}$  accounts for the energy of the system if image effects do not exist. In our case,  $U_{\text{nonel}}$  will be considered to correspond to the bond energies between atoms and groups of atoms.

Our problem, now, is to determine how these two terms are to be calculated for any value of the reaction coordinate. As a first step we will make an estimate of the total energy for the system in the initial and the "final" states and afterwards, using these results, a method of building up the corresponding potential energy curves will be presented.

*The energy of the initial state.*—Classically, a point charge  $q$  at a distance  $r$  from the surface of a perfect conductor produces an extra field equivalent, in vacuum, to that of a charge  $-q$  at the image point with respect to the plane of the conductor. Hence, in the absence of external fields, the energy of such a charge would be

$$U = -q^2/4r \quad [16]$$

As is well known, the classical image potential gives interaction energies that are too high when the distance to the surface becomes small, being the deviation due to the screening effect of the metal. To account for this screening capability the linearized Thomas-Fermi approximation (TFA) may be used (47).

The TFA is developed for cases in which the screening length of the metal ( $\lambda^{-1}$ ) is much bigger than the Fermi wavelength ( $\lambda_F$ ). Actually, most metals do not satisfy this ideality condition; nevertheless, calculations going beyond the TFA are cumbersome and there exist doubts whether the boundary conditions have been properly considered in these refined approximations (48-50). For this reason, and on account of its simplicity, the TFA will be maintained.

The response of a metallic surface to an external point charge within the TFA has been derived by Newns (50) who obtained, for the electrostatic energy of a charge  $q$ , a definite integral that depends on  $r$  and

$\lambda^{-1}$ . This integral may be calculated by numerical methods and it is seen that when  $r > \lambda^{-1}$  its value is well approximated by the Gomer-Swanson equation that considers a classical energy but with the surface recessed in  $\lambda^{-1}$  (51)

$$U = -q^2/4(r + \lambda^{-1}) \quad [17]$$

Considering the initial state, the distances between the metallic surface and the atoms in the hydroxonium ion are larger than the screening length; therefore, the Gomer-Swanson approximation (GSA) may be used in calculating the coulombic energy of this state. To do this, each atom in the hydroxonium ion will be considered to carry an electric charge. Contribution of terms depending on atomic polarizabilities may be disregarded within the distance range in which we are working, as is shown by the results of Antoniewicz (52).

Using reported charge densities for the planar configuration of the hydroxonium ion (43), the total energy at the initial state was calculated for Hg, Cu, Ni, and Au. Charge densities are 0.359  $e_0$  for the oxygen atom and  $-0.453 e_0$  for each hydrogen atom, where  $e_0$  is the electronic charge. Screening lengths for the different metals were obtained through the equation (53)

$$\lambda^{-1} = (E_F/6\pi n_0 e_0^2)^{1/2} \quad [18]$$

where  $E_F$  is the Fermi energy and  $n_0$  is the electron density per cubic centimeter, calculated under the consideration that the number of free electrons per atom is given by the number of the corresponding group in the Periodic Table.

The chemical energy for the proton-oxygen bond at the initial state is considered to be 180 kcal/mole (3, 43, 44). The results obtained for the metals under consideration are shown in Table II.

*The energy for the system metal-proton.*—If the total energy of the system formed by a proton adsorbed onto a metallic surface is to be calculated, one must be aware that at distances near the equilibrium bond length of the metal-proton system the TFA will not be reliable and, of course, the GSA will not be valid (54). A possible breakthrough for this problem is the use of results obtained from the "jellium" model (54, 55). This model considers a metal as a lattice of point positive charges immersed in an "electron gas," *i.e.*, a negative charge continuum. When surface effects are to be considered the inhomogeneity introduced by the presence of the surface is taken into account within the jellium model by assuming a negative charge distribution outside the plane of the metal. After calculating the energy of a free electron gas that corresponds to this model (56, 57), the influence of the positive ion lattice is included by considering the additional constraint that Poisson's equation must be satisfied point by point (46, 57). The energy arising when a proton approaches a metallic surface may also be calculated with this additional condition using the jellium model, and numerical results have been obtained for the case of a tungsten surface (46).

If the hypotheses of the jellium approach are considered, it is clear that this model will account basically for electrostatic interactions, since jellium does not consider surface states, nor represents the localized electron densities arising when chemical bonding exists.

Table II. Energy values for the initial state obtained considering the electrostatic term by the Gomer-Swanson approximation. The chemical bond for O-H in hydroxonium was taken to be 180 kcal/mole. Net charges on the ion atoms were taken from Ref. (43).

Metal	$\lambda^{-1}$ , Å	$E_{n=1}$ , kcal/mole
Hg	0.62	212
Cu	0.55	213
Ni	0.77	210
Au	0.59	212

For the same reason, potential energy curves for metal-proton systems obtained by the jellium model will only slightly vary in shape from metal to metal and the equilibrium energy will be basically modified according to work function differences. In consequence, the electrostatic energy arising when a proton interacts with a metallic surface will be considered as given by a potential energy curve of the same shape as that obtained for tungsten (46) but with its equilibrium energy modified by the corresponding work function difference

The chemical interaction that arises when a proton approaches a metallic surface is of a different kind and may be linked to hydride formation (58). Data for  $MH^+$  hydrides should be preferred in this case to those corresponding to neutral monohydrides. However, except for a few cases (Zn, Cd, Hg, Al, Mg),  $MH^+$  bond energies have not been determined (59); so, neutral monohydrides bond energies will be used as a first approximation, being aware that the value used will be smaller, in modulus, than that corresponding to the charged hydride. Nevertheless, this difference will be much less in the cases of Cu, Ni, and Au than that observed for Zn, Cd, and Hg for which values of the bond energy vary by a factor of 10 from  $MH^+$  to  $MH$ , because in the latter metals the  $s$ -orbital and the  $d$ -orbital are filled. Energy values for monohydrides were taken from Herzberg's tables (60). Work functions from the critical recompilation made by Trasatti (61) were used. The obtained results for the four metals under study are listed in Table III.

### The Classical Activation Energy for the Discharge Step Using Potential Energy Curves

In order to build up potential energy curves for the discharge step, it will be necessary to obtain the relation between the total energy of the system and some reaction coordinate for both the initial and "final" states. This reaction coordinate was implicitly defined in the original BEBO method by the hypothesis that total bond order is conserved all along the activation process. The particular conditions prevailing in an electrode reaction make necessary the revision of this fundamental postulate of the method.

Effectively, in stating this basic assumption of the method, Johnston extended the intuitive idea that reacting bonds should sum up a complete bond in the activated state. This extension was allowable on the basis that activation energies for proton-transfer reactions are five or more times less than bond energies involved in the process. Now, the explicit inclusion of electrostatic effects through calculations based on the jellium model shows that the activation energy for the backward reaction (*i.e.*, desorption of a proton bonded to the metallic surface and its combination with an  $OH_2$  group near the surface) is not as small as it should be; hence, Johnston's consideration will not apply in the case of the discharge step.

The fact that the final state and, in consequence, the backward reaction are hypothetical does not invalidate this argument. This is so because, the rate-determining event being the adiabatic transfer of the proton, what matters in the determination of the activation energy are the initial and final states of the adiabatic process, regardless of the fact that a nonadiabatic electron

transfer takes place before the "final" state is effectively attained.

These considerations show that in the case of the HER the assumption of total bond order conservation during the complete adiabatic transference of the proton is not valid. Nevertheless, in the case of the forward reaction the activation energy is far less than the total energy for the three "particle" system and, also, than the O-H bond energy. This fact suggests that as long as the system is in a configuration between the initial state and the activated complex, total bond order may be considered to be constant. However, once the activated complex has been attained, the great energy difference from it to the final state will not permit the conservation of bond order. This amounts to saying that, due to the energy difference between the initial and final states of the adiabatic process, the breaking of the first bond should be accompanied by a corresponding gradual buildup of the proton-metal bond, but once the configuration of the activated complex is achieved the great increase in electrostatic energy determines that the chemical link between the proton and the oxygen atom is rapidly lost and the  $OH_2$  group may eventually leave the metal-proton system.

With these considerations, the potential energy curve describing the evolution of the system for the adiabatic process will be obtained by superimposing the curve corresponding to the gradual destruction of the proton-oxygen bond and simultaneous appearance of the proton-metal bond with that corresponding to the metal-proton system. Since it is considered that total bond order in the activated complex is one, it is convenient to draw these potential energy curves as a function of bond order instead of bond length, thus defining a reaction coordinate.

*Energy curve for the initial state.*—According to the BEBO method the nonelectrostatic part of the total energy will be given by

$$U_{\text{nonel}} = D_{\text{HO}}n^p + D_{\text{HM}}(1 - n)^q \quad [19]$$

where, as before,  $D_{\text{HO}} = 180$  kcal/mole and  $D_{\text{HM}}$  is obtained from Herzberg's data for the neutral monohydrides of Cu, Ni, and Au, and the positive monohydride in the case of Hg. The electrostatic energy is calculated from the GSA according to the geometry of Fig. 1 and considering that the charge density on each atom varies linearly with bond order (20)

$$\delta_i = \delta_i^f + (\delta_i^f - \delta_i^o)n \quad [20]$$

where  $\delta_i$  is the charge density of atom  $i$ ,  $\delta_i^o$  is the charge density of atom  $i$  when the system is in the initial configuration, and  $\delta_i^f$  is the same quantity in the final state. Values for  $\delta_i^o$  are those from Conway (43);  $\delta_i^f$  is considered to be  $-e_0$  for the transferring proton and  $0.53 e_0$  for the oxygen atom. The final charge density on the oxygen atom was obtained considering a polarized water molecule at 2Å from the surface.

Since in the initial state the hydroxonium ion is not bonded to the metal, Pauling's relation between bond length and bond order, Eq. [3], will be considered to be valid for the proton-oxygen bond.

*Potential energy curve for the final state.*—In this case, as was described before, the electrostatic energy is obtained using the potential energy curve resulting for tungsten through application of the jellium model (46), taking into account the work function difference between tungsten and the metal in consideration. The nonelectrostatic interaction is taken into account by building the corresponding Morse curve for the monohydride from the data tabulated by Herzberg (60).

In order to build up the energy curve for the proton-metal system as a function of bond order, the objections presented to the direct use of Pauling's relation between bond length and bond order must be recalled. According to them, the original relation, Eq. [3], should be modified in order to account for the presence of the metallic surface. In doing so, it must be remembered

Table III. Energy values for metal-proton systems.  $U_{\text{elect}}$  is determined by analogy with the tungsten-proton system for which the work function is 4.55 eV and  $U_{\text{elect}}$  is 205 kcal/mole.

Metal	Work function, eV	$U_{\text{elect}}$ , kcal/mole	$U_{\text{nonel}}$ , kcal/mole	$E_{\text{no}}$ , kcal/mole
Hg	4.50	204	53	257
Cu	4.70	209	67	276
Ni	5.25	222	71	293
Au	4.78	210	71	281

that when the ion is relatively far from the metallic surface the GSA will hold as a first order correction to the classical point of view. This means that, in this case, the effective distance may be written as

$$R_{\text{eff}} = R_{\text{geom}} + \lambda^{-1} \quad [21]$$

where  $R_{\text{eff}}$  is the effective distance and  $R_{\text{geom}}$  the geometric or actual distance from the ion to the surface. Also, it must be considered that when bond order tends to zero, the effective distance will tend to the GSA and the relation between bond length and bond order should tend to Pauling's equation. With this basis, the following expression, valid at relatively low values of  $m$  (bond order for the proton-metal bond) is proposed (62)

$$R = R_s + \lambda^{-1} (1 - m) - 0.26 \ln m \quad [22]$$

In Fig. 2, the curves obtained for Hg are shown. Similar curves are obtained for the other three metals and from them classical activation energies are determined. Numerical results for the four metals under consideration are presented in Table IV.

### Conclusions

If calculated  $E_c$  data are compared with experimentally determined activation energies (Table IV), qualitative agreement is apparent since both magnitudes follow the sequence

$$\text{Hg} > \text{Cu} > \text{Ni} \sim \text{Au}$$

If these two activation energies are to be compared quantitatively, it is necessary to estimate a value for the "true" activation energy,  $E_o$ , in order to apply Eq. [12].

As has been pointed out before, the estimation of the "true" activation energy requires the vibrational analysis of the activated complex. This analysis cannot be carried out within the limits of the method presented in this paper because there does not exist an analytical function representing the energy curve of the systems in terms of bond order. Use of the vibrational analysis described by Johnston and Parr (31) cannot be made because of the observations made on the applicability of the method to electrode processes and because of the inaccuracies existing in the  $F_\sigma$  definition. We will, in consequence, limit ourselves to determining upper and lower limits for the "true" activation energies.

In order to make this determination, the fact that vibrational frequencies of reacting bonds are lower in the activated state than in the free molecules will be

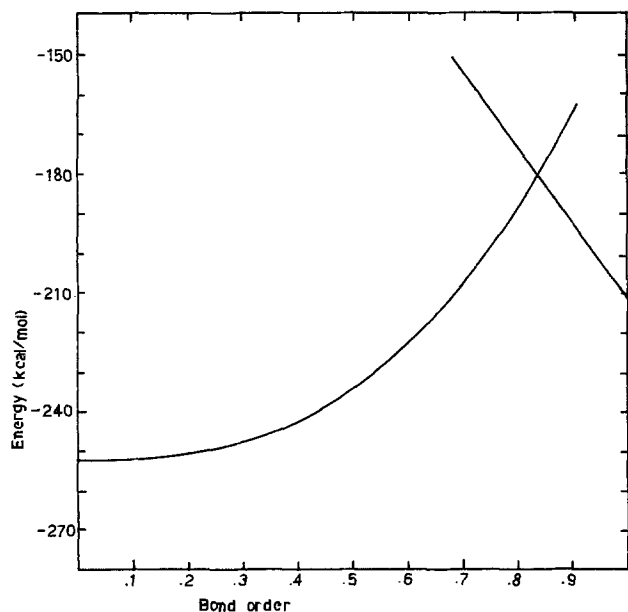


Fig. 2. Potential energy curves for  $(\text{H}-\text{OH}_2)^+$  and for  $\text{Hg}-\text{H}^+$  as a function of H-O bond order.

Table IV. Obtained  $E_c$  values and estimated "true" activation energies and enthalpy changes.

Metal	$E_c$ , kcal/mole	$E_o$ , kcal/mole	$E_{\text{exp}}$ , kcal/mole	$\Delta H$ , kcal/mole
Hg	30	25-30	21 (63)*	8-18
Cu	21	16-21	11 (32)	10-20
Ni	18	13-18	9 (32)	8-18
Au	18	13-18	9 (64)	8-18

\* Numbers in parentheses indicate references.

recalled. In consequence, since the O-H bonds that do not intervene directly in the reaction are considered to remain unmodified during the process, the lower limit for  $E_o$  will be given by

$$E_o = E_c - \frac{1}{2} h c \omega_{\text{H}^+}$$

where  $\omega_{\text{H}^+}$  refers to the initial frequency of the reacting bond and where it is considered, as a limited case, that the vibrational frequencies in the activated state are zero. Taking for the stretching frequency of the proton-oxygen bond a value about  $3500 \text{ cm}^{-1}$  (63), the correction term would be about 5 kcal/mole. The upper limit will be considered that for which the vibrational contribution in the activated state equals that of the reagents, i.e.,  $E_o = E_c$ . Possible ranges for  $E_o$  and for  $\Delta H$  are shown in Table IV.

The obtained results may also be considered from a mechanistic point of view. The energy values for HER on Hg suggest that, in this case, the discharge step is rate determining, in good accordance with experiment. In the cases of Cu, Ni, and Au the values calculated for activation energies do not permit a definite statement about the rate-determining step on these metals. Nevertheless, if it is recalled that MH bond energies were used instead of data for  $\text{MH}^+$  hydrides, it follows that calculated  $E_c$  and  $E_o$  values are higher than those that would result if the appropriate data were available. This would be in accordance with most experimental data suggesting that the discharge step is not rate determining in these metals (34, 64, 65).

The method compares favorably with the presentation by Salomon *et al.* (3) regarding both its reliability and capability of being improved. The first assertion arises from the fact that there is no need of explicit differentiation of empirical expressions. The improvement capability of the method is a consequence of the more rigorous way of considering the problem through theoretically defined models for the surface and the explicit recognition of image effects, as well as from the fact that all the experimental data that are necessary for the calculations come from fields different from electrochemistry and, thus, calculated values and experimental results are not interdependent.

Extension of the method to nonaqueous solvents as well as the study of the vibrational characteristics of the system as a function of bond order are currently being considered.

### Acknowledgments

This work is part of the requirements to be fulfilled by one of us (CMM) in order to obtain the Ph.D. degree. The authors gratefully recognize financial support for this investigation through Grant 31.26-S1-0335 of the Consejo de Investigaciones Científicas y Técnicas and from the Consejo de Desarrollo Científico y Humanístico (U.L.A.), Project C-24. Discussions with Dr. N. V. Joshi on surface properties and with Dr. B. Fontal on vibrational characteristics of the activated complex are warmly acknowledged.

Manuscript submitted June 24, 1974; revised manuscript received Aug. 20, 1975. This was Paper 331 presented at the San Francisco, California, Meeting of the Society, May 12-17, 1974.

Any discussion of this paper will appear in a Discussion Section to be published in the December 1976 JOURNAL. All discussions for the December 1976 Discussion Section should be submitted by Aug. 1, 1976.

Publication costs of this article were partially assisted by the Universidad de los Andes.

## REFERENCES

- B. E. Conway, "Theory and Principles of Electrode Processes," The Ronald Press Co., New York (1965).
- R. Parsons, in "Modern Aspects of Electrochemistry," Vol. 1, J. O'M. Bockris, Editor, Butterworths, London (1954).
- M. Salomon, C. G. Enke, and B. E. Conway, *J. Chem. Phys.*, **43**, 3989 (1965).
- J. O'M. Bockris and D. Drazic, "Electrochemical Science," Taylor & Francis Ltd., London (1972).
- R. A. Marcus, *J. Chem. Phys.*, **24**, 966 and 979 (1956).
- R. A. Marcus, *Discussions Faraday Soc.*, **29**, 21 (1960).
- R. A. Marcus, *J. Phys. Chem.*, **67**, 853 (1963).
- R. A. Marcus, *Ann. Rev. Phys. Chem.*, **15**, 155 (1964).
- R. A. Marcus, *J. Chem. Phys.*, **43**, 679 and 1598 (1965).
- R. A. Marcus, *Electrochim. Acta*, **13**, 995 (1968).
- V. G. Levich, in "Advances in Electrochemistry and Electrochemical Engineering," Vol. IV, P. Delahay, Editor, Interscience, New York (1966).
- R. R. Dogonadze, A. M. Kuznetsov, and V. G. Levich, *Electrochim. Acta*, **13**, 1025 (1968).
- V. G. Levich, R. R. Dogonadze, F. D. German, A. M. Kuznetsov, and Yu. Kharkats, *ibid.*, **15**, 353 (1970).
- V. G. Levich, in "Physical Chemistry," Vol. IXB, H. Eyring, D. Henderson, and W. Jost, Editors, Academic Press, Inc., New York (1970).
- R. R. Dogonadze, in "Reactions of Molecules at Electrodes," N. S. Hush, Editor, John Wiley & Sons, Inc., New York (1971).
- R. R. Dogonadze and Z. D. Urushadze, *J. Electroanal. Chem.*, **32**, 235 (1971).
- C. Lamy, *J. Chim. Phys.*, **70**, 823 (1973).
- A. J. Appleby, J. O'M. Bockris, R. K. Sen, and B. E. Conway, in "MTP International Review of Science, Physical Chemistry," Series One, Vol. 6, J. O'M. Bockris, Editor, Butterworths, London (1973).
- J. O'M. Bockris, K. L. Mittal, and R. K. Sen, *Nature (London) Phys. Sci.*, **234**, 118 (1971).
- C. M. Marschoff, Doctoral Thesis, Universidad de Buenos Aires (1975).
- J. Horiuti and J. C. Polanyi, *Acta Physicochim. U.R.S.S.*, **2**, 505 (1935).
- J. A. V. Butler, *Proc. Roy. Soc. (London)*, **A157**, 423 (1936).
- J. H. Davy, C. R. Guerra, H. S. Johnston, C. F. Weaver, and C. E. Young, *J. Chem. Phys.*, **41**, 1517 (1964).
- R. Parsons and J. O'M. Bockris, *Trans. Faraday Soc.*, **54**, 1053 (1958).
- B. E. Conway and J. O'M. Bockris, *Can. J. Chem.*, **35**, 1124 (1957).
- J. O'M. Bockris and D. B. Matthews, *Proc. Roy. Soc.*, **A292**, 479 (1966); *J. Chem. Phys.*, **44**, 298 (1966).
- J. O'M. Bockris, S. Srinivasan, and D. B. Matthews, *Discussions Faraday Soc.*, **39**, 219 (1965).
- A. J. Appleby, *J. Electroanal. Chem.*, **51**, 1 (1974).
- H. S. Johnston, *Advan. Chem. Phys.*, **3**, 131 (1960).
- H. S. Johnston and P. Goldfinger, *J. Chem. Phys.*, **37**, 700 (1962).
- H. S. Johnston and C. Parr, *J. Am. Chem. Soc.*, **85**, 2544 (1963).
- L. Pauling, *ibid.*, **69**, 542 (1947).
- R. M. Badger, *J. Chem. Phys.*, **2**, 128 (1934).
- J. O'M. Bockris, in "Modern Aspects of Electrochemistry," Vol. 1, J. O'M. Bockris, Editor, Butterworths, London (1954).
- A. Frumkin, in "Advances in Electrochemistry and Electrochemical Engineering," Vol. 1, P. Delahay, Editor, Interscience, New York (1961).
- B. E. Conway and M. Salomon, *Ber. Bunsenges. Physik. Chem.*, **68**, 331 (1964).
- B. E. Conway and M. Salomon, *J. Chem. Phys.*, **41**, 3169 (1965).
- M. Salomon and B. E. Conway, *Discussions Faraday Soc.*, **39**, 223 (1965).
- S. Glasstone, K. J. Laidler, and H. Eyring, "Theory of Rate Processes," McGraw-Hill Book Co., New York (1941).
- D. C. Grahame, *Chem. Rev.*, **41**, 441 (1947).
- D. C. Grahame, *J. Am. Chem. Soc.*, **79**, 2093 (1957).
- C. M. Marschoff and A. Jatem, To be published.
- B. E. Conway, in "Modern Aspects of Electrochemistry," Vol. 3, J. O'M. Bockris and B. E. Conway, Editors, Butterworths, London (1964).
- P. A. Kollman and C. F. Bender, *Chem. Phys. Letters*, **21**, 271 (1973).
- C. M. Criss and M. Salomon, in "Physical Chemistry of Organic Solvent Systems," A. K. Covington and T. Dickinson, Editors, Plenum Press, New York (1973).
- J. R. Smith, S. C. Ying, and W. Kohn, *Phys. Rev. Letters*, **30**, 610 (1973).
- N. H. March, *Advan. Phys.*, **6**, 1 (1957).
- J. W. Gadzuk, *Solid State Commun.*, **5**, 743 (1967).
- J. W. Gadzuk, *J. Phys. Chem. Solids*, **30**, 2307 (1968).
- D. M. Newns, *J. Chem. Phys.*, **50**, 4572 (1969).
- R. Gomer and L. W. Swanson, *ibid.*, **38**, 1613 (1963).
- P. R. Antoniewicz, *ibid.*, **56**, 1711 (1972).
- C. Kittel, "Introduction to Solid State Physics," 3rd ed., John Wiley & Sons, Inc., New York (1966).
- R. Smoluchowski, *Phys. Rev.*, **60**, 661 (1941).
- C. Herring and M. H. Nichols, *Rev. Mod. Phys.*, **21**, 228 (1949).
- P. Hohemberg and W. Kohn, *Phys. Rev.*, **136**, B864 (1964).
- J. R. Smith, *ibid.*, **181**, 522 (1969).
- A. Clark, "The Chemisorptive Bond," Academic Press, Inc., New York (1974).
- W. M. Mueller, J. P. Blackledge, and G. G. Libowitz, "Metal Hydrides," Academic Press, Inc., New York (1968).
- G. Herzberg, "Spectra of Diatomic Molecules," Van Nostrand Reinhold Co., New York (1950).
- S. Trasatti, *J. Electroanal. Chem.*, **39**, 163 (1972).
- C. M. Marschoff and P. J. Aragón, Submitted to *Acta Cient. Venezolana*.
- G. E. Walrafen, *J. Chem. Phys.*, **36**, 1035 (1962).
- B. E. Conway, "Electrochemical Data," Elsevier Publishing Co., Inc., Houston (1952).
- A. T. Kuhn and M. Byrne, *Electrochim. Acta*, **16**, 391 (1970).



## Cathodic Characteristics of a CuS Electrode in Liquid Ammonia

Yoshiharu Matsuda,\* Hiroaki Ueyama, and Yoshio Takasu

Department of Industrial Chemistry, Faculty of Engineering,  
Yamaguchi University, Tokiwadai, Ube 755, Yamaguchi, Japan

In the course of the investigation and the development of batteries whose electrolytes are nonaqueous solvents, a few papers (1-4) have presented the possibility of liquid ammonia as the electrolyte of high energy batteries. This solvent, liquid ammonia, is possible for use as the electrolyte at low temperatures and will contribute to the improvement of new batteries. On the other hand, a CuS cathode has often been used in organic electrolytes (5-11), but it has never been used in an electrolyte of liquid ammonia.

In this study, we examined some properties of liquid ammonia as the electrolyte and the cathodic performance of cupric sulfide (CuS) electrode in this electrolyte. The results revealed that this cathode showed excellent polarization characteristics and a possibility of stable discharge for a long time, and that it was changed to Cu in the discharge process.

### Experimental

Figure 1 shows a schematic diagram of the equipment. This system consists of pressure bottles and a temperature-controlled electrolytic cell (500 ml) composed of special glass for use under 20 atmospheric pressure. After the system was evacuated, ammonia was introduced into a pressure bottle of 300 ml cooled with a mixture of Dry Ice and organic solvent. Next, ammonia was distilled and transferred into another bottle containing solid sodium. Then it was transferred into the electrolytic cell containing thiocyanates and ammonium chloride. Conductivity measurements were made with two platinum plate electrodes whose dimensions were  $1 \times 1 \text{ cm}^2$ . A test electrode was prepared by pressing the mixture of pure commercial CuS, graphite, and polyethylene powders. This electrode, whose area was  $1.33 \text{ cm}^2$ , was mounted at the bottom of a glass tube with a glass diaphragm, and graphite powder and a carbon rod were used to make electrical contact. The counterelectrode was a platinum plate whose dimension was  $2 \times 3 \text{ cm}^2$ . The reference electrode was a Ag/AgCl/Cl<sup>-</sup>.

### Results and Discussion

Relations between specific conductivity of liquid ammonia with 4 mole/l of thiocyanates and temperature are shown in Fig. 2. Measurements were made with an a-c bridge at a frequency of 1 kHz and the order of the conductivity was  $\text{NH}_4\text{SCN} > \text{KSCN} > \text{NaSCN}$ . In Fig. 3, relations between equivalent conductivities of liquid ammonia with  $\text{NH}_4\text{SCN}$  and the square root of its concentration are shown. This figure suggests that the solutions are strong electrolytes.

Polarization characteristics of a CuS cathode are shown in Fig. 4. The composition of the electrode was 80 weight per cent (w/o) CuS, 5 w/o polyethylene,

and 15 w/o graphite, and the electrolyte was liquid ammonia containing 4 mole/l  $\text{NH}_4\text{SCN}$  and 0.5 mole/l  $\text{NH}_4\text{Cl}$ . The current density was  $42.8 \text{ mA/cm}^2$  at the electrode potential of  $-1.00\text{V}$  (vs. Ag/AgCl/Cl<sup>-</sup>) at  $25^\circ\text{C}$ . At  $-65^\circ\text{C}$ , the open-circuit voltage was  $-0.20\text{V}$  and the current density was  $9.39 \text{ mA/cm}^2$  at the electrode potential of  $-1.00\text{V}$ . The cathodic polarization characteristics of the CuS electrode were improved by elevating temperature. As shown in Fig. 4, linear relations between the current densities and the electrode potentials were found on the low polarization ranges, and these results suggest that the electrochemical process should be controlled by IR loss on these ranges.

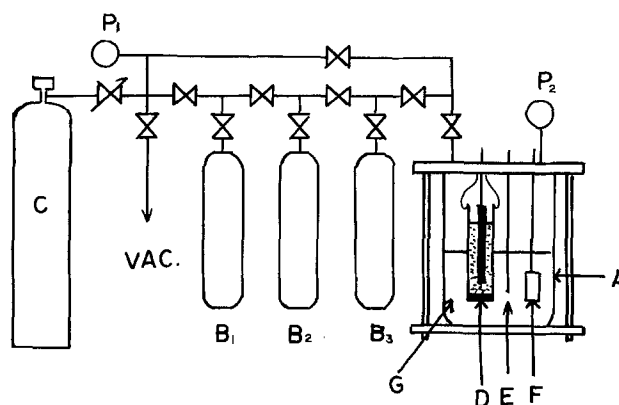


Fig. 1. Systematic diagram of the equipment. A: electrolytic cell; B<sub>1</sub>, B<sub>2</sub>, B<sub>3</sub>: pressure bottle; C: liquid NH<sub>3</sub> cylinder; D: test electrode; E: reference electrode; F: counterelectrode; G: electrolyte; P<sub>1</sub>, P<sub>2</sub>: pressure gauge; VAC: vacuum system;  $\times$ : stop cock.

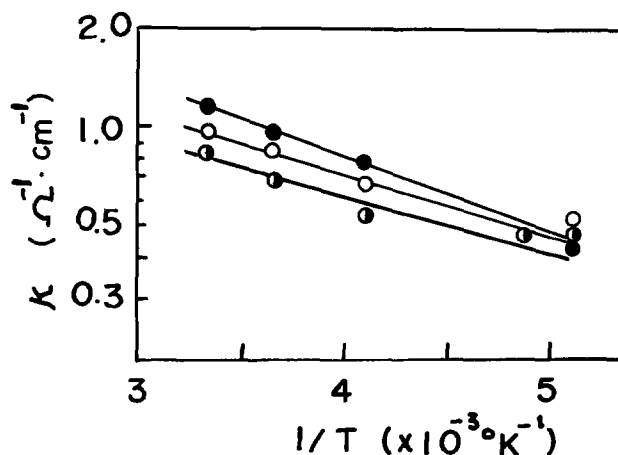


Fig. 2. Relations between specific conductivity and temperature for liquid ammonia with thiocyanates. Solute:  $\circ$  = 4 mole/l  $\text{NH}_4\text{SCN}$ ,  $\bullet$  = 4 mole/l  $\text{KSCN}$ ,  $\ominus$  = 4 mole/l  $\text{NaSCN}$ .

\* Electrochemical Society Active Member.  
Key words: cupric sulfide cathode in ammonia, electrode for liquid ammonia battery, liquid ammonia electrolyte of battery.

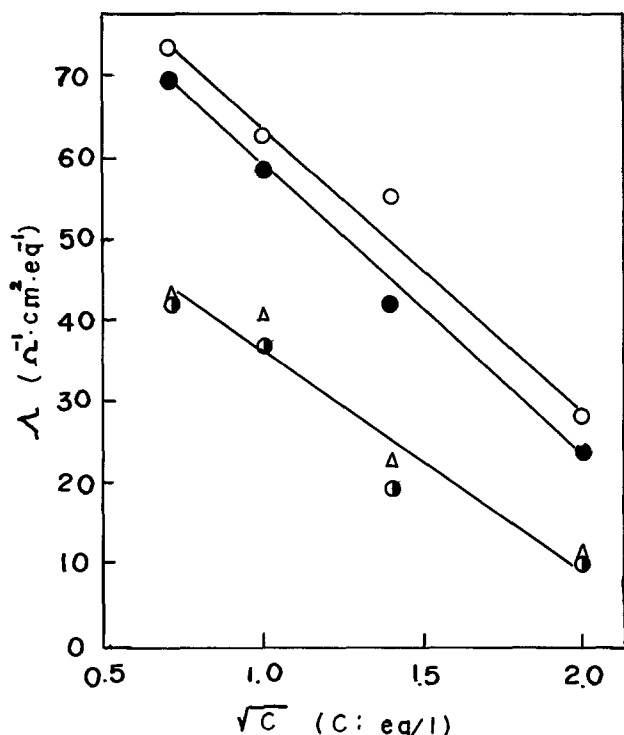


Fig. 3. Relation between  $\Delta$  and  $\sqrt{C}$  for liquid ammonia with  $\text{NH}_4\text{SCN}$  at several temperatures. Temperature:  $\circ = 30^\circ\text{C}$ ,  $\bullet = 0^\circ\text{C}$ ,  $\Delta = -65^\circ\text{C}$ ,  $\bullet = -75^\circ\text{C}$ . Solute:  $\text{NH}_4\text{SCN}$ .

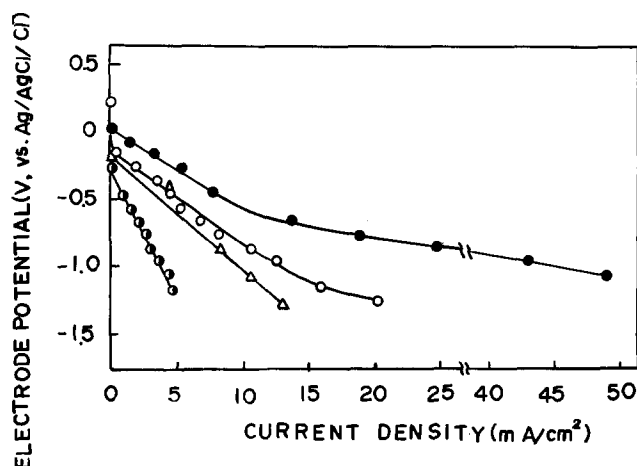


Fig. 4. Cathodic polarization curves for a CuS electrode. Electrode composition: CuS 80%, polyethylene 5%, graphite 15%. Solute: 4 mole/l  $\text{NH}_4\text{SCN}$  + 0.5 mole/l  $\text{NH}_4\text{Cl}$ . Temperature:  $\circ = 25^\circ\text{C}$ ,  $\bullet = 0^\circ\text{C}$ ,  $\Delta = -65^\circ\text{C}$ ,  $\bullet = -75^\circ\text{C}$ .

Figure 5 shows the results of the continuous discharge of this electrode. The measurements were made at  $0^\circ\text{C}$ , and currents applied were 5 and 10 mA. The efficiencies of the CuS electrode utilized were over 65% on the basis of a mechanism of two electrons per mole. Similar results were obtained in the measurements using electrode composed of 65 w/o CuS, 5 w/o polyethylene, and 30 w/o graphite. X-ray diffraction patterns from the cathode material are shown in Fig. 6. Curve 1 is the pattern before discharge and curve 2 is the pattern after discharge at 5 mA/1.33  $\text{cm}^2$  for 20 hr. These patterns suggested that CuS was reduced to Cu during cathodic discharge. Since the polarization curves of the constant discharge gave plateaus and no evidence of  $\text{Cu}_2\text{S}$  was found in x-ray diffraction patterns, the discharge of the electrode involved two electron processes.

Consequently, CuS was revealed to be a favorable material for a cathode in liquid ammonia. On the cath-

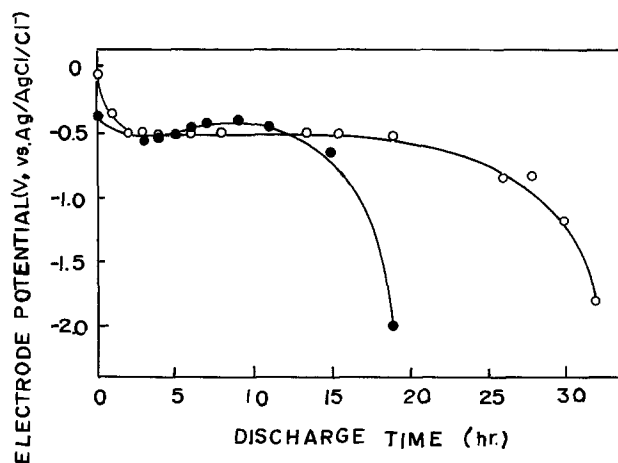


Fig. 5. Discharge curves at constant currents. Electrode composition: CuS 80%, polyethylene 5%, graphite 15%. Current density:  $\circ = 5 \text{ mA}/1.33 \text{ cm}^2$ ,  $\bullet = 10 \text{ mA}/1.33 \text{ cm}^2$ . Temperature:  $0^\circ\text{C}$ . Solute: 4 mole/l  $\text{NH}_4\text{SCN}$  + 0.5 mole/l  $\text{NH}_4\text{Cl}$ .

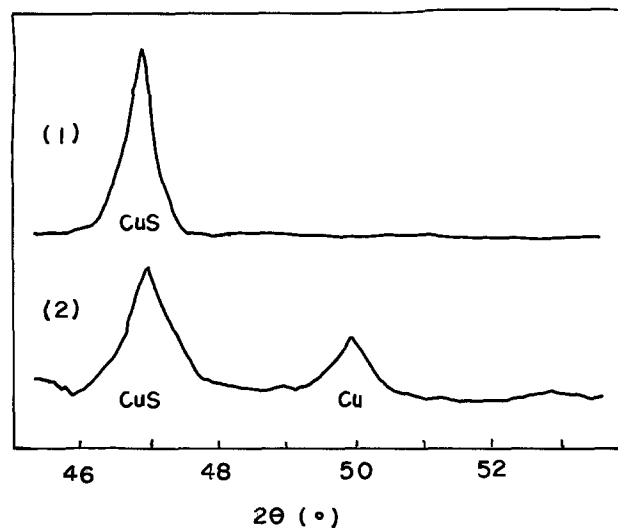


Fig. 6. X-ray diffraction patterns from cathodic material. Electrode composition: CuS 65%, polyethylene 5%, graphite 30%. Curve 1: before discharge, curve 2: after discharge at 5 mA/1.33  $\text{cm}^2$  for 20 hr. X-ray:  $\text{CuK}\alpha$ . Temperature (on discharge):  $0^\circ\text{C}$ .

odic discharge of CuS electrode, the performance was stable and the utilization of reactant was over 65%.

#### Acknowledgments

The authors would like to thank Mr. K. Ikeda of the Sanyo Electric Company Limited for his helpful support.

Manuscript submitted May 28, 1975; revised manuscript received Oct. 1, 1975.

Any discussion of this paper will appear in a Discussion Section to be published in the December 1976 JOURNAL. All discussions for the December 1976 Discussion Section should be submitted by Aug. 1, 1976.

Publication costs of this article were partially assisted by Yoshiharu Matsuda.

#### REFERENCES

- O. Adhart, Proceedings 14th Annual Power Sources Conference, p. 111 (1960).
- L. J. Minnick, Proceedings of the 17th Annual Power Sources Conference, p. 128 (1963).
- T. Saito, T. Kojima, N. Kashihara, and T. Takagaki, Preprints of 12th Battery Symposium, Electrochemical Society of Japan, p. 45 (1971).
- R. H. Comyn, J. T. Nelson, D. F. McMillen, and W. H. Steuernagel, Proceedings of the 23rd Annual Power Sources Conference, p. 153 (1969).
- J. Gabano, G. Gerbier, and J. Laurent, *ibid.*, p. 80 (1969).

6. L. R. McCoy, S. Lai, R. C. Saunders, and L. A. Heredy, Proceedings of the Annual Power Sources Conference, p. 68 (1974).
7. E. T. Seo, R. R. Sayano, M. L. McClanahan, and H. P. Silverman, *ibid.*, p. 74 (1974).
8. K. Teraji, S. Ikeda, Y. Takasu, and Y. Matsuda, Preprints of 15th Battery Symposium, Electrochemical Society of Japan, p. 14 (1974).
9. Fr. 1490725, August 4, 1967.
10. Fr. 1490725, August 4, 1967.
11. Fr. 1527783, June 7, 1968.

## Brief Communication



### Thin Film Deposition of Solid Electrolyte $\text{Ag}_{19}\text{I}_{15}\text{P}_2\text{O}_7$

M. R. Arora\* and J. Childs

Unican Electrochemical Products Limited, Montreal, Quebec, Canada

During the last few years, a considerable amount of work has been carried out on silver iodide based solid electrolytes such as  $\text{RbAg}_4\text{I}_5$ ,  $\text{Ag}_3\text{SI}$ ,  $\text{Ag}_{19}\text{I}_{15}\text{P}_2\text{O}_7$ , etc. All these materials are known to exhibit high ionic conductivity for silver at ambient temperatures. Pellets of these solid electrolytes, with suitable electrodes applied to them, have already been used successfully in the fabrication of devices such as coulometers, timers, batteries, etc. However, such devices tend to have high internal resistances and polarization losses due to poor solid-solid contacts. These problems can be overcome by the use of thin films since very small film thicknesses and excellent contacts between electrodes are possible. Recognizing this, Yamamoto and Takahashi (1), Vouros and Masters (2), Kennedy *et al.* (3, 4), Butherus and Broadhead (5), Takahashi *et al.* (6), and Fraser and Krishna (7) have prepared thin films of  $\text{Ag}_3\text{SI}$ ,  $\text{AgBr}$ , and  $\text{RbAg}_4\text{I}_5$ , but no literature is yet available on the thin films of oxy-anion substituted silver iodide solid electrolytes. The purpose of this communication is to describe our work on the thin films of  $\text{Ag}_{19}\text{I}_{15}\text{P}_2\text{O}_7$ .

The solid electrolyte  $\text{Ag}_{19}\text{I}_{15}\text{P}_2\text{O}_7$  was prepared in our laboratory by vacuum fusion by mixing the powders of  $\text{AgI}$  and  $\text{Ag}_4\text{P}_2\text{O}_7$  in a molar ratio of 15 to 1 with subsequent heating at  $250^\circ\text{C}$  for 20 hr under a reduced pressure following the method of Takahashi *et al.* (8). This product was then ground and sieved and only the particle sizes between mesh Tyler screens 40 and 70 for flash evaporation, and finer than 200 for rf sputtering, were used in all the experiments.

Our initial experiments using flash evaporation of  $\text{Ag}_{19}\text{I}_{15}\text{P}_2\text{O}_7$  resulted in films whose room temperature conductivity was rather low, being about  $10^{-5}$ - $10^{-6}$  ( $\text{ohm-cm}$ ) $^{-1}$ . To understand the problems involved in this process, use was made of a Micromass (Model Q8) mass spectrometer during the flash evaporation to monitor the vapor species, and the films formed were subsequently characterized using x-ray diffraction and scanning electron microscopy. It was found that the films which exhibited low conductivity were non-stoichiometric in nature, generally containing more iodine than required by stoichiometry.

After a large number of experiments, it was found that the film deposition parameters have to be strictly controlled within rather narrow limits in order to obtain films of high conductivity at room temperature. The main requirement is that the temperature of the evaporation source be greater than about  $1250^\circ\text{C}$ . But as the film deposition continues, the nozzle of the vibratory feeder steadily heats up due to its close proximity to the hot source and tends to get clogged

up. Therefore, the nozzle must be kept at a distance of at least about 4 cm from the hot source to reduce its heating. (Greater distances result in the particles spraying all over the vacuum chamber rather than going into the source itself.) Therefore, the experimental conditions used for all subsequent flash evaporation of  $\text{Ag}_{19}\text{I}_{15}\text{P}_2\text{O}_7$  were: an initial vacuum of about  $10^{-6}$  Torr, source temperature exceeding about  $1250^\circ\text{C}$ , distance between the feeder nozzle and the baffle-type evaporation source of about 4 cm, distance between the revolving substrate holder and the source of about 25 cm, and a film formation rate of about 20-60  $\text{\AA}/\text{sec}$ .

Rf sputtering of  $\text{Ag}_{19}\text{I}_{15}\text{P}_2\text{O}_7$  proved to be somewhat simpler than flash evaporation though the experimental parameters still had to be kept within narrow limits in order to consistently obtain films of high conductivity. The conditions used in this method were: argon gas pressure = 4 mTorr, spacing between target and the substrate = 4 cm, potential across the electrodes = 700-900V, and rate of film deposition = 15-60  $\text{\AA}/\text{sec}$ .

The conductivity of these films, measured using a Wayne Kerr Universal Bridge B221, was found to be quite satisfactory, being about 0.02-0.03 ( $\text{ohm-cm}$ ) $^{-1}$  for flash evaporation and about  $5 \times 10^{-3}$  ( $\text{ohm-cm}$ ) $^{-1}$  for rf sputtering. These values of conductivity compare well with 0.09 ( $\text{ohm-cm}$ ) $^{-1}$ , the conductivity of bulk  $\text{Ag}_{19}\text{I}_{15}\text{P}_2\text{O}_7$ . On storage, the conductivity of these films decreased during the first few hours but then remained essentially constant at about half of their initial value over a period of more than five weeks.

Sandwich-type cells of the type  $\text{Ag}/\text{Ag}_{19}\text{I}_{15}\text{P}_2\text{O}_7/\text{Au}$  were vacuum evaporated on glass slides to study their coulometric characteristics. The procedure employed in the fabrication of these cells has been described previously (7) and is essentially similar to that of Kennedy and Chen (3). Other crucial details of these cells are as follows:

Material	Film thickness, $\text{\AA}$	Surface area, $\text{cm}^2$
Au	1,500	0.13
$\text{Ag}_{19}\text{I}_{15}\text{P}_2\text{O}_7$	25,000-50,000	0.30
Ag	3,000	0.16

Currents of 5 and 10  $\mu\text{A}$  (40-80  $\mu\text{A}/\text{cm}^2$  at the gold electrode) were used and charges of up to 4000  $\mu\text{C}$  were employed in testing a large number of cells. Some of the results are summarized in Table I and a typical charging-discharging plot is given in Fig. 1. The charging and stripping of the cells were carried out using constant currents and the charges recovered were generally well within 2% when the stripping was carried out immediately after charging. However, when the charged cells were stored for vari-

\* Electrochemical Society Active Member.

Key words: thin films, solid electrolytes, coulometers.



Table I. Summary of charging-discharging measurements

Cell* number	Current, $\mu\text{A}$	Cutoff potential, mV	Time, sec charging	Time, sec dis- charging	Coulombic efficiency, %
A-1	5	300	200	200	100
A-2	5	400	200	200	100
A-3	10	400	60	60	100
A-4	10	400	100	98.5	98.5
A-5	10	400	120	118.5	98.75
A-6	10	400	200	199	99.5
A-7	10	400	300	298.5	99.5
A-8	10	400	400	396.5	99.1
A-9	10	500	100	100	100
B-1	10	500	120	120	100
B-2	10	500	150	150	100
B-3	10	500	200	198.5	99.25
B-4	10	500	400	397.5	99.4

\* A and B represent two different depositions each containing eleven cells.

ous time intervals, the loss of charge became somewhat greater, approaching about 10% after one day, though the rate of charge loss slowed down considerably after greater storage time intervals, with total charge loss approaching about 15-18% after over two weeks. These results are similar in nature to those observed by Kennedy *et al.* for  $\text{AgBr}$  and  $\text{RbAg}_4\text{I}_5$  (3, 4).

All these results are only preliminary in nature and more detailed work is now underway where attempts are being made to improve the characteristics of these films. Similar work is also being extended to other solid electrolytes such as  $\text{Ag}_7\text{I}_4\text{PO}_4$ ,  $\text{Ag}_7\text{I}_4\text{VO}_4$ , and  $\text{Ag}_6\text{I}_4\text{WO}_4$ , etc.

#### Acknowledgments

This work was partially funded under the Defence Industrial Research Program of the Defence Research Board of Canada (Project B-31).

Manuscript submitted Aug. 14, 1975; revised manuscript received Sept. 29, 1975.

Any discussion of this paper will appear in a Discussion Section to be published in the December 1976 JOURNAL. All discussions for the December 1976 Discussion Section should be submitted by Aug. 1, 1976.

Publication costs of this article were partially assisted by Unican Electrochemical Products Limited.

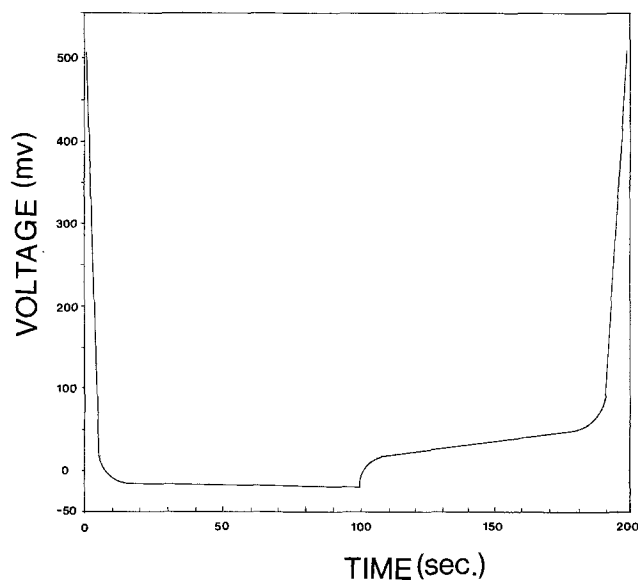


Fig. 1. Charging-discharging characteristics of an  $\text{Ag}_{19}\text{I}_{15}\text{P}_2\text{O}_7$  coulometer. Conditions used were current of  $10 \mu\text{A}$  for 100 sec to a cutoff potential of 500 mV.

#### REFERENCES

- O. Yamamoto and T. Takahashi, *Denki Kagaku*, **34**, 833 (1966).
- P. Vouros and J. I. Masters, *This Journal*, **116**, 880 (1969).
- J. H. Kennedy and F. Chen, *ibid.*, **118**, 1043 (1971).
- J. H. Kennedy, F. Chen, and J. Hunter, *ibid.*, **120**, 454 (1973).
- A. D. Butherus and J. Broadhead, Paper 10 presented at the Electrochemical Society Meeting, Miami, Florida, October 8-13, 1972.
- T. Takahashi, O. Yamamoto, and S. Ikeda, *J. Electrochem. Soc. Japan*, **44**, 796 (1971).
- G. H. Fraser and V. Krishna, Abstract 337, p. 804, The Electrochemical Society Extended Abstracts, Spring Meeting, San Francisco, California, May 12-17, 1974.
- T. Takahashi, S. Ikeda, and O. Yamamoto, *This Journal*, **119**, 477 (1972).



## Quantitative Analysis of Microsegregation in Silicon Grown by the Czochralski Method

A. Murgai, H. C. Gatos,\* and A. F. Witt\*

Department of Materials Science and Engineering and  
Department of Electrical Engineering and Computer Sciences,  
Massachusetts Institute of Technology, Cambridge, Massachusetts 02139

### ABSTRACT

Quantitative microsegregation analysis was carried out on Sb-doped silicon crystal pulled from the melt. Interference by thermal convection in the melt, invariably present in silicon growth at commonly used rates of pulling and seed rotation, was eliminated by introducing severe thermal asymmetry in the growth system. Interface demarcation was employed for the determination of the microscopic growth rates and spreading resistance measurements for obtaining composition profiles. For growth under forced convection conditions it was shown that the microsegregation behavior is controlled by the microscopic growth rate and is adequately accounted for by the Burton, Prim, and Slichter (BPS) model based on steady-state segregation. The small deviations from steady-state segregation were manifested as solute redistribution transients associated with the periodic growth rate variations (slight phase shift between dopant concentration and microscopic growth rate). For growth under thermal convection conditions, the microscopic growth rate is modulated by convective temperature fluctuations in the melt, but it does not control the microsegregation behavior because under these conditions the diffusion boundary layer thickness undergoes significant fluctuations. Accordingly, the BPS model, which assumes a constant diffusion boundary layer thickness, was found to be inapplicable to microsegregation in silicon grown under thermal convection.

Quantitative analysis of microsegregation associated with silicon growth by the Czochralski technique, at the generally employed rates of seed rotation (1), presents serious difficulties because of pronounced interference by thermal convection at the growth interface. Random compositional fluctuations invariably present in the silicon crystals (2) impair the systematic study of the relationship between the microscopic growth rate, the characteristics of the diffusion boundary layer, and the microsegregation behavior. It was reported recently (3), however, that during Czochralski growth, random compositional fluctuations in silicon, for aspect ratios (diameter over height of melt) greater than a critical value (*i.e.*, 2.5), are eliminated by introducing pronounced thermal asymmetry; under this thermal configuration the interference by thermal convection was eliminated, and forced convection conditions were achieved at commonly used rates of seed rotation.

In this communication a quantitative investigation of microsegregation in silicon is presented; the above thermal configuration is utilized and the interface demarcation technique is employed (4); spreading resistance measurements are used for dopant concentration microprofiling (5).

### Experimental

**Apparatus.**—A resistance-heated Czochralski puller was employed in this study. The main features of the puller and the modification which established the ther-

mal configuration making possible silicon growth under forced convection conditions have been described elsewhere (3).

Electrical contact with the seed for transmitting current pulses across the growth interface (interface demarcation technique) was made through the pulling shaft as in previously reported studies (4). Since the silicon melt is contained in an electrically insulating quartz linear and reacts with all available electrical conductors, a special technique was developed for achieving contact with the melt; molybdenum wire (0.5 mm in diameter) was inserted into a quartz capillary, one end of which was then sealed; one end of the wire was positioned a few millimeters inside the open end of the capillary and the other end was brought into contact with the power supply via the pedestal of the crucible; the open end of the capillary was inserted into the melt which rose into the tube and established electrical contact with the wire, a small portion of which it dissolved.

**Procedures.**—The samples employed in this study (about  $20 \times 20 \times 2$  mm) were cut in longitudinal segments along the rotational axis of (111) single crystals (about 2 cm in diameter and 10 cm long) pulled from melts doped with antimony ( $1.22 \times 10^{20}$  atoms/cm<sup>3</sup>). During pulling, current pulses (18A) of 0.05 sec duration at intervals of 0.5 or 1 sec were transmitted across the growth interface. Spreading resistance measurements at 5  $\mu$ m intervals were used for obtaining the microscopic dopant concentration

\* Electrochemical Society Active Member.

Key words: silicon, segregation analysis, Czochralski growth.

profiles, as described elsewhere (5); the spreading resistance measurements were reduced to dopant concentrations employing silicon standards whose carrier concentration was determined by Hall effect measurements; the dopant concentration was taken equal to the carrier concentration.

The following surface preparation procedure was developed and adopted for carrying out spreading resistance measurements and microscopic rate determinations directly on the same surface; the samples were cleaned in CP4 (5 parts  $\text{HNO}_3$  + 3HF + 3 $\text{CH}_3\text{COOH}$ ) rinsed with distilled water, and dried in a stream of nitrogen; they were then ultrasonically soldered onto brass disks with a 50 weight per cent (w/o) Pb: 50 w/o Sn alloy to obtain large ohmic contacts. Subsequently, the surface of each sample was polished with Syton-HT 30 and etched with Sirtl etchant (6): 1 part HF + 1 part (50 w/o aqueous solution)  $\text{CrO}_3$ ; optimum definition of the interface demarcation lines (intercepts of the periodically delineated growth interface with the surface) and of the dopant striations was obtained by about 12 successive immersions in the etchant; each immersion was of about 5 sec duration. For reproducible spreading resistance measurements it was found necessary to swab-clean the etched surface successively with  $\text{HNO}_3$ , hot water, and 1 part  $\text{H}_2\text{O}_2$  + 1 part (saturated aqueous solution) KOH; this cleaning sequence was repeated a few times (7).

Employing interface demarcation, the microscopic growth rate is obtained from the known frequency of the current pulses and the separation of the resulting interface demarcation lines (rate striations) (4). These values are the average growth rates for the regions between successive striations. In order to obtain rate values at any instant in time, the microscopic growth rate was taken as a Taylor (time) expansion series about a fixed origin in terms of its higher order derivatives. Thus, the rates were determined for the specific instants in time corresponding to the application of the individual current pulses (rather than for the time intervals between current pulses). Growth rate values corresponding to the concentration measurements at locations between successive rate striations were determined by means of parabolic time interpolation. In this interpolation it is taken into consideration that for a given time interval the fraction grown (distance) is proportional to the growth rate.

### Results and Discussion

*General remarks.*—A longitudinal cross section of a typical silicon crystal grown under severe thermal asymmetry with a pulling rate of 11  $\mu\text{m}/\text{sec}$  and a seed rotation of 5 rpm is shown in Fig. 1. It is seen that the initial segment of the crystal (upper part of figure)

exhibits well-defined periodic dopant striations with a period identical to that of the seed rotation (rotational striation); random dopant inhomogeneities are not present in this segment; these segregation characteristics indicate that forced convection conditions prevail during growth. The transition from growth under forced convection to growth under thermal convection (3) is abrupt and clearly visible. The dopant inhomogeneities in the segment grown under thermal convection exhibit no periodicity and are randomly distributed; such segregation behavior is invariably observed in silicon crystals pulled at the standard rates of seed rotation.

A detailed analysis of the prevailing thermohydrodynamics of the silicon melt in the present case has not been pursued. It appears, however, that for a specific range of melt aspect ratios, severe thermal asymmetry gives rise to a mode of convection leading to laminar flow at the growth interface, for seed rotation rates as low as 3 rpm. Without seed rotation, it was found that thermal convection at the growth interface (giving rise to nonrotational inhomogeneities) prevails for all aspect ratios of the melt.

*Segregation under forced convection conditions.*—Since pronounced thermal asymmetry was present during growth, backmelting occurred at the periphery of the crystal during each rotational cycle. Typical off-core segments grown without backmelting and with backmelting will be analyzed individually. No analysis of the on-core region will be presented.

*No backmelting.*—The photomicrograph in Fig. 2 shows a portion of the crystal segment grown under forced convection conditions at 9.5  $\mu\text{m}/\text{sec}$  and with a seed rotation of 5 rpm. Rotational striations spaced approximately 120  $\mu\text{m}$  from each other, rate striations introduced by the interface demarcation technique at 1 sec intervals, and the impact traces of the spreading resistance probe at a constant spacing of 5  $\mu\text{m}$  can be identified. The microscopic growth rates, and the corresponding dopant concentrations, are also shown in Fig. 2. It is seen that the growth rate varies periodically. The rotational striations coincide with the dopant concentration minima. The microscopic growth rate minima and maxima occur slightly in advance of the corresponding concentration minima and maxima. (This displacement is more pronounced in the backmelting case, see below.)

A direct analysis of the relationship between the dopant concentration in silicon pulled from the melt and the microscopic growth rates can now be performed. In the present analysis the theoretical model of Burton, Prim, and Slichter (8) (BPS) is employed which relates the dopant concentration in the crystal,

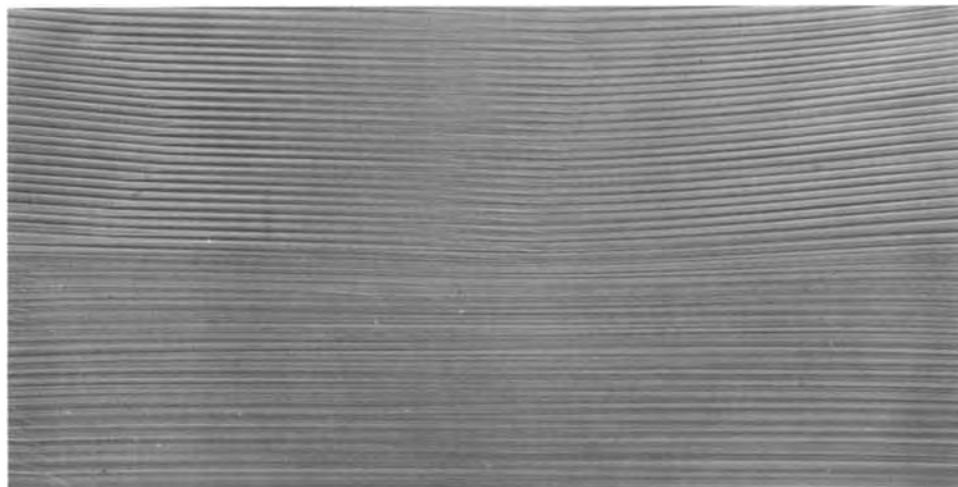
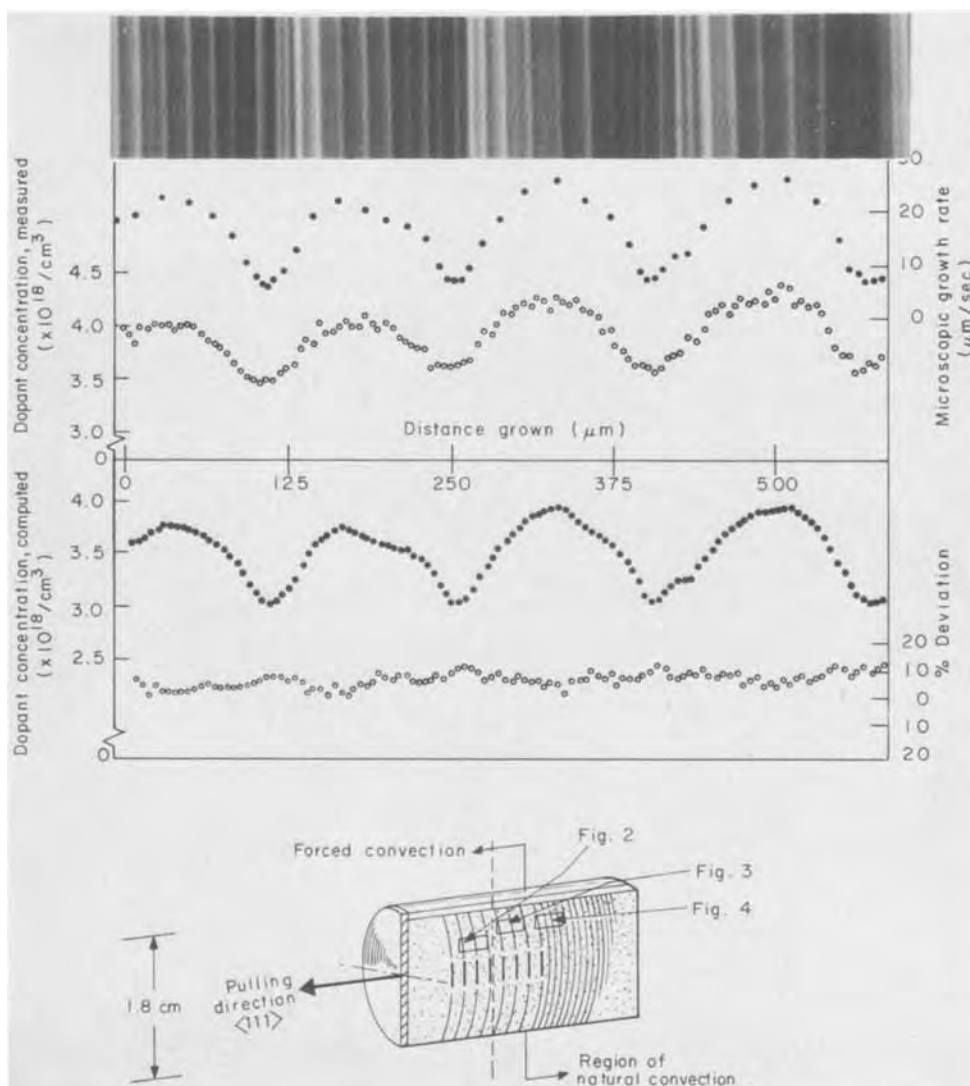


Fig. 1. Longitudinal cross section of silicon crystal pulled at 11  $\mu\text{m}/\text{sec}$  with a seed rotation of 5 rpm. In the upper portion of the crystal segment shown growth took place under forced convection; periodic (rotational) striations are clearly defined; their period is the same as the period of rotation; pronounced backmelting is associated with the rotational striations at the outer parts of the crystal, no random inhomogeneities are present. The abrupt transition to growth under interference by thermal convection is visible near the middle of the figure; the lower portion grown under these conditions exhibits nonperiodic (random) inhomogeneities typical of silicon crystals pulled at commonly employed rates of rotation. Magnification 12X.

Fig. 2. Microsegregation analysis of a differentially etched portion of the crystal (see sketch at bottom of figure) pulled at 9.5  $\mu\text{m}/\text{sec}$  and with a seed rotation rate of 5 rpm; no back-melting took place during its growth; rate striations and the impact traces of the spreading resistance probe are visible; the uppermost curve (black dots) is the microscopic growth rate plot as a function of distance grown; the second curve from the top is the corresponding dopant concentration plot. The theoretical dopant concentration computed on the basis of the BPS model (black dots) and the deviation between the experimental and the theoretical dopant concentration,  $[(C_{\text{exp}} - C_{\text{theor}})/C_{\text{exp}}]100$ , are shown in the lower part of the figure (see text). The positions of all portions of the crystal analyzed in this paper are shown in the sketch; the segment on the left-hand side of the vertical dotted line in the sketch was grown at 9.5  $\mu\text{m}/\text{sec}$  and the segment on the right-hand side was grown at 11  $\mu\text{m}/\text{sec}$ .



$C_s$ , to the growth rate, assuming diffusion controlled steady-state segregation

$$C_s = \frac{C_L k_0}{k_0 + (1 - k_0) \exp(-V\delta/D)} \quad [1]$$

where  $C_L$  is the dopant concentration in the bulk of the melt,  $k_0$  is the equilibrium distribution coefficient,  $V$  is the (microscopic) growth rate,  $\delta$  is the diffusion boundary layer thickness, and  $D$  is the diffusion coefficient of the dopant in the melt.

From the above relationship the dopant concentration in the crystal,  $C_s$ , was computed as follows: The experimental growth rate values were used; the value for  $C_L$  was obtained from experimental parameters using the normal freezing relationship

$$C_L = C_L^0 (1 - g)^{(k_{\text{eff}} - 1)} \quad [2]$$

where  $C_L^0$  is the original concentration of the dopant in the melt prior to solidification,  $g$  is the fraction solidified, and  $k_{\text{eff}}$  is the effective distribution coefficient;  $C_L^0$  was determined from the amount of dopant (Sb) initially added to a known weight of silicon melt. This value of  $1.22 \times 10^{20}/\text{cm}^3$  was found to be in good agreement with the value determined from the concentration in the silicon immediately adjacent to the original growth interface ( $C_{S^{0+}} = 2.64 \times 10^{18}/\text{cm}^3$ ) and the equilibrium distribution coefficient ( $k_0 = 0.023$ ), i.e.,  $C_L^0 = C_{S^{0+}}/k_0 = 1.15 \times 10^{20}/\text{cm}^3$ .  $k_{\text{eff}}$  was obtained from the average dopant concentration in the crystal segment first to solidify ( $C_s = 3.8 \times 10^{18}/\text{cm}^3$ ) and the value of  $C_L^0$ . For  $\delta/D$ , which is required to be constant in the BPS model, a value of 133.3

sec/cm was determined, by trial and error, so that both the amplitude of the dopant variation and the mean dopant concentration obtained from Eq. [1] are as close as possible to those determined by spreading resistance measurements.

The dopant concentration thus computed from Eq. [1] is shown in Fig. 2. Since the experimental measurements of the dopant concentration were carried out at 5  $\mu\text{m}$  intervals the computation of the concentration was also carried out for 5  $\mu\text{m}$  intervals; the required growth rate values for points between successive rate striations were determined by parabolic interpolation as pointed out earlier. The deviation between experimental and theoretical concentrations is also shown in Fig. 2; it is seen that most of the theoretical values deviate by less than 10% from the experimental ones.

From the value of  $\delta/D = 133.3$  cm/sec (found to give the best agreement of the experimental results with the BPS model) a thickness for the diffusion boundary layer  $\delta = 0.0266$  cm is found, taking  $D = 2 \times 10^{-4}$   $\text{cm}^2/\text{sec}$  (9). Using Cochran's analysis (10) for the employed seed rotation (5 rpm) a value of  $\delta = 0.044$  cm is obtained. An assessment of the difference between these two values will not be attempted at this time; it should be pointed out, however, that there are uncertainties associated with the precision of the diffusion constant  $D$  and the kinematic viscosity,  $\nu$ , in Cochran's relationship.

An inspection of the two concentration plots in Fig. 2 shows that the positions of the maxima and minima do not coincide and that the maxima and minima of the experimental plot are slightly lagging; i.e., the

microscopic rate maxima and minima occur somewhat in advance of the corresponding (experimental) concentration maxima and minima. This phase shift is associated with the slow (diffusion controlled) redistribution of the solute at the interface. Thus, within each rotational cycle, and in the absence of fluctuations in diffusion boundary layer thickness, the dopant concentration at the interface remains higher than required by steady-state segregation (11). Accordingly, the mean concentration in the solid must be higher than that expected for steady-state concentration. Indeed, the mean dopant concentration determined from the measured values shown in Fig. 2 is  $3.81 \times 10^{18}/\text{cm}^3$  as compared to  $3.45 \times 10^{18}/\text{cm}^3$  obtained from the computed values.

The analysis of microsegregation in silicon taking into consideration solute redistribution kinetics, is being quantitatively pursued and will be presented in a future communication.

*Periodic backmelting.*—The photomicrograph in Fig. 3 shows another portion from the same crystal segment used for the above segregation analysis (see sketch in Fig. 2). This portion was grown at a pulling rate of  $11.0 \mu\text{m}/\text{sec}$  with a seed rotation of 5 rpm. Here also the period of the rotational striations (broad lines) is the same as the period of seed rotation; the rate striations (narrow lines) were introduced at intervals of 0.5 sec. In this portion (located closer to the periphery of the crystal than the portion shown in Fig. 2) pronounced backmelting is associated with the rotational striations. Since the time interval between successive rotational striations is 12 sec (period of rotation) and since only about 10 rate striations of a period of 0.5 sec are visible between rotational striations, an apparent backmelting, for at most 7 sec, is associated with each rotational striation. It is seen that the rotational striations coincide with the concentration minima. The transition from the concentration maxima to the concentration minima is typical for rotational backmelting striations.

As in the case presented in Fig. 2, here also the theoretical dopant concentration was computed from the experimental microscopic growth rates employing the BPS model by determining a value of  $\delta/D$  so that the theoretically computed mean concentration and the amplitude of the concentration fluctuations were as close to the experimentally determined values as possible; Eq. [2] was used for determining the value of  $C_L$ , the fraction solidified being 0.15. As in Fig. 2, here also it can be seen that the dopant concentration maxima are displaced with respect to the growth rate maxima. The deviation between the experimentally determined and theoretically computed dopant concentrations is also shown in Fig. 3. It is, thus, seen that the dopant segregation is essentially controlled by the microscopic rate and that the BPS model accounts quite satisfactorily for the prevailing segregation conditions, although not as well as in the absence of backmelting.

It is of interest to point out that the dopant concentration in the segments first to solidify after backmelting is about 22% higher than if the concentration at the interface were  $C_L$ . This behavior indicates that the dopant concentration gradient at the original interface position does not vanish during backmelting.

The value of  $\delta/D$  which gave the best agreement between the computed dopant concentrations and the experimentally determined ones is  $166.6 \text{ sec}/\text{cm}$  as compared to  $133.3 \text{ sec}/\text{cm}$  found in the case of Fig. 2. The apparent increase of  $\delta/D$  in the present case (although the rate of seed rotation was the same for both cases) reflects the fact that, following backmelting, the dopant concentration at the growth interface at the onset of regrowth is higher than the value of  $C_L$  used in the present analysis.

*Thermal convection conditions.*—A crystal portion grown after the transition from forced convection to thermal convection conditions (see sketch in Fig. 2) is shown in the photomicrograph of Fig. 4. This portion was grown at a pulling rate of  $11 \mu\text{m}/\text{sec}$  with a seed

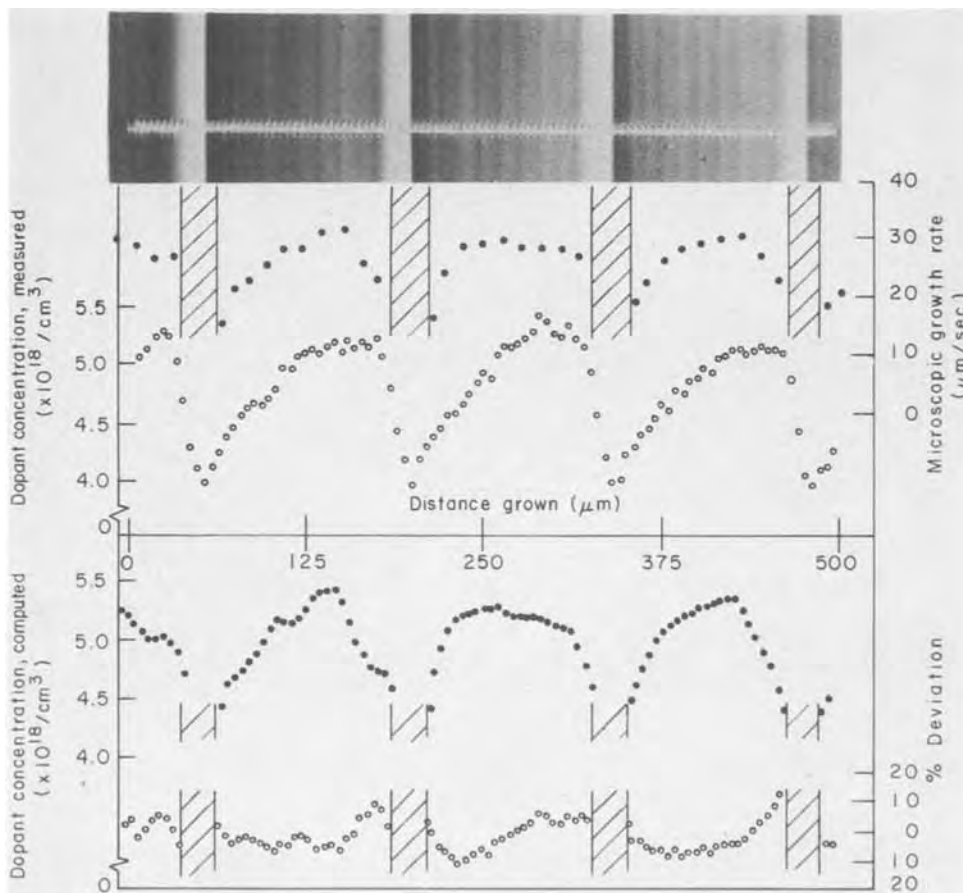


Fig. 3. Microsegregation analysis of a differentially etched portion of the crystal (see sketch in Fig. 2); backmelting is associated with the rotational striations (broad lines); the rate striations (fine lines) and the impact traces of the spreading resistance microprobe are visible (the apparent overlapping of the impact traces resulted from re-etching the surface for photomicrography after the spreading resistance measurements were made). The microscopic growth rates are shown on the top plot of the figure (dark dots); no measurements could be made in the regions of the broad striations. The measured dopant concentrations are shown on the second plot (from the top) in the figure. The theoretical dopant concentration (dark dots) and the deviation between experimental and theoretical values are shown in the lower part of the figure (see text).

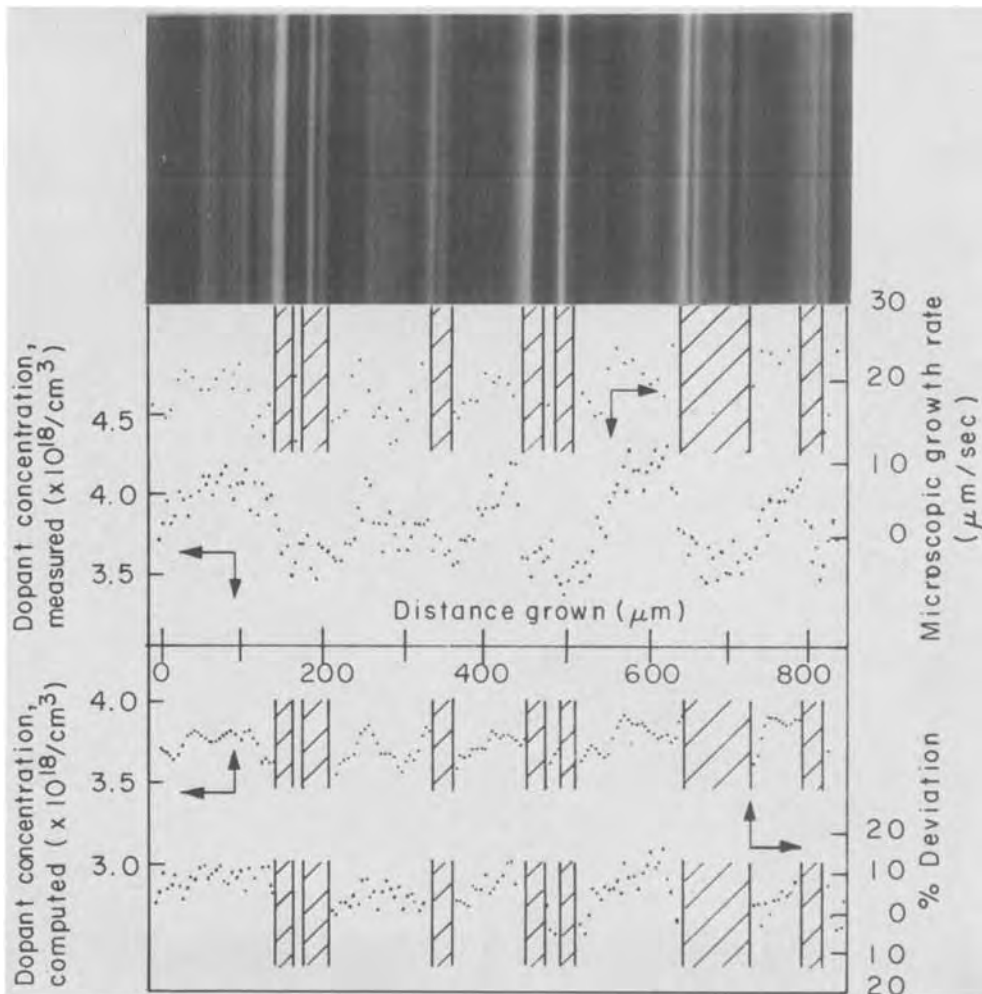


Fig. 4. Microsegregation analysis of a differentially etched portion of the crystal grown under thermal convection (see sketch in Fig. 2). A periodic pattern of dopant inhomogeneities is not apparent; rate striations can be identified in some parts of the portion shown. The microscopic growth rate, the measured dopant concentration, the theoretical dopant concentration, and the deviation (between the theoretical and experimental concentration) plots are shown in that order from top to bottom (see text).

rotation rate of 5 rpm. Current pulses for interface demarcation were transmitted at intervals of 0.5 sec. It is seen that the dopant inhomogeneities do not exhibit a well-defined periodic pattern. The rate striations (fine lines) can be identified in some areas of the crystal portion shown, but not throughout, because of interference by random dopant inhomogeneities; a comprehensive microsegregation analysis is not possible in this case. Nevertheless, from the dopant concentration profiles and from the best possible determination of the microscopic growth rates (using the identifiable rate striations), a comparison can be made with the microsegregation under forced convection conditions.

As seen in Fig. 4, there is no consistent correlation between the dopant concentration and the microscopic growth rate; nor is there a constant correspondence between dopant striations and the growth rate maxima or minima. Thus, the variation of the dopant concentration is not controlled solely by the variations in the microscopic growth rate, but also by variations in the diffusion boundary layer characteristics (thickness and compositional profile); the effects of these variations cannot be quantitatively isolated. Figures 3 and 4 show that fluctuations of the dopant concentration are smaller under thermal convection.

For a comparison with the previous two cases the BPS model was employed; an effective value of  $\delta/D = 80$  sec/cm was determined (by trial and error) so that the computed mean dopant concentration value best matches the experimentally determined one. As seen in Fig. 4, the amplitude of the dopant fluctuations in the computed plot is generally smaller (up to approximately a factor of two) than in the experimental plot. Furthermore, the details in the pattern of the dopant fluctuations differ in the computed and the experimental plots. It is, thus, seen that on the basis of this

analysis the diffusion boundary layer thickness is not constant and fluctuates toward smaller values than that required for steady-state segregation. Consistent with this analysis the mean dopant concentration decreased abruptly, i.e., the mean  $k_{\text{eff}}$  decreased from 0.033 to 0.026, in going from forced convection to thermal convection conditions. Furthermore, due to the decrease in the diffusion boundary layer thickness the amplitude of the dopant fluctuation in this crystal portion is smaller than in the crystal portion grown at the same pulling rate and at the same distance from the periphery of the crystal but under forced convection (Fig. 3). It is thus clear that the BPS model is not applicable to segregation under thermal convection because in addition to the microscopic growth rate, the diffusion boundary layer thickness also undergoes significant fluctuations.

It is of interest to note that as in periodic backmelting here also the dopant concentration in the parts of the segment first to solidify after backmelting is higher (by about 18%) than  $k_0 C_L$ , but less than the corresponding value in the periodic backmelting case; this result indicates again that the mean diffusion boundary layer thickness is smaller in the presence of thermal convection than under forced convection conditions. Under thermal convection, however, backmelting is on occasions sufficiently extensive so that the initial diffusion boundary layer vanishes and the concentration in the portion first to solidify is smaller than  $k_0 C_L$ , indicating that the concentration at the interface becomes less than  $C_L$  due to backmelting of a relatively large crystal portion with a dopant concentration ( $k_{\text{eff}} C_L$ ) appreciably less than  $C_L$ .

#### Summary

Forced convection conditions (laminar flow at the growth interface) were attained for silicon growth at

seed rotation rates above 3 rpm by introducing severe thermal asymmetry into a standard Czochralski-type apparatus. Crystal segments grown under these conditions exhibited only periodic rotational striations rather than random compositional inhomogeneities, which are invariably present in silicon crystals pulled at commonly employed rates of seed rotation. An abrupt transition from growth under forced convection conditions to growth under convective interference was found to occur at a critical aspect ratio of the melt.

The elimination of convective interference made possible the quantitative microsegregation analysis in silicon. Employing the BPS model it was shown that near steady-state microsegregation takes place under these conditions (with and without periodic backmelting). The observed deviation between the experimental results and the BPS model was manifested as solute redistribution transients associated with the variations in the microscopic growth rate (phase shift between dopant concentration and microscopic growth rates). The agreement of the experimental results with the BPS model was found to be better in the case of silicon than in the case of germanium growth reported earlier (5); this finding is not surprising since steady-state conditions should be more readily attainable for silicon growth (in the absence of convective interference) because of the significantly higher dopant difficulties in silicon melts.

It was shown that thermal convection (invariably present under the commonly employed conditions in silicon crystal pulling) leads to random fluctuations, not only of the microscopic growth rate but also of the diffusion boundary layer thickness; furthermore, under these conditions the mean diffusion boundary layer thickness decreases. Consequently, the effective distribution coefficient as well as the amplitude of the dopant concentration fluctuations are smaller in silicon growth under thermal convection than in silicon grown under forced convection. Because of the concurrent fluctuations of the microscopic growth rate and the diffusion boundary layer thickness, the BPS model is not applicable to the microsegregation in silicon pulled under thermal convective interference. Detailed studies of various aspects of microsegregation (including solute redistribution during growth rate transients and radial

concentration gradients) in silicon crystals pulled from the melt are being pursued employing the presently reported experimental approach.

### Acknowledgment

The authors are indebted to the National Science Foundation for financial support. The authors are also grateful to Mr. M. Lichtensteiger, Ms. M. Cretella, and Mr. W. Fitzgerald for their contribution in developing the experimental techniques employed in this investigation.

Manuscript submitted June 4, 1975; revised manuscript received Sept. 20, 1975.

Any discussion of this paper will appear in a Discussion Section to be published in the December 1976 JOURNAL. All discussions for the December 1976 Discussion Section should be submitted by Aug. 1, 1976.

Publication costs of this article were partially assisted by Massachusetts Institute of Technology.

### REFERENCES

1. See for example, A. Müller and M. Wilhelm, *Z. Naturforsch.*, **19A**, 254 (1964); W. R. Wilcox and L. D. Fullmer, *J. Appl. Phys.*, **36**, 2201 (1965); K. M. Kim, A. F. Witt, and H. C. Gatos, *This Journal*, **119**, 1218 (1972).
2. See for example, B. K. Jindal, V. V. Karelin, and W. A. Tiller, *This Journal*, **120**, 101 (1973).
3. A. Murgai, A. F. Witt, and H. C. Gatos, *ibid.*, **122**, 1276 (1975).
4. M. Lichtensteiger, A. F. Witt, and H. C. Gatos, *ibid.*, **118**, 1013 (1971).
5. A. F. Witt, M. Lichtensteiger, and H. C. Gatos, *ibid.*, **120**, 1119 (1973).
6. V. E. Sirtl and A. Adler, *Z. Metallk.*, **52**, 529 (1961).
7. W. A. Porter, A. Gupta, and D. L. Swindle, *This Journal*, **120**, 589 (1973).
8. J. A. Burton, R. C. Prim, and W. P. Slichter, *J. Chem. Phys.*, **21**, 1987 (1953).
9. H. Kodaera, *J. Appl. Phys. Japan*, **2**, 212 (1963).
10. J. A. Burton and W. P. Slichter, in "Transistor Technology," vol. 1, p. 71, H. E. Bridgers, J. H. Scaff, and J. N. Shive, Editors, D. Van Nostrand Co., Inc., New York (1959).
11. D. T. J. Hurle and E. Jakeman, *J. Crystal Growth*, **5**, 227 (1969).

## Sulfidation Kinetics of Iron and Ferritic Iron-Cobalt Alloys

D. J. Young\* and W. W. Smeltzer\*

Department of Metallurgy and Materials Science, McMaster University, Hamilton, Ontario, Canada

### ABSTRACT

Pure Fe and ferritic Fe-Co alloys react with H<sub>2</sub>S/H<sub>2</sub> atmospheres in the range  $8 \times 10^{-8} \leq p_{S_2} \leq 6 \times 10^{-5}$  atm at temperatures of 533°-700°C to form a solid single-phase scale of (FeCo)<sub>1-δ</sub>S. Parabolic scaling kinetics are observed in all cases, the magnitude of the rate constant, its activation energy, and its p<sub>S<sub>2</sub></sub> dependence being independent of alloy composition. The sulfidation of iron is shown to be controlled by lattice diffusion of iron through the sulfide and the quantitative applicability of Wagner's parabolic scaling theory is verified.

A preliminary investigation (1) of the reaction between Fe-Co alloys and H<sub>2</sub>S/H<sub>2</sub> atmospheres at 700°C showed that scales of a single-phase solid-solution monosulfide (FeCo)<sub>1-δ</sub>S grew by parabolic kinetics on two ferritic alloys. It was argued then that in view of the close similarities in thermodynamics and structure of the binary sulfides Fe<sub>1-δ</sub>S and Co<sub>1-δ</sub>S, both of which possess metal deficit NiAs structures, that

the scaling kinetics observed for the alloys should be amenable to analysis from the standpoint of ternary diffusion theory.

Prior to attempting such an analysis it is necessary to quantify the reaction kinetics as a function of alloy composition, ambient sulfur partial pressure, and temperature. As the behavior of the alloys is compared to that of pure Fe, it is important to establish the mechanism of the iron-sulfur reaction.

Considerable evidence already exists (2-6) that the sulfidation of iron is controlled by solid-state diffu-

\* Electrochemical Society Active Member.

Key words: diffusion, Fe-Co alloys, sulfidation kinetics, (FeCo)<sub>1-δ</sub>S scales.



sion and accordingly that the reaction is described by Wagner's theory (7) for scaling of pure metals. The recent publication (8) of accurate tracer diffusivity data for  $\text{Fe}_{1-\delta}\text{S}$  as a function of  $(\delta, T)$  together with existing information (9) on the variation of  $\delta$  with  $(p_{\text{S}_2}, T)$  and the electrical properties of  $\text{Fe}_{1-\delta}\text{S}$  (10) makes possible the quantitative verification of Wagner's treatment. Such a test is of interest as the degree of nonstoichiometry in  $\text{Fe}_{1-\delta}\text{S}$  is large, ranging up to  $\delta \approx 0.25$ .

No diffusivity data is available for  $\text{Co}_{1-\delta}\text{S}$  although qualitative evidence can be found from sulfidation studies. Marker experiments (11, 2) show that in both  $\text{Co}_{1-\delta}\text{S}$  and  $\text{Fe}_{1-\delta}\text{S}$  the metal is much more mobile than sulfur, and it may be assumed that this is the case also in the ternary sulfide. The variation of  $\delta$  in  $\text{Co}_{1-\delta}\text{S}$  has been measured (12) as a function of  $(p_{\text{S}_2}, T)$ . Comparison of this data with analogous data for  $\text{Fe}_{1-\delta}\text{S}$  shows that in a wide range of  $p_{\text{S}_2}, T$  values, both  $\text{Co}_{1-\delta}\text{S}$  and  $\text{Fe}_{1-\delta}\text{S}$  are the stable binary sulfides. Experimental conditions employed in this work fall within this range.

### Experimental

Single-phase ferritic alloys containing 0.00, 10.0, 19.9, 30.7, 40.0, 50.1, and 61.4 weight per cent (w/o) Co were fabricated from iron (>99.975 w/o pure) and cobalt (>99.997 w/o pure). They were sulfidized in  $\text{H}_2\text{S}/\text{H}_2$  atmospheres corresponding to  $8 \times 10^{-8} \leq p_{\text{S}_2} \leq 6 \times 10^{-5}$  atm at temperatures of 533°, 600°, 657°, and 700°C and the kinetics measured thermogravimetrically. Experimental details have been previously described (1).

### Results

Reaction kinetics were parabolic and examples are shown in Fig. 1. The straight lines in this figure represent the result of linear regression to the rate equation

$$\Delta W/A + W' = (k_p t)^{1/2} \quad [1]$$

where  $\Delta W/A$  is the weight change per unit area measured after time,  $t$ . This form of the parabolic rate equation was chosen to allow for the initial, unobserved period of reaction.

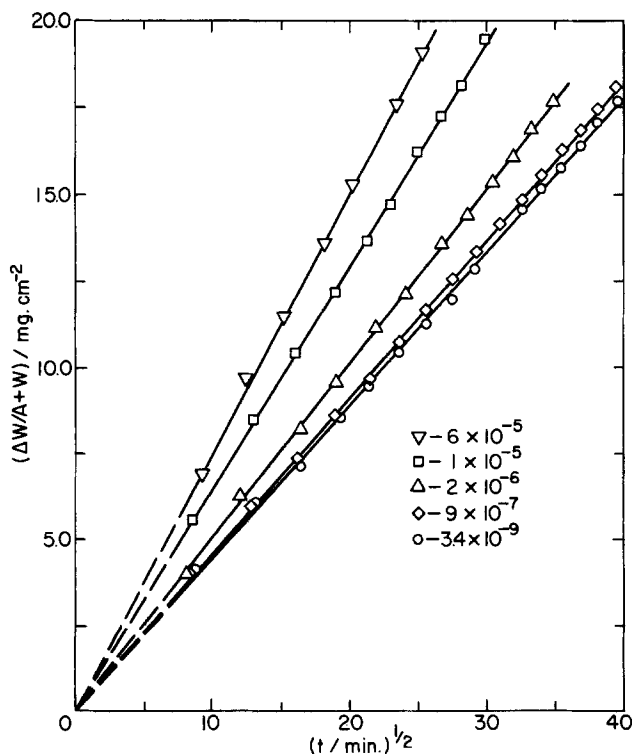


Fig. 1. Sulfidation kinetics of Fe-40 w/o Co at 700°C and several sulfur partial pressures. Continuous lines are regression lines found from Eq. [1].

The sulfur pressure dependence of the parabolic rate constant was determined for each of the alloys at 700°C and the results are displayed in Fig. 2. Linear regression of the data to the equation

$$\log k_p = \frac{1}{n} \log p_{\text{S}_2} + \text{constant} \quad [2]$$

yields a value for  $n$  of  $5.6 \pm 0.5$ . Values of  $n$  for the various alloys do not differ at a 0.05 level of significance. The  $p_{\text{S}_2}$  dependence of  $k_p$  was also determined at 600°C for Fe-40 Co and pure Fe. The results are shown in Fig. 3 and yield  $n = 5.5 \pm 0.3$ . The influence

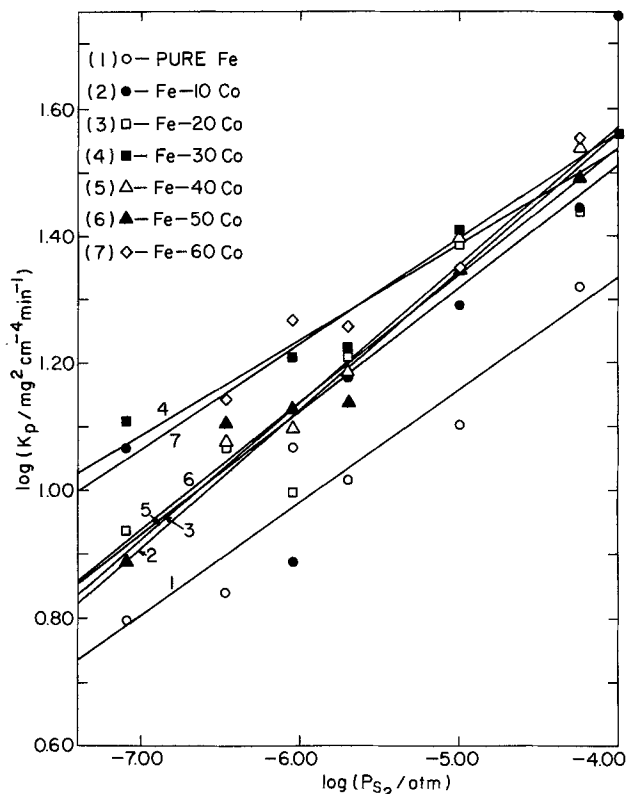


Fig. 2. Dependence of the parabolic rate constant on  $p_{\text{S}_2}$  at 700°C for each of the alloys. Straight lines found by regression on Eq. [2].

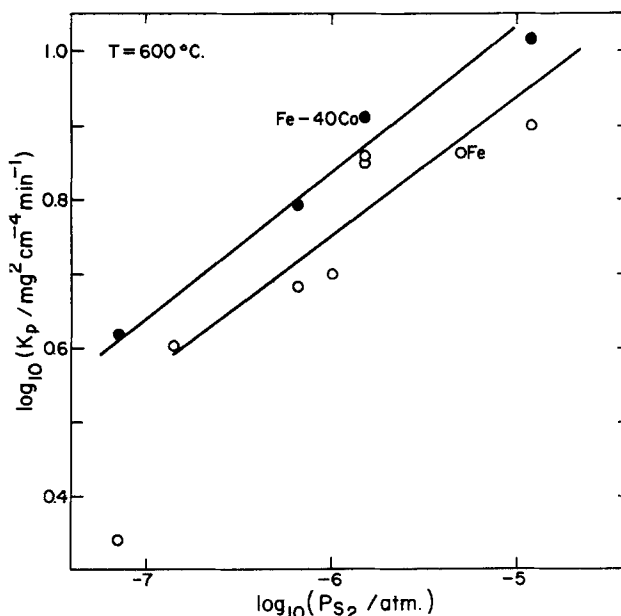


Fig. 3. Dependence of the parabolic rate constant on  $p_{\text{S}_2}$  at 600°C for Fe and Fe-40 w/o Co. Straight lines found by regression on Eq. [2].



of temperature on the sulfidation rate of each alloy at  $p_{S_2} = 2 \times 10^{-6}$  atm was determined. Arrhenius plots of the results are shown in Fig. 4 which also gives the deduced activation energies,  $E_A$ . The relatively large error in  $E_A$  is a consequence of the small temperature range employed.

The effect of alloy composition on the parabolic rate constant was determined at  $p_{S_2} = 2 \times 10^{-6}$  atm and the results are shown in Fig. 5. Inspection of the error bars on this figure reveals that no statistically

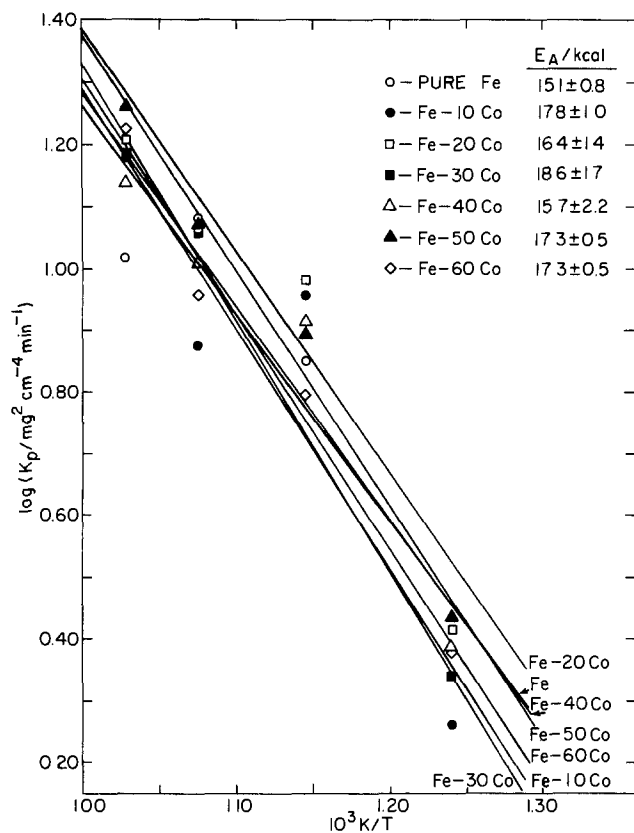


Fig. 4. Temperature dependence of the parabolic rate constant at  $p_{S_2} = 2 \times 10^{-6}$  atm for each of the alloys. Straight lines found by regression on the Arrhenius equation.

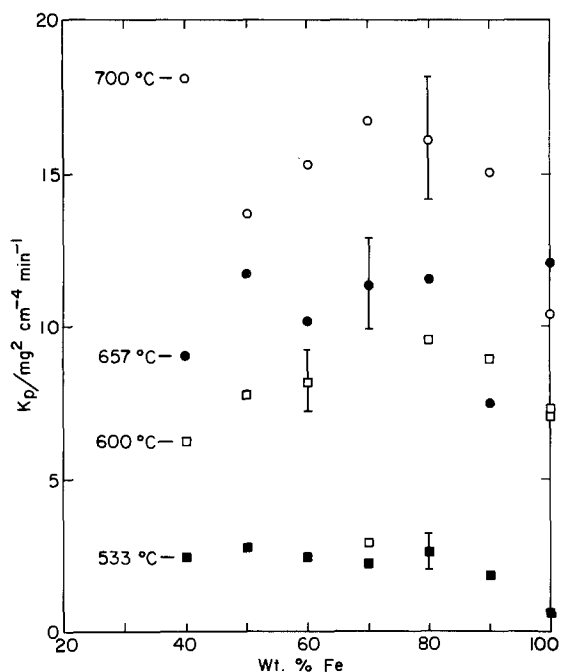


Fig. 5. Variation of parabolic rate constant with alloy composition at  $p_{S_2} = 2 \times 10^{-6}$  atm and various temperatures.

significant variation of reaction rate with alloy composition is found at any of the temperatures employed.

The appearance of the sulfide scales formed is typified by the micrographs in Fig. 6. The scales are seen to be compact, tightly adherent to the metal surface, and of very large grain size. As was reported earlier (1) the sulfidation product was the monosulfide  $(FeCo)_{1-\delta}S$  which, when sufficiently rich in Co, decomposed upon cooling via a eutectoid reaction (12) to yield  $(CoFe)_9S_8$  and  $(CoFe)_3S_4$ .

In order to investigate the applicability of Wagner's theory (7) for growth of a reaction product layer, the composition of the scale formed on pure iron was determined by microprobe analysis as a function of position within the scale. The results are shown in Fig. 7.

### Discussion

*Sulfidation of pure iron.*—The formation of a compact sulfide scale in a reaction which follows parabolic kinetics suggests that the process is controlled by solid-state diffusion. In this case, the theory of Wagner (7) should describe the reaction rate as a function of  $T$  and  $p_{S_2}$ . On the assumptions that only metal cations and electronic species are mobile in  $Fe_{1-\delta}S$  and that local equilibrium is attained, the theory predicts for the flux of metal through the scale

$$J_{Fe} = C_{Fe} D_{Fe} \frac{Z_{Fe}}{2|Z_S|} \frac{d \ln p_{S_2}}{dx} \quad [3]$$

where  $J$  is the flux,  $C$  the concentration,  $D$  the self-

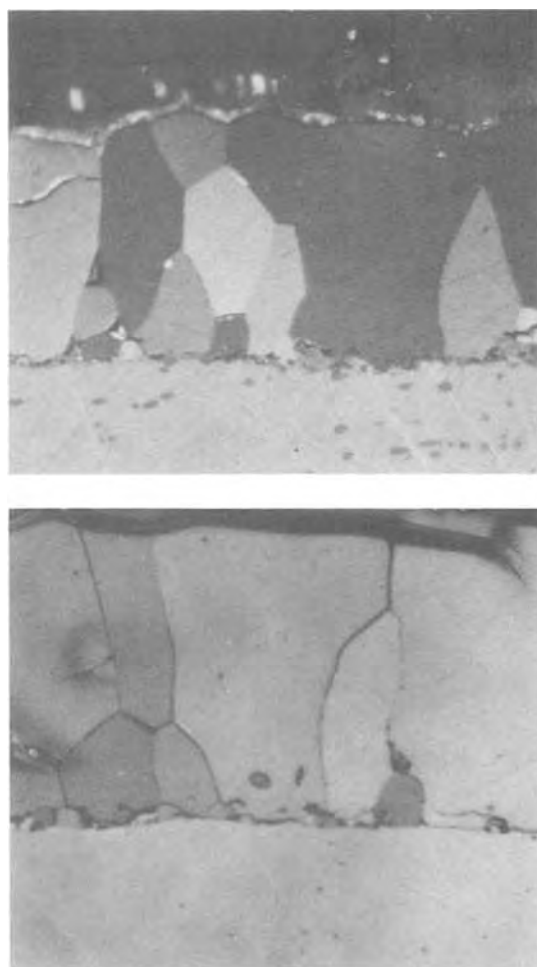


Fig. 6. Cross sections of sulfidized samples. Upper micrograph: pure Fe reacted at 700°C with  $p_{S_2} = 8 \times 10^{-8}$  atm for 22.5 min, magnification 380X. Lower micrograph Fe-40 w/o Co reacted at 600°C with  $p_{S_2} = 2 \times 10^{-6}$  atm for 39.3 min, magnification 380X.

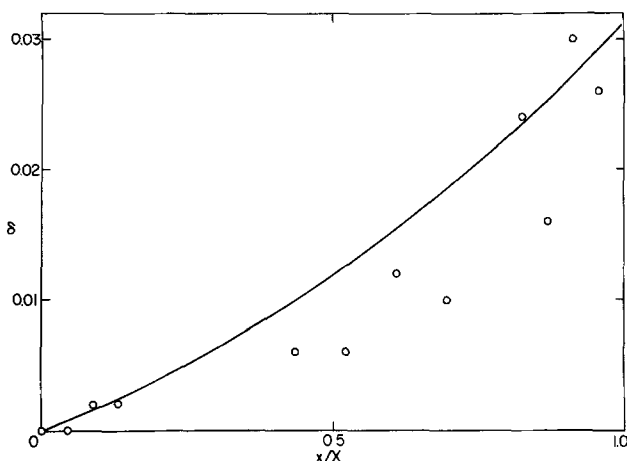


Fig. 7. Variation of stoichiometry with position in an  $\text{Fe}_{1-\delta}\text{S}$  scale formed on Fe at  $700^\circ\text{C}$  and  $p_{\text{S}_2} = 8 \times 10^{-8}$  atm. Continuous line calculated on the basis of divergence-free flux and local thermodynamic equilibrium; circles represent experimental measurements obtained on an electron microprobe.

diffusion coefficient,  $Z$  the effective valence, and  $x$  the position coordinate within the growing scale. Use has been made of the fact (10) that the electronic transport number  $\approx 1$ . The value for  $|Z_{\text{S}}|$  is taken as 2 and, therefore,  $Z_{\text{Fe}} = 2/(1 - \delta)$ . If the flux is assumed position independent, Eq. [3] integrates to yield the parabolic rate law with the rational rate constant expressed as

$$2k_{\text{r}} = c_{\text{eq}} \int_{p'_{\text{S}_2}}^{p''_{\text{S}_2}} \frac{Z_{\text{Fe}}}{|Z_{\text{S}}|} D_{\text{Fe}} d \ln p_{\text{S}_2} \quad [4]$$

where  $c_{\text{eq}}$  is the average concentration, in equivalents, of sulfide in the scale;  $p'_{\text{S}_2}$ ,  $p''_{\text{S}_2}$  are the sulfur partial pressures at the metal-scale and scale-gas interfaces.

The fundamental assumptions of the theory are: that local thermodynamic equilibrium is obtained; that the mechanism of mass transport is diffusion; and, finally, that the flux of matter within the scale is position independent. Both the flux equation [3] and the rate equation [4] are employed to investigate these assumptions.

The self-diffusion of S is very much slower (8) than that of Fe in  $\text{Fe}_{1-\delta}\text{S}$  and may be neglected. It follows then that if the deviation from stoichiometry in  $\text{Fe}_{1-\delta}\text{S}$  is small, the deviation from a constant value of  $J_{\text{Fe}}$  within the scale is also small. If Eq. [3] applies, then the quantity  $(D_{\text{Fe}} d \ln p_{\text{S}_2} / dx)$  should also be nearly independent of position. The variation of tracer-diffusion coefficient,  $D_{\text{Fe}}^{\text{T}}$ , with stoichiometry has been measured (8) in single crystal  $\text{Fe}_{1-\delta}\text{S}$  as

$$D_{\text{Fe}}^{\text{T}} = D_0 \delta \exp[-(19.4 + 20.1\delta)/RT] \quad [5]$$

and thus  $D_{\text{Fe}}^{\text{T}}$ , and hence  $D_{\text{Fe}}$ , is dependent upon composition for  $\delta$  small but practically constant for larger values. It follows therefore from [3] that the gradient  $d \ln p_{\text{S}_2} / dx$  in the FeS scale also is approximately position independent under these conditions. If the further assumption of local equilibrium is correct, it is possible from a knowledge of the composition of  $\text{Fe}_{1-\delta}\text{S}$  as a function of  $p_{\text{S}_2}$  to calculate the compositional gradients in a scale which is growing by solid-state diffusion. Many authors have measured  $\delta$  as a function of  $T$  and  $p_{\text{S}_2}$  and the data of Toulmin and Barton (9) has been employed in performing the present calculation. The results are compared with experimental measurements on a scale grown at  $700^\circ\text{C}$  in Fig. 7. Agreement is seen to be excellent except very near the metal-scale interface where  $\delta$  approaches zero and  $D_{\text{Fe}}$  is composition dependent.

Narita and Nishida (6) measured the elemental distributions within a  $\text{Fe}_{1-\delta}\text{S}$  scale grown at  $700^\circ\text{C}$  and found compositional gradients near the scale interfaces but an almost flat concentration profile in the

Table I. Scaling constant for sulfidation of iron

T/K	$p_{\text{S}_2}$ /atm	$k_{\text{r}}$ /equiv., $\text{cm}^{-1}\text{-sec}^{-1}$	
		Measured	Predicted
973	$8 \times 10^{-8}$	$2.0 \times 10^{-9}$	$6.3 \times 10^{-9}$
	$3 \times 10^{-7}$	$2.2 \times 10^{-9}$	$1.0 \times 10^{-8}$
	$2 \times 10^{-6}$	$3.2 \times 10^{-9}$	$1.3 \times 10^{-8}$
	$1 \times 10^{-5}$	$3.9 \times 10^{-9}$	$1.6 \times 10^{-8}$
	$6 \times 10^{-5}$	$6.5 \times 10^{-9}$	$2.0 \times 10^{-8}$
973	$2 \times 10^{-6}$	$3.2 \times 10^{-9}$	$1.3 \times 10^{-8}$
930		$3.8 \times 10^{-9}$	$8.3 \times 10^{-9}$
873		$2.3 \times 10^{-9}$	$4.7 \times 10^{-9}$
806		$6.9 \times 10^{-10}$	$2.2 \times 10^{-9}$

interior of the scale. This result was taken to imply a much higher value for  $D_{\text{Fe}}$  in the region of the very small gradient. Metallographic examination revealed that this interior region of the scale was cracked and porous, thereby providing an explanation for the enhanced diffusion. In the present case, the scales are nonporous (Fig. 6) and Eq. [3] is directly applicable with values for  $D_{\text{Fe}}$  characteristic of single crystal  $\text{Fe}_{1-\delta}\text{S}$ .

As the assumption of a position-independent flux, which is necessary for the integration of Eq. [3], is apparently a viable approximation, the utility of the integrated form [4] is now examined. The parabolic rate constant, as measured in  $\text{g}^2\text{-cm}^{-4}\text{-sec}^{-1}$ , is related to the rational rate constant, expressed in equivalent  $\text{cm}^{-1}\text{-sec}^{-1}$ , by the expression

$$k_{\text{r}} = \frac{1}{2} V_{\text{eq}} k_{\text{p}} / A^2 \quad [6]$$

where  $V_{\text{eq}}$  is the equivalent volume of  $\text{Fe}_{1-\delta}\text{S}$  and  $A$  is the atomic weight of S. Equation [4] was integrated numerically using the data of Toulmin and Barton (9) for the variation of  $Z_{\text{Fe}}$  with  $p_{\text{S}_2}$  and Eq. [5] for the variation of  $D_{\text{Fe}}$  with  $\delta$  and hence with  $p_{\text{S}_2}$ , on the assumption that  $D_{\text{Fe}} = D_{\text{Fe}}^{\text{T}}$ . The diffusion of Fe in  $\text{Fe}_{1-\delta}\text{S}$  is in fact anisotropic with  $D_{\text{c}} \approx 1.8D_{\text{a}}$  (8), where a and c refer to the basal and prismatic directions, respectively. An average value of  $D_{\text{c}} = 2.35 \text{ cm}^2\text{-sec}^{-1}$  in Eq. [5] was employed. Values of  $V_{\text{eq}}$  taken from Meussner and Birchenall (2) were employed in Eq. [6] to compare the predicted and measured rate constants. The results are summarized in Table I and shown as functions of  $p_{\text{S}_2}$  and  $T$  in Fig. 8 and 9.

The predicted and measured rate constants recorded in Table I are within half an order of magnitude, which is remarkably good agreement for the type of measurement involved. However, the error is nonrandom, the measured rates being consistently lower than those predicted. A possible reason for this discrepancy is that diffusion has been assumed uncorrelated in calculating  $D_{\text{Fe}}$  from the tracer diffusion coefficient,  $D_{\text{Fe}}^{\text{T}}$ . In fact  $D_{\text{Fe}} = fD_{\text{Fe}}^{\text{T}}$  where  $f$ , the correlation co-

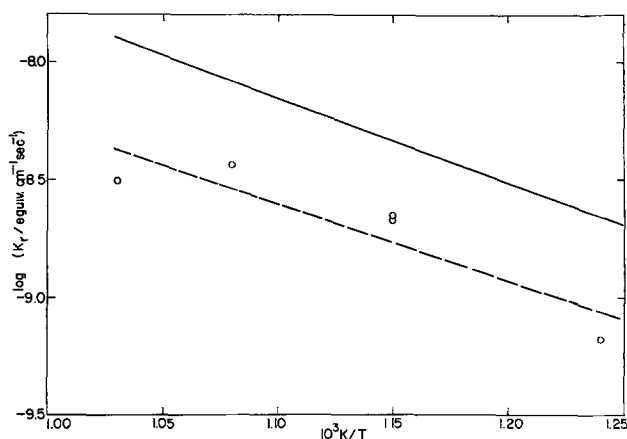


Fig. 8. Measured temperature dependence of iron sulfidation rates at  $p_{\text{S}_2} = 2 \times 10^{-6}$  atm compared with prediction of Wagner's theory (continuous line).

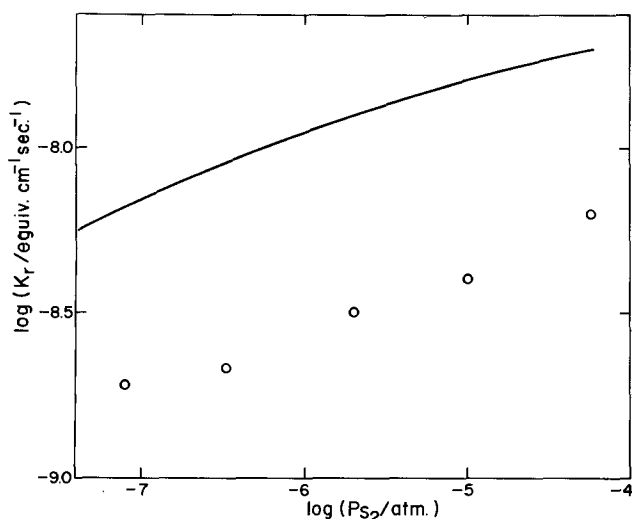


Fig. 9. Measured  $p_{S_2}$  dependence of iron sulfidation rates at 700°C compared with predictions of Wagner's theory (continuous line).

efficient, is unknown for  $Fe_{1-\delta}S$  but is certainly less than one for noninterstitial diffusion. It is emphasized that the errors in the original determinations of  $D_{Fe}^T$  and of  $\delta = f(p_{S_2})$  are large enough to account for the discrepancy between the measured and calculated values.

The predicted rate dependence on  $p_{S_2}$  and  $T$  are closely obeyed. The activation energy for reaction at  $p_{S_2} = 2 \times 10^{-6}$  atm is 15.1 kcal whereas the activation energy for the tracer diffusion (8) of Fe in  $Fe_{1-\delta}S$  is  $(19.4 + 20.1\delta)$  kcal. The difference arises through the temperature dependence of both  $p'_{S_2}$  and the functional relationship between  $Z_{Fe}$  and  $p_{S_2}$ . Since  $D_{Fe} \approx \bar{D}_{Fe} \neq f(p_{S_2})$ , then from [4]

$$k_r \approx C_{eq} \bar{D}_{Fe} \int_{p'_{S_2}}^{p''_{S_2}} \frac{Z_{Fe}}{|Z_S|} d \ln p_{S_2}$$

The temperature coefficient of the above integral can be evaluated numerically from the data of Toulmin and Barton (9) to yield, for  $p''_{S_2} = 2 \times 10^{-6}$  atm

$$\frac{d \ln (\text{Integral})}{d(1/T)} = + 5.4 \text{ kcal}$$

Hence it can be deduced from the kinetic activation energy for iron sulfidation that the activation energy of  $\bar{D}_{Fe}$  is 20.5 kcal, in excellent agreement with the tracer diffusion results which yield an average activation energy of 20.2 kcal for  $p_{S_2} = 2 \times 10^{-6}$  atm.

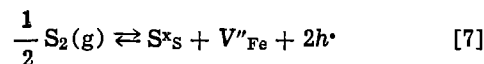
Self-diffusion activation energies have been estimated from the sulfidation reaction by other authors, by further approximating the integrated rate equation as

$$k_r = \frac{C_{eq} \bar{D}_{Fe}}{|Z_S|} [Z''_{Fe} \ln p''_{S_2} - Z'_{Fe} \ln p'_{S_2}]$$

This procedure can lead to substantial error. Meussner and Birchenall (2) deduced as average value of 20.6 kcal for  $0.12 < \delta < 0.25$  whereas the actual self-diffusion activation energy,  $Q$ , is  $22 < Q < 24.4$  in this region of nonstoichiometry (8). Turkdogan (4) deduced a value of 26.4 kcal for  $\delta \approx 0.13$  compared to  $Q = 22.0$  kcal, and a value of 20 kcal for  $\delta = 0.008$  which compares well with  $Q = 19.6$  kcal. Thus the above approximation of the integrated rate equation is viable only as  $\delta$  approaches zero.

The pressure dependence of the parabolic rate constant may be described empirically by Eq. [2] with  $n = 5.7$  at 700°C. Previous studies, carried out at higher values of  $p_{S_2}$ , yielded  $n = 5.7$  (5),  $n = 6$  (2, 4), and  $n = 7$  (3). At 500°C a value of 7.8 was found (13) for  $n$ . A value for  $n$  of 6 has in the past been ascribed to

rate control by diffusion of doubly ionized vacancies. Such a model is based on the proposed gas solid equilibrium



and the approximate formulation of charge balance

$$2[V''] = [h^{\bullet}] \quad [8]$$

where the point defect notation of Kroger and Vink (14) has been employed. With the further assumption of ideal or Henrian solution behavior, Eq. [7] and [8] yield

$$[V''] = (K/4)^{1/3} p_{S_2}^{1/6} \quad [9]$$

where  $K$  is the equilibrium constant for the process [7]. However it has been shown (9, 12) that the solution behavior of  $Fe_{1-\delta}S$  is not ideal nor Henrian, and as a consequence (8) the Wagner equation predicts a pressure dependence which is strong for small  $\delta$  but which decreases as  $\delta$  increases. The observation of a particular pressure dependence is therefore an insufficient basis for the deduction of a particular point defect mechanism.

Independent evidence exists (10) that the electronic conductivity,  $\sigma$ , of  $Fe_{1-\delta}S$  is metallic in type, and obeys the relation

$$\sigma = \text{const } p_{S_2}^{1/30}$$

Both observations appear to be inconsistent with the defect model posed above. The conductivity is however related to both the concentration and the mobility of the free carriers. It is conceivable that the mobility is dictated largely by the stoichiometry of the solid (e.g., through the existence of specific scattering centers whose concentration is stoichiometry dependent) and hence that the conductivity experiments and the defect model are possibly reconcilable. Kinetic studies of the Fe-S reaction, accordingly, do not resolve the question of the defect model for  $Fe_{1-\delta}S$ .

It is concluded that, under the present experimental conditions, the sulfidation of pure iron is controlled by lattice diffusion of Fe through the growing scale for the following reasons. The distribution of components within the sulfide scale is in accord with the known thermodynamic and diffusion properties of  $Fe_{1-\delta}S$  and with the assumption of a position-independent flux. The functional form of the kinetics and the magnitude of the rate constants are as predicted by Wagner's theory of scale growth. The magnitude and temperature dependence of the deduced value for  $D_{Fe}$  are in good agreement with independent measurements, in single crystal  $Fe_{1-\delta}S$ , of  $D_{Fe}^T$ . Finally, the pressure effect on the reaction rate constant is consistent with independent measurements of the thermodynamics of  $Fe_{1-\delta}S$ .

*Sulfidation of the alloys.*—The sulfidation properties of the alloys are in all respects closely similar to those of pure iron. Again parabolic kinetics and compact, large-grain sulfide scales were observed. The parabolic rate constants of pure Fe and the different alloys under given experimental conditions were the same within 95% confidence limits (Fig. 5). Similarly, the  $p_{S_2}$  and  $T$  dependencies of the rate constant (Fig. 1-4) were independent of alloy cobalt content at a 0.10 level of significance. These results imply that sulfidation of the alloys is also solid-state diffusion controlled and that the self-diffusion coefficients of Co and Fe are very similar in magnitude, in  $T$  dependence and in  $p_{S_2}$  dependence.

#### Acknowledgment

The authors gratefully acknowledge the sponsorship of this research by the National Research Council of Canada.

Manuscript submitted July 7, 1975; revised manuscript received Sept. 19, 1975.

Any discussion of this paper will appear in a Discussion Section to be published in the December 1976 JOURNAL. All discussions for the December 1976 Discussion Section should be submitted by Aug. 1, 1976.

Publication costs of this article were partially assisted by McMaster University.

#### REFERENCES

1. D. J. Young, P. Mayer, and W. W. Smeltzer, *This Journal*, **121**, 889 (1974).
2. R. A. Meussner and C. E. Birchenall, *Corrosion*, **13**, 677t (1957).
3. K. Haufler and A. Rahmel, *Z. Phys. Chem.*, **199**, 152 (1952).
4. E. T. Turkdogan, *Trans. AIME*, **242**, 1665 (1968).
5. T. Narita and K. Nishida, *Trans. Japan. Inst. Met.*, **14**, 439 (1973).
6. T. Narita and K. Nishida, *ibid.*, **14**, 447 (1973).
7. C. Wagner, in "Atom Movements," p. 153, ASM, Cleveland (1951).
8. R. H. Condit, R. R. Hobbins, and C. E. Birchenall, *Oxidation of Metals*, **8**, 409 (1974).
9. P. Toulmin and P. B. Barton, *Geochim. Cosmochim. Acta*, **28**, 641 (1964).
10. H. I. Kaplan and W. L. Worrell, in "The Chemistry of Extended Defects in Non-metallic Solids," p. 561, L. Eyring and M. O'Keeffe, Editors, North Holland/American Elsevier, New York (1970).
11. D. Coutouradis and A. Davin, in "High Temperature Metallic Corrosion of Sulfur and Its Compounds," Z. A. Foroulis, Editor p. 132, The Electrochemical Society Softbound Symposium Series, New York (1970).
12. T. Rosenqvist, *J. Iron Steel Inst.*, **176**, 37 (1954).
13. K. N. Strafford and R. Manifold, *Corrosion Sci.*, **9**, 489 (1969).
14. F. A. Kroger and H. J. Vink, *Solid State Phys.*, **3**, 307 (1956).

## Resistivity-Temperature Characteristics of Boron- and Antimony-Doped Tin Oxide Films

J. P. Marton

Welwyn Canada Limited, London, Ontario, Canada N6A 4G7

and D. A. Lepic<sup>1</sup>

McMaster University, Hamilton, Ontario, Canada

#### ABSTRACT

Freshly deposited films are found to exhibit irreversible changes in resistivity when cycled in the range of  $-60^{\circ}$  to  $+175^{\circ}\text{C}$ , but the resistivity may be stabilized by heat-treatment for a few hours at  $200^{\circ}\text{C}$ . Reversible changes in resistivity of stable films with temperature are found to depend in a unique way on the concentration of the dopants and the film thickness. An empirical relation has been developed to describe the resistivity-temperature relation of films as a function of doping concentration. Practical applications include the possibility of electrical resistors with controlled temperature coefficient of resistance in the range of near zero to  $+500$  ppm/ $^{\circ}\text{C}$  at room temperature.

$\text{SnO}_2$  single crystals and films have been investigated extensively because of the unique combination<sup>2</sup> of their useful electrical and optical properties. The electrical properties of single crystals (1, 2) are understood reasonably well, but the mechanism of conduction in films (3, 4) remains obscure. The latter depends strongly on the method of preparation, subsequent heat-treatments in various ambients, and the nature and concentration of dopants introduced.

Tin dioxide in its pure form is an n-type wide band-gap semiconductor with conduction electron concentration of about  $10^{17}$   $\text{cm}^{-3}$  at room temperature. This may be increased near metallic densities by doping with elements from Group V of the Periodic Table (e.g., Sb). Doping tin dioxide with Group III elements (e.g., In or B) also changes the carrier concentration and at high levels renders the host p-type.

The study of  $\text{SnO}_2$  films is complicated in a twofold manner. First, the process of film deposition is such that it renders the film oxygen deficient (5) and it introduces chlorine (4) into the film. Second, the films are polycrystalline with film thickness dependent on degrees of disorder. The first set of defects acts as dopants and may or may not be thermally stable, while the second class of disorders influences the electrical

conductivity through carrier scattering which may also be thermally unstable. However, if samples are prepared carefully and are thermally stabilized after film deposition, the effects of donor and acceptor doping and film thickness on the electrical resistivity and its temperature dependence may be studied. The present work is such a study aimed at characterizing thermally stable  $\text{SnO}_2$  films doped with antimony and boron.

#### Experimental

Samples were prepared by high temperature hydrolysis of  $\text{SnCl}_4$  in a  $\text{H}_2\text{O}$  and  $\text{HCl}$  atmosphere using the reaction  $\text{SnCl}_4 + 2\text{H}_2\text{O} \rightleftharpoons \text{SnO}_2 + 4\text{HCl}$  (endothermic). High alumina cylindrical ceramic substrates, with a submicron surface roughness,  $\frac{1}{4}$  in. diameter by 1 in. long were heated in a furnace to  $800^{\circ}\text{C}$  and were passed through the deposition zone. The latter was a chamber through which a vaporized firing solution<sup>3</sup> was passed. The solution was vaporized by passing the liquid through a quartz capillary heated to  $200^{\circ}\text{C}$ .

Doping was done by mixing the chlorides of antimony and boron in the  $\text{SnCl}_4$  solution in various quantities. In this work we refer to doping in terms of mole per cent of  $\text{SnO}_2$ . A 4% B and 0.6% Sb doping means that the firing solution contained 0.04 moles of B and 0.006 moles of Sb for every mole of  $\text{SnO}_2$  assumed to be formed. As all constituents appeared in the vapor at the same proportion as they had been

<sup>1</sup> Present address: Computing Devices Limited, Ottawa, Ontario, Canada.

Key words: doped tin oxide films, electrical conduction.

<sup>2</sup> The resistivity of  $\text{SnO}_2$  may be made to approach that of alloys (viz., be as low as  $1000$   $\mu\text{ohm-cm}$ ) and, in its undoped form, it is optically transparent in the visible range of wavelengths.

<sup>3</sup> The firing solution used in the experiments was made up of  $\text{SnCl}_4$  ( $351$   $\text{cm}^3$ ),  $\text{H}_2\text{O}$  ( $108$   $\text{cm}^3$ ),  $\text{HCl}$  ( $250$   $\text{cm}^3$ ),  $\text{H}_3\text{BO}_3$  (variable),  $\text{SbCl}_5$  (variable).

introduced into the firing solution, it was assumed that the concentration of B and Sb in the  $\text{SnO}_2$  films was proportional to their concentration in the firing solution. The doping of films was then varied by the amount of B and Sb in the firing solution.

Films were deposited with a large number of firing solutions containing different amounts of dopants, each group divided into four subgroups with room temperature resistances of 14, 20, 28, and 40 ohms. The resistance was controlled by the thickness of the films which in turn was adjusted by the deposition time. The film thickness ranged from 1.5 to  $3\mu$  and the deposition time was adjusted between 5 and 10 sec. The rate of deposition was kept constant for all groups of samples at 3000 A/sec by a suitable adjustment of the firing solution vapor flow rate. For all samples, other deposition conditions, *i.e.*, temperature, pressure, substrate feed rate, etc., were kept constant.

After deposition, the samples were allowed to come to room temperature in the normal laboratory atmosphere without attempts to anneal them in any special way. The samples were then provided with terminals and their resistance was measured between  $-60^\circ$  and  $+175^\circ\text{C}$ . Stabilization followed at  $200^\circ\text{C}$  for 5 hr and the resistance was measured again in the same range of temperatures.

The resistivity of film material was calculated from the resistance and film dimensions. Film thickness was measured by weighing the samples, removing the film by chemical means, and reweighing the bare substrates again. The differential weight and bulk density of  $\text{SnO}_2$  was used to obtain the film thickness.

In Table I, some typical groups used in the experiments are listed, along with their approximate volume resistivity and film thickness.

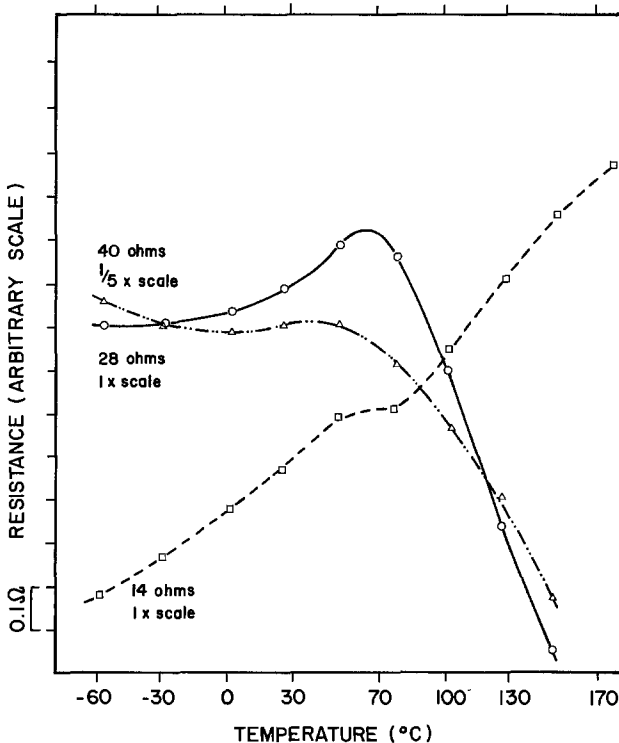
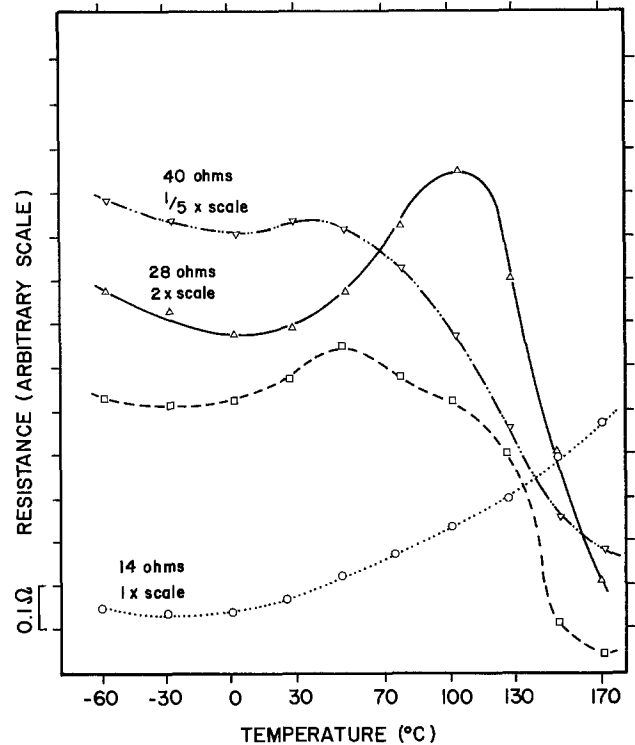
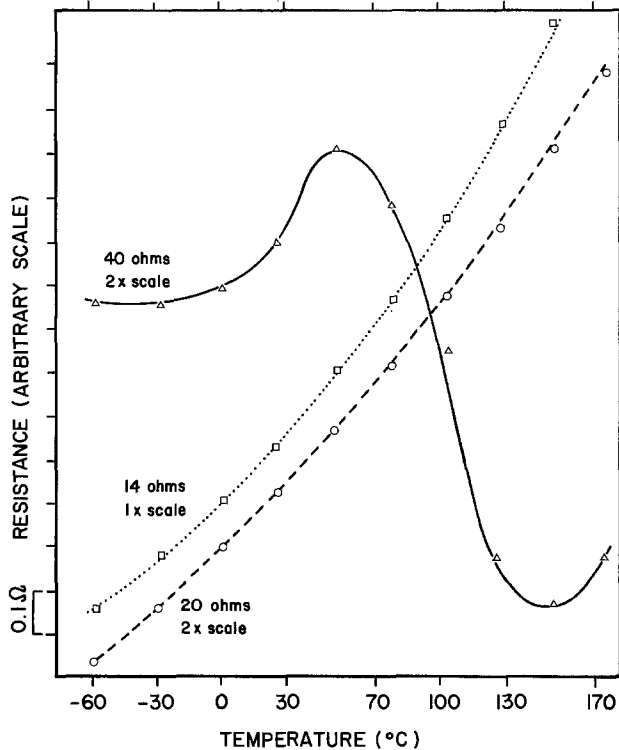


Fig. 1. Resistance vs. temperature of samples having three different doping levels (a, above left) 4.0% B, 0.27% Sb, (b, above right) 6.0% B, 0.4% Sb, and (c, left) 9.0% B, 0.9% Sb. Lower resistance films appear to behave similar to elemental semiconductors. Higher resistance films show anomalous behavior above  $50^\circ\text{C}$ . The anomaly extends to lower resistances for higher doping levels. The notes 1x and 2x etc. mean resistance divisions to be read as 0.1 and 0.2 ohm, respectively.

Table I. Some groups of samples used in the experiments along with their approximate volume resistivity and film thickness

Doping	Resistivity (mohm-cm)/film thickness ( $\mu$ )			
	14 ohms	20 ohms	28 ohms	40 ohms
4% B, 0.27% Sb	—	3.40/2.20	4.10/1.90	—
4% B, 0.4% Sb	2.10/2.0	2.40/1.70	—	—
4% B, 0.6% Sb	2.27/2.1	2.66/1.86	3.17/1.55	3.92/1.35
6% B, 0.4% Sb	2.86/2.60	—	4.54/2.15	—
9% B, 0.9% Sb	3.10/2.80	3.57/2.50	4.24/2.10	—

Table II. Activation energy measurements

Doping	Activation energy, eV
6.0% B, 0.60% Sb-40 ohms	0.0126
6.0% B, 0.90% Sb-20 ohms	0.0065
6.0% B, 0.90% Sb-40 ohms	0.0132
9.0% B, 0.90% Sb-40 ohms	0.0127
9.0% B, 1.35% Sb-40 ohms	0.0131

### Results and Discussions

*Irreversible effects.*—The characteristic temperature dependence of resistance of as-deposited films depends on the doping level and on the film thickness.  $R(T)$  curves of lightly doped thick films appear characteristic of elemental semiconductors, but at higher doping levels and for thinner films there appears an anomalous decrease of resistance with increasing temperatures above 50°C.

Typical curves are shown in Fig. 1 where the doping concentrations for Fig. 1a, b, and c are, respectively, 4.0% B, 0.27% Sb; 6.0% B, 0.4% Sb; and 9.0% B, 0.9% Sb. The anomalous decrease was measured for several samples, and activation energies for the decrease were calculated in the linear region. The results are listed in Table II, and a typical  $\log 1/R$  vs.  $1/T$  plot is shown in Fig. 2.

From the results, an average activation energy of 0.013 eV could be assigned to the resistance decrease, which was assumed to be associated with annealing of

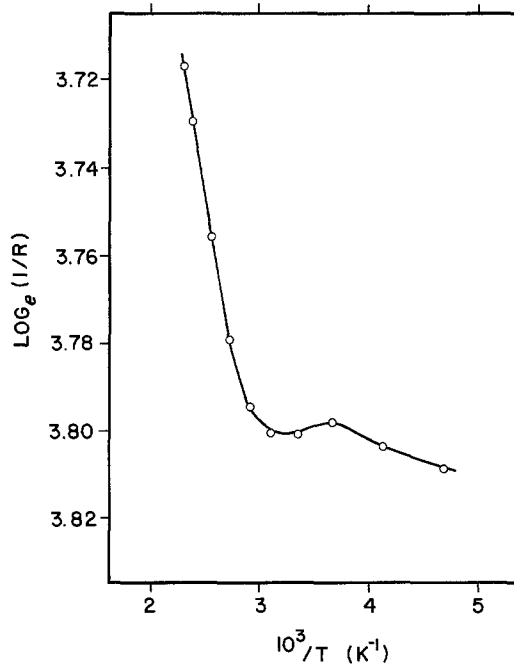


Fig. 2. Activation energy determination of the anomalous resistance decrease for films with 9.0% B, 0.9% Sb doping.

defects (6) in the film. These defects may be grain boundaries, which are known to occur at high densities in deposited films having a film thickness dependence. When annealed, the number of grain boundaries would decrease which would manifest itself in a decreasing resistance. In order to test this assumption, samples were cycled between  $-60^\circ$  and  $+175^\circ\text{C}$  and the resistance was monitored. Irreversible changes in resistance were indeed detected and their degree was found to depend on the doping concentration and film thickness. Typical results are shown for samples doped with 9% B, 1.35% Sb in Fig. 3 where the curves in 3a

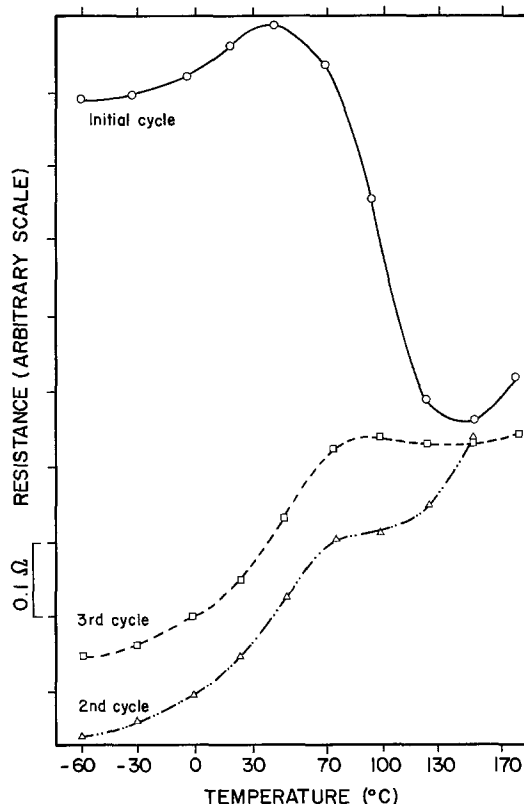
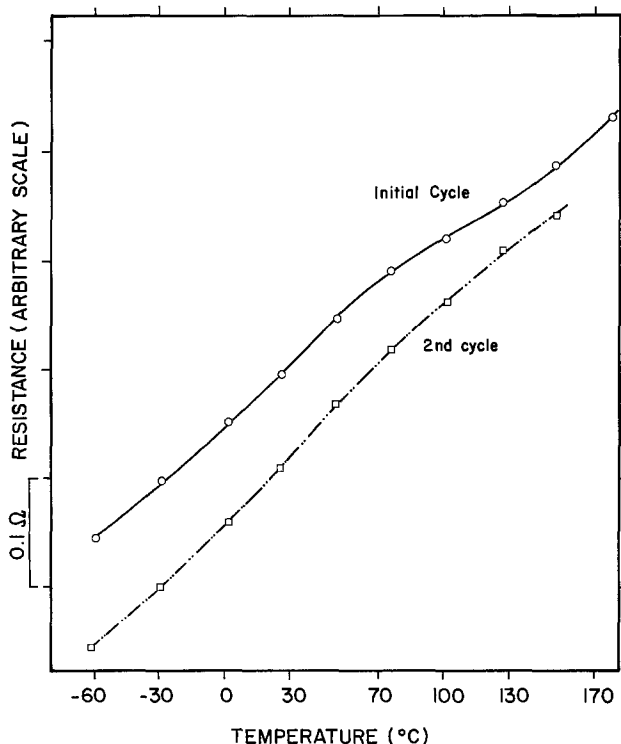


Fig. 3. Hysteresis of resistance on thermal cycling of films doped 9.0% B, 1.35% Sb. (a, above left) 14 ohm group (b, above right) 28 ohm group.

and b were measured on 14 and 28 ohm sample groups, respectively. For lighter doping levels and for lower resistances (thicker films) the irreversible changes are less than those for higher doping levels and thinner films.

In Fig. 3b we may note that the  $R(T)$  curve after the third cycle is above that measured after the second cycle. This was due to a slow cooling in cycle two, which annealed defects, and a fast cooling in cycle three, which reintroduced defects. The same behavior was observed for several other sample groups.

**Structural (thin film) effects.**—The volume resistivity  $\rho_v$  of freshly deposited films was measured in an attempt to determine whether any orderly film thickness dependence of resistivity exists at the different doping concentrations used. The thickness of films and their resistivity were obtained by differential weighing and by measuring the width and length of films. It was assumed that the density of  $\text{SnO}_2$  films was that of the bulk crystal.

Typical results are shown in Fig. 4 where the bulk resistivity is plotted against the reciprocal film thickness for several different doping levels. Although the plots are linear, a numerical comparison of the experimental values with the Fuchs theory (7) for thick films

$$\rho_v/\rho_{vo} = 1 + (3l/8d) \quad [1]$$

yields unreasonable values of several microns for the mean free paths of carriers. In the above expression,  $\rho_{vo}$  is the bulk resistivity of the crystal,  $l$  is the carrier mean free path, and  $d$  is the film thickness.

From the results we may speculate that the film thickness dependence of resistivity does not come about by film boundary scattering of carriers as predicted by the Fuchs theory, but rather by defect and grain boundary scattering of carriers. The density of defects and grain boundaries are known to depend on film thickness of films with a given concentration of impurities and a given thermal history; thus it may be the density of defects which causes the film thickness-dependent resistivity.

This idea conforms to the observed irreversible changes in resistance of freshly deposited films dis-

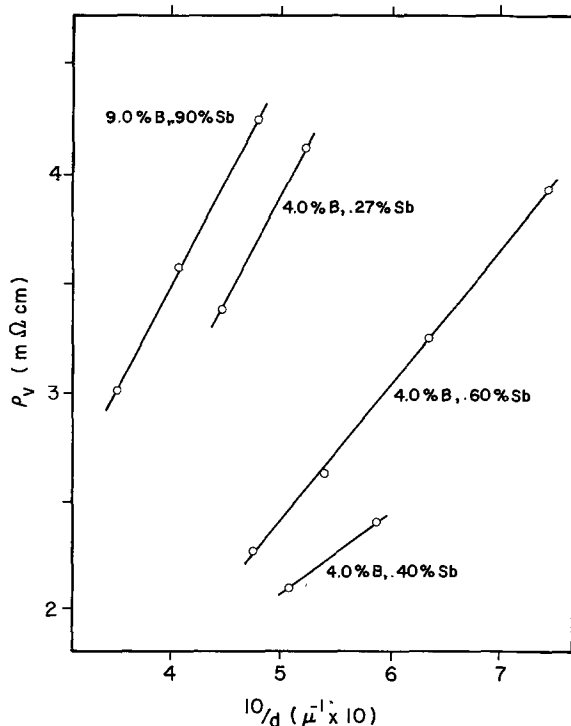


Fig. 4. Volume resistivity  $\rho_v$  plotted against inverse film thickness  $d$  for various doping levels to illustrate film thickness dependence of resistivity.

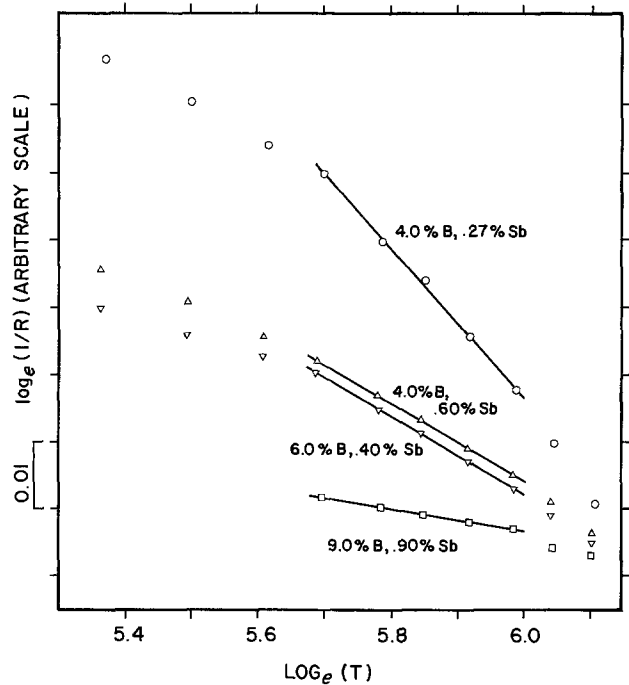


Fig. 5. Stable resistance vs. temperature of 20 ohm films with different doping levels. The slope of the curves decreases with increasing doping level.

cussed above as defects and grain boundaries may be decreased (or increased) by heat-treatment.

**Effect of doping.**—The effect of doping on the resistivity and its temperature dependence was measured on films that were stabilized at  $200^\circ\text{C}$  for several hours. In Fig. 5  $\log 1/R$  is plotted against  $\log T$  for 20 ohm films in order to isolate a power law relation. In the region of interest where solid lines are drawn through the data points, the  $R(T)$  relation may be written as

$$R(T) = R_0 T^\alpha \quad [2]$$

where  $R_0$  is the resistance at the reference temperature and where  $\alpha$  appears to be some function of doping.  $T$  is the absolute temperature.

Measurements on a large number of 14 and 20 ohm samples yielded fairly reliable values for  $\alpha$  at different doping concentrations. The results are listed in Table III and are plotted in Fig. 6. The plot is  $\alpha$  vs. the reciprocal of the product of B and Sb concentration in mole per cent. The film thickness dependence of  $\alpha$  is also contained in the figure, with the 14 and 20 ohm groups representing thicker and thinner films, respectively.

It is apparent from Fig. 6 that increasing doping levels decrease  $\alpha$  and that this decrease saturates at some moderate doping concentration. It is also apparent that it is the product of B and Sb concentrations that controls  $\alpha$ . In fact, we see from Table III that samples with 6% B, 0.4% Sb and 4% B, 0.6% Sb have the same  $\alpha$  value. A lower limit for  $\alpha$  appears to exist for both

Table III. Temperature exponent vs. doping level

Doping	Temperature exponent $\alpha$	
	14 ohms	20 ohms
2.7% B, 0.90% Sb	0.101	—
4.0% B, 0.27% Sb	0.163	0.118
4.0% B, 0.40% Sb	—	0.097
4.0% B, 0.60% Sb	—	0.063
6.0% B, 0.27% Sb	—	0.086
6.0% B, 0.40% Sb	—	0.063
6.0% B, 0.60% Sb	0.069	0.035
6.0% B, 0.90% Sb	0.073	—
9.0% B, 0.40% Sb	—	0.035
9.0% B, 0.90% Sb	0.055	0.018
9.9% B, 1.35% Sb	0.038	0.021

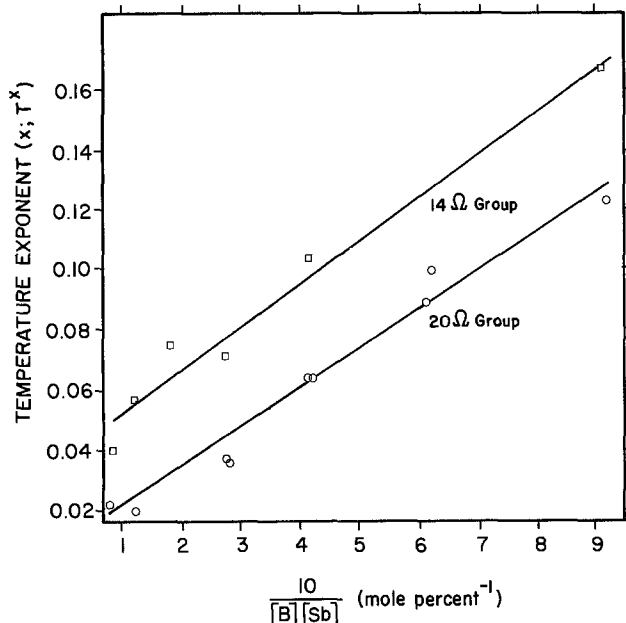


Fig. 6. Temperature exponent in Eq. [2] plotted against inverse doping concentration for 14 and 20 ohm groups of films.

resistance groups measured. For the 14 and 20 ohm group they are, respectively, 0.038 and 0.015.

Finally, we note that the slope of both curves in Fig. 6 is the same; thus we may write a final expression for  $R(T)$  in the temperature range of 25°-125°C as

$$R = R_0 T^{F(d)} T^{G(B,Sb)} \quad [3]$$

where  $F$  and  $G$  are functions of film thickness and doping concentration, respectively. For our specific case

$$F(d) = 0.015 \text{ for the 20 ohm group}$$

$$= 0.038 \text{ for the 14 ohm group}$$

$$G(B, Sb) = 0.118 / ([B][Sb])$$

This expression provides a "recipe" to fabricate electrical resistors with a desired temperature coefficient of resistance in the temperature range 25°-125°C. The TCR defined as

$$\frac{1}{R_0} \frac{\partial R(T)}{\partial T}$$

may be calculated from Eq. [3] to range from near zero to 500 ppm/°C for typical samples used in this work. The  $R(T)$  relationship can not be predicted by Eq. [3] however, outside this temperature range.

### Conclusions

The thermal instability of freshly deposited SnO<sub>2</sub> films doped with B and Sb was found to depend on film thickness and doping level. Irreversible changes in resistance were found to be greater for thinner films and for those with a higher concentration of dopants. These instabilities were suggested to be due to defect and grain boundary annealing.

It has been found that freshly deposited films may be stabilized by heating them at 200°C for several hours and then cooling them slowly to room temperature. Reversible  $R(T)$  characteristics of stabilized films showed a unique film thickness and doping concentration dependence in the temperature range 25°-125°C, and it was possible to write an empirical expression describing this relationship.

It was suggested that the results of this work may be used to design electrical resistors with a desired temperature coefficient of resistance in the present temperature range of interest.

### Acknowledgment

This work was supported in part by the National Research Council of Canada.

Manuscript submitted Sept. 13, 1973; revised manuscript received Sept. 8, 1975.

Any discussion of this paper will appear in a Discussion Section to be published in the December 1976 JOURNAL. All discussions for the December 1976 Discussion Section should be submitted by Aug. 1, 1976.

Publication costs of this article were partially assisted by Welwyn Canada Limited.

### REFERENCES

1. E. E. Kohnke, *J. Phys. Chem. Solids*, **23**, 1557 (1962).
2. C. G. Fonstad and R. H. Rediker, *J. Appl. Phys.*, **42**, 2911 (1971).
3. R. E. Aitchison, *Australian J. Appl. Sci.*, **5**, 10 (1954).
4. J. A. Aboaf, V. C. Marcotte, and N. J. Chou, *This Journal*, **120**, 701 (1973).
5. C. A. Vincent, *ibid.*, **119**, 515 (1972).
6. F. P. Koffyberg, *J. Appl. Phys.*, **36**, 844 (1965).
7. K. Fuchs, *Proc. Cambridge Phil. Soc.*, **34**, 100 (1938).

## Preparation and Properties of CVD Oxides with Low Charge Levels from SiH<sub>4</sub>-CO<sub>2</sub>-HCl-H<sub>2</sub> System

A. K. Gaid,\* G. K. Ackermann,<sup>1</sup> A. Nagarajan, and R. L. Bratter

IBM System Products Division, East Fishkill Facility, Hopewell Junction, New York 12533

### ABSTRACT

When SiO<sub>2</sub> is deposited from the SiH<sub>4</sub>-CO<sub>2</sub>-HCl-H<sub>2</sub> system at ~1000°C, the resulting films are equivalent to or better than dry O<sub>2</sub> grown SiO<sub>2</sub> in electrical properties. The addition of HCl to the SiH<sub>4</sub>-CO<sub>2</sub>-H<sub>2</sub> system reduces the Q<sub>ox</sub>. This is believed to be due to the reaction of unbonded Si with HCl, which prevents the incorporation of unbonded Si in the depositing SiO<sub>2</sub> matrix. The investigated properties, such as mobile charge density, index of refraction, etch rate, and density, were not affected by the presence of HCl. Postdeposition anneal (1050°C for 15 min in N<sub>2</sub>) deteriorates the films by causing an increase in fixed oxide charge level and in fast surface-state density.

Chemical vapor deposited (CVD) oxides find extensive applications in planar semiconductor device proc-

\*Electrochemical Society Active Member.

<sup>1</sup> Present address: IBM Boeblingen, West Germany.

Key words: deposition rates, flatband charge, annealing, fast surface-state density.

essing. These applications have been discussed elsewhere (1-7). The use of CVD oxides in the gate region of a field effect transistor (FET), however, is almost unknown. The high fixed-charge level (1-7) (Q<sub>ox</sub> = 1 - 20 × 10<sup>11</sup>) as determined at flatband condition, by

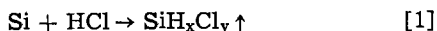


the usual C-V technique (8, 9), is one factor that has inhibited the use of CVD oxides for the above application. The mobile ions in these oxides are not a problem, since they can be reduced by increasing the deposition temperature (3, 7). In fact, at a deposition temperature of 1000°C, "as-deposited" oxide films from the  $\text{SiH}_4 + \text{CO}_2 + \text{H}_2$  system (6) show a low mobile charge density of  $2.7 (\pm 0.5) \times 10^{10} \text{ cm}^{-2}$ . Again it was shown (6) that the fast surface-state density ( $N_{\text{FS}}$ ) is  $1.5 (\pm 0.5) \times 10^{10} \text{ cm}^{-2} \text{ eV}^{-1}$  for CVD oxides deposited at 1000°C. The low mobile charge and the fast surface-state density, coupled with other physical and electrical properties, show that it is possible to deposit CVD oxides superior or equivalent in all respects, except the fixed-charge level, to the thermal oxides grown from dry oxygen.

Deal *et al.* (9) have hypothesized that the cause of fixed charges in the thermal oxides is excess ionic silicon, present at the Si-SiO<sub>2</sub> interface during oxidation, waiting to react with the oxidizing species that has to diffuse through the already-grown oxide. This hypothesis does not explain either the source of ionic silicon or any other cause of high charge levels in CVD oxides.

It is postulated here that the ionic silicon comes from the pyrolysis or reduction of silicon-bearing compounds used for the CVD oxide deposition. For example, in the  $\text{SiH}_4\text{-CO}_2\text{-H}_2$  system,  $\text{SiH}_4$  oxidation reaction must proceed simultaneously and in parallel with the decomposition of  $\text{SiH}_4$ . We feel that the latter reaction is responsible for free silicon in CVD oxides.

If, by some means, the rate of decomposition of  $\text{SiH}_4$  could be reduced or silicon formed by this means eliminated, then the fixed charge level in the CVD oxides would also be reduced. One way of reducing the free silicon is to add small amounts of HCl in the gas phase during the CVD deposition (10) so that the following reaction can occur



The result may be a reduction of the fixed (*i.e.*, flat-band) charge level in CVD oxides. As will be seen later, the experimental results met the above expectation.

This paper deals with the deposition rate of SiO<sub>2</sub> from the  $\text{SiH}_4 + \text{CO}_2 + \text{HCl} + \text{H}_2$  system and with the physical and electrical properties of the oxides so deposited.

### Experimental

**Equipment.**—The equipment used for the entire experimental investigation was a vertical, cold-wall, barrel-type, induction-heated reactor (11). The silicon "wafers" were placed on an SiC-coated graphite susceptor. Figure 1 gives a schematic cross-sectional view of the reactor. The fused-quartz chamber is 18 in. (~45 cm) long, with an internal diameter of 9 in. (~23 cm). The susceptor is placed in the chamber so that its

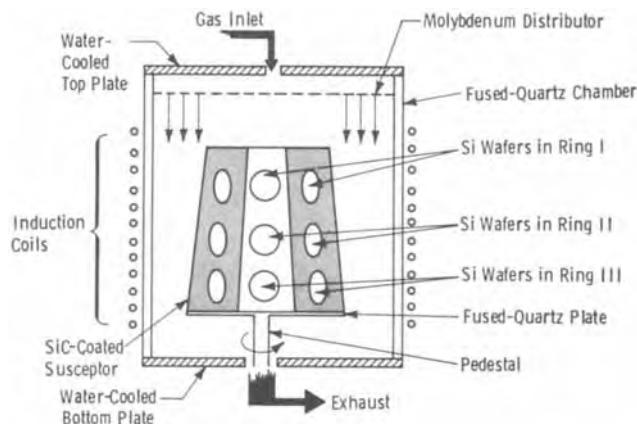


Fig. 1. Schematic cross-sectional view of reactor

leading edge is ~5 in. (12.7 cm) from the molybdenum distributor. The susceptor is hexagonal and is divided into three tiers, or "rings." Each of the six faces of the susceptor makes an angle of ~3 degrees with the central vertical axis. The susceptor is placed on a fused-quartz plate, which in turn is supported by a fused-quartz pedestal. The susceptor, approximately 8.25 in. (21 cm) long, was rotated at about 8 rpm throughout this experimental work. The volume of the annulus between the susceptor and the chamber (*i.e.*, the volume of the deposition zone) is ~5 liters. The surface area of the susceptor is  $\sim 1.1 \times 10^2 \text{ cm}^2$ .

The temperature was measured with an optical pyrometer.<sup>2</sup> All temperatures reported were corrected for system transmission losses and for emissivity (12). The reacting and carrier gases were introduced from the top of the reactor after each had been separately metered. All gases, except  $\text{SiH}_4$ , were metered through calibrated rotometers. The  $\text{SiH}_4$  (5% mixture in hydrogen) was controlled by a mass-flow controller.

**Typical deposition conditions and measurement technique.**—Three 2¼ in. (5.7-cm) Si, 11-25 ohm-cm, p-type, <100> wafers were processed in each experimental run, unless otherwise indicated. One wafer each was placed in rings 1, 2, and 3, at a predetermined fixed position. The remaining positions on the susceptor were filled with dummy wafers. Before loading in the reactor, wafers were cleaned ultrasonically in hot (85°C) deionized water (for 5 min), followed by  $\text{H}_2\text{SO}_4/\text{HNO}_3$  (3:1, at 120°C) cleaning (for 10 min), followed by a 10:1 dilute HF dip (for 10 sec). The wafers were then rinsed in running deionized water (for 5 min) and subsequently spin-dried. The wafer surface was hydrophobic after this cleaning.

During the experimental work, the  $\text{H}_2$  flow rate, typically, was 110 liters/min; the  $\text{SiH}_4$  flow rate (5% in  $\text{H}_2$ ) was varied between 60 and 1000  $\text{cm}^3/\text{min}$ . The  $\text{CO}_2:\text{SiH}_4$  ratio was changed between 15:1 and 250:1. The deposition temperature range was 850°-1050°C; the deposition time was never less than 5 or greater than 25 min. The HCl volume percentage was varied between 0.1% and ~1%. Without exception, HCl gas was introduced at the start of deposition and its flow terminated within 30 sec of the end of deposition.

The resulting SiO<sub>2</sub> film thicknesses were measured by CARIS<sup>3</sup> and by ellipsometry. In most cases, one thickness measurement per wafer was taken because the typical within-a-wafer thickness uniformity was  $\leq 2\%$ . The typical within-a-run deposition uniformity was  $\leq \pm 5\%$  at 1000°C, at a total flow rate of ~110 liters/min; the worst-cast within-a-run uniformity at any temperature and flow (within the experimental range) was  $\sim \pm 15\%$ . The deposition rates used in this report are therefore averaged deposition rates over three rings, and thus, as a first approximation, we neglected the  $\text{SiH}_4$  concentration variations along the susceptor length.

The electrical properties of the resulting oxides were investigated by means of MOS capacitors. These capacitors were formed by evaporating 20-mil (~0.05 cm) Al dots from a resistance heat source. Blanket Al was evaporated on the back side of these wafers to facilitate electrical contact. Following Al evaporation, all wafers were annealed for a half-hour in  $\text{N}_2$  at 400°C.

### Results

**Deposition rates.**—The parameters whose effect on the deposition rate of SiO<sub>2</sub> was investigated are HCl mole fraction,  $\text{SiH}_4$  mole fraction, deposition temperature,  $\text{CO}_2:\text{SiH}_4$  ratio, and  $\text{H}_2$  flow rate.

**Deposition rate vs. HCl mole fraction.**—Figure 2 shows the effect on the SiO<sub>2</sub> deposition rate of increasing the HCl mole fraction at a constant deposition temperature (*i.e.*, 1000°C) and at two  $\text{SiH}_4$  mole fractions, 3.8 ×

<sup>2</sup> The temperature along the susceptor length is  $\pm 10^\circ\text{C}$  of any reported value.

<sup>3</sup> Constant angle reflection interference spectroscopy.

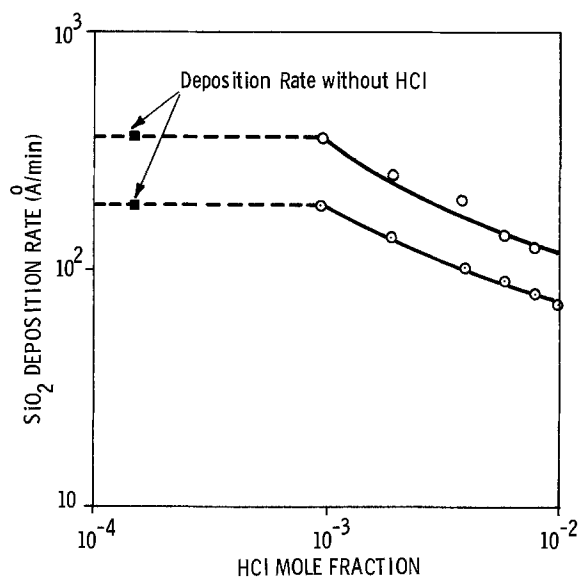


Fig. 2. Deposition rate of SiO<sub>2</sub> as a function of HCl mole fraction at two SiH<sub>4</sub> mole fractions: ○,  $1.9 \times 10^{-4}$ ; ○,  $3.8 \times 10^{-4}$ . Deposition temperature, H<sub>2</sub> flow rate, and CO<sub>2</sub> mole fraction are constant at 1000°C, 110 liters/min, and  $1.14 \times 10^{-2}$ , respectively.

10<sup>-4</sup> and  $1.9 \times 10^{-4}$ . The deposition rate for SiO<sub>2</sub> in the absence of HCl is also given for both SiH<sub>4</sub> mole fractions. Note that (i) at low HCl mole fractions, i.e.,  $\sim 9.55 \times 10^{-4}$ , there is no measurable change in deposition rate of SiO<sub>2</sub> when compared with the deposition rate of SiO<sub>2</sub> in the absence of HCl, and (ii) the deposition rate begins to decrease with increasing HCl concentration and continues even at an HCl:SiH<sub>4</sub> ratio of 50:1, though there is a slight evidence of leveling off.

This slight indication of saturation can be best seen in Fig. 3, where  $\Delta d_{\text{SiO}_2}$ , the difference in SiO<sub>2</sub> deposition rate with and without HCl, is plotted against the HCl mole fraction for two silane concentrations. Note that, as the HCl mole fraction is increased beyond  $\sim 4 \times 10^{-3}$ , the slope of the curve is reduced from 0.85 to 0.42.

**Deposition rate vs. SiH<sub>4</sub> mole fraction.**—Figure 4 shows the effect of SiH<sub>4</sub> concentration on SiO<sub>2</sub> deposition rate at three HCl mole fractions. Deposition rates without

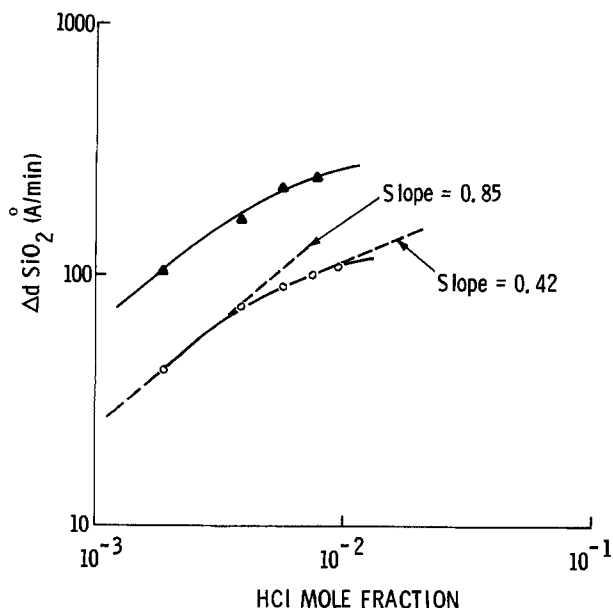


Fig. 3. Change in deposition rate of SiO<sub>2</sub> with and without HCl (i.e.,  $\Delta d_{\text{SiO}_2}$ ) as a function of HCl mole fraction; two SiH<sub>4</sub> mole fractions: ▲,  $3.8 \times 10^{-4}$ ; ○,  $1.9 \times 10^{-4}$ . Other deposition conditions same as Fig. 2.

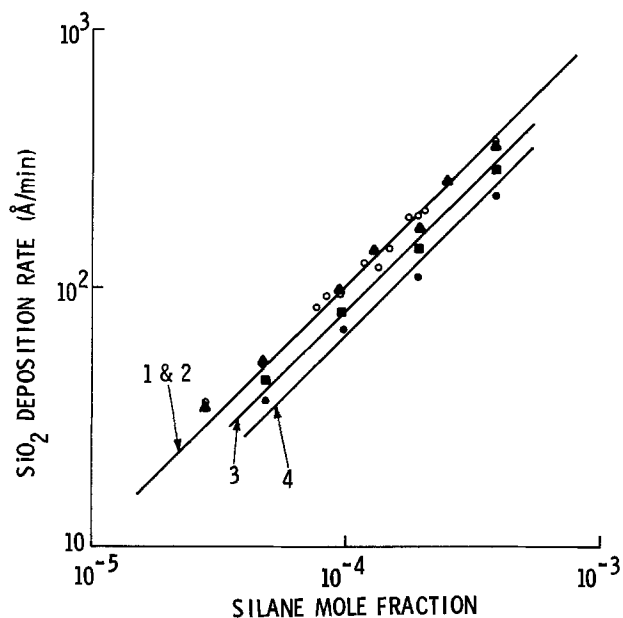


Fig. 4. Deposition rate of SiO<sub>2</sub> as a function of SiH<sub>4</sub> mole fraction, with HCl mole fraction as parameter. HCl mole fraction: ○, zero (curve 1); ▲,  $9.55 \times 10^{-4}$  (curve 2); ■,  $1.91 \times 10^{-3}$  (curve 3); ●,  $3.82 \times 10^{-3}$  (curve 4). Other deposition conditions same as Fig. 2.

HCl are also given. Note that (i) at low HCl mole fractions, i.e.,  $9.55 \times 10^{-4}$ , there is no measurable difference in deposition rate with and without HCl for any silane concentration within experimental range; (ii) all curves in Fig. 4 have been drawn with a slope of 1, the experimental points closely approximating these slopes, indicating that the reaction responsible for SiO<sub>2</sub> deposition is still a first-order reaction with respect to SiH<sub>4</sub> (6); and (iii) the drop in deposition rate is a function of SiH<sub>4</sub> concentration, i.e., when the drop in deposition rate does occur, the higher the SiH<sub>4</sub> concentration, the larger the drop for a fixed HCl concentration. This is shown in Fig. 5, where  $\Delta d_{\text{SiO}_2}$  is plotted for varying SiH<sub>4</sub> concentration, with the HCl mole fraction as a parameter.

**Deposition rate vs. deposition temperature.**—The reduction of SiO<sub>2</sub> deposition rate in the presence of HCl is a

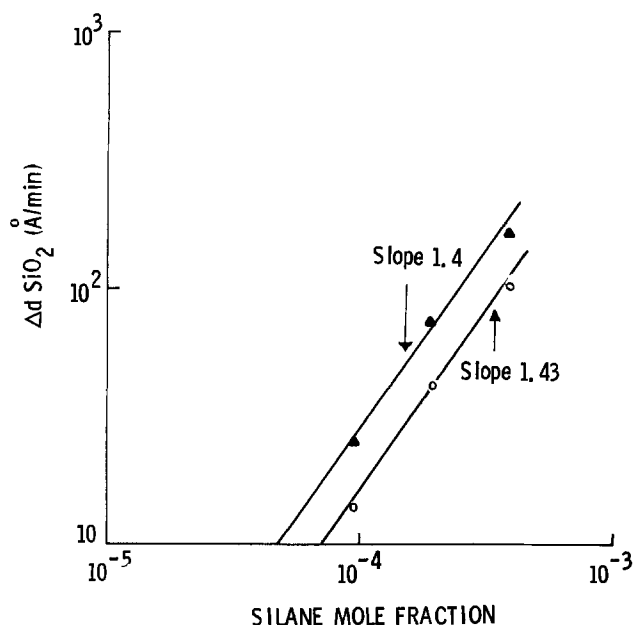


Fig. 5.  $\Delta d_{\text{SiO}_2}$  as a function of SiH<sub>4</sub> mole fraction at two HCl mole fractions: ▲,  $3.82 \times 10^{-3}$ ; ○,  $1.91 \times 10^{-3}$ . Other deposition conditions same as Fig. 2.

very temperature-sensitive phenomenon. This can readily be seen in Fig. 6, where the log of deposition rate is plotted as a function of the inverse of absolute temperature. The data for Fig. 6 were generated at a constant  $H_2$  flow rate of 110 liters/min and with constant  $SiH_4$  and  $HCl$  mole fractions, i.e.,  $1.9 \times 10^{-4}$  and  $1.91 \times 10^{-3}$ , respectively. The  $CO_2:SiH_4$  ratio was kept constant at 40:1. The curve for  $SiO_2$  deposition rate without  $HCl$  is also provided for comparison. Note that (i) at  $\sim 925^\circ C$ , deposition rate reduction ceases, and (ii) the reduction in deposition rate is a strong function of temperature, as shown in Fig. 7, where  $\Delta d_{SiO_2}$  is plotted against  $1/T$ . The activation energy value for the deposition rate reduction phenomenon is  $\sim 65$  kcal/g mole as calculated from Fig. 7.

**Deposition rate vs.  $CO_2:SiH_4$  ratio.**—At a constant  $H_2$  flow rate (110 liters/min), deposition temperature of  $1000^\circ C$ ,  $SiH_4$  mole fraction of  $1.9 \times 10^{-4}$ , and  $HCl$  mole fraction of  $1.91 \times 10^{-3}$ , the  $CO_2:SiH_4$  ratio was varied from 15:1 to 250:1 by varying the  $CO_2$  flow rate. The deposition rate was a constant within the experimental error and run-to-run reproducibility ( $\sim \pm 4\%$ ). Similar observations were made when no  $HCl$  was used (6).

**Deposition rate vs.  $H_2$  flow rate.**—In this experiment, the  $SiH_4$ ,  $HCl$ , and  $CO_2$  mole fractions were kept constant. The deposition temperature was also a constant at  $1000^\circ C$ . The  $H_2$  flow rate was varied from 60 to 130 liters/min. The deposition rate was found to be independent of  $H_2$  flow rate variation within this experimental range. Similar results were obtained without  $HCl$  (6). This experiment showed that the deposition rate of  $SiO_2$  is limited by surface chemical reaction, both with and without  $HCl$ . These results are consistent with the fact that the calculated mass transfer coefficient [estimated using Pohlhausen's approximation for isothermal flow (13)] for both  $SiH_4$  and  $HCl$  are

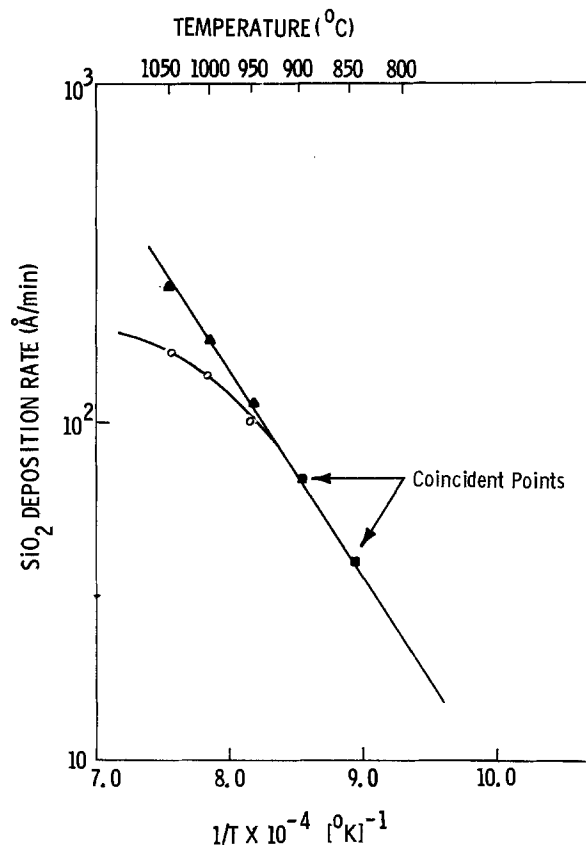


Fig. 6. Deposition rate of  $SiO_2$  as a function of deposition temperature:  $\blacktriangle$ , without  $HCl$ ;  $\circ$ ,  $HCl$  mole fraction of  $1.91 \times 10^{-3}$ ;  $\blacksquare$ , coincident points.  $SiH_4$  mole fraction,  $H_2$  flow rate, and  $CO_2$  mole fraction are constant at  $1.9 \times 10^{-4}$ , 110 liters/min, and  $7.64 \times 10^{-3}$ .

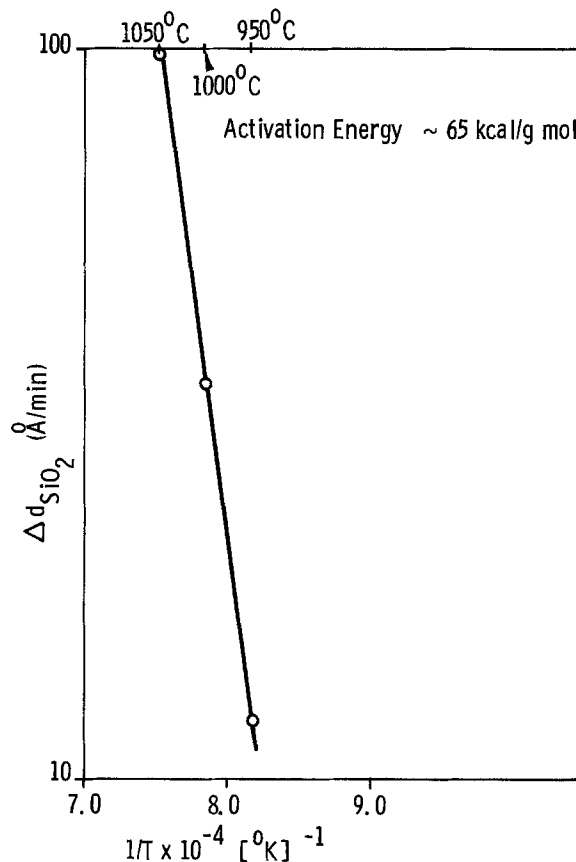


Fig. 7.  $\Delta d_{SiO_2}$  as a function of deposition temperature. All other deposition parameters same as Fig. 6.

$\sim$  four orders of magnitude larger than the surface chemical rate constant for  $SiO_2$  deposition with and without  $HCl$  at  $1000^\circ C$ , and at flows within the experimental range.

To summarize the effect of  $HCl$  on the deposition rate of  $SiO_2$ : (i) the presence of  $HCl$ , in general, reduces the deposition rate of  $SiO_2$ ; (ii) the exception to this occurs when low mole fractions of  $HCl$  and  $SiH_4$  are used; (iii) the drop in deposition rate due to the addition of  $HCl$  is highly temperature-sensitive (at  $\sim 925^\circ C$ , the drop in  $SiO_2$  deposition rate is no longer discernible); and (iv) the presence of  $HCl$  does not alter the fundamental nature of the reaction which results in  $SiO_2$  deposition, i.e., the  $SiO_2$  deposition rate is still first order with respect to  $SiH_4$ , independent of  $CO_2:SiH_4$  ratio and  $H_2$  flow rate.

**Physical properties.**—No significant difference was found in refractive index, etch rate, density, pin-hole density, and infrared absorption spectra between oxides deposited with and oxides deposited without  $HCl$ . As an example, Table I presents the index of refraction for selected samples deposited at  $1000^\circ C$ . For all the samples, the refractive index lay between 1.45 and 1.46, irrespective of various levels of processing variables considered in this paper. The physical properties without  $HCl$  are discussed in detail in Ref. (6).

Table I. Index of refraction as a function of  $HCl$  mole fraction CVD oxides deposited at  $1000^\circ C$

$CO_2:SiH_4$ ratio	$HCl$ mole fraction $\times 10^{-3}$	Index of refraction at 5460Å	Sample thickness (Å)
20	0	1.458	1142
20	0.955	1.454	1090
50	1.91	1.455	980
250	3.82	1.453	1080
60	5.73	1.460	1361
60	7.8	1.454	1200
60	9.55	1.459	1048

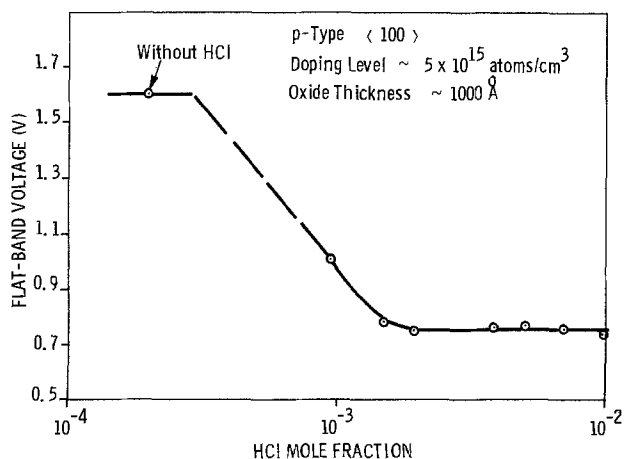


Fig. 8. Flatband voltage as a function of HCl mole fraction for oxide thickness of  $\sim 1000 \text{ \AA}$  on p-type  $\langle 100 \rangle$  Si. Doping level of silicon  $\sim 5 \times 10^{15}$  atoms/cm<sup>3</sup>. Flatband voltage without HCl, but for otherwise identical deposition conditions, also provided for comparison.

**Electrical Properties.**—The electrical properties were studied using MOS capacitors formed by the procedure outlined in the experimental section. It should be noted that, in general, these oxides were not exposed to any higher temperature anneal after deposition unless stated otherwise.

**Changes in flatband voltage as a function of HCl mole fraction ( $1000^\circ\text{C}$  deposition).**—The flatband voltage was measured by the usual C-V technique (8,9). The change in flatband voltage as a function of increasing HCl concentration and at a constant  $\text{SiH}_4$  concentration ( $1.9 \times 10^{-4}$ ) is shown in Fig. 8. The oxide thickness was kept constant at  $\sim 1000 \text{ \AA}$ . Though Fig. 8 shows data for p-type  $\langle 100 \rangle$  Si substrates, similar results were obtained on n-type  $\langle 100 \rangle$  Si substrates. Note that the flatband voltage first reduces very rapidly and then saturates at a value approximately equal to the  $\phi_{\text{MS}}$  value. These results are consistent with the hypothesis presented in the introduction.

**Flatband charge ( $Q_{\text{ox}}$ ) as a function of HCl mole fraction ( $1000^\circ\text{C}$  deposition).**—Table II presents  $Q_{\text{ox}}$  as a function of increasing HCl mole fraction at a constant  $\text{SiH}_4$  concentration. The oxide thickness is a variable between  $\sim 600$  and  $2600 \text{ \AA}$ . Note once again that, as HCl concentration increases for a fixed  $\text{SiH}_4$  mole fraction, the  $Q_{\text{ox}}$  decreases. In fact, at high HCl mole fractions, the  $Q_{\text{ox}}$  appears to be negative, i.e., the flatband voltage is less negative than the  $\phi_{\text{MS}}$  value. This is most likely due to the uncertainty of the  $\phi_{\text{MS}}$  value. The  $Q_{\text{ox}}$  values in Table II are average values obtained from both p- and n-type  $\langle 100 \rangle$  Si substrates. The last column of

Table II. Effect of increasing HCl concentration on  $Q_{\text{ox}}$  and deposition rate

HCl mole fraction $\times 10^{-3}$	$Q_{\text{ox}}$ (cm <sup>-2</sup> ) $\times 10^{10a,b}$	Drop in deposition rate
0	28 ( $\pm 2$ )	—
0.955	7 ( $\pm 2$ )	No
1.91	1.3 ( $\pm 0.3$ )	Yes
3.82	1.2 ( $\pm 0.2$ )	Yes
5.73	-2.5 ( $\pm 1$ )	Yes
7.64	-1.5 ( $\pm 0.5$ )	Yes

- Results are average of n- and p-type  $\langle 100 \rangle$  silicon.
  - $\text{SiH}_4$  mole fraction is constant at  $1.9 \times 10^{-4}$ .
  - Oxide thickness is variable, 625-2580  $\text{ \AA}$ .
  - Deposition temperature is constant at  $1000^\circ\text{C}$ .
- <sup>a</sup> The  $\phi_{\text{MS}}$  value in volts used to determine the  $Q_{\text{ox}}$  was calculated from the relationship  $-0.4 \pm \phi_{\text{B}}$ , where  $-0.4 \text{ V}$  is the Al silicon work function for intrinsic silicon (16) and  $\phi_{\text{B}}$  is the potential difference between the fermi level and the mid bandgap for doped silicon.
- <sup>b</sup> Numbers in parentheses are twice the standard deviation.

Table II shows whether there is a drop in the  $\text{SiO}_2$  deposition rate at that HCl concentration, when compared with the  $\text{SiO}_2$  deposition rate without HCl. At HCl mole fraction of  $9.55 \times 10^{-4}$ , there is no drop in deposition rate and yet there is a significant reduction (factor of 4) in  $Q_{\text{ox}}$ . This is consistent with the hypothesis.

**Flatband charge ( $Q_{\text{ox}}$ ) vs.  $\text{SiH}_4$  mole fraction ( $1000^\circ\text{C}$  deposition).**—From the hypothesis it was expected that for a constant HCl mole fraction, if the  $\text{SiH}_4$  concentration in the gas phase were increased, the  $Q_{\text{ox}}$  would increase. Table III presents the results of such an experiment, where the HCl mole fraction is kept constant at  $0.955 \times 10^{-3}$  and  $\text{SiH}_4$  is increased. The thickness is variable from  $\sim 600$  to  $2300 \text{ \AA}$ . The results of Table III are consistent with the hypothesis.

**Flatband charge ( $Q_{\text{ox}}$ ) vs. HCl: $\text{SiH}_4$  ratio ( $1000^\circ\text{C}$  deposition).**—It has been shown that HCl and  $\text{SiH}_4$  concentrations, when considered independently, had a marked effect on  $Q_{\text{ox}}$  (Table II and III). The question next was whether maintaining a certain ratio of HCl: $\text{SiH}_4$  was a sufficient condition for obtaining reproducibly low  $Q_{\text{ox}}$  values. Table IV shows the results of such an experiment, with HCl: $\text{SiH}_4$  kept at approximately 10:1 but at varying levels of  $\text{SiH}_4$  and HCl concentrations. Even though the HCl: $\text{SiH}_4$  ratio is nearly constant, markedly different  $Q_{\text{ox}}$  values result. Thus, the HCl: $\text{SiH}_4$  ratio is not an important parameter to control  $Q_{\text{ox}}$  values.

**Mobile charge ( $Q_{\text{m}}$ ) ( $1000^\circ\text{C}$  deposition).**—Mobile charges were measured by applying  $\pm 2 \times 10^6 \text{ V/cm}$  for 10 min at  $200^\circ\text{C}$ . This technique is similar to the one used by Kriegler *et al.* (14). The shift in flatband under positive bias was converted into mobile charge. For  $1000^\circ\text{C}$  deposited samples, the shift in the flatband under negative bias was not taken into account, because, in all cases, the flatband shift was negligible (i.e.,  $\leq 10 \text{ mV}$ ). This also means that the mobile charges were present at the metal/ $\text{SiO}_2$  interface.

The mobile charges were investigated as a function of  $\text{SiH}_4$  and HCl concentration variations. The  $\text{SiH}_4$  mole fraction was varied from 0.28 to  $3.8 \times 10^{-4}$ ; the HCl mole fraction, from 0 to  $7.64 \times 10^{-3}$ . No systematic variation of  $Q_{\text{m}}$  was found as a function of either  $\text{SiH}_4$  or HCl mole fraction. The mobile charge for all samples can be adequately represented as  $\sim 2.5 \times 10^{10}$  charges/cm<sup>2</sup>. The sample-to-sample variations were from  $\leq 1$

Table III. Effect of increasing  $\text{SiH}_4$  concentration on  $Q_{\text{ox}}$  at fixed HCl mole fraction

$\text{SiH}_4$ mole fraction $\times 10^{-4}$	$Q_{\text{ox}}$ (cm <sup>-2</sup> ) $\times 10^{10a,b}$
0.475	$< 1$
0.95	6.5 ( $\pm 1$ )
1.91	7.0 ( $\pm 2.0$ )
3.82	5.5 ( $\pm 2$ )

- Results are an average of n- and p-type  $\langle 100 \rangle$  silicon.
  - HCl mole fraction is constant at  $0.955 \times 10^{-3}$ .
  - Oxide thickness is variable 585-2340  $\text{ \AA}$ .
  - Deposition temperature is constant at  $1000^\circ\text{C}$ .
- <sup>a</sup> See footnote <sup>a</sup> in Table II.  
<sup>b</sup> See footnote <sup>b</sup> in Table II.

Table IV. Effect of HCl: $\text{SiH}_4$  ratio on  $Q_{\text{ox}}$

$\text{SiH}_4$ mole fraction $\times 10^{-4}$	HCl mole fraction $\times 10^{-3}$	HCl: $\text{SiH}_4$ ratio	$Q_{\text{ox}}$ (cm <sup>-2</sup> ) $\times 10^{10a,b}$
0.95	0.955	10.05	6.5 ( $\pm 1$ )
1.91	1.91	10.05	1.3 ( $\pm 0.3$ )
3.80	3.82	10.05	4.5 ( $\pm 4$ )

- Results are average of n- and p-type  $\langle 100 \rangle$  silicon.
  - Oxide thickness is variable, 850-2580  $\text{ \AA}$ .
  - Deposition temperature is constant at  $1000^\circ\text{C}$ .
- <sup>a</sup> See footnote <sup>a</sup> in Table II.  
<sup>b</sup> See footnote <sup>b</sup> in Table II.

$\times 10^{10}$  to  $4 \times 10^{10}$ . These variations were most likely due to run-to-run variations of Al evaporation. Thermal-oxide monitor wafers from each metallization run were also checked, and they showed a similar variation in mobile charge.

The inability of HCl to affect the mobile charge is in total contradiction to the observations reported with HCl-grown thermal oxides (14). This contradiction is not surprising, however, for two reasons: (i) the CVD oxides deposited from  $\text{SiH}_4\text{-CO}_2\text{-H}_2$  at  $1000^\circ\text{C}$  have very low mobile-charge levels, as reported earlier (6) and verified during these experiments, and (ii) the HCl concentration, in our case, is very small, i.e.,  $\ll 1\%$ . Our experiments with HCl thermal oxidation show that comparable low HCl concentration does not significantly improve mobile charges in thermal oxide, either, for  $1000^\circ\text{C}$  oxidation, especially when the mobile-charge levels are low without HCl.

**Fast surface-state density ( $N_{FS}$ ) ( $1000^\circ\text{C}$  deposition).**—Fast surface-state density was measured by the quasi-static technique of Khun (15), modified after Castrange (16) and Kerr (17). The modifications involve the use of high-frequency C-V trace as the ideal.

The fast surface-state densities at mid bandgap were measured on samples with oxide thickness between 800 and  $1200\text{\AA}$ . The value of the fast surface-state density at mid bandgap was unaffected by either  $\text{SiH}_4$  or HCl concentration variations and can be adequately represented by  $\sim 1.5 \times 10^{10}$  charges  $\text{cm}^{-2} \text{eV}^{-1}$ . The  $\text{SiH}_4$  mole fraction was varied from 0.28 to  $3.8 \times 10^{-4}$ , and the HCl mole fraction from 0 to  $7.64 \times 10^{-3}$ . We attribute these low  $N_{FS}$  values to the use of  $\text{H}_2$  during deposition.

The lack of relationship between  $Q_{ox}$  and the fast surface-state density ( $N_{FS}$ ) is shown in Fig. 9 for these CVD oxides. Note that the  $Q_{ox}$  varies by larger than one order of magnitude and the  $N_{FS}$  shows only sample-to-sample variations. It is important here to recall that these samples were not exposed to high-temperature anneal after deposition. This behavior is in contradiction to that of thermal oxides, where the  $N_{FS}$  is usually proportional to  $Q_{ox}$  (18). Figure 9 also shows that at least for these CVD oxides the causes for  $Q_{ox}$  and  $N_{FS}$  may be unrelated.

**Effect of deposition temperature on  $Q_{ox}$ ,  $Q_m$ , and  $N_{FS}$ .**—Table V presents an overview of the effect of deposition temperature on various charges. These oxides were not exposed to high-temperature postdeposition anneal, the  $\text{SiH}_4$  and HCl mole fractions were kept constant, and the deposition time was adjusted to obtain  $\sim 1000\text{\AA}$  of  $\text{SiO}_2$ . Note that, as the deposition temperature is dropped below  $1000^\circ\text{C}$ , the  $Q_{ox}$  increases as a step function. This is consistent with the hypothesis.

During the measurement of mobile charges, it became evident that the shift in flatband was significant (i.e., 50-100 mV) at  $200^\circ\text{C}$  and  $-2 \times 10^6 \text{ V/cm}$  for oxides deposited below  $1000^\circ\text{C}$ . This shift, which was

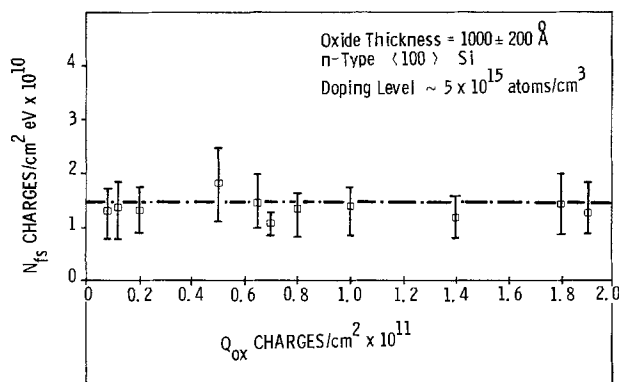


Fig. 9. Lack of dependence of fast surface-state density at mid bandgap on  $Q_{ox}$  in as-deposited CVD oxides. Oxide thickness was  $1000 \pm 200\text{\AA}$  on n-type  $\langle 100 \rangle$  Si; doping level of silicon  $\sim 5 \times 10^{15}$  atoms/ $\text{cm}^3$ .

Table V. Effect of deposition temperature on electrical properties

Deposition temperature ( $^\circ\text{C}$ )	$Q_{ox}$ ( $\text{cm}^{-2}$ ) $\times 10^{10a,b}$	$Q_m$ ( $\text{cm}^{-2}$ ) $\times 10^{10b}$	$N_{FS}$ ( $\text{cm}^{-2} \text{eV}^{-1}$ ) $\times 10^{10b}$
1050	<1	3.0 ( $\pm 0.5$ )	1.1 ( $\pm 0.5$ )
1000	1.3 ( $\pm 0.3$ )	2.1 ( $\pm 0.5$ )	1.0 ( $\pm 0.5$ )
950	7.0 ( $\pm 2$ )	4.0 ( $\pm 0.2$ )	1.2 ( $\pm 0.2$ )
900	7.0 ( $\pm 3$ )	4.2 ( $\pm 0.5$ )	1.5 ( $\pm 0.5$ )
850	4.5 ( $\pm 1$ )	2.8 ( $\pm 0.2$ )	3.0 ( $\pm 1$ )

1. Results are average of n- and p-type  $\langle 100 \rangle$  silicon.
  2.  $\text{SiH}_4$  mole fraction is constant at  $1.9 \times 10^{-4}$ .
  3. HCl mole fraction is constant at  $1.91 \times 10^{-3}$ .
  4. Sample thickness is  $\sim 1000\text{\AA}$ .
- <sup>a</sup> See footnote <sup>a</sup> in Table II.  
<sup>b</sup> See footnote <sup>b</sup> in Table II.

taken into account in the mobile-charge data presented in Table V, also implies that at least part of the mobile charges ( $\sim 33\%$ ) are distributed in the bulk of the oxides when the oxides are deposited below  $1000^\circ\text{C}$ .

The deposition temperature also appears to affect the fast surface-state density at mid bandgap. For example, the  $850^\circ\text{C}$  deposited samples showed very nearly the highest fast surface-state density measured during this experimental work. The value of  $N_{FS}$  for  $850^\circ\text{C}$  samples is 2-3 times the value of  $N_{FS}$  for  $1000^\circ\text{C}$  samples.

**Effect of annealing.**—The effect of postdeposition high-temperature anneal ( $1050^\circ\text{C}$ ) for 15 min in  $\text{N}_2$  is shown in Table VI. As-deposited wafers were divided into halves: one half was annealed at high temperature ( $1050^\circ\text{C}$  in  $\text{N}_2$  for 15 min); subsequently, both halves were metallized (Al) and annealed at  $400^\circ\text{C}$  for a half-hour in  $\text{N}_2$ . Note that the  $Q_{ox}$  and the fast surface-state density at mid bandgap are consistently higher in high-temperature annealed samples. The detrimental effect of annealing on  $V_{FB}$  stability when the MOS capacitors are exposed to  $\pm 2 \times 10^6 \text{ V/cm}$  at  $200^\circ\text{C}$  for 50 hr is discussed in the section about electrical stability. Mobile charges appear to be unaffected. There is also 2-4% densification, as shown in the  $T_{ox}$  (oxide thickness) column. The breakdown field ( $E_B$ )<sup>4</sup> does not appear to be a strong function of annealing. The distribution of  $E_B$  was extremely tight, without any early failures (0 out of 400 capacitors tested). A comparison between MOS capacitors made with CVD oxide and those made with dry  $\text{O}_2$  grown thermal oxide showed that the standard deviation of  $E_B$  in the latter case was larger (5-10 times), and that 2-5% of capacitors, also in the latter case, showed early breakdown (as much as 50% below the mean value). Osborne (19) reported similar wide distribution of  $E_B$  for MOS capacitors made with dry  $\text{O}_2$  grown oxides.

It is pertinent here to point out that HCl does not affect the  $E_B$  distribution for CVD oxides. Similar tight distributions were observed when CVD oxides were deposited without HCl, under otherwise identical conditions (6).

**Dielectric constant.**—A comparison of the oxide thickness measurements by ellipsometry and capacitance measurements agreed within  $\pm 3\%$  in almost all cases. Thus, the dielectric constant lies between 3.8 and 4.0, indicating that the presence of HCl during deposition did not affect the dielectric constant of CVD oxides.

**Electrical stability.**—It was our aim to investigate the effect of three variables on electrical stability (i.e., flatband voltage stability): (i) high-temperature postdeposition anneal, (ii) HCl mole-fraction variation, and (iii)  $\text{SiH}_4$  mole-fraction variation. Selected samples  $\sim 1000\text{\AA}$  thick were therefore stressed with  $\pm 2 \times 10^6 \text{ V/cm}$  at  $200^\circ\text{C}$  for  $\sim 50$  hr.

Figure 10 shows the results of a sample deposited with low  $\text{SiH}_4$  and HCl mole fractions,  $2.8 \times 10^{-5}$  and  $1.44 \times 10^{-3}$ , respectively, and at a deposition temperature of  $1000^\circ\text{C}$ . After deposition, the wafer was broken

<sup>4</sup> The procedure for measuring breakdown field is described in Ref. (6).

Table VI. Effect of high-temperature (1050°C, 15 min, N<sub>2</sub>) annealing on electrical properties CVD oxides deposited at 1000°C on n-type <100> Si

SiH <sub>4</sub> mole fraction × 10 <sup>-5</sup>	HCl mole fraction × 10 <sup>-3</sup>	Q <sub>ox</sub> (cm <sup>-2</sup> ) × 10 <sup>10a,b</sup>	N <sub>FS</sub> (cm <sup>-2</sup> , eV <sup>-1</sup> ) × 10 <sup>10b</sup>	T <sub>ox</sub> (Å)	E <sub>B</sub> 10 <sup>6</sup> V/cm <sup>b</sup>	Drop in deposition rate?	Postdeposition anneal?
2.8	1.44	<1	1.5 (±0.5)	850	8.4 (±0.4)	No	No
2.8	1.44	3.1 (±0.4)	3.8 (±0.5)	826	7.8 (±0.4)	—	Yes
2.8	2.88	1.5 (±0.4)	1.8 (±0.2)	1130	8.3 (±0.2)	No	No
2.8	2.88	1.8 (±0.6)	3.1 (±0.5)	1090	8.4 (±0.2)	—	Yes
9.5	1.91	<1	<1	820	8.5 (±0.4)	Yes	No
9.5	1.91	3.0 (±0.4)	3.9 (±1)	810	8.5 (±0.4)	—	Yes
2.8	0.955	<1	1.1 (±0.1)	440	9.1 (±0.6)	No	No
2.8	0.955	2.0 (±0.5)	—	432	—	—	Yes

<sup>a</sup> See footnote <sup>a</sup> in Table II.

<sup>b</sup> See footnote <sup>b</sup> in Table II.

Table VII. Fast surface states as a function of temperature bias stress and postdeposition high-temperature anneal (1050°C, 15 min, N<sub>2</sub>) with and without HCl

Deposition condition	Sample	N <sub>FS</sub> cm <sup>-2</sup> eV <sup>-1</sup> (at mid bandgap) × 10 <sup>10a</sup>		
		Initial	After 20 hr of + 2 × 10 <sup>6</sup> V/cm	After 20 hr of - 2 × 10 <sup>6</sup> V/cm and 200°C
Without HCl	As-deposited	1.2 (±0.3)	1.3 (±0.3)	2.5 (±0.3)
	Annealed	1.7 (±0.2)	3.2 (±0.5)	6.6 (±0.7)
With HCl	As-deposited	1.3 (±0.5)	1.3 (±0.5)	2.1 (±0.5)
	Annealed	2.2 (±0.5)	2.8 (±0.8)	4.2 (±1)

<sup>a</sup> Numbers in parentheses are twice the standard deviation.

in half, and one half was annealed at 1050°C for 15 min in N<sub>2</sub>. Both halves were then metallized. As shown in Fig. 10, the behavior of the annealed half is markedly different from the unannealed half under negative bias. The electrical-stability behavior of CVD oxides deposited without HCl is identically affected by high-temperature anneal (6). Note that under positive bias the flatband shifts by ~75 mV within the first hour, with subsequent rapid leveling off. This shift is consistent with the mobile charge in the sample.

Negative shift of flatband under negative bias in thermal oxide is attributed to an increase of Q<sub>ox</sub> (18) and/or of N<sub>FS</sub> (18, 20). To see whether the fast surface states, in fact, showed a larger increase in the annealed

half of the sample after negative-bias stress, several MOS capacitors from both halves of the wafer were stressed for 20 hr at 200°C under a bias of ±2 × 10<sup>6</sup> V/cm. The fast surface states were measured before and after the stress. The results are presented in Table VII. The results of similar experiments on CVD oxides deposited without HCl, but with otherwise identical conditions, are also presented. Note that the annealed half of the wafer, when compared with the as-deposited half, irrespective of whether the oxides are deposited with or without HCl, shows larger (~2 times) N<sub>FS</sub> after 20 hr of stress at -2 × 10<sup>6</sup> V/cm. Thus, negative-bias instability is directly related to high-temperature postdeposition anneal.

To verify the results of Fig. 10 and to investigate the impact on stability of doubling the HCl mole fraction, a sample was prepared at SiH<sub>4</sub> and HCl mole fractions of 2.8 × 10<sup>-5</sup> and 2.88 × 10<sup>-3</sup>, respectively, at a deposition temperature of 1000°C. The rest of the sample preparation was identical with the sample of Fig. 10. The results of the stability test are presented in Fig. 11. Once again, the annealed half of the sample behaves like thermal oxides, whereas the nonannealed sample appears to characterize CVD oxides. Note also that changing the HCl mole fraction had no significant effect.

Several additional samples (all unannealed) were subjected to the stability test. In these samples, the SiH<sub>4</sub> mole fraction was varied from 0.28 × 10<sup>-4</sup> to 3.8 × 10<sup>-4</sup>, and the HCl mole fraction was kept constant at 3.82 × 10<sup>-3</sup>. Data from two of these samples (SiH<sub>4</sub> mole fractions 1.9 and 3.82 × 10<sup>-4</sup>, respectively) are presented as an example in Fig. 12. Note that the change in SiH<sub>4</sub> mole fraction does not significantly affect the behavior of these oxides; the same is true for threefold variations in HCl (compare nonannealed data from Fig. 10, 11, and 12).

## Discussion

In the introductory section, two points were made in the hypothesis outlined: (i) adding HCl in the gas phase during the CVD deposition of SiO<sub>2</sub> reduces the fixed charges; (ii) the fixed charges are reduced because HCl reacts with unbonded Si atoms and thus prevents their incorporation in the depositing layers of SiO<sub>2</sub>. Implicit in these two statements is the hy-

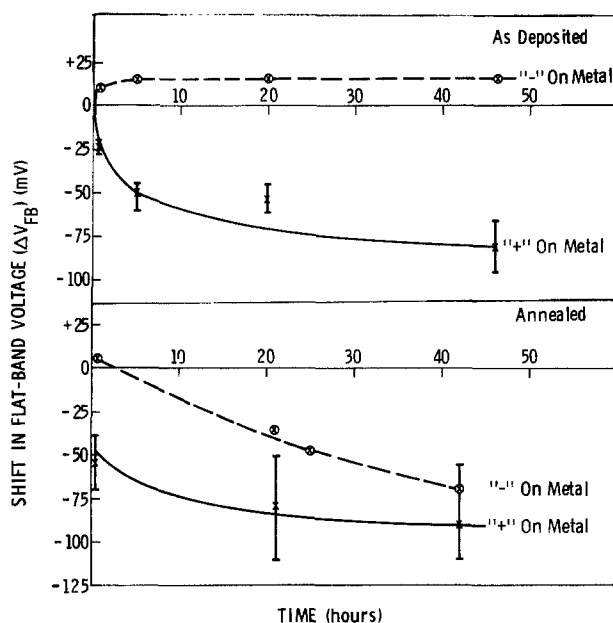


Fig. 10. Results of temperature (200°C) bias ± 2 × 10<sup>6</sup> V/cm stress on flatband voltage stability. Shown is the effect of high-temperature (1050°C, 15 min, in N<sub>2</sub>) postdeposition anneal. Samples deposited at SiH<sub>4</sub> and HCl mole fractions of 2.8 × 10<sup>-5</sup> and 1.44 × 10<sup>-3</sup>, respectively. Deposition temperature was 1000°C; sample thickness, 850Å on n-type <100> Si.

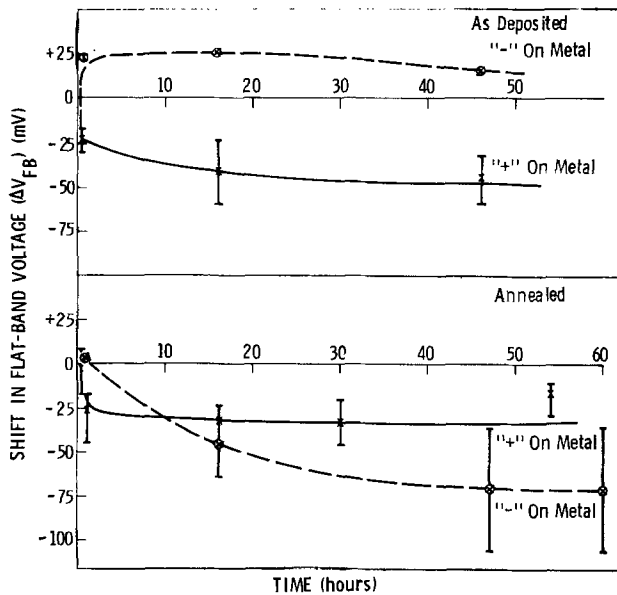


Fig. 11. Same as Fig. 10, except sample deposited with  $2.88 \times 10^{-3}$  mole fraction HCl. Sample thickness was  $1100 \text{ \AA}$ .

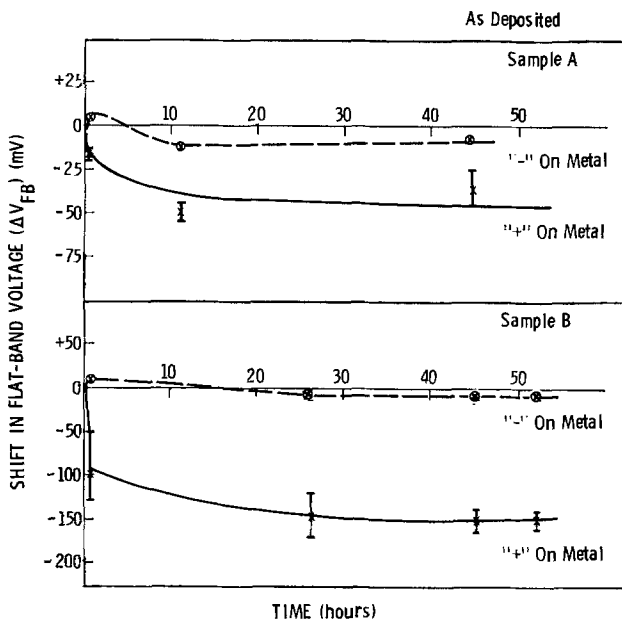


Fig. 12. Results of temperature ( $200^\circ\text{C}$ ) bias  $\pm 2 \times 10^6 \text{ V/cm}$  stress on flatband voltage stability. Sample A was deposited at  $\text{SiH}_4$  and HCl mole fractions of  $1.9 \times 10^{-4}$  and  $3.82 \times 10^{-3}$  and deposition temperature of  $1000^\circ\text{C}$ . Sample B preparation was identical with sample A except  $\text{SiH}_4$  mole fraction was 3.82. Sample A and B thicknesses were 950 and  $1150 \text{ \AA}$  on n-type  $\langle 100 \rangle \text{ Si}$ .

pothesis, after Deal *et al.* (9), that free silicon is the major cause of fixed charges in  $\text{SiO}_2$ . Our experimental results prove the first point without doubt. It should also be obvious that we cannot prove point (ii) of the hypothesis by the present experimental work; we can merely show consistency.

The drop in the  $\text{SiO}_2$  deposition rate in the presence of HCl was unexpected. We questioned whether perhaps a drop in deposition rate was necessary to reduce  $Q_{\text{ox}}$ , but found many combinations of  $\text{SiH}_4$  and HCl concentrations where there was no measurable drop in deposition rate and yet the  $Q_{\text{ox}}$  was very small (for example, see Table VI, lines 1, 3, and 7). Low  $\text{SiH}_4$  and/or low HCl mole fractions generally produce the results described above. Thus, the experimental data, where there is no drop in deposition rate of  $\text{SiO}_2$  because of HCl and low value of  $Q_{\text{ox}}$ , are consistent with point 2 of the hypothesis. The consistency of the ex-

perimental results presented in Tables II-V with the hypothesis has already been shown.

We are uncertain as to the precise cause of the decrease in the  $\text{SiO}_2$  deposition rate in the presence of HCl. However, since  $\Delta d_{\text{SiO}_2}$  is a quantitative function of  $\text{SiH}_4$  and HCl concentration (Fig. 3 and 5) and is temperature-dependent (Fig. 7), the drop in deposition rate is probably due to  $\text{SiH}_4$ -HCl reaction, resulting in a compound whose reaction rate with  $\text{CO}_2$  is small, in the experimental temperature range, to deposit  $\text{SiO}_2$ . Other equally probable and complex causes could also explain the decrease in deposition rate.

Some of the electrical properties of CVD oxides deposited from  $\text{SiH}_4$ - $\text{CO}_2$ -HCl- $\text{H}_2$ , though not unexpected, are different from thermal oxides. For example, it is accepted that  $N_{\text{FS}}$  is proportional to  $Q_{\text{ox}}$  (18) in thermal oxides. In these CVD oxides, an order-of-magnitude variation in  $Q_{\text{ox}}$  showed no significant variation in  $N_{\text{FS}}$  (Fig. 9), i.e., for as-deposited samples, the  $Q_{\text{ox}}$  and  $N_{\text{FS}}$  are unrelated. These results, we believe, are due to the high deposition temperature and  $\text{H}_2$  used during the deposition of these oxides. The increase in  $N_{\text{FS}}$  upon postdeposition high-temperature annealing (Table VI), however, has been reported for thermal oxides (18). The phenomenon of an increase in  $Q_{\text{ox}}$  as a result of high-temperature postdeposition anneal is also known in thermal oxides (18), i.e.,  $> 60 \text{ min}$  at  $1200^\circ\text{C}$  in an inert ambient. It is important to note here, however, that we saw an increase in  $Q_{\text{ox}}$  after only a 15 min anneal at  $1050^\circ\text{C}$  in  $\text{N}_2$  (Table VI). This high sensitivity to annealing in an  $\text{N}_2$  ambient could be due to the fact that these oxides in as-deposited condition had a small charge. Again, from the data of Fig. 10, 11, and 12, it is clear that the phenomenon of "drift VI" (18) is almost nonexistent in as-deposited CVD oxides. However, upon annealing, these CVD oxides behave much like thermal oxides as far as drift VI phenomenon is concerned (Fig. 10 and 11). Thus, from the point of view of CVD oxides, high-temperature postdeposition annealing causes drift VI.

Finally, we have clearly demonstrated that the effect of HCl in the case of CVD oxides is to reduce  $Q_{\text{ox}}$  (Fig. 8), unlike thermal oxides, where the presence of HCl reduces mobile charge. The lack of impact by HCl on mobile charge in these oxides was not unexpected, for two reasons: (i) CVD oxides deposited  $\sim 1000^\circ\text{C}$  without HCl in our reactor have low mobile charges ( $\leq 3 \times 10^{10}$ ) and (ii) the HCl concentration in the gas phase is small (usually  $\ll 1\%$ ). It is therefore possible that a small quantity of HCl in the gas phase may not be sufficient to reduce the already low level of mobile charges present in these CVD oxides.

### Conclusion

We have demonstrated the effect of HCl on deposition rates (i.e., deposition rate reduction) and on the properties of CVD oxides deposited from  $\text{SiH}_4$ - $\text{CO}_2$ - $\text{H}_2$  in the temperature range of  $850^\circ\text{C}$ - $1050^\circ\text{C}$ . In marked contrast to thermal oxides, the presence of HCl during CVD oxide deposition affects  $Q_{\text{ox}}$ . There is no detectable effect of HCl on mobile charges in these CVD oxides; however, the mobile-charge levels were low without HCl ( $\leq 3 \times 10^{10} \text{ cm}^{-2}$ ).

We have reported some significant differences in the electrical properties of CVD oxides and thermal oxides, such as a lack of relationship of  $Q_{\text{ox}}$  and  $N_{\text{FS}}$  (Fig. 9), the effect of high-temperature postdeposition anneal on  $Q_{\text{ox}}$  and  $N_{\text{FS}}$  (Table VI), and the lack of drift VI (18) in as-deposited CVD oxides (Fig. 10, 11, and 12). It is our hope that these differences in the electrical properties of thermal and CVD oxides will enhance the understanding of Si/ $\text{SiO}_2$  interface and associated charges.

We have not shown the location of  $Q_{\text{ox}}$  in these CVD oxides, that not being our purpose. Our interest was to produce CVD oxides with very nearly ideal flatband voltages, irrespective of the location of charge. We have done this, though with a somewhat limited range of oxide thickness ( $\sim 600$ - $2600 \text{ \AA}$ ).

We have also shown the consistency of our experimental results with the hypothesis that the cause of  $Q_{ox}$  is unbonded silicon in  $SiO_2$  matrix.

Finally, the CVD oxides deposited from  $SiH_4-CO_2-HCl-H_2$  at  $\sim 1000^\circ C$  are eminently suitable for application in the gate region of FET's.

### Acknowledgments

We are deeply indebted to Messrs. A. Kozul and T. Williams for preparing the test samples.

Manuscript submitted Nov. 18, 1974; revised manuscript received Oct. 21, 1975. This was Paper 150 presented at the Toronto, Canada, Meeting of the Society, May 11-16, 1975.

Any discussion of this paper will appear in a Discussion Section to be published in the December 1976 JOURNAL. All discussions for the December 1976 Discussion Section should be submitted by Aug. 1, 1976.

Publication costs of this article were partially assisted by the IBM Corporation.

### REFERENCES

1. M. J. Rand, *This Journal*, **114**, 274 (1967).
2. M. J. Rand and J. L. Ashworth, *ibid.*, **113**, 48 (1966).
3. T. L. Chu, J. R. Szedon, and G. A. Gruber, *Trans. Met. Soc. AIME*, **242**, 532 (1968).
4. R. C. G. Swann and A. E. Payne, *This Journal*, **116**, 1014 (1969).
5. W. J. Kroll, R. L. Titus, and J. B. Wagner, Abstract 13, p. 31, The Electrochemical Society Extended Abstracts Spring Meeting, Houston, Texas, May 7-11, 1972.
6. A. K. Gaiind, G. K. Ackermann, V. J. Lucarini, and R. L. Bratter, *This Journal*, To be published.
7. T. Miyazaki, I. Yoshida, M. Horiuchi, and T. Tokuyama, in "Chemical Vapor Deposition, Second International Conference," John M. Blocher and James C. Withers, Editors, p. 571, The Electrochemical Society Softbound Symposium Series, New York (1970).
8. A. S. Grove, B. E. Deal, E. H. Snow, and C. T. Sah, *Solid-State Electron.*, **8**, 145 (1965).
9. B. E. Deal, M. Sklar, A. S. Grove, and E. Snow, *This Journal*, **114**, 226 (1967).
10. A. K. Gaiind and R. L. Bratter, U.S. Pat. pending.
11. E. O. Ernest, D. J. Hurd, and G. Seely, U.S. Pat. 3,424,629.
12. F. G. Allen, *J. Appl. Phys.*, **28**, 1510 (1957).
13. R. B. Bird, W. E. Stewart, and E. L. Lightfoot, "Transport Phenomena," John Wiley and Sons, Inc., New York (1960).
14. R. J. Kriegler, Y. C. Cheng, and D. R. Colton, *This Journal*, **119**, 388 (1972).
15. M. Khun, *Solid-State Electron.*, **13**, 873 (1970).
16. R. Castange and C. Y. Lebd. Se'anc, *Acad. Sci. (Paris)*, **267**, 866 (1968).
17. D. Kerr, Private communication.
18. B. Deal, *This Journal*, **121**, 198C (1974).
19. C. Osborn, *ibid.*, **12**, 809 (1974).
20. A. Goetzberger, A. D. Lopez, and R. J. Strain, *ibid.*, **120**, 90 (1973).

## $YVO_4:Eu^{3+} + SiO_2$ , A Diluted Phosphor System

A. Wachtel\*

Westinghouse Research Laboratories, Pittsburgh, Pennsylvania 15235

### ABSTRACT

Combinations of  $YVO_4:Eu^{3+}$  with  $SiO_2$  can display fluorescence intensity which is higher than predicted on the basis of phosphor concentration. The effect is observed when the phosphor particles are encapsulated by vitreous  $SiO_2$  and is due to increased optical efficiency of excitation.

A diluted phosphor system may be defined as a combination between a phosphor and an optically transparent diluent in which the absorption and emission of a given amount of phosphor, excited by a given radiation density of diffuse u.v., can be higher than it would be in the absence of the diluent. Relatively few diluted phosphor systems have been reported in the past; one is the  $Zn_3(VO_4)_2-ZnO$  system described by Bernikov and Zelikin (1) in which the authors speak of a "microphase" of  $Zn_3(VO_4)_2$  dispersed in ZnO, and another is the heterogeneous halide-silica system recently published by Lehmann (2). The present system is based on original observations by Corth (3).

### Experimental

Samples were prepared by coprecipitating  $Y_{0.93}Eu_{0.07}VO_4$  by known methods (4,5) followed by filtration and washing. Aliquots of the moist filter cake were then slurried with the appropriate amounts of flux and silicic acid prior to drying and firing, usually at  $1150^\circ C$   $2 \times 1$  hr in air. Fired phosphors were ground and washed with dilute HCl to remove traces of unreacted matter.

Fluorescence was measured under 254 nm excitation, using three types of targets: (i) conventional powder plaques, (ii) conventional lehr layers prepared on  $1\frac{1}{2}$  in.  $\times$   $90^\circ$  sections of T-12 fluorescent lamp tubing, and (iii) single-particle layers deposited on microscope

slides coated with a pressure-sensitive adhesive. Measurements of the latter two were taken from the side opposite to that of excitation. Reflectance of 254 nm u.v. was measured by the method of Thornton (6).

### Results

Preliminary observations showed that the plaque output of silica containing compositions is increased by the presence of a flux during firing. Suitable fluxes are alkali halides, borates, or carbonates. Most of the compositions in this study were prepared with 10 mole silica/1 mole phosphor and Fig. 1 shows the fluorescence

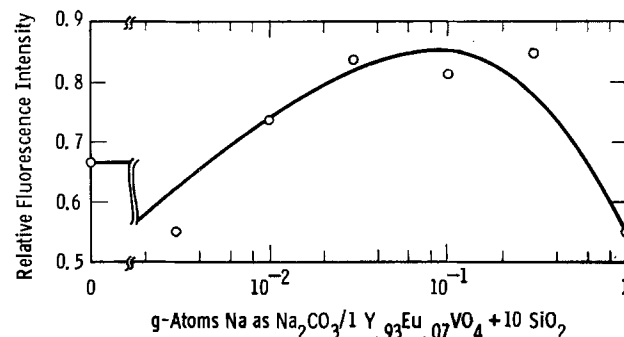


Fig. 1. Fluorescence intensity of  $YVO_4:Eu + 10 SiO_2$  as a function of  $Na_2CO_3$  flux.

\* Electrochemical Society Active Member.

Key words:  $YVO_4:Eu^{3+}$ , excitation, powder optics.



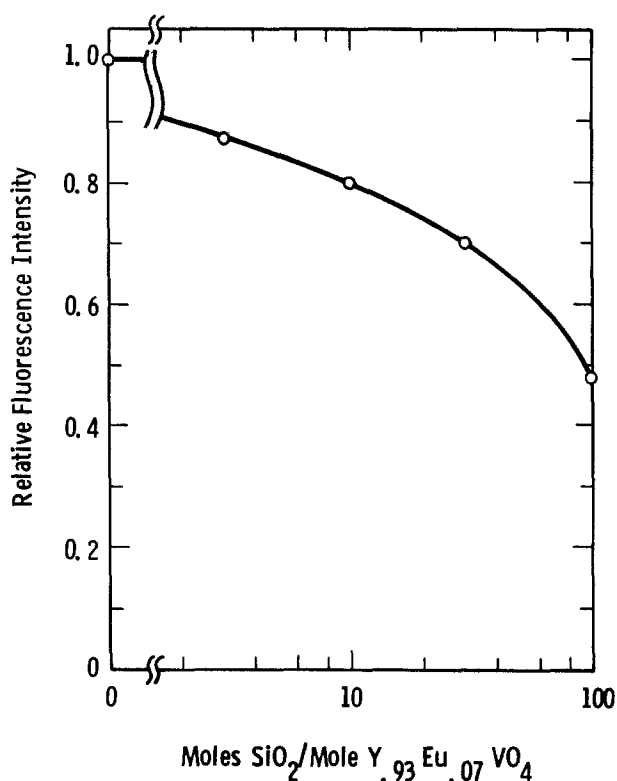


Fig. 2. Fluorescence intensity of  $YVO_4:Eu$  as a function of  $SiO_2$ .  $Na_2CO_3 = 0.003 \times SiO_2$ .

obtained with this as a function of  $Na_2CO_3$  added, based on the fluorescence of undiluted phosphor. In general, optimum flux amounted to 0.1 alkali metal/1  $YVO_4:Eu^{3+} + 10 SiO_2$ .

Figure 2 shows the fluorescence in plaques over the range of 0-100  $SiO_2/1 YVO_4:Eu^{3+}$  where the flux addition consisted of 0.03  $Na_2CO_3/1 SiO_2$ . At the 1 to 10 molar ratio of phosphor to silica, the concentration of  $YVO_4:Eu^{3+}$  is about 12% by volume, yet the fluorescence is still about 80% of that of undiluted phosphor and more highly optimized samples with this  $SiO_2$  concentration ranged as high as 96% (Table I). At the 1 to 100 molar ratio, the corresponding figures are 1.6%  $YVO_4:Eu^{3+}$  and 48% fluorescence intensity. Phosphate containing preparations behaved similarly.

Figure 3 shows the effect of flux on the morphology of pure phosphors and aliquots of the same precipitates fired with silica. Unfluxed  $YVO_4:Eu^{3+}$  (a) obtains in particles which are only 0.2-0.4  $\mu$  in size. In the presence of  $SiO_2$  (b) it can be seen that the phosphor particles form a dense layer over the  $SiO_2$ . The magnification here was reduced so as to show more than one coated particle of silica. Fluxed  $YVO_4:Eu^{3+}$  (c) forms rather well-faceted crystals which are typically 0.5-1.5  $\mu$  in size, while in the presence of silica and flux (d) these are no longer evident while the silica shows signs of fusion which resulted in encapsulation of the phosphor.

Table I summarizes the optical properties of these materials which, for convenience, are also identified with the appropriate letter of Fig. 3. In order to compare the effect of the physical arrangement between phosphor and silica with that of simple dilution, additional samples were prepared by mechanically mixing portions of the pure phosphors (a, c) with separately fired silica in the same ratio. These are indicated under "mixed." SEM of these were considered impractical because of the likelihood of segregation during settling of the suspensions on the copper blocks. We note, for instance, that the u.v. absorption ( $1 - R_{254}$ ) of the mechanical mixtures is appreciably lower than that of the undiluted phosphors, as is expected. On the other hand, the absorption of the fired combinations is only slightly lower. Considering the measured fluorescence intensities, we note that the unfluxed phosphor (a) performs normally in deep plaques but decreases in output with decreasing layer thickness. In combination with silica (b) fluorescence is drastically reduced in plaques, but the relative reduction decreases with decreasing layer thickness. This is seen in the ascending values of the ratios shown in the right-hand side of the table. In particular, we note that the performance of (b) equals that of (a) in single-particle layers. The mechanical mixture performs relatively well in plaques and lehr layers<sup>1</sup> in spite of the lower u.v. absorption.

The fluxed phosphor (c) is typical of normal production type  $YVO_4:Eu$ ; hence, the fluorescence is similar to the standard in all cases. In combination with silica (d), the plaque performance is very high but rapidly decreases with layer thickness. In contrast to the unfluxed preparation (b), this decrease is due to the silica (dilution) as seen by the descending values of ratio shown in the right-hand side of the table. The mechanical mixture performs much more poorly and, again in contrast to the previous case, drops to a very low value in single particle layers. In general, the data show that the effect of encapsulation as compared to random distribution of phosphor and silica particles increases with decreasing layer thickness.

### Discussion

The decreased fluorescence intensity of unfluxed  $YVO_4:Eu^{3+}$  in the single-particle layer is easily explained by the small particle size which limits the total amount of phosphor on the target. Since, however, the addition of silica caused no further reduction and resulted in a fluorescence intensity of 53.0 (Table I) which is actually higher than that of the fluxed system (49.5), it would seem that an enhancement effect was obtained in both cases. That this is not so is seen by reference to Fig. 3 which shows that a single particle layer of (b) contains approximately twice as much phosphor as a single particle layer of (a). The "dilution" of (b), while real in bulk, consists in this case merely of the separation of the phosphor layers by the silica particles and is optically of no consequence. On

<sup>1</sup> Since fluorescence output through lehr layers is a function of layer thickness, and optimum thickness depends on phosphor particle size and shape [phosphor (a) is much smaller than the  $SiO_2$ , "comparable" layers are difficult to prepare. Thus, the value of 68.3 for (a) +  $SiO_2$  compared to 64.7 for pure (a) is due such complications and all data for lehr layers should be considered to be very approximate.

Table I. Optical properties of  $Y_{0.93}Eu_{0.07}VO_4$  as a function of  $SiO_2$ , flux, and layer thickness

Flux	$SiO_2$	Fig. 3	$1-R_{254}$ Plaque	Fluorescence*			+ $SiO_2$ / - $SiO_2$ ratio		
				Plaque	t. Layer**	s.p. Layer**	Plaque	t. Layer**	s.p. Layer**
-	-	a	0.98	103.4	64.7	53.0			
-	+	b	0.94	75.0	58.5	53.0	0.77	0.905	1.00
-	mixed***	-	0.89	88.6	68.3	42.0	0.86	1.055	0.785
+	-	c	0.98	102.5	112.5	100.0			
+	+	d	0.96	98.5	91.3	49.5	0.96	0.81	0.495
+	mixed***	-	0.66	63.0	62.4	8.9	0.615	0.555	0.089

\* In per cent of an arbitrary standard phosphor.

\*\* t = thick (from paint, lehr), s.p. = single particle.

\*\*\* Mechanical mixtures of pure phosphors (a,c) with prefired  $SiO_2$ .

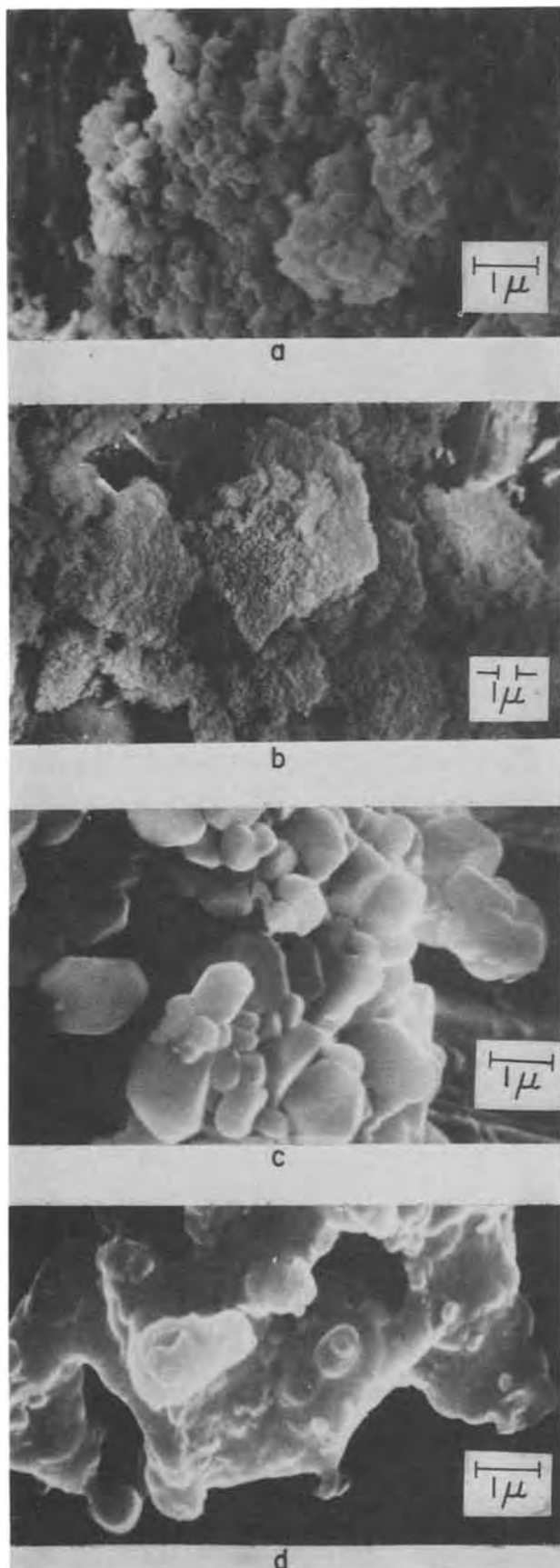


Fig. 3. Scanning electronphotomicrographs of compositions: a =  $\text{YVO}_4:\text{Eu}$ , unfluxed; b =  $\text{YVO}_4:\text{Eu} + 10 \text{SiO}_2$ , unfluxed; c =  $\text{YVO}_4:\text{Eu}$ , fluxed; d =  $\text{YVO}_4:\text{Eu} + 10 \text{SiO}_2$ , fluxed. Magnification: a, c, d = 10,000X; b = 3000X.

the other hand, a single particle layer of (d) still contains only the proportion of phosphor which is present

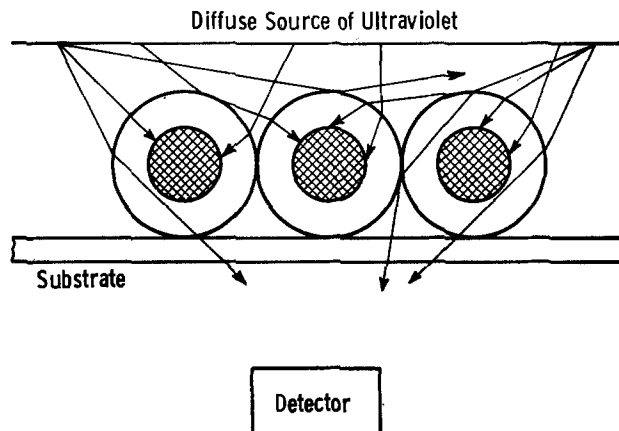


Fig. 4. Schematic representation of some optical paths in the excitation of fluxed  $\text{YVO}_4:\text{Eu} + 10 \text{SiO}_2$ .

in bulk, *i.e.*, 0.12 by volume. Since the phosphor particles are randomly oriented, their surface exposed to the exciting source equals  $0.12^{2/3} = 0.243$  of the total surface. One would therefore expect this layer to display 0.243 of the fluorescence intensity of the layer of undiluted phosphor. The measured intensity ratio of 0.495 shows that there exists enhancement by a factor of  $0.495/0.243 = 2.04$ . Owing to the complexity of the system (irregularly shaped particles with random inclusions whose morphology and distribution depend on numerous experimental details), this figure should serve only as an indication that the effect exists and, in the present system, has about this order of magnitude.

The process which seems to be primarily responsible for the observed effect is indicated in Fig. 4 which shows an array of particles which are idealized in the form of concentric spheres of phosphor and silica. As shown, the ratio of diameters is 0.5 to 1 which roughly corresponds to 12 volume per cent (v/o) phosphor ( $0.12^{1/3} = 0.493$ ). The linear magnification of a concentric sphere equals the refractive index of the shell which is 1.51 for vitreous silica at 254 nm. The total area of phosphor seen by the exciting source is therefore  $1.51^2 = 2.28$  times greater for all angles of incidence except grazing where shadowing of particles by their neighbors occurs and the magnification decreases towards the linear value of 1.51. The figure indicates the optical path of a number of rays, several of which contact the phosphor cores only by virtue of refraction at the silica surfaces. In real (irregular) silica particles each containing a number of randomly dispersed phosphor inclusions, the process is likely to be less efficient but fundamentally no different because all angles of incidence are equally represented.

It is possible that a small additional contribution obtains from the effect of the silica as a low refractive index coating which may decrease reflection losses of the exciting and emitted radiations. No efforts were made to evaluate it.

In layers of practical thickness, there is, of course, the additional effect in which the diluent serves to involve a greater depth of the layer in efficient absorption and emission. Although Table I shows that high ratios of fluorescence intensity of mechanical mixtures of fine particle size phosphor and silica compared to pure phosphor (a) are obtainable, the actual fluorescence intensities are relatively low. In the encapsulated system (d), on the other hand, the fluorescence can become quite high in lehrred layers and be almost undiminished in plaques.

#### Acknowledgments

The author wishes to thank Miss I. Walinski for sample preparations, Dr. W. A. Thornton for reflectance measurements, and Drs. F. M. Ryan, W. Lehmann, and N. T. Melamed for helpful discussions.

Manuscript submitted Sept. 10, 1975; revised manuscript received Oct. 24, 1975. This was Paper 203 presented at the Toronto, Canada, Meeting of the Society, May 11-16, 1975.

Any discussion of this paper will appear in a Discussion Section to be published in the December 1976 JOURNAL. All discussions for the December 1976 Discussion Section should be submitted by Aug. 1, 1976.

Publication costs of this article were partially assisted by the Westinghouse Electric Corporation.

## REFERENCES

1. S. L. Bernikov and Y. M. Zelikin, *Opt. Spectr.* **19**, 339 (1965).
2. W. Lehmann, *This Journal*, **122**, 748 (1975).
3. R. Corth, Unpublished.
4. R. C. Ropp, U.S. Pat. 3,630,946 (1971).
5. V. S. Krylov, R. L. Magunov, M. N. Puring, K. S. Bagdasarov, R. F. Sagina, and V. I. Popov, U.S. Pat. 3,667,701 (1972).
6. W. A. Thornton, *This Journal*, **116**, 286 (1969).

## Zn Diffusion in GaAs under Constant As Pressure

A. Luque, J. Martín, and G. L. Araújo

Laboratorio de Semiconductores de la E.T.S.I. de Telecomunicación,  
Universidad Politécnica de Madrid, Madrid, Spain

### ABSTRACT

Zn diffusion at different temperatures has been performed in GaAs keeping the arsenic pressure at the same value for all the temperatures. The effective diffusion coefficient and the surface concentration obtained under those conditions are temperature dependent and temperature independent, respectively. A generalization of the interstitial-substitutional model is presented to account for these facts.

It is a well-known fact that the diffusion coefficient of Zn in GaAs increases with the zinc concentration, which gives steeper diffusion profiles than the erfc profile appearing when the diffusion coefficient is a constant.

Allen and Cunnell (1, 2) proposed a model in which the zinc diffuses simultaneously in neutral and ionized forms. This model leads to a smaller variation of the diffusion coefficient,  $D$ , with zinc concentration than the observed one. Kendall and Jones (3) suggested that  $D$  is proportional to the concentration of positively ionized gallium vacancies; though this model shows a concentration dependence of  $D$  near that observed, it predicts the increase of  $D$  with the vacancy concentration and therefore with the arsenic vapor pressure, which is in disagreement with the experimental results of Rupprecht and Le May (4).

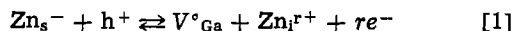
To date, the most widely accepted model is the so-called interstitial-substitutional model proposed by Longini (5) in 1962. This model assumes that the interstitial zinc diffuses much faster than the substitutional zinc, which becomes interstitial zinc on leaving a neutral gallium vacancy; the diffusion is therefore mainly controlled by the rate of production of interstitial zinc.

In the following, we first consider the dependence of the diffusion coefficient with Zn concentration and As pressure established by the interstitial-substitutional model. Then we study the diffusion conditions which allow As pressure to be kept under control in order to perform experiments of constant As pressure. Finally, the experimental results are interpreted on basis of a generalization of the interstitial-substitutional model.

### The Interstitial-Substitutional Model

In this model two forms of zinc impurities are assumed to be present; substitutional zinc and interstitial zinc. The two forms diffuse with different diffusion coefficients  $D_s$  and  $D_i$ ,  $D_i$  being much higher than  $D_s$ . However the most abundant form is the substitutional one. The diffusion process is therefore limited by the rate of production of interstitial zinc, which diffuses very rapidly.

The interstitial zinc reacts with a neutral gallium vacancy to produce substitutional zinc according to the equation



Key words: Zn diffusion, GaAs, compound semiconductors, semiconductor technology, interstitial-substitutional model.

Well-established evidence exists that the substitutional zinc is a single acceptor. However it is not clear if the interstitial zinc has to be considered as a single donor (6) or as a double donor (7).

Using  $k_0$  as the equilibrium constant of Eq. [1] with the relationships  $np = n_i^{r+}$  and  $p = [\text{Zn}_s^-]$  we may write

$$[\text{Zn}_i^{r+}] = \frac{k_0 [\text{Zn}_s^-]^{r+2}}{n_i^{2r} [\text{V}^\circ_{\text{Ga}}]} \quad [2]$$

Fick's laws for this diffusion process establish that

$$\begin{aligned} \frac{\partial}{\partial x} \left( D_s \frac{\partial [\text{Zn}_s^-]}{\partial x} + D_i \frac{\partial [\text{Zn}_i^{r+}]}{\partial x} \right) \\ = \frac{\partial}{\partial t} ([\text{Zn}_s^-] + [\text{Zn}_i^{r+}]) \end{aligned} \quad [3]$$

Considering  $[\text{Zn}_i^{r+}] \ll [\text{Zn}_s^-]$

$$\frac{\partial}{\partial x} \left[ \left( D_s + D_i \frac{\partial [\text{Zn}_i^{r+}]}{\partial [\text{Zn}_s^-]} \right) \frac{\partial [\text{Zn}_s^-]}{\partial x} \right] = \frac{\partial [\text{Zn}_s^-]}{\partial t} \quad [4]$$

An effective diffusion coefficient appears as

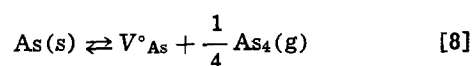
$$D = D_s + D_i \frac{\partial [\text{Zn}_i^{r+}]}{\partial [\text{Zn}_s^-]} \quad [5]$$

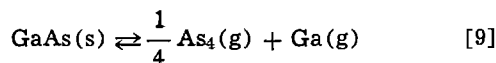
and considering Eq. [2] we obtain

$$D = D_s + D_i (r + 2) \frac{k_0 [\text{Zn}_s^-]^{r+1}}{n_i^{2r} [\text{V}^\circ_{\text{Ga}}]} \quad [6]$$

Unless the  $[\text{Zn}_s^-]$  is very small, the dominant term in Eq. [6] is the second one. So the process is limited by the diffusion rate of interstitial zinc that decreases with increasing neutral gallium vacancy concentration.

The dependence of  $D$  on  $[\text{V}^\circ_{\text{Ga}}]$  implies its dependence on the partial arsenic pressure  $p_{\text{As}}$  within the diffusion ampul. The generation of arsenic and gallium vacancies are regulated by the following equations





The mass-action law relationships for these equations are

$$k_1 = p_{\text{Ga}} [V^\circ_{\text{Ga}}] \quad [10]$$

$$k_2 = p_{\text{As}_4}^{1/4} [V^\circ_{\text{As}}] \quad [11]$$

$$k_3 = p_{\text{As}_4}^{1/4} p_{\text{Ga}} \quad [12]$$

From [10] and [12] we obtain

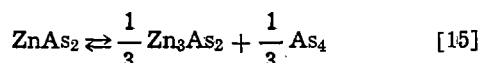
$$[V^\circ_{\text{Ga}}] = \frac{k_1}{k_3} p_{\text{As}_4}^{1/4} \quad [13]$$

Thus the result is that  $D$  decreases with increasing arsenic pressure for high zinc concentrations ( $\sim 10^{19}$ ) in good agreement with the experimental evidence reported by Rupprecht and Le May (4). For these concentrations and taking Eq. [13] into account, Eq. [6] can be written as

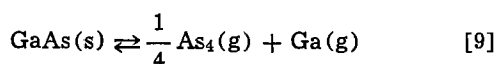
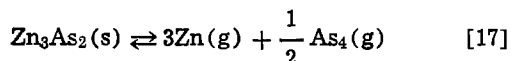
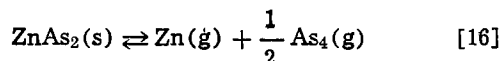
$$D = D_s + D_1 \frac{k_0 k_3}{k_1} \frac{r+2}{n_i^{2r}} \frac{1}{p_{\text{As}_4}^{1/4}} [\text{Zn}_s^-]^{r+1} \quad [14]$$

### Diffusion Source

$\text{ZnAs}_2$  has been used as a zinc diffusion source to provide a controlled arsenic pressure in addition to the zinc pressure. This arsenic pressure must be high enough to prevent As evaporation from the GaAs wafer which would damage the surface and produce anomalous diffusion fronts for shallow diffusions. Since  $\text{ZnAs}_2$  dissociates after the reaction



for temperatures below 744°C (the ternary eutectic temperature of the system  $\text{ZnAs}_2$ - $\text{Zn}_3\text{As}_2$ -GaAs),  $\text{Zn}_3\text{As}_2$  and GaAs are present in equilibrium with  $\text{As}_4$ , Zn, and Ga vapors. This equilibrium is provided by the reactions



The mass-action law relationships for these equations are

$$k_6 = p_{\text{Zn}} p_{\text{As}_4}^{1/2} \quad [18]$$

$$k_7 = p_{\text{Zn}}^3 p_{\text{As}_4}^{1/2} \quad [19]$$

$$k_3 = p_{\text{As}_4}^{1/4} p_{\text{Ga}} \quad [12]$$

Equations [18] and [19] give the  $\text{As}_4$  equilibrium vapor pressure; this pressure is the same for the ternary system and for the binary system  $\text{ZnAs}_2$ - $\text{Zn}_3\text{As}_2$ , because relations [18] and [19] hold for both systems. Figure 1 shows the As equilibrium vapor pressure vs.  $1/T$  reported by Lyons (8) for the binary system.

Using  $\text{ZnAs}_2$  as a diffusion source almost all the arsenic in the vapor phase is supplied through reaction [15] by this compound, which is much more volatile than the GaAs. The amount of  $\text{ZnAs}_2$  per unit volume of the diffusion ampul to obtain a certain arsenic vapor pressure,  $p_{\text{As}_4}$ , is given by

$$m_{\text{ZnAs}_2} = \frac{10.35}{T(^{\circ}\text{K})} p_{\text{As}_4} (\text{Torr}) \text{mg/cm}^3 \quad [20]$$

taking into account reaction [15] and assuming that  $\text{As}_4$  behaves as a perfect gas. The maximum vapor pressure that can be obtained is the ternary system equilibrium pressure and formula [20] will give the

minimum amount of  $\text{ZnAs}_2$  necessary to reach this pressure. The variation with temperature of the equilibrium vapor pressure and the minimum amount of  $\text{ZnAs}_2$  is shown in Fig. 2.

For temperatures over 744°C and below 1015°C (melting point of  $\text{Zn}_3\text{As}_2$ ) an invariant ternary liquidus richer in zinc than the  $\text{ZnAs}_2$  is formed in equilibrium with the GaAs and the  $\text{Zn}_3\text{As}_2$ . Again, in this case, if the amount of  $\text{ZnAs}_2$  is small enough the ternary equilibrium is not reached and the arsenic vapor pressure is given by [20].

The minimum amount of  $\text{ZnAs}_2$  to supply the arsenic vapor pressure that avoids the surface damage produced by the arsenic evaporation from the GaAs surface is much smaller and can be obtained also by using [20] together with the equilibrium  $p_{\text{As}_4}$  value for GaAs, given by Fig. 2.

### Experimental

To study the zinc diffusion into GaAs, 30 diffusions were performed using the sealed ampul technique. The

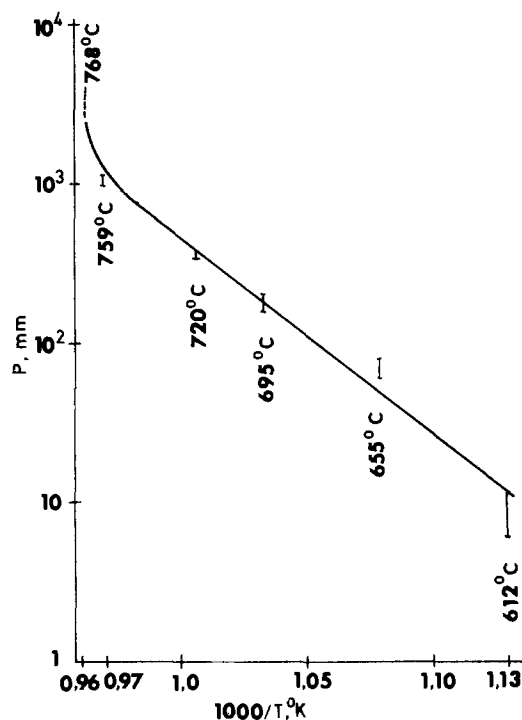


Fig. 1. As equilibrium vapor pressure [after Lyons (8)]

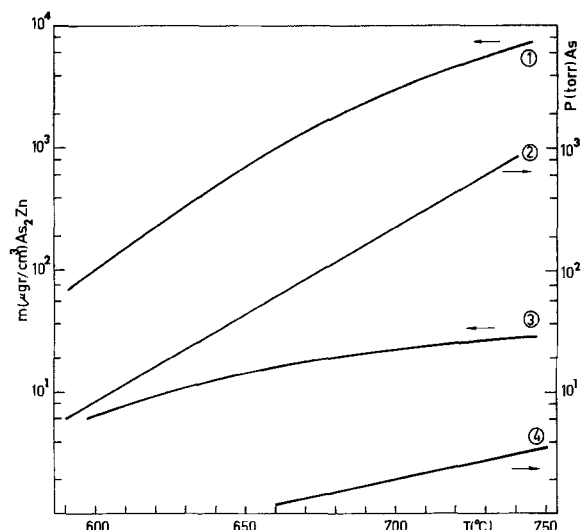


Fig. 2. As pressure vs. temperature in equilibrium with  $\text{ZnAs}_2$  (plot 2) (8) and with GaAs (plot 4) (18) and minimum amount of  $\text{ZnAs}_2$  vs. temperature to reach the As equilibrium vapor pressure with  $\text{ZnAs}_2$  (plot 1) and with GaAs (plot 3).

temperature was varied between 700° and 875°C and the diffusion time between ½ and 16 hr.

Selenium-doped wafers from Wacker-Chemitronic, grown in the (111) direction, were used. The resistivity for these wafers ranged from  $3.1 \times 10^{-3}$  to  $1.6 \times 10^{-3}$  ohm·cm and the mobility from 3320 to 2560 cm<sup>2</sup>/V-sec corresponding to a concentration between  $6 \times 10^{17}$  and  $1.5 \times 10^{18}$  cm<sup>-3</sup>. In each experiment a  $6 \times 10$  mm specimen of wafer was used.

The amounts of ZnAs<sub>2</sub> put as a dopant source in each ampul were lower than the minimum necessary to reach the equilibrium with a ternary system. Therefore, the diffusions were performed only in the presence of Zn<sub>3</sub>As<sub>2</sub> and GaAs under an arsenic vapor pressure given by

$$p_{As_4}(\text{Torrr}) = \frac{T(^{\circ}\text{K}) \cdot m_{ZnAs_2}(\text{mg/cm}^3)}{10.35} \quad [21]$$

The ampul volume was about 2.5 cm<sup>3</sup> in each case, varying due to the handling of the glass during the sealing process. For this reason it was not important to use an exact amount of ZnAs<sub>2</sub>. Table I shows the amount used in each case.

The value of  $p_{As_4}$  obtained from formula [21] is  $610 \pm 10\%$  mm considering the spreading of  $m_{ZnAs_2}$  and the variation of  $T$ . Therefore the experiments can be considered as performed under a constant arsenic pressure.

After each diffusion process,  $x_j$  and  $V/I$  were measured and the results are presented in Table I. To measure  $x_j$  the grooving cylinder technique was used for the shallower diffusions and the beveling technique for the deeper ones. The staining solution (100g of CuSO<sub>4</sub> and 5 cm<sup>3</sup> of FH 49% in a liter of water) was used under an intensive illumination.

The  $V/I$  was measured by the four-point technique. The average resistivity,  $\bar{\rho}$ , can be obtained from the  $V/I$  and  $x_j$  data by using the formula

$$\bar{\rho} = K(V/I)x_j \quad [22]$$

where  $K$  depends on the size of the specimen. In our case the value of  $K$  is 4.49 as obtained from the data reported by Logan (9).

### Results

The partial differential equation of diffusion

$$\frac{\partial}{\partial x} \left[ D \frac{\partial C}{\partial x} \right] = \frac{\partial C}{\partial t} \quad [23]$$

can be changed into an ordinary differential equation using the Boltzmann transformation

$$y = \frac{x}{2\sqrt{D_{\text{surf}} t}} \quad [23a]$$

and a solution of  $C(y)$  can be found provided  $D$  depends only on  $C$  and  $C_{\text{surf}}$  is time independent during the diffusion process.

Therefore, if these conditions hold in our case, a proportionality will exist between  $x_j$  and  $\sqrt{t}$ .

In Fig. 3 the experimental values of  $x_j$  vs.  $\sqrt{t}$  for the different diffusion temperatures are plotted. As can be

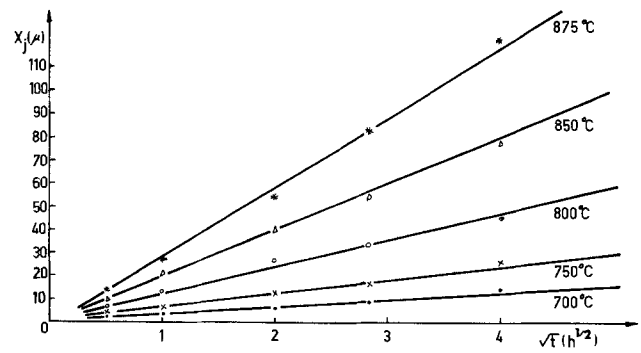


Fig. 3. Measured values of the junction depth as a function of the square root of the diffusion time.

seen the linear relationship theoretically predicted is experimentally found for each temperature. We can conclude that an equilibrium of vacancies is reached during the diffusion process causing  $D$  and  $C_{\text{surf}}$  to be time independent.

Recently irregularities in diffusion profiles have been interpreted (10) as coming from nonequilibrium sources of gallium vacancies of the surface and inside the bulk. In our experiments these nonequilibrium conditions were not observed perhaps because our diffusions were shallower.

Weisberg and Blanc (6) solved the diffusion equation for diffusion coefficients of the form

$$D = D_{\text{surf}} (C/C_{\text{surf}})^m \quad [24]$$

for  $m = 1, 2$ , and  $3$ , using the Boltzmann variable transformation (11). Since the profiles are very steep and the bulk concentration  $C_B$  is much lower than  $C_{\text{surf}}$ , the function position is independent of  $C_B$  and corresponds to

$$y_j = \frac{x_j}{2\sqrt{D_{\text{surf}} t}} \quad [25]$$

where  $y_j = 0.808$  for  $m = 1$ ,  $y_j = 0.546$  for  $m = 2$ , and  $y_j = 0.436$  for  $m = 3$  as obtained by Weisberg and Blanc (6).

$D_{\text{surf}}$  can be obtained from relationship [25]

$$D_{\text{surf}} = \frac{1}{4y_j^2} \left( \frac{x_j}{\sqrt{t}} \right)^2 \quad [26]$$

$x_j/\sqrt{t}$  being the slope of the lines plotted in Fig. 3. The values of  $D_{\text{surf}}$  calculated in this way for the different temperatures are presented in Table II for  $m = 2$  and  $3$ . A new value for  $m = 2.5$  is estimated by interpolation.

$C_{\text{surf}}$  can be obtained from the experimental values of  $V/I$  and  $x_j$ , which allows  $\bar{\rho}$  to be computed using Eq. [22] and considering that

$$\frac{1}{\rho} = \frac{1}{x_j} \int_0^{x_j} \frac{dx}{\rho} \quad [27]$$

where the expression for  $\rho$  is that reported by Gardner (12).

$$\rho(\text{ohm}\cdot\text{cm}) = 9.85 \times 10^{11} C^{-0.744} (\text{cm}^{-3}) \quad [28]$$

Table I. Experimental results of diffusions

Hr	700°C+			750°C+			800°C+			850°C+			875°C+		
	a	b	c	a	b	c	a	b	c	a	b	c	a	b	c
½	17	1100	1.90*	12	550	3.86*	12	340	5.60*	15	200	13 <sup>Δ</sup>	16	150	19 <sup>Δ</sup>
1	12	640	3.6*	13	450	5.1*	13	230	11 <sup>Δ</sup>	16	130	20 <sup>Δ</sup>	22	115	23 <sup>Δ</sup>
2	12	590	4.6*	15	320	8.7*	15	150	17 <sup>Δ</sup>	17	100	28 <sup>Δ</sup>	22	72	35 <sup>Δ</sup>
4	12	410	6*	14	210	14 <sup>Δ</sup>	12	100	26 <sup>Δ</sup>	16	75	37 <sup>Δ</sup>	12	50	47 <sup>Δ</sup>
8	12	270	9*	15	150	17 <sup>Δ</sup>	15	77	30 <sup>Δ</sup>	15	46	45 <sup>Δ</sup>	13	35	74 <sup>Δ</sup>
16	11	190	15*	12	100	26 <sup>Δ</sup>	12	50	40 <sup>Δ</sup>	14	32	69 <sup>Δ</sup>	14	25	109 <sup>Δ</sup>

\* a. ZnAs<sub>2</sub> weight, milligram. b.  $V/I$  measured value, millohm. c. Junction depth, micron.

• Grooving technique measurement.

Δ Bevel technique measurement.

Table II.  $D_{\text{surf}}$  ( $\text{cm}^2 \cdot \text{sec}^{-1}$ ) for different temperatures and different values of  $m$ 

Temp, °C	$m = 2$	$m = 2.5$	$m = 3$
700	$5.26 \times 10^{-11}$	$7.10 \times 10^{-11}$	$8.25 \times 10^{-11}$
750	$9.83 \times 10^{-11}$	$1.33 \times 10^{-10}$	$1.54 \times 10^{-10}$
800	$2.82 \times 10^{-10}$	$3.80 \times 10^{-10}$	$4.42 \times 10^{-10}$
850	$7.65 \times 10^{-10}$	$1.03 \times 10^{-9}$	$1.20 \times 10^{-9}$
875	$1.60 \times 10^{-9}$	$2.17 \times 10^{-9}$	$2.52 \times 10^{-9}$

Table III.  $y_j, I = (1/y_j) \int_0^{y_j} (C/C_{\text{surf}})^{0.744} dy$ , and  $C_{\text{surf}}$  values for different values of  $m$ 

	$m = 2$	$m = 2.5$	$m = 3$
$y_j$	0.548	0.470	0.436
$I$	0.407	0.380	0.352
$C_{\text{surf}}$	$1.75 \times 10^{20} \text{ cm}^{-3}$	$1.57 \times 10^{20} \text{ cm}^{-3}$	$1.57 \times 10^{20} \text{ cm}^{-3}$

The expression for  $C_{\text{surf}}$  is thus

$$C_{\text{surf}} = \left[ \frac{9.85 \times 10^{11} (I/V)/x_j}{K(1/y_j) \int_0^{y_j} (C/C_{\text{surf}})^{0.744} dy} \right]^{1/0.744} \quad [29]$$

Equation [29] shows that  $I/V$  must be proportional to  $x_j$  for diffusion processes performed at the same temperature and different diffusion times.

Figure 4 shows  $I/V$  vs.  $x_j$ . As can be observed all the experimental points can be joined by a single straight line implying that not only the surface concentration is temperature independent but is temperature independent too.

To obtain the value of  $C_{\text{surf}}$  the integral

$$\frac{1}{y_j} \int_0^{y_j} (C/C_{\text{surf}})^{0.744} dy$$

has been computed for  $m = 1, 2$ , and  $3$  from the data of Ref. [6]. A new value for  $m = 2.5$  has been also estimated by interpolation. The value of  $(I/V)/x_j$  is obtained from the slope of the straight line of Fig. 4. Data corresponding to  $m = 2, 2.5$ , and  $3$  is presented in Table III.

The diffusion coefficients vs. concentration, as reported by several authors, are plotted in Fig. 5. The values of the exponent  $m$ , deduced from the slope of the straight lines, range from 2 to 3.3. The graphic representation of Eq. [24] has also been drawn in this figure for  $m = 2.5$  and  $T = 850^\circ\text{C}$  using the values of  $C_{\text{surf}}$  and  $D_{\text{surf}}$  obtained in the present paper (Table IV). As can be seen curve 8 lies between the Rupprecht and Kendall curves. Since Rupprecht diffusion experiments were performed with a greater arsenic pressure than in ours and the Kendall diffusion was carried out with a lower arsenic pressure, it can be concluded that the diffusion coefficient is strongly dependent on the arsenic vapor pressure and that this parameter has to

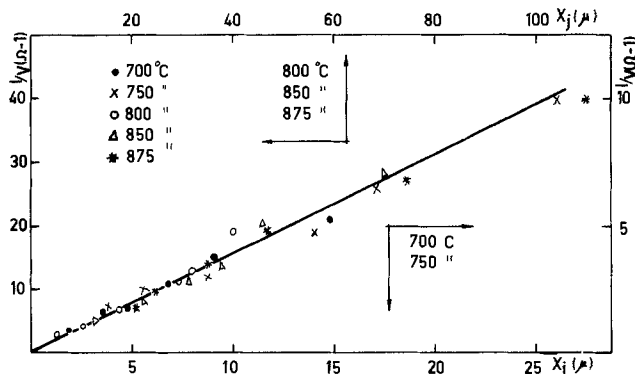


Fig. 4. Measured values of the sheet conductance as a function of the junction depth.

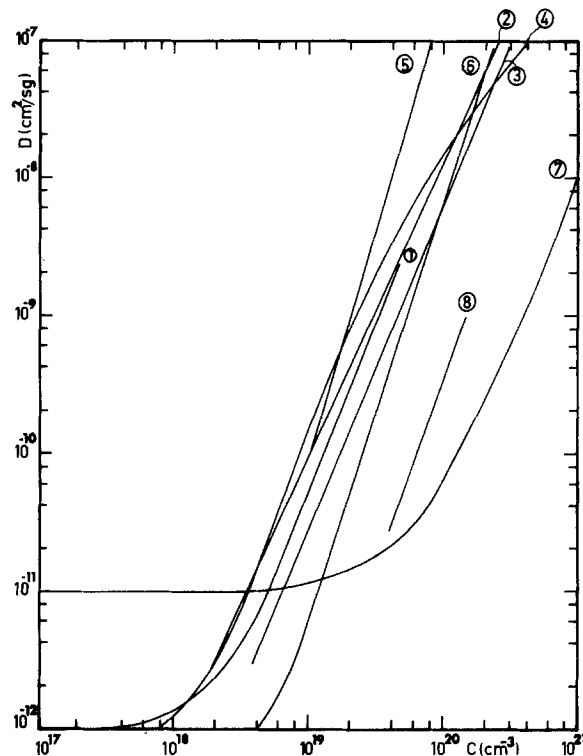


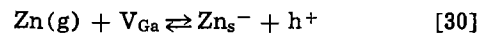
Fig. 5. Effective diffusion coefficient of Zn in GaAs after different authors: plot 1, Tuck (15); plot 2,  $y$ ; plot 3, Kadin and Tuck (16); plot 4, Chang and Pearson (7); plot 5, Pearson (17) and Kendall (3); plot 6, Kendall (3); plot 7, Rupprecht (4); and plot 8, present article. The diffusion temperatures and logarithmic slopes appear in Table IV.

be kept under control in order to obtain good repeatability.

Since the surface concentration is temperature independent the variation of  $D_{\text{surf}}$  ( $C_{\text{surf}}, T$ ) can only be attributed to the temperature variation. This result is not in agreement with other previously reported results [13], which may be attributed to the fact that these other results were obtained under a temperature variable arsenic pressure.  $D_{\text{surf}}$  vs.  $1000/T$  is plotted in Fig. 6 for three different values of  $m$ .

### Discussion

The incorporation reaction of zinc atoms in the vapor state to solid substitutional zinc is



The action-mass law for this reaction is

$$\frac{[\text{Zn}_{\text{s}}^-]p}{p_{\text{Zn}}[V_{\text{Ga}}]} = k_5 \quad [31]$$

with  $p = [\text{Zn}_{\text{s}}^-]$ , we obtain from Eq. [13] and [31]

$$[\text{Zn}_{\text{s}}^-] = \left( \frac{k_1 k_5}{k_3} \right)^{1/2} p_{\text{Zn}}^{1/2} p_{\text{As}_4}^{1/8} \quad [32]$$

During the diffusion process an equilibrium state exists between the zinc and arsenic vapors and the solid  $\text{Zn}_3\text{As}_2$ , so that, considering Eq. [19], Eq. [32] becomes

$$[\text{Zn}_{\text{s}}^-] = \left( \frac{k_1 k_5}{k_3} \right)^{1/2} k_7^{1/6} p_{\text{As}_4}^{1/24} \quad [33]$$

Table IV. Diffusion temperatures and logarithmic slopes in Fig. 5

Plot number	1	2	3	4	5	6	7	8
Diffusion temperature, °C	1000	1000	1000	900	900	750	850	850
Slope	2.3	2.2	2.2	2.5	2.9	3.4	2.0	2.5

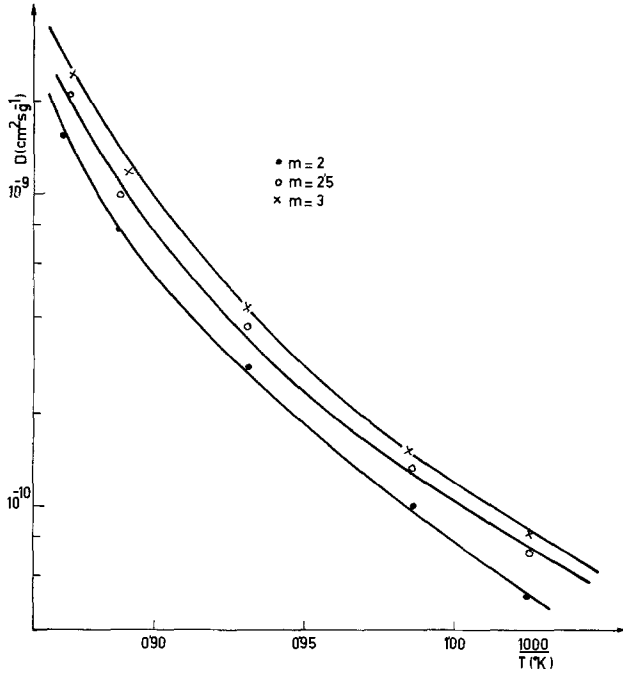


Fig. 6. Effective diffusion coefficients of Zn in GaAs vs. temperature for different values of  $m$ .

From this equation we observe that  $[Zn_s^-]$  varies very slowly with  $p_{As_4}$ . Therefore the lack of accuracy in the arsenic pressure referred to earlier, is not important when considering Eq. [33] as the relative error is reduced by 1/24.

Since a mass-action law constant  $k$  is of the form (14)

$$k = \exp\left(-\frac{\Delta G}{kT}\right) = \exp\left(\frac{\Delta S}{k}\right) \cdot \exp\left(-\frac{\Delta H}{kT}\right) \quad [34]$$

The main dependence of  $k$  on  $T$  is given by  $\exp(-\Delta H/kT)$ .  $\Delta G$ ,  $\Delta S$ , and  $\Delta H$  are, respectively, the increments of free energy, entropy, and enthalpy during the reaction.

Therefore the constants of Eq. [33] are (see Eq. [7], [9], [30], and [17])

$$k_1 \propto \exp\left[-\frac{H_{Ga}(g) + H_{V_{0Ga}}}{kT}\right] \quad [35]$$

where  $H_{Ga}(g)$ , is the enthalpy necessary to remove a Ga atom from the GaAs surface and  $H_{V_{0Ga}}$  is the enthalpy necessary to generate a gallium vacancy, the value about half the Ga-As bonding energy.

$$k_3 \propto \exp\left[-\frac{H_{As_4}(g) + H_{Ga}(g)}{kT}\right] \quad [36]$$

$H_{As_4}(g)$  is the enthalpy necessary to remove an As atom from the GaAs surface and form an  $As_4$  molecule.

$$k_5 \propto \exp\left[\frac{H_{Zn_s}(g)}{kT}\right] \quad [37]$$

where  $H_{Zn_s}(g)$  is the enthalpy necessary to remove a substitutional zinc atom from a gallium site.

$$k_7 \propto \exp\left[\frac{-H_{Zn_3As_2}}{kT}\right] \quad [38]$$

$H_{Zn_3As_2}$  is the formation enthalpy of  $Zn_3As_2$ .

Substituting [35], [36], [37], and [38] in Eq. [33] we may write

$$[Zn_s^-] \propto p_{As_4}^{1/24} \exp\left[\frac{H_{As_4}(g) + H_{Zn_s}(g) - H_{V_{0Ga}} - 1/3H_{Zn_3As_2}}{2kT}\right] \quad [39]$$

Although the values of the enthalpies in expression [39] are not known, the fact that two of them are positive and the other two negative could give a very small value of the exponent in [39]. This would explain the temperature independence of  $[Zn_s^-]$  experimentally observed.

As shown in Fig. 6 the diffusion coefficient increases with temperature. Regardless of the value of  $m$ , the activation energy of  $D$  increases with temperature between 1.3 and 2.6 eV, approximately, for temperatures ranging from 700° to 875°C. This variation could be explained if we consider that the interstitial zinc can simultaneously exist in single and double ionized forms. In this case the effective diffusion coefficient could be written, using a straightforward generalization of Eq. [6], as

$$D = D_s + \frac{3k_o^+}{n_i^2} \frac{[Zn_s^-]^2}{[V_{0Ga}]} D_{i^+} + \frac{4k_o^{++}}{n_i^4} \frac{[Zn_s^-]^3}{[V_{0Ga}]} D_{i^{++}} \quad [40]$$

where  $D_{i^+}$  and  $D_{i^{++}}$  are, respectively, the diffusion coefficients of the single and double ionized forms and  $k_o^+$  and  $k_o^{++}$  are action-mass law constants of reaction [1] for  $r = 1$  and  $r = 2$ , respectively. The temperature dependence of these constants are

$$k_o^+ \propto \exp\left[-\frac{H_{Zn_{i^+}}}{kT}\right] \quad [41]$$

and

$$k_o^{++} \propto \exp\left[-\frac{H_{Zn_{i^{++}}}}{kT}\right] \quad [42]$$

$H_{Zn_{i^+}}$  and  $H_{Zn_{i^{++}}}$  being the increment of enthalpy in the corresponding reactions.

The difference in activation energy of the second and third terms of Eq. [40] is

$$-\Delta E_a = -E_g + (H_{Zn_{i^{++}}} - H_{Zn_{i^+}}) + (E_{i^{++}} - E_{i^+}) \quad [43]$$

where the temperature independence of  $[Zn_s^-]$  has been considered and  $E_{i^+}$  and  $E_{i^{++}}$  are the activation energies of  $D_{i^+}$  and  $D_{i^{++}}$ , respectively.

Since the differences in parenthesis in Eq. [43] are probably small,  $\Delta E_a$  must differ very little from  $E_g$ , which in GaAs at 700°C is 1.1 eV. This value is in reasonable agreement with the experimentally found value of 1.3 eV.

## Conclusions

A set of diffusions was performed at a constant arsenic vapor pressure. It was found that the junction depth increased linearly with  $\sqrt{t}$  and that  $I/V$  increased linearly with  $x_j$  for each temperature implying that an equilibrium of vacancies exists in the diffusion process.

Using for the diffusion coefficient a law of the form  $D = D_{surf}(T) [C/C_{surf}(T)]^m$ ,  $D_{surf}(T)$  and  $C_{surf}(T)$  were obtained from experimental data.  $C_{surf}(T)$  was found to be temperature independent and this fact is discussed in terms of the interstitial-substitutional model. On the other hand  $D_{surf}(T)$  increases exponentially with  $1/T$  through an activation energy which varies between 1.3 and 2.6 eV for temperatures ranging from 700° to 875°C.

The behavior of  $D_{surf}$  vs.  $T$  can be attributed to a diffusion of interstitial zinc mainly in its doubly ionized form for the lower temperatures and in its singly ionized form for the higher ones. Therefore the exponent  $m$  changes from 3 to 2 when the temperature increases.

## Acknowledgments

This work has been partially supported by the U.S.A.-Spain Agreement N.S.F. Funds and by the Spanish III Plan of Development Funds.

The authors are indebted to Professor Kuper for helpful discussions.

Manuscript submitted April 9, 1975; revised manuscript received ca. Sept. 1, 1975.

Any discussion of this paper will appear in a Discussion Section to be published in the December 1976 JOURNAL. All discussions for the December 1976 Discussion Section should be submitted by Aug. 1, 1976.

Publication costs of this article were partially assisted by the Universidad Politecnica de Madrid.

#### LIST OF SYMBOLS

$D$	effective diffusion coefficient
$D_i$	diffusion coefficient of interstitial zinc
$D_s$	diffusion coefficient of substitutional zinc
$D_{surf}$	effective surface diffusion coefficient
$k_i$	mass-action law constants
$[Zn_s^-]$	substitutional zinc concentration
$p_{As_4}$	partial arsenic pressure, mm Hg
$m_{ZnAs_2}$	amount of $ZnAs_2$ per unit of volume to obtain a given partial arsenic pressure, $mg/cm^3$
$C$	impurity concentration
$C_{surf}$	impurity surface concentration
$H_{Ga}(g)$	enthalpy to remove a Ga atom from the GaAs surface
$H_{V_{Ga}}$	enthalpy to generate a gallium vacancy
$H_{As_4}(g)$	enthalpy to remove an arsenic atom from the GaAs surface
$H_{Zn_s}(g)$	enthalpy to remove a substitutional zinc atom from a gallium site
$H_{As_2Zn_3}$	formation enthalpy of $As_2Zn_3$
$D_i^+$	diffusion coefficient of single ionized zinc
$D_i^{++}$	diffusion coefficient of double ionized zinc
$H_{Zn_i}^+$	incremental enthalpy of Eq. [1] for $r = 1$

$H_{Zn_i}^{++}$	incremental enthalpy of Eq. [1] for $r = 2$
$\Delta E_a$	incremental activation energy
$E_i^{++}$	activation energy of $D_i^{++}$
$E_i^+$	activation energy of $D_i^+$

#### REFERENCES

1. J. Allen and F. Cunell, *Nature*, **182**, 1158 (1958).
2. J. W. Allen, *J. Phys. Chem. Solids*, **15**, 134 (1960).
3. D. L. Kendall and M. E. Jones, AIEE-IRE Device Research Conference, Stanford University (1961).
4. H. Rupprecht and C. Z. Le May, *J. Appl. Phys.*, **35**, 1970 (1964).
5. R. L. Longini, *Solid State Electron.*, **5**, 127 (1962).
6. L. R. Weisberg and J. Blanc, *Phys. Rev.*, **131**, 1548 (1963).
7. L. L. Chang and G. L. Pearson, *J. Appl. Phys.*, **35**, 1960 (1964).
8. V. S. Lyons, *J. Phys. Chem.*, **63**, 1142 (1959).
9. M. A. Logan, *Bell System Tech. J.*, **40**, 885 (1961).
10. J. Blanc, *J. Appl. Phys.*, **45**, 1948 (1974).
11. J. Crank, "The Mathematics of Diffusion," p. 148, Oxford University Press (1970).
12. Cf. M. H. Pilkuhn and H. Rupprecht, *Trans. Met. Soc. AIME*, **230**, 296 (1964).
13. C. H. Ting and G. L. Pearson, *J. Appl. Phys.*, **42**, 2247 (1971).
14. G. H. Barrow, *Quimica Fisica*, p. 435, Reverté (1972).
15. B. Tuck, *J. Phys. Chem. Solids*, **30**, 253 (1969).
16. M. A. H. Kadhin and B. Tuck, *J. Material Sci.*, **7**, 68 (1972).
17. G. L. Pearson *et al.*, *Bull. Am. Phys. Soc.*, St. Louis Meeting (1963).
18. J. Boomgard and K. Schof, *Philips Res. Rept.*, **12**, 127 (1957).

## Raman Scattering Spectroscopy Applied to the Study of Chemical Vapor Deposition Systems

T. O. Sedgwick\* and J. E. Smith, Jr.

IBM Thomas J. Watson Research Center, Yorktown Heights, New York 10598

#### ABSTRACT

Gas phase Raman scattering spectroscopy is being used as a new tool to study chemical processes taking place at high temperatures in chemical vapor deposition (CVD) systems. This technique allows measurement of changes in species concentration as well as gas temperature with spatial resolution of 0.1–0.5 mm without perturbing the CVD system. Studies of the decomposition of  $NH_3$  and  $SiH_4$  in a typical CVD system are presented as an example of the application of this technique. Measurements of  $NH_3$  concentration profiles, both normal and parallel to an rf-heated susceptor in  $H_2$ - $N_2$  gas mixtures, are presented. Attempts to measure  $SiH_4$  concentration profiles were thwarted by fluorescence from a trace impurity in the same spectral region.

Detailed understanding of gas phase chemical reactions important in CVD systems has been severely hampered by the lack of a technique for the detection of molecular vapor species, and measurement of their concentration and their concentration gradients in the heated zone of a CVD reactor. Similarly, until recently there has been no satisfactory technique for the measurement of temperature in a highly nonisothermal situation such as occurs in an rf-heated CVD reactor. Deposition rate and mass balance measurements combined with equilibrium thermodynamic calculations can sometimes give enough information to allow characterization of an over-all reaction as input mass transport or kinetically limited. However, because of the lack of local concentration and temperature information, little is known about the details of the chemical reactions taking place. The existence of intermediate

reaction products, the understanding of the variation of deposition rate as a function of position in the reactor, and the acquisition of quantitative kinetic and mass transport data depend in part upon being able to measure concentration and temperature profiles within a reactor.

The recent application of mass spectrometry to sample gases at elevated temperatures is beginning to yield important information about the species present in open tube CVD systems operated at atmospheric pressure (1). However, the mass spectrometric technique requires the use of a capillary-like sampling probe. The probe itself disturbs the flow of gases locally in a laminar flow reactor and the necessary expansion of the gas within the probe gives rise to some uncertainty as to whether the molecules reaching the spectrometer are representative of the gas composition in the reactor. U.V. and infrared absorption spectroscopy have been used to measure chemical equilibria at elevated

\* Electrochemical Society Active Member.

Key words: light scattering, Si deposition,  $NH_3$ ,  $SiCl_4$ , gas phase chemical reaction.



temperatures, but the inability to sample a small, well-defined sample volume as a function of position in the reactor, which may have a very nonhomogeneous chemical composition, limits the utility of these techniques. Possible excitation of the gas molecules in u.v. spectroscopy and the interference of the furnace infrared radiation in infrared spectroscopy are also problems. Temperature profiles in a CVD reactor measured by thermocouples have not been reported on in detail presumably because, once again, the probe (thermocouple) disturbs the local gas flow, and because radiation and conduction effects may be large and are difficult to evaluate.

Raman scattering has unique advantages for the study of gases and has developed rapidly in the last few years with the advent of the laser. It has been used primarily for molecular structure and bonding studies at room temperature (2, 3). However, it has also been used for molecular structure studies at high temperature, and for qualitative studies of chemical equilibria in an isothermal cell up to 1000°C (4-7). The use of Raman scattering as an analytical tool for species identification in gas mixtures and concentration measurements for process control, pollution monitoring, or atmospheric composition has been proposed, and some preliminary data is available (8-13). Similarly, the use of Raman scattering to measure gas temperature has been proposed, but until recently (13-14) no substantial use of the technique has been reported. In the present study we have used Raman scattering to determine species concentration and temperature as a function of position in a CVD reactor. In order to achieve the sensitivity and resolution needed it has been necessary to use more elaborate equipment than has been used in the above-cited studies. We will describe this apparatus below.

The properties of Raman scattering which may be used to advantage in the detection of molecules in the hot gas of a CVD reactor are:

(i) The Raman spectrum is unique for a molecular species and is usually composed of several narrow ( $\ll 50 \text{ cm}^{-1}$  wide) peaks.

(ii) A sample volume of gas is analyzed *in situ* at operating temperature and pressure.

(iii) Positioning of the detector at right angles to the laser beam allows the sampling of a small volume ( $\sim 1 \text{ mm}^3$  is easily achieved) which can be moved throughout the reactor volume.

(iv) Gas temperature can be measured simultaneously by a Raman technique.

(v) The Raman spectrum is detected in a spectral region away from the peak of the black-body radiation emitted by the reactor, reducing interference from this source.

In this paper, data will be presented showing concentration profiles of  $\text{NH}_3$  in a  $\text{H}_2\text{-N}_2$  carrier, and attempts to measure  $\text{SiH}_4$  concentration profiles in various reacting environments will be discussed.

### Raman Scattering

The Raman effect (15) is the inelastic scattering of light. Photons are scattered with energy shifted from that of the incident photons, and the energy difference is taken up by quantum transitions of the scattering system. In this paper, where the light is Raman scattered by a molecular gas, the transitions measured are between quantized molecular vibrational states. (The discussion could equally well be applied to transitions between rotational or mixed rotational-vibrational states, but the vibrational transitions have proved more useful in the applications we have made of the technique.)

The intensity,  $I$ , of Raman scattered light is given by the expression

$$I = K (\omega_L \pm \omega_V)^4 I_L \rho_i \sigma_1(\omega_V) G_{\pm}(\omega_V, T) \quad [1]$$

where  $\omega_L$  is the frequency of the incident light,  $\rho_i$  the number density of the gas,  $\sigma_1(\omega_V)$  the Raman cross

section for the vibrational transition of energy  $\omega_V$  of molecules of type identified by the subscript  $i$ ,  $I_L$  is the incident light intensity,  $K$  is a proportionality constant dependent upon measurement system geometry and response, and  $G_{\pm}(\omega_V, T)$  is a statistical factor described below. Although the scattered light is shifted both down (Stokes scattering) and up (anti-Stokes scattering) in energy, we have used only Stokes scattering for concentration measurements, and anti-Stokes scattering will not be considered further here. For Stokes scattering, the minus sign is appropriate in the factor  $(\omega_L \pm \omega_V)^4$  and  $G_{-}$  is

$$G_{-}(\omega_V, T) = 1 + \frac{1}{e^{\hbar\omega_V/kT} - 1} \quad [2]$$

where  $\hbar$  is Planck's constant,  $k$  Boltzmann's constant, and  $T$  is temperature.

Several qualitative statements can be made about Raman scattering based on these equations. Raman cross sections are very small, so in order to produce an easily detectable signal intensity,  $I$ , it is desirable to excite a Raman spectrum with the most intense light source possible, a laser. For the same reason the factor  $(\omega_L \pm \omega_V)^4$  in Eq. [1] dictates the use of the highest frequency laser possible. (In general,  $\omega_L \gg \omega_V$ .) More precisely, the factor  $I_L (\omega_L \pm \omega_V)^4$  should be maximized, since there is a trade-off between  $I_L$  and  $\omega_L$  in the choice of a suitable laser. An argon ion laser operating at wavelength of 4880Å (a deep blue light) seems to be the best available choice at this time.

The Raman scattered light is scattered in all directions relative to the exciting laser beam, with only a slow, smooth dependence on relative direction. The optical detection system is located on a line normal to the laser beam, so it is possible to define a small, easily located volume for measurement. This feature makes it possible to make gradient measurements on a fine spatial scale. It also enables measurements to be made in the hot part of a reactor, without being affected by temperatures or concentrations near the walls.

The Raman cross section is generally independent of exciting wavelength. The exception to this is when either the incident or scattered photons are in resonance with (equal in energy to) one of the allowed electronic transitions of the molecule under study. This is called resonance Raman scattering or resonance fluorescence scattering. In this case the cross section can be enhanced by five or six orders of magnitude with a resulting rise in sensitivity of the measurement. Resonance light scattering is not important for most gases of interest, since the allowed transitions lie above the range of energies covered by usefully powerful lasers. However, resonance fluorescence has been observed in the Si-Cl system (13) and is due to a high temperature Si-Cl compound, probably  $\text{SiCl}_2$ . In the present work we have observed a similar signal which is associated with the presence of a trace impurity in the  $\text{SiH}_4$ . This will be discussed below.

The Raman cross section for most molecules is very small and does not vary by more than an order of magnitude for most common gases. Table I shows the absolute cross section for  $\text{N}_2$  and the relative cross section and scattered energy shift for the most useful vibrational transitions of some common gases. Raman scattering is roughly equally sensitive for most common gases. In the present system, described below, the detection sensitivity for gases at room temperature at 1 atm total pressure is about 10-100 ppm. Since spectral peaks are  $< 50 \text{ cm}^{-1}$  wide, it is easy to see from Table I that at least several species can be detected simultaneously.

In order to obtain chemical composition data in a reacting system with a temperature gradient, we have reduced the raw data in the following manner. The number density,  $\rho$ , of a molecular reactant or product species is obtained directly from the Raman spectrum using Eq. [1]. In a system with a temperature gradient,

Table I. The Raman scattering cross sections of various gases relative to that of N<sub>2</sub>. The incident light of 5145Å was vertically polarized. The Raman scattered light was measured at 90° in the horizontal plane, and was not analyzed for its polarization (15).\*

Gas	$\Delta\nu$ (cm <sup>-1</sup> )	$\sigma_{\text{gas}}/\sigma_{\text{N}_2}$
O <sub>2</sub>	1103	4.0
CH <sub>4</sub>	2914	8.0
	3020	0.79
C <sub>2</sub> H <sub>2</sub>	867	2.4
	2890	5.8
NO	1877	0.55
N <sub>2</sub> O	1287	2.7
	2223	0.53
H <sub>2</sub>	4160	2.2
O <sub>2</sub>	1555	1.2
CO	2143	0.91
CO <sub>2</sub>	1388	1.5
CO <sub>2</sub>	1286	1.0
SO <sub>2</sub>	1151	5.5
H <sub>2</sub> S	2611	6.6

\* Differential Raman cross section of N<sub>2</sub> ( $d\sigma/d\Omega$ ) =  $(4.4 \pm 1.7) \times 10^{-31}$  cm<sup>2</sup>/sr (15).

the density will change as a function of temperature variation according to the ideal gas law even in the absence of chemical reactions. Therefore, in a non-isothermal system it is useful to obtain a measure of gas composition or relative concentration, such as mole fraction or partial pressure, which is independent of temperature or ideal gas law effects for use in mass transport or kinetic calculations. The composition of a gas mixture is obtained by dividing the number densities of its constituent gases by the density of a constituent whose relative concentration in the mixture does not change, but whose number density is governed by the ideal gas law.

The mole fraction,  $X_A$ , of species A in a gas mixture containing a component B whose relative concentration in the mixture does not change can be approximated, in the limit  $X_A \ll X_B$ , by

$$X_A(T) = G' \frac{I_A(T) I_B(T_0)}{I_B(T) I_A(T_0)} X_A(T_0),$$

$$G' = \frac{G_-(\omega_{VB}, T) G_-(\omega_{VA}, T_0)}{G_-(\omega_{VA}, T) G_-(\omega_{VB}, T_0)} \quad [3]$$

where  $I_A$  and  $I_B$  are the measured Raman scattering intensities of species A and B, and must be measured at the desired point in space both at temperature  $T$  and at some convenient reference temperature  $T_0$ .  $T_0$  is usually room temperature, but may be any temperature below which the gases do not react and change composition from the known input value  $X_A(T_0)$ . The factor  $G'$  is easily calculated knowing the measured  $\omega_{VA}$ ,  $\omega_{VB}$ ,  $T$ , and  $T_0$  values. For many cases of relatively low temperature and large  $\omega_{V}$ , the term  $e^{h\nu/kT} \gg 1$ , and the functions  $G_-$  and hence  $G'$  may be approximately 1. By using Eq. [3] to obtain the relative concentration, errors due to variations in window transmission are also eliminated.

### Experimental Apparatus and Procedures

*Optical equipment and measuring technique.*—A schematic diagram of our experimental apparatus is shown in Fig. 1. The laser is a Spectra Physics Model 170 argon ion laser operating at a peak intensity, feedback stabilized, of 9W with photon energy of 20,492 cm<sup>-1</sup> (wavelength 4880Å). This is chopped at a frequency of 108 Hz. The scattered light is collected with a  $f/1.5$ , 135 mm focal length Soligor lens located about 20 cm from the beam with its axis normal to the beam. The lens images a segment of the laser beam into the entrance slit of a Spex Model 1301  $f/7$  double monochromator with 1200 groove/mm gratings blazed at 5000Å. The monochromator is operated with slits 300–500  $\mu$ m wide, corresponding to an instrumental resolution of 11–21 cm<sup>-1</sup>.

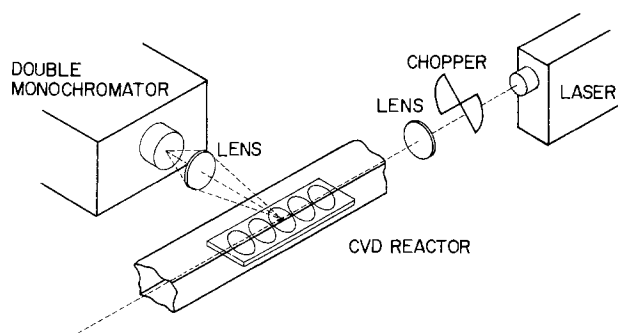


Fig. 1. Schematic of Raman scattering and chemical vapor deposition apparatus.

Light from the monochromator is focused on the cathode of a RCA C31034 photomultiplier tube (PMT) operated at  $-20^\circ\text{C}$ . The signal from the PMT is analyzed by photon counting techniques with a SSR Model 1110 digital synchronous computer. This instrument also functions as a digital lock-in amplifier operating synchronously with the laser chopper, accumulating signal plus noise during the time the laser is on and noise (i.e., black-body radiation, PMT dark count, stray room light, etc.) during the "off" periods; the difference is computed by the instrument and recorded on a strip chart recorder.

To measure the concentrations of SiH<sub>4</sub> and NH<sub>3</sub>, the Raman intensity,  $I$ , was measured by scanning through the principal scattering peak and integrating the signal to get the peak area. From this area was subtracted a background which was obtained from an identical scan, where the gas in question was not flowing in the reactor. Only at the lower concentrations was the background a significant fraction of the total signal. Table II shows the principal peak position, typical scan ranges, and counting times used for a slit width of 500  $\mu$ . The reference gas used in the concentration measurement and designated as B in Eq. [3] was N<sub>2</sub>; the amount of N<sub>2</sub> produced by decomposition of NH<sub>3</sub> was assumed negligible compared with the N<sub>2</sub> in the carrier gas.

*CVD reactor and gas flow conditions.*—The reactor, shown in Fig. 2, is a horizontal open tube of cross section  $3.5 \times 3.5$  cm with a flat, rf-heated, graphite susceptor  $1.1 \times 3.4 \times 17.0$  cm in the bottom of the tube serving as the heat source. The system is open in the sense that a dilute mixture of SiH<sub>4</sub> and/or NH<sub>3</sub> in a carrier gas of N<sub>2</sub> or a H<sub>2</sub>-N<sub>2</sub> mixture is constantly flowing through the tube. The total flow of gas is 3.9 liter/min through the tube which has 8.4 cm<sup>2</sup> of unobstructed cross section, resulting in a room temperature average gas velocity of 7.7 cm/sec. Flow visualization experiments using TiO<sub>2</sub> "smoke" in the tube showed that H<sub>2</sub> gives a very smooth laminar flow, while N<sub>2</sub> results in a rather unstable flow due to thermal convection. Because we wanted a relatively large concentration of both H<sub>2</sub> (to promote laminar flow) and N<sub>2</sub> (to use as reference gas) we chose a carrier gas mixture of 50% H<sub>2</sub>-50% N<sub>2</sub> in all but one experiment. This mixture gives a relatively smooth laminar flow with only a slight flutter in the stream lines appearing over the last half of the susceptor.

The NH<sub>3</sub> and SiH<sub>4</sub> were obtained from Matheson. The SiH<sub>4</sub> was a 5% mixture in N<sub>2</sub> (Fig. 5, data only), or a 10% mixture in H<sub>2</sub> with a trace impurity of SiCl<sub>4</sub> as

Table II. Experimental parameters for composition measurements

Species	Raman shift (cm <sup>-1</sup> )	Scan range (cm <sup>-1</sup> )	Scan time (min)
N <sub>2</sub>	2327	40	6.67
NH <sub>3</sub>	3332	60	10
SiH <sub>4</sub>	2187	60	10

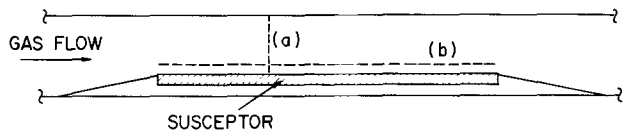


Fig. 2. Schematic of reactor. Data shown in Fig. 3-6 were taken at positions along dashed lines (a) 5.3 cm from front of susceptor, and (b) 0.25 cm above susceptor. Ramps are located at the leading and trailing ends of the susceptor to encourage the smoothest possible flow.

measured by Raman scattering. The  $N_2$  was boil-off from liquid  $N_2$ .

The susceptor was graphite and became coated with polycrystalline Si or silicon nitride during the experiments. The walls of the reactor tended to become coated with deposit after running several hours, depending on the input concentration of  $SiH_4$ , the gas composition, and the flow rate. Under some experimental conditions where  $SiH_4$  was present, it was found that the laser beam was made visible in a region over the susceptor by highly scattering particles, presumably consisting of polycrystalline Si or silicon-nitrogen compounds.

The concentration gradients in Fig. 3-6 were measured along the dashed lines as indicated in Fig. 2. The temperatures referred to in the figures and in the text were obtained with an optical pyrometer calibrated at the melting point of Ge and always refer to the temperature of the susceptor surface at the position (a), (in Fig. 2, 5.3 cm from the front of the susceptor). Gas temperature gradients have been measured by the Raman technique for this same reactor and have been published elsewhere (14).

### Results and Discussion

**Ammonia decomposition.**—Figure 3 shows the measured  $NH_3$  mole fraction as a function of vertical position [dashed line (a) in Fig. 2] above the susceptor. The input gas was 46%  $H_2$ , 46%  $N_2$ , and 8%  $NH_3$  at a susceptor temperature of 750° and 950°C. The relative concentration of  $N_2$  was assumed constant for the calculations in Fig. 3. The decrease in  $NH_3$  mole fraction as the susceptor is approached at both temperatures is presumed due to the decomposition of  $NH_3$  according to



The logarithms of the equilibrium constants for Eq. [4] at 1200° and 1000°K are 3.233 and 3.716, respectively, and so at thermal equilibrium in the temperature range studied (17) essentially complete decomposition of  $NH_3$  is expected. In fact, only slight decomposition of  $NH_3$  at 750°C is observed, indicating that the reaction is kinetically limited. The 950°C data show, however, complete decomposition at the susceptor surface. Without more information it cannot be determined whether the decomposition takes place in the gas phase or at the surface or both. Thus, the shape of this curve could be

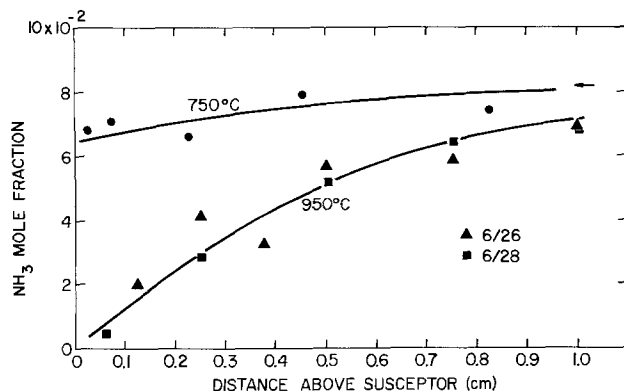


Fig. 3.  $NH_3$  concentration vs. distance above susceptor (Fig. 2, line a) at 750° and 950°C.

determined by both mass transport and kinetic factors. Unlike the 750°C case, the curve at 950°C does not extrapolate to the indicated input concentration of 8.2% mole fraction  $NH_3$ . Although the difference is within the observed scatter of the data, it is expected that there will be some depletion of  $NH_3$  far above the susceptor along its length.

Figure 4 shows the concentration of ammonia as a function of distance along the susceptor [dashed line (b) in Fig. 2]. The susceptor surface was at 950°C in the center, but it exhibited a considerable decrease in temperature at each end, particularly the front or gas inlet end. The decrease in concentration of  $NH_3$  as a function of distance indicates a depletion of reactant as would be expected from the comments on Fig. 3 above. It should be mentioned, however, that the Raman measurements give some evidence, not shown here in detail, that reactant concentrations and temperatures are effected by subtle changes in reactor geometry, wall cooling rates, or possibly even changing catalytic properties of the susceptor surface. For example, the  $NH_3$  concentration at the intersection point (5.3 cm along and 0.25 cm above the susceptor) of the two curves, Fig. 3 and Fig. 4, are not the same. This may have been due to the fact that different reactors and susceptors were used in these two experiments.

**Silane decomposition.**—Silane was observed to decompose rapidly above 500°C in a carrier gas of pure  $N_2$  as indicated by polycrystalline deposits of Si on the susceptor and quartz tube walls. Figure 5 shows the apparent mole fraction  $SiH_4$ , calculated from Eq. [3], as a function of vertical position above the susceptor at about 650°C. However, the apparent increase in  $SiH_4$  mole fraction, as the susceptor is approached, occurred at the same time as a qualitative change in the spectrum indicating the presence of a new gas species. At first we thought the new species to be disilane because of the similarity of the new spectrum with that of disilane in the 2140-2220  $cm^{-1}$  region. Subsequent measurements on the Si-Cl and Si-Cl-H systems, however, revealed a Si-Cl compound (probably  $SiCl_2$ ) which has a spectrum very similar to the presently observed species throughout the spectral range studied (13).  $SiCl_2$  is observed to fluoresce rather than Raman scat-

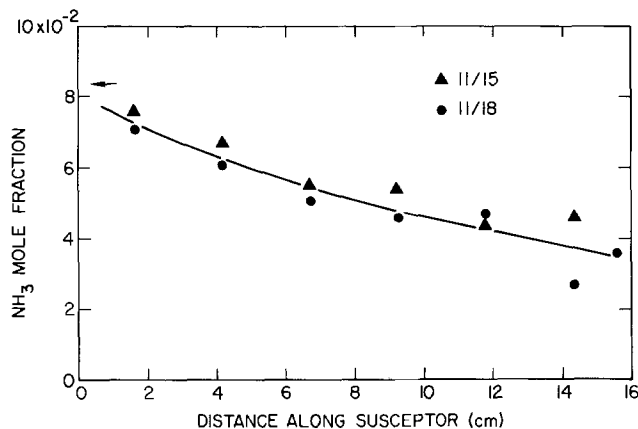


Fig. 4.  $NH_3$  concentration vs. distance along susceptor (Fig. 2, line b).

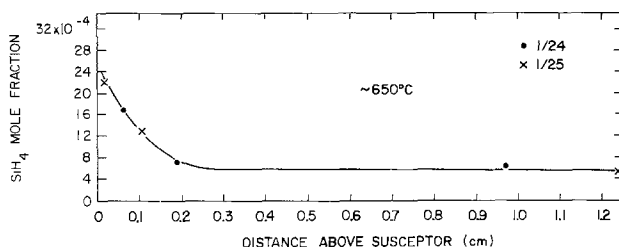


Fig. 5. Apparent  $SiH_4$  concentration vs. distance above susceptor (Fig. 2, line a) in a  $N_2$  ambient at ~650°C

ter, and therefore can be seen with at least a factor of  $10^3$  greater sensitivity than a Raman scattering molecule. Although there was no intentional introduction of Cl into the present system, there is an impurity of  $\text{SiCl}_4$  as well as possibly other Si-Cl-H compounds in commercial  $\text{SiH}_4$ . Thus,  $\text{SiCl}_2$  is apparently produced from the  $\text{SiCl}_4$  impurity in the hot gas and, because it fluoresces, it dominates the spectrum and makes concentration measurements of  $\text{SiH}_4$  impossible in its presence. The apparent increase in signal as the susceptor is approached occurs because of the strong fluorescence.

**Reaction of  $\text{SiH}_4 + \text{NH}_3$  in  $\text{H}_2\text{-N}_2$ .**—Figure 6 shows the mole fraction of  $\text{SiH}_4$  in a 46%  $\text{H}_2$ , 46%  $\text{N}_2$ , 8%  $\text{NH}_3$  mixture as a function of position above the susceptor for three different temperatures. This is a gas mixture which is commonly used to grow silicon nitride films. At both 750° and 850°C the observed mole fraction of  $\text{SiH}_4$  corresponds to the input concentration 0.065%, and does not change right up to the susceptor. Thus  $\text{H}_2$ , and we suspect also  $\text{NH}_3$ , suppresses formation of  $\text{SiCl}_2$  as well as the decomposition of  $\text{SiH}_4$  at least up to 850°C.

At 950°C the "hump" in the mole fraction  $\text{SiH}_4$  curve from 0.1 to 0.6 cm again correlates with the appearance of the  $\text{SiCl}_2$  fluorescence spectrum. The data curve decreases to zero at the susceptor surface, indicating that the  $\text{SiCl}_2$  is produced in the gas phase by a homogeneous gas reaction. Apparently both the  $\text{SiCl}_2$  as well as the  $\text{SiH}_4$  concentration is reduced to very small values as the susceptor is closely approached. The slightly higher-than-input level of the signal above 0.6 cm is presumably caused by the diffusion of  $\text{SiCl}_2$  out into the bulk gas.

### Conclusions

For the first time data is presented on chemical concentration gradients in a CVD reactor. These results, along with previously reported Raman gas temperature measurements (14), demonstrate the value of Raman spectroscopy for the detailed characterization of CVD

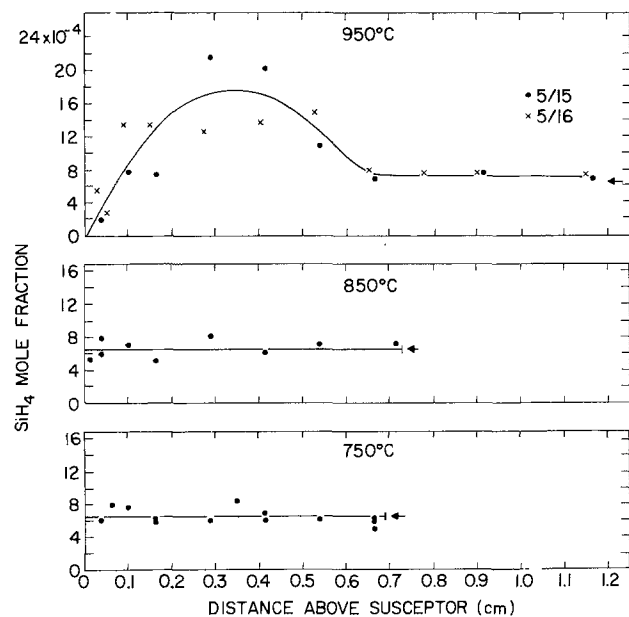


Fig. 6. Apparent  $\text{SiH}_4$  concentration vs. distance above susceptor for 750°, 850°, and 950°C in a 46%  $\text{N}_2$ -46%  $\text{H}_2$ -8%  $\text{NH}_3$  ambient (Fig. 2, line a).

systems. The results on  $\text{SiH}_4$  and  $\text{NH}_3$  decomposition in various ambients are preliminary, but they do show that it is possible to observe a chemical-kinetic limited reaction ( $\text{NH}_3$  decomposition), and detect a reaction intermediate (a Si-Cl compound formed by the reduction of the trace contaminant  $\text{SiCl}_4$ ). Clearly the possibility of sensing a fluorescing molecule, in this case the Si-Cl compound which is probably  $\text{SiCl}_2$ , makes the detection of the other major gas species more difficult. At the same time, the great sensitivity for detecting a fluorescing species will make this technique potentially very powerful for probing systems where the fluorescing species is the main species of interest.

The technique is limited whenever reactions deposit opaque films on the viewing window. Data acquisition is relatively slow, requiring 5-20 min per point, and measurements above 1000°-1100°C will require either longer counting times, changes in reactor design, or improvement in the optical equipment. Because the system must be at steady state for data acquisition, a stable laminar flow is necessary.

In conclusion it appears that Raman scattering offers considerable potential for the study of high temperature CVD and other chemical reactions.

### Acknowledgments

We are indebted to A. B. Fowler for valuable discussions leading up to this research, to A. Reisman for his support of this work, to R. Ghez, E. Irene, and A. Reisman for critical reading of the manuscript, and to R. R. Hebard for capable technical assistance.

Manuscript submitted Jan. 13, 1975; revised manuscript received Oct. 20, 1975.

Any discussion of this paper will appear in a Discussion Section to be published in the December 1976 JOURNAL. All discussions for the December 1976 Discussion Section should be submitted by Aug. 1, 1976.

Publication costs of this article were partially assisted by the IBM Corporation.

### REFERENCES

1. V. S. Ban, *This Journal*, **118**, 1473 (1971); Paper 155 presented at The Electrochemical Society Meeting, San Francisco, California, May 12-17, 1974; *This Journal*, **119**, 761 (1972).
2. R. J. Clark and D. M. Rippon, *J. Molecular Spectroscopy*, **44**, 479 (1972).
3. H. W. Kattenberg and A. Oskam, *ibid.*, **49**, 52 (1974).
4. I. R. Beattie and G. A. Ozin, *J. Chem. Soc.*, (A), 1691 (1969).
5. I. R. Beattie, G. A. Ozin, and R. O. Perry, *ibid.*, 2071 (1970).
6. G. A. Ozin, *ibid.*, 2307 (1970).
7. J. R. Beattie and J. R. Harder, *ibid.*, 2655 (1969).
8. A. M. Karger, R. P. English, and R. J. D. Smith, *Appl. Opt.*, **12**, 2083 (1973).
9. E. R. Schildkraut, American Laboratory, p. 23 (December 1972).
10. G. F. Widhoff and S. Lederman, *AIAA J.*, **9**, 309 (1971).
11. S. H. Melfi, J. D. Lawrence, Jr., and M. P. McCormick, *Appl. Phys. Letters*, **15**, 295 (1969).
12. S. Lederman, *Appl. Opt.*, **11**, 2088 (1972).
13. T. O. Sedgwick, J. E. Smith, Jr., R. Ghez, and M. E. Cowher, *J. Cryst. Growth*, To be published.
14. J. E. Smith, Jr. and T. O. Sedgwick, *Letters Heat Mass Transfer*, **2**, 329 (1975).
15. R. A. Smith, *Proc. Roy. Soc. (London) Ser. A*, **323**, 305 (1971).
16. D. G. Fouche and R. K. Chang, *Appl. Phys. Letters*, **18**, 579 (1971); *ibid.*, **20**, 256 (1972).
17. JANAF Thermochemical Tables Published by U.S. Department of Commerce (1971).

# Electrolytic Etching of Boron Phosphide

T. L. Chu,\* M. Gill,† and Shirley S. Chu

Institute of Technology, Southern Methodist University, Dallas, Texas 75275

## ABSTRACT

The electrolytic etching of boron phosphide in various electrolytes was investigated. Conditions to polish p-type boron phosphide were determined, but an insoluble film tended to form on the surface of n-type material. For electrode potentials near and above 1V, the removal of p-type material proceeded at a rate more than 100 times faster than the removal rate of n-type material. This difference in the etch rates allows selective removal of material, and mesa-type p-n homojunction and boron phosphide-silicon carbide heterojunction structures were fabricated.

Etching and polishing techniques are important processes for the study of semiconductors and for semiconductor device fabrication. For elemental semiconductors and some of the compound semiconductors, convenient chemical etchants are available for surface preparation and for certain types of selective etching. However, there are materials which are either inert to ordinary chemical etchants or are attacked very irregularly. In the case of boron phosphide, the only known etchants are fused alkalis at 400°-500°C and hydrogen chloride near 1100°C. The former etchant attacks boron phosphide very nonuniformly, and with the latter etchant, the decomposition of material at 1100°C is a problem. As a consequence, electrolytic etching may be the most useful etching technique for boron phosphide.

The purpose of this paper is to describe the experimental results obtained from an investigation of electrolytic etching of boron phosphide. Both p-type and n-type materials were studied, although more extensive data were obtained from p-type boron phosphide. The difference in the etching behavior of (111) and  $(\bar{1}\bar{1}\bar{1})$  faces was investigated. Also, electrolytic etching was used as a selective etching process in the fabrication of junction devices.

## Experimental

Electrolytic etching studies were carried out with both n-type and p-type boron phosphide platelets, which were grown by recrystallization from a nickel phosphide solution (1). Boron phosphide crystals up to  $7 \times 4 \times 3$  mm have been obtained recently (2) by the accelerated container rotation technique (3,4). The main faces of the platelets have a (111) orientation; usually one face is smooth and the other face is rough. The two faces could also be distinguished by chemical etching in a 3:1 molten mixture of sodium hydroxide and sodium peroxide at 400°-500°C. Dislocation etch pits were observed on the smooth face and not on the other. It is well established that the chemical etching of other III-V compound semiconductors produces etch pits on the Group III face and not on the Group V face (5). If the etching behavior of boron phosphide is similar to that of other III-V compound semiconductors, then the face which developed dislocation etch pits on the boron phosphide crystals is the boron, or the (111), face. The room temperature carrier concentration of the solution-grown boron phosphide crystals, determined by measurements on Schottky barrier diodes, was on the order of  $10^{18} \text{ cm}^{-2}$  or above (6).

Prior to electrolytic etching, rough faces of the boron phosphide platelets were polished with  $0.3 \mu\text{m}$  alumina abrasive; the as-grown smooth faces were etched without mechanical polishing. Because of the high carrier

concentration in solution-grown crystals, ohmic contact to the back side of the boron phosphide crystals was readily made by electroless nickel plating followed by an annealing in hydrogen or argon at 800°-850°C for 1 hr. For the etching process, Apiezon W wax was used as a mask so that only the desired region of the crystal surface was exposed to the electrolyte. Silicon monoxide and silicon dioxide were also used for masking purposes and were found to be more reliable than Apiezon W wax for controlling small area geometries in the fabrication of mesa structures.

A schematic of the electrolytic cell used for the etching and polishing of boron phosphide is shown in Fig. 1. The current density-potential relationships were determined, and the crystal-electrolyte potential difference was measured relative to a calomel reference electrode. Measurements were made both in the dark and with illumination. The solution was continuously agitated by nitrogen bubbled into the electrolyte near the anode. A uniform removal of material without undercutting of etching masks was obtained with the boron phosphide platelets near the axis of a cylindrical molybdenum cathode, as shown in Fig. 1. A simple parallel plane electrode configuration was used for some of the basic measurements. The electrolytes investigated were aqueous solutions of common alkalis and acids, and a few chemical etchants previously used for other III-V semiconductors. With these techniques, mesa-type heteroepitaxial boron phosphide-silicon carbide junction and boron phosphide p-n junction structures were isolated.

## Results

Typical current density-potential relationships and rest potential values for p-type and n-type boron phosphide crystals in a 10% sodium hydroxide solution at room temperature in the dark are shown in Fig. 2.

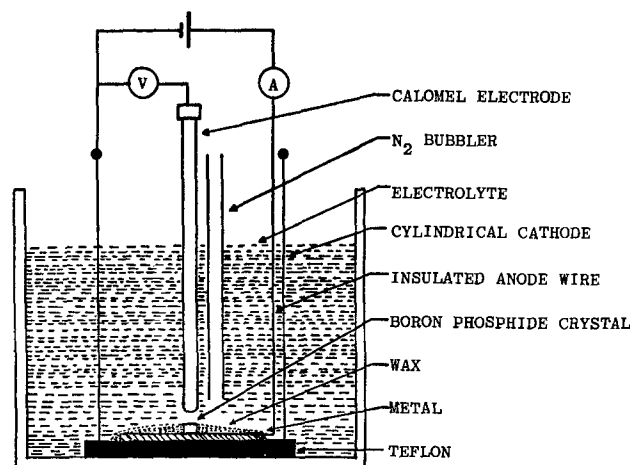


Fig. 1. Schematic of the electrolytic cell used for measurements and etching.

\* Electrochemical Society Active Member.

† Electrochemical Society Student Member.

Key words: boron phosphide, electrolytic etching, electrolytic polishing, selective etching.

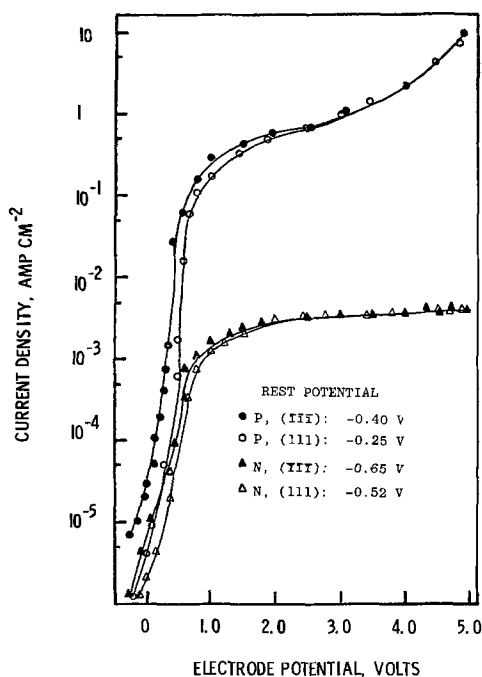


Fig. 2. Current density vs. electrode potential for (111) and  $(\bar{1}\bar{1}\bar{1})$  faces of n-type and p-type boron phosphide in a 10% NaOH solution in the dark.

As expected, current saturation was observed in all of the experiments with n-type boron phosphide crystals. The p-type material was readily dissolved, and it drew much larger currents than n-type material. At low anode potentials, the  $(\bar{1}\bar{1}\bar{1})$  face of both n-type and p-type boron phosphide drew larger current densities at a particular electrode potential than did the (111) face. At anode potentials higher than about 1V, the difference between the currents drawn by the (111) faces and the  $(\bar{1}\bar{1}\bar{1})$  faces is very small.

The rest potentials of n-type and p-type boron phosphide were measured in a number of electrolytes in addition to sodium hydroxide, and the rest potential for n-type crystals was always more negative than the rest potential for p-type crystals. A similar relationship was reported for gallium phosphide rest potentials (7). For both n-type and p-type boron phosphide, the rest potential was more positive for the (111) face. This polarity effect has also been observed for a number of other III-V compound semiconductors, and the Group III element face was reported to have a more positive rest potential (5, 7, 8). This observation agrees, therefore, with the tentative assignment of the smooth (111) face of the crystals to the boron face.

The following observations were made specifically from the etching of p-type boron phosphide. Twin lines and other gross crystallographic defects were revealed with current densities of 0.01 A/cm<sup>2</sup> or lower. For current densities between 0.01 and about 0.2 A/cm<sup>2</sup>, etch pits formed on the faces. At larger current densities, above about 0.5 A/cm<sup>2</sup>, the (111) and  $(\bar{1}\bar{1}\bar{1})$  faces had different etching characteristics. On the (111) face, a film tended to form; this film was, however, easily removed by rinsing with water. The texture of the etched (111) face was rough as shown in Fig. 3a. On the  $(\bar{1}\bar{1}\bar{1})$  face, however, there was no evidence of film formation, and a smooth, mirrorlike surface finish shown in Fig. 3b was produced. These observations are very similar to the results reported for gallium phosphide (7); at high current densities, the gallium face developed a rough texture and the phosphorus face became smooth. A few experiments were carried out with other electrolytes, and the etching characteristics of p-type boron phosphide in potassium hydroxide solutions and common acids were

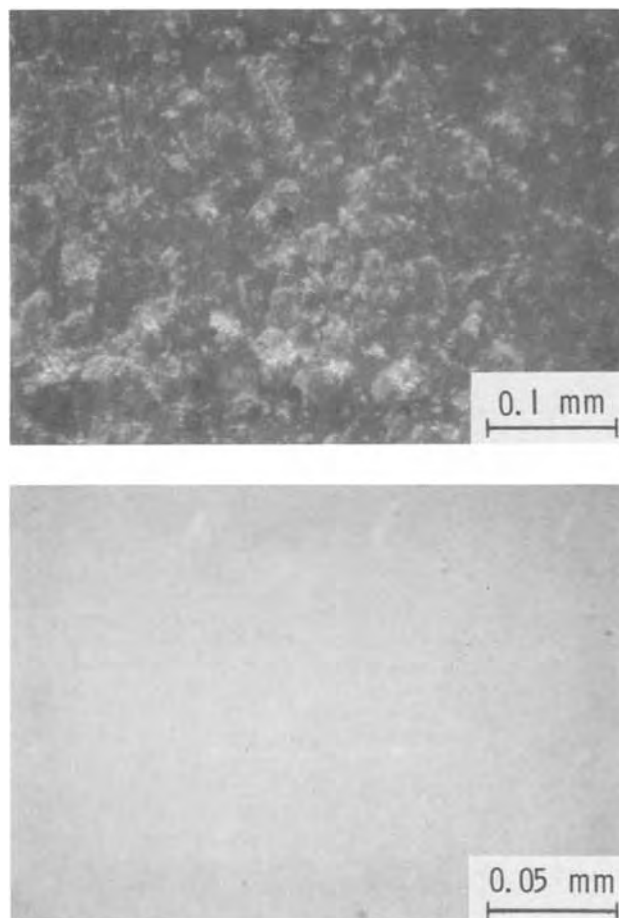


Fig. 3. Electrolytically etched surfaces of p-type boron phosphide with a current density of 0.5 A/cm<sup>2</sup>: (a, top), (111) face; (b, bottom),  $(\bar{1}\bar{1}\bar{1})$  face.

found to be similar to the characteristics obtained with the use of sodium hydroxide solutions.

In contrast to the etching of p-type boron phosphide, the etching of n-type boron phosphide was complicated by the formation of surface films at current densities higher than about 10<sup>-3</sup> A/cm<sup>2</sup>. At this current density, a film was observed with a 15 min etching period; with higher current densities, the film grew faster. The film could not be completely removed from the surface of the crystal even with ultrasonic agitation during etching, and the film was not soluble in hot alkali mixtures. X-ray measurements indicated that the films were predominantly boron phosphate (BPO<sub>4</sub>).

With current densities above 1 A/cm<sup>2</sup> through n-type boron phosphide, a porous, brittle, fiberlike film formed on the surface. Reflection electron diffraction examination showed that these films were monocrystalline boron phosphide of (111) orientation. It was concluded, therefore, that anodic disintegration of n-type boron phosphide at high current densities occurred preferentially in  $\langle 111 \rangle$  directions, and a surface layer which is a skeleton of the original crystal remained. Similar results were obtained from an etching study of gallium arsenide (9).

Various approaches were investigated to determine the conditions for the electrolytic polishing of n-type boron phosphide. A variety of electrolytes in addition to sodium hydroxide were used without success; an insoluble film formed in all cases. The effect of illumination on the etching of n-type boron phosphide was also investigated. A 650W incandescent lamp with a color temperature of 3400°K was used as the light source, so that a significant portion of the lamp output had an energy greater than the bandgap of boron

phosphide. A negative shift of about 0.2V or more of the rest potentials was observed with illumination, but very little difference in the cell currents was found. Consequently, the anodic dissolution behavior was not significantly affected by the illumination. N-type boron phosphide was successfully etched without film formation only under one condition: the n-type material exposed to the electrolyte was one side of a shallow, forward biased p-n junction. This observation supports the well-known fact that a supply of holes is required for electrolytic etching (10,11).

#### Selective Etching

It can be seen from Fig. 2 that the current density at, for example, 3V is about 300 times higher for p-type boron phosphide than for n-type material. This current density ratio corresponds approximately to the etch rate ratio between p-type and n-type boron phosphide, suggesting the possibility of selective removal of p-type material from boron phosphide p-n structures. The preferential etching of p-type material was initially investigated with a number of solution-grown boron phosphide crystals with built-in p-n junctions on a crystal face. Selective removal of p-type boron phosphide was obtained with current densities between 0.1 and 10 A/cm<sup>2</sup>. To prevent the formation of a surface film on the n-type regions, either very low current densities with a long etching time or very high currents for a very short time were used. Figure 4 shows one solution-grown crystal which was selectively etched; the p-type region developed a mirror-

like finish, and no removal of n-type material was observed. With low current densities and short etching times, electrolytic etching was also used to delineate thin epitaxially grown p-n junctions in boron phosphide.

Since electrolytic etching is selective, it can be used to produce mesa junction structures in boron phosphide. Mesa diodes were formed with both homoepitaxially and heteroepitaxially grown junctions. Both n-type and p-type layers of boron phosphide were deposited on solution-grown boron phosphide crystals and on hexagonal silicon carbide platelets by the thermal reduction of a boron tribromide-phosphorus trichloride mixture (12). To isolate the mesas, either silicon dioxide or silicon monoxide was used to define the mesa pattern, and the exposed boron phosphide was electrolytically removed. In the preparation of the boron phosphide-silicon carbide heterojunctions, a sharp decrease in the current indicated the complete removal of the boron phosphide layer exposed to the electrolyte. At that stage, the electrolyte was replaced by a 1N solution of hydrofluoric acid, and a slight anodic etching of the silicon carbide was carried out. This latter step improved the characteristics of the mesa junctions. The removal of n-type boron phosphide on silicon carbide occasionally required mechanical means to remove a surface film near the edge of the mesa. Figure 5 shows photomicrographs of two mesa junctions fabricated by anodic dissolution of boron phosphide. Figure 5a shows a homojunction made by selective removal of a portion of an n-type

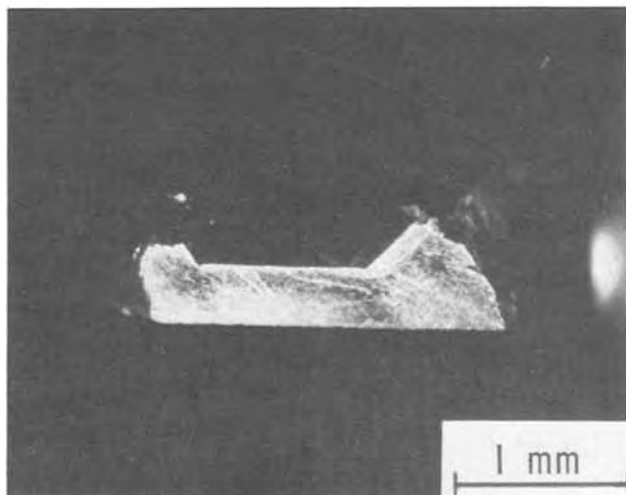
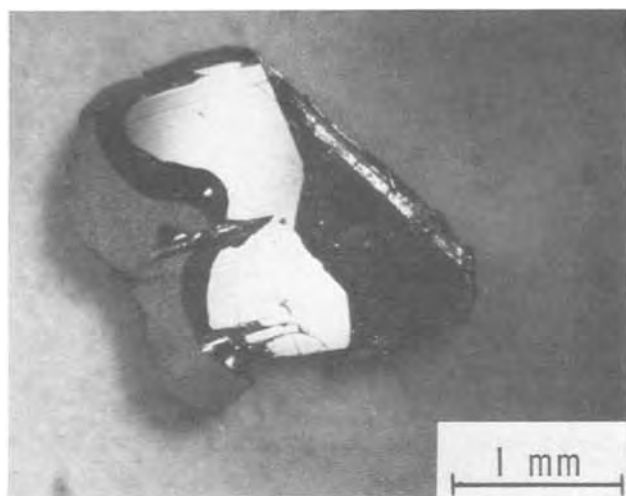


Fig. 4. Photomicrographs of an electrolytically etched boron phosphide crystal which has both n-type and p-type regions. Etching was done at 10 A/cm<sup>2</sup> for 10 sec: (a, top), top view; (b, bottom), cross-sectional view.

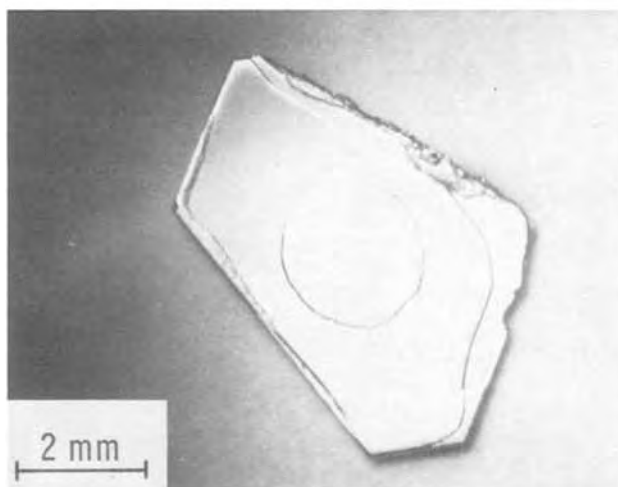
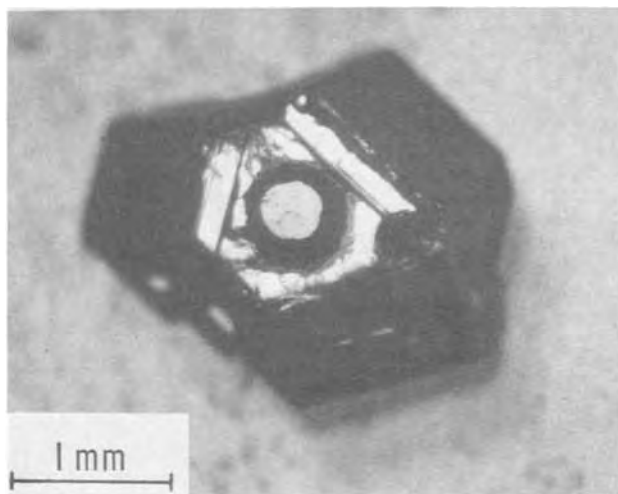


Fig. 5. Two mesa structures fabricated by electrolytic etching: (a, top) boron phosphide p-n homojunction; (b, bottom) boron phosphide-silicon carbide heterojunction.



epitaxial layer on a p-type substrate, and Fig. 5b shows a p-type boron phosphide mesa on n-type silicon carbide. These devices have rectifying characteristics, and easily visible, red, p-n junction electroluminescence was observed in some of the homojunction and heterojunction structures (13).

### Summary

Electrolytic etching of boron phosphide was investigated for device applications, since there is no suitable chemical etchant for this material. A technique was developed to etch and polish p-type boron phosphide. In contrast, an insoluble film tended to form on n-type boron phosphide, and material removal was very slow. Due to a large differential etch rate ratio between p-type and n-type material, boron phosphide p-n junction interfaces were delineated by electrolytic etching. Electrolytic etching was also applied to the fabrication of mesa-type boron phosphide p-n junctions and boron phosphide-silicon carbide heterojunction structures. Because of the inert nature of boron phosphide, electrolytic etching is the most suitable means available to remove p-type material and to isolate mesa-type junctions.

### Acknowledgment

The authors wish to thank Dr. R. K. Smeltzer for discussions and critical reading of the manuscript. This work was supported by the Langley Research Center of the National Aeronautics and Space Administration under Grant NGL-44-007-042.

Manuscript submitted July 11, 1975; revised manuscript received Oct. 1, 1975.

Any discussion of this paper will appear in a Discussion Section to be published in the December 1976 JOURNAL. All discussions for the December 1976 Discussion Section should be submitted by Aug. 1, 1976.

### REFERENCES

1. T. L. Chu, J. M. Jackson, and R. K. Smeltzer, *This Journal*, **120**, 802 (1973).
2. T. L. Chu, M. Gill, and R. K. Smeltzer, *J. Crystal Growth*, In press.
3. H. J. Scheel and E. O. Schulz-DuBois, *ibid.*, **8**, 304 (1971).
4. H. J. Scheel, *ibid.*, **13/14**, 560 (1972).
5. H. C. Gatos and M. C. Lavine, *This Journal*, **107**, 427 (1960).
6. H. B. Morris, M. S. Thesis, Southern Methodist University, Dallas, Texas (1973).
7. R. L. Meek and N. E. Schumaker, *This Journal*, **119**, 1148 (1972).
8. M. E. Straumanis, J. P. Krumme, and W. J. James, *ibid.*, **115**, 1050 (1968).
9. J. P. Krumme and M. E. Straumanis, *Trans. Met. Soc. AIME*, **239**, 395 (1967).
10. W. H. Brattain and C. G. B. Garrett, *Bell System Tech. J.*, **34**, 129 (1955).
11. H. Gerischer, in "Physical Chemistry," IXA, p. 523, H. Eyring, Editor, Academic Press, New York (1970).
12. T. L. Chu, J. M. Jackson, A. E. Hyslop, and S. C. Chu, *J. Appl. Phys.*, **42**, 420 (1971).
13. T. L. Chu and M. Gill, To be published.

## Fabrication and Thermal Stability of W-Si Ohmic Contacts

V. Kumar

Bell Laboratories, Murray Hill, New Jersey 07974

### ABSTRACT

W-Si ohmic contacts have been fabricated using rf-sputtered W and bulk-doped n- and p-type Si. The investigated doping range is  $\sim 5.5 \times 10^{18}$ – $\sim 1.2 \times 10^{20}/\text{cm}^3$  for B (p-type) and  $\sim 4.5 \times 10^{18}$ – $\sim 8 \times 10^{19}/\text{cm}^3$  for As (n-type); with corresponding contact resistance ranging as  $1.5 \times 10^{-4}$ – $5 \times 10^{-7}$  ohm- $\text{cm}^2$  and  $1.2 \times 10^{-5}$ – $8 \times 10^{-7}$  ohm- $\text{cm}^2$ , respectively. Steam-grown and deposited oxide ( $\text{SiO}_2$ ) were used as the mask to study the effect of impurity redistribution during steam oxidation on contact resistance. Chemical (100:1 buffered HF) and sputter etch cleaning were used to remove the native oxide from contact windows before W deposition. Metallurgical and electrical stability of these contacts was studied up to  $\sim 830^\circ\text{C}$ . The unannealed contacts (using steam oxide mask) are ohmic if the Si has  $>10^{19}/\text{cm}^3$  As but the minimum B needed is  $\sim 10^{20}/\text{cm}^3$ . This difference stems from two reasons: (i) B is lost from Si during steam oxidation whereas As concentrates in Si; (ii) the native oxide growing on p-Si seems to be electrically quite different from that on n-Si. Contacts improve with annealing up to  $\sim 800^\circ\text{C}$  (1 hr treatments), but if higher temperatures are used high resistance or "opens" may occur. Sputter etching is found to be more effective in cleaning the contact windows than the chemical cleaning.

Tungsten has been extensively studied for use as a refractory gate material for a new MOS-LSI technology (1). Some of the important reasons for selecting W as the first level metallization are (i) high melting temperature which is essential if the IC chip is to withstand the high temperature CVD (chemical vapor deposition) steps of intermediate insulator and/or the  $\text{Si}_3\text{N}_4$  encapsulation, (ii) good adhesion to both  $\text{SiO}_2$  and Si, (iii) the best (of all metals) matching of thermal expansion with Si, (iv) no low temperature melting eutectic with Si, (v) low electrical resistivity (only about 2.5 times that of Au in bulk), and (vi) its ability to act as a good mask during ion implantation for self-aligned structures.

Key words: ohmic contacts, metal-Si contacts, W metallization, dopant redistribution,  $\text{WSi}_2$  (tungsten disilicide).

It is therefore desirable to be able to form W-Si ohmic contacts while keeping the number of processing steps to a minimum. The beam lead technology utilizing a trilayer metallization, Ti-Pt (or Pd)-Au, uses PtSi at the contact sites to obtain ohmic contacts to both p- and n-type Si. Quite a number of workers (2-8) have experimentally investigated the PtSi-Si contacts and used the metal-semiconductor barrier contact as the theoretical model. For low resistance ohmic contacts this model requires a low and/or thin potential barrier. Although the barrier height is fixed for a given metal-Si pair, the width of the barrier (the depletion layer) can be progressively decreased by increasing the doping level of Si. W-Si Schottky barrier diodes have been fabricated in the past (16, 18) and the reported barrier height for W-(n)Si is intermediate between



Table I. Schottky barrier heights to Si at 300°K  
(data from forward I-V characteristics)

Material	Silicon type	$\phi_B$ (eV)	Reference
PtSi	n	0.85	(2)
PtSi	p	0.25	(2)
PtSi	n	0.84	(19)
Mo	n	0.59	(18)
Mo	n	0.55	(19)
W	n	0.67	(18)
WSi <sub>2</sub>	n	0.86	(17)
W	n	(0.59-0.68)*	(16)

\* WSi<sub>2</sub> formation at the interface was detected in samples with  $\phi_B$  greater than 0.65.

that for PtSi-(n)Si and PtSi-(p)Si as shown in Table I. Thus the extension of the barrier model suggests the feasibility of W-Si ohmic contacts without the use of an intermediate contact material like PtSi. Furthermore, the W-PtSi-Si system has been found to be not very stable at high temperatures (>750°C) (9).

This work was undertaken to evaluate the possibility of fabricating W-Si ohmic contacts and their metallurgical and electrical stability under various high temperature treatments including the encapsulation by CVD-Si<sub>3</sub>N<sub>4</sub>.

### Experimental

#### Sample preparation.—

(i) *Substrates.*—Bulk-doped, (As,  $4.5 \times 10^{18}$ - $1.2 \times 10^{20}$ /cm<sup>3</sup> and B,  $5.5 \times 10^{18}$ - $2 \times 10^{20}$ /cm<sup>3</sup>), (100) Si wafers were used for the investigation in order to ensure a well-known surface dopant-concentration for the W-Si contact.

(ii) *Oxide masking.*—It is known that when B-doped Si is thermally oxidized to cover the wafer with a masking oxide, the B concentration in Si at the interface is reduced considerably because of preferential B accumulation in the growing oxide. On the other hand, there is an enrichment in As which is preferentially retained in the Si (21) during oxide growth. Thus if steam oxide is used as a mask, the contact resistance data obtained would not correspond to the respective bulk dopant concentrations. However, an enhanced carrier concentration in Si at the interface is beneficial for making a contact ohmic and so As-doped (n-type) Si does not pose a problem for contacts opened through a steam oxide mask. The redistribution problem is absent if windows are opened through a vapor-deposited oxide. In view of the above, both a steam-grown and a deposited oxide were used as masks for opening contact windows. Contact windows were opened through the oxide mask using standard photolithography.

(iii) *Cleaning and W deposition.*—A free Si surface exposed to air (or any oxidizing ambient) for any length of time becomes covered with native oxide. Experiments have shown that the nature (refractive index, etc.) and growth rate of this oxide depend greatly on the Si surface (orientation, dopant type and concentration, and also the mode of doping). In general, doped Si shows a greater growth rate than the undoped and the rate is greater if the dopant has been introduced by diffusion rather than by addition to the melt. This thin native oxide has been observed to control the extent of reaction between Si and W (10). An insulating interlayer of silicon oxide between W and Si is obviously undesirable for a good contact. It is thus essential that steps be taken to remove the native oxide before W is deposited. Two schemes were used to remove this oxide before carrying out the next step of rf sputtering  $\sim 3000\text{Å}$  W.

In the first scheme the samples were given a 100:1 buffered HF clean for 2 min, spin dried, and loaded in the vacuum system for W deposition. Toward the end of the investigation, a water spray test (11) which tests the cleanliness of Si through hydrophobicity was used to monitor the slices before W deposition. The

test setup is shown in Fig. 1 and the test results on Si and SiO<sub>2</sub> surfaces in Fig. 2. This test turned out to be quite useful and some wafers were detected which had to be given extra cleaning (more time in 100:1 HF) before they were loaded for W deposition.

In the second scheme the oxide from the windows was sputter etched following which  $\sim 3000\text{Å}$  W was sputter deposited in the same system. Only the samples with steam oxide mask were used in this case. *In situ* sputter etching has the advantage of the Si surface not being exposed to an oxidizing ambient before W deposition but it can also cause damage to the exposed Si surface, the effects of which on a contact are not known. Wafers for the two cleaning methods were taken from the same crystal in order to have identical bulk doping.

After the W deposition, the test pattern shown in Fig. 3 was etched out using standard photolithography. Following a thorough clean, contact resistance measurements were made as described below. The measurements were repeated after various heat-treatments. The treatments consisted of 1 hr anneals in dry H<sub>2</sub> or in vacuum ( $\sim 10^{-7}$  Torr) between 600°-830°C. Each treatment was preceded by a thorough clean. Some samples were processed for a CVD Si-nitride encapsulation (680°C, 30 min) followed by removal of the cap in phosphoric acid for measurements. Metallurgical changes in the contact windows were followed with optical microscopy, SEM, and x-ray diffraction. The

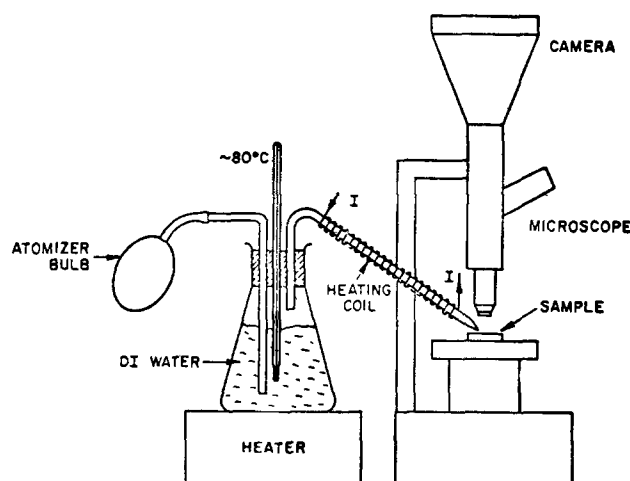


Fig. 1. Spray test setup

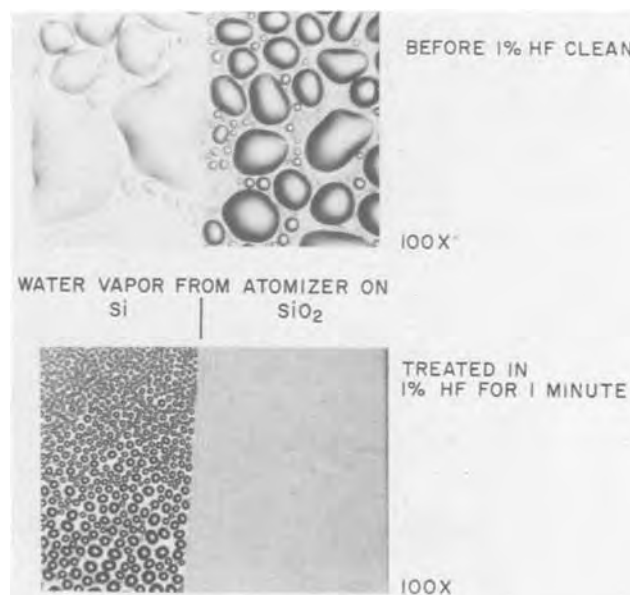


Fig. 2. Photographs of condensed water vapor on Si and SiO<sub>2</sub> before and after cleaning in 100:1 HF.

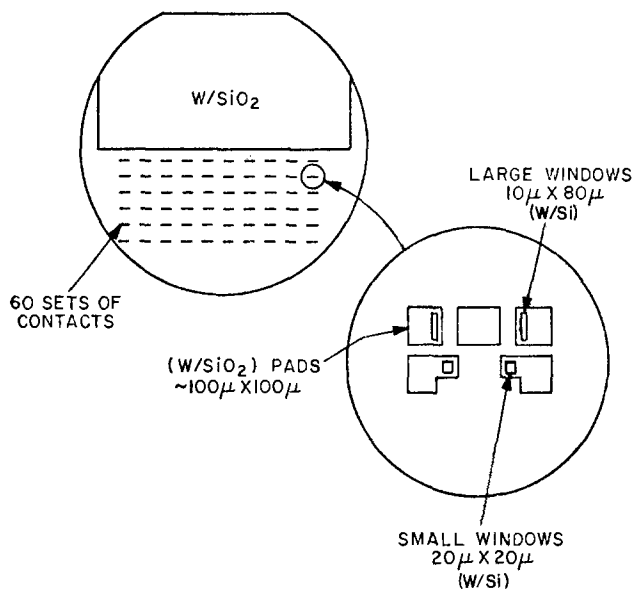


Fig. 3. Tested pattern

large W/SiO<sub>2</sub> area was used to monitor changes in the sheet resistivity of the W film as a result of heat-treatments.

**Measurement procedure.**—Contact resistance was estimated by taking the difference between resistance values obtained in a two-probe measurement on two sizes of contact windows. Each sample has 60 sets of two small (20 × 20 μ<sup>2</sup>) and two large (10 × 80 μ<sup>2</sup>) contact windows, with the connecting pads (~100 × 100 μ<sup>2</sup>) in the pattern shown in Fig. 3. In a two-probe measurement, the voltage developed across the probes (in mV) when a current of 1 mA is flowing in the circuit will be expressed by

$$V_L = 2R_{CL} + 2R_W + 2R_P + R_{SL}$$

for large area contacts and

$$V_{Sm} = 2R_{CSm} + 2R_W + 2R_P + R_{SSm}$$

for small contacts. Here  $R_C$  is the resistance of the contact, i.e., of the W-Si interface,  $R_W$  that of the W pad,  $R_P$  that of the probe, and  $R_S$  is the resistance of Si between the two contacts including the spreading term from each contact.

Probe tips were placed near the edges of the contact windows to minimize the  $R_W$  term, and  $R_P$  for the two cases was adjusted (by the probe-pressure adjustment) to be nearly equal. Taking the difference of the two voltages we get

$$\Delta V \cong 2(R_{CSm} - R_{CL}) + \Delta R_S$$

$\Delta R_S$  being close to the difference in the spreading resistance for the two cases.

Spreading resistance at an isolated contact is expressed as

$$R_{SP} = K \frac{\rho_s}{l}$$

where  $\rho_s$  is the substrate resistivity,  $l$  is a linear dimension of the contact, and  $K$  is a geometrical factor for the shape of the contact. For a circular contact of diameter  $D$ ,  $R_{SP} = \rho_s/2D$ . This is also roughly true for a square contact ( $L^2$ ) if we use  $D = L(4/\pi)^{1/2}$ . For the rectangular (10 × 80 μ) contact, the value of  $K$  turns out to be such that (12)

$$(R_{SP})_{Sm} \sim 2(R_{SP})_L$$

where the small contact is (20 × 20 μ). The contact resistance is expressed as

$$R_C = \frac{\rho_c}{\text{Area}}$$

where  $\rho_c$  is the specific contact resistance in ohm-cm<sup>2</sup>. Since the contact areas are 400 μ<sup>2</sup> (small) and 800 μ<sup>2</sup> (large)

$$R_{CSm} = 2R_{CL}$$

and therefore

$$2(R_{CSm} - R_{CL}) = R_{CSm} = \rho_c/4 \times 10^{-6} \text{ ohm}$$

Keeping in mind the spreading contribution, we can write that as an upper limit

$$\rho_c \leq \Delta V \times 4 \times 10^{-6} \text{ ohm-cm}^2$$

All reported values therefore include a spreading contribution.

The two-probe method itself places a lower limit on the determined  $\rho_c$ . Since a metal-Si contact is generally asymmetrical, the two-probe method measures the greater of the two resistances, because one of the two contacts is in reverse bias. However, at the high dopant concentrations and low currents involved, there is no asymmetry in the forward and reverse characteristics. This was confirmed by measuring forward and reverse characteristics of a single contact by using a thin Al film on the back of the slice (providing a large area back contact with very small ohmic resistance), with currents up to 10 mA. Contact resistance of a sample (3.5 × 10<sup>19</sup>/cm<sup>3</sup> B, ~900 Å PtSi, metallized with W) when measured with this two-probe technique was calculated to be 3.4 × 10<sup>-6</sup> ohm-cm<sup>2</sup>. The value obtained by using the "single front contact to large area back contact" method (13) on the same sample was 3.7 × 10<sup>-6</sup> ohm-cm<sup>2</sup>. The results are essentially the same, considering the variation generally observed in  $\rho_c$  measured with different techniques (14). Before doing the actual measurements, a scan of about 30 contact pairs was taken in the form of a multiple exposure I-V trace to assess the uniformity and ohmicity of the contacts.

## Results and Discussion

Measured  $\rho_c$  values are summarized in Tables II and III for chemically cleaned and sputter etch cleaned samples, respectively. It is noticed that as-deposited contacts for n- and p-type silicon are quite different. W-(n)Si contacts are nearly always ohmic, whereas W-(p)Si contacts are not and especially so when the masking oxide is steam grown and the bulk B concentration less than 10<sup>20</sup>/cm<sup>3</sup>. Also, for the p-type samples sputter etching leads to better contacts. In all cases the contacts improve with annealing. I-V traces of contacts from two samples with substrates from the same crystal (~10<sup>19</sup>/cm<sup>3</sup> B) but cleaned chemically (1BP; F-2) and by sputter etching (1BP; J-2) are shown in Fig. 4. The sputter cleaned sample shows better contacts (lower resistance and less spread) even though the annealing temperature is 50° lower while the anneal time is the same (1 hr). One sample (chemical window clean) showed nonohmic contacts up to a 730°C anneal. Even after the 780°C anneal (Fig. 4), this sample showed a large number of contacts which were nonohmic and had high resistance (a set of I-V curves very close to the V axis).

Chemical cleaning is found to be ineffective in cleaning the contact windows uniformly. Entire windows are left covered with the thin native oxide in some wafers. 1BP; F-series (~1.5 × 10<sup>19</sup>/cm<sup>3</sup>, B) of samples show this effect quite well. All contacts on these samples were nonohmic and had high resistance (5-10K ohm at 1 mA) as deposited. However, after a 730°C (1 hr, H<sub>2</sub>) anneal, some contacts became ohmic (R ~ 100 ohm) while the rest remained high and nonohmic. There was an indication (from optical microscopy at magnifications of 100× or less so that depth of focus was appropriate) of an incipient reaction in the windows where the contacts had become ohmic, but on

Table II. Measured  $\rho_C$  (ohm-cm<sup>2</sup>) for chemically cleaned samples

Doping cm <sup>-3</sup>	Oxide type	As-deposited	After 600°C 1 hr anneal	After 700°C 1 hr anneal	After 730°C 1 hr anneal
1.2 × 10 <sup>20</sup> , B	Steam	(5-8) × 10 <sup>-5</sup>	(3-8) × 10 <sup>-6</sup>	5 × 10 <sup>-7</sup> -2 × 10 <sup>-6</sup>	3 × 10 <sup>-6</sup>
1.2 × 10 <sup>20</sup> , B	CVD	(2-4) × 10 <sup>-6</sup>	7 × 10 <sup>-7</sup> -10 <sup>-6</sup>	(5-8) × 10 <sup>-7</sup>	
1.2 × 10 <sup>20</sup> , B	CVD (No cleaning in 1% HF)	N.O.*	N.O.	N.O.	N.O.
4 × 10 <sup>19</sup> , B	Steam	N.O.	(4-8) × 10 <sup>-5</sup>	7 × 10 <sup>-6</sup> -2 × 10 <sup>-5</sup>	(5-7) × 10 <sup>-6</sup>
4 × 10 <sup>19</sup> , B	CVD	(2-5) × 10 <sup>-6</sup>	(3-5) × 10 <sup>-6</sup>	(2.5-3.5) × 10 <sup>-6</sup>	
2 × 10 <sup>19</sup> , B	Steam	N.O.	N.O.		1.6 × 10 <sup>-5</sup> -3 × 10 <sup>-4</sup>
1.5 × 10 <sup>19</sup> , B	Steam	N.O.	N.O.		(1.5-2) × 10 <sup>-4</sup> (if reacted)
1.5 × 10 <sup>19</sup> , B	CVD	(6-9) × 10 <sup>-5</sup>	(4-6) × 10 <sup>-5</sup>	(2-3) × 10 <sup>-5</sup>	(4-5) × 10 <sup>-5</sup> (if reacted after 780°C)
1.2 × 10 <sup>19</sup> , B	CVD	N.O.	(3-7) × 10 <sup>-6</sup>	(2-3) × 10 <sup>-5</sup>	
1.2 × 10 <sup>19</sup> , B	Steam	N.O.	N.O.	Ohmic up to ~100 μA, (1-2) × 10 <sup>-3</sup>	
5.5 × 10 <sup>18</sup> , B	Steam	N.O.	N.O.	N.O.	
5.5 × 10 <sup>18</sup> , B	CVD	N.O.	N.O.	2 × 10 <sup>-4</sup> (Ne.O.)	
7.5 × 10 <sup>18</sup> , As	Steam	(1-5) × 10 <sup>-6</sup>	8 × 10 <sup>-7</sup> -1.5 × 10 <sup>-6</sup>	8 × 10 <sup>-7</sup> -1.5 × 10 <sup>-6</sup>	~10 <sup>6</sup>
7.5 × 10 <sup>18</sup> , As	CVD	(3-6) × 10 <sup>-6</sup>	(1.6-2) × 10 <sup>-6</sup>	(1.5-2) × 10 <sup>-6</sup>	~10 <sup>6</sup>
4 × 10 <sup>18</sup> , As	Steam	(5-8) × 10 <sup>-6</sup>			(5-9.5) × 10 <sup>-6</sup>
2 × 10 <sup>18</sup> , As	Steam	8 × 10 <sup>-6</sup> -1.5 × 10 <sup>-5</sup>	7 × 10 <sup>-6</sup> -1.4 × 10 <sup>-5</sup>	(5-9) × 10 <sup>-6</sup>	
2 × 10 <sup>18</sup> , As	CVD	N.O.	Ne.O. (2.4-4.7) × 10 <sup>-4</sup>	6 × 10 <sup>-5</sup> -2 × 10 <sup>-4</sup>	
4 × 10 <sup>18</sup> , As	Steam (No cleaning in 1% HF)	(1-2) × 10 <sup>-6</sup>	(1-2) × 10 <sup>-6</sup>		9 × 10 <sup>-6</sup> -1.5 × 10 <sup>-5</sup>
7 × 10 <sup>18</sup> , As	Steam	~6 × 10 <sup>-5</sup>	~6 × 10 <sup>-5</sup>		~6 × 10 <sup>-5</sup>
4.5 × 10 <sup>18</sup> , As	Steam	N.O.	Ne.O.		~1.2 × 10 <sup>-4</sup>

\* N.O. = nonohmic, Ne.O. = nearly ohmic.

Table III. Measured  $\rho_C$  (ohm-cm<sup>2</sup>) for sputter-cleaned samples

Doping	Oxide type	As-deposited	After 600°C anneal (1 hr)	After 700°C anneal (1 hr)	After 750°C anneal (1 hr)
1.2 × 10 <sup>20</sup> , B	Steam	(1-2) × 10 <sup>-5</sup>	(6-9) × 10 <sup>-6</sup>	(4-8) × 10 <sup>-6</sup>	(1.8-4) × 10 <sup>-6</sup>
4 × 10 <sup>19</sup> , B	Steam	~5 × 10 <sup>-5</sup>	~3 × 10 <sup>-5</sup>	~8 × 10 <sup>-6</sup>	~3.2 × 10 <sup>-6**</sup>
~1.5 × 10 <sup>19</sup> , B	Steam	N.O.	N.O.	?	~8 × 10 <sup>-6</sup>
~7.5 × 10 <sup>18</sup> , As	Steam	(3.6-6) × 10 <sup>-6</sup>	(3.2-6) × 10 <sup>-6</sup>	?	(4.5-6) × 10 <sup>-5</sup>
~7.5 × 10 <sup>18</sup> , As	Steam	3.6 × 10 <sup>-6</sup>	3.6 × 10 <sup>-6</sup>	4.5 × 10 <sup>-6*</sup>	(2.8-7) × 10 <sup>-6</sup>
~7.5 × 10 <sup>18</sup> , As	Steam	4.5 × 10 <sup>-6</sup>	4.5 × 10 <sup>-6</sup>	6 × 10 <sup>-6</sup>	3 × 10 <sup>-6**</sup>

\* Si<sub>3</sub>N<sub>4</sub> (2000Å, ~680°C) was deposited and etched off for testing.

the surface these contacts were still covered with W and no reaction product appeared over the W. Etching away the W from these contacts revealed that there was formation of granular WSi<sub>2</sub> (structure confirmed by x-ray diffraction) in the contact area. As shown in Fig. 5, only parts of the contact area have reacted. This confirms the nonuniformity of chemical cleaning (native oxide removal) within a window. In contrast, the reaction in the 1BP series of samples cleaned by sputter etching was uniform over the entire sample and also within each contact window. Figure 6(a) shows one such window before the W was removed and the reacted area (made up of WSi<sub>2</sub>/Si) is shown in Fig.

6(b); W and the surrounding SiO<sub>2</sub> having been etched off.

A further anneal of 1BP; F-samples for 1 hr at 780°C caused more reaction at the already reacted contacts and started it at some previously unreacted. Electrically, the freshly reacted and the previously reacted contacts were identical (R ~ 7 ohm). At this stage one of the samples (out of four) showed reaction at all contacts while on another sample there were many contacts without reaction which were nonohmic and had a high resistance. One such pair of neighboring sets on this sample is shown in Fig. 7. Figure 8 shows these two types of contacts as seen with a SEM. A layer

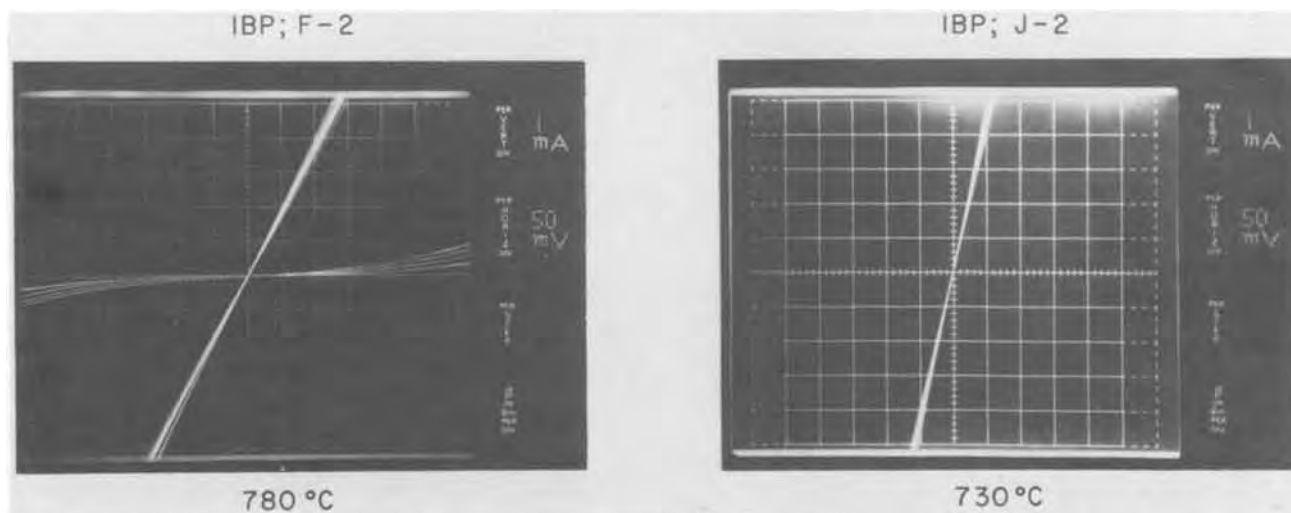


Fig. 4. Multiple exposure I-V trace of small contacts on samples 1BP; F-2 after a 780°C, 1 hr anneal and 1BP; J-2 after a 730°C, 1 hr anneal.

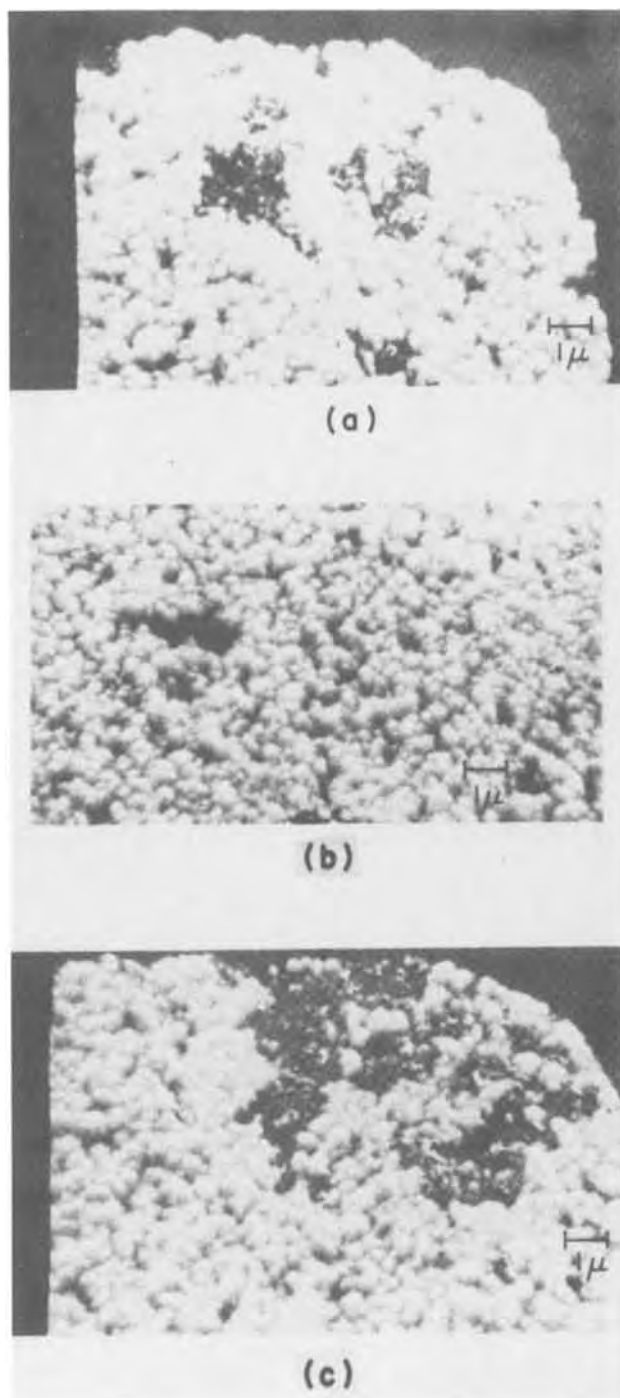


Fig. 5.  $WSi_2$  formation at W-Si interface in a small contact window on sample 1BP; F-2 after  $730^\circ\text{C}$ , 1 hr anneal.

of interfacial oxide is evidently responsible for both the absence of reaction and a good electrical contact. An attempt to cause reaction at more contacts by further annealing (one more hour) at  $780^\circ\text{C}$  resulted in more reaction (without any resistance change) at the reacted contacts but none at all in the unreacted ones. A cleaved section through a reacted contact at this stage showed it to be continuous as shown in Fig. 9. Even an anneal at  $830^\circ\text{C}$  (1 hr,  $\text{H}_2$ ) could not induce any reaction in the unreacted contacts. However, the reacted contacts experienced even more severe reaction and most of these actually "opened up" due to cracks as shown in Fig. 10.

As can be seen from a comparison of Fig. 6 and 7, the native oxide removal (which is also necessary for W-Si reaction) is more complete and uniform in back-sputter-cleaned samples. As-deposited contacts in the sputter-cleaned samples ( $\sim 1.2 \times 10^{20}/\text{cm}^3$  B) are

nearly ohmic ( $R_c \sim 10$  ohm). Annealing (1 hr,  $\text{H}_2$ ) at temperatures from  $600^\circ\text{C}$ - $730^\circ\text{C}$ , progressively reduces this value (down to  $\sim 1$  ohm). The distribution of the measured contact resistivity over 60 sets after each treatment is shown in Fig. 11 for one of these samples.

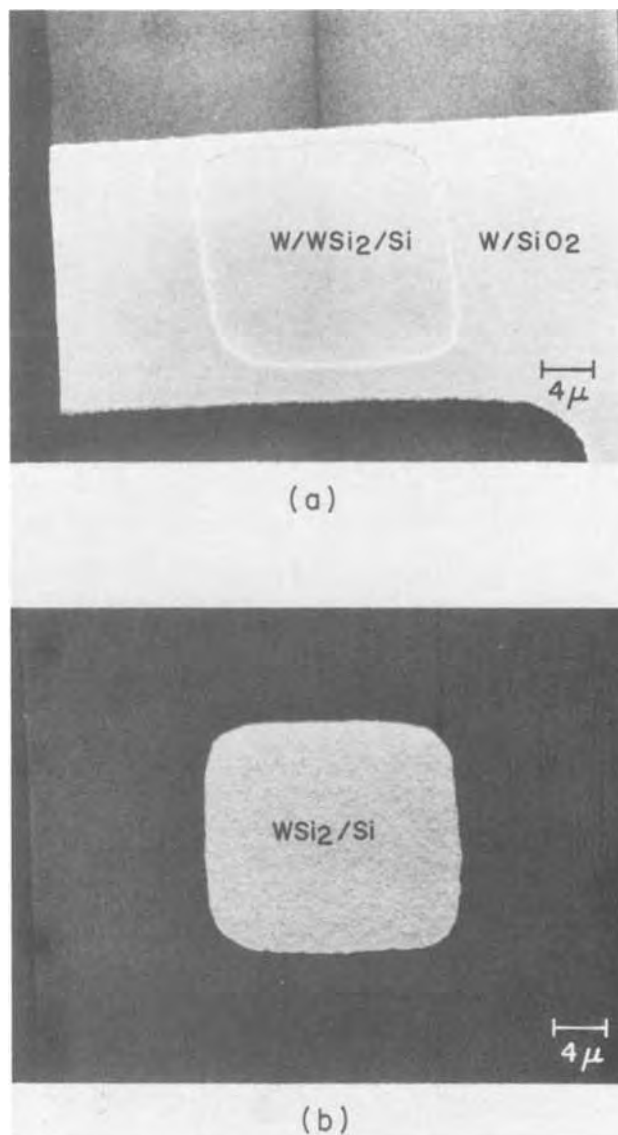


Fig. 6.  $WSi_2$  formation at W-Si interface in a small contact window on sample 1BP; J-2 after  $730^\circ\text{C}$ , 1 hr anneal.

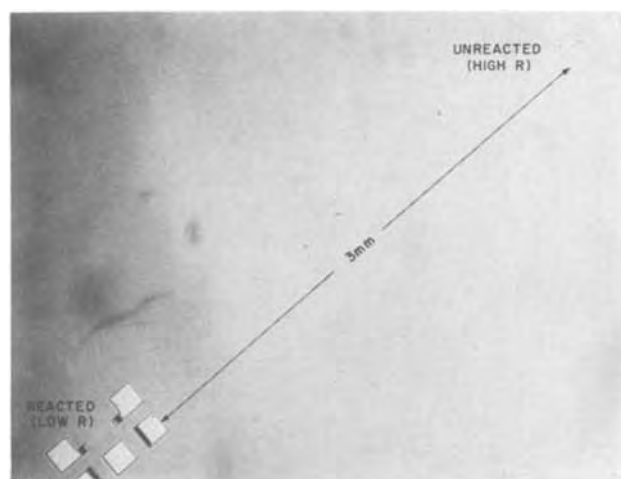


Fig. 7. Two neighboring sets ( $\sim 3$  mm apart) of contact windows on sample 1BP; F-4 after  $730^\circ\text{C}$ , 1 hr anneal.

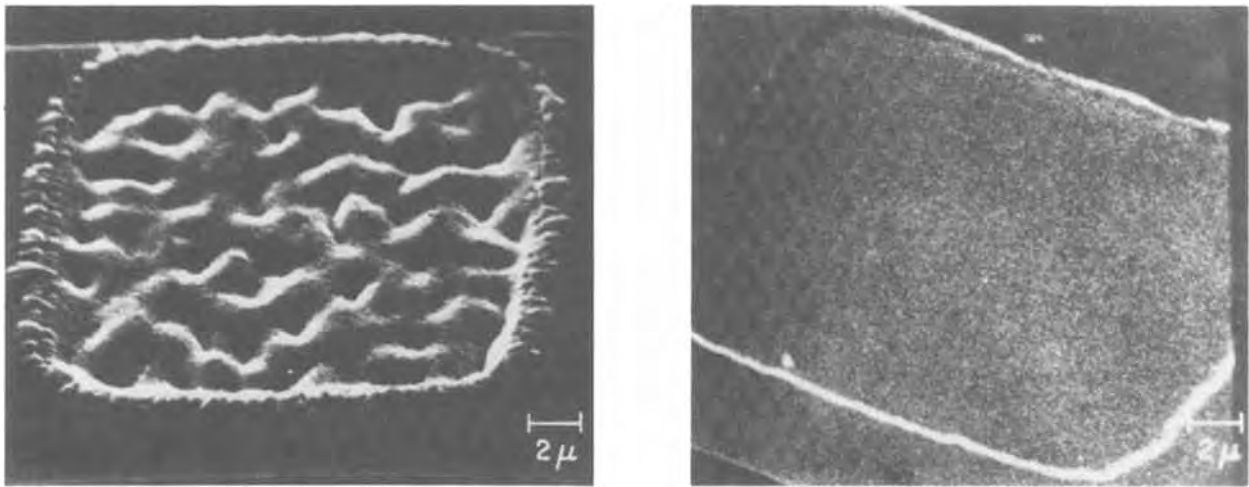


Fig. 8. Magnified view of two types of contact windows shown in Fig. 7

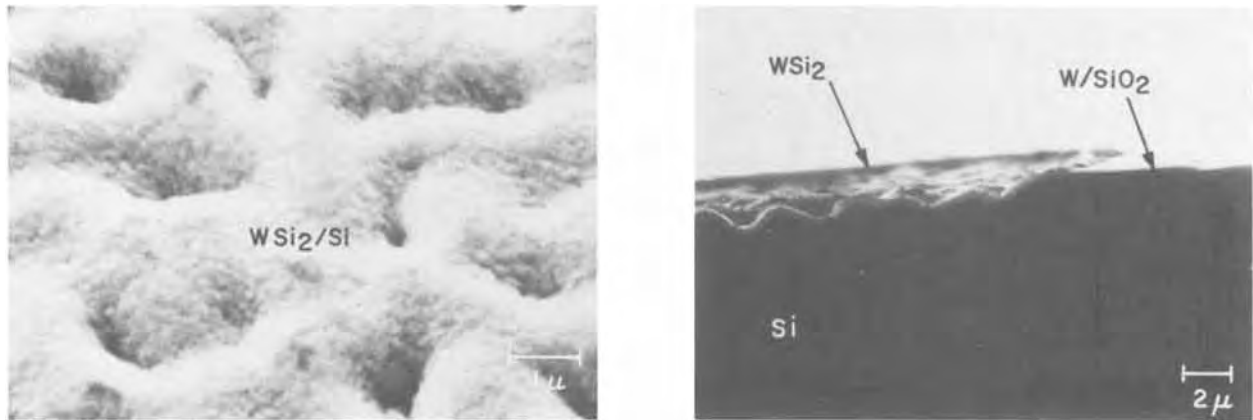


Fig. 9. Cleaved-through section of a completely reacted contact window on sample 1BP; F-4, after 730°C, 1 hr anneal

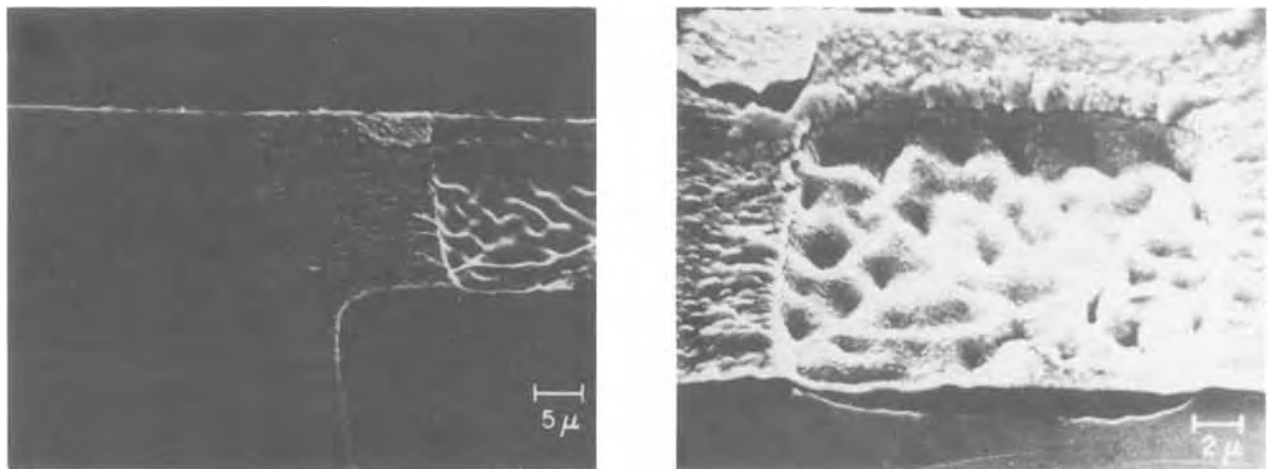


Fig. 10. An overreacted contact window after 830°C, 1 hr anneal showing cracks

Figure 11 includes the distribution obtained after  $\text{Si}_3\text{N}_4$  encapsulation (CVD at 680°C, 30 min,  $\sim 2000\text{\AA}$  thick film) and removal. It is clear that no significant degradation of contacts occurs as a result of this process.

The effect of impurity redistribution during steam oxidation on contact resistance is clearly seen in Table II. Since the barrier width is determined by the dopant concentration at (or near) the Si surface, the depletion of B from the Si surface in p-type samples leads to a thicker barrier compared to that expected for the bulk concentration. The reverse happens for the As-doped samples. This effect is not present when the oxide is a

deposited one. Thus as-deposited contacts to  $\sim 4 \times 10^{19}$  B/cm<sup>3</sup> Si are ohmic for CVD oxide mask and nonohmic for steam oxide whereas for  $\sim 2 \times 10^{19}$  As/cm<sup>3</sup> the situation is reversed. One of the reasons that the so far discussed 1BP; F-samples ( $\sim 10^{19}$  B/cm<sup>3</sup>) show such an improvement with annealing and  $\text{WSi}_2$  formation is probably the fact that during the W-Si reaction the Si layer with reduced ( $< 10^{19}$ ) B concentration is consumed and deeper Si with higher B level ( $\sim 10^{19}$ ) comes into contact with the metallic  $\text{WSi}_2$ . Boron diffusion in Si is too small ( $\sim 3 \times 10^{-17}$  cm<sup>2</sup>/sec) at these temperatures to lead to any appreciable flux from the

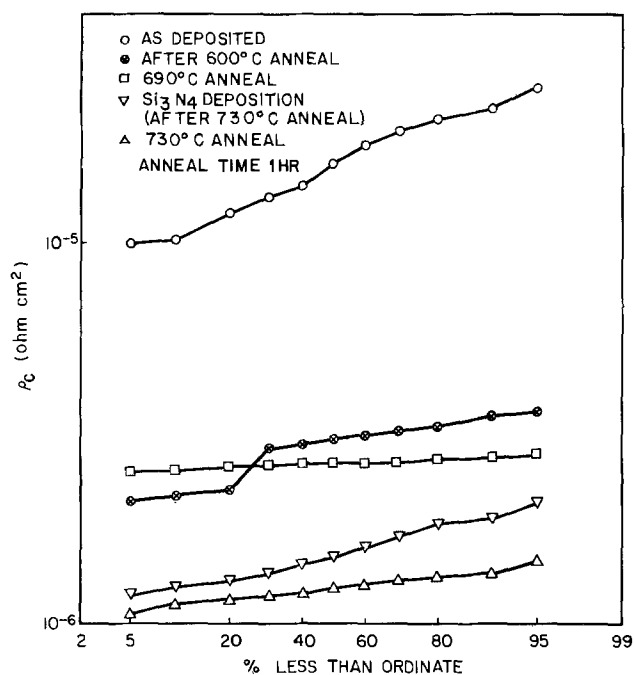


Fig. 11. Distribution of  $\rho_c$  over 60 contacts in 2BP; J-3 at various stages of heat-treatment.

bulk to the depleted surface. However, it can be seen from Table III that sputter etching of a  $4 \times 10^{19}$  B/cm<sup>3</sup> substrate leads to ohmic contacts (as deposited) even though the masking oxide is steam grown. It was argued and confirmed that in addition to the native oxide, sputter etching also removed some Si from the surface, thus exposing the Si with higher B concentration and improving the as-deposited contacts. The amount of Si removed by sputter etching was found to depend on the doping type. p<sup>+</sup>-Si sputtered at a faster rate ( $\sim 1.2$  times) compared to n<sup>+</sup>-Si. Since both the boron concentration profile in Si following the oxidation and the sputter etch depth will determine the concentration at the W-Si interface, the sputter etching does not always lead to a good contact. The lower the bulk concentration, the greater the etch depth required for a "good" contact provided the bulk concentration is high enough to yield an ohmic contact. Samples with  $\sim 1.5 \times 10^{19}$  B formed good W-Si contacts using chemical clean and CVD oxide mask but failed to give good contacts with sputter etch clean (steam oxide mask) until after annealing at 750°C (1 hr).

There seems to be no difficulty in making ohmic contacts to n-type Si by either of the cleaning processes and the thermal stability is excellent for up to one hour exposures to H<sub>2</sub> at 730°C. The contacts are not too stable above 800°C, when excessive WSi<sub>2</sub> formation can result in cracking or lifting up of W in the contact windows leading to "opens" or very high resistance. In contrast with the p-type samples which required a 100:1 HF clean not more than  $\sim 5$  min before loading, an n-type sample ( $8 \times 10^{19}$ /cm<sup>3</sup> As, steam oxide) when loaded in the W-deposition system after being exposed to air for over a week after the 100:1 HF clean (but kept in a plastic container for cleanliness) showed ohmic contacts in the "as-deposited" condition with a resistance value only slightly greater than the corresponding value in Table III. This indicates that the effectiveness of the native oxide whose thickness was measured to be only  $\sim 15$ Å for p-type samples 5 min after clean and  $\sim 22$ Å for n-Si after a week as a barrier to conduction is quite different for the two types of Si (B- or As-doped). It is possible that the redistribution of impurities between Si and oxide at the interface is responsible for this effect. However, removal of the native oxide by one of the methods (just prior to W deposition) was found to be essential

for making ohmic contacts to n-Si with As less than  $\sim 4 \times 10^{19}$ /cm<sup>3</sup>.

Measured values from all samples are summarized in Fig. 12. Here  $\rho_c$ , which includes the spreading contribution, is plotted against the dopant concentration. Since the dominant transport mechanism at high dopant concentration is tunneling (15), the calculated theoretical curves for a tunneling controlled contact are also shown. These curves have been obtained by using the expression (2)

$$\rho_c = g_o^{-1}$$

where

$$g_o = 10^{-4} \left( \frac{e}{h} \right)^2 \frac{\sqrt{2em^*\phi_o}}{\omega} \exp \left( - \frac{4\pi\omega}{h} \sqrt{2em^*\phi_o} \right) \text{ (mho/cm}^2\text{)}$$

in which  $e$  is the electronic charge,  $m^*$  is the carrier effective mass,  $\omega$  is the width of the barrier (depletion layer), and  $\phi_o = 1/2 \sqrt{\phi_B}$ , where  $\phi_B$  is the barrier height.

Due to absence of available data on the carrier effective masses in heavily doped (100) Si, values of (0.19) $m$  for n-Si and (0.17) $m$  for p-Si have been used. Since effective mass increases with doping, the real curves for calculated  $\rho_c$  lie lower than those shown in Fig. 12. In any case, the agreement with theoretical calculations based on tunneling alone is poor, especially in terms of the slope of  $\rho_c - N_{D,A}$  curve; theory predicts a much steeper slope. Strictly speaking, the influence of the thin native oxide barrier should also be included in the above expression. But as the experiments show, the electrical properties of the oxide are

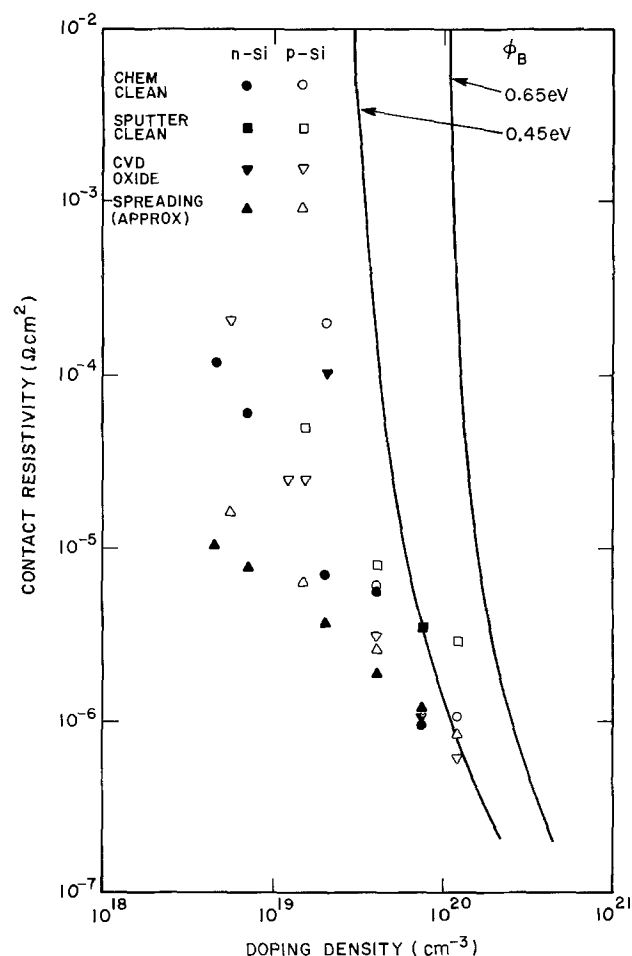


Fig. 12. Results of  $\rho_c$  variation with doping density. Two curves show the theoretical values expected for tunneling dominated contacts.

dependent on the substrate and the quantitative introduction of such an effect is impossible. Figure 12 also shows the approximate (geometric factor  $K$  is unknown) values of corresponding spreading resistance for each sample.

Figure 13 shows similar experimental data and theoretical curves for PtSi contacts (13). W-Si experimental data points are also shown in Fig. 13. In view of the fact that W-Si and PtSi-Si contact data are closer to one another and deviate from theory very sharply, it is believed that the measured  $\rho_c$  has a significant contribution from the spreading resistance. Spreading resistance depends only on the contact size (and shape) and substrate resistivity and is independent of the resistance of the interface. However, since the interface resistance (true contact resistance) and the spreading resistance are in series it suggests that the true contact resistance is probably smaller than measured. Experiments where contact windows were opened using electron beam lithography indicate that for contacts larger than on the order of a few square microns, the spreading term is indeed dominant (20). An additional argument for the interface not controlling the total resistance is the fact that on n-type Si, the resistance goes down even after the formation of  $WSi_2$  which has a higher barrier height to n-Si than W.

### Conclusions

1. W-Si ohmic contacts can be made by using rf-sputtered W on n-type as well as p-type Si.
2. The lowest measured contact resistivity to B-doped Si ( $5.5 \times 10^{18}$ - $1.2 \times 10^{20}/\text{cm}^3$ ) ranges from  $1.5 \times 10^{-4}$  to  $5 \times 10^{-7}$  ohm-cm<sup>2</sup> and for As-doped Si ( $4.5 \times 10^{18}$ - $8 \times 10^{19}/\text{cm}^3$ ) from  $1.2 \times 10^{-5}$  to  $8 \times 10^{-7}$  ohm-cm<sup>2</sup>.
3. The measured values include a large contribution from the spreading resistance.
4. Contact resistance decreases with annealing (1 hr,  $H_2$ ) from 600°C up to 800°C. This heat-treatment causes W and Si to react to form  $WSi_2$ .
5. In order to form a contact the thin layer of native oxide on Si has to be removed before depositing W. This can be accomplished by a simple chemical clean (100:1 HF for 1 min) or by sputter etching the oxide. The latter is found to be more effective.
6. Steam oxidation for obtaining oxide mask prior to contact formation has opposite effects for p-type (B)

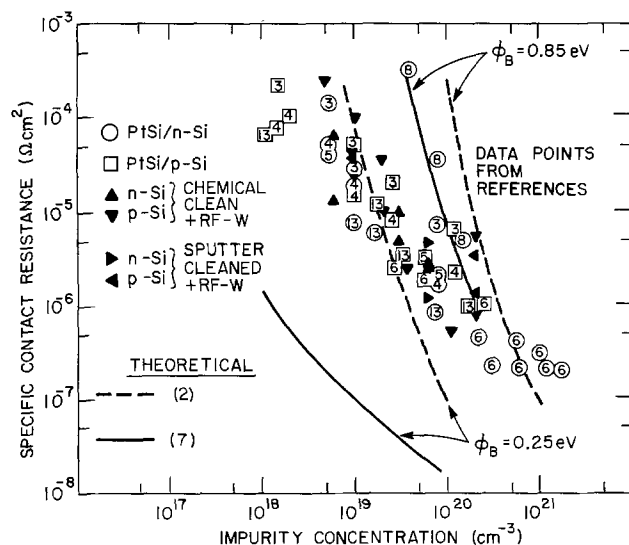


Fig. 13. Comparison of  $\rho_c$ - $N_{D,A}$  variation for W-Si and PtSi contacts.

and n-type (As) Si. Boron tends to concentrate in the oxide thus reducing its concentration in Si and leading to higher contact resistance as deposited. The opposite happens for As-doped Si. This effect is confirmed by using deposited and steam-grown oxide on similar substrates.

7. The native oxide growing on n-Si seems to be electrically different from that on p-Si. This difference may also be a result of the redistribution at Si-oxide interface.

### Acknowledgments

The author is thankful to W. J. Bertram for critically reading the manuscript. He sincerely appreciates the encouragement provided by R. S. Wagner in completing the work. Discussions with H. J. Levinstein were very useful. W films were deposited by F. B. Alexander and J. Sosniak. SEM pictures were obtained by S. E. Haszko.

Manuscript submitted March 20, 1975; revised manuscript received Oct. 1, 1975.

Any discussion of this paper will appear in a Discussion Section to be published in the December 1976 JOURNAL. All discussions for the December 1976 Discussion Section should be submitted by Aug. 1, 1976.

Publication costs of this article were partially assisted by Bell Laboratories.

### REFERENCES

1. R. S. Wagner, A. K. Sinha, T. T. Sheng, H. J. Levinstein, and F. B. Alexander, *J. Vacuum Sci. Technol.*, **11**, 582 (1974).
2. M. P. Lepselter and J. M. Andrews, in "Ohmic Contacts to Semiconductors," B. Schwartz, Editor, p. 159, The Electrochemical Society Softbound Symposium Series, New York (1969).
3. D. Shinoda, *ibid.*, p. 200.
4. H. Sello, *ibid.*, p. 277.
5. L. E. Terry and R. W. Wilson, *Proc. IEEE*, **57**, 1580 (1969).
6. C. Y. Ting and C. Y. Chen, *Solid-State Electron.*, **14**, 433 (1971).
7. C. Y. Chang, Y. K. Fang, and S. M. Sze, *ibid.*, **14**, 541 (1971).
8. A. Y. C. Yu, *ibid.*, **13**, 239 (1970).
9. A. K. Sinha, M. H. Read, and T. E. Smith, *J. Appl. Phys.*, **44**, 3465 (1973).
10. J. A. Borders and J. N. Sweet, in "Proceedings of the International Conference on Applications of Ion Beams to Metals," Picraux, Eernisse, and Vook, Editors, p. 179, Plenum Press, New York (1973).
11. J. M. Andrews, Private communication.
12. Ragner Holm, "Electric Contacts," p. 17, Hugo Gebers Forlag, Stockholm (1946).
13. A. K. Sinha, *This Journal*, **120**, 1767 (1973).
14. H. H. Berger, *ibid.*, **119**, 507 (1972).
15. C. A. Mead, in "Ohmic Contacts to Semiconductors," B. Schwartz, Editor, p. 3, The Electrochemical Society Softbound Symposium Series, New York (1969).
16. F. Koch, Unpublished.
17. Y. Itoh and N. Hashimoto, *J. Appl. Phys.*, **38**, 899 (1967).
18. S. M. Sze, "Physics of Semiconductors," p. 399, Wiley-Interscience, New York (1969).
19. Jack Saltich, in "Ohmic Contacts to Semiconductors," B. Schwartz, Editor, p. 187, The Electrochemical Society Softbound Symposium Series, New York (1969).
20. F. B. Koch, R. F. W. Pease, and A. U. Mac Rae, Paper 269 presented at The Electrochemical Society Meeting, Miami Beach, Florida, October 8-13, 1972.
21. A. S. Grove, "Physics and Technology of Semiconductor Devices," p. 69, John Wiley & Sons, Inc., New York (1967).



# Chemical Vapor Deposition of Antimony-Doped Tin Oxide Films Formed from Dibutyl Tin Diacetate

James Kane and H.P. Schweizer

Laboratories RCA Limited, Zurich, Switzerland

and Werner Kern\*

RCA Laboratories, Princeton, New Jersey 08540

## ABSTRACT

A CVD process for the preparation of transparent conducting layers of antimony-doped tin oxide has been developed utilizing dibutyl tin diacetate, antimony pentachloride,  $O_2$ ,  $H_2O$ , and  $N_2$  as carrier gas at a substrate temperature of 400°-550°C. It was designed to fulfill a need for more highly conducting coatings than those obtainable without doping, in the sheet resistance range 50-100 ohm/square, but still possessing an optical transmission in excess of 80% throughout the visible spectrum. Coatings to this specification are used extensively for a variety of electro-optic devices. A set of optimized deposition conditions is presented together with important optical, electrical, structural, and chemical properties of the films. Typical  $SnO_2:Sb$  films have film thicknesses ranging from 1500-3600Å with a sheet resistance of 50-150 ohm/square, a specific resistivity of 0.0015-0.0032 ohm-cm, an n-type carrier concentration of  $1.2 \times 10^{20} \text{ cm}^{-3}$ , and a Hall mobility of 23  $\text{cm}^2/\text{V-sec}$ . They exhibit a light transmission of 85-91% net, and have an optimum dopant concentration within the range of 0.6-2.7 atomic per cent of antimony. The films are free of volatile chlorine, are chemically inert, and may be heated in air for prolonged periods without noticeable deterioration. Samples on sapphire substrates were heated in air to 1000°C for several hours without change in the sheet resistance.

Transparent, electrically conducting thin films are required in many modern opto-electronic devices. Numerous materials, prepared by a variety of physical and chemical techniques (1,2), have been reported but in practice only two materials, tin oxide doped with antimony and indium oxide doped with tin, are widely used. Antimony-doped tin oxide coatings are conventionally prepared by spray hydrolysis of tin tetrachloride-antimony chloride mixtures (1-16), but for the high quality coatings required in electronic devices more sophisticated deposition techniques are needed. Sputtering techniques (1, 2, 17-20) have been used with better success. Chemical vapor deposition (21-22) could offer economic advantages of lower equipment cost and simpler processing.

A chemical vapor deposition process for the preparation of transparent conducting coatings of non-stoichiometric tin oxide has been described in a previous paper (22). The subject of the present investigation is an important modification of this basic process by which a controlled quantity of an antimony dopant, which greatly increases the conductivity of the film, is introduced into the tin oxide. A full description of the apparatus and the proposed advantages of the CVD technique over spray hydrolysis were presented in the previous paper (22). Also given were extensive literature references on undoped tin oxide films; references in the present paper are therefore confined essentially to antimony-doped tin oxide films.

In addition to lower conductivity, a second disadvantage of the undoped tin oxide is that it is non-stoichiometric and is therefore only a metastable phase. If it is subjected to any high temperature processing after deposition the conductivity is usually decreased. Prolonged heat-treatments eventually produce a high resistivity form of tin oxide. In contrast, antimony-doped tin oxide remains highly conducting and, provided that the substrate material is inert, it does not deteriorate even after prolonged heating in nonreduc-

ing ambients. Several samples deposited on sapphire were heated to 1000°C in air for several hours and there was no apparent deterioration in either the film quality or the conductivity. The material is more thermally stable in air than most of the substrates with which it is normally employed.

On quartz substrates heat-treatments in excess of 750°C produce a rapid deterioration in the sheet resistance due to chemical interaction of the tin oxide with the silicon dioxide substrate. On alkali-containing glass substrates the coatings deteriorate rapidly when heated above 500°C, due to the diffusion of alkali metal ions from the glass into the tin oxide.

## Film Deposition

*Choice of dopant compound.*—In preliminary experiments attempts were made to use various halide-free organometallic antimony compounds as dopant sources. This approach is attractive since it eliminates the possibility of halide contamination of the tin oxide; however, these doping experiments were only partially successful. The main disadvantage of antimony organometallic compounds is that they are too thermally stable and therefore are not entirely decomposed within the reaction chamber.

Antimony trichloride was examined but found to be troublesome because this compound is a solid at room temperature. Difficulties arise due to the accumulation of nonvolatile impurities on the surface of the melted  $SbCl_3$ , thus lowering its effective vapor pressure. In addition, due to poor thermal contact between the solid and the walls of the container, the effective vapor pressure of the solid is not constant.

It was eventually decided to optimize the process using antimony pentachloride ( $SbCl_5$ ) as the dopant source. This compound has a number of advantages over the other materials that were considered. Since it is a volatile liquid it can be transported at room temperature in a stream of inert gas; this transport can be achieved conveniently and in a reproducible manner by bubbling nitrogen through the liquid. Antimony

\* Electrochemical Society Active Member.

Key words: doped tin oxide, CVD, transparent conductors, thin films, semiconductors.



pentachloride is a corrosive and highly reactive material which is readily hydrolyzed by water. The ease of hydrolysis is, to a certain extent, an advantage since it ensures that the compound is entirely decomposed within the reaction chamber. Water vapor was introduced by passing nitrogen through a water bubbler, as indicated in Table I. A certain amount of water vapor is present during the reaction even without its extraneous addition since considerable quantities of water are generated in the vapor phase combustion of the organic constituents from the tin compound; complete exclusion of water is therefore not readily possible. The addition of water vapor was merely to ensure that excess was present in the reaction chamber. If proper handling precautions are observed, such as minimal exposure to air, this compound has proved to be a very convenient dopant source. Its one disadvantage is that it introduces chloride contamination into the tin oxide, but this seems to have no derogatory effects. Furthermore, we proved by very careful measurements that no chlorine or chlorides are given off from the films during heating in reduced pressure.

**Study of deposition parameters.**—The effects of the deposition variables were systematically explored to define the optimum processing conditions for the preparation of antimony-doped tin oxide coatings, with a sheet resistance of less than 200 ohm/square and an optical transmission in excess of 80% throughout the visible spectrum. The deposition parameters affecting the deposition rate and uniformity had already been investigated at length in previous work with the undoped tin oxide (22). The present study was required primarily to determine the optimum antimony concentration in the reactant gas stream and the effect of other parameters, such as substrate temperature, on the incorporation of this dopant into the tin oxide. The optimum quantity of antimony dopant was defined empirically as the maximum quantity which could be introduced into the chamber without producing any discoloration of the films. If this optimum concentration was exceeded the films became light blue in color and there was a consequent loss in optical transmission. After these optimum conditions for preparing doped coatings on an inert substrate had been defined, additional experiments were then undertaken to determine what changes were necessary to process borosilicate-type glasses and whether coating of soda lime glass would be feasible. Due to the rapid thermal diffusion of alkali ions at temperatures approaching the deposition temperature, these substrate materials are not chemically inert and this places additional constraints on the deposition process.

Table I. Materials and typical conditions for CVD of antimony-doped tin oxide films

1. Substrate material	Glass plates
2. Tin source material	Dibutyl tin diacetate
3. Tin source temperature	98°C
4. Organotin carrier flow rate	6750 cm <sup>3</sup> N <sub>2</sub> /min
5. Antimony source material	SbCl <sub>5</sub>
6. Antimony source temperature	25°C
7. Antimony carrier flow rate	420-850 cm <sup>3</sup> N <sub>2</sub> /min
8. H <sub>2</sub> O source temperature	25°C
9. H <sub>2</sub> O carrier flow rate	2100 cm <sup>3</sup> N <sub>2</sub> /min
10. Oxidant flow rate	380 cm <sup>3</sup> O <sub>2</sub> (H <sub>2</sub> O)/min
11. Substrate temperature	450°-475°C
12. Thermal equilibration	5 min
13. Deposition time	15-20 min
14. Postdeposition purge	0.5 min N <sub>2</sub>

**Deposition apparatus.**—The deposition system used in the present study was basically the same as that described for the preparation of undoped tin oxide coatings (22). A number of modifications in the construction of the apparatus were necessary to obtain satisfactory incorporation of the antimony dopant. Specifically the points of entry of the organometallic tin compound and the oxygen were repositioned and separated in order to avoid homogeneous gas phase nucleation with the consequent formation of hazed films containing particulate defects. A schematic diagram of the modified deposition system is shown in Fig. 1 and typical deposition conditions are summarized in Table I.

**Substrates for film deposition.**—Plates of polished vitreous (fused) quartz served as inert standard substrates on which to optimize the deposition parameters. They were later used as standards with which to compare other substrate materials. To establish the optimum antimony content and to determine which trace impurities are present in the system, representative deposits were prepared on high resistivity, (100)-oriented, and polished silicon wafers. These samples were then analyzed by mass spectroscopy, infrared spectroscopy, and ellipsometric measurements.

To demonstrate the high temperature stability of the antimony-doped tin oxide, coatings were prepared on several polished sapphire substrates of various crystallographic orientations. When annealed at 1000°C in air for several hours the tin oxide crystallized, but there was no apparent deterioration in either the optical or electrical properties of the coatings. X-ray examination revealed a high degree of preferred orientation in the annealed samples. This phenomenon is considered in more detail later.

In contrast to these substrate materials, soda lime glass substrates are not chemically inert at the temperatures required for chemical vapor deposition. To

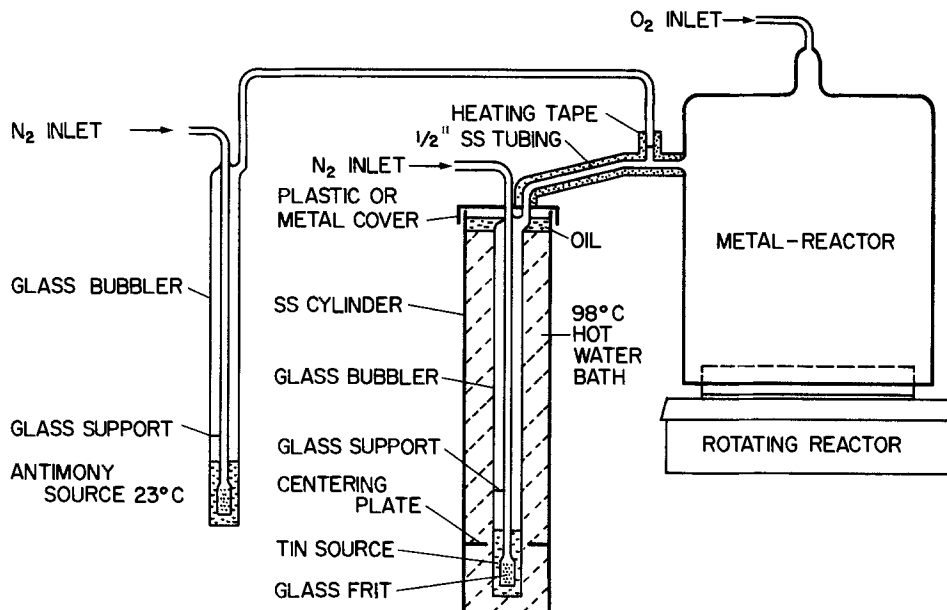


Fig. 1. Schematic representation of the modified CVD system used for preparing antimony-doped tin oxide films.

process glass substrates the optimum conditions must therefore be reestablished. The problem is caused by the diffusion of the highly mobile alkali metal ions out of the glass and into the growing tin oxide layer. The alkali metals apparently act as p-type doping agents in the n-type tin oxide, thus neutralizing some of the charge carriers. An even more unacceptable result of alkali impurities is hazing of the films, which makes them unsatisfactory for optical applications. Borosilicate glasses have usually a sufficiently low alkali metal content so that there is generally no difficulty in processing this type of substrate.

Soda lime glasses have a high alkali content and without special prior surface treatment it was not possible to prepare satisfactory coatings on this material. Several approaches were examined, as discussed in the following section.

*Surface treatment of soda lime substrate glasses.*—For commercial applications it is desirable to use soda lime float glass as substrates since this material is cheap and readily available. Float glass is also flat as prepared, requiring no surface polishing. This eliminates one of the major cost factors in the preparation of Pyrex glass or vitreous quartz substrates.

The rate of film deposition was found to be dependent on the substrate material. It is believed to be due to impairment or differences in initial film nucleation of the oxide layer rather than in a difference in the subsequent growth rate once full coverage is attained. For some substrate materials, notably untreated soda lime glass, the inability of the oxide to uniformly nucleate sometimes results in patchy deposition with large areas of the substrate remaining uncoated. If the soda lime glass is untreated prior to the tin oxide deposition, a hazy, highly resistive tin oxide coating is also formed due to the out-diffusion of alkali metal ions from the glass. Removal of the alkali metal ions from the surface of the glass is therefore necessary if high quality tin oxide coatings are to be prepared. This is especially true for high temperature CVD processing as the rate of diffusion is temperature dependent.

Two different surface treatments of the glass were evaluated, viz., surface ion depletion (SID) and acid leaching. Of the two treatments, surface ion depletion (23) was found to be the more effective.

It was found that the SID treated glass behaved in a similar manner to vitreous quartz with respect to the rate of tin oxide deposition and the electrical and optical properties of the resulting coatings. The sheet resistances were up to 30% higher than comparable layers on fused quartz, but were better (lower) than those achieved on polished borosilicate glasses with a low alkali metal content. The layers were haze free and the optical transmission was identical to that on quartz. The substrates could be processed at temperatures approaching the softening point of the glass without hazing.

Leaching of the alkali from the surface of the glass with a mineral acid is also a useful treatment. For this to be effective the glass substrates required boiling in

1:1 diluted hydrochloric or sulfuric acid for periods of at least 1 hr. The removal of the surface ions is not permanent or as deep as in the SID treatment, so that the substrates require close control of the deposition process to obtain the best results. The substrate temperature is especially critical, the optimum processing temperature being 475°C. Above this temperature the rate of alkali diffusion is increased and the electrical and optical properties of the coatings deteriorate. Below 475°C the sheet resistance gradually increases due to incomplete incorporation of the antimony dopant. Low sheet resistances can be obtained but the control of the deposition parameters becomes critical. For the preparation of SnO<sub>2</sub>:Sb films on soda lime glass, having a sheet resistance of about 100 ohm/square, the SID treatment is recommended. The deposition parameters are less critical in this case since higher surface temperatures do not result in the diffusion of alkali ions to the surface.

A comparison of film properties resulting from using fused quartz and variously acid-leached soda lime glass substrates is presented in Table II. The data show that the sheet resistance of the quartz continued to decrease at temperatures above 475°C, while there is a drastic increase in the sheet resistance of the soda lime glass. This is accompanied by hazing and a consequent decrease in optical transmission, resulting in films of unacceptable quality. Quartz is, therefore, a consistently better substrate material than either acid-leached or SID soda lime glass.

### Film Properties

*Electrical and compositional properties.*—The electrical resistance of the films was measured with a conventional four-point probe. The point separation of the probe was 10 mil. In order to calculate the specific resistivity, measurements of film thickness were made using a Sloan "Dektak," equipped with a 25 μm stylus. For this measurement a step was etched in the layer with HCl/Zn powder slurry.

The optimum concentration of the antimony dopant was determined from resistivity data recorded in three series of experiments. In the first series the antimony concentration was increased from zero to a level at which the layers became blue in appearance. The sheet resistance decreased with increasing antimony content until a blue coloration appeared. At this point a further increase in the antimony content produced a rapid deterioration in the optical transmission, with no further decrease in resistivity. The optimum doping level of antimony was taken to be the concentration which yielded films of minimum specific resistivity and maximum light transmission.

The second series of experiments was designed to determine the influence of substrate temperature on the effective incorporation of the antimony dopant. In this series the antimony dopant concentration was set within the previously determined range of values and the substrate temperature was varied from 350° to 550°C.

Table II. Comparison of coated quartz and variously acid-leached soda lime glass substrates as a function of deposition temperature

Deposition temp, °C	Acid leaching treatment of glass	Treated glass		Untreated quartz	
		Rs, ohm/sq.	Appearance	Rs, ohm/sq.	Appearance
420	Room temperature, 12M HCl, 1 hr	1500	Hazed	—	—
475		630	Hazed	—	—
420	Room temperature, 18M H <sub>2</sub> SO <sub>4</sub> , 1 hr	1000	Hazed	—	—
475		950	Hazed	—	—
420	Boiled in 6M HCl, 1 hr	275	Clear	—	—
400		650	Clear	300	Clear
425	Boiled in 50 volume per cent H <sub>2</sub> SO <sub>4</sub> , 1 hr	290	Clear	210	Clear
450		165	Clear	130	Clear
475		80	Clear	70	Clear
475		67	Clear	60	Clear
500		500	Hazed	50	Clear

Table III. Electrical resistivity and Sb/Sn ratio of films deposited at different temperatures and dopant concentrations

Substrate temp, °C	Sb-N <sub>2</sub> flow rate, cm <sup>3</sup> /min	Film thickness, Å	Fused quartz substrates			Surface treated soda lime glass	
			Sheet resistance, ohm/sq.	Specific resistivity, ohm-cm	Atom ratio,* Sb/Sn	Sheet resistance, ohm/sq.	Specific resistivity, ohm-cm
400	550	2450	300	$7.1 \times 10^{-3}$	0.0025	650	$1.7 \times 10^{-2}$
425	420	1600	390	$6.2 \times 10^{-3}$	0.0023	550	$8.8 \times 10^{-3}$
425	550	1300	270	$3.5 \times 10^{-3}$	0.0088	270	$3.5 \times 10^{-3}$
425	700	1500	185	$2.8 \times 10^{-3}$	0.022	150	$2.3 \times 10^{-3}$
425	850	1400**	240	$3.4 \times 10^{-3}$	0.11	295	$\sim 6.2 \times 10^{-3}$
450	420	3100	160	$5.0 \times 10^{-3}$	0.0030	185	$5.7 \times 10^{-3}$
450	550	2250	100	$2.3 \times 10^{-3}$	0.0075	115	$2.5 \times 10^{-3}$
450	700	3000	100	$3.0 \times 10^{-3}$	0.0063	105	$3.2 \times 10^{-3}$
450	850	3100**	70	$2.2 \times 10^{-3}$	0.025	77	$2.2 \times 10^{-3}$
475	420	3400	145	$4.9 \times 10^{-3}$	0.0029	150	$5.1 \times 10^{-3}$
475	550	3600	73	$2.6 \times 10^{-3}$	0.0090	86	$3.1 \times 10^{-3}$
475	700	3600	53	$1.9 \times 10^{-3}$	0.015	60	$2.2 \times 10^{-3}$
475	850	3150**	48	$1.5 \times 10^{-3}$	0.089	52	$1.6 \times 10^{-3}$
500	550	$\sim 800$	50	$\sim 4.0 \times 10^{-4}$	0.0075	550 (hazed)	$\sim 4.0 \times 10^{-3}$

\* Net intensity ratio  $SbL\alpha/SnL\alpha$  from x-ray fluorescence analysis.

\*\* Blue-grayish coloration of high light absorbance.

CVD conditions as stated in Table I except for temperature; films on quartz and glass substrates were codeposited.

In a third series of tests, further refinements in the CVD conditions were examined for different substrate materials.

Representative data from the first two series of experiments are recorded in Table III. Plates of vitreous fused quartz and surface-treated soda lime glass were used as substrate materials in 15 min deposition periods. The chemical composition of the  $SnO_2:Sb$  films is expressed as atom ratio Sb/Sn and was determined by x-ray fluorescence analysis described in a later section. The measured sheet resistances of the films obtained at 425°, 450°, and 475°C are plotted as a function of the antimony dopant input (gas flow rate  $Sb-N_2$  cm<sup>3</sup>/min) in Fig. 2. The

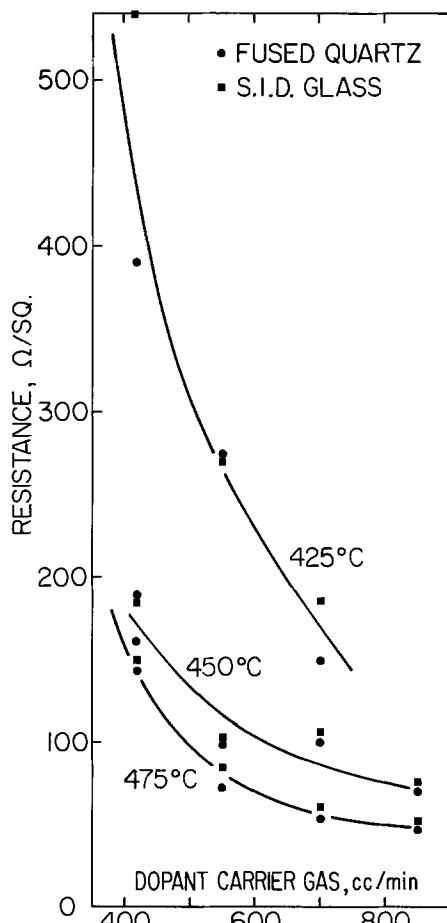


Fig. 2. Sheet resistance of  $SnO_2:Sb$  films on two substrate materials as a function of antimony dopant input ( $Sb-N_2$  flow rate) for three different deposition temperatures. (Film thicknesses vary as shown in Table III.)

sheet resistance is seen to decrease as the dopant input increases, and also as the temperature increases. This type of graph is useful in practical applications where sheet resistance is specified regardless of film thickness. However, part of these resistance changes are caused by differences in the film thickness which varies for the various CVD conditions. The same data are therefore plotted in Fig. 3 in terms of specific resistivity to eliminate effects of film thickness.

The effect of the dopant input on the Sb/Sn atom ratio of  $SnO_2:Sb$  films on quartz for the 425°, 450°, and 475°C samples from Table III is shown graphically in Fig. 4. It is seen that the Sb/Sn ratio increases nearly exponentially with the dopant carrier gas ( $Sb-N_2$ ) flow rate over the range studied. Apart from the wide spread of two of the 450°C data, which we cannot explain, there is little difference in the Sb/Sn ratios between the low and high temperature films.

The lowest resistivity ( $2-3 \times 10^{-3}$  ohm-cm) with highest light transmission ( $>85\%$  net) was obtained with films deposited at 450°C with intermediate doping level. The best film had a Sb/Sn ratio of 0.0075

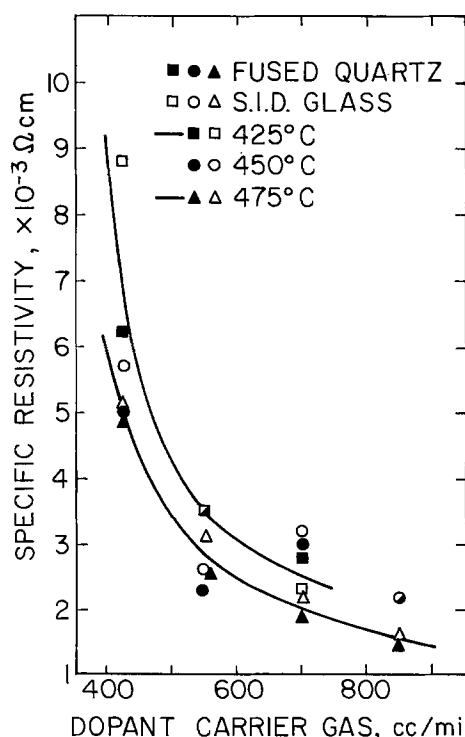


Fig. 3. Data from Fig. 2 plotted in terms of specific resistivity to normalize film thickness effects.

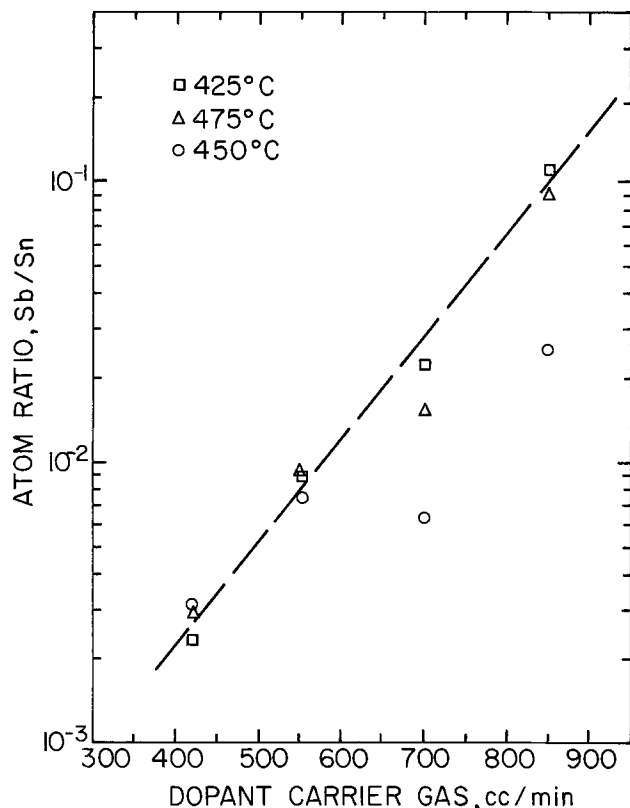


Fig. 4. Atom ratio Sb/Sn of  $\text{SnO}_2\text{:Sb}$  films on fused quartz plates as a function of  $\text{Sb-N}_2$  flow rate for low and high deposition temperatures. (Data from x-ray fluorescence analysis.)

which corresponds to about 0.6 atomic per cent (a/o) Sb in  $\text{SnO}_2\text{:Sb}$ .

In Table IV several physical properties of coatings prepared under optimum conditions on a number of different substrate materials are recorded. The Sb/Sn atomic ratios, determined by x-ray fluorescence analysis, were in the range 0.025-0.034 (2.0-2.7 a/o Sb in  $\text{SnO}_2\text{:Sb}$ ). These values are considerably higher than was expected from the results listed in Table III, but values in the same range were also obtained by electron probe microanalysis (Table V). The reason for the difference in dopant concentration is not understood, but it may have been due to minor modifications to the gas inlet system. Although the results in Tables IV and V are mutually consistent they can therefore not be strictly compared with those in Table III. The values of specific resistivity for this series (in Table IV) are in the range  $1.1 \times 10^{-3}$  to  $1.8 \times 10^{-3}$  ohm-cm, the lowest being for a film on a sapphire substrate. For comparison, values cited in the literature for  $\text{SnO}_2\text{:Sb}$  films prepared by various methods range typically from  $7 \times 10^{-4}$  to  $6 \times 10^{-3}$  ohm-cm (5, 13, 15, 19, 20, 24, 25).

Hall measurements were performed at room temperature using the standard Van der Pauw technique. The

magnetic field employed was 16 kG. The layers examined were deposited under optimum conditions on quartz substrates and had a measured thickness of 2800 Å. The layers were found to be n-type with a carrier concentration of  $1.2 \times 10^{20} \text{ cm}^{-3}$  and a mobility of  $23 \text{ cm}^2/\text{V-sec}$ . For comparison, undoped layers were also n-type but had a carrier concentration of  $9.0 \times 10^{18} \text{ cm}^{-3}$  and a Hall mobility of  $10 \text{ cm}^2/\text{V-sec}$ .

**Optical properties.**—The index of refraction and thickness of a single sample on silicon were determined by ellipsometry. The thickness of the sample was measured to be 2013 Å and the refractive index at a wavelength of 5461 Å was 1.8912, within the experimental limits 1.8855-1.8969. The refractive index of the tin oxide is to a large extent dependent on the deposition conditions, especially the presence of water vapor in the reaction gas stream which produces films of lower index (22).

In thin layers the thickness and uniformity of tin oxide coatings could be readily estimated simply by observing their color in reflection. This is a very sensitive technique for comparing run-to-run uniformity or for determining variations in the deposit thickness across the deposition zone. The reflection color which corresponds to a given thickness depends on the substrate material and the refractive index of the film. With experience and a set of calibrated samples one can determine the thickness quite accurately by observing the color in reflection, providing one knows or ascertains the order of interference. This technique is especially useful since the thickness range in which it is most sensitive corresponds to thicknesses of tin oxide films used in practical devices. For example, the films in the thickness range of 2200-2500 Å listed in Table IV exhibit a blue-violet interference color.

The visible light transmission was measured throughout the range of 4000-7200 Å. The transmission data is recorded in Table IV as per cent transmittance measured with an uncoated substrate in the reference beam. Due to interference effects the light transmission can be peaked at any given wavelength in the visible by a correct choice of film thickness. In Fig. 5 the transmission and reflectance spectra of a 2800 Å thick layer on quartz is shown. This figure illustrates the variations in transmission produced by interference effects.

The introduction of the antimony dopant had no measurable effect on the optical transmission [as compared to undoped tin oxide (22)] until a certain threshold concentration was exceeded. At this value, which varies with CVD conditions employed (Table III), the films became blue in appearance and there was a consequent decrease in optical transmission. Further increases in the dopant concentration produced a very rapid deterioration in the optical transmission.

To record the infrared spectrum of the antimony-doped tin oxide, a coating was prepared on an infrared transparent silicon wafer. The observed Sn-O band structure was very weak in the lattice band region near  $600 \text{ cm}^{-1}$ . The Sb-O band structure which

Table IV. Electrical and optical properties of antimony-doped CVD tin oxide films deposited under optimum conditions on various substrate materials

Substrate material	Film thickness, Å	Sheet resistance, ohm/sq.	Specific resistivity, ohm-cm	Optical transmission in %, at wavelength stated, (Å)									Avg
				4000	4400	4800	5200	5600	6000	6400	6800	7200	
Fused quartz	2200	72	$1.6 \times 10^{-3}$	92.6	85.5	81.8	82.8	85.0	82.2	91.0	93.3	94.4	88.3
SID* soda lime glass	2300	67	$1.5 \times 10^{-3}$	87.0	86.7	81.6	78.1	79.9	83.0	87.1	90.1	90.8	84.9
A.L.** soda lime glass	2000	76	$1.5 \times 10^{-3}$	95.2	88.1	85.0	84.2	88.0	92.0	94.7	95.3	94.3	90.8
A.L.** soda lime glass	2200	82	$1.8 \times 10^{-3}$	91.8	85.2	84.8	85.8	90.0	92.8	94.5	94.7	92.8	90.3
Borosilicate glass	2350	72	$1.7 \times 10^{-3}$	94.0	86.7	82.7	83.3	86.7	90.0	93.3	94.5	94.4	89.5
1120 Sapphire	2500	40	$1.1 \times 10^{-3}$	—	—	—	—	—	—	—	—	—	—

\* SID = surface ion depleted.

\*\* A.L. = acid leached by boiling in 50 volume per cent  $\text{H}_2\text{SO}_4$  for 1 hr.

CVD conditions: 450°C, 20 min,  $\text{Sb-N}_2$  650  $\text{cm}^3/\text{min}$ ; other conditions as stated in Table I. Film composition: Sb/Sn atom ratio = 0.025-0.034 (2.0-2.7 a/o Sb in  $\text{SnO}_2\text{:Sb}$ ).

Table V. Electrical resistivity and Sb/Sn ratio of films deposited under various conditions on different substrates

Substrate material	Sb-N <sub>2</sub> flow rate, cm <sup>3</sup> /min	Deposition temp, °C	Deposition time, min	Film thickness, Å	Sheet resistance, ohm/sq.	Specific resistivity, ohm-cm	Atom ratio,* Sb/Sn
Fused quartz	420	425	20	1400	260	3.6 × 10 <sup>-3</sup>	0.012
Fused quartz	420	450	20	1800	180	3.2 × 10 <sup>-3</sup>	0.0079
Fused quartz	420	475	15	1500	200	3.0 × 10 <sup>-3</sup>	0.0087
Fused quartz	420	500	15	2250	150	3.4 × 10 <sup>-3</sup>	0.0080
Fused quartz	420	525	10	1500	140	2.1 × 10 <sup>-3</sup>	0.011
Fused quartz	420	550	7.5	1200	220	2.6 × 10 <sup>-3</sup>	0.0078
Borosilicate glass	420	500	2.5	~600	1180	~7.1 × 10 <sup>-3</sup>	0.020
Borosilicate glass	420	500	5.0	1900	500	9.5 × 10 <sup>-3</sup>	0.021
Borosilicate glass	420	500	7.5	2720	354	9.6 × 10 <sup>-3</sup>	0.014
Borosilicate glass	420	500	10	~3500	200	~7.0 × 10 <sup>-3</sup>	0.020
Borosilicate glass	420	475	10	3100	295	9.2 × 10 <sup>-3</sup>	0.013
SID glass**	550	450	15	2250	115	2.6 × 10 <sup>-3</sup>	0.0087
SID glass**	650	450	20	2300	67	1.5 × 10 <sup>-3</sup>	0.029
Fused quartz	650	450	20	2200	70	1.5 × 10 <sup>-3</sup>	0.029
A.L. glass***	650	475	20	2200	80	1.8 × 10 <sup>-3</sup>	0.018
A.L. glass***	650	475	20	2800	80	2.2 × 10 <sup>-3</sup>	0.015
SID glass**	700	450	15	3000	105	3.2 × 10 <sup>-3</sup>	0.0083

\* Net intensity ratio SbL<sub>α1</sub>/SnL<sub>α1</sub> from electron probe microanalysis.

\*\* SID = surface ion depleted, soda lime glass.

\*\*\* A.L. = acid leached, microscope slide glass.

occurs in the same spectral region was also weak. Since the Sn-O bandgap transition occurs in the near u.v. (approximately 4 eV), the absorption occurring in the region 4000-2000 cm<sup>-1</sup> was free carrier absorption due to doping of the SnO<sub>2</sub> film. Absorption in the 4000 cm<sup>-1</sup> region as related to doping has been studied by Summitt and Borrelli (26).

*Surface morphology.*—The general features of the tin oxide surfaces were established by visual examination and by low power optical microscopy, including Nomarski differential interference contrast. Samples deposited under optimum conditions exhibited very smooth, structureless surfaces. Details of the surface morphology were studied at magnifications up to 20,000× by scanning electron microscopy in the secondary electron emissive mode with a Cambridge Stereoscan. The photographs in Fig. 6 for films deposited on SID glass and acid leached glass exhibit a fine-grained surface with few defects. No pretreatment of the specimens was required, since the SEM image is generated by secondary electrons emitted from the surface being scanned.

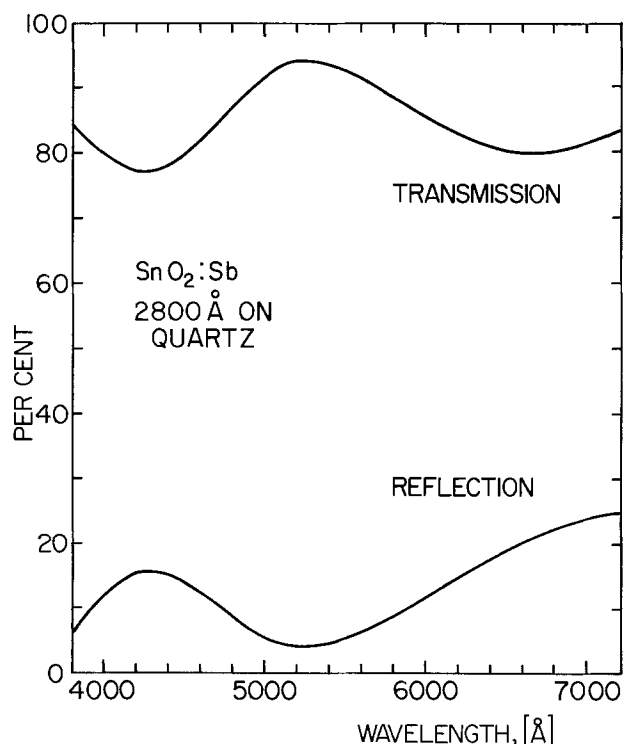


Fig. 5. Transmission and reflectance spectra of a 2800 Å thick layer of SnO<sub>2</sub>:Sb deposited on fused quartz.

Under certain gas flow or deposition temperature conditions where homogeneous gas phase nucleation was appreciable, hazy tin oxide films were obtained. These coatings were similar in appearance to those obtained on untreated soda lime glass substrates. The films also exhibited an excessive number of particulate defects. Hazed tin oxide coatings are unacceptable for most applications; therefore, considerable effort was devoted to ascertaining the cause of the haze and defining deposition conditions which minimized this effect.

*X-ray and electron diffraction studies.*—Samples from doped tin oxide layers deposited on fused quartz plates at substrate temperatures in the range 425°-500°C were destructively removed from the substrate by scraping with a diamond stylus and were

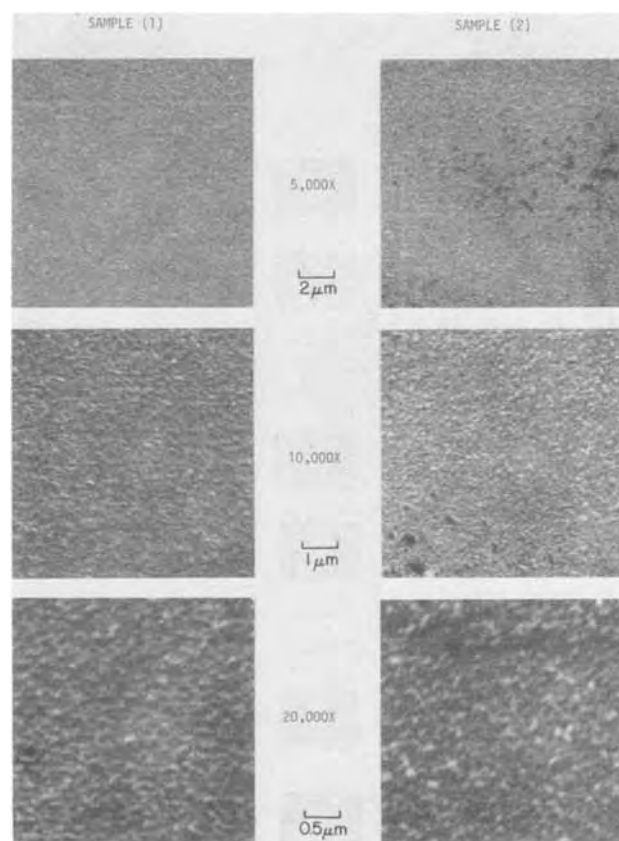


Fig. 6. Scanning electron micrographs of antimony-doped tin oxide films deposited at 450°C on two different substrate materials: sample 1, SID glass and sample 2, acid-treated soda lime glass. (Samples from Table IV.)

examined by x-ray diffraction. The x-ray powder patterns obtained were essentially the same for all samples. They showed that the layers were crystalline and composed almost entirely of tetragonal tin oxide ( $\text{SnO}_2$ ), similar to the results for undoped films reported by us (22) and also noted in the literature for undoped  $\text{SnO}_2$  films deposited from  $\text{SnCl}_4$  (27).

Surface examination of the same samples by electron diffraction confirmed this result for the films deposited at  $500^\circ\text{C}$ ; these were identified as polycrystalline tin oxide with azimuthal ordering about the (200)-axis. All other samples showed complex patterns which were most closely identifiable as polycrystalline antimony oxide ( $\text{Sb}_2\text{O}_3$ ) with azimuthal ordering about the (200)-axis. In addition, some unidentified second phase appeared to be present. The electron diffraction studies revealed the tin oxide to have a high degree of preferred orientation.

A number of attempts were made to produce epitaxial transparent conducting layers of tin oxide on single crystal substrate materials. Of all the materials examined sapphire appears to be the most promising. The tin oxide layers in thicknesses up to  $1\ \mu\text{m}$  were deposited on sapphire under the conditions described in Table I. They were subsequently annealed in air at  $1000^\circ\text{C}$  for 1 hr. On the inert sapphire substrates the optical and electrical properties of the tin oxide are not significantly changed by this treatment. Two orientations of sapphire (0001 and  $\bar{1}\bar{1}02$ ) were used in this investigation. Epitaxial growth was not achieved on either orientation but there were strong indications that given the correct choice of sapphire orientation epitaxial growth should be possible. Two typical Laue photographs for these sapphire orientations are presented in Fig. 7 for illustration.

On the  $\bar{1}\bar{1}02$  orientation the tin oxide was single-crystal-like in a direction perpendicular to the wafer face. The tin oxide  $\langle 101 \rangle$  coincided with the perpendicular to the  $\{1\bar{1}02\}$  of the sapphire. The tin oxide "a" axis was in the plane of the wafer and parallel to the sapphire  $1\bar{1}20$  axis. This results in two different tin oxide domains since the "a" axis of the tin oxide can align itself positive or negative with respect to the sapphire "a" axis. On the sample examined the two domains were not present in equal numbers; they were in a ratio of approximately 6 : 1. This observation would lead one to believe that it might be possible to misorient the substrate so as to

bias the growth of a single domain and produce epitaxy.

The tin oxide layer on the 0001 sapphire orientation was also single-crystal-like in a direction perpendicular to the wafer face. In this case the tin oxide "a"  $\langle 100 \rangle$  axis was aligned in the plane of the wafer with the sapphire "a" axis. Since there are three different sapphire "a" axes in the plane of the wafer this results in three different tin oxide domains each having a  $\langle 100 \rangle$  axis perpendicular to the wafer face. In this case misorientation of the wafer might also favor the growth of a single domain and produce epitaxy.

*X-ray fluorescence analysis.*—The concentration of the antimony dopant in the tin oxide was monitored by x-ray fluorescence spectroscopy. Since the elements antimony and tin are adjoining in the Periodic Table and have no interfering absorption edges, the relative intensities of spectroscopic lines should correspond closely to the relative concentrations of the elements. This was later confirmed by mass spectrographic analysis discussed in the section on trace impurity analysis.

For x-ray fluorescence spectroscopic analysis the type of substrate material was found to be critical. Earlier attempts to analyze doped tin oxide layers deposited on glass were unsuccessful due to the interference of strong x-ray fluorescence from calcium and potassium present in the glass. These samples on glass substrates were subsequently analyzed by electron probe microanalysis (see next section). Samples suitable for analysis by x-ray fluorescence were obtained by depositing the tin oxide on quartz substrates. The analytical results reported in Table III for films co-deposited on quartz and surface-treated soda lime glass were obtained by x-ray fluorescence analysis of the films on quartz. The film composition ranged from an atomic ratio Sb/Sn of 0.002-0.11.

*Electron-probe microanalysis.*—A number of samples of variously antimony-doped tin oxide coatings on glass and quartz deposited at various temperatures to different thicknesses were examined by electron-probe microanalysis for the reasons pointed out above. The results obtained were consistent with those obtained by x-ray fluorescence. The results are summarized in Table V, together with deposition parameters and other physical properties of the coatings. The antimony dopant concentration is expressed as the intensity ratio

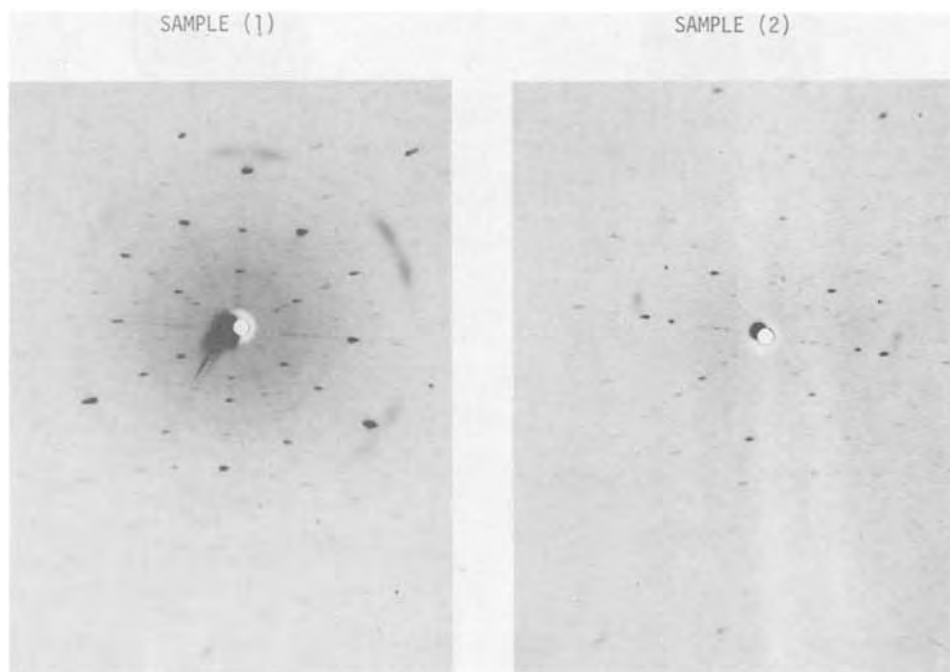


Fig. 7. Laue photographs of  $\text{SnO}_2\text{:Sb}$  coatings on single crystal sapphire substrates: sample 1, 0001 orientation and sample 2,  $\bar{1}\bar{1}02$  orientation.

(SbL $\alpha_1$ )/(SnL $\alpha_1$ ), which was assumed to correspond closely to atomic ratio. For L $\alpha_1$  lines of elements of consecutive atom number in this region of the Periodic Table, net intensity ratio should be substantially equivalent to mass concentration ratio. Several samples on quartz were analyzed by both x-ray fluorescence and electron-probe microanalysis to verify this assumption; the results obtained by the two analytical methods are in good agreement.

**Trace impurity analysis.**—One typical antimony-doped tin oxide layer, deposited on a polished wafer of 100 ohm-cm high purity silicon at a substrate temperature of 475°C under optimum conditions, was examined by spark source solids mass spectroscopy to identify and quantitate any chemical impurities. Besides the high concentration of antimony which was intentionally added to the tin oxide, the only other major impurity found was chlorine at a concentration of 0.05 a/o.

Other impurities identified were minor concentrations of transition metals (Zn 19, Fe 8.4, and Cu 1.3 ppm). The origin of these impurities is not known, but since only reagent quality chemicals were employed it was not entirely unexpected.

For many applications the presence of volatile impurities in the tin oxide is undesirable. To ascertain the nature and quantity of these impurities, several tin oxide coatings on glass were analyzed by means of an AEI MS-10 gas mass spectrometer. The samples were heated in an evacuated stainless steel container to temperatures up to 140°C and the gases evolved examined in the mass spectrometer. The experimental data showed that the bulk of the outgassing products was derived from the substrate material and not from the tin oxide coating. The principal gases evolved were carbon dioxide and water, but in no case were chlorine or chlorine-containing species present.

### Conclusions

It has been established that highly conducting antimony-doped tin oxide coatings can be prepared at deposition temperatures as low as 425°C by modifying the CVD process based on dibutyl tin diacetate, O<sub>2</sub>, H<sub>2</sub>O, and N<sub>2</sub> as carrier gas (22). This is accomplished by introduction of antimony as dopant in the form of SbCl<sub>5</sub> vapor.

The antimony concentrations measured in the films that were deposited under widely varying temperature and reactant flow conditions ranged from 0.002 to 0.11 atomic ratio Sb/Sn. The optimum dopant concentration was found to be within the range of 0.6-2.7 a/o (or mol per cent) Sb in SnO<sub>2</sub>:Sb.

Typical samples are 1500-3600Å thick with sheet resistance values of 50-150 ohm/square, and have a specific resistivity in the range  $1.5 \times 10^{-3}$  to  $3.2 \times 10^{-3}$  ohm-cm. Light transmission in the visible region of the spectrum ranges from 85 to 91% net. The films are free of volatile chlorine or chlorides. Coatings are thermally stable in air up to 1000°C, provided that the underlying substrate material is inert. Coatings prepared on single crystal sapphire did not deteriorate when heated to 1000°C in air for several hours. When heated in hydrogen the coatings were rapidly destroyed due to reduction of the oxide, as expected.

The films can be readily, reproducibly and uniformly deposited on different types of substrate material. Substrate plates of fused quartz, borosilicate glass, and treated soda lime glass have been used successfully. Surface ion depletion of soda lime glass by application of an electric field to the glass effected sufficient alkali ion depletion to yield film resistivities comparable to those of quartz. Provided that the substrates are treated by a less effective boiling acid leaching prior to the tin oxide deposition and the deposition temperature does not exceed 475°C, the coatings can be ap-

plied even to glass substrates with a high alkali content.

### Acknowledgments

The authors would like to thank the following persons for their contributions in the instrumental analysis part of the project: E. Meier and H. Meier (Zurich); E. P. Bertin, E. M. Botnick, D. C. McCarthy, J. J. McGinn, D. A. Kramer, C. W. Magee, R. J. Paff, B. J. Seabury, J. M. Shaw, R. D. Vibronek, and P. J. Zanzucchi (Princeton); we are indebted also to H. McCandless and L. A. Goodman (Princeton) for many fruitful discussions during the course of this investigation.

Manuscript submitted March 12, 1975; revised manuscript received Sept. 2, 1975. This was Paper 277RNP presented at the New York, New York, Meeting of the Society, Oct. 13-17, 1974.

Any discussion of this paper will appear in a Discussion Section to be published in the December 1976 JOURNAL. All discussions for the December 1976 Discussion Section should be submitted by Aug. 1, 1976.

Publication costs of this article were partially assisted by RCA Corporation.

### REFERENCES

1. L. Holland, in "Vacuum Deposition of Thin Films," chap. 16, p. 493, Chapman and Hall Ltd., London (1963).
2. L. I. Maissel, in "Handbook of Thin Film Technology," L. I. Maissel and R. Glang, Editors, chap. 18, McGraw-Hill Book Co., New York (1970).
3. J. M. Mochel, U.S. Pat. 2,564,707 (1951).
4. R. E. Aitchison, *Australian J. Appl. Sci.*, **5**, 10 (1954).
5. A. Fischer, *Z. Naturforsch.*, **9a**, 508 (1954).
6. I. Imai, *J. Phys. Soc. Japan*, **15**, 937 (1960).
7. J. A. Lely and J. G. Bos, U. S. Pat. 3,014,815 (1961).
8. Union des Verrieries Mecaniques Belges, Brit. Pat. 892,708 (1962).
9. R. Groth, E. Kauer, and P.C.v.d. Linden, *Z. Naturforsch.*, **17a**, 789 (1962).
10. H. Sasaki, Y. Nishimura, and T. Yamamoto, "Proc. Electronic Comp. Conf.," IEEE, p. 79 (1966).
11. R. W. Gress, J. A. Murphy, and A. T. Talawalkar, *ibid.*, p. 164 (1968).
12. T. Inagaki, J. Nakajima, and Y. Nishimura, *Fujitsu Sci. Tech. J.*, **5**, 235 (1969).
13. D. Elliott, D. L. Zellmer, and H. A. Laitinen, *This Journal*, **117**, 1343 (1970).
14. A. R. Peaker and B. Horsley, *Rev. Sci. Instr.*, **42**, 1825 (1971).
15. F. Möllers and R. Memming, *Ber. Bunsenges. Phys. Chem.*, **76**, 469 (1972).
16. A. Rohatgi, T. R. Viverito, and L. H. Slack, *J. Am. Ceram. Soc.*, **57**, 278 (1974).
17. W. R. Sinclair, F. G. Peters, D. W. Stillinger, and S. E. Koonce, *This Journal*, **112**, 1096 (1965).
18. V. M. Vaynshteyn, *Soviet J. Opt. Technol.*, **34**, 45 (1967).
19. J. L. Vossen, "Proc. (3rd) Symp. on the Dep. of Thin Films by Sputtering," p. 80, University of Rochester (1969).
20. J. L. Vossen and E. S. Poliniak, *Thin Solid Films*, **13**, 281 (1972).
21. R. Muto and S. Furuuchi, *Oyo Buturi*, **41**, 1 (1972).
22. J. Kane, H. P. Schweizer, and W. Kern, *This Journal*, **122**, 1144 (1975).
23. D. E. Carlson, K. W. Hang, and G. F. Stockdale, *J. Am. Ceram. Soc.*, **57**, 295 (1974).
24. S. P. Lyashenko and V. K. Miloslavskii, *Opt. Spectroscopy*, **19**, 55 (1965).
25. W. M. Feist, S. R. Steele, and D. W. Ready, in "Physics of Thin Films," G. Hass and R. E. Thun, Editors, Vol. 5, p. 310, Academic Press, New York (1969).
26. R. Summit and N. F. Borelli, *J. Phys. Chem. Solids*, **26**, 921 (1965).
27. J. A. Aboaf, V. C. Marcotte, and N. J. Chou, *This Journal*, **120**, 701 (1973).

# Chemical Vapor Deposition of Amorphous Boron on Massive Substrates

L. Vandenbulcke and G. Vuillard

Centre de Recherches sur la Chimie de la Combustion et des Hautes Températures,  
C.N.R.S., 45045 Orleans, Cedex, France

## ABSTRACT

Compact coatings of amorphous boron were deposited on the smooth surface of substrates such as graphite, refractory metals, iron, and stainless steel using the reduction of boron trichloride by hydrogen. With a constant surface temperature and a low deposition efficiency, a constant thickness is obtained if transport limitations are avoided at all points of the surface. Extension of the results is proposed for a deposition on larger surfaces and substrates of complex shape. The rate of deposition was studied at temperatures ranging from 950° to 1200°C. The apparent activation energy was found equal to 31.4 kcal/mole. Adherence and absence of cracks are a function of the specific nature of the substrate. The most satisfactory coatings were obtained on graphite, refractory metals of Group Vb, iron, and stainless steel. On iron and stainless steel, a diffusion barrier was first deposited by pack cementation, which avoids the transport of the metals and slows down the boron diffusion. Boron morphology regularity is shown to be a function of nucleation.

The rate at which a substance is deposited from chemically reactive vapors can be governed by either chemical kinetics or mass transport of reactants and products. The relative rate of transport to and from the reaction surface and the rate of chemical conversion in turn determine local concentrations and supersaturation which may influence deposit morphology. The relative importance of the diffusional and kinetic factors during chemical vapor deposition of boron by hydrogen reduction of boron trichloride on a hot filament was studied in detail by P. E. Gruber (1) and H. E. Carlton *et al.* (2). Generally a horizontal resistance heated wire is used. In this case, mass transport in the vapor phase is important whatever the geometry of the deposition cell. It is always equal to or greater than the mass transport by natural convection, and up to 1050°-1100°C, the deposition rate is governed by chemical kinetics (1-3).

On a massive substrate, the rate of deposition is generally limited by mass transport at these temperatures and crystals of boron nucleate very rapidly (4). To avoid this crystallization, a deposition cell was built to produce a stream of reactants flowing at high velocity normal to the center of the substrate, then flowing at high velocity in a parallel direction. In this case, it is very difficult to specify mass transport properties, but it was possible to increase experimentally the mass transfer by increasing the mass flow rate. The rate of mass flow was determined by the rate of reactants metered with flowmeters and by the shape and size of the deposition cell. In all cases where the deposition rate is governed by chemical kinetics at all points of the substrate, uniform coatings of "amorphous" boron are produced.

## Experimental Techniques

The experimental set up is shown in Fig. 1. The details of the deposition cell are shown in Fig. 2. The apparatus is made of Pyrex glass except for the reactor which is made of silica. The desired flow rates of  $\text{BCl}_3$  and  $\text{H}_2$  are adjusted by metering valves, and metered by flowmeters. The mixing gas is introduced in the reactor or bypassed outside through a valve. This valve provides for a flow of He introduced in the reactor and for a flow of the reactants bypassed outside, and vice versa. The stream of either He or the reactants is introduced at a high velocity normal to the substrate in a 0.8 cm diam cylindrical nozzle. The substrate is a disk

of 2 to 3 cm diam, 0.5 to 1 cm thick. It is heated by a high frequency generator regulated by a thermocouple fitted at 0.05 cm under the surface to be coated. The surface temperature of the substrate is measured by this thermocouple. The maximum temperature fluctuations are  $\pm 2^\circ\text{C}$ .

The experimental procedure is as follows: the desired flow rates of  $\text{BCl}_3$ ,  $\text{H}_2$ , and He metered by rotameters are set and the power supply adjusted to a predetermined value for the desired temperature. The substrate

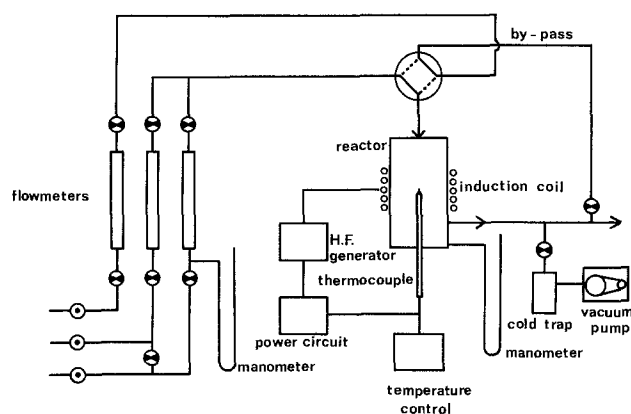


Fig. 1. Schematic diagram of experimental apparatus

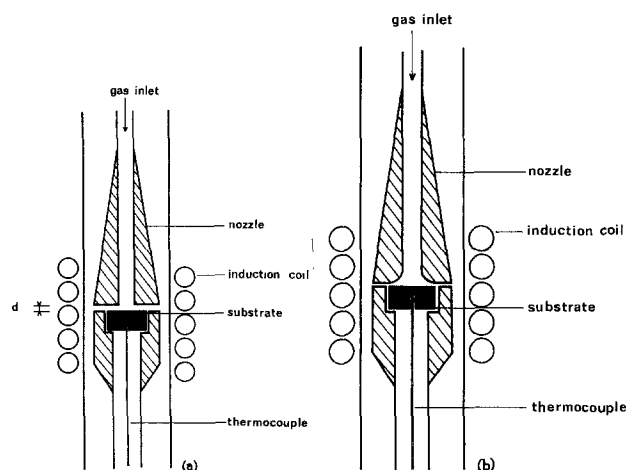


Fig. 2. Details of deposition cell showing high velocity nozzles

Key words: mass transport, kinetic, refractory metals, steel morphology.



is heated to the desired temperature in helium. Timing of the experiment is started with the reactants flow in the reactor. The volume measured between the bypass valve and the substrate is about 10 cm<sup>3</sup> and is flushed during a very small time (<1 sec in our experimental conditions). Timing of the experiment is stopped when the helium flow is turned into the reactor. The substrate and the boron deposited are cooled in helium. The helium flow rate is determined in order to avoid temperature fluctuations larger than during deposition at the start and the end of the experiment.

In all experiments, the ratio of BCl<sub>3</sub>:H<sub>2</sub> is equal to 2:3 without any addition of inert gas and the pressure is 1 atm. Hydrogen used in these experiments is of 99.995% by volume purity. CP-grade boron trichloride, 99.9% pure (manufacturer's specification) was used. The experimental apparatus is flushed before and after each reaction with helium of 99.995% pure by volume. The substrates used are: fine-texture prepolished graphite of average density 1.75, cleaned in alcohol in an ultrasonic device and dried; the refractory metals titanium, zirconium, niobium, tantalum, molybdenum, and tungsten of 99.9% purity (all surfaces are prepolished, in some cases optically polished and/or annealed); iron (99.95% purity), and stainless steel with average composition (C < 0.03, Cr = 18, Ni = 10%). In the case of iron and stainless steel it was necessary to first deposit a film to act as a diffusion barrier for boron. This was obtained by diffusion of tantalum produced by a pack-cementation process.

#### Influence of Mass Transport and Chemical Kinetics: Experiment and Discussion

The effect of flow rate, position of the substrate, and temperature on deposition rate were studied on a graphite substrate. Thickness of boron deposits was measured with an optical microscope on the prepolished vertical plane of the disk.

Figure 3 shows the thickness of boron deposits as a function of the radial distance on the disk with varying flow rates of reactants (H<sub>2</sub> + BCl<sub>3</sub>). Figure 2a shows the nozzle that was employed and the distance *d* between the nozzle and the deposition surface (*d* = 0.3 cm). The reaction time was always 120 sec and the temperature 1100°C. Figure 3 shows that the thickness is constant in the center of the substrate in front of the nozzle. When the flow rate is equal to or greater than 40 cm<sup>3</sup>/sec (0.14 g/cm<sup>2</sup> · sec of BCl<sub>3</sub>), it does not influence the boron-deposited thickness in the center of the substrate. At smaller flow rates the thickness is a function of the flow rate. The deposition rate is limited in one case by chemical kinetics, and by mass transfer in the vapor phase in the other. When the distance from the center of the substrate is greater than 0.4 cm, mass transfer in the vapor phase is small and the thickness falls quickly.

Figure 4 shows the thickness of boron deposits as a function of the diametral distance on the dish with

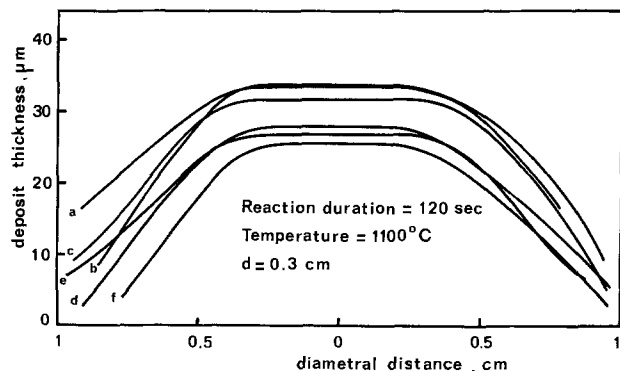


Fig. 3. Effect of flow rates of reactants on deposit thickness along the sample diameter: a = 50, b = 40, c = 34, d = 28, f = 16 cm<sup>3</sup>/sec.

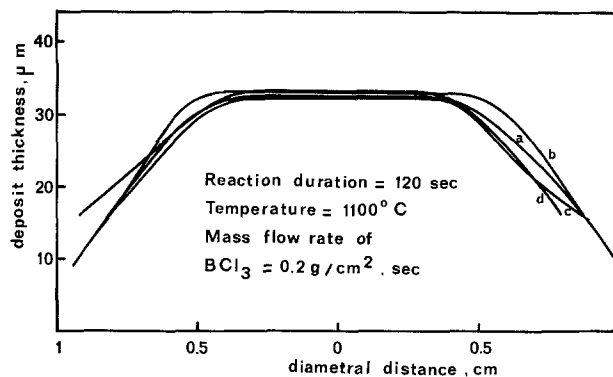


Fig. 4. Effect of *d* on deposit thickness along the sample diameter: a = 0.3, b = 1, c = 2, d = 3 cm.

varying distance *d* (Fig. 2a). The effect of *d* is very small over the range investigated, the flow of reactants remaining normal to the deposition surface. In the center of the substrate, the deposition rate is only limited by chemical kinetics.

The above studies show that the deposition rate is only limited by chemical kinetics when the stream of reactants is flowing at a rate equal to or greater than 80 cm/sec normal to the deposition surface at a temperature of 1100°C. However, the diameter of the nozzle cannot be increased extensively since in that case mass flow becomes considerable. It is possible to increase the rate of reactants flowing in a parallel direction to the substrate by reducing the distance *d* (*d* < 0.05 cm), but the boron deposit is always scaled off at a distance of 0.4 cm from the center of the deposition surface (circumference of the nozzle). Another nozzle type (Fig. 2b) was constructed to avoid this scaling. Figure 5 shows the boron-deposited thickness as a function of the diametral distance on two different substrates, graphite and molybdenum. The distance *d* is smaller than 0.5 mm, but our apparatus was not accurate enough to adjust *d* at a fixed value ±0.1 mm and to position the substrate in a horizontal plane. The reaction time was 120 sec, the temperature 1100°C, and the flow rate 100 cm/sec. Line a in Fig. 5 shows that the deposit thickness is slightly smaller at the periphery of the deposition surface; *d* was too large. Line b shows that the substrate surface was slightly at an angle and the mass transfer in the vapor phase was too small on one side of the substrate. The higher circumference thickness was produced by the temperature being higher at the periphery than in the center of the substrate which was cooled by the stream flow of the reactants. The two effects, mass transfer too low and temperature too high, can be a way to obtain constant thickness deposits. The deposition efficiency is very low (generally 0.2%) and it is not necessary to take the production of hydrogen chloride into account. Then, it is easier to pre-

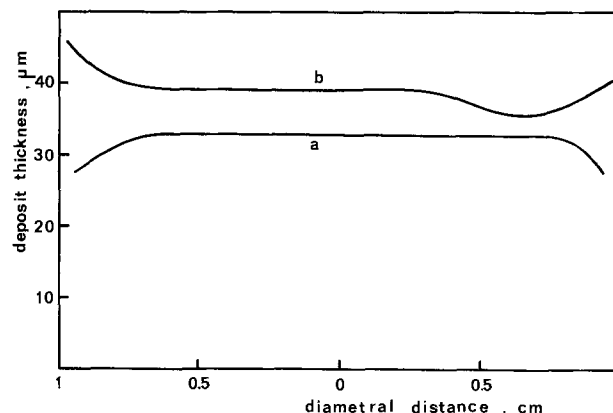


Fig. 5. Deposit thickness along the sample diameter with the nozzle of Fig. 2b: a = graphite, b = Mo.

heat the reactants and to deposit boron on a constant temperature substrate if the stream of reactants flows at a normal rate, then parallel to the substrate as high to produce a chemical kinetics limited deposition rate and without any pressure increase. It becomes obvious that amorphous boron could be deposited on a more complex shape if we adapt each deposition cell to each shape.

The effect of temperature on deposition rate is shown in Fig. 6, with a constant flow rate of 50 cm<sup>3</sup>/sec, 0.2 g/cm<sup>2</sup> · sec of BCl<sub>3</sub>. The final thickness of the boron deposit is observed to be directly proportional to the reaction time, except for 1200°C when the reaction time is greater than 180 sec. We can explain the shifting of the zero of the straight line by the nucleation occurring at a rate which is a function of the temperature. The apparent activation energy determined from the slope of the line in Fig. 7 is about 31.4 kcal/mole in the range of 950°-1100°C. Above 1100°C, the deposition rate is limited by the mass transfer in the vapor phase. Up to 1150°C, the boron deposit is amorphous during the first minutes of reaction. At 1200°C boron crystallizes very quickly (in the first minute).

### Deposition on Metallic Substrates

Boron was deposited on two types of metallic substrate: first, the refractory metals of the Groups IVb, Vb, and VIb where the interaction of the deposition reaction with the substrate is only a diffusion of boron in the metal; second, metals or alloys like iron and stainless steel where there is an interaction of H<sub>2</sub>/BCl<sub>3</sub> compositions with Cr and Fe which are transported as CrCl<sub>2</sub> along with the deposition of boron. In these cases, it was necessary to first deposit a barrier to avoid partially or entirely the transport of the metals and to reduce the diffusion rate of boron in the substrate. This barrier was of tantalum diffused into the substrate by a pack-cementation process which will be explained in detail elsewhere (5). On iron, the diffused tantalum formed an intermediate phase Ta<sub>3</sub>Fe<sub>7</sub> as determined by x-ray diffractometry and electron microprobe analysis. The thickness of this layer was 10-60 μ and constituted a new substrate. On stainless steel the structure of the layer is TaC(n) type. It is a very thin layer (0.4 μ)

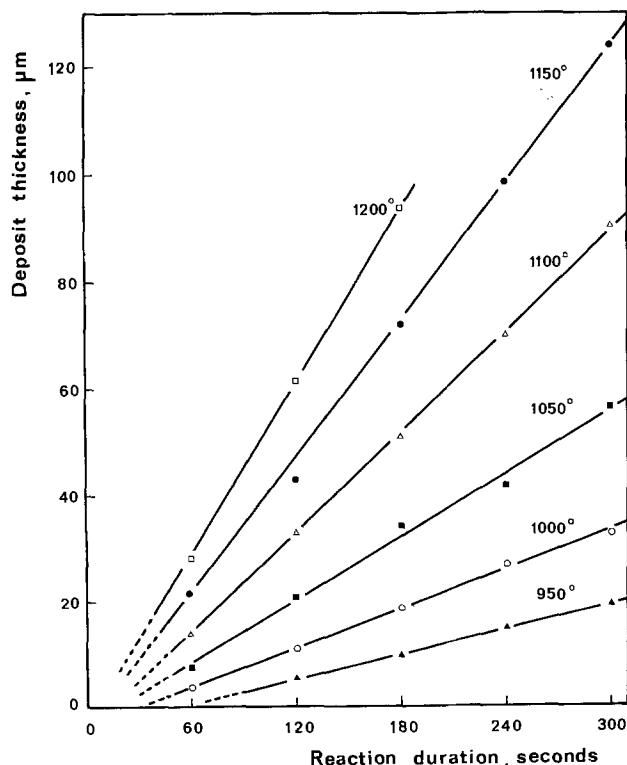


Fig. 6. Effect of temperature on deposition rate

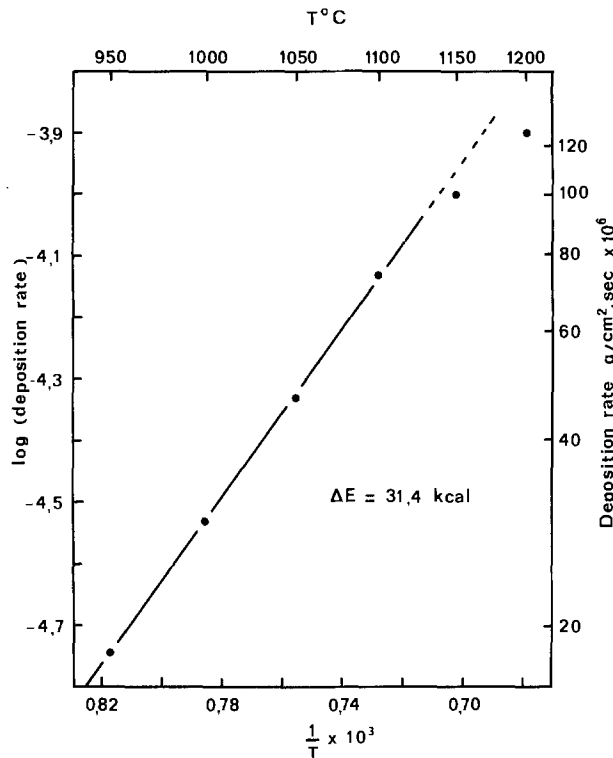


Fig. 7. Arrhenius plot of the boron deposition

which prevents the transport of metals as chlorides and slows down the boron diffusion in steel.

Coatings were studied by x-ray diffraction directly on the substrate coated with boron. The boron has a very small absorption coefficient and the different borides were identified as TiB<sub>2</sub>, ZrB<sub>2</sub>, NbB<sub>2</sub>, TaB<sub>2</sub>, Mo<sub>2</sub>B<sub>5</sub>, and W<sub>2</sub>B<sub>5</sub>. We have never obtained lines for other borides and pure metals. With molybdenum and tungsten as substrate, two layers of borides are identified by optical microscopy on a cross section. Studies of the inner layers by electron microprobe analysis show that presumably they are MoB and WB, the precision of the analysis, however, is unsatisfactory (Fig. 8). Optical studies did not reveal other borides of the other metals Ti, Zr, Ta, and Nb. The observed boride layers formed under the same conditions of time and

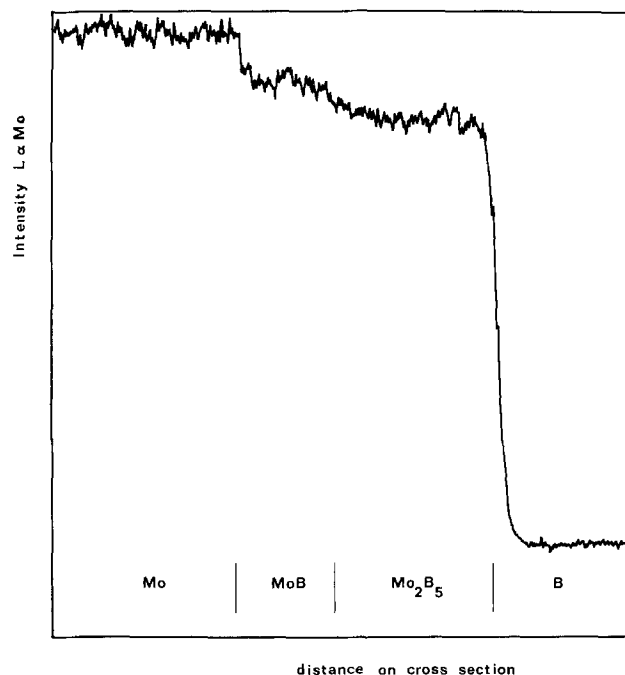


Fig. 8. Electron microprobe scan across a B coating on Mo

temperature show that the rate of boriding increases when going from the metals of Group IV to those of Group VI. These results are in agreement with the results of Epik (6). On tantalumized iron, the diffusion of boron forms two mixed borides of tantalum and iron. The x-ray lines of the borides are very close to those of  $TaB$  and  $TaB_2$ . This shows that iron is certainly inserted in the lattice. Figure 9 is a scanning of iron on a cross section of boron deposited on tantalumized iron which successively shows the different layers: boron, the two borides,  $Ta_3Fe_7$ , and pure iron. On stainless steel, there was boriding of the tantalumized layer and of the inner steel. The x-ray studies show a small displacement of the cementation layer lines and the formation of a complex boride of iron, chromium, and nickel. The EMA studies confirmed the boriding of steel through the cementation layer. Figures 10 and 11 show the diffusion being slowed down. All these results will be developed elsewhere (5).

The precipitation of borides at the interface is an important fact which regulates the adherence of boron to the substrate. It is essentially a diffusion of the small atoms of boron with a very slow diffusion of the metallic atoms in the opposite direction. This rapid one-way diffusion of boron fairly often produces an accumulation of vacancies which creates porosities in the interface proximity. These porosities increase when going from the metals of Group IV to those of Group VI (Fig. 12b-e). The deposits of boron on tantalumized iron do not show porosities when the deposition surface is strictly prepared. In the case of iron, the opposite diffusion of iron in boron is important as seen on iron

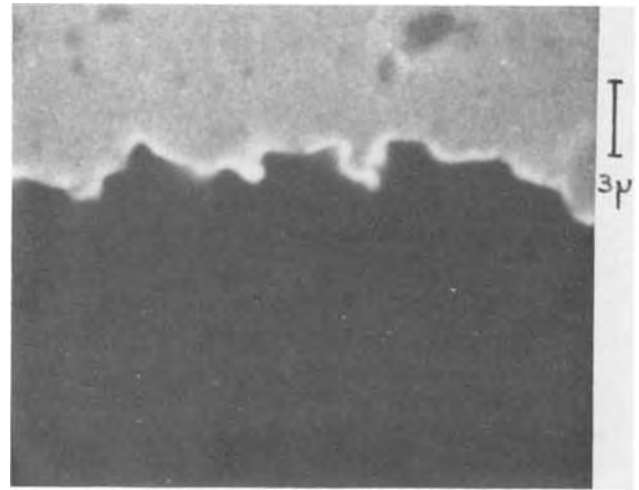


Fig. 11. Backscattered image

scanning of Fig. 9. The deposits on tantalum stainless steel never show porosities (Fig. 12f and g).

Another important aspect of the defects lies in the cracks that are produced normal to the deposit surface during the cooling of the sample. These cracks were observed with titanium or zirconium substrates which present a martensitic transformation which causes deep striation of the metal by itself (Fig. 12b). When the substrate was niobium or tantalum no cracks were

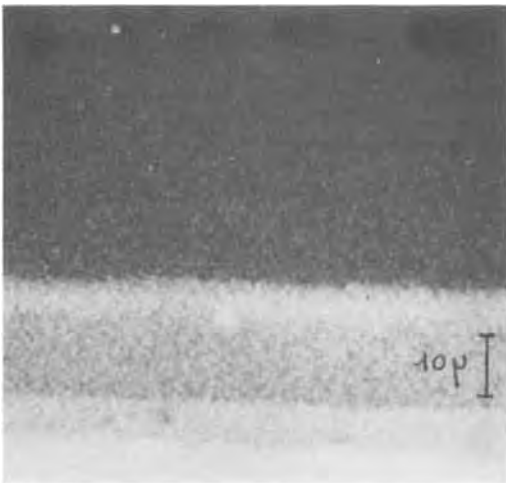


Fig. 9. Microprobe scan for Fe



Fig. 12a. B coating on graphite



Fig. 10. Absorbed electron image

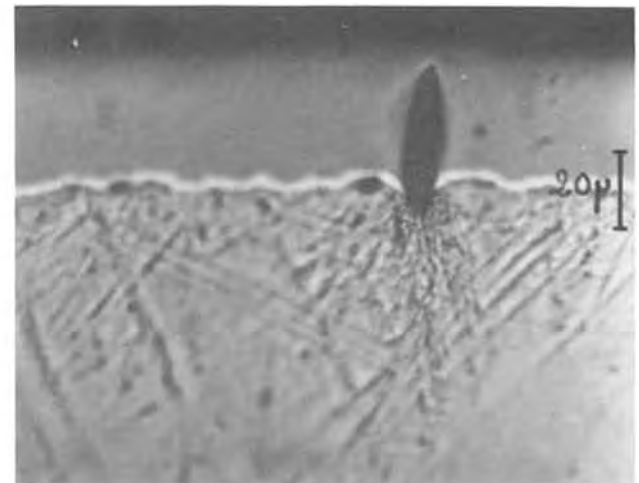


Fig. 12b. B coating on Ti

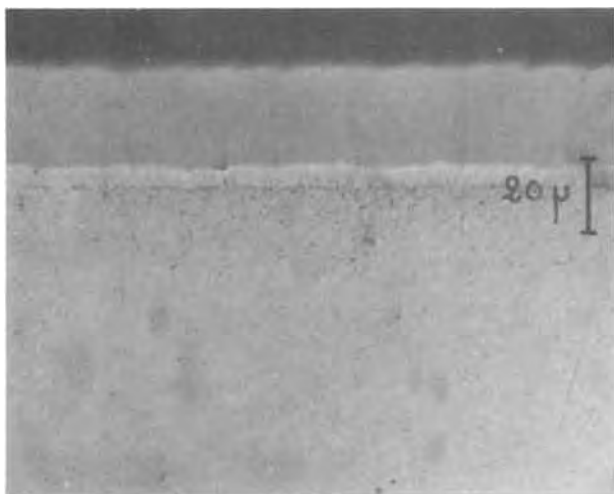


Fig. 12c. B coating on Ta

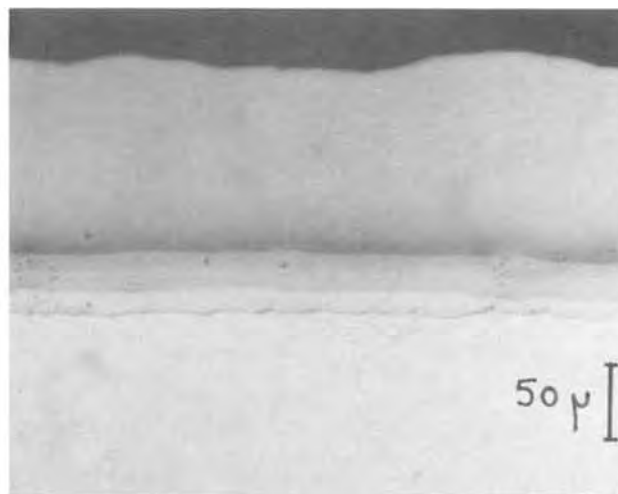


Fig. 12f. B coating on Fe(Ta)

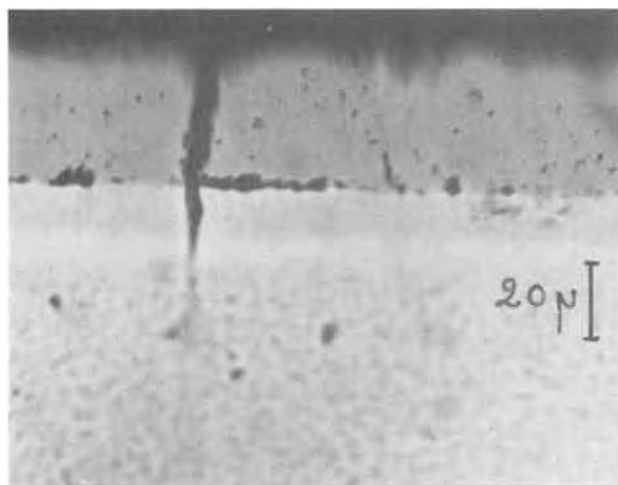


Fig. 12d. B coating on Mo

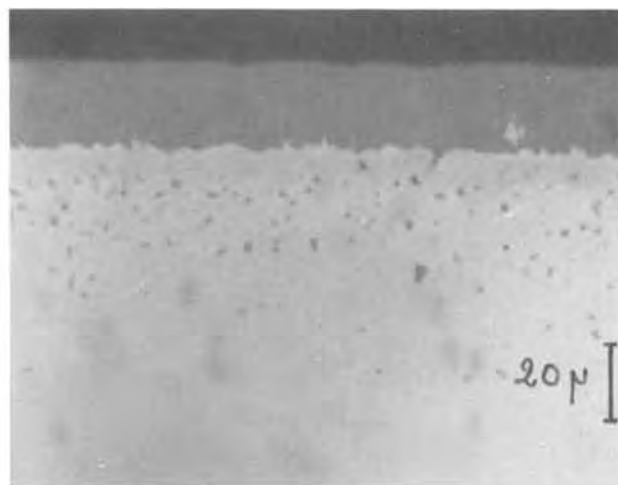


Fig. 12g. B coating on stainless steel

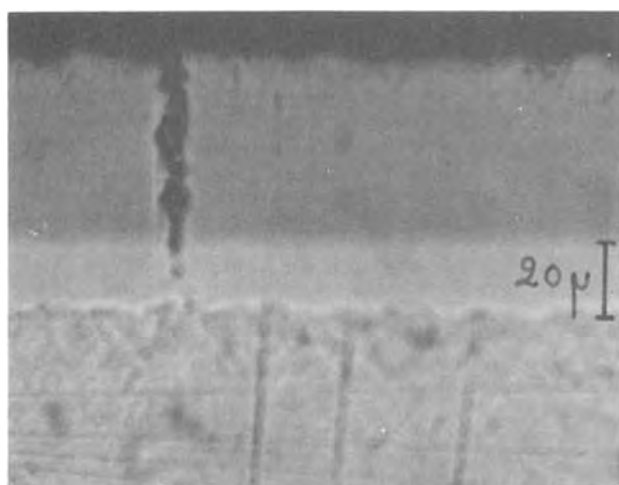


Fig. 12e. B coating on W

observed, but the metal does not present any transformation and the diffusion of boron forms only one boride ( $\text{NbB}_2$  and  $\text{TaB}_2$ ), the thermal expansion coefficient of which is of the same order as those of the pure metal and the amorphous boron ( $6.5\text{--}8.5 \times 10^{-6}/^\circ\text{C}$ ) (Fig. 12c). When boron is deposited on molybdenum and tungsten, the diffusion of boron forms two borides, and the cracks could arise from the difference between thermal expansion coefficients (Fig. 12d

and e). In all cases, cracks cross over the boron cones (Fig. 13).

Complete breakage of the boron deposit can arise during cooling down of the sample when the substrate-like carbides have a low ductility. So, boron deposited on steel coated with layers of carbide ( $\geq 5\mu$ ) presented an explosive splintering during cooling, although the thermal expansion coefficient is of the same order.

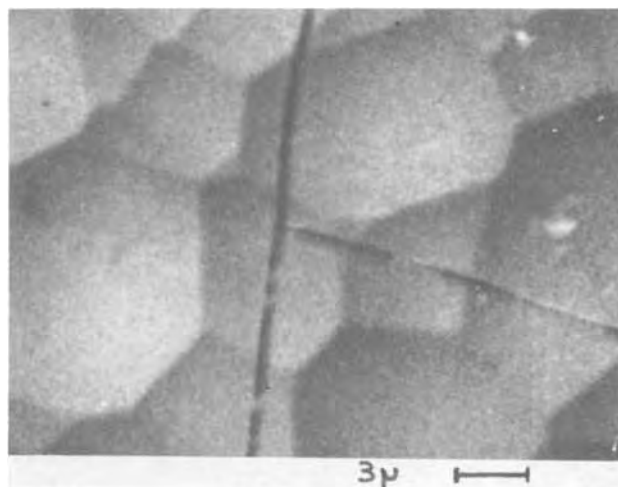


Fig. 13. Morphology of B coating on Mo

Complete scaling arises when crystallized boron is deposited on iron and steel.

The surface morphology of the boron deposits depends upon a number of factors connected to the substrate characteristics and the thickness of boron deposited. Figure 14 shows the surface morphology of amorphous boron deposited on tantalumized iron as a function of the deposition time. We shall show elsewhere (7) that amorphous boron presents a mononucleated morphology with growing cones. It is clear that the deposit morphology depends upon the physical aspect of the surface and is more regular on polished surfaces. Figure 15 shows the boron deposited on different substrates under the same conditions. Deposits are

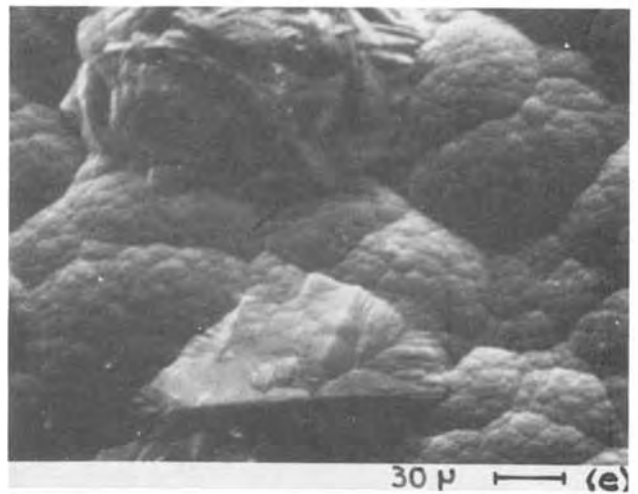
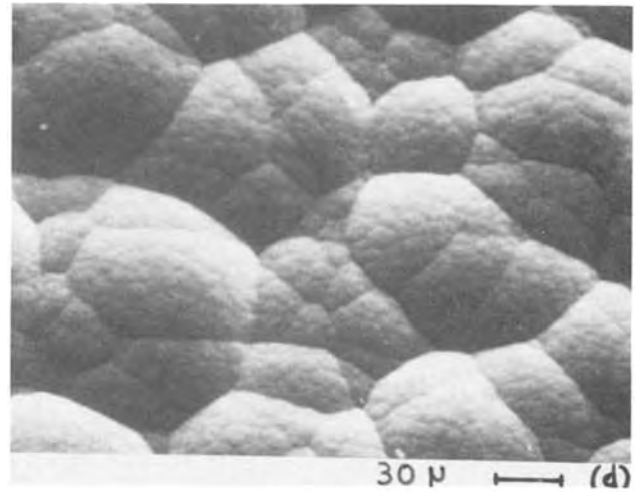
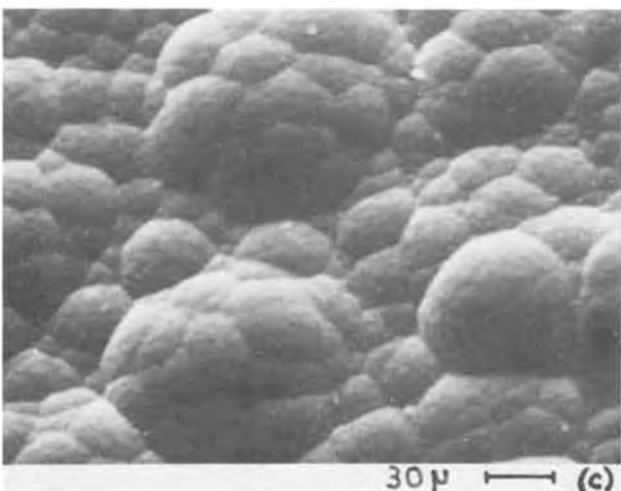
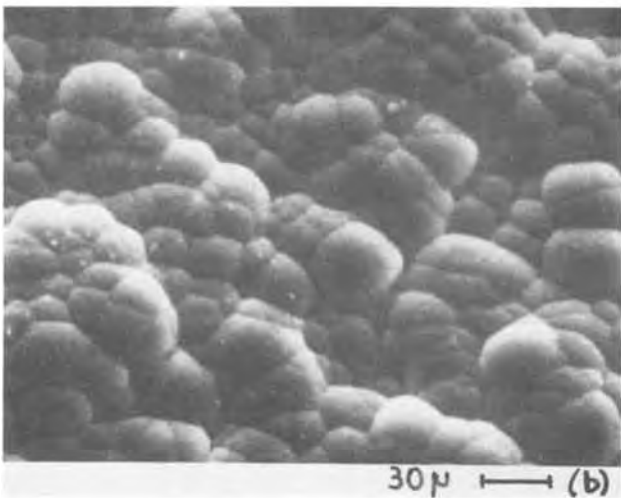
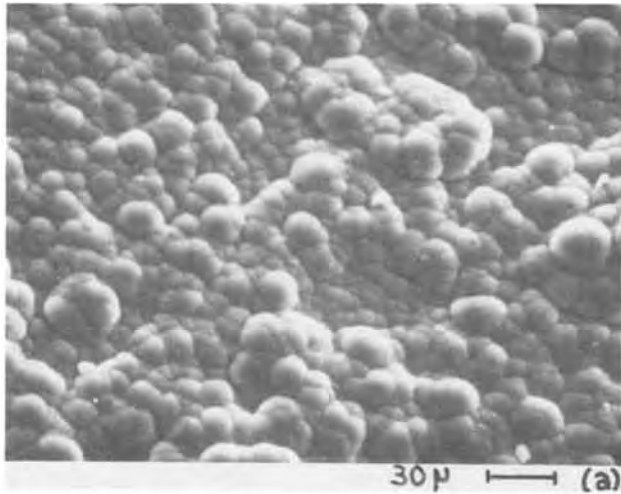


Fig. 14. Morphology of B deposited on Fe (Ta): (a) during 60 sec, (b) during 180 sec, (c) during 300 sec, (d) during 420 sec, (e) during 600 sec.

more regular when nucleation occurs on nonprivileged sites or when these sites are distributed statistically. Since the nucleation occurs faster on privileged sites another important factor is the recrystallized state of the metals. On an optically polished metal, these sites are essentially the grain boundaries. When the average grain size of the metal is of the same order as the size of the boron nucleus, the boron deposit is regular (Fig.

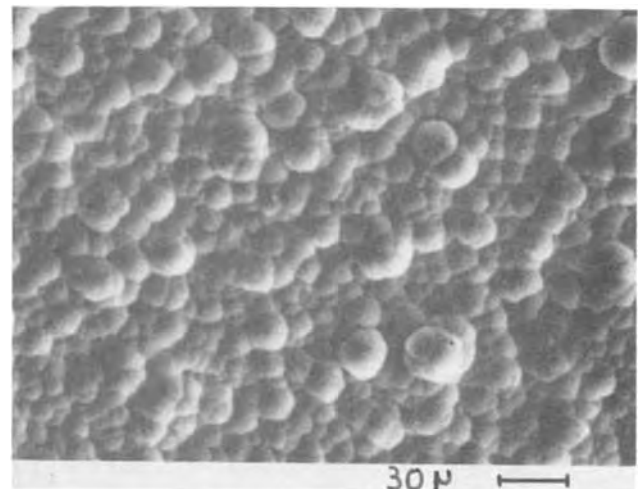


Fig. 15a. Morphology of B deposited in 120 sec at 1000°C on graphite.

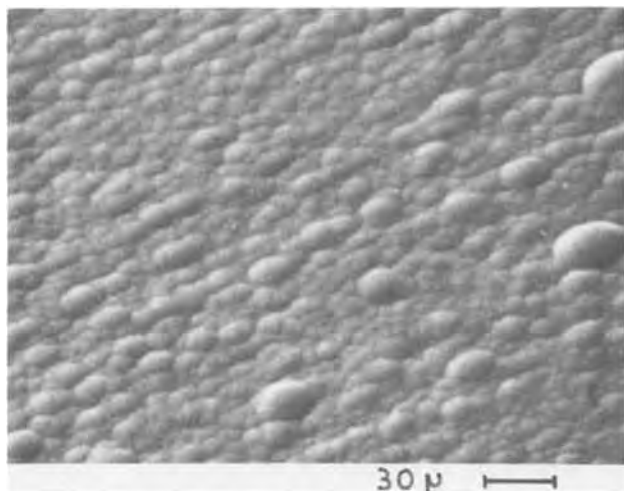


Fig. 15b. Morphology of B deposited in 120 sec at 1000°C on prepolished Nb.

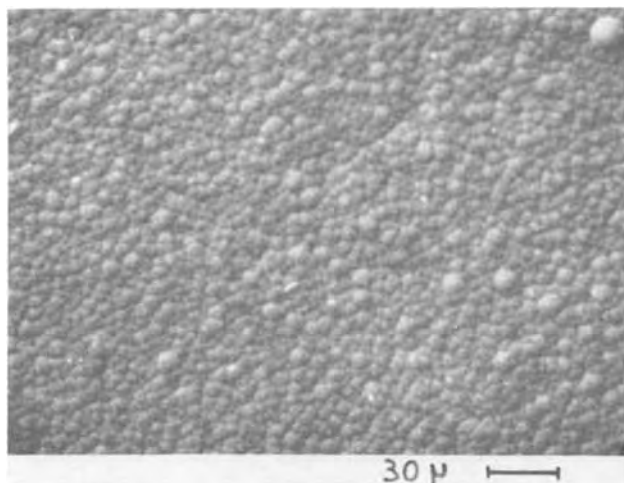


Fig. 15c. Morphology of B deposited in 120 sec at 1000°C on optically polished Ta.

16). When the average grain size is greater than the size of boron nucleus, the boron deposit is irregular. This effect occurred with annealed metals (Fig. 17). The nucleation occurs first on the grain boundary, then on the grain surfaces as a function of the crystalline orientation of the grains. The final boron thickness was

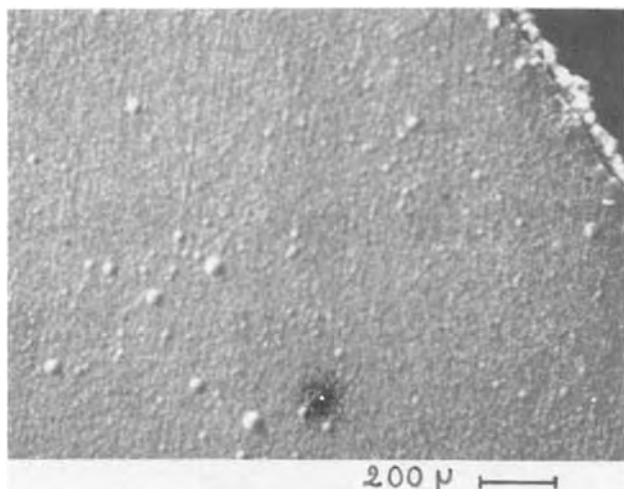


Fig. 16. B coating on a prepolished Mo sample

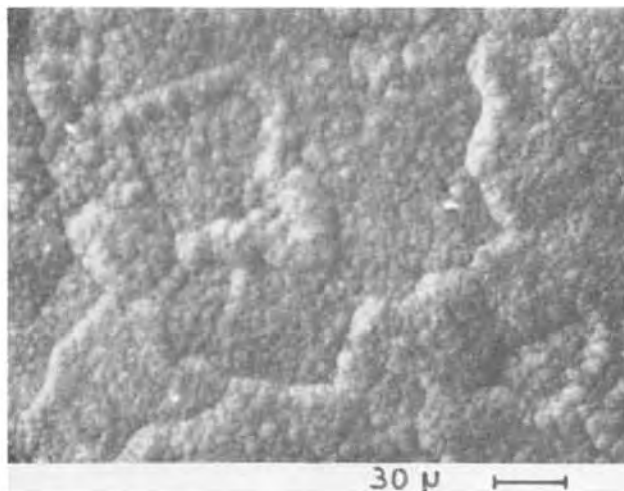


Fig. 17. B coating on a polished and annealed Mo sample

accordingly greater on the boundary layer and on some grains.

The microhardness of amorphous boron was measured on the cross section of the layers deposited on various substrates with thickness greater than  $50\mu$ . The Knoop microhardness values found were  $3350 \pm 50$  ( $\text{kg} \cdot \text{mm}^2$ ) with a 100g load.

### Conclusion

Mass transport limitations can be avoided in the deposition of boron from boron trichloride reduction by hydrogen on a massive substrate when the deposition cell provides for a stream of reactants flowing at high velocity normal to the substrate, subsequently flowing at a higher velocity in a parallel direction. Under these conditions deposition of amorphous boron occurs during a time that is a function of the temperature, and constant thickness of the deposit is achieved in all points of constant temperature if deposition efficiency is low. Then amorphous boron could be deposited on a complex-shaped substrate if one adapts each deposition cell to each shape. The deposition rate of boron increases sharply with the temperature. The apparent activation energy is about 31.4 kcal/mole.

Good coatings are achieved on graphite. On refractory metals, the best deposits, without cracks, are obtained with the metals of Group Vb. On iron and stainless steel, it is necessary to first deposit a barrier to avoid the transport of the metals and to reduce the diffusion rate of boron. It is a diffusion of tantalum produced by a pack-cementation process. Good coatings without any cracks and interfacial porosities are achieved on iron and stainless steel under strictly reproducible conditions for the preparation of the deposition surface. Complete scaling of the deposits occurs on hard substrates or hard layers such as carbides except when the hard layer is very thin.

The regularity of the deposit morphology is a function of the nucleation. Statistical nucleation arises when the surface does not present physical or structural privileged sites, or when these sites are statistically distributed at small distances, of the order of the size of one nucleus.

### Acknowledgments

The authors wish to thank A. Quilgars, M. Guérin, and Y. Auger, respectively, for the boron deposition equipment, power circuit realization, and samples preparation. We also gratefully acknowledge R. Herbin for her assistance in all the experimental work. The electron scanning micrograph studies and the electron microprobe analysis were made by B.R.G.M., Orléans.

Manuscript submitted May 20, 1975; revised manuscript received Sept. 22, 1975.



Any discussion of this paper will appear in a Discussion Section to be published in the December 1976 JOURNAL. All discussions for the December 1976 Discussion Section should be submitted by Aug. 1, 1976.

Publication costs of this article were partially assisted by University Orleans.

## REFERENCES

1. P. E. Gruber, in "Chemical Vapor Deposition, Second International Conference," M. Blocher, Jr. and J. C. Withers, Editors, p. 25, The Electrochemical

- Society Softbound Symposium Series, New York (1970).
2. H. E. Carlton, J. H. Oxley, E. H. Hall, and J. M. Blocher, Jr., *ibid.*, p. 209.
  3. J. Cueilleron and Y. Roux, *Ann. Chim.* **7**, 175 (1972).
  4. A. Luque, *Compt. Rend. Acad. Sci. (Paris)*, **274**, 286 (1972).
  5. L. Vandenbulcke and G. Vuillard, To be published.
  6. A. P. Epik, *Poroshkovaya Met. Akad. Nauk Ukr. SSR*, **3**, 21 (1963).
  7. L. Vandenbulcke and G. Vuillard, To be published.

## Coating of Cemented Carbide Cutting Tools with Alumina by Chemical Vapor Deposition

R. Funk, H. Schachner, C. Triquet,<sup>1</sup> M. Kornmann, and B. Lux

Battelle, Geneva Research Centre, 7, Route de Drize, CH-1227 Carouge-Genève, Switzerland

## ABSTRACT

Alpha-Al<sub>2</sub>O<sub>3</sub> has been chosen as the coating material for cemented carbide cutting tool inserts. The coatings have been prepared by chemical vapor deposition via hydrolysis of AlCl<sub>3</sub>. The hard, dense and adherent alumina layers consisted of α-Al<sub>2</sub>O<sub>3</sub> when deposited at temperatures above 850°C. Depending on the choice of the deposition parameters, the layer growth rate varied between a few tenths to 20 μm/hr. Machining tests carried out with cast iron and steel have shown that the presence of the alumina coating considerably increases the lifetime of the tool insert, reduces the number and the size of "cutting microholes" on the work piece, and decreases the amount of heat generated.

The quality of the cutting tool is of particular importance for the productivity of the metal cutting operation. Failure of tools used for cutting at high speeds is due to wear, plastic deformation, or rupture of the tool (1).

Wear of the surface of the tool is related to abrasion and adhesion processes taking place at the interface between the tool and the chip. In the case of cutting tools of cobalt-bonded tungsten carbide which are used for machining steel, diffusion of iron from the chip into the cobalt binder and of cobalt from the tool into the chip is particularly important in degrading the tool resistance (2). Furthermore, brittle and low melting carbides of tungsten and iron are sometimes formed at the tool/chip interface (3).

Plastic deformation (cratering) of the tool as well as the above-mentioned diffusion processes are accelerated by an increased temperature of the tool.

Rupture of the tool is mainly caused by mechanical shocks or vibrations.

Taking these factors into account, high performance from a cutting tool can be expected if: (i) The bulk of the tool has a high compressive strength, a high Young's modulus, a high creep resistance, and a high toughness, and (ii) the surface of the tool has good chemical resistance against the material to be machined, has a high hardness, and minimizes the absorption of heat by the tool.

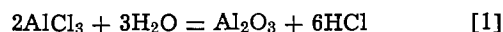
A single material cannot combine the optimum values required for both the surface and the bulk of the tool. Cemented carbides satisfy the conditions required of the bulk but not those demanded of the surface of the tool. Therefore, an increased performance can be expected for tools made of cemented carbide, the surface of which is covered with a suitable coating. Titanium carbide and titanium nitride coatings pro-

duced by CVD have already found industrial application.

Applying the above criteria for the choice of an efficient coating (see the comparisons given in Table I) α-Al<sub>2</sub>O<sub>3</sub> appears as a very promising coating, especially for the machining of steel at high temperatures, i.e., at high cutting speed. This choice is supported by the fact that massive alumina tools are already used in industry and that the low wear of tools when machining steels that have been deoxidized with aluminum seems to be related to a thin layer of alumina formed at the surface of the tool during the cutting operation (5).

## Experimental

*Deposition procedure.*—Alumina layers have been deposited on cemented carbide tools by chemical vapor deposition in a flow-type laboratory reactor which is shown schematically in Fig. 1, using one of the following reactions



The feed rates of the gases participating in the process (H<sub>2</sub>, CO<sub>2</sub>, CO, and HCl) were metered at atmospheric pressure and room temperature. The AlCl<sub>3</sub> vapor was produced by conversion of HCl over aluminum chips heated to about 250°C. The water vapor required for reaction [1] was introduced by bubbling H<sub>2</sub> as carrier gas through a saturator held at a constant temperature. Heating of the substrate was carried out by high frequency induction. The temperature was measured with a thermocouple and an optical pyrometer.

The substrates were commercial tool inserts of grade ISO P30 (S4) produced by SANDVIK AB (chip face 1.61 cm<sup>2</sup>, total surface 4.5 cm<sup>2</sup>). Experiments were also carried out with inserts precoated with layers of TiC, TiN, and Cr. Before coating the tool inserts were ultra-

<sup>1</sup> Present address: Sté Cuivre et Zinc, 10 Boulevard Froidmont, B-4000 Liège, Belgium.

Key words: chemical vapor deposition, alumina coatings, cutting tools.

Table I. Comparison of properties of cemented carbide and some possible coating materials

	Cemented carbide	TiC	TiB <sub>2</sub>	TiN	Si <sub>3</sub> N <sub>4</sub>	Al <sub>2</sub> O <sub>3</sub>	ZrO <sub>2</sub>
Reaction between tool and workpiece materials at elevated temperature (4)	Extensive (reaction between steel and cobalt binder)	Slight	Moderate	Moderate	Slight	No interaction	Moderate
Oxidation resistance in air at elevated temperature	Poor	Fair	Fair	Fair	Fair	Good	Good
Vickers hardness (kg/mm <sup>2</sup> )	1400-1800	3200	3250	1950	3100	3000	1100
Thermal conductivity (cal/cm·sec·°C)	0.20-0.30	0.078	0.062	0.048	0.04	0.081	0.0045
		0.099	0.11	0.063	0.013	0.014	0.0056

sonically cleaned, followed by vapor degreasing with Freon TF solvent or isopropyl alcohol.

Heating up and cooling down in the CVD reactor was carried out under hydrogen.

The values of the experimental parameters of the deposition runs are given in the figures and tables which summarize the results.

**Examination of coated samples.**—The difference in weight of the insert before and after coating permitted an estimation of the average layer thickness (1 mg  $\approx$  1  $\mu$ m). It corresponds reasonably well to the values measured directly on polished sections. The coating thickness is not completely uniform and increases toward the edge of the chip face (Fig. 2, 3).

Comparative wear tests were carried out with uncoated, TiC-coated, and Al<sub>2</sub>O<sub>3</sub>-coated tool inserts.

#### Influence of Deposition Parameters upon Layer Growth Rate and Structure

**Reaction 1 (H<sub>2</sub>O process).**—Figure 4 shows the deposition rate, expressed as the weight increase in mg·hr<sup>-1</sup>, as a function of the substrate temperature in the interval of 600°–1000°C. The decrease in the deposition rate with temperature might be related to an

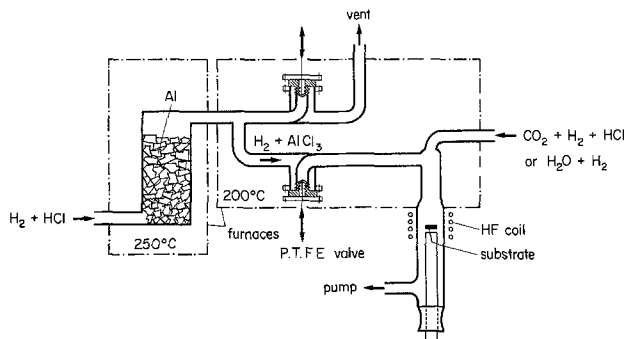


Fig. 1. Apparatus for chemical vapor deposition of Al<sub>2</sub>O<sub>3</sub> (schematic).

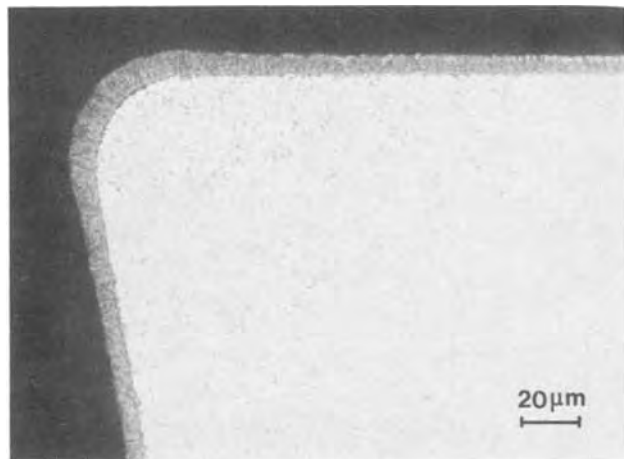


Fig. 2. Photomicrograph of a polished section through a tool insert (ISO P30) coated with  $\alpha$ -Al<sub>2</sub>O<sub>3</sub>, etched with hot phosphoric acid.

increasing degree of formation of Al<sub>2</sub>O<sub>3</sub> in the vapor phase. At higher total pressures (20 and 50 Torr) the deposition rate at a substrate temperature of 1000°C was negligible. These results are in agreement with observations made when Al<sub>2</sub>O<sub>3</sub> was deposited on aluminum at lower temperatures (400°–600°C) by the same process (6).

**Reaction 2 (H<sub>2</sub>O-CO<sub>2</sub> process).**—**Substrate temperature.**—For the CO<sub>2</sub>-H<sub>2</sub> process the deposition rate increases rapidly with temperature (Fig. 5) which indicates that it is controlled mainly by a chemical reaction step. The "activation energy," calculated according to the Arrhenius equation is about 40 kcal/mole.

**Total pressure.**—The deposition rate as a function of total pressure in the deposition chamber presents a maximum between 50 and 100 Torr (Fig. 6). The experiments were carried out at constant mass flow rate.

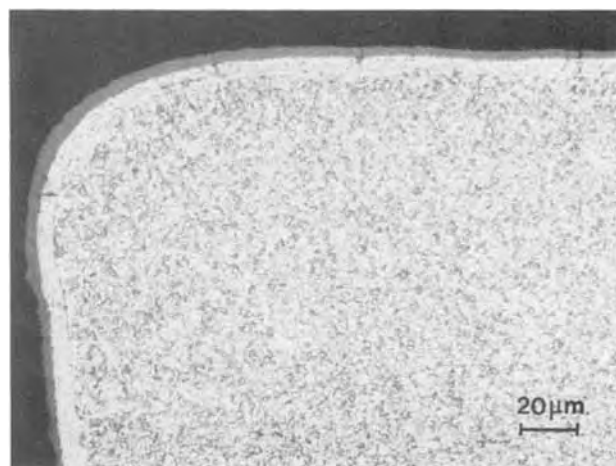


Fig. 3. Photomicrograph of a polished section through a tool insert coated with TiC and  $\alpha$ -Al<sub>2</sub>O<sub>3</sub>, etched with NaOH and KMnO<sub>4</sub>.

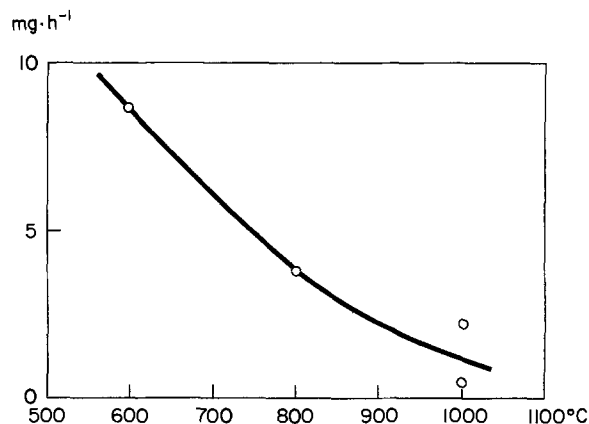


Fig. 4. H<sub>2</sub>O process. Deposition rate as a function of substrate temperature. (Substrate, ISO P30. Total pressure, 5 Torr. Partial pressures: AlCl<sub>3</sub>, 0.02; H<sub>2</sub>O, 0.06; and H<sub>2</sub>, 4.92 Torr. Linear gas velocity at 200°C, 9.4 cm·sec<sup>-1</sup>.)



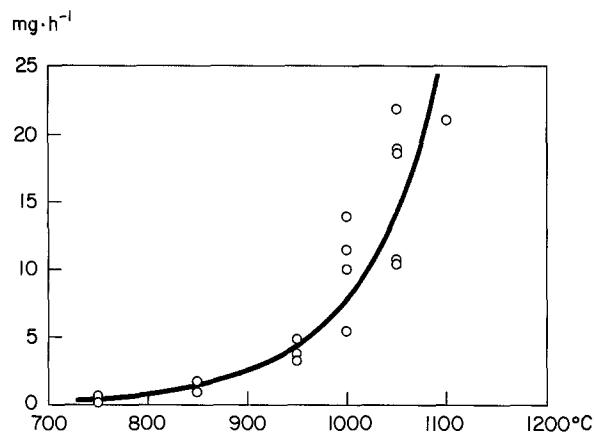


Fig. 5.  $H_2$ - $CO_2$  process. Deposition rate as a function of substrate temperature. (Substrate, ISO P30. Total pressure, 50 Torr. Partial pressures:  $AlCl_3$ , 0.2;  $CO_2$ , 24.9; and  $H_2$ , 24.9 Torr. Linear gas velocity at  $200^\circ C$ ,  $9.4 \text{ cm} \cdot \text{sec}^{-1}$ .)

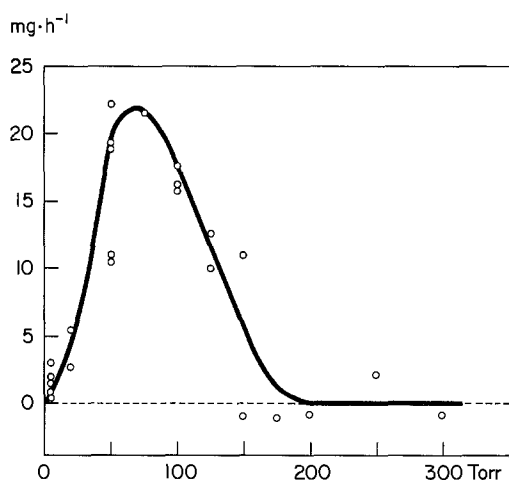


Fig. 6.  $H_2$ - $CO_2$  process. Deposition rate as a function of total pressure at constant mass flow rate. (Substrate, ISO P30. Substrate temperature,  $1050^\circ C$ . Gas composition:  $AlCl_3$ , 0.4%;  $CO_2$ , 49.8%; and  $H_2$ , 49.8%. Linear gas velocity at 50 Torr and  $200^\circ C$ ,  $9.4 \text{ cm} \cdot \text{sec}^{-1}$ .)

The decreasing deposition rate at higher pressure might be due to undesirable homogeneous reactions which lead to powder formation. These reactions are favored by the residence time of the reactants in the hot zone and the occurrence of free convective currents, the importance of which increases with pressure, *i.e.*, with decreasing flow velocity.

Sparrow *et al.* (7) derive the ratio  $Gr/Re^2$ , ratio of buoyancy forces to inertial forces, as the criterion for judging the nature of gas flow over a hot surface

$$\frac{Gr}{Re^2} = \frac{gH(T_1 - T_0)}{4T_0v^2}$$

with  $Gr$  the Grashof number;  $Re$  the Reynolds number;  $g$  the gravity;  $H$  the length dimension: distance between substrate and reactor wall, according to Curtis and Dismukes (8);  $T_1$  the substrate temperature;  $T_0$  the wall temperature; and  $v$  the gas velocity.

$Gr/Re^2$  increases with pressure. For pure forced convection this value should be less than 0.3 or 0.06 according to the criteria which are chosen (7). Furthermore, in the present experiments, for which the buoyancy force has a component opposite to the free stream velocity ("opposing flow"), a separation of flow occurs if  $Gr/Re^2$  is  $>1$ ; near the surface the gas flow is then upward and no longer downward (7).  $Gr/Re^2$  is calculated to be about 0.4 for a pressure of 100 Torr and about 1.6 for 200 Torr. If the average gas flow is directed upward there is no separation of flow due to

Table II. Deposition of  $Al_2O_3$  on cemented carbide cutting tools (ISO P30): Deposition rate as a function of gas composition (substrate temperature,  $1000^\circ C$ ; total pressure, 50 Torr; gas entrance temperature,  $200^\circ C$ ; linear gas velocity at  $200^\circ C$ ,  $9.4 \text{ cm} \cdot \text{sec}^{-1}$ )

No.	Partial pressures (Torr)						Deposition rate (mg·hr <sup>-1</sup> )
	$p_{AlCl_3}$	$p_{H_2}$	$p_{CO_2}$	$p_{Ar}$	$p_{CO}$	$p_{HCl}$	
1	0.2	24.9	24.9	—	—	—	10.4*
2	0.5	24.8	24.8	—	—	—	8.5
3	0.8	24.6	24.6	—	—	—	6.2
4	1.5	24.3	24.3	—	—	—	7.2
5	1.5	16.2	32.3	—	—	—	4.4
6	1.5	4.9	43.6	—	—	—	6.8
7	1.5	2.1	46.4	—	—	—	8.7
8	1.5	32.3	16.2	—	—	—	5.8
9	1.5	43.6	4.9	—	—	—	2.3
10	1.5	44.6	3.9	—	—	—	1.5
11	1.5	46.7	1.8	—	—	—	1.3
12	0.2	24.9	12.5	12.5	—	—	10.9
13	0.2	24.9	12.5	—	12.5	—	3.9
14	0.2	24.9	12.5	—	—	12.5	0.5

\* Mean value of four experiments.

buoyancy, and the decrease of the deposition rate with pressure is lower. An experiment at 300 Torr, with upward flow under the conditions indicated in Fig. 6, gave a deposition rate of  $11.3 \text{ mg} \cdot \text{hr}^{-1}$ .

**Gas composition.**—Table II summarizes the deposition experiments carried out with different partial pressures of the constituents of the vapor phase, but with an almost constant total pressure of 50 Torr and a substrate temperature of  $1000^\circ C$ . The deposition rate decreases slightly with  $p_{AlCl_3}$  (No. 1-4) and  $p_{H_2}$  (No. 5-7). Within the limits of reproducibility of the experiments, however, the measured values fall. The deposition rate increases approximately proportionally with  $p_{CO_2}$  (No. 8-11). Figure 7 shows deposition rates as functions of  $p_{CO_2}:p_{H_2}$  and  $p_{H_2}:p_{CO_2}$ . Addition of CO or HCl to the feed mixture reduces the deposition rate as shown in three experiments (No. 12-14) in which identical amounts of Ar, CO, and HCl were added.

**Structure of the coatings.**—The columnar growth structure of the  $Al_2O_3$  layers is shown in the metallographic section of Fig. 2. The coatings contained  $\alpha$ - $Al_2O_3$  over the range of substrate temperatures from  $850^\circ$  to  $1100^\circ C$ . In most cases no noticeable change of the substrate occurred and only the initial phases of the cemented carbide (monocarbides and Co) have been detected by x-ray diffraction in addition to the  $\alpha$ - $Al_2O_3$  of the coating. In a few cases only, the presence of  $\eta$ -carbides has been determined.

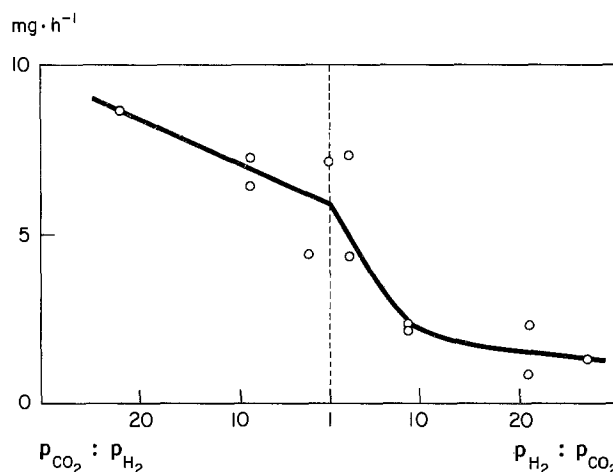


Fig. 7. Deposition rate as a function of  $p_{CO_2}:p_{H_2}$  and  $p_{H_2}:p_{CO_2}$ . (Substrate, ISO P30. Substrate temperature,  $1000^\circ C$ . Total pressure, 50 Torr.  $p_{AlCl_3}$ , 1.5 Torr. Linear gas velocity at  $200^\circ C$ ,  $9.4 \text{ cm} \cdot \text{sec}^{-1}$ .)

### Deposition of $\text{Al}_2\text{O}_3$ on WC, Co, and Precoated Tool Inserts

Deposition experiments have been carried out separately on the constituents of cemented carbides (WC and Co) as well as on inserts precoated with intermediate layers of TiC (Fig. 3), TiN, and Cr.

Very adherent layers of  $\alpha\text{-Al}_2\text{O}_3$  have been obtained on WC whereas on Co the formation of loose deposits was observed. TiC and TiN as intermediate layers were found to favor the adherence of the  $\text{Al}_2\text{O}_3$  coating, while on Cr nonadherent deposits were formed. The nonadherence on Co and Cr could be explained by substrate attack, possibly by HCl, and hence disturbance of the nucleation and layer growth. This view would agree with observations made by Bryant and Meier (9) in the case of other CVD reactions involving chlorides.

Observations concerning the nucleation of  $\text{Al}_2\text{O}_3$  coatings on TiC-coated and uncoated cemented carbide substrates have been reported earlier (10).

Table III. Machining condition for cast iron and high carbon steel

Materials machined	Lamellar gray cast iron	SANDVIK high carbon steel (C-0.96, Si-0.27, Mn-0.25, P-0.019, S-0.015, Cr-0.15%)
Dry cutting		
Advance	0.1 mm/rev	0.3-0.4 mm/rev
Depth of cut	0.5 mm	2.0 mm
Initial diameter of bars	40 mm	144 mm
Speed of first pass	190 m/min	140-200 m/min

### Results of Machining Tests

Comparative cutting tests have been carried out with  $\text{Al}_2\text{O}_3$ -coated, TiC-coated and uncoated tools; cast iron and high carbon steel have been machined mainly under the conditions given in Table III.

The main results of machining tests are the following: The wear of uncoated or TiC-coated tools is greater than that of the  $\text{Al}_2\text{O}_3$ -coated tools tested under the same conditions. This result is obtained both with high carbon steel and with lamellar gray cast iron (Fig. 8 and 9).

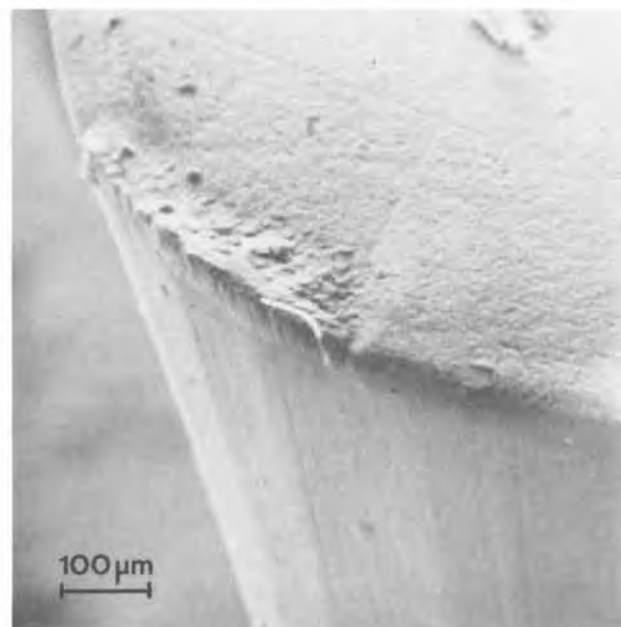
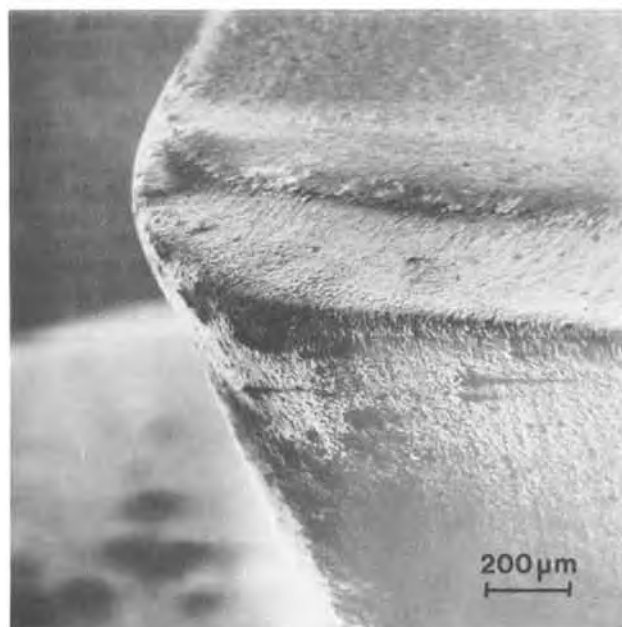
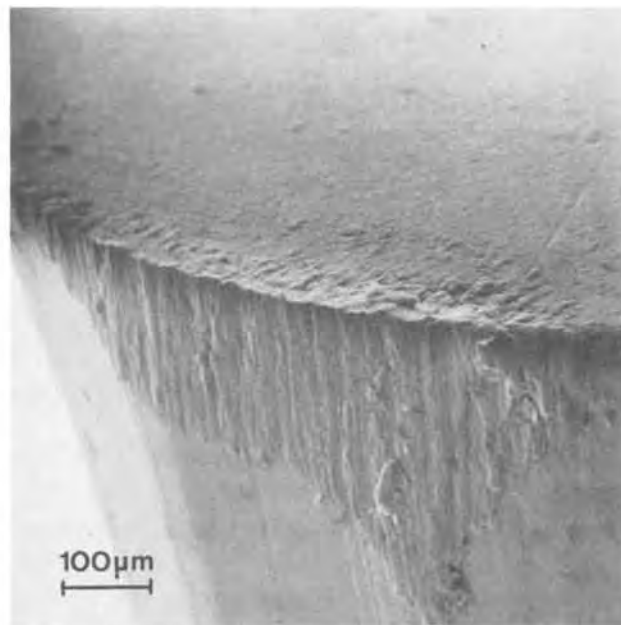
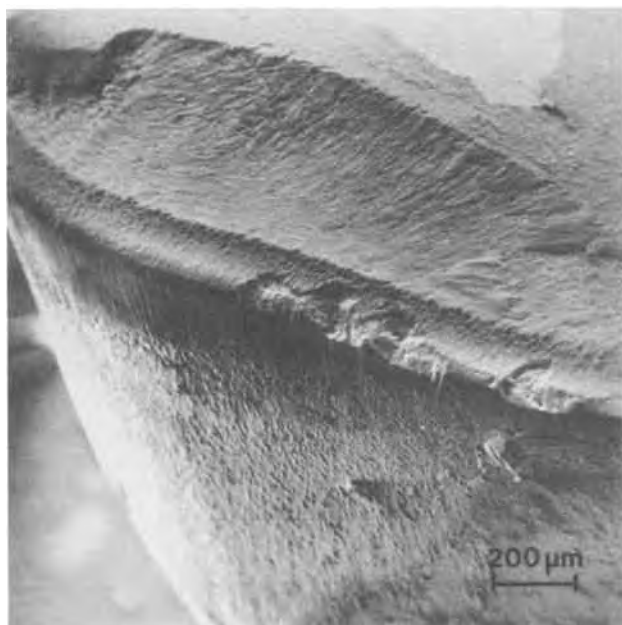


Fig. 8. Comparison of wear of  $\text{Al}_2\text{O}_3$ - and TiC-coated tools after cutting high carbon steel at 180 m/min for a duration of 10 min. (a, top) TiC-coated tool, (b, bottom)  $\text{Al}_2\text{O}_3$ -coated tool.

Fig. 9. Cutting edges of (a, top) uncoated and (b, bottom)  $\text{Al}_2\text{O}_3$ -coated (1  $\mu\text{m}$ ) carbide tool after cutting cast iron for a duration of 1 min.

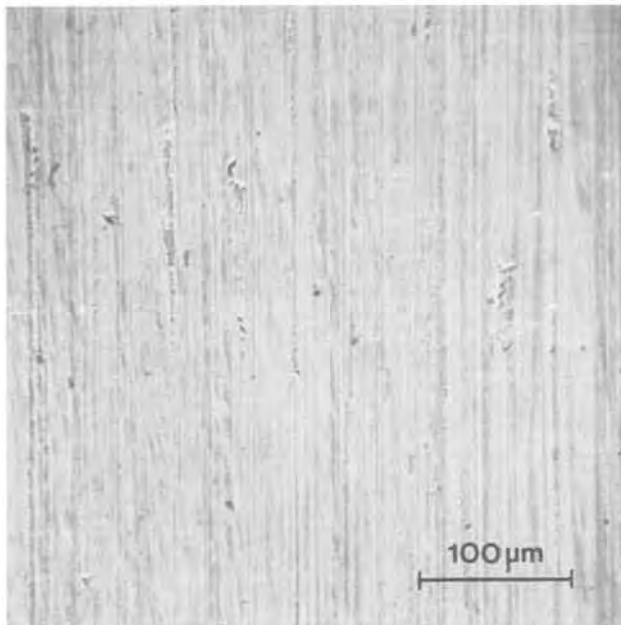
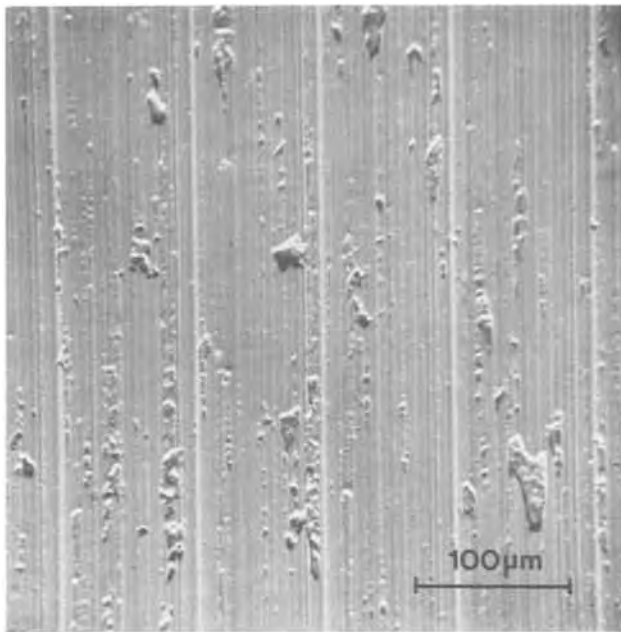


Fig. 10. Surface of high carbon steel workpieces cut with (a, top) an uncoated carbide tool and (b, bottom) an  $\text{Al}_2\text{O}_3$ -coated carbide tool.

For example, in machining tests with high carbon steel carried out at a speed of 140 m/min the lifetime of the  $\text{Al}_2\text{O}_3$ -coated tool insert was about twice that of a TiC-coated one and more than 10 times as long as that of an uncoated tool insert.

$\text{Al}_2\text{O}_3$  coatings with a thickness as low as 1  $\mu\text{m}$  have been effective (Fig. 9).

When cutting steel, the  $\alpha\text{-Al}_2\text{O}_3$  coating on the tool reduces the number and the size of "cutting micro-holes" on the work-pieces (Fig. 10). This effect is more marked at high cutting speeds (e.g., 180 m/min) than at lower speeds (e.g., 145 m/min).

#### Acknowledgments

The work has been carried out under contract with SANDVIK AB, Stockholm. Permission to publish this paper is gratefully acknowledged. The authors wish to thank W. Ohlsson, S. Ekemar, S. Amberg, and J. Lindström for many suggestions and stimulating discussions. The assistance of O. Baumberger and P. Neury from Battelle Geneva in the experimental work is acknowledged.

Manuscript submitted May 20, 1975; revised manuscript received Sept. 22, 1975. This paper was presented at the Fifth International Conference on Chemical Vapor Deposition at Stoke Poges, Buckinghamshire, England, Sept. 21-25, 1975.

Any discussion of this paper will appear in a Discussion Section to be published in the December 1976 JOURNAL. All discussions for the December 1976 Discussion Section should be submitted by Aug. 1, 1976.

Publication costs of this article were partially assisted by Battelle Geneva Research Centre.

#### REFERENCES

1. T. H. C. Childs and G. W. Rowe, *Rep. Prog. Phys.*, **36**, 223 (1973).
2. M. C. Shaw, "Metal Cutting Principles," 3rd ed., MIT Press, Cambridge (1961).
3. E. M. Trent, *Proc. Inst. Mech. Eng.*, **166**, 64 (1952).
4. E. D. Whitney, *Powder Metallurgy International*, **6**, 73 (1974).
5. H. Opitz, W. König, and N. Diederich, *Stahl Eisen*, **88**, 978 (1968).
6. H. Schachner and H. Tannenberger, *Ber. Deut. Keram. Ges.*, **49**, 76 (1972).
7. E. M. Sparrow, R. Eichhorn, and J. L. Gregg, *Phys. Fluids*, **2**, 319 (1959).
8. B. J. Curtis and J. P. Dismukes, in "Chemical Vapor Deposition, Fourth International Conference," G. F. Wakefield and J. M. Blocher, Jr., Editors, p. 218, The Electrochemical Society Soft-bound Symposium Series, Princeton, N. J. (1973).
9. W. A. Bryant and G. H. Meier, *J. Vacuum Sci. Technol.*, **11**, 719 (1974).
10. M. Kornmann, H. Schachner, R. Funk, and B. Lux, *J. Crystal Growth*, **28**, 259 (1975).

# Crystal Growth and Some Properties of Titanium Monophosphide

S. Motojima, T. Wakamatsu, Y. Takahashi, and K. Sugiyama

Department of Synthetic Chemistry, Faculty of Engineering, Gifu University, Kakamigahara, Gifu, 504 Japan

## ABSTRACT

Well-formed hexagonal whiskers of TiP (5-10 mm in length and 0.5-25  $\mu\text{m}$  in diameter) were obtained by chemical vapor deposition on a quartz substrate at 850°-1150°C using Au metal as an impurity to promote crystal growth, whereas platelet crystals were obtained at 1250°C using Pd or Pt. The effects of temperature, gas composition, and the kind of impurities on the growth rates were examined. Electrical resistivity and thermoelectric power of whiskers and platelet crystals indicated anisotropy. The tensile strength of whiskers was found to be about 1000 kg/mm<sup>2</sup> for 1  $\mu\text{m}$  samples. The whiskers showed a considerable oxidation resistance in air below 1000°C, probably because of the formation of Ti<sub>2</sub>O<sub>7</sub> and TiO<sub>2</sub> layers.

A number of compounds of borides, carbides, and nitrides of transition metals have been extensively investigated during the past decades. However, only a few studies on the phosphides have been performed, although some of the phosphides are of much interest in view of their physical and chemical properties.

Previously it was reported that the reactions of titanium metal with red phosphorus (1-2), phosphine (3-6), and calcium phosphide (7), or of titanium hydride with phosphine (2) at elevated temperatures gave titanium phosphides with various compositions depending on the reaction conditions used: TiP<sub>2</sub>, TiP, Ti<sub>2</sub>P, Ti<sub>3</sub>P, Ti<sub>3</sub>P<sub>2</sub>, etc.

Titanium monophosphide, TiP, is very stable to heat without appreciable vaporization of phosphorus even at 1100°C (1), is highly resistant to oxidation (3, 5), and is metallic in conduction. Its space group (8) is P6<sub>3</sub>/mmc and the unit cell dimensions are  $a = 3.499\text{\AA}$  and  $c = 11.700\text{\AA}$ .

However, there is no work reported in the literature on single crystal growth of TiP, much less about the preparation of whiskers from the vapor phase. In this paper, with the objective of obtaining the well-formed and long whiskers of TiP from a gas mixture of TiCl<sub>4</sub>, PCl<sub>3</sub>, and H<sub>2</sub>, the reaction conditions were examined, and some physical and chemical properties of the crystals were investigated in some detail.

## Experimental

**Materials.**—Commercial reagent grade titanium tetrachloride and phosphorus trichloride were used without further purification. Argon was purified by passing over titanium sponge kept at 800°C, and hydrogen was refined by passing through concentrated sulfuric acid and phosphorus pentoxide, sequentially.

**Preparation of TiP.**—The apparatus is shown in Fig. 1. A quartz tube 7, (8 mm OD and 65 mm in length), in which a SiC heater 8 was inserted, was placed as a substrate in the center of the reaction tube (quartz of 19 mm ID). The substrate was heated at 900°-1250°C. Hydrogen was bubbled into a titanium tetrachloride evaporator, 1, and was flowed through a condenser, 2. The temperature of coolant in the condenser was regarded as the saturating temperature. Phosphorus trichloride was also carried into the reaction tube by passing hydrogen through a saturator, 3. Argon was used for cleaning the reaction system before each experiment.

The surface temperature of the substrate was measured by an optical pyrometer through a window and

Key words: CVD (chemical vapor deposition), whisker, VLS (vapor-liquid-solid) growth.

the ambient temperature inside the reaction tube was monitored by a Chromel-Alumel thermocouple.

Aqueous solutions of MnSO<sub>4</sub> · 4H<sub>2</sub>O, Fe<sub>2</sub>(SO<sub>4</sub>)<sub>3</sub> · 9H<sub>2</sub>O, CoCl<sub>2</sub>, NiCl<sub>2</sub>, RhCl<sub>3</sub> · 4H<sub>2</sub>O, PdCl<sub>2</sub>, H<sub>2</sub>PtCl<sub>6</sub>, HAuCl<sub>4</sub>, etc. were used as the source of various impurities to promote crystal growth, and these were painted on a substrate scratched by abrasives, followed by decomposition or reduction into corresponding metals inside the reactor at a temperature below that used for the TiP crystal growth.

The range of the whisker length reported in this paper refers to that measured under 150 $\times$  magnification of about twenty of the longest samples obtained in any one growth experiment.

**Observation and analysis of deposits.**—The deposits were examined by x-ray diffraction, scanning electron microscopy, and x-ray microanalysis. Quantitative analysis of titanium in the deposits was carried out by back titration of cupric ion with EDTA using pyridyl-azo-naphthol as an indicator (9).

**Electrical resistivity.**—The four-point probe method was applied where each probe was separated by 0.5 mm from the other, and the crystal was contacted with probes by silver paint. Voltage of 10V from a d-c Wheatstone bridge was applied between the outer two probes and the voltage drop between inner two probes was measured by a microvoltmeter.

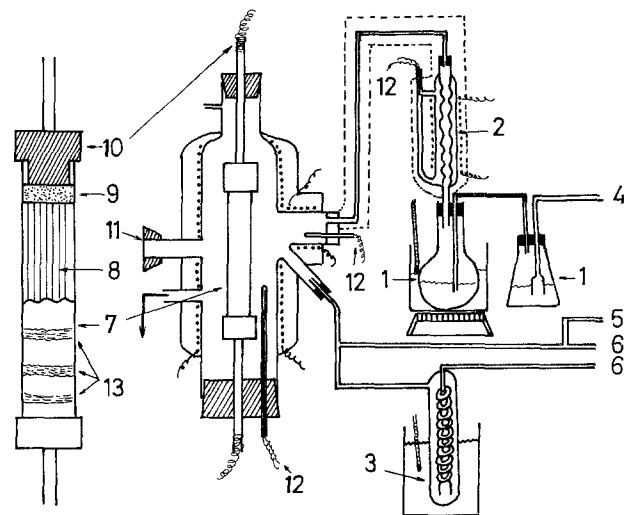


Fig. 1. Experimental apparatus. 1, TiCl<sub>4</sub> evaporator; 2, TiCl<sub>4</sub> condenser; 3, PCl<sub>3</sub> saturator; 4, H<sub>2</sub>; 5, Ar; 6, H<sub>2</sub>; 7, quartz substrate; 8, SiC heater; 9, graphite powder; 10, graphite conductor; 11, window; 12, thermocouple; 13, impurity painted zone.

**Thermoelectric power.**—The crystal was bridged between two copper plates (3 × 5 mm), which were separated by 2 mm from each other and one of which was heated by a Nichrome heater, and was contacted using silver conducting paint on the plates. The temperature difference of the two sides of crystal was measured by a 100 μm diameter iron-Chromel thermocouple. Thermoelectric power was measured in an argon atmosphere, and the temperature difference across the specimen was held at 1°–1.5°C.

**Tensile strength.**—Measurements of the tensile strength of the whiskers were carried out by a spring-type apparatus at room temperature.

**Stability for oxidation.**—A gravimetric method was adopted to check the progress of the oxidation reaction. TiP whiskers of about 100 mg (*w*) were heated at a given temperature in a flow of air (about 2 cm<sup>3</sup>/sec) during which weight change ( $\Delta w$ ) was measured at every time interval. The results were expressed in terms of  $\Delta w/w$ .

## Results and Discussion

**Identification of products and impurity effect.**—In a preliminary experiment, polycrystals or whiskers were observed in the absence or presence of gold impurity, respectively, at 1050°C. In the presence of palladium, however, platelet crystals were obtained at 1250°C. X-ray diffraction peaks of polycrystals or whiskers as grown, shown in Fig. 2A, were consistent with those reported by Schönberg (3) for pulverized TiP (Fig. 2D), and no other peaks were observed. Chemical analysis of titanium in the TiP crystals showed the atomic ratio of Ti/P to be 0.99. The whiskers were also identified as TiP by x-ray diffraction (Fig. 2B) which was conducted by placing a collection of whiskers on a holder plate along the growth direction and perpendicular to the x-ray beam. The growth direction was found to be parallel to the *c*-axis. A Laue photograph with the x-ray beam perpendicular to a face of the platelet crystal showed six-fold symmetry, and the diffraction peaks obtained from the platelet crystal attached on a holder plate keeping the face parallel to the plate face are shown in Fig. 2C. From these results, the face of the platelet crystal was assigned as the (001) plane.

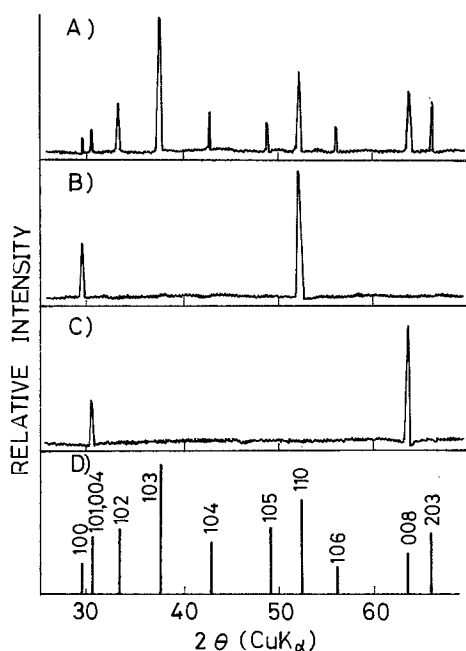


Fig. 2. X-ray diffraction profiles. A, As-grown whiskers; B, whisker aligned along the growth direction; C, platelet crystal keeping the face perpendicular to the x-ray beam; and D, TiP data from Schönberg (3).

Table I. Impurity effects.

Metals	Painted forms	Impurity effects*	Eutectic temperature (°C)**	
			Titanium impurity	Phosphorus impurity
Cr	CrCl <sub>3</sub>	—	—	1370°C
Mn	MnSO <sub>4</sub>	+ +	1175°C (60.8)	960°C (13.1)
Fe	FeCl <sub>3</sub>	—	1085 (~71)	1050 (17.1)
Co	CoCl <sub>2</sub>	—	1025 (~76)	1023 (19.9)
Ni	NiCl <sub>2</sub>	—	955 (75.5)	880 (19)
Rh	RhCl <sub>3</sub>	+ +	—	~1300 (~25)
Pd	PdCl <sub>2</sub>	+	1160 (60)	796 (32.7)
Cu	CuCl <sub>2</sub>	—	ca. 880 (34)	714 (15.7)
Ag	AgNO <sub>3</sub>	+	—	878 (~3.4)
Au	HAuCl <sub>4</sub>	+ +	1123† (11)	—
Sb	SbCl <sub>3</sub>	+ +	—	—
Nd	Nd(NO <sub>3</sub> ) <sub>3</sub>	—	—	—
Pt	H <sub>2</sub> PtCl <sub>6</sub>	+	1310 (84.4)	588 (20)

Reaction conditions: temperature 1040°C; PCl<sub>3</sub>/TiCl<sub>4</sub>/H<sub>2</sub> = 0.013/0.13/1.86 (cm<sup>3</sup>/sec); reaction time 15 min.

\* (—) No effects. (+) Weak positive effects (up to 3 mm long). (+ +) Strong positive effects (longer than 3 mm).

\*\* Atomic per cent of titanium or phosphorus at each eutectic point is shown in parenthesis.

† Peritectic temperature.

The variations of reaction temperature of 850°–1250°C and of the ratio PCl<sub>3</sub>/(PCl<sub>3</sub> + TiCl<sub>4</sub>) of 0.1–0.9 did not result in other products than TiP. In the absence of an impurity, no whiskers or platelet crystals were formed at any condition, indicating the essential role of the impurity in crystal growth.

In Table I, the effect of various metal impurities on whisker growth is shown together with the eutectic temperature of the corresponding binary alloys (10–11). Chromium, iron, cobalt, nickel, copper, and neodymium resulted in no effect on whisker growth, and deposition took place in a form of uniform coatings or polycrystals. On the other hand, manganese, rhodium, gold, and antimony showed a strongly positive effect, giving straight and thin whiskers (up to 3 mm in length), gold was particularly effective giving well-formed whiskers (above 5 mm in length).

Palladium and platinum exhibited a weak effect on whisker growth at 1040°C, but a strong effect at 1150°C; however, runs at 1250°C gave thin platelet crystals of longer than 3 mm in diagonal. The role of an impurity on the growth mechanism of crystals is discussed in a later section.

Gold was used hereafter unless otherwise indicated because of the convenience in handling. Although the concentration of gold may play a role in whisker growth the surface concentration of gold was fixed at about 50 μg/cm<sup>2</sup> of substrate area in this experiment.

Whiskers grown at 1040°C are shown in Fig. 3A and platelet crystals grown at 1250°C with the use of Pd impurity are shown in Fig. 3B. It can be seen that the whiskers and platelet crystals grow only on the impurity-painted zone and their growth direction tends to be vertical to the substrate surface. In Fig. 4, photomicrographs of a typical whisker obtained at 1040°C and the cross section are shown. They have the appearance of regular hexagonal pillars with an average size of 5–10 μm in length and 0.5–2.0 μm in diameter. Sometimes rectangular pillar crystals were also observed, and the growth direction may be judged from their appearance to be vertical to the *c*-axis.

**The effect of substrate temperature.**—Substrate temperature exhibited a strong effect on whisker growth. An average length of 5–6.5 mm was observed at 1020°–1050°C, and at higher or lower temperatures than 1020°–1050°C the length decreased abruptly. Above the optimum temperature, crystals grew in radial directions resulting in considerable branching. Sometimes platelet crystals of 1 ~ 3 × 0.5 ~ 2 mm, 0.5 ~ 5 μm thick were grown mixed with whiskers above the optimum temperature. At a temperature higher than 1100°C, they are apt to grow thick and have continuous growth steps (Fig. 5). Figure 5C shows a regular hexagonal pyramid frequently formed on the platelet crystals, on the tip of which a deposit is observed.

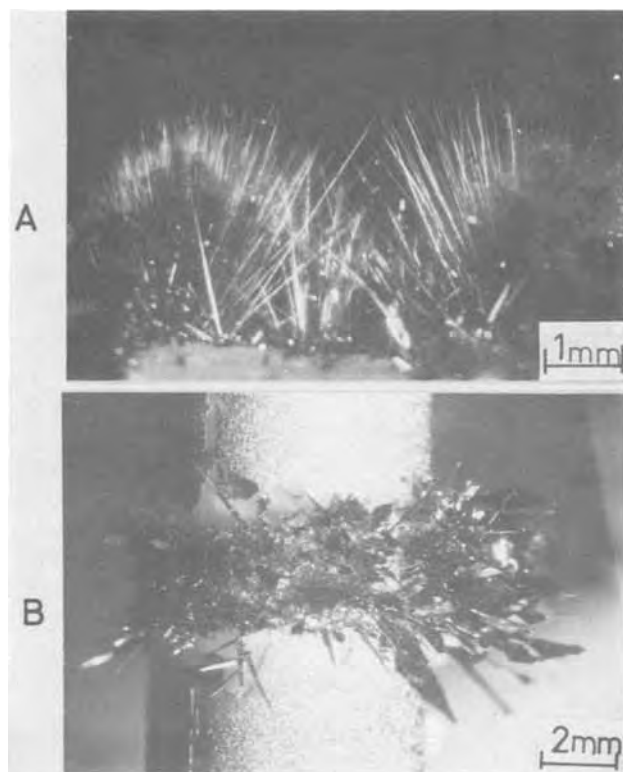


**Fig. 3.** Appearance of whiskers and platelet crystals. A, Whiskers, reaction temperature  $1040^{\circ}\text{C}$ ; reaction time 15 min;  $\text{PCl}_3/\text{TiCl}_4/\text{H}_2 = 0.015/0.12/2.0$  ( $\text{cm}^3/\text{sec}$ ), impurity Au. B, Platelet crystals, reaction temperature  $1250^{\circ}\text{C}$ ; reaction time 30 min;  $\text{PCl}_3/\text{TiCl}_4/\text{H}_2 = 0.02/0.2/2.2$  ( $\text{cm}^3/\text{sec}$ ), impurity Pd.

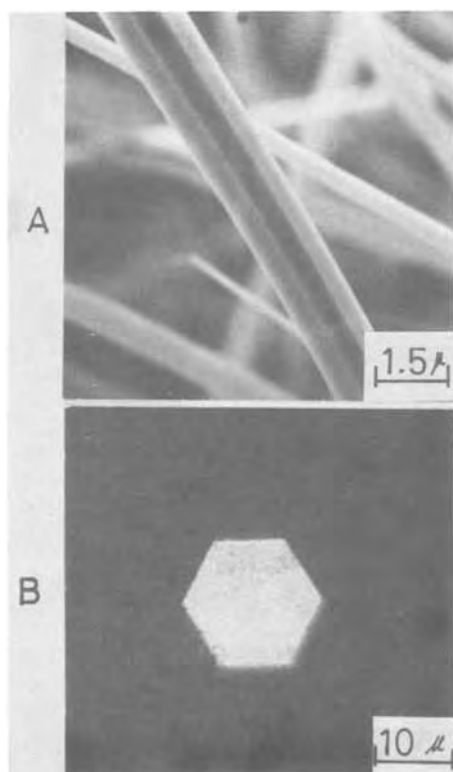


**Fig. 4.** A whisker of hexagonal pillar and its cross section. Reaction temperature  $1050^{\circ}\text{C}$ , reaction time 20 min,  $\text{PCl}_3/\text{TiCl}_4/\text{H}_2 = 0.03/0.2/2.0$  ( $\text{cm}^3/\text{sec}$ ), impurity Au. A, Appearance of whisker; B, its cross section.

The lowest temperature for the growth of TiP whiskers was approximately  $850^{\circ}\text{C}$  when gold was used as an impurity. In the case of palladium and platinum,

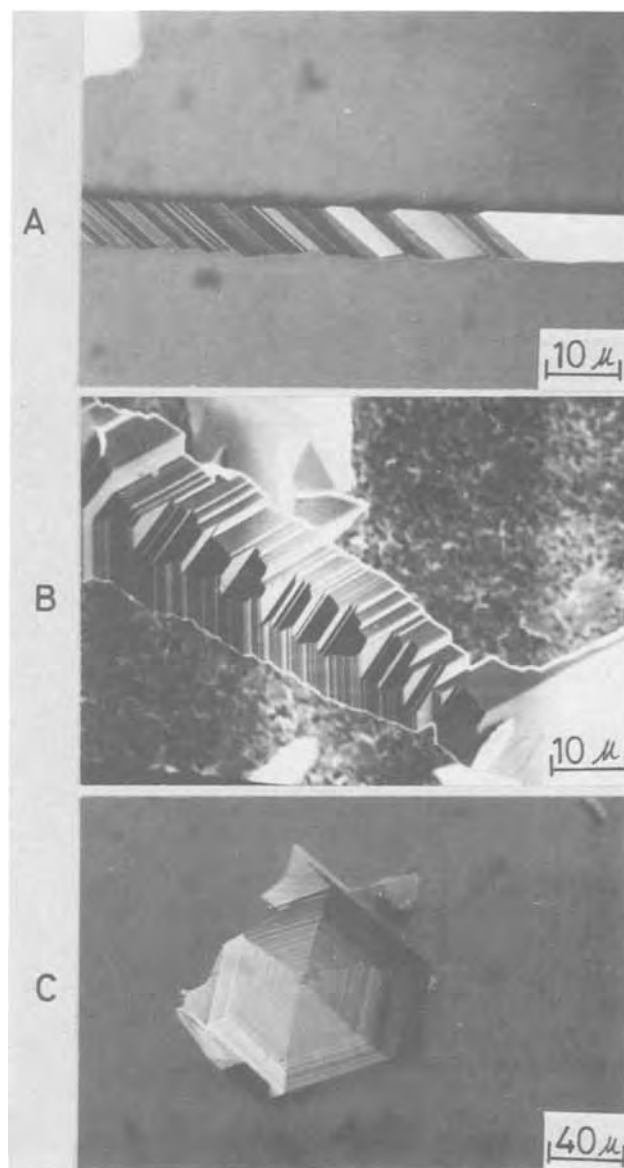


**Fig. 5.** Growth steps. A, Rectangular pillar, reaction temperature  $1130^{\circ}\text{C}$ ,  $\text{PCl}_3/\text{TiCl}_4/\text{H}_2 = 0.03/0.15/2.3$  ( $\text{cm}^3/\text{sec}$ ). B, Hexagonal pillar, reaction temperature  $1130^{\circ}\text{C}$ ,  $\text{PCl}_3/\text{TiCl}_4/\text{H}_2 = 0.03/0.15/2.0$  ( $\text{cm}^3/\text{sec}$ ). C, Hexagonal pyramid deposited on a platelet crystal, reaction temperature  $1100^{\circ}\text{C}$ ,  $\text{PCl}_3/\text{TiCl}_4/\text{H}_2 = 0.03/0.13/2.2$  ( $\text{cm}^3/\text{sec}$ ).

the lowest temperature for the whisker growth was found to be  $1050^{\circ}\text{C}$ , and the optimum temperature was in the range of  $1100^{\circ}\text{C}$ - $1150^{\circ}\text{C}$ ; on the other hand, platelet crystals were mainly obtained at a temperature higher than  $1200^{\circ}\text{C}$ . Although the system Au-Ti-P, Pd-Ti-P, or Pt-Ti-P have not been reported, the difference of the lowest or optimum temperature for the whisker growth among the impurities may be attributed to the eutectic temperature in the expected ternary system, impurity-titanium-phosphorus.

*Effects of gas composition and flow rate on whisker growth.*—The effect of the concentration of  $\text{PCl}_3$  and  $\text{TiCl}_4$  on whisker growth (solid line) and polycrystalline growth (broken line) are shown in Fig. 6, where the total chloride flow rate was fixed at  $0.25 \text{ cm}^3/\text{sec}$ . The longest whiskers were not obtained at the ratio of  $\text{PCl}_3/(\text{PCl}_3 + \text{TiCl}_4) = 0.5$ , which corresponds to the stoichiometric ratio of the reactions,  $\text{PCl}_3 + \text{TiCl}_4 + 7/2 \text{ H}_2 = \text{TiP} + 7\text{HCl}$ , but at  $\text{PCl}_3/(\text{PCl}_3 + \text{TiCl}_4) = 0.08\text{--}0.11$ .

Such a tendency for phosphide whiskers to grow from a gas mixture having a poorer  $\text{PCl}_3$  composition

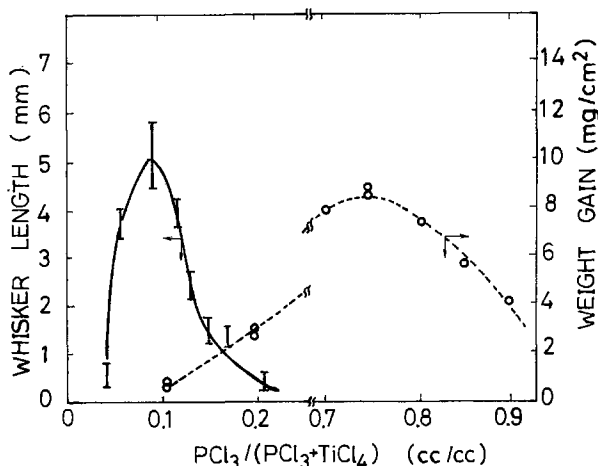


Fig. 6. Influence of  $\text{PCl}_3$  and  $\text{TiCl}_4$  composition on whisker and polycrystalline growth. —, Whisker (with Au), reaction temperature  $1050^\circ\text{C}$ , reaction time 15 min,  $\text{PCl}_3 + \text{TiCl}_4 = 0.25 \text{ cm}^3/\text{sec}$ ,  $\text{H}_2 = 2.25 \text{ cm}^3/\text{sec}$ . - - -, Polycrystalline (without Au), reaction temperature  $1050^\circ\text{C}$ , reaction time 15 min,  $\text{PCl}_3 + \text{TiCl}_4 = 0.2 \text{ cm}^3/\text{sec}$ ,  $\text{H}_2 = 2.2 \text{ cm}^3/\text{sec}$ .

than expected from stoichiometry has been found in the cases of ZrP (12) and BP (13) in the systems  $\text{ZrCl}_4 + \text{PCl}_3 + \text{H}_2$  and  $\text{BCl}_3 + \text{PCl}_3 + \text{H}_2$ , respectively. When no impurity was used, on the other hand, maximum growth rate of polycrystalline films was observed at  $\text{PCl}_3 / (\text{PCl}_3 + \text{TiCl}_4) = 0.7-0.8$ , that is, in a  $\text{PCl}_3$ -rich region. The fast growth of polycrystalline films may require the ratio  $\text{PCl}_3 / (\text{PCl}_3 + \text{TiCl}_4)$  of 0.5 in gaseous layer over the growing surface. However,  $\text{PCl}_3$  is easily reduced to the element of phosphorus which deposits on the inner wall of the reaction tube. Therefore, a ratio of  $\text{PCl}_3 / (\text{PCl}_3 + \text{TiCl}_4)$  of larger than 0.5 is reasonable in the flow system. On the contrary, the small value of the ratio for optimum condition to whisker growth suggests the phosphorus transport to be rate determining in whisker growth at least in its early stage of growth.

The total chloride flow rate also exhibited a pronounced effect on whisker growth, where the ratio of  $\text{PCl}_3$  and  $\text{TiCl}_4$  was fixed at  $\text{PCl}_3 / \text{TiCl}_4 = 0.1$ . An average length of 8-10 mm was obtained at  $\text{PCl}_3 + \text{TiCl}_4 = 0.12-0.15 \text{ cm}^3/\text{sec}$  (linear velocity  $\approx 0.27 \text{ cm}/\text{sec}$  at  $1040^\circ\text{C}$ ), and at a ratio higher or lower than this the length decreased abruptly below 2 mm and curled or woolly whiskers were obtained.

Growth rates of woolly whiskers were determined at about 2-3 mm/min, which is a considerably larger value than that of the pillar whisker of 0.2-0.6 mm/min.

The influence of total gas flow rate on whisker growth was also examined, where the flow ratio of the relevant gases was fixed at  $\text{PCl}_3 / \text{TiCl}_4 / \text{H}_2 = 0.0065 / 0.065 / 1$ . Whiskers grew to an average length of 6.5-7.5 mm at a flow rate of 1.8-2.2  $\text{cm}^3/\text{sec}$  (linear velocity is roughly estimated as 3.7-4.5  $\text{cm}/\text{sec}$  at  $1040^\circ\text{C}$ ).

*Mechanism of whisker growth.*—In order to clarify the role of the impurity, its location on the growing crystals is very important, since one of the indications for the tip vapor-liquid-solid (VLS) mechanism (14) is the existence of drops of impurity on their tips.

The tip part of most whiskers had a shape of a long hexagonal pyramid, and a droplike solid was seldom found on the tip, suggesting that a tip VLS mechanism does not take part in the growth, although a rapid VLS growth followed by slow VS growth in a radial direction cannot be ruled out at this time.

Similar appearances of the tip were also observed in the case of ZrP whisker growth (12) in which the tip was a clear-cut square or tetragonal pyramid.

Photomicrographs of the cross section of a base of a whisker display the presence of a thick and continuous layer, from which the whisker emerged. A result of x-ray microanalysis on this layer is shown in Fig. 7, indicating that the layer consists of a uniform composition of titanium-phosphorus-gold.

This observation suggests a growth mechanism by a center axial screw dislocation proposed by Frank *et al.* (15). However, as mentioned above, the present result can also be explained by the VLS mechanism (16), at least during the initial stage of growth.

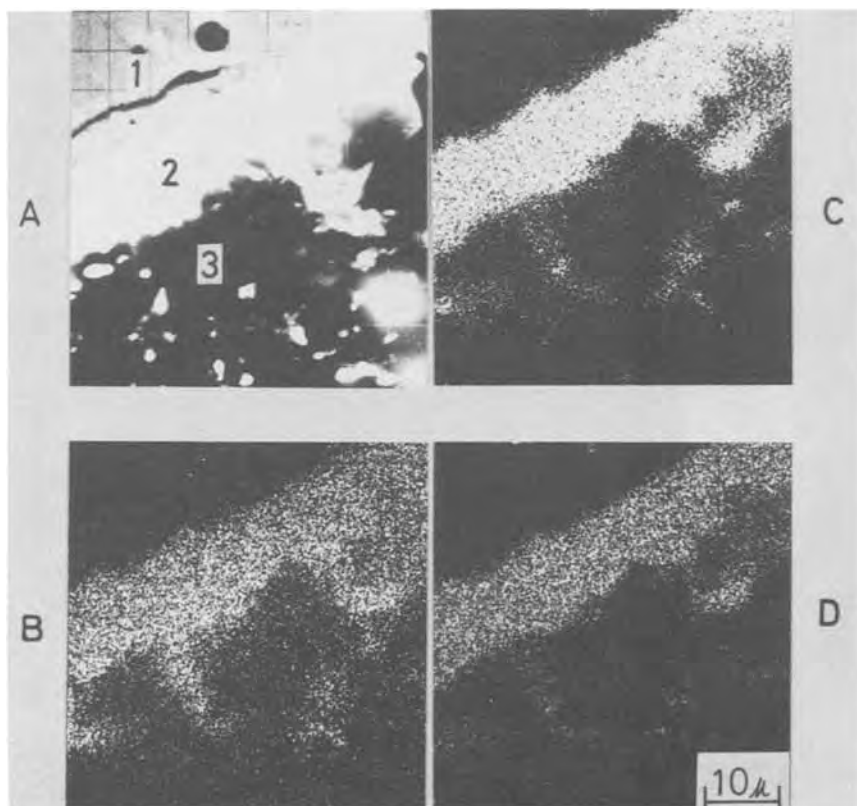


Fig. 7. Profiles of x-ray microanalysis. A: 1, Quartz substrate; 2, TiP layer; 3, whisker part molded in resin. X-ray: B,  $\text{PK}\alpha$ ; C,  $\text{TiK}\alpha$ ; D,  $\text{AuM}\alpha$ .



**Properties of TiP crystals.—Electrical resistivity.**—The resistivities of well-formed whiskers of hexagonal pillar (5–10 mm in length and about 10  $\mu\text{m}$  in diameter) and platelet crystals ( $3 \sim 6 \times 2 \sim 5$  mm,  $2 \sim 5$   $\mu\text{m}$  thick) are shown in Fig. 8, where the direction chosen for measurements of electrical resistivity and thermoelectric force (see next section) of crystal plates is in some direction within (001) plane of the plate. Although the measurements were carried out on three crystals of each type, the results were characteristic of each type within experimental error. In Fig. 8, the resistivity increases linearly with the temperature, characteristic of metallic conduction, and the whisker and the platelet crystals have resistivities of  $2.5 \times 10^{-4}$  and  $3.5 \times 10^{-5}$  ohm  $\cdot$  cm at room temperature, respectively. The activation energies are also estimated as 0.65 and 0.83 eV, respectively.

**Thermoelectric power.**—The thermoelectric power of the crystals are shown in Fig. 9. The thermoelectric power of whiskers relative to copper increased with temperature and showed 18 and 30  $\mu\text{V}/^\circ\text{C}$  at 25° and 200°C, respectively. These values are similar to those of  $\text{TiP}_2$  (17). On the other hand, the thermoelectric power of platelet crystals was independent of temperature and showed 8  $\mu\text{V}/^\circ\text{C}$ .

**Tensile strength.**—The tensile strength of hexagonal pillar whiskers was measured at room temperature as shown in Fig. 10, which indicates that the tensile strength increases with decrease of diameter and has values of 100 and 1000  $\text{kg}/\text{mm}^2$  for whiskers of 20 and 1  $\mu\text{m}$  in diameter, respectively.

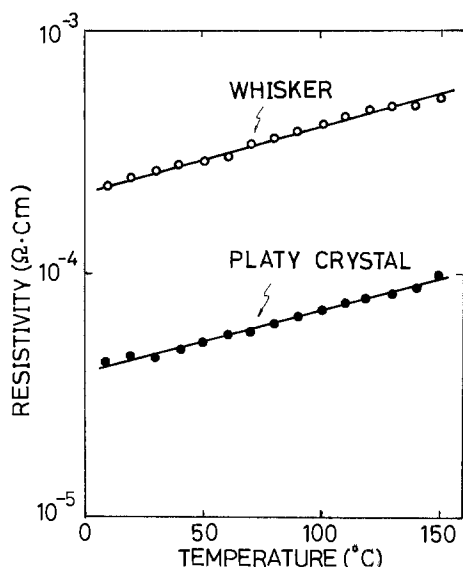


Fig. 8. Temperature dependence of electrical resistivity

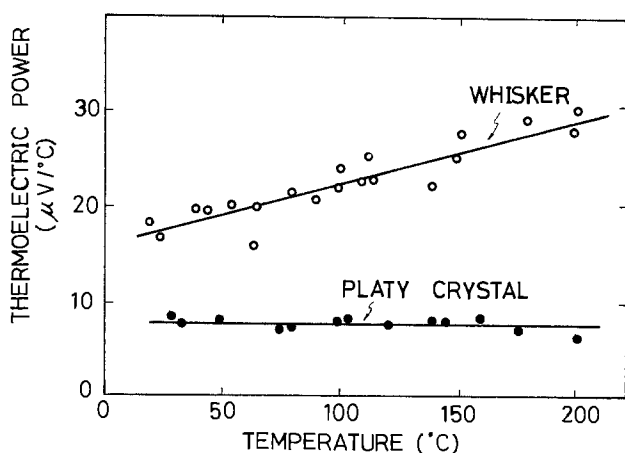
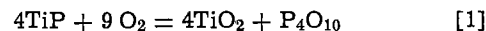


Fig. 9. Temperature dependence of thermoelectric power

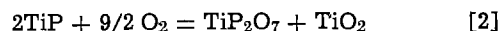
**Stability for oxidation in air.**—Figure 11 shows the change of weight ratio with time at various temperatures between 400° and 1000°C. The weight ratio increased with increasing temperature above 400°C, and at each temperature studied, the ratio quickly increased to a limiting value and remained constant with time. For example, at 1000°C, the ratio increased steeply to 0.56 after 5 min, and remained unchanged after 90 min.

The ratio of weight increase expected by the reaction



is as small as 1.0 weight per cent if phosphorus pentoxide is lost into the gaseous phase. Therefore, the real weight increase cannot be explained by the above reaction.

X-ray diffraction profiles of the products obtained at 1000°C for 30 min are assigned to both  $\text{TiP}_2\text{O}_7$  and  $\text{TiO}_2$ , indicating that the products consist mainly of  $\text{TiP}_2\text{O}_7$  and  $\text{TiO}_2$  in separate phases. But the x-ray pattern indicates little TiP remained at this temperature. It is reasonable to assume that TiP is susceptible to air oxidation at elevated temperatures according to the reaction



but a tight double layer of  $\text{TiP}_2\text{O}_7$  and  $\text{TiO}_2$  formed on the surface of crystals protects the bulk from further oxidation.

The oxidation product of ZrP, an analogous phosphide of TiP, was solely  $\text{ZrO}_2$  (12), probably due to the difference in the stability of the respective pyrophosphates.

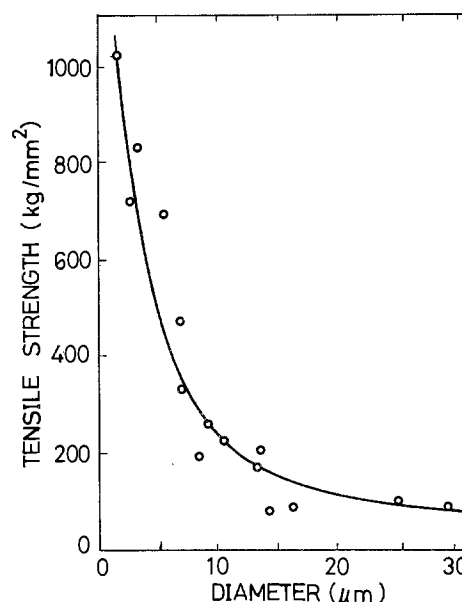


Fig. 10. Tensile strength vs. diameter of pillar whisker

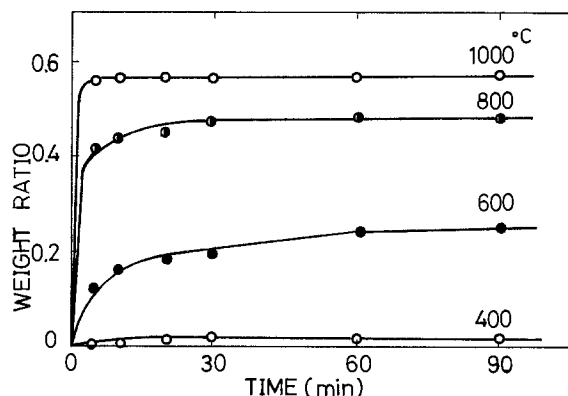


Fig. 11. Rates of oxidation resistivity in the temperature range of 400°–1000°C.



### Conclusions

1. Titanium monophosphide single crystals were obtained by chemical vapor deposition from a system,  $TiCl_4$ ,  $PCl_3$ , and  $H_2$  on a quartz substrate at 850°-1250°C.

2. Manganese, rhodium, gold, and antimony had a beneficial effect on whisker growth at 1040°C. In the case of gold, whiskers with an average length of 5-10 mm and a diameter of 0.5-25  $\mu m$  and with well-formed hexagonal cross section were obtained in the temperature range of 1020°-1050°C in 15 min. Palladium promoted platelet crystal growth at 1250°C.

3. The growth direction of whisker was the c-axis and the face of platelet crystals was assigned as the (001) plane.

4. The longest whisker was obtained at a substrate temperature of 1020°-1050°C,  $PCl_3/(PCl_3 + TiCl_4)$  ratio of 0.08-0.11, total flow rate of  $PCl_3 + TiCl_4$  of 0.12-0.15  $cm^3/sec$ , and a total gas flow rate (mainly  $H_2$ ) of 1.8-2.2  $cm^3/sec$ .

5. A droplike solid was seldom found on the tip part of most whiskers, and layers with uniform Ti-P-Au compositions were observed in the bottom part of whiskers. It is presumed that a screw dislocation or a bottom site VLS mechanism is responsible for the growth of TiP whiskers rather than a tip VLS mechanism.

6. The whisker and platelet crystals had  $2.5 \times 10^{-4}$  and  $3.5 \times 10^{-5}$  ohm · cm resistivity at room temperature along the direction of the growth axis and some direction in (001) plane, respectively.

7. The whisker and platelet crystal had 18 and 8  $\mu V/^\circ C$  thermoelectric power at room temperature along the direction as above, respectively.

8. The whiskers of 20 and 1  $\mu m$  in diameter had tensile strengths of 100 and 1000  $kg/mm^2$ , respectively.

9. TiP crystal was inert in air below 400°C, but oxidized at higher temperature. A layer of titanium pyrophosphate and titanium oxide formed in an early stage of oxidation prevented further oxidation and gave a high temperature stability up to about 1000°C in air. But the x-ray pattern indicates little TiP remained at this temperature.

10. TiP whiskers 5-10 mm long could be easily obtained by the CVD method using a gold impurity. Furthermore, they have a high stability to oxidation at elevated temperatures. Therefore, TiP whiskers are

expected to be one of the interesting materials for high temperature composite.

Manuscript submitted April 14, 1975; revised manuscript received Sept. 16, 1975.

Any discussion of this paper will appear in a Discussion Section to be published in the December 1976 JOURNAL. All discussions for the December 1976 Discussion Section should be submitted by Aug. 1, 1976.

Publication costs of this article were partially assisted by Gifu University.

### REFERENCES

1. W. Biltz, A. Rink, and F. Wiechmann, *Z. Anorg. Allgem. Chem.*, **238**, 395 (1938).
2. M. Knausenberger, G. Brauer, and K. A. Gingerich, *J. Less-Common Metals*, **8**, 136 (1965).
3. N. Schönberg, *Acta Chem. Scand.*, **8**, 226 (1954).
4. L. L. Vereikina and G. V. Samsonov, *Zh. Neorgan. Khim.*, **5**, 1888 (1960) (*C. A.*, **57**, 1834 (1962)).
5. G. V. Samsonov, L. L. Vereikina, and O. I. Popova, *Tr. Seminara po Zharostoikim Materialam, Akad. Nauk Ukr. SSR, Inst. Metallokeram. i Spets. Splavov, Kiev*, **6**, 75 (1960) (*C. A.*, **56**, 13546 (1962)).
6. G. V. Samsonov and L. L. Vereikina, U.S.S.P. Pat. 127,028 (1960) (*C. A.*, **54**, 18912 (1960)).
7. R. L. Ripley, *J. Less-Common Metals*, **4**, 496 (1962).
8. P.-O. Snell, *Acta Chem. Scand.*, **21**, 1773 (1967).
9. D. H. Wilkins, *Anal. Chem. Acta*, **20**, 113 (1959).
10. M. Hansen and K. Anderko, "Constitution of Binary Alloys," 2nd ed., pp. 39, 511, 512, 549, 607, 693, 723, 942, 958, 1027, 1050, 1085, 1087, McGraw-Hill Book Co., New York, Toronto, London (1958).
11. R. P. Elliott, "Constitution of Binary Alloys," 1st Suppl., pp. 97, 438, 736, 751, McGraw Hill Book Co., New York (1965).
12. S. Motojima, Y. Takahashi, and K. Sugiyama, *J. Crystal Growth*, **30**, 1 (1975).
13. S. Motojima, Y. Miura, Y. Takahashi, and K. Sugiyama, *Bull. Chem. Soc. Japan*, **48**, 3161 (1975).
14. R. S. Wagner and W. C. Ellis, *Appl. Phys. Letters*, **4**, 89 (1964); *Trans. AIME*, **233**, 1053 (1965).
15. F. C. Frank, *Discussion Faraday Soc.*, **5**, 48 (1949); W. K. Buton, N. Cabrera, and F. C. Frank, *Phil. Trans. Roy. Soc.*, **243**, 299 (1951).
16. M. H. Christmann, K. A. Jones, and K. H. Olsen, *J. Appl. Phys.*, **45**, 4295 (1974).
17. F. Hulliger, *Nature*, **204**, 775 (1964) (*C. A.*, **62**, 4719 (1965)).

## Low Temperature Migration of Gold Through Thin Films of Silicon Monoxide

D. V. Morgan, M. J. Howes, and C. J. Madams

Department of Electrical and Electronic Engineering, The University of Leeds, Leeds LS2 9JT, England

### ABSTRACT

A study of gold migration in silicon monoxide in the temperature range 200°-600°C has been carried out using the Rutherford scattering technique. It has been found that for plane sources, diffusion occurs which can be characterized by the normal Arrhenius form. For thick gold sources this temperature relation is followed until the silicon-gold eutectic temperature is exceeded at which point a rapid migration of the gold occurs and a high concentration is established in the film.

This investigation was initiated with a view to characterizing some of the less well investigated properties of the material commonly referred to as "silicon monoxide," and which has been used extensively as the amorphous material in the investigation of electrical switching phenomena in amorphous oxide films (1).

Key words: silicon monoxide, thin films, gold migration.

As the properties of silicon monoxide depend markedly on its method of preparation we have restricted our investigation to the study of the migratory behavior of gold in films which have been vacuum deposited from an electrically heated boat source. As silicon monoxide thus prepared is nonstoichiometric, we will refer to it as  $SiO_x$ , where the  $x$  refers to the material stoichiometry.

etry and which is given an experimentally determined value where appropriate.

### Experimental Techniques

Films of  $\text{SiO}_x$ , of thickness ranging from 200 to 500 nm, were prepared by the thermal deposition ( $10^{-6}$  Torr, 1-2 nm/sec) of solid silicon monoxide lumps from a boat source onto polished vitreous carbon substrates. It was found necessary to heat the substrate to  $200^\circ\text{C}$  to promote adhesion and to eliminate the stress cracking which occurs when deposited films cool to room temperature after deposition onto a cold substrate.

To facilitate depth profiling by Rutherford scattering, measurements of film density were made by including a clean microscope slide in the vacuum system and exposing this to the  $\text{SiO}_x$  flux during the evaporation. Microbalance and Talysurf thickness measurements on the slide enabled the density of the deposited oxide to be determined to an accuracy of 4%.

After the substrates had cooled to room temperature a gold evaporation was carried out through a mask containing 5 mm diameter holes to produce circular areas of gold on the surface of the deposited  $\text{SiO}_x$  layer. The resulting gold layers were of two thicknesses,  $\sim 3$  and 30 nm, as determined by a crystal film thickness monitor. The specimens were then annealed in an open tube, nitrogen gas ambient, furnace at temperatures in the range  $200^\circ\text{--}600^\circ\text{C}$  and for periods in the range 200-0.25 hr.

### Methods of Analysis

*Thin gold layer.*—A thin diffusion source approximates to a perfect plane source of zero thickness providing certain conditions are fulfilled (1). In general these conditions will be met if the resulting diffusion depth is large compared to the original source thickness. If the diffusion mechanism can be described by Fick's law then the resulting diffusion profile will have a half-Gaussian form. This particular case is extremely simple to analyze using the Rutherford scattering technique as the concentration of the diffusing species does not contribute significantly to the over-all stopping power of the substrate material and the concentration of substrate atoms can be assumed constant with depth. The over-all stopping power of the  $\text{SiO}_x$  film can be determined by Bragg's rule (2) (3) from tabulated data, and a check on the validity of the rule made against the known thickness of the  $\text{SiO}_x$  film.

If we consider the initial high energy side of a diffusion profile in a Rutherford scattering spectrum and assumes depth/energy linearity then a simple calculation

enables the contribution of the analyzing system to the FWHM of the profile to be calculated. For a diffusion profile FWHM greater than a factor of five times the detector and system FWHM the contribution from the measuring system is less than 2% of the profile FWHM. This is only true if the surface broadening, which is due solely to the system resolution, is removed. This may be accomplished by adding complementary channels about the surface half maximum point on the profile. For our results, our system resolution of 14 keV contributes less than 0.28 keV to the FWHM's of the profiles under these conditions. After this initial correction, the resulting data points were smoothed by truncating their Fourier transforms (4, 5) and the smoothed diffusion profiles extracted by iteratively computing channel depths (Fig. 1). A plot of log counts vs. channel depth squared, results in a graph whose slope yields the value of the diffusion coefficient. The values thus obtained may then be plotted against reciprocal temperature to obtain the diffusion parameter  $D_0$   $\text{cm}^2/\text{sec}$  (Fig. 2). This procedure was checked by comparing the diffusion coefficients of gold in silicon as obtained from Rutherford scattering, with those obtained from the extrapolation of known data (6). We find that there is satisfactory agreement between the different results (see Table I).

*Thick gold source.*—For the thick gold source case the analysis is not as simple, and we have been unable to make quantitative measurements on the migration of the gold into the  $\text{SiO}_x$  layer. Previous authors (7) have relied on existing knowledge of compound densities in determining the stopping power of alloy formations at interfaces. However these generally imply a semi-infinite substrate and the question of the growth direction of the interfacial layer does not arise. When dealing with film thickness of only 500 nm it becomes important, when analyzing the data, to determine whether material is moving out from the film into the surface layers or vice versa and whether the over-all specimen thickness remains constant. Unfortunately it is rarely possible to determine this from the Rutherford scattering spectrum. Nevertheless it is possible to draw some qualitative conclusions from the Rutherford scattering results.

The method of smoothing data by the truncation of its Fourier transform is only useful when applied to individual peaks on a Rutherford scattering spectrum. The spectra obtained from the thick film specimens were smoothed by a least squares, (fourth difference) curve fit applied to the entire spectrum.

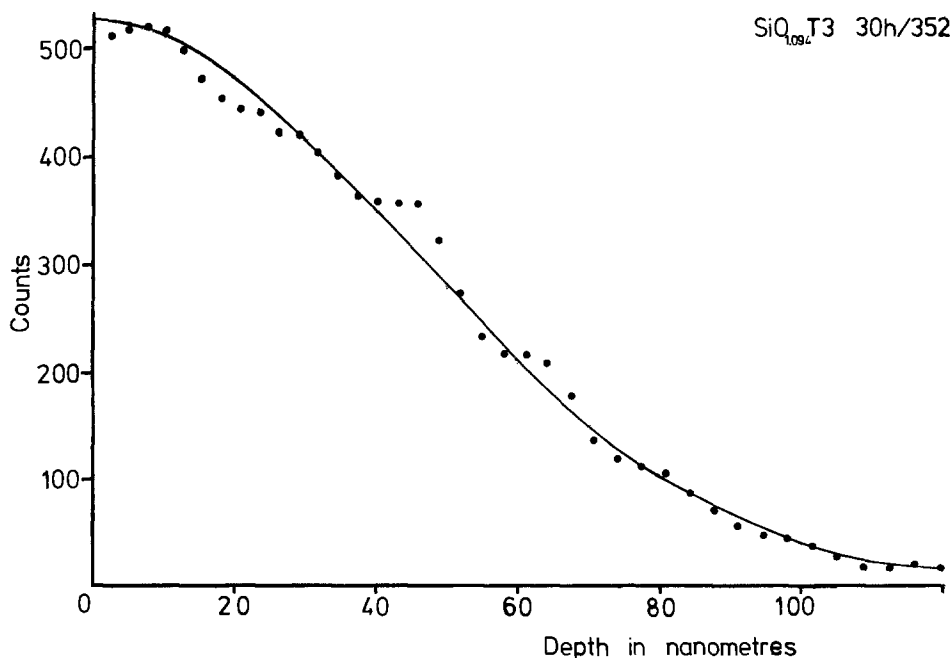


Fig. 1. Depth profile of a thin film diffusion of gold in  $\text{SiO}_{1.094}$  after computer analysis. The solid line represents the theoretical half-Gaussian shape that ideal results should have.

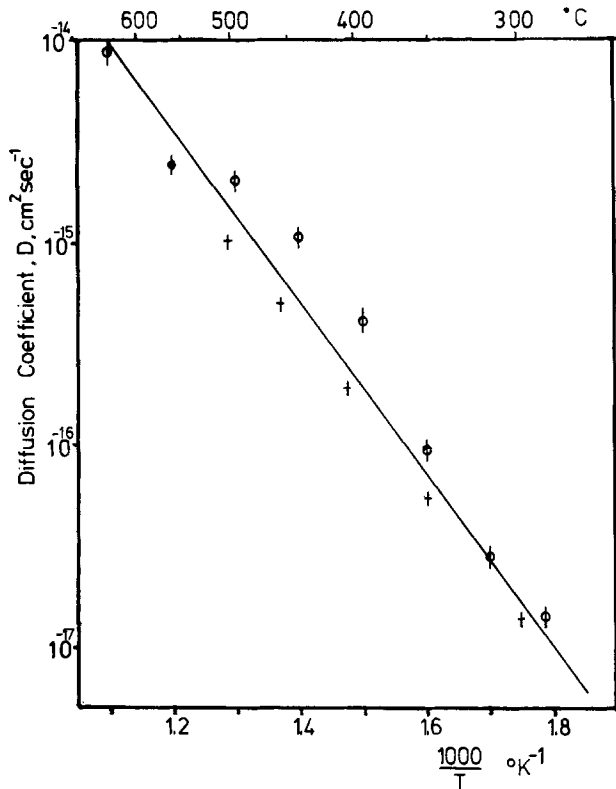


Fig. 2. Low temperature plane source diffusion coefficients of gold in  $\text{SiO}_x$ . The points  $\phi$  are from data obtained with a film of stoichiometric proportions of  $\text{SiO}_{1.096}$  and density  $2.08 \text{ g/cm}^3$ , those points  $+$  refer to films of stoichiometry  $\text{SiO}_{1.192}$  and density  $2.13 \text{ g/cm}^3$ .

### Results

*Thin gold source.*—We have obtained data from several sets of thin gold film specimens prepared at different times and which have different densities and stoichiometries. However, it is stressed that these results apply to films prepared by thermal deposition and with stoichiometric proportions near to  $\text{SiO}$ . These results should not be extrapolated to all values of stoichiometry up to  $\text{SiO}_2$ . [We have, however, observed significant gold diffusion in rf sputtered silicon dioxide (stoichiometrically  $\text{SiO}_{1.8}$ ) at  $390^\circ\text{C}$  after 16 hr.]

Our measured values of the diffusion parameters for  $\text{SiO}_x$

Table I. Comparison of calculated gold in silicon diffusion parameters

	$D_0$ $\text{cm}^2 \text{sec}^{-1}$	$\Delta E$ eV
Determined from plane source diffusions analyzed by Rutherford scattering ( $200^\circ\text{--}600^\circ\text{C}$ )	$1.4 \cdot 10^{-9}$	1.23
Radiotracer determination by sectioning (8) ( $800^\circ\text{--}1200^\circ\text{C}$ )	$1.1 \cdot 10^{-9}$	1.12

$$D_0 = 5 \cdot 10^{-10} \text{ cm}^2/\text{sec}, \quad \Delta E = 0.85 \text{ eV} [200^\circ\text{--}600^\circ\text{C}]$$

differ markedly from those obtained for  $\text{SiO}_2$  by Badalov and Shuman (8)

$$D_0 = 8.5 \cdot 10^{-5} \text{ cm}^2/\text{sec}, \quad \Delta E = 3.7 \text{ eV} [850^\circ\text{--}1000^\circ\text{C}]$$

albeit over a different temperature range. Optical and scanning electron microscopy examinations of the gold deposition areas after annealing showed that within instrumental resolution, the gold penetration occurred uniformly over the surface and no regions of irregularity (pinholes, etc.) could be detected.

All of the  $\text{SiO}_x$  films were deposited from either molybdenum boats covered with stainless steel mesh or from a tantalum boat which had a cover, also of tantalum, with a single 5 mm diameter hole. The tantalum boat was designed to minimize "spitting" of the silicon monoxide source material due to uneven heating. In general good quality films were produced by both types of boat.

No significant differences in the results on the thin gold source specimens deposited under the conditions described could be attributed to the different types of boat used, but there is some evidence that this is not the case with some of the thick gold film structures.

*Thick gold source.*—Devices fabricated with thick gold sources ( $\sim 30 \text{ nm}$ ) exhibited a similar type of diffusion to that of the thin gold source devices up to temperatures of about  $370^\circ\text{C}$ . Above this temperature a rapid migration of the gold occurs with a nearly rectangular depth distribution. The leading edges of the silicon and oxygen peaks in the Rutherford scattering spectrum have moved to an energy corresponding to surface scattering (Fig. 3). As is illustrated in Fig. 3, once this initial penetration has occurred the "normal" mode diffusion process continues until eventually total film penetration results (Fig. 4) and a high gold concentration, estimated at approximately  $10^{22} \text{ atoms cm}^{-3}$  is established within the film.

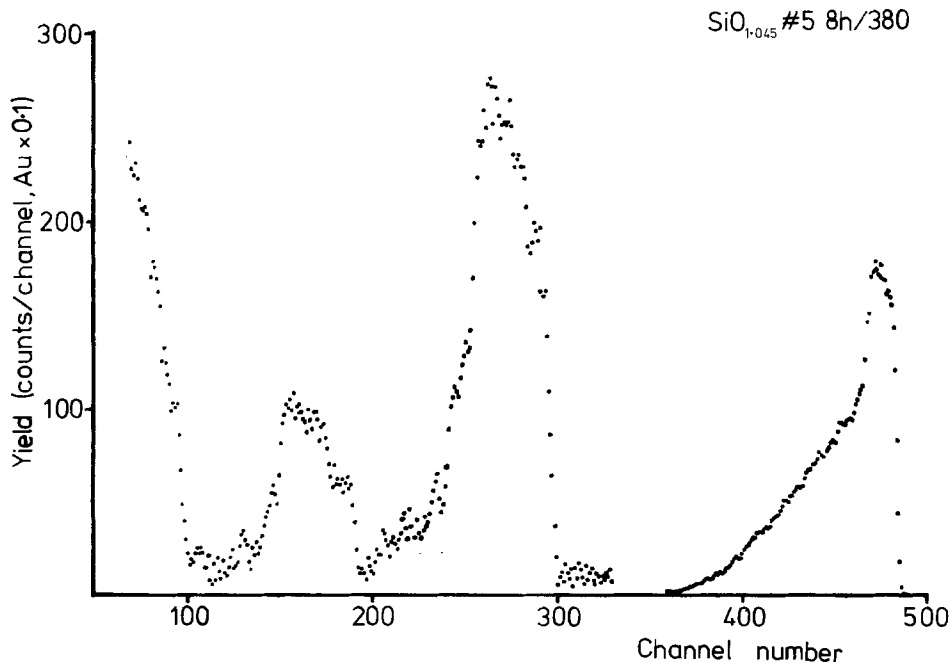


Fig. 3. Rutherford scattering spectrum,  $\theta = 16^\circ$ ,  $E_0 = 2 \text{ MeV}$ , of thick gold source specimen after annealing for 8 hr at  $385^\circ\text{C}$  showing initial penetration and subsequent diffusion of the gold.

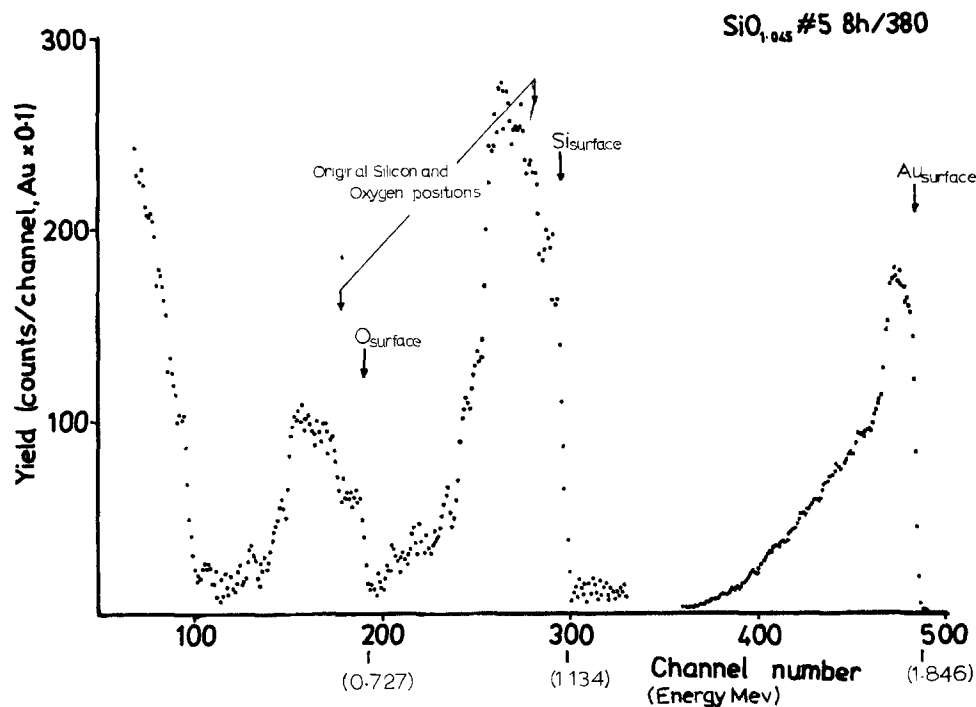


Fig. 4. Rutherford scattering spectrum after 16 hr at 388°C. Total film penetration has occurred.

The depth of this initial penetration depends on the original source thickness, but the rate at which the reaction occurs appears to vary with density and/or stoichiometry. However we have been unable to resolve whether it is the density or the stoichiometry of the  $\text{SiO}_x$  which plays the more significant role although we suspect it may be the latter.

As qualitative results are based largely on a visual interpretation of Rutherford scattering spectra we should consider possible sources of error in our interpretations.

It is known that surface irregularities can occur when thin metal films are annealed. The metal can withdraw into globules under the influence of surface tension resulting in a highly irregular surface. Although the absolute size of the surface irregularity may vary it is generally difficult to detect these by microscopy. The Rutherford scattering spectrum from such a specimen is ambiguous since it may show an apparent "profile" which is identical to that obtained when strong interpenetration has occurred.

Gold films 50 nm thick which were deposited as stripes across both the  $\text{SiO}_x$  layer and the vitreous carbon surface showed "island" formation after 10 min anneals at 500° and 600°C. Optical examination with an interferometer clearly showed the "islands" to be thick (300 nm) regions of gold and the Rutherford scattering spectra shows "profiles" which are almost twice as thick as the  $\text{SiO}_x$  film itself. Had a thinner gold film or a thicker  $\text{SiO}_x$  layer been used one might have erroneously assumed that significant penetration had occurred.

Annealing the thick gold source specimens below 500°C produced no evidence of the surface agglomeration as judged by optical microscopic examination.

As a further check that the Rutherford scattering data was correctly interpreted a theoretical spectrum to simulate surface agglomeration of the gold was computed for scattering from an  $\text{SiO}_x$  film which had 50% of its surface covered with a 50 nm gold film. Ignoring straggling effect (which was assumed to be minimal) but including the detector and system resolution (14 keV) a comparison may be made between the shape of the silicon peak of Fig. 3 and the computed silicon peak of Fig. 5. As there are no points of similarity between the two figures it is concluded that the spectrum in Fig. 3 does not result from surface accumulation.

Silicon oxide ( $\text{SiO}_x$ ) films deposited in a similar manner but with a slow evaporation rate (0.2 nm/sec) and a higher background pressure ( $10^{-5}$  Torr) show

heavy contamination from the boat source. The stoichiometry of these films is  $\text{SiO}_{1.15}\text{Mo}_{0.02}$ . Although the normal diffusion process may be observed in these films the expected rapid gold migration above 370°C did not occur. Above 500°C surface agglomeration of the gold was evident both over the  $\text{SiO}_x$  and carbon substrate and penetration which occurred was masked in the Rutherford scattering spectrum by the pseudoprofile from the surface agglomeration.

**Electrical measurements.**—Some simple electrical measurements were performed on devices made by depositing 100 nm of gold onto 500 nm of  $\text{SiO}_x$  on a carbon substrate.

The electroforming (1), of such thick  $\text{SiO}_x$  films, was unsuccessful and resulted only in dielectric breakdown. After annealing for 2 hr at 500°C, devices were found to electroform and exhibited voltage controlled negative resistance and bistable switching.

A few devices annealed for 8 hr at 390°C were found to be irreversibly in a short-circuit condition implying complete gold penetration of the  $\text{SiO}_x$  film.

### Conclusions

We have shown that for thermally deposited  $\text{SiO}_x$ , over a restricted range of stoichiometries, the plane

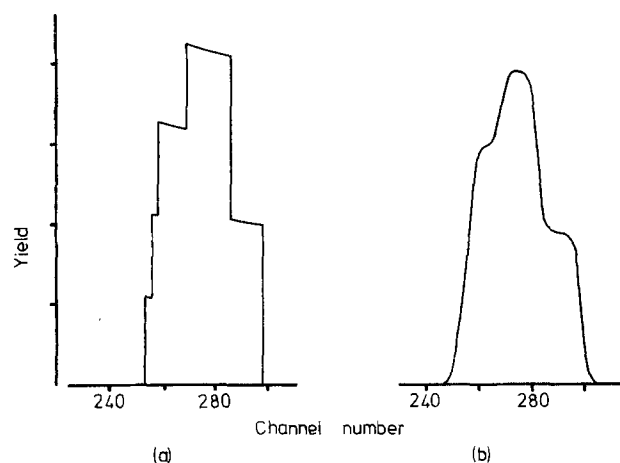


Fig. 5. Calculated shape of the backscattered spectrum from silicon in 200 nm  $\text{SiO}_{1.14}$  film with 50% of the analyzed surface covered with a 50 nm gold film.  $\theta = 168^\circ$ , 2 MeV alphas. (a) Assuming perfect detection system and negligible straggling. (b) Incorporating a 14 keV FWHM detection resolution.

source diffusivity of gold may be expressed as

$$D = 5.10^{-5} \exp(-0.85/KT) \text{ cm}^2/\text{sec} \quad (200^\circ\text{-}600^\circ\text{C})$$

Increasing the available source concentration, by increasing the gold layer thickness, has no effect on the diffusivity until the anneal temperature exceeds  $370^\circ\text{C}$ . This is the gold-silicon eutectic point (11), and the resultant rapid migration of the gold into the  $\text{SiO}_x$  may be described as a form of alloying of the gold with free silicon (12, 13) in the  $\text{SiO}_x$ . This results in a more rapid penetration of the  $\text{SiO}_x$  than would be the case if the gold migration was diffusion limited.

High concentrations of molybdenum, from the molybdenum boat source, in the  $\text{SiO}_x$  film appear to inhibit this alloying behavior, possibly by modifying the structure of the  $\text{SiO}_x$  (14).

The high electrical conductivity of the  $\text{SiO}_x$  observed after gold penetration has occurred is similar to that observed when thin film devices are switched into their low resistance state. The Bistable memory switching of  $\text{SiO}_x$  films in air has been reported by Manhart. The high conductivity state results from electrode migration along a high temperature region which has been initiated by thermal runaway.

It has previously been considered that in these amorphous oxide devices a high temperature ( $1000^\circ\text{C}$ ) (16) must be established, under conditions of thermal runaway or avalanche ionization, for structural changes to occur in either the insulating film or the electrodes. Our results have shown that, for gold on  $\text{SiO}_x$ , rapid migration can occur at a markedly lower temperature than this and, considering that the metal counterelectrodes used in these devices are biased positively (10, 15) the migration may also be enhanced by the applied field if the metal ionizes under extreme conditions such as avalanching.

#### Acknowledgment

The authors are indebted to Professor G. Carter and Dr. A. Carter of Salford University for the use of the accelerator facilities, to Professor Hogsted-Phim for his critical comments, and the Applied Physics Division AERE, Harwell for supporting this work.

Manuscript submitted April 25, 1975; revised manuscript received Sept. 29, 1975. This was Paper 127 presented at the Toronto, Canada, Meeting of the Society, May 11-16, 1975.

Any discussion of this paper will appear in a Discussion Section to be published in the December 1976 JOURNAL. All discussions for the December 1976 Discussion Section should be submitted by Aug. 1, 1976.

#### REFERENCES

1. G. Dearnley, A. M. Stoneham, and D. V. Morgan, *Rept. Prog Phys.*, **33**, 1129 (1970).
2. R. M. Burger and R. P. Donovan, Editors "Fundamentals of Silicon Integrated Device Technology," Vol. 1, p. 205, Prentice-Hall Inc., Englewood Cliffs, N. J. (1967).
3. W. H. Bragg and R. Kleeman, *Phil Mag.*, **10**, 318 (1950).
4. J. F. Ziegler and W. K. Chu, *Atomic Data and Nuclear Data Tables*, Vol. 13, p. 463 (1974).
5. C. Z. Lanazos, "Applied Analysis," Chap. 5, Pitman, London (1964).
6. J. F. Ziegler, G. W. Cole, and J. Baglin, *J. Appl. Phys.*, **43**, 3809 (1972).
7. D. Shaw, Editor, "Atomic Diffusion in Semiconductors," Plenum Press, London and New York (1973).
8. D. J. Coe, E. H. Rhoderick, P. H. Gerzon, and A. W. Tinsley, *Institute of Physics Conference Series No. 22*.
9. A. Z. Badalov and V. B. Shuman, *Fiz. Tech Poluprovodn*, **2**, 741 (1968).
10. C. J. Madams, D. V. Morgan, and M. J. Howes, *J. Appl. Phys.*, **45**, 5088 (1974).
11. M. Hansen, "Constitution of Binary Alloys," McGraw-Hill Book Co., New York (1958).
12. A. Cachard, J. A. Roger, J. Pivot, and C. M. S. Dupuy, *Phys. Status Solidi*, **A5**, 637 (1971).
13. M. V. Coleman and D. J. D. Thomas, *Phys. Status Solidi*, **22**, 593 (1967).
14. J. M. Stevels, *Philips Tech. Rev.*, **22**, 300 (1960).
15. S. Manhart, *Phys. D*, **6**, 82 (1973).
16. A. C. Warren, *Electronics Letters*, **5**, 461 (1962).
17. D. V. Morgan, M. J. Howes, R. D. Pollard, and D. G. P. Waters, *Thin Solid Films*, **15**, 127 (1973).

## Monolithic Studs as Interlevel Connectors in Planar Multilevel LSI

G. C. Schwartz\* and V. Platter

IBM System Products Division, East Fishkill Facility, Hopewell Junction, New York 12533

Planar aluminum and aluminum alloy interconnection metallization for multilevel integrated circuits was first made possible by the substitution of anodic conversion for subtractive etching (1-3). The anodic process results in a planar structure of interconnection metallization embedded in anodic oxide; there are no metal edges which subsequently must be covered by the interlevel insulator. Therefore the interlevel insulation can be significantly thinner than that required when standard processing is used. Nevertheless, a step is formed when the via holes are etched, so that the resultant structure is no longer completely planar.

A method for complete planarization was proposed by Sato *et al.* (4). They described a scheme which uses "bumps" as interlevel connectors and polyimide as a planarizing insulator to cover the conventionally etched metal. However, this excellent idea requires three separate metal depositions to form a two-level structure, five to form three levels, etc. This introduces additional vacuum steps, but more important, it introduces additional interfaces. It is well known that aluminum rapidly grows an oxide film as soon as it is exposed to air; this thin insulating layer adds to the interlevel resistance.

Anodic processing can be used to form the interconnection metallization pattern and the interlevel "bumps" or "studs" from a single metal film as described below.

**Step 1.**—The appropriate metal film is deposited upon the semiconductor substrate. A hafnium underlay is used when the metallization pattern includes elec-

trically "floating" conductors (5). When the metal used for the interconnection pattern is not pure aluminum, an appropriate alloy is deposited between the underlay and the aluminum cap (3). The composite metal film which is shown in Fig. 1a is deposited sequentially in a single evaporation in a multisource system.

**Step 2.**—A thin porous anodic oxide layer is formed on the surface of the aluminum, in oxalic acid, to insure adhesion of the photoresist layer which is then applied. Using standard photolithography, openings are made in the photoresist layer at the location of the studs, as shown in Fig. 1b.

**Step 3.**—A barrier layer is formed to about 75V in ammonium borate in ethylene glycol; the photoresist layer is removed by ashing; the structure in Fig. 1c results.

**Step 4.**—The barrier layer protects the area it covers from subsequent anodization in oxalic acid (1). The rest of the film is anodized in oxalic acid so that a thickness of aluminum equal to the thickness of the required interlevel insulator is anodized, producing the structure in Fig. 1d.

**Step 5.**—The anodic oxide is removed in an etch which dissolves the oxide without attacking the underlying aluminum (3), leaving the stud as shown in Fig. 1e.

**Step 6.**—A thin porous anodic oxide is formed again for resist adhesion, and a photoresist mask which leaves the interconnection metallization pattern areas uncovered (which include the previously formed studs) is produced. A barrier layer is formed to about 75V in the exposed regions; the stud is completely encapsulated in barrier layer, as shown in Fig. 1f.

**Step 7.**—The resist is removed and the exposed

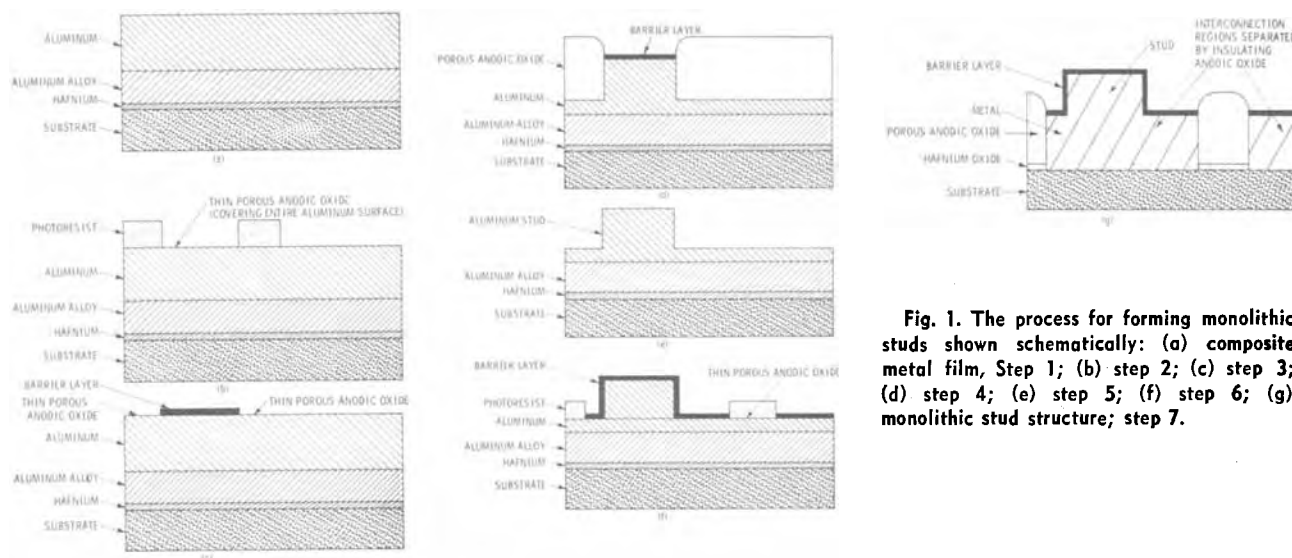


Fig. 1. The process for forming monolithic studs shown schematically: (a) composite metal film, Step 1; (b) step 2; (c) step 3; (d) step 4; (e) step 5; (f) step 6; (g) monolithic stud structure; step 7.

\* Electrochemical Society Active Member.

Key words: multilevel metallization, planar metallization, large-scale integrated circuits, anodic oxidation, aluminum alloy metallurgy.

aluminum and aluminum alloy are completely anodized as described previously (3) and the hafnium underlay is converted to an insulating layer by anodization followed by steam oxidations (5). At the temperature of the steam oxidation, the aluminum (aluminum alloy) and hafnium interdiffuse, so that there is no longer a discrete layer of hafnium at the substrate interface (5). Also it is unlikely that a sharp boundary still exists between the aluminum cap and the underlying alloy. If the hafnium underlay is required on upper levels, its oxidation temperature may have to be reduced (and the time increased) to be compatible

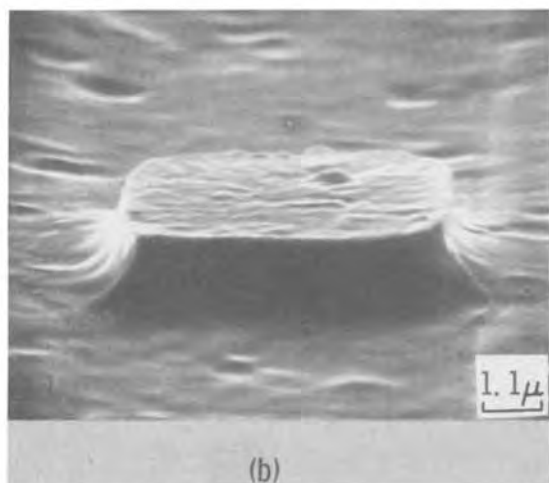
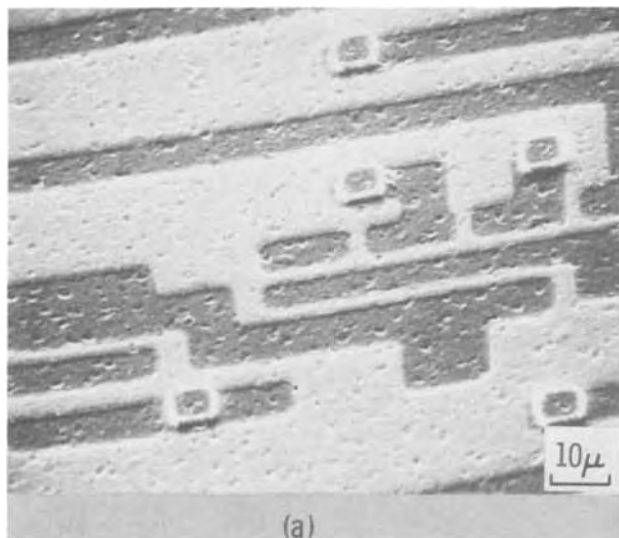


Fig. 2 (a) Scanning electron micrograph of a monolithic stud and interconnection metallization pattern formed by anodic processing. (b) Scanning electron micrograph of a stud only; higher magnification.

with the underlying polyimide. The final structure is shown schematically in Fig. 1g.

The polyimide is applied after the completion of the composite structure. It is then etched uniformly using rf reactive ion etching at high pressure (6) followed by a short rf sputter clean at the appropriate argon pressure to remove the anodic oxide which had protected the top of the stud during the processing.

The interconnection metallization is not completely planar since the barrier layer process of Tsunemitsu and Shiba (1) was used. However, this process was chosen because the barrier layer provides the best protection for the tall, narrow stud. Moreover, it is not the planarizing capability of the anodic processing that is important in this application; it is the ability to form the structure from a single metal film. However, an added dividend of anodic processing is the increased cross-sectional area of the conductors thus formed (compared to subtractive etch) with the attendant increase in current carrying capability (3).

A scanning electron micrograph of a stud formed by this process is shown in Fig. 2. It can be seen that some undercutting has occurred during the formation of the stud, but it is substantially less than that which results from subtractive etching.

### Conclusion

A description has been given of an anodic process by which it is possible to form both the interconnection metallization pattern and the interlevel connectors ("studs") from a single (composite) metal layer.

Manuscript submitted July 24, 1975; revised manuscript received Sept. 25, 1975.

Any discussion of this paper will appear in a Discussion Section to be published in the December 1976 JOURNAL. All discussions for the December 1976 Discussion Section should be submitted by Aug. 1, 1976.

Publication costs of this article were partially assisted by IBM Corporation.

### REFERENCES

1. H. Tsunemitsu and H. Shiba, Abstract 18.4, IEEE International Electron Devices Meeting, October 1969; NEC Research and Development, April 1972.
2. W. R. McMahon, Abstract 7.1, IEEE International Electron Devices Meeting, October 1970.
3. G. C. Schwartz, Abstract 3, p. 13, The Electrochemical Society Extended Abstracts, Spring Meeting, San Francisco, California, May 12-17, 1974; G. C. Schwartz and V. Platter, *This Journal*, **122**, 1508 (1975).
4. K. Sato, S. Harada, A. Saiki, T. Kimura, T. Okubo, and K. Mukai, Proceedings of the Electronic Components Conference, p. 15, 1973.
5. G. C. Schwartz and V. Platter, *This Journal*, **123** (1976).
6. L. Zielinski and G. C. Schwartz, Abstract 53, p. 117, The Electrochemical Society Extended Abstracts, Spring Meeting, Toronto, Canada, May 11-16, 1974.

# Influence of Trichloroethylene on Room Temperature Flatband Voltages of MOS Capacitors

D. L. Heald, R. M. Das, and R. P. Khosla<sup>1</sup>

University of California, Department of Electrical Engineering and Computer Science,  
Santa Barbara, California 93106

The ever increasing interest in growing high quality SiO<sub>2</sub> is well documented by the large number of recent papers in this area (1). Although the stabilization of the thermally grown SiO<sub>2</sub> can be achieved by a film of phosphosilicate glass (PSG), the use of HCl (2, 3) during the oxidation process has gained considerable attention.

This process provides a reduction in the instabilities due to the presence of mobile ions in the oxide. It also improves the dielectric breakdown characteristics of the oxide, reduces the surface-state density at the Si-SiO<sub>2</sub> interface, and increases the minority carrier lifetime in the silicon surface.

Most of these improvements are attributed to the presence of chlorine in HCl and are well substantiated by recent work of Van der Meulen *et al.* (4). It is believed that some chlorine is always incorporated in the oxide near the Si interface, which helps in neutralizing and immobilizing the sodium ions that are drifted toward the interface under an electric field at an elevated temperature. Since HCl is very corrosive and dangerous to handle, attempts have been made to use other compounds that contain chlorine and are easy to handle.

Chen and Hile (5) and Declerck *et al.* (6) have investigated the effects of trichloroethylene (TCE) on the characteristics of MOS devices subjected to bias-temperature stress. Van der Meulen *et al.* (4) noted that oxides grown in Cl<sub>2</sub> were electrically unstable at room temperature and that oxides grown in HCl exhibited flatband voltage shifts after room-temperature bias stress. It is the purpose of this paper to report on the room-temperature stability of oxides grown in TCE.

MOS capacitors were fabricated on n-type (100) Si substrates having 2-5 ohm-cm resistivity. The wafers were cleaned in a sulfuric acid-hydrogen peroxide solution, followed by an HF dip and DI H<sub>2</sub>O rinse. The furnace tube was cleaned and acclimatized with TCE and O<sub>2</sub> for a period of 10 hr.<sup>2</sup> All the wafers were oxidized at 1060°C, using the following sequence: (i) 1000 cm<sup>3</sup>/min of dry O<sub>2</sub> for 5 min; (ii) TCE/He at 0-105 cm<sup>3</sup>/min and dry O<sub>2</sub> at 1000 cm<sup>3</sup>/min for 60 min; (iii) 1000 cm<sup>3</sup>/min dry O<sub>2</sub> for 15 min; (iv) N<sub>2</sub> anneal for 15 min prior to removal of wafers. Thus the total oxidation time for each wafer was 80 min. The TCE bubbler was kept at room temperature, 23°C [Declerck *et al.* (6) kept the TCE bubbler at 34°C]. Immediately after removal, 30-mil aluminum dots for the metal gates were evaporated from tungsten filaments through a metal mask. Then oxide from part of the wafers was carefully etched in HF to allow contact to the substrate. Photoresist steps were completely avoided. The wafers were annealed for 15 min at 525° in N<sub>2</sub>. Conventional C-V measurements were made with and without room-temperature bias stress.

Figure 1 shows a plot of oxide thickness *vs.* TCE/He flow. The increased rate of the growth of SiO<sub>2</sub> is consistent with the observations reported both in the presence of HCl (3) as well as TCE (6). The growth rate of SiO<sub>2</sub> increased as the flow rate increased but satu-

rated beyond 70 cm<sup>3</sup>/min. The oxide thickness varied from 900 to 1650Å. The initial values of the flatband voltage, V<sub>FB</sub>, *vs.* TCE/He flow prior to any bias stress is shown in Fig. 2 (solid line). It was found that the optimum region of this curve occurs between 37-42 cm<sup>3</sup>/min of TCE/He, which is consistent with results of Van der Meulen *et al.* (4) and Declerck *et al.* (6) for high quality halogen-grown oxides. The improvement in flatband voltage afforded by low TCE/He flow rates is most probably a result of the compensation of positive oxide charge.

At the highest flow rate, 105 cm<sup>3</sup>/min of TCE/He, the C-V plots exhibit a small degree of low frequency behavior, indicative of increased recombination/generation activity. This is in general agreement with the reduced storage time for large percentages of TCE observed by Declerck *et al.* (6). The increased magnitude of the flatband voltage at the higher TCE/He flow rates has not previously been reported and is probably caused by an increase in positive charge density or a decrease in negative charge density in the oxide. It should be noted that for higher concentrations of TCE, Declerck *et al.* (6) did observe an increase in surface-state density.

The gates on the MOS capacitors were subjected to a negative bias at room temperature for times up to 20

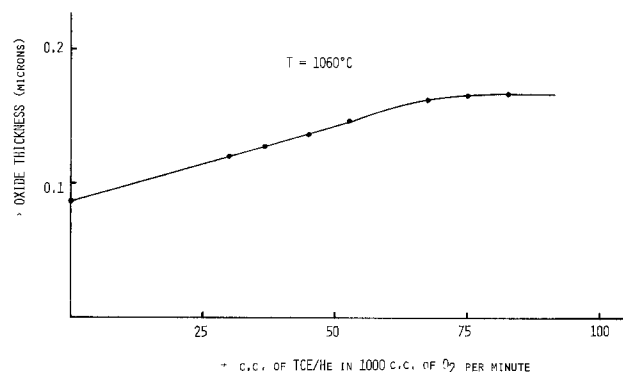


Fig. 1. Oxide thickness vs. TCE flow rate

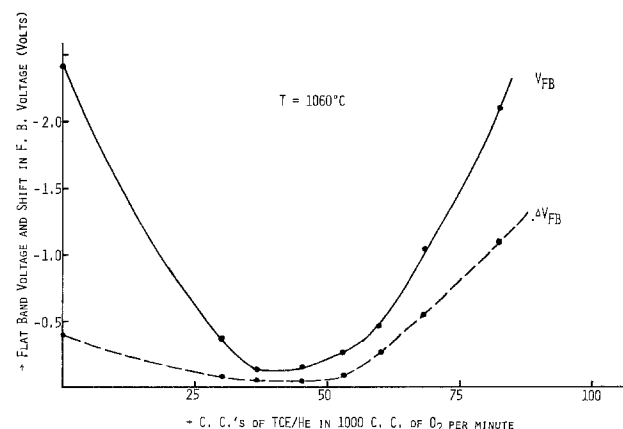


Fig. 2. Flatband voltage and shift in flatband voltage vs. TCE flow rate. Bias of +15V was applied for 5 min at room temperature, measurements were made as soon as possible.

<sup>1</sup> Visiting Scholar from Kodak Research Laboratories, Eastman Kodak Company, Rochester, New York 14650.

<sup>2</sup> At the early stages of the experiments carbon deposition in the furnace tube was frequently observed, even at low concentrations of TCE. But after substantial use we were unable to reproduce the conditions resulting in carbon deposition.

Key words: halogen oxidation, chlorine incorporation, flatband voltage shifts.



hr and fields up to  $6 \times 10^6$  V/cm. For a 15 min bias stress of  $10^6$  V/cm, no flatband voltage shifts could be detected except for the sample corresponding to  $105 \text{ cm}^3/\text{min}$  of TCE/He, in which a positive shift of  $0.55 \text{ V}$  was observed. It would be consistent with the initial flatband measurements if this shift were due to the motion of mobile charge acquired in the sample oxidized with the high TCE/He flow rate. The ions  $\text{H}^+$  or  $\text{H}_3\text{O}^+$  which are mobile at room temperature (7) are possible candidates. The actual role and fate of the hydrogen contained in the TCE has not been established. Van der Meulen *et al.* (4) have indicated that some sodium may be mobile at room temperature.

For extremely high fields ( $6 \times 10^6$  V/cm) and negative gate bias, the samples oxidized with  $105 \text{ cm}^3/\text{min}$  of TCE/He exhibited a transient flatband instability similar to that observed by Van der Meulen *et al.* (4) for  $\text{Cl}_2$ -grown oxides, although the instability was less pronounced. The flatband voltage first shifted in the positive direction and then for long times (on the order of 10 hr) shifted slightly in the negative direction, the flatband voltage never changing sign, however. A positive bias stress of  $10^6$  V/cm inhibited this negative bias instability completely. At field strengths normally encountered in device operation, the oxides were more stable.

Next the effects of positive bias stress were investigated. The resulting shift in flatband voltage is shown in Fig. 2 (dashed line). The minimum shift in the flatband voltage  $\Delta V_{\text{FB}}$  is  $0.062 \text{ V}$  for samples which were grown with flow rates of  $40\text{--}50 \text{ cm}^3/\text{min}$  of TCE/He. At flow rates below this minimum, both the reduction in flatband voltage and the reduction in flatband voltage shift can most easily be explained by the neutralization and trapping of mobile oxide charge. Introducing trap

sites for electrons in the oxide will not account for this behavior. A flatband shift of  $0.062 \text{ V}$  corresponds to a mobile charge density of about  $5 \times 10^9$  charges/ $\text{cm}^2$ .

For higher flow rates of TCE/He the flatband shift increases. At a concentration of  $105 \text{ cm}^3/\text{min}$  of TCE/He, not shown in Fig. 2, the shift was about  $2.5 \text{ V}$  (corresponding to a mobile charge concentration of  $2.85 \times 10^{11}/\text{cm}^2$ ), and substantial hysteresis appears in the C-V characteristics. Figure 3 shows the recovery of this shift with time and the observed hysteresis. (No hysteresis was observed for samples oxidized with low concentrations of TCE.) The dramatic increase in  $V_{\text{FB}}$  and  $\Delta V_{\text{FB}}$  implies high concentrations of mobile oxide charges or donor-like oxide traps, either of which could also cause the observed hysteresis.

In summary we have shown that TCE can be effectively used to lower oxide charge mobile at room temperature (mostly  $\text{H}^+$  or  $\text{H}_3\text{O}^+$  and perhaps some alkali ions) to values as small as  $5 \times 10^9/\text{cm}^2$ . Because of ease of handling, TCE may be a good substitute for HCl in growing high quality oxides. For extremely high fields (larger than those normally encountered in device operation) the TCE-grown oxides exhibited a room-temperature instability similar to that observed in  $\text{Cl}_2$ -grown oxides. For high quality oxides there is an optimum flow rate of TCE during oxidation of about 4-5%. Above this point, the introduction of additional positive mobile charge or donor-like traps in the oxide degrade the C-V characteristics. The incidence of low frequency behavior for large TCE flow rates indicates increased recombination/generation activity at the interface or bulk silicon near the surface.

Manuscript submitted June 9, 1975; revised manuscript received Aug. 25, 1975.

Any discussion of this paper will appear in a Discussion Section to be published in the December 1976 JOURNAL. All discussions for the December 1976 Discussion Section should be submitted by Aug. 1, 1976.

Publication costs of this article were partially assisted by the University of California.

#### REFERENCES

1. See a list of references in R. J. Kriegler, "Digest of Technical Papers," ISSCC, 55 (1975).
2. P. H. Robinson and F. P. Heiman, *This Journal*, **118**, 141 (1971).
3. R. J. Kriegler, Y. C. Cheng, and D. R. Colton, *ibid.*, **118**, 73C (1971); **119**, 388 (1972).
4. Y. J. Van der Meulen, C. M. Osburn, and J. F. Ziegler, *ibid.*, **122**, 284 (1975).
5. M. Chen and J. W. Hile, *ibid.*, **119**, 223 (1972).
6. G. J. Declerck, T. Hattori, G. A. May, J. Beaudouin, and J. D. Meindl, *ibid.*, **122**, 436 (1975).
7. B. E. Deal, *ibid.*, **121**, 198C (1974).

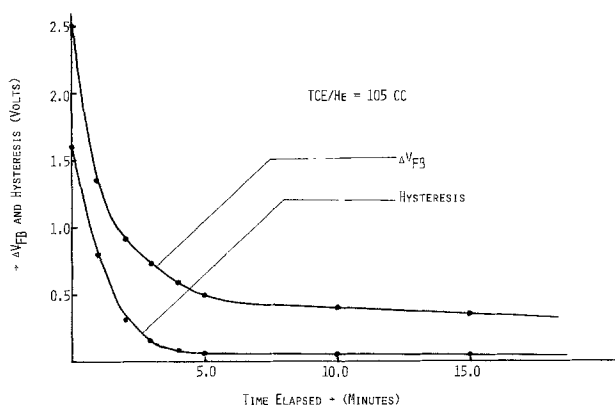


Fig. 3. Shift in flatband voltage and hysteresis vs. time elapsed after the bias of  $15 \text{ V}$  was applied at room temperature for 5 min.

## The Effect of Substrate Bias on the Properties of Reactively Sputtered Silicon Nitride

A. W. Stephens,<sup>1</sup> J. L. Vossen,\* and W. Kern\*

RCA Laboratories, David Sarnoff Research Center, Princeton, New Jersey 08540

There have been several reports (1-13) on the properties of sputtered silicon nitride films. In most cases optimum film properties have been achieved by re-

\* Electrochemical Society Active Member.  
<sup>1</sup> Present address: 95 Meadow Drive, Hightstown, New Jersey 08520.  
 Key words: silicon nitride films, bias sputtering, reactive sputtering, thin films.

active sputtering using high-purity Si targets rather than direct sputtering of hot-pressed  $\text{Si}_3\text{N}_4$ . Most of the reported work has been done by rf sputtering without direct control over the substrate bias. In general, the results of others indicate that optimum film properties (low etch rate, good barrier to alkali ions, etc.) are achieved when the deposition rate is high and the

discharge gas pressure is low. These sputtering conditions are known to lead to relatively high substrate bias voltages (14). With electrically floating substrates, it has been found (2, 6, 12) that films of high quality could not be produced at discharge pressures greater than about 15 mTorr, and the suggestion has been made that a high, negative self-bias is responsible for the improved film properties because of an increase in film density. Such an increase in film density could arise from two mechanisms: (i) enhanced surface mobility of depositing atoms and (ii) resputtering of weakly bound deposited species (12, 14).

In this note, we report direct evidence for improvement of the properties of rf reactively sputtered  $\text{Si}_3\text{N}_4$  using a sputtering system in which the substrate bias can be controlled, independent of the other rf glow discharge conditions.

### Experimental

The system for rf sputtering with controlled rf-induced substrate bias has been described in detail elsewhere (15). Briefly, there are two identical rf sputtering targets ( $\sim 20$  cm diameter) mounted concentrically in the top and bottom of the vacuum chamber. The separation between the targets was 2.85 cm. The lower target serves as a substrate platform. Both targets were 99.999+ % cast Si. The voltage on each target can be controlled independently of the other, and of other discharge conditions (e.g., pressure). The vacuum chamber is cylindrical (65 cm diameter by 16.5 cm high), and is pumped with a liquid-nitrogen-baffled oil diffusion pump/mechanical pump combination that was ordinarily pumped to  $2 \times 10^{-7}$  Torr prior to all deposition runs. The substrates (Si) were not thermally attached to the lower target. Substrate temperature was monitored with an infrared pyrometer calibrated for the emissivity of the  $\text{Si}_3\text{N}_4$  surface and for losses from absorption and reflection in the optical path. The substrate temperature did not vary much with differing deposition conditions and averaged  $130^\circ \pm 30^\circ\text{C}$ .

The upper (deposition) target voltage was held constant at 1500V (d-c sheath potential) and the discharge parameters that were varied were substrate bias voltage, partial pressure of  $\text{N}_2$  in Ar, and total gas pressure. The etch rate of the films in buffered HF was used as an indicator of the quality of the films.

Figure 1 illustrates the variation in etch rate with substrate bias. The etch rate decreases by about two orders of magnitude as the bias is increased from 0 to  $-50\text{V}$ , and then remains nearly constant for higher bias voltage. Under the conditions shown in Fig. 1, the deposition rate varies from about 200  $\text{\AA}/\text{min}$  at 0V to 150  $\text{\AA}/\text{min}$  at  $-300\text{V}$ . The other varied parameters (partial pressure of  $\text{N}_2$  in Ar, Fig. 2; and total gas pressure, Fig. 3) had a very much smaller influence on the etch rate of the films. The over-all trend was toward lower etch rates at higher deposition rates. The etch rate could be lowered by a factor of about 2-3 by heat-treating the films in  $\text{N}_2$  at  $1000^\circ\text{C}$  for 15-20 min, indicating that the films were not completely dense as deposited.

Electron diffraction analyses indicated that the films were amorphous. Infrared analysis showed a typical  $\text{Si}_3\text{N}_4$  spectrum with no evidence of oxygen. However, Auger electron spectroscopic analysis showed about 1% oxygen content. The only other film impurities observed were Ar and C. The carbon content was about 3.5 a/o. No Auger calibration for Ar was available, but the amount incorporated was probably high. The infrared absorption spectrum of the as-deposited films show, in addition to the typical  $\text{Si}_3\text{N}_4$  absorption bands, a very weak band near  $2100\text{ cm}^{-1}$ , suggesting the as-deposited films contain Si-H functional groups. After heat-treatment in  $\text{N}_2$  at  $1000^\circ\text{C}$ , there is a slight change in the refractive index and/or the film thickness. The Si-N band at  $850\text{ cm}^{-1}$  narrows slightly, but the band

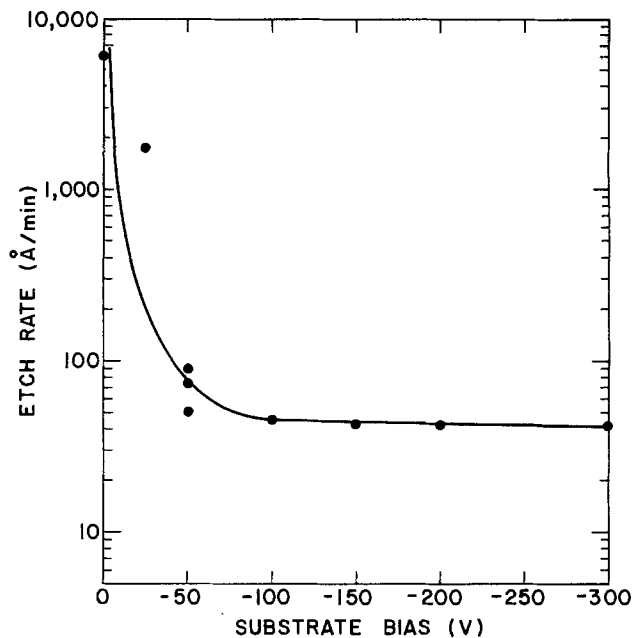


Fig. 1. Etch rate (buffered HF)<sup>2</sup> vs. substrate bias (total pressure = 48 mTorr; 6.5%  $\text{N}_2$ ).

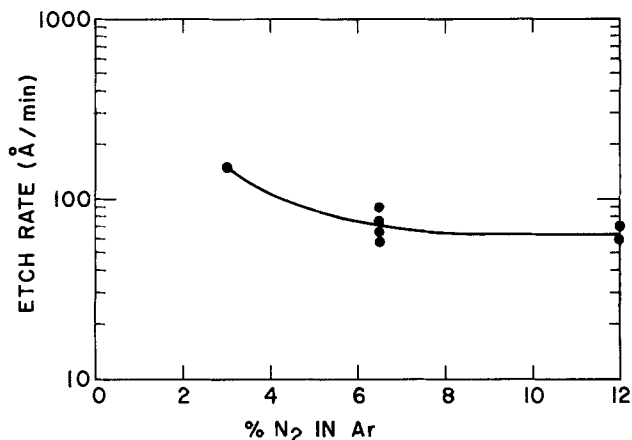


Fig. 2. Etch rate (buffered HF)<sup>2</sup> vs. per cent  $\text{N}_2$  in Ar (total pressure = 48 mTorr; substrate bias =  $-50\text{V}$ ).

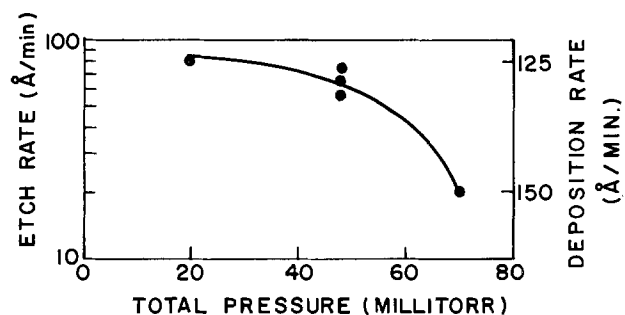


Fig. 3. Etch rate (buffered HF)<sup>2</sup> vs. total gas pressure (6.5%  $\text{N}_2$ ; bias voltage =  $-50\text{V}$ ).

<sup>2</sup> Composition of buffered HF: 1 part by weight 48-49% HF plus 5.75 parts by weight of 39-40%  $\text{NH}_4\text{F}$  solution.

center does not shift. Si-H absorption is not observed after the heat-treatment.

Ellipsometric measurements of the refractive index of the films yielded values ranging from 1.55 to 2.18 depending on the substrate bias and deposition rate. For bias voltages greater than 50V and deposition rates in excess of 200  $\text{\AA}/\text{min}$ , the refractive index was  $2.165 \pm 0.025$ , which is somewhat higher than the bulk value of 1.98.

Stress was measured by beam bending (unclamped Si beam). Films were deposited to a thickness of 2  $\mu\text{m}$

under conditions that yielded moderately low etch rates. The total stress measured was  $3.4 \times 10^9$  dyne/cm<sup>2</sup> (compressive).

### Discussion and Conclusions

The data presented here clearly indicate that the major determinant of rf reactively sputtered Si<sub>3</sub>N<sub>4</sub> film quality is the substrate bias, as was earlier hypothesized. The use of controlled substrate bias allows good quality films to be deposited with a wide range of gas pressures, whereas self-bias of the magnitude required (> -50V) can only be achieved at low gas pressures. [It should be noted that the bias voltages quoted are measured with respect to ground. As has been pointed out (16, 17) there is a systematic error involved in these measurements because the plasma potential is somewhat positive with respect to ground.] The data tend to indicate that increased film deposition rate improves the film properties, but, by comparison to the substrate bias, it is a second order effect.

### Acknowledgments

We are grateful for the help of several of our colleagues, R. Vibronek for many of the etch rate measurements, M. D. Coutts for electron diffraction analyses, D. G. Fisher for Auger electron spectroscopic analyses, P. Zanzucchi for some of the infrared analyses, and G. L. Schnable for several helpful discussions and review of the manuscript.

Manuscript submitted Sept. 4, 1975; revised manuscript received Oct. 16, 1975.

Any discussion of this paper will appear in a Discussion Section to be published in the December 1976 JOURNAL. All discussions for the December 1976 Discussion Section should be submitted by Aug. 1, 1976.

Publication costs of this article were partially assisted by RCA Laboratories.

### REFERENCES

1. S. M. Hu, *This Journal*, **113**, 693 (1966).
2. S. M. Hu and L. V. Gregor, *ibid.*, **114**, 826 (1967).
3. S. M. Hu, D. R. Kerr, and L. V. Gregor, *Appl. Phys. Letters*, **10**, 97 (1967).
4. L. F. Cordes, *ibid.*, **11**, 383 (1967).
5. A. R. Janus and G. A. Shirn, *J. Vacuum Sci. Technol.*, **4**, 37 (1967).
6. L. V. Gregor, Interim Report on U.S. Air Force Contract AF 33615-67-C-1886 (March 31, 1968).
7. P. J. Burkhardt and R. F. Marvel, *This Journal*, **116**, 864 (1969).
8. T. E. Burgess, J. C. Baum, F. M. Fowkes, R. Holmstrom, and G. A. Shirn, *ibid.*, **116**, 1005 (1969).
9. J. L. Vossen, *J. Vacuum Sci. Technol.*, **8**, 751 (1971).
10. W. Rothmund and C. R. Fritzsche, *Thin Solid Films*, **15**, 199 (1973).
11. P. C. Y. Chen, *ibid.*, **21**, 245 (1974).
12. C. J. Mogab, P. M. Petroff, and T. T. Sheng, *This Journal*, **122**, 815 (1975).
13. G. J. Kominiak, *ibid.*, **122**, 1271 (1975).
14. J. L. Vossen, *J. Vacuum Sci. Technol.*, **8**, S12 (1971).
15. J. L. Vossen, U.S. Pat. 3,860,507 (1975); *J. Vacuum Sci. Technol.*, **12**, 1052 (1975).
16. J. W. Coburn and E. Kay, *J. Appl. Phys.*, **43**, 4965 (1972).
17. O. Christensen and P. Jensen, *J. Phys. E.*, **5**, 86 (1972).

## A Comparison of the Process-Induced Gettering of Atomic Platinum and Gold in Silicon

K. P. Lisiak\*<sup>1</sup> and A. G. Milnes\*\*

Department of Electrical Engineering, Carnegie-Mellon University, Pittsburgh, Pennsylvania 15213

Platinum has recently been shown (1) to have two active sites in Si. One of these sites, the Pt<sub>II</sub> acceptor, has been found (2) to be a good lifetime controller. Based on energy position, the Pt levels can be expected to have less generation leakage for a given lifetime reduction than gold (2, 3). Also, Pt-doped diodes have lower forward volt drop than gold-doped diodes, at equal lifetime values (3). Since Pt is apparently a more promising lifetime controller than gold, a significant question is whether Pt suffers unintentional gettering during processing cycles.

Impurity gettering has been studied along two basic lines. One approach attempts to remove all deep impurities introduced into the silicon crystal in the growth and diffusion process (4-8). Techniques for this purpose use either some form of available chlorine in a gas flow during heat soaking or a phosphorous diffusion into the back surface. Studies of gold doping in Si, for example, have shown atomic gold to pile up in n<sup>+</sup> regions (9, 10). A second approach (11, 12) has been to study the unintentional loss of desired lifetime-controlling impurity species during subsequent device processing steps or by aging processes at operating temperatures or higher (13, 14).

Using neutron activation analysis, platinum has been studied here for its resistance to unintentional gettering by processing cycles accompanying its introduction into the silicon lattice. Distribution of atomic Pt within the various layers and loss of atomic Pt from the bulk are both monitored by this technique.

Adamic and McNamara (11) and Nakamura *et al.* (12) have conducted neutron activation studies of gold loss by phosphorous and boron glass getters. They used the Au<sup>198</sup> radioactive isotope as a tracer by irradiating samples of pure gold as the source material for Au deposition and saturation diffusions. For our work with Pt, the use of preirradiated metal in diffusions was not convenient. The most prevalent Pt isotopes, Pt<sup>197</sup> and Pt<sup>199</sup>, have half-lives of 18.5 hr and 31 min, respectively. These isotopes are produced in lower concentrations than is Au<sup>198</sup> from Au<sup>197</sup>. Also, the shorter half-lives of the Pt isotopes make elapsed time more critical. The Au<sup>199</sup> isotope which forms from the decay of Pt<sup>199</sup> has a sufficiently long half-life; however, if used in diffusion it would presumably behave as gold and not as platinum. To use this longer (3.15 day) half-life isotope in Pt work it is thus necessary to irradiate samples at the completion of all high temperature processing steps.

Processing was done in sealed Spectrosil ampuls. The initial experiment used Pt- and Au-saturated silicon which is subjected to diffusion using 3000-4000Å of

\* Electrochemical Society Student Member.

\*\* Electrochemical Society Active Member.

<sup>1</sup> Present address: Hewlett-Packard Laboratories, Palo Alto, California.

Key words: silicon, gettering, platinum, gold.

the Emulsitone products phosphorosilica film (P-SiO<sub>2</sub>), borosilica film I (B-SiO<sub>2</sub>), and silica film (E-SiO<sub>2</sub>). These films have been shown useful in Si device processing (15) and allow the use of closed-tube processing. This experiment models the situation where the Pt (or Au) must be inserted prior to the last high temperature cycle. Subsequent experiments compared the behavior of Pt and Au when diffused for a short time (15 min) in the presence of doped oxides and heavily doped diffused Si layers. This models the introduction of the deep impurity into the p-n junction regions as the last diffusion step.

### Silica Film Gettering

Samples of silicon saturated with platinum (48 hr, 900°C diffusion and quench) were cleaned of all surface alloys by etching and lapping to remove 1-2 mil per side. One slice received a phosphorosilica film layer on each side, another received borosilica film, and a third was coated with undoped silica film. The films were densified at 250°C and then each slice was sealed into a Spectrosil ampul. As a further control on the gettering process, a Pt-saturated slice was sealed into an ampul without any silica coating. The ampuls were then heat-soaked for 1 hr at 1100°C and quenched in a water bath. A second group of silica slices, saturated with gold, were gettered in a similar fashion.

The ampuls were then neutron irradiated, along with standards containing known amounts of Pt and Au. Nonheat-treated slices containing Pt or Au were also included for comparison. Following irradiation, each slice was counted in the Ge(Li) detector and the weight and concentration of Pt or Au determined from counts of the standard ampuls.

The doped silica films were then removed by etching in buffered HF. The Pt or Au concentration in the etched layer was determined from the differences of the successive slice weighings and the gamma count of the etch bath. An aqua regia etching (20 min, hot, 3:1 of HCl:HNO<sub>3</sub>) and count step was used to determine the presence of interface metal layers. Surface (p<sup>+</sup> or n<sup>+</sup>) region concentrations were investigated by successive etching of the slice in freshly made CP4.

Samples, diffused at 900°C to yield  $1.5 \times 10^{15} \text{ cm}^{-3}$  Pt and  $1.2 \times 10^{15} \text{ cm}^{-3}$  Au, were gettered at 1100°C for 1 hr in sealed ampuls with P-SiO<sub>2</sub>, B-SiO<sub>2</sub>, or E-SiO<sub>2</sub>. For this experiment a low concentration of Pt or Au was used so that surface (or bulk) impurity depletion might be noticeable if extreme gettering was encountered.

The results show that Pt is not gettered by the spin-on oxide films. Figure 1 shows the concentration of Pt in each slice (solid symbols) after surface etching to be comparable to the concentration in the heat-treated control. The concentrations of Pt in the P-SiO<sub>2</sub> and E-SiO<sub>2</sub> oxide etches show no significant gettering by these oxides. Only the B-SiO<sub>2</sub> gettered slice showed a significant amount of Pt concentrated near the surface. However, as Fig. 1 shows, this slice had twice the initial Pt concentration of the other Pt samples in this run. Since all Pt samples were initially diffused together until saturated with Pt, this discrepancy indicates some undissolved Pt was present on or in the sample. This excess Pt was then removed in subsequent etching of the gettered slice and was not gettered by the B-SiO<sub>2</sub> film.

All the Pt samples which received the 1100°C gettering cycle (P-SiO<sub>2</sub>, B-SiO<sub>2</sub>, E-SiO<sub>2</sub>, and heat-soaked control) showed some excess Pt in the first Si slice etch. This is apparently due to a tendency to form a layer of heavily Pt-doped Si at a damaged surface. These samples were not mirror-smooth polished or etched to strain relieve the surface. O'Shaughnessy *et al.* (9) showed that Au similarly accumulates at a lapped surface in their experiments. The close agreement of the Pt concentrations in the etch bath of the control slices with the etch baths of the P-SiO<sub>2</sub> or B-SiO<sub>2</sub> slices

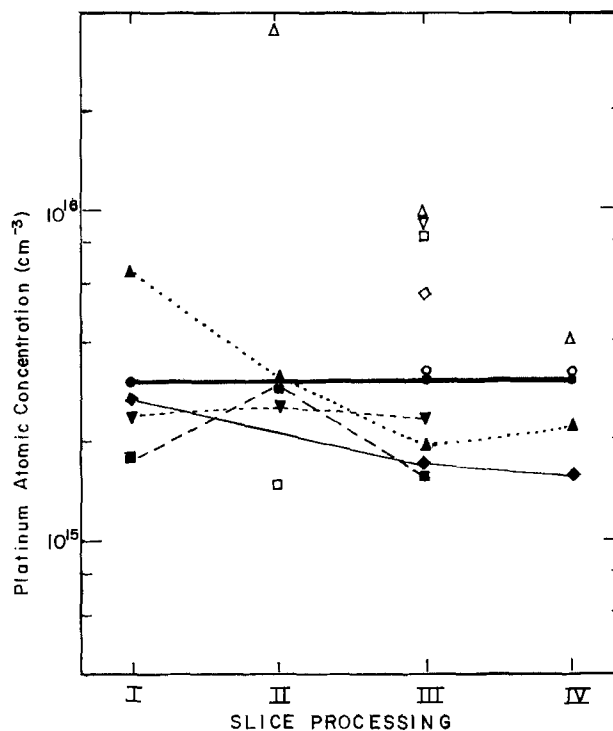


Fig. 1. Neutron activation results for gettering of Pt by Emulsitone film diffusions. Solid symbols are the average concentrations of platinum in each slice following a particular step in the etching sequence. The hollow symbols represent the concentration determined for the layer removed by the etch. Key:  $\square$  phosphorosilica film I,  $\triangle$  borosilica film,  $\nabla$  silica film,  $\diamond$  heat-treatment only,  $\circ$  untreated control, (I) as irradiated, (II) oxide removed by HF, (III) first Si etch (about 6  $\mu\text{m}$  per face), (IV) second Si etch (about 8  $\mu\text{m}$  per face).

(shown by the hollow symbols in Fig. 1 column III) suggests that no significant Pt gettering is caused by the p<sup>+</sup> or n<sup>+</sup> doping but that a damaged Si surface will getter Pt to some extent.

Au is gettered into P-SiO<sub>2</sub> layers and tends to form an interface layer between the B-SiO<sub>2</sub> layer and the silicon. While the oxides constituted less than 1% of sample weight, nearly 10% of Au in the P-SiO<sub>2</sub> sample was found in the oxide and 15% of Au in the B-SiO<sub>2</sub> sample was at the interface. These Au results agree qualitatively with the findings of Adamic and McNamara (11) and Nakamura *et al.* (12). Backscattering studies (10) have failed to find Au gettering into diffusion source phosphor glasses. Presumably this is because the sensitivity of backscattering techniques ( $10^{18} \text{ cm}^{-3}$ ) does not match that of neutron activation studies, which for Au is capable of reaching  $10^{12} \text{ cm}^{-3}$  and for Pt,  $10^{13}$ - $10^{14} \text{ cm}^{-3}$ .

### Thermal Oxide Gettering

Another experiment was performed to observe the uniformity of Pt diffusion in the presence of the thermal oxides P<sub>2</sub>O<sub>5</sub>, B<sub>2</sub>O<sub>3</sub>, and SiO<sub>2</sub>. Similar specimens were diffused with Au to provide a direct comparison. For this experiment, chemically polished Si slices were cleaned by the H<sub>2</sub>O<sub>2</sub> process (16) and one group was oxidized at 1150°C by wet O<sub>2</sub> for 60 min to grow 1  $\mu\text{m}$  of SiO<sub>2</sub>. A second group was placed in a furnace at 1150°C in a flow of O<sub>2</sub> over POCl<sub>3</sub> to grow P<sub>2</sub>O<sub>5</sub> until the n<sup>+</sup> layer was 2-4  $\mu\text{m}$  deep. The third group was oxidized with B<sub>2</sub>O<sub>3</sub> at 1100°C from the decomposition of BBr<sub>3</sub> to form 2-4  $\mu\text{m}$  of p<sup>+</sup> Si.

Slices which were to be Pt or Au diffused had the oxide and diffused layer removed from the back by lapping. These slices were recleaned by the H<sub>2</sub>O<sub>2</sub> process and the backs were covered with Au or Pt from spin-on solutions. Following bakeout of the films, the slices of each metal-oxide pair were sealed into sepa-

Table I. Gettering results of Pt and Au by thermal oxides during a 15 min 1100°C diffusion

Treatment (15 min 1100°C)	Concentration after alloy removal (cm <sup>-3</sup> )	Concentration after oxide removed from front surface by HF* (cm <sup>-3</sup> )	Concentration after first etch of front in CP4 (-4μm) (cm <sup>-3</sup> )	Concentration after second etch of front in CP4 (-4μm) (cm <sup>-3</sup> )	Concentration after third etch in CP4 (-8μm) (cm <sup>-3</sup> )
Pt + P <sub>2</sub> O <sub>5</sub>	2.48 × 10 <sup>16</sup>	2.96 × 10 <sup>16</sup>	2.79 × 10 <sup>16</sup>	1.90 × 10 <sup>16</sup>	1.78 × 10 <sup>16</sup>
Pt + B <sub>2</sub> O <sub>3</sub>	2.50 × 10 <sup>16</sup>	3.02 × 10 <sup>16</sup>	2.79 × 10 <sup>16</sup>	2.69 × 10 <sup>16</sup>	2.53 × 10 <sup>16</sup>
Pt + SiO <sub>2</sub>	2.72 × 10 <sup>16</sup>	2.72 × 10 <sup>16</sup>	2.74 × 10 <sup>16</sup>	2.68 × 10 <sup>16</sup>	2.78 × 10 <sup>16</sup>
Au + P <sub>2</sub> O <sub>5</sub>	2.84 × 10 <sup>16</sup>	2.95 × 10 <sup>16</sup>	9.9 × 10 <sup>15</sup>	—	—
Au + B <sub>2</sub> O <sub>3</sub>	2.05 × 10 <sup>16</sup>	9.16 × 10 <sup>15</sup>	9.22 × 10 <sup>15</sup>	—	—
Au + SiO <sub>2</sub>	1.61 × 10 <sup>16</sup>	1.65 × 10 <sup>16</sup>	1.60 × 10 <sup>16</sup>	—	—

\* The B<sub>2</sub>O<sub>3</sub> oxide was removed by hot H<sub>2</sub>SO<sub>4</sub>:HCl; HNO<sub>3</sub>:H<sub>2</sub>O of 1:2:4:20. The results shown are the slice concentrations, after each particular etch step, as the volume average of the atomic Pt detected in the slice. Steps not shown were not performed. Variations of 10% are not statistically significant.

rate Spectrosil ampuls. One oxidized slice from the same group was also included without a metal film. These controls served to check contamination and to indicate the amount of metal that could be vapor transported from the oxide surface. After a 15 min diffusion at 1100°C, the samples were removed to a water-bath quench. The ampuls were then opened and the metal-diffused slices were lapped on their backs (reducing one thickness by 1-2 mil) and trimmed along the edges to remove all alloyed Si. The results for the Pt- and Au-diffused experimental specimens are listed in Table I.

The Pt-diffused specimens all show an initial average concentration of Pt that is in good agreement with the 1100°C solubility of Pt (1). The final average concentration of the Pt + P<sub>2</sub>O<sub>5</sub> sample does show that there has been some loss of Pt to the n<sup>+</sup> surface layer. This is confirmed by the counts of the etch baths which show excess Pt in the n<sup>+</sup> Si. The variation in the Pt + B<sub>2</sub>O<sub>3</sub> concentration appears to be a statistical fluctuation since only slightly more Pt is found in the oxide etch of this sample than in that of the Pt + SiO<sub>2</sub> slice. This suggests that Pt diffusion produces a uniform Pt concentration profile in the presence of n<sup>+</sup>- or p<sup>+</sup>-doped material and that P<sub>2</sub>O<sub>5</sub> and B<sub>2</sub>O<sub>3</sub> do not significantly getter Pt.

The gold slices again show accumulation of gold into the front surface regions. Since the gold (and platinum) were diffused in the presence of the oxides and p<sup>+</sup> or n<sup>+</sup> regions, the initial concentrations are not fixed to the bulk solubility as in the previous run. Initially, the Au + P<sub>2</sub>O<sub>5</sub> and Au + B<sub>2</sub>O<sub>3</sub> slices show a higher average concentration than the Au + SiO<sub>2</sub> slice whose concentration agrees with the 1100°C solubility of gold (17). Subsequent etching showed the gold in the bulk of the Au + P<sub>2</sub>O<sub>5</sub> and Au + B<sub>2</sub>O<sub>3</sub> slices to be slightly lower than in the Au + SiO<sub>2</sub> sample. The gamma counts of the respective etch baths confirm this gold was present in the oxide and surface layers. Thus, Au diffusion produces a markedly non-uniform Au concentration profile in the presence of n<sup>+</sup> Si and is gettering by P<sub>2</sub>O<sub>5</sub> and B<sub>2</sub>O<sub>3</sub> glasses.

Control slices showed the processing to be sufficiently clean. Au in the control samples included with Pt samples was about 10<sup>12</sup> cm<sup>-3</sup>. Pt in these control samples approached the detectability limit of Pt(10<sup>14</sup> cm<sup>-3</sup>). Some Au was found in the Au control specimens, caused by the vapor transport of gold.

The possible solubility enhancement of Pt in p<sup>+</sup> or n<sup>+</sup> Si was more closely examined in a final experiment. Slices of very low resistivity n<sup>+</sup> and p<sup>+</sup> Si were saturated with Pt at 1150° for 24 hr and irradiated. Following the removal of surface alloys by trimming, lapping, and etching, both slices show a somewhat larger Pt concentration than previous 1150°C diffusions. An n<sup>+</sup> Si slice with 10<sup>19</sup> cm<sup>-3</sup> phosphorous showed 1.6 × 10<sup>17</sup> cm<sup>-3</sup> Pt and a p<sup>+</sup> Si slice with 10<sup>19</sup> cm<sup>-3</sup> boron showed 1.3 × 10<sup>17</sup> cm<sup>-3</sup> Pt. Although this is approximately twice the concentration of Pt found in diffusions into higher resistivity Si, some slight solubility enhancement is expected since lattice strains in low resistivity material and increased dislocations may cause pre-

cipitates to form in the Si material. These Pt results can be contrasted with the 10<sup>2</sup>-10<sup>3</sup> solubility enhancement reported for gold in heavily doped n-type Si (11, 12).

### Conclusions

Pt was not gettering by phosphosilica film or silica film layers on Pt-saturated Si during a 1 hr soak. The result for borosilica film was inconclusive because excess Pt was present on that sample. Gold was clearly gettering by the phosphosilica film and formed an interface layer under borosilica film. These gold results agree qualitatively with measurements of gold gettering by thermal oxides. The tendency of Pt to self-getter at a lapped surface is noted; however, the effect on the bulk is not significant for  $N_{Pt} = 3 \times 10^{15}$  cm<sup>-3</sup>.

Pt diffusion was not found to be affected by the presence of P<sub>2</sub>O<sub>5</sub>, B<sub>2</sub>O<sub>3</sub>, or thermal SiO<sub>2</sub> in a 15 min cycle. The measurements show no significant oxide gettering and only a factor of two enhancement of  $N_{Pt}$  for p<sup>+</sup> or n<sup>+</sup> Si over p or n Si. A 15 min diffusion cycle has also been shown to be as practical a means for insertion of Pt at 1100°C as it is for Au. Au diffusion is affected by the presence of P<sub>2</sub>O<sub>5</sub> or B<sub>2</sub>O<sub>3</sub> and the nonuniform profile confirms the gettering of Au noted in the literature. Thus, evidence presented, which is limited to observation of atomic (total) concentrations, suggests that Pt can be inserted in Si more reliably than can Au. This, together with related work on the recombination role of Pt in Si (2), suggests that Pt may be more effective than Au as a lifetime controller in silicon.

### Acknowledgments

This work was supported in part by the National Science Foundation and the Fannie and John Hertz Foundation.

Manuscript submitted May 12, 1975; revised manuscript received Oct. 13, 1975.

Any discussion of this paper will appear in a Discussion Section to be published in the December 1976 JOURNAL. All discussions for the December 1976 Discussion Section should be submitted by Aug. 1, 1976.

Publication costs of this article were partially assisted by the Carnegie-Mellon University.

### REFERENCES

1. K. P. Lisiak and A. G. Milnes, *Solid-State Electron.*, **18**, 533 (1975).
2. K. P. Lisiak and A. G. Milnes, *J. Appl. Phys.*, To be published.
3. R. F. Bailey, U.S. Pat. 3,640,783 (1972) and J. Sander, 3,783,049 (1974).
4. M. C. Chen and J. W. Hile, *This Journal*, **119**, 223 (1972).
5. R. J. Krieger, Y. C. Cheng, and D. R. Colton, *ibid.*, **119**, 388 (1972).
6. P. H. Robinson and F. P. Heiman, *ibid.*, **118**, 141 (1971).
7. R. S. Ronen and P. H. Robinson, *ibid.*, **119**, 747 (1972).
8. J. L. Lambert and M. Reese, *Solid-State Electron.*, **11**, 1055 (1968).
9. T. A. O'Shaughnessy, H. D. Barber, D. A. Thompson, and E. L. Heasell, *This Journal*, **121**, 1350 (1974).

10. R. L. Meeck, T. E. Seidel, and A. G. Cullis, *ibid.*, **122**, 786 (1975).
11. J. W. Adamic, Jr. and J. E. McNamara, Paper 153 presented at the Electrochemical Society Meeting, Washington, D. C., October 11-15, 1964.
12. M. Nakamura, T. Kato, and N. Oi, *Japan. J. Appl. Phys.*, **7**, 512 (1968).
13. K. D. Glinchuk and N. M. Litovchenko, *Soviet Phys.—Solid State*, **6**, 2963 (1965).
14. F. S. Shaklee, J. L. Larkin, and D. L. Kendall, *Proc. IEEE*, **57**, 1481 (1969).
15. J. A. Becker, *Solid-State Electron.*, **17**, 87 (1974).
16. W. Kern and D. A. Puotinen, *RCA Rev.*, **31**, 187 (1970).
17. W. M. Bullis, *Solid-State Electron.*, **9**, 143 (1966).

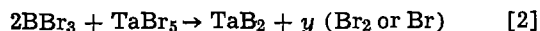
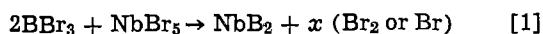
## Chemical Vapor Deposition of NbB<sub>2</sub> and TaB<sub>2</sub> through Heating by Concentration of Solar Radiation

B. Armas, C. Combescure, and F. Trombe

*Laboratoire de l'Energie Solaire, C.N.R.S., Odeillo, 66120 Font-Romeu, France*

According to some authors (1) molybdenum, tungsten, niobium, and tantalum borides cannot be produced in a suitable manner if hydrogen is used to reduce a mixture of a metal halide and a boron halide. The metal halide would be reduced first at rather low temperature. In that case one observes no reaction or only an incomplete one between boron and the metal. This procedure often leads to a mixture of boron and free metal or to some powdery deposits.

An alternative method is a direct thermal decomposition of mixtures of appropriate halides in the absence of hydrogen. Thermodynamic considerations have led us to use those halides which have the same dissociation domain (2). Since the hexagonal NbB<sub>2</sub> and TaB<sub>2</sub> structures have a domain of homogeneity, they are the easiest compounds to prepare. We attempted to prepare niobium and tantalum borides by the following reactions



### Apparatus

A solar furnace was used for heating. A flat mirror following the apparent sun motion receives the incident rays and reflects them parallel to the axis of a fixed parabolic mirror, 2m diameter and 0.85m focal length, which concentrates the solar radiation in its focus. In practice the total energy (1600W) lies inside of a 16 mm diameter circle. The representation of energy distribution in the focal plane is given by a bell-shaped curve which decreases rapidly and shows symmetry relative to the optical axis. The vapor deposition apparatus is shown in Fig. 1. The samples used were 12 mm diameter cylinders, 1 mm thick, placed in the focal plane. The temperature is measured with a micro-optical pyrometer "Pyro." The system can measure up to 3000°C but lower temperatures can be determined if desired by adjusting the luminous flux with two shutters.

### Experimental

*The gas phase effect.*—Experimental conditions were: temperature ( $T$ ) = 1500°C, pressure ( $P$ ) =  $2.10^{-1}$  Torr, gas flow ( $D$ ) =  $400 \text{ cm}^3 \cdot \text{hr}^{-1} \cdot \text{cm}^{-2}$ . The composition of the gas phase is given by the ratio  $\rho$  = boron halide weight to metal halide weight. The theoretical ratios are  $\rho_1 = 1.015$  for NbB<sub>2</sub> and  $\rho_2 = 0.86$  for TaB<sub>2</sub>. An x-ray diffraction analysis shows that a metal-boron diagram can be derived by modifying the gas phase composition.

**Key words:** niobium, tantalum, halides, borides.

*Pressure and temperature effect.*—The NbB<sub>2</sub> case.— $D = 400 \text{ cm}^3 \cdot \text{hr}^{-1} \cdot \text{cm}^{-2}$ ,  $\rho_1 = 1.015$ ,  $T = \text{variable temperature}$ . Curves plotting efficiency vs. temperature are given in Fig. 2. To determine the efficiency curves a slightly different but more practical device for systematic experiments was used. Heating was obtained through high frequency induction as was described in a previous paper (3). Curve 1 ( $P = 2.10^{-1}$ ) and curve 2 ( $P = 2.5 \cdot 10^{-2}$ ) show efficiency increasing with temperature. But, on both sides of  $T = 1040^\circ\text{C}$ , the variation of the efficiency with the pressure is inverted. Furthermore, above 1300°C the efficiency does not depend on the temperature. Moreover, the deposit composition is a strong function of the temperature: three types of deposits are obtained.

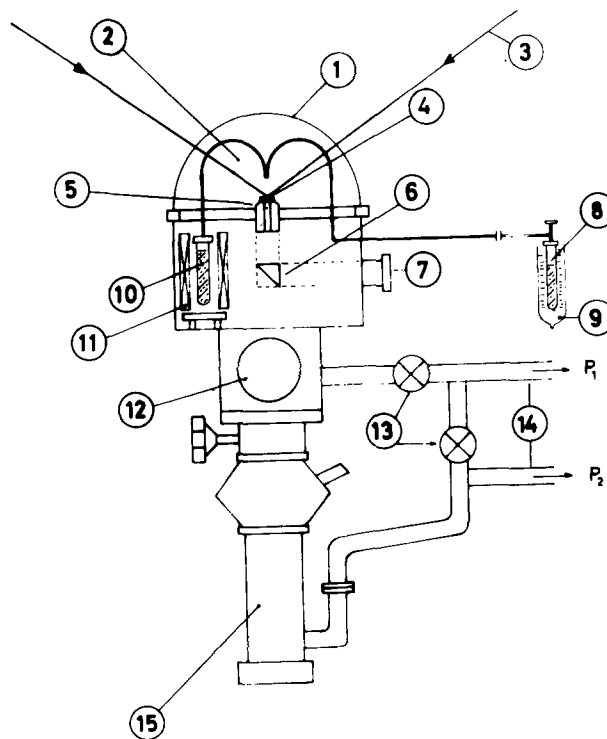


Fig. 1. Experimental apparatus used: (1) Pyrex cover, (2) reaction vessel, (3) solar radiation, (4) substrates, (5) water jacket, (6) prism, (7) observation window, (8) boron halide, (9) cooled condenser, (10) metallic halide vaporizer, (11) furnace, (12) cool trap for halides, (13) valves, (14) vacuum pumps, (15) diffusion vacuum pump.

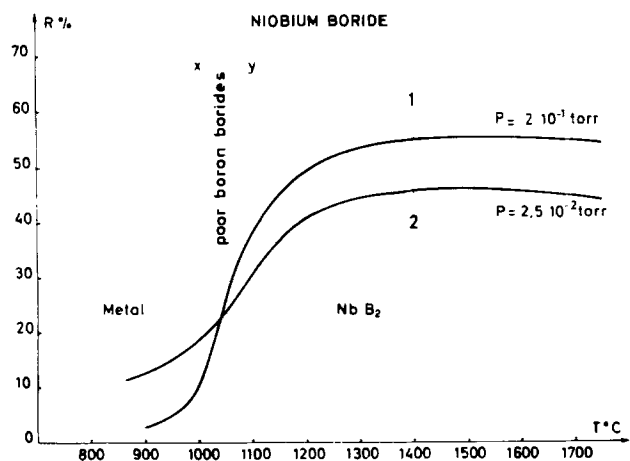


Fig. 2. Experimental efficiency curves.  $R\%$  is the ratio of the weight of the deposited boride to the maximum weight of boride available from the input gas mixture.

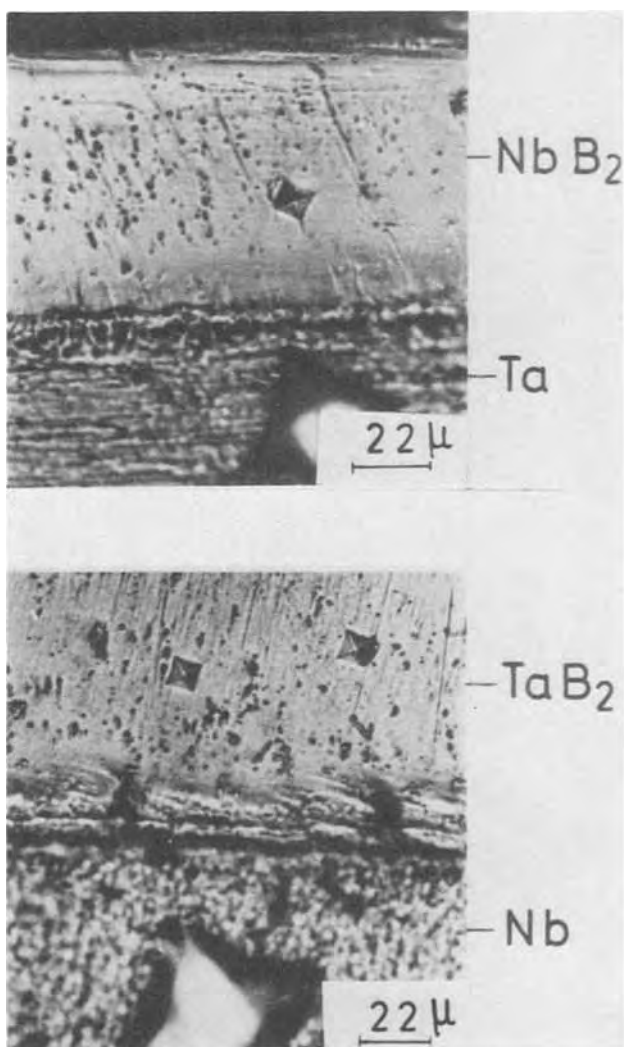


Fig. 3. (a, top) NbB<sub>2</sub> deposit on Ta,  $P = 1.5 \cdot 10^{-1}$  Torr,  $T = 1500^\circ\text{C}$ ,  $D = 400 \text{ cm}^3 \cdot \text{hr}^{-1} \cdot \text{cm}^{-2}$ ,  $\rho_1 = 1.015$ , Vickers microhardness 2200 kg/mm<sup>2</sup>. (b, bottom) TaB<sub>2</sub> deposit on Nb,  $P = 1.5 \cdot 10^{-1}$  Torr,  $T = 1500^\circ\text{C}$ ,  $D = 400 \text{ cm}^3 \cdot \text{hr}^{-1} \cdot \text{cm}^{-2}$ ,  $\rho_2 = 0.26$ , Vickers microhardness 2600 kg/mm<sup>2</sup>.

In the high frequency heating method, the substrates we used presented a 50°C difference of temperature between the center and the border of the sample. An inference from curves 1 and 2 is that we should operate between 1300° and 1600°C in order to obtain uniformity in deposit thickness. In this temperature

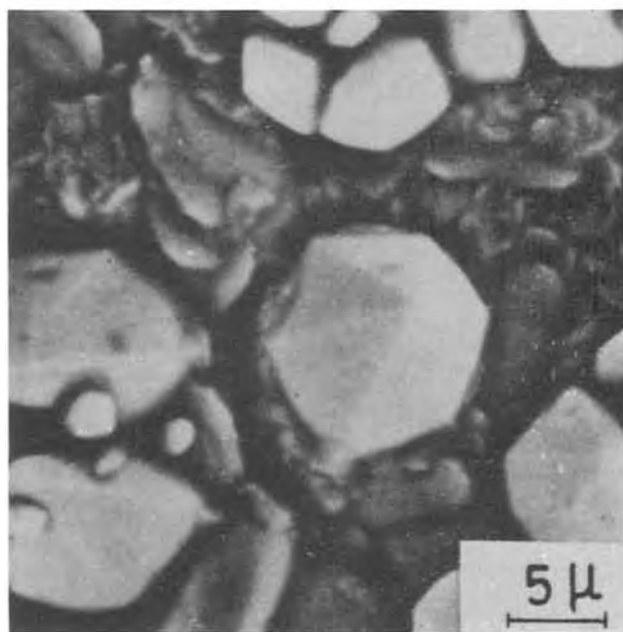
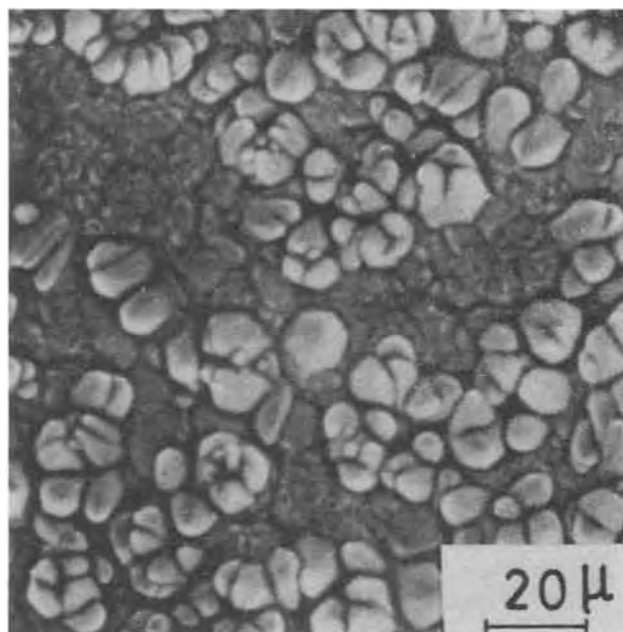


Fig. 4. (a, top) TaB<sub>2</sub> deposit on Nb,  $P = 2.5 \cdot 10^{-2}$  Torr,  $T = 1400^\circ\text{C}$ ,  $D = 150 \text{ cm}^3 \cdot \text{hr}^{-1} \cdot \text{cm}^{-2}$ ,  $\rho_2 = 0.86$ . (b, bottom) Same conditions of deposition as (a).

range, one can master the deposit composition by bringing the gas phase composition under absolute control. Stoichiometrical borides were obtained under the various conditions of temperature and pressure that were the best.

*The TaB<sub>2</sub> case.*—The corresponding curves presented the same form as the NbB<sub>2</sub> case, but the dissociation temperature was higher. This was consistent with our thermodynamic study.

*The halide flow effect.*—Efficiency remains constant if the flow is less than 400 cm<sup>3</sup> · hr<sup>-1</sup> · cm<sup>-2</sup> and decreases regularly with flow up to 700 cm<sup>3</sup> · hr<sup>-1</sup> · cm<sup>-2</sup>. The decrease becomes faster with higher flows.

#### Deposit Characterization

NbB<sub>2</sub> deposition was performed on Ta substrates and, conversely, TaB<sub>2</sub> was deposited upon Nb.

*Compact deposits.*—Compact and adhesive deposits are shown on the micrographs Fig. 3. Deposit compact-



ness is destroyed when conditions referred to in the legend of Fig. 3 are not respected. As the flow increases, the deposit gets more porous. As the temperature increases, very strong deposit-substrate interactions occur. At temperatures higher than 1700° and 1860°C for NbB<sub>2</sub> and TaB<sub>2</sub>, respectively, brilliant particles appeared in the gas jet denoting powder formation.

*Oriented deposits.*—Under the experimental conditions  $T = 1500^{\circ}\text{C}$ ,  $D = 400 \text{ cm}^3 \cdot \text{hr}^{-1} \cdot \text{cm}^{-2}$ ,  $\rho_1 = 1.015$  and  $\rho_2 = 0.86$  but with a lower pressure, porosities became visible on a line perpendicular to the substrates. With  $P = 2.5 \cdot 10^{-2}$  Torr, we got a basaltic deposit oriented in the C axis direction. These borides were not very adhesive and showed a cleavage plane parallel to the deposition surface. With the same value of  $P$  but with reduced gas flow we observed isolated nuclei shaped like small hexagonal-based pyramids. An attempt was undertaken to develop some of these nuclei and to study their behavior during the initial phase of the deposition process.

In these experiments, the halide flow was reduced to  $150 \text{ cm}^3 \cdot \text{hr}^{-1} \cdot \text{cm}^{-2}$ . We found that surface microcrystals can be observed if first a polycrystalline deposit is used which is oriented in no preferential direction and which is not amorphous. This particular feature is contrary to some cases of boride deposition (4). These small surface crystals are shown in Fig. 4(a); they are sometimes very distorted by their neighbors. Figure 4(b) presents one of them much more enlarged. Hexagonal symmetry can be clearly observed.

Therefore, development of well-defined microcrystals can be easily performed by reducing the halide concentration at the substrate level. However, their development is limited in the horizontal plane due to

the large number of nuclei. The microcrystals rarely measure more than 15 or 20 $\mu$ . The bigger ones come into contact with their neighbors and become distorted. Derivation of bigger monocrystals seems unlikely under the indicated operating conditions. One would probably need to use an amorphous substrate and decrease the total concentration of halides (5) to reduce the number of nuclei.

Under the previous operating conditions, the deposition temperature seems to have a slight effect on the crystals' characteristics. On the other hand, interactions with the substrates increase rapidly with the temperature of deposition.

Manuscript submitted May 20, 1975; revised manuscript received Sept. 24, 1975.

Any discussion of this paper will appear in a Discussion Section to be published in the December 1976 JOURNAL. All discussions for the December 1976 Discussion Section should be submitted by Aug. 1, 1976.

*Publication costs of this article were partially assisted by C.N.R.S.*

#### REFERENCES

1. C. F. Powell, "Vapor Deposition," Chap. III, p. 346, J. Wiley & Sons, Inc., New York (1966).
2. B. Armas, M. Ducarroi, in "Chemical Vapor Deposition, Fourth International Conference," G. F. Wakefield and J. M. Blocher, Jr., Editors, p. 181, The Electrochemical Society Softbound Symposium Series, New York (1973).
3. B. Armas, Université de Toulouse (1973).
4. A. Luque, *Compt. Rend.*, **274**, 286 (1972).
5. H. Schäfer, "Chemical Transport Reactions," Academic Press, Inc., New York (1964).





## Leclanché Electrolyte Compositional Studies for Thin Film Batteries

Alf M. Bredland

*ESB Incorporated, Ray-O-Vac Division, Madison, Wisconsin 53711*

and Michael N. Hull\*

*ESB Incorporated, Technology Center, Yardley, Pennsylvania 19067*

### ABSTRACT

The effect of zinc oxide dissolution and pH rise on the crystallization behavior of a series of Leclanché electrolytes has been determined with reference to their use in thin film batteries such as the ESB-P70. An electrolyte (2725) consisting of 27% ammonium chloride and 25% zinc chloride was identified as exhibiting increased solubility of zinc oxide, increased resistance to both pH rise and harmful crystal formation when compared to the presently employed 2210 composition.

Within the last five years, research and development of thin film batteries have accelerated in many parts of the battery industry. ESB has developed a thin film Leclanché battery for use in the Polaroid SX-70 cameras (1-5). In this particular battery, a small volume of 22:10 (22%  $\text{NH}_4\text{Cl}$  and 10%  $\text{ZnCl}_2$ ) electrolyte is exposed to a large surface area of the active materials. It would be anticipated that under these conditions, the electrolyte would be highly susceptible to changes in both composition and pH because of the chemical and electrochemical interaction between the electrolyte and the electrodes under open- or closed-circuit conditions. The question which arises is whether or not 22:10 is the most suitable electrolyte composition for use in a thin film format.

In the round cell configuration, experience has shown that 22:10 combines good conductivity with a tolerable corrosion rate of the anode and although crystals of  $\text{Zn}(\text{NH}_3)_2\text{Cl}_2$  are known to form on stand, such crystals in this configuration are relatively harmless (6-9). In the thin film format, however, conductivity may not be of prime importance due to the close proximity of the opposing electrodes while the formation of elongated crystals of  $\text{Zn}(\text{NH}_3)_2\text{Cl}_2$  could damage the separator. Again, in the round cell design, the zinc oxide content of the zinc can constitute a very small percentage of the total anode weight, while in the thin film case, the zinc oxide content of the zinc powder can have a typical value of the order of 5%. Furthermore, this zinc oxide is in intimate contact with the small volume of electrolyte and has a tendency to dissolve into it. Thus, in this latter case, both the pH and zinc ion composition of the electrolyte will be altered and it is therefore necessary that an initial electrolyte composition be chosen which can dissolve a substantial proportion of the zinc oxide from the anode without undergoing a large pH increase and without precipitating

zinc diammine crystals throughout the limited volume of electrolyte. In addition, the electrolyte should have a conductivity equal to or greater than the standard 22:10 composition.

It was decided to investigate the effect of electrolyte composition on each of the following factors: (a) pH rise and buffering capacity on the addition of  $\text{NH}_4\text{OH}$ , (b) type of crystal formation, (c) pH rise and type of crystal formation on the addition of  $\text{ZnO}$ . On the results of this information, one could then adjust the Leclanché electrolyte composition to give the best discharge performance for the particular configuration and cell materials employed.

### Experimental

As a starting point, electrolyte compositions along the iso-pH curve of 4.7 shown in Fig. 1 were investigated (6). For several of these compositions, the relative molar concentrations of each of the ions in solution is given in Table I and in particular, attention should be drawn to the  $\text{NH}_4^+:\text{Zn}^{++}$  ratio. This is an important parameter, since the solubility of  $\text{ZnO}$  would be expected to increase with increase in the concentration of  $\text{NH}_4^+$  species due to the formation of the soluble complex species  $\text{Zn}(\text{NH}_3)_4^{++}$ . Again, the relative tendency of  $\text{Zn}(\text{NH}_3)_2\text{Cl}_2$  crystals to be formed in preference to  $\text{ZnCl}_2 \cdot 4\text{Zn}(\text{OH})_2$  should be more favored in the compositions having the higher  $\text{NH}_4^+:\text{Zn}^{++}$  ratio, all other conditions being equal.

The titration of 13:00, 22:10, and 00:25 electrolytes with 29.4%  $\text{NH}_4\text{OH}$  is shown in Fig. 2. As expected, the 13:00 electrolyte shows an immediate rise into the alkaline region with the addition of  $\text{NH}_4\text{OH}$ . No precipitation products are produced and further additions of  $\text{NH}_4\text{OH}$  result only in a gradual increase of the solution pH. On the other hand, electrolyte 00:25 forms an immediate dense, white precipitate at point D [reported to be  $\text{ZnCl}_2 \cdot 4\text{Zn}(\text{OH})_2$ ] (6) and by continuously precipitating with further additions of  $\text{NH}_4\text{OH}$ , buffers

\* Electrochemical Society Active Member.

Key words: Leclanché electrolytes, thin film batteries, crystal formation, zinc oxide solubility.



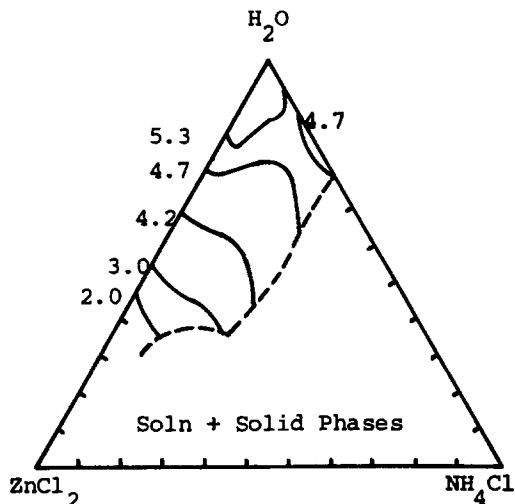


Fig. 1. Phase diagram for the system  $\text{ZnCl}_2\text{-NH}_4\text{Cl-H}_2\text{O}$  showing iso-pH lines from pH 2 to pH 5.3 at  $25^\circ\text{C}$ .

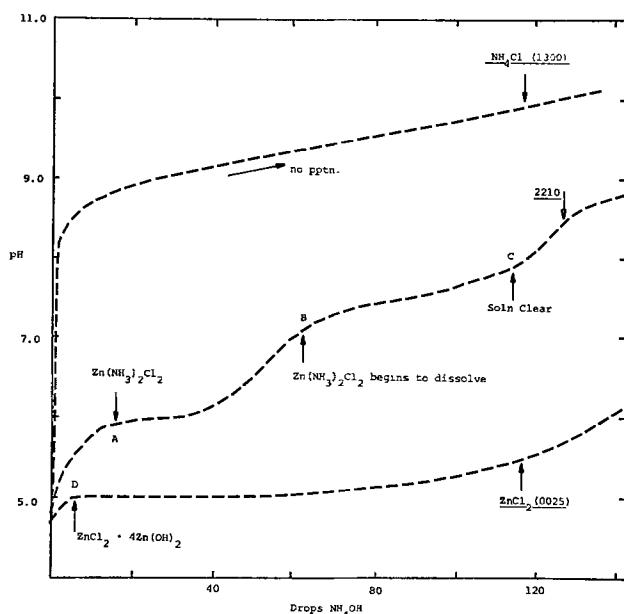


Fig. 2. pH variation of 20 ml amounts of 13%  $\text{NH}_4\text{Cl}$ , 22:10 and 25%  $\text{ZnCl}_2$  on the addition of 0.05 ml drops of 29.4%  $\text{NH}_4\text{OH}$ . pH measurements were recorded three days after the addition of hydroxide to allow time for equilibrium to be established.

the solution at a pH of approximately 5.0. Addition of  $\text{NH}_4\text{OH}$  to 22:10 causes the pH to rise slowly and at approximately pH 5.9, (point A), the solution is buffered by the precipitation of  $\text{Zn}(\text{NH}_3)_2\text{Cl}_2$ . After the addition of approximately 40 drops, precipitation is complete and the pH rises to a second buffered region (at B) where redissolution of the  $\text{Zn}(\text{NH}_3)_2\text{Cl}_2$  as  $\text{Zn}(\text{NH}_3)_4^{++}$  occurs. Complete redissolution has occurred at point C in the figure.

With change of the electrolyte composition from that of 22:10, having an  $\text{NH}_4^+:\text{Zn}^{++}$  ratio of 5:58, to lower values of this ratio, one finds that there is a transition point at a composition between 12:13 (2:36) and 11:14 (2:01) below which formation of the  $\text{ZnCl}_2\cdot 4\text{Zn}(\text{OH})_2$  is favored over that of the  $\text{Zn}(\text{NH}_3)_2\text{Cl}_2$ . This is illustrated in Fig. 3 where two compositions on each side of this transition point are shown. It is seen that with 15:10 (3:82) and 10:15 (1:70), both the crystalline (diammine) and the amorphous (zinc hydroxy chloride) precipitates can be distinguished both by the regions of inflection in the pH curves and by visual inspection of the solutions. With 15:10, formation of the crystalline precipitate precedes that of the amor-

Table I. Molar concentration of each of the ions and the  $\text{NH}_4^+:\text{Zn}^{++}$  ratios for each of the electrolytes investigated along the 4.7 iso-pH curve

Electrolyte*	$[\text{NH}_4^+]^\dagger$	$[\text{Zn}^{++}]^\dagger$	$[\text{Cl}^-]^\dagger$	$[\text{NH}_4^+]:[\text{Zn}^{++}]$
13:00	2.53	—	2.53	—
27:12	5.85	1.02	7.89	5.74
22:10	4.69	0.84	6.37	5.58
15:10	3.17	0.83	4.83	3.82
13½:11	2.84	0.91	4.65	3.12
12:13	2.55	1.08	4.72	2.36
11:14	2.37	1.18	4.73	2.01
10:15	2.16	1.27	4.70	1.70
09½:16	2.04	1.35	4.73	1.51
09:17	1.92	1.40	4.77	1.36
08½:18	1.80	1.45	4.65	1.21
08:19	1.77	1.65	5.07	1.07
07:20	1.54	1.72	4.99	0.9
00:25	—	2.26	2.26	—

\* First 2 digits are concentrations of ammonium chloride, last 2 digits are concentrations of zinc chloride in per cent by weight.  
† Concentrations are given in moles/liter.

phous while the reverse is true with 10:15. Figure 4 summarizes the relationship between the amount of  $\text{NH}_4\text{OH}$  required to form each type of precipitate and the initial  $\text{NH}_4^+:\text{Zn}^{++}$  ratio for each of the nine electrolyte compositions examined. The  $\text{NH}_4^+:\text{Zn}^{++}$  ratio is that of the solution prior to the  $\text{NH}_4\text{OH}$  addition. It is evident that there is an extremely rapid rise in the amount of  $\text{NH}_4\text{OH}$  required for precipitation of the diammine crystals for electrolyte compositions having an initial ratio  $<2:5$ . However, at these low  $\text{NH}_4^+:\text{Zn}^{++}$  ratios, the amorphous precipitate is readily formed and buffering of the electrolyte occurs at pH values somewhat below that when the diammine salt is the first precipitate formed (as in 22:10).

It would appear, therefore, from Fig. 4 that, if it is desirable to have a Leclanché electrolyte with an initial pH of 4.7 and maximum resistance to the formation of precipitated salts, the composition 11:14 should be chosen. However, one must choose the electrolyte composition by considering what the final  $\text{NH}_4^+:\text{Zn}^{++}$  ratio will be at the onset of precipitation. Reconsidering the 11:14 electrolyte from Fig. 4, it is evident that 21 drops of 29.4%  $\text{NH}_4\text{OH}$  were necessary for precipitation.

Now, 29.4%  $\text{NH}_4\text{OH}$  contains 15.43 moles/liter.

Hence, 21 drops (of 0.05 ml each) contain 0.016 mole.

This was added to 20 cm<sup>3</sup> of 11:14 electrolyte.

Thus the increase in the  $\text{NH}_4^+$  concentration of 11:14 was 0.8 mole.

In 11:14  $[\text{Zn}^{++}] = 1.18$  moles/liter  
 $[\text{NH}_4^+] = 2.37$  moles/liter  
 and  $[\text{NH}_4^+]:[\text{Zn}^{++}] = 2.01$ .

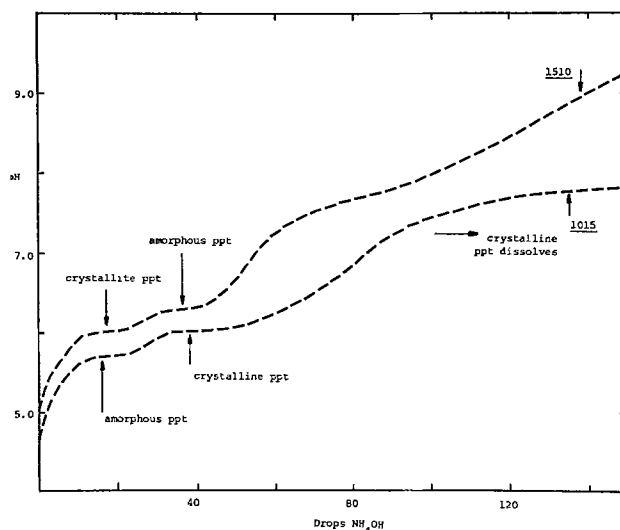


Fig. 3. Titration of 15:10 and 10:15 electrolytes under conditions identical to those of Fig. 2.

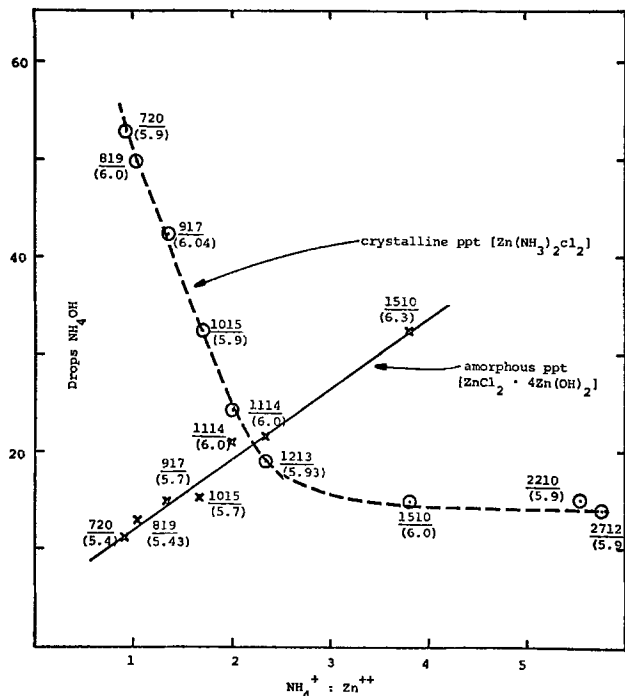


Fig. 4. Volume of  $\text{NH}_4\text{OH}$  as a function of the  $\text{NH}_4^+:\text{Zn}^{++}$  ratio required to precipitate  $\text{Zn}(\text{NH}_3)_2\text{Cl}_2$  and  $\text{ZnCl}_2 \cdot 4\text{Zn}(\text{OH})_2$  from  $20 \text{ cm}^3$  aliquots of Leclanché electrolytes along the iso-pH line 4.7. Each drop  $\sim 0.05 \text{ ml}$ . Figures beside points give electrolyte composition while figures in brackets refer to solution pH at point of precipitation.

After addition of 0.80 mole  $\text{NH}_4^+$ , the ratio now becomes  $(2.37 + 0.80)/1.18 = 2.69$ . This means that an electrolyte with an initial pH of 4.7 and having an  $\text{NH}_4^+:\text{Zn}^{++}$  ratio of approximately this final value, can best resist the formation of precipitates.

Considering, now, the effect on the solution pH of the addition of zinc oxide to Leclanché electrolytes along the 4.7 iso-pH curve, one finds that there is a gradual rise in pH of each electrolyte as ZnO is added (Fig. 5 shows two examples) until an amorphous or a crystalline deposit is formed beyond which point the pH will remain constant. Figure 6 shows the variation in grams of ZnO as a function of the initial  $\text{NH}_4^+:\text{Zn}^{++}$  ratio required to just form a precipitate in the solution. As the initial  $\text{NH}_4^+:\text{Zn}^{++}$  ratio rises, the amount of ZnO

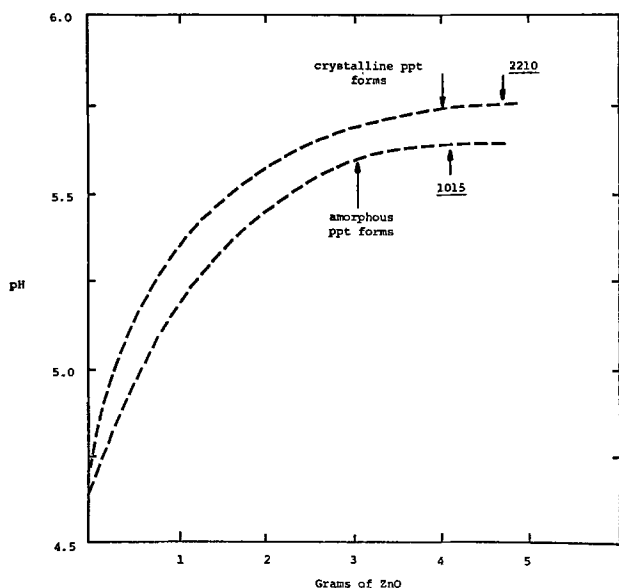


Fig. 5. Variation in the pH of  $200 \text{ cm}^3$  amounts of 22:10 and 10:15 electrolytes with the addition of zinc oxide.

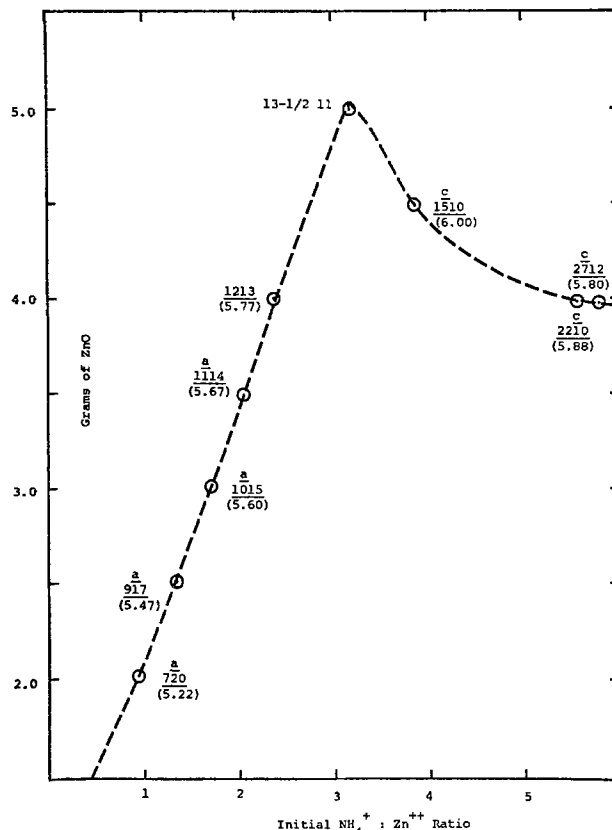


Fig. 6. Minimum amount of zinc oxide, plotted as a function of the  $\text{NH}_4^+:\text{Zn}^{++}$  ratio, which is required to cause permanent precipitation in  $200 \text{ cm}^3$  of various electrolytes along the 4.7 iso-pH curve. Letter gives type of precipitate: a = amorphous, c = crystalline. Figures in brackets refers to solution pH at point of precipitation.

which can be accepted by the electrolyte also rises and passes through a maximum of  $13\frac{1}{2}:11$ . ZnO is known to increase in solubility as the concentration of  $\text{NH}_4^+$  in the solution is increased, so a rise to  $13\frac{1}{2}:11$  in the apparent solubility of ZnO is not unexpected. Above an  $\text{NH}_4^+:\text{Zn}^{++}$  initial ratio of  $\sim 3$ , the solubility appears to decline. This is due to the fact that at these ratios sufficient ZnO is soluble to raise the pH to the value at which  $\text{Zn}(\text{NH}_3)_2\text{Cl}_2$  is precipitated and further addition of ZnO causes further precipitation of this diamine.

Once again, if one calculates the final  $\text{NH}_4^+:\text{Zn}^{++}$  ratio after the addition of the required amount of ZnO to  $13\frac{1}{2}:11$  for precipitation, one obtains the following:

5g of ZnO in  $200 \text{ cm}^3$  of  $13\frac{1}{2}:11$  raise the electrolyte composition to approximately 13:13  
Specific gravity of 13:13 is 1.14

In 1000g of 13:13, there are 130g  $\text{NH}_4\text{Cl}$  and 130g  $\text{ZnCl}_2$

1000g of 13:13 have a volume of  $877 \text{ cm}^3$

therefore

1000  $\text{cm}^3$  of 13:13 contains 148.2g  $\text{NH}_4\text{Cl}$  and 148.23g  $\text{ZnCl}_2$

Thus  $[\text{NH}_4^+] = 2.77\text{M}$   
 $[\text{Zn}^{++}] = 1.09\text{M}$

and  $\text{NH}_4^+:\text{Zn}^{++} = 2.54$

It is seen that the final  $\text{NH}_4^+:\text{Zn}^{++}$  ratio is close to that observed for minimum crystallization tendency on the addition of  $\text{NH}_4\text{OH}$ .

For electrolytes with an initial pH of 4.7, the composition  $13\frac{1}{2}:11$  will show the least salt formation if a substantial amount of the ZnO present in a powdered

Table II. Molar concentration of each of the ions and the  $\text{NH}_4^+:\text{Zn}^{++}$  ratios for the electrolytes having a fixed  $\text{NH}_4^+$  concentration of 27%

Electrolyte	$[\text{NH}_4^+]$	$[\text{Zn}^{++}]$	$[\text{Cl}^-]$	$[\text{NH}_4^+]:[\text{Zn}^{++}]$
27:05	5.61	0.41	6.43	13.68
27:08	5.74	0.67	7.07	8.57
27:12	5.85	1.02	7.89	5.74
27:15	5.97	1.30	8.57	4.59
27:25	6.53	2.37	11.27	2.76

zinc anode is dissolving in the electrolyte. However, the lower conductivity of this electrolyte compared to 22:10 (~30% less) outweighs its advantages over 22:10 in respect to crystal formation and hence its utility as an alternative thin film battery electrolyte would appear to be limited for those applications requiring high drain rates.

Since there is normally an appreciable amount of ZnO present in a powdered zinc anode which will cause the electrolyte pH to rise rapidly after cells are constructed, it was considered unnecessary to restrict the initial electrolyte pH to that of 22:10 since the important parameter is the final electrolyte pH after the battery has had time to equilibrate. Hence, a series of electrolyte compositions were investigated keeping the  $\text{NH}_4^+$  concentration fixed and as high as possible (27%) while varying the  $\text{Zn}^{++}$  concentration and thus the  $\text{NH}_4^+:\text{Zn}^{++}$  ratio. In this case, the initial pH of the electrolyte is lowered as the  $\text{Zn}^{++}$  concentration is increased but the final electrolyte pH is determined by the ZnO content of the final equilibrated electrolyte.

The electrolyte compositions investigated are given in Table II with the corresponding  $\text{NH}_4^+:\text{Zn}^{++}$  ratios. Figure 7 gives the pH titration curves of the three compositions 27:05, 27:10, and 27:25 with the addition of 29.4%  $\text{NH}_3$ . With 27:05 and 27:10, two plateaus are observed in which the first reflects buffering of the electrolyte by formation of  $\text{Zn}(\text{NH}_3)_2\text{Cl}_2$  and the second by dissolution of the  $\text{Zn}(\text{NH}_3)_2\text{Cl}_2$  as  $\text{Zn}(\text{NH}_3)_4\text{Cl}_2$ . With 27:25, the point of dissolution of the  $\text{Zn}(\text{NH}_3)_2\text{Cl}_2$  is not reached within the limits of the amount of ammonium hydroxide added in this experiment. Two main points should be noted from Fig. 7: (a) the buffering action begins at an increasingly higher pH as the  $\text{NH}_4^+:\text{Zn}^{++}$  ratio goes up, and (b) the buffering capacity due to formation of  $\text{Zn}(\text{NH}_3)_2\text{Cl}_2$  decreases as the  $\text{NH}_4^+:\text{Zn}^{++}$  ratio goes up. Note also that a greater addition of alkali is required as the ratio goes down before diammine formation is observed. These observations mean that fewer diammine crystals will be formed in a 27:05 electrolyte than in 27:25 before the electrolyte pH will rise to the second plateau and dissolution

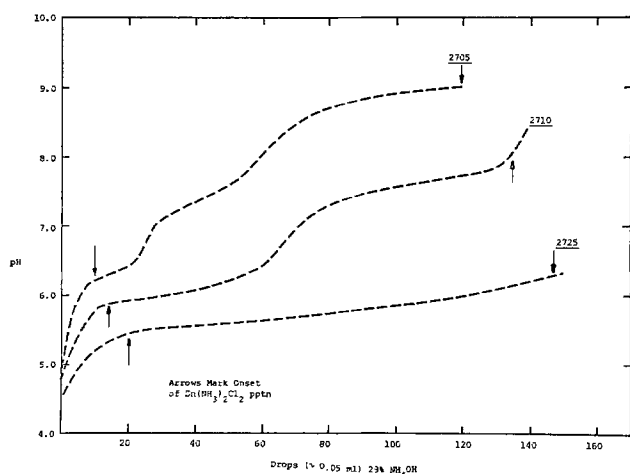


Fig. 7. Titration of 27:05, 27:10, and 27:25 electrolytes under conditions identical to those of Fig. 2 and 3.

of the crystals will begin. However, during the period when the buffering action is operative, the cathode discharge performance will be better with the 27:25 electrolyte in view of the lower pH value.

Figure 8 shows the minimum amount of ZnO required to form a precipitate of  $\text{Zn}(\text{NH}_3)_2\text{Cl}_2$  for each of the five compositions and gives the pH of the solution at the point of precipitation. A similar trend is seen for the iso-pH 4.7 electrolytes presented in Fig. 6, in that, as the  $\text{NH}_4^+:\text{Zn}^{++}$  ratio goes down, the amount of zinc oxide which can be taken up by the electrolyte before diammine formation occurs, goes up. As further points it may be noted that the buffered electrolyte pH is lowest with the lowest  $\text{NH}_4^+:\text{Zn}^{++}$  ratio and that the average crystal length of the precipitating diammine increases by about one order of magnitude between the electrolyte composition of 27:25 and that of 27:05. The longest and hence potentially more detrimental crystals are observed in the 27:05 electrolyte.

With a 22:10 electrolyte, 4g of ZnO per 200  $\text{cm}^3$  of electrolyte will cause diammine formation. This ratio of ZnO weight to electrolyte volume is approximately the same as that in the ESB P-70 thin film cell assuming 5% ZnO in the anode. Hence such an anode with 22:10 in the P-70 electrolyte will rapidly establish an electrolyte pH of approximately 5.9 and slow formation of diammine will have commenced. With 27:25, however, 4.0g of ZnO in 200  $\text{cm}^3$  electrolyte is insufficient for diammine formation and even at a level of 7.5g per 200  $\text{cm}^3$ , the pH cannot rise above ~5.4. Hence it may be advantageous when using a 27:25 electrolyte to allow the ZnO present in the anode to remain rather than attempt to remove it in order that the initially low pH value of 27:25 would be pulled up rapidly to 5.4 and thus anode corrosion be kept at a minimum. Compared to 22:10, however, the 27:25 electrolyte will always operate at least one-half of a pH unit lower than 22:10 and should thus give better discharge performance of the  $\text{MnO}_2$ .

### Conclusions

The main conclusion to be drawn from this work is that when a specific composition of Leclanché electrolyte is used, it should be tailored to fit the battery configuration, internal chemistry, and drain rate of that

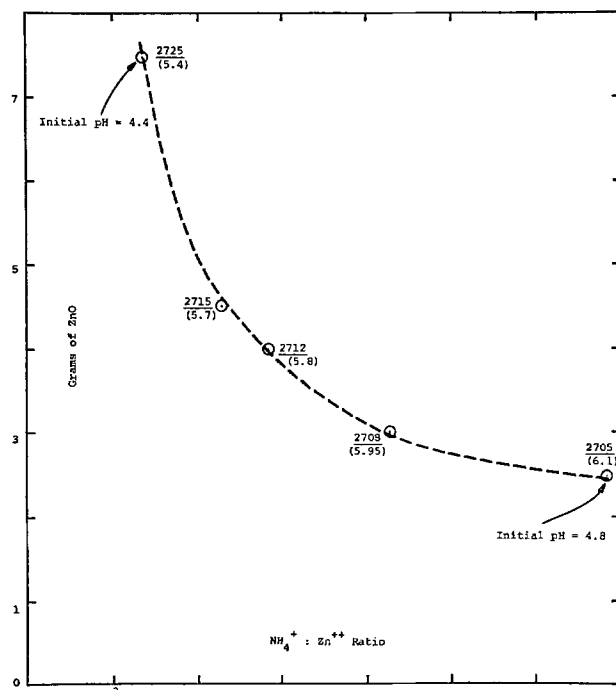


Fig. 8. Minimum amount of ZnO required for precipitation of the electrolytes having fixed  $\text{NH}_4^+$  concentration of 27%. Conditions identical to those of Fig. 6.

particular system in which it is employed. Clearly, an important consideration is not the initial composition of the electrolyte, but rather what the composition will be after equilibration with the active cell materials. Further, this equilibrated composition must have the correct pH for good anode stability and  $\text{MnO}_2$  discharge performance. In addition, one needs to consider how susceptible the electrolyte will be toward diammine crystal formation and if such crystals are formed, is the configuration such that rapid cell failure will result?

In the particular case of the ESB P-70 system in which diammine formation is undesirable and in which the zinc oxide content of the anode is relatively high, it appears that a composition of 27%  $\text{NH}_4\text{Cl}$  and 25%  $\text{ZnCl}_2$  constitutes the most suitable electrolyte.

Manuscript submitted June 10, 1975; revised manuscript received Oct. 16, 1975.

Any discussion of this paper will appear in a Discussion Section to be published in the December 1976

JOURNAL. All discussions for the December 1976 Discussion Section should be submitted by Aug. 1, 1976.

*Publication costs of this article were partially assisted by ESB Incorporated.*

#### REFERENCES

1. B. C. Bergum, U.S. Pat. 3,770,504 (1973).
2. J. M. Bilhorn, U.S. Pat. 3,741,814 (1973).
3. B. C. Bergum, J. M. Bilhorn, and K. V. Anderson, U.S. Pat. 3,734,780 (1973).
4. W. J. Dermody and J. E. Oltman, U.S. Pat. 3,701,690 (1972).
5. B. C. Bergum, J. M. Bilhorn, K. H. Kenyon, W. R. Macaulay, and J. A. Youngquist, U.S. Pat. 3,770,505 (1973).
6. N. C. Cahoon, *Trans. Electrochem. Soc.*, **92**, 162 (1947).
7. H. F. McMurdie, D. N. Craig, and G. W. Vinal, *ibid.*, **90**, 509 (1946).
8. E. Otto, C. K. Morehouse, and G. W. Vinal, *ibid.*, **90**, 419 (1946).
9. G. S. Bell, *Electrochim. Acta*, **13**, 2197 (1968).

## The Role of Ternary Phases in Cathode Reactions

M. Stanley Whittingham\*

*Exxon Research and Engineering Company, Corporate Research Laboratories, Linden, New Jersey 07036*

#### ABSTRACT

The cell reactions between lithium and several transition metal oxides and sulfides have been found to produce ternary phases and not the formation of lithium oxide or sulfide as previously proposed. These reactions, at 25°C, take place with essential retention of the crystalline lattice, thus facilitating secondary cathodic behavior. It is found that cell reversibility is optimized when no chemical bonds are broken during discharge, that is, where ternary phases are formed by an intercalation reaction and where a broad range of nonstoichiometry exists as in the system  $\text{Li}/\text{TiS}_2$ . Where some chemical bonds are broken as for  $\text{V}_2\text{O}_5$  and  $\text{TiS}_3$  partial or difficult reversibility is found, but when all the bonds are broken as for example in  $\text{CuS}$ , the cell only exhibits primary characteristics.

There has been much recent work in ambient temperature batteries using lithium anodes and cathodes comprising metallic compounds of the halides, oxides, and chalcogenides. Very little is known concerning the mechanism of cathodic reduction of such materials or even of the products of reaction. Thus frequently the observed emf's bear little, if any, relation to those calculated for simple reduction reactions. For  $\text{V}_2\text{O}_5$  reduction to  $\text{VO}_2$ , an emf of 2.4V is expected (1) but the observed cell emf is 3.5V (2, 3), for  $(\text{CF})_n$  going to graphite and  $\text{LiF}$  the free energy change corresponds to 4.6V and yet only 2.8V is observed experimentally (4, 5), and for  $\text{MoO}_3$  giving  $\text{MoO}_2$  and  $\text{Li}_2\text{S}$  the values are 2.2 (1) and 2.8V (2, 6). In the case of cupric sulfide the cell emf is that expected for the formation of  $\text{Li}_2\text{S}$  and  $\text{Cu}$ , 2.3V (7), and in many cases there is no discrepancy for the halides.

At low temperatures reactions in the solid state tend to go by the easiest route, that is, by the one involving minimal structural change. Thus in the reduction of tungsten trioxide by hydrogen at ambient temperatures hydrogen is incorporated into the lattice without any significant structural changes giving a hydrogen tungsten bronze,  $\text{H}_x\text{WO}_3$  (8). At temperatures,  $\sim 350^\circ\text{C}$ , above the stability limit of the bronze, reduction occurs by abstraction of oxygen along discrete planes with the formation of shear planes at definite intervals (9, 10). The remainder of the crystal-

line structure remains unchanged during this process, so here again there is no bulk rearrangement of atoms. Further reduction occurs directly to tungsten metal and no evidence is found for the presence of any intermediate oxides, which have very different crystalline structures although many are known. Thus where such simple structural changes cannot occur, the lattice will react by complete destruction to the metal. On the discharge of  $\text{MnO}_2$  (11) and  $\text{V}_2\text{O}_5$  (12) cathodes in aqueous solution it has been proposed that hydrogen atoms are incorporated into the lattice forming nonstoichiometric compounds analogous to  $\text{H}_x\text{WO}_3$ . It is therefore proposed that many of the cathode discharge reactions in lithium cells are governed by the same structural considerations. Such considerations are expected to dominate whenever the cathode material is insoluble in the electrolyte medium, that is, where liquid dissolution recrystallization processes cannot occur.

This paper describes the evidence for the formation of ternary phases during the reduction by lithium of a number of oxides and sulfides, and of their formation by topochemical reactions. The important role of topology in solid-state reactions has recently been reviewed by Thomas (13) and its important role in electrochemical reactions has also been suggested (2, 14).

#### Experimental

The oxides and sulfides were obtained from Alfa Inorganics or were prepared by direct reaction of the

\* Electrochemical Society Active Member.

Key words: cathode, secondary battery, sulfide, oxide, nonaqueous cell, lithium, ternary phases, nonstoichiometry.

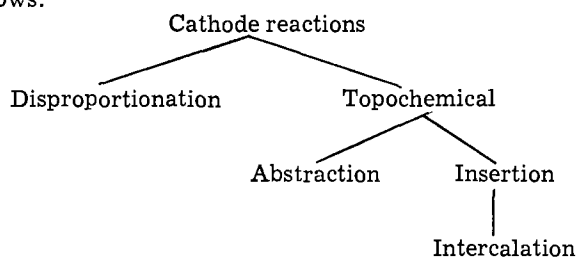
elements. They were then pressed into expanded metal screens using Teflon as a binder and with the addition of some graphite powder as conductor for those materials that are electronic insulators in the pure state. Lithium foil was used as the anode. The electrochemical experiments were performed using a Princeton Applied Research potentiostat, coulometer, and programmer. Open-circuit potentials were recorded only after at least an overnight stand under zero current flow. The lithium content of the cathode was changed by coulometric titration, and x-ray analysis was made at periodic intervals.

A major part of the structural analysis was performed on samples lithiated chemically using n-butyl lithium (15, 16). This technique has a number of advantages over the electrochemical method. It is much simpler and therefore quicker and there is no possibility of any side reactions due to the presence of graphite or of a polar solvent.

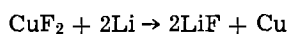
Samples were prepared for x-ray analysis in a helium glove box and were protected from reaction with air or moisture by a film of Mylar as described elsewhere (17). All the x-ray patterns were taken on a Philips diffractometer using  $\text{CuK}\alpha$  radiation, and the lattice parameters were calculated with the aid of a PDP 8E computer.

### Results and Discussion

The possible cathode reactions can be classified as follows:



A disproportionation reaction here is one such as is found with the copper halides



where the crystalline structure of the cathode is completely broken down. A topochemical reaction is one in which the structure of the product bears a close relationship to that of the reactant, and in which any atomic rearrangements can be accomplished by simple transformations. The shear structures, described above, are an example of such a structural change as are also the dehydration reactions of the molybdenum oxide hydrates which are shown schematically in Fig. 1. In the first step of this reaction water is simply lost from between the layers, which are built up by bonding between  $(\text{MoO}_5 \cdot \text{OH}_2)$  octahedron; in the second step the water in the bonding octahedra themselves is lost and a double layer of  $\text{MoO}_6$  octahedra are formed (18). A feature of these topochemical reactions is the frequent obtaining of good x-ray patterns, often closely related to that of the reactant; in contrast disproportionation reactions at ambient temperatures tend to give products amorphous to x-rays. In addition there is usually an increase in

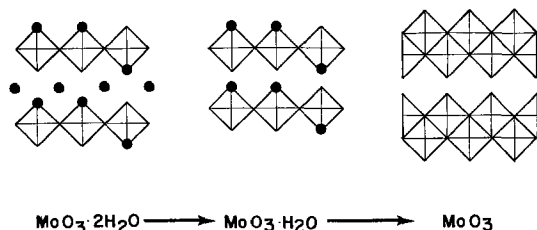
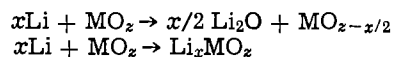


Fig. 1. The topochemical dehydration of molybdenum trioxide dihydrate,  $\text{MoO}_3 \cdot 2\text{H}_2\text{O}$ .  $\square$   $\text{MoO}_6$  or  $\text{MoO}_5 \cdot \text{OH}_2$  octahedra;  $\bullet$   $\text{H}_2\text{O}$ .

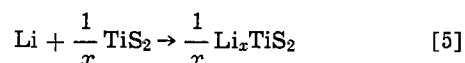
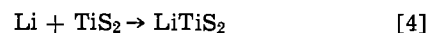
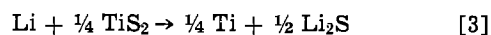
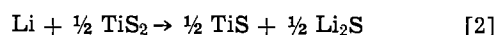
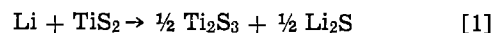
the BET surface area in the latter case due to the breakdown of the crystal, whereas for topochemical reactions the crystallites maintain their integrity and hence the BET areas usually remain constant (10). For lithium reactions, there may be two subsets, one in which anions are abstracted from the crystalline lattice and the other where lithium is inserted into the structure. In the former two binary phases are formed whereas in the latter a ternary phase is found



These reactions do not necessarily have to involve stoichiometric ratios of reactants, as the products can be nonstoichiometric phases such as the well-known sodium tungsten bronzes,  $\text{Na}_x\text{WO}_3$  where  $0 \leq x \leq 1$  (19).

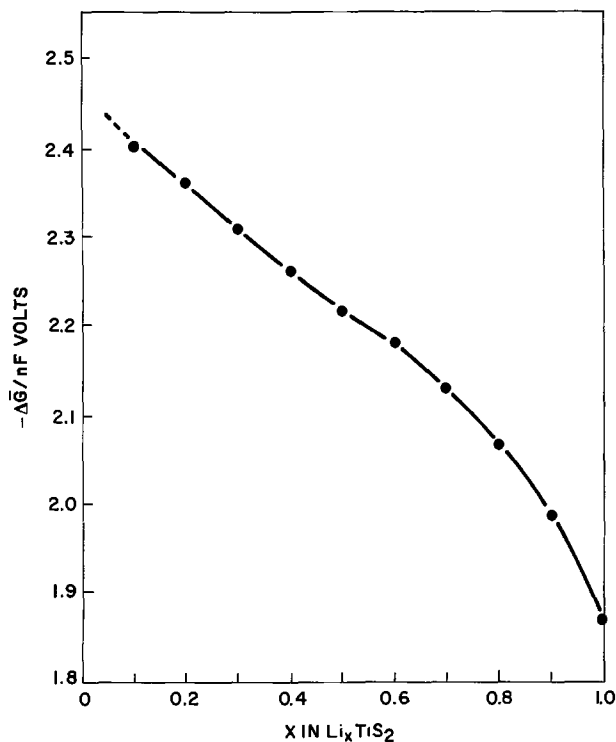
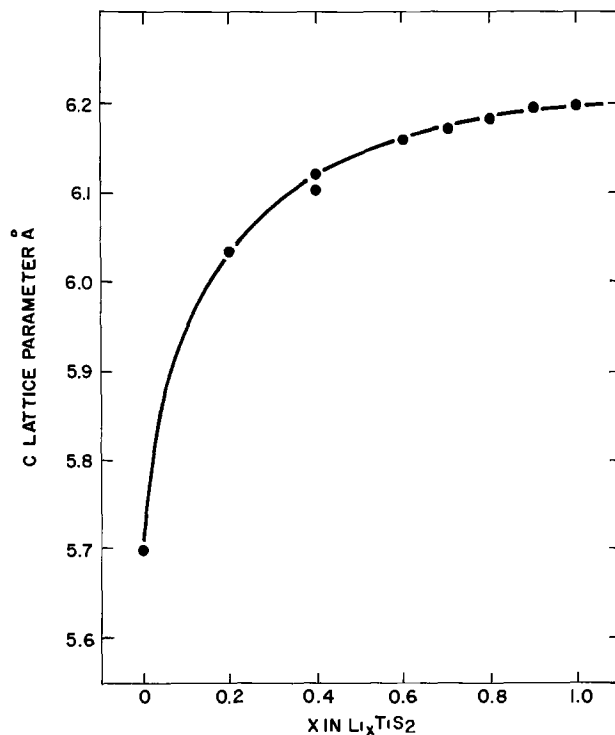
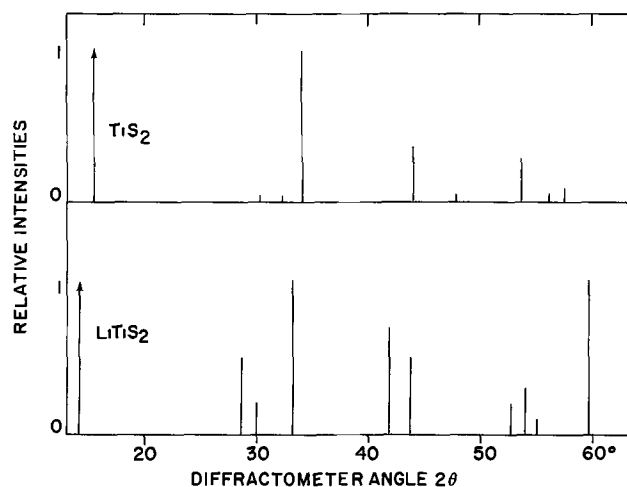
Intercalation reactions are a special case of a ternary insertion process in which the reactant has a layered structure and where lattice expansion occurs perpendicular to the basal planes to allow the insertion of the intercalate. In a true intercalation compound, where the host structure remains unchanged during formation, the reaction should be reversible. Graphite is perhaps the best known example of a lamellar material that can form such intercalation complexes, it is amphoteric in nature, forming compounds with both electron donors, such as potassium, and electron acceptors, such as bromine. Many of the dichalcogenides of the group IVB, VB, and VIB transition metals also form layer compounds in which anion layers are held together by weak Van der Waals forces and between which many electron donors can be intercalated including metals such as lithium and many organic nitrogen compounds, e.g., pyridine (16, 17, 20, 21).

As the intercalation reaction is the simplest to visualize, an example of it is described first. Although the layered disulfides were described as being electrochemically inactive and were merely used as inert substrates for electrochemically active materials such as iodine (22), titanium disulfide has recently been proposed as an active cathode material in both lithium (23, 24) and sodium cells (25). This could react with lithium in the following ways



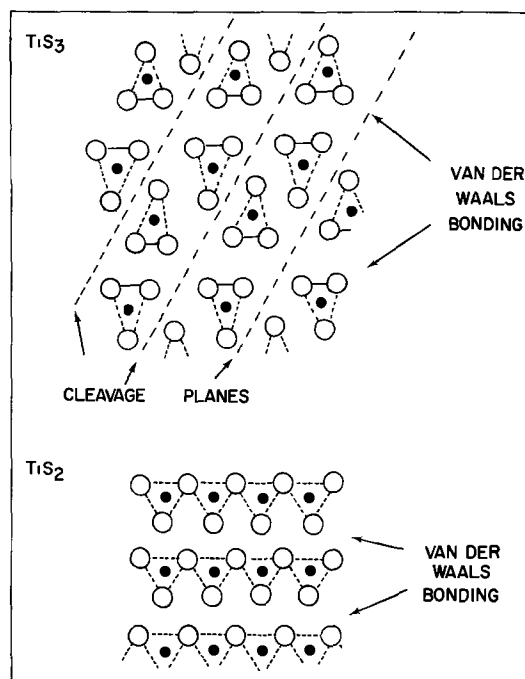
The associated calculated cells emf's for reactions [1] through [3] are 2.24, 1.87, and 1.38V, respectively (1). The experimentally determined values are given in Fig. 2. These were determined using as electrolyte a solution of lithium hexafluorophosphate in propylene carbonate, but were found to be independent of both salt and solvent. Clearly these cell potentials do not fit the calculated values for reactions [1], [2], or [3]. They are higher in all cases as observed for the oxides of vanadium and molybdenum. The variation with lithium content suggests the formation of a single compound with a continuously changing composition such as in  $\text{Li}_x\text{TiS}_2$  where  $0 \leq x \leq 1$ , as proposed in reaction [5]; reaction [4] would give a cell potential independent of state of reaction as  $\text{TiS}_2$  and  $\text{LiTiS}_2$  are in equilibrium with one another until the reaction is completed. This thermodynamic data thus suggests the formation of a ternary nonstoichiometric phase analogous to the well known sodium tungsten bronzes,  $\text{Na}_x\text{WO}_3$ .

An x-ray study of titanium disulfide before and after reaction with lithium shows little change as is shown in Fig. 3. The diffraction lines for  $\text{LiTiS}_2$  have

Fig. 2. Partial molar free energy of formation of  $\text{Li}_x\text{TiS}_2$ Fig. 4. Variation of c-lattice parameter with x in  $\text{Li}_x\text{TiS}_2$ Fig. 3. Schematic of x-ray diffractograms of  $\text{TiS}_2$  and  $\text{LiTiS}_2$ 

shifted to slightly lower angles,  $2\theta$  values, indicating a fractional increase in the hexagonal lattice parameters. Thus for  $\text{TiS}_2$  itself,  $a_0 = 3.407\text{\AA}$  and  $c_0 = 5.697\text{\AA}$ , whereas for  $\text{LiTiS}_2$ ,  $a_0 = 3.455\text{\AA}$  and  $c_0 = 6.195\text{\AA}$  (17), an increase of about 10% in the c-direction. These x-ray results were found to be identical for  $\text{TiS}_2$  reacted in an electrochemical cell and for the sulfide reacted with n-butyl lithium. Care had however to be taken in both cases. In the former the solvent could also intercalate the structure along with the lithium, causing a substantial lattice expansion, up to 18, 19, and  $24\text{\AA}$  in the case of propylene carbonate. In the latter, because the n-butyl lithium reaction is not reversible, lengthy reaction times were necessary to ensure equilibration of the lithium throughout the solid for x-values less than unity. Figure 4 shows the continuous variation of the c-lattice parameter with lithium content. This is consistent with the cell emf data and again shows the formation of a single ternary phase of formula  $\text{Li}_x\text{TiS}_2$  for all x-values. This variation in lattice parameters is in agreement with previous qualitative x-ray data (26).

Inspection of the crystal structure (Fig. 5) shows how this reaction can take place. Between the sulfur-

Fig. 5. Comparison of the structures of  $\text{TiS}_3$  and  $\text{TiS}_2$  looking down the b-axis.  $\circ$ , Sulfur;  $\bullet$ , titanium. The atoms are not all in the same plane.

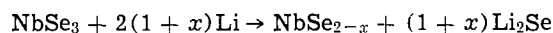
titanium-sulfur sandwiches there is no chemical bonding, just weak Van der Waals bonding, so that the lithium ions can be rather readily inserted between these layers without radically altering the over-all structure. The lithium and titanium ions occupy octahedral interstices (17) in the close-packed sulfur lattice. Although these holes are sufficiently large,  $\sim 0.7\text{\AA}$  radius, to accommodate lithium ions,  $0.7\text{\AA}$  radius, without any expansion of the lattice, an expansion is, nonetheless, observed. This is probably related to a fractionally decreasing ionicity of the lithium with increasing x; thus for x tending to zero the lithium is probably completely ionized whereas for x close to unity the ionization drops about 10% (assuming a linear change in the lithium volume with change of

ionicity).  $\text{Li}^7$  nuclear magnetic resonance studies (27) of  $\text{Li}_x\text{TiS}_2$  as a function of lithium content also indicate a decreasing ionicity of the lithium with increasing  $x$ . The Knight shift and quadrupole coupling constant both increased almost linearly with  $x$ .

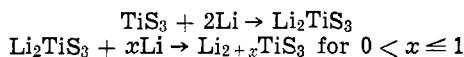
Clearly in the case of titanium disulfide, lithium reacts in an electrochemical cell by forming a ternary phase which is nonstoichiometric. In addition the crystalline structure of the initial material determines the final structure, that is, the material's topology is critical. This type of cell reaction is not restricted to lithium but has been shown by the author (21) and others (28, 29) to be general. Thus organics, such as pyridine and trimethylamine, as well as metals such as copper and silver, can be readily electrointercalated into these layered dichalcogenides. However, the existence of such a layered structure does not necessarily mean that the reaction will be thermodynamically allowed; thus, for example, tungsten disulfide is reduced directly to metallic tungsten (17) by lithium.

Titanium forms a trisulfide as well as the disulfide discussed previously. The trisulfide has the formula  $\text{TiS}(\text{S}-\text{S})$ , i.e., it contains one sulfide sulfur and one polysulfide group (30). Its structure, which superficially resembles the disulfide, is shown in Fig. 5. The Van der Waals layer is lined with polysulfide groups rather than the sulfide ions found in  $\text{TiS}_2$ . In addition the titanium atoms are in distorted trigonal prismatic sites as contrasted with octahedral sites of  $\text{TiS}_2$ . The trigonal prisms in the two rows between the Van der Waals gap are displaced perpendicular to the plane of the figure by half their height so that there is weak bonding between the sulfide,  $\text{S}^=$ , ion in one prism with the titanium in the adjacent prism. This weak bonding creates additional cleavage planes which cause the crystals to grow as fibers rather than the platelets of  $\text{TiS}_2$ ; thus the only strong bonding is along the axis of the trigonal prisms. This one-dimensional structure of  $\text{TiS}_3$  is compared with the two-dimensional structure of  $\text{TiS}_2$  in Fig. 5.

The reaction of titanium trisulfide and niobium triselenide with lithium has been proposed as the basis of a secondary lithium battery (22, 31) and to be



with  $x$  approaching 0.5. Such a disproportionation reaction is unlikely to be reversible and moreover is unlikely to occur at ambient temperatures for the reasons discussed at the beginning of this paper. An electrochemical discharge of  $\text{TiS}_3$  gave an open-circuit emf, of 2.17V, almost independent of lithium content up to two lithium with a gradual fall-off as a third was added. This is consistent with the two reactions



In the first reaction the lithium reacts by insertion into the structure forming a ternary compound and breaks the polysulfide bond. X-ray analysis of  $\text{TiS}_3$  cathodes after reaction showed an expansion of  $\sim 0.4\text{\AA}$  from  $8.73\text{\AA}$  to  $9.11\text{\AA}$  of the crystalline lattice perpendicular to the Van der Waals layer. A complete study of the reaction of titanium trisulfide with *n*-butyl lithium (32, 33) using x-ray and infrared techniques has clearly shown that ternary phases are formed and that the polysulfide bond is broken on reaction. A continuing x-ray analysis program (34) indicates that the chains of trigonal prisms are probably distorting toward the more stable octahedral coordination of the sulfur around the titanium. This formation of ternary phases has been independently ascertained (35).

Contrary to the original reports (31), our studies on titanium trisulfide indicate that it is only marginally rechargeable. At most one of the three lithium in  $\text{Li}_3\text{TiS}_3$  can be recovered and then only at very low current densities, for example under trickle charge.

Clearly the lithium that causes the breakage of the polysulfide bond cannot be reclaimed; this is probably related to a conversion of the titanium coordination polyhedron from a trigonal prism to the more stable octahedron. Thus in titanium trisulfide where a ternary phase is formed by a topochemical reaction in which some chemical bonds are irreversibly broken, secondary cathodic behavior is marginal. In contrast our electrochemical tests on niobium triselenide indicate that in this case complete reversibility for three lithium is found in agreement with prior work (31). The Se-Se bond in  $\text{NbSe}_3$  is variable in length and longer than that normally associated with the polychalcogenide bond (36), so that little disruption probably occurs on breakage. More important, however, is that niobium atoms do not have any preference for octahedral over trigonal prismatic sites (37), so that the initial breaking of the Se-Se bond does not lead to subsequent reorganization of the host structure as in  $\text{TiS}_3$ . These results on the trichalcogenides indicate that ternary phase formation in itself is not a sufficient criterion for reversibility.

Like the sulfides discussed above, we have found that many transition metal oxides also form ternary phases with lithium in electrochemical cells. Vanadium pentoxide has been extensively studied as the cathode in primary lithium cells (3) and recently has been shown to be rechargeable (38). The open-circuit emf on the  $\text{Li}/\text{V}_2\text{O}_5$  cell is almost constant for one lithium at  $\sim 3.4\text{V}$  (2) and then falls abruptly to  $\sim 2.5\text{V}$  for a second lithium. The x-ray pattern of the reaction product of  $\text{V}_2\text{O}_5$  and 1 mole of *n*-butyl lithium is compared in Fig. 6 with the x-ray patterns of  $\text{V}_2\text{O}_5$  and  $\text{LiV}_2\text{O}_5$  formed at  $600^\circ\text{C}$  by a solid-state reaction. This pattern bears a close resemblance to both known compounds, and the strong 001 reflection decreasing and the weak 200 reflection increasing in  $2\theta$  on reaction, but not as far as at high temperatures.

Figure 7 shows the structure of  $\text{V}_2\text{O}_5$ . The vanadium resides in a highly distorted octahedron of oxygen and much closer to one of the oxygen so that the bond to this oxygen is essentially of the type  $\text{V}=\text{O}$ . This allows for ready cleavage of the structure in the plane of these bonds permitting the inclusion of alkali and other metals. Thus for small amounts of lithium,  $x < 0.13$ , and sodium,  $x < 0.02$ , this structure is maintained as shown in Fig. 7b (39); these are the  $\alpha$ -alkali vanadium bronze phases,  $\text{M}_x\text{V}_2\text{O}_5$ . In the case of sodium, the compound  $\text{NaV}_2\text{O}_5$  has the same structure (Fig. 7c) but for the high temperature formed  $\text{LiV}_2\text{O}_5$ , the  $\text{VO}_5$  distorted square pyramids have a different orientation to that found in  $\text{V}_2\text{O}_5$  itself. Thus

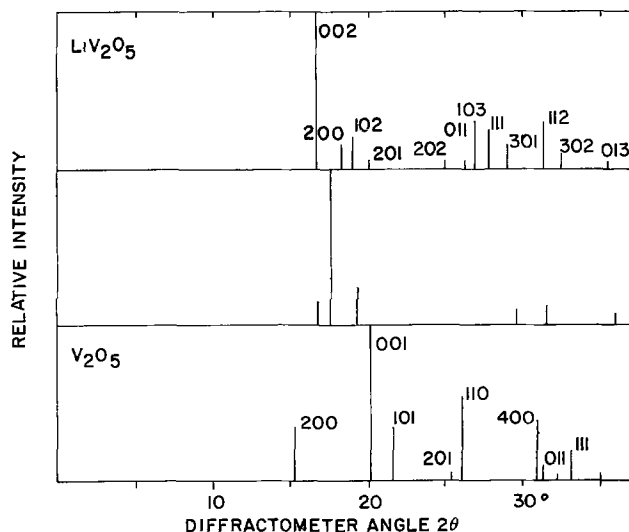


Fig. 6. Schematic of x-ray diffractograms of  $\text{LiV}_2\text{O}_5$ ,  $\text{V}_2\text{O}_5$ , and ambient temperature formed  $\text{LiV}_2\text{O}_5$ .



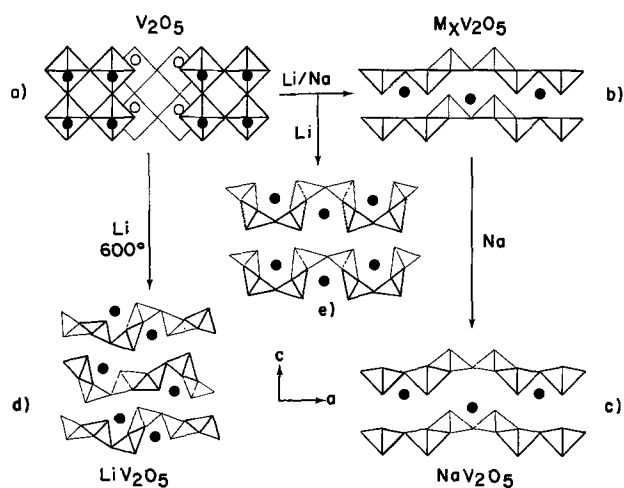


Fig. 7. Structures of vanadium pentoxides looking down the *b*-axis. (a)  $V_2O_5$ ; (b)  $M_xV_2O_5$  for low  $x$  values; (c)  $NaV_2O_5$  formed at high temperature; (d)  $LiV_2O_5$  formed at high temperature; and (e)  $LiV_2O_5$  formed at ambient temperature.

in  $LiV_2O_5$  the base of the pyramids alternate up and down singly, whereas in  $V_2O_5$  itself they alternate up and down in pairs. Although at high temperatures this change can readily take place, it is unlikely that it can occur at ambient temperatures. Therefore, it is proposed that on discharge in a lithium cell, vanadium pentoxide tends toward this same structure but maintains its pair alternation giving the structure shown in Fig. 7e. This structure has a *c*-parameter smaller than that of  $LiV_2O_5$  but larger than that of  $V_2O_5$ , and the converse for the *a*-cell parameter in agreement with the x-ray data of Fig. 6. Heating of this phase at  $600^\circ C$  converts it to the high temperature form of  $LiV_2O_5$ .

In the reaction of the alkalis with vanadium pentoxide the vanadium is reduced from the +5 valent state to the +4 state, with the electron localized on the vanadium (19) as the  $V=O$  bond is presumably broken. So here as for  $TiS_3$  bond breaking occurs, followed by structural distortion, and recharging is difficult, though it has been accomplished recently at low discharge depths,  $\sim 0.25 Li$  (38). An added complication in this case is the decomposition of the organic electrolyte that occurs at the emf's,  $> 3.5V$ , necessary for recharge so that the degree of reversibility cannot be determined for certain.

Molybdenum trioxide reacts readily with lithium forming ternary phases, as expected from its layered structure which is shown in Fig. 1. However, we have found at least two well-defined discharge products from the x-ray data which are different, but similar, to the known high temperature  $Li_2MoO_3$  (40) as found in the case of  $V_2O_5$ . Their structures are now being analyzed. The existence of two discharge plateaus, consistent with the above x-ray data, has been previously reported (41), but the suggestion that a primary reaction product reacts further with  $MoO_3$  to form polymolybdates, as originally proposed in a high temperature molten salt environment (42), is extremely unlikely. As discussed earlier such reactions are not likely to occur at low temperatures unless the reactants are at least partially soluble in the electrolyte. We have found similar x-ray evidence for ternary phase formation for  $MnO_2$  and  $TiO_2$ . The high emf found for the so-called  $CrO_3$  intercalate of graphite,  $3.9V$  for sodium (15) and lithium cells (measured by us on "Seloxcette" obtained from Alfa Chemicals) is probably due to the formation of a ternary complex. This might be  $LiCr_3O_8$  as "Seloxcette" has been claimed to be merely a mixture of graphite and  $Cr_3O_8$  (43). To determine the exact reaction paths of these ternary oxides will require x-ray analysis of

single crystals because of the complexities of their structures.

A number of metal compounds react with the formation of the metal and the simple lithium salt. Cupric sulfide apparently reacts with lithium in a one-step reduction step giving copper metal and lithium sulfide (44), the calculated and observed cell emf's,  $2.3V$ , are in good agreement. This class of reaction in which all the chemical bonds are broken is not normally reversible unless a partial solubility of the reactants in the electrolyte occurs. Thus  $NiS$  and  $CuS$  cells have been found to be irreversible and this was associated with the insolubility of  $Li_2S$  in the electrolyte (45).

### Conclusions

For some time now it has been postulated that the reversibility of alkali metal based cells should be enhanced if the crystalline structure of the cathode material is maintained during discharge and the subsequent charging (15, 46, 47). That the alkali metal tungsten and vanadium oxides bronzes,  $M_xWO_3$  and  $M_xV_2O_5$  where  $x < 1$ , could be used as ionically reversible electrodes (48, 49) for the measurement of the conductivity of the data aluminas focused attention on them for initial studies. However, although their thermodynamic properties and nonstoichiometry requirements were ideal for cathodic use, the diffusion of the alkali ions was much too small to maintain any significant current density (2). Emphasis was then shifted away from these high temperature phases to lower temperature reactions.

This study of the ambient temperature reaction between lithium and transition metal oxides and sulfides indicates that in many cases ternary phases are formed rather than simpler lower oxides or sulfides and lithium oxide or sulfide as had been previously suggested. The structure of this ternary product is determined by the crystal lattice of the initial reactant and minimum structural change occurs for intercalation reactions. The reversibility of the discharge reaction is maximized when no chemical bonds are broken during discharge (intercalation reaction) and minimum when all the chemical bonds are broken, that is, where the structure is completely broken down as for example found in the case of  $CuS$ ,  $CuF_2$ , and  $AgCl$ . When some but not all the chemical bonds are broken and the structure distorts as in  $TiS_3$  and  $V_2O_5$  partial and/or difficult rechargeability is found.

In many cases, such as for  $V_2O_5$  and  $MoO_3$ , the phases formed in these cells are different from the phases formed at elevated temperatures and may be metastable.

If nonstoichiometric phases are formed on discharge, then the rate of reaction and reversibility are likely to be enhanced as it is unnecessary to nucleate new phases. Reversibility is thus optimized when a single ternary phase is formed which is nonstoichiometric and exists over the entire phase region from reactant to final product, as in  $Li_xTiS_2$ ; the structure of this phase should remain essentially unchanged during reaction and no chemical bonds should be broken. These criteria become less important at higher temperatures. As the group VIA anions form such compounds much more often than the halides it is amongst the former that reversible ambient temperature cathodes are likely to be found. Naturally the existence of high electrical conductivity in many of these ternary phases is a strong asset from both discharge rate and reversibility considerations. Here an inert conductive matrix, such as carbon, which must make good contact with the electrochemically active material, need not be added.

Manuscript submitted July 7, 1975; revised manuscript received Oct. 10, 1975. This was Paper 40 presented at the Toronto, Canada, Meeting of the Society, May 11-16, 1975.

Any discussion of this paper will appear in a Discussion Section to be published in the December 1976 JOURNAL. All discussions for the December 1976 Discussion Section should be submitted by Aug. 1, 1976.

Publication costs of this article were partially assisted by Exxon Research and Engineering Company.

## REFERENCES

- J. G. Gibson and J. L. Sudworth, "Specific Energies of Galvanic Reactions and Related Thermodynamic Data," Chapman and Hall, London (1973).
- M. S. Whittingham, *This Journal*, **122**, 713 (1975).
- A. N. Dey, Abstract 54, p. 132, The Electrochemical Society Extended Abstracts, Fall Meeting, Boston, Massachusetts, Oct. 7-11, 1973.
- H. F. Hunger and G. J. Heymach, *This Journal*, **120**, 1161 (1973).
- A. J. Valerga, R. B. Badachhape, G. D. Parks, P. Kamarchik, J. L. Wood, and J. L. Margrave, Final Report, Contract DAAB07-73-C-0056, March 1974.
- L. Companella and G. Pistoia, *This Journal*, **118**, 1905 (1971).
- F. W. Dampier, *ibid.*, **121**, 656 (1974).
- P. G. Dickens, J. H. Moore, and D. J. Neild, *J. Solid State Chem.*, **7**, 241 (1973).
- P. Gado, *Acta Phys. Hung.*, **18**, 111 (1965).
- M. S. Whittingham and P. G. Dickens, in "Reactivity of Solids," Vol. 7, p. 640, Chapman and Hall, London (1972).
- J. P. Gabano, J. Seguret, and J. F. Laurent, *This Journal*, **117**, 147 (1970).
- K. R. Newby and A. B. Scott, *ibid.*, **117**, 152 (1970).
- J. M. Thomas, *Phil. Trans. Roy. Soc.*, **277**, 251 (1974).
- M. S. Whittingham, *This Journal*, **122**, 526 (1975).
- M. B. Armand, in "Fast Ion Transport in Solids," W. van Gool, Editor, North-Holland Publishing Co., Amsterdam (1973).
- M. B. Dines, *Mater. Res. Bull.*, **10**, 287 (1975).
- M. S. Whittingham and F. R. Gamble, Jr., *ibid.*, **10**, 363 (1975).
- H. R. Oswald, J. R. Gunter, and E. Dubler, *J. Solid State Chem.*, **13**, 330 (1975); *ibid.*, **5**, 354 (1972).
- P. G. Dickens and M. S. Whittingham, *Quart. Rev. Chem. Soc.*, **22**, 30 (1975).
- F. R. Gamble, J. H. Osiecki, M. Cais, R. Pisharody, F. J. DiSalvo, and T. H. Geballe, *Science*, **174**, 488 (1971).
- M. S. Whittingham, *J. Chem. Soc., Chem. Comm.*, 328 (1974).
- F. A. Trumbore, J. Broadhead, and T. M. Putvinski, Abstract 61, p. 149, The Electrochemical Society Extended Abstracts, Fall Meeting, Boston, Massachusetts, Oct. 7-11, 1973.
- M. S. Whittingham, *Science*, To be published.
- G. L. Holleck, F. S. Shuker, and S. B. Brummer, Abstract 52, p. 129, The Electrochemical Society Extended Abstracts, Fall Meeting, New York, New York, Oct. 13-17, 1974.
- D. A. Winn and B. C. H. Steele, *This Journal*, **122**, 68C (1975).
- J. Bichon, M. Danot, and J. Rouxel, *Compt. Rend.*, **276C**, 1283 (1973).
- B. G. Silbernagel and M. S. Whittingham, *J. Chem. Phys.*, In press.
- R. Schollhorn and H. Meyer, *Mater. Res. Bull.*, **9**, 1237 (1974).
- G. V. Subba Rao and J. C. Tsang, *ibid.*, **9**, 921 (1974).
- Von W. Kronert and J. Plieth, *Z. Anorg. Allgem. Chem.*, **336**, 207 (1965).
- J. Broadhead and F. Trumbore, Abstract 178, p. 445, The Electrochemical Society Extended Abstracts, Spring Meeting, Chicago, Illinois, May 13-18, 1973, and U.S. Pat. 3,864,167.
- R. R. Chianelli and M. B. Dines, *Inorg. Chem.*, **14**, 2417 (1975).
- R. R. Chianelli and M. B. Dines, *This Journal*, **122**, 182C (1975).
- R. R. Chianelli, M. B. Dines, and M. S. Whittingham, Paper 35 presented at The Electrochemical Society Meeting, Dallas, Texas, Oct. 5-9, 1975; submitted to *This Journal*.
- D. W. Murphy and F. A. Trumbore, *This Journal*, **122**, 68C (1975).
- A. Meerschant and J. Rouxel, *J. Less Common Metals*, **39**, 197 (1975).
- F. R. Gamble, *J. Solid State Chem.*, **9**, 358 (1974).
- C. R. Walk and J. S. Gore, *This Journal*, **122**, 68C (1975).
- P. Hagemuller, J. Galy, M. Pouchard, and A. Casalot, *Mater. Res. Bull.*, **1**, 45 (1966).
- J. M. Reau, C. Fouassier, and C. Gleitzer, *Bull. Soc. Chim. Fr.*, 4294 (1967).
- N. Margalit, *This Journal*, **121**, 1460 (1974).
- B. N. Popov and H. A. Laitinen, *ibid.*, **120**, 1346 (1973).
- L. B. Ebert, R. A. Huggins, and J. I. Brauman, *Carbon*, **12**, 199 (1974).
- Y. Matsuda, Y. Takasu, and H. Ueyama, *This Journal*, **122**, 69C (1975).
- G. Pistoia, *ibid.*, **118**, 153 (1971).
- M. S. Whittingham and R. A. Huggins, "Fast Ion Transport in Solids," W. van Gool, Editor, p. 645, North-Holland, Amsterdam (1972).
- B. C. H. Steele, *ibid.*, p. 103.
- M. S. Whittingham, *ibid.*, p. 434.
- M. S. Whittingham and R. A. Huggins, *J. Chem. Phys.*, **54**, 414 (1971).

# Structure and Anodic Discharge Behavior of Lithium-Boron Alloys in the LiCl-KCl Eutectic Melt

S. D. James\* and L. E. DeVries

Electrochemistry Branch, Naval Surface Weapons Center, White Oak, Maryland 20910

## ABSTRACT

Anodic discharge curves in the LiCl-KCl eutectic melt have been obtained for two lithium-boron alloys (70 and 80 weight per cent Li) between 673° and 873°K (400° and 600°C) and from 2-8 A/cm<sup>2</sup>. The behavior of Li contained in wicks of porous Ni was also studied for comparison. Calculated Li contents for Li-B alloy anodes, at the main break in curvature of discharge curves, clustered closely around 0.67 mole fraction Li. We consider this strong evidence for the existence of a compound Li<sub>2</sub>B in this alloy system. Between 748° and 873°K (475° and 600°C) and up to at least 8 A/cm<sup>2</sup>, there is no diffusional limitation to the anodic extraction of Li from the Li-B alloys. The shape of discharge curves, the lack of anodic diffusional limitation, and the longer low-V plateaus of the alloy richer in Li, are consistent with the following picture of the discharge process. The discharging material behaves like a sponge of solid Li<sub>2</sub>B compound containing a Li-rich, Li-B liquid alloy, probably a conjugate phase to the Li<sub>2</sub>B compound. Lithium anodizes into the melt at constant V out of this liquid alloy until it is wholly transformed to solid Li<sub>2</sub>B. This process constitutes the main plateau of alloy discharge curves. At this point (the main break in discharge curves) voltage rises to values where tighter-bound Li can be anodized out of the decomposing compound. The Li-B alloy electrodes are markedly superior to the Li-Ni wicks both in gravimetric coulombic capacity and in the ability to retain Li at high temperatures. Useful coulombic capacities of the Li-B alloys ranged up to 7700 coulombs/g of (Li + B) at about 3V vs. a chlorine reference electrode.

Presently used molten salt batteries yield only a small proportion of their theoretical energy. This is often due to failure of their Ca or Mg anodes. Calcium anodes react chemically with the electrolyte and both Ca and Mg anodes are passivated at high drains, becoming coated with resistive films of solid salt (1). Lithium, the most electronegative and one of the lightest of the elements, is a prime anode material. It does not react extensively with the LiCl-KCl melt and does not readily passivate in it. However, at the temperatures of these melts lithium is a highly corrosive liquid. This presents severe materials problems which may be mitigated by using a lithium alloy with a high melting point, as for example the LiAl compound (2). Of particular interest in the present work is the behavior of some alloys of lithium and boron which remain solid at high temperatures yet can be easily shaped by machining or pressing at room temperature. Their anodic behavior has been studied by obtaining discharge curves in the LiCl-KCl eutectic melt as a function of alloy composition, melt temperature, and discharge rate. Data were obtained between 673° and 873°K (400° and 600°C) for two alloy compositions [70 and 80 weight per cent (w/o) Li corresponding to 78.4 and 86.2 atomic per cent (a/o) Li] and three discharge current densities (2, 4, and 8 A/cm<sup>2</sup>). The behavior of Li contained in Ni Feltmetal wicks was also studied for comparison.

## Experimental

**Preparation of test electrodes.**—Lithium-boron alloys.—All the manipulations described below relating to Li-containing materials were done in high-purity He-atmosphere glove boxes. Alloy ingots were made using lithium of 99.9% purity from Foote Mineral Company, and boron, "Crystalline Lump, 99.9%, D1263" from Atomergics Chemetals Company. Alloy electrodes were prepared by pressing the alloy into the cylindrical hole of a steel cup (stainless steel Type 303) called the electrode holder. Alloy disks were pressed into the electrode holder as shown in Fig. 1a. During pressing,

the alloy filled the 8 mm diameter by 6 mm deep hole in the electrode holder and excess material extruded up through the 1 mm hole in the form of 0.04-0.1g of "spaghetti." This spaghetti was retained, weighed, and chemically analyzed for its Li content. Thus we arrived at an Li content of the alloy in that part of the ingot immediately adjacent to each individual sample to be discharged. Weighing the electrode holder before and after gave the mass of alloy in each test electrode. This averaged about 0.25g with the 70% alloy and 0.21g with the 80% alloy.

**Li wick electrodes.**—These were made as shown in Fig. 1b. From a 1 in. thick sheet of Ni Feltmetal (Brunswick Corporation, "Grade FM131, 18% dense" average pore size 50 μm) were machined cylindrical plugs slightly oversize (by 0.001-0.002 in.) in diameter but within 0.001 in. of the correct length. These then were pressed into the same electrode holders used for displaying Li-B alloys and placed for 1 min in molten Li at 1073°K (800°C) as in the diagram. Weighing the electrode holder before and after gave the mass of Li taken up by the Ni wick. This generally ranged from 0.12-0.14g of Li.

**Discharge cell and procedure.**—Figure 2 shows the experimental setup for discharging test electrodes. This setup was contained in a Pyrex glass pot (not shown). An atmosphere of dry argon gas was maintained inside

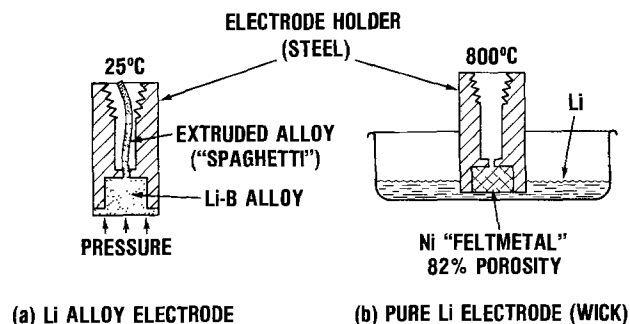


Fig. 1. Preparation of test electrodes

\* Electrochemical Society Active Member.  
Key words: anodes, electrodes, lithium, boron, molten salt batteries.

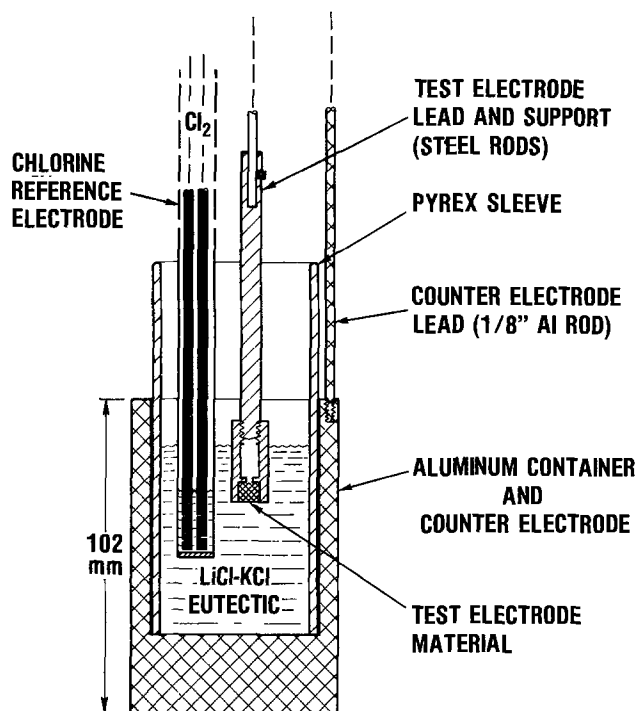


Fig. 2. Cell for discharging test electrodes. Drawing is to scale

the pot by flowing predried high purity (99.995%), water-pumped Ar through it. Before heating to the experimental temperature, the cell, containing powdered salt and reference electrode, was evacuated overnight at 553°K (280°C) to effect drying. A constant current ( $\pm 0.1\%$ ) was driven between test and counterelectrodes so as to anodically dissolve test electrode material while its voltage was measured with a high-impedance recorder and voltmeter. The test electrode was contained in the electrode holder already described, held centrally in the cell by threaded steel connecting rods as shown. The melt container was an Al pot (Type 1100, 99+Al) which also served as counter-

electrode, absorbing Li cathodically deposited on it during anodic discharge of the test electrode. The reference electrode was the chlorine electrode—the carbon/chlorine system inside a 8 mm fritted Pyrex tube. The Pyrex sleeve snugly fitting into the Al container served as an electrical insulator to restrict current to the bottom part only of the Al, thus favoring a uniform current density at the test electrode. After positioning the test electrodes in the melt it took from 20-40 min before steady temperature was recovered and discharge was begun. At the end of discharge the discharged electrode was normally withdrawn from the cell within 5 min for subsequent chemical analysis of its residual Li content.

Lithium contents were measured by extracting samples in aqueous solution and titrating the equivalent OH<sup>-</sup> produced. After the run in which the Li wicks were discharged, cell materials were analyzed for Li by atomic absorption and acidimetry. Of the 1.783g of Li introduced into the cell in this run, 1.077g (60.4%) was found as lithium oxide or silicate in a black skin adhering to Pyrex glass surfaces. The Al pot contained 0.657g of Li (36.9%) and smaller amounts totaling 0.015g (0.8%) were found in the solidified melt and on cooler glass surfaces above the cell. Finally, 0.015g (0.8%) of residual Li was found in the 15 discharged wick electrodes. This left 0.0185g, only 1.0% of the introduced Li, unaccounted for.

The present article is based on interpretation of data from the discharge of 76 Li-B alloy electrodes and 16 Li-wick electrodes. These data were obtained over the course of seven runs, each employing a fresh charge of salt and a new Al container.

### Results and Discussion

When discharged Li-B alloy electrodes were withdrawn from the experimental cell, it was apparent that a drastic shrinking of the sample had usually occurred. In extreme cases the shrinkage was from the initial 8 to 6.5 mm in diameter and from the initial 6 to 4 mm in length.

*Shape of discharge curves.*—Figure 3 shows discharge curves normalized by replotting the X-axis in terms of

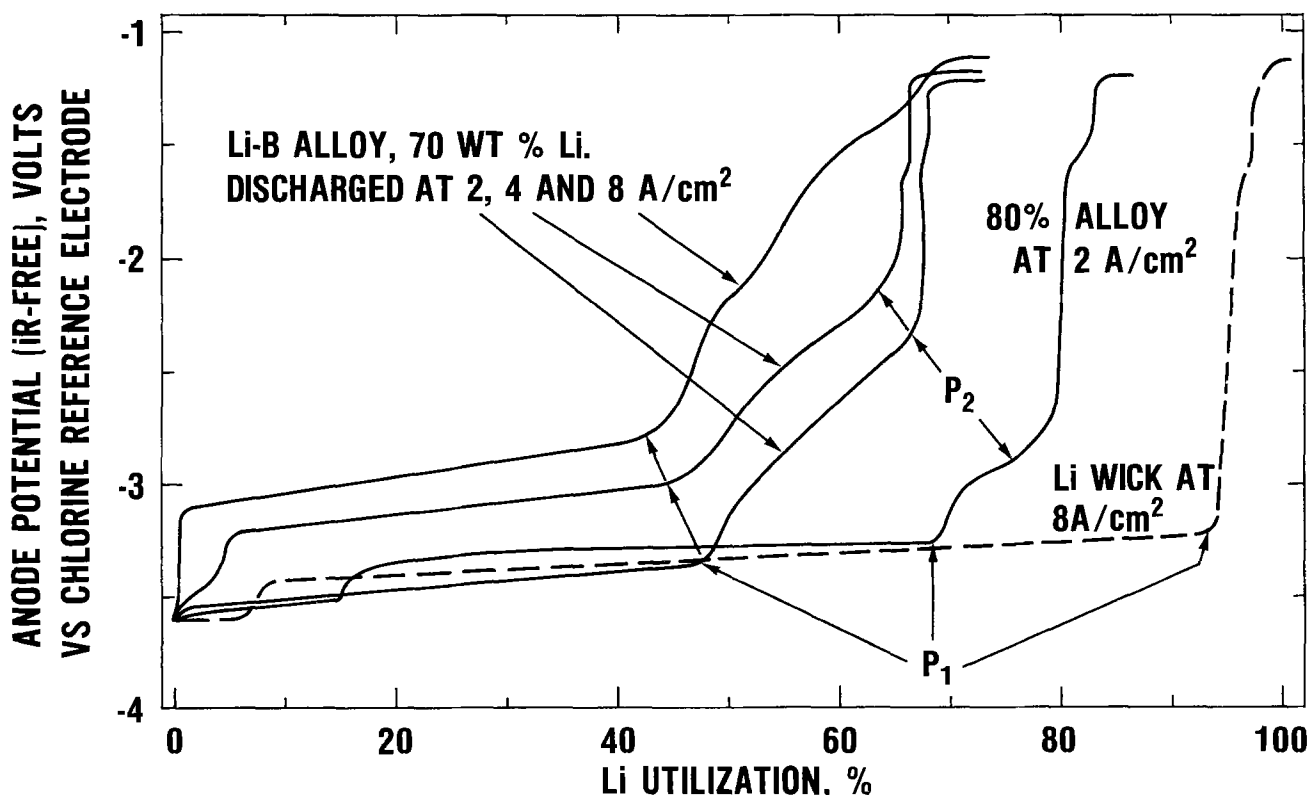


Fig. 3. Discharge curves normalized with respect to per cent utilization of the Li in each electrode. LiCl-KCl at 773°K (500°C)

per cent utilization of the Li in each electrode. The alloy discharge curves although referring mainly to the 70% alloy at 773°K (500°C) are actually typical of both alloys in the temperature range 723°-873°K (450°-600°C). Also shown for comparison is a typical Li-wick discharge curve. Current densities labeled on the curves are the ratio of current to the cross-sectional area of the mouth of the electrode holder (0.500 cm<sup>2</sup>).

All of the Li-B alloy discharge curves have the same general shape as follows: (i) a relatively brief and rather flat plateau close to the Li potential, (ii) a long gently sloping plateau, (iii) an intermediate region where voltage rises faster and is heavily inflected, and (iv) a long and quite flat final plateau. The first plateau was present in only 62% of the samples discharged. There was no apparent correlation between its appearance and any pretreatment or composition factor. Its duration was usually quite brief as in Fig. 3 but on occasion it lengthened to be as long as the second region (ii). In view of its closeness in potential to pure Li, it is probably associated with the discharge of relatively small amounts of free Li, unalloyed with boron. The Li balance (accountability) data discussed below are consistent with the view that regions (i), (ii), and (iii) represent the discharge of Li only; anodic oxidation of boron does not contribute appreciably to the current over this voltage range. The final plateau is controlled by anodic dissolution of stainless steel (Type 303) of the electrode holder. This was shown by anodizing a Type 303 steel rod in the melt and duplicating the voltage of this final plateau (about -1V vs. the chlorine electrode). As Fig. 3 shows, even on this final plateau the 70% alloys still retained one third of their original Li. So a minor part of the current on this plateau could be due to the anodic dissolution of this residual Li.

Considering the three 70% alloy curves, it is apparent that Li utilization at P<sub>1</sub> and P<sub>2</sub>, the two main breaks in curvature, falls only slightly with increasing current density with average values of about 45% for P<sub>1</sub> and 65% for P<sub>2</sub>. With respect to the usefulness of these alloys as battery anodes, the Li utilized at low voltages (i.e., prior to P<sub>1</sub>) is of particular interest. If the main break at P<sub>1</sub> was caused by concentration polarization, then Li utilization at this point would vary inversely with current density. The minor effect of current density upon Li utilization at P<sub>1</sub> shows therefore that, up to 8 A/cm<sup>2</sup> there is essentially no diffusional limitation to the anodic extraction of this Li from the 70% alloy at 773°K (500°C). Table III shows that this statement holds true for both 70 and 80% alloys at 773° and 873°K (500° and 600°C). For the 80% alloy the low-voltage plateau is significantly longer, i.e., a definitely larger proportion of the richer alloy's Li is utilizable at low voltage than is so for the 70% alloy. Again, Table III shows that this behavior is typical both at 773° and 873°K. Comparing the 8 A/cm<sup>2</sup> curve of the 70 w/o alloy with that of the Li wick shows the wick to utilize its Li twice as efficiently as the alloy and at about 0.5V lower voltage. However, as discussed below, the alloys are markedly superior to

the wicks both in gravimetric coulombic capacity and in the ability to retain Li at high temperatures.

The Li-wick discharge curve presumably approximates that of free liquid Li. Thus the long low-voltage plateau in the alloy discharges corresponds closely with that of free Li at 2 A/cm<sup>2</sup> and parallels it with increasing overvoltage at the higher current densities. So this low-voltage part of the alloy's Li content is relatively loosely bound in the alloy. However, subsequent to P<sub>1</sub>, the alloy's Li is discharged at much higher overvoltages from states of steadily stronger binding. The two inflections between the initial and final plateaus show the discharge process is not simple.

*Escape of Li from anode materials.*—Table I shows the results of our attempt to keep track of the Li content of our electrodes. This was done in terms of a "Li balance" defined in the table footnote. "Li residue" and "Li initial" were calculated from weighings and chemical analysis for Li. "Li anodized" was calculated from the quantity of electricity passed assuming it all involved merely Li → Li<sup>+</sup> + e<sup>-</sup>. If Li balance exceeds one then some other anodic process must be occurring in addition to Li → Li<sup>+</sup> + e<sup>-</sup>. An Li balance less than one means that Li is escaping from the electrode by some means other than anodic dissolution, e.g., by dissolution in the melt. The fact that the data of Table I never exceeded unity for Li-B alloys supports our assumption that only Li (not B) is anodically dissolving in the voltage range of Fig. 3. However, some of the data were significantly less than one so anodic dissolution was not the only way that the Li-B alloys were losing Li. We see from the table that alloy composition has little or no effect on Li loss whereas there is a clear tendency for more Li to escape from alloys discharged in the hotter melts. Below 773°K (500°C), Li balances tend to unity. Data were obtained using two separate ingots of each alloy composition. These ingots behaved essentially the same with respect to Li loss. To aid wetting and thereby good electrical contact between alloy samples and the steel electrode holders, some electrodes were preheated in He for 2 min at 1023°K (750°C). Two correlations in the table on preheating effect show a big loss of Li for preheated 70% alloy but little or no loss for the 80% alloy. On the whole it is clear that significant amounts of Li escape from these Li-B alloys at the higher temperatures of this study.

The loss of Li from test electrodes, noted above for Li-B alloys, was even more noticeable in the case of the Li-wick electrodes. Table I shows that the wicks (like the alloys) suffered essentially no Li loss during the conditions of a 773°K discharge. However, at 873°K a very definite loss of Li occurred from the wicks. While there is no direct correlation in the table between wicks and alloys it is clear that Li escaped faster from the wicks; at 873°K Li balance for the wicks was 0.78 while it was 0.82 and 0.83 for the alloys even though the alloys were preheated while the wicks were not. Figure 4 shows the results of varying the time for which wick electrodes were kept at open circuit in the melt at 873°K before discharging at 2 A/cm<sup>2</sup>. For a

Table I. Li balance<sup>a,b</sup> for Li-B alloy and Li wick electrodes

Anode material			Discharge temperature					
			673°-723°K (400°-450°C)		773°K (500°C)		873°K (600°C)	
			Preheat	No preheat	Preheat	No preheat	Preheat	No preheat
w/o of Li in Li-B alloy	70	Ingot 1		1.01	0.84	0.98		
		Ingot 2			0.89		0.82	
Li-Ni Feltmetal wicks	80	Ingot 1	1.02		0.94	0.97		
		Ingot 2			0.90		0.83	
						1.04		0.78

<sup>a</sup> Li balance = (Li anodized + Li residue) ÷ Li initial.

<sup>b</sup> Each datum is the average of results of from 2-8 similarly treated electrodes; mean deviations ranged from ±0.01 to ±0.07.

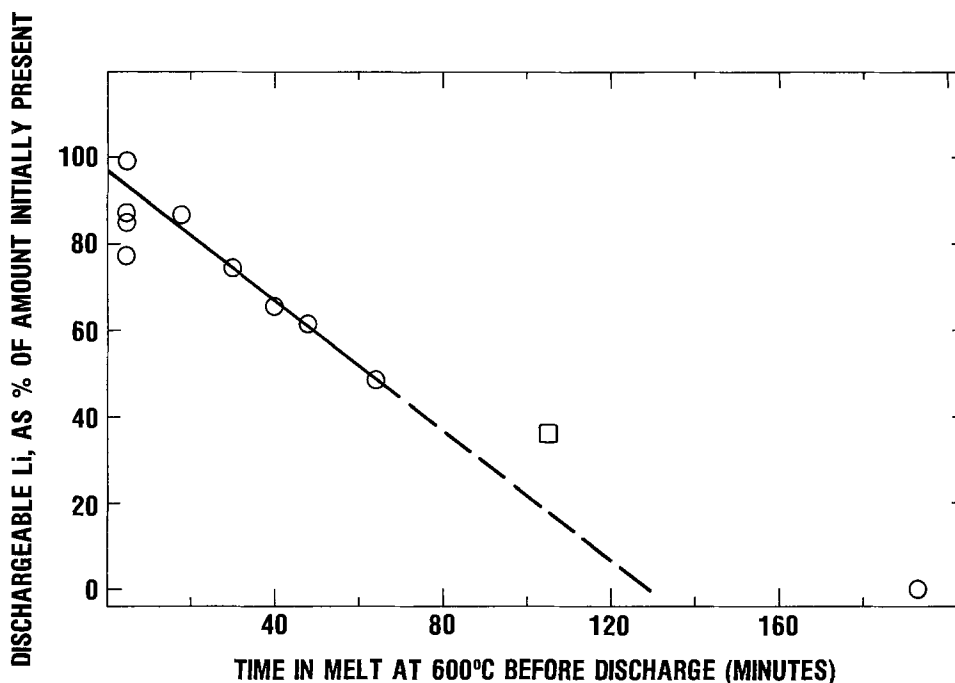
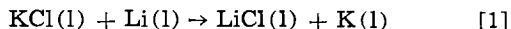


Fig. 4. Loss of Li from Ni felt-metal wicks vs. soaking period in melt at 873°K (600°C) prior to discharge. Dischargeable Li is that per cent anodically extracted up to point  $P_1$  of the 2 A/cm<sup>2</sup>, 873°K discharge curves. Square data point: Li-B alloy electrode, 80 w/o Li (see text).

series of wicks, Li remaining in the electrodes (as calculated from the discharge curves) fell drastically and linearly with soaking period. Extrapolation showed all Li would be lost after about 130 min; in fact, one electrode soaked for 193 min had no dischargeable Li left. Chemical analysis of the Ni wicks of these discharged electrodes showed them to contain only 0.8% of their initial Li content, i.e., no significant quantity of Li was being tied up in the form of an undischARGEABLE Li-Ni alloy. The rate of Li loss from the wicks at 873°K is equivalent to a self-discharge current of about 400 mA/cm<sup>2</sup> of anode surface. We did not do a systematic study of Li escape from alloy electrodes comparable to that of Fig. 4, with the wicks. Alloys were routinely discharged about 30 min after dipping them into the melt. However, due to instrument-problems, one alloy electrode spent 105 min in a 873°K melt before discharge at 4 A/cm<sup>2</sup> and 873°K (in addition it spent 20 hr in the Ar stream above the discharge-cell at 643° ± 25°K). Figure 4 shows that, in spite of this protracted preheating, its dischargeable Li was 36% vs. an extrapolated 18% for the wicks. After escaping from test electrodes, Li dissolved in the melt and then reacted with the various Pyrex glass surfaces contacted by melt. At the end of each run these surfaces were found to be coated with an adherent black layer which was essentially elemental Si plus lithium oxide or silicate.

It was suggested by one of the referees that the low Li balances of Table I were caused by the reaction of Li in electrodes with K<sup>+</sup> in the melt to produce metallic K vaporizing out of the cell (3, 4). The equilibrium constant for reaction [1] based on data at 800°K (5) is 0.137



Thus one might expect continuing reaction as K vapor is swept away from the melt by the stream of Ar cover gas. However the following data showed this was not the case. After a series of Li wicks had been discharged at 773° and 873°K, a detailed analysis for Li was done on the cell materials. Although the over-all Li balance for these discharges was 0.90, i.e., 10% had escaped discharge, all but 1.0% was found in the cell. Furthermore we found no K (and very little Li) condensed on the cooler glass surfaces above our melt or in room-temperature traps in the effluent Ar stream. The lack of K generation in our system must be ascribed to the extensive surface of Pyrex glass that con-

tacted our melt. Silica reacts rapidly with Li (6-11) according to reaction [2]



Potassium however forms a protective silicate film and reacts very slowly (7, 9). Furthermore in our temperature range Li reduces potassium oxides (5) and metasilicate (12). Thus it is reasonable to suppose that Pyrex glass would remove Li from the melt in preference to K and drive reaction [1] to the left. The melts of Ref. (4) and (5), where K generation was observed, were free from efficient getters of Li.

To sum up, the data indicate that under our discharge conditions, both Li-B alloys and Li wicks lose a significant proportion of their Li, only above 773°K. The results indicate that at 873°K the wicks lose Li about two or three times faster than the alloys.

*Composition of alloy electrodes at points  $P_1$  and  $P_2$  of discharge curves.*—It is reasonable to expect that well-defined breaks in the discharge curves may, in some cases, coincide with the arrival of the discharging alloy at a composition corresponding to some simple stoichiometric compound (since a compound has a well-defined free energy of decomposition, Li should discharge out of it at a characteristic voltage). This has been found to be true, e.g., in the case of charge-discharge curves in the Li-Al system (2). Thus the analysis of discharge curves can give valuable information concerning compound formation in alloy systems. This assumes of course that the discharging alloy is very close to states of equilibrium. In this case, changes in alloy voltage correspond to changes in the equilibrium activity of the potential determining species in the alloy sample (in our case, Li). Equilibrium will strictly be followed only in an infinitely slow discharge when composition is precisely uniform throughout the system. In a faster discharge, concentration changes (of Li and Li<sup>+</sup>) at the alloy/melt interface may themselves cause sudden large voltage steps which could be mistaken for those due to compounds. A distinction is possible however, because concentration polarization usually disappears after a few minutes at open circuit.

Our discharge curves generally had two quite well-defined breaks indicated as  $P_1$  and  $P_2$  on Fig. 4. It was invariably true that, within 2 min after opening the discharge circuit, the voltage had recovered and fallen below the value of  $P_2$ . Thus we must be careful of

Table II. Calculated Li atom-fraction<sup>a</sup> at points P<sub>1</sub> and P<sub>2</sub>, the main breaks in curvature of alloy discharge curves.

	Initial composition, w/o Li	Discharge temperature					
		773°K (500°C)			873°K (600°C)		
		2 A/cm <sup>2</sup>	4 A/cm <sup>2</sup>	8 A/cm <sup>2</sup>	2 A/cm <sup>2</sup>	4 A/cm <sup>2</sup>	8 A/cm <sup>2</sup>
P <sub>1</sub>	70	0.67	0.65	0.66	0.67	0.68	0.70
	80	0.67	0.67	—	0.70	0.71	0.74
P <sub>2</sub>	70	0.54	0.50	0.50	0.55	0.55	0.56
	80	0.58	0.54	0.51	0.61	0.58	0.71

<sup>a</sup> Each datum is the average of results of from 2-5 similarly discharged electrodes. The deviations ranged from  $\pm 0.01$  to  $\pm 0.05$  at P<sub>1</sub> and  $\pm 0.001$  to  $\pm 0.04$  at P<sub>2</sub>. The size of these mean deviations is paralleled by and probably arises from a heterogeneity in Li content of the Li-B ingots which was revealed by the "spaghetti" analyses. Due to this heterogeneity, spaghetti composition, in spite of being from material interfacial with the discharged sample, may differ slightly from it in Li content.

interpreting Li content at P<sub>2</sub> in terms of compounds; concentration polarization was certainly involved to some extent in this voltage step. However, voltage recovery subsequent to recovery of the P<sub>2</sub> value was much slower. For five samples, we followed the open-circuit voltage for an hour after discharge. In only one case did it reach the P<sub>1</sub> value, in the others it leveled out significantly above this value. Thus we are on much firmer ground in discussing Li content at P<sub>1</sub> than at P<sub>2</sub> in terms of compound formation.

For the two main breaks, we calculated the atom fraction of Li remaining in the sample by subtracting from the initial Li content the amount of Li taken out anodically. The calculated values at P<sub>1</sub> and P<sub>2</sub> are collected in Table II. Here, Li fraction at P<sub>1</sub> shows a definite clustering around the figure 0.67. This strongly suggests that a compound Li<sub>2</sub>B is arrived at at this point on the discharge curves. Proof of such a compound's existence must of course await more direct structural studies such as x-ray spectroscopy on the material. There is no definite trend in Li fraction at P<sub>1</sub> as a function of current density or of composition of the starting material. There is a possibly significant rise in tabulated Li fractions at 873°K vs. those at 773°K. This may be associated with the tendency, already discussed, for the alloy to lose Li more readily in the hotter melt. Our calculations assumed the samples were losing Li only by anodic discharge so the real compositions would be smaller than the tabulated values if additional Li were escaping. At the second main break in curvature, P<sub>2</sub>, calculated values of Li fraction show some tendency to group around 0.50 especially for samples discharged at 773°K. However, the divergences are much greater than those from the value 0.67 at P<sub>1</sub>. The most we can say about P<sub>2</sub> is that, at this point in the discharge, there is the possibility of an LiB compound being arrived at. As with the P<sub>1</sub> data, calculated Li contents are generally higher for samples discharged at 873°K due probably to a greater loss of Li from electrodes in the hotter melt.

#### Open-circuit voltage (OCV) of various Li electrodes.

—Figure 5 compares our data with other literature values. Our data includes the OCV of 76 Li-B alloy samples (673°-873°K), of 16 Li wick electrodes (773°-873°K) and of one electrode at 873°K where Li was cathodically deposited onto a steel rod dipped in the melt. Within  $\pm 5$  mV all of our data falls on the indicated line. The broken line in Fig. 5 shows Li voltages calculated from standard free energies of formation of LiCl(1) found in the JANAF compilation (5). These voltages were modified to the eutectic situation by equating salt activity to cation fraction. Also shown are the data of Anthony *et al.* (13) and Parassakis and Treadwell (14). These latter data seem definitely anomalous. This may be due to the presence in their cell of a porcelain membrane separating the electrodes. A bias potential across this membrane may have contributed to their OCV's.

It remains therefore to discuss the relatively small deviations among our data, Anthony's data, and the calculated (JANAF) Li OCV's. Our OCV's lie about 30 mV negative of the JANAF-derived Li line with Anthony's data in between. Differences of this order

are not uncommon in measurements on reactive materials at high temperatures; they may arise through variation in experimental procedures and materials used by different groups of workers. Furthermore, the calculated values may be in error due to the assumption that the LiCl activity in the eutectic is equal to the Li<sup>+</sup> cation fraction.

*Lithium utilization and nature of discharge process.*—Table III collects together Li utilization data for the alloy and wick anodes and includes the lower temperature discharges. It shows the per cent Li utilization (coulombic discharge efficiency) for the anodes at two points on the discharge curves; firstly at P<sub>1</sub>, the end of the main, low voltage plateau and secondly, in parenthesis, at an arbitrary value of 2V (*i*R-free) vs. the chlorine reference electrode.

Comparing Li utilization to P<sub>1</sub> for the two Li-B alloys, it is clear (except at 723°K) that a higher proportion of the 80% alloy's Li is utilizable at low voltage. In other words, as seen graphically in Fig. 3, the 80% alloy's extra Li (*vs.* the 70% alloy) goes towards extending the low voltage plateau. Current density has a relatively small effect on the utilization of Li in Li-B alloys. As noted before in discussing Fig. 3, there is a tendency for utilization to fall as current density rises. This effect is especially marked at the 2V point which usually occurs on the steeply rising part subsequent to P<sub>2</sub>. However, even here the effect is much smaller than the inverse first power dependence associated with pure diffusion control. So above about 750°K, there is essentially no diffusional limitation to the anodic extraction of Li from these Li-B alloys (below 8 A/cm<sup>2</sup>).

Together with data discussed in the two previous sections this is consistent with the following view of alloy discharge curves. The discharging material behaves like a sponge of solid Li<sub>2</sub>B compound containing a Li-rich, Li-B liquid alloy, probably a conjugate phase to the Li<sub>2</sub>B compound. Lithium anodizes into the melt out of this liquid alloy at constant voltage until it is wholly transformed to solid Li<sub>2</sub>B. This process con-

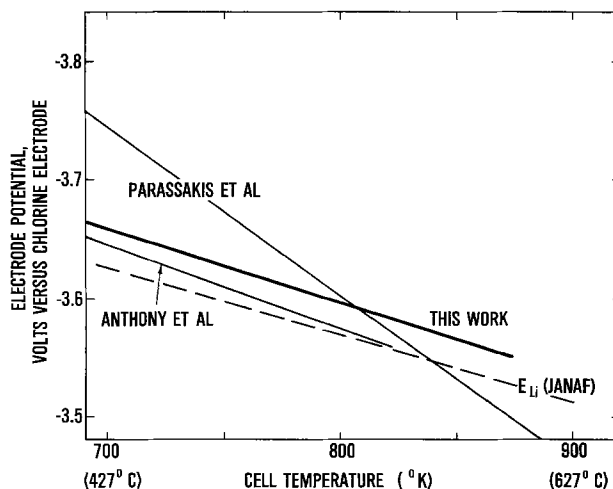


Fig. 5. Open-circuit voltage of various Li electrodes in LiCl-KCl eutectic melt.

Table III. Percentage lithium-utilization<sup>a</sup> during discharge of Li-B alloy anodes and Li/Ni-wick anodes. (a) to point P<sub>1</sub>, the first main break in curvature in discharge curves (b) in parenthesis, to a voltage of -2V (*i*R-free) vs. a chlorine reference electrode.

Anode material		Discharge temperature					A/cm <sup>2</sup>
		673°K 400°C	723°K 450°C	748°K 475°C	773°K 500°C	873°K 600°C	
w/o Li in Li-B alloy	70	6 (6)	51 (67)	49 (63)	52 (70)	45 (69)	2
		6 (8)	35 (38)	43 (60)	52 (65)	48 (63)	4
		6 (6)			50 (56)	46 (59)	8
	80		44 (45)		69 (77)	66 (74)	2
			32 (32)		68 (79)	64 (73)	4
					(49)	55 (65)	8
Li-Ni wicks				94 (98)	87 (90)	2	
				97 (100)		4	
				102 (103)	87 (88)	8	

<sup>a</sup> Calculated from the ratio of coulombs obtained at the appropriate point to the theoretical coulomb equivalent of the mass of Li in each anode. Each datum is the average of results of from 2-5 similarly discharged electrodes. Mean deviations ranged up to  $\pm 0.06$  at P<sub>1</sub> and up to  $\pm 0.10$  at 2V.

stitutes the main plateau of alloy discharge curves. At this point (P<sub>1</sub>, the main break in discharge curves) voltage rises to values where tighter bound Li can be anodized out of the decomposing compound. This view (of a Li-rich liquid alloy of constant composition wicking to the melt interface) explains the flatness of the main discharge plateau and the essential independence of Li utilization on discharge rate. It is consistent also with the appearance of the discharged alloy: a porous, hard, black and coke-like mass. We have recently obtained direct evidence for the essential plausibility of this picture. Alloy samples, 70 w/o in Li (78.4 a/o), surrounded with close-fitting mantles of Ni Feltmetal were heated to 973°K. At this temperature, substantial amounts of Li-rich, Li-B liquid alloy wicked from the solid Li-B alloy into the porous Ni. Work is continuing to establish the composition of solid and liquid phases in this alloy system. The slightly lowered activity of Li in the Li-B liquid alloy would account for the observed slower escape of Li from alloys compared with that from the Li-Ni wicks. At point P<sub>2</sub> it is possible that a second compound, Li-B, is arrived at. This over-all picture at present is a tentative one; it needs to be verified and supplemented by studies which probe structure more directly.

Table III shows that Li-B alloy anode performance falls off very sharply below about 723°K. At 673°K the alloys never gave more than about 10% of their capacity before voltage rose sharply to the final plateau value. A possible cause of this low temperature anode failure is a mass transport limitation either of Li<sup>+</sup> ions through melt away from the interface or of Li atoms through alloy toward the interface. However, the total lack of any rate dependence of Li utilization at 673°K argues against this view. Perhaps the Li-B liquid alloy, which was considered above to be the main source of dischargeable Li, solidifies between 723° and 673°K. More work is needed to clarify this point.

Li-B alloy anodes show great promise for use in high energy and power density, molten salt batteries. Table III shows that they consistently deliver between 50 and 70% of their theoretical coulombic capacity even up to 8 A/cm<sup>2</sup>. This is in striking contrast to the presently used Ca and Mg anodes which cannot be used above about 0.1 A/cm<sup>2</sup> due to solidification of resistive salt films on their surface. Providing melt temperature is above about 748°K, the Li-B alloy anodes seem virtually immune to this problem. Table III shows the 80% alloy to be clearly superior to the 70% alloy to point P<sub>1</sub> of the discharge curves. However, to the 2V point, this superiority is much less marked; it is in fact roughly halved. Table III demonstrates that the Li wicks definitely outperform the Li-B alloys with respect to Li dischargeability. At 773°K the wicks utilize virtually 100% of their Li. At 873°K though still outdoing the alloys, performance of the wicks has fallen somewhat due to the accelerated escape of Li from wick anodes in the hotter melt. Nevertheless the

Table IV. Useful coulombic capacities and plateau voltages of Li anodes

	Lithium-boron alloys w/o of Li		Lithium wicks (in Ni- Feltmetal)
	70	80	
Coulombs/cm <sup>3</sup> <sup>a</sup>	3900	5400	5500
Coulombs/g <sup>a</sup>	4800	7700	2600
Plateau voltage <sup>b</sup>	2 A/cm <sup>2</sup>	3.3	3.5
	8 A/cm <sup>2</sup>	2.9	3.3

<sup>a</sup> Coulombic capacity up to point P<sub>1</sub> of discharge curves [i.e., end of low-voltage plateau (see Fig. 3)]. Coulombs per cm<sup>3</sup> or g of (Li + B) for alloys and of (Li + Ni) for wicks. Wick capacities at 600°C are about 10% smaller than tabulated values.

<sup>b</sup> Average voltage (*i*R-free) up to point P<sub>1</sub> of discharge curves vs. chlorine reference electrode.

wicks, although excellent at discharging their Li, cannot contain as much, nor grip it as tenaciously as the boron alloys do. Both the 70 and 80 w/o Li-B alloys contain about 0.56g of Li per cubic centimeter of alloy whereas only an average of 0.41g of Li was absorbed in 1 cm<sup>3</sup> of our 82% porosity Ni Feltmetal wicks. On a weight basis a much bigger penalty is paid for using the wicks; they contain only about 0.19g of Li per gram of wick compared with 0.7 and 0.8g Li per gram of the two alloys. Furthermore, as shown earlier, Li escape from electrodes into the melt is about 2-3 times faster with wicks vs. alloys. Table IV compares briefly some of the battery aspects of alloy and wick performance.

### Acknowledgments

The authors acknowledge the contributions of Elmer Gubner who performed the chemical analysis, of Frederic M. Bowers for test electrode preparation and valuable suggestions, and of Raymond A. Sutula who prepared the Li-B ingots and first demonstrated the usefulness of these alloys as anode materials for molten salt batteries. This work was supported by the Independent Research Program of the Naval Surface Weapons Center, White Oak, Maryland.

Manuscript submitted March 24, 1975; revised manuscript received Nov. 7, 1975.

Ay discussion of this paper will appear in a Discussion Section to be published in the December 1976 JOURNAL. All discussions for the December 1976 Discussion Section should be submitted by Aug. 1, 1976.

Publication costs of this article were partially assisted by the Naval Surface Weapons Center.

### REFERENCES

1. R. P. Clark and K. R. Grothaus, *This Journal*, **118**, 1680 (1971).
2. S. D. James, *Electrochim. Acta*, **21**, 157 (1976).



3. M. S. Foster, S. E. Wood, and C. E. Crouthamel, *Inorg. Chem.*, **3**, 1428 (1964).
4. R. N. Seefurth and R. A. Sharma, *This Journal*, **122**, 1049 (1975).
5. JANAF Thermochemical Tables, 2nd ed. NRDS-NBS-37, U.S. Government Printing Office, Washington, D.C. (1971).
6. R. Bunsen, *Ann. Chem. Pharm.*, **94** 107C (1855).
7. E. Wiederman and G. C. Schmidt, *Ann. Phys. Chem.*, **57**, 447 (1896).
8. G. Masing and G. Tammann, *Z. Anorg. Chem.*, **76**, 183 (1910).
9. G. Tammann and A. Sworykin, *Z. Anorg. Allgem. Chem.*, **168**, 218 (1928).
10. L. Hackspill, *Helv. Chim. Acta*, **11**, 1003 (1928).
11. E. E. Schumacher and W. C. Ellis, *This Journal*, **61**, 91 (1932).
12. JANAF Thermochemical Tables, 1974 Supplement, *J. Phys. Chem. Ref. Data*, **3**, 453 (1974).
13. R. G. Anthony, B. J. Welch, and R. J. Steele, *Australian J. Chem.*, **21**, 789 (1968).
14. G. Parassakis and W. D. Treadwell, *Helv. Chim. Acta*, **38**, 1749 (1955).

## The Kinetics of the Self-Discharge Reaction in a Sealed Lead-Acid Cell

Kathryn R. Bullock\* and Donald H. McClelland\*

*The Gates Rubber Company, Denver, Colorado 80217*

### ABSTRACT

The kinetics and mechanism of the self-discharge reaction in a sealed, lead-acid cell have been investigated. The unique cell design and the purity of the materials used produce a slower rate of self-discharge and a different mechanism than the traditional lead-acid battery. Particular attention is given to the effects of expander composition and phosphoric acid concentration on the reaction. Rates of the reaction are determined for temperatures in the range of 35°-65°C.

A number of studies have been reported on the kinetics and mechanism of the self-discharge reaction in a vented, lead-acid cell (1-4). Particular emphasis has been placed on the effects of grid alloys (5-8), the electrolyte concentration (9), the presence of impurities (10), the formation temperature (11), and the storage temperature (12).

Although the self-discharge reaction in the lead-acid battery has been extensively studied, the unique construction of the Gates cell makes a reevaluation of this phenomenon necessary. There are three important differences between the Gates cell and the traditional lead-acid battery with respect to the self-discharge reaction. First, the grids in the Gates cell do not contain antimony. Therefore, the self-discharge mechanism which has been well established in the literature (1-8), whereby antimony is oxidized at the positive plate and reduced at the negative plate to form a local cell, cannot occur in the Gates cell. Secondly, the Gates cell is "dry," since all the electrolyte is absorbed either in the plates or in the porous glass separator. The capacity of the cell is thermodynamically limited by the volume and concentration of electrolyte in the cell. Thirdly, the Gates cell is sealed. Therefore, the possibility that gases given off during self-discharge are recombined within the cell must be considered.

The purpose of this study is twofold: (i) to examine the kinetics of the self-discharge reaction in a sealed cell at various temperatures, and (ii) to determine the effects of the expander composition and phosphoric acid concentration on the self-discharge reaction.

### Experimental

A cross section of a standard Gates "X" cell is shown in Fig. 1. The wound plates and separator are sealed in a polypropylene liner which is encased in a metal can crimped around the edge of the plastic top. The cell is filled with electrolyte through the tube in the center, and this tube is then sealed with

a Bunsen valve which will vent at approximately 50 psi.

The lead and lead oxides used in the grid, posts, and paste are at least 99.99% pure. The electrolyte is prepared from reagent grade acid and deionized water.

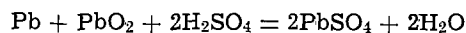
Voltage measurements were made as a function of time on standard Gates "X" and "D" cells and on experimental "D" cells at temperatures up to 65°C using a high impedance digital voltmeter. The data were analyzed using BASIC programs written for an IBM 370 computer.

Three sets of experimental "D" cells were constructed. In the first set, the quantities of phosphoric acid in the electrolyte and of lignin and barium sulfate in the negative plate expander were varied. These cells did not contain any carbon black in the expander. In the second set of cells, the amounts of carbon black and barium sulfate in the expander were varied, while the amount of lignin remained constant. In the third set of cells, the amount of phosphoric acid in the electrolyte was varied.

Measurements of the weights of the positive grid in the standard cells were made at several points in the self-discharge reaction. The positive active material was removed from the grids by slowly adding hydrazine to a hot solution of 5M ammonium acetate. After the positive active material was removed, the grids were washed in distilled water, blotted dry with a paper tissue, dried at 60°C for 15 min, and weighed.

### Results and Discussion

The open-circuit voltage of a lead-acid cell is related to the activity of the electrolyte by the Nernst equation for the cell reaction



$$E = E_o + \frac{RT}{F} \ln \frac{a_a}{a_w}$$

where  $a_a$  is the activity of the sulfuric acid and  $a_w$  is the activity of the water.

\* Electrochemical Society Active Member.

Key words: shelf-life, phosphoric acid, expander, first-order reaction, grid corrosion.

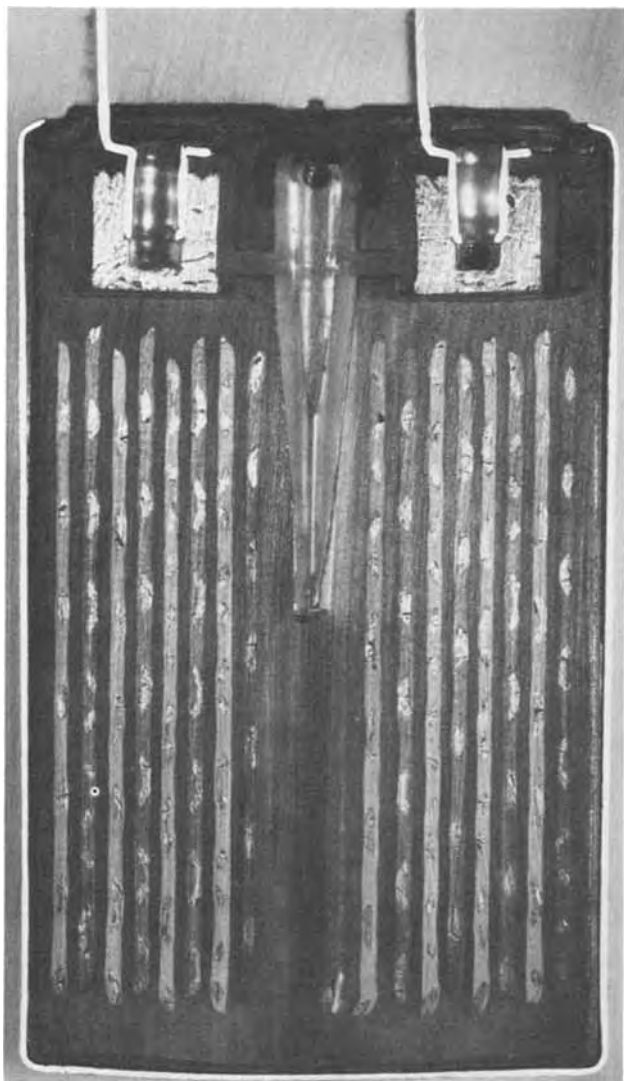


Fig. 1. Cross section of Gates "X" cell

If complete dissociation of the bisulfate ion is assumed, then  $a_a = 4 \gamma_{\pm}^3 m^3$  where  $\gamma_{\pm}$  is the mean ionic activity coefficient of sulfuric acid and  $m$  is the molality of the electrolyte. The values of  $a_a$  and  $a_w$  used in these calculations were calculated from the data of Harned and Hamer (13-15) at the temperatures specified.

In most of the self-discharge reactions which have been proposed (4) for the lead-acid battery, sulfuric acid reacts with a solid material such as lead or lead dioxide. Thus, it is reasonable to assume that the self-discharge reaction is pseudo-first-order with respect to sulfuric acid. The kinetic equation for such a reaction may be written as

$$\ln a_a - \ln (a_a)_0 = -kt$$

where  $t$  is the time,  $k$  is the rate constant,  $a_a$  is the acid activity at time  $t$ , and  $(a_a)_0$  is the initial acid activity.

Activities are used in this calculation instead of concentrations because of the high initial acid concentration and the wide concentration range covered during the shelf-life of the cell.

According to this equation, a plot of  $\ln a_a$  vs. time should be linear with a slope of  $-k$ . Some typical examples of such plots are shown in Fig. 2 for Gates "X" cells stored at three different temperatures. Below an  $\ln a_a$  value of about  $-3$ , which corresponds to an open-circuit voltage of about 2, the plots are linear. The self-discharge reaction, therefore, is first-

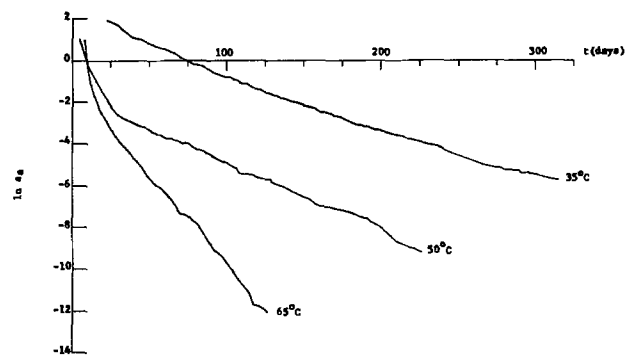


Fig. 2.  $\ln a_a$  activity of sulfuric acid as a function of time at several temperatures.

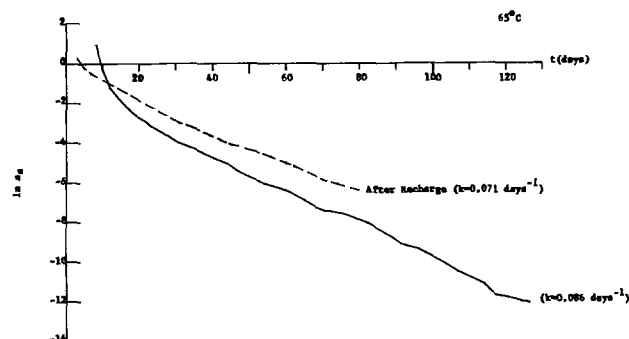


Fig. 3.  $\ln a_a$  activity of sulfuric acid as a function of time before and after recharge.

order with respect to sulfuric acid below about 2V. The mechanism remains the same throughout the remaining shelf-life of the cell even though the concentration of the sulfuric acid changes by three orders of magnitude.

The slopes of the lines were evaluated by the method of least squares. Correlations were excellent, with beta coefficients varying between 0.996 and 0.999. The average rate constant and standard deviation for five cells at each temperature are shown in Table I.

In Fig. 3, the 65°C curve shown in Fig. 2 is plotted on an expanded scale so that the change in slope at a  $\ln a_a$  value of about  $-3$  is more apparent. The last point on the curve corresponds to an electrolyte molality of 0.04. After this deep self-discharge, the cell was recharged with a constant current of 100 mA for one week at room temperature and was again stored at 65°C. The dashed curve in the figure shows the self-discharge of the cell after this recharge. The initial part of the curve has now straightened out almost entirely and the slope of the line has decreased slightly. The rate constant is now 0.071 days<sup>-1</sup> with a standard deviation of 0.001. A similar phenomenon was observed by Zachlin for cells with pure lead grids (7).

The fact that the cell is rechargeable after such an extreme self-discharge is in itself surprising. Figure 4 shows the capacity retention of a standard "X" cell which was allowed to self-discharge at 50°C to a voltage of 1.654 and was then recharged at 2.5V for 16 hr and cycled. A voltage of 1.654 at 50°C corresponds to an electrolyte molality of 0.014 and an  $\ln a_a$  value of  $-13.8$ . The cell recovered capacity rela-

Table I. Self-discharge rate constants for standard "X" cells

Average for 5 cells		
Temp. (°C)	$k$ (days <sup>-1</sup> )	$1\sigma$
35	0.020	0.002
50	0.034	0.001
65	0.090	0.004

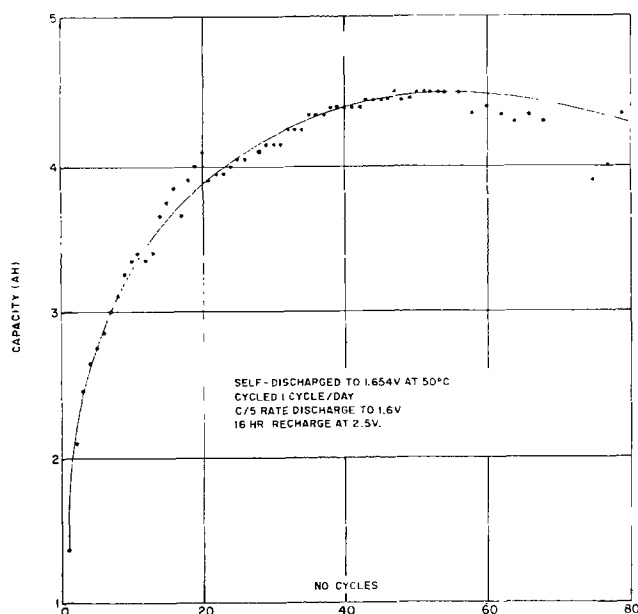


Fig. 4. Capacity retention after deep self-discharge

tively quickly and eventually delivered the full nominal capacity at the C/5 rate.

The results of the first set of tests on experimental cells are summarized in Fig. 5. A series of 57 "D" cells was constructed with concentrations of BaSO<sub>4</sub> and lignin ranging from 0.2 to 0.4% and from 0.4 to 0.8% of the dry, negative oxide weight, respectively, and with 0.1 or 0.8 weight per cent (w/o) phosphoric acid in the electrolyte. The cells were allowed to self-discharge at temperatures of 25°, 45°, 55°, and 65°C. Three standard "D" cells were discharged simultaneously at each of the four temperatures as controls. None of the experimental cells had any carbon black in the expander.

The upper curve in Fig. 5 represents the results from two cells. Both contained 0.1% phosphoric acid and 0.3% BaSO<sub>4</sub>, but one contained only 0.4% lignin while the other contained 0.8% lignin. Since the self-discharge curves of the two cells are indistinguishable, doubling the amount of lignin in the expander has no observable effect. The two lower curves represent the results from cells containing 0.8% phosphoric acid. One cell contains 0.2% BaSO<sub>4</sub> and 0.4% lignin,

Table II. Rate constants for production "D" cells

% H <sub>3</sub> PO <sub>4</sub>	k (days <sup>-1</sup> ) (1 σ)			
	50°C	55°C	60°C	65°C
0	0.049 (0.002)		0.10 (0.007)	0.16 (0.096)
0.1	0.045 (0.003)	0.049 (0.002)	0.089 (0.008)	0.13 (0.004)
0.8	0.036 (0.009)	0.041 (0.002)	0.063 (0.003)	0.12 (0.010)

while in the other cell these concentrations have been doubled. These self-discharge curves are also the same within experimental error. Thus, the concentrations of BaSO<sub>4</sub> and lignin have no apparent effect on the self-discharge reaction.

The difference between the two sets of self-discharge curves comes from the change in phosphoric acid concentration from 0.1 to 0.8%. Of particular interest is the change in the limiting slope of the curves, indicating that the phosphoric acid inhibits the self-discharge reaction. These trends were observed throughout the temperature and concentration ranges of the experiment.

Since none of these cells contained any carbon black in the expander, a second set of "D" cells was constructed which contained either 0 or 0.2% carbon black in the expander. One group of cells contained 0.4% BaSO<sub>4</sub> and 0.4% lignin, while the other group contained 0.2% BaSO<sub>4</sub> and 0.4% lignin. Standard Gates "D" cells were again used as controls. The cells were stored at 65°C. Varying the carbon black concentration in the expander had no effect on the self-discharge reaction within the limits of experimental error.

Further experiments were conducted at 50°, 60°, and 65°C on standard "D" cells which were filled with electrolyte containing 0, 0.1, and 0.8% phosphoric acid. Some results at 65°C are shown in Fig. 6. It is again apparent, from the limiting slopes of these curves, that the rate of the self-discharge reaction decreases as the phosphoric acid concentration is increased. Thus, phosphoric acid apparently inhibits the self-discharge reaction. The tests at the other two temperatures showed the same trend.

Table II summarizes the effect of phosphoric acid concentrations on the rate of the self-discharge reaction. The rate constants given at 50°, 60°, and 65°C are averages of the results from three "D" cells tested under each set of conditions. The data at 55°C are taken from the first set of experiments. The rate constants for cells containing 0.1 and 0.8% phosphoric

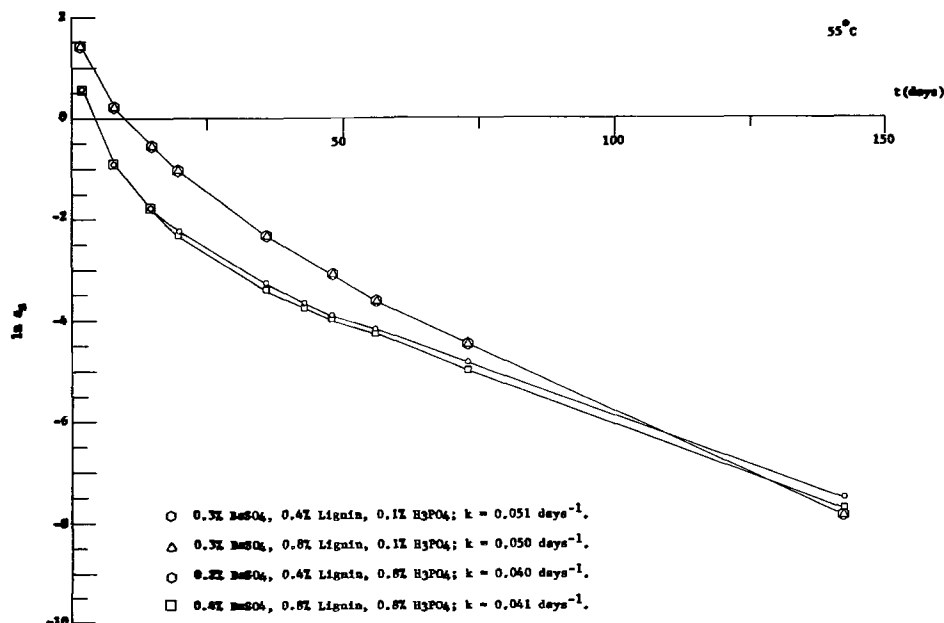


Fig. 5. Effect of expander composition and phosphoric acid concentration on self-discharge.

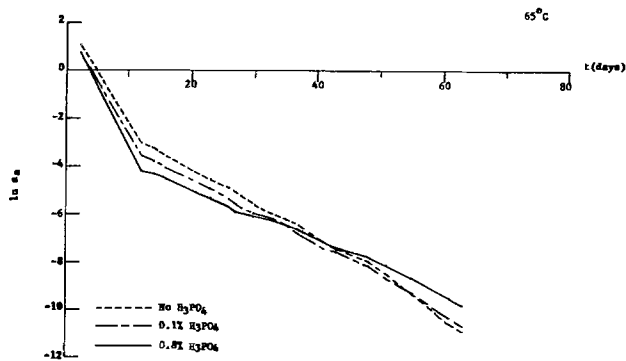


Fig. 6. Effect of phosphoric acid concentration on self-discharge

acid are averages for nine and six cells, respectively, with varying expander compositions.

The Arrhenius equation may be applied to these results in order to obtain the activation energy of the self-discharge reaction

$$\ln k = \ln A - \frac{E_a}{RT}$$

where  $A$  is the Arrhenius constant,  $E_a$  is the activation energy, and  $T$  is the absolute temperature.

An Arrhenius plot for standard "X" cells is shown in Fig. 7. The points are taken from the data given in Table I. The range of values obtained for the five cells tested at each temperature is also shown. The line shown was defined by the least-squares method. The data in Table II are plotted in the same manner in Fig. 8. The activation energy did not change significantly with the concentration of phosphoric acid in the electrolyte. Thus, it is apparent that phosphoric

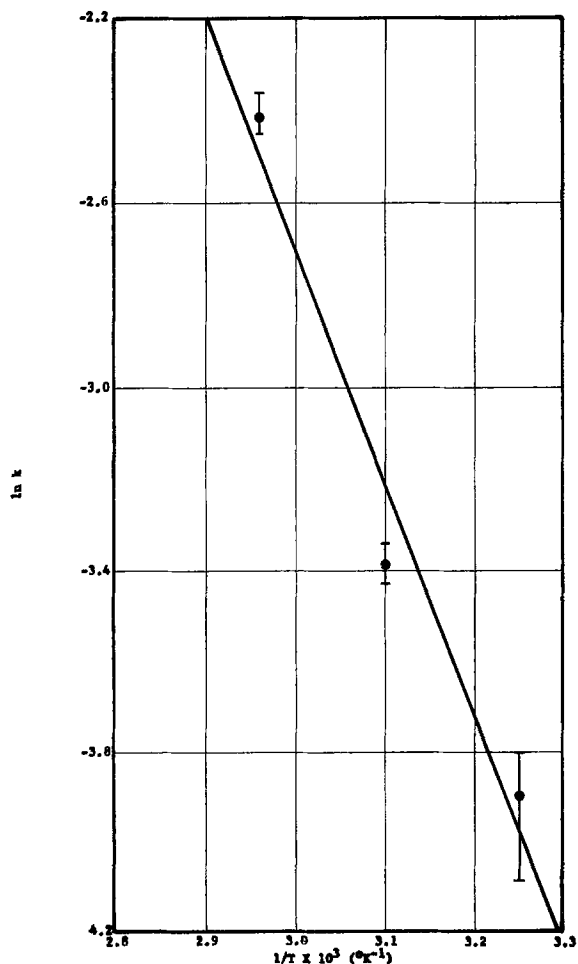


Fig. 7. Arrhenius plot for standard "X" cells

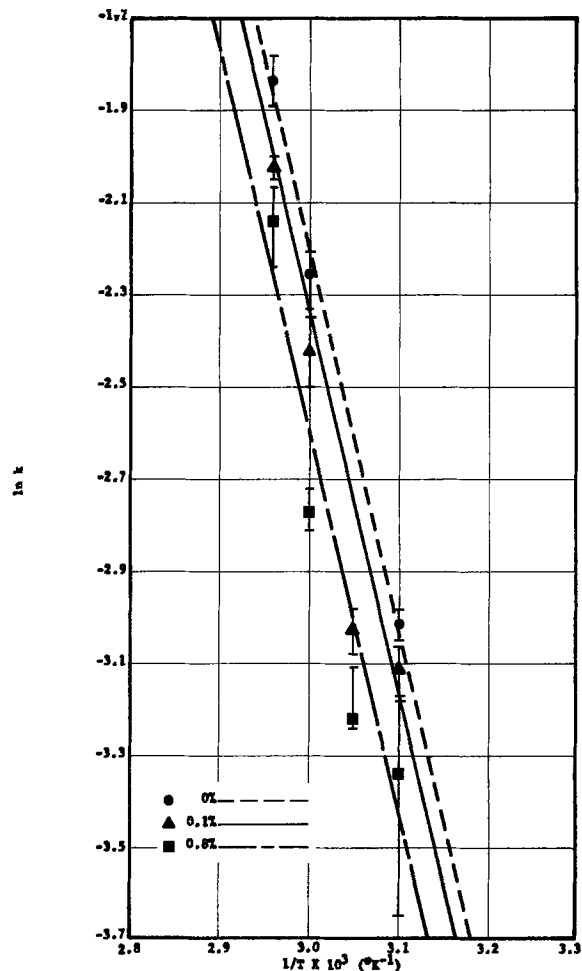


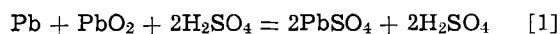
Fig. 8. Arrhenius plot for "D" cells with varying phosphoric acid concentrations.

acid decreases the rate of the self-discharge reaction but does not affect the reaction mechanism.

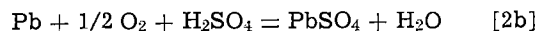
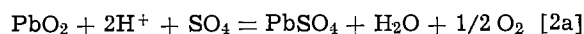
The activation energy obtained for all the cells tested is between 10 and 17 kcal/mole. More experiments are being done at lower temperatures in order to obtain more points and define this value more precisely. However, it will take a number of years for the cells to fully self-discharge at the lower temperatures.

There are three possible mechanisms for the self-discharge reaction in the Gates cell. These are:

Positive grid corrosion



The oxygen cycle



The hydrogen cycle



The over-all reaction for each of these three mechanisms is the double sulfate reaction. The oxidation of lignin at the positive electrode does not appear to be a significant part of the self-discharge reaction, since doubling the lignin concentration does not change the rate of the reaction (see Fig. 5).

Mahato, Weissman, and Laird (16) have recently shown that hydrogen and oxygen recombination (reactions [2b] and [3b]) proceed many times faster than the self-discharge reaction in a sealed cell. Therefore, the rate-limiting step in either the oxygen cycle or

the hydrogen cycle should be the gas-generating reaction (reactions [2a] and [3a]).

Values of activation energies which have been found in the literature range from about 8 to 18 kcal/mole for reaction [2a] (17-19), and from about 2 to 10.2 for reaction [3a] (17, 18, 20). Milner (18) has calculated an activation energy of 13.5 kcal/mole for reaction [1]. Thus, our value of 10-17 kcal/mole is in the right range for either reaction [1] or [2a].

In order to determine the influence of positive grid corrosion, positive grid weights were obtained on a series of 32 "D" cells from the same production lot. Twelve of these cells were stored at 65°C and allowed to self-discharge to an average voltage of 1.700 ( $1\sigma = 0.088$ ) at room temperature. Eight of the cells were stored at 65°C to an average voltage of 1.989 ( $1\sigma = 0.004$ ) at room temperature. The remaining 12 cells were stored at a cold temperature to minimize their self-discharge and had an average voltage of 2.144 ( $1\sigma = 0.003$ ). The weights of the positive grids in the cells discharged to 1.989 and to 1.700V were approximately the same and were about 2.45g lighter than the positive grids from the cells with high open-circuit voltages. Similar results were obtained on a set of standard Gates "X" cells. Apparently, the grid corrosion that does take place occurs early in the shelf-life before the cell has discharged to about 2V. About 1/3 of the sulfuric acid which reacts before this voltage is reached would be required to corrode 2.45g of grid. This can, at least in part, account for the initial high rate of self-discharge (see Fig. 1). However, the corrosion reaction does not occur to a significant extent below 2V and should not affect either the rates of the reactions shown in Tables I and II or the activation energy determined from the Arrhenius equation. Therefore, oxygen evolution (reaction [2a]) seems to be the most likely choice for the rate-determining step of the self-discharge reaction below 2V.

It should also be noted that a newly formed cell may contain "apparent PbO" and/or  $\alpha$ -PbO<sub>2</sub> in the positive plate (11, 21). These compounds are known to self-discharge at a higher rate than  $\beta$ -PbO<sub>2</sub> (22) and may also be part of the reason for the higher rate of self-discharge initially (23).

### Summary

The results of this study may be summarized as follows:

1. The self-discharge reaction is first-order with respect to sulfuric acid in a sealed, lead-acid cell.
2. The rate of the reaction increases with temperature, as predicted by the Arrhenius equation. The activation energy of the self-discharge reaction is between 10 and 17 kcal/mole.
3. Positive grid corrosion is a significant part of the self-discharge reaction early in the shelf-life of

the cell. Below about 2V, grid corrosion is not significant.

4. The cell can be recharged even after it has been completely self-discharged.

5. The composition of the negative expander does not affect the self-discharge reaction.

6. Phosphoric acid is an inhibitor of the self-discharge reaction.

### Acknowledgments

The authors are indebted to Karl Matthes, Phil Grossman, Barbara Papp, and Will Bundy for their help in collecting the data used in this paper and to Will Bundy and Don MacArthur for helpful discussions.

Manuscript submitted Oct. 14, 1975; revised manuscript received Nov. 13, 1975. This was Paper 17 presented at the Toronto, Canada, Meeting of the Society, May 11-16, 1975.

Any discussion of this paper will appear in a Discussion Section to be published in the December 1976 JOURNAL. All discussions for the December 1976 Discussion Section should be submitted by Aug. 1, 1976.

Publication costs of this article were partially assisted by The Gates Rubber Company.

### REFERENCES

1. J. W. R. Byfield, *Trans. Electrochem. Soc.*, **79**, 259 (1941).
2. John J. Lander, *This Journal*, **99**, 339 (1952).
3. G. Gabrielson, *J. Appl. Chem.*, **8**, 748 (1958).
4. P. Ruetschi and R. T. Angstadt, *This Journal*, **105**, 555 (1958).
5. J. T. Crennell and A. G. Milligan, *Trans. Faraday Soc.*, **27**, 103 (1931).
6. H. E. Haring and U. B. Thomas, *Trans. Electrochem. Soc.*, **68**, 293 (1935).
7. A. C. Zachlin, *ibid.*, **92**, 259 (1947).
8. J. Burbank, *This Journal*, **104**, 693 (1957).
9. R. H. Greenburg and J. A. Orsino, National Lead Co. Laboratory Publication No. 219-50, 1950.
10. H. C. Gillette, *Trans. Am. Electrochem. Soc.*, **41**, 217 (1922).
11. R. H. Greenburg and B. P. Caldwell, *Trans. Electrochem. Soc.*, **80**, 71 (1941).
12. A. C. Zachlin, *ibid.*, **82**, 365 (1942).
13. W. J. Hamer, *J. Am. Chem. Soc.*, **57**, 9 (1935).
14. H. S. Harned and W. J. Hamer, *ibid.*, **57**, 27 (1935).
15. H. S. Harned and W. J. Hamer, *ibid.*, **57**, 33 (1935).
16. B. K. Mahato, E. Y. Weissman, and E. C. Laird, *This Journal*, **121**, 13 (1974).
17. P. Ruetschi, J. B. Ockerman, and R. Amlie, *ibid.*, **107**, 325 (1960).
18. P. C. Milner, *Bell System Tech. J.*, **49**, 1321 (1970).
19. T. D. O'Sullivan, R. V. Biagetti, and M. C. Weeks, *ibid.*, **49**, 1335 (1970).
20. J. J. Lander, *This Journal*, **98**, 213 (1951).
21. V. H. Dodson, *ibid.*, **108**, 401 (1961).
22. P. Ruetschi, J. Sklarchuk, and R. T. Angstadt, *Electrochim. Acta*, **8**, 333 (1963).
23. V. H. Dodson, *This Journal*, **108**, 406 (1961).

# Effect of Temperature on Electrode Kinetic Parameters for Hydrogen and Oxygen Evolution Reactions on Nickel Electrodes in Alkaline Solutions

M. H. Miles,<sup>\*1</sup> G. Kissel, P. W. T. Lu,<sup>\*2</sup> and S. Srinivasan<sup>\*</sup>

Department of Applied Science, Brookhaven National Laboratory, Upton, New York 11973

## ABSTRACT

The electrode kinetic parameters for hydrogen and oxygen evolution were determined at temperatures of 80°, 150°, 208°, and 264°C on nickel electrodes in 50 weight per cent KOH solutions. Improvements in the exchange current density with increasing temperature were more significant for the oxygen evolution reaction than for the hydrogen evolution reaction. A favorable change in the Tafel slope for the oxygen evolution reaction occurs between 150° and 264°C which corresponds to an increase in the transfer coefficient from 0.67 to 3.3. This result supports the concept that a change in the reaction mechanism occurs for the oxygen electrode reaction near the Neel temperature of nickel oxide. At the higher experimental temperatures, the Tafel slope for the hydrogen evolution reaction changes from  $2RT/3F$  at low overpotentials to about  $2RT/F$  at high overpotentials suggesting a slow electrochemical desorption mechanism. The present study indicates that significant reductions in cell voltage for water electrolysis can be obtained by higher operating temperatures. At temperatures of about 150°C, it should be possible to approach a 100% energy efficiency (based on  $\Delta H$ ) at current densities commonly used in commercial water electrolyzers.

Hydrogen has attracted considerable attention as a possible fuel for the future (1-3). It is hoped that with abundant nuclear power, water could be decomposed to provide hydrogen as a portable fuel (1, 4, 5). There is also interest in producing hydrogen by water electrolysis, storing it as a metal hydride, and converting it to electricity in a fuel cell for load leveling and peak shaving operations in electric utilities (2, 6). Most commercial water electrolyzers use nickel electrodes and are operated at 70°-90°C in 25-35 weight per cent (w/o) potassium hydroxide solutions (7, 8). Voltage efficiencies range from 65 to 75% at current densities of about 200 mA/cm<sup>2</sup>. Increasing the operating temperature would obviously increase the efficiency of water electrolysis; however, quantitative information is unavailable since electrochemical studies of hydrogen and oxygen evolution reactions in alkali solutions at elevated temperatures are sparse (9). The objectives of the present study are to obtain fundamental kinetic parameters and to ascertain the efficiency gain at higher operating temperatures for water electrolysis. Tafel slopes, transfer coefficients, and exchange current densities are determined for both the hydrogen and oxygen evolution reactions on nickel electrodes in 50 w/o potassium hydroxide solutions at temperatures of 80°, 150°, 208°, and 264°C.

## Experimental

Major problems in designing electrochemical cells for use with aqueous systems at high temperatures include provisions for insulated electrode assemblies which are pressure tight, minimizing corrosion of metal parts, and finding a reference electrode which can operate at high temperatures. The reference electrode selected for this study was the dynamic hydrogen electrode (DHE) as described by Giner (10).

The main features of the stainless steel pressure vessel used for these studies is shown in Fig. 1. A

segment of 4 in. (ID) pipe was welded to a bottom plate 9 in. in diameter and 1/4 in. thick and to a top flange containing eight bolt holes. The cover was fabricated from 1/4 in. stainless steel with eight matching bolt holes and five experimental entry ports. Four entrance ports were tapped for 1/4 in. pipe thread fittings. Three insulated electrical feed-throughs were made from 1/8 in. diameter nickel rods threaded at each end and stainless steel Swagelock fittings with Teflon and plastic plug insulators. The voids were filled with RTV 630 silicone rubber which was the actual pressure seal. The fourth entrance port was fitted with a stainless steel Swagelock tee so that purge gas (argon or hydrogen) could be admitted and removed, and with a pressure gauge to monitor the vapor pressure of the solution as a function of temperature. The fifth entrance port, tapped for 1/8 in. pipe thread fitting, was used for a 1/16 in. Chromel-Alumel thermocouple clad with stainless steel. This thermo-

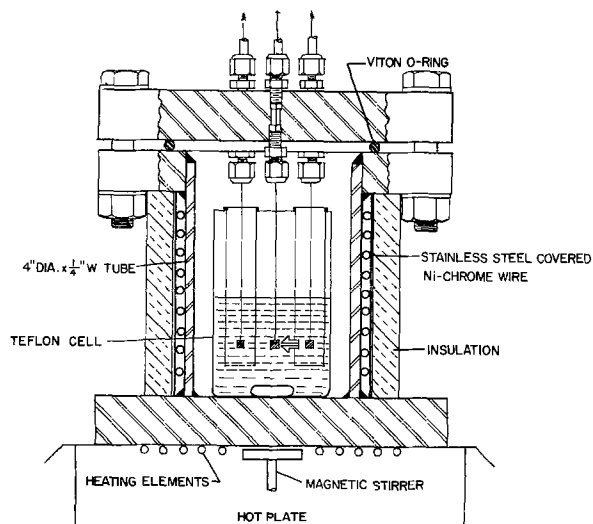


Fig. 1. Stainless steel pressure vessel and auxiliaries for high temperature studies of the hydrogen and oxygen evolution reactions on nickel electrodes in KOH solutions.

\* Electrochemical Society Active Member.

\*\* Electrochemical Society Student Member.

<sup>1</sup> Present address: Department of Chemistry, Middle Tennessee State University, Murfreesboro, Tennessee 37132.

<sup>2</sup> Present address: Department of Materials Science, State University of New York at Stony Brook, Stony Brook, New York 11794.

Key words: cell voltage, exchange current density, Tafel slope, transfer coefficient, water electrolysis.

couple was fed through a Swagelock fitting and then clad also with shrink Teflon and platinum so that it could serve a dual role as a counterelectrode for the dynamic hydrogen reference. The pressure gauge and thermocouple are not shown in Fig. 1. Prior calibration of the thermocouple showed that the measured temperatures were accurate to within 2°C.

In setting up a run, the three electrodes (anode, cathode, and reference) were connected to the three insulated electrical feed-throughs and positioned to fit into a Teflon cell which contained 300 ml of electrolyte. The alkaline solution was prepared from Baker analyzed KOH, low in chloride, and doubly distilled water. The three-compartment Teflon cell is shown schematically in Fig. 2. Each compartment was provided with holes at the top for venting the evolved gases to the pressure vessel. The Teflon cell cover minimized contamination problems due to any refluxing action within the pressure vessel. About 10 ml of water were placed outside the cell to compensate for the loss of water to the vapor phase at high temperatures and to reduce changes in the activity of water with increase of temperature. When the three electrodes and thermocouple were properly positioned in the Teflon cell, the pressure vessel cover was fastened to the flange by  $\frac{5}{8}$  in. steel bolts fitted with two washers. The gas seal was made using a  $\frac{1}{4}$  in. thick "O" ring positioned into a groove in an aluminum back-up plate. The walls of the vessel were heated with stainless steel encased Nichrome wire covered with asbestos, which in turn was insulated with a blanket of quartz wool about 1 in. thick. Magnetic stirring was used to agitate the KOH electrolyte during a run to reduce any temperature gradients within the cell, and the insulated magnetic stirring hot plate was used also to heat the bottom of the vessel. With 50 w/o KOH electrolyte, the pressure gauge reading increased from 0 psig at room temperature to about 210 psig at 264°C. Preliminary experiments using 30 w/o KOH were disbanded since vapor

pressure readings exceeded the safety limit of the vessel (about 300 psig).

Simultaneous studies of the hydrogen and oxygen evolution reactions were made by separately recording the current-potential relationships at the nickel electrodes. Each nickel electrode was mechanically polished using a series of emery papers followed by wet aluminum oxide powder polishing on a rotating felt wheel. The geometrical area of each electrode was 0.20 cm<sup>2</sup>. The electrochemical measurements were made using a PAR Model 173 potentiostat coupled with a PAR Model 175 programmer. Current-potential relationships were determined by steady-state, potentiostatic measurements in the direction of high currents to low currents. Before each experiment, currents of about 1 A/cm<sup>2</sup> were passed for at least several minutes to form an oxide layer on the nickel anode. Slow potential sweep rate (1 mV/sec) studies were used to check the results and usually gave good agreement with the potentiostatic measurements.

The potential of the DHE reference electrode *vs.* the reversible hydrogen electrode (RHE) was measured directly in the pressure vessel at the four experimental temperatures. After placing a second platinized platinum electrode about  $\frac{1}{2}$  cm above the DHE reference and bubbling pure hydrogen through the KOH solution overnight at room temperature, the cell was brought to the desired temperature. The hydrogen generated by the DHE reference could then be used to establish the reversible hydrogen potential on the second electrode.

The IR drop between the DHE reference electrode and the nickel electrode was determined by the interrupter technique (11). Due to the positioning of the Luggin capillary close to the oxygen electrode (Fig. 2), the IR drop at this electrode was about a factor of three times smaller than the IR drop measured at the hydrogen electrode.

## Results and Discussion

Three separate studies of the hydrogen and oxygen evolution reactions in 50 w/o KOH solutions in the Teflon cell and pressure vessel described above. These results were generally in good agreement with earlier preliminary measurements using a Teflon beaker in place of the three-compartment cell.

Figure 3 shows the averaged results for the three separate studies of the hydrogen and oxygen evolution reactions at temperatures of 80°, 150°, 208°, and 264°C. The experimental potentials have been corrected for the IR drop.

From Fig. 3 it is readily apparent that the increase in temperature has a more striking effect on the oxygen evolution reaction than on the hydrogen evolution reaction. Each temperature increase produces an obvious shift in the experimental lines to lower potentials for the oxygen evolution reaction. This is due to the slow kinetics of the oxygen electrode reaction (9, 12, 13). For the hydrogen evolution reaction, only small shifts in potential are observed at temperatures above 150°C. Nevertheless, substantial overpotentials are found for the hydrogen evolution reaction on nickel electrodes in alkaline solutions at lower temperatures (8).

Distinct, linear Tafel regions were observed at each temperature for both the hydrogen and oxygen evolution reactions. Dual Tafel regions were found for the oxygen evolution reaction at 208°C and also for the hydrogen evolution reaction at each of the three higher temperatures.

The exchange current densities for the hydrogen and oxygen evolution reactions can be determined at each temperature from Fig. 3 if the reversible electrode potentials *vs.* the DHE reference are known. For the hydrogen electrode reaction, the reversible potential,  $E_{RHE}$ , is given by

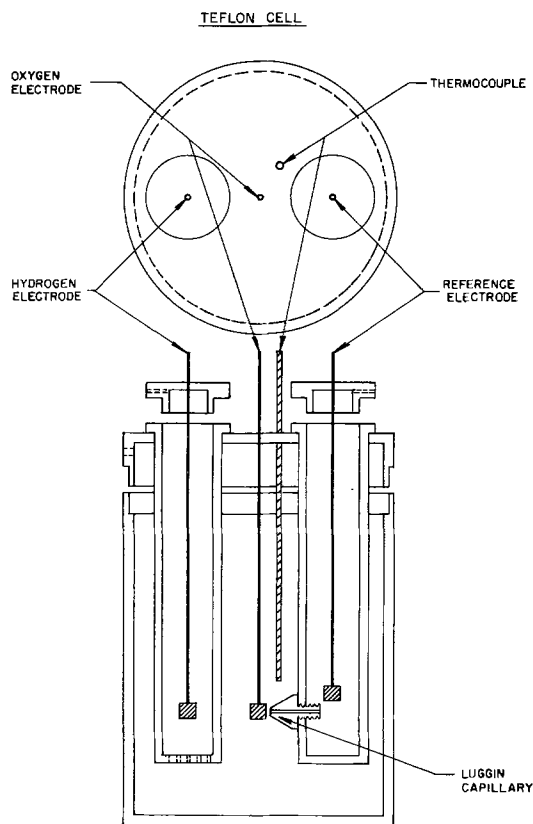
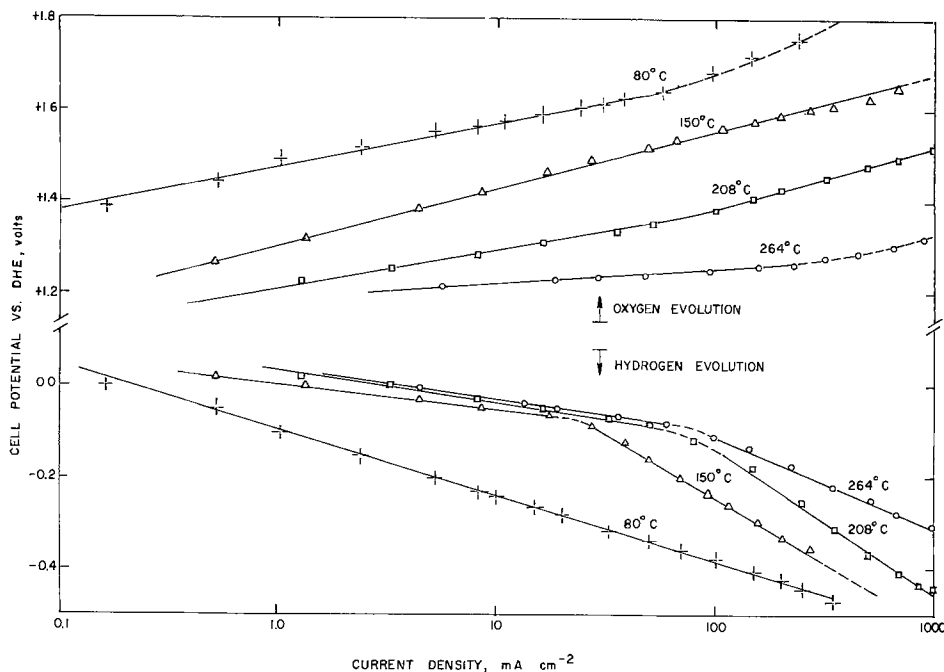


Fig. 2. Schematic diagram of the three compartment Teflon cell used in the pressure vessel.

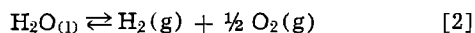
Fig. 3. Potential vs. current density relationships for hydrogen and oxygen evolution on polished nickel electrodes in 50 w/o KOH solutions at temperatures of 80°, 150°, 208°, and 264°C. Both nickel electrodes had a geometrical area of 0.20 cm<sup>2</sup>.



$$E_{\text{RHE}} = |\eta_{\text{DHE}}| \quad [1]$$

where  $\eta_{\text{DHE}}$  represents the overpotential of the DHE reference electrode at 1 mA/cm<sup>2</sup> as measured vs. the RHE electrode. Experimentally determined  $\eta_{\text{DHE}}$  values at the four temperatures are given in Table I. Similar to the observations by Giner (10), the overpotential for the DHE reference in KOH solutions decreases only slightly with increasing temperature.

Considering the cell reaction



the reversible potential for the oxygen evolution reaction,  $E_{\text{ROE}}$ , can be calculated from the expression

$$E_{\text{ROE}} = |\eta_{\text{DHE}}| + |E^0| + \frac{2.303RT}{2F} \log \frac{P_{\text{H}_2} \cdot (P_{\text{O}_2})^{1/2}}{a_{\text{H}_2\text{O}}} \quad [3]$$

where  $P_{\text{H}_2}$  and  $P_{\text{O}_2}$  represent the partial pressures in atmospheres of the evolved gases at the electrode surfaces, and  $a_{\text{H}_2\text{O}}$  represents the activity of water in the KOH solution. Changes in the standard reversible cell potential,  $E^0$ , with temperature are given by

$$\left( \frac{\partial E^0}{\partial T} \right)_P = \frac{\Delta S^0}{2F} \quad [4]$$

The minimum applied voltage needed to decompose water at standard conditions, decreases from 1.229V at 25°C to 1.027V at 264°C. Since hydrogen and oxygen will not be evolved until the partial pressures at the electrode surfaces equal the pressure above the solution, the experimental gauge pressure can be used to obtain the values for  $P_{\text{H}_2}$  and  $P_{\text{O}_2}$  needed in Eq. [3]. The gauge pressure can also be used to calculate the

Table I. Experimental and calculated quantities used to determine reversible electrode potentials vs. the DHE reference electrode

T (°C)	$ \eta_{\text{DHE}} $ (V) <sup>a</sup>	$E^0$ (V)	log term (V) <sup>b</sup>	$E_{\text{ROE}}$ (V)
80	0.045	1.183	0.025	1.25
150	0.043	1.123	0.041	1.21
208	0.037	1.074	0.077	1.19
264	0.035	1.027	0.123	1.19

<sup>a</sup> Experimentally measured in the pressure vessel.

<sup>b</sup> Calculated assuming partial pressures of hydrogen and oxygen at the electrode surfaces are equal to the total pressure above the solution, and using  $a_{\text{H}_2\text{O}} = 0.3$  in 50 w/o KOH solutions.

activity of water at high temperatures in 50 w/o KOH using the relationship

$$a_{\text{H}_2\text{O}} = P_{\text{H}_2\text{O}}/P^0_{\text{H}_2\text{O}} \quad [5]$$

where  $P_{\text{H}_2\text{O}}$  is the experimental vapor pressure for the solution at a given temperature and  $P^0_{\text{H}_2\text{O}}$  is the vapor pressure of pure water at that same temperature. For the three higher temperatures where  $P_{\text{H}_2\text{O}}$  was more accurately measurable, the activity of water calculated using Eq. [5] was  $0.3 \pm 0.1$ . Results reported by Bro and Kang (14) indicate that the activity of water in 50 w/o KOH (13M) at 25°C is about 0.3 and that this activity changes little with temperature. Table I presents the calculated results for the various terms in Eq. [3] along with the end result for  $E_{\text{ROE}}$  vs. the DHE reference electrode.

The Tafel slopes, transfer coefficients, and exchange current densities at the four experimental temperatures are presented in Table II for the hydrogen evolution reaction and in Table III for the oxygen evolu-

Table II. Kinetic parameters for the hydrogen evolution reaction on polished nickel electrodes in 50 w/o KOH solutions

T (°C)	Tafel slope (V)		Transfer coefficient*		Exchange current density (A/cm <sup>2</sup> )	
	low $\eta$	high $\eta$	low $\eta$	high $\eta$	low $\eta$	high $\eta$
80	—0.14—		—0.50—		— $1.1 \times 10^{-4}$ —	
150	0.054	0.28	1.6	0.30	$1.8 \times 10^{-4}$	$9.5 \times 10^{-3}$
208	0.070	0.32	1.4	0.30	$8.0 \times 10^{-4}$	$3.0 \times 10^{-2}$
264	0.066	0.20	1.6	0.53	$9.3 \times 10^{-4}$	$2.0 \times 10^{-2}$

\* Transfer coefficient =  $2.303 RT/bF$  where  $b$  is the Tafel slope.

Table III. Kinetic parameters for the oxygen evolution reaction on polished nickel electrodes in 50 w/o KOH solutions

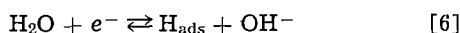
T (°C)	Tafel slope (V)		Transfer coefficient*		Exchange current density (A/cm <sup>2</sup> )	
	low $\eta$	high $\eta$	low $\eta$	high $\eta$	low $\eta$	high $\eta$
80	—0.095—		—0.74—		— $4.2 \times 10^{-6}$ —	
150	—0.125—		—0.67—		— $1.8 \times 10^{-4}$ —	
208	0.085	0.135	1.1	0.71	$6.0 \times 10^{-4}$	$3.5 \times 10^{-3}$
264	—0.032—		—3.3—		— $1.0 \times 10^{-3}$ —	

\* Transfer coefficient =  $2.303RT/bF$  where  $b$  is the Tafel slope.

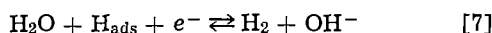


tion reaction. Where two Tafel regions exist, results for both the low overvoltage and high overvoltage regions are listed.

For the hydrogen evolution reaction at 80°C, the transfer coefficient of  $\alpha = 0.5$  indicates a rate-determining step involving an electron transfer such as the discharge step

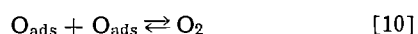
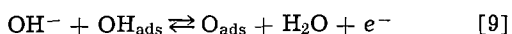
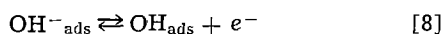


or the electrochemical desorption step



Previous studies suggest a slow discharge-fast recombination mechanism on nickel in alkaline solutions at room temperature (15, 16). The unusual Tafel slope of  $2RT/3F$ , i.e.,  $\alpha = 1.5$ , observed at low overpotentials at the higher temperatures, indicates either a fast discharge-slow electrochemical desorption mechanism under conditions of low hydrogen coverage ( $\theta \approx 0$ ) or a slow discharge-fast electrochemical desorption mechanism under conditions of high coverage ( $\theta \approx 1$ ) (17). Either mechanism predicts that the Tafel slope will change from  $2RT/3F$  to  $2RT/F$ , i.e.,  $\alpha = 0.5$ , at high overpotentials as observed experimentally. The coverage of adsorbed hydrogen on nickel at low overpotentials in 2M NaOH is reported to be small at room temperature (16). Since LeChatelier's principle predicts a decreasing equilibrium coverage of adsorbed hydrogen atoms with increasing temperature, the condition of low coverage at low overpotentials seems even more probable at the higher temperatures; hence a slow electrochemical desorption step is suggested.

For the oxygen evolution reaction, the anodic transfer coefficient changes from 0.67 to 3.3 as the temperature increases from 150° to 264°C, suggesting a change in the reaction mechanism. Dual mechanisms which are influenced by the overpotential seem to operate at the intermediate temperature of 208°C. Although many mechanisms are possible for the oxygen evolution reaction (12, 13), the most generally accepted mechanisms on various electrodes involve steps such as



where one of the electron-transfer steps is rate determining (12, 13, 18-20). Possible stages in the reaction mechanism are illustrated in Fig. 4. The observed transfer coefficient of about 0.7 at 80° and 150°C is

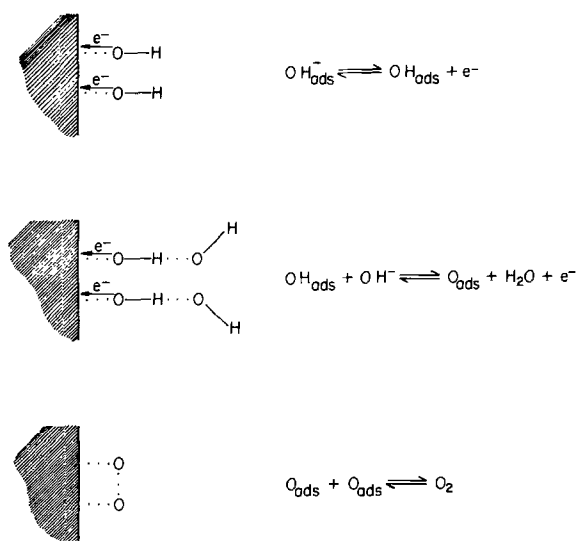


Fig. 4. Possible stages in the oxygen evolution reaction,  $4 \text{OH}^- \rightleftharpoons \text{O}_2 + 2\text{H}_2\text{O} + 4e^-$ , in alkaline solutions.

consistent with a slow electron-transfer step. If the recombination of adsorbed oxygen atoms becomes rate limiting at higher temperatures, an increase in the transfer coefficient to about 4 would be expected under Langmuirian adsorption conditions at low overpotentials. Considering the limitations of the theory and the experimental errors, the observed transfer coefficient of 3.3 at 264°C seems to support the slow recombination step rather than a slow electron-transfer step at high temperatures.

The change in mechanism for the oxygen evolution reaction may be related to the Neel temperature ( $T_N$ ) for nickel oxide. At 250°C, nickel oxide undergoes a magnetic transition from antiferromagnetic to paramagnetic. A change in the mechanism of  $\text{O}_2$  chemisorption occurs near  $T_N$  (21, 22), and Winter (22) has suggested that oxygen is dissociatively chemisorbed above  $T_N$ .

Stronger bonding of  $\text{OH}^-$ ,  $\text{OH}$ , and  $\text{O}$  species with nickel oxide above  $T_N$  would increase the rates of the electron-transfer steps and decrease the rate of the recombination step. Studies of the electrochemical reduction of oxygen by Bevan and Tseung (23) suggest that above  $T_N$  oxygen is dissociatively adsorbed on nickel oxide and then reduced directly to hydroxide ions without forming the peroxide intermediate. Their proposed mechanism is similar to the one given above for the oxygen evolution reaction since the electron-transfer steps for both involve single oxygen atoms.

Due to the changes in reaction mechanism producing large changes in the Tafel slopes, it is difficult to compare the exchange current densities,  $i_0$ . However, the exchange current density for the oxygen evolution reaction increased by more than three orders of magnitude from  $4.2 \times 10^{-6} \text{ A/cm}^2$  at 80°C to  $1.0 \times 10^{-3} \text{ A/cm}^2$  at 264°C. For the hydrogen evolution reaction, a smaller increase is observed from  $1.1 \times 10^{-4} \text{ A/cm}^2$  at 80°C to  $2.0 \times 10^{-2} \text{ A/cm}^2$  at 264°C. Where there is no change in reaction mechanisms, a heat of activation,  $\Delta H^\ddagger$ , can be calculated from

$$\Delta H^\ddagger = -2.303R \partial \log i_0 / \partial (1/T) \quad [11]$$

using the temperature dependency observed for  $i_0$ . From  $i_0$  values for the oxygen evolution reaction below the Neel temperature,  $\Delta H^\ddagger$  is about 18 kcal/mole. From  $\log i_0$  vs. reciprocal temperature plots at constant overvoltages of about 100 mV, an Arrhenius activation energy of approximately 15 kcal/mole is found. A break in the Arrhenius lines is observed when the data at 264°C are included, which again indicates a change in the reaction mechanism near this temperature. The change in  $\log i_0$  with  $1/T$  is not as linear for the hydrogen evolution reaction; however,  $\Delta H^\ddagger$  can be estimated to be about 8 kcal/mole from the  $i_0$  values determined at low overpotentials and about 14 kcal/mole from  $i_0$  values extrapolated from high overpotentials.

The cell potentials for water electrolysis at any desired current density can be readily determined from Fig. 3. Table IV presents the experimental cell voltages at current densities of 20 and 200 mA/cm<sup>2</sup> for the four temperatures. Most commercial electrolyzers operate at current densities in the range of about 200 mA/cm<sup>2</sup> using electrodes with high surface roughness factors. As shown in Table IV, operating cell potentials can be significantly reduced by increasing the temperature.

Table IV. Experimental cell voltages and voltage efficiencies for water electrolysis using nickel electrodes in 50 w/o KOH

$T$ (°C)	$E_{\text{cell}}$ at 20 mA/cm <sup>2</sup> (V)		$E_{\text{cell}}$ at 200 mA/cm <sup>2</sup> (V)	
		% Efficiency*		% Efficiency*
80	1.88	79%	2.17	68%
150	1.54	96%	1.92	77%
208	1.38	107%	1.66	89%
264	1.28	116%	1.43	103%

\* The efficiency obtained on the basis of  $\Delta H$ .

For water electrolysis to be competitive with other methods for hydrogen production, it is necessary to operate the cells at high current densities and at voltages close to the thermoneutral potential based on the enthalpy change for the cell reaction. This potential,  $E_H$ , is defined by the equation

$$E_H = -\Delta H/2F \quad [12]$$

where  $\Delta H$  is the enthalpy change for reaction [2] and  $F$  is the Faraday. This thermoneutral potential represents the operating voltage at which the electrical energy supplied is equal to the thermochemical energy required to decompose water; hence the cell can operate without producing any extraneous heating or cooling effects. Variation of the thermoneutral potential with temperature is very small, being  $-1.48V$  at  $25^\circ C$  at standard conditions and about  $-1.49V$  at  $1000^\circ C$ . Commercial water electrolyzers operate well above the thermoneutral potential; therefore, the excess electrical energy supplied appears as waste heat. When operating below  $E_H$ , the electrolysis cell would act as a refrigerator (24). This would be advantageous only if heat, such as waste heat from a nuclear reactor, is readily available to compensate for the cooling effect produced.

Assuming surface roughness factors in the range of 10-20 for nickel electrodes used in water electrolyzers as compared with the mechanically polished electrodes used in this study, Table IV suggests that voltage efficiencies of 100% (based on  $\Delta H$ ) are possible at current densities of 200-400 mA/cm<sup>2</sup> at temperatures as low as  $150^\circ C$ .

### Conclusions

1. Effects of temperature on electrode kinetic parameters are greatest for the oxygen evolution reaction. The exchange current density for this reaction increases more than three orders of magnitude from  $4.2 \times 10^{-6}$  A/cm<sup>2</sup> at  $80^\circ C$  to about  $1.0 \times 10^{-3}$  A/cm<sup>2</sup> at  $264^\circ C$ .

2. The transfer coefficient for the oxygen evolution reaction changes from 0.7 at temperatures of  $80^\circ$ ,  $150^\circ$ , and  $208^\circ C$  to 3.3 at  $264^\circ C$ . A change in reaction mechanism near the Neel temperature ( $250^\circ C$ ) for nickel oxide is suggested. Recombination of adsorbed oxygen atoms appears to be the rate-determining step at  $264^\circ C$  while electron-transfer steps are the likely slow steps at lower temperatures.

3. The dual Tafel slopes observed for the hydrogen evolution reaction suggest a slow electrochemical desorption step.

4. The efficiency of water electrolysis as a method for producing hydrogen can be greatly improved by increasing the temperature. At normal operating current densities, voltage efficiencies of about 100% based on  $\Delta H$  are possible at temperatures as low as  $150^\circ C$ . The extra energy input for carrying out water electrolysis at this temperature is negligible. The biggest problem in designing and developing a large scale water electrolysis plant to operate at  $150^\circ C$  will be in finding a substitute for asbestos as the separator material (25).

### Acknowledgments

The authors wish to thank Dr. R. H. Wiswall and Mr. F. J. Salzano for their interest and encourage-

ment of this work. The assistance of Mr. Warren Johnson and his colleagues in the construction of the pressure vessel is also appreciated. One of us (M.H.M.) gratefully acknowledges two summer appointments as a Visiting Scientist provided by the Brookhaven National Laboratory.

This work was performed under the auspices of the U.S. Energy Research and Development Administration.

Manuscript submitted July 23, 1975; revised manuscript received Nov. 14, 1975. This was Paper 398 presented at the Toronto, Canada, Meeting of the Society, May 11-16, 1975.

Any discussion of this paper will appear in a Discussion Section to be published in the December 1976 JOURNAL. All discussions for the December 1976 Discussion Section should be submitted by Aug. 1, 1976.

Publication costs of this article were partially assisted by Brookhaven National Laboratory.

### REFERENCES

1. W. E. Winsche, K. C. Hoffman, and F. J. Salzano, *Science*, **180**, 1325 (1973).
2. J. Fricke, *Phys. Unserer Zeit.*, **4**, 65 (1973).
3. D. P. Gregory, *Gas Waerme Int.*, **23**, 311 (1974).
4. H. Barnert, *Atomwirt. Atomtech.*, **18**, 408 (1973).
5. R. L. Costa and P. G. Grimes, *Chem. Eng. Progr.*, **63**, 56 (1967).
6. J. J. Reilly, K. C. Hoffman, G. Strickland, and R. H. Wiswall, in 26th Annual Proceedings Power Sources Conference, May 1974.
7. E. A. Chapman, *Chem. Process Eng.*, **46**, 387 (1965).
8. D. H. Smith, in "Industrial Electrochemical Processes," A. T. Kuhn, Editor, pp. 127-157, Elsevier, New York (1971).
9. M. H. Miles, *J. Electroanal. Chem.*, **60**, 89 (1975).
10. J. Giner, *This Journal*, **111**, 376 (1964).
11. K. R. Williams, "Introduction to Fuel Cells," pp. 57-63, Elsevier, New York (1966).
12. J. P. Hoare, "The Electrochemistry of Oxygen," Chap. 3, John Wiley & Sons, New York (1968).
13. J. O'M. Bockris and S. Srinivasan, "Fuel Cells: Their Electrochemistry," Chap. 8, McGraw-Hill Book Co., New York (1969).
14. P. Bro and H. Y. Kang, *This Journal*, **118** 1430 (1971).
15. J. O'M. Bockris and S. Srinivasan, *Electrochim. Acta*, **9**, 31 (1964).
16. M. A. V. Devanathan and M. Selvaratnam, *Trans. Faraday Soc.*, **56**, 1820 (1960).
17. S. Srinivasan, Thesis, University of Pennsylvania, Philadelphia, Pa. (1964).
18. A. Damjanovic, A. Dey, and J. O'M. Bockris, *This Journal*, **113**, 739 (1966).
19. J. W. Schultze and K. J. Vetter, *Electrochim. Acta*, **18**, 889 (1973).
20. A. J. Appleby and C. J. Van Drunen, *J. Electroanal. Chem.*, **60**, 101 (1975).
21. H. B. Charman, R. M. Dell, and S. S. Teale, *Trans. Faraday Soc.*, **59**, 453 (1963).
22. E. R. S. Winter, *J. Catalysis*, **6**, 35 (1966).
23. H. L. Bevan and A. C. C. Tseung, *Electrochim. Acta*, **9**, 201 (1974).
24. K. J. Vetter, "Electrochemical Kinetics," pp. 15-16, Academic Press, New York (1967).
25. G. Kissel, P. W. T. Lu, M. H. Miles, and S. Srinivasan, Proceedings of Tenth IECEC, p. 1194 (1975).

# Unique Transparent Film Deposited on Glass at Room Temperature

Charles B. Greenberg

PPG Industries, Incorporated, Glass Research Center, Pittsburgh, Pennsylvania 15238

## ABSTRACT

Thin, transparent, essentially metallic films may be deposited on glass at room temperature by electroless reduction from solution. By partial chemical replacement of the electroless metal by another more noble metal, a new film is formed. In one very interesting case, using  $S_2O_3^{2-}$  and  $NH_3$  in solution, the film develops significant nonmetallic character and an unusually low reflectance from the glass-air interface. In addition to silver metal the film consists of  $Cu_2O$  and a sulfur-containing species, probably  $Cu_2S$ . The resulting film is atypical within the family of generally metallic films deposited chemically on glass for purposes of solar and thermal insulation in architectural construction. In the course of developing this film as a commercial product, experimental data have been generated which suggest an interesting oxidation reaction.

Metals are, in general, excellent reflectors of thermal radiation at room temperature. For silver, gold, aluminum, and copper deposited to opacity in vacuum, spectral reflectance values in excess of 0.98 have been reported from 3  $\mu m$  to 20, 30, or 40  $\mu m$  (1, 2). For a radiating source at 25°C, 73% of the total emissive power lies between 3-20  $\mu m$ , 89% between 3-30  $\mu m$ , and 94% between 3-40  $\mu m$  (3). The bulk metals are of course also highly reflective in the spectral region of solar energy, about 99% of this energy being between 0.3-2.2  $\mu m$  at sea level (4). When deposited in vacuum or by electroless deposition as thin, partially transmitting films on glass, they still exhibit high reflectance in both the thermal and solar regions of radiation. Properties such as these have contributed to the considerable interest in coated windows for insulation in architectural construction, where, in part for reasons of chemical and mechanical durability, the uncoated glass surface usually faces the sun, while the coating itself faces inward. A second sheet of glass encapsulates it.

An electrolessly deposited, transparent film containing copper and silver, for example, in a weight ratio of about 6:1 has been characterized spectrally (5). Data are shown schematically in Fig. 1. The reflectance of incident solar spectral energy, as viewed in Fig. 1 from the side of the glass substrate which does not become coated, is quite high relative to uncoated glass. The reflectance from the film-air interface at 9.7  $\mu m$ , the peak of the spectral curve for thermal radiation incident at 25°C, is similarly high; the infrared reflectance is very much the same within at least the measured range of 2-15  $\mu m$ . The reflectance for the uncoated glass surface is peaked at 9.7  $\mu m$ , this wavelength corresponding to the Si-O-Si stretching band, but is elsewhere, within 2-15  $\mu m$ , generally lower.

Essentially metallic films are easily deposited chemically at room temperature from aqueous solution by established methods for electroless deposition. There are, of course, some chemical and mechanical manipulations to achieving uniformity on a large area. Not heretofore reported, to this writer's knowledge, are thin, transparent films on glass prepared by partial chemical replacement of one metal already present in the film by another from solution. Similar galvanic reactions are known for replacement in bulk metals (6, 7). In one particular instance on glass an unusually rapid oxidation reaction occurs in air also, yielding a very interesting film. It is this oxidation which, although not fully understood, constitutes the thrust of

the work to be described herein and the real novelty of the film.

## Experimental Procedures

*Replacement film preparation.*—The usual sequence for film formation at room temperature, using aqueous solutions and intervening rinses, all with demineralized water, is as follows. A thin, electroless silver layer is deposited, from an ammoniated solution of silver nitrate and dextrose, on the glass surface after sensitizing in a dilute solution of stannous chloride. Only one surface about 25-60  $cm^2$  in area is coated while horizontal. This is done by applying each solution as a puddle on a leveled surface. The thickness of the silver layer has not been measured, but for practical purposes is monitored by measuring the luminous transmittance. The target value is 0.80. The layer of silver acts as a catalyst for deposition of copper to a luminous transmittance of about 0.24. Deposition is from a basic solution containing cupric sulfate, nickel sulfate, sodium potassium tartrate, and formaldehyde. Similar solutions are well known. The electroless film may or may not be dried with flowing air at this point. Thereafter, still working in the horizontal position, copper is partially replaced by silver in 50 sec, using a solution containing in one liter 1.0g  $AgNO_3$ , 1.0  $cm^3$   $NH_4OH$  (28-30%  $NH_3$ ), and 3.0g  $Na_2S_2O_3 \cdot 5H_2O$ . Both  $NH_3$  and  $S_2O_3^{2-}$  are complexers for  $Ag^+$  and  $Cu^+$  (8, 9). A more concentrated version of this formula is known for replacement of copper from the bulk (10). This particular diluted version has been used for subsequent data except where otherwise stated. In one

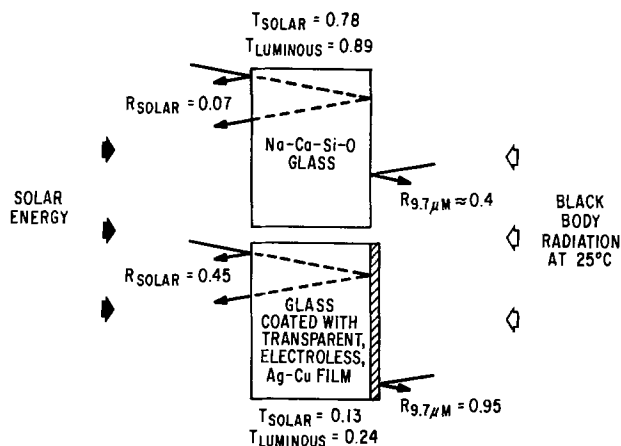


Fig. 1. Practical orientation of coated glass for architectural use. Reflectance (R) and transmittance (T) relative to uncoated glass.

Key words: thin film, sulfur-containing, replacement deposition, oxidation of copper.

case the replacement solution was further diluted 50% with demineralized water. The precursory electroless film was correspondingly thinner; luminous transmittance before replacement equal to 0.30 instead of 0.24. By dilution from the bulk concentration, the rate of replacement is more favorable for thin films. Replacement is terminated by rinsing followed by drying the film with pressurized air. Oxidation within the film occurs rapidly and spontaneously thereafter in the ambient air. In the broadest sense, it is continuing, having certainly begun in aqueous solution and during the brief final drying period (11).

In one instance oxidation was inhibited by following the otherwise final rinse with a passivating step. The film was exposed to an aqueous solution containing 0.13 g/liter of 3-amino-1H-1,2,4 triazole for 4 min at room temperature (12). This was followed by an additional rinse. Then the film was dried.

In two instances the usual procedure was altered by substituting for  $S_2O_3^{2-}$  the disodium salt of  $C_2O_4^{2-}$  or ethylenediamine tetraacetate. Replacement times were 30 sec at room temperature for data shown, but 15-60 sec have been used with similar results.

**Observing the oxidation reaction.**—Immediately after sample preparation, the reflectance from the uncoated glass-air interface was monitored while the opposite, coated surface was exposed to either the ambient air or a selected environment. In all cases but one, the Gardner Precision Glossmeter Model GG-9100 (precision  $\pm 0.002$ ) was used. For the passivated sample the Gardner Multi-Angle Glossmeter Model GG-9095 (precision  $\pm 0.01$ ) was used. Not more than about 15 sec passed between the final step in preparation and the initial data point at "zero" time. For the ambient environment, a typical condition was 30-60% relative humidity at 24°C. For the selected environments, a glass enclosure was used to contain the sample. This resulted in spurious reflections which had the net effect of decreasing all reflectance values by about 0.04. These data are therefore reported as relative reflectance values. Selected environments included  $N_2$  and  $O_2$ , moistened in some instances by flowing over water at room temperature. It was not necessary to remove dissolved  $O_2$  from the water.

**Electroless copper samples.**—In a few instances unreplaced electroless copper films were deposited on glass. Palladium activation was used. These were treated with  $S_2O_3^{2-}$  or  $NH_3$ - $S_2O_3^{2-}$  solutions at room temperature prior to the final rinse and drying. Immediately thereafter the reflectance was monitored.

**Identification of film constituents.**—The usual replacement film and, for comparison, the precursory electroless film were analyzed quantitatively by atomic absorption spectroscopy to give the amounts of silver and copper present. Also, the replacement film was qualitatively compared to uncoated glass using a Norlco PW1212 automatic x-ray spectrometer to determine whether sulfur was present. As a second qualitative determination for sulfur, analysis was made by energy dispersive x-rays using a Princeton Gamma-Tech Model LS-30 attachment to a JSM-2 scanning electron microscope. Crystal phase analysis was by electron diffraction using a JEM-7 transmission electron microscope. For the latter two analyses it was necessary to facilitate sample preparation by deviating somewhat, but not importantly, from the usual procedure for sample preparation. Instead of beginning with a precursory, electroless copper film on glass, copper was deposited in vacuum on either collodion or carbon, supported on a mica substrate. This permitted the necessary easy release for collection on copper grids after treating in a puddle of the normal replacement solution. Samples were also exposed to aqueous solutions containing sodium thiosulfate alone. Rinsing in these instances was done essentially by diluting the puddle of

Table I. Film analysis

	Cu (Units/cm <sup>2</sup> )	Ag (Units/cm <sup>2</sup> )	Ni ( $\mu$ g/cm <sup>2</sup> )
Electroless film, prior to replacement	18.8 $\mu$ g	1.9 $\mu$ g	<0.3
After replacement, 50 sec at room temperature	8.1 $\mu$ g	15.9 $\mu$ g	<0.3
Weight gain	-10.7 $\mu$ g	+14.0 $\mu$ g	—
Molar gain	-0.17 $\mu$ m	+0.13 $\mu$ m	—

replacement solution or  $S_2O_3^{2-}$  with demineralized water within a confining tray.

## Results and Discussion

**Experimental evidence for replacement and oxidation in air.**—For the usual aqueous solution described, partial replacement is confirmed by the atomic absorption data in Table I. Because nickel sulfate is present in the precursory electroless copper solution, its content is also shown. In some way nickel sulfate promotes adherence, but it is not detectable within the film in measurable quantities. On a molar basis more copper has been removed from the film than silver deposited. That may be indicative of experimental error but side reactions are also likely. For the replacement film in Table I, the film thickness, by the method of Tolansky (13), is about 465Å. Partial oxidation within the film is implied by the curve with open data points in Fig. 2, although a less likely case for restructuring could be made. The reflectance for this unpassivated film decreased rapidly within the first 10 min and then decreased slowly. The film is relatively stable thereafter. Accompanying this change is a clear change in visual appearance by reflection, generally occurring within the brownish gray colors (14) by irradiation with illuminant C. A similar change did not occur when the film was chemically passivated with

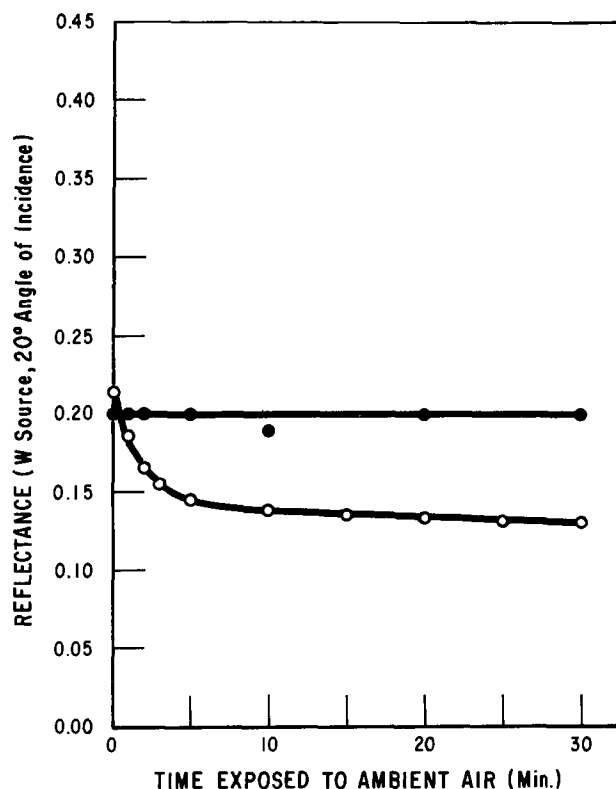


Fig. 2. Reflectance from the glass-air interface immediately after film deposition on one surface by electroless and replacement reactions: ○ film having partial replacement of electroless copper by silver from solution containing  $S_2O_3^{2-}$ ; ● similar film passivated prior to drying.

the triazole solution, as indicated by the curve with solid data points in Fig. 2.

A decrease in reflectance is also inhibited generally at room temperature by maintaining the sample in either partial vacuum or nitrogen, dry or moist, while monitoring. The curve in Fig. 3 indicates film stability in partial vacuum and moist nitrogen. The initial decrease in reflectance in partial vacuum is relatively small and can be accounted for by allowing for some time to reach 0.2 atmospheres. In this instance the replacement solution was, by 50%, a diluted version of the usual. The reflectance decreased quickly once air was admitted into the system. Moist oxygen caused a similar sharp decrease when introduced instead of  $N_2$ ; dry  $O_2$  did not.

The prior work of Germer (15) and Campbell and Thomas (16) suggests that residual copper in the replacement film, were it purely metallic, should oxidize to only about 10-20Å within the first 30 min of exposure to the ambient environment. The metallic silver component should not oxidize to any noticeable extent. Thereafter, the replacement film should be relatively stable. An oxide film 10-20Å thick should not be visible to the unaided eye. In the unpassivated films of Fig. 2 and 3, therefore, oxidation in air beyond this minimal thickness has been presumed.

**Phase analyses.**—There is evidence that the  $S_2O_3^{2-}$  replacement film contains Ag,  $Cu_2O$ , and probably  $Cu_2S$ . Vacuum-deposited copper exposed to the usual replacement solution for about 50 sec was shown qualitatively by electron diffraction to consist of at least crystalline silver and  $Cu_2O$ . There were no unidentified diffraction lines. By analysis with both energy dispersive x-rays and fluorescent x-rays, sulfur was detected qualitatively. Sulfur was only detected by electron diffraction after exposing another portion of the vacuum-deposited copper specimen to an aqueous solution of 3.0 g/liter  $Na_2S_2O_3 \cdot 5H_2O$  for about 30 min. A faint pattern for  $Cu_2S$  was discerned in some instances, suggesting this may also be the sulfur-containing species in the normal replacement film. The structure of  $Cu_2S$  is probably too poorly defined for easy identification by electron diffraction.

**Accelerated oxidation of Cu dependent on the presence of  $S_2O_3^{2-}$ .**—In Fig. 4 it is shown that an electroless copper film once exposed to  $S_2O_3^{2-}$  in the absence of a replacement reaction also suffers an exaggerated decrease in reflectance upon subsequent exposure to air. Its behavior is compared to that of similar copper films which were, as references, not exposed to  $S_2O_3^{2-}$ . Both references are relatively stable. In this way it has been demonstrated that supposedly enhanced oxidation within the replacement film can be explained in terms

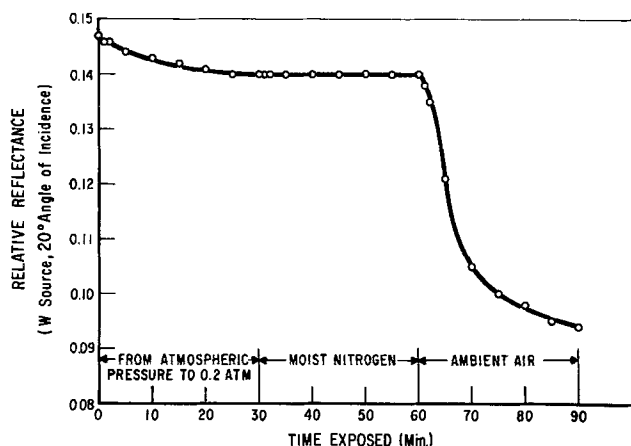


Fig. 3. Relative reflectance from the uncoated glass-air interface with an electroless-replacement film undergoing successive exposures to different environments. Electroless copper was partially replaced by silver from an aqueous solution containing  $S_2O_3^{2-}$ .

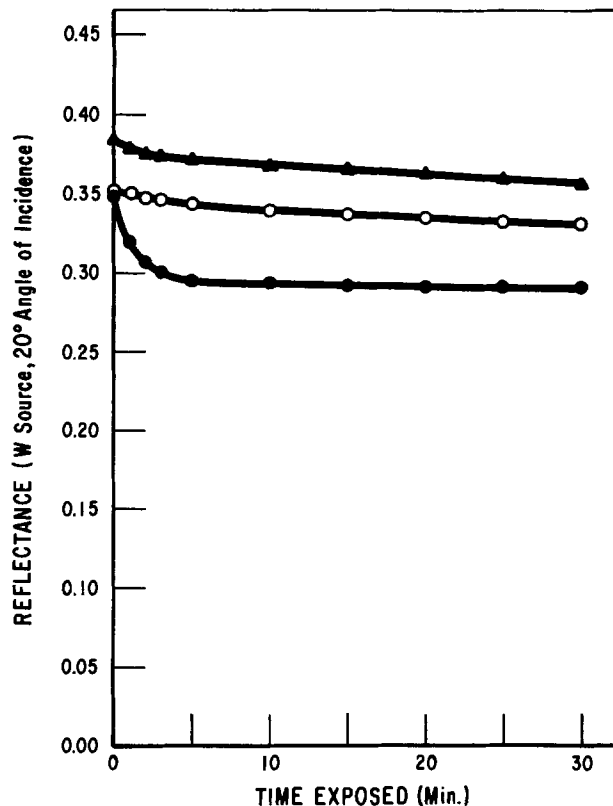


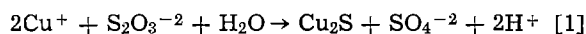
Fig. 4. Reflectance from the uncoated glass surface after deposition of electroless copper:  $\blacktriangle$  fresh film exposed to oxygenated water at room temperature;  $\circ$  fresh film exposed to the ambient air;  $\bullet$  film exposed to ambient air immediately after treatment in an aqueous solution of 3.0 g/liter  $Na_2S_2O_3 \cdot 5H_2O$  for 50 sec at room temperature.

of a reaction of copper or copper ions with  $S_2O_3^{2-}$ . In the case of electroless silver films deposited to approximately 150Å, no change in reflectance has been observed in air, with or without a pretreatment in aqueous solution containing  $S_2O_3^{2-}$ .

That the replacement reaction is favorable without the complexities of  $S_2O_3^{2-}$  is suggested by the samples in Fig. 5. Partial replacement, in these typical instances, was facilitated in the absence of  $S_2O_3^{2-}$  by known complexers for  $Cu^{+2}$ . There is no evidence for accelerated oxidation in air from the data in Fig. 5, further support for the special case with  $S_2O_3^{2-}$ .

An interesting parallel to the observed stability of copper in the replacement solutions of Fig. 5 is that stability can also be found with certain  $S_2O_3^{2-}$ - $NH_3$  solutions. This is shown by the curves in Fig. 6 for copper films exposed to two different  $S_2O_3^{2-}$ - $NH_3$  solutions. When the  $NH_4OH$  concentration was 1.25  $cm^3$ /liter, as compared to being 0.25  $cm^3$  (or absent), there was no evidence of a sharp decrease in reflectance.

**Possible reaction mechanism.**—One explanation for the curves in Fig. 6 follows from assuming that  $NH_3$  consumes copper ions as soluble complexes during the 50 sec of exposure to the  $S_2O_3^{2-}$  solution. This would work against precipitation involving dissolving copper ions and  $S_2O_3^{2-}$  by buffering copper ions. It would then be possible that with a low concentration of  $NH_4OH$  and a locally high concentration of dissolving  $Cu^+$



The standard free energy of formation for Eq. [1] is  $-41$  kcal (17). In the usual  $Ag^+$ - $NH_3$ - $S_2O_3^{2-}$  replacement solution, about three-fourths of the available  $NH_3$  could be consumed as  $Ag(NH_3)_2^+$ . Upon replacement  $Cu(NH_3)_2^+$  could form. Further oxidation to  $Cu(NH_3)_4^{+2}$  would consume  $NH_3$ . Notice that Eq. [1] does not appear to be in itself causing the sharp change in reflectance based on the results mentioned in con-

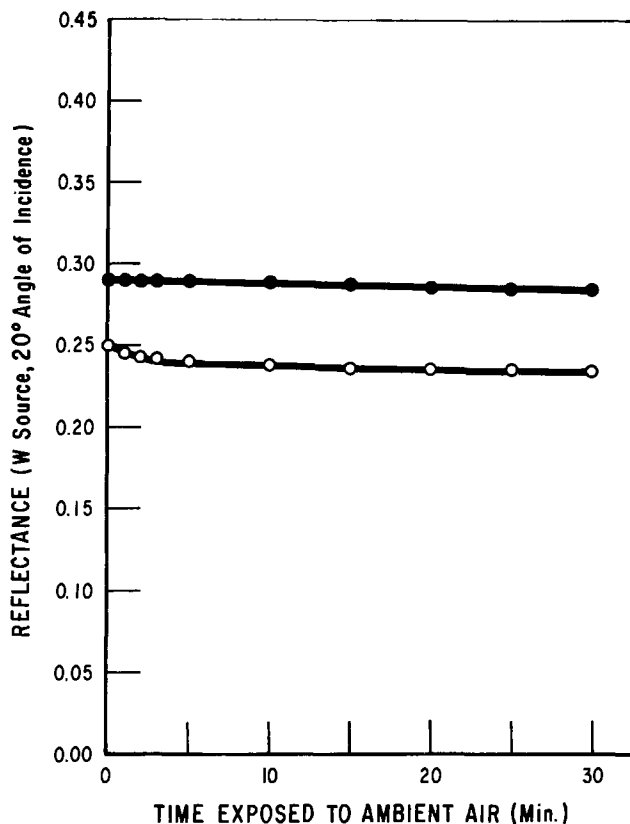


Fig. 5. Reflectance from the uncoated glass-air interface immediately after film deposition on one surface of glass by electroless and replacement reactions: ● 0.16 g/liter  $\text{Na}_2\text{C}_2\text{O}_4$  instead of  $\text{Na}_2\text{S}_2\text{O}_3 \cdot 5\text{H}_2\text{O}$ ; ○ 0.30 g/liter  $\text{Na}_2\text{C}_{10}\text{H}_{14}\text{O}_8\text{N}_2 \cdot 2\text{H}_2\text{O}$ . The luminous transmittance of the electroless precursor was 0.32-0.33.

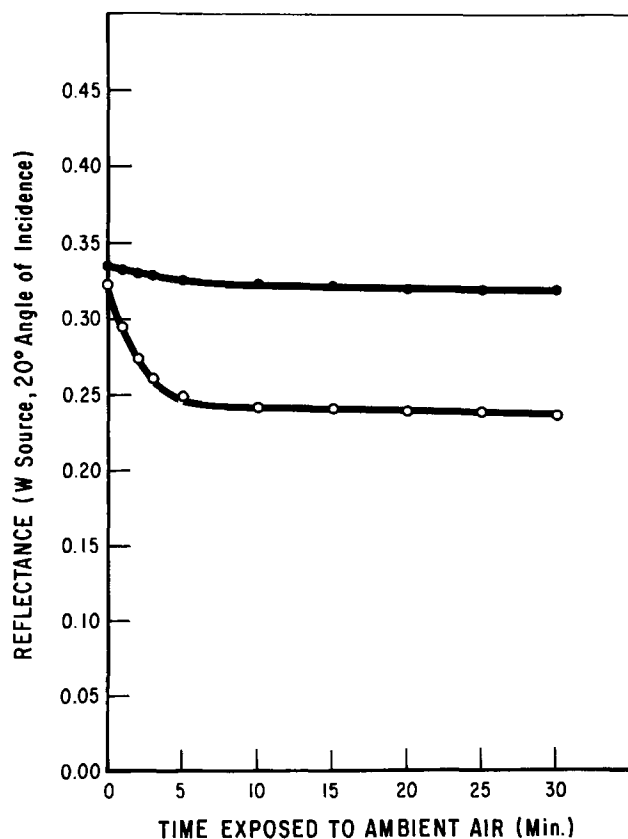
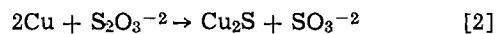


Fig. 6. Reflectance from the uncoated glass side with a deposit of electroless copper on one surface after the film was exposed at room temperature for 50 sec to an aqueous solution of 3.0 g/liter  $\text{Na}_2\text{S}_2\text{O}_3 \cdot 5\text{H}_2\text{O}$  with 1.25  $\text{cm}^3$ /liter  $\text{NH}_4\text{OH}$  (●) or 0.25  $\text{cm}^3$ /liter  $\text{NH}_4\text{OH}$  (○).

nection with Fig. 3. Air or moist  $\text{O}_2$  is necessary. Another thermodynamically favorable reaction is



but it is not obvious how this would depend on the concentration of  $\text{NH}_3$ .

With a precipitated sulfide present, accelerated oxidation in air is suggested by invoking the argument of an easy access for oxidation. The theory originally proposed by Cabrera and Mott (18), subsequently elaborated by many workers, characterizes slow logarithmic oxidation of pure copper by  $\text{O}_2$  as taking place by migration of cations driven in the field developed initially by the fast place exchange of adsorbed oxygen. Cation migration is facilitated in a more loosely bound structure or in grain boundaries (19, 20). The cuprous sulfide may, in some way, provide easy access for oxidation of residual copper metal in the film. It would be preventing the formation of a more protective, continuous oxide film which would normally slow oxidation.

### Summary

Using electroless copper films on glass as precursors, it has been possible to prepare new transparent films by partial chemical replacement with silver from aqueous solution at room temperature. Replacement solutions which were used contained  $\text{NH}_3$  and  $\text{S}_2\text{O}_3^{-2}$ ,  $\text{C}_2\text{O}_4^{-2}$ , or ethylenediamine tetraacetate, all complexing agents for silver and/or copper ions. An interesting secondary reaction, namely the apparently rapid oxidation of residual copper in air, occurred with some ammoniated  $\text{S}_2\text{O}_3^{-2}$  solutions. The film constituents which have been identified in this case are  $\text{Ag}$ ,  $\text{Cu}_2\text{O}$ , and a sulfur-containing species which may be  $\text{Cu}_2\text{S}$ . Consistent with the anticipated slow rate of oxidation of pure copper in oxygen and air at room temperature and with the data presented, a case can be made from prior literature for an easy access for oxidation by  $\text{O}_2$ . It may be that favorable structural defects and grain boundaries are formed by disruption of the growing  $\text{Cu}_2\text{O}$  lattice by sulfide in the presence of  $\text{O}_2$  and  $\text{H}_2\text{O}$ . The source of sulfur is  $\text{S}_2\text{O}_3^{-2}$  contained in the replacement solution. Among the various electroless and electroless-replacement films which have been prepared on glass at room temperature, the behavior in the presence of  $\text{S}_2\text{O}_3^{-2}$  seems to be unique.

### Acknowledgments

The writer is grateful to Mr. P. P. Harmon for his continual technical assistance, to Mr. C. J. McCafferty for data generated by x-ray fluorescence spectroscopy, to Ms. H. R. Golob for data generated by electron diffraction and energy dispersive x-rays, and to Ms. J. O. Bookmyer for information retrieval.

Manuscript submitted Aug. 11, 1975; revised manuscript received Oct. 25, 1975.

Any discussion of this paper will appear in a Discussion to be published in the December 1976 JOURNAL. All discussions for the December 1976 Discussion Section should be submitted by Aug. 1, 1976.

Publication costs of this article were partially assisted by PPG Industries, Incorporated.

### REFERENCES

1. H. E. Bennett and J. M. Bennett, in "Optical Properties and Electronic Structure of Metals," F. Abeles, Editor, p. 175, North-Holland Publishing Co., Amsterdam (1966).
2. L. F. Drummeter, Jr. and G. Hass, in "Physics of Thin Films," Vol. 2, G. Hass and R. E. Thun, Editors, p. 305, Academic Press, New York (1964).
3. R. V. Dunkle, *Trans. ASME*, **76**, 549 (1954).
4. P. Moon, *J. Franklin Inst.*, **230**, 583 (1940).
5. R. G. Miller, U.S. Pat. 3,457,138 (1969).
6. R. Sard, *This Journal*, **117**, 1156 (1970).
7. R. Glicksman, H. Mouquin, and C. V. King, *ibid.*, **100**, 580 (1953).

8. "Stability Constants, Part II: Inorganic Ligands," J. Bjerrum, G. Schwarzenbach, and L. G. Sillen, Editors, pp. 46 and 74, The Chemical Society, London (1958).
9. R. C. Brasted, "Comprehensive Inorganic Chemistry," Vol. 8, p. 162, D. Van Nostrand Company, Inc., Princeton, N. J. (1966).
10. Metal Finishing Guidebook Directory," 42nd ed., p. 531, Metals and Plastics Publications, Inc., Westwood, N. J. (1974).
11. J. Kruger, *Electrochem. Soc. Trans.*, **106**, 847 (1959); *ibid.*, **108**, 503 (1961); *ibid.*, **111**, 1038 (1964).
12. J. S. Ostrowski, U. S. Pat. 3,382,087 (1968).
13. S. Tolansky, "Multiple Beam Interferometry," pp. 8 and 147, Clarendon Press, Oxford (1948).
14. Inter-Society Color Council, National Bureau of Standards Color-Name Charts, Supplement to NBS Circular 553, Chips 63 and 64.
15. L. H. Germer, *Phys. Rev.*, **56**, 58 (1939).
16. W. E. Campbell and U. B. Thomas, *Electrochem. Soc. Trans.*, **76**, 303 (1939).
17. W. M. Latimer, "Oxidation Potentials," 2nd ed., pp. 72 and 184, Prentice-Hall, Inc., New York (1952).
18. N. Cabrera and N. F. Mott, *Rept. Progr. Phys.*, **12**, 163 (1948-49).
19. F. P. Fehlner and N. F. Mott, *Oxide Met.*, **2**, 59 (1970).
20. K. R. Lawless, *Rept. Progr. Phys.*, **37**, 231 (1974).

## Phase Structure and Composition of Fe-W Alloy Electrodeposits

T. Omi, H. L. Glass,<sup>1</sup> and H. Yamamoto\*

College of Engineering, University of Osaka Prefecture, Sakai, Japan 591

### ABSTRACT

Parallel studies have been made of the phase structure, composition, and current-potential characteristics of iron-tungsten alloy electrodeposition from alkaline aqueous ammoniacal tartrate electrolytes. The presence of sodium, introduced with tungstate in the form of  $\text{Na}_2\text{WO}_4$ , was found to have profound effects on the deposition process. The deposits formed at low current densities consisted of a solid solution bcc phase containing a maximum of 13 atomic per cent (a/o) W. As the limiting current density for iron deposition was reached, an amorphous alloy phase, having a constant composition of 22.2 a/o W, began to form. This amorphous phase was identified as  $\text{Fe}_3\text{W}$  saturated with excess iron atoms and having a structure based on tetrahedral units. The initiation of amorphous phase deposition was correlated with the occurrence of multiple nucleation associated with increasing accumulation of sodium atoms at the electrode. When the cathode potential was made still more negative, further increase in sodium accumulation appeared to have been responsible for an observed decrease in the rate of deposition of the amorphous  $\text{Fe}_3\text{W}$ . However, an amorphous  $\text{Fe}_2\text{W}$  phase may have formed at extreme values of cathode potential. Such a phase was prepared by elevation of the electrolyte pH. From analysis of these results, a prescription is developed to account for the formation of homogeneous stoichiometric electrodeposits. This prescription, which may be applicable to many amorphous and crystalline alloy deposition systems, consists of three conditions which describe material balance and atomic interactions at the electrode surface.

For at least fifty years (1) it has been known that alloy electrodeposits may exhibit nonequilibrium structures. Two common examples of deviations from equilibrium are the formation of supersaturated solid solutions and phases which normally are produced only at elevated temperatures. It is also possible for alloy electrodeposits to exist in metastable phases which do not appear at all on the usual equilibrium phase diagrams. Although formation of nonequilibrium structures must be related to the kinetics of the electrodeposition process (2, 3), this relationship is not well understood.

The work described in this article deals with the electrodeposition of iron-tungsten alloys which can form a metastable amorphous phase having a fixed composition containing 22.2 a/o W. Parallel studies of structure, composition, and current-potential characteristics provide insight into certain electrodeposition mechanisms which appear to be responsible for initiating the amorphous phase. In addition, an earlier analysis of the origin of stoichiometry in amorphous Co-W electrodeposits (4) is generalized into a prescription which may be applicable to deposition in many alloy systems, both amorphous and crystalline.

### Experimental Procedure

Electrolytes were made up of special grade chemicals (Wako Pure Chemicals Industries, Limited) and deionized water. They were prepared in a nitrogen gas atmosphere in order to prevent oxidation of the ferrous complex (5). Unless otherwise stated, the pH of the electrolytes was kept constant at 8.50 by addition of ammonium hydroxide. Nitrogen was swept through the solution for at least 20 min prior to electrolysis.

Electrolysis was carried out at  $80^\circ \pm 0.2^\circ\text{C}$  without agitation. A 400  $\text{cm}^3$  Pyrex glass cell was used. The platinum anodes were separated from the cathode by glass disks in order to avoid contamination by anode products. Vertically held rectangular cold-rolled mild steel substrates with an area of 5.74  $\text{cm}^2$  were used as cathodes. These cathodes were prepared by mechanical polishing on 5/0 emery paper, electrolytic degreasing in warm aqueous alkaline solution, etching in sulfuric acid (diluted 1:20) for 30 sec, and then rinsing in flowing deionized water. A 0.3 mm (outside diameter) Luggin capillary with a tip cut at an obtuse angle and in light contact with the center of the cathode plane was used as the probe of the reference electrode, a saturated calomel electrode held at  $25^\circ \pm 1^\circ\text{C}$ . The potential drop due to the ohmic resistance between cathode and reference electrode was determined with the aid of a synchroscope by measuring the decay of

\* Electrochemical Society Active Member.

<sup>1</sup> Visiting Researcher, Supported by National Science Foundation Visiting Scientist Grant; Present address: Rockwell International, Electronics Research Division, Anaheim, California 92803.

Key words: amorphous alloy, stoichiometry, limiting current, sodium, cathode potential.

the electrode potential after cutting off the current (6).

**Alloy deposition.**—The solutions used for alloy deposition were made from  $\text{FeSO}_4$ ,  $\text{Na}_2\text{WO}_4$ , and ammonium tartrate. The total  $\text{Fe} + \text{W}$  concentration was kept equal to the tartrate concentration at a constant value of 0.26 mole/liter.

Over most of the range of alloy deposition, the current density varies rapidly with cathode potential. Therefore, measurements were made under galvanostatic conditions with the cathode potential measured on a Shimadzu 3P potentiometer after a quasi-static state had been attained. The time required to reach a quasi-static state ranged from about 1 min for high current densities to several minutes for low current densities. Over a range of very low current density, the potential varies quite slowly. In this range, potentiostatic conditions were employed with the quasi-static current measured on a Hokuto-Denko PS-500B potentiostat. The time dependence of cathode potentials or of cathode currents was recorded on a TOA Electronics stripchart recorder EPR-22A. This recorder has a high internal resistance (2 megohm) and fast response (above 500 mm/sec).

Wet gravimetric chemical analyses were carried out to determine the compositions of the deposits. Using deposits prepared under coulometric and galvanostatic conditions (0.0198 A·hr/cm<sup>2</sup> and taking ionic valences of 2 for iron and 6 for tungsten, the partial currents due to deposition of metals and hydrogen were calculated from the measured compositions.

The structures of electrodeposits were studied by x-ray diffraction or by electron microscopy. Coulometrically (0.0198 A·hr/cm<sup>2</sup>) formed alloys of about 10  $\mu\text{m}$  thickness were examined. A Shimadzu VD-1A scintillation counter diffractometer equipped with a step scanning mechanism, 1.2 kW cobalt target, and iron filter was used for x-ray diffraction. In order to irradiate the whole or a part of alloy deposits, suitable divergence slits were used. A JEM-200 electron microscope equipped with a JEM-AD3 high resolution electron diffraction attachment and operated at an accelerating voltage of 200 kV was used for electron microscopy. The electropolishing of alloy deposits for transmission electron microscopy was made after dissolving out the substrate in sulfuric acid (diluted 1:1). The deposits were then electropolished from both sides at a cell voltage of 7-13V using a large stainless steel cathode and ice-cold electrolyte of the composition 840 cm<sup>3</sup>  $\text{CH}_3\text{OH}$ , 150 cm<sup>3</sup>  $\text{H}_2\text{SO}_4$ , and 13 cm<sup>3</sup> HF.

**Iron deposition.**—Iron depositions were made from two different electrolytes. Both electrolytes were similar to those used for alloy deposition; however, in one case both sodium and tungstate were omitted and in the other case tungstate was omitted but sodium, in the form of sodium tartrate, was retained. The same apparatus and reagents of the same quality as employed for alloy deposition were used.

Deposition was carried out potentiostatically while the current was continuously recorded. The mean over-all current density as well as the current efficiency for deposition of iron was determined at each value of cathode potential from the recorded current and the weight gain of the samples. In a few cases the current exhibited a rapid increase with time. In these cases deposition was carried out for 10 min; otherwise longer deposition times were employed.

The surfaces of the deposits were analyzed by reflection electron diffraction using an accelerating voltage of 100 kV.

### Results

**Alloy deposition.**—Figure 1 shows the current-potential curves during alloy electrodeposition. For presentation, the potential axis is displaced for each solution. In the determination of partial current-

potential curves, at least two measurements were made of alloy composition and cathode current efficiency for each value of cathode current density. These determinations resulted in smooth dependences of partial currents on the over-all current density. These smooth dependences were used to draw the partial currents shown in Fig. 1. In this way the maximum for deposition of iron in curve 6 (41 mA/cm<sup>2</sup>) was found and verified.

Under the galvanostatic conditions employed for alloy deposition, certain regions of the polarization curves exhibited a kind of bistable behavior. In these regions, shown by the horizontal lines in Fig. 1, the cathode potential spontaneously fluctuated between two values. Though irregular, the fluctuations had periods of about 10 sec. In regions of these fluctuations the thick curves in Fig. 1 are the time averages of the fluctuations which are described by the enveloping thin curves.

In general, the galvanostatic measurements of alloy deposition were reproducible to  $\pm 4$  mV. However, for solutions 3 and 4, the reproducibility at current densities above the bistable region was about  $\pm 10$  mV. This poorer reproducibility may be due to unresolved bistable behavior at these higher currents.

The scale of Fig. 1 has been chosen to display the general forms of the current-potential curves. At this scale, however, many detailed features of the original current-potential data are lost. In particular, the original data exhibited numerous characteristic breaks, defined as points where there is an abrupt change in slope. Only a few of these breaks are discernible in Fig. 1; however, the breaks are more fully described below and in Table I. Examination of the breaks leads to a division of the six sets of curves in Fig. 1 into two groups. The first group consists of curves 1 and 2, corresponding to tungsten mole fractions of 0.09 or less. The second group, consisting of the remaining curves 3-6, corresponds to tungsten mole fractions of 0.23 or greater.

For the first group, the values of cathode potential at which breaks occur appear to be independent of electrolyte composition. Thus, the breaks  $\alpha$ ,  $\beta$ , and  $\gamma$  which appear in curve set 1 at 930, 1010, and 1020 mV are also found in curve set 2 at the same values of cathode potential.

For the second group, the values of cathode potential at which breaks occur vary with electrolyte composition; however, the relative change in partial currents are very similar for all of these solutions. This similarity is brought out in Fig. 2 and Table I. Figure 2 is a set of schematic current-potential curves showing various breaks. Table I lists the values of cathode potential at which the breaks occurred for solutions 3-6. Also given in Table I are the relative changes in slope of the hydrogen, iron, and tungsten partial current curves; a + sign corresponding to an increase in slope and a - sign to a decrease. In general, the

Table I. Cathode potentials of breaks in current-potential curves for different electrolytes and changes in partial currents  $\Delta i_j$

C*	P**				$\Delta i_j$		
	0.23	0.41	0.71	0.85			
A	920	920	920	—			
B	960	967	970	980			
N	980	996	1000	1007			
C	100C	1009	1014	1027	+H	+Fe	+W
D	1007	1013	1018	1027		-Fe	
E	1018	1013	1020	1022	-H		-W
F	1023	1023	1028	1035	+H	+Fe	+W
G	1035	1035	1039	1040	+H	+Fe	-W
H	1039	1042	1048	1042	+H	-Fe	-W
I	—	—	—	1050	-H	-Fe	+W
J	—	—	—	1059	+H	+Fe	+W
K	—	—	—	1062	-H	-Fe	-W

\* C: Electrolyte mole fraction of tungsten,  $c_w/(c_w + c_{Fe})$ .

\*\* P: Cathode potentials,  $-E_{\text{CSB}}$  (mV),  $\Delta i_j$ : rise (+j), suppression (-j).



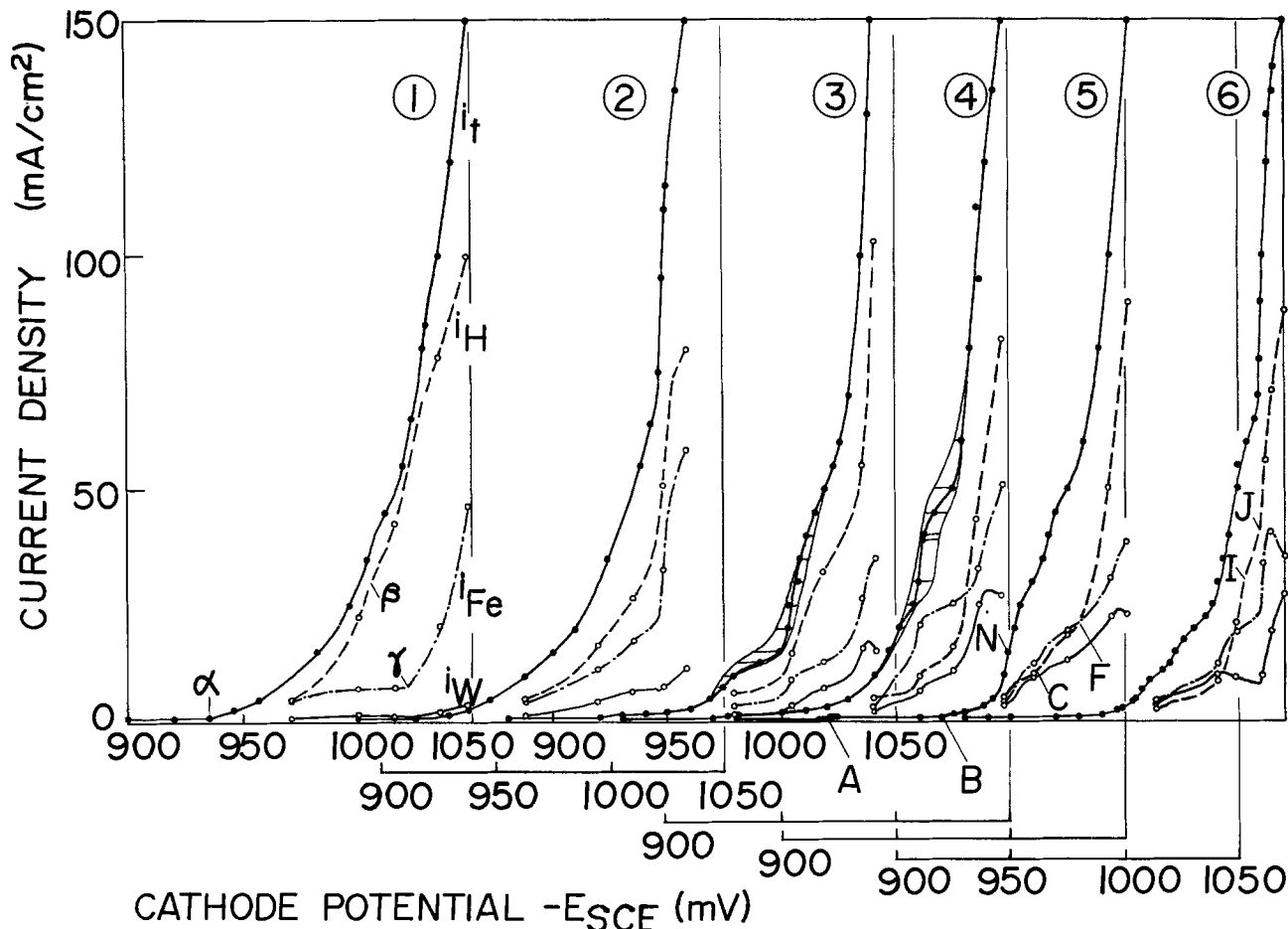


Fig. 1. Current-potential curves for alloy electrodeposition from ammoniacal alkaline tartrate electrolytes. The curves 1-6 correspond, respectively, to tungsten mole fractions  $c_W/(c_W + c_{Fe}) = 0.03, 0.09, 0.23, 0.41, 0.71,$  and  $0.85$ .  $(NH_4)_2C_4O_6H_4$  0.26 mole/liter, pH 8.50,  $80^\circ C$ .

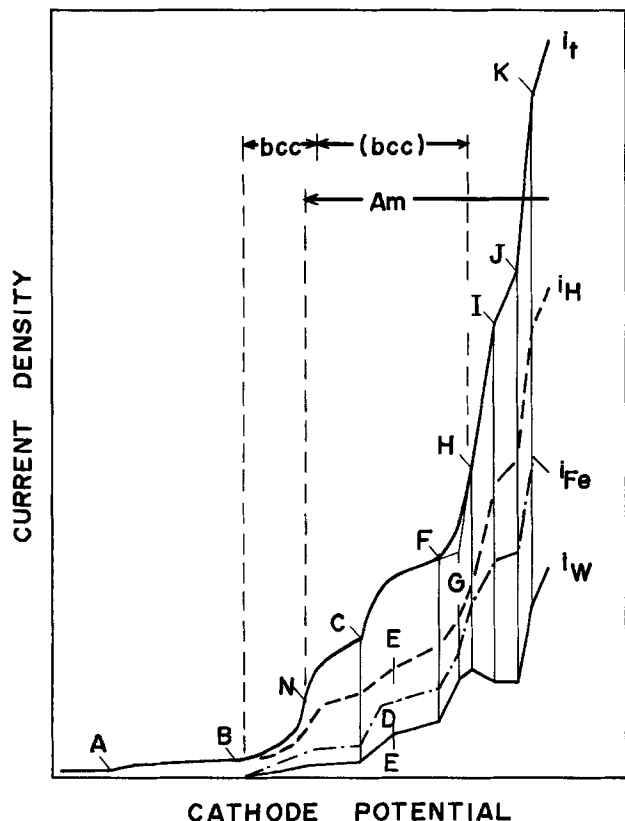


Fig. 2. Schematic current-potential curves for electrolytes of  $c_W/(c_W + c_{Fe}) = 0.23-0.85$ .

relative changes in slope are the same for hydrogen and iron; the break H being an exception.

*Alloy composition and structure.*—The structures of the alloy deposits were studied in detail for the solutions in which the tungsten mole fraction was 0.23 or greater; curves 3-6 in Fig. 1. For these solutions, alloy deposition initiated at a cathode potential slightly more negative than the break B in Fig. 2 and in Table I. At potentials less negative than this, no deposition of metal or alloy was observed. This is in agreement with Kudo's work which involved radioactive tracer in a similar solution (7).

At potentials more negative than B, two different structures were found. One structure was crystalline and may be described as a solid solution of tungsten in bcc iron. The second structure was an amorphous W-Fe alloy. As will be explained in the Discussion, this amorphous alloy appears to be isomorphous with amorphous  $Co_3W$  (4) which possesses neither crystal symmetry nor translational invariance. The occurrence of these two structures was found to be a function of cathode potential. This is indicated in Fig. 2 where the amorphous phase, denoted by Am, is shown to form when the cathode potential is more negative than N while the crystalline phase, denoted by bcc, is shown to form when the cathode potential is more negative than B. There is a range of overlap where both phases can deposit. This range of overlap depends on the tungsten mole fraction of the electrolyte. For solutions 5 and 6, having tungsten mole fractions of 0.71 and 0.85, the range of overlap is small, with the bcc region extending only slightly beyond N. For solutions 3 and 4, having tungsten mole fractions of 0.23 and 0.41, the range of overlap is quite large, extending all the way to the break H as indicated by the bcc in parentheses.

The extended range of overlap for solutions 3 and 4 corresponds to the region in which the cathode potential was observed to fluctuate as was shown in Fig. 1. For each value of current density in this region, the bistable fluctuations between two values of cathode potential were found to correlate with the structure of the deposit which formed near the Luggin capillary. When deposition was terminated at the less negative value of cathode potential, the x-ray diffractogram showed this portion of the deposit to be crystalline. For termination at the more negative value, this portion was amorphous. The two phases could also be distinguished by their visual appearance.

In those regions of Fig. 1 where the thick time-average curves for solutions 3 and 4 lie close to the more negative (right hand) enveloping curves, the deposit consisted mainly of amorphous phase. The crystalline phase occurred as embedded thin platelets lying parallel to the surface near the center of the sample where the Luggin capillary was located. These platelets were up to 8  $\mu\text{m}$  in diameter but only about 0.1  $\mu\text{m}$  in thickness. The converse structure, with amorphous phase platelets embedded in a crystalline phase matrix, was observed where the time-average curve lies close to the less negative enveloping curve. Thus, Fig. 1 indicates that within the extended range of overlap, N-H of Fig. 2, the formation of bcc phase occurs primarily in the range from C to D or E.

Since the platelets formed in the two-phase region had relatively large lateral dimensions, it was possible to use x-ray diffraction to measure the spatial variation of lattice parameter in the crystalline regions. It was found that this lattice parameter attains its maximum value, 2.940  $\text{\AA}$ , at the physical boundary where the crystalline and amorphous materials meet. This value of lattice parameter is found to correspond to a composition of 13 a/o W in bcc iron if one extrapolates the lattice parameter-composition relation obtained from deposits prepared in the single phase bcc region B-N of Fig. 2 where the tungsten content ranged from 3 to 9 a/o.

It is interesting to note that the maximum tungsten content of the electrodeposited bcc phase is the same as the maximum solubility of tungsten in bcc iron which is shown in the equilibrium phase diagram (8); however, this level of tungsten concentration is in equilibrium only at elevated temperatures. A similar relation was found for the maximum tungsten content in the crystalline phase of W-Co alloy electrodeposits (9).

Selected area diffraction in transmission electron microscopy yielded essentially identical patterns for the amorphous regions of two-phase samples and for the single phase amorphous samples. In the previously reported W-Co system (4, 9), the amorphous regions of two-phase deposits were found to contain small particles of the crystalline phase. These particles decreased in size and number as the cathode potential became more negative and as the over-all tungsten content of the deposits increased. In contrast to this behavior, selected area diffraction did not show any evidence of bcc particles in the amorphous regions of the two-phase W-Fe deposits.

Both the electron and x-ray diffraction patterns obtained from the amorphous W-Fe phase were nearly the same as the patterns from amorphous  $\text{Co}_3\text{W}$  (4). Actually, the so-called amorphous  $\text{Co}_3\text{W}$  was found to contain 22.2 a/o W (4) and should probably be viewed as a saturated solution of Co in  $\text{Co}_3\text{W}$ . Similarly, the chemical analyses of the single phase amorphous W-Fe electrodeposits revealed a tungsten content of 22.2 a/o.

As depicted in Fig. 2, the partial currents for iron and tungsten deposition are roughly parallel to each other in the ranges from N to C and from D or E to G; ranges where the deposits consisted mainly of the 22.2 a/o W amorphous phase. At G, however, the par-

tial current curves begin to diverge, with the curve for tungsten dropping off. Beyond J, as seen for solution 6 in Fig. 1, the tungsten partial current rebounds and the ratio of the increase of tungsten current to that of iron is about 1:5. This suggests that it may be possible to form an alloy of approximate composition  $\text{Fe}_2\text{W}$  if the tungsten mole fraction is sufficiently high and if the cathode potential is sufficiently negative. To explore this possibility, electrolytes of higher pH were prepared, since the maximum tungsten content found with the pH 8.50 solutions was 22.2 a/o. Figure 3 presents the results of chemical analyses of samples deposited galvanostatically from solutions having pH 9.00 and various tungsten mole fractions. Similar results were obtained for electrolytes of pH 9.40. Although these results are not sufficient to prove that an amorphous  $\text{Fe}_2\text{W}$  phase can be deposited, they do give some support to such an interpretation. A crystalline  $\text{Fe}_2\text{W}$  phase is shown in the equilibrium phase diagram (8).

*Iron deposit.*—Figures 4 and 5 present the current-potential curves for electrolytes analogous to solution 5 of Fig. 1 which had a tungsten mole fraction of 0.71. For Fig. 4 the tungstate was omitted but sodium was retained. For Fig. 5 both sodium and tungstate

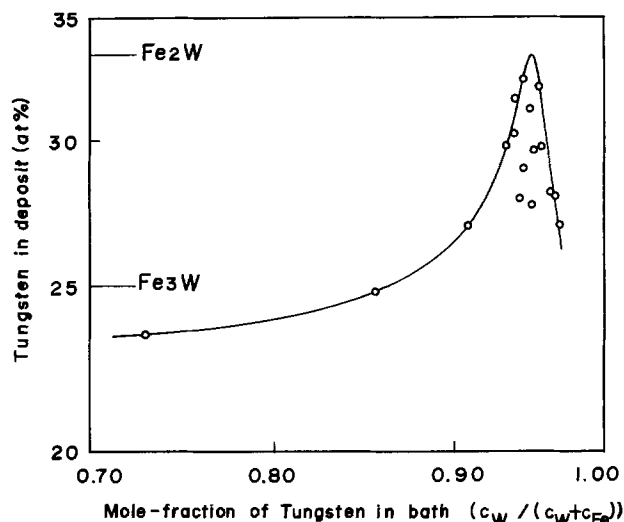


Fig. 3. Composition of deposits vs. tungsten mole fraction. 50  $\text{mA}/\text{cm}^2$ ; pH = 9.00, elevated by addition of  $\text{NH}_4\text{OH}$ .

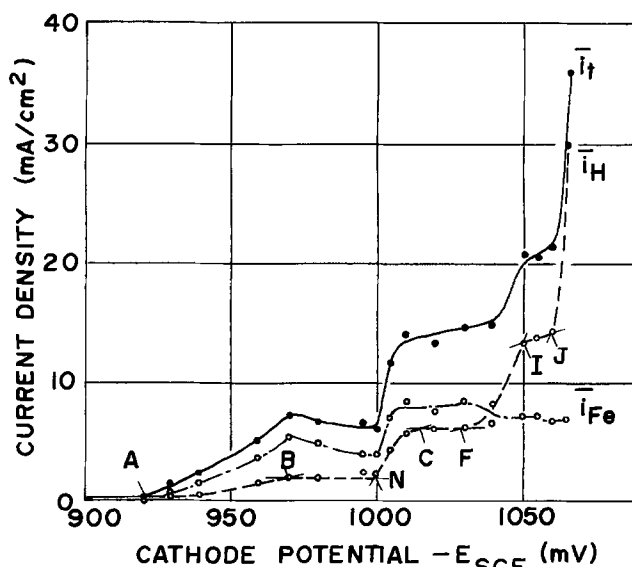


Fig. 4. Mean current-potential curves for deposition of iron in presence of sodium.  $(\text{NH}_4)_2\text{C}_4\text{O}_6\text{H}_4$ , 0.075 mole/liter;  $\text{Na}_2\text{C}_4\text{O}_6\text{H}_4$ , 0.185 mole/liter;  $\text{FeSO}_4$ , 0.075 mole/liter; pH = 8.50, 80°C.

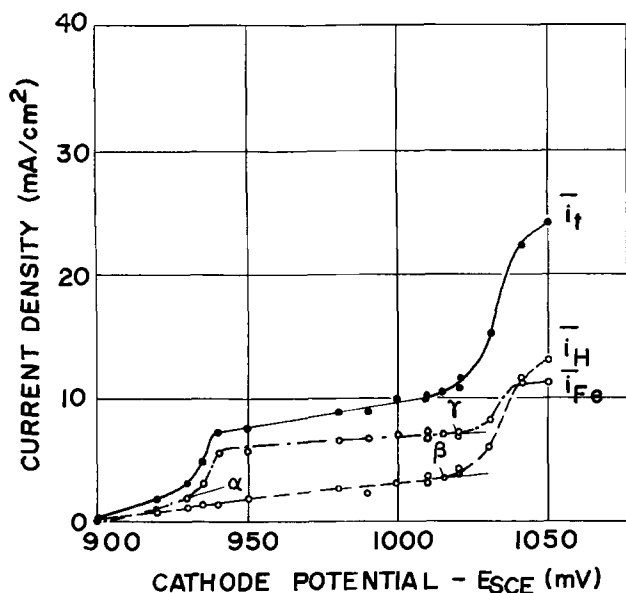


Fig. 5. Mean current-potential curves for deposition of iron in absence of sodium.  $(\text{NH}_4)_2\text{C}_4\text{O}_6\text{H}_4$ , 0.26 mole/liter;  $\text{FeSO}_4$ , 0.075 mole/liter; pH = 8.50, 80°C.

were omitted. The values of current which were measured for these potentiostatic depositions were reproducible to  $\pm 5\%$  for solutions containing sodium and to  $\pm 10\%$  for solutions without sodium.

Figure 4, for which sodium was present, exhibits a series of breaks similar to those of the analogous alloy curve of Fig. 1. The values of cathode potential at which the breaks occur are very nearly the same for both the alloy and iron depositions. On the other hand, Fig. 5, for which sodium was absent, does not exhibit breaks like those of the analogous alloy curve. Instead, Fig. 5 is similar to curve 1 of Fig. 1 for which the tungsten mole fraction and, therefore, the sodium concentration were minimum.

The current-potential curves in Fig. 6 correspond to an electrolyte analogous to solution 3 of Fig. 1, which had a tungsten mole fraction of 0.23, but with the tungstate omitted. Although less striking than Fig. 4, there is again a series of breaks which occur at the same values of cathode potential as those of the analogous alloy curve; at least up to the break N.

Figure 7 shows examples, for three different ranges of cathode potential, of the time dependence of the

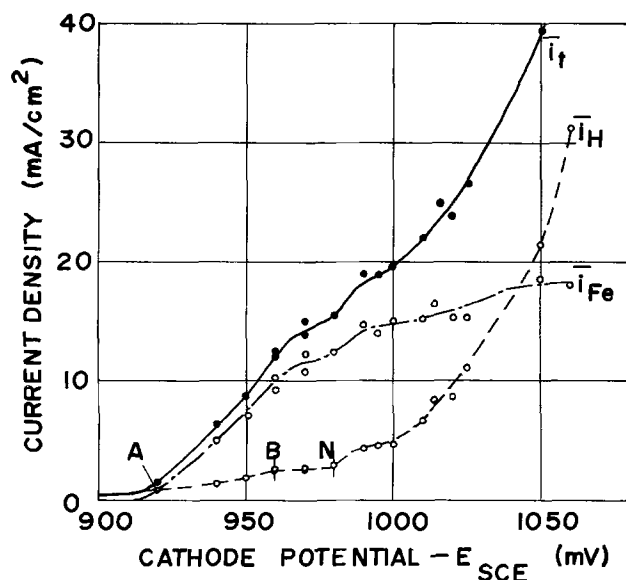


Fig. 6. Mean current-potential curves for deposition of iron in presence of sodium.  $(\text{NH}_4)_2\text{C}_4\text{O}_6\text{H}_4$ , 0.200 mole/liter;  $\text{Na}_2\text{C}_4\text{O}_6\text{H}_4$ , 0.060 mole/liter;  $\text{FeSO}_4$ , 0.200 mole/liter; pH = 8.50, 80°C.

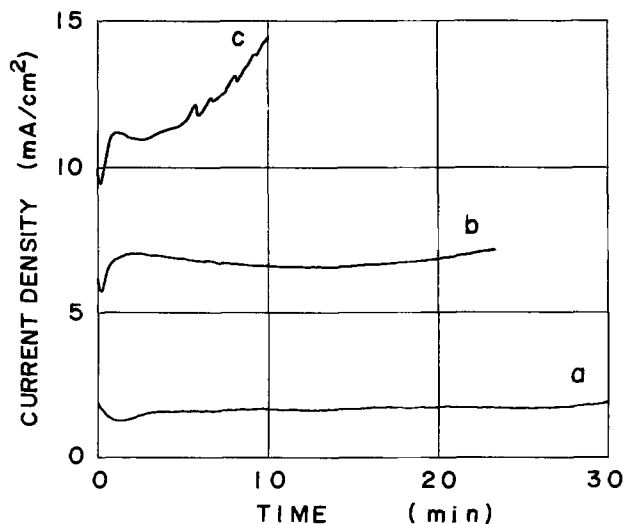


Fig. 7. Representative current-time behaviors observed during measurement of Fig. 4. a: behavior for the region  $-(920-940)$  mV<sub>SCE</sub>, measured at  $-930$  mV<sub>SCE</sub>; b: region  $-(960-995)$  mV<sub>SCE</sub>, measured at  $-995$  mV<sub>SCE</sub>; c: region  $-(1005-1055)$  mV<sub>SCE</sub>, measured at  $1005$  mV<sub>SCE</sub>.

deposition current observed during measurement of Fig. 4. Curve c, for the range of cathode potential beyond N, exhibits the fairly rapid increase of current with time which was found to be characteristic of iron deposition in this range of cathode potential. Because quasi-static conditions could not be attained, the current-potential curves for this range were obtained by keeping the deposition time constant at 10 min and using the time-averaged over-all current density.

Although the deposition current increased with time in the range beyond N, the current efficiency for iron decreased with time. This effect was especially pronounced for cathode potentials beyond 1040 mV. Another effect which was observed for the range beyond N was that the deposits were black in appearance rather than metallic gray as was seen at less negative potentials. All of these features, the increasing current, the decreasing current efficiency, and the blackening of the deposits, were observed for the electrolyte of Fig. 6 as well as that of Fig. 4. However, these effects were not observed for the solution of Fig. 5, which did not contain sodium.

The reflection electron diffraction patterns of the iron deposits failed to show evidence of any substances which could be responsible for the observed blackening. In spite of the difference in appearance, both the gray and black deposits gave diffraction patterns which were characteristic of bcc iron with a (321) preferred orientation.

### Discussion

Since cobalt and iron have nearly equal atomic scattering factors (for both x-ray and electron diffraction) and since the amorphous Fe-W alloys prepared in the range N-G in Fig. 2 and the amorphous  $\text{Co}_3\text{W}$  electrodeposits were both found to contain 22.2 a/o W, the close similarity of the diffraction patterns for the two amorphous alloy systems can be accounted for by the same atomic configuration. Therefore, adapting the configuration derived for amorphous  $\text{Co}_3\text{W}$  (4), the amorphous Fe-W electrodeposit may be described as a saturated solution of iron atoms in amorphous  $\text{Fe}_3\text{W}$  having as its basic structural unit a tetrahedron consisting of three iron atoms and one tungsten atom.

In the case of  $\text{Co}_3\text{W}$ , an equilibrium phase having an ordered crystalline structure is known. No corresponding  $\text{Fe}_3\text{W}$  phase appears in the equilibrium phase diagram for the Fe-W system (8). Nevertheless,

the generally close chemical similarity between cobalt and iron and the fact that the amorphous  $\text{Fe}_3\text{W}$  phase has a constant composition of 22.2 a/o W over a wide range of deposition conditions point to the existence of such a phase. Moreover, there is experimental evidence of a crystalline  $\text{Fe}_3\text{W}$  phase, isomorphous with crystalline  $\text{Co}_3\text{W}$ , localized at the surface of Fe-22.2 a/o W electrodeposits (10).

Because the amorphous deposits are nonequilibrium phases, their occurrence must be determined by the electrodeposition process. Several characteristics of this process are evident in the results of these experiments. First of all, it should be noted that the irregular fluctuations of cathode potential (Fig. 1) which were associated with transitions between crystalline and amorphous depositions are indicative of a diffusion-limited current density (6). From material balance considerations (11) and from the fact that the amorphous phase deposits at the negative end of the fluctuations, it follows that amorphous  $\text{Fe}_3\text{W}$  forms when the deposition of iron is diffusion controlled.

Additional information about the nature of the deposition process comes from a comparison of the iron deposition curves with the alloy curves. It is especially instructive to compare Fig. 4 for iron deposition in the presence of sodium and Fig. 5 for iron deposition in the absence of sodium with the results for the analogous alloy depositions from solution 5 in Fig. 1. Obviously, the essential form of the current-potential curves and the occurrence of most breaks are associated with the presence of sodium in the electrolyte. Further, on comparing Fig. 6, also for iron deposition in the presence of sodium, with its analog, solution 3 in Fig. 1, it is clearly seen that the values of cathode potential at which the breaks occur are controlled by the sodium and iron concentrations and are insensitive to the presence of tungstate.

While the form of the current-potential curve and the occurrence of breaks are associated with the presence of sodium, Fig. 2 and Table I show that there is a close correlation between the changes in hydrogen and iron partial currents at the breaks. The apparent connection between the presence of sodium and the deposition of hydrogen is expected to arise from the nature of the hydrogen electrode reaction which involves the deposition and accumulation of sodium atoms and their reaction with water molecules. The positive correlation between hydrogen and iron partial currents may be ascribed to convective effects associated with hydrogen evolution.

Both the hydrogen electrode reaction and the effects of hydrogen on iron deposition require elaboration. In this connection, the work of Matsuda and Notoya (12) on aqueous sodium hydroxide appears to be relevant. Their Fig. 8 in which the rate of sodium accumulation at a platinum electrode is plotted as a function of electrode potential, exhibits some interesting effects which seem to correspond to certain features of the Fe-W alloy deposition.

Matsuda and Notoya found that the accumulation of sodium atoms was initiated at a potential  $-E_{\text{SCE}} \approx 780$  mV. Similarly, preferential adsorption of tungsten (in some oxidation state) is known to occur on non-polarized electrodes only for electrolytes for which the open-circuit potential is more negative than  $-E_{\text{SCE}} \approx 780$  mV (10). This apparent connection between sodium accumulation and tungsten adsorption may be ascribed to the dissociation of the tungstate-tartrate complex brought about by the presence of sodium atoms at the electrode surface. The product tungstate then condenses.

Another feature noted by Matsuda and Notoya was a sharp maximum in the rate of sodium accumulation which occurred at  $-E_{\text{SCE}} \approx 1040$  mV irrespective of sodium concentration or electrolyte pH. In Fe-W alloy deposition, the break H (Table I) occurred at a potential very near this value. At this break, the

hydrogen partial current increased but the iron partial current exhibited a decrease in slope. This was the major exception to the observation that the relative changes in slope were the same for hydrogen and iron. The behavior at break H may be attributed, therefore, to a rapid increase in the number of sodium atoms at the electrode which results in an increase in hydrogen. The increased sodium at the electrode may obstruct iron deposition. The same mechanism would account for the pronounced decrease, with time, of the current efficiency of iron deposition which was observed beyond 1040 mV for those electrolytes which contained sodium but not tungstate. It should be remarked that an exact comparison with Matsuda and Notoya's results is hindered by the effects of concentration polarization and shielding by the Luggin capillary.

The effects of sodium appear to play a crucial role in establishing the amorphous alloy structure. Strong evidence for this was seen in the deposition of iron from those electrolytes which contained sodium, Fig. 4 and 6. In the range of cathode potentials beyond N the deposition current continually increased (Fig. 7) and the deposits became black in color; yet reflection electron diffraction showed no significant differences to account for the color change. These observations are consistent with the development of a more complex microprofile of the surface and an increase in defect density when the cathode potential exceeds N. These characteristics suggest the occurrence of multiple nucleation. However, the continued existence of crystallinity, as evidenced by the bcc electron diffraction patterns, implies a reasonably large particle size, probably no less than a few hundred atoms (13-15). It is not possible to determine whether this particle size arises directly through a nucleation and growth deposition process or by a rearrangement of atoms after deposition. In any case, the blackening occurs in the presence of sodium when the cathode potential exceeds N. These are the same conditions under which the amorphous phase deposits. Moreover, a similar relation between initiation of amorphous alloy deposition and blackening of metal deposits was found in the study of the Co-W system (9, 16).

The amorphous alloy structure must arise either because the deposition process produces mutually incoherent particles which are too small for the crystalline configuration to be energetically favored (13-15) or because the atoms do not bond together in the arrangement required for crystalline long-range order (4, 17). The occurrence of multiple nucleation along with the obstructive effects of sodium atoms and hydrogen atoms appears to be responsible for the initiation of the amorphous structure in the electrodeposits. This structure will be retained in the deposits if the atoms are unable to rearrange themselves into crystalline configurations. This will largely be determined by thermal vibration. In fact, amorphous alloys generally consist of a metal and a metalloid for example Ni-P (18) or Fe-P-C (19), so that strong bonding reduces thermal vibration; or the alloys contain an element having a high intrinsic Debye temperature, as in the tungsten alloys described here.

An important feature of the amorphous alloys, both  $\text{Co}_3\text{W}$  and  $\text{Fe}_3\text{W}$ , is that the chemical composition is constant and essentially stoichiometric over a wide range of deposition conditions. While stoichiometry in an ordered crystal structure is not surprising, the origin of stoichiometry in an amorphous structure may require elaboration. Certainly, the existence of an ordered crystal structure implies a preference for a local atomic configuration (short-range order) which can also exist in an amorphous structure of the same composition. However, by generalizing the criteria which were used to derive the structural model for amorphous  $\text{Co}_3\text{W}$  (4), a prescription may be written by which the deposition process can lead to the formation of a

stoichiometric alloy whether the structure is amorphous or crystalline.

An alloy of composition  $A_nB$  will be deposited if the following three conditions are met: (i) an  $n$ -atom cluster of A atoms forms a unique site on which a B atom can deposit; (ii)  $m$ -atom clusters of A atoms ( $m \geq n$ ) can form; (iii) the concentration of B atoms at the surface is much greater than the concentration of A atoms. Conditions i and iii are equivalent to statements that the deposition of B is catalyzed by  $n$ -atom clusters of A and that B atoms are available for deposition. Condition ii, which will be discussed in detail below, essentially means that the necessary  $n$ -atom clusters of A actually are formed. At this point it is clear why the conditions are independent of the degree of crystallinity of the structure; the stoichiometry involves interactions among only small numbers of atoms while crystallinity involves interactions among large numbers of atoms extending over large distances.

To discuss condition ii it is convenient to review Walton's theory (20) for nucleation in monatomic vapor deposition. Walton derived the equilibrium distribution of cluster sizes. This distribution depends upon a complicated balance among several factors including rate of incidence, substrate temperature, and the activation energy for surface diffusion. He found that under given deposition conditions one size of cluster dominates. This is the size  $m$  in condition ii. Walton also found that  $m$  is generally small and that the predominance of a particular value of  $m$  (at least when  $m$  is indeed small) extends over a substantial range of deposition conditions. The predominant cluster size will tend to shift to a smaller value if the rate of incidence increases, the temperature decreases, or the activation energy for surface diffusion increases.

If a Walton-type theory describes the nucleation of A atoms in alloy electrodeposition, there will be some equilibrium number density of  $n$ -atom clusters of A. When conditions i and iii are satisfied, a B atom will deposit on each of these  $n$ -atom clusters forming  $A_nB$  structural units. Furthermore, the deposition of B atoms may stabilize these clusters, thus effectively removing them from the equilibrium process of cluster formation and dissociation. If  $m = n$ , the  $n$ -atom clusters of A will predominate and nearly all of the deposited A atoms will be associated with B atoms in  $A_nB$  units. It is unlikely that there will be any clusters of A atoms of a size larger than  $n$ , for such clusters would form through atom-by-atom additions to  $n$ -atom clusters; but condition iii makes the formation of  $A_nB$  more probable. This is the significance of the term  $m \geq n$  in condition ii.

When  $m < n$ , there are additional considerations. If the deposition is dominated by an ordinary nucleation-and-growth process, the  $m$ -atom clusters will either dissociate or grow through atom-by-atom addition. In the latter case condition ii is superfluous, since the growing clusters will pass through the  $n$ -atom stage and, by conditions i and iii,  $A_nB$  structural units will be formed. This, of course, describes the formation of ordered crystalline alloy deposits. On the other hand, when multiple nucleation dominates the deposition process, as in the formation of amorphous alloy deposits, some  $m$ -atom clusters will attain size  $n$  and form  $A_nB$  units; however, many clusters smaller than  $n$  would probably become entrapped. The resulting deposit would be nonstoichiometric because of the excess A. The composition would vary with the degree of entrapment and, therefore, with the deposition conditions. Although the actual  $Fe_3W$  and  $Co_3W$  amorphous deposits contain excess iron and cobalt atoms, the compositions are constant at 22.2 a/o W for a wide range of deposition conditions. Thus, the departure from exact stoichiometry is not attributed to  $m < n$  effects; rather, the excess iron or cobalt is believed to be accommodated in sites which would otherwise be voids or clearances between the tetrahedral units (4).

The ranges of cathode potential in Fig. 2 can be described in terms of parameters  $m$  and  $n$ . In the range N-G, where amorphous  $Fe_2W$  deposits,  $n = 3$ . Beyond J it appears that  $Fe_2W$  is formed, so  $n = 2$ . To assign values of  $m$  to these ranges it is necessary to consider the partial currents. In the range N-G, where  $n = 3$  and the tungsten current increases,  $m = 3$  (or possibly  $m > 3$ ). In the range G-J the tungsten current drops off although the iron current increases. This is also the range in which sodium and hydrogen deposition increases. The obstructive effects of these elements may be equivalent to an increase in the activation energy for surface diffusion which could lower the value of  $m$ . If  $m = 2$ , then tungsten deposition would be retarded because  $m < n$ . The resumed increase in tungsten partial current beyond J may now be accounted for by the deposition of  $Fe_2W$  with  $n = 2$  so that condition ii is again satisfied. The fact that the  $Fe_2W$  composition was not actually attained in the pH 8.50 electrolytes may be ascribed to the violent agitation produced by hydrogen evolution at the high values of cathode potential in this range beyond J. With the higher pH solutions, as in Fig. 3, there was less agitation due to hydrogen and  $Fe_2W$  was obtained.

As described in the preceding paragraph, the adsorption of foreign substances is expected to lead to a small cluster size. Such effects would be common to many cases of deposition from solutions. Furthermore, small clusters are known to have catalytic effects (21, 22). Thus, in many cases of alloy deposition conditions i and ii will be satisfied and the occurrence of stoichiometry will be determined by condition iii. A factor which contributes to condition iii being satisfied for  $Fe_3W$  and  $Co_3W$  is that the stoichiometric alloy is deposited at the limiting current density for iron or cobalt. Under such circumstances the deposition of the A atoms (iron or cobalt) is diffusion limited and their concentration at the surface will be nearly zero; the concentration of the B atoms (tungsten) being finite at the surface leads to fulfillment of condition iii. Another system in which the three conditions seem to be met is Ag-Sn (23) in which the stoichiometric alloy  $Ag_3Sn$  forms under pulse electroplating at or near the limiting current density for Ag.

### Acknowledgments

Manuscript submitted May 13, 1975; revised manuscript received Oct. 22, 1975.

Any discussion of this paper will appear in a Discussion Section to be published in the December 1976 JOURNAL. All discussions for the December 1976 Discussion Section should be submitted by Aug. 1, 1976.

Publication costs of this article were partially assisted by Rockwell International.

### REFERENCES

1. H. Nakamura, *Sci. Papers Inst. Phys. Chem. Res. (Tokyo)*, **2**, 287 (1925).
2. K. M. Gorbunova and Yu. M. Polukalov, in "Electrodeposition of Alloys," V. A. Averkin, Editor, p. 29, IPST Ltd., Jerusalem (1964); and in "Electrodeposition of Metals and Alloys," N. E. Khomutov, Editor, p. 28, IPST Ltd., Jerusalem (1969).
3. N. P. Fedot'ev and P. M. Vyacheslavov, *Plating*, **57**, 700 (1970).
4. T. Omi, H. Yamamoto, and H. L. Glass, *This Journal*, **119**, 168 (1972).
5. M. Bobte.sky and J. Jordan, *J. Am. Chem. Soc.*, **67**, 1824 (1945).
6. K. J. Vetter, "Electrochemical Kinetics," p. 396, Academic Press, Inc., New York and London (1967).
7. T. Kudo, *J. Metal Finishing Soc. Japan*, **17**, 255 (1966).
8. M. Hansen, "Constitution of Binary Alloys", 2nd ed., McGraw-Hill Book Co., New York (1958).
9. S. Yoshioka, H. Yamamoto, and T. Omi, *J. Metal Finishing Soc. Japan*, **20**, 172 (1969).

10. T. Omi and H. Yamamoto, *ibid.*, **24**, 612 (1973).
11. T. Omi and H. Yamamoto, *ibid.*, **24**, 428 (1973).
12. A. Matsuda and R. Notoya, *J. Electrochem. Soc. Japan*, **34**, 619 (1966).
13. J. Farges, B. Raoult, and G. Torchet, *J. Chem. Phys.*, **59**, 3454 (1973).
14. M. R. Hoare and P. Pal, *J. Cryst. Growth*, **17**, 77 (1972).
15. M. R. Hoare and P. Pal, *Adv. Phys.*, **20**, 161 (1971).
16. T. Omi, Unpublished work.
17. J. F. Sadoc, J. Dixmier, and A. Guinier, *J. Non-Cryst. Solids*, **12**, 46 (1973).
18. B. G. Bagley and D. Turnbull, *J. Appl. Phys.*, **39**, 5681 (1968).
19. Pol Duwez and S. C. H. Lin, *ibid.*, **38**, 4096 (1967).
20. D. Walton, *J. Chem. Phys.*, **37**, 2182 (1962).
21. R. Van Hardeveld and A. Van Montfoort, *Surface Sci.*, **17**, 90 (1969).
22. R. Van Hardeveld and F. Hartog, *ibid.*, **15**, 189 (1969).
23. H. Leidheiser, Jr. and A. R. P. Ghuman, *This Journal*, **120**, 484 (1973).

## Tin (IV) Chloride Solution as a Sensitizer in Photoselective Metal Deposition

B. K. W. Baylis, A. Busuttill, N. E. Hedgecock, and M. Schlesinger\*

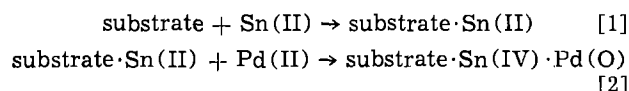
*Department of Physics, University of Windsor, Windsor, Ontario N9B 3P4, Canada*

### ABSTRACT

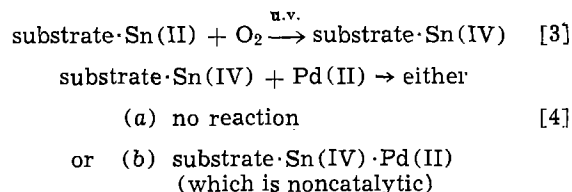
Experiments were conducted which show that Sn(IV) bound to a substrate is capable, in conjunction with Pd(II), of catalyzing Ni-P plating and that this effect can be inhibited by u.v. light. Some of the parameters affecting the quality of the plating and u.v. inhibition were determined. It was also found that in order for u.v. irradiation to inhibit Ni-P plating, the radiation must be applied after the Pd(II) activation step. In the case of copper, however, plating occurs only on the irradiated area of the catalyst. A mixture of Sn(IV) and Pd(II) was also found to catalyze Ni-P plating. The behavior of the catalyst deposited by this mixture was quite similar to that of the catalyst present after Pd(II) activation following Sn(IV) sensitization in the stepwise procedure.

The use of u.v. light to generate patterns in the catalytic surface of dielectric substrates has been well studied in recent years (1-4). The initial procedure was to immerse the substrate in a SnCl<sub>2</sub> solution (the sensitizer), to rinse, and then to irradiate with u.v. light through a quartz mask. After immersion in a PdCl<sub>2</sub> solution (the activator) and another rinse, the substrate was placed in a metallizing bath. Plating occurred wherever the u.v. light did not reach the catalyst.

The mechanism that has been proposed for the preparation of a catalytic layer by the conventional process is



The palladium metal is then the catalyst for the metallizing bath. U.V. light has been presumed to cause oxidation of the Sn(II) to Sn(IV), preventing reaction [2] (formation of the Pd(O) catalyst) and hence preventing metallization (2, 4)



That this mechanism does not give the complete explanation was shown [1] when it was discovered that u.v. light could cause inhibition of the catalyst even when applied after the activation step. It was in order to further probe this mechanism that the following study was undertaken, involving use of acidic Sn(IV) solution as a sensitizing bath.

### Experimental

All chemicals were supplied by Fisher or Canlab, A.C.S. reagent grade, and were used without further purification.

**Sensitizers.**—The stock solution used in this work was made by dissolving 10g SnCl<sub>4</sub>·5H<sub>2</sub>O in 10 ml concentrated HCl. To prepare a sensitizer bath, 2 ml of this stock solution were diluted to 200 ml using distilled water.

**Substrate.**—Glass slides were allowed to stand overnight in 10M NaOH, rinsed well with distilled water, dilute HCl, then distilled water and dried.

**Activator.**—1g PdCl<sub>2</sub> was dissolved in 10 ml concentrated HCl to make the stock solution. One ml of this was diluted to 200 ml for the activator bath.

**Mixed Sn(IV)·Pd(II) bath.**—One ml Sn(IV) stock solution plus 0.5 ml Pd(II) stock solution was diluted to 100 ml with distilled water.

**Ni-P bath.**—The nickel-plating bath consisted of 5.8g NiSO<sub>4</sub>·6H<sub>2</sub>O, 3.5g NaH<sub>2</sub>PO<sub>2</sub>·H<sub>2</sub>O, 2.9g disodium succinate, and 0.2g succinic acid dissolved in distilled water to make a 200 ml solution.

**Cu bath.**—Solution A consisted of 8g CuSO<sub>4</sub>·5H<sub>2</sub>O, 20g Rochelle's salt, and 5.6g NaOH dissolved in enough distilled water to make a 200 ml solution. Solution B consisted of 13g paraformaldehyde and 8.6g NaOH dissolved in enough distilled water to make a 200 ml solution. Two to three parts A were added to one part B to make the copper-plating bath.

**Test for Sn(II).**—A molybdate solution was prepared by dissolving 15g (NH<sub>4</sub>)<sub>2</sub>MoO<sub>4</sub> in 300 ml warm distilled water. The solution was cooled and 350 ml concentrated HCl was added. The cooled solution was diluted to 1 liter and stored in the dark.

A phosphate solution was prepared by dissolving 0.426g (NH<sub>4</sub>)<sub>2</sub>HPO<sub>4</sub> in distilled water and diluting to 1 liter.

\* Electrochemical Society Active Member.

Key words: electroless, sensitizer, tin(IV), photo selective.

For each test, 1-5 ml of tin(II) solution (ranging in concentration from 5 to 0.078 g/liter) was added to a freshly made mixture of 10 ml molybdate solution, 10 ml phosphate solution, and 20 ml distilled water. This solution was diluted to 50 ml, and a visible spectrum was recorded with a Cary-14 spectrophotometer as soon as possible. We were able to detect concentrations of Sn(II) as low as 3 mg/liter. This procedure is a slight modification of that described in Ref (5).

**Exposure system.**—The samples were exposed typically for 6 min to u.v. radiation from an Oriel low pressure mercury lamp Nr. C-13-61 at a distance of about 4 cm. Based on factory specifications, our luminance was calculated to be 1.17 mW/cm<sup>2</sup> at the  $\lambda = 2537\text{\AA}$  spectral line. This one is the dominant spectral component of the radiation from this particular light source. The masks used were Nichrome evaporated onto quartz, etched metal sheet, or simply opaque material supported over half the sample.

**Procedure.**—All solutions were used at room temperature. A slide was immersed in the sensitizer bath, the first distilled water rinse, and the activator bath for 2 min each. The slide was quickly dried in a hot airstream and irradiated with u.v. light for 6 min followed by a rinse in running distilled water. Times in the metallizing bath varied.

For some experiments, the drying and irradiation steps were performed either after the sensitizer bath, after the first rinse, or after the second (running water) rinse.

### Results

**Aging of Sn(II) sensitizer.**—It has been observed that use of aged SnCl<sub>2</sub> solution as the sensitizer results in better plating (6). "Aging" involves oxidation of the Sn(II) to Sn(IV) by atmospheric oxygen and subsequent colloid formation (7, 8). Adding SnCl<sub>4</sub> to the sensitizer has also been tried (6, 9, 10) but no improvement results unless the SnCl<sub>4</sub> is itself aged (11-13).

It has been hypothesized that aged Sn(IV) forms a colloidal dispersion which entraps Sn(II) ions. The latter has been presumed to be the active agent in the sensitizing process. According to Feldstein (11-14), an aged Sn(IV) component is adsorbed onto the substrate, and the Sn(II) attaches to the Sn(IV).

It has been noted (4) that, at least in the case of copper plating, oxygen is a prerequisite for the deactivation of fresh sensitizer by u.v. light (see Eq. [3]) and that no plating is obtained with aged sensitizer unless there is still some Sn(II) present (8). However, we obtained good Ni-P plating using a Sn(II) solution which had been aged for three weeks and, therefore, presumably contained almost exclusively Sn(IV). Further, using the same sensitizer we were able to get u.v. inhibition of plating, resulting in a "positive" image, i.e., a replica of the mask. In addition, we observed that u.v. deactivation of the catalyst even occurred in a pure nitrogen atmosphere. This means that our aged Sn(II) solution, which contains predominantly Sn(IV), was nevertheless still capable of interacting with Pd(II) to form a substance which catalyzes Ni-P plating. This substance is affected by u.v. irradiation, even in the absence of oxygen, in a way which destroys its ability to catalyze Ni-P plating.

**Nickel plating with Sn(IV) sensitizer.**—In order to clarify the role of Sn(IV) in the sensitizing procedure, we carried out a series of experiments using an acidic solution of SnCl<sub>4</sub>·5H<sub>2</sub>O<sup>1</sup> as the sensitizer. From Table I it can be seen that a uniform deposit is obtained only

<sup>1</sup> The test for Sn(II) described in the experimental section was employed to determine if any Sn(II) was present in the Sn(IV) solution or in our three-week-old Sn(II) solution. Both tests were negative, indicating that there was less than 3 mg/liter Sn(II) in both solutions.

Table I. Effect of aging Sn(IV) sensitizer on nickel plating

Appearance of sensitizer	Age of sens. (T ~ 21°C)	Quality of plating
Clear	0-1½ hr	Sometimes no plating. Otherwise nonuniform plating caused by uneven drying.
Clear	1½-11 hr	Nonuniform plating caused by uneven drying
Faintly hazy	12-21 hr	Transition to uniform
Opalescent	22-38 hr	Uniform plating
Cloudy	39-45 hr	Uniform plating
Cloudy to separating	After 45 hr	Nonuniform plating caused by uneven drying

if the age of the sensitizer solution is between 20 and 45 hr. This is evidently associated with better wetting of the substrate; for sensitizer ages outside this range, nonuniform plating due to uneven drying is observed. This observation is in agreement with that of Feldstein *et al.* (11) relating aging of Sn(IV) solution with better wetting.

The range in ages of the sensitizer during which uniform plating is observed is strongly affected by temperature. For example, if the room temperature is raised to 26°C, uniformity in plating is obtained for sensitizers 8-26 hr old. Lower temperatures have been observed to result in later times. Fortunately, higher temperatures also increase the rate of colloid formation, thus making the temperature effect quite visible. The appearance of the sensitizer bath is noted in Table I, because the correlation of the quality of plating with appearance of the sensitizer is better than that of the quality of plating with time, especially when fluctuations in room temperature are a problem.

When more stock solution was used in making the sensitizer bath, thus increasing not only the Sn(IV) but also the hydrochloric acid concentration, the evolution process shown in Table I was slowed. For instance, when the quantity of stock solution was increased by 30%, it required about 30% more time before smooth plating was observed.

Both the uniform and nonuniform plating are quite adherent to glass substrate. Once the samples are thoroughly dry, they are unaffected even by scrubbing with a brush.

**U.V. inhibition of nickel plating.**—If the substrate is dried and irradiated with u.v. light after the activation step or after the subsequent rinse, deposition of nickel is inhibited (see Table II). The effectiveness of the inhibition shows the same dependence on sensitizer age that the uniformity of plating does; that is, the most effective inhibition is obtained if the sensitizer is aged between 20 and 45 hr at an ambient temperature of 21°C. The sensitizer solutions appears faintly hazy to cloudy when it is capable of producing best "positive" images, i.e., replication of the photomask.

If in preparing the sensitizer bath additional HCl is used, the period of optimum photo-imaging is postponed considerably. The colloid also takes longer to

Table II. Results of drying and u.v. irradiation at different stages of the stepwise procedure for electroless deposition

	Ni-P	Cu
Drying and irradiation after:		
Sensitizer Sn(IV) ~24 hr old	u.v. No plating	No plating
	No u.v. Plating	No plating
Rinse H <sub>2</sub> O	u.v. No plating	No plating
	No u.v. Plating	No plating
Activator Pd(II)	u.v. No plating	Plating
	No u.v. Plating	No plating
Rinse H <sub>2</sub> O	u.v. No plating	Plating
	No u.v. Plating	No plating



appear. Hence, the correlation between appearance of the solution and its ability to produce good positive images still holds. However, it should be stressed that even during the period of optimum performance of the sensitizer, no inhibition is observed if drying and irradiation occur following sensitization or following the subsequent rinse (see Table II).

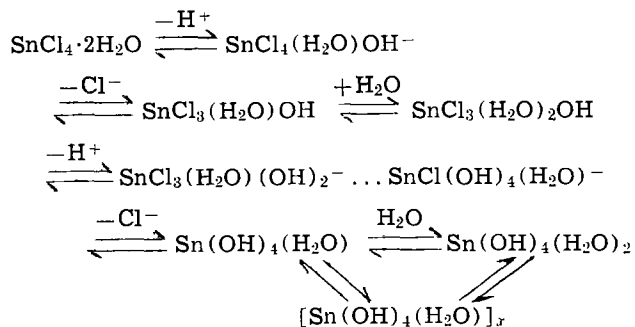
**Copper plating.**—D'Amico and DeAngelo observed (8) in their work that appreciable amounts of Sn(IV) were deposited on their substrate after immersion in a Sn(IV) sensitizer. Nonetheless, after activation and immersion in a Cu-plating bath, they observed no metallization. We also observed that copper does not plate under these conditions. However, when hot air drying and irradiation follow either the Pd(II) activation step or the second rinse, we observed copper plating on the u.v. irradiated areas. That is, a perfect negative results (see Table II). These negatives are only observed when the sensitizer is of the right age to also give good Ni-P positive images. Again, under these circumstances, we find that no plating at all is observed if irradiation follows Sn(IV) sensitization or the first rinse.

**Mixed sensitizer-activator.**—An acidic solution containing the same amount of Sn(IV) as in the sensitizer and the same amount of Pd(II) as in the activator was prepared as described in the experimental section. The variation observed in quality of plating and in imaging as the sensitizer-activator solution aged was as would be expected for the Sn(IV) sensitizer alone, especially if allowance is made for the delaying effect of slightly increased acidity. That is, the presence of the Pd(II) does not seem to alter the aging process of the Sn(IV). We find that good Ni-P positive images and good Cu negative images are obtained when hot air drying and u.v. irradiation are applied following immersion in the sensitizer-activator solution which has been aged from 24 to 48 hr.

### Discussion

**Aging of Sn(IV) solutions.**— $\text{SnCl}_4 \cdot 5\text{H}_2\text{O}$  is a covalent compound and requires a period of time before most or all the chlorine is present as chloride ions free in solution. This period of time has been known for about 70 years to be a function of many parameters, such as temperature, concentration, and hydrochloric acid concentration. The rate of the reaction is increased by increasing temperature, decreasing  $\text{SnCl}_4 \cdot 5\text{H}_2\text{O}$  concentration, and decreasing hydrochloric acid concentration. It has already been noted here and in Ref. (11) that these parameters also affect the length of time required for onset of optimum performance of the sensitizer, and in the same way. Thus the photosensitive species which may also be the one responsible for good wetting (hence uniform plating) must be one of the products of the reaction of water with  $\text{SnCl}_4 \cdot 5\text{H}_2\text{O}$ .

The mechanism assumed for the hydrolysis of  $\text{SnCl}_4 \cdot 5\text{H}_2\text{O}$  can be represented as (15)



The species of interest is one toward the end of the hydrolysis reaction, as indicated by the fact that some colloidal polymeric species is present in the solution when good wetting is observed. The improved

wetting observed by Feldstein *et al.* (11) with aged  $\text{SnCl}_4$  solution was attributed to "a  $\beta$ -stannic acid," which would correspond to our  $[\text{Sn}(\text{OH})_4(\text{H}_2\text{O})]_x$ . They picture this species as  $(\text{HO})_3\text{Sn}[\text{OSn}(\text{OH})_2]_n\text{OH}$ , where  $n$  may be 1, 2, 3, etc.

Some background plating in the irradiated sections (indicating incomplete inhibition of Ni-P plating) and nonuniform plating both occur when the sensitizer solutions are very cloudy and beginning to separate. These facts suggest that the species that does not wet well and is not photosensitive is the polymeric  $[\text{Sn}(\text{OH})_4 \cdot \text{H}_2\text{O}]_x$ , where  $x$  is relatively high. They also suggest that the species which does wet well and is perhaps also photosensitive could either be  $\text{SnCl}(\text{OH})_4(\text{H}_2\text{O})^-$ ,  $\text{Sn}(\text{OH})_4 \cdot (1 \text{ or } 2) \text{H}_2\text{O}$ , or  $[\text{Sn}(\text{OH})_4 \cdot \text{H}_2\text{O}]_x$ , where  $x$  is quite small. It is hoped that further study will clarify the nature of this species.

**Activation chemistry.**—As a result of the present work, we have been able to show that Sn(IV) can serve as an effective sensitizer for electroless plating. This we feel shows conclusively, as pointed out by us previously (1), that the effect of u.v. light cannot simply be explained by the mechanism shown in Eq. [3] and [4]. This mechanism requires that Sn(IV) which results from photo-oxidation of Sn(II) be incapable of interacting with Pd(II) to give a catalytic species. Our present experimental results indicate at the very least that the interaction between Sn(IV) bound to the substrate and Pd(II) results in a species that is catalytic for Ni-P plating.

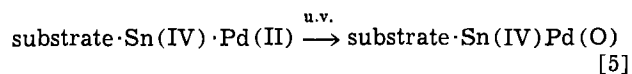
Our present results also indicate that the activation stage cannot be accounted for simply in terms of the redox reaction between Sn(II) and Pd(II) (Eq. [2]). It is well known that some Sn(IV) is present in Sn(II) sensitizer solutions, and we have shown that this Sn(IV) is also capable of reacting with Pd(II) to form a catalyst for Ni-P. Recently Kelly and Vondeling (16) reported that the Pd(II) present on their  $\text{TiO}_2$  bound to quartz was also capable of giving rise to metal plating "in certain cases." They suggest that the reducing agent in the metallizing bath reduces the Pd(II) to Pd(O), thus creating nucleation centers for plating. If this explanation is applicable to our case, it would appear from our results that the reducing agent,  $\text{H}_2\text{PO}_2^-$ , present in the Ni-P bath, is capable of reducing the bound Pd(II) to Pd(O), but formaldehyde, the reducing agent present in the copper bath, is not. It is also possible that there is a specific interaction between Ni(II) and the species resulting from the interaction between Sn(IV) and Pd(II), which might be designated substrate·Sn(IV)·Pd(II), that initiates the plating, and that Pd(O) is not necessary for catalyzing Ni-P plating.

Our work shows that the species substrate·Sn(IV)·Pd(II) must also be affected by u.v. light in such a way as to render it noncatalytic for Ni-P plating but still catalytic for Cu plating. Kelly and Vondeling further indicate that u.v. irradiation of  $\text{TiO}_2$  renders it capable of reducing Pd(II) to Pd(O). The mechanism for this has been discussed by Mollers *et al.* (17). Kelly and Vondeling also note that copper will plate on these Pd(O) nuclei, but that Ni-P will do so only under very specific conditions, *i.e.*, if a wetting agent was present in the Pd(II) solution or if the irradiation time was "not too long." The similarities between our results and theirs suggest strongly that the role of  $\text{SnO}_2$  in substrate·Sn(IV)·Pd(II) is very similar to that of  $\text{TiO}_2$  in the system  $\text{TiO}_2$ ·Pd(II).

The work on  $\text{TiO}_2$  suggests that the Pd(O) minimum coverage must be higher for Ni-P plating than for copper plating. Our previous work (1) on irradiation of the catalytic species present after the conventional activation step indicated that irradiation results in increased degree of crystallinity. It would appear from this and our present work that the more crystalline Pd-containing material is incapable of catalyzing



Ni-P plating. Thus it may be possible that the effect of u.v. radiation on the catalyst may be to reduce the Pd(II) to Pd(O)



In addition, it may decrease the density of noncrystalline Pd(O) sites below the threshold for Ni-P but not for Cu. It might also be possible that Pd(O) in this form is simply incapable of initiating Ni-P plating.

The above also suggests a reason that good wetting of the substrate correlates with photosensitivity. Good wetting means a uniform distribution of catalyst sites, making it possible for irradiation to decrease the density of noncrystalline Pd(O) sites below the Ni-P threshold. The Sn(IV) species giving good wetting could be, as discussed in the section on aging, either  $\text{SnCl(OH)}_4(\text{H}_2\text{O})^-$ ,  $\text{Sn(OH)}_4 \cdot (1 \text{ or } 2)\text{H}_2\text{O}$ , or polymeric  $[\text{Sn(OH)}_4\text{H}_2\text{O}]_x$ , where  $x$  is quite small.

### Conclusion

Sensitization with acidic Sn(IV) solutions followed by activation with a Pd(II) solution has been shown to catalyze Ni-P plating but not copper plating. The redox mechanism (Eq. [2]) that has been proposed [see Ref. (18)] to describe the reaction between Sn(II) and Pd(II) in the conventional activation step presumably has as its product  $\text{substrate} \cdot \text{Sn(IV)} \cdot \text{Pd(O)}$ . Our experiments show that  $\text{substrate} \cdot \text{Sn(IV)} \cdot \text{Pd(II)}$  catalyzes Ni-P plating, and it is well known that Sn(IV) is present in Sn(II) sensitizer baths. It is, therefore, obvious that Sn(IV)-containing species must also be included as active components in mechanisms for sensitization and activation of Ni-P plating. However, nonirradiated  $\text{substrate} \cdot \text{Sn(IV)} \cdot \text{Pd(II)}$  does not catalyze copper plating and, therefore, can be left out of mechanisms leading to copper plating.

The mechanism (Eq. [3] and [4]) proposed (2, 4) to explain the inhibiting effect of u.v. light when Sn(II) is the sensitizer implies that  $\text{substrate} \cdot \text{Sn(IV)} \cdot \text{Pd(II)}$  must be incapable of catalyzing metal plating. Our observation that  $\text{substrate} \cdot \text{Sn(IV)} \cdot \text{Pd(II)}$  does catalyze Ni-P plating seems to contradict this mechanism, at least in this simplified form. On the other hand, our copper plating results do not seem to contradict the mechanism in Eq [3] and [4].

Using a mixed Sn(IV) sensitizer-Pd(II) activator bath gives the same results as when these baths are separate. Drying and u.v. irradiation following immersion in this bath results in positive Ni-P images and negative Cu images.

Our experiments to date indicate the following procedure should be followed in order to obtain the best imaging with Ni-P plating using  $\text{SnCl}_4 \cdot 5\text{H}_2\text{O}$  in the sensitizer bath. A clean, dry microscope slide is im-

mersed first in an acidic ( $8.3 \times 10^{-2}\text{M HCl}$ ) tin (IV) chloride ( $2 \times 10^{-2}\text{M}$ ) solution that is between 20 and 45 hr old (for room temperature about 21°C). After the rinse and activation steps, the slide is dried in a hot airstream and irradiated with u.v. light through an appropriate mask. After a running water rinse and plating in a Ni-P metallizing bath, striking positives are obtained.

### Acknowledgments

This research was supported by the National Research Council of Canada.

Manuscript submitted Sept. 22, 1975; revised manuscript received Nov. 13, 1975.

Any discussion of this paper will appear in a Discussion Section to be published in the December 1976 JOURNAL. All discussions for the December 1976 Discussion Section should be submitted by Aug. 1, 1976.

Publication costs of this article were partially assisted by the University of Windsor.

### REFERENCES

1. S. L. Chow, N. E. Hedgecock, M. Schlesinger, and J. Rezek, *This Journal*, **119**, 1013 (1972).
2. R. L. Cohen, J. F. D'Amico, and K. W. West, *ibid.*, **118**, 2042 (1971).
3. J. F. D'Amico, F. A. Litt, and M. A. DeAngelo, *ibid.*, **119**, 956 (1972).
4. J. F. D'Amico, M. A. DeAngelo, J. F. Henrickson, J. T. Kenney, and D. J. Sharp, *ibid.*, **118**, 1695 (1971).
5. F. D. Snell and C. T. Snell, "Colorimetric Methods of Analysis," 3rd ed., pp. 215 ff and 660 ff., Van Nostrand, New York (1949).
6. G. Bernhardt, U.S. Pat. 3,616,296 (1971).
7. R. L. Cohen and K. W. West, *This Journal*, **119**, 433 (1972).
8. J. F. D'Amico and M. A. DeAngelo, *ibid.*, **120**, 1469 (1973).
9. D. M. Luce, B. L. Berdan, and M. L. Selker, U.S. Pat. 3,245,862 (1966).
10. J. S. Drotar, A. A. Parker, and K. A. Snyder, U.S. Pat. 3,573,973 (1971).
11. N. Feldstein, J. A. Weiner, and G. L. Schnable, *This Journal*, **119**, 1486 (1972).
12. N. Feldstein and J. A. Weiner, *ibid.*, **120**, 475 (1973).
13. N. Feldstein, S. L. Chow, and M. Schlesinger, *ibid.*, **120**, 875 (1973).
14. N. Feldstein and J. A. Weiner, *ibid.*, **119**, 668 (1972).
15. J. C. Bailar, Jr., "Chemistry of the Coordination Compounds," p. 446, Reinhold Publishing Corp., New York (1956).
16. J. J. Kelly and J. K. Vondeling, *This Journal*, **122**, 1103 (1975).
17. F. Mollers, H. J. Tolle, and R. Memming, *ibid.*, **121**, 1160 (1974).
18. W. Goldie, "Metallic Coating of Plastics," Vol. I p. 46, Electrochemical Publications Ltd., Middlesex, U.K. (1968).

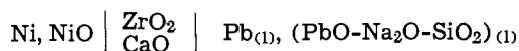
# A Thermodynamic Study of the PbO-Na<sub>2</sub>O-SiO<sub>2</sub> System

A. E. Grau and S. N. Flengas\*

University of Toronto, Department of Metallurgy and Materials Science, Toronto, Ontario, Canada

## ABSTRACT

The thermodynamic properties of PbO in the ternary melts PbO-Na<sub>2</sub>O-SiO<sub>2</sub> have been investigated by using solid electrolyte galvanic cells of the type

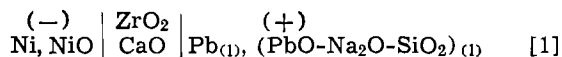


The results of this work, combined with those reported in previous publications from this laboratory (7, 23), cover the region of the ternary diagram lying between the PbO-SiO<sub>2</sub> side and the line joining the PbO corner with the sodium metasilicate compound. The results indicate that the addition of Na<sub>2</sub>O to the melt produces a significant increase in the activity of PbO. This type of behavior has also been observed in other ternary silicate systems. The partial molar enthalpies of mixing of PbO show a marked tendency toward positive values for increasing contents of Na<sub>2</sub>O in the solutions. This is interpreted as the presence of repulsive interactions between the PbO and Na<sub>2</sub>O components. A comparison of the available activity data for various metal oxides dissolved in sodium disilicate is presented.

The experimental thermodynamic study of molten silicates is difficult. Because of the very high temperatures involved, the choice of techniques is drastically reduced, and the problem of finding a container which will not contaminate the slag becomes critical. The only binary systems for which activity data have been directly determined are the FeO-SiO<sub>2</sub> (1-3), PbO-SiO<sub>2</sub> (4-9), MnO-SiO<sub>2</sub> (10), and CoO-SiO<sub>2</sub> (11). In the last two cases, however, the activities of the metal oxide component have been referred to the solid oxide as the standard state, and their expressions with respect to the liquid oxide cannot be accurately recalculated because of the lack of data for both the enthalpies of fusion and the heat capacities of the liquid metal oxides. Activities of SnO in the SnO-SiO<sub>2</sub> system have been reported in three different publications (12-14), but the results are in total disagreement. Reliable data for the enthalpies and entropies of mixing in binary silicates are available for the PbO-SiO<sub>2</sub> system only (7, 15).

Regarding ternary silicate melts, activity data are available for the systems FeO-CaO-SiO<sub>2</sub> (16, 17, 18), MnO-CaO-SiO<sub>2</sub> (10), and PbO-CaO-SiO<sub>2</sub> (19). Other systems such as NiO-Na<sub>2</sub>O-SiO<sub>2</sub> (20), FeO-Na<sub>2</sub>O-SiO<sub>2</sub> (21), and CoO-Na<sub>2</sub>O-SiO<sub>2</sub> (22) have been investigated only over very narrow composition ranges along the line joining the divalent metal oxide corner of the ternary diagram with the sodium disilicate compound. Systematic determinations of the enthalpies and entropies of mixing in ternary systems are unavailable in the literature.

In the present study, the thermodynamic properties of the PbO-Na<sub>2</sub>O-SiO<sub>2</sub> system have been investigated by employing solid electrolyte galvanic cells of the type



The cells were operated over a sufficiently wide temperature range in order to allow the calculation of not only the activities of PbO but also the partial molar enthalpies and entropies of solution of this component.

## Experimental

The experimental electrochemical cell used in this investigation is shown in Fig. 1, and its design was very

similar to that previously used in this laboratory for the investigation of the thermodynamic properties of a number of metal oxides (23).

The most important part of the cell was a 24 in. long tube of ZrO<sub>2</sub> stabilized with 5% CaO, commercially available from the Zirconium Corporation of America. The tube had one closed flat end, an inside diameter of 3/8 in., and an outside diameter of 1/2 in. Although the imperviousness of the tube is certified by the manufacturing company, it was subjected to helium leak detection tests in this laboratory using a Veeco Mass Spectrometer Leak Detector.

The reference electrode consisted of a mixture of Ni and NiO powders placed in a ceramic crucible at the bottom of the assembly. The electrical connection for this electrode consisted of several pieces of spectrographically pure nickel wire approximately 1/4 in. long.

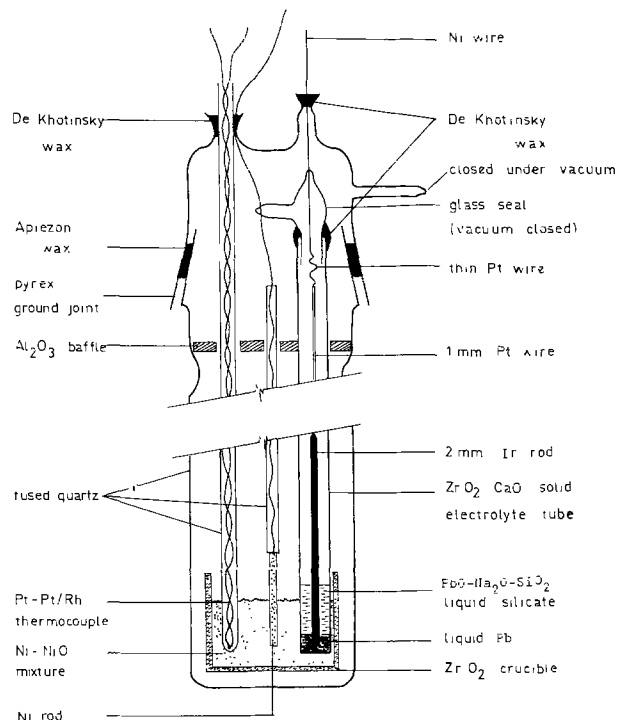


Fig. 1. Schematic diagram of "closed" solid electrolyte cell

\* Electrochemical Society Active Member.

Key words: PbO-Na<sub>2</sub>O-SiO<sub>2</sub> system, emf silicate melts, silicate thermodynamic data.

The nickel wire was welded to a platinum wire 0.020 in. in diameter which was insulated by means of an alumina tube and served as a lead wire to the potentiometer.

In some preliminary experiments, a Pt,O<sub>2</sub>(1 atm) electrode was used as the reference. However, the large oxygen chemical potential difference created across the solid electrolyte appeared to cause the permeability of this membrane to non-ionic oxygen, especially at high temperatures. This nonelectrochemical transfer of oxygen should explain the observed time dependence of the cell emf's when such a reference electrode was used. This phenomenon has also been reported in other publications (24, 25). The effect of oxygen permeation was unnoticeable when the low oxygen partial pressure electrode Ni/NiO was introduced.

Lead of 99.999% purity and the crushed ternary silicate were loaded inside the ZrO<sub>2</sub>-CaO tube. The electrical connection for this electrode was made by means of a 6 in. long iridium wire, 2 mm in diameter, partially immersed in the metal phase. Other metals like platinum or stainless steel were found to alloy with Pb. The iridium wire was welded to a platinum wire of 0.040 in. in diameter which was insulated with a fine alumina tube and brought to the upper part of the assembly to serve as the second lead wire to the potentiometer. The ZrO<sub>2</sub>-CaO tube was evacuated to 10<sup>-5</sup> atm and its open end closed under vacuum by means of a glass seal and "De Khotinsky" medium cement as indicated in Fig. 1.

Temperature measurements were made by means of a Pt/Pt-13% Rh thermocouple properly insulated and placed inside a 6 mm ID quartz tube closed at the lower end.

The entire cell was contained in a quartz tube of 45 mm ID with a closed flat end. A 50/60 quartz ground joint allowed the coupling of the quartz tube to the air-cooled Pyrex cap. This coupling was vacuum-sealed with Apiezon cement. The complete assembly was evacuated to 10<sup>-5</sup> atm and sealed under vacuum.

The alumina disk shown in Fig. 1 served both as a spacer and as a radiation baffle.

The bottom of the cell was placed in the 2 in. long constant temperature zone of a vertical furnace. The temperature was controlled within  $\pm 1^\circ\text{K}$  by means of a Brown Pyr-O-Vane controller from Honeywell Instruments. A grounded Inconel sheath was placed between the cell wall and the furnace tube to eliminate induced currents from the a-c field of the furnace windings.

The emf's originating from the Pt/Pt-13% Rh thermocouple were measured with a Leeds and Northrup K-3 potentiometer with the same furnace and over-all geometric arrangement. Corrections had to be applied for the use of cold junctions (44°C). All thermocouples used were standardized with respect to a calibrated couple.

Cell emf's were registered by means of a Keithley digital multimeter, Model 160, with an accuracy of  $\pm 0.1\%$  of recording. Polarization currents in such instruments are negligible. All cell emf readings were corrected for thermal emf's measured separately. Such corrections were of the order of 3 mV.

The main characteristic of the cell design described above is that the electrode compartments are completely isolated from each other, so that the only mass transfer which can take place between the electrodes is the electrochemical transfer of oxygen ions across the solid electrolyte. Since there is no gas diffusion from one electrode to the other, the oxygen partial pressure in each compartment reaches the equilibrium value, and both electrodes behave as closed thermodynamic systems. This type of cell is known as a "closed cell" and has been shown (23) to be free of mixed potential effects which are inherent in "open" type cells.

The system was systematically investigated along the three lines joining the PbO corner of the ternary dia-

gram with the sodium metasilicate, sodium disilicate and sodium trisilicate compounds. The compositions investigated are shown in Fig. 2. The shadowed area indicates the part of the phase diagram covered by this work combined with the phase diagram covered by this work combined with the work of Charette and Flengas (7) for the PbO-SiO<sub>2</sub> binary system.

The method adopted for the preparation of the slag samples was to prepare first the pure sodium silicate and then melt it with the amounts of PbO corresponding to the desired ternary compositions.

Na<sub>2</sub>O (in the form of Na<sub>2</sub>CO<sub>3</sub> anhydrous) and SiO<sub>2</sub> (obtained by dehydrating H<sub>4</sub>SiO<sub>4</sub> at 1250°-1300°K for 18-24 hr) were mixed in the proportions corresponding to the meta-, di-, and trisilicate. Each mixture was loaded into a large platinum crucible and heated slowly to about 1073°K in order to allow the decomposition of the carbonate. After a few hours, the temperature was raised to well above the melting point of the silicate and the sample left for 18 hr or so in order to assure its homogeneity. After this period of time, the crucible was removed from the furnace and cooled, with its contents, in a dessicator. When the presence of CO<sub>2</sub> bubbles or undissolved material was considerable, the silicate was ground and remelted in the same platinum crucible. The preparations obtained were finely ground and stored in a dessicator. Usually, about 50g of the sodium silicate was prepared at a time.

Both the sodium disilicate and sodium trisilicate formed colorless glasses while the metasilicate was obtained as a white nonglassy material.

For the preparation of the ternary slags, the sodium silicates were mixed with yellow PbO in the amounts corresponding to 10g samples. The mixtures were placed in small platinum crucibles provided with an alumina lid and introduced into a furnace preheated to about 1273°K where they were kept for 30 min.

After this time the slags were cooled, ground, and stored in a dessicator. The slags were homogeneous and yellow in color, the intensity of the color varying according to the PbO content. Some PbO volatilization was evidenced by a very light yellow deposit on the alumina lid, most of which may have been produced before the PbO dissolved in the slag. As indicated in Fig. 2, most of the compositions formed clear glasses upon solidification.

Five different samples were analyzed for PbO by dissolving the silicates in concentrated H<sub>2</sub>SO<sub>4</sub> and HF and evaporating to fumes to expel the silicon tetrafluoride. Pb was precipitated as PbSO<sub>4</sub>, which was filtered, washed, dried at 120°C, and finally weighed. The results agreed very well with the compositions calculated on weighing.

The electrochemical cells were operated on temperature cycles to a maximum of about 1273°K. Cell emf's

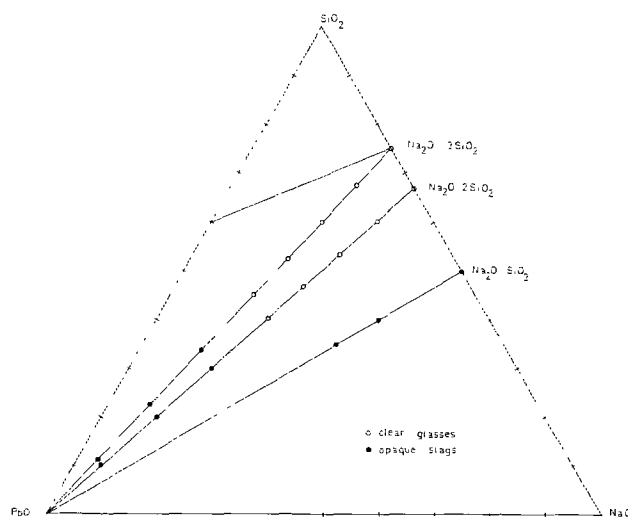


Fig. 2. Ternary compositions investigated

were read every 30° or 40°K and only when stable, so that the time between readings was usually 1-2 hr. The behavior of the cells may be described as follows:

(a) Cells containing PbO dissolved in either the sodium di- or trisilicate. They were run for period of at least 48 hr and in some cases up to 120 hr. The emf's were totally reproducible on repeated temperature cycling over an interval of about 250°K. After disassembling the cells, the following observations were always made: (i) The Ni-NiO mixture that served as the reference electrode formed a compact mass around the electrolyte tube and provided a very steady electrical contact. (ii) The Ir rod immersed in the silicate melt was unaffected by either Pb or the liquid slag. (iii) The ZrO<sub>2</sub>-CaO solid electrolyte tube did not show any effect of a possible interaction with the silicate melt. A barely visible yellow deposit on the inner wall at the bottom of the tube indicated some slight volatility of the PbO.

(b) Cells containing PbO dissolved in sodium metasilicate. These cells produced stable emf's during a period of 4-6 hr, after which time the emf fell to very low and unstable values. When the cells were disassembled, the lower part of the ZrO<sub>2</sub> tube was totally cracked and the liquid silicate had leaked to the outside of the tube. It was evident that the attack on the electrolyte was due to the higher concentration (and therefore higher activity) of the Na<sub>2</sub>O in the solution. Na<sub>2</sub>O shows a tendency to escape from the metasilicate in the form of a vapor which later decomposes in Na atoms and oxygen molecules (26). The small atoms of Na may then diffuse into the solid electrolyte causing its weakness and the eventual cracking.

### Results

The temperature dependence of the cell emf for all the slags investigated is shown in Fig. 3, 4, and 5. Figures 3 and 4 show the results obtained for compositions along the lines PbO-Na<sub>2</sub>O·3SiO<sub>2</sub> and PbO-Na<sub>2</sub>O·2SiO<sub>2</sub>, respectively, while Fig. 5 refers to compositions along the line PbO-Na<sub>2</sub>O·SiO<sub>2</sub>. In the last case because of the problem discussed above, only two compositions could be investigated. Other runs failed before producing any acceptable results.

According to the phase diagram for the PbO-Na<sub>2</sub>O-SiO<sub>2</sub> system due to Krakau and co-workers (27), reproduced in Fig. 6, the compositions  $X_{PbO} = 0.70$  and  $X_{PbO} = 0.85$  on the line PbO-Na<sub>2</sub>O·3SiO<sub>2</sub> and also the compositions  $X_{PbO} = 0.70$  and  $X_{PbO} = 0.85$  on the line PbO-Na<sub>2</sub>O·2SiO<sub>2</sub> lie in the stability field of PbO. This means that PbO is the first solid to appear during the cooling of the solutions and should be found in thermodynamic equilibrium with the PbO remaining in solution. These characteristics of this portion of the phase

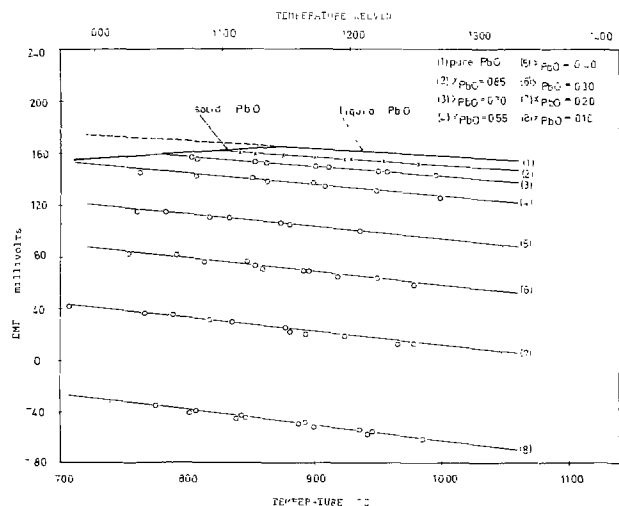


Fig. 3. Temperature dependence of emf for cell Ni, NiO/ZrO<sub>2</sub>-CaO/Pb, (PbO-Na<sub>2</sub>O-SiO<sub>2</sub>)Na<sub>2</sub>O:SiO<sub>2</sub> = 1:3.

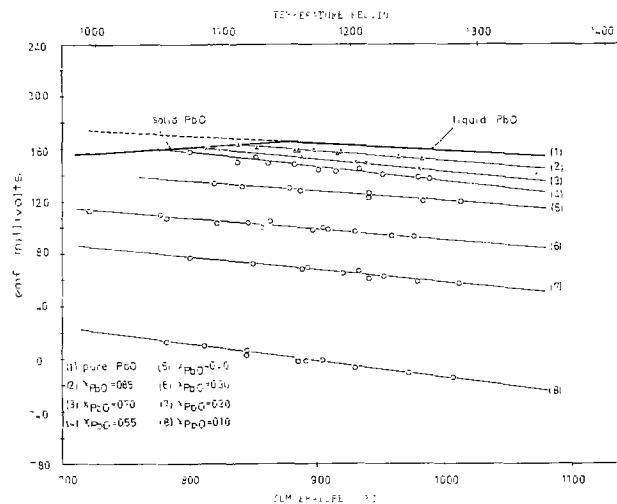


Fig. 4. Temperature dependence of emf for cell Ni, NiO/ZrO<sub>2</sub>-CaO/Pb, (PbO-Na<sub>2</sub>O-SiO<sub>2</sub>)Na<sub>2</sub>O:SiO<sub>2</sub> = 1:2.

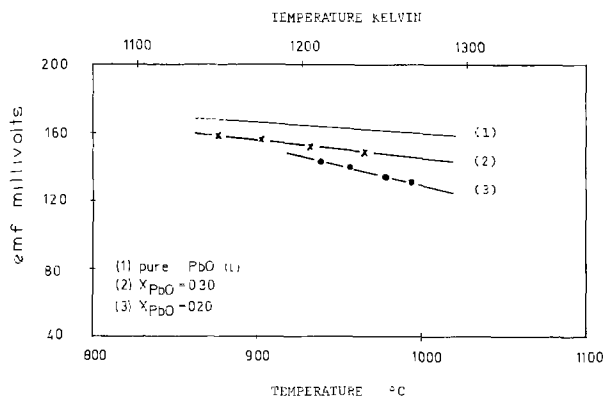


Fig. 5. Temperature dependence of emf for cell Ni, NiO/ZrO<sub>2</sub>-CaO/Pb, (PbO-Na<sub>2</sub>O-SiO<sub>2</sub>)Na<sub>2</sub>O:SiO<sub>2</sub> = 1:1.

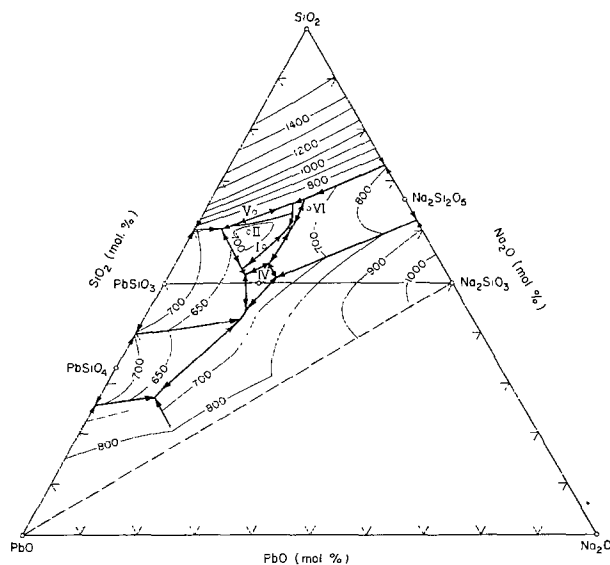


Fig. 6. Phase diagram of the PbO-Na<sub>2</sub>O-SiO<sub>2</sub> system [Ref. (27)]

diagram should be reflected in the emf data obtained for the above-mentioned compositions in the following way: (a) The emf vs. temperature lines should intersect the pure solid PbO line at the freezing point, and (b) all emf measurements below the freezing point should be coincident with the line corresponding to solid PbO.

As may be seen in Fig. 7, this behavior was strictly followed by the experiments. The obtained freezing points are in good agreement with those indicated in

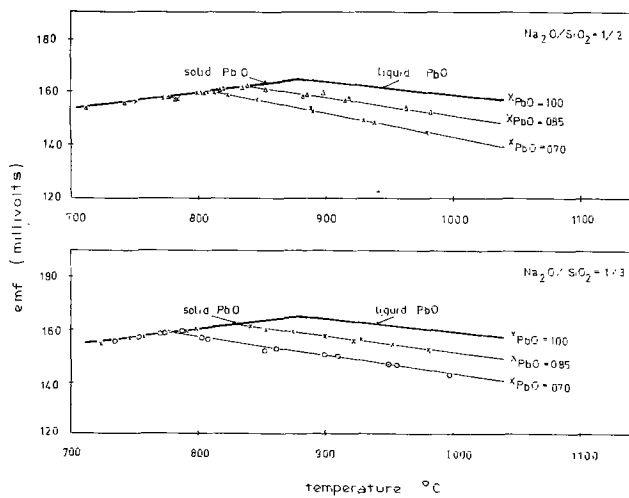


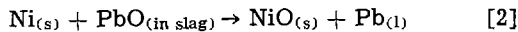
Fig. 7. Temperature dependence of emf for slags whose compositions lie in the stability field of PbO.

Fig. 6, and the emf data for lower temperatures coincide almost exactly with the line for solid PbO. These facts were taken as an excellent test for the accuracy of the emf data.

Each set of results represented in Fig. 3, 4, and 5 was subjected to a least squares analysis using a standard computer program, and the resulting linear relationships between cell emf and temperature have been included in Table I together with their corresponding standard deviation.

**Thermodynamic Calculations**

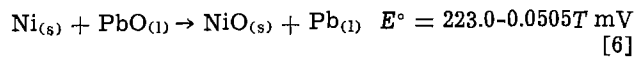
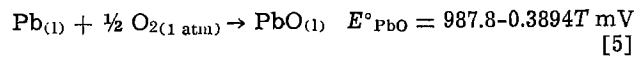
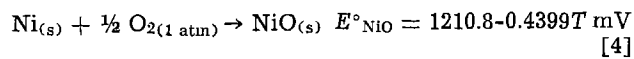
Considering the polarity of the cells indicated in the schematic representation [1], the cell reaction may be written as



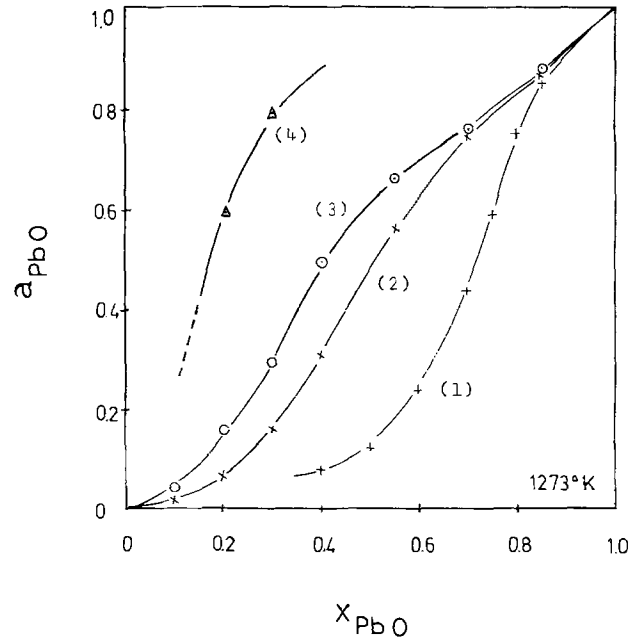
and the activities of the PbO in the ternary melts ( $a_{PbO}$ ) at  $T^\circ K$  may be calculated from the equation

$$E = E^\circ + \frac{RT}{2F} \ln a_{PbO} \quad [3]$$

where  $R$  is the gas constant,  $F$  the Faraday constant, and  $E$  the measured cell voltage.  $E^\circ$  represents the emf of the cell in which the slag phase has been replaced by pure liquid PbO.  $E^\circ$  was calculated from the available emf data (23) for the cell reactions as



Plots of the activity of PbO at 1273°K vs. the mole fraction of this oxide for different  $X_{Na_2O}/X_{SiO_2}$  ratios are shown in Fig. 8. It may be readily seen that, as



- (1) binary PbO-SiO<sub>2</sub><sup>(7)</sup>
- (2) Na<sub>2</sub>O / SiO<sub>2</sub> = 1 / 3
- (3) Na<sub>2</sub>O / SiO<sub>2</sub> = 1 / 2
- (4) Na<sub>2</sub>O / SiO<sub>2</sub> = 1 / 1

Fig. 8. Concentration dependence of the activities of PbO at 1273°K for various values of the ratio  $X_{Na_2O}/X_{SiO_2}$ .

the  $X_{Na_2O}/X_{SiO_2}$  ratio increases, the activity curves are consistently displaced toward more positive values. This observation follows the general rule for ternary silicate systems in the sense that the addition of a more basic metal oxide raises the activity of the other oxide in solution. The results plotted in Fig. 8 have also been used to obtain the isoactivity contours represented in Fig. 9 on an isothermal section of the ternary diagram at 1273°K.

From the analysis of the PbO activity data at different temperatures which are presented in Table II, it is readily concluded that the thermodynamic behavior of the solutions slowly approaches that of the ideal molecular model as the temperature increases. The knowledge of the temperature dependence of the activities of PbO was also used to calculate the partial molar enthalpies of mixing of liquid PbO,  $\Delta\bar{H}_{PbO}$ , by means of the van't Hoff equation

$$\frac{d(\ln a_{PbO})}{d(1/T)} = \frac{\Delta\bar{H}_{PbO}}{R} \quad [7]$$

Table I. Summary of emf data for the PbO-Na<sub>2</sub>O-SiO<sub>2</sub> system

$X_{PbO}$	$E = A - BT, \text{ mV}$								
	$X_{Na_2O}:X_{SiO_2} = 1:3$			$X_{Na_2O}:X_{SiO_2} = 1:2$			$X_{Na_2O}:X_{SiO_2} = 1:1$		
	A	B	Std dev.	A	B	Std dev.	A	B	Std dev.
0.10	88.2	0.1183	±1.1 mV	145.9	0.1255	±1.2 mV			
0.20	154.0	0.1126	±1.3	181.8	0.0972	±1.1	429.7	0.2356	±0.6 mV
0.30	197.3	0.1097	±1.3	187.3	0.0750	±1.3	279.6	0.1051	±0.3
0.40	210.9	0.0915	±0.6	213.3	0.0729	±0.9			
0.55	233.1	0.0831	±1.4	280.1	0.1130	±1.1			
0.70	232.7	0.0704	±0.4	256.5	0.0887	±0.3			
0.85	230.4	0.0823	±0.4	233.9	0.0647	±0.7			
1.00	223.0	0.0505	±1.0	223.0	0.0505	±1.0	223.0	0.0505	±1.0

X denotes mole fraction.

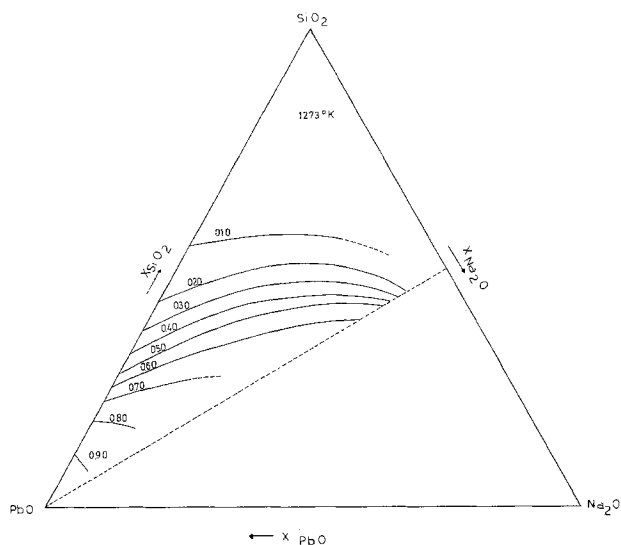


Fig. 9. PbO isoactivity lines at 1273°K

The concentration dependence of the partial molar enthalpies of mixing of liquid PbO dissolved in sodium silicates of different  $X_{\text{Na}_2\text{O}}/X_{\text{SiO}_2}$  ratios is shown in Fig. 10. It may be seen that the curves are of a rather unusual shape, going from negative to positive values and showing a minimum in the PbO-rich side of the diagram.

The partial molar entropies of mixing of liquid PbO,  $\Delta\bar{S}_{\text{PbO}}$ , were calculated from the standard expression

$$RT \ln a_{\text{PbO}} = \Delta\bar{H}_{\text{PbO}} - T\Delta\bar{S}_{\text{PbO}} \quad [8]$$

and the corresponding results are shown in Fig. 11. It may be noted that for the PbO-rich compositions,  $\Delta\bar{S}_{\text{PbO}}$  increases as the silica content increases, and that this tendency is completely reversed as the PbO concentration decreases. In order to follow such a drastic change, the curve corresponding to the ratio  $X_{\text{Na}_2\text{O}}/X_{\text{SiO}_2} = 1/2$ , goes through a peak which is characteristic of the presence of important configurational contributions to the entropy of the system.

The numerical values for both the partial molar enthalpies and the partial molar entropies of mixing of liquid PbO have been included in Table III. Because of the experimental difficulties experienced with slags having the ratio  $X_{\text{Na}_2\text{O}}/X_{\text{SiO}_2} = 1$ , the results obtained in such cases should be taken only as approximated values. These values have not been reported in the plots presented in this paper.

### Discussion

According to the general experimental evidence (10, 16-19), the addition of a more basic metal oxide  $M_{II}\text{O}$  to a silicate solution containing a metal oxide  $M_I\text{O}$ ,

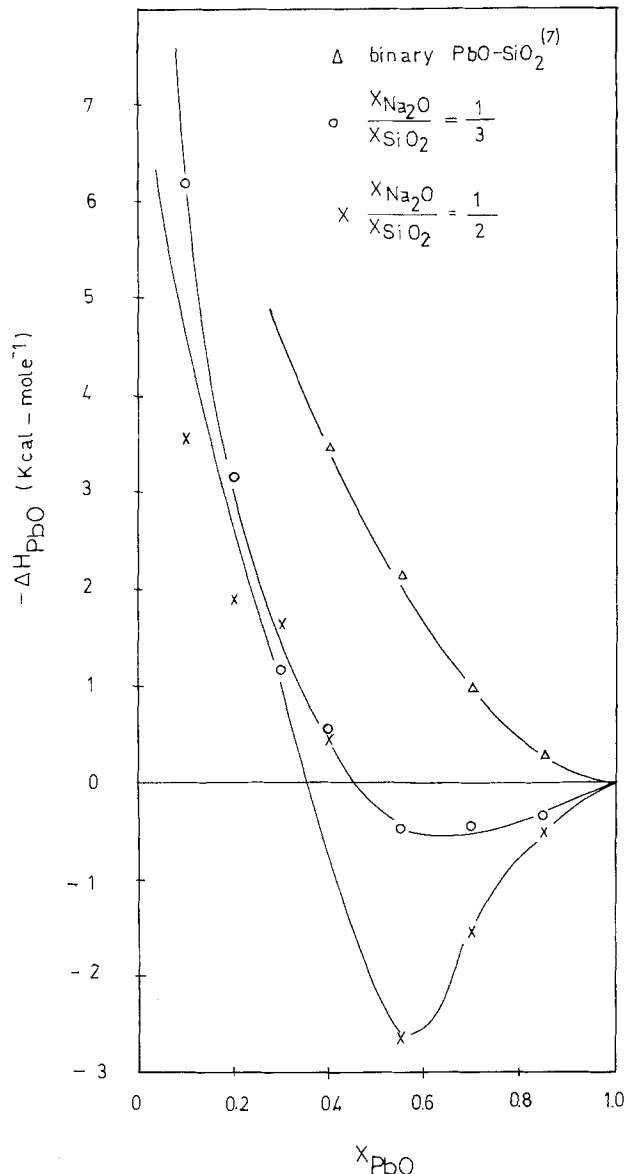


Fig. 10. Concentration dependence of the partial molar enthalpies of mixing of PbO for various values of the ratio  $X_{\text{Na}_2\text{O}}/X_{\text{SiO}_2}$ .

produces a rise in the activity of the latter. The explanation for this observation is that  $\text{SiO}_2$  reacts with  $M_{II}\text{O}$ , so that the proportion of  $M_I\text{O}$  left "unreacted" is increased and its activity also increases. Accordingly, for a given temperature and composition of the ternary slag, the highest activity of  $M_I\text{O}$  is reached when the nature of the  $M_{II}\text{O}$  component is such that it reacts completely with  $\text{SiO}_2$ . The phenomenon may be represented by the simplified reaction

Table II. PbO Activity data in the PbO-Na<sub>2</sub>O-SiO<sub>2</sub> system

$X_{\text{PbO}}$	Activities of PbO														
	$X_{\text{Na}_2\text{O}}:X_{\text{SiO}_2} = 0^*$ (binary PbO-SiO <sub>2</sub> )			$X_{\text{Na}_2\text{O}}:X_{\text{SiO}_2} = 1:3$				$X_{\text{Na}_2\text{O}}:X_{\text{SiO}_2} = 1:2$				$X_{\text{Na}_2\text{O}}:X_{\text{SiO}_2} = 1:1$			
	1123°K	1223°K	1273°K	1123°K	1173°K	1223°K	1273°K	1123°K	1173°K	1223°K	1273°K	1223°K	1273°K	1223°K	1273°K
0.0	0	0	0	0	0	0	0	0	0	0	0	0	0	0	0
0.10	—	—	—	0.013	0.014	0.016	0.018	0.036	0.038	0.041	0.043	—	—	—	—
0.20	—	—	—	0.057	0.060	0.064	0.067	0.145	0.149	0.155	0.160	0.688	—	0.590	—
0.30	—	—	—	0.149	0.152	0.155	0.159	0.271	0.280	0.288	0.295	0.824	—	0.790	—
0.40	0.068	0.076	0.081	0.301	0.304	0.307	0.310	0.487	0.490	0.495	0.498	—	—	—	—
0.55	0.165	0.169	0.171	0.578	0.574	0.568	0.564	0.763	0.725	0.693	0.664	—	—	—	—
0.70	0.410	0.424	0.440	0.771	0.764	0.758	0.753	0.822	0.798	0.777	0.758	—	—	—	—
0.85	0.832	0.845	0.852	0.885	0.881	0.876	0.871	0.902	0.892	0.884	0.877	—	—	—	—
1.0	1.00	1.00	1.00	1.00	1.00	1.00	1.00	1.00	1.00	1.00	1.00	1.00	1.00	1.00	1.00

\* Data from Charette and Flengas (7).

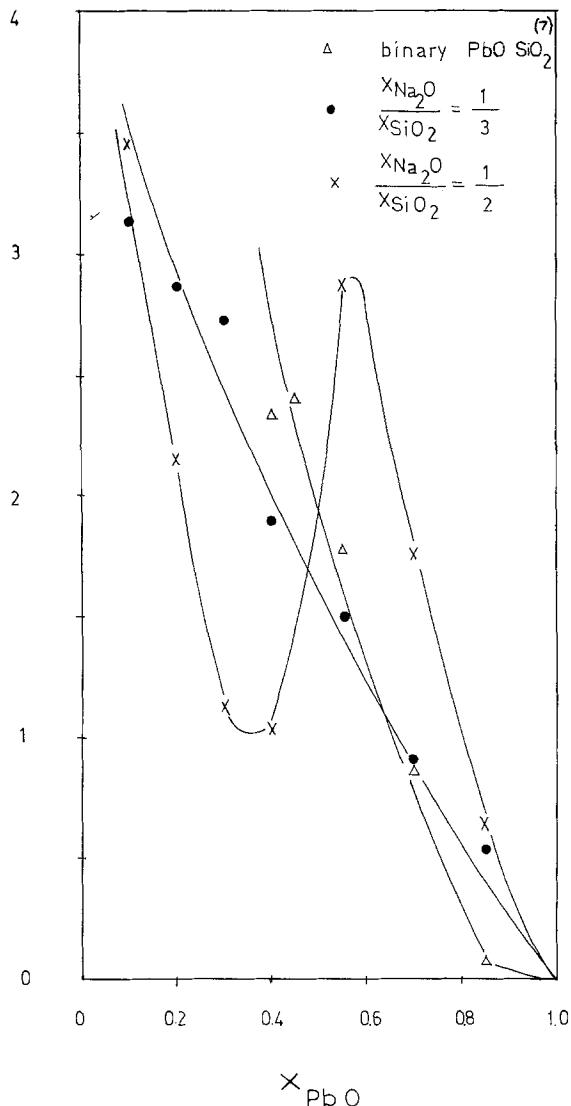
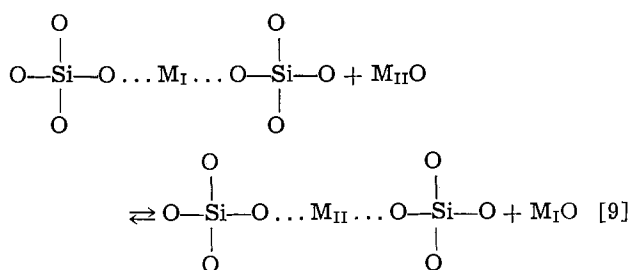


Fig. 11. Concentration dependence of the partial molar entropies of mixing of PbO for various values of the ratio  $X_{Na_2O}/X_{SiO_2}$ .



In the case of the PbO-Na<sub>2</sub>O-SiO<sub>2</sub> system, it is seen in Fig. 8 that the activities of PbO show a significant in-

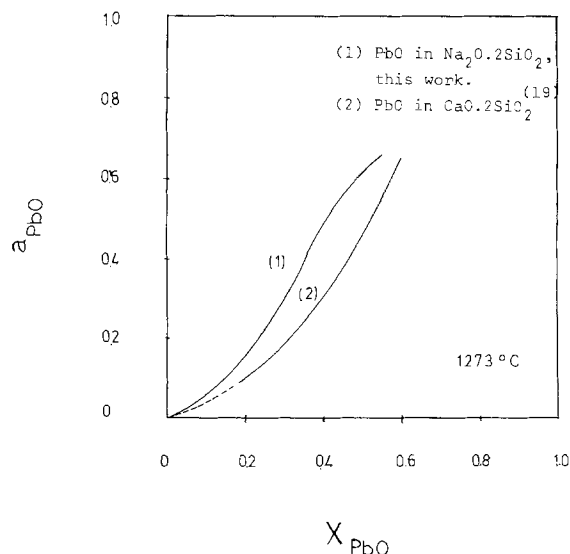


Fig. 12. Experimental concentration dependence of the activities of PbO dissolved in Na<sub>2</sub>O · 2SiO<sub>2</sub> and in CaO · 2SiO<sub>2</sub> at 1000°C.

crease with increasing concentrations of Na<sub>2</sub>O. Accordingly, the latter should be expected to behave as a highly reactive metal oxide with respect to silica. Since this characteristic is also a property of CaO, then the activities of PbO in the PbO-Na<sub>2</sub>O-SiO<sub>2</sub> melts should not be dramatically changed by replacing the Na<sub>2</sub>O component by CaO. The effect of this replacement is shown in Fig. 12, and it is interesting to note that Na<sub>2</sub>O appears to be more efficient than CaO in raising the activity of PbO. This observation could be of some use in metallurgical processes involving slag-metal reactions and where the recovery of a metal from the slag is largely affected by the activity of the corresponding metal oxide in this phase. However, from the available experimental data, it is not clear that this observation can be extended to systems containing metal oxides other than PbO.

The high escaping tendency of PbO from the PbO-Na<sub>2</sub>O-SiO<sub>2</sub> solutions seems to be partially caused by the existence of repulsive interactions between the PbO and Na<sub>2</sub>O components. This interpretation is suggested by the marked tendency toward positive heats of mixing evidenced in Fig. 10 and is supported by the activity data for a number of metal oxides dissolved in sodium disilicate melts which have been summarized in Fig. 13. From the tendencies observed in binary silicate melts, these activities are expected to decrease in the order NiO-CoO-FeO-PbO. This sequence is respected by the oxides of the transition metals Ni, Co, and Fe. However, the activities of PbO are seen to be higher than those of CoO and FeO. It appears, therefore, that there exist strong interactions between PbO and Na<sub>2</sub>O which are not comparable to similar interactions that may exist between the other metal oxides and Na<sub>2</sub>O.

Table III. Partial molar enthalpies and entropies of mixing of PbO in the PbO-Na<sub>2</sub>O-SiO<sub>2</sub> system

$X_{PbO}$	$X_{Na_2O}:X_{SiO_2} = 0^*$ (binary PbO-SiO <sub>2</sub> )		$X_{Na_2O}:X_{SiO_2} = 1:3$		$X_{Na_2O}:X_{SiO_2} = 1:2$		$X_{Na_2O}:X_{SiO_2} = 1:1$	
	$\Delta\bar{H}_{PbO}^\dagger$	$\Delta\bar{S}_{PbO}^\ddagger$	$\Delta\bar{H}_{PbO}^\dagger$	$\Delta\bar{S}_{PbO}^\ddagger$	$\Delta\bar{H}_{PbO}^\dagger$	$\Delta\bar{S}_{PbO}^\ddagger$	$\Delta\bar{H}_{PbO}^\dagger$	$\Delta\bar{S}_{PbO}^\ddagger$
0.10			-6220	3.14	-3560	3.46		
0.20			-3180	2.86	-1900	2.15	+9530	8.54
0.30			-1190	2.73	-1650	1.13	+2610	2.52
0.40	-3450	2.33	-560	1.89	-440	1.03		
0.55	-2150	1.78	+470	1.50	+2630	2.88		
0.70	-980	0.88	+450	0.92	+1540	1.76		
0.85	-300	0.09	+340	0.54	+500	0.65		
1.00	0	0	0	0	0	0	0	0

\* Data from Charette and Flengas (7).

†  $\Delta\bar{H}_{PbO}$  in cal/mole.

‡  $\Delta\bar{S}_{PbO}$  in cal/mole-°K.

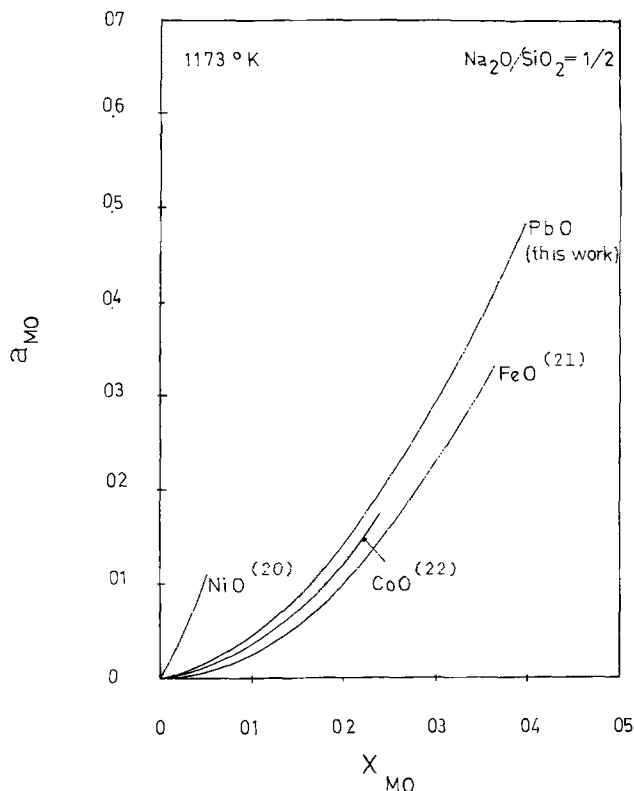
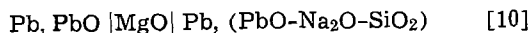


Fig. 13. Activity data at 1000°C for a number of metal oxides dissolved in  $\text{Na}_2\text{O} \cdot 2\text{SiO}_2$ .

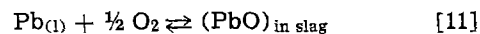
The activities of PbO in the PbO- $\text{Na}_2\text{O}$ - $\text{SiO}_2$  system have also been measured by Esin and co-workers (28) by using an electrochemical cell of the type



where the electrical contact for the electrodes was provided by means of graphite rods. Their results, however, are in total disagreement with those reported in this paper. These authors found that the replacement of  $\text{SiO}_2$  by  $\text{Na}_2\text{O}$  in the solutions (at constant mole fraction of PbO) results in a decrease of the activity of PbO. This is opposed to the behavior observed in the present work and in other thermodynamic investigations on ternary silicate melts (10, 16-19). Furthermore, the activities of PbO in the PbO- $\text{SiO}_2$  binary melts reported by Esin and co-workers (28) disagree completely with the well-established (4-9) concentration dependence of that property.

The reasons for the disagreement should be found in the experimental technique used by Esin. In the first place, it is now recognized that fused MgO is not a purely oxygen-ion conductor as it is in the case of the substitutional solid solutions  $\text{ZrO}_2$ - $\text{CaO}$ ,  $\text{ThO}_2$ - $\text{Y}_2\text{O}_3$ , etc. Thus, the use of the MgO membrane may have introduced an important error in the measured cell emf's. The second source of error should be found in the use of graphite as the electrical connection for the electrodes, since this will result in a value of the oxygen partial pressure different from the equilibrium

pressure that would coexist with pure liquid Pb and PbO in solution according to the reaction



### Acknowledgment

The authors are grateful to the National Research Council of Canada for its financial assistance in support of this work.

Manuscript submitted May 19, 1975; revised manuscript received Aug. 4, 1975.

Any discussion of this paper will appear in a Discussion Section to be published in the December 1976 JOURNAL. All discussions for the December 1976 Discussion Section should be submitted by Aug. 1, 1976.

Publication costs of this article were partially assisted by the University of Toronto.

### REFERENCES

1. R. Schuhmann, Jr. and P. J. Ensio, *Trans. AIME*, **191**, 401 (1951).
2. C. Bodsworth, *J. Iron Steel Inst. (London)*, **193**, 13 (1959).
3. P. A. Distin, S. G. Whiteway, and C. R. Masson, *Can. Met. Quart.*, **10**, 73 (1972).
4. F. D. Richardson and L. E. Webb, *Trans. Inst. Min. Met.*, **64**, 529 (1955).
5. R. Sridhar and J. H. E. Jeffes, *ibid.*, **76**, C44 (1967).
6. Z. Kozuka and C. S. Samis, *Met. Trans.*, **1**, 871 (1970).
7. G. G. Charette and S. N. Flengas, *Can. Met. Quart.*, **7**, 191 (1968).
8. M. L. Kappor and M. G. Froberg, *Arch. Eisenhüttenw.*, **42**, 5 (1971).
9. G. Papst and H. Schmalzried, *Z. Phys. Chem. N.P.*, **82**, 206 (1972).
10. K. P. Abraham, M. W. Davies, and F. D. Richardson, *J. Iron Steel Inst.*, **196**, 82 (1960).
11. I. B. Smith and C. R. Masson, *Can. J. Chem.*, **49**, 683 (1971).
12. D. M. Chizikov, M. E. Volvoka, and Yu. V. Isvetkov, *Izv. Akad. Nauk SSSR Met. Gorn. Delo*, **3**, 82 (1964).
13. Z. Kozuka, O. P. Siahaan, and J. Moriyama, *Trans. Japan. Inst. Metals*, **9**, 200 (1969).
14. J. Carbo and F. D. Richardson, *Trans. Inst. Min. Met.*, **81**, C131 (1972).
15. T. Østvold and J. Kleppa, *J. Inorg. Chem.*, **8**, 78 (1969).
16. K. L. Fetters and J. Chipman, *Trans. AIME*, **145**, 95 (1941).
17. C. R. Taylor and J. Chipman, *ibid.*, **154**, 228 (1953).
18. J. F. Elliot, *ibid.*, **203**, 485 (1955).
19. F. D. Richardson and T. C. M. Pillay, *Trans. Inst. Min. Met.*, **66**, 309 (1957).
20. A. M. Lacy and J. A. Pask, *J. Am. Ceram. Soc.*, **53**, 559 (1970).
21. A. M. Lacy and J. A. Pask, *ibid.*, **54**, 236 (1971).
22. A. M. Lacy and J. A. Pask, *ibid.*, **54**, 236 (1971).
23. G. G. Charette and S. N. Flengas, *This Journal*, **115**, 796 (1968).
24. E. T. Turkdogan and R. J. Fruehan, *Can. Met. Quart.*, **11**, 371 (1972).
25. C. B. Alcock and J. C. Chan, *ibid.*, **11**, 559 (1972).
26. L. Brewer and J. Margrave, *J. Phys. Chem.*, **59**, 421 (1955).
27. "Phase Diagrams for Ceramists," edited by the American Ceramic Society, p. 179, 2nd edition (1969).
28. O. A. Esin, I. T. Sryvalin, and V. V. Khlynov, *USSR J. Inorg. Chem.*, **2**, 237 (1957).



# Computer-Controlled Differential Capacitance Measurements

David M. Mohilner,\* Joyce C. Kreuser, and Hisamitsu Nakadomari<sup>1</sup>

Department of Chemistry, Colorado State University, Fort Collins, Colorado 80523

and Patricia R. Mohilner

Department of Computer Science, Colorado State University, Fort Collins, Colorado 80523

## ABSTRACT

The apparatus and technique for making differential capacitance measurements on a dropping mercury electrode under computer control are described. Sample results for electrolyte solutions and for aliphatic alcohol solutions are presented. A comparison of interfacial tension and differential capacitance measurements, both under computer control, reveals a source of systematic error in differential capacitance measurements which has generally been ignored in the past. Theoretical and experimental results are used to argue that differential capacitance is not a suitable experimental route to electro sorption isotherms for organic compounds.

For many years it was generally believed that differential capacitance measurements at a dropping mercury electrode (DME) based on the a-c impedance bridge method originated in 1941 by Grahame (1) were inherently more accurate than electrocapillary measurements and were therefore the best source of reliable information about the structure of the electrical double layer. A few years ago, however, a computer-controlled capillary electrometer was developed in this laboratory (2, 3) which is much faster and easier to use than the manual a-c bridge, and which was shown to yield data which are quite comparable to the best which can be obtained from a bridge for simple salt solutions. In the case of organic compounds, this computer-controlled capillary electrometer yields superior data, one reason for which is the difficulty of properly correcting capacitance measurements for frequency dispersion (4-6). A careful recent study (7) has indeed shown that the 95% confidence limits of the interfacial tension measured by the computer-controlled capillary electrometer do not exceed  $0.1 \text{ dyne cm}^{-1}$  and are independent of electrode potential, which implies a relative precision of about 1 part in 4000. Nevertheless, it seemed to us that it was not really fair to compare capacitance measurements obtained with a manual a-c bridge with computer-controlled electrocapillary data. Therefore we have designed a computer-controlled differential capacitance measuring instrument. In this paper we report on the design and operation of this instrument, and we evaluate its performance by direct comparison of integrated differential capacitance curves with electrocapillary curves on the same solution obtained with the computer-controlled capillary electrometer. One result of this direct comparison is that we have found a source of systematic error in differential capacitance measurements which may be serious in certain cases and which has generally been ignored in the literature (8). This particular source of systematic error probably could not have been detected from manual bridge measurements, but it is easily made manifest when the measurements are computer controlled.

## Experimental

**Apparatus.**—The a-c bridge was replaced by an operational amplifier potentiostat coupled with a phase sensitive current detector. This circuit was interfaced to a Digital Equipment Corporation (DEC) PDP-8/I minicomputer with 8K core and 32K fixed head disk.

\* Electrochemical Society Active Member.

<sup>1</sup> Present address: Department of Applied Science, Brookhaven National Laboratory, Upton, New York 11973.

Key words: electro sorption, surface excess, electrocapillarity, dropping mercury electrode.

The potentiostat circuit was similar to that described by deLevie and Husovsky (9). The phase sensitive current detector consists of an operational amplifier current-to-voltage converter coupled to a commercially available phase-lock amplifier (Ithaco Model 353, with Type D1 display unit, Type C1 demodulator, Type B1 amplifier, and Type H1 oscillator). The  $90^\circ$  phase angle switch on the front panel of the Type C1 demodulator was replaced by a mercury-wetted relay operating under computer control. A block diagram of the complete apparatus is shown in Fig. 1.

The d-c potential signal is supplied to the potentiostat by a 12-bit D/A converter on software command. The potentiostat input has a standard adder configuration. In addition to the d-c signal from the D/A converter, a d-c bias supply can be connected to the potentiostat input to permit the d-c potential of the electrode to be offset. The low frequency a-c signal for the capacitance measurements is supplied from the Type H1 oscillator, and the input resistance is normally chosen so that the controlled a-c potential of the electrode has an amplitude of 5 mV peak-to-peak. This same a-c signal from the Type H1 oscillator is connected to the reference input of the Type C1 demodulator to serve as the phase reference signal for the phase-lock amplifier. A second, high frequency (10 kHz), a-c oscillator can be connected to the potentiostat input via a computer-controlled mercury-wetted relay. This 10 kHz signal is connected to the DME momentarily before natural drop fall. The resulting 10 kHz a-c current is input to a birth detector

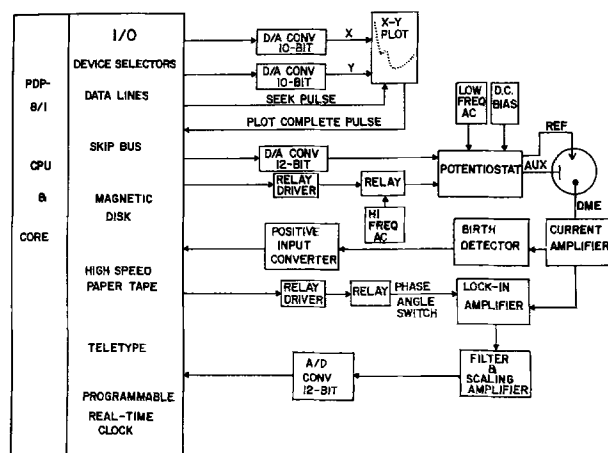


Fig. 1. Block diagram of apparatus for making computer-controlled differential capacitance measurements.

circuit similar to that described for the computer-controlled capillary electrometer (2). The birth detector circuit produces a sharp voltage pulse when the drop falls. This voltage pulse, signalling the beginning of a new drop, is input to the computer interface to start the programmable real-time clock which is used for timing the capacitance measurements. During capacitance measurement, the 10 kHz signal is disconnected from the potentiostat input by opening the relay contacts. The a-c current resulting from the 5 mV peak-to-peak controlled a-c potential is detected by a current-to-voltage converter whose output is input to the Type B1 amplifier of the Model 353 phase-lock amplifier system. This lock-in amplifier can be set by software command to detect either the in-phase or the 90° out-of-phase (quadrature) component. The output of the phase-lock amplifier is passed through a 50 Hz third-order Butterworth low-pass filter (10) into a Philbrick Model 1700 chopper stabilized operational amplifier which scales the signal appropriately and passes it to the sample-and-hold amplifier of the 12-bit A/D converter of the computer interface.

The three-electrode potentiostat can be connected either to the electrochemical cell or to a dummy cell consisting of a standard resistor and standard capacitor in series. The dummy cell is used for initial phase adjustments on the demodulator to compensate for the natural phase shifts of the potentiostat and current amplifiers. It is also used to adjust the phase angle switching circuitry so that on computer command the phase can be switched from exactly in-phase to exactly 90° out-of-phase. Finally the dummy cell is used to determine the calibration constant which is stored in the memory of the computer and is used to calculate the series capacitance and series resistance of the electrochemical cell from the measured in-phase and quadrature components of the a-c cell current.

An x-y plotter (Hewlett Packard Model 7004A) is interfaced to the computer so that a graphical display of the differential capacitance curve may be obtained during measurements. The digital data are typed on the teletype and are also punched on high speed paper tape for subsequent data analysis.

**Measurement procedure.**—Each time the a-c frequency is changed it is necessary to adjust the phase compensation for the operational amplifiers and the 90° phase angle switching circuitry. In order to make these adjustments more exact and more convenient, two modifications were introduced into the Type C1 demodulator. First, the single-turn phase angle adjustment potentiometer on the front panel (resistor R1) was replaced by a 10-turn Helipot with Duodial. Second, the single-turn variable resistor in the 90° phase angle switching circuit (resistor R97) which was originally located on the printed circuit board of the C1 demodulator was replaced by a 25-turn trimpot on the front panel.

The demodulator is first adjusted to compensate for the natural phase shifts of the operational amplifier circuitry by using a purely resistive dummy cell. For this purpose the phase angle switch of the demodulator is set to detect the quadrature component which should be exactly zero for a purely resistive dummy cell, and the Helipot is adjusted until the A/D reading is exactly zero. Next a dummy cell is inserted with the series resistor and capacitor selected so that the phase angle for the chosen a-c frequency is exactly 45°. The in-phase and quadrature components for this cell should be equal. The computer switches the phase angle to read alternately both of these components, and the A/D readings are typed out on the teletype. If the two A/D readings are not equal, the 25-turn trimpot is adjusted until they are equal. Since there is an interaction between this adjustment and the phase compensation adjustment, the latter is rechecked. Usually after two or three trials the two adjustments can be set so that a purely re-

sistive dummy cell gives a quadrature component which is exactly zero, and the dummy cell with 45° phase angle gives exactly equal in-phase and quadrature components. These two adjustments of the phase-lock circuitry, are vital for accurate differential capacitance measurements. They must be made every time the a-c frequency is changed, and even when one is operating at a single frequency they should be checked periodically.

The apparatus is calibrated using the same dummy cell with series standard resistance,  $R_{STD}$ , and standard capacitance,  $C_{STD}$ , so chosen that the phase angle is exactly 45°. For this purpose the computer first sets the phase angle switch of the demodulator to detect the current which is in-phase with the applied a-c potential and the voltage,  $V_D$ , which corresponds to the in-phase dummy cell current is measured by the A/D converter. Then the computer switches the detected phase angle to exactly 90° out-of-phase and the corresponding voltage,  $V''_D$ , is read by the A/D converter. The calibration factor,  $K$ , for the measurements is then calculated from the values of  $V_D$  and  $V''_D$  using the following formula which can be easily derived by standard a-c circuit analysis (11)

$$\begin{aligned} K &= C_{STD}/[V''_D + (V_D)^2/V''_D] \\ &= 1/(\omega R_{STD})[V''_D + (V''_D)^2/V''_D] \end{aligned} \quad [1]$$

In Eq. [1]  $\omega$  is the angular frequency of the applied a-c potential in radian sec<sup>-1</sup>. In all experiments described here the a-c frequency was measured with a Monsanto Model 110B programmable counter-timer.

The measured series resistance,  $R_s$ , and series capacitance,  $C_s$ , of the electrochemical cell at any electrode potential and at any instantaneous time in the drop life of the DME can then be determined by the following equations

$$(1/R_s) = \omega K[V'_m + (V''_m)^2/V'_m] \quad [2]$$

$$C_s = K[V''_m + (V'_m)^2/V''_m] \quad [3]$$

In Eq. [2] and [3]  $V'_m$  and  $V''_m$  denote the instantaneous values of the voltages read by the A/D converter corresponding to the in-phase and quadrature components of the cell current, respectively.  $C_s$  in Eq. [3] is equal to the capacitance of the electrical double layer of the DME provided that the surface area of the DME is negligibly small in comparison with the area of the auxiliary electrode (1, 8). In the measurements reported here the DME was placed in the center of a platinized cylindrical platinum gauze auxiliary electrode whose surface area was much larger than that of the DME. The differential capacitance per unit area,  $C$ , of the double layer is obtained by dividing  $C_s$  by the corresponding instantaneous area of the DME.

The computer is programmed so that for each value of the d-c electrode potential the in-phase voltage,  $V'_m$ , and the 90° out-of-phase voltage,  $V''_m$ , are measured at any desired times in the drop life on each of two successive drops. The timing sequence of the measurements is illustrated schematically in Fig. 2. Just before natural drop fall, the programmable real-time clock is stopped and its counter is zeroed. The fall of the drop causes the birth detector to issue a pulse which starts the clock recording the time in the life of the next drop. The computer then disconnects the 10 kHz input to the potentiostat and switches the phase angle switch on the demodulator to read the quadrature component. After waiting a specified period of time (for example, 2 sec) which is controlled by software command, the value of  $V''_m$  is read any desired number of times determined by the programmable clock and stored in memory. Then the 10 kHz signal is reconnected to the input of the potentiostat, the clock is stopped, and its counter is zeroed. When

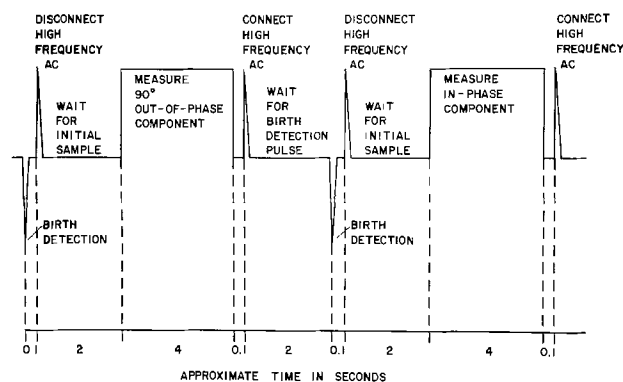


Fig. 2. Timing diagram for computer-controlled differential capacitance measurements.

the drop falls the clock is started again, the computer switches phase angle to in-phase, and after the same waiting period the value of  $V'_m$  is read at the same times in drop life as the  $V''_m$  readings, and the values are stored in memory. The d-c potential is then changed to the next value by the D/A converter, the 10 kHz a-c signal is connected again, and the sequence is repeated at the new electrode potential. After every two drops at a fixed d-c potential, the values of  $R_s$  and  $C_s$  are calculated for each of the times in drop life at which measurements were made by application of Eq. [2] and [3], and the differential capacitance,  $C$ , per unit area is calculated and plotted.

In the experiments described below the electrochemical cell and the calomel reference electrode were jacketed, and their temperatures were controlled at 25°C by pumping water from a thermostat through the jackets. The DME capillary was drawn from borosilicate glass to a fine tip, and the interior of the capillary was dewetted with the vapor of dichlorodimethylsilane by the method described previously (3). After dewetting, the capillary tip was recut so that the end of the capillary was wet by water. The sodium sulfate was reagent grade and was used without further purification. The mercury was triple vacuum distilled. The water used to prepare solutions was distilled from alkaline permanganate and then redistilled to prevent carry-over of traces of permanganate. The 2-butanol was distilled, and its purity was verified by gas chromatography.

### Results and Discussion

**Electrolyte solutions.**—It was decided that the best way to evaluate the performance of this instrument would be to compare directly the results of the capacitance measurements with electrocapillary measurements performed with the computer-controlled capillary electrometer on the same solution. Therefore we measured the differential capacitance of the DME in a solution of 0.05M sodium sulfate at 25°C. This solution is always used as the calibration solution for the capillary electrometer because an accurate, independent measurement by the sessile drop method of the interfacial tension of mercury at the electrocapillary maximum is available for it (12). Electrocapillary measurements were made on the same solution using the same reference electrode (a 0.1M KCl calomel electrode) employed in the capacitance measurements.

In the first experiments the computer was programmed to measure  $V'_m$  and  $V''_m$  at three different times 0.1 sec apart in the life of a drop, namely, 4.8, 4.9, and 5.0 sec. The area,  $A_{SPH}$ , of the electrode at each of these times was calculated, as in most published differential capacitance studies, by the following equation which assumes that the drop is spherical

$$A_{SPH} = (6m\sqrt{\pi}/d)^{2/3}t^{2/3} \quad [4]$$

In Eq. [4]  $m$  is the mass flow rate of the DME in  $g\text{-sec}^{-1}$ ,  $d$  is the density of mercury at 25°C in  $g\text{-cm}^{-3}$ , and  $t$  is the time in seconds in the drop life of the measurement. The series capacitance,  $C_s$ , of the electrochemical cell, which is the same as the differential capacitance of the DME, was calculated by means of Eq. [3] and the corresponding value of the differential capacitance per unit area,  $C$ , was calculated by dividing  $C_s$  by  $A_{SPH}$ . The precision of the measurement appeared to be very good. At all electrode potentials the relative standard deviation of  $C$  determined from the measurements of  $C_s$  at the three different times was about 0.05%. The differential capacitance per unit area,  $C$ , was then doubly integrated as a function of electrode potential,  $E$ , to obtain the interfacial tension,  $\gamma$ , by application of the equation from the thermodynamic theory of electrocapillarity (13)

$$\gamma = - \int_{\gamma_{\max}}^{\gamma} \int_{E_z}^E C dE dE + \gamma_{\max} \quad [5]$$

where  $\gamma_{\max}$  is the value of the interfacial tension at the electrocapillary maximum, and  $E_z$  is the potential of the electrocapillary maximum. The value of  $\gamma_{\max}$  is 426.2 dyne  $\text{cm}^{-1}$  (12) at 25°C, and the value of  $E_z$  was determined by digital computer fitting of the directly measured electrocapillary curve using the previously published digital computer techniques (14, 15).

The results of this double integration, which are shown in Fig. 3, were disturbing. In this figure, the smooth curve is the double integral of the differential capacitance, and the points are the interfacial tensions measured directly with the computer-controlled capillary electrometer. Except for the electrocapillary maximum, where there is a forced fit, the double integral of the differential capacitance lies systematically above the directly measured values of  $\gamma$ , and the magnitude of this systematic error increases progressively as the potential differs more and more from  $E_z$ . In fact, it can be seen from Fig. 3 that on the far cathodic branch of the electrocapillary curve the systematic error approaches 2 dyne  $\text{cm}^{-1}$ , which is 20 times the 95% confidence limits of the direct measurements of  $\gamma$  with the computer-controlled cap-

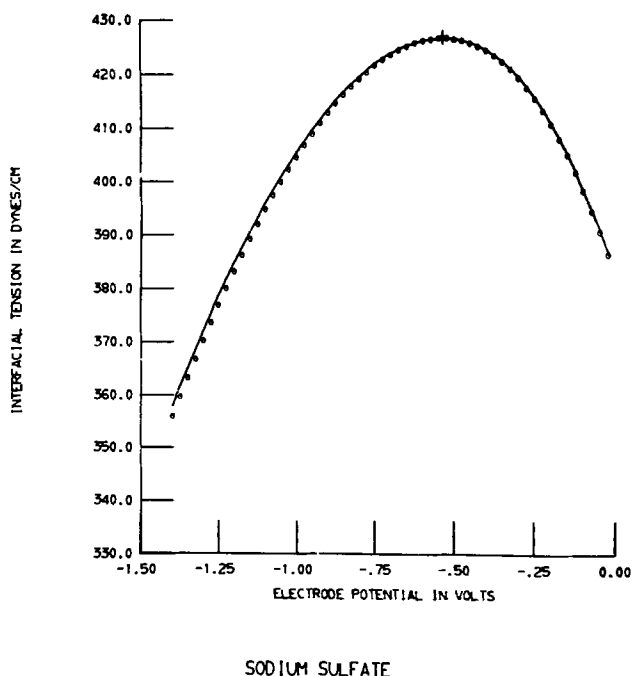


Fig. 3. Comparison of directly measured interfacial tension (circles) and doubly integrated differential capacitance (smooth curve) for 0.05M  $\text{Na}_2\text{SO}_4$  at 25°C before correction for excluded area due to capillary orifice.

illary electrometer. Such large systematic errors, clearly, could lead to serious errors in determination of relative surface excesses from the slopes of plots of  $\gamma$  at constant electrode potential vs. chemical potential of adsorbate (13).

In searching for a source of this systematic error, we decided to try measurements of  $V'_m$  and  $V''_m$  at different times in the drop life. It was observed that when the time interval between measurements was increased the relative standard deviation of  $C$ , the differential capacitance per unit area, determined from three measurements on one drop, also increased. For example, when the interval was increased from 0.1 to 2.0 sec the relative standard deviation increased from about 0.05 to 1.0%. This fact led us to record the value of the apparent capacitance per unit area,  $C$ , separately for each time of measurement. It was found that the apparent value of  $C$  at any fixed electrode potential increased as the time of measurement,  $t$ , increased. Typical results are illustrated in Fig. 4. The top curve in this figure gives  $C$  for 7.0 sec, the middle curve is for 5.0 sec, and the lowest curve is for 3.0 sec in drop life. Since  $C$  must be independent of the actual area of the electrode, this result suggested that the difficulty might lie in our calculation of the area of the drop as a function of time.

In the literature (8), there are numerous discussions of two possible sources of error in determining the correct area of a DME. The first source of error is the variation with time of the flow rate of mercury,  $m$ , due to the back pressure resulting from the interfacial tension. The second source of error is nonspherical shape. According to Payne (8a), "The absolute accuracy of the capacity measurement may be no better than 1% because of these factors." However, there is one even more obvious source of error in the calculation of the area of the drop which apparently has never been seriously considered (8b). This third source of error is simply the fact that even if the drop is truly spherical in shape its true area cannot be the area of a sphere of the same radius, because at the place where the drop connects with the column of mercury, i.e., at the orifice of the capillary, there is an excluded area not in contact with the solution. The true area,  $A_t$ , of the drop should therefore be

given by the area of the sphere,  $A_{SPH}$ , minus the area of the orifice,  $A_o$ . Therefore, assuming that the mass flow rate of mercury may be taken as a constant

$$A_t = A_{SPH} - A_o = (6m\sqrt{\pi}/d)^{2/3}t^{2/3} - A_o \quad [6]$$

The measured series capacitance,  $C_s$ , will then be given by

$$C_s = C(6m\sqrt{\pi}/d)^{2/3}t^{2/3} - CA_o \quad [7]$$

where  $C$  is the true differential capacitance per unit area.

We therefore changed the computer program to take the data in a new way in conformity with Eq. [7]. On one drop the computer samples the value of  $V''_m$  at 128 different times. On the next drop it samples the value of  $V'_m$  at the same times. Then the series capacitance,  $C_s$ , for each of these 128 different times is calculated from Eq. [3], and  $C_s$  is fitted to a least squares straight line as a linear regression on  $t^{2/3}$ . Typical results are shown in Fig. 5. It was found that at all potentials such least squares fits were very good. The differential capacitance at each potential was then calculated according to Eq. [7] from the slope of the least squares straight line. Figure 6 shows the differential capacitance curve for 0.05M  $\text{Na}_2\text{SO}_4$  at 25°C obtained by this new method. The value of  $C$  at any potential on this curve is higher than that calculated by the old method for any time in drop life (cf. Fig. 4) as it should be if Eq. [7] is correct.

The new differential capacitance curve was doubly integrated as a function of electrode potential and compared to the electrocapillary curve for the same solution directly measured by the computer-controlled capillary electrometer. The results are shown in Fig. 7. It can be seen from this figure that the agreement between the double integral of the capacitance and the directly measured electrocapillary curve is essentially perfect. In fact, the over-all difference between the two electrocapillary curves is within the 95% confidence limits ( $\pm 0.1$  dyne  $\text{cm}^{-1}$ ) of the directly measured interfacial tensions. Similar excellent agreement has been achieved with numerous other electrolyte solutions. We therefore believe that our new method of measuring the differential capacitance, tak-

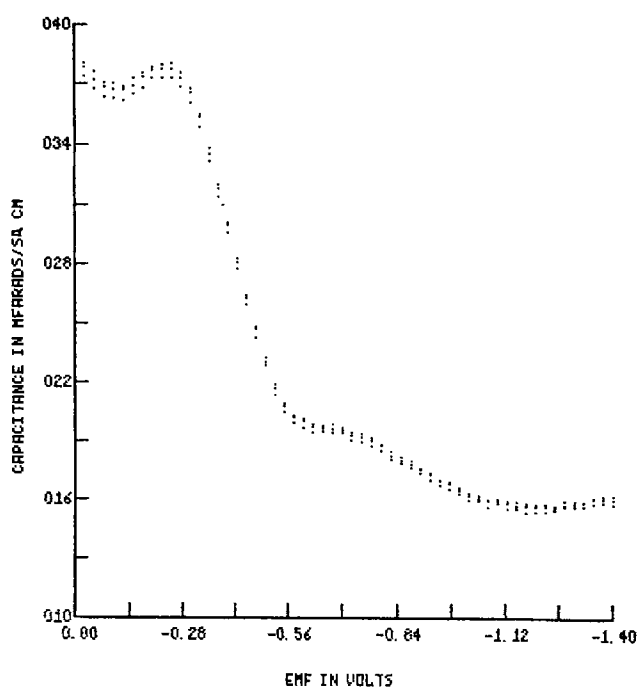


Fig. 4. Apparent differential capacitance per unit area for DME in 0.05M  $\text{Na}_2\text{SO}_4$  at 25°C measured at different times in drop life. Upper curve, 7 sec.; middle curve, 5 sec.; lower curve, 3 sec.

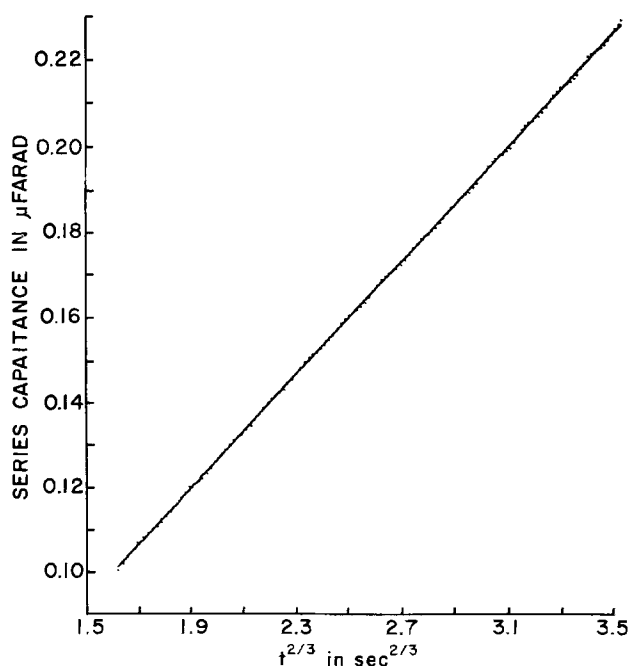


Fig. 5. Typical example of least squares straight line  $C_s$  vs.  $t^{2/3}$  0.05M  $\text{Na}_2\text{SO}_4$  at  $-0.525\text{V}$  vs. 0.1M KCl calomel electrode. The 128 points and the least squares straight line shown are the computer-plotted graph.

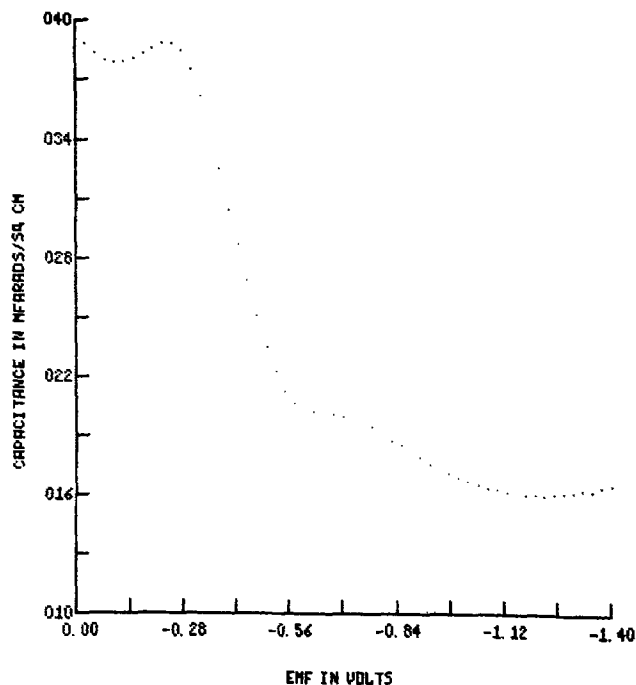


Fig. 6. Differential capacitance curve for 0.05M  $\text{Na}_2\text{SO}_4$  at 25°C obtained by taking account of excluded area due to capillary orifice.

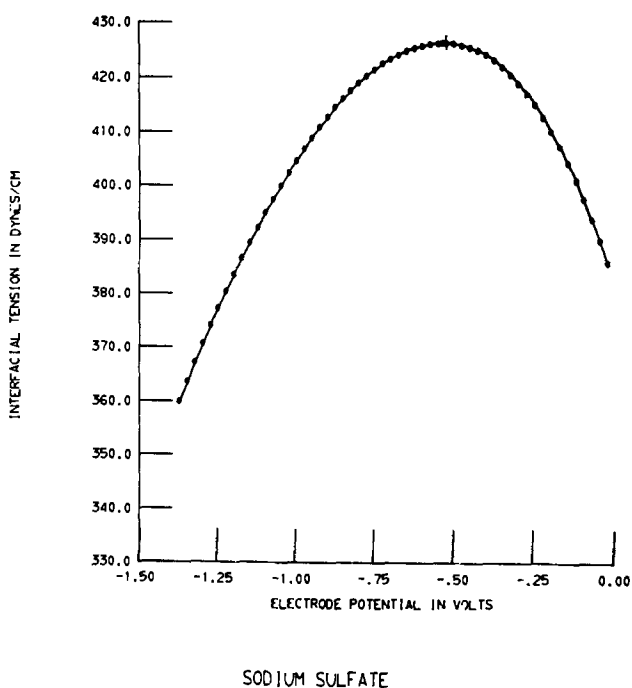


Fig. 7. Comparison of directly measured interfacial tension (circles) and doubly integrated differential capacitance (smooth curve) for 0.5M  $\text{Na}_2\text{SO}_4$  at 25°C after correction for excluded area due to capillary orifice.

ing account of the excluded area due to the capillary orifice according to Eq. [7], is the best way for obtaining thermodynamically meaningful differential capacitance curves. The excellence of the agreement between the doubly integrated capacitance and the directly measured electrocapillary curves seems to imply that the neglect of the excluded area of the orifice is the only serious error involved in obtaining the area of the drop as a function of time. Undoubtedly the back pressure effect and the nonsphericity effect are still present, but these must be second-order effects below the limits of error of the method of measurement. The fact that previously reported capacitance measurements using the manual a-c bridge have

neglected this source of error now casts some doubt on the absolute thermodynamic validity of those measurements. It would obviously be very difficult and tedious to determine the area of the capillary orifice by manual measurements but we would strongly urge that an attempt should be made in future manual capacitance measurements. Otherwise, this systematic error is bound to be present. Since all thermodynamic methods for determination of ionic surface excesses from differential capacitance, for example, the method of Grahame and Soderberg (16), necessarily involve integration of the capacitance, such systematic errors will be accentuated in the thermodynamic results. Because integration accentuates systematic error while smoothing out random error, such a systematic error can be especially insidious.

*Organic sorbates.*—It is also possible to measure the differential capacitance of the DME in the presence of organic sorbates using this computer-controlled apparatus. A typical example is the differential capacitance curve shown in Fig. 8 for a solution of 0.3M 2-butanol in a sodium sulfate solution in which the mean ionic activity,  $a_{\pm} = 0.07087$ , one of the solutions used in a recent study of the electroadsorption of 2-butanol (7, 17). The a-c frequency for this capacitance measurement was 102.4 Hz. This curve exhibits the typical shape which is usually observed for aliphatic compounds, i.e., two adsorption-desorption peaks and a low capacitance in the region of strong adsorption between the peaks. Such capacitance curves can be very useful for qualitative study of organic electroadsorption (18), and they are very quickly and easily measured with this computer-controlled apparatus. However, there are two serious complications involved in obtaining thermodynamic relative surface excesses of compounds from differential capacitance curves.

The first problem is that the differential capacitance which is actually measured (especially on the adsorption-desorption peaks) is frequency dependent, and the only capacitance which has thermodynamic significance is the limiting, zero frequency capacitance. Therefore, it is necessary to measure the capacitance at a series of frequencies and to extrapolate to zero frequency. This is simple enough if it is justifiable

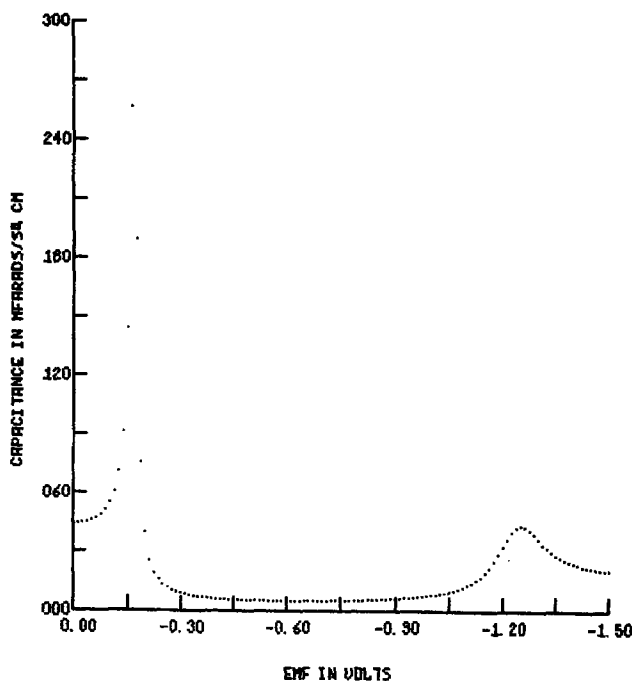


Fig. 8. Differential capacitance curve for 0.3M 2-butanol in  $\text{Na}_2\text{SO}_4$  solution with mean ionic activity of 0.07087 at 25°C. Frequency of measurement = 102.4 Hz. Electrode potential measured vs. 0.1M KCl calomel electrodes.

to plot the measured capacitance *vs.*  $\omega^{1/2}$  and take the intercept at  $\omega = 0$  as the true zero frequency or thermodynamic capacitance (5). Unfortunately, such a procedure can be very dangerous because, as Doblhofer and Mohilner (4) showed, it is possible to obtain plots of *C vs.*  $\omega^{1/2}$  which appear to be linear but which nevertheless yield too low values for the zero frequency capacitance. Therefore the only really safe method for extrapolating measured differential capacitance is the method of the Cole-Cole (19) plot as recommended by Armstrong *et al.* (6). This method requires that both the capacitance and the resistance due to the diffusion-controlled adsorption process be measured as a function of frequency at a sufficient number of frequencies to establish the Armstrong quarter-circle (6). Unfortunately, this requires a very accurate measurement of the series resistance of the cell as a function of time because the resistance due to the adsorption process is quite small and in series with the solution resistance. This means that in order to obtain the resistance due to the diffusion-controlled adsorption one must subtract two large numbers which are quite close to each other. We found that it was not possible to obtain the total cell resistance and the solution resistance with enough significant figures to yield, after subtraction, the resistance due to the diffusion-controlled adsorption with enough significant figures to permit a Cole-Cole analysis. It is possible that this problem might be overcome by adding a computer-controlled change in the amplification of the scaling amplifier which passes the output of the phase-lock amplifier to the A/D. However, we did not add this modification to the apparatus because it became clear that for any organic system the time required to take the capacitance and resistance data at enough different frequencies would be practically prohibitive. That is, the required electroadsorption data for an organic system could certainly be obtained in so much less time with the computer-controlled capillary electrometer (3) that it would be impractical to try to obtain the same information from capacitance data. Moreover, there is a second complication involved in the study of organic electroadsorption which has appeared as a result of a recent study carried out in this laboratory (7, 17, 20). We believe, in fact, that this second complication completely vitiates the idea of obtaining thermodynamic relative surface excesses of organic sorbates from differential capacitance measurements even if the frequency dispersion problem could be overcome.

Assuming that the proper zero frequency capacitances can be obtained, the only route (13) to thermodynamic relative surface excesses for the organic compound from differential capacitance data is still via the interfacial tension which can in turn only be obtained by double integration of the capacitance with respect to electrode potential. Such double integration requires prior knowledge of two integration constants, *i.e.*, the charge density,  $\sigma$ , and the interfacial tension,  $\gamma$ , at some electrode potential. Because  $E_z$  and  $\gamma_{\max}$  change drastically with increase of concentration of an organic sorbate (*cf.* Fig. 9) it is not feasible to carry out this double integration from the point of zero charge as in Eq. [5], for this would require prior measurement of the electrocapillary curve for each solution in order to obtain the required integration constants. It has been commonly believed that at electrode potentials far from  $E_z$ , where there is complete desorption of the organic compound, the electrocapillary curves for all solutions containing the organic compound merge with the electrocapillary curve for the base electrolyte solution. If this were true, then one could double integrate the differential capacitance from any potential in the region of total desorption, and the only integration constants required could be obtained from the electrocapillary curve of the base electrolyte solution. However, this

idea is actually incorrect both from a theoretical (13) and, as our recent study (7, 20) has shown, from a practical point of view.

According to the thermodynamic theory of electrocapillarity (13) the relative surface excess,  $\Gamma_{AW}$ , of the organic compound, A, with water, W, as the reference component is given by

$$\Gamma_{AW} = - (1/RT) (\partial\gamma/\partial \ln a_A)_{T,p,E,a_e} \quad [8]$$

where  $R$  is the gas constant,  $T$  is the absolute temperature,  $a_A$  is the bulk activity of the organic compound (21), and the subscripts T, p, E, and  $a_e$  indicate that the differentiation is carried out at constant temperature, pressure, electrode potential, and activity of the electrolyte (17) in the bulk solution. But  $\Gamma_{AW}$  is related to the true surface concentration of the organic compound,  $\Gamma_A$ , and of the adsorbed water,  $\Gamma_W$ , by the following equation (13)

$$\Gamma_{AW} = \Gamma_A - (x_A/x_W) \Gamma_W \quad [9]$$

where  $x_A$  and  $x_W$  are the bulk mole fractions of the organic compound and of the water, respectively. Now, clearly, if at some extreme electrode potential the organic compound is completely desorbed, *i.e.*,  $\Gamma_A = 0$ , it follows that  $\Gamma_{AW} < 0$ , since  $\Gamma_W$  will be positive. This implies that the interfacial tension will increase with increasing bulk activity of the organic compound. This means that in the potential region of total desorption of the organic compound the electrocapillary curve should rise progressively above the base electrolyte curve as the bulk activity of the organic compound is increased. This behavior is illustrated (7, 20) in Fig. 9 and 10 for the system 2-butanol in sodium sulfate solution. Figure 9 is the set of electrocapillary curves for the base electrolyte (0.1M  $\text{Na}_2\text{SO}_4$ ) and for 25 solutions containing successively increasing activities (21) of 2-butanol in solutions in which the mean ionic activity is the same ( $a_{\pm} = 0.07087$ ) as for the 0.1M  $\text{Na}_2\text{SO}_4$  in pure water (17). Examination of Fig. 9 shows that in the potential region in which adsorption of the organic compound occurs, the interfacial tension is progressively lowered and the potential of the electrocapillary maximum is progressively shifted in the anodic direction as the

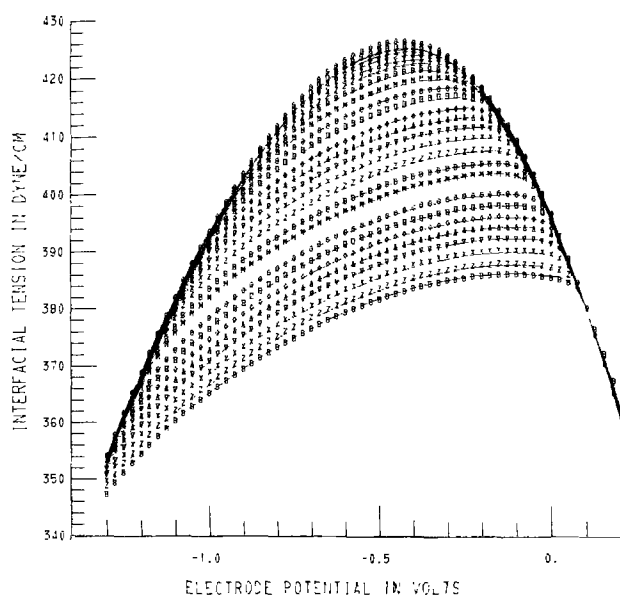


Fig. 9. Electrocapillary curves for 0.1M  $\text{Na}_2\text{SO}_4$  and 25 different activities of 2-butanol in solutions in which mean ionic activity is constant at 0.07087. Top curve in middle section is for base electrolyte. Other curves are for progressively increasing activities of 2-butanol from top to bottom [for details see Ref. (7) and (20)]. Electrode potential is measured vs. a Corning NAS 11-18 sodium ion glass electrode in same solution.

bulk activity of the 2-butanol is increased. However, on the far anodic side ( $E > +0.1V$ ) the 2-butanol is completely desorbed from the electrode surface. Since  $\Gamma_A = 0$ ,  $\Gamma_{AW} < 0$  and the interfacial tension rises at constant potential as the bulk activity of 2-butanol is increased. Simultaneously, the charge density at constant potential becomes less positive since the charge density,  $\sigma$ , is given by the Lippmann equation (13)

$$\sigma = -(\partial\gamma/\partial E)_{T,p,a_A,a_e} \quad [10]$$

This means that there is no electrode potential in the region of complete desorption of the organic compound in which the two integration constants required for integration of the differential capacitance are the same as on the base electrolyte electrocapillary curve. This behavior can be seen more clearly in Fig. 10 which is an expanded view of the same set of 26 electrocapillary curves in the electrode potential range  $+0.1$  to  $+0.2V$ . This result proves experimentally what was deduced above theoretically, that the old idea that the electrocapillary curves for the organic compound merge with the electrocapillary curve for the base electrolyte in the region of desorption is incorrect. Therefore the only way that the differential capacitance curves for the organic system can be integrated is to have a separate pair of integration constants for each concentration of the organic compound. This means that it would be necessary to have already measured the electrocapillary curves for every single solution.

The only other possible routes to organic electro-sorption isotherms from differential capacitance measurements involve various nonthermodynamic assumptions including those of congruence of the isotherm with respect to either the electrode potential (22) or the charge density (23, 24). Since our studies of organic electro-sorption (4, 7, 20) have indicated that organic electro-sorption isotherms are congruent with respect to neither of these electrical variables, we believe such approaches are unlikely to lead to correct results. We therefore recommend that the attempt to obtain electro-sorption isotherms for organic compounds from differential capacitance should be abandoned. The only valid route to such isotherms appears to be via interfacial tension measurements which can anyway be done more easily and more accurately

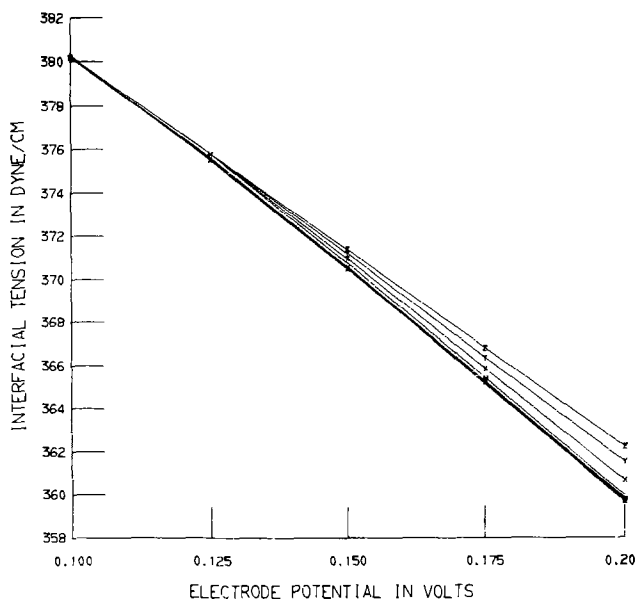


Fig. 10. Expanded view of electrocapillary curves shown in Fig. 9 for electrode potential region in which 2-butanol is desorbed. Lowest curve in this figure is for base electrolyte. Other curves are for progressively increasing activities of 2-butanol from bottom to top.

using the computer-controlled capillary electrometer (3) than can zero frequency differential capacitance measurements.

### Conclusions

A computer-controlled apparatus for measuring the differential capacitance of a dropping mercury electrode has been designed and evaluated. It was found that, provided account is taken of the excluded area due to the capillary orifice, the differential capacitance obtained with this instrument agrees with the electrocapillary curves obtained with a computer-controlled capillary electrometer within the confidence limits of the latter instrument. If account is not taken of the excluded area, serious systematic errors will occur. Such systematic errors must necessarily be present in most previously published differential capacitance measurements. This computer-controlled apparatus probably provides the easiest and most accurate method of obtaining differential capacitance curves for electrolyte solutions. An analysis of the problem involved in obtaining electro-sorption isotherms for organic sorbates from differential capacitance curves is given. It is concluded that except for qualitative purposes, differential capacitance should be abandoned as a route to thermodynamic electro-sorption isotherms for organic compounds. The best route to such isotherms is electrocapillary data obtained with a computer-controlled capillary electrometer.

### Acknowledgments

This work was supported by the U.S. Air Force Office of Scientific Research under Grant No. AF-AFOSR-70-1887. We thank Professor Robert deLevie, Georgetown University, and Dr. Roger Parsons, University of Bristol, for helpful discussion.

Manuscript submitted Aug. 15, 1975; revised manuscript received Oct. 17, 1975.

Any discussion of this paper will appear in a Discussion Section to be published in the December 1976 JOURNAL. All discussions for the December 1976 Discussion Section should be submitted by Aug. 1, 1976.

### REFERENCES

1. D. C. Grahame, *J. Am. Chem. Soc.*, **63**, 1207 (1941); *ibid.*, **68**, 301 (1946); *ibid.*, **71**, 2975 (1949).
2. J. Lawrence and D. M. Mohilner, *This Journal*, **118**, 259 (1971).
3. J. Lawrence and D. M. Mohilner, *ibid.*, **118**, 1596 (1971).
4. K. Doblhofer and D. M. Mohilner, *J. Phys. Chem.*, **75**, 1698 (1971).
5. R. Parsons and P. C. Symons, *Trans. Faraday Soc.*, **61**, 316 (1968).
6. R. D. Armstrong, W. P. Race, and H. R. Thirsk, *J. Electroanal. Chem.*, **16**, 517 (1968).
7. H. Nakadomari, D. M. Mohilner, and P. R. Mohilner, Submitted for publication.
8. (a) For a recent review in which methods for measuring differential capacitance are critically evaluated, cf., R. Payne in "Techniques of Electrochemistry," Vol. 1, E. Yeager and A. J. Salkind, Editors chap. 2, Wiley-Interscience, New York (1972).  
(b) The only reference in the prior literature of which we are aware in which the need for accounting for the excluded area due to the capillary orifice is mentioned is: G. H. Nancollas and C. A. Vincent, *Electrochim. Acta*, **10**, 97 (1965). We are indebted to one of the reviewers for calling this reference to our attention.
9. R. deLevie and A. A. Husovsky, *J. Electroanal. Chem.*, **20**, 181 (1969).
10. "Applications Manual for Computing Amplifiers," p. 75, G. A. Philbrick Researchers, Inc., Boston (1966) (Library of Congress Catalog Card No. 66-19610).
11. J. J. Brophy, "Basic Electronics for Scientists," 2nd ed., McGraw-Hill Book Co., New York (1972).
12. C. A. Smolders and E. M. Duyvis, *Rec. Trav. Chim.*, **80**, 635 (1961).



13. D. M. Mohilner, *Electroanal. Chem.*, **1**, 241 (1966).
14. D. M. Mohilner and P. R. Mohilner, *This Journal*, **115**, 261 (1968).
15. P. R. Mohilner and D. M. Mohilner, in "Computers in Chemistry and Instrumentation," Vol. 2, J. S. Mattson, H. B. Mark, Jr., and H. C. MacDonald Jr., Editors, chap. 1, Marcel Dekker, New York (1972).
16. D. C. Grahame and B. A. Soderberg, *J. Chem. Phys.*, **22**, 449 (1954).
17. D. M. Mohilner and H. Nakadomari, *J. Phys. Chem.*, **77**, 1594 (1973); *J. Electroanal. Chem.*, **65**, 843 (1975).
18. H. H. Bauer, H. R. Campbell, M. Langhorst, and A. K. Shallal, *J. Electroanal. Chem.*, **62**, 187 (1975).
19. K. S. Cole and R. H. Cole, *J. Chem. Phys.*, **9**, 341 (1941).
20. H. Nakadomari, Ph.D. dissertation, Colorado State University, 1974.
21. D. M. Mohilner, L. M. Bowman, S. J. Freeland, and H. Nakadomari, *This Journal*, **120**, 1658 (1973).
22. B. B. Damaskin, O. A. Petrii, and V. V. Batrakov, "Adsorption of Organic Compounds on Electrodes," Plenum Press, New York (1971).
23. R. Parsons, *J. Electroanal. Chem.*, **7**, 136 (1964).
24. R. Parsons, R. Peat, and R. M. Reeves, *ibid.*, **62**, 151 (1975).

## Current Distribution on a Disk Electrode for Redox Reactions

Peter Pierini, Peter Appel,<sup>1</sup> and John Newman\*

*Inorganic Materials Research Division, Lawrence Berkeley Laboratory, and Department of Chemical Engineering, University of California, Berkeley, California 94720*

### ABSTRACT

Current and concentration distributions on a rotating disk electrode are computed for general electrode reactions where the product concentrations must be included. The effect of migration on the surface concentration of the supporting electrolyte is also demonstrated.

Newman (1) introduced a method for the calculation of current and concentration profiles over the surface of a rotating disk electrode operated below the limiting current. The problem is complex, since the concentration variations near the electrode, the surface overpotential associated with the electrode reaction, and the ohmic potential drop in the bulk of the solution must be included in the analysis. The diffusion layer on a rotating disk electrode is thin compared with the characteristic dimensions of the electrochemical cells used in most experimental applications. This physical situation, in which the concentration changes rapidly in a region much smaller than the bulk of the solution where the potential continues to vary, was naturally formulated as a singular perturbation (6). Thus the potential in a large portion can be considered to satisfy Laplace's equation with the current density distribution on the boundaries matched to the mass flux entering the diffusion boundary layer. In the diffusion layer, the concentrations are determined from the appropriate mass transport equations with a mass flux at the electrode surface related by Faraday's law to the current density distribution on the electrodes, and with the concentrations approaching the bulk concentrations far from the electrode. The current distribution and concentrations at the electrode surface are further specified by the overpotential computed as the difference of the applied voltage, the equilibrium potential, and the ohmic drop in the solution (2). Marathe and Newman (3) experimentally proved the soundness of the theory by plating copper from a cupric sulfate-sulfuric acid solution and then measuring the thickness of the deposit. The potential mapping experiments of Miller and Bellavance (4) also agree quantitatively with theoretical predictions. Other verification exists in the work of Miller and Bruckenstein (11), and Smyrl and Newman (9, 12).

In an attempt to keep the treatment of the problem from being a quagmire of computational detail, com-

mon experimental situations were evaluated, and assumptions were made that would permit the broadest application of the theory. The flow was considered fully developed and laminar. The disk was designed to minimize edge effects. The mass transfer boundary layer must lie well within the hydrodynamic boundary layer; thus the Schmidt number must be large. Radial diffusion was neglected over the entire surface of the electrode, even at the outer edge. A mathematically convenient cell utilized a centered disk, embedded in an infinite insulating plane, and placed the counterelectrode at infinity. Actual cells must be carefully devised to approximate the condition of infinite dimension, or a correction to the potential description is necessary. Any electrochemical reaction may be studied except those evolving gas, but attention was restricted to metal deposition from a single salt solution and to an electrode reaction with an excess of supporting electrolyte, having a zero transference number and no dependence upon the product concentration.

Copper plating from a cupric sulfate solution is an example of the single salt reaction while the addition of enough sulfuric acid to suppress migration effects on the reactants illustrates the second type. Since the product does not remain in solution, it may be validly ignored. Any electrode reaction that involves only electron transfer usually requires that the effect of the product concentration be included. Redox couples and organic syntheses are in this class of reactions.

The alternating current response of a disk electrode has been investigated by Newman (13), but the effect of concentration variation was not included. Variations of double layer effects can be computed only if the concentrations of all the ionic species are known at the electrode surface. The supporting electrolyte does not participate in the surface reaction, but migration causes the surface concentration to deviate from the bulk solution. A future objective to treat the alternating current response more completely requires the knowledge of the local value of each component in solution.

We shall extend here the original perturbation scheme to general electrode reactions depending on both reactant and product concentrations and will de-

\* Electrochemical Society Active Member.

<sup>1</sup> Present address: Unilever Research, Vlaardinger, Holland.

Key words: current distribution, product dependent, supporting electrolyte concentration.



velop a procedure for determining the concentration of the supporting electrolyte. [See also Ref. (14).]

### Overpotential

The major departure from the formulation that omits the product dependence (1) lies in the treatment of the overpotential expressions and the variation of the exchange current density  $i_0$ . The necessary reaction parameters are conveniently introduced by the general electrode reaction



where  $s_i$  is the stoichiometric coefficient,  $M_i$  is the symbol for the chemical species,  $z_i$  is the species charge number, and  $n$  is the number of electrons participating in the reaction. The total voltage  $V$  applied to the cell is decomposed into the equilibrium potential  $U$ , ohmic drop  $\Phi_0$ , the concentration overpotential  $\eta_c$ , and the surface overpotential  $\eta_s$

$$V = U + \Phi_0 + \eta_c + \eta_s \quad [2]$$

The surface overpotential is defined by the Butler-Volmer expression

$$i = i_0 \left[ \exp\left(\frac{\alpha Z F}{RT} \eta_s\right) - \exp\left(-\frac{\beta Z F}{RT} \eta_s\right) \right] \quad [3]$$

The local value of the exchange current density  $i_0$  can be related to the concentrations of the reactants and products at the electrode surface by

$$i_0 = i_{0,\infty} \Pi \left( \frac{c_{i,o}}{c_{i,\infty}} \right)^{\gamma_i} \quad [4]$$

where  $i_{0,\infty}$  is a constant determined by the reaction properties and the constituents of the bulk solution, and  $Z$  is equal to  $-n$ . The kinetics parameters  $\alpha$ ,  $\beta$ , and  $\gamma_i$  are associated with the type of reaction occurring. The parameters of Eq. [3] and [4] may be measured experimentally; Newman (5) suggests rules for the evaluation of the exponents  $\gamma_i$ .

The concentration overpotential depends upon the variation of concentration through the diffusion layer in a complicated way. A relatively high electric conductivity which can be considered constant and enough supporting electrolyte to suppress the effect of migration on the reactants and products allow concentration dependent potential effects to be adequately represented by (6)

$$\eta_c = \frac{RT}{nF} \sum_i s_i \ln \left( \frac{c_{i,o}}{c_{i,\infty}} \right) \quad [5]$$

Although no formal arguments about the order of the perturbation approach have been given, Eq. [5] may be considered a first approximation which is justified by the small variation in electrical conductivity through the diffusion layer.

### Potential Distribution in the Bulk of the Solution Outside the Diffusion Layer

The potential distribution in the bulk of the solution outside the diffusion layer, where the concentrations are uniform, satisfies Laplace's equation. Rotational elliptic coordinates have proven both natural and convenient for the representation of the ohmic effects of rotating disk electrodes (1, 7). The expression for the potential at the surface of the electrode is

$$\Phi_0 = \frac{RT}{-nF} \sum_{m=0} B_m P_{2m}(\eta) \quad [6]$$

$P_{2m}(\eta)$  is the Legendre polynomial of order  $2m$  and  $\eta = \sqrt{1 - (r/r_0)^2}$  at the surface. The constants  $B_m$  are evaluated by taking the normal derivative of the potential distribution, then making use of the orthogonal properties of Legendre polynomials and the current

matching condition between the diffusion layer and the bulk solution.

### The Diffusion Layer

The mass balance is

$$v \cdot \nabla c_i = D_i \nabla^2 c_i + z_i u_i F \nabla \cdot (c_i \nabla \Phi) \quad [7]$$

Levich (8) advanced the idea of investigating the concentration distribution of all components in the solution by a perturbation technique. The method has been successfully applied to show the effect of ionic migration on the supporting electrolyte at the limiting current (15). For a solution that contains minor species and a binary indifferent electrolyte, the zero approximation omits the minor species. The potential and concentration profile associated with the supporting ions are then found to be constants, since the major species do not participate in the electrode reaction. Therefore, no current is passed, and the solution is the bulk concentration of the supporting ions,  $c_1^{(0)} = c_{1,\infty}$  and  $c_2^{(0)}$  is specified by electroneutrality. The first order approximation is

$$c_1 = c_1^{(0)} + c_1^{(1)}$$

$$c_2 = c_2^{(0)} + c_2^{(1)}$$

$$c_i = c_i^{(1)} \text{ where } i > 2 \quad [8]$$

Equation [8] is substituted into Eq. [7], and second order terms are dropped, which gives

$$v \cdot \nabla c_i^{(1)} = D_i \nabla^2 c_i^{(1)} \text{ for } i > 2 \quad [9]$$

$$v \cdot \nabla c_1^{(1)} = D_e \nabla^2 c_1^{(1)} + \sum_{i=3} \frac{z_i u_i (D_2 - D_i)}{z_1 u_1 - z_2 u_2} \nabla^2 c_1^{(1)} \quad [10]$$

The physical parameter  $D_e$  is the diffusion coefficient of the binary electrolyte

$$D_e \equiv \frac{z_1 u_1 D_2 - z_2 u_2 D_1}{z_1 u_1 - z_2 u_2} \quad [11]$$

The potential is eliminated between the two equations for the ions of the supporting electrolyte; then the electroneutrality condition is used to eliminate  $c_2^{(1)}$ .

The minor components are found by solving Eq. [9], the equation of convective diffusion that applies when the effect of migration can be ignored. Smyrl and Newman (9) have worked out a formal solution to Eq. [9] that can be applied to diffusion layers in laminar forced convection at high Schmidt numbers on axisymmetric bodies. The concentration derivative at the electrode surface, as a function of the surface concentration, is

$$\frac{\partial c_i}{\partial \zeta} \Big|_{\zeta=0} = \frac{-r}{\Gamma(4/3)} \int_0^r \frac{dc_{i,o}}{dr} \Big|_{r=r'} \frac{dr'}{(r^3 - r'^3)^{1/3}} \quad [12]$$

and Eq. [12] can be inverted

$$c_{i,o} - c_{i,\infty} = \frac{-1}{\Gamma(2/3)} \int_0^r \frac{\partial c_{i,o}}{\partial \zeta} \Big|_{\zeta=0} \frac{r' dr'}{(r^3 - r'^3)^{2/3}} \quad [13]$$

where the dimensionless distance from the surface is

$$\zeta = y (a\nu/3D_i)^{1/3} (\Omega/\nu)^{1/2} \quad [14]$$

All of the minor ionic species are either a reactant or a product in the general electrode reaction Eq. [1] which combined with Eq. [13] provides the relationship

$$\frac{c_{i,o} - c_{i,\infty}}{c_{j,o} - c_{j,\infty}} = \frac{s_i}{s_j} \left( \frac{D_j}{D_i} \right)^{2/3} \quad [15]$$

A great economy in computation can be achieved by using Eq. [15] to find the concentrations of all reaction species except for one, which must be determined from Eq. [12]. The reference ion will be taken to be the third species, and this can be conveniently regarded as the limiting reactant. The quantity  $D_i$  in Eq. [14] is now conveniently specified to be  $D_3$ .

Eq. [10] is solved subject to the boundary conditions

$$c_1^{(1)} \rightarrow c_{1,\infty}^{(1)} \text{ as } \zeta \rightarrow \infty \quad [16]$$

and zero flux of the supporting ions at the electrode surface. The Nernst-Einstein equation can be used to eliminate the mobilities from Eq. [10], which in terms of the Lighthill transformation becomes

$$\frac{d^2 c_1^{(1)}}{d\zeta^2} + 3\zeta^2 \frac{D_3}{D_e} \frac{dc_1^{(1)}}{d\zeta} = \frac{1}{z_2 - z_1} \sum_{i=3} z_i \left( 1 - \frac{D_i}{D_2} \right) \frac{d^2 c_i^{(1)}}{d\zeta^2} \quad [17]$$

with the boundary condition

$$\left. \frac{dc_1^{(1)}}{d\zeta} \right|_{\zeta=0} = \sum_{i=3} \frac{z_i}{z_2 - z_1} \frac{dc_i}{d\zeta} \quad [18]$$

The solution to Eq. [17] is first sought for the case of a constant surface concentration,  $c_{1,0}^{(1)}$ . The concentration derivatives of the minor species are expressed in terms of the reference ion concentration utilizing the solutions of Eq. [9] for a constant surface concentration (15) and Eq. [1]

$$\frac{d^2 c_1^{(1)}}{d\zeta^2} + 3\zeta^2 \frac{D_3}{D_e} \frac{dc_1^{(1)}}{d\zeta} = \frac{-3\zeta^2 (c_{3,\infty}^{(1)} - c_{3,0}^{(1)})}{\Gamma(4/3) (z_2 - z_1)} \sum_{i=3} z_i \frac{D_3}{D_i} \left( \frac{D_3}{D_i} - \frac{D_3}{D_2} \right) \frac{s_i}{s_3} e^{\frac{D_3}{D_i} \zeta^3} \quad [19]$$

The solution to Eq. [19] is

$$\frac{c_1^{(1)} - c_{1,\infty}^{(1)}}{c_{3,\infty}^{(1)} - c_{3,0}^{(1)}} = \frac{1}{\Gamma(4/3)} \left[ \left( \frac{D_3}{D_e} - \frac{D_3}{D_2} \right) \sum_{i=3} \frac{z_i}{z_2 - z_1} \frac{1}{\left( \frac{D_i}{D_e} - 1 \right)} \int_{\infty}^{\zeta} e^{-\frac{D_3}{D_e} x^3} dx + \sum_{i=3} \frac{z_i}{z_2 - z_1} \frac{s_i}{s_3} \frac{D_3}{D_i} \left( \frac{D_i}{D_3} - 1 \right) \int_{\infty}^{\zeta} e^{-\frac{D_3}{D_i} x^3} dx \right] \quad [20]$$

which at  $\zeta = 0$  becomes

$$\frac{c_{1,0}^{(1)} - c_{1,\infty}^{(1)}}{c_{3,\infty}^{(1)} - c_{3,0}^{(1)}} = - \sum_{i=3} \frac{z_i}{z_2 - z_1} \left[ \frac{\frac{D_1}{D_2} - 1}{\frac{D_i}{D_e} - 1} \left( 1 - \left( \frac{D_e}{D_1} \right)^{1/3} \right) + \left( \frac{D_e}{D_1} \right)^{1/3} \right] \left( \frac{D_3}{D_i} \right)^{2/3} \quad [21]$$

Since the differential equations are linear, the solutions for the constant surface concentration may be extended by a superposition integral (16) to the situation where  $c_{3,0}^{(1)}$  varies arbitrarily. The superposition integral reduces to Eq. [21], thus simply relating the two concentrations. The remaining concentration,  $c_2^{(1)}$ , is calculated from the condition of electroneutrality.

### Numerical Example

For a numerical example, a fast redox reaction equimolar in the bulk concentrations of minor species, such as the ferro-ferricyanide couple with sodium fluoride

as the supporting electrolyte, was chosen for a system that would exhibit significant differences between a product dependent and a product independent treatment. Many other systems would serve just as well. The dimensionless groups that characterize the solutions are (1, 10)

$$N = - \Gamma(4/3) \frac{nF r_0 i_{lim}}{RT \kappa_\infty} \quad [22]$$

and

$$J = \frac{i_{0,\infty} r_0 n F}{RT \kappa_\infty} \quad [23]$$

The basic solution procedure for the set of equations is similar to that of Parrish and Newman (10) with the addition of Eq. [5] for the concentration of the product and Eq. [18] for the concentration of the supporting electrolyte.

Concentration and current distributions are calculated with a given average current rather than a specified fraction of the limiting current at the center of the disk, by adding an extra loop (3) to the basic iteration (1). The parametric dependence of the computations on the dimensionless stirring rate  $N$  is thus clearly emphasized in Fig. 1 and 2. Increasing  $N$  produces larger differences between the product dependent and independent approaches. The concentration of the supporting electrolyte cation differs from the bulk value as shown in Fig. 3. The effect is small, but it must be taken into account for alternating current impedance calculations or double layer investigations.

Figure 2 for the reactant concentration is related to Fig. 1 for the current distribution by means of Eq. [12] or Eq. [13]. The product concentration  $c_{1,0}$  would be higher than the bulk concentration by an amount proportional to the depletion of the reactant in Fig. 2, and could be computed through Eq. [15]. The supporting cation in Fig. 3 reflects the current distribution also, but this is through the reactant and product concentrations according to Eq. [21].

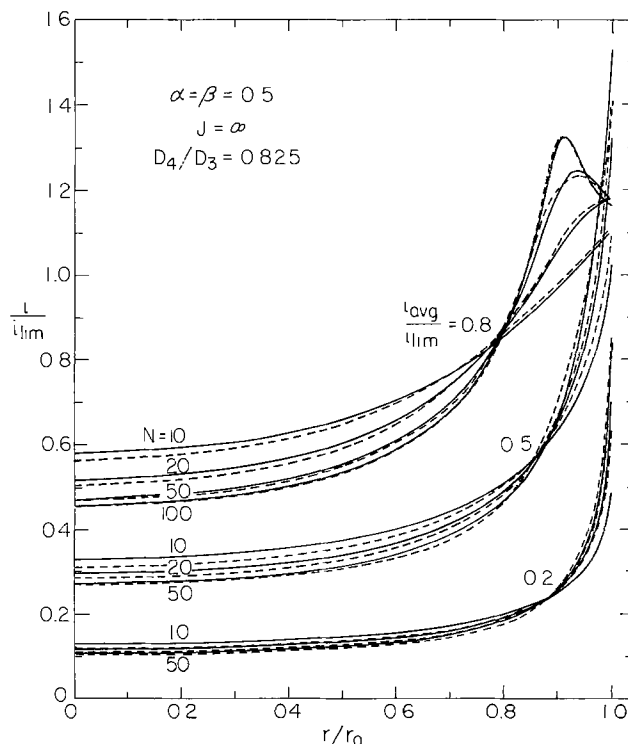


Fig. 1. Current distribution: dashed lines represent the product-independent reaction and solid lines are for the product-dependent reaction (reduction of ferricyanide with equal bulk concentrations of ferricyanide and ferrocyanide).  $D_4/D_3$  is the ratio at infinite dilution.

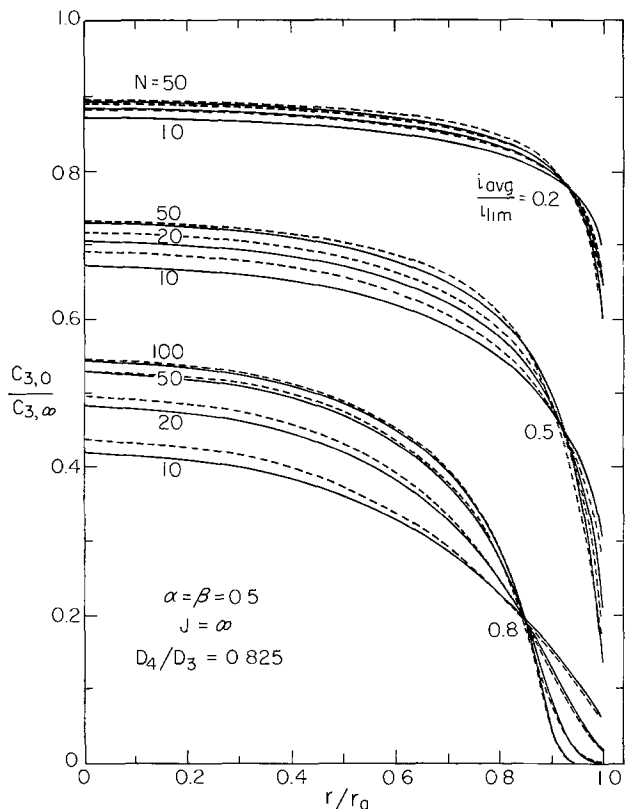


Fig. 2. Concentration distribution: dashed lines represent the product-independent reaction and the solid lines are for the product-dependent reaction.

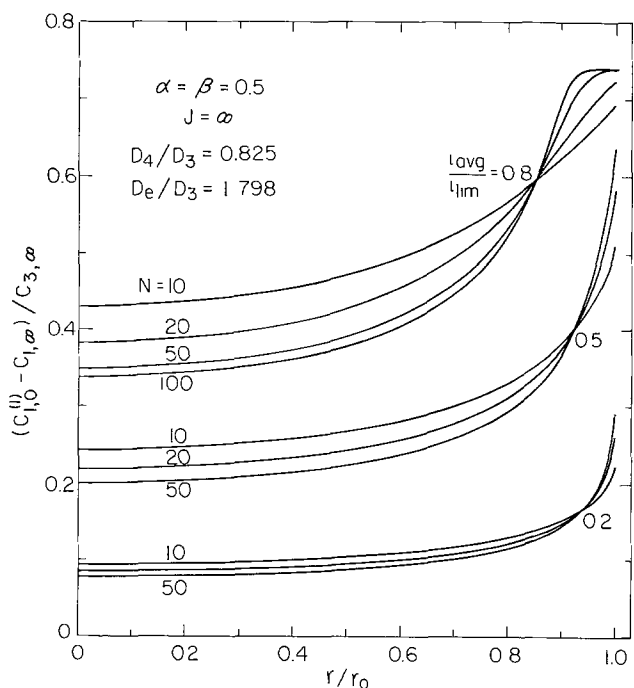


Fig. 3. Concentration distribution of the cation of the uni-univalent supporting electrolyte for the product- and reactant-dependent reaction.  $D_e/D_3$  is the ratio at infinite dilution.

### Acknowledgments

This work was supported by the U.S. Energy Research and Development Administration.

Manuscript submitted March 25, 1975; revised manuscript received Oct. 27, 1975.

Any discussion of this paper will appear in a Discussion Section to be published in the December 1976

JOURNAL. All discussions for the December 1976 Discussion Section should be submitted by Aug. 1, 1976.

Publication costs of this article were partially assisted by the University of California, Berkeley.

### LIST OF SYMBOLS

#### English characters

$a$	0.51023
$B_m$	coefficients in series for potential
$c_i$	concentration of $i$ th species, mole/cm <sup>3</sup>
$c_i^{(j)}$	concentration of $i$ th species in the $j$ th perturbation, mole/cm <sup>3</sup>
$c_{i,0}$	concentration of the $i$ th species at the electrode surface, mole/cm <sup>3</sup>
$c_{i,\infty}$	concentration of the $i$ th species in the bulk solution, mole/cm <sup>3</sup>
$D_e$	diffusion coefficient of the binary electrolyte, cm <sup>2</sup> /sec
$D_i$	diffusion coefficient of the $i$ th species, cm <sup>2</sup> /sec
$F$	Faraday's constant, coulomb/equiv
$i$	normal current density at electrode surface, A/cm <sup>2</sup>
$i_0$	exchange current density, A/cm <sup>2</sup>
$i_{0,\infty}$	characteristic exchange current density, A/cm <sup>2</sup>
$i_{lim}$	current density at the limiting current, A/cm <sup>2</sup>
$J$	dimensionless exchange current density
$M_i$	chemical symbol for $i$ th species
$N$	dimensionless stirring rate
$n$	number of electrons produced in the reaction
$P_{2m}$	Legendre polynomial of order $2m$
$R$	universal gas constant, joule/mole-deg
$r$	radial coordinate, cm
$r_0$	radius of disk electrode, cm
$s_i$	stoichiometric coefficient of species $i$
$T$	absolute temperature, °K
$U$	open-circuit cell potential, volt
$u_i$	mobility of species $i$ , cm <sup>2</sup> -mole/joule-sec
$V$	applied potential, volt
$y$	normal distance from disk, cm
$z_i$	charge number of species $i$
$Z$	negative number of electrons produced in the reaction

#### Greek Characters

$\alpha, \beta$	parameter in Butler-Volmer kinetic expression
$\gamma_i$	parameter in exchange current relation (see Eq. [4])
$\zeta$	dimensionless normal distance (see Eq. [14])
$\eta$	elliptic coordinate
$\eta_c$	concentration overpotential, volt
$\eta_s$	surface overpotential, volt
$\kappa_\infty$	electrical conductivity of bulk solution, ohm <sup>-1</sup> cm <sup>-1</sup>
$\nu$	kinematic viscosity, cm <sup>2</sup> /sec
$\Phi$	electrostatic potential, volt
$\Phi_0$	electrostatic potential extrapolated to the electrode surface, volt
$\Omega$	rotation speed, radians/sec

### REFERENCES

- J. Newman, *This Journal*, **113**, 1235 (1966).
- J. Newman, "Electrochemical Systems," Chap. 21, Prentice-Hall, Inc., Englewood Cliffs, N. J. (1973).
- V. Marathe and J. Newman, *This Journal*, **116**, 1704 (1969).
- B. Miller and M. I. Bellavance, *ibid.*, **120**, 42 (1973).
- J. Newman, "Electrochemical Systems," p. 174, Prentice-Hall, Inc., Englewood Cliffs, N. J. (1973).
- J. Newman, *Intern. J. Heat Mass Transfer*, **10**, 983 (1967).
- J. Newman, *This Journal*, **113**, 501 (1966).
- V. Levich, *Acta Physicochim. URSS*, **17**, 257 (1942).
- W. H. Smyrl and J. Newman, *This Journal*, **119**, 212 (1972).
- W. R. Parrish and J. Newman, *ibid.*, **116**, 169 (1969).
- S. Bruckenstein and B. Miller, *ibid.*, **117**, 1044 (1970).
- W. H. Smyrl and J. Newman, *ibid.*, **119**, 208 (1972).
- J. Newman, *ibid.*, **117**, 198 (1970).
- J. Newman, "Electrochemical Systems," p. 380, Prentice-Hall, Inc., Englewood Cliffs, N. J. (1973).
- J. Newman, *ibid.*, p. 364.
- Francis B. Hildebrand, "Advanced Calculus for Applications," pp. 451-454, Prentice-Hall, Inc., Englewood Cliffs, N. J. (1963).

# Ion Exchange Capacity of Cellulose Acetate Membranes

H.-U. Demisch and W. Pusch

Max-Planck-Institut für Biophysik, 6 Frankfurt am Main, Germany

## ABSTRACT

The fixed charge concentration of asymmetric cellulose acetate membranes caused by a small amount of carboxyl groups of the cellulose acetate was determined by titrating the corresponding  $H^+$  ions using the method of Heymann and Rabinov. The fixed charge concentration,  $C_{X^-}^0$ , was thus estimated to be  $3.4 \cdot 10^{-3}$  mequiv/g wet membrane. This value is compared with the effective fixed charge concentration determined by means of streaming potential measurements using NaCl solutions and asymmetric cellulose acetate membranes annealed at  $82.5^\circ C$ . Furthermore, the effect of the pH of the outside solution on the effective fixed charge concentration of the asymmetric cellulose acetate membrane is theoretically discussed assuming a dissociation equilibrium for the carboxyl groups. Thus, it is shown that the effective fixed charge concentration,  $C_{X^-}$ , of weak ion exchangers depends strongly on the pH as well as on the electrolyte concentration of the outside solution, and on the valency of the counterions. Since the theoretical treatment of the influence of pH on the effective fixed charge concentration is based on approximations, only a semiquantitative agreement between experimental findings and theoretical results is obtained.

During the late fifties Reid and Breton (1) proved homogeneous cellulose acetate membranes to be highly impermeable to salts but quite permeable to water. Parallel to these investigations with homogeneous cellulose acetate membranes, Loeb and Sourirajan (2) developed so-called modified or asymmetric cellulose acetate membranes possessing the same high salt rejection as the homogeneous ones but a much larger water permeability at nearly the same over-all thickness of the membranes. This difference in the water permeability was proved by Merten *et al.* (3, 4) to be due to the asymmetric structure of the modified membranes. Because of their essentially larger water permeability, these asymmetric cellulose acetate membranes became very important in the field of brackish and sea water desalination. Since the transport behavior of these membranes was investigated primarily with brine solutions of larger electrolyte concentrations, and the resulting salt rejection explained by a solution-diffusion mechanism (5), these membranes were believed not to be permselective (6). Only recently, Spiegler and Minning (7) as well as Pusch (8) reported that asymmetric cellulose acetate membranes possess a low fixed charge concentration and behave, therefore, as cation exchange membranes at very low electrolyte concentrations ( $< 10^{-2}$  mol/liter). These conclusions were drawn from streaming and membrane potential measurements. Because of these experimental findings, it was desirable to get further support of the cation exchange properties of these membranes as well as to get a more accurate value for the fixed charge concentration in lieu of the approximation which is obtained primarily from membrane potential measurements. Thus, we determined the fixed charge concentration by analytical methods and by means of "streaming potential" measurements.

## Experimental

The following experiments were performed with asymmetric cellulose acetate membranes annealed at  $82.5^\circ C$ . The membranes were prepared from Cellit K 700 cellulose acetate (39.1% acetyl) produced by Bayer AG of Leverkusen, Germany, according to the procedure of Manjikian, Loeb, and McCutchan (9). First, the fixed charge concentration,  $C_{X^-}^0$ , of these membranes was determined using the method of Heymann and Rabinov (10). For this reason, a suitable membrane sample

was imbibed in distilled water for several days. Thereafter, the sample was treated with 0.1N HCl to remove any cation other than  $H^+$  ions from the membrane. Then, the membrane sample was washed with distilled water until the rinse water was neutral (checked by methyl orange) and free from any chloride. The final rinse water was stored in order to be used later for the determination of a blank value of titration. This wet membrane sample was put in a 0.1M calcium acetate solution and kept in a closed Erlenmeyer flask for about 2 hr. During this time the Erlenmeyer flask, surrounded by an ice-water bath, was stored in a refrigerator. After this treatment, the membrane sample was squeezed and repeatedly washed, collecting all wash water in a suitable container. The collected rinse water was then titrated using 0.01M  $Ba(OH)_2$  solution with an automatic burette, carefully excluding  $CO_2$ . The last rinse water was also titrated in the same way. The difference in the amounts of  $Ba(OH)_2$  solution consumed in both cases results in the fixed charge concentration of the membrane. A series of determinations yielded the following mean value for the fixed charge concentration of the membrane with an error of  $\pm 10\%$

$$C_{X^-}^0 = 3.4 \cdot 10^{-3} \text{ mequiv/g wet membrane}$$

or

$$C_{X^-}^0 = 5.0 \cdot 10^{-3} \text{ equiv/liter pore volume}$$

using a water content of the entire asymmetric membrane of  $0.68 \text{ cm}^3/\text{g}$  wet membrane.

It should be mentioned that one obtains a fixed charge concentration which is only one-half of the one obtained if the membrane sample is not treated with 0.1N HCl.

In addition, three transport coefficients of the phenomenological relationships of thermodynamics of irreversible processes (11) were determined, which allow the estimation of the fixed charge concentration by means of the Schmid relationship (12), relating the electro-osmotic coefficient,  $l_{ep}$ , to the effective fixed charge concentration,  $C_{X^-}$ , the mechanical permeability,  $L_P$ , and the electrical resistance,  $R_e$ , of the membrane by the following relationship

$$l_{ep} \equiv (L_{EP}/L_E) = -F \cdot \omega \cdot C_{X^-} \cdot L_P \cdot R_e \quad [1]$$

where  $l_{ep} = -(\Delta E/\Delta P)_{i=0}$  = measured "streaming potential coefficient" under the boundary condition of zero electrical current (mV/atm);  $L_{EP}$  = electro-osmotic coefficient which relates an electrical current

Key words: streaming potential, membrane resistance, electro-osmotic coefficients, pH effect, asymmetric cellulose acetate membranes.

across the membrane to a pressure difference (mA/atm);  $L_E$  = electrical conductivity of the membrane ( $\text{ohm}^{-1} \text{cm}^{-2}$ );  $R_e = 1/L_E = (\Delta E/i)_{\Delta P=0}$  = electrical membrane resistance ( $\text{ohm}\cdot\text{cm}^2$ );  $L_P = (q/\Delta P)_{\Delta E=0}$  = mechanical or hydrodynamical permeability of the membrane ( $\text{cm}/\text{sec}\cdot\text{atm}$ ) under the boundary condition  $\Delta E = 0$ ;  $q$  = volume flux through the membrane ( $\text{g}/\text{cm}^2\cdot\text{sec}$  or  $\text{cm}/\text{sec}$ );  $i$  = electrical current density across membrane ( $\text{mA}/\text{cm}^2$ );  $\Delta E$  = electrical potential difference across membrane measured by reversible electrodes such as Ag/AgCl electrodes in the presence of chloride ions in the outside solutions (mV);  $\Delta P$  = hydrostatic pressure difference across membrane (atm);  $\omega = +1$  or  $-1$  for anion or cation exchange membranes, respectively;  $C_{X-}$  = effective fixed charge concentration (mol/liter pore volume);  $F$  = Faraday number (As/equiv).

Rearranging Eq. [1] and using the definition of  $l_{ep}$  and the approximation  $q \simeq L_P \Delta P$  (15), which was proved to be valid for asymmetric cellulose acetate membranes, the following relationship is obtained

$$(\Delta E)_{i=0} = F \cdot \omega \cdot C_{X-} \cdot R_e \cdot (q)_{i=0} \quad [2]$$

As can be seen from Eq. [2], the so-called "streaming potential,"  $\Delta E$ , depends on the product  $C_{X-} \cdot R_e \cdot q$  and not only on the effective fixed charge concentration,  $C_{X-}$ . Therefore, the "streaming potential" of high fixed charge ion exchange capacity membranes is of the same order of magnitude as the "streaming potential" of the asymmetric cellulose acetate membranes, although the fixed charge concentration of ion exchange membranes with high capacity is about 1000 times larger than the fixed charge concentration of cellulose acetate membranes. On the other hand, the hydrodynamic permeability (volume flux) and the electrical resistance of common ion exchange membranes are much lower than those for asymmetric cellulose acetate membranes.

Since the Schmid relationship is only valid at low electrolyte concentrations, a salt concentration of 0.02M NaCl was chosen for measuring the electro-osmotic coefficient,  $l_{ep}$ , the mechanical permeability,  $L_P$ , and the electrical resistance,  $R_e$ . This electrolyte concentration is also very convenient for an accurate measurement of the over-all ohmic resistance of the membrane assembly plus salt solution by means of conductivity bridges such as a Weyne-Kerr bridge. In addition, it should be mentioned that the pH of the NaCl solutions was always 5.8 because of the presence of  $\text{CO}_2$ .

Using a dialysis cell described in detail elsewhere (13-15), with salt solutions of equal concentrations on both sides of the membrane, the mechanical permeability,  $L_P$ , was measured at 25°C by means of volume flow measurements (16, 17). The following procedure was used to measure the streaming potential coefficient,  $l_{ep}$ , under the boundary condition  $i = 0$ . A pressure difference,  $\Delta P$ , was established across the membrane and the resulting electrical potential difference,  $\Delta E$ , was measured as a function of time,  $t$ , with Ag/AgCl electrodes by means of a compensation recorder. The desired electrical potential difference,  $\Delta E$ , was then obtained from the difference of the two measured steady-state values  $\Delta E(q) - \Delta E(q = 0)$ , where  $q = 0$  corresponds to  $\Delta P = 0$  thus, eliminating asymmetry potentials. Plotting this potential difference as a function of  $\Delta P$ , a straight line is obtained as is shown in Fig. 1. The slope of this straight line yields the streaming potential coefficient,  $l_{ep}$ .

In other experiments, the electrical resistance,  $R_e$ , of the asymmetric cellulose acetate membrane was determined by a difference method (18-20) using so-called Luggin capillaries (Pt/Ag/AgCl electrodes with a suitable salt bridge). On each side of the membrane a Luggin capillary was arranged at a distance,  $d$ , from the corresponding membrane surface, and the capillary endings were adjusted in such a way that they touched

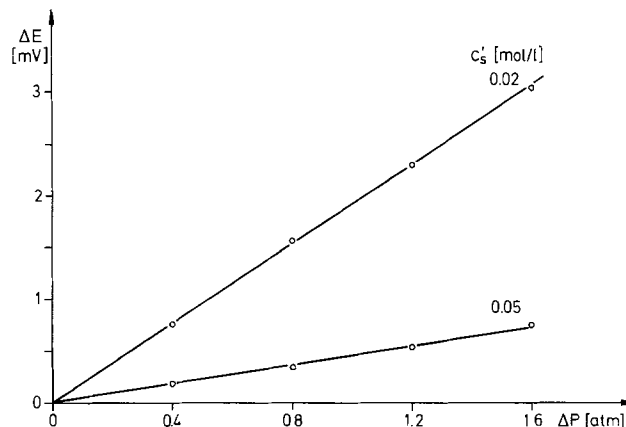


Fig. 1. "Streaming potential,"  $\Delta E$ , as a function of the hydrostatic pressure difference,  $\Delta P$ , with the boundary condition  $c'_s = c''_s$  at 25°C using an asymmetric cellulose acetate membrane annealed at 82.5°C.

the corresponding membrane surface at  $d = 0$ . Adjusting a constant electrical current across the membrane by means of the Ag/AgCl electrodes, the resistance between the two capillary endings was measured as a function of the distance,  $d$ . Now, the measured resistance is composed of the membrane resistance,  $\rho_m \delta$ , and the resistance of the solution between the capillary end and the corresponding membrane surface,  $\rho_s d$ . Thus the measured over-all resistance is related to these resistance components as follows

$$R = (1/A) (2\rho_s d + \rho_m \delta) \quad [3]$$

where  $R$  = measured over-all resistance (ohm);  $A$  = effective membrane area ( $\text{cm}^2$ );  $\rho_s$  = specific resistance of salt solution ( $\text{ohm}\cdot\text{cm}$ );  $\rho_m$  = specific resistance of the membrane ( $\text{ohm}\cdot\text{cm}$ );  $d$  = distance between capillary ending and membrane surface (cm);  $\delta$  = membrane thickness (cm).

Plotting the measured resistance,  $R$ , as a function of  $d$ , a straight line is obtained for distances,  $d$ , larger than the diameter of the capillary end. At distances smaller than the capillary diameter deviations from the straight line are observed in agreement with similar experimental findings by Guillou *et al.* (21). Extrapolating the straight line obtained for larger distances to  $d = 0$  yields the membrane resistance,  $R_e = \rho_m \delta$ . With a 0.02M NaCl solution the following experimental results have been obtained

$$L_P = 2.83 \cdot 10^{-4} \text{ cm}^4/\text{V As}^2 = 2.77 \cdot 10^{-5} \text{ cm}/\text{sec}\cdot\text{atm}$$

$$l_{ep} = 1.89 \cdot 10^{-2} \text{ cm}^3/\text{As} = 1.85 \text{ mV}/\text{atm}$$

$$R_e = 325 \pm 26 \text{ ohm}\cdot\text{cm}^2$$

$$\omega = -1$$

Substituting these values into Eq. [1], the following effective fixed charge concentration results

$$C_{X-} = 2.3 \cdot 10^{-3} \text{ equiv}/\text{liter pore volume}$$

Taking into account the different methods of determination of the fixed charge concentration, one can conclude that there is reasonable agreement between the two values obtained for the fixed charge concentration of an asymmetric cellulose acetate membrane. In this connection, one must consider the influence of the electrolyte concentration and the pH of the outside solution on the effective fixed charge concentration,  $C_{X-}$ , which is discussed later in more detail. In addition, it should also be pointed out that with the underlying model, the counterions in the membrane are assumed to move with the same velocity as the water. But, as Spiegler (22) has reported, this assumption is not completely valid because of the interaction of the counterions and fixed charges. This interaction can be

taken into account by a so-called conductivity factor,  $f_A$ , in Eq. [1] and [2]. This conductivity factor can be assumed to be about 0.5, implying that the fixed charge concentration obtained from Eq. [1] has to be doubled in order to yield a more certain value. This correction results in a much better agreement between the two values obtained for the fixed charge concentration of the asymmetric cellulose acetate membrane.

### Effective Fixed Charge Concentration of Weak Ion Exchangers

As Rabek (23) reported and reviewed, potentiometric titration curves of weak acidic or basic ion exchange materials are a good tool for the investigation of the reactive groups and a conformation analysis of an ion exchange material. These titration curves are often used in order to characterize the range of action of these ion exchange materials which is understandably different, depending on the activity of the ion exchange groups. It is well known that these titration curves are strongly affected by electrolytes which are present during titration (24). Whereas many theoretical investigations on the uptake of ions by ion exchange materials, in the presence of complexing agents, have been performed (24), no theoretical analysis of the effect of pH and electrolyte concentration on the effective capacity of weak ion exchange materials has been reported, as far as the authors are aware. Therefore, such an analysis is given below.

Assuming a dissociation equilibrium for the acidic active groups, such as  $\text{COO}^-$  groups of weak ion exchange materials, with an acidity constant,  $K_a$ , the following relationship between the effective fixed charge concentration,  $C_{X^-}$ , and the fixed charge concentration at complete dissociation,  $C_{X^-}^0$ , as well as the pH or  $\text{H}^+$  ion concentration,  $C_H$ , of the surrounding solution in the ion exchange phase is obtained

$$C_{X^-} = (K_a C_{X^-}^0) / (K_a + C_H) \quad [4]$$

Using the well-known Donnan relationship (25) for the distribution of the ions between outside solution and membrane phase without taking into account individual distribution coefficients of the ions, the electroneutrality condition within the membrane phase, and the ion product of water, the following four additional equations are obtained if an univalent acid, HA, and an  $x$ -valent metal salt,  $\text{MeA}_x$ , of this acid are considered

$$C_H \cdot C_A = c_H (c_a + x c_e) \quad [5]$$

$$C_{\text{Me}} = (c_e / c_{xH}) \cdot C_{xH} \quad [6]$$

$$C_{\text{OH}} = K_w / C_H \quad [7]$$

$$x C_{\text{Me}} + C_H = C_{\text{OH}} + C_A + C_{X^-} \quad [8]$$

where  $c_a$  = concentration of acid, HA, in the outside solution (mol/liter);  $c_H$  = concentration of  $\text{H}^+$  ions in the outside solution (mol/liter). Because of the electroneutrality condition in the outside solution,  $c_H$  and  $c_a$  are not independent but correlated to each other by the following relation:  $c_H = c_a + K_w / c_H$ ;  $c_e$  = concentration of metal salt  $\text{MeA}_x$  in the outside solution (mol/liter);  $x$  = valency of metal ion;  $K_a$  = acidity constant of active groups of membrane (mol/liter);  $K_w$  = ion product of water ( $\text{mol}^2/\text{liter}^2$ );  $C_H$ ,  $C_{\text{OH}}$ ,  $C_{\text{Me}}$ ,  $C_A$ , and  $C_{X^-}$  are the  $\text{H}^+$ ,  $\text{OH}^-$ ,  $\text{Me}^{x+}$ ,  $\text{A}^-$ , and fixed charge concentration, respectively, within the membrane phase (mol/liter pore volume).

Substituting Eq. [4], [5], [6], and [7] into the electroneutrality condition [8] and rearranging, the following polynomial equation for  $C_H$  is obtained

$$\{C^{x+2}H + K_a C^{x+1}H\} \cdot (x c_e / c_{xH}) + C^3H + K_a C^2H - \{K_a C_{X^-}^0 + K_w + c_H (c_a + x c_e)\} \cdot C_H - \{K_w + c_H (c_a + x c_e)\} \cdot K_a = 0 \quad [9]$$

Equation [9] is valid for  $\text{pH} \leq 7$ . At  $7 < \text{pH} \leq 14$  one has to add  $\text{Me}(\text{OH})_x$  instead of HA. This leads to a somewhat different equation which is not considered here.

This equation yields a cubic equation for  $x = 1$ , a fourth degree polynomial equation for  $x = 2$ , and a fifth degree polynomial equation for  $x = 3$ , as well as the same cubic equation for every  $x$  in the case  $c_e = 0$ . All these polynomial equations can easily be solved by means of a calculator such as the HP 65, for instance, with the corresponding programs. Assuming a suitable value for  $K_a$  of  $1.78 \cdot 10^{-5}$  mol/liter, the theoretical results presented graphically in Fig. 2a, b, and c were obtained. There, the ratio of the effective fixed charge concentration over the fixed charge concentration at complete dissociation,  $C_{X^-} / C_{X^-}^0$ , is plotted as a function of the pH of the outside solution using different parameter values of the metal salt concentration,  $c_e$ .

The following points should be noted. (i) Activity coefficients have been assumed to be unity replacing thermodynamic activities by concentrations. This as-

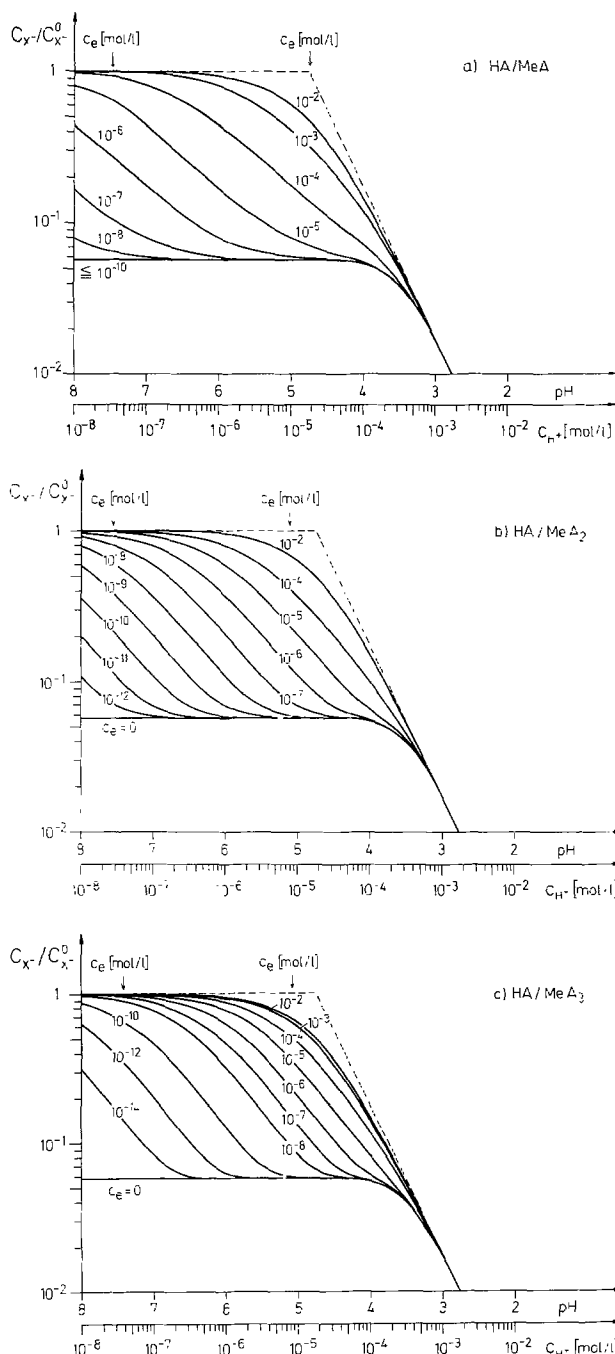


Fig. 2. Ratio of effective to total fixed charge concentration of a weak cation-exchange membrane as a function of pH in the presence of a monovalent acid and a monovalent (a), a divalent (b), and a trivalent (c) salt as calculated from Eq. [9] using an acidity constant  $K_a = 1.78 \cdot 10^{-5}$  mol/liter.

sumption will become increasingly invalid at higher solute concentration. (ii) No individual distribution coefficients for the ions have been taken into account. But, this could easily be done further for the metal salt by using an effective metal salt concentration  $K_s c_e$  of the outside solution with the distribution coefficient,  $K_s$ , of the salt.

As can be seen from Fig. 2a, b, and c, there exists a strong effect of the pH and the electrolyte concentration of the outside solution on the effective fixed charge concentration of the membrane. On the other hand, if no electrolyte, other than the acid, is present in the outside solution ( $c_e = 0$ ), the effective fixed charge concentration is strongly lowered ( $C_{X-}/C_{X-}^0 \approx 0.06$ ), but independent of the pH up to a pH value which corresponds to about the  $pK_a$  value of the active groups of the membrane. This theoretical result can easily be understood by a brief calculation. When no additional electrolyte is present except the acid, the only counterion which can balance the fixed charges is the  $H^+$  ion. Thus the concentration  $C_H$  within the membrane has always to be equal to the effective fixed charge concentration,  $C_{X-}$ , if the small amount of  $OH^-$  ions is neglected. With this condition, Eq. [4] yields  $C_{X-}/C_{X-}^0$  directly without further calculations. The square root of the corresponding quadratic equation yields the effective fixed charge concentration for the case  $c_e = 0$  at  $pH < pK_a$ .

From Fig. 2a, b, and c it can also be seen that there exists only a small effect of the pH on the effective fixed charge concentration,  $C_{X-}$ , at electrolyte concentrations larger than  $10^{-2}$  mol/liter or even  $10^{-3}$  mol/liter, depending on the valency of the corresponding cation. Furthermore, the change of the effective fixed charge concentration with increasing pH becomes more pronounced with increasing valency of the metal ion. At the same outside electrolyte concentration, the effective fixed charge concentration is lower at lower pH values in the presence of higher valency metal ions, whereas the opposite is true at larger pH values. On the other hand, the effective salt concentration, which determines the effective fixed charge concentration, is always lower than the salt concentration of the surrounding solution because of a distribution coefficient,  $K_s$ , for the salt, which is less than unity. Therefore, there will exist a strong dependence of the effective fixed charge concentration on the pH of the outside solution even at salt concentrations exceeding  $10^{-3}$  mol/liter. Thus, determining fixed charge concentrations of weak ion exchange membranes by methods other than analytical, will yield values for the effective fixed charge concentration which depend strongly on the composition of the outside solution. Also, every transport property of a weak ion exchange membrane, which is influenced by the effective fixed charge concentration, is affected by the pH of the outside solution. This was recently demonstrated by de Körösy (26) and Vacik *et al.* (28), for instance, by measuring electrical resistances of an amphoteric membrane as a function of the pH of the outside solution and formerly by Ohki (29) measuring the resistance of lipid bilayers which contained zwitterionic groups.

Finally, some remarks should be made on the use of the Schmid relationship for the determination of the fixed charge concentration of asymmetric cellulose acetate membranes. With the experimental setup and the corresponding boundary conditions used to measure  $C_{X-}$ , it is assumed that there exist no electrical potentials other than the streaming potential in the membrane. But this assumption is no longer valid for asymmetric membranes, as was shown recently (8). Because of the concentration gradient within the porous sublayer of an asymmetric cellulose acetate membrane (14), there exist two diffusion potentials and additional Donnan potentials within the membrane, even when the electrolyte concentrations on both sides of the membrane are equal (27). The two diffusion potentials

may possess opposite signs, depending on the ratio  $D_+/D_-$  in the active layer and the porous sublayer of the asymmetric cellulose acetate membrane ( $D_+$ ,  $D_-$  = diffusion coefficient of the cation and anion, respectively, within the active layer or porous sublayer). A detailed analysis indicates (15) that the two diffusion potentials of opposite sign and the resulting Donnan potentials nearly cancel for an asymmetric cellulose acetate membrane annealed at 82.5°C, using a salt concentration of 0.02M NaCl on both sides of the membrane. Thus, this detailed analysis of the electrical potential situation across an asymmetric cellulose acetate membrane leads to the conclusion that the Schmid relationship may be used for the determination of effective fixed charge concentrations of asymmetric membranes, if special boundary conditions are chosen. Under such special boundary conditions, the over-all membrane potential of an asymmetric membrane corresponds nearly to a pure streaming potential within the error of measurement. These assumptions are supported by further detailed analyses of the potential situation in asymmetric cellulose acetate membranes.

Summarizing, it should be stated that a comparison of fixed charge concentrations of weak ion exchange membranes, determined on the one hand by analytical methods such as titration, and on the other hand by measuring transport coefficients and/or streaming potentials, may fail since the former analysis leads to the total amount of fixed charges, whereas in the latter case, only an effective fixed charge concentration is delineated. The effective fixed charge concentration may differ strongly from the total fixed charge concentration due to the effect of pH and electrolyte concentration of the outside solutions on the amount of dissociated active groups of the membrane material. The pH of the 0.02M NaCl solutions used was always around 5.8. This means that the effective fixed charge concentration,  $C_{X-}$ , must be smaller than the fixed charge concentration,  $C_{X-}^0$ , determined by titration. Our experimental results are in qualitative agreement with this requirement, when all necessary semiquantitative corrections have been made.

Furthermore, it is, in principle, impossible to measure pure streaming potentials using asymmetric membranes with the corresponding experimental setup because of the additional diffusion and Donnan potentials which are present, even at equal electrolyte concentrations on both sides of the membrane. Thus, the effective fixed charge concentration can only be compared to the total fixed charge concentration if a detailed analysis of all additional electrical potential effects is conducted. With regard to the experimental findings reported here, this detailed analysis was performed yielding reasonable agreement between total and effective fixed charge concentration of an asymmetric cellulose acetate membrane.

### Acknowledgments

The authors are indebted to Professor R. Schlögl for his interest in this work and some stimulating discussions. The authors would also like to thank Mr. R. Gröpl for preparing the asymmetric cellulose acetate membranes and Mr. R. McKinney for reading the proofs. The work was financially supported by the Bundesminister für Forschung und Technologie, Bonn, Germany.

Manuscript submitted June 24, 1975; revised manuscript received Oct. 27, 1975.

Any discussion of this paper will appear in a Discussion Section to be published in the December 1976 JOURNAL. All discussions for the December 1976 Discussion Section should be submitted by Aug. 1, 1976.

Publication costs of this article were partially assisted by Max-Planck-Institut für Biophysik.

### REFERENCES

1. C. E. Reid and E. J. Breton, *J. Appl. Polymer Sci.*, **1**, 133 (1959).

2. S. Loeb and S. Sourirajan, *Advan. Chem. Ser.*, **38**, 117 (1962).
3. R. L. Riley, J. O. Gardner, and U. Merten, *Science*, **143**, 801 (1964).
4. R. L. Riley, U. Merten, and J. O. Gardner, *Desalination*, **1**, 30 (1966).
5. U. Merten, in "Desalination by Reverse Osmosis," U. Merten, Editor, pp. 19-22, The M.I.T. Press, Cambridge, Mass. (1966).
6. C. E. Reid and H. G. Spencer, *J. Polymer Sci.*, **4**, 354 (1960).
7. K. S. Spiegler and Ch. P. Minning, Proc. Nato Advanced Study Inst. "Polyelectrolytes II," Forges-les-Eaux, 1973, E. Sélégny, Editor, Reidel Publishing Co., Dordrecht, Holland (In preparation).
8. W. Pusch, *ibid.*
9. S. Manjikian, S. Loeb, and J. W. McCutchan, "Proceedings 1st International Desalination Symposium," Paper SWD/12, Washington, D. C. (1965).
10. E. Heymann and G. Rabinov, *J. Phys. Chem.*, **45**, 1152, 1167 (1941).
11. R. Schlögl, "Stofftransport durch Membranen." Dr.-Dietrich-Steinkopff-Verlag, Darmstadt (1964).
12. G. Schmid, *Z. Elektrochem.*, **54**, 424 (1950); *ibid.*, **55**, 229 (1951); *ibid.*, **56**, 181 (1952); G. Schmid and H. Schwarz, *ibid.*, **55**, 295 (1951); *ibid.*, **55**, 684 (1951); *ibid.*, **56**, 35 (1952).
13. W. Pusch, *Chem.-Ing.-Tech.*, **20**, 1216 (1973).
14. W. Pusch, *Desalination*, **16**, 65 (1975).
15. H.-U. Demisch, Dissertation, In preparation.
16. W. Pusch, Proceedings International Symposium "Structure of Water and Electrolyte Solutions," W. Luck, Editor, Verlag Chemie/Physik Verlag, Weinheim (1974).
17. W. Pusch, in "Permeability of Plastic Films and Coatings," H. B. Hopfenberg, Editor, Plenum Publishing Corp., New York (1974).
18. K. S. Spiegler, R. J. Moore, J. Leibovitz, and R. M. Messalem, "Study of Permeability Characteristics of Membranes," Sea Water Conversion Laboratory, U.C. at Berkeley, Combined Quarterly Reports No. 15 and 16 (January 1972).
19. G. Wiedner, Dissertation, Frankfurt am Main, Germany (1971).
20. A. Despić and G. J. Hills, *Trans. Faraday Soc.*, **51**, 1260 (1955).
21. M. Guillou, D. Guillou, and R. Buvet, "Membranes à Perméabilité Selectivé," pp. 131-152, Editions du Centre National de la Recherche Scientifique, Paris (1969).
22. K. S. Spiegler, *This Journal*, **100**, 303C (1953).
23. R. I. Rabek, "Polyelektrolyte (Allgemeine Einführung)," pp. 9-14, Akademie-Verlag, Berlin (1967).
24. F. Helfferich, "Ionenaustauscher," Bd. I, pp. 73-81, Verlag Chemie GmbH, Weinheim/Bergstrasse, Germany (1959).
25. F. G. Donnan, *Z. Elektrochem.*, **17**, 572 (1911).
26. F. de Kőrösy, *Desalination*, **16**, 85 (1975).
27. H.-U. Demisch and W. Pusch, The First Chemical Congress of the North American Continent, Nov. 30-Dec. 5, 1975, Mexico City, Mexico.
28. J. Vacik and J. Kopeček, *J. Appl. Polymer Sci.*, **19**, 3029 (1975).
29. Sh. Ohki, *J. Colloid Interface Sci.*, **30**, 413 (1969).

## Anodic Oxide Films as Barriers to Charge Transfer in O<sub>2</sub> Evolution at Pt in Acid Solutions

A. Damjanovic\*<sup>1</sup>

Xerox Corporation, Webster Research Center, Webster, New York 14580

and B. Jovanovic

Laboratory of Solid State Physics, Institute for Nuclear Science, "Boris Kidric," Belgrade, Yugoslavia

### ABSTRACT

The kinetics of oxygen evolution reaction at platinum anodes in acid solutions with different pH's is examined, and possible reaction mechanisms are discussed. The activity of the reaction at initially prerduced electrodes brought to a constant potential, or kept at a constant current density, decreases with time. Only at the electrodes initially subjected for a given time either to a high potential, or to a high anodic current density, it is possible to observe in "run down," or subsequent "run up" experiments a linear  $V$ -log  $i$  relationship for over several decades of current density with a slope close to 115 mV. The positions, but not the slopes of Tafel lines, are affected by time or conditions of pretreatments of electrodes (various  $V$  or  $i$ ). The decrease in the activity is attributed to the increase in average thickness of anodically formed surface oxide films. Only when it is assured that the film thickness remains practically unaltered during the  $i$ - $V$  measurements, meaningful kinetic parameters for the oxygen evolution reaction are obtained. The reaction order with respect to  $H^+$  is then found to be negative and fractional according to the over-all rate equation

$$i = kc^{-1/2} \exp \left( \frac{F\Delta V}{2RT} \right)$$

A model is suggested according to which a surface oxide film forms a barrier to charge transfer in series with the double-layer barrier. The fractional reaction order is accounted for with this model. A chemical step that follows a charge transfer step is rate determining. It is suggested that oxygen atoms in the surface oxide films participate in the oxygen evolution reaction.

The rate of oxygen reduction at potentials below 1.0V vs. hydrogen electrode (HE) is significantly lower

\* Electrochemical Society Active Member.

<sup>1</sup> Present address: 809 Harbor Square, Rochester, New York 14617.

Key words: oxygen evolution, dual barrier, anodic films, electrocatalysis.

at anodically preoxidized than at prerduced noble metal electrodes (1-3). This decrease in catalytic activity has been attributed to the presence of a thin oxide film over the surface of an anodically oxidized metal (1-4). Meyer (5) has suggested that the surface



oxide films at zirconium electrodes form a potential barrier for charge transfer in oxygen reduction. The barrier is in series with the double layer barrier and with the latter controls the over-all rate of oxygen reduction. The same concept has been used by MacDonald and Conway (6) to account for the unusually high Tafel slopes for oxygen evolution reaction at gold, palladium, and gold palladium alloy electrodes. In most of the studies of the kinetics and mechanisms of oxygen evolution reaction at platinum, little attention has been paid to the presence of thin surface oxide films that form (7-13) anodically over the metal surface. The presence of the films, and in particular the film thickness, which varies with time and experimental conditions (9, 10, 13), is expected to affect kinetic parameters (12, 14). Any analysis of the reaction mechanism may be invalid if the effect of film thickness on the kinetics is not taken into account.

In order to assess the importance of the surface oxide films at platinum electrodes, the kinetics of the oxygen evolution reaction in sulfuric acid solutions of different pH's is reexamined at conditions of controlled electrode pretreatment. A mechanism for the reaction is sought that would take into account the presence of oxide films at electrodes.

### Experimental

An all glass, three compartment cell used for most of the present experiments is similar to those already described (2, 15). A large platinized platinum gauze in a separate vessel attached to the cell was used to purify solutions (16). For additional pH measurements, another two compartment cell was made. Both the test and reference compartments of this cell are connected to two solution reservoirs each. Solutions in the first two reservoirs were saturated with  $O_2$  and in the other two with oxygen. With this arrangement it has been possible to replace in a few seconds solutions in both compartments with a solution of different pH.

Platinum (stated purity 99.998%) wire (diam = 0.5 mm) electrodes with geometrical areas of  $1 \text{ cm}^2$  were "sealed" into Pyrex tubes fitting the true bore inlets in the test compartment. Electrodes were washed with sulfuric acid and quadruply distilled water. The cell and electrodes were finally washed *in situ* with water redistilled directly into the cell.

Solutions are prepared from quadruply distilled water, including distillation from permanganate and bichromate solutions, and analyzed reagents  $H_2SO_4$ . Water is distilled directly into the cell. A required amount of sulfuric acid is introduced into the cell from a burette attached to the counterelectrode compartment. Solutions are finally purified by adsorption of residual impurities at a large platinized platinum gauze (16) kept at 0.3V. Oxygen, nitrogen (or argon), and hydrogen are purified by passing through systems of columns each with specific purification function (17).

Prior to an experiment the test electrode was anodically polarized at 1.9V for 1 min and then kept at 0.5V for 5 min (prereduced electrodes). Roughness factor of such electrodes has previously been found (18, 19) to be about 1.7. Current density data are scaled here with this roughness factor. Unless otherwise stated, all potentials refer to the reversible hydrogen electrode in the same solution (HE).

### Results

**Reproducibility of  $V-i$  relationships.**—The potential current density relationship at a prereduced electrode is shown in Fig. 1. An anodic current increases slowly with potential up to about 1.4V after which potential it increases more rapidly. However, points on the  $i-V$  curve from A to B do not represent a "true" steady state: current at any potential decreases with time at first rapidly and then very slowly. No linear  $V-\log i$  relationship can be obtained in this first "run up" experiment. Only after an electrode has been kept at a

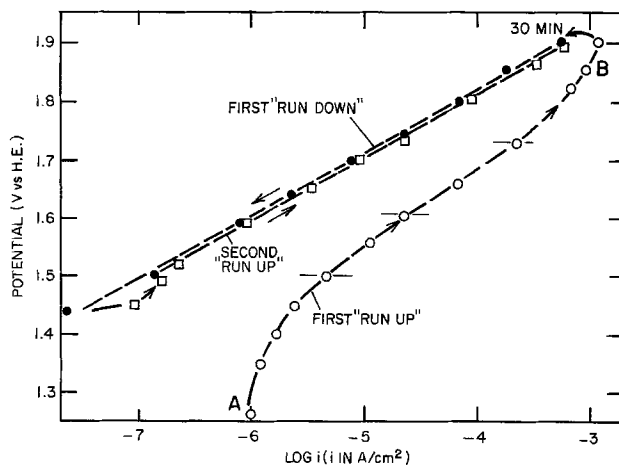


Fig. 1.  $V-\log i$  relationships at Pt in  $H_2SO_4$  solution with  $pH = 0.3$ . (○), First "run up" experiment; (●), first "run down" experiment after the electrode was kept for 30 min at 1.9V; and (□), subsequent "run up" measurement.

high potential (e.g.,  $\geq 1.70V$ ), or has been polarized with a high constant anodic current density (e.g.,  $i \geq 10^{-4} \text{ A/cm}^2$ ) for some time (e.g., 5 min or longer), is the current potential relationship in the process of decreasing electrode potential, or decreasing current density, practically independent of time. In this "run down" measurement a Tafel relationship is observed with a slope close to  $2RT/F$  over several decades of current.<sup>1</sup> Basically the same  $V-\log i$  relationship is retraced when subsequently the potential, or current density, is increased in steps but only up to the potential, or current density, of the initial polarization. If an electrode is brought in the first "run down" measurement to a potential below about 1.40V, and is kept there for some time ( $\sim 30$  min or longer), then the Tafel line in the subsequent "run up" measurement is slightly ( $\sim 20\%$ ) shifted towards higher current densities.

The same  $V-\log i$  relationships are obtained only when the electrodes are pretreated in the same way, e.g., only when they are initially prereduced and then kept for the same time at a given potential or current density. If either of these factors is changed, the  $V-\log i$  lines are shifted parallel with respect to each other. The  $\partial V/\partial \log i$  slopes are, however, unaffected by the electrode pretreatment. The examples are given in Fig. 2, 3, and 4.

**$V-\log i$  relationships.**— $V-\log i$  relationships for prereduced electrodes kept at 2.0V in 1N  $H_2SO_4$  solution for 5, 10, or 40 min are shown in Fig. 2. The longer the time of polarization, the lower is the activity of the electrode. The  $\partial V/\partial \log i$  slopes are all close to 115 mV. In Fig. 3, data are given for the prereduced electrodes that have been kept at different potentials for 30 min [except data marked by ( $\Delta$ )]. After the lapse of this time,  $V-\log i$  relationships are obtained by decreasing either current density or potential. It is evident that the higher the potential of initial polarization, the lower is the activity of the electrodes.

In Fig. 4, data are shown obtained in 0.1N  $H_2SO_4$  solution [except data marked ( $x$ )]. The activity of an electrode kept for 30 min at 2.0V is nearly an order of magnitude less than the activity of an electrode kept for the same time at 1.6V. The same trend holds for electrodes that are initially kept for 10 min at 1.8 and 1.5V. The  $\partial V/\partial \log i$  slopes are again close to 115 mV. In  $10^{-2}N$   $H_2SO_4$  solutions too, basically the same trend for the dependence of activity on electrode pretreatment is observed [compare ( $\Delta$ ) and ( $x$ ) in Fig. 3 and 4].

**pH dependence.**—From Fig. 3 and 4, it follows that at the same current density (e.g.,  $10^{-4} \text{ A/cm}^2$ ) potential

<sup>1</sup> Cf., Ref. (15), (17), (20), and (21).

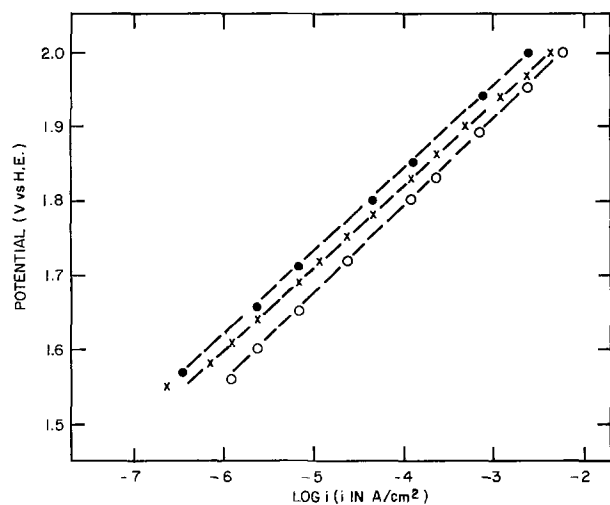


Fig. 2. Tafel lines for prereduced electrodes kept at 2.0V for (○), 5; (×), 10; and (●), 40 min in 1N H<sub>2</sub>SO<sub>4</sub>.

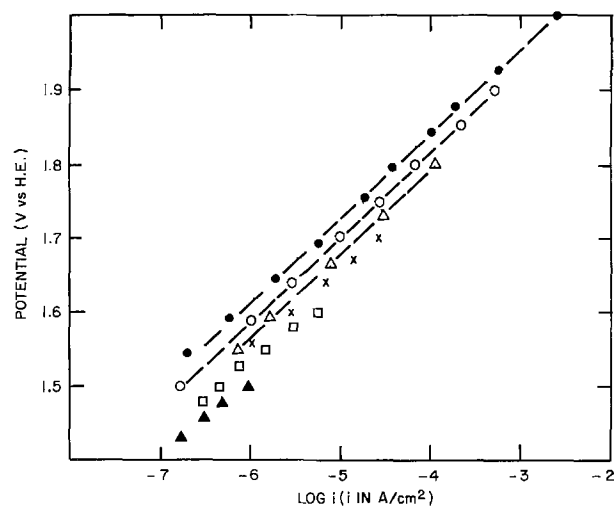


Fig. 3. V-log  $i$  relationships for prereduced electrode kept for 30 min in 1N H<sub>2</sub>SO<sub>4</sub> at different potentials, except for (Δ) when the electrode was kept for the same at 1.8V in 10<sup>-2</sup>N H<sub>2</sub>SO<sub>4</sub>.

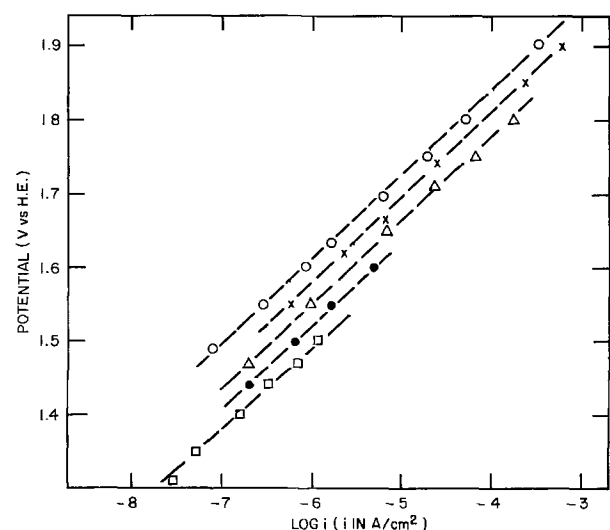


Fig. 4. V-log  $i$  relationships. (●), 30 min at 1.6V; (○), 30 min at 2.0V (part of the V-log  $i$  is shown only); (□) and (Δ), 10 min at 1.5 and 1.8V, respectively. Solution 0.1N H<sub>2</sub>SO<sub>4</sub>. Data (×) obtained in 10<sup>-2</sup>N H<sub>2</sub>SO<sub>4</sub> after 30 min at 1.9V.

with respect to a pH independent scale decreases with increasing pH. The  $\partial V/\partial \text{pH}$  is close to  $-60$  mV, as shown in Fig. 5 for electrodes initially kept at 1.9 and 2.0V (HE) for the same time.

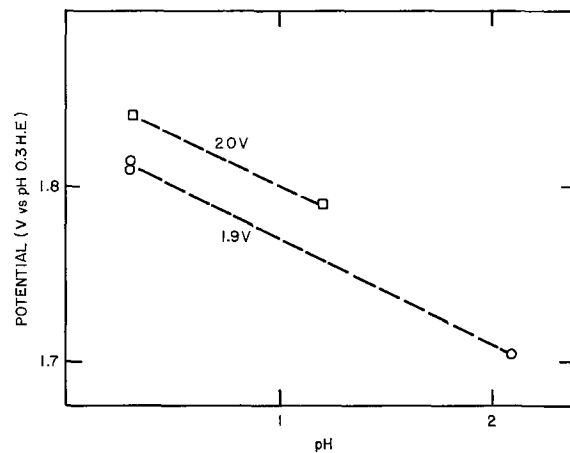


Fig. 5. pH dependence at electrode initially kept at 2.0 or 1.9V (vs. HE) for 30 min (see text). The potentials, that now refer to the hydrogen electrode in pH 0.3 solution, are read off at 10<sup>-4</sup> A/cm<sup>2</sup>.

To check whether this pH dependence is a true characteristic of the reaction or it reflects a difference in electrode activities arising entirely (or partially) from different degrees of oxidation state of electrode surfaces, e.g., from differences in thickness of surface oxide films that are anodically formed in solutions of different pH, in a second series of experiments after an electrode has been subjected to a constant anodic current for a given time (1 to 2 hr), solutions in both the test and reference electrode compartments were rapidly replaced with solutions of a different pH. The electric circuit during the replacement of solutions was not broken. The electrode potential referred to HE remained essentially unchanged in these experiments. If the oxidation state, e.g., thickness of the oxide films, does not change during the replacement of solutions, as assumed here, then the observed pH dependence reflects the true dependence of the oxygen evolution reaction on pH. Again,  $(\partial V/\partial \text{pH})_1$  with respect to a pH independent scale is  $-60$  mV.<sup>2</sup>

In a few experiments K<sub>2</sub>SO<sub>4</sub> has been added to H<sub>2</sub>SO<sub>4</sub> solutions to a constant ionic strength. No effect of excess of salt on the kinetics has been detected in the solution exchange experiments. As to the dependence on O<sub>2</sub> partial pressure, the same V-log  $i$  relationships are obtained regardless whether solution has been saturated with oxygen or argon, i.e.,  $\partial V/\partial \log p_{\text{O}_2} = 0$ .

For convenience, data are summarized in Table I. In the same table, some literature data are included for comparison and convenience.

### Discussion of the Results

**Comparison of the V-log  $i$  in the first "run-up" and subsequent "run-down" measurements.**—Above 1.0V an oxide phase forms (7-11, 15, 40-45) over platinum surface. Oxygen evolution occurs therefore only at oxide-covered platinum electrodes. Thickness of the oxide film at an electrode that is initially prereduced increases with increasing electrode potential (7 8). As the thickness,  $d$ , increases, the activity for oxygen evolution reaction, expressed as the exchange current density,  $i_0$ , decreases according to (12, 14)

$$i_0 = k \exp\left(-\frac{\delta d}{2}\right) \quad [1]$$

where  $k$  and  $\delta$  are constants. Consequently, as the potential in the first "run-up" measurements at a prereduced electrode is increased in a gradual or stepwise manner and the oxide film becomes progressively thicker, the current density decreases according to (12, 14)

<sup>2</sup> Previously reported pH dependence of  $-30$  mV (see Table I) is in error probably due to insufficient care of electrode pretreatment.

Table I. Parameters for O<sub>2</sub> evolution at Pt in acid solutions

	$\frac{dV}{d \log i}$	$\frac{dV^a}{dpH}$	$\frac{dV}{d \log P_{O_2}}$	$\left(\frac{dV}{dt}\right)$ $i = \text{const}$	$\left(\frac{di}{dt}\right)$ $V = \text{const}$
Present data	110-120 mV	-60 mV	0	> 0	< 0
Literature	$2.3 \frac{2RT^b}{F}$	-30 mV (15)		> 0 (39) <sup>e</sup>	< 0 <sup>f</sup>
	$2.3 \frac{2.17RT^c}{F}$	-60 mV (28)			
	~100 mV (37)				
	~185 mV <sup>d</sup>				

<sup>a</sup> With respect to NHE.

<sup>b</sup> References: (15, 17, 20-35).

<sup>c</sup> At 96°C. Reference (36).

<sup>d</sup> At high current densities. References (35, 38).

<sup>e</sup>  $dV/d \log i \sim 110$  mV. Reference (15).

<sup>f</sup>  $d \log i/d \log t \approx -0.5$ . Reference (40).

$$i = k \exp\left(-\frac{\delta d}{2}\right) \exp\left(\frac{FV}{2RT}\right) \quad [2]$$

i.e., it changes less than expected for a constant value of the exchange current density. In other words, due to the progressive increase in the oxide thickness, the  $\partial V/\partial \ln i$  slope in the first "run-up" experiment is higher than expected for an unchanged electrode (i.e.,  $\partial V/\partial \ln i > 2RT/F$ ). As shown in Fig. 1, the slope is not constant but changes with electrode potential.<sup>3</sup>

A different situation exists in the "run-down" and subsequent "run-up" experiments at potentials lower than that at which the electrode has been anodically pretreated. After an electrode has been kept at a high potential (e.g., 1.8-2.0V) for some time (e.g., 5-20 min), and after an oxide film has grown to a nearly constant thickness, the  $V$ - $\log i$  relationship is observed with the constant value of  $\partial V/\partial \ln i$  equal to  $2RT/F$ . This is because once the potential at an anodically pretreated electrode is decreased, the oxide films virtually stop growing (12, 46), i.e., there is a hysteresis in the thickness, and  $V$ - $\log i$  relationship holds for a constant thickness of the oxide film. Since the  $\partial V/\partial \log i$  slopes obtained at such electrodes are unaffected by the thickness itself (see below), it follows that the mechanism of reaction too is unaffected by the thickness of the oxide film. What changes in the first "run-up" experiments is therefore only the catalytic activity, or the exchange current density, as discussed above.<sup>4</sup>

**Change of the catalytic activity with time.**—The catalytic activity of a pre-reduced electrode decreases also with time of polarization at a given potential. For instance, at 2.0V current densities after 5, 10, or 40 min are close to 6, 4, or  $2.5 \times 10^{-3}$  A/cm<sup>2</sup>, respectively (cf., Fig. 2 and 6). The decrease can now be related to the reported slow (logarithmic) increase in the thickness of the oxide film: as the thickness increases with time, the catalytic activity at the same potential decreases. The same trend is evident in experiments when an electrode is kept for the same time at different potentials. This is illustrated in Fig. 7 in which the current densities observed in "run-down" experiments at 1.5V are plotted vs. the potential at which a pre-reduced electrode has been anodically polarized for 30 min prior to making measurements. Again, the change in the activity reflects the change in the thickness of oxide films.

It follows from the above discussion that anodic oxide films at platinum form a barrier to electron

<sup>3</sup> If an electrode is reduced before each measurement at a given potential then, for a fixed time of polarization,  $\partial V/\partial \ln i$  becomes again constant. Its value however, is now close to  $3RT/F$  instead of  $2RT/F$ . This is because of a particular dependence of thickness on electrode potential (12).

<sup>4</sup> Anodic current below 1.2V, i.e., below the reversible O<sub>2</sub>/H<sub>2</sub>O potential, is apparently due to simultaneous dissolution of platinum (47) and formation of anodic oxide film. As the potential increases and as the electrode, due to the oxide film formation, "passivates," oxygen evolution becomes the major reaction. Only at such passive electrodes when the dissolution rate drops (47) below  $10^{-9}$  A/cm<sup>2</sup>, is it possible to follow oxygen evolution down to  $10^{-9}$  A/cm<sup>2</sup>.

transfer in oxygen evolution reaction. Resistance to the transfer is not of the ohmic type since an extended, logarithmic dependence of potential on current density (for over six decades), that has frequently been reported,<sup>5</sup> cannot be accounted for in terms of such resistance. A significant drop of potential within the oxide phase is suggested in Fig. 1-4. For the same current density the potential at a more strongly pre-oxidized electrode is easily higher by 100-150 mV than the potential at a less strongly preoxidized electrode. This drop of potential has to be taken into account in any analysis of the mechanism of the reaction. Fur-

<sup>5</sup> See for instance Ref. (4).

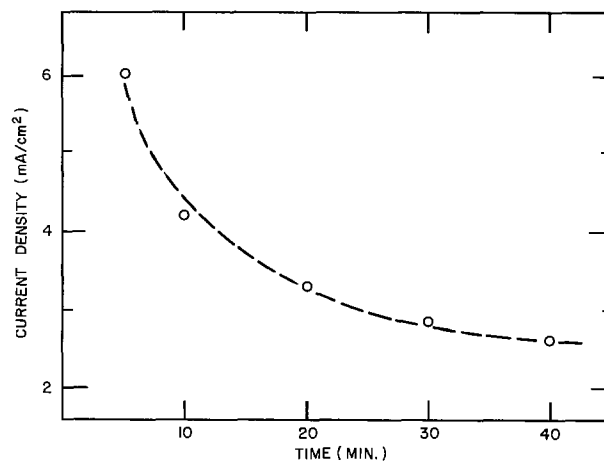


Fig. 6. Change with time of the catalytic activity expressed as current density at 2.0V. 1N H<sub>2</sub>SO<sub>4</sub>.

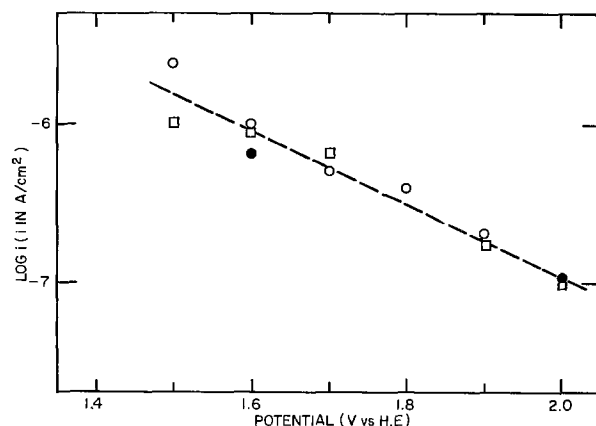


Fig. 7. Current density at 1.5V (HE) vs. potential at which an electrode was kept for 30 min prior to making measurements. (○), (●), and (□) refer to  $10^{-2}$ , 0.1, and 1N H<sub>2</sub>SO<sub>4</sub> solutions.

ther, for the experimentally obtained kinetic parameters, such as pH or oxygen partial pressure dependence, to be representative of the reaction mechanism, it is essential to ensure that they are obtained for the same oxidation state of the electrode surface. This has been aimed for in the present study.

### Mechanism of the Oxygen Evolution Reaction

With the kinetic parameters given in Table I, the rate equation for oxygen evolution at platinum in acid solutions can be written in the form

$$i = k[a_{H^+}]^{-1/2} \exp \left[ \frac{FV}{2RT} \right] \quad [3]$$

Here,  $k$  is a constant for a given thickness (and possibly type) of the surface oxide film; it decreases as thickness increases.

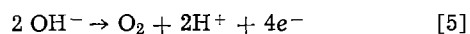
The following are the characteristic features of the kinetics. First, the order of reaction with respect to  $a_{H^+}$  is fractional and negative. Second, a simple linear Tafel relation, according to [3], extends for several decades (4). Such an extended relationship suggests that the mechanism and rate-determining step remain the same in the whole potential region examined, and that the reaction occurs in the absence of a diffusion control process.

*Mechanism under Langmuir conditions of adsorption.*—For the reaction



under Langmuir conditions of adsorption the negative reaction order of the reaction products,  $H^+$ , means that some hydrogen atoms in  $H_2O$  have reached the final stage of oxidation,  $H^+$ , without passing through the rate-determining step. With water molecules as reactants, the algebraic product of this reaction order with stoichiometric number ( $\nu$  from 1 to 4), which gives the number of hydrogen ions that have bypassed the rate-determining step for a single act of the over-all reaction,<sup>6</sup> is either  $-1/2$ ,  $-1$ ,  $-3/2$ , or  $-2$ . The values of  $-1/2$  and  $-3/2$ , and therefore the stoichiometric numbers 1 and 3, can be discarded because the product has to be an integer. The value  $-1$  corresponds to  $\nu = 2$ . With  $\nu = 2$  an even number of products can be formed either in or after the rate-determining step. However, three  $H^+$  are required to complete the over-all process. Similarly, for  $-2$  ( $\nu = 4$ ), either none or  $4H^+$  ions should be formed in or after the rate-determining step, but only two are required to complete the over-all process. Hence, neither  $\nu = 2$  nor  $\nu = 4$  can be ascribed to the rate-determining step. With this simple analysis, therefore, it is not possible to account for the observed pH dependence of the reaction. In a previous study, it was suggested (15) that  $\partial V/\partial pH = 0$  in spite of the observed dependence of  $-30$  mV. This then led to the conclusion that the first charge transfer step under Langmuir conditions with water molecules as reactants was rate determining. In view of the pH dependence obtained in the present work under controlled conditions of electrode pretreatment, this conclusion seems invalid.

If, instead of [4], it is assumed that, although in acid solution, the over-all reaction is



then again the fractional reaction order cannot be accounted for by this simple analysis. The observed pH dependence precludes, therefore, any simple analysis under Langmuir conditions of adsorption.

*Kinetics under Temkin conditions of adsorption.*—With any reasonable value for the change of heat of adsorption with coverage, Temkin conditions can hold (17) only for a relatively narrow region of potentials

( $\Delta V \approx 200$ – $300$  mV). This is because the coverage in the range, say,  $\theta = 0.1$ – $0.9$  changes rapidly with electrode potential, as shown for oxygen adsorption at oxide-free platinum (18). In the latter case, Temkin conditions hold only for about 150 mV. In view of the extended Tafel region for oxygen evolution reaction, Temkin conditions of adsorption apparently do not hold for oxygen evolution at platinum.

*Kinetic equations based on the dual barrier model.*—Since the catalytic activity for oxygen evolution decreases as the thickness of the anodic oxide film increases, the film itself is a barrier to charge transfer and a potential difference must exist across the film. The potential difference across the metal solution interface,  $\Delta V$ , is then a sum of the potential difference across the oxide film,  $\Delta V_{of}$ , and double layer,  $\Delta V_{dl}$

$$\Delta V = \Delta V_{of} + \Delta V_{dl} \quad [6]$$

In a steady state, when the current for oxide growth is negligible,  $\Delta V_{of}$  and  $\Delta V_{dl}$  for the same  $\Delta V$  adjust themselves in such a way that

$$i_{dl} = i_{of} \quad [7]$$

Here,  $i_{dl}$  and  $i_{of}$  are current densities across the double layer and oxide film, respectively.

The concept of the dual barrier control in a series type of arrangement has been advanced by Meyer (5) in an analysis of cathodic processes at passive Zr electrodes. MacDonald and Conway (6) have used this concept to explain some unusual Tafel slopes in oxygen evolution at Au and Pd electrodes.<sup>7</sup> Here, this concept is used to explain the unusual pH dependence of the oxygen evolution reaction at platinum anodes.

For any constant thickness of the oxide film, combining [3] and [7] one obtains

$$i_{\text{observed}} = i_{dl} = i_{of} = kc^{-p} \exp \left[ \frac{\alpha F \Delta V}{RT} \right] \quad [8]$$

where  $c$  is the activity of  $H^+$  ions,  $\alpha$  is the over-all transfer coefficient ( $= 1/2$ ), and  $p$  ( $= 1/2$ ) is the negative of the reaction order for  $H^+$ . In a simple analysis used here, it is assumed that  $i_{dl}$  for a given pH is a function of  $\Delta V_{dl}$  only, and not of  $\Delta V_{of}$ . Then the current across the double layer is given in the usual way by

$$i_{dl} = B c^n \exp \left[ \frac{\alpha_{dl} F \Delta V_{dl}}{RT} \right] \quad [9]$$

It follows that  $i_{of}$  is also in the form

$$i_{of} = A c^m \exp \left[ \frac{\alpha_{of} F \Delta V_{of}}{RT} \right] \quad [10]$$

Here,  $\alpha_{dl}$  and  $\alpha_{of}$  are the transfer coefficients, and  $m$  and  $n$  orders of the reactions with respect  $H^+$ .  $A$  and  $B$  are constants. By combining [8] and [9], taking logarithm and with [6] after rearranging one obtains

$$\Delta V_{dl} = \frac{\alpha_{of} \Delta V + (RT/F) \ln[(A/B)c^{m-n}]}{\alpha_{of} + \alpha_{dl}} \quad [11]$$

and

$$\Delta V_{of} = \frac{\alpha_{dl} \Delta V - (RT/F) \ln[(A/B)c^{m-n}]}{\alpha_{of} + \alpha_{dl}} \quad [12]$$

These equations relate the potential difference across the oxide film and double layer to the potential difference across the whole interface. With either [11] into [9], or [12] into [10], and rearranging, a kinetic equation based on the dual barrier model is obtained

$$i = \{A^{\alpha_{dl}} B^{\alpha_{of}} c^{(\alpha_{dl} m + \alpha_{of} n)}\} \frac{1}{\alpha_{dl} + \alpha_{of}} \exp \left[ \frac{\alpha_{of} \alpha_{dl} F \Delta V}{(\alpha_{of} + \alpha_{dl}) RT} \right] \quad [13]$$

<sup>6</sup> Cf., Ref. (48).

<sup>7</sup> See also Ref. (49) and (50).

Table II. Permissible ( $\alpha_{of}$ ,  $\alpha_{dl}$ ) for various values of  $n$  and  $m$ 

$m$	0	-1	-2	-3	-4
$n = 0$	—	(1, 1)	(2, 2/3)	(3, 3/5)	(4, 4/7)
-1	(1, 1)	—	—	—	—
-2	(2/3, 2)	—	—	—	—
-3	(3/5, 3)	—	—	—	—
-4	(4/7, 4)	—	—	—	—

Comparison of [13] and [8] yields

$$k = [A^{\alpha_{dl}} B^{\alpha_{of}}] \frac{1}{\alpha_{dl} + \alpha_{of}} \quad [14]$$

$$\alpha = \frac{\alpha_{dl}\alpha_{of}}{\alpha_{dl} + \alpha_{of}} [= 1/2] \quad [15]$$

$$p = -\frac{n\alpha_{of} + m\alpha_{dl}}{\alpha_{of} + \alpha_{dl}} [= 1/2] \quad [16]$$

These equations are used in the analysis of the mechanism of reaction.

It can be shown, using similar arguments as in the preceding section, that  $m$  and  $n$  must be either negative integers or zero. Also,  $n \neq m$ , for if  $m = n$  then, from [16],  $n = -1/2$ . In Table II, calculated values of  $\alpha_{of}$  and  $\alpha_{dl}$  are given for various values of  $m$  and  $n$ . Now, from [15], neither  $\alpha_{dl}$  nor  $\alpha_{of}$  can be zero. Also, any pair of ( $\alpha_{of}$ ,  $\alpha_{dl}$ ) with at least one negative coefficient is not a real solution; it would mean that the current decreases as potential increases. An inspection of Table II shows that with these restrictions there are eight solutions. For two solutions both with  $\alpha_{dl} = \alpha_{of} = 1$ , either  $m = 0$  and  $n = -1$ , or  $m = -1$  and  $n = 0$ . The solution with  $m = 0$  is preferred because the rate of the reaction across the oxide-solution interface is more likely to depend on pH than the rate of the reaction across the oxide film. For the same reason, only solutions in the first column ( $m = 0$ ) are acceptable. Solutions with  $n = -3$ , or  $-4$ , involve rather complex mechanisms both for the reaction across the double layer<sup>8</sup> and for the charge transfer across the oxide film. Furthermore, for the solution with  $n = -4$ , a chemical step that follows four electron transfers is rate determining. This, in turn, requires cathodic Tafel lines with an infinite slope.

Available data for the oxygen reduction at oxide-covered electrodes, however inaccurate due to gradual dissolution of oxides at potentials below about 1.0V, indicate (1, 15, 17, 22) that the slope is close to  $-100$  mV. As for the solutions with  $n = -3$ , it requires much higher ( $\sim 160$  mV) cathodic slopes than observed. For these reasons, both solutions with  $n = -3$  and  $-4$  are not considered further.

The rate equations for the two acceptable pairs of solutions are obtained from [9] and [10]. They are

$$i_{dl} = B c^{-1} \exp \left[ \frac{F\Delta V_{dl}}{RT} \right] \quad [17]$$

and

$$i_{of} = A \exp \left[ \frac{F\Delta V_{of}}{RT} \right] \quad [18]$$

for solution with  $n = -1$ , and

$$i_{dl} = B c^{-2} \exp \left[ \frac{2F\Delta V_{dl}}{RT} \right] \quad [19]$$

and

$$i_{of} = A \exp \left[ \frac{2F\Delta V_{of}}{3RT} \right] \quad [20]$$

for solution with  $n = -2$ . Current densities  $i_{dl}$  for these two solutions are analyzed in turn.

*Mechanism of the reaction for the solution with  $n = -2$ .*—From [19]

<sup>8</sup> Cf., Ref. (17).

$$\frac{\partial \Delta V_{dl}}{\partial \ln i} = \frac{RT}{2F} \quad [21]$$

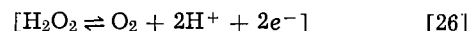
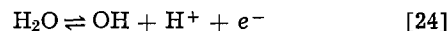
Now, for Langmuir conditions, for which [19] holds, this slope is given by<sup>9</sup>

$$\frac{\partial \Delta V_{dl}}{\partial \ln i} = \frac{RT}{F} \left\{ \beta_k r_k + \frac{1}{\nu_k} \sum_{j=1}^{k-1} (\nu_j r_j) \right\}^{-1} \quad [22]$$

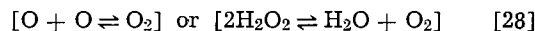
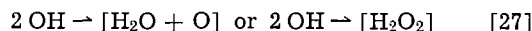
Here,  $\nu_j$  and  $\nu_k$  are stoichiometric numbers,<sup>10</sup> and  $r_j$  and  $r_k$  are the numbers of electrons transferred in a single act of the step  $j$  and the rate-determining step  $k$ , respectively.  $\beta$  is the symmetry factor usually taken as  $1/2$ . Values of  $r$  can be either zero or one.<sup>11</sup>  $\sum (\nu_j r_j)$  is equal to number of electrons transferred before the rate-determining step for one act of the over-all reaction. With [22], it is possible to fix the position of the rate-determining step with respect to the number of electrons transferred before or in the rate-determining step. From [21] and [22] it follows that

$$\sum_{j=1}^{k-1} (\nu_j r_j) = \nu_k (2 - \beta_k r_k) \quad [23]$$

This equation gives two solutions, both for  $r_k = 0$  and hence for a chemical step as rate determining. In the first,  $\nu_k = 1$  and  $\sum (\nu_j r_j) = 2$ . This is the case of a chemical recombination step as rate determining, for instance according to (17)



In the second solution,  $\nu_k = 2$  and  $\sum (\nu_j r_j) = 4$ . The following reaction path is an example (which, however, would have an infinite cathodic slope)



From data obtained on the anodic side only, no conclusion can be made about the products in the rate-determining step or in the steps that follow. This is indicated by brackets in [25], [26], [27], and [28]. In the second paths too, a chemical recombination step is rate determining. It is questionable whether relatively high current densities (e.g.,  $10^{-2}$  A/cm<sup>2</sup> at 2.0V) can be maintained by a chemical recombination step when coverage with reaction intermediates, e.g., OH, is low. Were the coverage high, a chemical recombination step would be independent of potential (51).

For solutions with  $n = 2$ , current density across the oxide film is given by [20]. No account for this rate expression is apparent. For this reason, and because high currents cannot be accounted for by a recombination step, solutions with  $n = 2$  are not suggested.

*Mechanism of the reaction for the solution with  $n = -1$ .*—From [17]

$$\frac{\partial \Delta V_{dl}}{\partial \ln i} = \frac{RT}{F} \quad [29]$$

and with [29] into [22] and with  $\beta = 1/2$ , it follows

$$\sum_{j=1}^{k-1} (\nu_j r_j) = \nu_k \left[ 1 - \frac{r_k}{2} \right] \quad [30]$$

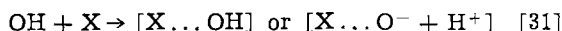
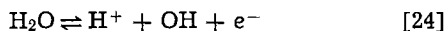
The only simple solution for  $n = -1$  and four electrons

<sup>9</sup> Cf., Ref. (17) and (19).

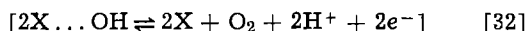
<sup>10</sup> Strictly speaking stoichiometric number refers to a rate-determining step. Here, however, it is applied to any step  $j$  and means the number of times the step  $j$  occurs for a single act of the over-all reaction.

<sup>11</sup> Simultaneous two electron transfers are considered unlikely.

in the over-all reaction is with  $\nu_k = 0$ ,  $\nu_k = 2$ , and  $\Sigma(\nu_j r_j) = 2$ . Again, a chemical step after a first charge transfer step is rate determining. Two  $H^+$  ions ( $-\nu_k n = 2$ ) are formed before and have, therefore, bypassed the rate-determining step. A reaction path satisfying this condition would be

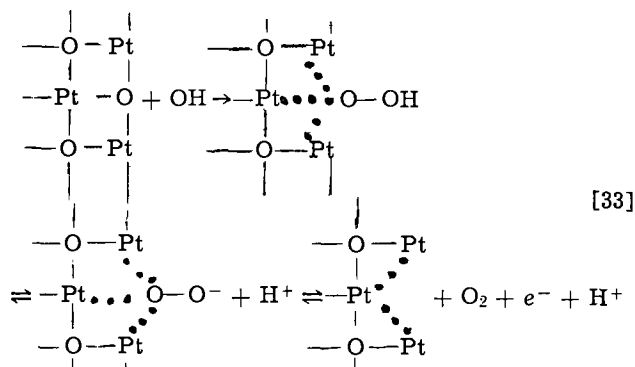


where X stands for a site on the surface of the oxide film. The reaction proceeds according to



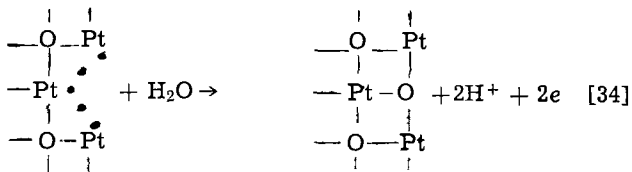
If X represents an oxygen atom in the oxide film after the completion of the over-all reaction the same oxygen atom, according to this model, remains in its position. Again, however, there is a difficulty of high current densities for a recombination step that must follow (cf., e.g., [32]).

*Direct participation of oxygen atoms in oxide film in  $O_2$  evolution.*—An attractive reaction path for the solution with  $n = -1$  is suggested here. According to this path, an oxygen atom in the oxide film directly participates in the oxygen evolution reaction. For instance, after step [24] the reaction proceeds according to



with the second step as rate determining.<sup>12</sup>

It may be noted that for this model and sequence of steps, including the rate-determining step, the stoichiometric number would be equal to 1 (instead of 2). Also,  $\Sigma(\nu_j r_j) = 1$ , and  $(-\nu_k n) = 1$ . Oxygen vacancy in the surface of the oxide film is subsequently replenished in a parallel reaction with the sequence of steps such as [24] and [31] and oxidation



Since this oxygen atom is already in the lattice of the oxide, it enters as a constant term in the over-all rate expression for the oxygen evolution reaction. For this reaction path there is no need for a high coverage with reaction intermediates.

An evidence that an oxygen atom in the surface oxide film participates directly in oxygen evolution reaction is provided by Rosenthal and Veselovski (52). These workers have found, using tracer technique with  $^{18}O$ , that if the platinum surface oxide film is initially enriched with  $^{18}O$  (by anodic polarization in  $^{18}O$  enriched solutions), then the first gas anodically evolved at platinum (in  $^{18}O$  unenriched solutions) is enriched with  $^{18}O$ . At silver electrodes too, direct participation of oxygen in surface oxides in oxygen evolution in alkaline solution has been detected (53).

*The over-all rate equation.*—According to the dual barrier model, the rate of oxygen evolution reaction

across the double layer is best described by [17]. In this rate expression, there is no fractional reaction order with respect to  $H^+$ . The corresponding rate equation across the oxide film is then given by [19], and the over-all observed rate, by [13]. The latter rate can be written as

$$i = (AB)^{1/2} c^{-1/2} \exp \left[ \frac{F\Delta V}{2RT} \right] \quad [35]$$

and a fractional reaction order appears in the over-all rate expression. This order now becomes fully accounted for in terms of the dual barrier control of the reaction. The rate across the double layer is controlled by a chemical step that follows a charge transfer step such as in sequences [24] and [31] or [24] and [33].

Factor A in Eq. [18] depends exponentially on the tunneling distance, that is on the average thickness of the surface oxide film (12). A is a constant for a given thickness of the film; it sharply decreases as the film thickness increases. This factor appears also in the over-all rate expression [35] and accounts for the change of the observed rate with time in terms of the change in the thickness of the oxide with time.

### Acknowledgment

One of us (A.D.) wishes to thank Dr. Anthony Ward for discussions and helpful suggestions and Ms. Carol Troy for care in technical preparation of the manuscript.

Manuscript submitted March 15, 1974; revised manuscript received Sept. 2, 1975.

Any discussion of this paper will appear in a Discussion Section to be published in the December 1976 JOURNAL. All discussions for the December 1976 Discussion Section should be submitted by Aug. 1, 1976.

Publication costs of this article were partially assisted by the Xerox Corporation.

### REFERENCES

1. A. Damjanovic and J. O'M. Bockris, *Electrochem. Acta*, **11**, 376 (1966).
2. A. Damjanovic, A. Dey, and J. O'M. Bockris, *This Journal*, **113**, 739 (1966).
3. D. Sepa, M. Vojnovic, and A. Damjanovic, *Electrochim. Acta*, **15**, 1355 (1970).
4. A. Damjanovic, in "Modern Aspects of Electrochemistry," J. O'M. Bockris and B. E. Conway, Editors, p. 369. Plenum Press, New York (1969).
5. R. E. Meyer, *This Journal*, **107**, 847 (1960).
6. J. J. MacDonald and B. E. Conway, *Proc. Roy. Soc.*, **269**, 419 (1962).
7. A. K. N. Reddy, M. A. Genshaw, and J. O'M. Bockris, *J. Chem. Phys.*, **48**, 671 (1968).
8. S. H. Kim, W. Paik, and J. O'M. Bockris, *Surface Sci.*, **33**, 617 (1972).
9. K. J. Vetter and J. W. Schultze, *J. Electroanal. Chem.*, **34**, 131 (1972).
10. K. J. Vetter and J. W. Schultze, *ibid.*, **34**, 141 (1972).
11. J. L. Ord and F. C. Ho, *This Journal*, **118**, 46 (1971).
12. A. Damjanovic, A. T. Ward, and M. O'Jea, *ibid.*, **121**, 1186 (1974).
13. A. Damjanovic, A. T. Ward, B. Ulrick, and M. O'Jea, *ibid.*, **122**, 471 (1975).
14. J. W. Schultze and K. J. Vetter, *Electrochim. Acta*, **18**, 889 (1973).
15. J. O'M. Bockris and A. K. M. S. Huq, *Proc. Roy. Soc.*, **A237**, 227 (1956).
16. A. Damjanovic, M. A. Genshaw, and J. O'M. Bockris, *This Journal*, **114**, 466 (1967).
17. A. Damjanovic, A. Dey, and J. O'M. Bockris, *Electrochim. Acta*, **11**, 791 (1966).
18. M. Paucirova, D. M. Drazic, and A. Damjanovic, *Acta Electrochem.*, **18**, 945 (1973).
19. A. Damjanovic and V. Brusic, *Electrochim. Acta*, **12**, 615 (1967).
20. D. V. Kokoulina, Yu. I. Krasovitskaya, and L. I. Krystalik, *Elektrokhimiya*, **7**, 1218 (1971).
21. W. Visscher and M. A. V. Devanathan, *J. Electroanal. Chem.*, **8**, 127 (1964).
22. T. P. Hoar, *Proc. Roy. Soc.*, **A142**, 628 (1933).
23. F. P. Bowden, *ibid.*, **A126**, 107 (1930).

<sup>12</sup> "Bonds" and "positions" of atoms only illustrate the model.

24. A. Rius, J. Llopis, and P. Gaudia, *Anales Real Soc. Espan. Fis. Quim. (Madrid)*, **46B**, 225 and 279 (1950).
25. N. A. Izgaryshev and E. A. Efimov, *Zh. Fiz. Khim.*, **30**, 1807 (1956).
26. E. A. Efimov and N. A. Izgaryshev, *ibid.*, **30**, 1606 (1956).
27. T. Erdev-Grúz and O. Golopencza-Bajor, *Acta Chim. Hung.*, **34**, 281 (1962).
28. T. Erdev-Grúz, M. Gallyas, and E. Szetey, *Acta Chim. (Budapest)*, **69**, 433 (1971).
29. H. A. Laitinen and C. G. Enke, *This Journal*, **107**, 773 (1960).
30. A. N. Frumkin and V. V. Sobol, *Dokl. Akad. Nauk SSSR*, **141**, 917 (1961).
31. J. P. Hoare, *This Journal*, **112**, 602 (1965).
32. J. P. Hoare, *Electrochim. Acta*, **11**, 203 (1966).
33. S. Schuldiner, T. B. Warner, and B. J. Piersma, *This Journal*, **114**, 343 (1967).
34. G. N. Afonshin, G. F. Volodin, and Yu. M. Tyurin, *Elektrokhimiya*, **7**, 1338 (1971).
35. I. I. Pyshnograeva, A. M. Skundin, Yu. B. Vasilev, and V. S. Bagotskii, *ibid.*, **6**, 142 (1970).
36. A. J. Appleby and A. Borucka, *This Journal*, **116**, 1212 (1969).
37. V. S. Bagotskii, E. I. Khrushevano, and N. A. Shimilova, *Elektrokhimiya*, **6**, 1746 (1970).
38. Yu. M. Tyurin and G. F. Volodin, *ibid.*, **5**, 1203 (1969).
39. H. A. Laitinen and C. G. Enke, *This Journal*, **104**, 773 (1960).
40. J. W. Schultze, *Z. Physik. Chem. Neufolge*, **73**, 29 (1970).
41. S. Shibata, *Electrochim. Acta.*, **17**, 395 (1972).
42. W. Visscher and M. Blijlevens, *ibid.*, **19**, 387 (1974).
43. F. C. Anson, and J. J. Lingane, *This Journal*, **70**, 4901 (1957).
44. P. Stonehart, H. A. Kozlovskia, and B. E. Conway, *Proc. Roy. Soc. (London)*, **A310**, 541 (1969).
45. L. B. Harris and A. Damjanovic, *This Journal*, **122**, 593 (1975).
46. D. Gilroy and B. E. Conway, *Can. J. Chem.*, **46**, 875 (1968).
47. A. N. Chemodanov, Ya. M. Kolotyrkin, M. A. Dembrovskii, and T. V. Kudrayavina, *Dokl. Akad. Nauk SSSR*, **171**, 1384 (1966).
48. J. O'M. Bockris, in "Modern Aspects of Electrochemistry," Vol. 1. p. 180, Butterworths, London (1954).
49. H. Göhr and E. Lange, *Z. Elektrochem.*, **63**, 673 (1958).
50. V. I. Veselovskii, Proceedings of the 4th Conference on Electrochemistry, Moscow (1956).
51. J. O'M. Bockris, *J. Chem. Phys.*, **24**, 817 (1956).
52. K. I. Rozenthal and V. I. Veselovskii, *Dokl. Akad. Nauk USSR*, **111**, 647 (1956).
53. K. I. Rozenthal and V. I. Veselovskii, *Zh. Fiz. Khim.*, **35**, 2481 (1961).

## Technical Note



### Silicon Epitaxial Growth by Electrodeposition from Molten Fluorides

Uri Cohen\* and Robert A. Huggins\*\*

Center for Materials Research, Stanford University, Stanford, California 94305

Molten fluoride baths based upon the alkali fluorides have been shown to yield excellent diffused silicide coatings (1), and superior coherent layers can be deposited on many refractory metals (2, 3). It is believed that the fluorides act as fluxing agents for surface oxides, exposing clean metallic surfaces to the solutions. This is essential for the deposition of high quality coatings with good adherency. It is also believed that the stable fluoride ion complexes help to decrease diffusion-control effects, which are responsible for increased interfacial roughness and eventually result in porous, dendritic, or powdery growth. Other attractive features of the alkali fluoride salts are their low melting eutectics, low vapor pressures, low viscosity, high ionic conductivity (and low electronic conductivity), and large decomposition potential range ( $> 3V$ ). All these features combine to make them ideal electrolytes for the deposition of many elements and compounds.

When applied to materials such as silicon, the electrocrystallization epitaxy (ECE) technique has a number of unique and attractive features. The operating temperature, e.g.,  $750^{\circ}C$ , is quite low compared with typical CVD techniques, whose operating temperatures are about  $1200^{\circ}C$ . Thus ECE should yield sharper junctions, without the deleterious effects of interdiffu-

sion and dopant redistribution, typical of high temperature processes. Lower operating temperatures are also beneficial with regard to avoiding thermal stresses, and for reasons related to materials handling, compatibility, and energy conservation.

ECE is also a much safer process in some ways, as it does not utilize hazardous gases such as  $H_2$  and  $SiCl_4$  or  $SiH_4$ , which are extensively used in the CVD techniques.

Probably of most importance, the ECE technique is isothermal and controlled by simple electrical parameters, such as current magnitudes and duration, which may easily be controlled by electronic instrumentation to facilitate precision in the film thickness and morphology. In principle, very thin films, well below the micron range, which might find uses in very fast devices, should be easily prepared by this technique. Thicker layers, as well as quite complex substrate shapes may be coated. These may find future uses in the processing of crystals or devices of various shapes.

Another unique feature of the electrodeposition process is that growth occurs on electrically conductive surfaces only. Insulating masks, through which windows can be cut, might be used to confine the growth, thereby providing a method of device isolation. Insulating masks should, of course, be stable in fluoride melts. Thus, silicon oxide is an inappropriate choice as it is quite soluble in fluorides. Silicon nitride, however, might be attractive for this purpose.

\* Electrochemical Society Student Member.

\*\* Electrochemical Society Active Member.

Key words: silicon epitaxy, electrodeposition, molten fluorides, electrocrystallization, semiconducting layers, thin-film deposition.

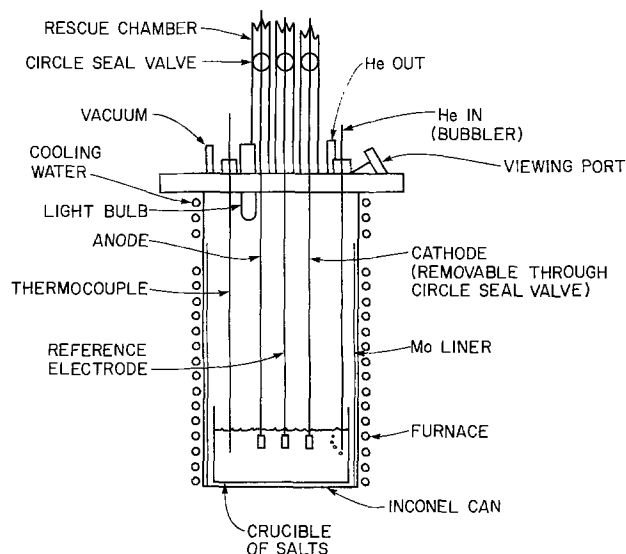


Fig. 1. Schematic drawing of the experimental apparatus

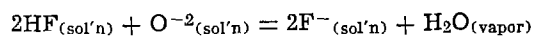
This paper reports experiments which show that such fluoride systems can be used to deposit high quality epitaxial layers of silicon upon single crystalline silicon substrates.

#### Experimental Procedures

Electrodeposition was done from a fluoride bath held in a molybdenum crucible contained within a

molybdenum-lined vacuum tight-chamber filled with an atmosphere of purified helium. Special insulated and vacuum-sealed chambers, equipped with helium and vacuum inlets, allow lowering, raising, and replacement of the various electrodes without changing the bath temperature. A viewing port with a sapphire window and an illumination bulb facilitate observation of the melt and electrodes. This apparatus is illustrated schematically in Fig. 1.

KF-LiF (1:1, mp = 492°C) was used as the solvent, with 5 mole per cent (m/o)  $K_2SiF_6$  as a solute. The mixture was first melted under vacuum with some of the KF replaced by  $KHF_2$ . The latter decomposed to KF and HF, which reacted with any residual oxides according to the equilibrium reaction



This equilibrium was shifted to the right under vacuum, removing the water vapor. This was followed by purging the melt with purified helium to expel any dissolved HF. The purification procedure was completed by a pre-electrolysis step, during which any metallic ions more noble than silicon, as well as some silicon, were plated onto a sacrificial molybdenum strip cathode. The combination of these two purification methods, which remove different types of impurities, was found to be necessary in this case. Elimination of the deoxidation procedure was investigated, but it was found to have especially deleterious effects upon the morphology of the silicon deposit.

High purity silicon was used as a dissolving anode, and a constant current of 2 mA/cm<sup>2</sup> was maintained for 12 hr.

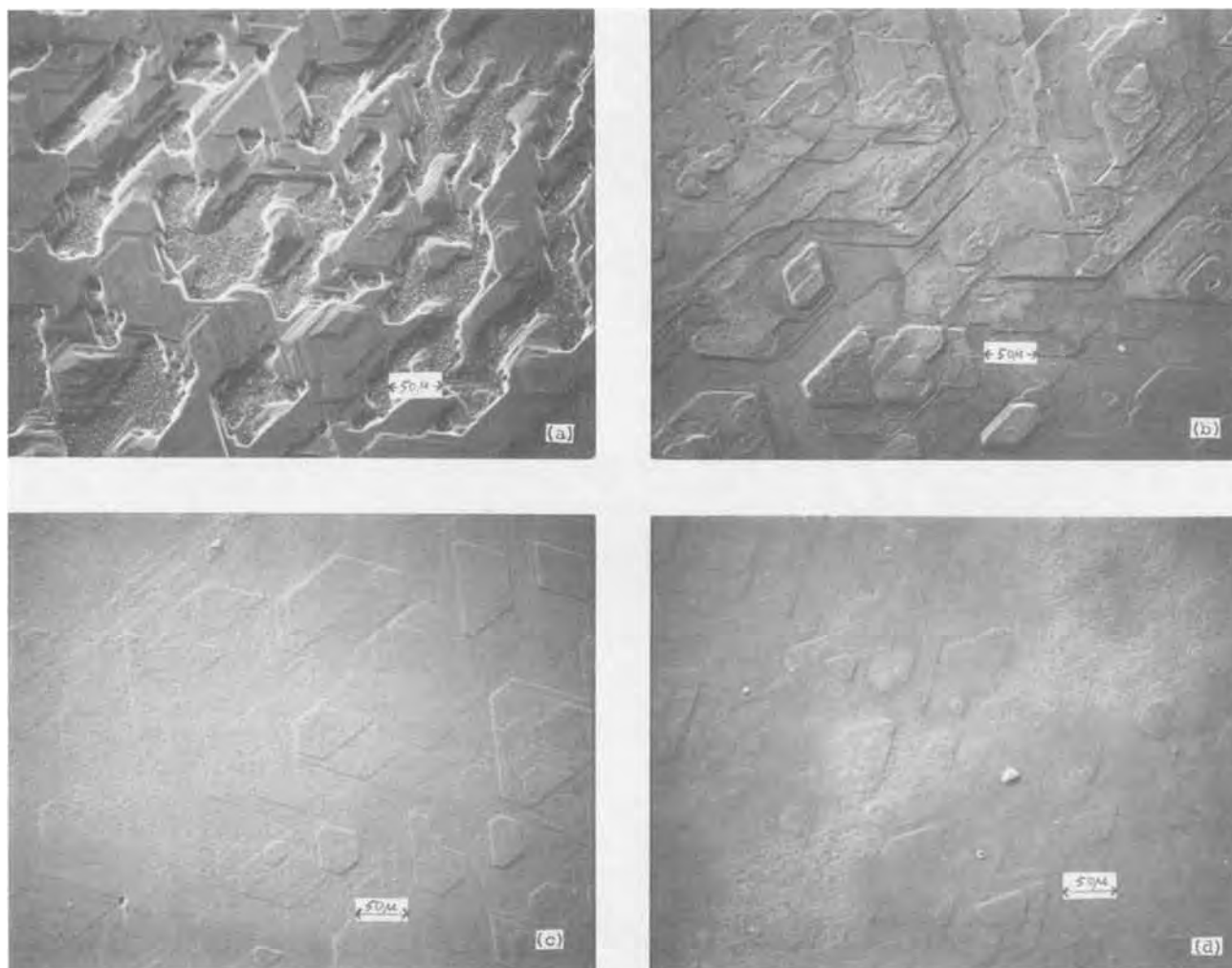


Fig. 2. SEM photographs of (111) Si epitaxial layers grown at (a) 1 mA/cm<sup>2</sup> (10μ thick); (b) 2 mA/cm<sup>2</sup> (10μ thick); (c) 4 mA/cm<sup>2</sup> (2μ thick); (d) 6 mA/cm<sup>2</sup> (10μ thick).



The coated molybdenum strip was then removed, and a silicon wafer with a (111) orientation and a mirror-polished face was introduced into the melt. An anodic current pulse of 50 mA/cm<sup>2</sup> was then applied for 1 sec. This served to achieve an *in situ* etching of the wafer (approximately 150Å). The polarity was then reversed, the Si wafer becoming the cathode, and constant current electrodeposition established for a predetermined period of time. The sample was then removed, cleaned, and examined. A potentiostat (PAR 173) was used for current control.

### Results

Epitaxial deposition of silicon readily occurred upon the single crystal substrate. The current density was found to have an important influence upon the morphology of the deposit. Figure 2(a) shows a scanning electron micrograph of the epitaxial growth obtained at 1 mA/cm<sup>2</sup>. Poor coverage of the substrate surface, and a hillock and layer structure can be seen. Such a structure is believed to be due to the adsorption of foreign species, probably oxygen or oxides, which hinder the propagation of kinks and steps.

If the adsorption rate is constant for a given impurity concentration and temperature, increased current density (or rate of deposition) should favor step propagation and more uniform growth. This effect can easily be seen in Fig. 2(b-d), which show deposits obtained at 2, 4, and 6 mA/cm<sup>2</sup>, respectively. It should be noted that the epitaxial layer in Fig. 2(c) is only 2μ thick, whereas the others are 10μ thick.

Deposit uniformity across the substrate surface was found to be greatly affected by the current distribution. Since Si is a poor electronic conductor, the current density is greater in areas with a shorter current path within the silicon wafer. This results in an enhanced and more uniform growth close to the melt surface, with poorer growth in remote areas.

To produce a more uniform current distribution, a metallic layer with greater conductivity may be attached to the back side of the wafer, either by a mechanical attachment, or as a coating or film. The metal in contact with the back side of the wafer should be compatible with silicon. It must not have a low melting point alloy or eutectic with silicon, and its solid solubility in Si at the operating temperature must be as small as possible. It may also be important that this

layer can be easily removed without damaging the wafer.

It was found that a layer of Ag metal 0.5μ thick, obtained by sputtering, resulted in a substantial improvement in the uniformity of the epitaxial layer. Thicker coatings should produce even more uniform layers. Silver may be removed by dipping in dilute HF, which will not attack silicon. Its solid solubility in silicon at 750°C is extremely low, and the Si-Ag system has one eutectic at 840°C.

Back-reflection Laue x-ray patterns have demonstrated that these layers are epitaxially related to the (111) substrate, even when the growth morphology appears rather rough. Results obtained by Auger spectroscopy and electron microprobe analysis have shown the deposit to be of high purity. Some carbon and oxygen were both found upon the surface after growth by Auger spectroscopy. They disappeared from the signal after a layer about 500Å thick was removed by sputtering. Electron microprobe analysis, with a sensitivity of about 100 ppm, detected no impurities beneath the surface.

### Acknowledgments

This work was supported by the Advanced Research Projects Agency and the Office of Naval Research. The authors wish to thank Mr. L. J. Anderson for his capable SEM photography, and Mr. W. H. Holmes for his invaluable assistance in sample preparation.

Manuscript submitted Oct. 20, 1975; revised manuscript received Nov. 10, 1975. This was Paper 259 RNP presented at the Dallas, Texas, Meeting of the Society, Oct. 5-9, 1975.

Any discussion of this paper will appear in a Discussion Section to be published in the December 1976 JOURNAL. All discussions for the December 1976 Discussion Section should be submitted by Aug. 1, 1976.

Publication costs of this article were partially assisted by Stanford University.

### REFERENCES

1. N. C. Cook, U. S. Pat. Re. 25,630 (1964).
2. S. Senderoff, G. W. Mellors, and W. J. Reinhart, *This Journal*, **112**, 840 (1965).
3. S. Senderoff and G. W. Mellors, *ibid.*, **112**, 266 (1965); *ibid.*, **113**, 60 (1966); *ibid.*, **113**, 66 (1966); *ibid.*, **114**, 586 (1967); *ibid.*, **118**, 220 (1971).

## Brief Communication



### The Fluid Motion Due to a Rotating Disk

Ralph White,\* Charles M. Mohr, Jr.,\*<sup>1</sup> and John Newman\*\*

*Inorganic Materials Research Division, Lawrence Berkeley Laboratory, and Department of Chemical Engineering, University of California, Berkeley, California 94720*

The solution of the Navier-Stokes equation for fluid motion due to a rotating disk includes characteristic parameters as presented below. We report here the most accurate values available for three of these parameters and compare to them values obtained by a numerical integration technique developed by Newman (3, 5).

\* Electrochemical Society Student Member.

\*\* Electrochemical Society Active Member.

<sup>1</sup> Present address: Aerojet Nuclear Company, Idaho Falls, Idaho 83401.

Key words: laminar flow.

In 1921, von Kármán (2) presented a separation of variables solution technique for the motion of an incompressible, Newtonian fluid which transformed the Navier-Stokes equation into a set of coupled, nonlinear, ordinary differential equations. By defining the following dimensionless variables  $\zeta = z\sqrt{\Omega/\nu}$ ,  $P = p/\mu\Omega$ ,  $G = v_\theta/r\Omega$ ,  $F = v_r/r\Omega$ , and  $H = v_z/\sqrt{\nu\Omega}$ , the transformed equations may be written as

$$2F + H' = 0 \quad [1]$$

$$F^2 - G^2 + HF' = F'' \quad [2]$$

$$2FG + HG' = G'' \quad [3]$$

$$HH' + P' = H'' \quad [4]$$

where the prime designates differentiation with respect to  $\zeta$ . The boundary conditions are

$$H = F = 0, G = 1 \text{ at } \zeta = 0 \quad [5]$$

and

$$F = G = 0 \text{ at } \zeta = \infty \quad [6]$$

Cochran (1) solved Eq. [1-3] (subject to boundary conditions [5] and [6]) by expanding the components of the velocity field first in power series in the dimensionless distance from the disk, which were assumed to be valid near the disk

$$F = a\zeta - \frac{1}{2}\zeta^2 - \frac{b}{3}\zeta^3 + \dots \quad [7]$$

$$G = 1 + b\zeta + \frac{1}{3}a\zeta^3 + \dots \quad [8]$$

$$H = -a\zeta^2 + \frac{1}{3}\zeta^3 + \frac{b}{6}\zeta^4 + \dots \quad [9]$$

and second in exponential series which were assumed to be valid far from the disk

$$F = Ae^{-\alpha\zeta} - \frac{(A^2 + B^2)e^{-2\alpha\zeta}}{2\alpha^2} + \frac{A(A^2 + B^2)e^{-3\alpha\zeta}}{4\alpha^4} + \dots \quad [10]$$

$$G = Be^{-\alpha\zeta} - \frac{B(A^2 + B^2)}{12\alpha^4}e^{-3\alpha\zeta} + \dots \quad [11]$$

$$H = -\alpha + \frac{2A}{\alpha}e^{-\alpha\zeta} - \frac{(A^2 + B^2)}{2\alpha^3}e^{-2\alpha\zeta} + \frac{A(A^2 + B^2)}{6\alpha^5}e^{-3\alpha\zeta} + \dots \quad [12]$$

We (5) followed Cochran's suggestion and required the two sets of expansions to yield, at  $\zeta = 1$ , the same values of the functions as well as the derivatives of  $F$  and  $G$ . In this manner we obtained the following values for the characteristic parameters<sup>2</sup>

$$a = 0.51023262, b = -0.61592201, \alpha = 0.88447411, \\ A = 0.92486353, B = 1.20221175 \quad [13]$$

Benton (7) solved this problem by utilizing a technique suggested by Fettis (8) and has tabulated to four significant figures the velocity field, its derivatives, and the pressure field.<sup>3</sup>

To demonstrate the utility of Newman's (3-5) solution technique, estimates of the parameters  $a$ ,  $b$ ,  $\alpha$ ,  $A$ , and  $B$  were obtained by solving this boundary value problem numerically. The governing Eq. [1-3] were first linearized (3-5) about trial values and then cast in finite-difference form accurate to order  $h^2$ . The boundary conditions given by Eq. [5] were applied directly, whereas it was necessary to approximate those given by Eq. [6] at some finite value of  $\zeta_{\zeta, \max}$ . The following expressions, derived from Eq. [10] and [11], were used for that purpose

$$F' = H_x F - \frac{(F^2 + G^2)}{2H_x} + \dots \quad [14]$$

and

$$G' = H_x G + \dots \quad [15]$$

where  $H_x$  was our estimate of  $-\alpha$  according to

<sup>2</sup> Values for  $a$  and  $b$  accurate to 12 significant figures are available in Ref. (6).

<sup>3</sup> Unfortunately, a minus sign for the pressure derivative in his equation (10) is missing; consequently, the sign of the entries in his Table 2 for  $P - P_0$  should be changed.

$$H_x = H + \frac{2F}{H_x} + \frac{(F^2 + G^2)}{2H_x^3} \left( 1 + \frac{F}{3H_x^2} \right) + \dots \quad [16]$$

which was developed from Eq. [12]. Equations [14], [15], and [16] were also linearized about trial values and expressed in finite-difference form accurate to order  $h^2$ . The resulting system of equations was solved by technique developed (3, 4) and extended (5) by Newman. Estimates of the five parameters obtained this way are

$$a = 0.51023262, b = -0.61592201, \alpha = 0.88447410, \\ A = 0.92486322, B = 1.20221104 \quad [17]$$

Clearly, these are very accurate estimates of the parameters given by Eq. [13]. The poorest estimate is for  $B$ , which is in error by only seven digits in the eighth significant figure.

The very attractive feature of Newman's solution technique, in addition to its accuracy, is its suitability for solving complicated boundary value problems directly without the development of specialized techniques, such as Cochran's for the present problem.

### Acknowledgments

This work was supported by the U.S. Energy Research and Development Administration.

Manuscript submitted Sept. 18, 1975; revised manuscript received Nov. 10, 1975.

Any discussion of this paper will appear in a Discussion Section to be published in the December 1976 JOURNAL. All discussions for the December 1976 Discussion Section should be submitted by Aug. 1, 1976.

Publication costs of this article were partially assisted by the University of California, Berkeley.

### LIST OF SYMBOLS

English characters:

$a$	characteristic parameter equal to $F'(0)$
$b$	characteristic parameter equal to $G'(0)$
$A$	characteristic parameter
$B$	characteristic parameter
$F$	dimensionless radial velocity
$G$	dimensionless velocity component in the tangential direction
$H$	dimensionless velocity component in the normal direction (from the disk)
$h$	dimensionless step size
$P$	dimensionless dynamic pressure
$p$	dynamic pressure, dyne/cm <sup>2</sup>
$r$	radial distance from the axis of the disk, cm
$v_r$	velocity component in the radial direction, cm/sec
$v_\theta$	velocity component in the tangential direction, cm/sec
$v_z$	velocity component in the normal direction, cm/sec
$z$	normal distance from the disk, cm

Greek characters:

$\alpha$	characteristic parameter equal to $-H(\infty)$
$\zeta$	dimensionless normal distance from the disk
$\mu$	viscosity of fluid, g/cm-sec
$\nu$	kinematic viscosity of fluid, cm <sup>2</sup> /sec
$\Omega$	rotation speed of the disk, sec <sup>-1</sup>

### REFERENCES

- W. G. Cochran, *Proc. Cambridge Phil. Soc.*, **30**, 365 (1934).
- Th. v. Kármán, *Z. Angew. Math. Mech.*, **1**, 233 (1921).
- J. S. Newman, "Electrochemical Systems," Prentice-Hall, Inc., Englewood Cliffs, N. J. (1973).
- J. Newman, in "Electroanalytical Chemistry," Vol. 6, A. J. Bard, Editor, pp. 187-352, Marcel Dekker, New York (1973).

5. R. White, C. M. Mohr, Jr., P. Fedkiw, and J. Newman, "The Fluid Motion Generated by a Rotating Disk: A Comparison of Solution Techniques," (LBL-3910) Lawrence Berkeley Laboratory, University of California, Berkeley (1975).
6. E. Levart and D. Schuhmann, *Intern. J. Heat Mass Transfer*, **17**, 555 (1974).
7. E. R. Benton, *J. Fluid Mech.*, **24**, 781 (1966).
8. H. E. Fettis, Proceedings of the 4th Midwestern Conference on Fluid Mechanics, Purdue (1955).

## Erratum

---

In the paper, "Lead-Acid Batteries: Use of Carbon Fiber-Lead Wire Grids at the Positive Electrode," by J. L. Weininger and C. R. Morelock, which appeared on pp. 1161-1167 in the September 1975 JOURNAL, Vol. 122, No. 9, the following resistivity for carbon fibers, lead, and lead dioxide should replace the incorrectly stated conductivities of the same materials in column 1, p. 1161:

pyrolyzed polyacrylonitrile fibers

$$\rho_{\text{Cfiber}} = 0.86 \times 10^{-3} \text{ to } 2.5 \times 10^{-3} \text{ ohm-cm}$$

$$\text{lead: } \rho_{\text{Pb}} = 2.1 \times 10^{-5} \text{ ohm-cm}$$

$$\text{lead dioxide: } \rho_{\alpha\text{-PbO}_2} = 1 \times 10^{-3} \text{ ohm-cm}$$

$$\rho_{\beta\text{-PbO}_2} = 4 \times 10^{-3} \text{ ohm-cm}$$



## Bulk and Surface Conduction in CVD SiO<sub>2</sub> and PSG Passivation Layers

Robert B. Comizzoli\*

RCA Laboratories, Princeton, New Jersey 08540

### ABSTRACT

Measurements of electrical conduction in the bulk of chemical vapor deposited (CVD) SiO<sub>2</sub> and phosphosilicate glass (PSG) passivation layers typically used for over-metal IC protection are reported. Moisture uptake increases the bulk conductivity, and the moisture effects depend on phosphorus content. The bulk current thermal activation energy of CVD SiO<sub>2</sub> (0.6 eV) is constant with varying moisture exposure. Before moisture exposure, phosphorus-containing glass has an activation energy of 0.8 eV, and it decreases with moisture exposure. Surface conductivity is also reported as a function of relative humidity. Conductivity values are related to IC leakage currents, and it is suggested that bulk currents in PSG should not contribute to aluminum corrosion in the absence of defects, such as cracks or pinholes.

SiO<sub>2</sub> and phosphosilicate glass (PSG) are important materials in silicon device passivation (1). Thin layers of PSG (hundreds of angstroms) have been described as useful for Na-gettering under gate metal of MOS devices (2-4). Thin layers must be used to avoid instabilities due to PSG polarization (3, 5-7). For over-metal passivation of IC's, thicker layers (about 10<sup>4</sup>Å) can be used (since polarization of the PSG is unimportant in this geometry). Generally, over-metal layers are deposited by chemical vapor deposition (CVD) (8-11). The phosphorus addition lowers intrinsic stress over aluminum metal and provides Na-gettering capability (12), which is particularly useful in plastic packaged devices. In addition, the passivating glass over metal provides important scratch protection during the device production process (13), and serves as insulating protection against loose conducting particles in hermetic packages (14).

The bulk and surface electrical properties of CVD passivation over metal are important in understanding Na-gettering (4, 15) device leakage as affected by lateral charge spreading (16-21), metal corrosion (22-25), and moisture effects (24, 25).

In this report, measurements of bulk electrical conductivity as a function of water uptake and temperature, and surface conductivity as a function of relative humidity (RH) are reported for CVD SiO<sub>2</sub> and CVD PSG. The data are used in estimating electrical and moisture effects typical for IC's.

### Sample Preparation

The glass layers were deposited on degenerate n-type (0.01 ohm-cm) silicon wafers at 450°C at a growth rate of about 1000 Å/min to a total thickness of 1 μm, using a reactor described by Kern (11, 26). Phosphorus concentrations, determined by etch rate analysis, are 0, 4.8, and 8.5 weight per cent (w/o) P in the glass. No postdeposition heat-treatments were applied.

Aluminum was evaporated to a thickness of 8700Å on the surface of the CVD layers and delineated by photolithography into an interdigitated electrode pattern. By proper electrical connection, this pattern allows measurement of bulk conductivity through the glass between one aluminum surface electrode and the silicon wafer, with the other surface electrode acting as a partial guard band, or it allows measurements of surface conduction between the two surface electrodes. The interdigitated pattern has an electrode spacing of 1.3 × 10<sup>-3</sup> cm, an effective electrode width of 0.23 cm, and an electrode area (used for bulk measurements) of 10<sup>-3</sup> cm<sup>2</sup>.

The wafers were subdivided into chips containing four interdigitated patterns each, and some chips were mounted on headers without hermetic cover for bulk measurements. This provided convenient handling and circuit connection, and allowed exposure to steam. On each header-mounted chip, three surface electrode pairs were connected to leads by means of bonded wire and one connection was provided to the silicon substrate. Other chips were not mounted on headers but were tested "as is" in a probe station for both bulk and surface measurements. Conductive silver-epoxy pastes were used as back electrodes in all cases.

### Measurement and Test Procedure

**Bulk electrical conductivity.**—In all electrical measurements a Keithley 602 or 610B electrometer was used, and a strip chart recorder continuously monitored the current.

Preliminary measurements of bulk and surface current as a function of voltage, temperature, ambient (air or N<sub>2</sub> with varying relative humidity), and autoclave exposure time (in steam at 15 psig, 121°C) established the following:

1. In dry N<sub>2</sub> ambient, measurements of current flow between one surface electrode and the silicon substrate could be made without surface current contributions, thus permitting measurement of bulk properties of the glass. The other surface electrode was used as

\* Electrochemical Society Active Member.

Key words: IC's, corrosion, passivation glass, reliability, moisture effects.

a partial guard band to establish that no surface current was detected in dry  $N_2$ . Thus, a guard band was not needed.

2. In most cases the time rate of change of current decreased 10-100 times 1 min after voltage application compared to initial values, and after 1 min, the current level was approximately linear with voltage, in the voltage range from 50 to 200V. Little dependence on polarity was observed.

3. Leakage current of the TO-5 header itself was negligible. It was always less than 10% of the sample currents. Based on these preliminary results a test procedure was established and carried out as follows:

(a) The current between one surface contact and the substrate was measured in dry  $N_2$  flow at 100V. The current level 1 min after voltage application was selected for evaluation.

(b) Measurements were done at three temperatures: 20°, 60°, and 95°C. Initially, all chips used were measured at the three temperatures. After autoclave stress treatment, each chip was measured at only one of the three temperatures for all succeeding measurements. In the data to be presented each data point at 0 hr autoclave time represents an average of 24 measurements, while each data point after autoclave exposure represents an average of eight measurements.

(c) The samples were placed in the steam phase of the autoclave with a cover arrangement to minimize condensate dripping. Exposure was usually 5 hr at a time, with current measurements made at the end of each stress period. After removal from the autoclave the samples were dried for 5 min in dry  $N_2$  flow at room temperature to remove surface water, and the measurements were done immediately thereafter. The current was measured in a small oven whose temperature was continuously monitored; variation was less than  $\pm 2^\circ C$ .

**Surface electrical conductivity.**—For these measurements the chips were placed in a probe station to which mixtures of dry and wet  $N_2$  were admitted to achieve controlled, variable relative humidity. All these measurements were done at  $23^\circ \pm 2^\circ C$ , and no autoclave stress was used. Two probes were used to contact the interdigitated patterns on the pellet, and the four patterns on each pellet were measured at 100V in the dark. The substrate was grounded. Again, the 1 min current level was chosen for analysis. For  $RH \gtrsim 60\%$  current reached steady state within 1 min. For lower relative humidity the current decayed very slowly.

### Experimental Results

**Bulk conductivity.**—The time dependence of the current after voltage application depends on the presence of phosphorus. For  $SiO_2$  the current increases slowly to a steady-state value, while with the 4.8 and 8.5 w/o P samples the current decreases after voltage application. This behavior is shown in Fig. 1. As mentioned previously, currents at 1 min are chosen for evaluation in all succeeding analyses. For all samples, evidence of a polarization process exists. If the sample is shorted after voltage application, a reverse current is measured for several minutes.

At 95°C the current in the  $SiO_2$  sample decays upon reaching a maximum value after the initial slow increase. The decay lasts more than 1 hr, and at the end of 1 hr it has decayed to 25% of its peak. For the PSG at all temperatures the decay also continues for at least 1 hr, and the current decreases about an order of magnitude from the 1 min level. Current levels at 1 min were used for analysis for convenience.

As expected, the bulk current increases with cumulative steam exposure. The 0 and 4.8% phosphorus samples show an initial bulk conductivity increase which saturates at about 10 hr moisture exposure. The 8.5% samples show a smaller initial conductivity increase followed by a second increase at about 20 hr. After

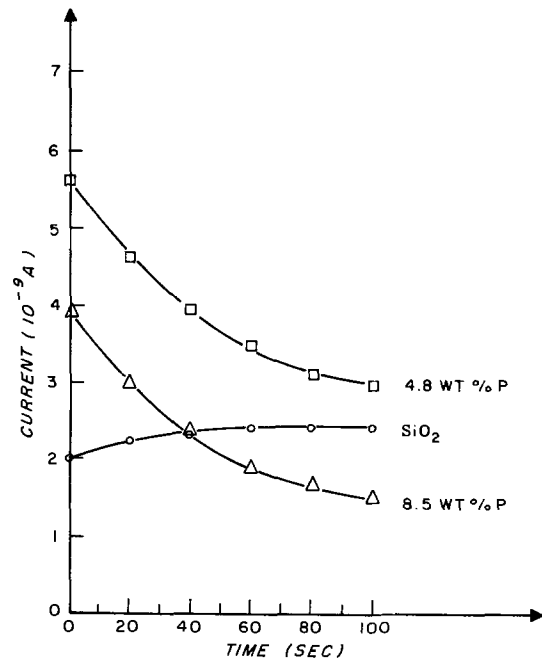


Fig. 1. Bulk current vs. time after voltage application for  $SiO_2$  and PSG at 95°C after 17 hr autoclave stress.

20 hr the conductivity of the 8.5% samples is generally higher than that of the 0 and 4.8% samples. This general dependence was found at all three measurement temperatures. A typical case is shown in Fig. 2.

The dependence of the current level on the phosphorus concentration varies with autoclave time. Before autoclave stress, the current of the phosphorus-containing glass is lower than that of the phosphorus-free glass ( $SiO_2$ ). This is shown in Fig. 3 for three temperatures. At 10 hr steam exposure, the current is greatest for the 4.8% sample and lowest for the 8.5% sample, as shown in Fig. 4. At 25 hr, Fig. 5 shows that the current level increases with increasing phosphorus content.

The temperature dependence of the current is different for the  $SiO_2$  as compared to the phosphorus-containing glass. As shown in Fig. 6-8, the current-temperature dependence of the  $SiO_2$  is well characterized

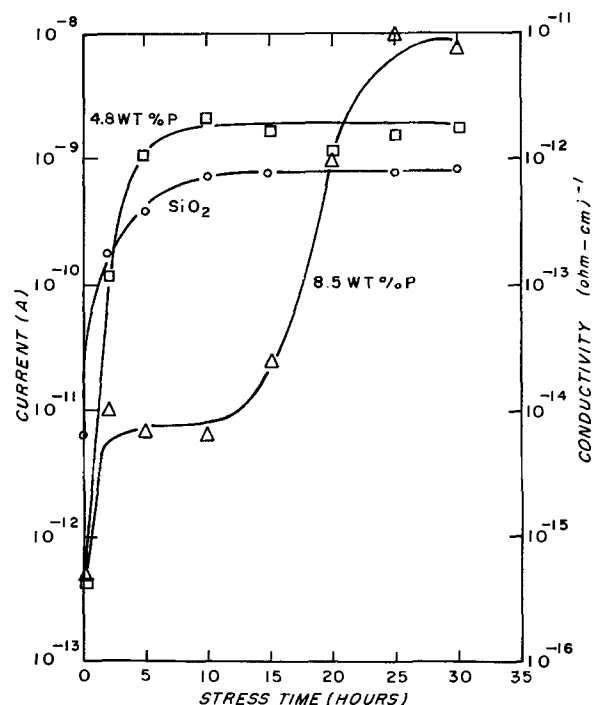


Fig. 2. Bulk current at 60°C vs. autoclave stress time

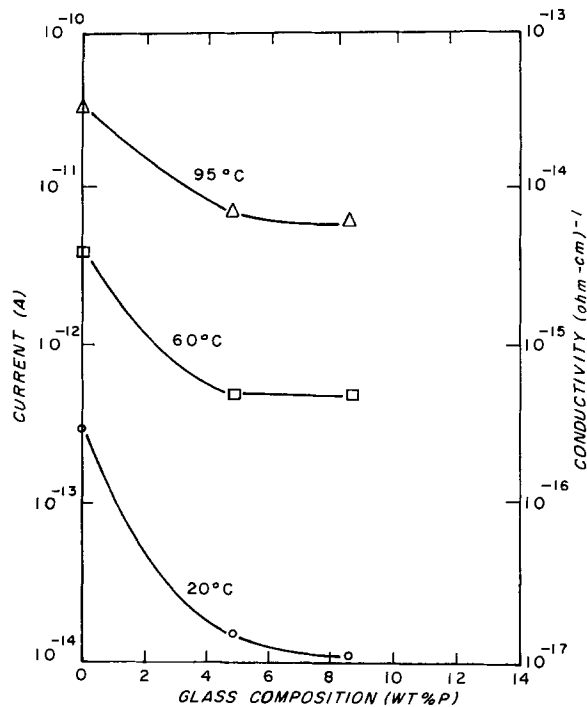


Fig. 3. Bulk current vs. phosphorus content before autoclave stress.

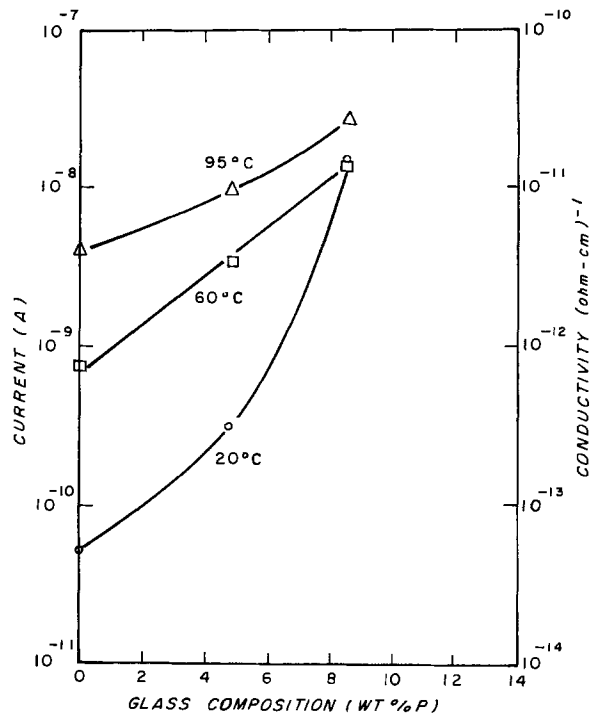


Fig. 5. Bulk current vs. phosphorus content after 25 hr autoclave stress.

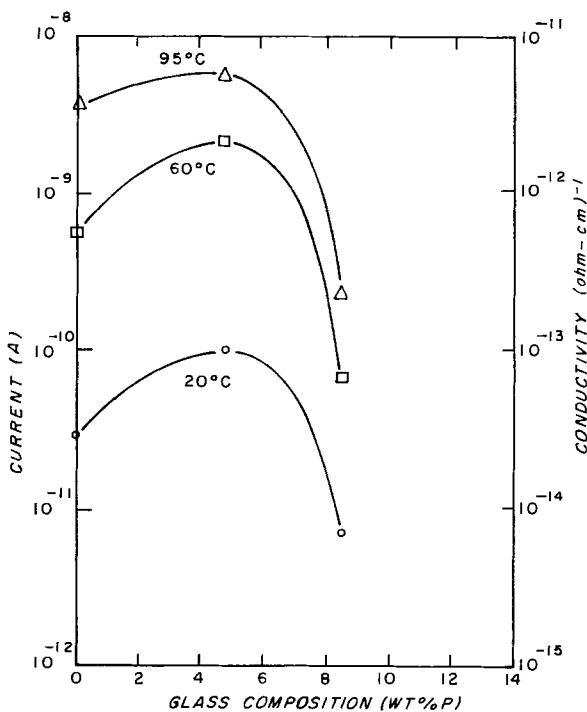


Fig. 4. Bulk current vs. phosphorus content after 10 hr autoclave stress.

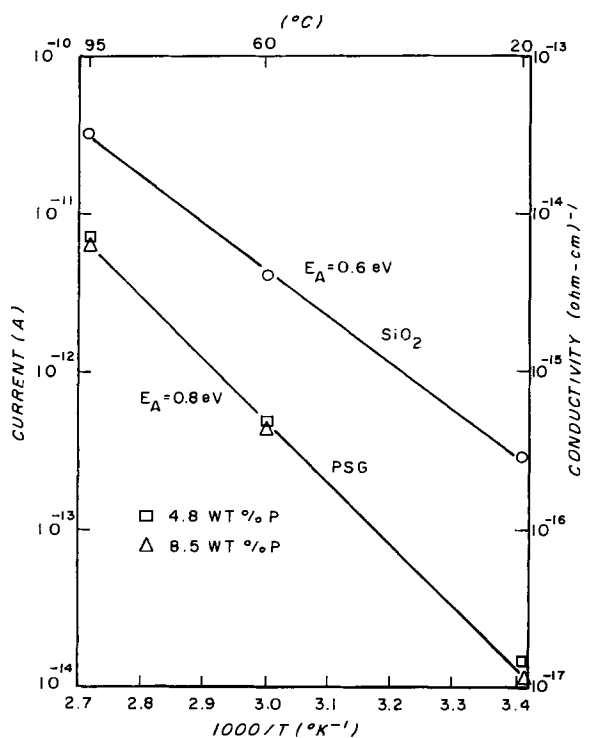


Fig. 6. Bulk current vs. temperature before autoclave stress

by a single activation energy of 0.6 eV, and this energy is independent of autoclave exposure. The current level increases with autoclave exposure, but the activation energy is unchanged. The phosphorus-containing glass before autoclave stress has an activation energy of 0.8 eV, independent of phosphorus concentration, as shown in Fig. 6. After steam exposure, the activation energy tends to decrease for these samples, as shown in Fig. 7 and 8, and in some cases a thermally activated process is not indicated.

For the 8.5% P samples after long autoclave exposure, it was found that a decrease in measured conductivity occurred for the elevated temperature measurement due to the several minute delay between

placing the sample in the oven and performing the current measurement. This was at most a decrease of 40% and has little effect on the activation energy determinations.

*Surface conductivity.*—The current at 23°C is constant and very low below about 30% RH and begins to increase above that value. Below 30% RH the current reflects bulk contributions. The SiO<sub>2</sub> above 30% RH has a greater surface current than the PSG samples as shown in Fig. 9, at least up to about 70% RH.

*Effect of cracks in PSG.*—In a separate experiment the effect of cracks in PSG over metal was determined. An Al line pair pattern on thermal SiO<sub>2</sub> with electrode

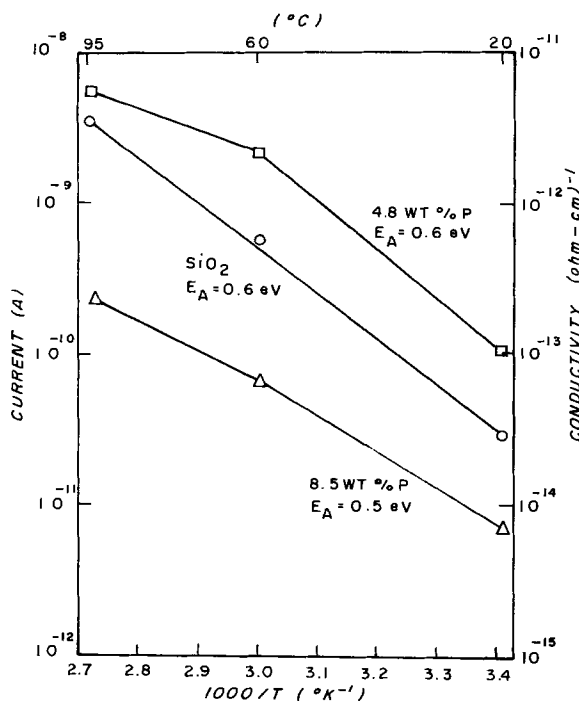


Fig. 7. Bulk current vs. temperature after 10 hr autoclave stress

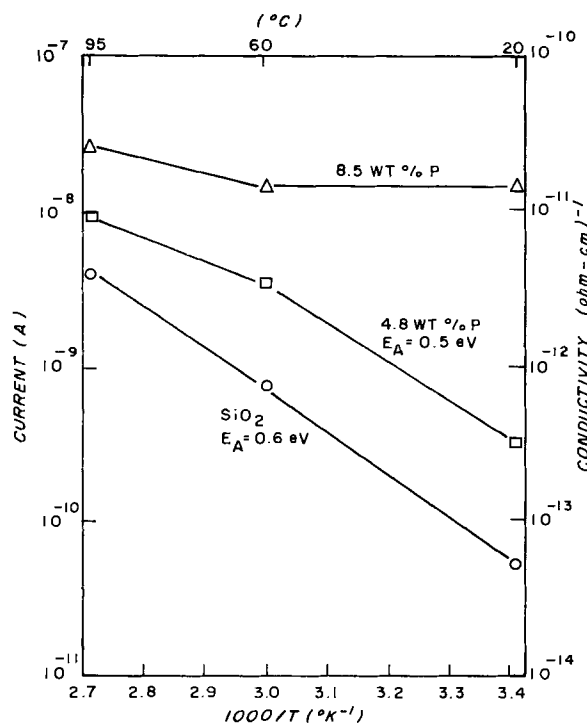


Fig. 8. Bulk current vs. temperature after 25 hr autoclave stress

gap of  $1.0 \times 10^{-3}$  cm and line length of  $7.5 \times 10^{-2}$  cm was overcoated with about  $1.0 \times 10^{-4}$  cm of 5 w/o PSG. In humid  $N_2$  (RH 60%) the current at 100V between line pairs was determined to be about  $5 \times 10^{-13}$ A. Probes were then used to crack the glass over each of the metal line pairs, and the current level increased to about  $5 \times 10^{-10}$ A. Upon introducing a dry  $N_2$  ambient, the current decreased to about  $10^{-14}$ A.

### Discussion

**Conductivity and activation energies.**—The difference in time dependence of the bulk current between the  $SiO_2$  and PSG samples and the fact that before autoclave stress the  $SiO_2$  conductivity is higher than that of the PSG suggests that Na ion motion in the  $SiO_2$  ac-

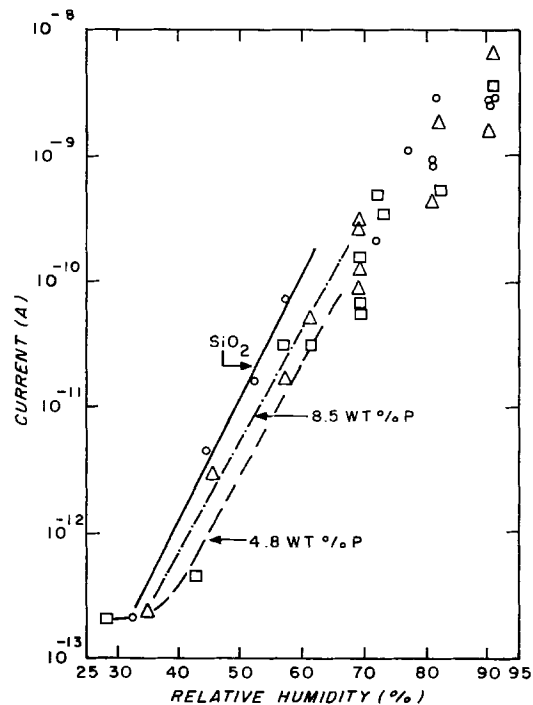


Fig. 9. Surface current vs. relative humidity at 23°C

counts for all or a large part of the observed current. CVD films frequently have high Na content (18). Sources of Na in the films discussed here are not known, but are probably numerous since Na-free Al was not used and MOS fabrication procedures were not followed. Atomic absorption analysis indicated a Na content of about  $1 \times 10^{13}/cm^2$  in these films as deposited.

The long-term steady-state value of current in the  $SiO_2$  samples (greater than that of the PSG) suggests a large reservoir of Na at the aluminum contact interface or at the Si interface. This large reservoir contributes a constant release rate of charge which results in a constant current. At 95°C the release rate is high enough that an effective decrease in the reservoir is observed, leading to a gradually decreasing current. For the PSG samples, Na motion is inhibited so the currents, before autoclave moisture is introduced, are lower.

The activation energy of the bulk conductivity for the  $SiO_2$  layer does not change with moisture content. The value of 0.6 eV may be compared with that of 0.5 eV for thermal  $SiO_2$  contaminated with  $1.0 \times 10^{13}$  Na/cm<sup>2</sup> (4), and with 0.6 eV (thermal oxide) previously reported (27). It should be pointed out that activation energies of Na motion in  $SiO_2$  and PSG depend both on the Na and the P concentration (4). The 0.8 eV activation energy for PSG before autoclave exposure is also in the range reported previously for Na drift in PSG (3, 4).

For thermal  $SiO_2$  at 200°C, resistivity values of  $2 \times 10^{15}$  and  $5 \times 10^{16}$  ohm-cm have been reported for phosphorus doped and undoped layers, respectively (28). Extrapolation of data in Fig. 6 to 200°C yields about  $5 \times 10^{11}$  ohm-cm for both phosphorus doped and undoped CVD  $SiO_2$ . CVD PSG films are less dense and have higher etch rates than densified PSG films of similar composition (10), and, thus, greater conductivities might be expected in low temperature CVD films.

As pointed out previously, the  $SiO_2$  is more conducting than the PSG before autoclave exposure. With sufficient autoclave exposure the PSG layers are more conducting than the  $SiO_2$ . Note that the  $SiO_2$  and 4.8% PSG currents increase to a saturation value in about 10 hr of steam exposure, while the 8.5% PSG layer

increases in two steps to a saturation value at about 25 hr. These times are functions not only of the glass properties but also of the sample and electrode geometry. In the test samples used in this study, water must penetrate the glass surface and diffuse laterally under the metal to result in current increase. For PSG used as over-metal passivation on an IC it is expected that moisture penetration into the PSG would be faster under the same conditions we describe.

The much greater increase of conductivity after autoclave exposure of the PSG as compared to the SiO<sub>2</sub> is not unreasonable in view of possible phase segregation of the PSG into small pockets of a phosphorus-rich phase in a SiO<sub>2</sub> matrix (29). The presence of two phases furnishes interface paths for water penetration and enhanced electrical conduction. At high autoclave steam temperatures (200°C) it has been reported (30) that the P<sub>2</sub>O<sub>5</sub> is actually leached out of the PSG, leaving behind a network structure (30). The authors state that this does not occur at 120°C (30). Phosphorus leaching into saturated water vapor at 120°C has been reported (31) for PSG films of high phosphorus content (about 10 mol per cent P<sub>2</sub>O<sub>5</sub> for films deposited at 450°C). This leaching out is easily detected by microscopic examination (30). None of the samples considered here showed this effect. In addition, infrared absorption measurements showed no decrease in P content after cumulative treatment for 1 hr each in water at 25°C, boiling water, and autoclave steam at 15 psig, 121°C (32).

**Surface current.**—The behavior of the surface current in Fig. 9 is consistent with the presence of Na on the surface and with previous results (19). At low RH (below about 70%) the phosphorus blocks Na ion motion compared to the SiO<sub>2</sub> samples. The large scatter from sample to sample above about 80% RH may reflect the presence of more than a monolayer of water and widely varying Na contamination of the surface from sample to sample.

**Leakage effects in IC's.**—In this section, a worst case estimate of leakage current for a typical IC in plastic is made, based on the highest bulk and surface conductivities described previously. These values are those after 25 hr of autoclave treatment with current measured at 95°C. For the typical IC we assume the following geometry: electrode gap of  $2 \times 10^{-3}$  cm, length of 0.1 cm, and metal line width of  $10^{-3}$  cm. A metallization overcoat of  $5 \times 10^{-5}$  cm of 8.5 w/o PSG is also assumed. Figure 10 shows the possible current paths in a schematic IC cross section. Path c is an interface path between the thermal oxide and the PSG interface. This current contribution is neglected. Path A represents the bulk conduction through the PSG between buried metal lines. Paths B and b represent the bulk and surface components of the surface path not involving openings in the PSG. Path b alone represents current flow between conductors which have discontinuities in the PSG above them. Leakage current flowing between open bond pad areas to other bond pads or to metallization lines is assumed small compared to that flowing between closely spaced metal interconnects since lateral bond pad spacing is usually large compared to interconnect lateral spacing. We ignore

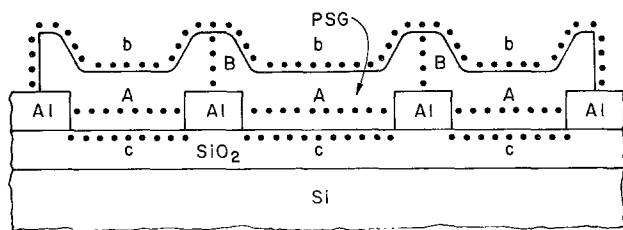


Fig. 10. Schematic cross section of IC showing various current paths associated with PSG passivation layer.

current at the thermal SiO<sub>2</sub>-PSG interface and in the SiO<sub>2</sub> and calculate the parallel contributions of the bulk flow component through the PSG between metal lines (path A) and of the surface component (path B-b), which has a series bulk term (path B) for current flow from the line to the surface, and from the surface back through the PSG to the other line. At 95°C, after 25 hr autoclave exposure, the bulk resistivity is about  $5 \times 10^{10}$  ohm-cm (Fig. 8). The surface resistance in humid ambient is about  $2 \times 10^{12}$  ohm/square, obtained by using the value measured at room temperature and extrapolating to 95°C using Koelmans' activation energy of 0.35 eV (24). (We assume that the plastic, at least for a short time, traps water at the PSG surface and that the chip is thus effectively in a humid environment, since we are interested in worst case estimates.) Using these values, and the assumed geometry, we calculate a bulk resistance between lines of  $2 \times 10^{13}$  ohm, and a surface path resistance of  $9 \times 10^{10}$  ohm. This latter term consists of the actual surface component of  $4 \times 10^{10}$  ohm and the two bulk components in series with this of  $2.5 \times 10^{10}$  ohm each. Thus, in this worst case, the surface path contributes essentially all the current and at 15V the contributed leakage current is about  $1.5 \times 10^{-10}$ A. This is negligible for almost all applications and is about four or five orders of magnitude below specified leakage currents for most IC applications.

In a separate experiment (33), a typical IC metallization pattern over thermal SiO<sub>2</sub> (no contact to silicon) overcoated with  $5 \times 10^{-5}$  cm of 8.5 w/o PSG and packaged in plastic showed a leakage current of  $3 \times 10^{-11}$ A at 95°C after 24 hr autoclave. The electrode length in this structure was 0.06 cm; for comparison then, the current should be approximately doubled, yielding  $6 \times 10^{-11}$ A, in reasonable agreement with the previously calculated value of  $1.5 \times 10^{-10}$ A.

Even though bulk and surface leakage currents are negligibly small, they can have indirect effects related to surface charge inversion (16-19, 21). Using a specially fabricated MOS IC, an inversion-induced leakage after autoclave stress was observed (33). The increased leakage occurred between the positively biased N-type regions of the IC and the negatively biased P regions. Upon voltage applications at 60°C, the leakage was constant at  $10^{-9}$ A. After about 30 sec the leakage increased with a time constant of several minutes to  $5 \times 10^{-9}$ A. The increase was limited to this easily tolerable level by proper channel stoppering. In a poorly designed IC (no channel stoppers) the effect could be disastrous, however.

**Aluminum corrosion effects.**—In this section estimates of the time for complete corrosion of an aluminum line are made. The possibility of cathodic aluminum corrosion in the presence of PSG of sufficiently high P content and water has been reported (25). Several hypothetical test situations are possible, and current between Al lines of the geometry described in the previous section are calculated. From the estimated currents, times for complete corrosion of the negative Al line are determined, assuming a Faraday efficiency of one and uniform current distribution.

The mass of Al available for corrosion is  $2.7 \times 10^{-8}$ g for the geometry used for the previous leakage current calculation and for Al thickness of  $10^{-4}$  cm and the charge needed for complete corrosion is  $3 \times 10^{-4}$  coulomb. This value is used to estimate corrosion time.

Autoclave stress followed by voltage application in dry ambient at elevated temperature is not expected to result in Al corrosion. In this situation the bulk resistance of  $2 \times 10^{13}$  ohm at 95°C for the typical electrode pattern limits the current to  $5 \times 10^{-13}$ A at 10V (path A). The surface conduction in dry ambient is negligible. In time the current will decay, and  $5 \times 10^{-14}$ A is a reasonable value for long-term estimates. This results in a corrosion time of 190 years.



Exposure of a device to humid ambient at room temperature without previous autoclave exposure is also not expected to result in Al corrosion, except at bonding pads, pinholes, or cracks as found previously (25, 32). Paulson and Kirk found that corrosion occurred in areas where the PSG was not continuous over the Al, such as at a bonding pad (25). This indicates that the bulk path resistance (path B) through the PSG to the surface is not grossly affected by long-term high humidity exposure. Thus, we ignore the bulk path resistance (path A) in this case, and note that the surface path resistance is limited by the metal-to-surface resistance through the PSG (path B). This is about  $5 \times 10^{13}$  ohm in this situation. The current is then  $2 \times 10^{-13}$ A, and the corrosion time is 45 years.

The presence of discontinuities at bonding pads, pinholes, or cracks in the PSG layer over the Al acts to shunt out the high bulk resistance of the PSG in surface path conduction (path b). For the conditions of the previous paragraph the surface path resistance is reduced to  $4 \times 10^{11}$  ohm for a surface current of  $2.5 \times 10^{-11}$ A at room temperature. The corrosion time is then 115 days. At 95°C the corrosion time would be reduced to about 10 days using Koelmans' (24) or Paulson and Kirk's (25) temperature acceleration factors. With specially prepared samples containing deliberate cracks and pinholes in the PSG, noticeable cathodic Al corrosion after three days in humid ambient for PSG with greater than 8 w/o P was found (32). The effects of current concentration would decrease further the corrosion times at cracks and pinholes compared to the estimate made here. Since cracks and pinholes can occur over closely spaced metal lines it is expected that these open areas are much more serious corrosion sites than the open bond pad areas, which are much more widely spaced. Even if some corrosion of bond pad metal occurs, it should not affect device performance since on three sides of the pad there is no connection to the circuit, and on the fourth side design consideration can minimize the effects of corrosion.

The three order increase in current between line pairs under PSG in humid ambient resulting from cracking of the PSG establishes directly that surface path conduction is greatly enhanced when openings in the PSG over metal can act to short out the bulk resistance of the surface path conduction (path B of Fig. 10). The decrease in current upon introducing dry N<sub>2</sub> ambient confirms that the increased current after cracking the PSG is actually a moisture-induced surface current.

The occurrence of corrosion at cracks and pinholes is consistent with the observation that cathodic corrosion is much more probable than anodic corrosion (25, 32). If anodic corrosion begins at a pinhole or crack over metal, then the anodizing process will result in an electrically insulating product, which will cut off or decrease current flow in the absence of chloride (24). The anodic current then is furnished at some other crack or pinhole or by a bonding pad area. No such self-limiting process occurs at the cathode.

### Summary

The bulk and surface conduction of CVD SiO<sub>2</sub> and PSG have been measured as functions of P concentration. The temperature dependence of the bulk current was also investigated. Effects of autoclave stress were determined. The measured electrical properties of these typical passivation layers were related to IC leakage and were shown to have no direct contribution to leakage currents, apart from the possibility of surface inversion effects. Estimates of times for cathodic Al corrosion were made, and, based on the results, it was shown that the high bulk resistivity of the PSG limits the current sufficiently so that corrosion occurs only at discontinuities in the PSG coverage of the aluminum.

### Acknowledgments

The author wishes to acknowledge advice and discussion with G. L. Schnable in all aspects of this paper. R. E. Allen performed the experimental measurements. The CVD work and metallization were done by A. W. Fisher. Samples for the PSG cracking test were supplied by M. Polinsky. Discussions with A. W. Fisher, K. Hang, and W. Kern were useful.

This work was supported in part by the Air Force Materials Laboratory, Wright-Patterson Air Force Base, Ohio, under contract No. F33615-74-C-5146.

Manuscript submitted June 19, 1975; revised manuscript received Oct. 15, 1975.

Any discussion of this paper will appear in a Discussion Section to be published in the December 1976 JOURNAL. All discussions for the December 1976 Discussion Section should be submitted by Aug. 1, 1976.

Publication costs of this article were partially assisted by RCA Laboratories.

### REFERENCES

1. G. L. Schnable, W. Kern, and R. B. Comizzoli, *This Journal*, **122**, 1092 (1975).
2. D. R. Kerr, J. S. Logan, P. J. Burkhardt, and W. A. Pliskin, *IBM J. Res. Develop.*, **8**, 376 (1964).
3. P. Balk and J. M. Eldridge, *Proc. IEEE*, **57**, 1558 (1969).
4. J. M. Eldridge, and D. R. Kerr, *This Journal*, **118**, 986 (1971).
5. E. H. Snow and B. E. Deal, *ibid.*, **113**, 263 (1966).
6. J. M. Eldridge, R. B. Laibowitz, and P. Balk, *J. Appl. Phys.*, **40**, 1922 (1975).
7. L. Kasprzak and A. Hornung, *IBM J. Res. Develop.*, **19**, 127 (1975).
8. W. Kern and A. W. Fisher, *RCA Rev.*, **31**, 715 (1970).
9. W. Kern and R. C. Heim, *This Journal*, **117**, 562 (1970).
10. W. Kern and R. C. Heim, *ibid.*, **117**, 568 (1970).
11. W. Kern, Paper 93, IEEE National Aerospace and Electronics Conference, Dayton, Ohio, June 1975.
12. M. M. Schlachter, E. S. Schlegel, R. S. Keen, R. A. Lathlaen, and G. L. Schnable, *IEEE Trans. Electron Devices*, **ED-17**, 1077 (1970).
13. L. K. Karstadt, W. G. Burger, C. M. Hsieh, and W. A. Cosgrove, *Solid State Technol.*, **16**, 41 (1973).
14. W. McQuitty and C. R. Lively, *Electronic Pkg. Prod.*, **11**, No. 11, 112 (1971).
15. T. W. Hickmott, *Phys. Rev. Letters*, **32**, 65 (1974).
16. W. Shockley, W. W. Hooper, H. J. Queisser, and W. Schroen, *Surface Sci.*, **2**, 277 (1964).
17. E. S. Schlegel, G. L. Schnable, R. F. Schwarz, and J. P. Spratt, *IEEE Trans. Electron Devices*, **ED-15**, 973 (1968).
18. E. S. Schlegel and G. L. Schnable, *ibid.*, **ED-16**, 386 (1969).
19. E. S. Schlegel, R. S. Keen, and G. L. Schnable, 8th Annual Proceedings on Reliab. Phys., p. 9 (1971).
20. R. Castagne, P. Hesto, and A. Vapaille, *Thin Solid Films*, **17**, 253 (1973).
21. G. A. Brown, K. Lovelace, and C. Hutchins, 11th Annual Proceedings on Reliab. Phys., p. 203 (1973).
22. R. S. Alwitt, *This Journal*, **121**, 1322 (1974).
23. S. C. Kolesar, 12th Annual Proceedings on Reliab. Phys., p. 155 (1974).
24. H. Koelmans, *ibid.*, p. 168 (1974).
25. W. M. Paulson and R. W. Kirk, *ibid.*, p. 172 (1974).
26. W. Kern, *RCA Rev.*, **29**, 525 (1968).
27. M. Kuhn and D. J. Silversmith, *This Journal*, **118**, 966 (1971).
28. E. H. Snow and B. E. Deal, *ibid.*, **113**, 263 (1966).
29. P. F. Schmidt, W. vanGelder, and J. Drobek, *ibid.*, **115**, 79 (1968).
30. J. Sato, Y. Ban, and K. Maeda, 9th Annual Proceedings on Reliab. Phys., p. 96 (1971).
31. N. Nagasima, H. Suzuki, K. Tanaka, and S. Nishida, *This Journal*, **121**, 434 (1974).
32. W. Kern, R. B. Comizzoli, A. W. Fisher, and G. L. Schnable, "Improved CVD Techniques for Depositing Passivation Layers on ICs," AFML-TR-75-160, Air Force Materials Laboratory, October 1975.
33. R. B. Comizzoli, Unpublished results.

# Electrical and EPR Studies of Electrolytically Grown TiO<sub>2</sub> (Rutile)

G. V. Chandrashekar and R. S. Title

IBM Thomas J. Watson Research Center, Yorktown Heights, New York 10598

## ABSTRACT

An electrolytic technique for growing rutile is described. The crystals obtained show n-type electrical conductivity. The defect structure was studied by EPR. The behavior of the conductivity and the changes in the defect structure as a result of heat-treatment in an oxidizing atmosphere shows the as-grown crystals to be oxygen deficient. An EPR spectrum of Pt<sup>3+</sup> in rutile is reported for the first time and a spectrum previously attributed to substitutional Ti<sup>3+</sup> is confirmed as such.

The tetragonal form of TiO<sub>2</sub>, rutile, has been extensively studied for many years (1-5). The electrical conductivity properties are especially interesting. The resistivity ranges from 10<sup>8</sup> ohm-cm in stoichiometric rutile down to 10<sup>-2</sup> ohm-cm in oxygen deficient rutile (5). The conductivity is n-type and is *via* a polaron mechanism (2-3). Although the defect structure in oxygen deficient rutile has been thoroughly investigated by optical (6-9) and electron paramagnetic resonance (EPR) techniques (10-13), there is no general agreement as to whether the defects are oxygen vacancies or Ti interstitials or some combination of these and other impurities.

Almost all of the crystal growth of rutile to date has been by the Verneuil process, a flame fusion technique in an oxy-hydrogen flame. In this paper we describe an electrolytic technique that yields oxygen-deficient rutile crystals. The electrical properties of these crystals are described. We also report EPR studies on several impurities. An observation of Pt<sup>3+</sup> substitutional on a Ti<sup>4+</sup> site is reported for the first time and evidence is given that a previously reported resonance is indeed due to Ti<sup>3+</sup> substitutional at Ti<sup>4+</sup> sites.

A comparison is made between the oxygen deficient crystals produced by the electrolytic and flame fusion techniques.

## Crystal Preparation

As part of a program of synthesis and crystal growth of inorganic transition metal compounds by the fused salt electrolysis technique, a mixture of TiO<sub>2</sub> (United Mineral and Chemical Corporation, 0.9999 pure) and Na<sub>2</sub>Ti<sub>3</sub>O<sub>7</sub> (prepared by heating Na<sub>2</sub>CO<sub>3</sub> and TiO<sub>2</sub> at 1000°C) was electrolyzed in a sodium borate-sodium fluoride bath (10% NaF). A platinum double cell similar to the ceramic double cell of Kunmann and Ferretti (14) was employed. A platinum disk (~1 cm<sup>2</sup>) was used as the cathode and the electrolysis was carried out at 850°C for up to 60 hr with a current density of about 25 mA/cm<sup>2</sup>. Dark green crystals that formed on the cathode were extracted from the adhering melt with dilute HCl. An x-ray powder pattern identified the crystals to be rutile. Optical emission analysis showed the following impurities in ppm by weight: B:1000; Si:300; Co:100; Pb:100; Cr:30; Pt:50; Ga:50; Mg:1. Other impurities were looked for, but all were below the detection limits for optical emission.

Unlike the solid crystals of TiO<sub>2</sub> that one generally associates with flame fusion growth (1), the electrolytically grown TiO<sub>2</sub> crystals were generally hollow rods a few mm long and about 1 mm wide. The long axis of the rods was found to lie along the crystalline c-axis and several crystals had flat (110) faces on their sides.

Key words: TiO<sub>2</sub>, rutile, electrolytic growth, electrical conductivity, electron paramagnetic resonance.

## Electrical Measurements

Electrical contacts to the crystals were made by indium soldering. The crystals were too small to use ultrasonic soldering techniques (2). The surface was, instead, repeatedly punctured by a fine-pointed soldering iron as the indium contacts were applied. Ohmic contacts were obtained. Four contacts were used, two for current and two for the voltage. Because of the hollow nature of the crystals care had to be taken in obtaining resistivity constants from the resistance measurements. The contacts were extended around as much of the diameter of the hollow rods as possible. Even with this precaution, the variation of the cross-sectional area along the length of a crystal does not allow an accurate determination to be made of the area through which the current flows. One can, however, set an upper limit on the cross-sectional area (namely, the entire area of the rod) and, hence, an upper limit on the resistivities determined from the resistance measurements. The upper limits to the resistivities of several as-grown samples were thus determined and found to be in the range 10-40 ohm-cm. A hot probe was used to determine the conductivity type which was found to be n-type. Heat-treatment of the as-grown samples at 1000°C in an oxygen atmosphere for three days caused the resistivity to increase to 10<sup>4</sup> ohm-cm. The relatively high n-type conductivity of the as-grown samples with a subsequent decrease in conductivity on heat-treatment in an oxygen atmosphere may be due to two different causes. One possibility is that it may be due to an oxygen deficiency in the as-grown samples. Rutile deficient in oxygen has been shown to be highly conducting n-type with a polaron conduction mechanism (3). Besides the presence of native defects (oxygen vacancies or Ti interstitials) that could give rise to n-type conductivity, there is also the possibility of the presence of impurity defects. These may be either substitutional (halogens on oxygen sites or Group V elements on Ti sites) or there may be interstitial cation impurities, all of which could give n-type conductivity. To help distinguish the defects responsible for the n-type conductivity, EPR studies were carried out.

## EPR Studies

There has been a rather extensive number of EPR studies on TiO<sub>2</sub> (15) and a large number of defects both substitutional and interstitial have been identified. The crystal structure of TiO<sub>2</sub> is especially well suited to distinguish substitutional sites from interstitial sites (15). The EPR studies were performed at 9.16 GHz at temperatures between 1.8°K and room temperature.

The as-grown crystals showed four defect resonances all due to trivalent impurities substitutional at Ti<sup>4+</sup> sites. Two of these Cr<sup>3+</sup> and Fe<sup>3+</sup> have previously been

observed in rutile (16, 17). These two spectra could be observed at all temperatures. Samples heat-treated at 1000°C for three days in an oxygen atmosphere still showed the Cr<sup>3+</sup> and Fe<sup>3+</sup> EPR spectra, but with diminished intensity. An EPR spectrum due to Pt<sup>3+</sup> substitutional at a Ti<sup>4+</sup> site, previously unreported in TiO<sub>2</sub>, was observed in the as-grown crystals. This EPR spectrum is shown in Fig. 1 for the orientations of the magnetic field corresponding to the principal directions of the g tensor, namely the [001] direction (c axis) and the [110] and  $[\bar{1}\bar{1}0]$  directions. (The  $[\bar{1}\bar{1}0]$  direction has a spectrum identical to that of the [110] direction.) The lines due to Pt<sup>3+</sup> are the groups of three lines, each consisting of a central line bracketed by two lines approximately one-fourth as intense. A line due to DPPH at  $g = 2.0036$  (about 3250G at X-band) is also shown in the figure. The Pt is undoubtedly incorporated from the Pt cathode or from the walls of the Pt crucible in which the TiO<sub>2</sub> crystals were electrolytically grown. The spectrum was identified as due to substitutional Pt<sup>3+</sup> from its g tensor (see Appendix) and from the hyperfine interaction with the 33.7% abundant isotope Pt<sup>195</sup> (nuclear spin 1/2). It is this hyperfine interaction that leads to the two weaker lines about each Pt<sup>3+</sup> central line. A description and analysis of the Pt<sup>3+</sup> spectrum is given in the Appendix. Heat-treatment of the as-grown samples at 1000°C in O<sub>2</sub> for 3 days caused the Pt<sup>3+</sup> spectrum to disappear.

We also observed a fourth EPR spectrum which we attribute to Ti<sup>3+</sup> substitutional at a Ti<sup>4+</sup> site. The parameters are given in Table I. The spectrum was only observed at temperatures below 77°K. At about 18°K the spectrum is axial. Below 18°K the spectrum has a g tensor that indicates the orthorhombic symmetry expected for a defect substitutional at a Ti<sup>4+</sup> site.

The spectra that we observed at 8.5°K are shown in Fig. 2 for orientations of the magnetic field along the principal directions of the g tensor ([001], [110], and  $[\bar{1}\bar{1}0]$  directions). The spectrum for the magnetic field parallel to the [100] or [010] directions is also shown. The fact that only a single line is observed in this direction is indicative of substitutional Ti<sup>3+</sup> and not interstitial Ti<sup>3+</sup>.

Gerritsen (15) at 4.2°K observed a spectrum with g values similar to those we observe at 8.5°K (Table I), which he also attributed to Ti<sup>3+</sup> substitutional at a Ti<sup>4+</sup> site. He reports, but gives no details, of a complicated hyperfine structure. The hyperfine structure is crucial in the identification of the center since there

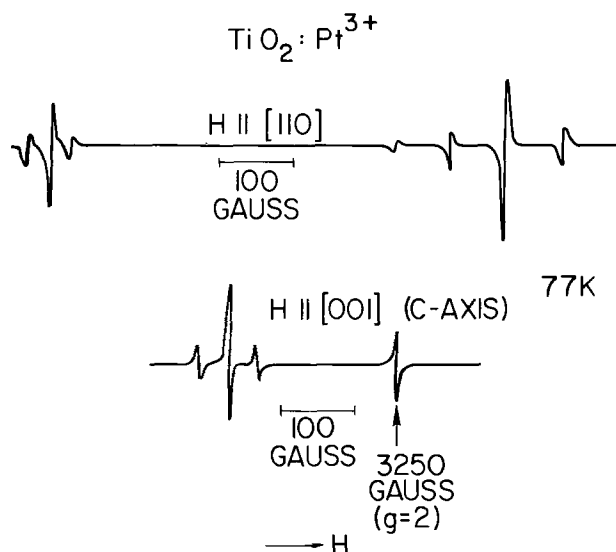


Fig. 1. EPR spectrum of substitutional Pt<sup>3+</sup> for the magnetic field parallel to the [110] and [001] directions. The  $g = 2$  reference marker is lined up for the two directions.

Table I. EPR principal values for substitutional Ti<sup>3+</sup>

T	$g_c = g_{001}$	$g_{110}$	$g_{\bar{1}\bar{1}0}$
8.5°K	1.9436 ±0.0005	1.9777 ±0.0005	1.9743 ±0.0005
T	$g_{\parallel} = g_c = g_{001}$		$g_{\perp}$
30°K	1.9436 ±0.0005		1.9762 ±0.0005

are quite a number of centers that have been observed in rutile with g tensors very similar to those of Table I (10-13).

For a general orientation of the magnetic field with respect to the crystalline axes, our hyperfine spectrum was difficult to resolve because of overlapping lines from the two equivalent orientations of the defect and due to the low natural abundances of Ti<sup>47</sup> and Ti<sup>49</sup>. However, for the magnetic field oriented along the [100] or [010] directions (midway between the [110] and  $[\bar{1}\bar{1}0]$  axes) a single line is observed with a clearly resolved hyperfine structure. The spectrum in this direction is shown with increased gain in Fig. 3. The pattern observed is clearly consistent with the natural abundances and nuclear spins of Ti<sup>47</sup> (7.75% abundant  $I = 5/2$ ) and Ti<sup>49</sup> (5.51% abundant and  $I = 7/2$ ). The value of the hyperfine tensor,  $A_{100}$ , in this direction was found to be the same for Ti<sup>47</sup> and Ti<sup>49</sup> as expected (17) and equal to  $7.06 \times 10^{-4} \text{ cm}^{-1}$ . This value of the hyperfine tensor is more consistent with the hyperfine tensor usually observed (18-21) for Ti<sup>47,49</sup> than with the much smaller superhyperfine tensor that results from the superhyperfine interaction of the other defects with Ti<sup>47,49</sup> in TiO<sub>2</sub> (22). Also the g tensor of Table I is consistent with what would be expected for a single 3d electron on a substitutional Ti<sup>4+</sup> site and with a  $a|x^2 - y^2\rangle + \sqrt{1 - a^2}|3z^2 - r^2\rangle$  ground state (23). We conclude that the center we are observing is a substitutional Ti<sup>3+</sup> defect.

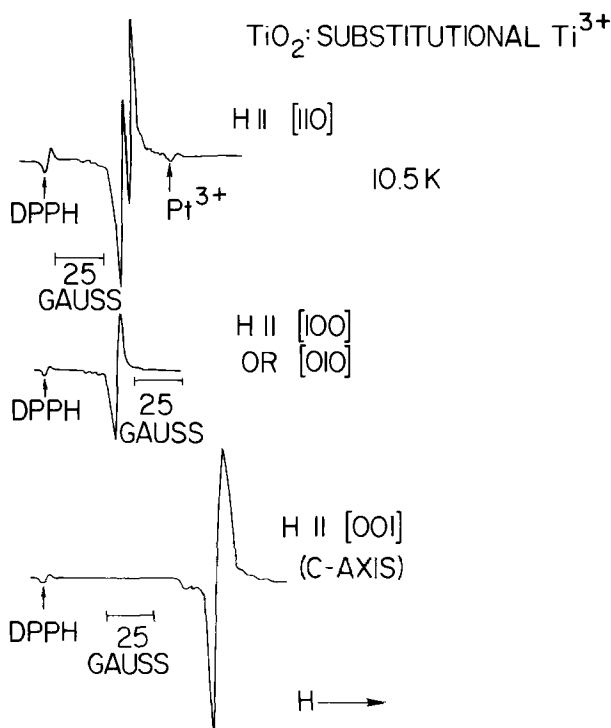


Fig. 2. EPR spectrum of Ti<sup>3+</sup> substitutional at a Ti<sup>4+</sup> site. The spectra are for the magnetic field along the [110], [100], and [001] axes. The three spectra are aligned with respect to the DPPH reference. A signal due to Pt<sup>3+</sup> is visible for the magnetic field in the [110] direction.

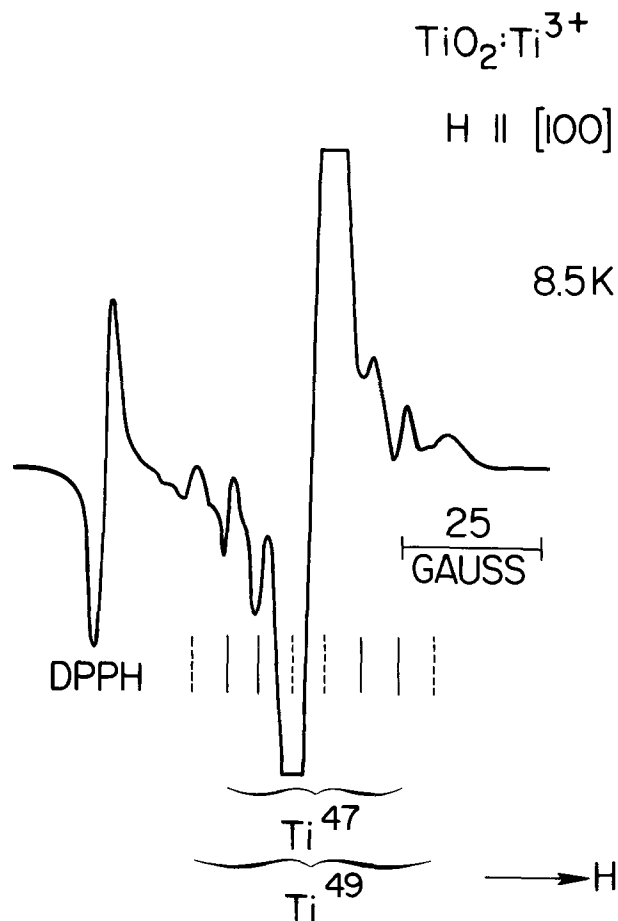


Fig. 3. The spectrum at increased gain for substitutional  $\text{Ti}^{3+}$  with the magnetic field along the  $[100]$  direction.

On annealing the as-grown crystals at  $1000^\circ\text{C}$  for 3 days in an  $\text{TiO}_2$  atmosphere the  $\text{Ti}^{3+}$  resonance disappears, as did the  $\text{Pt}^{3+}$  resonance.

It is also worthwhile reporting a negative result in the EPR studies. There have previously been several reports (10-13) of EPR spectra in conducting rutile which have been attributed to various forms of native defects. The  $g$  values of the EPR spectra, but not necessarily their principal axes, are very similar to those of Table I. There is no agreement on the native defects responsible for these EPR spectra. Those that have been suggested include various forms of polarons (10), an oxygen vacancy (11), and interstitial  $\text{Ti}^{3+}$  (15). More recently, Shen *et al.* (3) from a study of the effects on conducting rutile of treatment in various atmospheres, have suggested that hydrogen must be present in the crystal for the reported spectra (10, 15) to be observed.

Because the electrolytic technique for making conducting rutile differs from the flame fusion growth technique used by the previous workers and because of the controversy as to whether native defects are observable by EPR in conducting rutile, we made a thorough search for the EPR spectra attributed to these native defects (10-13) and found none. Our negative result is in accord with the conclusion of Shen *et al.* (13) that hydrogen is a necessary impurity for the observation of the spectra attributed to native defects. There is no reason for hydrogen to be present in the electrolytically grown conducting rutile.

### Discussion

There are a number of conclusions that can be made from the results of the measurements on electrolytically grown rutile. It is clear that in order for rutile to plate out as crystals in an electrolytic process, the crystals must be conducting. This is confirmed by the electrical measurements which in addition show the

conductivity to be n-type. The EPR studies, which were undertaken to determine the defects or impurities responsible for the n-type conductivity, detected no defects which alone could give n-type conductivity. Rather a number of trivalent impurities,  $\text{Cr}^{3+}$ ,  $\text{Fe}^{3+}$ ,  $\text{Pt}^{3+}$ , and  $\text{Ti}^{3+}$  were observed substitutional on  $\text{Ti}^{4+}$  sites. These centers have given up one less electron than the host  $\text{Ti}^{4+}$  they replace and hence the site containing such an impurity is effectively singly negatively charged with respect to the lattice. In order to preserve charge neutrality, centers of positive charge must exist in the lattice to compensate these negative charges. One possibility is the existence of holes, which at low temperature would be localized at the trivalent impurities but at higher temperatures would be free. P-type conductivity should then be observed and not the n-type that is observed. The observation of n-type conductivity is not consistent with compensation by holes and leads us to believe that the electrolytically grown rutile crystals contain native defects (unobserved by EPR) which provide the n-type carriers and may also provide the charge compensation necessary to observe trivalent impurities substitutional on  $\text{Ti}^{4+}$  sites. Since both the high n-type conductivity and the presence of substitutional trivalent impurities is either considerably diminished or eliminated on exposing the crystals to an oxidizing atmosphere, it is concluded that the native defects result from an oxygen deficiency. It is known that rutile with oxygen as low as  $\text{TiO}_{1.992}$  does exist (24). Controversy exists as to whether this results in the presence of oxygen vacancies or titanium interstitials (1, 6, 25-31). We did not observe the EPR signals that others have attributed to these defects and conclude that perhaps other impurities in conjunction with defects are required to make these observable (13).

In summary a new technique or growing rutile crystals has been described. The electrical and defect properties of the crystals have been determined and compared with the more conventionally grown rutile crystals.

### Acknowledgments

We would like to thank G. Arbach for growing the crystals and R. E. Fern and W. J. Fitzpatrick for help in determining their electrical and resonance properties.

Manuscript submitted July 3, 1975; revised manuscript received Nov. 14, 1975.

Any discussion of this paper will appear in a Discussion Section to be published in the December 1976 JOURNAL. All discussions for the December 1976 Discussion Section should be submitted by Aug. 1, 1976.

Publication costs of this article were partially assisted by IBM Corporation.

### APPENDIX

#### The $\text{Pt}^{3+}$ EPR Spectrum

The Hamiltonian for the Zeeman and hyperfine interactions is given by

$$\mathcal{H} = \beta S \cdot \bar{g} \cdot H + S \cdot \bar{A} \cdot I \quad [1]$$

where  $\beta$  is the Bohr magneton,  $S$  the effective electron spin,  $H$  the magnetic field,  $I$  the nuclear spin, and  $\bar{g}$  and  $\bar{A}$  the  $g$  and hyperfine tensors, respectively. It was observed that the maximum extension of the  $\text{Pt}^{3+}$  spectrum occurs when the magnetic field is oriented along the  $[110]$  or  $[\bar{1}\bar{1}0]$  directions (see Fig. 1). This indicates that the principal axes of the  $g$  tensor are along the  $[110]$ ,  $[\bar{1}\bar{1}0]$ , and  $[001]$  ( $c$  axis) axes. The principal axes of the  $A$  tensor were also found to be along these axes. The fact that the principal values of the  $g$  and  $A$  tensors are along the observed axes identifies the  $\text{Pt}^{3+}$  as substitutional at a  $\text{Ti}^{4+}$  site.  $\text{Pt}^{3+}$  at an interstitial site would have the axes of the  $g$  tensor deviate from the  $[110]$  and  $[\bar{1}\bar{1}0]$  axes.

Table II. EPR principal values for Pt<sup>3+</sup> in TiO<sub>2</sub> at 87°K

g <sub>c</sub> = g <sub>001</sub>	g tensor		10 <sup>4</sup> cm <sup>-1</sup>		
	g <sub>110</sub>	g <sub>110</sub>	A <sub>c</sub> = A <sub>001</sub>	A <sub>110</sub>	A <sub>110</sub>
2.1485	1.9137 + 0.0005	2.3338	81.5 ±1.0	134.7 ±1.0	59.1 ±1.0

The parameters for Pt<sup>3+</sup> in TiO<sub>2</sub> are given in Table II. The values for the g and A tensors are within the ranges that one usually observes (32) for Pt<sup>3+</sup> (5d<sup>7</sup>), though the value of g<sub>110</sub> is somewhat smaller than has been observed in other crystals. The g tensor (including the low g<sub>110</sub>) may be understood if it is assumed that the spitting of the d orbitals by the orthorhombic crystalline field at a Ti<sup>4+</sup> site is as shown in Fig. 4 (23, 33). Each d orbital is doubly degenerate. Further, it is required that six of the seven 5d electrons fill the lowest three orbitals and that there is one electron in the  $a|3z^2 - r^2\rangle - \sqrt{1-a^2}|r^2 - y^2\rangle$  orbital, the so-called high field, low spin, filling scheme (34). Because of spin-orbit coupling there will be an admixture of the  $|xy\rangle$  level from above and the  $|yz\rangle$  and  $|xz\rangle$  levels from below into the  $a|3z^2 - r^2\rangle - \sqrt{1-a^2}|x^2 - y^2\rangle$  orbital (level 4). It is the admixture of the  $|xy\rangle$  orbital from above that causes the comparatively large departure of g<sub>110</sub> from the free spin value of 2.

With the spin-orbit coupling taken into consideration and using formulae given in the literature (23, 35), one can analyze the observed g tensor and account for it in terms of the spin-orbit splitting parameter,  $\lambda$ , and the separations of level 4 from energy levels 2, 3, and 5 (Fig. 4). Neglecting any covalent effects, but taking second order correction terms (23, 35) into account, one obtains

$$\frac{\lambda}{E_4 - E_5} = -0.1501 \quad [2]$$

$$\frac{\lambda}{E_4 - E_3} = \frac{\lambda}{E_4 - E_2} = 0.0448$$

and  $a = 0.965$

where  $a$  is the coefficient in the level 4 orbital,  $a|3z^2 - r^2\rangle - \sqrt{1-a^2}|x^2 - y^2\rangle$ . The spin-orbit parameter,  $\lambda$ , is not known for Pt<sup>3+</sup> in TiO<sub>2</sub> (27). For the free Pt ion it is 3368 cm<sup>-1</sup> (36). The parameters show that  $|E_4 - E_5|$  is about 0.3  $|E_4 - E_3|$ , which is approximately the ratio observed for these 3d orbitals in TiO<sub>2</sub> (28).

With the parameters of [2], one can analyze the A tensor by use of the formulae already given in the literature (23, 35). The only unknowns in these formulae are  $\kappa$ , the spin-dependent exchange parameter between the d electrons and the paired core electrons, and  $\langle r^{-3} \rangle$ , where  $r$  is the radius of the 5d

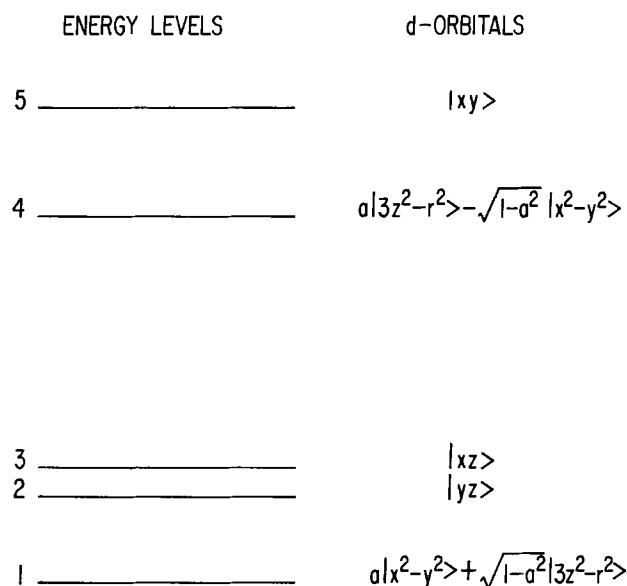


Fig. 4. The splitting of the d orbitals in the orthorhombic point symmetry at a Ti<sup>4+</sup> site [after Ensign et al. (33)].

electron orbit. It is found that the observed A tensor can be fitted with the parameters of [2] and with the values

$$\kappa = -0.02 \quad [3]$$

$$\langle r^{-3} \rangle = 9.75 \text{ atomic units}$$

The small negative value of  $\kappa$  indicates a small contribution of 6s electron character in the 5d orbital (37). No values of  $\langle r^{-3} \rangle$  are generally available for 5d orbitals (34), but they are expected to be larger than  $\langle r^{-3} \rangle$  for the isoelectronic 3d and 4d orbitals (34). For 3d<sup>7</sup> of Ni<sup>3+</sup>,  $\langle r^{-3} \rangle = 7.790$  a.u. and, for the 4d<sup>7</sup> of Pd<sup>3+</sup>,  $\langle r^{-3} \rangle = 8.487$  a.u. The value obtained for Pt<sup>3+</sup> in Eq. [3] fits the expected order.

## REFERENCES

- F. A. Grant, *Rev. Mod. Phys.*, **31**, 649 (1959).
- H. P. R. Frederikse, *J. Appl. Phys. Suppl.*, **32**, 2211 (1961).
- V. N. Bogomolov and V. P. Zhuse, *Soviet Phys.-Solid State*, **8**, 1904 (1967).
- W. D. Ohlsen, O. W. Johnson, and P. I. Kingsbury, *Phys. Rev.*, **175**, 1099 (1968).
- For a general review of all transition metal oxides including rutile, see C. N. R. Rao and G. V. Subba Rao, NSRDS-NBS 49, U.S. Department of Commerce (1974).
- A. von Hippel, J. Kalnajs, and W. B. Westphall, *J. Chem. Phys.*, **23**, 779 (1962).
- B. H. Soffer, *ibid.*, **35**, 940 (1961).
- D. C. Cronmeyer, *Phys. Rev.*, **113**, 1222 (1959).
- O. W. Johnson, W. D. Ohlsen, and P. J. Kingsbury, Jr., *ibid.*, **175**, 1102 (1968).
- P. F. Chester, *J. Appl. Phys. Suppl.*, **32**, 2233 (1961).
- V. N. Bogomolov and L. S. Sochova, *Soviet Phys.-Solid State*, **9**, 2647 (1968).
- P. I. Kingsbury, Jr., W. D. Ohlsen, and O. W. Johnson, *Phys. Rev.*, **175**, 1091 (1968).
- L. N. Shen, O. W. Johnson, W. D. Ohlsen, and J. W. DeFord, *ibid.*, **B10**, 1823 (1974).
- W. Kunmann and A. Ferretti, *Rev. Sci. Instr.*, **35**, 465 (1964).
- A review of EPR studies up to 1962 is given by H. J. Gerritsen, in "Paramagnetic Resonance," Vol. I, W. Low, Editor, p. 1, Academic Press, New York (1963).
- D. L. Carter and A. Okaya, *Phys. Rev.* **118**, 1485 (1960).
- H. J. Gerritsen, S. E. Harrison, and H. R. Lewis, *J. Appl. Phys.*, **31**, 1566 (1960).
- J. J. Davies and J. C. Wertz, *J. Mag. Res.*, **1**, 500 (1969).
- P. P. J. Van Engelen and J. C. M. Henning, *Phys. Letters*, **25A**, 733 (1967).
- E. L. Waters and A. H. Maki, *Phys. Rev.*, **125**, 233 (1962).
- B. R. McGarvey, *J. Chem. Phys.*, **38**, 388 (1961).
- E. Yamaka and R. G. Barnes, *Phys. Rev.*, **35**, A144 (1964).
- T. Shimizu, *J. Phys. Soc. Japan*, **23**, 248 (1967).
- R. N. Blumenthal and D. H. Whitmore, *This Journal*, **110**, 92 (1963).
- R. R. Hasiguti, *J. Metall. (Japan)*, **9**, 95 (1963).
- T. Hurlen, *Acta. Chem. Scand.*, **13**, 365 (1959).
- R. N. Blumenthal, J. Baukus, and W. M. Hirthe, *This Journal*, **114**, 175 (1967).
- R. R. Hasiguti, E. Iguchi, and S. Takahashi, Proc. 9th Int. Conf. Phys. Semiconductors, Moscow, 1968, Vol. 2, p. 1142.
- R. R. Hasiguti, E. Yagi, and M. Aono, *Radiation Effects*, **4**, 137 (1970).
- E. Iguchi and K. Yajima, *J. Phys. Soc. Japan*, **32**, 1415 (1972).
- E. Iguchi, K. Yajima, J. Asahina, and Y. Kanamori, *J. Phys. Chem. Solids*, **35**, 597 (1974).
- A. Abragam and B. Bleaney, "Electron Paramagnetic Resonance of Transition Ions," p. 487, Oxford University Press, New York (1970).
- T. C. Ensign, Te-Tse Chang, and A. H. Kahn, *Phys. Rev.*, **188**, 703 (1969).
- Ref 32, Chap. 8, pp. 472-490.
- B. Bleaney, K. D. Bowers, and M. H. L. Pryce, *Proc. Roy. Soc. Ser. A*, **228**, 166 (1955).
- C. E. Moore, "Atomic Energy Levels as Derived from Analyses of Optical Spectra," Vol. III. National Bureau of Standards No. 467, U.S. GPO, Washington, D.C. (1958). Vol. III.
- J. F. Gibson, D. J. E. Ingram, and D. Schonland, *Discussions Faraday Soc.*, **26**, 72 (1958).

# Quantum Efficiency Standard for Ultraviolet and Visible Excitation

A. Brill\* and A. W. de Jager-Veenis

Philips Research Laboratories, Eindhoven, The Netherlands

## ABSTRACT

To determine quantum efficiencies of powder phosphors as a function of exciting wavelength, sodium salicylate is usable in the ultraviolet but not in the visible region. As a powder standard in the excitation region, 200-550 nm red luminescent lumogen powder is proposed. The absolute quantum efficiency has been measured. It varies between 40 and 60% in this region and it has a high absorption.

To determine the efficiencies of powder phosphors it is very helpful to have standard phosphors with which efficiencies of other phosphors can be compared. In this way absolute measurements, which are generally time consuming, can be avoided. Some of the conditions that standard phosphors are required to fulfill is that they should be readily available, stable, and show agreement on the value of the efficiency. However, even when there is some uncertainty about the accuracy it is important to be able to make a comparison between a sample with unknown efficiency and the standard.

For excitation in the wavelength region near 250 nm, the standards issued by the National Bureau of Standards (NBS) in Washington are very suitable. The efficiencies of these phosphors have been measured by us earlier (1), together with other properties like decay time and temperature dependence. For many applications, however, it is often necessary to know the efficiency at other exciting wavelengths in the ultraviolet and visible regions.

For the ultraviolet exciting region up to a wavelength of about 350 nm sodium salicylate is often used, which has a constant efficiency as a function of wavelength from the far ultraviolet up to 350 nm at the long wavelength side. The quantum efficiency of sodium salicylate has been measured by several workers.

Table I gives some data for 254 nm excitation taken from Samson's book on far ultraviolet (2) together with our values.

Allison, Burns, and Tuzzolino (3) found for the quantum efficiency of sodium salicylate a figure very near unity. In our opinion this cannot be right, as can be readily seen from the fact that at liquid nitrogen temperature the efficiency increases by about 25%, as Kristianpoller and Knapp (4) showed. Nygaard (5) found originally 50% but in a later paper (6) he states the value of Ref. (3) to be right. The low value found by Inokuchi (7) is probably due to the use of very thin layers, so that the exciting radiation is not quite absorbed. The figures of Studer (8), Kristianpoller (9), Vasseur and Cantin (10), and Wrighton, Gingley, and Morse (11) are in agreement with our values. For the intrinsic quantum efficiency we found a value of 60%, i.e., a correction has been made for the absorption of the emitted luminescence in the layer (12). Not corrected for this absorption, the quantum efficiency is found to be 55%.

A disadvantage of sodium salicylate is that its emission is in the blue, so that constant quantum efficiency and high absorption are only found up to about 350 nm. At  $\lambda_{exc} = 365$  nm we found a lower quantum efficiency, in agreement with measurements reported by Hamman (13). For longer wavelength excitation use can be made of very diluted solutions of, e.g., rho-

Table I. Absolute quantum efficiency  $q$  of sodium salicylate<sup>1</sup>  
 $\lambda_{exc} = 253.7$  nm

Observer	$q$ (%)	Layer thickness	Reference
Allison <i>et al.</i>	99	2-4 mg/cm <sup>2</sup>	3
Vasseur and Cantin	65	2 mg/cm <sup>2</sup>	10
Nygaard	50	1-2 mg/cm <sup>2</sup>	5
Kristianpoller	64	6 mg/cm <sup>2</sup>	9
Inokuchi <i>et al.</i>	25	?	7
Studer	60	2 mm	8
Wrighton <i>et al.</i>	53	?	11
Morgenshtern <i>et al.</i>	50	1.5	18
Present work	60	2 mm	

<sup>1</sup> See J. A. R. Samson, "Techniques of Vacuum Ultraviolet Spectroscopy," John Wiley & Sons, Inc., New York (1967).

damine B or 6G, fluorescein, etc., which are known to show a nearly constant quantum efficiency as a function of exciting wavelength up to their emission region [see the paper by Velapoldi (14)]. Rhodamine B, for instance, emits in the red spectral region, so that it is suitable for excitation up to relatively long wavelengths.

Liquid samples like the ones mentioned, however, are less suitable as standards for comparison with powder phosphors because of the different geometry of the setup needed for the measurement. Another drawback of these liquid samples is that the efficiency is about constant as a function of the exciting wavelength, but the absorption and, as a consequence, the light output vary enormously through the spectrum. This is shown in Fig. 1, where the absorption is given for rhodamine B [see also Eastman (15)]. Low absorption and low light output in the ultraviolet and blue are found with a large maximum near 540 nm and a smaller maximum near 360 nm.

Kristianpoller and Dutton (16), Vavilov (17), Mor-

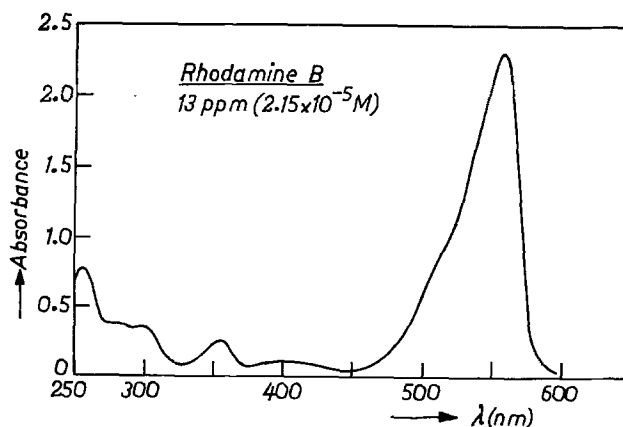


Fig. 1. Spectral absorption of rhodamine B

\* Electrochemical Society Active Member.

Key words: quantum efficiency, standard phosphors, luminescence, fluorescence, lumogen.

genshtern, Neustruev, and Epshtein (18), and Küttner, Selzle, and Schlag (19) described luminescent "lumogens" with a rather constant efficiency.

For the measurement of efficiencies at still longer exciting wavelengths we chose a red luminescent "lumogen T red GG" as a standard. It is one of a series of "lumogen" pigments available from the B.A.S.F. Company in Ludwigshafen, Germany (20). The luminescence properties of this material are described below.

### Experimental

The spectral power distribution was determined with a Spex 1700 II monochromator, which was automatically corrected for the wavelength-dependent instrumental response as was described previously (21). The instrument was equipped with a thermoelectrically cooled EMI Type 9659 QA photomultiplier (S20 response) and a liquid nitrogen-cooled Philips 150 CVP photomultiplier (S1 response). The setup was calibrated with the aid of a calibrated tungsten-halogen standard lamp of the NBS (Washington, D.C.).

The excitation spectra were determined with a Perkin-Elmer-Hitachi grating spectrofluorimeter MPF2A equipped with a red-sensitive Hitachi R446F photomultiplier. The sources used were a deuterium lamp for the ultraviolet and a tungsten-halogen lamp for the visible region. The relative quantum output in the u.v. region was determined as a function of wavelength with respect to that of sodium salicylate, assuming a constant quantum efficiency for the latter (see above). From 160 to 260 nm the excitation spectra were determined with a McPherson Seya-Namioka monochromator Type 235 in combination with an argon-flushed deuterium lamp and a thermoelectrically cooled calibrated EMI 9558 Q photomultiplier.

For the absolute measurements of the efficiency at  $\lambda = 365, 405, 436,$  and  $546$  nm, a Philips HPK 125W mercury vapor discharge source was used; the exciting lines were isolated with filters. Measurements were carried out with two detectors: (i) a thermoelement (flat power response) and (ii) a Philips 150 CVP photomultiplier (S1 photocathode), specially selected in view of a nearly flat response between 400 and 650 nm (not used for  $\lambda_{\text{exc}} = 365$  nm). The excitation intensity was determined with the aid of diffuse reflection against pure Eastman Kodak  $\text{BaSO}_4$  (22).

Two measurements were carried out on  $\text{BaSO}_4$  and each phosphor [for details of the method used see Ref. (1)]. One measurement was done without a filter in front of the photomultiplier and the other measurement with a filter that passes only the luminescence (for  $\text{BaSO}_4$  the output is then evidently zero). From the two measurements the reflection and radiant efficiency can be determined. The value of the reflection thus calculated should be about the same as the one found in a direct way in a spectrophotometer (see below).

Actually, the radiant efficiencies were determined from which the quantum efficiencies were calculated. For measurements at liquid nitrogen temperature, a setup was used similar to that described in Ref. (1).

Diffuse reflection measurements were carried out on a Perkin-Elmer Model 13 U spectrophotometer (detector EMI 9558 QA photomultiplier, source deuterium lamp) in the absorption region of the sample. The latter was placed in a specially made Perkin-Elmer attachment (sample between source and monochromator). In the emission region a Beckman DK2 spectrophotometer with Ulbricht sphere was used (sample between monochromator and detector). The absorption of liquids was measured on a Cary Model 17 spectrophotometer.

### Results and Discussion

The spectral power distribution of the lumogen T red GG at room temperature is given in Fig. 2. The maximum of the emission is found at a wavelength

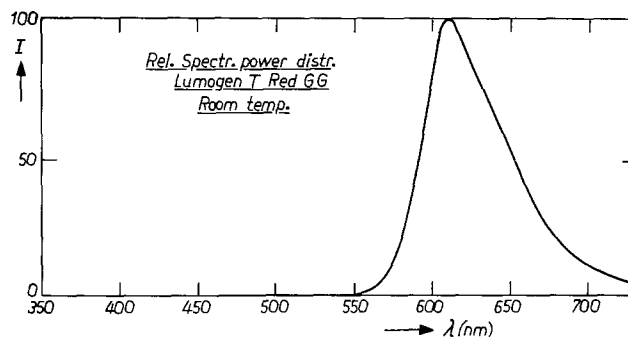


Fig. 2. Relative spectral power distribution of lumogen T red GG at room temperature.  $I$  denotes the spectral radiant power in arbitrary units.

between  $\lambda = 610$  and  $615$  nm. The spectral power distribution at liquid nitrogen temperature is given in Fig. 3, showing two peaks at  $\lambda = 600$  and  $640$  nm, respectively.

We measured the quantum efficiency as a function of the exciting wavelength (layer thickness about 2 mm). It proved to be not quite constant, but it varies only in a limited range between 40 and 60% in the spectral region between 220 and 550 nm. This is shown in Fig. 4, where the diffuse reflection curve is also given. An important advantage is that the absorption is high in the whole region; the lowest value is 78% near  $\lambda = 380$  nm (diffuse reflection = 22%).

The excitation spectrum was determined in the following way:

1. For  $\lambda = 254$  nm the absolute value of the quantum efficiencies was determined in a relative way with the aid of the NBS standard phosphors willemite and Mg-arsenate activated with Mn. The method used has been described in Ref. (1), where the determined absolute values of the latter phosphors are also given.

2. Absolute efficiencies were determined at the excitation wavelengths of the mercury discharge lines:

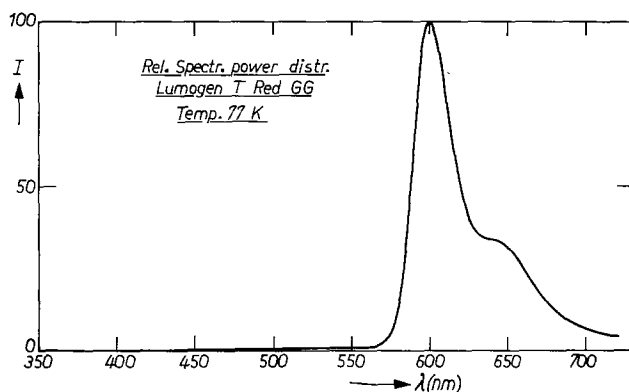


Fig. 3. Relative spectral power distribution of lumogen T red GG at 77°K.  $I$  denotes the spectral radiant power in arbitrary units.

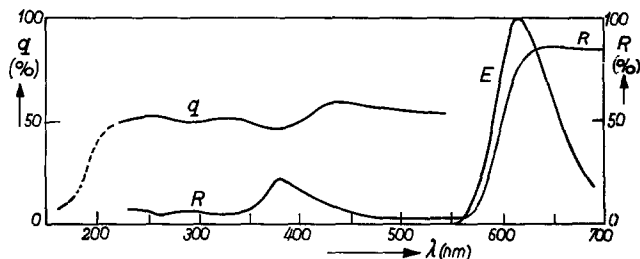


Fig. 4. Quantum efficiency  $q$ , diffuse reflection  $R$ , and spectral power distribution  $E$  of lumogen T red GG as a function of wavelength.

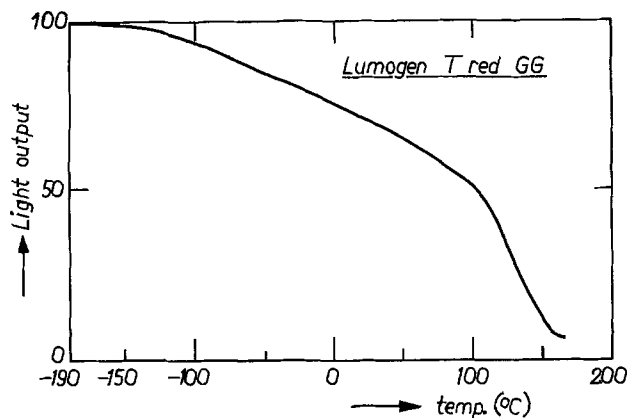


Fig. 5. Temperature dependence curve of lumogen T red GG

$\lambda = 365, 405, 436,$  and  $546$  nm with a method similar to that described in Ref. (1).

3. In the middle and near u.v. the relative excitation spectrum was determined with the aid of sodium salicylate as has been explained before, down to 160 nm.

4. To determine the quantum efficiency between 500 and 540 nm, use is made of rhodamine B as a reference. The ratio of the efficiencies of lumogen and rhodamine were determined at  $\lambda = 540$  and 365 nm where rhodamine has maxima in light output. A constant quantum efficiency is assumed for the rhodamine. Then the efficiency between 500 and 540 nm can be calculated from that at 365 nm, which has been determined in an absolute way as is mentioned above.

The measurements mentioned under 2-4 lead to a fairly constant quantum efficiency in the u.v. and visible region.

Part of the variation in quantum efficiency may be due to the influence of absorption in the polyvinyl chloride in which the luminescent material is dissolved. This may also be the reason for differences in efficiency between various batches of lumogen. (We found a difference of about 10% for two batches.) It is therefore necessary to calibrate every batch.

In addition to the spectral power distribution at the temperature of liquid nitrogen (see Fig. 4), we also determined the quantum efficiency ( $\lambda_{\text{exc}} = 365$  nm) at that temperature which proved to be about 40% higher than its value at room temperature. In Fig. 5 the temperature dependence curve of the relative light output is given.

### Acknowledgments

The authors are indebted to Miss R. E. Engelen for part of the measurements and to Mr. P. Vries for the response measurements of the photomultiplier.

Manuscript received Oct. 27, 1975. This was Paper 204 presented at the Toronto, Canada, Meeting of the Society, May 11-16, 1975.

Any discussion of this paper will appear in a Discussion Section to be published in the December 1976 JOURNAL. All discussions for the December 1976 Discussion Section should be submitted by Aug. 1, 1976.

Publication costs of this article were partially assisted by Philips Research Laboratories.

### REFERENCES

1. A. Bril and W. Hoekstra, *Philips Res. Rept.*, **16**, 356 (1961); *ibid.*, **19**, 296 (1964); A. Bril, in "Luminescence of Organic and Inorganic Materials," Kallman-Spruch, Editor, p. 479, John Wiley & Sons, Inc. New York (1962).
2. J. A. R. Samson, "Techniques of Vacuum Ultraviolet Spectroscopy," p. 216, John Wiley & Sons, Inc., New York.
3. R. Allison, J. Burns, and A. J. Tuzzolino, *J. Opt. Soc. Am.*, **54**, 747 (1964).
4. N. Kristianpoller and R. A. Knapp, *Appl. Opt.*, **3**, 915 (1964).
5. K. J. Nygaard, *Brit. J. Appl. Phys.*, **15**, 597 (1964).
6. K. J. Nygaard, *J. Opt. Soc. Am.*, **55**, 944 (1965).
7. H. Inokuchi, Y. Harada, and T. Kondow, *ibid.*, **54**, 842 (1964).
8. F. J. Studer, *ibid.*, **55**, 613A (1965).
9. N. Kristianpoller, *ibid.*, **54**, 1285 (1964).
10. J. Vasseur and M. Cantin, XI Coll. Spectr. Int. Beograd. (1963).
11. M. S. Wrighton, D. S. Ginley, and D. L. Morse, *J. Phys. Chem.*, **78**, 2229 (1974).
12. See A. Bril and H. A. Klasens, *Philips Res. Rept.* **7**, 401 (1952), especially p. 406.
13. J. F. Hammann, *Z. Angew. Phys.*, **10**, 187 (1958).
14. R. A. Velapoldi, in "Accuracy in Spectrophotometry and Luminescence Measurements," U.S. Dept. of Commerce, Washington, D.C. (1973).
15. J. W. Eastman, *Photochem. Photobiol.*, **6**, 55 (1967).
16. N. Kristianpoller and D. Dutton, *Appl. Opt.*, **3**, 287 (1964).
17. V. S. Vavilov, *J. Chem. Phys. Solids*, **8**, 223 (1959).
18. Z. L. Morgenshtern, V. B. Neustruev, and M. I. Epshtein, *J. Appl. Spectr. (SSSR)*, **3**, 35 (1965).
19. H. G. Kuettner, H. L. Selzle, and E. W. Schlag, *Z. Naturf.*, **29a**, 224 (1974).
20. Lumogen pigments, Technical Data BASF, Ludwigshafen, Federal Republic of Germany, 1972.
21. A. Bril, G. Blasse, and J. A. de Poorter, *This Journal*, **117**, 346 (1970).
22. F. Grum and G. W. Luckey, *Appl. Opt.*, **7**, 2289 (1968).

## Factors Influencing the Photoluminescence Behavior of Thoria

P. J. Harvey and J. B. Hallett

Atomic Energy of Canada Limited, Chalk River Nuclear Laboratories, Chalk River, Ontario, Canada K0J 1J0

### ABSTRACT

The photoluminescence of single crystals of thoria excited with u.v. light consists of sharp line spectra, characteristic of accidentally incorporated rare earth impurities and broad band spectra of the host lattice and other impurities. The effects of (i) the annealing atmosphere, the duration of the anneal, and the cooling rate, (ii) the deliberate addition of aliovalent  $\text{Ca}^{+2}$ ,  $\text{Y}^{+3}$ , and  $\text{Ta}^{+5}$  impurities, and (iii) the time and temperature of the u.v. excitation on the photoluminescence behavior are discussed.

Early studies on the optical properties of  $\text{ThO}_2$  (1-3) indicated that vacuum or air annealing could change the optical absorbance spectra. Other work on  $\text{ThO}_2$

**Key words:** thoria, photoluminescence, impurities, temperature dependence, thermoluminescence.

was carried out by Bates (4) and more recently by the present authors (5). Some impurity effects on the optical properties of  $\text{ThO}_2$  have also been examined (6, 7). The results of these studies showed many more basic differences than could be accounted for by the varied



experimental techniques employed. It was evident that progress in the identification of defect centers in ThO<sub>2</sub> was being impeded because different research groups were working with crystals from a variety of sources and prepared under a variety of conditions. There was insufficient, well-characterized quantitative optical data. The aims of the present paper are to document well-characterized data on the photoluminescence of thoria, to point out that many factors can influence the photoluminescence behavior, and to illustrate these effects. In addition, the present paper correlates the time and temperature dependence of the photoluminescence behavior with recently obtained thermoluminescence data (8).

### Experimental

High purity ThO<sub>2</sub> powder obtained from the American Potash Chemical Corporation, West Chicago, Illinois, was subjected to arc fusion by the Norton Research Corporation (Canada) Ltd., Chippawa, Ontario. Single crystals of ThO<sub>2</sub> were cut from the arc-fused boule using a diamond wire saw. Crystals were polished to optical flatness using a series of diamond pastes. The crystal dimensions were 0.25 mm thick and approximately 80 mm<sup>2</sup> surface area. The main impurities, determined by spark source mass spectroscopy, of a nominally pure crystal are listed in Table I. Doped crystals were prepared by adding 0.14 mole per cent (m/o) Y<sub>2</sub>O<sub>3</sub>, Ta<sub>2</sub>O<sub>5</sub>, or 0.28 m/o CaO to the ThO<sub>2</sub> powder before arc fusion.

The crystals were annealed at 1675°K in one of four atmospheres so that the effect of oxygen partial pressure on the photoluminescence could be studied. These atmospheres were: (i) air,  $p_{O_2} \sim 2.026 \times 10^4$  Pa ( $2 \times 10^{-1}$  atm), (ii) carbon dioxide,  $p_{O_2} \sim 1.013 \times 10^2$  Pa, (iii) carbon monoxide,  $p_{O_2} \sim 1.013 \times 10^{-8}$  Pa, and (iv) dry hydrogen,  $p_{O_2} \sim 1.013 \times 10^{-17}$  Pa. Crystals annealed in air or carbon dioxide will be referred to as oxidized; whereas crystals annealed in carbon monoxide or dry hydrogen will be referred to as reduced. Annealing times of  $3.60 \times 10^2$ ,  $8.64 \times 10^4$ , and  $7.20 \times 10^5$  sec were chosen and two cooling rates from the annealing to ambient temperature employed. The first, known as the fast cool, occurred when the crystal holder was completely removed from the furnace and cooled with a jet of cold air. From 1675° to 1000°K the cooling rate was  $\sim 3.5^\circ \text{sec}^{-1}$ . Furnace cooling, the slow cool, gave a rate of  $0.35^\circ \text{sec}^{-1}$  over the same temperature range.

All the photoluminescence measurements were made on a Perkin-Elmer MPF-3 spectrofluorimeter using a

Xenon arc lamp as the excitation source and a multi-alkali u.v. glass R446 photomultiplier as the detector. The spectral range examined was restricted to 400-800 nm with a 10 nm band pass. Reflected light made it difficult to make meaningful measurements below 400 nm and no attempts were made to investigate emission in the infrared region of the spectrum. The photoluminescence spectra were corrected for variations in the photomultiplier response. The crystals were mounted on a specially designed copper finger enclosed in an evacuated water-cooled quartz jacket. The specimen temperature was monitored using a precalibrated iron-constantan thermocouple embedded in the copper directly behind the specimen. The temperature dependence of the photoluminescence efficiency was measured at a linear heating rate of  $0.83^\circ \text{K sec}^{-1}$ . The same heating rate and crystal geometry were used when studying the thermoluminescence.

### Results

The effects of varying the u.v. excitation wavelength on the photoluminescence are illustrated in Fig. 1. For a pure crystal annealed in air at 1675°K, fast cooled, and measured at 80°K, a broad asymmetric band is observed at 450 nm with 255 nm optimum excitation. With 280 nm excitation a sharp line doublet is observed with peaks at 497 and 503 nm. An additional broad band occurs at 540 nm resulting from 320 nm excitation and 345 nm excitation produces a peak at 785 nm. The only positive identification is that of the sharp line doublet attributed to transitions from the <sup>3</sup>P<sub>0</sub> and <sup>3</sup>P<sub>1</sub> 4f levels to the <sup>3</sup>H<sub>4</sub> ground state for the trivalent rare earth Pr<sup>+3</sup> (9).

The effects of the different annealing treatments on the emission intensities for the different types of crystals are shown in Table II. The significant results in this table may be summarized as follows:

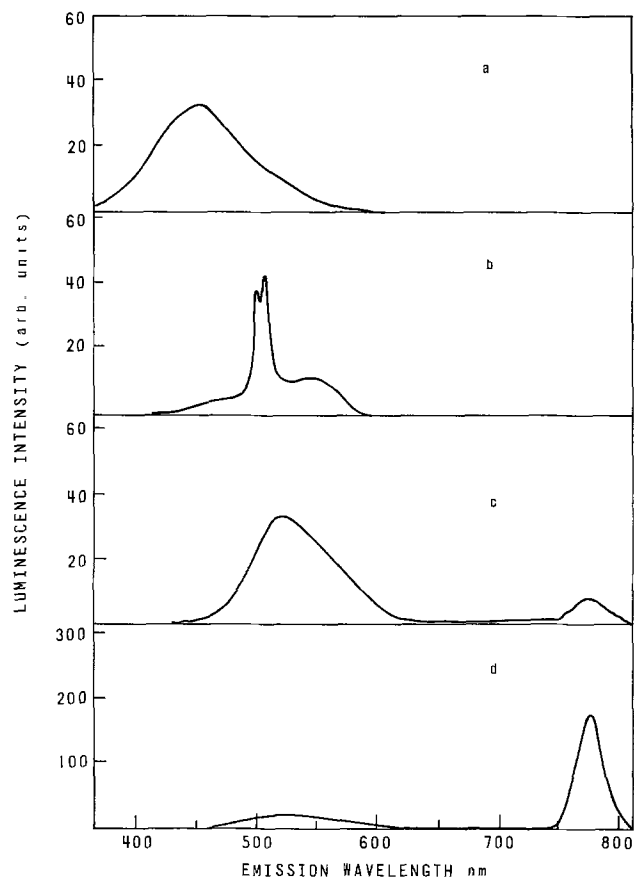


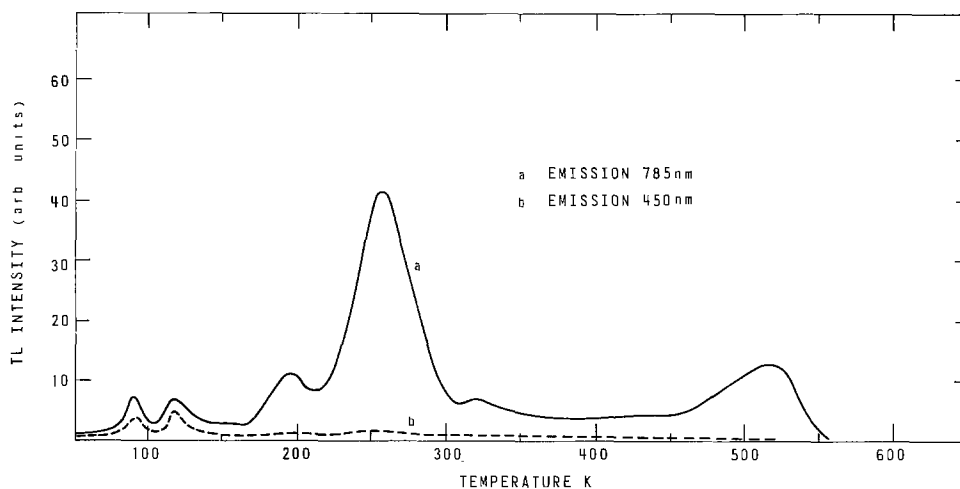
Fig. 1. Luminescence of pure ThO<sub>2</sub> at 80°K after an air anneal at 1675°K. a, 255 nm excitation; b, 280 nm excitation; c, 320 nm excitation; d, 345 nm excitation.

Table I. Impurity analysis of pure ThO<sub>2</sub>

Element	Atomic conc (ppm)*	Element	Atomic conc (ppm)*
F	8	Nb	0.6
Na	15	Mo	0.3
Mg	25	Rh	4
Al	35	Ag	0.8
Si	35	Ba	6
P	1	La	3
S	25	Ce	6
C	15	Pr	2
Ar	3	Nd	4
K	7	Sm	1
Ca	22	Gd	10
Sc	2	Tb	0.6
Ti	12	Dy	0.8
V	0.5	Ho	1
Cr	6	Er	0.5
Mn	0.6	Tm	0.3
Fe	18	Yb	0.3
Ni	2	Lu	0.3
Cu	1	U	6
Zn	1		
Ga	1		
Ge	2		
Rb	0.3		
Sr	0.5		
Y	3		
Zr	1.5		

\* Limit of detection for most elements is 0.3 ppm.

Fig. 2. Thermoluminescence of pure  $\text{ThO}_2$  resulting from: curve a, 345 nm excitation at 80°K on oxidized  $\text{ThO}_2$ ; curve b, 255 nm excitation at 80°K on reduced  $\text{ThO}_2$ .



1. Reducing anneals increase the 450 nm emission intensity.

2. The intensity of the 450 nm emission is also increased for  $\text{Ca}^{+2}$ - and  $\text{Y}^{+3}$ -doped crystals which have been subjected to the oxidizing anneals.

3. Doping with  $\text{Ta}^{+5}$  decreases the intensity of the 450 nm emission in reduced crystals.

4. Doping with  $\text{Ca}^{+2}$  directly increases the intensity of the 450 nm emission, whereas doping with  $\text{Y}^{+3}$  introduces an additional band at  $\sim 400$  nm and doping with  $\text{Ta}^{+5}$  introduces a long wavelength shoulder at 472 nm.

5. The 500 nm emission ( $\text{Pr}^{+3}$ ) is most severely decreased by doping with  $\text{Ca}^{+2}$  and  $\text{Y}^{+3}$  in air-annealed crystals. The relative effectiveness for decreasing the 500 nm emission is  $\text{Y}^{+3} > \text{Ca}^{+2} \gg \text{Ta}^{+5}$ .

6. The intensity of the 540 nm emission is generally decreased by doping.

7. A new band appears at 565 nm when  $\text{Ca}^{+2}$ -doped crystals are annealed in carbon monoxide.

8. When pure crystals are annealed in dry  $\text{H}_2$  a very large and complex band structure develops with broad maxima at 525 and 600 nm, and a sharp line shoulder at 655 nm. The complex new bands mask any 540 nm emission. The complex band structure is eliminated by doping.

9. The 785 nm emission is only observed in oxidized crystals and the intensity decreases on doping.

In general, emission intensities were decreased when the crystals were subjected to the slower cooling rate. In particular, the complex band structure in hydrogen-annealed crystals was almost completely eliminated by slow cooling. The emission intensities did not

change with annealing time after a minimum of  $\sim 7.2 \times 10^3$  sec at 1675°K. Shorter anneals, however, appeared to produce only partially oxidized and reduced crystals.

The effect of the excitation time on the photoluminescence emission intensity was also studied. At 80°K excitation of oxidized pure crystals with 345 nm light caused the intensity of the 785 nm emission to decrease with time, whereas excitation with 255 nm light on the reduced pure crystals did not cause the intensity of the 450 nm emission to change with time. The consequences of this behavior are illustrated by the thermoluminescence (TL) glow curves for oxidized and reduced pure  $\text{ThO}_2$  in Fig. 2. When reduced  $\text{ThO}_2$  is excited with 255 nm light at 300°K the intensity of the 450 nm emission increases with time for both  $\text{Ca}^{+2}$ -doped and pure crystals, and decreases with time for  $\text{Y}^{+3}$ -doped crystals. This time-dependent behavior has long been associated with charge trapping (10, 11). In the present study the increase with time is greatest for  $\text{Ca}^{+2}$ -doped crystals and should be evident in the TL glow curves. The TL data are presented in Fig. 3. A detailed study of the TL of pure  $\text{ThO}_2$  has been made by the authors (12). The present study on doped  $\text{ThO}_2$  indicates that, contrary to the results of the time-dependent increases, the TL intensity for  $\text{Ca}^{+2}$ -doped  $\text{ThO}_2$  is much lower than that for pure  $\text{ThO}_2$ .

Thermal quenching of luminescence has also been known for many years (10, 11). An important aspect of the present work was to study the temperature dependence of the luminescence intensity for  $\text{ThO}_2$  crystals, both pure and doped, oxidized and reduced. Since it has previously been observed (this paper) that the luminescence intensity is time dependent, the measurements of luminescence intensity as a function of increasing temperature were performed at discrete temperature intervals rather than by continuous monitor-

Table II. Effects of impurities and annealing treatments on the intensity of the photoluminescence induced by u.v. excitation

Crystal type	Emission intensities at				Annealing atmosphere
	450 nm	500 nm	540 nm	785 nm	
Pure $\text{ThO}_2$	30	40	40	200	Air
$\text{Ca}^{+2}$ -doped $\text{ThO}_2$	500	5	15	150	Air
$\text{Y}^{+3}$ -doped $\text{ThO}_2$	300†	5	10	150	Air
$\text{Ta}^{+5}$ -doped $\text{ThO}_2$	30*	40	5	50	Air
Pure $\text{ThO}_2$	20	35	35	200	$\text{CO}_2$
$\text{Ca}^{+2}$ -doped	650	35	30	150	$\text{CO}_2$
$\text{Y}^{+3}$ -doped	400†	25	15	150	$\text{CO}_2$
$\text{Ta}^{+5}$ -doped	50*	35	15	50	$\text{CO}_2$
Pure $\text{ThO}_2$	450	80	50	<5	$\text{CO}$
$\text{Ca}^{+2}$ -doped	700	60	55‡	<5	$\text{CO}$
$\text{Y}^{+3}$ -doped	400†	30	10	30	$\text{CO}$
$\text{Ta}^{+5}$ -doped	50*	50	10	<5	$\text{CO}$
Pure $\text{ThO}_2$	500	60	(Complex)		Dry $\text{H}_2$
$\text{Ca}^{+2}$ -doped	500	40	<5	<5	Dry $\text{H}_2$
$\text{Y}^{+3}$ -doped	300†	10	<5	<5	Dry $\text{H}_2$
$\text{Ta}^{+5}$ -doped	30*	70	<5	<5	Dry $\text{H}_2$

† Additional large emission band at 400 nm

\* Additional emission band at 472 nm.

‡ Emission shift to 565 nm maximum.

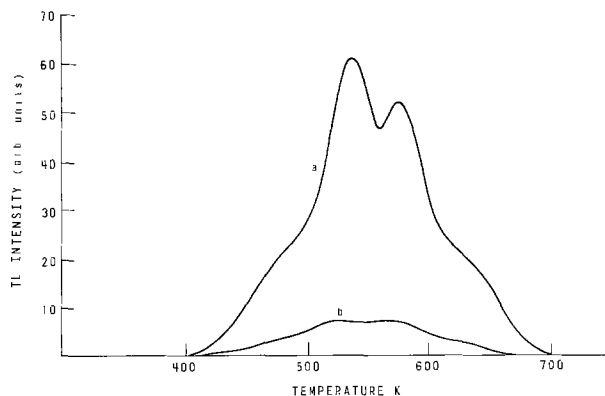


Fig. 3. Thermoluminescence of reduced  $\text{ThO}_2$  after 255 nm excitation at 300°K. Curve a, pure  $\text{ThO}_2$ ; curve b,  $\text{Ca}^{+2}$ -doped.

ing to minimize the time-dependent effects. The temperature dependence of the intensities of the 450 and 500 nm emissions are illustrated in Fig. 4 and 5, respectively.

It can be seen from Fig. 4 that not only does doping with  $\text{Ca}^{+2}$  and  $\text{Y}^{+3}$  enhance the intensity of the 450 nm emission at 80°K but the temperature dependence of the emission differs in the pure and doped material. The temperature dependence of the emission intensity also differs for the oxidized and reduced pure crystals. The annealing effects, however, in the doped crystals are much less important than the dopant. For the 500 nm emission the main points to note in Fig. 5 are:

1. Only for reduced pure  $\text{ThO}_2$  is there significant 500 nm emission above 400°K.

2. The quenching profiles for  $\text{Ca}^{+2}$ -,  $\text{Y}^{+3}$ -, and  $\text{Ta}^{+5}$ -doped  $\text{ThO}_2$  all differ; but are all self-consistent for different annealing atmospheres.

3. In doped crystals, the annealing atmosphere affects the 500 nm emission more than the 450 nm emission.

### Discussion

At least four emission bands are observed in  $\text{ThO}_2$  as a result of u.v. excitation. One of these consists of a sharp line doublet and is attributed to 4f transitions in the accidentally incorporated trivalent rare earth praseodymium,  $\text{Pr}^{+3}$ . Impurity analysis indicates that Pr is only present to a concentration of 2 ppm (Table I). While it is well known that  $\text{ThO}_2$  is an excellent host for rare earth activators (13), the low Pr concentration and the fact that other rare earth impurities, e.g., Ce, Gd, and Nd, while present in higher concentrations (5-10 ppm) do not show detectable lumi-

nescence suggest that the emission from  $\text{Pr}^{+3}$  is possibly being activated by a charge transfer type of process with neighboring ions (14).

Information regarding the nature of the center or centers responsible for the broad asymmetric 450 nm emission band can be obtained from examination of Table II. The intensity of the emission is enhanced by reduction which increases the oxygen vacancy concentration. The emission intensity is also enhanced by doping with  $\text{Ca}^{+2}$  and  $\text{Y}^{+3}$ . Charge neutrality requires an increase in the oxygen vacancy concentration when a  $\text{Th}^{+4}$  ion is substitutionally replaced by a  $\text{Ca}^{+2}$  or a  $\text{Y}^{+3}$  ion. Furthermore, doping with  $\text{Ta}^{+5}$  which decreases the oxygen vacancy concentration also decreases the 450 nm emission. The evidence suggests that the 450 nm emission is directly dependent on the oxygen vacancy concentration.

Arguments may be proposed that variable valence impurities, e.g.,  $\text{Fe}^{+2}$ , are solely responsible for the 450 nm emission. It seems to the authors, however, that total charge compensation by relatively small amounts of variable valence impurities is highly improbable. The precise role of the oxygen vacancies is not known. One may be observing the F center in  $\text{ThO}_2$  (2 electrons trapped at a single anion vacancy). Absorption of 255 nm light may convert some F centers to  $\text{F}^+$  centers (15). For MgO the F and  $\text{F}^+$  bands overlap and the presence of the  $\text{F}^+$  center can only be detected by EPR (16). Although many EPR studies have been made on single crystals of  $\text{ThO}_2$  (17-21) no undisputed evidence has yet been advanced for the F or  $\text{F}^+$  center. Many of the previous EPR studies either concentrated on signals from deliberately added rare earth impurities, or the

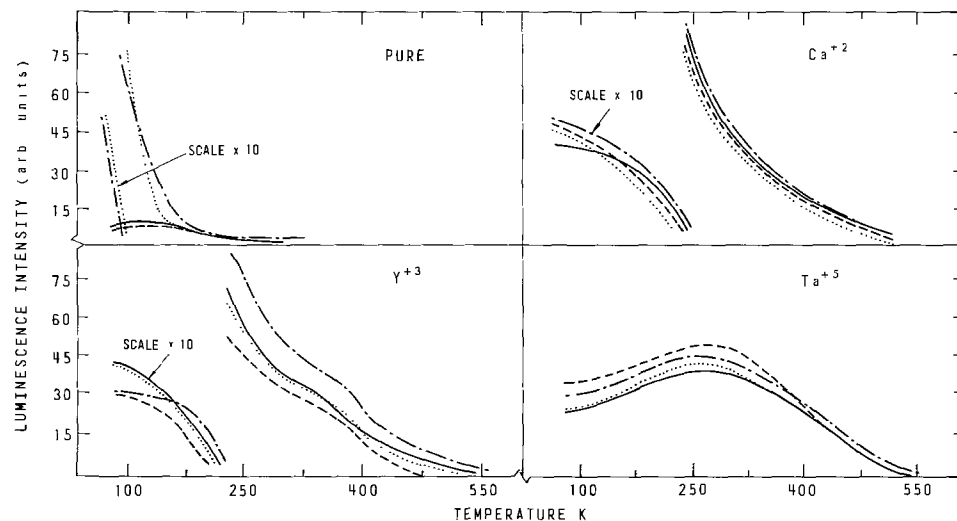


Fig. 4. Effects of the annealing atmosphere on the temperature dependence of the 450 nm emission resulting from 255 nm excitation in pure and doped  $\text{ThO}_2$ . —, Air annealed; ---,  $\text{CO}_2$  annealed; - · - ·, CO annealed; · · · ·,  $\text{H}_2$  annealed.

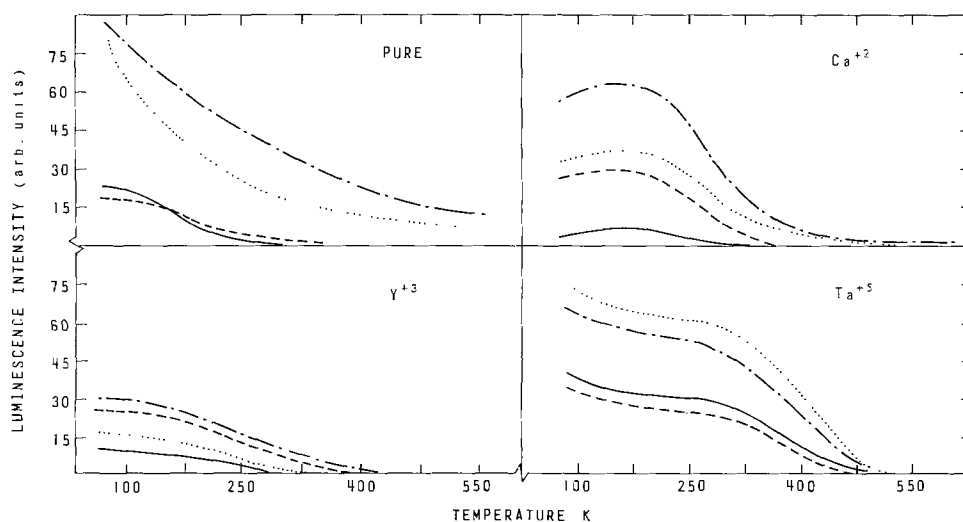


Fig. 5. Effects of the annealing atmosphere on the temperature dependence of the 500 nm emission ( $\text{Pr}^{+3}$ ) resulting from 280 nm excitation in pure and doped  $\text{ThO}_2$ . —, Air annealed; ---,  $\text{CO}_2$  annealed; - · - ·, CO annealed; · · · ·,  $\text{H}_2$  annealed.

crystals were sufficiently impure that signals from  $Gd^{+3}$  or  $Pb^{+3}$  ion impurities masked other effects. Detailed EPR studies on well-characterized  $ThO_2$  crystals of high purity, both before and after exposure to u.v. irradiation, are required to resolve this problem, although lack of sufficient nuclei spin in  $ThO_2$  may make positive identification difficult (22).

The identity of the center(s) responsible for the 540 nm emission is not known. TL data (12) indicate that  $Tb^{+3}$  and  $Er^{+3}$  also act as recombination sites in  $ThO_2$ . These rare earths luminesce around 540 nm in  $ThO_2$  (9) but they should show sharp line rather than broad band emission.

The 785 nm emission is only present for oxidized crystals and may be associated with variable valence transition metal ion impurities.  $V^{+3}$ ,  $Cr^{+3}$ , and  $Mn^{+4}$  luminesce near this wavelength in other materials (23-25).  $Cr^{+3}$  has been unambiguously shown to luminesce above 700 nm in oxidized MgO crystals (26). Present impurity analysis, however, would tend to favor Ti or Fe and taken in conjunction with oxidation-reduction potentials suggest that  $Fe^{+3}$  may be the impurity ion responsible for the 785 nm emission. Selective ion implantation studies are attempting to resolve this uncertainty.

The appearance of a band at 400 nm on doping with  $Y^{+3}$  suggests that one or both the  $Y^{+3}$  ions remain in the vicinity of the oxygen vacancy they create to maintain charge neutrality. The emission characteristics of the center would then be altered. It appears that doping with  $Ta^{+5}$  which produces the 472 nm shoulder is involved in a similar process. While doping with  $Ca^{+2}$  directly enhances the intensity of the 450 nm emission, a new band at 565 nm is observed in crystals annealed in carbon monoxide. The  $Ca^{+2}$  ions may be complexing with the centers responsible for the 540 nm emission thereby producing a new center which luminesces at 565 nm.

The higher luminescence with faster cooling is simply evidence of the nonequilibrium quenching of defects and impurities. While the attempts to correlate the emission centers with defects is of necessity highly speculative it is important to remember that the luminescence behavior of  $ThO_2$  is critically dependent on the purity and annealing treatment of the crystals used.

The luminescence efficiency of rare earth ions in various host lattices has been widely studied during the last decade (27-29). The well-known configuration coordinate models (30,31) are always invoked to explain the presence or absence of luminescence and it has been established that the difference,  $\Delta r$ , between the equilibrium configuration of the excited state of a defect center and that of the ground state must be small if luminescence is to occur. Blasse and Brill (28) have shown that  $\Delta r$  depends on the size of the host lattice ion for which the rare earth has been substituted and on the magnitude of the charge and size of the lattice ions surrounding the rare earth. In the present investigation the rare earth  $Pr^{+3}$  is surrounded by highly charged  $Th^{+4}$  ions which in the pure crystal give the host lattice great bonding strength, which causes  $\Delta r$  to be relatively small. The introduction of lower charged  $Ca^{+2}$  and  $Y^{+3}$  ions into the lattice weakens the lattice bonding and increases  $\Delta r$ . The luminescence efficiency of the rare earth ion should, therefore, be lowered in  $ThO_2$  by doing with  $Ca^{+2}$  and  $Y^{+3}$ . This is in agreement with the results of Table II. The effect of  $Ta^{+5}$  doping, however, cannot be explained in this manner.  $Ta^{+5}$  should increase the bonding strength and thereby decrease  $\Delta r$  and increase the luminescence. This effect is not observed. Other factors which affect  $\Delta r$  are changes in ionic radius of surrounding ions and changes in the symmetry of the immediate lattice environment. Symmetry effects are frequently very significant (32). Generally the higher the symmetry around a rare earth ion, the lower the intensity of the rare earth emission. Although the factors previously mentioned

are undoubtedly important, no completely self-consistent explanation of the changes in luminescence intensity with doping can be advanced at present.

The configuration co-ordinate models also schematically explain the temperature dependence of the luminescence. Nonradiative return from the excited state to the ground state of a defect center is possible via the point of intersection of the two parabolas. The situation at the intersection point, however, is complicated by the intersection of the ground excited states at this point. Little quantitative evidence is available on the effects of changing the ion size, charge, etc. on the temperature dependence of the luminescence. Indeed it is only very recently (33) that the energy levels and wave functions necessary to construct an accurate configuration co-ordinate diagram have been calculated for the F and  $F^+$  in MgO and CaO, and even in these relatively simple centers and simple oxides the temperature dependence effects are still being evaluated (34). It is also only recently in other materials that theoretical studies have been undertaken of the temperature quenching of narrow line and broad band emissions using quantum mechanical single configuration co-ordinate models (35).

The fact remains, however, that doping with  $Ca^{+2}$  and  $Y^{+3}$  produces dramatic changes in the temperature dependence of the 450 and 500 nm emissions in  $ThO_2$  (Fig. 4 and 5). One of the implications of this is that previously obtained TL data on doped  $ThO_2$  can now be explained.

As was pointed out earlier in this paper the increase of 450 nm luminescence with time of 255 nm excitation was greater for  $Ca^{+2}$ -doped  $ThO_2$  than for the pure crystal. Effects of this increase, indicative of trap filling, were not apparent when the glow curves of the pure and  $Ca^{+2}$ -doped  $ThO_2$  were measured. Figure 3 shows that the TL intensity is approximately 15 times greater for pure  $ThO_2$  than for  $Ca^{+2}$ -doped  $ThO_2$ . Previous studies (8, 12) have indicated that in  $ThO_2$  the rare earth ions, in particular  $Pr^{+3}$  (500 nm emission), act as the electron-hole recombination sites. The TL intensity, therefore, must be proportional to the luminescence efficiency of the rare earth ion ( $Pr^{+3}$ ) at the temperature at which the electron-hole recombination takes place. Figure 5 indicates that in the temperature region 400°-600°K the luminescence efficiency of the  $Pr^{+3}$  is much less for  $Ca^{+2}$ -doped  $ThO_2$  than for pure  $ThO_2$ . Hence the observed TL intensity is also much less for  $Ca^{+2}$ -doped crystals than for pure  $ThO_2$ .

The presence of  $Ca^{+2}$  and  $Y^{+3}$  ions also influences the temperature dependence of the 450 nm emission intensity (Fig. 4). Both  $Ca^{+2}$  and  $Y^{+3}$  greatly enhance the 450 nm emission in the region 100°-350°K. The centers giving rise to the 450 nm emission act as the main recombination centers for electron-hole recombination at temperatures below 400°K (12). One would expect, therefore, that the TL emission intensity in this temperature range would be greater for  $Ca^{+2}$ - and  $Y^{+3}$ -doped  $ThO_2$  than for pure  $ThO_2$ . Recent results (36) indicate that this is indeed the case.

### Conclusions

Photoluminescence occurs in  $ThO_2$  as a result of u.v. excitation. A broad asymmetric emission band at 450 nm may be due to closely overlapping F and  $F^+$  centers possibly associated with the reduced state of variable valence impurities. A doublet at 497 and 503 nm results from rare earth impurity  $Pr^{+3}$ . A second broad band occurs at 540 nm whose origin is unknown. Finally an emission band at 785 nm which probably arises from the presence of transition metal impurities is present in oxidized crystals.  $Fe^{+3}$ ,  $Cr^{+3}$ , or  $Ti^{+2}$  are possible sources.

The photoluminescence can be altered by varying the annealing atmosphere, the duration of the anneal, the cooling rate, the time of u.v. excitation, and the temperature of excitation. The photoluminescence can also

be changed by deliberate doping with  $\text{Ca}^{+2}$ ,  $\text{Y}^{+3}$ , or  $\text{Ta}^{+5}$ . Impurities have a very marked effect on the temperature dependence of the luminescence efficiency of the emission centers. These effects can explain many of the variations observed in the thermoluminescence of pure and doped  $\text{ThO}_2$ .

#### Acknowledgments

The spark source mass spectrometry analysis was performed by Mr. I. H. Crocker.

Manuscript submitted July 14, 1975; revised manuscript received Oct. 27, 1975. This was Paper 196 presented at the Toronto, Canada, Meeting of the Society, May 11-16, 1975.

Any discussion of this paper will appear in a Discussion Section to be published in the December 1976 JOURNAL. All discussions for the December 1976 Discussion Section should be submitted by Aug. 1, 1976.

Publication costs of this article were partially assisted by Atomic Energy of Canada Limited.

#### REFERENCES

- O. A. Weinreich and W. E. Danforth, *Phys. Rev.*, **88**, 953 (1952).
- W. E. Danforth, "Thoria in Electronics," *Advances in Electronics*, Vol. 5, Academic Press, New York (1953).
- J. H. Bodine and F. B. Thiess, *Phys. Rev.*, **98**, 1532 (1955).
- J. L. Bates, AEC Report BNWL 457 (1967).
- B. G. Childs, P. J. Harvey, and J. B. Hallett, *J. Am. Ceram. Soc.*, **53**, 431 (1970).
- R. C. Linares, *J. Phys. Chem. Solids*, **28**, 1285 (1967).
- P. J. Harvey, B. G. Childs, and J. Moerman, *J. Am. Ceram. Soc.*, **56**, 134 (1973).
- P. J. Harvey and J. B. Hallett, *J. Solid State Chem.*, **12**, 219 (1975).
- J. R. Saranathan, V. A. Fassel, and E. L. DeKalb, *Anal. Chem.*, **42**, 325 (1970).
- J. T. Randall and M. H. F. Wilkins, *Proc. Roy. Soc. London, Ser. A*, **184**, 366 (1945).
- G. F. J. Garlick and M. H. F. Wilkins, *ibid.*, **184**, 408 (1945).
- P. J. Harvey and J. B. Hallett, *Proceedings 4th International Conference on Luminescence Dosimetry*, Cracow, Poland, pp. 489-505 (August 1974).
- A. K. Trofimov, *Bull. Acad. Sci. USSR, Phys. Ser.*, **25**, 453 (1961).
- M. S. Orlov and I. G. Saitkulov, *Izv. Akad. Nauk SSSR, Ser. Fiz.*, **37**, 458 (1973).
- J. C. Kemp, W. M. Ziniker, and E. B. Hensley, *Phys. Letters*, **25A**, 43 (1967).
- Y. Chen, J. L. Kolopus, and W. A. Sibley, *Phys. Rev.*, **186**, 865 (1969).
- W. Low and D. Shaltiel, *J. Phys. Chem. Solids*, **6**, 315 (1958).
- V. I. Neely, J. B. Gruber, and W. J. Gray, *Phys. Rev.*, **158**, 809 (1967).
- G. S. Tint, Ph.D. Thesis, Temple University, Philadelphia (1970).
- M. M. Abraham, R. A. Weeks, G. W. Clark, and C. B. Finch, *Phys. Rev.*, **137A**, 138 (1965).
- M. M. Abraham, R. A. Weeks, and E. J. Lee, *J. Phys. Chem. Solids*, **26**, 1249 (1965).
- J. L. Kolopus, C. B. Finch, and M. M. Abraham, *Phys. Rev.*, **2B**, 2040 (1970).
- M. D. Sturge, *ibid.*, **130**, 639 (1963).
- A. L. Schawlow, *J. Appl. Phys. (Suppl)*, **33**, 395 (1962).
- B. Henderson and T. P. P. Hall, *Proc. Phys. Soc.*, **90**, 511 (1967).
- J. E. Wertz and P. Auzins, *Phys. Rev.*, **139A**, 1645 (1967).
- B. G. Wynbourne, Editor, "Spectroscopic Properties of Rare Earths," Interscience Publishers, New York (1965).
- G. Blasse and A. Bril, *Philips Tech. Rev.*, **31**, 333 (1970).
- R. Reisfeld, *Nat. Bur. Std., Special Publ.* 378, 203 (1973).
- F. Seitz, *Trans. Faraday Soc.*, **35**, 74 (1939).
- D. L. Dexter, C. C. Klick, and G. A. Russell, *Phys. Rev.*, **100**, 603 (1955).
- J. L. Sommerdijk, W. L. Wanmaker, and J. G. Verriet, *J. Luminescence*, **S**, 297 (1972).
- R. F. Wood and T. M. Wilson, *Solid State Comm.*, **16**, 545 (1975).
- J. B. Bates and R. F. Wood, *ibid.*, To be published.
- C. W. Struck and W. H. Fonger, *J. Luminescence*, **11**, 1 (1975).
- P. J. Harvey and J. B. Hallett, To be published.

## Growth and Structure of Polycrystalline Indium Phosphide Layers on Molybdenum Sheets

Tadashi Saitoh, Sunao Matsubara, and Shigekazu Minagawa\*

Central Research Laboratory, Hitachi, Limited, Kokubunji, Tokyo, Japan

#### ABSTRACT

Pinholeless polycrystalline indium phosphide layers were grown on molybdenum sheets at temperatures lower than 600°C using indium and phosphorus trichloride as the source materials. The low activation energy of the deposition rates and weak dependence of the rates on the partial pressure of indium monochloride suggest that surface processes play an important role in the growth of polycrystalline films. It was ascertained by an x-ray diffraction measurement that the {110} and {331} orientations become noticeable with increasing thickness at higher temperatures, whereas the <111> orientation is dominant at lower growth temperatures. The development of the <110> orientation produces films with a columnar structure, which could be explained by the dependence of the growth rate on the crystallographic orientation.

Indium phosphide is a promising material for solar cells because the indium phosphide cell has high theoretical conversion efficiency (1). In order to obtain low-cost solar cells for terrestrial use, it is necessary to

fabricate thin-film solar cells of polycrystalline indium phosphide on low-cost substrate materials.

To date, few papers have been published on the preparation of polycrystalline indium phosphide, although research on the epitaxial growth had been carried out (2-4). In this paper, polycrystalline layers were de-

\* Electrochemical Society Active Member.

Key words: deposition rates, grain size, orientation.

posited on thin molybdenum sheets by the reaction of indium with phosphorus trichloride in a hydrogen atmosphere. The indium transport reaction and the process for the deposition of pinhole-free indium phosphide were examined. The rate-determining step of the deposition is discussed. The grain size of the deposited film, which is generally required to be larger than the minority-carrier diffusion length, was measured as a function of deposition conditions since highly oriented polycrystalline films may be essential to realize efficient solar cells (5, 6). The orientation of the polycrystalline films was characterized by the x-ray method and reflection electron micrography.

### Experimental

**Film growth.**—Polycrystalline indium phosphide was deposited on 50  $\mu\text{m}$  thick molybdenum sheets by reaction of In and  $\text{PCl}_3$  in hydrogen. The molybdenum sheets were selected because of the small thermal expansion coefficient mismatch between molybdenum and indium phosphide and because of its chemical stability in a growth atmosphere. Prior to growth, the sheets were ultrasonically cleaned in trichloroethylene and subsequently in methanol, and chemically etched in a  $1 \text{ H}_2\text{SO}_4\text{-1 HNO}_3\text{-3 H}_2\text{O}$  solution.

The deposition was carried out in a horizontal reactor with a conventional gas feed system (2, 3), typical for an epitaxial growth of III-V semiconducting materials. The temperature of the indium source was held at  $750^\circ\text{C}$  and the temperature of the molybdenum sheets was in the range of  $450^\circ\text{C}$ – $650^\circ\text{C}$ . A typical flow rate of the hydrogen gas was  $200 \text{ cm}^3/\text{min}$  (at room temperature). The partial pressure of  $\text{PCl}_3$  in the feed gas was  $2\text{--}13 \times 10^{-3} \text{ atm}$ . The thickness of the deposited layers was determined by measuring the surface line profiles of step-etched samples.

**Structure.**—Measured x-ray intensities ( $\text{CuK}_\alpha$  radiation) were normalized by the theoretical values calculated by the following equation (7)

$$I = C \cdot M \cdot P \cdot L \cdot |F|^2 \cdot A \cdot T \quad [1]$$

where  $C$  is a constant,  $M$  the multiplicity of the planes,  $P$  the polarization factor,  $L$  the Lorentz factor,  $F$  the structure factor,  $A$  the absorption factor, and  $T$  the temperature factor. For powder samples with a plate-like shape, the absorption factor is described as (7)

$$A = A_0 \left\{ 1 - \exp\left(-\frac{2\mu t}{\sin \theta}\right) \right\} \quad [2]$$

where  $A_0$  is a constant,  $\mu$  the linear absorption coefficient,  $t$  the thickness, and  $\theta$  the x-ray diffraction angle.  $A$  is almost equal to  $A_0$  if the thickness,  $t$ , of indium phosphide is more than  $20 \mu\text{m}$ . The equations used to calculate other factors are those found in Guinier's book (7).

### Results and Discussions

**Transport of indium.**—A source temperature of  $750^\circ\text{C}$  was adopted in this experiment because a transport efficiency defined below was reported to saturate and approach an equilibrium value at temperatures higher than  $700^\circ\text{C}$  (8). First, the amount of indium consumed during the reaction was measured as a function of the reaction time at a linear flow rate of  $0.75 \text{ cm}/\text{sec}$ , calculated at  $750^\circ\text{C}$ . The amount was found to increase in proportion to the reaction time at  $\text{PCl}_3$  partial pressures of  $2.3 \times 10^{-3}$ – $1.2 \times 10^{-2} \text{ atm}$ . As for the effect of the  $\text{PCl}_3$  partial pressures in the feed gas, the transport rate of indium increased in proportion to the  $\text{PCl}_3$  partial pressure as indicated in Fig. 1.

The transport efficiency, defined by the ratio of the number of moles of indium transported to the number of moles of chlorine fed during the growth time, was 95%. This is in good agreement with the 99% obtained by thermodynamic calculation and an observed value reported for the same reaction in a vertical reactor (4). The result shows that the transport reaction around the source occurs under equilibrium conditions.

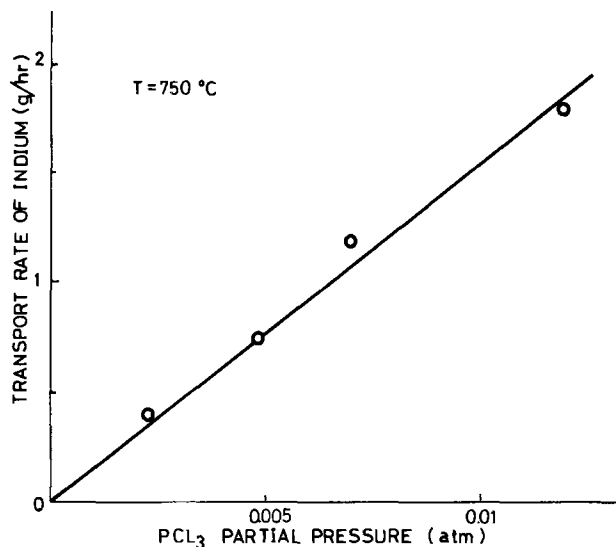
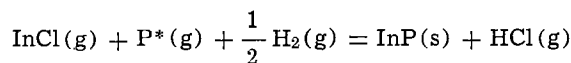


Fig. 1. Transport rate of indium as a function of  $\text{PCl}_3$  partial pressure. The temperature of the indium source is  $750^\circ\text{C}$ .

**Deposition of indium phosphide.**—The deposition of polycrystalline indium phosphide was carried out at temperatures lower than  $650^\circ\text{C}$  which had been used previously for epitaxial growth on single crystal substrates (2-4). In a film deposited at  $650^\circ\text{C}$ , there existed small holes where molybdenum surfaces could be seen, although the grain size was larger than that in a film prepared at lower temperatures. Temperatures lower than  $600^\circ\text{C}$  were found to be useful to obtain homogeneous films without pinholes. This suggests that sufficient supersaturation is necessary for uniform polycrystalline growth.

The thicknesses of the polycrystalline deposits were found to increase in proportion to the deposition time except in the initial stage of the deposition. From an Arrhenius plot of the deposition rates shown in Fig. 2, the activation energy was determined to be 15 kcal/mole. This agrees approximately with the activation energies of epitaxial growth on low-index planes (4).

Mass spectroscopic analysis (8) of gases in the deposition zone has shown that indium monochloride reacts with phosphorus compounds according to the reaction



where  $\text{P}^*$  represents  $\text{P}_2$  and  $\text{P}_4$ . Assuming that the

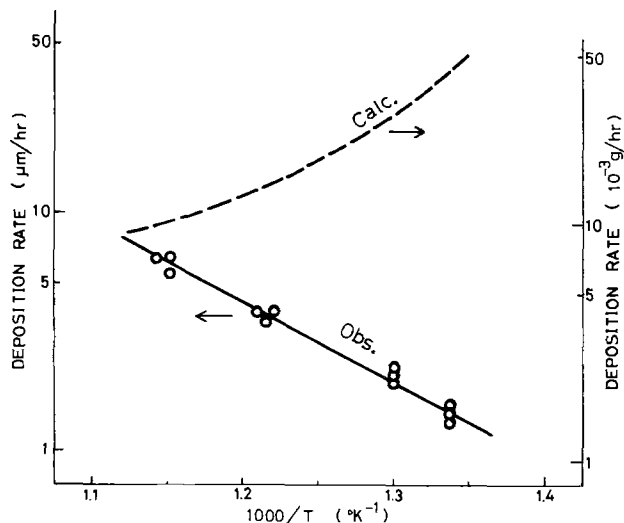


Fig. 2. Arrhenius plot of deposition rate for polycrystalline indium phosphide. The dashed line is calculated under thermodynamic equilibrium. The  $\text{PCl}_3$  partial pressure is  $7.2 \times 10^{-3} \text{ atm}$ .

phosphorus compound in the gas phase is the tetramer, deposition rates were calculated using the above equation. As indicated by the dashed line in Fig. 2, differences were observed on the Arrhenius plots between calculated and observed values. This result shows that the deposition reaction cannot be described as being carried out under thermodynamic equilibrium.

The deposition rate was examined as a function of the  $\text{PCl}_3$  partial pressure which corresponds to one-third of the  $\text{InCl}$  partial pressure appearing in Eq. [3]. The rate increases only slightly with increasing  $\text{PCl}_3$  partial pressure as shown in Fig. 3.

The weak dependence of the deposition rate on the partial pressure suggests that the deposition process is not limited by mass transfer of reactants in a gas phase but by surface processes such as surface reaction, surface diffusion, adsorption and desorption processes.

**Grain size.**—The grain size of the polycrystalline indium phosphide layers tends to increase both with increasing deposition temperature and thickness; moreover, the grain size is not always homogeneous. In the case of a layer deposited at  $600^\circ\text{C}$ , the mean value of the grain size measured by the Fullman method (9) was about  $7\ \mu\text{m}$  (about  $1\ \mu\text{m}$  in a film deposited at  $500^\circ\text{C}$ ). Roughness of the surface was about  $2\ \mu\text{m}$  for a  $12\ \mu\text{m}$  thick film deposited at  $600^\circ\text{C}$ .

The mean grain size increased and saturated with increasing film thickness as shown in Fig. 4. This tendency is related to the observation that small nuclei on a molybdenum surface grow in size and finally coalesce with each other.

A columnar structure in a cross section of the film shown in Fig. 5 suggests the saturation of the grain size. The columnar structure indicates that each grain grows mostly perpendicular to the substrate. The columns were found to develop with increasing growth temperature and thickness, which relates to the development of preferred orientation as mentioned below. However, the columns were found not to grow immediately from the substrate and not to exist in layers deposited at temperatures lower than about  $500^\circ\text{C}$ .

**Preferred orientation.**—X-ray diffraction spectra of InP films consisted primarily of diffraction peaks of low-index faces such as  $\{111\}$ ,  $\{110\}$ ,  $\{311\}$ , and  $\{331\}$ . Also, relative intensities of the diffracted peaks were found to vary with the growth temperature and the thickness of the film. For a film deposited at  $600^\circ\text{C}$ ,  $\{110\}$  and  $\{331\}$  faces developed, whereas  $\{111\}$  and  $\{311\}$  planes diminished with the thicknesses for films thicker than  $5\ \mu\text{m}$  as shown in Fig. 6. On the other hand, layers thinner than  $5\ \mu\text{m}$  were random in orientation. As for a film deposited at  $500^\circ\text{C}$ , the diffracted

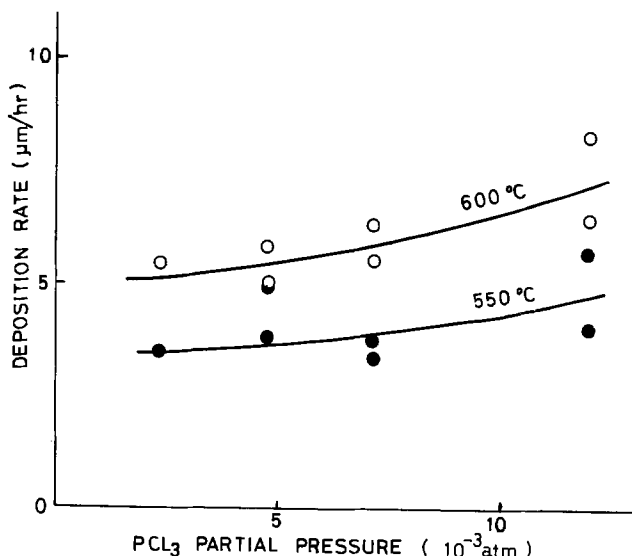


Fig. 3. The effect of  $\text{PCl}_3$  partial pressure in the feed gas on the deposition rate of polycrystalline layers.

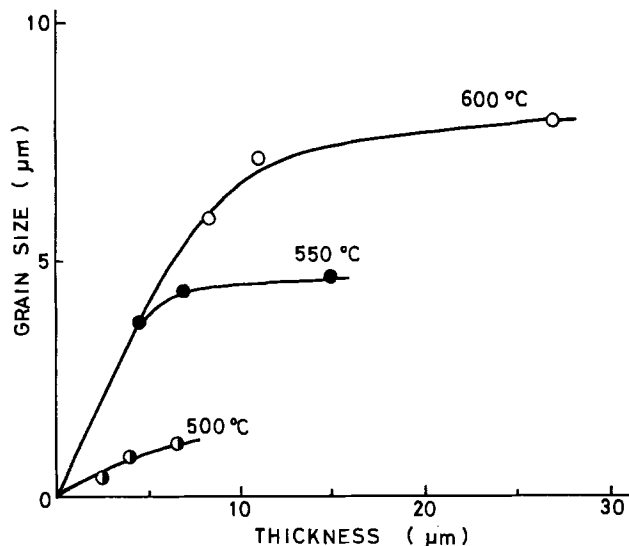


Fig. 4. The variation of grain size with thickness at various substrate temperatures.

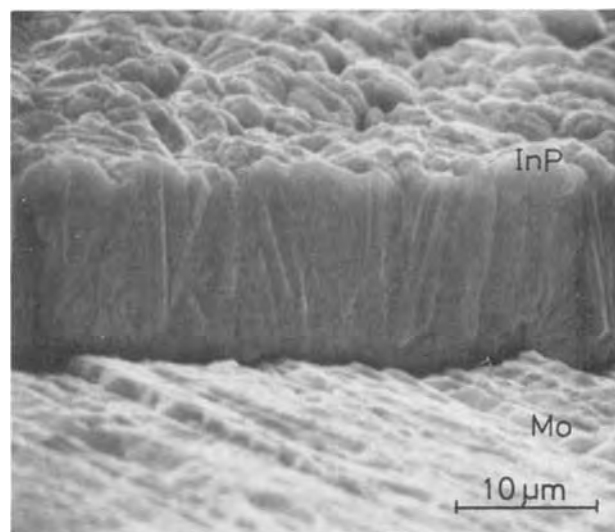


Fig. 5. Scanning electron micrograph of InP polycrystalline deposit on molybdenum.

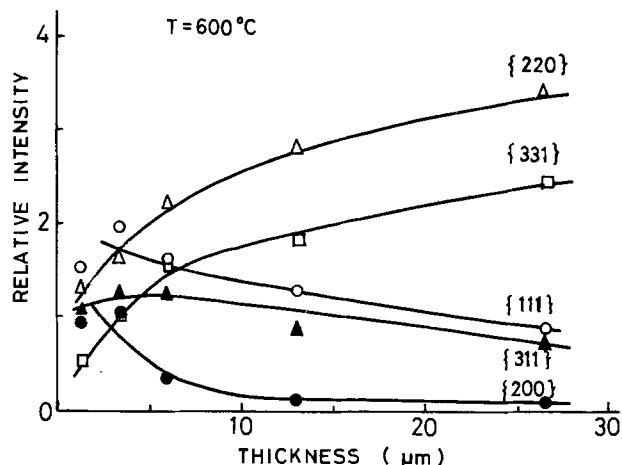


Fig. 6. The variation of relative intensity of x-ray diffraction with thickness for various crystal planes in the films deposited at  $600^\circ\text{C}$ .

intensities decreased in the order of  $\{111\} > \{220\} > \{311\} > \{331\} \cong \{200\}$  and the tendency held for films varying in thickness. However, the degree of preferred orientation was not found strong.

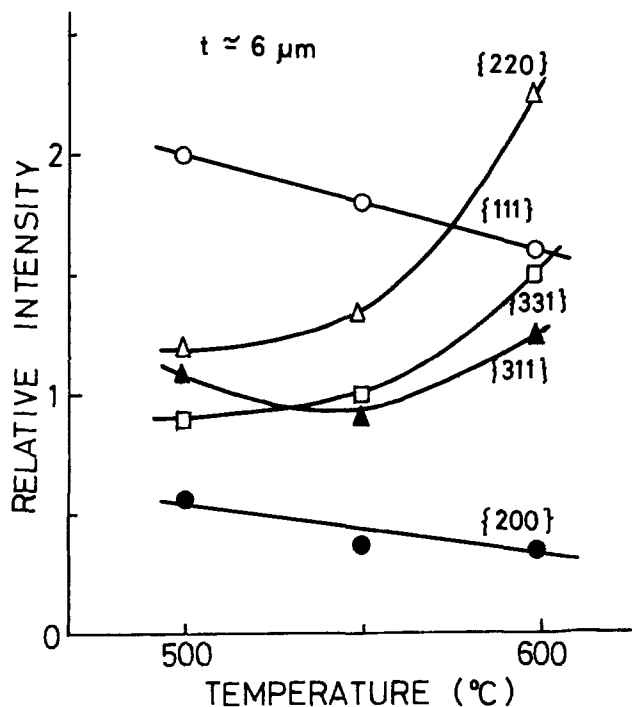


Fig. 7. The variation of relative diffracted intensity with deposition temperature for various crystal planes in the films with thickness of about  $6 \mu\text{m}$ .

Next, we examined the effect of growth temperature on the orientation of the films. In the case of thin films (about  $1 \mu\text{m}$ ), relatively random orientation was obtained irrespective of various growth temperatures, although  $\{111\}$  orientation developed to some extent. For the thicker film ( $6 \mu\text{m}$ ) shown in Fig. 7,  $\{110\}$  and  $\{331\}$  planes developed,  $\{111\}$  and  $\{100\}$  planes diminished, and the  $\{311\}$  plane did not change with increasing growth temperatures. The inverse tendency between the  $\{110\}$  and  $\{111\}$  orientations for increasing temperature is also similar to the result obtained for polycrystalline silicon films prepared by pyrolysis of silane on an oxidized silicon surface (10).

In order to examine the effect of the partial pressure of reactants on the orientation, the partial pressure of  $\text{PCl}_3$  was varied from  $2 \times 10^{-3}$  to  $1 \times 10^{-2}$  atm. However, no effect in preferred orientation was observed.

In the x-ray method, the information is obtained over an x-ray penetration depth of tens of microns, while reflection electron microscopy provides information on the degree of preferred orientation with less than a micron of the crystal surface. The reflection electron micrographs of the film deposited at  $600^\circ\text{C}$  showed random spots. This indicates that the surface consists of relatively large grains with random orientation. As the  $\{220\}$  intensity was dominant in the x-ray diffraction, the crystallites are oriented in the  $\langle 110 \rangle$  growth direction, but have randomly oriented surfaces.

On the other hand, for films grown at temperatures less than  $550^\circ\text{C}$ , the electron micrographs consisted of Debye rings. And the micrographs showed that among the various planes, the  $\{111\}$  plane was relatively parallel to the substrate surface, but the  $\{110\}$  face was inclined or random in the orientation. Especially, the orientation of the  $\{111\}$  face is consistent with that obtained by x-ray diffraction. This indicates that the orientation near the surface is equal to that in the film.

The  $\langle 110 \rangle$  preferred orientation of InP films prepared at  $600^\circ\text{C}$  is in agreement with that of polycrystalline silicon films (10). The  $\{110\}$  face was reported to be the plane with the fastest growth rate among low index planes for InP (4) and Si (11). In addition, for an epitaxial growth of indium phosphide, the growth rate was in the order of  $\{110\} > \{111\}\text{B} > \{100\}$  surfaces (4), corresponding to the order of the orientation. Therefore, in the polycrystalline growth of InP, the planes with higher growth rates grow preferentially and, thus, other planes cannot grow in the direction parallel to the substrate surface. As a result, the preferred orientation is formed for the planes with higher growth rates.

### Conclusions

Polycrystalline indium phosphide was deposited on molybdenum substrates by vapor-phase growth to investigate the growth mechanism and the structure of the film. The conclusions obtained are as follows:

1. The indium transport reaction with phosphorus trichloride occurs under thermodynamic equilibrium.
2. Homogeneous polycrystalline films are obtained at temperatures lower than  $600^\circ\text{C}$ . The activation energy of 15 kcal/mole and the dependence of the deposition rate on the partial pressure of the reactant suggests that surface processes determine the deposition rate.
3. The grain size depends on the deposition temperature but is independent of the partial pressure of  $\text{PCl}_3$  in the feed gas.
4. The crystal grains are oriented in the direction of  $\{111\}$  at low temperatures, but the  $\{110\}$  orientation and orientations near the  $\langle 110 \rangle$  directions developed at higher temperatures and with increasing the thickness.

### Acknowledgments

The authors wish to thank R. Takahashi for his advice on the vapor deposition and K. Ohbuchi for performing the x-ray diffraction experiments. The authors are also grateful to Dr. E. Maruyama for his critical reading of this manuscript and Drs. Y. Otomo and T. Tokuyama for their encouragement.

Manuscript submitted Sept. 22, 1975; revised manuscript received Nov. 4, 1975.

Any discussion of this paper will appear in a Discussion Section to be published in the December 1976 JOURNAL. All discussions for the December 1976 Discussion Section should be submitted by Aug. 1, 1976.

Publication costs of this article were partially assisted by Hitachi, Limited.

### REFERENCES

1. J. J. Wysocki and P. Rappaport, *J. Appl. Phys.*, **31**, 571 (1960).
2. H. Seki and M. Kinoshita, *Japan. J. Appl. Phys.*, **8**, 1142 (1968).
3. M. C. Hales, J. R. Knight, and C. W. Wilkins, Proc. 3rd Int. Symp. on Gallium Arsenide, p. 50 (1970).
4. O. Mizuno, *Japan. J. Appl. Phys.*, **14**, 451 (1975).
5. F. A. Shirland, *Advanced Energy Conversion*, **6**, 201 (1966).
6. P. H. Fang and L. Ephrath, *Appl. Phys. Letters*, **25**, 523 (1974).
7. A. Guinier, "X-ray Crystallographic Technology," Hilger and Watts Ltd., London (1952).
8. V. S. Ban and M. Ettenberg, *J. Phys. Chem. Solids*, **34**, 1119 (1973).
9. R. L. Fullman, *J. Metals*, March, 447 (1953).
10. T. I. Kamins and T. R. Cass, *Thin Solid Films*, **16**, 147 (1973).
11. S. K. Tung, *This Journal*, **112**, 436 (1965).



# A High Speed X-Ray Topographic Camera for Semiconductor Wafer Evaluation

D. L. Parker and W. A. Porter

*Institute for Solid State Electronics, Department of Electrical Engineering,  
Texas A&M University, College Station, Texas 77843*

## ABSTRACT

A new x-ray topographic camera is described which reduces the exposure time for the production of useful topographs of semiconductor wafers by at least one order of magnitude. The gain is achieved by holding the wafer with a curved vacuum chuck such that rays from a distant point source strike every portion of the wafer at the Bragg angle. Thus the Rowland focusing feature which has previously been used in many x-ray instruments for spectroscopy and diffractometry has been incorporated in the new camera. Included is an x-ray topograph of an entire 2 in. silicon wafer made on dental film during a 30 sec exposure.

For the past several years x-ray topography has been recognized as the best nondestructive means for the assessment of crystal lattice damage created during each processing step in the fabrication of semiconductor devices (1). However, essentially all previous applications have been in the research groups of the larger semiconductor manufacturers, government labs, and academic institutions. The high cost per topograph has prevented any widespread application of the technique in production process control. The high cost is due to a combination of the expensive equipment required, highly trained personnel, and long exposure times that have been required using conventional techniques. The new x-ray camera described here can be expected to significantly reduce the cost per topograph through the reduced exposure time required.

### The Camera Design

The new camera is of the Berg-Barrett type with the additional feature that the specimen is elastically deformed such that all rays from a distant point source of x-rays simultaneously satisfy the Bragg condition for a given set of lattice planes. Thus, the fraction of the total flux from the source that is actually used is increased with a corresponding reduction in exposure time. The exact shape into which the wafer must be deformed can be understood from the diagram in Fig. 1. The curved line represents the path whose tangent line at any point makes a constant angle  $\psi$  with a ray from the origin to that point. Elementary calculus may be used to show that the locus is an exponential spiral, i.e.

$$\rho = d \exp [\phi / \tan \psi]$$

where  $\rho$  and  $\phi$  are the plane polar coordinates and  $d$  is a constant. The local radius of curvature is given by

$$R = \rho / \sin \psi$$

The wafer is, of course, a three-dimensional object which requires compound bending in order to simultaneously satisfy the Bragg condition at all points on its surface for rays diverging from a distant point source. Careful consideration will show that the necessary wafer curvature in planes perpendicular to the central scattering plane is not unique. It is only necessary that the wafer surface take the curved shape shown in Fig. 1 in all planes which (i) contain the point source, and (ii) are perpendicular to the diffracting planes. In practice the wafer curvature (if any) in planes perpendicular to the central scattering plane is of minor importance just as is the case in conventional topography.

Key words: dislocation, quality control, silicon, processing, diffraction.

Several wafer-bending schemes were tried before a curved vacuum chuck was selected as the most reliable and adaptable technique. A concave spherical shape is currently being used for the vacuum chuck instead of the exact spiral cross section discussed above. A spherical shape was chosen for the following practical considerations:

1. No satisfactory means was found for accurately machining the exponential spiral shape within the necessary tolerances.

2. Random variations in the crystallographic orientation from wafer to wafer (small variations in  $\psi$ ) make the achievement of perfect bending of all wafers difficult.

3. The symmetry of the spherical chuck allows two alignment axes to be used without remounting the specimen after the initial alignment prior to the exposure.

In order to predict the error introduced by using the spherical chuck the following calculation can be made. Let a circle of radius  $d/\sin\psi$  osculate the spiral at the point  $x=d$  and  $y=0$ . The slope of the circle at points intercepted by rays from the origin is given by

$$\left. \frac{dy}{dx} \right|_{\text{circle}} = \tan(\gamma + \phi)$$

where

$$\gamma = \cos^{-1}(\cos\phi \cos\psi)$$

The slope of the spiral at points intercepted by the same rays is given by

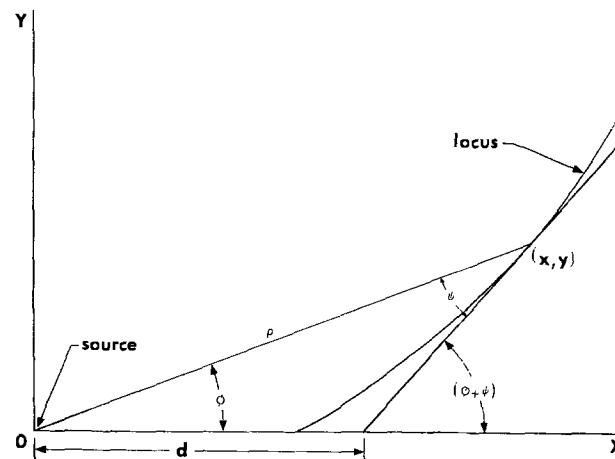


Fig. 1. The curved line is the exponential spiral  $\rho = d \exp(\phi / \tan \psi)$  which is the locus that intersects all rays from the origin at the same angle  $\psi$ .

$$\left. \frac{dy}{dx} \right|_{\text{spiral}} = \tan(\phi + \psi)$$

Thus, the angular error,  $\delta$ , is given by

$$\delta = \gamma - \psi$$

This theoretical angular error is considerably smaller than the experimental errors observed to date. Indeed, significant improvements in the chuck design are still possible. The failure of the wafer to conform exactly to the chuck shape is related to the partial vacuum pressure, the distribution and size of the vacuum feed points, as well as the hardness of the chuck material. Work continues on improving the chuck design to approach the predicted perfection of the exponential spiral. The problem that no single setting of the deformed wafer will simultaneously diffract x-rays from all portions of its surface is overcome by a slight rotation of the crystal (with film) during the exposure. This rotation is done about an axis through the center of the wafer and perpendicular to the central scattering plane. Thus, all portions of the wafer have equal opportunity to participate in the formation of the image provided the rate of rotation is constant.

### Experimental

Although the curved wafer technique is applicable to a wide variety of materials and radiations, work to date has only been done on (111) silicon using copper target radiation and the (440) reflection. This choice makes the angle  $\psi$  about  $18.1^\circ$  and the total scattering angle ( $2\theta$ ) for  $\text{CuK}\alpha_1$   $106.71^\circ$ . Thus, the diffracted rays leave the wafer at about  $88.6^\circ$  or almost normal to the slice. The distance from the x-ray source to the center of the specimen was chosen to be 30 in. The vacuum chuck is 3 in. in diameter, made of glass, with a spherical depression whose lowest point is at the center of the chuck. The radius of the chuck curvature was chosen as 96 in. which matches the exact spiral shape at the center. With a single vacuum feed hole in the center, the chuck can receive any size slice up to 3 in. in diameter. Of course, each combination of radiation, Bragg reflection, and crystal orientation in general, requires a separate vacuum chuck. A scatter tube is used along with various lead collimators positioned in a slot on the end nearest the specimen. Each lead collimator has a different size elliptical hole to allow total illumination of several wafer sizes and to minimize unwanted scattering from the chuck itself. The film is placed parallel to and 1 in. from the specimen. This distance is optimum to prevent interference with the incoming x-rays from the source.

The essential features of the camera are shown in Fig. 2. Provision is made to rotate the chuck about an axis through the center of the wafer and perpendicular to the drawing in Fig. 2. This rotation is used both for the initial setting of the camera as well as the short scan during the exposure. The film rotates with the

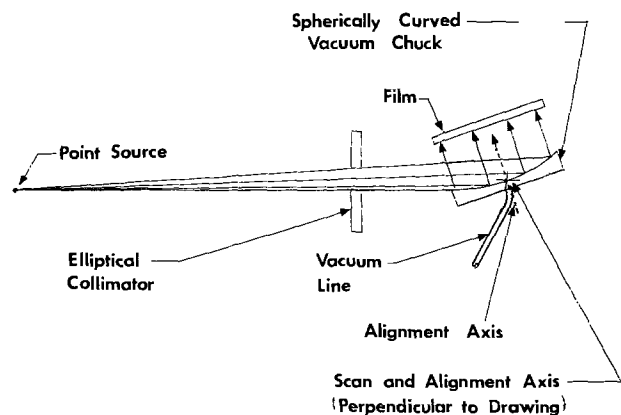


Fig. 2. Schematic diagram of the x-ray camera

chuck about this axis. Provision is also made for rotation of the chuck about an axis in the plane of the drawing, through the center of the wafer, and perpendicular to the wafer. This rotation is used in the initial setting of the camera. A flat edge attached to the face of the chuck to match the wafer flat allows a sequence of wafers from the same batch to be photographed with a minimum of initial adjustments from wafer to wafer.

The x-ray topograph shown in Fig. 3 is of a 2 in. silicon wafer. The wafer had completed all thermal processing steps including metallization and annealing. The devices visible in the topograph are various sized diodes and capacitors. The slip-plane damage near the top and sides was deliberately introduced after the diffusion step as part of a defect-device performance correlation experiment.

The x-ray source was a Rigaku rotating anode generator with copper target operating at 35 kV and 100 mA. The target focus was  $0.5 \times 5$  mm with a  $6^\circ$  take-off angle using one of the point source windows. The film was Kodak Dental Type DF46 ( $2\frac{1}{4} \times 3$  in.) with a 30 sec exposure. The scan during the exposure was  $0.25^\circ$  centered on the  $\text{K}\alpha_1$  diffraction peak. This effectively excludes most of the  $\text{K}\alpha_2$  image since the angular separation of the two peaks is about  $0.2^\circ$  for this reflection. The rotation during exposure effectively fills in the otherwise washed-out areas that are due to improper bending. However, rotation does reduce the resolution somewhat. If the wafer were perfectly spherically bent no rotation would be required due to the finite angular size of the focal spot. High resolution topographs can be made with the camera in the stationary mode with typical washed-out areas representing 20-40% of the total area of a 2 in. wafer. With the rotating anode generator the optimum exposure time for a  $25 \mu\text{m}$  emulsion nuclear tracking plate is less than 2 min and about 2 hr for a high resolution plate.

One subtle, although significant, advantage of this new camera is its immunity to the usual difficulties encountered in attempting to make topographs of bowed wafers. Conventional topographic cameras require an oscillating or automatic Bragg angle control feature to produce adequate topographs of processed wafers due to the inevitable bowing. Further, this camera is relatively immune to backside lapping damage.

During the development of this camera it was discovered that too much partial vacuum on the chuck will produce high stress points in the wafer. These

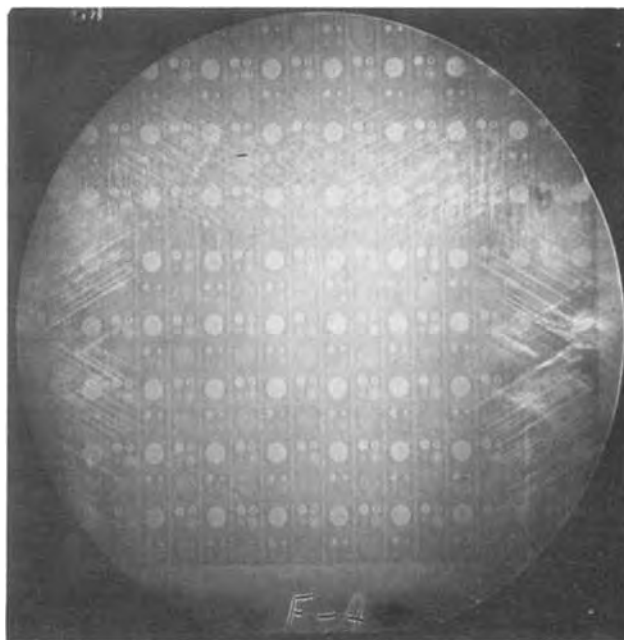


Fig. 3. An x-ray topograph (positive) of a 2 in. silicon wafer made on dental film with a 30 sec exposure.

stress points appear in the topographs as "dimples" particularly at the vacuum feed points. This problem is controlled by the use of a partial vacuum regulator. Typically, 10-15 mil wafers require only about 30 mm Hg differential pressure for bending. The stress required for bending the wafer is several orders of magnitude less than the localized stress produced by impurity atom mismatch and crystal defects. Thus, there is no evidence of the bending in the topograph and no evidence of residual damage to the wafer after the slight bending required during exposure.

### Conclusions

In the camera's present configuration and with an automatic dental film processor with a daylight loading hood, one person can produce 20-30 x-ray topographs per hour. A commercial version of the camera designed for rapid wafer loading and alignment could double this throughput. Also, at least two cameras may be operated simultaneously with the same x-ray tube. Further, real-time TV inspection is a possibility (2). These considerations make 100% evaluation of high reliability devices as well as routine quality control in-

spection at every stage of wafer processing economically feasible.

### Acknowledgments

This research is supported by NASA, Marshall Space Flight Center and Rome Air Development Center under contract NAS8-26379.

Manuscript submitted July 29, 1975; revised manuscript received Nov. 17, 1975.

Any discussion of this paper will appear in a Discussion Section to be published in the December 1976 JOURNAL. All discussions for the December 1976 Discussion Section should be submitted by Aug. 1, 1976.

Publication costs of this article were partially assisted by Texas A&M University.

### REFERENCES

1. B. Piwczyk, "X-rays Disclose an Integrated Circuit's Defects," *Solid State Technol.*, 30 (1973).
2. J.-I. Chikawa, I. Fujimoto, S. Endo, and K. Mase, in "Semiconductor Silicon 1973," H. R. Huff and R. R. Burgess, Editors, p. 448, The Electrochemical Society Symposium Series, Princeton, N.J. (1973).

## Boron Segregation at Si-SiO<sub>2</sub> Interface as a Function of Temperature and Orientation

J. W. Colby and L. E. Katz\*

*Bell Telephone Laboratories, Incorporated, Allentown, Pennsylvania 18103*

### ABSTRACT

The ion microprobe has been used to study the effects of crystal orientation and oxidation temperature on the segregation of boron at the silicon-silicon dioxide interface. The segregation coefficient was determined by measuring directly the total boron concentration in the oxide and the silicon at the interface, for (100) and (111) silicon, oxidized at 1000°, 1100°, and 1200°C in dry oxygen. It was found that boron segregation coefficients for (111) silicon are higher than those for (100) silicon for corresponding oxidation temperatures, and that these segregation coefficients decrease with increasing temperature. The experimental values of the boron segregation coefficient,  $m$ , may be described by

$$m_{(100)} = 0.03 \exp(0.52/kT)$$

$$m_{(111)} = 0.05 \exp(0.52/kT)$$

Diffusion coefficients were extracted from the experimental data using a modeling technique and agree well with the generally accepted values. The diffusion coefficients obtained for oxidizing ambient are given by

$$D_{(100)} = 0.19 \exp(-3.22/kT)$$

$$D_{(111)} = 2.04 \exp(-3.57/kT)$$

Upon thermal oxidation of silicon, an interface is formed which separates the solid silicon from the solid SiO<sub>2</sub> and which advances into the Si as oxidation proceeds. Impurities will redistribute at the interface until their chemical potentials on each side of the interface are equal. The ratio of the equilibrium concentration of boron in silicon dioxide to the equilibrium concentration of boron in silicon at the interface is called the equilibrium segregation coefficient. It is possible that the equilibrium segregation coefficient may not be identical to the experimental segregation coefficient. This will primarily be determined by the chemical potential differences and the kinetics of redistribution at the interface. The experimental segregation coefficient is called the effective or interface segregation coefficient.

Theoretical work has not determined the equilibrium segregation coefficient but merely bracketed it within

\* Electrochemical Society Active Member.

Key words: diffusion, ion microprobe, segregation coefficient.

the range of 10<sup>-3</sup>-10<sup>+3</sup> (1). Several studies (2-8) have been made in which a model for diffusion has been formulated, diffusion profiles experimentally determined in the silicon, and a value of the segregation coefficient chosen to force the data to fit the model. Values determined in this way have generally been in the range of 1-10.

Prince and Schwetmann (9) have studied segregation of boron from an implanted source, following steam oxidation. They used both step anodization and ion microprobe analysis to obtain profiles in the silicon and then used a modeling procedure to obtain the segregation coefficient. Their values of segregation coefficient for (111) wafers ranged from ~1.8 at 1200°C to ~5 at 1050°C.

The ion microprobe has been used in this study to determine the boron concentration on both sides of the interface thus providing a direct measure of the segregation coefficient. This avoids dependence on a modeling procedure as required by the above studies

(2-8). Such a technique has been employed (10, 11) previously. In one such study a value  $\sim 2$  for the segregation coefficient of boron in silicon is quoted, however, such details as temperature of diffusion are not presented. We present here a study of the effect of orientation and temperature on the segregation coefficient of boron in silicon.

### Experimental

Wafers from Czochralski grown crystals, boron doped ( $\sim 2 \times 10^{19}/\text{cm}^3$ ), with (100) and (111) orientations were used for these studies. Following appropriate cleaning, wafers of each orientation were oxidized (100% dry  $\text{O}_2$ ) at 1000°, 1100°, and 1200°C for 20, 8, and 5 hr, respectively. The times were chosen to keep the oxide thickness approximately in the 4000-5000Å range.

Both the ion microprobe mass analyzer (IMMA)<sup>1</sup> and the direct imaging ion microscope<sup>2</sup> were utilized in the study. The bombarding or primary ions were  $^{16}\text{O}_2^+$  at current densities (in the static beam of  $\sim 3\text{-}5 \text{ mA}/\text{cm}^2$ ). The beams were rastered in both machines and the secondary ions  $^{11}\text{B}^+$ ,  $^{30}\text{Si}^+$ , and  $^{28}\text{Si}^{++}$  were monitored and apertured to reduce crater sidewall effects. Values obtained from both machines agreed within two sigma limits.

The oxides were thinned to approximately 300Å and the oxide on the back of the wafer was completely removed prior to profiling, to reduce the effects of charging. As long as the oxide is sufficiently thin to allow some leakage current to flow, space charge does not become a problem, and stable profiles may be obtained even with a positive primary beam. The profiling was initiated in the oxide and continued across the interface into the silicon. The data were reduced to concentration by comparison with uniformly doped standards (boron-doped silicon and silica) which had previously been analyzed by the electron microprobe. Analyses obtained in this way have been shown to be accurate to within  $\pm 5\%$  relative (12). Depth calibration is accurate to within  $\pm 2\%$  (12). It should also be mentioned that for equivalent conditions of current density and accelerating potential,  $\text{SiO}_2$  sputters approximately 8% faster than silicon. This difference in sputtering rate must be taken into account when converting ion probe data to depth profile.

### Results and Discussion

A typical ion probe profile, reduced to concentration, is shown in Fig. 1. The boron concentration is shown in depth through the oxide, across the interface and into the silicon. The bulk silicon value,  $C_B$ , was measured at a depth  $>5 \mu\text{m}$  and is also shown.

Once the data has been appropriately reduced to concentration values as discussed above, the segregation coefficient of boron at the Si-SiO<sub>2</sub> interface is directly obtained by dividing the maximum value of boron concentration in the SiO<sub>2</sub> ( $C_0$ ) immediately adjacent to the interface by the minimum boron concentration in the silicon ( $C_s$ ) immediately adjacent to the interface as shown by Fig. 1 This has been done for the three temperatures and two orientations considered and the results are shown in Fig. 2. The results presented in Fig. 2 are an average of three or more determinations. The two sigma limits are also shown. It is immediately obvious that the segregation coefficient for (111) orientation is higher than for (100) orientation over the 1000°-1200°C temperature range considered. From the data, one obtains the following equations describing the segregation coefficient as a function of temperature

$$m = 0.03e^{0.52 \text{ eV}/kT} \quad (100) \quad [1]$$

$$m = 0.05e^{0.52 \text{ eV}/kT} \quad (111) \quad [2]$$

The average values and the two sigma limits for the segregation coefficient vary from  $2.95 \pm 0.25$  at 1200°C

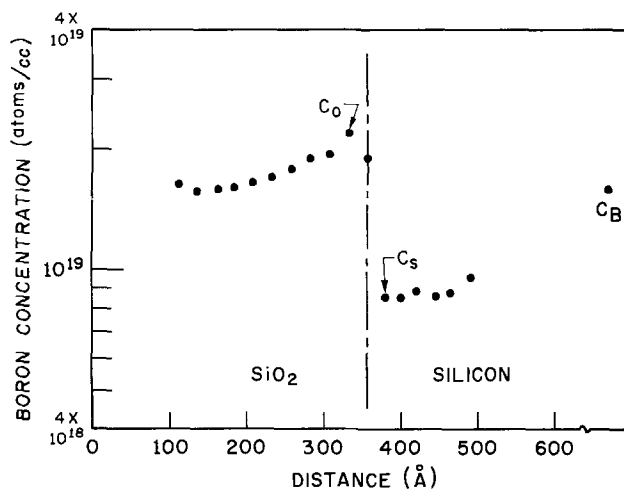


Fig. 1. Ion probe profile reduced to concentration, (100) orientation, 1100°C.

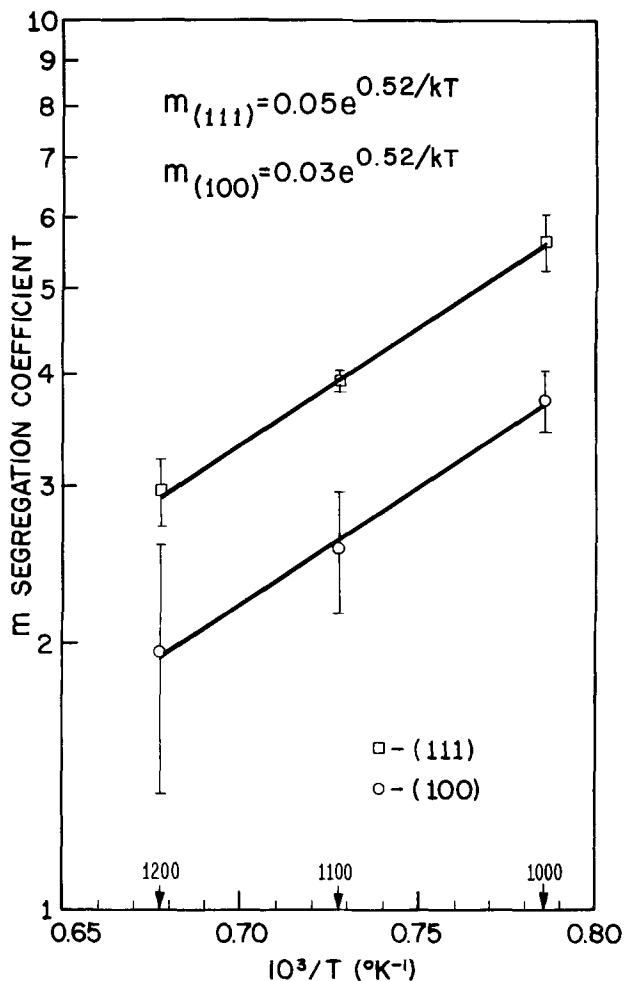


Fig. 2. Segregation coefficient as a function of temperature and orientation.

to  $5.63 \pm 0.41$  at 1000°C for (111) and from  $1.96 \pm 0.61$  at 1200°C to  $3.74 \pm 0.29$  at 1000°C for (100). These values for bulk samples and dry oxidations are in reasonable agreement with the values of Prince and Schwettmann (9) obtained by modeling for implanted wafers and steam oxidations for (111) orientations; the only reported data on variation of segregation coefficient with temperature. Comparison of segregation coefficient values must be made carefully since diffusion sources, wafer orientation, temperature of diffusion, ambient, and modeling techniques are different in many cases. There are indications (7, 8) however, that

<sup>1</sup> Manufactured by Applied Research Laboratories, Incorporated.

<sup>2</sup> Manufactured by Cameco Instruments.

concentration and oxidation rate may not affect segregation coefficient. The general range of segregation coefficient measured in these experiments is in line with various values reported for modeling techniques with varying experimental conditions. Refinement of modeling techniques (7) has suggested that a value of  $\sim 4$  at 1100°C for (111) is more valid than higher reported values (4, 5, 13) also based on modeling techniques. The value of 4 at 1100°C for (111) agrees extremely well with our experimentally determined value of  $3.93 \pm 0.09$ . Comparison with the only other experimentally determined (10, 11) value ( $\sim 2$ ) is difficult since the diffusion temperature was not published.

The orientation dependence of the segregation coefficient implies that the measured values for at least one of the orientations is not an equilibrium value and that the kinetic reaction rate across the interface determines the measured value. On the basis of equilibrium thermodynamics, one would not expect to observe an orientation dependence.

Some further interesting results may be obtained from the experimentally determined concentrations, if we take the ion probe values for  $C_s/C_B$  and  $m$  and consider the model of Grove *et al.* (3) for redistribution of boron upon oxidation of bulk silicon wafers, a value for the diffusion coefficient of boron in silicon can be determined by fitting their model to our experimental data. The model (3) considers solution of the diffusion equation with a moving boundary and the results describe redistribution from uniformly doped silicon. The resulting points are shown in Fig. 3. Least square fitting of these points yields

$$D_{(100)} = 0.192e^{-3.22/kT} \quad [3]$$

$$D_{(111)} = 2.04e^{-3.57/kT} \quad [4]$$

These functions are plotted as straight lines in Fig. 3. The orientation dependence of  $D$  is, of course, well known (14-24). The diffusivities converge at higher temperature as expected (22). Kendall and De Vries (25) have surveyed the literature and present various values of diffusion coefficients, as well as their estimates for the most valid values based on the experimental conditions and analysis of data. For boron in silicon, the values of Kurtz and Yee (26) are chosen. These values were obtained for surface concentrations generally in the mid  $10^{18}/\text{cm}^3$  range and apply for temperature from 1050° to 1350°C. The equation is

$$D_{(111)} = 1.4e^{-3.51/kT} \quad [5]$$

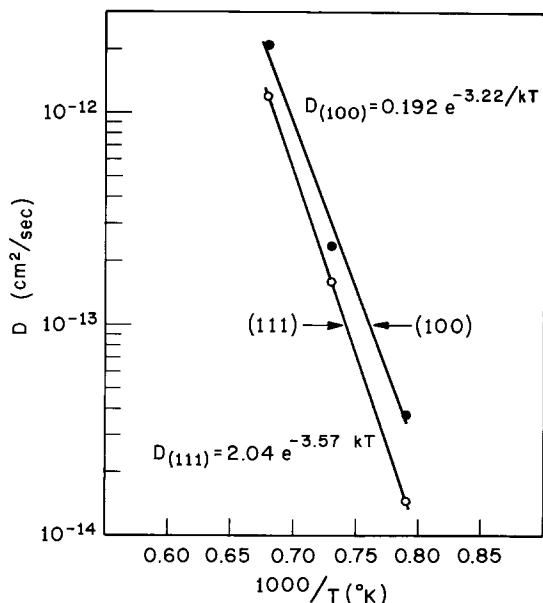


Fig. 3. Diffusion coefficient of boron in silicon-oxidizing ambient

which compares very favorably with the value obtained here (Eq. [4]) based on ion probe data and the model of Grove *et al.* (3).

Using the model of Grove *et al.* (3) for out-diffusion from a bulk wafer during oxidation,  $C_s/C_B$  can be calculated as a function of oxidation temperature, assuming  $m$  is independent of temperature. Ion probe data and necessary constants were used for such a calculation using the value of  $m$  at 1100°C for each orientation. The solid curves shown in Fig. 4 represent this calculation. Performing an identical calculation, but allowing  $m$  to vary with temperature as experimentally observed, generates the dotted curves shown in Fig. 4. Inclusion of the orientation and temperature variation of  $m$  in modeling calculations provides a more accurate description of the segregation at the oxidizing interface.

### Conclusion

The ion microprobe has been used to determine both the temperature and orientation dependence of the segregation coefficient of boron at the silicon-silicon dioxide interface. Observations show that the boron segregation coefficient decreases with increasing temperature in the range investigated, 1000°-1200°C and that boron segregation coefficient values for (111) oriented silicon are greater than (100) oriented silicon at corresponding temperatures over the same temperature range. Diffusion coefficients for boron in (100) and (111) silicon have been extracted from the experimental data using the modeling technique of Grove *et al.* (3). The values agree well with published data. The effect of the variation of the segregation coefficient with temperature and orientation has been demonstrated modeling  $C_s/C_B$ , the ratio of the boron surface concentration to the bulk boron concentration, as a function of temperature.

The orientation and temperature variation of the segregation coefficient should be included in device design and modeling techniques.

### Acknowledgment

The authors wish to thank P. H. Langer for use of his computer program based on the equations of Grove *et al.*, and for performing the various diffusion calculations using that program.

Manuscript submitted June 9, 1975; revised manuscript received Oct. 20, 1975. This was Paper 60 presented at the San Francisco, California, Meeting of the Society, May 12-17, 1974.

Any discussion of this paper will appear in a Discussion Section to be published in the December 1976

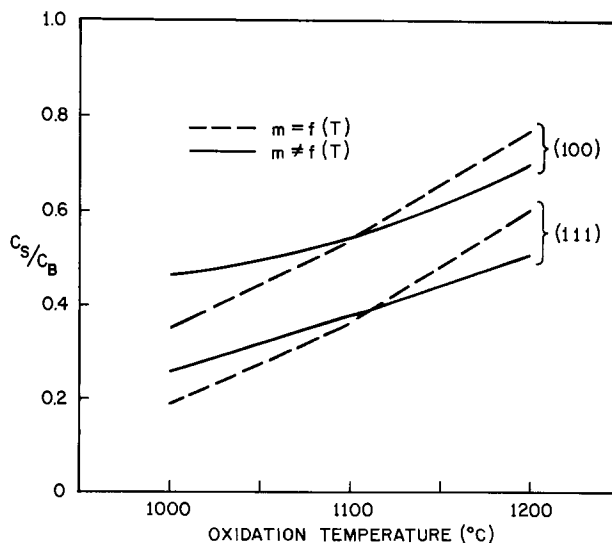


Fig. 4. Calculated  $C_s/C_B$  vs. oxidation temperature

JOURNAL. All discussions for the December 1976 Discussion Section should be submitted by Aug. 1, 1976.

Publication costs of this article were partially assisted by Bell Laboratories.

#### REFERENCES

1. C. D. Thurmond, "Properties of Elemental and Compound Semiconductors," H. C. Gatos, Editor, Interscience Publishers, New York (1962).
2. A. S. Grove, O. Leistiko, Jr., and C. T. Sah, *J. Phys. Chem. Solids*, **25**, 985 (1964).
3. A. S. Grove, O. Leistiko, Jr., and C. T. Sah, *J. Appl. Phys.*, **35**, 2695 (1964).
4. T. Kato and Y. Nishi, *Japan. J. Appl. Phys.*, **3**, 337 (1964).
5. J. S. T. Huang and L. C. Welliver, *This Journal*, **117**, 1577 (1970).
6. W. H. Chen and W. S. Chen, *ibid.*, **114**, 1297 (1967).
7. G. Masetti, P. Negrini, S. Solmi, and G. Soncini, *Acta Freqenza*, **XLII**, 346 (1973).
8. G. Masetti, S. Solmi, and G. Soncini, *Electron. Letters*, **9**, 226 (1973).
9. J. L. Prince and F. N. Schwettmann, *This Journal*, **121**, 705 (1974).
10. B. Blanchard, N. Hilleret, and J. Monnier, *Mat. Res. Bull.*, **6**, 1283 (1971).
11. B. Blanchard, N. Hilleret, and J. B. Quoirin, *J. Radio-analytical Chem.*, **12**, 85 (1972).
12. J. W. Colby, in "Scanning Electron Microscopy and Electron Probe Microanalysis," J. I. Goldstein, Editor, Plenum Press, New York (1975).
13. K. J. S. Cave, *Solid State Electron*, **8**, 991 (1965).
14. J. F. Shepard, R. J. Dendall, and P. Balk, Abstract 196, p. 87, The Electrochemical Society Extended Abstract, Fall Meeting, Philadelphia, Pennsylvania, Oct. 9-14, 1966.
15. G. N. Wills, *Solid State Electron*, **12**, 133 (1969).
16. R. A. Kovalev, V. B. Bernikov, Y. I. Pashintsev, and V. A. Marasnov, *Soviet Phys. Solid State*, **11**, 1571 (1970).
17. L. E. Katz, Symposium on Silicon Device Processing, *NBS Spec. Publ.* 337 (1970).
18. W. G. Allen and K. V. Anand, *Solid State Electron*, **14**, 397 (1971).
19. T. C. Chan and C. C. Mai, *Proc. IEEE*, **58**, 588 (1970).
20. M. Okamura, *Japan. J. Appl. Phys.*, **9**, 848 (1970).
21. H. Higuchi, M. Maki, and Y. Takano, Abstract 78, p. 190, The Electrochemical Society Extended Abstracts, Spring Meeting, Washington, D. C., May 9-13, 1971.
22. W. G. Allen, *Solid State Electron*, **16**, 709 (1973).
23. R. B. Fair, RNP 269 presented at The Electrochemical Society Meeting, New York, New York, Oct. 13-17, 1974.
24. S. M. Hu, *J. Appl. Phys.*, **45**, 1567 (1974).
25. D. L. Kendall and D. B. DeVries, in "Semiconductor Silicon," R. R. Haberecht and E. L. Kern, Editors, p. 358, The Electrochemical Society Softbound Symposium Series, New York (1969).
26. A. D. Kurtz and R. Yee, *J. Appl. Phys.*, **31**, 303 (1960).

## H<sub>2</sub>-Induced B Diffusion in MOS Devices

Dale M. Brown\*

General Electric Company, Corporate Research and Development, Schenectady, New York 12301

#### ABSTRACT

High temperature H<sub>2</sub>-induced B diffusion through self-aligned thin film Mo-gate MOSFET's is described. Mo-gate MOSFET threshold voltage and C-V curve shifts are used to detect the increase in B concentration in the Si substrate beneath the Mo gate. This phenomenon is explained by the catalyzed H<sub>2</sub> reduction of B<sub>2</sub>O<sub>3</sub> at the Mo-borosilicate glass interface. This occurs because the reaction rate at a given temperature is increased through the change in the free energy due to the entropy increase arising from the interstitial dissolution of the B in the Mo crystal lattice. With this model, it can thus be explained why oxides of elements from the lower rows of the periodic table (e.g., Si, P, and As) are not similarly reduced whenever they are components of a doped glass diffusion source and why Mo films are absolute diffusion blocks for these elements when they are present as oxides at interfaces. The study may shed some detailed insight into the catalytic activity of Mo and Fe in the synthesis of NH<sub>3</sub> from H<sub>2</sub> and N<sub>2</sub> and of other metallic hydrogenation catalysts.

B diffusion through the Mo gate of MOS structures was described previously (1). However, this phenomenon was never completely understood and further experimentation showed that very small amounts of H<sub>2</sub> in the diffusion ambient drastically reduce the masking ability of Mo films against its diffusion. The importance of the enhanced diffusion of B in SiO<sub>2</sub> when heated in H<sub>2</sub> and H<sub>2</sub>O ambients (2) has had important consequences for B-doped polysilicon-gate MOSFET's and has been described by others (3-6). Heat-treatment of Si-gate MOSFET's in H<sub>2</sub> and H<sub>2</sub>O ambients has been observed to decrease the p-channel enhancement mode MOSFET threshold or produce p-channel depletion mode devices instead of the desired enhancement mode device. Similar effects are observed for Mo-gate p-channel devices when H<sub>2</sub> is introduced into the diffusion ambient.

It is the purpose of this article to explain how and why this happens. The model also explains why Mo

films can be absolute diffusion barriers for other elements in glass films (e.g., Si, P, and As in their oxidized states) even when heated at high temperature in H<sub>2</sub>-containing ambients. The study also provides insight into a possible basic reason for catalytic activity not previously discussed in detail.

#### Experiments, Methods, and Results

Annular self-registered Mo-gate MOSFET's were made as described in Ref. (7), using a borosilicate glass diffusion source containing 28% B<sub>2</sub>O<sub>3</sub> as determined by the infrared absorption technique (8). Gate oxide thicknesses were approximately 1000Å, Mo film thicknesses were about 2000Å. The self-aligning Mo-gate MOSFET source and drain diffusions were carried out as a function of time in Ar, N<sub>2</sub>, and 10% H<sub>2</sub> in He at 1100°C.

Two types of MOSFET measurements were carried out: (i) gate threshold voltage measurements and gate C-V curves with the source and drain connected to the substrate give the characteristic low frequency C-V curve, (ii) C-V curves with source and drain float-

\* Electrochemical Society Active Member.

Key words: Mo catalysis, B<sub>2</sub>O<sub>3</sub> H<sub>2</sub> reduction, MOSFET's.

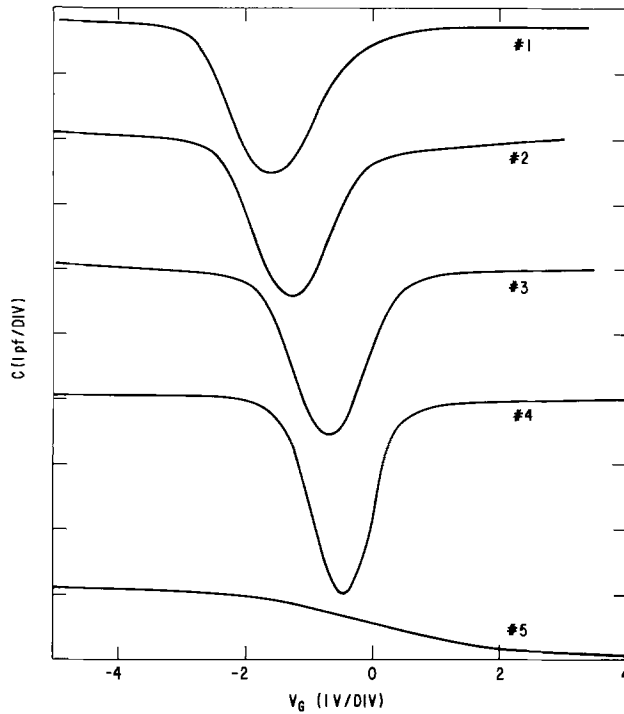


Fig. 1. Gate MOS C-V curves after diffusion with conditions as given in Table I. Capacitance curves are arbitrarily spaced on the C ordinate. Source and drain connected to substrate.

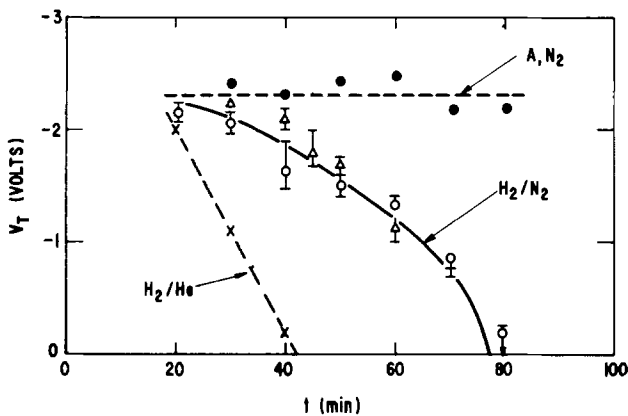


Fig. 2. 10  $\mu$ A gate threshold voltages vs. diffusion time in three different diffusion ambients, Ar, 10% H<sub>2</sub> in N<sub>2</sub>, and 10% H<sub>2</sub> in He. Silicon substrate crystal is n-type (111) phosphorous doped 3-5 ohm-cm.

ing give the high frequency C-V curves with a minimum inversion capacitance occurring at the maximum semiconductor depletion capacitance. The results of these measurements are given in Fig. 1 and 2 and summarized in Table I.

The observed shifts in threshold and C-V curves are caused by the increases in surface resistivity caused by B compensation of the phosphorus ionized donors.

Table I

No.	Ambient	Time (min)	V <sub>T</sub> (1 $\mu$ A)*	N <sub>D</sub> ** / cm <sup>3</sup>	(N <sub>D</sub> - N <sub>A</sub> )† / cm <sup>3</sup>
1	Ar, N <sub>2</sub>	30-80	-1.8	$2 \times 10^{15}$	$1.6 \times 10^{15}$
2	10% H <sub>2</sub> /N <sub>2</sub>	30	-1.5	$8 \times 10^{14}$	$\sim 10^{15}$
3	10% H <sub>2</sub> /N <sub>2</sub>	50	-0.8	$< 10^{13}$	$\sim 6 \times 10^{14}$
4	10% H <sub>2</sub> /N <sub>2</sub>	60	-0.6	$< 10^{13}$	$\sim 6 \times 10^{14}$
5	10% H <sub>2</sub> /N <sub>2</sub>	75	$\cong +5$	—	$-1.5 \times 10^{14}$

\* Measured threshold voltages are specified for a 1  $\mu$ A channel current using an aspect ratio, W/L = 20, device [Ref. (7)]. Silicon substrate is phosphorous doped with (111) surface orientation.

\*\* N<sub>D</sub> from V<sub>T</sub> assuming uniform doping and  $\phi_{MS} = 0.4$  [Ref. (7)].  
 † N<sub>D</sub> from C-V minimum depletion capacitance [Ref. (9)] which also assumes a uniform doping density (see discussion in text).

As boron atoms penetrate the gate structure, the resultant compensation decreases the ionized donor densities resulting in decreasing thresholds and depletion capacities as shown by the data in Fig. 1 and 2. Some of these results are summarized in Table I for the Ar, N<sub>2</sub>, and H<sub>2</sub> in N<sub>2</sub> diffusion ambients. The net ionized donor densities in the next to last column are estimated from standard threshold calculations for Mo-gate devices on (111) surfaces assuming a uniform doping profile and a fixed oxide charge of  $2.1 \times 10^{11}$ /cm<sup>2</sup> (7). The last column is the net uncompensated donor density arrived at using the gate MOS depletion capacitance which also assumes a uniform doping profile (9). This assumption is, of course, incorrect and probably accounts for the large differences in the estimated ionized donor densities arrived at using those two methods as the threshold approaches and passes through zero. Any detailed analysis of these threshold shifts would therefore have to take into account the nonuniformity of the doping profile caused by the B penetration and ensuing donor compensation. In turn, experimental samples would have to be subjected to detailed profile measurements using the MOSFET deep depletion  $d(1/C^2)/dV$  methods recently described (10). Sample 5 is a p-channel depletion mode device as indicated by the positive gate threshold and p-type MOS C-V curve. Threshold changes caused by changes in fixed oxide charge during B penetration of the gate oxide should not be a factor as indicated by previous experiments (1, 6).

Enhancement mode threshold data are shown in Fig. 2. The data are quite reproducible. The spread in the data at each point represents the threshold variation observed in scanning the wafer from left to right and top to bottom. Two sets of data are also shown using two different tanks of N<sub>2</sub> + 10% H<sub>2</sub>. Threshold data for He + 10% H<sub>2</sub> are also included in Fig. 2 and in this instance the B penetration occurs much more rapidly. It is obvious from the data that whereas total masking of B is possible for at least 1.5 hr in Ar or N<sub>2</sub> ambients even when very thin Mo films and gate oxides are used (7), the introduction of H<sub>2</sub> results in a drastic reduction in Mo-film diffusion masking. Furthermore, none of these effects have ever been observed when phosphorous-doped glass is used as a diffusion source (11). That is to say, no phosphorous penetration through the gates of self-aligned n-channel Mo-gate MOSFET's has been detected even when the diffusions are carried out in 10% H<sub>2</sub> + N<sub>2</sub> at 1100°C for periods of time as long as 1.5 hr. These observations are very striking and their explanation has to be based on an analysis of the chemical and physical properties of the system.

## Discussion

From a chemical point of view, the system is quite "clean," consisting of a lightly doped Si substrate, a thin (approximately 1000Å) film of thermally grown SiO<sub>2</sub> and a thin (approximately 2000Å) film of Mo covered with the B<sub>2</sub>O<sub>3</sub>-SiO<sub>2</sub> diffusion source. This structure is heated in gaseous ambients and, upon completion of the MOSFET structure by providing appropriate contacts, the Si substrate can be used as a B detector by simple measurements of MOSFET threshold.

One would anticipate that the rate of production of atomic B at the Mo-B<sub>2</sub>O<sub>3</sub> interface would be very small since the chemical reduction of B<sub>2</sub>O<sub>3</sub> by Mo or H<sub>2</sub> is strongly endothermic. In fact, P<sub>2</sub>O<sub>5</sub> should be much more easily reduced by H<sub>2</sub> than B<sub>2</sub>O<sub>3</sub>. This is shown by the magnitudes of the free energies of formation calculated using the JANAF Thermochemical Tables (12) for these reactions and summarized in Table II. P could, however, not go into interstitial position and diffuse interstitially through Mo whereas B is a small enough atom to do this. Elemental B has a radius of 0.88Å compared to 1-1.2Å for P or Si (13). The cubic body-centered cell of Mo has a radius for the largest interstitial space equal to 0.87Å at 1100°C. However,

Table II. Chemical reactions at 1100°C

Reaction	$\Delta G$ (kcal/mole)	$\Delta g$ (eV/atom)
$2B_2O_3 + 3Mo \rightarrow 3MoO_3 + 4B$	+198	2.15
$B_2O_3 + Mo \rightarrow MoO_3 + 2B$	+126	2.75
$B_2O_3 + 3H_2 \rightarrow 3H_2O + 2B$	+99	2.15
$SiO_2 + 2H_2 \rightarrow 2H_2O + Si$	+77	3.3
$P_2O_5 + 5H_2 \rightarrow 5H_2O + 2P$	+6	0.13

these considerations are not sufficient to explain the data in Fig. 2. Why, for instance, is the B diffusivity so much smaller in the  $N_2 + H_2$  ambient than in  $He + H_2$ ?

### Catalytic Reduction of $B_2O_3$

Heterogeneous catalytic reactions are normally considered to be determined by the adsorption and rearrangement of the reactants on the surface of the catalyst. Possible dissociation and a lowering of the free energy barrier in the transition state are assumed to accompany this surface adsorption and to account for low temperature catalytic reactivity. One of the most famous examples of this is the catalytic synthesis of ammonia from  $H_2$  and  $N_2$ . Although the absorption and catalytic activity of a surface is usually thought to have something to do with "active centers" and "the specific steric arrangement of its atoms" (14) there has been no rigorous statistical thermodynamic analysis of any specific system in the literature of the subject. This is not surprising since the chemical systems studied experimentally have been ill defined and complex. As described previously, the system being studied here is relatively simple; and the presence of the semiconductor substrate gives us a good method of monitoring relative rates of reaction.

Mo is an excellent catalyst for the synthesis of ammonia although for economic reasons Fe is used. Both of these materials have body-centered cubic (bcc) crystal structures. The interstitial space in the body-centered cell of Mo will accommodate elements of the first row including N ( $r = 0.7\text{\AA}$ ) but not, as pointed out previously, the large atoms of the second row.

In the system under discussion, it appears that the fact that B can dissolve interstitially in Mo at the reaction temperature whereas Si and P cannot plays an essential role in the reduction of the  $B_2O_3$  glass component on the Mo substrate. The free energy change during the endothermic reaction is reduced by  $T\Delta S$  where  $\Delta S$  arises from the entropy of dissolution of the B atoms in the Mo. At low B concentrations in Mo,  $\Delta S$  has a large incremental value because of the form of the curve of  $\Delta S$  as a function of the mole fraction of interstitial B in Mo. A low concentration of B can be produced by  $H_2$  reduction of  $B_2O_3$  and can diffuse through the Mo and be detected. The mechanism which is proposed to account for the observed phenomena is analogous to the structural disordering of a solid with the introduction of point defects which occurs with increasing temperature. The production of point defects is an endothermic process, but their distribution in the solid is accompanied by an increase in the entropy of the system. As a consequence, the free energy of the disordered system at a temperature at which the diffusion of point defects is possible is lower than that of the ordered system. The theory of the structural disordering of crystals which is discussed in many publications (15-17) can be adapted to the present problem.

The changes in the Gibbs free energy,  $\Delta G$ , in Table II are calculated from the change in the enthalpy,  $\Delta H$ , and the change in the thermal entropy. Changes in entropy associated with the formation of two dimensional adsorbed layers on catalytic surfaces have been discussed (18). The concept that the free energy of a reaction can be lowered by the much larger entropy changes associated with the interstitial substrate dissolution of

a product within the volume of the catalyst has not, so far as is known, ever been introduced. Yet this is clearly possible and could occur in the reduction of B by  $H_2$  on a Mo substrate and in the dissociation of  $H_2$  and other molecules on metallic substrates in catalytic hydrogenation reactions.

The entropy of interstitial dissolution of B in Mo can be calculated by the methods of statistical mechanics. The number of the largest interstitial sites/cm<sup>3</sup> in the Mo lattice is given by  $N = 3M/2$ , where M is the total number of Mo atoms/cm<sup>3</sup>. The number of ways of distributing solute atoms over these interstitial sites is

$$\frac{N!}{n!(N-n)!}$$

where n is the number of solute atoms/cm<sup>3</sup>. The corresponding entropy of dissolution is then given by

$$S = k[N \ln(N) - (N-n) \ln(N-n) - n \ln(n)]$$

making use of Stirling's theorem.

The free energy change in the reaction  $\Delta G^*$ , when it occurs on the Mo substrate, is therefore reduced from  $\Delta G$  by  $T\Delta S$  giving

$$\Delta G^* = \Delta G - T\Delta S = n\Delta g - kT[N \ln N - (N-n) \ln(N-n) - n \ln n]$$

where  $\Delta g$  is the free energy change associated with the production of one B atom by the reduction of  $B_2O_3$  by  $H_2$ . In the equilibrium state,  $\partial \Delta G^* / \partial n = 0$  which gives

$$n/(N-n) \simeq n/N = e^{-\Delta g/kT}$$

The approximation is valid because of the low concentration of the B in Mo at the temperature of reduction.

The number of interstitial positions can be calculated using the unit cell volume, atomic weight, and density of Mo and gives

$$N = 9.6 \times 10^{22}/\text{cm}^3$$

Using the Gibbs free energy data in Table II, the equilibrium concentration of interstitial B produced by the  $H_2$  reduction of  $B_2O_3$  at 1100°C (with  $\Delta g = 2.15$  eV) is

$$n = 1.2 \times 10^{15}/\text{cm}^3$$

The calculation thus demonstrates that a reaction which could not occur in the absence of a catalyzing system can give rise to B atoms in the Mo substrate which can then diffuse interstitially and be detected by their influence on the properties of the MOSFET. It is clear that since neither Si nor P will dissolve and diffuse interstitially in Mo,  $SiO_2$ , and  $P_2O_5$  will not be reduced by  $H_2$  in contact with Mo in agreement with the experimental observations.

The reduction in the B diffusivity in the presence of  $N_2$  is probably accounted for by the catalyzed formation at the surface of  $NH$  diatomic molecules by reaction between  $N_2$  molecules adsorbed at the surface and H atoms reaching the surface from dissociated  $H_2$  dissolved interstitially in the Mo substrate. The  $NH$  molecules can dissociate at the surface ( $\Delta h = 3.2$  eV) with interstitial dissolution of both the N and the H. The presence of interstitially dissolved nitrogen would reduce the entropy of dissolution of the B by reducing the number of available interstitial sites. This would reduce the concentration of B dissolved in the Mo substrate.

### Summary

The importance of the dissolution of B in the Mo substrate explaining the  $H_2$  reduction of  $B_2O_3$  and subsequent diffusion of B through thin Mo films has led to a catalytic model which explains the striking diffusion phenomena associated with Mo-gate MOSFET's. More specifically, it explains the high B diffusivity through the gate into the underlying Si whenever  $H_2$  is introduced into Ar, He, or  $N_2$  diffusion ambients.



Furthermore, this model explains the inertness of Mo films with other glass components like SiO<sub>2</sub>, P<sub>2</sub>O<sub>5</sub>, and As<sub>2</sub>O<sub>3</sub> which explains the observed diffusion-masking ability of Mo films against P. This study points out clearly for perhaps the first time the importance of the bulk crystallographic structure of a catalytic agent.

#### Acknowledgments

Mr. George J. Charney made all the samples and took all the data reported here. The author is especially thankful to Prof. J. W. Mitchell of the Department of Physics at the University of Virginia for pointing out the importance of a decrease in the free energy as a result of the interstitial dissolution of a product in explaining the catalytic phenomena discussed in this paper. Thanks also to Dr. D. W. McKee for reading the manuscript.

Manuscript submitted June 6, 1974; revised manuscript received Nov. 5, 1975.

Any discussion of this paper will appear in a Discussion Section to be published in the December 1976 JOURNAL. All discussions for the December 1976 Discussion Section should be submitted by Aug. 1, 1976.

Publication costs of this article were partially assisted by the General Electric Company.

#### REFERENCES

1. A. El-Hoshy, D. M. Brown, and W. E. Engeler, *Appl. Phys. Letters*, **17**, 261 (1970).
2. A. S. Grove, O. Leistiko Jr., and C. T. Sah, *J. Appl. Phys.*, **35**, 2695 (1964).
3. M. Ghezzi and D. M. Brown, *This Journal*, **120**, 146 (1973).
4. W. E. Armstrong and D. L. Tolliver, *ibid.*, **121**, 307 (1974).
5. K. Simakura, T. Suzuki, and Y. Yadoiwa, Abstract 155, p. 398, The Electrochemical Society Extended Abstracts, Fall Meeting, Boston, Massachusetts, October 7-11, 1973.
6. J. T. Clemens and E. F. Labuda, Abstract 46, p. 125, The Electrochemical Society Extended Abstracts, Spring Meeting, San Francisco, May 12-17, 1974.
7. D. M. Brown, W. R. Cady, J. W. Sprague, and P. J. Salvagni, *IEEE Trans. Electron Devices*, **ED-18**, 931 (1971).
8. A. S. Tenney, *This Journal*, **118**, 1658 (1971).
9. K. H. Zaininger and F. P. Heiman, *Solid State Technol.*, **13**, 49 (1970).
10. D. M. Brown, R. J. Connery, and P. V. Gray, *This Journal*, **122**, 121 (1975).
11. D. M. Brown, W. E. Engeler, M. Garfinkel, and P. V. Gray, *Solid-State Electron.*, **11**, 1105 (1968).
12. *JANAF Thermochemical Tables*, Second Edition, National Bureau of Standards, Washington, D. C. (1971).
13. *Handbook of Chemistry and Physics*, Chemical Rubber Publishing Co., Cleveland, Ohio.
14. P. H. Emmett, Editor, "Catalysis III," p. 224, Reinhold Publishing Corp., New York (1955).
15. R. H. Fowler and E. A. Guggenheim, "Statistical Thermodynamics," The Macmillan Company, New York (1939).
16. R. W. Gurney, "Introduction to Statistical Mechanics," McGraw-Hill Book Company, New York (1949).
17. R. A. Swalin, "Thermodynamics of Solids," John Wiley & Sons, Inc., New York (1962).
18. B. M. W. Trapnell, "Chemisorption," Butterworths, London (1955).

## Mixed Electrical Conduction in the Fluorite-Type Ce<sub>1-x</sub>Gd<sub>x</sub>O<sub>2-x/2</sub>

T. Kudo and H. Obayashi

Central Research Laboratory, Hitachi, Limited, Higashi-koigakubo, Kokubunji, Tokyo, 185, Japan

#### ABSTRACT

The CeO<sub>2</sub>-Gd<sub>2</sub>O<sub>3</sub> solid solutions exhibit high ionic conduction due to the migration of O<sup>2-</sup> ions via oxygen ion vacancies. The emf of a galvanic cell, O<sub>2</sub>(p<sub>O<sub>2</sub> = 1 atm), Pt|Ce<sub>1-x</sub>Gd<sub>x</sub>O<sub>2-x/2</sub>|Pt, O<sub>2</sub>(p<sub>O<sub>2</sub>), is measured within the temperature range between 700° and 800°C as a function of p<sub>O<sub>2</sub></sub>. At such high oxygen pressures as in air, the emf changes according to  $-(RT/4F) \ln p_{O_2}$  indicating the ionic transference number in the solid solution is unity. With decreasing oxygen pressure, however, the observed emf becomes smaller than the theoretical value. This indicates the onset of electronic conduction generated by the reduction of the solid solution. The dependence of the emf(*E*) on p<sub>O<sub>2</sub></sub> is described by</sub></sub>

$$E = \frac{RT}{F} \ln [(1 + p^*_{O_2}) / (p_{O_2}^{1/4} + p^*_{O_2}^{1/4})]$$

where p<sup>\*</sup><sub>O<sub>2</sub></sub> is a constant corresponding to the oxygen partial pressure at which the ionic transference number of the solid solution becomes 0.5. From the temperature dependence of p<sup>\*</sup><sub>O<sub>2</sub></sub>, partial molar enthalpy changes (Δ*H*) for the reduction of Ce<sub>1-x</sub>Gd<sub>x</sub>O<sub>2-x/2</sub> are calculated.

Ionic conduction in doped CeO<sub>2</sub> has been reported by Kevane (1), Blumenthal (2), Takahashi (3), and others. It is known that ionic conduction results from the migration of O<sup>2-</sup> ions over vacant ion sites which are produced by the partial replacement of Ce<sup>4+</sup> by such dopant ions as Ca<sup>2+</sup> or La<sup>3+</sup>. The present authors have also reported the oxygen ion conduction of the fluorite-type solid solution Ce<sub>1-x</sub>Ln<sub>x</sub>O<sub>2-x/2</sub> (Ln =

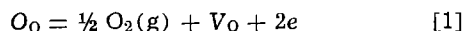
Key words: ionic conductor, solid electrolyte, cerium-gadolinium oxide, mixed conductor.

lanthanoid elements) (4), revealing that the CeO<sub>2</sub>-Gd<sub>2</sub>O<sub>3</sub> system exhibits excellent electrolytic conduction; the specific conductivity of Ce<sub>1-x</sub>Gd<sub>x</sub>O<sub>2-x/2</sub> (x = 0.23) at 750°C is 6.7 × 10<sup>-2</sup> (ohm-cm)<sup>-1</sup>, which rivals the value of calcia-stabilized zirconia at 1000°C.

The ionic transference number of Ce<sub>1-x</sub>Gd<sub>x</sub>O<sub>2-x/2</sub> has been proved to be substantially unity by the emf measurement of the galvanic cell, O<sub>2</sub>(p<sub>O<sub>2</sub> = 1 atm), Pt|Ce<sub>1-x</sub>Gd<sub>x</sub>O<sub>2-x/2</sub>|Pt, O<sub>2</sub>(p<sub>O<sub>2</sub> = 0.21 atm) (4). At lower oxygen pressures, however, electronic conduction</sub></sub>

seems to set in as reported for the  $\text{CeO}_2\text{-La}_2\text{O}_3$  system (5). The present study investigates the mixed conduction of  $\text{Ce}_{1-x}\text{Gd}_x\text{O}_{2-x/2}$  in order to provide the data needed for fuel cells and other applications. In addition, thermodynamic data for the reduction of  $\text{Ce}_{1-x}\text{Gd}_x\text{O}_{2-x/2}$  in a reducing atmosphere are also derived from analyses of emf data obtained by the present study.

Mixed ionic-electronic conduction in solid electrolytes has been studied by Schmalzried and Tare (6, 7) on a theoretical basis. In the present work, this theory is applied to  $\text{Ce}_{1-x}\text{Gd}_x\text{O}_{2-x/2}$ . Electronic conduction under a reducing atmosphere results from excess electrons generated by the reaction



where  $\text{O}_0$  and  $\text{V}_0$  represent oxygen ions at normal lattice sites and doubly ionized oxygen ion vacancies. The equilibrium constant  $K$  for the reaction [1] is

$$K = n_V n_e^2 p_{\text{O}_2}^{1/2} \quad [2]$$

where  $n_V$  and  $n_e$  are the concentration of vacancies and electrons, respectively. Assuming the number of oxygen ion vacancies generated by Eq. [1] to be negligible compared with that produced by replacement of  $\text{Ce}^{4+}$  by  $\text{Gd}^{3+}$  [ $\text{V}_0$ ]

$$n_e = (K/[\text{V}_0])^{1/2} \cdot p_{\text{O}_2}^{-1/4} \quad [3]$$

Thus, the electronic conductivity is given by

$$\sigma_e = (e\mu) (K/[\text{V}_0])^{1/2} \cdot p_{\text{O}_2}^{-1/4} \quad [4]$$

where  $e$  is the charge of an electron and  $\mu$  is its mobility. By substituting Eq. [4] into the equation defining the ionic transference number

$$t_i = \frac{\sigma_i}{\sigma_i + \sigma_e} \quad [5]$$

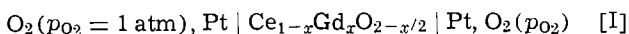
we obtain

$$t_i = \frac{1}{1 + (p_{\text{O}_2}/p^*_{\text{O}_2})^{-1/4}} \quad [6]$$

where

$$p_{\text{O}_2} = (\mu e/\sigma_i)^4 (K/[\text{V}_0])^2 \quad [7]$$

Here,  $\sigma_i$  represents the ionic conductivity. Since  $\sigma_i$  is considered to be independent of  $p_{\text{O}_2}$ ,  $p^*_{\text{O}_2}$  is a constant corresponding to an oxygen partial pressure at which the ionic transference number becomes 0.5. On the other hand, the emf ( $E$ ) of the galvanic cell



is given by

$$E = \frac{RT}{4F} \int_{p_{\text{O}_2}}^{p'_{\text{O}_2}} t_i d \ln p_{\text{O}_2} \quad [8]$$

By substituting  $t_i$  in Eq. [8] by Eq. [6], and integrating, we obtain

$$E = \frac{RT}{F} \ln \left( \frac{1 + p^*_{\text{O}_2}{}^{1/4}}{p_{\text{O}_2}{}^{1/4} + p^*_{\text{O}_2}{}^{1/4}} \right) \quad [9]$$

This provides the theoretical background for the following discussion.

### Experimental

**Sample preparation.**—Ceria powder (99.99% pure, Shin-etsu Chemical Company) and  $\text{Gd}_2\text{O}_3$  powder (99.9% pure, same supplier) were weighed, mixed in an agate mortar for 30 min, and heated in air at  $1300^\circ\text{C}$  for 8 hr. An x-ray analysis of the resultant specimen showed the diffraction pattern of the fluorite structure only. This specimen was reground in an agate mortar to 325 mesh size. In order to obtain a dense specimen, 3 mole per cent (m/o) of magnesium was added in the form of  $\text{Mg}(\text{NO}_3)_2$ . Methyl cellulose was added to this as a binder and the treated powder was cold pressed into 20 mm diameter pellets. The pellets were

heated in air at  $1800^\circ\text{C}$  for 2~3 hr in a Pt-40% Rh basket. The pellets in their final state were ca. 1.5 mm thick and ca. 16 mm diameter. Apparent density of the pellets was more than 98% of the theoretical value calculated from the lattice constant.

**EMF measurements.**—The test pellet was provided with platinum paste electrodes (5 mm diameter) on both sides. The platinum paste (No. 8103, Tokuriki Chemical Company) was baked at  $1000^\circ\text{C}$  for 1 hr. SEM observations showed the electrodes to be of a very porous structure, ensuring that equilibrium oxygen pressures would be attained quickly at the electrode/electrolyte interface. This test specimen was attached to an emf measurement apparatus, in which one side of the electrodes was exposed to pure oxygen and the other side to a gas mixture of  $\text{O}_2/\text{N}_2$  or  $\text{CO}_2/\text{H}_2$ . The specifications of the apparatus have been given in a previous paper (4).

High oxygen pressures ( $1 \sim 10^{-5}$  atm) were achieved by using  $\text{O}_2/\text{N}_2$  mixtures. Low oxygen pressures ( $10^{-13} \sim 10^{-20}$  atm at  $850^\circ\text{C}$ ) were obtained with  $\text{CO}_2/\text{H}_2$  mixtures by using gas flow meters to control their flow ratio. The  $\text{H}_2$  to  $\text{CO}_2$  mixing ratio ranged from 0.1 to 250 (or infinite). The gas mixture and oxygen were passed at a total pressure of 1 atm and linear speeds of about 0.5 cm/sec (at room temperature), assuring that the gases were heated to the equilibrium furnace temperatures.

The emf of the galvanic cells was measured by using a potentiometer (Yokogawa Electric, Type P-1). Conductivity measurements were carried out employing a d-c four-probe method. The details of the apparatus used in the conductivity measurements were given in a previous work (4). In all experiments, temperatures were controlled to within  $\pm 1^\circ\text{C}$ .

### Results and Discussion

The temperature dependence of the total conductivity ( $\sigma T$ ) vs.  $1/T$  in air for  $\text{Ce}_{1-x}\text{Gd}_x\text{O}_{2-x/2}$  is presented in Fig. 1. The temperature dependence observed for low dopant concentrations ( $x = 0.1 \sim 0.3$ ) may be described in the form

$$\sigma = [T (A_1 \exp(E_1/RT) + A_2 \exp(E_2/RT))]^{-1} \quad [10]$$

as reported by Bauerle and Hrizo (8) for a  $\text{ZrO}_2\text{-Y}_2\text{O}_3$  electrolyte.

The electrical conduction in air at temperatures between  $700^\circ$  and  $850^\circ\text{C}$  was proved to be ionic by using cell [I] in which  $p_{\text{O}_2} = 0.21$  atm. In the same manner, it was found that the ionic transference number for  $\text{Ce}_{1-x}\text{Gd}_x\text{O}_{2-x/2}$  ( $x = 0.1 \sim 0.5$ ) is larger than 0.98 for  $p_{\text{O}_2}$  from  $10^{-1}$  to  $10^{-5}$  atm at temperatures between  $700^\circ$  and  $850^\circ\text{C}$ .

To illustrate the oxygen pressure dependence of the emf given by the galvanic cell [I] under lower oxygen pressures, two isotherms for the compositions  $\text{Ce}_{1-x}\text{Gd}_x\text{O}_{2-x/2}$  ( $x = 0.2$  and  $0.5$ ) are plotted in Fig. 2. For comparison, the observed emf's of the same type  $\text{Zr}_{1-x}\text{Y}_x\text{O}_{2-x/2}$  ( $x = 0.10$ ) galvanic cell are also plotted. In the case of  $\text{ZrO}_2\text{-Y}_2\text{O}_3$ , the  $p_{\text{O}_2}$  dependence of the emf is described by

$$E = \frac{RT}{4F} \ln (p'_{\text{O}_2}/p_{\text{O}_2}) \quad [11]$$

the relation obtained when  $t_i = 1$ , or  $p^*_{\text{O}_2} \ll p_{\text{O}_2}$  in Eq. [9]. Although  $p^*_{\text{O}_2}$  for  $\text{Zr}_{1-x}\text{Y}_x\text{O}_{2-x/2}$  ( $x = 0.1$ ) has not yet been reported, it seems to be less than  $10^{-10}$  atm at  $750^\circ\text{C}$ , since Schmalzried (6) has reported that  $p^*_{\text{O}_2}$  for  $\text{Zr}_{1-x}\text{Ca}_x\text{O}_{2-x}$  ( $x = 0.15$ ) is  $10^{-13}$  atm at  $800^\circ\text{C}$ . Contrary to yttria-stabilized zirconia, the plotted emf's of  $\text{Ce}_{1-x}\text{Gd}_x\text{O}_{2-x/2}$  cells show a deviation from the  $p_{\text{O}_2}$  dependence expressed by Eq. [11]. This indicates that the electronic conduction in  $\text{Ce}_{1-x}\text{Gd}_x\text{O}_{2-x/2}$  is not negligible as compared with the ionic conduction under the oxygen pressures employed in

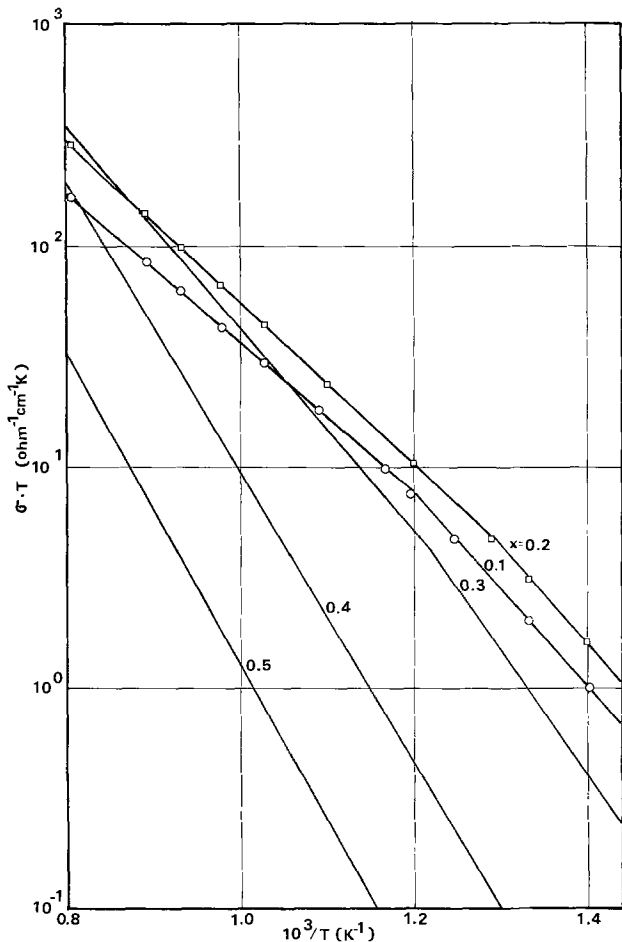


Fig. 1. Conductivity-temperature behavior for  $Ce_{1-x}Gd_xO_{2-x/2}$ . For the sake of clarity only a few of the measured data points for  $x = 0.1$  and  $0.2$  are shown.

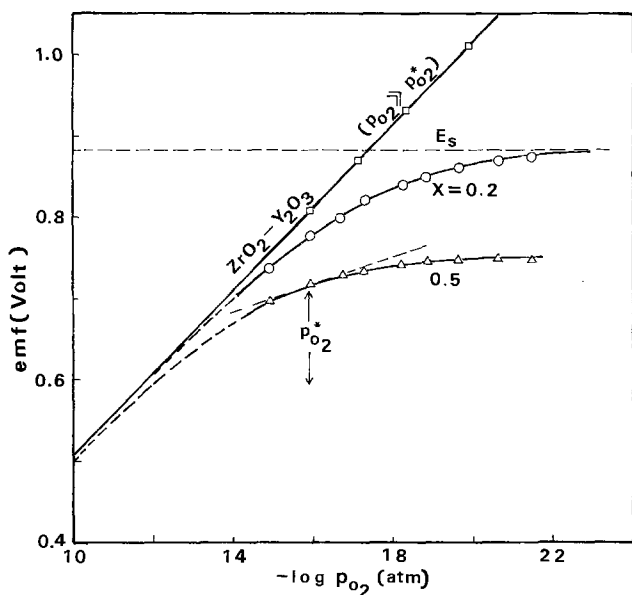


Fig. 2. EMF for galvanic cells,  $O_2$  (1 atm),  $Pt | Ce_{1-x}Gd_xO_{2-x/2}$  ( $x = 0.2$  and  $0.5$ )  $| Pt, O_2 (p_{O_2})$ , as a function  $p_{O_2}$  at  $750^\circ C$ . For comparison, data for  $Zr_{1-x}Y_xO_{2-x/2}$  ( $x = 0.1$ ) are shown.

these experiments. The dependence of the emf on  $p_{O_2}$  is in good agreement with Eq. [9] yielding values for  $p^*_{O_2}$  of  $3.92 \times 10^{-18}$  and  $1.38 \times 10^{-15}$  atm for  $x = 0.2$  and  $0.5$ , respectively. According to Eq. [9], the emf saturates to a value  $E_S$

Table I.  $p^*_{O_2}$  (atm) values for  $Ce_{1-x}Gd_xO_{2-x/2}$

$x$	$T$ ( $^\circ C$ )	700	750	800	850
0.1		$1.30 \times 10^{-17}$	$2.53 \times 10^{-16}$	$2.43 \times 10^{-15}$	$3.65 \times 10^{-14}$
0.2		$1.24 \times 10^{-19}$	$3.92 \times 10^{-18}$	$9.2 \times 10^{-17}$	$1.73 \times 10^{-15}$
0.3		$3.16 \times 10^{-19}$	$5.6 \times 10^{-18}$	$8.5 \times 10^{-17}$	$9.0 \times 10^{-16}$
0.4		$9.3 \times 10^{-19}$	$8.8 \times 10^{-18}$	$6.3 \times 10^{-17}$	$3.85 \times 10^{-16}$
0.5		$1.46 \times 10^{-16}$	$1.38 \times 10^{-15}$	$1.12 \times 10^{-14}$	$6.5 \times 10^{-14}$

$$E_S = \frac{RT}{F} \ln \frac{1 + (p^*_{O_2})^{1/4}}{(p^*_{O_2})^{1/4}} \quad [12]$$

The emf's observed when hydrogen with a dew point of ca.  $-30^\circ C$  was introduced into the cells corresponded to  $E_S$  calculated from Eq. [12] using  $p^*_{O_2}$  derived for  $Ce_{1-x}Gd_xO_{2-x/2}$  ( $x = 0.1 \sim 0.5$ ). These are tabulated in Table I. The temperature dependence of  $p^*_{O_2}$ , which is to be discussed later, gives a straight line in Arrhenius plots.

From the values for  $p^*_{O_2}$ , the ionic transference number  $t_i$  can be calculated as a function of  $p_{O_2}$  employing Eq. [5]. This is given in Fig. 3 for the composition  $Ce_{1-x}Gd_xO_{2-x/2}$  ( $x = 0.2$ ). The calculated transference number is  $\sigma_i / (\sigma_i + \sigma_e)$ . This should be distinguished from the "mean" transference number  $t_m$  given by

$$t_m = E / \frac{RT}{4F} \ln (p'_{O_2}/p_{O_2}) \quad [13]$$

where  $p_{O_2}$  and  $p'_{O_2}$  are oxygen pressures in the same asymmetrical cell as cell [I]. The value of  $t_m$  defined by Eq. [13] is an important criterion when applications of electrolytes to fuel cells are considered. It is shown in Fig. 3 only for  $700^\circ C$ .

The  $t_i$  isotherms at  $p_{O_2} = 10^{-20}$  atm and  $t_m$  for  $p'_{O_2} = 1$  atm and  $p_{O_2}$  (in Eq. [13]) =  $10^{-20}$  atm are given in Fig. 4 as a function of dopant ( $Gd^{3+}$ ) concentration,  $x$ . A maximum in  $t_i$  appears around  $x = 0.2$  at  $700^\circ C$ , but at higher temperatures the maximum point shifts to higher  $Gd^{3+}$  concentrations. A maximum in  $t_m$  appears at the composition which gives the maximum in  $t_i$ .

Though  $t_i$  does not exceed 0.37 for all compositions investigated,  $t_m$  at  $700^\circ C$  is as large as 0.91 for  $x = 0.2$ . This suggests that the utilization of  $Ce_{1-x}Gd_xO_{2-x/2}$  ( $x = 0.2$ ) in fuel cells is likely to be successful, contrary to  $Ce_{1-x}La_xO_{2-x/2}$  solid electrolytes (9). In the case of  $Ce_{1-x}La_xO_{2-x/2}$ , the transference number is improved by increasing  $x$ , while the conductivity is

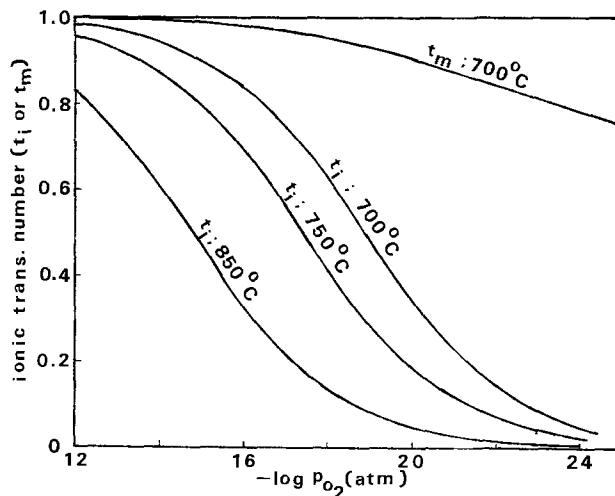


Fig. 3. The ionic transference number,  $t_i$ , for  $Ce_{1-x}Gd_xO_{2-x}$  ( $x = 0.2$ ) as a function of  $p_{O_2}$  as derived from  $p^*_{O_2}$  in Table I. The mean transference number,  $t_m$  (see text), is also shown for  $700^\circ C$ .

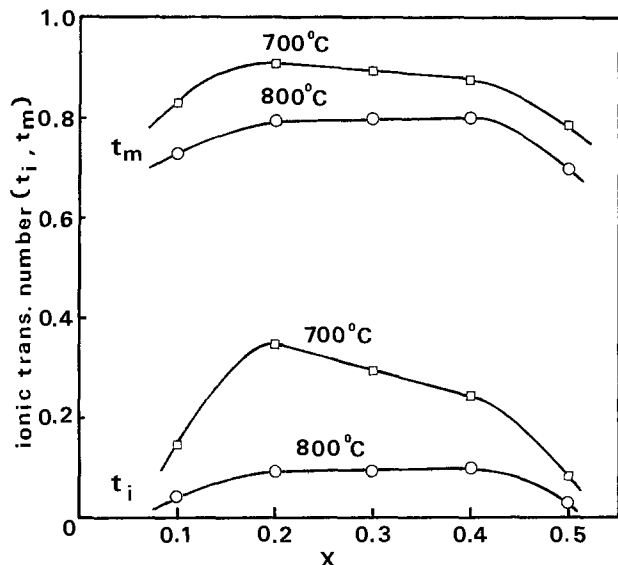


Fig. 4. The ionic transference numbers ( $t_i$  and  $t_m$ ) as a function of  $x$  in  $Ce_{1-x}Gd_xO_{2-x/2}$ .

sacrificed (10). However,  $Ce_{1-x}Gd_xO_{2-x/2}$  exhibits the highest transference number at the composition ( $x = 0.2$ ) where the conductivity is approximately maximized (cf. Fig. 1 and 4). Moreover, the conductivity of  $Ce_{1-x}Gd_xO_{2-x/2}$  at 700°C almost equals the value of calcia-stabilized zirconia at 1000°C.

Let us consider how the composition ( $x$ ) dependence of the transference number (or  $p^*_{O_2}$ ) arises. As Eq. [5] indicates, the ionic transference number becomes, in general, larger if ionic conductivity increases. At the same time, if the reduction of  $Ce^{4+}$  to  $Ce^{3+}$  is suppressed, the transference number also increases because the number of excess conduction electrons is decreased. Higher vacancy concentration, i.e., higher  $x$ , will shift the reaction given by Eq. [1] to the left-hand side and the concentration of  $Ce^{3+}$  ions will decrease. This results in an increase in the ionic transference number. For the  $CeO_2-La_2O_3$  system, the relation between the stability of  $Ce^{4+}$  and the dopant  $La^{3+}$  concentrations has been studied (10, 11); however, the conclusions are not really clear.

The stability of  $Ce^{4+}$  may be determined by the equilibrium constant  $K$  of the reaction given by Eq. [1], which has the form

$$K = K_0 \exp(-\Delta\bar{H}/RT) \quad [14]$$

where  $\Delta\bar{H}$  is the enthalpy change of the reaction.<sup>1</sup> Thus, the temperature dependent variables in Eq. [7] are  $K$ ,  $\sigma_i$ , and  $\mu$ . The dependence of  $\sigma_i$  on temperature is expressed by Eq. [10]. However, this is well approximated for all compositions in the temperature range between 700° and 850°C by

$$\sigma_i = \frac{\sigma_{i0}}{T} \exp(E_i/RT) \quad [15]$$

where  $E_i$  is the activation energy of oxygen ion conduction. This value ranges from ca. 0.55 to 1.3 eV as calculated from Fig. 1. On the other hand,  $\mu$  may be given by

$$\mu = \frac{b}{T} \exp(-E_e/RT) \quad [16]$$

assuming electrons migrate by a hopping mechanism in this case. Since  $E_e \ll E_i$  ( $E_i$  is equal to at least 0.5 eV for  $Ce_{1-x}Gd_xO_{2-x/2}$ ,  $x = 0.1 \sim 0.5$ ), Eq. [7] can be rewritten as

$$p^*_{O_2} = \left[ \frac{be}{\sigma_i} \right]^4 \cdot \left[ \frac{K}{[V_O]} \right]^2 \quad [17]$$

or

<sup>1</sup>  $\Delta\bar{H}$  = partial molal quantity discussed later.

$$(p^*_{O_2})^{1/4} \sigma_i = be[V_O]^{1/2} \cdot K^{1/2} \equiv \alpha \quad [18]$$

Equation [17] requires that the temperature dependence of  $p^*_{O_2}$  be exponential. This requirement is met as mentioned before. Taking logarithms of Eq. [18] and differentiating with respect to  $(1/T)$ , one may derive

$$\frac{\partial \ln \alpha}{\partial (1/T)} = \frac{1}{2} \frac{\partial}{\partial (1/T)} \ln K = -\frac{\Delta\bar{H}}{2R} \quad [19]$$

Hence,  $\Delta\bar{H}$  can be calculated from the slope of each line given in Fig. 5, in which  $\alpha$  for  $Ce_{1-x}Gd_xO_{2-x/2}$  is plotted vs.  $1/T$ .

The  $\Delta\bar{H}$  value obtained should be considered as the partial molal enthalpy change for the reduction of the solid electrolytes represented by Eq. [1] at the composition  $Ce_{1-x}Gd_xO_{2-x/2-\delta}$  at which  $\delta \approx 0$ . These are plotted in Fig. 6 as a function of  $x$ , where bars at each point indicate the possible errors estimated by a regression analysis of Fig. 5.  $\Delta\bar{H}$  is a measure of the stability of  $Ce^{4+}$  in the crystal lattice, i.e., the stability increases with an increase of  $\Delta\bar{H}$ . Since the dependence of  $\Delta\bar{H}$  on  $x$  is not simple (as seen in Fig. 6), one cannot conclude that dopant  $Gd^{3+}$  ions enhance the stability of  $Ce^{4+}$ . Moreover, it should be noted that all  $\Delta\bar{H}$ 's obtained for  $Ce_{1-x}Gd_xO_{2-x/2}$  are smaller than that for  $CeO_2$  (107 kcal/½ mole  $O_2$ ) (12) at the stoichiometric composition.

The complicated relation between  $\Delta\bar{H}$  and  $x$  causes the somewhat queer shapes of  $t_i$  shown in Fig. 4. The sharp increase in  $t_i$  between  $x = 0.1$  and  $0.2$  at 700°C corresponds to the  $\Delta\bar{H}$  increase in the same composition region. At larger  $x$ , however,  $\Delta\bar{H}$  changes marginally with the variation of  $x$  and, as a result,  $t_i$  is controlled mainly by  $\sigma_i$  instead of the stability of  $Ce^{4+}$ .

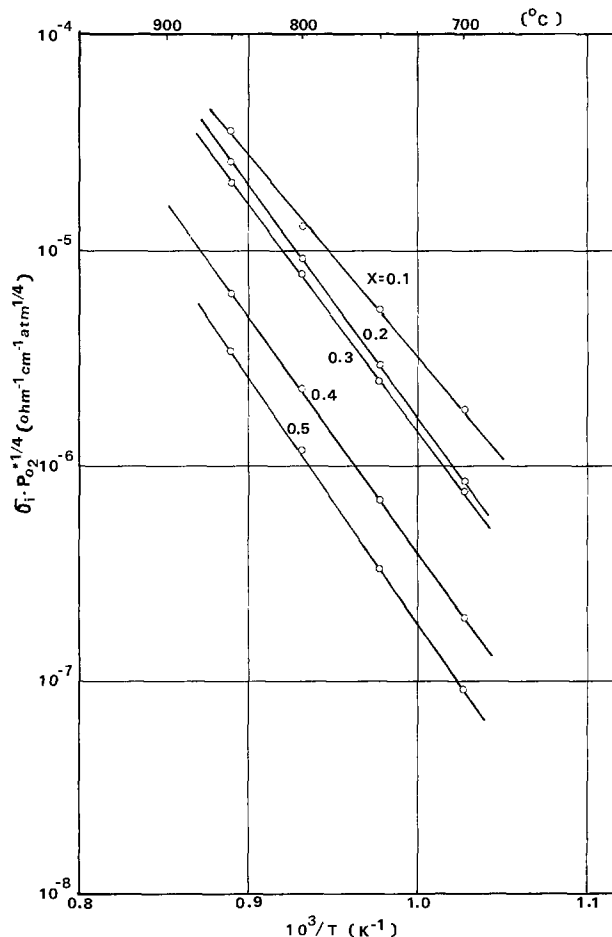


Fig. 5. Variation of  $(\sigma_i \cdot p^*_{O_2})^{1/4}$  with reciprocal absolute temperature for  $Ce_{1-x}Gd_xO_{2-x}$ .

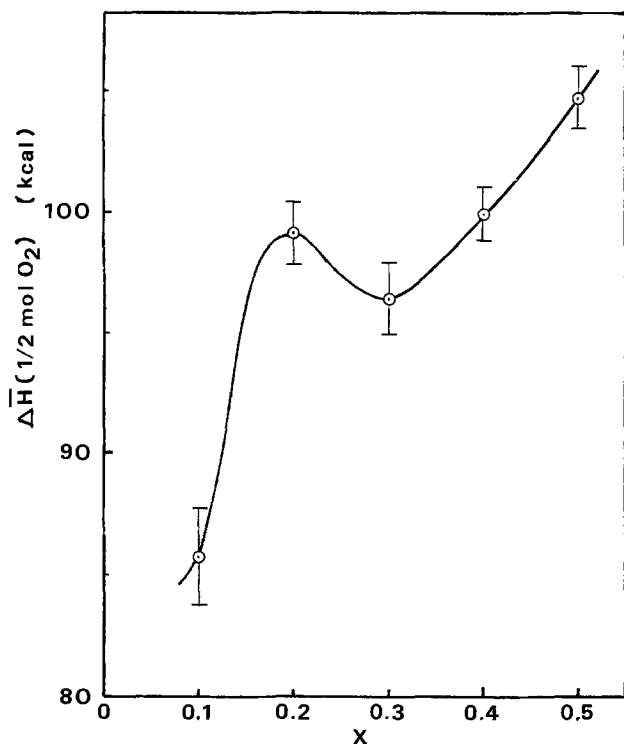


Fig. 6. The partial molal enthalpy change ( $\Delta\bar{H}$ ) for the reaction  $O_2 = \frac{1}{2} O_2(g) + V_O + 2e$  at the compositions  $Ce_{1-x}Gd_xO_{2-x/2}$  as a function of  $x$ .

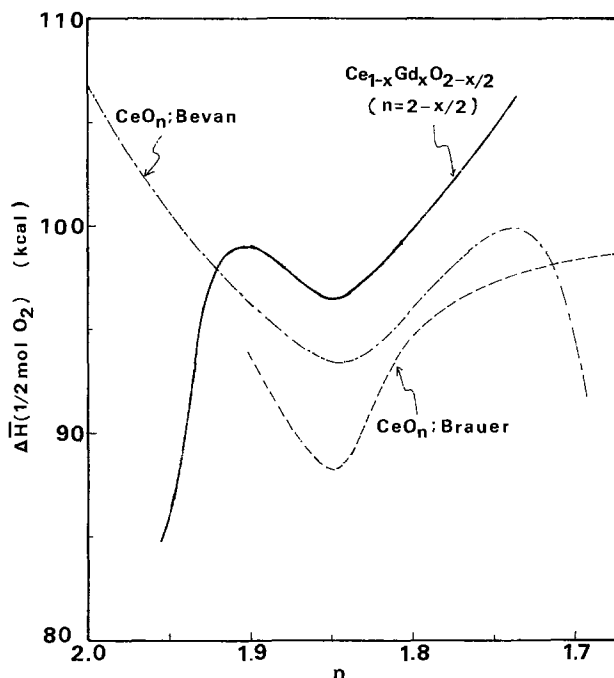


Fig. 7. Comparison of  $\Delta\bar{H}$  for  $Ce_{1-x}Gd_xO_{2-x/2}$  with those for  $CeO_n$  reported by Bevan (12) (---) and by Brauer (13) (-·-·-) as a function of  $n$ . For  $Ce_{1-x}Gd_xO_{2-x/2}$ ,  $n$  is  $(2-x/2)$ .

Nevertheless, at higher temperatures the effect of an increase in  $\Delta\bar{H}$ , which offsets that of  $\sigma_i$ , becomes appreciable. This effect shifts the maximum in the  $t_1$  curve for 800°C to larger  $x$ .

Finally, some consideration of the shape of the plot in Fig. 6 is needed. This plot is again shown in Fig. 7 with the partial molal enthalpy composition data for nondoped  $CeO_n$  reported by Bevan *et al.* (12) and Brauer *et al.* (13). Here the abscissa represents  $n$  in  $CeO_n$  instead of  $x$ , where  $n$  is  $(2-x/2)$  for  $Ce_{1-x}Gd_xO_{2-x/2}$ . This figure makes it clear that oxygen ion vacancies generated by the reduction of  $CeO_2$  and those produced by the dopant  $Gd^{3+}$  have the same effects on  $\Delta\bar{H}$  as long as  $n < 1.9$ . All three curves in Fig. 7 show similar profiles which have their minima at the same composition ( $n = 1.85$ ) in the region where  $n < 1.9$ , indicating that oxygen vacancies produced by the two different mechanisms influence  $\Delta\bar{H}$  in the same manner when defects of the oxygen ion lattice dominate.

In the region where  $n > 1.9$ , however,  $\Delta\bar{H}$  for  $Ce_{1-x}Gd_xO_{2-x/2}$  drastically decreases towards  $n = 2.0$  in contrast to the results for  $CeO_n$ . In the case of  $CeO_n$ , the decrease in  $\Delta\bar{H}$  to a minimum at the composition  $CeO_{1.85}$  can be interpreted as an effect associated with the increase in oxygen ion vacancies, with the increase after the minimum being an effect related to an ordering of lattice defects.

A remarkable decrease in  $\Delta\bar{H}$  seen in the small  $x$  region for  $Ce_{1-x}Gd_xO_{2-x/2}$  should not be attributed to the effect of oxygen vacancies but to the solution of  $Gd^{3+}$  itself. Perhaps a complex state between  $Gd^{3+}$  and  $O^{2-}$  with smaller binding energy is formed in a dilute solid solution, and the maximum at  $x = 0.2$  could be interpreted as the result of rapid disappearance of the complexes between the composition  $x = 0.1$  and 0.2.

Manuscript submitted July 29, 1975; revised manuscript received Nov. 19, 1975.

Any discussion of this paper will appear in a Discussion Section to be published in the December 1976 JOURNAL. All discussions for the December 1976 Discussion Section should be submitted by Aug. 1, 1976.

Publication costs of this article were partially assisted by Hitachi, Limited.

#### REFERENCES

1. C. J. Kevane, E. L. Holverson, and R. O. Watson, *J. Appl. Phys.*, **34**, 2083 (1963).
2. R. N. Blumenthal and B. A. Pinz, *ibid.*, **38**, 2376 (1967).
3. T. Takahashi and H. Iwahara, *Denki Kagaku*, **34**, 906 (1966).
4. T. Kudo and H. Obayashi, *This Journal*, **122**, 142 (1975).
5. T. Takahashi, in "Physics of Electrolytes," Vol. 2, J. Hladik, Editor, p. 989, Academic Press, London (1972).
6. H. Schmalzried, *Z. Elektrochem.*, **66**, 572 (1962).
7. V. B. Tare and H. Schmalzried, *Z. Physik. Chem. N.F.*, **43**, S30 (1964).
8. J. E. Bauerle and J. Hrizo, *J. Phys. Chem. Solids*, **30**, 565 (1969).
9. T. H. Etsell and S. N. Flengas, *Chem. Rev.*, **70**, 368 (1970).
10. T. Takahashi, K. Ito, and H. Iwahara, *Rev. Energ. Primaire*, **2**, 27 (1966).
11. A. D. Neumin, S. F. Pal'guyev, and V. N. Chebotin, in "Electrochemistry of Molten and Solid Electrolytes," Vol. 2, M. V. Snirnov, Editor, p. 79, Consultants Bureau, New York (1964).
12. D. S. M. Bevan and J. Kordis, *J. Inorg. Nucl. Chem.*, **26**, 1509 (1964).
13. G. Brauer, K. A. Gengerich, and U. Holtschmidt, *ibid.*, **16**, 77 (1960).

# An Improved Photolithographic Method of Metallization Applied to Fabrication of Planar Gunn-Effect Devices

O. Wada, S. Yanagisawa, and H. Takanashi

Fujitsu Laboratories Limited, Kamikodanaka 1015, Nakahara-ku, Kawasaki, Japan

## ABSTRACT

It is difficult to provide a fine pattern of metal electrode across a step included in the substrate. In order to overcome this difficulty, we have developed a method in which a deposition mask is constructed photolithographically by using a composite with the multilayer structure of negative photoresist layer-metal layer-positive photoresist layer. The electrode metal is evaporated through the windows opened in the composite mask. The principle of the present method and detailed procedure are described. The effect of the geometrical configuration of the evaporation setup on the broadening of the defined metal edge is also discussed. This method is applied in order to fabricate a planar Gunn-effect device. A Schottky gate electrode with a width of  $2\ \mu\text{m}$  is delineated across a bevel with a height of  $3.5\ \mu\text{m}$ .

Recently, many workers have investigated the application of the Gunn-effect device with planar structure for high speed logic circuits, using an n-GaAs layer epitaxially grown on a semi-insulating GaAs substrate (1-4). Fabrication of these devices is performed by etching the unwanted area of the n-GaAs layer and preparing ohmic and Schottky contacts (2-4) on the active area which is protected during the etching. In these processes, steps are formed at the peripheries of the active areas. Usually, the height of the step is a few microns or larger (5). From the viewpoint of photolithography, however, the existence of the step is disadvantageous in delineating fine patterns of the electrodes, particularly in preparing the Schottky gate electrode across the step. Both the standard photolithographic method, in which etch-resistant photoresist is used, and the so-called "lift-off method" (7, 8), in which the photoresist pattern is formed prior to metal deposition, are not used successfully (9). On the contrary, improvement of the device characteristics, such as trigger sensitivity (3, 6), is achieved by preparing fine electrodes and controlling the separation between them. Bachem and co-workers avoided such a disadvantage with a completely planar structure (9) in which the n-GaAs layer is protected under the ohmic and Schottky contact patterns including the electrode leads during the sputter etching. However, this structure could possibly degrade the electrical characteristics of the device, due to inhomogeneities of the electric field or the gate capacitance under the electrode lead, especially for devices with minute dimensions.

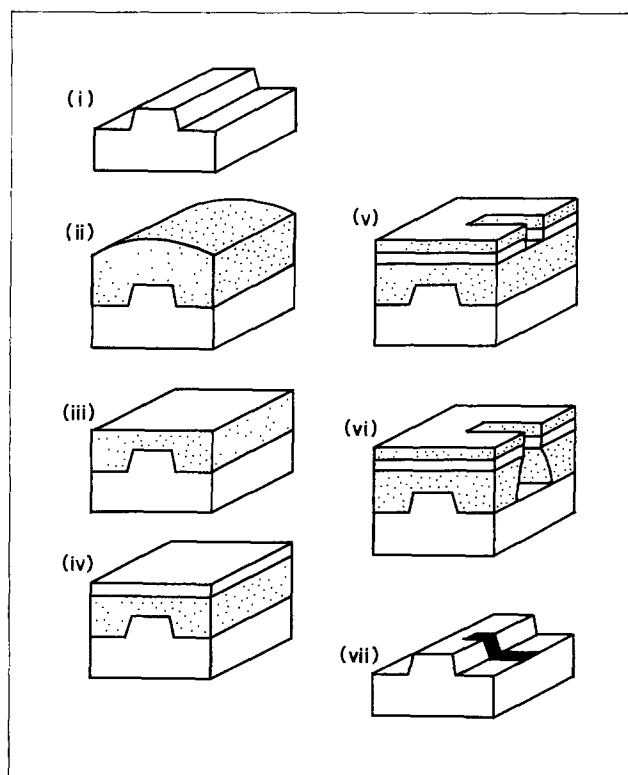
In this paper, we wish to describe an improved method of defining the electrode patterns across the steps on the substrate. This method utilizes a composite of a photoresist layer, an overlying metal, and a photoresist layer as a deposition mask during the evaporation of the electrode metal. The use of this composite mask has been proposed by Grebe and co-workers (10) for the case where no step is involved. We have extended the method for use in the fabrication of planar Gunn-effect devices. The structure includes steps with  $3.5\ \mu\text{m}$  height and line widths of  $2\ \mu\text{m}$ .

## Method

Figure 1 illustrates the sequence of the processes used to form a fine pattern of electrode across a step on the substrate. Only the key part of the device is

Key words: pattern delineation, bevel, deposition mask, ohmic contacts, Schottky gate electrodes.

shown, and the Schottky gate formation is used as an example; essentially the same process is applied



■ photoresist    □ metal

Fig. 1. Schematic representation of the method used to delineate a fine pattern of the metal electrode (Schottky gate) across a bevel on the substrate: (i) etching of the substrate to form a bevel, (ii) coating of the substrate with a positive photoresist layer followed by prebaking, (iii) thinning and smoothing of the resist layer, (iv) evaporation of a metal on the whole surface of the resist layer, (v) pattern formation on the metal layer by chemical etching with a mask produced by a negative photoresist layer using usual photolithographic technique, (vi) overexposure of the positive resist layer followed by development, (vii) evaporation of a metal film through the window in the composite layers and subsequent removal of the layers by immersion in acetone, thus leaving the desired pattern of the metal electrode.

to the ohmic contact formation. Here, we consider a GaAs layer with (100) surface.

(i) First, removal of the unwanted area of GaAs layer is performed by usual photoresist protecting technique and chemical etching. In this process, a bevel shape must be formed for the benefit of electrode crossing. The direction of the step edge should be chosen parallel to the  $\langle 011 \rangle$  crystal axis (11, 12). An etchant, the rate of which is reaction limited (12), is effectively used to obtain the bevel shape.

(ii) Positive photoresist, e.g., AZ-1350J,<sup>1</sup> with a thickness large enough to cover the whole substrate surface including the bevel top is coated and baked well (a few hours at 70°-80°C for AZ-1350J).

(iii) A flat photoresist surface is needed to minimize the deleterious effect of optical diffraction in the subsequent photoresist process. For this purpose, the resist surface is mechanically polished and smoothed to a thickness about 3-10  $\mu\text{m}$  larger than the bevel height. This process is performed in a way similar to the polishing of various semiconductor surfaces. The resist surface is smoothed by polishing with alumina powder (grain size of 3-0.3  $\mu\text{m}$ ) dissolved in water on a flat plate the surface of which is coated with a silk cloth, and is then finished by polishing in flowing water. Shallow scratches which are passively made in this process are not too harmful because the resist layer acts only as a spacer between the substrate surface and the overlying metal layer; the latter is prepared in the subsequent process. Thus, a carefully performed process results in a good uniformity of the residual resist thickness excluding the small area neighboring the wafer edge.

(iv) A metal layer is deposited on the whole surface of the resist layer. It is recommended that the procedure (ii) to (iv) be carried out under dark-room conditions.

(v) The electrode pattern is delineated by the usual protecting method and chemical etching. In this process, a positive photoresist layer is applicable as described by Grebe *et al.* (10). In that case, however, the resist is also removed in the next procedure in which the exposure and development of the lower resist layer are carried out. When a negative resist is used, it can still remain on the metal surface during the subsequent process. The use of a negative photoresist layer is advantageous in forming a good deposition mask even when the undercut of the metal layer occurs during etching procedure because the remaining negative photoresist edge works as the pattern-defining mask during the following metal evaporation process.

(vi) By the exposure of the whole area followed by the development, the exposed portion of the positive photoresist layer upon which no overlying metal exists is removed. The residual upper resist layer together with the metal layer can work as the deposition mask in the next process. The exposure time should be long enough for the bottom width of the hole in the resist to exceed the width of the metal deposited in the subsequent process. Overexposure is needed to control the pattern definition property only by the deposition process, not by other conditions. This aspect is useful to exclude the critical nature of the exposure and development of a thick resist layer.

(vii) Next, the electrode metal is evaporated at an angle normal to the surface, then the resist layers and the upper metal layers are removed by immersion of the substrate in acetone. These processes result in the desired structure.

In the last step of these processes, the configuration of the evaporation setup influences the quality of the deposited metal edge. The schematic illustration of the setup is shown in Fig. 2. As can be seen in Fig. 2, the broadening,  $b$ , and the tilting distance,  $t$ , of the edge are expressed by  $s(l - m)/2(h - s)$  and  $sl/(h - s)$ , respectively. In order to reduce these values for a given pattern width,  $m$ , it is important to select a large source-substrate separation,  $h$ , a small source dimension,  $l$ , and a small resist thickness,  $s$ . Although a greater amount of metal is required as  $h$  increases, broadening and tilting of the edge are greatly suppressed.

### Results and Discussion

To demonstrate the performance of the present method, an experimental result is described. A GaAs crystal with (100) surface was etched into bevel shapes, the height of which were 5.8  $\mu\text{m}$ , using the  $8\text{H}_2\text{O}_2 \cdot 1\text{H}_2\text{SO}_4 \cdot 1\text{H}_2\text{O}$  system (12). Then the composite mask was constructed using AZ-1350J, an Au layer ( $\approx 0.2 \mu\text{m}$ ), and spin-coated OMR-83<sup>2</sup> ( $\approx 1 \mu\text{m}$ ). The lower resist layer was thinned to about 11  $\mu\text{m}$  on the bevel bottom surface and to about 5  $\mu\text{m}$  on the bevel top surface. The uniformity of the resist thickness was good in the whole wafer area, excluding the area within 150  $\mu\text{m}$  from the wafer edge. After the delineation of the patterns on the Au layer, the positive resist was exposed to ultraviolet light for 10 min by means of a conventional photoresist exposure apparatus. Then the Au layer with 0.7  $\mu\text{m}$  thickness was deposited by using an evaporation source with effective surface dimensions of 1.3 cm  $\times$  0.7 cm ( $l \approx 1.3 \text{ cm}$ ). The substrate was set at a distance of 25 cm from the source ( $h = 25 \text{ cm}$ ). Figure 3 presents scanning electron micrographs showing the cross sec-

<sup>2</sup> Tokyo Ohka Kogyo Company, Limited, Kawasaki, Japan.

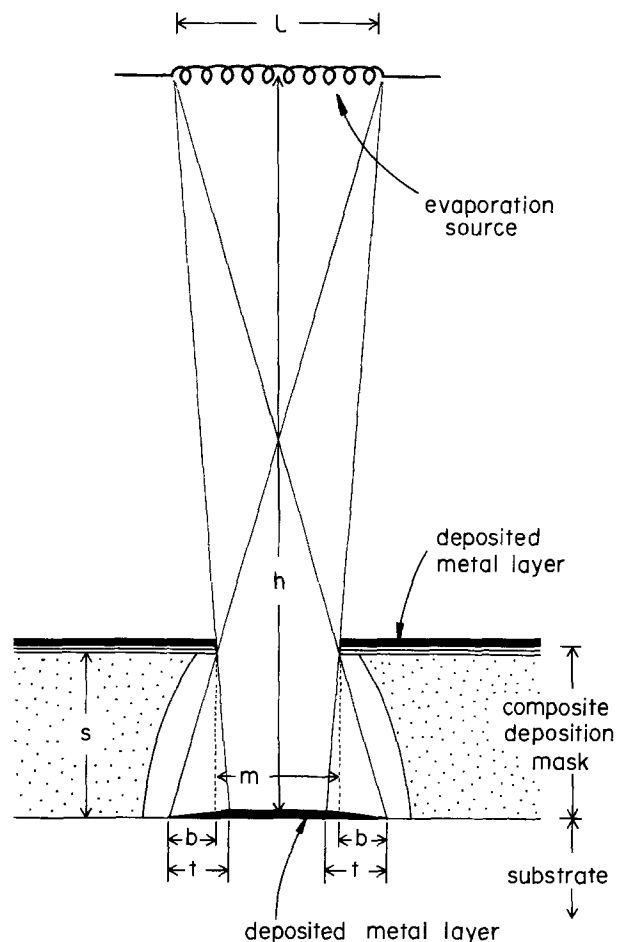


Fig. 2. Schematic drawing of the geometrical configuration of the evaporation source, the composite mask, and the substrate surface.

<sup>1</sup> Shipley Company, Incorporated, Newton, Massachusetts.

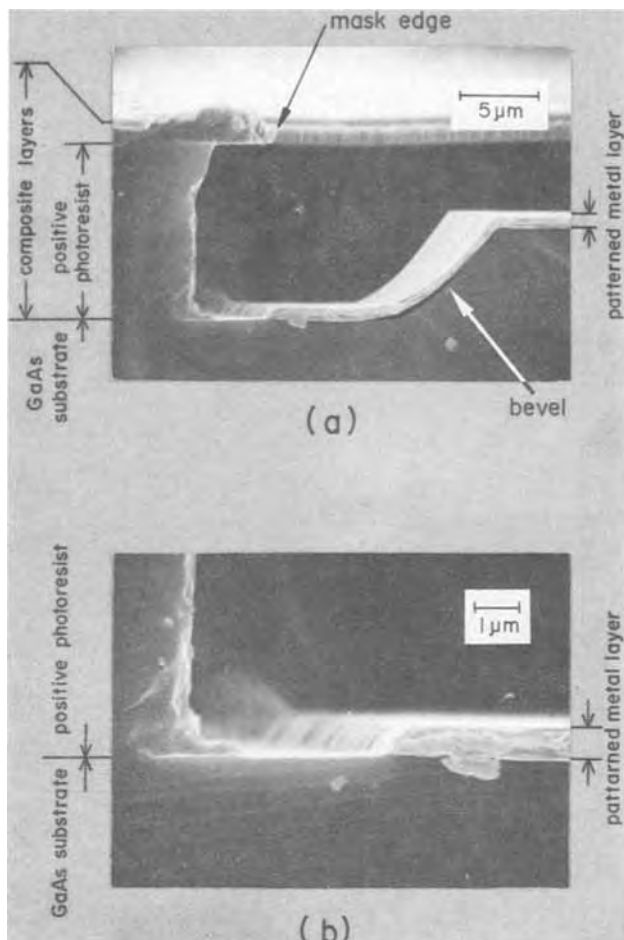


Fig. 3. Scanning electron micrograph of the structure of the substrate which is cross sectioned just after the evaporation of the gold layer. The structure observed for the area near the bevel is shown.

tion of the substrate after metal evaporation. The figure indicates that the deposited metal is delineated by the edge of the upper deposition mask, and that the overexposed lower resist layer works as a spacer. Taking  $h \gg s$  and  $l \gg m$  into account, we can calculate the dimensions of the deposited metal edge. In this case, the tilting distance is calculated to be  $0.6 \mu\text{m}$  on the bevel bottom surface and  $0.3 \mu\text{m}$  on the bevel top surface, and the corresponding broadening is one-half of that on each surface. From Fig. 3(b), the tilting distance is measured to be approximately  $0.5 \mu\text{m}$  on the bevel bottom surface. As is expected, this value agrees with the calculated one. Figure 4 shows the scanning electron micrograph of the Au pattern which was revealed after removal of the composite mask. Both the left-hand and the right-hand parts of the photograph show the top and the bottom surfaces of the bevel. A thick metal layer with well-defined edges is formed on each surface. It is also worth noticing that some pile-up of the deposited metal on the edge of the composite deposition mask occurs, as shown in Fig. 3(a). This may cause a narrowing of the window opened in the mask during the course of metal evaporation, particularly in the case where a very thick metal layer is delineated. The tilting of the upper edge of the deposited metal with an angle smaller than the expected one (Fig. 4) may be attributable to this window-narrowing effect.

Planar Gunn-effect devices were fabricated using the same method. An n-GaAs layer with (100) surface grown on a Cr-doped GaAs substrate was etched into a bevel with a height of  $3.5 \mu\text{m}$ . Then the composite mask was formed as described above. To form the ohmic contacts, an Au-Ge-Ni mixture was evapo-

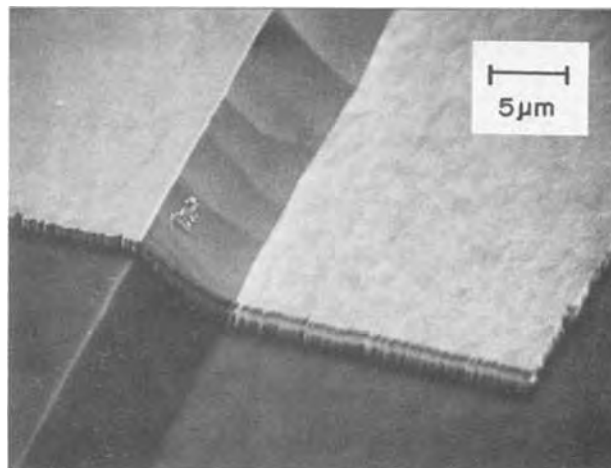


Fig. 4. Scanning electron micrograph of the bevel metallized by a thick metal layer showing the structure after removal of the composite mask. Note that the metal edges both on the top surface (left-hand side) and on the bottom surface (right-hand side) are appreciably well defined.

rated to a thickness of about  $3000\text{\AA}$ . Removal of the composite mask and subsequent alloying of the Au-Ge-Ni films at  $430^\circ\text{C}$  for 40 sec provided good ohmic contacts. The Schottky gate electrode was prepared by an aluminum layer with  $3000\text{\AA}$  thickness. In this fabrication, a smaller source dimension ( $l = 0.7 \text{ cm}$ ) and a larger source-substrate separation ( $h > 30 \text{ cm}$ ) than those used in the previous experiment were selected. Figure 5 shows the whole structure of the resultant device. The separation between the gate and the cathode and the small width of the gate are both  $2 \mu\text{m}$  on the top of the bevel. It has been confirmed by large magnification measurement that any additional broadening of the gate line width cannot be detected within the measurement accuracy even on the bevel bottom surface.

Figure 6 shows the waveforms of the triggering input and the current output obtained on a device with a gate-anode separation of  $25 \mu\text{m}$ . The device

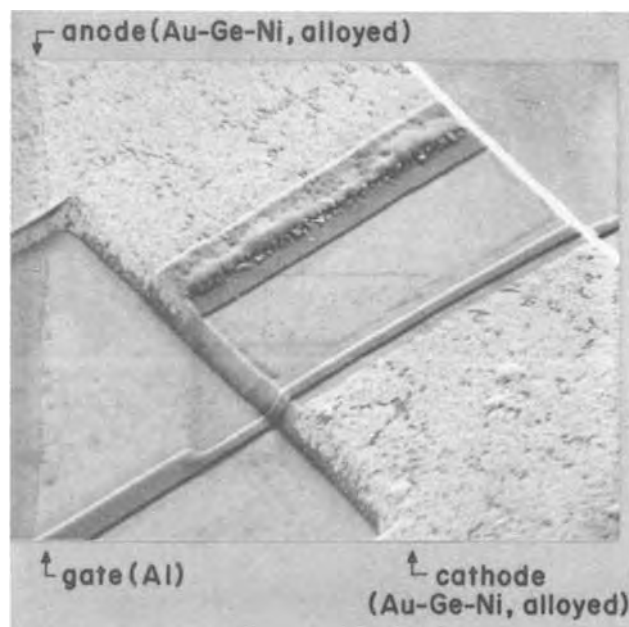


Fig. 5. Scanning electron micrograph of a planar Gunn-effect device with a Schottky gate prepared by using the metallization method described in the text. The distance between the gate and the anode, the width of the active layer, and the bevel height are  $20 \mu\text{m}$ ,  $60 \mu\text{m}$ , and  $3.5 \mu\text{m}$ , respectively. The gate width is only  $2 \mu\text{m}$ .



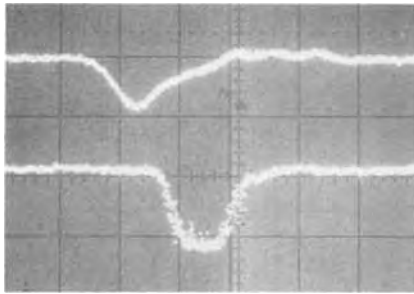


Fig. 6. Waveforms of the triggering signal fed into the gate (upper trace) and the current output detected by a 50 ohm load resistor (lower trace). The device is d-c biased at the subthreshold state. The vertical scale is 100 mV/div, and the horizontal scale is 250 psec/div. The time scale for the upper trace advances that for the lower one by about 100 psec in this photograph.

was d-c biased and the output was controlled by the triggering signal fed into the gate. A rapid response with 300 psec pulse width was obtained on the output by a gate input as small as 80 mV. In fabricating a device with such a large pulse repetition rate, and therefore having such fine dimensions, the method described in this paper is useful.

### Conclusions

An improved photolithographic method makes it possible to delineate a fine pattern of the electrode metal across a bevel on the substrate. The method utilizes a deposition mask with a multilayer structure composed of a negative photoresist layer, a metal layer, and a positive photoresist layer. In this method, the deleterious effect of optical diffraction is minimized by using an exposure mask in intimate contact with the flat surface of the upper negative photoresist layer. To obtain the flat surface, the lower photoresist layer surface is mechanically polished. Then windows are opened in the lower photoresist layer using the pattern-defined upper metal layer as an exposure mask. Thus the pattern-defining deposition mask is formed by the upper photoresist layer together with the metal layer. The broadening and tilting of the resulting pattern edge are minimized in the subsequent metal evaporation process by adopting an evaporation source with a small area and by setting the substrate far from the source.

The method has been applied in the fabrication of planar Gunn-effect devices with bevel heights of 3.5

$\mu\text{m}$ . A Schottky gate electrode with a width of 2  $\mu\text{m}$  has been delineated across the bevel. A rapid response characteristic has been achieved, largely due to the fine electrode patterns.

Delineation of a fine pattern across bevels on the substrate is greatly improved by this method. Adding to this, a greater thickness of the deposited metal does not impede the pattern formation. By this method, it is possible to make a narrow, thick metal stripe across a bevel, which has a small longitudinal resistance. Moreover, owing to these features, this method is considered to be of further usage in the microfabrication of GaAs.

### Acknowledgments

The authors are indebted to Dr. T. Misugi, Y. Fukukawa, and Y. Tōyama for their constant encouragements and discussions. They are also grateful to Dr. M. Abe and T. Ogawa for their useful discussions.

Manuscript submitted April 14, 1975; revised manuscript received Sept. 22, 1975.

Any discussion of this paper will appear in a Discussion Section to be published in the December 1976 JOURNAL. All discussions for the December 1976 Discussion Section should be submitted by Aug. 1, 1976.

Publication costs of this article were partially assisted by Fujitsu Laboratories Limited.

### REFERENCES

1. M. Takeuchi, A. Higashisaka, and K. Sekido, *IEEE Trans. Electron. Devices*, **ED-19**, 125 (1972).
2. T. Sugeta, H. Yanai, and K. Sekido, *Proc. IEEE*, **59**, 1629 (1971).
3. T. Sugeta, M. Tanimoto, T. Ikoma, and H. Yanai, *IEEE Trans. Electron. Devices*, **ED-21**, 504 (1974).
4. K. Mause, A. Schlachetzki, E. Hesse, and H. Salow, *IEEE Trans. Commun.*, **COM-22**, 1435 (1974).
5. A. Schlachetzki and K. Mause, *Electron. Letters*, **8**, 640 (1972).
6. K. Heime, *ibid.*, **7**, 610 (1971).
7. L. I. Maissel and R. Glang, "Handbook of Thin Film Technology," pp. 7-48, McGraw-Hill, New York (1970).
8. H. I. Smith, F. J. Bachner, and N. Efremow, *This Journal*, **118**, 821 (1971).
9. K. H. Bachem, J. Engemann, and K. Heime, *Japan. J. Appl. Phys. Suppl.*, **43**, 222 (1974).
10. K. Grebe, I. Ames, and A. Ginzberg, *J. Vacuum Sci. Technol.*, **11**, 458 (1974).
11. J. J. Gannon and C. J. Nuese, *This Journal*, **121**, 1215 (1974).
12. S. Iida and K. Ito, *ibid.*, **118**, 768 (1971).

## Vapor Pressure Dependence of the Relative Composition of III-V Mixed Crystals in Vapor Phase Epitaxy

Kenji Kajiyama

*Nippon Telegraph and Telephone Public Corporation,  
Electrical Communication Laboratories, Musashino, Tokyo 180, Japan*

### ABSTRACT

It is thermodynamically deduced that the composition  $x$  of  $\text{In}_x\text{Ga}_{1-x}\text{As}$  depends on the arsenic vapor pressure in a vapor phase epitaxy. Calculated results agree with the experiments. A simplified formula of the equilibrium relation is also deduced in the conventional reaction system without excessive arsenic pressure.

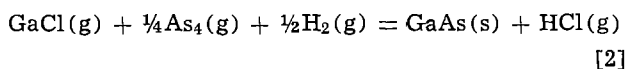
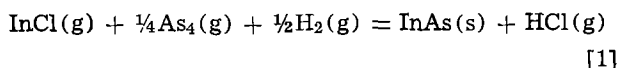
Mixed crystals of III-V compounds are promising materials in various applications. Taking the  $\text{In}_x\text{Ga}_{1-x}\text{As}$

Key words: III-V,  $\text{In}_x\text{Ga}_{1-x}\text{As}$ , arsenic vapor, vapor phase epitaxy, distribution relation.

system as an example, the distribution relation of In vs. Ga between the source vapor phase and the crystal phase should depend on the As vapor pressure. A simple derivation of the distribution relation is pre-

sented here, along with a comparison with experimental results. Experiments have been carried out with an (In-Ga)-AsCl<sub>3</sub>-As-H<sub>2</sub> system (1). As<sub>4</sub> and HCl are produced by the reaction of AsCl<sub>3</sub> with H<sub>2</sub> at 850°C. Resulting HCl reacts with In-Ga metal to form InCl and GaCl (870°C). The most significant feature of this system is that the main As source is metallic As, which is evaporated by heating at a temperature from 350° to 460°C. Evaporated As pressure is much larger than the decomposed As pressure from AsCl<sub>3</sub>. H<sub>2</sub> is used as a carrier gas.

Assuming equilibrium



with the equilibrium constant  $K$

$$K_{\text{InAs}} = a_{\text{InAs}} p_{\text{HCl}} p_{\text{InCl}}^{-1} p_{\text{As}_4}^{-1/4} p_{\text{H}_2}^{-1/2}$$

and

$$K_{\text{GaAs}} = a_{\text{GaAs}} p_{\text{HCl}} p_{\text{GaCl}}^{-1} p_{\text{As}_4}^{-1/4} p_{\text{H}_2}^{-1/2}$$

where  $a$  is the activity and  $p$  is the partial pressure (atm) in the crystal growth region. The above formulas are valid in any reaction system with chlorides for the transport of III-group components and H<sub>2</sub> as the carrier gas. Using the regular solution model (2), activities are given with the interaction parameter  $\alpha$

$$a_{\text{InAs}} = x \exp[\alpha(1-x)^2/RT],$$

$$a_{\text{GaAs}} = (1-x) \exp[\alpha \cdot x^2/RT]$$

In the usual experimental temperature region,  $p_{\text{InCl}_2} \ll p_{\text{InCl}}$ ,  $p_{\text{InCl}_3} \ll p_{\text{InCl}}$ ,  $p_{\text{GaCl}_2} \ll p_{\text{GaCl}}$ ,  $p_{\text{GaCl}_3} \ll p_{\text{GaCl}}$ , and  $p_{\text{Cl}_2} \ll p_{\text{HCl}}$ , which have been confirmed by mass spectrometry (3) and the equilibrium constants (4). The molar ratio  $y = n_{\text{In}}/(n_{\text{In}} + n_{\text{Ga}})$  of In to the total III-group components in the source vapor is approximated as

$$y/(1-y) = p'_{\text{InCl}}/p'_{\text{GaCl}} \\ = (p_{\text{InCl}} + x p_{\text{HCl}})/(p_{\text{GaCl}} + (1-x)p_{\text{HCl}}) \quad [3]$$

where  $p'_{\text{InCl}} - p_{\text{InCl}} = \gamma \cdot \Delta n_{\text{InAs}} = \gamma \cdot x \cdot \Delta n_{\text{In}_x\text{Ga}_{1-x}\text{As}} = x \cdot p_{\text{HCl}}$  and  $p'_{\text{GaCl}} - p_{\text{GaCl}} = \gamma \cdot \Delta n_{\text{GaAs}} = \gamma(1-x) \Delta n_{\text{In}_x\text{Ga}_{1-x}\text{As}} = (1-x) p_{\text{HCl}}$  ( $p'$  is the starting partial pressure,  $\Delta n$  is the depositing rate of crystal, and  $\gamma$  is the experimental constant), since, in the In-Ga source region, HCl is almost fully consumed by the In-Ga source to form InCl and GaCl (3) and, in the crystal growth region, HCl is regenerated from InCl and GaCl to deposit InAs and GaAs, respectively.

The composition dependence on As pressure is then deduced, using  $p_{\text{H}_2} = 1 - p_{\text{As}_4}$ . In the usual experimental condition,  $p_{\text{InCl}} \ll 1$ ,  $p_{\text{GaCl}} \ll 1$ ,  $p_{\text{HCl}} \ll 1$ , and  $p_{\text{As}_2} \ll p_{\text{As}_4}$ . The last inequality is approved by the equilibrium constant  $K = p_{\text{As}_2}^2/p_{\text{As}_4} \ll 10^{-3}$  ( $T < 1100^\circ\text{K}$ ) of the equilibrium  $\text{As}_4(g) = 2\text{As}_2(g)$  (4)

$$p_{\text{As}_4}^{1/4} (1 - p_{\text{As}_4})^{1/2} = \frac{1}{y-x} \left\{ \frac{x(1-y)}{K_{\text{InAs}}} \exp \frac{\alpha(1-x)^2}{RT} - \frac{(1-x)y}{K_{\text{GaAs}}} \exp \frac{\alpha x^2}{RT} \right\} \quad [4]$$

As the left-hand side of Eq. [4] has a maximum  $\sqrt[3]{4/27}$  at  $p_{\text{As}_4} = 1/3$  and a minimum 0 at  $p_{\text{As}_4} = 0$  or 1, the range of  $x$  is restricted for a given  $y$ . If  $p_{\text{As}_4} \ll 1$ , which corresponds to the minimum condition and is the conventional case without metallic As source, Eq. [4] becomes simpler. In this case, the consumption of the III-group components in the crystal growth region is small ( $y/(1-y) = p'_{\text{InCl}}/p'_{\text{GaCl}} \approx p_{\text{InCl}}/p_{\text{GaCl}}$ )

$$y/(1-y) = (K_{\text{GaAs}}/K_{\text{InAs}}) \{x/(1-x)\} \\ \exp\{\alpha(1-2x)/RT\} \quad [5]$$

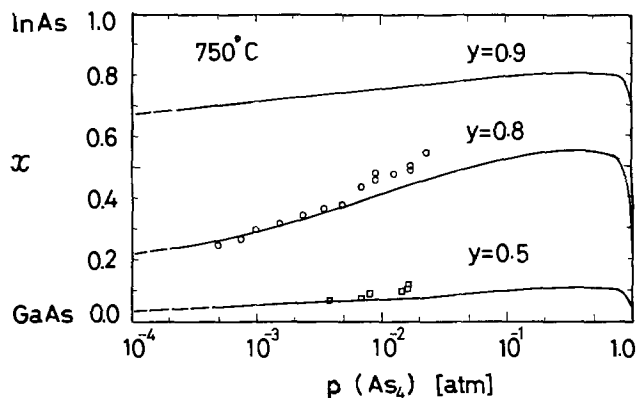


Fig. 1. Composition  $x$  of  $\text{In}_x\text{Ga}_{1-x}\text{As}$  crystal vs. arsenic vapor pressure  $p_{\text{As}_4}$  with the starting molar ratio  $y$  of In. —: calculated result; point: experiment (1);  $\circ$ :  $z = 0.9$  ( $y = 0.83$ );  $\square$ :  $z = 0.7$  ( $y = 0.61$ ).

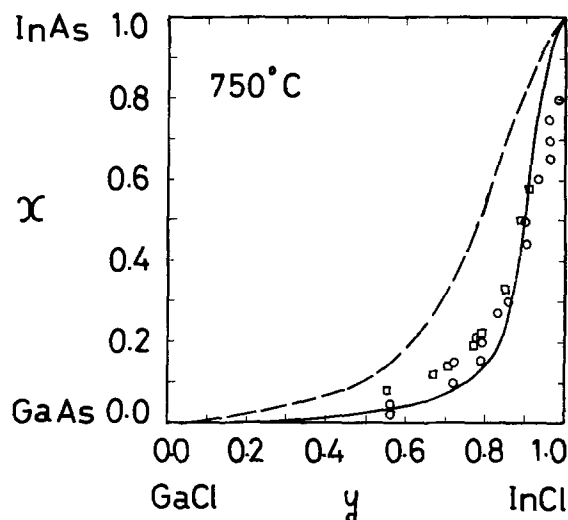


Fig. 2. Distribution relation of the III-group component between  $y$  in the starting source vapor and  $x$  in the grown crystal. —: calculated result for the minimum (the case in the conventional experiments); - - -: calculated result for the maximum;  $\circ$ : experiment (7);  $\square$ : experiment (8).

The As pressure dependence of the distribution relation (Fig. 1) and the range of  $x$  (Fig. 2) have been calculated using the thermodynamic coefficients:  $\alpha = 3000$  cal/mole (2),  $\log_{10}K_{\text{InAs}} = -7.68 + 7595/T$  (5),  $\log_{10}K_{\text{GaAs}} = -8.04 + 6990/T + 0.35 \times 10^{-3} T + 0.22 \ln T$  (4). The calculated As pressure dependence agrees with the experimental results (1).<sup>1</sup> The starting As pressure in the source gas does not exactly equal the equilibrium As pressure in the crystal growth region. But the difference between them, which results from crystal deposit, is small. ( $p'_{\text{As}_4}$  is much larger than  $p'$  of any other component gas in metallic As source system.)

As the In-Ga source has been used in the experiment, the distribution relation between  $y$  and the molar ratio  $z$  of In in the In-Ga source is needed. The  $y$ - $z$  relation is deduced in a similar way to Eq. [5], assuming a thermoequilibrium condition in the In-Ga source region

$$y/(1-y) = (K_{\text{Ga}}/K_{\text{In}}) \{z/(1-z)\} \\ \exp\{\alpha_{\text{In-Ga}}(1-2z)/RT\} \quad [6]$$

with

$$K_{\text{In}} = p_{\text{InCl}} p_{\text{H}_2}^{1/2} a_{\text{In}}^{-1} p_{\text{HCl}}^{-1}$$

$$K_{\text{Ga}} = p_{\text{GaCl}} p_{\text{H}_2}^{1/2} a_{\text{Ga}}^{-1} p_{\text{HCl}}^{-1}$$

<sup>1</sup> If a small quantity of the In-Ga source is used,  $x$  increases during the series of experiments, because Ga is consumed faster than In, as shown by the following  $y$ - $z$  relation.

where  $p'_{\text{InCl}_2} \ll p'_{\text{InCl}}$ ,  $p'_{\text{InCl}_3} \ll p'_{\text{InCl}}$ ,  $p'_{\text{GaCl}_2} \ll p'_{\text{GaCl}}$ ,  $p'_{\text{GaCl}_3} \ll p'_{\text{GaCl}}$ , and  $p'_{\text{Cl}_2} \ll p'_{\text{HCl}}$  are assumed in the In-Ga source region (3, 4). Calculated  $y$  values for the experimental  $z$  values are shown in the caption of Fig. 1. The following thermodynamic coefficients were used:  $\alpha_{\text{In-Ga}} = 1060$  cal/mole (6),  $K_{\text{In}}(900^\circ\text{C}) = 4.56$  (3),  $K_{\text{Ga}}(900^\circ\text{C}) = 5.67$  (3).

The calculated  $x$ - $y$  relation for the minimum condition agrees with the experimental results (7, 8), but differs somewhat from other detailed calculated results (9). The reason is a difference in the adopted thermodynamic coefficients but not in the simplified theory. The distribution relation depends weakly on the temperature because  $K_{\text{GaAs}}/K_{\text{InAs}}$  and  $\exp\{\alpha(1 - 2x)/RT\}$  vary slowly with temperature.

In a conventional reaction condition, where the partial pressure of the reactant gas is low ( $< 10^{-3}$  atm), the distribution relation of III-V mixed crystal is generally simplified<sup>2</sup>

$$y/(1-y) = [(K_1/K_2)\{x/(1-x)\}]$$

$$\exp\{\alpha(1-2x)/RT\}^m \quad [17]$$

where  $m$  is the number of relevant atoms in a molecule participating in the thermoequilibrium. For example,  $m = 1$  in the  $\text{In}_x\text{Ga}_{1-x}\text{As}$  system (In in InCl and Ga in GaCl) and  $m = 4$  in the  $\text{InAs}_x\text{P}_{1-x}$  system (10) (As in  $\text{As}_4$  and P in  $\text{P}_4$ ). And the distribution relation depends on the partial pressure of the common atom, e.g.,  $p_{\text{As}_4}$  in the  $\text{In}_x\text{Ga}_{1-x}\text{As}$  system and  $p_{\text{InCl}}$  in the  $\text{InAs}_x\text{P}_{1-x}$  system (10).

<sup>2</sup> A detailed discussion of the deduction will appear later with another good example of  $\text{InAs}_x\text{P}_{1-x}$ .

### Acknowledgments

The author would like to thank Mr. M. Yamaguchi for unpublished data and Dr. Y. Mizushima for his encouragement.

Manuscript submitted Aug. 27, 1974; revised manuscript received ca. Nov. 7, 1975.

Any discussion of this paper will appear in a Discussion Section to be published in the December 1976 JOURNAL. All discussions for the December 1976 Discussion Section should be submitted by Aug. 1, 1976.

Publication costs of this article were partially assisted by the Nippon Telegraph and Telephone Public Corporation.

### REFERENCES

1. H. Okamoto and S. Sakata, *Appl. Phys. Soc. (Japan)*, **2**, 315 (1972); M. Yamaguchi *et al.*, Unpublished.
2. M. B. Panish and M. Ilegams, "Progress in Solid State Chemistry," Vol. 7, Pergamon Press, Inc., New York (1972).
3. V. S. Ban, *J. Cryst. Growth*, **17**, 19 (1972).
4. D. J. Kirwan, *This Journal*, **117**, 1572 (1970).
5. O. Mizuno and K. Arai, *Japan. J. Appl. Phys.*, **13**, 1955 (1974).
6. J. P. Bros, R. Castanet, and M. Laffitte, *Compt. Rend.*, **264C**, 1804 (1967).
7. R. W. Conrad, P. L. Hoyt, and D. D. Martin, *This Journal*, **114**, 164 (1967).
8. R. E. Enstrom, D. Richman, and M. S. Abrahams, *Proc. 3rd Int. Symp. GaAs*, 30 (1970).
9. H. Nagai, T. Shibata, and H. Okamoto, *Japan. J. Appl. Phys.*, **10**, 1337 (1971); S. Minagawa, H. Seki, and E. Eguchi, *ibid.*, **11**, 855 (1972); J. B. Mullin and D. T. J. Hurle, *J. Luminescence*, **7**, 176 (1973).
10. K. Kajiyama, *Japan. J. Appl. Phys.*, **14**, 1057 (1975).

## The Preparation of High $T_c$ $\text{Nb}_3\text{Ge}$ Superconductors by Chemical Vapor Deposition

L. R. Newkirk, F. A. Valencia, and T. C. Wallace

Los Alamos Scientific Laboratory, Los Alamos, New Mexico 87544

### ABSTRACT

Bulk layers of  $\text{Nb}_3\text{Ge}$  have been deposited on copper substrates at  $900^\circ\text{C}$  by the hydrogen reduction of the chlorides of niobium and germanium with resistive  $T_c$ 's as high as  $22.5^\circ\text{K}$  and current densities up to  $1.8 \times 10^8$  A-cm<sup>-2</sup> at  $13.8^\circ\text{K}$ . This paper provides a detailed description of the coating process as well as empirical correlations between deposition parameters and  $T_c$ . Quantitative chlorination of Nb was found to be possible at  $T \approx 250^\circ\text{C}$  and for  $T > 900^\circ\text{C}$  extending the range of delivery rates below those obtainable by powder feeding of  $\text{NbCl}_5$ . Coatings in the range of 10-60  $\mu\text{m}$  thick have been produced with a typical deposition efficiency of 50-65% for mass flow rates of the order of 1g of salt per minute. The superconducting transition temperature has been correlated with a parameter of the form mole ratio  $\times$  dilution  $\times$  Reynolds number<sup>0.22</sup>, where mole ratio is defined by moles Nb: moles (Ge + O) in the gas stream, and dilution by moles gas: moles salt. In addition, the relationship between mole ratio and dilution which determines the phase produced ( $\text{Nb}_3\text{Ge}$  or  $\text{Nb}_5\text{Ge}_3$ ) is defined over the region of major interest. Lattice spacings are presented over a range of  $T_c$ 's, and microstructure and substrate adherence are discussed.

With the discovery that careful sputtering could produce  $\text{Nb}_3\text{Ge}$  with a transition temperature from  $22^\circ$  to  $23^\circ\text{K}$  (1, 2) this previously unexciting material was thrust to the forefront of high-temperature superconductors. In order to study properties requiring bulk quantities of material as well as to show potential for commercial or industrial development, a technique was required which is capable of generating bulk quantities

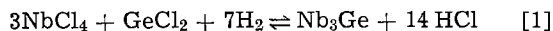
of this material. The authors (3) and others (4-7) have demonstrated that the technique of chemical vapor deposition (CVD) is capable of producing  $\text{Nb}_3\text{Ge}$  with superconducting onsets above  $22^\circ\text{K}$  in quantities sufficient for a variety of measurements, and in layers of sufficient thickness to be useful technologically. The superconducting properties of these deposits have been detailed in Ref. (3) and (4), and it is the intent of this paper to describe the deposition process itself and to examine the effects of the various coating parameters.

Key words: superconductivity, niobium-germanide, beta-tungsten, vapor deposition.

### Coating Technique

**Basic apparatus.**—The basic apparatus used in these experiments is depicted schematically in Fig. 1. Argon and hydrogen mixed in the desired proportions are preheated in a  $2.5 \times 30$  cm cylindrical nickel chamber maintained at  $500^\circ\text{C}$ , and then mixed in a stainless steel tee at  $350^\circ\text{C}$  with  $\text{NbCl}_5$  vapor generated by one of the methods described later.  $\text{GeCl}_4$  vapor, produced by passing Ar through liquid  $\text{GeCl}_4$  in the  $\text{GeCl}_4$  saturator, is introduced into the gas stream, and the resulting combination passed directly into the mixing chamber. This  $5 \times 30$  cm stainless steel chamber contains 10 nickel baffles which prevent any channeling of the gas through the chamber, and is maintained at  $500^\circ\text{C}$ . The plumbing connecting these components is made of Ni tubing or pipe, except where couplings necessitate the use of stainless steel.

After preheating and mixing, the gases and chlorides pass into the coating chamber where reduction takes place at  $900^\circ\text{C}$  according to the following reaction



The  $\text{NbCl}_4$  and  $\text{GeCl}_2$  which enter the reaction are generated from the  $\text{NbCl}_5$  and  $\text{GeCl}_4$  by thermal decomposition as the salt temperatures are increased through the coating train, with the excess chlorine reacting to  $\text{HCl}$ . The deposition area itself consists of the inside surface of a cylindrical hard drawn Cu tube  $2.2 \times 60$  cm with a wall thickness of 1 mm, surrounded by a 1 in. Ni pipe. The Ni pipe serves to protect the Cu tube from direct exposure to the atmosphere as well as to improve the uniformity of the substrate temperature. Temperature is measured by 4 Chromel-Alumel thermocouples placed in mechanical contact with the substrate at  $\sim 8, 23, 38,$  and  $53$  cm from the inlet end. Before being exhausted, the unused gases leaving the coating chamber are passed through an oil bubbler to prevent the back diffusion of air.

**Niobium delivery.**—Both  $\text{NbCl}_5$  powder and Nb chlorination were used successfully as sources of  $\text{NbCl}_5$  vapor.  $\text{NbCl}_5$  powder of reactor grade purity, but containing significant amounts of  $\text{NbOCl}_3$ , was screened to  $-100$  mesh and entrained on an Ar gas stream by means of a commercial powder feeder (Plasmatron by Plasmadyne Division of Geotel Incorporated). Feed rates varying from 0.8 to 2 g/min were employed with the lower feed rate limited by the equipment. Rates were measured by monitoring an electronic load cell connected to the Plasmatron, with an estimated accuracy of  $\pm 5\%$ . The entrained powder is then passed into a 20 liter stainless steel chamber maintained at  $400^\circ\text{C}$ , where the  $\text{NbCl}_5$  is vaporized. This large volume serves the additional function of smoothing fluctuations in the  $\text{NbCl}_5$  flow caused by irregularities in the Plasmatron or packing of the chloride into small pellets. The argon- $\text{NbCl}_5$  vapor mixture is then either passed into the coating train or exhausted through an oil bubbler, depending on the positions of the valves shown in Fig. 1.

The alternate technique of Nb chlorination is carried out in a  $5 \times 30$  cm cylindrical nickel chamber maintained at  $250^\circ\text{--}260^\circ\text{C}$ , containing reactor grade niobium

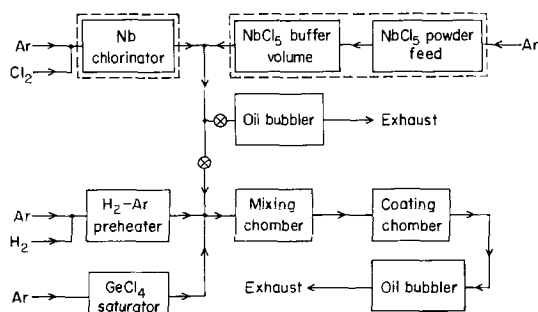


Fig. 1. Flow diagram for CVD apparatus

tubing either in the form of strips or cuttings. A chlorine-argon mixture in the ratio of  $\sim 1:4$  is introduced into the chamber, and chlorination to  $\text{NbCl}_5$  takes place. This process is sufficiently free of fluctuations that the  $\text{NbCl}_5$  vapor can be introduced directly into the coating train following chlorination, without the necessity of passing through a large buffering volume.

### Experimental Procedures

**Lattice spacings.**—Crystal structure and lattice spacings are determined by means of both powder patterns and a diffractometer. Powder patterns are obtained using a 114.6 mm Debye-Scherrer camera with copper radiation, and diffractometer patterns are produced with a Picker Model 3488 K, also using copper radiation. In both cases lattice spacings are determined by a least squares (8) extrapolation against the Nelson-Riley function, and are estimated to be accurate to  $\pm 0.002\text{\AA}$ .

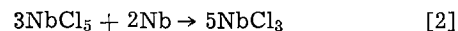
**Superconducting transitions.**—Superconducting transitions are measured both inductively ( $f = 23$  Hz) and resistively ( $J < 10$  A-cm $^{-2}$ ). A complete explanation of measurement techniques and thermometer calibration is found in Ref. (3). In general, temperatures are estimated to be  $\pm 0.2^\circ\text{K}$  for both the inductive and resistive measurements.

**Oxygen analysis.**—The method employed in this study to determine oxygen content depends on the use of a Pt melt to form stable platinides of Nb and Ge, allowing the liberation of oxygen as carbon monoxide (9). A portion of the sample to be analyzed (20-40 mg) is placed in a graphite crucible containing  $\sim 3$ g of Pt. The crucible is placed in a vacuum system and evacuated to a pressure of  $\sim 2 \times 10^{-6}$  Torr, following which the system is sealed off and the crucible rapidly heated to  $2000^\circ\text{C}$  for 1 min. The pressure rise in the system is measured using a thermocouple gauge and the oxygen content calculated on the basis of the system volume. Any material suspected of containing small amounts of NbH is first dehydrided by heating to  $\sim 700^\circ\text{C}$  in a vacuum of  $2 \times 10^{-6}$  Torr for 2 min. Samples of the evolved gas for the first 15 specimens examined were analyzed on a gas chromatograph and found to consist entirely of carbon monoxide. Oxygen composition determined by this method is estimated to be accurate to  $\pm 10\%$  of the measured value.

**Metallography.**—Samples examined metallographically were subjected to standard grinding and polishing procedures through  $0.05 \mu\text{m}$  alumina. Etching was carried out for times ranging from 15-60 sec in a mixture of  $90\text{H}_2\text{SO}_4$  and  $10\text{HF}$  by volume. Samples were etched by immersion and pumped in a vacuum chamber for 10-15 min following washing to remove any trace of etchant.

### Experimental Results

**Chlorination of Nb.**—The feasibility of Nb chlorination was studied over the full range of possible temperatures (ambient to  $950^\circ\text{C}$ ) with the intent of determining if the quantitative production of one of the chlorides was possible. The primary hindrance to achieving this is the formation  $\text{NbCl}_3$  by the reaction of  $\text{NbCl}_5$  with the excess Nb according to Eq. [2]



$\text{NbCl}_3$ , which has a range of homogeneity (10), does not vaporize, but rather slowly decomposes as a function of temperature and  $\text{NbCl}_5$  vapor pressure, to  $\text{NbCl}_5$  or possibly  $\text{NbCl}_4$  if the temperature is sufficiently high. Since the chlorinator must contain excess Nb to insure that all the  $\text{Cl}_2$  is reacted, the formation of  $\text{NbCl}_3$  must be prevented by the choice of temperature. Two temperature ranges have been found where this is possible. Above  $900^\circ\text{C}$   $\text{NbCl}_3$  does not form, and the Nb is reacted directly to  $\text{NbCl}_4$ , in substantial agreement with the chlorination technique used in Ref. (4). The disadvantage of this technique seems to be in the necessity

Table I. Nb consumption

Series	Calculated Nb consumption	Actual Nb consumption	Error
1	125.9g	120.4g	4.4%
2	200.9g	190.1g	5.4%

of keeping the chloride vapor at a relatively high temperature from production to reaction. Failure to do this can result in decomposition to NbCl<sub>3</sub> destroying the quantitative aspects of the process.

The second temperature where quantitative chlorination is possible, and the one employed in this study, is  $T = 260^\circ\text{C}$ . Although NbCl<sub>5</sub> is stable at this temperature, the reaction of NbCl<sub>5</sub> with Nb does not proceed if the partial pressure of NbCl<sub>5</sub> is maintained at or below 0.1 atm. Four chlorinators were examined after producing 150-200g of NbCl<sub>5</sub> each and the remaining Nb removed. The Nb was quite clean, indicating the absence of any NbCl<sub>3</sub> (a blue-black deposit). The Nb strips were etched or attacked only at the inlet end, indicating complete consumption of the Cl<sub>2</sub>. For two of the chlorinators records were maintained of the total chlorine flow over the life of the chlorinators, and the expected Nb consumption was calculated with the results shown in Table I. It is important to note that this technique is quantitative only if the partial pressure of NbCl<sub>5</sub> is maintained at or below the value indicated, by dilution with Ar or another inert gas. If it is allowed to approach 1 atm, NbCl<sub>3</sub> formation occurs and quantitative transfer of Nb is lost.

**Superconducting onset.**—The variation of superconducting onset with deposition parameters is shown in Fig. 2. For this figure data were used only for samples taken between 15 and 30 cm from the inlet end since  $T_c$  has been found to vary along the length of the coating chamber. For these correlations  $T_c$  is determined inductively at 23 Hz and in general is 1-1.5°K lower than the resistively determined onset. The parameter mole ratio  $\times$  dilution  $\times$  Reynolds number<sup>0.22</sup> was arrived at empirically and its possible significance will be discussed later. The mole ratio used in this figure is the mole ratio of NbCl<sub>5</sub> to GeCl<sub>4</sub> introduced into the apparatus, adjusted for the amount of oxygen found in the deposit. This adjustment is made with the assumption that the oxygen is in solid solution in the A-15 structure and is found on Ge lattice sites. Although no direct evidence exists that this is the case (i.e., neutron or x-ray ordering studies), all attempts to correlate  $T_c$  with deposition parameters failed without this assumption. Dilution is defined as the ratio of total moles of gas to total moles of chlorides passed through the system.

Figure 3 shows deposition efficiency as a function of the same parameter. Efficiency was defined as the weight of the deposit divided by the weight of Nb and

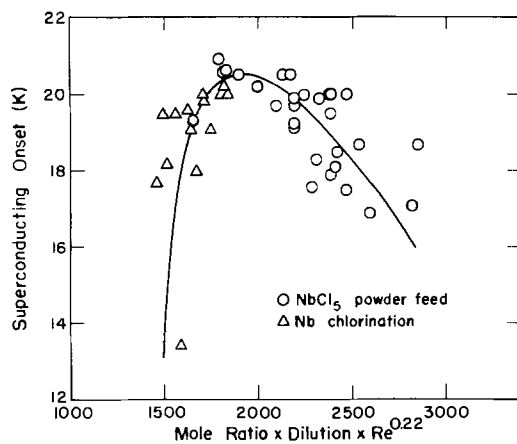
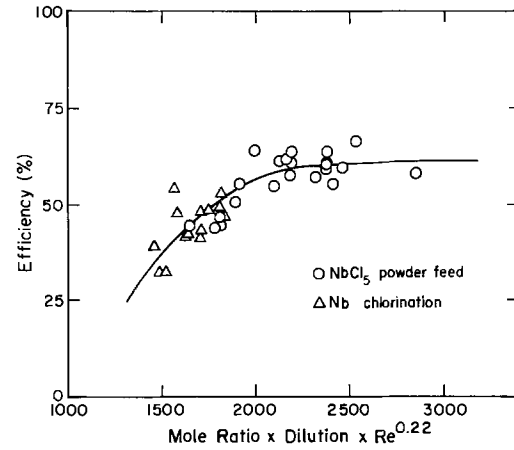
Fig. 2. Variation of  $T_c$  with correlation parameter

Fig. 3. Variation of efficiency with correlation parameter

Ge delivered, and varies between 30 and 65%. The data from which Fig. 2 and 3 were derived is tabulated in Tables II and III.

**Phase relationships.**—Figure 4 shows the relationship between deposition parameters and the phase produced. The boundary between the Nb<sub>3</sub>Ge region and the Nb<sub>5</sub>Ge<sub>3</sub> region does not seem to be sharp and indicates that the phases can coexist over a range of compositions. Whether this overlap is a property of the system or is the result of an inadequate choice of deposition parameters is not clear with the data available. A somewhat better boundary is possible if the scaling

Table II. Deposition efficiency as a function of the same parameter for NbCl<sub>5</sub> powder feed

NbCl <sub>5</sub> (g/30 min)	GeCl <sub>4</sub> (g/30 min)	H <sub>2</sub> (liters/min)	Ar (liters/min)	Oxygen (w/o)	Yield (g)	$T_c$ (inductive onset K)
25.5	6.60	5	7.8	0.73	4.9	19.3
27.5	7.95	10	7.8	0.77	6.2	20.5
31.5	8.38	10	7.8	0.82	6.4	20.6
28	7.88	10	7.8	1.22	5.5	20.6
27.3	7.90	10	7.8	1.15	5.3	20.9
25	8.03	10	7.8	0.83	7.3	20.2
24.5	6.52	10	7.8	0.87	3.3	20.0
23.3	6.39	10	7.8	1.44	5.6	19.7
26.3	6.20	10	7.8	1.31	3.2	18.3
27	5.80	10	7.8	1.28	5.5	18.5
26.8	4.85	10	7.8	2.15	6.0	18.1
25.3	5.60	10	7.8	1.92	4.1	19.2
25.8	6.20	12.5	7.8	1.72	6.6	17.9
33	6.84	12	7.8	0.75	4.6 (15 min)	18.7
31.8	7.20	12	7.8	0.71	4.0 (15 min)	20.0
31	7.64	15	7.8	1.82	4.1 (15 min)	20.5
30	7.56	15	7.8	1.40	3.9 (15 min)	20.0
26.5	7.04	15	7.8	2.16	3.8 (15 min)	19.9
29	6.70	15	7.8	2.07	3.5 (15 min)	19.9
25.8	6.74	15	7.8	1.95	3.6 (15 min)	19.5
25	6.90	12	7.8	1.38	3.5 (15 min)	19.1
28.5	7.10	20	7.8	1.68	3.6 (15 min)	18.7
27	7.90	12.5	7.8	0.97	7.4	20.5
26.8	4.85	10	7.8	1.38	6.0	17.1
27	5.80	10	7.8	0.96	5.5	16.9
26.8	4.85	10	7.8	2.84	6.0	17.9
25.25	5.60	10	7.8	1.33	4.1	17.5
29	8.00	15	7.8	1.18	4.1	17.6
61.25	14.80	20	15.5	0.85	13.0	20.0

Table III. Deposition efficiency as a function of the same parameter for Nb chlorination

Cl <sub>2</sub> (cm <sup>3</sup> /min)	GeCl <sub>4</sub> (g/30 min)	H <sub>2</sub> (liters/min)	Ar (liters/min)	Oxygen (w/o)	Yield (g)	$T_c$ (inductive onset K)
150	5.05	6.0	4.5	0.84	4.4	13.4
123	4.95	6.0	4.5	0.92	4.22	19.3
127	4.95	6.0	4.5	0.98	—	19.7
120	4.85	6.0	4.5	0.63	1.8	19.1
120	5.10	6.0	4.5	0.88	2.5	18.2
120	5.00	6.0	4.7	0.49	3.2	<4
120	5.30	6.0	4.7	0.30	3.3	19.1
120	5.00	6.0	4.7	0.48	3.7	19.9
120	4.75	6.0	4.7	0.46	4.0	20.4
120	5.00	6.0	4.7	0.36	3.8	19.2
120	4.90	6.0	4.7	0.21	3.6	20.1
120	5.00	6.0	4.7	0.76	3.2	19.6
123	4.95	6.0	4.5	1.48	2.5	19.5

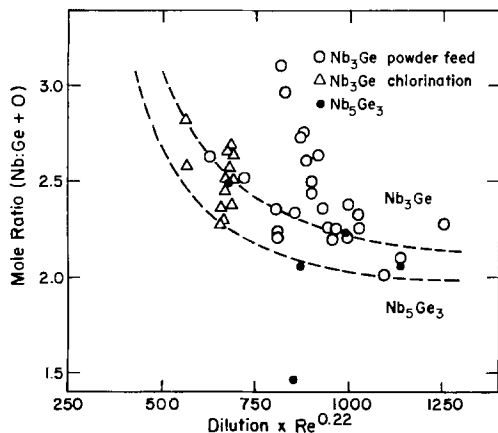


Fig. 4. Phase relationship of  $\text{Nb}_3\text{Ge}$  and  $\text{Nb}_5\text{Ge}_3$

parameter on the x axis is chosen to be dilution only, but the product of dilution  $\times$  Reynolds number<sup>0.22</sup> was used to be consistent with the parameters used in Fig. 2 and 3.

**Oxygen content.**—The oxygen content of  $\sim 45$  samples has been measured and values ranging from 0.1 to 2.1 weight per cent (w/o) were found. The primary source of this oxygen is  $\text{NbOCl}_3$  contained in the  $\text{NbCl}_5$  powder. When chlorination of Nb is carried out carefully instead of the use of  $\text{NbCl}_5$  powder, material with an oxygen content of 0.1 w/o can be consistently produced. The presence of significant amounts of oxygen does not seem to be harmful to the superconducting properties; in fact, the very best material produced (inductive  $T_c$ 's of 20.6–20.9°K and  $J_c$ 's of  $1.0\text{--}1.8 \times 10^6$  A-cm<sup>-2</sup> at 13.8°K) contained from 1.0 to 1.2 w/o oxygen. A similar effect was also noticeable in the x-ray powder patterns, with deposits containing  $\sim 1.0$  w/o oxygen having the greatest number of lines resolved into  $\alpha_1$  and  $\alpha_2$  doublets.

As noted in the section on superconducting onset, the oxygen content must be taken into account in calculating the A to B atom ratio in the  $\text{A}_3\text{B}$  structure. In addition to the major effect on  $T_c$  of altering the A to B atom ratio, it is also important to determine the effect of replacing Ge atoms by O atoms while maintaining the same A to B atom ratio. For the alloys studied, this effect, if it is present, seems to be smaller than the scatter in the data for both  $T_c$  and lattice spacings. As a result, neither  $T_c$  nor  $a_0$  provides direct evidence that the oxygen is in solid solution in the A-15 structure. Due to the difficulty in obtaining completely single-phase material (typical deposits are 80–90% A-15), ordering studies which may provide direct evidence concerning the location of oxygen atoms have not been completed.

**Lattice spacings.**—Figure 5 shows the inductive transition temperature as a function of lattice spacing. Several types of data are displayed in this figure in the following manner. The points shown for  $\text{NbCl}_5$  powder feed (with buffer), and Nb chlorination are believed to represent relatively homogeneous material for the reasons explained in the description of the coating technique. Those points labeled  $\text{NbCl}_5$  powder feed (without buffer) almost certainly contain significant compositional inhomogeneities as evidenced by visible fluctuations in the flow of  $\text{NbCl}_5$  powder and metallographic evidence of a layered structure in the deposit. The first set of data represents the actual variation of lattice spacing with  $T_c$ , and an extrapolation of this data is in good agreement with arc-melted specimens. The second set of data is included to show the error inhomogeneities can cause in determining a relationship of this type. The measurement of lattice spacings from a powder pattern is a true average over the thickness of the material, while a measurement of  $T_c$ , even at 23 Hz, tends to be somewhat biased toward the best

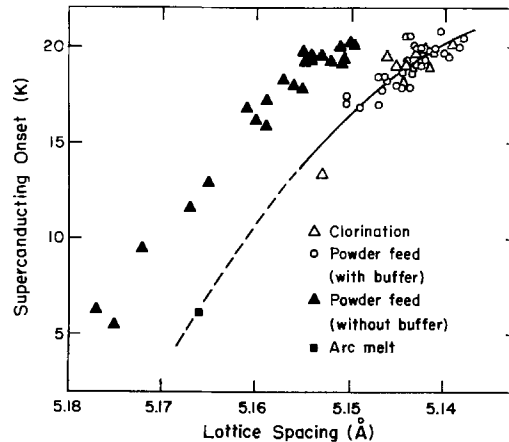


Fig. 5. Variation of  $T_c$  with lattice spacing

material present due to a shielding of the poorer material from the flux. For reasons such as this it is always necessary to be certain of the homogeneity of the material before trying to correlate any parameter which is clearly a bulk average with another property which can be influenced by small amounts of material.

**Additional properties.**—Figure 6 shows a photomicrograph typical of the microstructure of a homogeneous  $\text{Nb}_3\text{Ge}$  deposit. The grains are of the order of a few micrometers in size and seem to be elongated in the direction of growth. In addition, the interface between the  $\text{Nb}_3\text{Ge}$  deposit and the Cu substrate seems to indicate very intimate contact, probably a diffusion bond considering the solubility of Ge in Cu and the reducing properties of  $\text{H}_2$  on Cu at 900°C. The only evidence of vapor phase attack on the Cu substrate is the presence in the deposit of 1000 ppm Cu when analyzed spectrographically. This copper is probably concentrated near the deposit substrate interface.

The effects of lower deposition temperatures and several heat-treatments are discussed in Ref. (3). In addition, heat capacity measurements are detailed in Ref. (10), critical current measurements in Ref. (11), and the effects of 1 MeV neutron irradiation in Ref. (12).

### Discussion

Although the parameter used to define  $T_c$  and efficiency in Fig. 2 and 3 was arrived at empirically, some

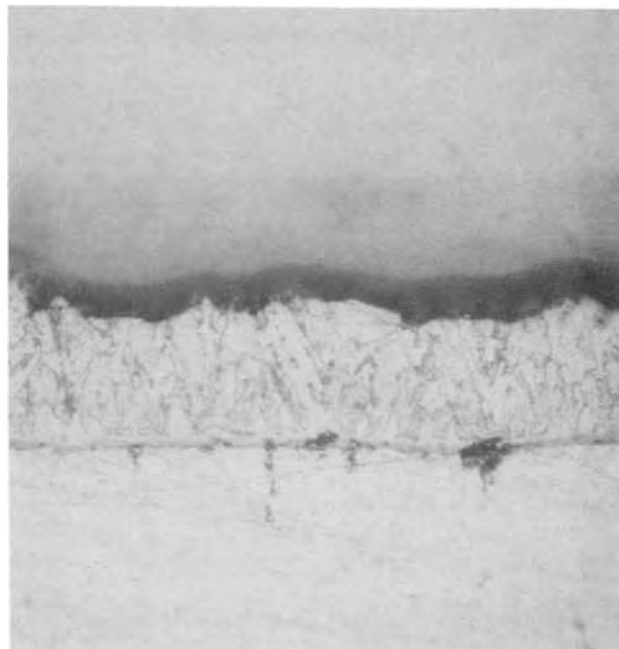
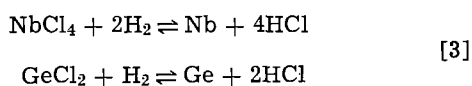


Fig. 6. Photomicrograph of  $\text{Nb}_3\text{Ge}$  deposit X545

insight is possible if the various processes involved in the deposition are considered. Any attempt to understand this dependence probably must begin with the assumption that a relationship exists between  $T_c$  and the composition of the deposit. If this is the case, the problem is reduced to finding the relationship between the stoichiometry of the deposit and the composition of the gas stream at the inlet. If one assumes that the composition of the deposit is determined by the relative concentrations of NbCl<sub>4</sub> and GeCl<sub>2</sub> at the deposition surface, and their respective reduction rates, then it is clear that the initial mole ratio of NbCl<sub>5</sub> to GeCl<sub>4</sub> and the relative diffusivities of NbCl<sub>4</sub> and GeCl<sub>2</sub> in the vapor mixture must play a role. While the calculation of these diffusivities in the five component system (Ar, H<sub>2</sub>, HCl, NbCl<sub>4</sub>, and GeCl<sub>2</sub>) is extremely complicated, it seems likely that both the dilution and viscosity (the latter being contained in the Reynolds number) will be a factor. The other factor to be considered is the relative reduction rates, which depend in part on the products of the reaction. If the reduction is examined as two separate reactions as in Eq. [3]



it is seen that the production of HCl for the Nb reduction is considerably larger than that for the Ge. As a consequence, a change in dilution should have different effects on the rates of the two reactions, resulting in a change in the composition of the deposit.

It is clear from an examination of Fig. 2 that it is possible to produce high  $T_c$  material over a wide range of flow conditions and mole ratios. Since, however, this is entirely an empirical relationship and its physical basis is understood in only the most tenuous way, great caution must be exercised in applying the relationship outside the experimentally studied ranges of these parameters. These ranges cover Reynolds numbers from 600 to 2000 (including partial pressures of H<sub>2</sub> from 0.35 to 0.70 atm), mole ratios from 2.0 to 3.0, and dilutions from 140 to 230. The large degree of data scatter in Fig. 2 may be the result of inaccuracies in measuring the various parameters involved, or it may indicate that the correlation parameter used does not have the correct form. For this reason all the original data used to construct Fig. 2 and 3 is presented in Tables II and III in order that the reader is enabled to correlate  $T_c$  to parameters which may be more meaningful.

If the assumption is made that the best material produced contains ~25 a/o Ge then an interesting exercise is possible. Based on arc melt data of 5.166Å at 18-19 a/o Ge and CVD data of 5.142Å at 25 a/o Ge, an extrapolation to 0 a/o Ge shows that the lattice spacing of hypothetical A-15 Nb<sub>3</sub>Nb might be expected to be

in the range of 5.23-5.24Å, a value in close agreement with that obtained by Vieland *et al.* (7). A number of deposits made early in the study showed lattice spacings as large as 5.21-5.22Å, and were not superconducting to 4°K. If the above extrapolation is meaningful, this suggests that Nb<sub>3</sub>Ge containing as little as 5-6 a/o Ge can be prepared with the A-15 structure. Since the major area of interest is stoichiometric Nb<sub>3</sub>Ge, sufficient data was never acquired concerning the location of the Ge deficient phase boundary to draw any firm conclusions.

### Acknowledgments

The authors wish to express their thanks to A. L. Giorgi and E. G. Szklarz for the inductive  $T_c$  measurements, and to B. T. Matthias for his help in undertaking and pursuing this project.

This work was completed under the auspices of the Energy Research and Development Administration.

Manuscript submitted May 20, 1975; revised manuscript received Oct. 14, 1975. This paper was presented at the Fifth International Conference on Chemical Vapor Deposition, Stoke Poges, Buckinghamshire, England, Sept. 21-25, 1975.

Any discussion of this paper will appear in a Discussion Section to be published in the December 1976 JOURNAL. All discussions for the December 1976 Discussion Section should be submitted by Aug. 1, 1976.

Publication costs of this article were partially assisted by Los Alamos Scientific Laboratory.

### REFERENCES

1. J. R. Gavaler, *Appl. Phys. Letters*, **23**, 480 (1973).
2. L. R. Testardi, J. H. Wernick and W. A. Royer, *Solid State Comm.*, **15**, 1 (1974).
3. L. R. Newkirk, F. A. Valencia, A. L. Giorgi, E. G. Szklarz, and T. C. Wallace, *Proceedings 1974 Applied Superconductivity Conf.*, p. 221.
4. J. R. Gavaler, M. A. Janoko, A. I. Braginski, and G. W. Roland, *Proceedings 1974 Applied Superconductivity Conf.*, p. 192.
5. A. I. Braginski and G. W. Roland, *Appl. Phys. Letters*, **25**, 762 (1974).
6. H. Kawamura and K. Tachikawa, *Phys. Letters*, **50A**, 29 (1974).
7. L. J. Vieland and A. W. Wicklund, *ibid.*, **49A**, 407 (1974).
8. R. E. Vogel and C. P. Kempter, *Acta Cryst.*, **14**, 1130 (1961).
9. William G. Smiley, *Anal. Chem.*, **27**, 1098 (1955).
10. J. M. E. Harper, T. H. Geballe, L. R. Newkirk, and F. A. Valencia, *Journal of Less Common Metals*, To be published.
11. R. J. Bartlett, H. L. Laquer, and R. D. Taylor, *Proceedings 1974 Applied Superconductivity Conf.*, p. 405.
12. A. R. Sweedler, D. E. Cox, and L. R. Newkirk, *J. Electronic Mater.*, To be published.

# High Temperature Electrical Conductivity of Aluminum Nitride

R. W. Francis

*Exxon Research and Engineering Company, Linden, New Jersey 07036*

and W. L. Worrell\*

*Department of Metallurgy and Materials Science, University of Pennsylvania, Philadelphia, Pennsylvania 19174*

## ABSTRACT

The electrical conductivity of high purity (99.8 pct) AlN has been determined using both a-c and d-c techniques. Measurements were made at temperatures between 700° and 1000°C and in a nitrogen pressure range of 1-10<sup>-5</sup> atm. The electrical conductivity is independent of nitrogen pressure. Galvanic cell results indicate that ionic conduction is negligible. Over the experimental temperature range, the electrical conductivity of AlN follows the equation

$$\sigma(\text{ohm}^{-1}\text{-cm}^{-1}) = 6.89 \times 10^3 \exp(-E/kT)$$

where the activation energy ( $E$ ) is  $1.82 \pm 0.06$  eV. It is concluded that the conduction process is extrinsic due to carbon impurities (~350 ppm) present in the AlN.

Aluminum nitride is a potentially useful refractory material, particularly at elevated temperatures. Its oxidation in air at temperatures up to 600°C is low (1, 2), and it is resistant to attack by acids, molten metals, and water vapor (1, 3). Recent studies indicate that AlN is very resistant to chemical attack by lithium at 400°C (4); thus AlN may be a suitable electronic insulator in alkali metal-molten salt batteries. Aluminum nitride also has potential applications in elevated temperature semiconductor devices (5-7). Although these various applications require a detailed knowledge of its conductivity at elevated temperatures, there is considerable variation in the activation energy and magnitude of the electrical conductivity of AlN measured by previous investigators (1, 3, 6, 8-12). In this study the electrical conductivity of high purity (>99%) AlN has been measured using a-c and d-c techniques at temperatures between 700° and 1000°C and at nitrogen pressures between 1 and 10<sup>-5</sup> atm.

## Experimental

Hot-pressed polycrystalline AlN samples were prepared by Cerac/Pure Incorporated. Aluminum nitride powder was synthesized by the electric discharge method (3) and hot-pressed without binder in a graphite die at ~1600°C under a nitrogen atmosphere. The 1 cm diameter AlN rod was machined to remove surface-impregnated carbon and then cut into pellets of different thicknesses. Sample porosity did not exceed 5%. The pellets were annealed in our laboratory at 1400°C for 76 hr in high purity nitrogen. Chemical analyses performed by the supplier both before and after annealing are listed in Table I. It should be emphasized that the purity of the annealed samples (99.8%) is higher than AlN samples used in previous studies.

Gold electrical contacts, which were used in the a-c conductivity measurements, were fabricated using the following procedure. The flat surfaces of the AlN pellets were polished and then rinsed in acetone and petroleum ether. After coating the flat surfaces with du Pont thermosetting gold paste (No. 5780), the pellets were heated slowly in air to 200°C, held for 10 hr, and then annealed for 2 hr at 400°C. Coherent gold contacts with less than 0.1 ohm resistance across

Table I. Chemical analysis (w/o)

Hot-pressed AlN pellets as received from Cerac

Al	66.10	B	0.001
N	33.0	Mn	0.001
Si	0.03	Cr	0.001
C	0.035	Cu	0.001
Ni	0.01	Sn	0.001
Fe	0.01	Ti	0.001
Mg	0.001		

Total measured content = 99.19

Remainder impurity assumed to be oxygen = 0.81%

After annealing in N<sub>2</sub> gas at 1400°C for 76 hr

Al 65.31% (theoretically 65.81%)  
N 34.45% (theoretically 34.19%)  
AlN = 99.8%

each contact surface were obtained. For the d-c conductivity measurements, aluminum powder was added to the gold paste to make gold-rich solid solutions (~0.5 atom per cent Al), which formed coherent electrodes after a similar annealing procedure. A two-phase presintered Cr,Cr<sub>2</sub>N mixture was also used to provide electrical contact in one d-c conductivity experiment.

After preparing the electrical contacts, the AlN sample was sandwiched between two gold foils in an alumina reaction tube (Fig. 1). A spring-loaded arrangement was used to maintain good electrical contact between the sample and the gold foils. Platinum wires, which were spot-welded to the gold foils, provided electrical contact to the external equipment. A grounded platinum foil enclosed the alumina reaction tube to minimize any electrical noise originating from the a-c resistance windings.

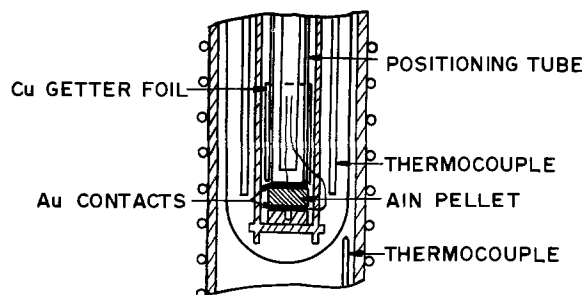


Fig. 1. Experimental arrangement

\* Electrochemical Society Active Member.

Key words: extrinsic conduction in AlN, effect of carbon impurities, electronic conductivity in AlN, chromium nitride electrodes.



The AlN sample was equilibrated with nitrogen gas at 1 atm or with N<sub>2</sub>/Ar gas mixtures to establish nitrogen pressures at 10<sup>-2</sup>, 10<sup>-4</sup>, and 10<sup>-5</sup> atm. Before being introduced into the apparatus, high purity nitrogen (no detectable impurities in parts per million) was passed through anhydrous CaSO<sub>4</sub> and through copper chips at 500°C to remove water vapor and oxygen. High purity argon was passed through CaSO<sub>4</sub> and Zr-Ti chips at 850°C. An internal copper foil was placed inside the reaction tube near the sample to further minimize any oxidation effects.

Two-probe a-c conductivity measurements were made using a Wayne-Kerr B221 transformer ratio-arm bridge operating at 1592 Hz and a General Radio 1232-A tuned amplifier and null detector. Voltage across the sample varied from 0.03 to 0.3V rms depending on the bridge range. With the bridge balanced, parallel conductance and capacitance were measured. A Wayne-Kerr S121 audio signal generator was used to vary the frequency from 50 to 20 kHz. For the d-c measurements, a Keithley 630 potentiometric electrometer (input impedance of 10<sup>13</sup> ohm) was used to measure the potential drop across the AlN sample and across a standard resistor. A variable 12 megohm limiting resistor was used to maintain constant currents between 1 and 50 μA (±5 × 10<sup>-3</sup> μA). All components and lead wires were electrically shielded.

After positioning an AlN sample in the reaction tube, the tube was evacuated and checked for gas leaks. Gas flow was then introduced at 20 cm<sup>3</sup>/min, and the furnace temperature was increased at 200°C/hr to 800°C. Readings were taken over a period of 5-8 hr before the temperature was increased stepwise to 1000°C. Deviations in the measured values were less than 1 pct at each temperature. Cycling the temperature back to 700°C gave subsequent measurements within ±2.5% of those originally observed. The nitrogen pressure was then changed, and the same procedure was followed. Some samples were held at temperature for 1-2 days with no variation in conductance greater than 3%.

### Results

**A-C conductivity.**—The a-c conductivity of each sample is equal to  $Gt/A$ , where  $G$  is the measured parallel conductance,  $t$  is sample thickness, and  $A$  is the cross-sectional area. Conductivity results for one sample under 1 atm nitrogen are shown in Fig. 2. Results below 650°C are clearly influenced by impurities and/or grain boundary conduction. It may be significant that the observed activation energy of 0.17 ± 0.01 eV at temperatures between 100° and 300°C is close to the activation energy (0.18 eV)

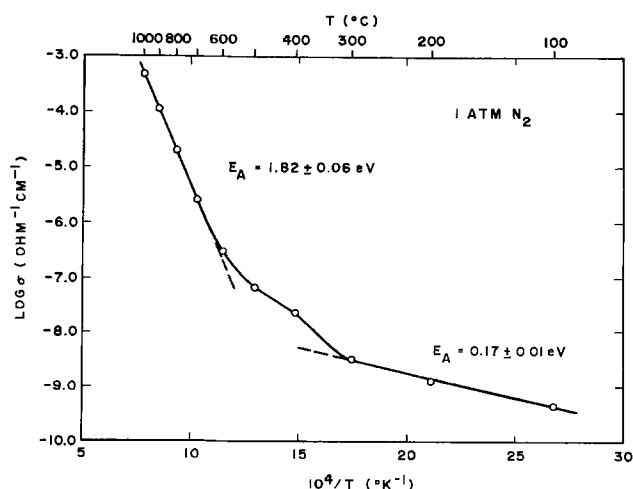


Fig. 2. Electrical conductivity over an extended temperature range.

observed for iron-impurity conduction in GaAs (13). As shown in Table I, iron is present (100 ppm) as an impurity in our AlN samples.

At temperatures above 650°C, results for the a-c conductivity are extremely reproducible. Data obtained at 1592 Hz and 1 atm nitrogen pressure are shown in Fig. 3 for four samples, one of which is twice as thick as the other three. A frequency of 1592 Hz is selected for determining the bulk a-c conductivity, because the observed conductivity is constant above 1592 Hz within the experimental uncertainty (±10%). At frequencies below 1592 Hz, the conductivity decreases rapidly with decreasing frequency. A least squares treatment of the data yields the following equation for the straight line shown in Fig. 3

$$\sigma (\text{ohm}^{-1}\text{-cm}^{-1}) = 6.89 (\pm 0.04) \times 10^8 \exp(-1.82 (\pm 0.06) / kT) \quad [1]$$

where 1.82 eV is the activation energy. The quoted experimental uncertainty in Eq. [1] is two standard deviations, i.e., 95% of the data are within the specified uncertainty. This is equivalent to a ±10% deviation in the conductivity.

As shown in Fig. 4, the a-c conductivity is independent of nitrogen pressure at pressures between 1 and 10<sup>-5</sup> atm. The solid line in Fig. 4 is calculated from Eq. [1], and the uncertainty bars represent the experimental scatter observed at 1 atm. All conductivity data obtained at lower nitrogen pressures are within the uncertainty bars and are in excellent agreement with those observed at 1 atm.

The effect of carbon concentration on the electrical conductivity is also illustrated in Fig. 4. "Low carbon" AlN samples (~350 ppm carbon) yield results represented by the solid line. However, results obtained with samples having a tenfold increase in analyzed carbon content (~3400 ppm) are a factor of five higher. As shown in Fig. 4, a dotted line, which is parallel to the solid line, provides an excellent fit to the data obtained from the "high carbon" samples.

**D-C conductivity.**—D-C conductivity data are shown in Fig. 5, in which the solid line is calculated from

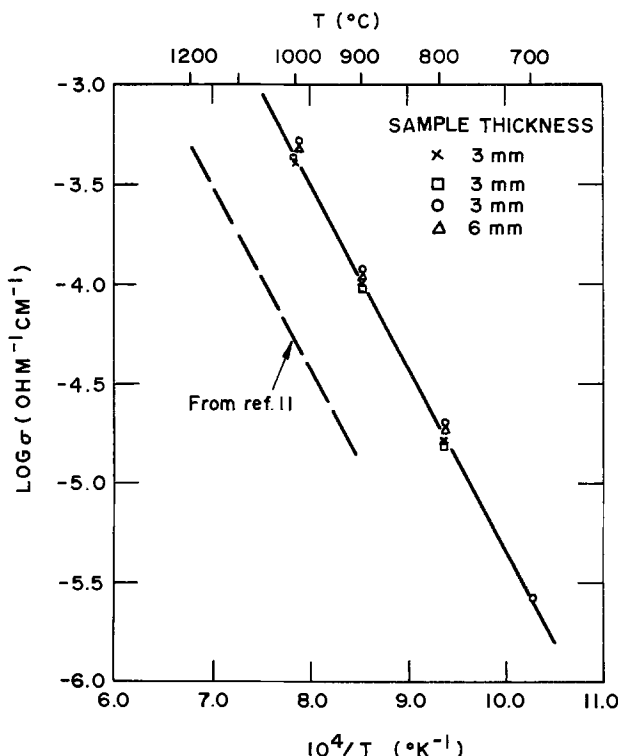


Fig. 3. Temperature dependence of electrical conductivity at 1 atm nitrogen.

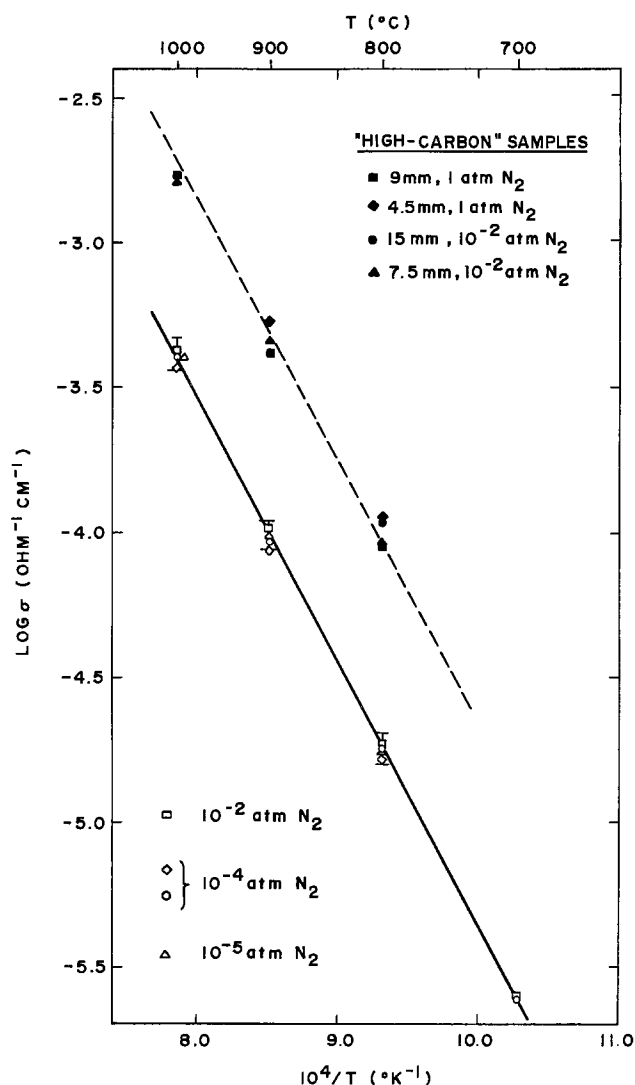


Fig. 4. Effect of nitrogen pressure and carbon concentration on the electrical conductivity.

Eq. [1]. Excellent agreement is observed between the a-c and d-c results using a Cr,Cr<sub>2</sub>N electrode. Although the data obtained using two gold alloy electrodes are about 80% higher than the a-c data, the activation energy is identical. The d-c conductivity data are independent of voltage polarity. With reversal of the applied voltage, no current transients or decays have been observed, which indicates negligible interfacial polarization (14, 15).

**Galvanic cell measurements.**—The observed independence of conductivity with nitrogen pressure (Fig. 4) indicates that AlN is either an ionic conductor or an electronic conductor having a large concentration of electronic defects. Thus, galvanic cell measurements have been carried out to determine if significant ionic conductivity occurs in AlN. Using Cr,Cr<sub>2</sub>N, and Cr<sub>2</sub>N,CrN mixtures as two-phase electrodes, the emf established across an AlN electrolyte has been measured. The percentage of ionic conductivity in AlN is equal to the measured cell emf divided by the calculated emf. Cell emf's, which vary between 107 (700°C) and 122 mV (900°C), are calculated from available thermodynamic data for the chromium nitrides (16). Using three different AlN samples, cell emf's have been measured over a period of 2-20 hr with deviations less than 0.2 mV at temperatures between 700° and 900°C. EMF values between +1.0 and -0.3 mV have been obtained, presumably due to thermoelectric effects in AlN (11). A one degree temperature gradient across the cell would account

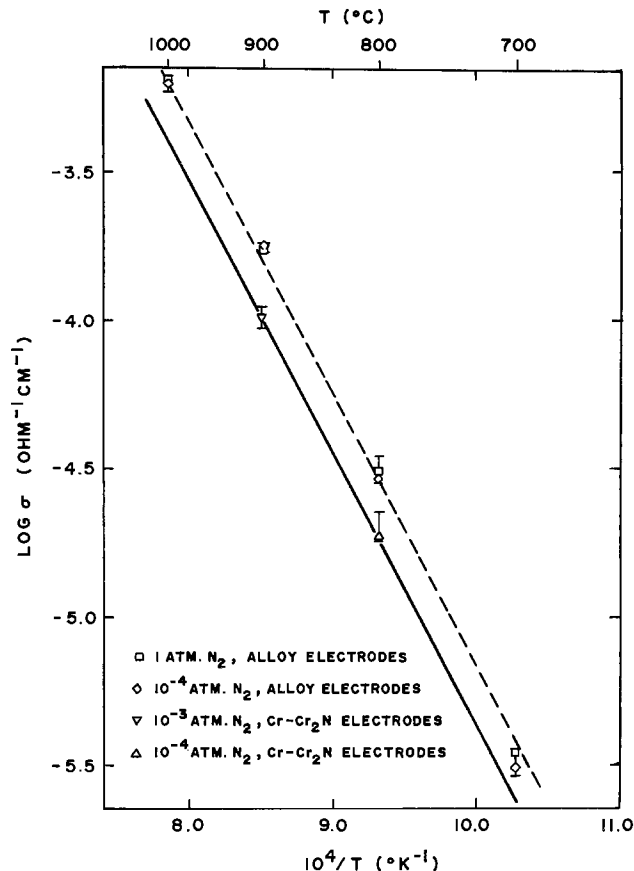


Fig. 5. Temperature dependence of d-c electrical conductivity

for the generation of such small emf's. Thus ionic conduction in our AlN samples is negligible.

## Discussion

**Previous results.**—Eight investigations of the electrical conductivity have been reported (1, 3, 6, 8-12). In one study (9), results from different samples varied by three orders of magnitude, and no precise data were obtained. In three investigations (1, 3, 10), results are difficult to evaluate because of the high porosity and/or low purity of the AlN samples. A measured activation energy of 2.8 eV was attributed to impurity conduction associated with excess aluminum in two single crystal (~98% pure) studies (6, 8). Using two-probe a-c measurements on hot-pressed samples, conductivity data have recently been obtained at temperatures between 1100° and 1700°C (12). However, a resistivity decrease with increasing gas flow rate was observed, presumably due to spurious electrical transport in the nitrogen gas. Similar phenomena have been observed in measurements of the high temperature resistivity of Al<sub>2</sub>O<sub>3</sub> (17). Gorbатов and Kamyshev (11) have measured the a-c conductivity at temperatures between 1000° and 1300°C and under nitrogen pressures of 1 and 10<sup>-4</sup> atm. To obtain a sample density greater than 95%, they hot-pressed samples in graphite dies. As shown in Fig. 3, their results are lower than those obtained in this study. However, their measured activation energy of 1.9 eV is in good agreement with our value of 1.82 eV.

**Conduction mechanism.**—The independence of the conductivity on nitrogen pressure (Fig. 4) and the galvanic cell results establish the predominance of electronic conduction in our AlN samples. Before forming conclusions about the conduction mechanism, it is essential to discuss the influence of interfacial effects and gas conduction processes on our results. The independence of the conductivity with sample thickness (Fig. 3 and 4) is experimental evidence

that interfacial resistances are negligible. A particularly striking example is that of the high carbon samples (Fig. 4), in which sample thicknesses vary from 4.5 to 15 mm with no observable effect. Furthermore, all a-c data are obtained in a frequency-independent region, in which interfacial, including grain boundary, effects are presumably negligible. With regard to the possibility of gas conduction processes, it should be noted that the conductivity of air (which is a reasonable estimate for pure nitrogen) is two to three orders of magnitude less than that of AlN in our experimental temperature range (18).

Although the conductivity of the high carbon samples is about a factor of five higher than the low carbon results, the observed activation energy is in excellent agreement, as is illustrated by the parallel lines in Fig. 4. The agreement in observed activation energy indicates a similar conduction process in both the low and high carbon samples, and we conclude that the conduction process in our AlN samples is extrinsic, due to carbon impurities. Because of the similarities in preparation, the carbon concentration in Gorbатов and Kamyshov's samples should be comparable to those used in this study, and one would expect the close agreement in activation energy which is observed (1.9 vs. 1.82 eV).

An extrinsic conduction mechanism is consistent with a number of other experimental observations. When one of our AlN samples is reused, the conductivity of the sample increases but the activation energy remains constant. For example, the data shown in Fig. 5 for the Au-Al alloy electrodes are obtained with AlN samples which have been used twice previously. Such conductivity increases can be attributed to an increase in carbon concentration originating from the organic resin in the gold paste. After experimental runs, a small, thin, black residue, presumably carbon, has been observed in isolated areas between the gold contacts and the AlN sample. Chemical analysis of reused samples shows a qualitative increase in carbon concentration with no detectable changes in the concentrations of the other major impurities listed in Table I.

Although no measurements of the oxygen content of AlN were made, Table I indicates that annealed samples could contain a maximum of 0.2 weight per cent (w/o) oxygen, which is almost as high as the concentration of carbon in the high carbon samples. However, there are several reasons why the effect of oxygen has been ignored in the interpretation of our conductivity results. Oxygen in AlN is most likely an acceptor and would either compensate a carbon donor or decrease the conductivity of n-type AlN. Oxygen absorption bands in AlN are at 4.53 and 4.80 eV (19), which are much higher than the impurity ionization energy of 3.64 eV calculated from our measured activation energy ( $2 \times 1.82$ ). Optical absorption measurements on AlN crystals prepared in graphite surroundings show an increase in absorption coefficient at  $\sim 3.5$  eV (19, 20), which is consistent with our impurity ionization energy.

The bandgap for AlN is between 5.7 and 6.2 eV (19, 20). A carbon-impurity ionization energy of 3.64 eV requires that carbon occupies a deep-lying impurity level. Theoretically, carbon in AlN could be either an electron donor or an acceptor. Using thermoelectric emf measurements, Gorbатов and Kamyshov have observed n-type electronic conductivity in car-

bon-contaminated AlN (11). This observation together with the observed increase in electrical conductivity with increasing carbon content (Fig. 4) indicates that carbon acts as an electron donor in AlN.

### Acknowledgments

Financial support of this work by the U.S. Atomic Energy Commission and the Advanced Research Projects Agency through the Laboratory for Research on the Structure of Matter at the University of Pennsylvania is gratefully acknowledged.

This paper is based upon a dissertation submitted by R. W. Francis in partial fulfillment of the requirements of the degree of Doctor of Philosophy at the University of Pennsylvania.

Manuscript submitted July 28, 1975; revised manuscript received Oct. 24, 1975. This was Paper 179 presented at the San Francisco, California, Meeting of the Society, May 12-17, 1974.

Any discussion of this paper will appear in a Discussion Section to be published in the December 1976 JOURNAL. All discussions for the December 1976 Discussion Section should be submitted by Aug. 1, 1976.

Publication costs of this article were partially assisted by the Exxon Research and Engineering Company.

### REFERENCES

1. K. M. Taylor and C. Lenie, *This Journal*, **107**, 308 (1960).
2. N. G. Coles, D. R. Glasson, and S. A. A. Jayaweera, *J. Appl. Chem.*, **19**, 178 (1969).
3. G. Long and L. M. Foster, *J. Am. Ceram. Soc.*, **42**, 53 (1959).
4. E. J. Cairns and R. A. Murie, in "Corrosion Problems in Energy Conversion and Generation," C. S. Tedmon, Jr., Editor, pp. 3-19, The Electrochemical Society Softbound Symposium Series, Princeton, N. J. (1974).
5. T. L. Clu, D. W. Ing, and A. J. Noreika, *Solid-State Electron.*, **10**, 1023 (1967).
6. K. Kawabe, R. H. Tredgold, and Y. Inuishi, *Elec. Eng. Japan*, **87**, 62 (1967).
7. R. H. Tredgold, "Space Charge Conduction in Solids," Elsevier Publishing Co., Amsterdam (1966).
8. G. A. Cox, D. O. Cummins, K. Kawabe, and R. H. Tredgold, *J. Phys. Chem. Solids*, **28**, 543 (1967).
9. J. Lagrenaudie, *J. Chim. Phys.*, **53**, 222 (1956).
10. J. V. Andreeva, I. G. Barantseva, E. M. Dudnik, and V. L. Yupko, *Teplofiz. Vysokikh Temperatur*, *Akad. Nauk SSSR*, **2**, 829 (1964).
11. A. G. Gorbатов and V. M. Kamyshov, *Poroshkovaya Met.*, *Akad. Nauk Ukr. SSR*, **10**, 61 (1970).
12. W. A. Fischer and B. Schuh, *Arch. Eisenhuettenw.*, **45**, 745 (1974).
13. J. Blanc, R. H. Bube, and L. Weisberg, *J. Phys. Chem. Solids*, **25**, 225 (1964).
14. A. R. von Hippel, "Dielectrics and Waves," John Wiley & Sons, Inc., New York (1954).
15. J. Volger, in "Progress in Semiconductors," Vol. IV, A. F. Gibson, R. E. Burgess, and P. A. Aigrain, Editors, p. 206, John Wiley & Sons, Inc., New York (1960).
16. T. Mills, *J. Less-Common Metals*, **22**, 373 (1970).
17. R. J. Brook, J. Yee, and F. A. Kröger, *J. Am. Ceram. Soc.*, **54**, 444 (1971).
18. O. T. Ozkan and A. J. Moulson, *Brit. J. Appl. Phys.*, **3**, 983 (1970).
19. J. Pastrňák and L. Roskovcová, *Phys. Status Solidi*, **26**, 591 (1968).
20. W. M. Yim, E. J. Stofko, P. J. Zanzucchi, J. I. Pankove, M. Ettenberg, and S. L. Gilbert, *J. Appl. Phys.*, **44**, 292 (1973).

## Minimizing Process-Induced Slip in Silicon Wafers by Slow Heating and Cooling

A. Wayne Fisher and G. L. Schnable\*

RCA Laboratories, Princeton, New Jersey 08540

The formation of slip regions in single crystal silicon wafers and its influence on device parameters has been studied by numerous investigators. The general conclusion is that the slip and its associated edge dislocations can degrade electrical parameters, especially if precipitation of metals or dopant atoms occurs at their sites.

A number of authors have discussed thermally induced slip in silicon wafers, and the effects of radial thermal gradients arising during high temperature processing sequences (1-9). Although several authors have mentioned that heating rates are a factor (1, 7, 9) in the formation of thermally induced dislocations, the relative importance of heating rates *vs.* cooling rates has not been indicated. A number of papers deal only with cooling rates, and thus imply that cooling rates are the most important factor in determining the amount of thermally induced slip (2, 3, 4, 6, 8).

Several techniques have been described for minimizing slip by reducing the radial thermal gradients (4, 8). Mechanical slow pullers have been used to insert and retract wafers from the furnace slowly, and thus reduce the thermal gradients which cause warpage and slip.

The purpose of this paper is to indicate that in fabricating silicon devices, slow heating of the silicon wafer is as important as slow cooling of the wafer in avoiding slip, and to show that the use of programmable mechanical pullers is a technique for controlling heating and cooling rates.

To evaluate the use of slow pullers as a method for reducing slip, a group of 80 5-cm diameter silicon wafers (0.045 mm thick, (100) orientation, polished on one side) was divided into four lots of 20 wafers each. The wafers were furnace at 1150°C in dry O<sub>2</sub> by inserting and retracting them from the furnace at different rates. The wafers were held vertically, perpendicular to the gas stream in a 25 cm long slotted quartz boat with supporting slots spaced 2.5 mm center to center. The center portion of the boat was loaded to a length of about 5 cm. Each lot was cycled three times from room temperature to 1150°C, and each time allowed to stabilize at 1150°C for 10 min before being removed for cooling to room temperature.

The work described in this paper was performed in a Lindberg Heavy Duty Furnace<sup>1</sup> with a uniform horizontal heat zone of 60 cm at a temperature of 1150°C. The temperature at the end of the flat heat zone dropped from 1150° to 800°C (800°C is below the temperature at which slip is believed to occur) in a distance of approximately 28 cm. The four lots were temperature cycled in and out of the furnace by the following procedures. Lot No. 1 was inserted and removed rapidly from the furnace, *i.e.*, from the end of the tube into the 1150°C zone in approximately 5 sec, stabilized for 10 min, then retracted to the end of the tube in approximately 5 sec. Upon removal it was

observed that the end wafers had cooled uniformly. The wafers in the center region of the boat remained hotter for a longer period of time and their periphery cooled first. The wafers were stripped of the oxide in aqueous HF and Dash etched (12 parts CH<sub>3</sub>COOH, 3 parts 70% HNO<sub>3</sub>, 1 part 49% HF) (10) for 16 hr to reveal slip regions. The slip was progressively worse on wafers located toward the center of the boat, with the center wafers being warped as well as heavily slipped. Figure 1a shows two wafers taken from the center of the boat after Dash etching for 16 hr.

The second lot of wafers was inserted into the hot zone rapidly (5 sec) and cooled slowly at a rate of 13 cm/min. All wafers appeared to cool uniformly as they traveled from the hot zone to the cold zone of the furnace. However, after oxide removal and Dash etching, all wafers, including the two end ones, had developed slip. As before, the slip was more severe on the wafers in the center of the boat (Fig. 1b). However, the degree of slip was less than observed on the wafers that were inserted fast and retracted fast, and warpage was not present.

The third lot was inserted into the hot zone slowly and cooled slowly at a rate of 13 cm/min for each step. Oxide stripping and Dash etching revealed no appreciable slip on any of these wafers (Fig. 2a).

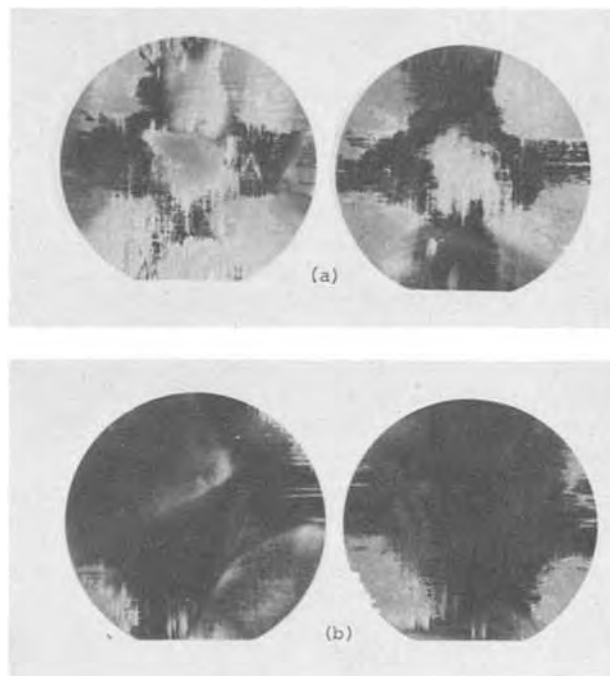


Fig. 1. Wafers taken from center of boat and etched 16 hr in Dash etch: (a) wafers inserted fast and retracted fast, (b) wafers inserted fast and retracted at 13 cm/min.

\* Electrochemical Society Active Member.

Key words: crystallographic slip, slow heating, slow cooling, mechanical pullers.

<sup>1</sup> Lindberg Engineering Company, Watertown, Wisconsin.

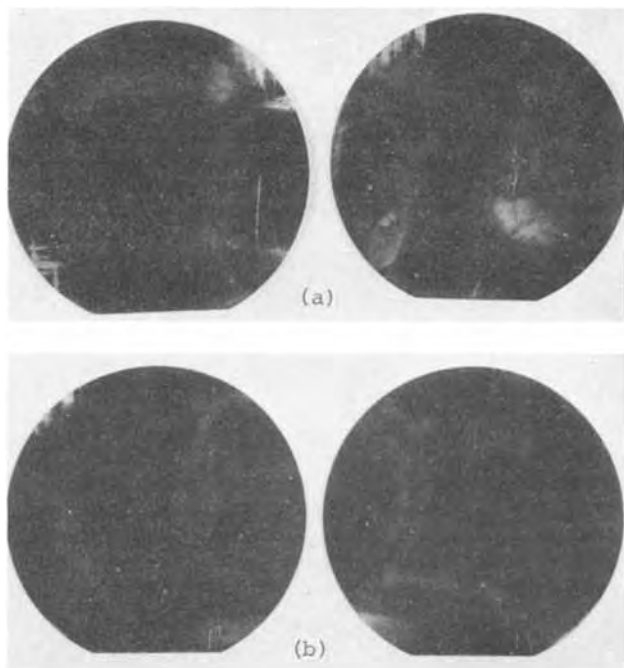


Fig. 2. Wafers taken from center of boat and etched 16 hr in Dash etch: (a) wafers inserted and retracted at 13 cm/min, (b) wafers inserted at 13 cm/min and retracted at 6.5 cm/min.

The fourth lot was inserted into the hot zone at a rate of 13 cm/min and removal was conducted at a rate of 6.5 cm/min. Oxide stripping and Dash etching again revealed essentially no slip (Fig. 2b).

#### Discussion and Conclusions

Tests have shown that slow retraction of wafers from high temperature furnaces by itself does not eliminate the crystallographic slip. Radial temperature gradients present when wafers are inserted into the furnace also generate crystallographic slip; thus it is necessary to insert the wafers slowly as well as remove them slowly. Slow insertion and slow retraction of silicon wafers into and out of high temperature furnaces at a rate of 13 cm/min using mechanical pullers is a method of reducing the radial temperature gradients to a level where crystallographic slip and associated edge dislocations are minimized.

One disadvantage of this technique is that as the wafers pass into and out of the furnace, the wafers at one end of the boat are heated for a longer time. For some heat-treatments (such as thermal oxidation, pocket

diffusion, isolation diffusion, and p+ diffusions), where the total time of heat-treatment is long, this time difference is negligible. For an insertion and pull rate of 13 cm/min, the time differential from one end of a 25-cm boat to the other is about 4 min. For base and emitter diffusions, where control over junction depth is very critical and diffusion times are shorter, this technique will be limited. One possible means of overcoming the problem is to insert wafers at one end of the furnace and remove them from the other, thus averaging out the time when temperature gradient occurs along the length of the boat.

The technique of using mechanical pullers to achieve both slow heating and slow cooling is applicable to many production lines, and is especially desirable to avoid process-induced slip in wafers containing narrow-base bipolar transistors. Various types of equipment are now available for controlled mechanical insertion and removal of boats from furnaces (11). Commercially available slow pullers have independent speed controls for the insertion and retraction portion of the cycle, and travel speeds are adjustable in the range of about 1.2-25 cm/min.

#### Acknowledgment

The authors wish to thank R. Matenkoski for providing the furnace used in these experiments.

Manuscript submitted Aug. 18, 1975; revised manuscript received Nov. 26, 1975.

Any discussion of this paper will appear in a Discussion Section to be published in the December 1976 JOURNAL. All discussions for the December 1976 Discussion Section should be submitted by Aug. 1, 1976.

Publication costs of this article were partially assisted by RCA Laboratories.

#### REFERENCES

1. K. Morizane and P. S. Gleim, *J. Appl. Phys.*, **40**, 4104 (1969).
2. S. M. Hu, *ibid.*, **40**, 4413 (1969).
3. G. H. Schwuttke, *Microelectronics and Reliability*, **9**, 397 (1970).
4. G. H. Schwuttke, 8th Ann. Proc. Rel. Phys., pp. 274 (1971) (IEEE Cat. No. 70C59-PHY).
5. W. A. Porter, D. D. Drew, and J. S. Linder, *J. Appl. Phys.*, **43**, 1477 (1972).
6. S. M. Hu, *Appl. Phys. Letters*, **22**, 261 (1973).
7. A. Yoshinaka and Y. Sugita, Abstract 67, p. 171, The Electrochemical Society Extended Abstracts, Spring Meeting, San Francisco, California, May 12-17, 1974.
8. E. W. Hearn and G. H. Schwuttke, *This Journal*, **121**, 208C (1974).
9. C. J. Varker, *ibid.*, **121**, 376C (1974).
10. W. C. Dash, *J. Appl. Phys.*, **27**, 1193 (1956).
11. G. Hillman, *Solid State Technol.*, **17**, 68 (1974).

## Latent Heat Measurement of Phase Transformations in Potassium Nitrate

E. Y. Wang

Department of Electrical Engineering, Wayne State University, Detroit, Michigan 48202

Potassium nitrate ( $\text{KNO}_3$ ) can exist in three possible phases at normal atmospheric pressure. At room temperature, the structure is orthorhombic and aragonite (phase II) (1). Upon heating to temperature  $401^\circ\text{K}$ , the structure transforms to rhombohedral (phase I) and remains the same structure until melting. Upon cooling, the material solidifies in the rhombohedral form which is ferroelectric (phase III). Fur-

Key words: latent heat, potassium nitrate, differential scanning calorimetry.

ther cooling generally returns the structure to the orthorhombic form (phase II). All phase transformations are first order and involve latent heats. In this note, we used differential scanning calorimetry (DSC) to obtain directly the latent heats of phase transformations in  $\text{KNO}_3$ . Results obtained by DSC method for phase II $\rightarrow$ I are compared with those by differential thermal analysis (2) and other methods (3). Latent heat measurement by a direct method from phase III $\rightarrow$ II is reported here for the first time. In addition,

Table I. Latent heats in  $\text{KNO}_3$  by DCS method

Heating and cooling cycle run No.	Phase II $\rightarrow$ I transition		Phase I $\rightarrow$ III transition		Phase III $\rightarrow$ II transition*	
	Temperature in $^{\circ}\text{K}$	Latent heat in cal/mole ( $Q_{21}$ )	Temperature in $^{\circ}\text{K}$	Latent heat in cal/mole ( $Q_{13}$ )	Temperature in $^{\circ}\text{K}$	Latent heat in cal/mole ( $Q_{32}$ )
1	401	1290	—	—	—	—
2	401	1295	389	720	369	575
3	401	1289	389	718	367	571
4	401	1290	389	721	346	569
5	401	1292	389	719	338	573

\* Deduced by assuming that  $Q_{21} = Q_{13} + Q_{32}$ .

the effect of moisture content on the transformation temperature from phase III  $\rightarrow$  II has been studied.

### Experimental Results

DSC measurements were made on  $\text{KNO}_3$  by using a Perkin-Elmer DSC-1B apparatus. Unlike previous methods (2, 3) DSC yields direct recording of heat quantities by using a close-loop, negative feedback control of the power supplied to specimen and reference systems. When the specimen absorbs or emits energy (heat), more or less power is required to maintain the specimen in equilibrium with the reference system at the same temperature. The differential power is then recorded continuously according to the energy (heat) requirement of the specimen. The specimen was initially in powdered form of 99.0% purity. The powder was placed in an aluminum sample pan and was heated to the melting temperature. The sample pan was mechanically sealed during entire measurements. Figures 1 and 2 show the thermal spectrum. In the heating cycle, the two endothermic peaks correspond to the phase II  $\rightarrow$  I transformation and melting. In cooling cycles, the peaks correspond to crystallization and the phase I  $\rightarrow$  III transformation. The heats of fusion in melting and crystallization are 28.1 cal/g which agrees with previous values (4). The crystallization occurs at a lower temperature than the melting temperature because of supercooling effect, and on subsequent cooling the specimen does not convert from phase III to phase II until exposed to moisture. Moisture was introduced by removing the cover of the sample pan and exposing the specimen to room atmosphere over night. Figure 3 shows the results of cooling cycles for a "wet" specimen and its subsequent thermal cooling cycling. The thermal spectra are "identical" in heating cycles; however, in cooling cycles the phase III  $\rightarrow$  II transformation depends on the amount of moisture content in the  $\text{KNO}_3$ . As the number of thermal cycles increases, the moisture content is decreased and the transformation temperature from phase III  $\rightarrow$  II is lowered; eventually the  $\text{KNO}_3$  remains in phase III "indefinitely." Re-

Table II. Comparisons of latent heats with previous works

Authors and reference	Method	Latent heats		
		$Q_{21}$ (cal/mole)	$Q_{13}$ (cal/mole)	$Q_{32}$ (cal/mole)
Kracek (2)	Differential thermal analysis measurement	1060	558	502
Miekkoja (3)	Specific heat measurements	1295	—	—
Mustajoki (5)	Differential calorimetric measurements	1195	720	560
Wang (present work)	DSC measurements	$1291 \pm 13$	$720 \pm 7$	$571 \pm 6$

peated measurements for different amounts of  $\text{KNO}_3$  under the same conditions yield essentially the same results. Latent heats calculated from the thermal spectra are summarized in Table I. A comparison of latent heats with previous works is shown in Table II. It

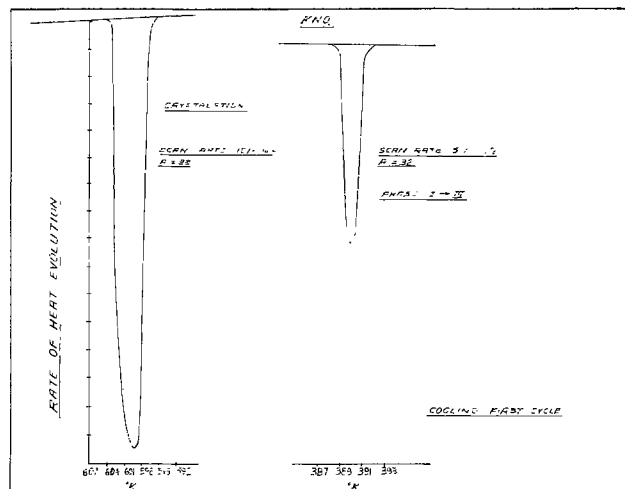


Fig. 2. Cooling cycle of a typical thermal spectrum

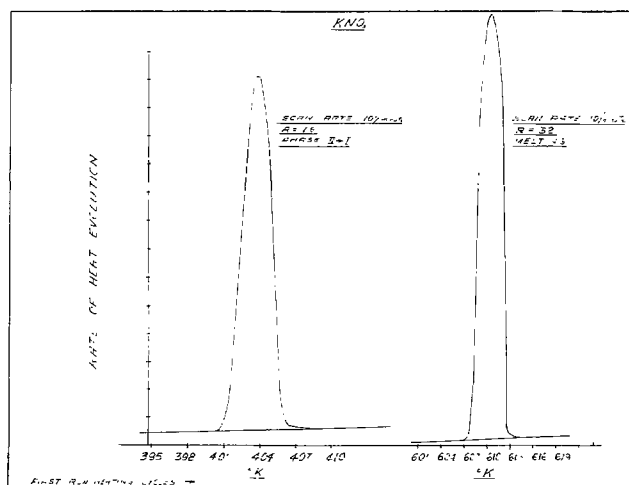


Fig. 1. Heating cycle of a typical thermal spectrum

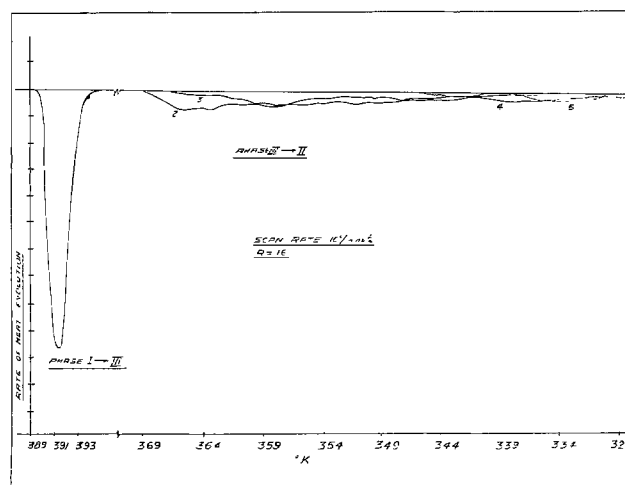


Fig. 3. Subsequent cooling cycles of a typical thermal spectrum

should be pointed out that in the DSC method transition temperatures depend on scan rate; however, the latent heat is independent of scan rate.

### Conclusions

In conclusion, we have used the DSC method to obtain the latent heats for all of the phase transformations in  $\text{KNO}_3$ . We believe the values obtained here are more accurate in view of the nature of the DSC method. The error in latent heat values is estimated to be within  $\pm 1\%$ . Particularly, we believe that latent heat measurement from phase III $\rightarrow$ II is reported here for the first time by a direct method. By direct method we mean that latent heat values were obtained directly from measurements instead of other material parameters such as transition temperature, specific heat, and others. The moisture effect on the transformation temperature of phase III $\rightarrow$ II is also consistent with previous observations (2-6).

## Temperature Asymmetries and Fluctuations in a Barrel Reactor

B. J. Curtis\*

Laboratories RCA Limited, Zurich, Switzerland

The work reported in this paper is concerned with a study of thermal conditions in a barrel reactor, similar to but smaller than those used in the production of homoepitaxial silicon. This is a continuation of the investigations reported in Ref. (1-3).

As has been mentioned previously (1, 2), the effects of certain process parameters such as temperature gradients and hydrodynamic effects on the homogeneity and uniformity of melt-grown crystals is relatively well understood. In the case of growth from the vapor phase however, this subject has received detailed attention only during the past few years. In view of the importance of the epitaxial silicon process, any information that can be gained about the prevailing conditions inside the reactor is of potential use in improving the yield and quality of devices. Experience has shown that reactors built nominally to identical specifications behave differently under the same operating conditions. In addition, with the increasing application of large-scale integration, the demand for thin homoepitaxial silicon layers may increase and it seems likely that the growth of such layers will require closer control than the thicker layers that are grown in production at present.

### Experimental

A number of factors influenced the design of the reactor. The size was limited by the available rf generator which had a maximum output of 12.5 kW. In designing the reactor, an attempt was made to incorporate as much flexibility as possible so that the same chamber could be operated with either air- or water-cooled walls. Provision was also made for the addition of baffles near the gas inlet should this have been necessary. In addition, the thermocouple used for the temperature measurements was built into the rotatable susceptor since the effects of rotation had not been studied previously. This posed some problems since a gas-tight rotary feed-through was required for the susceptor supporting shaft and thermocouple.

The final design of the reactor is shown in Fig. 1 in which the left side of the drawing shows the reactor

Manuscript submitted May 2, 1974; revised manuscript received Nov. 6, 1975.

Any discussion of this paper will appear in a Discussion Section to be published in the December 1976 JOURNAL. All discussions for the December 1976 Discussion Section should be submitted by Aug. 1, 1976.

Publication costs of this article were partially assisted by Wayne State University.

### REFERENCES

1. C. Finbak and O. Hassel, *Z. Physik. Chem.*, **37**, 75 (1937).
2. F. C. Kracek, *J. Phys. Chem.*, **34**, 225 (1930).
3. Heikki Miekko-oja, *Ann. Acad. Sci. Fennicae: Ser. A I*, **7**, (1941).
4. R. C. Weast, "Handbook of Chemistry and Physics," 53rd ed., R. C. Weast, Editor, p. B 243, Chemical Rubber Publishing Co., Cleveland, Ohio (1972).
5. A. Mustajoki, *Ann. Acad. Sci. Fennicae: A VI*, **99**, (1962).
6. H. W. Sturmer and C. E. Bleil, *General Motors Research Publication*, 932 (1969).

with water-cooled walls and the right side with air-cooled walls. Two demountable water-cooled stainless steel end plates sealed the vitreous silica reactor tube and, if required, the Pyrex glass cooling water jacket by o-rings held in compression by four Teflon support rods. These support rods were surrounded by gold-coated glass tubes which shielded them from the radiation from the hot susceptor. The tapered, hexagonal carbon susceptor (for exact dimensions see Fig. 3) was supported by a carbon rod attached to a hollow, stainless steel shaft, the rotary seal to the base plate being achieved by a water-cooled o-ring. The leads from the Chromel-Alumel thermocouple passed through the hol-

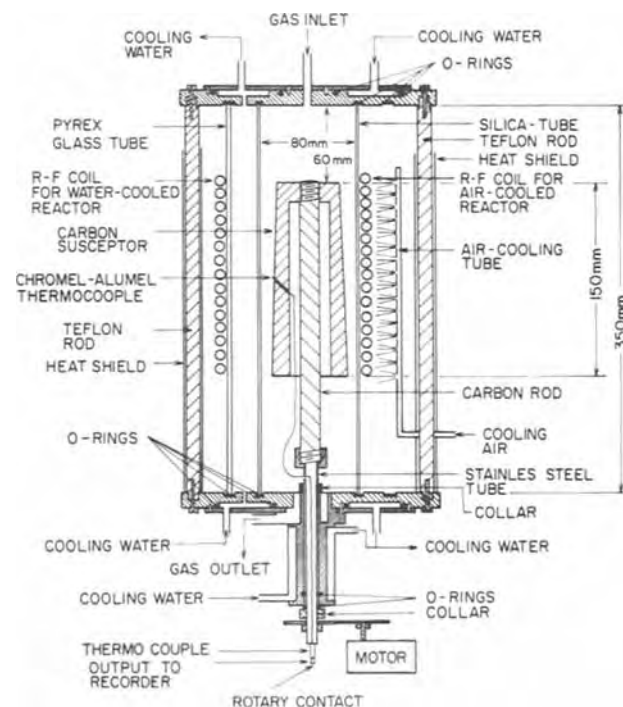


Fig. 1. Barrel reactor with air- or water-cooled walls

\* Electrochemical Society Active Member.

Key words: silicon, reactor technology, temperature stability.



low shaft to a rotary contact (see also Fig. 2). Some initial problems arose with hydrogen leaking from a

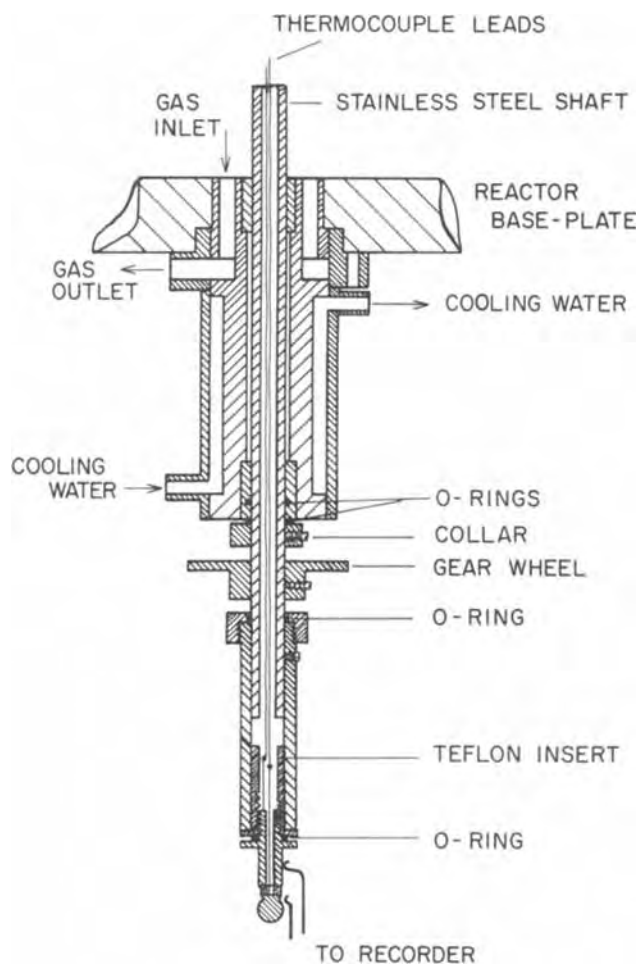


Fig. 2. Rotary feed-through for susceptor support and thermocouple

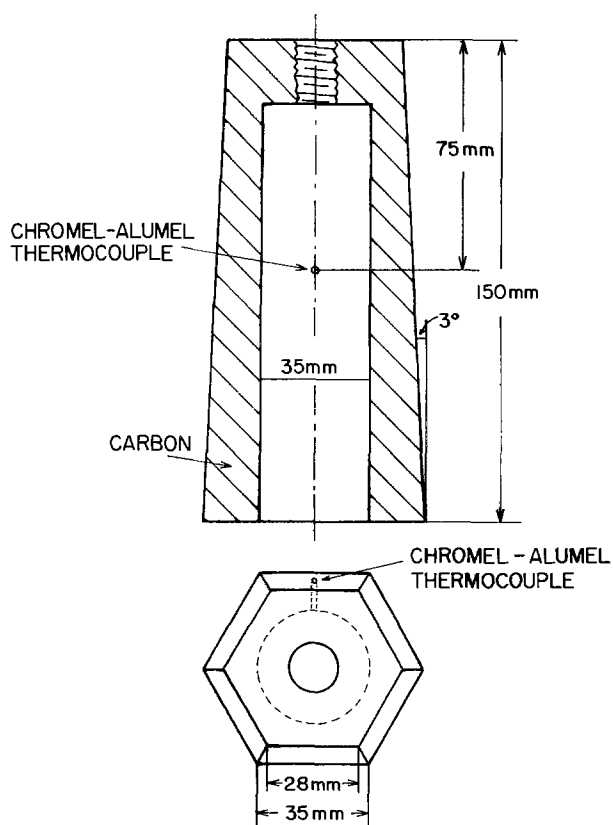


Fig. 3. Carbon susceptor

number of points which was eliminated by additional o-rings. The Chromel-Alumel thermocouple itself was fabricated from 100 $\mu$  diameter wire sheathed in stainless steel with powdered magnesium oxide insulation (Omega Company Type 304-K-MO-020). The stainless steel sheath was found to react with the carbon susceptor at 1200°C and so a piece of alumina tubing was inserted between the thermocouple and the susceptor. The tip of the thermocouple projected 1 mm from the susceptor surface at the midpoint of one of its faces. Since the susceptor could be rotated, a rotary contact was required for the thermocouple. For this purpose, a small co-axial plug and socket was used which proved to be quite suitable at the low rotation speeds used (maximum 6 rpm). As mentioned previously, the reactor could be either water-cooled or air-cooled, the latter being accomplished either by contact with the ambient air (natural air cooling) or by four perforated tubes (Fig. 1 right side) disposed symmetrically around and spaced 35 mm from the vitreous silica tube (forced air cooling).

The output from the thermocouple was partially compensated with a stable millivolt source and displayed on a chart recorder so that temperature changes of about 0.25°C could be detected. A power controller with a feedback loop placed close to the rf coil was used to ensure that the power delivered to the susceptor was held constant. Once the conditions had stabilized, the recorded temperature remained constant to within  $\pm 0.5^\circ\text{C}$  over periods of a few minutes with a drift of a few degrees over longer periods.

## Results and Discussion

Investigations in a smaller, water-cooled barrel reactor (3) indicated that under certain conditions, temperature instabilities appeared in the gas phase near the hot susceptor which increased as the gas velocity was increased. This effect was large at a position 25 mm downstream on the susceptor surface; at a point 50 mm downstream the effects were small but still detectable.

The measurements to be reported here were made at one thermocouple position as mentioned above and as shown in Fig. 1. This position was 75 mm downstream on the susceptor, thereby allowing the gas a reasonable time to equilibrate and, from previous results (3), relatively stable thermal conditions would be expected at that point. Nevertheless, temperature fluctuations were still detected which tended to increase in magnitude with increasing gas velocity. The gas velocities quoted in this paper are the room temperature values. When corrected for the actual gas temperature, the real gas velocity would be approximately three times the indicated values.

In hydrogen, with the susceptor stationary, temperature fluctuations began at a gas velocity of about 18 cm/sec with air-cooled walls and at 8 cm/sec with water-cooled walls. The maximum amplitude of the fluctuations was 0.5°C in the former and 1.5°C in the latter case. These results illustrate the slightly decreased stability of the water-cooled reactor as compared to the air-cooled reactor. These effects seen in hydrogen were relatively small and are probably not of great importance in practice.

Temperature asymmetries were detected when the susceptor (and with it, the thermocouple) was rotated. With constant power input to the susceptor, the temperature registered by the thermocouple varies in a regular manner as shown in Fig. 4. The upper portion (a) shows the effect with hydrogen; the period of the fluctuations was one revolution and their amplitude increased with increasing gas velocity up to about 5°C at 34 cm/sec. Figure 4(b) shows the effect of turning on the forced-air cooling. Superimposed on the general asymmetry seen in (a) were four peaks, each one resulting from one of the air-cooling tubes. Again, their amplitude increases with increasing gas velocity up to about 8°C at 34 cm/sec.



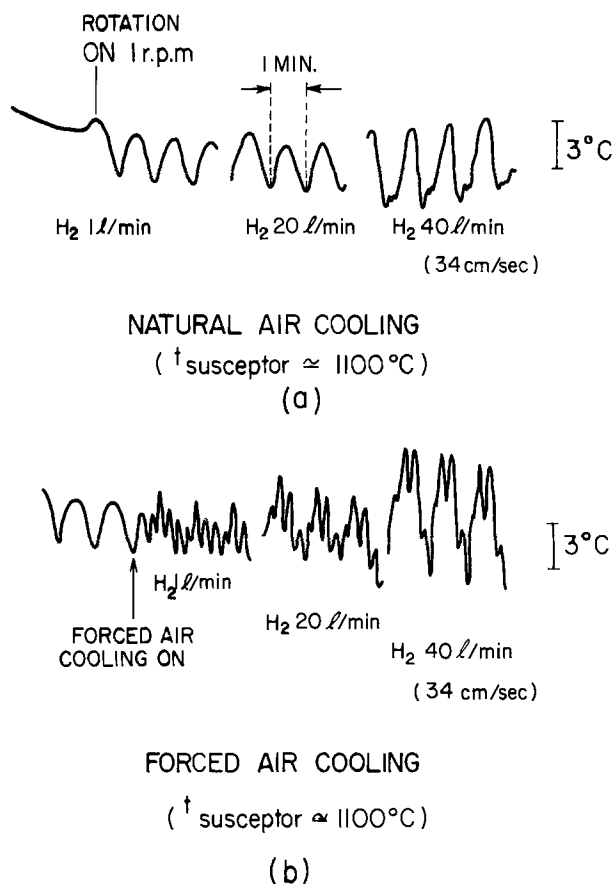


Fig. 4. Rotational temperature asymmetries in hydrogen (1 rpm): (a) with natural air cooling, (b) forced air cooling.

Since the susceptors in production reactors are rotated at 6 rpm, the drive was changed to give this increased speed since it was possible that the effects measured at 1 rpm would be smoothed out at this higher speed. This was not the case, however; the peaks were merely moved closer together but could still be easily resolved. When nitrogen is substituted for hydrogen, the amplitude of the temperature fluctuations increases to about 35°C as compared to about 8°C for hydrogen. The differences between air and water cooling were not so great but since the susceptor temperature was lower in the latter case, it seems quite likely that the effect would be greater in that instance for equivalent susceptor temperatures.

The type of fluctuations observed with the stationary susceptor is superimposed on the rotational fluctuations. This is shown in Fig. 5 for a water-cooled reactor and a rotation rate of 6 rpm. Between 8.4 and 13.0 cm/sec the stationary fluctuations begin and can be seen in the trace taken at 13 cm/sec. The amplitude of the rotational and stationary fluctuations can be seen to increase with increasing gas velocity. A similar effect was seen with the air-cooled reactor.

### Conclusion

Similar effects were seen with the longer susceptor as had been seen earlier (3) with a shorter susceptor without rotation, but their magnitude was probably not sufficient to cause any great problems as regards uniformity or crystal perfection in a practical growth system. In any case, the susceptor used in production reactors has a minimum of 15 cm free surface before the reacting gases reach the substrates so that the stationary fluctuations will be of even smaller amplitude. The presence of the rotational fluctuations, however, could be one factor which causes differences in behavior in apparently identical reactors. It is unlikely that temperature fluctuations in the gas phase would affect the

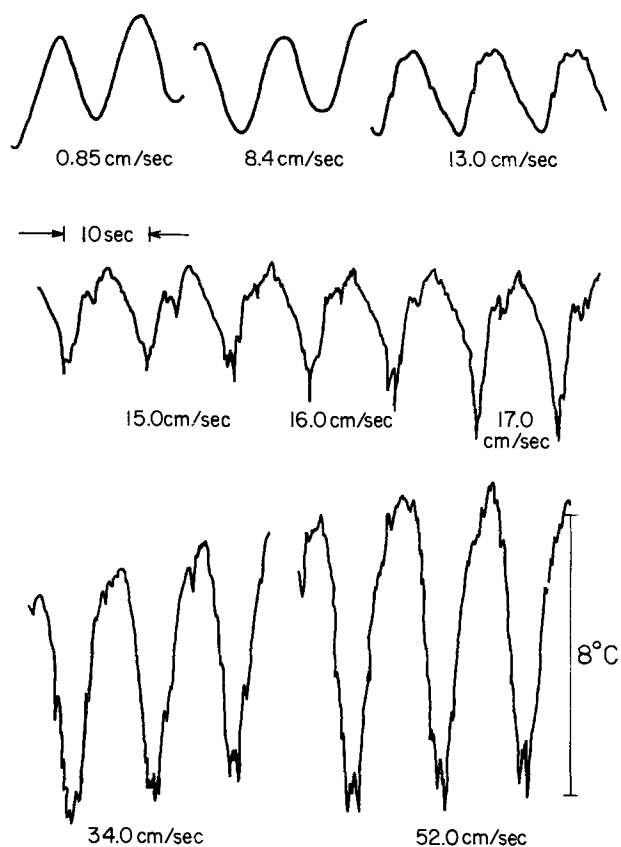


Fig. 5. Effect of gas velocity on rotational temperature fluctuations in hydrogen with a water-cooled reactor.

substrate temperature since the thermal mass of the substrate and susceptor is large. But the possibility exists that the diffusive flux of reactants and reaction products to and from the substrate would be affected since diffusion is a temperature-dependent process. This could, then, lead to inhomogeneities and nonuniformities in the grown layer.

The origin of the rotational fluctuations is not entirely clear. The fact that their magnitude is larger with nitrogen than with hydrogen shows that the effect is, to some extent, gas dependent. This, together with the velocity dependence of their amplitude, indicates that their origin is probably a combination of flow and geometrical factors.

### Acknowledgments

The author wishes to thank A. E. White for his technical assistance and D. Richman for helpful discussions.

Manuscript submitted April 14, 1975; revised manuscript received Nov. 10, 1975.

Any discussion of this paper will appear in a Discussion Section to be published in the December 1976 JOURNAL. All discussions for the December 1976 Discussion Section should be submitted by Aug. 1, 1976.

Publication costs of this article were partially assisted by Laboratories RCA Limited.

### REFERENCES

1. B. J. Curtis and J. P. Dismukes, *J. Cryst. Growth*, **17**, 128 (1972).
2. J. P. Dismukes and B. J. Curtis, in "Semiconductor Silicon 1973," H. R. Huff and R. R. Burgess, Editors, p. 258, The Electrochemical Society Softbound Symposium Series, Princeton, N.J. (1973).
3. B. J. Curtis and J. P. Dismukes, in "Chemical Vapor Deposition, Fourth International Conference," G. F. Wakefield and J. W. Blocher, Jr., Editors, p. 218, The Electrochemical Society Softbound Symposium Series, Princeton, N.J. (1973).

# The Dissociation Energy of BiS and the Vapor Composition over Bi-S Melts

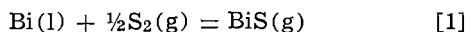
Daniel Cubicciotti\*

Stanford Research Institute, Menlo Park, California 94025

## Dissociation Energy

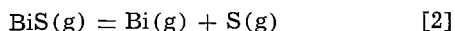
The stability of the BiS molecule relative to the elements was determined in a transpiration experiment (1) a few years ago and the molecule identified in a mass spectrometer study (2). Since that time the molecular constants of the molecule have been measured by Barrow *et al.* (3) so that its thermodynamic functions can be calculated. That information allows a careful interpretation of the transpiration data, as follows.

The equilibrium constants for the reaction



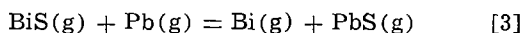
were taken from Ref. (1). The thermodynamic functions for BiS calculated from molecular constants are given in Table I, while those for Bi and S<sub>2</sub> are from Hultgren (4) and the JANAF Tables (5), respectively. The calculations of the third law enthalpies of reaction ( $\Delta H_{298} = -RT \ln K - T\Delta F$ ) are given in Table II and lead to an average value of  $27.9 \pm 1$  kcal/mole. The temperature coefficient of the equilibrium constant gave an enthalpy change of  $25 \pm 5$  kcal/mole at 1000°K which leads to a value of  $29 \pm 5$  at 298°K in good agreement with the third law value.

The dissociation energy of BiS is equal to the enthalpy change at 0°K for the reaction



The third law value above, when combined with the appropriate enthalpies of atomization from Ref. (4) and (5), leads to a dissociation energy of  $72.3 \pm 1$  kcal/mole for BiS.

Uy and Drowart (6) have measured the equilibrium constant for the reaction



by a mass spectrometer technique. The enthalpy change they measured for the reaction was  $-7.2 \pm 1$  kcal/mole at 0°K (with corrected *F* values). The dissociation energy of PbS is not yet well established. Uy and Drowart gave a value of  $80.4 \pm 1.5$  kcal from mass spectrometer data and  $81.8 \pm 0.4$  from spectroscopic data. The JANAF Tables reviewed the literature and gave  $82.4 \pm 1.5$  as a compromise. The dissociation energy of BiS calculated from those values are  $73.2 \pm 2.5$ ,  $74.6 \pm 1.5$ , and  $75.2 \pm 2.5$ , respectively.

Dissociation energies from spectroscopic data that are in good agreement with thermochemical values for a large number of molecules have been derived by a method due to Hildenbrand (8). In his method, the dissociation energy, *D*<sub>0</sub>, is related to the value calculated from a linear Birge-Sponer extrapolation, *D*(LBX), by the empirical equation

$$\frac{D_0}{D(\text{LBX})} = 0.448 + 0.365 \left( \frac{r_x}{r_e} \right) \quad [4]$$

in which *r*<sub>e</sub> is the equilibrium internuclear distance and *r*<sub>x</sub> is an estimate of the distance at which the ionic and covalent potential curves cross, given by

$$r_x = \frac{14.40 \text{ (eV)}}{(\text{ionization potential of metal atom, eV}) - (\text{electron affinity of nonmetal atom, eV})}$$

\* Electrochemical Society Active Member.

Key words: bismuth sulfide, dissociation energy, vapor composition.

Table I. Thermodynamic functions calculated for BiS (standard state, ideal gas)

Temperature, °K	$-\left(\frac{G^\circ_T - H_{298}}{T}\right)$ , cal/mole deg	Absolute entropy, <i>S</i> <sup>0</sup> , cal/mole deg	Enthalpy increment <i>H</i> <sub>T</sub> - <i>H</i> <sub>298</sub> , kcal/mole	Heat capacity, cal/mole deg
298	61.57	61.57	0.0	8.406
300	61.57	61.62	0.016	8.411
400	61.90	64.07	0.868	8.620
500	62.53	66.01	1.736	8.728
600	63.25	67.60	2.612	8.790
700	63.97	68.96	3.494	8.829
800	64.67	70.14	4.378	8.855
900	65.34	71.19	5.264	8.873
1000	65.97	72.12	6.152	8.886
1100	66.57	72.97	7.041	8.896
1200	67.13	73.75	7.931	8.903
1300	67.67	74.46	8.822	8.909
1400	68.18	75.12	9.713	8.913
1500	68.66	75.74	10.604	8.917

<sup>0</sup> *H*<sub>298</sub> - *H*<sub>0</sub> = 2.262 kcal/mole. Molecular constant used [from Barrow (3)]. *r*<sub>e</sub> = 2.319 Å; *ω*<sub>e</sub> = 409 cm<sup>-1</sup>. Ground state multiplicity (*g*) = 2 because of lambda doubling [see Ref. (7)]. The state with spin = 3/2 is expected to have an energy of the order of 8000 cm<sup>-1</sup> (personal communication from Professor R. F. Barrow).

Table II. Third law evaluation of enthalpy change for reaction [1]

Equilibrium constants measured in Ref. (1), Torr <sup>1/2</sup>	Temperature, °C	Δ <i>F</i> , cal/mole deg	Δ <i>H</i> <sub>298</sub> , kcal
0.1	705	-17.53	28.0
0.15	740	-17.40	28.0
0.31	800	-16.96	27.8
Average			27.9

For the BiS molecule we calculate *r*<sub>x</sub> = 2.76 so that *r*<sub>x</sub>/*r*<sub>e</sub> = 1.19 and *D*<sub>0</sub>*D*(LBX) = 0.883. The value of *D*(LBX) from Barrow's data is 81.1 kcal so that *D*<sub>0</sub> calculated by Hildenbrand's method is 71.6 kcal/mole in good agreement with the thermochemical value.

## Composition of Vapor over Bi-S Melts

The vapor phase in equilibrium with the condensed phases in the Bi-S system will consist primarily of the species S<sub>2</sub>, BiS, Bi<sub>2</sub>, Bi in various relative amounts depending on melt composition. There will also be smaller amounts of secondary species such as S and the more complex species, Bi<sub>4</sub>, Bi<sub>2</sub>S<sub>2</sub>, S<sub>8</sub>, etc. (9, 10). For the present discussion those secondary species are neglected.

The amounts of the primary species can be calculated from the available thermochemical data for the gases [sulfur species from Ref. (5), bismuth species from Ref. (4), BiS from this paper] and the thermodynamic activities of Bi and S in the melt given in Ref. (1). The results of such a calculation for 800°C (1073°K) are given in Fig. 1.

The predominant vapor species is S<sub>2</sub> over almost the entire composition range. At sufficiently small sulfur content in the melt (atom fraction sulfur < 0.05), the species Bi<sub>2</sub> is predominant. The pressure of BiS is al-

ways intermediate between those of S<sub>2</sub> and Bi<sub>2</sub>. In fact,

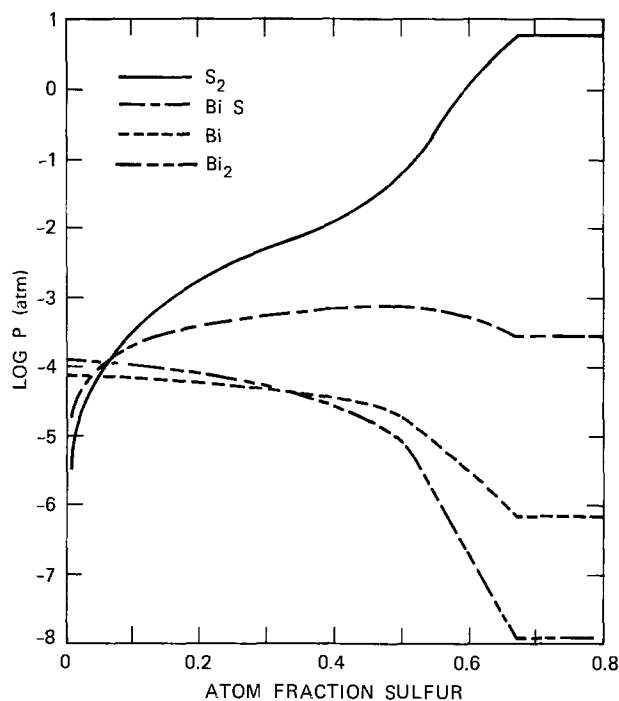


Fig. 1. Partial pressures of species over Bi-S melts at 800°C

as noted in an earlier paper, the dissociation energy of BiS is approximately the mean of those of Bi<sub>2</sub> and S<sub>2</sub> and since there are no large entropy effects the pressure of BiS is approximately the geometrical mean of those of S<sub>2</sub> and Bi<sub>2</sub>. The lower two curves in Fig. 2 show the total amounts of S and Bi in the vapor, i.e., the sums of pressures of all species containing S and Bi presented as pressures of monatomic S and Bi.

The curves at temperatures other than 800°C are qualitatively the same. The major differences arise because at temperatures below 775°C solid Bi<sub>2</sub>S<sub>3</sub> precipitates, at the melt compositions reported in the phase diagram (11). Above 775°C a second liquid phase separates. The activities of Bi and S are essentially the

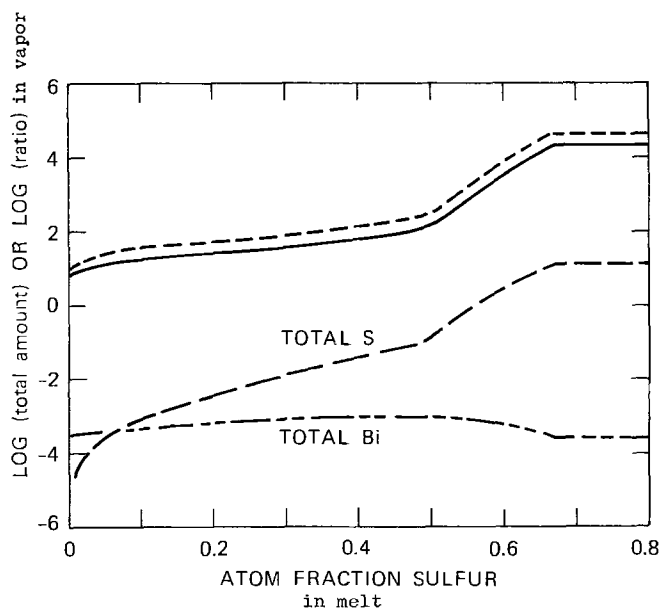


Fig. 2. Composition of gas phase at 800°C. Lower two curves: total amount of sulfur and bismuth in vapor; Total S =  $2 P(S_2) + P(BiS)$ ; Total Bi =  $2 P(Bi_2) + P(Bi) + P(BiS)$ . Upper two curves: composition of gas relative to melt; full curve = ratio of gram atoms of sulfur to bismuth in equilibrium gas (calculated from pressures of species) relative to ratio in melt; dotted curve = ratio of gram atoms of sulfur to bismuth in effused vapor (calculated from effusion rates of species) relative to ratio in melt.

same functions of composition over a wide temperature range (1).

The pressure of BiS goes through a maximum at 0.5 atom fraction of S in the melt. However the maximum has no particular significance. The maximum is a necessary consequence of the relationship of the pressure of BiS between the product of the activities of S and Bi in the system and the fact that those activities are monotonic functions of the composition variable (atom fraction S). Thus, in general (12), a vapor species Bi<sub>x</sub>S<sub>y</sub> will show a maximum in its pressure when the melt composition is given by  $N_S/N_{Bi} = y/x$ .

The ratio of the relative amounts of sulfur and bismuth in the vapor and in the melt are shown in Fig. 2 as the full curve. That ratio always exceeds unity and therefore there is no composition that evaporates congruently. (Congruent evaporation implies that the vapor composition calculated from the pressures is equal to the melt composition.) The vapor is always richer in sulfur than the melt. As the concentration of sulfur in the melt decreases that ratio drops to a limiting value (6.7 at 800°C). Therefore, in principle, equilibrium vaporization of the melt will always cause it to become enriched in bismuth.

It is interesting to consider vaporization of the melt controlled by an effusion orifice. In that case the ratio of species that evaporates is dependent on their molecular weights as well as their partial pressures. The Knudsen equation (13) for the rate of evaporation is

$$V \propto P \sqrt{MT} \quad [5]$$

in which  $V$  is the molecular rate of vaporization,  $P$  the pressure,  $M$  the molecular weight, and  $T$  the temperature. Because of the large differences in molecular weights of the species, there is a significant effect on the ratio of sulfur to bismuth that is vaporized. The ratios of amounts of sulfur to bismuth evaporated through an effusion orifice are shown as the dotted curve in Fig. 2. Vapor effused from the system always shows a larger sulfur to bismuth ratio than the equilibrium vapor pressures. The factor is approximately two except for small atom fractions of sulfur where it decreases to about 1.5.

That difference in the composition of the vapor removed from a system by different "equilibrium" processes can be important in an experimental test of the vapor composition of a system. Experimentally one often investigates the composition of the vapor of a system by evaporating a substantial fraction of a sample and analyzing the residue. The above analysis shows that the residue left after a Knudsen effusion evaporation would be poorer in sulfur than a true equilibrium vaporization. The effusion vaporization results could be corrected to the equilibrium situation only with a knowledge of the molecular weights of the vapor species and then relative amounts. In a Langmuir (open surface) vaporization the relative amounts of the components evaporated would be additionally complicated by the possibility of unequal vaporization coefficients. Therefore, the experimental test of vapor composition by measurements of the relative amounts removed by evaporation can give results that are not relevant to equilibrium vapor compositions.

Manuscript received May 9, 1975.

Any discussion of this paper will appear in a Discussion Section to be published in the December 1976 JOURNAL. All discussions for the December 1976 Discussion Section should be submitted by Aug. 1, 1976.

Publication costs of this article were partially assisted by the Stanford Research Institute.

#### REFERENCES

1. D. Cubicciotti, *J. Phys. Chem.*, **67**, 118 (1963).
2. D. Cubicciotti, *ibid.*, **67**, 1385 (1963).
3. R. F. Barrow, O. V. Stobart, H. Vaughn, *Proc. Phys. Soc.*, **90**, 555 (1967).

4. R. Hultgren *et al.*, "Selected Values of Thermodynamic Properties of Metals and Alloys," J. Wiley & Sons, Inc., New York (1963); Loose-leaf Supplement on Bi, 1968.
5. JANAF Thermochemical Tables, The Dow Chemical Co., Midland, Michigan (1974).
6. O. M. Uy and J. Drowart, *Trans. Faraday Soc.*, **65**, 3221 (1969). There is a systematic error in the values of the free energy functions in their Table 4. Also the values of A and B in their Table 2 are not consistent with their Table 1.
7. G. Herzberg, "Spectra of Diatomic Molecules," 2nd ed., pp. 227 and 471, D. Van Nostrand Co. New York (1950).
8. D. L. Hildenbrand, in "Advances in High Temperature Chemistry," Vol. 1, p. 193, (1967); D. L. Hildenbrand and E. Murad, *J. Chem. Phys.*, **51**, 807 (1969).
9. V. S. Ban and B. E. Knox, *ibid.*, **52**, 243 (1970); C. L. Sullivan, J. E. Prusaczyk, and K. D. Carlson, *ibid.*, **53**, 1289 (1970).
10. F. J. Kohl, O. M. Uy, and K. D. Carlson, *ibid.*, **47**, 2667 (1967).
11. D. Cubicciotti, *ibid.*, **66**, 1205 (1962).
12. The partial pressure of the species  $\text{Bi}_x\text{S}_y$  is related to the activities of the components by  $p(\text{Bi}_x\text{S}_y) =$

$K A^x(\text{Bi}) A^y(\text{S})$  in which  $K$  is the equilibrium constant. A maximum in the pressure will occur if the derivative with respect to composition is zero; so

$$0 = \frac{dp}{dN(\text{S})} = K \times A^y(\text{S}) A^{x-1}(\text{Bi}) \frac{dA(\text{Bi})}{dN(\text{S})} + y A^x(\text{Bi}) A^{y-1}(\text{S}) \frac{dA(\text{S})}{dN(\text{S})}$$

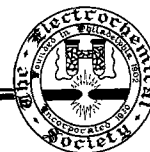
The Gibbs-Duhem equation can be written

$$\frac{N(\text{Bi})}{A(\text{Bi})} dA(\text{Bi}) = - \frac{N(\text{S})}{A(\text{S})} dA(\text{S})$$

and substitution into the above equation leads to the result  $N(\text{S})/N(\text{Bi}) = y/x$ . Thus a maximum in the pressure of a species will necessarily occur at a composition of the melt equal to the vapor composition of that species.

13. See, for example, "The Characterization of High Temperature Vapors," J. L. Margrave, Editor, Chap. 6, John Wiley & Sons, Inc., New York (1967).

## Brief Communication



### Anodic Passivation and Coating of AlAs in Aqueous Solutions

W. D. Johnston, Jr.

Bell Laboratories, Holmdel, New Jersey 07733

The close lattice match between AlAs and GaAs is well known and has made possible successful heterojunction semiconductor devices of great potential importance. The instability of pure AlAs in air due to water-vapor attack has hitherto limited interest in AlAs-GaAs systems to alloy compositions of  $\text{Al}_x\text{Ga}_{1-x}\text{As}$  with  $x \lesssim 0.8$ . Recently, high performance n-AlAs/p-GaAs large area solar cells prepared by vapor phase epitaxy (VPE) have been demonstrated (1). An essential element in practical solar cell devices is a stable, and preferably antireflective, top surface. We describe here the technique of anodic growth of a stable oxide layer on pure VPE AlAs. The anodic oxidation of GaAs,  $\text{Al}_x\text{Ga}_{1-x}\text{As}$ , and GaP is substantially similar and has been described in detail by Schwartz, Ermanis, and Brastad (2). We will emphasize here only the significant differences for pure AlAs. As in the work of Ref. (2), we employed a Pt cathode and Ta anode contact. We investigated anodic growth on n-AlAs layers ( $n \sim 10^{18} \text{ cm}^{-3}$ ,  $\rho \sim 0.05 \text{ ohm-cm}$ ,  $\mu \sim 120$ ) grown by VPE on (100) GaAs substrates (3), in pH-adjusted  $\text{H}_2\text{O}_2$  or  $\text{H}_2\text{O}$  electrolytes.

We found that uniform, controlled oxide growth on AlAs is even more critically dependent upon purity of the electrolyte with respect to halide or  $\text{NO}_3^-$  ion concentration than was found for the Ga compounds (2). We were unable, in fact, to obtain high quality large area anodic growth in 30%  $\text{H}_2\text{O}_2$  electrolyte anywhere in the pH 1.5-5.0 range, owing, we believe, to residual

(1 ppm)  $\text{Cl}^-$  impurity, although acceptable growth on GaAs was attainable. Similar difficulty was encountered with ordinary distilled  $\text{H}_2\text{O}$ . With multiply filtered, deionized (4)  $\text{H}_2\text{O}$  (18 megohm cm), to which  $\text{H}_3\text{PO}_4$  had been added to pH 1.9-2.0, however, excellent growth could be attained up to 2500 Å under constant current conditions. The final layer thickness was determined to be linearly dependent (approximately 10 Å/V) on supply compliance voltage setting. Current densities of  $\sim 2-8 \text{ mA/cm}^2$  were satisfactory for room temperature baths at pH 2.0. At higher current densities tapering of the oxide was observed, particularly for AlAs epilayers grown on high resistivity substrates. Nonuniformity and pinholing of the oxide occurs at lower current densities. At elevated temperatures a greater range of current densities is permitted, thicker films may be grown, but the optimum pH range of 1.9-2.0 remains unchanged. Our conclusion that  $\text{Cl}^-$  impurity is responsible for the poor anodization with  $\text{H}_2\text{O}_2$  and ordinary distilled water is based on the observation that addition of  $\sim 1$  ppm of  $\text{Cl}^-$  (from successive dilution of reagent HCl) to the highly pure water gave similarly poor anodization behavior.

Following anodization, the material was baked and annealed at 400°C for 1 hr in a dry  $\text{N}_2$  ambient. This serves to drive off water of hydration and improve the stability of the vitreous film. By analogy with Ref. (2), we believe the oxide film to be the form  $\text{Al}_2\text{O}_3 \cdot \text{As}_2\text{O}_3$ . At higher baking temperatures ( $\gtrsim 550^\circ\text{C}$ , 20 min) devitrification and loss of arsenic oxides sets in. The layers then fracture and "flake off" on cooling.

The unbaked anodic oxide film is significantly more resistant to attack by concentrated or dilute HCl than is the equivalent anodic oxide grown on GaAs. Total removal of a 1000Å film in 50% HCl takes a few seconds for the film on GaAs, and tens of minutes for the film on AlAs. If pinholes, imperfections, or edges are exposed, in fact, the film is detached by attack on the underlying AlAs which is attacked much more rapidly than the oxide. Unbaked films deteriorate over several weeks in room air. The properly baked films are stable in room air and resist deterioration in contact with the photoresists, waxes, glycol phthalate, and shellac-based cements used in device fabrication, all of which attack and deteriorate unprotected AlAs in varying degrees. The baked film is rapidly removed in 10% HF or H<sub>2</sub>SO<sub>4</sub> solutions but is not attacked by 20% Br<sub>2</sub>:CH<sub>3</sub>OH. It may also be removed rapidly in 1M KOH, which has less tendency to attack the underlying AlAs.

Preliminary measurements indicate a refractive index for the baked films of 1.7-1.8 at 600 nm. (The index does not vary from film to film, rather the uncertainty lies in our imperfect knowledge of the optical constants of AlAs, uncertainty in exact film thickness, residual surface roughness effects, etc.) The anodic oxide is thus eminently suitable for an antireflective coating [ $n_{\text{AlAs}} \sim 3.3 = (1.8)^2$ ] and we have in fact obtained reflectivities below 2% across the 570-750 nm band on the solar cell devices described in Ref. (1).

Recently, the anodization of GaAs in a solution of ethylene or propylene glycol, tartaric acid, and water was described (5). We have found that this electrolyte does not offer any advantage over pure H<sub>2</sub>O/H<sub>3</sub>PO<sub>4</sub> for anodization of AlAs or GaAs, and we were only able to obtain poor results, comparable to those with the H<sub>2</sub>O<sub>2</sub> bath for AlAs. We have also tried other conductivity/pH modifiers—citric, acetic and tartaric acids, NH<sub>4</sub>OH—in the highly pure water. Results in these electrolytes were less satisfactory, and the anodic oxides formed were less stable in air, whether baked or not.

In summary, stable, uniform anodic oxide films may be grown to reproducible and controlled thicknesses on AlAs by similar techniques as used (2) for GaAs, GaP,

and Ga<sub>1-x</sub>Al<sub>x</sub>As alloy. The stability of the properly baked film is at least as good against attack by water or mineral acid solutions as the films on the Ga-containing compounds, and AlAs treated in this fashion can be handled and processed without the random deterioration, oxidation, and/or hydration which has hitherto precluded much interest in use of this compound in practical devices.

#### Acknowledgments

We thank W. M. Callahan for growing and characterizing the VPE layers used in this work.

Manuscript submitted Sept. 29, 1975; revised manuscript received Nov. 10, 1975.

Any discussion of this paper will appear in a Discussion Section to be published in the December 1976 JOURNAL. All discussions for the December 1976 Discussion Section should be submitted by Aug. 1, 1976.

Publication costs of this article were partially assisted by Bell Laboratories.

#### REFERENCES

1. W. D. Johnston, Jr. and W. M. Callahan, *Appl. Phys. Letters*, **28**, 150 (1976). Briefly, we have obtained open-circuit voltages up to 0.92V and short-circuit current densities to 0.03A cm<sup>-2</sup> for devices of 2-3 cm<sup>2</sup> area at 100 mW/cm<sup>2</sup>, AM 1.4 conditions. Conversion efficiencies are 13-18% for our present devices, limited by the simple stripe contacts used, which give fill factors of 0.5-0.6. The VPE material appears to have similar potential to LPE Ga<sub>1-x</sub>Al<sub>x</sub>As - GaAs,  $x \sim 0.7-0.8$  material described by others. See for instance J. M. Woodall and H. J. Hovel, *J. Vacuum Sci. Technol.*, **12**, 1000 (1975).
2. B. Schwartz, F. Ermanis, and M. H. Brastad. Submitted to *This Journal*.
3. W. D. Johnston, Jr. and W. M. Callahan, Unpublished. A chloride-AsH<sub>3</sub> growth technique was employed similar to that described by A. G. Sigai, M. S. Abrahams, and J. Blanc, *This Journal*, **119**, 952 (1972).
4. Millipore Filter Corp. (Recirculating "Super Q" System).
5. H. Hasegawa, K. E. Forward, and H. L. Hartnagel, *Appl. Phys. Letters*, **10**, 567 (1975).



## Boundary Layer Replenishment and Unsteady-State Phenomena in Hydrogen-Oxygen Fuel Cells

Lyle F. Albright, T. G. Theofanous, and A. G. Rohrer<sup>1</sup>

*School of Chemical Engineering, Purdue University, West Lafayette, Indiana 47907*

### ABSTRACT

A one-dimensional (for diffusion) platinum electrode immersed in either dilute potassium hydroxide or sulfuric acid solutions was investigated for start-ups and restarts after partial rest periods. The experimental results for both the cathode and anode of the hydrogen-oxygen fuel cell were examined quantitatively to indicate the time periods for surface reaction control, diffusion control, and convection control.

When a fuel cell is started up, *i.e.*, when the circuit of the cell is closed after the cell has been rested, the current surges to a high value and then decays toward a steady-state value. As this occurs, the concentration of oxygen at the surface of the cathode decreases, and a boundary layer of electrolyte that is relatively depleted in absorbed oxygen forms next to the cathode. Hydrogen depletion also occurs at and near the anodic surfaces. When a cell is rested after it has been operated for extended periods of time, oxygen and hydrogen diffuse or transfer back in the regions on or near the cathodic and anodic surfaces, respectively. Relatively little quantitative information is available, however, on oxygen and hydrogen concentrations as a cell is initially rested or during the restarts (after a cell has been partially rested). Information on rest periods and on restarts would appear to be useful in clarifying phenomena that occur during cell operation.

The available information on start-up of a fuel cell indicates that several current-controlling steps may occur during start-up depending on the time after the circuit is closed and on the type of cell (or electrode) used (2-4, 7-10). In the time period immediately after the circuit is closed, the current is high and is sometimes relatively constant. Kinetic control is of major importance during this initial time period. With increased time after closing the circuit, the current often becomes essentially directly proportional to  $1/\sqrt{\text{time}}$ ; the diffusion (or transfer) step of hydrogen or oxygen through the electrolyte to the anode or cathode, respectively, is then the controlling step. A third controlling step, free or natural convection, often becomes important for vertical electrodes several minutes after the circuit is closed (6).

In the present investigation, experimental evidence was obtained relative to the start-ups and restarts (after partial rest periods) for one-dimensional electrodes. This information plus mathematical analysis of the data has helped clarify the phenomena occurring during start-up, the rest period, and restarts.

<sup>1</sup> Present address: E. I. du Pont de Nemours and Company, Houston, Texas 77001.

Key words: fuel cell, electrode, electrolyte, cathode, anode, sulfuric acid, potassium hydroxide.

### Equipment and Operating Procedure

The equipment and operating procedures were similar to those used by earlier investigators (2, 3). The test electrode was a piece of platinum foil that was 8 cm high, 3 cm wide, and 0.0125 cm thick. It was either completely or partially immersed in a vertical position in an electrolyte contained in a glass beaker. In some runs, the electrode was positioned in the middle of a 3 cm  $\times$  8 cm rectangular passageway constructed with Plexiglas plastic pieces that were 7 cm long. Since the passageway fitted closely around the edges of the electrode, diffusion of the absorbed gas in the electrolyte (oxygen or hydrogen depending on whether the electrode was being used as a cathode or anode) could, with this shielding, be only perpendicular to the plane of the electrode.

The surface roughness of the test electrode was increased by the electrodeposition of platinum from a 10% solution of chloroplatinic acid using a current density of 13 mA/cm<sup>2</sup> for 240 sec. DeVet (3) has earlier shown that such an electrodeposition technique increases the surface area by a factor of about 150, presumably indicating the presence of some platinum black on the surface.

When the test electrode was the cathode, the electrolyte in the main beaker was saturated with oxygen. The electrolyte around the counterelectrode was, however, saturated with hydrogen. For most runs of this investigation, 1N KOH was used as the electrolyte.

The differences in the potentials between the test electrode and the reference electrode (a saturated calomel electrode) were measured. After the open-circuit potential was determined using a Honeywell Model No. 2780 potentiometer, the desired potential difference was established and maintained to within 0.01V with a control system containing a potentiostat (Duffer's Model 600) and a dual power supply (Duffer's Model 620). Continuous measurement of the cell current was recorded on a Sargent SR recorder with a range up to 125 mA.

In some experiments, the fuel cell was modified so that the test electrode was the anode. The flows of oxygen and hydrogen were then reversed. In some cases,

dilute solutions of sulfuric acid were used as electrolyte.

The electrode to be tested was generally activated at the start of each day's operation; to do this it was immersed in 20% nitric acid maintained at a temperature just below its boiling point for 2 hr. The electrode was then rinsed with distilled water for 10 min; and then assembled with the fuel cell, which was immersed in a water bath.

The fuel cell was normally operated at room temperature, i.e., at 25°-29°C. The electrolyte solutions for the cathode and anode were saturated with oxygen and hydrogen, respectively, by bubbling these gases through the electrolyte for 1-2 hr. In order to allow for dissipation of the convection currents in the electrolyte, the gas flows were stopped for at least 20 min before the circuits were closed. This technique of saturating the electrolyte with oxygen and hydrogen is defined here as the initial rest period.

### Results

Several runs were made initially to determine if the shielded electrodes provided one-dimensional diffusion of the absorbed reactant gas through the electrolyte. Comparative runs made with a cathode completely immersed in 1N KOH, an anode in 1N KOH, and an anode in 1N H<sub>2</sub>SO<sub>4</sub> indicated that the currents generated by shielded electrodes were 5-10% less than currents with unshielded electrodes. Figure 1 shows the currents generated as a function of time after the circuit was closed for a shielded and freshly activated cathode immersed in 1N KOH at potentials of 0.2, 0.3, and 0.6V. In all start-up runs, the currents were initially high and decayed to more or less steady-state values after several minutes.

The results of these start-up runs with shielded electrodes were next compared with calculated values obtained using the well-known equation for one-dimensional diffusion of the absorbed gas in the electrolyte. In the case of the cathode, oxygen is the absorbed gas

$$i_s = AnFC(D/\pi t)^{0.5} \quad [1]$$

where  $i_s$  = start-up current, mA;  $A$  = submerged area of electrode, cm<sup>2</sup>;  $n$  = number of electrons transferred per mole of reactant gas;  $F$  = Faraday number,  $9.65 \times 10^7$  mA-sec;  $C$  = concentration of dissolved reactant in electrolyte, mole/cm<sup>3</sup>;  $D$  = diffusivity of dissolved reactant in electrolyte, cm<sup>2</sup>/sec;  $\pi$  = 3.1416; and  $t$  = time, sec.

A basic assumption of the above equation is that the reactant gas reacts immediately upon reaching the electrode and that the concentration of the reactant at the surface is zero. Values for diffusivity and for equilibrium solubilities of oxygen and hydrogen in dilute

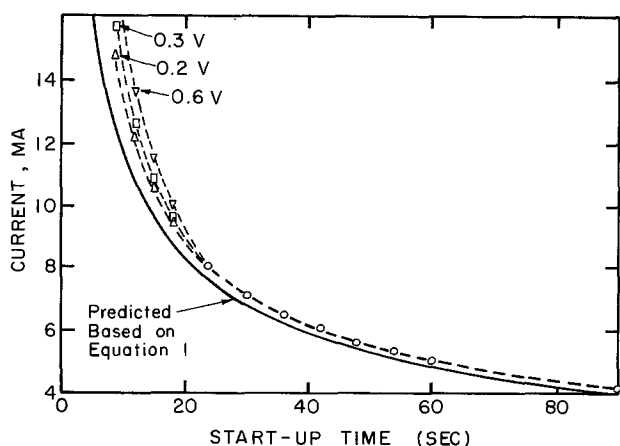


Fig. 1. Current as function of time after start-up of cathode completely immersed in 1N KOH at polarizations of 0.2, 0.3, and 0.6V.

electrolyte solutions, such as needed in Eq. [1], are reported in the literature (1, 5). Currents calculated using Eq. [1] agreed in all cases within 4% of the experimental currents for time periods from 15 to 200 sec after the circuit was closed.

Plots of the current vs.  $(1/t^{0.5})$  were most useful. The straight-line portion of such graphs was in all cases well represented by Eq. [1]. Figure 2 is an example for  $(1/t^{0.5})$  values from about 0.07 to 0.25. Other time portions of these graphs will be considered later.

The currents at start-up of other one-dimensional electrodes in addition to those tested in this investigation can probably also be predicted by means of Eq. [1]. To support this conclusion, Eq. [1] resulted in a 10-15% underprediction of the start-up currents obtained by DeVet (3) who used an unshielded cathode immersed in 1N sulfuric acid electrolyte.

After the shielded electrodes were found to result in one-dimensional diffusion, a series of runs was made in which a cathode immersed in 1N KOH was first started up, then partially rested, and then restarted. When the circuit is first closed (resulting in the start-up current), an oxygen-deficient boundary layer is formed, and it grows in thickness as the circuit remains closed, as confirmed with the appropriate one-dimensional diffusion equations. The length of the start-up period was controlled in a series of runs at either 1.0 or 2.5 min. Following the start-up period, the circuit was opened in order to rest the cell. During this period of time, oxygen diffused into the boundary layer. Longer rest periods replenished to a greater extent the reactant concentrations causing them to approach the equilibrium concentrations that resulted after "complete" resting. Rest periods of 0.5, 1.0, 1.5, 2, 2.5, 5, and 12.5 min were tested. Finally, the circuit was closed once more, and the resulting current is defined as the restart current,  $i_{rs}$ . When molecular diffusion is controlling, the magnitude of  $i_{rs}$  can be related to  $i_s$  by the following equation derived by Rohrer (7)

$$\frac{i_{rs}}{i_s} = \frac{1}{2} \int_0^\infty f(y) \left[ \frac{y}{Dt_{rs}} e^{-\frac{y^2}{4Dt_{rs}}} \right] dy + 1 \quad [2]$$

where

$$f(y) = \frac{1}{2\sqrt{\pi Dt_r}} \int_0^\infty \left[ \operatorname{erf} \left( \frac{u}{2\sqrt{Dt_r}} \right) - 1 \right] \left[ e^{-\frac{(y+u)^2}{4Dt_r}} + e^{-\frac{(y-u)^2}{4Dt_r}} \right] du \quad [3]$$

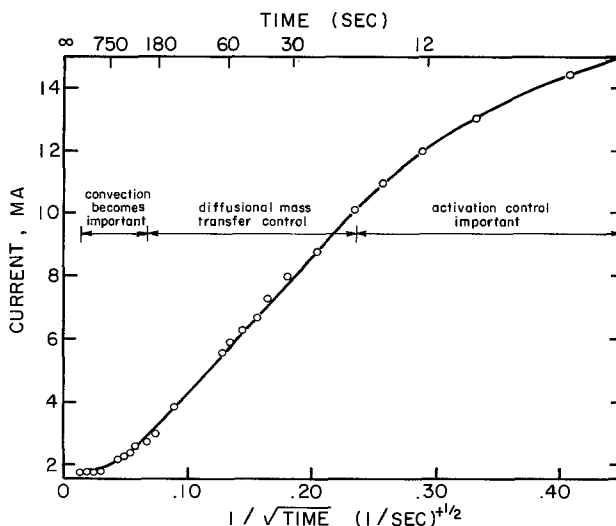


Fig. 2. Plot showing time regions for various controlling steps of start-up of hydrogen-oxygen fuel cell with 1.0N KOH electrolyte.

and  $t_{rs}$  = time elapsed after restart;  $t_r$  = total resting time;  $\tau$  = the start-up time.

The experimental results of the restarts are reported here as the ratio of the restart current to the start-up current, i.e.,  $i_{rs}/i_s$ . In all cases, predicted values of  $i_{rs}/i_s$  based on the derived mathematical model (7) agreed well with the experimental values in the diffusion-law region (about 15-200 sec). Figure 3 shows the results for runs with the cathode completely immersed in 1N KOH and with a polarization of 0.2V. Both increased rest periods and decreased periods of time of closed circuit during start-up resulted in higher  $i_{rs}/i_s$ .

The ratio  $i_{rs}/i_s$  is a function of only two dimensionless variables (7),  $v = t_{rs}/t_r$  and  $g = \tau/t_r$ . In fact, also using the substitutions

$$n = \frac{y}{2\sqrt{Dt_{rs}}} \text{ and } m = \frac{u}{2\sqrt{Dt_{rs}}}$$

Eq. [2] and [3] become

$$\frac{i_{rs}}{i_s} = 2 \int_0^\infty f(n,v,g) e^{-n^2} n \, dn + 1 \quad [4]$$

and

$$f(n,v,g) = \left(\frac{v}{\pi}\right)^{1/2} \int_0^\infty \left[ \operatorname{erf}\left(\frac{v^{1/2}m}{g^{1/2}}\right) - 1 \right] [e^{-v(n+m)^2} + e^{-v(n-m)^2}] dm \quad [5]$$

Figure 4 indicates how  $i_{rs}/i_s$  varies for various values of  $v$  and  $g$  based on the mathematical model. This graph indicated that a rest period as large as five times the start-up period ( $g = 0.2$ ) is insufficient to completely replenish the boundary layer formed during start-up. When the rest period becomes large as compared to the rest period, i.e.,  $v \gg 1$ , then the effect of increased resting becomes less since  $i_{rs}/i_s \rightarrow 1.0$ .

*Results of early time period of start-up.*—The current values calculated using Eq. [1] generally do not agree with the experimental values during the first 20 sec after start-up of a well-rested electrode. Figure 1 shows the results obtained with a cathode that had been freshly activated in nitric acid and was then immersed in 1N KOH. In this case, the experimental cur-

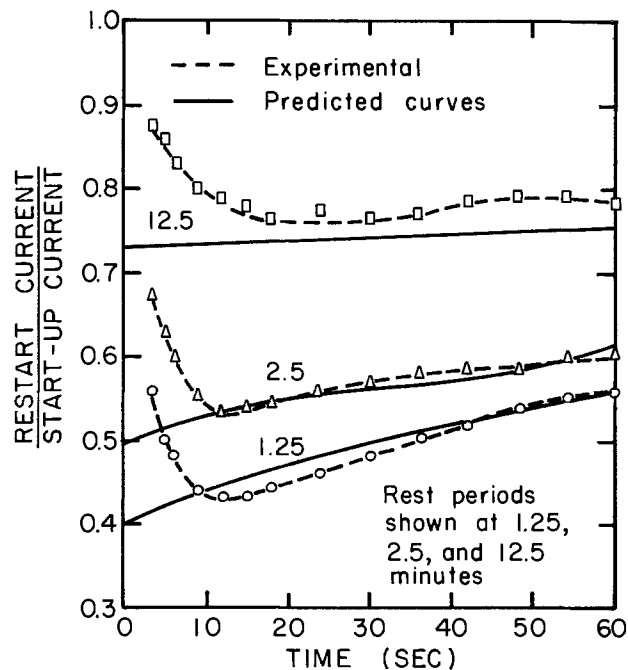


Fig. 3. Comparison of experimental and predicted ratio of restart to start-up currents for cathode immersed in 1N KOH and with polarization of 0.2V.

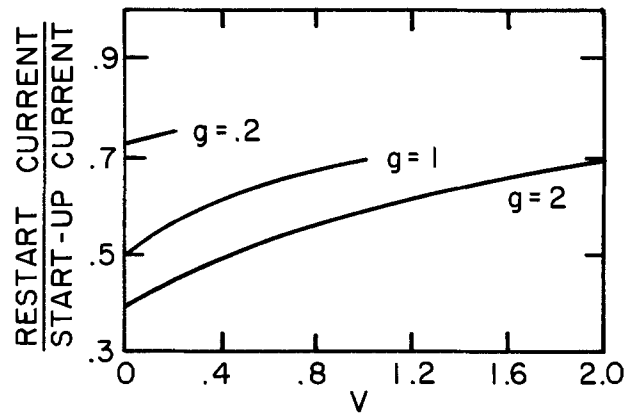


Fig. 4. Restart current/start-up current as function of dimensionless variables  $v$  and  $g$ .

rents in the range of about 2-20 sec after closing the circuit were higher than the calculated values. During this time period, the currents were also sensitive to the magnitude of the imposed voltage. For activated anodes immersed in either 1N KOH or 1N H<sub>2</sub>SO<sub>4</sub>, similar findings were also noted. These results can be explained by two factors. Adsorption of hydrogen on the anode and of oxygen on the cathodes during the rest period results in more reactants (and hence higher currents) than are predicted based just on diffusion transfer. At least partial kinetic control is occurring as indicated by increased currents with higher imposed voltages.

For restart runs with a cathode immersed in 1N KOH, the poor agreement as indicated by Fig. 3 between the experimental and calculated results in the time period of 2-15 sec can also be explained by oxygen adsorbed on the cathodic surface. During the rest period, part of the oxygen that transfer to the surface is adsorbed on the surface. This adsorbed oxygen is then responsible for currents higher than would be predicted assuming diffusion transfer was the only phenomenon that had to be considered.

Immersion of the cathode in 1N KOH slowly deactivated it and may have resulted in diminished adsorption of oxygen on the surface. This conclusion is based on comparative runs with a cathode immersed from 0 to 8 days in 1N KOH. As noted in Fig. 5, decreased currents were obtained in the 2-20 sec time period (i.e.,  $1/t^{0.5}$  from about 0.22 to 0.7) as the time of immersion increased. Extended immersions of an anode in 1N H<sub>2</sub>SO<sub>4</sub> also deactivated it.

The cathode that was used immediately after being immersed (i.e., zero days immersion) was most active. For values of  $1/t^{0.5}$  from about 0.22 to 0.30, the slope

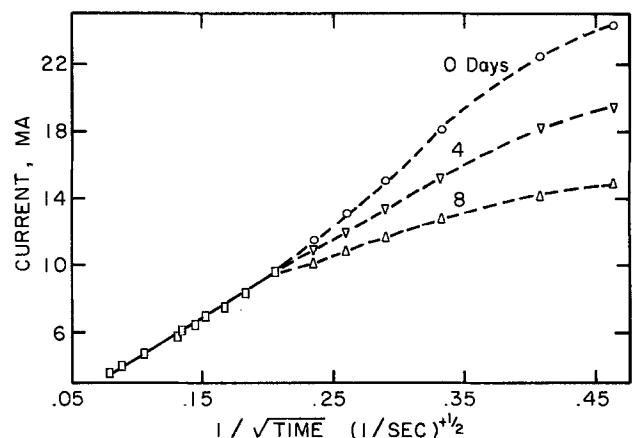


Fig. 5. Effect of aging of cathode in 1N KOH solution as related to start-up currents with 1N KOH electrolyte and with polarization of 0.2V.



increased rapidly, but at higher ( $1/t^{0.5}$ ) values, i.e., lower time values, the slope decreased and began to level out. For a constant current value, the electrode would be completely activation or kinetic controlled.

*Results for long time periods after start-up.*—For all electrodes tested, the current always became essentially constant several minutes after start-up. Equation [1], however, predicts that the current would continue to decrease with time until zero current would be obtained at infinite time. Free or natural convection most likely becomes of increased importance as a means of transferring oxygen (or hydrogen) to the electrode surface as the diffusional transfer decreases in importance (6).

Convection currents may also have increased somewhat as boundary layers deficient in oxygen (or hydrogen) were formed around the electrodes; in this latter case, some density gradients were most likely formed in the electrolyte solution near the electrode. The concentration of the electrolyte used sometimes has a significant effect on the current obtained after several minutes of operation. Currents obtained after 120 sec with a cathode immersed in 1N KOH were somewhat greater than currents in experiments using 1.5N KOH. More random convection currents probably occurred in the more dilute KOH solution because its lower viscosity would result in greater transfer of oxygen to the cathode surface. In addition, increased normality results in somewhat decreased oxygen diffusivity and solubility. It appears that for the electrodes used in this investigation that convection and diffusion steps are both partially controlling at the longer periods of time investigated.

### Discussion

Kinetic control, diffusion control, convection control, and adsorption of oxygen on the cathode and of hydrogen on the anode are important considerations needed to explain the results of start-up and restart experiments of this investigation. The levels of current (or current fluxes) that serve as transition regions from one type of control to another have been reported for the flat-plate vertical anode and cathode used in this investigation. Such transition regions will certainly vary with at least the following variables: surface activation and roughness of the electrode; type of electrode being investigated such as either anode or cath-

ode; type and concentration of electrolyte used; and the over-all geometry of the cell. Both roughness and the surface composition of the electrode should be further investigated in order to determine the levels of surface oxides, adsorbed species, etc. on the surface. Preliminary investigations here have already indicated that differences in surface compositions occur as a cathode is used in a fuel cell.

Other important areas that require further investigation are the mechanism of adsorption and the amount of oxygen (or hydrogen) that is adsorbed on the cathode (or anode) during the rest cycle and also the phenomena that occur during the initial stages of start-up when activation control is important.

### Acknowledgments

Indiana Gas Association provided generous financial support to this investigation. Messrs. J. J. Schmitz, J. B. Cavender, and R. W. Salnick all made significant contributions in development of the equipment and procedures employed.

Manuscript submitted April 4, 1975; revised manuscript received Oct. 27, 1975.

Any discussion of this paper will appear in a Discussion Section to be published in the December 1976 JOURNAL. All discussions for the December 1976 Discussion Section should be submitted by Aug. 1, 1976.

Publication costs of this article were partially assisted by Purdue University.

### REFERENCES

1. R. Davies, G. Horvath, and C. Tobias, *Electrochim. Acta*, **12**, 287 (1967).
2. H. J. Davitt and L. F. Albright, *This Journal*, **114**, 53 (1967).
3. J. O. DeVet, R. G. Barile, and L. F. Albright, *ibid.*, **117**, 417 (1970).
4. L. Hsueh and John Newman, *ibid.*, **117**, 1242 (1970).
5. International Critical Tables 3(272) National Research Council, McGraw-Hill, New York (1928).
6. R. N. O'Brien, *This Journal*, **119**, 589 (1972).
7. A. G. Rohrer, Masters Thesis, Purdue University, West Lafayette, Indiana (1973).
8. W. H. Smyrl and John Newman, *This Journal*, **118**, 1079 (1971).
9. H. Weber, H. Meissner, and D. Sama, *ibid.*, **109**, 884 (1962).
10. F. Will, *ibid.*, **110**, 145 (1962).

## Equilibrium Phases Between Lithium Sulfide and Iron Sulfides

Ram A. Sharma

General Motors Corporation, Electrochemistry Department, Research Laboratories, Warren, Michigan 48090

### ABSTRACT

The equilibrium phases in the lithium sulfide-ferrous sulfide system were determined by differential thermal analysis and x-ray diffraction analysis. A compound  $\text{Li}_2\text{S}\cdot\text{FeS}$ , which melts incongruently at  $885^\circ \pm 5^\circ\text{C}$  to  $\text{Li}_2\text{S}$ , and a liquid containing approximately 50.5 mole per cent (m/o) FeS, and has a transition at  $840^\circ \pm 5^\circ\text{C}$ , was found. A eutectic between  $\text{Li}_2\text{S}\cdot\text{FeS}$  and FeS was observed at 63 m/o FeS and  $858^\circ \pm 3^\circ\text{C}$ . The terminal liquidus curves, computed by the application of Temkin's model, were found to be in good agreement with those experimentally determined. X-ray diffraction studies confirmed the transition in the compound  $\text{Li}_2\text{S}\cdot\text{FeS}$  and also indicated compounds  $2\text{Li}_2\text{S}\cdot\text{Fe}_3\text{S}_4$  and  $\text{Li}_2\text{S}\cdot\text{Fe}_2\text{S}_3$ , between  $\text{Li}_2\text{S}$ , FeS, and  $\text{FeS}_2$ .

The lithium-sulfur system appears very promising for developing an electrochemical cell of a high-temperature molten salt battery for vehicular propulsion

\* Electrochemical Society Active Member.

Key words: equilibrium phases, lithium sulfide, iron sulfides.

(1). One of the major problems which has been encountered in developing this type of cell is the containment of sulfur in the positive electrode compartment. This problem arises because the cell operates at about  $400^\circ\text{C}$  at which temperature sulfur vapor pres-

sure is very appreciable (2), and, therefore, sulfur is lost by vaporization.

It has also been observed that a lithium-sulfur liquid of about 65.5 mole per cent (m/o) sulfur (3) which forms during the cell cycling, dissolves in the typical  $\text{LiCl-KCl}$  electrolyte to an appreciable extent. This dissolved lithium-sulfur liquid reacts with the lithium in the anode forming lithium sulfide. Lithium sulfide is practically insoluble in the electrolyte at the cell operating temperature (0.02 mole/liter) (4). The loss of sulfur-electrode capacity by this self-discharge mechanism is difficult to recover.

The use of  $\text{FeS}_2$  in place of sulfur circumvents the problems of sulfur loss by vaporization and the solution mechanism. Therefore, work is in progress to develop  $\text{Li-FeS}_2$  cells. Microscopic examination of samples of the positive ( $\text{FeS}_2$ ) electrode (4, 5) have indicated the presence of intermediate product phases during cycling. This investigation was conducted to determine the equilibrium phases in the  $\text{Li}_2\text{S-FeS}$  system and other possible compounds between  $\text{Li}_2\text{S}$ ,  $\text{FeS}$ , and  $\text{FeS}_2$ . This information should be useful in understanding the cell operation and in the design of practical cells.

### Experimental

**Materials.**—Lithium sulfide was white powder; its lithium content determined by chemical analysis was 29.8 weight per cent (w/o) (30.26 w/o theoretical). Its x-ray powder diffraction pattern indicated only  $\text{Li}_2\text{S}$ . Ferrous sulfide used was a black powder of 99.999% purity, as quoted by the supplier. Pyrite ( $\text{FeS}_2$ ) was technical grade. It was freed from silica or silicates by a "sink-float" technique using tetrabromomethane of specific gravity 2.96. Its chemical analysis gave ~ 97 w/o  $\text{FeS}_2$ .

**Apparatus and procedure for determining the equilibrium phases in the  $\text{Li}_2\text{S-FeS}$  system.**—The differential thermal analyzer used consisted of a small resistance heating element furnace suitable for use up to  $1600^\circ\text{C}$ ; an alumina enclosure for the sample and reference containers, allowing the maintenance of inert atmosphere (helium); a temperature programmer with a digital indicator; and a multipoint recorder for measuring sample temperatures and differential temperatures between the sample and a reference alumina sample, and sample weight. Platinum/platinum-10% rhodium thermocouples which were accurate within  $3^\circ$  in the range of temperature measured were used for temperature determination. Small, specially designed, dense graphite containers which could be closed nearly gastight with threaded caps were used for holding the samples. The graphite containers were fitted on the tops of the alumina thermocouple sheaths. Thin platinum foils were placed between the graphite containers and the thermocouple beads to avoid contamination of the thermocouple beads and to provide good contact between them and the graphite containers. The layout of the sample and reference containers inside the furnace is shown in Fig. 1.

Various salt compositions were prepared by taking weighed amounts of the components and mixing them thoroughly in an agate mortar. The accuracy of the compositions so prepared was checked by chemical analysis which indicated the intended composition within  $\pm 1\%$ . About 0.5g of the mixture was placed in the graphite container. The entire manipulation was done in a helium-atmosphere dry box. The graphite container with the sample was removed from the jar only to position it on the top of the alumina sheath of the thermocouple inside the enclosure. Helium was passed through the enclosure. Phase transition temperatures were obtained with heating and cooling rates from  $2^\circ$  to  $10^\circ\text{C}/\text{min}$ . A typical representation of these curves for a melt of composition of 60 m/o  $\text{FeS}$  and 40 m/o  $\text{Li}_2\text{S}$  at a rate of  $4^\circ\text{C}/\text{min}$  is shown in Fig. 2.

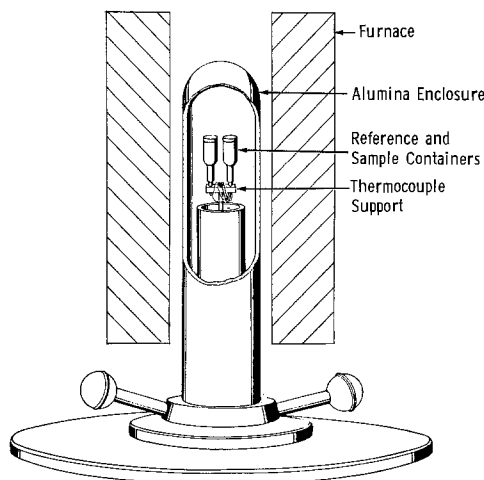


Fig. 1. Layout of samples inside the furnace

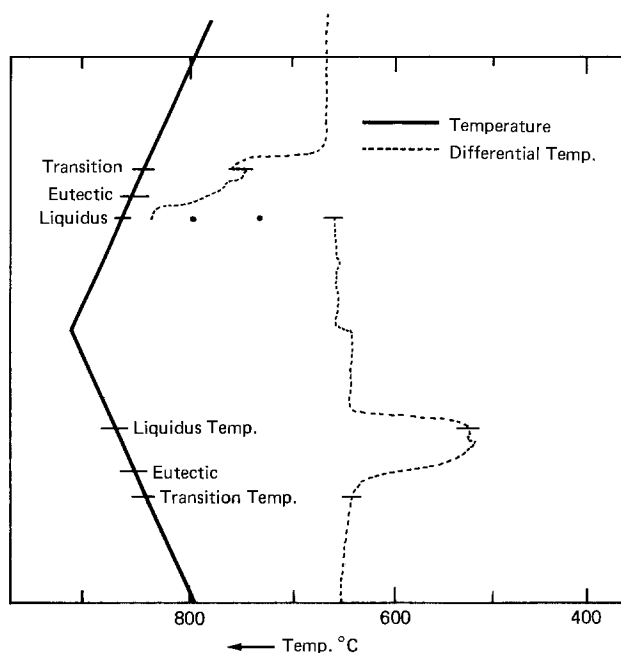


Fig. 2. A typical representation of the DTA curves obtained for a melt of 60 m/o  $\text{FeS}$  and 40 m/o  $\text{Li}_2\text{S}$  at  $4^\circ\text{C}/\text{min}$ .

By combining the measurements from the heating and cooling curves, the liquidus temperatures and eutectic temperature could be determined with good accuracy. The uncertainty could be further removed by having the measurements at different heating and cooling rates and, in the case of the eutectic temperature, at various compositions.

**Sample preparation and equipment for x-ray diffraction analysis.**—For x-ray diffraction analysis, the calculated amounts of  $\text{Li}_2\text{S}$ ,  $\text{FeS}$ , and  $\text{FeS}_2$  for the intended compound were mixed thoroughly in an agate mortar inside a helium-atmosphere dry box. About 5g of this mixture was taken into a dense-graphite container (6 cm high and 1 cm ID) which was placed inside a silica capsule. The silica capsule was sealed under vacuum and placed inside a tubular furnace at the desired temperature. After a certain period, the silica capsule was cooled, the sample was taken out of the graphite container and was crushed to a fine powder. The powder was reloaded into the graphite container, and proceeding as above, it was again placed at the desired temperature for another period. It was then taken out of the graphite container and crushed inside a helium atmosphere dry box. A small portion

of this powder was sealed in a fine silica capillary for x-ray diffraction analysis.

The equipment used for the x-ray diffraction analysis was a 143.2 mm camera mounted in conjunction with a vertical x-ray tube on a diffractometer instrument. A copper target tube could not be used because of the fluorescent effect of the copper radiation on the iron within the samples. A chromium target could not be used because of the heavy absorption of the radiation by the capillary (and the sample), and the x-ray powder pattern obtained contained only two lines because of the long wavelength radiation. So a molybdenum target tube CA-7 type with 0.002 in. reactor grade zirconium filter at the window to suppress  $K_{\beta}$  radiation was chosen.

Molybdenum radiation is short in wavelength and as a result the lines of the generated powder patterns are quite close together. This concentration of lines toward the front reflection region of the camera and the inaccuracies of the front reflection region are undesirable consequences of this radiation choice. However, a check of the two available lines obtained from a sample ( $2\text{Li}_2\text{S}\cdot\text{Fe}_3\text{S}_4$ ) showed identical readings using either molybdenum or chromium radiation.

The x-ray diffraction patterns obtained for FeS and  $\text{FeS}_2$  (pyrite) were also in complete agreement with the data reported in ASTM cards 11-151 for FeS and 6-0710 for pyrite.

### Results and Discussion

The differential thermal analysis data for the  $\text{Li}_2\text{S}$ -FeS system are given in Table I. The equilibrium phase diagram based on the data obtained from both heating and cooling curves is shown in Fig. 3. A compound,  $\text{Li}_2\text{S}\cdot\text{FeS}$ , occurs in this system, melting incongruently at  $885 \pm 5^\circ\text{C}$  to  $\text{Li}_2\text{S}$  and a liquid containing approximately 50.5 m/o FeS. A eutectic between  $\text{Li}_2\text{S}\cdot\text{FeS}$  and FeS occurs at  $858 \pm 3^\circ\text{C}$  and at the composition containing 63 m/o FeS. The compound  $\text{Li}_2\text{S}\cdot\text{FeS}$  also has a transition temperature at  $840 \pm 5^\circ\text{C}$ , as shown in Fig. 3.

The scanning electron microscope (SEM) pictures of the solidified melts, obtained from the differential thermal analysis runs, are shown in Fig. 4-7. These solidified samples were metallic black and brittle. They were easily tapped out of the graphite containers indicating that they shrank more than the graphite.

The SEM picture in Fig. 4 of the fractured surface of the solidified melt of 34.3 m/o FeS and 64.7 m/o  $\text{Li}_2\text{S}$ , consisting of 31.4 m/o  $\text{Li}_2\text{S}$  and 68.6 m/o  $\text{Li}_2\text{S}\cdot\text{FeS}$ , shows clearly two phases in accordance with the phase diagram. The lithium sulfide phase is of granular structure and the  $\text{Li}_2\text{S}\cdot\text{FeS}$  phase is of the fibrous (wood-like) structure. The compound  $\text{Li}_2\text{S}\cdot\text{FeS}$  appears to have a hexagonal structure which may be inferred from the careful examination of this phase in this picture, i.e., from the obtuse angles of the grains.

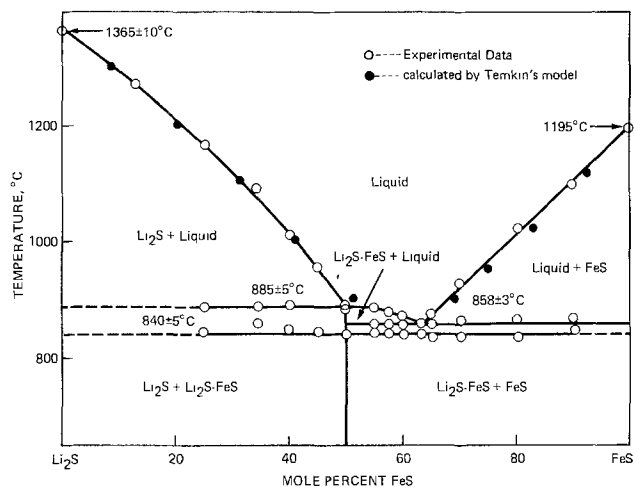


Fig. 3. The  $\text{Li}_2\text{S}$ -FeS system

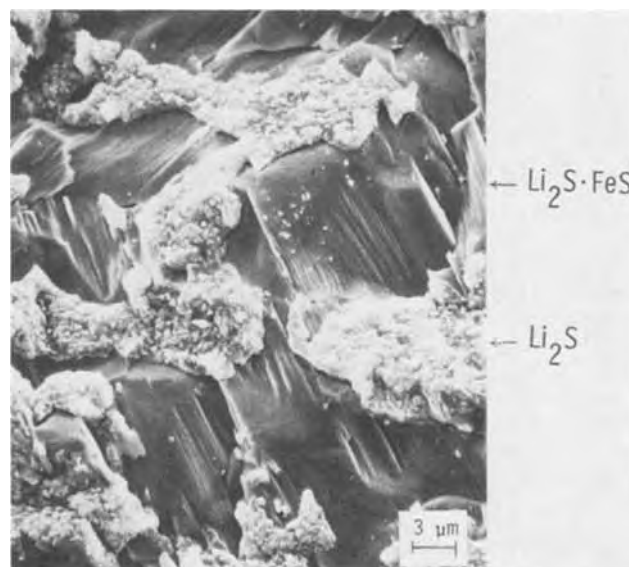


Fig. 4. Microstructure of the fractured surface of the solidified melt of 34.3 m/o FeS and 65.7 m/o  $\text{Li}_2\text{S}$  consisting of 31.4 m/o  $\text{Li}_2\text{S}$  and 68.6 m/o  $\text{Li}_2\text{S}\cdot\text{FeS}$ .

The SEM picture in Fig. 5 of the solidified melt of 50 m/o FeS and 50 m/o  $\text{Li}_2\text{S}$  consisting of  $\text{Li}_2\text{S}\cdot\text{FeS}$  compound indicates a single phase and the flaky structure of this compound.

The SEM picture in Fig. 6 of the fractured surface of the solidified melt of 63 m/o FeS and 37 m/o  $\text{Li}_2\text{S}$

Table I. Differential thermal analysis data for the  $\text{Li}_2\text{S}$ -FeS system

Composition FeS (m/o)	Transition temperature ( $^\circ\text{C}$ )			Eutectic temperature ( $^\circ\text{C}$ )			Liquidus temperature ( $^\circ\text{C}$ )		
	Heat	Cool	Mean	Heat	Cool	Mean	Heat	Cool	Mean
100	—	—	—	—	—	—	1195 $\pm$ 5	1195 $\pm$ 5	1195 $\pm$ 5
90	850	—	850	—	873	873 $\pm$ 3	1100	1093	1096 $\pm$ 4
80	837	—	837	—	866	866	1022	1020	1021 $\pm$ 1
70	838	—	838	—	868	868	928	932	930 $\pm$ 2
65	835	—	835 $\pm$ 5	858	865	861 $\pm$ 4	876	876	876 $\pm$ 1
63	835	845	840 $\pm$ 5	860	858	858 $\pm$ 2	—	—	—
60	835	845	840 $\pm$ 5	860	855	857 $\pm$ 3	873	867	870 $\pm$ 3
57.5	845	843	844 $\pm$ 1	861	855	858 $\pm$ 3	875	875	875
55	846	845	845	857	857	857	885	878	881 $\pm$ 4
				Melting point of $\text{Li}_2\text{S}\cdot\text{FeS}$ ( $^\circ\text{C}$ )					
50	840	—	840 $\pm$ 5	880	878	879 $\pm$ 1	885	883	884 $\pm$ 1
45	846	—	846 $\pm$ 1	883	890	886 $\pm$ 4	953	958	955 $\pm$ 3
40	848	—	848	888	895	890 $\pm$ 5	1008	1008	1008
34.3	858	—	858 $\pm$ 2	893	883	888 $\pm$ 5	1090	1085	1088 $\pm$ 2
25	855	835	845 $\pm$ 10	880	890	885 $\pm$ 5	1175	1160	1168 $\pm$ 8
12	—	—	—	—	—	—	1282	1260	1271 $\pm$ 11

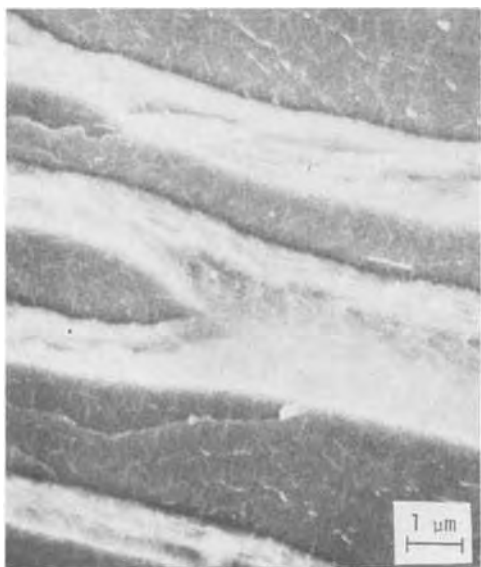


Fig. 5. Microstructure of the solidified melt of 50 m/o FeS and 50 m/o  $\text{Li}_2\text{S}$ , i.e., of the compound  $\text{Li}_2\text{S} \cdot \text{FeS}$ .

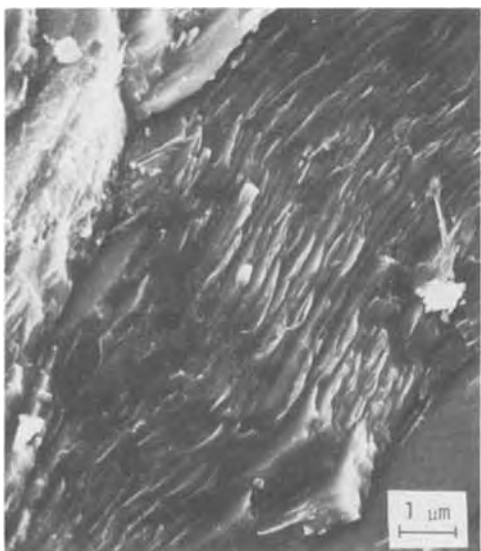


Fig. 6. Microstructure of the solidified eutectic melt of 63 m/o FeS and 37 m/o  $\text{Li}_2\text{S}$  consisting of 74 m/o  $\text{Li}_2\text{S} \cdot \text{FeS}$  and 24 m/o FeS.

shows the structure of the eutectic between the compounds  $\text{Li}_2\text{S} \cdot \text{FeS}$  and FeS. It is a typical pearlitic structure, commonly observed as that of a eutectic melt.

The SEM picture in Fig. 7 shows the structure of the solidified melt of 70 m/o FeS and 30 m/o  $\text{Li}_2\text{S}$  consisting of 60 m/o  $\text{Li}_2\text{S} \cdot \text{FeS}$  and 40 m/o FeS. Globular grains of FeS which might have precipitated during cooling between liquidus temperature and eutectic temperature, may be observed embedded in the  $\text{Li}_2\text{S} \cdot \text{FeS}$  matrix in this picture.

According to Temkin's model (6), the activity,  $a$ , of a component in an ideal fused salt solution is equal to the product of its cationic and anionic fractions, e.g., the activity of  $\text{Li}_2\text{S}$ ,  $a_{\text{Li}_2\text{S}}$ , in fused  $\text{Li}_2\text{S}$ -FeS melt is given as

$$a_{\text{Li}_2\text{S}} = (X'_{\text{Li}^+})^2 (X'^{\text{s}2-}) \quad [1]$$

assuming that the ionic species present are only  $\text{Li}^+$ ,  $\text{Fe}^{2+}$ , and  $\text{S}^{2-}$ , where

$$X'_{\text{Li}^+} = \frac{2X_{\text{Li}_2\text{S}}}{2X_{\text{Li}_2\text{S}} + X_{\text{FeS}}} = \frac{2X_{\text{Li}_2\text{S}}}{1 + X_{\text{Li}_2\text{S}}} \quad [2]$$

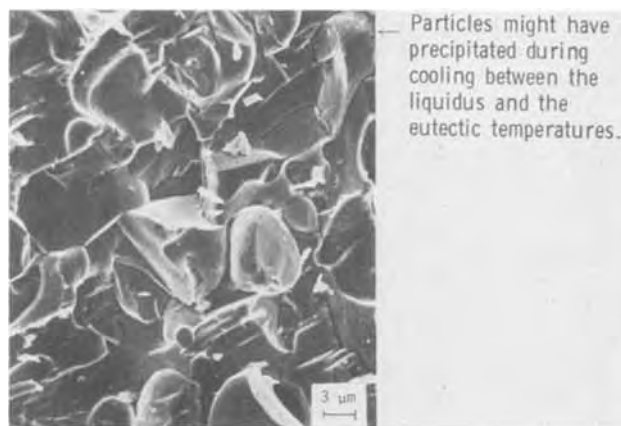


Fig. 7. Microstructure of the fractured surface of the solidified melt of 70 m/o FeS and 30 m/o  $\text{Li}_2\text{S}$  consisting of 60 m/o  $\text{Li}_2\text{S} \cdot \text{FeS}$  and 40 m/o FeS.

and  $X'^{\text{s}2-}$  is unity.  $X'$  and  $X$  are the mole fractions of the designated ions and components, respectively. Therefore

$$a_{\text{Li}_2\text{S}} = \left( \frac{2X_{\text{Li}_2\text{S}}}{1 + X_{\text{Li}_2\text{S}}} \right)^2 \quad [3]$$

and similarly

$$a_{\text{FeS}} = \frac{X_{\text{FeS}}}{2 - X_{\text{FeS}}} \quad [4]$$

The activity of  $\text{Li}_2\text{S}$  with respect to pure supercooled liquid  $\text{Li}_2\text{S}$  as standard state at a given temperature may be calculated by the equation

$$\ln a_{\text{Li}_2\text{S}} = -\frac{\Delta H_m}{RT} \left( \frac{T_m - T}{T_m} \right) + \frac{\Delta C_p}{RT} \left[ (T_m - T) - T \ln \frac{T_m}{T} \right] \quad [5]$$

where pure solid  $\text{Li}_2\text{S}$  is assumed to be in equilibrium with the melt,  $\Delta H_m$  is the heat of fusion of  $\text{Li}_2\text{S}$  at  $T_m$ , the melting point of  $\text{Li}_2\text{S}$  in degrees Kelvin,  $T$  is the equilibrium temperature, and  $\Delta C_p$  is the difference between the heat capacities of the liquid and the solid at temperature,  $T$ . The activity of FeS can also be calculated by a similar equation.

The numerical value of  $\Delta H_m$ , 7 kcal/mole of  $\text{Li}_2\text{S}$  is calculated assuming that Temkin's model applies to the melts and using the experimental liquidus compositions at low concentrations of FeS. The application of Temkin's model at the low concentrations of FeS appears not unreasonable when it applies well to the melts on the FeS liquidus side of the phase diagram as will be seen later. The value of  $\Delta H_m$ , 7.73 kcal/mole for FeS is reported in the literature (7);  $T_m = 1638^\circ\text{K}$  for  $\text{Li}_2\text{S}$  (3) and  $1468^\circ\text{K}$  for FeS (7); and  $\Delta C_p = 0$  for  $\text{Li}_2\text{S}$  is assumed and for FeS is calculated from the data in the literature (7).

Using the activities of  $\text{Li}_2\text{S}$  and FeS calculated from Eq. [5] and assuming the  $\text{Li}_2\text{S}$ -FeS melts obey Temkin's model, the mole fractions of  $\text{Li}_2\text{S}$  and FeS were calculated by Eq. [3] and [4] at different temperatures, respectively. They are shown as solid circles in Fig. 3. Agreement between the measured and calculated values of mole fractions for both  $\text{Li}_2\text{S}$  and FeS appears to be good, even for this melt of sulfides having cations of different valences.

The x-ray diffraction patterns of the other possible compounds between  $\text{Li}_2\text{S}$ , FeS, and  $\text{FeS}_2$  are discussed below.

$\text{Li}_2\text{S} \cdot \text{FeS}(\alpha)$ .—The composition for this compound, made by mixing thoroughly the weighed amounts of  $\text{Li}_2\text{S}$  and FeS, was kept at  $870^\circ\text{C}$  for 35 days. The x-ray

powder diffraction data of a sample from this composition are given in Table II. The pattern has about 13 d-values different from that of FeS and 17 d-values different from that of  $\text{Li}_2\text{S}$  (3). About 25 d-values of FeS and 33 d-values of  $\text{Li}_2\text{S}$  are not observed in this pattern. Therefore the x-ray diffraction data confirm the compound  $\text{Li}_2\text{S}\cdot\text{FeS}(\alpha)$  as indicated by the  $\text{Li}_2\text{S}\text{-FeS}$  phase diagram above  $840^\circ \pm 5^\circ\text{C}$ .

$\text{Li}_2\text{S}\cdot\text{FeS}(\beta)$ .—The x-ray diffraction data of the composition for this compound after keeping at  $700^\circ\text{C}$  for 20 days are also given in Table II. As may be seen from the d-values reported in this table, the x-ray diffraction pattern of this compound differs from those

of FeS,  $\text{Li}_2\text{S}$ , and  $\text{Li}_2\text{S}\cdot\text{FeS}(\alpha)$ . This is again in confirmation with the  $\text{Li}_2\text{S}\text{-FeS}$  phase diagram, according to which this compound forms below  $840^\circ \pm 5^\circ\text{C}$ . Compound  $\text{Li}_2\text{S}\cdot\text{FeS}$  has also been reported to be formed during cycling of  $\text{Li}\text{-FeS}_2$  cells at  $400^\circ\text{C}$  (5, 8).

The respective compositions for the prospective compounds,  $\text{Li}_2\text{S}\cdot\text{Fe}_3\text{S}_4$ ,  $2\text{Li}_2\text{S}\cdot\text{Fe}_3\text{S}_4$ ,  $\text{Li}_2\text{S}\cdot\text{Fe}_2\text{S}_3$ , and  $2\text{Li}_2\text{S}\cdot\text{Fe}_2\text{S}_3$  were kept at about  $670^\circ\text{C}$  for 2 weeks, then were ground and kept for additional 6 weeks at this temperature. The temperature,  $670^\circ\text{C}$ , was dictated by the decomposition vapor pressure of sulfur over pyrite, which increases sharply above this temperature (9).

Table II. X-ray diffraction data (d-values in Å) of the compounds  $\text{Li}_2\text{S}$ , FeS,  $\text{FeS}_2$  (pyrite), and the compositions corresponding to the other possible compounds

$\text{Li}_2\text{S}\cdot\text{FeS}(\beta)$	$\text{Li}_2\text{S}\cdot\text{FeS}(\alpha)$	$\text{Li}_2\text{S}\cdot\text{Fe}_3\text{S}_4$	$2\text{Li}_2\text{S}\cdot\text{Fe}_3\text{S}_4$	$\text{Li}_2\text{S}\cdot\text{Fe}_2\text{S}_3$	$2\text{Li}_2\text{S}\cdot\text{Fe}_2\text{S}_3$	$\text{Li}_2\text{S}$	FeS	$\text{FeS}_2$
			7.01					
6.35	6.35		6.35	6.16	6.89			
			5.81		6.07			
						5.57	5.40	
			4.68	5.28			4.74	
4.52	4.42	4.52	4.33	4.47	4.68			
	3.84	4.37	3.80		4.28	4.35		
			3.39		3.77	3.82		
	3.39		3.39			3.60		
	3.13				3.39	3.26		
3.09				3.09	3.16			3.13
	2.97	3.04	3.04			3.06		
					2.97	2.92	2.98	
						2.83		
						2.74		
	2.66	2.68	2.68	2.72	2.72		2.66	2.71
		2.52		2.52			2.52	
				2.41	2.413	2.53	2.42	2.42
						2.47		
						2.39		
2.32	2.31	2.292	2.31	2.31	2.305	2.32		2.21
				2.22	2.206	2.21		
				2.14			2.14	
	2.07	2.105	2.094		2.084		2.09	
2.02						1.989		
1.965	1.946		1.974		1.965			
		1.928		1.919	1.910		1.923	1.916
1.842			1.893			1.886		
	1.779	1.756	1.756	1.764	1.764	1.805		
							1.748	
							1.719	
						1.708		
1.671			1.678					
1.658	1.652		1.619	1.639	1.632	1.631	1.634	1.633
		1.632				1.583	1.596	
		1.559		1.565	1.577	1.563		1.564
						1.532		
		1.519	1.508	1.508	1.508		1.501	1.503
1.476			1.466	1.461			1.469	
1.426	1.426	1.456	1.431		1.436	1.415	1.445	1.448
							1.422	
		1.398					1.331	
1.311	1.311	1.298		1.315	1.319		1.319	
						1.299		
			1.283				1.284	
1.279					1.279	1.267	1.271	
					1.249			1.243
		1.203		1.241	1.206		1.224	1.211
				1.210			1.188	1.182
				1.183			1.179	
1.173	1.179		1.160		1.170			1.155
						1.156		
		1.124					1.135	
			1.121	1.118			1.119	1.106
1.095			1.092		1.098	1.091	1.108	
	1.084						1.091	
	1.073		1.057					
		1.044		1.037	1.042		1.054	1.043
		1.017						
1.003	1.003		1.015	1.001	1.003	1.003	1.024	1.006
							0.994	0.989
			0.9673	0.9896	0.9851			
			0.9763			0.960		0.958
0.963				0.9527	0.9529	0.947		
				0.9002				0.903
0.898					0.8984	0.899		
	0.889							
		0.8788	0.8753	0.872				0.879
0.867						0.868		
						0.858		0.857
		0.8314	0.8314		0.8519			
						0.822		0.826
				0.819				0.817
		0.7517	0.7529					
					0.7019			

The x-ray diffraction data of the samples from these compositions are given in Table II.

$\text{Li}_2\text{S}\cdot\text{Fe}_3\text{S}_4$ .—Almost all the d-values of this prospective compound were observed to have the corresponding values in the patterns of  $\text{Li}_2\text{S}$ ,  $\text{FeS}$ ,  $\text{FeS}_2$ , and  $2\text{Li}_2\text{S}\cdot\text{Fe}_3\text{S}_4$ . The present x-ray data discount the formation of this compound from  $\text{Li}_2\text{S}$ ,  $\text{FeS}$ , and  $\text{FeS}_2$ .

$2\text{Li}_2\text{S}\cdot\text{Fe}_3\text{S}_4$ .—About ten d-values of this compound were not observed in the patterns of  $\text{Li}_2\text{S}$ ,  $\text{FeS}$ ,  $\text{FeS}_2$ , and  $\text{Li}_2\text{S}\cdot\text{FeS}$ . Most of the d-values of the compounds  $\text{Li}_2\text{S}$ ,  $\text{FeS}$ , and  $\text{FeS}_2$  were not observed in the pattern of this compound. Therefore, the x-ray diffraction data indicate the possibility of the compound  $2\text{Li}_2\text{S}\cdot\text{Fe}_3\text{S}_4$ .

$\text{Li}_2\text{S}\cdot\text{Fe}_2\text{S}_3$ .—As may be observed from the d-values in Table II, the x-ray diffraction pattern of the composition for this compound differs greatly from those of  $\text{Li}_2\text{S}$ ,  $\text{FeS}$ ,  $\text{FeS}_2$ ,  $\text{Li}_2\text{S}\cdot\text{FeS}$ , and  $2\text{Li}_2\text{S}\cdot\text{Fe}_3\text{S}_4$ . Such compounds with sodium, potassium, rubidium, and cesium, such as  $\text{Na}_2\text{S}\cdot\text{Fe}_2\text{S}_3$ ,  $\text{K}_2\text{S}\cdot\text{Fe}_2\text{S}_3$ ,  $\text{Rb}_2\text{S}\cdot\text{Fe}_2\text{S}_3$ , and  $\text{Cs}_2\text{S}\cdot\text{Fe}_2\text{S}_3$  (10, 11), have also been reported in the literature. So the present x-ray diffraction data indicate the possibility of a compound  $\text{Li}_2\text{S}\cdot\text{Fe}_2\text{S}_3$ .

$2\text{Li}_2\text{S}\cdot\text{Fe}_2\text{S}_3$ .—Almost all the d-values of the composition for this compound are observed in the patterns of  $\text{FeS}_2$ ,  $\text{FeS}$ ,  $\text{Li}_2\text{S}$ ,  $\text{Li}_2\text{S}\cdot\text{FeS}$ , and  $\text{Li}_2\text{S}\cdot\text{Fe}_2\text{S}_3$ . The x-ray diffraction data of the present study do not indicate a compound  $2\text{Li}_2\text{S}\cdot\text{Fe}_2\text{S}_3$ , though the formation of this compound has been reported during the cycling of Li-Al/FeS<sub>2</sub> cells (8).

### Conclusions

The equilibrium phase diagram of  $\text{Li}_2\text{S}$ - $\text{FeS}$  system was determined. The important characteristics of this system are:

1. A compound,  $\text{Li}_2\text{S}\cdot\text{FeS}$ , incongruently melting at  $885^\circ \pm 5^\circ\text{C}$  to  $\text{Li}_2\text{S}$  and a 50.5 m/o  $\text{FeS}$  melt, and having a transition at  $840^\circ \pm 5^\circ\text{C}$  was found.
2. A eutectic between  $\text{Li}_2\text{S}\cdot\text{FeS}$  and  $\text{FeS}$  at 63 m/o  $\text{FeS}$  and  $858^\circ \pm 3^\circ\text{C}$  was observed.
3. Temkin's model for molten salt melts fits the terminal liquidus curves of the experimental data well, with a calculated value of  $\Delta H_m$ , 7 kcal for  $\text{Li}_2\text{S}$  and the literature value, 7.73 kcal for  $\text{FeS}$  (7).

The x-ray diffraction studies confirmed the compound,  $\text{Li}_2\text{S}\cdot\text{FeS}$  and its transition. They also indicated

the compounds  $2\text{Li}_2\text{S}\cdot\text{Fe}_3\text{S}_4$  and  $\text{Li}_2\text{S}\cdot\text{Fe}_2\text{S}_3$  between  $\text{Li}_2\text{S}$ ,  $\text{FeS}$ , and  $\text{FeS}_2$ .

### Acknowledgments

The author wishes to thank Dr. Seymour Katz of the Metallurgy Department and David W. Buttram of the Electrochemistry Department for assistance in the experimental work, Thomas P. Schreiber of the Analytical Chemistry Department for the SEM pictures, Miss F. A. Forster of the Chemistry Department and Ray Silver of Delco Electronics for x-ray analysis, and Drs. Elton Cairns and J. Dunning of the Electrochemistry Department for useful discussions.

Manuscript submitted June 2, 1975; revised manuscript received Oct. 28, 1975. This was Paper 24 presented at the Dallas, Texas, Meeting of the Society, Oct. 5-9, 1975.

Any discussion of this paper will appear in a Discussion Section to be published in the December 1976 JOURNAL. All discussions for the December 1976 Discussion Section should be submitted by Aug. 1, 1976.

Publication costs of this article were partially assisted by General Motors Corporation.

### REFERENCES

1. E. J. Cairns and R. K. Steunenberg, in "Progress in High Temperature Physics and Chemistry," Vol. 5, C. A. Rouse, Editor, p. 63, Pergamon Press, New York (1973).
2. E. H. Baker, *Trans. Min. and Met., Pt. C*, 93 (1971).
3. R. A. Sharma, *This Journal*, 119, 1439 (1972).
4. C. H. Liu, A. J. Zielen, and D. M. Gruen, *ibid.*, 120, 67 (1973).
5. P. A. Nelson and D. S. Webster, ANL 8064, Argonne National Laboratory, Argonne, Illinois, April 1974.
6. M. Temkin, *Acta Physicochem. URSS*, 20, 411 (1945).
7. O. Kubaschewski, E. LL. Evans, and C. B. Alcock, "Metallurgical Thermochemistry," Fourth Edition, Pergamon Press, Inc., New York (1967).
8. A. E. Martin, R. K. Steunenberg, and Z. Tomczuk, Paper 54 presented at The Electrochemical Society Meeting, New York, New York, Oct. 13-17, 1974.
9. L. D'Or, *J. Chim. Phys.*, 28, 377 (1931).
10. W. Bronger, *Naturwissenschaften*, 5, 158 (1965).
11. W. Bronger, *Z. Anorg. Allgem. Chem.*, 359, 225 (1958).

## A High Energy Density Solid-State Battery System

C. C. Liang\* and L. H. Barnette

P. R. Mallory & Company Incorporated, Laboratory for Physical Science,  
Northwest Industrial Park, Burlington, Massachusetts 01803

### ABSTRACT

The discharge and storage characteristics of a new solid-state battery system,  $\text{Li}/\text{LiI}(\text{Al}_2\text{O}_3)/\text{PbI}_2$ ,  $\text{PbS}$ ,  $\text{Pb}$  were investigated. Results of the discharge tests suggested that both  $\text{PbI}_2$  and  $\text{PbS}$  are cathode active and can be discharged efficiently. A discharge efficiency of 100% was realized on test cells with a stoichiometric capacity of 18 mA-hr/cm<sup>2</sup> at a drain rate of 10  $\mu\text{A}/\text{cm}^2$  at room temperature. Results of the storage tests showed that the system is stable on storage. Test cells experienced no capacity loss after a storage period of one year at room temperature, 45°, and 60°C. The discharge and storage characteristics indicate that the system is a practical, low rate solid-state battery system and the practical batteries have a volumetric energy density of 8 W-hr/in.<sup>3</sup> (0.49 W-hr/cm<sup>3</sup>) at a power level of 150  $\mu\text{W}/\text{in}^3$ .

It was reported in a previous article (1) that the ionic conductivity of polycrystalline  $\text{LiI}$  can be in-

\* Electrochemical Society Active Member.  
Key words: solid-state batteries, solid electrolyte cells, lithium, lithium iodide, lead sulfide, lead iodide.

creased from  $10^{-7}$  (ohm-cm)<sup>-1</sup> to  $10^{-5}$  (ohm-cm)<sup>-1</sup> at room temperature by the incorporation of  $\text{Al}_2\text{O}_3$ . The suitability of  $\text{LiI}(\text{Al}_2\text{O}_3)$  as a solid electrolyte material was demonstrated by the discharge and storage characteristics of the  $\text{Li}/\text{LiI}(\text{Al}_2\text{O}_3)/\text{PbI}_2$ ,  $\text{Pb}$  solid

electrolyte cells. The Li/LiI(Al<sub>2</sub>O<sub>3</sub>)/PbI<sub>2</sub>, Pb system is a low rate solid-state battery system which has an extremely long storage life. Hermetically sealed, practical batteries of this system have a volumetric energy density ranging between 3 and 3.5 W-hr/in.<sup>3</sup> (ca. 0.18 and 0.21 W-hr/cm<sup>3</sup>) at a power density of about 100 μW/in.<sup>3</sup> at room temperature. The relatively low energy density is due to the rather high electrochemical equivalent volume of the active cathode material, PbI<sub>2</sub>, and to the fact that a considerable amount of Pb and solid electrolyte material must be used in the cathode to facilitate the electronic and ionic conduction during discharge.

In our recent studies of the solid-state battery systems using the LiI(Al<sub>2</sub>O<sub>3</sub>) solid electrolyte we found that the volumetric energy density of the Li/LiI(Al<sub>2</sub>O<sub>3</sub>) system can be substantially increased by using a mixture of PbS and PbI<sub>2</sub> as the active cathode material. The results of these studies are reported in this article.

### Experimental

**Solid electrolyte preparation.**—The LiI(Al<sub>2</sub>O<sub>3</sub>) solid electrolyte was prepared according to the procedures described previously (1). A powder mixture of anhydrous LiI and Al<sub>2</sub>O<sub>3</sub> in a mole ratio of 2 to 1 was heated at 550°C for about 17 hr in a helium-filled dry box (Vacuum Atmospheres). The H<sub>2</sub>O and O<sub>2</sub> content in the dry box was maintained at less than 15 ppm.

**Solid electrolyte cell fabrication.**—Li/LiI(Al<sub>2</sub>O<sub>3</sub>)/PbI<sub>2</sub>, PbS, Pb solid electrolyte cells (Fig. 1) were fabricated in the dry box. The cathode powder was a well-blended mixture of 40 weight per cent (w/o) PbI<sub>2</sub>, 40 w/o PbS, and 20 w/o Pb and the anode was Li metal. The current collectors were Pb for the cathode and steel for the anode. The fabrication procedures were reported previously (1, 2). The cathode, the electrolyte, and the anode with a polypropylene retaining ring were consolidated by pressing in a 1.52 cm (0.6 in.) diameter steel die at 7030 kg/cm<sup>2</sup> (100,000 psi). The geometric area of the cathode was 1.81 cm<sup>2</sup> and that of the anode was 1.48 cm<sup>2</sup>. The thickness of the electrolyte was 0.02 ± 0.005 cm (0.008 ± 0.002 in.) and the stoichiometric capacity of the test cell was limited by the amount of cathode. Both single cell and multi-cell batteries were constructed using the solid electrolyte cells for various discharge and storage tests. The batteries which were discharged outside the dry box were hermetically packaged in steel battery housings with glass to metal seals.

**Discharge tests.**—The test batteries were discharged at various temperatures under either constant current or constant load conditions. Keithley Model 610B or Model 616 electrometers were used to measure the voltages of the test batteries. For short term discharge tests the voltages were recorded by strip chart recorders. For long term discharge tests the voltages were recorded manually at intervals.

**Storage tests.**—Solid electrolyte cells having a stoichiometric capacity of 33 ± 2 mA-hr were used for

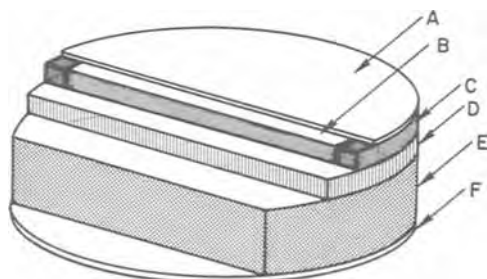


Fig. 1. Sectioned view of the solid electrolyte cell. A, Anode current collector; B, anode; C, anode retaining ring; D, solid electrolyte; E, cathode; F, cathode current collector.

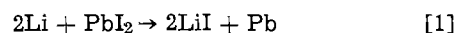
storage tests. They were stacked in glass vials with polyethylene covers and stored at ambient temperature, 45° ± 2°C, 60° ± 2°C, and 100° ± 2°C. Scientific Products temperature block module heaters were used to maintain the temperature above ambient. Since the test cells were not hermetically sealed the storage tests were conducted in the dry box under helium atmosphere.

Inasmuch as the capacity retention of the test cells upon storage was of principal interest for this study, accelerated discharge tests were carried out at 125°C on most of the test cells before and after storage to determine the storability.

### Results and Discussion

Approximately 250 solid electrolyte cells were made for various tests. The stoichiometric capacities of the test cells ranged between 14 and 136 mA-hr assuming that both PbI<sub>2</sub> and PbS are cathode active. Cells with stoichiometric capacities of 33 and 136 mA-hr were studied extensively and their characteristics are reported in this article.

It was assumed that the cell reactions are



The open-circuit voltage based on cell reaction [1] is 1.9V at 25°C (1, 3, 4). In order to calculate the open-circuit voltage based on reaction [2] the standard Gibbs free energy of formation ( $\Delta G^\circ_f$ ) for Li<sub>2</sub>S was determined from the open-circuit voltages of Li/LiI/Ag<sub>2</sub>S, Ag and Li/LiI/S, graphite solid electrolyte cells. At 25° ± 2°C the open-circuit voltages of the Li/Ag<sub>2</sub>S and Li/S cells were found to be 2.11 ± 0.01V and 2.31 ± 0.05V, respectively. These results are consistent with the fact that the  $\Delta G^\circ_f$  for Ag<sub>2</sub>S is -9.72 kcal/mole (3), therefore, the difference between the equilibrium potential of the Li/S cell and that of the Li/Ag<sub>2</sub>S cell should be 0.21V. Accordingly, we estimated the  $\Delta G^\circ_f$  for Li<sub>2</sub>S at -106 ± 2 kcal/mole and the open-circuit voltage according to cell reaction [2] at 1.80 ± 0.05V at room temperature (3, 4). The  $\Delta G^\circ_f$  (Li<sub>2</sub>S) value obtained from the present study agreed rather well with that due to Freeman (5). Freeman calculated the standard heat of formation ( $\Delta H^\circ_f$ ) for Li<sub>2</sub>S from the heat of solution data and obtained a value of -107 ± 2 kcal/mole. Furthermore, he estimated the standard entropy ( $S^\circ$ ) for Li<sub>2</sub>S at 14 cal/deg-mole. Based on the fact that the standard entropies of Li and S are 6.96 cal/deg-mole (4) and 7.6 cal/deg-mole, respectively, the standard entropy of formation ( $\Delta S^\circ_f$ ) for Li<sub>2</sub>S is calculated to be -7.52 cal/deg-mole. Accordingly, the  $\Delta G^\circ_f$  (Li<sub>2</sub>S) according to Freeman is -104.8 ± 2 kcal/mole. Nonetheless, since the  $\Delta G^\circ_f$  (Li<sub>2</sub>S) value of the present study was obtained from direct measurements of open-circuit voltage of voltaic cells and consistent results were obtained from cells with different cathodes (Ag<sub>2</sub>S and S) we selected to use the value of -107 ± 2 kcal/mole of this study for the calculation of the open-circuit voltage based on reaction [2].

The Li/LiI(Al<sub>2</sub>O<sub>3</sub>)/PbI<sub>2</sub>, PbS, Pb cell exhibited an initial open-circuit voltage of 2.00 ± 0.05V. However, after a small capacity had been discharged from the cell, the voltage recovered to 1.91 ± 0.01V upon open circuit indicating that the initial high open-circuit voltage might be due to impurities such as PbO and S in the cathode.

The assumption that both PbI<sub>2</sub> and PbS can be discharged was shown to be correct from the initial discharge tests. Test cells with cathodes weighing 0.23-0.26g were discharged under a 100 kohm load at room temperature. As shown in Fig. 2 a capacity of about 33 mA-hr was realized from each of the 12 test cells under these discharge conditions. The stoichiometric capacity of the test cells was 33 ± 2 mA-hr according to the cathode weight assuming that both PbI<sub>2</sub> and PbS

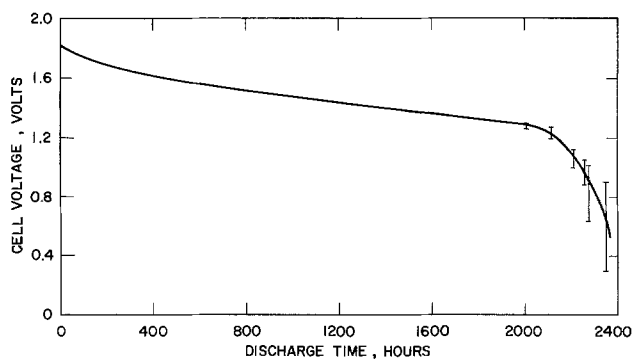


Fig. 2. Discharge curve of the 33 mA-hr cells under a 100 kohm load at room temperature.

are cathode active. The discharge curves of the 33 mA-hr cells at various constant currents at room temperature are shown in Fig. 3. The stoichiometric capacity was not realized at a discharge current of 36  $\mu\text{A}$  or higher.

The discharge characteristics of test cells having a stoichiometric capacity of 136 mA-hr were studied in detail and the results are discussed below.

Under a constant load of 100 kohm at room temperature a capacity of about 65 mA-hr was realized to a cutoff voltage of 1V as shown by the discharge curve in Fig. 4 which represents an average of six test cells. On the other hand, Fig. 5 shows that at higher drain rates (e.g., 36  $\mu\text{A}$  or higher) the realized capacities were about the same as those of the 33 mA-hr capacity cells. The following is a possible explanation for such a behavior. Since the electronically conductive Pb was evenly distributed in the cathode, and the electrolyte was a cationic conductor, the discharge reaction began at the electrolyte-cathode interface and extended to-

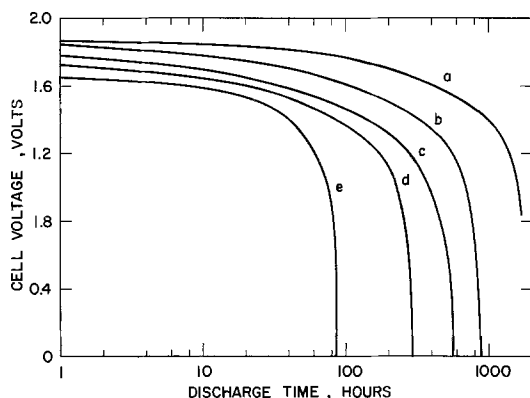


Fig. 3. Discharge curves of the 33 mA-hr cells under various constant currents at room temperature. Curve a, 18  $\mu\text{A}$ ; curve b, 36  $\mu\text{A}$ ; curve c, 54  $\mu\text{A}$ ; curve d, 72  $\mu\text{A}$ ; curve e, 90  $\mu\text{A}$ .

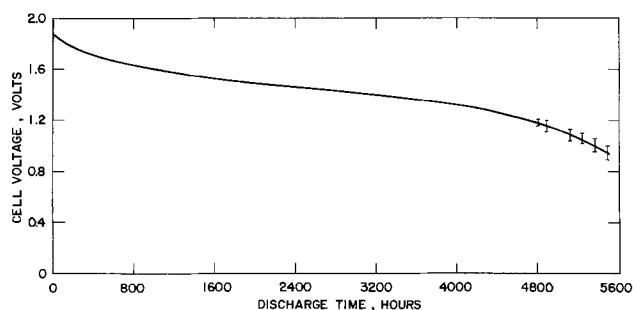


Fig. 4. Discharge curve of the 136 mA-hr cells under a 100 kohm load at room temperature.

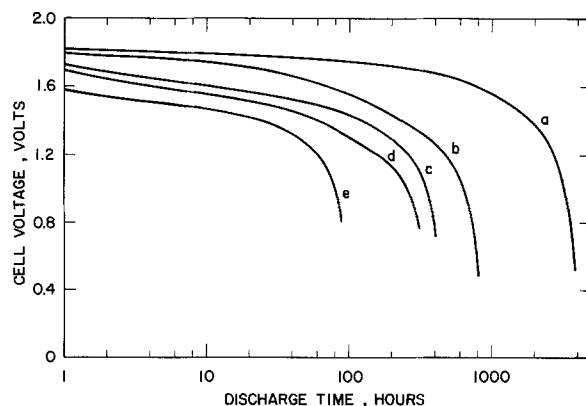


Fig. 5. Discharge curves of the 136 mA-hr cells under various constant currents at room temperature. Curve a, 18  $\mu\text{A}$ ; curve b, 36  $\mu\text{A}$ ; curve c, 54  $\mu\text{A}$ ; curve d, 72  $\mu\text{A}$ ; curve e, 90  $\mu\text{A}$ .

ward the cathode current collector. The accumulation of the discharge products had a net effect of reducing the geometric area and increasing the length of the path with respect to the lithium ion transport during discharge. Consequently, similar IR losses due to the cathode structure would be experienced by cells of the same diameter which were discharged under similar drain rates at similar discharged capacities.

Discharge tests were also conducted at 37°C for implantable pacemaker applications. As expected from the conductivity considerations both the realized capacity and the load voltage of the cells were higher at 37°C than at room temperature under otherwise similar discharge conditions as shown in Fig. 6 and 7.

It is noted that since the solid electrolyte cells do not contain any solution electrolyte and all the components are solid with extremely low vapor pressures, it is not necessary to contain the solid electrolyte cells in individual containers for the construction of multi-

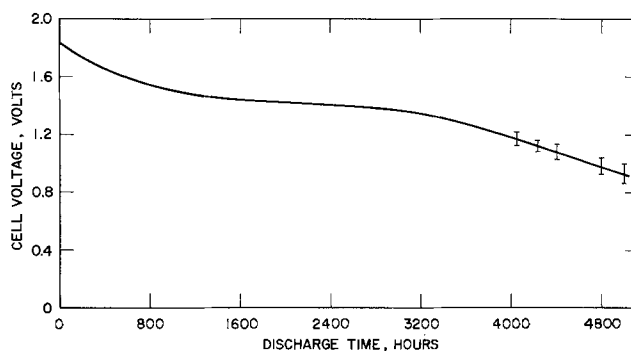


Fig. 6. Discharge curve of the 136 mA-hr cells under a 100 kohm load at 37° ± 2°C.

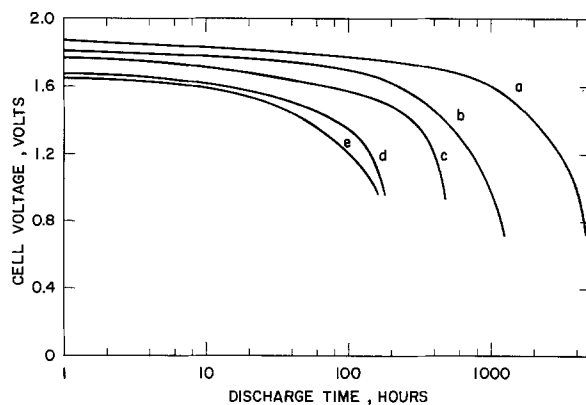


Fig. 7. Discharge curves of the 136 mA-hr cells under various constant currents at 37° ± 2°C. Curve a, 18  $\mu\text{A}$ ; curve b, 36  $\mu\text{A}$ ; curve c, 54  $\mu\text{A}$ ; curve d, 90  $\mu\text{A}$ ; curve e, 108  $\mu\text{A}$ .



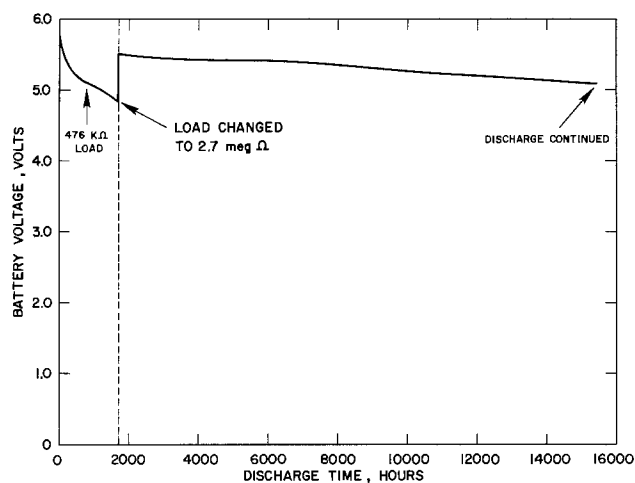


Fig. 8. Long term discharge curve of the single stack (3 cells in series) 6V, 136 mA-hr batteries at  $37^{\circ} \pm 2^{\circ}\text{C}$ .

cell batteries. Any number of the solid electrolyte cells may be connected in series and/or in parallel within a single battery housing. In view of these characteristics, the discharge current of practical batteries for some applications may be as low as  $1\text{--}1.5 \mu\text{A}/\text{cm}^2$  at  $37^{\circ}\text{C}$ . Accordingly, low drain rate tests were conducted on batteries containing three 136 mA-hr cells in series. Six batteries were used for this study. The battery was discharged at  $37^{\circ}\text{C}$  under a load of 476 kohm for 1700 hr. At this point the load was changed to 2.7 megohm for long term low drain tests. Figure 8 shows that after 15,000 hr the load voltage was still above 5V. It is estimated that these tests will be completed 5 years hence.

Accelerated discharge tests were conducted to determine whether or not the stoichiometric capacity of the 136 mA-hr cells can be realized and to determine load voltage at various depths of discharge at low drain rates. The first series of accelerated discharge tests was conducted on batteries containing either a 1 or 2 cells connected in parallel. The load voltage of the battery under a low drain rate was measured at  $37^{\circ}\text{C}$ , then the battery was discharged at  $100^{\circ}\text{C}$  at a considerably higher drain rate (a 10 kohm load for the single cell battery and a 5 kohm load for the 2-cell battery). After the depth of discharge had reached about 40% the load voltage was again measured at  $37^{\circ}\text{C}$  under the low drain rate. The cycle was repeated until the discharged capacity reached 130 mA-hr/cell. At this point the battery was discharged to completion at  $37^{\circ}\text{C}$  under the low drain rate. The results of these tests are summarized in Table I. It is noted from Table I that after a capacity of 130 mA-hr/cell had been discharged the load voltage under a drain rate of  $1.5 \mu\text{A}/\text{cm}^2$  was still above 1.3V at  $37^{\circ}\text{C}$ .

Similar tests were conducted on a battery containing 4-parallel stacks of 3 cells in series. The battery had an open-circuit voltage of 6V and a stoichiometric capacity of  $544 \pm 8$  mA-hr. The dimensions of the packaged battery were 0.67 in. OD  $\times$  1.1 in. long. After a capacity of about 540 mA-hr had been discharged under high drain rates and at higher temperatures, it was found that the load voltage of the battery at  $10 \mu\text{A}$  at  $37^{\circ}\text{C}$  remained above 4.3V for more than 200 hr. These results strongly suggest that under a drain rate of  $1\text{--}1.5 \mu\text{A}/\text{cm}^2$  at  $37^{\circ}\text{C}$  the stoichiometric capacity of 136 mA-hr/cell (about  $75 \text{ mA-hr}/\text{cm}^2$ ) can be realized.

Test cells having a stoichiometric capacity of  $33 \pm 2$  mA-hr were used for the storage tests. The results of these tests are summarized in Table II and discussed below.

Table I. Accelerated discharge test results

Discharge conditions				Battery voltage, V											
Load, kohm		Temp, $^{\circ}\text{C}$	Time, hr	No. 1	No. 2	No. 3	No. 4	No. 5	No. 6	No. 7	No. 8	No. 9	No. 10	No. 11	
No. 1-6	No. 7-11			No. 1	No. 2	No. 3	No. 4	No. 5	No. 6	No. 7	No. 8	No. 9	No. 10	No. 11	
180	360	37	0	1.93	1.93	1.94	1.94	1.90	1.92	1.94	1.90	1.91	1.90	1.90	
		38	3	1.86	1.85	1.85	1.87	1.85	1.85	1.86	1.85	1.85	1.85	1.85	
		38	19	1.88	1.87	1.88	1.85	1.88	1.87	1.88	1.87	1.87	1.87	1.87	
5	10	105	0	1.96	1.95	1.95	1.93	1.93	1.93	1.95	1.95	1.95	1.96	1.95	
		103	5	1.86	1.86	1.86	1.88	1.86	1.86	1.86	1.86	1.86	1.86	1.86	
		110	70	1.76	1.73	1.74	1.73	1.75	1.72	1.74	1.72	1.75	1.76	1.74	
		104	94	1.74	1.73	1.73	1.78	1.72	1.71	1.71	1.74	1.72	1.72	1.74	
		104	118	1.68	1.68	1.68	1.65	1.68	1.68	1.68	1.67	1.68	1.68	1.68	
		103	142	1.63	1.62	1.63	1.65	1.63	1.62	1.62	1.66	1.63	1.63	1.62	
		104	166	1.61	1.61	1.61	1.61	1.58	1.60	1.66	1.64	1.64	1.63	1.61	
		108	238	1.57	1.56	1.57	1.57	1.57	1.57	1.55	1.57	1.57	1.54	1.56	
		100	264	1.54	1.53	1.53	1.53	1.53	1.52	1.54	1.52	1.52	1.53	1.51	
		99	315	1.51	1.50	1.50	1.47	1.50	1.48	1.48	1.47	1.47	1.51	1.50	1.49
		Approx. discharged capacity: 104 mA-hr (battery No. 1-6); 52 mA-hr (battery No. 7-11)													
180	360	38	0	1.80	1.82	1.83	1.81	1.84	1.81	1.84	1.81	1.81	1.81	1.82	
		39	69	1.56	1.56	1.51	1.56	1.50	1.54	1.54	1.53	1.52	1.51	1.53	
5	10	101	0	1.55	1.52	1.51	1.51	1.50	1.50	1.52	1.51	1.49	1.51	1.50	
		99	24	1.39	1.37	1.37	1.33	1.37	1.34	1.34	1.29	1.37	1.36	1.34	
		103	48	1.33	1.31	1.34	1.31	1.34	1.30	1.31	1.30	1.33	1.31	1.30	
		101	72	1.31	1.29	1.30	1.27	1.30	1.30	1.27	1.27	1.30	1.29	1.27	
		101	140	1.30	1.27	1.23	1.25	1.21	1.21	1.22	1.21	1.23	1.23	1.21	
		104	235	1.20	1.20	1.19	1.20	1.18	1.17	1.17	1.17	1.16	1.19	1.19	
		108	307	1.20	1.20	1.20	1.17	1.17	1.17	1.17	1.17	1.16	1.17	1.17	
		108	360	1.19	1.17	1.14	1.14	1.14	1.17	1.14	1.14	1.14	1.14	1.14	
		104	451	1.10	1.10	1.10	1.08	1.10	1.08	1.10	1.10	1.08	1.10	1.10	
		101	500	1.06	1.06	1.05	1.04	1.07	1.05	1.07	1.06	1.05	1.07	1.07	
106	573	1.02	1.01	1.00	0.98	1.01	0.99	1.01	1.01	1.01	1.02	0.98	1.01		
Approx. discharged capacity: 242 mA-hr (battery No. 1-6); 121 mA-hr (battery No. 7-11)															
240	480	37	0	1.59	1.57	1.59	1.57	1.57	1.58	1.59	1.58	1.58	1.58	1.58	
		39	50	1.59	1.58	1.58	1.58	1.58	1.58	1.57	1.56	1.56	1.56	1.56	
5	10	100	0	1.31	1.30	1.30	1.30	1.30	1.30	1.31	1.30	1.30	1.30	1.31	
		101	21	1.01	0.98	1.01	1.00	0.98	0.97	0.98	0.97	0.97	0.97	0.97	
		101	45	0.98	0.97	0.96	0.96	0.96	0.40	0.96	0.96	0.97	0.96	0.96	
		102	117	0.81	0.80	0.80	0.75	0.80	—	0.80	0.72	0.80	0.71	0.72	
Approx. discharged capacity: 260 mA-hr (battery No. 1-6); 130 mA-hr (battery No. 7-11)															
240	480	37	0	1.48	1.48	1.44	1.45	1.44	—	1.48	1.44	1.45	1.44	1.44	
		39	268	1.31	1.34	1.34	1.32	1.35	—	1.31	1.28	1.35	1.24	1.31	

Table II. Results of the storage tests at various temperatures

Cell No.	Storage temperature	Storage periods	Discharge conditions	Realized capacity (mA-hr)
73515-10	Room	2 weeks	100 kohm, 25° ± 2°C	32
73515-11	Room	2 weeks	100 kohm, 25° ± 2°C	33
73516-9	Room	2 weeks	100 kohm, 25° ± 2°C	33
73530-4	Room	2 weeks	125 μA, 125° ± 2°C	32
73530-5	Room	2 weeks	125 μA, 125° ± 2°C	31
73515-12	Room	6 weeks	100 kohm, 25° ± 2°C	33
73515-13	Room	6 weeks	100 kohm, 25° ± 2°C	34
73516-11	Room	6 weeks	100 kohm, 25° ± 2°C	32
73517-1	Room	3 months	125 μA, 125° ± 2°C	32
73517-3	Room	3 months	125 μA, 125° ± 2°C	33
73517-9	Room	3 months	125 μA, 125° ± 2°C	33
73530-6	Room	6 months	125 μA, 125° ± 2°C	32
73530-10	Room	6 months	125 μA, 125° ± 2°C	32
73530-11	Room	6 months	125 μA, 125° ± 2°C	33
73515-12	Room	1 year	125 μA, 125° ± 2°C	34
73515-13	Room	1 year	125 μA, 125° ± 2°C	32
73530-12	Room	1 year	125 μA, 125° ± 2°C	32
73517-5	45°C	3 months	125 μA, 125° ± 2°C	32
73517-8	45°C	3 months	125 μA, 125° ± 2°C	32
73529-6	45°C	3 months	125 μA, 125° ± 2°C	32
73515-1	45°C	6 months	125 μA, 125° ± 2°C	31
73515-4	45°C	6 months	125 μA, 125° ± 2°C	32
73523-14	45°C	6 months	125 μA, 125° ± 2°C	33
73529-3	45°C	6 months	125 μA, 125° ± 2°C	32
73529-6	45°C	6 months	125 μA, 125° ± 2°C	33
73513-4	45°C	1 year	125 μA, 125° ± 2°C	32
73513-6	45°C	1 year	125 μA, 125° ± 2°C	32
73516-3	45°C	1 year	125 μA, 125° ± 2°C	31
73517-2	45°C	1 year	125 μA, 125° ± 2°C	32
73522-9	45°C	1 year	125 μA, 125° ± 2°C	33
73522-12	45°C	1 year	125 μA, 125° ± 2°C	33
73508-1	60°C	6 weeks	100 kohm, 25° ± 2°C	33
73508-2	60°C	6 weeks	100 kohm, 25° ± 2°C	31
73508-3	60°C	6 weeks	100 kohm, 25° ± 2°C	31
73515-8	60°C	3 months	Lithium nitride formed on the anode	
73529-2	60°C	3 months	Lithium nitride formed on the anode	
73522-14	60°C	3 months	125 μA, 125° ± 2°C	32
73523-2	60°C	3 months	125 μA, 125° ± 2°C	32
73523-9	60°C	3 months	125 μA, 125° ± 2°C	32
73523-17	60°C	3 months	125 μA, 125° ± 2°C	31
73530-2	60°C	3 months	125 μA, 125° ± 2°C	31
73523-13	60°C	6 months	125 μA, 125° ± 2°C	33
73517-1	60°C	6 months	125 μA, 125° ± 2°C	33
73517-4	60°C	6 months	125 μA, 125° ± 2°C	32
73517-7	60°C	6 months	125 μA, 125° ± 2°C	33
73515-3	60°C	1 year	125 μA, 125° ± 2°C	32
73515-5	60°C	1 year	125 μA, 125° ± 2°C	32
73516-2	60°C	1 year	125 μA, 125° ± 2°C	32
73522-5	60°C	1 year	125 μA, 125° ± 2°C	33
73523-13	60°C	1 year	125 μA, 125° ± 2°C	33
73523-14	60°C	1 year	125 μA, 125° ± 2°C	32

The test cells experienced no capacity loss after a storage period of 6 weeks, 3 months, 6 months, or 1 year at room temperature. Figure 9 shows the discharge curves of a 2 and a 6 week old cell under a 100 kohm load at room temperature. No significant difference in discharge characteristics was noted. Furthermore, a discharge efficiency of 100% was realized in both cells. The realized capacities of all the test cells after storage at room temperature are shown in Table II. The stoichiometric capacity of  $33 \pm 2$  mA-hr was realized in all the stored cells. It is noted that since the capacity retention of the test cells was of principal interest, accelerated discharge tests were carried out

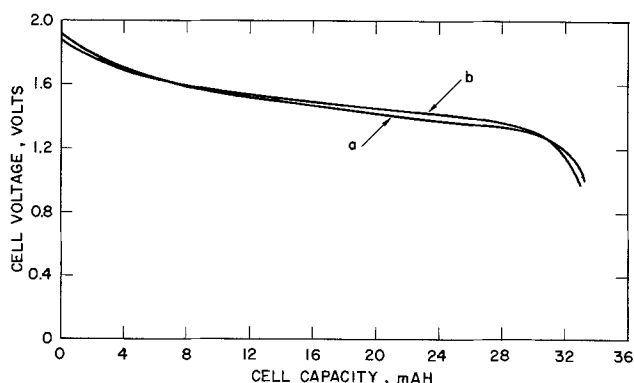


Fig. 9. Discharge curves of the 33 mA-hr cells before and after room temperature storage. Discharge conditions: 100 kohm load at room temperature. Curve a, cell No. 73515-11 (fresh cell); curve b, cell No. 73515-12 (stored at room temperature for 6 weeks).

on the 3 month, 6 month, and 1 year stored cells. The test cells were discharged at 125 μA at 125°C. The stoichiometric capacity was realized in all the tests indicating that no self-discharge process had taken place.

The results of the 45°C storage tests were similar to those of the room temperature storage tests. The test cells experienced no capacity loss after storage as shown in Table II.

Figure 10 shows the discharge curves of 2 test cells before and after a storage period of 1000 hr at 60°C. It is noted that no capacity loss was experienced by the stored cell. However, after a storage period of 3 months we noted that 2 of the 20 stored cells showed low open-circuit voltage. The 2 cells were positioned at the top of the stack in the glass vial. An examination of these 2 cells revealed a dark brown substance on the Li anode. Since an ammonia odor was clearly noted when water was dropped on the dark brown compound we concluded that it was lithium nitride. The nitride formation was caused by the small amount of residual nitrogen in the dry box. Evidently, the rate of nitride formation must be significant at 60°C to cause problems for the unsealed test cells. Nonetheless, 5 cells were selected at random from the remaining cells and discharged at 125 μA at 125°C. The stoichiometric capacity was realized. Consequently, we concluded that the failure of the 2 cells was due to causes other than the intrinsic properties of the system. In order to alleviate the nitride formation problem, the glass vial which contained the remaining test cells was heat sealed in two overlapping 10 mil polyethylene bags and the cells were returned to the 60°C storage.

The 6 month and 1 year stored cells were discharged at 125 μA at 125°C. No capacity loss was experienced by these cells as shown in Table II. Figure 11 shows the typical discharge curves of the test cells before and after a storage period of 1 year at 60° and 45°C.

All the test cells stored at 100°C showed lithium nitride formation on the anode after 3 months. Indeed, the anode of most of the test cells was completely covered with lithium nitride and separated from the electrolyte. It was concluded that lithium nitride formation at 100°C due to the residual nitrogen in the dry box had rendered the storage of the unsealed cells impractical. No attempt was made to discharge these cells.

The fact that the test cells experienced no capacity loss after various storage periods up to 1 year at room temperature, 45°, and 60°C showed that the Li/LiI(Al<sub>2</sub>O<sub>3</sub>)/PbI<sub>2</sub>, PbS, Pb batteries are stable on storage and have a long shelf life. It should be noted, however, that the laboratory cells were not hermetically sealed, the anodes stored at 100°C reacted with the residual nitrogen in the dry box and became defective. Consequently, no conclusion can be made in regard to

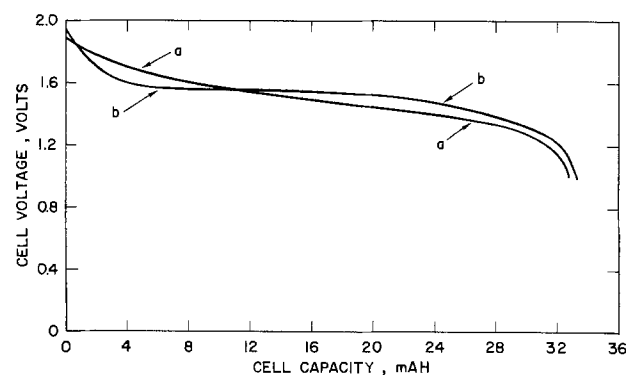


Fig. 10. Discharge curves of the 33 mA-hr cells before and after 60°C storage. Discharge conditions: 100 kohm load at room temperature. Curve a, cell No. 73515-11 (fresh cell); curve b, cell No. 73508-1 (stored at 60°C for 6 weeks).

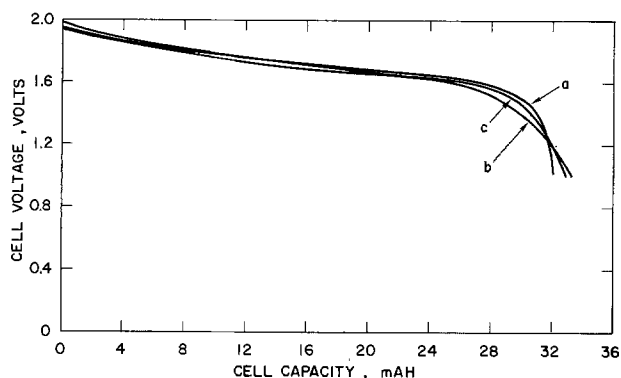


Fig. 11. Discharge curve of the 33 mA-hr cells before and after long term storage. Discharge conditions: 125  $\mu$ A at 125°C. Curve a, cell No. 73530-4 (fresh cell); curve b, cell No. 73522-12 (stored at 45°C for 1 year); curve c, cell No. 73522-5 (stored at 60°C for 1 year).

the storability of the laboratory type of Li/LiI(Al<sub>2</sub>O<sub>3</sub>)/PbI<sub>2</sub>, PbS, Pb batteries at 100°C.

The results of the discharge and storage tests showed that the Li/LiI(Al<sub>2</sub>O<sub>3</sub>)/PbI<sub>2</sub>, PbS, Pb system is a practical low rate, high energy density system. Indeed,

batteries containing parallel and series stacks of cells have been made for low rate applications. It is estimated based on the low rate and accelerated discharge test results that an energy density of 0.49 W-hr/cm<sup>3</sup> (8 W-hr/in.<sup>3</sup>) can be realized from these batteries.

Manuscript submitted Sept. 11, 1975; revised manuscript received ca. Nov. 15, 1975.

Any discussion of this paper will appear in a Discussion Section to be published in the December 1976 JOURNAL. All discussions for the December 1976 Discussion Section should be submitted by Aug. 1, 1976.

Publication costs of this article were partially assisted by P. R. Mallory & Company Incorporated.

#### REFERENCES

1. C. C. Liang, *This Journal*, **120**, 1289 (1973).
2. C. C. Liang, Proceedings of 1971 Intersociety Energy Convention, Engineering Conference, p. 673.
3. "Selected Values of Chemical Thermodynamic Properties," *Nat. Bur. Std. Tech. Notes* 270-3 and 270-4.
4. JANAF Thermodynamical Tables, 2nd ed., National Bureau of Standards, Washington, D. C. (June 1971).
5. R. D. Freeman, Oklahoma State University Research Foundation Report No. 60 (January 1962).

## The Role of Conductivity Variations Within Artificial Pits During Anodic Dissolution

Richard Alkire,\* Daniel Ernsberger,\*\* and David Damon<sup>1</sup>

Department of Chemical Engineering, University of Illinois, Urbana, Illinois 61801

#### ABSTRACT

Owing to restricted mass transport, the conductivity of electrolytic solution within occluded regions may be different from that of the bulk electrolyte outside the occluded regions. Experimental and theoretical investigations have been carried out on artificial copper pits (length to diameter ratio between 0.93 and 10.3) dissolving in binary copper sulfate solutions (0.001-0.5M at 25°C) in order to clarify conditions under which conductivity effects are appreciable. Both potentiostatic (50-1500 mV) and galvanostatic (1.2-6.8 mA/cm<sup>2</sup>) data agree with a mathematical model which includes charge transfer, ohmic, geometric, and unsteady-state mass transport processes. The model generates dimensionless criteria by which the importance of conductivity changes in other chemical systems can be estimated.

Because corrosion processes are complex, it is often difficult to design meaningful accelerated tests and/or to scale up laboratory results to field applications. Therefore model studies on simple analogs of corrosion processes can be helpful even though they may not account for the entire range of possible complexities which actual corrosion systems possess. That is, model studies on seemingly artificial systems can clarify the conceptual groundwork upon which is based intuitive judgments about real systems.

Models of localized corrosion processes, especially pitting and crevicing, have been proposed by several investigators in order to clarify effects of diffusion-limited behavior within the occluded region. Diffusion-limited attack eventually leads to the formation of concentration gradients within the occluded region. As a consequence, the kinetics of the corrosion reactions deep within the occluded region may be very different

from those occurring under bulk electrolyte conditions owing to the concentration dependence of the rate constants (1). Also, the increased concentration of species within the occluded region may increase the conductivity of the occluded solution, thereby reducing the ohmic resistance of the corroding system (2). Upon extended dissolution, the precipitation of salt films within the occluded region can eventually occur (3). These processes cause naturally corroding systems to be rather complicated owing to the many possible electrochemical reactions, the complex interfacial phenomena and solution chemistry, and the uncertain geometry of localized corrosion cells.

The purpose of the present study was to employ experiments and mathematical models to investigate the role of conductivity variations within artificial pits during the course of controlled metal dissolution. The program was designed to develop a predictive basis for estimating conditions under which auto-acceleration of dissolution rates in artificial pits can occur owing to conductivity variations (4, 5).

\* Electrochemical Society Active Member.

\*\* Electrochemical Society Student Member.

<sup>1</sup> Present address: Babcock and Wilcox Company, Alliance, Ohio 44601.

Key words: mathematical model, artificial pit, corrosion.

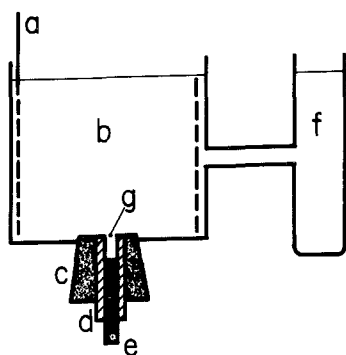


Fig. 1. Electrolysis cell. a, cathode screen; b, electrolyte compartment; c, rubber stopper; d, insulating side walls; e, wire anode; f, reference electrode compartment; g, artificial pit.

### Apparatus

Cylindrical artificial pits with inert side walls were fabricated by embedding copper wire<sup>2</sup> in epoxy resin and cutting off one end. The exposed surface was mechanically polished to 600 grade, and the copper was then dissolved to the desired depth by anodic dissolution in flowing sulfuric acid. A flat-bottomed polished surface was subsequently obtained by electropolishing in 50% phosphoric acid. Before and after pitting experiments, microscopic examination of the circular surface was made with an objective having a depth of focus of 0.01 mm, and it was found that every portion of the surface was in sharp focus. Artificial pits were placed facing upward in the corrosion cell as depicted in Fig. 1. The cylindrical cathode consisted of copper screen. A mercurous sulfate reference electrode was used in the side compartment. It was found that the behavior of the pit did not depend on cathode or reference electrode position provided that they were placed more than 1.5 cm (or 10 pit diameters) from the pit entrance. Similarly, it was found that pit behavior was independent of the amount of solution in the cell provided that the solution depth exceeded 1.5 cm. The solution in the cell was not agitated.

The uniformity of the current distribution in the vicinity of the pit mouth was measured analogically by using conductive paper cut in the shape of a two-dimensional slot. A slot with a length to width ratio of unity had a potential distribution that varied by 10% from the edge to the center of the slot mouth. The potential distribution in a circular pit will be less uniform than the slot geometry. Therefore pits with aspect length to diameter ratios appreciably less than unity were not investigated.

Experiments were conducted under both constant potential control (Wenking No. 68TS3) and constant current control (Electronic Measurements No. C633). During the course of some experiments, the potential

<sup>2</sup> See Table I for diameters.

distribution within the pit was measured directly by lowering a microcapillary probe into the pit. The electrolysis cell was placed on a microscope stage and the probe was mounted in place of the objective lens. The focus knob was connected to the shaft of a precision potentiometer thereby obtaining a voltage signal proportional to probe displacement. An X-Y recorder (Hewlett-Packard No. 7004B) displayed the measured potential as a function of position. The probe cross-sectional area was 8% of the pit cross-sectional area.

### Procedure

Four concentrations of electrolytic solution (0.001, 0.01, 0.1, and 0.5M) were prepared from AR hydrated copper sulfate and deionized, distilled water (conductivity  $4 \times 10^{-6}$  mho/cm).

After electropolishing, pits were rinsed with about 3500 pit volumes of distilled water (a few milliliters) and dried. The pit depth was measured to within 0.01 mm by mounting the pit on a microscope stage (Bausch & Lomb UK 128) and focusing first on the metal surface and then on the external epoxy surface; the fine focus micrometer provided a direct measure of pit depth. The pit was then placed in the electrolysis cell, and solution was added with a syringe to assure that no bubbles were trapped within the pit. The make-up solution was held at 25°C.

Constant potential experiments were carried out with solutions of several concentrations, while constant current experiments were carried out with a single solution as indicated in Table I. For each solution, a freshly prepared pit was used for measurements at four different conditions (either applied potential or applied current). The duration of each unsteady-state experiment ranged between 70 and 400 sec. Between each measurement the pit was rinsed with electrolyte of bulk concentration and temperature 25°C. During some constant potential experiments, the potential distribution within the pit was measured by lowering the microcapillary reference electrode probe into the pit until the tip hit the base and flexed; the probe was then withdrawn. Each traverse took about 5 sec.

Upon completion of experiments for each solution, the conductivity of the bulk solution was measured with a resistance bridge (Leeds & Northrup Series 4959). The diameter of the pit was measured optically to within 0.01 mm by placing the pit on the stage of a microscope having a calibrated scale in the eyepiece.

### Mathematical Model

The artificial pit geometry is described by a right circular cylinder of radius  $r$  and height  $h$ . The binary solution of electrolyte in the pit contains a soluble salt of the metal which is undergoing dissolution, for example copper sulfate in the case of copper dissolution. Only one electrochemical reaction occurs, metal dissolution; the metal does not corrode in the solution. During dissolution the metal surface is assumed to remain smooth and perpendicular to the side walls.

Table I. Experimental conditions

Figure No.	Applied potential (mV) or current ( $\mu$ A)	Concentration (mole/liter)	Conductivity (ohm-cm) <sup>-1</sup>	Pit diameter (mm)	Pit depth (mm)	Aspect ratio	Duration of experiment
1. Unsteady-state experiments							
(a) Constant potential electrolysis							
2	200, 300, 400, 500	0.01	0.00144	0.53	1.20	2.26	400, 300, 250, 250 sec
3	50, 100, 200	0.10	0.00867	0.56	1.20	2.15	400, 400, 400 sec
4	50, 75, 100, 200	0.10	0.00867	1.29	1.20	0.93	300, 250, 310, 200 sec
(b) Constant current electrolysis							
6	2, 5, 5.0, 10.0, 15.0	0.01	0.00144	0.53	1.20	2.26	340, 300, 200, 400 sec
2. Steady-state experiments							
Constant potential electrolysis							
7	100, 300, 500, 700	0.01	0.00144	0.251	1.13	4.50	95, 27, 18, 13 min
	500, 1000, 1500	0.001	0.00025	0.251	1.13	4.50	63, 30, 25 min
	50, 100, 150, 200	0.01	0.00144	0.812	8.40	10.35	1290, 1350, 1280, 3080 min

During dissolution, the solubility of the binary metal salt is not exceeded and therefore precipitation does not occur.

For diffusion of a binary electrolyte under stagnant conditions, the one-dimensional unsteady diffusion equation is

$$\frac{\partial c(y,t)}{\partial t} = D \frac{\partial^2 c(y,t)}{\partial y^2} \quad [1]$$

where it is assumed that the diffusion coefficient of the neutral salt,  $D$ , is independent of concentration (6). Symbols used in the equation are explained at the end of the text. A migration term does not appear in Eq. [1] since the concentration refers to the movement of the neutral binary salt, not individual ionic species. The initial condition which corresponds to the experimental procedure is that the concentration within the pit is uniform prior to application of power

$$c(y,0) = c_b \quad [2]$$

The boundary condition at the pit entrance ( $y = h$ ) which conforms to the experimental procedure is

$$c(h,t) = c_b \quad [3]$$

At the base of the pit ( $y = 0$ ), the concentration gradient in the metal salt is proportional to the current flowing through the pit

$$\frac{\partial c(0,t)}{\partial y} = - \frac{(1 - t_+)i}{nFD} \quad [4]$$

As the metal dissolves, the pit becomes longer. For the short duration unsteady-state experiments reported in Table I, however, the elongation is less than 0.03% of the initial length. For longer duration steady-state experiments, variation of pit length during dissolution was accounted for with use of Faraday's law.

The potential between the dissolving anode and the reference electrode can be resolved into four component overpotentials which arise owing to charge transfer, concentration differences, resistance effects within the pit, and resistance effects external to the pit mouth

$$\phi = \eta_s + \eta_c + \eta_r + \eta_m \quad [5]$$

The component overpotentials are related to the current density and concentration by

$$i = i_0 \left[ \frac{c(0,t)}{c_b} \right]^{0.42} (e^{(\alpha_a F/RT)\eta_s} - e^{-(\alpha_c F/RT)\eta_s}) \quad [6]$$

$$\eta_c = \frac{(1 + t_+)RT}{F} \ln \left[ \frac{c(y,t)}{c_b} \right] \quad [7]$$

$$\eta_r = \frac{ih}{\kappa^*} \quad [8]$$

$$\eta_m = \frac{\pi r i}{4\kappa_b} \quad [9]$$

where  $\kappa^*$  is the average conductivity of electrolyte in the occluded region. Equation [6] characterizes the Cu/CuSO<sub>4</sub> system (7) and Eq. [7] is the Nernst equation written for a binary salt (8). The conductivity of copper sulfate solutions varies with concentration (9-12); a parabolic least squares fit of the data was used (4) to give

$$\kappa = \kappa_b \left( \frac{c}{c_b} \right)^\gamma \quad \text{for } 10^{-8}\text{M} < c < 1.43\text{M} \quad [10]$$

where

$$\gamma = 0.706 - 0.214 \ln c_b - 0.0107 \ln \frac{c}{c_b} \quad [11]$$

The agreement between the conductivity data and Eq. [10] is everywhere within 8% of the experimentally measured conductivity. Equation [8] is Ohm's law

where the average conductivity is employed. It is recognized from transport theory that Ohm's law is not valid in the presence of concentration gradients owing to diffusion potentials; the suitability of simplifying the analysis by ignoring these restrictions will be in part justified by comparison of theoretical predictions with experimental data in the following sections. Equation [9] is Ohm's law where the resistance is computed for a flat disk embedded in an insulating plane with the counterelectrode at infinity (13).

### Method of Solution

The details of the calculations are given in Ref. (4) and are only summarized here. For constant current calculations, an analytical solution by separation of variables is available (4,14) for the concentration distribution as a function of time. Equations [5]-[9] were then employed to calculate the total overpotential.

For constant potential calculations, an IBM-360 digital computer was used in conjunction with the Crank-Nicolson finite difference scheme to obtain the unsteady-state concentration and potential distributions within the pit during dissolution. At each time step, the current density required by Eq. [4] was chosen by Newton-Raphson iteration such that Eq. [5]-[9] were satisfied under the prevailing concentration distribution. Numerical unsteady-state calculations were found to be insensitive to mesh size between 20-100 mesh points and to initial time increments ( $Dt/h^2$ ) less than  $10^{-5}$ . The size of the time step was increased by a factor of 1.1 with each successive step.

### Results and Discussion

During preliminary experiments, it was found that extended periods of dissolution would often lead to precipitation of a salt film onto the electrode surface owing to supersaturation of solution. Under constant applied current conditions, for example, a sudden voltage rise would occur some time after initiation of electrolysis, to be denoted the transition time. For semi-infinite diffusion, the transition time is related to the other parameters by (15)

$$t^{1/2} = \frac{nF\sqrt{\pi D}}{2i} (c_{pptn} - c_b)$$

Measurement of the transition time therefore provides a direct indication of the solute concentration at the electrode surface when precipitation occurs. Experiments performed in several solutions (0.01, 0.1, and 0.5M CuSO<sub>4</sub>) at applied current densities up to 250 mA/cm<sup>2</sup> gave the consistent result that precipitation occurred when the saturation concentration was exceeded by 2.2-fold.

The short-duration transient experiments reported below were conducted under such conditions that precipitation did not occur. Longer duration experiments were conducted until either a pseudo steady state was attained or else salt precipitation occurred. The results of both types of experiments are discussed separately.

*Short duration experiments.*—Table I (Part 1) provides conditions under which short duration experiments were performed; the parameters of the binary copper sulfate system for which data were obtained are provided in Table II. These values were used in making theoretical calculations with the above mathematical model. For 24 experiments of 26 performed, it was found that the predicted value of the initial current (or potential) averaged to within 5.0% of the measured value. The range was between 0 and 19% error.

Results of constant potential experiments and calculations are given for two concentrations and two aspect ratios in Fig. 2, 3, and 4. The solid lines corre-

Table II. System parameters

$D(0.001M)$	$= 7.5 \times 10^{-6} \text{ cm}^2/\text{sec}$
$D(0.01M)$	$= 6.79 \times 10^{-6} \text{ cm}^2/\text{sec}$
$D(0.1M)$	$= 5.63 \times 10^{-6} \text{ cm}^2/\text{sec}$
$\kappa_b(0.001M)$	$= 2.51 \times 10^{-4}/\text{ohm-cm}$
$\kappa_b(0.01M)$	$= 1.44 \times 10^{-3}/\text{ohm-cm}$
$\kappa_b(0.1M)$	$= 8.67 \times 10^{-3}/\text{ohm-cm}$
$\eta$	$= 2 \text{ g-equiv./g-mole}$
$i_0(0.001M)$	$= 0.144 \text{ mA/cm}^2$
$i_0(0.01M)$	$= 0.380 \text{ mA/cm}^2$
$i_0(0.1M)$	$= 1.0 \text{ mA/cm}^2$
$t_+(0.001M)$	$= 0.40$
$t_+(0.01M)$	$= 0.40$
$t_+(0.1M)$	$= 0.36$
$\alpha_a$	$= 1.5$
$\alpha_c$	$= 0.5$

spond to experimental measurements while the dashed lines correspond to theoretical calculations. In each figure, results are given for several different applied potentials. It is seen in every case that the current eventually increased above its initial value, sometimes passing through a minimum which was more or less shallow. In every case, the agreement between experiment and theory is within 10% of the measured value. The increase in current during constant potential elec-

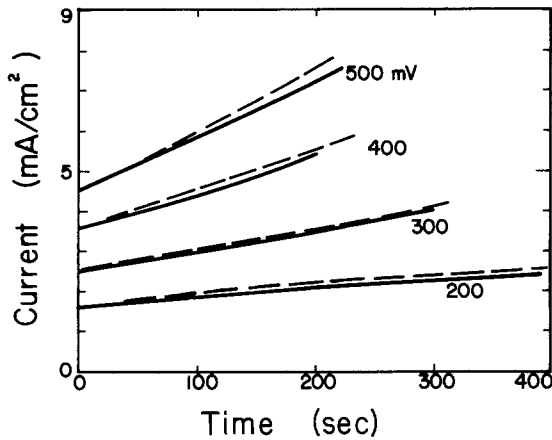


Fig. 2. Current response during constant potential electrolysis ( $c_b = 0.01M, h/D = 2.26$ ).

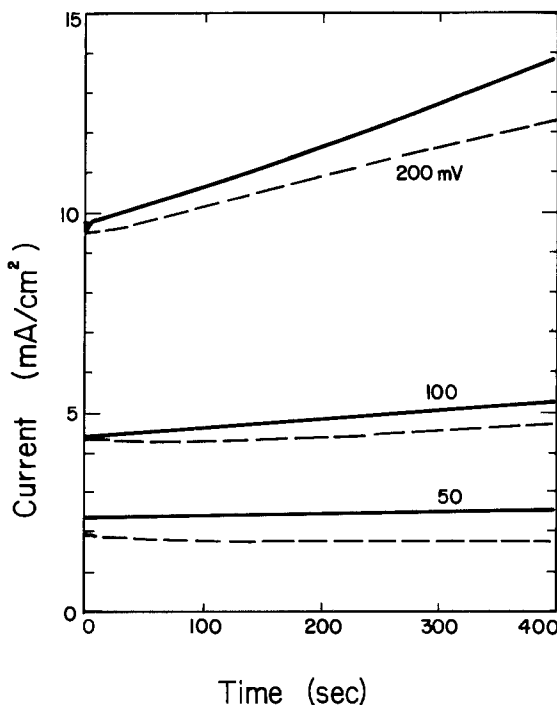


Fig. 3. Current response during constant potential electrolysis ( $c_b = 0.1M, h/D = 2.15$ ).

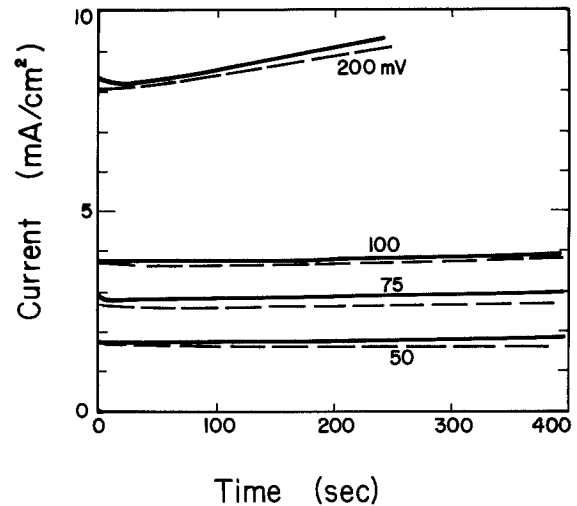


Fig. 4. Current response during constant potential electrolysis ( $c_b = 0.1M, h/D = 0.93$ ).

trolysis is due to increased conductivity of solution within the pore, not surface roughening. (If the solution in the pit is stirred part way through an experiment, the current returns to its initial value.) The minimum in the current occurs owing to the competing effects of concentration overpotential and conductivity variation.

A typical potential distribution measured within the pit during dissolution is given by the solid line in Fig. 5. The data show that potential variations external to the pit are important. The theoretical calculations indicated by the dashed line are in good agreement with these data. The hysteresis in the potential traverse is thought to arise from free movement in the microscope gears, not from disturbing the concentration profile; partial traverses showed that even when the probe did not enter the pit, a reversal in traverse direction was accompanied by hysteresis. Insertion of the measuring probe was found to disturb the current by less than 2% of the measured value.

Figure 6 shows results of four experiments on a pit operated at different applied constant currents. In each, the potential (measured between anode and reference electrode) eventually decreased during unsteady-state dissolution. The theoretical model predicted behavior, shown by the dashed lines, which is in accord with the experimental data.

*Long-duration experiments.*—Experimental conditions under which long-term dissolution experiments were conducted are given in Table I (Part 2). Theoretical calculations were made for each experiment performed. Results are given in Fig. 7 for one series of constant potential experiments in a solution of 0.01M

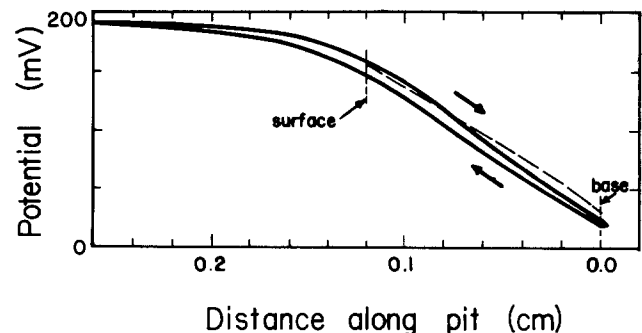


Fig. 5. Potential distribution in an artificial pit during electrolysis ( $c_b = 0.1M, h/D = 0.93, \text{time} = 28 \text{ sec}$  after onset of electrolysis).

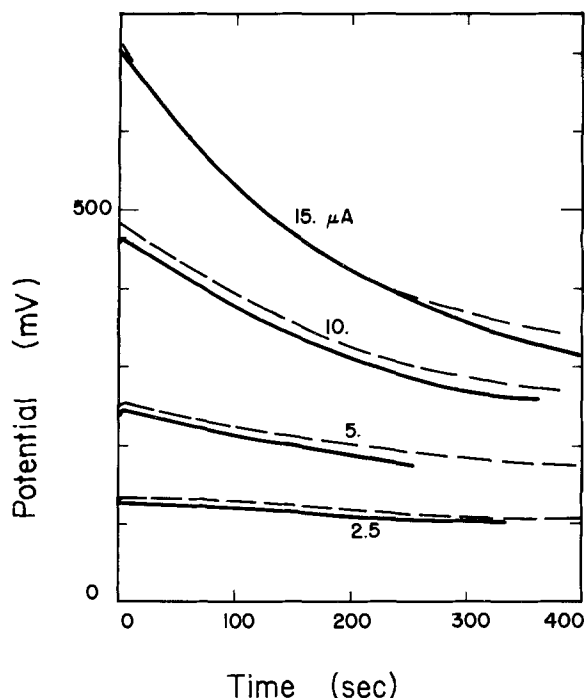


Fig. 6. Potential response during constant current electrolysis ( $c_b = 0.1M$ ,  $h/D = 2.26$ ).

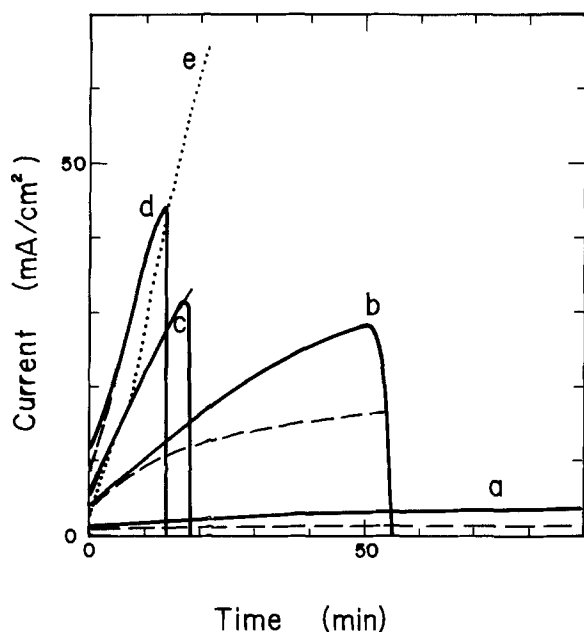


Fig. 7. Current response during constant potential electrolysis. a, 0.01M, 100 mV; b, 0.01M, 300 mV; c, 0.01M, 500 mV; d, 0.01M, 700 mV; e, 0.001M, 1500 mV.

$CuSO_4$ . At the higher applied potentials, the current increased by up to five times the initial current and then fell suddenly owing to precipitation within the pit. At lower applied potentials, a steady-state current was obtained. The dotted line marked "e" in Fig. 7 shows experimental data for a highly polarized elec-

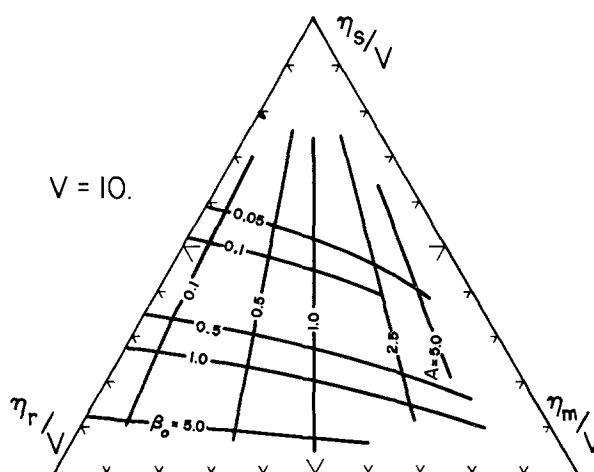


Fig. 8. Overpotential partitioning at onset of electrolysis

trode in very dilute electrolyte. At the moment of salt precipitation, the current had increased by more than 25-fold above the initial value at  $t = 0$ .

The theoretical calculations, shown by the dashed lines, are in good agreement with experimental trends. Table III summarizes the predicted and measured values of current at the end of the experiment (either attainment of steady state or else salt precipitation). It is seen that in every case investigated the theory provides a conservative estimate of the auto-acceleration effect.

*Theoretical model.*—The foregoing comparison of theory and experiment has been carried out over a wide range of operating conditions including mode of power supply, aspect ratio, pit diameter, solute concentration, rate of dissolution, and duration of experiment. Because the experiments were carefully designed in the sense that no adjustable or uncertain parameters were involved, the good agreement between theory and experiment indicates either that the assumptions were justified, or that any poor assumptions were inconsequential.

By writing the mathematical equations in dimensionless form, it is possible to develop criteria for estimating those situations where the ohmic overpotential is greater than the charge-transfer or concentration overpotentials so that auto-acceleration is possible. A procedure, outlined below, has been developed for predicting the maximum current which would be experienced under given operating conditions. The principal purpose of presenting these results is to provide an example of how dimensionless parameters can be used to assist in determining which physical phenomena control corrosion behavior, in determining what scale-up ratios apply, and in locating the window in parameter space within which the auto-acceleration effect is likely to be most destructive.

*Under what conditions is acceleration likely to occur?*—Acceleration will occur only if a major portion of the applied potential is consumed by the ohmic resistance within the pit. At the initial moment of switching on the circuit, Fig. 8 shows how overpotentials are distributed between ohmic and surface processes (concentration overpotential being absent). The figure cor-

Table III. Final currents, steady-state experiments

Applied potential (mV)	Concentration (mole/liter)	Aspect ratio	Final current observed (mA/cm <sup>2</sup> )	Final current predicted (mA/cm <sup>2</sup> )
100, 300, 500, 700	0.01	4.50	3.8, 28.6, 31.2, 44.3	1.7, 16.5, 31.2, 44.3
500, 1000, 1500	0.001	4.50	29.5, 47.6, 67.8	7.4, 17.7, 29.5
50, 100, 150, 200	0.01	10.35	0.091, 0.91, 0.98, 2.5	0.081, 0.56, 0.62, 1.8

responds to  $V = \phi_A nF/RT = 10$ , or 125 mV for a two-electron reaction. Because  $\eta_s$ ,  $\eta_m$ , and  $\eta_r$  sum to the applied potential, each point within the triangle represents a different partitioning between the three overpotentials. The partitioning depends on two dimensionless parameters

$$A = \frac{\pi r}{4h}$$

$$\beta_0 = \frac{i_0 nFh}{RT\kappa_b}$$

The parameter  $A$  is an aspect ratio, while  $\beta_0$  is the ratio of ohmic resistance to charge-transfer resistance insofar as it contains the ratio of  $i_0$  to  $\kappa$ . Figure 8 illustrates how the relative values of the three overpotentials depend on  $A$  and  $\beta_0$ . On this basis, it is seen that the ohmic resistance in the pit consumes an appreciable fraction (over 50%) of the applied potential under the conditions

$$A < 1$$

$$\beta_0 > 1 \quad [12]$$

Under the conditions given in Eq. [12], the auto-acceleration effect is likely to be observed.

*To what extent will acceleration occur?*—It is convenient to arrange the parameters of the system into dimensionless group as follows

$$\theta = -\frac{\kappa_b RT(1-t_+)}{c_b n^2 F^2 D}$$

The application of potential  $V = \phi_A nF/RT$  will cause flow of current (initially equal to  $\beta_i = i_0 nFh/RT\kappa_b$ ) which will change to some final steady-state value, ( $\beta_{ss} = i_{ss} nFh/RT\kappa_b$ ) provided that precipitation of insoluble salts does not occur. For a long narrow pit ( $r/h = 0.0127$ ), the ratio of  $\beta_{ss}/\beta_i$  is given in Fig. 9 for a wide variety of possible systems and operating conditions. It is seen that a final steady-state current of 50-fold greater than the initial current is possible for some systems. For shorter pits ( $r/h = 0.127$ ) the ratio of  $\beta_{ss}/\beta_i$  is also given in Fig. 9. It is seen that the auto-acceleration phenomenon is important under conditions such that  $h/r$ ,  $V$ ,  $\beta_0$ ,  $\theta$ , and  $\gamma$  are large.

### Conclusions

Dissolution of metal within artificial pits can increase the conductivity of solution within the pit suf-

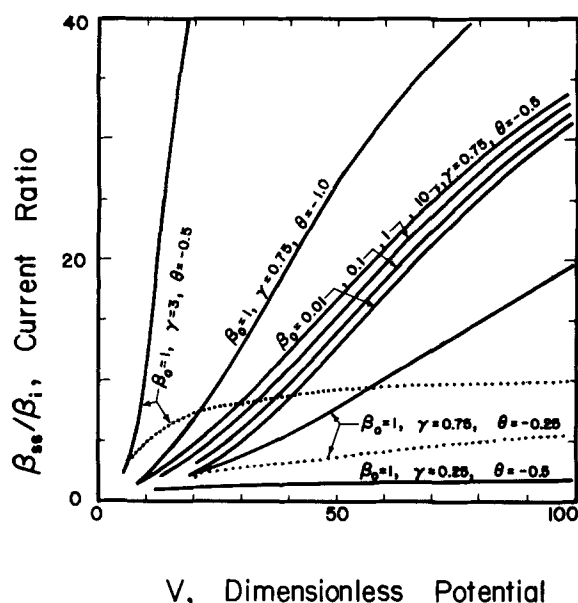


Fig. 9. Extent of auto-acceleration. —  $A = 0.01$  or  $r/h = 0.0127$ ; - - -  $A = 0.1$  or  $r/h = 0.127$ .

ficiently to initiate auto-acceleration of the dissolution rate. Under such conditions, the rate of dissolution can increase manifold over the initial rate. A mathematical analysis of concentration and potential variations within artificial pits is in good agreement with data on artificial pits containing binary electrolyte. The theory permits estimation of what conditions are likely to exhibit auto-acceleration and to what extent the dissolution rate is likely to increase. Similar effects occur in multicomponent electrolyte systems, and the methods used in this investigation could be extended to these systems without difficulty.

Naturally corroding pits and crevices are more complex than the artificial pits studied here. Whereas it is often difficult to assign values to the parameters of naturally corroding systems, modeling studies assist in clarifying the interpretation of complex data.

### Acknowledgments

The investigation received the support of the National Science Foundation via Grant NSF DMR 74-08716 and a du Pont Grant-in-Aid. Appreciation is extended to the Exxon Foundation for fellowship support for one of the authors (D. E.).

Manuscript submitted July 22, 1975; revised manuscript received Oct. 15, 1975.

Any discussion of this paper will appear in a Discussion Section to be published in the December 1976 JOURNAL. All discussions for the December 1976 Discussion Section should be submitted by Aug. 1, 1976.

Publication costs of this article were partially assisted by the University of Illinois.

### LIST OF SYMBOLS

$A$	$\pi r/4h$ , dimensionless aspect ratio
$c$	concentration, mole/cm <sup>3</sup>
$C_b$	bulk concentration, mole/cm <sup>3</sup>
$D$	diffusivity of neutral salt, cm <sup>2</sup> /sec
$F$	Faraday constant, coulomb/equivalent
$i$	current density, A/cm <sup>2</sup>
$i_i$	initial current density, A/cm <sup>2</sup>
$i_0$	exchange current density, A/cm <sup>2</sup>
$i_{ss}$	steady-state current density, A/cm <sup>2</sup>
$h$	pit length, cm
$n$	number of electrons in electrochemical reaction
$R$	gas constant, coulomb-V/g-mole °K
$r$	pit radius, cm
$t$	time, sec
$t_+$	cationic transference number
$T$	temperature, °K
$V$	$\phi_A nF/RT$ , dimensionless applied potential
$y$	spatial variable
$\alpha_a$	anodic transfer coefficient
$\alpha_c$	cathodic transfer coefficient
$\beta_i$	$i_0 nFh/RT\kappa_b$ , dimensionless initial current density
$\beta_0$	$i_0 nFh/RT\kappa_b$ , dimensionless exchange current density
$\beta_{ss}$	$i_{ss} nFh/RT\kappa_b$ , dimensionless steady-state current density
$\gamma$	empirical parameter defined by Eq. [11]
$\eta_c$	concentration overpotential, V
$\eta_m$	ohmic resistance overpotential external to the pit, V
$\eta_r$	ohmic resistance overpotential within the pit, V
$\eta_s$	surface overpotential, V
$\theta$	$-\kappa_b RT(1-t_+)/c_b n^2 F^2 D$ , dimensionless diffusion parameter
$\kappa$	electrolyte conductivity, (ohm-cm) <sup>-1</sup>
$\kappa_b$	electrolyte conductivity of bulk solution, (ohm-cm) <sup>-1</sup>
$\kappa^*$	average conductivity of electrolyte in occluded region, (ohm-cm) <sup>-1</sup>
$\phi_A$	applied potential, V

### REFERENCES

1. T. Suzuki, M. Yamabe, and Y. Kitamura, *Corrosion*, **29**, 18 (1973).
2. D. A. Vermilyea and C. S. Tedmon, Jr., *This Journal*, **117**, 437 (1970).
3. T. R. Beck, *Electrochim. Acta*, **18**, 815 (1973).
4. D. W. Ernsberger, M.S. Thesis, Department of Chemical Engineering, University of Illinois, Urbana, January 1975.



5. D. A. Damon, B.S. Thesis, Department of Chemical Engineering University of Illinois, Urbana, June 1971.
6. J. S. Newman, "Electrochemical Systems," p. 223, Prentice-Hall, Inc., Englewood Cliffs, N. J. (1973).
7. J. S. Newman, *ibid.*, p. 177.
8. J. S. Newman, *ibid.*, p. 385.
9. T. Richardson, *Trans. Am. Electrochem. Soc.*, **20**, 179 (1911).
10. C. Kern, *ibid.*, **41**, 181 (1922).
11. R. Skowronski, *ibid.*, **52**, 205 (1927).
12. G. Owen, *J. Am. Chem. Soc.*, **60**, 3074 (1938).
13. J. S. Newman, "Electrochemical Systems," p. 344, Prentice-Hall, Inc., Englewood Cliffs, N. J. (1973).
14. H. S. Carslaw and J. C. Jaeger, "Conduction of Heat in Solids," p. 113, Oxford University Press, New York (1959).
15. T. R. Beck, Paper 99 presented at The Electrochemical Society Meeting, Boston, Mass., Oct. 7-11, 1973.

## Transport Processes and the Mechanism of Pitting of Metals

Jose R. Galvele\*<sup>1</sup>

*The Ohio State University, Corrosion Center, Columbus, Ohio 43210*

### ABSTRACT

A pit model was developed on the assumption that the metal ions hydrolyze inside the pits and that the corrosion products are transported by diffusion. Concentrations of  $\text{Me}^{2+}$ ,  $\text{Me}(\text{OH})^+$ , and  $\text{H}^+$  ions, as a function of pit depth and current density, for Zn, Fe, Ni, Co, Al, and Cr were calculated. The main reason for passivity breakdown at the initial stages of pit growth, was found to be the localized acidification due to metal ions hydrolysis. Assuming a critical pH value for pit initiation, the following experimental facts could be explained: (i) the effect of the external pH on the pitting potential of Fe and stainless steel; (ii) the effect of sodium borate concentration on the pitting potential of Zn; (iii) the effect of weak acid salts on the pitting potential of Al; (iv) the oscillations of the electrode potential of stainless steel and nickel in solutions of  $\text{Cl}^- + \text{SO}_4^{2-}$  ions; (v) the existence of a pitting inhibition potential; and (vi) the existence of a pitting protection potential. Through analysis of the transport processes inside a pit it was also concluded that the pitting potential of a metal should change with the  $\text{Cl}^-$  ion concentration according to the equation

$$E_p = E_p^\circ - B \cdot \log [\text{Cl}^-]$$

$B = 0.059\text{V}$  being the slope of the curve at room temperature.

It is a generally accepted fact that pitting starts at a certain critical potential, known as pitting potential (1). Yet the nature of such a potential still remains uncertain. Several explanations have been given, such as zero charge potential, potential-induced ion migration, electrically produced mechanical breakdown, competitive adsorption, salt-formation equilibrium potential, etc. (1). Nevertheless, none of these mechanisms could account for the way in which variables such as pH, ionic concentration, and inhibitor concentration affect the pitting potential. In recent publications, Wexler and Galvele (2) and Alvarez and Galvele (3) reported that the pitting potential was the minimum potential at which localized acidity could be maintained inside a pit. The present paper, based on simple transport equations shows that such acidification can be obtained even at the very early stages of pitting, and that, as was recently reported (4), transport calculations inside the pit explain why variables such as an aggressive anion concentration, nonaggressive anion concentration, external pH, presence of weak acid salts, and alloying elements modify the pitting potential of a metal.

It is concluded that most of the observations made so far on the pitting potential can be explained simply by transport phenomena, and that processes like competitive adsorption, salt formation, film contamination,

etc., even though present during the pitting process, do not play a major role in fixing the pitting potential.

Several authors have shown that the solution inside a pit, as well as that inside a crack or crevice, has a composition quite different from that in the bulk solution (5-10). As early as 1937 Hoar (11) proposed a mechanism of "autocatalytic" pit propagation, which considered that the main cause of pitting was the drop of pH inside the pit. Other authors (12, 13) postulated that the condition for pitting initiation was an increase of chloride ion concentration on the metal-solution interface. In a similar way Kaesche (14) considered the formation of saturated  $\text{AlCl}_3$  inside a pit the necessary condition for the pitting of aluminum.

After studying the pitting of iron in various environments, Vetter and Strehblow (15, 16) questioned all mechanisms based on local composition changes. These authors assumed that the causes of pitting should be present in all the stages of pit growth, even in the smallest detectable pits. Pits as small as one micron in diameter, growing with current densities of the order of 1-9 A/cm<sup>2</sup> were detected in iron. According to their calculations, the origin of pitting could not be attributed to changes in pH, in potential, or in ionic concentration, since such changes would be meaningless in the initial stages of pitting. However, the pitting model developed by Vetter and Strehblow cannot be taken as a realistic model; according to their model the pH inside the pit increases during pit growth, while in practice the pH was found to decrease (5-10).

Pickering and Frankenthal (17) developed a much simpler pit model, and they analyzed the changes in

\* Electrochemical Society Active Member.

<sup>1</sup> On leave from the Comision Nacional de Energia Atomica, Departamento de Metalurgia, Buenos Aires, Argentina.

Key words: pitting of metals, pitting potential, transport processes, pitting inhibitors.

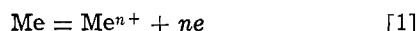
composition to be expected in the pit. Nevertheless, the model by Pickering and Frankenthal could not be applied in its original form to all pitting cases because, again, it would lead to pH increases inside the pit as the pit grew.

### Pit Model

In the present paper a pit model similar to that developed by Pickering and Frankenthal is used (Fig. 1). Their model was developed for a metal that would dissolve in an acid solution and consequently always resulted in a decrease in the pH inside the pit. To overcome this difficulty, the model used herein assumes that the pH of the bulk solution can take any value from acid to alkaline values.

The model by Pickering and Frankenthal takes into consideration the transport of ions both by diffusion and by electrical migration. In this way, complex formulae are obtained when the study of the hydrolysis of the metal ions, or modifications of the external pH are attempted. Since, as shown by Vetter and Strehblow (16), pitting initiation takes place with small changes in the electrolyte composition, it is reasonable to assume that the bulk solution acts as a supporting electrolyte for the metal ions and the hydrolysis products produced during pitting initiation. In this way the transport equations are considerably simplified, since only transport by diffusion remains important. The following are the main modifications introduced in the model used in the present paper:

(i) Instead of a single charge transfer reaction, a more general expression is used for the anodic reaction taking place inside the pit



The dissolution reaction is assumed to take place at the bottom of the pit, (Fig. 1) as in the model by Pickering and Frankenthal. No reaction takes place at the walls of the pit. In this way a unidirectional pit model is obtained, with a considerable simplification in the mathematical treatment.

(ii) Reaction [1] is assumed to occur in a sodium salt of an aggressive but noncomplexing anion. The pH of the bulk solution could have any value, and is given as a boundary condition.

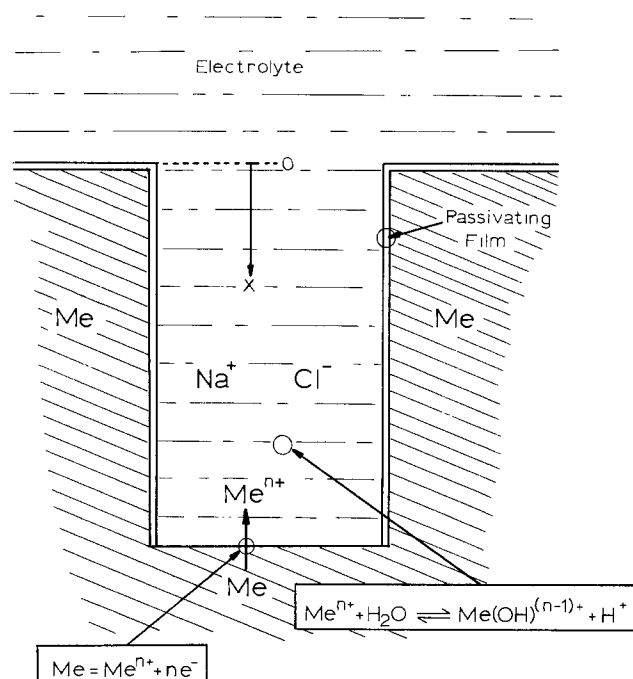
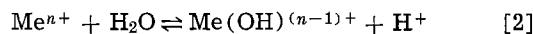


Fig. 1. Unidirectional pit model

(iii) It is assumed that reaction [1] is followed by a hydrolysis equilibrium of the type

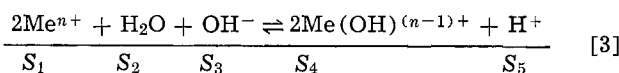


and that this equilibrium is very quickly reached (18).

Reaction [2] is a simplified description of the processes taking place inside a pit. Polynuclear complexes could be formed, or further degrees of hydrolysis could occur. Nevertheless, reaction [2] will give the minimum degree of acidification expected inside a pit. On the other hand, either no polynuclear complexes are reported for the metals used in the present work, or their formation rate is very slow (18, 19).

(iv) The last, and most important, modification introduced to the Pickering and Frankenthal model is the assumption that the aggressive anion salt acts as a supporting electrolyte for the ionic species formed in reactions [1] and [2].<sup>2</sup>

Since it is assumed that the bulk solution could have any pH value, reaction [2] has to be rewritten to account for the contribution of the OH<sup>-</sup> ions at pH values higher than 7



From Eq. [3] we find that inside the pit there are five species (S<sub>1</sub>-S<sub>5</sub>), the concentrations of which should be calculated. The detailed mathematical treatment for a system like this can be found in Vetter's work (20). The five unknown concentrations are calculated by resolution of the five following equations: the flow of the species containing Me atoms will be given by

$$D_1 \frac{dC_1}{dx} + D_4 \frac{dC_4}{dx} = \frac{i}{n \cdot F} \quad [4]$$

the flow of the species containing O atoms will be given by

$$D_2 \frac{dC_2}{dx} + D_3 \frac{dC_3}{dx} + D_4 \frac{dC_4}{dx} = 0 \quad [5]$$

and the flow of the species containing H atoms will be given by

$$2D_2 \frac{dC_2}{dx} + D_3 \frac{dC_3}{dx} + D_4 \frac{dC_4}{dx} + D_5 \frac{dC_5}{dx} = 0 \quad [6]$$

Finally, the two following equilibrium relations must be considered

$$*K_1 = \frac{C_4 \cdot C_5}{C_1} \quad [7]$$

which is the law of mass action applied to reaction [2] and

$$K_w = C_3 \cdot C_5 \quad [8]$$

which is the ionic product of water. In the above equations, D<sub>j</sub> is the diffusion coefficient in cm<sup>2</sup>/sec, C<sub>j</sub> is the concentration in mole/cm<sup>3</sup> of the species j, n is the charge of the metal ion as given in Eq. [1], F is the Faraday constant, \*K<sub>1</sub> is the equilibrium constant of reaction [2], i in A/cm<sup>2</sup> is the current density of reaction [1], and x is the pit depth in cm where x = 0 at the opening of the pit.

The assumed boundary conditions for x = 0 are C<sub>1</sub> = 0; C<sub>3</sub> = K<sub>w</sub> · 10<sup>-pH</sup> mole/liter; C<sub>4</sub> = 0; and C<sub>5</sub> = 10<sup>-pH</sup> mole/liter. As a first approximation all the diffusion coefficients, except those for H<sup>+</sup> and OH<sup>-</sup> ions, are taken as equal to 10<sup>-5</sup> cm<sup>2</sup>/sec; therefore D<sub>1</sub> = D<sub>2</sub> = D<sub>4</sub> = 10<sup>-5</sup> cm<sup>2</sup>/sec, D<sub>3</sub> = 5.3 × 10<sup>-5</sup> cm<sup>2</sup>/sec, and D<sub>5</sub> = 9.3 × 10<sup>-5</sup> cm<sup>2</sup>/sec. The equilibrium constants used were taken from the review by Sillen and

<sup>2</sup> This assumption is exact only when the supporting electrolyte is in great excess over the electroactive species. However, it has been shown [Ref. (20), p. 175] that even a minor addition of supporting electrolyte of the order of magnitude of the concentration of the electroactive species reduces to a large degree the influence of the electric field.

Table I. Hydrolysis constants and solubility constants (19)

Metal	Hydrolysis constant ( $*K_1$ )	Solubility constant ( $K_{s0}$ )
Cr <sup>3+</sup>	10 <sup>-4</sup> (M · 1 <sup>-1</sup> )	10 <sup>-30</sup> (M <sup>4</sup> · 1 <sup>-4</sup> )
Fe <sup>2+</sup>	10 <sup>-7</sup> (M · 1 <sup>-1</sup> )	10 <sup>-15.1</sup> (M <sup>3</sup> · 1 <sup>-3</sup> )
Co <sup>2+</sup>	10 <sup>-10</sup> (M · 1 <sup>-1</sup> )	10 <sup>-15</sup> (M <sup>3</sup> · 1 <sup>-3</sup> )
Ni <sup>2+</sup>	10 <sup>-10</sup> (M · 1 <sup>-1</sup> )	10 <sup>-15</sup> (M <sup>3</sup> · 1 <sup>-3</sup> )
Zn <sup>2+</sup>	10 <sup>-9.15</sup> (M · 1 <sup>-1</sup> )	10 <sup>-16.6</sup> (M <sup>3</sup> · 1 <sup>-3</sup> )
Al <sup>3+</sup>	10 <sup>-8.02</sup> (M · 1 <sup>-1</sup> )	10 <sup>-38</sup> (M <sup>4</sup> · 1 <sup>-4</sup> )

Martell (19), and the values chosen for the calculations are reported in Table I.

By multiplying Eq. [5] by 2 and subtracting from Eq. [6], the terms for S<sub>2</sub> are eliminated

$$-D_3 \frac{dC_3}{dx} - D_4 \frac{dC_4}{dx} + D_5 \frac{dC_5}{dx} = 0 \quad [9]$$

Equation [8] is solved for C<sub>3</sub>, and this expression is substituted for C<sub>3</sub> in Eq. [9]. Equation [7] is solved for C<sub>1</sub>, and the resultant expression is substituted for C<sub>1</sub> in Eq. [4]. By integration, the following two equations are obtained

$$\frac{n \cdot F \cdot D_1}{*K_1} C_4 \cdot C_5 + n \cdot F \cdot D_4 \cdot C_4 = x \cdot i + k \quad [10]$$

$$D_5 \cdot C_5 - D_3 \cdot K_w \frac{1}{C_5} - D_4 \cdot C_4 = k' \quad [11]$$

Using the above-mentioned boundary conditions, constants  $k$  and  $k'$  are calculated. Equation [11] is solved for C<sub>4</sub>, and the resulting expression is substituted for C<sub>4</sub> in Eq. [10]. By giving values to C<sub>5</sub>, the values of the parameter  $x \cdot i$  are calculated. With the same values of C<sub>5</sub>, the values of C<sub>4</sub> are calculated in Eq. [11]. Then C<sub>1</sub> is calculated in Eq. [7] and C<sub>3</sub> in Eq. [8]. No calculations are made for C<sub>2</sub>.

### Ionic Concentration Diagrams

The above-mentioned calculations were made for the ionic concentration diagrams of the following systems: Zn/Zn<sup>2+</sup> (Fig. 2); Fe/Fe<sup>2+</sup> (Fig. 3); Ni/Ni<sup>2+</sup> (Fig. 4); Al/Al<sup>3+</sup> (Fig. 5); and Cr/Cr<sup>3+</sup> (Fig. 6). The diagram in Fig. 4 applies also to Co/Co<sup>2+</sup>, since the same  $*K_1$  value was used for Ni and for Co (see Table I).

The pH values for the bulk solution were chosen so that the oxide film might be under thermodynamically stable conditions according to Pourbaix diagrams (21). The pH values used were pH 7 for aluminum and chromium, pH 9 for zinc, and pH 10 for iron, nickel, and cobalt.

The straight line  $C_{Me}^-$  in the diagrams indicates the total of the concentrations of all the species containing Me atoms. The line is broken for a concentration of 10 mole/liter to indicate that saturation of the Me salt should be reached. Actually, the present treatment is valid only for diluted solutions, and deviations from the calculated diagrams should be expected for such high concentrations.

The ionic concentration diagrams give the concentrations of Me<sup>n+</sup>, Me(OH)<sup>(n-1)+</sup>, and H<sup>+</sup> ions as functions of  $x \cdot i$ . If the current density inside the pit is known, the diagram will show the ionic concentrations along the pit. On the other hand, at a certain given pit depth the diagram will show the current density required to get a certain change in the ionic concentration. For example, let us consider the case of iron in 1.0M NaCl solution at pH 10 (Fig. 3). Let us assume that the iron sample has two pits different in size, one of them 10<sup>-6</sup> cm deep and the other 10<sup>-4</sup> cm deep. If the current density inside the pits is 1 A/cm<sup>2</sup>, the  $x \cdot i$  values will be 10<sup>-6</sup> and 10<sup>-4</sup> A/cm, respectively. From Fig. 3 it is concluded that the composition at the bottom of the shallower pit will be 10<sup>-5</sup>M Fe<sup>2+</sup>, 5.0 × 10<sup>-4</sup>M Fe(OH)<sup>+</sup>, and pH 8.5. On the other hand, the

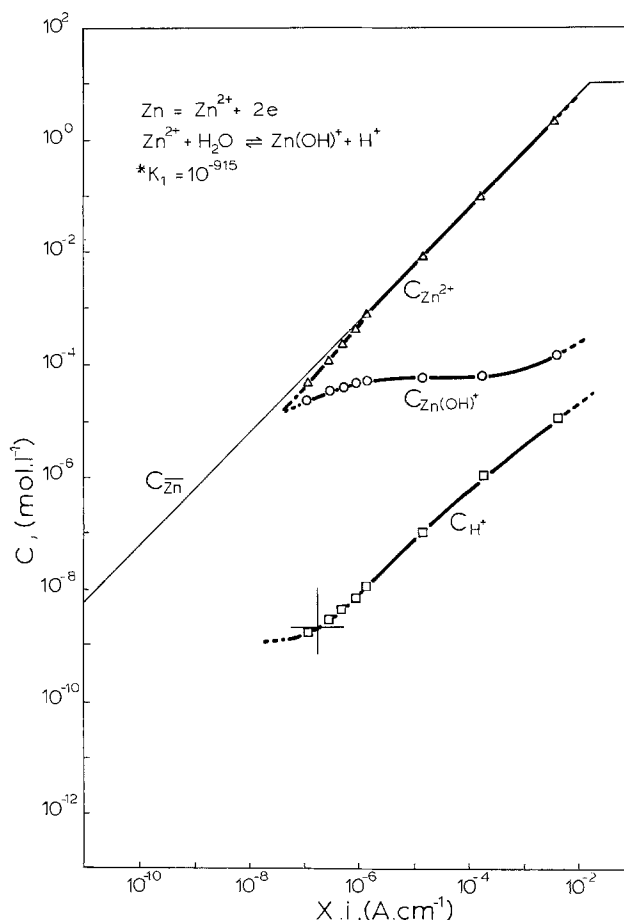


Fig. 2. Concentrations of Zn<sup>2+</sup>, Zn(OH)<sup>+</sup>, and H<sup>+</sup> as a function of the product of the depth  $x$  and the current density  $i$  is a unidirectional pit.

composition at the bottom of the deeper pit is going to be: 5.0 × 10<sup>-2</sup>M Fe<sup>2+</sup>, 5.6 × 10<sup>-4</sup>M Fe(OH)<sup>+</sup>, and pH 5.1. The diagram predicts that the larger changes in composition and in pH will be found at the bottom of the deeper pit.

We can also compare two different specimens, with pits of equal size, but with different current densities inside the pits. For example, if the pits are 10<sup>-3</sup> cm deep in both specimens, but the current density inside the pits is 10<sup>-1</sup> A/cm<sup>2</sup> in one of the samples and 10<sup>-4</sup> A/cm<sup>2</sup> in the other, the composition at the bottom of the pits is going to be 5.0 × 10<sup>-2</sup>M Fe<sup>2+</sup>, 5.6 × 10<sup>-5</sup>M Fe(OH)<sup>+</sup>, and pH 5.1 in the first specimen ( $x \cdot i = 10^{-4}$  A/cm), and 5.0 × 10<sup>-8</sup>M Fe<sup>2+</sup>, 5.0 × 10<sup>-5</sup>M Fe(OH)<sup>+</sup>, and pH 9.95 in the second ( $x \cdot i = 10^{-7}$  A/cm). While important changes in composition should occur with current densities of 1 A/cm<sup>2</sup>, virtually no changes should be expected for a current density of 10<sup>-4</sup> A/cm<sup>2</sup>.

No assumptions are made as to the way in which the current density could be obtained. In practice, it will mean that the electrode potential is properly changed. In most cases of acid solutions, such as those inside a pit, a logarithmic relation between current density and electrode potential should be expected.

Figures 2-6 show that, in spite of what Vetter and Strehblow have indicated, the H<sup>+</sup> ion concentration inside the pit undergoes important changes when the pit size or the current density inside the pit is changed. It is also shown that, as found in practice, the pH inside the pit is lower than that of the bulk solution. From the data in Fig. 3, the pH along a crevice or a crack in iron can be estimated. It was found (Fig. 7) that the pH predicted by the present model is somewhere between 3 and 4, for an external pH of 10. This

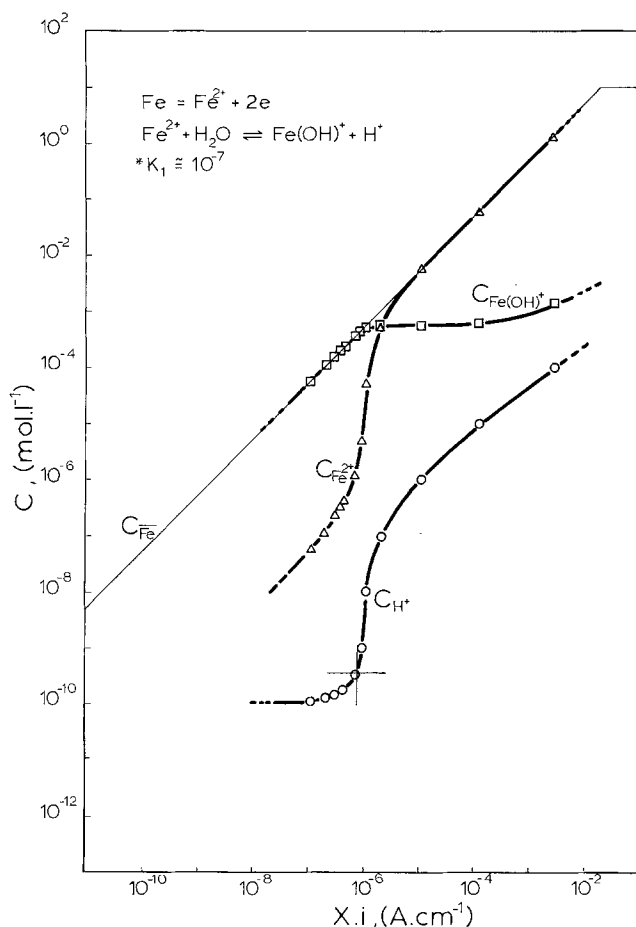


Fig. 3. Concentrations of  $Fe^{2+}$ ,  $Fe(OH)^+$ , and  $H^+$  as a function of the product of the depth  $x$  and the current density  $i$  in a uni-directional pit.

prediction is in good agreement with the experimental observations reported by Smith, Peterson, and Brown (6).

#### Critical $H^+$ Ion Concentration

To be able to use the present ionic concentration diagrams in the study of pitting it is necessary to find the minimum degree of acidification necessary for sustained pit activity.

As a first approximation, the criterion used by Pourbaix for the potential *vs.* pH diagrams (21) was applied in the present paper. Pourbaix separates the passivity zones from the corrosion zones as follows. The solubility product of the passivating oxide film being known, the pH value at which such oxide film will be in equilibrium with a solution containing traces of metal ions is calculated. The concentration of the metal ions is arbitrarily taken as equal to  $10^{-6}$  mole/liter. Such pH values are calculated herein by using the  $K_{s0}$  values reported in Table I. The calculated pH values are indicated in Fig. 2-6 by means of a cross (+) on the  $H^+$  ion concentration line. The pH values calculated are pH 9.5 for iron, cobalt, and nickel; pH 8.7 for zinc; pH 6.0 for chromium; and pH 5.0 for aluminum. All these values are in reasonably good agreement with those reported by Pourbaix (21), with the exception of chromium which, according to Pourbaix, should be somewhere between 3.5 and 4.8.

Due to the scattering of the  $K_{s0}$  reported values (19), and to the arbitrarily choosing  $10^{-6}$  mole/liter as the metal ion concentration, the calculated critical pH values have an error of at least plus or minus one unit pH. This criterion of choosing the critical pH values is clearly a rough approximation and experimental information is necessary. In the case of zinc,

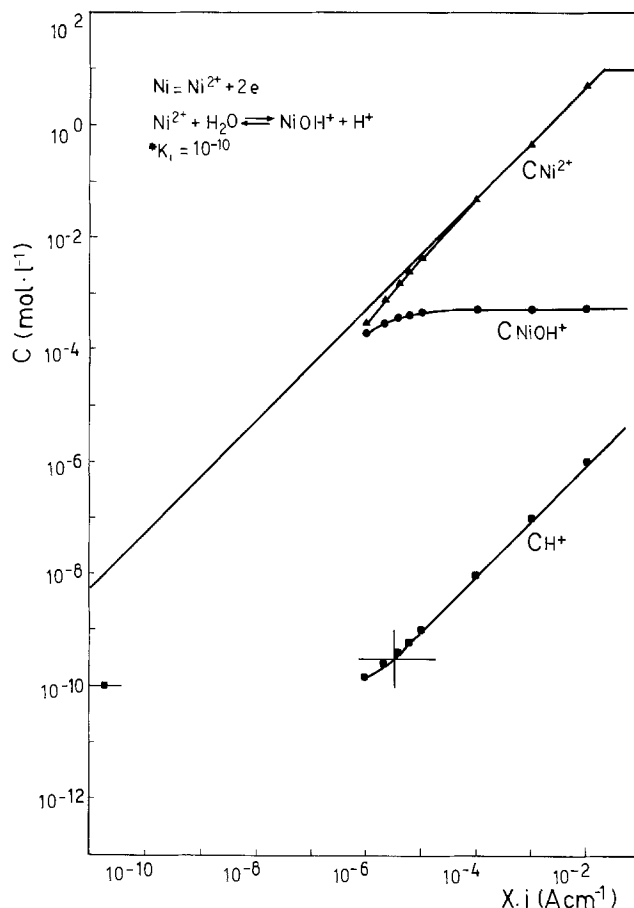


Fig. 4. Concentrations of  $Ni^{2+}$ ,  $Ni(OH)^+$ , and  $H^+$  as a function of the product of the depth  $x$  and the current density  $i$  in a uni-directional pit.

the pH value calculated, 8.7, is in good correspondence with the experimental results reported by Davies and Lotlikar (22). These authors found that zinc, in galvanostatic measurements, was passivated in solutions of pH 9.2, 10.0, and 11.0, and did not get passive in solutions at pH 8.2.

For iron the estimated pH value was 9.5. Vetter and Strehblow (23) reported passivity to pitting transitions for iron at pH values as low as 8.0. On the other hand, Alvarez and Galvele (24) found that the pitting potential of iron is pH independent for pH values lower than 10, and pH dependent at values higher than 10. It was then concluded that the critical pH for iron should be around 10.

No experimental information is available for other metals or alloys. Nevertheless, the concept of a critical pH for depassivation was applied to stainless steels by Defranoux and Tricot (25). These authors found that the presence of chloride ions produced an increase in the critical pH for depassivation of stainless steels.

#### Current Density inside the Pits

To be able to use the ionic concentration diagrams it is also necessary to know the current density inside the pits. For aluminum in NaCl solutions, Kaesche (14) reported that the minimum current density inside the pits was recorded at the pitting potential and had a value of 0.3 A/cm<sup>2</sup>. For aluminum in 4M NaCl solution, the current density inside the pits increased with the electrode potential, following what seemed to be a logarithmic law with a slope of  $b = 0.150V$ . At a potential 0.100V over the pitting potential the current density inside the pits was close to 1.1 A/cm<sup>2</sup>.

Szklarska-Smialowska and Janik-Czachor (26) measured the current densities within pits for Fe-16Cr alloy in 0.7N NaCl + 0.7N Na<sub>2</sub>SO<sub>4</sub> solution. They

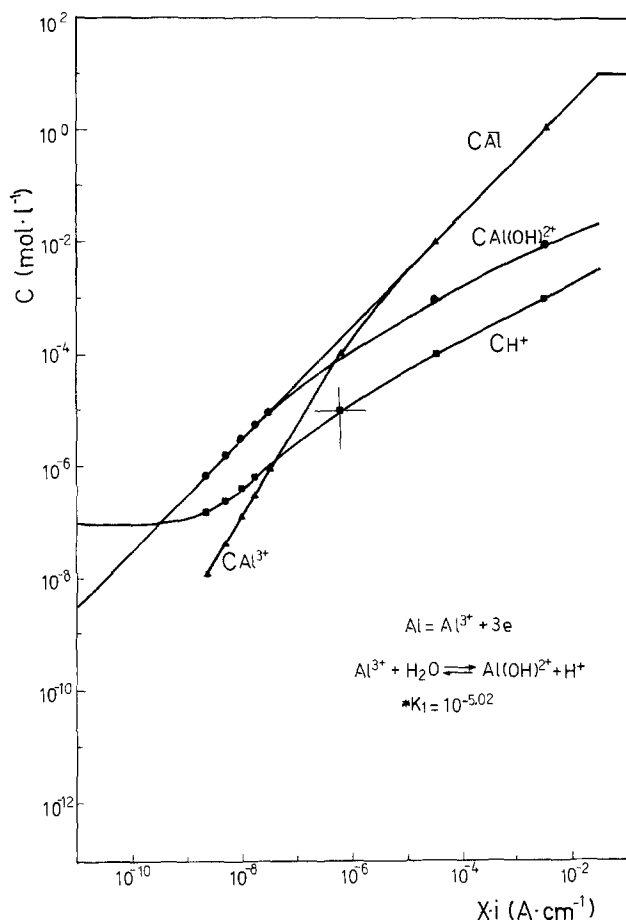


Fig. 5. Concentrations of  $\text{Al}^{3+}$ ,  $\text{Al(OH)}^{2+}$ , and  $\text{H}^+$  as a function of the product of the depth  $x$  and the current density  $i$  in a unidirectional pit.

found that the current density inside the pits was a function of potential, and according to the interpretation made by Sato *et al.* (27) it would follow a logarithmic law with a slope of  $b = 0.220\text{V}$ . For the Fe-16Cr alloy Szklarska-Smialowska and Janik-Czachor reported a pit initiation potential of about 0.50V (SCE) and a pit passivation potential of  $-0.05\text{V}$  (SCE). From Sato's paper it is inferred that the current density at the pit initiation potential was about  $8.0\text{ A/cm}^2$ , while at the pit passivation potential it dropped to  $0.1\text{ A/cm}^2$ .

Sato *et al.* (27) reported that in austenitic stainless steels, for potentials higher than  $0.60\text{V}$  (SCE) the current density inside the pits became potential independent, reaching a value of  $8\text{ A/cm}^2$ .

Schwenk (28), working with 18/10 chromium-nickel austenitic stainless steels, reported a current density inside the pits, at the pitting potential, of the order of  $0.5\text{ A/cm}^2$ . He also found that the reaction inside the pit followed a Tafel law, with a slope of  $b = 0.087\text{V}$ .

For pure iron, Vetter and Strehblow (15) reported pit initiation current densities ranging from  $0.9$  up to  $2.0\text{ A/cm}^2$ . For nickel pits of  $1\mu$  diameter, Vetter (29) reported current densities as high as  $50\text{--}70\text{ A/cm}^2$ .

From the above-mentioned results, it can be safely assumed that the current density inside a pit, at the initiation stage, is of the order of  $1\text{ A/cm}^2$ .

#### Pit Initiation Conditions

Figures 2-6 show that for most of the metals studied the critical pH is reached with  $x \cdot i$  values lower than  $10^{-6}\text{ A/cm}$ . Since at pit initiation conditions the current density inside the pit is at least  $1\text{ A/cm}^2$ , it is concluded that the necessary acidification can be obtained

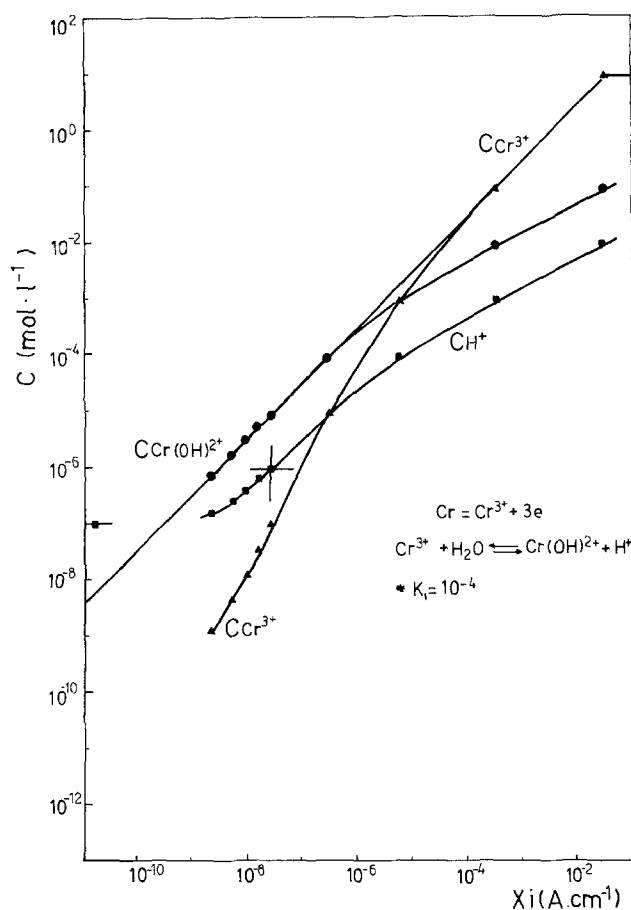


Fig. 6. Concentrations of  $\text{Cr}^{3+}$ ,  $\text{Cr(OH)}^{2+}$ , and  $\text{H}^+$  as a function of the product of the depth  $x$  and the current density  $i$  in a unidirectional pit.

in pits as small as  $10^{-6}\text{ cm}$ . This means that a crack in the passivating oxide film would give a diffusion path long enough to reach the critical pH. If such cracks are present, it would only be necessary to apply a potential high enough to reach the above-mentioned current density.

As for the existence of such cracks in the passive oxide film, there is abundant literature in favor of it. Current oscillations below the pitting potential were reported for aluminum (30), for zinc (31), and for stainless steels (32) showing the presence of a film rupture-reformation process. Vetter and Strehblow (16) reported that a change in the electrode potential, just before the injection of chloride ions, produced a noticeable increase in the pit density in iron. This was interpreted as a production of defects in the oxide film as a result of the potential shift. Sato (33) calculated the tensions induced in the oxide film by electrostriction, and concluded that they were high enough to produce mechanical breakdown of the oxide film. Fromhold (34) also found that the transport of ions through the passive film would produce stresses large enough to cause mechanical breakdown of the oxide film.

It can be concluded that film breakdown is constantly occurring on a passive metal. Nevertheless, the exposure of bare metal does not necessarily lead to localized corrosion. Straining metal experiments (2, 3, 30) have shown that the exposure to bare metal does not lead to pitting, unless the electrode potential is equal to, or higher than, the pitting potential.

Once the crack in the passive film is produced, if the electrode potential is high enough, a net anodic current density will circulate through the fissure. From the diagrams in Fig. 2-6 it should be possible to predict at which current density the critical acidification can be reached, or if the metal will repassivate.

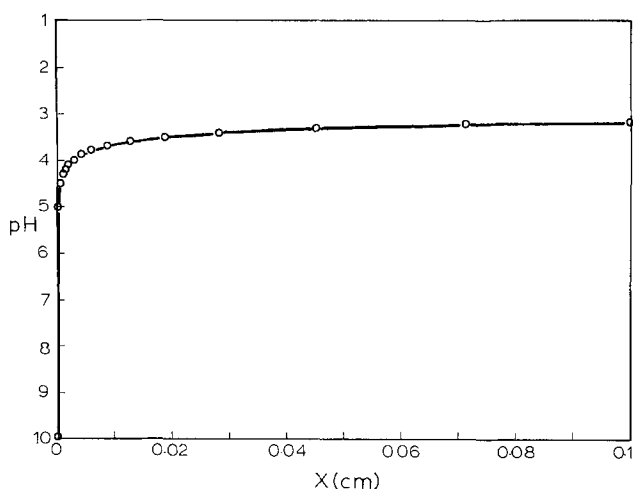


Fig. 7. Calculated pH profile for iron along a pit or crevice. External pH = 10, current density = 1 A/cm<sup>2</sup>, \*K<sub>1</sub> = 10<sup>-7</sup> mole/liter.

Figures 2-6 show that the critical acidification varies from metal to metal. For aluminum, for example, it is much higher than for iron or nickel. Nevertheless, in all cases the critical acidification is reached for very low  $x \cdot i$  values.

So far it has been assumed that the current density inside the pit is of the order of 1 A/cm<sup>2</sup>. For some metals, as is probably the case with chromium, it might happen that such high current densities could not be reached. Then the metal would not be susceptible to pitting. Nevertheless, the critical  $x \cdot i$  value can be reached even with small current densities, provided that a sufficiently long diffusion path is present. That would be the case in a crevice. In this way, a metal could be resistant to pitting, but susceptible to crevice corrosion. From the electrochemical point of view both processes would be equal, the only difference being the length of the diffusion path.

#### Effect of the External pH on the Pitting Potential

A large increase in the pH of the bulk solution inhibits the pitting process. Leckie and Uhlig (35) reported that the pitting potential of stainless steel was independent of the pH in the range of 1-7, but for pH values higher than 7 the OH<sup>-</sup> ion acted as pit inhibitor. In the same way, Venu *et al.* (36) and Rajagopalan *et al.* (37) reported that the presence of NaOH inhibited the passivity breakdown of steels in NaCl solutions.

By appropriate modification of the boundary conditions, it is possible to calculate the effect of the external pH on the concentration profiles in the ionic concentration diagrams. Calculations were performed for iron, assuming external pH values ranging from pH 7 to 12 (Fig. 8). The external pH was found to modify the shape of the H<sup>+</sup> ion concentration curve inside the pit. The critical pH for iron is somewhere between 9 and 10. If the pH of the bulk solution is 10, the critical pH value would be reached with  $x \cdot i$  values of about 10<sup>-6</sup> A/cm. By increasing the external pH to 11,  $x \cdot i$  values of 10<sup>-5</sup> A/cm are required. For pH 12 the critical acidification is reached only with  $x \cdot i$  values of 10<sup>-4</sup> A/cm. The experimental conditions being equal, this means that the current density has to increase one order of magnitude whenever the pH of the bulk solution is increased one unit. If the relation between potential and current density inside the pit follows a logarithmic law, then it should be expected that the pitting potential will follow a law of the type

$$E_p = A + b \cdot \log C_{OH^-} \quad [12]$$

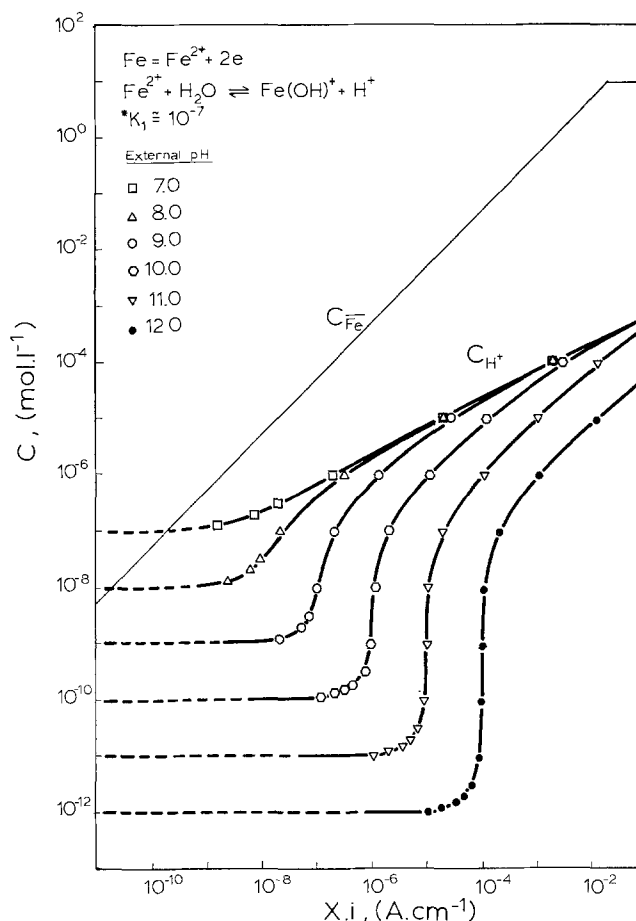


Fig. 8. Effect of the external pH on the concentration of H<sup>+</sup> as a function of the product of the depth  $x$  and the current density  $i$  in a unidirectional iron pit.

Through galvanostatic experiments with high purity iron in NaCl solutions, Alvarez and Galvele (24) found that the pitting potential of iron was independent of the pH between pH 7 and 10, but showed a logarithmic relation, as in Eq. [12], from pH 10 to pH 12; the slope of the curve being  $b = 0.020V$ .

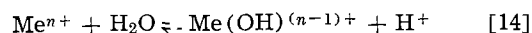
#### Presence of Anions of Weak Acid Salts

It is known that the presence of weak acid salts inhibits pitting by increasing the pitting potential. The pitting potential of aluminum is increased by the presence of soluble salts of acetate (38), benzoate (38), chromate (38,39) or tartrate (39). Pitting of zinc is inhibited by a borate buffer (40), and the pitting potential of iron in the presence of a borate buffer (23) is more than 100 mV higher than in its absence (41).

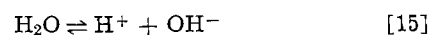
Anions of weak acids, because of their buffer properties, should modify the hydrogen ion concentration profiles in Fig. 2-6. Under these circumstances, the following equilibrium will take place inside the pit



where LH is the weak acid, and L<sup>-</sup> is the anion of the weak acid. The equilibrium constant of the reaction will be K<sub>a</sub>. The other equilibrium reactions are

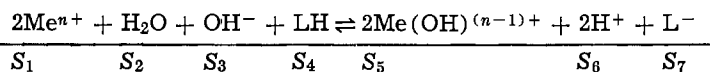


with the equilibrium constant \*K<sub>1</sub>, and



with the equilibrium constant K<sub>w</sub>.

The over-all reaction will be



[16]

The boundary conditions are chosen as above, making allowance for the fact that the concentration of protons in the bulk solution will be related to the concentration of the weak acid (LH) and that of its anion ( $\text{L}^-$ ) through Eq. [13].

Figure 9 shows the ionic concentration diagram for zinc in the presence of  $10^{-2}\text{M}$  borax plus  $1.0\text{M}$  NaCl solution. By comparison with Fig. 2, the presence of the borate salt is found to shift the hydrogen ion concentration line to higher  $x \cdot i$  values. This means that, under otherwise equal conditions, in the presence of borax higher current densities are required to reach the critical acidification. Figure 10 shows the degree of shifting of the hydrogen ion concentration line for various borax concentrations. For borax concentrations lower than  $10^{-4}$ , little effect should be expected from the weak acid salt. For higher borax concentrations an increase of one order of magnitude in the concentration of borax results in an increase of about one order of magnitude in the  $x \cdot i$  values. If the relation between potential and current density inside the pit follows a logarithmic law, it follows that the pitting potential of zinc should be related to the borax concentration by an equation of the type

$$E_p = A' + b' \cdot \log C_b \quad [17]$$

$C_b$  being the concentration of the buffer salt. The value of  $b'$  should be equal to the Tafel slope of the metal in a pitlike solution.

The results in Fig. 9 are in good agreement with the measurements of pitting potentials for zinc reported by Augustynski *et al.* (40). These authors found a

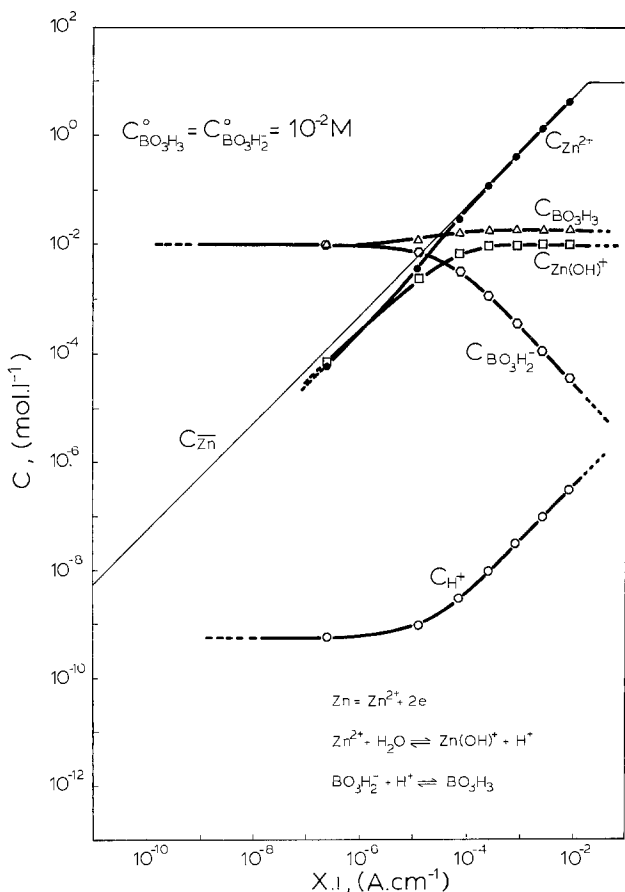


Fig. 9. Effect of  $10^{-2}\text{M}$  borax on the concentrations of  $\text{Zn}^{2+}$ ,  $\text{Zn}(\text{OH})^+$ , and  $\text{H}^+$  as a function of the product of the depth  $x$  and the current density  $i$  in a unidirectional zinc pit.

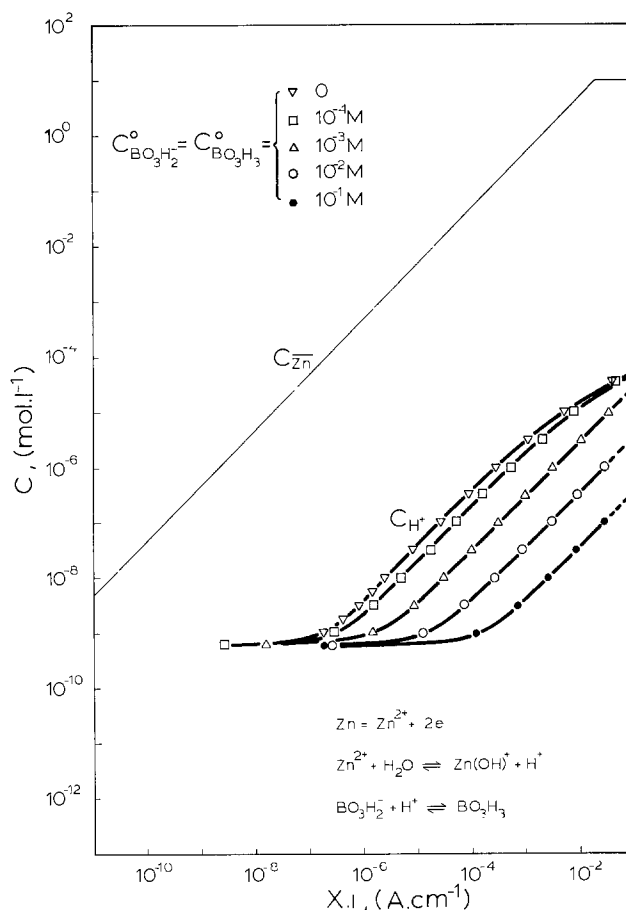


Fig. 10. Effect of the borax concentration on the  $\text{H}^+$  concentration as a function of the product of the depth  $x$  and the current density  $i$  in a unidirectional zinc pit.

logarithmic relation between the pitting potential and the buffer concentration for zinc in NaCl and in  $\text{NaClO}_4$  solutions. When the buffer concentration is higher than that of the aggressive anion, the pitting potentials measured by Augustynski *et al.* are higher than those predicted by Eq. [17]. The reason for this is that under such circumstances the aggressive anion is not acting as a supporting electrolyte, and the concentration buildup of the buffer anion inside the pit must be accounted for.

Diagrams similar to those in Fig. 10 were found for iron in the presence of borax. Vetter and Strehblow (23) reported a pitting potential of  $-0.17\text{V}$  (NHE) for iron in a  $1.0\text{M}$  NaCl solution containing  $0.029\text{M}$   $\text{KH}_2\text{BO}_3$  +  $0.021\text{M}$   $\text{H}_3\text{BO}_3$ . In the absence of buffers, Semino and Galvele (41) measured pitting potentials from  $-0.32$  to  $-0.34\text{V}$  (NHE). A diagram calculated for the solution used by Vetter and Strehblow shows that in their solution the  $x \cdot i$  values were about two orders of magnitude higher than in that used by Semino and Galvele. The Tafel slope for iron inside the pit should be somewhere between  $0.080$  and  $0.114\text{V}$  (42). Equation [17] predicts a difference of  $0.160$ – $0.230\text{V}$  in the pitting potential values, which fits very well with the difference of  $0.150$ – $0.170\text{V}$  found between the experimental results.

From Eq. [13] one would expect that salts from acids of different strength should have different effects on the ionic concentration diagrams. Figure 11 shows the effect of  $0.1\text{M}$  weak acid salt on the proton concentration line inside the pit for aluminum. The calculations were made for four different acid strengths, going from

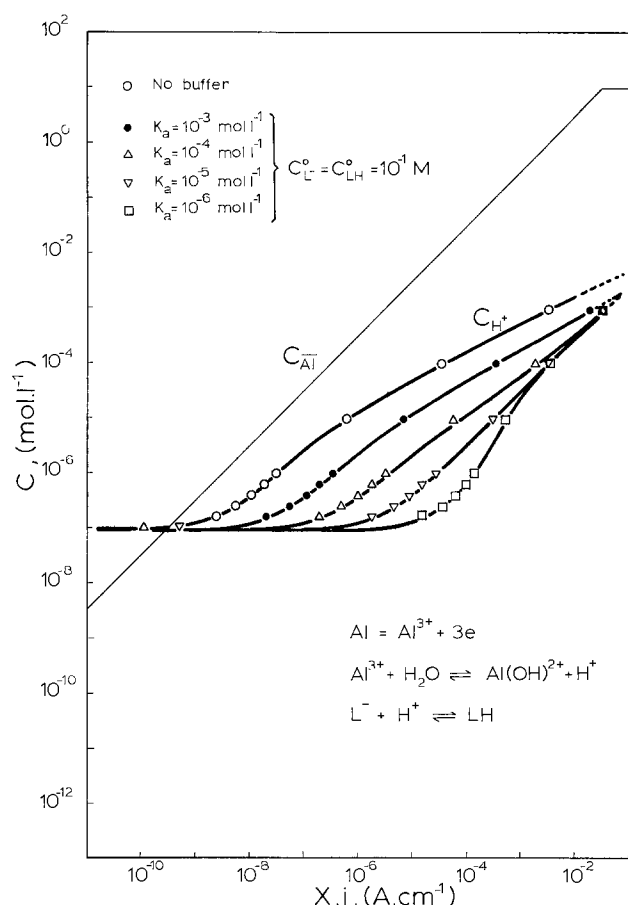


Fig. 11. Effect of the  $K_a$  of the buffer on the  $H^+$  concentration as a function of the product of the depth  $x$  and the current density  $i$  in a unidirectional aluminum pit.

$K_a = 10^{-6}$  up to  $K_a = 10^{-3}$  mole/liter. The lower the value of  $K_a$ , the higher the  $x \cdot i$  values. From Fig. 11 it is concluded that the salt with the lowest  $K_a$  should be the most effective pitting inhibitor. Table II shows  $K_a$  values for various weak acids. From Table II and from Fig. 11 it can be concluded that from among chromate, acetate, and benzoate, chromate should be the most effective and benzoate the least, in correspondence with the experimental results reported by Böhni and Uhlig (38). Tartrates should be the least effective inhibitors, as reported by De Micheli and Galvele (39). According to Table II silicates and borates should have good inhibitor properties.

The present model does not take into consideration the possibility of formation of insoluble compounds between the metal ions and the weak acid anions. Such precipitates would occlude the pits, thus enhancing the inhibition capacity of the weak acid salt.

### Aggressive Anion Concentration

If the concentration of the aggressive anion salt is changed over a wide range of values, the assumption that such salt is acting as a supporting electrolyte is not valid. In this case the electric field inside the pit cannot be ignored, and Eq. [4-6] are not valid. The following equations should be used [Ref. (20), p. 171]

Table II. Ionization constants of weak acids

Aqueous solution	pK <sub>a</sub> at 25°C	Reference
Acetic acid	4.76	43
Benzoic acid	4.20	43
Boric acid	9.23	43
Chromic acid	6.50	19
$H_2CrO_4 / CrO_4^{2-}$		
Silicate $K_1$	11.81	19
Tartaric acid $K_1$	3.03	43

$$\frac{i \cdot \nu_j}{n \cdot F} = D_j \left[ \frac{dC_j}{dx} + z_j \cdot C_j \cdot \frac{F}{R \cdot T} \cdot \frac{d\phi}{dx} \right] \quad [18]$$

for the reacting species, where  $\nu_j$  is the stoichiometric factor of the species  $S_j$ , and  $d\phi/dx$  is the electric field. For the nonreacting species the following equation is used

$$C_j = C_0 \cdot e^{-(z_j \cdot F/RT) \cdot \phi} \quad [19]$$

A further equation used is the condition of electro-neutrality

$$\sum z_j \cdot C_j = 0 \quad [20]$$

The resolution of the above equations for a system where hydrolysis equilibrium is included is quite complex. Nevertheless, the resolution for a simpler system gives very useful information.

Let us assume that the metal is dissolving according to reaction [1]. Neglecting for a while the hydrolysis reaction of the metal ions, we will assume that the only ionic species present are:  $Me^{n+}$ ;  $Na^+$ ; and  $Cl^-$ . Under these conditions the following set of equations has to be solved

$$\frac{i}{n \cdot F} = D_{Me} \left[ \frac{dC_{Me}}{dx} + n \cdot C_{Me} \cdot \frac{F}{R \cdot T} \cdot \frac{d\phi}{dx} \right] \quad [21]$$

for  $Me^{n+}$  ions

$$C_{Na} = C_0 \cdot e^{+\psi} \quad [22]$$

for  $Na^+$  ions, where  $\psi = F \cdot \phi / R \cdot T$

$$C_{Cl} = C_0 \cdot e^{-\psi} \quad [23]$$

for  $Cl^-$  ions, and the electroneutrality condition

$$n \cdot C_{Me} + C_{Na} - C_{Cl} = 0 \quad [24]$$

$C_{Na}$  and  $C_{Cl}$  in Eq. [24] are substituted for Eq. [22] and [23]

$$n \cdot C_{Me} = C_0 \cdot e^{+\psi} - C_0 \cdot e^{-\psi} \quad [25]$$

Equation [25] is substituted for  $n \cdot C_{Me}$  in Eq. [21]. By differentiating Eq. [25],  $dC_{Me}/dx$  is obtained, and it is substituted for in Eq. [21]. By integration of Eq. [22], and taking into account the following boundary conditions for  $x = 0$  ( $C_{Me} = 0$ ;  $C_{Na} = C_0$ ;  $C_{Cl} = C_0$ ; and  $\phi = 0$ ), Eq. [26] is obtained

$$i \cdot x = C_0 \cdot D_{Me} \cdot F \cdot [(n+1) \cdot e^{+\psi} + (n-1) \cdot e^{-\psi} - 2 \cdot n] \quad [26]$$

For  $n = 1$  the equation developed by Pickering and Frankenthal is obtained (17). By solving Eq. [26] for  $n = 3$ ,  $D_{Me} = 10^{-5}$  cm<sup>2</sup>/sec, and  $C_0 = 1.0M$ , the diagram in Fig. 12 is obtained. Up to  $x \cdot i$  values of  $10^{-3}$  A/cm, the line for  $C_{Me}$  in Fig. 12 is the same as  $C_{Al}$  in Fig. 5. For  $x \cdot i$  values higher than  $10^{-3}$  A/cm a small deviation is found. This indicates that the assumption of a supporting electrolyte, made while drawing Fig. 5 was valid, since the correction for  $\phi$  at low  $x \cdot i$  values is negligible.

According to Fig. 12, a measurable electrical potential,  $\phi$ , appears only for high  $x \cdot i$  values. For 1.0M NaCl solution at  $x \cdot i = 10^{-2}$  A/cm, the electrical potential could get up to some 0.035V. For lower  $C_0$  values higher electrical potentials are found (Fig. 13). In a  $10^{-3}M$  NaCl solution at  $x \cdot i = 10^{-2}$  A/cm, the electrical potential increases up to 0.200V.

If the value of  $x \cdot i$  is known, Fig. 13 can be used to evaluate the electrical potential,  $\phi$ , under the experimental conditions of pitting potential measurement. There is not any precise information available, and only a rough estimation can be made. From the information in the literature, as mentioned above, we can assume that the current density inside a pit is of the order of 1 A/cm<sup>2</sup>. As for the size of the pits, when measuring the pitting potential value they are usually visible under the optical microscope, so they must be at least  $10^{-2}$  cm big. Then, an estimate for  $x \cdot i$  value,



under stable pitting growth, would be  $x \cdot i \cong 10^{-2}$  A/cm. For such  $x \cdot i$  values Eq. [26] is reduced to

$$x \cdot i \cong (n + 1) \cdot C_o \cdot D_{Me} \cdot F \cdot e^{+\psi} \quad [27]$$

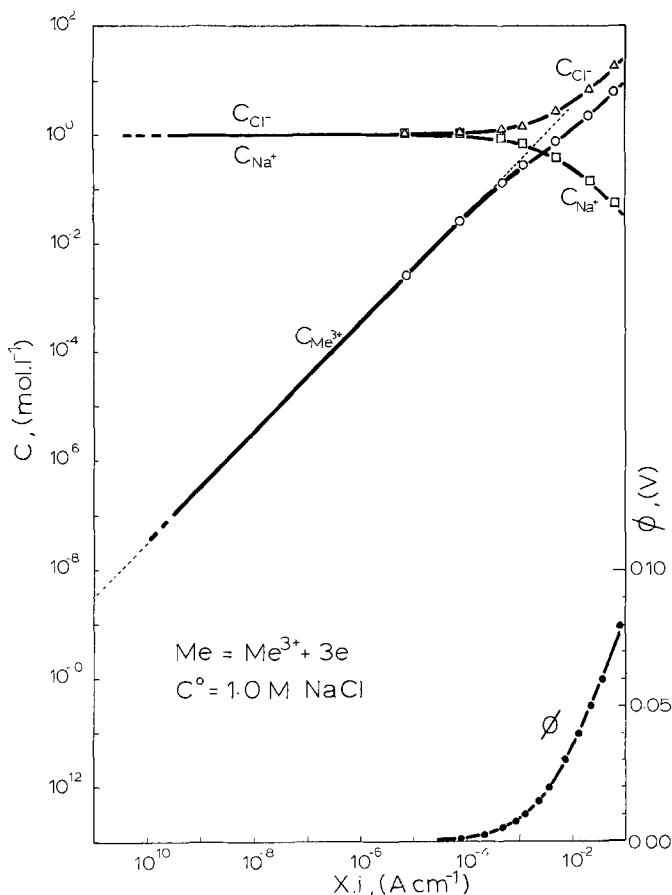


Fig. 12. Concentrations of  $Me^{3+}$ ,  $Na^+$  and  $Cl^-$ , and  $\phi$  as a function of the product of the depth  $x$  and the current density  $i$  in a unidirectional pit.

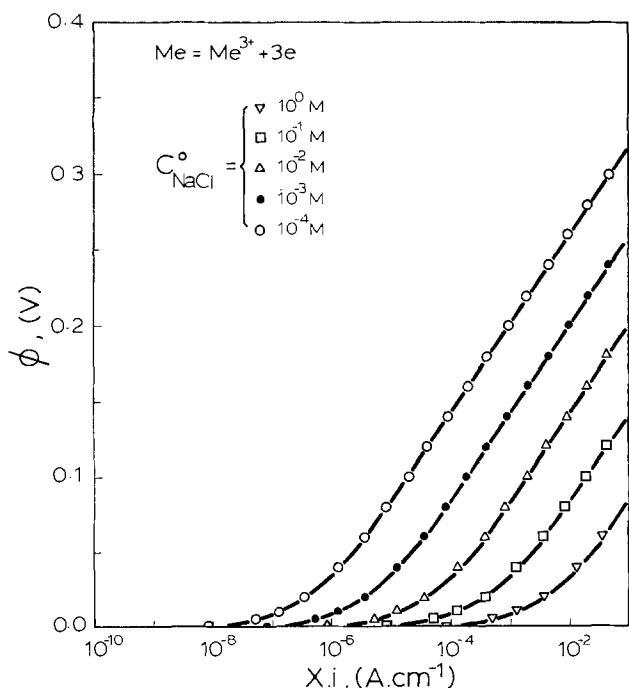


Fig. 13. Value of  $\phi$  for various aggressive anion concentrations as a function of the product of the depth  $x$  and the current density  $i$  in a unidirectional pit.

If the pitting potentials are measured at approximately constant  $x \cdot i$  values, then for two different NaCl concentrations we have

$$C_o^I \cdot e^{+\psi_I} = C_o^{II} \cdot e^{+\psi_{II}} \quad [28]$$

Replacing for the value of  $\psi$ , and taking logarithms

$$\ln C_o^I + \frac{F}{R \cdot T} \phi_I = \ln C_o^{II} + \frac{F}{R \cdot T} \phi_{II} \quad [29]$$

reordering and changing to decimal logarithms

$$\phi = \phi_o - \left[ \frac{R \cdot T}{F} \cdot \ln 10 \right] \cdot \log C_o \quad [30]$$

Equation [30] would give the change of electrical potential inside the pit when the pitting potential is measured as a function of the NaCl concentration. This electrical potential should be subtracted from the measured pitting potential value to get the real pitting potential.

Equation [30] has a negative slope, with a value  $b = 0.059V$  at  $25^\circ C$ . Table III shows experimentally measured slopes for pitting potentials vs. aggressive anion concentration. If, as assumed above, the  $x \cdot i$  values are close to  $10^{-2}$  A/cm, then the electrical potential inside the pits accounts for all the changes in the pitting potential found for iron (24), aluminum (44), aluminum-copper alloys (44), nickel (45), nickel-copper alloys (45), and zirconium (46), and perhaps for stainless steel (47). It also accounts for half the slope found for titanium (48). The agreement between Eq. [30] and the experimental results in Table III is very good in view of the fact that Eq. [30] is valid only for dilute solutions, and that the results in Table III have not been corrected for ohmic drops outside the pits.

Figure 12 also gives information about pit initiation conditions. According to some authors (12, 13) chloride ion buildup on the metal-solution interface would be the key factor for pit initiation. Figure 5 shows that the critical change in  $H^+$  ion concentration is obtained with  $x \cdot i$  values of the order of  $10^{-6}$  A/cm. On the other hand, Fig. 12 shows that to get any significant change in the chloride ion concentration  $x \cdot i$  values of the order of  $10^{-4}$ - $10^{-3}$  A/cm are required. This means that for pit initiation, where  $x$  values are of the order of  $10^{-6}$  cm, the critical proton concentration could be reached with current densities of 1 A/cm<sup>2</sup>, while any measurable change in the chloride concentration would require current densities as high as 100-1000 A/cm<sup>2</sup>. This consideration seems to exclude chloride ion buildup as a primary condition for pit initiation.

#### Mixed Electrolytes: NaCl + Na<sub>2</sub>SO<sub>4</sub> Solutions

Sulfate ions are known to inhibit pitting of stainless steels in chloride solutions (35). Equations [18-20] can also be used to study a mixed electrolyte such as NaCl + Na<sub>2</sub>SO<sub>4</sub> solutions. Equations [18] and [19] show that for anions of different charge, those with

Table III. Effect of the aggressive anion concentration on the pitting potential, experimental values for the slope of the curve  $E_p = A - B \log C_x$

Metal or alloy	Slope B, (V)	Medium	Reference
Aluminum	-0.073	NaCl solution	44
Al-4% Cu	-0.046	NaCl solution	44
Al <sub>2</sub> Cu	-0.055	NaCl solution	44
Cu-65.8Ni	-0.074	NaCl solution	45
Cu-82.6Ni	-0.078	NaCl solution	45
Iron	-0.059	NaCl solution	24
Fe-18Cr-8Ni	-0.088	NaCl solution	35
Fe-18Cr-8Ni	-0.044	Pitlike solution	47
Nickel	-0.071	NaCl solution	45
Titanium	-0.110	KBr/HBr solution	48
Zirconium	-0.058	NaCl solution	46

the highest charge will be preferentially accumulated at the metal-solution interface.

Calculations made for a 0.1M NaCl + 1.0M Na<sub>2</sub>SO<sub>4</sub> solution show that the main effect is a reduction of the electrical potential inside the pit due to the presence of the divalent SO<sub>4</sub><sup>=</sup> ion. In the absence of sulfate ions the electrical potential,  $\phi$ , for  $x \cdot i$  equal to 10<sup>-2</sup> A/cm is 0.085V. The addition of 1.0M Na<sub>2</sub>SO<sub>4</sub> to the solution reduces the electrical potential  $\phi$  to 0.010V.

More significant effects are found with lower ionic concentrations. For mixtures of 0.1M Na<sub>2</sub>SO<sub>4</sub> + 0.01M NaCl solution a remarkable buildup in sulfate ion concentration is found for  $x \cdot i$  values higher than 10<sup>-4</sup> A/cm (Fig. 14). Beginning with a SO<sub>4</sub><sup>=</sup>:Cl<sup>-</sup> concentration ratio of 10:1, ratios as high as 100:1 or higher are easily reached. As soon as a pit is nucleated, a sulfate ion concentration builds up inside the pit, and eventually the pit is repassivated. The pits will not be able to grow any further and sulfate anion would act as pitting inhibitor in NaCl solutions. Figure 14 also explains the potential oscillations, under galvanostatic conditions, found by Szklarska-Smialowska and Janik-Czachor (26) for iron-chromium alloys, and by Szklarska-Smialowska (49) for nickel in NaCl + Na<sub>2</sub>SO<sub>4</sub> solutions. As soon as the pits start to grow a buildup in sulfate ions takes place inside the pits, thus deactivating them. Later the diffusion of sulfate ions to the bulk solution reduces the content of sulfate ions inside the pit, and a continuous process of activation and deactivation of the pits is established.

#### Pitting Potential and Protection Potential

From potentiokinetic measurements, Pourbaix (50) reported two different potentials related to pitting: the pitting potential or rupture potential above which pitting starts, and the protection potential or the potential below which active pits will stop growing. According to Szklarska-Smialowska and Janik-Czachor (26) the real pitting potential is that which Pourbaix calls the protection potential. These authors found that this potential is equal to the galvanostatically measured pitting potential, and concluded that the higher pitting potential potentiokinetically found is the result of the measuring technique.

The present pitting model can be used to explain the existence of two potentials found in the potentiokinetic measurements. As mentioned above, the oxide film on the passive metal will suffer continuous breaks, thus exposing bare metal to the solution. The current density circulating in those fissures will be a function of the electrode potential. At each potential the cracks in the oxide will show a characteristic  $x \cdot i$  value given

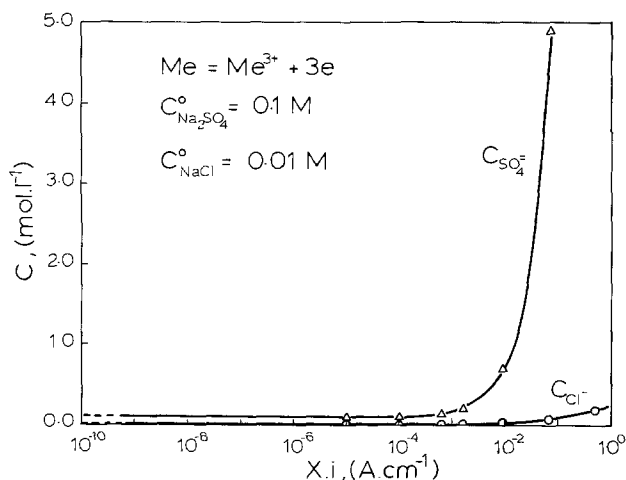


Fig. 14. Concentrations of SO<sub>4</sub><sup>=</sup> and Cl<sup>-</sup> as a function of the product of the depth  $x$  and the current density  $i$  in a unidirectional pit.

by the current density and by the length of the crack (Fig. 15a). As soon as the system reaches the minimum  $x \cdot i$  value for pit growth, which is  $x \cdot i = 1$  in Fig. 15, the pit will start to grow. If the potential remains constant, the current density will also be constant, but  $x$  will increase with time, as will  $x \cdot i$  ( $x \cdot i = 2$  in Fig. 15). If the potential is then lowered, the current density will drop, but the pit will continue to grow while the  $x \cdot i$  value is higher than 1. This means that pitting will grow at potentials lower than the initiation potential. Finally the pit will stop either because the  $x \cdot i$  value is lower than the minimum for pit growth, or because the electrode potential is lower than the corrosion potential inside the pit, and the acidification disappears as a result of hydrogen evolution.

Szklarska-Smialowska and Janik-Czachor's results can be used to find out whether the above-mentioned changes could take place during a potentiokinetic measurement. During potentiostatic measurements for Fe-16Cr in 0.7N Na<sub>2</sub>SO<sub>4</sub> + 0.7N NaCl solution, pitting could start at potentials as high as +0.50V (SCE). The reported current density inside the pits is about 8 A/cm<sup>2</sup>. Once started, the same pits will continue to grow at lower potentials, and they would stop at -0.05V (SCE). The current density inside the pits at this potential is 0.1 A/cm<sup>2</sup>. Assuming a value for minimum  $x \cdot i$  of 10<sup>-5</sup> A/cm, the pits will start to grow at 0.50V (SCE) in defects of about 1.3 × 10<sup>-6</sup> cm. When reducing the potential, the pits should have a minimum size of 10<sup>-4</sup> cm to be able to grow at the current density of 0.1 A/cm<sup>2</sup>. With a current density of 8 A/cm<sup>2</sup> a pit of 10<sup>-4</sup> cm takes less than 0.4 sec to grow. Since the critical  $x \cdot i$  values in Fig. 2-6 are lower than 10<sup>-5</sup> A/cm, a much shorter time will be required to obtain the two potentials reported by Pourbaix.

#### Conclusions

As shown in previous publications (2, 3) there is a potential below which no localized acidification can be maintained on the metal-solution interface. This potential is given by the corrosion potential of the metal in the acidified solution,  $E_c^*$ . The alloying elements affect the pitting potential mainly by modifying the corrosion potential inside the pit. When measuring the pitting potential, a positive polarization,  $\eta$ , is added to the corrosion potential,  $E_c^*$ , to maintain a net anodic

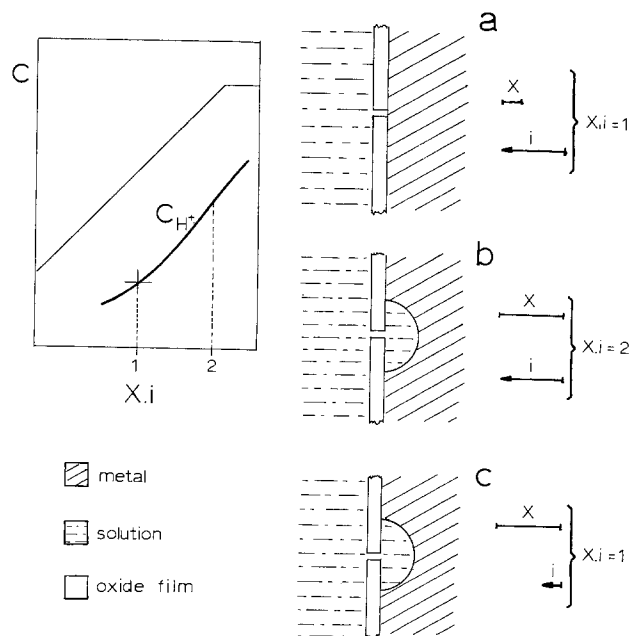


Fig. 15. Events leading to the measurement of pitting protection potentials different from pitting potentials in potentiokinetic experiments.

current density inside the pit, and secure the minimum  $x \cdot i$  value. From the present paper it is concluded that a further addition should be made,  $E_{inh}$ , when inhibitors like  $\text{OH}^-$  ions or buffer salts are present.

Since the current density inside the pit is high, another contribution due to the electrical potential,  $\phi$ , must be accounted for. In this way, the measured pitting potential is the total of the above mentioned factors

$$E_p = E_c^* + \eta + E_{inh} + \phi$$

All the observations reported so far in the literature on the pitting potential can be explained by transport phenomena. Processes like competitive adsorption, salt formation, film contamination, etc., even though present during the pitting process, do not play a major role in fixing the pitting potential.

### Acknowledgments

The author is grateful to Professor Roger W. Staehle for the encouragement and facilities received for the completion of the present work.

Parts of this work were sponsored by the Servicio Naval de Investigacion y Desarrollo of Argentina and by the Electric Power Research Institute through The Ohio State University Research Foundation.

Manuscript submitted Oct. 29, 1975; revised manuscript received Dec. 12, 1975.

Any discussion of this paper will appear in a Discussion Section to be published in the December 1976 JOURNAL. All discussions for the December 1976 Discussion Section should be submitted by Aug. 1, 1976.

Publication costs of this article were partially assisted by The Ohio State University.

### REFERENCES

- J. Kruger, Passivity and Its Breakdown on Iron and Iron Base Alloys, Japan-U.S.A. Seminar, Honolulu, Hawaii, March 10-12, 1975.
- S. B. de Wexler and J. R. Galvele, *This Journal*, **121**, 1272 (1974).
- G. Alvarez and J. R. Galvele, *Corrosion*, To be published.
- J. R. Galvele, Passivity and Its Breakdown on Iron and Iron Base Alloys, Japan-U.S.A. Seminar, Honolulu, Hawaii, March 10-12, 1975.
- G. Sandoz, C. T. Fujii, and B. F. Brown, *Corrosion Sci.*, **10**, 839 (1970).
- J. A. Smith, M. H. Peterson, and B. F. Brown, *Corrosion*, **26**, 539 (1970).
- J. A. Davis, in "Localized Corrosion," R. W. Staehle, B. F. Brown, J. Kruger, and A. Agrawal, Editors, p. 168, NACE, Houston (1974).
- B. E. Wilde and E. Williams, *Electrochim. Acta*, **16**, 1971 (1971).
- R. Piccinini, M. Marek, A. J. E. Pourbaix, and R. F. Hochman, in "Localized Corrosion," R. W. Staehle, B. F. Brown, J. Kruger, and A. Agrawal, Editors, p. 179, NACE, Houston (1974).
- T. Suzuki, M. Yamabe, and Y. Kitamura, *Corrosion*, **29**, 18 (1973).
- T. P. Hoar, "Electrode Processes," p. 299, Butterworths, London (1961).
- L. I. Freiman, Lap Le Min, and G. S. Raskin, *Zashchita Metallov*, **9**, 680 (1973).
- Y. Hisamatsu, Passivity and Its Breakdown on Iron and Iron Base Alloys, Japan-U.S.A. Seminar, Honolulu, Hawaii, March 10-12, 1975.
- H. Kaesche, *Z. Physik. Chem. (N.F.)*, **34**, 87 (1962).
- K. J. Vetter and H. H. Strehblow, *Ber. Bunsenges. Physik. Chem.*, **74**, 1024 (1970).
- K. J. Vetter and H. H. Strehblow, in "Localized Corrosion," R. W. Staehle, B. F. Brown, J. Kruger, and A. Agrawal, Editors, p. 240, NACE, Houston (1974).
- H. W. Pickering and R. P. Frankenthal, *This Journal*, **119**, 1297 (1972).
- J. P. Hunt, "Metal Ions in Aqueous Solutions," pp. 46 and 48, Benjamin Inc., New York (1963).
- L. G. Silen and A. E. Martell, "Stability Constants of Metal-Ion Complexes," Chemical Society Special Publication and Supplement 1, Social Publication 25, London (1964).
- K. J. Vetter, "Electrochemical Kinetics," p. 180, Academic Press, New York (1961).
- M. Pourbaix, "Atlas of Electrochemical Equilibria in Aqueous Solutions," Pergamon Press, Oxford (1966).
- D. E. Davies and M. M. Lotlikar, *Brit. Corros. J.*, **1**, 149 (1966).
- K. J. Vetter and H. H. Strehblow, *Ber. Bunsenges. Physik. Chem.*, **74**, 449 (1970).
- G. Alvarez and J. R. Galvele, To be published.
- J. M. Defranoux and R. Tricot, *Mem. Sci. Rev. Met.*, **69**, 323 (1972).
- Z. Szklarska-Smialowska and M. Janik-Czachor, *Brit. Corros. J.*, **4**, 138 (1969).
- N. Sato, T. Nakagawa, K. Kudo, and M. Sakashita, *Trans. Japan Inst. Metals*, **13**, 103 (1972).
- W. Schwenk, *Corrosion*, **20**, 129t (1964).
- K. J. Vetter, Private communication.
- J. R. Galvele, S. M. de De Micheli, I. L. Muller, S. B. de Wexler, and I. L. Alanis, in "Localized Corrosion," R. W. Staehle, B. F. Brown, J. Kruger, and A. Agrawal, Editors, p. 580, NACE, Houston (1974).
- M. M. Lotlikar and D. E. Davies, *Proc. Intern. Congr. Met. Corr.*, **3rd**, 167 (1966).
- Y. Hisamatsu, T. Yoshii, and Y. Matsumura, in "Localized Corrosion," R. W. Staehle, B. F. Brown, J. Kruger, and A. Agrawal, Editors, p. 427, NACE, Houston (1974).
- N. Sato, *Electrochim. Acta*, **19**, 1683 (1971).
- A. T. Fromhold, Passivity and Its Breakdown on Iron and Iron Base Alloys, Japan-U.S.A. Seminar, Honolulu, Hawaii, March 10-12, 1975.
- H. P. Leckie and H. H. Uhlig, *This Journal*, **113**, 1262 (1966).
- K. Venu, K. Balakrishnan, and K. S. Rajagopalan, *Corrosion Sci.*, **5**, 59 (1965).
- K. S. Rajagopalan and K. Venu, *ibid.*, **8**, 557 (1968).
- H. Böhni and H. H. Uhlig, *This Journal*, **116**, 906 (1969).
- S. M. de De Micheli and J. R. Galvele, *Metallurgia (ABM)*, **27**, 589 (1971).
- J. Augustynski, F. Dalard, and J. C. Sohm, *Corrosion Sci.*, **12**, 713 (1972).
- C. J. Semino and J. R. Galvele, *ibid.*, To be published.
- K. Schwabe and C. Voigt, *Electrochim. Acta*, **14**, 853 (1969).
- R. A. Robinson and R. H. Stokes, "Electrolyte Solutions," p. 517, Butterworths, London (1968).
- J. R. Galvele and S. M. de De Micheli, *Corrosion Sci.*, **10**, 795 (1970).
- T. Koizumi and H. H. Uhlig, *This Journal*, **121**, 1137 (1974).
- Y. M. Kolotyркиn, *Proc. Int. Congr. Met Corrosion*, **1st**, 10 (1961).
- T. Suzuki and Y. Kitamura, *Corrosion*, **28**, 1 (1972).
- T. R. Beck, in "Localized Corrosion," R. W. Staehle, B. F. Brown, J. Kruger, and A. Agrawal, Editors, p. 644, NACE, Houston (1974).
- Z. Szklarska-Smialowska, *Corrosion Sci.*, **11**, 209 (1971).
- M. Pourbaix, *Corrosion*, **26**, 431 (1970).

# Hydrogen Embrittlement of Electroless Copper Deposits

Y. Okinaka\* and S. Nakahara\*

Bell Laboratories, Murray Hill, New Jersey 07974

## ABSTRACT

Transmission and scanning electron microscopes were used to investigate the cause of brittleness of electroless copper deposits. Numerous voids were found in brittle deposits, whereas ductile deposits contained significantly fewer voids. These voids were 20–300Å in diameter and randomly distributed within a grain. Low angle grain boundaries contained larger voids. The ductility was found to improve considerably on prolonged standing even at room temperature. These results, in conjunction with chemical mechanistic considerations, have led to the conclusion that these voids contain hydrogen gas, and that the brittleness is due to the so-called "hydrogen embrittlement" phenomenon rather than the incorporation of  $\text{Cu}_2\text{O}$  or morphological effects postulated by some investigators.

Electroless copper deposits formed in the absence of a "ductility promoter" are known to be brittle. This poor ductility is attributed in the early literature to the incorporation of either hydrogen (1, 2) or  $\text{Cu}_2\text{O}$  in the deposit (3). However, no direct experimental evidence has yet been reported to show the presence of these inclusions. More recently, an attempt has been made to correlate physical properties with the deposit morphology (4), but no clear-cut relationship between ductility and morphology has been found. We carried out a transmission electron microscopic (TEM) study in search for the evidence of inclusions. Except for the surface oxide, we failed to find any  $\text{Cu}_2\text{O}$  within the deposit. On the other hand, it was discovered that a large number of voids ranging in diameter from 20 to 300Å are present in the deposit. On the basis of chemical mechanistic considerations, it is suggested that the voids are filled with hydrogen gas and may be regarded as gas bubbles, and that the poor ductility is due to the phenomenon known as hydrogen embrittlement.

## Experimental

Two plating solutions were used. Bath A contained 0.06M  $\text{CuSO}_4$ , 0.15M EDTA, 0.049M formaldehyde, 0.0017% phosphate ester wetting agent (5), and NaOH to make the pH equal to 11.85. This bath was operated at 60°C. Bath B contained  $2 \times 10^{-3}\text{M}$  NaCN in addition to the constituents of bath A, and it was operated at 75°C. The plating solutions were analyzed frequently using a polarographic method (6), and necessary replenishments were made to maintain the original concentrations. The plating rate was approximately the same for both baths: 2.8  $\mu\text{m/hr}$  for bath A and 3.0  $\mu\text{m/hr}$  for bath B.

The substrates used for obtaining the transmission electron micrographs shown in Fig. 1 and 2 were textured copper films prepared by cold-rolling and annealing a sheet of OFHC copper. The deposits used for all other observations and ductility measurements were plated on liquid-honed Plexiglas sheets sensitized and activated by the conventional  $\text{SnCl}_2$ - $\text{PdCl}_2$  method. Foil specimens for TEM observations were prepared by electropolishing the deposits about 15  $\mu\text{m}$  thick using the conventional window technique.

The ductility was measured with a portable ductility tester developed recently by the authors (7). In this technique the film is rigidly held in a fixture and pushed with a metal sphere in the direction of thickness until fracture. Scanning electron microscopy (SEM) was used to examine the fracture surface.

\* Electrochemical Society Active Member.

Key words: plating, ductility, electron microscopy, fractograph.

## Experimental Results

**TEM observations.**—The transmission electron micrographs shown in Fig. 1 and 2 were obtained using the so-called through-focus imaging technique (8, 9), in which the image is obtained under defocused conditions. The bright spots of various sizes surrounded by dark rings are believed to be images of voids contain-

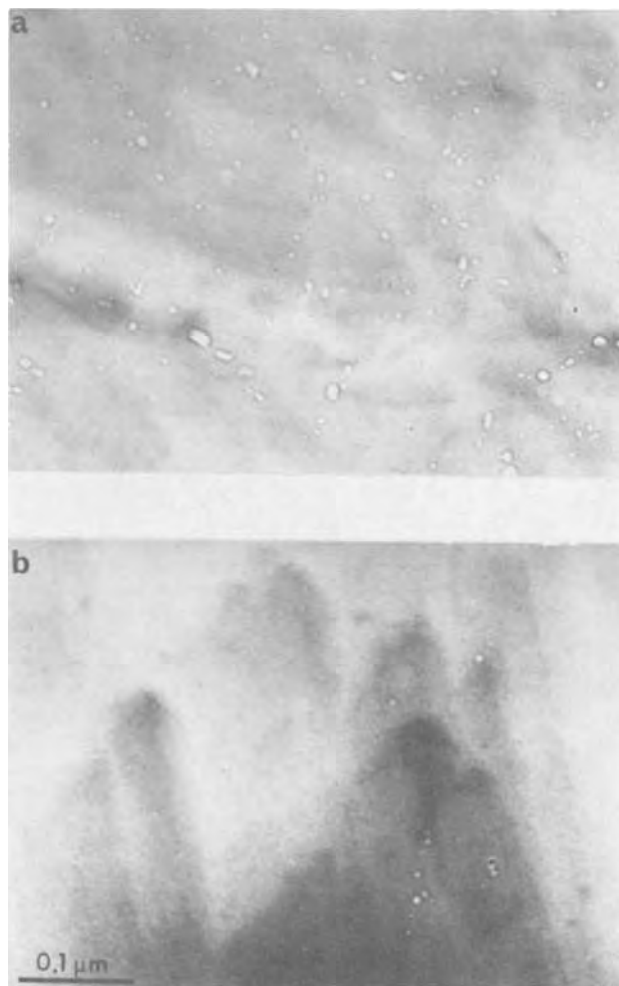


Fig. 1. TEM micrographs of electroless copper deposits formed on textured copper substrate in (a) bath A (no cyanide, 60°C) and (b) bath B ( $2 \times 10^{-3}\text{M}$  NaCN, 75°C). (Defocusing distance  $\Delta f = -3.9 \mu\text{m}$ ).

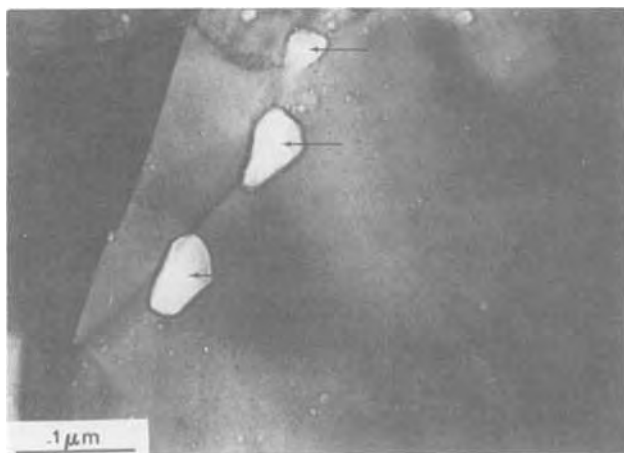


Fig. 2. TEM micrograph of low angle grain boundary region of deposit formed in bath A ( $\Delta f = -3.9 \mu\text{m}$ ).

ing hydrogen gas. Figure 1a was obtained with a deposit formed in bath A (no cyanide,  $60^\circ\text{C}$ ), while bath B (with cyanide,  $75^\circ\text{C}$ ) yielded a deposit shown in Fig. 1b. These two micrographs show images of a single grain. It is seen that the addition of cyanide and the higher plating temperature markedly decreased the void density. The void density calculated from Fig. 1a assuming a specimen thickness of  $1200\text{\AA}$  is equal to  $9 \times 10^{15}/\text{cm}^3$ , while the corresponding density value for Fig. 1b is about one order of magnitude less, i.e.,  $\sim 9 \times 10^{14}/\text{cm}^3$ . Using stereomicroscopy, we confirmed that these voids are randomly distributed within the grain (9).

Very large, somewhat faceted voids (up to  $500\text{--}750\text{\AA}$ ) were frequently found at low angle grain boundaries of the deposit formed in bath A as shown in Fig. 2. High angle grain boundaries did not contain such large voids.

Deposits formed on Plexiglas substrates were also examined by TEM. These deposits were not suitable for the observation of voids because they consisted of numerous small grains, and image features associated with many grain boundaries, growth twins, and dislocations obscured the image of the voids. The grain size of the deposits formed in baths A and B was approximately the same ( $0.5\text{--}1 \mu\text{m}$ ). Twin and dislocation densities in the two deposits were also comparable.

**Ductility.**—Cyanide is known as an effective ductility promoter for electroless copper (1-3). Plating at higher temperatures is also known to yield deposits with higher ductility (3). The ductility values, expressed in terms of percentage elongation, of the  $15 \mu\text{m}$  thick films deposited on Plexiglas in baths A and B were 1.2 and 3.6%, respectively.<sup>1</sup>

It has been reported that the ductility of electroless copper deposits improves significantly upon annealing at relatively low temperatures ( $100^\circ\text{--}400^\circ\text{C}$ ) (10, 11). We found that a dramatic improvement of ductility occurs even at room temperature if the films are left standing for an extended period of time. For example, the ductility of the two films mentioned above increased to 4.6% (bath A) and 4.8% (bath B) after standing at room temperature for about six months. It should be noted that the improvement of ductility was significant for both films, and that the two final ductility values were practically the same.

**SEM observations.**—The surface morphology of the films deposited on Plexiglas substrates in baths A and B is shown in Fig. 3. It is seen that bath A produced a coarser structure than bath B did. Much more dramatic difference was found in the morphology of fracture surfaces of these two films. This is illustrated by the

<sup>1</sup> The precision of the elongation measurement was approximately  $\pm 10\%$  of the measured values.

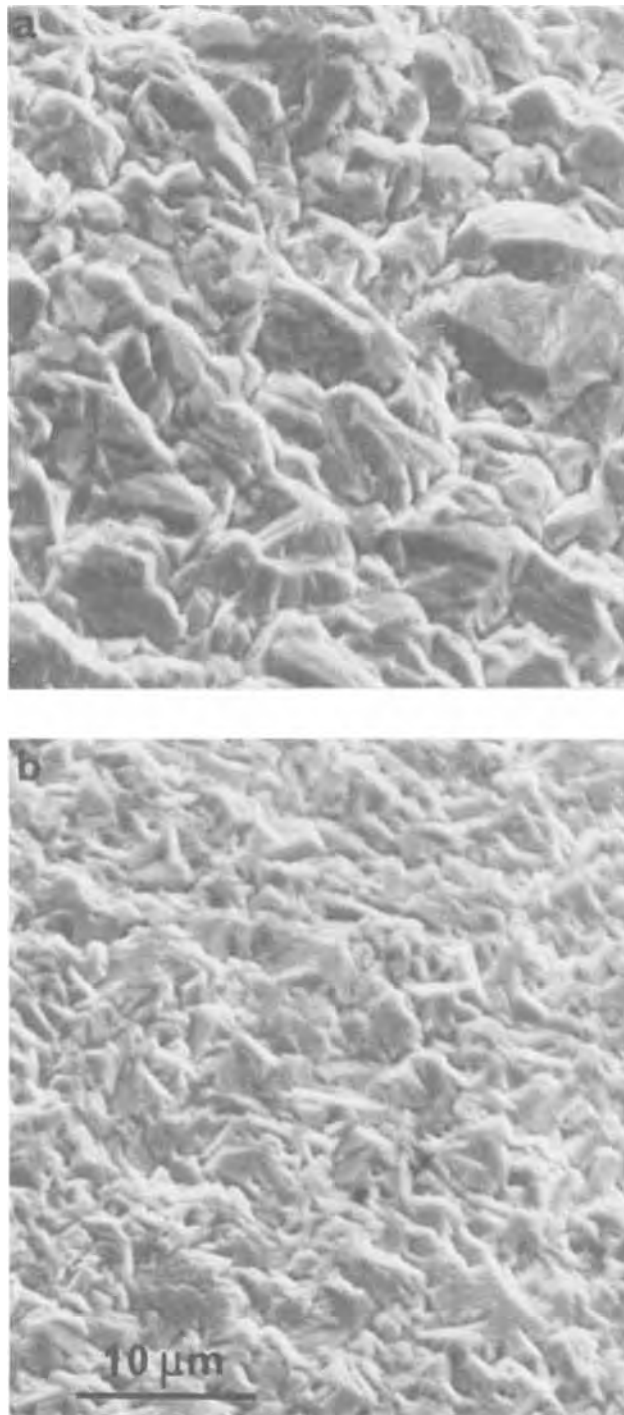


Fig. 3. SEM micrographs of the surface of electroless copper deposits formed on Plexiglas substrate in (a) bath A and (b) bath B.

SEM micrographs in Fig. 4, which were obtained with the as-deposited film specimens used for the ductility measurement. The fracture surface of the film plated in bath A was extremely rugged (Fig. 4a), whereas that of the film formed in bath B had a much smoother appearance with necking characteristics (Fig. 4b). The features seen in Fig. 4b were more or less comparable to those of ductile, annealed copper sheets. The specimens of the films tested for ductility after the prolonged standing at room temperature were also examined by SEM. It is significant to note that in spite of the considerable improvement in ductility, the morphology of fracture surfaces of these specimens was similar to that of the fresh films shown in Fig. 4.

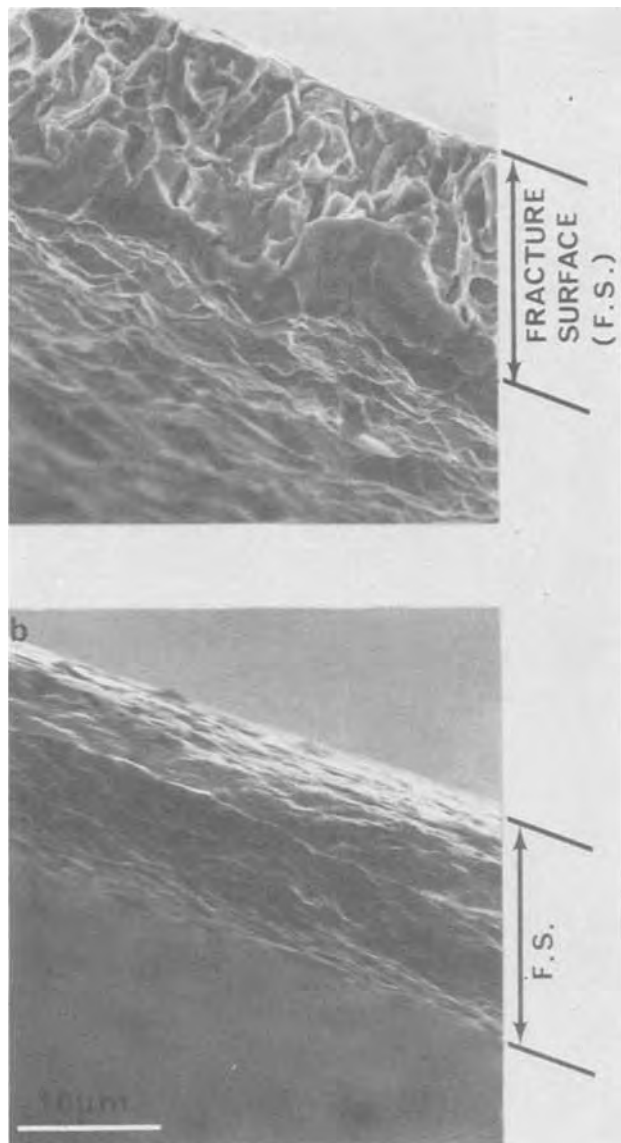
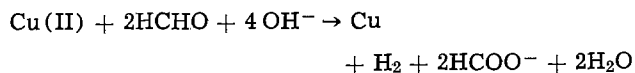


Fig. 4. SEM micrographs of fracture surface of electroless copper deposits formed on Plexiglas substrate in (a) bath A and (b) bath B.

### Discussion

It is well established that the electroless deposition of copper accompanies the evolution of hydrogen gas with the following over-all reaction (12, 13)



The isotope experiment carried out previously (13) using deuterated formaldehyde with  $\text{H}_2\text{O}$  and ordinary formaldehyde with  $\text{D}_2\text{O}$  showed that both hydrogen atoms in  $\text{H}_2$  in the above reaction come from the splitting of the C-H bond in the formaldehyde molecule. On the basis of these facts, it is reasonable to assume that if any hydrogen remains trapped within the deposit, an equilibrium exists between the hydrogen atoms in an adsorbed state and the hydrogen gas contained in the voids.<sup>2</sup> Such incorporated hydrogen is most likely to cause the phenomenon commonly known as "internal" hydrogen embrittlement (as opposed to "external" hydrogen-environment embrittlement which

<sup>2</sup> Lukes (12) proposed a reaction mechanism involving the formation of hydride ion,  $\text{H}^-$ , on the deposit surface. This mechanism was recently supported by Pearlstein (14). We thought that if this mechanism is indeed operative, copper hydride ( $\text{CuH}$ ) might exist and be detectable especially in brittle deposits. However, an electron diffraction analysis failed to yield any evidence for this compound.

occurs when metals are exposed to gaseous hydrogen atmospheres).

The internal hydrogen embrittlement is generally considered to result from either or both of the following two effects: a lowering of the lattice cohesion (atomistic embrittlement), and a build up of high internal pressure in microcracks or voids (pressure effect) (15). When the hydrogen concentration is low as compared to the lattice solubility, the atomistic embrittlement prevails, whereas the pressure effect dominates when the excess hydrogen content is sufficiently high. It is of interest to consider which of the two internal embrittlement mechanisms is predominant for electroless copper. The brittle deposit formed on Plexiglas in bath A was analyzed for total hydrogen using a vacuum fusion technique (Gollob Analytical Service Corporation, Berkeley Heights, New Jersey). The hydrogen content was found to be of the order of 100-200 ppm. On the other hand, the equilibrium solubility of hydrogen in copper is known to be extremely small: 0.055 ppm at 1 atm at  $500^\circ\text{C}$  (16) and less at lower temperatures. Thus, it can be concluded that practically all hydrogen found by the chemical analysis is present in the gaseous form within the voids. The internal pressure in the voids calculated using the above hydrogen concentration, the void density ( $9 \times 10^{15}/\text{cm}^3$ ), and the average diameter of voids ( $\sim 50\text{\AA}$ ) amounts to  $2-4 \times 10^4$  atm.<sup>3</sup> An inevitable conclusion is then that the brittleness of electroless copper deposits is due to the pressure effect associated with the internal hydrogen embrittlement. The improvement of ductility observed on heating at relatively low temperatures (10, 11) or on prolonged standing at room temperature is consistent with this conclusion in view of the known high mobility of hydrogen in metals (18).

The effect of cyanide ions on ductility can be interpreted on the assumption that they strongly adsorb on copper and facilitate the escape of hydrogen gas from the deposit surface. Apparently, the higher plating temperature also accelerates the desorption of hydrogen gas. However, the hydrogen content of the film plated even in bath B with cyanide at a temperature as high as  $75^\circ\text{C}$  apparently was significant, as is evidenced by the fact that its ductility did improve considerably (from 3.6 to 4.8%) on standing at room temperature.

The difference in roughness between the two fracture surfaces (Fig. 4) may be related to the corresponding difference observed on the as-deposited surface shown in Fig. 3. On the other hand, in the presence of large voids at grain boundaries (Fig. 2), it is probable that cracks initiate at such voids. This also may produce rugged fracture surfaces. Whatever the cause of the morphological differences may be, it is clear that the ductility is not determined by the deposit morphology; as already mentioned, the fracture surface showed no morphological change after the improvement of ductility on room temperature stand.

### Summary and Conclusions

1. Numerous voids ranging in diameter from 20 to 300 $\text{\AA}$  are present within grains of brittle electroless copper deposits. Low angle grain boundaries of such deposits contain voids as large as 500-750 $\text{\AA}$  in diameter. These voids are believed to be filled with hydrogen gas.
2. This study indicates that the brittleness of electroless copper deposits is due to the "hydrogen embrittlement" phenomenon rather than the incorporation of  $\text{Cu}_2\text{O}$  or deposit morphology.
3. An improved ductility results when the plating is performed under the conditions which facilitate the escape of hydrogen gas. The addition of cyanide and plating at higher temperature bring about this effect, although these conditions did not completely eliminate the inclusion of hydrogen in the present experiment.

<sup>3</sup> These values, which may seem extremely high, are actually lower than the internal pressure calculated for the hydrogen embrittlement of steel ( $10^6-10^8$  atm) (17).

4. Low temperature annealing or room temperature standing for an extended period of time appears to allow hydrogen to escape and hence further improve ductility.

Manuscript submitted Sept. 4, 1975; revised manuscript received Dec. 5, 1975.

Any discussion of this paper will appear in a Discussion Section to be published in the December 1976 JOURNAL. All discussions for the December 1976 Discussion Section should be submitted by Aug. 1, 1976.

Publication costs of this article were partially assisted by Bell Laboratories.

#### REFERENCES

1. F. W. Schneble, Jr., R. J. Zeblicky, and J. F. McCormack, U.S. Pat. 3,310,430 (1967).
2. F. W. Schneble, Jr., J. F. McCormack, R. J. Zeblicky, and J. D. Williamson, U.S. Pat. 3,615,737 (1971).
3. H. Hirohata, M. Oita, and K. Honjo, *J. Metal Finishing Soc. Japan*, **21**, 485 (1970).
4. T. L. Aycock, N. C. Huie, and G. Krauss, *Met. Trans.*, **5**, 1215 (1974).
5. F. W. Schneble, Jr., R. J. Zeblicky, and J. F. McCormack, U.S. Pat. 3,257,215 (1966).
6. Y. Okinaka and C. Wolowodiuk, Unpublished results.
7. S. Nakahara and Y. Okinaka, To be published.
8. L. Albert, R. Schneider, and H. Fischer, *Z. Naturforsch.*, **19A**, 1120 (1964).
9. S. Nakahara and Y. Okinaka, in "Properties of Electrodeposits—Their Measurements and Significance," R. Sard, H. Leidheiser, Jr., and F. Ogburn, Editors Chapter 3, The Electrochemical Society, Softbound Symposium Series, Princeton (1975).
10. J. J. Grunwald, H. Rhodenizer, and L. Slominski, *Plating*, **58**, 1004 (1971).
11. J. J. Grunwald, L. Slominski, and A. Landau, Proceedings of the Fourth Plating in the Electronics Industry Symposium, p. 13, American Electroplaters Society (1973).
12. R. M. Lukes, *Plating*, **51**, 1066 (1964).
13. Y. Okinaka, Paper 144 presented at The Electrochemical Society Meeting, Detroit, Michigan, October 5-9, 1969.
14. F. Pearlstein, in "Modern Electroplating," 3rd ed., F. A. Lowenheim, Editor, p. 734, John Wiley & Sons, Inc., New York (1974).
15. A. S. Tetelman, in "Hydrogen in Metals," I. M. Bernstein and A. W. Thompson, Editors, American Society for Metals, Metals Park, Ohio (1974).
16. C. L. Thomas, *Trans. Met. Soc. AIME*, **239**, 485 (1967).
17. A. R. Troiano, in "Hydrogen in Metals," I. M. Bernstein and A. W. Thompson, Editors American Society for Metals, Metals Park, Ohio (1974).
18. A. S. Tetelman and A. J. McEvily, "Fracture of Structural Materials," John Wiley & Sons, Inc., New York (1967).

## Design Considerations for Electrodeposition onto a High Resistance Electroless Flash in a Continuous Plater

J. F. D'Amico\* and M. A. De Angelo

Western Electric Company, Engineering Research Center, Princeton, New Jersey 08540

and L. D. Noble

Western Electric Company, Columbus, Ohio 43200

#### ABSTRACT

The buildup of copper by electrodeposition onto a high resistance electroless flash has been studied in a roll-to-roll continuous plater employing copper fluoborate at ambient temperature. Input to the plater was circuit-patterned polyimide tape having an initial deposit which ranged from 2.4  $\mu\text{in.}$  electroless copper through 146  $\mu\text{in.}$  electroless plus electroplated copper. Buildup of copper through one (or more) plating loops was traced by atomic absorption analysis of millimeter-sized pattern sections cut from the tape; this analysis followed an abrupt interruption in steady-state plating and a rapid ejection of the tape from the plater. By this technique, copper distributions along and across the tape were determined. Thickness buildups to 400  $\mu\text{in.}$  at tape speeds of 2.3 and 3.1 ft/min are reported. The copper distributions have been used to compute maximum and average cathodic current densities,  $J_{\text{max}}$  and  $J_{\text{ave}}$ , respectively, for selected plater configurations and input copper thicknesses. Significant asymmetries in local plating rate due to the high input tape resistance were observed and the ratio  $J_{\text{max}}/J_{\text{ave}}$  was as high as 12/1 in some cases. Since excessive cathodic current densities can degrade performance of the plated product, the regulation of  $J_{\text{max}}$  within definable limits is a critical aspect of plater design. A correlation of  $J_{\text{max}}$  to input thickness of the electroless flash and to applied plating currents is presented and its implications with respect to plater design examined.

The fabrication of flexible printed circuits by additive methods (1, 2) usually employs a continuous electroplating step to build up a thin, resistive electroless flash to the required conductor thickness. In this step the metallized flexible substrate, connected cathodi-

cally in the plating cell, may receive unwanted extremes of cathodic current density, even though the applied plating currents are set quite moderately. This occurs because the relatively high resistance of the electroless deposit forces a highly nonuniform deposition along the plater axis, with little or no plating at the high resistance (input) side, and well above average plating at the low resistance (exit) side of the

\* Electrochemical Society Active Member.

Key words: copper fluoborate plating, cathode current density, plating distributions, pattern plating, fusion current.



system. This effect must be adequately considered in the design and operation of a continuous plater to insure that the quality of the plated deposit is not adversely affected.

In this paper we shall describe experiments in which an electroless flash of 2.3  $\mu\text{in.}$  is built up in stages to as much as 400  $\mu\text{in.}$  by continuous plating in copper fluoborate. Measurements of the observed copper distributions will be presented and from these the average ( $J_{\text{ave}}$ ) and maximum ( $J_{\text{max}}$ ) cathodic current densities calculated for individual plating loops under various conditions. The ratio  $J_{\text{max}}/J_{\text{ave}}$  will be used as an index of the plating rate asymmetry in any loop.

The plating configuration used in our experiments is more complex than the idealized parallel plate configuration, the latter case being more amenable to computation and analysis. Nevertheless, we have attempted to look beyond the complexities introduced by our configuration to provide some understanding of the continuous plating problem.

The starting material in these experiments was patterned electroless copper on polyimide tape. Plating experiments under various combinations of input copper thickness, plating current, plating loop depth, and tape speed, were performed and analyzed to provide a detailed description of the system performance. The buildup of copper through one (or more) plating loops was traced by atomic absorption analysis of millimeter-sized pattern sections cut from the tape. This analysis followed an abrupt interruption in steady-state operations to provide a snapshot record of the plating distribution at all points. The copper distributions were used to compute the cathodic current density at selected positions in the plater.

Representative distributions along the tape have been plotted for runs at 2.3 and 3.1 ft/min tape speed. Results will be given for runs with normal i.e., standard, plater configuration and for two nonstandard configurations which employ either field shields at the plating loop exit, or added cathode connections in solution. The nonstandard configurations are attempts to reduce plating asymmetries and peak cathodic current densities.

The determinations of copper distribution for the normal configuration runs have been used to formulate a plater design based upon the limiting of cathodic current density to a specified maximum in the plater. This is an important first step in the establishment of a generalized design scheme for continuous plating onto high resistance electrodes.

### Background

In electroplating onto a high resistance cathode, the plating current flow produces a significant  $IR$  drop along the cathode (specimen) surface which thus may deviate appreciably from an ideal equipotential. The voltage gradients induced along the cathode act to vary the local surface overpotential and thus the rate of metal deposition. Such variations are in addition to any which occur due to mass or charge transfer effects.

The effects of ohmic electrode resistance on current and potential distributions in various plating cells have received considerable attention in the literature. Weisselberg (3) has reported current and potential distributions for a resistive anode rod suspended along the axis of a nonresistive cylindrical cathode. Wojtowicz *et al.* (4) have reported current and potential distributions for a thin wire resistive anode under conditions of negligible longitudinal potential drops in the electrolyte. Fomichev (5) has calculated current distributions in resistive parallel strip electrodes. Tobias and Wijsman (6) have considered the case of plane parallel electrodes of finite but uniform resistance.

The above papers describe steady-state systems and assume that resistive changes which result from the electrodeposition process are negligible. This assumption is not valid when the resistivity (thickness) varies

substantially along the substrate. The effects of spacial thickness variations have been analyzed by Alkire (7) for cathodic electrodeposition onto a thin stationary metal strip of high resistance.

The problem to be discussed in this paper involves steady-state plating in a continuous system. In this, as in all plating cells, the cathodic current distribution (and thus the deposit distribution) is determined by the interaction of several variables: cell geometry, electrolyte composition and temperature, electrolyte agitation and flow pattern, electrode resistances, plus the level of the applied plating current. Our experimental results show deposit distributions which are highly asymmetric along the plater axis when the input copper thickness is ultrathin, but which become more uniform and eventually linear as the input thickness increases. From this result we have surmised that the ohmic resistance of the deposit (cathode) is the main variable determining the cathodic current distribution, with kinetic (charge transfer) or concentration (mass transfer) polarization effects of secondary importance. The properties of the copper fluoborate electrolyte, the configuration applying uniform agitation to the electrolyte, and the relatively low levels of applied current are consistent with this conclusion.

By way of qualitative description, we refer to Fig. 1A which depicts an idealized single loop continuous plater with commonly connected anodes/cathodes. The upper rollers, grounded conductors, provide cathodic connection to the underside of the tape; contact to the reverse side occurs via plated through-holes in the tape. The through-holes are presumed sufficiently conductive to maintain a uniform potential  $V(X)$  on either side of the tape at coordinate  $X$  measured along the tape axis. The corresponding potential in the electrolyte just beyond the diffusion layer is denoted as  $V_s(X)$ , and  $V_o$  denotes the anode potential relative to ground (cathode). The currents collected on each side of the loop are denoted  $i$  and  $I$  as indicated. The lower roller is a nonconductor and blanks plating at the bottom of the loop on one side of the tape. The interelec-

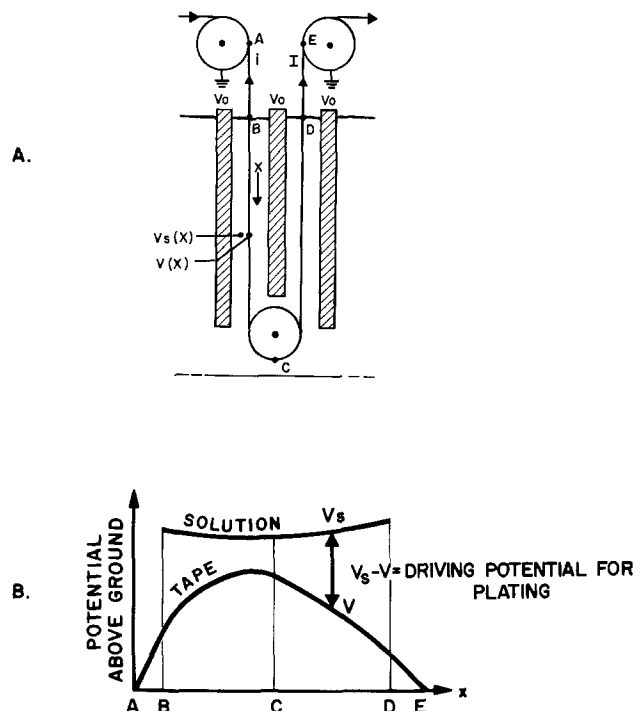


Fig. 1. (A) Schematic diagram of single loop, continuous plater with common anode ( $V_o$ ) and common cathode (grounded) connections. Coordinate  $X$  measures position along the tape while  $V(X)$  and  $V_s(X)$  are the respective potentials on the tape and in the electrolyte at  $X$ . (B) Schematic of potential distributions for the single loop plater.



trode spacing on either side or along the tape is uniform, and the circulation of electrolyte is presumed equivalent at all points. Edge effects near the air-electrolyte interfaces or near the bottom roller are neglected.

In Fig. 1B we sketch the tape and solution potential distributions for a typical plating loop. The difference  $V_s(X) - V(X)$  represents the driving potential for plating at  $X$ ; thus the plating rate varies along the loop. The potential difference  $V_s(X) - V(X) = \eta(X) + \phi$ , where  $\eta$  is the surface overpotential and  $\phi$  the reversible cell potential for the system. At any  $X$  the plating rate increases with  $V_s - V$ . (The plating rate dependence upon potential is usually given (8) as an exponential function of  $\eta$ .)

Due to the current flow in the resistive tape, a voltage rise must occur as one passes downward along the loop. At a point before C this trend is reversed and as we proceed toward the loop exit, the current reverses direction and flows toward the exit cathode roller. The magnitudes of  $i$  and  $I$  reflect the relative tape resistances in each portion of the loop. Since thickness increases as the tape passes through the loop,  $I > i$ . The solution potential  $V_s$  is presumed not to vary strongly with  $X$ , a reasonable assumption for electrolytes of high conductivity. We see in Fig. 1B that  $V_s - V$  (and thus the local deposition rate) decreases as we proceed away from the cathode rollers.

### Experimental

**Apparatus and plating conditions.**—A schematic of the plating system used is presented in Fig. 2. The left-hand sketch shows an unscaled elevation of the plater, the right-hand sketch a scaled plan view of a plater section. The tape orientation is vertical, the spacing between alternate rollers exceeding the 4 in. roller diameter by only 5/16 in. on each side. For the single pass runs, the tape was rethreaded to bypass all but one loop; pass 2 was used for plating at full

depth, pass 1 for plating at reduced depth. Anodes were oval-shaped OFHC copper rod, 3 in. nominal width, and centered on the tape in the plater.

For some of the single pass runs, the configuration was modified as shown in Fig. 3. These runs involved addition of shields at the loop exit (3A) or added cathode connections in the electrolyte (3B). The cathode connections were made using 1/4 in. formed copper rods, insulated except at their ends to contact the metallized center strip on the key side of the pattern (see Fig. 4).

The plating bath was copper fluoborate operated at ambient temperature. This bath was prepared by diluting two parts of fluoborate concentrate (Allied Chemical Company) with one part deionized water to obtain an electrolyte of 462 g/liter copper fluoborate (124 g/liter as Cu), 7.2 g/liter fluoboric acid, and 30.7 g/liter boric acid. During the runs, the plating solution was pumped and filtered continuously through carbon-charged polypropylene filters.

The electrolyte tank capacity was 70 gal and the circulation rate 5-8 gal/min. Circulation was from the exit side lower corner of the tank (inlet) diagonally across to the entrance side upper corner (exit).

**Tape generation and tape removal from the plater.**—The tapes for analysis were 2 mil polyimide (du Pont KAPTON®H Film) patterned in electroless copper by the photoselective metal deposition process (2). The patterns on each side are shown in Fig. 4. During plating, the bus side was in direct contact with the cathode rollers, the key side plating by contact via the through-holes. Experiments were performed by executing an abrupt interruption in steady-state operations. For the single loop experiments, the plater power was turned off and the tape section removed after cutting at positions marking the top of the input and output cathode rollers. The tape section was immediately rinsed in deionized water, then dried in air.

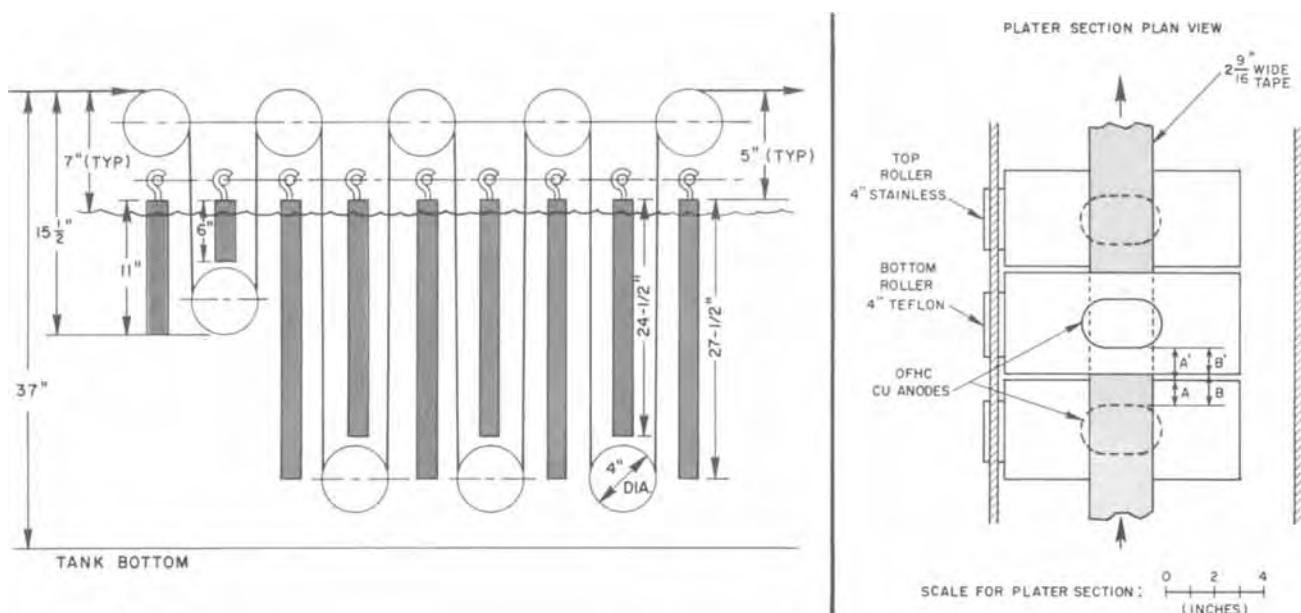


Fig. 2. Schematic of continuous plater in multipass mode (left) and plan view of scaled plater section (right). For single loop runs the tape was rethreaded to bypass the loops not being used. Anodes in the bypassed loops remained in place. The vertical pitch of the tape was as follows: tape to anode at top,  $A = 1$  in.,  $A' = 1 \frac{5}{16}$  in., at bottom,  $B = 1 \frac{5}{16}$  in.,  $B' = 1$  in.

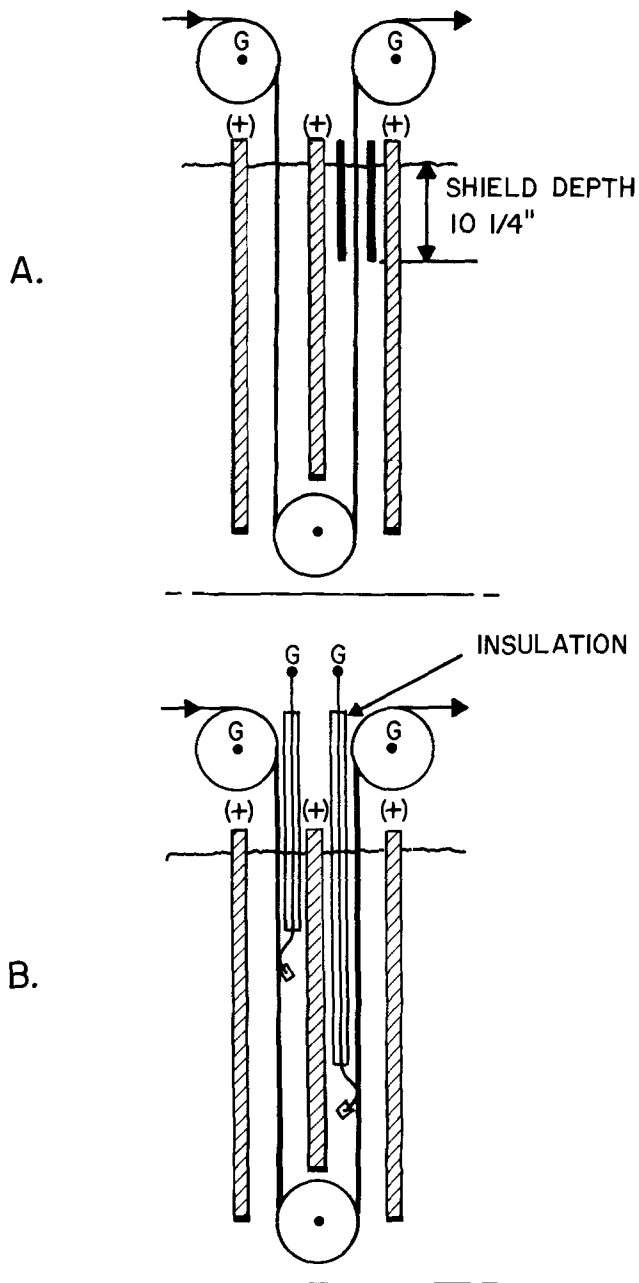


Fig. 3. Schematic diagram of nonstandard plating configuration. (A) Experiment using exit field shield. (B) Experiment using added cathode connections in the electrolyte. The G's indicate connection to ground.

For the multiloop experiments, the tape removal process took somewhat longer as it was necessary to raise the tape transport mechanism out of solution to remove the tape section. The lapsed time between power shutoff and the water rinse in this case was about 2½ min.

**Tape indexing and specimen designation.**—The center sprocket holes used to transport the tape in the plater provided a convenient coordinate along the tape axis. Thus all tapes were indexed by numbering the sprocket holes, with the zero position at the top of the input cathode roller. Conversion to distance in inches was made using the factor 0.627 in. per sprocket number.

Tape position in the plater at the time of its removal was recorded by fiducial marks locating the tape position at the top of each cathode roller. The location of the air-solution interface was made by ruler measurements on the machine at the time of each run.

The specimen labeling scheme is illustrated in Fig. 4. All measurements to be reported were made on the

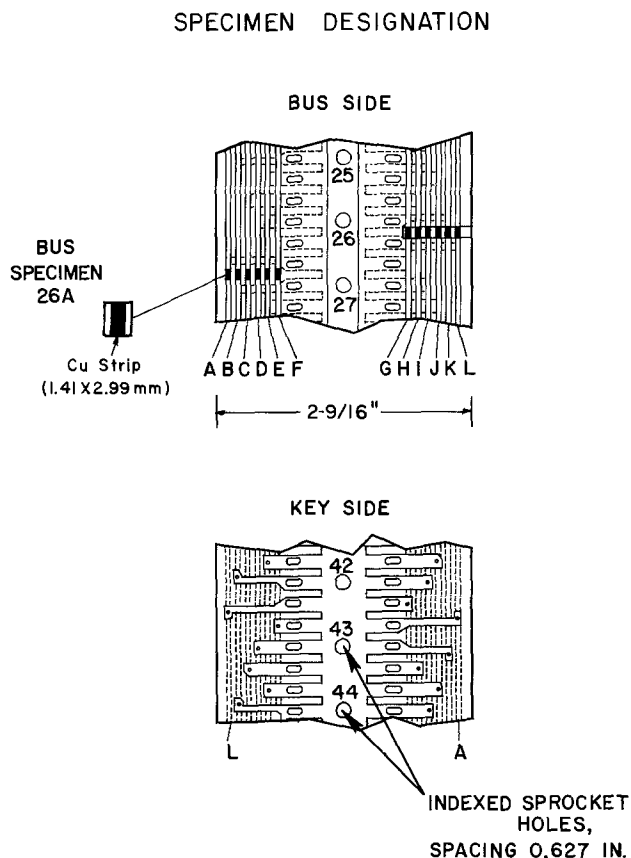


Fig. 4. Description of patterned tape and specimen designation. Specimens for atomic absorption analysis were taken from the bus side of the tape, cut into 1.41 × 2.99 mm strips at each bus. The center sprocket holes were used to register and transport the tape through the plater.

bus side of the pattern, the individual specimens carefully cut from the tape using a razor blade and a steel template.

The area of deposited copper on a specimen was computed from measured values of specimen length and pattern width. The measured dimensions averaged over 20 specimens were

Width:  $55.33 \pm 1.01^1$  mil =  $0.141 \pm 0.0025$  cm

Length:  $117.8 \pm 1.2^1$  mil =  $0.299 \pm 0.0029$  cm

Bus area:  $0.0422 \text{ cm}^2 \pm 2.8\%$

**Copper analysis by atomic absorption spectrometry.**—The specimens, cut to size, were immersed in a measured volume of aqua regia to dissolve the copper. The aqua regia was diluted 2 to 1 with deionized water. The volume of solvent varied from 2 to 400 ml depending upon the copper thickness. Dilution was made to maintain the copper concentration near a value of 2 ppm.

Analyses were carried out using a Jarrell-Ash No. 82-536 Atomic Absorption-Flame Emission Spectrometer, using an air-acetylene flame and the 3247.5 Cu line. Solution standards were prepared by an aqua regia dilution of a Spex 1000 ppm/ml spectroscopic standard solution.

The AA data permit determination of the mass per unit area of the deposited copper. Thickness determinations were made from these values using the bulk copper density, 8.93 g/cm<sup>3</sup>. Experimental errors in the copper analysis have been determined from the precision and accuracy of the AA analysis and the area measurements on each specimen. The AA analysis at 2 ppm copper concentration is estimated to have a precision of 3.5% and an absolute accuracy of 1%. The

<sup>1</sup> All reported errors are average deviations.

over-all precision in the copper determination is thus  $3.5\% + 2.8\%$  (error in area) =  $6.3\%$ . An additional systematic error in the copper thickness is introduced by the lateral growth as the plating proceeds. This error is approximately linear in total thickness plated and is a maximum of  $5\%$  for the thickest specimens.

**Calculation of cathodic current density.**—The cathodic current density at any position in the plater may be determined from the measured copper thickness distribution on the tape if the tape speed is known. A diagram of an elemental tape section proceeding vertically through the plating cell at speed  $v$  is shown in Fig. 5. The  $X$  coordinate, measured along the tape axis, locates position in the plater relative to fixed lab coordinates. Upon interruption of the steady state to obtain the plating loop the lab-fixed coordinates transfer to the tape in a one to one correspondence which relates distance along the tape to coordinate location in the plater.

In Fig. 5 a tape section between  $X$  and  $X + \Delta X$ , discharging ions across the element-electrolyte interface of area  $\approx W \Delta X$  receives a cathodic current  $I_c (\equiv J \cdot W \Delta X)$  and a deposit which increases the metal thickness by  $\Delta T$ . For steady state

$$I_d(X + \Delta X) = I_d(X) + J \cdot W \Delta X \quad [1]$$

where  $I_d(X)$  and  $I_d(X + \Delta X)$  are currents flowing through the deposit through cross sections  $W \cdot T(X)$  and  $W \cdot (T(X) + \Delta T)$ , respectively. The corresponding deposit current densities are  $J_d(X)$  and  $J_d(X + \Delta X)$ .

At speed  $v$  the deposit thickness increases by  $\Delta T$  in time interval  $\Delta X/v$ , thus the deposition rate is  $v \Delta T/\Delta X$ . Using Faraday's law and the bulk density,  $8.93 \text{ g/cm}^3$ , the cathodic current density  $J$  at any  $X'$  can be shown to be

$$J(X') (\text{asf}) = 12.8v (\text{ft/min}) \cdot (\Delta T/\Delta X)_{X'} (\mu\text{in./in.}) \quad [2]$$

### Results

The major results to be reported will relate to single loop experiments. These were preferred over the multipass common electrode experiments because they permit the setting of total current and thus the thickness deposited for each pass. However, no distinction is to be made between the two cases. We have included some results from the multipass work to underscore how resistance affects the plating distribution

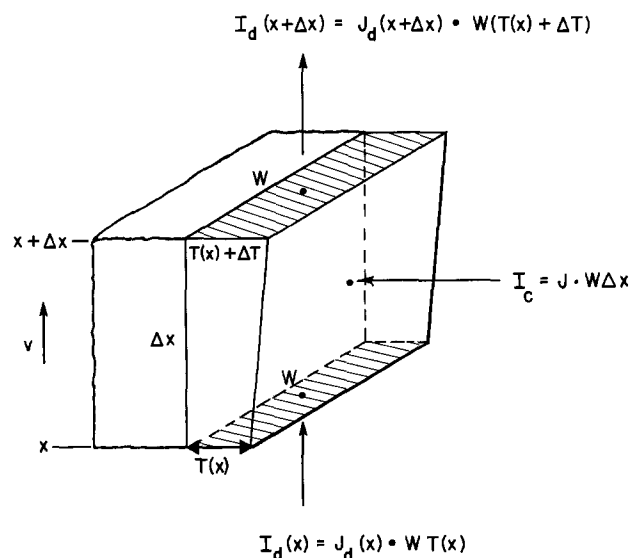


Fig. 5. Elemental tape section in the plater. The section, moving vertically at speed  $v$ , receives cathodic current  $I_c$  across interface  $W \cdot \Delta X$ . As a result, deposit thickness increases by  $\Delta T$  across span  $\Delta X$ . The deposit current  $I_d$  is also increased when this occurs.

when the individual passes have significantly different input resistances.

**Multipass operation.**—In Fig. 6 we present transverse copper distributions for a four-pass plating run at  $2.3 \text{ ft/min}$  and  $75\text{A}$ . The copper thickness at each bus is plotted vs. distance from the center of the tape for segments cut at the end of each completed pass. Input copper thickness ( $I$ ) was  $2.2 \mu\text{in.}$ . The average thickness over all buses at the respective exits was found to be: pass 1 (II)— $7.7 \mu\text{in.}$ ; pass 2 (III)— $31.7 \mu\text{in.}$ ; pass 3 (IV)— $104.8 \mu\text{in.}$ ; pass 4 (V)— $208 \mu\text{in.}$ . The copper deposit across the tape is seen to be highly nonuniform though symmetric about the tape axis, with an appreciably enhanced buildup at the edges.

For the purposes of comparison, we have plotted distributions predicted from the primary current distribution of plane parallel electrodes (9) of the same width and spacing as our electrodes. The primary distribution is based upon cell geometry and is independent of mass and charge transfer effects. (However, electrode kinetic and mass transfer effects would prevent the infinite current densities predicted at the electrode edges.) The primary current distribution curves have been normalized by matching the predicted average thickness with the measured average thickness of the buses. The observed thicknesses do not deviate appreciably from the theoretical curves, thus plater geometry is held primarily responsible for the nonuniformity of the transverse distributions.

In Fig. 6 variations in plating along the tape axis are also observed as we note nonuniform deposit increases in successive passes. A breakdown in the fraction of the total deposit received in each of the four passes, respectively, is  $0.011$ ,  $0.037$ ,  $0.154$ , and  $0.509$ . The peak

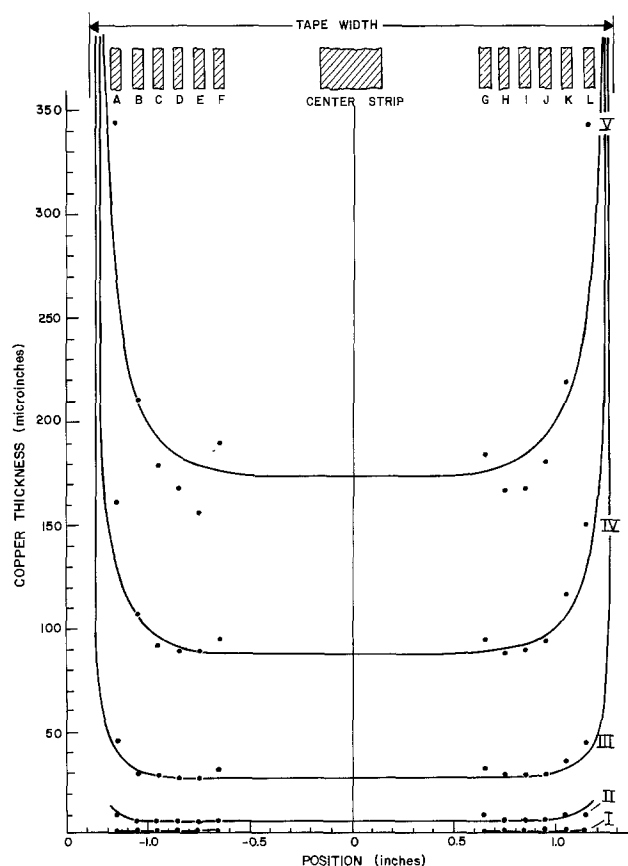


Fig. 6. Transverse copper distributions for multipass run 5/21,  $2.3 \text{ ft/min}$  at  $75\text{A}$ . Measurements at each bus for: I. input electroless deposit; II. exit of first pass; III. exit of second pass; IV. exit of third pass; and V. exit of final pass. The solid lines indicate results predicted from the primary current distributions of equivalent plane parallel electrodes (9).

cathodic current density is seen to occur in the final pass in the plater.

**Single pass distributions.**—The single pass results show transverse and axial distributions similar to those already discussed. The transverse distributions for single pass runs will not be specified further.

Before presentation of the axial results, it is useful to discuss the relation between the axial and transverse distributions. If the latter are determined by primary current distributions, thus plater geometry, then the axial and transverse depositions may be considered separately and independent of each other. This separation should be possible when ohmic effects control the deposition in the system. On the other hand, if electrolyte polarization effects are appreciable, the plating distributions will be sensitive to the over-all level of cathodic current, and thus the axial and transverse depositions will be related. We shall make some further comments on this separation in the Discussion section after presentation of experimental results. Needless to say, the separation in distributions permits a significant saving in effort since it forestalls the need for a separate axial deposition model at each lateral position.

The axial results presented refer exclusively to measurements at outer bus A. To predict the axial distribution at other positions, we presume that the bus A results could be multiplied by an appropriate scale factor such as that determined to predict the distributions for the plane parallel electrodes in Fig. 6.

Four sequences of single loop experiments were performed as follows: I and II, normal configuration at 2.3 and 3.1 ft/min, respectively; III and IV, speed 3.1 ft/min with modified plater configurations using a field shield or added cathodes in the electrolyte (note Fig. 3). A tabulation of experimental conditions and the corresponding values of peak and average cathodic current density for all runs is presented in Table I. The ratio  $J_{max}/J_{ave}$  defining A, the plating asymmetry factor, is also presented for each loop. The asymmetry is seen reduced as the input copper thickness is increased. (However, the effects due only to thickness changes are somewhat masked by the changes in the applied current). Values of  $J_{max}$  in the table were calculated in Eq. [2] from values of maximum slope ( $\Delta T/\Delta X$ ) determined from the respective copper distributions.

Axial distributions (measured at bus A in all cases) are presented in Fig. 7 and 8 for normal configurations at 2.3 and 3.1 ft/min, and in Fig. 9 and 10 for experiments at 3.1 ft/min using field shields and added solution cathodes, respectively. In these figures the vertical dashed lines indicate the location of the entrance and exit air-electrolyte interfaces. The vertical arrows indicate the lowest position of the tape in the

loop. The cathodic current densities  $J_{max}$  reported in the figures are higher than the average over the entire pattern since the plating rate at the outer bus is appreciably higher than the average over the entire pattern.

In Fig. 7 copper distributions for A (15A), B (20A), and C (55A) at 2.3 ft/min are presented. The A and B runs are comparable except for the shorter loop length of A. The effective plating zone for these runs of high input resistance is seen confined to a span of 8-10 in. near the exit air-electrolyte interface. The shortened loop length in A has little effect on the plating distribution in the first half of the loop. The situation is different in C where a less asymmetric plating occurs as a result of increases in input thickness and in the applied current.<sup>2</sup>

We note in Fig. 7 and 8 that the copper deposition does not halt abruptly at the exit interface but continues for 2-3 in. beyond. This effect occurs because an appreciable electrolyte meniscus is formed as the tape is pulled out of solution and is capable of plating until its copper ions are depleted. Current passage in electrolyte menisci has been reported for partially immersed parallel vertical electrodes by Will (10), Ben-nion and Tobias (11), and Burshtein *et al.* (12). In multipass runs we have also observed a delay in the resumption of plating upon reentry of the tape into the electrolyte. This phenomenon is presumably the result of surface blocking by the ion-depleted layer until mixing with the bulk electrolyte restores the ion concentration at the interface.

In Fig. 8 we observe results for A (10A), B (20A), and C (45A), with tape speed at 3.1 ft/min. A decrease in asymmetry is evident as the input copper thickness is increased. The effects on plating asymmetry due to speed or current variations are difficult to assess by superficial comparison of the two figures.

In Fig. 9 results for the exit field shield experiments are presented. The role of the shield is to reduce the local electric field, thus enhancing the plating rate elsewhere in the loop. Results in Fig. 9 for A (10A), B (10A), C (20A), and D (35A) were obtained at tape speeds of 3.1 ft/min. The region along the tape covered by the shield is indicated by the shading in the figure. In Fig. 9A we have also plotted the copper distribution from run 1/29, a comparable experiment without the shield. The presence of the shield is seen to expand the effective plating zone down into the electrolyte, thus reducing the value of  $J_{max}$ . In Fig. 9B and 9C we note that the shield flattens the slope at the exit interface, thus shifting the position of  $J_{max}$  to the inlet side of the loop. In Fig. 9D the shield completely blocks the plat-

<sup>2</sup> Further comments on this subject are made in the Discussion.

Table I. Tabulation of single loop runs\*

Group	Run	Figure	Speed (ft/min)	Current (A)	Input Cu thickness ( $\mu$ in.)	Peak cathodic current density $J_{max}$ (asf)	Avg cathodic current density $J_{ave}$ (asf)	Asymmetry factor $A = J_{max}/J_{ave}$
I	12/11/73	7B	2.3	20	3.0	370	47.0	7.9
	1/9/74**	7A	2.3	15	3.3	273	69.6	3.9
	12/14/73	7C	2.3	55	99.5	382	147.8	2.6
	1/15/74	—	2.3	32	146	80.0	79.9	1.0
II	1/29/74	—	3.1	10	2.8	302	25.3	11.9
	1/28/74	8A	3.1	10	3.2	145	19.2	7.6
	1/29/74-A	8B	3.1	20	39.6	386	49.0	7.9
	1/29/74-B	8C	3.1	45	96.0	321	109.7	2.9
III	3/5/74	9A	3.1	10	2.4	203	24.0	8.5
	3/6/74	9B	3.1	10	35.2	59.0	19.2	3.1
	3/6/74-A	9C	3.1	20	58.5	139	40.8	3.4
	3/6/74-B	9D	3.1	35	121	301	76.3	3.9
IV	3/13/74	10A	3.1	14	3.1	24.0	8.7	2.8
	3/14/74	10B	3.1	20	16.7	79.0	24.8	3.2
	3/15/74	—	3.1	40	59.0	128	72.4	1.8

\* All measurements for bus A.

\*\* Short pass.

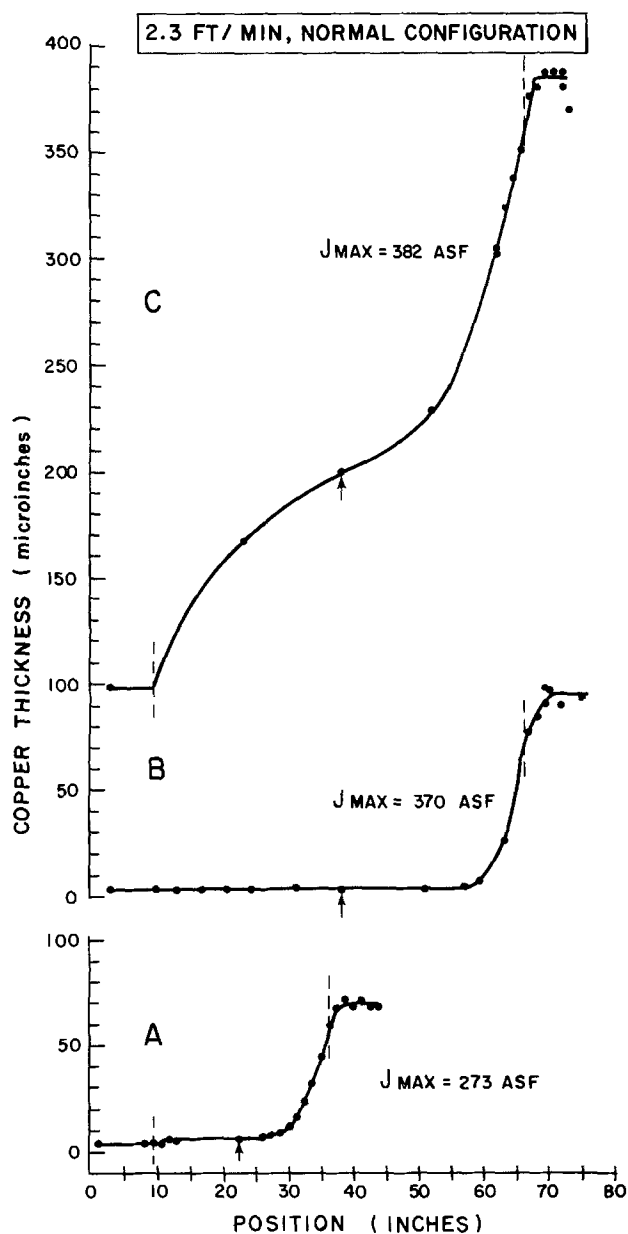


Fig. 7. Axial copper distributions, bus A, normal configuration, 2.3 ft/min: (A) run 1/9, 15A, short pass; (B) run 12/11, 20A; (C) run 12/14, 55A.

ing at the exit interface, again forcing the peak cathodic current to occur at the inlet side of the loop.

The experiments with added solution cathodes are presented in Fig. 10 with tape speed at 3.1 ft/min, A (14A) and B (20A). The locations of the solution connections are shown by the asterisks. The effect of these modifications is to enhance the deposition in the vicinity of the solution connections. (The connection near position 58 in. appears slightly mislocated, as the plating enhancement is found near the 53 in. position.)

**Constraints on plater operation.**—The axial plating asymmetries which have been noted suggest a need to limit average current densities,  $J$  (cathodic) or  $J_d$  (in the deposit), to values appreciably lower than those used in standard practice for the same electrolytes. This restriction anticipates that values of  $J$  or  $J_d$  may be excessive at some positions in the plating cell, leading to reduced quality of the plated product. The degradation may result from extremes in either or both variables.

The anticipated product difficulties are (i) fusion of the plated deposit, (ii) deposition of burned or nodular deposits, and/or (iii) damage to the substrate-deposit

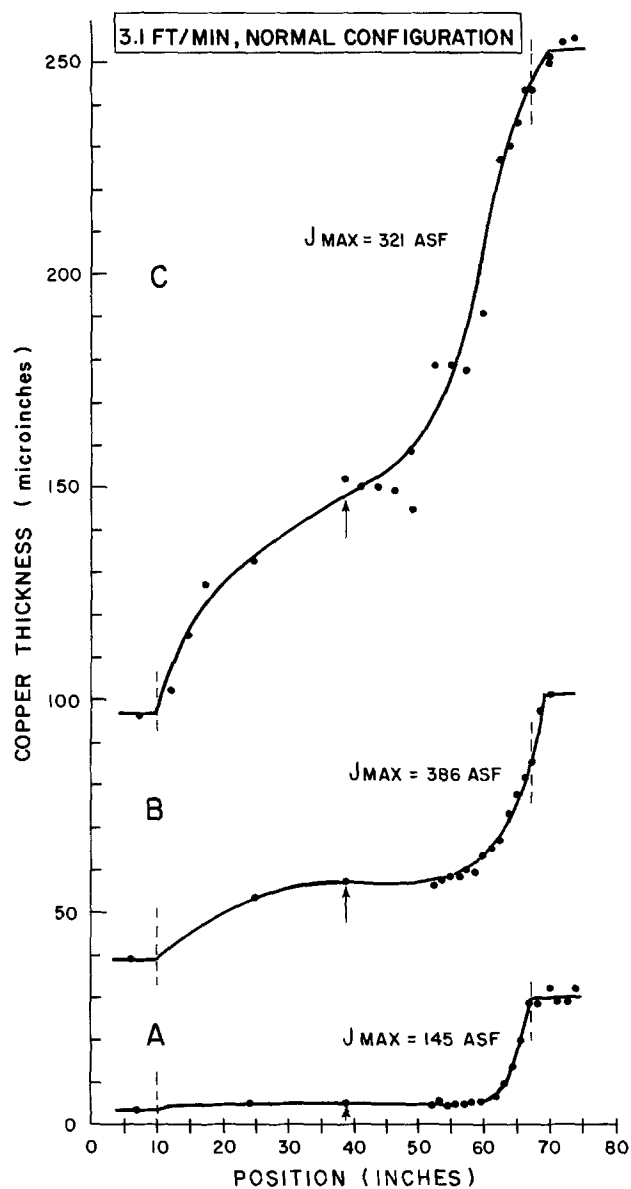


Fig. 8. Axial copper distributions, bus A, normal configuration, 3.1 ft/min: (A) run 1/28, 10A; (B) run 1/29-A, 20A; (C) run 1/29-B, 45A. Note improvement in deposit uniformity as the input thickness increases.

interface. These three aspects will be discussed separately in the sections which follow.

(i) **Deposit fusion.**—The occurrence of fusion requires the rate of ohmic heating produced by the deposit current  $I_d$  to appreciably exceed the rate of heat dissipation from the tape. For continuous plating as described here, the point where fusion will occur (if  $I_d$  is large enough) is at and beyond the exit air-electrolyte interface.

Figure 11 provides correlations of fusion current  $I_F$  vs. thickness of deposit for copper-metallized polyimide tapes, either blanket plated (13), or pattern plated (our results). Also plotted for reference are handbook results (14) for copper wire of equivalent rectangular cross section. Note that the units of current are normalized per unit conductor width. The tape results were obtained using 2 mil polyimide substrates metallized on both sides with electroless and electroplated copper and suspended vertically in air during the passage of current. The pattern results were obtained by using the configuration in Fig. 4, with pattern width at the minimum cross section used to normalize the fusion current. The fusion line shift downwards from pattern to blanket to wire reflects the decreasing ca-

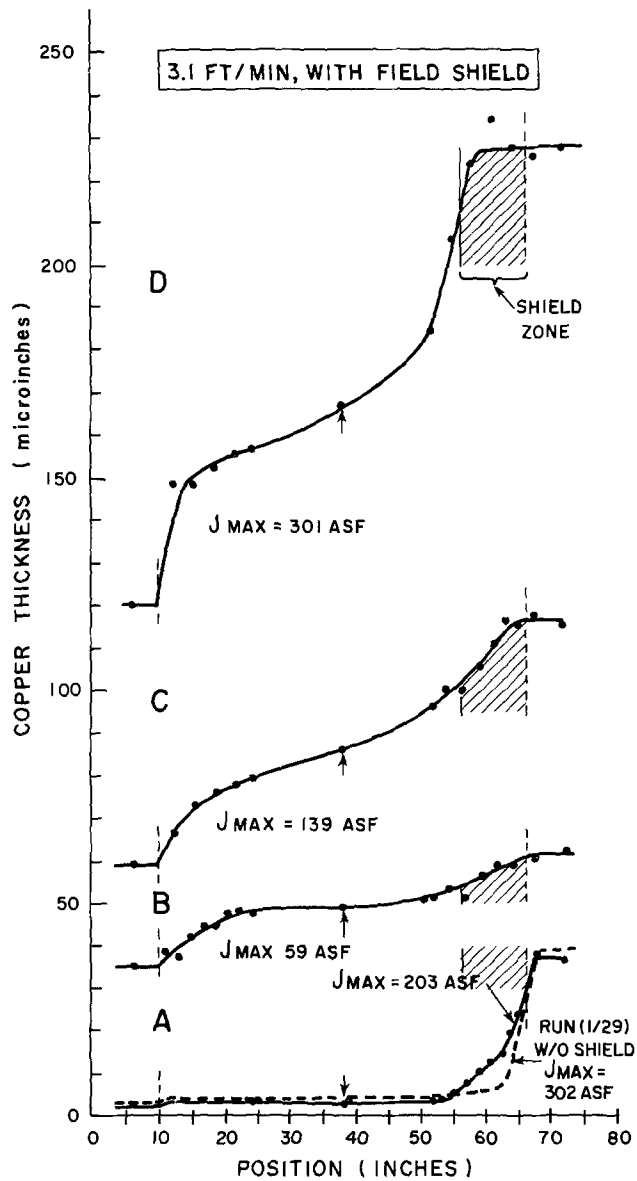


Fig. 9. Axial copper distributions, bus A, with exit field shield. Shield zone is indicated by the shaded area. (A) Run 3/5, 10A; also plotted run 1/29, 10A without shield. (B) Run 3/6, 10A. (C) Run 3/6-A, 20A. (D) Run 3/6-B, 35A. The shield reduces the thickness gradient at the loop exit while increasing the gradient at the entrance side. (An exception is Fig. 9A with 2.4  $\mu$ in. input.)

pability for heat dissipation of the respective configurations.

Also plotted in Fig. 11 is the correlation between applied plating current  $I$  (A/inch of width, mean cross section) and the resulting thickness of the patterned tape at the exit of the plating loop (dashed curve). This curve is based upon the faradaic equivalence of current and deposit and assumes an input thickness of 3  $\mu$ in. at a speed of 3.1 ft/min.

The occurrence of fusion may be predicted from Fig. 11 by comparing the current in the deposit at the loop exit,  $I_{d,exit}$  to current  $I_F$  at which fusion occurs. To avoid fusion  $I_{d,exit}$  must be less than  $I_F$  at the exit deposit thickness. As a matter of convenience we can estimate  $I_{d,exit}$  to be very nearly equal to the total plating current  $I$ , since very little current flows in the entrance side of the loop for input deposit thicknesses less than about 40  $\mu$ in. (see Fig. 7 and 8). The criterion for fusion avoidance thus becomes  $I < I_F$ .

To evaluate a specific case using Fig. 11, consider a loop in which a total current of 3 A/in. at 3.1 ft/min is applied to a 3  $\mu$ in. patterned or blanket-plated tape, respectively. At this current, fusion is predicted for

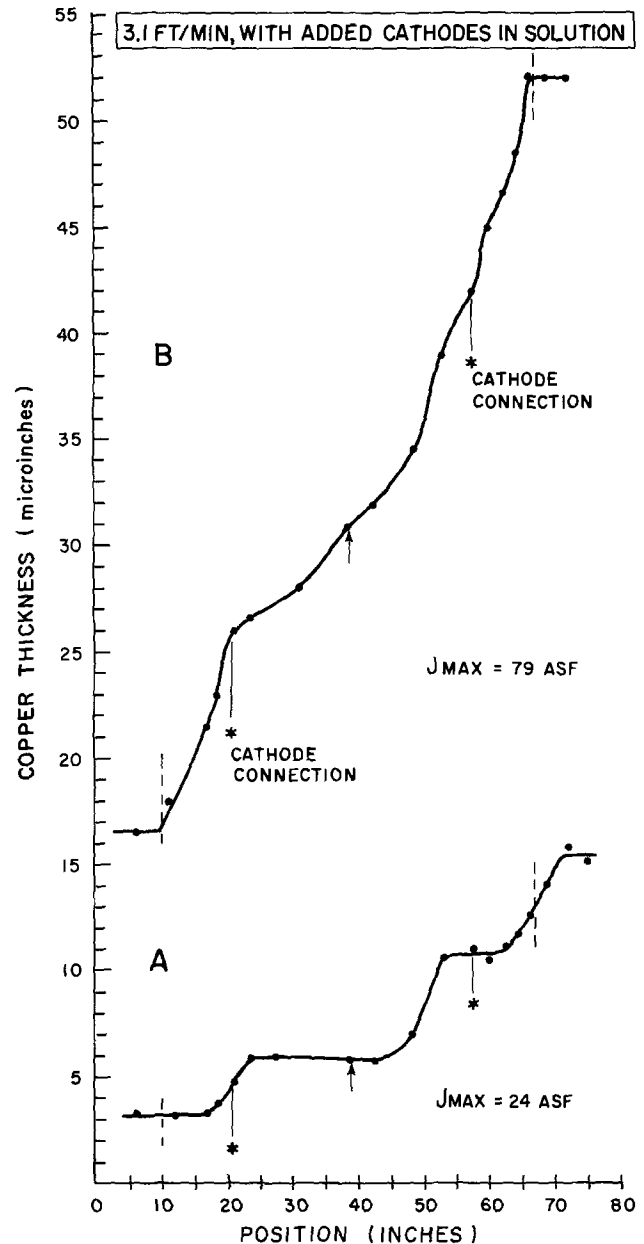


Fig. 10. Axial copper distributions, bus A, with added cathodes in solution, 3.1 ft/min. Position of the solution contacts is indicated by \*. (A) Run 3/13, 14A. (B) Run 3/14, 20A.

thicknesses less than or equal to 4  $\mu$ in. in the patterned tape. 5.8  $\mu$ in. in the blanket tape. The plating line predicts that the exit thickness will be 9.5  $\mu$ in., thus fusion is not possible in this case.

The fusion limitations described do not impose severe restrictions on our ability to plate at "useful" rates such as those employed in the work described.

(ii) Occurrence of burned or nodular deposits.—Burned or nodular deposits occur when the local cathodic current density  $J$  exceeds the limits of the electrolyte for the conditions of use. Avoidance of such deposits requires limiting the values of  $J_{ave}$  so that the corresponding values of  $J_{max}$  are not excessive. Alternatively, changes could be made in bath, cell, or tape speed, to reduce the  $J_{max}/J_{ave}$  ratio and thus reduce  $J_{max}$ .

(iii) Damage to substrate-deposit interface.—The final constraint involves more subtle effects inasmuch as a damaging of the substrate-deposit interface is not always readily evident without additional evaluations. If  $J$  or  $J_d$  are sufficiently high, excessive heating of the interface or the generation of internal stresses in the

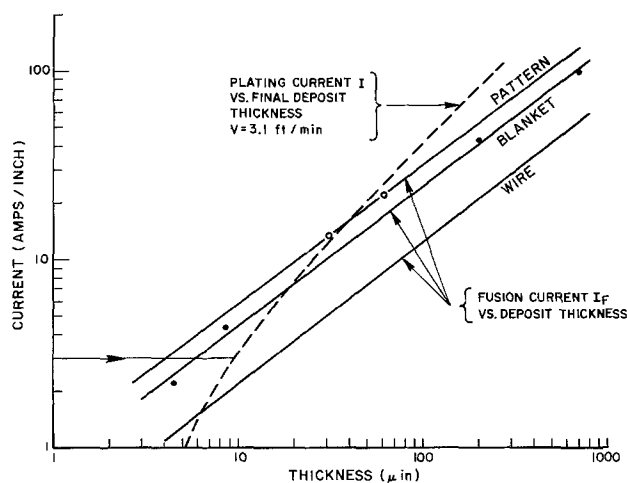


Fig. 11. Plating current  $I$  and fusion current  $I_F$  vs. copper thickness. The plating current line (dashed) describes the Faraday equivalent current-thickness relation at the exit of the plating loop, for an input thickness of  $3 \mu\text{in.}$  and a tape speed of  $3.1 \text{ ft/min.}$  Fusion lines describe current limits of specimens in air for wire (14), for blanket plated Cu/polyimide (13), and for patterned Cu/polyimide (our data). The line shifts upward reflect the improved heat dissipation of the respective geometries.

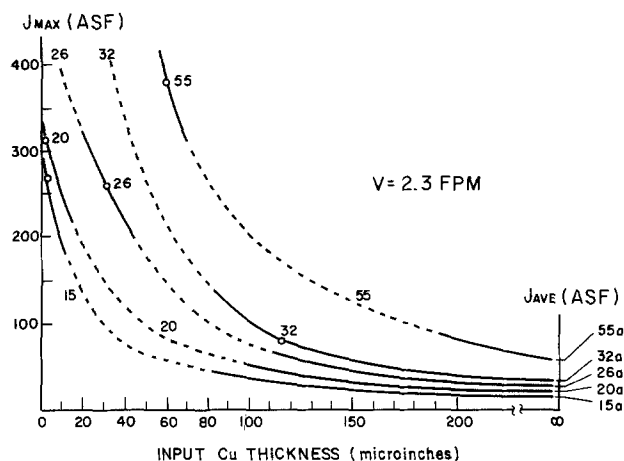


Fig. 12. Peak cathodic current density  $J_{\text{max}}$  vs. Cu thickness (average over all buses) at the plating loop input;  $v = 2.3 \text{ ft/min,}$  plating current  $I$  as a parameter. The curves are sketched using experimental results (open circles) plus the extrapolations:  $J_{\text{max}} = \infty$  at zero thickness,  $J_{\text{max}} = J_{\text{ave}}$  at  $\infty$  thickness.

deposit may lower the substrate-deposit adherence or induce preferential corrosion of pattern edges (undercutting) during plating. These aspects are strongly sensitive to the particulars of the materials plated, thus we cannot *a priori* specify the appropriate limiting values. Such limits must be empirically fixed by careful evaluations of product quality vs. the level of cur-

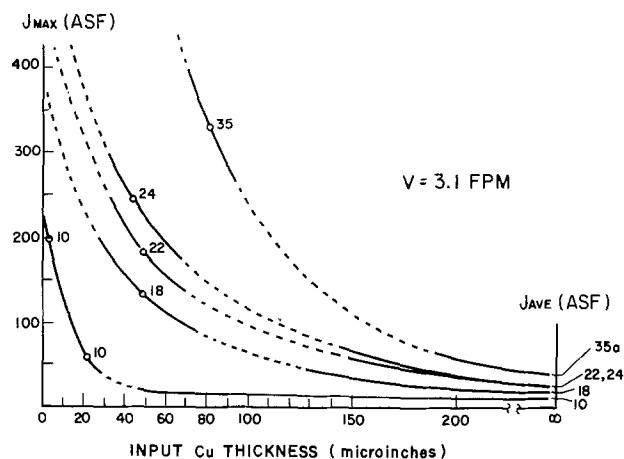


Fig. 13. Peak cathodic current density  $J_{\text{max}}$  vs. Cu thickness (average over all buses) at the plating loop input;  $v = 3.1 \text{ ft/min,}$  plating current  $I$  as a parameter.

rents applied. We do not assert that the cathodic or deposit current densities stand alone as determinants of plating quality, but must certainly be included as major factors.

*Plater design.*—An empirical scheme based upon the setting of an upper limit for  $J_{\text{max}}$  is sketched in Fig. 12 and 13 for tape speeds of  $2.3$  and  $3.1 \text{ ft/min,}$  respectively. In these figures experimental values of  $J_{\text{max}}$  (open circles) have been plotted vs. input copper thickness for respective single plating loops, with plating current  $I$  as a parameter. A family of curves has been sketched making use of the experimental results (open circles) and the following criteria: approaching zero input thickness, the curves must be asymptotic to the positive  $J_{\text{max}}$  axis; for very large thicknesses,  $J_{\text{max}}$  must approach  $J_{\text{ave}}$ . (Note  $J_{\text{ave}}$  is independent of the plating distribution. Figure 12 and 13 give an indication of how  $J_{\text{max}}$ , input thickness, and the individual loop currents  $I$  are related.)

A design can be accomplished by the following iterations:

1. For a specified  $J_{\text{max}}$  read or interpolate the allowed loop current  $I$  corresponding to the input Cu thickness.
2. For the indicated  $I$ , compute the thickness which will be added by plating (via Faraday's law).
3. Repeat for the next loop, using the incremented Cu thickness.

As an illustration, a plater design using  $J_{\text{max}} = 200 \text{ asf}$  as an upper limit is presented in Table II for speeds of  $2.3$  and  $3.1 \text{ ft/min.}$  The implementation of this design requires that each plater pass be electrically isolated from all others. The precision in  $J_{\text{max}}$  vs. thickness data (open circles) is estimated as  $10\text{--}15\%$ . For regions where no data is available (the dashed portions of the curves), the estimates of  $J_{\text{max}}$  should be accurate to  $20\text{--}40\%$ , based upon the degree of extrapolation.

Table II. Plater design for isolated plating loops. Upper limit of  $J_{\text{max}} = 200 \text{ asf;}$  tape speed  $2.3$  and  $3.1 \text{ ft/min.}^*$

Pass	$V = 2.3 \text{ ft/min}$			$V = 3.1 \text{ ft/min}$		
	Input Cu thickness	Allowed current $J_{\text{max}} = 200 \text{ asf}$	Equivalent Cu thickness**	Input Cu thickness	Allowed current $J_{\text{max}} = 200 \text{ asf}$	Equivalent Cu thickness***
I	$3 \mu\text{in.}$	13A	$39 \mu\text{in.}$	$3 \mu\text{in.}$	10A	$22 \mu\text{in.}$
II	$42 \mu\text{in.}$	25A	$75 \mu\text{in.}$	$25 \mu\text{in.}$	17A	$37 \mu\text{in.}$
III	$117 \mu\text{in.}$	57A	$171 \mu\text{in.}$	$62 \mu\text{in.}$	24A	$53 \mu\text{in.}$
IV				$115 \mu\text{in.}$	35A	$77 \mu\text{in.}$
Total		95A	$288 \mu\text{in.}$		86A	$192 \mu\text{in.}$

\* Assumptions: input electroless Cu thickness =  $3 \mu\text{in.}$ ; pattern area =  $0.196 \text{ ft}^2/\text{ft}$ ; tape length in solution =  $4.75 \text{ ft.}$

\*\* Conversion  $3.0 \mu\text{in./A.}$

\*\*\* Conversion  $2.2 \mu\text{in./A.}$

### Discussion

*Separation of transverse and axial distributions.*—The validity of treating the transverse and axial copper distributions as separable is supported by (i) experimental results relating  $J_{\max}$  and  $J_{\text{ave}}$  at different transverse positions and (ii) calculations of cathodic current distributions using the Tobias-Wijsman parallel electrode model (6). Thus:

(i) The ratio  $J_{\max}/J_{\text{ave}}$  used as an index of axial plating asymmetry is reported in Table I for measurements on bus A. For runs 12/11 and 12/14, the bus A results were 7.87 and 2.58, respectively. The corresponding ratios for center bus C were found to be 8.77 and 1.84, respectively. Thus the plating asymmetries at different lateral positions appear to be the same, even though the absolute plating rates differ by a transverse position dependent scale factor.

(ii) The Tobias-Wijsman calculation (6) of the current distribution in a pair of closely spaced long planar electrodes can be used to evaluate the relative effects of electrode *vs.* electrolyte resistance when cathodic currents are much less than the limiting current density, *i.e.*, negligible concentration polarization. The very high value of limiting current density<sup>3</sup> in fluoborate electrolytes (15) insures the validity of neglecting concentration polarization.

The Tobias-Wijsman parameter  $\phi$  expresses the degree of nonuniformity of the cathodic current density  $J$  along the resistive cathode

$$\phi = L \left\{ \frac{r}{b + d/K} \right\}^{1/2} \quad [3]$$

where  $L$  = electrode length,  $r$  = cathode resistance per unit length of a 1 cm strip,  $b$  = linear polarization parameter (model assumes  $b = d\eta/dJ$ , where  $\eta$  is the surface overpotential),  $d$  = the electrode spacing, and  $K$  = electrolyte conductivity. The expression in brackets denotes the ratio of electrode to electrolyte resistance. When this ratio is large, thus large  $\phi$ , the current density distribution is highly nonuniform.

Applying the above formulae to a typical half-pass in our plater

$$\begin{aligned} b &= 0.215 \text{ ohm-cm}^2 \text{ [calculated from results in Ref. (16)]} \\ K &= 0.15 \text{ ohm}^{-1} \text{ cm}^{-1} \text{ [from Ref. (15)]} \\ d &= 2.94 \text{ cm} \\ L &= 71.6 \text{ cm} \\ r &= 0.709/t \text{ ohm where } t = \text{the average copper thickness in the half-pass of the plater} \end{aligned}$$

Thus

$$\phi = 13.48 t^{-1/2} \quad [4]$$

Calculations of  $\phi$  and  $J_{\max}/J_{\text{ave}}$  *vs.* average electrode thickness were made with Eq. [XXX] of Ref. (6) and are presented in Table III. Note that  $J_{\max} = J(X = 0)$ . The calculations indicate that the electrode resistance

<sup>3</sup> The supplier's technical bulletin reports a limiting current density of 300 asf at 80°F without agitation, for the electrolyte used in our experiments.

Table III. Calculation of cathodic current distribution *vs.* mean copper thickness\*

Mean copper thickness ( $\mu\text{in.}$ )	$\phi$	$\frac{J_{\max}}{J_{\text{ave}}}$
0	$\infty$	$\infty$
5	6.03	6.03
10	4.26	4.26
20	3.01	3.02
50	1.91	2.00
100	1.35	1.54
200	0.953	1.29
$\infty$	0.00	1.00

\* Model of Tobias and Wijsman (6).

is appreciably greater than the electrolyte resistance up to about 100  $\mu\text{in.}$  deposit thickness. This supports the assumption that the observed distributions in the early stages of the copper buildup reflect mainly the effects due to cathode resistance.

*Effect of speed and current on axial distributions.*—The experimental results indicate that the plating distributions are affected by changes in tape speed or in applied current, as evidenced by variations in asymmetry factor  $A$ . To examine these variations more closely, it is useful to relate  $A$  to the measured variables. By using Eq. [2] for  $J_{\text{ave}}$  and  $J_{\max}$ , the factor  $A$  for a single loop of length  $L$ , speed  $v$ , and applied current  $I$  becomes

$$A = \frac{L}{T_f - T_o} (\text{grad } T)_{\max} = L \cdot v/I (\text{grad } T)_{\max} \quad [5]$$

where  $(\text{grad } T)_{\max}$  denotes the maximum thickness gradient  $dT/dX$  for the loop and  $T_f - T_o$  the increment in copper thickness. For two experiments at different  $I$  and  $v$  but constant  $L$

$$\begin{aligned} A_1/A_2 &= (v_1/v_2) (I_2/I_1) (\text{grad } T_1)_{\max}/(\text{grad } T_2)_{\max} \quad [6] \\ &= (v_1/I_1) (v_2/I_2)^{-1} (\text{grad } T_1)_{\max}/(\text{grad } T_2)_{\max} \quad [7] \end{aligned}$$

At constant speed, the  $A$  ratio is seen inversely proportional to the applied current ratio and directly proportional to the ratio of maximum thickness gradients. At constant current the  $A$  ratio is directly proportional to the speed ratio and to the ratio of maximum thickness gradients. For either speed or current variations, the plated copper increment  $T_f - T_o$  will vary and thus the copper distribution curves are difficult to compare and interpret.

An important case is that in which both input and exit copper thicknesses are identical though  $v$  and  $I$  are varied. This can occur if  $v_1/I_1$  equals  $v_2/I_2$ , thus

$$A_1/A_2 = (\text{grad } T_1)_{\max}/(\text{grad } T_2)_{\max} \quad [8]$$

In the plater described here we expect the kinetic and mass transfer resistances to be unaffected by the moderate speed or current level changes which have been made. For identical input and output thicknesses we expect identical  $T$  *vs.*  $X$  curves, thus the right side of Eq. [8] should equal unity and  $A_1 = A_2$ . A test of this assumption can be made using the correlations in Fig. 12 and 13. As an example, for speeds of 2.3 and 3.1 ft/min and input thicknesses of  $T_o = 10 \mu\text{in.}$ , we calculate  $A_1 = 18.4$ ,  $A_2 = 12.2$  for  $(v/I)_{1,2} = 0.115$ ;  $A_1 = 15.8$ ,  $A_2 = 12.2$  for  $(v/I)_{1,2} = 0.153$ ;  $A_1 = 14.5$ ;  $A_2 = 14.2$  for  $(v/I)_{1,2} = 0.230$ . The agreement above is only fair, reflecting the approximate nature of the Fig. 12 and 13 correlations.

*Single pass runs, normal configuration.*—The importance of the cathode resistance in determining the axial plating distribution is readily observed in Fig. 7 and 8. The deposit asymmetry is greatest when plating the thin electrode coating but is reduced as the input copper thickness is increased. In Table I for groups I and II we observe a decrease in asymmetry factor  $A$  with input thickness. ( $J_{\text{ave}}$  in these cases is steady or increasing with thickness.) At the highest input thickness, 146  $\mu\text{in.}$  in run 1/15,  $A$  becomes as low as 1.0, indicating that a uniform (linear) plating rate has been attained.

In group II, runs 1/28 and 1/29 were identical except for the input thicknesses, 3.2 *vs.* 2.8  $\mu\text{in.}$ , respectively. The strong dependence of the axial distribution on input thickness is seen in the higher  $A$  value for run 1/29. (The lack of complete agreement in values of  $J_{\text{ave}}$  for these two runs at the same current indicates that some run-to-run variation in copper distribution over the pattern has occurred; this type of variation is also seen in comparing several other runs of equal applied cur-



rents.) An additional factor which enhances the input thickness dependence of the axial distribution is the observed variation in electroless copper resistivity<sup>4</sup> with thickness, the thinnest deposits having the highest resistivity values. Thus the ohmic effects due to input thickness (resistance) will be larger than expected from the relative change in deposit thickness.

The preceding comments have generally ignored the question of interpreting the observed asymmetries in the light of changes in the applied current. The separation of asymmetry effects due to current *vs.* thickness changes is not readily accomplished and very likely requires additional experiments at constant current.

In attempting to interpret the asymmetry/thickness/current interaction, we note that the factor  $A$ , though proportional to  $J_{\max}$ , does not take into account the distribution of  $J$  values along the entire loop axis. Thus the integrated effects of the asymmetry are not completely taken into account. To examine this idea further, we have defined an additional index,  $F_{1/2}$ , the fraction of the total plating which occurs in the input half of the plating loop.

In Table IV, we have retabulated the results from normal configuration runs at full pass length, and have added computed values  $A \cdot I$  and  $F_{1/2}$ . The product  $A \cdot I$  is a current normalized asymmetry factor (cf., Eq. [5]), while  $F_{1/2}$  integrates the asymmetry over each half of the plating loop. For  $J_{\max} = J_{\text{ave}}$ ,  $A = 1.0$  and  $F_{1/2}$  approaches (but must be less than) 0.5. In Table IV,  $A \cdot I$  shows considerable scatter and does not indicate a strong correlation with input thickness above the scatter. The  $F_{1/2}$ , on the other hand, shows a clear correlation with input thickness. We expect that  $F_{1/2}$  is relatively insensitive to current changes, provided the corresponding values of  $J_{\max}$  are much less than limiting current values. We have interpreted the  $F_{1/2}$  results in Table IV as supporting our basic conclusion that the plating asymmetry along the loop axis decreases with input thickness of deposit.

*Single pass runs with exit field shield.*—The exit field shield experiments show that peak current density can indeed be reduced (note Fig. 9A). The measured  $J_{\max}$  for the runs with the shield (3/5) and without the shield (1/29) were 203 asf and 302 asf, respectively. The input tape thickness in run 3/5 was slightly less than that in run 1/29, thus the differences in maximum current density due to the presence of the shield should be even greater.

*Single pass runs with added cathodes in solution.*—The runs made using added cathode contacts in solution show noticeably enhanced plating rates in the vicinity of the cathode connections, note Fig. 10. They also show relatively low values of  $J_{\max}$ . These reduced values are largely the result of extraneous plating, as an appreciable fraction of the applied current is consumed by deposition onto the cathode connections. Thus Faraday's law cannot be used to predict the deposit thickness in this case. As an example, in run 3/13

<sup>4</sup>J. F. D'Amico and M. A. De Angelo, unpublished results. Four-point probe measurements of  $\frac{3}{8} \times 5$  in. electroless copper-polyimide strips produced with a similar bath gave resistivity values of 21  $\mu\text{ohm-cm}$  at 2.8  $\mu\text{in.}$ , 16  $\mu\text{ohm-cm}$  at 3.2  $\mu\text{in.}$ , and 4.5  $\mu\text{ohm-cm}$  at 10  $\mu\text{in.}$

Table IV. Computation of  $A \cdot I$  and  $F_{1/2}$  for normal configuration runs at full pass length

Run	Input Cu thickness ( $\mu\text{in.}$ )	Current (A)	Asymmetry factor $A$	$A \cdot I$	$F_{1/2}$
12/11, 2.3 ft/min	3.0	20	7.9	158	0.011
12/14, 2.3 ft/min	99.5	55	2.6	143	0.27
1/15, 2.3 ft/min	146	32	1.0	32	0.49
1/29, 3.1 ft/min	2.8	10	11.9	119	0.050
1/28, 3.1 ft/min	3.2	10	7.6	76	0.063
1/29-A, 3.1 ft/min	39.6	20	7.9	158	0.16
1/29-B, 3.1 ft/min	96.0	45	2.9	131	0.19

(Fig. 10A) with  $I = 14\text{A}$  at 3.1 ft/min, an average of 13  $\mu\text{in.}$  Cu was added to all buses while the deposit predicted by Faraday's law is 26  $\mu\text{in.}$ , a reduction of 50%. Over thicker deposits, e.g., run 3/14 (Fig. 10B), the copper loss was only 14% of the Faraday value. The practical application of this method awaits a useable cathode connection which can be continuously deplated of the deposited copper.

*Plater design via limits on  $J_{\max}$ .*—The plater design scheme outlined in Fig. 12 and 13 is presented not as a final solution but as a preliminary exercise on how to attack the continuous plating problem. The curve family which has been drawn through the available but limited data could be improved by addition of more data. We would also point out that the correlations presented are highly specific to our plater and electrolyte and should be extrapolated with caution. The lack of applicability of these results to other geometries and electrolytes restricts the usefulness of this approach and supports the formulation of a mathematical model to provide the needed generalization. The results of this work could be used to verify the predictions of such a model.

## Summary

The cathodic electrodeposition of copper onto high resistance platings has been studied in a continuous copper fluoborate electroplater. The effects of cathode resistance were found to dominate the plating distribution for high input resistances, producing highly asymmetric distributions of deposits along the plater axis. These asymmetries reflect the highly nonuniform cathodic current densities produced by the ohmic effects, and are in addition to thickness variations due to the primary current distribution or to electrolyte polarization effects. As thicker, less resistive electrodes are plated, the axial asymmetries were reduced, approaching a state of uniform plating.

In view of the observed asymmetries, the peak cathodic current densities possible in the plater, even at moderate values of applied current, can be excessive and may produce degradation of the physical properties of the plated deposits. Thus the effects of high input resistance must be carefully considered in the design and operation of this type of system.

A plater design scheme for continuous plating in copper fluoborate has been presented. This scheme, based upon imposed limits in cathodic current density, should prove useful as a starting point for the analysis of other continuous plating systems, and should provide a valuable input for the development of a theoretical model.

For any substrate-electrolyte combination, a definitive determination of cathodic current density *vs.* product quality must be developed as corollary information if a proper plating design is to be achieved.

## Acknowledgments

The authors gratefully acknowledge Mr. F. McLarson for his valuable critique, suggestions, and assistance, especially in the application of the Tobias-Wijsman model to this problem. They also acknowledge Mr. L. R. Johnson for his technical assistance during plater operations and tape sampling.

Manuscript submitted June 17, 1975; revised manuscript received Nov. 17, 1975.

Any discussion of this paper will appear in a Discussion Section to be published in the December 1976 JOURNAL. All discussions for the December 1976 Discussion Section should be submitted by Aug. 1, 1976.

Publication costs of this article were partially assisted by the Western Electric Company.

## REFERENCES

1. D. J. Sharp, *Plating*, **58**, 786 (1971).
2. J. F. D'Amico, M. A. De Angelo, J. F. Henrickson, J. T. Kenney, and D. J. Sharp, *This Journal*, **118**, 1695 (1971).
3. A. Weisselberg, *Trans. Electrochem. Soc.*, **90**, 235 (1946).
4. J. Wojtowicz, L. Laliberte, and B. E. Conway, *Electrochim. Acta*, **13**, 361 (1968).
5. V. Fomichev, *Soviet Electrochem.*, **4**, 708 (1968).
6. C. Tobias and R. Wijsman, *This Journal*, **100**, 459 (1953).
7. R. Alkire, *ibid.*, **118**, 1935 (1971).
8. See, for example, J. S. Newman, "Electrochemical Systems," Chap. 1, Prentice-Hall, Englewood Cliffs, New Jersey (1973).
9. *Ibid.* Chap. 18.
10. F. Will, *This Journal*, **110**, 145 (1963).
11. D. Bennion and C. Tobias, *ibid.*, **113**, 589 (1966).
12. R. Burshtein, M. Tarasevich, S. Chernyshov, and Y. Chirkov, *ibid.*, **4**, 1154 (1968).
13. L. D. Noble and R. Sinitski, Unpublished work.
14. W. H. Preece, *Proc. Roy Soc. (London)*, April 1884, Dec. 1887, and April 1888, referenced in "Standard Handbook for Electrical Engineers," 10th ed., D. G. Fink, Editor. McGraw-Hill, New York (1968).
15. "Modern Electroplating," 3rd ed., F Lowenheim, Editor, p. 185, John Wiley & Sons, New York (1974).
16. C. J. Milora, J. F. Henrickson, and W. C. Hahn, *This Journal*, **120**, 488 (1973).

## Mass Transfer on Horizontal Wires in the Presence of Free and Combined Forced and Free Convection

Aladar Tvarusko\*

Laboratoire Suisse de Recherches Horlogères, Neuchâtel, Switzerland

### ABSTRACT

Mass transfer was measured on horizontal copper and nickel wires (0.51 and 0.25 mm diameter) in acidified  $\text{CuSO}_4$  and alkaline ferro-ferricyanide solutions, respectively, in the presence of forced and free convection. The mass transfer measurements were made in practical overflow cells of two sizes over a limited range:  $1422 < \text{Sc} < 3433$ ,  $0.112 < \text{Re} < 4.40$ ,  $0.023 < \text{Gr} < 16.6$ ,  $37.9 < \text{Ra} < 5.7 \times 10^4$ . The mass transfer was proportional to  $\text{Re}^{0.4}$  and its magnitude was markedly affected by the concentration of the solution. Both forced and free convection are operative in most of the present forced-convection mass transfer measurements which correlate well if plotted as  $(\text{Sh}/\text{Re}^{1/2})(\text{Re}^2/\text{Gr})^{1/2}$  against  $\text{Gr}/(\text{Re}^2\text{Sc}^{1/3})$ . It is to be noted that the boundary layer thicknesses and the wire diameters are of comparable magnitude.

Heat and mass transfer to circular cylinders (tubes, wires) are of great technological importance and have been studied in various fluids under various geometrical and hydrodynamic conditions (1-3). The applications range from hot-wire anemometers (4) through heat-exchangers to chemical vapor deposition (5) and electrodeposition (6). Vertical and horizontal circular cylinders have been mostly studied.

Since heat and mass transfer are analogous, the results of either are of considerable interest to both. Most of the heat transfer measurements to horizontal cylinders, however, were done in air, i.e., at a low Prandtl number ( $\text{Pr} \approx 0.7$ ). The application of these heat transfer data to mass transfer in liquids of high Schmidt numbers ( $\text{Sc} \geq 1000$ ) is frequently not successful because of the marked influence of  $\text{Sc}$  on the processes involved (1-3).

The magnitude of mass and heat transfer is markedly affected by the fluid flow present. Heat and mass transfer measurements were made over a wide range of forced convection,  $10^{-5} < \text{Re} < 10^6$  and natural or free convection,  $10^{-9} < \text{Gr} < 10^9$ ,  $10^{-9} < \text{Ra} < 10^{11}$  (1-3, 7). The present mass transfer measurements were made over a limited range:  $1422 \leq \text{Sc} \leq 3433$ ,  $0.112 \leq \text{Re} \leq 4.40$ ,  $0.023 \leq \text{Gr} \leq 16.6$ ,  $37.9 \leq \text{Ra} \leq 5.7 \times 10^4$ . The author is unaware of any mass transfer measurements on horizontal cylinders under the aforementioned natural convection conditions. The mass transfer data of Dobry and Finn (8) are the only ones which were measured under forced convection conditions ( $\text{Sc} \approx$

$1200$ ,  $0.023 \leq \text{Re} \leq 8.1$ ) similar to those used in the present study. These data and other relevant heat transfer correlations are described in connection with the discussion of the present data.

In most heat and mass transfer measurements either the forced or free convection dominates and the other can be neglected. At certain combinations of  $\text{Re}$ ,  $\text{Gr}$ , and  $\text{Sc}$  ( $\text{Pr}$ ) numbers, however, both forced and free convection must be taken into consideration. Heat and mass transfer to horizontal cylinders have been studied in the presence of the extremely complex mixed convection in air (2-4, 7, 9-13) and reacting gases [ $\text{Pr} \sim 1$ , (5, 14, 15)], respectively. The mixed (combined) convection heat transfer has been theoretically analyzed for various Prandtl numbers (7, 16-18).

The subject of this paper is the mass transfer to horizontal copper and nickel wires in aqueous electrolytes of two types in a simple, practical overflow cell of two sizes in the presence of free and combined forced and free convection. The mass transfer is correlated in terms of appropriate dimensionless numbers.

### Experimental

A large portion of past heat and mass transfer studies on cylinders was made in carefully chosen geometries, such as a circular tube of large diameter with a large hydrodynamic entrance region which usually facilitated the correlation of the results. Cells or containers for these heat and mass transfer measurements are usually designed to maintain the fluid flow constant and well defined at and near the body being studied. This is not always the case in practical cells where other aspects must also be taken into considera-

\* Electrochemical Society Active Member.

Key words: mass transfer, wire, free convection, combined forced and free convection.

tion (e.g., engineering, economics). This means that the fluid flow in a cell is not necessarily well defined in a hydrodynamic sense but is characteristic for the cell in question.

The overflow cell, shown schematically in Fig. 1, is one of the simplest and most frequently used electrochemical cells. The solution enters near its bottom and flows through the cell and over some of its inner walls. Overflow cells of two lengths,  $L$ , 8.2 and 45.7 cm, and fluid flow cross-sectional areas,  $S$ , 38.7 and 667.7 cm<sup>2</sup>, respectively, were used. The design of these cells has been described in detail earlier (6, 19). Since the equivalent diameter of both overflow cells (using any definition) is greater than the entrance region, i.e., the distance between the horizontal wire and fluid entrance, the fluid flow cannot be considered to be fully developed. However, in view of the small average fluid velocities,  $U$ , used in these overflow cells (0.026–0.90 cm/sec) and the small wire diameters in a large volume of fluid in the cell (large  $S$ ), the fluid flow for all practical purposes is considered to be more or less uniform along the wire except at the highest  $U$  values in the long cell (0.036M CuSO<sub>4</sub>, 0.36M H<sub>2</sub>SO<sub>4</sub> solution).

The fluid after entering the cell suddenly expands, flows through it toward the overflow(s) at one or both end walls, and the angle of attack (the angle between stream direction and cylinder axis) at the wire may deviate from normal. According to Kutateladze (20), the heat transfer from a cylinder remains practically constant in the range of 90° ± 20° angle of attack outside of which it decreases substantially. In view of this and the small  $U$  values, the relatively large fluid volume in the cell, the small wire diameters, and the obtained results, the flow can be considered to be practically normal to the wire.

The mass transfer rates on the horizontal wires were obtained electrochemically by measuring potentiodynamically the cathodic limiting current density,  $I_L$ . The experimental details were described earlier (6, 21). Nickel and copper wires of 0.25 and 0.51 mm diameter,  $d$ , respectively, were used for the mass transfer measurements.

The  $I_L$  values were obtained in two types of aqueous solution. One was a deaerated 0.005 equimolar solution of the potassium ferro- and ferricyanide redox couple in 1M KOH and will be designated as 0.005M. The ferricyanide anion is reduced and only electron transfer takes place at the cathode. In the other solutions, the metal ion is reduced on the cathode to metal and removed from the solution. These solutions contained various amounts of CuSO<sub>4</sub> and ten-fold H<sub>2</sub>SO<sub>4</sub>. In both types of solution, the species to be reduced must diffuse through the diffusion layer to the cathode whereas only the ferrocyanide has to diffuse toward the bulk solution. Since the electroneutrality condition must be fulfilled, the concentration of the other species will also change in the diffusion layer(s) and must be esti-

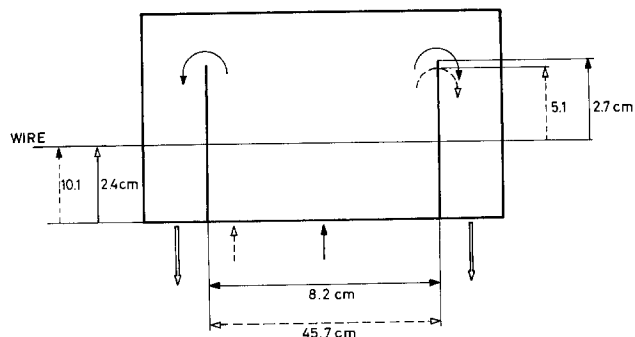


Fig. 1. Schematic diagram of an overflow cell. The solid and dashed lines indicate the most pertinent dimensions and fluid flow in the small and large overflow cell, respectively.

ated, especially in the case of free convection (22–25).

Free or natural convection is caused by the difference in solution density at and near the surface,  $\Delta\rho$ . These values were calculated by the procedure of Selman and Newman (23, 24) who state that the density difference calculated by the traditionally used method of Wilke, Eisenberg, and Tobias (25) can lead to appreciable errors. These two methods predict very different sulfuric acid concentrations at the cathode (23, 24) and thus, different  $\Delta\rho$  and Gr values are obtained. A complete dissociation of bisulfate ions to sulfate and hydrogen ions was assumed in the present calculations. The densities, viscosities, and diffusion coefficients of the solutions were calculated using the appropriate equations of Fenech and Tobias (26) and Gordon, Newman, and Tobias (27).

The data of Selman-Newman (23, 24) are strictly valid for the vertical electrode whereas the present mass transfer measurements relate to a horizontal electrode. Their estimation method for the interfacial concentrations is quite general and can be applied to other than vertical configurations by changing the power according to which the mass transfer coefficient,  $k$ , depends on the respective diffusion constants (23). According to Boeffard (28), the exponent in question is 2/3 for free convection at horizontal electrodes whereas it is 3/4 for vertical electrodes (23). The effect of this power change was calculated using the traditional Wilke-Eisenberg-Tobias procedure (25). The interfacial ferrocyanide concentrations were calculated (28) to be within 2% of each other for these two powers. In the case of the acidified CuSO<sub>4</sub> solutions, the difference in the Grashof numbers deviated by less than 2%; this was calculated with the densification coefficients,  $\alpha$ , of Selman and Newman (23, 24) using the formula of Fouad and Ibl (29). In view of these small errors in the interfacial concentration estimations, the data calculated by the Selman-Newman procedure were used in this study without any correction.

The dimensionless numbers were calculated with mean fluid properties ( $\rho$ ,  $\mu$ ,  $\nu$ ,  $D$ ), averaged between the bulk solution and electrode surface. The normalized density difference for Gr was calculated with fluid properties as required. The wire diameter was used for the characteristic length.

## Results and Discussion

**Forced convection.**—The limiting current densities were measured on two wires in two different solutions of various concentrations in overflow cells of two lengths. Figure 2 shows  $I_L$  to increase linearly with the

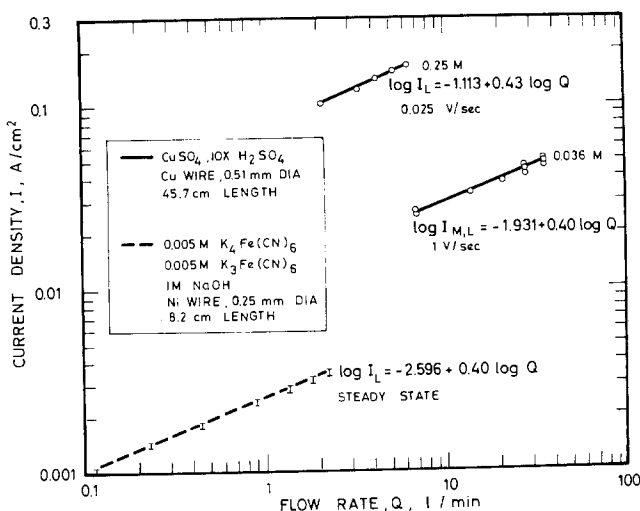


Fig. 2. Limiting current density as a function of volumetric flow rate in overflow cells of two sizes.

volumetric flow rate,  $Q$ , in a logarithmic plot in all cases. The slope is 0.40 at low concentrations regardless of the nature of the electroactive species and solution, cell length, and wire characteristics, but increases to 0.43 for the concentrated solution. The magnitude of  $I_L$  is markedly affected by the concentration of the electroactive species as expected.

The same  $I_L$  values are obtained under most conditions by steady-state and potentiodynamic measurements in a large number of simple redox and metal salt solutions (30). The steady-state  $I_L$  values are obtained from potentiostatic pulses located along the  $I_L$  plateau in the  $I$ - $V$  curves. It is more convenient to obtain  $I_L$  potentiodynamically. The  $I_L$  plateau is present only at low sweep rates of potential whereas at greater sweep rates  $I$  goes through a maximum and subsequent minimum (21, 31). It was shown elsewhere (31) that the  $I$  maximum and minimum ( $I_M$ ) in the  $I$ - $V$  curve are absent in the presence of fluid flow at markedly greater sweep rates than usually used. The permissible sweep rate increases with increasing fluid flow rate. The higher sweep rate leads to the minimization of the surface change along the  $I_L$  plateau in the presence of electrodeposition and also to time saving. The  $I$ - $V$  curves for the 0.036M acidified  $\text{CuSO}_4$  contained a shallow, very small current dip ( $I_M$ ) at the lowest flow rate at 1 V/sec sweep rate but  $I_M$  was absent at higher  $Q$ . The  $I_L$ - $Q$  correlation is not affected by taking these  $I_M$  values of negligible difference at the lowest flow rate used.

$\text{Sh}/\text{Sc}^{0.3}$  is widely used for the correlation of heat transfer. Figure 3 shows the data of Fig. 2 replotted in terms  $\text{Sh}/\text{Sc}^{0.3}$  and  $\text{Re}$ . It contains also the  $I_L$  values obtained in acidified  $\text{CuSO}_4$  solutions of various concentrations flowing at 6 liter/min which were described elsewhere (31). It is obvious that correlation of the present data is not satisfactory; the pre-exponential factors of the two extreme curves differ by a factor of two.

Figure 3 also shows some of the relevant heat and mass transfer correlations. Dobry and Finn (8) measured the  $I_L$  values in approximately 0.002M equimolar ferro-ferricyanide solutions with supporting electrolytes on 0.13 mm diameter Pt, Ni, and Cu wires and 0.025 mm diameter Cu wire. The equation given in Fig. 3 was obtained by regression analysis of all their data [Table I (8), using their solution properties]. The slope of this regression line is the same as those of the present data. The magnitude of their mass transfer however, is considerably smaller than that of the present study.

The broad-based heat transfer equations of Ulsamer [(32), recalculated from  $\text{Sh}/\text{Sc}^{0.31}$  to  $\text{Sh}/\text{Sc}^{0.3}$ ] and McAdams (1) are shown in Fig. 3 to be situated between the mass transfer data of Dobry and Finn (8)

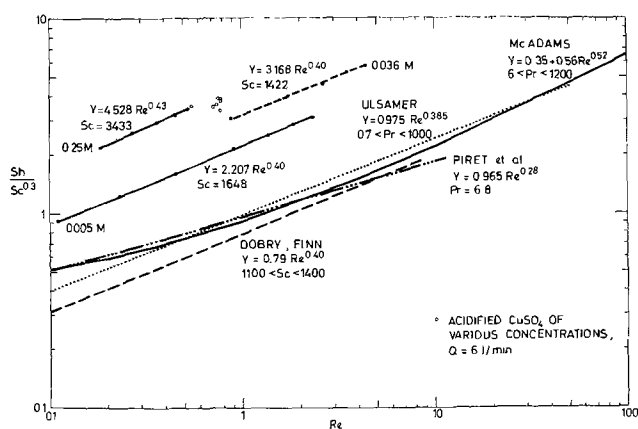


Fig. 3. Mass and heat transfer on horizontal cylinders in forced convection. The experimental data and the relevant correlations are expressed as  $\text{Sh}/\text{Sc}^{0.3}$ .

and the present ones. The heat transfer correlation for water by Piret *et al.* (33) is also shown. It can be seen that the indicated correlations predict practically similar heat transfer values at  $\text{Re}$  of interest here even though their coefficients differ markedly; this is possible for these forms of equations (4).

The discrepancy between these data and the present results is considerable. The greater mass transfer values could be due to the presence of upstream turbulence of the free stream and flow nonuniformity. The effect of turbulence was calculated by the Galloway-Sage equation modified by Brauer (3) and the results are shown in Fig. 4 in terms of the frequently used  $\text{Sh}/\text{Sc}^{1/3}$  ratio. This equation is given in Fig. 4 and is valid in the range of  $10^{-2} < \text{Re} < 4 \times 10^5$  and  $0.73 < \text{Pr} < 300$ . In view of the  $\text{Pr}$  limitation and  $\text{Sc}$  values of the present study (up to an order of magnitude greater), the results plotted in Fig. 4 can be considered only as approximative. The influence of  $\text{Sc}$  is small and is illustrated by the two  $Tu = 0$  curves where  $Tu$ , the intensity of turbulence, is the ratio of the root mean square of the velocity fluctuation and time-mean mainstream velocity (34, 35). Therefore, the effect of turbulence intensity is shown only for  $\text{Sc}$  of the acidified 0.25M  $\text{CuSO}_4$  solution. It can be clearly seen in Fig. 4 that the turbulence intensity cannot account for the present greater mass transfer in the  $\text{Re}$  region of interest, not even at the high  $Tu = 0.2$ ;  $\text{Sh}/\text{Sc}^{1/3}$  increased only by an additional 15% when  $Tu$  was increased to unity and is not shown. This is naturally subject to the assumption that the validity of the Galloway-Sage/Brauer equation can be extended to  $\text{Sc}$  of interest here without great error. It is to be noted that the magnitude of the error is likely to be smaller for an extrapolation from  $\text{Pr} \sim 300$  than only from  $\text{Pr} \sim 0.7$ . Furthermore, the effect of turbulence intensity at small  $\text{Sc}$  becomes significant only at significantly higher  $\text{Re}$  ( $\sim 10^4$ ).

It was mentioned earlier that the fluid flow is likely nonuniform near the horizontal cylinder (because of the short entrance region) especially in the acidified 0.036M  $\text{CuSO}_4$  solution. The mass transfer measurements clearly reveal (Fig. 3 and 4) that the data for the slower flowing acidified 0.25M  $\text{CuSO}_4$  are greater than those for the aforementioned solution. In view of this and the same functional dependence of  $\text{Sh}$  on  $\text{Re}$  (power of the 0.40-0.43) at low flow velocities, it can safely be assumed that the nonuniformity of fluid flow is not responsible for the deviation of the measured mass transfer.

Wire vibration could also be the cause of the greater mass transfer. However, no wire vibration was observed by the naked eye and the data in the acidified  $\text{CuSO}_4$  solutions in the same cell would again be con-

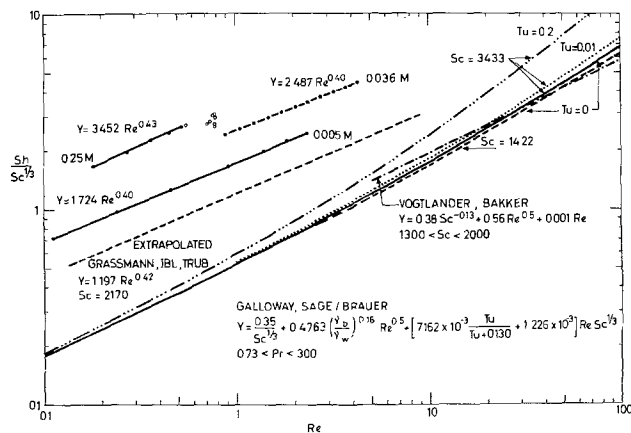


Fig. 4. Mass and heat transfer on horizontal cylinders in forced convection are given as  $\text{Sh}/\text{Sc}^{1/3}$ . The effect of turbulence intensity is calculated by the Galloway-Sage equation modified by Brauer.

tradictory. Furthermore, van der Hegge Zijnen (35) states that his data for turbulent air "show that the heat transfer from a wire vibrating in the direction of a uniform flow is somewhat lower than the heat transfer of a stationary wire in the same flow." In view of this, wire vibration is ruled out as being the cause for the deviation.

Figure 4 also shows the correlating equation of Vogtlander and Bakker (36) who measured the  $I_L$  in alkaline ferro/ferricyanide solution on short wires ( $0.5 < d < 1$  mm,  $L \sim 20$  mm) at higher  $Re$  ( $5 < Re < 100$ ). The extrapolation of their data to  $Re$  of interest here would yield considerably lower mass transfer than measured here. On the other hand, the extrapolated data of Grassmann, Ibl, and Trüb (37) for thin cylinders ( $d = 5$  mm,  $L = 40$  mm,  $200 < Re < 6000$ ) are closer to the present data even if the cylinder blockage is considered in the calculation of the fluid velocity (36). The data extrapolated from the correlation ( $Sh/Sc^{1/3} = 0.508 Re^{0.5}$ ) of Rao, Raju, and Rao (38) for horizontal cylinders ( $2.6 < d < 7.6$  mm,  $L = 50$  mm,  $100 < Re < 4000$ , reduction of ferricyanide) fall just below the Galloway-Sage/Brauer curve at  $Tu = 0$  and run parallel to it. They found that the mass transfer rate increased with decreasing cylinder diameter. The extrapolation of the mass transfer data to smaller  $Re$  is questionable, especially in view of the reported change in the form of the  $Nu-Re$  relationship taking place at  $Re = 44$  (4).

The correlations up to now contained  $Sc$  to power 0.3 or  $1/3$ . Two correlations contain  $Sc$  to 0.4 power which are shown in Fig. 5 together with the present data. Kutateladze's equation is valid at  $5 < Re < 80$  and  $Pr \neq 0.72$  (20) and  $Nu$  is proportional to  $Re^{0.4}$  just as found in the present data. The pre-exponential factor for the least concentrated solution (0.005M) is 14% higher than that of Kutateladze and considerably higher for the other two solutions. Kutateladze states that the validity of his equation is confirmed by experiments of various authors. The correlation of Perkins and Leppert (39) is valid at  $Re > 40$ , and  $0.7 < Pr < 300$ , and is close to that of Kutateladze in the overlapping region.

Hatton, James, and Swire (4) recently measured the heat transfer on horizontal cylinders ( $0.1 < d < 1.26$  mm,  $L = 121$  mm) in forced air ( $10^{-2} < Re < 45$ ) the direction of which was parallel, counter, or normal to the direction of gravity. Assuming a  $Sc^{0.4}$  dependence for the heat transfer, the equation in Fig. 5 was obtained for the present case, i.e., the forced flow is parallel with the direction of the free convection flow (counter to gravity). Their original equation contains a temperature loading factor the neglect of which (and its analogous ratio of kinematic viscosities) results in a maximum difference of  $-0.4\%$  in the magni-

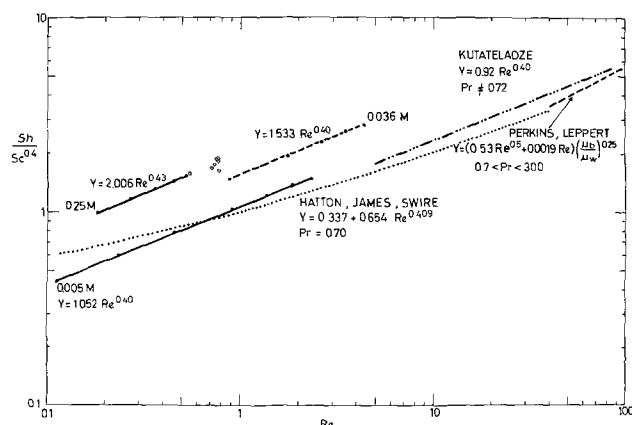


Fig. 5. Mass and heat transfer on horizontal cylinders in forced convection are shown as  $Sh/Sc^{0.4}$ . The correlations are given in their range of validity.

tude of  $Nu$ . Their curve runs close to the other two from literature (Fig. 5) and intersects the line for the least concentrated solution. They state that their correlation predicts higher  $Nu$  at  $Re < 5$ . The assumption of the  $Sc^{0.4}$  dependence of  $Sh$  is arbitrary since the heat transfer was measured only in air.

The separation of the data is not eliminated by increasing the power of  $Sc$  to 0.4 but the agreement of the data for the least concentrated solution has markedly improved. The deviation of the present data increases with the increasing concentration of the electroactive species. This clearly indicates the influence of a concentration-dependent variable which is the density difference. This determines the magnitude of the free convection the presence of which is clouded by the good correlatability of  $Sh$  with  $Re$  in all three solutions. Before discussing the combined forced and free convection, the results of free convection are discussed.

*Free convection.*—The local and over-all heat and mass transfers on horizontal circular cylinders under free convection have been widely studied [(1-3, 13, 40-42) and references therein]. The local heat and mass transfer around the circumference of the cylinder is very complex because of the presence of hydrodynamically stable and unstable conditions at the two extreme vertical positions and their combinations of various degrees around the circumference. The local heat and mass transfer is considerably higher in the hydrodynamically unstable region than in the stable region which in the present case (cathodic reduction) roughly corresponds to the upper and lower halves of the cylinder, respectively. This is well documented in the literature (3, 40, 41).

The over-all  $Sh$  is usually plotted as a function of  $Ra$ . Figure 6 shows the various correlations of the literature [(1, 3, 9), Tsubouchi, Masuda through Ref. (4)] which are different and their coefficients vary but the physical shape of the curves changes only little. The experimental data, obtained in acidified solutions of various  $CuSO_4$  concentrations (31), are more or less parallel to the correlations (dashed line) at the upper end of  $Ra$  studied whereas at the lower end of  $Ra$  the decrease of  $Sh$  with decreasing  $Ra$  is small (solid regression line). It is to be noted that Nagendra *et al.* (43) obtained a similar heat transfer behavior on vertical cylinders, i.e., the power of the  $Ra$   $d/L$  group decreased from 0.25 (short cylinders) with decreasing values of this group ( $Ra$  is diameter-based).  $Nu$  was found to be proportional to  $(Ra d/L)^{0.16}$  for long cylinders and 0.05 was the power for wires. In view of the closeness of the correlations for vertical and horizontal cylinders (1, 2), such a behavior could be expected for both cylinder orientations.

The experimental data are greater than those predicted by the heat transfer correlations (Fig. 6). According to Gebhart and Pera (13), the heat transfer

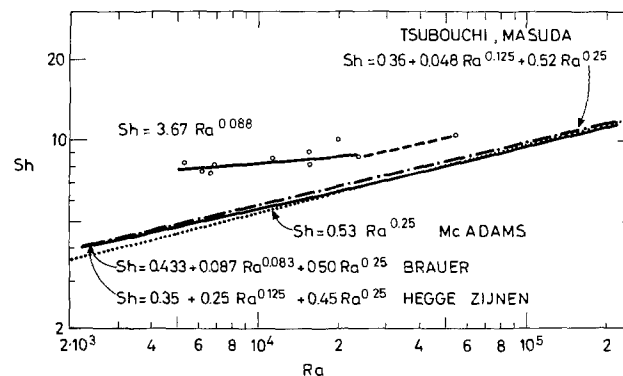


Fig. 6. Heat and mass transfer on horizontal cylinders in the presence of free convection as a function of Rayleigh number.

data at various Pr do not correlate well in the presence of natural convection and a systematic deviation of the data with Pr can be observed in past correlations (the  $Ra < 10^{-2}$  range is discussed). On the other hand, the mass transfer data in the range of  $Ra > 10^6$  are also somewhat above the corresponding heat transfer values [Fig. 7.13 in (3), (40, 42)].

It is to be noted that the boundary layer thicknesses are comparable to the wire diameter magnitudes. Therefore, only qualitative similarity can be expected with the results where the boundary layer thicknesses are very small in comparison to the cylinder diameter.

**Combined forced and free convection.**—In most heat and mass transfer cases, either the forced or free convection is dominating and the other can be neglected. Under certain conditions, however, both convections must be taken into consideration. It was shown that the mass transfer increases with increasing forced convection ( $Sh \propto Re^{0.4}$ ) and the magnitude of mass transfer ( $Sh/Sc^m$ ,  $0.3 \leq m \leq 0.4$ ) increases with increasing concentration of the electroactive species and the deviation is considerable. These aspects and the magnitude of Sh in the presence of free convection point toward the influence of both convections.

Heat transfer in the presence of combined (mixed) convection was studied on horizontal cylinders by several authors (2-4, 7, 9, 10-13) but the mass transfer was investigated only in the gas phase up to now (5, 14, 15). The local and over-all heat transfer in the presence of combined convection was also studied theoretically (7, 16-18). The heat and mass transfer is often correlated as a function of the vectorial sum of forced and free convection parameters (4, 5, 9, 14, 15). The vectorial addition is relevant only for the parallel forced and free convection flow (7). According to Acrivos (16), the two transfer mechanisms, however, are nonadditive and the transition between the two pure convections is gradual, especially at high Pr. The present mass transfer data could not be correlated on the basis of vectorial addition of Gr and Re.

The heat transfer on horizontal cylinders in the presence of combined convection is usually correlated as a function of the parameters  $Gr/Re^2$  (2, 3, 11, 12, 16, 17),  $Gr/Re^{2.5}$  (10, 18), or  $Pr Re^3/Nu Gr$  [to various powers at very small values of Re and Gr (7)]. Free convection is negligible if  $Gr/Re^2 \rightarrow 0$  and the forced convection can be neglected if  $Gr/Re^2 \rightarrow \infty$ . The influence of free convection is said to be negligible for a flat plate at  $Gr/Re^2 < 0.02$  for all Pr (16) or when the measured Nu values on horizontal cylinders are within 5% of the calculated parallel forced-flow values in air, i.e.,  $Gr/Re^2 < 0.28$  (11) or  $< 0.10$  (12). The range of present mass transfer data is  $0.0042 < Gr/Re^2 < 500$  which means that almost all data are within the combined convection zone. The correlation of  $Gr/Re^2$  vs. Sh normalized to a calculated pure forced-convective Sh (11, 12) or pure free-convective Sh shows a marked improvement over the correlations with vectorial addition of Gr and Re but is still not completely acceptable; its success depends entirely on the use of proper convective correlations which represent the data well.

According to Acrivos (17), the combined convection problem at large Pr values is characterized by the  $Gr/(Re^2 Pr^{1/3})$  group. The upper curve in Fig. 7 shows the present mass transfer data plotted as  $(Sh/Re^{1/2})(Re^2/Gr)^{1/2}$  against  $Gr/(Re^2 Sc^{1/3})$  instead of the originally proposed  $Gr/Re^2$  group (16). The data fall on a single curve the form of which is the same as the form of curves given by Acrivos for a vertical flat plate in an upward forced flow of fluid with  $Pr \leq 100$  (16). According to a subsequent analysis by Acrivos (17), the results given in his earlier paper (16) were "substantially in error" at high Pr values where the presence of two distinct boundary layers (heat transfer and hydrodynamic) was not accounted for. The mag-

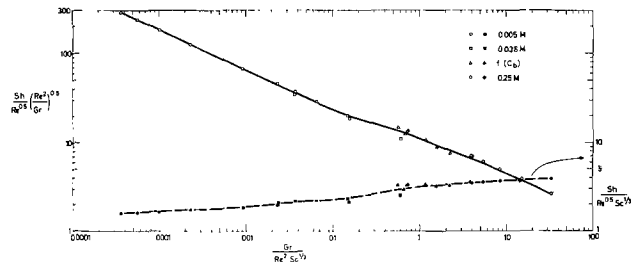


Fig. 7. Correlation of the present mass transfer data in the presence of combined parallel forced and free convection.

nitude of the error is unfortunately not given and therefore, no comparison can be made.

Acrivos (17) derived for general surface geometries that  $Nu_l/(Re^{1/2} Pr^{1/3})$  is a function of  $Gr/(Re^2 Sc^{1/3})$  where  $Nu_l$  is the local Nusselt number. Since the local and over-all heat and mass transfer equations are of similar forms, the over-all mass transfer values of the present study were also expressed as  $Sh/(Re^{1/2} Sc^{1/3})$  and are plotted in Fig. 7 as a function of  $Gr/(Re^2 Sc^{1/3})$ . This curve is similar to the curve given by Acrivos for the local heat transfer in the stagnation region of a constant temperature heated horizontal cylinder with upward flow at  $Pr \rightarrow \infty$ . The spread in the transition region between the pure forced and free convection zones ( $Gr/(Re^2 Sc^{1/3}) \sim 1$ ) is somewhat greater than in the corresponding region of the upper curve. Furthermore, the data at higher  $Gr/(Re^2 Sc^{1/3})$  values do not fall close to the assumable pure free convection asymptote (17). In view of the definite forced convection dependence of the mass transfer even at the highest Gr (0.25M solution), this deviation is not surprising. The effect of the forced convection seems to be better accounted for by the  $(Sh/Re^{1/2})(Re^2/Gr)^{1/2}$  group than by the other group. It is unfortunate that these two curves (Fig. 7), which represent the present data well, cannot be directly and quantitatively compared with those of Acrivos (16, 17).

### Conclusions

Mass transfer in aqueous solutions in practical overflow cells increased with increasing forced convection and was proportional to the 0.40-0.43 power of the fluid flow; this is in good agreement with some of the previous correlations. The magnitude of mass transfer, however, was markedly higher in both forced and free convection than predicted by the various correlations given in the literature, and the difference increased with increasing concentration of the electroactive species. In most of the present forced-convection mass transfer measurements both forced and free convection are operative. The effect of the combined convection on the present mass transfer data could not be correlated on the basis of vectorial addition of Gr and Re whereas the normalized Sh (to a pure forced-convective Sh)  $Gr/Re^2$  curves yielded improved but still not completely acceptable correlations. The relations developed by Acrivos (16, 17) correlate the present mass transfer data well especially if plotted as  $(Sh/Re^{1/2})(Re^2/Gr)^{1/2}$  against  $Gr/(Re^2 Sc^{1/3})$ .

It is to be noted that the boundary layer thicknesses are comparable to the wire diameters used, and therefore only qualitative agreement can be expected with results for which the boundary layer thicknesses are small in comparison to the cylinder diameter. Furthermore, the theoretical correlations assume that the fluid properties remain constant in the boundary layers with the exception of fluid density. In order to account for fluid property changes in the boundary layers, the various dimensionless numbers were correlated with mean fluid properties.

It is shown that the data obtained in practical overflow cells can be correlated well by the relationship

developed, through and for carefully and purposely chosen experimental conditions and designs.

### Acknowledgment

The author wishes to thank Prof. C. W. Tobias for calling his attention to Ref. (28).

Manuscript submitted Aug. 26, 1975; revised manuscript received Nov. 14, 1975.

Any discussion of this paper will appear in a Discussion Section to be published in the December 1976 JOURNAL. All discussions for the December 1976 Discussion Section should be submitted by Aug. 1, 1976.

### LIST OF SYMBOLS

$a$	thermal diffusivity, $\text{cm}^2/\text{sec}$
$c$	concentration, $\text{mole}/\text{cm}^3$
$d$	wire diameter, $\text{cm}$
$D$	diffusivity, $\text{cm}^2/\text{sec}$
$F$	Faraday's constant, 96,487 coulomb/g-equiv.
$g$	acceleration of gravity, $\text{cm}/\text{sec}^2$
$I$	current density, $\text{A}/\text{cm}^2$
$I_L$	limiting current density, $\text{A}/\text{cm}^2$
$I_M$	current density at the minimum of $I$ - $V$ curves, $\text{A}/\text{cm}^2$
$k$	mass transfer coefficient, $= I_L/zF c_b$ , $\text{cm}/\text{sec}$
$L$	wire length, $\text{cm}$
$Q$	volumetric flow rate, liter/min
$Q^*$	volumetric flow rate, $\text{cm}^3/\text{sec}$
$S$	cross-sectional area of fluid flow, $\text{cm}^2$
$U$	average flow velocity, $= Q^*/S$ , $\text{cm}/\text{sec}$
$V$	electrode potential, $V$
$z$	valence of ionic species, g-equiv./mole
$\alpha$	densification coefficient, $= 1/\rho(d\rho/dc)$ , $\text{cm}^3/\text{mole}$
$\Delta$	difference between value in bulk and at electrode
$\mu$	dynamic viscosity, $\text{g}/\text{cm}\cdot\text{sec}$
$\nu$	kinematic viscosity, $\text{cm}^2/\text{sec}$
$\rho$	density, $\text{g}/\text{cm}^3$

### Dimensionless numbers

Gr	Grashof number, $= gd^3/\nu^2 \cdot (\rho_w - \rho_b)/\rho_b$
Nu	Nusselt number, $= kd/D$
$Nu_l$	local Nusselt number
Pr	Prandtl number, $= \nu/a$
Ra	Rayleigh number, $= Gr Pr$ , $= Gr Sc$
Re	Reynolds number, $= Ud/\nu$
Sc	Schmidt number, $= \nu/D$
Sh	Sherwood number, $= kd/D$
Tu	turbulence intensity, = ratio of the root mean square of the velocity fluctuation and time-mean mainstream velocity

### Subscripts

$b$	in the bulk
$w$	at the electrode wall

### REFERENCES

- W. H. McAdams, "Heat Transmission," Chap. 7 and 10, McGraw-Hill Book Co., New York (1954).
- H. Börner, *VDI-Forschungsh.*, **512**, (1965).
- H. Brauer, "Stoffaustausch einschliesslich chemischer Reaktionen," Chap. 7, Verlag Sauerländer, Aarau, Switzerland (1971).
- A. P. Hatton, D. D. James, and H. W. Swire, *J. Fluid Mech.*, **42**, 17 (1970).
- H. E. Carlton and J. H. Oxley, "Proceedings of the Conference on Chemical Vapor Deposition of Refractory Metals, Alloys, and Compounds," A. C. Schaffhauser, Editor, pp. 19-33, American Nuclear Society, Hinsdale, Ill. (1967).
- A. Tvarusko, *This Journal*, **119**, 43 (1972).
- S. Nakai and T. Okazaki, *Intern. J. Heat Mass Transfer*, **18**, 387, 397 (1975).
- R. Dobry and R. K. Finn, *Ind. Eng. Chem.*, **48**, 1540 (1956).
- B. G. van der Hegge Zijnen, *Appl. Sci. Res.*, **A6**, 129 (1956).
- G. K. Sharma and S. P. Sukhatme, *J. Heat Transfer, Trans. ASME*, **91**, 457 (1969).
- P. H. Oosthuizen and S. Madan, *ibid.*, **92**, 194 (1970).
- P. H. Oosthuizen and S. Madan, *ibid.*, **93**, 240 (1971).
- B. Gebhart and L. Pera, *J. Fluid Mech.*, **45**, 49 (1970).
- H. E. Carlton and J. H. Oxley, *Am. Inst. Chem. Engrs. J.*, **13**, 86 (1967).
- H. E. Carlton and J. H. Oxley, *ibid.*, **13**, 571 (1967).
- A. Acrivos, *ibid.*, **4**, 285 (1958).
- A. Acrivos, *Chem. Eng. Sci.*, **21**, 343 (1966).
- N. D. Joshi and S. P. Sukhatme, *J. Heat Transfer, Trans. ASME*, **93**, 441 (1971).
- A. Tvarusko, *Plating*, **58**, 983 (1971).
- S. S. Kutateladze, "Fundamentals of Heat Transfer," pp. 246-248, Edward Arnold (Publishers) Ltd., London (1963).
- A. Tvarusko, *Plating*, **60**, 345 (1973).
- N. Ibl and U. Braun, *Chimia (Aarau)*, **21**, 395 (1967).
- J. R. Selman and J. Newman, UCRL-20322, January 1971.
- J. R. Selman and J. Newman, *This Journal*, **118**, 1070 (1971).
- C. R. Wilke, M. Eisenberg, and C. W. Tobias, *ibid.*, **100**, 513 (1953).
- E. J. Fenech and C. W. Tobias, *Electrochim. Acta*, **2**, 311 (1960).
- S. L. Gordon, J. S. Newman, and C. W. Tobias, *Ann. N.Y. Acad. Sci.*, **70**, 414 (1966).
- A. J. -L. P. M. Boeffard, UCRL-16624, January 1966.
- M. G. Fouad and N. Ibl, *Electrochim. Acta*, **3**, 233 (1960).
- A. Tvarusko, *Plating*, **61**, 139 (1974).
- A. Tvarusko, *Electrodep. Surface Treat.*, **2**, 481 (1973/1974).
- J. Ulsamer, *Forsch. Gebiete Ingenieurw.*, **3**, 94 (1933).
- E. L. Piret, W. James, and M. Stacy, *Ind. Eng. Chem.*, **39**, 1098 (1947).
- A. H. P. Skelland, "Diffusional Mass Transfer," pp. 273-281, John Wiley & Sons, Inc, New York (1974).
- B. G. van der Hegge Zijnen, *Appl. Sci. Res.*, **A7**, 205 (1958).
- P. H. Vogtländer and C. A. P. Bakker, *Chem. Eng. Sci.*, **18**, 583 (1963).
- P. Grassmann, N. Ibl, and J. Trüb, *Chem.-Ingr.-Tech.*, **33**, 529 (1961).
- K. S. Rao, G. J. V. J. Raju, and C. V. Rao, *Indian J. Technol.*, **6**, 46 (1968).
- H. C. Perkins, Jr. and G. Leppert, *J. Heat Transfer, Trans. ASME*, **84**, 257 (1962).
- G. Schütz, *Intern. J. Heat Mass Transfer*, **6**, 873 (1963).
- R. Wilhelm, *VDI-Forschungsh.*, **531**, (1969).
- A. F. J. Smith and A. A. Wragg, *J. Appl. Electrochem.*, **4**, 219 (1974).
- H. R. Nagendra, M. A. Tirunaryanan, and A. Ramachandran, *J. Heat Transfer, Trans. ASME*, **92**, 191 (1970).



# Discharge Mechanism of MnO<sub>2</sub> Electrodes as Influenced by the Solubility of the Reaction Products

Paul Ruetschi\*

Leclanché S.A., 1400 Yverdon, Switzerland

## ABSTRACT

An ultrathin electrolytic cell has been used to study by means of microscopic observation morphological changes of MnO<sub>2</sub> particles at magnification of 1500× *in situ* during discharge in various electrolytes. It is shown that the solubility of three-valent manganese species plays an important role in certain electrolytes, depending on pH. The discharge mechanism is discussed in the light of the observed dissolution and on the basis of x-ray data of the solid reaction products.

Morphological changes occurring during electrochemical reduction of MnO<sub>2</sub> particles are difficult to observe by conventional microscopic means since the individual particles are very small and since MnO<sub>2</sub> electrodes contain normally acetylene black or graphite, which reduce optical contrast to unacceptable levels.

## Experimental

Recently, an ultrathin electrochemical cell was described (1) which allowed optical observation of electrode reactions *in situ* at maximum magnification. This technique was applied in the present study to MnO<sub>2</sub> electrodes.

The ultrathin MnO<sub>2</sub> electrodes were prepared by suspending 100 mg of finely ground electrolytic γ-MnO<sub>2</sub> (Tekkosha Type HH, BET area 43.2 m<sup>2</sup>/g) in 1 ml of chloroform and dipping a 2 mm wide and 20 mm long strip of very fine Ni or Pt screen (wire diameter 0.05 mm, 300 mesh) into this slurry. After drying, there remained 0.2-0.6 mg of MnO<sub>2</sub> on the screen. The electrode was then compressed at 5000 kg between polished steel dies and mounted flat, by means of epoxy resin, on a microscope slide, side by side with ultrathin counter- and reference electrodes. These latter consisted of 2 mm wide, 20 mm long, and 0.05 mm thick foils (Goodfellow Metals Ltd., Ruxley Towers, Claygate-Esher, Surrey, England) of amalgamated zinc (for KOH, NH<sub>4</sub>Cl, and ZnCl<sub>2</sub> solutions) or of electroformed porous lead (for H<sub>2</sub>SO<sub>4</sub> solutions). A cover glass of 0.15 mm thickness was placed on top of the electrodes and epoxy resin was applied around its periphery, effectively sealing the cell. The cell was filled with electrolyte through an intentional opening in the epoxy seal by applying vacuum (Fig. 1).

The electrodes were discharged at slow linear potentiodynamic sweep (3 mV/min) using a Wenking potentiostat 68 TA 1 and scanning potentiometer SMP 69. Photographs were taken at 1500× optical magnification using oil immersion, a 100× objective lens, vertical illumination through the microscope tube (Metallurgical Microscope Olympus, Type MF), and a Polaroid Type 107 film.

## Alkaline Solutions (KOH 10.2M)

Two peaks (Fig. 2) were observed in the current-voltage diagram (2), the first at 1.3V vs. Zn/ZnO and the second at 0.9V vs. Zn/ZnO. During the first peak no change in the shape of the original MnO<sub>2</sub> particles was observed. However, sudden dissolution of the grains started during the descending branch of the peak. Finally, only the bare substrate remained. During the second peak small hexagonal platelets of

Mn(OH)<sub>2</sub> began to crystallize out of solution onto the substrate (Fig. 3).

Growth of hexagonal crystals of Mn(OH)<sub>2</sub> can be followed even better in Fig. 4, obtained under similar conditions, Patience and luck combined determined if a good spot was chosen for one picture series.

The observation that partially reduced MnO<sub>2</sub> becomes quite soluble in KOH is of practical importance with respect to the self-discharge behavior and voltage recovery on open circuit of commercial alkaline cells.

The reaction mechanism in KOH can be represented as follows (3)

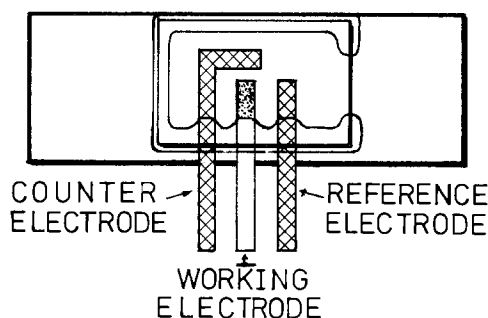
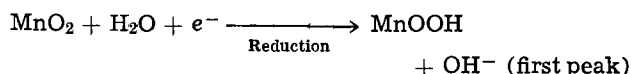


Fig. 1. Ultrathin cell for optical observation of electrode processes at 1500X magnification, viewed from the top.

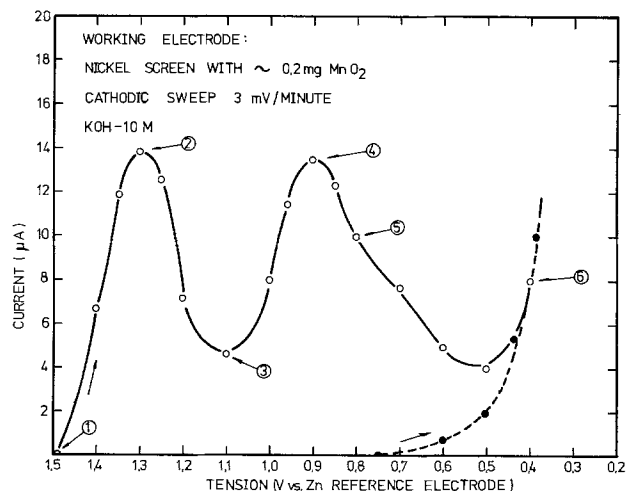


Fig. 2. Linear potentiodynamic cathodic sweep at 180 mV/hr in 10.2M KOH. Dotted line is run without MnO<sub>2</sub>.

\* Electrochemical Society Active Member.

Key words: Leclanché cells, dry cells, manganese dioxide electrodes, solubility of manganese compounds, electrochemistry of MnO<sub>2</sub>.



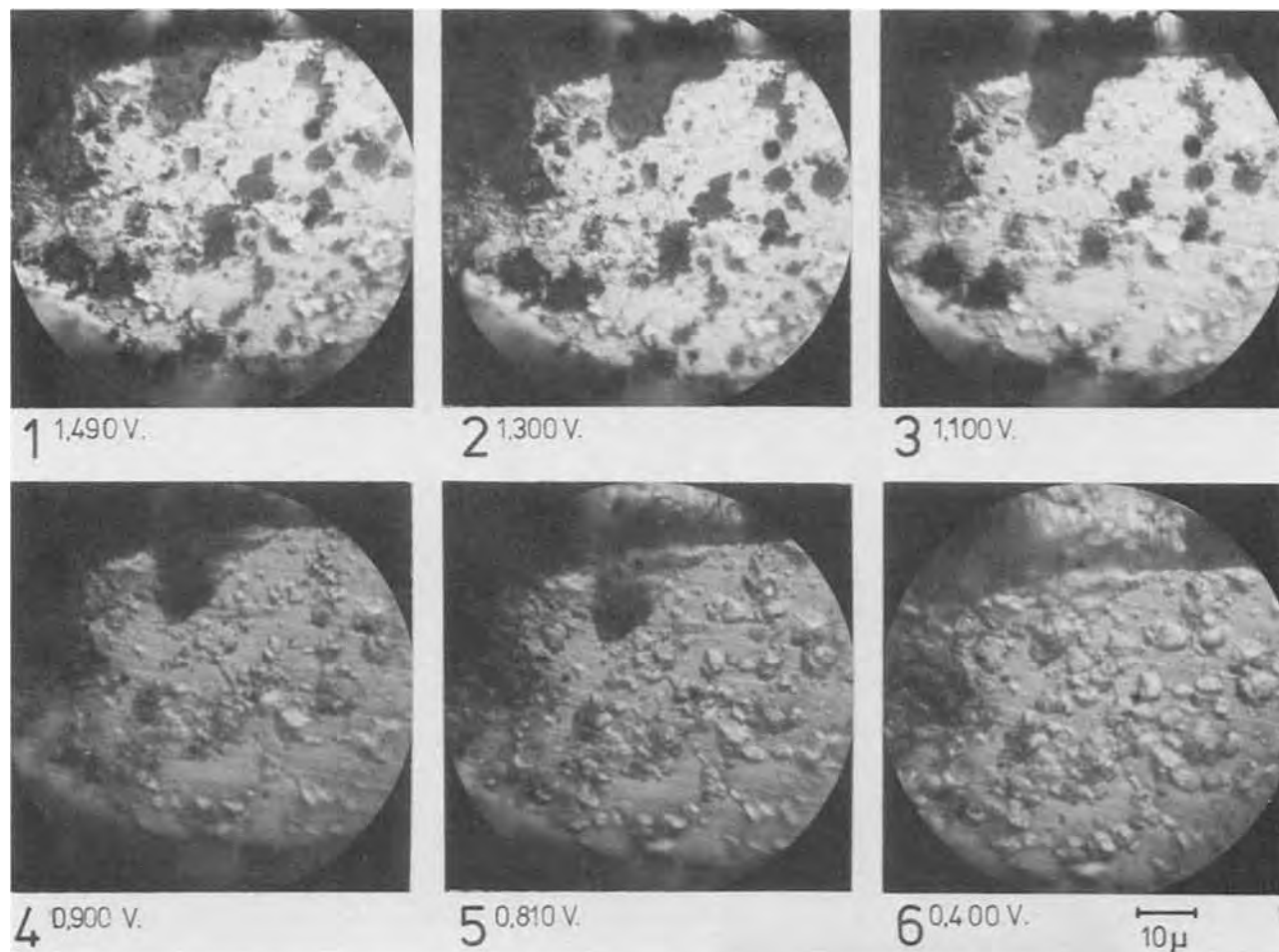
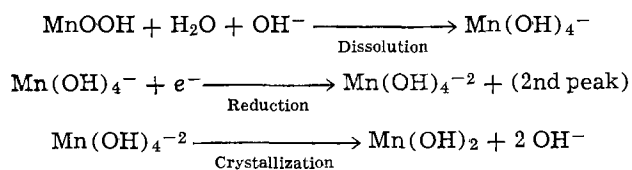


Fig. 3. Dissolution of  $\text{MnO}_2$  upon reduction in 10.2M KOH. Optical magnification 1500X. Pictures refer to the indicated points in Fig. 2



The height of the first current peak may vary from one run to the next, depending on the extent and strength of bonding achieved between substrate and  $\text{MnO}_2$  particles. No binders, and no carbon blacks or graphites, were used in these ultrathin electrodes, in order to facilitate optical observation.

In some runs, the nickel screen substrate was replaced by a thin pyrolytic graphite foil. Optical contrast was very poor and the second peak was much reduced in height, or disappeared completely. This means that reduction of  $\text{Mn}(\text{OH})_4^-$  requires a catalytically active, extended surface area.

The current decrease after the first peak is in part due to  $\gamma$ - $\text{MnO}_2$  depletion and in part to the formation of resistive  $\text{MnOOH}$  layers between remaining  $\text{MnO}_2$  grains and substrate.

The reaction mechanism shown above is supported by x-ray data, obtained with larger  $\text{MnO}_2$  samples (200 mg), pressed into a nickel screen electrode and reduced potentiostatically for 2 weeks at +0.7V vs. Zn in 10.2M KOH. Reflections due to  $\gamma$ - $\text{MnOOH}$  (manganite) were readily apparent. Furthermore, strong lines corresponding to  $\alpha$ - $\text{MnO}_2$  (cryptomelane) were visible. The  $\alpha$ - $\text{MnO}_2$  was apparently formed by reoxidation of  $\text{Mn}(\text{OH})_4^-$  and  $\text{Mn}(\text{OH})_4^{-2}$  ions in the presence of  $\text{K}^+$  ions, on  $\text{MnO}_2$  grains not in electrical contact with the substrate Ni screen. Such secondary processes, including also precipitation of  $\text{Mn}_3\text{O}_4$  (hausmannite) from solutions containing both two- and three-valent

manganese species, are not considered here, although they might be occurring in technical electrodes.

In order to detect and demonstrate the presence of reducible, three-valent manganese in solution, some ultrathin cells were mounted with an additional sensing electrode near the working electrode. The sensing electrode consisted of a 0.05 mm thick platinum foil, held potentiostatically at +0.7V vs. the Zn reference. The current to the sensing electrode was monitored and was found to increase from near 0 to 40 nA as the current to the working electrode decreased, following the first peak.

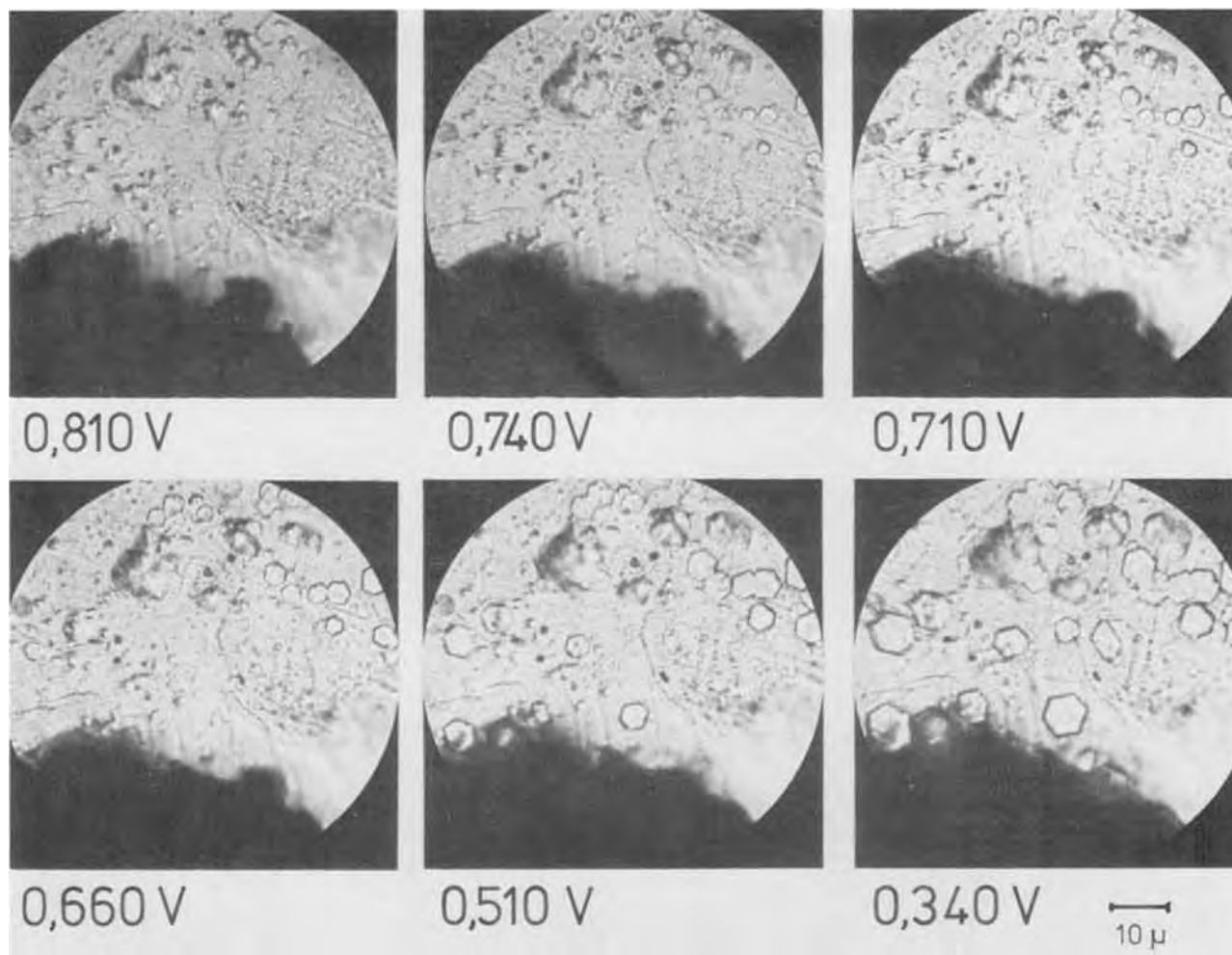
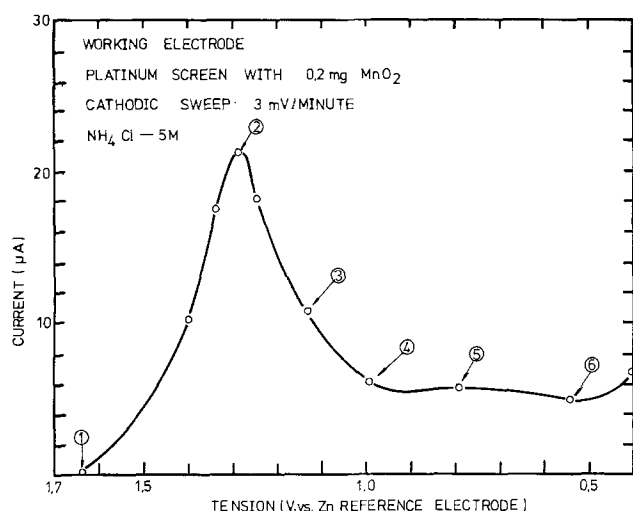
#### Neutral Solutions (5M $\text{NH}_4\text{Cl}$ or 3.5M $\text{ZnCl}_2$ )

Only one single peak (at 1.35V vs. Zn/ $\text{ZnCl}_2$ ) was discernible during the cathodic sweep (Fig. 5). Dissolution of  $\text{MnO}_2$  particles became apparent only after the peak, at 1.2V vs. Zn/ $\text{ZnCl}_2$  (Fig. 6). No precipitation or recrystallization was detectable under the conditions prevailing in the ultrathin cells, down to the potential of  $\text{H}_2$  evolution.

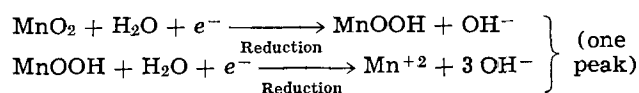
A very small second hump in the current-voltage curve, at about 0.75V vs. Zn, was sometimes observed, probably due to some dissolved three-valent manganese.

Since during reduction of  $\text{MnO}_2$ ,  $\text{OH}^-$  ions are generated the pH may locally increase at the reaction site, such that some  $\text{MnOOH}$  might dissolve as  $\text{Mn}(\text{OH})_4^-$  or mixed hydroxide-chloride complexes. However, these species would undergo disproportionation into  $\text{MnO}_2$  and  $\text{Mn}^{+2}$  when meeting a solution zone of lower pH.

Some  $\gamma$ - $\text{MnOOH}$  (manganite) was detected by x-ray analysis of larger  $\text{MnO}_2$  samples, pressed into Pt screens and reduced potentiostatically in 5M  $\text{NH}_4\text{Cl}$  for 2 weeks at +0.7V vs. Zn. In accordance with the pH-potential diagram, reduction in the pH range between

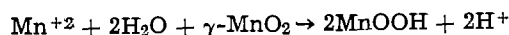
Fig. 4. Crystallization of Mn(OH)<sub>2</sub> from solutionFig. 5. Linear potentiodynamic cathodic sweep at 180 mV/hr in 5M NH<sub>4</sub>Cl.

0 and 7 can proceed directly to the two-valent state (Fig. 7). In other words, the reduction of the intermediate MnOOH should theoretically occur simultaneously with, and at the same potential of, that of  $\gamma$ -MnO<sub>2</sub>. The reduction mechanism can thus be written as



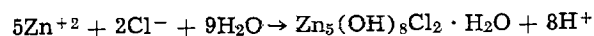
The second reaction indicated above might be considerably suppressed, or completely inhibited, by resistive effects, due to the poor conductivity of MnOOH. As already mentioned, it may involve partial dissolution of MnOOH and disproportionation into MnO<sub>2</sub> and Mn<sup>2+</sup>, as explained below in more detail for acid solutions.

In technical electrodes, the soluble two- and three-valent manganese species produced on discharge may be reoxidized electrochemically by unreacted  $\gamma$ -MnO<sub>2</sub> to form lower oxides, (MnO<sub>2</sub>)<sub>2n-3</sub> · (MnOOH)<sub>4-2n</sub> · mH<sub>2</sub>O, reducing, in turn, MnO<sub>2</sub> to a lower oxidation state electrochemically. In the simplest form the sum of the two individual processes then results in an over-all process which might be written schematically

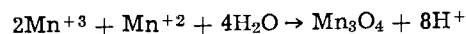


which is formally equivalent to "ion exchange" (Fig. 8).

In solutions containing many zinc ions, zinc hydroxychloride will precipitate, due to the increasing pH in the electrodes



Also, Mn<sub>3</sub>O<sub>4</sub> (hausmannite) might precipitate according to



The stability of three-valent manganese in solution will depend on pH, Cl<sup>-</sup>, and Mn<sup>2+</sup> ion concentration.

Experiments with ultrathin cells having been equipped with sensing electrodes, consisting of 0.05 mm thick Pt foil, held at +0.7V vs. Zn, did not reveal

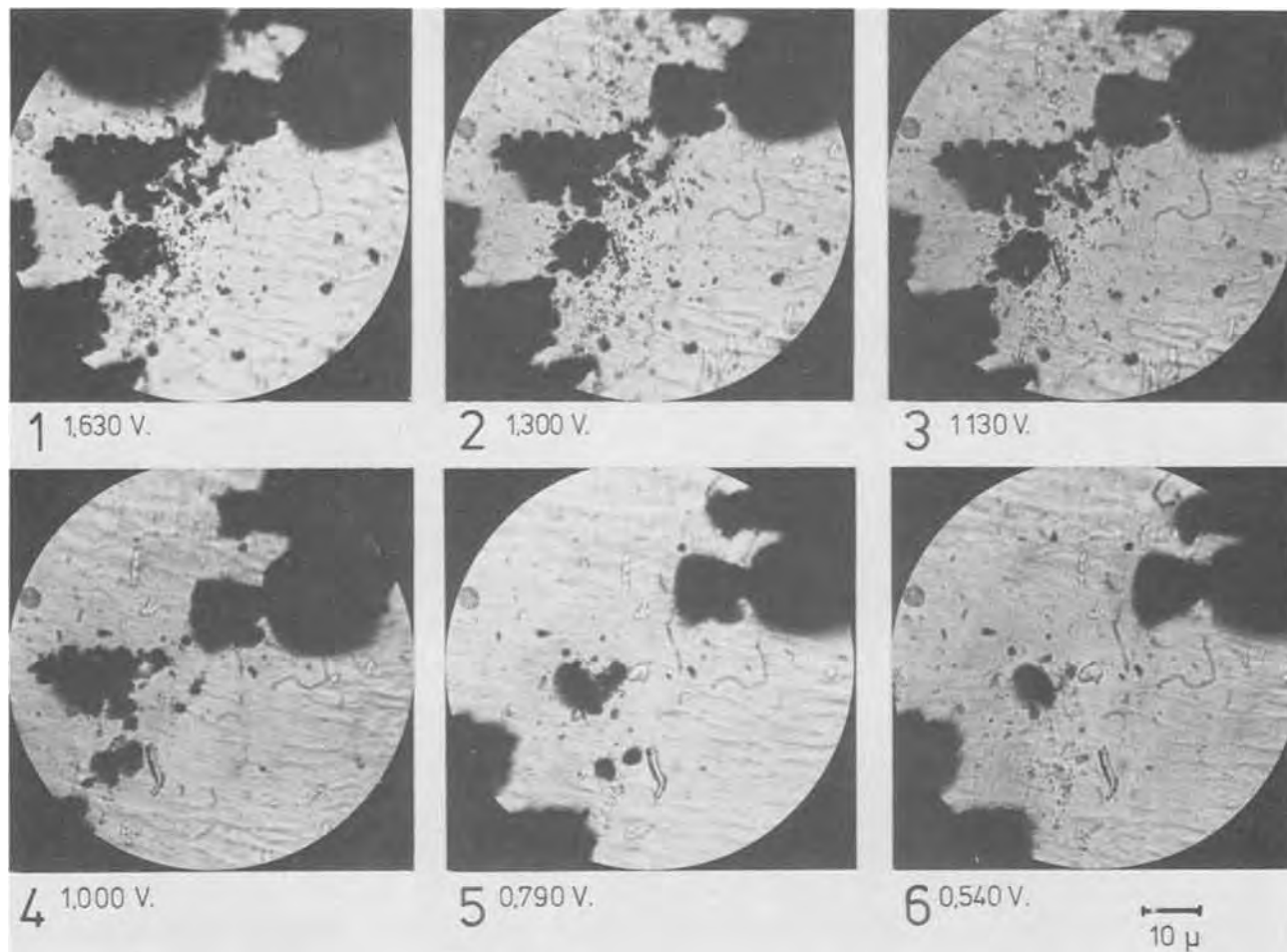


Fig. 6. Dissolution of  $\text{MnO}_2$  upon reduction in  $5\text{M NH}_4\text{Cl}$ . Optical magnification 1500X. Pictures refer to the indicated points in Fig. 5

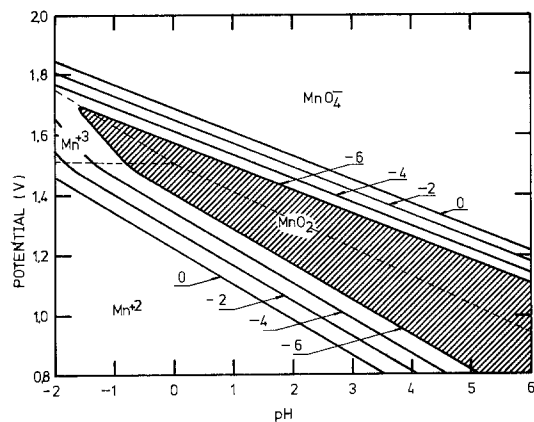


Fig. 7. pH-potential diagram of manganese dioxide in acid solution.

the presence of measurable amounts of  $\text{Mn}^{+3}$  in  $5\text{N NH}_4\text{Cl}$  solution, as long as the  $\text{Mn}^{+2}$  ion concentration remained small.

It was also noted that dissolution of  $\text{MnO}_2$  grains in ultrathin cells stopped completely when interrupting discharge at various potentials, between 1.3 and 0.7V vs. Zn. This indicates that dissolution of  $\text{MnOOH}$  in  $\text{NH}_4\text{Cl}$  is very slow or very small.

#### Acid Solutions ( $2\text{M H}_2\text{SO}_4$ )

In order to carry out experiments in  $2\text{M H}_2\text{SO}_4$  it was necessary to first equilibrate and saturate the acid with  $\gamma\text{-MnO}_2$ , otherwise spontaneous dissolution of  $\text{MnO}_2$  particles interfered with the observation of the discharge process. The spontaneous dissolution of  $\gamma$ -

$\text{Mn}^{2+}$  ion diffusion and electrochemical oxidation

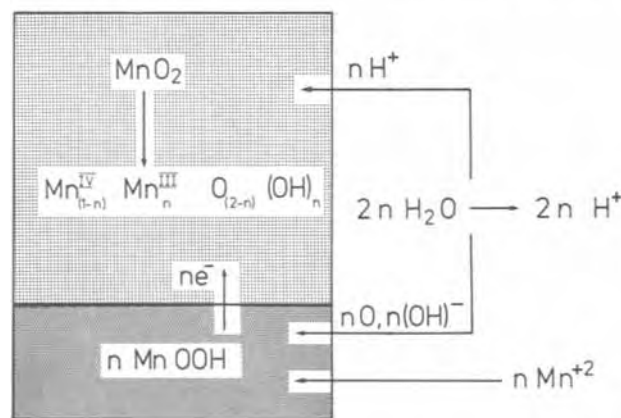
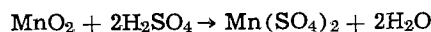
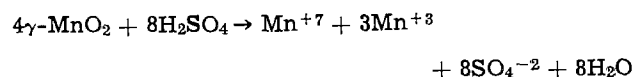


Fig. 8. Redox mechanism between dissolved  $\text{Mn}^{+2}$  and  $\text{MnO}_2$

$\text{MnO}_2$  in untreated  $2\text{M H}_2\text{SO}_4$  was much larger than expected, resulting in complete disappearance of entire grains in less than 24 hr. Dissolution could theoretically occur according to



(little is known about the stability of dissolved  $\text{Mn}^{+4}$ ) but could possibly be accompanied also by disproportionation



Three-valent manganese ions are stabilized at high acid concentration.

During discharge in MnO<sub>2</sub>-saturated H<sub>2</sub>SO<sub>4</sub> with slow potentiodynamic cathodic sweep, two current peaks were observed, one at 1.5V vs. Pb/PbSO<sub>4</sub> and the second at 0.8V vs. Pb/PbSO<sub>4</sub> (Fig. 9). Dissolutions of the grains had already started during the first peak (Fig. 10). It appeared that initially  $\gamma$ -MnO<sub>2</sub> was reduced to MnOOH and that the acid reacted rapidly with the discharge product, resulting in dissolution and loss of contact with the substrate.

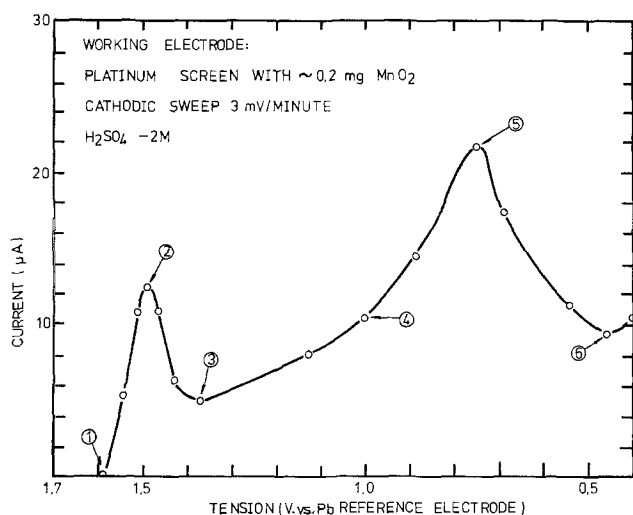


Fig. 9. Linear potentiodynamic cathodic sweep at 180 mV/hr in 2M H<sub>2</sub>SO<sub>4</sub>.

The second peak appeared to be due to a dissolved, reducible manganese species, probably a complexed Mn<sup>+3</sup> ion. Reduction of this species must be highly irreversible, involving a large cathodic overvoltage (see pH-potential diagram, Fig. 7).

The second peak was also present when the platinum screen support was replaced by a thin graphite foil.

Experiments with sensing electrodes of 0.05 mm platinum foil, held at + 0.5V vs. Pb/PbSO<sub>4</sub>, proved that a reducible species was removed from solution on the working electrode during the second peak. The current of the sensing electrode, due to reduction of soluble Mn<sup>+3</sup>, dropped rapidly as the working electrode went through the second peak.

A poorly reducible MnO<sub>2</sub> was possibly formed by disproportionation of Mn<sup>+3</sup> on top of remaining  $\gamma$ -MnO<sub>2</sub> grains. Reduction of this secondary MnO<sub>2</sub> might have been contributing to the background current in the current-voltage diagram. In thicker electrodes, Mn<sup>+3</sup> ions might also be reoxidized on unreacted MnO<sub>2</sub> particles, not in electric contact, to form manganese dioxide with a lower degree of oxidation, as discussed for neutral solutions. The reduction potential and availability for reduction of precipitated MnO<sub>2</sub> will depend on the extent and nature of substrate surface and binder material. These aspects are of practical importance for the manufacture of acidic MnO<sub>2</sub> cells (4).

The mechanism in acid can be summarized as follows

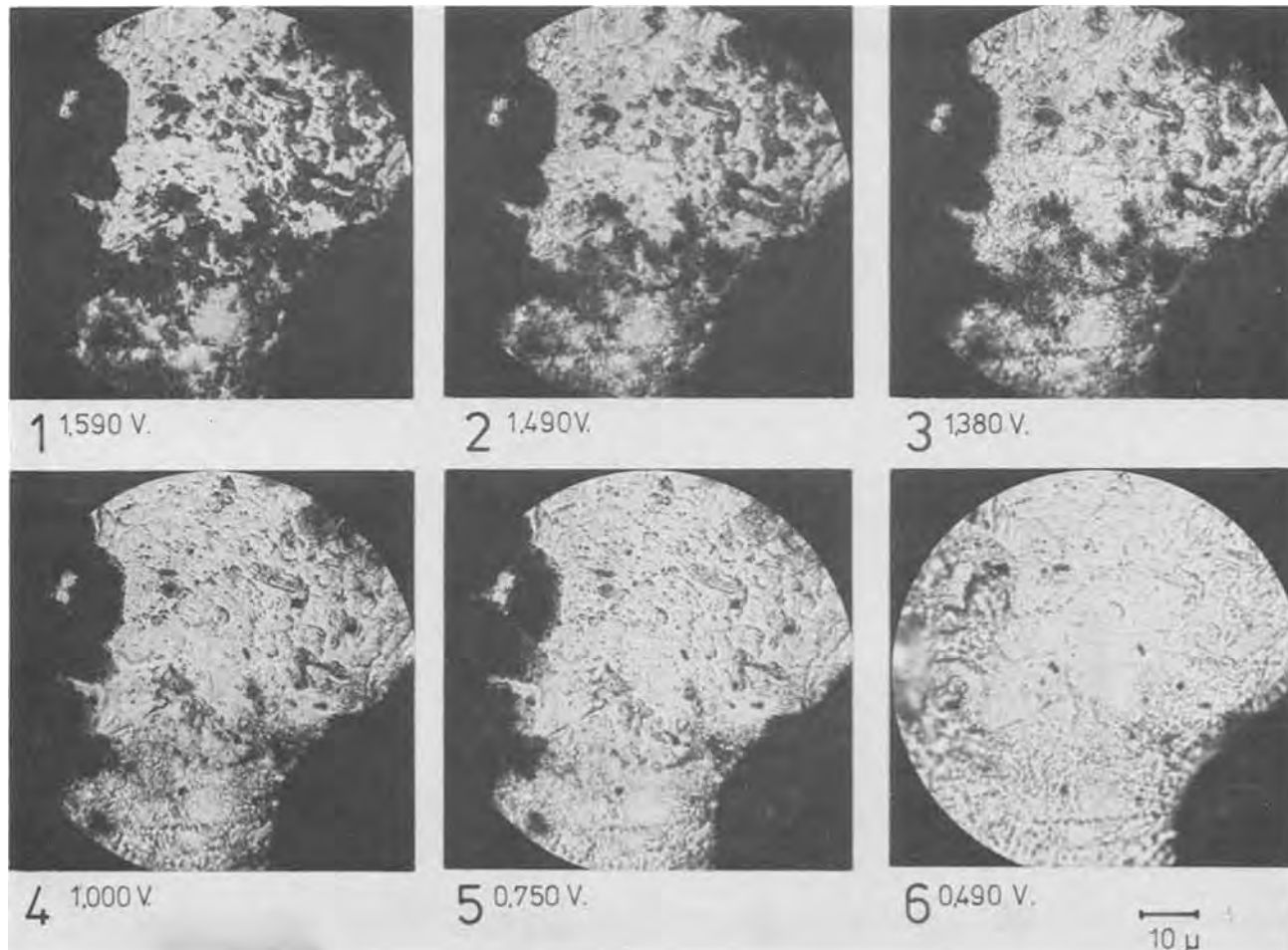
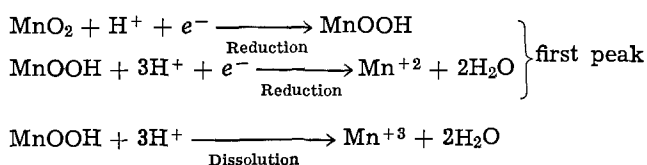
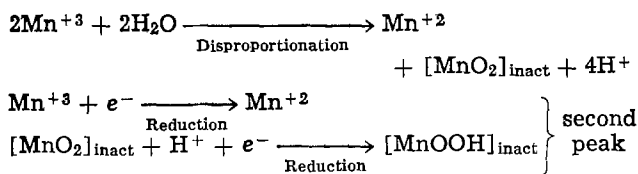


Fig. 10. Dissolution of MnO<sub>2</sub> upon reduction in 2M H<sub>2</sub>SO<sub>4</sub>. Optical magnification 1500X. Pictures refer to the indicated points in Fig. 9



The results of this investigation demonstrate the importance of dissolution-precipitation mechanisms in  $\text{MnO}_2$  electrodes (5). Dissolution processes may have considerable consequences in the performance of technical electrodes and cells.

Manuscript received Sept. 26, 1975. This was Paper 4 presented at the Dallas, Texas, Meeting of the Society, Oct. 5-9, 1975.

Any discussion of this paper will appear in a Discussion Section to be published in the December 1976 JOURNAL. All discussions for the December 1976 Discussion Section should be submitted by Aug. 1, 1976.

Publication costs of this article were partially assisted by Leclanché S. A.

## REFERENCES

1. P. Ruetschi, in "Power Sources 4," D. Collins, Editor, p. 392, Oriol Press, Newcastle upon Tyne, England (1973).
2. J. McBreen, "Proceedings of the 9th International Power Sources Symposium, Brighton, 1974," Paper No. 35; *Electrochim. Acta*, **20**, 221 (1975).
3. A. Kozawa, in "Batteries," Vol. 1, K. V. Kordesch, Editor, p. 392, Marcel Dekker, Inc., New York (1974).
4. K. Kordesch, Paper presented at the Battery Division Meeting of I.S.E., Marcoussis, France, May 1975.
5. P. Ruetschi, R. Giovanoli, and P. Bürki, Introductory lecture, International Symposium on Manganese Dioxide, Cleveland, 1975.

## Electrochemical Reduction of Beta-Ketoesters: The Tafel Rearrangement

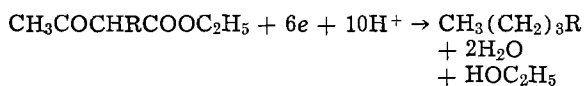
Stanley Wawzonek\* and Judith E. Durham

Department of Chemistry, The University of Iowa, Iowa City, Iowa 52242

## ABSTRACT

The electrochemical reduction of ethyl  $\alpha$ -butylacetoacetate at a lead cathode in aqueous sulfuric acid formed *n*-octane, 2-heptanone, 2-octanol, 3-octanol, 2-octanone, 3-octanone, 2,3-octanedione, ethyl caproate, and *erythro*- and *threo*-ethyl  $\alpha$ -*n*-butyl- $\beta$ -hydroxybutyrate. These products indicate that the Tafel Rearrangement proceeds through a cyclopropane intermediate. Studies of the reduction of 2-methyl-2-carbethoxycyclohexanone, 2,5-dicarbethoxycyclohexane-1,4-dione, and 2,5-dibenzyl-2,5-dicarbethoxycyclohexane-1,4-dione found that this method was not suitable for the preparation of cycloheptane and cyclooctane derivatives.

The electrochemical reduction of  $\alpha$ -alkylacetoacetic esters in a mixture of ethanol, water, and sulfuric acid at a lead cathode forms a straight chain saturated hydrocarbon by what has become to be known as the Tafel Rearrangement



Although this rearrangement has been known for more than 60 years and there has been speculation about its mechanism (1-5) no concrete evidence has been presented for the actual steps involved.

The present work reports studies of the mechanism of the Tafel Rearrangement and the application of this reaction to  $\beta$ -ketoesters in the cyclohexane series.

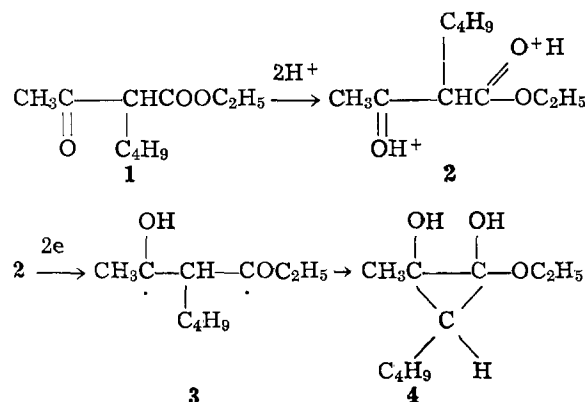
## Results and Discussion

Studies of the mechanism of the Tafel Rearrangement were based on an investigation of the electrochemical reduction of ethyl  $\alpha$ -*n*-butylacetoacetate in a mixture of ethanol, water, and sulfuric acid at 60°C; the result was a complex mixture of products. In agreement with Tafel (2), *n*-octane was obtained in good yields when the electrolysis was allowed to proceed for 6-8 hr. Other products obtained and isolated were 2-heptanone, 2-octanol, 3-octanol, 2-octanone, 3-octanone, ethyl caproate, and *erythro*- and *threo*-ethyl  $\alpha$ -*n*-butyl- $\beta$ -hydroxybutyrate. The yellow color and mass spectrum of one of the fractions indicated that

2,3-octanedione was also formed but the amount present was too small to isolate or characterize as a quin-oxaline.

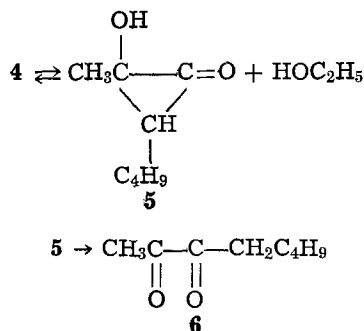
The electrochemical reduction of ethyl  $\alpha$ -*n*-butylacetoacetate was also studied at a mercury cathode in 50% aqueous acetonitrile. The ester shows in this medium a polarographic reduction wave at -2.14V (*vs.* mercury pool) using 0.2*N* tetra-*n*-butylammonium bromide as a supporting electrolyte. The products obtained were 2-heptanone, 2-heptanol, and ethyl caproate. The ketone and ester result from a basic cleavage of the starting material and 2-heptanol is formed by the electrochemical reduction of 2-heptanone.

Based on the products obtained the following steps are proposed for the Tafel Rearrangement



\* Electrochemical Society Active Member.

Key words: lead cathode, cyclopropanone intermediate, ethyl  $\alpha$ -*n*-butylacetoacetate.



The absence of rearranged products from the reduction of the ester **1** in nonacidic medium indicates that protonation of the ester is an important step in the rearrangement. Reduction of the protonated form **2** is considered to form a diradical **3** which cyclizes to a cyclopropane derivative **4**. Intermediates of this type have been proposed to explain the rearranged products obtained in the Clemmensen reduction of  $\beta$ -diketones (**6**) and  $\alpha,\beta$ -unsaturated ketones (**7**).

The possibility also exists for the addition of two electrons solely to the ketone carbonyl followed by an addition of the resulting carbanion to the ester group with the formation of **4**. Such a carbanion is apparently formed but is protonated rapidly and yields the ethyl  $\alpha$ -*n*-butyl- $\beta$ -hydroxybutyrates which were isolated.

Intermediate **4** exists in equilibrium with the hydroxycyclopropane **5** which can undergo a retroaldol condensation and form 2,3-octanedione **6**. This diketone upon further reduction would yield *n*-octane and the derivatives of *n*-octane isolated. Such a behavior was confirmed by the electrochemical reduction of 2,3-octanedione **6** under acid conditions; *n*-octane, 2-octanol, 2-octanone, 3-octanone, 3-octanol, and ethyl caproate were isolated and identified.

Ethyl caproate and 2-heptanone formed in the electrochemical reduction of ethyl  $\alpha$ -*n*-butylacetoacetate are formed mainly by chemical reactions of the latter with acid.

Attempts to trap the hydroxycyclopropanone **5** by carrying out the electrochemical reduction of ethyl  $\alpha$ -*n*-butylacetoacetate in the presence of anthracene and of 9,10-dimethylanthracene gave no Diels-Alder adduct. Cyclopropanones are known to react in such a manner with conjugated dienes at low temperatures (**8**). This result suggests that the concentration of the hydroxycyclopropanone **5** is low because of its rearrangement to 2,3-octanedione **6**.

The hemiacetal **4** cannot be ruled out as a precursor of 2,3-octanedione **6**. Cleavage of this compound **4** in a similar manner to that reported for the hemiacetal of 2,2,3,3-tetramethylcyclopropanone (**9**) would yield the diketone **6**, ethyl  $\alpha$ -*n*-butyl- $\beta$ -hydroxybutyrate, ethyl  $\alpha$ -methyl- $\alpha$ -hydroxyenanthate, and 2-hydroxy-4-ethoxy-3-octanone. The last two compounds were not detected, however, among the products of the electrolysis.

Studies of the applicability of the Tafel Rearrangement to 2-methyl-2-carbethoxycyclohexanone, 2,5-dicarbethoxycyclohexane-1,4-dione, and 2,5-dibenzyl-2,5-dicarbethoxycyclohexane-1,4-dione found that this reduction was not suitable for the preparation of synthetically useful cycloheptane and cyclooctane derivatives. The reduction of 2-methyl-2-carbethoxycyclohexanone gave a 56% yield of a liquid which, when examined by gas liquid chromatography was found to contain eleven compounds. The isomeric 2-carbethoxy-2-methylcyclohexanols were the main products and accounted for approximately 41.5% of the mixture. Other products isolated and identified were starting ester (13.4%), 3-methylcycloheptane (5%), and 2-methyl or 3-methylcycloheptanol (5%).

2,5-Dicarbethoxycyclohexane-1,4-dione was not reduced electrochemically at a lead cathode in a mix-

ture of ethanol or dioxane, water, and sulfuric acid. The dibenzyl derivative on the other hand gave mainly cleavage products of the cyclohexane ring from which only ethyl  $\alpha$ -benzylbutyrate was identified. The resistance of the first compound to electrochemical reduction can be ascribed to its dienolic structure. This behavior is different from that observed polarographically in alcohol-water solutions for 1,3-diketones; enolized 1,3-diketones were more easily reduced than nonenolized diketones (**10**). The results for the dibenzyl derivative parallels the observations reported for the reduction of 1,4-cyclohexanedione (**11**); 2,5-hexanedione was obtained with other products.

### Experimental

Infrared data were recorded using a Perkin-Elmer infrared double beam recording spectrometer and NMR data were obtained using a Varian A-60 or HA-100 spectrometer. Mass spectral data were obtained with a Hitachi RMU6E spectrometer.

Gas-liquid chromatographic (GLC) analyses were carried out with a Hewlett Packard Model 5750 B gas chromatograph and a F and M Model 5750 programmed temperature gas chromatograph. All preparative GLC's were carried out with the F and M instrument.

The following columns were used in the gas-liquid chromatographic separations and analyses:

Column A: 6 ft  $\times$   $\frac{1}{8}$  in., 5% SE-30 on 100-120 mesh Chromosorb P.

Column B: 6 ft  $\times$   $\frac{1}{4}$  in., 15% Carbowax 4000 on 100-120 mesh Chromosorb P.

Column C: 10 ft  $\times$   $\frac{1}{4}$  in., 15% SE-30 on 100-120 mesh Chromosorb P.

Column D: 10 ft  $\times$   $\frac{1}{4}$  in., 15% Carbowax 4000 on 100-120 mesh Chromosorb P.

*Electrolytic cells.*—Cell 1 consisted of a 800 ml beaker fitted with a porous unglazed porcelain cup (6 in. high  $\times$  2 in. in diameter). The anode was a cylindrical lead sheet (3 in. high  $\times$  3.25 in. in diameter) and surrounded the cathode compartment (cup). The cathode was a hollow lead pipe (2.5 in.  $\times$  0.75 in. in diameter) sealed at one end and cooled with water. The porous cup was sealed with a rubber stopper which held the cathode, thermometer, addition funnel, and a tube leading to a gas trap for collecting volatile compounds formed.

Cell 2 was similar to cell 1 and consisted of a 1 liter beaker fitted with a cylindrical lead sheet anode (4.5 in. high  $\times$  3.5 in. in diameter). The cathode compartment was a porous cup (5.125 in. high  $\times$  3 in. in diameter) and was sealed with a rubber stopper which held the cathode, thermometer, addition funnel, and a fitting which could be attached to a gas trap or condenser. The cathode was a hollow lead pipe (5.5 in. long and 1 in. in diameter) containing 12 holes (0.25 in. in diameter) which allowed the hydrogen formed to escape into the cathode compartment. The cathode was sealed with a rubber stopper.

Cell 3 consisted of an 800 ml beaker fitted with a porous cup (3.75 in. high  $\times$  2 in. in diameter) which served as the anode compartment. The anode was a platinum foil cylinder (1 in. high  $\times$  1 in. in diameter) and the cathode was a mercury pool.

*Electrolytic reduction of ethyl  $\alpha$ -*n*-butylacetoacetate.*

—*Isolation of *n*-octane.*—Using cell 1 ethyl  $\alpha$ -*n*-butylacetoacetate (**2**) (10g) and 30% sulfuric acid (30g) were diluted to 100 ml with ethanol and placed in the cathode compartment. The anode compartment was filled with 30% sulfuric acid. Electrolysis was carried out using a current of 3.5A for 6.5 hr at 60°C. Sixty per cent sulfuric acid was added as necessary during the electrolysis. Gases formed were trapped using a salt-ice bath as a coolant. Upon completion of the electrolysis the material in the trap was combined with the catholyte and the combined solutions extracted with ether. The ether extract was washed successively with



water, 10% sodium carbonate, and water until neutral. The ether layer was dried and the ether was removed using a fractionating column. The residue was distilled using a steam bath and gave a liquid (1.22g) which when analyzed by gas liquid chromatography contained diethyl ether and *n*-octane in a ratio of 1:1.1. The retention times using column A (He flow 30 ml/min; injection port 240°C; detector 270°C; column 79°C) were 24 and 60 sec, respectively, and agreed with those of authentic samples. Preparative chromatography using column C (He flow 40 ml/min; injection port 205°C; detector 225°C; column 125°C) gave a pure sample of *n*-octane which showed a mass spectrum identical to that of an authentic sample.

**Isolation of byproducts.**—Using electrolysis cell 2 ethyl  $\alpha$ -*n*-butylacetoacetate (25g) and 30% sulfuric acid (75g) were diluted to 250 ml with ethanol and added to the cathode compartment. The electrolysis was carried out at a current of 3.5A for 3 hr at 60° in a similar fashion to that given above. The product (23g) was isolated by the procedure given above and analyzed by gas liquid chromatography using columns C and D. Preparative GLC using column D (He flow 35 ml/min; injection port 208°C; detector 235°C; column 150°C) gave the following compounds (the retention times and relative areas are given in parenthesis): *n*-octane (1.3 min, 1.0), 2-heptanone (2.5 min, 2.3), ethyl caproate (6.4 min, 1.5), 2-octanone (8.1 min, 3.5), 3-octanone (9.1 min, 3.1), 2-octanol (13.0 min, 2.9), 3-octanol (13.9 min, 3.6), ethyl  $\alpha$ -*n*-butylacetoacetate (36.6 min, 11.6), and *erythro*- and *threo*-ethyl  $\alpha$ -*n*-butyl- $\beta$ -hydroxybutyrate (52.4 min. 6.9 and 61.8 min. 6.9).

*n*-Octane was identified by its mass spectrum. 2-Heptanone, ethyl caproate, and 2-octanone were identified by their infrared, NMR, and mass spectra.

The 3-octanone fraction was yellow in color and gave only one peak by GLC analysis. The mass spectrum showed the following fragments: *m/e* 144, 142, 129, 128, 117, 115, 112, 101, 99, 88, 72, 71, 57, 43 (base), and 41. An authentic sample of 2,3-octanedione showed the following mass spectrum: *m/e* 142, 99, 71, 57, and 43. An attempt to isolate the diketone as a quinoxaline by treating the fraction with *o*-phenylenediamine was not successful. This derivative was prepared from an authentic sample of the diketone and is a low melting solid.

The peak at 144 in this fraction is caused by a trace of ethyl caproate.

The 2-octanol and 3-octanol were isolated in amounts sufficient only for mass spectral analysis. The spectrum of the former was identical with that of an authentic sample. 3-Octanol gave an M-2 peak at *m/e* of 128, a peak at 101 for the loss of an ethyl group, and a peak at 59 for the  $C_8H_7O^+$  ion.

Ethyl  $\alpha$ -*n*-butylacetoacetate was identified by its retention time and infrared and mass spectra.

*Erythro*- and *threo*-ethyl  $\alpha$ -*n*-butyl- $\beta$ -hydroxybutyrate were identified by a comparison of their retention times and mass spectra with those of authentic samples (12).

**Electrochemical reduction of ethyl  $\alpha$ -*n*-butylacetoacetate at a mercury cathode in 50% aqueous acetonitrile.**—The ester (10g) was reduced in cell 3 in a 1:1 aqueous acetonitrile (400 ml) solution containing 0.2M tetrabutylammonium bromide using a current of 0.4A for 8 hr. Extraction with ether gave 8.9g of a liquid which by GLC analysis using column D (He flow 35 ml/min; injection port 206°C; detector 235°C; column 140°C) consisted of 2-heptanone, ethyl caproate, 2-heptanol, and starting material. Fractionation at 72°–93°C (10 mm) gave 0.83g of a mixture of the first three compounds in a ratio of 2.7:1.1:1.0.

**Electrochemical reduction of 2,3-octanedione.**—Using cell 1 and a gas trap, a mixture of 2,3-octanedione (5.0g) and 30% sulfuric acid was diluted to 100 ml with

ethanol and electrolyzed with a current of 2-4A at 60°C for 10 hr. The cooling trap contained pure *n*-octane (1 ml). Ether extraction of the catholyte gave a liquid (2.1g) which by preparative GLC on column D yielded the following compounds (the relative amounts are given in parenthesis): ethyl caproate (7.3), 2-octanone (1.0), 3-octanone (1.5), 2,3-octanedione (3.7), 2-octanol (1.2), and 3-octanol (1.5).

**Electrochemical reduction of 2-methyl-2-carbethoxycyclohexanone.**—Using cell 2 fitted with a condenser the ester (9.24g) and 60% sulfuric acid (45g) were diluted to 250 ml with ethanol and electrolyzed for 4 hr at 60° with a current of 3.5A. Extraction with ether in the usual manner gave 5.2g of a yellow liquid. Gas-liquid chromatographic analysis using column D (He flow 35 ml/min; injection port 205°C; detector 240°C; column 140°C) indicated the presence of about 11 compounds. By preparative GLC at 100° and 125° the following compounds were isolated in sufficient amounts for identification (the migration times and relative amounts are given in parenthesis): 3-methylcycloheptane (3 min, 4.0), 2-methyl-2-carbethoxycyclohexanone (19.0 min, 11.0), 2-methyl or 3-methyl-cycloheptanol (27.6 min, 4.1), and *erythro*- and *threo*-2-carbethoxy-2-methylcyclohexanols (74.6 min, 20.4 and 131.2 min, 13.6). Identification of all fractions except the starting material was made using mass spectral data. The starting ester was characterized by its migration time.

**Electrochemical reduction of 2,5-dibenzyl-2,5-dicarbethoxycyclohexane-1,4-dione (13).**—A mixture of *cis* and *trans*-2,5-dibenzyl-2,5-dicarbethoxycyclohexane-1,4-dione (6.5g), 30% sulfuric acid (75g), and ethanol (50 ml) was diluted to 350 ml with dioxane and electrolyzed in cell 2 at 70°C with a current of 2.5A for 23 hr. Extraction with methylene chloride gave 4.55g of a yellow oil. Thin layer chromatography on silica gel indicated the presence of numerous compounds. Column chromatography on a 3 ft  $\times$  1 in. silica gel column using benzene and methylene chloride as eluents followed by preparative layer chromatography on silica gel using methylene chloride gave six apparently pure compounds. Mass spectral analysis of two of these gave molecular ion peaks at *m/e* 206 which corresponds to ethyl  $\alpha$ -benzylbutyrate. Three of the components gave no molecular ion peaks; the highest discernible peaks were at *m/e* 320, 321, and 171. The last component gave a molecular ion at *m/e* 202.

**2-Methyl-3-pentylquinoxaline.**—A mixture of 2,3-octanedione (14) (0.71g) and *o*-phenylenediamine (0.5g) was heated at 100° for 1 hr. Upon cooling a solid (0.8g) was formed and recrystallized from a mixture of methanol and water; mp 45°–46°C.

*Anal.*: Calcd. for  $C_{14}H_{18}N_2$ : C, 78.50; H, 8.41; N, 13.08. Found: C, 78.94; H, 8.29; N, 13.12.

### Acknowledgments

This paper is part of the Ph.D. thesis of J. E. Durham, The University of Iowa.

Manuscript submitted Aug. 8, 1975; revised manuscript received Nov. 20, 1975.

Any discussion of this paper will appear in a Discussion Section to be published in the December 1976 JOURNAL. All discussions for the December 1976 Discussion Section should be submitted by Aug. 1, 1976.

### REFERENCES

1. J. Tafel and H. Hahl, *Ber.*, **40**, 3312 (1907).
2. J. Tafel and W. Jurgens, *ibid.*, **42**, 2548 (1909).
3. J. Tafel, *ibid.*, **45**, 437 (1912).
4. H. Stenzyl, Fr. Fichter, and H. Arni, *Helv. Chim. Acta*, **19**, 392 (1936).
5. L. Ebersson, in "Organic Electrochemistry," M. M. Baizer, Editor, Chap. 10, p. 420, Marcel Dekker, New York (1973).

6. N. J. Cusak and B. R. Davis, *J. Org. Chem.*, **30**, 2062 (1965).
7. I. Elphimoff-Felkin and P. Sarda, *Tetrahedron Letters*, 3045 (1969).
8. N. J. Turro and W. B. Hammon, *Tetrahedron*, **24**, 6017 (1968).
9. N. J. Turro, P. A. Leersmaker, H. R. Wilson, D. C. Neckers, G. W. Beyers, and G. F. Vesley, *J. Am. Chem. Soc.*, **87**, 2613 (1965).
10. E. Kariy, I. Hermolm, I. Rubinstein, and E. Gileadi, *Tetrahedron*, **27**, 1303 (1971).
11. E. Kariy and B. J. Cohen *J. Chem. Soc., Perkin II*, 509 (1972).
12. M. Giani, L. Moltemi, and A. Trebbi, *Farmaco (Pav.a) Ed. Sci.*, **14**, 784 (1959).
13. D. Y. Chang and M. C. Chan, *J. Org. Chem.*, **39**, 976 (1974).
14. H. Meister, *Ann. Chem.*, **724**, 128 (1969).

## Electrodissolution of Nickel in Molten LiCl-KCl

D. L. Piron,\* S. Asakura, and Ken Nobe\*

*School of Engineering and Applied Science, University of California, Los Angeles, California 90024*

### ABSTRACT

The electrodis-solution of nickel in molten eutectic LiCl-KCl has been investigated by quasi-steady-state potentiostatic and transient polarization techniques. The results indicate that electrodis-solution is diffusion controlled. In addition, anodic passivation behavior is observed. Passivation is surmised to be due to the deposition of a chloro-nickel complex. Diffusion coefficients of Ni(I) have been determined from the chronoamperometric and chronopotentiometric data and found in accord with values reported in the literature.

Studies of the anodic behavior of nickel and other transition metals in aqueous electrolytes have been quite extensive. On the other hand, there has been much less work reported on the anodic behavior of nickel and other common metals in molten salts. This paper reports on the anodic dissolution studies of nickel in molten LiCl-KCl eutectic mixture. Since the rate of electrodis-solution should be fast due to the high temperatures and highly corrosive environment, transient polarization techniques have been utilized.

Equations to describe diffusion-controlled metal electrodis-solution during chronopotentiometric and chronoamperometric experiments can be obtained by solutions of Fick's second law of diffusion

$$\frac{\partial C(x, t)}{\partial t} = D \frac{\partial^2 C}{\partial x^2} \quad [1]$$

with the following initial and boundary conditions

(i) chronopotentiometry

$$C(x, 0) = C^\circ \quad [2]$$

$$\frac{\partial C(0, t)}{\partial x} = \frac{i}{nFD} \quad [3]$$

$$C(\infty, t) = C^\circ \quad [4]$$

(ii) chronoamperometry

$$C(x, 0) = C^\circ \quad [2]$$

$$C(\infty, t) = C^\circ \quad [4]$$

$$C(0, t) = C^\circ \exp(nFE/RT) \quad [5]$$

Equation [2] is the initial condition for both cases where  $C^\circ$  is the bulk concentration of the metal cation. Equation [5] is the boundary condition at the metal-electrolyte interface during a chronoamperometric experiment, i.e., the electrode potential follows the Nernst equation.

For chronopotentiometry, Eq. [1]-[4] lead to Eq. [6]

$$i\sqrt{\tau} = \frac{nF}{2} \sqrt{\pi D} C^\circ \left[ \exp\left(\frac{nFE_\tau}{RT}\right) - 1 \right] \quad [6]$$

where  $\tau$  is the transition time and  $E_\tau$  is the electrode potential at  $\tau$ .

Equations [1], [2], [4], and [5] lead to Eq. [7] which describes the current transient for metal electrodis-solution during a constant potential pulse

$$i = \frac{nF\sqrt{D} C^\circ}{\sqrt{\pi t}} \left[ \exp\left(\frac{nFE}{RT}\right) - 1 \right] \quad [7]$$

### Experimental

Reagent grade LiCl and KCl were mixed in the mole ratio of 59/41 to prepare the eutectic salt. NiCl<sub>2</sub> (0.1 mole/kg of eutectic salt) was added to the electrolyte. Purification of the eutectic salt was performed with an HCl atmosphere to remove water, oxygen, and hydroxides during melting according to the method described by Laitinen *et al.* (1). After the purification process, nitrogen replaced the HCl atmosphere.

The test, auxiliary, and reference electrodes were prepared by sealing nickel 200 wire (0.4 mm diameter) in Pyrex tubes with differing lengths of wire exposed; 1 mm, 2 cm, and 70 cm, respectively. The latter was coiled to provide a more compact volume.

Appropriate function generators with an Anotrol controller were utilized to provide constant potentials, constant currents, and linear potential sweeps. Oscilloscopes, oscilloscopes, and a dual-channel recorder were used to measure current transients, potential transients, and potential-current behavior, respectively.

### Results

Quasi-steady-state potentiostatic anodic polarization of nickel was performed by applying each potential value for 30 sec, measuring the current at the end of this time interval and then increasing the potential to the next value. Figure 1 shows a typical anodic polarization curve. All potential values in this paper are given relative to the nickel reference electrode. An active-passive transition is observed at about 125 mV, and it is seen that the passivation current is about two orders of magnitude larger than the passive current.

Figure 2(a) shows typical current transient behavior during an anodic potential step. At low polarization values the current is inversely proportional to the square root of the time as shown in Fig. 2(b). Similar plots are obtained at higher temperatures up to 565°C

\* Electrochemical Society Active Member.

Key words: corrosion, molten salts, anodic dissolution.



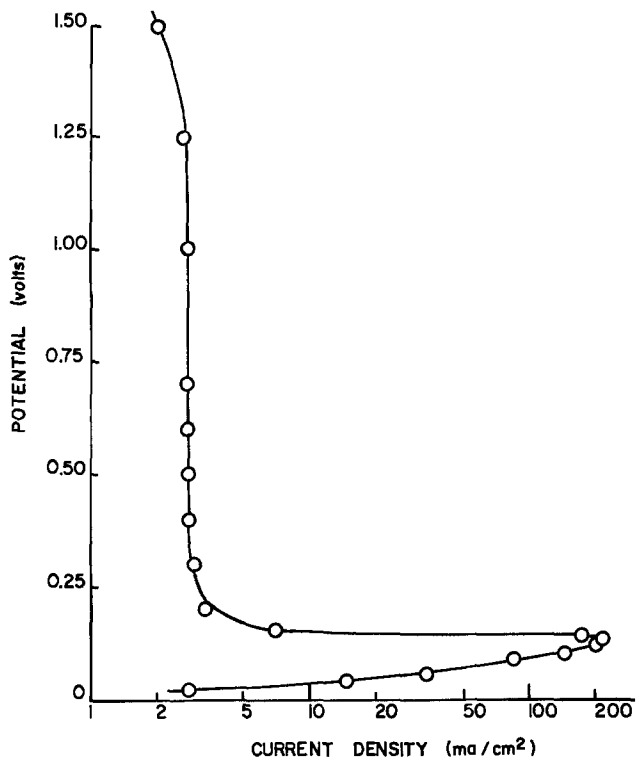


Fig. 1. Potentiostatic anodic polarization, 370°C

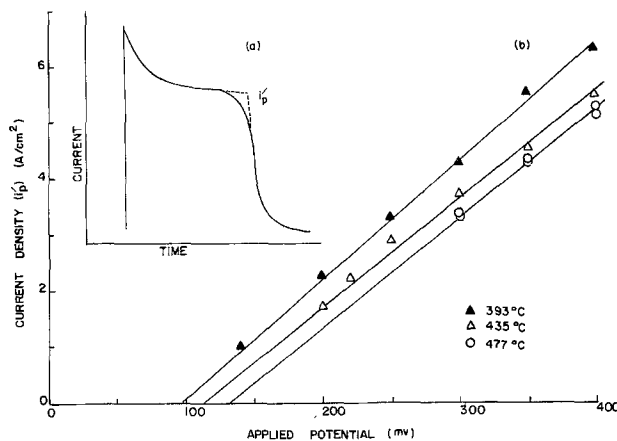


Fig. 4. Chronoamperometric results: (a) typical current transient at  $E > 150$  mV, (b)  $i'_p$  vs.  $E$  plots.

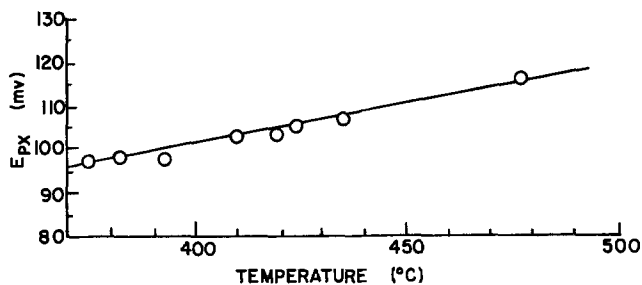


Fig. 5. Passivation potential ( $E_{px}$ ) vs. temperature

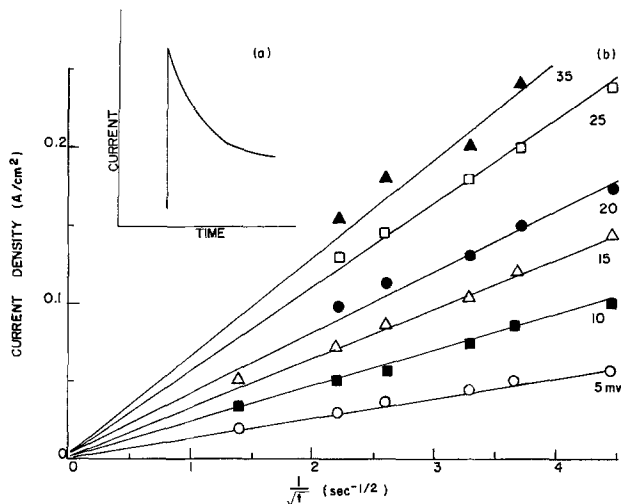


Fig. 2. Chronoamperometric results: (a) typical current transient at  $E \leq 40$  mV, (b) current vs.  $1/\sqrt{t}$  at 375°C.

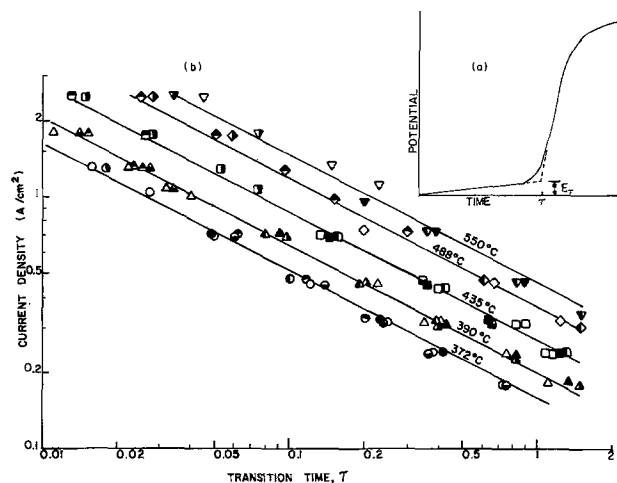


Fig. 6. Chronopotentiometric results: (a) typical potential transient, (b) current vs. transition time,  $\tau$  plots.

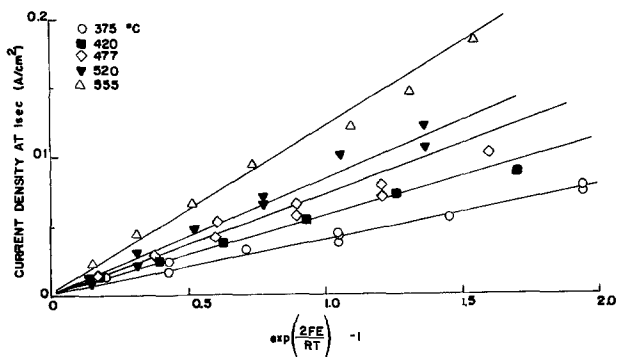


Fig. 3. Chronoamperometric results, current vs.  $[\exp(2FE/RT) - 1]$  plots.

and are given elsewhere (2). These linear  $i$  vs.  $1/\sqrt{t}$  plots are obtained up to a polarization of 40 mV. Figure 3 shows plots of  $i\sqrt{t}$  vs.  $[\exp(2FE/RT) - 1]$ . The slopes of these linear plots increased with increase in temperature. The linear relationships shown in Fig. 2(b) and 3 are in accord with Eq. [7], and indicate that the electrodisolution of nickel in the molten LiCl-KCl eutectic mixture is diffusion controlled.

Figure 4(a) shows typical current transient behavior at higher polarization potentials ( $>150$  mV). A current arrest ( $i'_p$ ) was observed during the decay. The current,  $i'_p$ , and the corresponding potential,  $E'_p$ , are the passivation parameters. A plot of  $i'_p$  vs.  $E'_p$ , as shown in Fig. 4(b), gives a linear relationship. By extrapolation of these plots to  $i'_p = 0$ , the passivation potential corrected for the ohmic potential drop,  $E_{px}$ , is obtained. Figure 5 shows that the passivation poten-

tial,  $E_{px}$ , varies linearly with the temperature.

A typical potential transient behavior during an anodic current step is shown in Fig. 6(a). A log-log plot of the current and the transition time,  $\tau$ , gives a linear relationship with a slope of  $-\frac{1}{2}$  as shown in Fig. 6(b). These results are in accord with Eq. [6] and indicate, as the chronoamperometric experiments, that the electrodisolution of nickel is diffusion controlled.

Active-passive polarization behavior similar to that obtained during quasi-steady-state potentiostatic anodic polarization was obtained for the linear potential sweeps as shown in Fig. 7. It is seen that the peak current,  $i_p$ , and the peak potential,  $E_p$ , both increase with increase in the sweep rate.

### Discussion

The diffusion coefficient in Ni(II) in molten LiCl-KCl can be determined from Eq. [6] and [7] and the chronopotentiometric and chronoamperometric data, respectively. The calculated diffusion coefficients at various temperatures are given in the Arrhenius plots of Fig. 8. A comparison with the diffusion coefficients obtained by other workers is presented in Table I. It is seen that there is good agreement between the values obtained in this work and others. The activation energies obtained from the slopes of the chronoamperometric and chronopotentiometric Arrhenius plots are 11.2 and 10.4 kcal/g mole, respectively. The activation energy reported by Poinet and Barbier (3) is 7.1 kcal/g mole, which is substantially lower than the values obtained in the present study.

Transient polarization techniques as well as the quasi-steady-state potentiostatic polarization experiments show that nickel in molten LiCl-KCl exhibited passivation behavior. In the active region, electrodisolution of nickel is shown to be diffusion controlled, and the concentration of Ni(II) at the metal-electrolyte interface,  $C(0,t)$ , can be determined by the Nernst relation (Eq. [5]). Since the bulk concentration of Ni(II),  $C^\circ$ , is 0.1 g mole/kg, eutectic salt,  $C(0,t)$  at 375°C and 100 mV (approximately the passivation potential) is 3.6 g mole/kg eutectic melt. The diffusion-controlled electrodisolution and the passivation behavior suggest a dissolution-precipitation mechanism for passivation. It is surmised that precipitation of a metal chloride salt, such as  $K_2NiCl_4$ , occurs when the concentration of Ni(II) reaches saturation conditions, e.g., at 100 mV and 375°C,  $C_{sat} = C(0,t) = 3.6$  g mole/kg eutectic melt). Passivation is ascribed to the deposition of this salt precipitate on the nickel surface. As long as saturation concentrations of Ni(II)

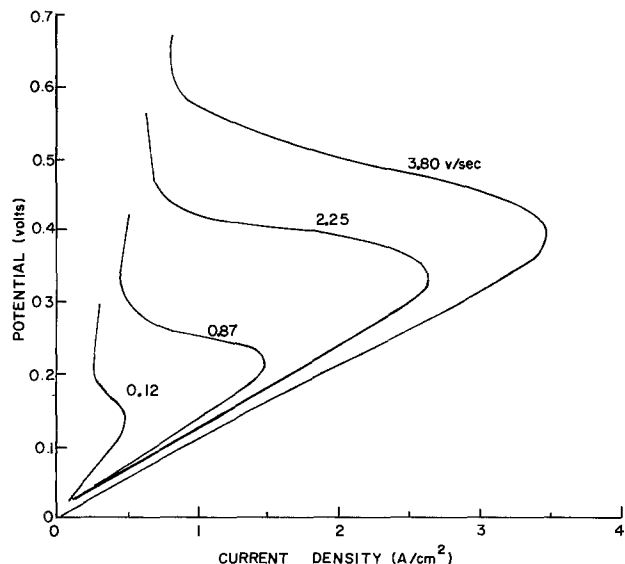


Fig. 7. Potential-current behavior at various sweep rates, 365°C

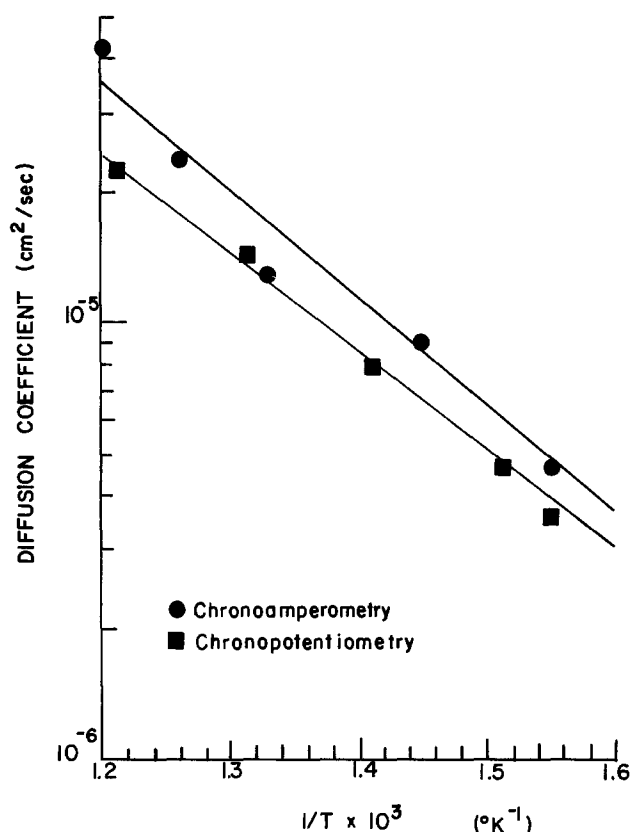


Fig. 8. Arrhenius plots for electrodisolution of nickel

exist at the metal-electrolyte interface passivation is maintained.

Piontelli *et al.* (6) had previously reported passivation of nickel in  $NiCl_2$ -KCl melts, and they have attributed this behavior to solid metal chloride deposits. Passivation of platinum in molten LiCl-KCl eutectic mixture at 450°C has been observed by DeHaan and van der Poorten (7) who ascribed this behavior to the formation of the chloroplatinum complex,  $K_2PtCl_6$ . Since previous work in this laboratory (8) has shown that chloride concentrations of 0.5 weight per cent (w/o) NaCl and greater precludes passivation of nickel in aqueous solution (1N  $H_2SO_4$ ), the chemical character of the passive film formed on nickel in aqueous solutions at room temperature must be substantially different than that formed on nickel in chloride melts at elevated temperatures.

### Acknowledgments

This work is part of the University of California seawater desalination program.

Manuscript submitted Feb. 3, 1975; revised manuscript received Dec. 31, 1975.

Any discussion of this paper will appear in a Discussion Section to be published in the December 1976 JOURNAL. All discussions for the December 1976 Discussion Section should be submitted by Aug. 1, 1976.

Table I. Diffusion coefficients of Ni(II) in molten KCl-KCl eutectic mixture at 450°C

Diffusion coefficients $\times 10^5$ cm <sup>2</sup> /sec	Reference
1.1	3
1.3	4
2.4	5
1.0* (chronopotentiometry)	This work
1.1* (chronoamperometry)	This work

\* Interpolated values.

## REFERENCES

1. H. A. Laitinen, W. S. Ferguson, and R. A. Osteryoung, *This Journal*, **104**, 516 (1957).
2. D. L. Piron, Ph.D. thesis, UCLA (1971).
3. J. C. Poignet and M. J. Barbier, *Electrochim. Acta*, **17**, 1277 (1972).
4. W. K. Behl, *This Journal*, **118**, 889 (1971).
5. E. Schmidt, *Electrochim. Acta*, **8**, 23 (1963).
6. R. Piontelli, G. Sternheim, and M. Francini, *J. Chem. Phys.*, **24**, 1113 (1956).
7. A. de Haan and M. van der Poorten, *C. R. Acad. Sci. Paris*, **261** (1965).
8. D. L. Piron, E. P. Koutsoukos, and Ken Nobe, *Corrosion*, **20**, 263 (1969).

## The Transient Behavior of an Ideally Polarized Porous Carbon Electrode at Constant Charging Current

M. Yaniv<sup>1</sup> and A. Soffer

Nuclear Research Centre, Negev, Department of Chemistry, Beer-Sheva, Israel

### ABSTRACT

The porous, high surface carbon electrode obeys the simple model of distributed resistivity and capacity, indicating that at least in transient behavior it approaches the ideally polarized electrode properties. Two potential transients at constant charging currents were simultaneously recorded at the (front) side facing the counterelectrode and at the opposite (rear) side, and compared with the theoretical curves. Some disagreement with theory was experienced at the front side, resulting in an apparently higher solution resistivity. This was attributed to micropore ionic resistivity which slows down the rate of charging of the front side. It is shown that direct and simple graphical means of calculating double layer capacity and electronic and ionic conductivity of the porous electrode phases are possible by measuring the rear side potential transients. At the front side, the solution resistivity of the porous electrode can only be obtained by curve fitting. Inserting a reference electrode in an isolated solution at the rear side of the porous electrode provides a simple means of measuring  $IR$  free electrode potential.

One of the major problems in practical electrochemistry is the slowness of the interfacial electrode reaction as compared to the rate of transport between the electrodes. In order to increase the rate of electrode reaction per unit of geometric surface area of electrode, it is necessary to increase the ratio  $A_i/A_a$  of the true to apparent surface areas. This frequently leads to a porous electrode structure.

The porous electrode is essentially three dimensional, i.e., the electrode process takes place within a volume rather than on a plane. However, the electrode process does not proceed evenly throughout the thickness of the electrode. It is faster on parts located closer to the counterelectrode. This is mainly because of two reasons: (i) the  $IR$  drop in the solution within the pores of the electrode and (ii) the screening by the electrode network, provided it is a better conductor than the solution. The screening effect is represented by appropriate impedances across the interface distributed along the porous electrode, in addition to the ohmic resistance of the solution.

Transient behavior is exhibited in cases where the above impedances are associated with local energy storage, i.e., concentration gradients and double layer capacitances in its generalized sense (1). This essentially includes all charge-consuming processes capable of changing the interfacial structure of the electrode surface.

The distributed impedances can be divided into four types, namely, ohmic, double layer capacitance, Faradaic reaction, and diffusion polarization. If all four or even three types of impedances are accounted for, the resulting equations are quite complex and are very difficult to compare with experimental results; this

is especially so in cases of transient behavior. In fact such trials are scanty and have been examined only for the steady state (2-4).

The combination of ohmic, Faradaic, and diffusion polarizations were studied by Rangarajan (5) and compared with calculated results of other authors. A most general case was also theoretically studied by De Levie (6) for the semi-infinite porous electrode. This model included ohmic, Faradaic, capacitance, and diffusion polarizations. Newman and Tobias (7) treated the steady-state behavior of a porous electrode where Faradaic and diffusion processes play a role.

The approximation of the heterogeneous porous electrode to a continuous medium of evenly distributed impedances was first introduced by Ksenzhek and Stender (8) and was adopted by many other authors. Later Ksenzhek and Stender treated galvanostatic transients for the case of combined double layer and Faradaic impedances (9).

The simplest case of distributed interfacial capacitance and solution resistance, namely, the case of the ideally polarized porous electrode, is of special interest. This is because it is easily approached by experiment (10-13) and the corresponding differential equations can be solved explicitly. Therefore, theory can be thoroughly compared with experiment. Moreover, once a satisfactory model is at hand, three important properties of the porous electrode can be experimentally determined from the shape of the current or voltage transients, i.e., the double layer capacity and the solution and electrode resistivities. The resistivities are of obvious importance for fuel cell technology, while the double layer capacity could play a role in energy storage available for high instantaneous discharge rate from a fuel cell of a lower, steady-state power (14).

This simple model had been treated by De Levie (15) for the case of a semi-infinite porous electrode.

<sup>1</sup> Present address: Department of Chemistry, Tel-Aviv University, Tel-Aviv, Israel.

Key words: double layer, porous electrode, transients.

The finite electrode case was considered by Bonemay *et al.* (16) for a fuel cell porous electrode terminating in a resistance  $R_f$  equivalent to the gas fuel cell reaction. The more general form of a finite electrode where the above resistance is absent is especially considered here. In this respect, Posey and Morozumi (17) had solved the problem for galvanostatic, potentiostatic, and triangular current modes. It is worth noting however, that the so-called current density  $j(x,t)$  distribution given in Fig. 4 of Ref. (17) is rather the derivative of the current  $i(x,t)$  with respect to the location  $x$ , and not the current itself passing in direction  $x$  within the electrode. The expression  $j(x,t)$  was obtained by Posey and Morozumi by differentiating with respect to time the expression of the potential  $\eta(x,t)$  given in Eq. [4] of their paper. The true current  $i(x,t)$  within the porous electrode had to be obtained by differentiating Eq. [4] with respect to  $x$ .

In this case, the steady-state distribution  $i(x,\infty)$  of the current should be linear, reading zero at  $x = 0$ , in agreement with the boundary condition, but the term  $j(x,t)$  approaches constant value at the steady state, as well as the derivative  $\partial i(x,t)/\partial x$ .

Recent publications by Gagnon (10, 11) together with a previous work (18) are perhaps the only experimental works on ideally polarized porous electrodes where the transient behavior is compared with theory. In the work by Gagnon the current transient due to triangular voltage sweep was followed. If any potential function is used the (experimentally non-avoidable) outer solution resistance between the reference and the porous electrode  $R_o$  will inherently influence the transient behavior of the system. The solutions obtained thence (16, 17, 19) contain transcendental expressions in  $R$ , the solution resistance of the porous electrode. This prevents one from obtaining an explicit expression of this important value, which can then be evaluated only by somewhat tedious curve fitting.

By using a galvanostatic step, however, the potential equations of the porous electrode edges contain both  $C$ , the double layer capacitance, and  $R$  in explicit forms and can be directly evaluated from experimental results as shown by Posey and Morozumi (17).

It will be shown that computing  $R$  from the potential function of the front edge (the side where the constant current is applied) of the electrode also involves some experimental difficulties.

The location of a reference electrode at the rear side of the porous electrode (opposite the auxiliary electrode) will be shown to make it possible to use a very simple graphical procedure of obtaining both  $C$  and  $R$ ; such a reference electrode enables the measurement of an almost  $IR$  free potential of the porous working electrode.

### Experimental

The electrochemical cell and the electrical instrumentation are described elsewhere (20). A scheme of the electrochemical cell and the corresponding equivalent circuit are given in Fig. 1. The rear side solution is electrically isolated from the entire cell solution at the front of the porous electrode. Obviously the two solutions are interconnected through the open pores of the electrode. The solution was aqueous NaCl, 0.10N. The experiments were performed at  $25^\circ \pm 0.1^\circ\text{C}$ . The porous carbon electrode was a Pure Carbon Product (St. Marys, Pennsylvania), Type FC-13. It has a BET surface area of  $450 \text{ m}^2/\text{g}$ . The electrodes were disk shaped, 9 mm in diameter, 1 and 3 mm thick. Its macropore and micropore volumes, given by the manufacturer, are respectively, 0.28 and  $0.24 \text{ cm}^3/\text{g}$ . The macropores, which are responsible for fluid permeability, have pore diameters in the range  $3.7\text{--}0.8\mu$ . The average micropore diameter is about  $21\text{\AA}$ . The micro-

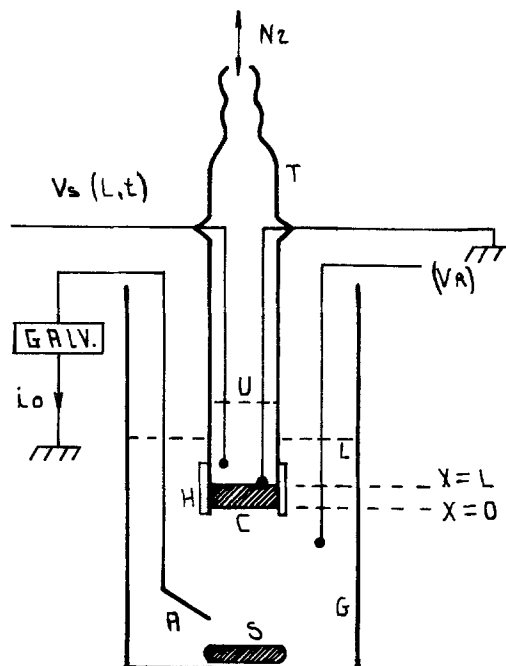


Fig. 1a. Schematic description of the system. A, Auxiliary electrode; C, porous carbon electrode; G, glass vessel; H, a special Teflon tube heat-contracted to fasten and seal porous electrode to glass tube; T,  $\text{N}_2$ , nitrogen pressure-vacuum pulses to pump solution through electrode; L, U, lower and upper (variable) solution levels.  $V_s(L,t)$ ,  $V(R)$ , reference electrode connections measuring appropriate potentials;  $i_o$ , constant current supplied by galvanostat, GALV.

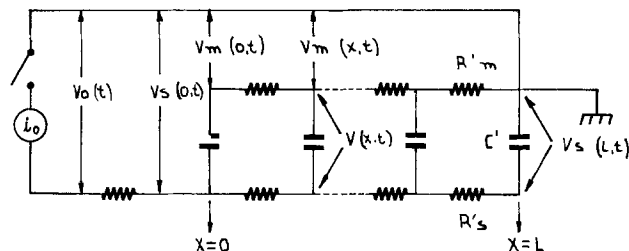


Fig. 1b. The equivalent circuit of the porous electrode.  $R'_m$  and  $R'_s$ , electronic and ionic resistivity per unit length of the porous electrode, respectively;  $V_o(t)$  and  $V_s(L,t)$  are, respectively, front and rear side reference electrode potentials vs. porous electrode. (The potentials  $V_o(t)$ ,  $V_s(L,t)$ , and  $V_m(0,t)$  are easily measurable.)

pores are responsible for the major part of surface area, and hence of capacity. Due to the enormous double layer capacity of the high surface porous electrode ( $\sim 45 \text{ farad/g}$ ), concentration changes could occur within the pores of the electrode because of ion adsorption or desorption (1). In order to keep constant concentration, the solution was pumped back and forth through the electrode by means of pressure-vacuum steps of nitrogen applied at the upper solution (Fig. 2). Constant concentration is essential for the fundamental assumption of the model presented, where the ionic conductivity within the pores is considered constant. It can, however, be easily shown that at sufficiently low charging currents and small charging periods, the diffusion flux is enough to prevent any significant concentration polarization in the pores. Pumping was therefore stopped whenever accurate voltage transients were recorded. At such conditions, potential jumps, probably streaming potentials, were experienced on reversal of pumping direction.

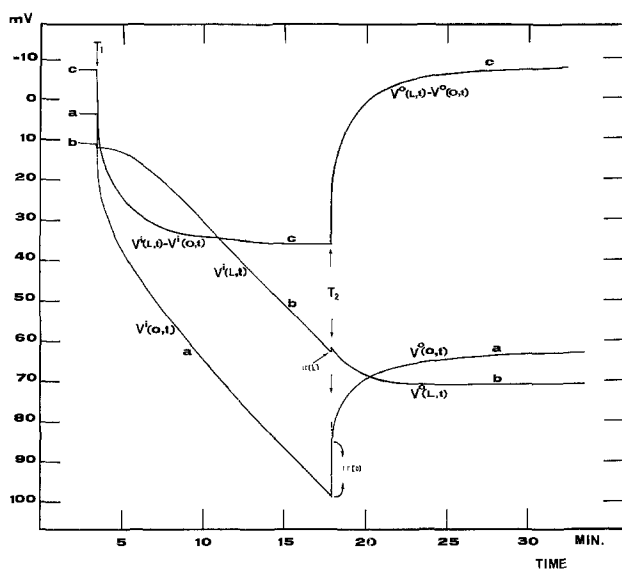


Fig. 2. Experimental voltage transients of the rear and front sides of the porous electrode.

### Results and Discussion

**Description of the model.**—The solution resistance of the porous electrode exists within the bulk of the pores while the double layer capacitance is associated with the interface, *i.e.*, with the walls surrounding the pore. An ionic unit charge, moving within the electrode pores, encounters ohmic and double layer capacitance impedances at different positions within the pore. If, however, the dimensions of the largest pores are much smaller as compared to the electrode dimension, the resistance and capacitance impedances of one pore unit become small compared to the corresponding over-all magnitudes. Under such conditions, the continuous model of distributed impedances is justified (8). It is treated hereafter for the unidimensional case, and later is discussed again.

Consider a porous electrode enclosed in an insulating tube of constant cross section and flooded by an electrolytic solution. The two ends of the tube are in contact with separate solutions of the same composition as is described in Fig. 1a.

The current  $i_0$  is passed between the porous (working) electrode through a contact at  $x = 0$  and a counterelectrode situated at the side  $x = 0$  of the porous electrode.

At any location  $x$ , Ohm's law is given for the solution phase by

$$i_s(x,t)R'_s = -\partial V_s(x,t)/\partial x \quad [1]$$

and for the metallic phase by

$$i_m(x,t)R'_m = -\partial V_m(x,t)/\partial x \quad [2]$$

where, as shown in Fig. 2b,  $i$  is the current and  $R'$  the resistivity per unit length of the electrode, along the  $x$  axis. The subscripts  $s$  and  $m$  denote the solution and electrode phases, respectively.  $V_m(x,t)$  is the electrode potential referred to the edge  $x = L$  (opposite the counterelectrode side) of the electrode phase, taken as  $V_m(L,t) = 0$ .  $V_s(x,t)$  is the solution potential (as obtained by a hypothetical reference electrode located within the pores) referred to the same point  $x = L$  at the electrode phase. The electroneutrality condition requires that

$$i = i_s = -i_m \quad [3]$$

By means of the last three equations and denoting  $V(x,t) = V_s(x,t) - V_m(x,t)$ , the expression

$$\partial V(x,t)/\partial x = -i(R'_m + R'_s) \quad [4]$$

is obtained.

The current  $i_s$  is in the direction  $x$ . The decrease of this current is equal to the rate of the double layer

charging associated with the increase  $\partial V/\partial t$  in the potential difference across the double layer, thus

$$\partial(V_s - V_m)/\partial t = \partial V(x,t)/\partial t = -(1/C')(\partial i(x,t)/\partial t) \quad [5]$$

It is assumed in this model that  $R'_m$ ,  $R'_s$ , and  $C'$  are constants in both time and location. Differentiating Eq. [4] with respect to  $x$  and substituting in Eq. [5] the expression

$$\frac{\partial^2 V}{\partial x^2} = R'C' \frac{\partial V}{\partial t} \quad [6]$$

is obtained (10, 17),<sup>2</sup> where  $R' = R'_s + R'_m$ .

**Step function current mode.**—The following boundary and initial conditions must exist for a constant current step beginning at  $t = 0$

$$i(L,t) = -\partial V(L,t)/\partial x = 0 \quad [7a]$$

$$i(0,t) = -(1/R')(\partial V(0,t)/\partial x) = i_0 \quad [7b]$$

$$i(x,0) = (1/R')(\partial V(x,0)/\partial x) = 0 \quad [8a]$$

$$V(x,0) = V_0 \quad [8b]$$

The last condition means that the porous electrode is at equilibrium at  $t = 0$ . The solution of Eq. [6] according to conditions [7] and [8] is

$$V^i - V_0 = i_0 R' L \left[ -\frac{2}{\pi^2} \sum_{n=1}^{\infty} \frac{1}{n^2} \exp\left(-n^2 \pi^2 \frac{t}{\tau}\right) \cos \frac{n\pi x}{L} + \frac{1}{2} \left(\frac{x}{L}\right)^2 - \frac{x}{L} + \frac{t}{\tau} + \frac{1}{3} \right] \quad (21, 17)^3 \quad [9]$$

where  $\tau = L^2 R' C'$ . The superscript  $i$  is for the step function current mode. The first term in Eq. [9] is a transient which decays with time. The second and third terms represent parabolic distribution of potential  $V - V_0$  after the transient decay. The fourth term shows a linear increase of  $V - V_0$  at long times.

The current function is obtained by differentiating Eq. [9] with respect to  $x$  and using Eq. [1]

$$i(x,t) = i_0 \left[ 1 - \sum_{n=1}^{\infty} \frac{2}{n\pi} \exp\left(-n^2 \pi^2 \frac{t}{\tau}\right) \sin \frac{n\pi x}{L} - \frac{x}{L} \right] \quad [10]$$

The current has a linear distribution at long times and is always zero at  $x = L$ .

**Interruption of prolonged step function current.**—In this case, the linear current distribution will serve as the initial condition, namely  $i(x,0) = i_0(1 - x/L)$  and substitution of the last expression in Eq. [1] gives

$$\frac{\partial V(x,0)}{\partial x} = -\frac{i_0}{R'} \left( 1 - \frac{x}{L} \right) \quad [11]$$

The solution of Eq. [6], subject to condition [11] can be shown to be

$$V^o - V_0 = \frac{2i_0 R' L}{\pi^2} \sum_{n=1}^{\infty} \frac{1}{n^2} \exp\left(-n^2 \pi^2 \frac{t}{\tau}\right) \cos \frac{n\pi x}{L} \quad [12]$$

The superscript  $o$  stands for the interrupted current mode.

<sup>2</sup> In Ref. (10) and (17), the resistivity of the electrode is neglected. This is a particular case where  $R' = R'_s$  and  $V = V_s$ , which is also the case in the experimental system presented here.

<sup>3</sup> The solution in Ref. (21) is given for the coordinate  $L - x$ . In Ref. (17) the terms  $\frac{1}{2} \left(\frac{x}{L}\right)^2 - \frac{x}{L}$  are included within the infinite series as a Fourier expansion.

The potential  $V_o$  is the equilibrium value approached at infinite time. The same transient is obtained as before but with the opposite sign.

The current function is accordingly

$$i = \frac{2i_o}{\pi} \sum_{n=1}^{\infty} \frac{1}{n} \exp\left(-n^2\pi^2 \frac{t}{\tau}\right) \sin \frac{n\pi x}{L} \quad [13]$$

*Particular cases.*—In an experimental setup it is very difficult to install potential measuring probes within the porous electrode (at  $0 > x > L$ ) without disturbing its macroscopic homogeneity. It is however easy to insert reference electrodes in the solution at the sides  $x = 0$  and  $x = L$ , as well as two electronic contacts with the porous electrode at  $x = 0$  and  $x = L$ . The last point will serve as the zero reference potential as assumed above. The measurable potentials at the other three points are  $V_m(0, t)$ ,  $V_s(0, t)$ , and  $V_s(L, t)$  (Fig. 1b).

The electronic potential  $V_m(0, t)$  results from the IR drop in the electrode phase and is obtained by integration of Eq. [10] and [13] and by using Eq. [2] and [3]

$$V_m^i(0, t) = -R'_m i_o L \left\{ \frac{1}{2} + \frac{2}{\pi^2} \sum_{n=1}^{\infty} \frac{1}{n^2} \exp\left(-n^2\pi^2 \frac{t}{\tau}\right) [(-1)^n - 1] \right\} \quad [14a]$$

$$V_o^m(0, t) = \frac{2R'_m i_o L}{\pi^2} \sum_{n=1}^{\infty} \frac{1}{n^2} \exp\left(-n^2\pi^2 \frac{t}{\tau}\right) [(-1)^n - 1] \quad [14b]$$

The amplitude of the transient in Eq. [14a, b] is given by

$$|V_m(0, 0) - V_m(0, \infty)| = \frac{1}{2} R'_m i_o L \quad [15]$$

which provides a direct experimental evaluation of  $R'_m$ .

In order to have an expression for  $V_s(0, t)$ , let us start from

$$V_s(0, t) = [V_s(0, t) - V_m(0, t)] + V_m(0, t)$$

The first term is obtained by substituting  $x = 0$  in Eq. [9] or [12], while the second is given by Eq. [14a, b]. Substituting accordingly,  $V_s(0, t)$  is given by

$$V_s^i(0, t) - V_o^i = i_o L \left\{ (R'_s + R'_m) \frac{t}{\tau} + \frac{2R'_s - R'_m}{6} - \frac{2}{\pi^2} \sum_{n=1}^{\infty} \frac{1}{n^2} \exp\left(-n^2\pi^2 \frac{t}{\tau}\right) [R'_s + R'_m(-1)^n] \right\} \quad [16a]$$

$$V_o^s(0, t) - V_o = \frac{2i_o L}{\pi^2} \sum_{n=1}^{\infty} \frac{1}{n^2} \exp\left(-n^2\pi^2 \frac{t}{\tau}\right) [R'_s + R'_m(-1)^n] \quad [16b]$$

Equation [16a] has a linear term in  $t$  which remains after the decay of the transient. The slope of this linear part is

$$\frac{dV_s^i(0, t \rightarrow \infty)}{dt} = \frac{i_o}{LC'} t \quad [17a]$$

Its intercepts with the time and potential axes are, respectively

$$t_{\infty} = \frac{2R'_s - R'_m}{6} C'L^2 \quad [18a]$$

which is a characteristic time of the transient term in Eq. [16a, b] and

$$V_{\infty} = \frac{2R'_s - R'_m}{6} i_o L \quad [18b]$$

The amplitude of the transient Eq. [16b] is given by

$$V_o^s(0, \infty) - V_o^s(0, 0) = \frac{i_o L}{6} (2R'_s - R'_m) \quad [18c]$$

Thus by measuring the amplitude [15], the slope [17a], and one of the magnitudes given on the left-hand side of Eq. [18a, b, c], it is possible to calculate the parameters  $R'_m$ ,  $C'$ , and  $R'_s$  of the porous electrode. However, in practice it is very difficult to measure  $V_s(0, t)$  and the associated values given in Eq. [18a, b, c]. This is because the IR drop between the electrode surface  $x = 0$  and the reference electrode at the front side  $x = 0$  is superimposed on the potential  $V_s(0, t)$ . Moreover, the initial slope of Eq. [16a, b] is infinite as well as that of the IR drop voltage step. This makes it impossible to subtract the IR drop contribution from the experimental potential measured by the reference electrode in order to obtain  $V_s(0, t)$ . Consequently the intercepts and the transient amplitude given in Eq. [18a, b, c] cannot be determined.

On the other hand, the potential-time curve recorded by means of the rear side reference electrode ( $x = L$ ) is almost completely free from IR drops, has finite initial slopes, and can thus provide much better means of calculating  $R'_s$ . The appropriate practical equations for this side are

$$V^i(L, t) - V_o^i = i_o L (R'_s + R'_m) \left[ -\frac{2}{\pi^2} \sum_{n=1}^{\infty} \frac{(-1)^n}{n^2} \exp\left(-n^2\pi^2 \frac{t}{\tau}\right) - \frac{1}{6} + \frac{t}{\tau} \right] \quad [19a]$$

$$V_o^s(L, t) - V_o = \frac{2i_o L}{\pi^2} (R'_s + R'_m) \sum_{n=1}^{\infty} \frac{(-1)^n}{n^2} \exp\left(-n^2\pi^2 \frac{t}{\tau}\right) \quad [19b]$$

By analogy with Eq. [17a] and [18a, b, c] one obtains from Eq. [19a, b]

$$\frac{dV^i(L, t \rightarrow \infty)}{dt} = \frac{i_o t}{LC'} \quad [17b]$$

$$t_{Lo} = \frac{\tau}{6} = \frac{(R'_m + R'_s) C'L^2}{6} \quad [20a]$$

$$V_{Lo} - V_o = -i_o L / 6 (R'_s + R'_m) \quad [20b]$$

$$V_o^s(L, \infty) - V_o^s(L, 0) = i_o L / 6 (R'_s + R'_m) \quad [20c]$$

Equations [20a, b, c] can serve to calculate  $R'_s$  from experimental results as is shown for Eq. [18a, b, c].

#### Comparison of Experimental Results with Theory

Considering the manufacturer's specifications of the porous carbon electrodes used in this work, their specific resistivities are some orders of magnitude smaller than that of the solution used. Therefore  $R'_m \ll R'_s$  and  $R'_m$  can be dropped from Eq. [16], [18], [19], and [20].

Typical graphs of the potentials of the rear and front sides of the porous electrode vs. time are given in Fig. 2. The complete separation of the rear and front side solutions in this system gives negligible IR drop;  $I \cdot R(L)$  for the rear side electrode as compared with  $I \cdot R(0)$  for the front side. This emphasizes the advantages of measuring the working electrode potential by means of a rear reference electrode, which

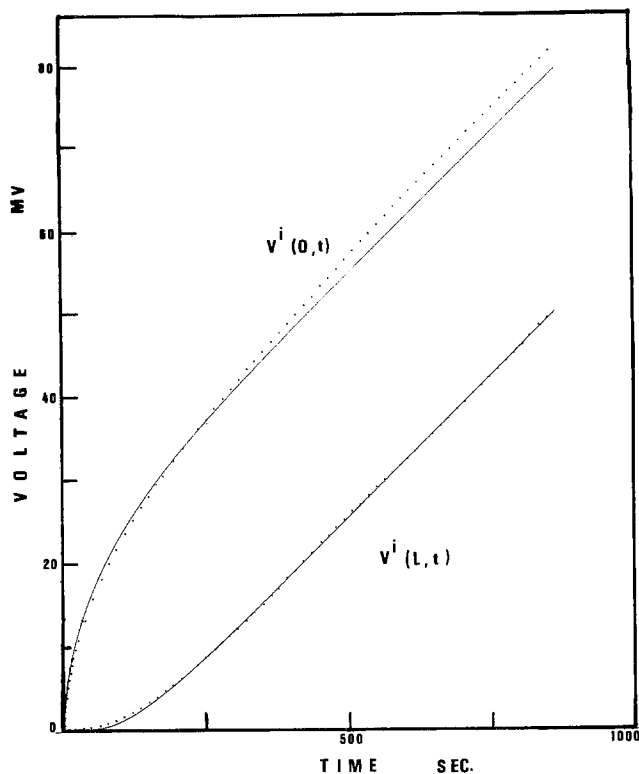


Fig. 3. Comparison between experimental (points) and theoretical (line, a computer plot) voltage transients of a 3 mm thick porous electrode, at the current step function mode. The curves  $V^i(0,t)$  and  $V^i(L,t)$  are, respectively, the front and rear side transients.

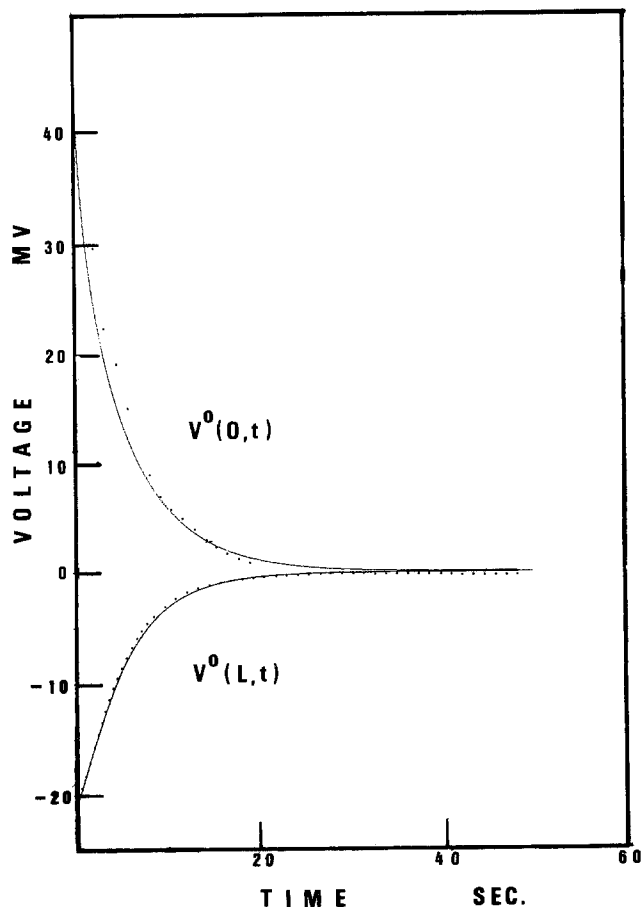


Fig. 4. The same as Fig. 3 but for the mode of interruption of prolonged current step function.

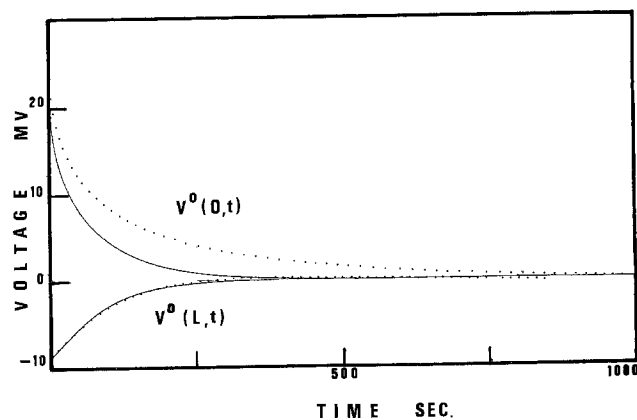


Fig. 5. The same as Fig. 4, but for 1 mm thick porous electrode

is screened from the IR drop by the porous working electrode.

The comparison of the theoretical and experimental curves is given in Fig. 3-5. The parameters  $C'$  and  $R'_s$  for the rear reference electrode potential  $V^i(L,t)$  (Fig. 3) were calculated by means of Eq. [17b] and [20b]; for  $V^0(L,t)$  (Fig. 4 and 5) by Eq. [17b] and [20c]. The specific capacitance  $C'$  for the front side reference electrode potentials  $V^i(0,t)$  and  $V^0(0,t)$  were calculated according to Eq. [17a], whereas  $R'_s$  for these curves was obtained by curve fitting rather than utilizing Eq. [18a, b, c]. This was because of the limitations discussed above.

The parameters  $C'$  and  $R'_s$  characterizing the ideally polarized porous electrode are calculated by the various experimental results and are given in Table I together with the tortuosity factor.

The tortuosity factor  $T$  is given by the expression

$$\rho_p = \rho_B T \cdot 100/P \quad [21]$$

where  $\rho_B$  is the specific resistivity of the bulk electrolyte solution and  $\rho_p$  is the apparent specific resistivity of the solution within the porous electrode assuming cell dimensions identical with that of the whole electrode.

The magnitude  $\rho_p$  is obtained experimentally from the transient amplitude  $V^i(L,t)$ .  $P$  is the porosity in volume per cent. It is given by  $100 V_P/d$ , where  $V_P$  and  $d$  are, respectively, the pore void volume and the density and are given by the manufacturer. The tortuosity  $T_{mac}$  given in Table I is calculated by the macroporosity volume per cent, while  $T_t$  is obtained according to the total (micro and macro) porosity. The tortuosity expresses the elongation of the conduction path as compared to straight tunnels parallel to the  $x$  axis. It must therefore be considerably greater than unity. As seen in Table I, this requirement is not fulfilled if only macroporosity is responsible for the ionic conductance of the pores.

It appears, therefore, that at least part of the micropores participate in ionic conduction.

It is seen from Fig. 3-5 that the coincidence of the experimental and theoretical curves is quite satisfactory for the rear side reference electrode  $V(L,t)$ . Significant discrepancy is shown however by the front side transient  $V(0,t)$ , especially in the case of the

Table I. Summary of properties of the 3 mm thick porous carbon electrode, calculated from various experimental voltage transients

Property	Type of transient			
	$V^i(L,t)$	$V^0(L,t)$	$V^i(0,t)$	$V^0(0,t)$
$\rho_p$ (ohm-cm)	366	366	442	442
$C$ ( $\mu F/cm^2$ )	9.5	—	9.5	—
$\tau_{mac}$	1.0	—	—	—
$\tau_{tot}$	1.8	—	—	—

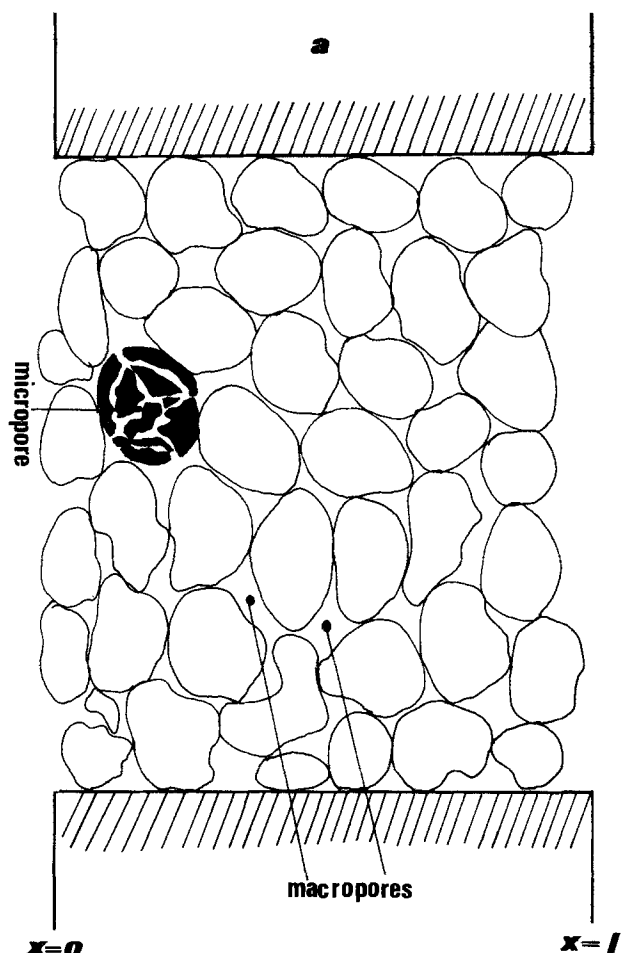


Fig. 6a. Schematic of the fine structure of the porous active carbon electrode. The micropores are shown in one granule only.

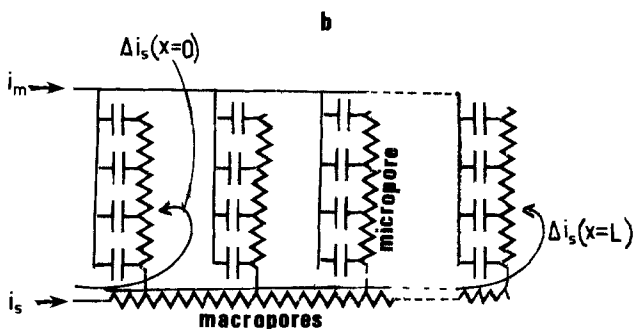


Fig. 6b. A modified equivalent circuit where micropore resistivity is taken into consideration.

thinner 1 mm electrode (Fig. 5). Also the value of  $R'_s$  (Table I) obtained by the front side transient through curve fitting is considerably higher than that obtained by the rear side transient. These discrepancies can be qualitatively explained by some more detailed description of the porous structure of the carbon electrode. Similar to many other types of activated carbons, the pore structure of the carbon studied exhibits two completely distinct ranges of pore radii. The micropores which practically accommodate all the surface area and double layer capacity are of an average pore diameter of  $21\text{\AA}$ .<sup>4</sup> These may be viewed as long and narrow branched tunnels terminating at the macro-

<sup>4</sup> Average pore diameters are calculated by  $\tau = 2V/s$ , where  $V$  is the pore void volume and  $s$  is the specific surface area per gram (22). The macropore distribution function of this carbon, provided by the manufacturers, shows practically no contribution to porosity at diameter ranges below  $8000\text{\AA}$ .

pores which are about thousandfold larger<sup>4</sup> in diameter. The corresponding equivalent circuit of such a structure must account for the combined resistive and capacitive impedances of the micropores and for the merely resistive contribution of the macropores. An appropriate circuit is given in Fig. 6 together with a schematic of the pore structure of the electrode. This equivalent circuit differs from the previous one (Fig. 2b) by an extra (distributed) micropore resistivity  $R_{mic}$  extending along the macropores. An ionic current  $\Delta i(x=L)$  charging the double layer of the rear side  $x=L$  of the porous electrode faces mainly the macropore resistivity  $R'_s L$  due to the long (1 or 3 mm) pathway  $L$ . The rear side transient is therefore insensitive to the micropore resistivity, that is why it is in good agreement with the simple model of Fig. 2. The front side, on the other hand, is charged through a very short pathway with the specific linear resistivity  $R'_s$ ; therefore, the contribution of  $R_{mic}$  is sensible. This results in a charging rate [slope of transients  $V(0,1)$ ] which is slower than that predicted by the simpler model, and in an apparently higher  $R'_s$  (Table I). The relative contribution of  $R_{mic}$  is obviously larger for the thinner (1 mm) electrode, therefore the greater variance of experiment from theory for the transient  $V(0,t)$  of that electrode.

The electrode model described in Fig. 6 will merit further study once it is accompanied by more experimental results to which theory should be compared.

Manuscript submitted Jan. 6, 1975; revised manuscript received Aug. 4, 1975.

Any discussion of this paper will appear in a Discussion Section to be published in the December 1976 JOURNAL. All discussions for the December 1976 Discussion Section should be submitted by Aug. 1, 1976.

#### REFERENCES

1. A. Soffer, *J. Electroanal. Chem.*, **40**, 153 (1972).
2. R. De Levie, *Electrochim. Acta*, **9**, 1231 (1964).
3. J. J. Coleman, *This Journal*, **98**, 26 (1951).
4. V. S. Daniel'-Bek, *Zh. Fiz. Khim.*, **22**, 697 (1948).
5. S. K. Rangarajan, *J. Electroanal. Chem.*, **22**, 89 (1969).
6. R. De Levie, *Electrochim. Acta*, **8**, 751 (1963).
7. J. S. Newman and C. W. Tobias, *This Journal*, **109**, 1183 (1962).
8. O. S. Ksenzhek and V. V. Stender, *Dokl. Akad. Nauk SSSR*, **106**, 487 (1956); *Zh. Fiz. Khim.*, **31**, 117 (1957).
9. O. S. Ksenzhek, *Zh. Fiz. Khim.*, **37**, 2007 (1963); **38**, 1846 (1964).
10. E. G. Gagnon, *This Journal*, **120**, 1052 (1973).
11. E. G. Gagnon, *ibid.*, **121**, 512 (1974).
12. A. Soffer and M. Folman, *J. Electroanal. Chem.*, **38**, 25 (1972).
13. M. Yaniv, M.Sc. Thesis, The Feinberg Graduate School, Weizmann Institute of Science, Rehovot, Israel, 1974.
14. E. Keren and A. Soffer, To be published.
15. R. De Levie, *Electrochim. Acta*, **8**, 751 (1963).
16. M. Bonnemay, G. Bronoel, E. Levart, and A. A. Pilla, *J. Electroanal. Chem.*, **13**, 44 (1967).
17. F. A. Posey and T. Morozumi, *This Journal*, **113**, 176 (1966).
18. A. Soffer, Ph.D. Thesis, Technion-Israel Institute of Technology, Haifa, 1969.
19. L. G. Austin and E. G. Gagnon, *This Journal*, **120**, 251 (1973).
20. M. Yaniv and A. Soffer, To be published.
21. H. S. Carslaw and J. C. Jaeger, "Conduction of Heat in Solids," p. 112, Oxford University Press (1959).
22. C. Orr and J. M. Dallavalle, "Fine Particle Measurement," p. 267, Macmillan Co., New York (1960).





## Mass Spectrometric Studies on High Temperature Reaction Between Hydrogen Chloride and Silica/Silicon

Sin-Shong Lin

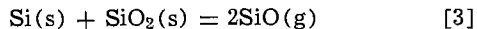
*Army Materials and Mechanics Research Center, Watertown, Massachusetts 02072*

The high temperature chemical reaction between hydrogen chloride and silica is widely employed in the fabrication of solid-state devices (1). This reaction is especially used to eliminate surface oxides of silicon substrates for epitaxial growth of silicon wafers. The reaction is carried out at 1200°C under 1 atm pressure of HCl by assuming that the interaction takes place according to



Thus the formation of silicon tetrachloride and water vapors eliminates oxide surfaces and exposes growth sites in bulk silicon substrates.

Although the chemical reaction is thermodynamically feasible, the reaction may not be the only reaction occurring at the surfaces of silicon substrates. Other interactions such as



are competitive and may occupy dominant roles in the elimination mechanism of surface oxides. Also the formation of high temperature silicon chloride vapor species is highly probable (2, 3), and these species may play more important roles in the reaction mechanism.

The work reported here is a part of research aimed to investigate the nitridation kinetics of silicon (4). Attempts have been made to modify and to accelerate the nitridation process by use of HCl to eliminate oxide layers of silicon. During the course of the present study, the interaction of HCl and SiO<sub>2</sub> is found to deviate considerably from the assumed reaction [1]. Thus the elucidation of this reaction becomes essential for a better understanding of the important industrial process.

The description of the present setup is detailed elsewhere (5, 6). The solid sample,<sup>1</sup> silica, silicon, or silicon monoxide (equimolar mixture of Si and SiO<sub>2</sub>), is loaded onto an alumina boat which is then placed near the tip of the closed end alumina combustion tube of a specially designed miniature furnace. A 0.006 in. diam orifice is drilled axially to the closed end so that all vapors in the reaction chamber are directed into a vacuum for sampling. Hydrogen chloride or an 8.1% HCl nitrogen mixture is introduced into the furnace at a flow rate of 10 cm<sup>3</sup>/min. The temperature of the furnace is set and regulated by a Pt-10% Rh/Pt thermocouple attached to a proportional temperature controller in a range 800°-1400°C. Under the given flow rate, the pressure of the chamber varies from 100 to 400 mm Hg depending on temperature, orifice, and

pumping speed. The effusates from the gas-solid interaction through the orifice are modulated and detected by a quadrupole mass spectrometer. The identity of an ion is established from the mass number and the isotopic distribution.

Some experimental results are tabulated in Table I. The first group of the experiments was performed between silica and HCl or the HCl/N<sub>2</sub> mixture. At temperatures below 1200°C, no reaction product was observed. Mass spectra consist solely of reactant ions, such as HCl<sup>+</sup>, Cl<sup>+</sup>, and Cl<sub>2</sub><sup>+</sup> (plus N<sub>2</sub><sup>+</sup> and N<sub>2</sub><sup>++</sup> in the HCl/N<sub>2</sub> run). Ion species resulting from the interaction begin to appear starting from 1250°C, and their relative abundances vary with increasing temperature up to 1400°C. Ions SiCl<sup>+</sup>, SiCl<sub>2</sub><sup>+</sup>, and SiCl<sub>3</sub><sup>+</sup> are observed, but SiCl<sub>4</sub><sup>+</sup> is never detected. A trace amount of O<sub>2</sub><sup>+</sup> and SiO<sup>+</sup> is detected only in the HCl runs. The presence of H<sub>2</sub>O<sup>+</sup> ion is hard to establish due to a high background peak at this mass.

The second run was made with SiO and the HCl/N<sub>2</sub> mixture. The interaction is so favorable that all ions containing Si and Cl atoms are observed such as SiCl<sup>+</sup>, SiCl<sub>2</sub><sup>+</sup>, SiCl<sub>3</sub><sup>+</sup>, and SiCl<sub>4</sub><sup>+</sup>. The relative abundances of these Si-Cl ion species are comparable to that of the unreacted HCl<sup>+</sup>. Moreover the first three Si-Cl species become more abundant than SiCl<sub>4</sub><sup>+</sup> as the temperature increases. The SiO<sup>+</sup> ion is clearly detected at 1400°C, and the intensity is comparable to that of SiCl<sup>+</sup>. Neither O<sub>2</sub><sup>+</sup> nor H<sub>2</sub>O<sup>+</sup> is observed.

The third run was made with silicon and the HCl/N<sub>2</sub> mixture. The interaction between them is so strong that all ions species described previously are observed at all temperatures of the experiments. The ion intensity ratios of SiCl<sup>+</sup>, SiCl<sub>2</sub><sup>+</sup>, and SiCl<sub>3</sub><sup>+</sup> to SiCl<sub>4</sub><sup>+</sup> are nearly constant except at the highest temperature of 1400°C. These ratios are found to increase significantly reflecting the contributions to these ions from other molecules. The H<sub>2</sub><sup>+</sup> ion is detected and separated from noisy background of low mass spectra.

From relative abundances of observed Si-Cl species, it is evident that the extent of the HCl + solid interaction decreases drastically from silicon to silicon monoxide, and to silica. At 1200°C large amounts of Si-Cl ion vapors are observed in the Si run, but no reaction product is observed in the SiO<sub>2</sub> run. Consequently little interaction occurs between HCl and SiO<sub>2</sub> at this temperature. Although reaction [1] is thermodynamically feasible, it is kinetically unfavorable and proceeds at a very slow rate. One might reason that the HCl pressure in the present experiments is not comparable to the 1 atm pressure commonly used. Since the pressures of these runs are about one-fourth of 1 atm, such deviation should not change the situation significantly.

The interaction between HCl and Si from 800° to 1200°C presumably produces SiCl<sub>4</sub> as a major gaseous species as shown in reaction [1]. Upon electron impact

Key words: mass spectrometry, silicon chlorides, silicon, etching of silicon.

<sup>1</sup> Sources of materials: Si, 99.99% pure, from Electronic Space Products, Inc.; SiO, 99.7% pure, from Alfa Products, Ventron Company; SiO<sub>2</sub>, spectrographic grade, from Spex Industries; HCl and HCl/N<sub>2</sub>, electronic grade, from Matheson Gas Products.

Table I. Relative ion intensities of vapor species observed in interaction between hydrogen chloride and silica/silicon

Run No.	Solid composition	Gas pressure, mm Hg	Temperature, °C	Relative ion intensity <sup>(d)</sup>						Remark <sup>(b)</sup>	
				N <sub>2</sub> <sup>+</sup>	HCl <sup>+</sup>	SiO <sup>+</sup>	SiCl <sup>+</sup>	SiCl <sub>2</sub> <sup>+</sup>	SiCl <sub>3</sub> <sup>+</sup>		SiCl <sub>4</sub> <sup>+</sup>
062375	SiO <sub>2</sub>	HCl/N <sub>2</sub> <sup>(a)</sup> 120-160	1400	6000	1750	—	4	24	4	—	
			1350	11500	1500	—	3	10	1	—	
			1300	8000	1150	—	1	3	0.5	—	
			1250	7500	800	—	—	2	—	—	
			1200	3500	350	—	—	—	—	—	
072475	SiO <sub>2</sub>	HCl	1400	—	37500	( <sup>c</sup> )	20	325	130	—	O <sub>2</sub> <sup>+</sup> present
			1400	—	27500	( <sup>c</sup> )	15	190	45	—	
072575	SiO <sub>2</sub>	HCl	1300	—	23500	( <sup>c</sup> )	4	8	4	—	O <sub>2</sub> <sup>+</sup> present
			1200	—	23500	( <sup>c</sup> )	—	—	—	—	
063075	SiO	HCl/N <sub>2</sub> <sup>(a)</sup> 150	1400	5400	850	50	670	300	90	15	No O <sub>2</sub> <sup>+</sup> ion
			1350	5400	1020	( <sup>c</sup> )	240	60	70	16	
			1300	4800	1100	( <sup>c</sup> )	130	40	70	16	
072175	Si	HCl/N <sub>2</sub> <sup>(a)</sup> 350-400	800	19200	840	—	1040	560	2850	600	H <sub>2</sub> <sup>+</sup> present
			1000	16800	840	—	1040	460	2200	460	
			1200	16800	800	—	1650	720	1260	140	
			1400	8800	760	—	840	610	290	15	

(<sup>a</sup>) The mixture contains 8.1% HCl by volume.

(<sup>b</sup>) H<sub>2</sub>O<sup>+</sup> is not detected due to high background.

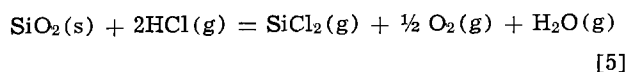
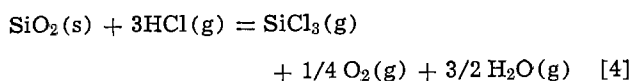
(<sup>c</sup>) Not recorded but observed in scan spectra.

(<sup>d</sup>) Electron energy = 40 eV. Ion intensities may vary from run to run. Intensities are those of most abundant peaks.

ionization, SiCl<sub>4</sub> dissociates (7, 8) extensively into SiCl<sub>4</sub><sup>+</sup>, SiCl<sub>3</sub><sup>+</sup>, SiCl<sub>2</sub><sup>+</sup>, SiCl<sup>+</sup>, and Si<sup>+</sup> (obscured by background N<sub>2</sub><sup>+</sup>), so that mass spectra obtained consist mostly of these peaks and reactants. The formation of chlorosilane is believed to be minor and is discounted, because no hydrogen containing Si-Cl ion is observed. As the temperature is increased to 1200°C or higher, the contribution to these fragmented ions from high temperature vapors SiCl<sub>2</sub> and SiCl<sub>3</sub> increases. Thus at the highest temperature of the experiment, the abundances of SiCl<sub>2</sub><sup>+</sup> and SiCl<sub>3</sub><sup>+</sup> increase more than would be expected from the fragmentation of SiCl<sub>4</sub>. This observation is consistent with available thermodynamic data. In Fig. 1, vapor pressures of Si-Cl neutral species calculated from the HCl + Si interaction under 1 atm pressure of HCl are plotted vs. temperature. At 1000°K SiCl<sub>4</sub> is the major species from the interaction, but above 1200°C, the vapor consists of comparable magnitudes of SiCl<sub>4</sub>, SiCl<sub>3</sub>, and SiCl<sub>2</sub>.

The appearance potential measurement made during the Si run also establishes that molecules SiCl<sub>2</sub> and SiCl<sub>3</sub> in addition to SiCl<sub>4</sub> exist at high temperatures. The appearance potentials of SiCl<sup>+</sup>, SiCl<sub>2</sub><sup>+</sup>, SiCl<sub>3</sub><sup>+</sup>, and SiCl<sub>4</sub><sup>+</sup> ions are 16.0, 12.6, 12.5, and 11.5 ± 0.7 eV, respectively, at 800°C. However at 1200°C, the appearance potentials of SiCl<sup>+</sup>, SiCl<sub>2</sub><sup>+</sup>, SiCl<sub>3</sub><sup>+</sup>, and SiCl<sub>4</sub><sup>+</sup> become 12.0, 10.0, 12.2, and 12.0 ± 0.7 eV, respectively. The lower appearance potentials of SiCl<sub>2</sub><sup>+</sup> and SiCl<sub>3</sub><sup>+</sup> suggest that at higher temperatures these ions are derived from other molecules in addition to SiCl<sub>4</sub>.

Although the interaction between HCl and SiO<sub>2</sub> does not occur to a measurable extent at 1200°C as described in the preceding paragraphs, it has taken place above this temperature. The ion species SiCl<sup>+</sup>, SiCl<sub>2</sub><sup>+</sup>, and SiCl<sub>3</sub><sup>+</sup> are detected from 1250° to 1400°C, but no SiCl<sub>4</sub><sup>+</sup> is detected within the sensitivity of the instrument. Since the largest Si-Cl ion observed in the system is SiCl<sub>3</sub><sup>+</sup>, the ion is probably derived from the direct ionization of SiCl<sub>3</sub> vapor. Moreover relative abundances of SiCl<sup>+</sup>, SiCl<sub>2</sub><sup>+</sup>, and SiCl<sub>3</sub><sup>+</sup> vary with increasing temperatures. Especially at 1400°C, the ion intensity of SiCl<sub>2</sub><sup>+</sup> increases more rapidly than that of SiCl<sub>3</sub><sup>+</sup>. This possibly indicates that SiCl<sub>2</sub> molecule exists and is a more dominant species than SiCl<sub>3</sub>. Therefore the reactions written in best agreement with the experiments are



The presence of SiCl in the vapor phase is not confirmed experimentally due to the fact that large portions of SiCl<sup>+</sup> are fragmented ions, but from the thermodynamic calculation, SiCl molecule is present in an insignificant amount. The vapor pressure data shown in Fig. 1 disagree with the present SiO<sub>2</sub> results. The calculated data indicate that SiCl<sub>4</sub> should be a dominant species at all temperatures of the experiment. An explanation of this discrepancy is that the formation of Si-Cl species with a large number of Cl

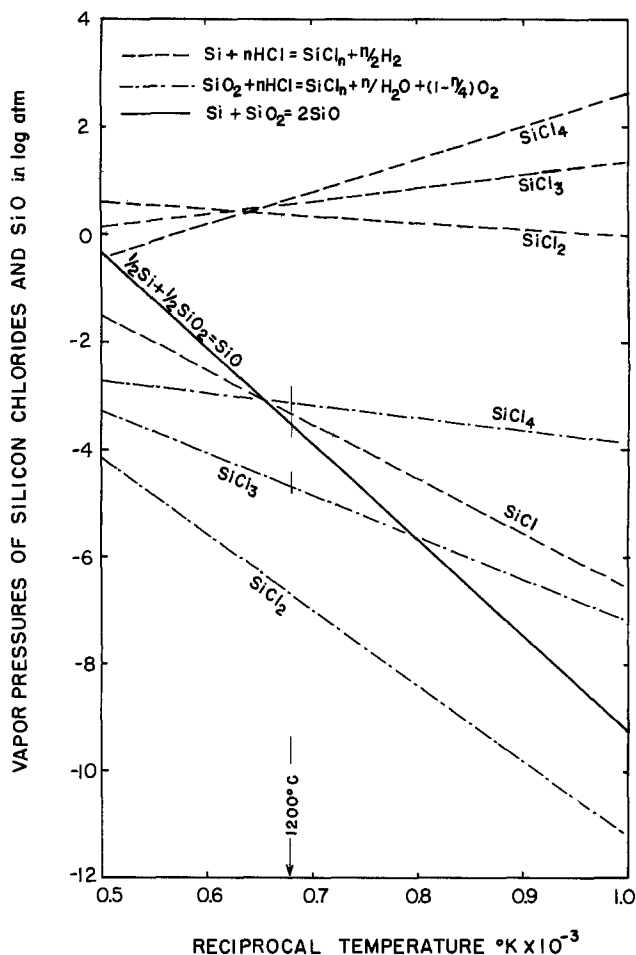


Fig. 1. Equilibrium vapor pressures of Si-Cl and SiO. The pressures are calculated from the gas-solid reactions indicated on the graph under 1 atm pressure of HCl and unity activity of solid. All thermodynamic data are taken from the JANAF tables.

atoms is kinetically unfavorable from the  $\text{HCl} + \text{SiO}_2$  interaction. Consequently  $\text{SiCl}_4$  is not observed, and  $\text{SiCl}_3$  is detected in a lesser amount.

The  $\text{SiO}^+$  is detected over the  $\text{SiO}$  sample and in some of the  $\text{SiO}_2$  runs. The vapor pressure of  $\text{SiO}$  over  $\text{Si}$  and  $\text{SiO}_2$  solids as indicated by reaction [3] become significant at temperatures above  $1200^\circ\text{C}$ . As shown in Fig. 1 the equilibrium vapor pressure of  $\text{SiO}$  is found to be greater than vapor pressures of  $\text{SiCl}_2$  and  $\text{SiCl}_3$  from the  $\text{HCl} + \text{SiO}_2$  reaction. Since  $\text{SiCl}_4$  is not detected during the  $\text{SiO}_2$  runs, the evaporation of  $\text{SiO}$  from the contaminated silicon surfaces is believed to be more competitive than any reactions between  $\text{SiO}_2$  and  $\text{HCl}$ . Moreover this evaporation is accelerated by escape of silicon chloride vapors resulting from the interaction between silicon substrate and  $\text{HCl}$ . The vapor pressure of  $\text{SiCl}_4$  resulting from the latter reaction is found to be five orders of magnitude larger than that of  $\text{SiO}$ , which does promote the  $\text{SiO}$  evaporation. The vapor phase reaction between  $\text{SiO}$  and  $\text{HCl}$  to form  $\text{Si-Cl}$  vapors is also a highly probable mechanism, however the present data cannot distinguish this alternative process.

In summary, the interaction between  $\text{HCl}$  and  $\text{SiO}_2$  produces high temperature vapors  $\text{SiCl}_2$  and  $\text{SiCl}_3$  but not  $\text{SiCl}_4$  above  $1250^\circ\text{C}$ , and no interaction is observed below  $1200^\circ\text{C}$ .  $\text{SiCl}_4$  molecule is found to be a major vapor species formed by the interaction between  $\text{HCl}$  and  $\text{Si}$  at low temperatures, and other species such as  $\text{SiCl}_2$  and  $\text{SiCl}_3$  may become important at higher temperatures. The elimination of contaminated silicon

surface oxides by  $\text{HCl}$  gas is mainly due to simple vaporization of  $\text{SiO}$  from the silicon substrates. This vaporization is further promoted by the formation of silicon chloride vapors from the interaction between  $\text{HCl}$  and  $\text{Si}$ . The direct interaction between  $\text{SiO}_2$  and  $\text{HCl}$  to form silicon chloride vapors and water plays a minor role in the etching process of the silicon substrates.

Manuscript submitted Sept. 8, 1975; revised manuscript received Nov. 10, 1975.

Any discussion of this paper will appear in a Discussion Section to be published in the December 1976 JOURNAL. All discussions for the December 1976 Discussion Section should be submitted by Aug. 1, 1976.

Publication costs of this article were partially assisted by the Army Materials and Mechanics Research Center.

#### REFERENCES

1. J. M. Blocher, Jr., *J. Vacuum Sci. Technol.*, **11**, 680 (1974).
2. R. H. Vought, *Phys. Rev.*, **71**, 93 (1947).
3. A. D. Rusin, O. P. Yakovlev, and A. Ereshko, *Vestn. Mosk. Univ., Khim.*, **28**, (3), 310 (1973).
4. Sin-Shong Lin, *J. Am. Ceram. Soc.*, **58**, 271 (1975).
5. Sin-Shong Lin, AMMRC TR 73-9, March 1973.
6. Sin-Shong Lin, *This Journal*, **122**, 1405 (1975).
7. H. J. Svec and G. R. Sparrow, *J. Chem. Soc.*, (A), No. 7, 1162 (1970).
8. V. S. Ban and S. L. Gilbert, *This Journal*, **122**, 1382 (1975).

---

### Erratum

In the paper, "Electrochemical Studies on Single Crystalline  $\text{CuCl}$  Solid Electrolyte," by A. V. Joshi and J. Bruce Wagner, Jr., which appeared on pp. 1071-1080 in the August 1975 JOURNAL, Vol. 122, No. 8, Fig. 3 and 13 were inadvertently interchanged in printing. The captions now read erroneously and must also be interchanged. In Fig. 4, the upper curve denotes the total

conductivity measured by a-c techniques and is essentially the ionic conductivity of  $\text{CuCl}$  equilibrated with copper [ $\sigma_{\text{ion}}^\circ$ ]. The lower curve denotes the electronic conductivity of  $\text{CuCl}$  equilibrated with copper [ $\sigma_e^\circ$ ]. In Ref. (13) the second author's name should be spelled Baudouin.

---



## Passivation of High Breakdown Voltage p-n-p Structures by Thermal Oxidation

R. E. Blaha and W. R. Fahrner

*Institut für Angewandte Festkörperphysik der Fraunhofer-Gesellschaft, 78 Freiburg, Germany*

### ABSTRACT

Experiments for the thermal oxidation of silicon power devices are carried out on symmetrical p-n-p junctions with breakdown voltages of 1.2 and 2.8 kV, respectively. A new etching procedure is developed for the surface cleaning. For the 1.2 kV samples, the oxidation procedure is optimized with respect to temperature, time, and cooling rate. The smallest leakage current is obtained when silicon boats are used during the thermal oxidation. No yield is found for a junction bevel angle larger than  $7^\circ$ . For the 2.8 kV diodes additional precautions must be taken, most important of which is the use of silicon furnace tubes. To obtain thick ( $\approx 1000\text{\AA}$ ) oxide layers, a dry-wet-dry oxidation cycle is used.

Long term stability of thyristors is improved by a passivation step which protects the critical p-n junctions of the structure. Very often passivation is carried out by depositing silicone rubber or glasses. These techniques are not always successful because they do not prevent ion migration. A better way consists of introducing a thermal oxidation step followed by a silicon nitride deposition. In this case, the main problem is the oxidation, especially when devices with a high breakdown voltage  $U_B$  (in our case approximately 1.2 and 2.8 kV) are to be passivated. The high temperature process introduces impurities which soften the abrupt I-V characteristics of the diode.

This paper deals with the technological conditions for a reduction of impurities. The investigations are carried out with two symmetrical p-n-p structures which are the essential part of the final thyristors. In Fig. 1, a cross section of a 3 kV device is shown. The starting material is nominally 110 ohm-cm n-type silicon. First of all, the wafer of 16 mm diameter and 700  $\mu\text{m}$  thickness is diffused with Al to a junction depth of 95-100  $\mu\text{m}$ . A second diffusion step introduces Ga to a junction depth of 50  $\mu\text{m}$ . Then, boron silicate gettering (10  $\mu\text{m}$ ,  $1-2 \cdot 10^{17}/\text{cm}^3$ ) removes the impurities in the preceding steps. The wafers are beveled at the edge with an angle between  $1.6^\circ$  and  $1.8^\circ$ . Finally, they are etched with Syton polish and CP 8 (1). The 1.2 kV wafers differ only slightly in doping level, in diameter (19 mm), and in thickness (550  $\mu\text{m}$ ). The above process steps are carried out by the BBC laboratories in Lampertheim, Germany, and Baden, Switzerland, respectively.

### Experiments and Results

The experiments are subdivided into two groups. In the first one, 19 mm diameter p-n-p structures of 1.2 kV breakdown voltage and  $3^\circ$  bevel angle are investigated. In the second one, p-n-p structures of 2.8 kV breakdown voltage and a bevel angle of  $1.6^\circ$  are examined. To obtain reliable statistics, more than 60 runs

Key words: p-n-p diode, junction passivation, thermal oxidation of Si diodes.

are carried out for either group. This means that the effects of each parameter quoted below are checked by the measurements of five or more runs.

An important condition for successful passivation is the cleaning of the surface of the device. The usual MOS cleaning is developed for polished surfaces and fails for our case of lapped surfaces. We find that these need a removal of more than  $1000\text{\AA}$  of the surface. In addition the MOS cleaning of 2 hr/run consumes too much time. After a trial and error procedure, we have obtained the best results by applying the following steps: (i) HF 40% (Merck suprapur), 30 sec; (ii) Millipore SQ-H<sub>2</sub>O rinse (18 Mohm-cm); (iii) perchlorate etch (74.5% volume HNO<sub>3</sub> of 65%, 7.5% volume CH<sub>3</sub>COOH of 96%, 10.5% volume HF of 40%, 7.5% volume HClO<sub>4</sub> of 70%, all Merck suprapur) for 10 sec, corresponding to a surface removal of  $1700\text{\AA}$ ; (iv) H<sub>2</sub>O as in (ii); and (v) drying with a spinner, 60 sec.

The sample is introduced into the furnace immediately after cleaning. The oxidation is carried out in a Heraeus-Heralux® quartz tube. For each sample, the I-V characteristics are measured first after the etch cleaning and then after oxidation and subsequent annealing. As a criterion for "acceptable characteristics," the manufacturers of power devices adopt a standard of 20 mA. In this investigation, we reduce this level to

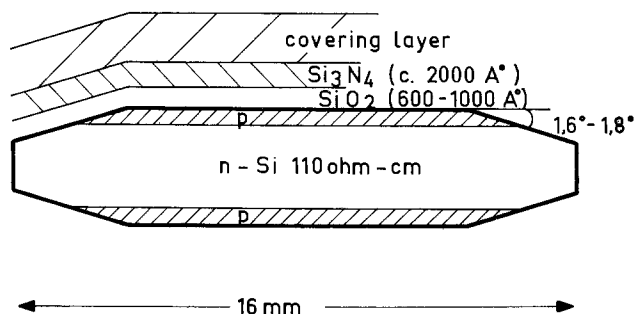


Fig. 1. Cross section of a typical p-n-p device

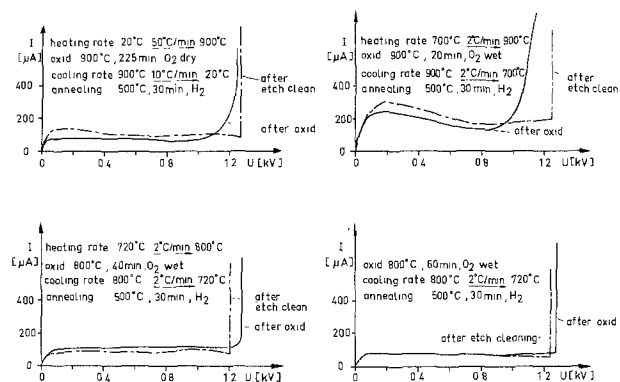


Fig. 2. I-V characteristics for different oxidation conditions

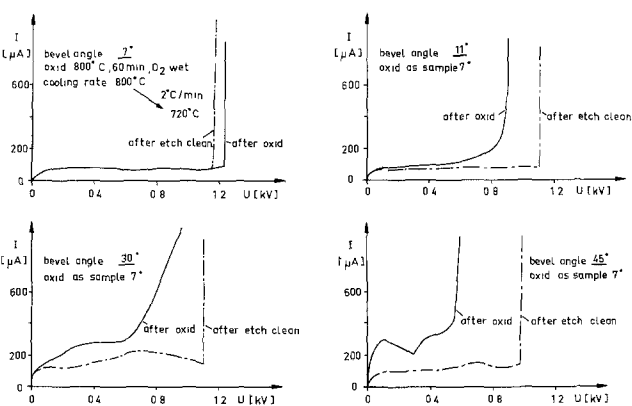


Fig. 3. Dependency of I-V characteristics on bevel angle

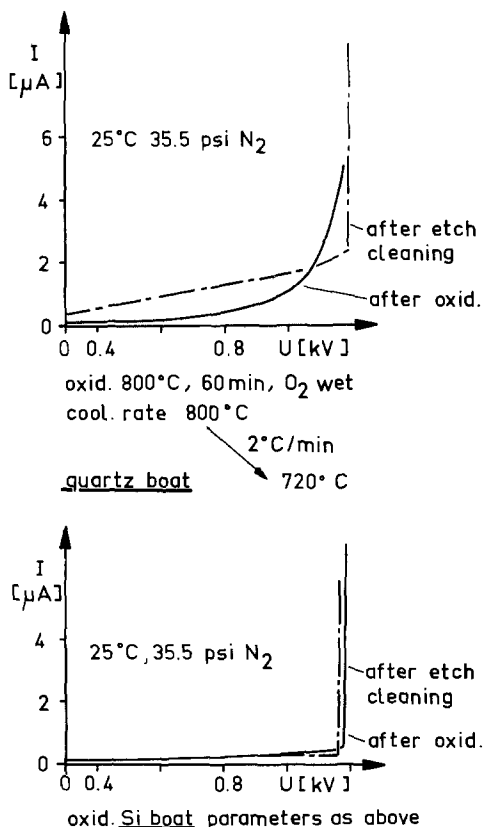


Fig. 4. Influence of different wafer-support materials during the oxidation. The indicated temperature of 25°C and 35.5 psi N<sub>2</sub> refer to the conditions during I-V measurements.

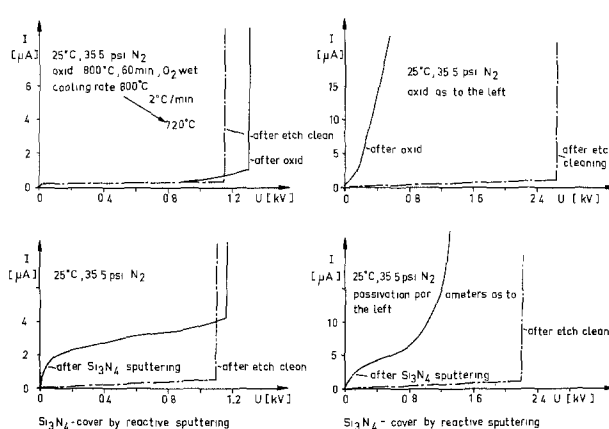


Fig. 5. Comparison of differently passivated 1.2 and 2.8 kV diodes which are identically processed.

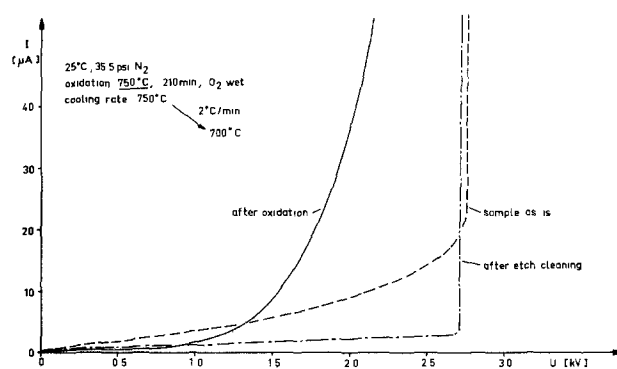


Fig. 6. I-V characteristics after reducing the oxidation temperature and varying the preparation of the tube and boat.

100  $\mu$ A. Furthermore we use the inverse radius of curvature at breakdown as a measure for "better" or "worse" characteristics. The breakdown point is given when the conductance increases to 100  $\mu$ A/10V. Since the characteristics are almost identical in either voltage direction, only the first quadrant is shown. In Fig. 2, I-V characteristics of 1.2 kV diodes with different oxidation conditions are plotted. The results obtained from these and other curves for higher oxidation temperature are the following: (i) Oxidation temperatures above 850°C do not give good I-V characteristics. (ii) The optimum condition is an oxidation temperature of 800°C and a constant cooling rate of 2°C/min from 800° to 720°C. (iii) A constant heating rate up to the oxidation temperature does not improve the diodes. Retaining the oxidation conditions (800°C, 60 min, wet oxygen, 2°C/min cooling from 800° to 720°C) we

now investigate the effects of a variation of the bevel angles. In Fig. 3, typical examples of diodes with 7°, 11°, 30°, and 45° are given. It turns out that only bevel angles up to 7° maintain abrupt I-V characteristics whereas a high leakage current and soft I-V characteristics are found for larger angles.

A further improvement is obtained by using silicon instead of quartz boats (Fig. 4). Two diodes otherwise identically processed show significantly different I-V characteristics. This is attributed to the different impurity concentrations in quartz and silicon (2). It is found, for instance, that the sodium content in Dow Corning and Siemens silicon used for the boats is negligible (0.0 to 0.6 ppba) whereas in quartz, high values (260 ppba) are measured. Note that the leakage current is below 1  $\mu$ A.

The know-how of the first experimental series must be extended when 2.8 kV diodes are to be oxidized as demonstrated in Fig. 5. In the upper half of the figure, the characteristics of a 2.5 kV diode and of a 1.2 kV diode are presented for comparison. The same problem arises for a nitride passivation, as shown in the lower half of the figure. After the etch cleaning, a  $\text{Si}_3\text{N}_4$  layer is deposited on a 1.2 and a 2.2 kV diode by reactive sputtering. All process parameters are identical. Due to these results we have to find new ways for preparing good oxides. We have varied the following parameters: the cleaning procedure, the tube and boat cleaning, the steam content, the oxide temperature, the oxidation time, and the cooling rate after oxidation. As shown in Fig. 6, a diode oxidized in wet oxygen for 210 min at 750°C and slowly cooled down to 700°C with 2°C/min exhibits soft characteristics and a high leakage current. The same result is obtained when the sample is oxidized at 800°C for 60 min in wet oxygen after the tube and the boat are precleaned with HCl at 1100°C for 5 hr.

In Fig. 7, (top), a dry 800°C oxide of 60 min oxidation time and a cooling rate of 2°C/min is shown. Again the results are unsatisfactory. This is also true for the sample shown below where dry oxygen of

1200°C for 15 min is applied. The cooling rate is 60°C/min until room temperature is reached. The blocking characteristics of the diode have completely disappeared due to impurities (mostly metal ions) induced by the high temperature.

In order to test the effects of impurities introduced by oxygen and steam, we replace the oxidation by a heat-treatment in nitrogen ambient of the same temperature as the oxidation. The results are given in Fig. 8. The upper curves correspond to a sample annealed for 5 min, the lower for 30 min. Two conclusions can be drawn from this figure: (i) the oxygen and steam are not responsible for the degradation of the diode, since the 30 min sample fails, and (ii) the degradation is proportional to a "contact time" with impurities in the furnace.

Finally the quartz environment (tube and boat) are identified as the essential source of contamination during the process. This is proved in Fig. 9. Two diodes are processed with identical conditions. The first one is oxidized in a quartz tube (upper half of the figure); for the second one, we use a silicon tube. This result of hard I-V characteristic and a low leakage current of less than 2  $\mu$ A is completely reproducible. In order to increase the oxide thickness, we use wet oxygen. Unsatisfactory results are obtained. However, when we switch over to a dry-wet-dry or a dry-wet cycle, the characteristics are as good as for the solely dry oxidation (Fig. 10). The dry-wet-dry oxidation conditions are: 33 min dry oxygen, 70 min wet oxygen, and 15 min dry oxygen. The cooling rate from 800° to 720°C is 2°C/min. For the dry-wet oxidation, we use 10 min dry oxygen, 8 min wet oxygen, and a cooling rate of 3.3°C/min. By comparison we find that low leakage currents are maintained by the initial dry oxidation.

### Conclusion

The experiments on the thermal oxidation of power devices are carried out first with symmetrical diodes of a breakdown voltage of 1.2 kV. Bevel angles are 3°, 6°, 7°, 11°, and 45°. The investigations are extended to diodes of a breakdown voltage between 2.2 and 3.1 kV and bevel angles of 1.6°-1.8°.

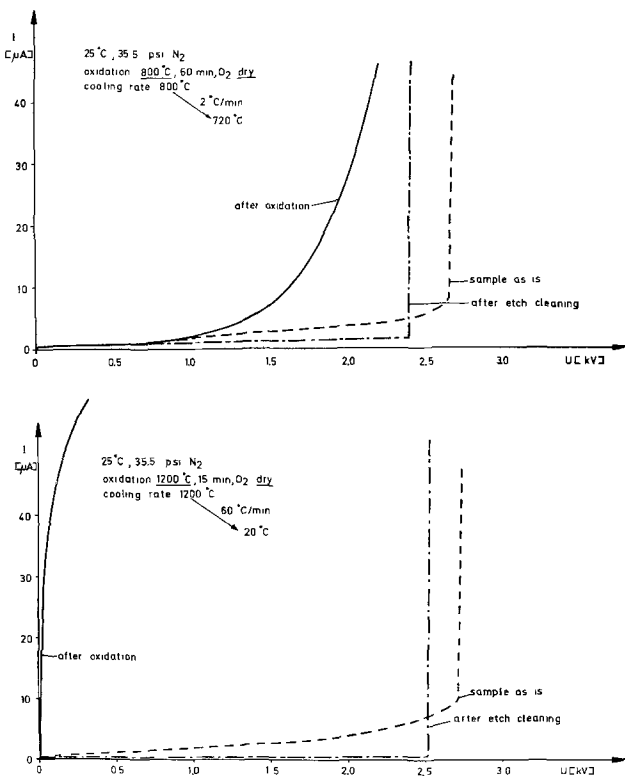


Fig. 7. I-V characteristics after dry oxidation (top) and oxidation at elevated temperature.

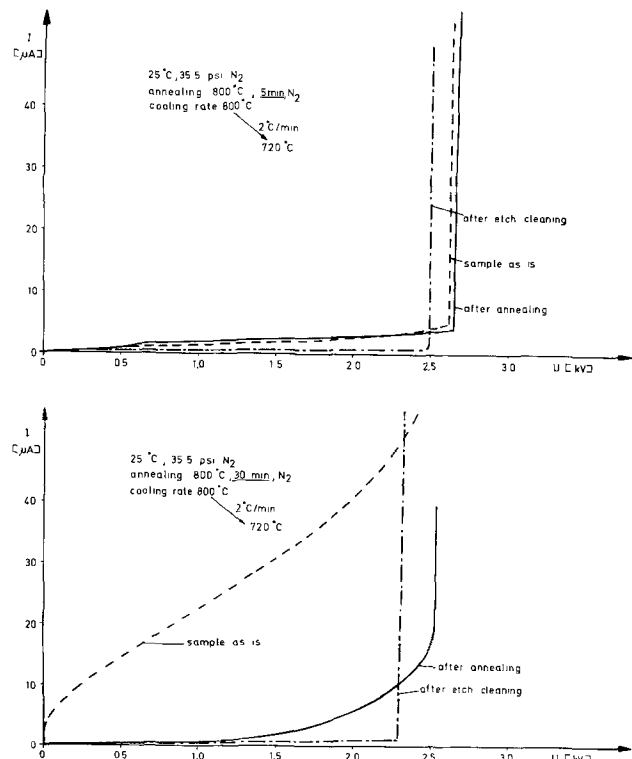


Fig. 8. I-V characteristics after annealing for different times

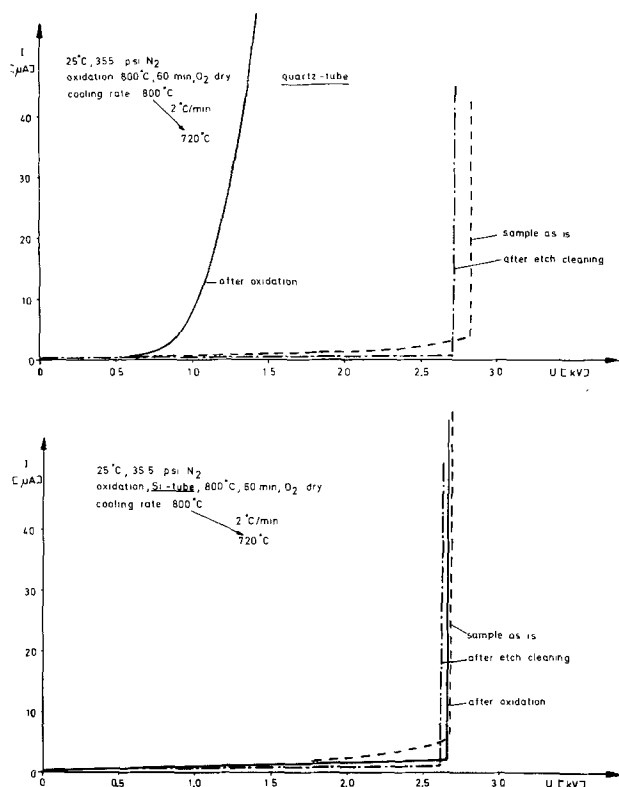


Fig. 9. The influence of the tube material on I-V characteristics. All other parameters are unchanged.

For the surface cleaning of the device, an etch cleaning is developed. For the 1.2 kV diodes, the best oxidation temperature in a quartz tube is  $800^\circ\text{C}$  with a subsequent cooling of  $2^\circ\text{C}/\text{min}$ . This procedure is successful for bevel angles up to  $7^\circ$ . A further improvement is obtained when silicon boats are used for the oxidation.

This technique fails in the case of the 2.8 kV diodes. It is found that the use of silicon tubes saves the initial abrupt I-V characteristics. Again, we use a dry oxidation temperature of  $800^\circ\text{C}$ , and a cooling rate of  $2^\circ\text{C}/\text{min}$ . It turns out that temperatures up to  $900^\circ\text{C}$  and cooling rates up to  $4^\circ\text{C}/\text{min}$  can be successfully applied with a silicon tube. To obtain thicker layers, a dry-wet-dry or dry-wet cycle is used. It can be concluded that for the first time, to our knowledge, passivation by thermal oxidation of 2.8 kV diodes can be carried out.

#### Acknowledgment

The authors are grateful to Drs. Jaecklin and Kuse of BBC Baden, Switzerland and Mr. Weimann of

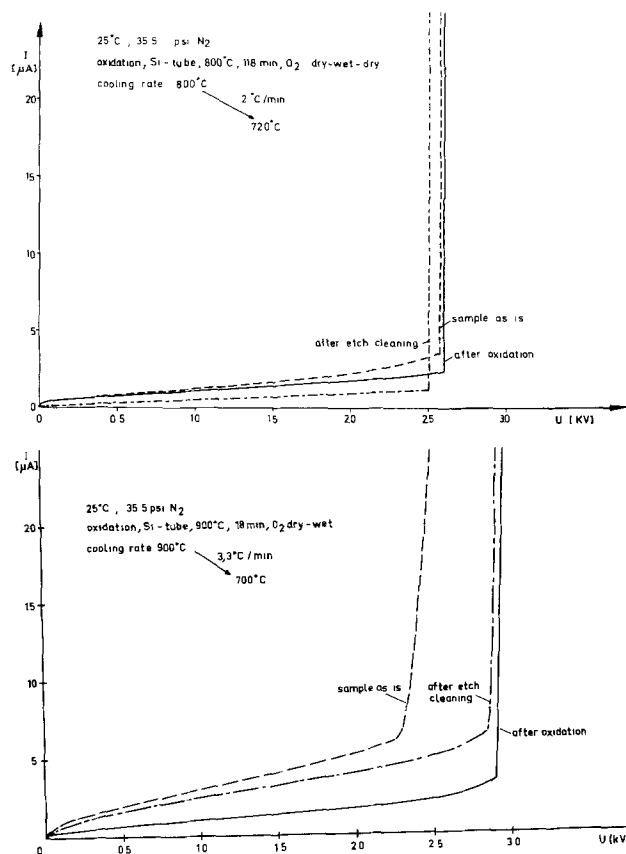


Fig. 10. Extension of the successful oxidation of Fig. 9 (bottom) to thicker oxide layers (800-1200Å) by a dry-wet-dry and a dry-wet oxidation cycle.

BBC Lampertheim, Germany for many discussions and supplying the wafers.

Manuscript submitted July 23, 1975; revised manuscript received Nov. 17, 1975.

Any discussion of this paper will appear in a Discussion Section to be published in the December 1976 JOURNAL. All discussions for the December 1976 Discussion Section should be submitted by Aug. 1, 1976.

Publication costs of this article were partially assisted by Institut für Angewandte Festkörperphysik.

#### REFERENCES

1. A. F. Bogenschütz, "Atzpraxis für Halbleiter," pp. 67-94 C. Hauser Verlag, München (1967).
2. W. Dietze, L. P. Hunt, and D. H. Sawyer, Paper 154 presented at The Electrochemical Society Meeting, Boston, Massachusetts, October 7-11, 1973.

# Chemically Vapor Deposited Fe<sub>2</sub>O<sub>3</sub> Films

Donald R. Mason\*

Harris Semiconductor, Melbourne, Florida 32901

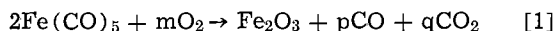
## ABSTRACT

The kinetics of the oxidation of iron pentacarbonyl by oxygen in the presence of water vapor have been investigated. Thin films having a composition closely resembling Fe<sub>2</sub>O<sub>3</sub> are obtained. The reaction sequence comprises, first, homogeneous nucleation and heterogeneous growth of particles which appear as smoke. Termination occurs by pyrolysis and oxidation of the smoke particles on the hot deposition surface. The H<sub>2</sub>O acts as an inhibitor on the film deposition rate. This mechanism is different from that normally proposed for homoepitaxy and from that proposed by Sladek for Si<sub>3</sub>N<sub>4</sub> deposition.

Metal oxide films for use as photolithographic masks have been prepared and evaluated by several investigators. Metal oxide masks are potentially superior to emulsion and some metal masks because they are harder (hence more scratch resistant) and partially transparent in the visible spectrum.

Sinclair, Sullivan, and Fastnacht (1, 2) evaluated a wide range of compositions of oxide films made by d-c reactive sputtering at 60 Torr and 10-100% O<sub>2</sub>. Requirements for good films would be that they transmit less than 1% of the incident energy below 4000Å, more than 30% of the incident energy above 5890Å, are etchable in reagents compatible with photoresist processes, and can resolve lines separated by 2 μm or less. Films of iron-vanadium oxide came closest to meeting the proposed properties desired for the masks.

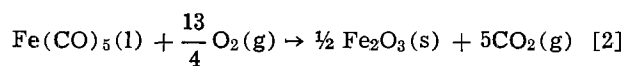
Meanwhile, MacChesney, O'Connor, and Sullivan (3) prepared iron oxide films on soda lime glass plates by chemical vapor deposition using iron pentacarbonyl (Fe(CO)<sub>5</sub>) vapor in an argon carrier gas and reacting it in ambient gas atmospheres of argon, carbon dioxide, oxygen, or oxygen-water vapor. These films met the proposed criteria if prepared properly. Upon oxidation, the over-all reaction which takes place is



The detailed mechanisms of these reactions are not yet known. In oxygen without water vapor, the rates were (3) "... approximately proportional to carrier gas flow rate and were not believed to be temperature dependent above 140°C." Water vapor not only drastically reduced the deposition rate, but the deposition rate *vs.* temperature now showed an activation energy of 12.7 kcal/mole. They postulated without discussion that the decomposition of iron pentacarbonyl to iron oxide proceeds by a surface catalyzed reaction (inferentially as the rate-limiting step.)

Peters, Sinclair, and Sullivan (4) have prepared FeO<sub>x</sub> films by sputtering and indicate that, at least for them, sputtering is more convenient than chemical vapor deposition. More recently, Sullivan (5) has indicated that good quality CVD films can be prepared at 100°C that meet all requirements, using CO<sub>2</sub> as a carrier gas.

Cotton, Fischer, and Wilkinson (6) investigated the structure and properties of iron pentacarbonyl. The latent heat of vaporization is +8.9 kcal/mole. The enthalpy of combustion at 298°K according to the reaction

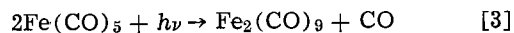


is -385.9 kcal/mole. This represents an energy release of 16.8 eV per molecule of Fe(CO)<sub>5</sub>(l) oxidized, or

\* Electrochemical Society Active Member.

Key words: CVD mechanism, iron oxide film, iron pentacarbonyl oxidation, photolithographic masks.

17.2 eV per molecule of Fe(CO)<sub>5</sub>(g) oxidized. Irradiation of Fe(CO)<sub>5</sub> with near u.v. light produces iron enneacarbonyl, Fe<sub>2</sub>(CO)<sub>9</sub>, and carbon monoxide (7)



When pure, it is unattacked by air. It is insoluble and nonvolatile, and unique among carbonyls. The compound decomposes at 100°C to give iron, CO, some Fe(CO)<sub>5</sub>, and some iron dodecacarbonyl, Fe<sub>3</sub>(CO)<sub>12</sub>. Iron dodecacarbonyl exists as green monoclinic crystals. It is volatile in steam without decomposition, but if heated alone above 100°C, it breaks down into metallic iron and carbon monoxide.

## Experimental

Our preliminary work was carried out using N<sub>2</sub> as a carrier gas for the Fe(CO)<sub>5</sub>, which was introduced by a bubbler. The remainder of the gas was made up of O<sub>2</sub> and CO<sub>2</sub>.

Following the over-all reaction mechanism given by Eq. [1], wherein all of the liberated CO is converted to CO<sub>2</sub>, then a maximum of 3.25 volumes of O<sub>2</sub> are needed for each volume of Fe(CO)<sub>5</sub>. This restriction was met in all cases; usually with more than a 100% excess of oxygen. Temperature ranges studied extended from 90° to 160°C.

In order to obtain reaction time-temperature relationships, the process observations were made by noting film color changes with time. The reaction was terminated when the appropriate color fringe on the film was observed, and the times noted. This technique is dependent on chamber-wall cleanliness and is also subjective, even with an experienced observer, with an error of typically ±5 sec.

The times required to form the first purple (950Å) fringe and the first red (1700Å) fringe were noted and the deposition rate over this thickness interval computed from the time interval difference. By using this "steady-state" deposition rate, the apparent elapsed time to form the first 950Å was calculated. By subtracting this time interval from the time noted to form the first purple fringe, an apparent induction period for the reaction was calculated. Time measurements were to the nearest 5 sec.

A gas control system was hard plumbed with copper tubing and equipped with thermoelectric coolers for temperature control of the iron carbonyl and water bubblers. The reaction chamber was an inverted 8 in. diameter funnel whose lip had been ground to give a snug fit onto the hot plate surface. Its volume was 1700 cm<sup>3</sup>. Depositions were made on 2½ in. square soft glass plates, polished on one side, and cleaned thoroughly just prior to deposition. All work was done in a laminar flow hood. Residual small particles on the glass often caused large pinholes. Typically, the carrier gas was saturated with iron carbonyl at room temperature and equilibrated by going through a second



bubbler maintained at 20°C. Water vapor at 0°, 10°, and 20°C was introduced in the oxidizer stream.

In order to assess the nonsteady-state conditions existing during reaction, the chamber was treated as a continuous stirred tank reactor system (8). In conditions of operation, a substrate plate was placed on the hot plate surface, and the reaction funnel placed over it, defining  $t = 0$ . The apparent start of deposition,  $t_0$ , was determined as above. During purging of the reactor, assuming this reaction to be first order with respect to iron carbonyl, the reactant concentration builds up in accordance with the relationship (8)

$$C_a = \frac{C_{a,0}}{Q} \left( 1 - \exp - \frac{Qt}{\theta} \right) \quad [4]$$

where  $Q = (k^* + F/V)\theta = (k^*\theta + 1)$ ;  $\theta = V/F$ , sec;  $k^*$  = first order reaction velocity constant,  $\text{sec}^{-1}$ ;  $F$  = total volumetric flow rate through the reactor,  $\text{cm}^3/\text{sec}$ ;  $V$  = volume of the reactor,  $\text{cm}^3$ ;  $C_a$  =  $\text{Fe}(\text{CO})_5$  concentration in reactor at time =  $t$ , mole fraction; and  $C_{a,0}$  =  $\text{Fe}(\text{CO})_5$  concentration in the feed gas stream, mole fraction. Initially, it was assumed that  $k^* \ll F/V$ . For example, at 115°C, 22.8  $\text{cm}^3$  per minute of  $\text{Fe}(\text{CO})_5$  were fed to the reactor for 4.22 min to form a film 1700Å thick. This corresponds to 223 mg Fe in the gas, from which only 19.5 mg Fe deposited on the hot plate areas.

The concentrations of  $\text{Fe}(\text{CO})_5$  were calculated using Eq. [4] at  $t = t_{950}$  and at  $t = t_{1700}$ , the times when the films were "950Å" (first purple) and "1700Å" (first red) thick. This corresponds to the time interval over which the deposition rate was measured.

With the increase in  $\text{Fe}(\text{CO})_5$  concentration, the  $\text{H}_2\text{O}$  concentration was also decreasing. Assuming a 50% relative humidity and nominal room temperature of 24°C ( $p_{\text{H}_2\text{O}} = 22$  mm Hg), then the chamber contained 14,500 ppm  $\text{H}_2\text{O}$  at the initiation of the purge cycle. The decrease in water vapor content with time is (9)

$$C_{\text{H}_2\text{O}} = C_{\text{H}_2\text{O},0} + (A_{\text{H}_2\text{O}} - C_{\text{H}_2\text{O},0}) \exp - t/\theta \quad [5]$$

where  $C_{\text{H}_2\text{O}}$  = actual water vapor concentration in reactor at time =  $t$ , ppm;  $C_{\text{H}_2\text{O},0}$  = water vapor concentration in reactant feed stream, ppm; and  $A_{\text{H}_2\text{O}}$  = initial water vapor concentration in reactor, assumed 14,500 ppm, as described above. The carbonyl and water concentrations were calculated at  $t_{950}$  and  $t_{1700}$  and a mean concentration used. Errors were typically about 5-10%.

A series of 39 additional sets of runs with from three to nine observations at each set of conditions was made varying iron carbonyl concentration (from 0.53 to 1.5%), water concentration (from 0.063 to 0.24%), and temperature (13 runs at 104°C, 13 runs as 115°C, and 13 runs at 127°C). Flow rate was typically 1350  $\text{cm}^3/\text{min}$ . All data were analyzed as outlined above. Results plotted on Fig. 1 and 2 show deposition rates in Å/min at 104°C, plotted vs. water vapor concentration and  $\text{Fe}(\text{CO})_5$  concentration in mole fraction, respectively. Similar plots were obtained at 115° and 127°C. Water vapor concentration was more difficult to control than carbonyl concentration.

The plots in Fig. 1 and 2 indicate that the deposition rate varies approximately with the iron carbonyl concentration to the 1.5 power, and with the water concentration to the -1 power. In order to evaluate these exponents more carefully as well as the pre-exponential coefficient,  $A$ , and the activation energy,  $\Delta E$ , the data were subjected to a multiple regression analysis on a computer. The results were

$$R^* = \frac{3.738 \times 10^7 (C_1)^{1.575}}{(C_2)^{0.93}} \exp \frac{-8124}{RT} \text{ Å/min} \quad [6]$$

where  $R^*$  = deposition rate, Å/min;  $C_1$  = iron carbonyl concentration, mole fraction;  $C_2$  = water con-

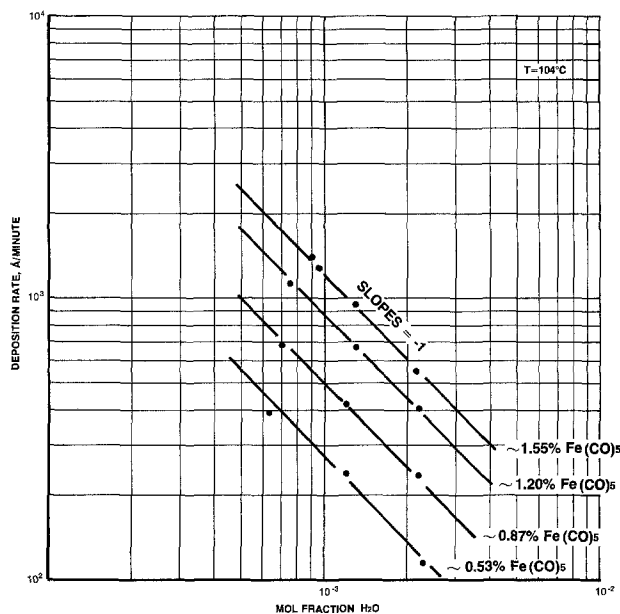


Fig. 1. Film deposition rate,  $R^*$ , in Å/min vs. water vapor concentration in mole fraction as functions of iron pentacarbonyl concentration at 104°C.

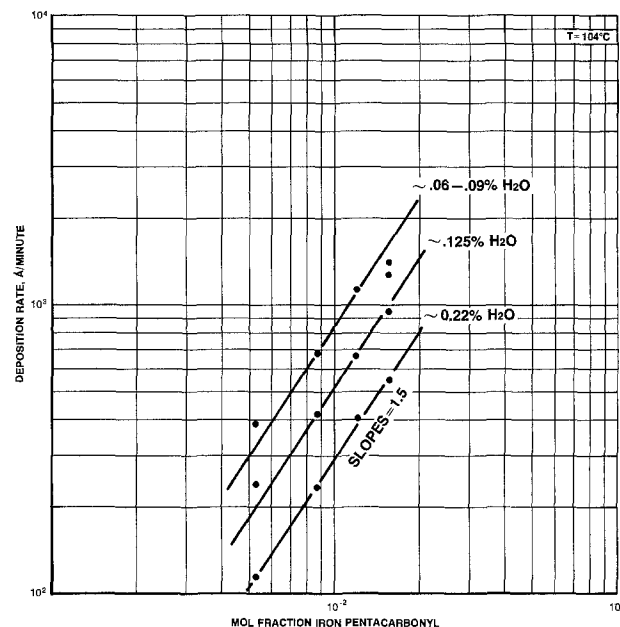


Fig. 2. Film deposition rate,  $R^*$ , in Å/min vs. iron pentacarbonyl concentration in mole fraction as functions of water vapor concentration at 104°C.

centration, mole fraction;  $A$  = pre-exponential coefficient =  $3.738 \times 10^7$ ;  $\Delta E$  = activation energy,  $-8124 \pm 366$  cal/g mole;  $m$  = concentration dependence of  $C_1$ ,  $1.575 \pm 0.030$ ; and  $n$  = concentration dependence of  $C_2$ ,  $-0.930 \pm 0.024$ , where the  $\pm$  values indicate one sigma limits.

At low water concentrations, the deposition rate was very rapid, and the chamber became smoky and cloudy very rapidly. Water vapor suppressed smoke formation and reduced deposition rate.

The sensitivity of the deposition rate to various operating parameters can be determined by differentiating the rate expression with respect to the independent variables. For example, a variation of  $\pm 2^\circ\text{K}$  in deposition temperature can cause a total of 10% change between minimum and maximum film thick-

ness. Good temperature control is necessary for good deposition rate reproducibility and film uniformity.

When compared to the activation energy found by MacChesney *et al.* of 12.7 kcal/mole, our significantly lower activation energy of 8.1 kcal/mole indicates that the presence of large amounts of CO<sub>2</sub> changes the reaction path. These activation energies were both determined for the reaction system containing water vapor.

### Results

When it was observed that small foreign particles on the substrate surface seem to exert a retarding influence on oxide film deposition well beyond the particle dimensions, it appeared that the system might be sensitive to electrostatic influences. To investigate this effect, two Al foil electrodes 2.5 cm square were placed in the reaction chamber about 5 cm apart and a potential ranging from 6 to 15 kV applied, while the reaction was proceeding under highly smoke-forming conditions. There was a large accumulation of negatively charged dark reddish brown soot containing 61.4 weight per cent (w/o) Fe around the positive electrode and a much smaller amount of positively charged blackish and gray-colored soot containing 46.3% Fe around the negative electrode. Hence ions are formed in the vapor as part of the reaction mechanism. This type of behavior is unusual for a vapor-phase reaction. At every high (15 kV) potential, the soot was cleared almost instantaneously from the vapor phase and deposition essentially ceased. When the potential was lowered to 6 kV, it reappeared. No detectable current was noted on a milliammeter.

To ascertain the degree of smoke particle formation, a fractional portion of the exhaust stream from the reactor was introduced into a particle counter. After 4 min, the rate of generation of particles greater than 0.5 $\mu$  in diameter attained a steady state of about 250,000 particles/ft<sup>3</sup> min.

To ascertain whether or not there actually is an induction period for deposition, plates were slid into and out of the funnel reactor while it was operating under steady-state conditions. Reproducible results were obtained but a negative induction period was indicated. This may possibly be attributed to a condensation on the glass plate surface as it is warming to reaction temperature, to an electrostatic effect which accelerates the initial deposition or retards later depositions, or to some other effect involving the initial deposition on the surface.

### Film Characterization

**Density.**—The density of a film was determined by measuring a 7.8 mg weight increase after deposition of a 4000Å thick film. On a 2½ in. × 2½ in. × 0.060 in. glass substrate

$$\rho = \frac{7.8 \times 10^{-3}}{40.4 \times 0.4 \times 10^{-4}} = 4.84 \text{ g/cm}^3 \quad [7]$$

A 1400Å film weighing 2900  $\mu$ g on one side of two 2 in. diameter silicon wafers gave a density calculation of 5.07 g/cm<sup>3</sup>. This is lower than that observed for any oxide of iron (Table I).

**Composition.**—Film compositions were measured using atomic absorption spectra intensities and comparing against standard solutions. Precision is expected to be about  $\pm$  0.5%. Results on films as-made as well as powders attracted to the positive electrode and negative electrode are listed in Table I along with properties of some iron compounds.

The film taken from the hot plate (69.4% Fe) apparently is Fe<sub>2</sub>O<sub>3</sub> (69.8% Fe), and was formed after prolonged exposure at the deposition temperature of 127°C. The normal film (68.6% Fe) has a higher iron composition than the negatively charged ions (61.4% Fe) or the positively charged ions (47.3% Fe) that are

Table I. Iron compositions of various samples and compositions, density and index of refraction of various iron compounds

Sample	w/o Fe	Density	Index of refraction (5896Å)
Normal film	68.6	4.84 (5.07)	3.0 $\pm$ 0.2
Powder at anode	61.4	(negatively charged ions)	
Powder at cathode	47.3	(positively charged ions)	
Film from hot plate	69.4		
Fe <sub>2</sub> O <sub>3</sub>	69.8	5.24	3.01 (5896Å) 2.94 (6708Å)
Fe <sub>3</sub> O <sub>4</sub>	72.3	5.18	2.42
FeO	77.6	5.7	2.32
FeCO <sub>3</sub>	47.6	3.8	1.663(?)
Fe(CO) <sub>5</sub>	28.0		
Fe <sub>2</sub> (CO) <sub>9</sub>	30.6	2.08	
Fe <sub>3</sub> (CO) <sub>12</sub>	33.2		
Fe <sub>2</sub> (CO) <sub>4</sub>	49.9		
Fe <sub>3</sub> (CO) <sub>5</sub>	44.2		
Fe(CO)	66.5		
MacChesney 155°C film	67.0		
MacChesney 200°C film	68.2		

formed during the reaction. This indicates that pyrolysis and oxidation does take place during the termination phase of the reaction after the smoke particles deposit on the hot glass surface. The positively charged ions (47.3% Fe) have an iron composition similar to FeCO<sub>3</sub> (47.6% Fe).

**Transmission electron microscope pictures.**—Transmission electron microscope pictures using the replica technique, and Talyscan surface profiles were made on some of the films. As the project progressed, various data were correlated to define an interpretation of the reaction kinetics (see below). As part of this study, two films at  $t = 10$  sec and  $t = 15$  sec showed characteristics different from each other and from the completed films. (Where  $t = 0$  is time of introduction of plates into the reactor.)

(i)  $t = 10$  sec.—It appeared that there was a substantial amount of initial deposition of reacted product on the glass surface. This supports the "negative induction period" observed with the kinetic studies. The particle size distribution was large with 2 particles/ $\mu^2$  having 0.2  $\mu$ m diameter or greater.

(ii)  $t = 15$  sec.—The particle size distribution became narrower, with fewer particles (1 per  $\mu^2$ ) having diameters greater than 0.2  $\mu$ m. A transmission electron microscope photograph at 21,000X is shown in Fig. 3.

(iii) *Completed films.*—These films (about 1700Å thick) showed even a narrower particle size distribution (1 per 20–25  $\mu^2$ ) and a much finer grained structure.

### Reaction Kinetics Interpretations

Our observations lead us to speculate on the nature of the reaction mechanism in order to explain the kinetic behavior of the system.

The presence of H<sub>2</sub>O promotes the oxidation of CO to CO<sub>2</sub> (3, 10) but inhibits the growth of FeO<sub>x</sub> films (3, this work).

The presence of smoke or fog in the reacting system indicates a homogeneous nucleation mechanism. By considering the limiting reaction step in the film growth rate to occur on the surfaces of smoke particles via a heterogeneous reaction mechanism, a good approximation can be made for the observed results. The iron content of the smoke particles lower than that of Fe<sub>2</sub>O<sub>3</sub> indicates that some CO is still held chemically to the iron at this stage. Hence, the final stage of film deposition is then assumed to occur by way of a combination of thermal decomposition and oxidation reaction of the smoke particles on the surface of the glass plate. Analysis of the as-made films (68.4 w/o Fe) indicates the probable inclusion of some CO.

A complete set of reaction step equations would be impossible to construct, but some speculations can be made nevertheless. It was desired to establish a model

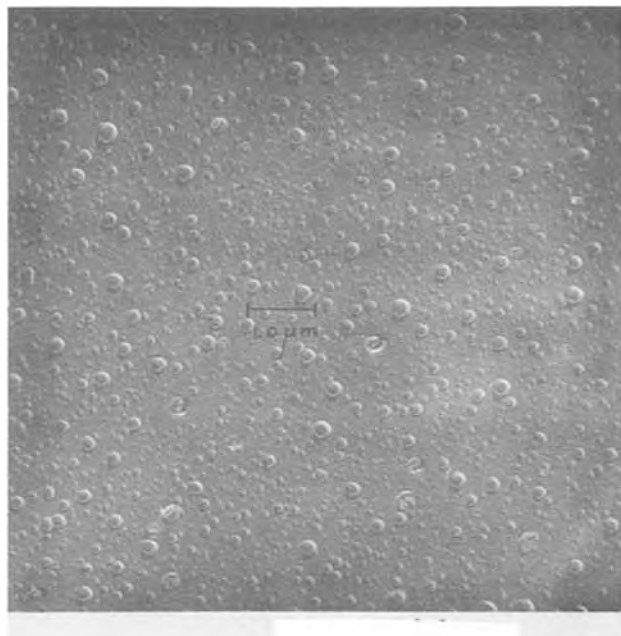
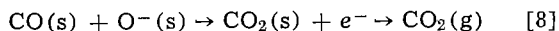


Fig. 3. Transmission electron microscope photograph of iron oxide film after initial 15 sec of deposition. Spheroidal particles, some partially shattered, demonstrate vapor-phase nucleation and particle growth, followed by pyrolysis on the glass surface. Composition change between particles and films indicates that oxidation accompanies pyrolysis (9000X after reduction).

so that the somewhat unusual values of the concentration exponents in Eq. [6] could be explained. It is assumed that the partially oxidized  $\text{FeO}_x$  particles have semiconductive properties, and the limiting step is the catalytic oxidation of adsorbed  $\text{Fe}(\text{CO})_5$  by  $\text{O}^-$  adsorbed on the smoke particles, leaving  $\text{Fe}(\text{CO})_4$  to be further oxidized and incorporated into the smoke particles as a semiconducting material.

Lee and Mason (11) have analyzed the possible conditions which can exist to promote the catalytic oxidation of CO by  $\text{O}_2$  on a semiconductor catalyst. This category of reaction involves the simultaneous adsorption of positive ( $\text{CO}^+$ ) and negative ( $\text{O}^-$ ) ions and oxygen atoms and CO molecules, with the most probable limiting step being the surface migration of adsorbed ions, atoms and molecules, to combine to form  $\text{CO}_2$  as the reaction product. For the reaction



Lee and Mason's theory can show that the rate equation can have the following form, if the adsorbed ions have surface concentrations so as to generate a negative space charge region beneath the semiconductor catalyst surface

$$R^* = \frac{K_1 p_{\text{O}_2}^{1/2} p_{\text{CO}}^{5/3}}{(1 + K_4 p_{\text{CO}_2})^{8/3}} \quad [9]$$

Under conditions relevant to these experiments, the positive adsorbed surface ion concentration ( $\text{CO}^+$ ) would have to be in excess of the negative adsorbed surface ion concentration ( $\text{O}^-$ ) in order to form the required negative space charge region beneath the surface of the smoke particles.

In the experimental section, it was found that the deposition rate varied as the 1.575 power of the iron carbonyl concentration, which is close to the predicted 1.67 power of the CO in this reaction mechanism. For the experimental evidence to be consistent with Lee and Mason's theory, the pressure of iron pentacarbonyl must be substituted for the pressure of carbon monoxide.

By using the narrow concentration ranges of  $\text{O}_2$  and  $\text{CO}_2$  which occurred more or less by accident in our

deposition system, the data were again subjected to a series of multiple regression analyses on the computer. In this situation, it was necessary to select values of  $K_4$  in order to generate the 8/3 exponent for the  $\text{CO}_2$  adsorption isotherm in the denominator. The results are

$R^*$

$$= \frac{8.459 \times 10^7 (p_{\text{Fe}(\text{CO})_5})^{1.34} (p_{\text{O}_2})^{0.26} \exp \frac{-8093}{RT}}{(p_{\text{H}_2\text{O}})^{0.924} (1 + 0.422 p_{\text{CO}_2})^{2.68}} \text{ A/min} \quad [10]$$

However, standard errors and F-level tests of statistical significance (one sigma limits) indicate that there was not sufficient variation in these quantities to verify their exponents quantitatively.

The inhibiting influence of water vapor may be explained by the competitive adsorption of ( $\text{H}_3\text{O}^+$ ) molecules on the surface in place of the ( $\text{CO}^+$ ) or equivalent molecules from the  $\text{Fe}(\text{CO})_5$ . This mechanism would decrease the adsorbed  $\text{Fe}(\text{CO})_5$  concentration and decrease the rate of smoke particle growth, without affecting the reaction order of the  $\text{Fe}(\text{CO})_5$ . The competitive adsorption of the nonreacting  $\text{H}_2\text{O}$  would probably introduce a term of  $(1 + K p_{\text{H}_2\text{O}})^{-1}$  into the rate expression.

The state of the theory is such that adsorption isotherms are not available for three species of charged particles simultaneously adsorbed on a semiconductor surface.

### Particle Growth Kinetics

During normal epitaxial deposition, it is generally assumed that one or more molecular species containing components of the epitaxial composition strikes the surface and becomes incorporated into the structure essentially as an atomic entity after reaction and desorption of carrier atoms. This assumption seems to be valid for silicon, germanium, III-V compounds perhaps, and many other systems.

More recently, Sladek (12) has considered the case of competition between reactions on the surface and homogeneous reactions which produce a powder in the gas phase which is not incorporated into the film. He cites experimental evidence for the formation of silicon nitride films to support his theory.

In the  $\text{Fe}_2\text{O}_3$  deposition reaction considered here, we postulate still a third mechanism. The reaction proceeds via homogeneous nucleation to form a smoke particle which grows via a heterogeneous mechanism. The smoke particles then form the epitaxial film through a termination reaction involving pyrolysis and oxidation. The film deposition rate may be controlled by the competition between adsorption of two similarly charged ions, only one of which contributes to the reaction mechanism. By occupying surface adsorption area, the second like-charged ion acts as a reaction inhibitor.

The experimental evidence (smoke, compositions, transmission electron microscope pictures) confirms the theory in the case of iron pentacarbonyl oxidation even though the quantitative kinetic evidence for the heterogeneous mechanism is far from conclusive.

### Summary

High quality, defect-free films of iron oxide that are suitable for making semitransparent photolithographic masks have been prepared on soft glass plates by oxidation of iron pentacarbonyl. These films correspond generally to the composition  $\text{Fe}_2\text{O}_3$ . The chemical vapor deposition kinetics have been analyzed and a film growth mechanism has been proposed.

### Acknowledgments

Mr. William J. Willis performed the experimental work and made many valuable suggestions. Mr. R. K.

Lowry performed the chemical analyses and Mr. R. E. Flutie took the transmission electron microscope pictures. Dr. P. W. Chiang participated in several discussions of the manuscript which increased the clarity of presentation. The clarity of this paper was improved significantly by the peer review system used by **This Journal**.

Manuscript received Sept. 8, 1975; revised manuscript received Dec. 8, 1975.

Any discussion of this paper will appear in a Discussion Section to be published in the December 1976 **JOURNAL**. All discussions for the December 1976 Discussion Section should be submitted by Aug. 1, 1976.

Publication costs of this article were partially assisted by Harris Semiconductor.

#### REFERENCES

1. W. R. Sinclair, M. V. Sullivan, and R. A. Fastnacht, *This Journal*, **118**, 341 (1971).
2. W. R. Sinclair, M. V. Sullivan, and R. A. Fastnacht, Abstract 125, p. 323, The Electrochemical Society Extended Abstracts, Spring Meeting, Los Angeles, California, May 10-15, 1970.
3. J. B. MacChesney, P. B. O'Connor, and M. V. Sullivan, Abstract 126, p. 325, *ibid.* Also *This Journal*, **118**, 776 (1971).
4. F. G. Peters, W. R. Sinclair, and M. V. Sullivan, *ibid.*, **119**, 305 (1972).
5. M. V. Sullivan, *ibid.*, **120**, 545 (1973).
6. F. A. Cotton, A. F. Fischer, and G. Wilkinson, *J. Am. Chem. Soc.*, **81**, 800 (1959).
7. P. J. Durrant and B. Durrant, "Introduction to Advanced Inorganic Chemistry," 2nd ed., pp. 1125-1162, John Wiley & Sons, Inc., New York (1970).
8. D. R. Mason and E. L. Piret, *Ind. Eng. Chem.*, **42**, 817 (Equation 3g) (1950).
9. *ibid.*, (Equation 3b).
10. S. W. Benson, "The Foundations of Chemical Kinetics," McGraw-Hill Book Co., New York (1960).
11. V. J. Lee and D. R. Mason, "Proc. Third Intern. Congr. on Catalysis-1964", pp. 556-576, North-Holland Publishing Co., Amsterdam (1965). See also V. J. Lee, Ph.D. Thesis, University of Michigan (1963).
12. K. J. Sladek, *This Journal*, **118**, 654 (1971).

## The Anodic Oxidation of Vanadium: Transport Numbers of Metal and Oxygen and the Metal/Oxygen Ratio in the Oxide Films

W. D. Mackintosh and H. H. Plattner

Atomic Energy of Canada Limited, Chalk River Nuclear Laboratories, Chalk River, Ontario, Canada

#### ABSTRACT

The techniques of ion implantation and Rutherford backscattering analysis have been used to determine the transport numbers of metal and oxygen during the anodic oxidation of vanadium. These were found to be  $0.28 \pm 0.05$  and  $0.72 \pm 0.05$ , respectively. The Rutherford backscattering analysis simultaneously gives the ratio of V/O in the film. This was found to be  $0.4 \pm 0.02$  thus indicating that the films are V<sub>2</sub>O<sub>5</sub>. The result was confirmed by use of the nuclear reaction <sup>16</sup>O(d,p)<sup>17</sup>O.

In 1965 Keil and Salomon (1) demonstrated that adherent oxide films could be grown on vanadium provided that an electrolyte of borax in glacial acetic acid was used. They also studied the film composition using Faraday's law, attenuated total reflectance spectroscopy, and electron paramagnetic resonance spectroscopy. In a later publication, Keil and Ludwig (2) explored the relationship between ion current migrating through the oxide films and the electrostatic field across the dielectric over a potential range of 100V utilizing the open-circuit transient method. Ellis, Hopper, and De Smet (3) simultaneously published a similar study. While investigating anodic oxidation and subsequent film stripping as a technique for sectioning vanadium, Arora and Kelly (4) devised a method for stabilizing the films so that they were not subject to reaction with the atmosphere which otherwise occurs within 60 sec of removal from the electrolyte. They also measured the rate of dissolution of vanadium in the electrolyte during anodic oxidation.

In this present work we have used ion implantation and nuclear analytical techniques to determine the transport numbers of metal and oxygen ions and to investigate the film composition. These objectives were achieved by a method similar to that described in a

previous publication (5) where it was shown that the energy spectra of He ions backscattered from aluminum, recorded before and after anodic oxidation, could be interpreted to give both the thickness of the oxide films and the final position of foreign atoms introduced into the surface layers of the metal before oxidation. Implanted noble gas atoms were used to act as an immobile marker and hence to deduce the transport numbers of metal and oxygen. It was also shown to be possible to establish whether or not the films were stoichiometric Al<sub>2</sub>O<sub>3</sub>. In this latter application the Rutherford backscattering method, unlike x-ray analysis, can be used on amorphous films and, unlike electron paramagnetic resonance spectroscopy, does not require that the film be dissolved from the substrate before analysis.

In addition, we have used the <sup>16</sup>O(d,p)<sup>17</sup>O reaction (6) to determine the oxygen content of the films. These measurements served to confirm the oxide thickness and the V/O ratio obtained by Rutherford backscattering.

#### Experimental

The vanadium specimens were cut from sheets, 0.5 mm thick, using a jig to ensure reproducibility. The areas were 4 × 1 cm except that a rectangular section was removed from one corner to leave a lug 5 × 3 mm

to which the electrical connections were made. Surfaces were prepared by abrading with fine metallurgical paper followed by vibratory polishing with 0.3  $\mu\text{m}$  alumina. Residual alumina was removed by ultrasonic cleaning in distilled water. The specimens were then rinsed in ethanol and dried in air. This was followed by three cycles in which the specimens were anodized then stripped of oxide in a dilute ( $\sim 0.1\%$ ) solution of KOH (4).

All anodizations were carried out in the electrolyte proposed in Ref. (1), namely glacial acetic acid containing 0.02 mole/liter  $\text{Na}_2\text{B}_4\text{O}_7 \cdot 10 \text{H}_2\text{O}$  and 1.0 mole/liter additional  $\text{H}_2\text{O}$ . The temperature was  $23^\circ\text{C}$ . For the most part the procedure followed that of Ref. (4), that is, the specimens were immersed in the electrolyte to a depth of 3.5 cm facing a larger platinum electrode at a distance of 1 cm. The vessel was open to the atmosphere and not stirred. The electrolyte was discarded after two hours' use. A constant voltage power supply was used and an external variable resistance was connected in the circuit so that limits to both the current and voltage could be preset. In anodizing in this manner, we standardized on a maximum current of 3 mA/cm<sup>2</sup> and a time of 6 min as this had been shown in Ref. (4) to be the optimum condition for obtaining the minimum loss of vanadium to the electrolyte. Immediately following anodization each specimen was rinsed briefly in glacial acetic acid to prevent deposition of the solid component of the electrolyte on the surface. The specimens were then rapidly dried in a jet of dry air.

Some specimens were anodized in a manner closer to that described in Ref. (1) *viz.* the electrolyte was contained in a closed vessel, and was purged with Ar to keep the solution stirred. In these cases the current was kept constant at 1 mA/cm<sup>2</sup> and the voltage allowed to rise to the desired value with no limitation on time. These too were washed in acetic acid and dried in a stream of air.

Noble gas ions accelerated to energies of 50 keV were implanted into specimens which were covered with an oxide film 25  $\mu\text{g}/\text{cm}^2$  thick. At this energy the implanted atoms were located entirely within the preformed oxide and served to mark this layer. The number of ions implanted was commensurate with the sensitivity of the Rutherford scattering method for each species;  $2 \times 10^{15}$  of Xe and  $4 \times 10^{15}$  atoms/cm<sup>2</sup> of Kr.

The experimental arrangement for obtaining the spectra of backscattered He ions was identical with that described in Ref. (5). Briefly, it consists of a Van de Graaff accelerator delivering a beam of 2 MeV He ions, a target chamber and a surface barrier detector (resolution 17 keV FWHM) placed to observe ions scattered through  $150^\circ$ , together with the usual electronics and pulse height analyzer. For oxygen analysis a beam of 900 keV deuterons was used and the detector was covered with Mylar 19  $\mu\text{m}$  thick (6); otherwise the arrangements were identical to those for backscattering.

The basis of the Rutherford scattering technique for surface analysis, for film thickness measurements, and for locating the position of foreign atoms has been described [Ref. (7) and references therein]. The essence of the method is that, if a He ion of known energy (in this case 2 MeV) is scattered from a surface atom, the resultant energy loss can be calculated from the kinematics of the system. Any additional energy loss observed is due to the fact that the struck atom is not on the surface and therefore the He ion suffers energy loss in both its ingoing and outgoing trajectories. This loss can be interpreted to give the depth of the atom.

The area of the peak obtained by backscattering from implanted ions is dependent on the number of implanted atoms present. It is possible to obtain the

absolute amounts (7), but for these experiments it was sufficient to compare areas after normalization to the same integrated beam current (*i.e.*, same number of incident particles) to observe any changes in the amount of implant occurring during anodization.

The details of how the spectra are interpreted are, again, given in Ref. (5). We present a very brief illustration by means of Fig. 1. It was obtained from a specimen of V after the oxide had been thickened to 60  $\mu\text{g}/\text{cm}^2$ . In the spectrum, the peak to the right is derived from scattering from the Xe. The continuum to the left containing a marked step is derived from scattering from the V atoms. The lower step is obtained from V atoms in the oxide, the higher from V atoms in the metal substrate. The peak on the substrate continuum is derived from backscattering from O atoms in the oxide layer. It has poor statistical significance and hence is unsatisfactory for determining the oxygen content.

The width of the step in the continuum, indicated by the vertical dashed lines in Fig. 1, is a measure of the oxide thickness and this can be calculated as described in Ref. (5). However, as noted in this reference, it is necessary to know the ratio of metal to O atoms in the oxide to carry out the calculation accurately as the energy loss sustained by the He ions is dependent upon the composition of the medium through which they are passing. We assumed that this ratio was not known with certainty and calculated two possible values for the rate of energy loss; one based on a composition of  $\text{VO}_2$  and one on  $\text{V}_2\text{O}_5$ . We then calculated for each of the two compositions what the ratio of the step heights should be and compared this calculated ratio with the observed ratio. The composition leading to the best fit was considered the correct one. The choice and additional evidence for the correctness of the choice are given below.

The position of the dashed vertical line above the Xe peak on the energy scale of Fig. 1 corresponds to Xe atoms if they were on the surface. The actual Xe position indicates that the Xe atoms are buried. The depth of the Xe is calculated from this energy shift. The precision obtainable for this measurement and for the thickness of the oxide film is 2  $\mu\text{g}/\text{cm}^2$ .

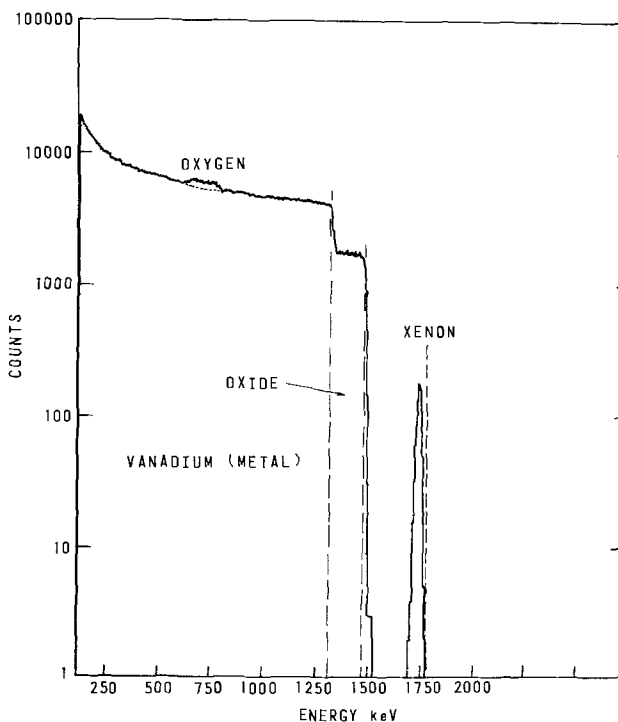


Fig. 1. Rutherford backscattered spectrum from xenon in anodized vanadium.

The procedure for the nuclear reactions  $^{16}\text{O}(d,p)^{17}\text{O}$  was much as described in Ref. (6). The peak in the spectrum derived from the proton product of the reaction was identified from its energy. The area of the peak was compared to that derived from a comparative standard exposed to the same integrated beam current. The comparative standard was Ta covered by an oxide layer known to be 2579 Å thick and to contain  $37 \mu\text{g}/\text{cm}^2$  of oxygen.

### Results

**Oxygen to vanadium ratio.**—In Fig. 2 the count data in the region of the step in the vanadium continuum have been replotted as a function of depth by interpolating into the data of Fig. 1. Figure 2A assumes the oxide is  $\text{V}_2\text{O}_5$ , Fig. 2B that it is  $\text{VO}_2$ . These show a difference of only  $3 \mu\text{g}/\text{cm}^2$  in the thickness as the energy to depth calculations are little affected by moderate differences in the composition of the oxide. The dashed lines represent the standard deviation of the least squares fit to the data points. The point  $\oplus$  is the fitted count in the first channel of data derived from the vanadium substrate. Using this number and assuming a stoichiometry for the oxide it is a straightforward matter to calculate the number of counts that should be obtained from the vanadium in the oxide film for the chosen stoichiometry. These calculated curves are shown as solid lines for  $\text{V}_2\text{O}_5$  and  $\text{VO}_2$  in Fig. 2A and 2B, respectively. (Curves for  $\text{V}_2\text{O}_3$  and  $\text{VO}$  diverge further from the data.) The relative standard deviation of the calculated curves was 2% (indicated by  $\uparrow$  in the figures), that of the observed data, 2.5% (indicated by the dashed lines in the figures). Of 30 spectra we have examined, the calculated curves based on a V/O ratio of 0.4 ( $\text{V}_2\text{O}_5$ ) fitted the observed data within these limits so it can be said that the V/O ratios were within 4.5% of stoichiometric  $\text{V}_2\text{O}_5$ .

Results obtained from another experiment confirm that the film is indeed  $\text{V}_2\text{O}_5$ . In Fig. 3 we show the weight of oxide per  $\text{cm}^2$  of surface for seven samples which were anodized at applied voltages of 40, 50, 60, 70, 80, and 90, respectively. In all cases the initial current was  $3 \text{ mA}/\text{cm}^2$  and the anodization time was 6 min. Each of the samples was analyzed in three ways: by weighing, by the  $^{16}\text{O}(d,p)^{17}\text{O}$  reaction, and by Rutherford backscattering. The values marked  $\nabla$  were obtained by converting the oxygen results found by the  $^{16}\text{O}(d,p)^{17}\text{O}$  reaction to oxide assuming the oxide was  $\text{V}_2\text{O}_5$  while those marked  $\blacksquare$  assume the oxide was  $\text{VO}_2$ . The precision of these results depends on two factors, counting statistics and the reproducibility

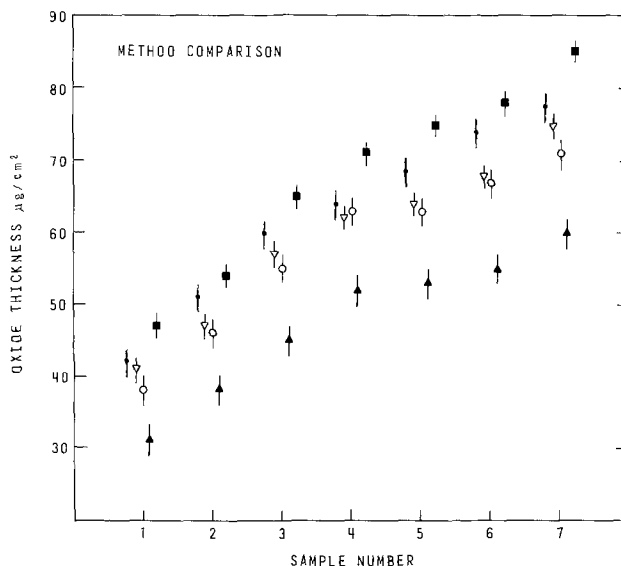


Fig. 3. The results of Rutherford backscattering analysis, nuclear reaction analysis, and conventional weighing. The assumption that the oxide is  $\text{V}_2\text{O}_5$  is compared with the results on the assumption the oxide is  $\text{VO}_2$ .  $\nabla$   $^{16}\text{O}(d,p)^{17}\text{O}$  if  $\text{V}_2\text{O}_5$ ;  $\circ$  Rutherford backscattering if  $\text{V}_2\text{O}_5$ ;  $\blacktriangle$  Rutherford backscattering if  $\text{VO}_2$ ;  $\blacksquare$   $^{16}\text{O}(d,p)^{17}\text{O}$  if  $\text{VO}_2$ ;  $\bullet$  conventional weighing.

of the measurement of incident beam dose on sample and comparative standard. The values plotted in the figure are the averages for triplicate analyses; the widest range observed was  $\pm 2 \mu\text{g}/\text{cm}^2$  for the thickest samples. The points  $\circ$  are the Rutherford backscattering results assuming  $\text{V}_2\text{O}_5$ ,  $\blacktriangle$  assuming  $\text{VO}_2$ . In this experiment these diverge more than the results shown in Fig. 2 because we tilted the specimens at an angle to the target beam to increase the total path length of the incident and emergent particles. Due to the increased path length the method is then more sensitive for distinguishing between the two possible oxides. The points marked  $\bullet$  are the values obtained from the difference in weight between the anodized specimen before and after stripping. The standard deviation found during weighing in quintuplicate was  $2.5 \mu\text{g}/\text{cm}^2$ . It can be seen from this figure, bearing in mind the precision of each result, that the weight calculated from Rutherford backscattering and the  $^{16}\text{O}(d,p)^{17}\text{O}$  reaction data on the assumption that the film is  $\text{V}_2\text{O}_5$

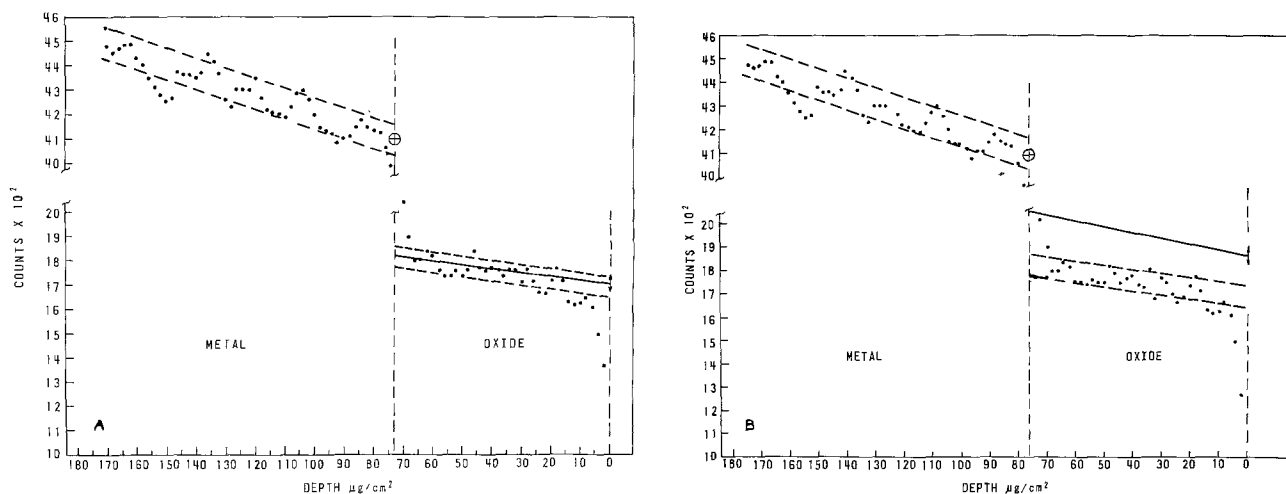


Fig. 2. Rutherford backscattering yield derived from the vanadium in the oxide and top layers of the substrate plotted as a function of depth. (A) The calculated spectrum shape in the oxide step (solid line) has been obtained on the assumption the oxide is  $\text{V}_2\text{O}_5$ , (B) on the assumption the oxide is  $\text{VO}_2$ .

agree quite closely. On the other hand, the points diverge in opposite directions when it is assumed the film is  $\text{VO}_2$ . In addition, weights determined by conventional weighing agree more closely with those obtained by Rutherford backscattering and the  $^{16}\text{O}(d, p)^{17}\text{O}$  reaction assuming the film is  $\text{V}_2\text{O}_5$  while converting the data to weight. It is therefore concluded that the oxide film is  $\text{V}_2\text{O}_5$ .

This conclusion is in contradiction to that of Keil and Salomon (1) who contended that the oxide was  $\text{VO}_2$ . Our normal method of oxidation differed from theirs. However, we anodized 8 specimens in their manner, i.e., in a closed vessel with Ar purging, at a constant current of 1 mA/cm<sup>2</sup>, and an electrode spacing of 1 cm. The oxide thicknesses produced ranged from 20 to 85  $\mu\text{g}/\text{cm}^2$ . In every case, the Rutherford backscattering spectra showed that the heights of the steps derived from the vanadium in the oxide film corresponded to  $\text{V}_2\text{O}_5$ . These differences in results are difficult to reconcile. The advantage of the Rutherford backscattering method is that the film is examined *in situ* while the electron paramagnetic resonance method used involved determination of the valence of V after dissolution. It would take little  $\text{SO}_3^{--}$  in the sulfate-bisulfate solution used to dissolve the oxide, to reduce  $\text{V}_2\text{O}_5$  to the vanadyl ion.

**Transport number.**—The metal transport number is given by the ratio  $D/T$  when  $D$  is the amount of oxide grown above an immobile marker and  $T$  is the total thickness of oxide grown during the anodization. The method by which this ratio is obtained from ion implantation and Rutherford backscattering experiments is illustrated in Fig. 4. The vertical lines denoted  $t_1$  represent the preformed oxide layer while the points X mark the position of the immobile marker atoms implanted within this film. The thickness of the film and the depth of the marker  $d_1$  are obtained from backscattering spectra of specimens before anodization. The depth  $d_2$  of the implant below the outer surface of the specimen and the thickness of the oxide  $t_3$  are likewise obtained from backscattering spectra after the specimen has been anodized. The thickness  $t_2$

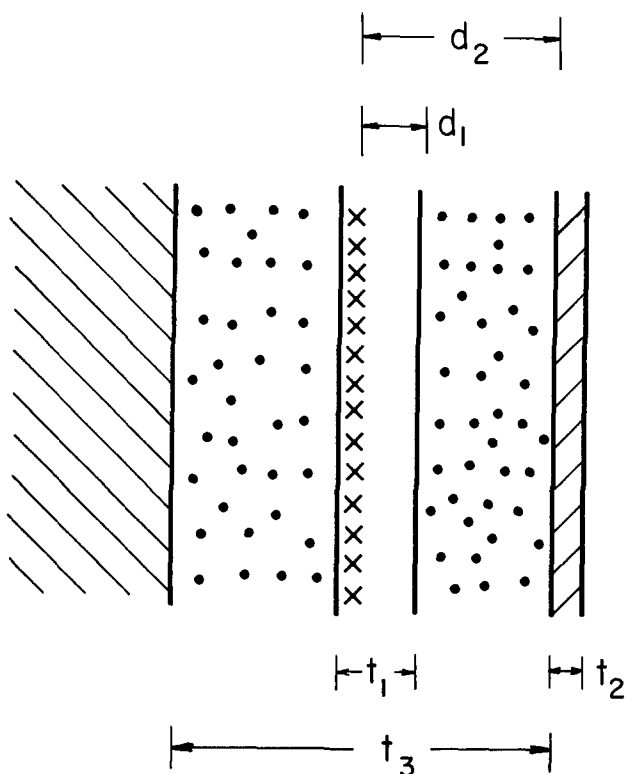


Fig. 4. Illustration of the parameters used in calculating the metal transport numbers.

represents the oxide equivalent of the amount of V that has been dissolved in the electrolyte during anodization. Expressing all depths in  $\mu\text{g}/\text{cm}^2$ , the required ratio  $D/T$  is therefore given by the following expression

$$\frac{d_2 - d_1 + t_2}{t_3 - t_1 + t_2}$$

Arora and Kelly (4) found that on anodizing for 6 min at 50V with an initial current limited to 2 mA · cm<sup>2</sup>, the loss of vanadium to the electrolyte was 4.2  $\mu\text{g}/\text{cm}^2$  which, as  $\text{V}_2\text{O}_5$ , would give a value of 7  $\mu\text{g}/\text{cm}^2$  for  $t_2$ . On the other hand, Keil and Salomon (1) found no loss on reanodizing a specimen to 100V at a constant current of 0.555 mA/cm<sup>2</sup> that had a preformed film formed at 20V. Since neither condition corresponded exactly with ours, we determined the value under our circumstances. Six weighed specimens were anodized to 40V with an upper limit to the current of 3 mA/cm<sup>2</sup> and for a time of 6 min. These were reweighed. Half of them were then stripped of oxide and weighed again. The remainder were reanodized to 80V again limiting the current to 3 mA/cm<sup>2</sup> and the time to 6 min. These were weighed, stripped, and reweighed. From the first set we found the loss of vanadium to average 7  $\mu\text{g}/\text{cm}^2$ , the second set averaged 11  $\mu\text{g}/\text{cm}^2$ . We therefore concluded that the vanadium loss in our marker experiments, i.e., during anodization of a specimen covered with a preformed oxide film, was the difference between these values, that is, 4  $\mu\text{g}/\text{cm}^2$  of V or 7  $\mu\text{g}/\text{cm}^2$  as  $\text{V}_2\text{O}_5$ , essentially in agreement with Arora and Kelly despite the fact that the conditions differed.

The metal transport numbers are given in Table I for a number of oxide thicknesses. Two additional specimens were anodized in the manner of Keil and Salomon (1) to voltages of 60 and 85, respectively. We found, as did Arora and Kelly, that specimens anodized in this way did not have oxides of even thickness right out to the edges of the specimens. However, the measurements were made in the region (75-85% of the total area) that was evenly colored. The transport numbers agreed with those for our normal method of anodizing, when the same allowance was made for vanadium loss to the electrolyte but would be half this value were there no loss as claimed in Ref. (1).

The table notes that the standard deviation of these results is 0.02. However, the same correction factor for vanadium loss to the electrolyte was applied to each calculation. When we add in the probable error of this correction factor ( $\pm 3 \mu\text{g}/\text{cm}^2$ ), the total error becomes 0.05.

The results could conceivably be in error if the presence of the implanted material effects a change in the oxidation process. The maximum concentration of noble gas atoms in the marked volume is  $\sim 5$  atom per

Table I. Oxide thickness and metal transport numbers

No.	Implant species	Oxide thickness, $\mu\text{g}/\text{cm}^2$	Transport number of metal
1	Xe	77	0.25
2	Xe	88.5	0.24
3	Xe	67	0.20
4	Xe	71	0.23
5	Xe	60	0.30
6	Xe	49	0.26
7	Xe	58	0.26
8	Xe	56	0.35
9	Xe	73	0.32
10	Kr	71.5	0.31
11	Kr	63.5	0.29
12	Xe	44	0.25
13	Xe	47.5	0.28
14	Xe	62	0.25
15	Xe	76	0.32
16	Xe	78.5	0.29
Average			0.28
Std. Dev.			0.02



cent (a/o). However, in the specimens used, the area of the implant covered only one-third of the total area. We were able, therefore, to determine oxide thickness and the V/O ratio both in the implanted and off-implant regions. Within the precision of the measurements no differences were ever detected although the implanted region was visually distinct, presumably due to the radiation damage producing a difference in reflectivity.

### Conclusions

In these experiments, V has been anodically oxidized in glacial acetic acid containing 0.02 mole/liter of  $\text{Na}_2\text{B}_4\text{O}_7 \cdot 10 \text{H}_2\text{O}$  and 1.0 mole of additional water. Some specimens were anodized in the manner of Keil and Salomon (1) and some in the manner of Arora and Kelly (4). Irrespective of the method used and whether or not the specimen is or is not covered by a preformed oxide layer, substantial loss of V to the electrolyte is obtained. Both methods yield films in which the V/O ratio is close to that of  $\text{V}_2\text{O}_5$  over the thickness range of 20 to 85  $\mu\text{g}/\text{cm}^2$ .

In both methods the oxidation takes place by both inward migration of O and outward migration of V. The metal transport number was found to be  $0.28 \pm 0.05$  for films ranging from 20 to 85  $\mu\text{g}/\text{cm}^2$  in thickness. This value is very similar to those for Ta, Nb, and W which have been reported to be in the ranges 0.24-0.31, 0.22-0.33, and 0.30-0.37, respectively (8, 9).

Manuscript received Aug. 29, 1975; revised manuscript received Nov. 24, 1975; This was Paper 99 presented at the Toronto, Canada, Meeting of the Society, May 11-16, 1975.

Any discussion of this paper will appear in a Discussion Section to be published in the December 1976 JOURNAL. All discussions for the December 1976 Discussion Section should be submitted by Aug. 1, 1976.

Publication costs of this article were partially assisted by Atomic Energy of Canada Limited.

### REFERENCES

1. R. G. Keil and R. E. Salomon, *This Journal*, **115**, 628 (1968).
2. R. G. Keil and K. Ludwig, *ibid.*, **118**, 864 (1971).
3. B. H. Ellis, M. A. Hopper, and D. J. De Smet, *ibid.*, **118**, 860 (1971).
4. M. R. Arora and R. Kelly, *ibid.*, **120**, 128 (1973).
5. F. Brown and W. D. Mackintosh, *ibid.*, **120**, 1096 (1973).
6. G. Amsel, J. P. Nadai, E. D'Artenare, D. David, E. Girard, and J. Marlin, *Nucl. Instr. Methods*, **92**, 481 (1971).
7. W. D. Mackintosh and J. A. Davies, *Anal. Chem.*, **41**, 26A (1969).
8. J. P. S. Pringle, *This Journal*, **120**, 398 (1973).
9. J. A. Davies, B. Domeij, J. P. S. Pringle, and F. Brown, *ibid.*, **112**, 675 (1965).

## Electrochromism and Photochromism in $\text{MoO}_3$ Films

Thomas C. Arnoldussen

General Motors Corporation, Research Laboratories, Warren, Michigan 48090

### ABSTRACT

Electrical properties of amorphous evaporated electrochromic  $\text{MoO}_3$  (molybdenum trioxide) films were studied in various ambients. It is shown that at a given applied voltage there is a "humidity threshold" below which coloration does not occur. The transient behavior of the current and remnant voltage in low humidity (precoloration), high humidity (postcoloration), and in the transition stage is shown to be consistent with an electrochemical interpretation of the coloration process. Changes in solubility upon electrical coloration and u.v. photocoloration verify that a chemical change accompanies the color change.

Electrochromic materials have been the subject of a number of recent studies (1-10). They are of interest for passive alphanumeric displays.  $\text{MoO}_3$  and  $\text{WO}_3$  have been most discussed, though other transition metal compounds and organics are possibilities.

Electrochromic materials can, in general, be colored by high energy irradiation (1-3) (u.v. light, ion bombardment, etc.) as well as by electrical means. Optical and electrically colored  $\text{MoO}_3$  and  $\text{WO}_3$  have been studied by Deb (1, 2) and Tubbs (3) and the absorption spectra have been found to be similar for both coloration techniques. The absorption shows a broad peak centered in the red portion of the spectrum (8000-10,000Å) with a minimum in the violet blue; hence the characteristic blue purple color.

Optically induced coloration can be produced in air or in vacuum. Electrical coloration was reported by Deb (2) to occur in air but not in vacuum, suggesting that water vapor may facilitate electrical coloration. He also reported (2) that amorphous, oxygen-deficient films colored more readily.

Deb (1, 2, 4) proposed that coloration is caused by electron injection and filling of color centers, e.g.,

oxygen vacancy electron traps present in the film as a result of the deposition process, analogous to alkali halide color centers. In recent work, others (5-9) have explored coloration of  $\text{WO}_3$  and other materials in electrochemical cells employing a liquid or gelled electrolyte such as  $\text{H}_2\text{SO}_4$ . Chang and Howard (5) pointed out the electrochemical redox nature of coloration in some such devices and showed the optical absorption spectrum of electrochemically reduced  $\text{WO}_3$  to be qualitatively similar to  $\text{WO}_3$  colored in air using Au electrodes; though higher contrasts were achievable with the  $\text{H}_2\text{SO}_4$  electrolyte. Hurditch (10) demonstrated the dependence of coloration time and voltage on the water content of hydrated  $\text{WO}_3 \cdot \text{H}_2\text{O}$  films postulating the dissociation of  $\text{H}_2\text{O}$  and formation of blue hydrogen tungsten bronze  $\text{WO}_{3-x}(\text{OH})_x$  at the cathode.

We show here that for evaporated  $\text{MoO}_3$  films there exists an ambient humidity threshold for coloration which, interpreted as an electrochemical reaction, is related to the voltage threshold for coloration in these materials. Moreover, the fact that  $\text{MoO}_3$  undergoes a drastic change of solubility in water when chemically reduced allows us to demonstrate that a chemical



change accompanies electrical coloration and u.v. optical coloration as well.

### MoO<sub>3</sub> Sample Preparation

MoO<sub>3</sub> was electron-beam evaporated from a pressed and sintered pellet of 99.9% pure MoO<sub>3</sub> powder. Parallel Au electrodes 1.88 mm wide, spaced 117 $\mu$  apart were deposited on a glass slide. A 0.67  $\mu$ m film of MoO<sub>3</sub> was then evaporated over the electrode gap with about 0.5 mm overlap on each electrode. X-ray diffraction showed the evaporated MoO<sub>3</sub> was amorphous. Electrical leads were attached to the Au pads with Ag paste.

### MoO<sub>3</sub> Electrical Characteristics in Vacuum and Air

Current vs. voltage characteristics were measured in a 10<sup>-6</sup> Torr vacuum. These results are shown in Fig. 1. Since the device structure is basically symmetric, the designated voltage polarity was arbitrarily chosen. It can be seen that at low voltages the I-V curve is slightly asymmetric while this asymmetry is not apparent in the range from 100 to 1000V ( $\sim 10^4$ - $10^5$  V/cm). In vacuum the response time for current upon change of voltage was much less than a second, and no coloration resulted.

With the sample chamber open to air and -100V applied, the current decayed exponentially with a time constant  $\sim 50$  min. After allowing the "charging current" to decay for 1½ hr, the voltage source was zeroed. The remnant voltage,  $V_R$ , on the sample was initially  $\sim 0.75$ V, with polarity in opposition to the original applied voltage, decaying to half that value in  $\sim 5$  min, followed by a slower decay. Time constants of this magnitude could not be accounted for by any electronic capacitance associated with the sample or measurement circuit. They are more characteristic of slow ion motion or chemical reactions.

The device was recharged in air and the remnant voltage monitored as the sample chamber was sequentially evacuated, reexposed to air, reevacuated, etc. Each evacuation caused  $V_R$  to drop to near zero ( $\lesssim 1$  kT/e) and each reexposure to air caused it to return to the original decay curve as shown in Fig. 2. The charging process did not produce coloration and the remnant voltage was typical of ionic polarization

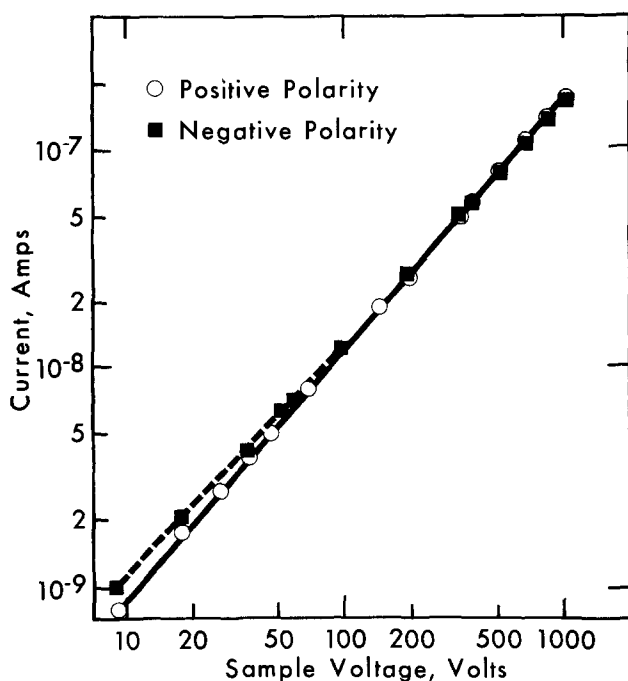


Fig. 1. Current vs. voltage in vacuum for sample of dimensions given in the text. Curve is slightly greater than linear,  $I \propto V^{1.18}$  at higher voltages.

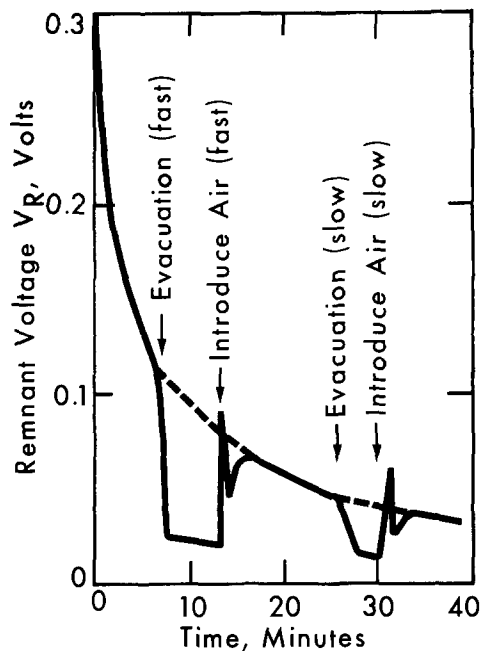


Fig. 2. Remnant voltage decay showing disappearance and re-appearance upon evacuating and reintroducing air into the sample chamber. This type of decay is characteristic of polarized but uncolored MoO<sub>3</sub> films. Colored films show a much slower  $V_R$  decay which also disappears and reappears when water vapor is removed or introduced.

rather than an electrochemical potential, as indicated by the comparatively rapid initial decay of  $V_R$ . Adsorbed water vapor was the suspected source of ions, giving rise to separated H<sup>+</sup> and OH<sup>-</sup> or MoO<sub>4</sub><sup>=</sup> ions. The drop in  $V_R$  upon evacuation is believed due to desorption of water from the surface with the resulting immobilization of the polarized ions. Hurditch (10) showed the apparent dependence of H<sup>+</sup> ion mobility on the water content of WO<sub>3</sub>. Because the MoO<sub>3</sub> is not a perfect electronic insulator, charge on the electrometer capacitance leaks off without replenishment (the decreased ion mobility freezes the relaxing ion polarization in place) resulting in a drop in measured voltage. When air is reintroduced the ions resume diffusion and the measured voltage increases. The  $V_R$  overshoot/undershoot occurring when air is reintroduced is probably due to competing charging discharging processes, the increased ion diffusion driving the electrometer voltage up and the electronic leakage resistance driving it down. The fact that the form and magnitude of this transient is roughly independent of the air reentry rate suggests that it is related to the absolute water vapor partial pressure.

### Electrical Characteristics in N<sub>2</sub>, O<sub>2</sub>, H<sub>2</sub>, and H<sub>2</sub>O Vapor

To ascertain that water vapor was responsible for the polarization behavior, the I-V and I-time characteristics of an identical device were observed in vacuum, in pure N<sub>2</sub>, pure O<sub>2</sub>, forming gas (96% N<sub>2</sub>, 4% H<sub>2</sub>), and forming gas plus O<sub>2</sub>. The electrical behavior was essentially the same as in vacuum for all of these ambients.

When water vapor was introduced by bubbling N<sub>2</sub> through water prior to leaking it into the sample chamber, the behavior was drastically changed. With 200V applied, the current (originally  $3.7 \times 10^{-8}$ A in vacuum) showed no change until the water vapor partial pressure reached  $\sim 1$  Torr, at which point the current began decreasing. As the pressure continued rising the current reached a minimum of  $1.8 \times 10^{-8}$ A (water vapor pressure  $\sim 5$  Torr), then sharply increased. As the total pressure reached  $\sim 1$  atm (water vapor partial pressure  $\sim 20$  Torr) the current reached a steady value of  $7.5 \times 10^{-6}$ A (see Fig.

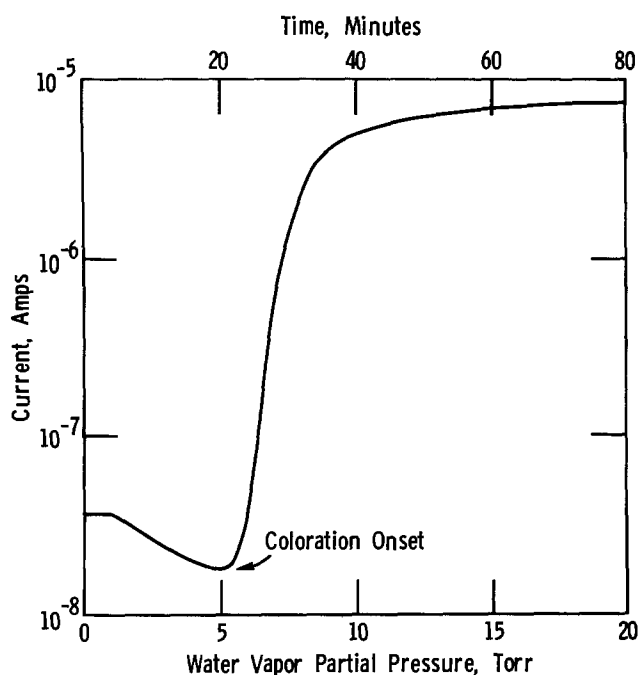


Fig. 3. Current vs. water vapor partial pressure and time for constant leak rate. Current is constant up to  $\sim 1$  Torr, decreases as ionic polarization proceeds, increases sharply above  $\sim 5$  Torr as coloration occurs, then saturates at high pressures.

3). During the time the current and water vapor were rising the device became colored dark purple. Evacuation caused the current to drop to  $5 \times 10^{-8}$  A as compared with  $3.7 \times 10^{-8}$  A before  $H_2O$  vapor introduction and coloration.

Microscopic inspection of this device revealed that dark purple coloration occurred in the  $MoO_3$  overlapping the Au cathode, while little color change was discerned in the gap region between cathode and anode. This is shown in Fig. 4. The deepest coloration occurred along the periphery of the Au cathode over-

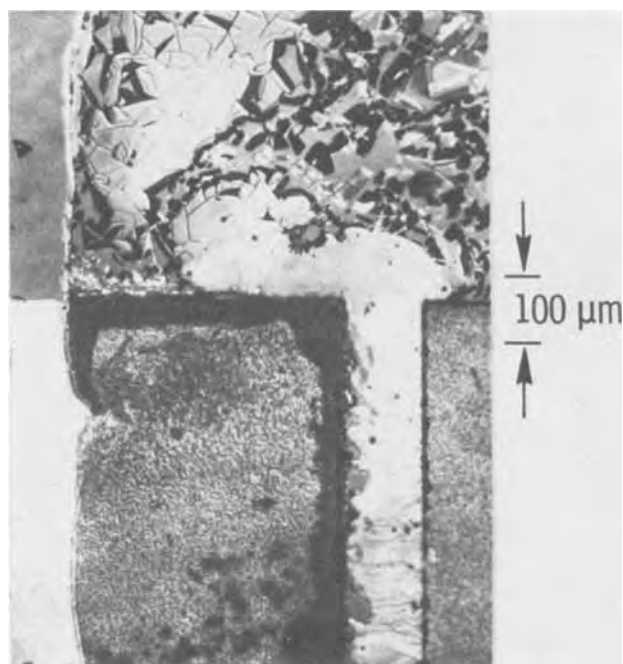


Fig. 4.  $MoO_3$  film colored to completion in high humidity. Coloration is principally along the cathode periphery (left). Striations between anode (right) and cathode suggest mass flow. Crystallization has occurred in the fringing field region (top).

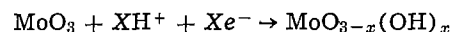
laid by  $MoO_3$ , not simply along the cathode edge adjacent to the gap. This form of the coloration coupled with the return of the current to near the precoloration value upon evacuation suggests a high surface ion conductance in the presence of high humidity.

We interpret the various stages of the above coloration process as follows:

(i) For water vapor pressures ( $p_{H_2O}$ ) ranging from vacuum to  $\sim 1$  Torr, the current is predominantly electronic and carried in the bulk of the film.

(ii) For  $1 \text{ Torr} \lesssim p_{H_2O} \lesssim 5 \text{ Torr}$ , the current decays monotonically without coloration. During this stage adsorbed  $H_2O$  is present in sufficient quantity to permit  $H^+$  migration and polarization to occur,  $H^+$  ions moving to and accumulating at the upper surface of the  $MoO_3$  over the cathode, forming an electrochemical double layer. During this stage the voltage drop across this double layer is insufficient to cause the chemical reduction of  $MoO_3$  to proceed. As  $p_{H_2O}$  increases the surface ion conductance increases, causing a larger voltage drop at the double layer.

(iii) As the water vapor reaches a critical pressure ( $\sim 5$  Torr), the double layer voltage drop is sufficient to permit electrochemical reduction of the  $MoO_3$  to occur. This is depicted in Fig. 5. The lower oxides of Mo and W are blue to black and metallic. An example of such a reduction reaction is



forming a hydrogen molybdenum bronze. One formulation of the well-known dye "moly blue,"  $(MoO_2)_2(MoO_4) \cdot H_2O$ —molybdenum molybdate, is also of this form.  $Mo^{+5}$  is usually identified with a blue color (11).  $MoO_3$  reduction (coloration) proceeds from the upper surface down to the Au cathode (e to f in Fig. 5). The effective cathode is moved to the top

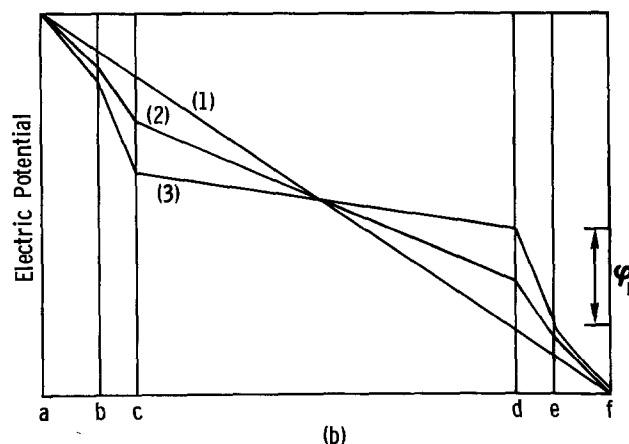
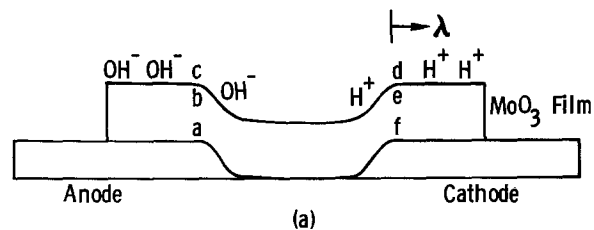


Fig. 5. (a) Cross section of  $MoO_3$  film with representative points  $a, b, c, d, e, f$  indicated  $ab = ef = \text{film thickness} = 0.67 \mu\text{m}$ .  $cd = \text{electrode gap} = 117 \mu\text{m}$ . (b) Potential profile using representative points from top figure for the case of (1) vacuum, (2) low water vapor, and (3) critical water vapor pressure. Potential drops through film and across double layers  $bc$  and  $de$  are exaggerated for clarity. When double layer potential drop becomes  $\geq \phi_r$ , the reaction potential, electrochemical redox reaction proceeds.

surface by virtue of the metallic nature of the  $\text{MoO}_{3-x}(\text{OH})_x$ .

(iv) At the high water vapor pressures attained here, the surface ion conductance dominates. Once the  $\text{MoO}_3$  over the cathode has been reduced, the dominant current path is from the Au cathode through the  $\text{MoO}_{3-x}(\text{OH})_x$  above the cathode and across the  $\text{H}_2\text{O}$  adsorbed surface. Further coloration of the  $\text{MoO}_3$  between the electrodes is short circuited by the surface where direct electrolysis of  $\text{H}_2\text{O}$  is suggested by the large constant current which disappears when the chamber is reevacuated.

One can show that for a film of bulk resistivity  $\rho_B$  (ohm-cm) and surface resistivity  $\rho_S$  (ohm/square) the potential at the top surface of the film overlapping the electrode falls off as

$$V(\lambda) = V_{\text{edge}} \exp \left[ -\lambda / \sqrt{l\rho_B/\rho_S} \right]$$

where  $V_{\text{edge}}$  is the potential directly above the electrode edge (point d in Fig. 5),  $l$  is the film thickness, and  $\lambda$  is the distance from this edge into the interior area defined by the electrode (Fig. 5). The potential is relative to the electrode. Thus within several lengths  $\sqrt{l\rho_B/\rho_S}$  the potential of the top surface of the film is at virtually the electrode potential. In the sample just described, if we assume the current measured in vacuum gives us  $\rho_B$ , and the current measured in high humidity gives us  $\rho_S$  then

$$\frac{V(\lambda)}{V_{\text{edge}}} = \exp \left[ \frac{-\lambda}{9.5 \mu\text{m}} \right] \cdot V(\lambda)/V_{\text{edge}} = 10^{-1}$$

$$\text{for } \lambda = 22 \mu\text{m}$$

Since the field through the film is appreciable only within a distance  $\sim \lambda$  of the electrode edge, we expect coloration to occur primarily in this region. Figures 4 and 6 do show the peripheral colored region to be  $\sim 25$ - $50 \mu\text{m}$  wide, in good agreement for this idealized model. This is further evidence that, for this device geometry and high humidity, the ionic conduction is principally on the surface rather than in the bulk.

Prolonged coloration resulted in irreversible effects seen in Fig. 4. Not only has coloration formed over the cathode, but crystallization has occurred in the region of the electrode fringing field. Notice also the striations in the electrode gap suggesting large scale mass flow.

#### Discharge Current

To observe whether the remnant voltage on a colored sample is characteristic of an electrochemical emf rather than a polarization voltage, another sample was placed in a water vapor-saturated  $\text{N}_2$  atmosphere with 200V applied until just the initial stages of coloration were observed. The voltage source was zeroed and coloration halted before any gross irreversible effects occurred. The remnant voltage was 1.08V and decayed less than 5% in 5 min; much slower than the remnant voltage decay observed in samples not brought to coloration. This would be expected if the emf were electrochemical in origin and associated with the coloration. The sample was removed for microscopic observation which revealed coloration only along the cathode periphery as before, but much fainter (Fig. 6).

A half-hour later, this sample was replaced in the measurement chamber open to air and  $V_R$  had decayed to only 0.5V. The current delivered by this emf was recorded as a function of time (Fig. 7). After  $13\frac{1}{2}$  hr, the current had decayed to about 1% of the initial value. The integrated current, or total charge delivered by the cell during this time, was  $2.4 \times 10^{-6}$  coulombs. This corresponds to  $\sim 10^{16}$  e/cm<sup>2</sup> based on the peripheral area colored. This charge stored in the electrical capacitance between the top  $\text{MoO}_3$  surface and the Au electrode would require a dielectric constant in excess of  $10^4$ . If stored in an electrochemical double layer capacitance, assuming (12) a hydrated double layer

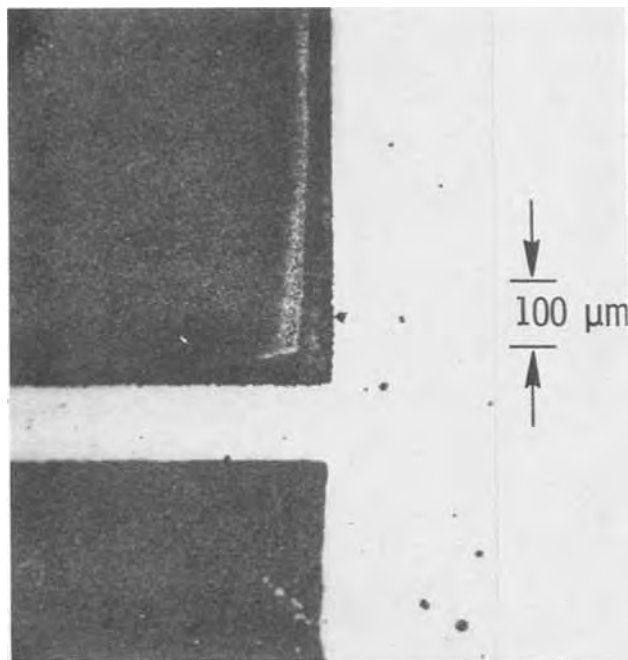


Fig. 6.  $\text{MoO}_3$  film brought to partial coloration in high humidity. Coloration, along cathode (top) periphery, was halted before gross irreversible effects occurred.

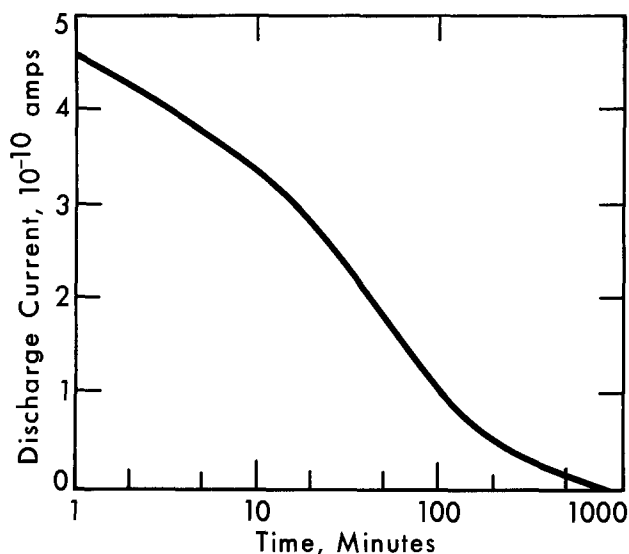


Fig. 7. Discharge current driven by  $V_R$  in air for partially colored device shown in Fig. 6. Total charge delivered in  $13\frac{1}{2}$  hr was 2.4  $\mu\text{C}$  or  $\sim 2 \text{ mC/cm}^2$  based on the peripheral area colored.

dielectric constant  $\sim 30$ , the voltage drop per angstrom of double layer would be  $\sim 5\text{V}$ , sufficient to cause almost any electrochemical reaction to proceed. We can only conclude that this charge is stored neutrally as a chemical potential of a newly formed chemical specie.

#### Solubility Change

Quantitative chemical analysis of dehydrated colored and uncolored EC films might resolve the question of whether the film is chemically changed. However, standard analysis techniques are of questionable value. Auger spectroscopy and electron microprobe analysis tend to generate sufficient heat to alter the film during measurement. In addition the latter is not particularly sensitive to oxygen. ESR can detect a change in  $\text{Mo}^{+5}$  concentration, but cannot distinguish between filling of color center traps already present in the film and  $\text{Mo}^{+5}$  formation by chemical reaction.

A wet chemical analysis technique does, however, provide qualitative evidence of a chemical change.  $\text{MoO}_3$  is quite soluble in water while reduced oxides and hydroxides are relatively insoluble. Immersing electrically colored samples in water caused the uncolored regions to dissolve while the colored regions remained insoluble. Neither coloration nor decreased solubility were observed in the crystallized region of the sample shown in Fig. 4. Furthermore, this same technique showed that films colored by  $\text{Ne}^+$  ion bombardment and by u.v. light became insoluble. Such a change in solubility is a thermodynamic characteristic of a phase change and in this case a chemical change.

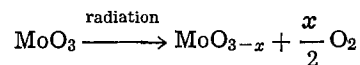
### Conclusion

Based on electrical characteristics correlated with observed solubility changes of  $\text{MoO}_3$  electrochromic films, we conclude that electrical coloration occurs by means of an electrochemical redox reaction with adsorbed water vapor as the electrolyte. Furthermore, it seems that optical coloration occurs by photochemical reduction.

It is believed that water vapor is adsorbed on the surface of the  $\text{MoO}_3$  film forming  $\text{H}_2\text{MoO}_4$  on the surface. As suggested by Hurditch (10), the  $\text{H}^+$  ions become increasingly mobile as the water content increases. For low water vapor pressures, ionic polarization occurs without coloration of the  $\text{MoO}_3$  film since voltages less than the electrochemical reaction potentials are dropped across the double layers due to the high surface electrolyte impedance. As the water pressure is increased, the  $\text{H}^+$  ion concentration and mobility increase, causing more of the voltage to be dropped across the double layers. At a critical water vapor pressure (for a given voltage), the ion conductance is great enough to cause the voltage drop across the electrochemical double layer to equal the reaction potential.

Beyond this point the electrochemical reduction reaction proceeds, accompanied by coloration and increased current. When the  $\text{MoO}_3$  over the cathode periphery has colored to completion, the large, steady current observed in high humidity is attributed to electrolysis of water on the surface. The counterpart of this "water vapor threshold" at fixed voltage would be the voltage threshold at fixed atmosphere reported by Deb (4) and at fixed water content of intentionally hydrated  $\text{WO}_3$  films reported by Hurditch (10).

In the case of optical (u.v.) coloration, it is believed that the high energy radiation actually results in photodecomposition such as



Ambient water vapor does not seem to be an essential factor since photochromism can occur even in vacuum though it is enhanced in humid atmosphere (2). However, water of hydration is known to be incorporated in vacuum evaporated  $\text{WO}_3$  and  $\text{MoO}_3$  (10,13) in significant quantities and may facilitate photodecomposition.

### Acknowledgments

I would like to thank Dr. Martin C. Steele for his continuing interest and the fruitful discussions we have had in this research.

Manuscript received Sept. 22, 1975.

Any discussion of this paper will appear in a Discussion Section to be published in the December 1976 JOURNAL. All discussions for the December 1976 Discussion Section should be submitted by Aug. 1, 1976.

Publication costs of this article were partially assisted by General Motors Corporation.

### REFERENCES

1. S. K. Deb and J. A. Chopoorian, *J. Appl. Phys.*, **37**, 4818 (1966).
2. S. K. Deb, *Phil. Mag.*, **27**, 801 (1973).
3. M. R. Tubbs, *Phys. Status Solidi (a)*, **21**, 253 (1974).
4. S. K. Deb, *Proc. Electron. Components Conf.*, p. 11, Washington, D. C., May 1974.
5. I. F. Chang and W. E. Howard, *Proc. IEEE Display Devices and Systems Conf.*, p. 148, New York, New York, October 1974.
6. R. S. Crandall and B. W. Faughnan, *Appl. Phys. Letters*, **26**, 120 (1975).
7. W. E. Kramer *et al.*, SID Conference, Washington, D. C., April 1975.
8. J. H. McGee *et al.*, *ibid.*, April 1975.
9. R. D. Giglia, *ibid.*, April 1975.
10. R. Hurditch, *Electron. Letters*, **11**, 142 (1975).
11. W. M. Latimer and J. H. Hildebrand, "Reference Book of Inorganic Chemistry," Macmillan, New York (1951).
12. Tibor Erdey-Gruz, "Kinetics of Electrode Processes," John Wiley & Sons, New York (1972).
13. N. E. Promisel, Editor, "The Science and Technology of Refractory Metals," Pergamon Press, New York (1964).

## Automatic Chemical Processing for Silicon Wafers

D. R. Oswald

Bell Laboratories, Allentown, Pennsylvania 18103

### ABSTRACT

Apparatus has been designed to make the treatment of silicon wafers with wet chemicals an automatic, unattended operation. The wafers remain in a single process vessel while reagents enter and leave in a preprogrammed sequence to make up a given total treatment procedure. The approach avoids a number of deterrents to good process control inherent with the traditional method of transferring wafers from vessel to vessel. For example, there is no potential for debris floating on a liquid surface being deposited onto the wafers because there is no withdrawal through a liquid-air interface. In addition, there is no chance of contaminants entering a treatment solution through the open-air pouring of chemicals or through the use of utensils that might be unclean.

### Description of the Apparatus

Figure 1 illustrates schematically how three component parts—a solenoid valve network, a process

Key words: chemical processing, wafer cleaning, silicon surfaces.

vessel, and a chemical metering and dispensing system—combine to make up the complete automated system. A fourth component, not shown, is a sequence programmer to operate the various valves.

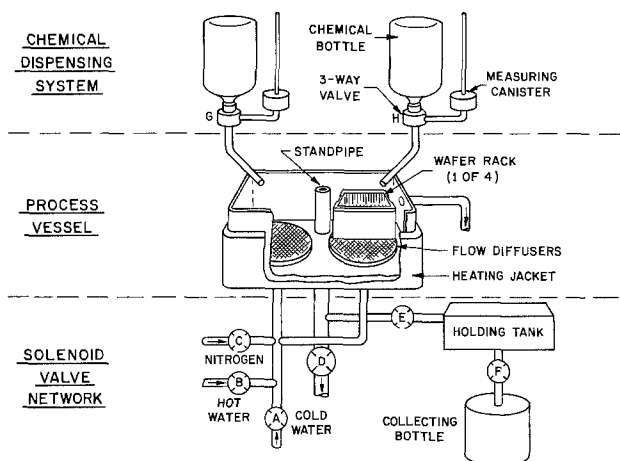


Fig. 1. Automatic processor diagram

**Solenoid valve arrangement.**—The valves designated A and B in Fig. 1 can permit either cold or hot water, respectively, to enter the process vessel from the bottom, through flow diffusers that create a uniform upward flow of water over essentially the whole horizontal area of the vessel. Through valve C, nitrogen can be bubbled into the vessel for the purpose of solution agitation and mixing.

Valve D can establish liquid volume in the vessel at two possible levels. When it is closed, the vessel can fill to an overflow level. In the open position, it operates in combination with valve E to establish a liquid level at the top of an adjustable-height standpipe and to direct the out-going flow to either a drain or a "holding tank."

**Process vessel.**—This is a rectangular tank of appropriate size for the type of wafer holders to be used and the number of them that are to be simultaneously accommodated. Materials of construction that have been used are stainless steel, either by itself or coated internally with "Kynar,"<sup>1</sup> and fused quartz.

**Chemical metering and dispensing system.**—Liquid chemicals are injected into the process vessel from above, directly from the container in which they were shipped, with no intermediate pouring, open-air exposure, or handling. To accomplish this, the screw cap of the jug or bottle in which the chemical was shipped is removed and a specially designed check valve is screwed on in its place. The container is then inverted and clamped into a measuring-dispensing system that positions it at a slightly higher elevation than the process vessel. Figure 2 shows the process vessel area of a typical processor, with three 1 gal polyethylene bottles and one 8 lb glass bottle clamped in position above the vessel. The manner in which the chemicals are metered and dispensed is illustrated in Fig. 3. As the bottle is clamped into position, a plunger opens the check valve that made possible its being inverted without spillage. Liquid can then flow from the bottle through a three-way Teflon solenoid valve into a measuring canister whose inside volume equals that to be dispensed (Fig. 3A). The liquid will fill the canister and will flow up the inside of an air-venting tube attached to the canister until it reaches the same level as the liquid in the bottle. A second venting tube, a permanent part of the screwed-on check valve assembly, admits air at the same time to the cavity above the liquid in the inverted container. When voltage is applied to the solenoid valve it switches to the position of Fig. 3B and the liquid in the canister empties into the process vessel. Because the volume of liquid that flows up the vent tube dispenses along with

<sup>1</sup> Kynar is a polyvinylidene fluoride, equal in inertness to polyethylene, that can be applied to a metallic base by spraying and baking.

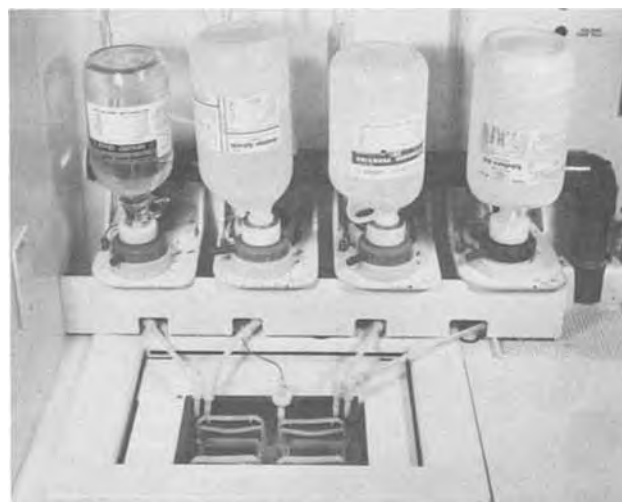


Fig. 2. Process vessel and chemical dispensers

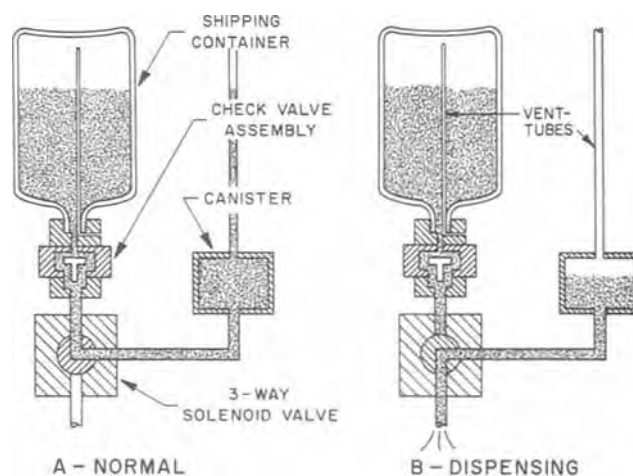


Fig. 3. Technique for metering chemicals

the canister volume, a small variation occurs from run to run in the total volume dispensed as the jug empties. A tube with an inside diameter of only 0.090 in. is adequate, however, and results in only a 1 ml difference from the full-bottle to empty-bottle conditions for a 1 gal container. For most applications such an error is tolerable.

**Valve programming system.**—The fourth and final major component of the automatic processor is an electrical control system for operating the solenoid valves to program the flow of chemicals and water into and out of the process vessel. A rotating-cylinder type of sequence timer, where switch activating buttons are inserted into slots on the cylinder's circumference, can provide suitable programmability and sequence flexibility. With this arrangement cylinders can be pre-programmed and stored so that a change from one chemical procedure to another is a simple matter of changing cylinders.

### Operation of the Automatic Processor

A chemical treatment for etching or cleaning silicon wafers typically requires the following procedure: (i) prepare a solution of one or more chemicals mixed with water; (ii) immerse rack-held wafers in the solution; (iii) heat the solution; (iv) maintain solution temperature for the necessary reaction time; (v) stop the reaction by flushing away the solution with water; (vi) discard the spent solution into a drain or, when it is ecologically harmful, into a collection vessel for

discarding by other means; (vii) rinse the wafers with flowing, high purity water.

The valve actions and liquid flows to automatically perform this simple but commonly used sequence proceed as follows:

**Action 1.**—(Fig. 4a) The apparatus is in its static, between-run condition here, with valve A open to admit cold, high purity water while all other valves are closed. This keeps water overflowing through the process vessel to avoid stagnation and the collection of environmental particulates. Rack-held wafers are inserted into the vessel while it is in this condition and the treatment sequence begins with valve A closing and valve B opening to replace the overflowing cold water with hot water.

**Action 2.**—(Fig. 4b) After sufficient hot-water overflow for temperature equilibrium in the vessel, valve B closes. Valve D opens to lower the water level in the vessel to the top of the open-ended standpipe, thereby establishing the volume of water with which the chemicals to be added as the next step will be diluted. Dilution ratios and vessel size are chosen such that the wafers remain fully immersed at this lowered water level.

**Action 3.**—(Fig. 4c) Valve D closes and valves G and H open to inject a premeasured volume of each of the chemicals into the vessel, while a heating tape surrounding the vessel maintains the desired bath temperature. Valve C bubbles nitrogen through the solution to mix the reagents and water.

**Action 4.**—(Fig. 4d) Valve A opens to introduce cold water and valve E opens to direct the resultant flow of rapidly diluting solution into a "holding tank." When the liquid reaches a level sensor in this tank, valve E closes and D opens to switch the continuing flow to a drain. This arrangement provides the means for collecting ecologically harmful chemicals that cannot enter a drain except in very dilute form. The volume of spent chemical that is collected in the holding tank before diversion to a drain, and therefore the dilution achieved before the drain is used, can be varied by adjusting the height of the level sensor in the holding tank. By means of push-button operated valve F, the holding tank can be emptied between runs into a larger collecting bottle. An essential safety feature is that sensors will not allow the electrical circuitry to operate in the automatic mode if either the holding tank or collecting bottle is full.

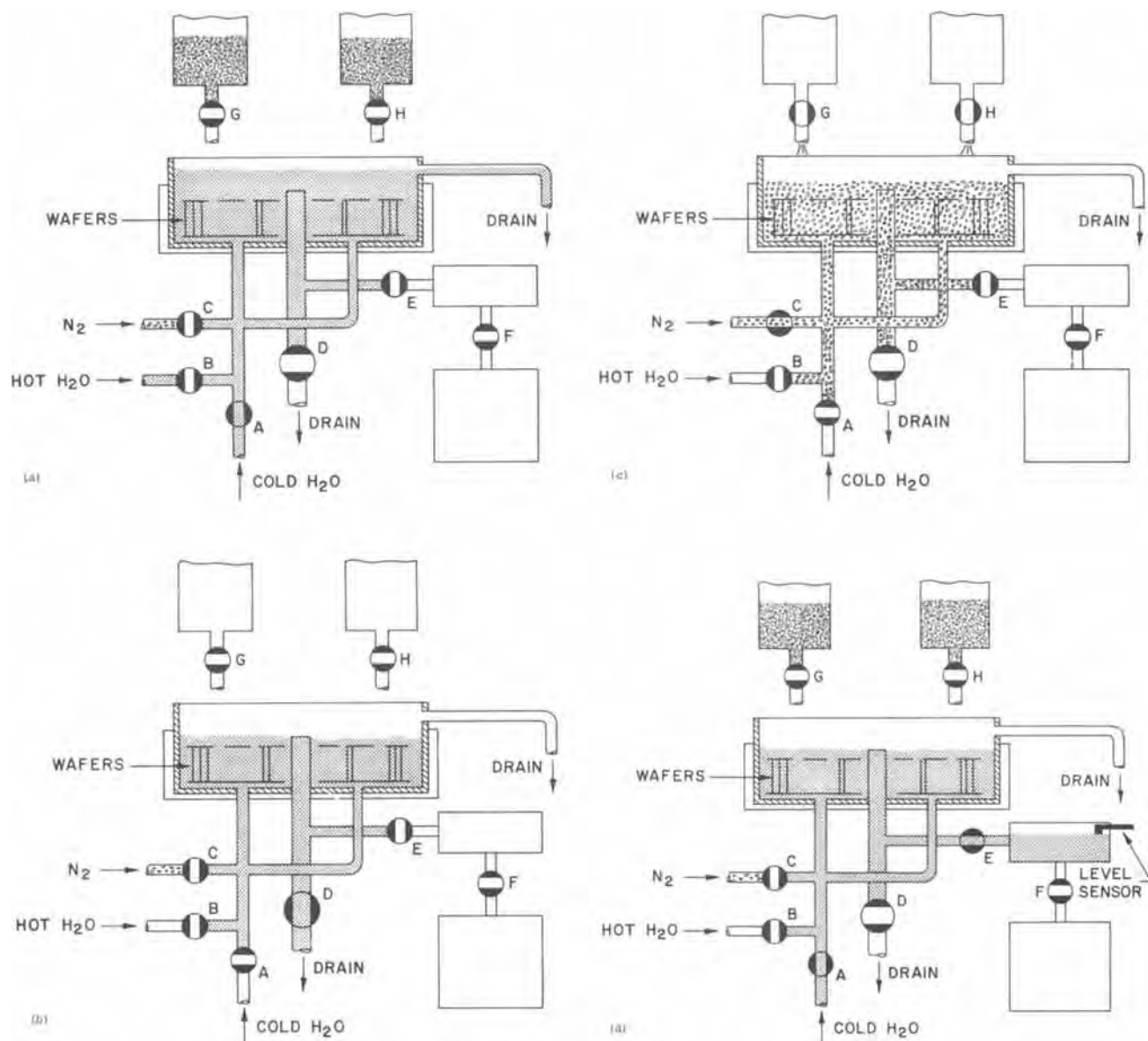


Fig. 4. A typical automatic sequence: (a) cold water overflow; (b) water volume adjustment; (c) dispensing chemicals; (d) collecting spent chemicals.

Action 5.—(Fig. 4a) As the final action, valve A opens to bring in cold water and return the apparatus to its original condition of overflow flushing. When the conductivity of the overflowing water indicates that rinsing has been adequate, the wafers are withdrawn and are dried by centrifugal spinning.

### Apparatus Performance as a Wafer Cleaner

One wet-chemistry procedure that has been automated with this apparatus, in which the sequence of valve actions and liquid flows proceeds essentially as in the example illustrated,<sup>2</sup> is the cleaning of wafers with a solution of hydrogen peroxide, ammonium hydroxide, and water (1,2) after they have been polished. Cleaning after polishing is necessary because some surface-deposited residue, especially in the form of discrete and scattered particulates up to a few microns in size, is practically unavoidable with the abrasive suspensions or slurries used for polishing. It is common practice after such postpolish cleaning to visually inspect the wafers to be sure the cleaning has been effective.

An instrument has been developed to perform such an inspection in a mechanized nonsubjective fashion by scanning a wafer surface with a laser beam to count the number of discrete residual defects, down to one micron in size, that are present on a surface (3). The data of Fig. 5, collected on several thousand 2 in. diameter polished wafers, show an improvement in the effectiveness of automatically performed  $\text{NH}_4\text{OH}-\text{H}_2\text{O}_2-\text{H}_2\text{O}$  cleaning over the manual, bath-to-bath transfer method for the same procedure. The median count of defects left after cleaning was reduced from

<sup>2</sup> The only deviation from the described sequence is that the spent solutions enter a drain directly for disposal and are not collected.

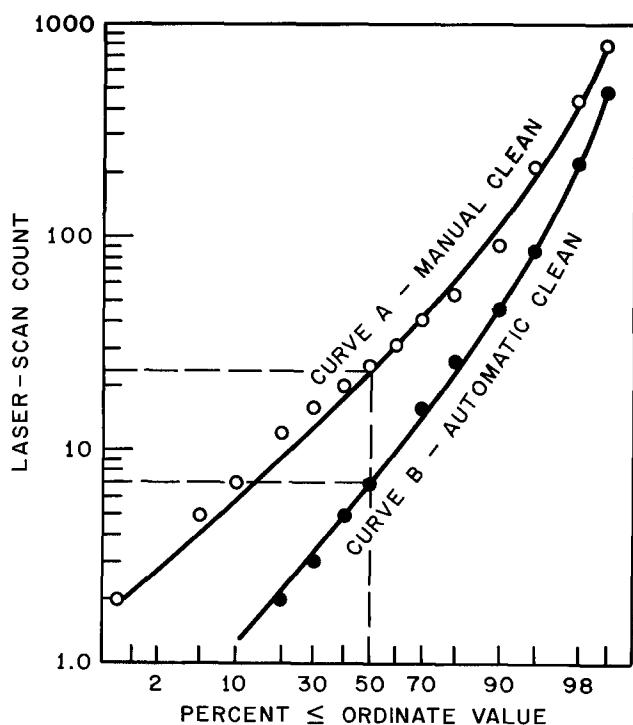


Fig. 5. Laser scan data to compare manual and automatic wafer cleaning.

23 to 7 by the automation. To avoid a possible influence on the count by particles collected on the wafer surfaces during the interval between cleaning and inspecting, each wafer was scrubbed before entering the laser scanning instrument in apparatus that uses a brush and detergent solution to dislodge and wash away loosely attached particles (4).

### Summary

The automated concept for wet-chemistry as implemented by the apparatus described provides significant benefits over traditional bath-to-bath transfer methods for sequential chemical treatments. They can be summarized as follows:

1. Opportunities for residue deposition often associated with the draining of liquid across wafer surfaces or evaporation of liquid films from the surfaces are eliminated because there is no wafer withdrawal from a liquid except at the end of a processing sequence, when the liquid is flowing, high purity water with no static meniscus to hold floating debris.

2. Solution composition is reproduced exactly from run to run because chemicals are measured by volume in a positive way.

3. Process parameters such as bath temperature and reaction times require no operator judgment or attention because they are under the automatic and repeatable control of a sequence programmer.

4. Structural materials for components that contact the chemicals or reagents are limited to inert materials (Teflon, polyethylene, quartz). There is no metallic exposure and no ionic contamination of solutions. Liquid movement is by gravity flow to avoid a need for pumps or other corrosion-prone components.

5. Performing a given chemical treatment sequence in automated fashion is much more efficient than an equivalent procedure performed manually. For the wafer cleaning procedure and the particular apparatus described here, for instance, total process time is 15 min for 100 wafers. The only operator attention needed besides the loading-unloading function is to occasionally replenish the chemical supply by clamping new bottles into position, which can be done while a cycle is in progress so no time is lost. One person can easily operate more than one apparatus or can perform additional functions.

6. In procedures where the chemicals are normally discarded after one use, automation can result in more efficient use of chemicals. In the illustrated cleaning process, for example, chemical consumption for a given number of wafers has been halved over the manual process the automation has replaced.

Manuscript received Feb. 27, 1975.

Any discussion of this paper will appear in a Discussion Section to be published in the December 1976 JOURNAL. All discussions for the December 1976 Discussion Section should be submitted by Aug. 1, 1976.

Publication costs of this article were partially assisted by Bell Laboratories.

### REFERENCES

1. W. Kern, *RCA Rev.*, **31**, (1970).
2. R. C. Henderson, *This Journal*, **119**, 772 (1972).
3. D. R. Oswald and D. F. Munro, *J. Electron. Mater.*, **3**, (1974).
4. R. J. Jaccodine and D. R. Oswald, U.S. Pat. 3,585,668 (1971).



# The Effects of High Temperature Annealing on MNOS Devices

James A. Topich\* and Eugene T. Yon

Engineering Design Center, Case Western Reserve University, Cleveland, Ohio 44106

## ABSTRACT

The effects of high temperature annealing on the conduction and memory properties of MNOS memory devices was studied. The results showed that the conductivity of the nitride increased with annealing time and temperature and that the memory retention qualities of the device were degraded. These results can be explained by the hypothesis that the heat-treatment has increased the number of traps in the silicon nitride. The correlation of the theoretical and experimental results indicates that the traps are uniformly distributed through the silicon nitride layer and are not localized at the oxide nitride interface.

Annealing as one step in the fabrication process for producing MNOS memory devices has been used by many workers in this field (1-4). However, no detailed investigation into the effects of this step on the properties of the devices was undertaken. In this study, all samples used were fabricated in an identical manner and then subjected to annealing treatments for various times from 5 to 120 min and at various temperatures in the range 800°-1000°C. After the devices were completed, the conduction and memory properties were analyzed in order to provide information about the effects of the annealing on certain parameters which characterize the silicon nitride film.

## Fabrication Procedure

All devices tested were fabricated on phosphorous-doped (111) polished silicon wafers of 0.5-0.88 ohm-cm resistivity. The silicon wafers were degreased using 3 min soaks in hot trichloroethylene, acetone, and methanol; followed by a rinse in deionized water down to 10 megohm-cm; a 1 min etch in buffered HF; and a second water rinse. The silicon surfaces were further cleaned using a 5 min soak in a hot solution of 5 parts deionized water, 1 part ammonium hydroxide, and 3 parts of hydrogen peroxide; a rinse in deionized water; a 5 min soak in a hot solution of 5 parts deionized water, 1 part hydrochloric acid, and 2 parts of hydrogen peroxide; and a final rinse in deionized water.

Ellipsometric measurements showed that after the cleaning procedure approximately 10Å of silicon dioxide was present on the silicon surface, as has been reported by others (5, 6). Since the primary purpose of this work was to investigate the silicon nitride layer, no additional oxide was grown.

Immediately after being cleaned, 750-1000Å of silicon nitride was pyrolytically deposited at 700°C on the wafers using silane and ammonia with hydrogen as a carrier gas. The silane and ammonia were in the ratio of 1 to 100 and were purchased from Matheson under the trade name N-gas.

Following the silicon nitride deposition, the samples were annealed in dry nitrogen at either 800°, 900°, 950°, or 1000°C for various lengths of time. For each batch of samples fabricated, one wafer was left as a control to which the experimental data could be compared. Table I lists the various samples along with their annealing temperatures and times.

Next, aluminum was evaporated on top the Si<sub>3</sub>N<sub>4</sub> and photolithography was used to outline circular electrodes 35 mils in diameter giving an area of 6.23 × 10<sup>-3</sup> cm<sup>2</sup>. To provide a good electrical contact to the back side, it was cleaned and etched prior to the

evaporation of an aluminum layer. After metallization, the wafers were tested without being diced.

## Theory

The theory and equations which are given below are presented so that the experimental data could be used to extract values for some of the parameters which characterize the silicon nitride. This material has been presented and expounded on by many without complete agreement by all of the authors. These differences will be discussed in the text as they come up. The main thrust of this work was to determine the effect of annealing on these parameters and then to go back and try to correlate the results with some of the variations in the theories.

*Conduction properties.*—Because of the thin oxide employed in the devices which were studied, the conduction properties will be dominated by the silicon nitride. It has been shown (7-10) that at room temperature and with electric fields in the range of 10<sup>6</sup>-10<sup>7</sup> V/cm, the current density in the silicon nitride is governed by the Poole-Frenkel field-enhanced thermal excitation of trapped carriers. The equation describing this mechanism is

$$J_N = C_N E \exp \left\{ \left( \frac{e^3 E}{\pi \epsilon_N \epsilon_0} \right)^{1/2} - e \phi_t \right\} / r k T \quad [1]$$

where  $J_N$  is the current density,  $E$  the electric field in the layer,  $e$  the electronic charge,  $\phi_t$  the trap depth,  $k$

Table I

Sample	Annealing temp, °C	Annealing time, min
T-C-1		
T-C-2	1000	10
T-C-3	1000	20
T-C-4	1000	30
T-C-5		
T-C-6	1000	10
T-C-7	1000	20
T-C-8	1000	30
T-E-1		
T-E-2	1000	5
T-E-3	1000	10
T-E-4	1000	20
T-F-1		
T-F-2	800	10
T-F-3	800	20
T-F-4	800	30
T-F-5	800	60
T-F-6	800	120
T-G-1		
T-G-2	900	10
T-G-3	900	20
T-G-4	900	30
T-G-5	900	60
T-H-1		
T-H-2	950	10
T-H-3	950	15
T-H-4	950	20
T-H-5	950	25

\* Electrochemical Society Student Member.

Key words: charge trapping, silicon nitride, nonvolatile memory, heat-treatment, tunneling.



Boltzmann's constant,  $T$  the absolute temperature,  $\epsilon_0$  the permittivity of free space,  $\epsilon_N$  the high frequency dielectric constant of the silicon nitride, and  $C_N$  and  $r$  are constants which will be discussed later.

The value for the high frequency dielectric constant which has been used by most authors is given by  $\epsilon_N = n^2$  where  $n = 2$  is the index of refraction in the visible range (10-12). Sze (9), however, points out that the dielectric constant for visible wavelength is not necessarily the correct value to use. His calculations show that the dielectric constant in the infrared region might be more appropriate for the Poole-Frenkel effect in silicon nitride. In this work, a value of 5.5, as taken from Sze (9), was used for the high frequency dielectric constant. As far as the results presented here are concerned, the uncertainty in the value which should be used for the dielectric constant is not of major importance for two reasons; first, it is the square root of the dielectric constant which is employed in the calculations, so even large variations in the value of the dielectric constant would result in much smaller variations in other calculated values, and secondly, in this work concern was for variations in parameters caused by the annealing which would show up regardless of the value used for  $\epsilon_N$ .

$C_N$ , the preexponential factor in Eq. [1], has the units of conductivity. It is generally accepted that  $C_N$  is a function of the density of traps (7, 9-12), but there are differences in terminology which can cause confusion as to the correct functional form. What Kendall (7), Sze (9), and Brown *et al.* (13) refer to as traps are called donor sites by Yeargan *et al.* (10) and Simmons (11). Simmons' (11) neutral traps are the acceptor sites of Yeargan *et al.* (10). In this work the term "trap" is used instead of donor site, and compensation takes place by means of the acceptor sites. Once the differences in terminology are taken into account, all of the above-mentioned works show that an increase in the trap density,  $N_t$ , will result in an increase in  $C_N$  and that  $C_N$  is also a function of the acceptor site density  $N_a$ . The exact functional form varies as the relative densities vary, with  $C_N$  proportional to  $N_t^{1/2}$  for traps only and proportional to  $(N_t - N_a)/N_a$  with compensation.

The parameter  $r$  is a unitless constant whose value can range from 1 to 2 depending on the relative position and density of traps and acceptor sites in the silicon nitride (7, 10, 12). As with the factor  $C_N$ , some confusion can arise because of the differences in terminology used by various authors, but if one uses the terminology employed in this work then  $r$  approaches 1 as compensation of traps by acceptor sites takes place.

When the conduction data is plotted as  $\ln(J/E)$  vs.  $E^{1/2}$ , a straight line should result if the conduction mechanism is due to the Poole-Frenkel effect. From the slope of the plot, the value of  $r$  can be calculated using the equation

$$r = (e^3/\pi\epsilon_N\epsilon_0)^{1/2}/SkT \quad [2]$$

where  $S$  is the slope of the plot. Once a value for  $r$  is determined, a value for  $C_N$  can be calculated from the experimentally measured currents and voltages. Any change of the trap density in the silicon nitride should be reflected in a change in  $C_N$ . Even though it is possible to calculate a value for  $C_N$ , it is not possible to extract an exact value for the trap density because (i) both traps and acceptor sites play a role in the conduction mechanism and (ii) one of the terms in  $C_N$  is the mobility for which published values vary by at least two orders of magnitude (10). Nevertheless, changes in  $C_N$  will indicate qualitatively what changes may have occurred in the trap density.

By measuring the current through the devices at a constant electric field but at different temperatures, a value for the trap depth,  $\phi_t$ , can be determined. The resulting data are plotted as  $\ln(I_N)$  vs.  $T^{-1}$ , and the

slope,  $S$ , of the plot is then used in Eq. [3] below to calculate the value of  $\phi_t$

$$\phi_t = -(Sk/e) + (eE/\pi\epsilon_N\epsilon_0)^{1/2} \quad [3]$$

Thus, by the proper manipulation of the conduction data obtained from devices which have undergone varied annealing treatments, an understanding of the effects of annealing on the silicon nitride layer can be deduced.

**Memory retention.**—Since the major functional use of thin oxide MNOS devices is for nonvolatile memory applications, the effects of annealing on the memory properties were also investigated. Earlier work on MNOS devices (13, 14) leads investigators to conclude that the charges were trapped at the oxide nitride interface. If this were the case, then the decay of the threshold voltage would be a simple exponential characterized by a single time constant. However, it has been reported by many that the decay is logarithmic (15, 16) and this can be explained theoretically with a spatial distribution of trapped charges in the silicon nitride.

The theory which was used in this work to explain the flatband-voltage decay was first published by Lundkvist, Lundström, and Svensson (6) and was based on a direct tunneling theory using the WKB method. A similar result was obtained by Ross and Wallmark (17), but for the charging of MNOS devices as a function of the applied voltage and time. Figure 1 shows the band structure used in the theory (1, 2) and Fig. 2 shows the assumed trapped charge density in a

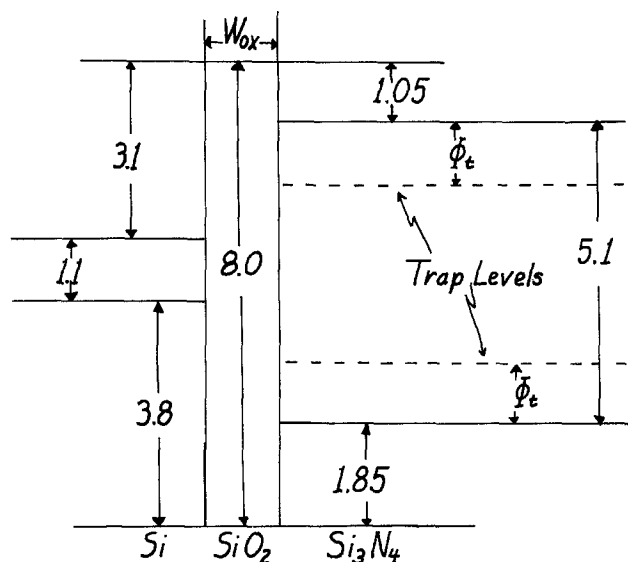


Fig. 1. Energy band diagram of the MNOS structure

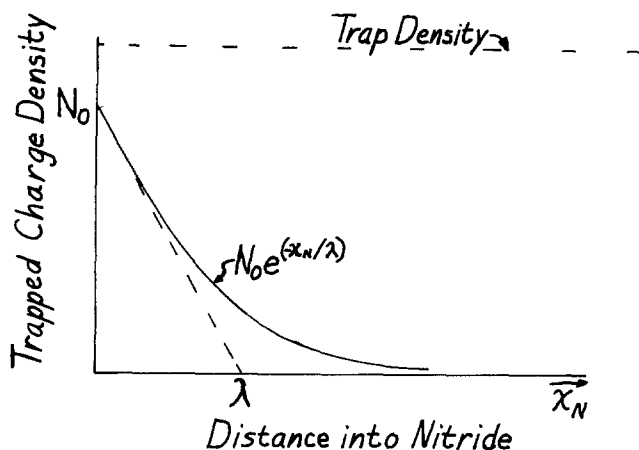


Fig. 2. Trapped charge distribution used in the discharge theory

spatially uniform distribution of traps. One should note that the maximum for the trapped charge density,  $N_o$ , which is a function of the applied voltage, is less than the trap density  $N_t$ , and that the total number of trapped charges is given by  $N_o\lambda$ , where  $\lambda$  is a mean trapping distance which is inversely proportional to the density of traps. The resulting equation describing the quantity of charge remaining in the silicon nitride at a time  $t$  is given by

$$Q_t = Q_o \{1 - (2.3B_N/\lambda) \log (t/\tau_1)\} \quad [4]$$

where  $Q_o$  is the initial charge stored in the nitride as given by  $eN_o\lambda$ ,  $\tau_1$  is a characteristic time constant associated with the start of the discharge after the end of the switching pulse and is a function of the oxide thickness, and  $B_N$  is a constant given by  $2(2m^*e/\hbar^2)^{1/2}\phi_t^{1/2}$ .

If the traps were to saturate because of a switching pulse, then the resulting trapped charge density would have approximately a rectangular shape with the total number of trapped charges given by  $N_t d$ , where  $d$  is the maximum distance into the nitride at which charges are trapped. If this were the trapped charge density then Eq. [4] would be modified to

$$Q(t) = eN_t d \{1 - (2.3B_N/d) \log (t/\tau_1)\} \quad [4a]$$

From Eq. [4a] the decay rate would be given by  $e2.3B_N N_t$  which is independent of the applied voltage. On the other hand, Eq. [4] gives a decay rate of  $eN_o 2.3B_N$  which is a function of the applied switching voltage because of the factor  $N_o$ . Results to be presented below show that the decay rate is a function of applied voltage, which supports the assumed exponential trapped charge density.

Since it is much easier to measure the flatband-voltage rather than charge decay, Eq. [4] can be modified from charge to flatband-voltage decay by dividing  $-Q(t)$  by  $C_o$ , the capacitance of the device. In doing this the metal-silicon work function difference is ignored since it is more than an order of magnitude smaller than the initial flatband voltages which are considered. The theoretical expression for the flatband-voltage decay rate,  $D_N$ , of thin oxide MNOS devices can be expressed as

$$D_N = -V_{FBO} 2.3B_N/\lambda \quad [5]$$

with  $V_{FBO}$  the initial flatband voltage immediately after pulsing. From Eq. [5], the observed decay rate should increase in magnitude with a decreasing mean trapping distance  $\lambda$ . Since  $\lambda$  is inversely proportional to the trap density, as the number of traps increase the decay rate should also increase.

In order to compare the various samples in the study it would be more appropriate to focus attention on what will be referred to as a normalized decay rate,  $D_{NO}$ , which is obtained by dividing the observed decay rate by minus the initial flatband-voltage after pulsing. The theoretical expression for the normalized decay rate is then given by

$$D_{NO} = D_N/(-V_{FBO}) = 2.3B_N/\lambda \quad [6]$$

where  $D_{NO}$  is a function of the trap depth and the mean trapping distance which is inversely proportional to the number of traps.

### Experimental Procedures and Results

Due to the various methods of silicon nitride deposition and the wide variations in deposition parameters, there is no one published value for the dielectric constant which can be universally used. Because the electric field needs to be accurately known in order to derive meaningful numbers, it was imperative that an accurate value for the dielectric constant be obtained for the devices under test. Knowing the area of the capacitor and dielectric constant, the thickness of the nitride film can be calculated from a capacitance mea-

surement and the electric field determined from the applied voltage.

The multiple beam interferometer method of Tolansky (18) was used in conjunction with capacitance measurements to calculate the dielectric constant for the silicon nitride at 1 MHz. Both annealed and unannealed samples were tested and a value of 5.6 was calculated irrespective of the annealing treatment.

For the conduction measurements the samples were placed in a shielded box and held down by a small vacuum pump on a metal plate which could be heated. The applied voltages were obtained from a 90V battery and a simple voltage divider. Before each device was tested, the capacitance was measured under heavy accumulation in order that the nitride thickness could be calculated. This was done so that all measurements could be made at known electric fields, thus enabling different devices to be unambiguously compared.

Figure 3 shows the resulting data for three samples from the batch annealed at 950°C. The parallel displacement of the curves indicated that the preexponential term,  $C_N$  in the Poole-Frenkel equation has increased in value with the annealing. From this increase it can be inferred that the trap density has also increased with annealing. Since the plotted lines are almost parallel, the values of  $r$  calculated from the slopes using Eq. [2] will be very nearly the same. For all samples tested,  $r$  was calculated to be  $1 \pm 0.08$ . This implies that there are both traps and acceptor sites and that their relative ratio is not affected by the annealing. Similar changes in the conduction properties were obtained for all annealing temperatures except 800°C where there were no observed changes in the conduction properties. This is reasonable since all measured quantities varied the least for the 800°C anneal.

A second set of conduction measurements was made on the two batches of samples annealed at 1000°C. In these tests the electric field in the nitride was held constant at  $5.5 \times 10^6$  V/cm and the temperature of the device was varied. Figure 4 shows the resulting data for a number of devices. Using the slope,  $S$ , of these plots and Eq. [3], the value of the trap depth,  $\phi_t$ , was calculated. The values obtained from all of the plots

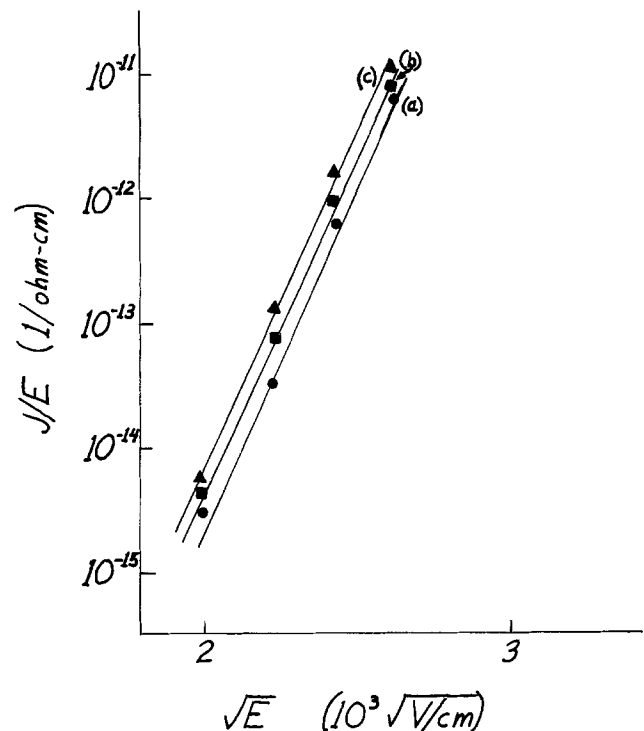


Fig. 3. Poole-Frenkel plot of the conduction data: (a) T-H-2, (b) T-H-3, and (c) T-H-5.

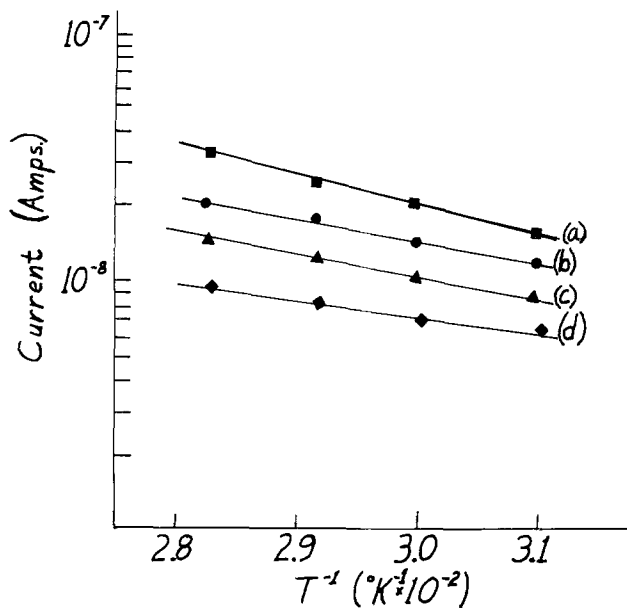


Fig. 4. Log of the current vs.  $T^{-1}$  at a constant electric field: (a) T-C-8, (b) T-C-5, (c) T-E-2, and (d) T-E-4.

varied between 0.9 and 0.996V with an average of 0.946V, but there was no trend to the variations which could be correlated with the annealing treatment. Since the 1000°C anneal was the most severe heat-treatment any sample was to undergo and since there was no apparent effect on the trap depth due to the annealing, this type of measurement was not made on the samples annealed at other temperatures and a value of 0.95 was used for  $\phi_t$  in subsequent calculations.

The second area of study was the effect of annealing on the memory retention properties of the devices. For each device tested a high frequency C-V plot was made and by knowing the substrate resistivity the flatband capacitance was calculated (19). Knowing the flatband capacitance, an automatic recording setup was adjusted so as to periodically record the flatband voltage of the device under test. The duration of the recording process was only 1 sec, and the voltages applied to the device were less than that needed to induce the switching action, thus minimizing the possibility of enhancing the discharge process. Before being connected to the recording setup, each device was subjected to a +40V pulse of 5 sec duration and then a -40V pulse of like duration. Immediately following the end of the negative pulse the device was connected to the automatic measurement circuitry and the discharge recorded.

The results for samples annealed at 950°C are shown in Fig. 5. As can be seen from the plots, there is no apparent trend in the observed decay rates which can

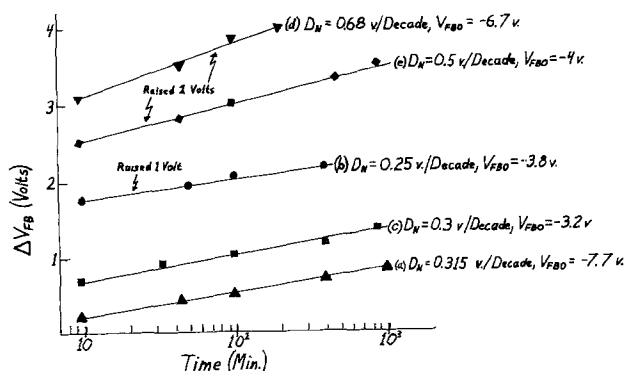


Fig. 5. Change in the flatband voltage vs. time after switching: (a) T-H-1, (b) T-H-2, (c) T-H-3, (d) T-H-4 and (e) T-H-5.

be correlated with the annealing time. If one goes back to Eq. [5], it can be seen that the decay rates are influenced not only by the physical properties of the silicon nitride, but also by the initial flatband-voltages to which the devices were shifted. Thus valid comparisons can be made by looking at the normalized decay rate,  $D_{NO}$ , given by Eq. [6].

Before doing this, it will be shown that the concept of a normalized decay rate being a property of the device is legitimate. Figure 6 is a plot of normalized decay rates vs. initial flatband-voltage for a sample in the T-H batch. As can be seen from the plot, the initial flatband voltages varied by a factor of three whereas the normalized decay rates were within 5% of each other. This constancy of the normalized decay rate justifies its use as a device property.

Results of the comparisons of the normalized decay rates for all samples are shown in Fig. 7. The linear dependence of normalized decay on annealing time is evident along with the fact that at higher annealing temperatures the rate of increase is larger. The variations of the intercepts on the ordinate axis are most probably due to slight processing variances.

In order to unify analysis of the data for different annealing temperatures, the slopes of the four lines in Fig. 7 were plotted vs. the reciprocal of the annealing temperature in degrees Kelvin. This plot is shown in Fig. 8 along with the activation energy of 1.59 eV which was calculated from the slope of the line. From

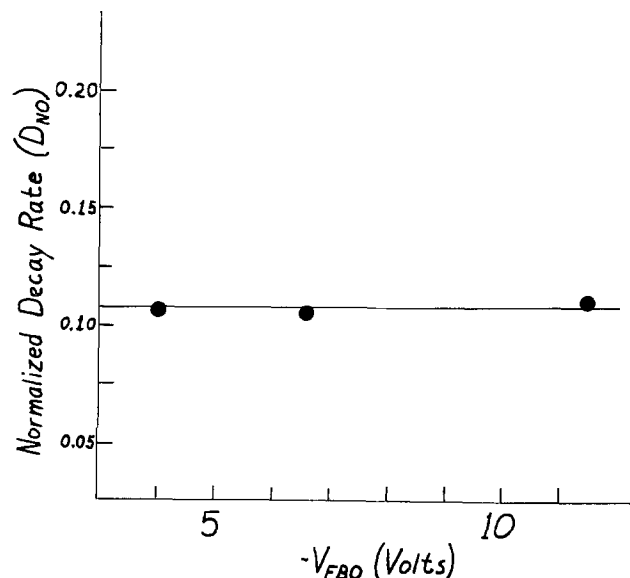


Fig. 6. Normalized decay rate vs. initial flatband voltage for a device on sample T-H-4.

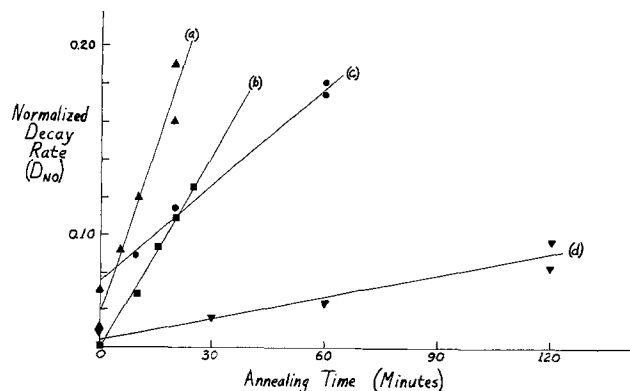


Fig. 7. Normalized decay rates vs. annealing: (a) 1000°C anneal, (b) 950°C anneal, (c) 900°C anneal, and (d) 800°C anneal.

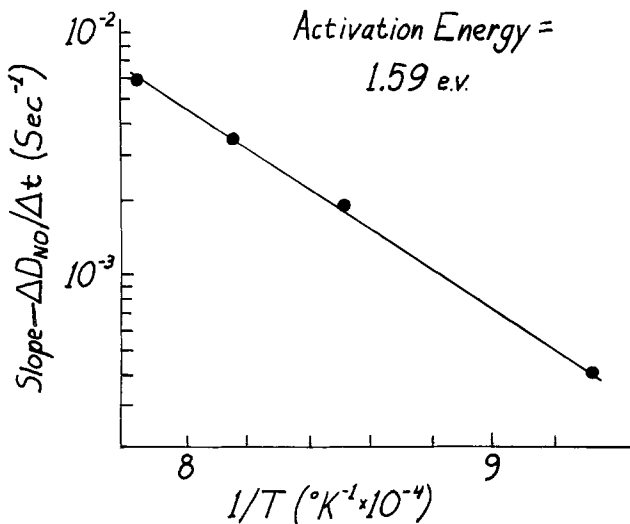


Fig. 8. Slope of the plots in Fig. 7 vs. the reciprocal of the annealing temperature.

the information contained in Fig. 7 and 8, an empirical formula can be written for the normalized decay rate as a function of both the annealing time,  $t$ , and the annealing temperature,  $T$ , as follows

$$D_{NO} = D_0 + D_1 t \exp(-E_{ACT}/kT) \quad [7]$$

where  $D_0$  and  $D_1$  are constants which will depend on the silicon nitride deposition parameters and  $E_{ACT}$  is the activation energy mentioned above.

From the normalized decay rates, the value of  $\lambda$  for each device can be calculated using Eq. [6] and a value of  $10^{10}m^{-1}$  for  $B_N$ . In this work,  $\lambda$  varied from  $58\text{\AA}$  for the smallest decay rate to  $12\text{\AA}$  for the largest. From the observed decrease in  $\lambda$  with increased annealing time and temperature, it can be inferred that the trap density in the silicon nitride has increased because of the annealing step.

### Summary and Conclusion

This study of the effects of high temperature annealing on MNOS devices has demonstrated the detrimental effects that a high temperature processing step can have on the memory performance of a device if it is done after the nitride deposition.

Two independent sets of data, conduction and decay, along with the theoretical works presented show that the observed changes are consistent with an increase in the trap density. This increase can be associated with an increase in the number and size of small crystalline regions in the otherwise amorphous film. The presence of these traps would be caused by the incomplete bonding structure present at the edges of the small crystallites due to a deficiency of one of the atomic species (16, 20). The additional traps would be generated when the thermal energy of the annealing

process initiates further growth of these small crystallite regions. Electron diffraction patterns showed that these crystallites are present and that their size is on the order of  $10\text{\AA}$ , but no information as to the number of crystallites present could be obtained from the pictures taken.

The results of this work also provide further evidence for the theory that the memory property of MNOS devices is not due to interface traps as was originally believed, but rather that the trap sites are an inherent property of the silicon nitride and that the trapped charges are spatially distributed in the nitride. The thin oxide merely acts as a barrier which enhances the critical voltage needed to initiate the switching action.

### Acknowledgments

This work was partially supported by the National Institute of Health under Grants RR-00857-01A1 and NIGMS 2-P01-GM14267-09.

Manuscript submitted Feb. 13, 1975; revised manuscript received Aug. 25, 1975.

Any discussion of this paper will appear in a Discussion Section to be published in the December 1976 JOURNAL. All discussions for the December 1976 Discussion Section should be submitted by Aug. 1, 1976.

### REFERENCES

1. K. I. Lundström and C. M. Svensson, *IEEE Trans. Electron. Devices*, **ED-19**, 826 (1972).
2. J. T. Wallmark and J. H. Scott, *RCA Rev.*, **30**, 335 (1969).
3. L. G. Carlstedt and C. M. Svensson, *IEEE J. Solid State Circuits*, **SC-7**, 382 (1972).
4. T. L. Chu, J. R. Szedon, and C. H. Lee, *Solid-State Electron.*, **10**, 897 (1967).
5. M. H. White and J. R. Cricchi, *IEEE Trans. Electron. Devices*, **ED-19**, 280 (1972).
6. L. Lundkvist, I. Lundström, and C. Svensson, *Solid-State Electron.*, **16**, 811 (1973).
7. E. J. M. Kendall, *Can. J. Phys.*, **46**, 2509 (1968).
8. J. R. Yeargan and H. L. Taylor, *This Journal*, **115**, 273 (1968).
9. S. M. Sze, *J. Appl. Phys.*, **28**, 2951 (1967).
10. J. R. Yeargan and H. L. Taylor, *ibid.*, **39**, 5600 (1968).
11. G. A. Brown, W. C. Robinette, and H. G. Carlson, *This Journal*, **115**, 948 (1968).
12. J. G. Simmons, *Phys. Rev.*, **155**, 657 (1967).
13. F. A. Sewell, H. A. R. Wegener, and E. T. Lewis, *Appl. Phys. Letters*, **14**, 45 (1969).
14. M. Pulver and G. Dorda, *Phys. Status Solidi (a)*, **1**, 65 (1970).
15. E. C. Ross and J. T. Wallmark, *RCA Rev.*, **31**, 467 (1970).
16. S. M. Hu, *This Journal*, **113**, 696 (1966).
17. E. C. Ross and J. T. Wallmark, *RCA Rev.*, **30**, 360 (1969).
18. S. Tolansky, "Surface Microtopography," Wiley Interscience, New York (1960).
19. S. M. Sze, "Physics of Semiconductor Devices," Wiley Interscience, New York (1969).
20. E. J. M. Kendall and J. W. Haslett, *IEEE Trans. Electron. Devices*, **ED-19**, 287 (1972).

# The Influence of Fixed Interface Charges on the Current-Gain Falloff of Planar n-p-n Transistors

Wolfgang M. Werner

Institut für Theoretische Elektrotechnik, Technische Hochschule Aachen, 51 Aachen, Templergraben 55, Germany

## ABSTRACT

The influence of the fixed interface charge,  $Q_{sc}$ , at the surface of the base region on the common emitter current gain of planar n-p-n transistors has been investigated. Various values of  $Q_{sc}$  were realized by means of appropriate annealing processes and by using differently oriented substrates. The value of  $Q_{sc}$  was measured by applying the MOS capacitance-voltage technique. It was shown that the current gain at low collector currents increases with decreasing interface charge density. To obtain the lowest possible value of  $Q_{sc}$ , diffusion and oxidation processes were carried out in an MOS furnace. The transistors produced in this way show a current gain which is constant over six decades of collector current.

It is well known that in silicon planar technology each p-n junction is limited by a Si-SiO<sub>2</sub> interface. This fact results in interface effects influencing the characteristics of a p-n junction. The Si-SiO<sub>2</sub> interface itself is characterized mainly by the positive fixed interface charge,  $Q_{sc}$ , and the interface states  $N_{ss}$  (1-5), which are both located in a 20Å thick layer at the Si-SiO<sub>2</sub> interface (6). This sheet charge causes an accumulation of majority charge carriers on the surface of n-doped silicon and a depletion of majority charge carriers on the surface of p-doped silicon. With a higher charge density, inversion can also occur on the surface of p-doped silicon. In connection with experiments carried out with gate-controlled planar silicon diodes, Grove *et al.* (7) show that the recombination-generation current is considerably dependent on the gate voltage which simulates interface charges. Figure 1 shows the current of a forward-biased diode as a function of the gate voltage (7). As can be seen, the current increases considerably, especially at low forward voltages, if the surface under the gate electrode becomes depleted. The current maximum occurs if the surface is approximately intrinsic. This is the case for the transition between depletion and weak inversion. Interface states, which act as recombination centers, are responsible for this current maximum, because only those centers whose energy levels are near the intrinsic Fermi level contribute significantly to the recombination rate. The current decreases again, although not to its original value, when the surface becomes strongly inverted. The latter is easily explained by the actual enlargement of the diode area.

According to Grove *et al.* (7), an estimation of the recombination current of a forward-biased diode (see Fig. 1) is given by

$$I_{rec} = \frac{1}{2} q n_i \left[ \frac{W}{\tau_J} A_J + \left( \frac{d}{\tau_s} + S_o \right) A_s \right] \exp \left( \frac{qV_F}{2kT} \right) \quad [1]$$

where  $A_J$  is the area of the metallurgical p-n junction,  $A_s$  is the area of the depleted surface,  $\tau_J$  and  $\tau_s$  are the effective lifetimes in the corresponding regions, and  $W$  is the thickness of the space-charge region of the metallurgical p-n junction. The width of the space-charge region at the surface  $d$  is proportional to the total interface charge density

$$d = \frac{Q_{sc}}{qN_A} \quad [2]$$

Key words: interface charges, recombination centers, low power devices, depletion region, MOS preparation technique.

where  $N_A$  is the impurity concentration of the p-doped region. This equation is valid for the cases of depletion and weak inversion.

The surface recombination velocity,  $S_o$ , is proportional to the interface state density

$$S_o = \sigma v_{th} N_{ss} \quad [3]$$

Here,  $\sigma$  is the capture cross section of the generation-recombination centers and  $v_{th}$  is the thermal carrier velocity.

In the case of an NPN transistor, all of the recombination current will appear as a base current. Since the current caused by recombination in the space-charge regions decreases with the factor  $q|V_F|/2kT$ , whereas the collector current decreases with the factor  $q|V_F|/kT$ , the current gain  $h_{fe} = I_C/I_B$  will decrease with decreasing collector current.

Reddie (8) has shown by means of a gate-controlled n-p-n transistor that the current-gain falloff at low current levels is strongly influenced by the gate voltage. In the work of Khajezadeh *et al.* (9), two different interface charge densities were realized employing <100> and <111> oriented material. The transistors fabricated with <100> oriented silicon slices result in a considerably smaller current-gain falloff, which is caused by the lower interface charge density, in opposition to <111> material.

In this paper the influence of the fixed interface charge,  $Q_{sc}$ , on the current gain at low current levels has been investigated. The transistors with the lowest value of  $Q_{sc}$  show a current gain which is constant

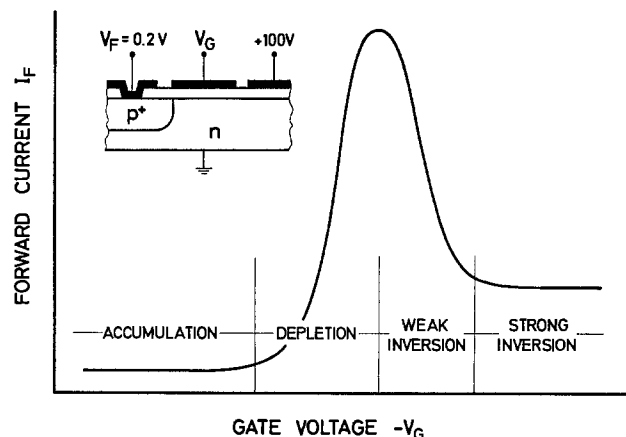


Fig. 1. Forward current as a function of gate voltage for the gate-controlled diode shown in the insert.

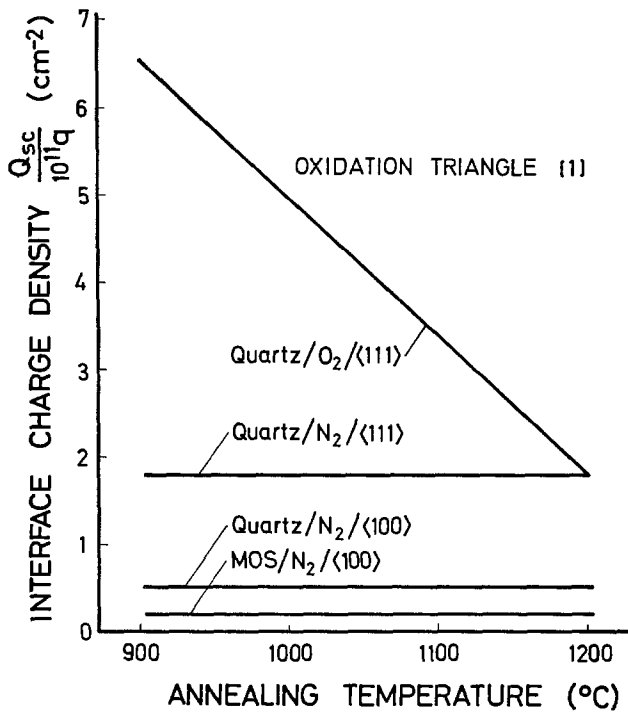


Fig. 2. Illustration of the dependence of fixed interface charge on the annealing parameters and the crystal orientation.

over six decades of collector current. The development of such devices is important for low power and low noise applications.

#### Sample Preparation

Various values of  $Q_{sc}$  were realized by annealing the samples in nitrogen or oxygen at the end of the emitter diffusion process, and by using  $\langle 111 \rangle$  and  $\langle 100 \rangle$  oriented substrates. Moreover, two different diffusion and oxidation furnaces, a quartz-tube furnace and a special MOS furnace with an SiC tube, were used. Figure 2 shows in principle the dependence of the fixed interface charge on the above-mentioned parameters and on the temperature of the final heat-treatment. The highest value of  $Q_{sc}$  was observed when  $\langle 111 \rangle$  oriented silicon slices, a quartz-tube furnace, and an annealing process in  $O_2$  were employed. The lowest possible value of  $Q_{sc}$  was obtained using  $\langle 100 \rangle$  oriented material, the MOS furnace, and an annealing process in  $N_2$  (1).

The starting material for the production of n-p-n transistors was phosphorus-doped silicon with an impurity concentration of  $2.5 \cdot 10^{15} \text{ cm}^{-3}$ . This has an etch-pit density of  $4000 \text{ cm}^{-2}$ . The base and emitter regions were formed using two different diffusion sources: doped oxides (10) and gaseous sources. When using doped oxides, the surface concentrations are about  $1.5 \cdot 10^{18} \text{ cm}^{-3}$  for the base region (see Table I)

Table I: Dependence of the fixed charge  $Q_{sc}$ , the impurity concentration at the surface of the base region, and the normalized current gain on the annealing ambient, the silicon orientation, and the diffusion furnace used

Type of diffusion furnace	Crystal orientation	Annealing ambient at 1000°C	$\frac{Q_{sc}}{q 10^{11} \text{ cm}^{-2}}$ Collector	$\frac{Q_{sc}}{q 10^{11} \text{ cm}^{-2}}$ Base	$C_s$ $10^{18} \text{ cm}^{-3}$ Base	$\frac{h_{fe}}{h_{fe \max}}$ at 1μA
Quartz-tube furnace	$\langle 111 \rangle$	$O_2$	5.2	18.0	1.10	0.75
		$N_2$	1.8	7.8	1.54	—
	$\langle 100 \rangle$	$O_2$	1.9	11.0	1.60	—
		$N_2$	0.5	4.6	2.06	0.97
MOS furnace	$\langle 100 \rangle$	$O_2$	1.3	5.2	1.30	0.94
		$N_2$	0.2	2.6	1.90	1.00

and about  $5 \cdot 10^{19} \text{ cm}^{-3}$  for the emitter region (LCE, low concentration emitter). Applying the gaseous sources,  $B_2H_6$  for the base and  $POCl_3$  for the emitter, the surface concentrations are  $1 \cdot 10^{18} \text{ cm}^{-3}$  and  $5 \cdot 10^{20} \text{ cm}^{-3}$  for the base and emitter regions, respectively (HCE, high concentration emitter). The base surface concentrations were determined by MOS capacitance-voltage measurements and the emitter surface concentrations were calculated from the sheet resistance and the junction depth applying Irvin curves (11). The metallization of the slices with aluminum was carried out by an electron gun. The substrate temperature was kept at room temperature during the evaporation process. Before the last photoresist operation step, the samples were annealed at  $500^\circ\text{C}$  in nitrogen in order to reduce fast surface states. The base area of the transistors was  $50 \times 40 \mu\text{m}^2$  and the emitter area was  $17.5 \times 25 \mu\text{m}^2$ . The material used for the production of the MOS samples, which are required for the measurement of  $Q_{sc}$ , was boron-doped  $\langle 100 \rangle$  and  $\langle 111 \rangle$  oriented silicon slices with an impurity concentration of  $6 \cdot 10^{15} \text{ cm}^{-3}$ . These slices were treated exactly like the n-p-n transistors with respect to the high temperature and annealing processes. After the first oxidation, which yields the masking oxide for the base, the oxide was entirely etched away before the base diffusion was carried out. After the emitter diffusion process the oxide was etched down to an oxide thickness of about 1300Å. Reduction of the oxide thickness is necessary to reach a sufficient sensitivity for the measurement of  $Q_{sc}$ . The field plates were prepared by evaporating aluminum through a metal mask resulting in circular dots  $500 \mu\text{m}$  in diameter. After this evaporation process, the samples were annealed in the same way as the n-p-n transistors. The value of  $Q_{sc}$  was measured applying the MOS capacitance-voltage technique (12, 13), using a work function difference of  $\phi_{MS} = -\phi_F - 0.22\text{V}$  (14) where  $\phi_F = -(E_F - E_1)/q$ .

#### Results and Discussion

The d-c common emitter current gain  $h_{fe} = I_C/I_B$  of the n-p-n transistors was measured at an applied voltage of  $U_{BE} = U_{CE}$ , if not otherwise indicated. Table I shows the values of  $Q_{sc}$  at the surface of the base region and the normalized current gain at a collector current of  $1 \mu\text{A}$  as a function of the annealing ambient, crystal orientation, and type of diffusion furnace used. In this case, base and emitter regions were formed applying doped oxides. As can be seen, the normalized current gain increases with decreasing interface charge. For the lowest value of  $Q_{sc}$ , the current-gain falloff is zero. The calculations to determine  $Q_{sc}$  also provide the surface concentration of the base area. They are specified in the sixth column. As can be seen, the surface concentrations of the samples annealed in  $N_2$  are about 30% higher than those annealed in  $O_2$ . This can be explained by the segregation coefficient of boron at the Si-SiO<sub>2</sub> interface which is in the range of 0.3 (15). For comparison, the values of  $Q_{sc}$  at the surface of n-doped silicon with an impurity concentration of  $2.5 \cdot 10^{15} \text{ cm}^{-3}$ , which is also the starting material for the n-p-n transistors, are specified in the fourth column. These values are much lower than those at the surface of the base region. Thus it is evident that the base diffusion process generates fixed interface charges. The measured fixed interface charge density at the surface of the base region of the devices produced with gaseous sources is in the same order of magnitude as that of the devices fabricated with doped oxides. They are  $8.7 \cdot 10^{11} \text{ qcm}^{-2}$  and  $4.5 \cdot 10^{11} \text{ qcm}^{-2}$  for  $\langle 111 \rangle$  and  $\langle 100 \rangle$  oriented slices, respectively, both being annealed in nitrogen.

As mentioned above, interface states are also responsible for current-gain falloff. Therefore it is of interest to note that normally there exists a strong correlation between interface states and interface charges (16). For the annealing parameters used in

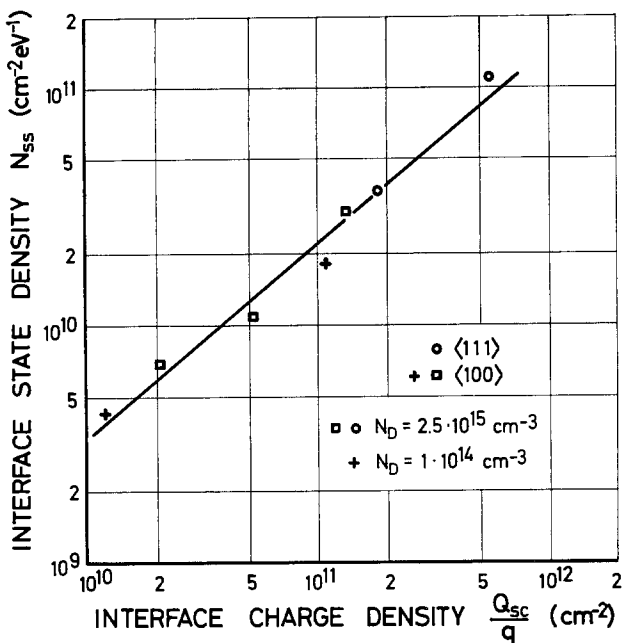


Fig. 3. Illustration of the correlation between interface charges and interface states.

this work, this correlation is shown in Fig. 3, for n-doped <100> and <111> oriented slices with impurity concentrations of  $2.5 \cdot 10^{15}$  and  $1 \cdot 10^{14} \text{ cm}^{-3}$ . The values of  $N_{ss}$  represented in Fig. 3 are located in the middle of the energy gap.  $N_{ss}$  was measured by means of the quasi-static technique of Kuhn (7).

Figure 4 shows the normalized current gain as a function of the collector current. Parameters are the diffusion furnace used, the annealing ambient, the crystal orientation, and the surface concentration of the emitter region. When comparing the curves marked quartz/ $N_2$ / $\langle 100 \rangle$ /LCE and quartz/ $N_2$ / $\langle 100 \rangle$ /HCE, it becomes evident that the impurity concentration of the emitter region also influences the current-gain falloff. The current gain of the transistors characterized by the parameters MOS/ $N_2$ / $\langle 100 \rangle$ /LCE is constant over nearly six decades of collector current, the parameters corresponding to the lowest value of  $Q_{sc}$ . In this case the base current is composed entirely of neutral-region recombination (diffusion) terms, which increase exponentially with  $qV_{BE}/kT$ . From these results it can be concluded that the current-gain falloff of the low concentration emitter devices is caused by the recombination centers at the surface of the base region. The current-gain falloff of the high concentration emitter devices is mainly caused by recombination mechanisms in the emitter-base space-charge region because

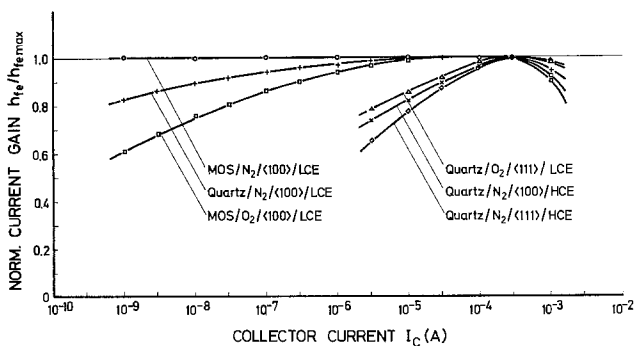


Fig. 4. Normalized current gain as a function of collector current. Parameters are the diffusion furnace used, the annealing ambient, the crystal orientation, and the surface concentration of the emitter region.

the interface charge density at the surface of the base region of these devices is in the same order of magnitude as that of the devices fabricated with doped oxides. The variations of collector and base currents as a function of the base-emitter voltage are shown in Fig. 5. It is clearly seen that the slope of the base current of the devices with the lowest interface charge current. Figure 6 shows typical curves of the current gain vs. collector current of these devices. Parameter is the base width. It was  $0.58 \mu\text{m}$  for a current gain of 500 and  $0.98 \mu\text{m}$  for a current gain of 35. The curve with the highest current gain shows a slight deviation from ideal beta-linearity. The increase of current gain at low current levels is caused by the reverse current of the collector-base junction. This is demonstrated in Fig. 7, where the current gain is shown as a function of the collector current with the collector-base voltage as parameter. As can be seen, the current gain in the linear region is also dependent on the collector-base voltage. This is caused by the actual shortening of the

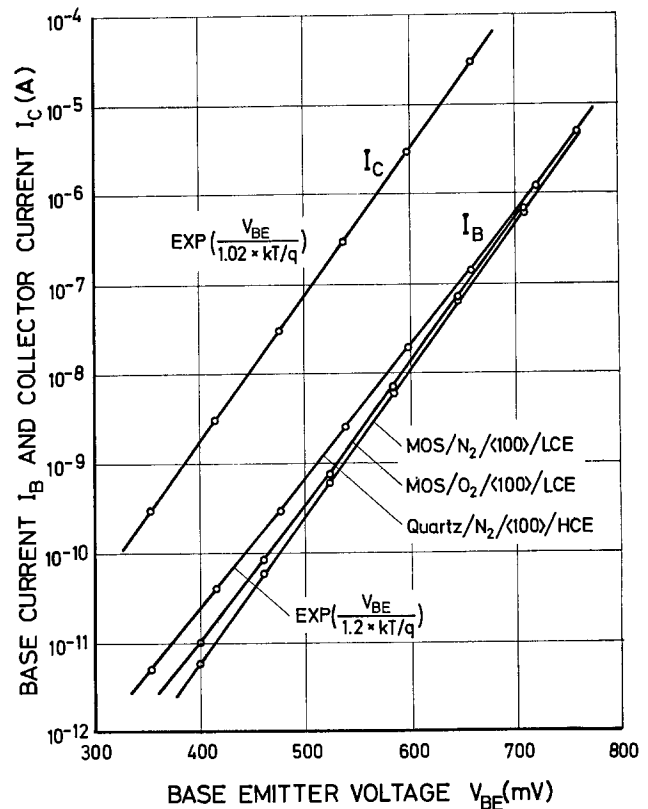


Fig. 5. Collector and base current as a function of emitter-base forward bias. Parameters are the same as in Fig. 7.

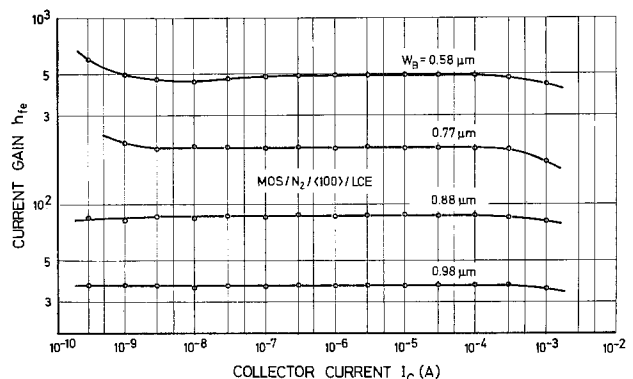


Fig. 6. Common emitter current gain vs. collector current of n-p-n transistors with the lowest possible value of  $Q_{sc}$ . Parameter is the base width.

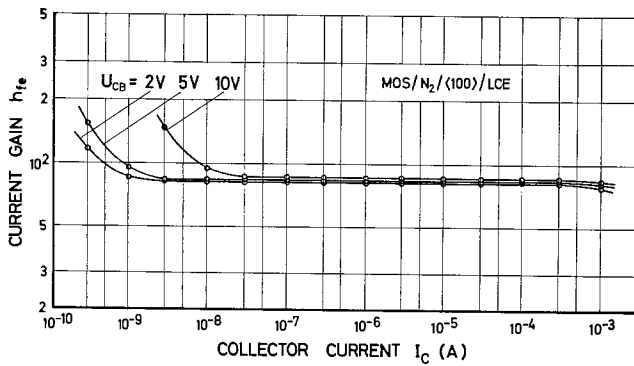


Fig. 7. Current gain as a function of the collector current with the collector-base voltage as parameter.

base width as a result of the expansion of the base-collector space-charge region.

### Conclusion

The influence of the fixed interface charge at the surface of the base region on the d-c common emitter current gain of planar n-p-n transistors has been investigated. The results obtained indicate that the current gain at low collector currents increases with decreasing interface charge density. It was shown that it is possible to produce n-p-n transistors without current-gain falloff at low collector currents. This was obtained by employing MOS preparation techniques, which yield the lowest possible value of  $Q_{sc}$ .

### Acknowledgments

The author would like to thank Professor Dr. W. L. Engl for his interest and support of this work, Dr. J. A. Becker for helpful discussions, and Mr. H. J. Gahle for

his assistance with the measurements of the current gain.

Manuscript submitted May 14, 1974; revised manuscript received July 21, 1975. This was Paper 24 presented at the San Francisco, California, Meeting of the Society, May 12-17, 1974.

Any discussion of this paper will appear in a Discussion Section to be published in the December 1976 JOURNAL. All discussions for the December 1976 Discussion Section should be submitted by Aug. 1, 1976.

Publication costs of this article were partially assisted by the Institut für Theoretische Elektrotechnik.

### REFERENCES

1. B. E. Deal, M. Sklar, A. S. Grove, and E. H. Snow, *This Journal*, **114**, 266 (1967).
2. E. Kooi, *Philips Res. Rept.*, **21**, 477 (1966).
3. P. V. Gray and D. M. Brown, *Appl. Phys. Letters*, **8**, 31 (1966).
4. E. A. Fogels and C. A. T. Salama, *This Journal*, **118**, 2003 (1971).
5. F. Montillo and P. Balk, *ibid.*, **118**, 1463 (1971).
6. R. J. Powell and C. N. Berglund, *J. Appl. Phys.*, **42**, 4390 (1971).
7. A. S. Grove and D. J. Fitzgerald, *Solid-State Electron.*, **9**, 783 (1966).
8. V. G. K. Reddi, *ibid.*, **10**, 305 (1967).
9. H. Khajezadeh and T. T. McCaffrey, *Proc. IEEE*, **57**, 1518 (1969).
10. J. A. Becker, Private communication.
11. I. C. Irvin, *Bell System Tech. J.*, **41**, 387 (1962).
12. A. S. Grove, B. E. Deal, E. H. Snow, and C. T. Sah, *Solid-State Electron.*, **8**, 145 (1965).
13. L. M. Terman, *ibid.*, **5**, 285 (1962).
14. W. M. Werner, *ibid.*, **17**, 769 (1974).
15. A. S. Grove, O. Leistiko, Jr., and C. T. Sah, *J. Appl. Phys.*, **35**, 2965 (1964).
16. A. Goetzberger, V. Heine, and E. H. Nicollian, *Appl. Phys. Letters*, **12**, 95 (1968).
17. M. Kuhn, *Solid-State Electron.*, **13**, 873 (1970).



# Dependence of Recombination in p-Type GaP(Zn,O) on Dopant Concentrations

J. A. W. van der Does de Bye

Philips Research Laboratories, Eindhoven, The Netherlands

## ABSTRACT

The luminescence of p-type GaP(Zn,O), a semiconducting material for light emitting diodes, is controlled by the transitions of the excited free electrons and by those of the electrons bound to the luminescent nearest-neighbor ( $Zn_{Ga}Op$ ) complexes. The results of the determination of the internal quantum efficiency ( $\eta$ ) on a large number of samples, prepared by solution growth and by liquid phase epitaxy and covering a zinc concentration range of  $10^{17}$ - $5 \cdot 10^{18}$   $cm^{-3}$ , lead to the conclusion that an Auger effect acting on the bound electrons is the dominant cause of the reduction of the internal efficiency of the samples with a free hole concentration ( $p$ ) above  $4 \cdot 10^{17}$   $cm^{-3}$ , where also the trapping by "killers" becomes negligible. The Auger constant was derived, being  $\approx 3 \cdot 10^{-11}$   $cm^3 sec^{-1}$ . Below this concentration the thermalization of the electrons bound to the complexes is the more important effect enhancing the otherwise relatively small action of the killers. The best value for  $\eta$  is  $\approx 40\%$  at  $p \approx 5 \cdot 10^{17}$   $cm^{-3}$ . Decay time ( $\tau$ ) measurements, using pulsed and sine-wave modulated excitation, provide insight in the effect of screening by free holes on the radiative and Auger transitions by using in the interpretation of the data the quantity ( $\eta/\tau$ ) which is proportional to the effective radiative recombination rate (including the effect of screening mentioned). Both radiative and Auger transition probabilities are reduced by a common screening factor as low as 0.2. Electron diffusion length measurements on the epitaxial samples show a strong decrease of the minority carrier lifetime with increasing zinc concentration which is ascribed mainly to the trapping by the (ZnO) complexes whose concentration increases with the zinc dope. This study also provides information on the oxygen incorporation during the crystal growth. This incorporation probably takes place at thermal equilibrium between the oxygen source and the solid GaP. [O] increases with [Zn] reaching  $\approx 10^{18}$   $cm^{-3}$  at [Zn]  $\approx 5 \cdot 10^{18}$   $cm^{-3}$ .

Semiconductor diodes that emit visible light are of increasing importance for certain applications, *i.e.*, for indication and for display of symbols. The luminescence efficiency of such diodes is generally much below 100%. Various causes exist for this circumstance part of which are peculiar to the semiconductor material used and to the devices made from them. These causes are still a matter of conjecture. In this respect the subject of this paper, p-type gallium phosphide doped with zinc and oxygen, is no exception. Partly these causes arise from the properties of the light emitting layer, *i.e.*, p-type GaP(Zn, O). Another cause, generally of minor importance for this type of material, is the limited efficiency of injection of electrons into this layer.

A study of dopant-dependent recombination in p-type GaP(Zn, O) is useful to elucidate the relevant properties of this layer with respect to both bulk efficiency and injection efficiency.

With regard to the bulk efficiency results have been published by Dishman, DiDomenico, and Caruso (1) and Jayson, Bhargava, and Dixon (2). They used the dopant dependence of two observables, quantum efficiency and decay time. In Ref. (1) it was tried to determine the internal quantum efficiency, a difficult experimental problem, while Ref. (2) emphasized the decay measurements. In view of the large number of model parameters *a priori* statements on some of these parameters were used, partly based on a theoretical study by Sinha and DiDomenico (3). References (1) and (2) essentially used a recombination model for which Fig. 1 shows a simplified level and transition diagram. It is seen that the losses arise from two groups of nonradiative transitions labeled  $\tau_{nk}$  and  $\tau_n$  which act on the free and bound electrons, respectively, and which parallel the transitions  $\tau_{nt}$  and  $\tau_r$  that

lead to the luminescence. The luminescent centers  $N_t$ , to whose concentration the rate of transitions  $\tau_{nt}$  is proportional, are nearest-neighbor complexes of one zinc ion and one oxygen ion (4) (on the gallium and phosphorus sites, respectively). These complexes have an electron binding energy  $E_t \approx 0.3$  eV. The thermal emission ( $\tau_{tn}$ ) in which  $E_t$  is active has the effect of enhancing the electron losses through the path  $\tau_{nk}$ . This effect (5), causing a temperature-dependent reduction of the efficiency, can be important at room temperature for the p-type GaP(Zn, O) used in light emitting diodes. The transitions  $\tau_{nk}$ ,  $\tau_n$ , and  $\tau_r$  which are not specified in detail in Fig. 1 terminate in hole levels. For  $\tau_n$  and  $\tau_r$  such levels are close to both valence band and equilibrium Fermi level, requiring the knowledge of hole statistics in the recombination studies (5).  $\tau_r$  was found to arise from two radiative mechanisms, *i.e.*, exciton annihilation and complex-to-zinc-acceptor transitions both of which contribute to the red luminescence (4, 6). The former mechanism is generally the stronger one.

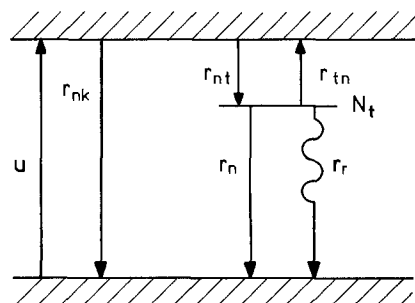


Fig. 1. A simplified recombination model for p-GaP(Zn,O)

Key words: light emitting diodes, quantum efficiency, oxygen incorporation, free carrier screening.

A different approach which involves few *a priori* statements was used by Henry, Bachrach, and Schumaker (7) who invoked the decay behavior of the free electrons, measured through the green exciton luminescence, to obtain data on the competition between the transitions  $r_{nt}$  and  $r_{nk}$ . Using these measurements in addition to internal quantum efficiency results and decays of the red emission, data were found on the competition between the transitions  $r_r$  and  $r_n$ . For the study of the dopant dependence of the competition between  $r_{nk}$  and  $r_{nt}$  the method of using the green exciton decay is, however, not suitable owing to the immeasurably short lifetimes of the free electrons in samples of high zinc concentration. This is borne out by our findings on the diffusion length (also to be discussed in the present paper). For the study of the energy losses through the paths  $r_{nk}$  and  $r_n$  the present paper emphasizes the dopant dependence of the internal quantum efficiency of the red luminescence. As it will be shown this approach involves only a few *a priori* assumptions. The efficiency ( $\eta$ ) is conveniently expressed by the quantity  $(1 - \eta)/\eta$  to show the effects of the two energy losses. The decay time ( $\tau$ ) of the red luminescence plays a secondary role and serves to provide information on the effects of screening and hole statistics on the bound excitons that yield most of the red luminescence. The study of these effects uses the quantity  $\eta/\tau$  that is free from many model parameters that act on the separate quantities  $\eta$  and  $\tau$ .

Another subject is discussed in the present paper, namely, the rate of transitions  $r_{nt}$  which is connected with the diffusion length of the electrons in p-GaP(Zn, O) through the minority carrier lifetime. Findings on this quantity are helpful in understanding the injection efficiency of a light emitting diode containing the GaP(Zn, O). The present paper, however, deals with these findings in a different context, *i.e.*, that of the rather intangible problem of the oxygen incorporation in GaP. The connecting link with  $r_{nt}$  is the proportionality of  $r_{nt}$  with the concentration of the (ZnO) complexes.

The following section covers the preparational and experimental techniques. It contains a somewhat extended discussion on the problem of determining the internal quantum efficiency. In subsequent sections are discussed the measurements; the results of decay and efficiency measurements in order to assess the importance of killers ( $r_{nk}$ ) and Auger transitions ( $r_n$ ); and the diffusion length measurements in order to reach conclusions on the oxygen incorporation.

### Preparation of the Samples and Experimental Techniques

Two techniques were used for the crystallization of GaP from a saturated solution in pure Ga (6N, Alusuisse). Both use as the starting material GaP which was synthesized from  $\text{PH}_3$  and Ga yielding spectrochemically pure crystals<sup>1</sup> which contain less than 1 ppm of sulfur. One technique of sample preparation is by spontaneous growth in an evacuated and sealed quartz ampul ("solution-grown" or SG samples). The other technique is by liquid phase epitaxy (LPE samples) (9) using n-type GaP substrates being themselves LPE material or GaP obtained by the liquid encapsulation technique<sup>2</sup> (LEC crystals). The LPE technique also provides the p-n junctions to enable the measurement of diffusion lengths.

The SG samples were grown by cooling the solution from 1130° to 800°C with a rate of 5° or 13°C/hr while the data for the LPE samples are 1050 (10) 500°C, followed by an anneal at 500°C for 12-14 hr. This annealing which also occurs during a good part of the time of growth promotes the formation of the luminescent

(ZnO) complexes. For the SG samples this annealing was carried out separately at 500°C in air for 168 hr, with a preanneal at 560°-600°C.

Both techniques use zinc additions to the solution so as to cover a zinc acceptor concentration range from  $1 \cdot 10^{17}$  to  $5 \cdot 10^{18}$   $\text{cm}^{-3}$ . Sufficient oxygen was added, as  $\text{Ga}_2\text{O}_3$ , to obtain amply saturated solutions in Ga for the LPE technique whereas for the SG technique the amounts added vary, being  $10^{-1}$ ,  $2 \cdot 10^{-2}$ , and  $4 \cdot 10^{-3}$  mol per cent. It is convenient to state in this section that in a previous investigation of a large number of SG samples no clear correlation was found between the  $\text{Ga}_2\text{O}_3$  admixture and the two physical quantities measured on the SG material, *i.e.*, efficiency and decay time. Therefore no discussion is given on effects of variation of the  $\text{Ga}_2\text{O}_3$  admixture in the present paper.

In addition to the internal quantum efficiency and the decay time constant of the luminescence which were determined on all samples, the electron diffusion length and the free hole concentration were measured on the LPE samples. For the latter quantity a conventional Hall measurement technique was applied using the van der Pauw method (10). Regarding the SG samples batch averages were determined for the zinc concentration using an atomic absorption analysis preceded by the extraction of the zinc from GaP which was dissolved in aqua regia (11).<sup>3</sup> With regard to the Hall effect results a finding by Foster, Woods and Lewis (12)<sup>4</sup> must be mentioned.  $p$  as measured was found to be approximately equal to  $[\text{Zn}]$  and is therefore larger than the true value of  $p$ . In the discussion of the concentration-dependent recombination it is to be understood that  $p$ , acting as an independent variable, is the measured quantity, in accordance with the practice in Ref. (1) and (2). The values of quantities that multiply  $p$  in equations are therefore different from the true values. Inasmuch as the measured value of  $p$  is approximately proportional to the true value no essential change is necessary in the interpretation of the recombination results.

Using a scanning electron microscope electron diffusion lengths were determined by the evaluation of the electron beam induced currents in the p-n junctions of the LPE samples (13). The technique and types of results are similar to those described by Hackett, Saul, Dixon, and Kammlott (14).

Two methods were used to determine the decay time constants, *i.e.*, sine-wave modulated excitation and pulsed excitation. In the former method a 514.5 nm laser beam from a Coherent Radiation argon ion laser, Model 52, was modulated by a Lasermetrics electro-optical modulator, Model EOM 3064, up to 50 MHz, using a built-in electrical network to match the output circuit of a wideband amplifier, Model GA-15, from the same firm. Both laser beam and luminescence were perceived by photomultipliers with a trialkali cathode, Philips or Amperex Type 56TVP, which provided the luminescence and reference signals for a Hewlett Packard vector voltmeter, Model 8405 A. This instrument measured the phase difference ( $\phi$ ) between the luminescence and the excitation as a function of the frequency ( $F$ ). The interpretation uses the relation between  $\phi$  and the decay time  $\tau$

$$\tan \phi = 2\pi \cdot F \cdot \tau \quad [1]$$

which is appropriate for systems having a single decay time. The results are generally in good agreement (within 10-20%) with those obtained by the other method which used 350 kV electron pulses of 2 nsec duration and 1 mA peak current. In the latter method the decay was measured by photon counting using a "delayed coincidence" method (15) or storage in a

<sup>1</sup> The crystals were prepared in a production facility of Philips at Maarheeze, The Netherlands, according to a procedure described by Grimmeis, Kischio, and Scholz (8).

<sup>2</sup> LEC crystals were grown by Mr. H. J. A. van Dijk at this laboratory.

<sup>3</sup> The  $[\text{Zn}]$  determination was carried out by Mr. L. H. Bastings and co-workers of this laboratory using a dithizon extraction method according to Ref. (11).

<sup>4</sup> According to our calculations on the oxygen incorporation the concentration of the zinc incorporated is higher than the measured free hole concentration by a factor of roughly 1.5.

fast multichannel buffer memory (16). Generally the decays measured were exponential over at least one decade of intensity and frequently over  $1\frac{1}{2}$ -2 decades.

The internal quantum efficiency was determined from a set of values of the external quantum efficiency applying immersion of the sample in liquids of different indices of refraction. Each liquid was contained in a spherical glass vessel which was positioned in an integrating sphere which provided the required  $4\pi$  geometry. The excitation was by the same laser source mentioned earlier. The detection of the excitation and luminescence light employed a calibrated photomultiplier in combination with suitable filters.<sup>5</sup> The samples, i.e., planparallel epitaxial samples and more irregular solution-grown samples, were reduced in size to achieve a good transparency. At sufficient size reduction the external efficiency should approach the internal efficiency. Nevertheless immersion in liquids of increasing optical density still leads to an increasing efficiency value. The immersion fluids used were air, ethanol, trichloroethylene, and in a few cases methylene iodide having indices of refraction equal to 1, 1.359, 1.4765, and 1.738, respectively.

In the interpretation of the efficiency results a Stern plot (17) is used where it is assumed that the external and internal efficiencies are related to an average transfer function  $T_{avg}$  by

$$\eta_{int}/\eta_{ext} = 1 + S/T_{avg} \quad [2]$$

A plot of  $1/\eta_{ext}$  against  $1/T_{avg}$  should then extrapolate to  $1/\eta_{int}$  at  $1/T_{avg} = 0$ .  $T_{avg}$  is the probability for a photon to exit into the less dense outer medium when arriving at the interface. The slope constant  $S$  in Eq. [2] varies considerably between samples. Obviously a small value of this constant is favorable. This is also true from a theoretical point of view. In deriving Eq. [2] it is supposed that (i) a photon undergoes a large number of reflections prior to exit into the outer medium, and (ii) this large number leads to randomization of the propagation directions within the sample. These assumptions may not remain true when the ratio of the indices of refraction approaches unity. A deviation from Eq. [2] might therefore occur when the experiment could be continued with outer media of higher optical density implying that the extrapolated value would differ from the true value of the internal efficiency. This difference is probably lessened by reducing the slope constant.

### Experimental Results

The experiments to be described were all carried out at room temperature.

**Bulk quantities.**—Internal quantum efficiency ( $\eta$ ) and decay time constant ( $\tau$ ) were measured at 293°K. Figure 2 shows  $\eta$  against  $p$ . It is seen that  $\eta$  decreases with increasing  $p$  from a maximum of about 40% at  $p \approx 5 \cdot 10^{17} \text{ cm}^{-3}$ . This decrease is discussed later. The symbol  $\dagger$  refers to a measurement of Ref. (7). Figure 3 shows  $\tau$  against  $p$  and includes the measurement of Ref. (7) and those of Ref. (2). The results on our SG samples were plotted by interpolation between those on our LPE samples for which  $p$  is known in order to assign  $p$  values to the SG samples.<sup>6</sup> This interpolation enabled the plots of other quantities against  $p$ , including the plot in Fig. 2. Since Fig. 3 will not be directly involved in the interpretation of the measurements (nor will Fig. 2) in the section on efficiency and decay results, some discussion is given here. In contrast to  $\eta$ , Fig. 2, the scatter in  $\tau$  is small. This is understandable as the sample dimensions that influence the efficiency determination are not expected to have an influence on  $\tau$ . Some of the scatter may arise as the value of  $p$  may change by the reduction in size of the samples

<sup>5</sup> Care was taken to avoid saturation of the luminescent complexes in the samples for both  $\eta$  and  $\tau$  determinations.

<sup>6</sup> This procedure is supported by the batch data on the zinc incorporated in the SG samples assuming  $p \approx [\text{Zn}]$  (12).

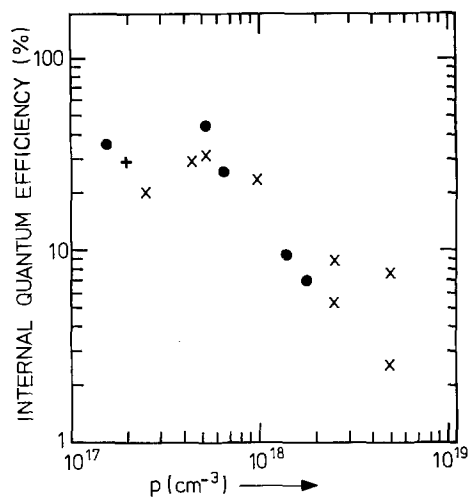


Fig. 2. Internal quantum efficiency of the red luminescence against free hole concentration. The dots indicate solution-grown samples; the crosses, liquid phase epitaxial samples. Symbol  $\dagger$  refers to a measurement of Ref. (7).

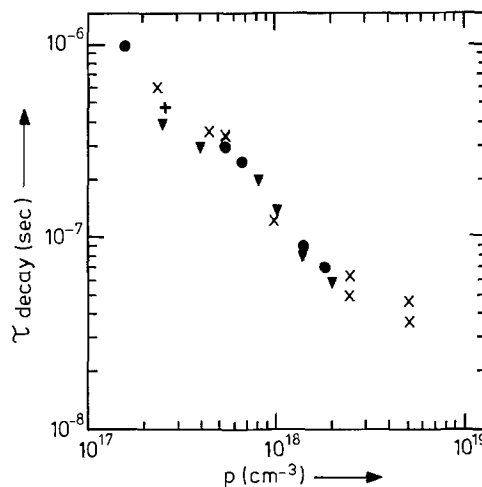


Fig. 3. Decay time of the red luminescence of the same samples as in Fig. 2 and in addition those of Ref. (2) (triangles).

that was necessary for the  $\eta$  measurements. This change in  $p$  may arise from the separation of a small part from a somewhat inhomogeneous, large sample on which the Hall measurement was carried out. The results of Ref. (2) and of the present paper are in fair agreement.

The  $\eta$  and  $\tau$  results will be used to find information on the energy losses by killers and by an Auger effect and on screening, in a later section.

**Diffusion length.**—For the technique and interpretation reference can be made to Hackett *et al.* (14). Short diffusion lengths, down to  $0.16 \mu\text{m}$ , as occur in samples with a high [Zn] value, could be determined without much difficulty. This is shown in Fig. 4a along with a case of a longer diffusion length of a sample with a low [Zn] value (Fig. 4b). The linear parts from which the diffusion length is determined generally exceed one decade of the electron beam induced current. Figure 4a shows the effect of the finite excitation volume becoming comparable to the diffusion length, the slope from which this length was determined being far from the  $p$ - $n$  junction. The electron beam current was a few times  $10^{-12}\text{A}$  at 10 kV.

Results (on LPE samples only) are stated in terms of the minority carrier lifetime ( $\tau_{MIN}$ ) which is related to the diffusion length by the known expression

$$L_{ep}^2 = D_{ep} \cdot \tau_{MIN} \quad [3]$$

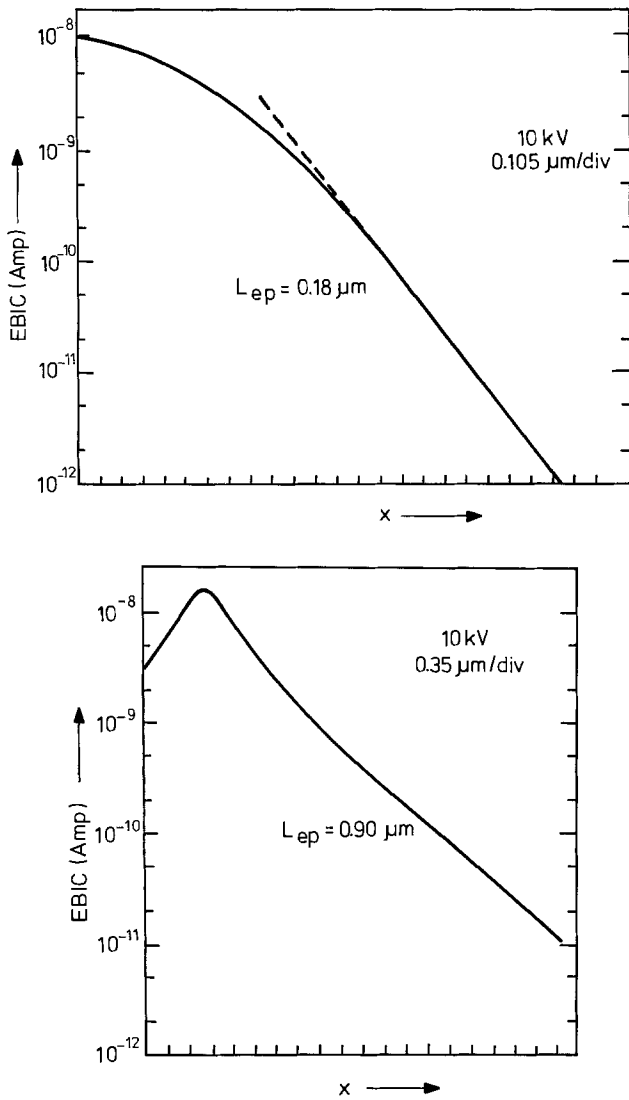


Fig. 4. Typical plots for the electron-beam-induced current (EBIC) as functions of the position  $x$  in the p-n diode, measured with a scanning electron microscope on: (a, top) a sample having a high zinc concentration and a short diffusion length ( $L_{ep}$ ), and (b, bottom) a sample having a lower zinc concentration and a longer diffusion length.

$D_{ep}$  taken to be  $2.5 \text{ cm}^2\text{-sec}^{-1}$ . The results are plotted in Fig. 5 and show a strong decrease of  $\tau_{MIN}$  with increasing free hole concentration.

A comparison is made in Fig. 5 with results (18) on GaP(Zn), without intentionally added oxygen, for which a representative curve was drawn (curve 3). It is seen from this comparison that there is a reduction of the minority carrier lifetime with respect to the oxygenless samples, pointing to the involvement of oxygen in the creation of the relevant capturing centers. In view of the dopant dependence of  $\tau_{MIN}$  zinc must also be involved in the creation of these centers. It is reasonable to identify these centers with the luminescent (ZnO) complexes. A few results from Ref. (14) on GaP(Zn, O) are also included in Fig. 5, part of which agrees with our findings. One point, however, shows a rather large upward deviation. In view of our conclusion on the involvement of O and Zn we would suspect a (relative) oxygen deficiency for the sample in question.

**Discussion of the Efficiency and Decay Results**

In the discussion of Fig. 1 two causes for the reduction of the efficiency were mentioned, i.e., the recombination through killers and the Auger effect, as well as an additional cause, i.e., the thermal quenching

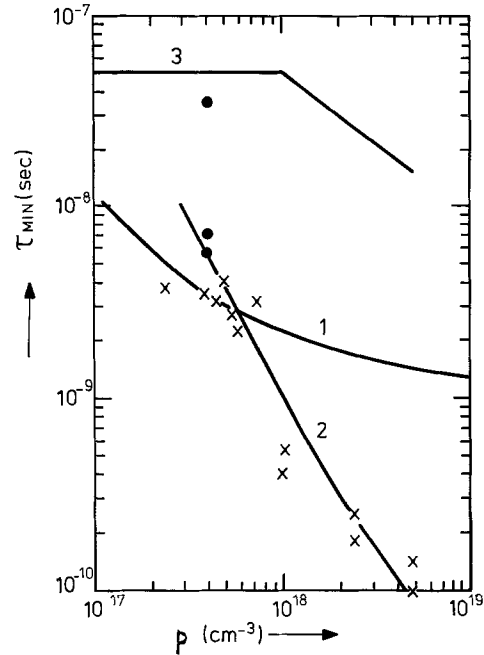


Fig. 5. The minority carrier lifetime ( $\tau_{MIN}$ ) as functions of the amount of zinc incorporated ( $[Zn]$ ). Curves 1 and 2 describe the cases of nonequilibrium and equilibrium incorporation of oxygen in GaP. Oxygen and zinc are involved in the formation of (ZnO) complexes which trap most of the minority carriers. Results obtained on our samples are indicated by crosses. Similar results of Ref. (14) are indicated by dots. Curve 3 represents the higher lifetime values of Ref. (18) measured on p-GaP(Zn) not containing intentionally added oxygen. In the calculation of curves 1 and 2 account was taken of the thermalization of the captured electrons which is important at low  $p$ .

which depends on the presence of killers. An extension of this discussion is now necessary to take account of the existence of two excited states of the luminescent center (4) as well as of the influence of the hole statistics which cause these states (the single electron and exciton states) to change into each other by the transfer of the exciton hole from and to the valence band. Figure 6 shows the relevant level and transition scheme. (See List of Symbols.)<sup>7</sup> Linearized expressions for  $\eta$  and  $\tau$  were derived in Ref. (1 and 2). The linearization is justified by the application of low excitation densities to the samples so as to avoid saturation of the luminescent centers. Various radiative and Auger transitions involving the luminescent centers have been discussed in Ref. (1-3). We shall only invoke the

<sup>7</sup> These symbols are the same as in Ref. (1-3) except that time constant  $\tau$  is replaced by its reciprocal, rate  $\gamma$ , for a more convenient statement of various equations.

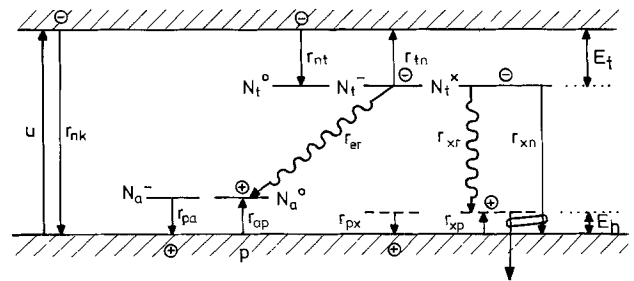


Fig. 6. Recombination model describing the three states of the (ZnO) complexes and various transitions in p-GaP(Zn, O). (See List of Symbols.) For the Auger effect ( $r_{xn}$ ) it is assumed that the exciton hole is the particle to carry off the transition energy (19). Two types of radiative transitions occur ( $r_{xr}$  and  $r_{er}$ ). The single electron transitions ( $r_{er}$ ) are negligible.

stronger ones, *i.e.*, the annihilation of the exciton states by radiation and by the Auger effect (rates  $r_{xr}$  and  $r_{xn}$ ). The resulting expression for  $\eta$

$$\frac{1-\eta}{\eta} = \frac{1-s}{s} + \frac{1-s}{s} \cdot \frac{p_h}{p} \cdot \frac{r_{tn}}{r_{xr}} + \frac{1}{s} \cdot \frac{B_0 p}{r_{xro}} \cdot \frac{g_a}{g_r} \quad [4]$$

is stated so as to expose the three causes of efficiency reduction mentioned above, each in terms of competition between two types of transition. The first term on the right-hand side is the killer term where  $s (= r_{nt}/[r_{nt} + r_{nk}])$  is the ratio of branching of the excited free electrons to the luminescent centers ( $N_t$ ). The loss through killers is enhanced by the thermal quenching. The second term is an extension of the first term by including the competition between the thermal emission ( $r_{tn}$ ), affecting the single electron states ( $N_t^-$ ), and the radiative transitions ( $r_{xr}$ ) of the exciton states ( $N_t^*$ ). This competition invokes the relative probabilities of finding these excited states, *i.e.*, respectively  $(1-f)$  and  $f$ . Assuming thermal equilibrium between these states these probabilities are represented by the factor  $p_h/p$ , a Boltzmann-type expression which depends on the ionization energy  $E_h$  of the exciton hole, the density of states of the valence band, and a degeneracy factor. The Auger effect ( $r_{xn}$ ) is expressed by the third term to be in competition with the radiation, rewriting their rates as  $B_0 \cdot p \cdot g_a$  and  $r_{xro} \cdot g_r$  to show the dependence on  $p$  and that on screening. The screening factors  $g_a$  and  $g_r$ , both being below unity, multiply the basic constants  $B_0$  and  $r_{xro}$ . The second and third terms, depending on  $p$ , allow 45° line approximations in a double log plot of  $(1-\eta)/\eta$  against  $p$ .

Figure 7 shows the experimental  $(1-\eta)/\eta$  results for the more efficient samples selected from Fig. 2. It is seen that for  $p$  above  $4 \cdot 10^{17} \text{ cm}^{-3}$  the experimental

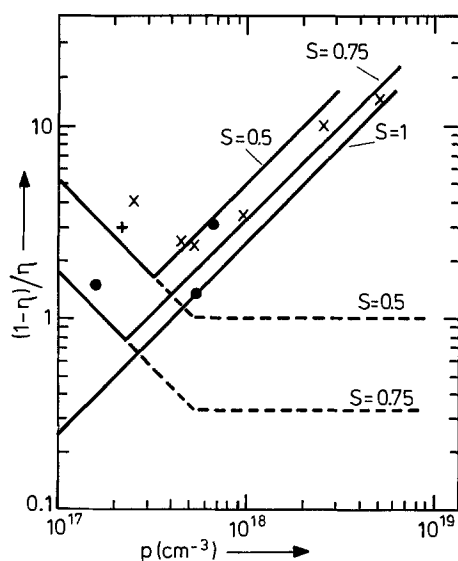


Fig. 7.  $(1-\eta)/\eta$  against  $p$ . The theory (Eq. [4]) is approximated here by sets of straight lines, having the free electron branching ratio  $s$  as the parameter. The lines with slope  $+1$  indicate the Auger effect to be the dominant effect in reducing the efficiency. The  $s$ -values indicated were assigned to the sets of lines, taking  $s = 1$  for the lower one. The lines with slope  $-1$  describe the detrimental effect of the thermalization of the captured electrons at low  $p$ . The horizontal lines describe the action of killers without assistance of this thermalization and are relatively unimportant. Most samples have high values of  $s$ , in most cases above  $1/2$ . The symbols have the same meaning as in Fig. 2. It is seen from this presentation of our experimental efficiency values that the combined action of the Auger and thermalization effects suggests an optimum  $p$ -value around  $4 \cdot 10^{17} \text{ cm}^{-3}$ . Incidentally this is also close to practical values for light emitting diodes.

points can be approximated by a straight line under 45° pointing to the dominance of the third term of Eq. [4]. This implies that the multiplier of  $p$  in this term is essentially constant. Excluding the possibility of covariance of  $s$  and  $g_a/g_r$  as functions of  $p$  it is fair to assume  $g_a/g_r = 1$ , as it was done in Ref. (1-2), and  $s = \text{constant}$ . Regarding  $s$  it is implausible to use a value much below unity. The reason for taking  $s \approx 1$  follows from the discussion of the minority carrier lifetimes in the next section; the trapping rate  $r_{nt}$  of the luminescent complexes, being proportional to  $[ZnO]$  which increases with  $p$ , would require the killer action to increase proportionally to maintain a constant value of  $s$  being smaller than unity. For such proportionality no plausible model is, however, known. Using then  $g_a/g_r = s = 1$  as fair conclusions (20) from the application of Eq. [4] to experiment,  $B_0/r_{xro}$  can be estimated at  $2.5\text{-}3.8 \cdot 10^{-18} \text{ cm}^3$ . Assuming the low temperature value of  $r_{xro}$ , being  $10^7 \text{ sec}^{-1}$  (6), to be applicable to GaP(Zn, O) at room temperature we obtain  $B_0 = 2.5\text{-}3.8 \cdot 10^{-11} \text{ cm}^3 \cdot \text{sec}^{-1}$ .

Figure 7 contains various broken line approximations of Eq. [4] using  $s$  as the parameter and  $B_0 = 2.5 \cdot 10^{-11} \text{ cm}^3 \cdot \text{sec}^{-1}$ . It is seen that for the values of  $s$  used the first term of Eq. [4] is unimportant. In contrast to the third term no confirmation can be found for the dependence on  $p$  of the second term, which gives the other (negative) 45° approximation, owing to the small number of samples for which  $p$  is known [including one measurement of Ref. (7)]. For these samples accidental killers may play a role giving rise to differences in  $s$ . Using values  $4.5 \cdot 10^6 \text{ sec}^{-1}$  for  $r_{tn}$  (2) and  $1.2 \cdot 10^{18} \text{ cm}^{-3}$  for  $p_h$  (to be discussed later) a few low- $p$  samples are still found to have  $s$  values in excess of 0.5.

We emphasize the following findings from Fig. 7, using Eq [4]. The loss through killers is unimportant above  $p = 4 \cdot 10^{17} \text{ cm}^{-3}$ , more so in comparison with the loss by the Auger effect. The basic rate constant of the Auger effect,  $B_0$ , was found to be  $\approx 3 \cdot 10^{-11} \text{ cm}^3 \cdot \text{sec}^{-1}$ , using these efficiency results only. The free electron branching ratio  $s$  is high, exceeding 0.5 for most samples and being probably equal to unity at high  $p$ . The screening by free holes affects the radiative and Auger transitions in about the same way. At  $p < 4 \cdot 10^{17} \text{ cm}^{-3}$  the killers predominate mainly through the thermal quenching (at room temperature).

In discussing the effects of screening we shall use a single screening factor,  $g$ , and express  $\eta$  in a different way<sup>8</sup>

$$\eta = s \cdot (r_r \cdot \tau) \quad [5]$$

where  $\eta$  is seen to be reduced below unity in two steps, *i.e.*, branching of the free electrons ( $s$ ) and branching between the radiative and all other transitions to which the electrons on the luminescent centers are subject. The former transitions (rate  $r_r$ ) and latter transitions constitute the decay rate  $1/\tau$ . Putting the observable quantities  $\eta$  and  $\tau$  on one side and re-expressing  $r_r$  by  $f \cdot g \cdot r_{xro}$  we obtain

$$\eta/\tau = s \cdot f \cdot g \cdot r_{xro} \quad [6]$$

$f$  being, as stated earlier, the probability of finding the excited luminescent center in the exciton state.

When  $s$  is known, using the findings on  $\eta$  of Fig. 7, it is possible to use Eq. [6] to obtain information on the screening. Figure 8 shows the experimental  $\eta/\tau$  results along with a theoretical curve to be discussed later in this section. According to the findings on  $\eta$ ,  $s$  is close to unity for  $p > 4 \cdot 10^{17} \text{ cm}^{-3}$ . Taking as before  $r_{xro} = 10^7 \text{ sec}^{-1}$  it is then immediately concluded that the product  $f \cdot g$  is of the order of 0.1-0.2 for most samples. In other words the radiative lifetime is then effectively 0.5-1  $\mu\text{sec}$ . Since  $f$  will be close to unity at

<sup>8</sup> See also Eq. [A5b] of Ref. (2); Ref. (5) contains a similar equation [8b].

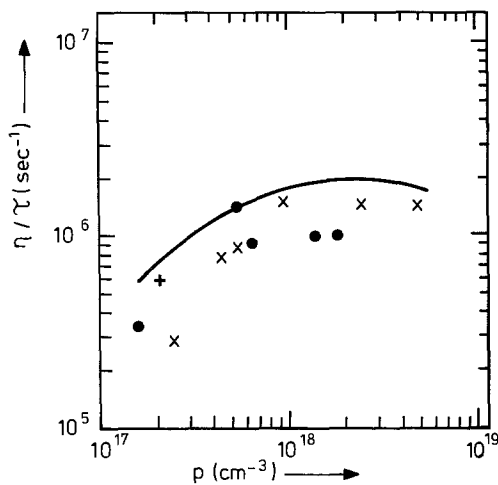


Fig. 8. Quantity  $\eta/\tau$  against  $p$ . This quantity is the free electron branching ratio,  $s$ , divided by the effective radiative lifetime,  $(f \cdot g \cdot r_{xro})^{-1}$  (see Eq. [6]). In view of the values  $r_{xro} = 10^7 \text{ sec}^{-1}$  [Ref. (6)] and  $s \approx 1$  this plot shows a strong action of the screening ( $g$ ) and the occupancy ( $f$ ) of the exciton hole level on the radiative transitions. The theoretical curve was calculated, using a mathematical approach for  $f$  and  $g$  and taking  $s = 1$ .

high  $p$  (in view of  $f = p/(p + p_h)$ ),  $g$  can therefore be estimated at, say, 0.2 implying a strong reduction of the transition probability by screening.

No confirmation of some screening model was found possible using the  $\eta/\tau$  findings. Known theories (1-3) employ a few parameters for which we could not obtain a unique set of values. Another consequence is that we are not well able to establish separate functions for  $f$  and  $g$ . The theoretical curve in Fig. 8 is based on an arbitrary mathematical approach of the screening effect. At the lower  $p$  values, however, where the screening should be weak ( $g \approx 1$ )  $f$  may be estimated leading to the value of  $p_h$  we have applied in the discussion of the  $(1 - \eta)/\eta$  results, i.e.,  $1.2 \cdot 10^{18} \text{ cm}^{-3}$ .

The considerations in this section depend critically on the assumption of a value for the basic quantity  $r_{xro}$ . In view of Eq. [4] the basic Auger rate constant  $B_o$  also depends on this assumption. It may be tried to reduce both quantities by a same factor in order to obtain an alternative interpretation for the findings of Fig. 7 and 8. The screening will then decrease and becomes absent when this factor is about 3. The fit of theory to Fig. 3 ( $\tau$  against  $p$ ) is, however, best using the accepted value for  $r_{xro}$ .

At this point it may be useful to comment on findings on Auger effect and screening by other workers. Assuming *a priori* certain values of the screening parameters  $B_o = 3 \cdot 10^{-11} \text{ cm}^3 \cdot \text{sec}^{-1}$  was arrived at in Ref. (2) while in Ref. (1 and 3) higher values were proposed, i.e., respectively  $5 \cdot 10^{-11}$  and  $10^{-10} \text{ cm}^3 \cdot \text{sec}^{-1}$ . The latter values must be considered too high, predicting a stronger decrease in efficiency with increasing  $p$  than we have actually found. The same conclusion applies to the value of  $5.5 \cdot 10^{-11} \text{ cm}^3 \cdot \text{sec}^{-1}$  we have derived from findings in Ref. (7). The latter result is rather surprising since in this reference no modifiable assumption could be found.

Various opinions on screening also exist differing mainly in the adjustment of parameters (1, 2). It was objected by Dapkus, Hackett, Lorimor, and Bachrach (21) that the screening as described in Ref. (2) would be too strong for the existence of "green" excitons (bound to isoelectronic nitrogen centers in GaP) at values of  $p$  above a few times  $10^{17} \text{ cm}^{-3}$ . The effect of screening was therefore deemed overestimated for both green and "red" excitons. Our results supporting those of Ref. (2), however, imply that the objection of

Ref. (21) is not justified with regard to the red excitons.

Concluding the discussion on screening it can be said that, using the  $(1 - \eta)/\eta$  and the  $\eta/\tau$  results in combination, plausible experimental evidence on the effect of screening on the red exciton annihilation could be obtained. This evidence shows this effect to be quite appreciable.

### Minority Carrier Lifetime and Oxygen Incorporation

In this section we try to deduce from the minority carrier lifetime results data on the oxygen incorporation. The connecting link between lifetime ( $\tau_{\text{MIN}}$ ) and this incorporation is provided by the (ZnO) complexes which act as capturing centers for the minority carriers (electrons).

Such deduction is complicated by the thermalization of the electrons from the (ZnO) complexes.  $\tau_{\text{MIN}}$  does therefore not arise from a simple addition of the trapping rates of the complexes and the killers ( $r_{nt}$  and  $r_{nk}$  of Fig. 1). Above a certain value of  $p$  the Auger effect will, however, dominate the thermalization, enabling this simple addition. It was also found that the killer action is probably weak for most samples (see preceding section). For large values of  $p$ ,  $\tau_{\text{MIN}}$  can therefore be approximated by the expression

$$\tau_{\text{MIN}}^{-1} = B_{nt} \cdot [\text{ZnO}] \quad [7]$$

where  $B_{nt}$  is the capture rate constant of the complexes. Assuming for  $B_{nt}$  a value of about  $10^{-8} \text{ cm}^3 \cdot \text{sec}^{-1}$  (22) it can be directly inferred from the experimental data (see Fig. 5) that  $[\text{ZnO}]$  can reach values up to  $10^{18} \text{ cm}^{-3}$ , a result that has not been thought probable before.

The remaining part of this section is concerned with the functional behavior of  $[\text{ZnO}]$  in order to provide insight in the oxygen incorporation. This incorporation and the complex formation which occur at different temperatures, i.e.,  $\approx 1000^\circ\text{C}$  and  $\approx 500^\circ\text{C}$ , are two problems of defect chemistry. At these temperatures zinc and oxygen, acting as acceptors and donors on the gallium and phosphorus sites, respectively, are completely ionized. Assuming that in their interaction these ion species remain on the sites mentioned and that no vacancies<sup>9</sup> are involved we shall apply for the complex formation a model by Wiley (23). This model uses the electrostatic binding energy of the two ion species to calculate the reaction constant in

$$[\text{Zn}^-] \cdot [\text{O}^+] = K_c \cdot [\text{ZnO}] \quad [8]$$

which is a first approximation. In the calculations we have followed the refinements in Ref. (23) taking non-nearest-neighbor complexes into account. Clearly data on  $[\text{Zn}]$  and  $[\text{O}]$  must be provided.  $[\text{Zn}]$  was applied as an independent variable. For  $[\text{O}]$  some theory is necessary. For such theory we tried ideas of Jordan, Trumbore, Wolfstirn, Kowalchik, and Roccasecca (24) who suggested that oxygen might be incorporated in an "equilibrium" or a "nonequilibrium" mode. This problem was also studied by Peters and Vink (25). In the nonequilibrium case the oxygen incorporation is assumed to be surface controlled owing to a fixed Fermi level at the surface (26). This implies a constant value of  $n$  in the reaction equation

$$n \cdot [\text{O}^+] = K_1 \cdot [\text{O}_{\text{source}}] \quad [9]$$

In the other case no such restriction on the incorporation occurs owing to, presumably, inclusions of  $\text{Ga}_2\text{O}_3$  which are forced into the solid GaP by a supersaturation of the Ga liquid with this oxide.<sup>10</sup> As it is proper for an equilibrium case the following equations are invoked to control the value of  $n$ , i.e.

$$n \cdot p = n_1^2 \quad [10]$$

<sup>9</sup> Lacking data on energy and charge state we have not taken the P- and Ga-vacancies into account.

<sup>10</sup> This occurred in the preparation of our LPE samples.

and the neutrality condition, neglecting other donors and acceptors

$$p + [O^+] = [Zn^-] + n \quad [11]$$

For the two cases of nonequilibrium and equilibrium incorporation theoretical curves were calculated for Fig. 5 using in both cases Eq. [8] and [9]. For the former case the quantities  $n$ ,  $K_1$  and  $[O_{source}]$  of Eq. [9] may be assumed to be constant for the LPE samples investigated. This implies a constant oxygen addition to the solid GaP; for curve 1  $[O^+] = 10^{17} \text{ cm}^{-3}$  was taken. With regard to the equilibrium case, curve 2, we have taken for the relevant quantities the following values:  $n_i = 1.6 \cdot 10^{17} \text{ cm}^{-3}$ ;  $K_1 \cdot [O_{source}] / n_i^2 = 0.4$ ; and  $B_{nt} = 10^{-8} \text{ cm}^3 \cdot \text{sec}^{-1}$ . Clearly the experimental data are best explained assuming the equilibrium mode of incorporation to occur. The steps in the calculation for the equilibrium case are illustrated in Fig. 9 which shows the dopant dependence of the various oxygen concentrations which are linked by Wiley's theory.

The above determination of the oxygen incorporated depends on the value taken for the capture rate constant  $B_{nt}$ . Other values are known, i.e., a value of  $\approx 4 \cdot 10^{-8} \text{ cm}^3 \cdot \text{sec}^{-1}$  that was derived from measurements of the decay time of the red luminescence by Jayson, Bachrach, Dapkus, and Schumaker (27), and a value of  $\approx 2 \cdot 10^{-8} \text{ cm}^3 \cdot \text{sec}^{-1}$  inferred from a transient capacitance study on a p-n junction by Lang (28), a more direct determination. Application of the latter value would reduce the concentration values of Fig. 9 by a factor of two to a first approximation. Lang also determined the concentration of the (ZnO) complexes and the O donors, i.e.,  $4.3\text{--}11 \cdot 10^{15} \text{ cm}^{-3}$  and  $1.1\text{--}1.9 \cdot 10^{16} \text{ cm}^{-3}$ , respectively, the latter value being supported by a photocapacitance study by Kukimoto, Henry, and Merritt (29) on the same sample. These concentration values are lower than the values predicted by Fig. 9 (for a zinc concentration of  $\approx 4 \cdot 10^{17} \text{ cm}^{-3}$ ), being  $\approx 3 \cdot 10^{16} \text{ cm}^{-3}$  and  $\approx 10^{17} \text{ cm}^{-3}$ , by a factor of five (or a factor of 2-3 using Lang's value for  $B_{nt}$ ). The discrepancy found above may, as also indicated in Ref. (25), be explained by differences in sample preparation.

### Conclusions

Measurements of the internal quantum efficiency which were carried out on samples of small size and

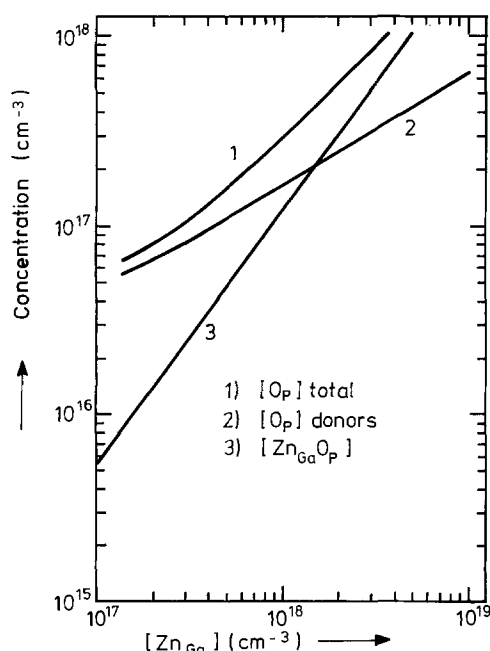


Fig. 9. Various concentrations of oxygen in GaP as function of  $[Zn]$  assuming the incorporation of O in GaP to take place in equilibrium. Curve 3 was used in Fig. 5 to describe  $\tau_{MIN}$ .

good transparency show an Auger effect to be the dominant cause of losses by nonradiative transitions above  $p \approx 4 \cdot 10^{17} \text{ cm}^{-3}$ . In addition the other nonradiative transitions, i.e., trapping by killers, become negligible. Below this  $p$  value the effect of the killers is noticeable owing to the thermalization of the minority carriers from the luminescent (ZnO) complexes. The better efficiency values are found in the lower  $p$  range with a maximum of  $\approx 40\%$ . A fairly direct determination was found possible for the rate constant of the Auger effect, i.e.,  $\approx 3 \cdot 10^{-11} \text{ cm}^3 \cdot \text{sec}^{-1}$ .

Using the decay time results in addition to the efficiency results screening by free holes was found to have an appreciable effect on both radiative and Auger transition probabilities of the excitons bound to the (ZnO) complexes. The theoretical interpretation does not allow a confirmation of a screening theory, however.

The measurement of the diffusion length against  $p$  provides an insight in the problem of the oxygen incorporation into GaP, the oxygen being connected with the main electron trapping centers, i.e., the (ZnO) complexes. The oxygen concentration increases with  $p$ , becoming  $\approx 10^{18} \text{ cm}^{-3}$  at  $p \approx 5 \cdot 10^{18} \text{ cm}^{-3}$ . This increase points to an equilibrium mode of oxygen incorporation in our samples which is presumably made possible by the presence of  $Ga_2O_3$  inclusions in the solid GaP during the crystal growth.

### Acknowledgments

The author is indebted to Dr. A. J. Bosman, Dr. A. T. Vink, and Mr. R. C. Peters of this laboratory and to Dr. R. N. Bhargava of the Philips Laboratories, North American Philips Corporation, for their helpful comments. Moreover he is grateful to Messrs. Vink and Peters for the preparation and part of the measurements of the samples. The assistance by Mr. P. H. J. M. Verberne, Mr. R. L. A. van der Heijden, and Mr. A. C. van Amstel is gratefully acknowledged.

Manuscript received Oct. 2, 1975. This was Paper 73 presented at the San Francisco, California, Meeting of the Society, May 12-17, 1974.

Any discussion of this paper will appear in a Discussion Section to be published in the December 1976 JOURNAL. All discussions for the December 1976 Discussion Section should be submitted by Aug. 1, 1976.

Publication costs of this article were partially assisted by Philips Research Laboratories.

### LIST OF SYMBOLS

$N_t$	concentration of the (ZnO) complexes
$N_t^0, N_t^-, N_t^x$	<i>idem.</i> , applying to the ground state, the single electron state, and the exciton state, respectively
$\tau_{nt}$ and $\tau_{tn}$	single-electron trapping and thermalization rates ( $\text{sec}^{-1}$ ). For $\tau_{tn}$ a value of $4.5 \cdot 10^6 \text{ sec}^{-1}$ was taken (2)
$E_t$	energy of binding the single electron to a complex, being approximately 0.3 eV and a parameter of $\tau_{tn}$
$B_{nt}$	rate constant of $\tau_{nt}$ and $\tau_{tn}$ , approximately $10^{-8} \text{ cm}^3 \cdot \text{sec}^{-1}$
$r_{nk}$	rate of the nonradiative transitions of the free electrons
$u$	generation rate ( $\text{cm}^{-3} \cdot \text{sec}^{-1}$ )
$r_{xn}$	exciton annihilation rate by the Auger effect which is proportional to $p$
$B$	rate constant ( $\text{cm}^3 \cdot \text{sec}^{-1}$ ) in $r_{xn} = B \cdot p$ , which is reduced by free hole screening, the basic rate constant being $B_0$
$r_{xr}$ and $r_{er}$	radiative rates for the excitons and the complex-acceptor pairs. $r_{xr}$ is also reduced by the screening from a basic rate $r_{xro}$ , its value being $10^7 \text{ sec}^{-1}$ [Ref. (6)]
$r_{px}$ and $r_{xp}$	rates of trapping and thermalization of the exciton hole, being proportional to $p$ and $p_h$ , respectively
$p$ and $p_h$	free hole concentration and effective valence band density of states, referred to

$E_h$  the exciton hole level.  $p_h$  is subject to the screening, which modifies the basic rate  $p_{ho}$ , for which the value of  $1.2 \cdot 10^{18} \text{ cm}^{-3}$  was taken. At low  $p$ ,  $p_h \approx p_{ho}$

$f$  exciton binding energy, being implicit in  $p_h \cdot E_h$  is reduced by screening from a basic energy  $E_{ho}$

$s$  occupancy of the exciton hole level

$g_a$  and  $g_r$  fraction of the excited free electrons captured by the (ZnO) complexes

screening factors, modifying the Auger and radiative transition probabilities. Usually replaced by single factor  $g$

## REFERENCES

- J. M. Dishman, M. DiDomenico, Jr., and R. Caruso, *Phys. Rev.*, **B2**, 1988 (1970).
- J. S. Jayson, R. N. Bhargava, and R. W. Dixon, *J. Appl. Phys.*, **41**, 4972 (1970).
- K. P. Sinha and M. DiDomenico, Jr., *Phys. Rev.*, **B1**, 2623 (1970).
- T. N. Morgan, B. Welber, and R. N. Bhargava, *ibid.*, **166**, 751 (1968); C. H. Henry, P. J. Dean, and J. D. Cuthbert, *ibid.*, **166**, 754 (1968).
- J. A. W. van der Does de Bye, *ibid.*, **147**, 589 (1966).
- J. D. Cuthbert, C. H. Henry, and P. J. Dean, *ibid.*, **170**, 739 (1968).
- C. H. Henry, R. Z. Bachrach, and N. E. Schumaker, *ibid.*, **B8**, 4761 (1973).
- H. G. Grimmeiss, W. Kischio, and H. Scholz, *Philips Tech. Rev.*, **26**, 156 (1965).
- R. C. Peters, "Proceedings of the Fourth International Symposium on GaAs and Related Compounds, Boulder, 1972," Institute of Physics, London, Conference Series No. 17, p. 55 (1973).
- L. J. van der Pauw, *Philips Res. Rept.*, **13**, 1 (1958).
- G. Iwantscheff, *Angew. Chem.*, **69**, 472 (1957).
- L. M. Foster, J. F. Woods, and J. E. Lewis, *Appl. Phys. Letters*, **14**, 25 (1969).
- M. Klerk, (this laboratory), Unpublished results.
- W. H. Hackett, Jr., R. H. Saul, R. W. Dixon, and G. W. Kammlott, *J. Appl. Phys.*, **43**, 2857 (1972).
- L. M. Bollinger and G. E. Thomas, *Rev. Sci. Instr.*, **32**, 1044 (1961).
- J. A. W. van der Does de Bye, A. C. P. van den Bosch, C. M. Hart, M. Saitoh, A. Slob, and P. Verhoog, *ibid.*, **43**, 1468 (1972).
- F. Stern, *Appl. Opt.*, **3**, 111 (1964); M. R. Lorenz and G. D. Pettit, *J. Appl. Phys.*, **38**, 3983 (1967); W. B. Joyce, R. Z. Bachrach, R. W. Dixon, and D. A. Sealer, *J. Appl. Phys.*, **45**, 2229 (1974).
- R. Z. Bachrach and O. G. Lorimor, *J. Appl. Phys.*, **43**, 500 (1972); P. D. Dapkus, W. H. Hackett, Jr., O. G. Lorimor, G. W. Kammlott, and S. E. Haszko, *Appl. Phys. Letters*, **22**, 227 (1973).
- G. F. Neumark, *Phys. Rev.*, **7**, 3802 (1973).
- J. A. W. van der Does de Bye and A. T. Vink, *J. Luminescence*, **5**, 108 (1972), supporting the high  $s$  values.
- P. D. Dapkus, W. H. Hackett, O. G. Lorimor, and R. Z. Bachrach, *J. Appl. Phys.*, **45**, 4920 (1974).
- J. A. W. van der Does de Bye, Unpublished results.
- J. D. Wiley, *J. Phys. Chem. Solids*, **32**, 2053 (1971).
- A. S. Jordan, F. A. Trumbore, K. B. Wofstirn, M. Kowalchik, and P. P. Roccasecca, *This Journal*, **120**, 791 (1973).
- R. C. Peters and A. T. Vink, Paper presented at the 5th International Symposium on GaAs and Related Compounds, September 1974, Deauville, France.
- K. H. Zschau and A. Vogel, "Proceedings of the Third International Symposium on GaAs and Related Compounds, Aachen, Germany, 1970," Institute of Physics, London, Conference Series No. 9, p. 100.
- J. S. Jayson, R. Z. Bachrach, P. D. Dapkus, and N. E. Schumaker, *Phys. Rev.*, **B6**, 2357 (1972).
- D. V. Lang, *J. Appl. Phys.*, **45**, 3014, 3023 (1974).
- H. Kukimoto, C. H. Henry, and F. R. Merritt, *Phys. Rev.*, **B7**, 2486 (1973).

## Sulfur Hexafluoride Etching Effects in Silicon

L. J. Stinson\*

Hewlett Packard Associates, Palo Alto, California 94304

and J. A. Howard and R. C. Neville

Department of Electrical Engineering and Computer Science,  
University of California, Santa Barbara, California 93106

### ABSTRACT

The performance of sulfur hexafluoride as an *in situ* etchant for silicon during epitaxial growth processes has been examined as a function of temperature and partial pressure. Below 1060°C etching was preferential, producing pitted substrates, while above 1060°C etching was smooth. However, above 1060°C, both the SiO<sub>2</sub> masking layers on the substrates and the quartz reactor walls were attacked during the etching of the silicon. This occurred in both helium and hydrogen ambients. High resistivity silicon substrates were etched *in situ* with SF<sub>6</sub>. Silicon epitaxial layers were deposited subsequent to *in situ* etching with SF<sub>6</sub>. Both etched substrates and etched substrates with epitaxial layers were examined optically for the presence of active sulfur donor sites. The concentration of active sulfur donor sites resulting from etching with SF<sub>6</sub> was found to be less than  $1 \times 10^{13} \text{ cm}^{-3}$  in both the etched substrates and the silicon layers deposited subsequent to SF<sub>6</sub> etching.

As modern semiconductor devices have grown in complexity and performance, it has become increasingly important to reproducibly grow high-quality

silicon epitaxial layers on silicon or sapphire substrates. Since semiconductor devices are usually fabricated in the epitaxial layer, the critical physical processes which determine the electronic characteristics of these devices take place in the epitaxial layer. This close relationship between semiconductor device

\* Electrochemical Society Active Member  
Key words: silicon etching, epitaxial deposition, impurities, silica etching, sulfur hexafluoride.



performance and the physical nature of the epitaxial layer makes work toward improving this incompletely understood process worthwhile.

In the ideal situation, the epitaxial deposition process gives control over the dopant concentration profile while maintaining a high degree of perfection in the crystalline structure of the deposited material. In order to adequately accomplish this task it is necessary that the surface layers of the substrate be essentially ideal. The introduction of an etchant before silicon epitaxial deposition has been used to obtain better uniformity in the deposited layer thickness (1). Surface oxides, films, and mechanical damage on the substrates can introduce severe perturbation into the crystal structure if they are not removed prior to epitaxial growth. Because of this, substrates are etched *in situ* by vapor etching prior to epitaxial deposition. The vapor etchants which have been reported to be suitable for this purpose are  $\text{Cl}_2$  (2),  $\text{HI}$  (3),  $\text{HBr}$  (4),  $\text{HCl}$  (3, 5),  $\text{H}_2\text{S}$  (6, 7),  $\text{SF}_6$  (8), and water vapor (9).

Although hydrogen chloride is the etchant most commonly used for this purpose, the high temperature required (1100°-1200°C) and the transport of impurities by  $\text{HCl}$  cause severe impurity redistribution problems (10-12). In addition, the highly corrosive nature of  $\text{HCl}$  causes expensive periodic replacement of gas regulators, mass flow controllers, lines, etc. Gupta has found that even the introduction of very small amounts of  $\text{HCl}$  degrades both the surface of the deposited layer and the impurity concentration profile. The undesirable characteristics of  $\text{HCl}$  has led to the investigation of alternate sources of a less corrosive etchant which will allow etching at a lower temperature. Of the etchants which have been investigated  $\text{SF}_6$  seems to be most promising for this and many other applications in semiconductor processing. Many of these applications and the physical and thermodynamic properties of sulfur hexafluoride have recently been reviewed by Adler and Yaws (14).

Rai-Choudhury (8) has investigated the feasibility of utilizing  $\text{SF}_6$  as a low temperature *in situ* etchant for the Si epitaxial deposition process. The reported results indicated that the etched surfaces were very smooth and the subsequently deposited silicon layers were high quality. The entire etching and deposition process could be carried out at temperatures less than 1100°C.

Gupta (13) has suggested the use of sulfur hexafluoride during epitaxial growth at low concentrations to improve epitaxial deposition uniformities since sulfur hexafluoride gives good surfaces at lower temperatures and does not degrade the impurity concentration profile as severely as  $\text{HCl}$ . Although  $\text{SF}_6$  appears to be quite promising, little has been reported about the effects on the electrical and optical properties of sulfur doping in the epitaxial layer resulting from etching with  $\text{SF}_6$ . The diffusion rate of sulfur in silicon is quite rapid,  $1 \times 10^{-8}$   $\text{cm}^2/\text{sec}$  at 1100°C and  $2 \times 10^{-9}$   $\text{cm}^2/\text{sec}$  at 1000°C (15). The maximum solubility of sulfur in silicon has been reported by Carlson *et al.* (15) to be  $3 \times 10^{15}$  atoms/ $\text{cm}^3$ , easily high enough to significantly affect the electrical behavior of the deposited layers. Sulfur is a two level donor in silicon with energy levels at 0.18 and 0.37 eV below the conduction band edge (16). The properties of these donor states have been studied both experimentally (16, 17) and theoretically (18, 19). The hole capture cross section is small, but electrons are easily captured.

It is the purpose of this study to investigate the performance of  $\text{SF}_6$  as an *in situ* etchant for the silicon epitaxial deposition process and to investigate the effect of sulfur doping on the characteristics of the deposited material.

### Experimental Procedure

Silicon wafers were etched with  $\text{SF}_6$  *in situ* in an epitaxial reactor over a wide range of temperatures and  $\text{SF}_6$  partial pressures. The epitaxial reactor used

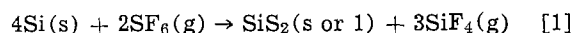
for this work consisted of a 20 kW, computer-controlled RF (450 kHz) heated horizontal reactor with a 3 in. diam round tube configuration which was cooled by forced air. The silicon wafers were mounted on a silicon carbide coated graphite susceptor which was adjusted to provide optimum flow characteristics for uniform layer etchant or growth characteristics. The sulfur hexafluoride was injected into the main gas stream of palladium purified hydrogen. The reactant flow rates were monitored and controlled with automatic mass flow controllers accurate to within 2%. The substrate surface temperatures were directly monitored with an infrared radiometer viewing normal to the wafer surface. The temperature readings were corrected for emissivity errors and absorption losses. The silicon wafers were (1, 1, 1) oriented,  $\sim 50$  ohm-cm p-type with acceptor concentration (boron) of  $1.0\text{-}1.5 \times 10^{14}$   $\text{cm}^{-3}$ . The wafers were mechanically and chemically polished. To minimize substrate surface contamination, a thorough cleaning and degreasing procedure was given the wafers prior to entering the reactor.<sup>1</sup> The etch rates were measured by weight loss techniques using an analytical balance accurate to 20  $\mu\text{g}$ . The etched surfaces were examined under a scanning electron microscope for evidence of preferential etching or pitting.

After a suitable range in temperatures and  $\text{SF}_6$  partial pressures was found, a series of silicon wafers, coated with thermally grown oxide and strips of the oxide removed by standard photoresist and etch techniques, was etched in  $\text{SF}_6$ . These wafers were examined under a scanning electron microscope to make qualitative measurement of the degree of attack and of undercutting of the oxide masks by the  $\text{SF}_6$ . In addition, other wafers without the oxide were etched and several microns of silicon deposited over the layers using  $\text{SiH}_4$  as the silicon source. These were also examined under the scanning electron microscope for the presence of crystal defects. Defects would indicate an inadequate removal of surface impurities or of preferential etching.

The samples were optically studied for the evidence of sulfur doping using a MacPherson monochromator in the experimental setup described in the Appendix. Samples were prepared by lapping the back (non-doped) side of each slice and then etching it down in silicon etch to a thickness of 3-8 $\mu$ . Transmission samples were placed with one flat side perpendicular to the beam between the output slit and the photomultiplier tube. Measurements were taken for wavelengths from 12.0 to 1.0 $\mu$  in search of evidence of active sulfur donor sites.

### Results

Sulfur hexafluoride etches silicon according to the reaction



The free energy of the reaction is -706.81 kcal/mole at 1400°C (11). Thus sulfur hexafluoride etches silicon spontaneously and irreversibly producing volatile sulfides and fluorides of silicon.

The silicon etch rate dependence on temperature found is shown in Fig. 1 for a  $\text{SF}_6$  concentration of 0.1%. As indicated in Fig. 1, the etch rate tends to level off at a value determined by either the mass transfer of the reactants to the substrate surface or by the mass transfer of the reaction byproducts away from the surface. For temperatures less than 1100°C and a fixed partial pressure of  $\text{SF}_6$  the etch rate ( $R'$ ) dependence on temperature is as given in Eq. [2]

$$R' \propto \exp\left(\frac{-Ea}{RT}\right) \quad [2]$$

In the foregoing expression,  $Ea$  is the activation energy, determined to be  $\sim 17$  kcal/mole,  $R$  is the gas constant, and  $T$  is the absolute substrate temperature.

<sup>1</sup> The cleaning process involved immersion in transistor grade TCE, acetone, and methyl alcohol with a 15 min boil in nitric acid.

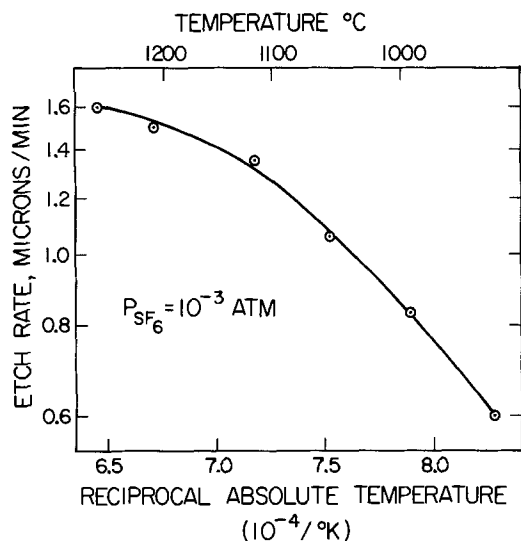


Fig. 1. Silicon etch rate vs. substrate temperature for  $SF_6$  pressure of  $10^{-3}$  atm.

Sulfur hexafluoride etching was found to be preferential for temperatures of  $1050^{\circ}C$  and below over an  $SF_6$  concentration range of 0.01-0.1% by volume. The preferential etching produced cloudy surfaces, which, as revealed by scanning electron microscopy, were the result of pitting. A typical substrate surface which was etched at a temperature below  $1050^{\circ}C$  is shown in Fig. 2. The etchant is judged unsuitable for use at temperatures below  $1050^{\circ}C$  due to the morphology problems which would result from epitaxial deposition on such a pitted surface.

The silicon etch rate dependence on  $SF_6$  partial pressure was characteristic of a first-order reaction with the etch rate being approximately directly proportional to the  $SF_6$  partial pressure. The silicon etch rate de-

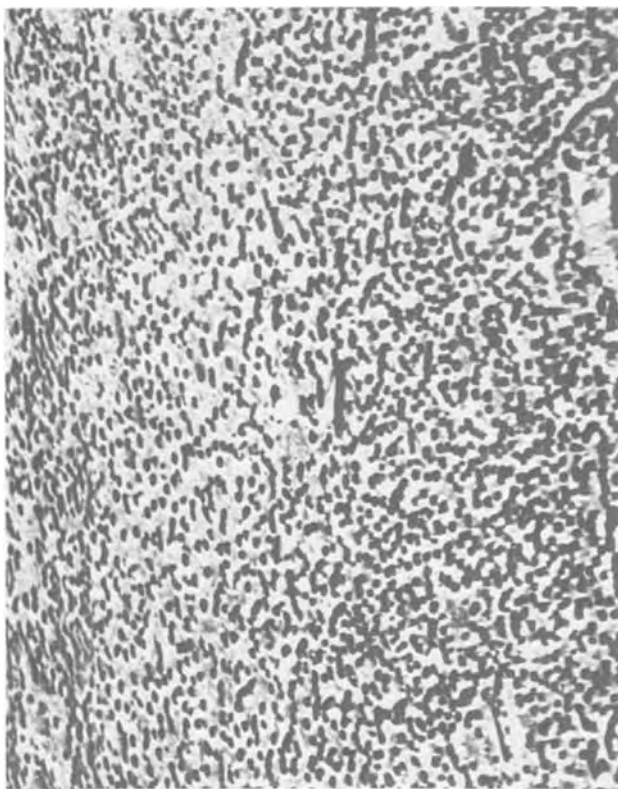


Fig. 2. Pitted substrate surface from  $SF_6$  etching at  $T < 1050^{\circ}C$ . Scanning electron microscope at a magnification of  $80\times$ .

pendence on  $SF_6$  partial pressure for a substrate temperature of  $1060^{\circ}C$  is shown in Fig. 3. As indicated on Fig. 3, the  $SF_6$  partial pressure range investigated was from  $10^{-4}$  to  $10^{-3}$  atm.  $SF_6$  partial pressures of less than  $10^{-4}$  atm were not used since the etch rate was too low to be of economic interest. Increasing the  $SF_6$  concentration above  $10^{-3}$  atm resulted in a white fibrous growth of material along the gas exit end of the susceptor. The use of higher carrier gas velocities ( $\sim 100$  cm/sec) to sweep away the reaction byproducts was found to be effective for reducing the amounts of the deposits. Etching at  $SF_6$  partial pressures of  $10^{-4}$ - $10^{-3}$  atm resulted in no observable deposits on either the reactor chamber or the substrate.

Etching at temperatures above  $1060^{\circ}C$  produced smooth mirrorlike surfaces. Epitaxial layers subsequently deposited on the silicon surfaces which were etched at temperatures greater than  $1060^{\circ}C$  were of high quality with a stacking fault density of  $< 2/cm^2$ . Although etching produced smooth surfaces at the higher temperatures, the oxide masks on each wafer and quartz reactor walls were attacked. Repeated etching with  $SF_6$  resulted in frosting the quartz reactor tube in the warmest areas surrounding the susceptor. This was, however, a slow process requiring a period of several months (approximately 20-30 runs) before any reactor tube had to be discarded. This may not present a problem in those cases where a water-cooled reactor tube is used.

The  $SF_6$  attack of the oxide mask presents a more serious problem. At a substrate temperature of  $1275^{\circ}C$  and  $SF_6$  concentration of 0.06% the oxide attack was of such severity that a half-micron oxide mask was entirely consumed in approximately 2.0 min. Reducing the  $SF_6$  concentration to 0.01% resulted in a somewhat lower oxide etch rate. However, the half-micron thick oxide layer was consumed in approximately 7 min. Reducing the substrate temperature to  $1100^{\circ}C$ , approaching the minimum temperature of interest, resulted in a more preferential etching of the oxide and again within about 15 min the  $SF_6$  had penetrated the mask to the silicon underneath. The oxide etch rate was found to be more sensitive to temperature than to  $SF_6$  concentrations but even at the lower temperatures was at least an order of magnitude higher than the maximum allowable. Etching in a helium ambient to eliminate the possibility of HF formation and subsequent attack of the oxide yielded no apparent change. Again the half-micron thick oxide was penetrated in less than 7 min. Etching in both ambients is consistent with the model holding that the fluorine ion is responsible for the oxide attack. A typical oxide which had undergone  $SF_6$  attack in a helium ambient is shown in Fig. 4 at the point of ultimate failure of the oxide mask.

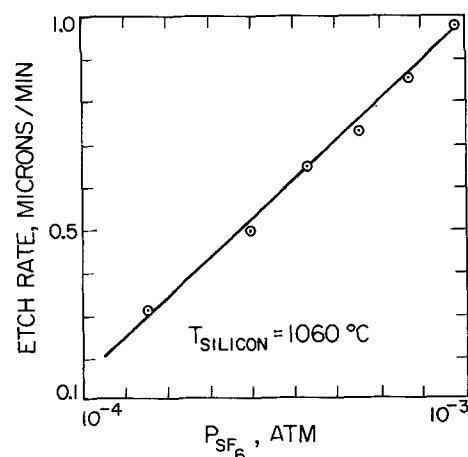


Fig. 3. Silicon etch rate vs.  $SF_6$  partial pressure

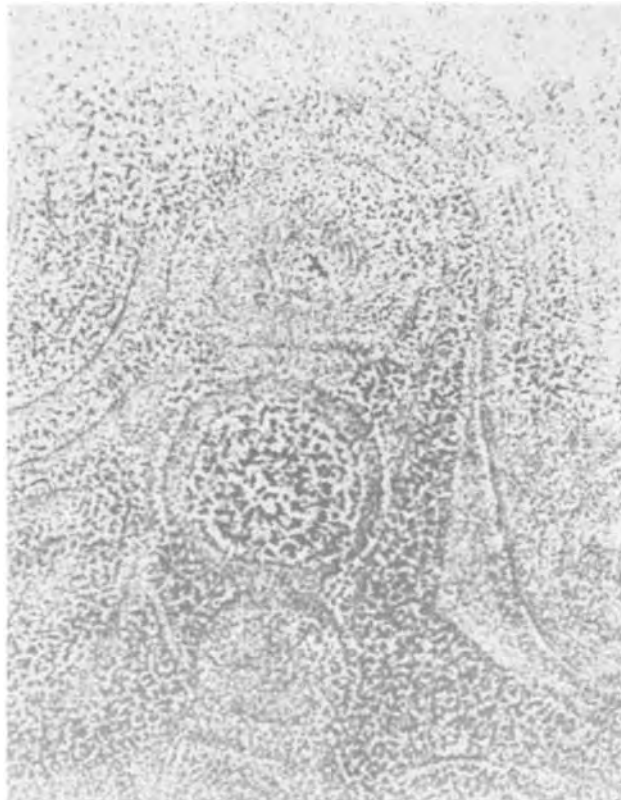


Fig. 4. Silica mask attack by  $\text{SF}_6$  in He ambient. Scanning electron microscope at a magnification of  $120\times$ .

As a result of the work, we judge that most sulfur hexafluoride etching will take place between  $1050^\circ$  and  $1100^\circ\text{C}$  in order to strike a balance between preferential etching and the effects such as outdiffusion, autodoping, etc. brought on by high temperature operations. At these temperatures the diffusion constant,  $D$ , will be in the  $5\text{--}10 \times 10^{-9} \text{ cm}^2/\text{sec}$  range and the maximum sulfur concentration in the silicon will lie close to  $10^{15}/\text{cm}^3$ .

High resistivity p-type silicon wafers with acceptor (boron) concentrations of  $1\text{--}1.5 \times 10^{13}/\text{cm}^3$  were etched in the temperature range of  $1050^\circ$  and  $1100^\circ\text{C}$ . Testing for the presence of active sulfur donors was done optically using a MacPherson monochromator in the procedure described in the Appendix. Measurements were taken for wavelengths from  $12.0$  to  $1.0\mu$ . No evidence of an active sulfur donor was found in either the etched substrates or in the deposited epitaxial layers. A slice of the original p-type material was placed in a small furnace and sulfur diffused at  $1100^\circ\text{C}$  for 16 hr. It was prepared for transmission measurements and the presence of sulfur at both  $0.18$  and  $0.37 \text{ eV}$  was observed. A capacitance-voltage analysis of gold and aluminum Schottky barriers on epitaxial layers deposited on  $\text{SF}_6$  etched substrates gave no indication of the presence of sulfur. We conclude that after sulfur hexafluoride etching sulfur is not present in silicon in amounts greater than  $1 \times 10^{13}/\text{cm}^3$ .

### Summary

In summary, sulfur hexafluoride was found to be an effective etchant for *in situ* etching of silicon at substrate temperatures above  $1060^\circ\text{C}$ . The low etching temperatures of this process, together with deposition from silane, allow the complete epitaxial deposition operation to take place at temperatures of less than  $1100^\circ\text{C}$ . The attack on the oxide masks by this etchant over the temperature range required for nonpreferential etching renders the etchant unusable in those instances where localized etching and deposition are desired. Measurement of sulfur doping in either sub-

strates etched with  $\text{SF}_6$  or in silicon epitaxial layers deposited subsequent to *in situ* etching with  $\text{SF}_6$  indicated that sulfur was not present down to the detection limit of the measurement technique ( $\sim 10^{13}/\text{cm}^3$ ).

Manuscript submitted Aug. 25, 1975; revised manuscript received Nov. 12, 1975. This was Paper 97 presented at the Chicago, Illinois, Meeting of the Society, May 13-18, 1973.

Any discussion of this paper will appear in a Discussion Section to be published in the December 1976 JOURNAL. All discussions for the December 1976 Discussion Section should be submitted by Aug. 1, 1976.

## APPENDIX

### Optical Transmission Measurements

A schematic of the optical experimental apparatus is shown in Fig. 5. Input power from a Jarrell-Ash light source cooled by a small electric fan is modulated by a 200-Hz Bulova chopper. A single-grating MacPherson monochromator selects the wavelength and the beam passes through the quartz beam-splitter at A. The reflected beam (about 2% of the input power above  $3000\text{\AA}$ ) is measured with a United Detector Technology u.v.-sensitive silicon photodetector (Model 500-UV) B, and the transmitted beam strikes the output mirror C, and is reflected through the output slit D, and into the photomultiplier tube E. The photomultiplier output is processed by a PAR lock-in amplifier.

Calibration measurements were made with no samples in the path of the beam. The beam-splitter at A introduces three possible sources of error in the measurements. The first of these is caused by the approximately  $40^\circ$  angle between the beam direction and the normal to the quartz plate. This causes an effective shift in wavelength which is a function of the angular dispersion  $A$  of the monochromator grating, the angle of incidence on the beam-splitter, the beam-splitter thickness  $t$ , and the index of refraction  $n$  of the quartz. The path difference  $\Delta$  introduced by the beam-splitter is shown in Fig. 5, and is given by Snell's law (assuming the index of refraction of air is unity) as  $\Delta = (t \sin \theta)/n$ . For a  $1/16$  in. quartz slide this gives a  $\Delta$  of  $6.2 \times 10^{-4}m$ . (The index of refraction of quartz is approximately 1.55 throughout the visible and near infrared regions.) The angular dispersion of the grating is given by

$$\frac{\Delta\phi}{\Delta\lambda} = \frac{m}{d \cos \phi}; \quad \Delta\phi = \frac{d\Delta\phi \cos \lambda}{m} \quad [\text{A-1}]$$

Here  $d$  is the grating spacing and  $m$  is the order number of the spectrum. The worst-case shift is in the first-order spectrum. The path length,  $L$  from grating to beam-splitter is  $1.58$  met and hence  $\Delta\phi$ , the angular separation of the reflected spectral lines, is  $t/L = 1.01 \times 10^{-3}$  rad. The approximate angle of reflection from the grating is  $15^\circ$ , so a calculation yields  $\Delta\lambda = 16\text{\AA}$ . This is a function of wavelength and must be applied to the lock-in amplifier output spectrum. The corresponding energy error is  $0.005 \text{ eV}$ .

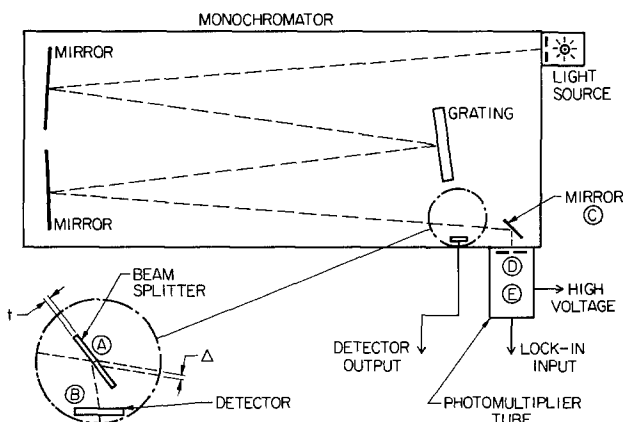


Fig. 5. Optical measurement apparatus

The second error due to the beam-splitter is a result of the finite width of the photodetector. Fluctuations in amplitude of the light source output cause fluctuations in detector output over a bandwidth of wavelengths given by Eq. [A-1]. The angular separation  $\Delta\phi$  is calculated using  $L$  as before and  $W$ , the detector width, as  $0.5 \text{ in.} = 1.3 \times 10^{-2}$ . Calculating as before the value  $\Delta\lambda = 120\text{\AA}$  is obtained. Thus a variation in intensity of the light source over the range  $\lambda - \Delta\lambda$  to  $\lambda + \Delta\lambda$  will be measured by the detector while the monochromator output signal will respond only to changes in the intensity over the wavelength range covered by the slit. This will not cause significant error provided the percentage change in intensity output of the lamp is constant with wavelength over the range  $\lambda - (\Delta\lambda/2)$  to  $\lambda + (\Delta\lambda/2)$ . Since the fluctuations in light source intensity were observed to be of a short-term, random nature (by measuring light source output with the photomultiplier tube at constant wavelength every 10 sec for 15 min and every 15 min thereafter for 2 hr) rather than statistical fluctuations as in Johnson noise, then it is assumed that the variations in intensity result from power supply transients. Thus it can reasonably be assumed that the relative intensity distribution will not change over the range  $\lambda - (\Delta\lambda/2)$  to  $\lambda + (\Delta\lambda/2)$ , only the total intensity will vary.

The final possible error resulting from insertion of the beam-splitter occurs in wavelength regions where the rate of change of the quartz transmission coefficient with frequency is much greater than the light source intensity variation. The transmission is constant at wavelengths greater than  $3300\text{\AA}$ , the region used.

The minimum amount of sulfur detectable by the system was determined as follows: Several samples of silicon were prepared by pulling (111) oriented ingots from melts containing a known amount of sulfur. The maximum solubility of sulfur in silicon is approximately  $4 \times 10^{16}$  (20) and the calculated concentrations of sulfur in the test ingots was kept well below this ( $10^{14}$ ,  $10^{13}$ ,  $10^{12}$ , and  $10^{11}/\text{cm}^3$ ). Samples from each of these ingots were placed in the beam of the monochromator and a search made for the absorption peaks at 0.18 and 0.37 eV. Evidence was strong at the  $10^{14}/\text{cm}^3$  and slight at the  $10^{13}/\text{cm}^3$  impurity concentrations. No evidence was seen at  $10^{12}$  or  $10^{11}/\text{cm}^3$ . A cross check was then made by using sample wafers into which sulfur diffusions had been made. The diffusion

profile was calculated for the sulfur and the wafers polished down to the regions of desired maximum sulfur concentration. For samples with sulfur concentration ranging from  $10^{14}$  to  $10^{13}/\text{cm}^3$  we could observe absorption with the monochromator. With samples with sulfur concentrations between  $10^{13}$  and  $10^{12}/\text{cm}^3$  we could observe some slight absorption and none at all was observable for any sample with maximum concentration below  $8 \times 10^{12}/\text{cm}^3$ . (For the UCSB monochromator system and using 3-8 mm thick samples we find the minimum detectable sulfur concentration to be  $10^{13}/\text{cm}^3$ .)

#### REFERENCES

1. W. K. Burton, N. Cabrera, and F. C. Frank, *Phil. Trans. Roy. Soc. London, Ser. A*, **243**, 299 (1951).
2. J. P. Dismukes and R. Ulmer, *This Journal*, **118**, 634 (1971).
3. T. H. Chu, G. A. Gruber, and R. Stickler, *ibid.*, **113**, 156 (1966).
4. L. V. Gregor, P. Balk, and F. J. Campagna, *IBM J. Res. Dev.*, **9**, 327 (1965).
5. G. A. Lang and T. Stavish, *RCA Rev.*, **24**, 488 (1963).
6. P. Rai-Choudhury and A. J. Noreika, *This Journal*, **116**, 539 (1969).
7. T. L. Chu, *ibid.*, **115**, 1207 (1968).
8. P. Rai-Choudhury, *ibid.*, **118**, 266 (1971).
9. T. L. Chu and R. L. Tallman, *ibid.*, **111**, 1306 (1964).
10. D. C. Gupta and R. Vee, *ibid.*, **116**, 1561 (1969).
11. S. E. Mayer and D. E. Shea, *ibid.*, **111**, 550 (1964).
12. W. H. Shepherd, *ibid.*, **115**, 652 (1968).
13. D. C. Gupta and J. L. Porter, *Nat. Bur. Std., Special Publication No. 337* (Nov. 1970).
14. L. S. Adler and C. L. Yaws, *Solid State Technol.*, **18**, 35 (1975).
15. R. O. Carlson, R. N. Hall, and E. M. Pell, Jr., *Phys. Chem. Solids*, **8**, 81 (1959).
16. A. A. Lebedev, N. A. Saltonov, and V. M. Tachkevich, *Fiz. Tekh. Poluprov.*, **5**(1), 31 (1971).
17. A. A. Lebedev, A. T. Mamadalina, and N. T. Saltanaov, *ibid.*, **5**(1), 17 (1971).
18. T. H. Ning and C. T. Sheh, *Phys. Rev.*, **B4**, 3482 (1971).
19. T. G. Castner, Jr., *ibid.*, **B3**, 4911 (1970).
20. F. A. Trambore, *Bell System Monograph* 3483 (1960).

## Nucleation of $\text{Al}_2\text{O}_3$ Layers on Cemented Carbide Tools

J. N. Lindström and R. T. Johannesson<sup>1</sup>

Sandvik AB, Coromant Research Center, S-126 12 Stockholm 42, Sweden

#### ABSTRACT

Aluminum oxide was deposited with a CVD technique onto polished TiC-coated and uncoated cemented carbide substrates. Experiments of short duration were performed with varying process parameters. The density of  $\text{Al}_2\text{O}_3$  nuclei on the (Ti, W)C phase in cemented carbide and on the TiC coating was measured for each experiment. The corresponding chemical equilibria of the gas phase were calculated. The supersaturations of reactants ( $p_{i,\text{in}}/p_{i,\text{eq}}$ ) were compared with the nuclei densities. It was found that the densities of nuclei vary with the supersaturation of the oxygen donors ( $\text{CO}_2$  and  $\text{H}_2\text{O}$ ). In these experiments there was a relative shortage of oxygen donors. The early stage of the  $\text{Al}_2\text{O}_3$  deposition is supposed to influence the adhesion of the coating in two ways. First, voids that form in the cemented carbide substrate surface during heating up may cause pores, which decrease the strength of the interface. Second, too sparse a nucleation weakens the bond between the coating and the substrate. By using TiC-coated cemented carbide as the substrate it is possible to avoid the void formation and to obtain an evenly distributed nucleation.

For half a decade  $5 \mu\text{m}$  CVD titanium carbide layers deposited on cemented carbide cutting tools have proved their efficiency in increasing the wear resist-

ance, especially in turning operations (1-3). Titanium nitride, carbonitride, and similar compounds have also been used (4).

The improvements achieved by these thin layers seem to be caused mainly by the retardation of chemical processes contributing to the wear, especially dif-

<sup>1</sup>Present address: Linköping University, S-581 83 Linköping, Sweden.

Key words: chemical vapor deposition, titanium carbide, supersaturation, density of nuclei, whiskers.

fusion and oxidation. Thus in the case of uncoated tool tips the workpiece tends to react with the cemented carbide binder (cobalt alloy) at the high cutting temperatures of about 1000°C. Therefore the chemically resistant oxide layers, e.g., aluminum oxide ought to be even more suitable for this application than carbides and nitrides.

The important question in the production of coatings is which of the parameters are the critical ones in the control of the nucleation process and of the growth process. The supersaturation is such an important factor for the growth morphology of whiskers as shown by Campbell (5). It may be regarded as a measure of the driving force of the nucleation process (6-7).

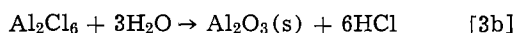
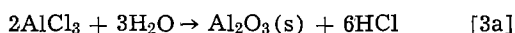
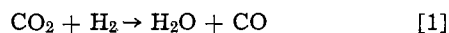
The nucleation in turn is important and often critical in determining the adhesion and the kind of subsequent growth of a desired layer. Therefore the influence of supersaturation on the nucleation process for aluminum oxide onto cemented carbide has been studied in our laboratory (8) and elsewhere (9). The nucleation on the multiphase cemented carbide substrate was found to be different on the different phases in the surface at given process conditions.

A possibility for avoiding this difficulty is to deposit an Al<sub>2</sub>O<sub>3</sub> layer using an intermediate TiC coating. The purpose of the present work is to study empirically the interaction between supersaturation (different process conditions) and nucleation on TiC-coated cemented carbides compared with uncoated cemented carbide in the pilot plant scale.

### Experimental

**Equilibrium calculations.**—Among the different conventional systems possible to use for depositing Al<sub>2</sub>O<sub>3</sub> coatings, the H<sub>2</sub>O/AlCl<sub>3</sub> system seems to be too reactive (9, 10), whereas the O<sub>2</sub>/AlCl<sub>3</sub> system is very slow (10). Therefore the experiments were done in the system CO<sub>2</sub>/H<sub>2</sub>/AlCl<sub>3</sub>.

The components of the following reactions were considered



Due to the relatively moderate deposition temperatures used (<1350°K), some possible compounds might be regarded as present only in negligible amounts, e.g., the lower aluminum chlorides (10) and oxides (11-12). Aluminum oxychlorides are formed only at relatively low temperatures (13).

The thermodynamic data for the equilibrium calculations were taken from Kubaschewski (14).

For the process conditions used the equilibrium according to reactions [1]-[3] was found to be considerably shifted to the right. From the input partial pressures  $p_{i,\text{in}}$ , and the equilibrium partial pressures  $p_{i,\text{eq}}$  of each component  $i$ , a supersaturation  $\Sigma_i$ , was calculated according to equation

$$\Sigma_i = p_{i,\text{in}}/p_{i,\text{eq}} \quad [4]$$

$\Sigma_{\text{H}_2\text{O}}$  is defined  $p_{\text{CO}_2,\text{in}}/p_{\text{H}_2\text{O},\text{eq}}$  due to reaction [1], which is supposed to be completely converted.  $\Sigma_{\text{Al}_2\text{Cl}_6}$  is defined analogously with regard to  $\Sigma_{\text{AlCl}_3}$  and reaction [2].

The supersaturations of the components are given in Table I.

### Experimental Procedure

In comparison with previous investigations (8) extra precautions were taken in order to minimize the moisture remaining in the apparatus.

The remaining experimental procedure was performed in accordance with the previous investigations (8).

The nucleation of Al<sub>2</sub>O<sub>3</sub> on cemented carbide substrates and TiC-coated cemented carbide substrates was studied in a pilot plant CVD apparatus (Fig. 1-2). The volume of the reaction chamber was 0.015m<sup>3</sup> and it was heated by a resistance furnace. The temperature was measured with thermocouples placed in a sealed tube inserted into the reactor from above. The accuracy of the temperature measurements was ±8°K.

Twenty-five per cent of the gas came from an AlCl<sub>3</sub> generator. The AlCl<sub>3</sub> was formed by reacting HCl with small aluminum pieces (99.8% pure, main impurities Fe and Si). The AlCl<sub>3</sub> flow was analyzed before each experiment to guarantee a complete conversion of HCl. The AlCl<sub>3</sub> part of the flow was thoroughly mixed in extended pipes with the CO<sub>2</sub>-containing flow (75%) before entering the reactor. The hydrogen was purified in a Pd-Ag diffusion cell. The purity of HCl and CO<sub>2</sub> was 99.98%. A Reynold's number of about 50 implies a laminar flow.

The substrates were cemented carbide inserts, Type SPUN 120308, of a ISO P30 grade containing 86% WC, 5.5% Co, and the balance cubic carbides TiC, TaC, and NbC (forming  $\gamma$ -phase). Some inserts were TiC coated. In order to make the Al<sub>2</sub>O<sub>3</sub> nuclei visible the samples were polished on one side. They were placed on alsint supports in a tube of alsint.

A rather extended heating up period was needed due to the relatively large pilot plant deposition reactor.

Table I. Process conditions, supersaturations, and nuclei densities

Exp No.	Temperature, °K	Pressure (total), kPa	Inlet gas		Time, sec	Supersaturations				Nuclei density ( $\mu\text{m}$ ) <sup>-2</sup>	
			CO <sub>2</sub> , kPa	AlCl <sub>3</sub> , kPa		CO <sub>2</sub>	H <sub>2</sub> O	AlCl <sub>3</sub>	Al <sub>2</sub> Cl <sub>6</sub>	on TiC	on (Ti, W)C
1	1150	8	0.24	0.16	60	4,500	46	700	48	140	130
2	1200	8	0.24	0.16	60	4,000	36	490	39	d.*	o.g.**
3	1250	8	0.24	0.16	60	3,600	29	350	32	80	50
4	1300	8	0.24	0.16	60	3,200	24	260	27	70	100
5	1350	8	0.24	0.16	60	2,900	20	190	23	50	d.*
6	1250	8	0.24	0.053	60	570	1.5	6,400	10 <sup>5</sup>	50	o.g.**
7	1250	8	0.24	0.16	60	3,600	29	350	32	80	50
8	1250	8	0.24	0.48	60	12,000	108	130	1.5	70	80
9	1250	8	0.08	0.16	60	85,000	220	80	1.5	100	80
10	1250	8	0.24	0.16	60	3,600	29	350	32	80	50
11	1250	8	0.72	0.16	60	56	1.6	13 · 10 <sup>4</sup>	5 · 10 <sup>5</sup>	70	o.g.**
12	1250	2	0.06	0.04	60	6,700	55	260	70	80	110
13	1250	8	0.24	0.16	60	3,600	29	350	32	80	50
14	1250	32	0.96	0.64	60	1,900	16	490	16	50	50
15	1250	8	0.24	0.16	180	3,600	29	350	32	50	50
16	1250	8	0.24	0.16	540	3,600	29	350	32		
17	1250	8	0	0.16	60						
18	1250	8	0.24	0	60						
19	1250	8	0	0	60						

Experiments 7, 10, and 13 are pure repetitions.

\* d. = dense (>120).

\*\* o.g. = overgrown.

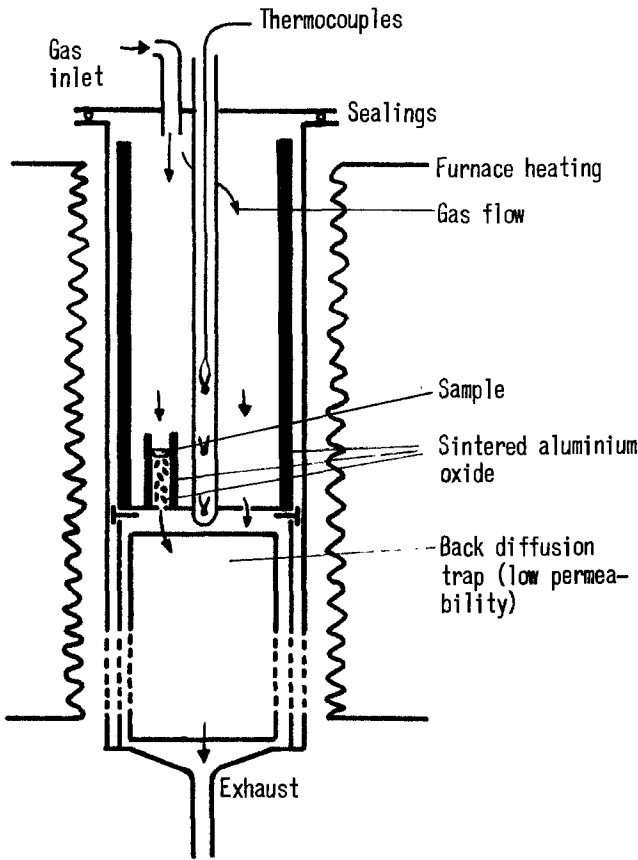


Fig. 1. Deposition chamber

During this heating the  $AlCl_3$  generator was started by feeding  $HCl + H_2$  through it. This flow bypassed the deposition reactor. During the last minute before the deposition the desired flow rates of the gases were adjusted while being bypassed and the two gas flows were then simultaneously shunted over to the reaction chamber. The process was continued for 60 sec in most of the experiments and was then terminated by passing the remaining flow directly to the exhaust, followed by an evacuation of the reactor to about 0.05 kPa. After refilling the reactor with hydrogen the furnace was removed. The minimum time of deposition for consistency of the process conditions was about 20 sec. The process conditions are shown in Table I.

Blank runs (experiments 17-19) were carried out in order to make the distinction between  $Al_2O_3$  and titanium oxide nuclei possible (Fig. 3 and 4).

In the central variant of each chain of process conditions ( $AlCl_3$  and  $CO_2$  partial pressures, temperature, and pressure) the ratio  $p_{AlCl_3,in}/p_{CO_2,in}$  is stoichiometric. The substrates were studied in the scanning electron microscope (SEM), where the density of nuclei on TiC and on the  $\gamma$ -phase (cubic carbides) of the cemented carbide surface was counted. The same techniques were used as in the previous investigation (8).

**Results and Discussion**

The transformation of the surface to be coated starts during heating up in  $H_2$ . On uncoated cemented carbide the binder (Co alloy) diffuses away leaving voids behind (Fig. 3). Probably the binder covers the carbide surface with a thin layer. The moisture that inevitably is present in the gas slightly attacks the cemented carbide surface and the TiC-coated surface, respectively, by oxidation. The WC phase is at least partially

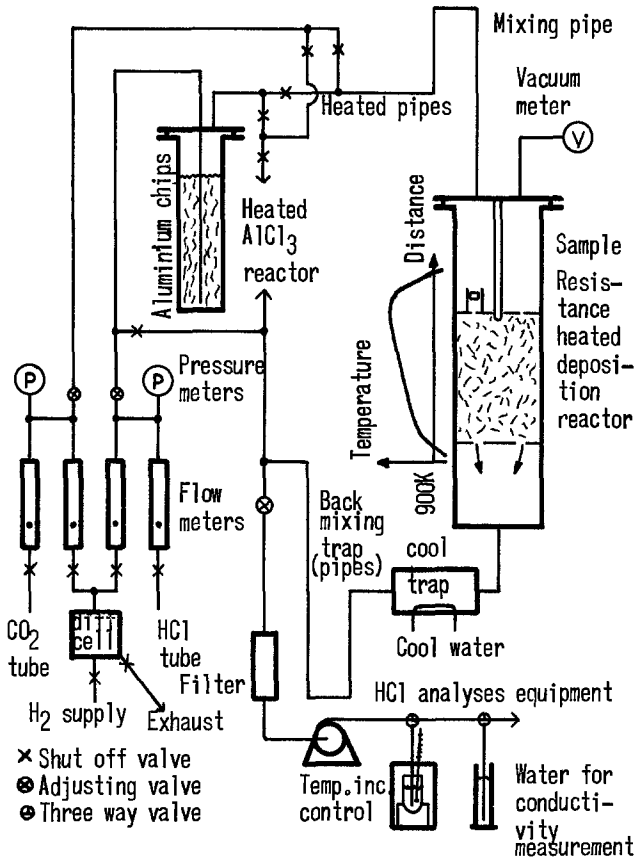


Fig. 2. Gas supply and exhaust system

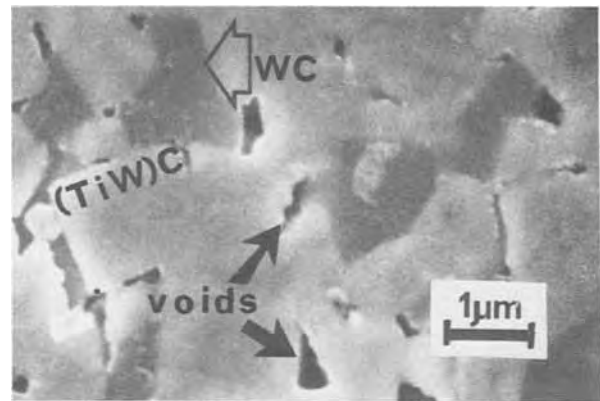


Fig. 3. Cemented carbide surface of run No. 18 in Table I (blank run, no  $Al_2O_3$  nuclei). SEM image.

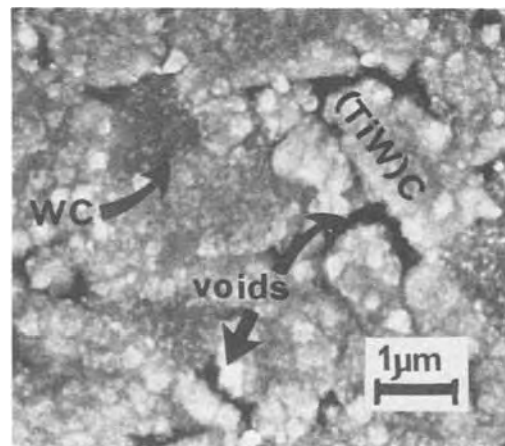


Fig. 4. Cemented carbide surface run No. 12 in Table I with  $Al_2O_3$  nuclei.



converted to carbide of  $\eta$ -phase type (e.g.  $\text{Co}_6\text{W}_6\text{C}$ ). However, in all experiments, where the gas contained  $\text{AlCl}_3$ , the attack was so mild that it was possible to count the  $\text{Al}_2\text{O}_3$  nuclei both on the (Ti, W)C grains of the uncoated surfaces of the cemented carbide (Fig. 4) and on the polished surfaces of the TiC-coated inserts (Fig. 5). The densities of nuclei in the different experiments are given in Table I. We note that the nuclei density varies with temperature,  $\text{AlCl}_3$  content,  $\text{CO}_2$  content, and total pressure in a significant way. Of course the uncertainty in the measurement of nuclei density is too large to put significance to every single figure. However, the trends are quite clear for nucleation on TiC-coated substrates but less clear for the nucleation on uncoated cemented carbide substrates.

Let us distinguish between the supersaturation of (a) aluminum donors (the chlorides) and (b) oxygen donors ( $\text{CO}_2$  and  $\text{H}_2\text{O}$ ). If we let only the temperature vary, experiments 1-5, we note that all supersaturations increase, which is also true for the density of nuclei (Table I). If we let the input pressure of  $\text{CO}_2$  decrease by altering the content of  $\text{CO}_2$ , experiment 9-11, we obtain an increase in the supersaturation of oxygen donors, while the supersaturation of the aluminum donors decreases. The density of nuclei follows the supersaturation of oxygen donors under these conditions. If we increase the content of  $\text{AlCl}_3$ , experiments 6-8, the conditions are somewhat more complicated. The supersaturations of the oxygen donors decrease while those of the aluminum donors increase. Possibly there is a certain decrease in the density of nuclei showing a weak relationship with the supersaturation of the oxygen donors. If we increase the total pressure keeping the percentage of reactants constant, experiments 12-14, the supersaturations of the aluminum donors remain relatively constant ( $\text{AlCl}_3$  decreases and  $\text{Al}_2\text{Cl}_6$  increases) while the supersaturation of the oxygen donors increases. The density of nuclei increases with the supersaturation of the oxygen donors.

In conclusion the density of nuclei on TiC-coated substrates seems to agree with the supersaturation of the oxygen donors. Also the nucleation on cemented carbide, on the (Ti, W)C phase, shows the same trend (Table I) although as mentioned previously with less significance.

When concluding the comparison we should bear in mind, that the differences between the calculated supersaturations of the different gas compositions (experiments 6-11) are exaggerated compared to the ones encountered by the samples. The gas is partly converted before reaching the substrate surface.

These results seem to be in disagreement with those reported previously for nucleation on uncoated cemented carbide substrates (8). We discuss this below.

When comparing CVD experiments in the same chemical system, it is obvious that we must consider experiments with similar values of the process parameters. In our previous study of the nucleation of alumina on the (Ti, W)C phase in cemented carbide we used  $\text{AlCl}_3/\text{CO}_2$  ratios around 0.33 and in the present

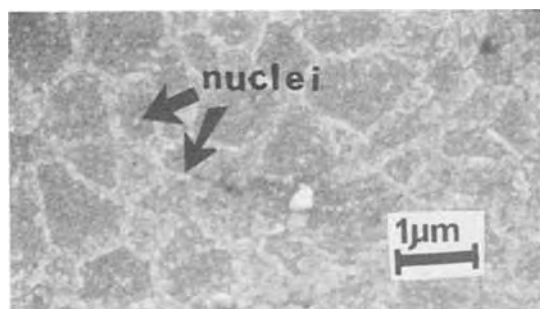


Fig. 5. TiC-coated cemented carbide surface of run No. 9 in Table I. Sparsely nucleated with  $\text{Al}_2\text{O}_3$ .

study ratios around 0.67. Thus in the previous series of experiments the aluminum donors were in relative shortage and the density of nuclei was governed by the supersaturation of the aluminum chlorides while in this series of experiments the oxygen donors were in relative shortage. Furthermore the current experimental series was carried out under as moisture-free conditions as possible.

Hence, it seems natural to assume that the critical event in the nucleation of a CVD coating is the formation of stable "clusters" of some intermediate products of that reactant which is in shortage.

The two series of experiments agree in that the same temperature-nuclei density relationship was established.

From a production point of view TiC coating of the substrates prior to alumina coating has two aspects. First, the adhesion of the coating seems to be bad if the initial density of nuclei is too low due to incorrect supersaturation. Bad adhesion can also result from the deterioration of the substrate surface during heating up in hydrogen. Using TiC-coated substrates will improve adhesion by giving an even density of nuclei and by preventing substrate deterioration. Second, difficulties will arise in large production charges due to small amounts of cobalt being dissolved probably as chlorides from uncoated cemented carbide substrates. This will cause the coating to grow by a whiskerlike structure. Compare the structure of a coating obtained in a small charge (Fig. 6) to that obtained in a large charge (Fig. 7). In the latter case the reactant gas

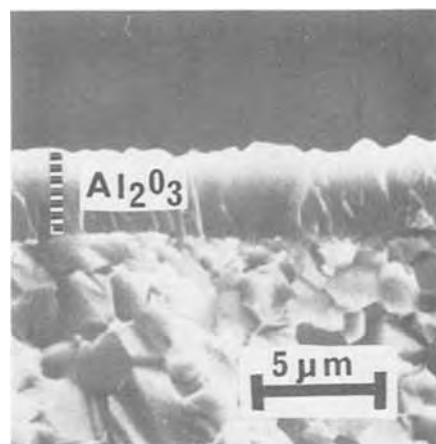


Fig. 6. Cemented carbide with a  $4 \mu\text{m}$   $\text{Al}_2\text{O}_3$  layer produced in laboratory scale. Fracture section in scanning electron microscope (SEM).

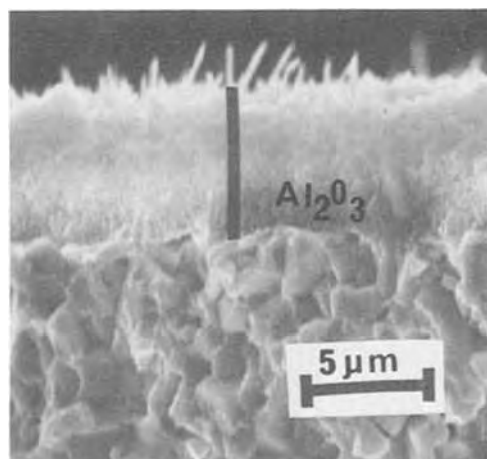


Fig. 7. Cemented carbide with a  $6 \mu\text{m}$   $\text{Al}_2\text{O}_3$  layer produced in pilot plant scale. Fracture section in SEM.

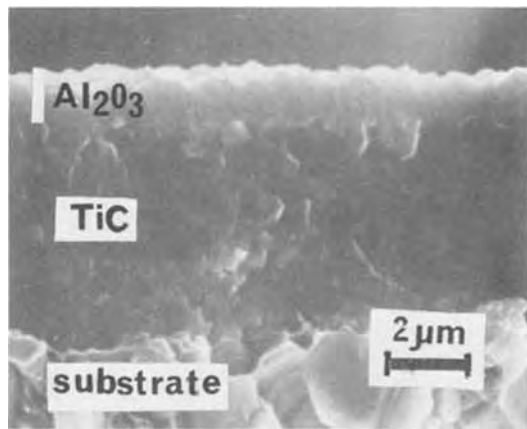


Fig. 8. Cemented carbide with a  $1\ \mu\text{m}$   $\text{Al}_2\text{O}_3$  layer (on top) and a  $5\ \mu\text{m}$  TiC layer (below) from production. Fracture surface in SEM.

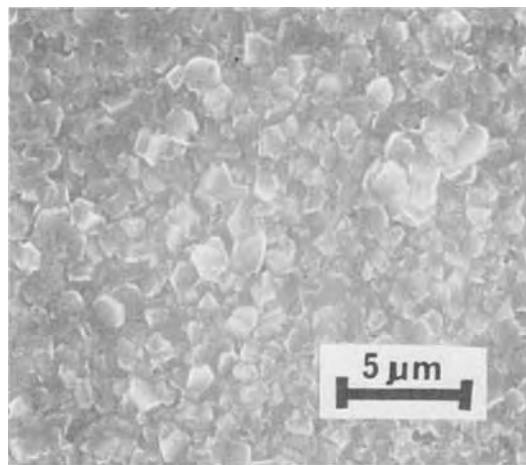


Fig. 9. Surface appearance of a  $1\ \mu\text{m}$   $\text{Al}_2\text{O}_3$  layer on top of a  $5\ \mu\text{m}$  TiC layer on cemented carbide. Production coated. A SEM image.

contained dissolved cobalt chlorides. Again using TiC-coated substrates will reduce the tendency to whisker formation by protecting the cobalt from being attacked by the reactants.

### Conclusions

The supersaturation of reaction components for  $\text{Al}_2\text{O}_3$  layer formation is shown to have a pertinent influence on the nuclei density and thus subsequently on the adhesion of the layer.

The deposition of  $\text{Al}_2\text{O}_3$  on TiC-coated cemented carbide is found to be advantageous. First, it isolates the cobalt and stops it from interfering with the alumina nucleation and growth and, second, it secures an even density of alumina nuclei.

Manuscript submitted May 20, 1975; revised manuscript received ca Nov. 12, 1975. This paper was presented at the Fifth International Conference on Chemical Vapor Deposition, Stoke Poges, Buckinghamshire, England, Sept. 21-25, 1975.

Any discussion of this paper will appear in a Discussion Section to be published in the December 1976 JOURNAL. All discussions for the December 1976 Discussion Section should be submitted by Aug. 1, 1976.

Publication costs of this article were partially assisted by Sandvik AB.

### SYMBOLS

- $p_{i,\text{in}}$  input partial pressure of ith component, atm  
 $p_{i,\text{eq}}$  equilibrium partial pressure of ith component, atm  
 $\Sigma_i$  supersaturation of ith component  
 $K_p$  equilibrium constant for the total reaction, atm

### REFERENCES

1. W. Ruppert, U.S. Pat. 2,962,388 (1960).
2. H. E. Hintermann, H. Gass, and J. N. Lindström, "Proceedings of the 3rd International Conference on CVD," F. A. Glaski, Editor, p. 352, American Nuclear Society, Hinsdale, Ill. (1972).
3. R. Ljungqvist, *ibid.*, p. 383.
4. G. F. Wakefield and J. A. Bloom, *ibid.*, p. 397.
5. W. B. Campbell, *Chem. Eng. Progr.*, **62**, 68 (1966).
6. J. M. Blocher, Jr., "Proceedings of the (1st) International Conference on CVD," A. C. Schaffhauser, Editor, p. 3, American Nuclear Society, Hinsdale, Ill. (1967).
7. J. M. Blocher, Jr., *J. Vacuum Sci. Technol.*, **11**, 680 (1974).
8. R. T. Johannesson and J. N. Lindström, *ibid.*, **12**, 854 (1975).
9. R. Funk, M. Kornmann, B. Lux, and H. Schachner, *J. Crystal Growth*, **28**, 259 (1975).
10. P. Wong and McD. Robinson, *J. Am. Ceram. Soc.*, **53**, 617 (1970).
11. H. Yanagida and F. A. Kröger, *ibid.*, **51**, 700 (1968).
12. G. I. Volkodav, *Fiz. Khim. Obrabot. Mat.*, **5**, 78 (1973).
13. K. Iida and T. Tsujide, *Japan. J. Appl. Phys.*, **11**, 772 (1971).
14. O. Kubaschewski, E. Ll. Evans, and C. B. Alcock, "Metallurgical Thermochemistry," 4th ed., pp. 421-424, Pergamon Press, Oxford (1967).
15. D. R. Messier and P. Wong, *This Journal*, **118**, 772 (1971).
16. B. F. Johnson, J. N. Lindström, and F. W. J. O. Ohlsson, U.S. Pat. 3,837,896 (1974).



# Surface Oxidation of Silicon Nitride Films

S. I. Raider,<sup>\*1</sup> R. Flitsch, J. A. Aboaf,<sup>\*</sup> and W. A. Pliskin<sup>\*</sup>

IBM System Products Division, East Fishkill Facility, Hopewell Junction, New York 12533

## ABSTRACT

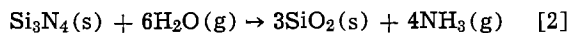
ESCA is used to characterize silicon nitride surface oxidation. Si 2p, N 1s, and O 1s binding energies and photoelectron line intensities of oxidized nitride films are compared with the corresponding lines from thick reference films of silicon, silicon nitride, silicon dioxide, and a series of oxynitrides. Rapid initial oxidation of silicon nitride surfaces occurs at room temperature on exposure of nitride films to air. A graded oxidized nitride film forms between the film surface and the nitride. Similarly, oxynitride films with gradations in composition are obtained upon oxidation of nitride films at high temperatures.

Silicon nitride thin films deposited on silicon or on silicon dioxide have received considerable attention for applications in semiconductor device structures because of their cited chemical stability and resistance to diffusion of impurities. However, an Si-N bond is chemically reactive and should oxidize when exposed to air. The free-energy changes (1) for silicon nitride oxidation in oxygen or water vapor, *i.e.*



$$\Delta F_{298^\circ\text{K}} = -304 \text{ kcal/mole}$$

and



$$\Delta F_{298^\circ\text{K}} = -147 \text{ kcal/mole}$$

indicate that nitride surface oxidation at room temperature is thermodynamically feasible. Silicon nitride films have been intentionally oxidized in oxygen or water at temperatures  $\geq 900^\circ\text{C}$  (2). The kinetics of nitride surface oxidation indicate that the conversion process at these temperatures is slow. Little is known of nitride reactivity at lower temperatures. Sato *et al.* (3) have reported on chemical instabilities at a silicon nitride surface when films were exposed to high-pressure water or to water vapor in an autoclave at temperatures up to  $300^\circ\text{C}$ . From Auger spectra, Maguire and Augustus (4) have recently identified oxygen at a nitride surface, but have suggested that a high-temperature reaction with either oxygen or water vapor impurities in the carrier gas stream led to surface oxidation.

The presence of an oxidant impurity in a reactant gas stream during nitride-film deposition at elevated temperatures results in the formation of homogeneous oxynitride films. These films form a continuous series of compounds with changing oxygen and nitrogen content rather than a mixture of silicon dioxide and silicon nitride (5, 6). The oxygen content of oxynitrides can be related to the film index of refraction ( $n$ ) (7), which ranges from about 2.0 for silicon nitride to 1.46 for silicon dioxide. The indices of refraction of oxynitride films, obtained from measurements of reflective interference minima at two angles of incidence at an energy of about 2 eV, have been found to vary linearly with the oxygen content of the film (7).

In this investigation, products of surface oxidation of nitride films formed at room temperature and at  $1070^\circ\text{C}$  are characterized using x-ray photoelectron spectroscopy (ESCA) (8). ESCA spectra of oxidized reaction products at nitride surfaces are compared with spectra of silicon dioxide, of silicon nitride, and of homogeneous oxynitride reference films.

\* Electrochemical Society Active Member.

<sup>1</sup> Present address: IBM Thomas J. Watson Research Center, Yorktown Heights, New York 10598.

Key words: x-ray photoelectron spectroscopy (ESCA), dielectric, thin film, silicon oxynitride.

## Experimental

**Film preparation.**—Silicon nitride samples were prepared by chemical vapor deposition on cleaned silicon substrates at  $800^\circ\text{C}$ . The silicon wafers were induction-heated on a carbon susceptor coated with silicon carbide. A reaction mixture of silane (semiconductor grade) and ammonia (99.99% pure) in a ratio of 1:100 was carried by nitrogen gas into a quartz reaction chamber. Some silicon nitride films were prepared from silicon tetrabromide (9); some were prepared by reactively sputtering silicon with nitrogen gas (10). Oxynitride films were deposited at  $1000^\circ\text{C}$  by adding oxygen to the silicon nitride reaction mixture. Silicon dioxide films were prepared by oxidation of silicon in dry oxygen at  $1000^\circ\text{C}$ . The thickness and refractive index of each film on silicon substrates were measured with a Rudolph ellipsometer. Film thicknesses ranged from 400 to  $2000\text{\AA}$ .

The reactivity of silicon nitride films in air at temperatures of  $25^\circ \pm 2^\circ\text{C}$  and 30-50% relative humidity was examined by exposure to air in a clean hood for times up to one month. Nitride films were also oxidized in dry oxygen at  $1070^\circ\text{C}$  for times up to 7 hr. The oxide films which formed after oxidation at  $1070^\circ\text{C}$  were etched at  $25^\circ\text{C}$  with buffered HF (7 parts 40%  $\text{NH}_4\text{F}$ : 1 part 49% HF) diluted with 10 parts water. The etch rates for silicon dioxide and silicon nitride films are 2.2 and 0.075  $\text{\AA}/\text{sec}$ , respectively. Silicon oxynitride films etch at intermediate rates depending on the oxygen content of the film. In some cases, silicon nitride films were etched in a 10:1 diluted HF solution to remove surface oxide which might have formed in air.

**ESCA.**—Data were obtained with an AEI ES 100 electron spectrometer. Samples were mounted on a copper block fixed to the end of a rotatable probe and inserted into the spectrometer. A magnesium-targeted x-ray source ( $\text{Mg K}\alpha_{12}$  radiation = 1253.6 eV) was used to analyze most of the samples, but an aluminum source ( $\text{Al K}\alpha_{12}$  radiation = 1486.6 eV) was also used. The spectrometer was examined for linearity by measuring the photoelectron lines corresponding to the Cu  $2p^{3/2}$  (932.8 eV) and the Au  $4f^{7/2}$  (83.8 eV) levels (11) with  $\text{Mg K}\alpha_{12}$  and  $\text{Al K}\alpha_{12}$  x-ray radiation. Photoelectron lines obtained using these two x-ray sources should differ in energy by 233.0 eV. Appropriate adjustments were made to the spectrometer high-voltage supply to obtain this difference between the atomic levels for both Cu  $2p^{3/2}$  and Au  $4f^{7/2}$ . After these adjustments had been made, the correction factor for the spectrometer was evaluated using the Au  $4f^{7/2}$  line.

A broad energy scan of all samples was first obtained at 2 eV/sec. The strong photoelectron lines were then scanned over a 15V range at a rate of 0.02 eV/sec. All data were referenced to the Au  $4f^{7/2}$  line to correct for surface charging effects. The O 1s, N 1s, C 1s, and Si 2p

lines were examined from each sample. The C 1s line is due to carbon contamination found on all samples.

Intensity data were obtained by integration of the photoelectron line areas. Intensity ratios of ESCA data are compared so as to eliminate errors resulting from surface contamination. The sample plane was generally tilted  $10^\circ$  from the normal to the electrostatic analyzer entrance slit to obtain maximum line intensities. Some intensity data were obtained as a function of sample inclination to the analyzer entrance slit to vary the emitted-electron sampling depth. A decrease in angle between a sample surface and the detector slit results in a decrease in sampling depth from which photoemitted electrons are collected (12).

### Results

**ESCA spectra of  $\text{Si}_3\text{N}_4$ .**—A typical ESCA broad-energy scan of a  $0.1 \mu\text{m}$  thick unetched silicon nitride film with a refractive index of 2.00 is shown in Fig. 1. In addition to nitrogen, silicon, and carbon photoelectron lines, an oxygen line is also observed. This sample was subsequently heated to  $350^\circ\text{C}$  in the spectrometer vacuum chamber. The C 1s line intensity was somewhat decreased by this heat-treatment, whereas the O 1s line intensity was not decreased. An oxygen line was also present on ESCA spectra of reactively sputtered silicon nitride films and on deposited films, independent of whether the reactant used to form silicon nitride was silicon tetrabromide or silane. The surfaces of all silicon nitride films examined appeared to be rich in oxygen.

Chemically etching the silicon nitride surface with diluted HF (1:10) reduces the O 1s photoelectron line intensity (Fig. 2a) when compared with the nonetched surface (Fig. 1). However, the O 1s line of an etched sample increases in intensity on exposure to air at room temperature. The increase in O 1s line intensity after 3 days and after 30 days is shown in Fig. 2b and c, respectively. The thickness of the surface film formed in air at room temperature, in terms of silicon dioxide film thickness, is estimated from ESCA line intensities (13) to be 2-3Å for a freshly etched film, 3-5Å after 3 days, and from 6 to 9Å after one month's exposure.

**Comparison of Si 2p, N 1s, and O 1s binding energies, half-widths, and intensities.**—ESCA spectra of silicon, of silicon dioxide, and of a series of oxynitride films were compared with data from etched and nonetched silicon nitride spectra. Shifts in Si 2p, N 1s, and O 1s binding energies for the various samples are illustrated in Fig. 3. As the oxygen content of the films increases, the binding energies increase. For example, the binding energies of the oxynitride films increase as their refractive indices approach the value of 1.46 for silicon

dioxide. The magnitude of the binding energy changes for the photoelectron lines examined and decreases in the order Si 2p (4.4 eV) > N 1s (0.9 eV) > O 1s (0.4 eV). Compositional differences in the surface regions of these films are most readily identified from the Si 2p photoelectron spectra for which the largest changes in binding energies are observed.

The Si 2p binding energy for nonetched silicon nitride ( $n = 2.00$ ) is less than that of etched silicon nitride ( $n = 1.99$ ), but coincides with the Si 2p line for silicon oxynitride with a refractive index of 1.90. The Si 2p binding energy data clearly indicate that the oxygen that is present on nonetched nitride or that appears on etched nitride films (Fig. 1 and 2) is chemically bound to the silicon at the film surface. Changes in refractive indices obtained from ellipsometry are indicative of the composition of an entire film rather than only of a film surface.

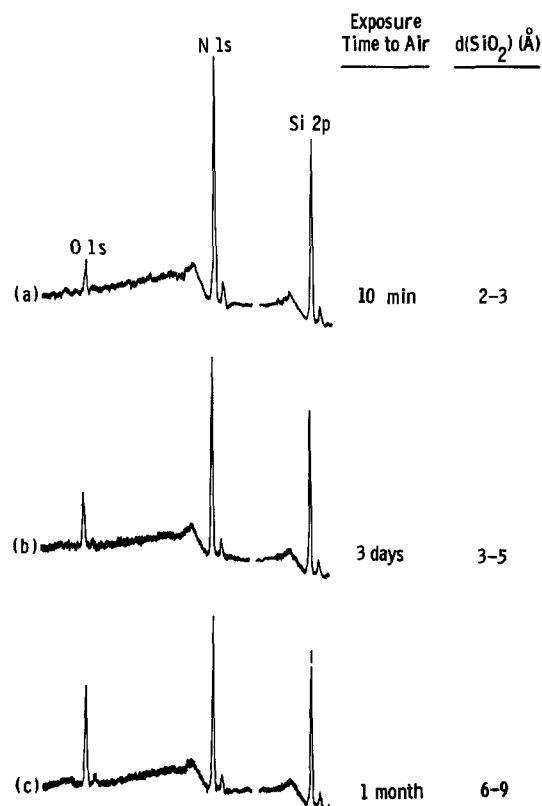


Fig. 2. Changes in O 1s photoelectron line intensity as a function of exposure time to air at room temperature after etching a silicon nitride surface with dilute (1:10) HF. Film thickness,  $d(\text{SiO}_2)$ , estimated from O 1s/Si 2p intensity ratio.

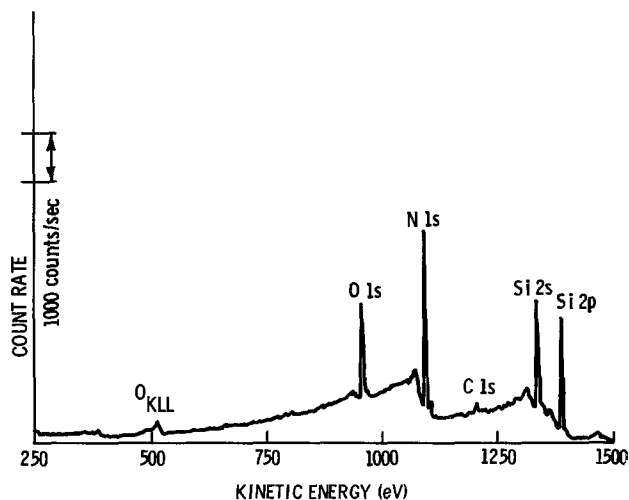


Fig. 1. Broad-energy ESCA spectrum of nonetched silicon nitride

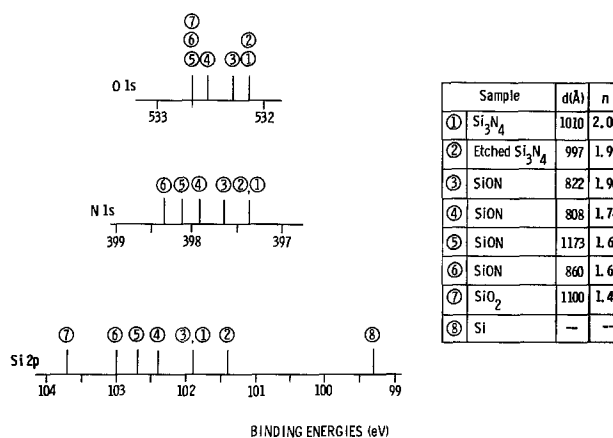


Fig. 3. Comparison of Si 2p, N 1s, and O 1s binding energies as a function of oxygen content in different samples.

Differences are observed in the half-widths of the photoelectron lines. The largest variation in half-widths is observed for Si 2p lines

HW(Si 2p): Si substrate (1.4 eV) < SiO<sub>2</sub>

= etched Si<sub>3</sub>N<sub>4</sub> (1.8 eV) ≅ Si<sub>3</sub>N<sub>4</sub> (1.9 eV)

< SiO<sub>x</sub>N<sub>y</sub> (2.1 eV)

An increase in half-width can indicate that a greater distribution of species with different binding energies is contributing to an observed photoelectron line. A broader range of silicon compounds contributes to the oxynitride films than to the nitride, etched nitride, or dioxide, while the narrowest range of energies contributes to the silicon single crystal line.

The relative photoelectron line intensities are plotted in Fig. 4 for those compounds whose binding energies are shown in Fig. 3. On the basis of similar correlations (7), the film index of refraction is plotted as a linear function of photoelectron line intensity ratios over the continuous range of homogeneous compounds extending from silicon dioxide to silicon nitride. Refractive indices and relative photoelectron line intensities of silicon dioxide and of etched silicon nitride films are used as reference points for the lines drawn in Fig. 4. A comparison of etched and nonetched silicon nitride indicates that the oxygen line intensity is relatively high and the nitrogen line intensity low in the non-etched sample. The O 1s/Si 2p intensity data for oxynitride films are high with respect to the reference line, whereas the nitrogen intensity data fit the nitrogen reference line.

*Variation in sampling depth for emitted photoelectrons.*—Photoelectron line intensity ratios are plotted in Fig. 5 as a function of angle,  $\theta$ , of sample inclination from perpendicularity to the detector slit (12). As the sample angle,  $\theta$ , decreases with respect to the detector slit, the photoelectron line intensity from a carbon contamination surface film is increased while line intensities from the bulk film are decreased.

The O 1s/N 1s and O 1s/Si 2p intensity ratios for a nonetched silicon nitride film increase as the angle of inclination decreases. A greater increase in intensity ratio is observed for the O 1s/N 1s ratio. The N 1s/Si 2p intensity ratio decreases with decrease in angle  $\theta$ . No change is observed in the binding energies of the photoelectron lines with variation in sample angle.

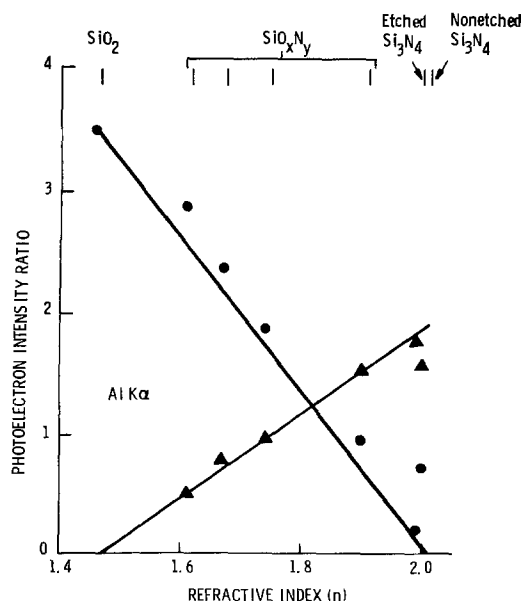


Fig. 4. O 1s/Si 2p (●) and N 1s/Si 2p (▲) photoelectron line intensity ratios as a function of sample refractive index.

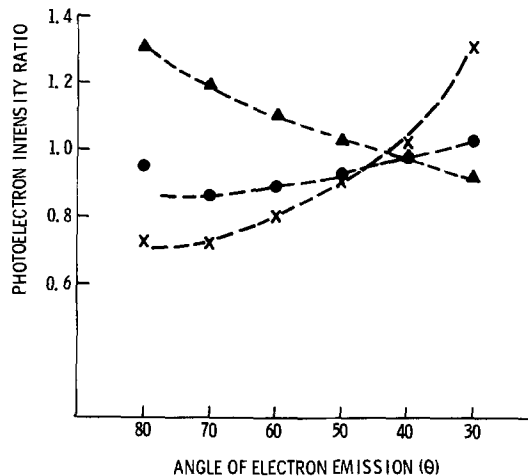
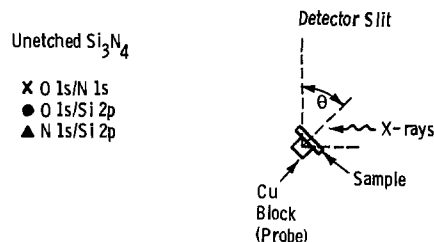


Fig. 5. Photoelectron line intensity ratios for a nonetched silicon nitride film as a function of variation of sample angle,  $\theta$ , of inclination from perpendicularity to the detector slit.

However, the Si 2p line half-width increases about 20% with a 60° decrease in sample angle of inclination, whereas the O 1s line increases about 10%; no change in half-width is observed for the N 1s line.

*Oxidation of silicon nitride at an elevated temperature.*—Nitride films were oxidized in dry oxygen at 1070°C for times from ½ to 7 hr, and the films formed were characterized using ESCA. Binding-energy and line half-width data are given in Table I, and intensity ratios of observed photoelectron lines are plotted in Fig. 6. Single Si 2p lines are observed for each sample, although the line half-widths increase and pass through a maximum after 1 hr of oxidation. As the oxidation time is increased, the Si 2p binding energies of the oxidized samples approach the Si 2p binding energy of silicon dioxide. After oxidation for 7 hr, the binding energy and the line half-width are close to those of silicon dioxide. From etch-back data, the oxidized film is estimated to be 188Å thick after 4 hr of oxidation and 292Å thick after 7 hr. The large half-

Table I. Silicon nitride surface film composition after oxidation at 1070°C in dry oxygen as a function of oxidation time in terms of (a) Si 2p binding energies and half-widths and (b) thickness of oxide film formed, estimated from etching data and from  $I(N\ 1s)/I(Si\ 2p)$  intensity ratios<sup>(a)</sup>

Sample	Oxidation time (hr)	Si 2p binding energy (eV)	Si 2p half-width (eV)	Etching		ESCA Est. $d(SiO_2)$ from Fig. 7 (Å)
				$d(Si_3N_4)$ oxidized (Å)	Est. $d(SiO_2)$ (Å)	
Etched Si <sub>3</sub> N <sub>4</sub>	0	101.4	1.9	3	6	—
Si <sub>3</sub> N <sub>4</sub> <sup>(b)</sup>	—	101.9	2.2	15	30	1
Si <sub>3</sub> N <sub>4</sub>	0.5	102.6	2.5	24	48	11
Si <sub>3</sub> N <sub>4</sub>	1	102.7	2.4	47	94	22
Si <sub>3</sub> N <sub>4</sub>	4	103.7	2.2	94	188	34
Si <sub>3</sub> N <sub>4</sub>	7	103.7	1.9	146	292	49
SiO <sub>2</sub>	—	103.7	1.8	—	—	—

(a) Al K $\alpha_{12}$  radiation, Au reference.

(b) Oxidation resulting from exposure to air at 25°C.

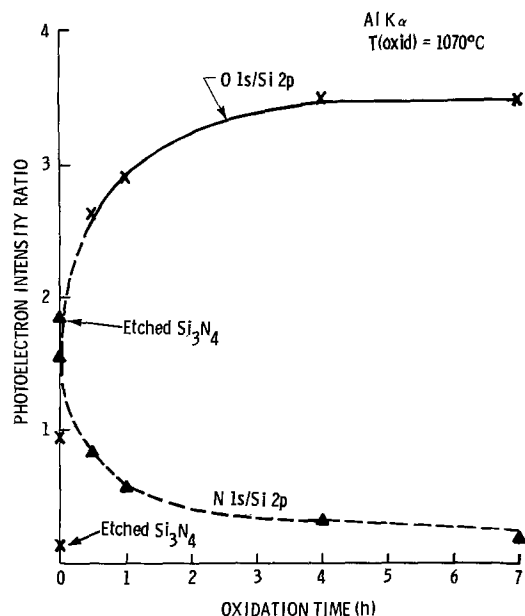


Fig. 6. O 1s/Si 2p and N 1s/Si 2p photoelectron line intensity ratios as a function of oxidation time of silicon nitride in dry oxygen at 1070°C.

widths of the Si 2p lines for samples oxidized for a half-hour and for 1 hr indicate that a distribution of components contributes to these lines. The oxygen-to-silicon intensity ratio is not equal to that of silicon dioxide until the nitride has been oxidized for  $\geq 4$  hr. A trace of nitrogen is still detected in the sample oxidized for 7 hr. More nitrogen and less oxygen are present in the samples oxidized for shorter times.

### Discussion

**ESCA.**—ESCA binding energies of an element are related to the fractional atomic charge about an element and, therefore, to the electronegativities of neighboring atoms. Pauling electronegativities of the elements of interest increase in the order  $\text{Si}(1.8) < \text{N}(3.0) < \text{O}(3.5)$ . The binding energy of a photoelectron line increases as the electronegativity of a neighboring atom increases.

The magnitude of the binding energy is a function of core electron promotion from a particular atom in a solid to the reference Fermi level of that solid. Any change in reference level in going from one material to another is assumed to modify the magnitudes of the respective Si 2p, N 1s, and O 1s binding energies equally.

The intensity of photoelectrons of a given energy from a homogeneous material is proportional to the density of the film attenuated by a factor  $e^{-x/\Lambda}$ , where  $x$  is the distance through the material that the photoelectron must travel and  $\Lambda$  is the mean escape depth of an electron and depends on the energy of the photoelectron and on the nature of the material. Photoelectron lines with kinetic energies of about 1 keV have mean escape depths of  $<30\text{\AA}$ . Contributions to the intensity of a photoelectron line are therefore significantly affected by the composition of the film surface. Surface contamination, film inhomogeneities, or multilayer structures will alter the intensity of a single line. A decrease in the sample angle of inclination with respect to the electron detector slit effectively decreases the sampling depth from which electrons are collected. The signal from the film surface is therefore maximized relative to the bulk and spectral contributions from the surface, and the underlying substrate may be differentiated.

**ESCA of reference films.**—Silicon, silicon dioxide, etched silicon nitride, and oxynitride films were chosen as homogeneous reference materials to be charac-

terized by ESCA from which the silicon nitride surface oxidation products could be identified. The Si 2p binding energies increase with increasing electronegativity of the neighboring atoms in changing from silicon (99.3 eV) to etched silicon nitride (101.4 eV) to silicon dioxide (103.7 eV). The increases in binding energy of silicon nitride and silicon dioxide with respect to silicon are about one-half the bandgaps of these dielectric films. Intermediate Si 2p binding energies located between those of etched silicon nitride and those of silicon dioxide are observed in each of the spectra of the oxynitride films.

The absence of distinct Si 2p lines at 99.3 and 103.7 eV indicates that Si-(O)<sub>4</sub> and Si-(Si)<sub>4</sub> tetrahedral groups, found in silicon dioxide and silicon, respectively, do not make a significant contribution to the nitride or oxynitride structures. From the Si 2p data, silazane (Si-N-Si) bridge structures found in silicon nitride are apparently changed by oxidation to siloxane (Si-O-Si) bridge structures and these structures are the predominant ones present in the oxynitride films. The ESCA Si 2p data indicate that  $\text{SiO}_x\text{N}_y$  is not a mixture of silicon dioxide and silicon nitride, but rather that siloxane and silazane groups are blended on a molecular scale. Chemical bonding near the surfaces of  $\text{SiO}_x\text{N}_y$  films, as determined from ESCA spectral data, is consistent with models of chemical bonding in bulk  $\text{SiO}_x\text{N}_y$  films deduced from optical properties of the films (14).

Smaller increases in N 1s and O 1s binding energies are observed as the oxygen content of the films is increased. These data are insufficient to uniquely identify corresponding changes in the films. It is likely that changes in composition from  $\text{N}_3\text{Si-N-SiN}_3$  to  $\text{O}_3\text{Si-N-SiO}_3$  and from  $\text{N}_3\text{Si-O-SiN}_3$  to  $\text{O}_3\text{Si-O-SiO}_3$  are the causes of a significant portion of the observed binding-energy shifts. Modifications of surface charging (15) resulting from the higher oxygen content of the films, or the formation of species such as Si-O-N-Si and Si-O-O-Si, may also contribute to the observed binding-energy changes.

A linear relationship was established between oxygen content and refractive indices of homogeneous oxynitride reference films (7). A similar linear relationship between photoelectron line intensity ratios of N 1s and O 1s relative to Si 2p and change in refractive index of homogeneous reference films is to be expected and is observed in Fig. 4. The O 1s/Si 2p ratios for the oxynitride films are somewhat high when compared with the O 1s/Si 2p reference and indicate that the films may be oxygen rich near the film surfaces. The N 1s/Si 2p data do not indicate that these films are nitrogen deficient. However, the N 1s/Si 2p reference line is determined from the intensity ratio for etched silicon nitride, which is already nitrogen deficient at the film surface because it is partially oxidized.

**Silicon nitride surface oxidation.**—Oxygen detected in the ESCA spectrum of unetched silicon nitride shown in Fig. 1 is a component of an oxidized surface film. Evidence that nitride surfaces are oxidized is provided by ESCA binding energy and intensity data. Silicon atoms at the unetched film surface are bound to oxygen atoms, which are more electronegative than nitrogen atoms and cause the Si 2p line maximum to be shifted to a higher binding energy. The surface oxide layer significantly shifts the binding energy of the Si 2p line, since the contributions to the line intensity are exponentially dependent on the depth from which the electrons are emitted. As a result, the silicon nitride film with an oxidized surface layer ( $n = 1.99$ ) has a binding energy similar to that of an oxynitride film, with a refractive index of 1.90. Refractive indices are characteristic of bulk, rather than surface, properties. If the oxidized surface layer on the nitride surface were silicon dioxide, separate Si 2p lines at 101.4

and 103.7 eV would have been observed. The oxidized surface is likely to be a graded oxynitride layer, which is oxygen rich at the surface.

The O 1s and N 1s intensities, relative to the Si 2p intensity, also indicate that an unetched nitride film is oxygen rich and nitrogen deficient when compared with these components in an etched silicon nitride film. Nitride surface oxidation partially results in a replacement of nitrogen bound to silicon with oxygen bound to silicon. The intensity ratios for unetched silicon nitride are similar to the intensity ratios for an oxynitride film, with a refractive index of about 1.91 indicating good agreement between binding energy and intensity data.

The angular dependence of the intensity offers a means of differentiating surface and bulk species. A comparison of line intensity from the surface to the bulk film is significantly enhanced at small angles  $\theta$  of emission (12). Variations in relative photoelectron intensity with sampling depth (Fig. 5) from spectra of nonetched silicon nitride give further indications of nonuniform nitride-film composition. An increase in O 1s/N 1s and O 1s/Si 2p intensity ratios with a decrease in angle is consistent with the formation of an oxidized surface film on silicon nitride. The larger increase in O 1s/N 1s intensity ratio with a decrease in angle is related to the increase in oxygen content and to the decrease in nitrogen content near the film surface. An oxidized silicon nitride surface deficient in nitrogen near the film surface also causes the N 1s/Si 2p intensity ratio to decrease with a decrease in sample angle.

Changes in the O 1s line intensity in spectra of etched silicon nitride upon exposure to air as a function of time (Fig. 2) indicate that the nitride surface, initially, is rapidly oxidized in air at room temperature. The oxidant at room temperature may be either oxygen or water vapor in the air. The oxidation rate is greater for water vapor than for oxygen at elevated temperatures, but little is known of their relative reactivity at room temperature.

The reactivity of nitride films with oxidants at room temperature has not been previously recognized although oxygen has been identified as an impurity in silicon nitride films. Bound oxygen, if present, is generally believed to be located at the nitride-silicon interface because of rapid surface oxidation of silicon. Nuclear microanalysis data obtained by Croset *et al.* (16), indicating the presence of oxygen in a nitride film on silicon, were interpreted in terms of oxide at the interface, but might also have been partly explained as due to rapid oxynitride formation at the nitride surface. Rapid surface oxidation of a nitride film is also consistent with the result of Maguire and Augustus (4), in which oxygen was identified at a silicon nitride surface by Auger spectroscopy.

**High-temperature oxidation of silicon nitride.**—An oxidized film is present at a silicon nitride surface after oxidation at 1070°C in dry oxygen. Binding-energy data indicate that silicon dioxide is not a major component of the oxidized film unless the nitrates are oxidized for more than 1 hr. The film formed after oxidation for one-half hour is mainly oxynitride on silicon nitride, with no evidence of the presence of significant silicon dioxide. N 1s photoelectrons are detected even in the film oxidized for 7 hr. The oxidized film surfaces are oxygen rich and resist etching in a nitride etchant (boiling phosphoric acid).

The thickness of an oxide film formed at elevated temperatures can be estimated in terms of silicon dioxide from etching and ESCA intensity data. A decrease in nitride film thickness after etching the oxidized film in buffered HF provides one basis for estimating oxide film thickness (Table I). The thickness of the oxidized film is also estimated from the N 1s/Si 2p intensity ratio of the oxidized surface layer. The

intensity of N 1s photoelectron lines from an underlying layer is calculated by assuming that the oxidized film, *i.e.*, the oxide equivalent of the silicon nitride film removed by etching, is silicon dioxide (Table I). In Fig. 7, a normalized N 1s/Si 2p intensity ratio,  $R$ , is determined as a function of the silicon dioxide film thickness,  $d(\text{SiO}_2)$ , and of the mean escape depth,  $\Lambda(\text{N } 1s)$ , for nitrogen photoelectrons attenuated by a silicon dioxide film, from the equation

$$R = \frac{I(\text{N } 1s)}{I(\text{Si } 2p)} \bigg/ \frac{I(\text{N } 1s)_{\text{Si}_3\text{N}_4}}{I(\text{Si } 2p)_{\text{Si}_3\text{N}_4}} = \frac{D^{\text{N}}_{\text{Si}_3\text{N}_4} e^{-d(\text{SiO}_2)/\Lambda(\text{N } 1s)}_{\text{SiO}_2}}{D^{\text{Si}}_{\text{SiO}_2} + (D^{\text{Si}}_{\text{Si}_3\text{N}_4} - D^{\text{Si}}_{\text{SiO}_2}) e^{-d(\text{SiO}_2)/\Lambda(\text{Si } 2p)_{\text{SiO}_2}}$$

where  $I$  = photoelectron intensity,  $\Lambda(\text{Si } 2p)_{\text{SiO}_2}$  = mean escape depth of Si 2p photoelectrons in silicon dioxide = 25Å,  $D^{\text{N}}_{\text{Si}_3\text{N}_4}$  = concentration of nitrogen atoms per unit volume of silicon nitride =  $[(4 \times \text{atomic weight of nitrogen}) / (\text{molecular weight of Si}_3\text{N}_4)] \times \rho_{\text{Si}_3\text{N}_4}$ ,  $\rho_{\text{SiO}_2}$  = silicon dioxide density = 2.3 g/cm<sup>3</sup>, and  $\rho_{\text{Si}_3\text{N}_4}$  = silicon nitride density = 3.4 g/cm<sup>3</sup>. The experimentally observed intensity ratio is normalized with respect to etched silicon nitride. Though  $\Lambda(\text{N } 1s)$  is not known, it is assumed to be between  $\Lambda(\text{O } 1s)$  and  $\Lambda(\text{Si } 2p)$  in silicon dioxide (20Å) (13, 17).

The experimentally obtained N 1s/Si 2p intensity ratios are not in agreement with calculated density ratios obtained by extrapolation of the experimental data to the  $\Lambda(\text{N } 1s)$  curve equal to 20Å (Fig. 7). The oxide-film thickness estimated from etching data is greater than the oxide film thickness estimated from ESCA data. This is to be expected for a graded oxynitride film. Etching in buffered HF removes silicon dioxide and oxynitride and overestimates the silicon dioxide film thickness. ESCA underestimates the oxide-film thickness by assuming that the oxidized film is silicon dioxide and that N 1s photoelectrons are emitted from an underlying silicon nitride layer. The intensity data are consistent with binding-energy data and indicate that the oxidized films are generally incompletely oxidized and contain nitrogen.

The N 1s/Si 2p and O 1s/Si 2p intensity ratio data for a nitride film oxidized at 1070°C do not correspond to a single homogeneous oxynitride film with a specific refractive index value (Table II). Refractive indices of oxynitride films formed at 1070°C were determined from Fig. 4 with intensity ratio data obtained for the oxidized films. The O 1s/Si 2p intensity ratios yield lower estimates of refractive indices than the N 1s/Si 2p intensity ratios. The oxidized films are apparently not homogeneous, but are graded, being oxygen rich near the surface and nitrogen rich as the oxygen-free nitride film is approached. In such a case, the refractive index determined from O 1s/Si 2p in-

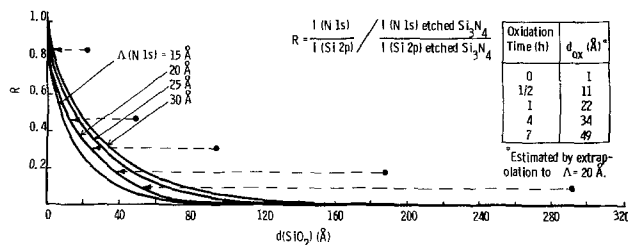


Fig. 7. Comparison between a calculated and an observed (normalized) N 1s/Si 2p photoelectron line intensity ratio for an oxide film of variable thickness on a thick silicon nitride film. It is assumed in calculating the intensity ratio that the oxide film, whose thickness is determined by etching and ellipsometry, is pure silicon dioxide. Silicon dioxide film thickness,  $d(\text{SiO}_2)$ , is estimated by extrapolation of the experimental N 1s/Si 2p intensity data (●) to the  $\Lambda(\text{N } 1s)$  curve = 20Å.

Table II. Comparison of  $I(\text{N } 1s)/I(\text{Si } 2p)$  and  $I(\text{O } 1s)/I(\text{Si } 2p)$  intensity ratios between silicon nitride films oxidized at  $1070^\circ\text{C}$  in dry oxygen and homogeneous oxynitride films

Oxi- dation time (hr)	$I(\text{N } 1s)$	Homo- geneous oxynitride refractive index (n)	$I(\text{O } 1s)$	Homo- geneous oxynitride refractive index (n)
	$I(\text{Si } 2p)$	(from Fig. 4)	$I(\text{Si } 2p)$	(from Fig. 4)
0.5	0.85	1.70	2.62	1.59-1.62
1	0.58	1.62	2.92	1.55-1.57
4	0.34	1.56	3.5	1.46
7	0.19	1.51	3.5	1.46

tensity ratio data overestimates the amount of oxygen present, whereas N 1s/Si 2p intensity ratio data underestimate the amount of nitrogen present.

### Conclusions

An ESCA study of reaction products of silicon nitride oxidation and of homogeneous oxynitride films indicates that oxidation of a silicon nitride surface occurs rapidly at room temperature in air. The oxidation product of room-temperature oxidation is an oxynitride film. A graded oxynitride film, which is oxygen rich at the surface, is formed after oxidation of silicon nitride at  $1070^\circ\text{C}$  in oxygen. The ESCA data also indicate that the homogeneous oxynitride reference films are composed of a range of species blended on a molecular scale and are not mixtures of silicon dioxide and silicon nitride.

### Acknowledgments

The authors thank P.-C. Li for the preparation of some of the oxynitride samples used in this study and F. W. Anderson and R. A. Pollak for helpful discussions. The technical assistance of L. Forget, J. Hollis, and M. J. Palmer is gratefully acknowledged.

Manuscript submitted April 9, 1975; revised manuscript received ca. Nov. 19, 1975.

Any discussion of this paper will appear in a Discussion Section to be published in the December 1976 JOURNAL. All discussions for the December 1976 Discussion Section should be submitted by Aug. 1, 1976.

Publication costs of this article were partially assisted by IBM Corporation.

### REFERENCES

- JANAF Interim Thermochemical Tables, The Dow Chemical Co., Midland, Michigan.
- I. Franz and W. Langheinrich, *Solid State Electron.*, **14**, 499 (1971).
- J. Sato, Y. Ban, and K. Maeda, *Annual Rel. Phys. Sympos.*, **9**, 96 (1971).
- H. G. Maguire and P. D. Augustus, *This Journal*, **119**, 791 (1972).
- C. M. Drum and M. J. Rand, *J. Appl. Phys.*, **39**, 4458 (1968).
- N. C. Tombs, F. A. Sewell, Jr., and J. J. Comer, *This Journal*, **116**, 862 (1969).
- D. M. Brown, P. V. Gray, F. K. Heumann, H. R. Philipp, and E. A. Taft, *ibid.*, **115**, 311 (1968).
- K. Siegbahn, C. Nordling, A. Fehlgren, R. Nordberg, K. Hamrin, J. Hedman, G. Johansson, T. Bergman, S.-E. Karlsson, and I. Lindberg, "ESCA—Atomic, Molecular and Solid State Structure Studied by Means of Electron Spectroscopy," Almquist and Wiksells, Uppsala, Sweden (1967).
- J. A. Aboaf, *This Journal*, **116**, 1736 (1969).
- S. M. Hu and L. V. Gregor, *ibid.*, **114**, 826 (1967).
- G. Johansson, J. Hedman, A. Berndtsson, M. Klason, and R. Nilsson, *J. Electron Spectrosc.*, **2**, 295 (1973).
- W. A. Fraser, J. V. Florio, W. N. Delgass, and W. D. Robertson, *Surface Sci.*, **36**, 661 (1973).
- R. Flitsch and S. I. Raider, *J. Vacuum Sci. Technol.*, **12**, 299 (1975).
- H. R. Philipp, *This Journal*, **120**, 295 (1973).
- M. F. Ebel and H. Ebel, *J. Electron Spectrosc.*, **3**, 169 (1974).
- M. Croset, S. Rigo, and G. Amsel, *Appl. Phys. Letters*, **19**, 33 (1971).
- C. D. Wagner, *Anal. Chem.*, **44**, 1050 (1972).

## Elimination of Process-Induced Stacking Faults by Preoxidation Gettering of Si Wafers

### II. $\text{Si}_3\text{N}_4$ Process

P. M. Petroff,\* G. A. Rozgonyi,\* and T. T. Sheng

Bell Laboratories, Murray Hill, New Jersey 07974

### ABSTRACT

A simple and novel process which prevents the formation of oxidation-induced stacking faults (SF) during the fabrication of Si devices is described. The process involves the deposition of a  $\text{Si}_3\text{N}_4$  film on the back of the wafer followed by a preoxidation annealing. This procedure eliminates the nucleation centers and impurities, which occur during the oxide growth, involved in the formation of SF. The  $\text{Si}_3\text{N}_4$  process has also been found to effectively reduce the wafer contamination by impurities such as Cu and Au. Application of this preoxidation gettering process to device processing is shown to be effective in drastically reducing leakages in p-n junctions and in eliminating the nucleation centers associated with the SF tetrahedron often found in the fabrication of Si bipolar devices.

There is now a large body of literature (1-5) dealing with crystallographic defects in silicon and their role on device performance. One type of electrically active structural defect which is often found in Si device

structures is the oxidation-induced stacking fault (hereafter designated as SF). Studies on these defects, which form during a high temperature oxidation treatment of the Si wafer, have produced the following results:

(a) Oxidation-induced SF produce leakages in p-n junction devices (2-6).

\* Electrochemical Society Active Member.  
Key words: silicon defects, transmission electron microscopy, gettering, silicon device processing.

(b) Oxidation-induced SF may be nucleated at centers which are introduced during the crystal growth (4, 5, 9) or at centers introduced by the processing operations preceding or concurrent to the oxide growth (7, 11, 13). In the case of process-induced SF nucleation centers, small precipitates which form at or near the SiO<sub>2</sub>-Si interface have been identified (7, 8, 10). In the case of SF nucleation centers introduced during the crystal growth, the oxidation-induced SF distribution usually follows a swirl distribution for float-zone silicon (5, 11) or a coring distribution (11) for Czochralski silicon. The swirl distribution of stacking faults suggests that the precipitates and dislocation loops observed (14) in the swirl pattern of dislocation-free float-zone silicon act as nucleation centers to the SF introduced during oxidation.

(c) The oxidation-induced SF have an extrinsic nature and grow by a climb mechanism from an interfacial Frank dislocation presumably emitted by precipitates (7, 8).

(d) In some instances impurities have been found to play an important role in promoting the formation of SF (7, 11). A wafer surface orientation dependence on the appearance of SF has also been reported (12, 13). In the case of HF-treated, wet oxidized Si wafer, it has been found that {111} surfaces (13) or surfaces with orientation 3° to 10° "off" {100} (11) do not show stacking faults after oxidation.

This apparent wealth of experimental results has not yet produced an oxide formation process which could prevent the SF formation during the fabrication of Si devices and it would appear that a number of important questions still need to be answered before their formation mechanism is understood and a solution for their elimination could be proposed. Among these unanswered questions are: (a) the nature of the precipitates which act as nuclei to the SF formation, (b) the nature of the impurities and point defects involved in the precipitate formation and the growth of SF, and (c) the nature of the extrinsic fault. The SF could be composed of an oxygen-rich plane (15), as some recent data seem to indicate, or of an extra plane of Si atoms.

Since the answers to these questions require complex analytical techniques in many cases not yet available, an empirical solution to the SF problem has been sought after by using gettering methods. The leading idea behind these gettering experiments was that such methods could eliminate the impurity nucleation centers and affect the growth mechanism of the SF. These gettering methods which are applied to the Si wafer prior (16, 17) to or during the oxidation treatment have proven effective in eliminating oxidation-induced SF. The present work describes in detail a simple and novel processing scheme which relies on the gettering action of a Si<sub>3</sub>N<sub>4</sub> film deposited on one side of the Si wafer to suppress the formation of SF on the device side of the wafer. The possible mechanisms for the SF suppression are discussed. Examples of the effectiveness of this technique which is compatible with most device processing operations are given for the case of p-n junctions and for the case of Si epitaxial films on {111} Si substrates.

### Experimental

Si<sub>3</sub>N<sub>4</sub> films have been deposited by low temperature (300°C) rf sputtering or by chemical vapor deposition (at 800°C) on the back side of Si wafers; the front side of the wafers were Syton polished and were used to study the SF. The wafer orientation was {100} or {111} and both Czochralski and float-zone, dislocation-free, n-type silicon were used in these experiments. The wafer thicknesses ranged from 275 to 425 μm and the Si<sub>3</sub>N<sub>4</sub> film thicknesses deposited were typically 4000 Å for the sputtered and the CVD Si<sub>3</sub>N<sub>4</sub> films.

The defect distribution in the wafers after these processing treatments was revealed by etching in a Secco etch solution (18) for 10 min. Examination of the etch features was carried out by optical microscopy

with a Zeiss ultraphot microscope using Nomarski interference contrast optics. In some instances the defect nature and distribution were obtained by transmission electron microscopy (TEM) and x-ray topography (XRT).

*Preoxidation gettering of defects.*—To evaluate the gettering process on the same wafer only one-half of each wafer was covered with the Si<sub>3</sub>N<sub>4</sub> film. A half-silicon wafer was used as a mask to limit the Si<sub>3</sub>N<sub>4</sub> coverage to one-half of the back of the wafer. After Si<sub>3</sub>N<sub>4</sub> deposition and standard cleaning the wafers were annealed in N<sub>2</sub> + 1% O<sub>2</sub> or in Ar atmosphere; the annealing temperatures were varied from 1000° to 1200°C and annealing times ranged from 1 to 4 hr.

*Gettering of oxidation-induced defects.*—Some of the wafers which were preannealed as described above were cleaned and steam oxidized to grow 4000 Å of SiO<sub>2</sub> at 1050°C for 35 min. The Si<sub>3</sub>N<sub>4</sub> layer was left on the back of the wafers during the oxide deposition; for some pregettered wafers the Si<sub>3</sub>N<sub>4</sub> layer was removed prior to the oxide growth. After a Secco etching treatment of 10 min the defect nature and distribution in these wafers were then inspected by optical microscopy, XRT, and TEM.

*Chemical impurity analysis.*—The chemical impurities in the starting material and in the wafers subsequent to the Si<sub>3</sub>N<sub>4</sub> deposition, annealing and oxidation steps were measured by neutron activation analysis. In addition, several impurity profile distributions through the wafer thickness were obtained after repeated thinning of the gettered wafers. The wafers were thinned by mechanical lapping; a careful rinse in a jet of nonpreferential Si etch solution followed the lapping operation to completely remove small particulates left on the sample by the lapping operation. A final rinse in DI water preceded the neutron activation analysis. The relative amount of material removed during the thinning operation was obtained from weight measurements of the samples with a microbalance.

*Device applications of the pregettering Si<sub>3</sub>N<sub>4</sub> process.*—The effectiveness of the pregettering method in producing lower p-n junction leakage and higher device yields was tested on two types of structures. First, leakage currents in p-n junction devices which were part of a typical integrated circuit test pattern were measured on wafers which had been pregettered with the Si<sub>3</sub>N<sub>4</sub> process prior to the first oxidation. These leakage measurements were compared to the leakages of the same devices in monitor wafers which were not pregettered. Both pregettered and ungettered wafers were processed simultaneously. Twelve wafers, each containing 100 devices, were measured for leakage at 28V on devices with a 35V breakdown voltage with an automatic prober. A more detailed description on the application of the Si<sub>3</sub>N<sub>4</sub> gettering process to device processing is given in Ref. (20).

### Results

In the remainder of this paper, the elimination of defects is referred to as "gettering" of defects by analogy to the well-known gettering of impurities.

*Preoxidation gettering of defects.*—The difference in the defect structures between the gettered and ungettered parts of an unoxidized Si wafer are shown in the photomicrograph in Fig. 1A and in the optical micrograph in Fig. 1B. These micrographs show the front side of a wafer which was gettered on only one-half of the wafer back side. The etch features associated with defects in the silicon are clearly visible only on the ungettered part of the wafer in Fig. 1B. In the higher magnification micrographs in Fig. 2B-D these etch features appear as saucer pits with a density between 1-4 × 10<sup>6</sup>/cm<sup>2</sup> in the ungettered part of the wafer while the front surface of the gettered half of the wafer the pit density is from zero to 10 cm<sup>2</sup>. The



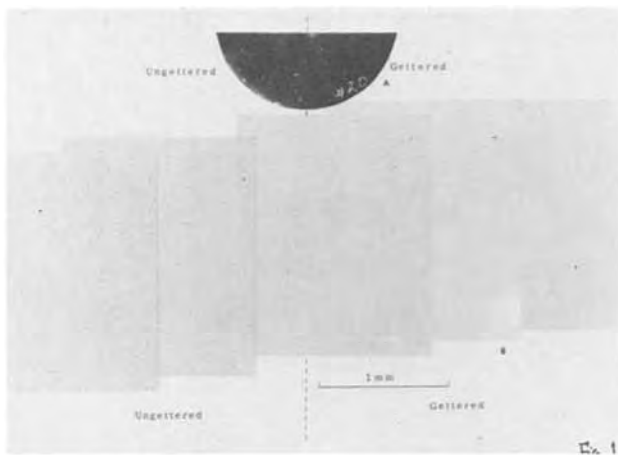


Fig. 1. A, Photomicrograph of the front side of a half Si wafer which was annealed in  $N_2 + 1\% O_2$  for 1 hr at  $1000^\circ C$ . Prior to the annealing half of the wafer back surface was coated with  $4000\text{\AA}$  of sputtered  $Si_3N_4$ . The differences between the gettered and ungettered part of the wafer have been revealed by an 8 min Secco etching treatment. B, Optical micrograph of the front side of a gettered wafer showing the boundary between the gettered and ungettered parts of the wafer. The etch features in the ungettered part have been revealed by 8 min etching in Secco etch.

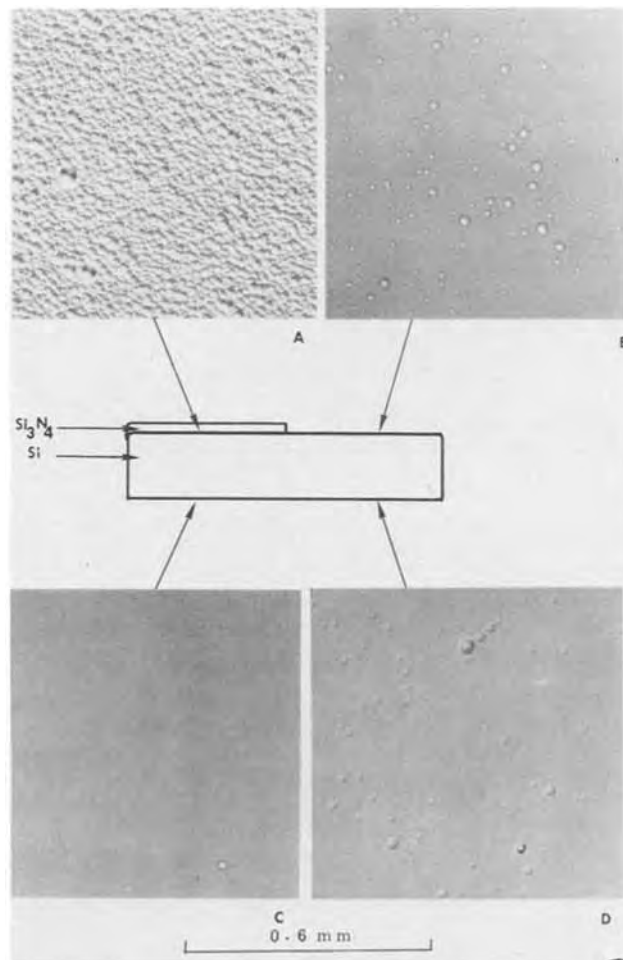


Fig. 2. Etch features of a Si wafer after annealing at  $1000^\circ C$  in  $N_2 + 1\% O_2$  for 1 hr. Prior to annealing half of the wafer back surface was coated with  $4000\text{\AA}$  of  $Si_3N_4$ . Magnification,  $600\times$ . A, Si surface after removal of the  $Si_3N_4$  film. B, Surface of the ungettered half of the wafer back side. C, Surface of the gettered half of the wafer front side. D, Surface of the ungettered half of the wafer front side.

CVD  $Si_3N_4$  and the sputtered  $Si_3N_4$  gave identical results for a 1 hr anneal at  $1050^\circ C$ .

*Elimination of oxidation-induced stacking faults.*—The wafers, which were subjected to a preoxidation gettering as described above, exhibited, after a steam oxidation ( $\approx 3000\text{\AA}$  of  $SiO_2$ ) process, a distinctly lower defect concentration from that in ungettered wafers. Figure 3A and B illustrate for a pregettered and steam-oxidized wafer the absence of etch features characteristic of stacking faults on the side of the wafer opposite to the  $Si_3N_4$  film. Higher magnification micrographs of the front side of an oxidized wafer which was pregettered are seen in Fig. 4A and B. The etch features seen in the ungettered part of this wafer (Fig. 4B) have indeed been correlated with the different etching stages of SF as shown in the transmission electron micrographs in Fig. 5. The x-ray topograph shown in Fig. 6 illustrates the effectiveness of the pregettering process in preventing the SF formation. If a wafer

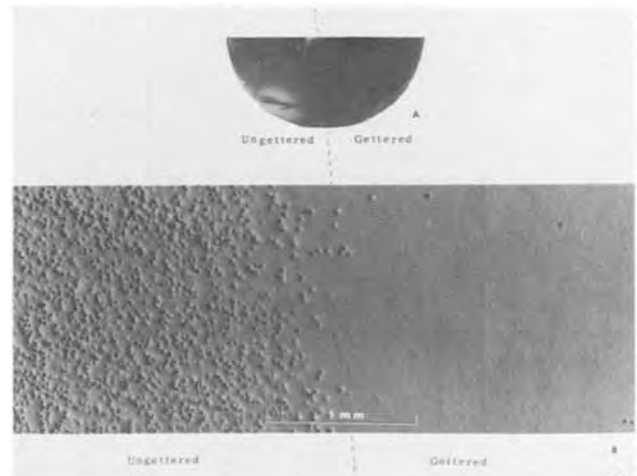


Fig. 3. A, Photomicrograph of the front side of a half Si wafer after preoxidation gettering (in  $N_2 + 1\% O_2$  for 1 hr at  $1050^\circ C$ ) and oxidation (wet oxide at  $1050^\circ C$ , 2 hr). Prior to the annealing half of the wafer back surface was coated with  $4000\text{\AA}$  of sputtered  $Si_3N_4$ . The difference between the gettered and ungettered part of the wafer have been revealed by an 8 min Secco etching treatment. B, Optical micrograph of the front side of the same wafer showing the boundary between the gettered and ungettered parts of the wafer.

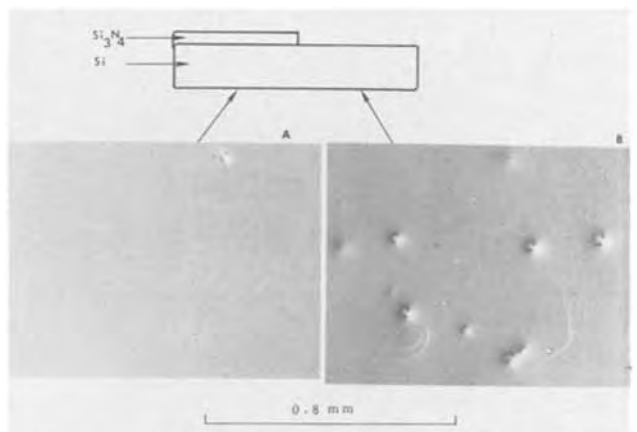


Fig. 4. Etch features of a Si wafer after preoxidation gettering and oxidation (annealing at  $1050^\circ C$  in  $N_2 + 1\% O_2$  for 1 hr, oxidation at  $1050^\circ C$  for 35 min wet oxide). Half of the wafer back surface was coated with  $4000\text{\AA}$  of sputtered  $Si_3N_4$  prior to the annealing and oxide deposition. Prior to etching the oxide was removed. A, Surface of the gettered half of the wafer front side. B, Surface of the ungettered half of the wafer front side. Etch features are characteristic of stacking faults (see Fig. 4). Magnification,  $800\times$ .



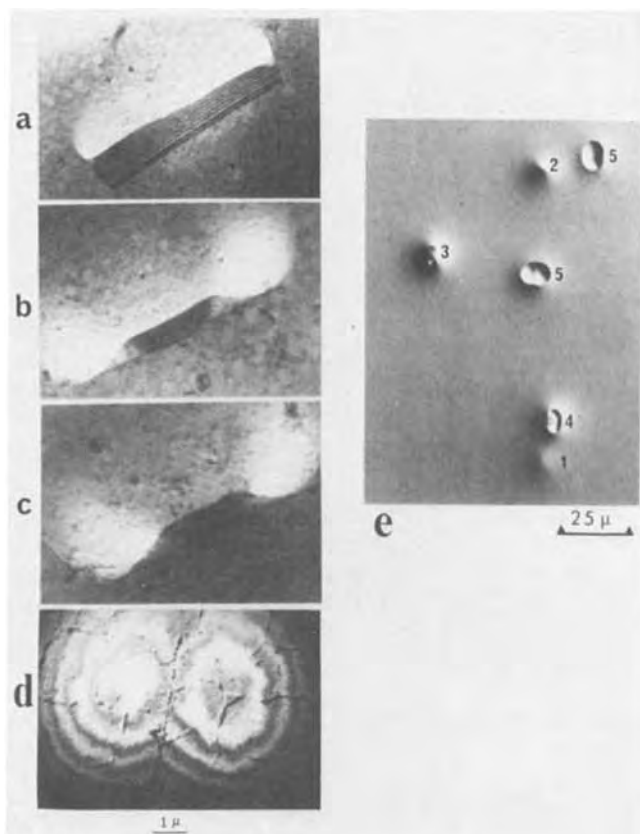


Fig. 5. Transmission electron micrographs of different etching stages of oxidation-induced stacking faults, A to D. Magnification, 10,000 $\times$ . E, Optical micrograph of etch features due to oxidation-induced stacking faults. Etch pit 1 corresponds to a stacking fault below the Si surface. Etch pits 2 to 5, respectively, correspond to the various etching stages of the stacking faults shown in the micrographs A to D.

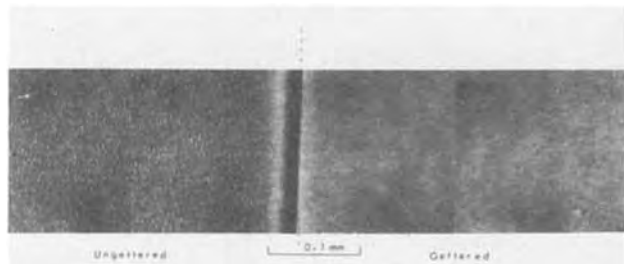


Fig. 6. Transmission x-ray topograph of a wafer after preoxidation gettering and oxidation (wet oxide deposited at 1050°C for 2 hr). The right part of the micrograph which corresponds to the half of the wafer coated with Si<sub>3</sub>N<sub>4</sub> on the back is essentially free of defects. The left part of the micrograph corresponds to that half of the wafer not coated with the Si<sub>3</sub>N<sub>4</sub>; a high density of SF associated with black-white spots is observed in this half of the wafer.

was pregettered as indicated above the suppression of the SF was equally effective when the Si<sub>3</sub>N<sub>4</sub> layer was removed prior to the oxide growth.

**Metallic impurity gettering.**—A number of authors have reported (10, 11, 13) on the importance of metallic impurities in promoting the SF formation during steam oxidation. Since the Si<sub>3</sub>N<sub>4</sub> preoxidation gettering process was proved to be effective in suppressing the SF formation, its possible role as a metallic impurity gettering process was also checked by neutron activation analysis. The results of neutron activation analysis on 14 wafers taken at various stages of the processing are summarized in Table I along with the chemical analysis of control wafers. These analyses

Table I. Neutron activation analysis

Sample No.	Au concentration (atoms $\times$ cm <sup>-3</sup> )	Cu concentration (atoms $\times$ cm <sup>-3</sup> )	Wafer treatment
1	$1.4 \times 10^{11}$	$3.9 \times 10^{13}$	Cleaned
2	$1 \times 10^{11}$	$1.3 \times 10^{13}$	
3	$1.3 \times 10^{13}$	$1.3 \times 10^{14}$	Si <sub>3</sub> N <sub>4</sub> sputter deposited
4	$5.2 \times 10^{12}$	$1.6 \times 10^{14}$	
5	$2.2 \times 10^{12}$	$1 \times 10^{13}$	Si <sub>3</sub> N <sub>4</sub> sputter deposited. Removed
6	$3.8 \times 10^{12}$	$2.2 \times 10^{14}$	Same treatment as No. 5 then sample annealed 2 hr, 1000°C in N <sub>2</sub> + 1% O <sub>2</sub>
7	$5 \times 10^{11}$	$9.8 \times 10^{13}$	Cleaned. Annealed 2 hr, 1100°C in N <sub>2</sub> + 1% O <sub>2</sub>
8	$4 \times 10^{12}$	$2 \times 10^{14}$	Si <sub>3</sub> N <sub>4</sub> sputter deposited; removed. Sample annealed 2 hr, 1100°C in N <sub>2</sub> + 1% O <sub>2</sub>
9	$5 \times 10^{12}$	$2.2 \times 10^{14}$	Si <sub>3</sub> N <sub>4</sub> sputter deposited. Sample annealed 2 hr, 1100°C in N <sub>2</sub> + 1% O <sub>2</sub>
10	$4 \times 10^{12}$	$1.7 \times 10^{13}$	Same sample as No. 9; Si <sub>3</sub> N <sub>4</sub> removed
11	$2.3 \times 10^{13}$	$3.4 \times 10^{14}$	Si <sub>3</sub> N <sub>4</sub> sputter deposited; annealed 1000°C 1 hr in N <sub>2</sub> + 1% O <sub>2</sub>
12	$1 \times 10^{13}$	$2.7 \times 10^{14}$	
13	$8.5 \times 10^{12}$	$4.2 \times 10^{13}$	Same sample as No. 11 and 12, respectively, but Si <sub>3</sub> N <sub>4</sub> was removed.
14	$6.3 \times 10^{12}$	$3 \times 10^{13}$	

indicated that two sources of metallic impurities, namely, Cu and Au, were introduced during the wafer processing. A comparison of the Au and Cu concentrations in samples 1,2 and 3,4 indicated that the Si<sub>3</sub>N<sub>4</sub> deposited by rf sputtering was contaminated with Au and Cu. The origin of these metallic elements was traced to the lining of the anode in the sputtering system used for the Si<sub>3</sub>N<sub>4</sub> deposition. Both Au and Cu are very fast diffusing elements (19) in Si at temperatures higher than 1000°C and the sputtered Si<sub>3</sub>N<sub>4</sub> is then expected to behave as a Cu and Au source during the preoxidation gettering. The second source of contamination is introduced by annealing in the ovens as shown by comparing the Au and Cu concentrations in samples 1,2,5 and 6,7 and 8. Both these contamination sources increase the Cu and Au content in the wafers by roughly an order of magnitude. After the preoxidation gettering, the measurements on samples 9,11,12 and 10,13,14 indicated that the Si<sub>3</sub>N<sub>4</sub> retained and trapped the Cu and Au atoms and in effect acted as a gettering medium for both these elements. The concentration of Cu in the preoxidation gettered wafers was essentially that found in clean uncontaminated wafers (compare the measurements on samples 1,2 and 9,13 and 14). The gettering action of the Si<sub>3</sub>N<sub>4</sub> layer was also evident in the Cu and Au concentration profiles shown in Fig. 7 and 8. The precision in the Cu concentration measurements was not as good as for Au as indicated by the error bars and was essentially limited by the short lifetime of the Cu radioisotope. These figures also showed that the trapping action of the Si<sub>3</sub>N<sub>4</sub> film was less pronounced for Au than for Cu.

**Applications of the Si<sub>3</sub>N<sub>4</sub> preoxidation gettering process to device processing.**—Application of the Si<sub>3</sub>N<sub>4</sub> gettering process to the fabrication of devices revealed that the effectiveness of this process on (100) wafers depends, in part, on the origin of the stacking faults. Recent work by Rozgonyi and Kushner (20) describes two classes of oxidation-induced SF: surface- or contamination-induced SF, and bulk or native defect nucleated SF. The electrical properties and device yields have been studied in detail for both preoxidation gettered and ungettered wafers (20). The results reported by Rozgonyi and Kushner (20) indicate that for (100) or (111) wafers which would normally form surface SF, the Si<sub>3</sub>N<sub>4</sub> gettering will produce p-n junctions completely free of SF with correspondingly lower leakage currents and increased device yields. However, the Si<sub>3</sub>N<sub>4</sub> preoxidation gettering procedure is not as effective for eliminating

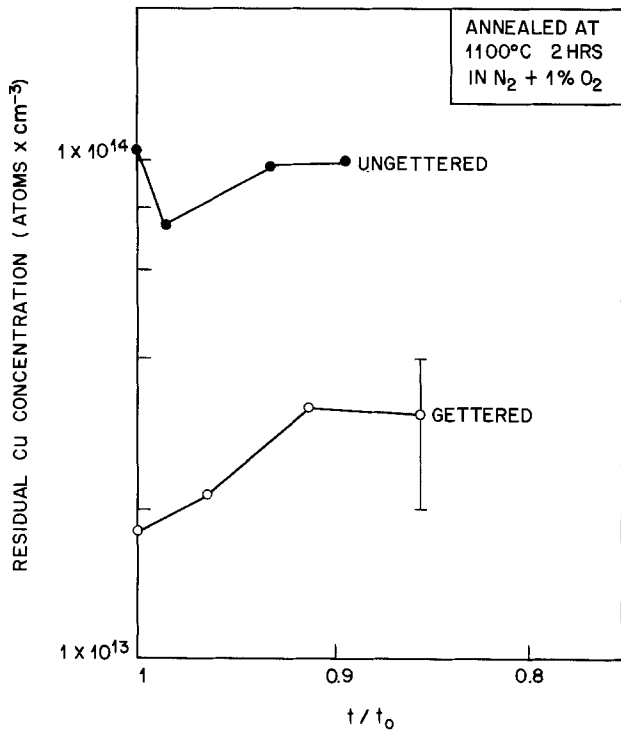


Fig. 7. Distribution of the residual Cu concentration as a function of the relative wafer thickness  $t/t_0$ ;  $t_0$  and  $t$  correspond respectively to the wafer thickness prior to and after successive polishing of the back side of the wafer. The concentration profiles are shown after a preoxidation gettering for the gettered half and the ungettered half of the same wafer.

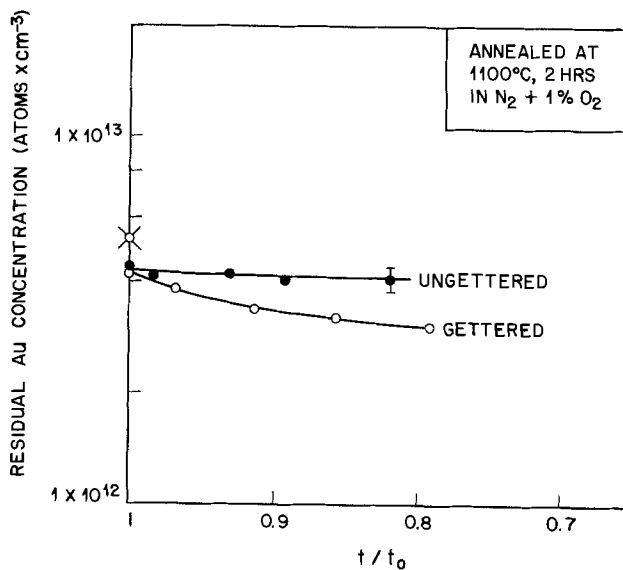


Fig. 8. Distribution of the residual Au concentration as a function of the relative wafer thickness  $t/t_0$ ;  $t_0$  and  $t$  correspond respectively to the wafer thickness prior to and after successive polishing of the back side of the wafer. The concentration profiles are shown after a preoxidation gettering for the gettered half and ungettered half of the same wafer.

the formation of bulk SF as opposed to the surface SF. In this case a more severe preoxidation gettering, e.g., introduction of misfit dislocations (16, 20) on the back of the wafers must be used to improve the device yields.

### Discussion

As pointed out at the beginning of this paper, the understanding of the SF formation process during steam oxidation is still very poor. However, the pre-

vious studies (11, 16, 17) on this problem have shown that both the crystal growth and the wafer processing introduce the nucleation centers (C), the point defects (N), and impurities (I) needed to the SF formation. The experiments described in this paper confirmed that the successful suppression of the SF formation may be achieved by trapping or elimination of either C, N, or I. Indeed, the chemical impurities analysis of gettered wafers indicated that the  $\text{Si}_3\text{N}_4$  film was actively trapping metallic impurities such as Au and Cu. In addition the results on preoxidation gettered wafers from which the  $\text{Si}_3\text{N}_4$  layer was removed prior to the oxide deposition, suggest that the elimination of nucleation centers is also a major mechanism in the elimination of SF.

The gettering mechanism which effectively eliminates the nucleation centers or the impurities or the point defects is now discussed. First, the effects of the internal stresses of the  $\text{Si}_3\text{N}_4$  film should be considered as a possible source of driving forces in the gettering mechanism. The stress measurements in CVD  $\text{Si}_3\text{N}_4$  (21) indicate that in the temperature range  $25^\circ\text{C} \leq T \leq 1000^\circ\text{C}$  the stresses are tensile and range between 1 and  $3 \times 10^{10}$  dynes/cm<sup>2</sup>. No stress measurements in the sputtered  $\text{Si}_3\text{N}_4$  films are available at high temperature; however, room temperature stress measurements (22) in these films showed compressive stresses in the range  $5 \times 10^9$  to  $1 \times 10^{10}$  dynes/cm<sup>2</sup>. It is surprising that the gettering is equally effective in wafers strained in tension or compression at room temperature since the strain gradient  $\partial\epsilon/\partial z$  through the wafer thickness is expected to control the gettering kinetics. If we assume that a point defect concentration gradient  $\partial c/\partial z$ , is rapidly established (i.e., nonequilibrium condition), the total flux of defects leaving the sample is given by

$$J = c \frac{\partial G}{\partial \epsilon} \frac{D}{kT} \frac{\partial \epsilon}{\partial z} - D \frac{\partial c}{\partial z} \quad [1]$$

where  $D$  and  $c$  are respectively the defect diffusion coefficient and concentration;  $\partial G/\partial \epsilon$  is the change in the defect-free energy along the  $z$  direction orthogonal to the wafer surfaces. When the stress is changed from tensile to compressive, the sign of  $\partial\epsilon/\partial z$  is reversed and different solutions are expected for Eq. [1]. The influence of the strain gradient sign on  $\partial G/\partial \epsilon$  is negligible with the result that impurities or point defects should be gettered on opposite sides of the wafers when the strain gradient is reversed. To account for the effectiveness of the gettering for both the tensile and compressive  $\text{Si}_3\text{N}_4$  films, one is led to the conclusion that the stress in the compressive films becomes tensile at high temperatures ( $T > 1000^\circ\text{C}$ ). Recent stress measurements at high temperatures (24) indeed suggest that this is the case for plasma-deposited  $\text{Si}_3\text{N}_4$  films which are compressively strained at room temperature.

Simultaneously to the strain enhanced elimination of point defects and nucleation centers, a gettering due to the nonstoichiometry of the  $\text{Si}_3\text{N}_4$  may also occur. Recent density and composition measurements (23) of sputtered  $\text{Si}_3\text{N}_4$  indicate that the deposited films are not stoichiometric and that in general they are deficient in Si. At high temperatures the diffusion of Si atoms across the Si- $\text{Si}_3\text{N}_4$  interface could take place to form one or several layers of the stoichiometric  $\text{Si}_3\text{N}_4$  films at the interface. The resulting gradient in the point defect concentration in the Si wafers may then provide the additional driving force for the point defect elimination.

### Conclusions

We have shown that a novel process which involves the deposition of a  $\text{Si}_3\text{N}_4$  film on the back of Si wafers followed by a preoxidation annealing effectively eliminates the formation of contamination-induced stacking faults on the device side of the wafers. The gettering of the  $\text{Si}_3\text{N}_4$  layer has been found to effectively

reduce the contamination of the wafers by impurities such as Cu and Au. The defect gettering action of the  $\text{Si}_3\text{N}_4$  film is probably related to the stress induced in the Si wafers by the  $\text{Si}_3\text{N}_4$  film. Application of this preoxidation gettering process to actual device processing was proved to be effective in drastically reducing leakages in p-n junctions and in eliminating the nucleation centers which are associated with the formation of contamination-induced stacking faults.

### Acknowledgments

The authors wish to thank S. P. Murarka and V. Kumar for their valuable help with the neutron activation analytical part of this work. R. Kushner, D. Boulin, B. Deysher, and C. Pearce are also thanked for having applied this gettering process to the fabrication of Si devices.

Manuscript submitted Sept. 2, 1975; revised manuscript received Nov. 26, 1975.

Any discussion of this paper will appear in a Discussion Section to be published in the December 1976 JOURNAL. All discussions for the December 1976 Discussion Section should be submitted by Aug. 1, 1976.

Publication costs of this article were partially assisted by Bell Laboratories.

### REFERENCES

1. S. Yoshikawa and J. Chikawa, *Appl. Phys. Letters*, **23**, 1 (1973).
2. K. V. Ravi, C. J. Varker, and C. E. Volk, *This Journal*, **120**, 533 (1973).
3. K. V. Ravi and C. J. Varker, "Semiconductor Silicon," H. R. Huff and R. R. Burgess, Editors, pp. 136, 670, The Electrochemical Society Soft-bound Symposium Series, Princeton, N.J. (1973).
4. H. Shiraki, *Japan. J. Appl. Phys.*, **13**, 1859 (1974).
5. A. J. R. de Kock, *Philips Res. Rept, Supplement No. 1* (1973).
6. K. V. Ravi and C. J. Varker, *J. Appl. Phys.*, **45**, 263 (1974).
7. C. M. Hsieh and D. M. Maher, *ibid.*, **44**, 1302 (1973).
8. W. W. Tice and T. C. Huang, *Appl. Phys. Letters*, **24**, 4, 157 (1974).
9. A. Staudinger and J. Patel, Unpublished results.
10. L. Dyer and F. W. Voltmer, *This Journal*, **120**, 82 (1973).
11. D. I. Pomerantz, *This Journal*, **119**, 255 (1972).
12. Y. Sugita, T. Kato, and M. Tamura, *J. Appl. Phys.*, **42**, 5847 (1971).
13. C. M. Drum and W. van Gelder, *J. Appl. Phys.*, **43**, 4465 (1972).
14. P. M. Petroff and A. J. R. de Kock, Abstract 143, p. 338, The Electrochemical Society Extended Abstracts, Spring Meeting, Toronto, Canada, May 11-16, 1975; *J. Cryst. Growth*, **30**, 117 (1975).
15. N. Sato, K. Kajiwara, and A. Shibata, *Phys. Status Solidi A*, **16**, K63 (1973).
16. G. A. Rozgonyi, P. M. Petroff, and M. H. Read, *This Journal*, **122**, 1725 (1975).
17. D. Pomerantz, *J. Appl. Phys.*, **38**, 13, 5020 (1967).
18. F. Secco D'Aragona, *This Journal*, **119**, 948 (1972).
19. S. M. Hu, "Atomic Diffusion in Semiconductors," D. Shaw, Editor, p. 217, Plenum Press, New York (1973).
20. G. A. Rozgonyi and D. Kushner, *This Journal*, **123**, 570 (1976).
21. M. Tamura and H. Sunami, *Japan J. Appl. Phys.*, **11**, 8 (1971).
22. C. J. Mogab, P. M. Petroff, and T. T. Sheng, *This Journal*, **122**, 6, 816 (1975).
23. A. K. Sinha, T. E. Smith, G. Quintana, S. E. Haszko, and E. Jugujo, Unpublished results.
24. A. K. Sinha and T. E. Smith, Unpublished results.

# The Elimination of Stacking Faults by Preoxidation Gettering of Silicon Wafers

## III. Defect Etch Pit Correlation with p-n Junction Leakage

G. A. Rozgonyi\* and R. A. Kushner

Bell Laboratories, Murray Hill, New Jersey 07974

### ABSTRACT

Recently described procedures for the elimination of oxidation-induced stacking faults have been incorporated into a device processing line to yield data on the leakage in p-n junction tester diodes. The gettering processes, which take place on the back side of a wafer before the first oxidation, include the deliberate introduction of misfit dislocations and/or the deposition of a highly strained layer of  $\text{Si}_3\text{N}_4$ . The results show that leakage currents can be reduced by several orders of magnitude and diode yields<sup>1</sup> increased from about 10% to greater than 90%. By doing "post mortem" chemical etch pit studies on previously electrically mapped  $10 \times 10$  arrays of diodes the relative effectiveness of the two gettering schemes are compared. Factors such as the type of stacking fault, whether it be related to a native or process-induced source, or whether it is clean or decorated are discussed as well as the influence of slip-type dislocations.

It has recently been shown (1, 2) that a preoxidation gettering of the other side, i.e., the back of silicon wafers (hereafter called the POGO approach) will result in a front side that is free of stacking faults. The basic idea is that removal or isolation of stacking fault nuclei before the initial oxidation will prevent stack-

ing faults from forming during the actual oxidation step itself. The POGO approach is to be distinguished from those gettering treatments (3, 4) which effect a deactivation or annihilation of previously formed stacking faults. That is, the gettering process is aimed at removing stacking fault nucleation sites and not stacking faults. In addition, by maintaining the gettering source on the back side, it is possible to protect the wafer from process-induced nuclei which may be

\* Electrochemical Society Active Member.

<sup>1</sup> Per cent of diodes with junction leakage less than 100 nA  $\text{cm}^{-2}$  at 28V.

Key words: silicon defects, defect gettering, device leakage.

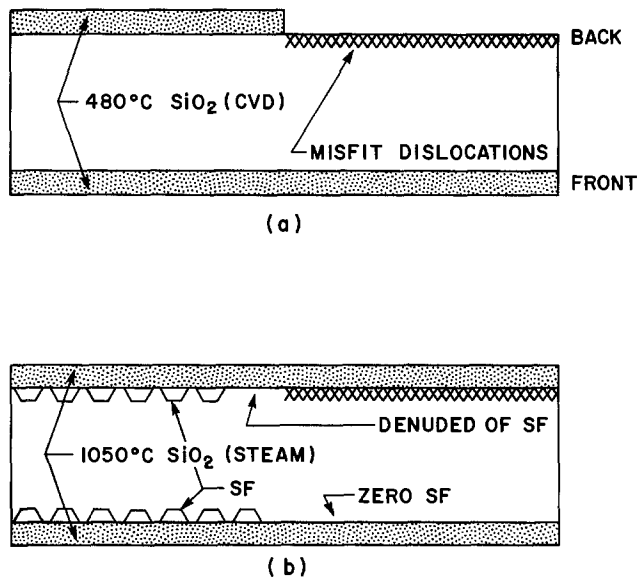


Fig. 1. Schematic of preoxidation gettering sequence for POGO I process. (a) Misfit dislocations on half of back side of wafer masked with a low temperature oxide. (b) Stacking faults nucleated after steam oxidation are confined to nongettered half of wafer.

introduced, not only during the initial oxidation, but also at later stages of device fabrication. In this regard the process differs from preoxidation gettering by high temperature annealing (5), which only operates on native defects.

Two gettering schemes have been successfully used on as-received, Syton polished, silicon wafers. One depends on the gettering action of misfit dislocations (1) which are deliberately introduced by diffusion of phosphorus into the back side of a wafer. The second procedure is to deposit a layer of  $\text{Si}_3\text{N}_4$ , also on the back surface, where it is believed that the strain gradients (2) introduced in the substrate by the highly stressed nitride layer will getter stacking fault nuclei. Although the precise nature of the defect interactions, gettering species, stacking fault nuclei, etc., are not fully understood, the two procedures themselves were found effective enough to warrant limited introduction into a device processing line.

The initial defect studies indicated that misfit dislocations (1) were effective in gettering stacking fault nuclei whose origins were either process-induced (contamination) or growth-induced (native defects). The  $\text{Si}_3\text{N}_4$  process (2), which is basically an elastic effect and introduces much less lattice distortion than misfit dislocations, was found to be mainly effective in suppressing process-induced nuclei. However, native defects such as the so-called "swirl" of A and B complexes (6, 7) were not eliminated or deactivated by a  $\text{Si}_3\text{N}_4$  POGO treatment. The differences between stacking faults that result primarily from processing and those related to a bulk source are discussed in this report. However, the main objective of the present paper is to correlate the presence or absence of stacking faults with the leakage in individual p-n junction diodes and thereby evaluate the effectiveness of these

POGO processes in an actual device. In addition to the oxidation-induced stacking faults, the electrical effects of process-induced dislocations were also studied.

### Experimental Procedures

The wafers used in this study were grown by the Czochralski technique and supplied by Western Electric. The wafers were (100) oriented with the back side chemically etched and the front side Syton polished. They were 2 in. diameter,  $400\ \mu\text{m}$  thick, p-type, with a nominal resistivity of 6-12 ohm-cm.

The as-received wafers were divided into groups, depending on the initial treatment they were to receive. One group received no preoxidation gettering treatment and served as a control. Prior to any POGO treatment the remaining wafers all had  $1\ \mu\text{m}$  of chemical vapor deposited (CVD) silicon dioxide deposited on the front side at  $480^\circ\text{C}$  in a Silox reactor. This was done in order to confine diffusion-induced dislocations to the back side of the wafers. Some wafers, for which gettering of only half the wafer was desired, also received a deposited oxide on the back side. Standard photolithographic procedures were used on these wafers to strip the oxide from half the back. At this point the wafers were further divided into two groups. One POGO group had  $2000\text{\AA}$  of CVD silicon nitride deposited on the back side in a Nitrox reactor at  $800^\circ\text{C}$  to generate a strain gradient. This was followed by  $4000\text{\AA}$  of CVD silicon dioxide. The silicon dioxide was deposited to protect the nitride from reaction during subsequent device processing and was retained at each photolithographic step. The second POGO group received a phosphorus diffusion from a  $\text{POCl}_3$  source for 60 min at  $1100^\circ\text{C}$  which served to generate misfit dislocations as shown schematically in Fig. 1a. This group also received back side layers of CVD silicon nitride and silicon dioxide which provided a cap over the heavy phosphorus layer and prevented transfer of this dopant to the front sides of other wafers during subsequent processing. The deposited masking oxide was then removed from the front side of all the wafers and the control group was added. Table I summarizes the two gettered structures which will be referred to as the POGO I and POGO II processes, while the etch pit and leakage results on various wafers are listed in Table II.

In order to monitor the effectiveness of the POGO treatment some wafers from the POGO I group were removed prior to the CVD  $\text{Si}_3\text{N}_4$  cap and given an oxidation in steam at  $1050^\circ\text{C}$  to grow  $4000\text{\AA}$  of oxide. Examination usually revealed stacking faults on the ungettered halves of the wafers, as shown schematically in Fig. 1b. A denuded region, N, was observed at the boundary of the gettered and ungettered portions of the wafer back side which was at least as wide as the wafer thickness, as described previously (1).

The device fabrication sequence followed was the same as that used to fabricate memory devices in the Murray Hill MOS laboratory. The order of operations was retained and all thermal cycles were included. A mask set was utilized which generated a  $10 \times 10$  array of test chips, each of which had, among other features, a large area diode ( $4.8 \times 10^{-4}\ \text{cm}^2$ ) and a substrate contact. The diode was formed by  $\text{PBr}_3$  predeposition at  $1000^\circ\text{C}$  and subsequent diffusion during steam re-oxidation to give a diode with a resistance of  $15\ \text{ohm}/\square$

Table I. Preoxidation gettering summary

Label	Primary gettering component	Gettering procedure	Additional steps*	Stacking faults Gettered
POGO I	Misfit dislocations	Phosphorus diffusion at $T \cong 1100^\circ\text{C}$	Encapsulate n-skin with $\text{Si}_3\text{N}_4$	Bulk and surface
POGO II	Strain gradient	$\text{Si}_3\text{N}_4$ layer with $\sigma > 1 \times 10^{10}\ \text{d-cm}^{-2}$	Anneal $\text{Si}_3\text{N}_4$ layer at $1000^\circ\text{C}$ for 60 min	Surface

\* The gettering medium is retained throughout all subsequent device processing.

Table II. Summary data on samples in Fig. 4-8

Sample	Treatment	Etch pits	Figure	Yield,* %	Leakage map
G30	Monitor	Slip + SF <sub>s</sub>	4a	13	—
G25	POGO I	Slip only	4b	72	Fig. 5
G22	POGO II	Slip + SF <sub>B</sub>	4c	36	Fig. 6
D-1	POGO I plus slow cooling	Low SF <sub>B</sub> clean	8a	87	—
D-2	POGO I plus slow cooling	No SF <sub>B</sub>	7b	98	—
E-5	POGO II slow cooling	SF <sub>B</sub>	—	38	—
F-8	Monitor slow cooling	SF <sub>B</sub> , decorated	8b	5	—

\* Per cent of devices with a leakage less than 100 nA-cm<sup>-2</sup>.

and a junction depth of 2.5  $\mu\text{m}$ . The substrate contact step followed the junction formation step and was generated by a 1050°C BN predeposition (sheet resistance = 20 ohm/ $\square$ ) and a steam reoxidation. The processing included a boron chanstop implant to raise the surface acceptor concentration in order to pin the breakdown voltage of the n<sup>+</sup>-p junctions at about 35V. The chanstop implant was done early in the processing and any implant damage was annealed during the subsequent 1200°C drive-in. The particular device whose junction leakage required improvement has the specification that the leakage current be less than 100 nA-cm<sup>2</sup> at 28V reverse bias. This is a rather severe restriction in light of the 35V breakdown voltage. The 10  $\times$  10 array was mapped for junction leakage using an automatic prober. The metal and underlying oxides were then removed prior to the preferential etch pit procedure. In this way it was possible to correlate the measured electrical characteristics of the p-n junctions with the observed defect characteristics.

Defects were delineated using the Secco etch (8) and studied using Nomarski interference contrast microscopy. Two kinds of structural defects are discussed in this report, stacking faults and dislocations. The oxidation-induced stacking faults have been further divided into two groups which are designated as bulk or surface. The bulk stacking faults are most easily identified by their occurrence in a striated or "swirled" pattern, as shown in Fig. 2a, which can readily be traced to the nonuniform distribution of native defects, i.e., stacking fault nuclei, incorporated in certain material during crystal growth (6, 9). Surface stacking faults, on the other hand, will often have a spotty and essentially random distribution, see Fig. 2b. These defects are generally related to contamination of the wafer or of the oxidation furnace, or to process-induced surface damage, and can be distinguished from the bulk stacking faults by the nature of the etch pits, as shown in Fig. 3. Note that a wafer with bulk stacking faults will have pits of varying size, as shown by arrows SF<sub>B</sub> in Fig. 3a. Also, new pits will appear as the sample is step-etched. However, surface stacking faults are all the same size, see arrows SF<sub>S</sub> in Fig. 3b, and do not change their density if the sample is step-etched to obtain a depth profile.

A dislocation-free wafer which undergoes slip due to thermal asymmetries produced during high temperature processing will typically have a defect distribution as shown in Fig. 2c where the dislocation density is highest in the four corners, near the flat, and in the central core region. Etch pits of slip dislocations are shown in Fig. 3 by the arrows D.

### Experimental Results

Macrophotographs of three device wafers which have been given a "post-mortem" preferential etch after electrical mapping and stripping down to the substrate are shown in Fig. 4. The wafer in Fig. 4a was not gettered prior to oxidation, while those in Fig. 4b and c were respectively gettered according to the POGO I and POGO II schedules outlined in Table I. The over-

riding defect common to all wafers is the high dislocation density in the four corners of each wafer. Diode junction leakage is always high and device yield low in these corners where the dislocation density is greater than 10<sup>6</sup> cm<sup>-2</sup>. The rest of the wafer will gen-

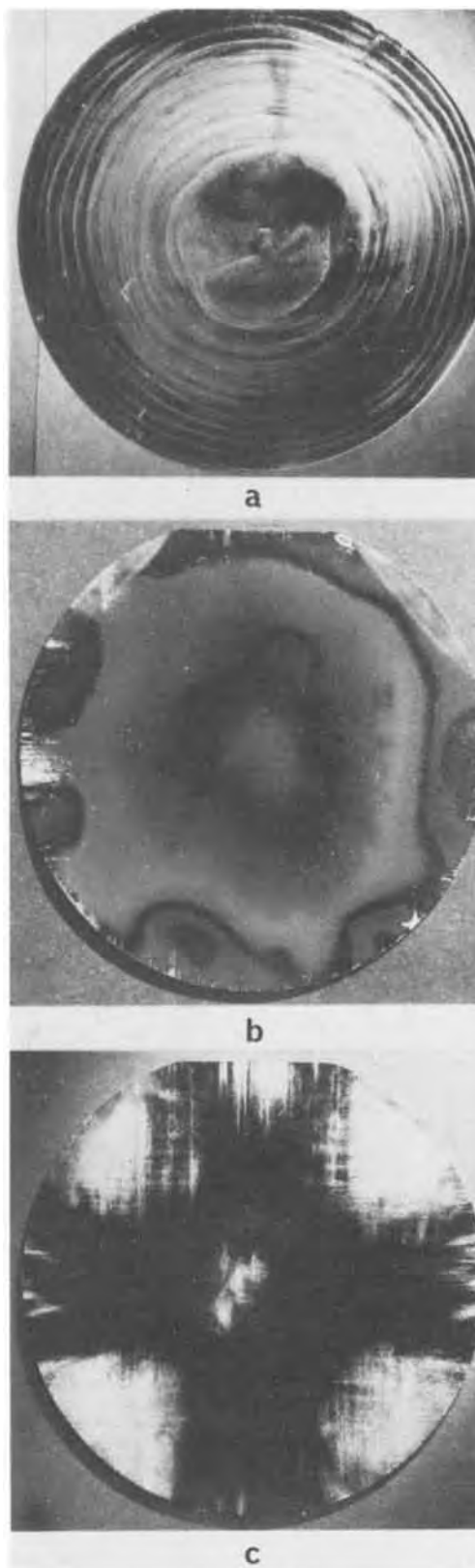


Fig. 2. Macrophotographs of Secco etched 2 in. diameter wafers illustrating: (a) swirl distribution of bulk stacking faults; (b) spotty distribution of surface stacking faults; and (c) typical distribution of "slip" type dislocations in (100) wafer.

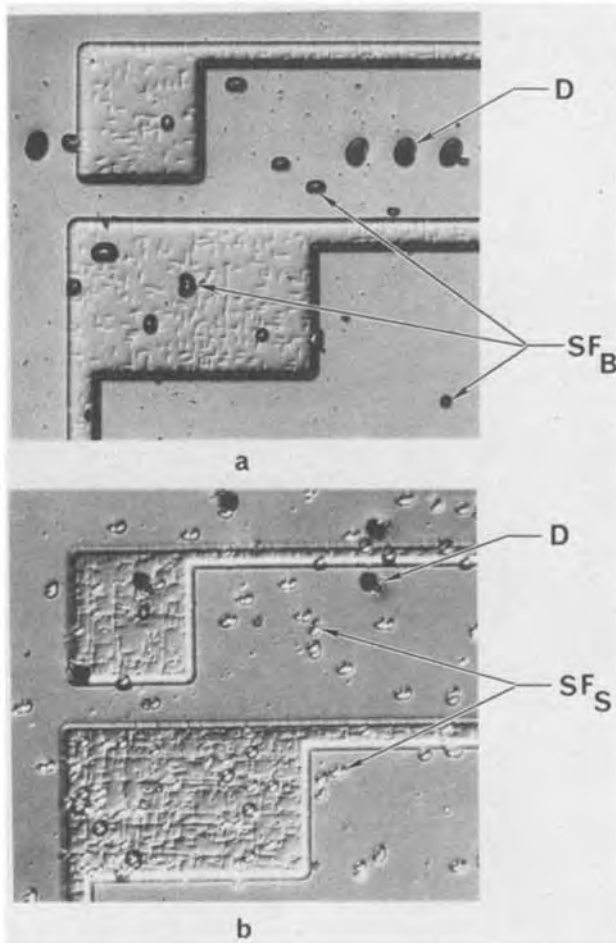


Fig. 3. Comparison of etch pits of dislocations, arrows D; stacking faults with a bulk origin, arrows SF<sub>B</sub> in (a); and stacking faults with a surface origin, arrows SF<sub>S</sub> in (b).

erally have from  $10^4$  to  $10^5$  dislocations/cm<sup>2</sup> except for the central core region where the dislocation density may be  $10^6$  cm<sup>-2</sup> locally, compare Fig. 4b and 2c. A diode leakage map of sample G25 (Fig. 4b) is shown in Fig. 5 with an outline of the wafer superimposed. The map scale is such that one unit equals  $10 \times 10^{-12}$ A, which can be converted to a leakage density of  $22 \times 10^{-9}$  A-cm<sup>-2</sup>. The double asterisk corresponds to numbers greater than 999. If those diodes with leakages greater than 100 picoA are isolated from the rest of the  $10 \times 10$  array the resulting profile of the map in Fig. 5 matches the wafer slip pattern, see Fig. 4b. Therefore, any attempts at correlating gettering of stacking faults with device properties must be done on wafers with a process-induced dislocation density less than  $10^5$  cm<sup>-2</sup>. The fact that most of the wafer, with a dislocation density from  $10^4$  to  $10^5$  cm<sup>-2</sup>, has extremely low diode leakage is consistent with a companion study on diode leakage in p-tub CMOS devices where it was shown that a dislocation density of less than  $5 \times 10^4$  cm<sup>-2</sup> will not influence the diode leakage (10). Because this report is primarily devoted to the effects of stacking faults, and since slip dislocations can be suppressed by proper control of the wafer heating and cooling cycles (11), to be discussed below, the differences in leakage for the 3 wafers shown in Fig. 4 will only be compared where the dislocation density is low.

If the slip dislocations are neglected, the 3 wafers shown in Fig. 4 represent three different stacking fault situations. The first, monitor wafer G30, is dominated by surface stacking faults, compare the hazy regions of Fig. 4a with Fig. 2b; while the third sample, POGO II wafer G22 (see Fig. 4c), illustrates a swirl

pattern typical of bulk stacking faults (recall Fig. 2a). No stacking faults at all are present in wafer G25 (see Fig. 4b) which had the POGO I treatment. The diode leakage map for this stacking fault free sample (see Fig. 5) gave an average leakage of about  $60 \times 10^{-12}$ A, for the 50 diodes which were not in the heavily

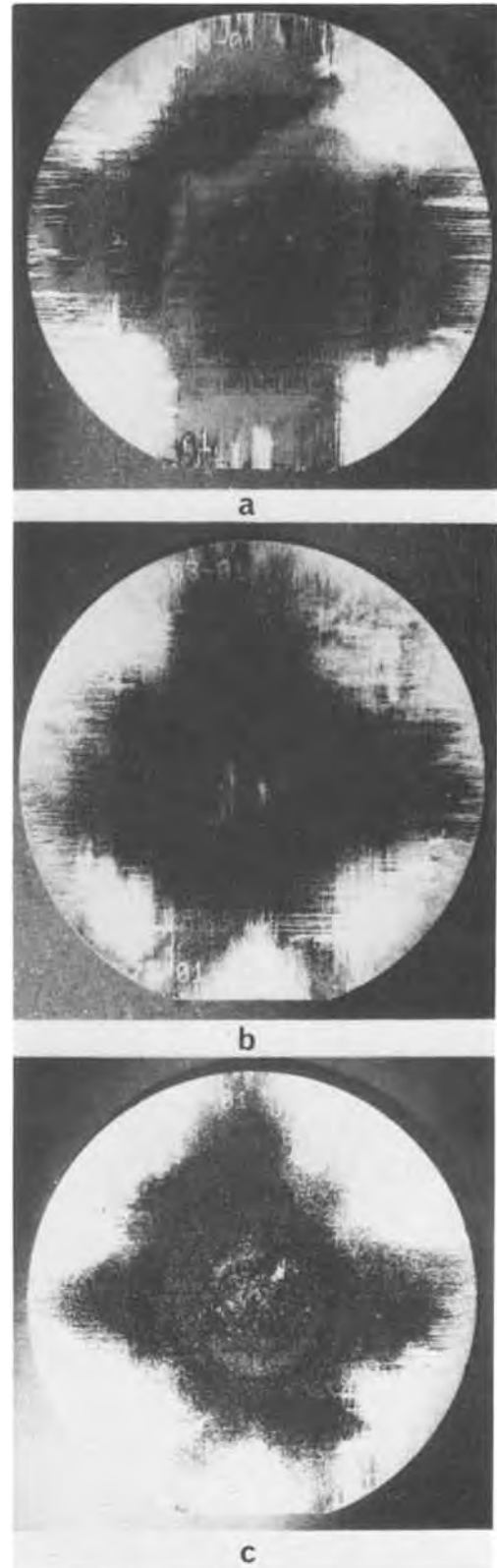


Fig. 4. Secco etched wafers with  $10 \times 10$  array of tester diodes processed (a) without preoxidation gettering, sample G30, (b) with misfit dislocation POGO I process, sample G25, and (c) with Si<sub>3</sub>N<sub>4</sub> POGO II process, sample G22.



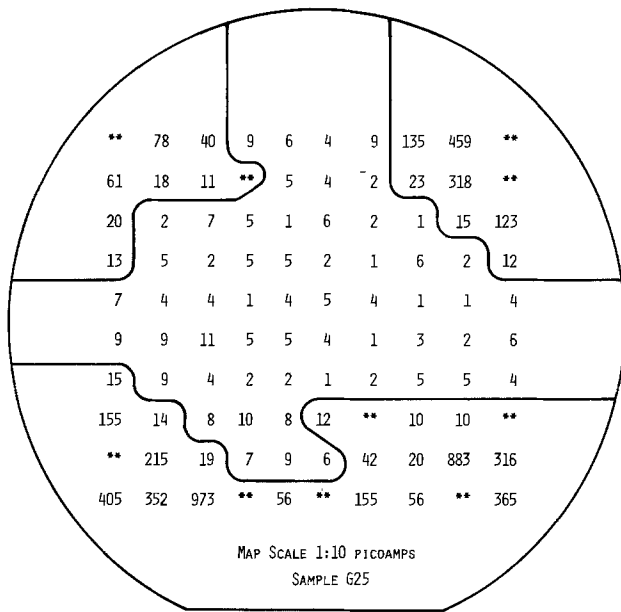
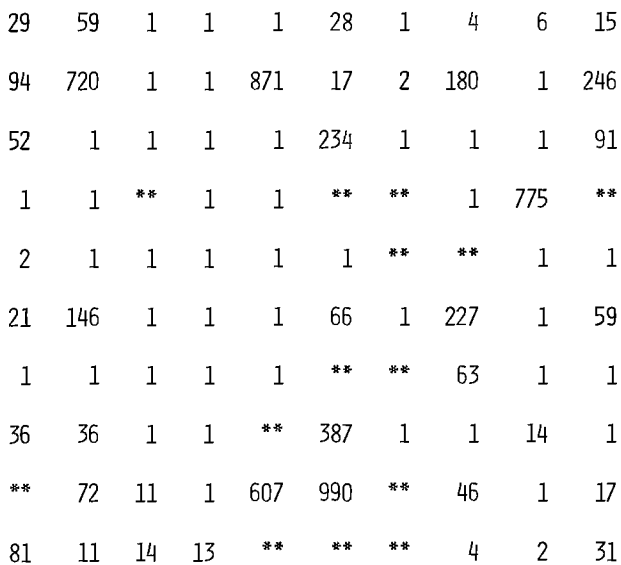


Fig. 5. Diode leakage map of sample G25 whose Secco etch photo is shown in Fig. 4b. A one corresponds to  $10 \times 10^{-12}$ A and \*\* indicates a leakage at least 1000 times greater.



MAP SCALE 1:1 NANOAMP  
SAMPLE G22

Fig. 6. Diode leakage map of sample G22 whose Secco etch photo is shown in Fig. 4c. A one corresponds to  $1 \times 10^{-9}$ A and \*\* indicates a leakage at least 1000 times greater.

slipped regions. This should be compared to an average of  $30 \times 10^{-9}$ A for similar regions of the non-POGO treated wafer, G30. Sample G22 was processed using the  $\text{Si}_3\text{N}_4$  POGO II sequence, which did not appear to suppress bulk stacking faults, as shown in Fig. 4c, and yielded the leakage map presented in Fig. 6. These data vary quite erratically with asterisks found next to ones in many cases. Note that the map scale in Fig. 6 has been increased by a factor of 100 over that in Fig. 5 in order to illustrate this apparently erratic distribution. At this point it was necessary to microscopically examine each individual diode to determine the local dislocation and stacking fault density. When this was done it was found that all of the diodes with leakages of  $1 \times 10^{-9}$ A or less (a 1 on the map), were

free of stacking faults. Adjacent diodes with asterisks, which were often located along a swirl band, would have bulk stacking faults within the diode area, similar to those shown in Fig. 3a.

We can, therefore, conclude from these data that both bulk and surface stacking faults will increase the leakage in p-n junction diodes. Also, it appears that the  $\text{Si}_3\text{N}_4$  POGO II process is only effective in suppressing the formation of surface stacking faults, whereas the POGO I treatment is required to produce diodes free of stacking faults.

By combining the POGO approach with suitable modifications (11) of the wafer cooling rates following all high temperature treatments it is possible to reduce the density of slip dislocations as well as the stacking faults. This reduction in slip is illustrated in Fig. 7 which shows samples F-8 and D-2 which are monitor and POGO I wafers from the same device processing lot. Dislocations did not play a role in the evaluation of the diode leakage maps for these wafers. Although the reduction in slip is not complete it is significantly reduced over the wafers in Fig. 4. Also, once the dislocations are suppressed the swirl pattern of bulk stacking faults becomes more prominent in the nongettered monitor wafer F-8, see Fig. 7a. The leakage map of this device showed a yield of only 5%, i.e.,

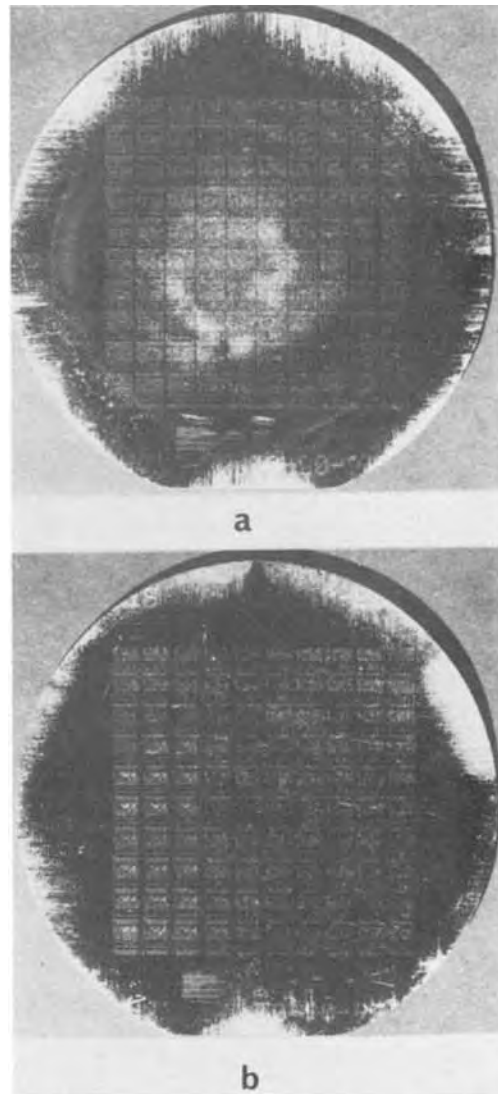


Fig. 7. Secco etched wafers with  $10 \times 10$  array of tester diodes which were slow cooled during all high temperature processes illustrating reduced density of "slip" type dislocations in addition to (a) heavy swirl of bulk stacking faults in wafer F-8 which did not receive a POGO treatment. (b) POGO I treated wafer.

diodes with junction leakage less than  $100 \text{ nA-cm}^{-2}$ . It should be noted that the monitor wafer with a high density of slip dislocations, see Fig. 4a, actually had a 15% yield. It is possible that wafers with process-induced dislocations may provide a beneficial "self-gettering" for a small number of devices in regions where the dislocation density is low enough not to produce high leakage paths on its own.

This reduction in yield has also been observed (12) when comparing the storage times of arrays of MOS tester devices which were gradually or rapidly withdrawn from the oxidation furnace. The slow cooling eliminated the slip but gave rise to a high density of stacking faults which essentially wiped out the whole wafer. However, the fast cooling with slip produced a lower stacking fault density and a reasonable yield away from the slipped corners. This potential interaction between different kinds of defects which depends, in part, on the nature of the starting material, makes it extremely difficult to empirically optimize furnace operations and wafer cooling cycles. It is essential, therefore, that the microstructure of the defects be examined before and after any perturbation of the high temperature process.

Returning to the slow cooled wafer which also had a POGO I treatment (D-2, Fig. 7b) we note a combined reduction in slip and absence of the heavy swirl observed in Fig. 7a. The diode leakage map of sample D-2 showed a yield of 98%, which should be compared to the 5% yield of the non-POGO monitor wafer F-8, and the 72% yield of the fast cooled, POGO I wafer G25, previously discussed in Fig. 5 and 4b. A third slow cooled wafer which had the POGO II process had a yield of 36%. This wafer did have bulk stacking faults and a prominent swirl pattern, similar to Fig. 7a. However, the 36% yield indicated that the stacking faults of the POGO II wafer did not appear to be as electronically active as those in the monitor wafer. This can be explained as follows. Although the POGO II process is not as effective as POGO I in suppressing stacking fault formation, it will reduce the amount of contamination in the bulk of the wafer which will then lead to a cleaner, less decorated stacking fault with reduced electrical activity.

Support for the idea of stacking faults with varying amounts of decoration and electrical activity was obtained by microstructure examination of pits in sample D-1, a POGO I wafer which did have a low density of bulk stacking faults, although none were evident in the macrophoto. Figure 8 gives a comparison of clean stacking fault etch pits from wafer D-1 with decorated pits from a monitor wafer, F-8, which was processed with D-1. Note that the black pits in Fig. 8a are symmetric with relatively smooth side walls. Also, the small background "saucer" pits are isolated entities. However, in the non-POGO treated, heavily swirled wafer (see Fig. 8b) the black pits are irregularly shaped with a knobby structure, while the background saucer pits tend to aggregate into clusters (see arrows A in Fig. 8b). This distinction between clean and decorated defects has been observed previously (13) when comparing dislocation etch pits in saucer-pit free GaP LPE layers with GaP substrates containing  $10^7$  saucer pits/cm<sup>2</sup>.

The reason for the occurrence of stacking faults, i.e., the incomplete nature of the POGO I treatment for sample D-1, is believed to be related to the quality of the starting material, other samples of which had an unusually high density of native microdefects. Work is in progress both on evaluating defects in the as-received wafers and in using the SEM in the EBIC mode to examine the differences between clean and decorated stacking faults. For example, leakage currents at 28V of samples D-1 and F-8, Fig. 8a and b, were typically  $22 \text{ nA-cm}^{-2}$  or  $1 \text{ } \mu\text{A-cm}^{-2}$ , respectively. However, the 87% yield of wafer D-1 was noticeably lower than

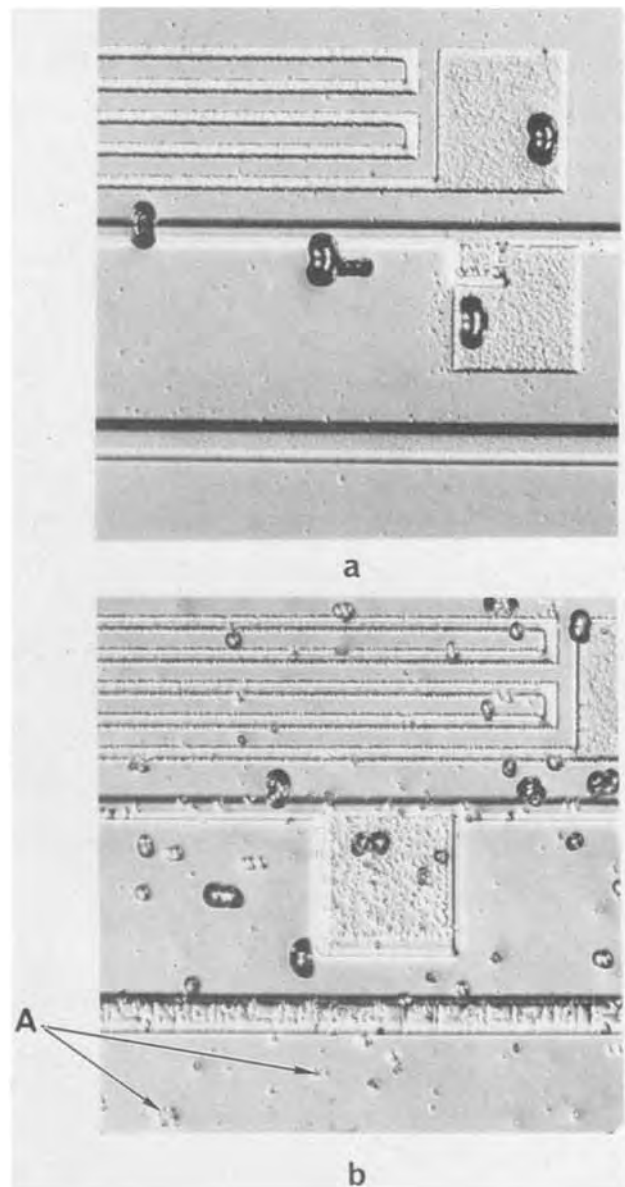


Fig. 8. Comparison of etch pits of bulk stacking faults which are (a) clean (wafer D-1), and those which are (b) decorated (wafer F-8). Note aggregates of saucer pits, arrows A in (b).

the 96-98% yield of other POGO I wafers from this group. Since most of the 13 bad devices were in the higher stacking fault density regions it is likely that, like slip dislocations, a high enough density of clean stacking faults will increase the diode leakage.

### Summary and Conclusions

The results of this study can be briefly summarized in the following statements:

1. Both dislocations and stacking faults can cause increased diode leakage and reduced yield for devices with leakage requirements less than  $1 \text{ } \mu\text{A-cm}^{-2}$  at 28V, especially if the defects are decorated and their density is greater than  $10^4 \text{ cm}^{-2}$ .

2. The suppression of stacking faults by preoxidation gettering with misfit dislocations will reduce leakage currents by two to three orders of magnitude and increase yields of tester diodes from 10% to greater than 90%, provided the slip dislocation density is below  $5 \times 10^4 \text{ cm}^{-2}$ .

3. Preoxidation gettering with the  $\text{Si}_3\text{N}_4$  process is not effective in eliminating bulk stacking faults which have native defect origins, although surface stacking faults related to processing are gettering. However, the



level of decoration of the bulk stacking faults is reduced compared to nongettered wafers, with a resulting improvement in device yields from about 10 to 30 or 40%.

4. The occurrence of bulk stacking faults and the completeness of the misfit dislocation gettering process appears to be related to the density of native defects in the starting material.

#### Acknowledgments

The authors would like to thank Mrs. M. H. Read for carrying out the chemical etching procedures reported in this study. Also, discussions with P. M. Petroff and D. M. Boulin proved most useful and are gratefully acknowledged. Comments on the final manuscript by R. B. Marcus and E. N. Fuls are also appreciated.

Manuscript submitted Sept. 12, 1975; revised manuscript received Nov. 16, 1975.

Any discussion of this paper will appear in a Discussion Section to be published in the December 1976 JOURNAL. All discussions for the December 1976 Discussion Section should be submitted by Aug. 1, 1976.

Publication costs of this article were partially assisted by Bell Laboratories.

#### REFERENCES

1. G. A. Rozgonyi, P. M. Petroff, and M. H. Read, *This Journal*, **122**, 1725 (1975).
2. P. M. Petroff, G. A. Rozgonyi, and T. T. Sheng, *ibid.*, **123**, 565 (1976).
3. J. E. Lawrence, in "Semiconductor Silicon" R. R. Haberecht and E. L. Kern, Editors, p. 596 (1969) and references therein.
4. C. M. Hsieh, J. R. Mathews, H. D. Seidel, K. A. Pickar, and C. M. Drum, *Appl. Phys. Letters*, **22**, 238 (1973); T. E. Seidel and R. L. Meek, in "Ion Implantation in Semiconductors," B. L. Crowder, Editors, Plenum Publishing Corp., New York (1973); R. L. Meek, T. E. Seidel, and A. G. Cullis, *This Journal*, **122**, 786 (1975).
5. H. Shiraki, *Japan J. Appl. Phys.*, **13**, 1514 (1974).
6. A. J. R. de Kock, *Philips Res. Rept., Supplement No. 1* (1973).
7. P. M. Petroff and A. J. R. de Kock, *J. Cryst. Growth*, **30**, 117 (1975).
8. F. Secco D'Aragona, *This Journal*, **119**, 948 (1972).
9. K. Ravi and C. J. Varker, *J. Appl. Phys.*, **45**, 263 (1974).
10. G. A. Rozgonyi and J. Dishman, Unpublished data.
11. K. Moerschel, Private communication.
12. G. A. Rozgonyi and E. N. Fuls, Unpublished data.
13. G. A. Rozgonyi and T. Iizuka, *This Journal*, **120**, 673 (1973).

## Technical Notes



### The Effect of Structural Change on Electrical Conductivity in InSe

Kazuaki Imai and Yutaka Abe<sup>1</sup>

Department of Nuclear Engineering, Hokkaido University, Sapporo 060, Japan

Indium selenide, a layered semiconductor, has been investigated by several authors with respect to the optical (1-3) and electrical (4-6) properties. However, these experimental results seem to depend on the process by which the crystal was grown and the perfection of the crystals.

In this note, we report the several characteristic changes in activation energies of the electrical conductivity in InSe and the relation between a structural change and the conductivity in the high temperature range.

#### Experimental

For the measurements of electrical conductivity, single crystals of InSe which had been grown by the Bridgman method were cut from the ingot and cleaved perpendicular to the C axis. The typical dimensions of the specimens were  $3 \times 7 \times 0.5$  mm<sup>3</sup>. In order to measure the temperature dependence of electrical conductivity, the samples were cooled in a vacuum cryostat and heated in a vacuum furnace.

Te-Au contacts were attached to the specimens. These contacts had good ohmic characteristics at room temperature and below. Below 190°K there was a slight deviation from the ohmic behavior but the de-

viation was less than 15% and could be neglected. Above room temperature, Cu pressure contacts were used. These contacts also showed good ohmic behavior.

The electrical conductivity was measured along the cleaved surface, i.e., parallel to the C plane, of the specimens. The dark conductivity of our specimens at room temperature was  $2.2 \times 10^{-5}$  (ohm-cm)<sup>-1</sup>, with a variation of this value for different specimens of about 10%.

The typical temperature dependence of electrical conductivity from 80° to 950°K is shown in Fig. 1. These curves are qualitatively similar to those in Ref. (4). The characteristics can be divided into five distinct temperature regions, namely, (I) below 190°K, (II) 190°~429°K, (III) 429°~600°K, (IV) 600°~827°K, and (V) above 827°K. In region I, the conductivity seems to be limited by crystal purity. In regions II, III, and 600°~750°K in IV, there is a linear relation  $\log \sigma - 1/T$ , and in these regions the activation energies are calculated as II = 0.42 eV, III = 0.34 eV, and IV = 1.05 eV, respectively. In region V, the conductivity has a metallic temperature dependence.

In order to find the relation between the variation of activation energies and the crystallographic change in our specimens, we have investigated the change of x-ray diffraction patterns using a high temperature Debye-Scherrer camera.

<sup>1</sup> Present address: Division of Engineering, Brown University, Providence, Rhode Island 02912.

Key words: electrical conductivity, structural change, phase change.

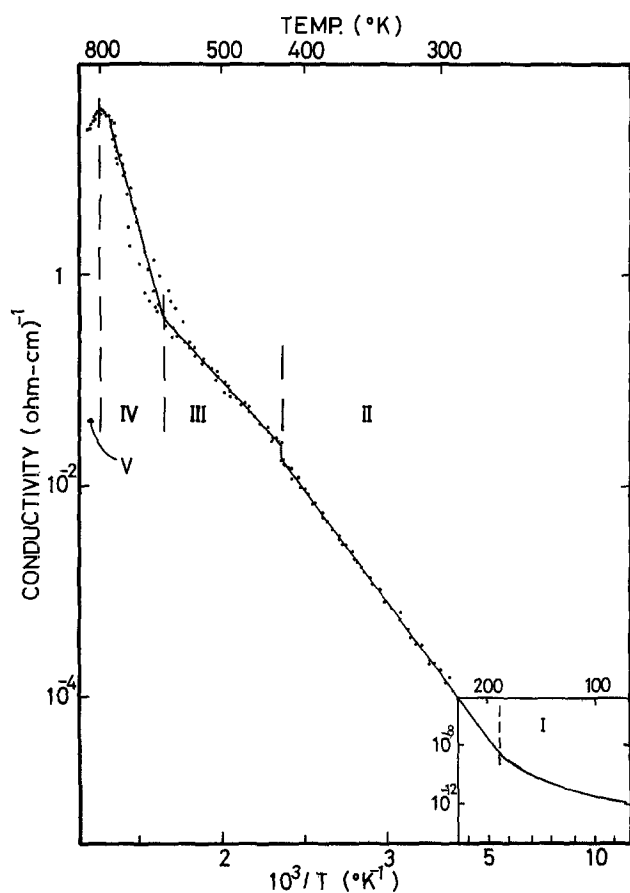


Fig. 1. The temperature dependence of electrical conductivity. The experimental results in the lowest temperature region are plotted on a different scale.

The specimens for this experiment were prepared as follows: stoichiometric amounts of indium (99.999%) and selenium (99.999%) were enclosed in a quartz holder in a vacuum of  $10^{-5}$  Torr. After fusion, cooling of the melt led to formation of a polycrystal of InSe. This crystal was cut in pieces of  $0.4 \times 0.4 \times 7$  mm<sup>3</sup>.

CuK $\alpha$  line was used as an x-ray beam. A typical result is shown in Fig. 2. The calculated lattice parameters of InSe in a hexagonal structure at room temperature are  $a = 4.001 \pm 0.003$  Å and  $c = 16.639 \pm 0.005$  Å. No appreciable change in the patterns is observed at 429° and 827°K, whereas a drastic change is found around 600°K as easily seen in Fig. 2. This structural change is irreversible: when the specimen is cooled slowly to room temperature, no change around 600°K is observed.

### Discussion

In this note, we deal mainly with regions II, III, and IV. As indicated by optical absorption, the indirect energy gap of InSe is 1.187 eV (3). On the other hand, the two activation energies in regions II and III in our experiments are 0.42 eV (190°~429°K) and 0.34 eV (429°~600°K), respectively. This fact indicates that the electrical conductivity of our specimens is trap controlled even in the higher temperature ranges.

We could not find a definite structural change around 429°K by x-ray analysis but we have observed a distinct peak in the specific heat measurement (7) in our specimens, which indicates that a slight phase change might occur at this temperature. We conjecture that the step in the activation energy at 429°K is correlated with this slight phase change.

As described above, we found a drastic change of x-ray patterns around 600°K. Above 600°K, InSe cannot be considered to have structures such as D<sub>3h</sub>,

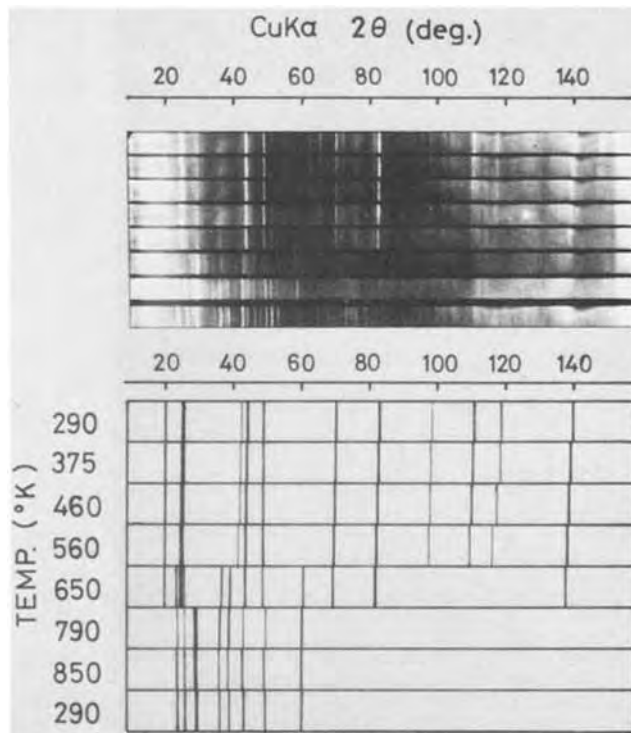


Fig. 2. The temperature dependence of x-ray Debye-Scherrer patterns. Strong lines taken from the photographs are shown in the lower figure.

D<sub>3h</sub>, or C<sub>3v</sub>; there is a complex change in crystal structure. This transition occurs at the point where there is a kink in the electrical conductivity. If we alternatively assume the onset of intrinsic conduction in this temperature range, our experimental results would yield an energy gap width of 2.1 eV which was almost twice as large as the energy gap obtained by optical experiments. Therefore it must be concluded that electric conduction of InSe above 600°K is entirely controlled by the structural change rather than by intrinsic conduction.

Also, we would like to point out that the structural change of InSe may be very sensitive to the external pressure of Se vapor. We have observed that a slight amount of excess Se added in the process of heat-treatment of InSe effectively quenched the phase change. We conjecture that vapor pressure of Se in our specific heat measurement on InSe, where we used quartz capillary packed entirely by InSe, was high enough for the quenching and therefore we could not observe the large phase change around 600°K.

More detailed experiments on the phase diagram with the temperature and external pressure, in particular with respect to the partial pressure of Se, are now in progress and will be reported elsewhere.

### Acknowledgments

The authors would like to thank Professor K. Watanabe and Dr. M. Fukuchi of the Department of Metallurgical Engineering for provision of the high temperature Debye-Scherrer camera.

This work was partially supported by the Takeda Science Foundation.

Manuscript submitted Sept. 17, 1975; revised manuscript received Dec. 12, 1975.

Any discussion of this paper will appear in a Discussion Section to be published in the December 1976 JOURNAL. All discussions for the December 1976 Discussion Section should be submitted by Aug. 1, 1976.

Publication costs of this article were partially assisted by Hokkaido University.

## REFERENCES

1. J. C. Brice, P. C. Newman, and H. C. Wright, *Brit. J. Appl. Phys.*, **9**, 110 (1958).
2. P. Fielding, G. Fischer, and E. Mooser, *J. Phys. Chem. Solids*, **8**, 434 (1959).
3. M. Yu. Sakhnovskii, V. B. Timofeev, and A. S. Yakimova, *Sov. Phys.—Semicond.*, **2**, 168 (1968).
4. R. W. Damon and R. W. Redington, *Phys. Rev.*, **96**, 1498 (1954).
5. S. Sugaike, *Mineral. J.*, **2**, 63 (1957).
6. S. Mori, *J. Phys. Soc. Japan*, **18**, 308 (1963).
7. K. Imai, M. Sato, and Y. Abe, *This Journal*, **121**, 1674 (1974).

## Effects of Oxide Thickness and Substrate Dopants on Irradiated MOS Capacitors

W. R. Haller,<sup>1</sup> S. Share, and A. S. Epstein

Harry Diamond Laboratories, Adelphi, Maryland 20783

and V. Kumar and W. E. Dahlke

Lehigh University, Bethlehem, Pennsylvania 18015

In our previous publications dealing with the effect of oxide thickness on oxide charge buildup in MOS (metal-oxide-silicon) structures (1, 2), there were indications that the density of radiation-induced fast interface states was dependent on the oxide thickness. In the following note, we have explored this dependence more fully. In addition, the effect of various p-type substrate dopants on the interface-state density is discussed.

The dopants, their concentrations, and oxide thicknesses ( $t_{ox}$ ), are listed in Table I. The oxides were grown on <111> oriented silicon substrates by a wet oxide technique, described elsewhere, at a temperature of 925°C (1). The thermal oxidation of silicon can permit the incorporation of the substrate dopants (in our study, Ga, In, Al, or B) at the interface and into the oxide (3-6). Aluminum contacts were used on the oxide, and either gold or aluminum served as the back contact to the silicon substrates. The areas of the MOS capacitors ranged from  $5 \times 10^{-4}$  to  $2 \times 10^{-3}$  cm<sup>2</sup>. An effective thickness of the oxide was calculated from the oxide capacitance in accumulation, the metal electrode area, and by assuming a dielectric constant for the oxide of 3.8.

The capacitors were irradiated at <sup>60</sup>Co gamma source (dose rate  $2 \times 10^6$  rads(Si)/hr) to a dose of  $10^6$  rads(Si). Measurements were initiated within 1 hr after the irradiation. The samples were unbiased (floating) during the irradiation (7).

Changes in oxide charge density and fast interface-state density resulting from irradiation of the MOS capacitors were obtained from capacitance-voltage (C-V) measurements at frequencies of 1 MHz and 100 Hz. Additional confirmation of the interface-state

density was provided by conductance-voltage (G-V) measurements (8). Ionizing irradiation normally causes a parallel shift,  $\Delta V$ , of the C-V characteristics toward the negative voltage direction (Fig. 1). This shift is generally interpreted as a buildup of positive charge in the oxide. Calculation of the oxide-charge density from C-V data requires a knowledge of the distribution of oxide charge over the oxide layer.

Since this is difficult to attain, an effective value (image) of the oxide charge density can be calculated from  $\Delta Q_{ox} = q\Delta N_{ox} = \epsilon_{ox}\Delta V/t_{ox}$  where  $\epsilon_{ox}$  is the SiO<sub>2</sub> dielectric constant,  $q$  is the charge of an electron,  $t_{ox}$  is the oxide thickness, and  $\Delta N_{ox}$  is an effective density of the radiation-induced oxide states. The shift of the flatband voltage in high frequency (1 MHz) C-V curves (Fig. 1) was used to obtain values of  $\Delta V$ , since the high frequency curves minimize the contribution of fast interface states. Ionizing radiation also causes large changes in the low frequency C-V characteristic (i.e., increased dispersion) as shown in Fig. 1. This is usually attributed to an increase in the fast interface-state density. Using high (1 MHz) and low (100 Hz) frequency C-V characteristics, the interface-state density distribution can be obtained by a procedure outlined by Castagne and Vapaille (9) both before and after  $10^6$  rads(Si) irradiation. The interface-state distribution of some of the samples was also obtained from the G-V data by a procedure outlined by Nicollian and Goetzberger (8), using a single time-constant surface-state circuit model. The effects of inhomogeneities and lateral nonuniformities are not considered in our discussion.

The effect of irradiation on MOS capacitors with various oxide thicknesses and dopants is found in Table I. The data are arranged in the order of decreasing oxide thickness. Listed in Table I along with the oxide thicknesses,  $t_{ox}$ , are the effective density of radiation-induced oxide states,  $\Delta N_{ox}$ , after  $10^6$  rads(Si) ir-

<sup>1</sup> Work performed while summer student at Harry Diamond Laboratories. Present address: Department of Electrical Engineering, Lehigh University, Bethlehem, Pennsylvania 18015.

Key words: radiation, dopants, oxide thickness, interface states, charge buildup.

Table I. Sample fabrication data, interface-state densities, and oxide charge buildup for irradiated samples with various oxide thicknesses and substrate dopants

Sample No.	Dopant	Dopant concentration (cm <sup>-3</sup> )	$t_{ox}$ (Å)	$\Delta N_{ox}$ ( $\times 10^{11}$ cm <sup>-2</sup> )	$N_{ss}$ ( $\times 10^{11}$ cm <sup>-2</sup> V <sup>-1</sup> )	$\Delta N_s$ ( $\times 10^{11}$ cm <sup>-2</sup> )	$\Delta N_{ox}/\Delta N_s$
Ga-2	Gallium	$1 \times 10^{17}$	1336	40	93	8.2	4.9
Al-4	Aluminum	$1 \times 10^{18}$	968	45	70	14	3.2
In-5	Indium	$1 \times 10^{17}$	968	44	63	15	2.9
B-3	Boron	$2 \times 10^{18}$	750	35	47	12	2.9
In-3	Indium	$1 \times 10^{18}$	347	24	27	8.4	2.9
B-1	Boron	$2 \times 10^{18}$	308	17	29	6.2	2.8
B-16	Boron	$2 \times 10^{18}$	160	20	12.5	6.0	3.3
B-9	Boron	$2 \times 10^{18}$	90	5	6.5	1.5	3.3

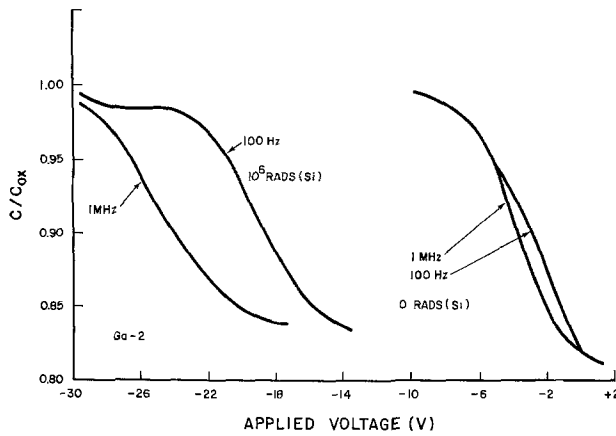


Fig. 1. C-V data for gallium-doped substrate sample Ga-2 showing 1 MHz and 100 Hz data for pre- and post-irradiated [ $10^6$  rads (Si)] condition. Note shift of C-V curve to more negative voltage following the  $^{60}\text{Co}$  irradiation.

radiation, the peak values of the fast interface-state density distribution after  $10^6$  rads (Si) irradiation,  $N_{ss}$ , and the change of the total density of fast-interface states ( $\text{cm}^{-2}$ ) induced by irradiation,  $\Delta N_s$ . The latter is obtained by taking the difference between the total density of interface states after and before  $10^6$  rads (Si) irradiation. For all except the Ga-doped sample, the values of  $N_{ss}$  and  $\Delta N_s$  increase with increasing oxide thickness. The peak energy of the state distribution lies at about 0.30-0.35 eV above valence band edge. The value of the total density of interface states prior to irradiation is on the order of  $10^{11} \text{ cm}^{-2}$  for all oxide thicknesses. The variation of  $\Delta N_s$  with oxide thickness as noted in Table I has, to our knowledge, not been reported so directly before. A result similar to this has recently been inferred from radiation experiments performed on CMOS integrated circuits (10). On the other hand, the increase of  $\Delta N_{ox}$  with oxide thickness has been noted in our previous work (1). This latter trend was found to be indicative of a buildup of positive charge in the oxide located within 160Å of the Si-SiO<sub>2</sub> interface. Reference to the last column in Table I reveals that the ratios of  $\Delta N_{ox}$  to  $\Delta N_s$  for all the thicknesses of the B-doped samples as well as the In- and Al-doped samples are approximately equal ( $\sim 3$ ). This suggests that  $\Delta N_s$  is directly proportional to  $\Delta N_{ox}$  and that there is a direct relation between the effect of oxide charge buildup and radiation-induced fast interface states; namely, the thickness dependence of both processes are similar for the wet oxides studied here.

The total radiation-induced interface-state density,  $\Delta N_s$ , shows a difference for the Ga-doped substrate dopant as seen by the larger ratio of  $\Delta N_{ox}$  to  $\Delta N_s$  in Table I. It is not immediately obvious why the Ga-doped sample should have a reduced density of radiation-induced fast interface states. It may be related to the higher diffusion coefficient of Ga in SiO<sub>2</sub> (4). If the density of fast-interface states is related to an impurity, then the deeper the dopant diffuses into

the oxide, the less likely the communication of the interface state with the silicon.

These results have been deduced from a straightforward analysis of C-V data. Castagne and Vapaille have shown in their analysis of C-V data that the effects of oxide charge inhomogeneities can produce apparent changes in the fast interface-state density (11). The probability that the radiation-induced interface state densities in our experiment are due to inhomogeneities is considered unlikely since analyses of both C-V and G-V data provide similar state distributions (11).

### Conclusion

A variation of the radiation-induced fast interface-state density ( $\Delta N_s$ ) with oxide thickness has been observed in MOS capacitors fabricated by the wet oxide technique. Comparing the effect of oxide charge buildup  $\Delta N_{ox}$  with  $\Delta N_s$  for each thickness yields a constant value of  $\Delta N_{ox}/\Delta N_s$  ( $\sim 3$ ) for all devices fabricated on B-doped substrates. This result can also be extended to include other p-type substrate dopants, including Al and In. A larger value of  $\Delta N_{ox}/\Delta N_s$  ( $\sim 5$ ), however, has been found for the Ga-doped sample because of the smaller value of  $\Delta N_s$ .

### Acknowledgments

We thank R. Cohen of the Massachusetts Institute of Technology, Lincoln Laboratories, for supplying the silicon substrates.

Manuscript submitted Oct. 21, 1975; revised manuscript received Dec. 16, 1975.

Any discussion of this paper will appear in a Discussion Section to be published in the December 1976 JOURNAL. All discussions for the December 1976 Discussion Section should be submitted by Aug. 1, 1976.

Publication costs of this article were partially assisted by Harry Diamond Laboratories.

### REFERENCES

1. S. Share, A. S. Epstein, V. Kumar, W. E. Dahlke, and W. Haller, *J. Appl. Phys.*, **45**, 4894 (1974).
2. S. Share and R. A. Martin, *IEEE Trans. Electron. Devices*, **ED-22**, 619 (1975).
3. A. S. Grove, "Physics and Technology of Semiconductor Devices," pp. 69-77, John Wiley & Sons, New York (1967).
4. H. Wolf, "Semiconductors," pp. 342-370, John Wiley & Sons, New York (1971).
5. A. S. Grove, O. Leisteko, Jr., and C. T. Sah, *J. Appl. Phys.*, **35**, 2695 (1964).
6. B. E. Deal, A. S. Grove, E. H. Snow, and C. T. Sah, *This Journal*, **112**, 308 (1965).
7. Self-biasing effects may arise due to metal-semiconductor work function difference, oxide charge buildup, and photocurrent production in the SiO<sub>2</sub> during irradiation.
8. E. H. Nicollian and A. Goetzberger, *Bell System Tech. J.*, **46**, 1055 (1967).
9. R. Castagne and A. Vapaille, *Surface Sci.*, **28**, 157 (1971).
10. J. G. Fossum, G. F. Derbenwick, and B. L. Gregory, Paper A-12 presented at IEEE Conference on Nuclear and Space Radiation Effects, July 1975, Arcata, California.
11. R. Castagne and A. Vapaille, *Electron. Letters*, **6**, 691 (1970).

# Selective Etching of GaP Crystals with Hot Phosphoric Acid

T. Uragaki, H. Yamanaka, and M. Inoue

Matsushita Electronics Corporation, Research Laboratory, Takatsuki, Osaka, Japan

The chemical etching of GaP is one of the important processes in the fabrication of the light emitting devices (1, 2). Aqua regia (3) has been conventionally used for groove formation on a  $(\bar{1}\bar{1}\bar{1})$  wafer, along which the individual chips are mechanically separated. However, irregularly grooved patterns are often observed in prolonged etching as a result of lateral etching at the mask edges. In addition, the mechanical cutting of the shallow grooves for chip separation, by a diamond saw or a laser beam, gives rise to profound surface damages to the crystal which may degrade the device performance.

This report describes a new technique for pattern etching of GaP crystals with phosphoric acid. Well-defined grooves, uniform in width and depth, are formed on the  $(\bar{1}\bar{1}\bar{1})$  surface regardless of the pattern orientation. The cross-sectional view of the grooves obtained is so sharply V shaped that no mechanical cutting process should follow for chip separation. The pattern etching technique can use a vacuum-deposited film of gold or gold alloy as the mask, which will be contact electrodes.

## Experimental Procedure

The GaP wafers used for the etching experiments are (111),  $(\bar{1}\bar{1}\bar{1})$ , or (100) oriented and doped with sulfur to a carrier concentration of  $4\sim 8 \times 10^{17} \text{ cm}^{-3}$ . The etch pit density was  $3\sim 5 \times 10^5 \text{ cm}^{-2}$ . The mechanically polished wafers were further etched chemically with a solution of 2 vol HCl + 1 vol HNO<sub>3</sub> + 2 vol H<sub>2</sub>O (4) at 60°C for 1~2 min.

For the mask etching, a gold film of 3000Å thickness was deposited in vacuum onto the wafer surface at 300°C, being followed by pattern formation with a mixed solution of 25g I<sub>2</sub> + 50g KI + 500 ml H<sub>2</sub>O.

The etching was carried out with reagent-grade H<sub>3</sub>PO<sub>4</sub> (85%) at a temperature of 150°~200°C. Gas evolution during etching provides vigorous stirring of the etching solution. Measurements of the etch depth and width were made with a microscope. For detailed geometrical observation of the revealed surfaces, the scanning electron microscope was used.

## Results and Discussion

**Etching rate.**—The etching rate was determined for the (111),  $(\bar{1}\bar{1}\bar{1})$ , and (100) surfaces. Figure 1 shows the change in wafer thickness with increasing etching time. The decrease in wafer thickness is seen to be a linear function of time up to 10 min and the etching rate, which is defined as the thickness removed per unit time, is therefore constant. The etching rate at 180°C for the  $(\bar{1}\bar{1}\bar{1})$  wafer was found to be about 20 times higher than that for the (111) or (100) wafer, probably due to the crystallographic anisotropy in chemical reactivity of the zinc blende structure.

The temperature dependence of the etching rate for the  $(\bar{1}\bar{1}\bar{1})$  surface is shown in Fig. 2. The etching rate is practically controllable between 5 and 25  $\mu\text{m}/\text{min}$  by varying the temperature from 150° to 200°C.

**Pattern etching.**—Using a vacuum-deposited gold film on the  $(\bar{1}\bar{1}\bar{1})$  surface of GaP as an etch mask, the exposed circular region of 60  $\mu\text{m}$  diameter was etched

Key words: mesa formation, GaP LED, chemical etch, III-V compounds, H<sub>3</sub>PO<sub>4</sub>.

with H<sub>3</sub>PO<sub>4</sub> at 180°C. Figures 3(a) and 3(b) are the  $\langle\bar{1}\bar{1}\bar{1}\rangle$  top view and the  $\langle\bar{1}\bar{1}0\rangle$  cross-sectional view of a hollow formed by 6 min etching, respectively, in which the hollow is found to be of threefold symmetry surrounded by the  $(\bar{2}\bar{2}\bar{1})$  and  $(\bar{1}\bar{1}\bar{7})$  facets.

A selective etching was also carried out for stripes of 60  $\mu\text{m}$  width oriented in the  $[\bar{1}\bar{1}0]$  direction. Figure 4 [(a) to (e)] shows the change in shape and size of the cross section of the grooves during the successive etching for 1~8 min. At the first stage of etching the grooves were flat bottomed [Fig. 4(a) and (b)] and then grew to be asymmetrical V shaped [Fig. 4(e)]. It was observed that the angles between the revealed facets and the  $(\bar{1}\bar{1}\bar{1})$  surfaces were unchanged throughout the etching period. These angles were measured to be 45° and 55°, and are in good agreement with the calculated angles of 44.5° and 54.7° assuming the  $(\bar{1}\bar{1}\bar{7})$  and  $(\bar{2}\bar{2}\bar{1})$  planes for the revealed surfaces.

For the practical application of stripe etching, there is a need to know the dependence of the resulting groove profile on the crystallographic direction of the mask pattern. Grooves parallel to three typical directions,  $[\bar{1}\bar{1}0]$ ,  $[\bar{1}\bar{1}\bar{2}]$ , and 45° off  $[\bar{1}\bar{1}0]$ , were formed on a  $(\bar{1}\bar{1}\bar{1})$  wafer, of which cross sections are compared in Fig. 5. As is seen in Fig. 5, the V shapes formed are not so much different from one another, where the bottom angles between the revealed surfaces are in the range of 70°~80°. The strictly symmetrical cross

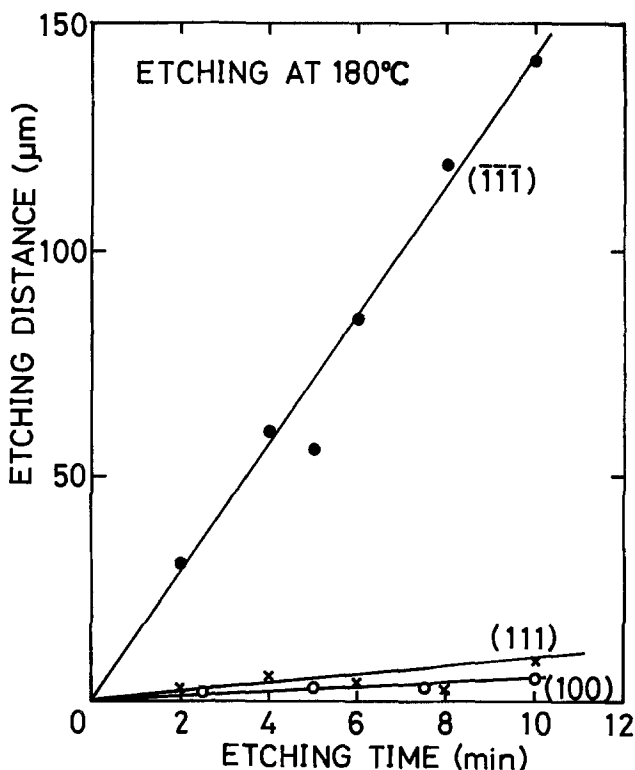


Fig. 1. Change in wafer thickness with etching time. The crystal orientations are  $\langle 111 \rangle$ ,  $\langle \bar{1}\bar{1}\bar{1} \rangle$ , and  $\langle 100 \rangle$  and etching temperature is 180°C.

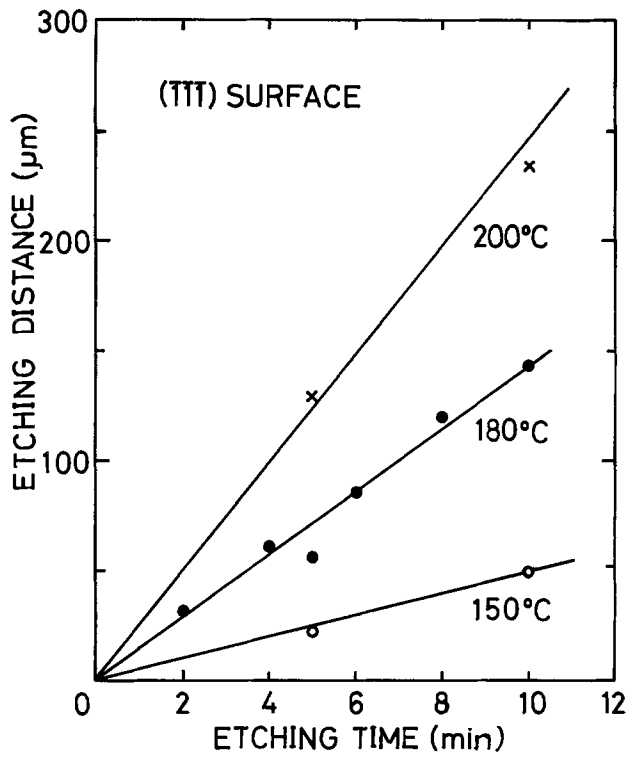


Fig. 2. Temperature dependence of etching rate for the  $(\bar{1}\bar{1}\bar{1})$  surface.

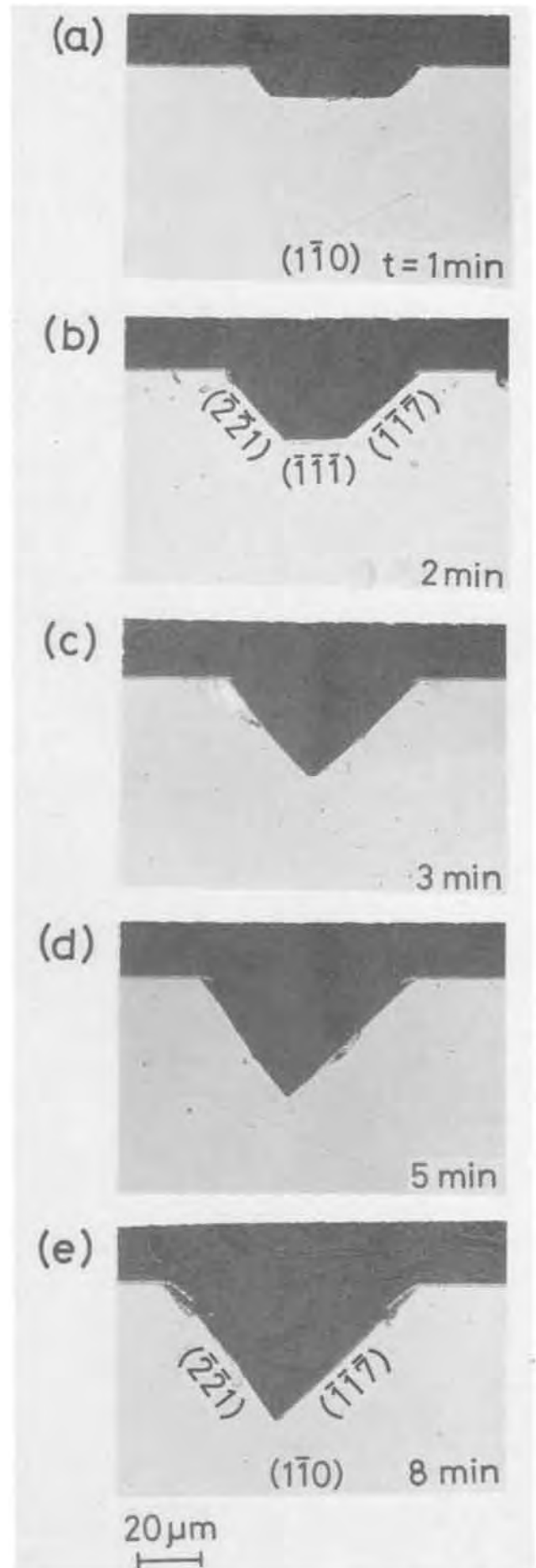


Fig. 4. Change in shape and size of the cross section of the grooves during the successive etching.

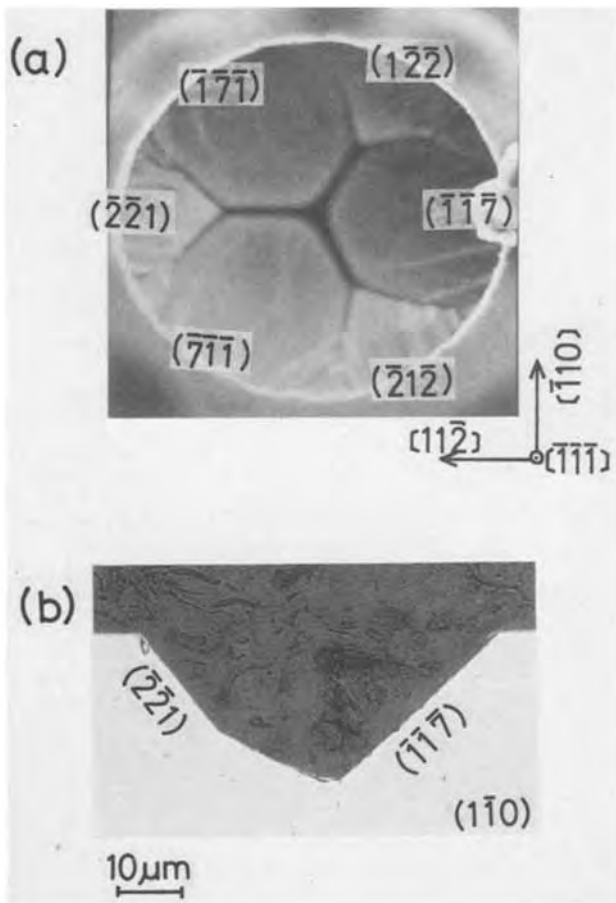


Fig. 3. The  $\langle \bar{1}\bar{1}\bar{1} \rangle$  top view (a) and the  $\langle \bar{1}\bar{1}\bar{0} \rangle$  cross-sectional view (b) of a hollow engraved on a  $(\bar{1}\bar{1}\bar{1})$  surface.

Fig. 5. Cross sections of the grooves parallel to three typical directions, (a)  $[1\bar{1}0]$ , (b)  $[1\bar{1}2]$ , and (c)  $45^\circ$  off  $[1\bar{1}0]$ .

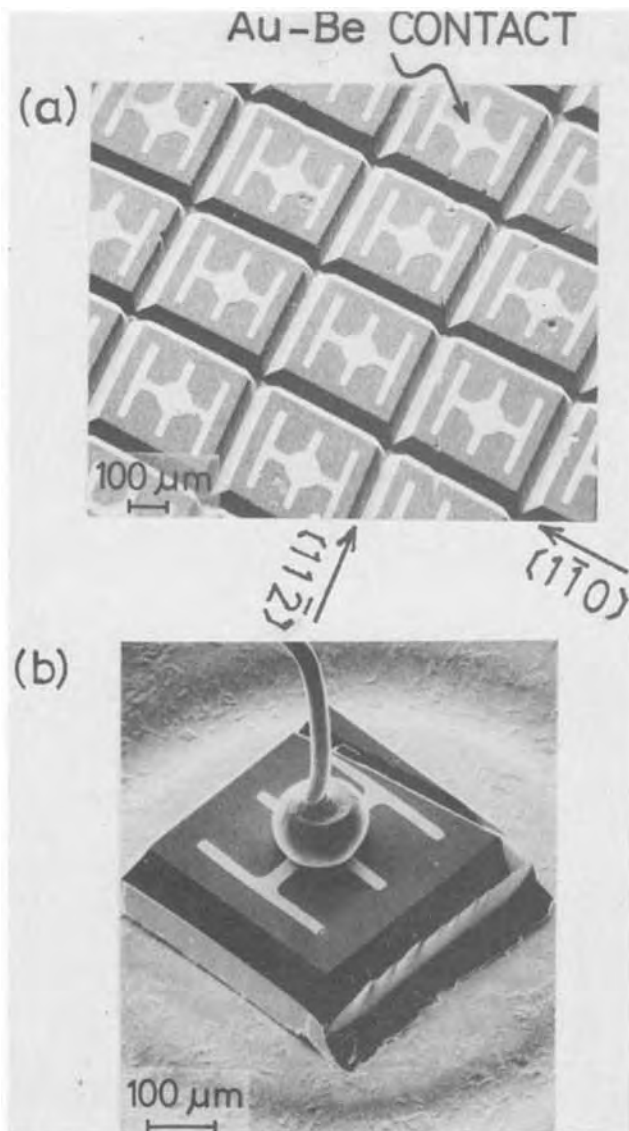
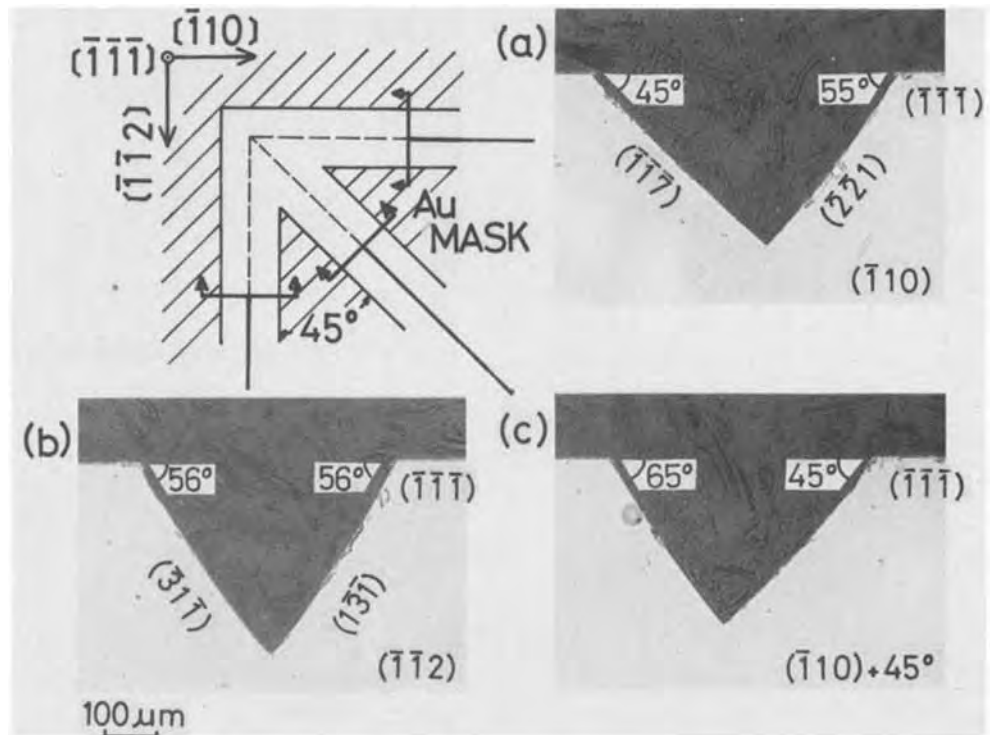


Fig. 6. Scanning electron micrographs of a mesa-etched wafer (a) and an LED chip mounted on a TO-18 stem (b).

section is obtained only when the stripe is parallel to the  $[1\bar{1}2]$  direction.

#### Application to Device Fabrication

The etching technique with  $H_3PO_4$  was applied to the mesa-formation process of GaP LED's. A  $(\bar{1}\bar{1}\bar{1})$  LPE wafer of p/n/n<sup>+</sup> structure was pattern etched using an Au-Zn or Au-Be alloy film as the mask. The stripe lines were directed parallel to the  $[1\bar{1}0]$  and  $[1\bar{1}2]$  directions in  $400\ \mu\text{m}$  intervals, as shown in Fig. 6(a). The width and depth of the V-shaped grooves obtained were  $60\ \mu\text{m}$  and  $40\ \mu\text{m}$ , respectively. After the mesa etching, the Au-alloy film was again photoetched in order to leave the electrode patterns for ohmic contact to the p-layer. The separation of individual chips was easily accomplished by bending the wafer with a roller after reduction of the wafer thickness to about  $200\ \mu\text{m}$ . Figure 6(b) shows an LED chip mounted p-side up on a TO-18 stem. When the diode is mounted p-side down, the inclined facets formed by the mesa etching act as efficient internal reflectors giving rise to an increase of light output.

#### Acknowledgments

The authors wish to thank Dr. I. Teramoto and S. Fujwara for encouragement and comments, and T. Matsuda for technical assistance.

Manuscript submitted Dec. 3, 1975; revised manuscript received Jan. 14, 1976.

Any discussion of this paper will appear in a Discussion Section to be published in the December 1976 JOURNAL. All discussions for the December 1976 Discussion Section should be submitted by Aug. 1, 1976.

Publication costs of this article were partially assisted by the Matsushita Electronics Corporation.

#### REFERENCES

1. R. A. Logan, H. G. White, and W. Wigmann, *Solid-State Electron.*, **14**, 55 (1971).
2. R. H. Saul, J. Armstrong, and W. H. Hackett, *Appl. Phys. Letters*, **15**, 229 (1969).
3. N. E. Schumaker, M. Kuhn, and R. A. Furnage, *IEEE Trans. Electron. Devices*, **ED-18**, 627 (1971).
4. R. H. Saul, *This Journal*, **115**, 1184 (1968).

# Profile Parameters of Implanted-Diffused Arsenic Layers in Silicon

Richard B. Fair\* and Joseph C. C. Tsai

Bell Laboratories, Reading, Pennsylvania 19604

In a previous paper, the diffusion of ion-implanted As in <100> Si was discussed as well as the electrical quality of implanted-diffused layers. It is the purpose of this paper to derive equations that describe the important characteristic profile parameters, and to support these equations with experimental data. A discussion of total As surface concentration, junction depth, and profile gradient will be presented, which will be followed by an analysis of the sheet resistance of implanted-diffused As layers and the surface concentration of the electrically active As.

## Analysis

*Total As surface concentration,  $C_{T0}$ , and junction depth,  $x_J$ .*—It was shown previously (1) that the implanted-diffused total As profile shape is approximately described by the equation

$$C = C_{T0} (1 - 0.87Y - 0.45Y^2) \quad [1]$$

where

$$Y = x(8C_{T0}D_it/n_i)^{-1/2} \quad [2]$$

$t$  is the diffusion time (sec),  $D_i$  is the intrinsic As diffusivity ( $\text{cm}^2/\text{sec}$ ),  $n_i$  is the intrinsic electron concentration, and  $C_{T0}$  is the As surface concentration (atom/ $\text{cm}^3$ ) assumed to be greater than  $\sim 1 \times 10^{19} \text{ cm}^{-3}$ .

Equation [1] is a Chebyshev polynomial approximation to the solution of the diffusion equation with a linear concentration-dependent diffusion coefficient and constant surface concentration,  $C_{T0}$ . It is probable that the polynomial coefficients are time-dependent for the case of nonconstant  $C_{T0}$ , such as the case of a redistributing impurity distribution. For the case of implanted As in Si,  $C_{T0}$  decreases as  $t^{-1/3}$ , and the constant  $C_{T0}$  approximation is not an unreasonable assumption. In any case, the functional form of  $Y$  would not be different (Eq. [2]).

In order to solve for the junction depth as a function of time, temperature, and implant dose, Eq. [1] can be solved for  $Y$  at  $C(x_J)$  and the result substituted into Eq. [2]. Thus, at the junction

$$x_J = (8C_{T0} D_i t / n_i)^{1/2} \frac{\left(0.64 - 0.45 \frac{C(x_J)^{1/2}}{C_{T0}} - 0.435\right)}{0.45} \quad [3]$$

When  $0.45 C(x_J)/C_{T0} \ll 0.64$ , then Eq. [3] becomes

$$x_J = 2.3 (C_{T0} D_i t / n_i)^{1/2} \quad [4]$$

and  $Y_J = 0.81$ .

When diffusion occurs from a predeposited As layer in Si, the total concentration,  $Q_T$  (atom/ $\text{cm}^2$ ), remains constant. Thus, integrating Eq. [1] over  $x$  gives the result that

$$Q_T = K C_{T0} x_J \quad [5]$$

with  $K = 0.45$  (valid for  $C_{T0} \gtrsim 1 \times 10^{19} \text{ cm}^{-3}$ ). For the case of a redistributing implanted layer,  $K$  would be slightly time dependent to balance the nonconstant  $C_{T0}$ .  $Q_T$  vs.  $C_{T0} \cdot x_J$  data from the measured As profiles described in Ref. (1) are plotted in Fig. 1, and it is found that  $K$  averages out to be  $(1.9)^{-1} \approx 0.53$

(50 keV implantations). Thus the time dependence of the polynomial coefficients and, thus,  $K$ , is not significant.

Substitution of Eq. [5] into Eq. [4] yields

$$x_J = K_1 \left( \frac{Q_T D_i t}{n_i} \right)^{1/3} \quad [6]$$

with  $K_1 = 2.16$ . Data are shown in Fig. 2 where  $x_J$  values at  $C = 0.01 C_{T0}$  as determined by direct profile measurement by secondary ion mass spectrometry are plotted as a function of implant dose and diffusion time and temperature. The data represent diffusions in the temperature range of  $1000^\circ\text{--}1250^\circ\text{C}$ . For diffusions performed in neutral ambients or in oxygen, Eq. [6] can be used to fit these data slightly better with  $K_1 = 2$ . Thus

$$x_J = 2 \left( \frac{Q_T D_i t}{n_i} \right)^{1/3} \quad [7]$$

for  $C_{T0} \gtrsim 1 \times 10^{19} \text{ cm}^{-3}$ .

Diffusions performed in steam ambients represent a special case, and are discussed in Ref. (1). It can be seen, however, in Fig. 2 that the discrepancy in  $x_J$  between diffusions performed in steam ambients and  $\text{N}_2$  or  $\text{O}_2$  ambients decreases as  $x_J$  increases. This result indicates that the As diffusion in steam is being controlled by a surface effect associated with the oxidation process.

The time and temperature dependence of the surface concentration,  $C_{T0}$ , can now easily be obtained by combining Eq. [5] and [7]. Thus

$$C_{T0} = 0.94 \left( \frac{Q_T^2 n_i}{D_i t} \right)^{1/3} \quad [8]$$

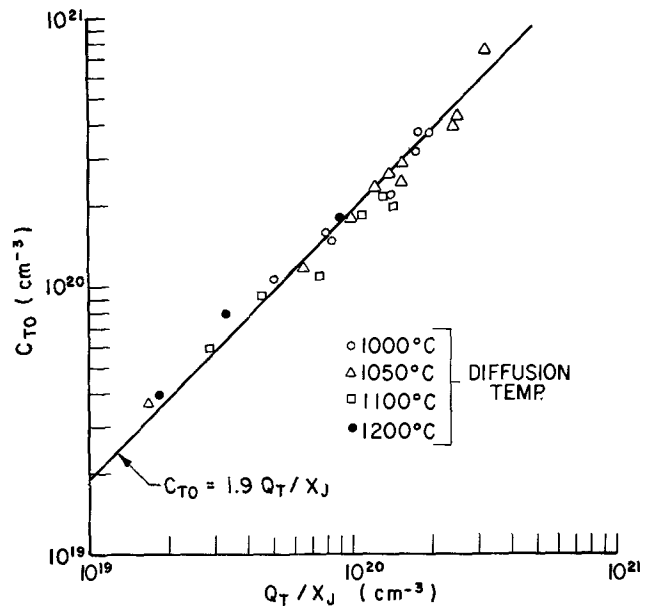


Fig. 1. Total As surface concentration vs. the average doping for implanted-diffused layers in Si.

\* Electrochemical Society Active Member.

Key words: ion implantation, arsenic diffusion, sheet resistance, junction depth.



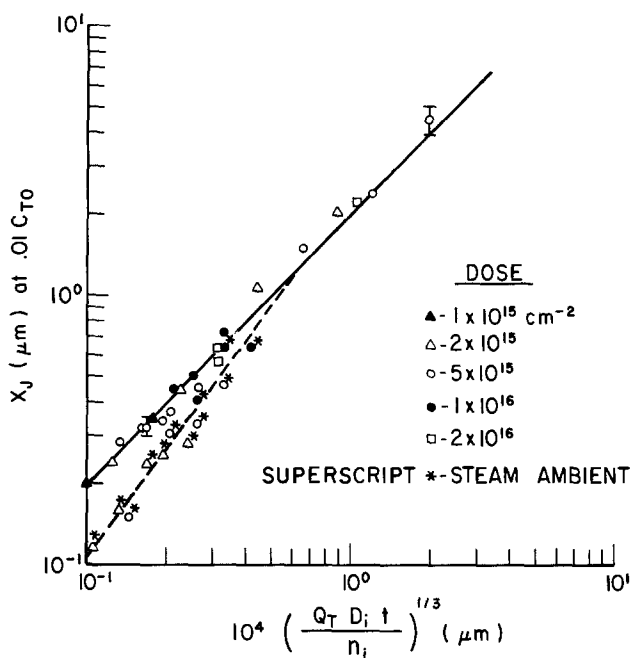


Fig. 2. Time, temperature, and dose dependence of the junction depth of implanted As layers diffused in N<sub>2</sub>, O<sub>2</sub>, and steam ambients.

Equation [8] predicts that for a given temperature and dose, the surface concentration will decrease as  $t^{-1/3}$ . The data plotted in Fig. 3 (from measured profiles) agree quite well with Eq. [8].

*Profile gradient calculation.*—The gradient of the As profile at the junction can be calculated by differentiating Eq. [1] and substituting Eq. [2]. Thus, for  $C(x_j) \ll C_{T0}$

$$\left. \frac{dC}{dx} \right|_{x=x_j} = -0.565 (C_{T0} n_i / D_i t)^{1/2} \quad [9]$$

or

$$\left. \frac{dC}{dx} \right|_{x=x_j} = -1.24 C_{T0} / x_j \quad [10]$$

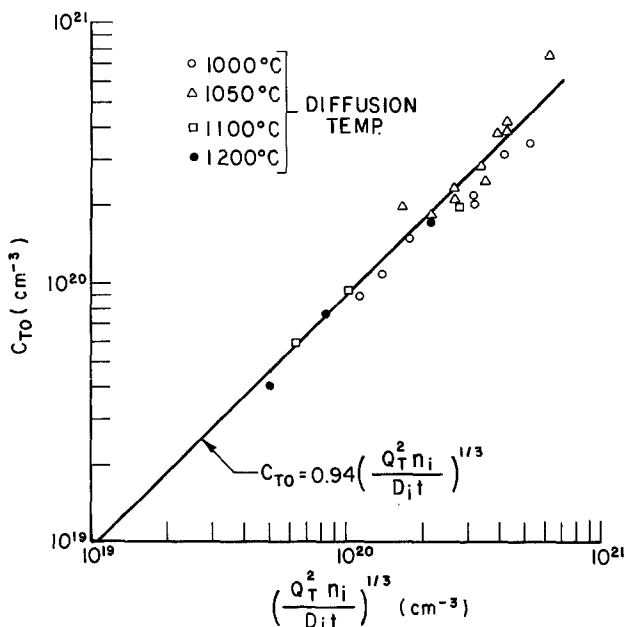


Fig. 3. Time, temperature, and dose dependence of implanted-diffused As surface concentration.

Gradient data from measured implanted-diffused As profiles, plotted in Fig. 4, show that Eq. [10] is applicable at  $C(x_j) = 0.1 C_{T0}$ . Data from chemical source As diffusions ( $\blacktriangle$ —data) are also shown. However, the gradient is not constant with decreasing concentration for a given value of  $C_{T0}/x_j$ . At  $C(x_j) = 0.01 C_{T0}$  the gradient has decreased by a factor of 4 below the value at  $C = 0.1 C_{T0}$ . The significance of this result is unclear in view of the uncertain accuracy of the measurements.

*Sheet resistance and electrically active As surface concentration.*—The expression for the sheet resistance of a diffused layer is

$$R_s = 1 / \left( q \bar{u} \int_0^{x_j} C_A dx \right) \quad [11]$$

where  $C_A$  is the electrically active As concentration and  $\bar{u}$  is the effective bulk carrier mobility (cm<sup>2</sup>/V-sec) given by

$$\bar{u} = \frac{\int_0^{x_j} u C_A dx}{\int_0^{x_j} C_A dx} \quad [12]$$

When the implanted-diffused As is 100% electrically active, i.e.,  $C_{T0} = C_{A0}$  (active As surface concentration), then using Eq. [5] and [11],  $C_{A0}$  can be expressed in terms of the measurable quantities  $R_s$  and  $x_j$ . Thus

$$C_{A0} = \frac{1.9}{q \bar{u} R_s x_j} \quad [13]$$

In order to determine the concentration dependence of  $\bar{u}$ , use will be made of the mobility data in Ref. (4, 5) which can be described approximately by the expression

$$u = \frac{28.2 \times 10^7}{C_A^{1/3}} \text{ cm}^2/\text{V-sec} \quad [14]$$

for the As concentration range of  $10^{19} \text{ cm}^{-3} < C_A < 6 \times 10^{20} \text{ cm}^{-3}$ . Substituting Eq. [1], [2], and [14] into Eq. [12], the effective mobility can be determined from numerical integration. However, using the fact that the As profile is almost a step function and the average doping is approximately  $Q_T/x_j = 0.53 C_{A0}$ , a simple expression for  $\bar{u}$  has been found which is

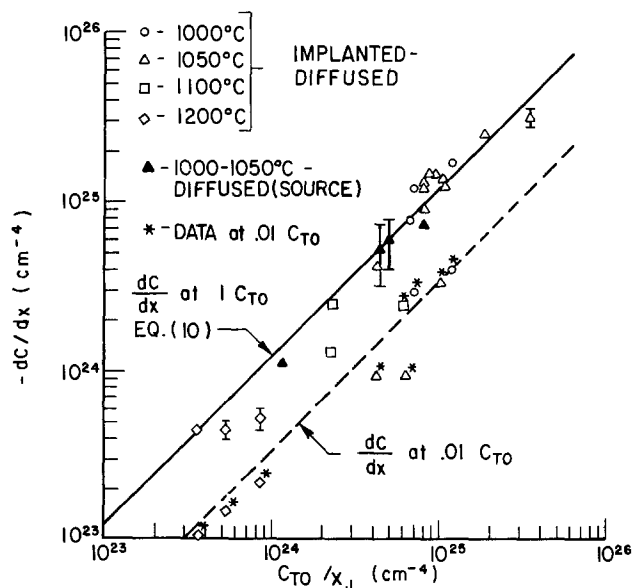


Fig. 4. Arsenic layer junction profile gradient vs. surface concentration/junction depth at two concentrations.

$$\bar{u} = \frac{28.2 \times 10^7}{(0.53 C_{A0})^{1/3}} \quad [15]$$

The  $0.53 C_{A0}$  term represents an equivalent uniform As distribution over the diffused layer. Substituting Eq. [15] in Eq. [13], the following expression for  $C_{A0}$  is obtained

$$C_{A0} = \frac{6.26 \times 10^{15}}{(R_S x_J)^{3/2}} \quad [16]$$

This equation for  $C_{A0}$  differs from the result obtained for diffusion from a chemical source (2) where a constant mobility was assumed

$$C_{A0} = \frac{1.56 \times 10^{17}}{R_S x_J} \quad [17]$$

Experimental data of  $C_{A0}$  vs.  $(R_S x_J)$  are shown plotted in Fig. 5 along with Eq. [16] and [17]. The experimental values of  $C_{A0}$  were determined from differential conductivity measurements on implanted-diffused As layers and the revised resistivity vs. electron concentration curve for As in Si [Fig. 1 of Ref. (1)]. The effect of using the revised  $\rho$  vs.  $n$  curve for As is to increase the magnitude of the slope of the  $C_{A0}$  vs.  $R_S x_J$  curve (on log-log scales), as compared to using Irvin's  $\rho$  vs.  $n$  curve (6). Irvin's curve underestimates electron concentration,  $n$ , when  $\rho > 8 \times 10^{-4}$  ohm-cm. Most of the data displayed in Fig. 5 showed 100% electrical activity. However, at high doses and short diffusion times,  $C_{T0}$  may be greater than the solid solubility of active As,  $C_{A,SOL}$  (1). Data for which  $C_{T0} > C_{A,SOL}$  are indicated in Fig. 5 by an (\*).

Sheet resistance can be determined as a function of implant dose and diffusion time and temperature by combining Eq. [11] with the expression for  $\bar{u}$  of Eq. [15] to yield

$$R_S = \frac{1.7 \times 10^{10}}{Q_T^{7/9}} \left( \frac{n_i}{D_i t} \right)^{1/9} \quad [18]$$

Equation [18] predicts that for a fixed temperature and dose,  $R_S \propto t^{-1/9}$ . This expression is shown plotted in Fig. 6 along with sheet resistance data obtained

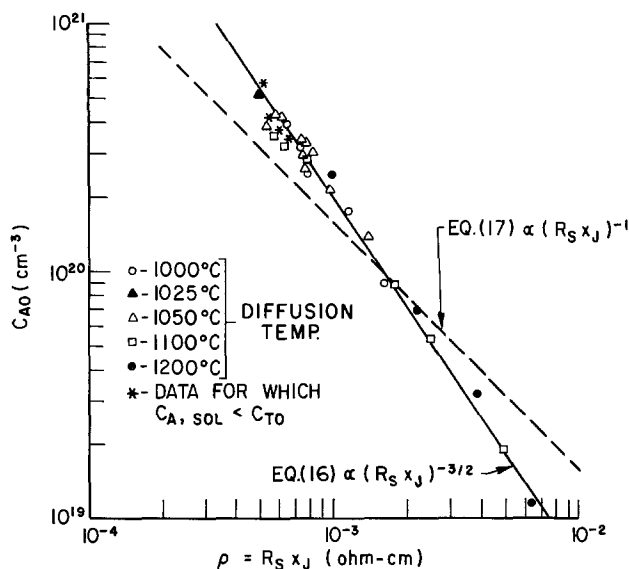


Fig. 5. Electrically active As surface concentration vs. the implanted-diffused layer resistivity. The dashed line was obtained from data on chemical-source As diffusions in Si.

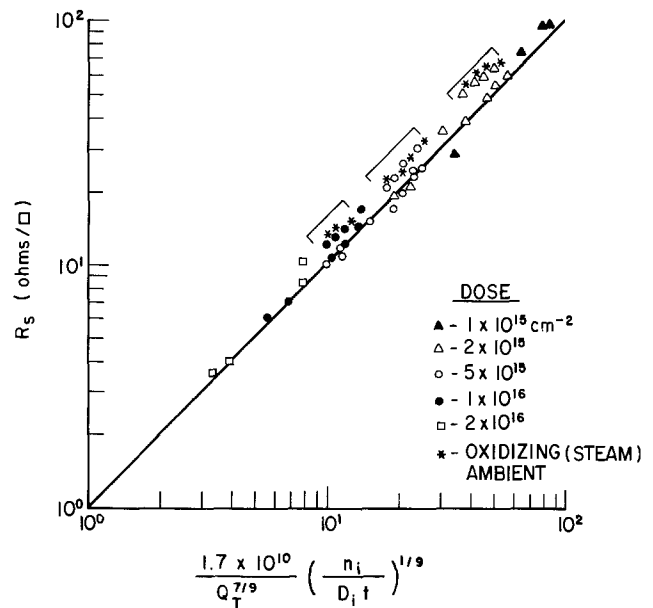


Fig. 6. Time, temperature, and dose dependence of the implanted-diffused As layer sheet resistance.

over the range  $1000^\circ < T < 1250^\circ\text{C}$ . For diffusions performed in neutral ambients or in oxygen, the agreement with theory is good. However, diffusions in steam consistently yield  $R_S$  values that are 10-20% higher than predicted. This result is consistent with the fact that As diffusion in steam yields shallower junctions and higher (lower  $\bar{u}$ ) average concentrations than diffusions in  $O_2$  or  $N_2$ .

### Discussion

It should be pointed out that the curves in this paper are derived for 50 keV As predepositions. The energy of the predeposition implantation is important for shallow junction diffusions. The projected range and standard deviation (7) for 50 keV As in Si are  $R_P = 324\text{\AA}$  and  $\Delta R_P = 120\text{\AA}$ , respectively. For 100 keV As in Si,  $R_P = 584\text{\AA}$  and  $\Delta R_P = 211\text{\AA}$ . Thus, a junction depth difference of  $\sim 500\text{\AA}$  should be expected for shallow junction drive-ins from 100 keV implants. However, for buried layer-type diffusions ( $>1 \mu\text{m}$ ), little difference, if any, should be expected between 50 and 100 keV predepositions. It is also expected that the results in the present study are applicable for an implant energy of 30 keV.

### Summary and Conclusions

Equations have been derived that describe the important profile variables that are required to characterize the diffusion of As implanted layers for which the surface concentration is greater than  $\sim 1 \times 10^{19} \text{ cm}^{-3}$ . In addition, data obtained from differential conductivity profile measurements and SIMS profile measurements (1) have been used to obtain experimental parameters for these equations.

Manuscript submitted Oct. 6, 1975; revised manuscript received Nov. 24, 1975.

Any discussion of this paper will appear in a Discussion Section to be published in the December 1976 JOURNAL. All discussions for the December 1976 Discussion Section should be submitted by Aug. 1, 1976.

Publication costs of this article were partially assisted by Bell Laboratories.

### REFERENCES

1. R. B. Fair and J. C. C. Tsai, *This Journal*, **122**, 1689 (1975).
2. R. B. Fair, *J. Appl. Phys.*, **43**, 1278 (1972).
3. R. B. Fair and G. R. Weber, *ibid.*, **44**, 273 (1973).

4. H. Müller, H. Kranz, H. Ryssel, and K. Schmid, *Appl. Phys.*, **4**, 115 (1974).  
 5. V. I. Fistul', "Heavily Doped Semiconductors," p. 129, Plenum Press, New York (1969).

6. J. C. Irvin, *Bell Syst. Tech. J.*, **41**, 387 (1962).  
 7. W. S. Johnson and J. F. Gibbons, "Projected Range Statistics in Semiconductors," Stanford University Press, California (1970).

## In Situ Thickness Monitoring of Thick Polycrystalline Silicon Film and Its Application to Silicon Epitaxial Growth

Katsuro Sugawara,\* Yukiyoishi Nakazawa, and Takeo Yoshimi

Hitachi, Limited, Semiconductor and Integrated Circuits Division, Kodaira, Tokyo, Japan

The development of high performance silicon semiconductor bipolar devices has increased the requirement for precise control of silicon epitaxial layers. One of the precise control methods is an "in process" monitoring system. Dumin first devised a monitoring method using optical interference to control the thickness of the SOS (silicon-on-sapphire) epitaxial layer (1), and this method was extended to monitor thickness in  $\text{Al}_2\text{O}_3$  (2), sputtered  $\text{SiO}_2$  (3), CVD  $\text{SiO}_2$  (4), and polycrystalline silicon (5, 6) film formation. In this note, the monitoring of polycrystalline silicon film thickness was investigated to evaluate the monitoring capability of silicon epitaxial layer thickness which was inferred by measuring the thickness of simultaneously deposited polycrystalline silicon films on insulator-covered substrates.

The following problems were anticipated in the case of monitoring silicon epitaxial growth which took place in a hotter atmosphere than amorphous or polycrystalline CVD film formation:

(i) Intensity of background in the infrared radiation emitted from the substrate was stronger.

(ii) The substrate covered with insulating film degraded in severe ambient conditions such as hot hydrogen and hydrogen chloride.

(iii) Correlation between the deposition rate of the polycrystalline silicon film and that of the single crystalline silicon layer when the thickness of the silicon epitaxial layer was indirectly monitored as the polycrystalline silicon film thickness.

Both methods of infrared radiation (1, 5) and infrared laser (6) were tried for this purpose and the improved former method was selected due to the larger monitoring capability for higher temperature deposition.

The experiment was carried out in a horizontal epitaxial reactor of rf-heated type with a SiC-coated graphite susceptor. The cross section of the reactor tube was  $120 \times 65$  mm. In this reactor, polycrystalline silicon films produced by  $\text{SiCl}_4\text{-H}_2$  or  $\text{SiH}_2\text{Cl}_2\text{-H}_2$  (7, 8) system were deposited on two kinds of substrates; thermally grown  $\text{SiO}_2$  films of  $1.2 \mu\text{m}$  in thickness and CVD  $\text{Si}_3\text{N}_4$  films of  $3000\text{\AA}$  formed on silicon substrates. The silicon deposition was performed at a  $\text{SiCl}_4/\text{H}_2$  ratio of 0.005 in the temperature range from  $1060^\circ$  to  $1330^\circ\text{C}$  for the  $\text{SiCl}_4\text{-H}_2$  system and  $\text{SiH}_2\text{Cl}_2/\text{H}_2$  ratio of 0.005 from  $950^\circ$  to  $1280^\circ\text{C}$  for the  $\text{SiH}_2\text{Cl}_2\text{-H}_2$  system at  $\text{H}_2$  flow rate of 60 liter/min. The reaction temperature was corrected for emissivity according to Allen's data (9).

During the deposition, the infrared radiation emitted from the substrate was received by a PbS photocell with a filter (10) which allowed only  $2.0 \mu\text{m}$  wave-

length to pass through. The signal from the photocell was then amplified and recorded as an interference wave pattern. Since the peak-to-peak of waves corresponded to the deposition film thickness, the thickness of the epitaxial layer could be estimated from the correlation curve between the polycrystalline silicon thickness and the silicon epitaxial layer growth. After the deposition, the thickness of the silicon epitaxial layer and that of the polycrystalline silicon film were determined by means of an angle lapping and staining technique in addition to Talystep measurements.

Figure 1 shows a typical pattern obtained in the case of a polycrystalline silicon film deposition at  $1120^\circ\text{C}$  on  $\text{Si}_3\text{N}_4$  film using the  $\text{SiH}_2\text{Cl}_2\text{-H}_2$  reaction. One cycle of the interference wave was approximately  $0.28 \mu\text{m}$  in film thickness when glancing angle of the photocell was  $40^\circ$ . Under these conditions the maximum monitoring thickness,  $d_{\text{max}}$ , which was the thickness at the point where the amplitude of the observed signal could not be recognized, reached nearly  $3.9 \mu\text{m}$  for the polycrystalline silicon film. With increase of film thickness the interference wave drawn in the polycrystalline silicon deposition was observed to decay rapidly.

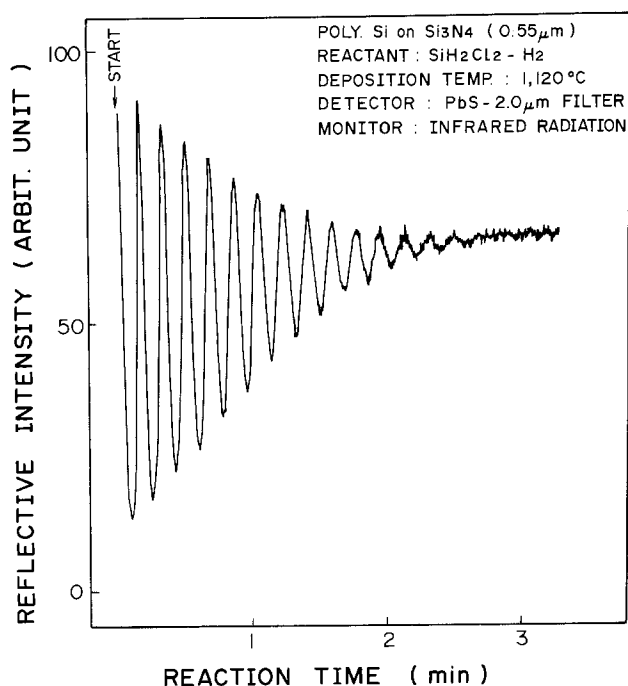


Fig. 1. Observed pattern of interference wave when the polycrystalline silicon film was formed by the  $\text{SiH}_2\text{Cl}_2\text{-H}_2$  reaction on the  $\text{Si}_3\text{N}_4$  substrate.

\* Electrochemical Society Active Member.

Key words: polycrystalline silicon deposition, infrared radiation,  $\text{SiCl}_4\text{-H}_2$  reaction,  $\text{SiH}_2\text{Cl}_2\text{-H}_2$  reaction, precise control of film thickness.

The temperature dependence of  $d_{max}$  was plotted for the thermally grown  $\text{SiO}_2$  substrate in Fig. 2 and for the CVD  $\text{Si}_3\text{N}_4$  substrate in Fig. 3 as a function of deposition temperature. In both reactions  $d_{max}$  showed a tendency of increasing to a maximum, then decreasing. From these figures, the following features could be discerned: (i)  $d_{max}$  deposited at  $1120^\circ\text{C}$  by the  $\text{SiH}_2\text{Cl}_2\text{-H}_2$  reaction was a little larger than that at  $1220^\circ\text{C}$  by the  $\text{SiCl}_4\text{-H}_2$  reaction; (ii) thickness monitoring of the  $\text{SiH}_2\text{Cl}_2\text{-H}_2$  reaction was applicable in a wider temperature range than that of the  $\text{SiCl}_4\text{-H}_2$

reaction; and (iii)  $\text{Si}_3\text{N}_4$  film was less liable to degenerate than  $\text{SiO}_2$  film (11) in such a hot hydrogen atmosphere. However, the difference of the optical refractive index between Si and  $\text{Si}_3\text{N}_4$  was a little smaller than between Si and  $\text{SiO}_2$  and hence this difference brought about a smaller interference intensity.

Accuracy control of the film thickness could be obtained by selecting the wavelength of the filter used independent of the film thickness. A filter of  $2.0 \pm 0.05 \mu\text{m}$  was selected in this experiment because it was at this wavelength that one received the maximum radiation energy emitted from a black body heated at  $1400^\circ\text{K}$  (12) which corresponded to the deposition temperature in this experiment.

Figure 4 shows the correlation between the thickness of the polycrystalline silicon film on the thermally grown  $\text{SiO}_2$  of  $1.2 \mu\text{m}$  in thickness and that of the epitaxial layer on a boron-doped  $\langle 111 \rangle$  oriented silicon substrate with a resistivity of 10 ohm-cm. Both wafers were adjacent to each other on the susceptor and the deposition was done at  $1120^\circ\text{C}$  by the  $\text{SiH}_2\text{Cl}_2\text{-H}_2$  reaction. The relation of the single crystal thickness,  $y \mu\text{m}$ , to the polycrystalline silicon thickness,  $x \mu\text{m}$ , was given by the following experimental formula shown by a dashed line (Fig. 4)

$$y = 0.95x \quad [1]$$

The solid line indicates the relation of  $y = x$ . Single crystal film grew 5% thinner than the polycrystalline one.

For the purpose of precise control of the silicon epitaxial layer thickness, the thickness monitoring of the CVD films was further developed for thick polycrystalline silicon film. An improved thickness monitoring method using infrared radiation through a filter with a definite wavelength was adapted for this aim. Values of maximum monitoring thickness were: (i)  $3.9 \mu\text{m}$  in the polycrystalline silicon film, corresponding to  $3.7 \mu\text{m}$  in the single crystal layer, deposited at  $1120^\circ\text{C}$  by the  $\text{SiH}_2\text{Cl}_2\text{-H}_2$  reaction, and (ii)  $2.8 \mu\text{m}$  in the polycrystalline film, grown at  $1220^\circ\text{C}$  by the  $\text{SiCl}_4\text{-H}_2$  reaction on the  $\text{Si}_3\text{N}_4$  substrate, corresponding to  $2.7 \mu\text{m}$  in the epitaxial layer.

The observed rapid decay of refractive intensities in the interference wave with increasing film thick-

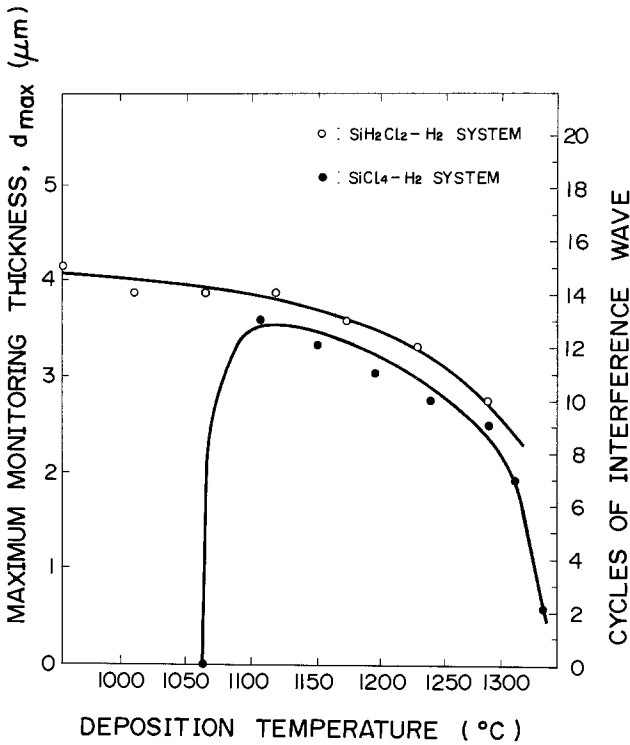


Fig. 2. Dependence of the maximum monitoring thickness,  $d_{max}$ , on the deposition temperature when the polycrystalline film was deposited on the thermally grown  $\text{SiO}_2$  substrate.

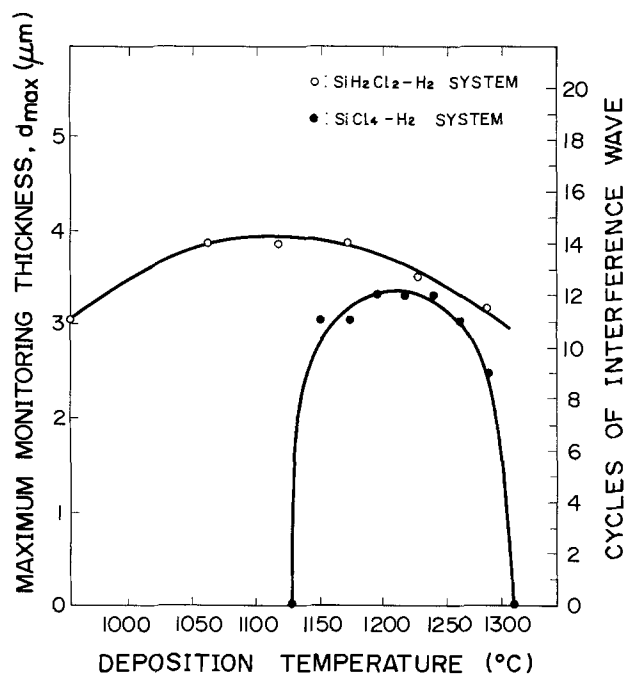


Fig. 3. Dependence of the maximum monitoring thickness,  $d_{max}$ , on the deposition temperature when the polycrystalline silicon film was deposited on the CVD  $\text{Si}_3\text{N}_4$  substrate.

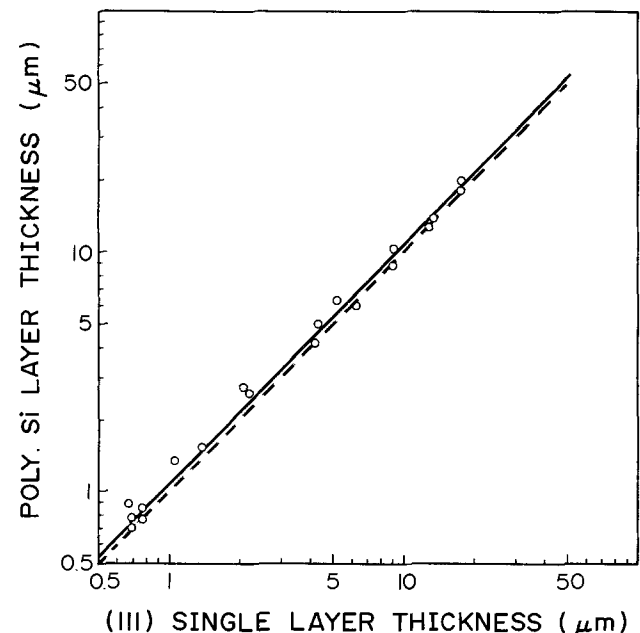


Fig. 4. Correlation between the thickness of the polycrystalline silicon film on the thermally grown  $\text{SiO}_2$  and that of the silicon epitaxial layer grown on the  $\langle 111 \rangle$  oriented silicon substrate.

ness may be caused by scattering by the grains or the surface roughness of the polycrystalline silicon film or an increased absorption coefficient in the silicon substrate at high temperature. The interpretation of this decay will be pursued in the next paper (13).

#### Acknowledgments

The authors express their sincere appreciation to Mr. S. Nishida, Mr. M. Ono, and Dr. Y. Sugita for valuable discussions and continued support throughout this work and to Mr. S. Yasuda for the technical discussion of the epitaxial growth.

Manuscript submitted Aug. 5, 1975; revised manuscript received Dec. 29, 1975.

Any discussion of this paper will appear in a Discussion Section to be published in the December 1976 JOURNAL. All discussions for the December 1976 Discussion Section should be submitted by Aug. 1, 1976.

Publication costs of this article were partially assisted by Hitachi, Limited.

#### REFERENCES

1. D. J. Dumin, *Rev. Sci. Instr.*, **38**, 1107 (1967).
2. J. F. Roberts, C. A. Clark, and A. C. Dumbi, *ibid.*, **41**, 247 (1970).
3. R. Glang, in "Handbook of Thin Film Technology," L. I. Maissel and R. Glang, Editors, pp. 1-114, McGraw-Hill Book Co., New York (1970).
4. K. Sugawara, T. Yoshimi, H. Okuyama, and T. Shirasu, *This Journal*, **121**, 1233 (1974).
5. T. I. Kamins and C. J. Dell'Oca, *ibid.*, **119**, 112 (1972).
6. K. Sugawara, T. Yoshimi, H. Okuyama, and Y. Homma, *ibid.*, **121**, 1235 (1974).
7. D. J. DeLong, *Solid State Technol.*, **October**, 29 (1972).
8. N. Goldsmith and P. H. Robinson, *RCA Rev.*, **34**, 358 (1973).
9. F. G. Allen, *J. Appl. Phys.*, **28**, 1510 (1957).
10. I. Honda, N. Hashimoto, M. Ashikawa, and S. Muto, Abstract 23, 7th Symposium on Semiconductor and Integrated Circuits Technology of the Electrochemical Society of Japan, Nov. 21-22, 1974 (in Japanese).
11. K. Sugawara, *This Journal*, **118**, 110 (1971).
12. E. W. Washburn, in "International Critical Tables of Numerical Data, Physics, Chemistry and Technology," Chap. 5, p. 238, McGraw-Hill Book Co., New York (1929).
13. K. Sugawara, T. Yoshimi, Y. Nakazawa, and K. Ito, *This Journal*, To be published, May (1976).

## Brief Communication



### Raman Line Broadening in the Superionic Conductors, $\text{Ag}[\text{HgI}]_2$ , and $\text{Cu}[\text{HgI}]_2$

D. F. Shriver, G. Joy III, and D. Greig

Department of Chemistry and Materials Research Center, Northwestern University, Evanston, Illinois 60201

In this communication we report observations on the Raman linewidths of some solid-state ionic conductors and suggest that measurements of this type may be useful in screening potential ionic conductors. Silver mercuric iodide and copper mercuric iodide, which have been well characterized by conductivity and x-ray structural studies (1-6) are known to undergo a transition somewhat above room temperature into a disordered phase which exhibits high  $\text{Ag}^+$  or  $\text{Cu}^+$  mobility. We investigated the variation of the Raman bandwidths as these two materials are taken through the order-disorder phase transition, and these results are compared with a related thallium compound,  $\text{Tl}_2[\text{HgI}_4]$ , which does not exhibit high ionic mobility.

The salts were prepared by literature methods (7, 8) and characterized by x-ray powder patterns and elemental analysis for Ag, Hg, Tl, and Cu. The samples were contained in 12 mm outside diameter Pyrex tubes which were rotated in a variable temperature spinning sample holder (9), and spectra were recorded with a Spex 0.85m double monochromator using backscattering sample illumination and digital data acquisition. Owing to instability of the samples under blue or green laser irradiation, the laser excitation wavelengths 632.8, 676.4, or 799.3 nm were employed. To minimize instrumental line broadening, the mono-

chromator bandpass was maintained at one-half wave-number or less. The laser power was typically between 5-15 mW, which in conjunction with the use of a line focus and sample spinning insures that local heating was negligible. Temperatures were measured by means of an iron-constantan thermocouple placed in close proximity to the sample.

The dominant feature in the spectra of all samples is a band at ca.  $123 \text{ cm}^{-1}$  (Fig. 1) which is assigned as the symmetric  $\text{HgI}_2^{2-}$  stretching mode by analogy with data on this species both in solution and in the solid state (10, 11). The A symmetry designation applies to this mode for the two  $\text{HgI}_2^{2-}$  ions in the  $\text{S}_2^2$  unit cell characteristic of the  $\beta$ -phase. The corresponding formal designation is  $A_1$  for the disordered (high temperature)  $\alpha$ -phase which belongs to the  $\text{T}_d^2$  space group. Other features in this general region of the spectrum include two peaks at 80 and  $105 \text{ cm}^{-1}$  in the  $\beta$ -phase, which transform to a very broad feature centered around  $84 \text{ cm}^{-1}$  in the  $\alpha$ -phase. From data on  $\text{AgI}$  (12) and a variety of  $\text{AgI}$  complexes (13), these bands are assigned as silver-iodine stretching modes. It is significant that these bands are broad at room temperature even though there is no evidence for disorder.

As shown in Fig. 1, the phase transition at  $323^\circ\text{K}$  for the silver salt brings about two very noticeable changes in the  $123 \text{ cm}^{-1}$  region: the  $123 \text{ cm}^{-1}$  feature

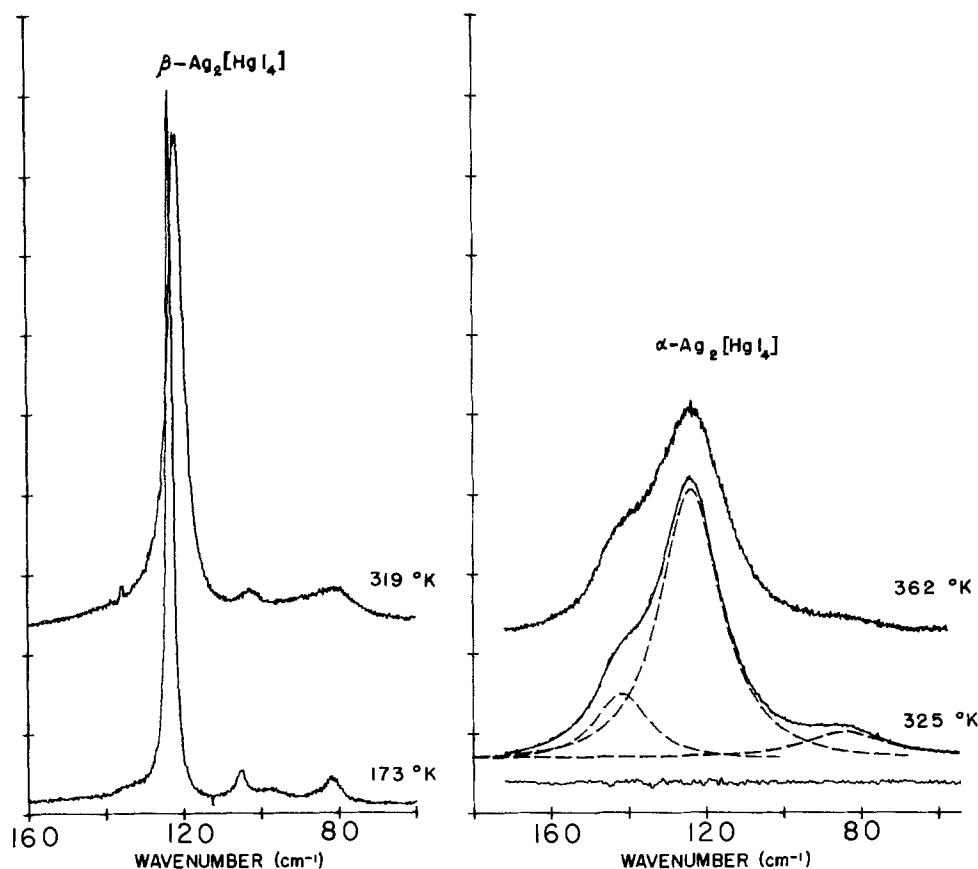


Fig. 1. Raman spectrum for the low and high temperature phases of  $\text{Ag}_2[\text{HgI}_4]$  in the vicinity of  $120\text{ cm}^{-1}$ . For the  $\alpha$ -phase, resolved components of the spectrum are shown as dashed lines, and the difference between the observed and calculated spectra is displayed at the bottom.

is broadened considerably, and a distinct shoulder appears around  $141\text{ cm}^{-1}$ . A similar broadening is observed for the corresponding band in  $\text{Cu}_2[\text{HgI}_4]$  when the sample undergoes the order-disorder transition at  $343^\circ\text{K}$ , but it is not observed for  $\text{Tl}_2[\text{HgI}_4]$ , which does not appear to have a solid phase transition, and which is not a good ionic conductor (Table I).

Since disorder is a common feature in superionic conductors, the detection of disorder via Raman spectroscopy should be useful for identification of potential new conductors (14, 15). The utility of various screening techniques for ionic conductors has been discussed by Whittingham, who lists direct measurement of ionic conductivity, ion exchange, dielectric loss, and nuclear magnetic resonance as useful methods (16). As with NMR, the Raman measurement is a spectroscopic tool which can be applied very readily to polycrystalline samples if the basic Raman instrumentation is available. For example, we routinely employ Raman spectroscopy to characterize new heavy metal halide phases. The measurement may be carried out directly on the Pyrex or fused silica tube in which the sample was prepared, and as the Raman scattering cross sections for heavy metal halides are quite large, high sensitivity is obtainable. It also is a straightforward

matter to perform the Raman measurements at a series of temperatures to detect the onset of disorder.

The scope of the Raman method is different from that of NMR line narrowing because Raman spectroscopy is not limited by the existence of suitable nuclear properties for the mobile ion. On the other hand, Raman spectroscopy is not highly sensitive to light metal oxides, and therefore is not an attractive tool for  $\beta$ -alumina type systems where fluorescence from impurities tends to obscure the Raman spectrum unless careful sample preparation is employed. As with NMR, a positive Raman test will not ensure that the sample will be a good ionic conductor, but will indicate that the more complex conductivity measurements are warranted. High ionic conductivity will not accompany Raman line broadening if the disorder is localized between sites which do not communicate with the remainder of the crystal, or if the disorder is static, with little ion motion between sites. In principle, infrared line broadening could be used analogously to the Raman technique; however, the latter will generally be the most convenient, particularly with heavy metal halides.

There are several possible origins for the broadening of certain infrared and Raman modes in disordered phases. In the disordered phase, the wave vector,  $k$ , no longer retains its meaning so the  $k \approx 0$  selection rule is relaxed with the resulting observation of transitions over a range of the phonon dispersion. Disorder also introduces new decay channels for the lifetime broadening of optical transitions (17). Additional broadening will occur if the correlation time for ion motion occurs on an appropriate time scale (18). Finally, it is possible that a variety of discrete new structures in the disordered phase will produce a series of overlapping bands which give the appearance of simple line broadening. Clearly, the line broadening experiments contain potentially useful information beyond their application in screening; however, the unraveling of individual contributions to the broadening may be difficult.

Table I. Linewidths at half-height vs. temperature\*

$\text{Ag}_2[\text{HgI}_4]$ ( $122\text{ cm}^{-1}$ band)				
Temperature, $^\circ\text{K}$	173	319	332	391
Linewidth, $\text{cm}^{-1}$	2.0	4.7	19.8	24.5
$\text{Cu}_2[\text{HgI}_4]$ ( $127\text{ cm}^{-1}$ band)				
Temperature, $^\circ\text{K}$	153	342	355	
Linewidth, $\text{cm}^{-1}$	1.4	4.1	ca. 18	
$\text{Tl}_2[\text{HgI}_4]$ ( $129\text{ cm}^{-1}$ band)				
Temperature, $^\circ\text{K}$	153	295	405	
Linewidth, $\text{cm}^{-1}$	2.5	2.9	6.5	

\* Transition temperatures:  $\text{Ag}_2[\text{HgI}_4]$ ,  $323^\circ\text{K}$ ;  $\text{Cu}_2[\text{HgI}_4]$ ,  $343^\circ\text{K}$ .

The origin of the  $141\text{ cm}^{-1}$  shoulder in the Raman spectrum of  $\alpha\text{-Ag}_2[\text{HgI}_4]$  is not obvious, but two alternate explanations appear likely. It may correspond to a maximum in the phonon density of states which is observed owing to a breakdown of the periodicity, or it may correspond to a discrete structural feature which is unique to the disordered phase. A likely new structure is the  $\text{Hg}_2\text{I}_7$  moiety, which would arise in the crystal by the occupation of two adjacent tetrahedral sites by  $\text{Hg}^{2+}$  ions. Normal coordinate analyses on isolated  $\text{HgI}_4^{2-}$  and  $\text{Hg}_2\text{I}_7^{3-}$  indicate that a high frequency mode should appear in the spectrum of the latter. Since the details are not essential to the purpose of the present note, further discussion of the  $141\text{ cm}^{-1}$  feature will be deferred.

#### Acknowledgments

This research was sponsored by the National Science Foundation through the Northwestern University Materials Research Center.

Manuscript received Nov. 5, 1975.

Any discussion of this paper will appear in a Discussion Section to be published in the December 1976 JOURNAL. All discussions for the December 1976 Discussion Section should be submitted by Aug. 1, 1976.

Publication costs of this article were partially assisted by Northwestern University.

#### REFERENCES

1. J. A. A. Ketelaar, *Z. Krist.*, **80**, 190 (1931); *ibid.*, **87**, 436 (1934).
2. J. A. A. Ketelaar, *Z. Physik Chem.*, **B26**, 327 (1934); *ibid.*, **B30**, 53 (1935); *Trans. Faraday Soc.*, **34**, 874 (1938).
3. J. Rothstein, *Phys. Rev.*, **98**, 271 (1955).
4. R. Weil and A. W. Lawson, *J. Chem. Phys.*, **41**, 832 (1964).
5. S. Geiler, in "Fast Ion Transport in Solids," W. Van Gool, Editor, p. 607, North-Holland, Amsterdam, (1973).
6. K. W. Browall, J. S. Kasper, and H. Wiedemeier, *J. Solid State Chem.*, **10**, 20 (1974); J. S. Kasper and K. W. Browall, *ibid.*, **13**, 49 (1975).
7. E. P. Hensel, *Ber.*, **3**, 123 (1970).
8. H. F. Walton, "Inorganic Preparations," p. 79, Prentice-Hall, Englewood Cliffs, N. J. (1948).
9. D. F. Shriver and J. B. R. Dunn, *Appl. Spectros.*, **28**, 319 (1974).
10. D. A. Long and J. Y. H. Chau, *Trans. Faraday Soc.*, **58**, 2325 (1962).
11. M. A. Hooper and D. W. James, *Aust. J. Chem.*, **24**, 1331 (1971); N. Krauzman and J. P. Mathieu, *Compt. Rend. Acad. Sci. (Paris)*, **173**, 232 (1921).
12. G. L. Bottger and C. V. Damsgard, *J. Chem. Phys.*, **57**, 1215 (1972).
13. M. Batista-Leal, Unpublished observations, 1975.
14. W. J. Pardee and G. D. Mahan, *J. Solid State Chem.*, in press.
15. M. J. Rice, S. Strässler, and G. A. Toombs, *Phys. Rev. Letters*, **32**, 596 (1974).
16. M. S. Whittingham, in "Fast Ion Transport in Solids," W. Van Gool, Editor, p. 429, North-Holland, Amsterdam (1973).
17. S. Kern and C.-Y. She, *Chem. Phys. Letters*, **25**, 287 (1974).
18. P. da R. Andrade and S. P. S. Porto, *Solid State Communications*, **14**, 547 (1974), and references therein.



## Energy—The Short and Long of It<sup>1</sup>

John S. Foster, Jr.

TRW Incorporated, Redondo Beach, California 90278



Thank you very much, President Beck, for that very generous and flattering introduction. At the outset I want to express my appreciation for the honor and privilege of being invited to present the semiannual Electrochemical Society Lecture.

I should begin with a few words about the title chosen for this lecture. Each of you has been called upon to make presentations and speeches from time to time. In addition you are asked to supply a subject and title. In my case the subject came easily—ENERGY. The rest of the title, however, was born out of a sense of frustration—frustration being experienced by almost everyone involved in energy; those who search for new sources and development and production, processes, distribution, and final use. And also those who are frustrated by the difficult and tedious social, political, economic, environmental, legislative, and legal aspects. This frustration has been growing for the last twenty years.

Perhaps it started with the debates in the early 1950's culminating in the 1954 congressional decision to regulate the price of gas at the wellhead. The subsequent controls to keep the price of gas low held down prices for oil and reduced our use of coal. We went to

the Middle East for cheaper oil and became dependent on that source to fuel the future growth of America. And all the while we have been debating the pros and cons of our actions. We chose the course of enforcing cheaper fuel prices for energy at the risk of not facing up to the costs of energy for the long haul. In 1973 OPEC pulled the string on our short-term strategy realizing that by then we were ill prepared to do without them. So in spite of two decades of debate, the short and the long of it is that we are drifting deeper and deeper into trouble. It was the sense of frustration that despite endless debates we have stuck to the wrong course that prompted me to assume it might be possible to say something succinct, hence the title, "Energy—The Short and Long of It."

America and the rest of the world may have finally awakened to the fact that we have an energy crisis on our hands, and that it's going to get worse before it gets better.

Our energy needs are increasing while our supplies of oil and gas are dwindling. We're at the mercy of the petroleum exporting countries, more so today than we were at the time of the embargo back in 1973. We may have to deal with a shortage of natural gas this winter. And both oil and gas supplies are limited. One day they're going to be gone.

It's everyone's problem—government, industry, universities, the man on the street. The solution is going to be devilishly difficult, and everyone is going to have to get involved.

We need a plan of action, for both the short term and long term, if we're going to solve the dilemma. And that's a part of what I want to talk about today, at the risk perhaps of belaboring the obvious. Some things do bear repeating, lest we get so busy fighting alligators that we forget that our original objective was to drain the swamp.

It seems to me that the energy crisis and the way out of it can best be understood if we look at three fairly well-defined aspects of the problem. First off, there is the people problem, which has to do with the general public and its relationship to the energy crisis. Make no mistake about it, if we can't solve this one, if we can't get the public behind us, then "Project Independence" isn't likely to be any more successful than "Project Prohibition" was half a century ago.

Second, we have the problem of method and approach; how we're going to attack the energy crisis, arrive at decisions about what to do, the associated risks, and how best to use the nation's capabilities.

Third, there are the specific programs, schedules, and approvals for achieving our objectives. If the schedule slips too much, if we make too many wrong guesses about what we ought to be doing, the crisis is going to turn into a full-scale disaster.

Now let's look at the short and long of it for each of these categories.

*The people problem.*—Some of the shorts and longs of the "people problem" are: we're short on energy

<sup>1</sup>This is The Electrochemical Society Lecture delivered at the Dallas, Texas, Meeting of the Society, October 6, 1975.



resources, long on waste. Short on action and decisions, long on proposals, ideas, and schemes. Short on trust, long on suspicion. Short on personal concern and commitment, long on fingerpointing and accusations. Short on enabling legislation, long on restrictive legislation. Long on political profit, short on economic profit.

It's very difficult to get people, except those already deeply and professionally involved with energy, to realize that we do have a crisis. To most people, the energy crisis has come and gone. They want to keep their heavy and low-mileage cars. They want the thermostat up to 75° or 80° in the winter and down to 70° or 75° in the summer. We're short on the long view, long on the short view.

What we're going through right now is kind of like a remission in cancer: some of the symptoms have disappeared, but the disease is still there. We'd better do something to treat it, because it can be terminal.

The people are recovering, or trying to recover, from a series of painful blows. In the past few years, we've seen America all but torn apart by the controversy over Vietnam. We've lived through the shame and shambles of Watergate. We've held our breath and tried to resolve the Middle East crisis before it blows up in our faces. We've tried and are still trying to cope with runaway inflation in the midst of a recession. (Perhaps recession is not the right word. If your neighbor is out of work, that's an "economic readjustment." If you're out of work, that's a "recession." And if your wife is out of work, that's a "depression.")

Now, after all these overlapping traumas and crises, we're told that we have to learn to live with less oil for our furnaces and cars and electric power plants. Is it any wonder that people are either apathetic about the energy problem, or simply refuse to believe that it is a problem? Or that some are convinced that it's another high-level conspiracy designed to line the pockets of the "haves" at the expense of the "have-nots"?

Of course, it's actually a cop-out to even talk about the problem in the context of our own country exclusively. The fact is, and we all know this even though we may not like to admit it, the energy problem is a global one. Anything we do to cope with it on a national basis is only going to be a stopgap measure at best. We already consume 35% of the world's energy with only 6% of its population. How much longer can we get away with that?

There are some very tough choices that have to be made. President Ford realized this when he began to review the Project Independence Blueprint during his Christmas vacation last year. Every alternative seemed to have two or three unacceptable aspects to it. Some alternatives would play hell with the economy, others would further degrade the environment, almost all of them present severe economic problems. Everything interacts with everything else. We don't just have an energy problem, we have the Four Big E's: Energy, Environment, Economics, and Education.

Everyone who tries to cope with these problems suffers from some kind of built-in bias. Any program the President proposes has, of necessity, a political aspect and requires negotiation and compromise with the Congress. Each member of Congress has a constituency back home to answer to, with their own sets of built-in biases and regional interests. The same applies to industry; any changes they propose have to be evaluated in terms of profit-and-loss and accountability to the stockholders. Who among us is going to volunteer to become a nonprofit corporation in order to save a few barrels of oil? But the fact is we can save energy and make more profit.

It comes down to this: we're short on self-sacrifice, long on self-interest. That's what created the energy problem in the first place, and that's what's delaying the solution. It's going to take nothing less than a restructuring of all the old thought patterns, from the top down and from the bottom up. We've got to start living by the Golden Rule instead of just giving it lip

service. And since America has been the biggest consumer of energy, I think it's pretty much up to us to take the lead in alleviating the crisis.

*The method and approach.*—How should we approach this amorphous mass known as the energy crisis? Some of the shorts and longs that apply here are: we're short on incentives, long on requests. Short on trained people, long on unemployed people. We're short on coordinated, integrated programs, long on individual pet projects. Worst of all, we're short on time, long on problems to be solved in time.

Dr. Edward Teller, in his report to the Energy Panel of the Commission on Critical Choices for Americans, said that we should not try to solve the energy problem forever. We can't expect to provide answers to all the new problems and possibilities that may show up in the 21st century. I think that's an important point to remember. It provides a sharper focus and makes the over-all problem a little more manageable.

We need to look at the whole picture, the four Big E's that I mentioned. In one sense, there's no such thing as solving the energy problem, the environmental problem, the economic problem, the education problem any more than we can expect to solve the old age problem or the health care problem. We can only improve the situation in each case by solving hundreds and thousands of individual problems, one at a time.

It's different than going to the moon or fighting a war and it's even more complex. But some of the same tools and skills can be used and are being used. The systems approach, computer modeling and synthesis, these techniques help identify key elements of the problem, analyze various functions and how they interact, but the name of the game is to spot the leverage points that can increase the energy supply, reduce the cost, improve the environment, and motivate people to do their part.

There are a lot of dedicated people in industry, government, and education working on these problems. Of these the most immediate and pressing burden falls on those in government, for without question it is their judgments and actions which will chart our course toward energy independence. Unfortunately, almost all of these civil servants are terribly overloaded. Those at the top are very able people who must be involved in an enormously complicated and demanding range of activities. The coordination of government agencies, preparation and presentation of testimony, speaking engagements, program development and review are just part of the burden. To the levels below them falls the responsibility for creating analyses of important questions, program detail, endless meetings with support contractors, etc. With such heavy loads there is a tendency to handle each problem as it comes up and not be able to devote the time necessary to address and resolve the major problems.

It seems to me that the effectiveness of various agencies could be significantly improved, particularly in the energy areas, if the largest or more important efforts could be identified, and government/industry teams selected to give them the attention they deserve. While this may seem to be quite a departure from present practice, it is just the method we have used in the past—in World War II to produce synthetic rubber, in the late fifties to overcome the missile gap, and in the sixties to go to the moon and return successfully. In the same way, it seems to me we can forge government/industry teams to accelerate the development of *in situ* coal and shale, liquefaction and gasification of coal, and other areas where the name of the game is to reduce technical and economic uncertainties. In this regard one of the things our government does best is to take those actions necessary to improve the market environment by the removal of technical risk, provision of front end capital, etc. One of the things that government frequently does not do well is the implementation of programs; hence, the reason for suggesting a government/industry team.

It will take years to perform a complete analysis of the over-all energy problem and all the alternative solutions. But in the meantime, we can and must begin working on some of the major requirements that have already been identified, like expanding our coal production and usage, building more nuclear power plants, intensifying the search for new oil and gas deposits, and doing extensive research and development on new energy sources such as oil from shale, gas from coal, and solar energy conversion.

Of course the energy problem is nothing new to electrochemists. You've been working on more efficient ways to convert and store energy ever since the discovery of electricity back in the 18th century, and the contributions of electrochemists include batteries, fuel cells, and solar cells. Your work has made possible self-starting cars, portable radios, flashlights, calculators, manned flight, and long-term planetary probes. And today, electrochemistry still faces a host of challenges. The world needs low-cost, efficient ways of reducing our dependence on fossil fuels. Fuel cells, for example, can nearly double the efficiency of converting fossil fuels to electricity, provided low-cost, long-life catalysts can be found. Inexpensive photogalvanic or photovoltaic devices can provide us with an almost inexhaustible supply of energy. And economical, long-life, efficient secondary batteries can provide the load leveling needed to operate large coal and nuclear power plants at maximum efficiency. There's no doubt about it, you've got your work cut out for you. We all have.

*Programs and schedules.*—The things we have to do to deal with the energy crisis are related to our two major objectives: reduce energy demands and find new energy resources. It sounds a lot simpler than it really is.

For the short term, I see at least six steps that need to be taken, all of which will help for the long term, too. They are: conservation, building a reserve supply, finding new gas and oil deposits, switching from petroleum to coal wherever possible, stepping up construction of nuclear power plants, and, last but by no means least, training the necessary talent. For the long term, we have only one step to take, but it's a giant one: we have to find new substitutes, in addition to nuclear power and coal, to replace the oil and gas which will all be gone within the next generation or two unless of course we can gain a little time through the unlikely discovery of major new deposits that we don't yet know about.

Eliminating waste through conservation can relieve the energy crunch faster than any other single step. This will also alleviate the economic crunch to some extent and, in many cases, ease the environmental pollution problem. It's amazing but true that even a one per cent saving or improvement in efficiency would reduce our oil consumption by 100 million barrels each year. At today's prices, that's more than a billion dollars saved. There are other fringe benefits, too. For instance, the 55 mile-per-hour national speed limit, even though it's pretty loosely enforced, not only saved a lot of gas but reduced highway fatalities by 20% in 1974. (Apparently this idea of taking things slower is catching on with the younger generation. My secretary tells me that the kids are not only driving slower, they're even dancing slower, and closer, too.)

The automotive industry has finally embarked on a program of conversion to energy-saving cars. It's been a slow and painful process, but it's working. To the rest of industry, conservation means planning for the future in new ways like more efficient heating and cooling systems, more efficient machines and equipment and use of materials. To labor, conservation may mean the loss of some jobs for the short term, but it will mean more jobs in the long run as more energy becomes available for critical industrial needs, and as new sources of energy are developed.

But what about the man on the street again? What can be done on an individual basis to make people stop wasting energy? The whole thrust of the American way of life has been the idea of upward mobility, increasing our standard of living, and that means burning up more energy. But we must have the cooperation of the general public or we're not going to solve the energy problem. Government and industry need the public's support and confidence. We've got to work like the devil to restore the people's faith in their leaders and in science and technology. Beyond that, we've got to somehow get people to do what's best for the greater number, even if it means giving up some of their personal conveniences. This may require rationing and enforced scarcity, unless we can find the kinds of incentives that will make it happen voluntarily.

Close on the heels of this conservation program, we need to begin building a reserve stockpile of gas and petroleum. We should start small, say, a six-month supply, while continuing to study the situation to figure out whether we really need a six-month, two-year, four-year supply or whatever. This will help take us out of the panic mode and also put us in a little better negotiating position. Naturally, this plan is not going to work unless we can make the first step, conservation, work.

We've got to keep looking for more oil and gas, that goes without saying. We need to explore the outer continental shelf, in spite of the risk of pollution. The techniques to avoid blowouts and spills or to minimize their consequences are improving every day. The risk is small, but in my view it is one that we have to take. It is, after all, a much smaller risk than the one we're already taking—the risk of running out of oil altogether before we have a viable substitute.

Further, we need to switch from oil and gas to coal wherever possible and to step up production of coal, for which the supply is numbered in hundreds rather than tens of years. To make the switch, we have to solve some economic problems and environmental problems, but they are within the reach of today's technology. We can't just sit back and say that we mustn't burn coal because it pollutes, or because it's too expensive to convert the power plants. We can raise the money and we can control the pollution.

Nuclear power offers one of the most promising ways to get out from under our petroleum dependency, in spite of the economic problem and public controversy associated with it. There is concern about reactor safety, radiation exposure, waste management, and terrorism. Some of these fears are valid, but so is the need to build reactors. We should get to work in both areas, but with a new partnership between government and industry.

Finally, we need to increase the supply of trained professionals in the energy fields. We look to the universities and colleges for the solution to this problem but government and industry can help by publicizing their needs. We need specialists in fossil energy, solar energy, geothermal energy, and nuclear energy reactors. And we need people whose interests and education span more than one discipline. We've got to avoid the kind of polarization we've seen in recent years that pits the environmentalists and the energists against one another, and the economists against both.

For the long term, we must start now to look for the substitutes that will keep us going after the gas and oil run out. There are enormous uncertainties, and it's going to take continuing study and experimentation to remove these uncertainties so we can decide where to spend our time and money.

For example, we need to work the oil shale, particularly in situ approaches to find out whether the oil can be extracted economically and what the environmental considerations are. We need to drill more geothermal wells to find out whether in fact we have enough resources to provide the estimated 20,000 megawatts of

electric power we need by 1985. There's little point in solving the technological problems if the resources aren't there. We need to put a lot of effort into experimenting and evaluating the opportunities from solar energy. But here again, there are a host of social, and financial as well as technical problems to be identified and solved.

The short and the long of it is that we have perhaps two to three years to adjust the international political and economic situation to avoid the strangulation of several of our allies. We have from five to ten years to find several major new sources of oil and gas, and fifteen to twenty-five years to develop alternative energy sources before the oil and gas are gone. These are the milestones we must pass, and on schedule.

It isn't going to happen by accident, or by executive fiat, or by legislation. It will happen only if everyone works together instead of at cross-purposes; scientists, energists, environmentalists, politicians, economists, businessmen, and educators being concerned and working together for the common good.

During the next four days of sessions and discussions many of you will have your minds on the general subject of energy, and within the discipline of electrochemistry which permits us to solve many of the problems that limit not only the availability of energy, but also the flexibility and efficiencies in its use. I hope these remarks will turn out to be of some value in your deliberations. My time is up as of this minute, I thank you for yours.



## Marcel J. N. Pourbaix—Palladium Award Medalist

R. W. Staehle<sup>1</sup>



R. W. Staehle delivers introductory remarks about the Palladium Award Medalist.

It is a great honor for me to introduce Marcel Pourbaix on the occasion of his receiving the 1975 Palladium Medal from The Electrochemical Society. Pourbaix represents not only a specific set of contributions but signifies an important era in the development of corrosion science and engineering. It is certainly appropriate that The Electrochemical Society bestow its highest honor on a person who has contributed so extensively and so generously.

I should like first to review briefly important aspects of his early history. Secondly, I should like to comment on Pourbaix the man since the products of a man are so closely related to his personal inclinations.

The task of preparing this presentation was facilitated by a recently published biography of Pourbaix prepared by B. F. Brown describing Pourbaix's background (1) on the occasion of his seventieth birthday.

Pourbaix was born in 1904 in Myshega, Russia, of Belgian parents. He was graduated from high school in 1922 and received, for his scholarship, the Prix d'Excellence from the Belgian government. In the same year he was admitted to the Faculty of Applied Science of the Université Libre de Bruxelles.

In 1927 Pourbaix graduated "with great distinction" from the Université Libre de Bruxelles and served as

an assistant from 1927-1928. He received his first exposure to engineering during the period of 1928-1934 while he was an engineer in the Belgian Chemical Union. Thereafter, he returned to U.L.B. where he has been ever since. Here, he worked on problems of general chemistry, electrochemistry, applied physical chemistry, catalysis, and metallurgy.

By 1938 he had devised a potential-*pH* diagram and first published it in the bulletin of the Belgian Chemical Society (2).

In 1940 Pourbaix delivered to the Faculty of Sciences an extensive dissertation entitled: "Experimental Contributions to the Study of Corrosion on Ferrous Metals." This large thesis was accompanied by three ancillary ones; the title of one was "Thermodynamics of Dilute Aqueous Solutions" which was submitted to the Technical University of Delft with F. E. C. Scheffer and W. G. Burgers as sponsors. He finally received two doctoral degrees, one from the Technical University of Delft and one from the University of Brussels.

Even before World War II U. R. Evans had been impressed by the elegance of Pourbaix's presentation and had encouraged him. Following the War, Evans arranged for John Agar to translate "The Thermodynamics of Dilute Aqueous Solutions;" this was published in 1949 by Arnold publishers (3) with an extensive foreword by U. R. Evans.

In Evans' foreword to Pourbaix's first book he noted: "It is likely that the research group at the Université Libre de Bruxelles, which Dr Pourbaix is now organizing, will come to be one of the world's centers for the experimental and theoretical development of the numerous subjects on which he is now working."

We have seen Evans' prediction realized. Most of the details since that time are chronicled in the article by Brown (1).

Turning now to Pourbaix, the man, and his effect on his science, I wish to enumerate three themes which seem to characterize him. First, he has a highly developed intuitive concern for the structure of things. This applies not only to his technical views but also to the structure of institutions in which the technical processes must be encouraged and developed. The potential-*pH* diagram, i.e., the Pourbaix diagram, provides such a structure for arranging important information with respect to key thermodynamic variables. His selection of potential and *pH* was a master stroke in organizing information relative to corrosion. The potential controls the solubility of metals relative to their ions; and the *pH* controls the stability of the protective films. Pourbaix was always careful to point out that the diagrams furnished a framework within which kinetic process might be interpreted, but that the thermodynamic predictions were never a substitute for kinetic information. The potential-*pH* diagram furnishes a framework within which the kinetic information can be organized, much the same as the binary equilibrium diagram of metallurgy, with its coordinates of temperature and composition, furnishes a similar

<sup>1</sup> Introductory remarks by R. W. Staehle, Department of Metallurgical Engineering, The Ohio State University, on the occasion of the presentation of the Palladium Medal Award to Marcel J. N. Pourbaix on October 7, 1975, at the Dallas Meeting of the Society.

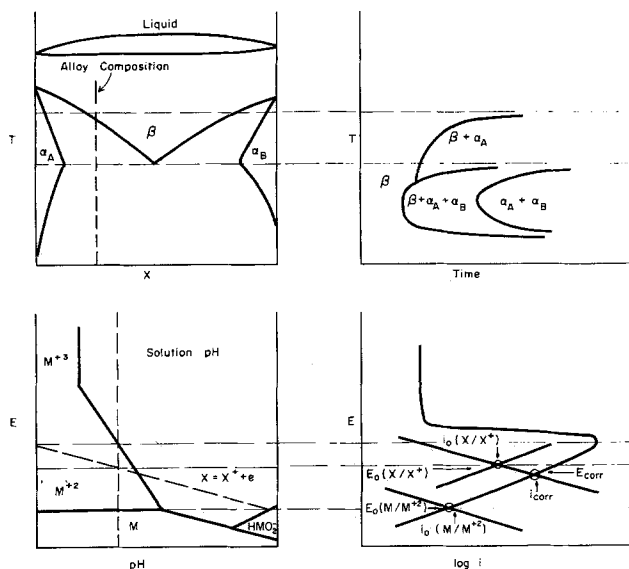


Fig. 1. Upper two diagrams show schematic relationship between binary equilibrium diagrams and TTT curve. Lower two diagrams show relationship between Pourbaix diagrams and polarization curve. Diagrams at left are thermodynamic and at right are kinetic.

framework for the TTT curves. This correspondence is shown in Fig. 1.

On this occasion, it would be somehow inappropriate not to show a sample of his diagrams and the appropriate one is for palladium shown in Fig. 2. The regions pertinent to corrosion are shown as based upon the solubility or boundary lines. Here palladium is in its immune state below line 2 where the metallic palladium is stable. Above line 2 a succession of hydroxides and oxides are stable and provide the circumstance of passivity. To the left,  $\text{Pd}^{++}$  is stable and suggests the possibility of corrosion.

An important aspect of his concern for structure is his early observation that the diagrams applied not only to corrosion but also to a broad range of chemical phenomena. In particular they supply a framework within which to consider geochemistry, electroplating, batteries, water treatment, and both homogeneous and heterogeneous chemical processes.

Pourbaix's concern for the structure of things has also produced important institutional pillars within which corrosion science and technology operate. This includes significant publications as well as organizations devoted to corrosion and electrochemistry. The encyclopedic "Atlas of Electrochemical Equilibria in Aqueous Solutions" (4) provides immediate access to these important diagrams. These diagrams have served as models for the development of other equilibrium

diagrams which describe chemical stability. A relatively recent noteworthy development applies the concept of these diagrams to hot salt corrosion in gas turbines where the stability diagram for aluminum in sulfur-containing environments has been developed, by Goebel *et al.* (5). The correspondence of the hot salt and aqueous diagram is shown in Fig. 3. Finally, his recent publication, "Lectures on Electrochemical Corrosion," embraces both the thermodynamic and kinetic bases which underlie corrosion.

Pourbaix founded CITCE in 1949. CITCE is an acronym for the International Committee for Electrochemical Thermodynamics and Kinetics where both the kinetic and thermodynamic aspects for corrosion and electrochemistry are subjects of joint consideration. He founded CEBELCOR in 1951 which serves as the institutional basis for combining science and engineering in the service of corrosion. CEBELCOR is again an acronym, for the Belgium Corrosion Center.

In 1952 Pourbaix founded the Electrochemistry Commission of the International Union of Pure and Applied Chemistry; he was the founder of working group six (test and control methods) for the European Federation of Corrosion. In 1970 he formed the corrosion department of the University of Brussels and in 1972 developed a collaboration with the University of Florida.

The second thematic stream in Pourbaix's background seems to be based upon a strong incentive to relate fundamental understandings to the needs of the world at large. In the present vernacular this is called "technology transfer." However, Pourbaix's personal efforts have epitomized the concepts in technology transfer throughout his career. He is the first of the corrosion missionaries. He has established short courses, which he terms "corrosion weeks," in Brussels, Pittsburgh, Gainesville, Lisbon, Rio de Janeiro, Dubrovnic, and Clermont. He has been unceasing in his enthusiasm for spreading the gospel of corrosion. To use the words energetic and peripatetic in this enterprise seem most appropriate. The zeal and selflessness which he has exhibited in this enterprise deserve, by themselves, the Palladium Medal.

Finally, and perhaps most characteristic of Pourbaix is his personal generosity. He encourages young workers to dedicate their enthusiasm and confidence to unravelling the complications of corrosion problems. He never recoils from starting yet again with still another young mind. He has especially encouraged the development of new groups in developing countries.

Another side of this generous spirit is epitomized in his charming tradition of sending postcards to corrosionists throughout the world. He always arranges for a card to be sent to U. R. Evans from significant meetings and often arranges to have those present add their

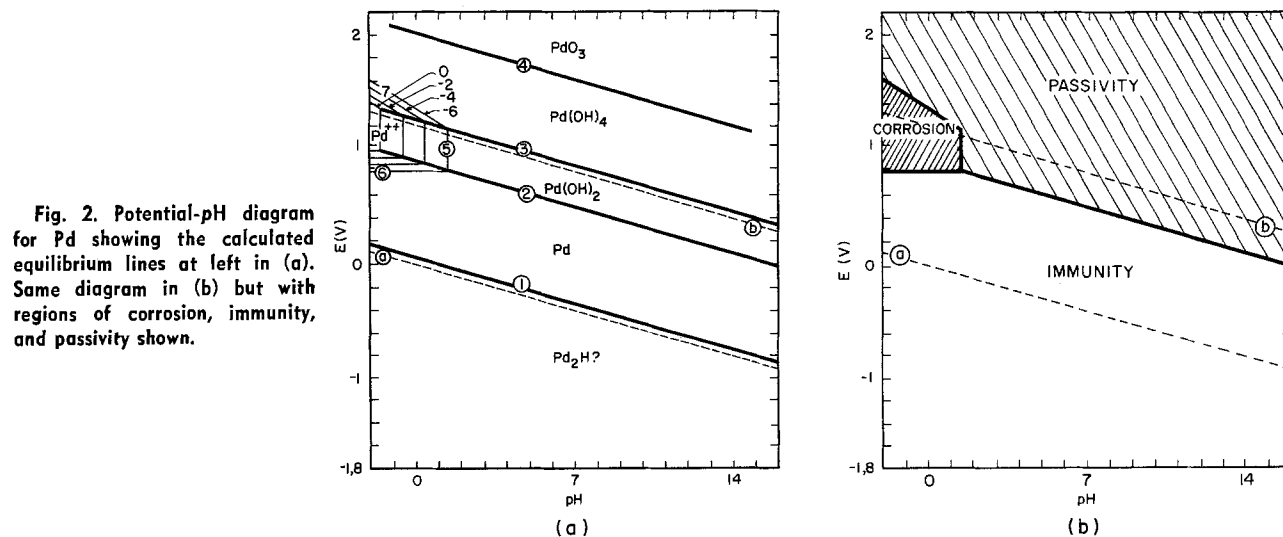


Fig. 2. Potential-pH diagram for Pd showing the calculated equilibrium lines at left in (a). Same diagram in (b) but with regions of corrosion, immunity, and passivity shown.

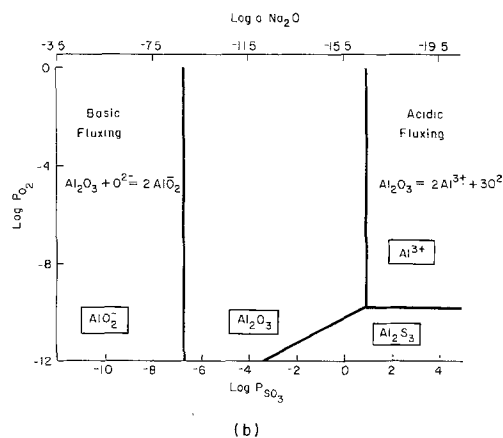
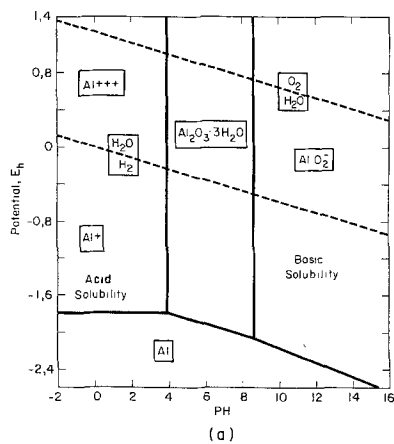


Fig. 3. Comparison of thermodynamic diagrams of the stability of aluminum in water at left (a) and in molten sulfates at right (b). The water developed for 25°C and the other for 1000°C. The reversal in location of acid and basic regions arises from conventions in the respective technologies.

signatures. He is unflinching in this acknowledgment of those who have gone before him and who have contributed to the foundations upon which his work has spread still further.

It is especially appropriate to conclude this introduction by acknowledging his wife, Marcelle. He gives her loyal and unflinching support which she returns to him. They have three children. One is an architect, one a doctor, and one his successor. They have a charming country home outside Brussels where Mme. Pourbaix raises flowers from seeds obtained during their corrosion travels. In addition to being a charming companion, Mme. Pourbaix is a significant artist in her own right and specializes particularly in sculpture.

I omit an enumeration of the honors which have been accorded to Pourbaix. These may be found readily in the article by Brown. Further, listing the honors

which he has received would be redundant. For Pourbaix the honor has always been in the giving.

#### REFERENCES

1. B. F. Brown, *Corrosion*, **31**, 307 (1975).
2. Thermodynamique des solutions aqueuses diluées. Potentiel d'oxydo-réduction (résumé de conférence). Bull. Soc. Chim. Belgique, Vol. 48, XLVIII (decembre 1938).
3. M. Pourbaix, "Thermodynamics of Dilute Aqueous Solutions," Arnold Publication, London, 1949.
4. M. Pourbaix, "Atlas of Electrochemical Equilibria in Aqueous Solutions," Pergamon Press, London.
5. J. A. Goebel, F. S. Pettit, and G. W. Goward, "Deposition of Corrosion in Gas Turbines," A. B. Hart and A. J. B. Cutler, Editors, John Wiley & Sons, New York (1973).

## Some Applications of Potential-pH Diagrams to the Study of Localized Corrosion

Marcel Pourbaix<sup>2</sup>



Marcel J. N. Pourbaix presents the Palladium Medal Address

Dear Roger, you are really, as everybody knows, a fine, fair, and faithful friend. Thanks a lot for your very kind words.

Dear Ted and Mr. President, first of all I wish to express to The Electrochemical Society and to you my feelings of deep gratitude for having extended to me such a high distinction, which enables me, as Palladium Medallist, to join eleven outstanding friends of the United States and of other countries, among whom two are present today: Herb Uhlig and Norman Hackerman. Referring to the six non-American medallists (Carl Wagner, Ulick Evans, the late Karl Bonhoeffer, Aleksandr Frumkin, Thomas Hoar, and Veniamin Levich), as well as to Paul Delahay who is also from Belgium, I may tell you how much the Palladium Medal since the day it was created, has been appreciated throughout the whole world, and how much it has contributed to promoting international friendship and collaboration, which is a duty for all of us. In the kind presentation which was published in the September issue of the *Journal* of your Society, the creation of CITCE in 1949 was mentioned. I wish to remind you that one of those who has actively contributed to the creation of CITCE is Pierre Van Rysselberghe, who, for reasons of health, is unable to attend the present meeting, who also comes from Belgium, who is presently retired from Stanford Uni-

<sup>2</sup> Palladium Medal Address delivered October 7, 1975 at the Dallas Texas, Meeting of The Electrochemical Society. The medal was struck from palladium supplied by the International Nickel Company, 67 Wall Street, New York, New York 10005.

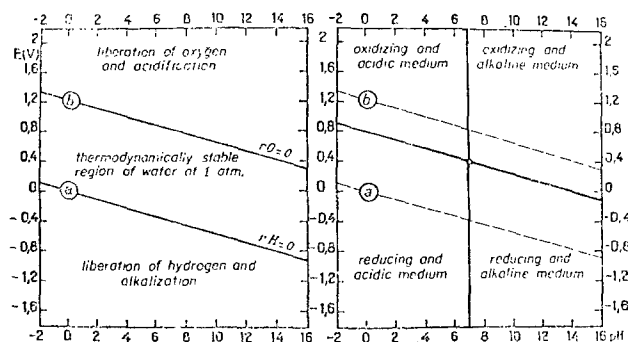


Fig. 1. Domain of thermodynamic stability of water at 25°C under 1 atm pressure (line  $\alpha$  corresponds to the equilibrium conditions of reaction  $2H^+ + 2e^- = H_2$  under 1 atm). Acid, alkaline, oxidizing, and reducing media.

versity, and who was the first president of CITCE. I also wish to pay tribute to my many friends, and especially to the members of the team of CEBELCOR, who have collaborated on the work which is crowned today by the Palladium Medal.

**Passivation by Palladium**

Mr. President, ladies and gentlemen, as you all know, palladium is really a fine metal, which altogether is corrosion-resistant in most environments and has practically no overpotential for the hydrogen evolution. This means that, if palladium is in contact with another metal under conditions where hydrogen may be evolved under atmospheric pressure, its electrode potential is along the "hydrogen line"  $\alpha$  of the potential-pH diagrams (Fig. 1). If this line is in the corrosion area of another metal, as is generally the case for iron (Fig. 2), it will promote corrosion of this metal because it will increase its corrosion affinity, which is measured by the vertical distance between the electrode potential of the metal and its immunity potential. But if the hydrogen line  $\alpha$  is in the passivity area of a metal or alloy, and above its corrosion area, palladium may promote passivity, and thus reduce or even stop corrosion. This is in agreement with the work which

was begun in 1953 by N. D. Tomashov and co-workers concerning the influence of "cathodic additions" (Cu, Ag, Pt, Pd, Re) on the passivating ability and the corrosion resistance of some high-alloy steels (1) [see details in Ref. (2)], it's being understood that such an effect may be beneficial only if the corrosion area of the alloy steel (Fig. 3 and 4), which depends notably upon the nature of the steel, is not too close to the hydrogen line; if too close, or if the passivity is not perfect due for instance to a too high chloride content of the solution, palladium may be harmful instead of being beneficial. Palladium should thus be used only with precautions for improving the corrosion resistance of alloy steels. A similar, and more spectacular and safe effect of palladium, exists on titanium which, as shown in Fig. 5, has a corrosion area far below the hydrogen line and may be perfectly passive even in the presence of chloride. And this is why, as shown by the fine work begun in 1958 by M. Stern (3) and begun in 1961 by N. D. Tomashov (2, 4), the addition of palladium to titanium may be very beneficial. As said in 1970 by M. G. Fontana (5), "one of the great triumphs of corrosion science is the development of titanium alloys containing noble metal additions." However, it should be borne in mind that these noble metal additions may be effective only when the dangerous "corrosion triangle shown in Fig. 3, 4, and 5, is entirely below the hydrogen line  $\alpha$ , and preferably far below, so that any danger of localized corrosion (crevice corrosion, and eventually stress corrosion cracking) be avoided. In the cases of both alloy steels and titanium, palladium may be used either as alloy-element or as a deposit on the metal (2).

But, Ted, I think that you know more than I about titanium. As far as palladium is concerned, I hope that I shall resist the temptation to use the beautiful specimen which International Nickel and you just gave to me for making corrosion and protection experiments.

I shall now present two examples of the application of potential-pH diagrams to the study of localized corrosion phenomena and to the setting up of remedies to such corrosion relating respectively to copper, to iron, and to their alloys.

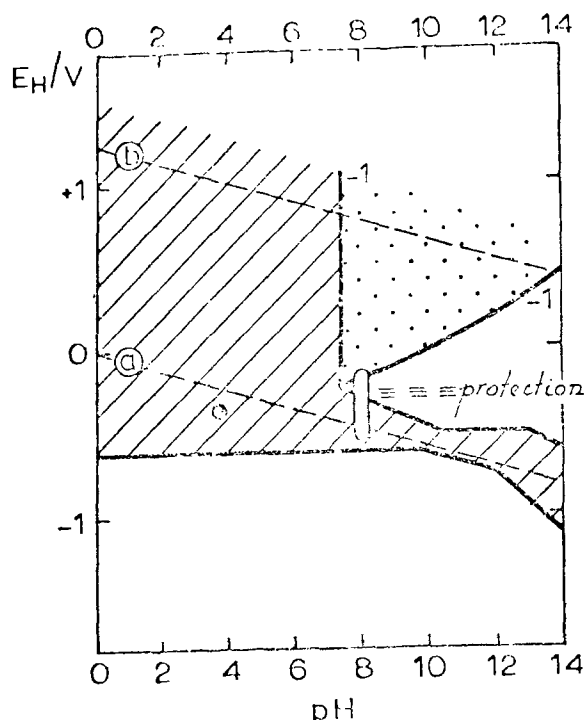


Fig. 2. Corrosion, immunity, and passivation conditions for iron at 25°C ( $Cl^- 10^{-1}M$ ) (schema).

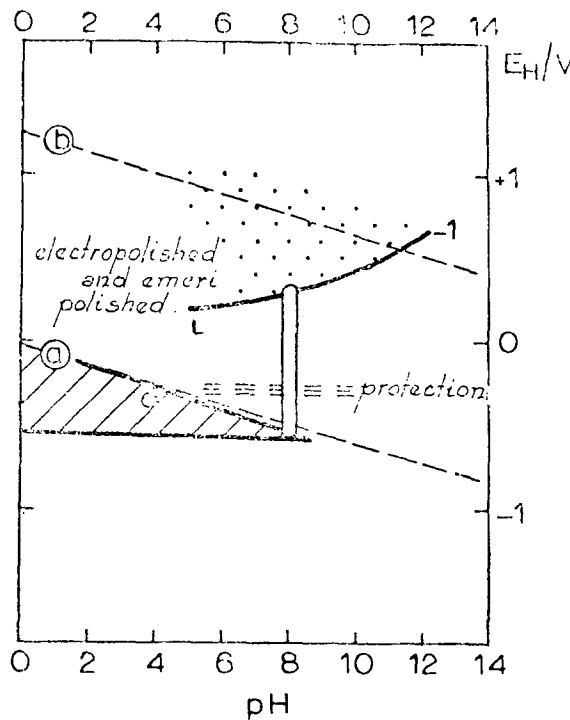


Fig. 3. Corrosion, immunity, and passivation conditions for chromium-steel AISI 410 ( $Cl^- 10^{-1}M$ ) (schema).

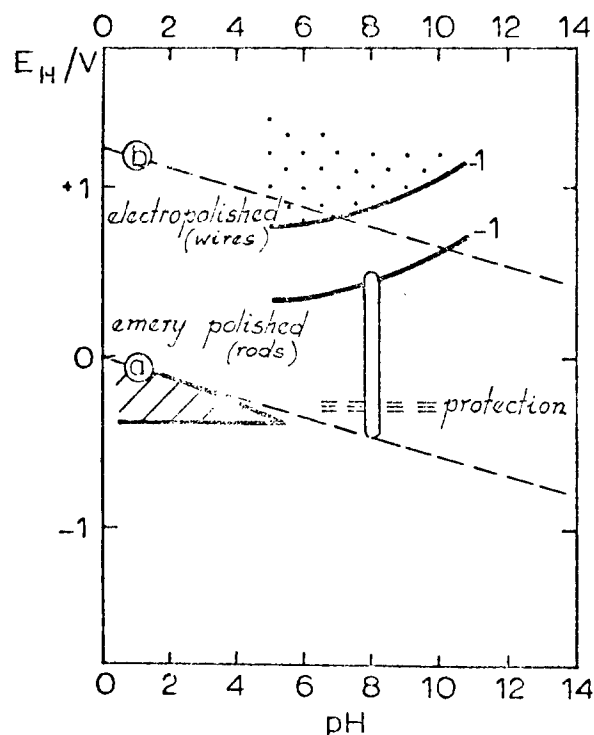


Fig. 4. Corrosion, immunity, and passivation conditions for chromium-nickel steel AISI 304 ( $Cl^- 10^{-1}M$ ) (schema).

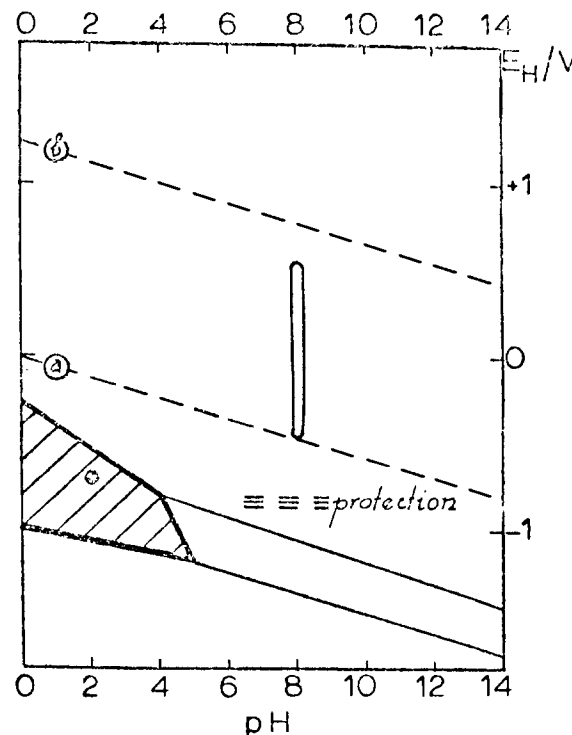


Fig. 5. Corrosion and passivation conditions for titanium (schema)

### Localized Corrosion of Copper and of Copper Alloys

In 1961, the International Copper Research Organization, INCRA, asked CEBELCOR to try to elucidate some fundamental electrochemical aspects of the pitting corrosion of copper tubes in cold water, which was at that time a severe problem in several countries such as Belgium, Germany, The Netherlands, the United Kingdom, and the U.S.A., but not in France.

Thanks to pioneer work performed in the U.K. in the early fifties by H. S. Campbell (6) and R. May (7), it was already known that most copper pits contained white cuprous chloride,  $CuCl$  (7); and that the existence of pits was often associated with the presence on the surface of the metal of a carbonaceous film formed during manufacture of the tubes (6a) attributed to breakdown of drawing lubricant residues during bright annealing of the half-hard tubes. However, copper tubes covered with such a "deleterious film" did not pit in all waters: no trouble occurred in some surface waters, such as the water of the river Thames, containing an unidentified organic fluorescent inhibitor (6b). The circulation of electric currents between external cathodic areas and internal anodic cavities had already been observed, but it was also observed by R. May that, for some unknown reason, the currents sometimes flowed "in the wrong direction": the pit sometimes became "cathodic" instead of "anodic."

In the research which we undertook in this field (8), we first tried to form artificially a pit similar to the natural ones by simply immersing in running Brussels water a copper plate on which was sealed a thin plastic tube containing some  $CuCl$  (Fig. 6); but, after about a month of immersion, we observed with surprise just the contrary of what we expected: instead of a pit there was a deposit of metallic copper under the  $CuCl$ -containing tube. We then used another experimental device (Fig. 7) consisting of a series of glass tubes containing open sections of copper tubes cut at  $120^\circ$ . Water was passed continuously through the glass tubes at a velocity of 20 mm/sec, and, as a function of time, we measured the values of the electrode potentials of the copper specimens and we observed visually their surface conditions. Tests were also made on thin copper wires, where the development of a pit was detected by a rupture of the wire.

Figure 8 shows a typical electrode potential-time curve for 10%  $PO_4H_3$ -pickled electrolytic copper in flowing Brussels water. During a first period of about ten days, the electrode potential remains at relatively low values (about  $-50$  to  $-10$  mV<sub>sce</sub>) and the surface becomes covered with a reddish deposit of cuprous oxide  $Cu_2O$ ; during a second period of about ten days, the potential increases steadily to about  $+40$  mV<sub>sce</sub>, and some greenish flakes of basic carbonate malachite  $CuCO_3 \cdot Cu(OH)_2$  are progressively formed on the surface; during a third period, periodic drops and rises of electrode potential occur.

We observed that illumination of the copper with a 200W tungsten flash lamp (which we used occasionally for observing the surface condition of the metal) does not affect its electrode potential during the first period shown in Fig. 8 (after 1 hr at  $-38$  mV<sub>sce</sub>) (Fig. 9), but during the third period (after 145 days at  $+77$  mV<sub>sce</sub>) it promotes very quickly, during a fraction of a second, a considerable potential drop of about 320 mV (until  $-250$  mV<sub>sce</sub>), which is only temporary. We also observed that a stagnation of the water (Fig. 10) leads, during the first period, to a slight increase (of about 20 mV) of the electrode potential, but that, during the

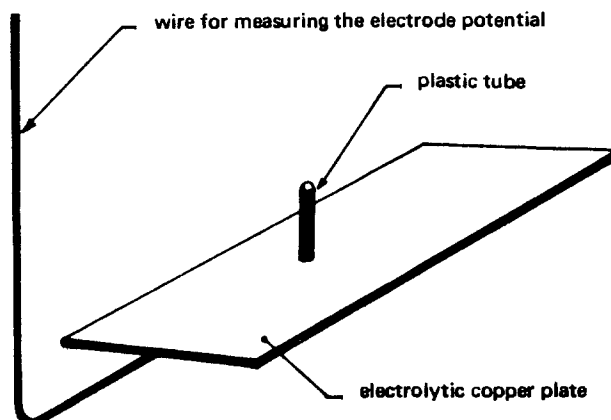


Fig. 6. Copper specimen used in experiments for attempting to produce artificial pits (first attempt).



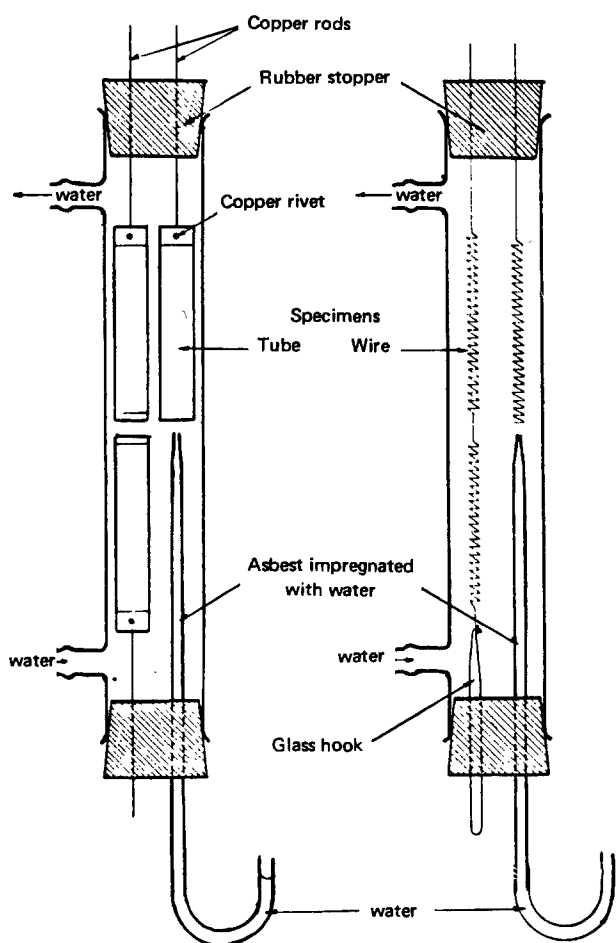


Fig. 7. Apparatus for corrosion testing of tube and wire specimens. At left is the corrosimeter for tubes, at right the corrosimeter for wires.

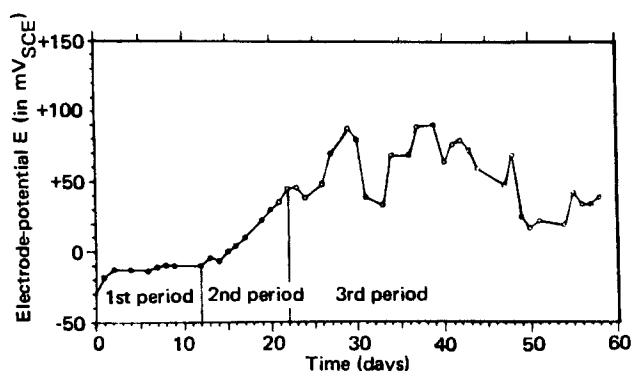


Fig. 8. Influence of immersion time on the electrode potential of electrolytic copper vertically immersed in continuously flowing Brussels water.

third period, it promotes a slow and important decrease of the potential to the same value as does illumination ( $-250 \text{ mV}_{\text{SCE}}$ ), and this also temporary. I have to confess that these funny results were at that time quite incomprehensible to us, and that they even led some members of the team working with us to question the interest and the validity of electrode potential measurements. Besides this, we had performed numerous potentiokinetic and potentiostatic experiments, most of which were helpless and hopeless, until finally, after having tested for about 155-367 days 207 specimens of different composition (electrolytic copper, deoxidized phosphorous, arsenic, etc.), of different initial surface conditions (pickled, as coming from the factory, with or without "aquablasting," etc.), isolated

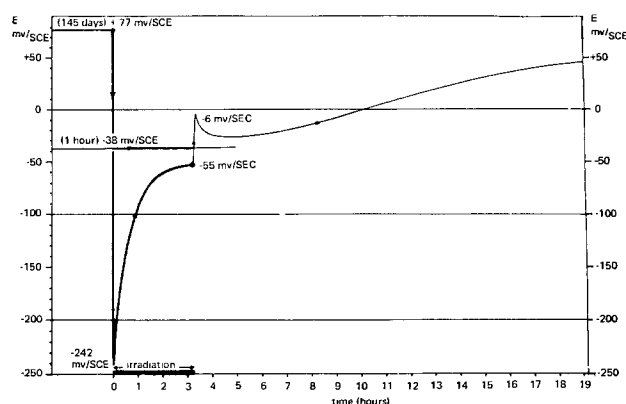


Fig. 9. Influence of temporary illumination of electrolytic copper on its electrode potential after 1 hr and 145 days immersion in circulating Brussels water.

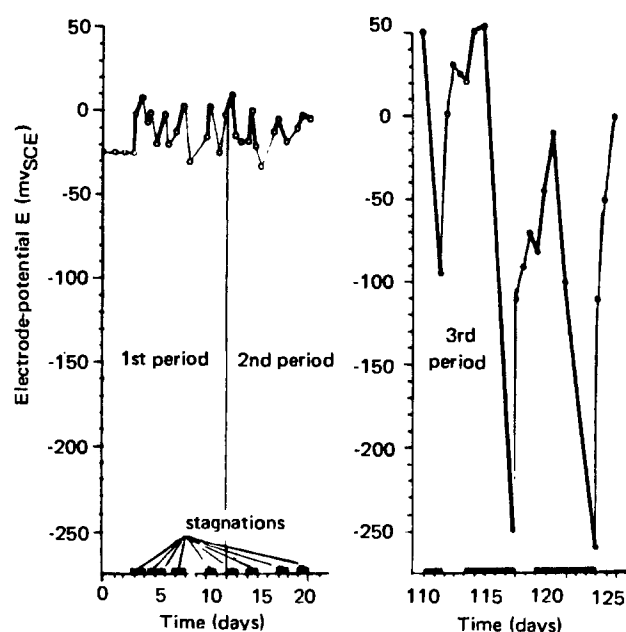


Fig. 10. Influence of water stagnation on the electrode potential of electrolytic copper immersed vertically.

or coupled with graphite or with different metals (gold, platinum, rhodium, silver, tin), with or without some additions ( $\text{Fe}^{++}$ ,  $\text{MnO}_2$ ,  $\text{NaClO}$ ) to the Brussels water we were using for the tests, we made an unexpected observation which brought hope and confidence back to us (Fig. 11 and 12).

Among these 207 specimens, 51 did show pitting and the 156 others did not. And, all the 51 pitted specimens had reached, during the third period of the experiments conducted with the device shown in Fig. 7, an electrode potential higher (i.e., more positive) than a critical value, which was about  $+100 \text{ mV}_{\text{SCE}}$  for wires and  $+170 \text{ mV}_{\text{SCE}}$  for tubes; these specimens were the only ones which reached such high values: all the 156 other specimens, which did not show pitting, had lower potentials. In trying to understand our experimental observations, we looked to cross sections through copper pits and we used potential-pH equilibrium diagrams.

Figure 13 shows a cross section through a copper pit in Brussels water. At the bottom of the pit there is some white cuprous chloride,  $\text{CuCl}$ , and a large amount of reddish cuprous oxide,  $\text{Cu}_2\text{O}$ ; the top of the pit is covered with green malachite  $\text{CuCO}_3 \cdot \text{Cu}(\text{OH})_2$  (with some white calcium carbonate,  $\text{CaCO}_3$ ). Needless to say, the solution in the presence of which the copper pit develops is not the bulk of the water, but a solution saturated in both  $\text{CuCl}$  and  $\text{Cu}_2\text{O}$ . Figure 14 shows a

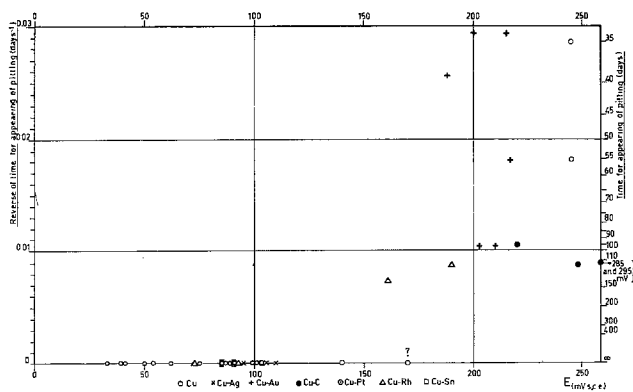


Fig. 11. Corrosimetric test on pickled copper tubes in the presence of circulating Brussels water. Relationship between the maximum electrode potential and the time when corrosion pits appear.

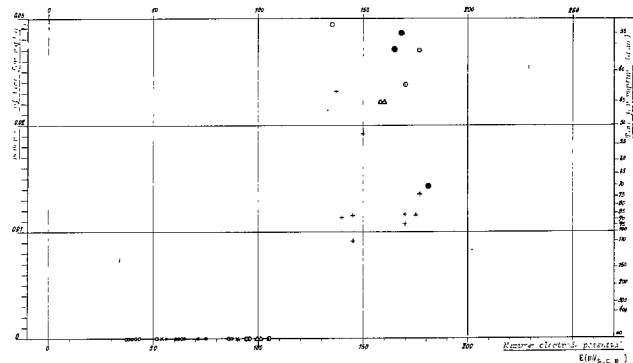


Fig. 12. Corrosimetric tests on electrolytic copper wires in the presence of Brussels water flowing continuously (11.5 cm · sec<sup>-1</sup>). Relation between the maximum electrode potential and the time when rupture occurs. (Results after 250 days).

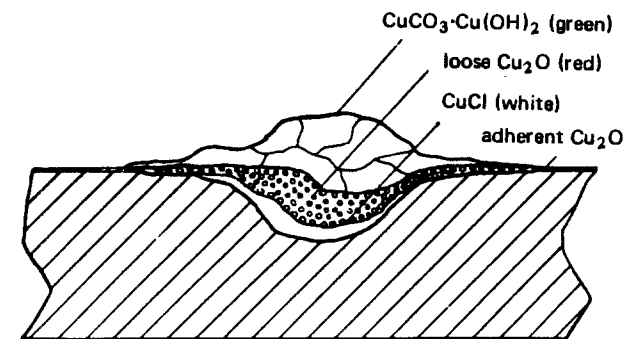


Fig. 13. Copper pit. Cross section showing the presence of red Cu<sub>2</sub>O and white CuCl beneath a mushroom of green malachite.

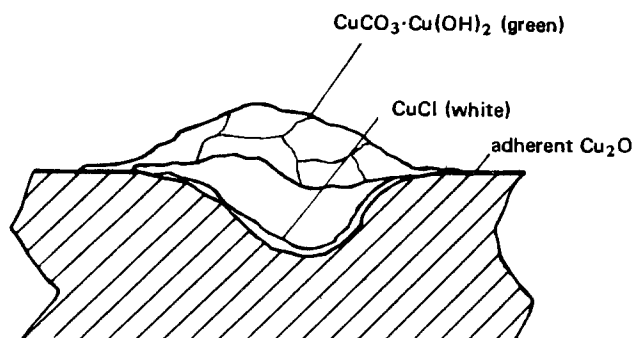


Fig. 14. Copper pit. Cross section of the pit shown in Fig. 13 after removal of the loose deposit of Cu<sub>2</sub>O.

further cross section through a copper pit, similar to the one shown in Fig. 13, which clearly shows that

most of the Cu<sub>2</sub>O has disappeared from the cavity and is thus a loose secondary corrosion product.

Figure 15 shows a potential-pH equilibrium diagram for the binary system Cu-H<sub>2</sub>O, at 25°C where, notably, the equilibrium conditions of Cu, Cu<sub>2</sub>O, and CuO, may be seen; in the presence of pure water of pH 7, the stable oxidation product of copper is Cu<sub>2</sub>O if no oxygen is present; it is CuO if oxygen is present. Figure 16 shows a potential-pH equilibrium diagram for the

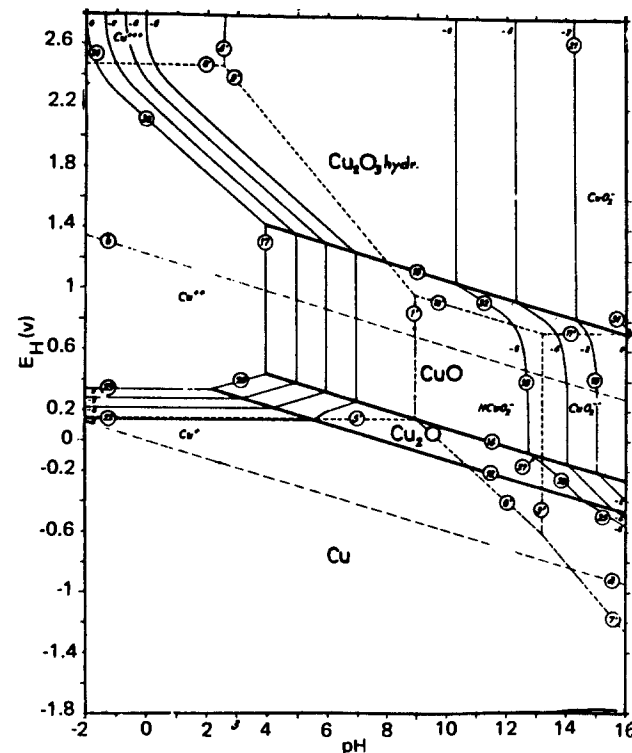


Fig. 15. Potential-pH equilibrium diagram for the copper-water system at 25°C.

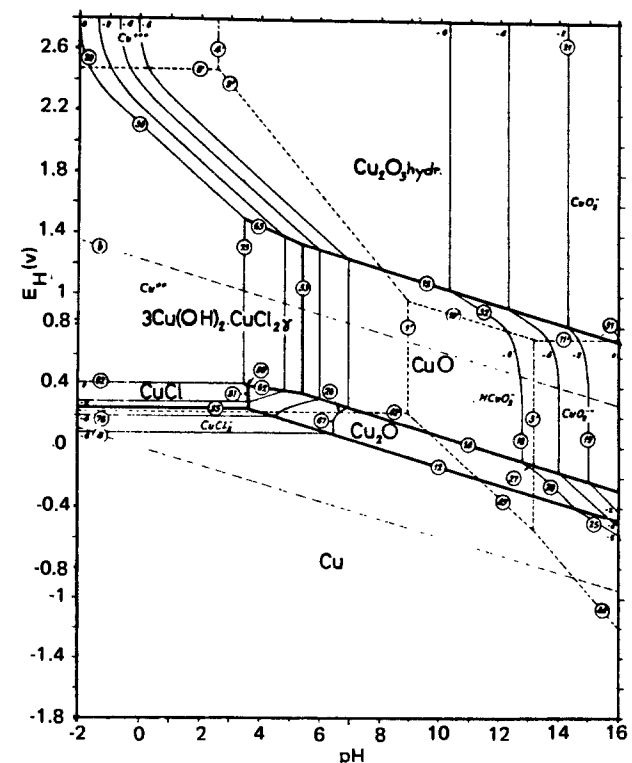


Fig. 16. Potential-pH equilibrium diagram for the three-component system, Cu-Cl-H<sub>2</sub>O, for solutions containing 355 ppm Cl<sup>-</sup> (10<sup>-2</sup> g · ion/liter).

ternary system Cu-Cl-H<sub>2</sub>O valid for solutions containing 10<sup>-2</sup> g-ion Cl<sup>-</sup>/liter, which is about the amount of Cl<sup>-</sup> in a solution saturated in CuCl. This figure shows that CuCl is not stable in a neutral solution of pH 7, where the stable form of univalent copper is Cu<sub>2</sub>O; CuCl should thus, in such a solution, hydrolyze according to the reaction  $2\text{CuCl} + \text{H}_2\text{O} \rightarrow \text{Cu}_2\text{O} + 2\text{H}^+ + 2\text{Cl}^-$ . The only point of the diagram where Cu, Cu<sub>2</sub>O, and CuCl, which are coexisting at the bottom of a pit, are simultaneously stable, is the point of intersection of the three lines 12, 51, and 55. This point, whose coordinates are  $E = +270 \text{ mV}_{\text{ehs}}$  and  $\text{pH} = 3.5$ , thus represents the equilibrium conditions at the bottom of the pit. For this point, the equilibrium concentrations in dissolved copper are, assuming that the solution is "perfect": 10<sup>-2.44</sup> as Cu<sup>++</sup>, 10<sup>-3.37</sup> as CuCl<sub>2</sub><sup>-</sup>, and 10<sup>-4.31</sup> as Cu<sup>+</sup>, i.e., a total of 10<sup>-2.43</sup> (or 234 ppm) dissolved copper; the equilibrium concentrations in dissolved Cl are 10<sup>-2.17</sup> as Cl<sup>-</sup> and 10<sup>-3.07</sup> as CuCl<sub>2</sub><sup>-</sup>, i.e., a total of 10<sup>-2.12</sup> at.g/liter or 270 ppm dissolved Cl. Under these conditions of electrode potential and pH, the corrosion reaction of copper is reversible; it is thus easy to understand that any such pit will grow if the electrode potential inside the pit is higher (more positive) than +270 mV<sub>she</sub> (i.e., +20 mV<sub>sce</sub>); on the contrary, such a pit will be stifled, with redeposition of metallic copper, if this electrode potential is lower (more negative) than +270 mV<sub>she</sub>. And this is the very simple criterion which governs the problem of copper pitting in waters containing some chloride: for avoiding the development of copper pits in such waters, it is necessary and sufficient to prevent any increase of the electrode potential inside the cavities above +270 mV<sub>she</sub> (or +20 mV<sub>sce</sub>). As electrode potentials inside cavities are usually not easily measurable, it is convenient to correlate them with the electrode potentials outside the cavities (Fig. 17) which, due to the existence of a diffusion potential, are generally about 80-150 mV higher (about +350 to +420 mV<sub>she</sub> or +100 to +170 mV<sub>sce</sub>). And we thus have the explanation of the critical protection potential against copper pitting (about +100 to +170 mV<sub>sce</sub>) which was observed experimentally.

Figure 18 shows, together with the theoretical corrosion-immunity and passivation conditions of copper in water at 25°C, the equilibrium conditions inside a copper pit ( $E = +270 \text{ mV}_{\text{she}}$  and  $\text{pH} = 3.5$ ) and the possible extreme electrode potential values of copper in the presence of water of pH 8 (from 0 to about +600 mV<sub>she</sub> according to the oxygen content of the water and to the surface condition of the metal). One sees that the protection potential against copper pitting (about +350 to +420 mV<sub>she</sub>) lies between these two possible extreme values, and that copper pits may thus, in fact, grow or be stifled.

This criterion was in harmony with all previously known facts and has opened the way to new methods of protection and control. The presence of carbon on the surface of copper, which, thanks to H. S. Campbell (6a), has been known since 1950 to promote pitting, increases the electrode potential of more or less per-

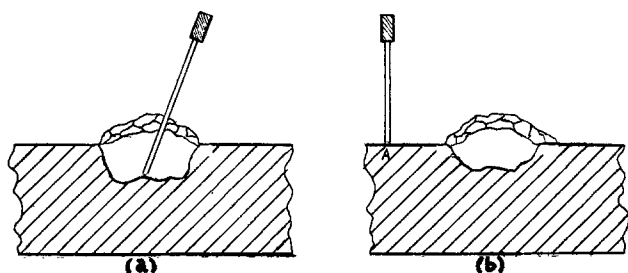


Fig. 17. The electrode potential of pitted copper (a) as measured within the pit; (b) as measured outside the pit, giving the "mixed potential."

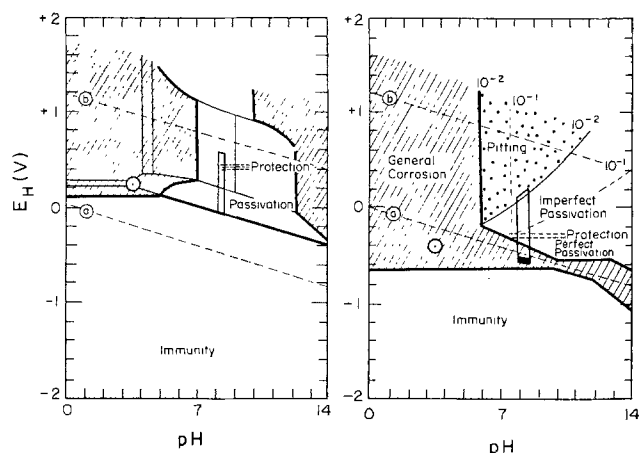


Fig. 18. (left) Copper in Brussels water. pH and electrode potential conditions inside pits in equilibrium:  $\text{pH} = 3.5$ ,  $E = +270 \text{ mV}_{\text{she}}$ . Possible electrode potentials outside pits at  $\text{pH} = 8$ :  $E = 0$  to +600 mV<sub>she</sub>. Protection potential against localized corrosion: about +350 to +420 mV<sub>she</sub>.

Fig. 19. (right) Armco iron in solutions containing chloride (10<sup>-2</sup> and 10<sup>-1</sup> g · ion/liter). pH and electrode potential conditions inside oxygen-free living pits:  $\text{pH} = 3.8$ ,  $E = -325 \text{ mV}_{\text{she}}$ . Possible electrode potentials outside pits at  $\text{pH} = 8$ :  $E = -0.5-0 \text{ mV}_{\text{she}}$  for 10<sup>-2</sup> g · ion Cl<sup>-</sup>/liter. Protection potential against localized corrosion: about -300 mV<sub>she</sub>.

fectly passive copper up to about +300 mV<sub>sce</sub>, i.e., much above the critical value (8b). The addition of ferrous sulfate to seawater, which was shown in 1961 by T. W. Bostwick to prevent the pitting corrosion of brass exchanger tubes (9), depresses the electrode potential below this critical value. Extensive exposure trials of different kinds of copper tubes in different water supplies with measurements of the electrode potentials have been recently performed by F. J. Cornwell, J. Wildsmith, and P. T. Gilbert (10). As shown by Fig. 20 and 21, all the results of these tests are in full agreement with the above-mentioned criterion: whatever the metal and whatever the water, pitting only occurs (and always occurs) if the electrode potential is higher than about +100 to +170 mV<sub>sce</sub> (i.e., +350 to +420 mV<sub>she</sub>).

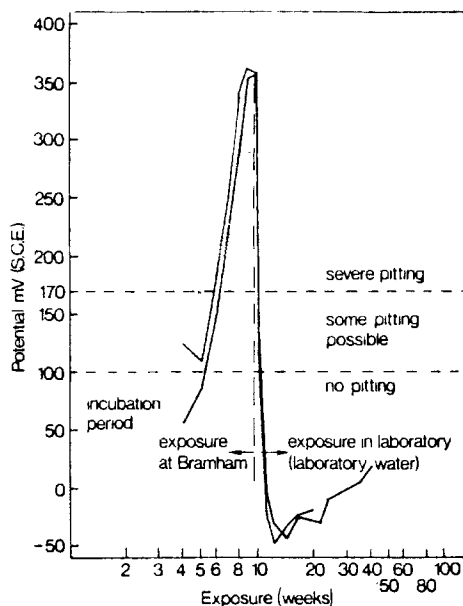


Fig. 20. Effect of transferring uncleaned copper tubes undergoing pitting at Bramham to the laboratory (Leeds water), after Cornwell et al.

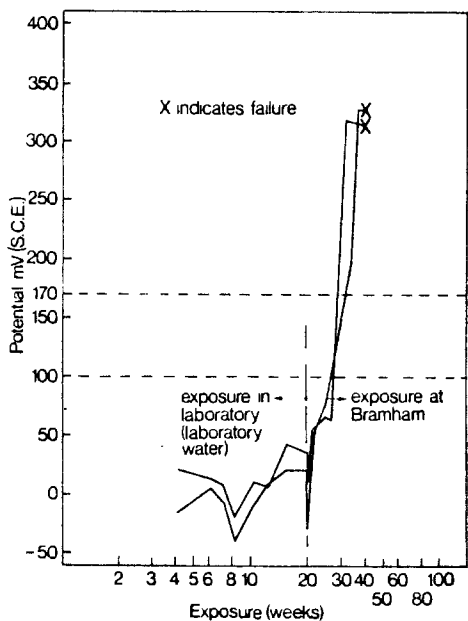


Fig. 21. Effect of transferring uncleaned copper tubes from the laboratory (Leeds water) to Bramham, after Cornwell et al.

Since 1962, new precautions and new remedies have been suggested as a result of this criterion, being understood that, if not only pitting corrosion but also any general corrosion should be avoided, the protection potential should be dropped from +270 to +100 mV<sub>she</sub> (or from +20 to -150 mV<sub>sce</sub>). When in the presence of a corrosive water or of a corrosive atmosphere, copper should not be in contact with any substance whose zero-current electrode potential in the considered environment is higher than the critical one, such as carbon and gold, for example; and this explains the recently observed deterioration of so many bronze sculptures which were covered with a porous gold deposit (the doors of the Baptistery in Firenze, the horses of Praxiteles in Venice, etc.). Silver and tin have lower electrode potentials and are thus not harmful to copper, and this is why silvered and tinned copper utensils may be used for cooking. Since about 1966, the copper hot-water tanks placed on the roofs of many houses in London, whose corrosion has been for many years the source of great concern, have been protected cathodically after a recommendation of B.N.F.M.R.A., using temporary so-called "protector rods" of aluminum alloys which depress the electrode potential below +100 mV<sub>she</sub> (11). A general method has been proposed for checking the pitting susceptibility of different sorts of copper and of copper alloys in different waters (Fig. 25) (8d, f, g), as well as for clarifying the mechanism of dealloying copper alloys, such as the removal of nickel from copper nickels and the removal of zinc from brasses (12, 13). However, much work remains to be done before these problems might be considered as really mastered.

Now, coming back to the experiments which were mentioned at the beginning of this talk, what is the mechanism of copper pitting? What is the explanation of the "funny results" which were obtained concerning the influence of light and stagnation on the electrode potential?

During the first stage of the experiment, whose results are shown in Fig. 8, copper undergoes general corrosion in the bulk of the water (Fig. 22) with formation of Cu<sup>+</sup> and Cu<sup>2+</sup> ions and, eventually, solid CuCl which hydrolyzes, for instance according to the reaction 2CuCl + H<sub>2</sub>O → Cu<sub>2</sub>O + 2H<sup>+</sup> + 2Cl<sup>-</sup>, with formation of solid Cu<sub>2</sub>O which deposits on the metal and of hydrochloric acid HCl which is washed away by the water. According to Fig. 23, which is the equilib-

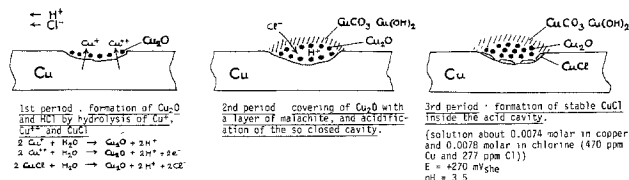


Fig. 22. Initiation and evolution of a copper corrosion pit in the presence of water containing chloride.

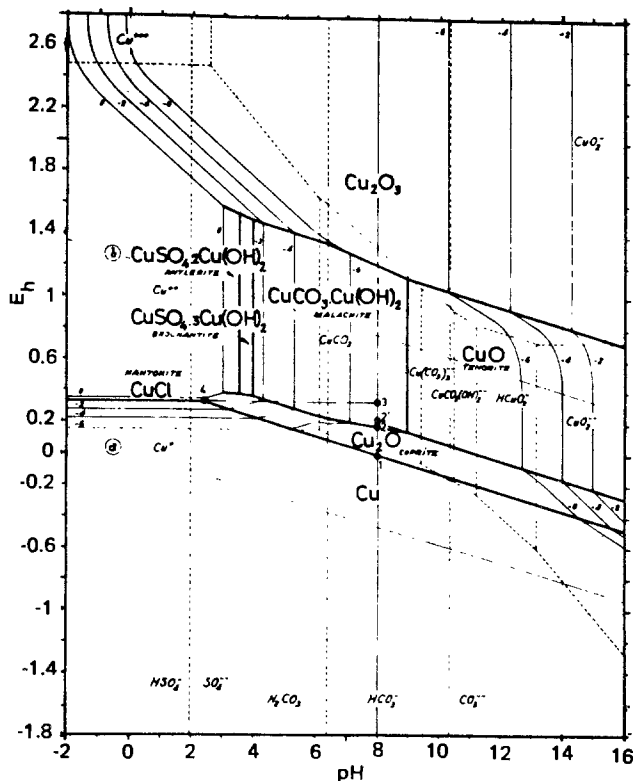


Fig. 23. Potential-pH equilibrium diagram for the five component system Cu-Cl-CO<sub>2</sub>-SO<sub>3</sub>-H<sub>2</sub>O at 25°C for solutions containing 229 ppm CO<sub>2</sub> (10<sup>-2.28</sup> g · ion/liter), 46 ppm SO<sub>3</sub> (10<sup>-3.24</sup> g · ion/liter), and 22 ppm Cl (10<sup>-3.21</sup> g · ion/liter).

rium potential-pH diagram of the quinary system Cu-Cl-CO<sub>2</sub>-SO<sub>3</sub>-H<sub>2</sub>O for the contents of Cl, CO<sub>2</sub>, and SO<sub>3</sub> existing in Brussels water, malachite CuO<sub>3</sub>·Cu(OH)<sub>2</sub> is the stable form of copper in the presence of aerated Brussels water of pH 8 (e.g., at point 3) and this is why, during the second stage of the experiment, Cu<sub>2</sub>O becomes progressively covered with malachite which, being relatively protective (8e), forms a screen which progressively prevents the hydrochloric acid from being washed away by the bulk of the water. The pH inside the cavity thus decreases until, when the third stage is reached, the solution inside the cavity becomes saturated in CuCl which is being deposited on the metal; the solution inside the cavity then has a pH of about 3.5 and is then about 0.01M in CuCl; as previously stated, the cavity increases in depth with dissolution of copper if the electrode potential is higher (more positive) than +270 mV<sub>she</sub>; on the contrary, the pit heals with redeposition of metallic copper if the electrode potential is lower (less positive) than +270 mV<sub>she</sub>.

As we have seen, both an illumination of the metal and a stagnation of the water lead, during the third stage of the experiment, to a temporary potential drop (which is sudden in the case of illumination and slow in the case of stagnation), and this to the same value: -250 mV<sub>sce</sub> (i.e., 0 mV<sub>she</sub>). As may be seen in Fig. 23 (point 1), this value 0 mV<sub>she</sub> is, for the pH 8 of Brussels water, the equilibrium electrode potential of the

system Cu-Cu<sub>2</sub>O. It is thus likely that, during the third stage of the experiment, both an illumination of the copper and a stagnation of the water lead to a temporary contact of truly metallic copper with the bulk of the water. We think, without having had so far the opportunity to check this extensively, that:

(i) This sudden action of illumination of copper during the third stage of the experiment is due to an immediate photochemical action of light on CuCl with formation of metallic Cu (as the action of light on AgCl with formation of Ag in photography). Such an effect of light should thus indicate the presence of CuCl on the surface of the copper, and might thus detect an early stage of pit formation.

(ii) This slow action of stagnation of the water is due to a progressive opening of some active cavities (Fig. 24), probably as a result of a chemical attack of the external malachite layer by the internal chlorhydric acid, with formation of "chimneys" through which gaseous CO<sub>2</sub> escapes from the cavity and the bulk of the water penetrates to the bottom of the cavity, where copper is really in a pickled metallic state. Such an effect of stagnation should thus detect an advanced stage of pit formation.

(iii) Both these actions are temporary because, due to the presence of oxygen in the bulk of the water, metallic copper becomes quickly oxidized.

As a result of all this, the testing device shown in Fig. 25 has been established. Water is passed through a series of four corrosimeters containing copper specimens, recording the electrode potentials of these specimens as a function of time. In the corrosimeters No. 1, 2, and 3, which are intended for checking the behavior of different samples of copper and/or copper alloys in a given water, water is continuously passed in darkness (No. 2), in darkness with periods of stagnation (No. 3), and continuously with periods of illumination (No. 1). In corrosimeter No. 4, which is intended for appreciating the danger of pitting in a given water, the water to be tested is continuously passed in the darkness on pickled copper partially covered with gold, supposed to represent a "deleterious surface condition."

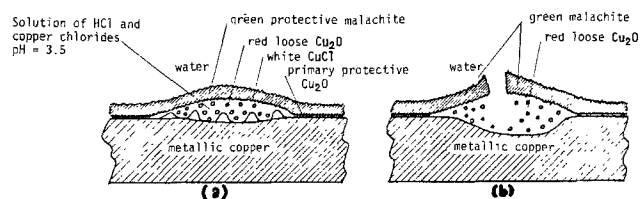


Fig. 24. Copper pit. (a) closed pit (in running water)  $E = +20$  to  $+77$  mV<sub>SCE</sub>; (b) open pit (in stagnant water)  $E = -250$  mV<sub>SCE</sub>.

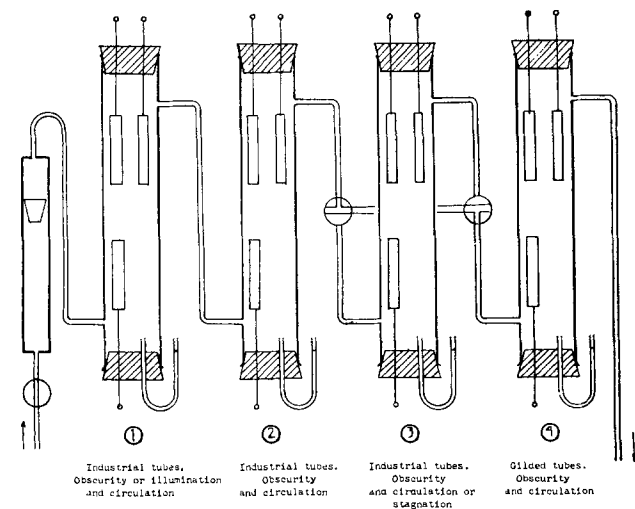


Fig. 25. Device for testing the pitting behavior of copper in water

Now, why is the pitting corrosion of copper tubes for cold-water delivery not a problem in France, as it is in many other countries? Probably because France mostly uses hard tubes which, contrary to the soft ones, are not annealed in a reducing atmosphere and are free of the deleterious carbon film likely to be formed by the cracking of some oils.

Before closing this statement on copper, I wish to remind that, as has been emphasized by R. M. Garrels (14), potential-pH equilibrium diagrams may be useful in geology. Figure 26 indicates some stability conditions of the chlorides nantokite and  $\gamma$  paratacamite (which is the Chilean copper mineral). Figure 27 may be useful for checking the conditions of stability of the basic copper carbonates malachite and azurite. Figure 28 may be useful for checking the conditions of stability of the basic copper sulfates brochantite and antlerite, as well as the conditions where patinas formed on copper roofing may be the black tenorite or the green brochantite.

### Localized Corrosion of Iron and Steels

Figure 29 shows a theoretical potential-pH diagram for the Fe-H<sub>2</sub>O system at 25°C. Figure 30a shows experimental potentiokinetic polarization curves for iron in the presence of chloride-free aqueous solutions of different pH's and Fig. 30b shows the corresponding experimental potential-pH conditions for immunity, general corrosion, and passivity of iron (15). Figure 31a shows experimental potentiokinetic polarization curves for iron in the presence of solutions similar to those of Fig. 30a, but containing chloride; these curves show, besides passivation potentials which are the same as in Fig. 30a, pitting potentials and protection potentials against localized corrosion, and make it possible to represent at Fig. 31b experimental potential-pH conditions for immunity, general corrosion, pitting corrosion, imperfect passivity where no new pits are formed but

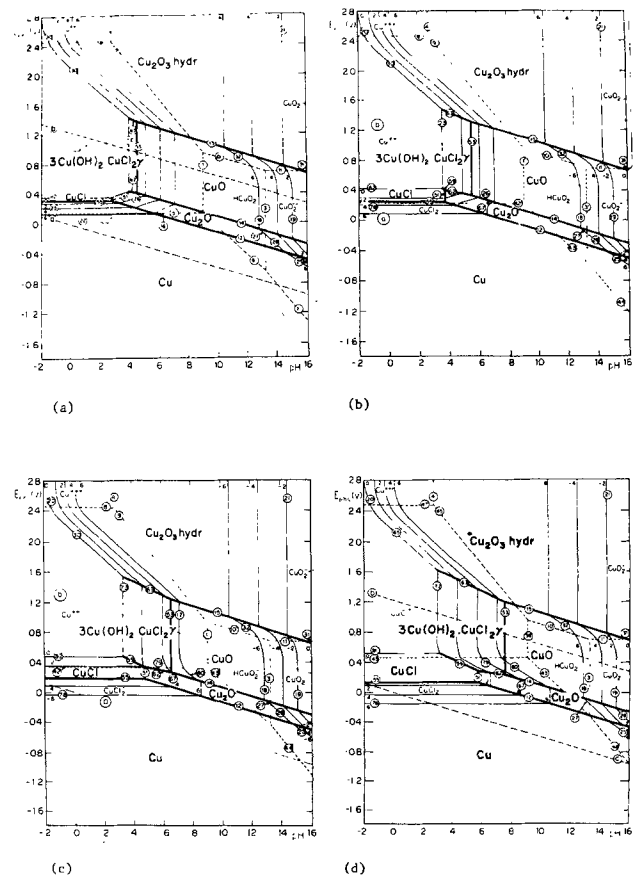


Fig. 26. Potential-pH equilibrium diagrams for the ternary system Cu-Cl-H<sub>2</sub>O at 25°C for (a) 10<sup>-3</sup>, (b) 10<sup>-2</sup>, (c) 10<sup>-1</sup>, and (d) 1 g · ion Cl<sup>-</sup>/liter (35, 355, 3550, and 35,500 ppm).

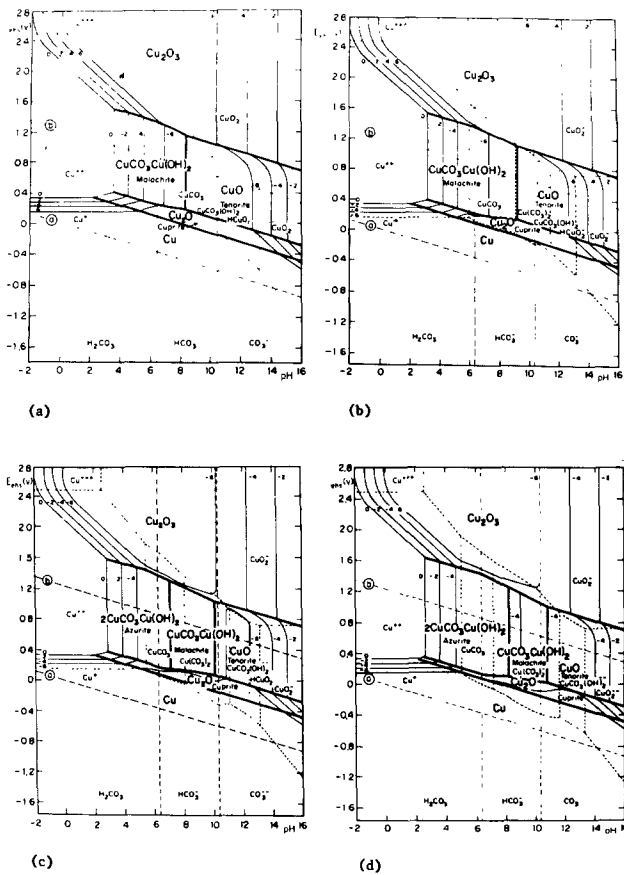


Fig. 27. Potential-pH equilibrium diagrams for the ternary system Cu-CO<sub>2</sub>-H<sub>2</sub>O at 25°C for (a) 10<sup>-3</sup>, (b) 10<sup>-2</sup>, (c) 10<sup>-1</sup>, and (d) 1 mole total dissolved CO<sub>2</sub> per liter (44, 440, 4400, and 44,000 ppm).

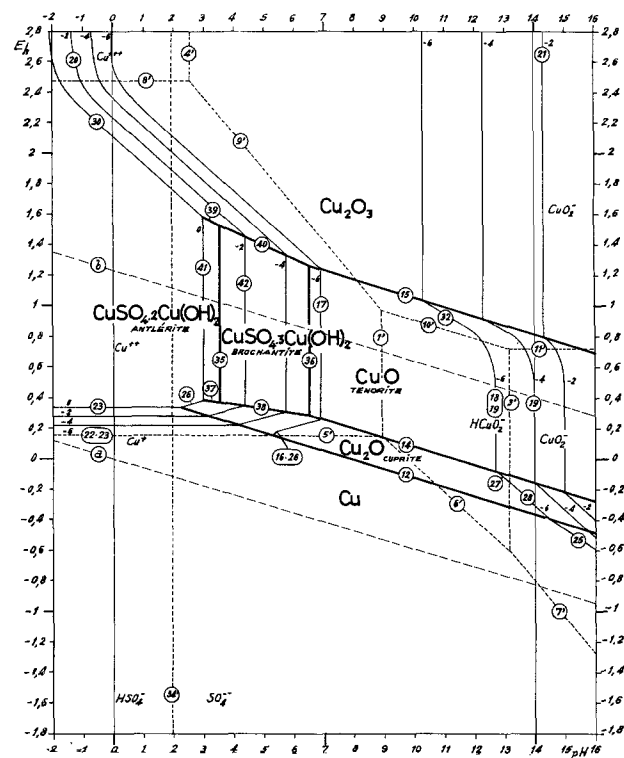


Fig. 28. Potential-pH equilibrium diagram for the ternary system Cu-SO<sub>3</sub>-H<sub>2</sub>O at 25°C for 10<sup>-3.24</sup> mole dissolved SO<sub>3</sub> per liter (46 ppm).

where previously formed pits may grow, and perfect passivity where these pits do not grow.

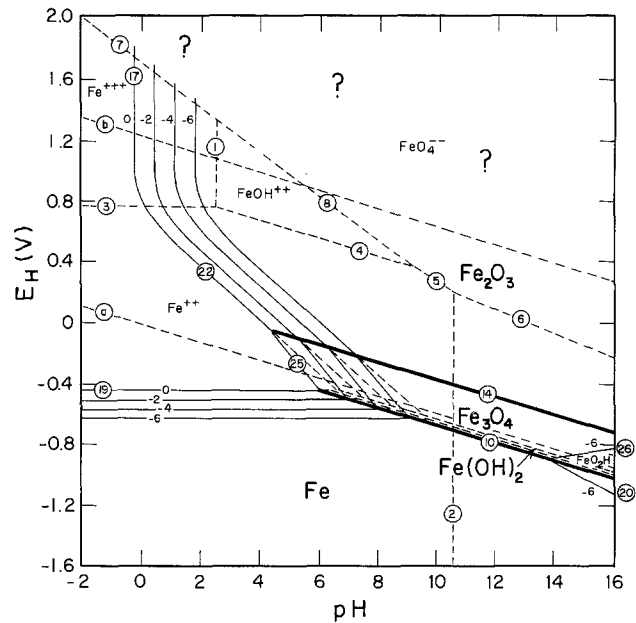


Fig. 29. Potential-pH equilibrium diagram for the iron-water system at 25°C.

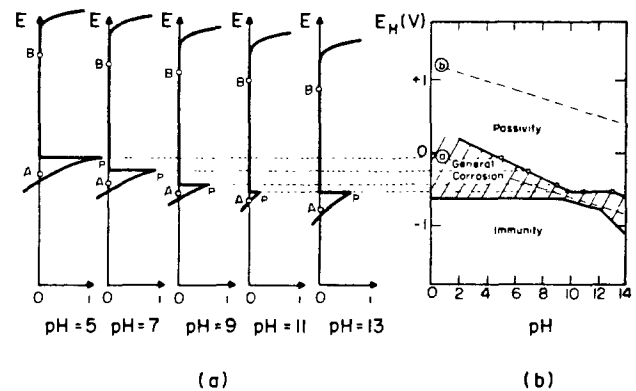


Fig. 30. Behavior of iron in chloride-free solutions. (a) polarization curves in the presence of solutions for pH 5-13; (b) experimental conditions of immunity, general corrosion, and passivity.

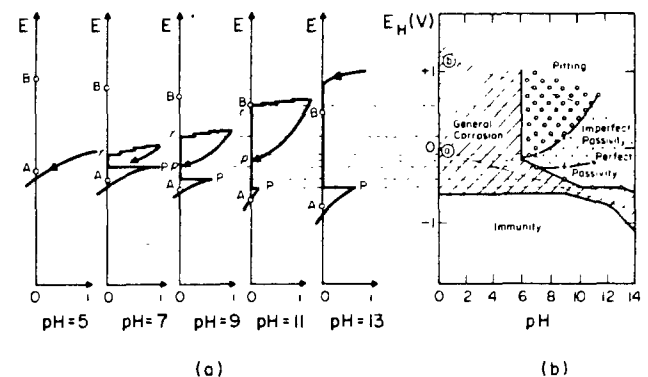


Fig. 31. Behavior of iron in solutions containing chloride (355 ppm): (a) polarization curves in the presence of solutions for pH 5-13; (b) experimental conditions of immunity, general corrosion, perfect and imperfect passivity, and pitting. Protection potential against localized corrosion.

Figure 19 shows, together with the experimental potential-pH conditions of immunity, general corrosion, pitting corrosion, and perfect and imperfect passivity shown in Fig. 31b, the potential and pH conditions inside an active oxygen-free corrosion pit or crevice, or other "occluded corrosion cell" or OCC as it has been called by B. F. Brown ( $E = -325 \text{ mV}_{\text{she}}$  and  $\text{pH} \approx 3.8$ ), and the possible extreme electrode potential values of iron in the presence of water of pH 8 (from about  $-550$  to  $+100 \text{ mV}_{\text{she}}$  according to the oxygen content of the water). One sees in this figure that the protection potential against localized corrosion of iron is, as it is for copper (Fig. 18), very close to the electrode potential inside an active OCC.

Figure 32 shows a device which permits, by passing oxygen and nitrogen on, respectively, the external and the internal part of a duplex iron specimen, the production on the internal part, as a result of differential aeration, of a crevice under conditions which notably permit the measurement of the pH and the electrode potential on both the cathodic and the anodic areas (which is an "occluded corrosion cell"). Figure 33 shows, as a result of experiments performed with such a device by J. Van Muylder *et al.* (16), the influence of a slow external cathodic polarization on the potential and pH conditions inside an iron crevice. It is seen that this polarization progressively increases the pH

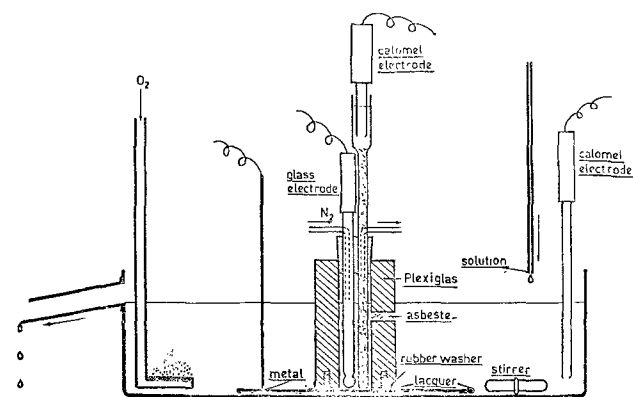


Fig. 32. Device for studying crevice corrosion

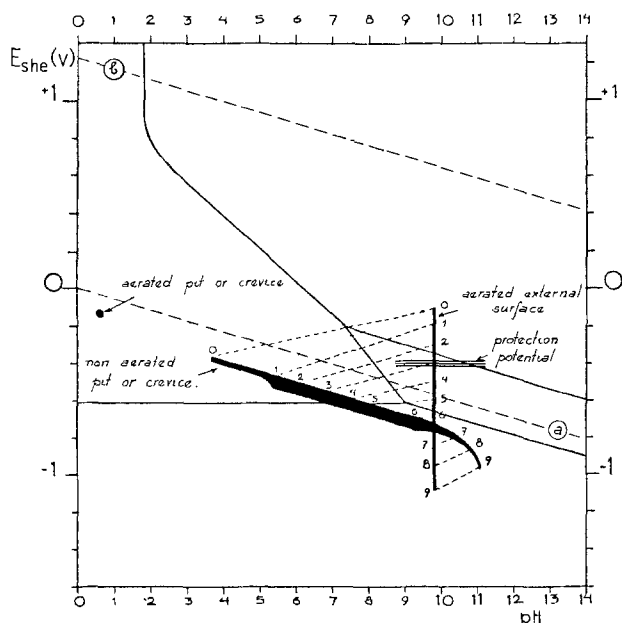


Fig. 33. Influence of a slow cathodic polarization on the potential and pH conditions inside a crevice (mild steel with an aerated solution of 0.001M NaOH and 0.001M NaCl), after J. Van Muylder, L. Sathler *et al.*

inside the cavity and that, when the external potential reaches the "protection potential against localized corrosion," this solution is not acid anymore and the iron has become immune; however, there is still inside the cavity a hydrogen evolution whose affinity, which is measured by the vertical distance between the line relating to the crevice and the hydrogen equilibrium line  $\alpha$  (about 100 mV), remains about the same until the solution becomes neutral and increases very much when the solution has become definitely alkaline. When measuring, during a rapid external cathodic polarization, the current flow between a large external area and a small internal cavity of pH 5.5, Antoine Pourbaix has observed the two polarization curves shown in Fig. 34 (17). It may be seen that, when the external cathodic polarization is increased, the cavity progressively ceases to act as an anode, reaches at  $-0.43 \text{ mV}_{\text{she}}$  the state of zero current, and afterwards acts as a cathode. When the protection potential  $-0.38 \text{ mV}_{\text{she}}$  is reached on the external area, the potential inside the cavity has become  $-0.44 \text{ mV}_{\text{she}}$ ; the cavity has then become immune and the cathodic current density, which is about  $2 \mu\text{A}\cdot\text{cm}^{-2}$ , totally corresponds to a hydrogen evolution. Figure 35 shows the results obtained by B. F. Brown in his famous work on the cathodic polarization of steel cracks when using his freezing method (18). One sees that Brown's curve on cracks is very similar to Van Muylder's curve on crevices, and this confirms the assumption that the chemistry and the electrochemistry of crevices and cracks, as well as of any other form of OCC (pits, cor-

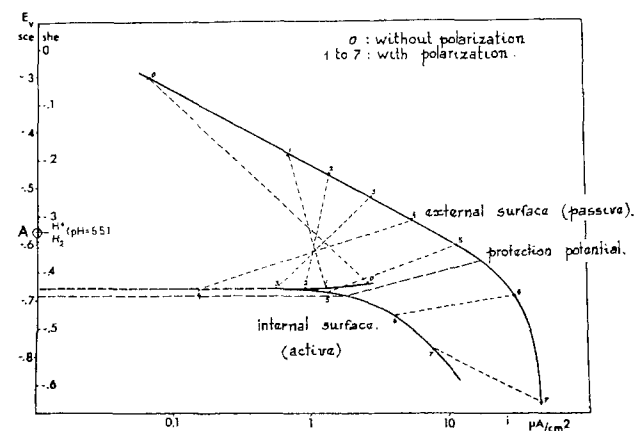


Fig. 34. Influence of a rapid external cathodic polarization on the electrochemical behavior of mild steel outside and inside a crevice (external pH = 9.5; internal pH = 5.5), after Antoine Pourbaix.

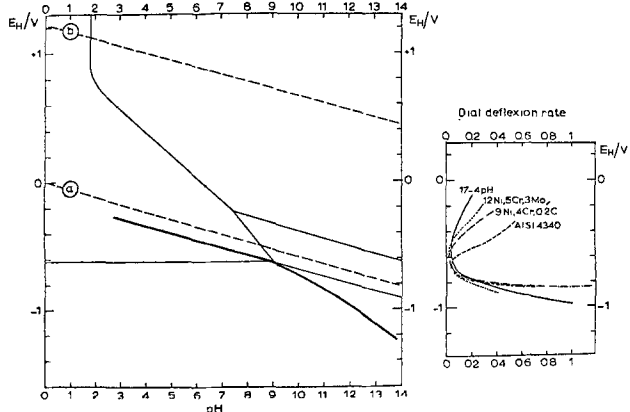


Fig. 35. Influence of a cathodic polarization on the electrochemical characteristics and propagation rate of a stress corrosion crack (chromium steel AISI 4340 in contact with NaCl 3.5% solution), after B. F. Brown.

rosion in recesses, intergranular corrosion, etc.), is the same.

As the representative point of the OCC in both Fig. 33 and 35 is below the "hydrogen line"  $\alpha$ , hydrogen is being evolved inside both crevices and cracks, even if the bulk of the solution is alkaline. This means that cathodic protection below the "protection potential against localized corrosion" (usually about  $-200$ – $-400$  mV<sub>she</sub>), which may often prevent any localized corrosion of iron and steels, may be fully effective against deterioration of the material only if this material is not susceptible to hydrogen embrittlement. Needless to say, this is of particular importance for stress corrosion cracking.

### Conclusions

Coming to the end of this rapid survey, I wish to raise attention to the fact that, in the cases of both copper and iron in the presence of solutions containing chloride which we have been considering in the present lecture, the solution existing inside the OCC is, in fact, a solution of a chloride of the considered metal (CuCl or FeCl<sub>2</sub>·4H<sub>2</sub>O) which is thermodynamically unstable in the bulk of the water and thus hydrolyzes, with formation of a stable oxide (Cu<sub>2</sub>O or Fe<sub>3</sub>O<sub>4</sub>), with decrease of the pH and increase of the chloride concentration until the solution becomes saturated in this chloride (about 0.01M and pH 3.5 for CuCl, and about 4.6M and pH 3.8 for FeCl<sub>2</sub>·4H<sub>2</sub>O). The system then ceases to be univariant and becomes invariant.

Such solutions may be prepared synthetically by simply saturating oxygen-free water with this chloride in the presence of the metal in powder form. This makes it possible to prepare very easily a solution similar to the solution really existing inside a crevice or a crack, or along a corroding grain-boundary, or in any other OCC, and this in any desirable quantity (100 cm<sup>3</sup> or 1000 cm<sup>3</sup>, or more) which might be suitable for any analysis and electrochemical experiment. This was done for copper in 1962 by Jean Van Muylder (8), and for iron in 1973 by C. T. Fujii (19) and in 1974 by Lucio Sathler (20). Both C. T. Fujii and L. Sathler have obtained for the OCC of iron in chloride solutions at 25°C a very concentrated solution, respectively 4.2 and 4.6M in FeCl and pH 3.8. According to L. Sathler, isolated iron corrodes in this solution with a velocity of 1.2  $\mu\text{A}\cdot\text{cm}^{-2}$  (13  $\mu\text{m}\cdot\text{year}^{-1}$ ), and passivates at  $-185$  mV<sub>she</sub> with a passivation current of 2.5 mA·cm<sup>-2</sup> (27 mm·year<sup>-1</sup>). If oxygen penetrates into this solution, the pH decreases from 3.8 to about 0.6, and the zero-current electrode potential of iron increases from  $-325$  mV<sub>she</sub> to  $-125$  mV<sub>she</sub> (Fig. 33), where it corrodes with a velocity of about 0.7 mA·cm<sup>-2</sup> (8 mm·year<sup>-1</sup>) and may not become passive.

Finally, I think that it is important to realize fully that, in any case where localized corrosion is to be considered, such corrosion does not develop in the bulk of the solution and at the electrode potentials existing on the external surfaces, but inside an OCC where the composition of the solution and the electrode potential of the metal may be very different from what it is outside these cavities. For instance, many problems related to intergranular corrosion might be better understood by systematic research related to the electrochemical behavior of substances existing along these grain boundaries in these solutions.

Besides this, as stated recently (21), it is likely that by adding to copper, to iron or to other metals alloying elements which when dissolving in the solutions existing inside the OCC of these metals would render these solutions less aggressive and/or lead to the deposition of a less soluble salt or element under the existing conditions of pH and electrode potential, etc., it would be possible to better explain than presently the beneficial influence of some alloying elements to nonferrous metals (As and Fe in copper alloys? Sb and Bi in aluminium alloys?) and to some steels (Mo?), and to

set up new and better alloys as far as their resistance to localized corrosion is concerned.

This last phrase was written several months ago, at a moment when no proof of the exactitude of this statement was available, as far as I know. Today, three hours ago, at 2.30 p.m., T. Kodama and J. R. Ambrose, co-workers of Jerry Kruger at the National Bureau of Standards, presented at the present meeting of The Electrochemical Society an outstanding paper (Abstract 75) entitled "Effect of Molybdate Ion on the Repassivation Kinetics of Iron in Sodium Chloride Solutions." According to this paper, and in full agreement with the present theory, molybdenum would dissolve in an iron OCC as molybdate ions and would form with the dissolved ions insoluble ferrous molybdate FeMoO<sub>4</sub>. It is most likely that this is the fundamental reason of the beneficial effect of molybdenum on the pitting and crevice behavior of alloy steels (such as the AISI 316); the just-mentioned concept for setting new and better alloys might thus perhaps be correct.

As a conclusion, I wish to emphasize that any time one has to study localized corrosion, and notably crevice corrosion, intergranular corrosion, and stress corrosion cracking which have a so-great practical importance, there is a great interest in the measurement of electrode potential and pH values outside and inside the cavities, and to interpret the so-obtained values on the basis of both electrochemical thermodynamics and electrochemical kinetics. Such researches would preferably include a thorough study of the chemistry and of the electrochemistry of the solutions existing inside the occluded corrosion cells and of the anodic and cathodic behavior of the constituents of the considered metal or alloy in these solutions (23).

### Acknowledgments

International collaboration related to this work was supported by the North Atlantic Treaty Organization (NATO) under research grants SA. 5-2-05B(688) 482(73) and SA. 9-5-02/SRG-001(74) 121/AR.

### REFERENCES

1. N. D. Tomashov *et al.*; (a) *Proc. USSR Acad. Sci.*, **89**, 121 (1953); (b) *Usp. Khim.*, **24**, 453 (1955); (c) *Metallurgizdat*, p. 73 (1963).
2. M. Pourbaix, (a) *CEBELCOR Rappt. Tech.*, **120**, (RT 205), 33 (1972); (b) *Corrosion Sci.*, **14**, 25 (1974); (c) Proceedings of the 5th International Congress on Metallic Corrosion, Tokyo, Japan, May 1972, p. 17, NACE, Houston (1974).
3. M. Stern *et al.*, (a) *This Journal*, **105**, 638 (1958); (b) *Trans. Am. Soc. Metals*, **50**, 438 (1958); (c) *This Journal*, **106**, 755 (1959); (d) *ibid.*, **106**, 759 (1959); (e) *Trans. Am. Soc. Metals*, **52**, 239 (1960); (f) *Corrosion*, **17**, 86 (1961); (g) *J. Metals*, **12**, 144 (1961).
4. N. D. Tomashov, R. M. Altovsky, and G. P. Chernova, *This Journal*, **108**, 113 (1961).
5. M. G. Fontana, *Met. Trans.*, **1**, 3251 (1970).
6. H. S. Campbell, (a) *J. Inst. Metals*, **77**, 345 (1950); (b) *Proc. Soc. Water Treat. Exam.*, **3**, 100 (1954); (c) Proceedings of the 2nd International Congress on Metallic Corrosion, New York, New York, 1963, p. 243, NACE, Houston (1966). (d) Proceedings of the U. R. Evans Conference on Localized Corrosion, Williamsburg, Virginia, 1971, p. 625, NACE, Houston (1974).
7. R. May, *J. Inst. Metals*, **32**, 65-74 (1953).
8. M. Pourbaix, J. Van Muylder, P. Van Laer, N. de Zoubov and A. Pourbaix, *CEBELCOR's Technical Reports (RT)*, (a) **RT 125** (1965); (b) **RT 126** (1965); (c) **RT 127** (1965) and **E 61** (1967); (d) **RT 128** (1965) and **E 62** (1967); (e) **RT 133** (1965); (f) **RT 161** (1969); (g) **RT 201** (1972).
9. T. W. Bostwick, *Corrosion*, **17**, 12 (1961). See also *Tech. Bull. No. 7 of Yorkshire Imperial Metals, Ltd.* (revised 1970).
10. F. J. Cornwell, G. Wildsmith, and P. T. Gilbert, *Brit. Corrosion J.*, **8**, 202 (1973).
11. H. S. Campbell, Proceedings of the U.R. Evans Conference on Localized Corrosion, Williamsburg, Virginia, 1971, p. 625, NACE, Houston (1974).



12. Ph. A. Parrish, Ph.D. Thesis, University of Florida (1970).
13. E. D. Verink and M. Pourbaix, *CEBELCOR Rappt. Techn.*, **117**, RT 191 (1971).
14. R. M. Garrels, (a) "Mineral Equilibria at Low Temperature and Pressure," Harper & Row, Publishers, New York (1960); (b) (in collaboration with C. L. Christ), "Solutions. Minerals and Equilibria," Harper & Row, Publishers, New York (1965).
15. M. Pourbaix, (a) Ph.D. Thesis, Université Libre de Bruxelles (1945) and *Publication CEBELCOR*, **F21**, (1951); (b) *CEBELCOR Rappt. Techn.*, **109**, RT 157 (1969); (c) "Lectures on Electrochemical Corrosion," Plenum Press, New York (1973).
16. M. Pourbaix, *CEBELCOR Rappt. Techn.*, **111**, RT 166 (1969).
17. A. Pourbaix, *ibid.*, **118**, RT 198 (1971).
18. B. F. Brown, (a) (in collaboration with C. T. Fujii and E. P. Dahlberg), *This Journal*, **116**, 218 (1969); (b) *CEBELCOR, Rappt. Techn.*, **112**, RT 170 (1970).
19. C. T. Fujii, *ibid.*, **123**, RT 213 (1974).
20. L. Sathler and J. Van Muylder, *ibid.*, **126**, RT 224 (1975).
21. M. Pourbaix, (a) Seminar on "Passivity and Its Breakdown on Iron and Iron-base Alloys," Honolulu, Hawaii, March 10-12, 1975. Discussion to be published by the Japan Corrosion Society and by NACE; (b) Preprint 4th European Symposium on Corrosion Inhibitors, Ferrara, Italy, Sept. 15-19, 1975, p. 674.
22. T. Kodama and J. R. Ambrose, Paper 75 presented at The Electrochemical Society Meeting, Dallas, Texas, October 5-9, 1975.
23. M. Pourbaix, (a) *CEBELCOR Rappt. Techn.*, **118**, RT 199 (1971); (b) Proc. NATO Science Committee Research Evaluation Conference, "The theory of stress corrosion cracking in alloys," J. C. Scully, Editor, pp. 17-63 (1971).

## English as the World Language of Science

G. Wranglén\*

Royal Institute of Technology, Stockholm, Sweden

Throughout the Middle Ages and well into modern times, Latin was used by scholars of all kinds as the international language of learning. At the universities, Latin was generally used in lectures until about 1750 and in dissertations until about 1850. With the rise of nationalism and the development of the national languages, the role of Latin as a common language of scholars gradually disappeared. An attempt to revive Latin in simplified form for use within the sciences has been made in our time. The result, Interlingua, as romantic as Romanic, was published in 1951 and has met with some favorable response in medical circles. However, the chances for a more general acceptance of this artificial language would seem very small indeed. On the other hand, English is rapidly developing into an international language of science with a standing similar to that once held by Latin. That rational, practical, and economic factors contribute toward this fortunate development is apparent in many different ways.

Until ten to fifteen years ago, it was still usual to provide simultaneous translations at international scientific conferences. Apart from the fact that such translations were usually unsatisfactory, this practice has now had to be abandoned for economic reasons. Instead, contributors to such conferences are required or at least encouraged to speak in English. A natural consequence is that the corresponding paper is also published in that language.

At national or regional conferences or symposia, e.g., in the Scandinavian countries, it is now common practice that although the papers are presented in the author's own native tongue or in some regional language understandable to all participants, the papers are simultaneously or later published in a common volume in English and hence made available to a worldwide audience of readers.

The situation is similar with national scientific journals, with the unfortunate result that valuable material has been buried and forgotten in publications in uncommon languages and with small circulations. While it is still important and necessary to publish technical, commercial, and educational articles in Journals using the language of the country concerned, it is becoming more and more usual, particularly in small countries, to use English as the preferred or exclusive language for material of a purely scientific nature. This usually

means a highly increased circulation of and efficiency in the journal concerned.

A number of multilingual international journals, published in Western Europe, present a special problem. These journals publish articles in either English, German, or French and abstracts of each individual article in all of these three languages and occasionally in Russian. These journals are often official organs of international scientific societies with the majority of their members in West European countries and with English, German, and French as official languages, although English is by far most generally used by the members. Publishers are finding it increasingly difficult and costly to publish these multilingual journals due to the lack of trained personnel in the printing works capable of handling articles in several languages and the excess time taken and cost involved in setting such material. Abstracts in several languages are likewise time consuming and costly to translate and set. Because of lack of expertise by the translators, they are often inaccurate. For these reasons, some publishers have concluded that they can no longer publish multilingual journals and have consequently decided to accept papers and publish abstracts in English only. This is a fortunate development which should be greeted with satisfaction. In order to assure a scientific contribution as large a circle of readers as possible, there is no question but that it should be published in English. It should therefore be in the interest of both the author himself and the journal concerned that a contribution be published in that language. Particularly among young authors of various nationalities, it is becoming common practice to publish their papers in English. It is natural, therefore, that the proportion of non-English papers has been continuously decreasing in multilingual journals in recent years, even before the decisive impact of economic considerations.

The only opposition to this natural and inevitable development seems to come from French-speaking scientists. Other nationalities seem to welcome or at least accept the use of English as the sole means of communication both at international meetings and in international journals. This is particularly true of non-European scientists, such as Japanese and Indians who usually cannot understand or read any European language other than English. Indeed, the same seems to be true of many Americans.

In this context, some statistics may be of interest. According to a study carried out a few years ago and

\* President, International Society of Electrochemistry.

presented in "An Overview of Worldwide Chemical Information Facilities and Resources,"<sup>1</sup> the languages used in articles dealing with the chemical sciences and reported in "Chemical Abstracts" in the period 1962-1966 had a percentage distribution as follows

English	55%
Russian	21%
German	7%
French	5%
Japanese	3%
Italian	2%
Polish	2%
Other languages	5%
	<hr/> 100%

In addition, about three-fourths of the articles in Russian were translated into English, which means that about 70% of the contents of chemical journals was available in the English language. If a similar study were made today, the dominance of English would probably be found to be still greater.

These figures reflect the very desirable development toward the use of English as the world language of science. In view of these figures, it seems hard to find rational, not only historical, reasons for maintaining German and French as official languages of journals which pretend to be truly international and not only West European. If abstracts should be published in, say, two languages in such journals, these languages should obviously be English and Russian, not English and

French. However, Eastern Europe has apparently adapted itself to a situation with Russian as a common regional language of science and English as a common world language of science. It might be argued that this gives West an unfair advantage over East. Actually, this is not so. Since most Russian and other East European scientists today can read and understand English while only a very few in the West have a command of Russian, we are the handicapped ones.

It is sometimes argued, furthermore, that the use of only English in a journal instead of, say, English-German-French would make the journal less international in character. Indeed, just the opposite is true. Whereas practically all prospective readers, and even those preferring German or French, can immediately understand an article published in English, a great many, and perhaps a majority of those outside Western Europe, would have to resort to a translation or at least a dictionary in order to comprehend the content of an article published in German or French. Hence, much is gained and little is lost by using English as the sole language of publication.

In conclusion, it would seem, therefore, that the development of English toward the world language of science and hence as the sole means of communication in international journals and at international scientific meetings is not only a practical and economic necessity but also a great service to the scientific community of the world. A common world language of science facilitates communication and personal contacts and favors friendship among scientists of different nationalities. It is also to be hoped that it may therefore contribute to international understanding and friendship on a larger scale and in a broader sense.

<sup>1</sup>Published by the National Science Foundation, Washington, D.C. (1967).



## Molten Salt Metallizing of Nickel Alloys<sup>1</sup>

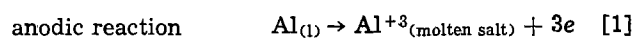
Ned Godshall<sup>\*,2</sup>

Imperial College of Science and Technology, University of London, London SW7, England

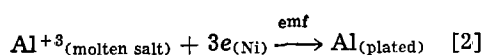
The electrodeposition and metallizing of nickel-base alloys to improve high temperature strength and stress-corrosion properties in connection with gas turbine applications has long been viewed as a desirable goal. Specifically, the aqueous plating and subsequent surface diffusion of aluminum, cobalt, chromium, platinum, and yttrium into nickel-base alloys has been observed to impart these enhanced properties. However, established electrolytic techniques are (i) unable to deliver these metallizing elements to the surfaces of restricted areas, such as turbine blade cooling holes (approximately 0.030 in. diameter) or (ii) may deliver them unevenly, e.g., to yield unfavorable accumulation at sharp curvatures of turbine blades.

For these reasons, a molten salt electrochemical technique was sought to establish a means by which aluminum could be coated onto the surface of nickel-base alloys and concurrently diffused into the interior approximately 2-6 $\mu$ . The high temperature aspect of the molten salt technique would have the added advantage of providing essentially a one-step technique; not requiring the additional heat-treating step necessary with standard electrolytic plating processes for the diffusion of the metallizing element beyond the surface.

The general electrochemical and diffusional equations may be illustrated by



cathodic reaction



where NiAl represents the various dispersion-hardening compounds.

### Experimental Procedure

**Cell design.**—All experiments were conducted in a molten salt bath under an inert argon atmosphere at a temperature of 800°C (1472°F). Equimolar sodium-potassium chloride (NaCl-KCl) was selected as the fused-salt medium because of its relatively high thermal stability and the proximity of its melting point (660°C, 1220°F) to that of aluminum (657°C, 1215°F), the metallizing element under study. In addition, equimolar NaCl-KCl retains its favorable electrical transport properties at elevated temperatures; specifically, high ionic conduction and low electronic conduction.

300g NaCl-KCl were contained in a 70 mm diameter alumina crucible, which was enclosed within a 20.32 cm (8 in.) Inconel cylinder (Fig. 1). The cylinder was capped with a specially designed brass head which

included movable vacuum-tight ports for the electrode assemblies, argon circulation, and specimen ingress/egress.

The electrode assemblies were composed of (i) a Nimonic cathode (working electrode), (ii) a liquid aluminum anode (counterelectrode), (iii) a reference bulb electrode (0.1M silver chloride, AgCl; balance: equimolar NaCl-KCl), and (iv) a platinum foil auxiliary electrode (4.50 cm<sup>2</sup>). A schematic diagram of the electrode arrangement is given in Fig. 2.

**High temperature aspects.**—Standard fused-salt procedures were utilized as much as possible during experimentation; however, operation at the elevated experimental temperature, 800°C (1472°F), necessitated several significant changes.

(i) A liquid aluminum anode was required. This was provided by containing 14.0g of high purity aluminum in an alumina crucible suspended above the molten salt surface. The crucible was lowered into the melt when both the NaCl-KCl and aluminum reached the liquid state.

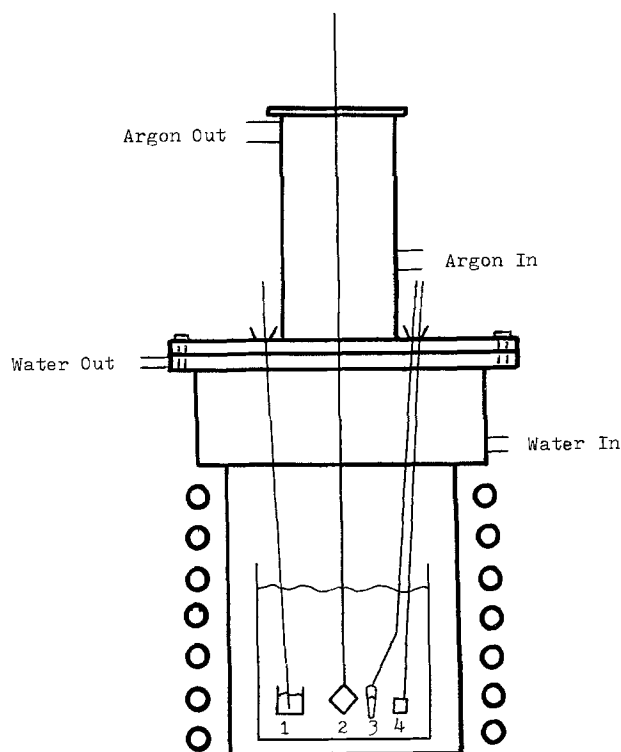


Fig. 1. Cell design: 1. liquid aluminum anode; 2. Nimonic specimen cathode; 3. AgCl reference bulb electrode; 4. platinum reference electrode.

<sup>1</sup> 1975 F. M. Becket Memorial Award Report.

<sup>\*</sup> Electrochemical Society Student Member.

<sup>2</sup> Present address: Department of Materials Science, Stanford University, Stanford, California 94305.

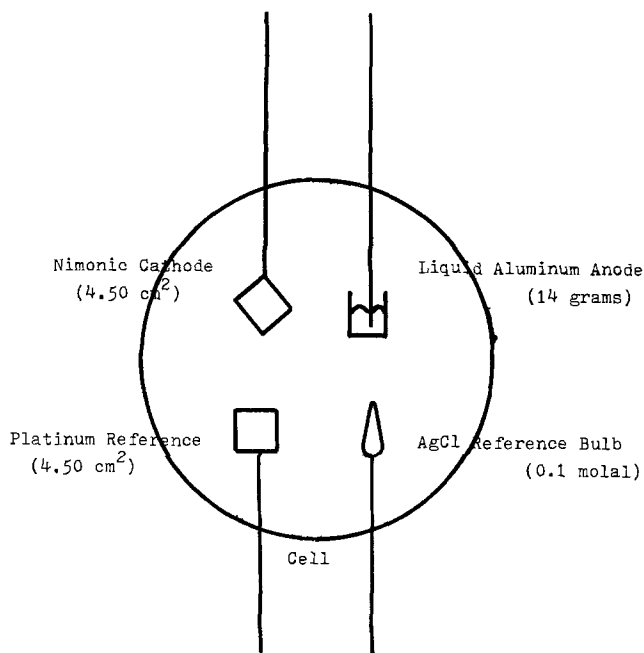


Fig. 2. Electrode assemblies

(ii) All electrodes were necessarily constructed of either high quality quartz or alumina, rather than of the lower melting point Pyrex glasses commonly used in molten salt experiments.

(iii) An extensive fused-salt drying process was required to minimize attack of the quartz electrodes by residual water and to prevent the fused-salt from "bumping" due to gas evolution during the initial testing. This was accomplished by predrying the fused-salt mixture, followed by 72 hr of concurrent vacuum treatment and slow incremental heating, until the melting point of the salt was reached (660°C, 1220°F).

(iv) Drying and purification of the inert argon atmosphere used during experimentation was likewise found necessary in order to eliminate water and oxygen from the cell environment.

**Test material.**—The nickel-base alloy selected as the substrate for experimentation was Nimonic 80A (carbon: 0.10%, Cr: 20.5%, Mn: 0.80%, Fe: 3.0%, S: 0.010%, Cu: 0.2%, Al: 1.4%, Ni: balance; manufactured by Henry H. Wiggins, Limited, England). Nimonic 80A was chosen as the test material because of its age-hardenable, creep-resisting properties, and service temperature of 815°C (1499°F). In addition, its major applications currently lie within the gas turbine industry.

**Electrical circuitry.**—A 50V d-c power supply provided the emf for the electrodeposition reaction. The electrical parameters of the aluminum deposition reaction were monitored using the electrical circuit illustrated in Fig. 3. The Hermes coulombic integrator was initially calibrated by shorting the cell from the circuit, which allowed a direct coulombic measurement of aluminum ion transport within the cell.

A bismuth "starter" electrode was originally used as the cathode, in place of the Nimonic test specimens, to establish an initial concentration ( $10^{-2}M$ ) of aluminum ions ( $Al^{+3}$ ) in the NaCl-KCl melt. Steady-state aluminum ion concentration was maintained thereafter, since an equal number of  $Al^{+3}$  ions were released from the liquid aluminum anode as were deposited onto the cathodic test specimens.

### Discussion of Results

**Aluminum ion instability in NaCl-KCl.**—Nimonic test specimens were immersed in the NaCl-KCl melt

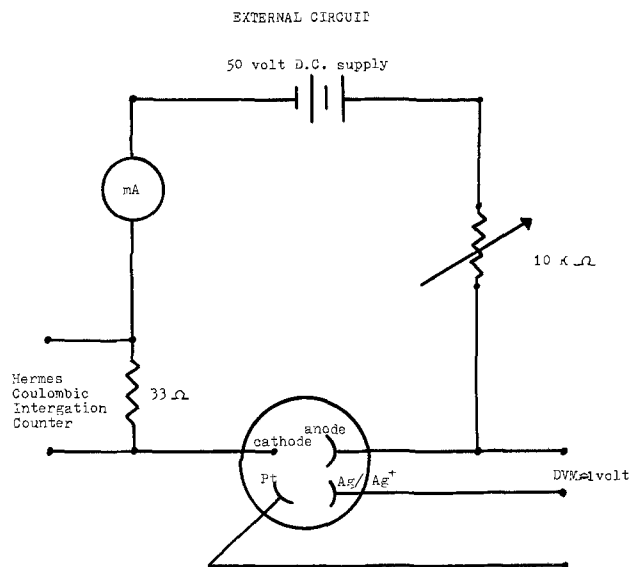


Fig. 3. External circuit

and subjected to alluminiding conditions and potentiostatic measurements. The length of immersion time and the current density were independently varied. The effects of time and current density variation were determined by visual inspection, x-ray fluorescence, and microhardness measurements (Table I).

It was concluded that little or no elemental aluminum adhered to, or diffused into, the Nimonic 80A test specimens despite the fact that coulombic measurements indicated high levels of  $Al^{+3}$  ion transport to the specimen surface.

**Fluoride additions.**—Aluminum fluoride ( $AlF_3$ ) and sodium fluoride (NaF) were added to the equimolar NaCl-KCl melt at concentrations of  $2 \times 10^{-2}$  and  $1.5 \times 10^{-2}M$ , respectively, in order to reduce the volatility and vapor pressure of the melt and to provide for greater stability of the aluminum ions. Significant changes in the surface properties and weight of the test samples were detected (Table II).

**Experimentation time and current density effects.**—The effect of reaction time on the weight change for specimens immersed in both fluoride-doped and fluoride-free melts is illustrated in Fig. 4. The weight gain of a sample was found to increase exponentially with time rather than linearly as was expected from con-

Table I. Surface property results without fluoride additions to the melt

Time of experiment (min)	Current density (mA/cm <sup>2</sup> )	Weight change $\Delta W$ (mg)	Surface microhardness (GKN scale)
45	1.378	0.0	158
45	2.756	0.1	180
45	5.511	0.1	158
20	2.756	0.0	165
80	2.756	0.1	172

Table II. Surface property results with fluoride additions to the melt

Time of experiment (min)	Current density (mA/cm <sup>2</sup> )	Weight change $\Delta W$ (mg)	Surface microhardness (GKN scale)
45	0.323	0.6	168
45	1.378	1.6	182
45	2.756	1.6	191
45	5.511	0.9	186
20	5.511	0.3	172
30	5.511	0.4	168
80	5.511	4.7	205

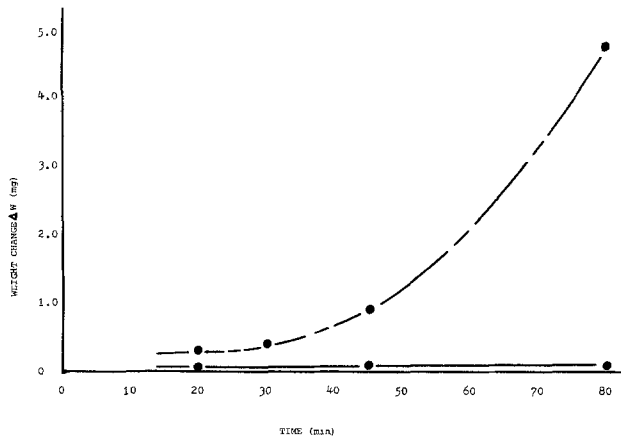


Fig. 4. Weight change vs. time, — without fluorides, - - - with fluorides.

stant current, constant  $Al^{+3}$  ion transport reasoning. This exponential character has been attributed to a diffusion-limiting step whereby much of the aluminum reaching the specimen surface in the early minutes of testing is unable to diffuse beyond the surface before dripping off the specimen, back into the melt.

The effect of current density on weight change seemed somewhat more limited than the effect of time (Fig. 5). The weight gain of specimens reached a plateau at a current density of approximately  $2 \text{ mA cm}^{-2}$ , above which an increase yielded no increase in coated or diffused aluminum on the samples.

**Microhardness measurements.**—The effects of time and current density on the mechanical properties of the specimens were determined by means of GKN microhardness tests. Surface hardness increased sharply with reaction time, when fluorides were present in the melt, due to the development of NiAl dispersion-hardening compounds (Fig. 6). The less-pronounced increase in hardness during fluoride-free tests was attributed to secondary thermal treatment of the substrate nickel alloy and not to any NiAl development, since x-ray fluorescence measurements detected little aluminum on or near these surfaces.

Surface hardness increased with increasing current density (Fig. 7). Once again, however, an increase in current density beyond approximately  $2 \text{ mA cm}^{-2}$  yielded no increase in physical properties, indicating the point at which interface transport and subsurface diffusion reach a steady state.

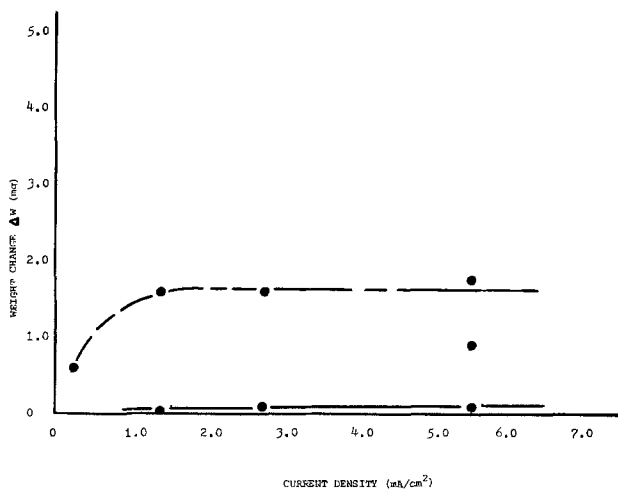


Fig. 5. Weight change vs. current density, — without fluorides, - - - with fluorides.

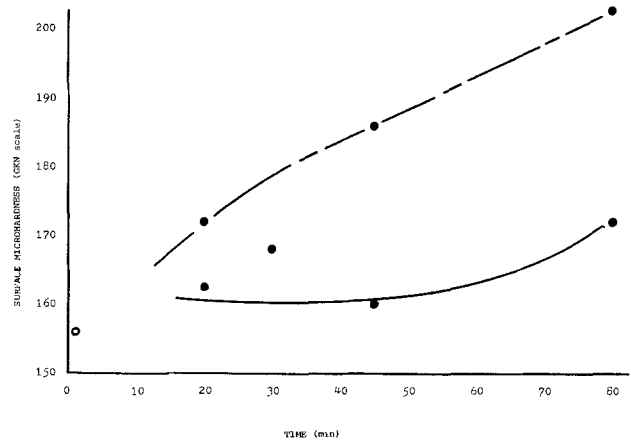


Fig. 6. Surface microhardness vs. time, ○ original hardness, — without fluorides, - - - with fluorides.

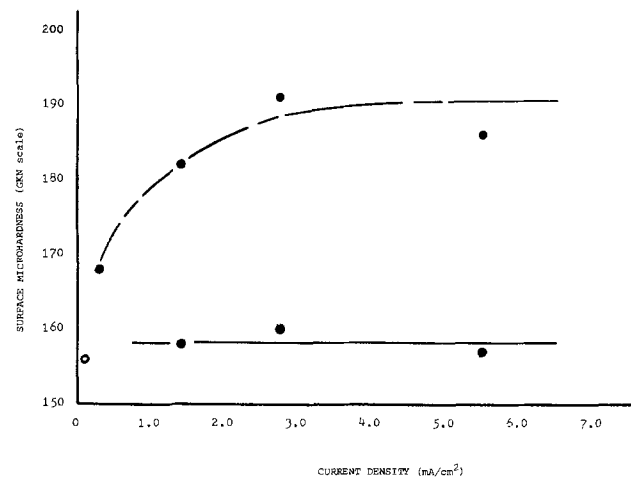
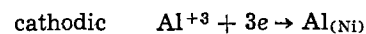
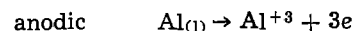


Fig. 7. Surface microhardness vs. current density, ○ original hardness, — without fluorides, - - - with fluorides.

**Shape effects.**—The effect of complicated shape changes was evaluated by bending and drilling 0.030 in. (0.76 mm) diameter holes in several specimens prior to testing. Samples were sectioned and examined metallographically and were qualitatively found to exhibit no unusual amounts of aluminum at points of stress concentration, such as at acute or obtuse bends or at small diameter openings.

**Self-driven process.**—The over-all metallizing reaction, shown in Eq. [1]-[3] was found to be self-sustaining and not dependent on an external power source. The 50V d-c source was removed from the circuit and the anode "shorted" to the cathode (Table II, first experiment). The resultant current flow and aluminum deposit indicated a free energy decrease ( $-\Delta G$ ) and the self-sustaining nature of the reactions



The electrode potentials were calculated using the Nernst equation

$$E = E^{\circ} - \frac{RT}{3F} \ln a_{Al^{+3}}$$

and were found to correspond adequately with observed results. The potentials of the Nimonic specimens (cathode) usually approximated  $-1.65V$  with respect to the 0.1M AgCl reference, while the potential of the liquid aluminum (anode) averaged  $-0.95V$  with

respect to the reference. Variance, in both cases, was  $\pm 0.15V$ .

**Process efficiency.**—The weight of aluminum which was available for adherence to the Nimonic specimens ( $Al_{Th}$ ) was calculated through the use of the coulombic integrator shown in the external electric circuitry (Fig. 3). The calculated ( $Al_{Th}$ ) (see Appendix) varied widely from that observed experimentally ( $Al_{Ex}$ ), leading to reaction efficiencies ( $Al_{Ex}/Al_{Th}$ ) of 45-60% for the melts with fluoride additions.

### Conclusions

The stability of the aluminum ion ( $Al^{+3}$ ) in equimolar NaCl-KCl is much too low for it, alone, to be a realistic molten salt aluminum transport medium. However, the addition of small amounts of fluorides greatly enhances the stability of aluminum ions and, therefore, greatly improves the prospects of molten salt metallizing. However, increased chemical attack of quartz by fluorides has been observed, so that cell design should be modified in future work.

Current molten salt metallizing processes are, unfortunately, very time and temperature dependent because of the diffusion-limiting steps involved. High current densities are unable to shorten the time requirement. The rate of diffusion of aluminum into the Nimonic is slow compared with the rate of deposition of aluminum onto the Nimonic surface.

Smooth, uniform deposition of aluminum over large areas has been attained. This uniform coating is, however, possible only when fluorides are present in the melt. In addition, the electrodeposition and diffusion of aluminum into small diameter openings seems feasible, although more in-depth study is required to define the limitations.

The deposition reaction can be carried out on a self-sustaining basis on a laboratory scale. However, longer deposition times are required because of the low currents generated when no external source is utilized.

The current efficiency of the experiments carried out to date has been low. Further elucidation of the causes of this poor current efficiency is necessary before development of higher electrodeposition and diffusion rates is possible.

### Recommendations

The sodium chloride-potassium chloride molten salt system is unsuitable for aluminum electrodeposition work at high temperatures. Therefore, in the future, all work should be carried out in melts where fluorides are at least present, preferably in fluoride-based systems.

The effect of temperature should be studied because diffusion has been found to be the rate-limiting step.

In addition, the concentration of aluminum ions in the melt could be treated as a variable in future work to ascertain the causes for the low current efficiencies observed to date. Likewise, stirring or bubbling gas through the melt could be introduced to determine the effects of mixing.

The electrodeposition of metals other than aluminum should be explored. Elemental yttrium and/or platinum are promising substitutes.

Continued work could also easily incorporate corrosion studies of prepared specimens, and would be highly informative since corrosion resistance is an important criterion in the use of the diffused substrate.

### APPENDIX

#### Calculation of Theoretical Aluminum Deposit ( $Al_{Th}$ )

Example

$$\text{Current} = 12.4 \text{ mA}$$

$$\text{Area of specimen} = (1.5 \text{ cm}^2) \times 2 = 4.50 \text{ cm}^2$$

$$\text{Current density} = I/A = 2.755 \text{ mA/cm}^2$$

$$\text{Number of integrator units (empirical)} = 1217 \text{ units}$$

$$1 \text{ coulomb} = 36.07 \text{ units at } 0.410V \text{ across the integrator}$$

$$1217 \text{ units} \times 1 \text{ coulomb}/36.07 \text{ units} = 33.74 \text{ coulombs}$$

$$\text{Number of moles} = C/nF$$

$$\text{Number of moles} = 33.74 \text{ coulombs}/(3)(96,500) = 1.166 \times 10^{-4} \text{ moles}$$

$$1.166 \times 10^{-4} \text{ moles} \times \frac{27g \text{ Al}}{1 \text{ mole Al}} = 3.15 \times 10^{-3}g$$

$$Al = 3.15 \text{ mg Al}$$

$$(Al_{Th}) = 3.15 \text{ mg Al}$$

#### Efficiency Calculation

The actual weight of aluminum deposited onto the above sample ( $Al_{Ex}$ ) was 1.6 mg. Therefore

$$\text{Efficiency} = (Al_{Ex})/(Al_{Th}) = \frac{1.60 \text{ mg}}{3.15 \text{ mg}} = 51\%$$



## Interfacial Na<sup>+</sup> Transport in the Beta Alumina/Propylene Carbonate System

Gregory C. Farrington\*

General Electric Company, Research and Development Center, Schenectady, New York 12301

### ABSTRACT

Na<sup>+</sup> transport across a polycrystalline  $\beta$ -alumina/propylene carbonate interface has been studied at 23°C as a function of current density from 1.0 to 6600  $\mu\text{A}/\text{cm}^2$  under dry and hydrated conditions. Constant current transient analysis from  $10^{-7}$  to  $10^2$  sec was used to distinguish interfacial and bulk resistivity components during ion entry into and exit from  $\beta$ -alumina. The resistance associated with Na<sup>+</sup> exit increases significantly after exposure of the  $\beta$ -alumina to water vapor. Interfacial current/voltage relationships for dry and hydrated samples are nonlinear but qualitatively similar. Na<sup>+</sup> entry phenomena are obscured by a steadily increasing interfacial resistance which accompanies ion transport into the  $\beta$ -alumina, a process reversed by extended electrolysis out of the interface. The results suggest that interfacial transport involves an adsorbed intermediate state and is influenced by an equilibrium between adsorbed Na<sup>+</sup>/H<sub>2</sub>O and Na<sup>+</sup>/H<sub>3</sub>O<sup>+</sup> substituted into the  $\beta$ -alumina.

Ion transport across a solid electrolyte/liquid electrolyte interface involves a fundamental change in ionic environment. Restricted motion within the solid electrolyte contrasts with ionic association, solvation, and random diffusion in the liquid. Clearly, this step is influenced by the molecular structure and dielectric constant of the liquid electrolyte and by the structure of the solid electrolyte.

Beta alumina (ca. 1.2 Na<sub>2</sub>O·9Al<sub>2</sub>O<sub>3</sub>) is a solid electrolyte of interest in a variety of novel electrochemical energy storage systems. It is stable in a range of chemical environments and has high conductivity for several monovalent cations, especially Na<sup>+</sup>. It is also ideally suited for the study of ionic transport between dissimilar phases.

Ion transport across solid electrolyte/liquid electrolyte interfaces has been previously examined in ion exchange membrane/aqueous electrolyte systems. Kressmen and Tye (1) and Peers (2) discussed the effects of ionic depletion at specific ion selective membrane interfaces. Sandblom, Eisenman, and Walker (3, 4) presented a theoretical examination of ideally permselective, liquid ion exchange membranes, specifically addressing ion transport effects within the membranes. Results of a preliminary examination (5) of  $\beta$ -alumina/propylene carbonate interfacial transport at 25°C performed in this laboratory revealed that a large increase in interfacial impedance for Na<sup>+</sup> entry and exit ensues from exposure of the  $\beta$ -alumina to water vapor. Similar effects were noted by Voinov and Tannenberger (6) who speculated that protons may be irreversibly driven into the  $\beta$ -alumina under the influence of an electric field, increasing its resistivity.

The present work was undertaken to examine Na<sup>+</sup> transport across a propylene carbonate/ $\beta$ -alumina interface under nominally anhydrous conditions and

in the presence of adsorbed water. To separately distinguish interfacial and bulk resistivity effects and differentiate Na<sup>+</sup> entry into the solid electrolyte from Na<sup>+</sup> exit, a fast risetime, constant current technique was used.

### Experimental

Beta alumina ceramic rods were prepared from Alcoa XB-2  $\beta$ -alumina powder. The powder was ground with ZrO<sub>2</sub> grinding media, dried under vacuum, screened, and hydrostatically pressed into rods approximately 1.6 cm in diameter and 15 cm long. The rods were cut into 1.6 cm segments and fired at 1700°C. The resulting ceramic was single phase, polycrystalline  $\beta$ -alumina of 98% theoretical density, containing approximately 1% MgO and 1% ZrO<sub>2</sub>.

Rods were sliced with a diamond saw into disks 1.3 cm in diameter and 4 mm thick. A 0.6 mm hole was drilled 3 mm into each disk from its circumference halfway between each face. Sample faces were polished through 600A grit SiC paper, washed in methanol, and fired for 24 hr at 700°C. Between individual experiments, samples were wet polished with methanol through 600A grit SiC paper, rinsed with methanol, and baked at 400°C in vacuo. They were transferred in vacuo to a Vacuum Atmospheres Ar dry box and polished briefly on dry 600A grit SiC paper immediately before use.

In the following experiments "dry"  $\beta$ -alumina is that which has been treated as above. "Hydrated"  $\beta$ -alumina was prepared identically except for exposure to 100% relative humidity at 23°C for 20 min or 28 hr before analysis.

Samples were mounted in the Teflon experimental cell shown in Fig. 1 and held in place with silicone rubber gaskets. Burdick and Jackson "Spectroscopic" propylene carbonate was dried by multiple percolation through a 16 × 2 cm column of alumina which had been activated at 500°C in vacuo for 24 hr.

\* Electrochemical Society Active Member.

Key words: solid electrolyte, electrolysis, ion transport, water.

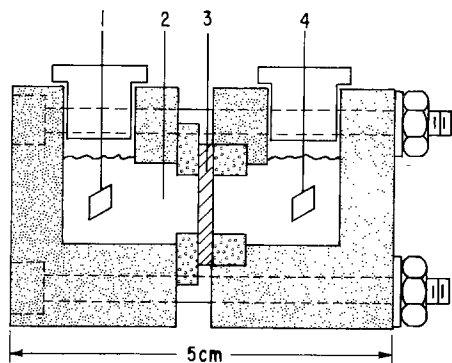


Fig. 1. Experimental cell constructed of Teflon; gaskets of silicone rubber; drawn to scale.

Baker anhydrous reagent NaI and Southwestern Analytical anhydrous tetrabutylammonium tetrafluoroborate (TBABF<sub>4</sub>) were baked 48 hr at 110°C in vacuo, weighed into appropriate volumetric glassware, and baked a second time under identical conditions before dilution. Two electrolyte solutions were prepared: solution 1, 0.010M NaI + 0.100M TBABF<sub>4</sub>; and solution 2, saturated NaI and TBABF<sub>4</sub>. Solution 1 was the test solution and is referred to in this paper by its Na<sup>+</sup> concentration. The second was used in the unmonitored compartment of the experimental cell.

The assembled cell incorporated four electrodes, an outer current carrying pair of Pt foil (electrodes 1 + 4) and an inner reference pair (electrodes 2 + 3). Each reference electrode was an Au wire into which either Tl or Na amalgam was dissolved. No difference in results was observed between Tl or Na electrodes. A small amount of electrolyte was injected into the disk reference electrode hole to improve contact. Observed with a Keithley Model 616 digital electrometer, these electrodes established a potential difference satisfactorily stable for the experiments described here.

Galvanostatic data (10<sup>-7</sup>-10<sup>-3</sup> sec) were obtained by applying single, fast risetime (<5 × 10<sup>-8</sup> sec) constant current square waves to electrodes 1 + 4 while monitoring the differential voltage response across electrodes 2 + 3. A broad range of elapsed time was covered by applying pulses of differing widths. The result is a plot of voltage drop associated with ion transport between electrodes 2 and 3 at constant current from 10<sup>-7</sup> to 10 sec from current initiation. Voltage *vs.* time was converted to resistivity *vs.* time by dividing by current and multiplying by the geometrical β-alumina surface area exposed to propylene carbonate. All the transient data reported were obtained at a current density of 138 μA/cm<sup>2</sup>. The pulse generator used has been previously described (7).

Potential transients were captured with a Tektronix 7633 storage oscilloscope using a 6B53A time base and 6A11 vertical amplifier. The probe-oscilloscope combination has a 60 MHz bandwidth, 5.9 × 10<sup>-9</sup> sec risetime, and vertical deflection accuracy of 3%. Stored traces were photographed for subsequent manual retrieval of potential-time data. The apparatus was operated in a single pulse mode by triggering the oscilloscope and pulser with a Tektronix Model 115 pulse generator.

Experimentation in the 10<sup>-1</sup>-100 sec time range was performed with a PAR Model 173 potentiostat/galvanostat, PAR Model 175 programmer, Keithley Model 616 digital electrometer, and Hewlett-Packard 7004 x-y recorder.

### Results and Discussion

*Dry β-alumina-Na<sup>+</sup> exit.*—Typical data from galvanostatic analysis of Na<sup>+</sup> exit from β-alumina into propylene carbonate across a dry interface are plotted in Fig. 2. Three major resistivity components comprise the response shown: (a) propylene carbonate

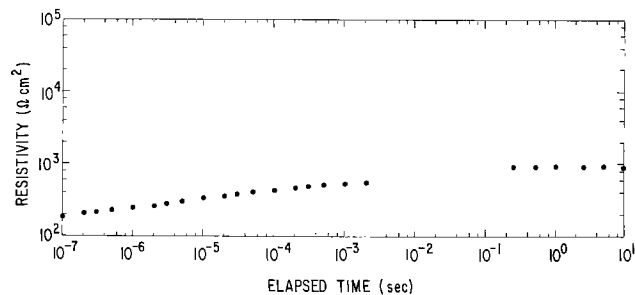


Fig. 2. Na<sup>+</sup> exit from β-alumina through dry interface; 0.010M Na<sup>+</sup> at 23°C.

electrolyte resistance; (b) interfacial polarization; and (c) bulk resistivity of polycrystalline β-alumina. These components occur electrically in series; each can be approximated by a simple parallel RC circuit. The circuit shown in Fig. 3, then, approximates the resistivity-time behavior in this system.

The resistance-time response of each individual RC pair in Fig. 3 upon perturbation by a constant current square wave has been previously derived (7) and is shown in Eq. [1]. Figure 4 is a plot of R<sub>t</sub> as a function of t as predicted by Eq. [1]

$$R_t = R(1 - e^{-t/RC}) \quad [1]$$

From Fig. 4, it is clear that if the time constant of the RC components shown in Fig. 3 are sufficiently different and each falls within the range of analysis, a staircase resistivity-time behavior will be observed for the model circuit from which all values of R and C can be calculated. Moreover, so long as (RC)<sub>int</sub> is 10<sup>2</sup>-10<sup>3</sup> times larger than (RC)<sub>PC</sub> and (RC)<sub>beta</sub>, interfacial polarization can be separated from solution and β-alumina resistance.

The anticipated time constant for propylene carbonate relaxation shown in Fig. 3 was confirmed experimentally. Time constants for the β-alumina were

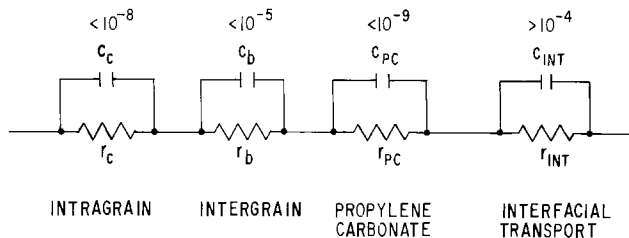


Fig. 3. Model circuit approximating ion transport across a polycrystalline β-alumina/propylene carbonate interface; figures above each RC pair are anticipated time constants in seconds.

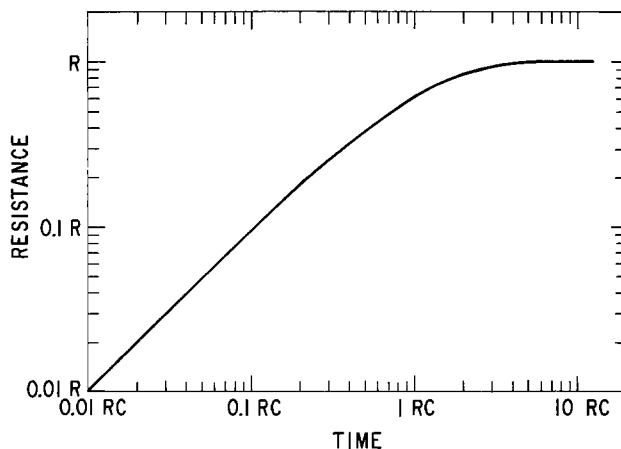


Fig. 4. Resistivity *vs.* elapsed time response of an ideal RC parallel circuit upon application of a constant current square wave of infinitely short risetime.



determined by a four-probe galvanostatic technique previously described (7). Interfacial response was estimated by considering double layer capacitance to be  $10^{-5}$  F/cm<sup>2</sup> and interfacial resistivity to be  $10^2$ - $10^3$  ohm-cm<sup>2</sup>. At  $t > 10^{-5}$  sec, therefore, the resistivity associated with ionic transport within  $\beta$ -alumina and propylene carbonate is constant. Any further resistance increase results from interfacial polarization.

No interfacial resistivity component can be clearly distinguished in Fig. 2. However, a detailed examination of the relationship between total voltage drop across the interface, including bulk IR drop in each electrolyte, and constant current magnitude, shown in Fig. 5, reveals a significant nonohmic component that cannot be associated with bulk effects.

Four different curves are displayed in Fig. 5: I, taken immediately after cell assembly; II, after the first, and III, after  $2 \times 10^{-2}$  coulombs of Na<sup>+</sup> had been electrolyzed out of the  $\beta$ -alumina sample at  $1640 \mu\text{A}/\text{cm}^2$ . The decreased polarization observed in curves II and III at low current densities is temporary; both gradually rise to meet I as more relaxation time is introduced between one electrolysis and the next.

Background voltage drop arising from bulk resistance of the propylene carbonate and  $\beta$ -alumina, which is expected to be ohmic, is the fourth plot in Fig. 5. It was derived by considering the resistivity observed at  $10^{-5}$  sec in Fig. 2 to be bulk resistivity exclusive of interfacial polarization. The validity of this assumption is discussed in a following section.

The divergence of curves I-III at low currents and their sensitivity to prior electrolysis suggest that sustained Na<sup>+</sup> electrolysis out of the interface temporarily removes a species inhibiting transport. Trace water, present in the propylene carbonate electrolyte despite scrupulous precautions, can easily be suspected of involvement with these effects.

In gathering data for Fig. 5, total voltage was constant from 0 to 20 sec after constant current initiation for currents less than  $1000 \mu\text{A}/\text{cm}^2$ ; points were taken at 3 sec. At higher current densities, the voltage wave had a positive slope. This imparts an increasing slope to data in Fig. 5 at higher current densities. A hypothesis explaining this is presented in a later section.

*Dry  $\beta$ -alumina-Na<sup>+</sup> entry.*—Experimental examination of Na<sup>+</sup> entry into  $\beta$ -alumina is complicated by

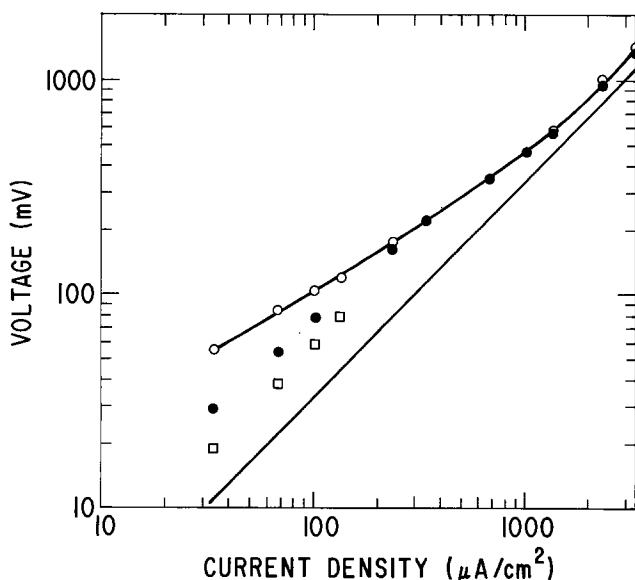


Fig. 5. Interfacial transport through dry interface; Na<sup>+</sup> exit into 0.010M Na<sup>+</sup>; total voltage vs. current density. Straight line is background voltage due to bulk  $\beta$ -alumina and propylene carbonate resistance. 23°C; ○, curve I; ●, curve II; □, curve III.

interfacial Na<sup>+</sup> depletion and accumulation of impurities transported into the solid electrolyte as the result of current passage. Interfacial Na<sup>+</sup> depletion produces a gradual increase in interfacial resistivity with time. Impurity accumulation results in spurious and nonreproducible resistivity behavior.

Na<sup>+</sup> interfacial depletion was observed by electrolyzing Na<sup>+</sup> into  $\beta$ -alumina from a quiescent solution of 0.010M Na<sup>+</sup> with a linearly increasing controlled current. Theory (8) predicts that the total voltage will increase slowly until the interfacial Na<sup>+</sup> concentration is zero. At this critical "transition" time, the rate of Na<sup>+</sup> transport into the electrolyte exceeds its rate of diffusion to the interface. The voltage should increase sharply until it is artificially limited or a second cation capable of injection into the solid electrolyte is produced.

Figure 6 shows the experimental results. Curve I was recorded immediately after cell assembly and has a transition time of 4.5 sec as measured at the intersection of tangents drawn on each of the curve legs.

Murray and Reilley (8) have derived a theoretical relationship (Eq. [2]) between mobile ion concentration ( $C$ ), diffusion coefficient ( $D$ ), current sweep rate ( $B$ ), and the critical time ( $t$ ), at which the interfacial mobile ion concentration becomes zero. Assuming  $C = 0.010M$ ,  $B = 164 \mu\text{A}/\text{cm}^2/\text{sec}$ ,  $n = 1$ , and  $D = 10^{-6}$  cm<sup>2</sup>/sec, Eq. [2] predicts a critical time of 3.9 sec. Both  $D$  and  $B$  were estimated in this calculation, the first in the absence of an exact value and the second because a precise measure of the actual conducting surface area of the  $\beta$ -alumina is not known. Since the sample is polycrystalline, interfacial transport across some portions of the surface is blocked by improper grain orientation, making the actual current density greater than that estimated from the apparent geometric surface area. Considering these uncertainties, the agreement between observed and calculated transition times is surprisingly good.

$$t^{3/2} = \frac{3nFD^{1/2}\pi^{1/2}C}{4B} \quad [2]$$

More interesting in Fig. 6 are curves II and III. The former was recorded under identical conditions to I but after  $1.2 \times 10^{-2}$  coulombs of Na<sup>+</sup> was electrolyzed into the solid electrolyte. This extended electrolysis of Na<sup>+</sup> into the interface clearly resulted in adsorption or injection of species which drastically increase interfacial polarization. Initial response is restored after extended Na<sup>+</sup> electrolysis out of the interface.

This electrolysis-dependent polarization is similar to that shown in Fig. 5 in which Na<sup>+</sup> exit interfacial polarization was found to decrease temporarily after extended Na<sup>+</sup> electrolysis out of  $\beta$ -alumina. It precludes further examination of Na<sup>+</sup> interfacial entry. The suspicion that trace water may be involved in

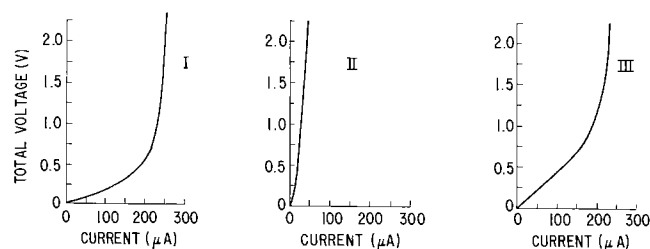


Fig. 6. Interfacial transport through dry interface; Na<sup>+</sup> entry from 0.010M Na<sup>+</sup>; linear current sweep at  $50 \mu\text{A}/\text{sec}$ ; exposed  $\beta$ -alumina area =  $0.304 \text{ cm}^2$ , (curve I) initial, (curve II) after  $1.2 \times 10^{-2}$  coulombs Na<sup>+</sup> entry at  $329 \mu\text{A}/\text{cm}^2$ , (curve III) following curve II but after  $1.7 \times 10^{-2}$  coulombs Na<sup>+</sup> exit at  $329 \mu\text{A}/\text{cm}^2$ ; 23°C.

these effects prompted more detailed examination of its effects on interfacial transport.

**Hydrated  $\beta$ -Alumina- $\text{Na}^+$  exit.**—Galvanostatic data in Fig. 7 contrast  $\text{Na}^+$  exit into 0.010M  $\text{Na}^+$  from dry  $\beta$ -alumina and from  $\beta$ -alumina after 20 min hydration. Both curves are essentially identical at short times, corroborating the assertion that this region ( $10^{-7}$ - $10^{-4}$  sec) represents bulk IR effects in the two electrolytes. Both diverge at longer times, the hydrated response to a value constant at  $t > 10^{-2}$  sec. There is clear evidence of an interfacial resistivity component at  $10^{-3}$  sec.

Voltage as a function of constant current for  $\text{Na}^+$  exit into 0.010M  $\text{Na}^+$  from  $\beta$ -alumina hydrated 20 min and 28 hr is plotted in Fig. 8. Little difference is apparent.

Figure 8 also contrasts  $\text{Na}^+$  exit from dry and hydrated  $\beta$ -alumina. Voltage drop for the hydrated sample is greater than that observed with the dry sample, especially at low current densities. However, all three curves are qualitatively similar. In both hydrated and dry experiments, constant current densities greater than  $1000 \mu\text{A}/\text{cm}^2$  produce steadily rising voltage/time relationships. This rise is resolved for the hydrated case in the curious behavior seen in Fig. 9, in which at  $3290 \mu\text{A}/\text{cm}^2$  a large interfacial voltage transition occurs after several seconds.

**Interfacial transport mechanism.**—Interfacial polarization is a significant nonohmic component of the total voltage arising from  $\text{Na}^+$  transport through a  $\beta$ -alumina/propylene carbonate interface. The current/

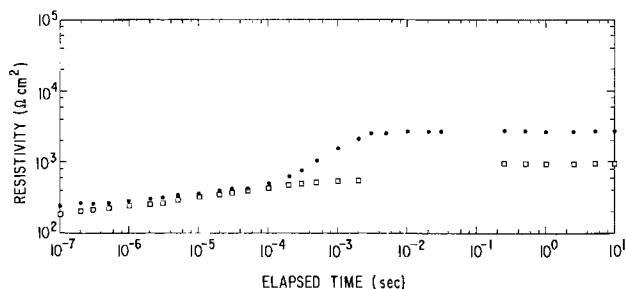


Fig. 7. Interfacial transport;  $\text{Na}^+$  exit into 0.010M  $\text{Na}^+$ ; ● interface hydrated 20 min; □ nominally dry interface; observed with constant current of  $138 \mu\text{A}/\text{cm}^2$ ;  $23^\circ\text{C}$ .

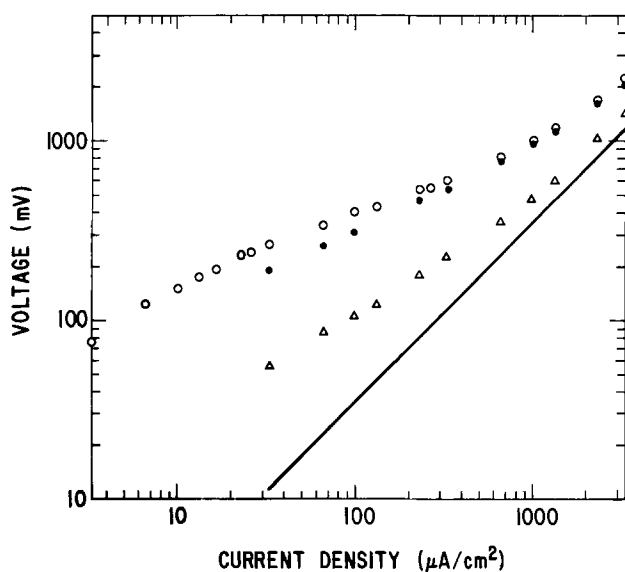


Fig. 8.  $\text{Na}^+$  exit into 0.010M  $\text{Na}^+$ ; total voltage vs. current density; straight line is background voltage drop; ○ interface hydrated 20 min, ● interface hydrated 28 hr, △ dry interface;  $23^\circ\text{C}$ .

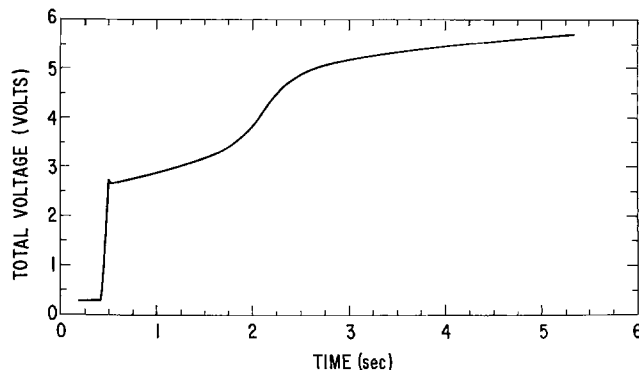


Fig. 9. Interfacial transport through hydrated interface;  $\text{Na}^+$  exit into 0.010M  $\text{Na}^+$ ; 28 hr hydration time; total voltage vs. elapsed time during galvanostatic perturbation at  $3290 \mu\text{A}/\text{cm}^2$ ;  $23^\circ\text{C}$ . Sharp rise at 0.5 min represents initial application of current.

voltage relationships for  $\text{Na}^+$  exit from  $\beta$ -alumina into propylene carbonate under dry and hydrated conditions (Fig. 8) are similar in general structure. Both deviate from bulk IR resistivity at low current densities, approach bulk IR resistivity at higher currents, and again diverge at highest current densities. Extended  $\text{Na}^+$  entry into both dry and hydrated interfaces results in resistivity increases which are reversed only upon sustained  $\text{Na}^+$  exit (Fig. 6). These observations suggest that adsorbed water significantly affects  $\beta$ -alumina/propylene carbonate interfacial transport.

Various aluminas are adsorbents for a number of species including  $\text{H}_2\text{O}$  and  $\text{Na}^+$ . Raman analysis of water adsorbed on  $\alpha$ -alumina concludes that  $\text{Na}^+$  ions and water molecules compete for Lewis acid sites (9).  $\text{Na}^+$  adsorption is thought to cause  $\alpha$ -alumina catalyst "poisoning" in  $\text{Na}^+$ -containing environments. Infrared spectroscopic analysis of pyridine adsorption on  $\alpha$ -alumina concludes that pyridine adsorbs at non-protonic Lewis acid sites in the absence of water. Proton activity is observed in the presence of water.

A variety of data also implies that water is adsorbed directly into the conducting planes of  $\beta$ -alumina. Kline *et al.* (10), in broadband NMR measurements, found that the  $^{23}\text{Na}$  spectrum in  $\beta$ -alumina, which is sharply narrowed by rapid localized ion motion at room temperature, broadens in the presence of water vapor. One inference from this is that diffusion of water into the conduction plane significantly decreases local  $\text{Na}^+$  motion, and, as a consequence,  $\text{Na}^+$  conductivity. Heating restores a normal spectrum. Weight change measurements corroborate the reversibility of the exchange (11).

Thus, water adsorbed at a  $\beta$ -alumina, interface may diffuse into the  $\beta$ -alumina, lowering bulk conductivity in the interfacial region, and is also a source of ionic hydrogen species such as  $\text{H}_3\text{O}^+$  and  $\text{H}^+$ . Both these ions can replace  $\text{Na}^+$  in  $\beta$ -alumina.

$\text{H}_3\text{O}^+$   $\beta$ -alumina has been prepared by exchanging  $\text{Na}^+$   $\beta$ -alumina in concentrated  $\text{H}_2\text{SO}_4$  (12).  $\text{H}^+$   $\beta$ -alumina is synthesized by exposing  $\text{Ag}^+$   $\beta$ -alumina to a reducing atmosphere of  $\text{H}_2$  (13). Both  $\text{H}^+$  and  $\text{H}_3\text{O}^+$  ions, therefore, are capable of diffusing spontaneously or under the influence of a field into  $\beta$ -alumina.

The preceding information suggests that water adsorbs on the  $\beta$ -alumina surface and ionic hydrogen species, such as  $\text{H}_3\text{O}^+$ , diffuse into the solid electrolyte, partially exchanging with surface  $\text{Na}^+$  ions. The result is a mixture of  $\text{Na}^+$ ,  $\text{OH}^-$ , and  $\text{H}_2\text{O}$  adsorbed on the electrolyte surface and a mixed  $\text{H}_3\text{O}^+/\text{Na}^+$  composition within the conducting planes adjacent to the surface.

Under the influence of an appropriate field, both  $\text{Na}^+$  and  $\text{H}_3\text{O}^+$  move out of the interface, both initially to adsorption sites on the surface. Subsequent

solvation and desorption steps maintain Na<sup>+</sup>/H<sub>2</sub>O equilibrium at the interface. The locally elevated Na<sup>+</sup> concentration alters the adsorption equilibrium at the interface as long as current flows, and increases the Na<sup>+</sup>/H<sub>2</sub>O and Na<sup>+</sup>/H<sub>3</sub>O<sup>+</sup> ratios on the surface and in adjacent conducting planes.

Sustained Na<sup>+</sup> exit temporarily decreases the concentrations of adsorbed H<sub>2</sub>O and exchanged H<sub>3</sub>O<sup>+</sup> and results in the temporary decrease in interfacial polarization observed at low current densities in Fig. 5. Similarly, ion entry increases the proportion of H<sub>3</sub>O<sup>+</sup> in the conduction planes, decreasing conductivity. This is reversed by extended ion transport out of the interface, as seen in Fig. 6.

Na<sup>+</sup> exit, thus, is hypothesized to involve an intermediate adsorbed state at low current densities. If the current is increased to the point at which surface adsorption sites become saturated, ion transition must take place through a secondary mechanism requiring greater energy. This results in the upwardly sloping voltage/time curves observed at higher currents during ion exit and culminates in the voltage transition shown in Fig. 9.

### Conclusions

Interfacial polarization associated with Na<sup>+</sup> transport across a polycrystalline  $\beta$ -alumina/propylene carbonate interface is nonohmic and can be separately distinguished from bulk resistivity. It is increased by water adsorbed on the interface. Interfaces which have been dried exhibit significantly lower polarization than those purposely hydrated by exposure to water vapor.

The results presented are consistent with the hypothesis that interfacial Na<sup>+</sup> ion transport occurs through an intermediate state in which Na<sup>+</sup> is adsorbed on the  $\beta$ -alumina surface, transport between the conducting planes and surface being more rapid than transport directly to the solvated state. Water competes with Na<sup>+</sup> for surface adsorption sites and provides a source of ionic hydrogen species, such as H<sub>3</sub>O<sup>+</sup>, which can diffuse into  $\beta$ -alumina. A dynamic equilibrium between adsorbed Na<sup>+</sup>/H<sub>2</sub>O and Na<sup>+</sup>/H<sub>3</sub>O<sup>+</sup> substituted into the adjacent conducting planes is established and results in increased interfacial

resistivity in the presence of water. Extended Na<sup>+</sup> electrolysis into  $\beta$ -alumina gradually enlarges the region of decreased conductivity by transporting ionic hydrogen species more deeply into the electrolyte. Extended electrolysis out reverses the effect, essentially "cleaning" the interface.

### Acknowledgment

Dr. R. W. Powers kindly supplied the  $\beta$ -alumina samples used in this work.

Manuscript submitted Aug. 26, 1975; revised manuscript received Dec. 14, 1975.

Any discussion of this paper will appear in a Discussion Section to be published in the December 1976 JOURNAL. All discussions for the December 1976 Discussion Section should be submitted by Aug. 1, 1976.

Publication costs of this article were partially assisted by General Electric Company.

### REFERENCES

1. T.R.E. Kressman and F. L. Tye, *Discussions Faraday Soc.*, **21**, 185 (1956).
2. A. M. Peers, *ibid.*, **21**, 124 (1956).
3. J. Sandblom, G. Eisenman, and J. L. Walker, *J. Phys. Chem.*, **71**, 3862 (1967).
4. J. Sandblom, G. Eisenman, and J. L. Walker, *ibid.*, **71**, 3871 (1967).
5. G. C. Farrington, Abstract, Symposium on Interfacial Phenomena, American Institute of Chemical Engineers, 67th Meeting, Washington, D.C., December 1974.
6. M. Voinov and H. Tannenberger, *Electrochim. Acta*, **19**, 959 (1974).
7. G. C. Farrington, *This Journal*. To be published.
8. R. W. Murray and C. N. Reilley, *J. Electroanal. Chem.*, **3**, 64 (1962).
9. G. Careri, V. Mazzacurati, M. Sampoli, and G. Signorelli, *J. Catalysis*, **26**, 494 (1972).
10. D. Kline, H. S. Story, and W. L. Roth, *J. Chem. Phys.*, **56**, 5180 (1972).
11. W. L. Roth, General Electric Research and Development Center, Report No. 74CRD954 (1971).
12. H. Saalfeld, H. Matthies, and S. K. Datta, *Ber. Deut. Keram. Ges.*, **45**, 212 (1968).
13. G. P. Kummer, "Progress in Solid State Chemistry," Vol. 7, A. Reiss and J. O. McCaldin, Editors, Pergamon Press, New York (1972).

## Oxidation and Corrosion of Tin-Coated Zircaloy-4

K. Hauffe\* and V. Martinez\*

*Institute of Physical Chemistry, University of Göttingen, 34 Göttingen, West Germany*

### ABSTRACT

Because of the lack of the adhesion of the growing oxide layer on zirconium alloys, tin-coated Zircaloy-4 has been oxidized in 250 Torr oxygen at 500°C and corroded in high pressure water at 349°C and 176 atm. The rate of both reactions was decreased with increasing thickness of the tin layer (up to 0.1  $\mu$ m). Simultaneously, the transition point was shifted to longer periods. Presumably this enhancement was caused by the tin layer which exists between the alloy and the oxide operating as liquid agent.

A great number of atomic reactors, such as stationary units for electrical power supply or for ship reactors, operate as high pressure water reactor type, where Zircaloy-2 and -4 are used as construction material. The use of these alloys continues to be attractive for fuel cladding and pressure tubing applications. Besides the creep strength, the corrosion behavior of these alloys is very important for the durability and

security of these reactors. Besides Zircaloy-2 and -4, zirconium-niobium alloys with 2.5-3.5 weight per cent (w/o) Nb, either without or with about 1 w/o Sn, have become of importance because of their higher creep strength with similarly good corrosion resistance under reactor conditions (1). All these alloys form, at high temperatures under high pressure water, zirconium oxide containing more or less amounts of foreign ions caused by immigration of alloying elements. However, the oxide layers exhibit only a limited

\* Electrochemical Society Active Member.

Key words: plasticity, layer, interface, crevices, stresses.

adherence which is responsible for the premature destruction of this material.

As today it is well known on the basis of an extensive study and of experience, the ductility of  $ZrO_2$  is rather small. Therefore, when the oxide layer has attained a critical thickness, the shearing stresses between the alloy and the growing oxide become so large that crevices and pores are formed in the oxide scale. Associated with this is transition to prevailing transport of  $O_2$  molecules in these crevices and pores, causing a faster oxidation or corrosion characterized by a transition from a parabolic rate law to an approximately linear rate law of oxidation. Simultaneously, a color change of this oxide layer occurs from dark gray, in consequence of an oxygen deficiency, to white, due to its attaining a stoichiometric composition. Initially, near the transition point white spots appear in the gray oxide layer which become larger during the oxidation. As known, this color is connected with a postoxidation of the initial nonstoichiometrically composed oxide layer oxygen vacancies and free electrons in consequence of an oxygen deficit.

As long as the contact of the oxide layer with the alloy is not interrupted and the number of pores and crevices per unit area of the oxide layer is not too large, sufficient oxygen ion vacancies and free electrons are available in the oxide layer for the transport of oxygen ions to the alloy-oxide interface. In the later period of oxidation, however, the density of crevices and pores has become so large that transport of oxygen as  $O_2$  molecules in crevices and pores prevails. In consequence of this fact the oxide layer is oxidized to a stoichiometric composition in which the concentration of oxygen ion vacancies and of free electrons has been strongly reduced. The oxide layer becomes white. This transition, which is correlated with the appearance of a porous oxide layer and with an increase in the rate of oxidation, can be easily recognized by a break in the oxidation-time curve (Fig. 1).

While, in the pretransition oxidation period, the rate of oxidation is determined mainly by a transport of electrons and/or holes and of oxygen ions via vacancies and/or via interstitial positions, characterized by a parabolic rate law, the subsequent oxidation period fits a linear rate law of oxidation rather well, because transport processes through the porous oxide layer no longer determine the oxidation rate. However, other rate laws, for instance a cubic and a logarithmic rate law in the pretransition period, have been found (2). The problem which had to be solved was by what means the rate of oxidation could be decreased, a question which is correlated with the shift of the transition point to longer oxidation time. This problem is intimately connected with the aim of preventing the ap-

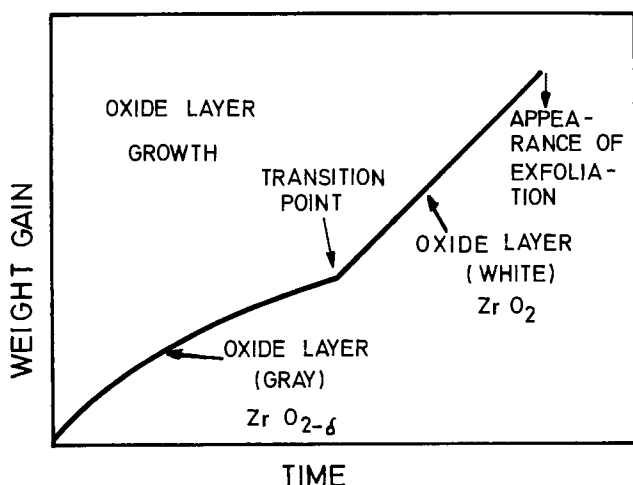


Fig. 1. Schematic representation of the kinetics of oxidation of Zircaloy.

pearance of pores and crevices in the oxide layer. Ignoring the various possible ways of solving this problem discussed elsewhere (3), only one possibility was tentatively employed which seemed to offer some success. This was the introduction of a plastic or a liquid layer between the alloy and the growing oxide layer.

The introduction of a plastic oxide layer is a rather complicated problem because the oxide must have not only a predominantly defect structure, but must also exhibit a high mobility of the lattice defects at temperatures between 280° and 350°C, the temperature range of an operating high pressure water atomic reactor. These requirements are necessary in order to decrease the shearing stresses at the oxide/alloy interface due to diffusion of oxygen ion vacancies into the interface, and to prevent the formation of crevices and pores. Attempts to solve this problem which have met with success are not known.

The second way, in which a plastic or liquid metal layer is deposited between the alloy and the growing oxide layer, and which remains unoxidized during the corrosion, seems to be more successful. The application of this method was stimulated by experiments on the high temperature oxidation of Fe-Cu and Fe-Sn alloys, where the noble metals Cu and Sn are precipitated at the interface steel/oxide. These metals, because of the high oxidation temperature of > 1000°C are in a liquid state and act simultaneously as a liquid interface and as a blocking layer to prevent a porous structure in the oxide layer and decrease the rate of oxidation (4).

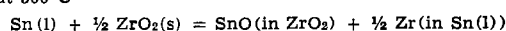
On account of the favorable influence of tin on the oxidation behavior of Zircalloys and its low melting point, which promises to prevent shearing stresses due to its liquid state at the temperature of an operating reactor, tin was selected as liquid metal layer. It was deposited in various thicknesses on Zircaloy-4 sheets and tubes before oxidation. To what extent other metals would operate in this manner between 280° and 400°C is unknown. However, only metals with a low melting point (< 280°C, the lowest operating temperature of a reactor) can be employed. Furthermore it must be taken into account that a quick diffusion of zirconium atoms must occur through the metal interlayer, so that the following arrangement is present

zirconium alloy/liquid tin layer/zirconium oxide [I]

and a SnO and/or  $SnO_2$  growth must not occur. In the first stage of oxidation, however, involving a layer of "dark  $ZrO_2$ " before the transition point, the activity of SnO in  $ZrO_2$ ,  $a_{SnO(in ZrO_2)}$ , next to the interface liquid Sn/ $ZrO_2$  is extremely low so that tin is practically not converted to SnO as can be estimated from thermodynamic data.<sup>1</sup> Unfortunately in the later period of oxidation after the transition point tin is not sufficiently inert (3) and a mixed-oxide can be formed.

In spite of this complex mechanism, described by Douglass and Wagner (6) in more detail, we want to show here that indeed a liquid tin layer is acting favorably between the alloy and zirconium oxide in the manner mentioned above.

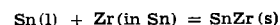
<sup>1</sup> According to Wagner (private communication) after the equilibrium at 500°C



practically no formation of SnO can be expected because one obtains

$$a_{SnO(in ZrO_2)} \approx 10^{-18}/a_{Zr(in Sn)}$$

and if the value for  $a_{Zr(in Sn)} \approx 10^{-4}$  is introduced employing the equilibrium



with

$$a_{Sn} \times a_{Zr(in Sn)} = \exp(\Delta G^\circ_{SnZr}/RT)$$

with  $\Delta G^\circ_{SnZr} = -14,000$  cal/mole [see Wagner (5)] then we obtain

$$a_{SnO(in ZrO_2)} \approx 10^{-14}$$

as an upper limit if saturation of liquid tin with the intermetallic SnZr governs. On the basis of this calculation we may assume that  $a_{SnO(in ZrO_2)}$  may be even lower than  $10^{-14}$  if the liquid alloy is not in equilibrium with the intermetallic SnZr.

First of all, corrosion experiments with flowing water were carried out in a high pressure autoclave in the Research Centre of the Atomic Reactor Station at Tsepshude (7). This autoclave was constructed with four mounting frames and a lock chamber in order to take out samples under high pressure during the experiments without any interruption of the corrosion of the remaining samples. This experimental arrangement is necessary in order to prevent a cooling of the remaining samples which causes thermal stresses in the oxide layer.

### Experimental

**Apparatus.**—The specimens were oxidized in oxygen at normal pressure in an oxidation apparatus well known in the literature. The oxidation in high pressure water vapor and the corrosion in high pressure water were measured in an autoclave.

The oxidation apparatus (Fig. 2) consisted of a vertical quartz tube connected with a Sartorius electronic microbalance capable of weighing to  $\pm 1 \mu\text{g}$ , this being completely enclosed in the vacuum system. The furnace temperature was controlled to  $\pm 1^\circ\text{C}$  with a temperature controller. Oxygen of a purity 99.995 volume per cent (v/o) supplied by Messer-Griesheim was used in the tests requiring an oxygen atmosphere. As carrier gas pure argon was employed.

For the corrosion of Zircaloy-4 samples in high pressure water an autoclave with lock chamber was constructed (Fig. 3). At the bottom of this autoclave are four drawing junction pieces which are correspondingly connected with four ball valves by means of intermediate water-cooled connections. On the lower junction of these ball valves the lock chamber is placed, connected with these ball valves through a flareless tube fitting. This lock chamber consists of lock tube, packroom, drain valve, and axially movable drawing rod. This arrangement makes possible the introduction or taking out of samples during the experiments. The autoclave can operate at a maximum temperature of  $500^\circ\text{C}$  and a maximum pressure of 250 atm. We feel that our experimental arrangement has several advantages over that of the other authors particularly for long time experiments. While taking out several samples it is not necessary to cool the reacting system and therefore probable crevice formation in the oxide layer of the remaining samples in consequence of thermal stresses is suppressed. In spite of its steel construction, the thermal isolation was so designed that in the middle of the autoclave the temperature accuracy in a width of 15 cm was  $\pm 0.5^\circ\text{C}$  at  $349^\circ\text{C}$  and 176 atm water pressure. Deionized water used as a corroding environment had 0.04–0.026 mg/liter  $\text{O}_2$ , a specific conductivity of  $0.5\text{--}1.7 \mu\text{mho}\cdot\text{cm}^{-1}$  and a pH

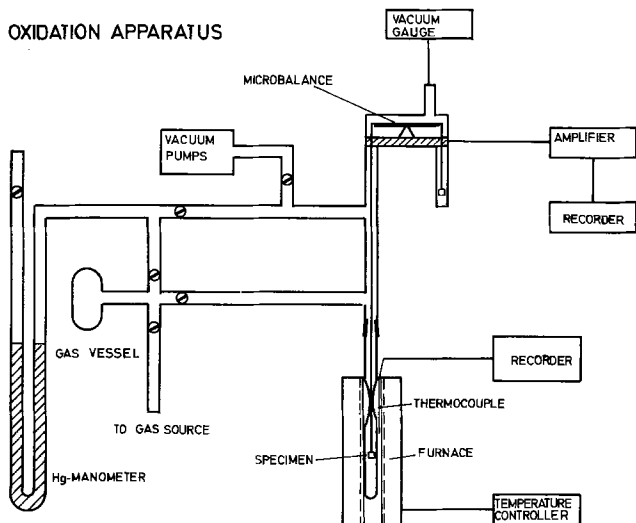


Fig. 2. Oxidation apparatus

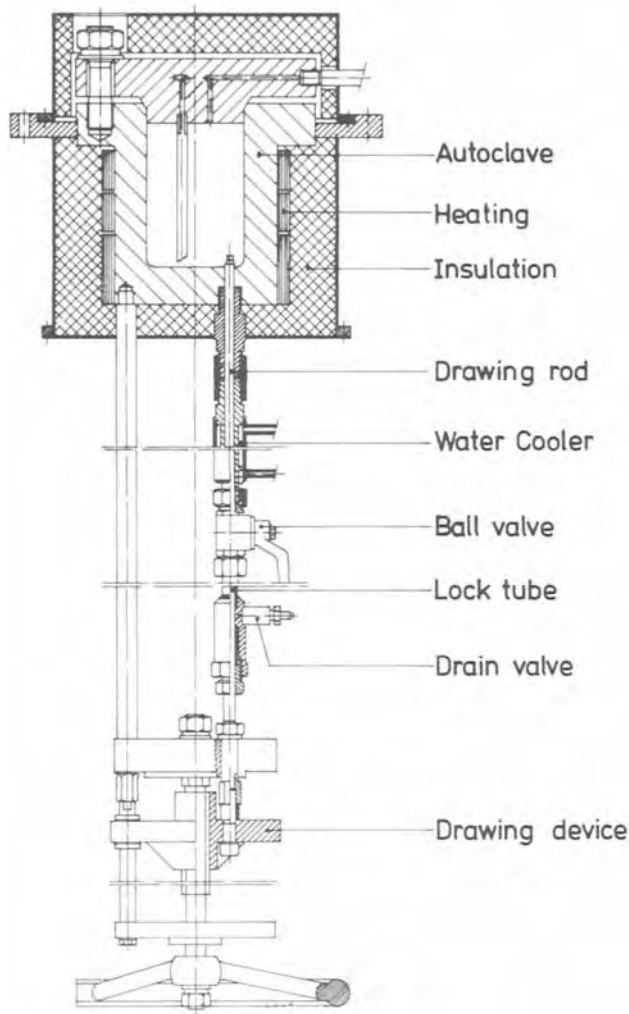


Fig. 3. Autoclave for high-pressure water oxidation experiments

value of 7.5–6.4. The applied flow rate of water was measured continuously during the experiments.

**Sample preparation.**—Zircaloy-4 samples<sup>2</sup> measuring  $15 \times 10 \times 0.8 \text{ mm}$  were cut from strips, polished on 800 grid silicon carbide paper, degreased, and then pickled in the following pickling solution: 45 v/o  $\text{HNO}_3$ , 5 v/o  $\text{HF}$  diluted with deionized water at about  $20^\circ\text{C}$ . Following this, we tried to deposit tin layers on Zircaloy-4 samples. First of all the samples were immersed, under vacuum and at  $700^\circ\text{C}$ , in a tin bath. At this temperature and greater, unfortunately, the undesirable and brittle  $\text{Sn}_2\text{Zr}$  principally was formed. The presence of this compound on the samples by no means reduces the oxidation rate (Fig. 4). Zirconium diffuses quickly through this alloy and reacts at the outer interface with the oxygen. At lower temperatures ( $< 600^\circ\text{C}$ ) longer time is necessary in order to get a thin compact layer with a tin content of larger than 95 w/o. Unfortunately this layer was not uniform and had a poor adherence.

No suitable tin layers were obtained by means of electrochemical methods, with and without adding organic compounds as inhibitors, at temperatures between  $20^\circ$  and  $90^\circ\text{C}$ . Thin and uniform tin layers were deposited therefore by evaporation under vacuum ( $10^{-5}$  Torr) with a Balzers microevaporator MIKRO-BA-3. The thickness of these evaporated tin layers was estimated through optical comparison of the samples with other Zircaloy-4 samples previously weighed and calibrated by light absorption of evaporated tin onto glass.

<sup>2</sup> Zircaloy-4 is a zirconium alloy which mainly contains 1.2–1.7 w/o Sn; 0.07–0.13 w/o Cr; 0.18–0.24 w/o Fe, and 0.10–0.15 w/o  $\text{O}_2$  (8).

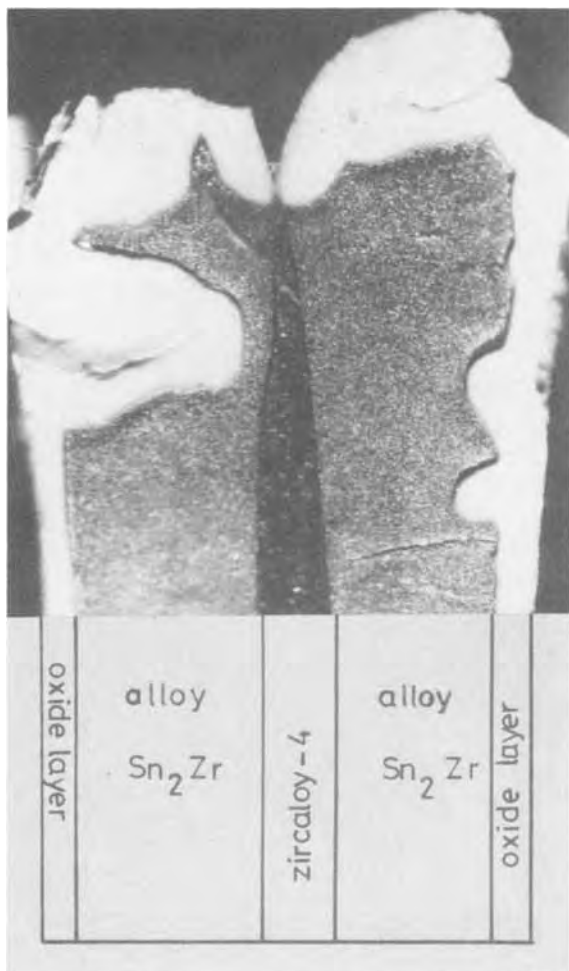


Fig. 4. Cross-section photograph of an oxidized tin coated Zircaloy-4 sample ( $T = 500^{\circ}\text{C}$ ;  $p_{\text{O}_2} = 300$  Torr;  $t = 4$  days) (X63).

### Experimental Results

**Oxidation with oxygen.**—First, samples with tin coatings of different thickness were oxidized in 250 Torr oxygen at  $500^{\circ}\text{C}$ . Figure 5 shows that the oxidation rate decreases with the thickness of the tin layer. In spite of the scatter in results, we found a shift of the transition point to longer oxidation times. In the pretransition period the initial oxidation rate of the samples with thick tin coatings (between 0.1 and  $0.3 \mu\text{m}$ ) is higher than the oxidation of the samples with thinner tin coatings ( $< 0.1 \mu\text{m}$ ). This unexpected initial weight increase probably is caused by the simultaneous oxidation of tin.

On the other hand, Fig. 5 shows that transition time increases up to  $800\text{\AA}$  tin and this dependence is approximately linear as shown by Fig. 6. The dependence of the parabolic rate constant on the thickness of the tin layers in the first period of oxidation is shown in Fig. 7. Figure 5 represents also the kinetics of the post-transition oxidation, the time dependence now being linear. Practically no change of the oxidation rate in this post-transition period by means of these coatings was observed. On account of their lack of effectiveness for oxidation resistance, thick tin layers ( $\geq 0.1 \mu\text{m}$ ) were not employed in subsequent experiments.

Figure 8 shows the increasing dependence of the oxidation rate on the oxygen pressure of a Zircaloy-4 sample with a  $400\text{\AA}$  thick tin coating at  $500^{\circ}\text{C}$ . Furthermore in Fig. 9 there is plotted the parabolic rate constant  $k_p$ , vs. the oxygen pressure in a logarithmic scale yielding  $k_p \sim p_{\text{O}_2}^{1/8}$ . Meanwhile, in the post-transition stage the linear rate constant  $k_L$  increases with a fourth root of the oxygen pressure as can be seen from

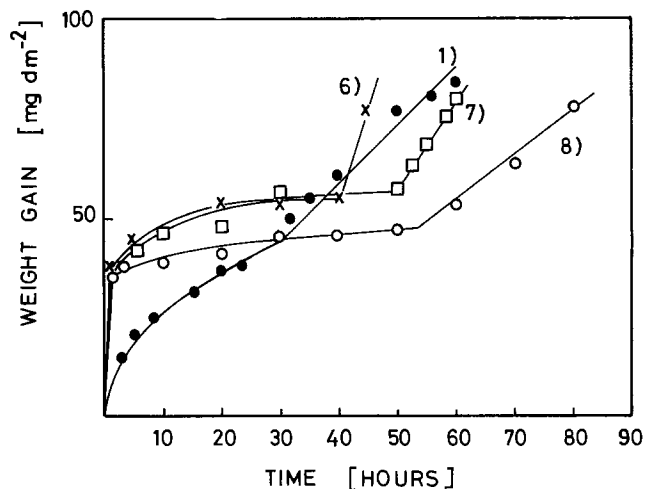
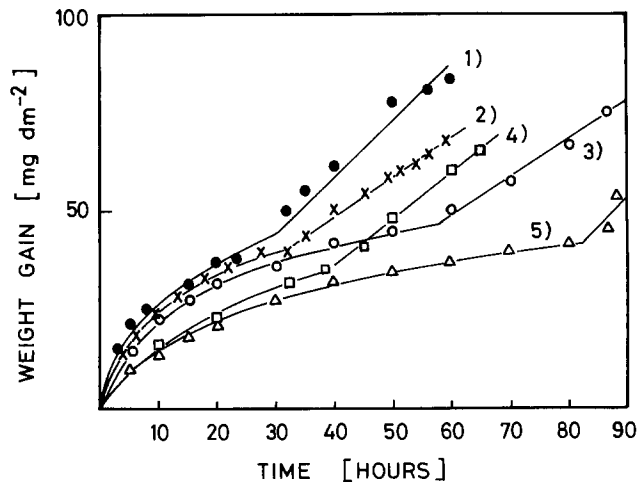


Fig. 5. (a, top) Oxidation of tin-coated Zircaloy-4 specimens at  $500^{\circ}\text{C}$  and 250 Torr oxygen: curve 1, no tin; curve 2,  $200\text{\AA}$ ; curve 3,  $300\text{\AA}$ ; curve 4,  $500\text{\AA}$  tin; curve 5,  $800\text{\AA}$  tin coating thickness. (b, bottom) Oxidation of tin-coated Zircaloy-4 samples at  $500^{\circ}\text{C}$  and 250 Torr oxygen: curve 1, no tin; curve 6,  $0.1 \mu\text{m}$ ; curve 7,  $0.18 \mu\text{m}$ ; curve 8,  $0.23 \mu\text{m}$  tin coating thickness.

Fig. 9. This dependence of the parabolic rate constant on the oxygen pressure forced us to assume that the rate-determining diffusion must occur in the p-type region of the oxide layer near the outer surface according to

Zr-alloy | n-type  $\text{ZrO}_2$ -p/n

transition-p-type  $\text{ZrO}_2$  | oxygen [II]

while the diffusion in the n-type region must be fast enough. A remarkable observation is also the decrease of the transition time with increasing oxygen pressure (Fig. 10) which seems to be correlated with a faster growing p-type oxide region.

The dependence of the oxidation rate of a Zircaloy-4 sample on the temperature with a  $800\text{\AA}$  thick tin coating in 250 Torr oxygen is shown in Fig. 11. The values of the oxidation constants were found to be increased with increasing temperature. From these results an activation energy of  $27.7 \text{ kcal/mole}$  was calculated. Since this value agrees with that for the oxidation of pure Zircaloy, the mechanism of both may be assumed to be identical.

By means of microprobe measurements with a microprobe analyzer (Geoscan), an enriched tin zone could be identified at the alloy/oxide interface. Figure 12 shows the distribution of both metals, tin and zirconium, in the oxide layer.

**High pressure water corrosion.**—In addition to the oxidation experiments, Zircaloy-4 samples with tin

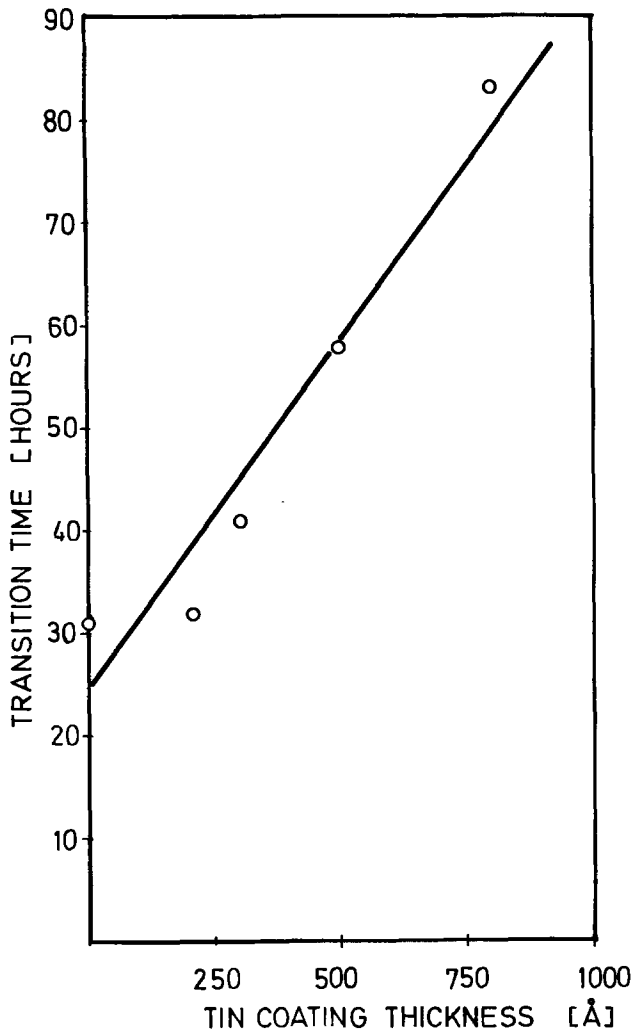


Fig. 6. Dependence of the oxidation transition time on the tin coating thickness at 500°C and 250 Torr oxygen.

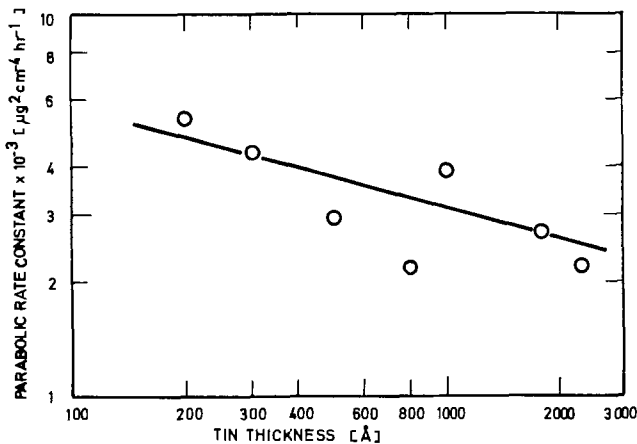


Fig. 7. Dependence of the parabolic oxidation rate constant on the tin coating thickness at 500°C and 250 Torr oxygen.

coatings were corroded in high pressure water in the autoclave at 349°C and 176 atm. Both the time dependence and the tin thickness dependence of the corrosion rate was measured. The samples were taken out without interrupting the corrosion of the remaining samples, as described in the experimental section. A small decrease of the oxidation rate with increase of the thickness of tin coatings was observed (Fig. 13).

**Water vapor oxidation.**—Zircaloy-4 samples with tin deposited were oxidized at 403°C and 48 atm water vapor pressure. In spite of the scatter in the results a

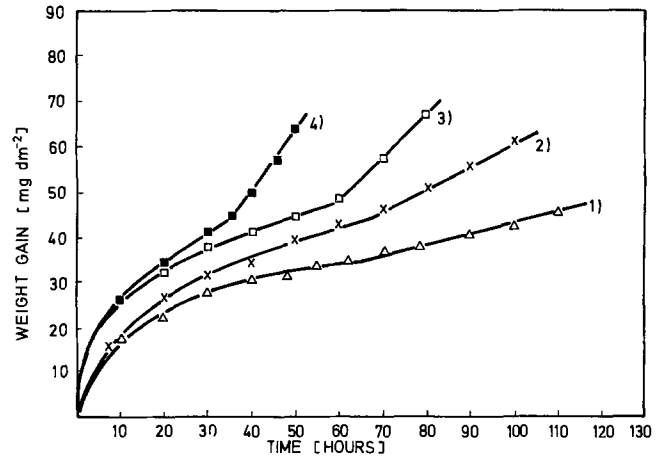


Fig. 8. Dependence of the oxidation rate on the oxygen pressure at 500°C and tin coating thickness of about 400Å: curve 1,  $8 \times 10^{-4}$  atm; curve 2,  $8.7 \times 10^{-3}$  atm; curve 3,  $3.3 \times 10^{-1}$  atm; curve 4,  $6.3 \times 10^{-1}$  atm.

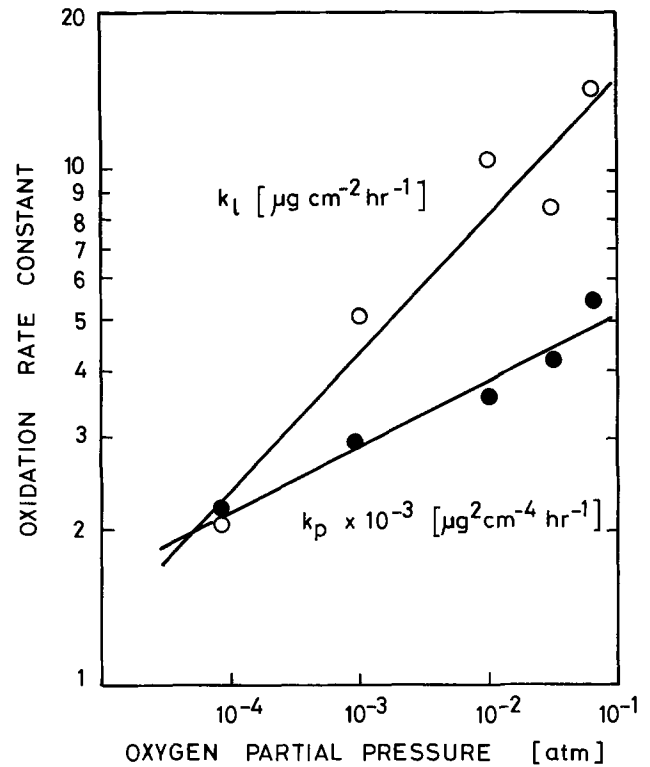


Fig. 9. Dependence of the parabolic and of the linear oxidation rate constant on the oxygen pressure at 500°C and tin coating thickness of about 400Å.

small decrease of the oxidation rate with increasing thickness of the tin layer was detected as shown in Fig. 14.

**Electron microscope photographs.**—On comparing an oxidized Zircaloy-4 sample without a tin coating (Fig. 15a) with an oxidized tin-coated Zircaloy-4 sample (Fig. 15b) it can be recognized that the oxide layer of the tin-free specimen exhibits a greater number of pores and crevices.

Photographs of these pore-free zones allow the conclusion that this tin treatment causes the growth of a more coherent oxide layer at 500°C and 250 Torr oxygen. The thicknesses of all these oxide layers have been obtained close by the transition point or in the linear oxidation region, i.e., beyond the transition point. This transition occurs at about 40-55 mg-dm<sup>-2</sup>.

**Discussion**

Since zirconium oxide exhibits an intrinsic lattice defect behavior according to

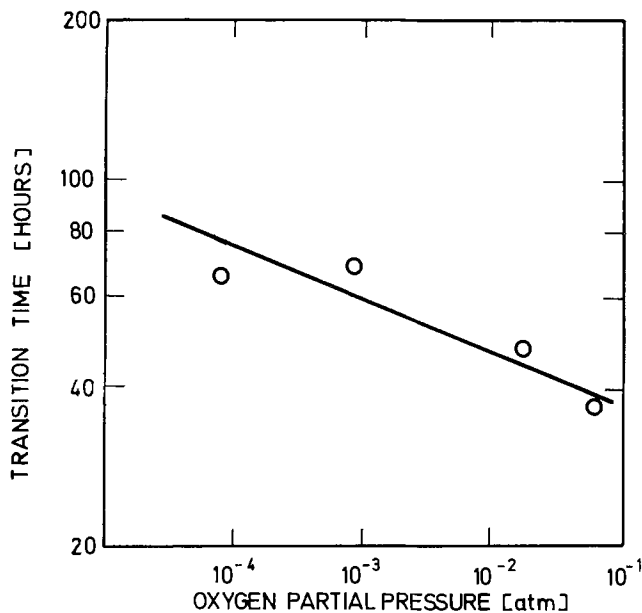


Fig. 10. Dependence of the oxidation transition time on the oxygen pressure at 500°C and tin coating thickness of about 400Å.

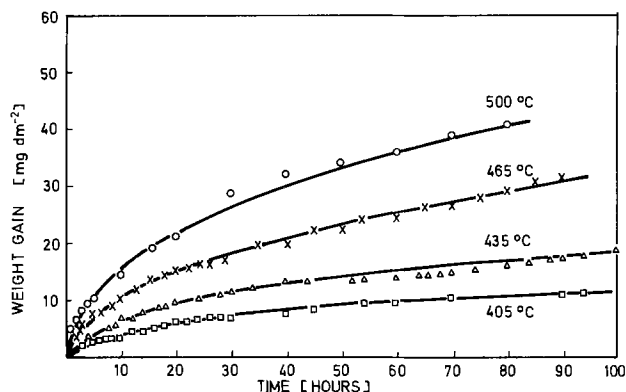
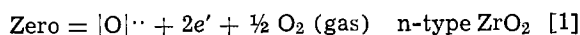


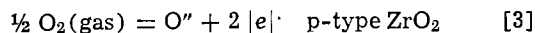
Fig. 11. Dependence of the oxidation rate of tin-coated Zircaloy-4 samples on the temperature at 250 Torr oxygen and tin coating thickness of about 800Å.



with the temperature-dependent equilibrium



and



with the temperature-dependent equilibrium



we may tentatively assume that the oxidation of zirconium and its alloys occurs by diffusion of oxygen ions through the oxide layer via oxygen ion vacancies  $|\text{O}| \cdot$  and  $|\text{O}| \cdot$  and via interstitial positions  $\text{O}''$  and  $\text{O}'$  with the equivalent number of free electrons  $e'$  and holes  $|e| \cdot$  for electroneutrality.

Taking into account the  $\Delta G^\circ$  values for the formation of  $\text{ZrO}_2$ ,  $\text{SnO}_2$ , and  $\text{SnO}$  at 500°C ( $-57$ ,  $-28$ , and  $-24$  kcal/equiv.) and the experimental results of the oxidation of zirconium alloys with Cu, Cr, Fe, and Mo additions (9), it is concluded that tin remains initially precipitated at the alloy/oxide interface. This metal separating the growing oxide from the alloy should decrease the shearing stresses between the alloy and the oxide. Because of the relative small quantity of tin in the alloy it is questionable whether a homogeneous precipitation of this metal at the interface is possible.

At the beginning of oxidation and corrosion of the Zircaloy-4 samples with thin tin coatings, at tempera-

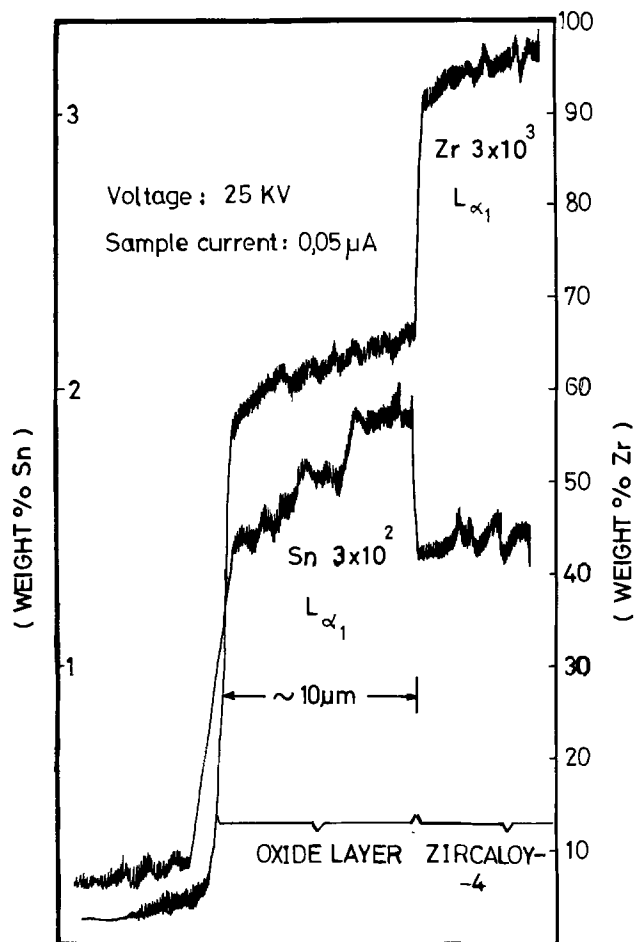


Fig. 12. Distribution of zirconium and tin in the oxide layer of an oxidized Zircaloy-4 sample (tin coating thickness 400Å;  $T = 500^\circ\text{C}$ ;  $p_{\text{O}_2} = 477$  Torr).

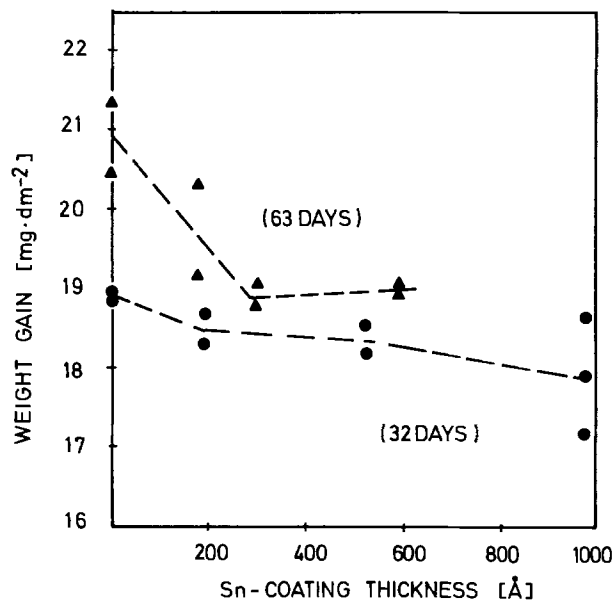
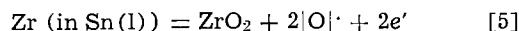


Fig. 13. Corrosion of Zircaloy-4 samples at 349°C and 176 atm water pressure ( $t_1 = 32$  days;  $t_2 = 63$  days).

tures between 350° and 500°C a liquid tin layer should be expected at the alloy/oxide interface. During corrosion zirconium dissolves in liquid tin and migrates through this tin layer toward the interface tin/oxide where the following reaction occurs



independent of the oxidizing ambient. During the oxi-



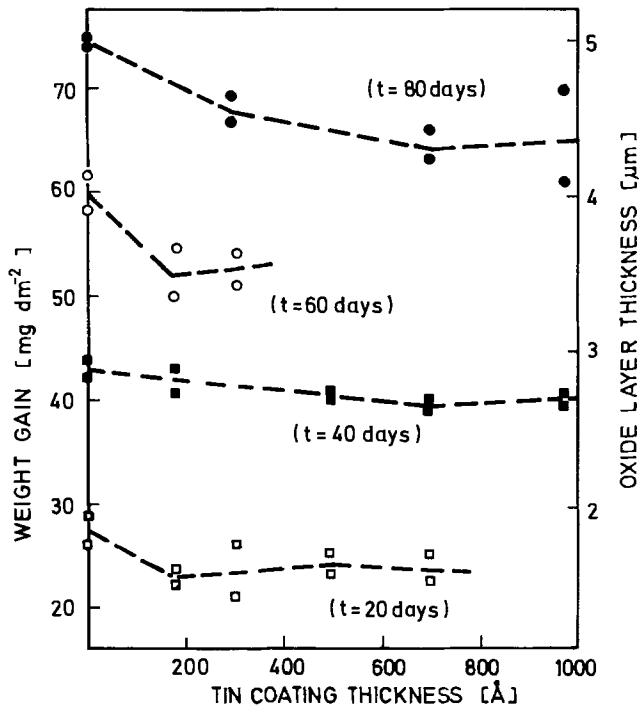


Fig. 14. Oxidation of Zircaloy-4 samples at 403°C and 48 atm water vapor pressure ( $t_1 = 20$  days;  $t_2 = 40$  days;  $t_3 = 60$  days;  $t_4 = 80$  days).

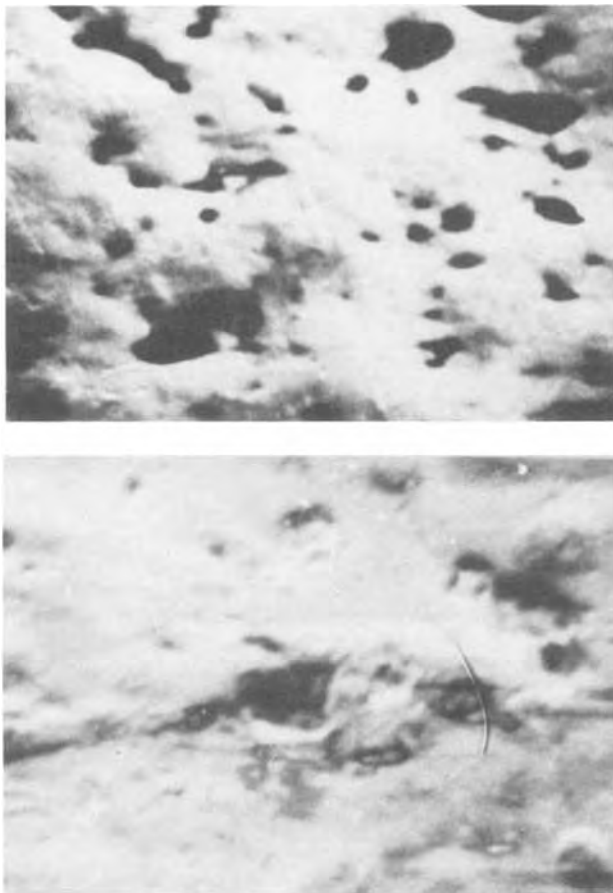


Fig. 15. Electron microscope photographs of oxidized Zircaloy-4 samples ( $T = 500^\circ\text{C}$ ;  $p_{\text{O}_2} = 250$  Torr;  $t = 85$  hr). (a, top) Weight gain:  $110 \text{ mg-dm}^{-2}$  ( $\times 300$ ). No tin. (b, bottom) Weight gain:  $95 \text{ mg-dm}^{-2}$  ( $\times 360$ ). Tin-coated sample.

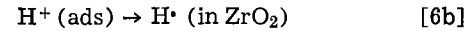
ation in oxygen, these oxygen ion vacancies  $|\text{O}|^\cdot$  migrate with free electrons in an ambipolar diffusion through the oxide layer only toward the p-type region,

where oxygen ions in interstitial positions and holes are the migrating species [3].

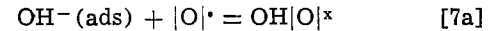
During the corrosion in high-pressure water, the growing oxide layer is homogeneously n-type due to the low oxygen pressure. Therefore, only free electrons are available besides oxygen ion vacancies produced by reaction step [5]. We can consider that the first reaction step is adsorption of  $\text{H}^+$  and  $\text{OH}^-$  onto the  $\text{ZrO}_2$  surface



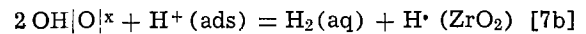
followed by entering of hydrogen into the oxide lattice



Simultaneously, the  $\text{OH}^-$  ions enter the oxide lattice occupying oxygen ion vacancies

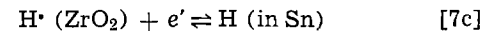


producing electrically neutral species which can react with protons at the surface

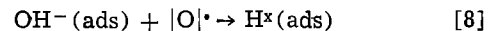


under formation of hydrogen dissolved in water and protons in the oxide lattice.

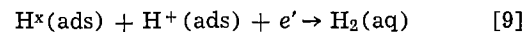
Assuming a fast migration of protons into the oxide lattice and a slow one for the electrons, mainly protons are discharged at the  $\text{Sn}/\text{ZrO}_2$  interface, according to



Since, however, the solubility of hydrogen in tin is very small, the reaction step [7c] is precluded. Therefore, in the presence of a tin layer one is forced to assume the following reaction sequence with hydrogen formation at the  $\text{ZrO}_2/\text{H}_2\text{O}$  interface, according to the following steps



and



Due to the tin coating we need free electrons and, therefore, a migration of electrons through the oxide layer is necessary in order to make possible the reaction steps [8] and [9].

As soon as the tin layer has disappeared during a longer oxidation period due to its inclusion in the oxide layer experimentally detected by our microprobe measurements, then the oxidation continues in the same way as an untreated Zircaloy-4 producing pores and crevices in the oxide layer which are responsible for the appearance of the transition to a faster rate of oxidation and a quasi-linear rate law. In this case we might suppose that the appearance of transition is closely connected with the disappearance of the liquid tin layer. At present, however, the available experimental results cannot be tendered in evidence.

In conclusion, the presence of a liquid tin layer at the alloy/oxide interface promotes the formation of a coherent and pore-free zirconium oxide layer which temporarily prevents a faster oxidation which occurs after the transition point is attained. Unfortunately, the initially precipitated tin disappears soon due to its dissolution in Zircaloy-4 and/or due to its inclusion in the oxide layer.

#### Acknowledgment

This work was sponsored by the Gesellschaft fuer Kernenergieverwertung in Schiffbau und Schifffahrt mbH, Geesthacht (GKSS) within a research program between this Society and the Institute of Physical Chemistry, University of Göttingen, West Germany. We would like to thank W. Spalthoff and A. Reymann for the stimulating cooperation in the reactor station. Furthermore, we are grateful to C. Wagner for a detailed discussion.

Manuscript submitted Aug. 26, 1975; revised manuscript received Nov. 5, 1975. This was Paper 253 presented at the Toronto, Canada, Meeting of the Society, May 11-16, 1975.

Any discussion of this paper will appear in a Discussion Section to be published in the December 1976 JOURNAL. All discussions for the December 1976 Discussion Section should be submitted by Aug. 1, 1976.

#### REFERENCES

1. W. Spalhoff and H. Wilhelm, Report of the GKSS, 70/46 (Sept. 1970).
2. K. Hauffe, "Oxidation of Metals," p. 228, Plenum

3. K. Hauffe, *Werkstoffe Korrosion*, **22**, 604 (1971).
4. R. G. Olssen, B. B. Rice, and E. T. Turkdogan, *J. Iron Steel Inst., London*, **207**, 1607 (1969).
5. C. Wagner, *Acta Met.*, **6**, 309 (1958).
6. D. L. Douglass and C. Wagner, *This Journal*, **113**, 671 (1966).
7. V. Martinez and A. Reymann, *Werkstoffe Korrosion*, **26** (9), 703 (1975).
8. Zirkonium-Documentation of the VDM-Zirkonium Gesellschaft.
9. B. De Gelas, G. Berganger, and P. Lacombe, *J. Nucl. Mater.*, **29**, 1 (1969).

## Corrosion of Lead Alloys at High Anodic Potentials

J. L. Weininger\* and E. G. Siwek

General Electric Company, Corporate Research and Development, Schenectady, New York 12301

#### ABSTRACT

The corrosion of expanded grids of lead-antimony, lead-calcium, and lead-calcium-tin alloys maintained at constant high float charge was measured metallographically. Linear growth rates were determined for oxide growth on all three alloys. X-ray scans and maps served to locate the presence of  $\text{PbSO}_4$  at the interfaces and in the bulk of the  $\text{PbO}_2$  corrosion product. The results are consonant with corresponding high temperature corrosion work.

Different alloys of lead are used in a variety of lead-acid battery designs and applications. This makes it necessary to examine the behavior of a given alloy under the conditions of its prospective use, for example, float charge.

The anodic corrosion of pure lead was first studied in detail by Lander (1). Combining a thermodynamic and a kinetic approach, he related the mechanism of the positive plate reactions to the actual conditions of battery service. Lander's work showed that the grid of the  $\text{Pb/PbO}_2$  electrode is passivated at a potential corresponding to mild overcharge, which is encountered in battery-"float" service. It had already been shown by Haring and Thomas (2), in their introduction of  $\text{Pb/Ca}$  alloys to the battery industry, that the  $\text{Pb/Ca}$  alloy corroded much slower than  $\text{Pb/Sb}$  and at a rate comparable to that of pure  $\text{Pb}$ . The  $\text{Pb/Ca}$  alloy was at first used in emergency standby batteries (3); it is now gaining acceptance in maintenance-free batteries and other applications (4).

The present work involves the corrosion of  $\text{Pb/Sb}$ ,  $\text{Pb/Ca}$ , and  $\text{Pb/Ca/Sn}$  alloys at a constant high anodic potential (overvoltage *vs.*  $\text{PbO}_2/\text{PbSO}_4 = 0.25\text{V}$ ) at room temperature. The pertinent electrochemistry has been discussed by Milner (5). A similar approach at elevated temperature is described by Cannone, Feder, and Biagetti (6) for accelerated corrosion and life tests of the Bell System's lead-acid battery. Very recently, another such accelerated life test of  $\text{Pb/Sb}$  grids for heavy duty cycling has been described by Maskalick (7).

#### Experimental

Different methods of observing the course of corrosion may be used. Willihnganz (3) and others (6) determined the percentage growth of the corroding grid over the original  $\text{Pb}$  grid thickness. Maskalick (7) measured the actual thickness loss of lead after removal of the corrosion product. In the present case, the depth of corrosion of the alloys was determined directly by metallographic observation. References (3) and (6) describe the axial extension of the grid where-

as the lateral dimensional changes (7), resulting directly from the conversion of lead to lead dioxide is used in the present work. The axial extension is caused by the lateral expansion; both are measures of grid corrosion to the extent that the grid growth is proportional to the depth of corrosion (8). The microscopic method was chosen in this work because the condition of room temperature corrosion, combined with a potential close to that of maximum anodic protection (9), resulted in very small rates of corrosion. Furthermore, small samples could be selected from relatively small test electrodes.

Expanded grids, prepared from the following three alloy compositions, were tested: (i)  $\text{Pb-5\% Sb}$  (standard antimonial grid alloy), (ii)  $\text{Pb-0.07} \pm 0.01\% \text{ Ca}$ , and (iii)  $\text{Pb-0.06} \pm 0.01\% \text{ Ca-0.84} \pm 0.05\% \text{ Sn}$ .

The following variables of electrode preparation or operation were used to observe their effect on grid corrosion.

(a) Grid preparation before pasting: (i) a phosphoric acid etch, which involved successive washings in acetone, ethanol, water, and a 10 min etch in 10%  $\text{H}_3\text{PO}_4$ ; and (ii) ultrasonic cleaning in a commercial cleaning solution containing tetrachloroethylene.

(b) Pasted *vs.* unpasted grids: One-half of each expanded grid was left unpasted in order to study the effect of the presence of the paste on the grid.

(c) Flooded *vs.* "starved" condition of electrodes: (i) The electrode was immersed in an ample supply of 1.28 sp gr acid, and (ii) the electrodes were wrapped with several layers of separator which extended into a pool of 1.28 sp gr acid and kept the electrode in a wet, but electrolyte-"starved" condition.

Fifteen electrodes with a surface area of  $2.5 \times 3.1$  cm (each side) were assembled in three test cells for the flooded and starved electrolyte conditions. (The  $\text{Pb/Sb}$  grids were tested only in the electrolyte-starved cell in order to avoid antimony poisoning of the negative electrodes which would occur in the flooded case). The positive test electrodes were interleaved with negative counterelectrodes. They were connected in parallel to a potentiostat for a constant overcharge at

\* Electrochemical Society Active Member.

Key words: lead-acid battery, corrosion, passivation, lead-calcium alloys, oxide growth, cell failure mechanism.

1.34V vs. a Hg/Hg<sub>2</sub>SO<sub>4</sub> reference electrode at room temperature. This corresponds to an overvoltage of 0.25V with respect to the theoretical PbSO<sub>4</sub>/PbO<sub>2</sub> potential, and also to a high float-charge according to Willihnganz (3), but in terms of the anodic passivation established by Lander (9), this potential is near the minimum of oxide growth and lower than the potential at which appreciable oxygen evolution occurs. Our own experiments with positive plates having Pb/Ca grids (10) showed that gas evolution just begins at this potential in a cell after substantial cycle life with a total cell charging voltage of about 2.45V. At the positive potential of 1.34V vs. Hg/Hg<sub>2</sub>SO<sub>4</sub>, the corrosion current densities for the flooded and starved cells were 50 and 43 μA/cm<sup>2</sup>, respectively.

Small samples were taken from the grids at periodic intervals over a total test time of 5000 hr. The samples were washed with distilled water, dried, and mounted for microscopic observation of the corrosion layer. Since intergranular corrosion was involved, the actual depth of corrosion was defined as the fraction of a line normal to the Pb/PbO<sub>2</sub> electrode-H<sub>2</sub>SO<sub>4</sub> electrolyte interface, which covered the oxide. An average of 20 readings per sample gave a measure of the corrosion depth within ± 20%.

In addition, at 2300 hr and at the end of the tests at 5000 hr, representative samples of the three alloys were mounted for an electron microprobe analysis, from which scanning electron micrographs, x-ray scans, and x-ray maps were obtained.

**Results**

The graphs in Fig. 1-3 show the corrosion of the three alloys as a function of time. The data were fitted by the least squares method by a linear equation (solid lines in Fig. 1-3)

$$\Delta y = k + m \cdot t \quad [1]$$

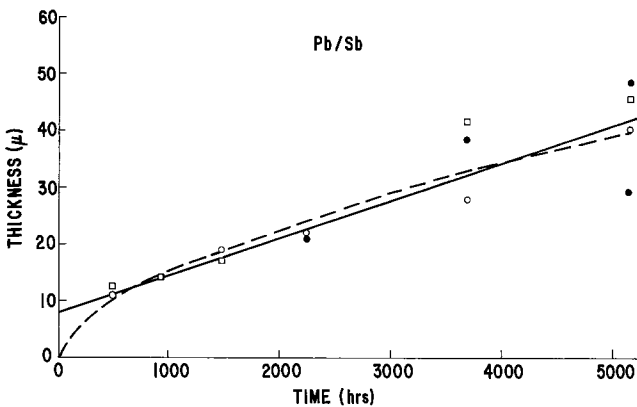


Fig. 1. Oxide growth on Pb-Sb alloy, starved electrolyte; ○ and □ bare grids; ● grids of pasted electrodes.

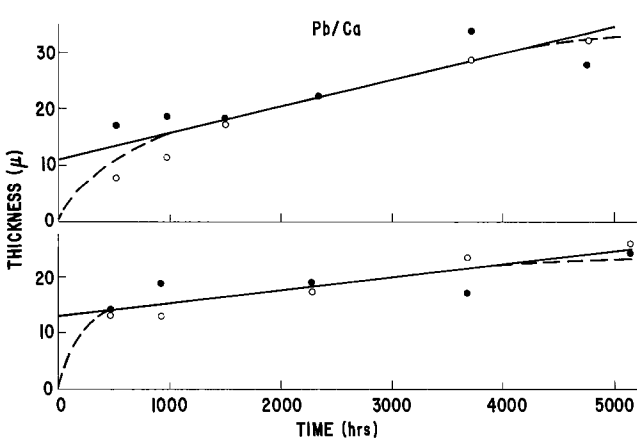


Fig. 2. Oxide growth on Pb-Ca alloy; top, flooded; bottom, electrolyte-starved cells; ○ bare grid; ● pasted grid.

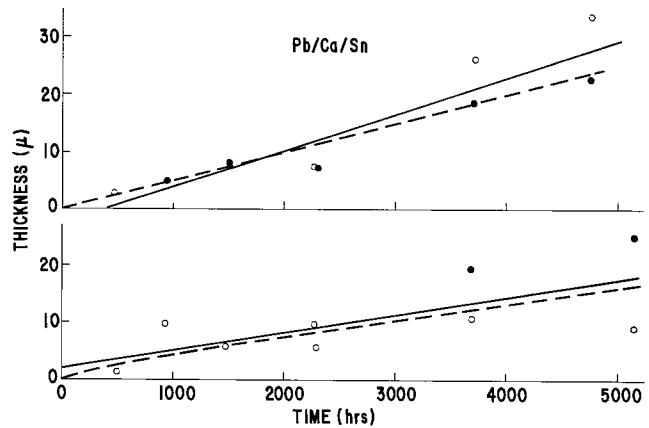


Fig. 3. Oxide growth of Pb-Ca-Sn alloy; top, flooded; bottom, electrolyte-starved cells; ○ bare grids; ● pasted grids.

and by an exponential equation (dashed lines in Fig. 1-3)

$$\Delta y = k' \cdot t^x \quad [2]$$

where Δy is the thickness of the oxide layer, grown at time t, and m is the linear growth rate. k, k', and x are constants.

Table I gives the numerical values of the constants in the rate expression. With these constants, the growth of the oxide was extrapolated from the seven-months experimental data, to periods of one, two, and five years (Table II).

Although the scatter in the experimental data is large, the data were also expressed in exponential equations because this type of relation has been encountered before (7) and, indeed, it is expected for a diffusion-controlled mechanism of corrosion. All fitted curves should pass through the origin. The extent to which this does not occur in the linear least square fits reflects the experimental error.

The error limit in individual determinations was about ± 20%. It was large because the experimental conditions combined to make the corrosion effect small. However, as seen in Fig. 1-3, for the first 5000 hr of corrosion at room temperature, the linear relation gives a larger corrosion rate than the exponential one.

As shown in Table II, under the given experimental conditions, the antimonial grid corroded two to three times as fast as the calcium alloys in the electrolyte-

Table I. Constants in Eq. [1] and [2]

		Linear form (Eq. [1])		Exponential form (Eq. [2])	
		k, μ	m, μ/hr	k', μ/(hr) <sup>x</sup>	x
Pb/Sb	s*	7.9	0.00662	0.282	0.580
Pb/Ca	f*	11.0	0.00468	0.517	0.487
Pb/Ca	s	13.0	0.00230	2.87	0.245
Pb/Ca/Sn	f	-2.6	0.00631	0.0039	1.03
Pb/Ca/Sn	s	2.2	0.00303	0.0102	0.868

\* s and f: electrolyte-starved and flooded cells.

Table II. Growth of lead alloys in microns at 1.34V. Anodic potential vs. Hg/Hg<sub>2</sub>SO<sub>4</sub>

Rates		One year		Two years		Five years	
		Linear	Exponential	Linear	Exponential	Linear	Exponential
Pb/Sb	s*	66	54	124	81	298	139
Pb/Ca	f*	52	43	93	60	216	94
Pb/Ca	s	33	27	53	31	114	39
Pb/Ca/Sn	f	52	44	108	91	273	233
Pb/Ca/Sn	s	29	27	55	49	134	110

\* s and f: electrolyte-starved and flooded cells.

starved cell. The Ca-alloys had a comparable corrosion rate, at least for the extrapolated first year value. They corroded twice as fast in the electrolyte-flooded as in the electrolyte-starved environment. Other variations in the preparation of the  $\text{PbO}_2$  electrodes, *i.e.*, the method of cleaning the grid before pasting, or the presence or absence of the paste on the grid, did not have any influence on the corrosion rates within the experimental error. Data for unpasted and pasted grids were combined in Fig. 1-3, and in the evaluation of the corrosion rates.

### Optical and Electron Microscopy

For microscopic examination, it was found that a coarse and fine mechanical polish was satisfactory for observing the oxide layer, but for x-ray scanning an ultra microtome cut gave an oxide surface with the least distortion. Figure 4 is a micrograph of such a cut. It represents the Pb/Ca/Sn alloy and its corrosion layer after 4800 hr on test. The grid had been originally cleaned with the solvent; it was pasted and tested in the flooded condition. Some fragments of the active material are still near the oxide-electrolyte interface.

Figures 5 through 7 are pairs of backscattered electrons (BSE) micrographs and sulfur x-ray maps of the same location for the three grid alloys. The BSE micrographs give a better indication of the topography of the sample than optical micrographs and they also serve to locate x-ray scans, as in Fig. 6. The sulfur x-ray maps were obtained by tuning the crystal spectrometer to the  $\text{K}\alpha$  line of sulfur.

Figure 4 shows clearly the intergranular nature of the oxide growth on the Pb-Ca-Sn alloy. Material in islands close to the oxide/electrolyte interface, stemming from the battery paste, contains a considerable amount of  $\text{PbSO}_4$  (Fig. 5a). This is noted in the sulfur x-ray map of the area (Fig. 5b). It was also observed in several sulfur x-ray scans (not shown) which indicated a surface concentration of  $\text{PbSO}_4$  at the oxide-electrolyte interface. The sulfur x-rays may have originated not only in the above-mentioned remnants of the active material, but also in a thin surface skin

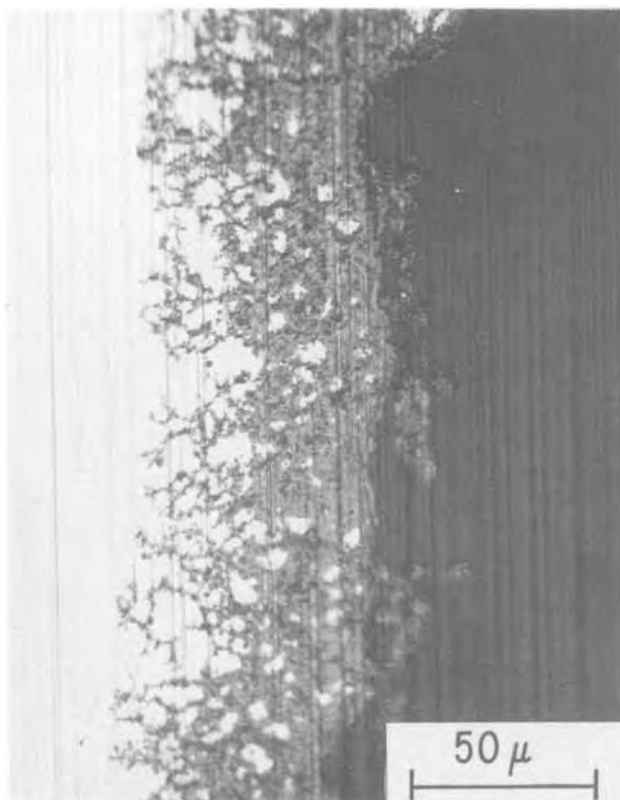


Fig. 4. Pb-Ca-Sn grid after 4800 hr of corrosion, 500X

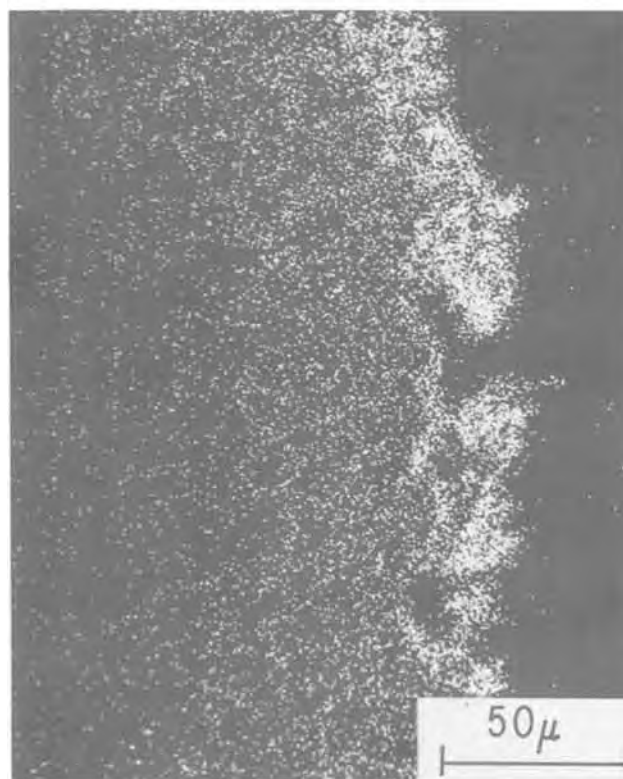


Fig. 5. (a, top) BSE micrograph of Pb-Ca-Sn; (b, bottom) sulfur x-ray map of same location as Fig. 4 and 5a. 500X.

of  $\text{PbSO}_4$  which could have formed during sampling of the electrode.

In the Pb-Sb sample, the sulfur content of the oxide layer, even at the electrolyte interface, was very low as shown by the scan in Fig. 6a and the uniform and scarce sulfur x-ray map in Fig. 6b.

However,  $\text{PbSO}_4$  accumulates at the grid-oxide interface in the case of the Pb-Ca alloys. Figure 7a shows the sulfur scan which corresponds to the interfaces and location of the x-ray map (Fig. 7b) as drawn

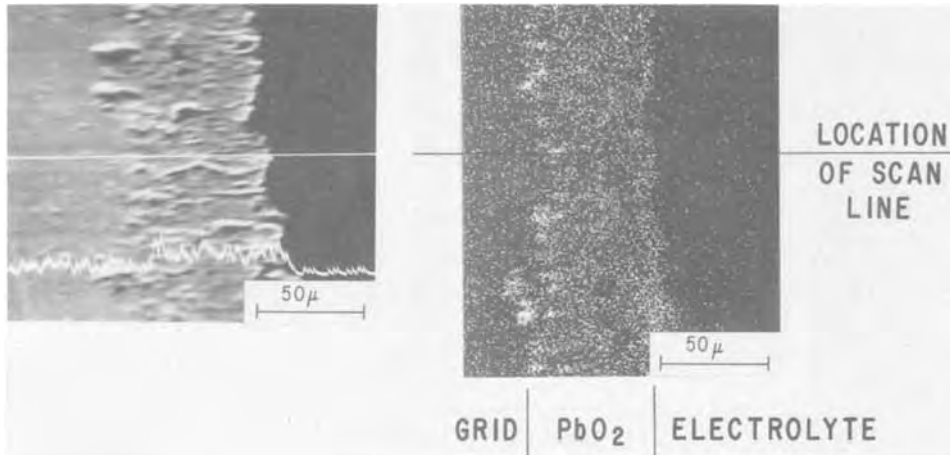


Fig. 6. (a, left) BSE micrograph of Pb-Sb with sulfur x-ray scan; (b, right) sulfur x-ray map of same location. 600X.

on the periphery of the micrographs. This location of  $\text{PbSO}_4$  at the grid-oxide interface was found consistently in different samples as well as in different locations on the same sample.

#### Discussion

The corrosion data of the lead alloys can be represented either by a linear or by an exponential growth rate. In the early stages of corrosion, these descriptions of the oxide growth are quite similar (Fig. 1-3). The last column of Table I gives a slope for the curve  $\log \Delta y = \log k' \pm x \cdot \log t$ . With one minor exception, this slope  $x$  has a value of one (linear rate) or smaller.

Extrapolation of high temperature results by others (3, 6, 7) to room temperature with an Arrhenius-type function would lead to the same conclusions for the beginning of corrosion. The mechanism of the corrosion process cannot be described precisely (1) without knowing the details of the film structure; for example, the extent of porosity. However, a linear rate implies that the reaction at one of the interfaces, rather than ionic migration through the film, is rate determining. While the film is still thin, this seems plausible. Furthermore, if it is assumed that for all cases a linear rate represented the maximum corrosion rate, it is

possible to make estimates of the minimum lifetime of a battery in which failure is due to grid corrosion.

It is possible to compare the results of this work with that of others, although each investigator chooses different experimental conditions and reports corrosion data differently. As pointed out above, lead alloy corrosion data have been given as percentage grid growth (5, 6) or in terms of the amount of lead removed during corrosion (4, 7). In this study, a direct metallographic procedure was chosen, which had been successful for the determination of silver tarnishing in halogen vapors (12). Assuming that the  $\text{PbO}_2$  film has a porosity of 20%, then  $1\mu$  of lead lost per square centimeter (1.135 mg) corresponds to a buildup of  $1.51\mu$  of oxide layer. If the original grid thickness is given, these relative measures can also be related to the percentage increases of the grid thickness.

In the Bell Laboratories work (6), pure Pb and the Pb-Ca alloys were described by a corrosion rate law with an exponential time dependence larger than linear. This is the one example in which the corrosion rate increased with time. The high temperature corrosion, extrapolated to room temperature and to shorter periods of time, gave 0.90 and  $18\mu/\text{yr}$  for Pb-Ca and Pb-Sb alloys as compared with the values of  $52\mu/\text{yr}$  (electrolyte-flooded) and  $66\mu/\text{yr}$  (electrolyte-starved) in the present work. The difference may be traced to and may be consistent with the use of different acid concentration (1.21 vs. 1.28 sp gr  $\text{H}_2\text{SO}_4$ ), different anodic potentials (1.17 vs. 1.34V), different grid design and preparation (cast vs. wrought), and also different surface area/cross-sectional area ratios. Finally, the Pb-Ca data were extrapolated in Ref. (6) by a quadratic equation which would give lower values for the initial stages of corrosion than a linear one.

In other reports on Pb-Ca grid corrosion, Willihnganz (3) measured over-all dimensional changes of the grid so that the observed percentage growth cannot be related to actual scale growth. However, Feliu *et al.* (13) determined weight losses corresponding to a growth of  $4.4\text{--}16\mu$  for oxide layers on Pb-Ca alloy in a 100-day period. The values depended on grain structure and current density and correspond to the present 100-day result of  $14\mu$  for the binary electrolyte-flooded Pb-Ca alloy.

A further interesting comparison exists in the case of Pb-Sb grids, which Maskalick (7) tested under the more rigorous condition of battery cycling, when the grid is in a lower, more active potential region for at least part of the test time. The corrosion rate extrapolated to  $25^\circ\text{C}$  was  $230\mu/\text{yr}$  as compared with  $66\mu/\text{yr}$

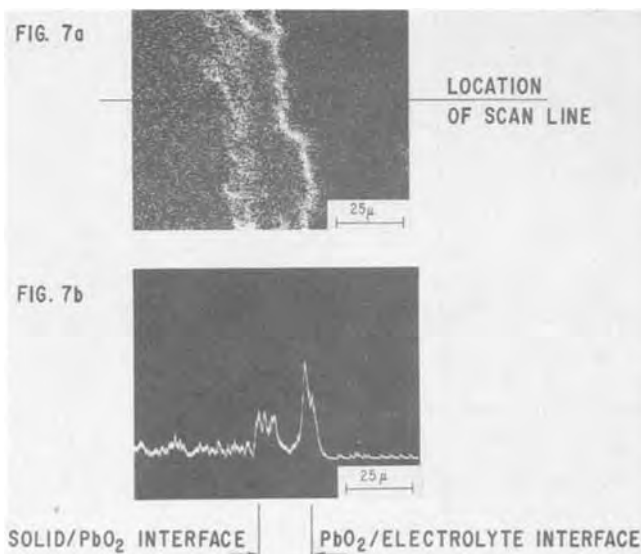


Fig. 7. (a, top) Sulfur x-ray scan on Pb-Ca alloy; (b, bottom) sulfur x-ray map of same location. 1000X.

for Pb-Sb in the electrolyte-starved condition of the present experiments.

The optical and electron microscopy showed the expected intergranular progress of the Pb/Ca alloy corrosion. It has been pointed out that the effect of grain structure on corrosion will be different for wrought and cast grids (4). In the present study, wrought grids were used; the binary Pb/Ca and ternary Pb-Ca-Sn showed about the same extent of corrosion. This was to be expected on the basis of the relation between corrosion rate and grain size (4). The latter were determined for the two alloys to have ASTM grain size numbers 11.5 and 11.1 (14). This corresponds to average grain sizes of 7.5 and 6.8 $\mu$ , respectively.

Another possibly important observation was that of a PbSO<sub>4</sub> layer between the metal and oxide. This was observed only in the case of the Pb-Ca alloy. The x-ray map and scan of Fig. 7 clearly show the presence of PbSO<sub>4</sub> at the location for the Pb-Ca alloy. They do not, however, indicate a continuous barrier layer which had been observed by others (11) during cycling tests. That work attributed poor cycle life of cells with Pb-Ca grids to the presence of the PbSO<sub>4</sub> interface layer, which was said to enhance shedding of active material. In our test, the site of PbSO<sub>4</sub> concentration may extend over a distance of about 1 $\mu$ . Only the presence of PbSO<sub>4</sub> is indicated, not the inhibition of an electrode reaction. At least for the overcharge condition, corrosion was neither accelerated nor inhibited by the presence of PbSO<sub>4</sub>.

#### Acknowledgments

The authors wish to thank D. G. Fink for the preparation of the metallographic samples and W. T. Hat-

field for the electron microprobe analysis. The binary and ternary calcium alloys were supplied by the St. Joe Minerals Corporation.

Manuscript submitted Sept. 11, 1975; revised manuscript received Nov. 20, 1975. This was Paper 29 presented at the Washington, D.C., Meeting of the Society, May 2-7, 1976.

Any discussion of this paper will appear in a Discussion Section to be published in the December 1976 JOURNAL. All discussions for the December 1976 Discussion Section should be submitted by Aug. 1, 1976.

Publication costs of this article were partially assisted by General Electric Company.

#### REFERENCES

1. J. J. Lander, *This Journal*, **103**, 1 (1956).
2. H. E. Haring and U. B. Thomas, *Trans. Electrochem. Soc.*, **68**, 293 (1935).
3. E. Willihnganz, *Electrochem. Technol.*, **6**, 338 (1968).
4. M. V. Rose and J. A. Young, 5th International Lead Conference, Paris, November 1974.
5. P. C. Milner, *Bell System Tech. J.*, **49**, 1321 (1970).
6. A. G. Cannone, D. O. Feder, and R. V. Biagetti, *ibid.*, **49**, 1279 (1970).
7. N. J. Maskalick, *This Journal*, **122**, 20 (1975).
8. J. J. Lander, *ibid.*, **98**, 220 (1951).
9. J. J. Lander, *ibid.*, **98**, 213 (1951).
10. J. L. Weininger and C. R. Morelock, *ibid.*, **122**, 1161 (1975).
11. S. Tudor, A. Weisstuch, and S. H. Davang, *Electrochem. Technol.*, **3**, 90 (1965); **4**, 406 (1966); **5**, 21 (1967).
12. J. L. Weininger, *This Journal*, **105**, 577 (1958).
13. S. Feliu, L. Galán, and J. A. González, *Werkstoffe Korrosion*, **23**, 554 (1972).
14. A. T. Balcerzak, Private communication.

## Effect of Heat-Treatments on Magnetic Properties of Electroless Nickel Alloys

Morton Schwartz\*<sup>1</sup> and Glenn O. Mallory\*

The Richardson Company, Allied-Kelite Products Division, Los Angeles, California 90012

#### ABSTRACT

Electroless deposits from various ammoniacal and acid formulations were evaluated for their ferromagnetic properties and the effects of artificial aging on these properties. Deposits from ammoniacal solutions were ferromagnetic as deposited. Deposits from acid solutions were nonferromagnetic. After heat-treatment, all deposits exhibited ferromagnetism through a maximum, the temperature-time relationship being different for each deposit. This phenomenon appeared to be related to the type of ligand in the solution and to the substrate rather than the phosphorus content of the deposit. Ammoniacal deposits retained magnetism at higher levels after heating for 96 hr at 400°C than any of the acid systems with the pyrophosphate deposit values being higher than citrate deposits. Deposits on aluminum substrates exhibited higher magnetization than on brass substrates or foils separated from substrates.

Electroless nickel deposits exhibit inferior magnetic properties when compared to electrodeposited nickel (1), in fact, deposits with high phosphorus content are nonferromagnetic (2). Such deposits are used as undercoats for subsequent hard magnetic cobalt alloys (containing phosphorus and other elements) in memory systems. The very fine polycrystalline solid solution, bordering on amorphous or liquid (glass)-like metastable structure (3-5) of electroless Ni-P deposits provides the structure required for nonferromagnetic behavior. Such structure also minimizes epitaxial growth of subsequent deposits.

For computer applications, it would be desirable to increase the hardness of the electroless nickel undercoats by suitable heat-treatments which have been studied extensively (6-8). Unfortunately, after artificial aging the electroless Ni-P deposits develop ferromagnetic properties which may affect the over-all magnetism of the memory disk or drum. This change in ferromagnetic behavior is a result of the developing equilibrium between the newly formed Ni<sub>3</sub>P intermetallic phase and the Ni phase, with increasing grain size and heterogeneity of the deposit.

It would also be desirable in some applications to eliminate the use of a thin deposit of rhodium or chromium as a final wear resistant surface (with its adverse effect on magnetism). In such cases, disks and drums are heated in air to produce the desirable thin

\* Electrochemical Society Active Member.

<sup>1</sup> Present address: 3017 Oakhurst Avenue, Los Angeles, California 90034.

Key words: electroless nickel, magnetism, heat-treatment, computer.

Table I. Electroless solution compositions and conditions for binary Ni-P alloys

Constituents, g/liter	Acid*				Alkaline*	
	1 Acetate <sup>a</sup>	2 Hydrac	3 Citrate <sup>a</sup>	4 Lactate+ propionate	5 Citrate	6 Pyro- phosphate
NiSO <sub>4</sub> · 6H <sub>2</sub> O	35	35	30 <sup>b</sup>	24	30 <sup>b</sup>	25
NaH <sub>2</sub> PO <sub>4</sub> · H <sub>2</sub> O	10	10	10	24	10	25
H <sub>2</sub> C-COONa · 3H <sub>2</sub> O	10	—	—	—	—	—
H <sub>2</sub> C-CH(OH)COONa	—	10 <sup>c</sup>	—	—	—	—
Na <sub>2</sub> C <sub>2</sub> O <sub>7</sub> · 2H <sub>2</sub> O	—	—	10	—	100	—
H <sub>2</sub> C-CH(OH)COOH <sup>d</sup>	—	—	—	30.7	—	—
H <sub>2</sub> C-CH <sub>2</sub> -COOH	—	—	—	2.2	—	—
NH <sub>4</sub> Cl	—	—	—	—	50	—
Na <sub>2</sub> P <sub>2</sub> O <sub>7</sub>	—	—	—	—	—	50
pH	5-5.5	5-5.5	5.2-5.8	4.5-5.0	9-9.5	10-10.5
T °C	90-95	90-95	90-95	90-95	90-95	70-75
Rate of deposition						
μm/min on brass	0.43	0.24	0.13	0.21	0.13	0.25
on Al	0.53	0.29	—	0.21	—	0.32
Thickness of deposit						
μm on brass	2.56	3.2	2.54	2.54	3.81	2.54
on Al	3.2	3.85	—	2.54	—	3.81
Foil	5.1	5.1	7.87 (6.33 <sup>a</sup> )	10.16	10.16	—
w/o P in deposit	7-9	7-9	7-9	9-10	5-7	4-6
Reference	1	1	1	13	1	14

\* NaOH used for neutralization in acid baths, NH<sub>4</sub>OH in alkaline baths.

<sup>a</sup> Although proprietary (General American Transportation Company), composition made up as published (with 0.002 ppm Pb<sup>++</sup> as stabilizer).

<sup>b</sup> Deposits from low pH (3.8-4.0) baths of same composition were also studied. The rate of deposition decreased to about 0.08 μm/min and the phosphorus content of the deposit increased to about 12-16 w/o P in all cases.

<sup>c</sup> NiCl<sub>2</sub> · 6H<sub>2</sub>O.

<sup>d</sup> A 50 g/liter Hydrac bath (Hydrac II) was also used. Deposits were dull and rough and did not exhibit any significantly different magnetic properties.

<sup>e</sup> Lactic acid, 88%.

oxide coating on the magnetic cobalt alloy surface which improves its wear characteristics and the "ridability" of the heads. When such thermal treatments are used, the electroless Ni-P undercoat may develop ferromagnetism.

This phenomenon of increasing ferromagnetic behavior has been reported by several investigators. Gorbunova and Nikiforova (9) reported quantitative data indicating that deposits from acid solutions are nonferromagnetic while deposits from alkaline (citrate) solutions are magnetic ( $H_c = 4.1$  oe,  $B_r = 45$  G,  $B_s = 140$  G). After heat-treatment at 400°C, 1 hr, both types of deposits showed increased magnetics with the coercive force ( $H_c$ ) reaching 140 oe, the alkaline solution deposits achieving  $B_r$  3000-3300G/ $B_s$  3400-3700G, and the acid deposits less than one-half of these values. Gorbunova *et al.* (9a) extended their studies on the ferromagnetic behavior of deposits (on copper substrates) from the ammoniacal citrate solutions and concluded that the as-plated magnetic properties depended on the phosphorus content of the deposit which, in turn, was determined by the composition of the solution. Further, the variations of magnetic properties of the deposits due to annealing temperatures were also considered as related to the phosphorus content and changes in phase and structural transitions. Bondar (10) reviewed results obtained mostly by Russian investigators relating the magnetic changes to P content and being due to structural transformations and formation of the Ni-Ni<sub>3</sub>P system; neither methods of measurement nor substrates used were indicated. Data (11) on the coercivity of deposits from various alkaline citrate formulations indicate that all these deposits exhibit low coercivities in the as-plated condition with increased values after heat-treatment at 350°C. Alberts *et al.* (12) observed that citrate formulations produced deposits with coercive forces ( $H_c = 10-80$  oe) when ammonia was used to maintain the pH of the solutions and that zero coercivity was obtained when sodium hydroxide was used; these results were reflected in the considerable differences in the phosphorus content of the deposits (3-6 w/o P in NH<sub>3</sub> controlled solutions and 10-17 w/o P in NaOH controlled solutions, devoid of ammonium ions).

The purpose of this investigation was to evaluate the magnetic characteristics of electroless nickel-alloy deposits from various electrolytes and to study the ef-

fects of brass and aluminum (6061) alloy substrates and thermal exposure on these properties. The selection of these substrates was determined by the practice of utilizing brass Hull cell panels as a convenient substrate to check out the solutions and then actually producing deposits on aluminum alloy disks or drums.

### Experimental

The electroless plating solutions were prepared from individually purified (carbon-treated) stock solution concentrates of the constituents. Deionized water was used exclusively. Tables I and II give the use compositions and conditions. (Bath 8 was made up with proprietary concentrates and used according to supplier directions.) The deposits produced from each bath are henceforth identified by the designated bath number.

A 100-125 cm<sup>2</sup>/liter area to volume relationship was employed, the total volume of each solution being 1.8 liter. Solutions were stirred by occasional manual agitation of the panel. Each panel was plated in a freshly prepared solution and was then sliced into test specimens for heat-treatment and testing, thus ensuring uniformity of deposit for each test.

The brass Hull cell panels (8.5 × 12.5 × 0.33 cm) were cleaned with solvent, followed by an alkaline cleaner and acid dip (10% v/v HNO<sub>3</sub>). Electroless

Table II. Proprietary electroless systems

Conditions	Binary	Ternary			Quaternary
	7 <sup>a</sup>	8 <sup>b</sup>	9	10	11 <sup>a</sup>
pH	9-9.5	4.5-5	4.5-5	10.5	4.5-5
T °C	90-95	90-95	90-95	70-75	90-95
Rate of deposition, μm/min					
Brass	0.12	0.09	0.29	0.17	0.29
Al	—	0.11	0.33	0.20	—
Thickness of deposits, μm					
Brass	2.54	2.54	2.54	2.54	2.54
on Al	2.6	3.18	2.92	2.92	—
Foil	—	12.7	10.16	22.86	—
Deposit composition, w/o	17 Mo -Ni	1 Cu 15 P -Ni	2 Cu 16 P -Ni	4 Cu 5 P -Ni	2 Cu 8 SN 16 P -Ni

<sup>a</sup> Patents applied for, Allied-Kelite Division, The Richardson Company.

<sup>b</sup> M. Gulla, Shipley Company, Incorporated, U. S. Pat. 3,764,352 (1973).



plating was initiated by contact with an aluminum wire.

The aluminum (6061) alloy panels ( $7.5 \times 15 \times 0.078$  cm) were prepared by cleaning in a suitable inhibited alkaline cleaner, followed by an acid cleaner and a 15-20 sec dip in a zincate solution. All electroless plating solutions were made up with nickel sulfate to minimize corrosive effects of the anion. The rate of deposition on the aluminum substrates was 10-25% higher than on brass substrates.

The electroless nickel foils were produced by plating on aluminum substrates which were masked on one side. The mask was removed with solvent and the aluminum dissolved in 1M NaOH containing sodium gluconate. The foils were cut into 0.64 cm (0.25 in.) wide strips and aged. Most of the (as-plated) electroless nickel foils were quite free of stress and easily handled; a notable exception being the deposit from the pyrophosphate solution which was under considerable tensile stress and could not be used. After heat-treatment (especially at 400°C), many of the foils became brittle and some were destroyed in handling.

The sulfamate nickel deposits were all plated from the same solution (3.5 liter) using the above preparation cycles and the technique of immersion into the plating solution with a "live" lead. Electrodeposited foils were produced by plating on a partially passivated stainless steel panel and removed by peeling off the deposit after grinding the edges. The foils were reduced 0.64 cm (0.25 in.) on each edge to minimize current density effects. The sulfamate solution composition and plating conditions were

nickel sulfamate (anhy.)	325 g/liter
(nickel metal)	75 g/liter)
boric acid	40 g/liter
chloride	2 g/liter
anti-pit	0.35 g/liter
pH	4.0
temperature	55°-60°C
current density	2.7 A/dm <sup>2</sup>
deposition rate	0.5-0.55 $\mu\text{m}/\text{min}$

All the deposit thicknesses were determined by supermicrometer measurements using 1 oz pressure on the anvil.

Heat-treatment of test strips (0.635 cm wide) was done in Hodgkins ovens, controlled with Weather-Measure TPC-N Type K controllers and powerstats to prevent overshooting. Chromel-Alumel thermocouples were attached to the specimen containers and checked with reference thermocouples and a Leeds & Northrup potentiometer. Temperature variations were determined to be within  $\pm 5^\circ\text{C}$ .

The heat-treatment was carried out in air. This was considered justified since it is "normal" practice in the magnetic plating of disks and drums. Further, it appeared that the superficial oxides formed did not seem to influence the magnetic measurements significantly. It should be noted that the interference oxide colors formed varied as a result of the type of solution used.

The magnetic characteristics were measured with a calibrated low frequency (60 Hz) hysteresis loop tester. This instrument consists of a large coil conducting sufficient current to provide a coercive field of 1000 oe. A smaller coil (wrapped around a Teflon tube) is adjusted (zeroed) to be at rest, eliminating any distortion. An 0.635 cm wide test strip (minimum length 3.2 cm),<sup>2</sup> attached to a micarta holder, is inserted into the Teflon tube. The test specimen, if magnetic, becomes saturated, distorting the field. This distortion is picked up and displayed on an oscilloscope

<sup>2</sup> Unfortunately, some of the aged electroless nickel foils were broken remnants and shorter. This could reduce the magnetization values ( $B_s$  and  $B_r$ ) but would not affect  $H_c$  significantly. No distinction of the shorter-length foils were noted at the time of measurement.

as the material's characteristic magnetic hysteresis loop.

The field intensity or field ( $H$ ) is measured on the x axis of the oscilloscope grid. The coercive force,  $H_c$  (oe), is the force required to demagnetize the material being tested and is measured at the loop intercept of the x axis.

The y axis of the grid measures the total flux (maxwells, cgs units) permeating the material. Since the field intensity ( $H$ ) is at least 4-5 times stronger than the coercive force,  $H_c$ , of the materials tested, it is assumed that the  $\phi_s$  measurements represent magnetic saturation.  $\phi_r$  or remanence is the magnetism retained when  $H = 0$  and is measured at the y intercept. These values are converted to flux density,  $B$  (G), by dividing the total flux (maxwells) by the total cross-sectional area (cm<sup>2</sup>) of the magnetic coating on the test specimen.

The values of  $B_s$ ,  $B_r$ , and  $H_c$  are required to characterize magnetic properties of the material. Hard magnetic materials are characterized by large  $B_r$  and large  $H_c$  values; soft magnetic materials have small  $H_c$  values. The ratio  $B_r/B_s$  can be used to indicate the squareness of the hysteresis loop. The ratio  $B_s/H_s$  is the permeability,  $\mu$ , of the material.

$B_s$  is a physical property of the composition of the magnetic alloy.  $B_r$  and  $H_c$  are structure sensitive which depend on strains, crystal structure and orientation, and anisotropy of the ferromagnetic phase (15). In precipitation-hardened alloys, such as these electroless nickel deposits, the ferromagnetic phase (Ni) results from the precipitation of the nonferromagnetic phase, Ni<sub>3</sub>P, from the supersaturated Ni-P alloys.

An increase in coercivity may involve the precipitation of individually high coercive particles which are small enough to exhibit single domain behavior. It may also be a result of an order-disorder transformation induced by heat-treatment.

Two dissimilarities with the hard magnetics of computers should be noted: (i) computers utilize frequencies in the megacycle range whereas the instrument required only 60 Hz, as stated, and (ii) bulk magnetics are measured, whereas a computer head measures some indefinite surface magnetism, the depth of which depends on the frequency, magnetic permeability, signal strength, gap, and (possibly) other parameters. Thus, the data obtained are valid for the magnetic properties of the coating per se, but require interpretation for application to computer memory systems or may be used as controls once correlation is established.

## Results and Discussion

The nickel electrodeposits exhibited similar saturation induction with some variation in remanent induction on both substrates and foil; the coercivities being the same. Table III shows the large changes and divergence in the induction which occurred as a result of the various heat-treatments. For example, the induction in foils increased 2.5-3X after aging 1 hr at 275°C, these increases being reduced by one-half when aged at 300°C for the same time. On aluminum substrates, induction increased 2-3X at 300°C, 48 hr treatment, while the smallest increase developed on brass substrates at 300°C, 1 hr. The effect on coercivity was reversed, i.e.,  $H_c$  reduced immediately for all deposits and then remained fairly constant with annealing times up to 72-96 hr. Thus there appears to be a temperature-time optimum, providing maximum ferromagnetism for each deposit, depending on the kind of substrate or lack of substrate.

*Ni-P deposits from ammoniacal solutions.*—The Ni-P alloys produced from ammoniacal solutions (baths 5 and 6) contained approximately the same phosphorus content yet exhibited different magnetic behavior as shown in Table IV. On substrates, the initial  $H_c$  of deposit 6 was higher than 5. The latter remained low (20-40 oe) until aged 72 hr at 300°C, or at higher tem-



Table III. Effect of heat-treatments on magnetic properties of sulfamate nickel electrodeposits

Heat-treatment Temp, °C	Time, hr	$H_c$ (oe)			$B_r$ (Gauss)			$B_s$ (Gauss)			$B_r/B_s$		
		f*	a#	b+	f	a	b	f	a	b	f	a	b
0	0	85	80	80	2725	2480	3285	3965	4335	4340	0.69	0.58	0.76
275	96**	45	35	45	8360	4335	4025	9910	5110	4645	0.84	0.85	0.87
300	1	30	40	40	4335	3250	4335	6810	4180	5775	0.64	0.78	0.78
	24	30	35	40	3715	5030	2355	5265	6035	2725	0.71	0.83	0.86
	48	X	30	40	X	6190	2480	X	8670	2785	X	0.71	0.89
	72	20	28	40	3095	6190	2785	4025	7275	3095	0.77	0.85	0.80
400	96	—	28	40	—	2100	1115	—	3470	1395	—	0.54	0.80
	1	20	40	40	4335	3960	3050	6810	5260	4100	0.64	0.75	0.74
	24	16	38	35	1980	2970	990	2660	4260	1395	0.74	0.70	0.71
	48	X	38	30	X	2600	865	X	3960	1360	X	0.66	0.64
	72	14	38	—	620	1980	S/I	1050	3400	S/I	0.59	0.58	—
	96	—	38	—	—	680	S/I	—	1175	S/I	—	0.58	—

\* Foils, deposit thickness = 5.1  $\mu$ m.# Aluminum (6061) substrate, deposit thickness = 2.54  $\mu$ m.+ Brass substrate, deposit thickness = 2.54  $\mu$ m.

\*\* 275°C, 1 hr aging for foils only.

X = lost (destroyed); S/I = slight indication of magnetism.

Table IV. Effect of heat-treatments on magnetic properties of deposits from ammoniacal solutions

Bath	Heat-treatment Temp, °C	Time, hr	$H_c$			$B_r$			$B_s$			$B_r/B_s$		
			f*	a**	b***	f	a	b	f	a	b	f	a	b
5	0	0	10		20	400		580	490		825	0.82		0.7
	275	96	—		20	—		1155	—		1490	—		0.78
	300	1	8		20	490		1155	640		1490	0.77		0.78
		24	12		40	735		1240	855		1570	0.86		0.79
		48	12		40	610		1240	920		1570	0.66		0.79
		72	14		140	535		1985	765		2315	0.7		0.86
		96	—		140	—		1570	—		1985	—		0.79
		375	2		120	—		2810	—		2895	—		0.97
	400	1	50		120	735		2230	855		2560	0.86		0.87
		2	—		120	—		2480	X		2810	X		0.88
		24	X†		120	X		1490	X		1985	X		0.75
		48	X		120	X		1410	X		1820	X		0.77
		72	X		120	X		1490	—		1655	—		0.9
		96	—		150	—		1075	—		1320	—		0.81
6	0	0	90	40		600	125		1200	370		0.5		0.34
	300	1	95	55		1410	1550		2050	2170		0.69		0.71
		24	100	70		1775	1860		2060	2540		0.86		0.73
		48	115	65		2375	2010		2875	2630		0.83		0.76
		72	110	60		1750	2710		2125	3250		0.82		0.83
	400	1	120	75		1875	3100		2500	3410		0.75		0.91
		24	110	80		1750	2710		2200	3020		0.8		0.9
		48	100	100		550	2475		650	2790		0.85		0.89
		72	—	105		S/I	2245		S/I	2555		—		0.88

\* Foil.

\*\* On aluminum.

\*\*\* On brass.

† Deposits too brittle to handle and oxidized.

peratures at which point  $H_c$  increased to 120-150 oe.  $H_c$  of deposit 6 increased gradually from 40 to 105 oe over the entire heat-treatment series. On aluminum substrates, the initial  $H_c$  was 90 oe, reaching a maximum of 120 oe at 400°C, 1 hr and decreasing as time was extended to 48 hr. A similar but reverse trend is shown for the magnetic induction, i.e., the deposit 5 initially was larger but was exceeded by 700-1000G by deposit 6 as a result of the heat-treatments, both deposits being on brass substrates.

Heating deposit 5 for 96 hr at 275°C produced the same magnetization as the 300°C, 1 hr treatment. Of the heat-treatment conditions tested, the maximum induction was obtained after aging at 375°C, 2 hr; this also gave the squarest hysteresis loop ( $B_r/B_s = 0.97$ ).

Number 5 foil gave much lower magnetisms. The maximum  $B_s$  was obtained after aging 48 hr at 300°C, while  $B_r$  reached a maximum after 24 hr at 300°C and 1 hr at 400°C. Heat-treatment at 400°C beyond 1 hr resulted in difficult to handle, brittle deposits which were quite oxidized. The  $H_c$  on the foils ranged between 8-14 oe.

Comparison of No. 6 deposits shows the magnetism induced was larger on aluminum substrates initially, reaching a maximum after 48 hr at 300°C and decreasing with further aging at 400°C. While the deposit on the brass substrate exhibited a flat "loop" with small induction, it responded immediately to heat-treatment exhibiting larger induction after 1 hr at 300°C, and

reached a maximum ( $B_r = 3100$ G,  $B_s = 3400$ G) after aging 1 hr at 400°C with a squareness of 0.91.

Figures 1 and 2a show the progressively increasing hysteresis loops and similarity of these ammoniacal

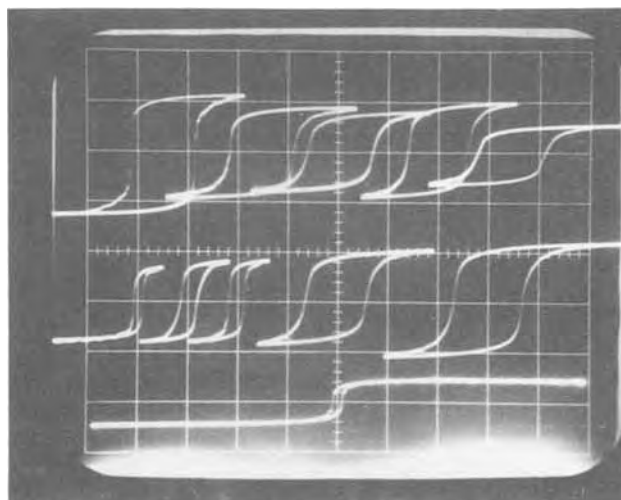


Fig. 1. Hysteresis loops; ammoniacal citrate deposits on brass. Left to right heat-treatment times: 1, 24, 48, 72, 96 hr. Lower series aged 300°C; upper, 400°C,  $\phi = 1$  maxwell/cm,  $H_c = 200$  oe/cm.

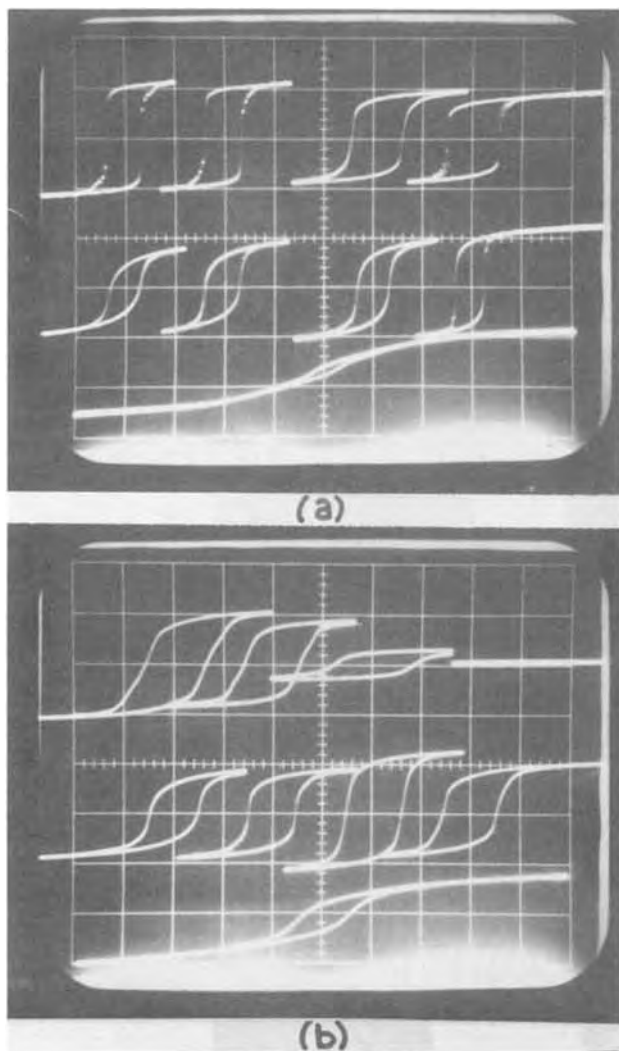


Fig. 2. (a) Hysteresis loops, ammoniacal pyrophosphate deposits on brass. Left to right heat-treatment times: 1, 24, 48, 72 hr. Lower series aged 300°C, upper, 400°C,  $\phi = 1$  maxwell/cm,  $H_c = 200$  oe/cm. (b) Hysteresis loops, ammoniacal pyrophosphate deposits on aluminum. Heat-treatment as (a),  $\phi = 1$  maxwell/cm,  $H_c = 200$  oe/cm.

solution deposits on brass when aged at 300°C and the decreasing magnetic induction and slightly increasing coercivity for the 400°C series. The effect of substrate on magnetic changes due to aging is seen when Fig. 2a and 2b are compared.

Along with bath 10 (see Table V) which was also an ammoniacal solution, the deposits from these solutions retained magnetism at considerably higher levels after heating at 400°C for 96 hr than any deposits from the acid baths.

*Ni-P deposits from acid solutions.*—Figures 3-6 show that the influences of the substrate and the solution's complexing ligand on the deposit's magnetic characteristics after various heat-treatments were also evident for acid solutions used at the usual pH ranges of 4.5-5.5.

With regard to brass substrates (Fig. 3), deposit 4 exhibited slightly larger magnetic induction than deposit 1, and continued to be magnetic after 96 hr at both 300° and 400°C whereas deposit 1 became nonmagnetic after 72 hr. Figures 4a and 5a show the actual hysteresis loops for these two deposits on brass. At 400°C, the citrate deposit (No. 3) was nonmagnetic after only 1 hr and the Hydrac deposit (No. 2) after 48 hr. The acetate deposit (No. 1) developed the same coercive and induction values for both temperatures, but showed a lower  $H_c$  (140 oe) and only slightly

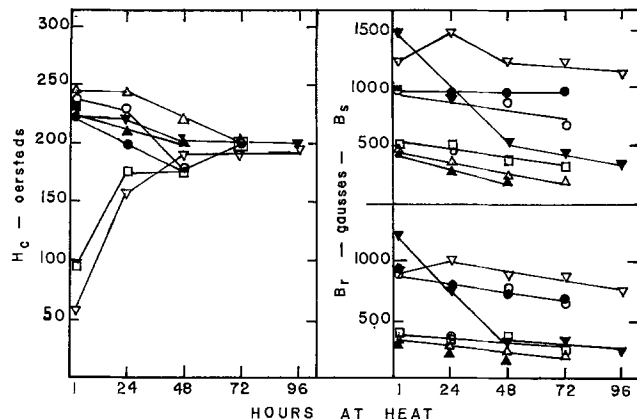


Fig. 3. Ferromagnetic properties of binary Ni-P alloys from acid solutions on brass. Acetate: ○ 300°C, ● 400°C; Citrate: □ 300°C, ■ 400°C; Hydrac: △ 300°C, ▲ 400°C; Lactate: ▽ 300°C, ▾ 400°C.

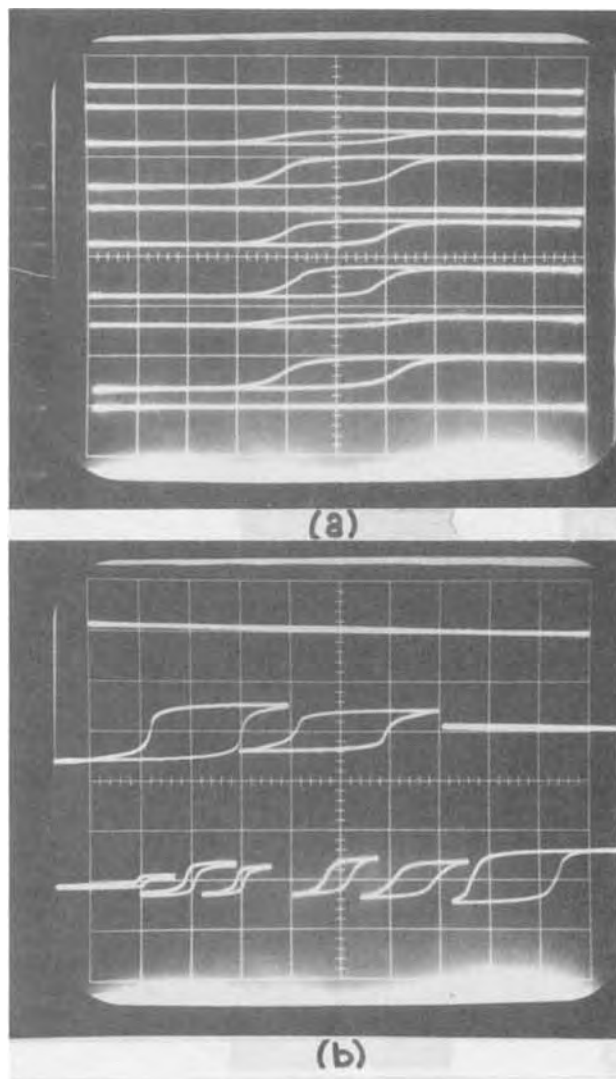


Fig. 4. (a) Hysteresis loops, acetate bath (pH 5.5) deposits on brass. Lower sequence, as plated; 2-6 aged 300°C, 1-96 hr, 7-10 aged 400°C, 1-72 hr,  $\phi = 1$  maxwell/cm,  $H_c = 200$  oe/cm. (b) Hysteresis loop, acetate bath (pH 5.5) deposits on aluminum. Lower series, left, as-plated, remainder aged 300°C, 1-96 hr. Upper series, aged 400°C,  $\phi = 1$  maxwell/cm,  $H_c = 200$  oe/cm.

smaller magnetic induction ( $B_r = 740$ G,  $B_s = 870$ G) when heated at 275°C for 96 hr. The  $H_c$  of deposits from all the baths varied through a range of 60-240 oe after 1 hr at heat, but converged to the narrower range of 190-200 oe after 72 hr. Saturation induction

Table V. Effect of heat-treatments on magnetic properties of ternary (Ni-Cu-P) deposits

Bath (deposit)	Heat-treatment		$H_c$ (oe)			$(B_r)$ (G)			$B_s$ (G)			
	Temp, °C	Time, hr	f	a	b	f	a	b	f	a	b	
8 (1 Cu 15 P -Ni)	0	0	0	0	0	0	0	0	0	0	0	
	300	1	S/I	S/I	S/I	S/I	S/I	S/I	S/I	S/I	S/I	
		24	80	60	30	12	150	125	20	300	370	
		48	105	40	30	50	200	250	55	500	620	
		72	120	80	30	37	300	250	50	700	500	
		96	—	120	30	—	500	125	—	750	250	
		1	120	190	120	25	300	370	35	450	620	
	400	24	200	220	200	50	350	370	65	500	620	
		48	210	S/I	200	60	S/I	250	80	S/I	310	
		72	230	S/I	220	35	S/I	250	45	S/I	310	
		96	—	0	240	—	0	125	—	0	185	
		0	0	0	0	0	0	0	0	0	0	
1		S/I	S/I	S/I	S/I	S/I	S/I	S/I	S/I	S/I		
9 (2 Cu 16 P -Ni)	300	24	S/I	40	S/I	110	S/I	S/I	S/I	270	S/I	
		48	80	60	S/I	60*	215	S/I	*	325	S/I	
		72	60	120	S/I	60*	215	S/I	*	270	S/I	
		1	80	S/I	35	60*	S/I	150	*	S/I	340	
		24	100	S/I	75	75*	S/I	125	*	S/I	250	
		48	100	S/I	S/I	60*	S/I	S/I	*	S/I	S/I	
	400	72	80	S/I	S/I	45*	S/I	S/I	*	S/I	S/I	
		0	0	48	10	10	140	540	2250	360	1620	2600
		300	1	24	16	12	220	3340	2230	330	3560	2480
			24	(75)	20	24	220	3020	1000	240	3180	2230
			48	16	14	22	5100	3235	750	660	3500	2000
			72	16	16	24	500	3570	1100	660	3775	1550
96	—		15	—	—	2965	—	—	3235	—		
1	20		85	50	600	4580	3470	830	5400	3530		
400	24	32	100	70	520	3910	2470	760	4450	3220		
	48	28	110	75	480	2965	2480	760	3500	2785		
	72	32	110	80	600	1890	2170	825	2150	2480		
	96	—	100	90	—	1620	2000	—	1750	2230		

\* Poor loops, difficult to measure; approximations only.  
S/I = slight indication of magnetism, f = foil, a = on aluminum, b = on brass.

generally followed the same trends as remanent induction.

Deposits from these solutions (citrate not run) on aluminum substrates (Fig. 6) developed a somewhat different pattern. All deposits were still magnetic after 96 hr at 300°C. At 400°C, deposit 4 was magnetic after 48 hr while the others became nonmagnetic after 24 hr. The coercivities remained spread over a wide range. Deposit 1 aged at 300°C behaved differently from the other deposits with a rising curve for both its lower coercivity and larger induction.

The changing hysteresis loops for deposits from baths 1 and 4 are shown in Fig. 4 and 5. While the changes in magnetics for deposit No. 4 are quite similar for both substrates, the differences due to substrates are quite evident with regard to acetate deposits.

The data obtained with foils produced from these acid solutions are shown in Fig. 7. The  $H_c$  of deposit 2 ranged from 140 to 200 oe, followed by deposit 4 and deposit 1. Deposit 3 showed large variations in  $H_c$  due to aging temperatures with aging at 400°C producing the highest  $H_c$ . At 300°C, only deposit 1 was magnetic after 1 hr aging, the other deposits required longer times to develop magnetic properties.

Deposits from acid baths operated at pH's below 4 contain at least 13-16% phosphorus. As-plated deposits from the citrate and acetate baths showed no ferromagnetism. Figure 8 shows the effect of aging these deposits. At 300°C, both deposits were ferromagnetic with the flux density and coercivity of the acetate deposit increasing steadily from 1 hr aging ( $B_r = 310G$ ,  $B_s = 620G$ ,  $H_c = 60$  oe) to 96 hr at heat ( $B_r = 930G$ ,  $B_s = 1240G$ ,  $H_c = 160$  oe). The citrate deposit exhibited maximum induction ( $B_r = 250G$ ,  $B_s = 500G$ ) after 24 hr at heat and became nonmagnetic after 72 hr with  $H_c$  increasing very closely to that of the acetate bath.

Aging at 400°C resulted in higher  $H_c$  (180-200 oe) but the magnetism was lost after 24 hr for the acetate deposit and after only 1 hr for the citrate deposit.

*Electroless ternary (Ni-Cu-P) alloys.*—The ternary deposits produced from proprietary acid formulations (baths 8 and 9, Table II) generally exhibited somewhat lower ferromagnetism (after heat-treatment)

than binary deposits from acid solutions. However, the amount of copper in the deposit influenced the magnetic properties as shown in Table V.

Neither deposit exhibited magnetism after aging at 300°C for 1 hr. Deposit 8 developed magnetism on both substrates and foil within 24 hr whereas deposit 9 gave only slight indications of magnetism (not measurable) on brass and considerably lower values on aluminum substrates.

Aging at 400°C initially resulted in increased magnetism for deposit 8 on both brass and aluminum substrates with the deposit on brass retaining some magnetism after 96 hr while only slight indications of magnetism were obtained after 24 hr on aluminum substrate.

Deposit 9 on brass substrates showed only slight indication of magnetism at 300°C with magnetism developing at 400°C within 1 hr but lost after 24 hr. The results obtained with aluminum substrates were reversed. These deposits developed less magnetism at either heat-treatment temperature, the difference being twice the copper content.

Table V also shows large increases in the coercivity of these deposits as a result of the higher aging temperature, especially for deposit 8 on brass.

The lower magnetic properties developed by deposits from these baths was also evidenced in foils. The  $H_c$  of foils produced in bath 9 was lower and decreased with time while the  $H_c$  of foil 8 increased with time at both temperatures.

The ternary deposit (Ni-4Cu-5P) from the ammoniacal bath 10 developed considerable magnetism while aging, being higher for deposits on aluminum substrates than on brass substrates. There was a gradual decrease in magnetic induction with time at both temperatures. This followed the same trend as the ammoniacal binary deposits with the hysteresis loops being very similar. The principal difference was the continued low coercivity at 300°C and the larger induction values. These deposits exhibited and retained the highest magnetic induction of all alloys tested.

*Electroless quaternary (Ni-2Cu-8Sn-16P) alloys.*—This alloy was interesting since it had the same composition as that from bath 9 with the added 8 w/o tin. However, this alloy also developed ferromagnetic prop-

Table VI. Effect of heat-treatments on magnetic properties of quaternary (Ni-Cu-Sn-P) deposits

Heat-treatment Temp, °C	Time, hr	$H_c$	$B_r$	$B_s$	$B_r/B_s$
0	0	—	0	0	—
250	1	—	S/I	S/I	—
	48	—	S/I	S/I	—
260	6	10	155	310	0.5
275	24	40	185	245	0.76
300	2	20	215	430	0.5
	24	50	435	745	0.58
	48	80	370	680	0.54
	72	120	620	805	0.77
325	2	100	1550	2165	0.72
350	2	120	1800	3100	0.6
375	2	140	310	370	0.84
400	2	140	310	370	0.84
	24	140	495	680	0.73
	48	135	435	620	0.7
	72	—	S/I	S/I	—
	96	—	0	0	—

S/I = slight indication of magnetism.

erties on aging, as shown in Table VI. Deposit 11 developed magnetism on brass substrates at 275°C reaching a maximum at 350°C ( $B_r = 1850\text{G}$ ,  $B_s = 3100\text{G}$ ,  $H_c = 120\text{ oe}$ ) which reduced sharply at 375°C. Referring to deposit 9, Table VI, it is seen that the ternary deposit exhibited only slight unmeasurable indications of magnetism at 400°C which was lost after 24 hr,

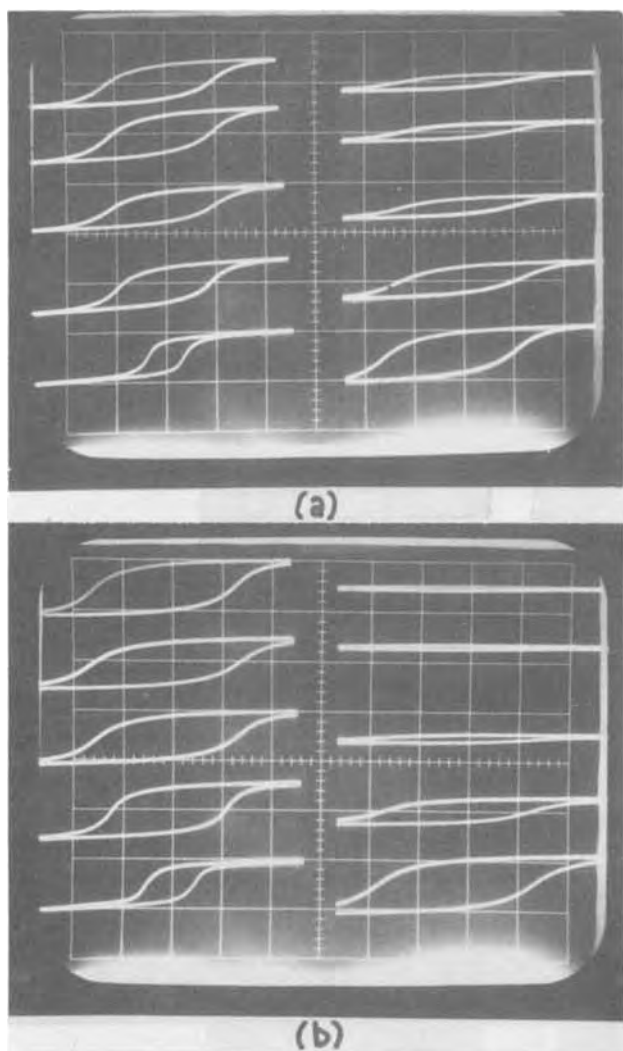


Fig. 5. Hysteresis loops, lactate-propionate deposit on brass. Left column, aged 300°C, 1-96 hr. Right column, aged 400°C, 1-96 hr,  $\phi = 1\text{ maxwell/cm}$ ,  $H_c = 200\text{ oe/cm}$ . (b) Hysteresis loops, lactate-propionate deposit on aluminum. Same order as (a),  $\phi = 1\text{ maxwell/cm}$ ,  $H_c = 200\text{ oe/cm}$ .

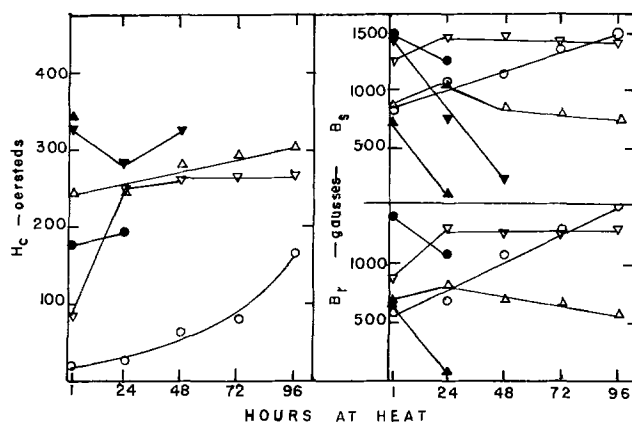


Fig. 6. Ferromagnetic properties of binary Ni-P alloys on aluminum from acid solutions. Acetate:  $\circ$  300°C,  $\bullet$  400°C; Hydrac:  $\triangle$  300°C,  $\blacktriangle$  400°C; Lactate:  $\nabla$  300°C,  $\blacktriangledown$  400°C.

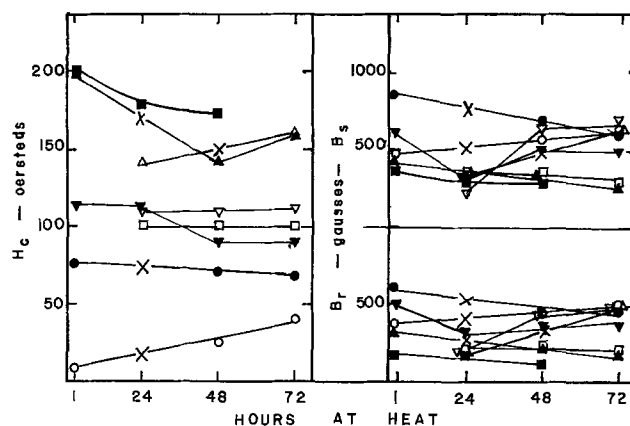


Fig. 7. Ferromagnetic properties of binary Ni-P alloy foils from acid solutions. Acetate,  $\circ$  300°C,  $\bullet$  400°C; Citrate:  $\square$  300°C,  $\blacksquare$  400°C; Hydrac:  $\triangle$  300°C,  $\blacktriangle$  400°C; Lactate:  $\nabla$  300°C,  $\blacktriangledown$  400°C.

whereas the quaternary alloy retained a larger magnetism until after 48 hr at heat. Thus it appeared that the tin increased the magnetization of the alloy due to artificial aging, probably by competing for the phosphorus with tin-phosphorus compounds forming at lower temperatures. It is suspected that the quaternary alloy is also deposited as a supersaturated solution.

*Electroless nickel-molybdenum alloy.*—Emission spectrographic analysis of deposit 7 (Table II) indicated that it was a nickel alloy containing 17 w/o Mo (a slight trace of phosphorus reported, 0.2%). This alloy did not show any evidence of ferromagnetism as deposited or after aging at 300° and 400°C for 96 hr. These negative results were obtained with 2.54  $\mu\text{m}$  deposits on both aluminum and brass substrates and 5  $\mu\text{m}$  thick foil (which did not appear stressed).

X-ray diffraction studies of this deposit on a steel substrate and as foil revealed a poorly ordered structure with crystallite size approximately  $60 \pm 10\text{ \AA}$ . The foil sample showed a higher degree of orientation in the (111) direction than in the (200) direction. A discrepancy between the broadening measurements for the (200) direction on the foil vs. the deposit on the substrate was attributed as most likely due to stress factors.

Heat-treatment of the plated substrate at 400°C, 1 hr in air showed only minor changes which could be attributed to stress relief. Heat-treatment at 500°C, 1 hr showed some structural changes and crystal growth with the (200) reflection indicating a grain size of approximately 150Å. However no evidence of new phase transformation was found. At 680°C, 1 hr (in nitrogen) considerable change was noted with the

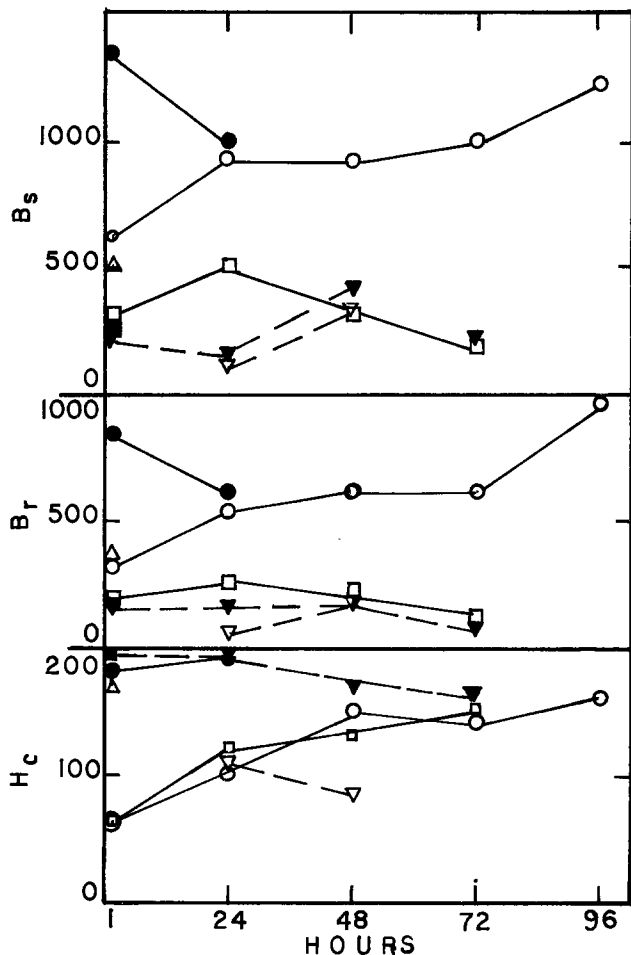


Fig. 8. Ferromagnetic properties of binary Ni-P alloys for low pH (<4) solutions. Acetate: ○ 300°C, ● 400°C; Citrate: □ 300°C, ■ 400°C, △ 375°C; Citrate foil: ▽ 300°C, ▼ 400°C.

crystallite size growing to about 800Å as determined from the (200) peaks.

When foils were heated at 600°C for 1 hr in air, a structural change occurred and a strong NiO phase was found along with a trace of MoO<sub>2</sub>.

These results help explain the absence of ferromagnetic properties after aging at 400°C. A further observation with regard to this alloy was that very little visible oxidation developed during aging at 400°C, even after 96 hr.

Deposit 4 on the aluminum substrate was selected for x-ray diffraction studies since it exhibited a gradual increase in magnetic induction at 300°C and a gradual decrease at 400°C aging cycles; these were accompanied by continued increasing coercivities (Fig. 5a and 5b). The as-deposited specimen indicated an amorphous appearing deposit, with an approximate crystallite size of 10-50Å. An aluminum substrate signal strongly showed through the deposit. The 400°C, 1 hr heat-treatment produced a marked change in crystal structure; the nickel showed a crystal size in excess of 1000Å and the new Ni<sub>3</sub>P phase with a minor amount of surface oxide (NiO) appeared. Aging for 48 hr produced a somewhat stronger Ni<sub>3</sub>P phase with some evidence of diffusion with the substrate producing a NiAl<sub>3</sub> phase. Deposits aged at 72 and 96 hr appeared to be similar with Ni<sub>3</sub>P and NiAl<sub>3</sub> peaks becoming stronger; elemental Ni showed up only as a minor constituent or phase.

These observations agree quite well with the sequence of hysteresis loops in Fig. 5b. The development of crystal order is one of the transformations induced by heat-treatment; this alters the magnetic properties significantly. The high coercivities exhibited by most of these electroless alloys appears to be the result of

an order-disorder transformation with the ordered phase precipitating in a matrix of the disordered solid solution (15). The amount of phosphorus in the deposit determines the relationship of the phases developing (3, 6) and influences the magnetic properties. The influence of substrate being plated and the type of ligand in the plating solution on the magnetic properties of as-deposited film may be explained by composition of deposit and stresses produced. However, their continued effects after artificial aging remain unclear.

### Summary and Conclusions

Deposits from all ammoniacal solutions studied were ferromagnetic directly as plated. Of the acid solutions studied, only the acetate deposit on aluminum substrates showed some evidence of magnetism ( $B_r = 75G$ ,  $B_s = 175G$ ,  $H_c = 7.5$  oe) (Fig. 4b). The sulfamate nickel electrodeposits were considerably more magnetic.

Artificial aging increased magnetic induction of all deposits through some maximum, the temperature-time relationship being different for each deposit. The coercive force was also usually increased; however,  $H_c$  was lowered by one-half or more for the nickel electrodeposits.

The ferromagnetic properties of the deposits and their changes due to heat-treatment varied significantly on the two substrates as well as free foils. These variations were also related to the different ligands in the electroless solutions. Mallory (16) drew similar conclusions with regard to the corrosion characteristics of electroless deposits.

The ferromagnetism induced in foils deposited from acid solutions increased with aging at 300°C and decreased with aging at 400°C. This effect appeared to be related to the solution's complexing ligands in the following order: acetate > lactate-propionate > hydroxy-acetate > citrate. The order was reversed for increasing coercivities.

The same relationships might be considered for the deposits on substrates (from the same acid solutions). In the case of deposits on brass substrates heat-treated at 300°C, however, the order was slightly changed with lactate-propionate > acetate > citrate > hydroxy-acetate.

The low pH (high P) deposits also exhibited magnetism after aging at 300°C within 1 hr, with acetate deposits continuing to increase with time and the citrate deposit remaining fairly constant. At 400°C, the citrate deposit became nonmagnetic after 1 hr, the acetate deposit after 24 hr. It is suggested that whatever free nickel exists is dispersed in the developing predominant Ni<sub>3</sub>P matrix.

Ternary deposits from acid solutions developed only slightly lower induction than the binary alloys, the 2 w/o copper alloys being less magnetic than the 1 w/o copper alloy. The ternary (Ni-4Cu-5P) alloy from the ammoniacal solution, however, exhibited the largest magnetic induction with the lowest coercive force of all the alloys studied, suggesting a more complete transformation of a Cu<sub>3</sub>P phase with a larger amount of a nickel phase remaining.

Additions of 8 w/o tin to the Ni-2Cu-16P alloy resulted in increased magnetization of the alloy after artificial aging, reaching a maximum at 350°C and reducing sharply at 375°C. This also suggests a competing transformation with the presence of a nickel phase.

A Ni-17Mo electroless alloy did not develop any ferromagnetism with aging up to 400°C. This result was in agreement with the fact that no phase transformation occurred below approximately 600°C as determined by x-ray diffraction studies.

### Acknowledgments

The authors are indebted to Burton Magnekote Incorporated and especially its general manager, Mr. Mel

Sackter for extended use of the B-H loop tester and the many helpful discussions, to Professor J. R. Cady and the University of Southern California for use of the metallurgical laboratory and oven equipment. We thank C. Johnson and J. Foreman of The Richardson Company, Allied-Kelite Division, for preparation of the special alloy deposits.

Manuscript submitted Sept. 11, 1975; revised manuscript received Jan. 9, 1976. This was Paper 123 presented at the New York, New York, Meeting of the Society, Oct. 13-17, 1974.

Any discussion of this paper will appear in a Discussion Section to be published in the December 1976 JOURNAL. All discussions for the December 1976 Discussion Section should be submitted by Aug. 1, 1976.

Publication costs of this article were partially assisted by The Richardson Company.

#### REFERENCES

1. A. Brenner and G. Riddell, *J. Res. Nat. Bur. Std.*, **37**, 31 (1947); *ibid.*, **39**, 385 (1947); *Proc. AES*, **33**, 23 (1946); *ibid.*, **34**, 156 (1947); U. S. Patents 2,532,283-4 (1950).
2. W. Wesley, *Plating*, **37**, 732 (1950).
3. A. H. Graham, R. W. Lindsay, and H. J. Read, *This Journal*, **112**, 401 (1965).
4. A. W. Goldenstein, W. Rostoker, F. Schossberger, and G. Gutzeit, *ibid.*, **104**, 104 (1957).
5. (a) J. P. Marton and M. Schlessinger, *ibid.*, **115**, 16 (1968); (b) S. L. Chow, N. E. Hedgecock, M. Schlessinger, and J. Rezek, *ibid.*, **119**, 1614 (1970).
6. K. T. Ziehlke, W. S. Dritt, and C. H. Mahoney, *Metal Progr.*, **77**, 84 (1960).
7. W. G. Lee, *Plating*, **47**, 288 (1960).
8. J. P. Randin and H. E. Hintermann, *ibid.*, **54**, 523 (1967).
9. K. M. Gorbunova and A. A. Nikiforova, "Physico-Chemical Principles of Nickel Plating," (1960), Translated from Russian by the Israel Program for Scientific Translations, OTS 63-11003, Jerusalem (1963).
- 9a. K. M. Gorbunova, A. A. Nikiforova, Ym. M. Polukarov, and V. P. Moiseev, *Russ. J. Phys. Chem.*, **38**, 854 (1964).
10. V. V. Bondar, "Electrochemistry 1966." Translated from Russian by the Israel Scientific Translations, pp. 48-63, TT 70-50035, Jerusalem (1970).
11. W. Safranek, Editor, "The Properties of Electrodeposited Metals and Alloys," pp. 467-470, Elsevier, Amsterdam (1974).
12. G. S. Alberts, R. H. Wright, and C. C. Parker, *This Journal*, **113**, 687 (1966).
13. G. Gutzeit, *Plating*, **46**, 1158, 1275, 1377 (1959); **47**, 63 (1960); U. S. Pat. 2,882,294 (1958).
14. M. Schwartz, *Proc. AES*, **47**, 176 (1960).
15. "Cobalt Monograph," Edited by Centre D'Information DuCobalt, Chap. 9, pp. 296ff, France (1960).
16. G. O. Mallory, *Plating*, **61**, 1005 (1974).

## New Solid Conductors of Na<sup>+</sup> and K<sup>+</sup> Ions

J. Singer, W. L. Fielder, H. E. Kautz, and J. S. Fordyce\*

National Aeronautics and Space Administration, Lewis Research Center, Cleveland, Ohio 44135

#### ABSTRACT

A search through 40 structure types for solid conductors of Na<sup>+</sup> and K<sup>+</sup> ions has produced three types capable of ion transport with conductivities in the vicinity of 10<sup>-5</sup> (ohm-cm)<sup>-1</sup> at 25°C: (i) the pyrochlores NaTaWO<sub>6</sub> and NaTa<sub>2</sub>O<sub>3</sub>F; (ii) the bcc-Im3 phase of NaSbO<sub>3</sub>; and (iii) the Na and K niobates near the composition 2M<sub>2</sub>O·3Nb<sub>2</sub>O<sub>5</sub>. Of these five compounds, only the K niobate (whose structure has not been elucidated) can be fully sintered without transformation. A number of phase diagrams have been developed during the course of the work.

A search for new solid conductors of alkali metal ions was initiated after the publication of the work on beta alumina (1, 2) for the purpose of finding additional types of electrolytes for high energy-high power density secondary batteries. The approach was to select a variety of "open" structures, to prepare alkali metal representatives of these structures, and to screen them in the form of preliminary preparations by a suitable fast method. Direct measurement of ionic transport upon improved specimens was reserved for compounds showing promise in the screening. This report considers principally the five best conductors found in the search through about 40 structure types. Additional information related to this report may be found in the separate publications from the three laboratories involved, as referred to below.

#### Background and Structural Aspects of Materials with

$$\sigma_{\text{ION}} = 10^{-5}(\text{ohm-cm})^{-1}$$

*NaSbO<sub>3</sub> bcc, Im3.*—This phase was first reported by Kafalas (10) as the K analogue resulting from the high pressure transformation of the ilmenite form of KSbO<sub>3</sub>. On the basis of their structure analysis, Hong *et al.* (11) predicted and confirmed that the new phase would readily undergo ion exchange with salts of monovalent

ions and that, among the MBO<sub>3</sub> analogues, the Na exchange product would exhibit the highest ion mobility. They further report that (i) NaSbO<sub>3</sub> (Im3 phase) indicated in preliminary a-c measurements on ionic conductivity like that of  $\beta$ -alumina; (ii) its metastability prevents sintering to dense specimens; and (iii) in ceramic form, it is slowly attacked by molten Na.

The structure of the Im3 phase may be briefly described as follows (11): M<sup>+</sup> ions in disordered partial occupancy of sites in tunnels which consist of face-shared octahedra running parallel to the [111] directions. The mobility of a given M<sup>+</sup> ion depends on its size relative to the openings of the oxygen octahedra, Na<sup>+</sup> appearing to be at an optimum.

During the course of this work, it was first suggested that the F<sup>-1</sup> ion could stabilize the Im3 phase to permit 1 atm direct synthesis (12) and then demonstrated that this was feasible (5, 6, 12, 13). Also, it was found (5) that the Na compound produced by ion exchange from TlSbO<sub>3</sub> or KSbO<sub>3</sub> may incorporate up to 25% more Na than the ion displaced.

*Pyrochlores.*—The general formula of the fully occupied pyrochlore structure of the cubic space group Fd3m may be written as A<sub>2</sub>B<sub>2</sub>X<sub>6</sub>X' or A<sub>2</sub>B'B''X<sub>6</sub>X' (14). Structural features of this structure type are: (i) the B<sub>2</sub>X<sub>6</sub> or B'B''X<sub>6</sub> groups represent a subarray of octahedra with the B atoms, like Ta, Nb, Sb, and others,

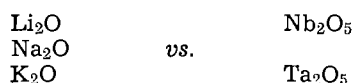
\* Electrochemical Society Active Member.

Key words: sodium pyrochlores, sodium antimonate, alkali niobates, solid electrolyte.

in the centers of the octahedra of the X<sub>6</sub> ions (which are usually O<sup>2-</sup>, OH<sup>-</sup>, Cl<sup>-</sup>, or F<sup>-</sup>); (ii) the A cations (of mono-, di-, or trivalent atoms) may be in any of several crystallographic sets, depending on the ions' size, charge, and number, thus offering ways to control A-ion mobility; (iii) the "seventh" anion (14, 15), X', which is similar to but not necessarily the same as X, is not bound to the octahedra; its site occupancy determines whether A ions have a clear path through the structure.

The ability of the pyrochlore structure to accommodate a wide range of atom species and to permit some degree of control over site occupancies is what made it a promising candidate. The defect pyrochlores measured in this program are NaTaWO<sub>6</sub> and NaTa<sub>2</sub>O<sub>5</sub>F. The former was suggested by Raveau (16-18) who also supplied a powder sample for the first specimens. The oxyfluoride was decided upon as possibly more resistant to reaction with a Na electrode than the W-containing pyrochlore might be. Both these pyrochlores are of the AB'B''X<sub>6</sub> type (19); the absence of the X' anion promised the maximum openness of the structure for the A cation. The size of the Na<sup>+</sup> ion is distinctly optimal for passage, with the handicaps that Na pyrochlores have to be made by ion exchange from the other alkali metal analogues and, concomitantly, are unstable at the temperatures required for sintering to fully dense bodies.

*Niobates* 2Na<sub>2</sub>O·3Nb<sub>2</sub>O<sub>5</sub>, 2K<sub>2</sub>O·3Nb<sub>2</sub>O<sub>5</sub>.—A number of compounds found in the six binary systems (6)



were tested for ionic conductivity by the methods described elsewhere (4). Among these, the only structure type found capable of appreciable alkali ion transport was the niobate close to, but not exactly at, the 2:3 composition, most probably at 41 K<sub>2</sub>O·59 Nb<sub>2</sub>O<sub>5</sub>. This compound has an orthorhombic unit cell with *a* = 7.822Å, *b* = 33.019Å, *c* = 6.481Å, and crystal growth of this phase was first reported by Nassau (21). Geometrical considerations have led to postulating that the K<sup>+</sup> ions are in layers between the Nb-O octahedra and that they should be mobile (6) as was demonstrated subsequently (see below). The crystal structure analysis has yet to be done.

Most of the other alkali niobates and tantalates, found to be tunnel structures more or less related to the bronzes, were screened out as being poor conductors.

### Experimental

*Specimen preparation.*—NaSbO<sub>3</sub>, Im3 phase.—A special high pressure apparatus was employed to transform KSbO<sub>3</sub> from the ilmenite form to the Im3 polymorph at about 20 k bar and 700°C (11). The pure transformation product, as verified by x-ray diffraction, was powdered and mixed with 10 times its molar quantity of molten NaNO<sub>3</sub>. The exchanged compound was water leached to remove excess nitrates and finally checked by x-ray diffraction for single phase. Disks of the NaSbO<sub>3</sub> were then made by pressing finely powdered material (~ 1μ) in a tungsten carbide die in a partial vacuum at 30,000 psi and held at pressure (~ 1μ) at 600°C for ~ 1 hr; 2 weight per cent (w/o) NaNH<sub>2</sub> was mixed with the starting powder to help achieve the high densities of the disks, ~ 95% of theoretical.

*NaSbO<sub>3</sub>·1/6 NaF, Im3.*—The K analogue was made by reacting a 2:1 weight ratio of K<sub>2</sub>H<sub>2</sub>Sb<sub>2</sub>O<sub>7</sub>·4H<sub>2</sub>O and KF at 900°C for 2 hr. Excess KF and KSbO<sub>3</sub> ilmenite was then leached with water and the pure fluorinated antimonate, probably Pn3, ion exchanged three times in molten NaNO<sub>3</sub> at 325°C. The product, Im3 with a nominal composition at about NaSbO<sub>3</sub>·1/6 NaF, was

analyzed chemically and by x-ray structure analysis (13). The F<sup>-</sup> stabilization of the phase unfortunately did not extend to permit sintering the Na compound without a protective atmosphere, and disks of NaSbO<sub>3</sub>·1/6 NaF had to be made the same way as the NaSbO<sub>3</sub> without F<sup>-</sup>; similar densities were obtained.

*NaTaWO<sub>6</sub>, pyrochlore.*—The first measurements were made on disks pressed from powder (supplied by Professor B. Raveau of Caen). The highest densities without transformation were obtained at 40,000 psi at 500°C with 2% by weight NaNH<sub>2</sub> added. Other preparations behaved similarly; they were made by ion exchanging the K analogue which had been synthesized from K<sub>2</sub>CO<sub>3</sub>, WO<sub>3</sub>, and Ta<sub>2</sub>O<sub>5</sub> by conventional techniques.

*NaTa<sub>2</sub>O<sub>5</sub>F, pyrochlore.*—This type of pyrochlore offered the possibility of greater chemical inertness than the W compound (5). The Rb analogue, but not the K, could be made directly from the components. RbF and Ta<sub>2</sub>O<sub>5</sub> were fired at 750°C in argon for two days; grinding and refiring had to be repeated for a total of three times to produce single phase. Single crystals were also prepared using excess RbF as a flux. A single 1150°C firing of a 4:1 molar ratio of RbF and Ta<sub>2</sub>O<sub>5</sub> yielded small crystals suitable for structure analysis. The Na exchange in this pyrochlore required two stages, first Rb → K, followed by K → Na.

Ceramic disks of NaTa<sub>2</sub>O<sub>5</sub>F were pressed under conditions similar to those for NaSbO<sub>3</sub>; however, lower densities were obtained. As with NaTaWO<sub>6</sub>, the oxyfluoride probably had some H<sub>2</sub>O in the lattice.

*2M<sub>2</sub>O·3Nb<sub>2</sub>O<sub>5</sub>.*—As fully described elsewhere (7), anhydrous disks of the K and Na compounds were difficult to prepare. The synthesis of single phase powder of the K compound by conventional solid-state reaction procedures required the exact ratio of K<sub>2</sub>CO<sub>3</sub>:Nb<sub>2</sub>O<sub>5</sub> for the composition 41K<sub>2</sub>O:59Nb<sub>2</sub>O<sub>5</sub>. The product, as well as the Na analogue made by ion exchange in molten NaNO<sub>3</sub>, was extremely moisture sensitive, and the following schedule was required to fabricate a sound, dense disk: single phase powder → prepress, 700 psi → isostatically press, 20,000 psi → dry at 220°C, 0.5 hr → sinter, 1050°C, 2 hr → seal into evacuated capsule; operations were conducted in a dry box or, where that was not possible, above 220°C, where H<sub>2</sub>O is not absorbed, all with minimal exposure to air.

*Electrical measurements.*—The five materials described in the foregoing were investigated by two- and four-probe a-c and d-c conductivity methods; elimination of the majority of candidate materials was based on special a-c methods, such as dielectric loss, which were less dependent on specimen perfection (3, 4) than conventional a-c methods. Blocking electrodes (sputtered Pt or C paint) were used for a-c conductivity measurements over a range of frequencies. Reversible electrodes were either (i) Na<sub>x</sub>WO<sub>3</sub> made directly on the sample (for Na compounds only) (20), (ii) propylene carbonate solutions (PC) of Na- or K-PF<sub>6</sub>, as appropriate, (iii) molten alkali metal, or (iv) fused NaNO<sub>3</sub>. The d-c current usually employed was 14 μA.

### Results

The data obtained are summarized in Table I and Fig. 1-4. Figure 3 includes conductivity data for beta alumina (curves 1 and 2) which are presented as validation of the simpler two-probe PC electrode procedure generally employed to evaluate ionic transport.

Table I. Ionic conductivity at 25°C for new ionic conductors

Substance	ΔE, kJ/m	σ 25°C, (ohm-cm) <sup>-1</sup>
NaSbO <sub>3</sub> , bcc (with or without 1/6 NaF)	42	10 <sup>-5</sup>
NaTaWO <sub>6</sub> and NaTa <sub>2</sub> O <sub>5</sub> F; pyrochlores	21	10 <sup>-5</sup>
2NaO·3Nb <sub>2</sub> O <sub>5</sub> and 2K <sub>2</sub> O·3Nb <sub>2</sub> O <sub>5</sub>	17	10 <sup>-5</sup>



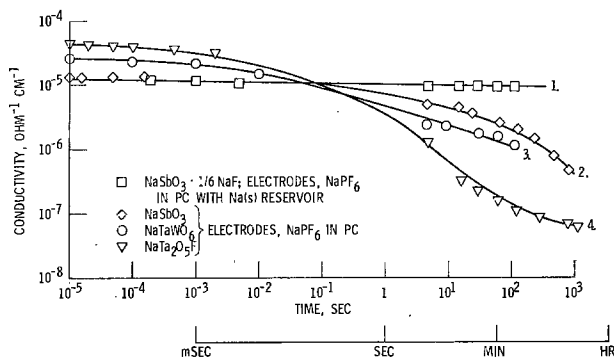


Fig. 1. D-C conductivity of cubic materials with time (300°K)

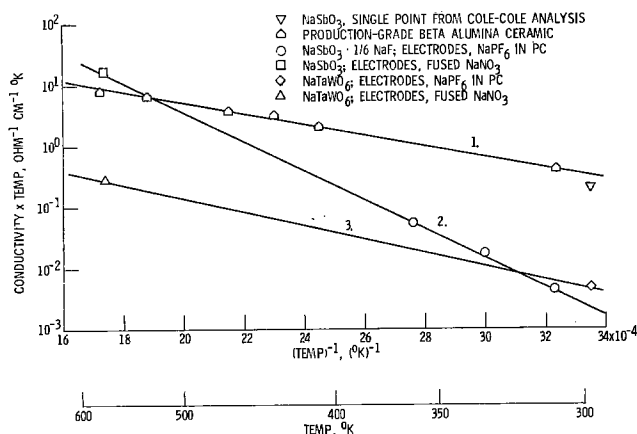


Fig. 2. Conductivity of cubic materials with temperature; comparison with "production" beta alumina ceramic.

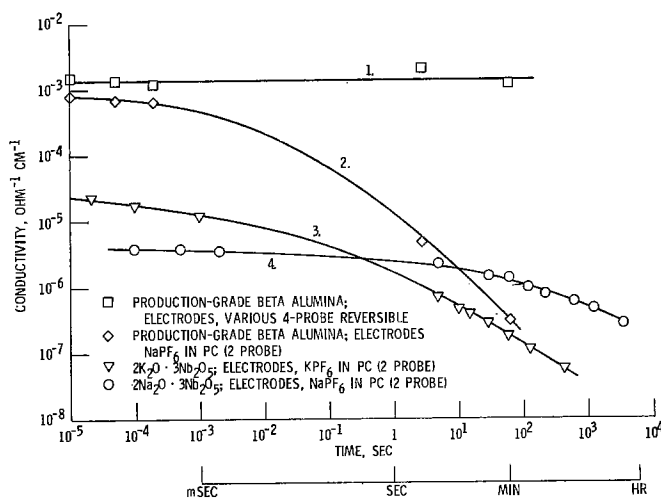


Fig. 3. D-C conductivity of planar materials with time (300°K)

The validation consists of the observation of but little more polarization occurring in the first  $10^{-2}$  sec after application of field in the two-probe experiment (curve 2) compared with the absence of polarization over the entire time of measurement where more completely reversible electrodes were used (curve 1). A similar comparison is presented in Fig. 1 for NaSbO<sub>3</sub>-Im3, where curve 1, taken with the more reversible electrodes (due to solid Na availability), coincides for  $10^{-1}$  sec with the two-probe PC data (curve 2). Rejected candidates showed early onset of polarization, from  $10^{-6}$  sec after application of field, and much more rapid polarization continuing linearly with time (9).

The conductivity values used in constructing Fig. 2 and 4 were the values given by extrapolation to the zero time axis of the two-probe PC data plus other types of data as indicated. Activation energies calculated from Fig. 2 and 4 are included in Table I.

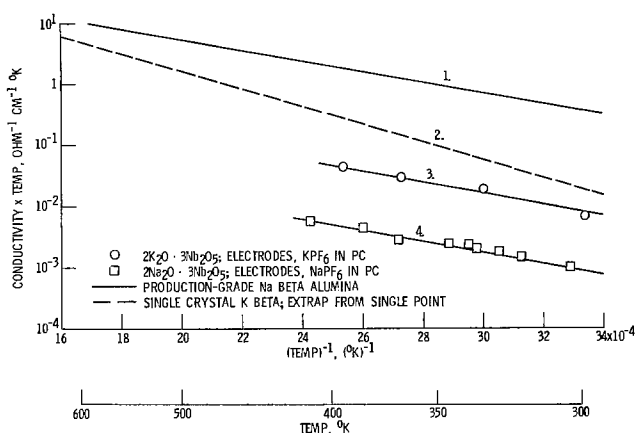


Fig. 4. Conductivity of planar materials with temperature; comparison with beta alumina.

## Discussion

About 40 structure types were surveyed in the total study (9). The five compounds of Table I, representing altogether three structure types, were the ones whose properties came closest to the goals of the survey. Among those eliminated were a number of "tunnel" types, i.e., with cations in unidirectional linear channels. Some of those screened out which have appeared elsewhere as being of some interest are hollandite (3, 22) and  $\beta$ -eucryptite (23).

Further development might increase the conductivities given in Table I. Ceramic quality could be improved for each of the compounds. For the pyrochlores, compositions other than those given here could well be explored, particularly for the purpose of trying more and less than eight alkali ions per unit cell. In the present work, further, the specimens of the pyrochlores at the time and conditions of measurement were probably not truly anhydrous, and water molecules in the lattice would be in sites to inhibit cation motion.

Of particular interest among the findings are: (i) the antimonate has about the same Na<sup>+</sup> ion conductivity as beta alumina at about 280°C, and (ii) the K niobate has about the same K<sup>+</sup> ion conductivity as K-beta ceramic may be presumed to have.

## Summary

Five compounds in three structure types have been discovered to be good solid conductors of alkali metal ions. A unique bcc form of NaSbO<sub>3</sub>, a unique orthorhombic layer structure of the composition 2M<sub>2</sub>O · 3Nb<sub>2</sub>O<sub>5</sub> (M = Na or K), and the Na pyrochlores NaTa<sub>2</sub>O<sub>5</sub>F, NaTaWO<sub>6</sub>, each show alkali ion transport with conductivities of  $\sim 10^{-5}$  (ohm-cm)<sup>-1</sup> at 25°C. Ion exchange is required to make each of these Na compounds; only the 2K<sub>2</sub>O · 3Nb<sub>2</sub>O<sub>5</sub> can, so far, be synthesized directly from the oxides, and so is the only one which can be sintered readily. The niobate is about as good a conductor of K<sup>+</sup> ion as is K-beta alumina; the NaSbO<sub>3</sub> compares well with Na beta at 280°C.

## Acknowledgments

The contributions to this work by the Sections under John B. Goodenough at Lincoln Laboratory and under Robert S. Roth at the National Bureau of Standards are gratefully acknowledged.

Manuscript submitted Dec. 2, 1975; revised manuscript received Jan. 13, 1976.

Any discussion of this paper will appear in a Discussion Section to be published in the December 1976 JOURNAL. All discussions for the December 1976 Discussion Section should be submitted by Aug. 1, 1976.

Publication costs of this article were partially assisted by NASA.



## REFERENCES

- J. T. Kummer and N. Weber, *Proc. Ann. Power Sources Conf.*, **21st**, (1967).
- J. T. Kummer and N. Weber, U. S. Pat. 3,404,035 (1968).
- J. Singer, H. E. Kautz, W. L. Fielder, and J. S. Fordyce, NASA TN D-7157 (January 1973).
- H. E. Kautz, J. Singer, W. L. Fielder, and J. S. Fordyce, NASA TN D-7146 (March 1973).
- J. B. Goodenough, J. Kafalas, and H. Y-P. Hong, NASA Contract C-43205-C, Final Report CR-134836 (March 1975).
- R. S. Roth, H. S. Parker, W. S. Brower, and D. B. Minor, NASA Contract C-29933-C, Final Report CR-134599 (April 1974), NBSIR 74-440.
- R. S. Roth, W. S. Brower, H. S. Parker, D. B. Minor, and J. L. Waring, NASA Contract C-50821-C, Final Report CR-134869 (July 1975), NBSIR 75-754.
- W. L. Roth and O. Muller, General Electric Co. Tech. Report SRD-74-034, NASA CR-134610 (April 1974).
- J. Singer, H. Kautz, W. Fielder, and J. Fordyce, Summary Report, NASA TM X-71753 (August 1975).
- J. A. Kafalas, NBS Special Publication 364, p. 287 (1972).
- H. Y.-P. Hong, J. A. Kafalas, and J. B. Goodenough, *J. Solid State Chem.*, **9**, 345 (1974).
- W. S. Brower, D. B. Minor, H. S. Parker, and R. S. Roth, *Mat. Res. Bull.*, **9**, 1045 (1974).
- H. Y-P. Hong, J. A. Kafalas, J. B. Goodenough, C. H. Anderson, Jr., and D. M. Tracy, *MIT Solid State Res. Rpt.*, (1974:2) p. 20.
- F. Jona, G. Shirane, and R. Pepinsky, *Phys. Rev.*, **98**, 903 (1955).
- B. Darriet, M. Rat, J. Galy, and P. Hagenmuller, *Mat. Res. Bull.*, **6**, 1305 (1971).
- B. Raveau and J.-C. Thomazeau, *C. R. Acad. Sci. Paris, C*, **266**, 540 (1968).
- C. Michel and B. Raveau, *ibid.*, **268**, 323 (1969).
- B. Raveau and C. Michel, Private communications (1972); C. Michel, Thesis, University of Caen, France (1974).
- J. L. Fourquet, C. Jacobini, and R. dePape, *Mat. Res. Bull.*, **8**, 393 (1973).
- H. E. Kautz, W. L. Fielder, J. Singer, and J. S. Fordyce, NASA TM X-2985 (1974).
- K. Nassau, J. W. Schiever, and J. L. Bernstein, *This Journal*, **116**, 348 (1969).
- T. Takahashi and K. Kawahara, *J. Chem. Soc. Japan*, **10**, 1883 (1974).
- R. T. Johnson, B. Morosin, M. L. Knotek, and R. M. Biefield, *This Journal*, To be published.

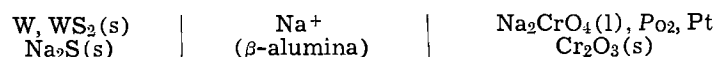
## The Standard Free Energy of Formation of Liquid Na<sub>2</sub>CrO<sub>4</sub>, 1100°-1220°K

Winston W. Liang\* and John F. Elliott\*\*

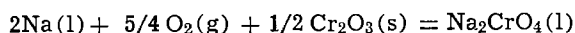
Department of Materials Science and Engineering,  
Massachusetts Institute of Technology, Cambridge, Massachusetts 02139

### ABSTRACT

The standard free energy of sodium chromate has been determined employing the reversible cell

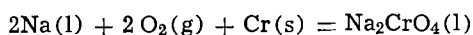


The results of the measurements give



$$\Delta G^\circ = -648,900 + 106.94T \text{ (J/mole)}$$

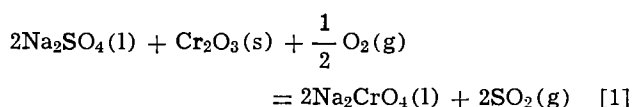
and



$$\Delta G^\circ = -1,209,900 + 233.1T \text{ (J/mole)}$$

These results are valid in the vicinity of 900°C.

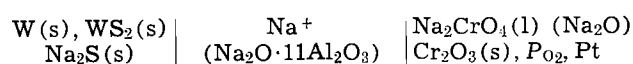
Chromium is the vital alloying element for corrosion resistance of stainless steels and iron-, nickel-, and cobalt-based superalloys. Deposits of liquid sodium sulfate have been associated with accelerated corrosion of these metals (1), and during simulated sodium sulfate-induced hot corrosion of nickel-based alloys, sodium chromate has been found as a corrosion product (2-6). The formation of sodium chromate was suggested to result from the reaction of sodium sulfate with the protective oxide, Cr<sub>2</sub>O<sub>3</sub>



However, lack of accurate information on the standard

free energy of formation of fused sodium chromate did not allow an adequate thermodynamic description of the reaction. The only available thermochemical data on sodium chromate was its standard heat of formation at 298°K which was determined calorimetrically (7). This information and recently determined data on the low and high temperature heat capacities and enthalpy increments of the compound have permitted calculation of  $\Delta G^\circ_f$  for Na<sub>2</sub>CrO<sub>4</sub> at elevated temperatures (8).

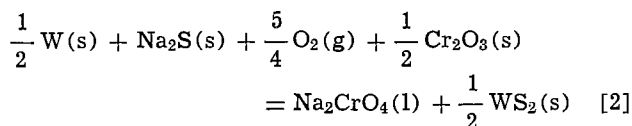
The recent development of a sodium reference electrode using  $\beta$ -alumina as the solid electrolyte (9, 10) makes it possible to investigate the thermodynamic properties of fused sodium chromate by the cell



[A]

The over-all cell reaction may be written

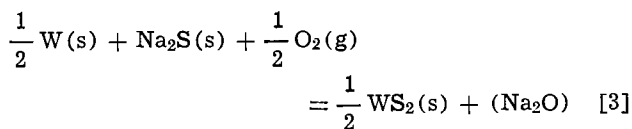
\* Electrochemical Society Student Member.  
\*\* Electrochemical Society Active Member.  
Key words: thermodynamics, sodium chromate, emf measurements.



For which

$$\Delta G^\circ_2 = -2F\epsilon + 5/4 RT \ln P_{\text{O}_2}$$

$F$  is Faraday's constant and  $\epsilon$  is the reversible potential of the cell. The liquid chromate is saturated with  $\text{Cr}_2\text{O}_3(\text{s})$ . Alternatively, the over-all cell reaction may be written



where the sodium oxide is in solution in liquid sodium chromate at the cathode. By reaction [3], the activity of sodium oxide relative to pure sodium oxide can be determined from the reversible potential of the cell when the oxygen pressure in the cathode chamber is fixed

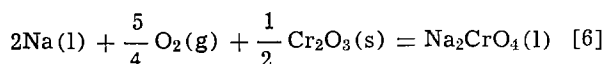
$$-2F\epsilon = \frac{1}{2} \Delta G^\circ_f(\text{WS}_2) + \Delta G^\circ_f(\text{Na}_2\text{O}) - \Delta G^\circ_f(\text{Na}_2\text{S}) \\ + RT \ln a_{\text{Na}_2\text{O}} - \frac{1}{2} RT \ln P_{\text{O}_2} \quad [4]$$

Similarly, the standard free energy of formation of liquid sodium chromate can be obtained from  $\epsilon$  and  $P_{\text{O}_2}$

$$-2F\epsilon = \frac{1}{2} \Delta G^\circ_f(\text{WS}_2) + \Delta G^\circ_f(\text{Na}_2\text{CrO}_4) - \Delta G^\circ_f(\text{Na}_2\text{S}) \\ - \frac{1}{2} \Delta G^\circ_f(\text{Cr}_2\text{O}_3) - \frac{5}{4} RT \ln P_{\text{O}_2} \quad [5]$$

It is to be noted that the experimental cell potential must be corrected for the thermoelectric effect of the W-Pt junction (20-30 mV) to obtain the values of  $\epsilon$  used in Eq. [4] and [5].

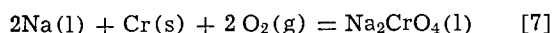
The standard free energy of formation of sodium chromate by the reactions



can be obtained from Eq. [5] utilizing the data in Table I

$$\Delta G^\circ_6 = -2F\epsilon + \frac{5}{4} RT \ln P_{\text{O}_2} - 267,350 + 46.06T \quad [6a]$$

and for the formation from the elements



$$\Delta G^\circ_f(\text{Na}_2\text{CrO}_4) = -2F\epsilon + 2 RT \ln P_{\text{O}_2} \\ - 828,370 + 172.2T \quad [7a]$$

Thus the information obtained from the cell can be used to determine the standard free energy of liquid sodium chromate.

### Experiments

The anode materials consisted of 99.9% pure tungsten powder and reagent grade  $\text{WS}_2$  and  $\text{Na}_2\text{S}$ . These

Table I. Thermodynamic data

Compound*	$\Delta G^\circ = \Delta H^\circ - T\Delta S^\circ$ , J/mole	Reference
$\text{Cr}_2\text{O}_3(\text{s})$	$-1,122,040 + 252.3T$	(11)
$\text{Na}_2\text{S(s)}$	$-435,550 + 124.3T$	(12)
$\frac{1}{2} \text{WS}_2(\text{s})$	$-168,200 + 78.24T$	(13)
$\text{Na}_2\text{O(l)}$	$-353,550 + 88.91T$	(12)

\* Reference states: Na(l), Cr(s), W(s),  $\text{O}_2(\text{g})$ , and  $\text{S}_2(\text{g})$ ; all at 1 atm pressure.

materials were mixed in the molar ratio of 1:1:4 and were dried overnight at 80°C before use. The cathode materials consisted of reagent grade  $\text{Na}_2\text{CrO}_4$  and  $\text{Cr}_2\text{O}_3$ . The chromium oxide was either in the form of a powder or small pieces that were obtained by sintering the powder at 1600°C in argon having an oxygen pressure of approximately  $10^{-12}$  atm. The density of the pellets was 3.87 g/cm<sup>3</sup>. In the case that the chromium oxide powder was used, 2g of it and 20g of powdered sodium chromate were dried at 220°C under vacuum for 1 week prior to use (14). If the chromium oxide pellet was used, the sodium chromate powder was dried as described and the pellet was added to the cell along with the powder.

The crucibles of  $\beta$ -alumina used for the electrolyte were processed from Monofrax H bricks (Carborundum Company). The bricks were crushed to +8 mesh particles. The crushed material was ground in an alumina ball mill for 30-40 hr. Then 2 weight per cent (w/o)  $\text{Na}_2\text{CO}_3$ , 1 w/o MgO, and  $\frac{1}{2}$  w/o  $\text{Y}_2\text{O}_3$  in powder form were added and mixed in a tumble mixer for 10 hr. The resulting mixture was calcined in a platinum crucible for 1 hr in air (15). This calcined material was reground in an alumina ball mill for 10-15 hr to obtain a final particle size of 0.5-1  $\mu\text{m}$ . Cylindrical rods 12.5 mm  $\times$  6-8 cm long of this material were obtained by first pressing them in a die at 2000 psi followed by isostatically pressing at 32,000 psi. The rods were pre-fired at 1100°C for 1 hr while packed in coarse  $\beta$ -alumina powder. They were then drilled with a 6 mm drill, packed in coarse  $\beta$ -alumina powder, and fired in air at 1750°C (16). The maximum temperature was held for a period of 20-30 min. These sintered crucibles were 93% dense and crack free, and had no open porosity. The electrochemical characteristics of  $\beta$ -alumina which makes it suitable as the electrolyte in the cell are well described (17, 18).

The arrangement of the cell is shown in Fig. 1. When used, the  $\beta$ -alumina electrolyte was a straight-walled crucible 11 mm OD  $\times$  6 mm ID  $\times$  60 mm high. The anode chamber containing W,  $\text{WS}_2$ , and  $\text{Na}_2\text{S}$  powders and the W lead was sealed with soft glass as the cell was brought to temperature.

The cathode consisted of a platinum wire within an alumina tube. The tip of the tube was positioned approximately 5 mm below the surface of the liquid sodium chromate. A gas of known composition, Ar +  $\text{O}_2$  or air, was bubbled through the melt at a rate of a few centimeters (STP) per minute. The gases were carefully dried before they entered the cell and the Vycor furnace tube was maintained at a pressure

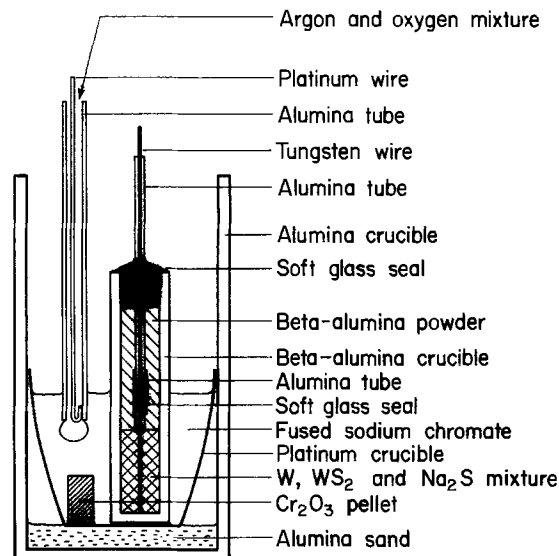


Fig. 1. Cell arrangement

slightly in excess of atmospheric by throttling the outflow of the gas.

The temperature of the cell was measured with a Pt/Pt-10% Rh thermocouple and it was known with an uncertainty of not more than  $\pm 1.0^\circ\text{C}$ . The cell potential was measured with a Beckman pH meter ( $10^{14}$  ohms impedance).

After being brought to temperature, the cell required 8 hr for its potential to stabilize. Subsequently the potential was very steady and reproducible. When the temperature was changed, the potential reached a new steady state within 1-2 hr which was approximately the time required by the system to reach thermal equilibrium. If the temperature was altered and then returned to the original value, the cell potential was reproducible within 1 or 2 mV. The potential also varied less than 1 mV when the gas flow was changed in the range of 0-5 cm<sup>3</sup>/min (STP). All measurements were made at a rate of 2 cm<sup>3</sup>/min. With a change in oxygen pressure in the cathode gas, the cell reached a new steady value in 7-9 hr. Polarization of the cell with a current of 50 mA for 10 sec in either direction caused a displacement of the cell potential by 350 mV above or below the previous steady-state reading. The potential returned to the previous value within 30 sec after the polarizing current was turned off.

### Experimental Results and Discussion

The experimental measurements are shown in Table II and the results in terms of  $\Delta G^\circ_2$  are shown in Fig. 2. The line is the least squares line for all points; its equation is

$$\Delta G^\circ_2 = -381,500 + 60.88T \quad [3a]$$

with uncertainties of approximately  $\pm 1500$  J/mole in free energy,  $\pm 3000$  J/mole in enthalpy, and  $\pm 3$  J/mole $\cdot^\circ\text{K}$  in entropy. Inserting these results into Eq. [6a] gives

$$\Delta G^\circ_6 = -648,900 + 106.94T \quad [6b]$$

and into Eq. [7a] gives for the liquid

$$\Delta G^\circ_f(\text{Na}_2\text{CrO}_4) = -1,209,900 + 233.1T \quad [7b]$$

with uncertainties of approximately  $\pm 12,000$  J/mole $\cdot^\circ\text{K}$  in free energy,  $\pm 14,000$  J/mole in enthalpy, and 9 J/mole $\cdot^\circ\text{K}$  in entropy.

There are no direct measurements at elevated temperatures of the standard free energy of Na<sub>2</sub>CrO<sub>4</sub>

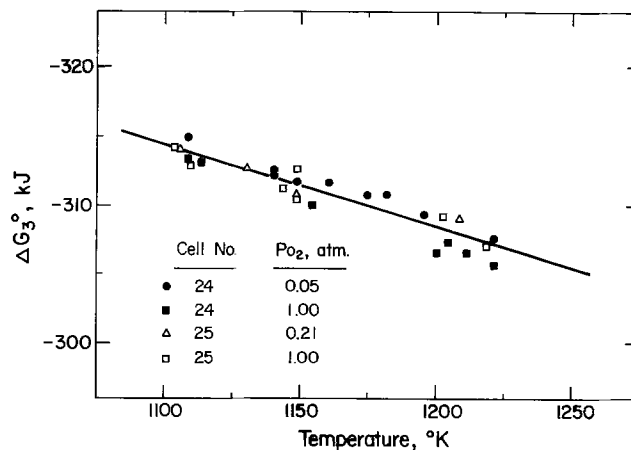


Fig. 2. Experimental results in terms of Eq. [2]

which can be used for comparison with the present results. There are, however, data on the specific heat and the enthalpy increment by Ferrante, Stuve, and Krug (8) and the standard enthalpy of formation of the compound at 298 $^\circ\text{K}$  by Nelson, Moss, and Hepler (7). These data permit calculation of the thermodynamic properties of Na<sub>2</sub>CrO<sub>4</sub> in the temperature range of this study (8). The resulting equation for the liquid is

$$\Delta G^\circ_f(\text{Na}_2\text{CrO}_4) = -1,278,600 + 301.25T \quad [7c]$$

Subtracting from this one-half the standard free energy of formation of Cr<sub>2</sub>O<sub>3</sub>(c) gives

$$\Delta G^\circ_6 = -717,600 + 175.10T \quad [6c]$$

It is to be seen that at 1100 $^\circ\text{K}$  the results obtained from the experiments reported are lower than those obtained from the thermochemical data (7, 8, 11) by approximately 6200 joules (1500 cal). At 1200 $^\circ\text{K}$  the differences are approximately 13,000 joules (3000 cal). The agreement in the values of the standard free energies is felt to be reasonably good considering the diverse data that have been used in obtaining the two sets of equations.

The set of equations [6b] and [7b] differ from the set [6c] and [7c] principally in the entropy terms. If one back calculates from reaction [6] and Eq. [6b] using the appropriate data from Table I to get an equation for  $\Delta G^\circ_2$ , one obtains a line in Fig. 2 based on the thermal data that crosses the experimental line but which has a much greater (negative) slope. The disagreement appears to be much greater than that which results from the uncertainties in the various data used in determining these two lines. It may be due to either, or both, of the following reasons:

(a) Uncertainties in the thermochemical data for Na<sub>2</sub>S and WS<sub>2</sub> which may be large because of the experimental difficulties when working with these compounds.

(b) The entropy term in Eq. [7b], which is derived from the cell measurement, may include a term that is related to a change in composition with temperature of Na<sub>2</sub>CrO<sub>4</sub> when saturated with Cr<sub>2</sub>O<sub>3</sub>(s).

The possible change in composition of Na<sub>2</sub>CrO<sub>4</sub> with temperature mentioned above probably would be small in view of the very low activity of Na<sub>2</sub>O in the salt and also the fact that it does not change appreciably either with a change in oxygen pressure or temperature. It is to be noted that there was no evidence during the experimental work that the composition of the liquid chromate deviated appreciably from Na<sub>2</sub>CrO<sub>4</sub>.

For conditions in which liquid sodium chromate and Cr<sub>2</sub>O<sub>3</sub> coexist, it is concluded that the free energy of formation of Na<sub>2</sub>CrO<sub>4</sub> according to Eq. [7b] should be used.

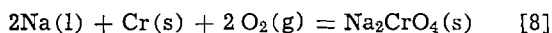
Using the data of Ferrante and co-workers (8) on the melting of Na<sub>2</sub>CrO<sub>4</sub> ( $\Delta H_m = 24,300$  J/mole,  $T_m =$

Table II. Experimental measurements

Cell No.	P <sub>O<sub>2</sub></sub> , atm	Temp, $^\circ\text{K}$	Cell emf,* V	$-\log a_{\text{Na}_2\text{O}}$
24	0.05	1141	1.435	11.630
		1161	1.429	11.424
		1182	1.421	11.201
		1141	1.436	11.639
		1175	1.422	11.260
		1196	1.411	11.018
		1221	1.398	10.740
		1149	1.431	11.533
		1109	1.454	12.060
24	1.0	1155	1.604	12.346
		1201	1.589	11.826
		1222	1.584	11.617
		1109	1.624	12.955
		1114	1.623	12.897
		1205	1.593	11.827
		1212	1.589	11.738
		1109	1.589	11.738
25	1.0	1144	1.613	12.525
		1104	1.629	13.050
		1149	1.621	12.549
		1203	1.603	11.927
		1219	1.592	11.707
		1149	1.609	12.444
		1110	1.622	12.927
		1110	1.622	12.927
25	0.21	1149	1.514	11.949
		1106	1.535	12.512
		1131	1.526	12.208
		1209	1.500	11.359
		1209	1.500	11.359

\* Corrected for W-Pt thermoelectric effect.

1065°K), one obtains for the reaction to form the solid

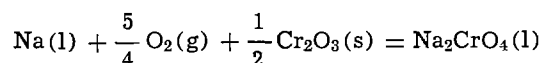


$$\Delta G^\circ_f = -1,234,200 + 255.92T \quad [8a]$$

This equation applies to the superheated solid phase in the temperature range of 900°-1200°C.

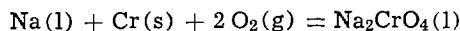
### Summary and Conclusions

The standard free energy of formation of sodium chromate has been measured by a high temperature emf cell. The results apply to the reaction



$$\Delta G^\circ_R = -648,900 + 106.94T$$

and to



$$\Delta G^\circ_f = -1,209,900 + 233.1T$$

The equations are based on measurements obtained in the temperature range of 1100°-1220°K.

### Acknowledgments

The authors gratefully acknowledge financial support of the work reported by the Energy Research and Development Administration. The help of Mr. R. Stanton who made the  $\beta$ -alumina electrolytes is acknowledged with appreciation. Helpful suggestions by Professor H. K. Bowen on the preparation and properties of the electrolytes were appreciated.

Manuscript submitted Oct. 21, 1975; revised manuscript received Dec. 29, 1975.

Any discussion of this paper will appear in a Discussion Section to be published in the December 1976 JOURNAL. All discussions for the December 1976 Discussion Section should be submitted by Aug. 1, 1976.

Publication costs of this article were partially assisted by Massachusetts Institute of Technology.

### REFERENCES

1. A. M. Beltran and D. A. Shores, "Superalloys," C. T. Sim and W. C. Hagel, Editors, p. 317, John Wiley & Sons, Inc., New York (1972).
2. A. U. Seybolt, "High-Temperature Metallic Corrosion of Sulfur and Its Compounds," Z. A. Foroulis, Editor, pp. 159-169, The Electrochemical Society Softbound Symposium Series, New York (1970).
3. N. S. Bornstein, M. A. DeCrescente, and H. A. Roth, *Met. Trans.*, **4**, 1799 (1973).
4. J. A. Goebel, F. S. Pettit, and G. W. Goward, *ibid.*, **4**, 261 (1973).
5. G. Romeo and D. W. McKee, *This Journal*, **122**, 188 (1975).
6. D. W. McKee, D. Chatterji, G. Romeo, and H. S. Spacil, "Metal-Slag-Gas Reactions and Processes," Z. A. Foroulis and W. W. Smeltzer, Editors, pp. 711-735, The Electrochemical Society Softbound Symposium Series, Princeton, N. J. (1975).
7. T. Nelson, C. Moss, and L. G. Hepler, *J. Phys. Chem.*, **64**, 376 (1960).
8. M. J. Ferrante, J. M. Stuve, and M. P. Krug, *U. S. Bur. Mines Rept. Invest. No. 7691* (1972).
9. W. W. Liang, H. K. Bowen, and J. F. Elliott, "Metal-Slag-Gas Reactions and Processes," Z. A. Foroulis and W. W. Smeltzer, Editors, pp. 608-624, The Electrochemical Society Softbound Symposium Series, Princeton, N. J. (1975).
10. W. W. Liang, H. K. Bowen, and J. F. Elliott, Unpublished work.
11. JANAF Thermochemical Tables, The Dow Chemical Co., Midland, Michigan, supplement to Dec. 1974.
12. JANAF Thermochemical Tables, Second edition, NBS 37, Published by U.S. Department of Commerce (1970).
13. J. P. Hager and J. F. Elliott, *Trans. AIME*, **239**, 513 (1967).
14. W. H. Hartford, *Ind. Eng. Chem.*, **41**, 1993 (1949).
15. S. P. Mitoff, Private communication.
16. T. L. Francis, F. E. Phelps, and G. MacZura, *Am. Ceram. Soc. Bull.*, **50**, 615 (1971).
17. Y. F. Yao and J. T. Kummer, *J. Inorg. Nucl. Chem.*, **29**, 2453 (1967).
18. M. S. Whittingham and R. A. Huggins, *J. Chem. Phys.*, **54**, 414 (1971).

## Electrochemical Oxidation of N-Substituted Iminodimethylenediphosphonic Acids

John H. Wagenknecht\*

Monsanto Company, Corporate Research Department, St. Louis, Missouri 63166

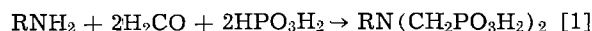
### ABSTRACT

The electrochemical oxidation of substituted iminodimethylenediphosphonic acids  $[\text{RN}(\text{CH}_2\text{PO}_3\text{H}_2)_2]$  in strong aqueous acid leads cleanly to the secondary amine  $(\text{RNHCH}_2\text{PO}_3\text{H}_2)$  in most cases. Voltammetric data, NMR data, and the products of the oxidations suggest that unprotonated amine is available for oxidation even in strongly acidic aqueous solution.

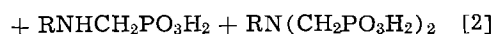
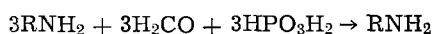
The only reported electrochemical oxidation of a simple phosphonic acid was that of methylphosphonic acid which led to cleavage of the carbon-phosphorus bond (1). Oxidation of N-phosphonomethyliminodiacetic acid, however, did not lead to cleavage of the phosphonate portion of the molecule (2). It has previously been reported that nitrilotrimethylenetriphosphonic acid may be electrochemically oxidized, resulting in cleavage of the methylenephosphonic acid group (3). The present study was made to determine if that was a general reaction, useful for the preparation of a

wide variety of secondary aminomethylenephosphonic acids.

Tertiary iminodimethylenediphosphonic acids are conveniently made by the reaction of an amine with formaldehyde and phosphorous acid (4)



Stoichiometric quantities of reagents, however, produce a mixture which is very difficult to separate (5), so that a simple, clean synthesis



\* Electrochemical Society Active Member.

Key words: N-substituted aminomethylenephosphonic acids, voltammetry, preparative electrolysis.

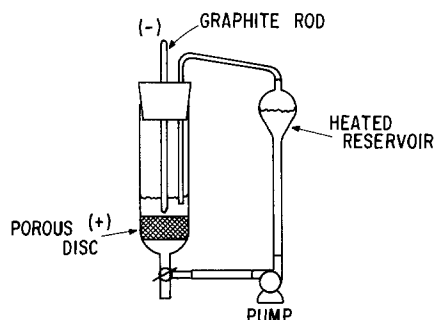


Fig. 1. Recirculating electrolysis system with a porous graphite anode.

of secondary aminomethylenephosphonic acids was unknown.

### Experimental

Cyclic voltammetry was carried out in a three-compartment cell with a glassy carbon anode (5 mm diameter button in glass tubing), Pt wire cathode, and a saturated calomel reference electrode. A Wenking Model 66TA1 potentiostat, Exact Electronics, Inc., Model 505 function generator, and Moseley 7035 AM X-Y recorder were used for obtaining voltammograms. A scan rate of 6.8 mV/sec was used, and the depolarizer concentration was 5 mM in 0.2M  $H_3PO_4$ , except for compounds X-XIII which were run in 50%  $H_3PO_4$  because they are insoluble in dilute acid.

NMR spectra were obtained with a Varian T-60 NMR spectrometer with 20% HCl or concentrated HCl as the solvent and 3(trimethylsilyl)propanesulfonic acid as the internal reference.

All of the starting tertiary amines were prepared by the procedure of Moedritzer and Irani (4) involving reaction of the primary amine with formaldehyde and phosphorus acid.

Most of the electrolyses were conveniently carried out in the apparatus shown in Fig. 1. However, equally good results may be obtained by electrolysis at a graphite plate anode in a beaker.

**Typical electrolysis procedure.**—A 40g sample of nitrilotrimethylenetriphosphonic acid was dissolved in 20 ml of 20% HCl by warming on a steam bath. The solution was added to the reservoir (Fig. 1) which was heated to maintain the solution at 70°C. The solution was circulated through the cell (8.5 cm<sup>2</sup> × 1 in. thick, Union Carbide PG45 porous graphite anode and graphite rod cathode) by a Gorman-Rupp MI-2095 metering pump at 100 ml/min. Current was supplied to the cell by a Harrison Model 865B constant-current power supply. After electrolysis at 1A for 4 hr (NMR indicated 57% conversion), the current was lowered to 0.6A and electrolysis was continued for an additional 5 hr. The NMR spectrum of the solution then indicated the absence of starting material. The solution was concentrated to an oil on a rotary evaporator. The oil was boiled with isopropanol, cooled in a refrigerator overnight, and filtered to give 25g (91%) of dried iminodimethylenediphosphonic acid, identical to an authentic sample (5).

Using the above procedure, the following oxidations were carried out as indicated in Table I. Order of presentation is starting material, product, product melting point, and product elemental analyses.

III,  $CH_3(CH_2)_{11}NHCH_2PO_3H_2 \cdot \frac{1}{2}H_2O$ , 230°–250° dec., calc for  $C_{13}H_{31}NO_{3.5}P$ : C, 54.21; H, 10.85; N, 4.86; P, 10.75. Found: C, 54.40, 54.15; H, 10.84, 11.23; N, 4.74, 4.65; P, 10.99, 11.03.

IV,  $C_6H_5CH_2NHCH_2PO_3H_2 \cdot H_2O$ , 277°–279°, calc for  $C_8H_{14}NO_3P$ : C, 43.83; H, 6.43; N, 6.39. Found: C, 43.36, 43.62; H, 6.42, 6.45; N, 6.33, 6.32 [in addition,  $HN(CH_2PO_3H_2)_2$  was formed in this reaction].

V,  $C_6H_5CH_2CH_2NHCH_2PO_3H_2 \cdot 2H_2O$ , 265°–270°, calc for  $C_9H_{18}NO_5P$ : C, 43.02; H, 7.72; N, 5.58; P, 12.33. Found: C, 43.99, 44.0; H, 6.09, 5.95; N, 5.46, 5.56; P, 12.60.

VII,  $HO_2C(CH_2)_3NHCH_2PO_3H_2$ , 177°, calc for  $C_5H_{12}NO_5P$ : C, 30.46; H, 6.14; N, 7.11; P, 15.71. Found: C, 29.64, 29.66; H, 6.39, 6.61; N, 7.11, 7.18; P, 15.74.

VIII,  $HO_2C(CH_2)_4NHCH_2PO_3H_2 \cdot \frac{1}{2}H_2O$ , 207°–209°, calc for  $C_6H_{15}NO_{5.5}P$ : C, 32.74; H, 6.87; N, 6.37; P, 14.07.

Table I. Voltammetry data and oxidation products of substituted iminodimethylenediphosphonic acids

Compound	Structure (Y = $CH_2PO_3H_2$ )	$E_p$ (V vs. SCE)	$i_p$ ( $\mu A$ )	Product(s) (Y = $CH_2PO_3H_2$ )
I	$NY_3$	0.92	108	$HNY_2$
II	Nitrilotrimethylenetriphosphonic acid $CH_3NY_2$	1.05	80	Iminodimethylenediphosphonic acid $CH_3NHY$
III	N-methyliminodimethylenediphosphonic acid $CH_3(CH_2)_{11}NY_2$			N-methylaminomethylenephosphonic acid $CH_3(CH_2)_{11}NHY$
IV	N-dodecyliminodimethylenediphosphonic acid $C_{12}H_{25}CH_2NY_2$	0.93	179	N-dodecylaminomethylenephosphonic acid $C_{12}H_{25}NH_2$ (60)
V	N-benzyliminodimethylenediphosphonic acid $C_6H_5CH_2CH_2NY_2$	0.95	141	N-phenylaminomethylenephosphonic acid $HNY_2$ (40) $C_6H_5CH_2CH_2NH_2$
VI	N-phenethyliminodimethylenediphosphonic acid $CH_2=CHCH_2NY_2$	1.02	83	N-phenethylaminomethylenephosphonic acid Complex mixture
VII	N-allyliminodimethylenediphosphonic acid $HO_2C(CH_2)_3NY_2$	1.02	112	$HO_2C(CH_2)_3NH_2$
VIII	4-(Iminodimethylenediphosphonic acid) Butyric acid $HO_2C(CH_2)_4NY_2$	1.00	96	4-(Aminomethylenephosphonic acid) Butyric acid $HO_2C(CH_2)_4NH_2$
IX	5-(Iminodimethylenediphosphonic acid) Valeric acid $HO_2C(CH_2)_5NY_2$	1.00	93	5-(Aminomethylenephosphonic acid) Valeric acid $HO_2C(CH_2)_5NH_2$
X	6-(Iminodimethylenediphosphonic acid) Caproic acid $Y_2NCH_2CH_2NY_2$	0.95	43	6-(Aminomethylenephosphonic acid) Caproic acid $YHNCH_2CH_2NH_2$
XI	Ethylenediamine-N,N',N'-tetramethylenetetraphosphonic acid $Y_2N(CH_2)_6NY_2$	1.05	40	Ethylenediamine-N,N'-dimethylenediphosphonic acid $HNY_2$ $YHN(CH_2)_6NH_2$
XII	Hexamethylenediamine-N,N',N'-tetramethylenetetraphosphonic acid $Y_2N(CH_2)_8NY_2$	1.05	52	Hexamethylenediamine-N,N'-dimethylenediphosphonic acid $YHN(CH_2)_8NH_2$
XIII	Octamethylenediamine-N,N',N'-tetramethylenetetraphosphonic acid $Y_2N-CH_2-\text{S}-CH_2NY_2$	1.00	93	Octamethylenediamine-N,N'-dimethylenediphosphonic acid $YHNCH_2-\text{S}-CH_2NH_2$
XIV	1,4-Bisaminomethylcyclohexane-N,N',N'-tetramethylenetetraphosphonic acid $(Y_2NCH_2CH_2)_2O$	1.04	149	1,4-Bisaminomethylcyclohexane-N,N'-dimethylenediphosphonic acid $(YHNCH_2CH_2)_2O$
XV	2,2'-Diaminodiethylether-N,N',N'-tetramethylenetetraphosphonic acid $(Y_2NCH_2CH_2)_2S$	1.03	160	2,2'-Diaminodiethylether-N,N'-dimethylenediphosphonic acid $(YHNCH_2CH_2)_2S$
	2,2'-Diaminodiethylthioether-N,N',N'-tetramethylenetetraphosphonic acid			2,2'-Diaminodiethylthioether-N,N'-dimethylenediphosphonic acid

Found: C, 32.70, 32.57; H, 6.76, 6.66; N, 6.52, 6.37; P, 14.68, 14.65.

IX,  $\text{HO}_2\text{C}(\text{CH}_2)_5\text{NHCH}_2\text{PO}_3\text{H}_2$ , 210°-212°, calc for  $\text{C}_7\text{H}_{16}\text{NO}_5\text{P}$ : C, 37.33; H, 7.16; N, 6.22; P, 13.75. Found: C, 36.27, 35.99; H, 6.74, 6.78; N, 6.00, 5.98; P, 13.39, 13.59.

X,  $\text{H}_2\text{O}_3\text{PCH}_2\text{NHCH}_2\text{CH}_2\text{NHCH}_2\text{PO}_3\text{H}_2 \cdot 2\text{H}_2\text{O}$ , 295°-300°, calc for  $\text{C}_4\text{H}_{13}\text{N}_2\text{O}_8\text{P}_2$ : C, 16.90; H, 6.38; N, 9.86; P, 21.80. Found: C, 17.24, 17.57; H, 6.28, 6.21; N, 9.97, 9.92; P, 20.97.

XI,  $\text{H}_2\text{O}_3\text{PCH}_2\text{NH}(\text{CH}_2)_6\text{NHCH}_2\text{PO}_3\text{H}_2 \cdot 2\text{H}_2\text{O}$ , 300°-302°, calc for  $\text{C}_8\text{H}_{26}\text{N}_2\text{O}_8\text{P}_2$ : C, 28.23; H, 7.70; N, 8.23; P, 18.21. Found: C, 27.69, 27.67; H, 7.41, 7.31; N, 8.12, 8.18; P, 18.19.

XII,  $\text{H}_2\text{O}_3\text{PCH}_2\text{NH}(\text{CH}_2)_3\text{NHCH}_2\text{PO}_3\text{H}_2 \cdot 4\text{H}_2\text{O}$ , 190°, calc for  $\text{C}_{10}\text{H}_{34}\text{N}_2\text{O}_{10}\text{P}_2$ : C, 29.70; H, 8.48; N, 6.93. Found: C, 29.13, 29.19; H, 6.50, 6.80; N, 6.67, 6.60.

XIII,  $\text{H}_2\text{O}_3\text{PCH}_2\text{NHCH}_2(1,4\text{-C}_6\text{H}_{10})\text{CH}_2\text{NHCH}_2\text{PO}_3\text{H}_2 \cdot \text{H}_2\text{O}$ , 305°-310°, calc for  $\text{C}_{10}\text{H}_{26}\text{N}_2\text{O}_7\text{P}_2$ : C, 34.47; H, 7.53; N, 8.04. Found: C, 34.21, 34.14; H, 7.49, 7.42; N, 7.25, 7.22.

XIV,  $(\text{H}_2\text{O}_3\text{PCH}_2\text{NHCH}_2\text{CH}_2)_2\text{O}$ , 289°-293°, calc for  $\text{C}_6\text{H}_{18}\text{N}_2\text{O}_7\text{P}_2$ : C, 24.66; H, 6.21; N, 9.59. Found: C, 23.98, 23.86; H, 5.96, 6.14; N, 8.80, 8.86.

**Electrolysis in a beaker.**—In a 100-ml beaker with graphite plate anode (35 cm<sup>2</sup>) and Pt wire cathode was placed 80 ml of 20% HCl and 8g of  $\text{CH}_3\text{N}(\text{CH}_2\text{PO}_3\text{H}_2)_2$  (II). This was electrolyzed at 250 mA for 26 hr at room temperature using a Harrison Model 865B power supply. The NMR spectra for the starting solution, partially oxidized solution, and completely oxidized solution are shown in Fig. 2. The solution was concentrated on a rotary evaporator and the residue crystallized from ethanol-water giving 3.7g (80%) of  $\text{CH}_3\text{NHCH}_2\text{PO}_3\text{H}_2$ , mp 274°-275°.

Analysis. calc for  $\text{C}_2\text{H}_8\text{NO}_3\text{P}$ : C, 19.21; H, 6.45; N, 11.20; P, 24.76. Found: C, 18.76, 18.85; H, 6.40, 6.35; N, 11.21, 11.43; P, 24.29.

**Isolation of formylphosphonic acid.**—The electrolysis was run in the cell shown in Fig. 1. Twenty grams of nitrilotrimethylenetriphosphonic acid in 100 ml of 0.1M HCl was electrolyzed at room temperature for 5.75 hr at 0.5A. The solvent was removed on a rotary evaporator and 100 ml  $\text{CH}_3\text{CN}$  was added to the residue to precipitate  $\text{HN}(\text{CH}_2\text{PO}_3\text{H}_2)_2$ . The filtrate was concentrated on a rotary evaporator and the residue extracted with acetone. The acetone extract was concentrated to a glass at reduced pressure. NMR analysis indicated

pure  $\text{HCPO}_3\text{H}_2$ . Elemental analysis: calc for  $\text{CH}_3\text{O}_4\text{P} \cdot \text{H}_2\text{O}$ : C, 9.38; H, 3.93; N, 0.00. Found: C, 9.15, 9.31; H, 3.97, 3.74; N, 0.78, 0.70.

The material did not form an insoluble semicarbazone (6) and would not form a precipitate with a saturated sodium bisulfite solution. A portion of the material was made basic with aqueous NaOH, heated, cooled, and reacidified with concentrated HCl. The acidification was accompanied by gas evolution (presumably  $\text{CO}_2$ ). Proton NMR indicated the presence of  $\text{HPO}_3\text{H}_2$  (upfield peak at  $\delta = 1.05$ ) and  $\text{HOCH}_2\text{PO}_3\text{H}_2$  ( $\delta = 3.98$ ,  $J_{\text{HP}} = 7$  Hz) in the acidified solution.

## Results

Cyclic voltammetry was carried out in 0.2M  $\text{H}_3\text{PO}_4$  at a glassy carbon anode. None of the compounds showed reversible oxidation. The peak potentials ( $E_p$ ) for the oxidations of the substituted iminodimethylenediphosphonic acids are shown in Table I.

The products of the macroelectrolyses are also shown in the table along with the melting point and elemental analysis. Many of the secondary amine products are shown as hydrates based on elemental analysis.

In each case another major product, formylphosphonic acid, was formed (as evidenced by its  $^1\text{H}$  NMR doublet at  $\delta = 5.38$ ) but was generally not isolated. A crude form of that compound was isolated, as is shown in the experimental section.

Except for  $\phi\text{CH}_2\text{N}(\text{CH}_2\text{PO}_3\text{H}_2)_2$ ,  $\text{CH}_2=\text{CHCH}_2\text{N}(\text{CH}_2\text{PO}_3\text{H}_2)_2$ , and  $(\text{H}_2\text{O}_3\text{PCH}_2)_2\text{NCH}_2\text{CH}_2\text{N}(\text{CH}_2\text{PO}_3\text{H}_2)_2$  the oxidations proceeded cleanly to the secondary amine as indicated by proton NMR. The reactions were easily followed by  $^1\text{H}$  NMR because the tertiary amines exhibit a sharp doublet at around  $\delta = 3.8$  with a separation of about 14 Hz. That signal which is due to the methylene between phosphorus and nitrogen shifts upfield and becomes a multiplet because of quadrupole coupling to nitrogen for the secondary amine products (see Fig. 2). In most cases it was difficult to initiate crystallization of the product so that product isolation was not optimized for each product.

## Discussion

The cyclic voltammetry data shown in Table I indicates that the site of the oxidation is the same in each case since the range of oxidation potentials is so narrow. Note that this is the same potential region in which tertiary amines are known to oxidize (7).

There seem to be several groupings of compounds based on peak current. First, compounds I, II, and VI-IX ( $i_p$  ranging from 80 to 112) might be considered to be the normal monoamine oxidation. Compounds XIV and XV have higher values of  $i_p$ , presumably because two amines are available on each molecule. Compounds X-XIII would be expected to have lower values of  $i_p$  because they were run in the more viscous

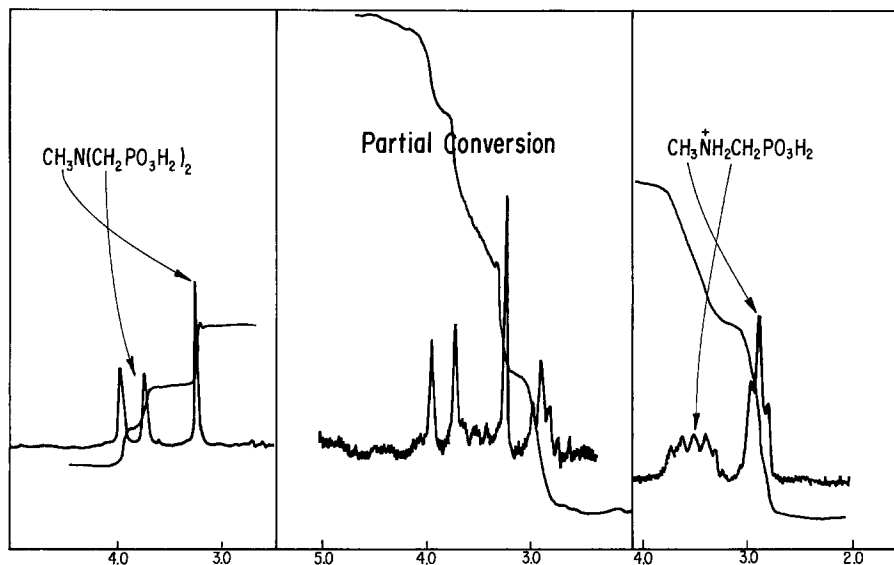
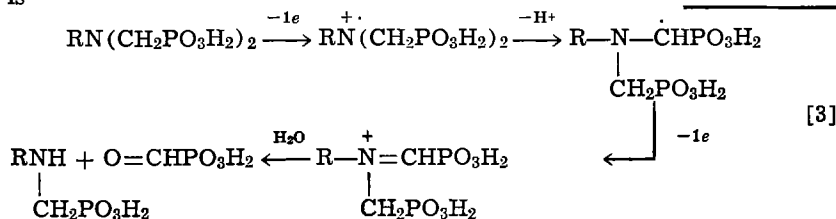


Fig. 2. Proton NMR spectra of N-methyliminodimethylenediphosphonic acid in 20% HCl, a partially electrolyzed solution and the final product.

medium of 50%  $\text{H}_3\text{PO}_4$ . It is not clear why compounds IV, V, and XIII have abnormally high values of  $i_p$ . Dodecyliminodimethylenediphosphonic acid (III) was not sufficiently soluble in 50%  $\text{H}_3\text{PO}_4$  to obtain a voltammogram.

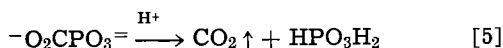
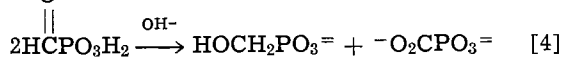
The general reaction path suggested by the product is



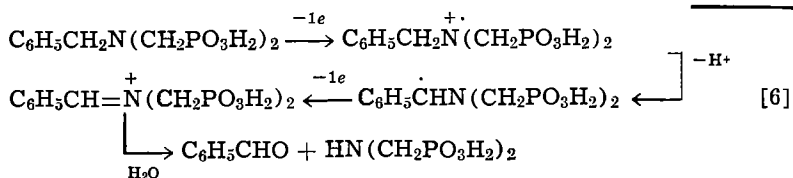
This is similar to the oxidation pathway suggested for simple tertiary aliphatic amines (8). However, the related  $\alpha$ -aminophosphonic acids were shown to cleave both the carbon-nitrogen and carbon-phosphorus bond on electrochemical oxidation (9). The evidence for the structure of the cleaved portion of the molecule

(HCPO<sub>3</sub>H<sub>2</sub>) includes the data in the experimental section. Further, the <sup>1</sup>H NMR spectrum in 20% HCl consists of a doublet ( $J_{\text{HP}} = 9$  Hz) at  $\delta = 5.38$  for the hydrogen attached to the carbonyl. The similar hy-

drogen on glyoxylic acid (HCCO<sub>2</sub>H) has a similar chemical shift. The disproportionation in basic solution parallels the reaction of glyoxylic acid in basic media (10)



As is indicated in Table I, some of the compounds gave more than one secondary amine product. For compound IV both methylenephosphonic acid and benzyl were cleaved in a nearly statistical amount. Presumably, the benzyl is cleaved according to the following pathway

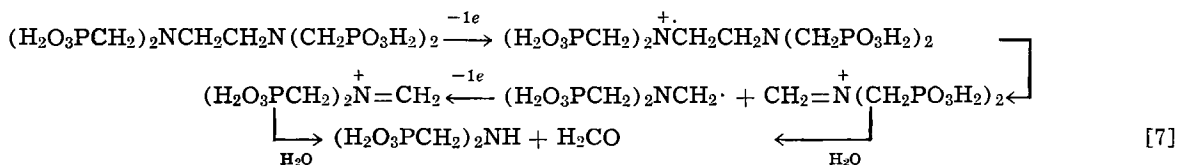


Benzaldehyde was detected in the NMR spectrum of the products.

Compound V was included because it was thought that benzyl cation might be cleaved from the intermediate cation radical; however, only methylenephosphonic acid cleavage occurred.

Compound VI probably underwent cleavage of both the allyl and the methylenephosphonic acid groups. Unfortunately, no single product could be isolated from the reaction mixture.

Compound X apparently has two cleavage pathways, the normal methylenephosphonic acid cleavage and cleavage of the carbon-carbon bond. The second pathway is visualized as follows



Formaldehyde was detected in the NMR spectrum of the products. A similar cleavage has been reported for the anodic oxidation of an aziridine ring (11).

The preparative electrolyses were carried out in 20% or concentrated HCl for several reasons. First, graphite anodes are unstable in phosphoric or sulfuric acids. HCl may be removed from the product by distillation. At the current densities used there is no problem of overoxidation of the product when HCl is used as the

solvent because the O<sub>2</sub> evolution potential is very near that of the tertiary amine oxidation. Therefore, when the starting material is completely consumed, only O<sub>2</sub> evolution occurs, so that a constant current power supply rather than a potentiostat may be employed. Aqueous HCl was not the solvent for voltammetry because the peaks were too close to the background.

Both the voltammetric data and reaction pathway suggest that these compounds behave as free amines even in concentrated aqueous acid. That is further supported by the <sup>1</sup>H NMR spectra of these compounds in 20% HCl. All of the tertiary amines show a doublet in the NMR spectrum, due to the hydrogens on the carbon attached to phosphorus. These appear as a doublet because of coupling to phosphorus. They are not further split by quadrupole coupling to nitrogen which generally occurs with protonated or quaternary nitrogen. However, secondary amines containing only one methylenephosphonic acid group do show quadrupole coupling to nitrogen, so that the methylene between nitrogen and phosphorus appears as a multiplet. [This was incorrectly attributed to coupling with hydrogen attached to nitrogen in the previous communication (3).] The NMR spectra shown in Fig. 2 illustrate this phenomenon. Note that the methyl group is a singlet for N-methyliminodimethylenediphosphonic acid, whereas the methyl on N-methylaminomethylenephosphonic acid is a triplet due to quadrupolar coupling to pro-

tonated nitrogen. Similarly, the methylene appears as a doublet (split by phosphorus) in the tertiary amine and as a multiplet in the secondary amine due to coupling to phosphorus and nitrogen.

#### Acknowledgment

The author would like to thank K. F. Koncki who did most of the laboratory work and R. S. Mitchell (Monsanto Industrial Chemicals Company) who supplied all of the tertiary amine starting compounds.

Manuscript submitted Oct. 30, 1975; revised manuscript received ca. Dec. 23, 1975. This was Paper 348

Any discussion of this paper will appear in a Discussion Section to be published in the December 1976 JOURNAL. All discussions for the December 1976 Discussion Section should be submitted by Aug. 1, 1976.

Publication costs of this article were partially assisted by Monsanto Company.

#### REFERENCES

1. I. M. Osadchenko, A. P. Tomilov, N. Sh. Fuks, and E. G. Bondarenko, *Russian J. Gen. Chem.*, **39**, 900 (1969).
2. H. W. Frazier, L. R. Smith, and J. H. Wagenknecht, U.S. Pat. 3,835,000 (1974).
3. J. H. Wagenknecht, *Syn. React. Inorg. Metal-Org. Chem.*, **4**, 567 (1974).
4. K. Moedritzer and R. R. Irani, *J. Org. Chem.*, **31**, 1603 (1966).
5. K. Moedritzer, *Syn. Inorg. Metal-Org. Chem.*, **3**, 75 (1973).
6. R. L. Shriner, R. C. Fuson, and D. Y. Curtin, "The Systematic Identification of Organic Compounds," p. 218, John Wiley & Sons, Inc., New York (1959).
7. C. K. Mann and K. K. Barnes, "Electrochemical Reactions in Nonaqueous Systems," p. 279, Marcel Dekker, Inc., New York (1970).
8. S. D. Ross, M. Finkelstein, and E. I. Rudd, "Anodic Oxidation," pp. 211-215, Academic Press, Inc., New York (1975).
9. G. H. Alt and J. H. Wagenknecht, *Syn. React. Inorg. Metal-Org. Chem.*, **4**, 255 (1974).
10. R. C. Fuson and H. R. Snyder, "Organic Chemistry," p. 311, John Wiley & Sons, Inc., New York (1942).
11. P. G. Gassman, I. Nishiguchi, and H. Yamamoto, *J. Am. Chem. Soc.*, **97**, 1600 (1975).

## Voltammetric and Related Studies of NbCl<sub>5</sub> in Molten Chloroaluminates

G. Ting,<sup>1</sup> K. W. Fung,<sup>2</sup> and G. Mamantov\*

Department of Chemistry, University of Tennessee, Knoxville, Tennessee 37916

#### ABSTRACT

The electrochemical reduction of NbCl<sub>5</sub> in AlCl<sub>3</sub>-NaCl melts of compositions varying from a NaCl saturated melt [~50-50 mole per cent (m/o)] to a 63 m/o AlCl<sub>3</sub> melt was investigated by chronoamperometry, linear sweep voltammetry, chronopotentiometry, and differential pulse polarography. The reduction mechanism is determined to a large extent by the melt composition and temperature which, in turn, determine the Lewis acidity of the melt. The formation of lower oxidation states results in dimerization and cluster formation. The standard electrode potential of the Nb(V)/Nb(IV) couple and the diffusion coefficient of Nb(V) in the NaCl saturated melt are reported.

Molten chloroaluminates (AlCl<sub>3</sub>-MCl mixtures where M<sup>+</sup> is an alkali cation) (1) are interesting solvents for electrochemical and spectral studies. The Lewis acidity (2-6) of these low-melting ionic liquids can be readily changed by varying the AlCl<sub>3</sub>-MCl ratio. The acidic compositions are particularly good media for stabilization of lower oxidation states, such as Cd<sub>2</sub><sup>2+</sup> (7), Bi<sup>+</sup>, Bi<sub>5</sub><sup>3+</sup> (8, 9), Hg<sub>3</sub><sup>2+</sup> (10), and Te<sub>2</sub><sup>2+</sup> and Te<sub>4</sub><sup>2+</sup> (11).

Recently we have become involved in electrochemical studies of selected metal ions of Groups IVB-VIB (refractory metals) in chloroaluminate melts. We are particularly interested in the effect of melt acidity, as determined by melt composition and temperature, on the redox chemistry and the mechanisms of electrode processes involving refractory metal ions. Possible formation of metal clusters (12) is also of interest. In a previous paper (13) we have reported on the electrochemistry of zirconium (IV) in these media. In this paper we report on the reduction of NbCl<sub>5</sub> in AlCl<sub>3</sub>-NaCl melts of different compositions by electrochemical techniques, such as chronoamperometry, chronopotentiometry, pulse polarography, and linear sweep voltammetry.

The electrochemistry of niobium in molten halides has been studied previously (14-27), mostly in the LiCl-KCl eutectic and the equimolar NaCl-KCl melt. In these studies niobium solute species were usually

produced by anodic dissolution of niobium metal; there is disagreement in the literature as to the nature of the niobium species produced. Gut (14) has studied the reduction of NbCl<sub>5</sub> in AlCl<sub>3</sub>-containing melts. He reported that Nb(V) is reduced to Nb(III) in two steps at a platinum electrode in the AlCl<sub>3</sub>-NaCl-KCl [50-25-25 mole per cent (m/o)] melt at 200°C; in the more acidic melt, AlCl<sub>3</sub>-NaCl-KCl (60-26-14 m/o), at 120°C the two steps almost overlap. Gut interpreted the process as being due to a one step two-electron reduction; however, *E* vs. log (*i*<sub>d</sub> - *i*)/*i* plot was not linear.

#### Experimental

Melt preparation, electrochemical cell, instrumentation, and procedures have been described previously (10, 28). Differential pulse polarograms were obtained with the Princeton Applied Research Model 174 polarographic analyzer. Both platinum and tungsten wires (electrode areas 0.10 cm<sup>2</sup>) were used as working electrodes. The reference electrode was an aluminum wire immersed in AlCl<sub>3</sub>-NaCl (63-37 m/o) and separated from the main compartment by a thin Pyrex membrane.

NbCl<sub>5</sub> (from Alfa Inorganics) was purified twice by sublimation through a Pyrex frit at 220°C. The yellow granular crystals were identified by Raman spectra (29).

#### Results and Discussion

*AlCl<sub>3</sub>-NaCl<sub>sat</sub> melt.*<sup>3</sup>—*Mechanism of the reduction of Nb(V).*—Polarograms constructed from current-time curves (10) for the reduction of Nb(V) at both

<sup>3</sup> The liquidus composition at 175°C is ~49.8 m/o in AlCl<sub>3</sub> (3).

\* Electrochemical Society Active Member.

<sup>1</sup> Present address: Institute of Nuclear Energy, Taiwan, Republic of China.

<sup>2</sup> Present address: Department of Chemistry, University of Hong Kong, Hong Kong.

Key words: niobium, chloroaluminates, NbCl<sub>5</sub>, AlCl<sub>3</sub>-NaCl melts.



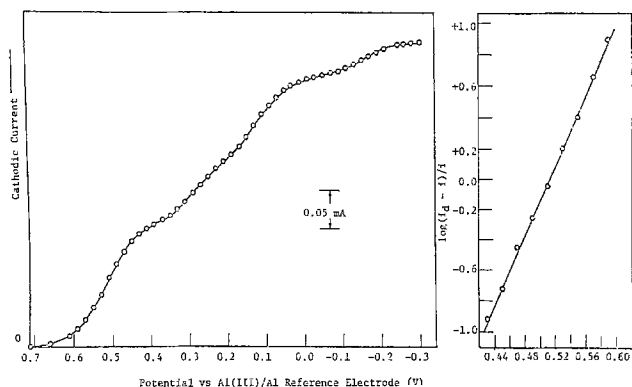


Fig. 1. Polarogram constructed from current-time curves for the reduction of Nb(V) at platinum electrode at 180°C; plot of  $E$  vs.  $\log(i_d - i)/i$  for the first wave. Melt composition,  $\text{AlCl}_3\text{-NaCl}_{\text{sat}}$ ; electrode area, 0.10 cm<sup>2</sup>; Nb(V) concentration,  $2.68 \times 10^{-2}\text{M}$ ; current measured at 5 sec.

platinum and tungsten working electrodes exhibit four reduction steps at longer current measuring times (5 sec) in the temperature range 160°-180°C (Fig. 1) (at > 180°C the over-all polarograms were ill-defined). The dependence of the diffusion currents on the concentration of Nb(V) is shown in Table I. Diffusion current ratios with respect to the first reduction step were approximately 1:0.5:0.5: (0.2-0.3). The first reduction step is well-defined; the slope  $2.3 RT/nF$  of the  $\log(i_d - i)/i$  vs.  $E$  plot for the first reduction step (Fig. 1) corresponds to a one-electron reversible process. At lower concentrations ( $6.8 \times 10^{-3}\text{M}$ ) and short current measuring times (0.1 and 0.02 sec) only two reduction steps were observed; the corresponding log plots (Fig. 2) result in  $n_1 = 0.97$  and  $n_2 = 0.92$ . Differential pulse polarographic, chronopotentiometric (at low current densities), and linear sweep voltammetric (at low scan rates,  $\leq 0.1$  V/sec) studies also resulted in four reduction steps. Typical chronopotentiograms and cyclic voltammograms are shown in Fig. 3 and 4, respectively. Chronopotentiograms taken at high current densities and linear sweep voltammograms taken at fast scan rates exhibit three reduction steps (the third reduction step was observed at higher concentrations than those corresponding to polarographic conditions of Fig. 2).

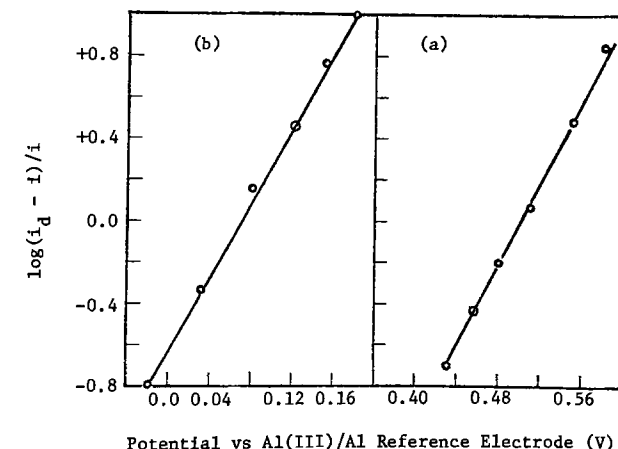
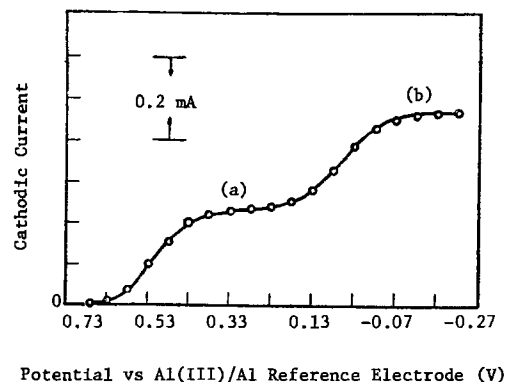


Fig. 2. Polarogram constructed from current-time curves at tungsten electrode at 180°C. Plot of  $E$  vs.  $\log(i_d - i)/i$  for the two waves shown. Melt composition,  $\text{AlCl}_3\text{-NaCl}_{\text{sat}}$ ; electrode area, 0.10 cm<sup>2</sup>; Nb(V) concentration,  $6.8 \times 10^{-3}\text{M}$ ; current measured at 0.1 sec.

The cyclic voltammogram for the first step is shown in Fig. 5; the summary of the voltammetric data for the first step at a platinum electrode is shown in Table II (similar results were obtained at a tungsten electrode). The peak current,  $i_{p(1)}$ , for the first reduction step was directly proportional to Nb(V) con-

Table I. Concentration dependence of the diffusion currents<sup>a</sup>

Nb(V) concentration (M)	$i_{d(1)}$ ( $\mu\text{A}$ )	$i_{d(1)}/C$ ( $\mu\text{A} \cdot \text{liter} \cdot \text{mole}^{-1}$ )	$i_{d(2)}$ ( $\mu\text{A}$ )	$i_{d(2)}/C$ ( $\mu\text{A} \cdot \text{liter} \cdot \text{mole}^{-1}$ )	$i_{d(3)}$ ( $\mu\text{A}$ )	$i_{d(3)}/C$ ( $\mu\text{A} \cdot \text{liter} \cdot \text{mole}^{-1}$ )	$i_{d(4)}$ ( $\mu\text{A}$ )	$i_{d(4)}/C$ ( $\mu\text{A} \cdot \text{liter} \cdot \text{mole}^{-1}$ )
$6.8 \times 10^{-3}$	37	$5.45 \times 10^3$	21	$3.00 \times 10^3$	20	$2.94 \times 10^3$	7	$1.02 \times 10^3$
$2.68 \times 10^{-2}$	150	$5.59 \times 10^3$	80	$2.98 \times 10^3$	84	$3.13 \times 10^3$	30	$1.11 \times 10^3$
$5.19 \times 10^{-2}$	288	$5.54 \times 10^3$	144	$2.77 \times 10^3$	168	$3.23 \times 10^3$	64	$1.15 \times 10^3$

<sup>a</sup> Melt composition,  $\text{AlCl}_3\text{-NaCl}_{\text{sat}}$ ; Pt electrode area, 0.10 cm<sup>2</sup>; temperature, 180°; current measured at 5 sec.

Table II. Voltammetric results for the reduction of Nb(V) to Nb(IV) at the platinum electrode.<sup>a</sup>  
Melt composition,  $\text{AlCl}_3\text{-NaCl}_{\text{sat}}$

NbCl <sub>5</sub> concentration (M)	Temperature (°C)	$(E_p^c - E_p^a)_{\text{calc.}}$ (mV)	$(E_p^c - E_p^a)_{\text{exp.}}$ (mV)	$(E_p - E_{p/2})_{\text{calc.}}$ (mV)	$(E_p - E_{p/2})_{\text{exp.}}$ (mV)	$i_p^a / i_p^c$	$E_p^a$ (V)	$E_{1/2}$ (V)	$D$ (cm <sup>2</sup> /sec)	
$6.8 \times 10^{-3}$	180	-89.7	-90 ± 5	-86.1	-90 ± 5	1.00	0.440	0.496	$7.0 \times 10^{-6}$	
	$1.34 \times 10^{-2}$	160	-85.7	-89 ± 5	-82.3	-90 ± 5	1.00	0.480	0.525	$6.6 \times 10^{-6}$
		180	-89.7	-90 ± 5	-86.1	-100 ± 10	0.99	0.460	0.516	$7.1 \times 10^{-6}$
		220	-97.6	-100 ± 5	-93.7	-110 ± 10	1.00	0.438	0.498	$11.2 \times 10^{-6}$
		260	-105.5	-110 ± 5	-101.3	-120 ± 10	0.98	0.416	0.476	$19.3 \times 10^{-6}$
$2.68 \times 10^{-2}$	300	-114.0	-130 ± 10	-109.4	-140 ± 10	1.03	0.413	0.458	$24.5 \times 10^{-6}$	
	160	-85.7	-90 ± 5	-82.3	-90 ± 5	1.01	0.50	0.540	$4.9 \times 10^{-6}$	
	180	-89.7	-95 ± 5	-86.1	-100 ± 10	1.02	0.474	0.524	$5.8 \times 10^{-6}$	
$5.19 \times 10^{-2}$	300	-113.4	-130 ± 10	-108.9	-120 ± 10	1.01	0.406	0.466	$20.8 \times 10^{-6}$	
	160	-85.7	-100 ± 10	-82.3	-95 ± 10	0.97	0.504	0.548	$4.8 \times 10^{-6}$	
	180	-89.7	-100 ± 10	-86.1	-100 ± 10	0.98	0.490	0.538	$6.6 \times 10^{-6}$	

<sup>a</sup> Electrode area, 0.10 cm<sup>2</sup>; scan rate, 0.1 V/sec; Al(III) ( $\text{AlCl}_3\text{-NaCl}$ , 63-37 m/o)/Al reference electrode.

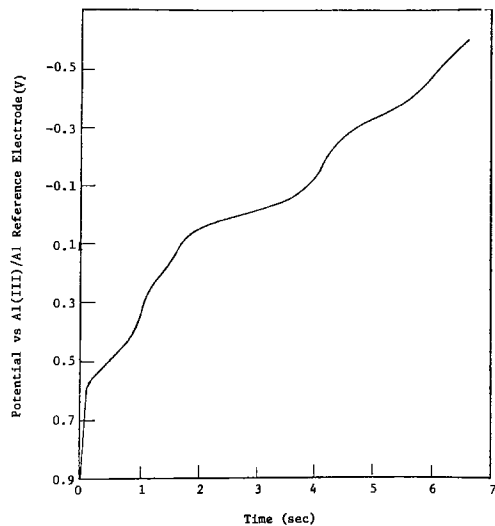


Fig. 3. Chronopotentiogram for the reduction of Nb(V) at tungsten electrode at 160°C. Melt composition,  $\text{AlCl}_3\text{-NaCl}_{\text{sat}}$ ; electrode area,  $0.10 \text{ cm}^2$ ; Nb(V) concentration,  $5.19 \times 10^{-2} \text{ M}$ ; current density,  $10 \text{ mA/cm}^2$ .

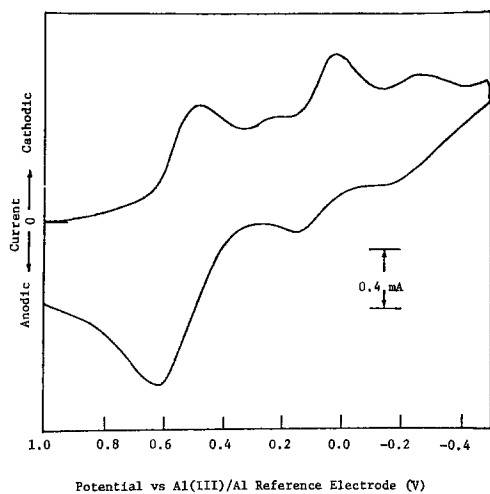


Fig. 4. Cyclic voltammogram (first scan) for the reduction of Nb(V) at platinum electrode at 160°C. Melt composition;  $\text{AlCl}_3\text{-NaCl}_{\text{sat}}$ ; electrode area,  $0.10 \text{ cm}^2$ ; Nb(V) concentration,  $5.19 \times 10^{-2} \text{ M}$ ; scan rate,  $0.1 \text{ V/sec}$ .

centration in the range studied; the parameter  $i_p/v^{1/2}$  is almost independent of the scan rate ( $v$  was varied from  $0.02$  to  $10 \text{ V/sec}$ ) at temperatures  $180^\circ\text{-}260^\circ\text{C}$ . Comparison of experimental and theoretical (30) peak potential separations ( $E_p^c - E_p^a$ ), peak widths ( $E_p - E_{p/2}$ ), and anodic and cathodic peak current ratios [ $i_p^a/i_p^c$ , calculated using Nicholson's semi-empirical formula (31)] leads to the conclusion that the first reduction step is essentially a one-electron reversible diffusion-controlled process. This conclusion was verified by: (i) peak width measurements of the first peak in the differential pulse polarogram (32); (ii) chronopotentiometric  $E$  vs.  $\log(\tau^{1/2} - t^{1/2})/t^{1/2}$  plot for the first reduction step; (iii) values of  $n_1$  of 1.01 and 1.05 determined from the ratio of voltammetric  $i_p/v^{1/2}$  to chronoamperometric  $it^{1/2}$  and chronopotentiometric  $i\tau^{1/2}$ . For these determinations of  $n$ , concentration, diffusion coefficient, and electrode area do not need to be known. These ratios are given as (33)

$$\frac{i_p/v^{1/2}}{it^{1/2}} = 86.31 (n/T)^{1/2} \quad [1]$$

$$\frac{i_p/v^{1/2}}{i\tau^{1/2}} = 54.86 (n/T)^{1/2} \quad [2]$$

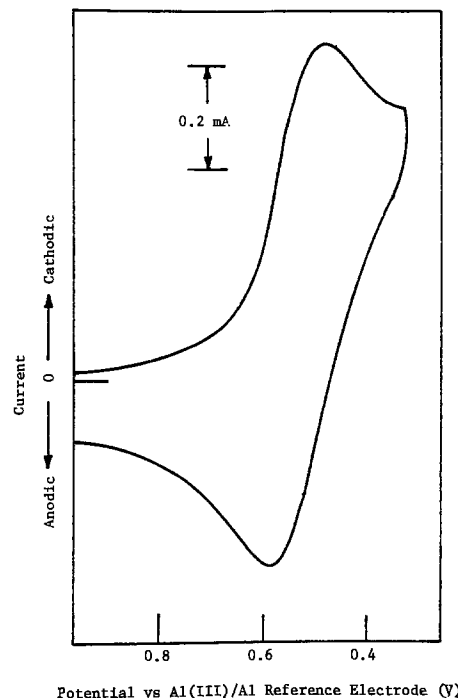


Fig. 5. Cyclic voltammogram for the reduction of Nb(V) at tungsten electrode at 180°C. Melt composition,  $\text{AlCl}_3\text{-NaCl}_{\text{sat}}$ ; electrode area,  $0.10 \text{ cm}^2$ ; Nb(V) concentration,  $2.68 \times 10^{-2} \text{ M}$ ; scan rate,  $0.2 \text{ V/sec}$ .

However, it should be noted (Table II and Fig. 6) that the voltammetric peak potential,  $E_{p(1)}^c$ , shifts anodically with increasing Nb(V) concentration. An anodic shift of  $E_p^c$  with increasing solute concentration for the case of the soluble product may be caused either by a mechanism involving reversible charge transfer followed by reversible or irreversible dimerization (34-38) or by a disproportionation reaction following a reversible charge transfer (39). The latter mechanism may be eliminated by the observed linear dependence of the peak current on concentration. According to Saveant and Vianello (36) for the case of reversible charge transfer followed by a reversible dimerization, when the extent of dimerization is small, the peak potential is given by

$$E_p = E_{1/2} - 0.70 RT/nF - RT/4nF \ln D_o/D_z - RT/2nF \ln K + RT/2nF \ln C \quad [3]$$

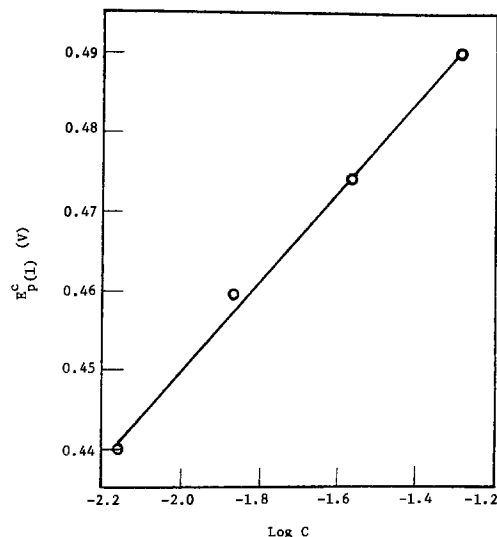


Fig. 6. Plot of  $E_{p(1)}^c$  vs.  $\log C$  for the reduction of Nb(V) to Nb(IV) at platinum electrode at 180°C. Melt composition,  $\text{AlCl}_3\text{-NaCl}_{\text{sat}}$ ; electrode area,  $0.10 \text{ cm}^2$ .

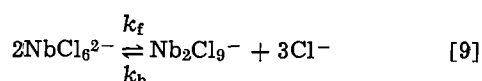
where  $D_o$  and  $D_z$  are diffusion coefficients of the oxidized and the dimer forms and  $K$  is the equilibrium constant for the dimerization process. Thus,  $E_p$  vs.  $\log C$  plot should be linear with a slope  $2.3 RT/2nF$ . The observed slope (Fig. 6) results in  $n_1 = 0.92$ , thus, providing strong evidence for the presence of some dimerization following the first reduction step.

The presence of a preceding chemical reaction before the second reduction step is also supported by a  $\sim 20\%$  decrease in the chronopotentiometric  $i_o\tau_2^{1/2}$  when the current density is increased from 6 to 25 mA/cm<sup>2</sup> (33).

The results obtained by several methods point to the reduction mechanism of the ECEEE type, at least at longer times (slower scan rates in linear sweep voltammetry and lower current densities in chronopotentiometry). The mechanism believed to be present is

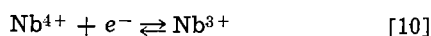
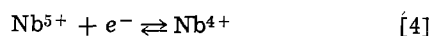


Decreasing  $K$  (see Eq. [5]) values for dimerization of Nb(IV) in more acidic melts are expected by considering a reaction, such as



This reaction will be driven to the right by the reaction of  $\text{Al}_2\text{Cl}_7^-$  ions with  $\text{Cl}^-$  ions to form  $\text{AlCl}_4^-$  ions. It would, therefore, be expected from equilibrium considerations that in the melt saturated with NaCl, complications due to dimerization in this basic melt composition should be only minor; this expectation is borne out by the experimental results. Saveant *et al.* (40) reported that a pure diffusion-controlled process should be seen for an ECE mechanism with a large  $K$  for the following chemical reaction. The number of electrons in the reduction steps occurring after the dimerization process is based primarily on the observed polarographic diffusion current ratios. The existence of  $\text{Nb}_2^{7+}$  (no conclusions may be drawn from the existing data regarding the number of Cl<sup>-</sup> ions associated with this or other entities) has not been reported as yet; however, Caton and Freund (15) have reported that niobium ions with an average  $n$  value of 3.64 were generated by controlled potential electrolysis in LiCl-KCl eutectic. Also Yang *et al.* (24) have found that mixed valence states between  $\text{Nb}^{3+}$  and  $\text{Nb}^{4+}$  prevailed in concentrated LiCl-KCl eutectic. Formation of  $\text{Nb}_3^{8+}$  in LiCl-KCl eutectic has been reported by Saeki and Suzuki (17, 25).

The results obtained at shorter times (or faster scan rates) indicate that the first two reduction steps involve simple reversible electrode reactions



The chemical reaction following the first reduction step does not have enough time to occur. The third reduction step observed in the chronopotentiograms and voltammograms is possibly due to a higher order electrode reduction of  $\text{Nb}^{3+}$ ; the observed flatness of the third wave is in agreement with the theoretical prediction (41) that the voltammograms for higher order processes are smaller and broader than the corresponding first order voltammograms.

*Standard electrode potential of the Nb(V)/Nb(IV) couple.*—The half-wave potential  $E_{1/2}$  for a reversible process  $O + ne^- = R$  may be taken as the voltammetric equivalent of the standard electrode potential  $E^\circ$ , assuming that the diffusion coefficients and activity coefficients are equal (33). The  $E_{1/2}$  values for the process  $\text{Nb(V)} + e^- \rightleftharpoons \text{Nb(IV)}$  are listed in Table II with respect to Al(III)/Al (in  $\text{AlCl}_3$ -NaCl, 63-37 m/o) reference electrode. Assuming that the complications due to dimerization of Nb(IV) are small at low solute concentrations and that the half-wave potential is a good estimate of the standard electrode potential, useful thermodynamic information may be obtained. At Nb(V) concentration of  $1.34 \times 10^{-2}M$ ,  $E$  vs.  $T$  plot is linear in the temperature range 160°-300°C resulting in

$$E = 0.732 - 4.79 \times 10^{-4}T \quad [11]$$

The entropy change for the cell reaction is

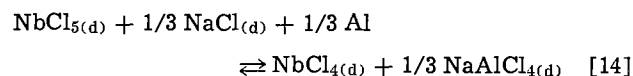
$$\Delta S = nF \left( \frac{\partial E}{\partial T} \right)_P = -11.05 \text{ (eu)} \quad [12]$$

After correcting for the potential difference due to melt composition difference between bulk and reference electrode compartments [ $\Delta E$  between  $\text{AlCl}_3$ -NaCl<sub>sat</sub> and the 63-37 m/o is 0.60V at 175°C (3, 5)], the cell voltage in the range 160°-300°C becomes

$$E = 1.33 - 4.79 \times 10^{-4}T \quad [13]$$

(in the above equation it is assumed that the temperature coefficient is independent of the melt composition).

The equilibrium quotient for the reaction



$Q = X_{\text{NbCl}_4}/X_{\text{NbCl}_5}$ , is, therefore, given by

$$\log Q = -2.41 + 6.70 \times 10^3/T \quad [15]$$

This equation shows that the lower the temperature the higher is the stability of Nb(IV) in the  $\text{AlCl}_3$ -NaCl<sub>sat</sub> melt. This result is in agreement with the previous observations (3, 42) that the Lewis acidity of chloroaluminates increases with decreasing temperature and that an increase in acidity favors the lower oxidation state.

*Diffusion coefficient of Nb(V).*—Assuming that the effect of dimerization is small, the diffusion coefficient of Nb(V) in molten  $\text{AlCl}_3$ -NaCl<sub>sat</sub> may be calculated from the Randles-Sevcik equation (see Table II). A linear  $\log D$  vs.  $1/T$  plot in the temperature range 160°-300°C was obtained for the Nb(V) concentration of  $1.34 \times 10^{-2}M$ . The resulting equation is

$$\log D = -2.70 - 1100/T \quad [16]$$

From this equation the activation energy for the diffusion of Nb(V) in this melt has been calculated as 5.0 kcal/mole.

The diffusion coefficient for Nb(V) at 180°C was also calculated from the chronopotentiometric data using the Sand equation; the values of  $4.9 \times 10^{-6}$  and  $4.5 \times 10^{-6}$  cm<sup>2</sup>/sec at Nb(V) concentration of  $2.68 \times 10^{-2}$  and  $5.19 \times 10^{-2}M$ , respectively, were obtained. Chronoamperometric results at short times (0.02 and 0.1 sec) resulted in the  $D$  value of  $\sim 4.8 \times 10^{-6}$  cm<sup>2</sup>/sec for the Nb(V) concentration of  $2.68 \times 10^{-2}M$ . Thus, the agreement between  $D$  values obtained by three different methods is at best reasonable; similar deviations were observed in studies of Ti(II) in molten chloroaluminates (42).

*Adsorption effects.*—At platinum (but not tungsten) electrode, sharp characteristic (43) adsorption-desorption peaks were observed in linear sweep voltammograms before the third reduction step after  $\sim 1$  day at

experimental temperature (220°C) at the Nb(V) concentration of  $2.68 \times 10^{-2}M$ . At lower scan rates ( $\leq 2$  V/sec) the adsorption and desorption peak currents are symmetric; at faster scan rates the adsorption peak shifts cathodically and the desorption peak anodically; the amount of this shift increases with increasing scan rate. The adsorption-desorption peaks become broad and skewed. The parameter  $i_p/v^{1/2}$  increased with scan rate as expected (43). These observations are consistent with the theory of linear sweep voltammetry of systems involving kinetic adsorption of the products (44).

**AlCl<sub>3</sub>-NaCl (55-45 m/o) melt.**—The melt composition has a pronounced effect on the reduction characteristics of Nb(V). The polarogram constructed from current-time curves using a platinum electrode at 180°C is shown in Fig. 7; two reduction steps are observed. Similar results were obtained at 260°C and with a tungsten electrode. A value of  $n = 1.9$  was obtained from the  $E$  vs.  $\log(i_d - i)/i$  plot for the first reduction step. Upon lowering the temperature to 140°-150°C the first step is split into two steps (Fig. 8) for which nonlinear log plots were obtained. Similar results were obtained by chronopotentiometry and linear sweep voltammetry. The experimental observations ( $n = 2$  for the first reduction step at 180°C, the splitting of this step into two steps of approximately equal height at 140°-150°C, and the nonlinearity of log plots) point to the formation of Nb<sup>4+</sup> followed by dimerization and further reduction to Nb<sub>2</sub><sup>6+</sup> in the first reduction step at 180°C or the first two steps at 140°-150°C. The reduction step at 0.26V (Fig. 7) occurs at approximately the same potential [after correcting

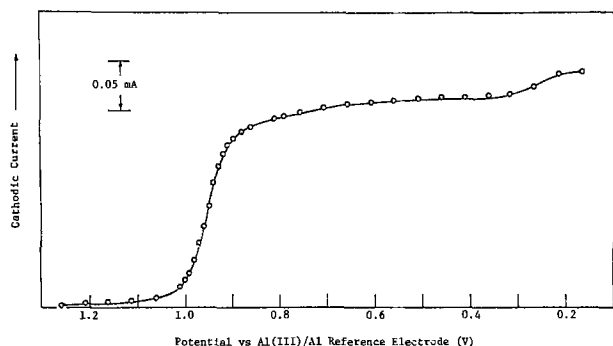


Fig. 7. Polarograms constructed from current-time curves for the reduction of Nb(V) at platinum electrode at 180°C. Melt composition, AlCl<sub>3</sub>-NaCl (55-45 m/o); electrode area, 0.10 cm<sup>2</sup>; Nb(V) concentration,  $1.42 \times 10^{-2}M$ ; current measured at 5 sec.

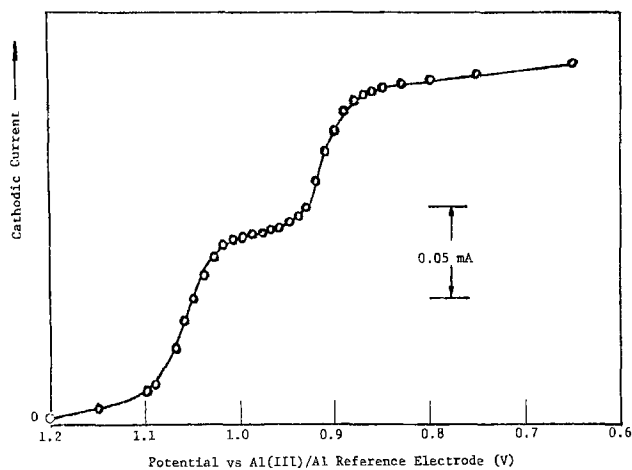


Fig. 8. Polarogram constructed from current-time curves for the reduction of Nb(V) at platinum electrode at 140°C. Melt composition, AlCl<sub>3</sub>-NaCl (55-45 m/o); electrode area, 0.10 cm<sup>2</sup>; Nb(V) concentration,  $1.42 \times 10^{-2}M$ ; current measured at 5 sec.

for melt composition difference (3, 5)] as the last step in the NaCl-saturated melt. This evidence as well as the observed diffusion current ratio and the broad nature of the peak at this potential in the cyclic voltammogram pointing to higher reaction order (41) lead us to conclude that the formation of Nb<sub>3</sub><sup>3+</sup> is probably involved at this potential. The splitting of the first reduction step at 180°C into two steps at 140°-150°C is probably caused by the increase in  $k_f$  value (or decreasing  $K$ ,  $K = k_b/k_f$ , see Eq. [5]) at lower temperatures due to the increasing acidity of the melt at lower temperatures. Saveant *et al.* (39) have reported that the peak potential should shift anodically with increasing  $k_f$  value (decreasing  $K$  value) for an ECE mechanism involving a reversible chemical reaction. According to Nicholson and Shain (45) anodic shift of the first wave and the appearance of a second wave should be observed at large values of  $k_f$  for an ECE mechanism with an irreversible chemical reaction. The observed results are in agreement with the theoretical predictions as stated above.

**AlCl<sub>3</sub>-NaCl (63-37 m/o) melt.**—The electrochemical behavior of Nb(V) in this very acidic melt at 180°-260°C is very similar to that in the 55/45 melt at 180°C. Two reduction steps were observed. For the first well-defined step  $E_{1/2} = 1.04V$  at 180°C; the voltammetric peak current is proportional to Nb(V) concentration. The second poorly defined step occurs at the same potential (after correcting for the composition difference) as the last step in the NaCl-saturated melt. The presence of kinetic complications in the first reduction step may be deduced from several experimental results, such as a very small reoxidation peak current at a potential 0.3-0.5V more anodic (depending on the scan rate) than the cathodic peak potential; a decrease in the  $i_p/v^{1/2}$  parameter with increasing scan rate, the anodic shift of the cathodic peak potential with increasing concentration, and nonlinear log plots using polarograms constructed from current-time curves. It is concluded that the reduction scheme of Nb(V) in this melt is the same as in the 55/45 melt.

## Conclusions

The results presented in this paper for the reduction of Nb(V) and in previous papers for the reduction of Zr(IV) and the oxidation of Ti(II) (13, 42) in molten chloroaluminates demonstrate that the electrochemical reduction pathway is, to a large extent, determined by the melt composition and temperature. Since both of these parameters determine the Lewis acidity of the chloroaluminate melts (2-6), a direct relationship to that parameter is apparent.

This work, as well as related studies on the electroreduction of Ta(V) and W(VI) (46), also illustrates that the formation of lower oxidation states of the refractory metal in these melts results in dimerization and cluster formation. This result is in agreement with those of McCarley and co-workers (47, 48). No evidence for the deposition of niobium metal in these melts has been obtained.

## Acknowledgments

This research was supported by the National Science Foundation Grants GP 32433X and MPS 74-10357 A01. One of the authors (G. T.) would like to acknowledge financial support from the Institute of Nuclear Energy Research, Taiwan, Republic of China.

Manuscript submitted Aug. 22, 1975; revised manuscript received Jan. 12, 1976.

Any discussion of this paper will appear in a Discussion Section to be published in the December 1976 JOURNAL. All discussions for the December 1976 Discussion Section should be submitted by Aug. 1, 1976.

Publication costs of this article were partially assisted by the University of Tennessee.

LIST OF SYMBOLS  
(Others are defined in the text)

$i_d$	polarographic diffusion current
$i_p^c$	cathodic peak current in linear sweep voltammetry
$i_p^a$	anodic peak current in linear sweep voltammetry
$v$	scan rate in linear sweep voltammetry
$E_p^c$	cathodic peak potential in linear sweep voltammetry
$E_p^a$	anodic peak potential in linear sweep voltammetry
$E_{p/2}$	half-peak potential in linear sweep voltammetry
$\tau$	chronopotentiometric transition time

## REFERENCES

- For a review, see C. R. Boston, in "Advances in Molten Salt Chemistry," Vol. 1, J. Braunstein, G. Mamantov, and G. P. Smith, Editors, pp. 129-163, Plenum Press, New York (1971).
- B. Tremillon and G. Letisse, *J. Electroanal. Chem.*, **17**, 371 (1968).
- G. Torsi and G. Mamantov, *Inorg. Chem.*, **10**, 1900 (1971).
- G. Torsi and G. Mamantov, *ibid.*, **11**, 1439 (1972).
- L. G. Boxall, H. L. Jones, and R. A. Osteryoung, *This Journal*, **120**, 223 (1973).
- A. A. Fannin, L. A. King, and D. W. Seegmiller, *ibid.*, **119**, 801 (1972).
- T. C. F. Munday and J. D. Corbett, *Inorg. Chem.*, **5**, 1263 (1966).
- N. J. Bjerrum, C. R. Boston, and G. P. Smith, *ibid.*, **6**, 1162 (1967).
- N. J. Bjerrum and G. P. Smith, *ibid.*, **6**, 1968 (1967).
- G. Torsi, K. W. Fung, G. M. Begun, and G. M. Mamantov, *ibid.*, **10**, 2285 (1971).
- N. J. Bjerrum, *ibid.*, **9**, 1965 (1970); **10**, 2578 (1971); **11**, 2648 (1972).
- See, for example, D. Brown, in "Comprehensive Inorganic Chemistry," Vol. 3, J. C. Bailar, Jr., H. J. Emeleus, R. Nyholm, and A. F. Trotman-Dickenson, Editors, pp. 568-573, Pergamon Press, Elmsford, N. Y. (1973).
- B. Gilbert, G. Mamantov, and K. W. Fung, *Inorg. Chem.*, **14**, 1802 (1975).
- R. Gut, *Helv. Chim. Acta*, **43**, 830 (1960).
- R. D. Caton, Jr. and H. Freund, *Anal. Chem.*, **36**, 15 (1964).
- J. Dartnell, K. E. Johnson, and L. L. Shreir, *J. Less Common Metals*, **6**, 85 (1964).
- Y. Saeki and T. Suzuki, *ibid.*, **9**, 362 (1965).
- Y. Saeki and K. Funaki, *Bull. Tokyo Inst. Technol.*, **86**, 1 (1968).
- V. F. Pimenov, *Izv. Vysshikh Uchebn. Zavedenil, Tsvetn. Met.*, **11**, 64 (1968); **12**, 90 (1969).
- D. Inman, R. S. Sethi, and R. Spencer, *J. Electroanal. Chem.*, **29**, 137 (1971).
- M. Sakawa and T. Kuroda, *Denki Kagaku*, **36**, 653 (1968); **37**, 99 (1969).
- Y. Saeki and T. Suzuki, *ibid.*, **34**, 691 (1966).
- V. F. Pimenov and Yu. V. Baimakov, *Soviet Electrochem.*, **4**, 1220 (1968).
- L. Yang, R. G. Hudson, and C. Y. Chien, "Physical Chemistry of Process Metallurgy," Part 2, Metallurgical Society Conference, Vol. 8, p. 925, Interscience, New York (1959).
- T. Suzuki, *Electrochim. Acta*, **15**, 127 (1970).
- L. E. Ivanovskii and M. T. Krasilnikov, *Electrochem. Molten Solid Electrolytes*, **7**, 48 (1969).
- S. Senderoff and G. W. Mellors, *This Journal*, **113**, 66 (1966).
- K. W. Fung and G. Mamantov, in "Comprehensive Analytical Chemistry," Vol. III, G. Svehla, Editor, pp. 305-370, Elsevier Publishing Co. (1975).
- J. R. Beattie, T. R. Gilson, and G. A. Ozin, *J. Chem. Soc., (A)*, **89**, 2765 (1968).
- R. S. Nicholson and I. Shain, *Anal. Chem.*, **36**, 706 (1964).
- R. S. Nicholson, *ibid.*, **38**, 1406 (1966).
- E. P. Parry and R. A. Osteryoung, *ibid.*, **37**, 1634 (1965).
- P. Delahay, "New Instrumental Methods in Electrochemistry," Interscience Publishers, Inc., New York (1954).
- M. S. Shuman, *Anal. Chem.*, **42**, 521 (1960).
- J. M. Saveant and E. Vianello, *Electrochim. Acta*, **10**, 905 (1965).
- J. M. Saveant and E. Vianello, *ibid.*, **12**, 1545 (1967).
- R. S. Nicholson, *Anal. Chem.*, **37**, 667 (1965).
- M. L. Olmstead, R. C. Hamilton, and R. S. Nicholson, *ibid.*, **41**, 260 (1969).
- M. Mastragostino, L. Nadjjo, and J. M. Saveant, *Electrochim. Acta*, **13**, 721 (1968).
- J. M. Saveant, C. P. Andrieux, and L. Nadjjo, *J. Electroanal. Chem.*, **41**, 137 (1973).
- M. S. Shuman, *Anal. Chem.*, **41**, 142 (1969).
- K. W. Fung and G. Mamantov, *J. Electroanal. Chem.*, **35**, 27 (1972).
- R. H. Wopschall and I. Shain, *Anal. Chem.*, **39**, 1514 (1967).
- M. H. Hulbert and I. Shain, *ibid.*, **42**, 162 (1970).
- R. S. Nicholson and I. Shain, *ibid.*, **37**, 178 (1965).
- G. Mamantov, D. L. Brotherton, and L. E. McCurry, Unpublished work.
- W. C. Dorman and R. E. McCarley, *Inorg. Chem.*, **13**, 491 (1974).
- R. E. McCarley, Private communication.

## Studies in Derivative Chronopotentiometry

### III. Application to Submillisecond Transition Times

P. E. Sturrock\*

School of Chemistry, Georgia Institute of Technology, Atlanta Georgia 30332

and R. H. Gibson\*

Department of Chemistry, University of North Carolina at Charlotte, Charlotte, North Carolina 28223

#### ABSTRACT

The derivative technique for the measurement of chronopotentiometric transition times is applied to millimolar solutions of cadmium and lead at the dropping mercury electrode. Linear Bard plots are obtained down to transition times of 15  $\mu$ sec with calculated chronopotentiometric constants having a relative accuracy of better than 3%. The present limitations to the measurement of short transition times, for reversible electrode reactions, appear to be due to instrumentation.

The chief disadvantage in chronopotentiometry is the strong influence that the double-layer charging has

over the output waveform and the concomitant difficulty in measuring the parameter of interest, the transition time. With the advent of derivative chronopotentiometry, the disadvantages of the conventional

\* Electrochemical Society Active Member.  
Key words: DME, current correction, reversible reactions.

technique are lessened or removed. In previous papers (1-2) we have discussed instrumentation, diffusion-controlled systems, and application to analysis. We present here some measurements of short transition times ( $<1$  msec). Since the measuring technique and double-layer influences were discussed in the previous two papers (1-2), that material and pertinent references will not be repeated here.

In order to make rapid repetitive chronopotentiometric measurements on a reproducible electrode, we decided to utilize the classical dropping mercury electrode, DME. Some results obtained on this electrode were presented previously (1-2). However, unless short transition times can be measured accurately, the use of the DME results in a rather narrow range of usable transition times. Thus, successful measurements of short transition times greatly enhance the practical applications of chronopotentiometry with the DME and also serve as a further check on the split-current model and correction techniques.

### Experimental

Derivative and conventional (200 mV) chronopotentiograms were obtained with two solutions: 1 mM  $\text{Pb}(\text{NO}_3)_2$  in 1M  $\text{KNO}_3$  and 1 mM  $\text{Cd}(\text{NO}_3)_2$  in 1M  $\text{KNO}_3$ . The chronopotentiograms were obtained with an instrument described previously (1) and recorded on a Tektronix 564A storage oscilloscope equipped with a 10 MHz dual-trace vertical amplifier. The chronopotentiograms were then photographed with a Tektronix C-12A camera and the data read from the photographs. At each current setting several repeats were made, each one on a fresh drop. In most cases the repeated traces superimposed so well that they appeared to be only one trace.

The experiments were first performed using a Beckman hanging mercury drop assembly to produce a 1  $\mu\text{l}$ iter HMDE. The area of this electrode is calculated to be 0.0484  $\text{cm}^2$ . Due to the current limitations of the instrument, the fastest transition time measured with this electrode was 261  $\mu\text{sec}$ . The experiments were then repeated on a DME. By varying the time between drop detachment and switching from prebias potential to constant current, different electrode areas could be utilized; therefore, higher current densities, leading to shorter transition times could be obtained within the current limitations of the instrumentation. While estimates of the DME area could be made by measuring the mercury flow rate and delay times, the areas reported were obtained by comparison with the transition times obtained with the HMDE.

The instrument can use either a diode gate (Philbrick SPG-1) or a mercury-wetted relay for switching from the prebias to current mode. The switching time for the diode gate is much faster than that of the relay, but the diode gate can pass a maximum of only 2.5 mA current and has the added disadvantage of having a small current offset, the magnitude of which is dependent upon duty cycle. The relay used was of the bridging type so that the current pulse was applied before the prebias was released. However, the prebias circuit has sufficient current capacity that the application of

the current pulse resulted in only a slight drift in the effective prebias while the relay was bridged. The small time delay for the relay switching adds to that of the timing circuit and results in increased time delays and consequently larger DME areas than when the diode gate was used. All of the experiments with the cadmium solution were performed using the relay switching while those with the lead solutions were performed with the diode gate. The difference in switching devices explains the larger DME area reported for the cadmium experiments. The use of the diode gate and its limited current capability required a second, smaller DME area for the lead experiments at the shortest transition times.

Positive feedback was not used to compensate for the double-layer charging in these experiments since the rise time of the compensator circuit limits its use to transition times of greater than 100  $\mu\text{sec}$ .

### Results

The experimental results are summarized in Table I. All experimental points are retained since, in no case, is the deviation of a single point more than 4 standard deviations from the average of the other points of that series. The large standard deviation of the cadmium results with the DME originates from the transition times below 12  $\mu\text{sec}$  where the current was  $> 5$  mA. If these 8 points are deleted, the chronopotentiometric constant for this series becomes  $435 \pm 7$ . However, the worst point (transition time = 3.25  $\mu\text{sec}$ ) is only high by 3.2 standard deviations from the series or a relative deviation of 10.1%.

The Bard-plot intercepts for the derivative data correspond to an average of 21.3 and 24.7  $\mu\text{f}/\text{cm}^2$ , respectively, for the cadmium and lead series.

Figure 1 shows the short transition time end of the DME series for both metals. The dotted lines are the best fit lines for the complete series of 45 and 50 points. Figure 2 shows the derivative HMDE series for both metals. The dotted lines are the best fit lines from the fast DME data, identical with the lines of Fig. 1.

The 200 mV technique results in higher values for the chronopotentiometric constant for both metals than does the derivative technique. This same trend can also be seen by comparing the results in Tables II and III of Ref. (1) and is probably due to the 200 mV interval extending past the point at which the surface concentration of the depolarizer reaches zero. Thus, the last portion of the curve included in the 200 mV region contains faradaic current in excess of the amount that should be contained in the transition time. The 200 mV technique also results in an intercept in the Bard plot that corresponds to a double-layer capacitance that is too large. The values for the cadmium and lead series in Table I are 36 and 41  $\mu\text{f}/\text{cm}^2$ , respectively. Nonan (3) suggested using the slope of the initial potential change in the  $E-t$  curve to evaluate the double-layer capacitance and hence the correction factor for the 200 mV technique. However, the results of this study indicate that even if the correct double-layer capacitance is obtained, the correction factor is

Table I\*

Solution	$\tau$ measurement	Electrode and area	Number of points	$\tau$ range	Bard-plot intercept	Chronopotentiometric constant
a**	200 mV	HMDE, 0.0484	35	1-98 msec	7.2	448 $\pm$ 6
a	Derivative	HMDE, 0.0484	35	0.53-82 msec	1.0	429 $\pm$ 5
a	Derivative	DME, 0.02926	50	3 $\mu\text{sec}$ -11 msec	0.8	430 $\pm$ 13
b***	200 mV	HMDE, 0.0484	25	0.59-85 msec	8.1	491 $\pm$ 7
b	Derivative	HMDE, 0.0484	25	0.26-72 msec	1.2	467 $\pm$ 6
b	Derivative	DME, 0.02912	38	54 $\mu\text{sec}$ -74 msec	1.1	467 $\pm$ 5
b	Derivative	DME, 0.01125	45	11-439 $\mu\text{sec}$	0.9	467 $\pm$ 6

\* Electrode areas are  $\text{cm}^2$ ; intercepts are  $\frac{\mu\text{f} \times \Delta E}{\text{cm}^2}$ ; chronopotentiometric constants are  $\frac{\text{A-sec}^{1/2}\text{-ml}}{\text{mole}}$ .

\*\* a =  $1.00 \times 10^{-3}\text{M}$   $\text{Cd}(\text{NO}_3)_2$  in 1M  $\text{KNO}_3$ .

\*\*\* b =  $1.00 \times 10^{-3}\text{M}$   $\text{Pb}(\text{NO}_3)_2$  in 1M  $\text{KNO}_3$ .

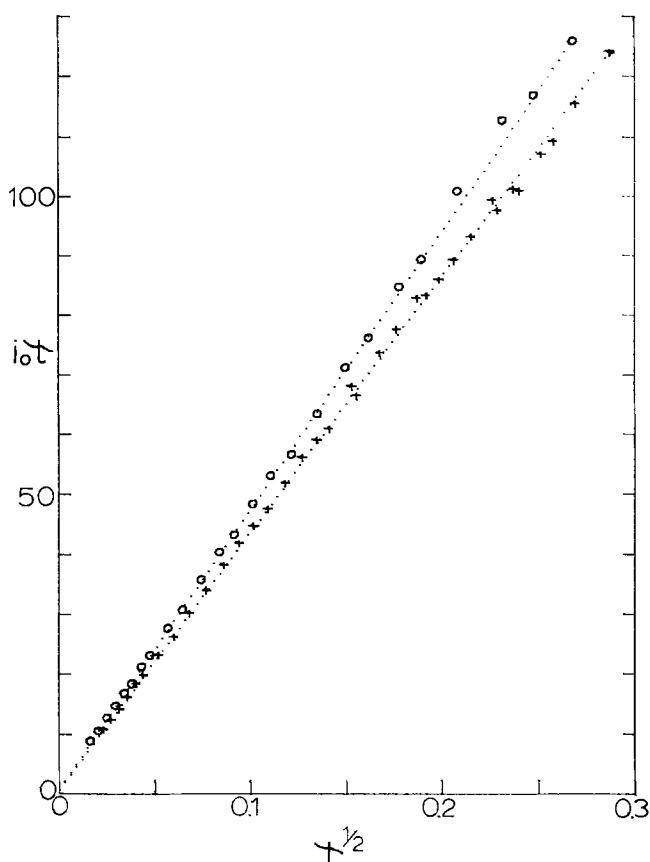


Fig. 1. Bard plot of short transition time data at DME: ○ = 1 mM  $\text{Pb}(\text{NO}_3)_2$  in 1M  $\text{KNO}_3$ ; + = 1 mM  $\text{Cd}(\text{NO}_3)_2$  in 1M  $\text{KNO}_3$ ;  $\tau$  is in sec,  $i_0$  is in  $\text{mA}/\text{cm}^2$ .

inadequate and the technique results in too large a value for the chronopotentiometric constant.

### Conclusions

Using our present equipment, it appears that transition times for reversible processes can be measured with a relative precision of 2-3% down to about 15  $\mu\text{sec}$ . Below that point the precision deteriorates. The present limitations on the measurement of fast transition times appear to be due to the instrumentation. The problems of current capacity and switching have been discussed above. The other instrumentation problem is the speed and accuracy of the differentiator. The amplifier used for this purpose is a Philbrick P-45AU with a nominal unity-gain bandwidth of 200 MHz and a current output of 20 mA. Even with this amplifier, it is difficult to design a stable differentiator circuit with a rise time significantly less than 1  $\mu\text{sec}$ . In addition, slight errors in the calibration of the differentiator lead to large errors in the corrected short transition times where the Bard-plot intercept is more than 50% of the total experimental  $i_0\tau$  values.

As was pointed out in Ref. (1), the charging current is a problem at short times and low concentrations. In Fig. 1 it can be seen that the charging current is about 50% of the total current for the fastest transitions measured in this study. If lower concentrations had been employed, the charging current would be a larger fraction of the total current at these transition times and

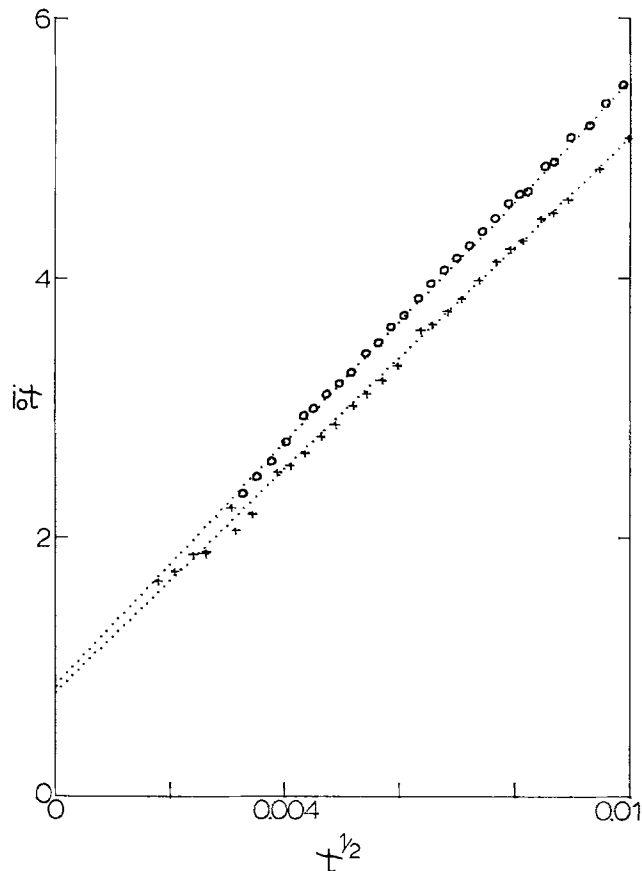


Fig. 2. Bard plot of transition time data at HMDE, symbols and units as in Fig. 1.

the scatter of calculated chronopotentiometric constants should be greater. Conversely, at higher concentrations the results should be improved or even faster transitions should be measurable.

With the extension of the measurement of transition times to  $< 10 \mu\text{sec}$  by the derivative technique, the use of the DME for chronopotentiometry now becomes much more feasible. Previously, a planar electrode was needed in order to obtain data over so many orders of magnitude. Thus, the application to analysis and kinetic studies appears more viable. Future papers in this series will deal with applications to chemical kinetics coupled to reversible charge-transfer reactions.

Manuscript submitted Oct. 28, 1975; revised manuscript received Jan. 14, 1976.

Any discussion of this paper will appear in a Discussion Section to be published in the December 1976 JOURNAL. All discussions for the December 1976 Discussion Section should be submitted by Aug. 1, 1976.

Publication costs of this article were partially assisted by the Georgia Institute of Technology.

### REFERENCES

1. P. E. Sturrock, J. Hughey, B. Vaudreil, G. O'Brien, and R. Gibson, *This Journal*, **122**, 1195 (1975).
2. P. E. Sturrock, B. Vaudreil, and R. H. Gibson, *This Journal*, **122**, 1311 (1975).
3. D. C. Noonan, Ph.D. Dissertation, Columbia University (1967).

# The Effect of Nonuniform Concentration on the Distribution of Potential and Electrochemical Reaction Rate in Molten Polysulfide Electrodes

Y. K. Kao and P. C. Wayner, Jr.

Department of Chemical and Environmental Engineering, Rensselaer Polytechnic Institute, Troy, New York 12181

## ABSTRACT

A nonuniform concentration model for the sulfur electrode of the Na/S battery is presented. Numerical results obtained using a hypothetical concentration distribution demonstrate that a concentration gradient in the polysulfide phase region of the phase diagram will cause a significant shift in the reaction distribution from that predicted by a uniform concentration model. The effect of concentration on the local double layer potential difference significantly enhances the operation of the sulfur electrode.

The use of the sodium sulfur fused salt systems as a secondary battery is desirable because of its high theoretical energy density, high open-circuit cell voltage, and the intrinsic low cost of the reactants. Current research on this battery concerns a device that consists of reservoirs of sodium and of sulfur which are separated by a solid ceramic electrolyte,  $\beta$ -alumina, which is a conductor of only the sodium ions. This system was first described by Kummer and Weber (1). Since that time considerable research has been done on this system (e.g., 2-5). The fully charged cathode usually consists of a conductive graphite felt matrix imbedded in a pool of the nonconductive liquid sulfur. During discharge, the sodium ions, having given up an electron to the external circuit, migrate through the solid electrolyte to form various polysulfides ( $\text{Na}_2\text{S}_x$ ) at the surface of the porous graphite cathode. The operating range of the cell is limited and complicated by the formation of various phases as described by its phase diagram (6). Upon discharge insoluble  $\text{Na}_2\text{S}_2$  precipitates out when the over-all composition reaches a critical value. When the amount of sulfur present in the cell is greater than that equivalent to an over-all composition of about  $\text{Na}_2\text{S}_5$ , two immiscible liquid phases (S,  $\text{Na}_2\text{S}_5$ ) coexist. Previous work (7) on the kinetics of the electrode reaction of carbon or graphite in  $\text{Na}_2\text{S}_3$ ,  $\text{Na}_2\text{S}_4$ ,  $\text{Na}_2\text{S}_5$  melts at 300°-350°C has revealed that the exchange current density is extremely high. The porous electrode operation is believed to be transport limited as a result of the high exchange current density, complicated phase relationship, and the nonconductivity of sulfur phase.

Using a uniform concentration model, Gibson (8), demonstrated that gross heterogeneity in the reaction distribution can severely limit the operation of the cell. However, a uniform concentration model cannot evaluate the more important effect on cell operation resulting from the high dependency of open-circuit voltage on composition. Herein, a model of the polysulfide/sulfur electrode which includes the effect of composition on cell operation is developed. The predominant effect of composition on cell operation is numerically demonstrated for various hypothetical composition distributions. This effect significantly enhances the operation of the sulfur electrode.

## Physical Parameters

The selection of a theoretical approach was influenced by a thorough search of the available data on the Na/S system. Fortunately, sufficient data was available so that the effect of concentration gradients could be

Key words: battery, porous sulfur electrode, sodium-sulfur cell.

included. Data on the transference number and activity of sulfur have been obtained by Cleaver and Davis (9). They report the Washburn number for sulfur which is defined as the number of moles of atomic sulfur which pass through a plane which is stationary with respect to the sodium ions per Faraday of charge. The open-circuit voltage data are available in Ref. (6, 9), and the conductivity data are presented in Ref. (9, 10). The conductivity of a representative graphite felt is also available along with some information on the limiting current at the polysulfide/graphite electrode (11).

The following interpolation equations for a temperature of 350°C, is obtained from Cleaver's experimental data for use in the computations described below.

1. The conductivity of the melt can be approximated by

$$k_1 = 1.5376 - 1.9264w_s \text{ (in } \text{ohm}^{-1}\text{-cm}^{-1}\text{)} \quad [1]$$

in which  $w_s$  is the weight fraction of atomic sulfur.

2. The density data are best fitted by

$$v = 37.1683 - 18.6457m_s \text{ (in } \text{cm}^3\text{/mole)} \quad [2]$$

in which  $v$ ,  $1/(c_1 + c_3)$ , is defined as the volume occupied by one mole of  $\text{Na}_2\text{S}$  and S, and  $m_s$  is defined as  $c_1/(c_1 + c_3)$ .

3. The chemical potential of atomic sulfur can be approximated by (in mV)

$$\frac{RT}{2F} \ln a(s) = -690.9970 + 384.9642x - 74.8151x^2 + 5.0553x^3 \quad [3]$$

where  $a(s)$  is the activity of atomic sulfur in  $\text{Na}_2\text{S}_x$  and  $x$  is the  $x$  in  $\text{Na}_2\text{S}_x$ .

## Sulfur Electrode Model

The sulfur electrode is composed of a graphite felt matrix immersed in a pool of molten sulfur and/or polysulfide. A cross-sectional diagram of the cylindrical electrode is shown in Fig. 1. It is bounded on the inner side by the ceramic tube, with outer radius  $R_0$ , which serves as sodium container. On the other side, it is bounded by a conductive tube which also serves as a container for the cathodic material. The space is filled with porous graphite felt which serves as an electronic path since sulfur is a nonconductive material.

The analysis herein follows the continuum model approach of Newman and Tobias (12) which assumes that the system is adequately described as the superposition of two continua: the electrolyte and the graphite matrix. The current-potential relationship for the graphite phase is described by Ohm's law



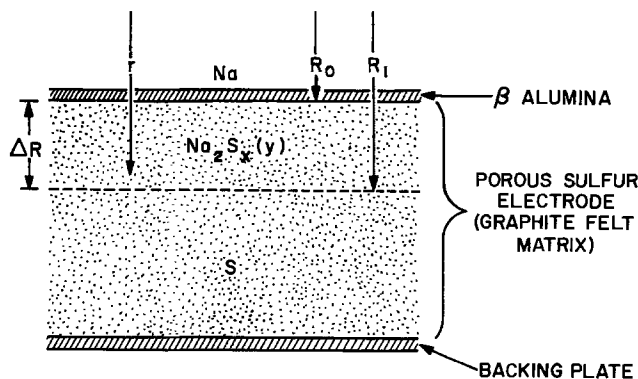


Fig. 1. Cross-sectional drawing of the cylindrical electrode

$$\frac{d\phi_2}{dr} = -\frac{1}{k_2} i_2 \quad [4]$$

The current-potential relationship for the melt phase with concentration gradient has to be developed, following the approach proposed by Newman, Bennion, and Tobias (13), from the multicomponent diffusion equation

$$c_i \nabla \mu_i = \sum_j K_{ij} (v_j - v_i) \quad [5]$$

Equations [6]-[8] are then obtained by assuming the melt is composed of the following species: (i) free sulfur atom, S, denoted by subscript 1; (ii) sodium ion, Na<sup>+</sup>, denoted by subscript 2; and (iii) sulfide ion, S<sup>2-</sup>, denoted by subscript 3.

$$c_1 \nabla \mu_1 = K_{12} (v_2 - v_1) + K_{13} (v_3 - v_1) \quad [6]$$

$$c_2 \nabla \mu_2 = K_{21} (v_1 - v_2) + K_{23} (v_3 - v_2) \quad [7]$$

$$c_3 \nabla \mu_3 = K_{31} (v_1 - v_3) + K_{32} (v_2 - v_3) \quad [8]$$

In these equations  $\mu_i$ ,  $K_{ij}$ , and  $v_i$  are the electrochemical potential, the drag coefficient, and the velocity. After choosing  $v_2$  as the reference velocity and introducing the current equation

$$i_1 = z_3 c_3 F (v_3 - v_2) \quad [9]$$

where  $z_3$  and  $c_3$  are the charge number and the concentration of species 3 and  $F$  is the Faraday constant, and using the chemical potential of the electrolyte which is defined as

$$c \nabla \mu = c_2 \nabla \mu_2 + c_3 \nabla \mu_3 = (K_{21} + K_{31}) (v_1 - v_2) - K_{31} (v_3 - v_2) \quad [10]$$

and after eliminating the  $v_i$ 's of Eq. [6]-[8] by [9] and [10] we arrive at the following expressions of the molar fluxes

$$N_1 = \frac{K_{31} c_1}{(K_{21} + K_{31}) c_3 z_3 F} \frac{i_1}{F} + \frac{c_1}{K_{12} + K_{13}} c \nabla \mu + c_1 v_2 \quad [11]$$

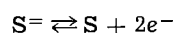
$$N_2 = c_2 v_2 \quad [12]$$

$$N_3 = \frac{i_1}{z_3 F} + c_3 v_2 \quad [13]$$

Eliminating  $v_1$ ,  $v_2$ , and  $v_3$  in Eq. [11]-[13], the following equation is obtained

$$c_3 \nabla \mu_3 = \frac{i_1}{z_3 c_3 F} \left\{ -\frac{(K_{31} K_{21} + K_{21} K_{32} + K_{31} K_{32})}{K_{21} + K_{31}} \right\} + \frac{K_{31}}{K_{21} + K_{31}} \frac{c}{c_3} \nabla \mu \quad [14]$$

Assuming the reference electrode has the reaction



one can define the potential gradient in the melt as

$$\nabla \mu_3 - \nabla \mu_1 = -2F \nabla \phi_1 \quad [15]$$

Applying Eq. [14] and the Gibbs-Duhem equation:  $c \nabla \mu + c_1 \nabla \mu_1 = 0$  one obtains the following

$$\begin{aligned} \nabla \mu_3 - \nabla \mu_1 &= \nabla \mu_3 \\ -\frac{c}{c_3} \nabla \mu &= \frac{i_1}{z_3 c_3 F} \left[ \frac{K_{31} K_{21} + K_{32} K_{21} + K_{31} K_{32}}{K_{21} + K_{31}} \right] \\ &+ \frac{K_{31}}{K_{21} + K_{31}} \frac{c}{c_3} \nabla \mu + \frac{c}{c_1} \nabla \mu = -2F \nabla \phi_1 \quad [16] \end{aligned}$$

Then define

$$i_1 = -k_1 \nabla \phi_1 \text{ when } \nabla \mu = 0$$

$$k_1 = \frac{-2F^2 c_3^2 z_3 (K_{31} + K_{21})}{(K_{31} K_{21} + K_{32} K_{21} + K_{31} K_{32})} \quad [17]$$

Hence, the current equation for the melt phase is

$$i_1 = -k_1 \nabla \phi_1 - \frac{k_1}{2F} \left[ \frac{1}{c_1} + \frac{1}{c_3} \frac{K_{31}}{K_{21} + K_{31}} \right] c \nabla \mu \quad [18]$$

According to Cleaver's result:  $K_{31} \gg K_{21}, K_{32}$ , therefore

$$i_1 = -k_1 \nabla \phi_1 + \frac{k_1}{2F} [1 - 2W_s] \nabla \mu_1$$

where  $W_s$  is called the Washburn number and is defined (9) to be  $-c_1/2c_3$ .

The above equation then becomes

$$i_1 = -K_1 \frac{d\phi_1}{dr} + \frac{k_1}{2F} \times \frac{d\mu_1}{dr} \quad [19]$$

The conservation of charge in each phase leads to the following equations

$$\frac{di_1}{dr} = -\frac{1}{r} i_1 - ai_s \quad [20]$$

$$\frac{di_2}{dr} = -\frac{1}{r} i_2 + ai_s \quad [21]$$

The conservation of charge, assuming there is no capacitance in the electrode, is given by one equation

$$(i_1 + i_2)r = I_{R_0} R_0 \quad [22]$$

Past research on electrokinetics (14, 15) indicated that the process was diffusion controlled. This result is substantiated, at least for part of the discharging cose near the reversible potential, in the recent comprehensive discussion of the electrokinetics of the sodium polysulfide electrodes (16). For the redox reaction  $S + 2e^- \rightleftharpoons S^=$ , the diffusional overpotential  $\eta$  can be expressed in terms of the limiting current densities of sulfide ion,  $i_{ds^=}$ , and sulfur,  $i_{ds}$ , by the following equation (17)

$$\eta = \frac{RT}{2F} \ln \frac{\left(1 - \frac{i_s}{i_{ds}}\right)}{\left(1 - \frac{i_s}{i_{ds^=}}\right)} \quad [23a]$$

where  $i_{ds}$  is negative and  $i_{ds^=}$  is positive. Taking  $|i_{ds^=} = |i_{ds}| = i_1$  in Eq. [23a] and assuming that the total overpotential is due to concentration polarization gives

$$i_s = -i_1 \tanh(\alpha \eta); \quad \eta = \phi_2 - \phi_1 - \Delta \phi_e, \quad \alpha = \frac{F}{RT} \quad [23b]$$

where  $i_1$  is the limiting current density and  $\Delta \phi_e$  is the value of  $\phi_2 - \phi_1$  at  $i_s = 0$ .

The boundary conditions are

$$\begin{aligned} i_1(r - R_0) &= I_{R_0} \\ i_2(r = R_0) &= 0 \\ \phi_1(r = R_0) &= 0 \\ i_2(r = R_1) &= I_{R_0}R_0/R_1 \end{aligned}$$

where  $R_1$  denotes the position where the polysulfide/sulfur interface, or the position of the backing plate. The active electrode lies between  $r = R_0$  and  $r = R_1$ .

Eliminating  $\phi_1$ ,  $\phi_2$ , and  $i_2$  between Eq. [4] and [19]-[23] the following single equation for  $i_1$  is obtained

$$\begin{aligned} \frac{d^2 i_1}{dr^2} &= -\frac{1}{r} \frac{di_1}{dr} + \frac{1}{r^2} i_1 \\ &+ ai_1 \alpha \left[ 1 - \left( \frac{1}{ai_1} \right)^2 \left( \frac{di_1}{dr} + \frac{1}{r} i_1 \right)^2 \right] \\ &\cdot \left[ \left( \frac{1}{k_1} + \frac{1}{k_2} \right) i_1 - \frac{I_{R_0} R_0}{k_2 r} - \frac{1}{F} (1 - 2W_s) \frac{d\mu_1}{dr} \right] \end{aligned} \quad [24]$$

Using,  $\mu_1 = \mu_1^* + RT \ln a(s)$  and introducing the dimensionless variable  $j = i_1/I_{R_0}$  and  $y = (r - R_0)/(R_1 - R_0)$ , the following equation is obtained

$$\begin{aligned} \frac{d^2 j}{dy^2} &= -C_t \frac{dj}{dy} + C_t^2 j + \left[ 1 - \beta^2 \left( \frac{dj}{dy} + C_{tj} \right)^2 \right] \\ &\cdot \left[ \gamma \left( j - \frac{k_1}{k_1 + k_2} \right) \left( \frac{R_0}{R_0 + y\Delta R} \right) \right. \\ &\left. - \delta \times (b' + 2c'x + 3d'x^2) \frac{dx}{dy} \right] \end{aligned} \quad [25]$$

where

$$\begin{aligned} C_t &= \frac{\Delta R}{y\Delta R + R_0} \\ \beta &= \frac{I_{R_0}}{ai_1\Delta R} \\ \gamma &= ai_1\Delta R^2\alpha \left( \frac{1}{k_1} + \frac{1}{k_2} \right) \\ \delta &= \frac{ai_1\Delta R}{I_{R_0}} \frac{\alpha RT}{2F} \end{aligned}$$

For this study,  $\alpha = F/RT$ , then

$$\delta = \frac{ai_1\Delta R}{I_{R_0}} = \frac{1}{\beta}$$

Equation [25] now becomes

$$\begin{aligned} \frac{d^2 j}{dy^2} &= -C_t \frac{dj}{dy} + C_t^2 j + \left[ 1 - \beta^2 \left( \frac{dj}{dy} + C_{tj} \right)^2 \right] \\ &\cdot \left[ \gamma \left[ j - \frac{k_1}{k_1 + k_2} \left( \frac{R_0}{R_0 + y\Delta R} \right) \right. \right. \\ &\left. \left. - \frac{x}{\beta} (b' + 2c'x + 3d'x^2) \frac{dx}{dy} \right] \right] \end{aligned} \quad [26]$$

where

$$\begin{aligned} b' &= \frac{bnF}{RT} \\ c' &= \frac{cnF}{RT} \\ d' &= \frac{dnF}{RT} \end{aligned}$$

with boundary conditions

$$j(0) = 1, \quad j(1) = 0$$

## Numerical Results

Equation [26] was solved using the orthogonal collocation method (18) with 10 interior collocation points. The limiting current density was assumed to be 50 mA/cm<sup>2</sup> and the surface area per unit volume,  $a$ , was assumed to be 100 cm<sup>-1</sup>, which was based on experimental results (11) and previous numerical experience. This value showed good agreement between the model predicted internal resistance and experimental results for cells operating in the two-phase region (3).

In Fig. 2 and 3, the reaction rate distributions and the corresponding reaction overpotentials for various values of  $\beta$  ( $\propto I_{R_0}/\Delta R$ ) at constant  $\gamma$  ( $\propto \Delta R^2$ ) are presented. In Fig. 4, the reaction overpotential distribution for various values of  $\gamma$  at constant  $\beta$  are presented. The broken curves denote the results for a uniform concentration whereas the solid curves represent the results for the following hypothetical concentration distribution: the concentration of Na<sub>2</sub>S in Na<sub>2</sub>S<sub>x</sub> varies linearly from a value of  $x = 5.0$  at  $y = 0$  to  $x = 5.25$  at  $y = 1$ . The broken curves in Fig. 2 show the effect of current load on the reaction rate distribution for an electrode of fixed thickness. The results are similar at low current loads, i.e.,  $I_{R_0} = 0.12345, 0.24690$  A/cm<sup>2</sup>. However, at higher current densities,  $I_{R_0} = 0.49380$ , the shape of the curve changes in the high rate region which is characteristic of this type of kinetics. At a reaction rate near its limiting value, the rate becomes much less sensitive to a change in the reaction overpotential. The corresponding curves of overpotential presented in Fig. 3 are all similar in shape. In addition, if linear polarization kinetics were used, Eq. [26] would be invariant to the current load,  $I_{R_0}$ . Then the broken curves in Fig. 2 and 3 would be exactly proportional to their current load. The broken curves presented in Fig. 4

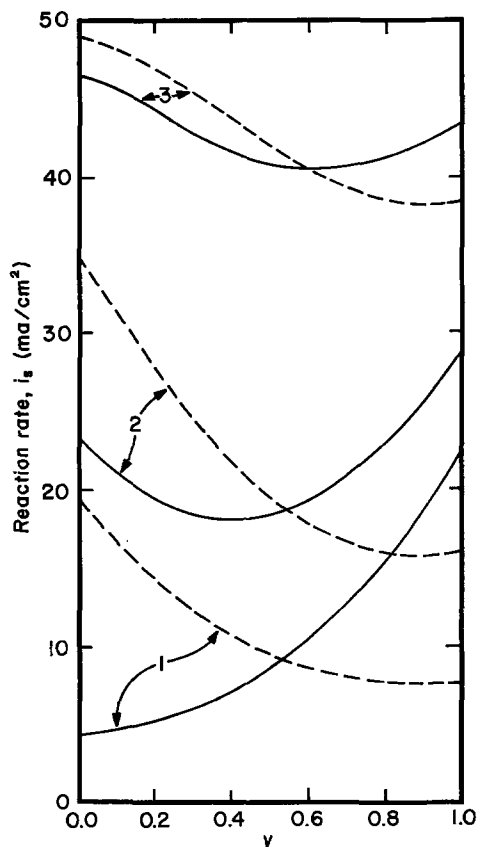


Fig. 2. Reaction rate distribution for: curve 1,  $I_{R_0} = 0.12345$  A/cm<sup>2</sup>; curve 2,  $I_{R_0} = 0.24690$  A/cm<sup>2</sup>; curve 3,  $I_{R_0} = 0.49380$  A/cm<sup>2</sup>. ( $R_0 = 0.3$  cm,  $\Delta R = 0.1$  cm,  $k_2 = 3$  ohm<sup>-1</sup>·cm<sup>-1</sup>,  $a = 100$  cm<sup>-1</sup>,  $i_1 = 0.05$  A/cm<sup>2</sup>). Solid curves represent nonuniform concentration and broken curves represent uniform concentration.

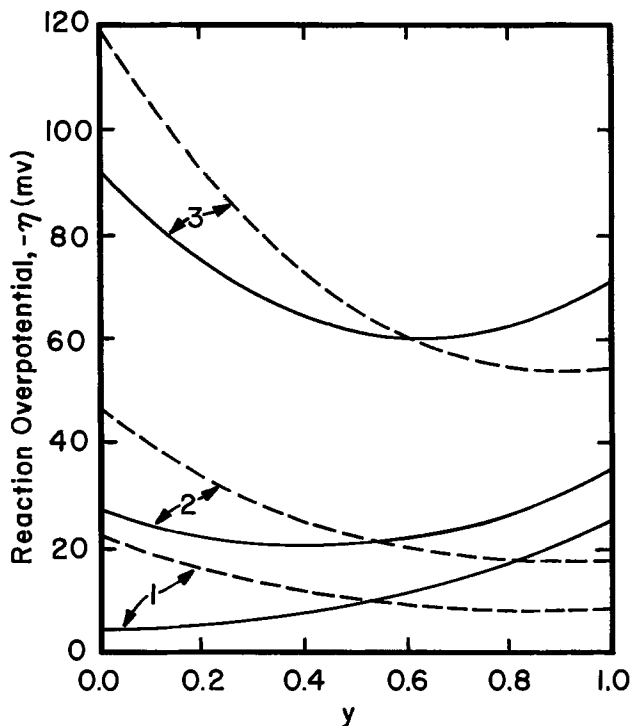


Fig. 3. Reaction overpotential distribution for conditions listed in caption for Fig. 2.

demonstrate that the reaction distribution becomes more heterogeneous as the thickness of the electrode increases.

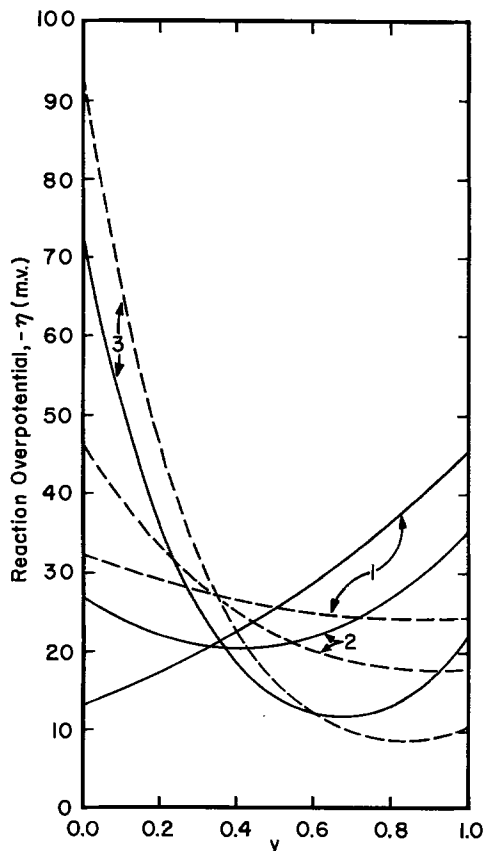


Fig. 4. Reaction overpotential distribution for: curve 1,  $I_{R_0} = 0.12345 \text{ A/cm}^2$ ,  $\Delta R = 0.05 \text{ cm}$ ; curve 2,  $I_{R_0} = 0.24690 \text{ A/cm}^2$ ,  $\Delta R = 0.1 \text{ cm}$ ; curve 3,  $I_{R_0} = 0.49380 \text{ A/cm}^2$ ,  $\Delta R = 0.2 \text{ cm}$ . ( $R_0 = 0.3 \text{ cm}$ ,  $k_2 = 3 \text{ ohm}^{-1}\text{-cm}^{-1}$ ,  $a = 100 \text{ cm}^{-1}$ ,  $i_1 = 50 \text{ mA/cm}^2$ .)

The concentration term of Eq. [26] is inversely proportional to the parameter  $\beta$ . As  $I_{R_0}$  becomes smaller, corresponding to smaller  $\beta$ , the concentration term becomes more dominant. As illustrated by the solid curves in Fig. 2 and 3 at lower current loads, the hypothetical concentration distribution shifts the high reaction zone located near  $y = 0$  in the uniform concentration case to  $y = 1$ . Therefore, the tendency for  $\text{Na}_2\text{S}_2$  to precipitate at the ceramic interface is reduced and the operation of the cell is improved. At a higher load, the concentration effect becomes less dominant. When  $\beta (\propto I_{R_0}/\Delta R)$  is kept constant while varying  $\gamma (\propto [\Delta R]^2)$ , the concentration effect becomes less dominant as the thickness of the electrode increases, which is illustrated by the solid curves in Fig. 4. Therefore, an increase in electrode thickness partially offsets the enhancement of cell operation resulting from the concentration effect.

In Fig. 5, the reaction overpotential distribution is presented for the case of  $k_2 = 0.3 \text{ ohm}^{-1}\text{-cm}^{-1}$ . (In the previously described results  $k_1 = 3.0 \text{ ohm}^{-1}\text{-cm}^{-1}$ .) For the uniform concentration cases, the reaction distribution is more symmetrical. For the same hypothetical concentration variation used previously, the reaction shifts toward the sulfur-rich region of the electrode. As the magnitude of the concentration variation increases, part of the electrode can operate in the charging mode while the average operation is one of discharge. This is shown in Fig. 6 for the case:  $\Delta R = 0.025 \text{ cm}$ ,  $I_{R_0} = 0.1234 \text{ A/cm}^2$ , and a concentration variation of  $x = 3.0$  at  $y = 0$  to  $x = 5.25$  at  $y = 1$ .

In Fig. 7, the variation of cell voltage with discharge is presented for different load conditions for the uniform concentration case. The slight density change is accomplished in this model by (i) changing the position of the polysulfide/sulfur interface in the two-phase region, and (ii) varying the position of the back-

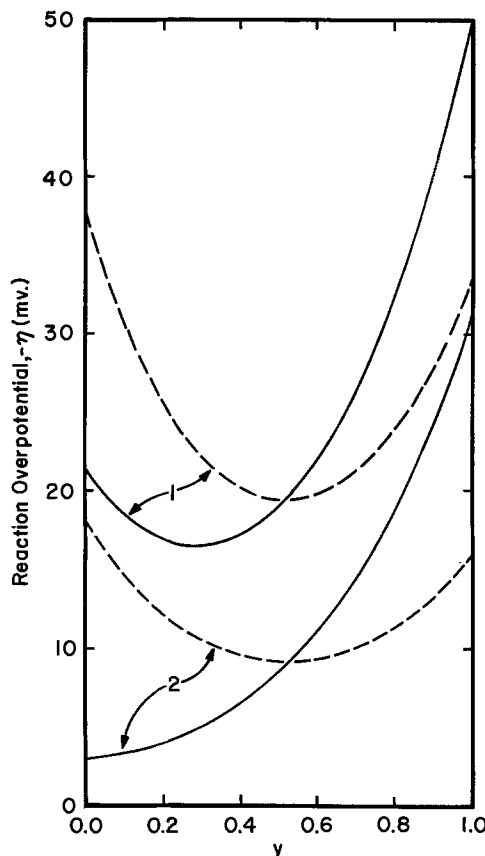


Fig. 5. Reaction overpotential distribution for melt and felt conductivities of the same order of magnitude. Curve 1,  $I_{R_0} = 0.24690 \text{ A/cm}^2$ ; curve 2,  $I_{R_0} = 0.12345 \text{ A/cm}^2$ . ( $k_2 = 0.3 \text{ ohm}^{-1}\text{-cm}^{-1}$ ,  $R_0 = 0.3 \text{ cm}$ ,  $\Delta R = 0.1 \text{ cm}$ ,  $a = 100 \text{ cm}^{-1}$ ,  $i_1 = 50 \text{ mA/cm}^2$ .)

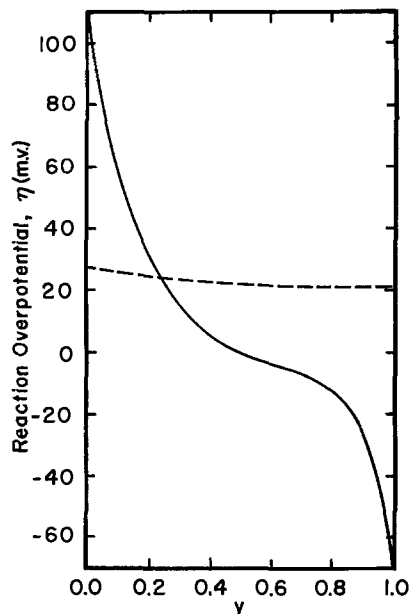


Fig. 6a. Reaction overpotential distribution for maximum concentration variation. ( $I_{R_0} = 0.12345 \text{ A/cm}^2$ ,  $\Delta R = 0.05 \text{ cm}$ ,  $k_2 = 3 \text{ ohm}^{-1}\text{-cm}^{-1}$ ,  $\alpha = 100 \text{ cm}^{-1}$ ,  $i_l = 50 \text{ mA/cm}^2$ .)

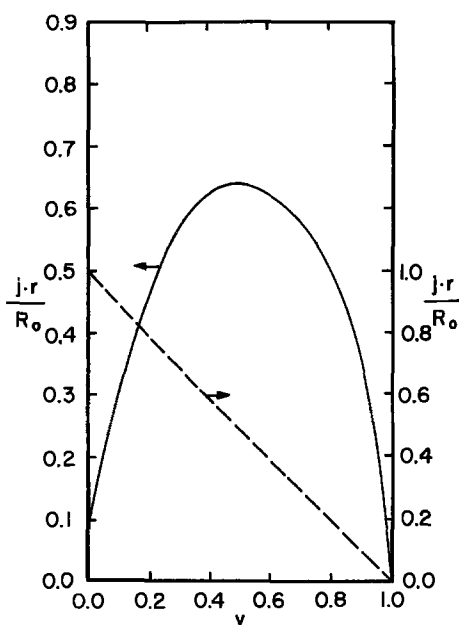


Fig. 6b. Current distribution for same conditions as listed in caption for Fig. 6a.

ing plate in the one-phase region. The equations that describe this effect are

$$R_1 \frac{dR_1}{dt} = \frac{I_{R_0} R_0}{2F} (2V_{\text{Na}} + V_s = + V_s) \quad [27]$$

for single phase region, and

$$R_1 \frac{dR_1}{dt} = \frac{I_{R_0} R_0}{2Fc_3}$$

for two-phase region.

The total potential loss is computed as the sum of the following four terms: (i) the total potential drop in the melt; (ii) the reaction overpotential loss at  $y = 1$ ; (iii) the ohmic potential loss in the ceramic electrolyte with ID = 0.4 cm, OD = 0.6 cm, and a resistivity of 5 ohm-cm; and (iv) the contact potential loss between the

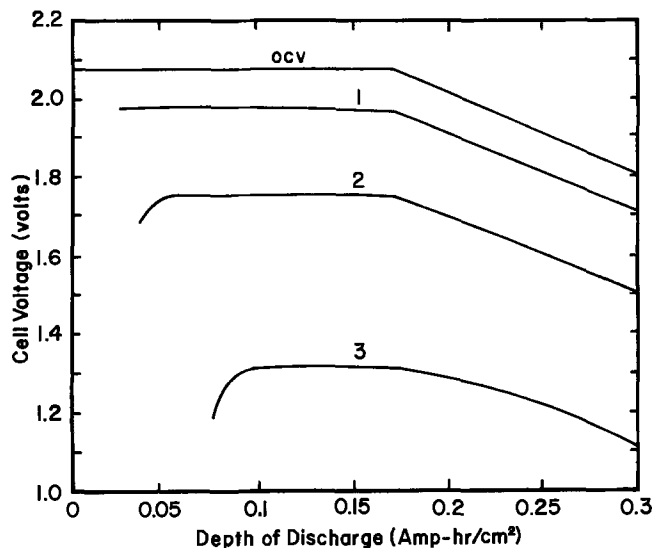
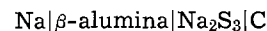


Fig. 7. Computed cell voltage of Na/S cell vs. depth of discharge for the uniform concentration model. Cell dimensions for fully charged state are  $R_0 = 0.3 \text{ cm}$  and  $\Delta R = 0.225 \text{ cm}$ . Curve 1,  $I_{R_0} = 0.1235 \text{ A/cm}^2$ ; curve 2,  $I_{R_0} = 0.37035 \text{ A/cm}^2$ ; curve 3,  $I_{R_0} = 0.823 \text{ A/cm}^2$ .

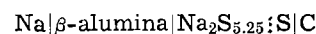
graphite felt and the backing plate with a resistance of  $0.1 \text{ ohm-cm}^2$ . There is an increase in the cell voltage at the earlier stage of discharge due to the reduction in the reaction overpotential loss as the thickness of the active electrode increases. Beyond this point the OCV decreases because the dominant effect now is the ohmic loss which increases as the electrode becomes thicker.

### Discussion

The numerical results for the uniform concentration case agree with the results of Newman and Tobias (12) and Gibson (8). Briefly, the region of most reaction is determined by the relative values of the melt and felt conductivities. Based on the results reported in an earlier modeling study of the Na/S battery by Gibson (8), the Na/S battery should not operate as well as it does (3). The very fact that the cell operates as well as it does when the felt conductivity is much greater than the melt conductivity can be explained by the inclusion of a concentration effect as developed herein. Simply stated, the dominant effect of concentration shifts the reaction to the region where the reactant is more abundant. This can be easily seen by comparing the following two cells



which has an OCV of 1.8V at  $350^\circ\text{C}$ ; and



which has an OCV of 2.078V. The sum of the overpotential losses in the melt, felt, and due to reaction is less than this 280 mV difference. Therefore, the particular heterogeneous reaction distribution predicted by the uniform concentration model cannot continue throughout the operating life of the cell.

The following is a more detailed account of the effect of concentration on the various overpotentials in the sulfur electrode (same conditions as Fig. 2). First, the computed cell voltages at the same depths of discharge are higher for the previously described concentration profile (Fig. 2) than for the uniform concentration profile.

In Table I the results in terms of potential losses of the highest OCV value of 2.078 excluding those ohmic losses in the solid electrolyte and due to the contact resistance between the graphite and the backing plate are summarized.

Table I. Potential losses (mV) in the sulfur electrode

$I_{R_0}$ (A/cm <sup>2</sup> )		$\Delta R$ (cm)			
		0.025	0.05	0.1	0.2
0.12345	u	111.67	43.94	34.24	34.05
	N	103.19	34.77	26.71	31.11
0.24690	u	*	107.34	59.92	59.09
	N	*	97.23	51.15	54.84
0.49380	u	*	*	134.19	116.18
	N	*	*	119.85	107.66

u = uniform, N = nonuniform.

\* Not available, because of the volume of the electrode is insufficient to sustain the current loads.

The concentration profile has four effects: (i) A cell operating at the assumed concentration profile has a higher OCV at  $y = 1$  than a cell operating at uniform concentration; (ii) the assumed concentration profile reduces the potential loss across the melt because of the migrating current contribution; (iii) the assumed concentration profile shifts the reaction distribution away from the ceramic resulting in an increase of reaction overpotential at  $y = 1$ ; and (iv) as a consequence of (iii), the ohmic potential drop in the melt increases because more current has to flow through a larger section of the melt. The first two effects depend on the concentration profile. The second effect has a slight variation due to the electrode dimension only because of the cylindrical geometry. These effects result in a gain in the cell voltage relative to the uniform concentration case of about 11 mV due to effect (i) and about 21 mV due to effect (ii). Effect (iii), the increase in reaction overpotential at  $y = 1$ , depends on the electrode thickness and varies slightly with the current load because of the nonlinear kinetics. These results are summarized in Table II. The fourth effect is summarized in Table III. Superficially, the results shown in Table I indicate that the effect of the concentration profile diminishes as the thickness increases. However, a larger variation in concentration is needed to obtain the same result with thicker electrodes.

Although the entire description of the porous electrode cannot be presented until the transport effects are included in a complete transient model, the results of the nonuniform concentration model presented herein are a better description of cell operation than those obtained using a uniform concentration model.

Table II. Increase in reaction overpotential at  $y = 1$ . Comparison of varying concentration case to the uniform concentration case (mV)

$I_{R_0}$ (A/cm <sup>2</sup> )	$\Delta R$ (cm)			
	0.025	0.05	0.1	0.2
0.12345	23.51	21.03	17.19	11.24
0.24690	*	21.74	17.34	11.29
0.49380	*	*	16.78	11.27

\* Not available, because of the volume of the electrode is insufficient to sustain the current loads.

Table III. Increase in ohmic losses in the melt due to the varying concentration profile

$I_{R_0}$ (A/cm <sup>2</sup> )	$\Delta R$ (cm)			
	0.025	0.05	0.1	0.2
0.12345	0	1.68	6.95	17.04
0.24690	*	0.12	1.12	15.90
0.49380	*	*	0.97	11.75

\* Not available, because of the volume of the electrode is insufficient to sustain the current loads.

### Acknowledgment

Support for this study was provided by the National Science foundation under a RANN program (NSF-C805) through the Ford Motor Company. We thank Mr. R. W. Minck of the Ford Motor Company for his useful discussions.

Manuscript submitted Sept. 10, 1975; revised manuscript received Jan. 5, 1976.

Any discussion of this paper will appear in a Discussion Section to be published in the December 1976 JOURNAL. All discussions for the December 1976 Discussion Section should be submitted by Aug. 1, 1976.

Publication costs of this article were partially assisted by Rensselaer Polytechnic Institute.

### LIST OF SYMBOLS

$a$	activity; surface area per unit volume
$b'$	$bnF/RT$ , $b = 384.9642$ mV
$c$	molar concentration
$c'$	$cnF/RT$ , $c = 74.8151$ mV
$C_t$	$\Delta R/(y\Delta R + R_0)$
$d'$	$dnF/RT$ , $d = 5.0553$ mV
$F$	Faraday
$i$	current density
$I_{R_0}$	current density at $r = R_0$
$j$	$i_1/I_{R_0}$
$k$	conductivity
$K$	drag coefficient
$N$	molar flux
$r$	radial position
$R$	gas constant
$R_0$	radius of ceramic outer surface
$R_1$	radius of outer surface of active electrode
$T$	temperature
$v$	molar volume, velocity
$W_s$	Washburn number
$w_s$	weight fraction of sulfur
$x$	$x$ in $Na_2S_x$
$z$	valence number
$\alpha$	$F/RT$
$\beta$	$I_{R_0}/ai_1\Delta R$
$\gamma$	$ai_1(\Delta R)^2 \alpha(1/k_1 + 1/k_2)$
$\delta$	$1/\beta$
$\Delta R$	active electrode thickness
$\eta$	reaction overpotential
$\mu$	electrochemical potential
$\phi$	potential

### Subscripts

1	melt, sulfur
2	felt, sodium ion
3	sulfide ion
l	limiting current

### REFERENCES

- J. T. Kummer and Neil Weber, Auto. Eng. Cong., Detroit, Michigan (1967) S.A.E. 670179.
- J. L. Sudworth, M. D. Hames, M. A. Storey, M. F. Azin, and A. R. Tilley, Proceedings 8th International Power Source Symposium (1972).
- "Research on Electrodes and Electrolyte for the Ford Sodium-Sulfur Battery," Annual Report, July 1974, NSF-RANN Contract 805.
- "Sodium-Sulfur Battery Development," Final Report, July 1974, EPRI Project RP 128.
- "Development Program for Solid Electrolyte Batteries," Final Report, October 1974, EPRI Project RP 127.
- N. K. Gupta and R. P. Tischer, *This Journal*, **119**, 1003 (1972).
- R. P. Tischer, Abstract 170, p. 434, The Electrochemical Society Extended Abstracts, Spring Meeting, Houston, Texas, May 7-11, 1972; also Private communication from N. K. Gupta.
- G. Gibson, *J. Appl. Electrochem.*, **4**, 125 (1974).
- B. Cleaver, et al., *Electrochim. Acta*, **18**, 719 (1973); **18**, 727 (1973); **18**, 733 (1973).
- M. D. Hames, M.Ph. Thesis, University of Southampton (1971).
- R. Minck, Private communication.
- J. Newman and C. W. Tobias, *This Journal*, **109**, 1183 (1962).
- J. Newman, D. Bennion, and C. W. Tobias, *Ber. Bunsenges, Phys. Chem.*, **69**, 608 (1965).

14. K. D. South, J. L. Sudworth, and G. Gibson, *This Journal*, **119**, 554 (1972).
15. S. H. Selis, *Electrochim. Acta*, **15**, 1285 (1970).
16. "Research on Electrodes and Electrolyte For the Ford Sodium-Sulfur Battery," Annual Report, July 1975, NSF-RANN Contract C-805.
17. K. J. Vetter, "Electrochemical Kinetics," Academic Press, New York (1967).
18. J. N. Viladsen, "Selected Approximation Methods for Chemical Engineering Problems," Institutet for Kemiteknik, Numerisk Institut Denmarks Techiske Hojskole, Copenhagen, Denmark (1970).

## Interfacial Phenomena at Solid Aluminum Electrodes in Solutions of $\text{AlBr}_3/\text{KBr}$ in Aromatic Hydrocarbons

A. Reger, E. Peled,\* and E. Gileadi\*

*Institute of Chemistry, Tel-Aviv University, Ramat-Aviv, Israel*

### ABSTRACT

Solutions of  $\text{AlBr}_3$  and  $\text{KBr}$  in toluene, mesitylene, or their mixture have been prepared under high purity conditions on a vacuum line. Anodic dissolution and cathodic deposition at a pure aluminum electrode were studied. Special attention was focused on the mechanism of rupture of the oxide film initially present on the surface and the formation of pits under the surface. The apparent exchange current density was found to depend on the anodic current density employed to activate the surface. The current density was found to be a linear function of potential over ca. 0.2V on both sides of the reversible potential. This was interpreted as being due to the solution resistance inside small flaws (pinholes) in the oxide layer on the surface.

Recent studies of the electrodeposition of aluminum from aromatic hydrocarbons containing  $\text{AlBr}_3$  with small amounts of  $\text{HBr}$  or water (1) or with an alkali bromide (2) have indicated that this system may be useful as a plating bath for a variety of industrial applications. While this system has been known since the early thirties (3, 4), an understanding of the fundamental electrode processes taking place during anodic dissolution and cathodic deposition is still lacking.

Aluminum bromide is quite soluble in toluene (5) and in other aromatic hydrocarbons (6). At low concentrations (in the millimolar range) the solutions are colorless but at high concentrations (1-3M) a pale yellow color is observed, depending on the hydrocarbon employed as the solvent (5).<sup>1</sup> The conductivity of these solutions is very low, but it has been observed in the earliest studies of this system (4) that addition of  $\text{KBr}$  or any other alkali bromide increases the conductivity significantly, to the point that electrochemical measurements can readily be made. The conductivity increases with increasing concentration of  $\text{KBr}$ , reaching a maximum in the range of 1-6  $\text{mMho}\cdot\text{cm}^{-1}$  (depending on the total concentration of  $\text{AlBr}_3$  and on the hydrocarbon employed) when the molar ratio  $\text{AlBr}_3/\text{KBr}$  is 2:1 (3, 4, 7, 8). This observation, combined with the fact that  $\text{KBr}$  itself is not soluble in aromatic hydrocarbons, implies that a complex of the type  $\text{Al}_2\text{Br}_7^-$  probably exists in solution. This was verified recently by preliminary transference number measurements (2b). Cryoscopic studies of these systems indicated that polyions of the type  $(\text{K}^+\text{Al}_2\text{Br}_7^-)_n$  where  $n \leq 4$  may also exist (9).

The first kinetic studies in this type of system were performed by Plotnikov and Yakubson in 1928 (8). An aluminum anode and a platinum cathode were used. Large current densities, in the range of 60-100  $\text{mA}/\text{cm}^2$  were employed. The faradaic efficiency was low both at the anode and at the cathode, some free bromine was formed, and the solution turned dark and viscous.

\* Electrochemical Society Active Member.

Key words: aluminum electrodes, interfacial phenomena, aromatic hydrocarbons, aluminum bromide, aluminum oxide.

<sup>1</sup> Recent experiments in our laboratory, to be reported elsewhere, indicated that persistent purification with an aluminum amalgam in contact with the solution results in a colorless solution even at high concentrations of  $\text{AlBr}_3$ .

The kinetics of electrodeposition and dissolution of aluminum has been studied in molten salts (10, 11). Values of the exchange current densities observed by different authors under similar conditions differ markedly, probably because not enough care has been taken to remove the surface oxide formed spontaneously on aluminum. In another study employing an  $\text{AlCl}_3/\text{MCl}$  melt (12), well-defined transition times were observed during anodic polarization. These were ascribed to the formation of a layer of poorly conducting  $\text{Al}_2\text{Cl}_6$  on the surface of the electrode.

In the present paper the results of studies of electrodeposition and dissolution of aluminum are reported. Toluene, mesitylene, or a mixture of both were used as the solvent. Aluminum bromide and potassium bromide in molar ratios of about 3:1 served as the electrolyte. Measurements were taken on high purity aluminum wires. Great care was taken to prepare highly purified and rigorously dried solutions and to prepare reproducible clean aluminum surfaces for evaluation of kinetic data.

### Experimental

**The cell and electrodes**—The cell and electrodes are shown in Fig. 1, together with the separate compartment used for preparation of solutions. A cylindrical geometry was employed to achieve a uniform current distribution on the working electrode and to minimize IR drop during measurements. An aluminum wire (Hopkin and Williams 99.99% purity) served as the working electrode. Another Al wire of the same purity, situated parallel to the working electrode at a distance of about 2 mm, served as the reference and a third such wire formed as a helix served as the counterelectrode. Electric contact was made to tungsten wires sealed through the cell cover. The cell was sealed with glass flanges employing neoprene O-rings which were not in direct contact with the solvent in the cell. Connection to the vacuum line was made through Rotaflo valves with Teflon heads. The cell could be evacuated to a pressure of less than  $10^{-4}$  mm Hg.

The Al electrodes were cleaned by degreasing in acetone, dipping in 1M  $\text{NaOH}$  at 60°C for about 30 sec, rinsing in triple distilled water, washing with AR grade acetone to remove the water, and pumping off

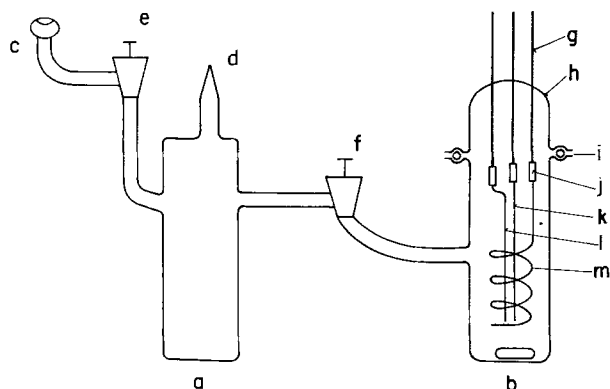


Fig. 1. The cell: a, solution preparation compartment; b, the electrochemical cell; c, connection to high vacuum line; d, connection to  $\text{AlBr}_3$  sublimation container; e, f, Rotaflo valves; g, tungsten wires; h, cell cover; i, O-rings, neoprene; j, stainless steel connectors; k, working electrode; l, reference electrode; m, counter-electrode.

the remaining acetone on the vacuum line to a pressure of about  $10^{-4}$  mm Hg. In some experiments aluminum-plated copper wire was used as the reference electrode, the copper wire was cleaned in an acid mixture consisting of equal volumes of  $\text{HNO}_3$ ,  $\text{CH}_3\text{COOH}$ , and  $\text{H}_3\text{PO}_4$  instead of dipping in alkali, all other steps being the same. Before measurements the working electrode was pretreated by pulsing it anodically at different current densities in the range of 0.2–70  $\text{mA}/\text{cm}^2$  with solution stirring. The reference electrode was pretreated in a similar manner. The copper reference electrode was plated in a stirred solution with a layer of ca.  $1\mu$  aluminum, at a current density of 2–10  $\text{mA}/\text{cm}^2$ . In a freshly prepared solution the thin layer of aluminum tended to dissolve after a few hours, probably due to small traces of impurities ( $\text{O}_2$  or  $\text{HBr}$ ) in the solution. After preelectrolysis the system was stabilized and the aluminum coating on copper dissolved only after several days. As a rule addition of mesitylene to toluene tended to stabilize the solution and decrease the rate of chemical dissolution of freshly deposited aluminum in it.

All measurements were taken at  $20^\circ \pm 2^\circ\text{C}$ .

**Preparation of solutions.**—A weighed amount of  $\text{KBr}$  (Baker Analyzed) was placed in the solution-preparation compartment (compartment a in Fig. 1) and held at  $150^\circ\text{C}$  for ca. 15 hr with continuous pumping to remove traces of water.  $\text{AlBr}_3$  (97% purity, obtained from Merck) was purified by subliming twice under vacuum at  $80^\circ\text{--}100^\circ\text{C}$ . In the second step the material was transferred through tube d into compartment a and the tube was sealed off while the cell was still under vacuum. White translucent crystals of  $\text{AlBr}_3$  were obtained in this manner. Toluene or mesitylene (Frutarom, analytical grade) was refluxed for several hours over sodium, then transferred for several hours to an evacuated flask containing  $\text{P}_2\text{O}_5$  or molecular sieve. Finally, the solvent was transferred under vacuum to compartment a through joint c and valve e. As soon as the solution was prepared the cell was wrapped with a black cloth to avoid photodecomposition which has been observed to occur in certain cases. The solution was transferred to the electrochemical cell b by opening valve f and tilting the whole assembly. This was usually done just before the experiments. The exact composition of the solution was determined at the end of a series of experiments by measuring the concentration of K and Al with an atomic absorption spectrophotometer (Perkin Elmer, Model 403). The concentrations of  $\text{AlBr}_3$  and  $\text{KBr}$  were around 2.5 and 0.8M, respectively, in all experiments.

Solutions prepared in the manner described above were colorless or pale yellow and were found to be stable in the dark for periods of several months.

**IR correction.**—The combination of a relatively low specific conductivity and high exchange current density (see below) makes it rather difficult to perform accurate measurements. In a typical case, the equivalent reaction resistance may be as low as 10–20% of the solution resistance in series with it, and accurate measurement of the latter hence becomes of major importance. All measurements were performed galvanostatically employing an Elron CHG-1 galvanostat with a risetime of 2  $\mu\text{sec}$ . The galvanostat was combined with a homemade pulse generator to provide square current pulses of any desired length from a few microseconds up to a few seconds. The solution resistance was determined from the fast initial jump in potential upon application of the pulse, as seen in Fig. 2. The overpotential was determined by measurement on a much slower time scale, as shown in Fig. 3. To check the values of  $IR$  obtained in this way another method was employed to measure the same quantity: A small a-c voltage  $V_{\text{wc}}$  was applied between the working and the counter-electrode and the resulting voltage  $V_{\text{wr}}$  developed between the working and the reference electrodes was measured. The effective resistance  $R_{\text{wr}}$  to be used in computing the  $IR$  correction was then calculated from the simple equation.

$$R_{\text{wr}} = R_{\text{wc}}(V_{\text{wr}}/V_{\text{wc}}) \quad [1]$$

The resistance  $R_{\text{wc}}$  between the working and the counterelectrodes was measured with a conductometer. All above measurements were performed at a constant frequency of  $3 \times 10^3$  Hz. Occasional comparison at higher frequencies gave identical results.

The values of  $IR$  obtained by the above a-c method agreed, within experimental error, with those calculated from the fast galvanostatic transients and the latter were used in all subsequent experiments.

## Results

**Reference electrodes.**—An aluminum wire or an aluminum-plated copper wire dipped in the solution was employed as the reference electrode. Thus all potentials measured (after  $IR$  correction) represent overpotential measurements for electrodeposition or dissolution of Al. To ensure that the reference electrodes operated properly, several such electrodes were introduced into the solution and the potential difference between them was measured for periods of several weeks. This was always found to be  $0 \pm 1$  mV, after an initial time for stabilization, which could be as long as several hours. The potential remained constant after activation by anodic pulses. A freshly formed Al surface on a copper wire exhibited the same potential. When the cell was opened in a glove box under an inert atmosphere and a new clean Al wire was put in the cell its potential also agreed with that of another refer-

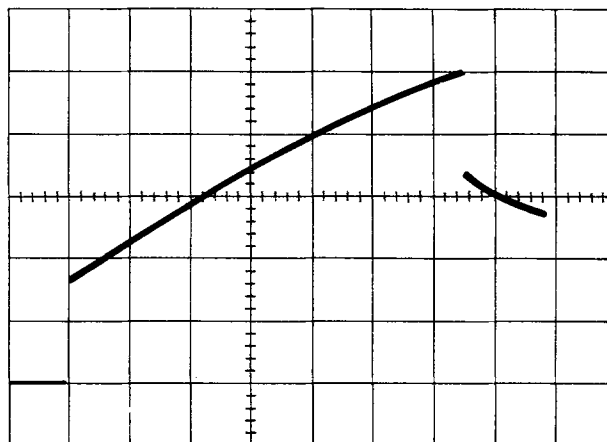


Fig. 2. Fast galvanostatic transient on Al wire. Scale: 1 mV/div; 20  $\mu\text{sec}/\text{div}$ ; electrode area,  $0.55 \text{ cm}^2$ . Current: 0.05 mA. Solvent: toluene 85%, mesitylene 15%.

ence electrode, which had been in the same solution for a long time, to within 1 mV.

**Effect of anodic pulses on the apparent exchange current density.**—Several anodic current pulses of a few seconds duration each were applied to the working electrode to try to remove the oxide layer which was formed between the time the wire had been taken out of the NaOH cleaning solution and the time it was placed in the cell solution. Figure 3 shows typical short anodic galvanostatic transients in the range of 0.11–0.44 mA/cm<sup>2</sup> following initial activation by anodic pulses (5–10 sec) of 4.4 mA/cm<sup>2</sup>. Transients in the cathodic direction were identical. The relationships between current density  $i$  and overpotential  $\eta$  (corrected for  $IR$ ) are shown in Fig. 4 for electrodes pretreated with anodic pulses at different current densities. The apparent exchange current densities were calculated from these lines employing the equation

$$i = i_0 \frac{nF\eta}{\nu RT} \quad [2]$$

in which  $n = 3^2$  and the stoichiometric number  $\nu$  is arbitrarily assumed to have a value of unity. These are shown in Table I together with the corresponding re-

<sup>2</sup> This represents the number of electrons needed to deposit one atom of Al. Recently it was shown (2b) that the over-all reaction may be rather more complicated and only 3/7 of an electron is required per molecule of AlBr<sub>3</sub> taking part in the over-all electrode reaction.

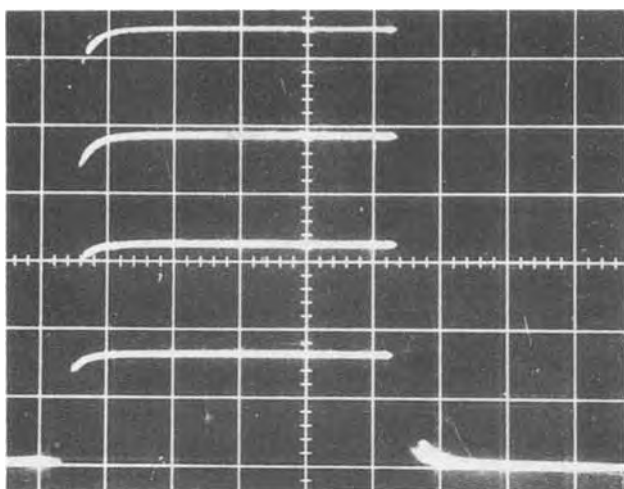


Fig. 3. Galvanostatic transient on Al wire electrode following anodic pretreatment at 4.4 mA/cm<sup>2</sup>. Scale: 2 mV/div; 0.1 msec/div; electrode area, 0.45 cm<sup>2</sup>. Polarization currents: 0.05, 0.10, 0.15, and 0.20 mA. Solvent: toluene 85%, mesitylene 15%.

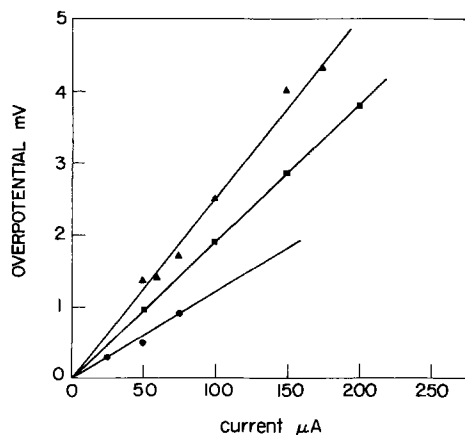


Fig. 4. Micropolarization measurements on Al wire electrodes (short pulses). Solvent: toluene 85%, mesitylene 15%. Anodic pretreatment of electrodes at (a)  $\blacktriangle$  2.2 mA/cm<sup>2</sup>; (b)  $\blacksquare$  4.4 mA/cm<sup>2</sup>; (c)  $\bullet$  30 mA/cm<sup>2</sup>.

Table I. Reaction resistance and apparent exchange current density as a function of current density during anodic activation

CD for activation, mA/cm <sup>2</sup>	1.0	2.2	4.4	30	70
Apparent $i_0$ , mA/cm <sup>2</sup>	0.06	0.75	1.0	3.2	>32
Reaction resistance, ohm · cm <sup>2</sup>	145	11.5	8.6	2.7	<0.27

action resistances. The values of  $i_0$  are referred to as "apparent" exchange current densities since, as is discussed below, the surface oxide film has not been entirely removed and the current/potential relationship observed cannot be related directly to the rate of exchange of electrons at a clean Al surface. When the electrode was activated with anodic pulses of 70 mA/cm<sup>2</sup>, the apparent exchange current density was too high to be measured properly and the result given in Table I above should only be considered as an estimate of the lower limit for this quantity.

**Differential capacitance of the interface.**—The capacitance  $C$  of the interface was estimated from the rising part of the galvanostatic transient just after the jump in potential due to  $IR$  drop, as can be seen in Fig. 2. From the equation

$$i = C(dV/dt)_{t \rightarrow 0} \quad [3]$$

the capacitance is obtained by measuring the initial value of  $dV/dt$ . In most measurements the value of  $C$  was obtained from the first 10–50  $\mu$ sec in the duration of the transient. Values ranged from 1 to 3  $\mu$ F/cm<sup>2</sup> and did not seem to be affected significantly by anodic pretreatment of the electrode up to ca. 30 mA/cm<sup>2</sup>. Activation of the electrode at higher anodic current densities increased the measured capacitance by more than an order of magnitude.

**Buildup of potential during high anodic polarization.**—In Fig. 5 a typical behavior of an Al wire freshly placed in solution during an anodic pulse can be seen. A few seconds after the current has been applied the potential jumps suddenly by 2–3V and reaches a new, nearly constant value. If the experiment is repeated, a higher anodic current density has to be used to obtain the same transient. The transition time and the height of the potential jump are not reproducible, but the general shape of the curve is the same in all experiments. This phenomenon is only observed during anodic polarization. In the cathodic branch the potential remains in the low region indefinitely.

**Polarization at high overpotential (short pulses).**—In Fig. 6 the  $\eta/i$  relationship is plotted over a wide range of overpotential, on both the anodic and the cathodic side of the reversible potential. A linear relationship is

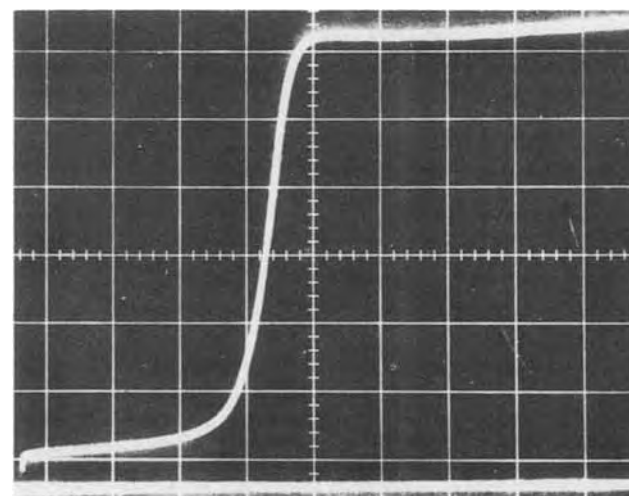


Fig. 5. Variation of potential during anodic dissolution. Scale: 0.5 V/div; 1 sec/div; electrode area, 0.60 cm<sup>2</sup>. Current: 1.0 mA. Solvent: toluene.



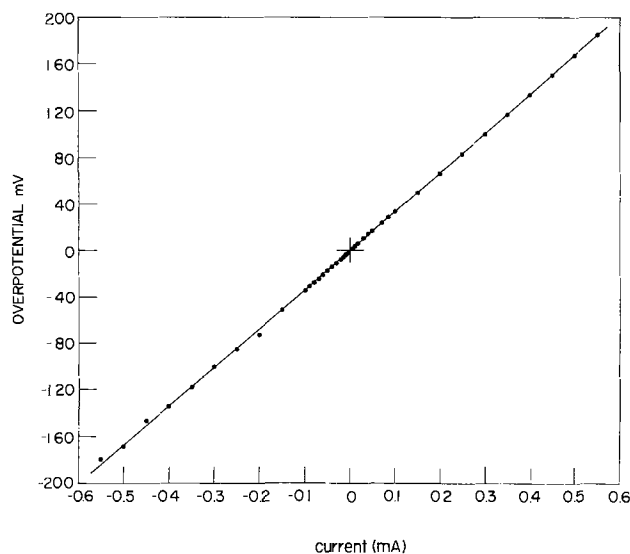


Fig. 6. Current/potential relationship (short pulses) after mild anodic pretreatment ( $1 \text{ mA/cm}^2$ ). Solvent: mesitylene. Electrode area:  $0.44 \text{ cm}^2$ .

observed throughout this range, contrary to expectation. In the experiment shown in Fig. 6 anodic pretreatment was rather mild, at  $1 \text{ mA/cm}^2$  only, and as a result the apparent exchange current density was low. However, the linearity in the  $\eta/i$  relationship was extended to  $0.1\text{--}0.2\text{V}$  in all cases, independent of the current density applied during pretreatment by anodic pulsing. If an electrode is not pretreated at all, the resistance due to the surface oxide film is in the range of  $10\text{--}50 \text{ kohm}\cdot\text{cm}^2$  in most experiments.

**Steady-state polarization measurements.**—When the variation of potential with time is viewed on a rather fast scale, as in Fig. 3, steady state is reached within less than  $0.1 \text{ msec}$ , and the potential does not seem to change at all during the next few milliseconds. If, however, the time scale is extended by about four orders of magnitude, the behavior shown in Fig. 7 is observed. The overpotential rises slowly and a new steady state is reached after  $10\text{--}15 \text{ sec}$ . The resulting  $\eta/i$  plot is shown in Fig. 8. The value of  $i_0$  calculated from these data is  $0.12 \text{ mA/cm}^2$ , compared to  $0.75 \text{ mA/cm}^2$  calculated above from short transients following anodic activation at the same current density. The steady-state overpotential after longer times depends on the current density during anodic pretreatment in much the same

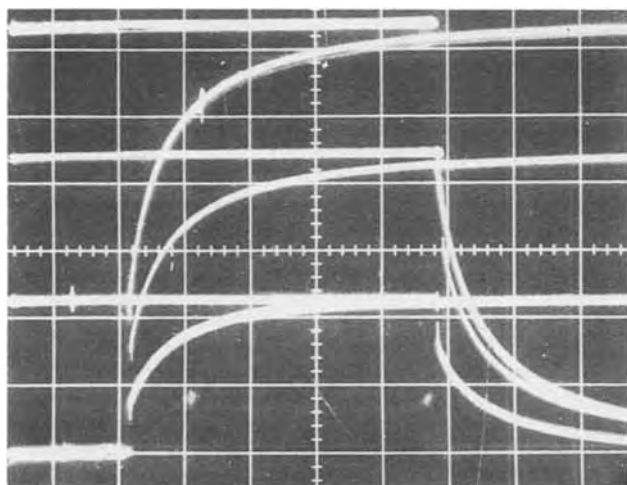


Fig. 7. Steady-state galvanostatic transients on Al wire electrode following anodic pretreatment at  $2.2 \text{ mA/cm}^2$ . Solvent: toluene 85%, mesitylene 15%. Scale:  $1 \text{ mV/div}$ ;  $1 \text{ sec/div}$ ; electrode area,  $0.45 \text{ cm}^2$ . Polarization currents:  $10, 20, \text{ and } 30 \mu\text{A}$ . Duration of each pulse:  $15 \text{ sec}$ .

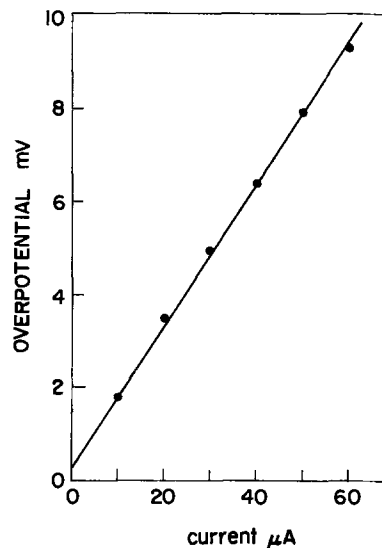


Fig. 8. Micropolarization measurements on Al wire electrodes from steady-state transients. Solvent: toluene 85%, mesitylene 15%.

way as shown in Fig. 4 for short-time measurements. Identical transients were obtained for anodic and cathodic polarizations.

### Discussion

While the chemistry and electrochemistry of the  $\text{AlBr}_3/\text{MBr}/\text{aromatic hydrocarbon}$  solvent system has been studied by a number of authors, little is known of the interfacial phenomena occurring when a solid electrode is dipped in this solution. This system is unique in that it possesses a fairly high conductivity combined with a low dielectric constant. The mechanism of charge transfer and the structure of the double layer at such a system is therefore of great interest. Apart from the fundamental aspects, this solvent system can be used as a plating bath for Al, and it is important therefore to understand the phenomena taking place both at the anode and at the cathode so that conditions can be chosen to obtain high quality electroplated products and long lifetimes of the baths. Of particular interest in this respect is the anodic behavior of Al electrodes, which are always covered with an oxide film (air formed after the anode has been cleaned in acid or alkali) since efficient anodic dissolution during plating operation is essential for the stability of the bath.

The reaction resistance of electrodes which have not been activated by anodic pulses is  $ca. 10\text{--}50 \text{ kohm}\cdot\text{cm}^2$  and the capacitance of the interface is in the range of  $1\text{--}3 \mu\text{F/cm}^2$ . Activation of the electrode by anodic pulses of up to  $30 \text{ mA/cm}^2$  caused a decrease of the reaction resistance to a few  $\text{ohm}\cdot\text{cm}^2$  (cf. Table I), but the capacitance remained essentially unaltered. Activation of the electrode at even higher anodic current densities caused a further decrease in the reaction resistance by an order of magnitude or more, while the capacitance tended to increase by about the same factor.

The thickness of the oxide layer on a fresh surface (which has not been activated) can be estimated from the capacitance of the interface. Assuming a dielectric constant of  $\epsilon = 5$  for the oxide this turns out to be  $ca. 15\text{--}50 \text{ \AA}$ , in agreement with values reported in the literature for air-formed oxide layers (13). In view of the fact that the capacitance of the interface is not significantly affected by anodic pulsing (up to  $30 \text{ mA/cm}^2$ ) it must be concluded that most of this layer is not removed by the activation process. The lowering of the reaction resistance, however, implies that the layer must be ruptured and a bare aluminum surface must be exposed to the solution as a result of activation by anodic pulses.

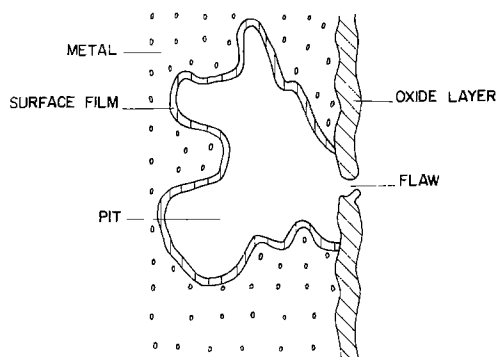


Fig. 9. Schematic representation of a flaw and pit model of an oxide-covered aluminum surface.

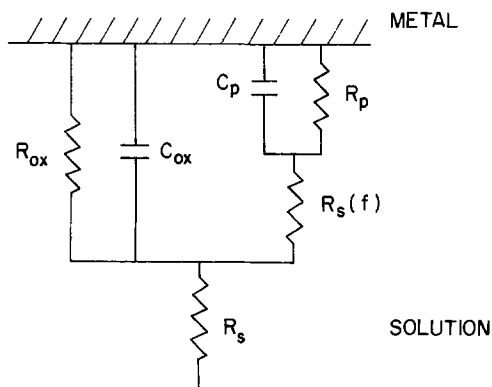


Fig. 10. Equivalent circuit for the model shown in Fig. 9.  $R_{ox}$ ,  $C_{ox}$ : resistance and capacitance of oxide film.  $R_p$ ,  $C_p$ : resistance and capacitance of interface inside pit.  $R_s(f)$ : resistance of solution inside flaw.  $R_s$ : solution resistance.

A model has been proposed by Richardson and Wood (13) to account for observations during the chemical corrosion and anodic dissolution of aluminum in aqueous solutions. It seems that a similar model may apply to our system as well. A modification of the model of Richardson and Wood is shown schematically in Fig. 9. The corresponding equivalent circuit is shown in Fig. 10. According to this model a fresh aluminum electrode (which has not been activated) is covered with an oxide film having a few flaws or pinholes. The total area of these holes is too small to affect the resistance of the interface, and the measured reaction resistance is that due to the oxide film ( $R_{ox}$ ). During anodic activation, pits are developed under the flaws. The area of the pits can be very much larger than the area of the flaws and as a result a certain degree of collapse of the film can occur causing an increase in the diameter of the flaw.<sup>3</sup> The resistance of the solution in the flaws and inside the pits ( $R_s(f)$ ) becomes smaller than the resistance of the oxide layer in parallel with it and this is probably the quantity given in Table I. As long as the resistance  $R_s(f)$  is large compared to the impedance associated with the capacitance of the interface inside the pit  $C_p$ , the latter will not affect the total capacitance measured, as found experimentally. If anodic activation is carried out at  $i > 30$  mA/cm<sup>2</sup> the radii of the flaws increases so that  $R_s(f)$  becomes negligible and one measures the capacitance ( $C_p$ ) and reaction resistance ( $R_p$ ) of the oxide-free surface inside the pits. It should not be concluded from the above reasoning that inside a pit the interface consists of a pure aluminum surface in contact with the solution. There is clear evidence (14) that corrosion of aluminum and attendant reduction of the solvent occur (even in ultrapure, colorless solutions) at such a rate

<sup>3</sup> It should be noted that during most of the polarization measurements the current is applied for only short periods of time, mostly less than 1 msec, while anodic activation is affected by several pulses of a few seconds duration each. It is thus unlikely that the area of the flaws would be significantly changed during polarization measurements.

that a film of reaction products a few monolayers thick could form on the surface within seconds. Preliminary experiments employing copper electrodes plated with aluminum *in situ* have indicated that such a film is indeed formed in the present system.

The model proposed above can also account for the linear  $\eta/i$  relationship found in a wide range of overpotential (cf. Fig. 6). It would seem that the apparent exchange current density and the corresponding reaction resistance measured on electrodes activated by anodic pulses are in fact a measure of the solution resistance  $R_s(f)$  in the flaws. Thus the linearity of the  $\eta/i$  plot is maintained over a wide range.

The slow approach to steady state shown in Fig. 7 is probably due to mass-transport limitation through the flaws, causing changes of concentration of reactants or products in the pits. As would be expected, the reaction resistance measured on this time scale also decreases with increasing current density during anodic activation, due to an increase in the diameter of the flaws.

The sudden change in potential shown in Fig. 5 for anodic polarization of an electrode which has not been activated by anodic pulses can be associated with blocking of the flaws in the oxide surface by reaction products (e.g.,  $Al_2Br_6$ ), a phenomenon which has also been observed during anodic dissolution of aluminum in an  $AlCl_3$  melt (12). A similar behavior is not observed when the electrode is polarized cathodically, since dendrite growth does not allow blocking of the surface.

#### Acknowledgments

This paper is dedicated to the memory of our student, Shmuel Ziegel.

We are indebted to the National Council for Research and Development, Prime Minister's Office, Jerusalem, Israel, for financial support of this work.

Manuscript submitted Sept. 2, 1975; revised manuscript received Jan. 5, 1976.

Any discussion of this paper will appear in a Discussion Section to be published in the December 1976 JOURNAL. All discussions for the December 1976 Discussion Section should be submitted by Aug. 1, 1976.

#### REFERENCES

- G. A. Capuano and W. G. Davenport, (a) *This Journal*, **118**, 1688 (1971); (b) *Plating*, **60**, 251 (1973).
- E. Peled and E. Gileadi, (a) *Plating*, **62**, 342 (1975); (b) *This Journal*, **123**, 15 (1976).
- (a) V. A. Plotnikov and E. Ya. Gorenbein, *J. Gen. Chem. USSR*, **7**, 372 (1937); (b) E. Ya. Gorenbein, *Univ. Etat Kiev, Bull. Sci. Rec. Chim.*, **1**, 101 (1935).
- (a) V. A. Plotnikov and S. I. Yakubson, *J. Gen. Chem. USSR*, **6**, 1690 (1936); (b) V. A. Plotnikov, I. A. Sheka, and V. A. Yankelevich, *ibid.*, **3**, 481 (1933); (c) V. A. Plotnikov, I. B. Barmashenko, and E. B. Gitman, *Mem. Inst. Chem. Acad. Sci. Ukr. SSR*, **5**, 3 (1938).
- (a) H. C. Brown and W. J. Wallace, *J. Am. Chem. Soc.*, **75**, 6265 (1953); (b) S. U. Choi and H. C. Brown, *ibid.*, **88**, 903 (1966); (c) E. Wertyporoch and B. Adamus, *Z. Phys. Chem. A*, **168**, 31 (1934); (d) J. F. Norris and D. Rubinstein, *J. Am. Chem. Soc.*, **61**, 1163 (1939).
- (a) H. H. Perkampus and G. Orth, *Angew. Chem.*, **78**, 908 (1966); (b) D. D. Eley and P. J. King, *J. Chem. Soc.*, 2517 (1952).
- S. I. Yakubson, *J. Phys. Chem. USSR*, **21**, 343 (1947).
- V. A. Plotnikov and S. Yakubson, *Z. Phys. Chem.*, **138**, 251 (1928).
- (a) E. Ya. Gorenbein, *J. Phys. Chem. USSR*, **20**, 547 (1946); (b) E. Ya. Gorenbein, *J. Gen. Chem. USSR*, **26**, 2985 (1956).
- K. Schulze and H. Hoff, *Electrochim. Acta*, **17**, 119 (1972).
- B. S. Del Duca, *This Journal*, **118**, 405 (1971).
- B. Gilbert, D. L. Brotherton, and G. Mamantov, *ibid.*, **121**, 773 (1974).
- J. A. Richardson and G. C. Wood, *ibid.*, **120**, 193 (1973).
- E. Peled, S. Ziegel, and E. Gileadi, In preparation.

## Influence of Inhibitors on the Structure of Silver Deposits Obtained by Electrolysis of Aqueous Nitrate Solutions

J. Vereecken\* and R. Winand\*

Laboratory of Metallurgy and Electrochemistry, Free University of Brussels, Brussels, Belgium

The aim of this study is to determine the experimental conditions for the electrolysis of aqueous solutions of silver nitrates to obtain a smooth and coherent deposit of pure silver at a silver cathode. Indeed the actual conditions of the industrial silver electrorefining from golden silver in silver nitrate solutions lead to dendritic deposits. This involves several disadvantages such as scrapers, great volume of the cells, difficult recovery of the pure metal, loss of electrolyte, and so on.

In order to find out whether it is possible to improve the structure of those deposits we studied systematically the influence of several parameters of the electrolysis: composition of the electrolyte (concentration in  $\text{AgNO}_3$ ,  $\text{NaNO}_3$ , and  $\text{HNO}_3$  and concentration in addition agent) cathodic current density, temperature, time of the electrolysis, and stirring.

We can find in the literature (1, 2) very important reviews concerning electrocrystallization in relation to inhibitors. For the purpose of this study, it is only necessary to summarize the different studies concerning the influence of inhibitors on electrocrystallization of silver from nitrate solutions. Studies on this subject are not numerous; one of the reasons being the very rapid change of the surface of the deposit during the electrolysis.

Glazunof, Teindl, and Halik (3) observed an increase in the smoothness of silver deposits with an addition of 0.03-0.15% agar-agar to the solution. Vagramyan (4) studied the influence of dextrine and benzoic acid and concluded that the nucleation rate is a function of the active surface area. Fischer (2, 5) found that nitric acid can have an inhibitor effect on the silver deposit. Taft and Hiebert (6) carried on investigations with 169 addition agents in an attempt to determine a relationship between the nature of the addition agent and the nature of the silver deposit: They found that certain products such as diglycol stearate, ammonium laurate, and particularly amino methane are good inhibitors. Taft and Horseley (7) and Hodge and Lutness (8) found that sodium acetate and ferrous sulfate improve the structure of the deposit. But they found no obvious relationship between the molecular structure of the wetting agent and the form of the deposit.

### Experimental Conditions

A particularly important problem in electrocrystallization is to avoid edge effects; this is why we used a parallelepipedic cell which was held at constant temperature. The useful area of the cathode was  $10 \text{ cm}^2$ . These electrodes were degassed, polished, and degreased prior to electrolysis. High purity reagents were used. During the electrolysis we recorded the cell voltage and the cathodic galvanic potential (the reference

\* Electrochemical Society Active Member.

Key words: silver, electrocrystallization, silver nitrate, organic inhibitor.

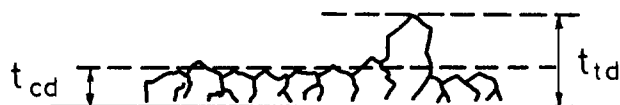


Fig. 1. Principle of the measurement of the quality of the deposit by means of metallographic cross sections:  $t_{cd}$ , thickness of coherent deposit;  $t_{td}$ , thickness of total deposit.

electrode was a mercurous sulfate electrode). The current efficiency was measured in a classical way. The quality of the deposit was evaluated as follows: We measured (Fig. 1) the thickness of coherent deposit  $t_{cd}$  and the thickness of total deposit  $t_{td}$  and we calculated the ratio  $t_{cd}/t_{td}$ . During the electrolysis we also observed the deposit with an optical microscope by means of a special electrolysis cell. After the electrolysis the structure of the deposit was observed with metallographic cross sections. Several different electrolytes were studied. They are mentioned in Table I.

### Results and Discussion

Microscopic observations made during galvanostatic pulse experiments enabled us to confirm the first part of the theory of Ibl (9): Dendrites appear at the transient time. Figure 2 represents the variation of the cathodic galvanic potential as a function of time during an electrolysis at constant current density. The cathodic galvanic potential increases with time but after the formation of the dendrites the potential begins to decrease. This is probably due to an increase of the surface.

We also found a good agreement with Sand's relationship: The product of the cathodic current density with the square root of the transient time is proportional to the concentration in silver ions (Fig. 3). This shows clearly that diffusion laws are obeyed, even for our relatively large electrodes. We are thus entitled to calculate the diffusion limiting current density on the basis of the theory summarized by Vetter (11) in the case of natural convection. Details about this calculation may be found in Ref. (12).

Table I. Characteristics of the different electrolytes used in this work

Electrolytes	$C_{\text{Ag}^+}$ (g/liter)	$C_{\text{NaNO}_3}$ (g/liter)	$C_{\text{HNO}_3}$ (g/liter)	$J_{e \text{ lim}}$ (A/dm <sup>2</sup> )
E <sub>1</sub>	15	100	2.26	1.24
E <sub>2</sub>	45	100	3.46	3.73
E <sub>3</sub>	135	100	2.7	11.2
E <sub>4</sub>	405	100	2.7	33.6
E <sub>5</sub> *	170	—	2.7	14.1
E <sub>6</sub> *	320	—	2.7	26.5
E <sub>7</sub> **	135	100	—	11.2
E <sub>8</sub> **	264	100	—	21.9
E <sub>7</sub>	300	50	2.7	24.8

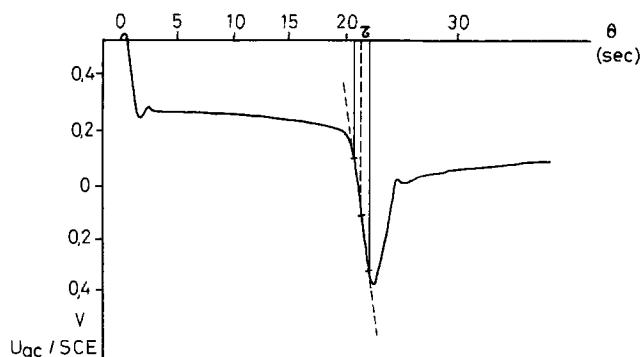


Fig. 2. Potential-time relationship during a constant current step ( $\tau$  is the transient time).

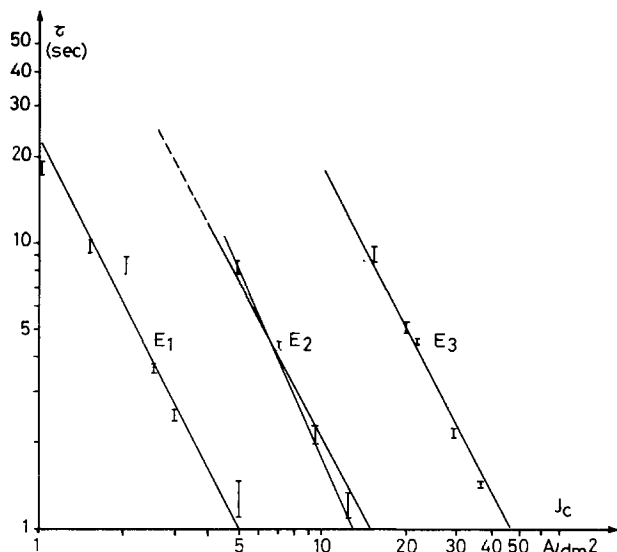


Fig. 3. Logarithmic plot of the transient time  $\tau$  as a function of the cathodic current density.

Our other experimental results, *i.e.*, long lasting electrolysis below the limiting current density, showing that the deposits obtained without inhibitors and with current density lower than the diffusion limiting current density are smooth only at the beginning of the electrolysis, the smoothness of the deposits decreasing when time increases. Thus deposits containing protruding single crystals can be obtained without reaching the diffusion limiting current density. This is in opposition with the second part of Ibl's theory (9).

Another conclusion of this study is that an increase in the duration of the electrolysis increases the thickness of coherent deposit only if the cathodic current density is low enough; a maximum time of electrolysis exists for each value of the current density above which the deposit becomes very rough.

The effect of other electrolysis parameters can be summarized as follows:

1. The quality of the deposit increases with the  $\text{Ag}^+$  ion concentration.
2. The presence of  $\text{NaNO}_3$  can lead to different results: With a constant concentration in  $\text{AgNO}_3$  the conductivity of the electrolyte increases. This improves the throwing power. On the other hand, according to Fischer (2)  $\text{NaNO}_3$  is an inhibitor for silver electro-deposition. But the presence of  $\text{NaNO}_3$  can increase the diffusion overpotential; that is why we worked with electrolytes with different concentrations in  $\text{NaNO}_3$  but constant conductivity. The final conclusion is that a decrease in the concentration in silver nitrate favors the formation of a good deposit.
3. The pH of the industrial electrolytes must be between 1 and 5 to avoid the precipitation of  $\text{Cu}(\text{OH})_2$  or  $\text{Ag}_2\text{O}$ . We studied the influence of nitric acid with

the same restriction as for  $\text{NaNO}_3$  and we concluded that the presence of nitric acid has a good influence on the formation of a coherent deposit (Fig. 4).

4. An increase in the temperature (in the range of  $25^\circ\text{--}45^\circ\text{C}$ ) and a stirring of the solution have no considerable influence on the structure of the deposit.

We conclude that it is impossible to find conditions to produce a smooth and coherent silver deposit without addition of inhibitor. We investigated different organic molecules and we found that thiourea improves the quality of the deposit (Fig. 5). It is unfortunately impossible to exceed a concentration of 100 mg/liter because of the small solubility of thiourea in the electrolyte. We also found that the presence of thiourea does not change the cathodic current efficiency and that the amount of thiourea occluded in the deposit is low. For example, at  $1 \text{ A/dm}^2$  the concentration in sulfur in the deposit is 0.55 ppm after spectrophotometric absorption determination.

A particularly interesting way to summarize the influence of some of the most important parameters of the electrolysis is to use the classification of Fischer (2) in the way proposed by Winand (13-15) in a graph with the ratio  $J_c/C_{\text{Me}^{z+}}$  in abscissa and the concentration of inhibitor in ordinate. In the present case, we found four different types of structure (Fig. 6): BR, basis-oriented reproduction type;  $\text{BR}^*$ , BR with partial coverage of the initial surface; FI, field-oriented isolation type; and UD, unoriented dispersion type.

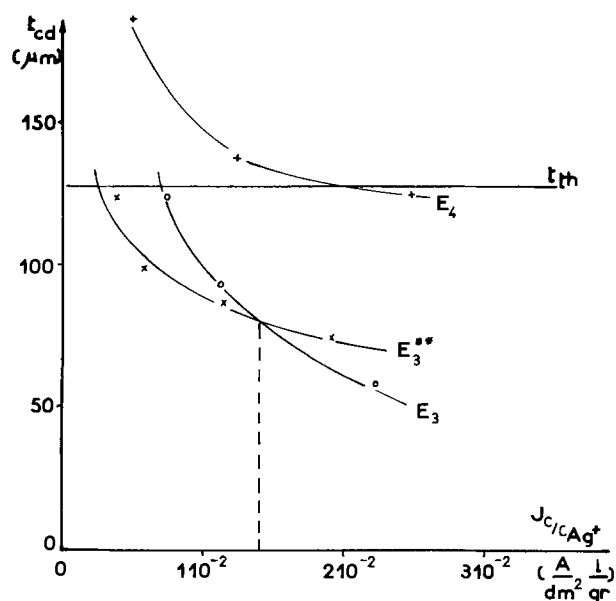


Fig. 4. Influence of the  $\text{HNO}_3$  concentration on the quality of the deposit. Comparison of  $t_{cd}$  as a function of the ratio  $J_c/C_{\text{Ag}^+}$  for three electrolytes described in Table I.

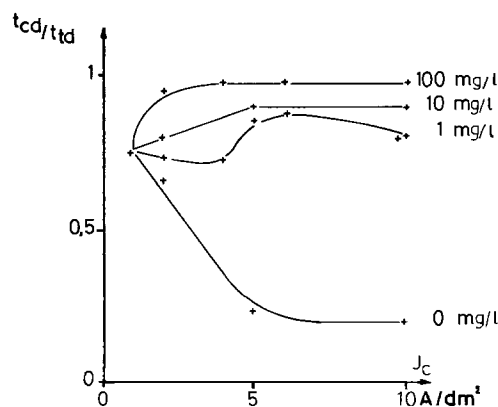


Fig. 5. Influence of the concentration of thiourea on the quality of the deposit.

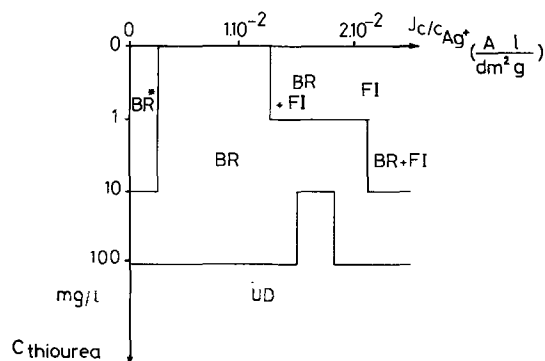


Fig. 6. Nature of the deposit in function of the ratio  $J_c/C_{Ag^+}$  and the concentration of thiourea; BR, basis-oriented reproduction type; FI, field-oriented isolation type; and UD, unoriented dispersion type.

We established also in a recent study (10) that potassium and sodium tartrate can very markedly improve the quality of the deposit (Fig. 7).

With a scanning microscope it is very easy to see the very different nucleation types of silver obtained from a silver nitrate electrolyte. Without inhibitor (Fig. 8) we observe a very irregular nucleation; the cathode is not completely covered and big crystals are growing besides very little ones.

In the presence of thiourea (Fig. 9), the electrode is completely covered with big uniform well-faced crystals. An addition of tartrate changes completely the shape of the crystals (Fig. 10) which are in this case very fine and badly formed.

We have thus found experimental conditions allowing us to produce a smooth and coherent deposit. These conditions are summarized in Table II. We intend to elucidate the way the inhibitor acts in future studies.

### Summary

The aim of this study was to determine the best experimental conditions to obtain a smooth and coherent silver deposit from a nitrate solution.

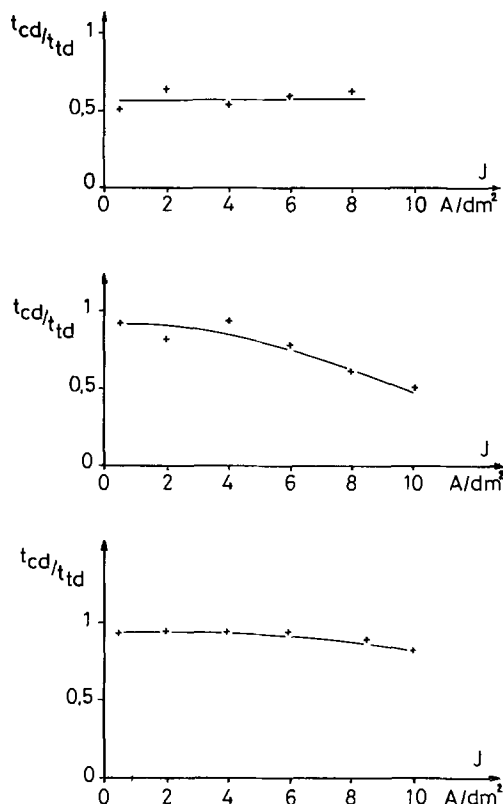


Fig. 7. Influence of the concentration of sodium potassium tartrate on the quality of the deposit. (a, top) 3 mmole/liter, (b, center) 1 mmol/liter, and (c, bottom) 0.5 mmol/liter.

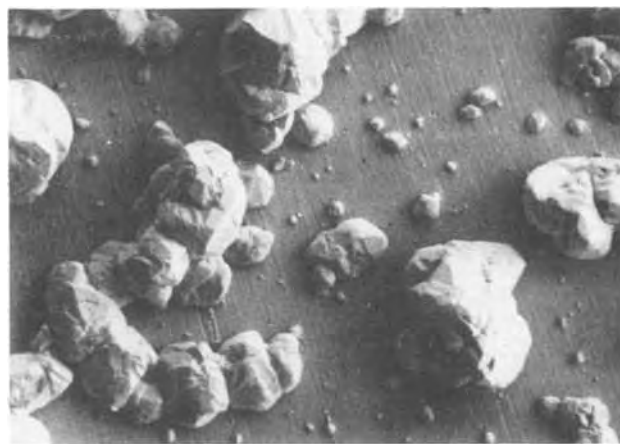


Fig. 8. Observation of the upper surface of a silver deposit obtained from a silver nitrate solution without inhibitor (scanning microscope 100X).



Fig. 9. Observation of the upper surface of a silver deposit obtained from a silver nitrate solution with thiourea (scanning microscope 100X).

We investigated first the classical electrolysis parameters: cathodic current density, duration of the electrolysis, composition of the electrolyte, tempera-

Table II. Summary of the best conditions to obtain coherent deposits of silver from silver nitrate solutions

$C_{Ag^+}$	>	200 g/liter*	
$C_{NaNO_3}$	>	50 g/liter*	
$C_{HNO_3}$	>	2.7 g/liter*	
$C_{thiourea}$		100 mg/liter	(1.31 mmol/liter)
$C_{tartrate}$		0.8 g/liter	(2.8 mmol/liter)
$J_c$	<	5 A/dm <sup>2</sup>	

\* These values are influenced by the industrial conditions.

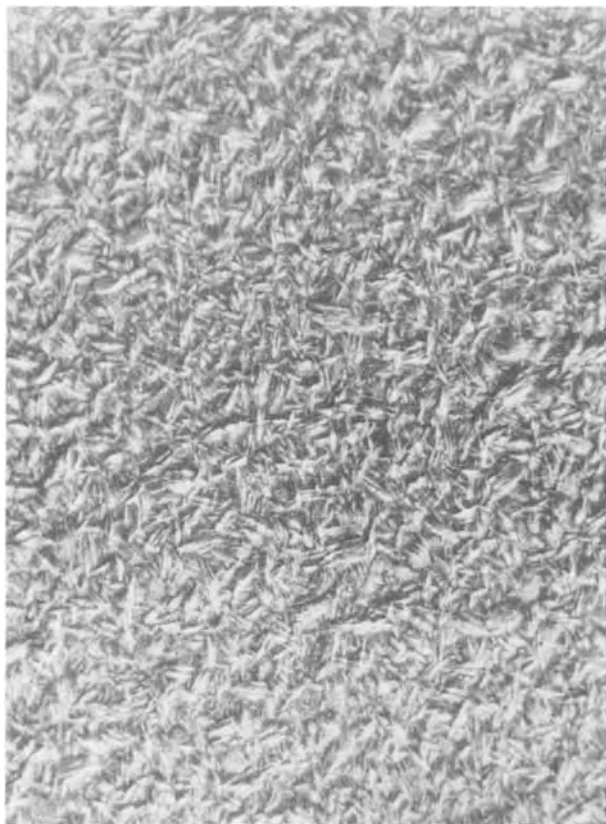


Fig. 10. Observation of the upper surface of a silver deposit obtained from a silver nitrate solution with sodium potassium tartrate (scanning microscope 100X).

ture, and stirring. It was impossible to obtain and keep a good cathodic deposit structure under any of the investigated conditions. Observing the deposit with a microscope while it was growing, we noticed that the dendritic growth took place even at a current density lower than the limiting current density. We thus added several inhibitors to the bath, and we observed that the

presence of thiourea and sodium and potassium tartrate diminished the roughness of the deposit.

The observed types of structures were interpreted in terms of Fischer's theory and were plotted as a function of the ratio  $J_c/C_{Ag^+}$  and the concentration of thiourea.

Manuscript submitted Oct. 23, 1975; revised manuscript received Dec. 19, 1975. This was Paper 135 presented at the Cleveland, Ohio, Meeting of the Society, Oct. 3-7, 1971.

Any discussion of this paper will appear in a Discussion Section to be published in the December 1976 JOURNAL. All discussions for the December 1976 Discussion Section should be submitted by Aug. 1, 1976.

Publication costs of this article were partially assisted by the Free University of Brussels.

#### REFERENCES

1. J. O'M. Bockris and G. A. Raz Umney, "Fundamental Aspects of Electrocrystallization," Plenum Press, New York (1967).
2. H. Fischer, "Elektrolytische Abscheidung und Elektrokristallisation von Metallen," Springer Verlag, Berlin (1954).
3. T. Glazunov, Teindl, and Halik, *Chem. Listy*, **29**, 117 (1935).
4. At. Vagramyan, *J. Phys. Chem. (USSR)*, **14**, 1182 (1940).
5. H. Fischer and Hf. Heiling, *Trans. Inst. Metal Finishing*, **31**, 90 (1954).
6. R. Taft and E. Hiebert, *Kansas Acad. Sci.*, **46**, 142 (1943).
7. R. Taft and E. Horseley, *Trans. Electrochem. Soc.*, **74**, 305 (1938).
8. J. E. Hodge and O. E. Lutness, Master's Thesis, Univ. of Kansas (1941).
9. N. Ibl, *Advan. Electrochem. Electrochem. Eng.*, **II**, p. 49, Interscience (1962).
10. M. Froment, G. Maurin, J. Vereecken, and R. Wiart, *C. R. Acad. Sci. Paris*, **271**, 253 (1970).
11. K. J. Vetter, "Elektrochemische Kinetik," pp. 170-174, Springer Verlag, Berlin (1961).
12. J. C. Evenepoel and R. Winand, *Rev. ATB Met.*, **10**, 132 (1970).
13. R. Winand, *Mem. Sci. Rev. Met.*, **58**, 25 (1961).
14. R. Winand and J. Vereecken, *Rev. ATB Met.*, **10**, 58 (1970).
15. R. Winand and J. Vereecken, *Trans. Inst. Min. Met.*, **84**, 67 (1975).

## Heterogeneous Charge Transfer Rates of the Ferrocene Oxidation in Sulfolane

N. R. Armstrong<sup>1</sup> and Rod K. Quinn\*

Sandia Laboratories, Albuquerque, New Mexico 87115

and N. E. Vanderborgh

The University of New Mexico, Albuquerque, New Mexico 87131

During investigations of the electrochemistry of several organic compounds in the aprotic solvent sulfolane, we have observed unusually low charge transfer rates for both heterogeneous and homogeneous reactions (1, 2, 3). The charge transfer involving the bimolecular reproporation of the *p*-nitrobenzaldehyde dianion with the parent species ( $k_f = 5 \times 10^2$  liter/mole-sec) and the heterogeneous charge transfer rates of both nitrobenzene and benzaldehyde reduc-

tion reactions ( $k_s$ , near  $10^{-3}$  cm/sec) appear anomalously slow. We discuss here cyclic voltammetric investigations for other charge transfer steps in sulfolane, especially the heterogeneous oxidation rates of ferrocene and heterogeneous reduction of nitrobenzene.

The deviation of these rates of charge transfer from predicted values is explored as well as the possible effect on charge transfer rate of varying electrode material (metal type and surface topography).

Predictions of charge transfer rates can be made by Marcus theory calculations provided estimates of solvent and intramolecular rearrangement energies can

\* Electrochemical Society Active Member.

<sup>1</sup> Present address: Department of Chemistry, Michigan State University, East Lansing, Michigan 48823.

Key words: vapor-deposited electrodes, heterogeneous charge transfer, Marcus rate theory, sulfolane.

be accurately made. Several examples of agreement of the predicted and observed rates of charge transfer for inorganic and organic redox couples are available in the literature (4). We made similar calculations for the ferrocene oxidation in sulfolane to test for this type of agreement in the rather unusual solvent sulfolane and found large deviations between predicted and observed rates of charge transfer. The reduction rates of nitrobenzene in sulfolane, being of the same order of magnitude, are also reported here. These results should stimulate further studies in similar solvent systems.

Previous studies have explored possible differences in charge transfer rates that might result when electrode materials were varied (5-8). In general, these investigations have demonstrated only small effects of electrode type, *e.g.*, Au, Pt, Pd, on charge transfer rate, for nonadsorbed reactant systems. Results presented here generally concur with these findings. The effect of varying electrode surface structure on reaction kinetics was tested using this ferrocene system. The investigations reported here use a number of different electrode materials to explore the effects of metal type and surface topography upon the charge transfer process. Unique vapor-deposition facilities permitted the fabrication of high purity metal electrodes as thin films on optically flat, inert substrates (9). Both the ferrocene oxidation and nitrobenzene reduction in sulfolane on Pt, Pd, and Au vapor-deposited electrodes are described.

### Experimental

Methods for purification of the chemicals used in this study have been previously described (1) except for ferrocene (Eastman Chemical Grade) which was purified by sublimation.

Electrochemical measurements were made in a cell similar to that used for spectroelectrochemistry (2, 3). This was fabricated of Teflon and had a solution volume of 2 ml. The reference electrode was made from a silver wire, 1.5 mm in diameter, positioned within 0.5 mm of the working electrode surface. This electrode was anodized in a perchlorate solution prior to use. The potential maintained by this electrode (AgRE) remained constant to  $< 2$  mV over the time period of an experiment. A difference of  $-740$  mV exists between the oxidation potential of ferrocene found with this reference electrode from that found with an isolated Ag/AgClO<sub>4</sub> reference described previously (1). The counterelectrode used here was a large platinum foil positioned along the cell wall. Working electrodes were mounted against one of the outer cell walls. Solution contacted the working electrode surface through a channel drilled into the cell maintaining a geometric area of 0.106 cm<sup>2</sup>. The working electrode was positioned by another Teflon cover bolted to the cell body. An O ring, positioned between the working electrode and the cell body, precisely defined the active electrode area. Electrical contact to the film electrodes was made through a platinum foil; contact resistance was less than 5 ohm. Thermostated oil, circulated through hollow bolts in the cell body, was used to maintain constant solution temperature. This temperature was monitored by a thermistor positioned in the solution.

Two different types of working electrodes were used. Highly polished bulk metal electrodes were positioned directly on the cell. Vapor-deposited thin films were prepared on flat quartz substrates (2, 9). These films, between 20 and 1000 nm thickness, were fabricated of platinum, gold, and palladium. Under conditions of high target bias and low background argon pressure in the sputtering step, relatively high density films were produced. Reversing these conditions, *i.e.*, low target bias and high argon pressure, produced more porous films. The porous films showed surface defects as large as 3000 nm.

Electrochemical measurements were made using either of two different potentiostats. One, previously described (1), was modified by including a positive feedback circuit to compensate for electrode and solution resistances. The other, a PAR 173 potentiostat equipped with a 179 digital coulometer and a 175 universal waveform source, also was equipped with this compensation circuitry. The rate coefficients for charge transfer were in the range where the cyclic voltammetric technique described by Nicholson (10) is valid.

Techniques used with ring-disk electrodes have been previously described (11). All electrodes were preconditioned prior to a measurement by scanning several times between  $-1$  to  $1$  V *vs.* AgRE in a solution not containing electroactive components.

### Results and Discussion

The oxidation of ferrocene is a one-electron process leading to a chemically stable cation, the ferricenium ion. This process is shown in the cyclic voltammogram in Fig. 1. Superimposed on this figure is a residual current trace taken with a platinum electrode in a 0.10M TBAP sulfolane solution. A wide potential window, between the cathodic and anodic limits, of 3.5V is available using this system. The chemical reversibility of the ferrocene oxidation was tested.

Cyclic voltammetric experiments showed the peak current ratio,  $i_{p,c}/i_{p,a}$ , is unity at voltage sweep rates as low as 10 mV/sec. This value suggests that the product cation has high stability. The chemical stability of the ferricenium cation was also explored using ring-disk voltammetry. The collection efficiency was measured as a function of angular velocity. During this experiment the potential of the disk was poised at the convection-limited current region of the ferrocene oxidation while the ring electrode was positioned at the convection-limited plateau of the opposite process, the reduction of the cation. Measured collection efficiencies were independent of the angular velocity (30-300 rad/sec) and, within limits of error, equal to the theoretical efficiency,  $N_0$ , of 0.308. All of these data emphasize the high stability of this cation in this solvent system. Similar chemical stability has not been observed in several other solvents (12-14). For example, Diggle and Parker (12) have demonstrated that the ferricenium cation reacts in aqueous and nonaqueous media through a slow chemical step thought to be a solvolysis reaction. The data do not suggest a similar process in sulfolane.

Data also indicate that the oxidation step is diffusion controlled. In Fig. 2, a linear relationship between peak current and the square root of scan rate is shown. The zero intercept suggests that no adsorption is involved. Under conditions of constant depolarizer concentration, the slope of this curve is proportional to the square root of the diffusion coefficient and to the electroactive area. The slope remained at a constant value as the supporting electrolyte was changed

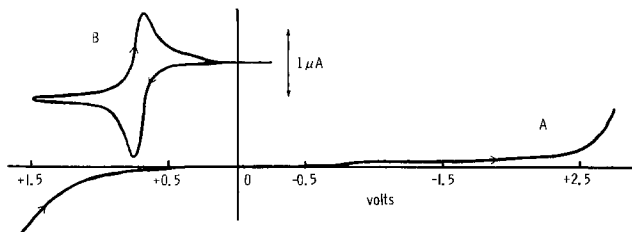


Fig. 1. Cyclic voltammetry of ferrocene in sulfolane. (A) Residual voltammogram taken at a Pt electrode in 0.1N TBAP/sulfolane. (B) Cyclic voltammogram of ferrocene oxidation in sulfolane. The potential axis is defined with respect to the AgRE pseudo-reference electrode. The applied scan rate was 16.7 mV/sec. The electrode area was 0.1064 cm<sup>2</sup>. The bulk concentration of ferrocene in (B) was  $2.0 \times 10^{-4}$  M.



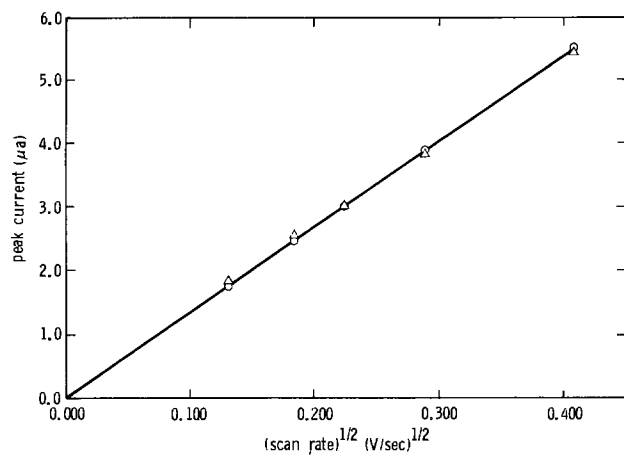


Fig. 2. Cyclic voltammetric peak current ( $i_{p,ra}$ ) ( $\mu\text{A}$ ) vs. (scan rate) $^{1/2}$  ( $\text{V}/\text{sec}$ ) $^{1/2}$  for the ferrocene oxidation in sulfolane;  $\circ$  = 0.1N TBAP solutions,  $\triangle$  0.1N  $\text{KClO}_4$  solutions.

from 0.1M TBAP to 0.1M  $\text{KClO}_4$ . This suggests that the diffusing species is unaffected by this change in the cation of the supporting electrolyte. Moreover, the slope remained constant when various electrode types, different metallic surfaces of various porosities, were used.

The diffusion constant for ferrocene has been previously measured using a RDE method (1). The determined value, calculated from the Levich equation, was  $1.03 \times 10^{-6} \text{ cm}^2/\text{sec}$ . This compared favorably with a determination made using Stokes' law ( $1.06 \times 10^{-6} \text{ cm}^2/\text{sec}$ ) and suggests that the diffusing species is neutral and unsolvated. Diffusion coefficients for ferrocene measured in other nonaqueous media are typically one order of magnitude larger (15). This lower value in sulfolane may be explained, in part, by the higher viscosity of this solvent. Sulfolane exhibits a liquid crystal phase near room temperature with extensive ordering in two dimensions (16). To some degree this ordered solvent structure might persist at the temperatures of these studies, 323°K. This possibility is explored later in this paper.

Separation of the cyclic voltammetric peak potentials was between 65-150 mV at sweep rates between 10-200 mV/sec. Measurements of the heterogeneous rate coefficients,  $k_s$ , of the ferrocene oxidation indicated a slow kinetic process which varied little in velocity as the electrode type was changed. These data are shown in Table I. Triplicate results were obtained for at least five scan rates between 10 and 200 mV/sec. The data in Table I are average values; the precision of these  $k_s$  measurements was  $\pm 10\%$ . The apparent activation energy was estimated by observing the variation in these rates between 303° and 353°K. Results showed that the activation energy is low, less than 3 kcal/mole, and virtually the same for each substrate. The rate coefficients were measured

Table I. Kinetic parameter for the oxidation of ferrocene and reduction of nitrobenzene in sulfolane

Substrate	$k_s$ (50°C),* cm/sec
Ferrocene:	
Pt bulk (polished)	$1.9 \times 10^{-3}$
Pt film (200Å) (annealed)	$1.8 \times 10^{-3}$
Pt film (200Å) dense	$5.0 \times 10^{-3}$
Pt film (200Å) porous	$3.5 \times 10^{-3}$
Au film (300Å) dense	$3.9 \times 10^{-3}$
Pd film (200Å) dense	$3.2 \times 10^{-3}$
Nitrobenzene:	
Pt bulk (polished)	$2.0 \times 10^{-3}$

\* Taken at 5 or more sweep rates between 10 and 200 mV · sec $^{-1}$  and averaged. Average deviation of rate coefficients at each electrode is less than  $\pm 10\%$ . All rates determined in 0.1N TBAP solutions at 50°C. Reactant concentrations were  $1.0 \times 10^{-3}M$ .

Table II. Standard rate coefficients of the oxidation of ferrocene as a function of supporting electrolyte

Substrate	$k_s$ (50°C), cm/sec
Pt bulk (0.1M TBAP)	$1.9 \times 10^{-3}$
Pt bulk (0.1M $\text{KClO}_4$ )	$0.9 \times 10^{-3}$
Pt film (200Å) annealed (0.1M TBAP)	$1.8 \times 10^{-3}$
Pt film (200Å) annealed (0.1M $\text{KClO}_4$ )	$0.9 \times 10^{-3}$

in both TBAP and  $\text{KClO}_4$  solutions; this data is shown in Table II. All data show slow charge transfer rates although those in  $\text{KClO}_4$  are consistently slower than those found in TBAP solutions. This lack of variation of the charge transfer rate with electrode material, combined with information proving diffusion control of the oxidative process, indicates an electron transfer process not involving direct electrode interaction. This is an expected consequence for charge transfer reactions involving nonadsorbed or deposited species (4, 7). The primary effect observed is electrostatic in nature. This effect was found to be small for the noble metal films reported even though the roughness factors varied considerably (17). Investigations of metal deposition reactions will be reported where the electrode interaction is more pronounced and obvious differences between the behavior of the thin film electrodes is observed (17). There are no data to suggest that other electrode processes, such as oxide formation, proceed concurrently with the charge transfer step. The reduction of *p*-benzoquinone in DMF on several bulk electrodes (Pt, Pd, Au, Ir, and Rh) has been recently reported (4). Rates of charge transfer for that process are similar to those reported here for the ferrocene oxidation and, like those, are invariant with electrode type.

The charge transfer rates in sulfolane will be influenced by the fact that the oxidation occurs at potentials removed from the zero charge potential for platinum. Differential capacitance experiments showed that the charge transfer step occurs at potentials slightly positive of the estimated zero charge potential in TBAP solutions (17). This leads to a calculated inner Helmholtz potential of 35 mV and would result in a relatively small (less than 50%) negative adjustment in the rate coefficients.

These experimental values for charge transfer were compared to those predicted theoretically (4, 18, 19). Assuming that work terms can be neglected, a value for the activation free energy ( $\Delta G^\ddagger$ ) was estimated from a combination of the solvent and internal rearrangement energies

$$\Delta G^\ddagger = (\lambda_i + \lambda_o)/4 \quad [1]$$

The solvent reorganization energy ( $\lambda_o$ ) can be evaluated as 0.119 eV using optical and bulk dielectric constants. We estimated an internal rearrangement energy,  $\lambda_i$ , using data from the activation energy of self-exchange of the ferrocene-ferricenium couple measured in methanol (20). An upper limit of 0.10 eV for  $\lambda_i$  was determined from this data. A worst-case assumption is suggested by the internal rearrangement measured for the ferri-ferrocyanide couple of 0.379 eV (4). For these estimates of  $\lambda_i + \lambda_o$ , the calculated value of  $\Delta G^\ddagger$  is consequently less than 0.12 eV.

Using this value and assuming a collision frequency of  $10^4 \text{ cm}^2/\text{sec}$ , the heterogeneous rate coefficient is estimated to be at least  $10^2 \text{ cm}^2/\text{sec}$ . Similar values can be predicted from the relationship between heterogeneous and homogeneous charge transfer (18, 19)

$$(k_{ex}/Z_{\text{homo}})^{1/2} = (k_s/Z_{\text{het}}) \quad [2]$$

A value of the homogeneous exchange coefficient of  $10^8 \text{ liter/mole} \cdot \text{sec}$  and values of  $10^4 \text{ cm}^2/\text{sec}$  and



$10^{11} \text{ sec}^{-1}$  for the heterogeneous and homogeneous collision frequencies (4), respectively, suggest a value of  $k_s$  of  $10^{2.5} \text{ cm/sec}$ .

Charge transfer steps for other redox couples in sulfolane appear similarly slow. An average value of the heterogeneous rate coefficient for the one-electron reduction of nitrobenzene, determined using the cyclic voltammetric technique, is included in Table I. The stability of the anion produced in this process has been previously demonstrated (1-3). The value of this rate coefficient,  $k_s = 2.0 \times 10^{-3} \text{ cm/sec}$ , is similar to that found for the ferrocene oxidation, and appears slow for a nitrobenzene reduction. Studies in other nonaqueous media show a  $k_s$  for this process in excess of 0.1-1.0 cm/sec (21-23). Double-layer corrections for the reduction rate coefficient were estimated to be less than one order of magnitude. Such slow electron transfer rates as found for the ferrocene oxidation have been explained by assuming localization of the unit charge. For instance, such slow rates for nitro-substituted hydrocarbons have been attributed to large differences in charge distribution between the parent and anion resulting in an unusually large rearrangement energy (21).

The charge transfer parameters for several inorganic and organic redox couples have been successfully predicted using the Marcus theory in both aqueous and nonaqueous solutions (9). The rates for these processes are typically large ( $k_s > 10^{-2} \text{ cm/sec}$ ) with corresponding small rearrangement energies. Oxidation of ferrocene should not involve large energies for rearrangement since both the neutral and charged species are essentially spherical (15). However, the solvent may contribute larger-than-predicted rearrangement energies. Evidence suggests that solvents such as DMSO and sulfolane exhibit long-range, second-order structuring (16, 24, 25). This type of order will not be reflected in either the optical or bulk dielectric constants (9).

This solvent structure may also be the cause of slow rates for homogeneous charge transfer and chemical reactions previously observed in sulfolane (1-3). The solvent effect may reflect itself in both the rearrangement energies which make up the activation free energy and in the preexponential term of the absolute rate equation. We have assumed for purposes of the above calculations that the collision frequency,  $Z$ , is only slightly affected by solvent viscosity. At most, such an effect would lead to less than an order of magnitude correction in the rate coefficient. Assessment of a possibly larger, more specific effect of solvent structure on the preexponential factor awaits a study of temperature dependence on rate coefficients in a variety of solvent media. Although our understanding of this phenomenon is only qualitative and considerable additional work is necessary to explore the reasons for these slow chemical and electron transfer steps, we suggest that similar retardation might be found in other structured solvents such as DMSO and hexamethylphosphoamide.

#### Acknowledgments

The authors acknowledge the contribution to this work made by D. M. Mattox and G. J. Kominiak who prepared the film electrodes used for these studies and the technical assistance of P. G. Neiswander. This

work was supported in part through an AWU/AEC Graduate Fellowship at Sandia Laboratories (to N.R.A.) granted by Associated Western Universities, and by the U.S. Energy Research and Development Administration (ERDA).

Manuscript submitted Sept. 16, 1975; revised manuscript received Jan. 9, 1976. This was Paper 349 presented at the San Francisco, California, Meeting of the Society, May 12-17, 1974.

Any discussion of this paper will appear in a Discussion Section to be published in the December 1976 JOURNAL. All discussions for the December 1976 Discussion Section should be submitted by Aug. 1, 1976.

Publication costs of this article were partially assisted by Sandia Laboratories.

#### REFERENCES

1. N. R. Armstrong, R. K. Quinn, and N. E. Vanderborgh, *Anal. Chem.*, **46**, 1759 (1974).
2. R. K. Quinn, N. R. Armstrong, and N. E. Vanderborgh, *J. Vacuum Sci. Technol.*, **12**, 160 (1975).
3. N. R. Armstrong, N. E. Vanderborgh and R. K. Quinn, Submitted for publication; N. R. Armstrong, Ph.D. Dissertation, University of New Mexico (1974).
4. J. M. Hale, in *Reactions of Molecules at Electrodes*, H. S. Hush, Editor, pp. 229-257, Wiley-Interscience, New York (1971).
5. A. Capon and R. Parsons, *J. Electroanal. Chem.*, **46**, 215 (1973).
6. R. Parsons, *Surface Sci.*, **2**, 418 (1964).
7. M. V. Vojnovic and D. B. Sepa, *J. Chem. Phys.*, **51**, 5344 (1969).
8. J. O'M. Bockris, R. J. Mannan, and A. Damjanovic, *ibid.*, **48**, (1968).
9. D. M. Mattox and G. J. Kominiak, *J. Vacuum Sci. Technol.*, **8**, 194 (1971).
10. R. S. Nicholson, *Anal. Chem.*, **37**, 1351 (1965).
11. N. R. Armstrong, R. K. Quinn, and N. E. Vanderborgh, *This Journal*, **122**, 615 (1975).
12. J. W. Diggle and A. J. Parker, *Electrochim. Acta*, **18**, 975 (1973).
13. R. E. Panzer and P. J. Elving, *This Journal*, **119**, 864 (1972).
14. J. Lelievre, C. LeFeuvre, and R. Gaboriaud, *C. R. Acad. Sci. (Paris) C*, **275**, 1455 (1972).
15. I. Ruff, V. J. Friedrich, K. Demeter, and K. Csillag, *J. Phys. Chem.*, **75**, 3303 (1971).
16. M. Della Monica, L. Jannelli, and U. Lamanna, *ibid.*, **72**, 1068 (1968).
17. R. K. Quinn, N. R. Armstrong, M. L. Knotek, and N. E. Vanderborgh, Submitted to *This Journal*; Abstract 395, p. 901, Abstract 396, p. 903, The Electrochemical Society Extended Abstracts, Spring Meeting, Toronto, Canada, May 11-16, 1975.
18. R. A. Marcus, *Ann. Rev. Phys. Chem.*, **15**, 155 (1964).
19. R. A. Marcus, *J. Chem. Phys.*, **43**, 679 (1965).
20. D. R. Stranks, *Discussions Faraday Soc.*, **29**, 73 (1960).
21. M. E. Peover and J. S. Powell, *J. Electroanal. Chem.*, **20**, 427 (1969).
22. M. E. Peover, in *Reactions of Molecules at Electrodes*, H. S. Hush, Editor, pp. 259-281, Wiley-Interscience, New York (1971).
23. M. E. Peover, in *Electroanalytical Chemistry*, Vol. 2, A. J. Bard, Editor, Chap. 1, Marcel Dekker, New York (1967).
24. B. Case, in *Reactions of Molecules at Electrodes*, H. S. Hush, Editor, pp. 45-134, Wiley-Interscience, New York (1971).
25. H. L. Schlafer and W. Schaffernicht, *Angew. Chem.*, **72**, 618 (1960).

# A Zinc Chlorine Molten Salt Cell

Samuel vonWinbush<sup>1</sup> and Anthony F. Sammells\*

Gould Incorporated, Gould Laboratories—Energy Research, St. Paul, Minnesota 55165

There are several high energy batteries currently being investigated that use molten salt electrolytes. These battery systems operate at temperatures significantly above ambient. For example, the proposed normal temperature of operation for the lithium/chlorine (1), lithium/iron sulfide (2), and aluminum/chlorine (3) cells are 650°, 425°, and 150°C, respectively. For these systems it is, of course, mandatory that the electrolyte used be a molten salt if the battery is to be rechargeable. Considerable work has been reported on the deposition of aluminum from organic nonaqueous electrolytes at ambient temperatures (4) which may at some time make an ambient temperature aluminum chlorine battery worth consideration.

The zinc chlorine aqueous battery system has been investigated over the last several years (5). This system operates at ambient temperatures and uses a flowing electrolyte of aqueous zinc chloride in which a gradual stoichiometric change takes place (6) during charge and discharge.

Until this time, little work has been done to determine the feasibility of a zinc chlorine molten salt cell. Pure molten zinc chloride is impractical for such a system because it is a highly viscous liquid consisting mainly of complex species such as  $(\text{ZnCl}_2)_n$ ,  $\text{ZnCl}_4^{2-}$ ,  $\text{ZnCl}_3^-$ , and  $\text{ZnCl}_2$  (7) with very little  $\text{Zn}^{2+}$  existing in the vicinity of the melting point. Molten zinc chloride has a relatively low conductivity, varying from  $1.31 \times 10^{-3} \text{ ohm}^{-1} \text{ cm}^{-1}$  at its melting point to  $8.4 \times 10^{-2} \text{ ohm}^{-1} \text{ cm}^{-1}$  at 501°C (8). Several investigators have shown that the addition of small amounts of alkali halides to molten zinc chloride greatly decreases its viscosity with a corresponding increase in the conductivity (8, 13). For example, the conductivity of zinc chloride at 475°C can be increased from about  $3.1 \times 10^{-2}$  to  $4 \times 10^{-1} \text{ ohm}^{-1} \text{ cm}^{-1}$  by the addition of 30 mole per cent (m/o) KCl. Upon discharge of a molten salt zinc chlorine cell, some increase in IR polarization will therefore be expected as a result of the stoichiometric change taking place in the melt.

Molten zinc chloride dissolves zinc metal to a small extent (0.61 m/o at 600°C) with the formation of a subhalide (9). This solubility, however, decreases with the addition of alkali chlorides which destabilize the apparent  $\text{Zn}_2^{2+}$  species in the melt (10).

Zinc chloride forms many eutectics with sodium chloride and potassium chloride and mixtures thereof. These eutectics enable one to work at temperatures below 300°C, with liquidus lines sufficiently shallow to allow moderate concentration changes to occur without precipitation of salts on the electrodes of a zinc chlorine cell. Preliminary work is reported here to determine the feasibility of such a system.

## Experimental

**Electrolyte preparation.**—Electrolyte melts were made from high purity NaCl, KCl, and  $\text{ZnCl}_2$  obtained from the Fisher Chemical Company. Mixtures initially prepared in the dry box were heated to 110°C under vacuum overnight and then at 190°C for two days to assure complete removal of moisture. Melts were then transferred under vacuum to the dry box. All melts used were clear and showed no discoloration.

**Dry box.**—All cell assembly and coulometric studies were performed in a Vacuum Atmospheres dry box with an HE-193-2 Vacuum Atmospheres dry train.

\* Electrochemical Society Active Member.  
<sup>1</sup> Present address: State University of New York, Old Westbury, New York 11568.  
Key words: molten salt electrolytes, coulombic efficiency, galvanic cell, zinc-chlorine couple.

Cell voltages were recorded on an HP3430A digital voltmeter.

Constant current source used in the coulometric study and in cell discharge was a J. Fluke Model 351A.

**Cell assembly.**—The eutectic mixtures used were first melted in the electrolyte holder of the cell in the dry box. The cell cap containing the electrode components was then inserted. A seal was achieved between the two halves by a suitable clamping device around the ground-glass lip. Cell temperatures were recorded via a Chromel-Alumel thermocouple. The porous chlorine electrode was fabricated from POCO AX grade graphite. UCAR C-34 graphite cement was used to seal the chlorine electrode to the tungsten feed-through.

Scanning electron microscope photographs were taken with a Cambridge Model S4-104 SEM.

## Results and Discussion

In order to determine coulombic efficiencies for zinc deposition and dissolution that might be expected in the molten salts studied, use was made of the coulombic efficiency cell shown schematically in Fig. 1. From the weight changes for the cathodic and anodic processes shown in Table I, it can be seen that coulombic efficiencies close to 100% were observed with all the melts investigated, the results shown representing typical values of repeated runs. Discrepancies from 100% coulombic efficiency can be explained by oxidation of the zinc after removal from the molten salt and prior to weighing. The interelectrode separation in this experiment was typically 0.5 cm.

The zinc deposited from the molten salts was typically crystalline as shown in the 20X SEM photograph (Fig. 2), the hexagonal appearance of the individual zinc crystals being shown in the 200X SEM photograph (Fig. 3). Altering the current density produced little change in the zinc morphology, except the occurrence of dendritic growths increased with current density.

The utility of these molten salts as an electrolyte in a zinc chlorine galvanic cell was then investigated. The experimental setup for the galvanic cell is shown in Fig. 4. The cell container was made from Pyrex glass and contained tungsten feedthroughs for electrode

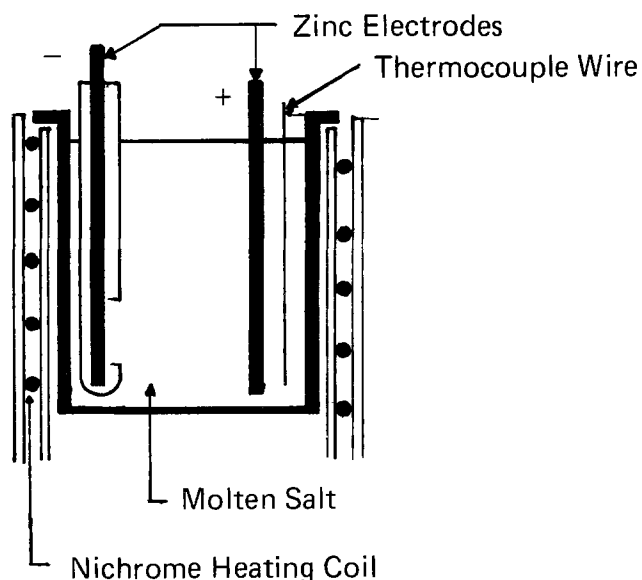
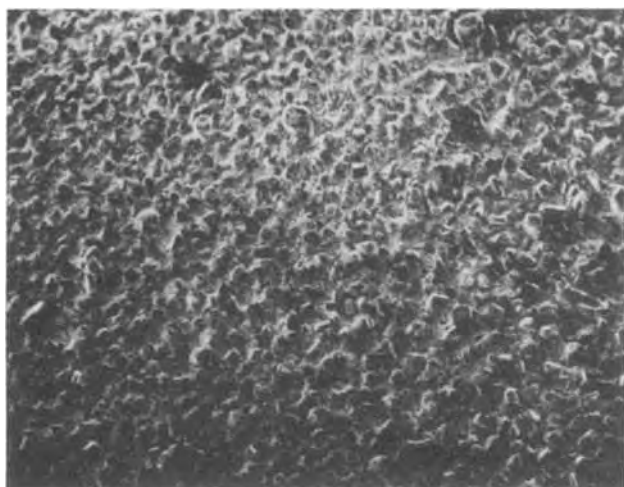


Fig. 1. Coulometric efficiency cell for zinc deposition from  $\text{ZnCl}_2$  containing molten salts.

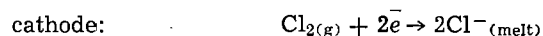
Table I. Coulombic efficiencies for ZnCl<sub>2</sub> containing molten salts

	ZnCl <sub>2</sub> -NaCl-KCl eut <sup>a</sup>			ZnCl <sub>2</sub> -NaCl eut <sup>b</sup>			ZnCl <sub>2</sub> -KCl eut <sup>c</sup>		
	mA/cm <sup>2</sup>	0.68	2.05	6.83	0.68	2.05	6.83	0.68	2.05
Zn loss at anode (g)	0.129	0.122	0.122	0.133	0.125	0.133	0.123	0.128	0.118
Zn gain at cathode (g)	0.122	0.127	0.157	0.121	0.136	0.132	0.121	0.128	0.109
Theoretical (g)	0.122			0.122			0.122		
		m/o ZnCl <sub>2</sub>	m/o KCl	m/o NaCl	m.p., °C				
	a	60.0	20	20.0	203				
	b	59.5		40.5	262				
	c	49.0	51		230				

contacts. The cell was initially run as a primary, at which time the graphite negative electrode was substituted for a high purity zinc strip of approximately the same dimensions. For this cell configuration, a load curve is shown in Fig. 5, where current densities at the chlorine electrode (the limiting electrode) of 7 mA/cm<sup>2</sup> could be achieved at 1.0V indicating considerable polarization at this electrode. The open-circuit potential for this system was found to be around 1.73V at temperatures of 288°C which compares with a zinc chloride breakdown potential of 1.71V at 300°C (11). This significant polarization indicated in Fig. 5 was partially due to IR losses caused by the fairly large interelectrode spacing of 0.7 cm, which was dictated by convenient experimental design.

Fig. 2. 20X SEM photograph of zinc deposited from ZnCl<sub>2</sub>-NaCl-KCl eutectic.Fig. 3. 300X SEM photograph of zinc deposited from ZnCl<sub>2</sub>-NaCl-KCl eutectic.

The electrode reactions in this system during discharge can be predicted as



A discharge curve for this cell configuration is shown in Fig. 6, using the ternary eutectic shown in Table 1, over a 30 hr period using a current density of 1.19 mA/cm<sup>2</sup>. The break in the discharge curve at around 24 hr was caused by deterioration of the graphite cement which was used to make contact to the positive lead. Erosion of the graphite cement in the molten salts used proved a serious experimental problem.

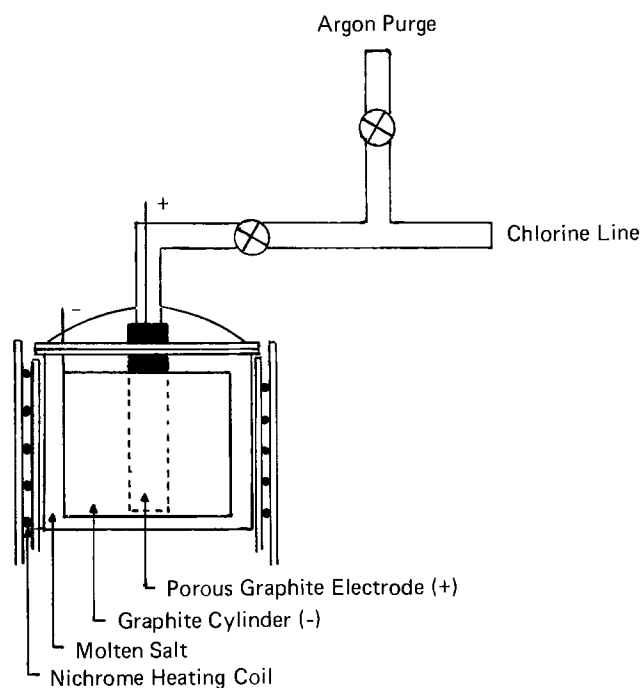
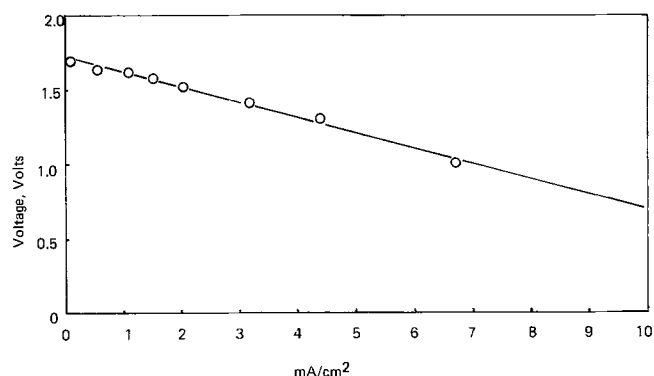


Fig. 4. Experimental arrangement of galvanic cell

Fig. 5. Load curve for Zn/Cl<sub>2</sub> molten salt cell

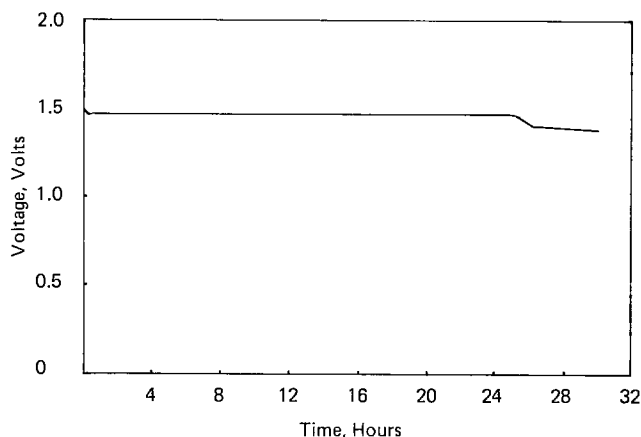
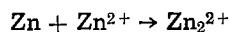


Fig. 6. Discharge curve for Zn/Cl<sub>2</sub> molten salt cell at 1.19 mA/cm<sup>2</sup>.

When using a graphite negative electrode, the cell was run in the secondary mode. The apparent coulombic efficiencies of cycled cells varied between 10 and 100%. A charge-discharge curve is shown in Fig. 7 for the cell initially charged at 7 mA/cm<sup>2</sup> (at the zinc electrode) and discharged at 0.7 mA/cm<sup>2</sup> giving apparently high coulombic efficiency. It should, however, be pointed out that this cell had cycled several times and this high efficiency may reflect the presence of excess zinc not removed during earlier cycles. Figure 7 does, however, give an idea of the electrochemical performance with the cell configuration used. The reduction in charging voltage during charge probably reflects a gradual reduction in polarization at the chlorine electrode.

Some difficulty was encountered in determining the coulombic efficiency that would be expected from this system, since the discharge performance was very sensitive to chlorine pressure at the porous graphite used as the chlorine electrode and required frequent adjustment. Presumably, maintenance of the optimized three-phase interface between the graphite, molten salt, and gaseous chlorine was greatly influenced by the chlorine gas pressure. Two other factors could also explain variations from 100% coulombic efficiency. The first of these was the generally poor adhesion of the electrodeposited zinc on the graphite cylinder upon charge. Such deposits could be expected to prematurely fall off the electrode upon discharge, giving a low round-trip coulombic efficiency in some runs. Secondly, it has been shown (9) that zinc has a finite solubility in molten ZnCl<sub>2</sub> caused by the reaction



giving the zinc subhalide species. It has been calculated

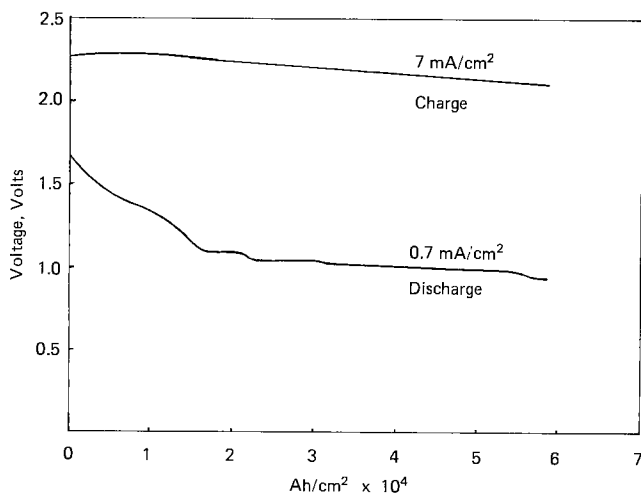
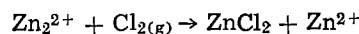


Fig. 7. Charge-discharge curve for Zn/Cl<sub>2</sub> molten salt cell

that the solubility of zinc in molten ZnCl<sub>2</sub> at 288°C is around 79 ppm. In the presence of alkali halides the Zn<sub>2</sub><sup>2+</sup> species is destabilized. It has been directly shown (12) that the addition of alkali halides to melts of CdCl<sub>2</sub> saturated with the species Cd<sub>2</sub><sup>2+</sup> is greatly decreased. For example in CdCl<sub>2</sub> melts containing KCl at concentrations comparable to the melt compositions used in this study, the dissolved Cd was reduced from 14 m/o to less than 0.02 m/o by the addition of the alkali halide. It would not be unreasonable to expect a similar reduction in dissolved zinc in the systems investigated in this study. We would expect the concentration of dissolved zinc to be less than 10 ppm. However, in the small cells used in this study, this represents around 0.019 mA-hr of zinc in the form of the subspecies Zn<sub>2</sub><sup>2+</sup> available for the direct reaction



Any coulombic losses by this path will therefore be dictated by the rate of the above reaction.

By reference to Fig. 8, the composition change that might be realized in the KCl-ZnCl<sub>2</sub> melt (66.7 m/o ZnCl<sub>2</sub>, 33.3 m/o KCl) upon cycling is shown. Starting with a galvanic cell that contains 10 ml of this electrolyte at a temperature of 288°C, it can be seen that the ZnCl<sub>2</sub> concentration can vary between 47 m/o upon complete cell charge to 77 m/o upon discharge as indicated by the arrow in Fig. 8. This represents a potential charge capacity of 8.7 A-hr. However, no cells are reported here that were cycled between these concentration limits.

### Conclusion

It therefore remains to be seen whether molten salt electrolytes can be of utility in the zinc chlorine system. It is clear from this study that considerable work will have to be performed on optimization of the zinc deposition in molten salts so as to ensure good adhesion to the substrate, together with a greater understanding of possible self-discharge mechanisms. It would seem unlikely that very high current densities are practical with the molten salts reported here. Greater discharge rates may result from increased electrolyte conductivities and optimization of the chlorine electrode performance. However, this preliminary work does show the couple feasible under these conditions even though not practical at this time.

### Acknowledgments

The partial support of this investigation by the National Science Foundation (NSF Faculty Research Participation Project, Grant No. HES-75-05080) is gratefully acknowledged.

Manuscript submitted Sept. 8, 1975; revised manuscript received Jan. 12, 1976.

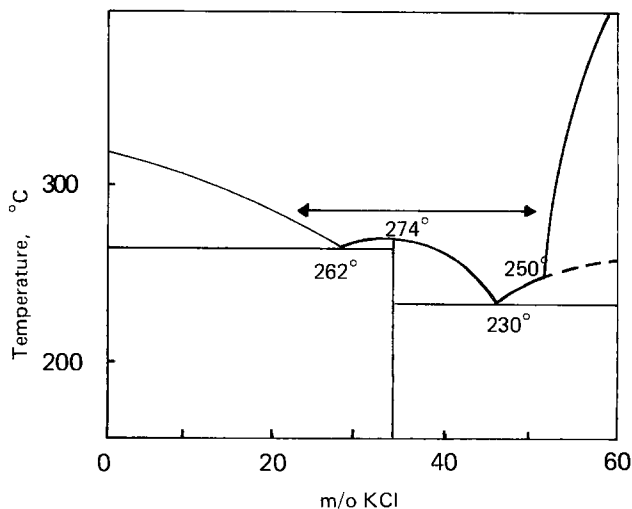


Fig. 8. Phase diagram for KCl-ZnCl<sub>2</sub> system

Any discussion of this paper will appear in a Discussion Section to be published in the December 1976 JOURNAL. All discussions for the December 1976 Discussion Section should be submitted by Aug. 1, 1976.

Publication costs of this article were partially assisted by Gould Incorporated.

## REFERENCES

1. D. A. J. Swinkels, *This Journal*, **112**, 62 (1966).
2. P. A. Nelson, E. C. Gay, and W. J. Walsh, Proc. 26th Power Sources Symposium, Atlantic City (1974).
3. J. Giner and G. L. Holleck, NASA Report No. CR-1541 (1973).
4. A. G. A. Capuano and W. G. Davenport, *This Journal*, **118**, 1658 (1971); A. Brenner, in "Advances in Electrochemistry and Electrochemical Engineering," Vol. 5, C. W. Tobias, Editor, John Wiley & Sons, New York (1967).
5. P. C. Symons, International Conf. on Electrolytes for Power Sources, Brighton, England, December 1973.
6. A. F. Sammells, Abstract 236, p. 600, The Electrochemical Society Extended Abstracts, Fall Meeting, Dallas, Texas, October 5-10, 1975.
7. R. B. Ellis, *This Journal*, **113**, 485 (1966).
8. H. Bloom and I. A. Weeks, *Trans. Faraday Soc.*, **67**, 1416 (1971).
9. S. vonWinbush, J. D. Corbett, and F. C. Albers, *J. Am. Chem. Soc.*, **79**, 3020 (1957).
10. J. D. Corbett and R. K. McMullen, *ibid.*, **77**, 4217 (1955).
11. Iu. K. Delimarskii and B. F. Markov, in "Electrochemistry of Fused Salts," R. E. Wood, Editor, p. 127, Sigma Press, New York (1961).
12. A. Cubicciotti and D. Cubicciotti, *J. Am. Chem. Soc.*, **74**, 1198 (1952).
13. F. R. Duke and R. A. Fleming, *This Journal*, **104**, 251 (1957).



## Predeposition in Silicon as Affected by the Formation of Orthorhombic SiP and Cubic $\text{SiO}_2 \cdot \text{P}_2\text{O}_5$ at the PSG-Si Interface

S. Solmi, G. Celotti, D. Nobili, and P. Negrini

C.N.R. LAMEL Laboratory, 40126 Bologna, Italy

### ABSTRACT

The phenomena limiting heavy phosphorus predeposition in silicon have been studied in the temperature range 850°–1000°C by using electrical measurements and x-ray diffraction, together with optical and electron microscopy and Rutherford backscattering of He ions. It is reported that increasing the flux of dopant across the oxide layer, either by reducing oxygen pressure or by increasing that of  $\text{POCl}_3$ , leads ultimately to anomalous doping kinetics associated to segregation of orthorhombic SiP and cubic  $\text{SiO}_2 \cdot \text{P}_2\text{O}_5$  at the PSG-Si interface, and to damage and loss of adhesion of the surface oxide. Increasing temperature acts in opposition to the onset of this phenomenon due to the increased competitiveness of bulk silicon diffusivity. Segregation is sensitive to the orientation of the slice: the (111) being the most favorable, followed by the (110) and (100), respectively. The parameters leading to interface segregation are analyzed and discussed.

An extensive investigation on the predeposition and solubility of phosphorus in silicon is underway in our laboratory, with the aim of contributing to clarification of the basic physicochemical aspects of the doping technology.

Previous research, carried out in the temperature range 850°–1200°C using  $\text{POCl}_3$  and oxidizing conditions (1), has shown that the total content,  $Q$ , of predeposited phosphorus increases with time following a parabolic law  $Q = \sqrt{Kt}$ . A similar kinetic,  $X_0 = \sqrt{Bt}$ , is observed for the thickness  $X_0$  of the surface oxide. The rate-determining step for both processes is the diffusion of the reacting species across the oxide layer.

With increasing  $\text{POCl}_3$  concentration in the gas, the chemical potential of phosphorus at the oxide-silicon interface and in the adjacent silicon matrix can overcome the value corresponding to the solubility limit, and silicon phosphide precipitates of orthorhombic structure (2) can nucleate and grow, in the course of the process, within the diffused region of the crystal.

Diffusion of the dopant in the bulk competes with the precipitation process, and the amount,  $Q_{\text{el}}$ , of phosphorus electrically active after predeposition is limited by the solubility and diffusivity of this element in silicon. These conditions are satisfied in a wide range of temperature, time, and flux composition typical of device technology. The fraction of electrically inactive dopant increases with the concentration of  $\text{POCl}_3$  and decreasing predeposition temperature.

The present research concerns the phenomena occurring with increasing dopant flux and concentration. The formation of phosphorus-rich compounds at the

interface of silicon and heavily doped PSG has been reported by several authors (3-6).

Kooi (3), after standard predeposition using a  $\text{P}_2\text{O}_5$  solid source, observed the presence at the PSG-Si interface of crystalline phosphorus-rich compounds. The structure of these phases was not analyzed.

Schmidt *et al.* (4) reported the presence of orthorhombic SiP in the surface layers of Si diffused from doped anodic oxide and observed that segregation depends on the orientation of the slice (5).

Segregation phenomena and the structure of the precipitates have not yet been systematically studied in function of the main parameters of the predeposition process. The present research aims at contributing to clarification of these problems which are of practical importance for device technology.

### Experimental

We used dislocation-free silicon slices about 300  $\mu\text{m}$  thick and mirror finished on one side as produced by Wacker. The (111) orientation has been studied more extensively; and a limited number of experiments was also performed on (100) and (110) oriented specimens. Our slices were of Czochralski type, boron doped, of nominally 1  $\text{ohm}\cdot\text{cm}$ .

Predeposition has been carried out mainly at 920° and 1000°C. Some treatments have also been performed at 850°C. We used oxidizing conditions, together with the apparatus and procedures described in our previous paper (1).

A set of predepositions has been carried out changing only the partial pressure of oxygen, and another set changing only that of the phosphorus oxychloride. In all cases the total gas flow was kept constant (1580 ml/min) by adjusting the main nitrogen flow. To remove

Key words: phosphorus predeposition, phosphosilicate compounds, silicon monophosphide, interface segregation, anomalous doping.

the doped oxide layer, a standard 3 min etching in 5% HF solution was performed before the drive-in treatments.

We have accurately measured the total and the electrically active phosphorus content,  $Q$  and  $Q_{el}$ , in the predeposited silicon slices. These quantities have been determined by using the techniques already reported in detail; that is, neutron activation analysis and electrical resistivity measurements. The latter were performed after predeposition as well as after suitable drive-in (1).

The features of the oxide films have been observed by using a Leitz M M 5 optical microscope, and their thickness and surface roughness accurately measured by a Talystep. The roughness has been analyzed by using a special sharp stylus of truncated pyramidal form (nominal tip dimensions  $\sim 0.1 \times 2.5 \mu\text{m}$ ) and applying a stylus force of about  $10 \mu$  newton.

The composition of the oxide film has been checked by Rutherford backscattering of He ions with energy 1.8 MeV, obtained from the 2 MeV Van der Graaf of the Laboratorio Nazionale of Legnaro (Italy). The overall resolution was estimated  $\sim 18$  keV and the beam divergence was kept lower than  $10^{-4}$  rad. The data analysis has been performed as described in Ref. (7).

In a range of experimental conditions, the oxide films turned out to be loose; therefore it was possible to collect powder specimens suitable for x-ray examinations. We verified the absence of contamination by comparing the spectra of powders obtained by using tools of different materials (glass, Plexiglas, and stainless steel).

The powders were observed by the Debye-Scherrer technique employing a Philips 114.6 mm  $\phi$  camera, and Cu  $K\alpha$  radiation. To detect the presence of small quantities of crystalline phases embedded in the amorphous oxide matrix, we performed rather long exposures on Kodak Kodirex film.

Parallel examinations have been performed directly on the oxide films lying on their silicon substrates, by using a Rigaku-Denki SG-7 powder diffractometer equipped with scintillation counter and potentiometric recording, Cu  $K\alpha$  radiation, and the usual Bragg symmetric reflection geometry. Photographic methods have been discarded because they were unsuccessful for both the transmission and reflection geometry, even with very long exposures.

The two techniques turned out to be complementary because the undesired scattering (amorphous  $\text{SiO}_2$  from matrix in Debye-Scherrer, and Si (111) from substrate with the diffractometer) masked different angular regions.

## Results

*Anomalous doping and oxide damage.*—We report first the values of total and electrically active phosphorus,  $Q$  and  $Q_{el}$ , for 27 min predepositions at  $920^\circ\text{C}$ .

In Fig. 1 these quantities are plotted vs. the concentration of  $\text{POCl}_3$  at a constant oxygen concentration of 5.7%. In Fig. 2  $Q$  and  $Q_{el}$  are reported vs. the concentration of  $\text{O}_2$  at a constant phosphorus oxychloride concentration of 0.27%.

In Fig. 3 and 4, respectively, we report the results of the corresponding predeposition experiments carried out at  $1000^\circ\text{C}$ . The concentration ranges explored in these latter experiments are about three times larger than in those performed at  $920^\circ\text{C}$ .

We notice that in a wide range of gas compositions the content of phosphorus,  $Q$ , increases with phosphorus oxychloride concentration. A sudden deviation from this trend takes place at about 0.5%  $\text{POCl}_3$  in the  $920^\circ\text{C}$  experiments. This phenomenon is observed at  $1000^\circ\text{C}$  only for the highest  $\text{POCl}_3$  concentrations.

As is shown in Fig. 2 and 4, in a wide range of flux compositions the content of phosphorus increases with decreasing oxygen concentration. A sudden deviation from this trend is observed at about 3% oxygen in the

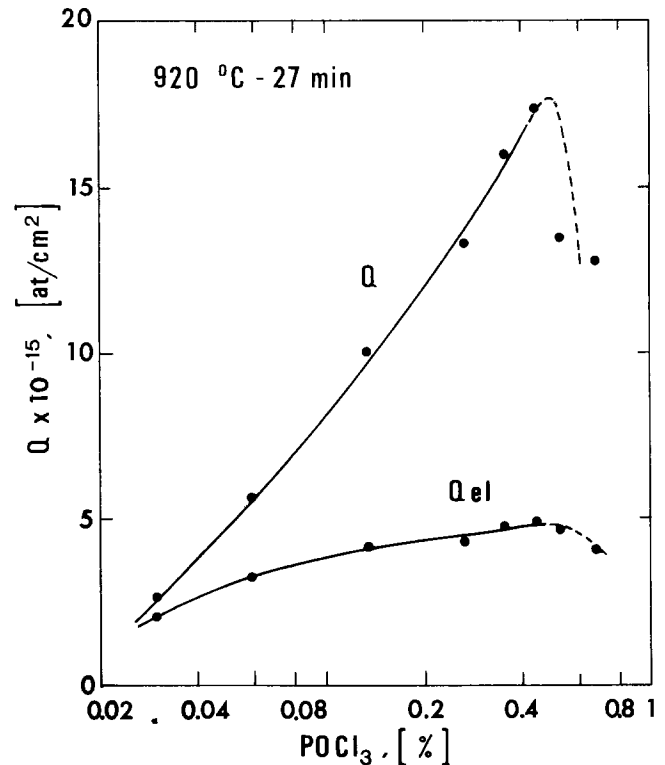


Fig. 1. Total,  $Q$ , and electrically active phosphorus,  $Q_{el}$ , vs.  $\text{POCl}_3$  concentration in constant time (27 min) predepositions at  $920^\circ\text{C}$ . Oxygen concentration is constant (5.7%).

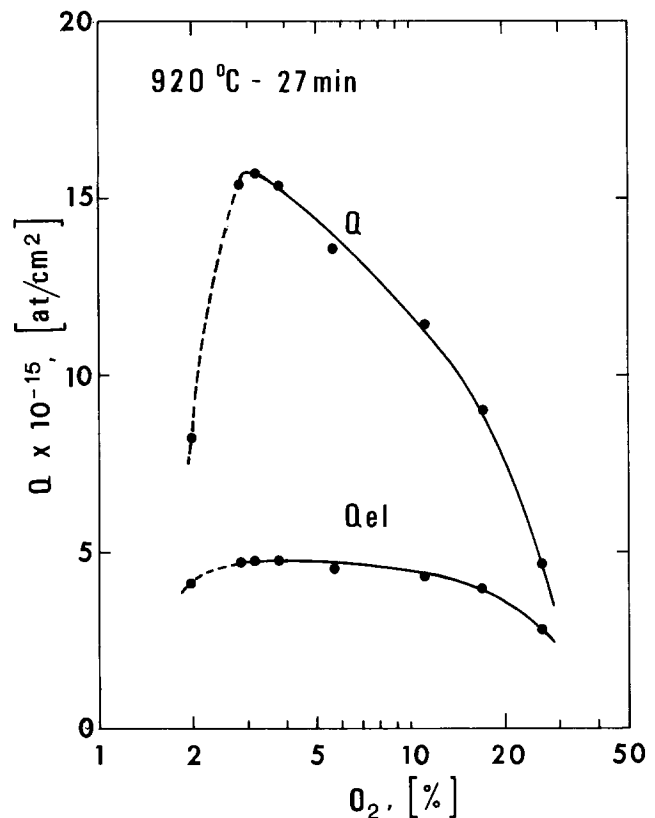


Fig. 2. Total,  $Q$ , and electrically active phosphorus,  $Q_{el}$ , vs. oxygen concentration in constant time (27 min) predepositions at  $920^\circ\text{C}$ .  $\text{POCl}_3$  concentration is constant (0.27%).

$920^\circ\text{C}$  predepositions. This phenomenon is absent at  $1000^\circ\text{C}$ .

To analyze the phenomena observed at  $920^\circ\text{C}$  we have studied the time dependence of the values of  $Q$  and  $Q_{el}$  for two distinct phosphorus oxychloride con-

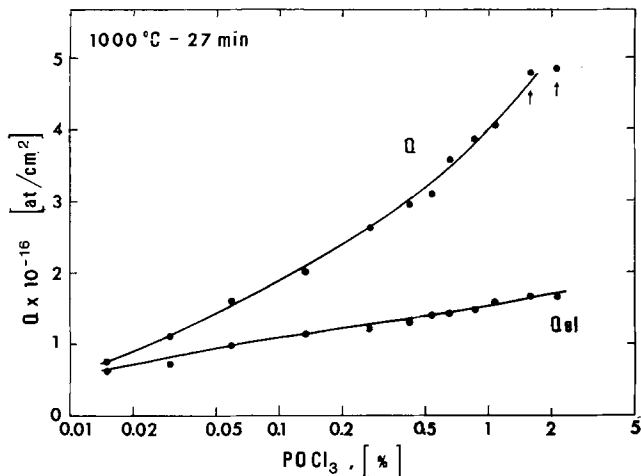


Fig. 3. Total, Q, and electrically active phosphorus, Q<sub>el</sub>, vs. POCl<sub>3</sub> concentration in constant time (27 min) predepositions at 1000°C. Oxygen concentration is constant (5.7%). The arrows indicate the samples analyzed by x-ray.

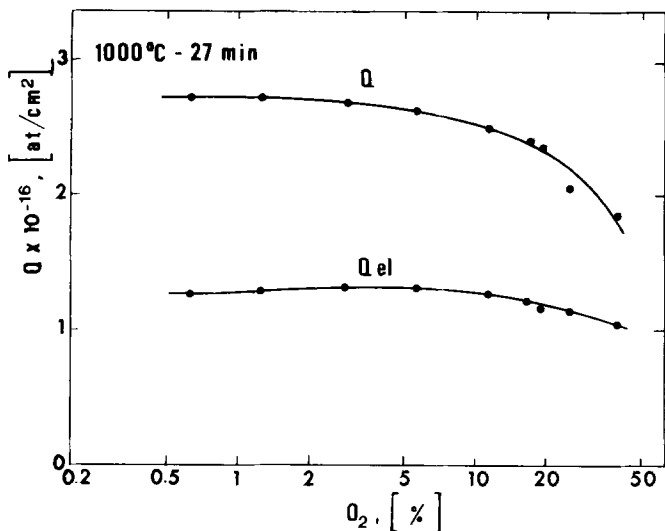


Fig. 4. Total, Q, and electrically active phosphorus, Q<sub>el</sub>, vs. oxygen concentration in constant time (27 min) predepositions at 1000°C. POCl<sub>3</sub> concentration is constant (0.27%).

centrations. Figures 5 and 6 show the results obtained with 0.27 and 0.53% POCl<sub>3</sub>, respectively. Oxygen per cent is kept constant (5.7%). It is observed that a deviation from the parabolic law of phosphorus doping,

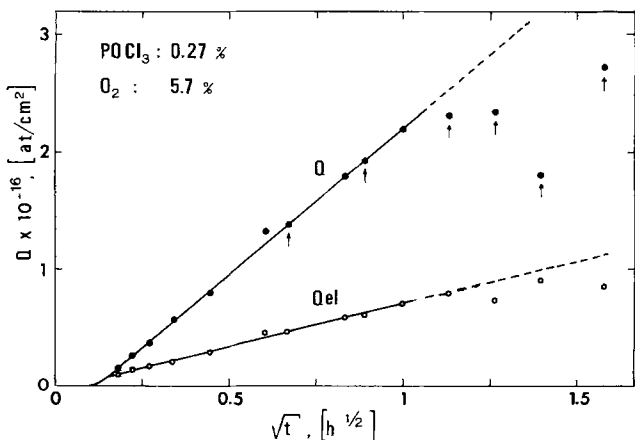


Fig. 5. Time square root dependence of the total, Q, and electrically active phosphorus, Q<sub>el</sub>, in predepositions carried out at 920°C. Doping gas composition is 0.27% POCl<sub>3</sub> and 5.7% O<sub>2</sub>. The arrows indicate the samples analyzed by x-ray.

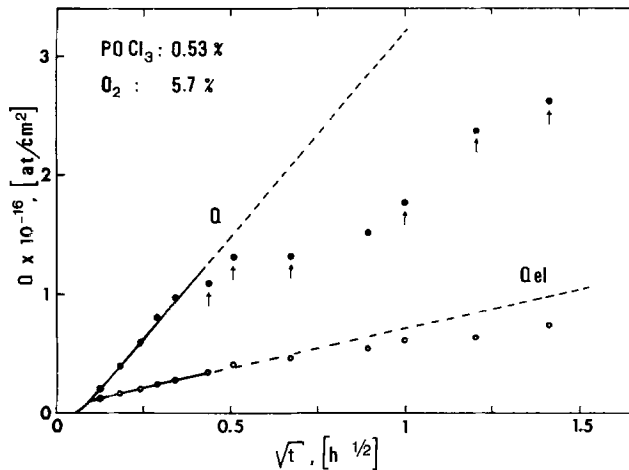


Fig. 6. Time square root dependence of the total, Q, and electrically active phosphorus, Q<sub>el</sub>, in predepositions carried out at 920°C. Doping gas composition is 0.53% POCl<sub>3</sub> and 5.7% O<sub>2</sub>. The arrows indicate the samples analyzed by x-ray.

$Q = \sqrt{Kt}$ , takes place at a time which decreases as the POCl<sub>3</sub> concentration increases. Above these limits (~60 and 10 min, respectively) the dopant content in the silicon matrix turns out to be markedly lower than expected.

The electrically active dopant, Q<sub>el</sub>, is a property less sensitive to the above phenomenon; this is probably the reason its occurrence remained unobserved. In Fig. 7 we report the values of the oxide thickness in the same predeposition experiments of Fig. 5 and 6. Also, these plots show a deviation, taking place at the above-mentioned times, from the well-known time dependence of the oxide growth  $X_o = \sqrt{Bt}$ .

In fact, both effects correspond to modifications in the doped oxide films which no longer appear uniform and smooth, but present a damage whose density and features depend on time and flux composition. An optical micrograph representative of the initial stage of damage at 920°C is reported in Fig. 8, associated with the corresponding roughness profile determined by the Talystep. In this stage the oxide presents circular defects of two distinct types: bubbles and small craters. These are also evidenced by the roughness profile. At longer predeposition times the whole surface of the slice is damaged and the defects overlap.

These modifications are associated with loss of adhesion and consistency of the oxide. The phenomenon involves the whole surface film including the region lying between isolated defects. The oxide becomes loose and can be easily scraped off, leaving the underlying silicon surface clean. Actually, Talystep measure-

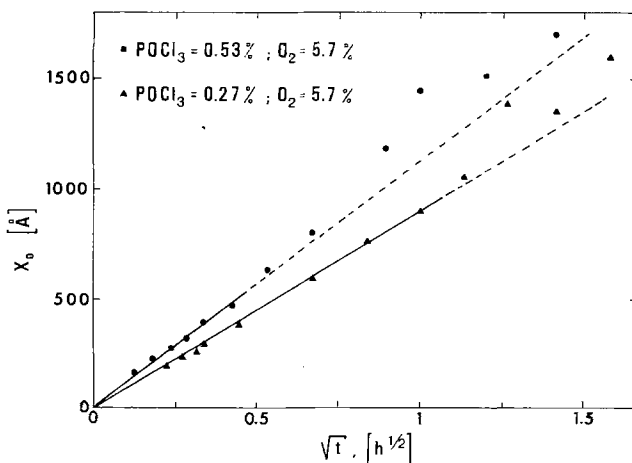


Fig. 7. Oxide thickness, X<sub>o</sub>, vs. square root predeposition time. The experimental conditions are the same as in Fig. 5 and 6.



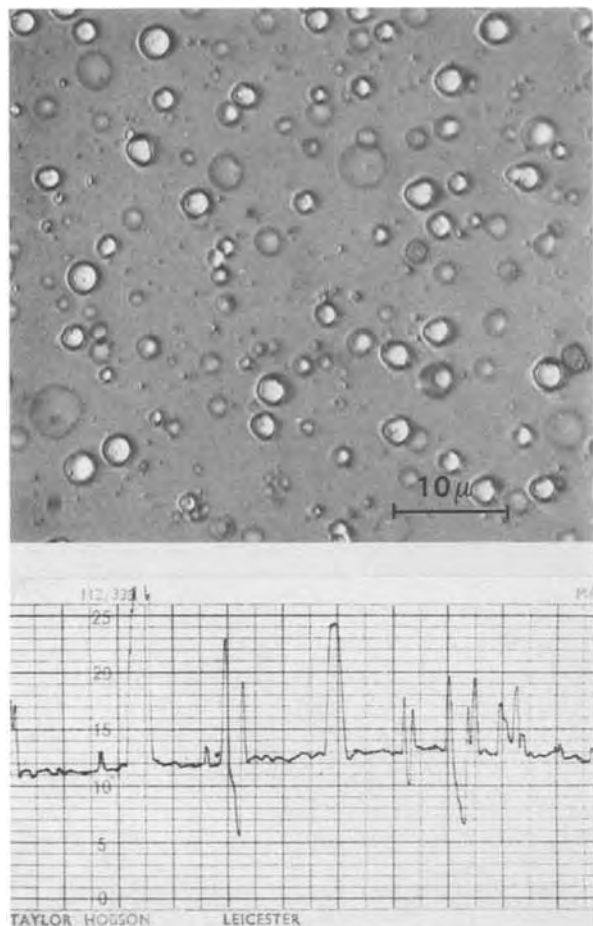


Fig. 8. Optical micrograph (top) of the damaged oxide grown during a predeposition of 17 min at 920°C. The doping gas composition is the same as in Fig. 6. Corresponding roughness profile (bottom) determined by the Talystep. The horizontal magnification is the same as the optical micrograph while the vertical magnification is 40Å per division.

ments have shown that the silicon surface is also made slightly rough and the amount of this effect increases with predeposition time.

The features and consistency of the oxide layers for specimens predeposited at 850°C under conditions giving rise to anomalous doping, are similar to those described above. At 1000°C the onset of damage was present only at the highest phosphorus oxychloride concentrations which could be realized, still maintaining a good reproducibility, in our predeposition apparatus. The oxide turned out to be simply softer than the normal one. As is shown in Fig. 9, the damage resulting at this temperature is associated with the formation of clusters of irregular shape which look like those observed by Ghezzi in arsenic glass at high temperature (8).

**Analysis of the surface film.**—In order to obtain information on the chemical composition of the oxide layers, we have performed some backscattering analysis of our specimens. Our spectra allow the exclusion of chlorine and nitrogen which, although in remarkable concentrations in the gas phase, are absent in the solid within the limits of sensitivity of this technique (about 0.1% for chlorine and 1% for nitrogen). As an example, we report in Fig. 10 the spectrum concerning a sample predeposited 11 min under the same conditions of Fig. 6. The peaks account for the presence of oxygen, silicon, and phosphorus, which are the only observed components. The energy corresponding to chlorine (1160 keV) is not reported in Fig. 10 due to the absence of any measurable effect.

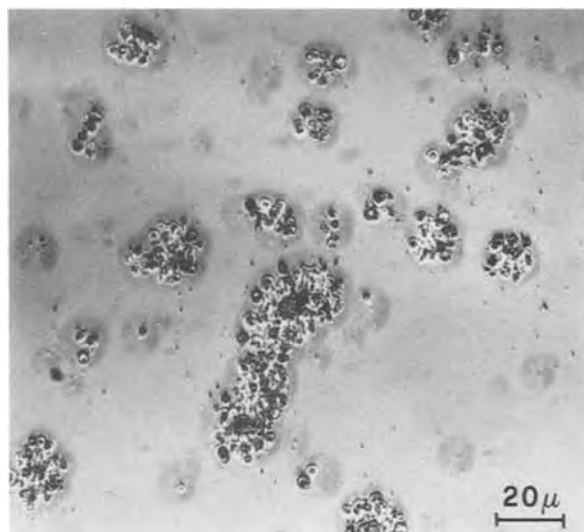


Fig. 9. Optical micrograph of the oxide grown during a predeposition of 27 min at 1000°C. Doping gas composition is 2.2%  $\text{POCl}_3$  and 5.7%  $\text{O}_2$ . Damage appears in the form of clusters of irregular shape.

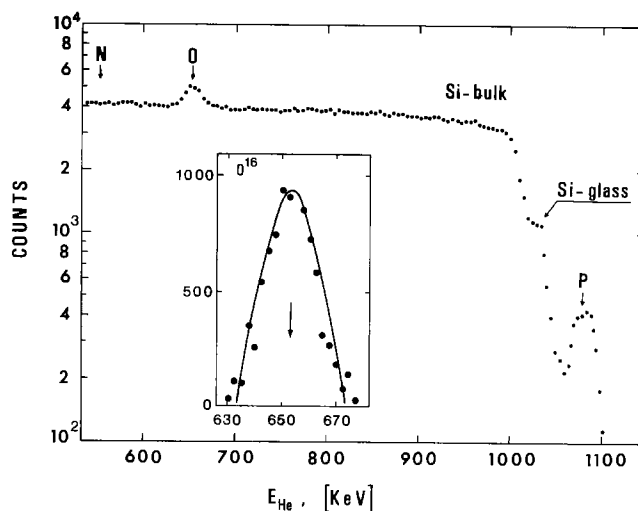


Fig. 10. Backscattering energy spectrum of 1.8 MeV-He ions incident on a silicon sample predeposited 11 min at 920°C, as in Fig. 6. The resulting oxygen peak is reported on the bottom. For better clarity we reported only half of the experimental points.

Considering the composition of a typical phosphorus glass, our surface layers show a defectiveness of oxygen; for example, the atomic percentages in Fig. 10 are approximately: 65% oxygen, 27% silicon, and 8% phosphorus. These results are in agreement with the presence, reported below, of remarkable concentrations of SiP in the defective oxide films.

In order to reveal the presence of crystalline phases in the surface layer, we performed a systematic x-ray analysis of the specimens shown by arrows in Fig. 3, 5, and 6. Loose oxide films were studied both by the diffractometer and the Debye-Scherrer technique.

Two crystalline phases have been found in the specimens predeposited under conditions giving rise to anomalous doping. Their reflections are reported in Tables I and II, respectively. The former shows those attributed to orthorhombic SiP, and, for comparison, the major powder reflections given by Wadsten (9, 10). The latter shows the interplanar distances that we attribute to cubic  $\text{SiO}_2 \cdot \text{P}_2\text{O}_5$  in comparison with the powder data of this phase, which Tien and Hummel call high temperature form (11) and Liebau *et al.* AI form (12). The data of these authors are complementary. We notice first that, accounting also for the

Table I. SiP (orthorhombic form)

Wadsten (9, 10) (Guinier)			This work* (Debye) (Diffractometer)			
$d_{obs}$ (Å)	$I_{obs}$	hkl	$d_{obs}$ (Å)	$I_{obs}$	$d_{obs}$ (Å)	$I_{obs}$
6.81	m	002	6.89	mw	6.81	s
3.123	m	130	3.13	w		
3.045	s	131	3.03**	s		
2.839	m	132	2.82	m		
2.560	m	080	—	—	2.52	w
1.909	s	190	1.92	ms	—	—
1.755	vs	200	1.76	vs	—	—

\* The empty region of the Debye column is due to diffuse scattering from amorphous  $\text{SiO}_2$ , that of the diffractometer to (111) single crystal reflection from Si substrate.

\*\* Superimposed to a strong line of cubic  $\text{SiO}_2 \cdot \text{P}_2\text{O}_5$ .

Table II.  $\text{SiO}_2 \cdot \text{P}_2\text{O}_5$  (cubic form)

Tien et al. (11) (diffractometer) Liebau et al. (12) (Guinier)			This work* (Debye) (Diffractometer)			
$d_{obs}$ (Å)	$I_{obs}$	hkl	$d_{obs}$ (Å)	$I_{obs}$	$d_{obs}$ (Å)	$I_{obs}$
7.5	vwv	300	—	—	7.44	mw
4.32	m	333	—	—	4.35	vw
3.74	vvs	600	—	—	3.74	vs
3.351	vvs	630	3.36	s	3.38	s
3.053	vvs	633	3.03**	vs	—	—
2.644	m	660	2.67	m	2.65	vw
2.380	m	922	—	—	2.40	vw
2.254	m	933	2.25	ms	2.25	vw
2.073	s	960	2.04	s	2.08	mw
1.814	s	966	—	—	1.80	w
1.811	m		—	—	—	—
1.634	m		—	—	—	—
1.629	m		12 · 6 · 3	1.64	m	1.64
1.441	s	999	—	—	1.44	w
1.417	m	11 · 11 · 3	1.39	w	—	—

\* The empty regions of the columns turn out as specified in Table I.

\*\* Superimposed to a strong line of orthorhombic SiP.

angular regions masked by undesired scattering, the agreement of the results of our two techniques is satisfactory.

The identification of the phases has also taken into account the intensity of the reflections, and is fairly sure. The line with  $d = 3.03\text{Å}$ , visible in Debye-Scherrer photographs, is the only superposition of strong reflections belonging to both crystalline compounds. In some cases, x-ray examinations have also shown clear evidence of the presence of  $\alpha$ -quartz.<sup>1</sup>

The diffractometric reflection spectra show the presence for both the SiP and the  $\text{SiO}_2 \cdot \text{P}_2\text{O}_5$  of orientation effects; in fact, to account for the observations of only two lines, which moreover are not the strongest ones, pertaining to the orthorhombic SiP, these crystallites have to present their (001) or (010) planes, parallel to the (111) surface of the silicon slice. As for the  $\text{SiO}_2 \cdot \text{P}_2\text{O}_5$ , the enhanced relative intensity of the (300) reflection in Table II suggests that this phase is partially oriented with its (100) faces parallel to the (111) planes of silicon.

Finally, we notice that the intensity of the lines associated with the SiP and the  $\text{SiO}_2 \cdot \text{P}_2\text{O}_5$  generally increases with predeposition time. Further, the intensity of the reflections of both compounds was slightly lower in the specimens predeposited at  $1000^\circ\text{C}$ , although, as shown in Fig. 3, the latter correspond to a flux much richer, by more than a factor 3, of  $\text{POCl}_3$ .

The diffractometric analysis of the specimens predeposited under conditions which did not result in anomalous doping, did not show any reflection. This result is not in contradiction with the presence, discussed in our previous work, of SiP precipitates in the

<sup>1</sup> Formation of crystalline phosphosilicates and  $\alpha$ -quartz was observed also in  $\text{SiO}_2$  heavily predeposited with phosphorus (13-15).

Si matrix. In fact, their prevalent orientations, determined by electron diffraction (2), are such that the observation is inhibited with our diffractometric method; only a small fraction, far below the sensitivity of our x-ray technique, is oriented with their (010) planes parallel to the (111) surface of the silicon slice (16).

*Localization of the crystalline phases.*—To define the position of the observed compounds within the oxide layer, we performed chemical etching of the surface films by HF solutions of different concentrations, followed by Talystep measurements of the thickness of the dissolved oxide and diffractometric examinations.

These observations have shown that in all cases the  $\text{SiO}_2 \cdot \text{P}_2\text{O}_5$  and the SiP were essentially localized at the oxide-silicon interface. These conclusions have also been confirmed by observations after mechanical abrasion of the oxide film performed in order to avoid effects due to selective etching.

A typical example of our results is shown in Fig. 11 which reports, in dependence of the degree of chemical etching, the intensity of characteristic x-ray diffractometer reflections in a specimen predeposited 150 min at  $920^\circ\text{C}$  with a flux composition of 0.27%  $\text{POCl}_3$  and 5.7%  $\text{O}_2$ . It can be noticed that a fraction of the crystalline compounds is still present after the last strong etching.

The above results have been further quantitatively confirmed by electrical resistivity measurements. These were performed on identical specimens, etched or mechanically abraded in order to obtain increasing surface removal (the most aggressive process was anodic

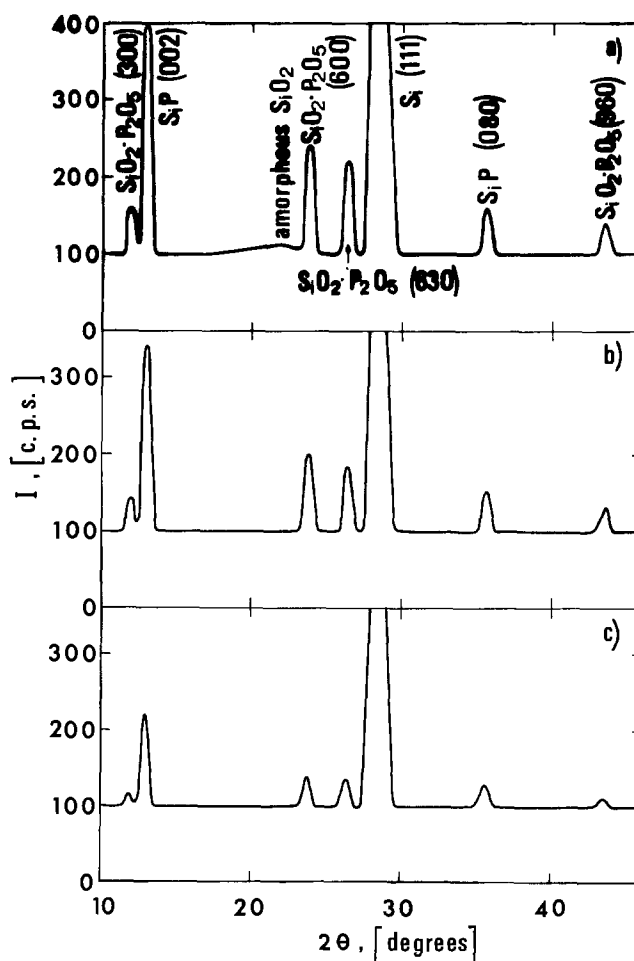


Fig. 11. Intensity of characteristic x-ray reflections of a specimen predeposited 150 min at  $920^\circ\text{C}$  with the same flux composition as in Fig. 5 (diffractometer,  $\text{CuK}\alpha$  radiation): (a) refers to the initial state, (b) after 5 min etching in 0.5% HF, and (c) after 5 min etching in 49% HF.

oxidation and dissolution), followed by surface resistivity measurements both before and after suitable drive-in treatments. These determinations give the electrically active,  $Q_{el}$ , and the total phosphorus,  $Q$ , respectively (1): the values of  $Q_{el}$  monitor the etching of the silicon matrix, while the differences of  $Q$  measure the phosphorus content of the etched material. An example of our results is reported in Table III.

In addition, these measurements confirm, with a sensitivity greater than that attributed to our x-ray technique, that the phosphorus-rich layer is absent in the specimens which present a normal doping behavior.

Finally, we noticed that the phosphorus content in the matrix of silicon in the anomalously doped specimens cannot be exactly defined any more; a remarkable fraction, about 50% in the above example, is in fact localized in an interfacial region, a few hundred angstroms thick.

**Effect of the crystallographic orientation of the slices.**—In order to verify whether the oxide-silicon interface plays a role in the nucleation and growth of the crystals of SiP and of  $\text{SiO}_2 \cdot \text{P}_2\text{O}_5$ , we have performed experiments at 920°C, processing together silicon slices of different orientations. A 30 min predeposition has been carried out in a flux with 0.53%  $\text{POCl}_3$  and 50, 80, and 150 min predepositions in a flux with 0.27%  $\text{POCl}_3$ . Oxygen per cent was kept constant (5.7%). These experiments have evidenced a remarkable effect of the crystallographic orientation of the surface of the slices: the (111) is the most favorable for the onset of the phenomenon of anomalous doping, followed in order by the (110) and by the (100) orientation.

TEM examinations suggest that surface diffusivity plays a role in the rapid growth of precipitates; as an example we report in Fig. 12 large SiP crystals grown at the oxide-silicon interface of a (111) oriented specimen processed as in Fig. 11. The size of these precipitates which lie along the  $\langle 110 \rangle$  directions of silicon is about 10 times that of those found inside the silicon matrix.

**Correlation between segregation at the interface and in the bulk silicon.**—The present results and those reported in Ref. (1) indicate that interface segregation is enhanced by the same parameters which increase the amount of electrically inactive phosphorus (SiP precipitates in the silicon matrix) formed in the stage preceding the onset of the phenomenon. This connection is further evidenced by predeposition experiments on slices previously oxidized in order to form thin oxide layers. These reduce the flux of phosphorus, thus decreasing the amount of SiP in the bulk silicon (1). All other conditions, except the concentration gradients, remain unaltered, after an initial transient, as long as SiP precipitates are present.

Oxide films of thickness 120, 200, and 380 Å have been obtained by thermal oxidation at 920°C in a dry oxygen atmosphere. These specimens have been processed 80 min at 920°C, together with unoxidized slices

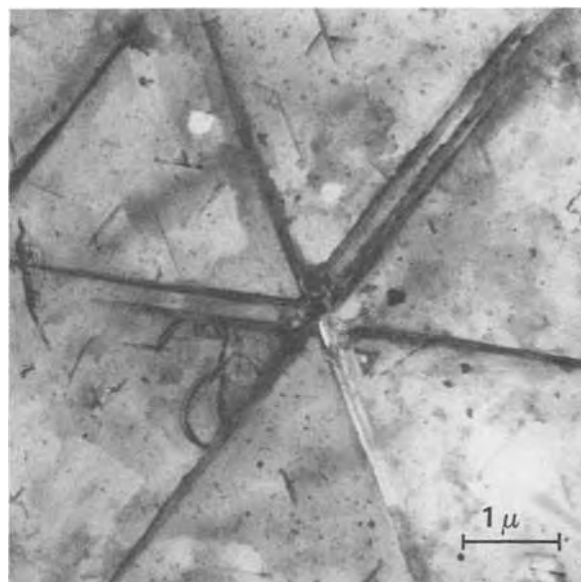


Fig. 12. Electron micrograph showing large SiP precipitates lying along  $\langle 110 \rangle$  directions. Specimen has been processed as those in Fig. 11.

of the same (111) orientation, in a flux with 0.27%  $\text{POCl}_3$  and 5.7% oxygen.

Oxide damage was observed only in the unoxidized slices and, in a very limited amount, in those slices with the thinnest preformed film ( $\sim 120\text{Å}$ ). The formation of SiP and of  $\text{SiO}_2 \cdot \text{P}_2\text{O}_5$  was revealed, by x-ray examinations, only in the unoxidized slices.

More detailed information results from the study of the effect of temperature. We show, as an example, in Fig. 13 the chemical and electrical concentration profiles of phosphorus in slices processed for the same time (27 min), in fluxes of the same composition (0.27%  $\text{POCl}_3$  and 5.7%  $\text{O}_2$ ), at 920° and 1000°C, respectively. These profiles have been obtained using the technique of neutron activation and that of electrical measurements already reported in detail (17, 18). The concentration dependence of mobility has been taken into account (19).

It is seen that, while the amount of electrically inactive dopant is comparable, the surface concentration attained in the process at 920°C is more than two times higher. This effect results from competition between the diffusivity across the oxide and that in the bulk silicon; the latter being characterized by a higher absolute value of the exponential term (1).

These experiments show that interface segregation is connected to the concentration of SiP in the region near the interface.

### Discussion and Conclusions

Our observations show that the kinetics of phosphorus predeposition can be altered by a phenomenon

Table III. Comparative effects of surface removal on regularly and anomalously doped slices

Predeposition $T = 920^\circ\text{C}$ $t = 27\text{ min}$ $\text{O}_2 = 5.7\%$	Technique of surface removal			$Q_{el}$	$Q$	$\frac{Q}{Q_{el}}$
				(at/cm <sup>2</sup> )	(at/cm <sup>2</sup> )	
$\text{POCl}_3 = 0.53\%$ Anomalously doped (see Fig. 6)	HF	0.5%	3 min	$4.40 \times 10^{15}$	$1.41 \times 10^{16}$	3.20
	HF	49%	5 min	$4.23 \times 10^{15}$	$9.65 \times 10^{15}$	2.28
	Mechanical abrasion					
	+ HF	0.5%	3 min	$4.32 \times 10^{15}$	$1.04 \times 10^{16}$	2.41
	Anodic oxidation (Si layer removed <200Å)					
	+ HF	0.5%	3 min	$4.08 \times 10^{15}$	$7.46 \times 10^{15}$	1.83
$\text{POCl}_3 = 0.27\%$ Regularly doped (see Fig. 5)	HF	0.5%	3 min	$4.73 \times 10^{15}$	$1.48 \times 10^{16}$	3.13
	HF	49%	5 min	$4.60 \times 10^{15}$	$1.44 \times 10^{16}$	3.13
	Anodic oxidation (Si layer removed <200Å)					
	+ HF	0.5%	3 min	$4.44 \times 10^{15}$	$1.35 \times 10^{16}$	3.04

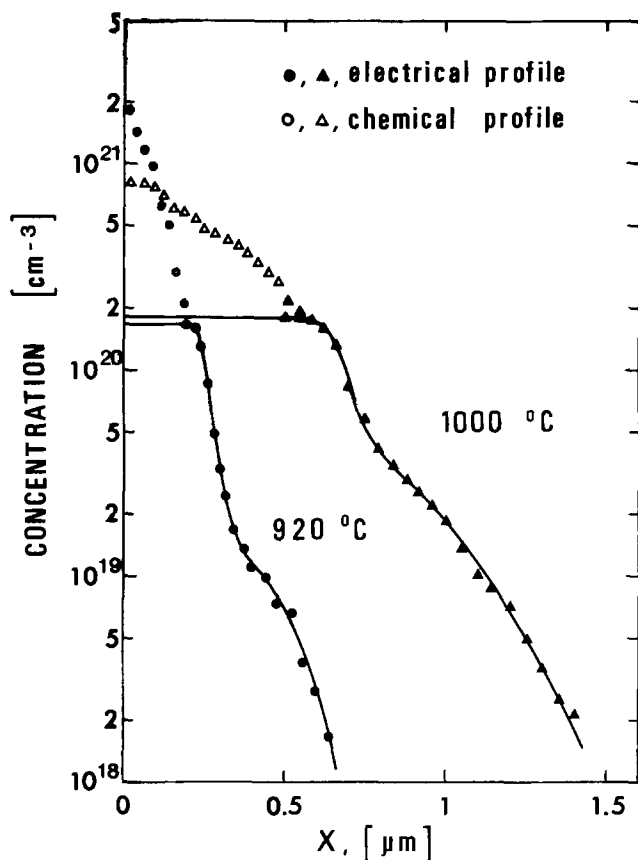


Fig. 13. Chemical and electrical phosphorus profiles for 27 min predepositions at 920°C and 1000°C, respectively. Gas composition is the same as in Fig. 5.

which reduces the amount of dopant in the silicon matrix and is associated with damage and loss of coherency of the doped oxide. The hypothesis of a chemical reaction between the furnace gas and the surface being responsible for this effect has been discarded on the basis of the composition results obtained by backscattering analysis. It is shown that the phenomenon results from segregation of orthorhombic SiP and cubic  $\text{SiO}_2 \cdot \text{P}_2\text{O}_5$  taking place at the PSG-Si interface.

As is evidenced by Fig. 5 and 6, the onset of interface segregation does not depend primarily on the amount,  $Q$ , of phosphorus predeposited in silicon, but on the flux of dopant across the surface oxide. These conclusions are confirmed by the observation that previous slight oxidation of the slices inhibits the segregation process. The flux can be increased either by increasing  $\text{POCl}_3$  concentration or by decreasing that of oxygen. This gives rise to the maximum in Fig. 1 as well as to the change of slope in Fig. 3; in fact, the specimens processed in a richer flux of  $\text{POCl}_3$  undergo interface segregation in shorter times. The maximum corresponds to the concentration of  $\text{POCl}_3$  just giving rise to the onset of segregation in the chosen predeposition time (27 min). The same reasoning accounts for the maximum observed in Fig. 2 with decreasing the concentration of oxygen.

The segregation phenomena depend on the crystallographic orientation of the surface of the slice; the (111) being the most favorable, followed in order by the (110) and the (100). These results and the observed preferential orientation of the precipitates indicate that the surface plays a role in the nucleation and growth processes.

As for the SiP, we observe that, contrary to what might be expected by considering only the supersaturation gradient, precipitation takes place first within the silicon matrix. This phenomenon, studied in our

previous work (1), is also evidenced by the chemical profiles in Fig. 13, representative of situations which precede interface segregation. Its occurrence shows that a higher supersaturation of dopant is needed for nucleation at the interface.

Steeper supersaturation gradients in the silicon matrix, as can be obtained either by increasing the flux across the surface oxide or by decreasing the temperature, result in local accumulation of the SiP and enhance the nucleation at the interface of suitably oriented crystals.

The nucleation of the  $\text{SiO}_2 \cdot \text{P}_2\text{O}_5$ , which is always found associated with the SiP, should be enhanced by the latter. In fact, phosphorus oxide concentration is maximum at the surface; nevertheless  $\text{SiO}_2 \cdot \text{P}_2\text{O}_5$  segregation takes place at the PSG-silicon interface.

We observe, finally, that the conditions for interface segregation are not unusual in predepositions at 920°C using  $\text{POCl}_3$ . They are satisfied also with other sources as is shown by the results reported by Schmidt *et al.* (4, 5) and suggested by those of Kooi (3). It is likely that interface segregation occurred also in the experiments using heavily doped oxide sources reported by Ghezzi (20); in fact, the surface damage that he observed looks like that shown in Fig. 8.

#### Acknowledgments

We wish to thank G. G. Bentini for having performed the backscattering analysis of our specimens; M. Servidori and A. Armigliato for their electron microscopy results and the useful discussion. Acknowledgments are due to E. Gabilli and S. Guerri for cooperation in setting up the experimental facilities.

Manuscript submitted July 29, 1975; revised manuscript received Dec. 14, 1975. This was Paper 172 presented at the Dallas, Texas, Meeting of the Society, Oct. 5-9, 1975.

Any discussion of this paper will appear in a Discussion Section to be published in the December 1976 JOURNAL. All discussions for the December 1976 Discussion Section should be submitted by Aug. 1, 1976.

Publication costs of this article were partially assisted by C.N.R.

#### REFERENCES

1. P. Negrini, D. Nobili, and S. Solmi, *This Journal*, **122**, 1254 (1975).
2. A. Armigliato and M. Servidori, *J. Mater. Sci.*, **10**, 306 (1975).
3. E. Kooi, *This Journal*, **111**, 1383 (1964).
4. P. F. Schmidt and R. Stickler, *ibid.*, **111**, 1188 (1964).
5. T. W. O'Keeffe, P. F. Schmidt, and R. Stickler, *ibid.*, **112**, 878 (1965).
6. C. G. Beck and R. Stickler, *J. Appl. Phys.*, **37**, 4683 (1966).
7. G. della Mea, A. V. Drigo, S. Lo Russo, P. Mazzoldi, S. Yamaguchi, and G. G. Bentini, *Appl. Phys. Letters*, **26**, 147 (1975).
8. M. Ghezzi and D. M. Brown, *This Journal*, **120**, 110 (1973).
9. T. Wadsten, *Acta Chem. Scand.*, **23**, 2532 (1969).
10. T. Wadsten, *Chem. Scripta*, **8**, 63 (1975).
11. T. Y. Tien and F. A. Hummel, *J. Am. Ceram. Soc.*, **45**, 422 (1962).
12. F. Liebau, G. Bissert, and N. Köppen, *Z. Anorg. Allgem. Chem.*, **359**, 113 (1968).
13. P. F. Schmidt, W. van Gelder, and J. Drobek, *This Journal*, **115**, 79 (1968).
14. D. R. Campbell, E. I. Alessandrini, K. N. Tu, and J. E. Lewis, *ibid.*, **121**, 1081 (1974).
15. E. I. Alessandrini and D. R. Campbell, *ibid.*, **121**, 1115 (1974).
16. A. Armigliato and M. Servidori, Private communication.
17. G. Restelli, F. Girardi, F. Mousty, and A. Ostidich, *Nucl. Instr. Methods*, **112**, 581 (1973).
18. E. Tannenbaum, *Solid-State Electron.*, **2**, 123 (1961).
19. G. Baccarani and P. Ostojica, *ibid.*, **18**, 579 (1975).
20. M. Ghezzi, *This Journal*, **119**, 1428 (1972).

# Diffusional Growth of Cobaltous-Ferrous Oxide Scales on Cobalt-Iron Alloys

P. Mayer\*<sup>1</sup> and W. W. Smeltzer\*

Department of Metallurgy and Materials Science, McMaster University, Hamilton, Ontario, Canada L8S 4M1

## ABSTRACT

Co-Fe alloys containing up to 10 weight per cent (w/o) Fe oxidize parabolically by formation of a cobaltous-ferrous oxide [(CoFe)O] scale when exposed at 1200°C to oxygen at 10<sup>-2</sup>, 10<sup>-1</sup>, and 1 atm. The values of the parabolic oxidation constants were directly dependent on the iron contents of the alloys. The iron profiles within the scales exhibited maxima which shifted toward the center of a scale away from its outer surface with increasing oxygen pressure. It is demonstrated on the basis of a ternary diffusional analysis that these findings are consistent with independent measurements on the ratio of metal self-diffusion coefficients in this oxide and with the postulate that the relative migration rate of cobalt and iron at positions in a scale is dependent upon the magnitude of the oxygen activity.

Cobalt and iron form a homogeneous solid solution at high temperatures. The oxygen potential Co-Fe-O phase diagram (1, 2) illustrates that (CoFe)O exists as the stable phase on alloys containing up to ~30% Fe in oxygen ranging to 1 atm pressure at 1200°C. We previously found, as anticipated, that cobalt alloys with iron ranging up to 10% oxidized parabolically by formation of a (CoFe)O scale when exposed at this temperature to oxygen at 10<sup>-4</sup> and 10<sup>-3</sup> atm (3). The iron gradients within the scales increased with increasing outward distance due to iron migrating more rapidly than cobalt. A diffusion model based upon equations derived by Wagner (4) for metal transport through a scale under chemical activity gradients led to a correlation between the parabolic oxidation constants and the iron gradients.

The metal self-diffusion parameters in (CoFe)O are unusual. Crow (5) has determined the tracer diffusion coefficients of cobalt and iron in this oxide. At 1200°C, the ratio  $D_{Fe}/D_{Co}$  equals 1.6 at oxygen pressures of 10<sup>-4</sup> and 10<sup>-3</sup> atm and it equals 0.7 at pressures greater than 10<sup>-1</sup> atm. One would, therefore, predict from the above diffusion model that an iron concentration profile exhibiting a maximum could develop in the (CoFe)O scale when an alloy containing up to 10% Fe is oxidized at oxygen pressures greater than 10<sup>-3</sup> atm. The present communication demonstrates that these predictions are actually valid.

## Experimental

Disk-shaped Co-Fe alloy specimens (10 × 2 mm) were metallographically polished to 1 $\mu$  diamond abrasive and oxidized at 1200°C for periods up to 30 min in flowing ultrahigh purity oxygen at pressures 10<sup>-2</sup>, 10<sup>-1</sup>, and 1 atm using a continuously weighing semi-microbalance. Measurements of the metal concentration profiles in cross-sectioned specimens were measured by an electron-microprobe analyzer. The preparation of the alloys, experimental assemblies, and methods have been described (3). The actual iron contents of the nominal 1, 2, 4, 6, 8, and 10 w/o Fe alloys are 0.93, 2.1, 4.1, 5.5, 7.7, and 9.6 w/o Fe, respectively.

## Results

It was found that the oxidation rate at each pressure followed a parabolic time dependence. Figures 1-3 show the oxidation curves plotted in parabolic form for cobalt and the six alloys at the three test pressures. The values of the parabolic oxidation constants, which

were accurate to within  $\pm 10\%$  based on the deviations from the average value of four runs completed on each alloy, are shown in Fig. 4. These constants show a direct dependence on the iron contents of the alloys.

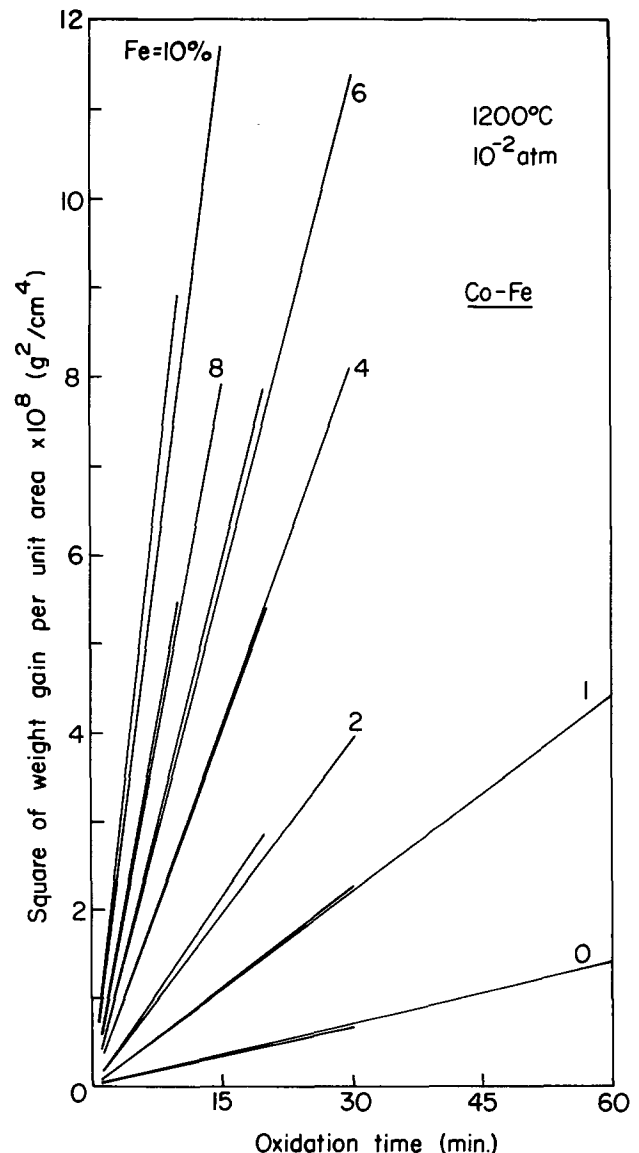


Fig. 1. Oxidation kinetics of the Co-Fe alloys exposed at 1200°C in oxygen at 10<sup>-2</sup> atm plotted in parabolic form.

\* Electrochemical Society Active Member.

<sup>1</sup> Present address: Ontario Research Foundation, Sheridan Park, Mississauga, Ontario, Canada.

Key words: Co-Fe alloy oxidation, cobaltous-ferrous oxide, diffusional scale growth.

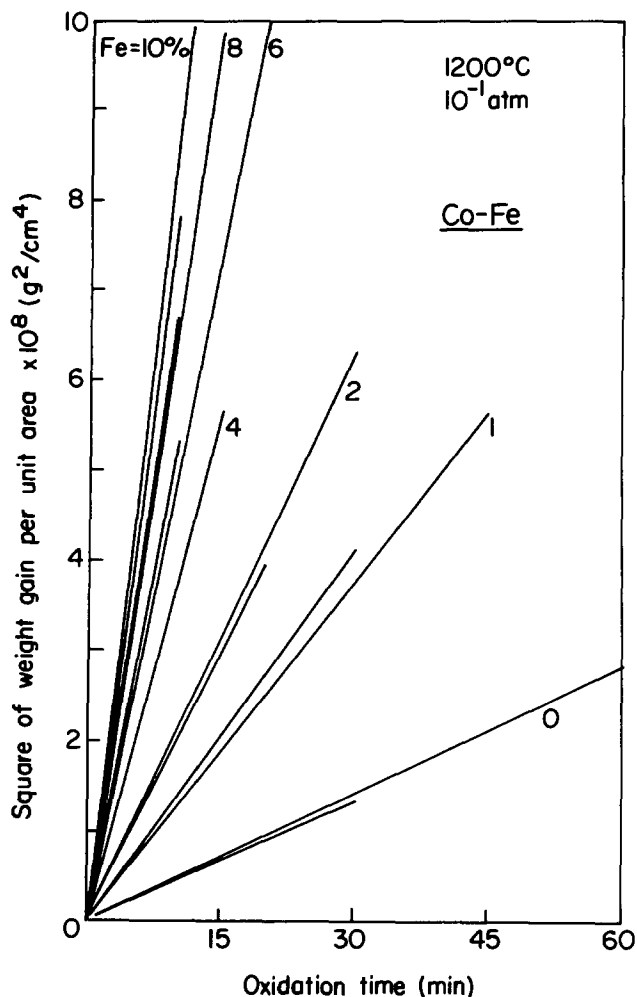


Fig. 2. Oxidation kinetics of the Co-Fe alloys exposed at 1200°C in oxygen at 10<sup>-1</sup> atm plotted in parabolic form.

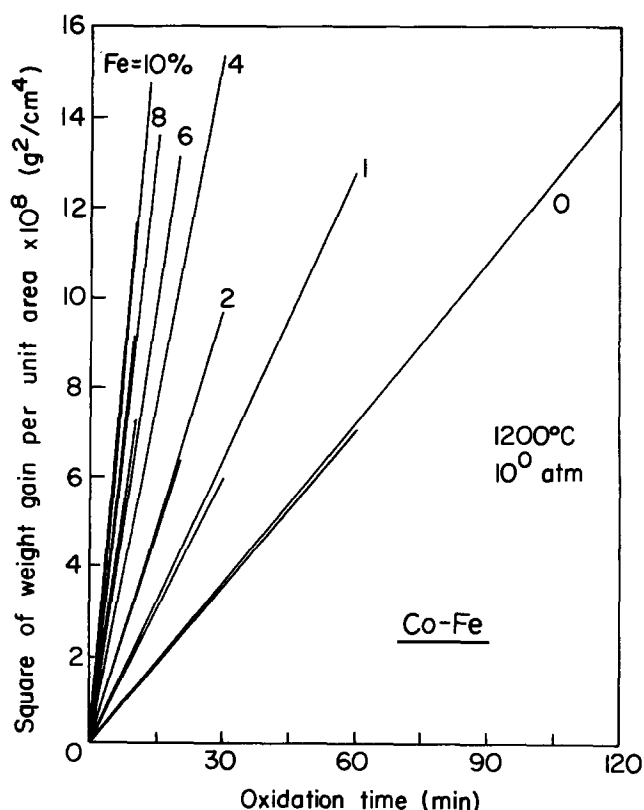


Fig. 3. Oxidation kinetics of the Co-Fe alloys exposed at 1200°C in oxygen at 1 atm plotted in parabolic form.

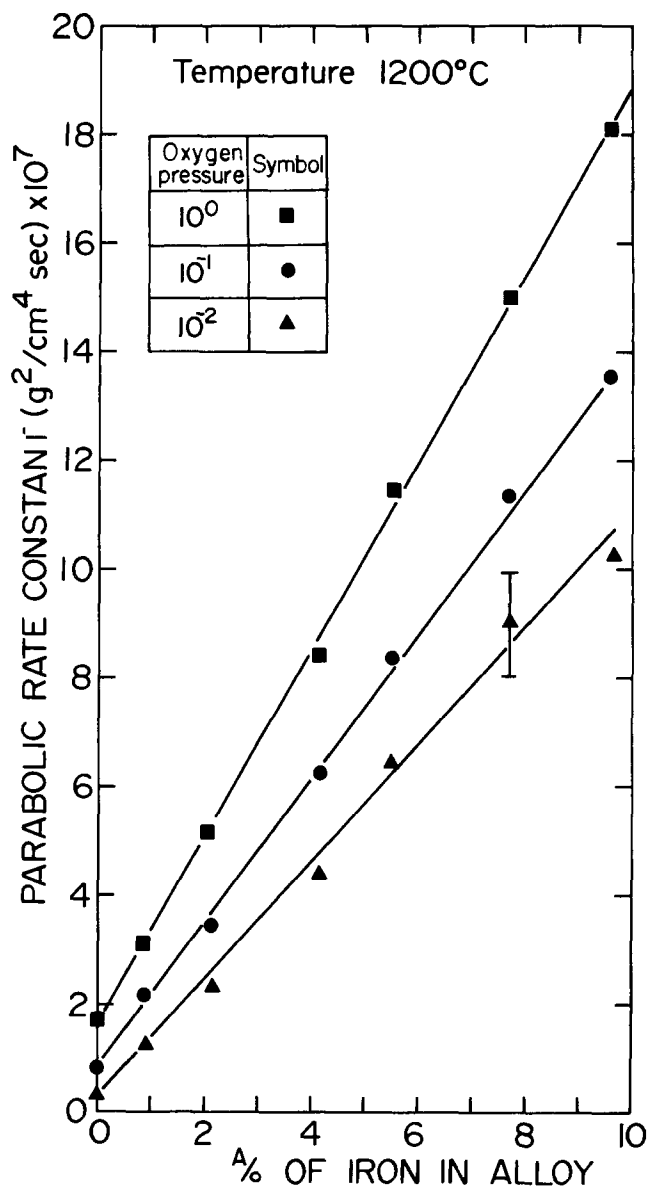


Fig. 4. Variation of the parabolic oxidation constants with alloy iron content of the Co-Fe alloys at 1200°C.

X-ray diffraction lattice parameter measurements on the powdered scales confirmed that they were composed of (CoFe)O. Figures 5 and 6 show typical scale cross sections. The alloy-oxide interfaces were planar and the alloys did not exhibit internal oxidation. Examination of several cross sections revealed that the scales were composed of large columnar grains and regions in the vicinity of the scale-gas interface of small discontinuous precipitates of submicron size (typically  $\sim 0.5\mu$ ); the density of these precipitates decreased with increasing iron content and decreasing oxygen pressure. These precipitates are believed to be (CoFe)<sub>3</sub>O<sub>4</sub> resulting from the quench of the specimens from the reaction temperature.

Iron compositions within the scales formed on each alloy expressed as the atom fraction of iron or mole fraction wustite in (CoFe)O at the three investigated pressures are shown in Fig. 7-9. These determinations are based on analysis taken from scales on each particular alloy at different times of exposure using the electron microprobe point count method at normalized distances  $y = x/x_s$  from the alloy surface where  $x_s$  is a total scale thickness. These normalized distances could be reproduced within  $\pm 10\%$ . Significant variations of iron concentration within the scales were not observed when measured parallel to an alloy surface. It was possible to conclude from these determinations

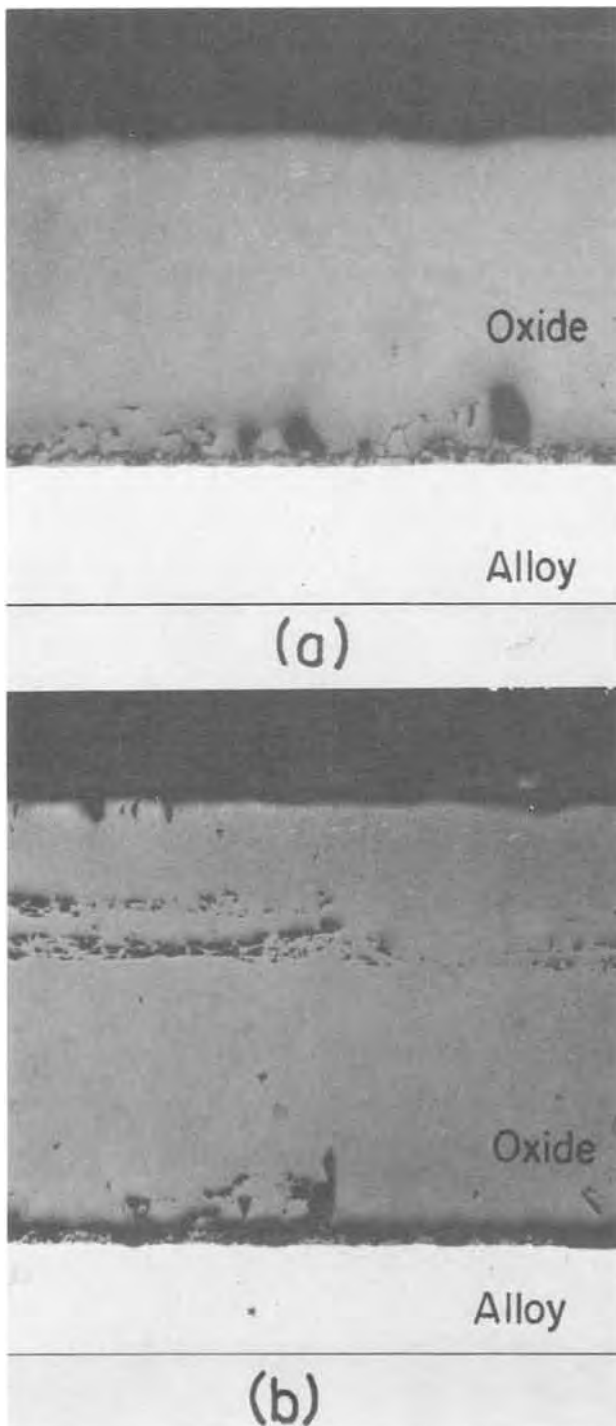


Fig. 5. Cross sections of oxide scales formed at 1200°C in oxygen at 1 atm pressure (200X): (a) Co-1 w/o Fe alloy oxidized for 60 min; (b) Co-10 w/o Fe alloy oxidized for 15 min.

that the iron content of a scale corresponded to that of the alloy and that the iron profiles exhibited maxima, the positions of these maxima shifting toward the center of a scale away from the outer interface with increasing oxygen pressure.

#### Discussion

In an earlier publication an excellent correlation was obtained between the parabolic reaction kinetics and the normalized metal profiles in the scales formed on the alloys of this investigation at oxygen pressures of  $10^{-4}$  and  $10^{-3}$  atm (3). This interpretation involving ternary diffusion in conjunction with compositional, diffusional, and thermodynamic data accounted for the uphill diffusion of iron against its concentration gradi-

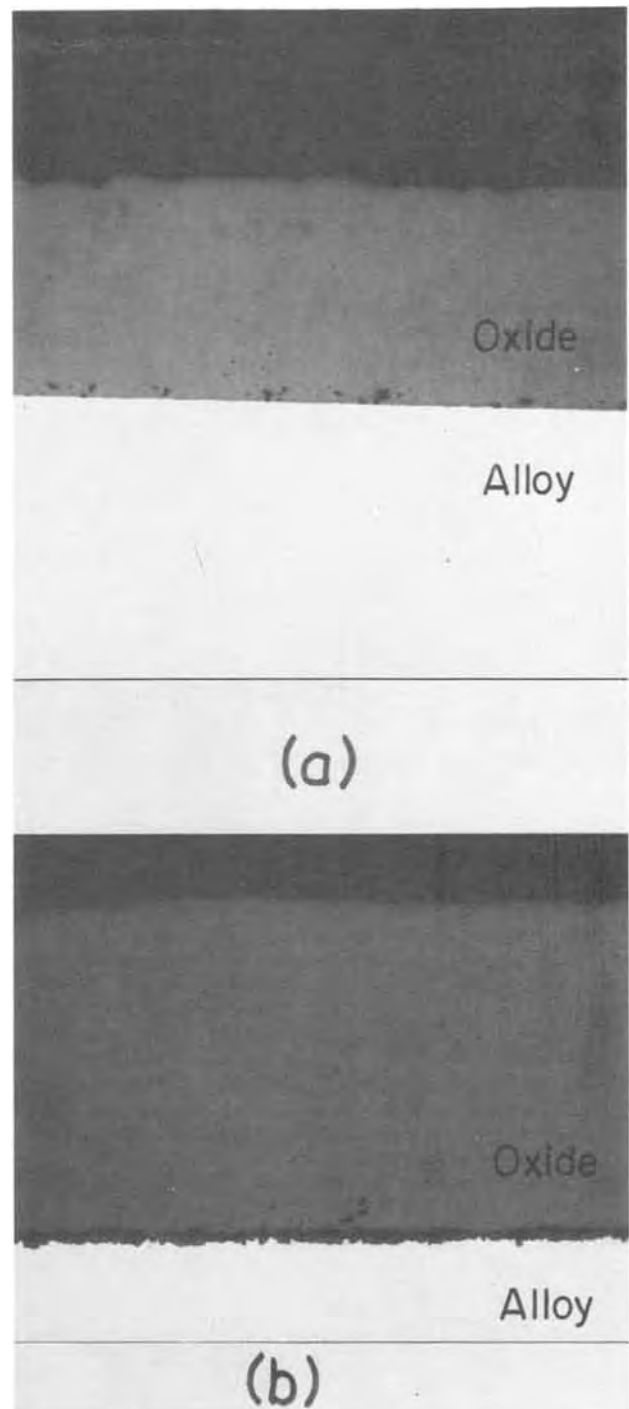


Fig. 6. Cross sections of oxide scales formed at 1200°C in oxygen at  $10^{-2}$  atm pressure (200X): (a) Co-1 w/o Fe alloy oxidized for 60 min; (b) Co-10 w/o Fe alloy oxidized for 15 min.

ent in the (CoFe)O scale by its more rapid diffusion (larger self-diffusion coefficient) under the influence of the oxygen activity gradient. We now demonstrate that the observed iron profiles exhibiting maxima in the scales can be calculated from the same basic diffusion model assuming a variation in the related rates of metal diffusion with oxygen activity. This ternary diffusion model was originally advanced by Wagner (4) and the reader is referred to his paper and to our previous paper for its application to the Co-Fe-O system (3), mathematical derivations, and applications of the diffusion flux and mass balance equations.

The (CoFe)O scale growth is determined by the outward diffusion of cobalt and iron via vacancies, and Eq. [11] from Ref. (4) for the parabolic oxidation constant becomes

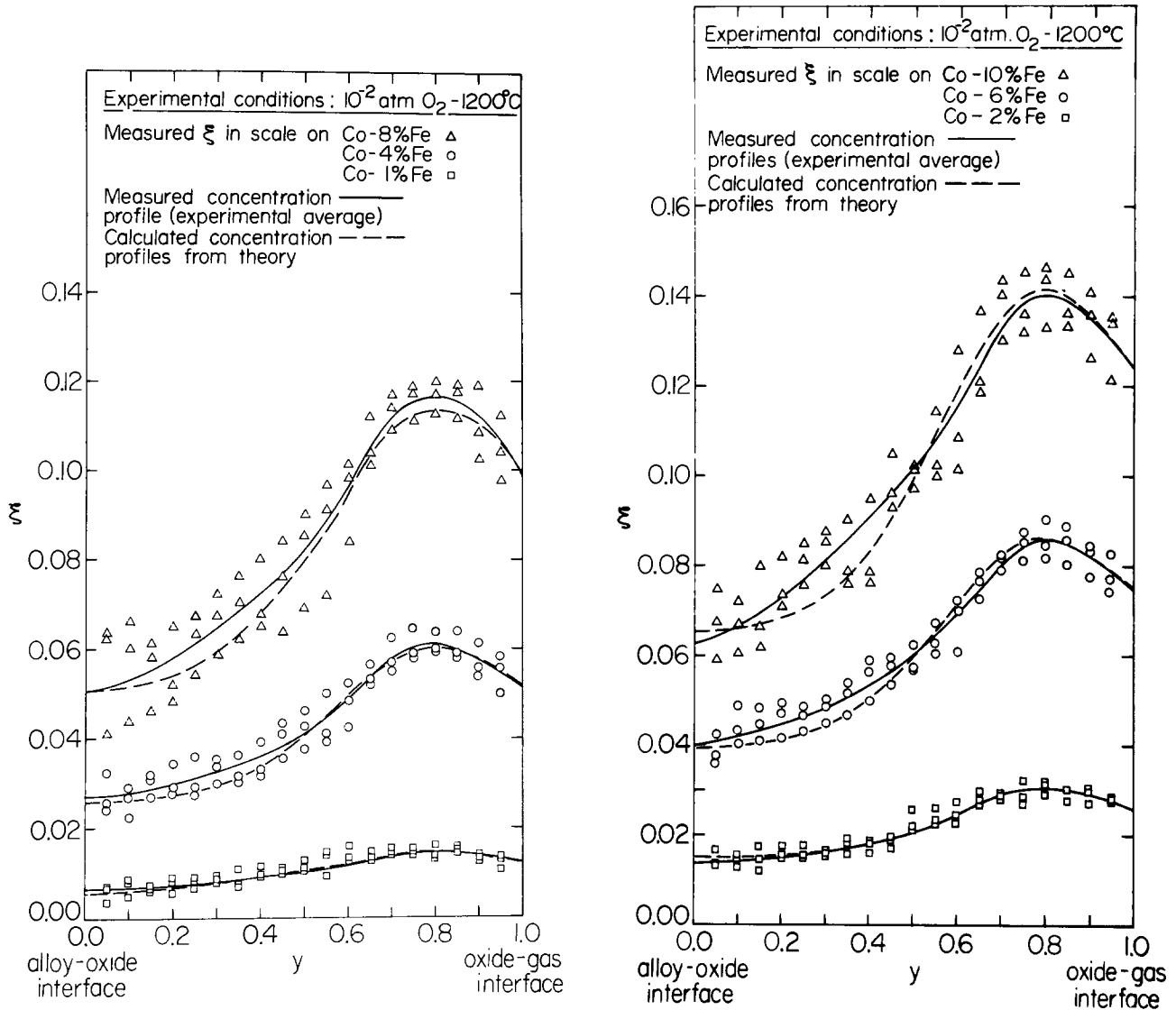


Fig. 7. Mole fraction FeO,  $\xi$ , as a function of normalized distance coordinate  $y$  in  $(\text{CoFe})\text{O}$  scales at  $10^{-2}$  atm oxygen pressure: (a, left) Co-1, 4, and 8 w/o Fe; (b, right) Co-2, 6, and 10 w/o Fe.

$$D_{\text{Co}}(1 - \xi) \left( \frac{-d \ln a_{\text{CoO}}}{d\xi} \frac{d\xi}{dy} + \frac{Z_{\text{Co}}}{Z_{\text{O}}} \frac{d \ln a_{\text{O}}}{dy} \right) + D_{\text{Fe}} \xi \left( \frac{-d \ln a_{\text{FeO}}}{d\xi} \frac{d\xi}{dy} + \frac{Z_{\text{Fe}}}{Z_{\text{O}}} \frac{d \ln a_{\text{O}}}{dy} \right) = k \quad [1]$$

In this expression,  $D$  is a metal self-diffusion coefficient,  $a$  is a local activity,  $Z$  is a valency,  $\xi$  is the atom fraction of iron or mole fraction of wustite in  $(\text{CoFe})\text{O}$ , and  $y = x/x_s$  is the normalized scale thickness.

For Henrian solution behavior of wustite in cobalt oxide,  $p = D_{\text{Fe}}/D_{\text{Co}} = D_{\text{Fe}^\circ}/D_{\text{Co}^\circ}$ ,  $Z_{\text{Co}} = Z_{\text{Fe}} = |Z_{\text{O}}| = 2$ ,  $k' = k/D_{\text{Co}^\circ}\gamma$  and  $N_V = \gamma a_{\text{O}}^n \xi$ , Eq. [1] becomes Eq. [8] of Ref. (3)

$$\frac{d \ln a_{\text{O}}}{dy} = \left[ \frac{k'}{a_{\text{O}}^n \xi} + (p - 1) \frac{d\xi}{dy} \right] / [1 + (p - 1)\xi] \quad [2]$$

In the above expressions,  $D_{\text{Co}^\circ}$  and  $D_{\text{Fe}^\circ}$  are the cobalt and iron vacancy diffusivities,  $N_V$  is the atom fraction of vacancies in  $(\text{CoFe})\text{O}$ ,  $\gamma$  and  $n$  are empirical constants.

Equation [19] from Ref. (4), which describes the metal gradient in a scale using the divergence equation for the metal flux, becomes Eq. [9] and [10] of Ref. (3)

$$y k \frac{d\xi}{dy} = \frac{-d}{dy} \left[ D_{\text{Fe}} \xi \left( \frac{d \ln a_{\text{FeO}}}{d\xi} \frac{d\xi}{dy} - \frac{d \ln a_{\text{O}}}{dy} \right) \right] \quad [3]$$

and after substitution

$$y k \frac{d\xi}{dy} = - \frac{d}{dy} \left[ p \cdot D_{\text{Co}^\circ} \cdot \gamma \cdot a_{\text{O}}^n \cdot \xi^2 \cdot \left( \frac{1}{\xi} \frac{d\xi}{dy} - \frac{d \ln a_{\text{O}}}{dy} \right) \right] \quad [4]$$

The intended differentiation of Eq. [4] after rearrangement leads to

$$\begin{aligned} \frac{d^2 \xi}{dy^2} = & \left\{ - \frac{y k'}{p a_{\text{O}}^n \xi^2} \cdot \frac{d\xi}{dy} - \left[ \frac{1}{p} \cdot \frac{dp}{dy} + \frac{2}{\xi} \frac{d\xi}{dy} \right. \right. \\ & \left. \left. + n \frac{d \ln a_{\text{O}}}{dy} \cdot \left( \frac{1}{\xi} \cdot \frac{d\xi}{dy} - \frac{d \ln a_{\text{O}}}{dy} \right) \right] + \frac{1}{\xi^2} \left( \frac{d\xi}{dy} \right)^2 \right. \\ & \left. - \frac{k'}{[1 + (p - 1)\xi] \cdot a_{\text{O}}^n \xi} \cdot \left( \frac{1}{\xi} \frac{d\xi}{dy} + \frac{n d \ln a_{\text{O}}}{dy} \right) \right. \\ & \left. - \left\{ \frac{d \ln a_{\text{O}}}{dy} / [1 + (p - 1)\xi] \right\} \right. \\ & \left. \cdot \left[ \frac{d\xi}{dy} (p - 1) + \frac{dp}{dy} \xi \right] + \frac{1}{[1 + (p - 1)\xi]} \cdot \frac{dp}{dy} \cdot \frac{d\xi}{dy} \right\} \\ & \cdot \frac{1}{\left( \frac{1}{\xi} - \frac{(p - 1)}{[1 + (p - 1)\xi]} \right)} \quad [5] \end{aligned}$$



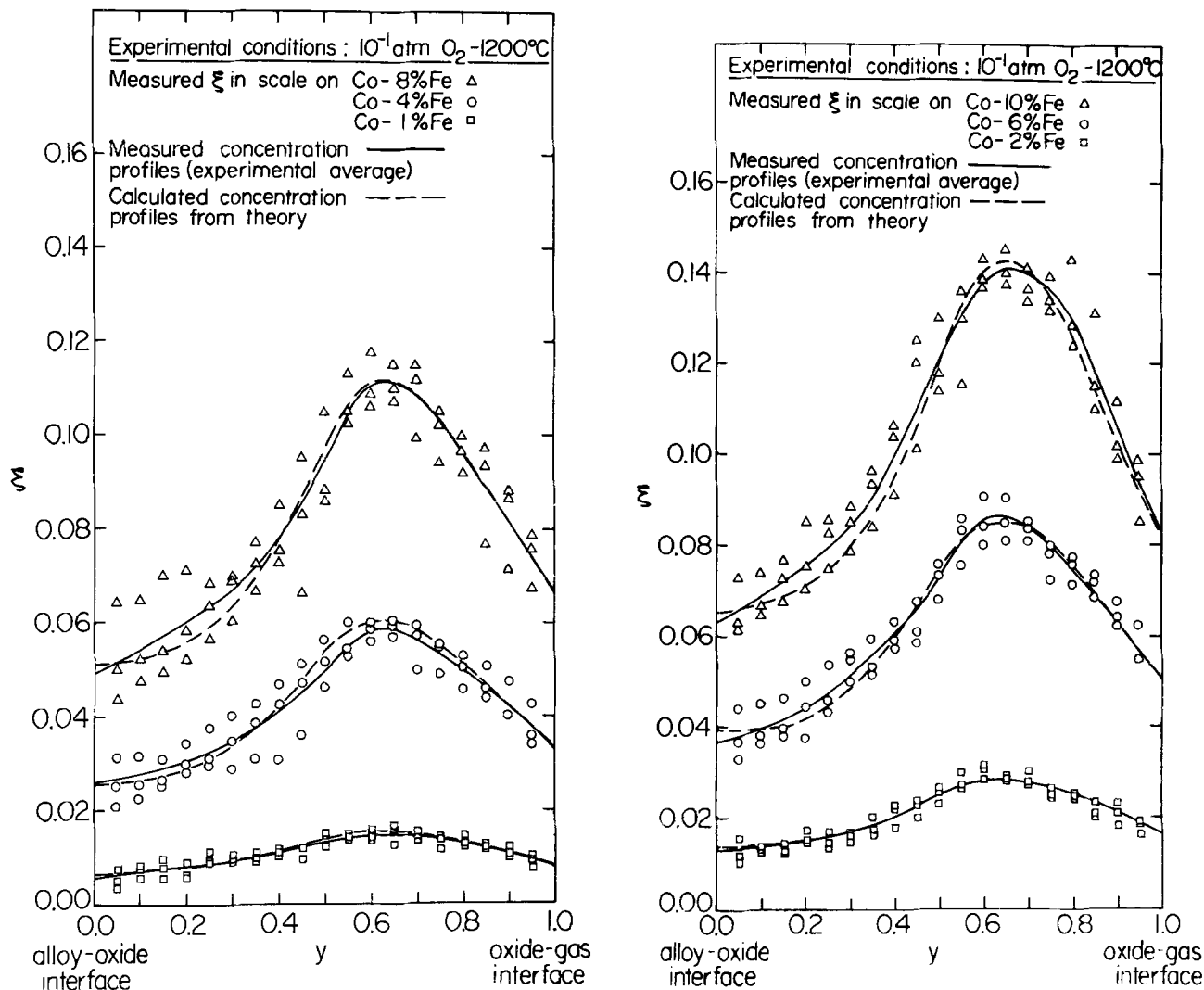


Fig. 8. Mole fraction of FeO,  $\xi$ , as a function of normalized distance coordinate  $y$  in (CoFe)O scales at  $10^{-1}$  atm oxygen pressure: (a, left) Co-1, 4, and 8 w/o Fe; (b, right) Co-2, 6, and 10 w/o Fe.

Equations [2] and [5] describe the variation of the mole fraction of FeO,  $\xi$ , and the oxygen activity,  $a_o$ , as a function of  $y$ . Unfortunately, the dependent variables  $\xi$  and  $a_o$  are inseparable and an analytical solution does not exist. Therefore, these differential equations must be solved simultaneously using a numerical method with appropriate conditions to obtain  $\xi$  and  $a_o$  as a function of  $y$ . The equation describing the material balance at the alloy-oxide interface can be employed as an auxiliary equation in this numerical analysis. Since an insignificant degree of internal oxidation occurred, the ratio for the flux of cobalt to iron in the scale at its inner interface is equivalent to the metal ratio in the bulk alloy. Equation [35] in Ref. (4) gives

$$\left( \frac{d\xi}{dy} \right)_{y=0} = \frac{k'}{a_o'^n \xi'} \left\{ \frac{p' \xi' - [1 + (p' - 1) \xi'] \xi_{\text{alloy}}}{p'} \right\} \quad [6]$$

where the prime refers to the inner scale surface and  $\xi_{\text{alloy}}$  is the atom fraction of iron in the alloy.

A stable fourth-order integration procedure (6) (modified Haming's predictor-corrector) was used to generate the iron concentration and oxygen activity profiles over the scale normalized thickness,  $y = 0$  to  $y = 1$ . We have shown in our previous paper that the empirical constants relating the cation vacancy concentration to the composition and the oxygen activity of (CoFe)O at  $1200^\circ\text{C}$  are  $\gamma = 0.60 \pm 0.11$  and  $n = 0.15 \pm 0.03$ . The vacancy diffusivity of cobalt was also shown to be  $D_{\text{Co}^\circ} = 1.46 \pm 0.04 \times 10^{-6}$  cm<sup>2</sup>/sec. The

ratio,  $p$ , of cobalt and iron vacancy diffusivities in (CoFe)O is estimated from the Co<sup>60</sup> and Fe<sup>55</sup> diffusion measurements on single crystals of pure and iron-doped CoO reported by Crow (5). The interpolated relation of  $p$  vs. oxygen pressure from these measurements is shown in Fig. 10. A value of  $k'$  was obtained from the parabolic oxidation constant,  $k_p$ , given in

$$\text{Fig. 4 from the relationship } k' = \frac{k_p}{2D_{\text{Co}^\circ} \gamma} (V/16)^2$$

where  $V$  is the molar volume of the oxide. The iron profiles were calculated from Eq. [2] and [5] as an initial value problem using the auxiliary Eq. [6] to relate  $(d\xi/dy)_{y=0}$  to  $\xi'$ ,  $a_o'$ ,  $k'$ , and  $p$ . These calculated profiles are compared to those experimentally obtained in Fig. 7-9.

The good agreement of the calculated to the measured iron profiles substantiates the basic tenets of the ternary diffusion model. An analysis based on these concepts, moreover, leads to an explanation of the hitherto unobserved observations on the growth of a solid solution oxide scale on a binary alloy in which a metal gradient exhibits maxima dependent on the growth rate of the scale governed by the magnitude of the atmospheric oxygen activity. From the diffusional analysis, we conclude that the observed metal profiles exhibiting maxima can be calculated based upon the variation of a kinetic parameter which in this case is the ratio of the metal self-diffusion coefficients,  $D_{\text{Fe}}/D_{\text{Co}}$ . Figure 11 depicts the oxygen activity profile in the scale which monotonically increases with increasing scale thickness. One can conclude by compar-

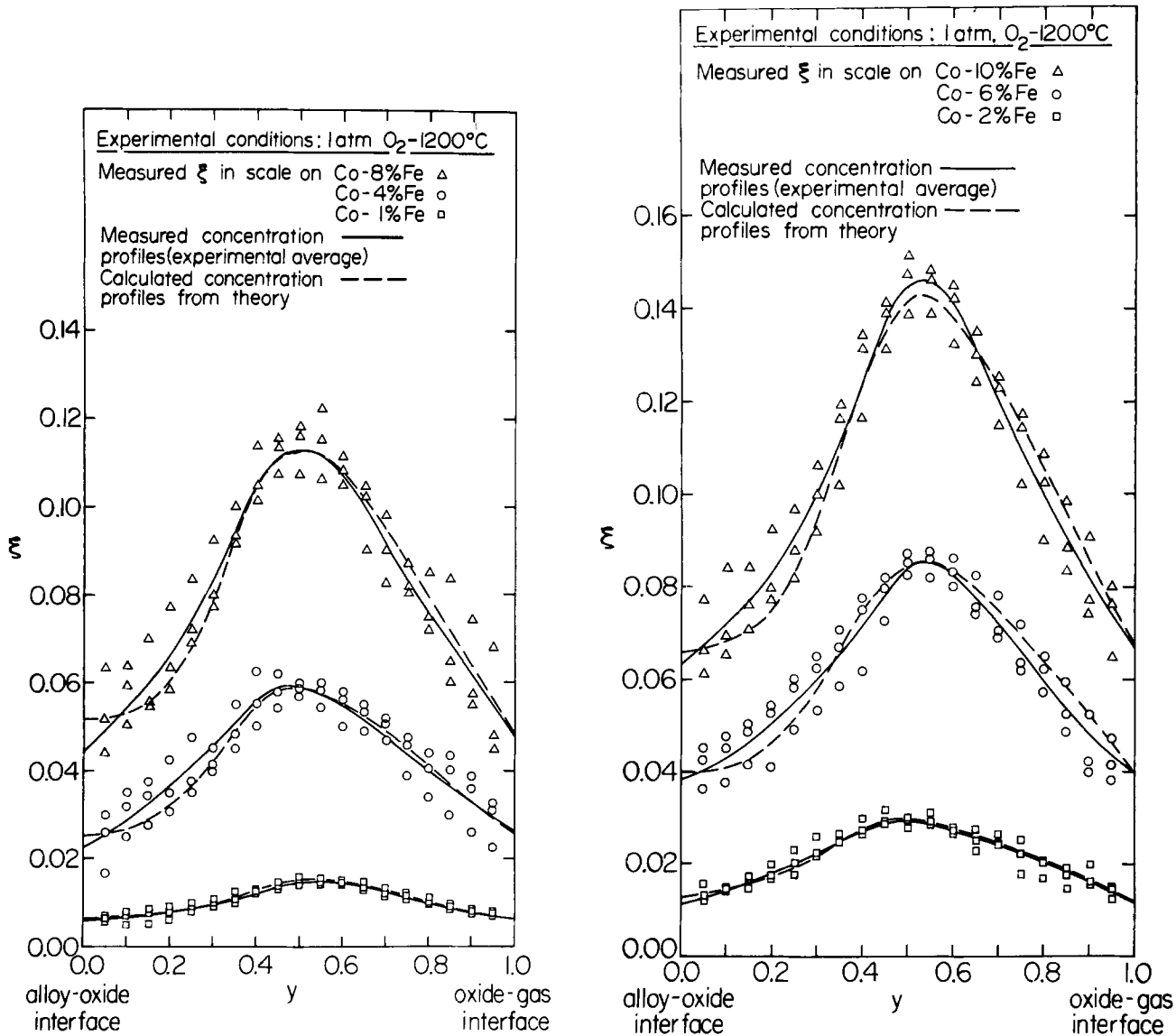


Fig. 9. Mole fraction of FeO,  $\xi$ , as a function of normalized distance coordinate  $y$  in the (CoFe)O scales formed at 1 atm oxygen pressure: (a, left) Co-1, 4, and 8 w/o Fe; (b, right) Co-2, 6, and 10 w/o Fe.

ing the graphs of Fig. 9, 10, and 11 that iron diffused more rapidly against its own gradient than cobalt down its own concentration gradient in the inner region of a scale at low oxygen activity less than  $10^{-3}$  atm because  $D_{Fe}/D_{Co} = 1.6$ . This tendency was reversed at higher oxygen activity since the above ratio

of diffusion coefficients underwent a transition from 1.6 to 0.7 over oxygen activities corresponding to the

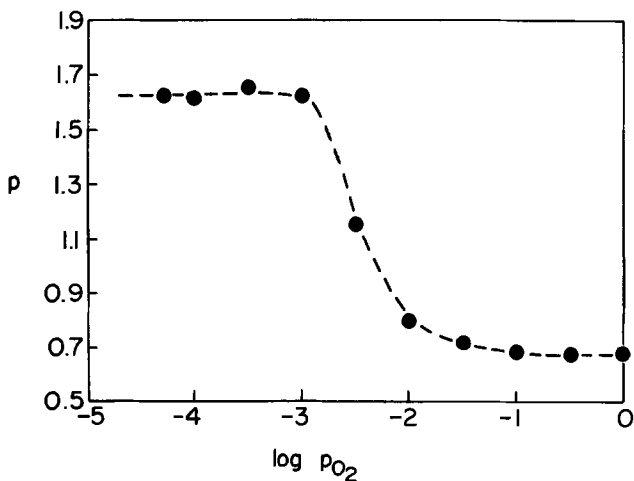


Fig. 10. Ratio of tracer diffusion coefficients of  $Fe^{55}$  and  $Co^{66}$  in single crystal CoO at 1200°C as a function of oxygen pressure.

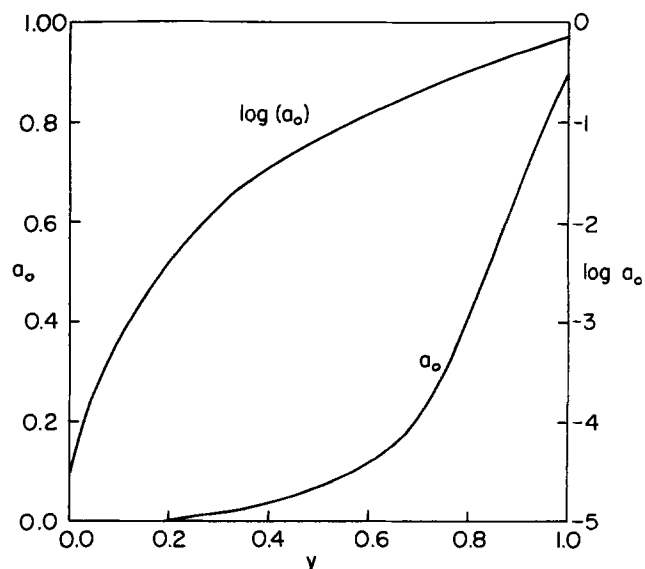


Fig. 11. Oxygen activity profile in the (CoFe)O scale formed on the Co-10 w/o Fe alloy at 1 atm oxygen pressure.

pressure range  $10^{-3}$ - $10^{-1}$  atm. Accordingly, more rapid cobalt diffusion and the subsequent decrease in iron concentration caused a maximum in the iron profile within a scale. The height and position of this maximum is interrelated to the kinetic diffusion coefficients and the oxygen activity gradient driving force. It is also interesting to note that the development of this maximum in the iron profile near the midpoint of a scale when the atmospheric pressure is 1 atm corresponds to a bell-shape profile.

We emphasize finally that the analysis based on ternary diffusion is to be regarded as a simplified empirical description of the oxidation properties of Co-Fe alloys under conditions for growth of a (CoFe)O scale. As illustrated in our earlier paper on this subject, a more fundamental analysis cannot be attempted until additional definitive knowledge becomes available on the structural, thermodynamic, and metal transport properties of (CoFe)O. The analysis, nonetheless, does lead to an explanation of metal profiles exhibiting maxima in an oxide scale formed on a binary alloy.

#### Acknowledgments

This work was carried out by P. Mayer in partial fulfillment of the requirements for award of the Ph.D.

degree by McMaster University under the auspices of the National Research Council of Canada. He gratefully acknowledges the award of a National Research Council of Canada Bursary for graduate studies.

Manuscript submitted Oct. 8, 1975; revised manuscript received Jan. 6, 1976.

Any discussion of this paper will appear in a Discussion Section to be published in the December 1976 JOURNAL. All discussions for the December 1976 Discussion Section should be submitted by Aug. 1, 1976.

Publication costs of this article were partially assisted by McMaster University.

#### REFERENCES

1. E. Aukrust and A. Muan, *Trans. AIME*, **230**, 1395 (1964).
2. E. Aukrust and A. Muan, *ibid.*, **227**, 1378 (1963).
3. P. Mayer and W. W. Smeltzer, *This Journal*, **121**, 538 (1974).
4. C. Wagner, *Corrosion Sci.*, **2**, 91 (1969).
5. W. B. Crow, Report ARL-70-0090, Project No. 7021, Office of Aerospace Research, United States Air Force, Wright-Patterson Air Force Base, Ohio (1970).
6. International Business Machine Inc., New York, Scientific Subroutine Package, System 360, Version III.

## D-C Field Dependence of Tantalum Film Capacitors

Peter W. Wyatt

*Bell Laboratories, Allentown, Pennsylvania 18103*

#### ABSTRACT

The capacitance of tantalum film capacitors changes on the order of 1% when a field of a few MV/cm is applied. It is shown in this paper that the  $C(E)$  dependence of anodic  $Ta_2O_5$  is produced by at least three separate physical processes. An equation for  $C(E)$  is given in which each process is represented by one term. The effects on each process of oxide thickness, anodization soak time, counterelectrode material, nitrogen doping, heat-treatment, measurement frequency and temperature, and the rate of rise of bias voltage during measurement are discussed. It is shown that one of the processes affects the capacitance through a field-dependent bulk polarizability. The other two processes may also involve field-dependent polarizability, but there is evidence that one or perhaps both of them are produced by a change in the oxide thickness with field. A physical model for the asymmetry in  $C(E)$  is proposed.

It is well known that the small-signal capacitance of Ta film capacitors depends on the d-c bias voltage (1, 2). In a previous paper (2) it was shown that the voltage, or more accurately the field, dependence at liquid nitrogen temperature is produced entirely by bulk oxide effects and not by interface effects. That is, the physical processes which cause the field dependence are distributed uniformly through the oxide thickness rather than being localized at the metal-oxide interfaces. This observation is particularly interesting in view of the asymmetry of the capacitance-field [ $C(E)$ ] curve, since it indicates that the amorphous  $Ta_2O_5$  dielectric must have a built-in anisotropy. In the present paper the nature of the processes which produce the field dependence is considered.

Capacitors have been made and measured with variations in several experimental parameters, described in the next two sections. The  $C(E)$  curve is complicated in shape, so to characterize the dependence on these parameters the curve must be separated into components which behave in a simple fashion.

An empirical equation is presented which accomplishes this separation, and it is shown that each of the three major terms of the equation represents a different physical process. The experimental results show how each process depends on the parameters which were varied. In the last section the nature of each process is discussed and a simple physical model for the anisotropy is presented.

#### Samples

All samples were made using standard processing (2), with modifications described below. Two sample geometries were used. The one illustrated in Ref. (2) is a planar arrangement in which none of the films is etched and no photoresist is used. In the other, which is more conventional, patterns are defined in both the Ta and counterelectrode using photoresist and the metals are chemically etched. These samples are not planar, since the edge of the Ta film is part of the capacitor area. Despite this substantial dissimilarity, no difference has been observed between the  $C(E)$  curves of the two patterns.

The capacitor consists of a layer of d.c.-sputtered Ta about 3000Å thick, an anodic  $Ta_2O_5$  dielectric

layer, and an evaporated metal counterelectrode. The substrate is glass or glazed ceramic protected by a thermal Ta<sub>2</sub>O<sub>5</sub> underlayer. No effect of substrate material on the capacitance-field characteristics has been observed.

The Ta film serves as one electrode and is anodically oxidized to form the dielectric. In most of these experiments it contains up to a few atomic per cent (a/o) nitrogen, added as a dopant in the sputtering gas, and has the  $\beta$  (tetragonal) crystal structure (3). Nitrogen is commonly added to  $\beta$ -Ta because it improves capacitor quality (4). In one experiment capacitors were made with nitrogen doping ranging from zero to a level sufficient to produce bcc Ta crystal structure (5).

The Ta<sub>2</sub>O<sub>5</sub> was produced in all cases by anodization in 0.01 weight per cent (w/o) citric acid in water at room temperature using a Ta sheet cathode. Samples were anodized at a current density of 0.16 mA/cm<sup>2</sup> until a final voltage,  $V_f$ , was reached.  $V_f$  was then held for a soak period,  $t_s$ . Standard values are 230V and 1 hr, which produce an oxide 4100Å thick, but each of these parameters was varied in some experiments. For the standard values the average electric field at the end of the soak period,  $E_f$ , is 5.5 MV/cm.

The standard counterelectrode is a thin film of NiCr (500Å) backed by a thicker film of Au (5000-15,000Å), sequentially evaporated by electron-beam heating. Evaporation from resistance-heated filaments was used in one experiment, and several other metals were used.

In standard processing the samples are not intentionally heated except during several cleaning steps, where the maximum temperature is 120°C for drying in air. They are also heated by radiation from the evaporant source during counterelectrode evaporation; the temperature reached is not known. One annealing experiment was done in which the finished capacitors were heated at 200°C for times from 15 min to 4 hr.

### Measurements

Capacitance-voltage data were recorded using the system described in Ref. (2). A slow linear ramp bias voltage is applied to the capacitor while the change of capacitance and phase angle is monitored with a General Radio 1654 impedance comparator. For the small values of interest the phase angle is essentially equal to the dissipation factor. The comparator uses a small a-c voltage added to the d-c bias to measure the capacitance, so that one actually measures a differential capacitance. The change in capacitance,  $\Delta C$ , normalized by the zero-voltage capacitance,  $C_0$ , is recorded *vs.* voltage both on an X-Y recorder and a digital printer. The change in phase angle is simultaneously recorded on the X-Y recorder. The voltage scale is converted to average electric field, defined as  $E = V/d$ , using the oxide thickness,  $d$ , determined by ellipsometry.

Both the bias rise rate and the magnitude of the a-c voltage have little effect on the measurement, so precise control is not required. For 230V capacitors, 1V/sec and 1  $V_{rms}$  were used. For other oxide thicknesses the bias rise rate was varied roughly in proportion to the thickness. The a-c voltage was reduced to 0.3  $V_{rms}$  for the thinnest oxides. The most commonly used frequency was 1 kHz, but many samples were also measured at 0.1, 10, and 100 kHz.

The accuracy of the  $\Delta C$  measurement is estimated to be about 0.01% of  $C_0$ . Random errors, such as noise, are clearly less than 0.01%. There are several known sources of systematic error, but none of them is likely to cause more than 0.01% of  $C_0$  distortion of the curve under the conditions of these measurements. An NPO ceramic capacitor measured under

similar conditions exhibited essentially zero  $C(V)$  dependence.

For a typical measurement the comparator is balanced at 0V d.c., the voltage ramp is started, and the change in capacitance is recorded. After a high voltage has been applied and removed, the sample remains partially polarized for a period of hours or even days. It is therefore not practical to measure a given sample more than once or, in particular, to use the same sample for both negative and positive bias voltages. Therefore, for most measurements two adjacent capacitors on the same substrate are used, one for positive and the other for negative bias.

Most samples were measured at room or liquid nitrogen temperature. Most of the analysis reported here is for measurements at 77°K, for which the capacitor was simply immersed in liquid nitrogen. A few measurements were also made of samples immersed in liquid helium at 4.2°K. A series of measurements between liquid nitrogen and room temperature were made using a Delta Design temperature chamber with liquid N<sub>2</sub> coolant. Temperature measurements in that case were made with an iron-constantan thermocouple, taped to the substrate, and a Leeds and Northrup potentiometer.

### Empirical Model

Typical data for liquid N<sub>2</sub> temperature are shown in Fig. 1 (solid line). The electric field is defined as positive when the Ta electrode is positive relative to the counterelectrode. The two capacitors used for this curve (one for +, the other for -) were standard units, *i.e.*, they were made using a 230V anodization with 1 hr soak and NiCr-Au counterelectrode. The a-c signal was 1  $V_{rms}$  at 1 kHz, and the bias rise rate was 1 V/sec.

It is evident that the change in capacitance produced by a d-c field is on the order of 1% or less, and that it is asymmetric. This asymmetry is apparent even at very low field and, as we shall see, at all temperatures and frequencies investigated.

When experimental parameters such as measurement temperature or anodization soak time are varied, this curve changes in a complex way. In order to describe these changes the field dependence must be separated into components which behave simply with the varied parameter. The means for such a separation can be developed by considering two experiments.

In the first, two groups of capacitors were made in which everything was the same except the anodization soak time.  $C(E)$  curves were recorded for a pair of units from each group (remembering that the oxide thickness depends on soak time), and the difference between the two curves was calculated. This difference, for samples with 2 min and 300 min soak time, is plotted in Fig. 2. It is obviously very close to linear in the field.

Now let us consider one of the  $C(E)$  curves, the 300 min one to be specific. By subtracting a straight line of the appropriate slope, corresponding to the line in Fig. 2, one finds the curve plotted in Fig. 3. The significance of this curve is that it is almost exactly symmetric in the electric field. Thus essentially all of the asymmetry of the  $C(E)$  curve can be expressed by a simple linear dependence. Moreover, the physical process which produces the asymmetry is affected by the anodization soak time, while those which produce symmetric changes in  $C$  are not. Therefore they must be different processes.

The curve in Fig. 3 can be further separated by considering the frequency dependence. Nominally identical pairs of samples were measured at 100 Hz and at 100 kHz, and the difference between the two curves was calculated. This difference is shown in Fig. 4, together with its symmetric and antisymmetric parts. (The symmetric part of a capacitance curve is  $[\Delta C(E) + \Delta C(-E)]/2C_0$  and the antisymmetric

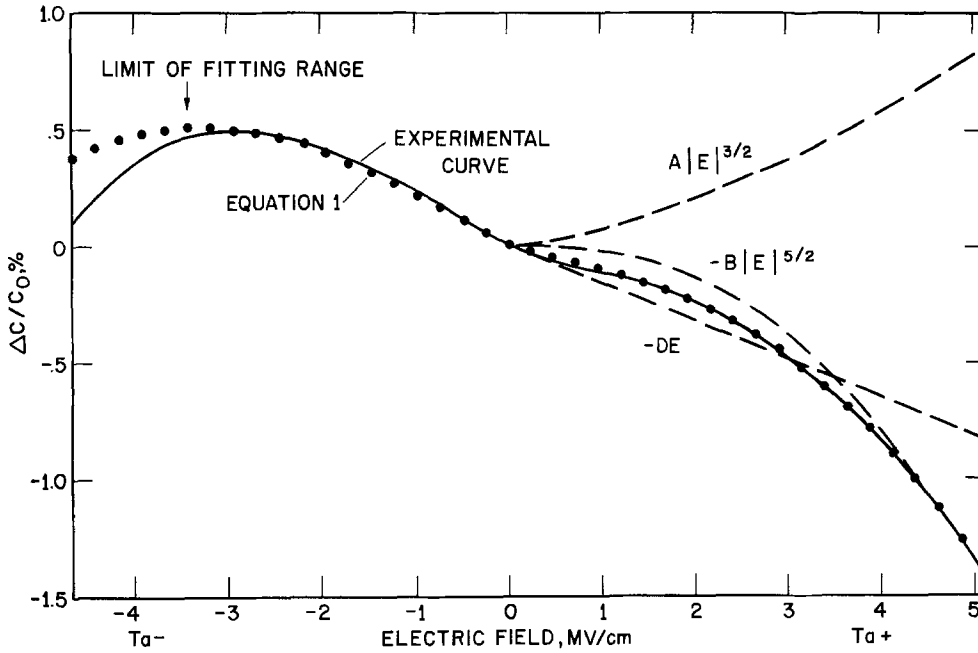


Fig. 1. Solid line: a typical  $C(E)$  curve for a pair of capacitors measured at 1 kHz and 77°K. Points: calculated values obtained by fitting Eq. [1] over the field range  $-3.4$  to  $+5.0$  MV/cm. Dashed curves: the three field-dependent terms of Eq. [1].

part is  $[\Delta C(E) - \Delta C(-E)]/2C_0$ , defined for  $E > 0$ .) Comparing the symmetric part with Fig. 3, one sees that taking the difference has eliminated the decrease

in  $\Delta C$  at high field. By plotting the symmetric part of the difference on log-log scales in Fig. 5 one finds that it varies essentially as  $E^{3/2}$ . Thus there are two symmetric contributions to  $C(E)$ . One is an increase in capacitance as  $E^{3/2}$  which is frequency dependent. The other is a decrease in capacitance which is independent of frequency, and which one finds by adjusting coefficients varied as  $E^{5/2}$ . By arguments directly analogous to those used in the soak time discussion, these two contributions must be produced by two different physical processes.

The above discussion can be neatly summarized in an equation for the normalized change in capacitance

$$\frac{\Delta C}{C_0} = A|E|^{3/2} - B|E|^{5/2} - DE + H \quad [1]$$

This equation can be fit to any given experimental

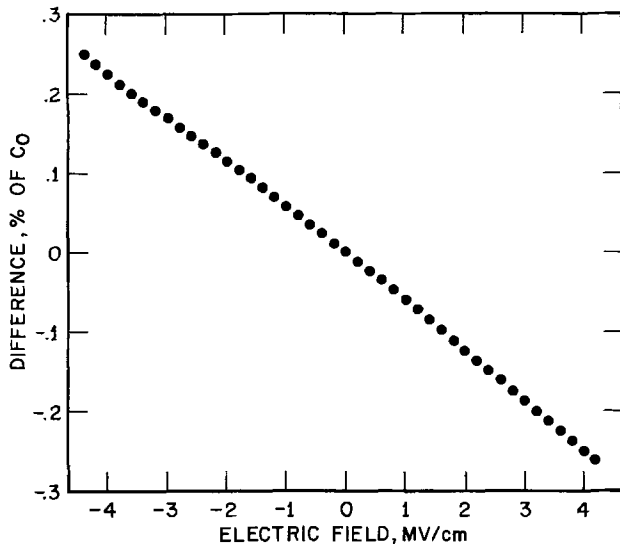


Fig. 2.  $\Delta C(E)/C_0$  for samples with 5 hr soak time minus  $\Delta C(E)/C_0$  for samples with 2 min soak time, plotted vs. field.

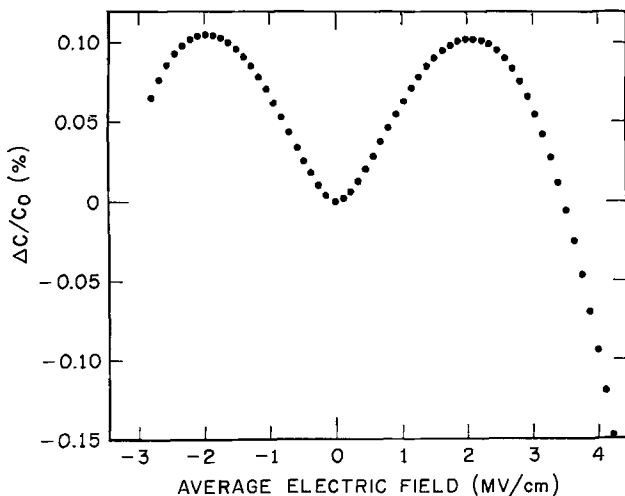


Fig. 3.  $\Delta C(E)/C_0$  for one of the samples in Fig. 2 minus a straight line. The curve is nearly symmetric.

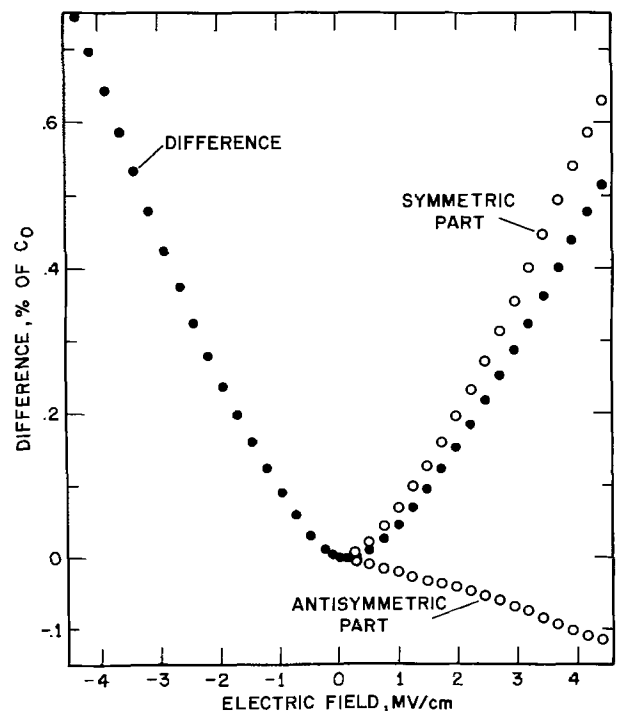


Fig. 4. Solid circles:  $\Delta C(E)/C_0$  measured at 0.1 kHz minus  $\Delta C(E)/C_0$  measured at 100 kHz. Open circles: the symmetric and antisymmetric parts of the difference.

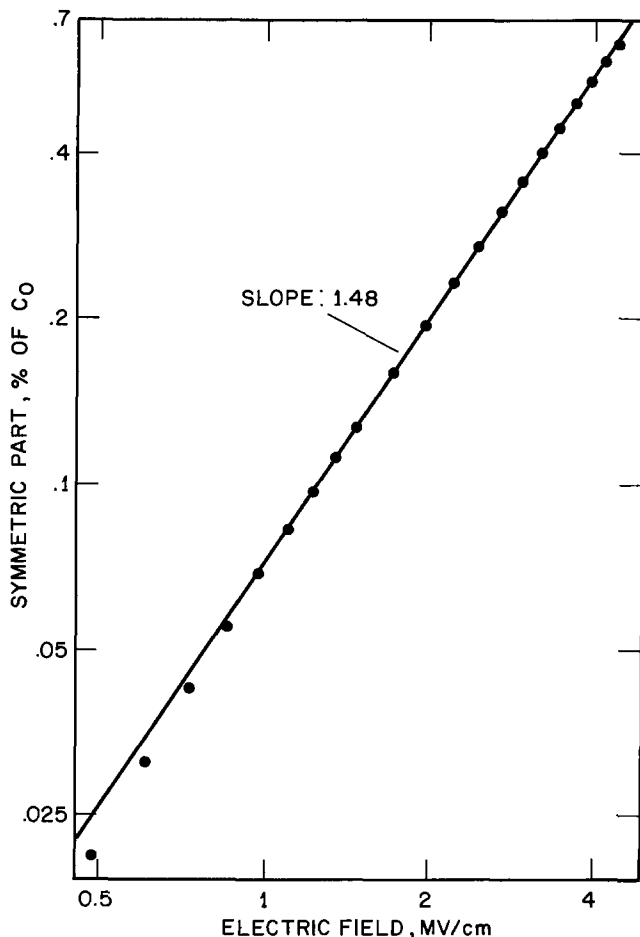


Fig. 5. The symmetric part of the difference curve from Fig. 4, replotted on log-log scales.

curve by adjusting the four coefficients,  $A$ ,  $B$ ,  $D$ , and  $H$ , using a computer library routine which weights all points equivalently. The result for one curve is shown by the dots in Fig. 1. The three field dependent terms are plotted separately as dashed lines. The constant,  $H$ , allows the  $E = 0$  point to be treated equivalently with all the others and improves the fit somewhat. It is always very small and has no apparent physical significance.

It is obvious in Fig. 1 that Eq. [1] fits the data very well except at high negative field, where evidently an additional mechanism becomes important. Because of this deviation the coefficients which one finds depend somewhat on the field range used for fitting. In Fig. 1 the range used was  $-0.6$  to  $+0.9 E_f$ , where  $E_f$  is the field at the end of anodization, 5.5 MV/cm. This dependence causes some confusion in data analysis, but if the same field range is used for fitting all curves in an experiment, meaningful results can be obtained. The dependence on field range is not large provided that (i) the negative limit is not much beyond  $-0.6 E_f$ , and (ii) the absolute value of the negative limit is less than the positive limit.

The importance of Eq. [1] lies in the fact that each of the field dependent terms represents a different

physical process, or perhaps more than one process. The exact form of each term is less important, since one or even all of them may not be precisely correct. The three terms are very different in form: the first is positive and symmetric, the second is negative and symmetric, and the third is antisymmetric. As a result the equation allows one to separate the data unambiguously and study the contribution from each physical process independently of the others. Thus, by doing experiments in which experimental parameters are varied one can learn how each process depends on those parameters.

The dissipation factor also depends on electric field, and a similar analysis can be done. The dependence at low temperature has the form

$$\Delta DF(E) = L|E|^{3/2} - ME \quad [2]$$

the same as Eq. [1] except that the negative symmetric term is missing. There is also an additive contribution due to electronic leakage current. The magnitude of the first term can be large; larger than the zero field value of the  $DF$ . The second term is much smaller. No attempt has been made to determine the effect on Eq. [2] of the various experimental parameters. Its significance in this paper lies in its resemblance to Eq. [1], discussed in a later section.

### Experimental Results

A considerable number of parameters have been varied in these experiments. The effects of each one are summarized in Table I. The oxide thickness was considered in Ref. (2). It was shown there that when the anodization for different thicknesses is done consistently the  $\Delta C/C_0$  vs.  $E$  curve, and hence all three coefficients of Eq. [1], are independent of oxide thickness over the range 2700-5400Å, and only very weakly dependent on thickness down to 900Å. From this result it was argued that  $\Delta C(E)$  must be produced by bulk oxide effects. The soak time and frequency experiments described in the last section and in more detail below tell us that at least three such effects must be involved.

*Soak time.*—In the soak time experiment six Ta films from the same sputtering batch were anodized together at constant current until 230V was reached. The voltage was then held constant and samples were removed at six different times, from 0 to 24 hr. During the 24 hr soak the oxide thickness increased from 3620 to 4460Å, determined by ellipsometry. Counter-electrodes were deposited simultaneously on all six samples, and measurements were taken as usual. Equation [1] was fit to the data at 77°K, 1 kHz over the range  $-2.8$  to  $+4.2$  MV/cm. The results are shown in Fig. 6. It is evident that within the expected sample-to-sample scatter of several per cent, the coefficients  $A$  and  $B$  of the two symmetric terms are independent of soak time,  $t_s$ , as expected from the previous discussion, while the coefficient  $D$  of the antisymmetric term increases approximately as  $\log t_s$ , at least for times larger than a few minutes. The sample with zero soak time, plotted to the left of the log scale, is consistent with the others. A somewhat better fit, including the  $t_s = 0$  point, is obtained by setting  $D = D_0 \log(t_s + t_0)/t_1$ , where  $t_1$  is a

Table I. Dependence of the coefficients of Eq. [1] on the varied parameters

Parameter	A	B	D
Oxide thickness	All three coefficients nearly independent	Independent	Independent
Increasing anodization soak time	Independent	Independent	Increases
Increasing frequency	Decreases	Nearly independent	Decreases slowly
Increasing temperature	Increases, $\rightarrow 0$ as $T \rightarrow 0$	Independent	Increases slowly, $> 0$ as $T \rightarrow 0$
Increasing bias rise rate	Increases very slightly	Independent	Increases very slightly
Counterelectrode material	Large variation is probably due to different heating during counterelectrode evaporation	Independent	Independent
Nitrogen doping of the Ta film	No effect for concentrations from $<< 1$ to 5 a/o N in the Ta	Independent	Independent
Heat-treatment at 200° C	Decreases	Independent	Decreases

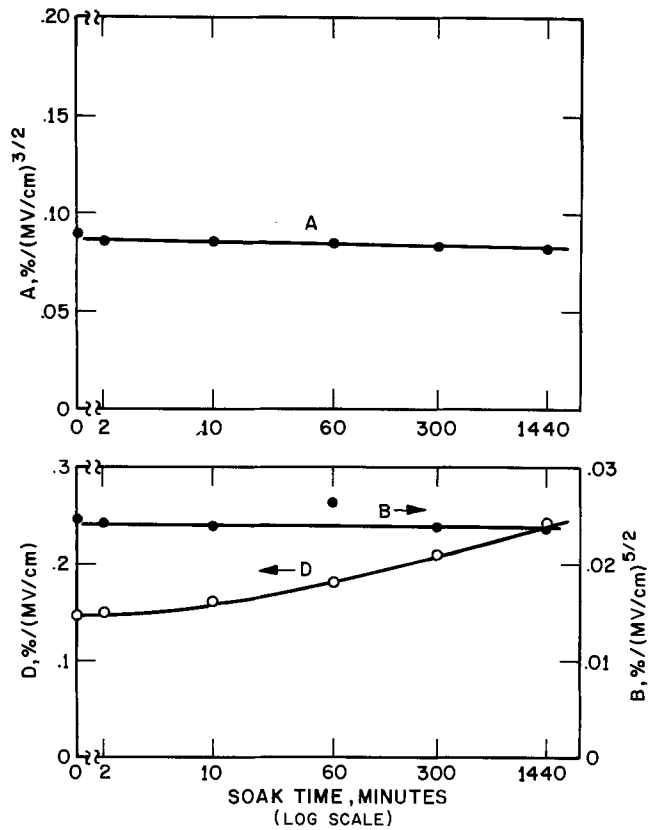


Fig. 6. Dependence of the coefficients of Eq. [1] on duration of the constant voltage soak period of anodization.

constant and  $t_0$  is about 5 min. Physically, this suggests that the effect of the soak period is also produced, to a small extent, by the constant-current part of the anodization.

**Frequency.**—Capacitance-field curves were measured at four different frequencies, 0.1-100 kHz. Data for a set of standard samples, recorded at 77°K and fit over the range  $-0.5$  to  $+0.75 E_f$ , are shown in Fig. 7. Similar data have been recorded for many sets of samples. In all cases  $A$  varies approximately as  $\log(1/f)$ , extrapolating to zero between a few MHz and a few tens of MHz.  $B$ , in contrast, varies only slowly if at all with frequency, usually decreasing slightly with increasing  $f$ . In some sets of capacitors it has appeared independent of  $f$  for the four frequencies measured, while in a few a slight increase occurred with increasing frequency. The difference in slope among different sets is probably due to variation among the capacitors of each set. These calculations confirm that the positive symmetric term in  $\Delta C(E)$  is strongly frequency dependent, while the negative symmetric term is nearly independent of  $f$ . The coefficient,  $D$ , of the antisymmetric term always decreases with increasing frequency, but much more slowly than  $A$ .

**Temperature.**—The temperature dependence of the three coefficients and the rms error for measurements at 1 kHz are shown in Fig. 8. The points from 77° to 182°K are from capacitors all on the same substrate. They were fit over the range  $-0.5$  to  $+0.7 E_f$ . The points at 4.2°K are from a single capacitor on a different substrate from the same processing group, fit over a different range,  $-0.17$  to  $+0.7 E_f$ . Smooth curves are drawn through the points above 100°K and extrapolated somewhat arbitrarily to absolute zero. The remarkably close agreement of these extrapolations with the 4.2°K data can only be considered fortuitous in view of the difference in field range.

The 77°K points do not lie on the same curves as the higher temperature ones. Also, the fit to Eq. [1]

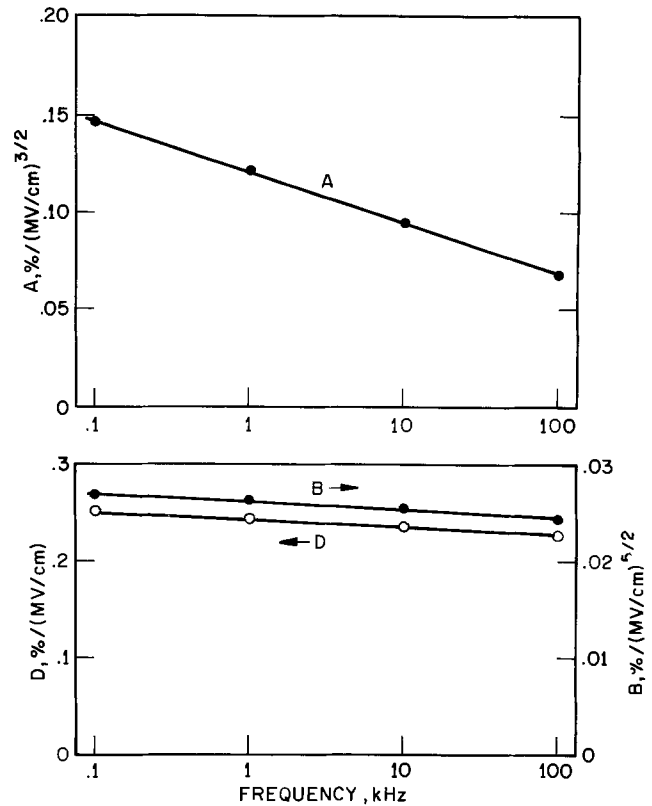


Fig. 7. Dependence of the coefficients on measurement frequency. The slope of  $B$  is often much less negative than for this sample.

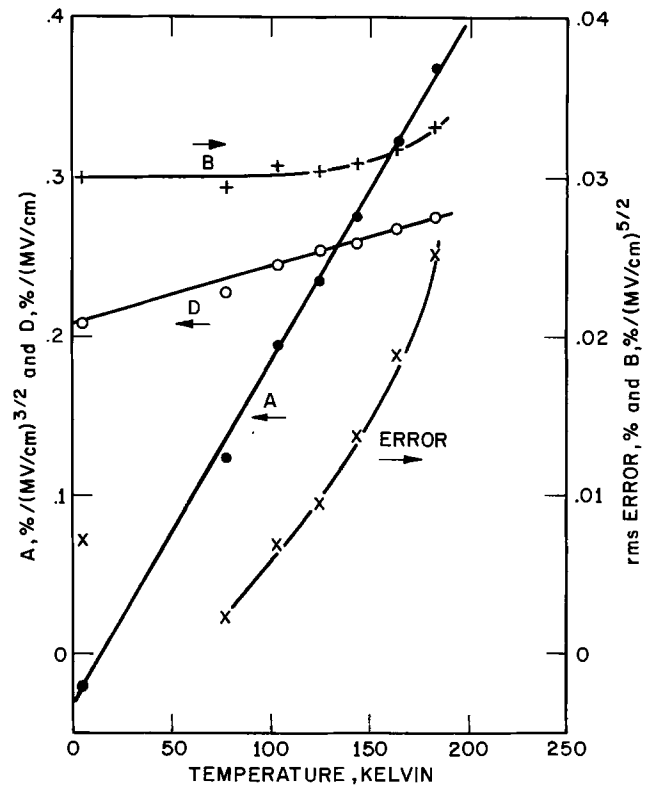


Fig. 8. Temperature dependence of the coefficients and rms fitting error of Eq. [1].

is not nearly as good at higher temperatures or at 4.2°K as it is at 77°K. The fixturing used at temperatures other than 77°K was not carefully designed and used substantial lengths of unshielded hookup wire. It is likely that this fixturing contributes to the inconsistency and possibly to the poor fit. It is also likely that temperature measurement inaccuracy and variation of temperature during the time required

to record a curve contribute additional errors at the higher temperatures.

The inconsistency of the data and the poor fit make it impossible to precisely determine the temperature dependence of the three coefficients. However, several points are nevertheless apparent in Fig. 8. (i) The coefficient,  $A$ , of the positive symmetric term decreases approximately linearly as the temperature is lowered, becoming very small as  $T \rightarrow 0$ . It is very unlikely that  $A$  actually becomes negative, as appears true in the rather poor fit at 4.2°K. (ii) The coefficient,  $B$ , of the negative symmetric term depends much less on temperature and does not become small as  $T \rightarrow 0$ . The apparent magnitude of  $B$  at the higher temperatures depends strongly on the field range used for fitting, but all reasonable ranges give approximately the same low temperature extrapolation. (iii) The coefficient,  $D$ , of the antisymmetric term decreases as  $T$  is lowered, but much more slowly than  $A$  does. The asymmetry clearly does not disappear at low temperature.

Equation [1] does not fit the  $C(E)$  curve at room temperature, so evidently additional physical processes contribute at such higher temperatures. These probably include some interface effects as well as the bulk processes which dominate at 77°K. Unfortunately, the data for 103°-182°K are not accurate enough for precise extrapolation to room temperature.

**Bias rise rate.**—The rate of rise of the bias voltage during measurement has been varied from 0.005 to 0.24 (MV/cm)/sec. The usual rate is 0.024 (MV/cm)/sec. No major difference is apparent between different rise rates. The coefficients  $A$  and  $D$  tend to increase slightly with increasing rate, but the difference is not much larger than typical capacitor-to-capacitor variation.

One sample was measured using a bias voltage which increased in steps of 10-30V instead of linearly. Each voltage was held constant for 1 hr and then a data point was recorded. One finds that the curve for stepped voltage differs from the others only by an amount comparable to typical capacitor-to-capacitor variation.

**Counterelectrode material.**—The effect of counterelectrode material is very complicated. The materials which have been used are: NiCr backed by Au (the standard), NiCr without Au, Ti backed by Pd and Au, Au alone, Cr, and Cu. The low temperature  $C(E)$  curves for all of these are qualitatively similar, and all fit Eq. [1] reasonably well. There are, however, quantitative differences as large as a factor of 1.5 between otherwise similar capacitors with different counterelectrode types. One is tempted to conclude that the counterelectrode material is responsible for these differences, but heating during deposition is a more likely cause.

Large differences in the coefficients are also found for nominally identical capacitors whose counterelectrodes were deposited in different evaporators, or to a lesser degree in the same evaporator at different times. It is likely that this variation results from different degrees of heating of the sample surface by radiation from the evaporant source, with a possible contribution by electron or ion bombardment from the source. One expects the degree of heating to be even more different for nonstandard counterelectrode materials or thicknesses, so this heating effect is probably the reason for the apparent dependence on counterelectrode material.

**Nitrogen doping.**—The size of the coefficients also depends somewhat on the nature of the Ta film, which may vary slightly for different sputtering runs. It is well known that other characteristics of Ta film capacitors are affected by details of the Ta film. A particularly striking example is the effect of nitrogen

incorporated into the Ta. Huttemann, Morabito, and Gerstenberg (4) have shown that 1 a/o nitrogen in the Ta reduces the leakage current at 50V by several orders of magnitude. This effect has not been explained, but to take advantage of it  $N_2$  is added to the sputtering gas for capacitor film. Even if it is not added intentionally, a small amount of nitrogen is likely to be present due to residual or leaking air in the vacuum system. When the Ta is anodically oxidized, the nitrogen is incorporated into the oxide with a nonuniform distribution (6), almost all the N atoms being in the 3/4 of the oxide nearer the Ta electrode.

Capacitors were made on Ta containing N concentrations from near zero to 4 a/o. Each group was anodized separately and had counterelectrodes deposited at different times, so that substantial differences in the coefficients, ~50%, were found even between groups made from the same lot of Ta. The dependence of the coefficients on N concentration was small compared with this large variation.

In another experiment, reported in Ref. (2), the oxide was chemically thinned after anodization. The Ta for those units contained about 1 a/o N, which as usual was incorporated nonuniformly into the oxide (7). Before thinning, the N was located only in the 60-70% of the oxide closest to the Ta. Thinning removed the N-depleted layer, so for the thinnest sample all the oxide contained some nitrogen (7). Despite this gross difference in N distribution, the  $C(E)$  curves for different degrees of thinning were essentially the same as for a sample which was not thinned (2).

Thus, it is quite clear that a high concentration of nitrogen impurity centers, typically present in Ta film capacitors, is not responsible for any of the three terms in the low temperature  $C(E)$  dependence. Note, however, that probably none of the samples in this experiment contained truly zero nitrogen. The possibility remains that low levels of N impurity might contribute to  $C(E)$  in an effect which saturates at much less than 1 a/o.

**Heat-treatment.**—The last parameter investigated was the effect of heat-treatment at 200°C after complete fabrication of the capacitor. Two substrates were investigated, each containing 24 capacitors. The samples were heat-treated by placing them in an oven at 200°C for periods of 15 min-4.3 hr. The coefficients of Eq. [1] for one substrate fit over the range  $-0.43$  to  $+0.65 E_f$  are plotted vs. heat-treatment time in Fig. 9. (Time = 0 is plotted at the left of the logarithmic scale.)

Before any heat-treatment the  $C(E)$  curves for capacitors of the two substrates were very different from each other, and on the one shown there were substantial differences from capacitor to capacitor. The two sets of points plotted at time = 0 indicate the difference for two pairs of capacitors. After heat-treatment for as short a time as 15 min, the samples became essentially identical and there was no longer any variation among capacitors on either sample. It is evident from Fig. 9 that heat-treatment at 200°C causes a decrease in magnitude of the positive symmetric term,  $A$ , and the antisymmetric term,  $D$ , of  $C(E)$ . The negative symmetric term,  $B$ , in contrast, is unaffected.

## Discussion

The experimental results summarized in the last section and in Ref. (2) constitute a sizable body of information about the behavior of Ta film capacitors. They demonstrate that at least three bulk processes contribute to the  $C(E)$  dependence at low temperature and that interface processes do not contribute significantly. They tell us much about the nature of the three processes, although it is still not possible to specifically identify the physical mechanisms involved. In this section, the behavior of the three processes,



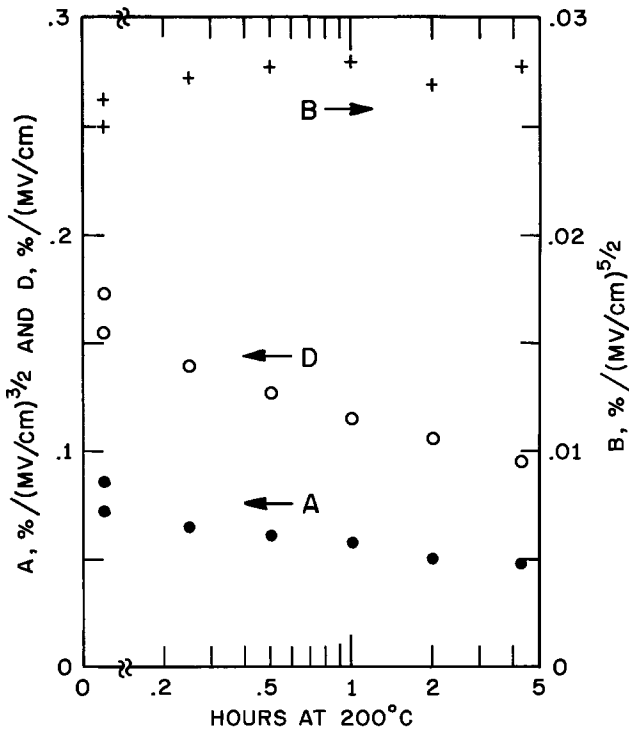


Fig. 9. Effect on the coefficients of heat-treatment at 200°C

each represented by a term in Eq. [1], is summarized and possible physical mechanisms are discussed.

*Positive symmetric term.*—The first term has the form  $A|E|^{3/2}$ , representing an increase in capacitance with increasing field. Its magnitude is frequency dependent, so the change in capacitance must be due to a change in polarizability rather than changes in thickness or area. The magnitude increases as the temperature is raised or the frequency is lowered. This change is in the same direction as for a Debye-type polarization. However, the form of the dependence is  $A \propto \log(1/f)$  and (approximately)  $A \propto T$ , which is entirely different than the form for a single relaxation time. Hence, one must assume that the modes which are responsible for this part of the polarizability are distributed over a wide range of relaxation times. Each mode contributes to the polarizability for frequencies much lower than the inverse of its relaxation time and not for frequencies much higher. For frequencies near the inverse of its relaxation time, the mode contributes to the field dependence of the dissipation factor, producing the dominant  $|E|^{3/2}$  term in  $DF(E)$ . The fact that the distribution of inverse relaxation times extends to rather low frequencies, 100 Hz or less, indicates that ionic motion is involved.

The magnitude of this term is reduced by heat-treatment at 200°C. This suggests that the polarization in question is associated with defects, that is, local instabilities which are annealed out at high temperature. One might expect that purely structural defects, involving unstable arrangement of Ta and O ions, would be reduced by a long anodization soak time, since the ionic current drops by a large factor during the soak period. However, we have seen that the positive symmetric term is not affected by the duration of the soak period. Hence it is plausible, though by no means proven, that impurities may be responsible for this polarization. Nitrogen, which is present in the films, is not a candidate unless the effect saturates at low concentrations.

*Negative symmetric term.*—The second term in Eq. [1],  $-B|E|^{5/2}$ , represents a decrease in capacitance with increasing field. Reference to Table I yields the

surprising result that this term is independent of every parameter which we have investigated within the accuracy of the determination. This independence suggests that the process involved is a fundamental property of anodic  $Ta_2O_5$ , not affected by impurities or other defects. There is no corresponding term in the field dependence of the dissipation factor.

Cornish and Young (8) have reported a similar phenomenon at visible light frequency and room temperature. They used an ellipsometer to study the index of refraction and thickness of an anodic  $Ta_2O_5$  film on single crystal bulk Ta with a sulfuric acid counterelectrode. They found that under an applied d-c electric field the oxide becomes uniaxially anisotropic, that both indices of refraction decrease, and that the oxide thickness increases. (The latter is in addition to any growth due to further anodization.) Both of these changes are proportional to the square of the electric field. The index of refraction is, of course, just the square root of the high frequency dielectric constant, so both of these changes with field would result in a high frequency capacitance decreasing as  $E^2$ .

The changes reported by Cornish and Young are in the same direction and of similar magnitude to the negative symmetric term observed in the present work. The form is not quite the same, but Young has indicated (9) that a  $5/2$  dependence might fit the optical data adequately. In similar ellipsometric work with a liquid counterelectrode, discussed further in the next subsection, Wang and Ord (10) have found that the index of refraction and oxide thickness do not vary simply as  $E^2$ . So it is quite possible that the negative symmetric term is the same effect as that which Cornish and Young observed at a frequency  $10^{12}$  times higher. Repeating the ellipsometric measurements at several other temperatures would probably show whether the two effects are the same. If so, the changes in thickness and index of refraction should be independent of temperature.

If the two observations are in fact the same, then clearly the nonlinearity in the dielectric response must be produced by electronic polarizability. Cornish and Young (8) have suggested five general mechanisms which might produce the optical effect. The first two, a direct modification of the electronic polarizability by the d-c field and an indirect modification of it due to small ionic displacements, are consistent with the present experiments. The last three, however, involve redistribution of ions or electrons or creation of defects, all of which would be very much slower at 77°K than at room temperature. Thus, while these mechanisms may explain the slow part of the ellipsometric results, they cannot explain the present results.

*Antisymmetric term.*—The third term in Eq. [1],  $-DE$ , expresses the asymmetry of  $C(E)$ . The fact that it is linear means that  $\Delta C(E)$  approaches zero at  $E = 0$  with a finite slope. Thus the physical mechanism responsible for the asymmetry is active even at low fields. This rules out any mechanism involving emission of carriers either from the electrodes or from bulk traps, since such processes involve an exponential field dependence and are negligible at low field. The linear dependence also indicates that the asymmetry does not result from anisotropy induced by the field, such as the uniaxial anisotropy reported by Cornish and Young (8). Rather, the anisotropy is already present, frozen into the oxide.

The antisymmetric term varies with frequency and temperature in the same direction as the first term of Eq. [1], but more slowly. Unlike the first term, it does not become small as the temperature approaches zero. Its magnitude is reduced by heat-treatment, but increased by increasing anodization soak time.

Cornish and Young (8), as discussed above, found that the oxide thickness and index of refraction vary as  $E^2$  for positive fields, a form which is not likely to be asymmetric. Wang and Ord (10), however, found that a linear term had to be added in order to fit their data. The thickness increase and index decrease could be fit equally well by  $AE + BE^2$  or  $A'E + B'E^2$ . Obviously, one would expect  $A''E + B''E^{5/2}$ , which matches the second and third terms of Eq. [1], to fit just as well. A crude comparison with some of Wang's data indicates that both terms are of the same order of magnitude in the two experiments. So there is a strong possibility that Wang and Ord are seeing with visible light the effects which produce both the negative symmetric and antisymmetric terms at audio frequencies. There is still, however, considerable doubt that the two observations are the same due to the apparent conflict between the two ellipsometric experiments (8, 10). The question of whether there is asymmetry in those measurements needs to be resolved. Ideally one would like to do the ellipsometric experiment using a transparent solid film counterelectrode so that reverse fields could be applied. In such an experiment any asymmetry would be immediately apparent, even at low fields.

If the thickness does in fact change linearly with field, it means that the amorphous oxide is piezoelectric, a remarkable result. If, in contrast, further ellipsometric work shows that there is no such dependence, then the asymmetry in  $C(E)$  at audio frequencies indicates an asymmetric polarizability, a result which is also rather surprising. A simple physical model for such a polarizability is discussed in the remainder of this section.

Anodic  $Ta_2O_5$  grows by transit of Ta and O ions through the existing oxide. From the point of view of an individual ion the amorphous oxide appears as an irregular set of possible occupation sites separated by potential barriers. These sites and barriers are formed by other ions, which are themselves capable of moving, so one must think of this as an instantaneous picture of a dynamic situation.

Because the oxide is amorphous, the barriers and occupation sites are not all the same. Some will have a much higher potential barrier on one side than on the opposite side. An ion which lands in such a site will tend to remain there much longer if the higher barrier is on the downfield side, i.e., in the direction of current flow for the ion in question, than if the lower barrier is on the downfield side. Pringle (11) has suggested as a result of work with radioactive tracers that the charge transfer event does not consist simply of one ion jumping between adjacent sites, but rather involves simultaneous motion of a group of both Ta and O ions. If this picture is correct, then when an ion leaves its site the surrounding ions are rearranged and the symmetry of the site is likely to be changed. A site with a low barrier downfield is more likely to lose its occupying ion than other sites, and therefore is more likely to be rearranged. Thus its lifetime is shorter, and in equilibrium the density of such sites is expected to be less than that of sites with a high barrier downfield. In this way a preferred orientation of asymmetric sites might be formed.

This picture can be made more explicit for a highly simplified case. We consider asymmetric sites only, and assume that there are only two types, those with the high barrier downfield (h) and those with the low barrier downfield (l). We further assume that when an ion leaves its site the disturbance is sufficient to completely rearrange the site so that the two orientations are equally likely.

In equilibrium, at a fixed ionic current density, the number of sites of each orientation being created must equal the number being destroyed. We have

assumed above that the two types of sites are created at the same rate, so in equilibrium they must be destroyed at the same rate. The rate of destruction of each type,  $R$ , is equal to the emission probability for that type,  $P_h$  or  $P_l$ , times the density,  $N_h$  or  $N_l$

$$R = P_h \times N_h = P_l \times N_l \quad [3]$$

The density of each type of site must adjust itself in consideration of the difference in emission probabilities to produce this equality.

The emission probabilities, according to the usual simple model of hopping from site to adjacent site, are

$$P_{h(l)} = P_0 \exp - (aW_{h(l)} - bE)$$

where  $W_{h(l)}$  is the height of the high (low) barrier and  $P_0$ ,  $a$ , and  $b$  are constants. Combining these equations shows that in equilibrium the difference in density of high and low sites is

$$\Delta N = N_h - N_l = \frac{R}{P_0} (e^{aW_h} - e^{aW_l}) e^{-bE} \quad [4]$$

So, indeed, a preferred orientation of asymmetric sites is formed, with the degree of orientation dependent on the degree of asymmetry. In the real oxide, of course, sites will have some distribution of degrees of asymmetry.

The response to an electric field of an ion in an asymmetric site is asymmetric. As a simple, one dimensional, classical example, consider a potential of the form  $V = ax^2 + bx^3$ , where  $a$  and  $b$  are both positive and we are interested only in small displacements. This potential has a minimum at  $x = 0$ , rises rapidly for  $x > 0$ , and rises more slowly for  $x < 0$ . Thus the preferred orientation of the preceding discussion is with  $+x$  in the downfield direction.

Applying a d-c electric field,  $E$ , adds a term  $-Ex$  to the potential, where  $E > 0$  is parallel to the anodization field and  $E < 0$  is antiparallel to it. The ion occupying this potential well is centered at the potential minimum, which is

$$x_0 = [-2a + (4a^2 + 12bE)^{1/2}]/6b$$

The small signal polarizability, which is essentially what is measured in these experiments, is proportional to the rate of change of  $x_0$  with respect to  $E$ . That is

$$\text{polarizability} \propto dx_0/dE = (4a^2 + 12bE)^{-1/2}$$

For small displacements all but the first order term can be neglected, and we have

$$\text{polarizability} \propto (1 - 3bE/2a^2)/2a$$

This polarizability is obviously asymmetric, and for a potential with the preferred orientation it is smaller for positive field than for negative. One expects to find in the amorphous oxide a wide range of degrees of asymmetry and sites with all orientations. But if there is a preference for one orientation due to the mechanism described above, then polarization of these sites will produce a  $C(E)$  curve with the observed asymmetry.

Now let us compare this model with the experimental results. The proposed polarization involves ionic motion so its speed is limited to about phonon frequencies, which are slower than visible light frequency. Therefore its absence in the Cornish and Young (8) experiment is expected. (Of course this conflicts with the Wang and Ord (10) result.) It is not temperature activated, so it should remain observable at very low temperature, in agreement with experiment. The polarization discussed above, however, would be independent of temperature and frequency, which does not agree with experiment, since the antisymmetric term does have a small dependence on those parameters. It is possible that quantum

effects could provide the required dependence, since an ion in a fixed potential well does not simply sit at the point of minimum potential. It is distributed over a small volume, and its average position in an asymmetric potential depends on its energy level which in turn depends on the temperature. Alternatively there could be more complex occupation sites, involving multiple minima separated by very low barriers, as discussed by Argall and Jonscher (12) for silicon oxide. So while the temperature and frequency dependence do not agree with this model in its simplest form, that does not necessarily invalidate the idea.

One would expect that exposure to a high temperature would, through diffusion, reduce the degree of preferred orientation of asymmetric sites and the asymmetry of the sites themselves. Thus heat-treatment should reduce the asymmetry of  $C(E)$ , in agreement with experiment.

The effect of anodization soak time is not so obvious. During the soak period the oxide continues to grow, so the electric field and hence the ionic currents decrease. One might expect the density of asymmetric sites to change due to that decrease. Unfortunately one cannot predict with any certainty the form or even the direction of such a change. This prediction would be a key test of the physical ideas of this model, but it would require a much more sophisticated treatment of the anodization process.

To summarize, a highly simplified, qualitative model for the asymmetry of  $C(E)$  has been discussed, based on the dynamics of the anodization process. It assumes that the asymmetry is not present at optical frequency, which agrees with the work of Cornish and Young (8) but conflicts with that of Wang and Ord (10). The model is not sufficiently detailed to allow precise derivation of the dependence on various experimental parameters. It agrees with the presence of asymmetry in  $C(E)$  at very low temperature and with the reduction in asymmetry due to heat-treatment. It does not explain in its simplest form the small frequency and temperature dependence of the asymmetry, but it is quite possible that this disagreement is due to oversimplification in the model, so it does not indicate that the physical idea is wrong. The model is not sufficiently sophisticated to predict a soak time dependence.

### Summary

The dependence of small-signal capacitance on d-c electric field at low temperature has been shown to be produced by at least three separate physical processes, all of which are bulk oxide effects (2). The first one causes the capacitance to increase as  $|E|^{3/2}$  when a field is applied. The data are consistent with a set of polarizations which require thermal activation and which have relaxation times corresponding to frequencies broadly distributed throughout and beyond the range 100 Hz to 100 kHz. It is likely that these polarizations are associated with defects in the oxide.

The second process causes the capacitance to decrease approximately as  $|E|^{5/2}$ . This process appears to be an inherent property of anodic  $Ta_2O_5$ , since its magnitude is not affected by any of the varied parameters. It is likely, though not certain, that this is the

same effect observed in ellipsometric measurements (8-10). If it is the same, then it is produced by an increase in oxide thickness with increasing field and an associated decrease in dielectric constant.

The third process produces the asymmetry in  $C(E)$  and is approximately linear in the field. It indicates that the amorphous oxide has a built-in anisotropy. It may be the same effect observed in one ellipsometric experiment (10), in which case the oxide is apparently piezoelectric. But if another ellipsometric experiment (8) is correct, then the asymmetry must be a measure of a nonlinear polarizability produced by ionic motion. Such a polarizability would result if ions are located in asymmetric sites which are preferentially oriented. A crude model was introduced to show how the dynamics of anodization might produce such a preferred orientation. This model agrees qualitatively with some of the experimental results, but a much more sophisticated version of it would be required to show whether the physical picture involved is consistent with other results.

### Acknowledgments

Thanks are due to W. P. Wang for providing some of his ellipsometric data and to L. Young for useful discussions.

Manuscript submitted Nov. 25, 1975; revised manuscript received Jan. 16, 1976. This was Paper 77 presented at the Toronto, Canada, Meeting of the Society, May 11-16, 1975.

Any discussion of this paper will appear in a Discussion Section to be published in the December 1976 JOURNAL. All discussions for the December 1976 Discussion Section should be submitted by Aug. 1, 1976.

*Publication costs of this article were partially assisted by Bell Laboratories.*

### REFERENCES

1. M. Nakamura, J. Yamazaki, W. Endou, and Y. Nishimura, *Electronics and Communications in Japan*, **55C**, 107 (1972).
2. P. W. Wyatt, *This Journal*, **122**, 1660 (1975).
3. M. H. Read and C. Altman, *Appl. Phys. Letters*, **7**, 51 (1965).
4. Robert D. Huttemann, J. M. Morabito, and D. Gerstenberg, *IEEE Trans., PHP*, **11**, 67 (1975).
5. The N concentration required to produce bcc Ta depends on the sputtering machine. For the machine used here, Huttemann *et al.* in Ref. (4) showed that about 6 a/o N produces bcc structure with no detectable intermixed  $\beta$ -phase.
6. R. T. Simmons, P. T. Morzenti, D. M. Smyth, and D. Gerstenberg, *Thin Solid Films*, **23**, 75 (1974). This paper discusses heavily N-doped Ta, but J. M. Morabito has found a similar distribution in some lightly N-doped Ta used for the present experiments.
7. Determined by J. M. Morabito using Auger electron spectroscopy combined with sputtering.
8. W. D. Cornish and L. Young, *Proc. Roy. Soc. London*, **A335**, 39 (1973).
9. W. D. Cornish, K. K. Yee, and L. Young, Paper 90 presented at The Electrochemical Society Meeting, Toronto, Canada, May 11-16, 1975.
10. W. P. Wang and J. L. Ord, Paper 89 presented at The Electrochemical Society Meeting, Toronto, Canada, May 11-16, 1975.
11. J. P. S. Pringle, *This Journal*, **120**, 398 (1973).
12. F. Argall and A. K. Jonscher, *Thin Solid Films*, **2**, 185 (1968).

# Preferential Etching of GaAs Through Photoresist Masks

Mutsuyuki Otsubo, Takao Oda, Hisao Kumabe, and Hidejiro Miki

Mitsubishi Electric Corporation, Central Research Laboratory, Itami, Hyogo, Japan

## ABSTRACT

The citric acid-hydrogen peroxide-water system has been developed for preferential etching of GaAs through photoresist masks. Etching rates depend strongly on the composition of the solution and on the crystal orientation of GaAs, with the rates in the order (111)B > (100) > (111)A. Flat-bottomed holes were obtained for all compositions of the solutions. The solution does not erode photoresist masks, thereby providing preferential etching of GaAs through such masks.

Significant progress in GaAs materials and device technology has been made such that it is now possible to produce reliable n-type GaAs Schottky-barrier field-effect transistors (MESFET's) with gate length of 1  $\mu\text{m}$  (1-3).

The active layer thickness of n-type GaAs MESFET's should be controlled with an accuracy of several hundred angstroms in order to adjust the pinch-off voltage. GaAs MESFET's are usually fabricated by a lift-off technique (4) in which the GaAs surfaces are chemically etched slightly through photoresist masks in order to clean the surfaces before evaporation of the metals. For this purpose, the etching solution should satisfy the following conditions: (i) It should have a slow etching rate; (ii) it should not erode the photoresist masks; and (iii) it should provide flat etching profiles when the crystals are etched through windows in photoresist masks.

Many etching solutions have been developed during the years. Most commonly used of these are the  $\text{H}_2\text{SO}_4\text{-H}_2\text{O}_2\text{-H}_2\text{O}$  solution (5-6), the  $\text{Br}_2\text{-CH}_3\text{OH}$  solution (7-8), the  $\text{NaOH-H}_2\text{O}_2\text{-H}_2\text{O}$  solution (9), and the  $\text{NH}_4\text{OH-H}_2\text{O}_2\text{-H}_2\text{O}$  solution (10-11). Since these all tend to erode photoresist masks, however, they cannot be used for preferential etching of GaAs crystals through photoresist masks.

In the present experiments, a new etching solution composed of citric acid [ $\text{C}_3\text{H}_4(\text{OH})(\text{COOH})_3\cdot\text{H}_2\text{O}$ ], hydrogen peroxide ( $\text{H}_2\text{O}_2$ ), and water has been developed for preferential etching of GaAs crystals through windows in photoresist masks. In this paper, the etching characteristics of GaAs crystals in this newly developed solution are described.

## Experimental

**Etching solution.**—The  $\text{C}_3\text{H}_4(\text{OH})(\text{COOH})_3\cdot\text{H}_2\text{O-H}_2\text{O}_2\text{-H}_2\text{O}$  solutions were prepared by mixing 50 weight per cent (w/o)  $\text{C}_3\text{H}_4(\text{OH})(\text{COOH})_3\cdot\text{H}_2\text{O}$  aqueous solution and 30 w/o  $\text{H}_2\text{O}_2$  prior to each etching experiment. The composition of the etching solution was varied by changing the proportions of 30 w/o  $\text{H}_2\text{O}_2$  and 50 w/o citric acid; the ratio (by volume measure) of citric acid to  $\text{H}_2\text{O}_2$  is defined by the parameter  $k$ , which was varied between 0.1 and 100 over the course of our experiments. The chemicals used were all of reagent grade. The temperature of the solution was varied between  $5^\circ$  and  $55^\circ \pm 0.5^\circ\text{C}$ .

**Sample.**—The physical and electrical properties of GaAs crystals used in the etching experiments are summarized in Table I. These wafers were sliced within  $1^\circ$  of the low-index planes and then lapped with 4000 mesh alumina abrasive. After being degreased and rinsed they were chemically etched in a

Key words: field effect transistors, compound semiconductors, citric acid, etching rate.

Table I. Physical and electrical properties of the samples used in these experiments

Sample	Crystal	Growth method	Dopant and type	Orientation	Carrier concentration ( $\text{cm}^{-3}$ )
A	GaAs	LEC	Sn n	100	$1.0 \times 10^{18}$
B	GaAs	H.B	Si n	100	$7.0 \times 10^{17}$
C	GaAs	H.B	None n	100	$2.0 \times 10^{18}$
D	GaAs	H.B	None n	111 A	$2.0 \times 10^{18}$
E	GaAs	H.B	None n	111 B	$2.0 \times 10^{18}$
F	GaAs	H.B	Cr S.I	100	$\rho > 10^6$ ohm·cm
G	GaAs	H.B	Cd p	100	$2.0 \times 10^{18}$
H	GaAs	H.B	Zn p	100	$2.0 \times 10^{17}$
I	InSb	H.B	Te n	100	$2.0 \times 10^{17}$
J	GaSb	H.B	None p	100	$2.0 \times 10^{18}$

10%  $\text{Br}_2\text{-CH}_3\text{OH}$  solution for 30 sec at room temperature and finally etched in a  $3\text{H}_2\text{SO}_4\text{-1H}_2\text{O}_2\text{-1H}_2\text{O}$  solution for 60 sec at  $60^\circ\text{C}$  prior to the etching experiments.

**Photoresist masks.**—A photoresist (AZ-1350 and/or OMR) was coated on the crystal surface, and rectangular windows, set parallel to the [110] directions, were cut into the masks by using standard photoresist techniques. The [011] and [0 $\bar{1}$ 1] directions in the (100) plane were distinguished with aid of Sirtl's etch figures as demonstrated in GaAs crystals (8, 12).

**Etching rate.**—Etched depth was measured from a step height between an etched and unetched surface by using Dektak (manufactured by Sloan Corporation). Average etching rate was calculated by dividing the measured depth by the elapsed etching time. The accuracy of the measurement was about 100Å.

## Results and Discussion

**Composition dependence of the etching rate.**—Figure 1 shows the dependence of the average etching rate on solution composition,  $k$ , for (100) planes of GaAs (sample A) etched for 10 min. The solution was kept at  $24^\circ\text{C}$  during etching experiments. In Fig. 1, the volume ratio of 50 w/o  $\text{C}_3\text{H}_4(\text{OH})(\text{COOH})_3\cdot\text{H}_2\text{O}$  aqueous solution to 30 w/o  $\text{H}_2\text{O}_2$ ,  $k$ , was chosen as a variable. Open and closed circles denote the etching rates as the etching was carried out with and without stirring, respectively. For low values of  $k$ , the etching rates increased with increasing  $k$  in both cases and reached a maximum value of 100 Å/sec at  $k = 2$ . The average etching rate then decreased with  $k$  increasing still further. No stirring effects were observed for solutions with  $k > 2$ . On the other hand, the etching rates considerably increased by stirring the solutions with composition  $k < 2$ . These curves show that the factors controlling the etching are different in the two compositional regions. It is desirable to use the solutions with composition  $k > 2$  in order to control the etched depth precisely and to eliminate stirring as a vari-

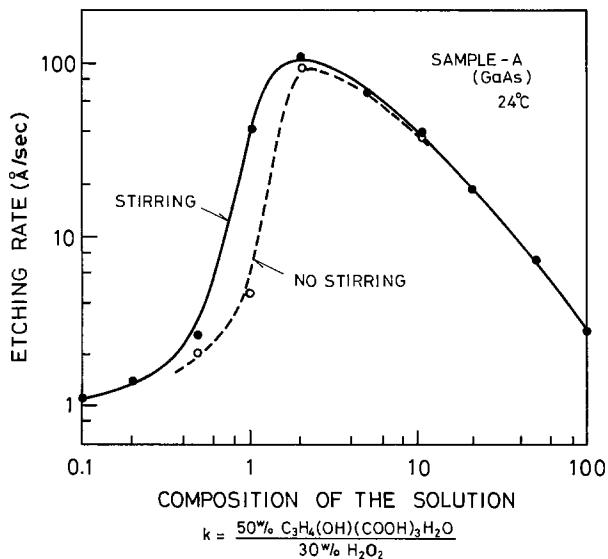


Fig. 1. Composition dependence of the etching rates for a sample A. ●, Stirring; ○, no stirring.

able in the etching process. For the fabrication of GaAs MESFET's, the slow etching rates demonstrated in Fig. 1 are highly desirable.

Etching rates of 1 ~ 4 Å/sec were obtained in the solution with  $k < 1$  and  $k > 30$ , such slow rates are also desirable for profiling the characteristics of thin films such as epitaxial layers for GaAs MESFET's, ion-implanted layers, and diffused layers. To date, anodic oxidation techniques have often been used for such evaluation (13-14).

*Temperature dependence of the etching rate.*—Figure 2 shows the temperature dependence of the etching rates in the solution with  $k = 10$  on three kinds of III-V compound semiconductors. In this experiment, InSb and GaSb were also etched in order to decide whether the etching process is reaction limited or diffusion limited. The etching rates increased exponentially with increasing etching temperature in all cases. The activation energies were obtained to be 11.2 kcal/mole for GaAs (sample A), 11.1 kcal/mole for InSb (sample I), and 12.7 kcal/mole for GaSb (sample J). The etching shows markedly different etching rates on these crystals. No stirring effects were observed on the GaAs crystals (sample A) in the solution, and the

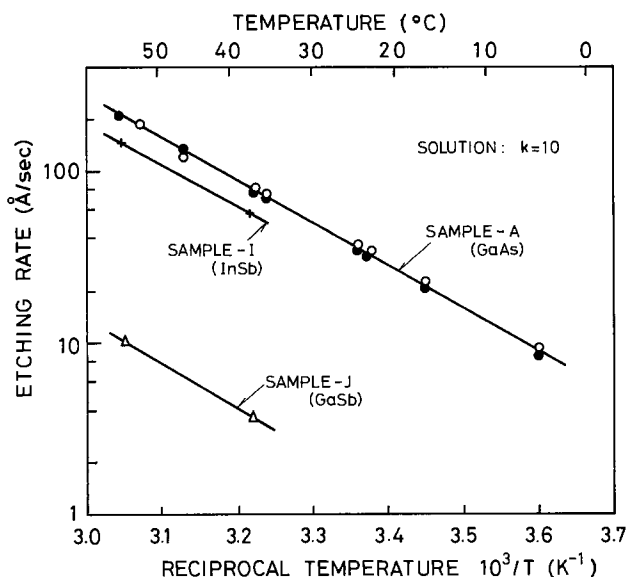


Fig. 2. Temperature dependence of the etching rates for GaAs (sample A), InSb (sample I), and a GaSb (sample J) in the solution with  $k = 10$ .

etched depth increased linearly with etching time as shown in Fig. 3. From the different etching rates, we conclude that the etching process in the solution with  $k > 2$  is chemical reaction rate limited.

Figure 4 shows the temperature dependence of the etching rates for the GaAs sample A in the solution with  $k = 1$ . Considerable stirring effects were observed. That is to say, the etching rates and the activation energy were increased when the solution was violently stirred. The activation energies obtained were 15.3 kcal/mole in the stirred solution and 8.4 kcal/mole in the unstirred solution. This suggests that a diffusion-controlled rate-limited process participates in the etching process for the solution with  $k = 1$ . Relation between etched depth and etching time in the solution with  $k = 1$  for sample A is shown in Fig. 5. The etched depth did not increase linearly with etching time, in contrast to that for the solution with  $k = 10$ . If the etching process in the solution with  $k = 1$  is controlled by a diffusion rate-limited process, the etched depth should increase in proportion to the square root of the etching time. Since this was not observed (as shown in Fig. 5), the etching process in the solution with  $k = 1$  is probably controlled by both a reaction rate-limited process and a diffusion rate-limited process.

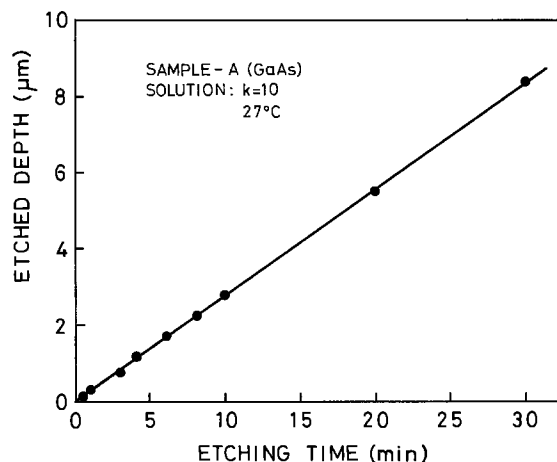


Fig. 3. Relation between etched depth and etching time in the solution with  $k = 10$  for sample A.

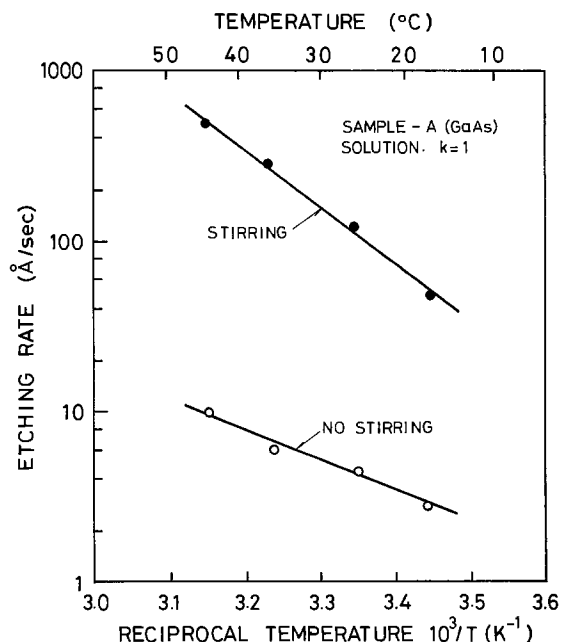


Fig. 4. Temperature dependence of the etching rates in the solution with  $k = 1$  for sample A.

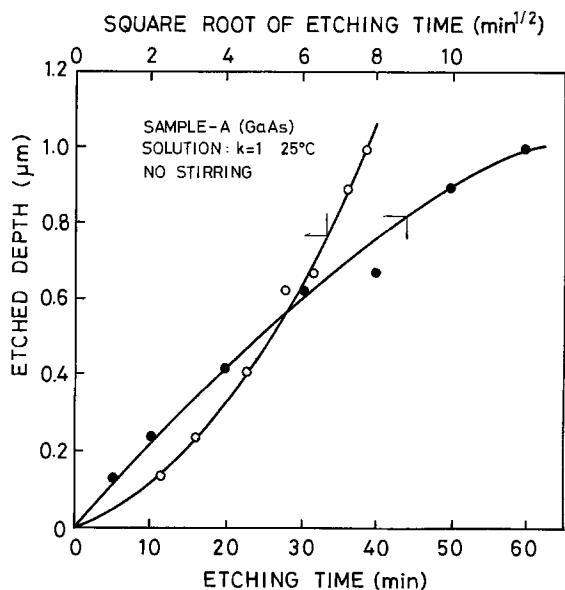


Fig. 5. Relation between etched depth and etching time in the solution with  $k = 1$  for sample A.

**Orientation dependence of the etching rate.**—Figure 6 shows the temperature dependence of the etching rates for the solution with  $k = 10$  for three different GaAs crystallographic planes. The order of magnitude of the etching rates was  $(111)B > (100) > (111)A$ . The etching rates on the  $(111)A$  surface were about 60% of that on the  $(100)$  surface and were the smallest of all surfaces investigated. The activation energies obtained for each of these planes were about the same (11.2 kcal/mole). This also indicates that the solution with  $k = 10$  is controlled by a reaction rate-limited process.

GaAs crystals with different doping concentration and with different dopants (as shown in Table I) were etched in the solution with  $k = 10$  at 29°C for 10 min. No doping concentration dependence was observed within our experimental conditions.

**Etching profile.**—The exposed GaAs surfaces defined by a photoresist mask (AZ-1350), whose geometry was shown in Fig. 7(a), were etched in the solution with  $k = 10$  at room temperature. The etching profiles were examined by cleaving the wafer along  $[011]$  and  $[0\bar{1}1]$  directions. The etching profiles are demonstrated in Fig. 7(b)–(d). Figure 7(b), (c), and (d) show the cross section cleaved along  $[011]$  and  $[0\bar{1}1]$  directions,

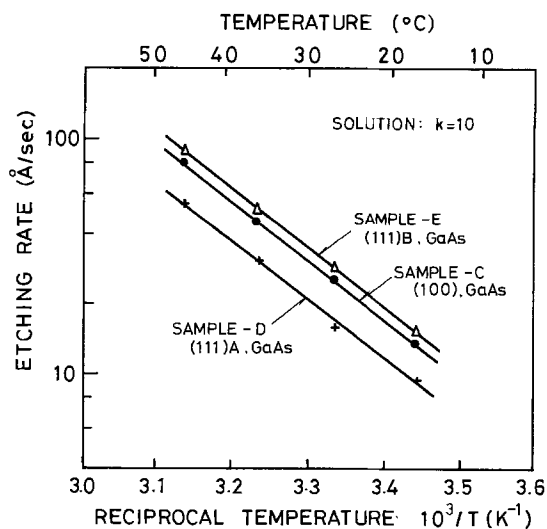


Fig. 6. Orientation dependence of the etching rates in the solution with  $k = 10$ .

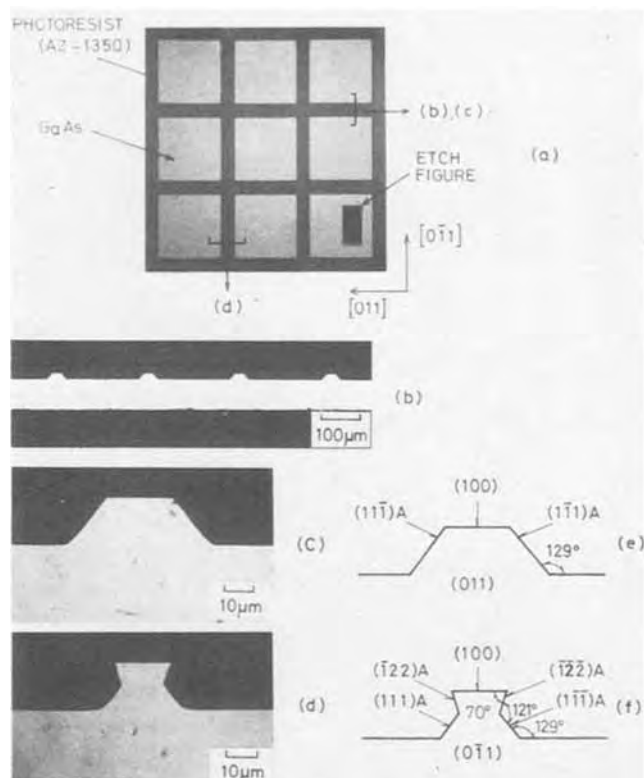


Fig. 7. Typical etching profiles on the cross section cleaved along  $[011]$  and  $[0\bar{1}1]$  directions for sample A (GaAs). The sample surfaces defined by a photoresist mask (AZ-1350) were etched in the solution with  $k = 10$ .

respectively. Flat-bottomed holes were obtained for all compositions of the solutions, as shown in Fig. 7(b).

A trapezoidal structure was formed on the cross section cleaved along  $[011]$  direction. These etching profiles were thought to occur due to the difference in the etching rates between  $(111)A$  planes and the other planes, as demonstrated in GaAs crystals etched with  $Br_2-CH_3OH$  solution (8),  $H_2SO_4-H_2O_2-H_2O$  solution (6), and  $NH_4OH-H_2O_2$  solution (11).

On the other hand, the etching profiles for the cross section cleaved along the  $[0\bar{1}1]$  direction were a hand-drum shaped structure, resembling a Japanese "tsuzumi," which was asymmetrical to that for cross sections cleaved along the  $[011]$  direction. The etching profiles also were different from that obtained by etching the  $(100)$  GaAs crystals in  $Br_2-CH_3OH$  (8),  $H_2SO_4-H_2O_2-H_2O$  (6), and  $NH_4OH-H_2O_2$  solutions (11), where reverse mesa-shaped structures were obtained. The observed angles and the most probable planes deduced from these angles are shown in Fig. 7(e) and (f). These planes are  $(111)A$  and  $(111)A$  on  $[011]$  cross section and  $(111)A$ ,  $(\bar{1}22)A$ ,  $(111)A$ , and  $(\bar{1}22)A$  on  $[0\bar{1}1]$  cross section.

Although the differences in our etching profiles and those observed for a  $Br_2-CH_3OH$  solution (5) are not clear, it is possible that these differences are due to the differences in the planes and the etching ratio  $(100)/(111)A$  for both solutions.

**Erosion of photoresist.**—The erosion of the photoresist used as a mask in the preferential etching of GaAs crystals with the  $C_3H_4(OH)(COOH)_3 \cdot H_2O-H_2O_2-H_2O$  solution was investigated to compare it with that used for etching with the  $H_2SO_4-H_2O_2-H_2O$  system. GaAs MESFET patterns were defined by a standard photoresist technique with AZ-1350, which is a positive-type photoresist, and with OMR, which is a negative one. The exposed GaAs surfaces were etched 5000Å. The times to etch 5000Å are 2.5 min for the

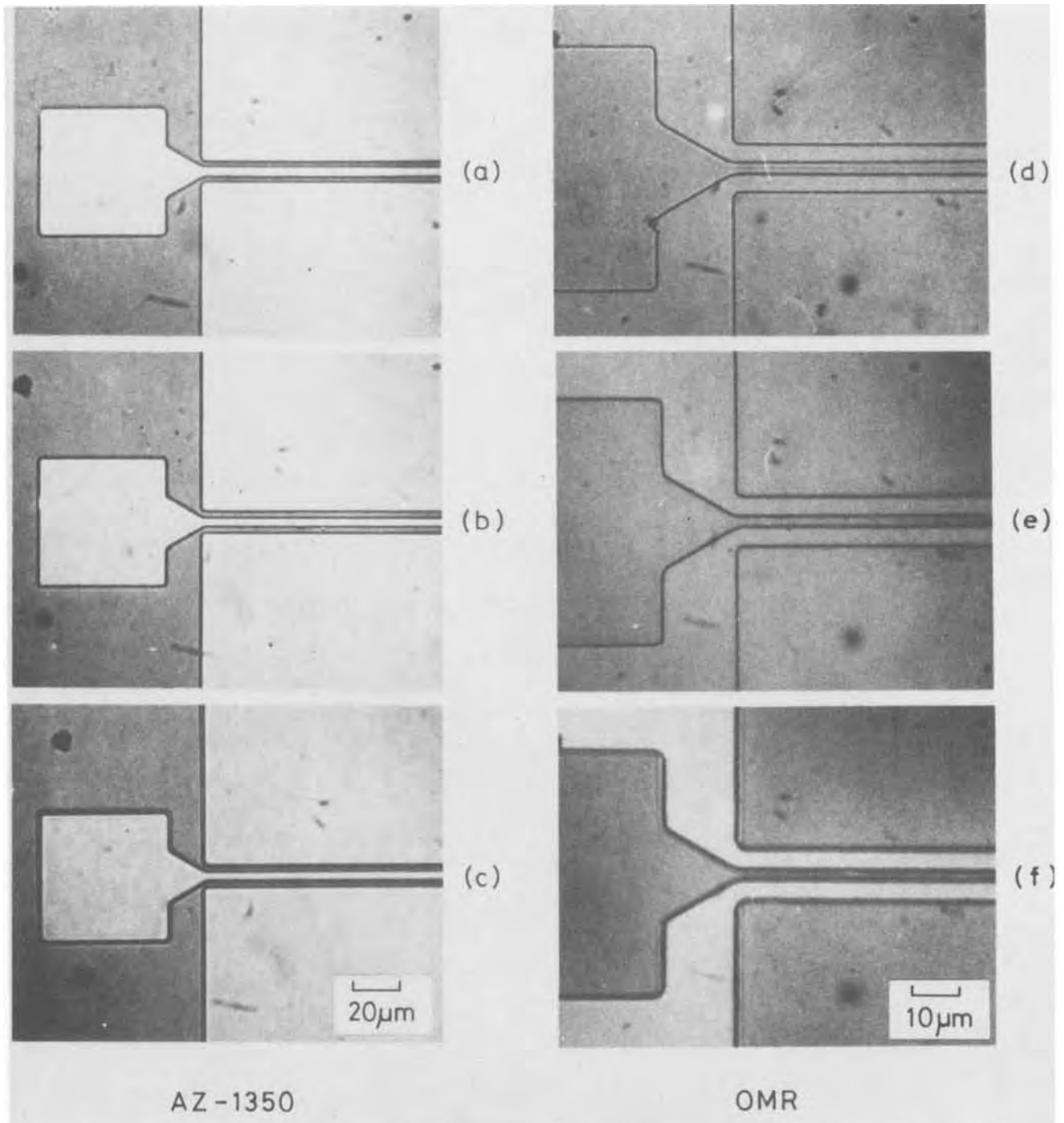


Fig. 8. Comparison of erosion of photoresist masks [(a)-(c) for AZ-1350, (d)-(f) for OMR] due to etching with the  $C_3H_4(OH)(COOH)_3 \cdot H_2O-H_2O_2-H_2O$  system and the  $3H_2SO_4-1H_2O_2-1H_2O$ . (a), (d) patterns before etching; (b), (e) etched in the solution with  $k = 10$  for 2.5 min ( $0.5 \mu m$ ); (c), (f) etched with  $3H_2SO_4-1H_2O_2-1H_2O$  at  $60^\circ C$  for 3 sec ( $0.5 \mu m$ ).

hydrogen peroxide-citric acid solution with  $k = 10$  at  $23^\circ C$ , and 3 sec for a  $3H_2SO_4-1H_2O_2-1H_2O$  solution at  $60^\circ C$ . The results are shown in Fig. 8. Figure 8(a) and (d) are the original patterns used in the experiment. The erosion of the photoresist masks by  $3H_2SO_4-1H_2O_2-1H_2O$  is apparently seen in Fig. 8(c) and (f). In this case, part of the photoresist masks have been dissolved into solution and the pattern size has changed. The  $Br_2-CH_3OH$ ,  $NaOH-H_2O_2$ , and  $NH_4OH-H_2O_2$  solutions also erode the photoresist masks as in the case of the  $H_2SO_4-H_2O_2-H_2O$  system.

On the other hand, no erosion of the photoresist masks by the solution with  $k = 10$  is observed, as shown in Fig. 8(b) and (e), and pattern size is the same as those in the original one. No erosion was observed for all compositions of the solution examined in

these experiments. The photoresists used in this experiment did not dissolve perceptibly in solution even when the etching was carried out for 60 min at room temperature.

From the above-described results, it is believed that the solution developed here should be of general use to GaAs device technology.

#### Summary

An etching solution for the preferential etching of GaAs through photoresist masks has been developed. The solution consists of citric acid, hydrogen peroxide, and water. Etching rates vary from 1 to 100  $\text{\AA}/\text{sec}$ , depending on the composition of the solution. The etching process for solutions containing a higher composition of citric acid ( $k > 2$ ) is chemical reaction



rate limited, for solutions containing a lower concentration of citric acid ( $k < 2$ ), it is chemical reaction rate limited and diffusion rate limited. The etching rates depend on crystal orientation, with the rates for the solution with  $k = 10$  decreasing in the order (111)B > (100) > (111)A.

Flat-bottomed holes are obtained for all compositions of the solution. However, the hole structures in preferential etching on the crystals display asymmetrical patterns.

This etching solution does not erode the photoresist masks, thereby providing improved resolutions and definition for fine photoresist patterns such as n-type GaAs MESFET's.

#### Acknowledgments

The authors wish to thank Drs. K. Shirahata and T. Hata for encouragement throughout this work.

Manuscript submitted Sept. 19, 1975; revised manuscript received Dec. 19, 1975.

Any discussion of this paper will appear in a Discussion Section to be published in the December 1976 JOURNAL. All discussions for the December 1976 Discussion Section should be submitted by Aug. 1, 1976.

Publication costs of this article were partially assisted by Mitsubishi Electric Corporation.

#### REFERENCES

1. K. E. Drangeid, R. Sommerhalder, and W. Walter, *Electron. Letters*, **6**, 228 (1970).
2. W. Baechtold, *IEEE J. Solid-State Circuit*, **SC-8**, 54 (1973).
3. C. A. Liechti and R. L. Tillman, *IEEE Trans. Microwave Theory Techniques*, **MTT-22**, 510 (1974).
4. R. M. Waner, Editor "Integrated Circuit," p. 323, McGraw Hill Book Co, New York (1965).
5. M. V. Sullivan and L. A. Pompliano, *This Journal*, **108**, 60C (1961).
6. S. Iida and K. Ito, *ibid.*, **118**, 768 (1971).
7. C. S. Fuller and H. W. Allison, *ibid.*, **109**, 880 (1962).
8. Y. Tarui, Y. Komiya, and Y. Harada, *ibid.*, **118**, 118 (1971).
9. D. W. Shaw, *ibid.*, **113**, 958 (1966).
10. J. C. Dymment and G. A. Rozgonyi, *ibid.*, **118**, 1346 (1971).
11. J. J. Gannon and C. J. Nuese, *ibid.*, **121**, 1215 (1974).
12. G. H. Olsen, M. S. Abrahams, and T. J. Zamerowski, *ibid.*, **121**, 1650 (1974).
13. D. L. Rode, B. Schwartz, and J. V. DiLorenzo, *Solid-State Electron.*, **17**, 1119 (1974).
14. H. Muller, F. H. Eisen, and J. W. Mayer, *This Journal*, **122**, 651 (1975).

## Ionic Conductivity in Solid Electrolytes Based on Lithium Aluminosilicate Glass and Glass-Ceramic

Ralph T. Johnson, Jr., R. M. Biefeld, M. L. Knotek, and B. Morosin

Sandia Laboratories, Albuquerque, New Mexico 87115

#### ABSTRACT

Ionic conductivity measurements on  $\text{Li}_2\text{O} \cdot \text{Al}_2\text{O}_3 \cdot 2\text{SiO}_2$ , i.e.,  $\text{LiAlSiO}_4$ , glass and glass-ceramic have shown these materials to be good lithium ion conducting solid electrolytes at high temperatures. This composition crystallizes in the  $\beta$ -eucryptite structure which is attractive for solid electrolyte applications because of its low thermal expansion. The glasses were prepared by quenching from the melt and were annealed to remove strain. The glass-ceramic ( $\beta$ -eucryptite) samples were crystallized (aided by  $\text{TiO}_2$  and  $\text{ZrO}_2$  nucleating agents) by using a heat-treatment determined through differential thermal analysis. The conductivity ( $\sigma$ ) was measured (to  $650^\circ\text{C}$ ) with a variety of techniques, including 2-terminal a.c., 3-terminal guarded a.c., 4-terminal a.c., 2-terminal d.c., and a pulsed method. Vapor-deposited Cr contacts were used. Different sample geometries, contact geometries, and measurement circuitries were employed. The results from the various measurements are in excellent agreement. The a-c techniques appear to be the most versatile and accurate of the methods examined. In these materials the conductivity is thermally activated ( $\sigma = \sigma_0 e^{-E/kT}$ ) with typical values of  $\sigma_0 = 1.9 \times 10^2$  ( $\text{ohm-cm}^{-1}$ ) and  $E \approx 0.68$  eV for the glasses, and  $\sigma_0 = 2.1 \times 10^4$  ( $\text{ohm-cm}^{-1}$ ) and  $E \approx 1.05$  eV for the glass-ceramics. The  $\text{TiO}_2$  and  $\text{ZrO}_2$  nucleating agents [concentrations up to 2.8 mole per cent (m/o)] did not appear to influence the ionic conductivity. Data were also taken on a ( $\beta$ -eucryptite) glass-ceramic with a composition near the  $\beta$ -eucryptite/ $\beta$ -spodumene phase boundary. The ionic conductivity of this material is lower than that of the  $\text{LiAlSiO}_4$  materials. Data are also provided on  $\beta$ -spodumene material.

This paper reports on the ionic conductivity in lithium aluminosilicate glasses and glass-ceramics. The materials examined have compositions near that of stoichiometric  $\text{Li}_2\text{O} \cdot \text{Al}_2\text{O}_3 \cdot 2\text{SiO}_2$ , i.e.,  $\text{LiAlSiO}_4$ . Materials of this stoichiometry form the basis of the class of materials which, when in crystalline form, exhibit the  $\beta$ -eucryptite structure (1-11). These materials are of interest for high temperature solid electrolyte applications (12), e.g., thermal batteries (13), because of the combined characteristics of low thermal expansion

(6-11) and high lithium ionic conductivity at elevated temperatures (14). In these studies, ionic conductivity measurements were made over the temperature range from room temperature to  $\sim 650^\circ\text{C}$  with a 3-terminal guarded a-c technique and a 4-terminal a-c technique. These experimental techniques are shown to give accurate values and are in excellent agreement with other experimental techniques examined. The data obtained on the stoichiometric  $\text{LiAlSiO}_4$  materials are compared with similar data taken on a glass-ceramic obtained from Corning Glass Works which also exhibits the  $\beta$ -eucryptite structure, but which has a composition near the  $\beta$ -eucryptite/

Key words: solid electrolytes, lithium ion conductors, ionic conductivity, lithium aluminosilicate glass and glass-ceramic,  $\beta$ -eucryptite structure.



$\beta$ -spodumene phase boundary. Data are also provided on material with the  $\beta$ -spodumene phase (4-8, 15-17).

The lithium aluminosilicate materials examined in this study are of the general class  $\text{Li}_2\text{O} \cdot \text{Al}_2\text{O}_3 \cdot n\text{SiO}_2$ . Compositions with  $n \approx 2$  crystallize in the  $\beta$ -eucryptite structure whereas for  $n \approx 4-11$  the  $\beta$ -spodumene phase is formed (4-8, 16, 17). These materials have low thermal expansion characteristics which are composition dependent (6-8, 17-19) and structure dependent (7, 20). A variety of commercial applications have utilized the low thermal expansion characteristics (18, 19, 21), but have not utilized the  $\text{Li}^+$  ionic conduction characteristics. The more notable applications to date include cookware, cooking surfaces, and heat exchangers which are based on  $\beta$ -spodumene materials (18, 19, 21). These materials have a lower Li content than the  $\beta$ -eucryptite materials. The commercial developments to date appear to have been directed toward reducing the  $\text{Li}_2\text{O}$  content in order to lower the conductivity of the material to avoid electrical shorting at high temperatures (19). However, for solid electrolyte applications it is obviously important to enhance the ionic conductivity, and for this reason we have examined the  $\beta$ -eucryptite materials.

Some information on ionic conductivity is available on lithium aluminosilicates in the  $\beta$ -spodumene phase (19, 22-24); however, there is very little information published on the  $\beta$ -eucryptite materials (24), and none on the glass or glass-ceramic. Recent nuclear magnetic resonance (NMR) experiments (25) in conjunction with Raman scattering experiments (26) have shown that  $\text{Li}^+$  motion does occur in  $\text{LiAlSiO}_4$  glass and glass-ceramic ( $\beta$ -eucryptite) materials. The results reported here on our ionic conductivity measurements on  $\text{LiAlSiO}_4$  show that at high temperatures ( $\approx 600^\circ\text{C}$ ) the  $\text{Li}^+$  ionic conductivity of these materials compares favorably with that of other lithium ion conductors of interest for solid electrolyte applications (22, 27).

In this paper, we first describe the method of preparation of the  $\text{LiAlSiO}_4$  glasses and glass-ceramics and the characteristics of the Corning glass-ceramic. The method of electrically contacting the samples is then discussed. This is followed by a section which outlines the methods used for measuring the ionic conductivity (which include 2-terminal a.c., 3-terminal guarded a.c., 4-terminal a.c., 2 terminal d.c., and a pulsed method). Another section then describes experiments designed to compare the measurement techniques and to establish the reliability of the measurements. The final section gives the results obtained from the ionic conductivity studies on the glass and glass-ceramic materials, and also mentions possible solid electrolyte applications.

### Material Properties

The glass-ceramic obtained from Corning Glass Works (Corning designation code 99QHA) was in the form of large slabs ( $15 \times 12 \times 0.3-0.6$  cm), and was a "good quality" glass-ceramic. This material had uniform compositional, structural, and electrical properties as determined from chemical analyses, x-ray diffraction, and ionic conductivity measurements. The exact composition and method of preparation (e.g., heat-treatment, etc.) are not completely known.

Table I gives the composition of the starting materials used by Corning (information provided by Corn-

ing), and the composition of the starting materials used in our laboratories for the preparation of the  $\text{LiAlSiO}_4$  glass and glass-ceramic materials. From this information, it is seen that the Corning glass-ceramic has a much lower  $\text{Li}_2\text{O}$  content, and that  $\text{TiO}_2$ ,  $\text{ZrO}_2$ , and  $\text{P}_2\text{O}_5$  were used as nucleating agents (28). Results from chemical analysis performed in our laboratories were consistent with the information provided by Corning on the starting materials. This material has a composition near the  $\beta$ -eucryptite/ $\beta$ -spodumene phase boundary and it can be considered as a  $\beta$ -eucryptite/ $\beta$ -quartz solid solution (6, 7).

In preparation of the  $\text{LiAlSiO}_4$  materials in our laboratories, reagent grade chemicals (99% purity or better) were used. The glasses were prepared by mixing about 250g of  $\text{Li}_2\text{CO}_3$  and the required oxides in a twin-cone blender for 1-2 hr and then melting in Pt crucibles at  $1600^\circ\text{C}$ . The melts were stirred with platinum stirrers for 17 hr and allowed to stand for 2 hr after stirring at  $1600^\circ\text{C}$ . The glass was then cast onto a water-chilled copper plate, cooled for 20 sec, and placed into an annealing furnace at  $370^\circ\text{C}$ . The temperature of the annealing furnace was then raised at a rate of  $20^\circ\text{C}/\text{min}$  to  $650^\circ\text{C}$ , held there for 5 min, and then cooled to room temperature at the natural cooling rate of the furnace. X-ray powder diffraction photographs of the glasses revealed no crystalline structure. The heat-treatment schedules used for producing the glass-ceramic materials varied and depended upon the nucleating agents (5, 28). The  $\text{LiAlSiO}_4$ -B material with the  $\text{TiO}_2$  nucleating agent (see Table I) was crystallized by heating the glass to  $925^\circ\text{C}$  at a rate of  $5^\circ\text{C}/\text{min}$ . The glass was held at that temperature for 5 hr and then the temperature was increased to  $960^\circ\text{C}$  and held there for 5 hr. The glass was then cooled to room temperature in 8 hr. The glass-ceramic with the  $\text{TiO}_2$  and  $\text{ZrO}_2$  nucleating agents ( $\text{LiAlSiO}_4$ -C) was produced by heat-treating the glass through a schedule which involved raising the temperature to  $560^\circ\text{C}$  at a rate of  $5^\circ\text{C}/\text{min}$ , holding at that temperature for 4 hr, and then increasing the temperature (over 1.5 hr) to  $930^\circ\text{C}$  and holding at that temperature for 4 hr. The material was then cooled to room temperature in 8 hr.

The above heat-treatments were determined from differential thermal analysis (DTA) performed on rapidly cooled and unannealed glass samples and from x-ray powder diffraction photographs taken of samples heated to different temperatures and then rapidly cooled. The DTA data were taken with a du Pont 990 thermal analyzer. The results are shown in Fig. 1. The DTA on  $\text{LiAlSiO}_4$ -B was carried out at a rate of  $10^\circ\text{C}/\text{min}$  with  $\text{Al}_2\text{O}_3$  as the reference. A glass transition temperature ( $T_g$ ) of  $650^\circ\text{C}$  was found. The phase

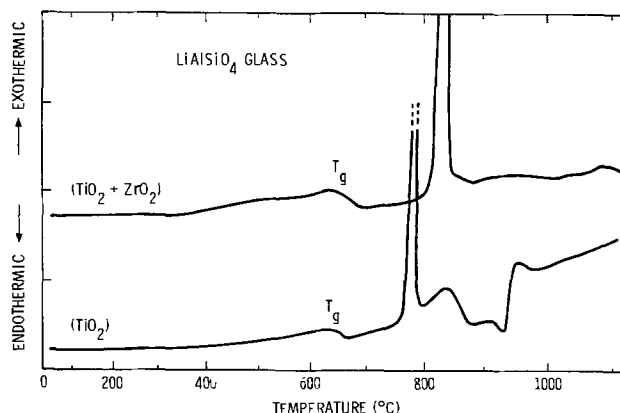


Fig. 1. Differential thermal analysis data on  $\text{LiAlSiO}_4$  glasses with nucleating agents of  $\text{TiO}_2$  and  $\text{TiO}_2 + \text{ZrO}_2$ . Composition information is given in Table I.  $T_g$  is the glass transition temperature. The exotherms result from crystallization as discussed in the text.

Table I. Composition derived from starting materials

Material	Composition (m/o)					
	$\text{Li}_2\text{O}$	$\text{Al}_2\text{O}_3$	$\text{SiO}_2$	$\text{TiO}_2$	$\text{ZrO}_2$	$\text{P}_2\text{O}_5$
$\text{LiAlSiO}_4$ -A	25	25	50			
$\text{LiAlSiO}_4$ -B	24.3	24.3	48.6	2.8		
$\text{LiAlSiO}_4$ -C	24.3	24.3	48.7	1.6	1.0	
Corning <sup>a</sup>	10.6	21.6	62.8	2.8	1.8	0.4

<sup>a</sup> From information provided by Corning Glass Works.

changes responsible for the observed heat effects between 770° and 950°C are due to the crystallization of  $\beta$ -eucryptite and an unidentified phase. These results are similar to those reported by Barry *et al.* (5) on similar materials except that they observed different (hexagonal and tetragonal) phases. In our studies, the intensities of the reflections due to the unidentified phase are stronger than the intensities of the  $\beta$ -eucryptite reflections following heat-treatment at low temperatures (770°-800°C); however, these unidentified reflections become weaker at higher heat-treatment temperatures (800°-850°C) and disappear above 950°C. Above this heat-treatment temperature only the  $\beta$ -eucryptite phase is detected. Thus, in the DTA of the  $\text{TiO}_2$ -nucleated  $\text{LiAlSiO}_4$ , the exotherm from 770° to 800°C can be associated primarily with the formation of the unidentified crystalline phase. The complex behavior observed from 800° to 950°C is probably caused by the conversion of this unidentified phase to the  $\beta$ -eucryptite phase.

The DTA results for the  $\text{LiAlSiO}_4$ -C glass ( $\text{TiO}_2$  and  $\text{ZrO}_2$  nucleating agents) reveal a  $T_g$  of 650°C and the existence of only one crystalline phase,  $\beta$ -eucryptite. The formation of this phase is responsible for the exotherm from 805° to 830°C.

X-ray analysis of the as-obtained Corning material revealed the presence of the  $\beta$ -eucryptite structure. However, heat-treatment of this glass-ceramic to 1120°C resulted in conversion to the  $\beta$ -spodumene phase (6). Similar heat-treatment of the  $\text{LiAlSiO}_4$  materials resulted in no new phases.

The density of these materials was determined by displacement with toluene. The densities of the  $\text{LiAlSiO}_4$ -B and -C glasses were found to be 2.45 and 2.49 g/cm<sup>3</sup>, respectively. After heat-treatment the densities of the corresponding glass-ceramics were slightly lower (2.38 and 2.41 g/cm<sup>3</sup>, respectively). The density of the "as-obtained" Corning glass-ceramic ( $\beta$ -eucryptite phase) was found to be 2.57 g/cm<sup>3</sup>. Scanning electron micrograph studies suggested that the as-obtained Corning material also contained more glassy phase (or smaller crystallites) than the  $\text{LiAlSiO}_4$  glass-ceramics. The density of this material increased to 2.62 g/cm<sup>3</sup> after conversion to the  $\beta$ -spodumene phase. These bulk densities may be compared with the theoretical crystal densities of 2.351, 2.391, and 2.399 g/cm<sup>3</sup> for  $n = 2$  ( $\beta$ -eucryptite) and  $n = 3$  and 4 [ $\beta$ -spodumene (16)], respectively.

### Electrodes

The samples used for the ionic conductivity measurements were cut with a diamond saw and were polished (first with dry emery paper then with an oil-based diamond polish) on the surfaces to be contacted. They then were cleaned with acetone and ethyl alcohol. Vacuum evaporated ( $\sim 10^{-6}$  Torr) thin-film electrodes of Cr, Al, or Li were applied. Results obtained with these electrodes were evaluated. For general discussions of important electrode and measurement criteria see Ref. (29) and (30).

For studies of thin-film Li electrodes, the Li was evaporated at  $\sim 150^\circ\text{C}$  utilizing the reaction:  $2\text{LiCl} + \text{Ca} \rightarrow \text{CaCl}_2 + 2\text{Li}$ . Only marginal results were obtained from these experiments. The contacts frequently appeared to be "ineffective" (possibly evaporated off the samples) as the sample temperature was increased. Generally, sample temperatures  $> 100^\circ\text{C}$  were needed in order for the sample conductance values to be in a range which could be measured with the instrumentation. The results which were obtained with Li electrodes were in agreement with those obtained with Cr and Al.

Good results were obtained with both Cr and Al electrodes. These contacts were evaporated onto the samples with the samples at  $300^\circ\text{C}$ . Contacts evaporated at this temperature were found to be more me-

chanically (and electrically) stable than those evaporated at room temperature. Electrical leads were then contacted by either spring loading or using silver paint. Some of the studies showed that contact effects can significantly influence the results. In several experiments where contacts were applied to the samples with various surface treatments, the conductivity was found to vary by an order of magnitude. For this reason, much care was exercised in sample surface preparation and in applying the electrodes. With properly applied contacts, our results indicated that while Cr and Al are not reference electrodes, there was no great effect due to their inactivity. Generally the results obtained with Cr and Al contacts were very similar, except that there was an indication of more polarization-related effects for the Al contacts at the higher conductivities. For this reason, most work was done with Cr electrodes, and only results obtained by using Cr electrodes are reported here.

### Electrical Measurement Techniques

Electrical measurements were made by using a variety of techniques which included 2-terminal a.c., 3-terminal guarded a.c., 4-terminal a.c., 2-terminal d.c., and a pulsed method. These methods were complementary in that the measurement circuitries and the sample and contact geometries were considerably different, e.g., area-to-length ratios differed by factors of up to  $\sim 10^3$ . By comparison and cross-correlation of results from the various techniques, a high reliability could be assigned to the conductivity data.

*2-Terminal d-c method.*—The 2-terminal d-c technique was used primarily as a check of the a-c and the pulsed method results. It also gave an indication of the extent of electronic conduction within the samples (31, 32). The measurements were made on samples with dimensions of approximately  $2 \times 2 \times 0.1$  cm. The contacts were evaporated onto the  $2 \times 2$  cm sample faces. The electrical measurements were made with a Keithley digital electrometer, Model 615 (fast current mode), in series with a constant voltage source (0.5V). When the circuit was closed, the instantaneous current was used to measure the total (ionic and electronic) current. The time variation in current through the sample gave an indication of the polarization which occurred at the electrodes. The final stabilized current is related to the electronic contribution to the conductivity (31, 32).

For measurements as a function of temperature, thermocouples were bonded to the sides of the sample with porcelainlike cement (Omega CC high temperature cement). The sample was encased in a thin ceramic holder which supported the electrical leads. This assembly was placed between two Ta strips which formed the heater arrangement. This entire assembly was mounted in a vacuum system, and measurements were made at  $\sim 10^{-6}$  Torr. The temperature gradient across the sample was  $1^\circ\text{-}2^\circ\text{C}$  at  $\sim 400^\circ\text{C}$ .

*Pulsed method.*—A pulsed method (2-terminal measurement) was examined since it is one of the techniques which can be used to measure ionic conductivity in the presence of polarization effects. The sample configuration is similar to that for the 2-terminal d-c method. As with the d-c technique, the pulsed method measures the "instantaneous" current. In this case the current is in response to a small-amplitude square-wave voltage pulse. The experimental arrangement is illustrated in Fig. 2, and is a modification of a method developed by Nissen and Carlsten (33). The basic circuit includes a pulse generator (Tektronix Type 114 with a Tektronix X10 attenuator), a current-sensing (standard) resistor in series with the sample (resistance a factor of  $\sim 10$  lower than that of the sample), and fast-rise oscilloscopes (Hewlett-Packard Models 180 and 183) for determining the sample voltage and

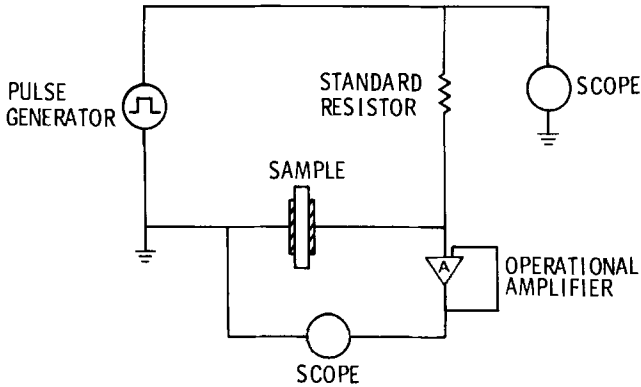


Fig. 2. Schematic diagram of the pulsed conductivity measurement circuit.

current. The operational amplifier (Burr-Brown Model 3503T) was used to increase the effective input impedance of the scope measuring the sample voltage. The scopes were triggered several microseconds before the pulse generator was triggered in order to record complete traces of the voltage and current pulses. Voltage pulses of  $\sim 100$  mV magnitude and  $\sim 200$   $\mu$ sec duration were used. This method was limited to measuring conductances  $\gtrsim 10^{-6}$  ohm $^{-1}$ .

**2- and 3-Terminal a-c methods.**—Both 2-terminal a-c and 3-terminal guarded a-c measurements were made on samples prepared in the same manner as for the d-c and pulsed experiments. The experimental arrangement is shown in Fig. 3. The measurements were made using a Hewlett-Packard 4800A vector impedance meter with a 4810A direct measurement plug-in. This instrument covers the frequency range from 5 to  $5 \times 10^5$  Hz. The impedance range is from 1 ohm to 10 megohm. The sample is connected to the instrument through two shielded coaxial cables. The shields are grounded at the instrument to minimize cable capacitance effects. The 2-terminal and 3-terminal measurements were the same except that the 3-terminal measurements were on samples which had a grounded (guard) electrode around the sample edge. This helped minimize problems due to leakage currents across the surface of the samples as well as to minimize field fringing effects. In preparing samples for the guarded measurements, a circular groove was cut through the Cr contacts with sand-blasting techniques (alignment of the grooves on opposite surfaces was within  $\approx 2\%$ ). This defined a center electrode area ( $\sim 0.35$  cm $^2$ ) and an outer electrode area on each surface. The center circular electrodes were used for the conductance measurements (the length-to-area ratio,  $l/A$ , used for conductivity determinations was  $\approx 0.35$  cm $^{-1}$ ). The leads to the outer electrodes were connected to the grounded shields on the coaxial cables which were also tied to a common system ground. For measurements of low conductances, a resistor ( $10^7$  ohm) was used in

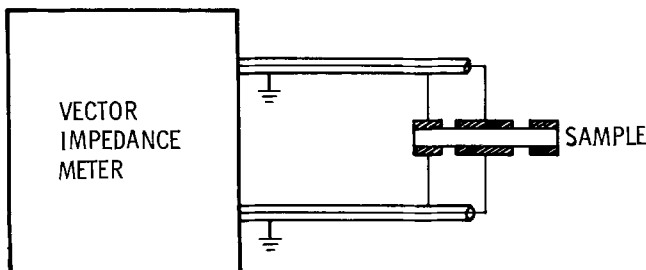


Fig. 3. Experimental arrangement for 2-terminal a-c and 3-terminal guarded a-c measurements. These measurements differ only in that for the 2-terminal measurements the outer guarded electrodes are either not used or are not grounded, i.e. no leads attached.

parallel with the sample to extend the lower limit of the effective sample conductance measurement range from  $\sim 10^{-7}$  to  $\sim 10^{-8}$  ohm $^{-1}$  (with some loss in accuracy). The rms voltage across the samples with this instrumentation varies from about 2.7 mV to 2.7 V (dependent upon the impedance), and has values  $< 270$  mV for conductances  $> 10^{-8}$  ohm. Conductance vs. frequency measurements were made over the frequency range from 50 to  $5 \times 10^5$  Hz.

**4-Terminal a-c method.**—The 4-terminal a-c measurements were made with the circuit and sample geometry shown in Fig. 4. Bar-shaped samples with dimensions of about  $1 \times 1 \times 15$  mm were used. Two electrodes were evaporated onto the ends of the sample and served as current lead contacts. The voltage contacts consisted of two strips 1 mm wide which encompassed three sides of the sample. These electrodes were  $\sim 7$  mm apart and were centered on the sample. With this arrangement  $l/A \approx 70$  cm $^{-1}$ .

The sample was coupled to the internal oscillator output from a Princeton Applied Research Model 124A lock-in amplifier through a voltage-to-current transducer, i.e., the sample was inserted in the feedback loop of an operational amplifier. The current through the feedback loop of the operational amplifier was determined by the output voltage of the oscillator,  $V(t)$ , and the input resistor,  $R$ , with  $i(t) = V(t)/R$ . Thus the sample was driven with a sinusoidal current whose phase was fixed relative to the input voltage  $V(t)$ . This alleviates the problems associated with polarization at the current contacts to the sample, since this configuration will always drive  $i(t)$  through the sample irrespective of any polarization that is occurring. Thus the only problem with polarization in this method is the polarization at the voltage contacts. This polarization, however, can be accurately monitored because any polarization will result in a phase shift between  $\phi(t)$  and  $i(t)$ . We need merely adjust the frequency of the measurement until the phase shift is negligible to get accurate values for the bulk conductance. Phase shifts of less than  $1^\circ$  could easily be measured. With this circuit, any impedance from 10 to  $10^8$  ohm could be accurately measured in the frequency range from 2 Hz to  $\approx 10$  kHz. The ability to use very low frequencies while alleviating polarization problems is important when inferring d-c conductivity from such measurements due to the intrinsic dispersion which is likely to be present in systems such as these. In the case of

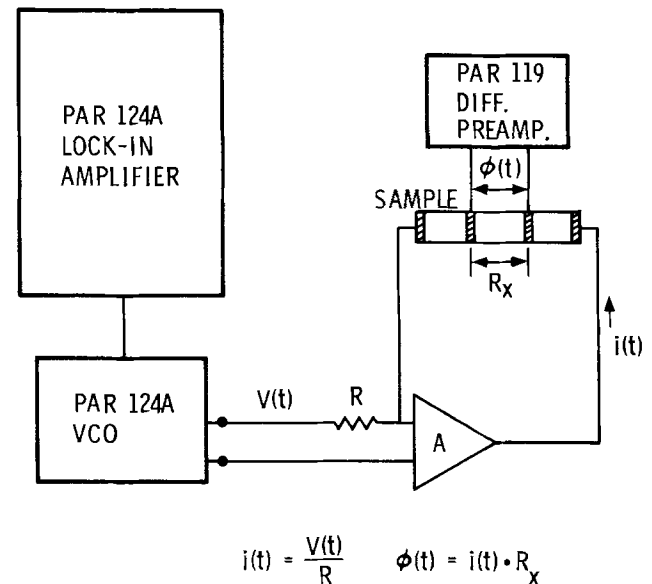


Fig. 4. Schematic diagram of the 4-terminal a-c measurement technique. The operational amplifier is an analog device Model 41L ultralow input offset bias current FET amplifier.

these materials, however, there appears to be no dispersion.

All measurements were taken with the peak-to-peak value of  $i(t) < 10^{-9}$ A. This resulted in a-c voltages  $\phi(t)$ , applied across the sample, of  $\leq 10$  mV. The measurement apparatus also contained a calibration resistor which could be inserted in place of the sample. Between data points the apparatus was switched to the calibration resistance and all leads to the sample were shorted to ground. This allowed any polarization which had built up to drain off. There was finite input offset bias current ( $\approx 10^{-12}$ A) present in the operational amplifier and the d-c polarization of the current contacts due to this current was monitored. This polarization was kept below 0.05V to avoid contact injection.

For measurements as a function of temperature, the sample was bonded to alumina plates with the Omega porcelain cement. One or more Chromel-Alumel thermocouples were affixed to the sample at various points by using the same cement. Nichrome wires were attached to the electrodes with Ag paint. This assembly was placed in a tube furnace and the data were taken with the sample in air. The data were taken at 7 Hz and the phase angle between the input current and the sample voltage was always  $< 5^\circ$ .

### Comparison of Measurement Techniques

In order to compare these conductivity measurement techniques and to investigate effects due to sample and contact geometry, two different sets of experiments were performed. The same material (the Corning  $\beta$ -eucryptite glass-ceramic and in some cases sister samples) was used in all the experiments. The first set of experiments was designed to compare the 2-terminal techniques (a.c., d.c., and pulsed), whereas the other experiments compared the 3- and 4-terminal a-c techniques.

**2-Terminal (a-c, d-c, and pulsed) experiments.**— These experiments were performed on the same sample, with the same contacts, and were mounted in the same sample holder. The attempt here was to vary only the measurement circuitry. Ring-shaped Cr electrodes were used. This contact configuration was chosen for evaluation as a possible base-electrode structure (electrically conductive) over which other more active, but possibly less conductive, electrodes (e.g., Li) could be deposited (or attached). It also provided a completely different electrode geometry than that used for the 3- and 4-terminal experiments. Since the ring-shaped electrode is not the normal (more conventional) electrode configuration and the effects of fringing fields are not known, the data are presented as conductance rather than conductivity, i.e., no attempt was made to determine the exact geometry factors appropriate for a conductivity determination.

The results obtained from the 2-terminal (a-c, d-c, and pulsed) measurements are shown in Fig. 5 and 6. Figure 5 gives the conductance values determined from the d-c and pulsed measurements as well as the frequency-dependent data obtained from the a-c measurements. The data were obtained for temperatures ranging from 100° to 450°C. The d-c results were obtained from the "instantaneous" (time = 0) current values obtained when the circuit was closed. The time-dependent results from the d-c measurements suggested that the current is carried by ions [presumably  $\text{Li}^+$  ions (25, 26)], in good agreement with recent NMR and Raman scattering experiments (25, 26). Furthermore, the electronic contribution to the conductivity is many orders of magnitude less than the ionic contribution. For example, measurements made at 400°C indicate that at this temperature the electronic conductivity is over three orders of magnitude less than the ionic conductivity. The ionic conductivity at this temperature is  $\sim 10^{-4}$  (ohm-cm) $^{-1}$ .

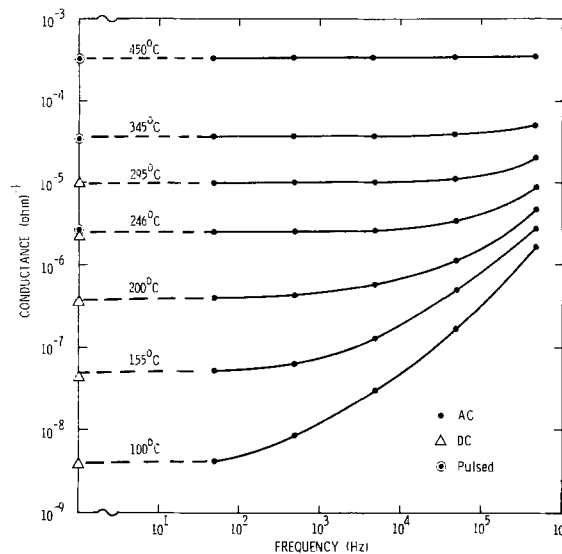


Fig. 5. Ionic conductance data obtained by using 2-terminal a-c, d-c, and pulsed measurement techniques on a glass-ceramic ( $\beta$ -eucryptite) sample at the temperatures indicated.

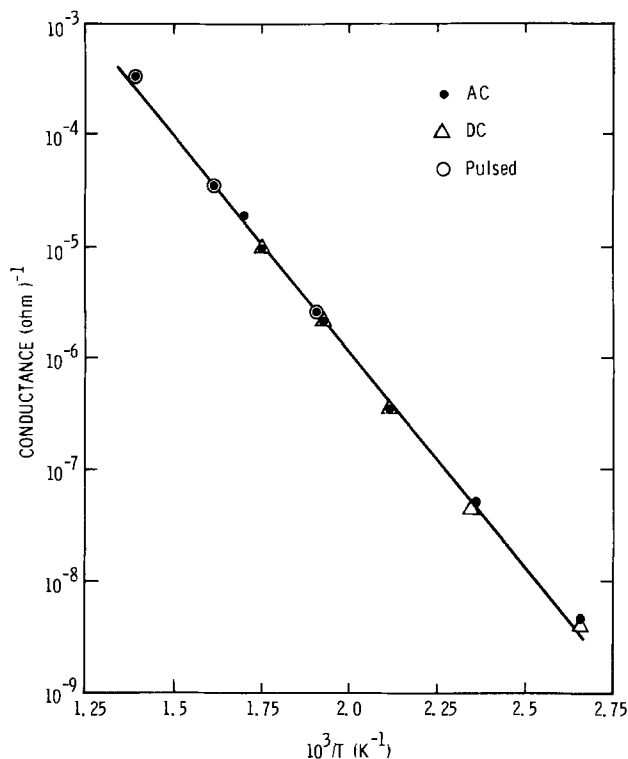


Fig. 6. Temperature dependence of the ionic conductance determined from the data in Fig. 5 for the  $\beta$ -eucryptite sample. The data were obtained with a-c, d-c, and pulsed 2-terminal techniques. Results show (i) excellent correlation between the measurement techniques, and (ii) that the conductivity is thermally activated with an activation energy of  $\sim 0.78$  eV for this sample.

Results in Fig. 5 from the pulsed measurements are, as they should be, in good agreement with the d-c results. The extrapolated a-c data, or a-c data in the frequency independent region, are also in good agreement with the d-c and pulsed results. In the frequency-dependent region, the a-c data indicate an increase in conductance with increasing frequency. This is especially pronounced for the low conductance (or low temperature) data, and is due to the experimental arrangement (cabling, etc.) and is not (necessarily) due to the sample. A similar frequency dependence was observed when the sample was replaced by a resistor. Any dispersion due to the sample was masked, in our case, by circuit effects.

These conductance results are compared further in Fig. 6 where conductance is plotted as a function of reciprocal temperature. The a-c conductance results are those obtained from the frequency-independent region. This plot also shows the excellent agreement obtained between the various techniques. Furthermore, the results show that the conductivity of this material (Corning  $\beta$ -eucryptite glass-ceramic) is thermally activated with an activation energy of  $\sim 0.78$  eV.

**3- and 4-Terminal a-c experiments.**—This set of experiments was designed to accurately determine the conductivity of the material. In order to provide completely independent determinations of the conductivity with these two techniques, different measurement circuitries, different sample geometries (slab vs. bar-shaped samples), different contact configurations ( $l/A$  ratios varied by  $\sim 200\times$ ), and different sample holder/heater arrangements were used. Even the ambient environment was changed.

The results from the 3- and 4-terminal measurements are shown in Fig. 7 (for the  $\beta$ -eucryptite phase). The agreement between results is within 10%. (Similar results were obtained on the  $\text{LiAlSiO}_4$  materials.) This is remarkable considering the factors that were different in the two measurements. The results are also in good agreement with the 2-terminal data (Fig. 6) in that the same activation energy is obtained. An estimate of the  $l/A$  ratio for the 2-terminal experiments gave conductivity values within less than a factor of 2 of the values in Fig. 7. As noted before, there is considerable uncertainty and error in this estimate of  $l/A$ , so this agreement appears to be reasonably good. All of these results give us confidence in our ability to measure the bulk ionic conductivity of these materials.

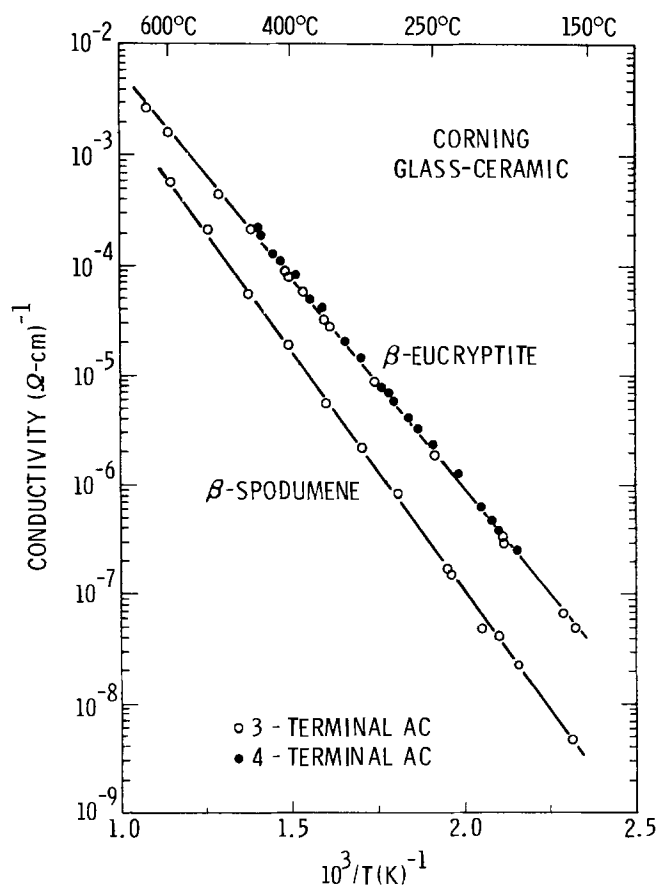


Fig. 7. Ionic conductivity of the Corning glass-ceramic in the as-obtained  $\beta$ -eucryptite phase and in the  $\beta$ -spodumene phase (induced by heat-treatment). Data were obtained by using 3- and 4-terminal a-c techniques and are in excellent agreement. Results are summarized in Table II.

**Conclusion.**—The study in this section has provided a useful comparison of five different ionic conductivity measurement techniques. The pulsed technique was the most difficult technique to use. This technique was also limited to measuring conductances  $\geq 10^{-6}$  ohm $^{-1}$ . The 2-terminal d-c technique was the most inaccurate method to use because of polarization effects encountered with inactive electrodes. For ionic conductivity determinations the most meaningful and useful techniques are the 4-terminal a-c and 3-terminal guarded a-c techniques. These techniques are complementary in that different sample geometries, contact configurations, and measurement circuitries are employed. The 4-terminal a-c measurement has the advantage (or at least has the potential) of minimizing undesirable contact effects. Where possible, both of these techniques should be used to measure the conductivity in order to establish the reliability of the data. Furthermore, these experiments have shown that the conductivity in these materials is not significantly dependent upon sample geometry, contact geometry, or the measurement circuitry. Thus it is concluded that ionic conductivity values obtained are those of the bulk material.

### Materials Ionic Conductivity Studies

Most of the studies of ionic conductivity in the glass and glass-ceramic materials were made with the 3-terminal guarded a-c and 4-terminal a-c techniques. Data were taken over the temperature range from room temperature to  $\sim 650^\circ\text{C}$ .

**Results.**—Results on the Corning material in both the  $\beta$ -eucryptite and  $\beta$ -spodumene phases are shown in Fig. 7. These data were obtained on the same sample; that is, the conductivity data for the sample in the  $\beta$ -spodumene phase were obtained after the sample had been converted (via heat-treatment) to the  $\beta$ -spodumene phase. The results show that the ionic conductivity ( $\sigma$ ) is thermally activated

$$\sigma = \sigma_0 e^{-E/kT}$$

with activation energies,  $E$ , of 0.78 and 0.87 eV for the  $\beta$ -eucryptite and  $\beta$ -spodumene materials, respectively. Values for  $E$  and the preexponential factor,  $\sigma_0$ , for all of the materials examined in this study are summarized in Table II.

The results in Fig. 7 show that the conductivity of the  $\beta$ -spodumene material is less than that of the  $\beta$ -eucryptite material in the temperature range examined ( $\leq 650^\circ\text{C}$ ). In the conversion of the  $\beta$ -eucryptite material to the  $\beta$ -spodumene material,  $E$  increased from  $\sim 0.78$  to  $\sim 0.87$  eV and  $\sigma_0$  increased from  $\sim 50$  to  $\sim 65$  (ohm-cm) $^{-1}$ . The degree to which this change is associated with the conversion to the  $\beta$ -spodumene crystalline structure as compared to changes in other materials properties, e.g., glass phase and/or relative amounts of glass and crystalline phases, is not known. For the  $\beta$ -spodumene phase, results published by Pizzini and co-workers (22, 23) on polycrystalline sintered pressed pellets show a larger activation energy ( $\sim 1.16$  eV) than that reported here, but a  $\sigma_0$  of about the same value. Thus the conductivity of the sintered polycrystalline  $\beta$ -spodumene samples they examined is even lower than that of our  $\beta$ -spodumene glass-ceramic

Table II. Activation energy,  $E$ , and preexponential factor,  $\sigma_0$ , determined from ionic conductivity measurements; using  $\sigma = \sigma_0 e^{-E/kT}$

Material	Structure	$E$ (eV)	$\sigma_0$ (ohm-cm) $^{-1}$
$\text{LiAlSiO}_4$ glass	Noncrystalline	0.68	$1.9 \times 10^3$
$\text{LiAlSiO}_4$ glass-ceramic	$\beta$ -eucryptite	1.05	$2.1 \times 10^4$
Corning glass-ceramic	$\beta$ -eucryptite	0.78	$5 \times 10^1$
Corning glass-ceramic	$\beta$ -spodumene	0.87	$6.5 \times 10^1$

samples. This would suggest that the crystalline phase alone does not dominate the electrical properties of these materials. In the polycrystalline sintered material the interface between the crystallites (grain boundaries, etc.) may significantly influence the electrical properties; whereas in the glass-ceramic, the glass phase as well as the interface between the glass and crystalline phases is probably important. The importance of the glass phase in glass-ceramics has recently been pointed out by McMillan (34). Furthermore, our experiments on the  $\text{LiAlSiO}_4$  materials (reported below) suggest that the glass phase may play a very important role in ionic transport in these materials.

The ionic conductivity data on the  $\text{LiAlSiO}_4$  glasses and glass-ceramics ( $\beta$ -eucryptite) are shown in Fig. 8, and are compared with the data (from Fig. 7) on the Corning  $\beta$ -eucryptite glass-ceramic. Results show that the conductivity of the  $\text{LiAlSiO}_4$  material is higher than that of the Corning material (at high temperatures), and is also higher than that reported for other  $\beta$ -eucryptite materials (24). The lower conductivity of the Corning materials may be due, at least in part, to the lower lithium content of these materials (see Table I). Some data reported by Hammel (19) suggest that the lithium content does significantly influence the ionic conductivity, in a manner which is consistent with our results.

The results in Fig. 8 also show that the conductivity of the  $\text{LiAlSiO}_4$  glass is greater than that of the glass-ceramic over the temperature range examined. In the conversion of this material from a glass to a glass-ceramic, both the activation energy increases (from  $\sim 0.68$  to  $\sim 1.05$  eV) and the  $\sigma_0$  value increases [from  $\sim 1.9 \times 10^2$  to  $\sim 2.1 \times 10^4$  ( $\text{ohm-cm})^{-1}$ ]. Similar changes in ionic conductivity have been observed in other glass and glass-ceramic systems (34, 35).

It is also seen from the data in Fig. 8 that nucleating agents do not affect the ionic conductivity in the glass phase (at least to the concentrations studied here). The glass-ceramic data presented here are for the glass-ceramic prepared with the  $\text{TiO}_2$  nucleating agents. Slightly higher  $E$  and  $\sigma_0$  values were observed for the glass-ceramic with the  $\text{TiO}_2 + \text{ZrO}_2$  nucleating agents, but whether this is due to the nucleating agents or

(more probably) other materials properties is not known.

**Comparison.**—In comparing the conductivity of  $\text{LiAlSiO}_4$  glass and glass-ceramic, and in interpreting the results, it is important to note that the composition of the glass and crystalline phases in the glass-ceramic should be about the same, i.e.,  $\text{LiAlSiO}_4$ , since the initial glass composition is near that of stoichiometric  $\beta$ -eucryptite. (This assumes, of course, only one glass phase and that this phase is the same as that for the  $\text{LiAlSiO}_4$  glass.) This feature plus the fact that the conductivity of the glass-ceramic is less than that of the glass suggests that, in the glass-ceramic, the contribution to the conductivity from the glass phase is greater than that from the crystalline phase. In arriving at this interpretation, one cannot ignore the possible importance of other properties, such as more than one phase (or a different phase) in the glassy region, effects associated with crystal anisotropies, and glass/crystalline interface effects. However, we want to emphasize that our results do strongly suggest that in these materials the glass phase is important in  $\text{Li}^+$  ion transport. Furthermore, the results from these experiments also suggest that it may be possible to further enhance the conductivity of the  $\beta$ -eucryptite materials by varying materials properties, such as composition.

**Applications.**—Since the  $\text{LiAlSiO}_4$  materials have conductivity values of the order of  $10^{-2}$  ( $\text{ohm-cm})^{-1}$  at high temperatures ( $\sim 600^\circ\text{C}$ ), they are of interest for high temperature solid electrolyte applications (12, 13). Other lithium silicates and lithium aluminosilicates also have conductivity values in this range. West (27) has recently reviewed some of this literature and it is clear that other materials at high temperatures exhibit lithium ionic conductivities with similar or in some cases even slightly higher conductivity values than those reported here. The advantage that the  $\beta$ -eucryptite materials possess for solid electrolyte applications is their low thermal expansion characteristics (6-8, 17-19). The  $\beta$ -spodumene materials also possess low thermal expansion characteristics but the conductivity is lower, possibly due to the lower lithium content.

Some possible applications for these  $\beta$ -eucryptite materials include thermal batteries (13) and special electrothermal devices, etc. (12), which would utilize  $\text{Li}^+$  ion transport. For many of these applications one would like a material with a higher ionic conductivity than that reported here. For example, for thermal battery applications one would like conductivity values about an order of magnitude higher, while maintaining about the same activation energy (that is, about 1 eV). Future efforts will be devoted to determining the extent to which the ionic conductivity of these materials can be increased and to defining potential solid electrolyte applications.

### Acknowledgments

The authors are indebted to D. L. Stewart for preparing some of the glass and glass-ceramic samples and for helping define the heat-treatment schedules; to J. F. Wolcott and J. C. Russell for performing chemical analysis; to D. D. Drummond for designing the modified pulsed measurement circuit and for assisting with all phases of the experiments; to R. A. Jaramillo for assistance with the experiments using the 4-terminal a-c technique; to W. B. Benedick for many helpful discussions and for obtaining the Corning materials; and to R. C. Hughes, R. J. Eagan, D. A. Nissen, and B. H. Van Domelen for stimulating discussions.

This work was supported by the U. S. Energy Research and Development Administration (ERDA).

Manuscript submitted May 13, 1975; revised manuscript received July 21, 1975.

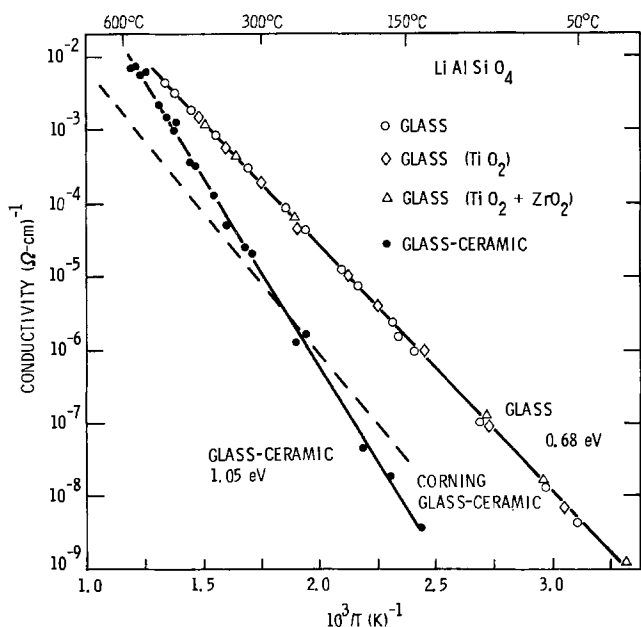


Fig. 8. Ionic conductivity of  $\text{LiAlSiO}_4$  glass, glass with nucleating agents, and glass-ceramic (see Table I). The glass-ceramic ( $\beta$ -eucryptite material) was prepared by heat-treating the glass. The dashed line is the data from Fig. 7 on the Corning ( $\beta$ -eucryptite) glass-ceramic. Conductivity results are summarized in Table II.

Any discussion of this paper will appear in a Discussion Section to be published in the December 1976 JOURNAL. All discussions for the December 1976 Discussion Section should be submitted by Aug. 1, 1976.

Publication costs of this article were partially assisted by Sandia Laboratories.

## REFERENCES

- H. G. F. Winkler, *Acta Cryst.*, **1**, 27 (1948).
- M. J. Buerger, *Am. Mineralogist*, **39**, 600 (1954).
- V. Tscherry, H. Schulz, and F. Laves, *Z. Krist.*, **135**, 161, 175 (1972).
- R. A. Hatch, *Am. Mineralogist*, **28**, 471 (1943).
- T. I. Barry, D. Clinton, L. A. Lay, R. A. Mercer, and R. P. Miller, *J. Mater. Sci.*, **5**, 117 (1970); *ibid.*, **4**, 596 (1969).
- R. A. Eppler, *J. Am. Ceram. Soc.*, **46**, 97 (1963).
- P. W. McMillan, "Glass-Ceramics," pp. 112, 160, and 174, Academic Press, New York (1964).
- F. A. Hummel, *J. Am. Ceram. Soc.*, **34**, 235 (1951).
- H. Schulz, *ibid.*, **57**, 313 (1974).
- F. H. Gillery and E. A. Bush, *ibid.*, **42**, 175 (1959).
- R. W. Lynch and B. Morosin, Papers F6 and I10, American Crystallographic Association Meeting, Jan. 31-Feb. 4, 1971.
- B. Morosin and R. T. Johnson, Jr., "Solid Electrolyte Materials," Sandia Laboratories Report SAND74-0296 (1974).
- D. A. Nissen and R. W. Carlsten, in "Fast Ion Transport in Solids: Solid State Batteries and Devices," Proceedings of the NATO Advanced Study Institute, Belgirate, Italy, September 5-15, 1972, W. van Gool, Editor, p. 675, North-Holland Publishing Company, Amsterdam-London (1973).
- R. T. Johnson, Jr., B. Morosin, M. L. Knotek, and R. M. Biefeld, *Bull. Am. Phys. Soc.*, **20**, 330 (1975).
- B. J. Skinner and H. T. Evans, Jr., *Am. J. Sci.*, **258-A**, 312 (1960).
- C. T. Li and D. R. Peacor, *Z. Krist.*, **126**, 46 (1968); *ibid.*, **132**, 118 (1970).
- W. Ostertag, G. R. Fischer, and J. P. Williams, *J. Am. Ceram. Soc.*, **51**, 651 (1968).
- G. H. Beall, in "Advances in Nucleation and Crystallization in Glasses," Symposium of the Glass Division of the American Ceramic Society, April 26-28, 1971, L. L. Hench and S. W. Freiman, Editors, p. 251, The American Ceramic Society, Inc., Columbus, Ohio (1971).
- J. J. Hammel, U.S. Pat. 3,834,911 (1974).
- S. W. Freiman and L. L. Hench, *J. Am. Ceram. Soc.*, **55**, 86 (1972).
- A. G. Pincus, in Ref. (18), p. 210.
- S. Pizzini, *J. Appl. Electrochem.*, **1**, 153 (1971).
- S. Pizzini, G. Monari, and R. Morlotti, *This Journal*, **118**, 796 (1971).
- I. D. Raistrick, L. E. Nagel, and R. A. Huggins, Abstract 21, p. 50, The Electrochemical Society Extended Abstracts, Spring Meeting, Toronto, Canada, May 11-16, 1975.
- H. T. Weaver and R. M. Biefeld, *Solid State Communications*, **18**, 39 (1976).
- B. Morosin and P. S. Peercy, *Phys. Letters*, **53A**, 147 (1975).
- A. R. West, *J. Appl. Electrochem.*, **3**, 327 (1973).
- For discussions of the role of nucleating agents in these materials see: J. J. Hammel, in Ref. (18), p. 1; D. R. Stewart, *ibid.*, p. 83; R. P. Hunt and K. N. R. Taylor, *J. Mater. Sci.*, **8**, 203 (1973); and H. Harper, P. F. James, and P. W. McMillan, *Discussions Faraday Soc.*, **50**, 206 (1970).
- M. S. Wittingham, in Ref. (13), p. 429.
- A. Kvist, in "Physics of Electrolytes," Vol. 1, J. Hladik, Editor, p. 319, Academic Press, New York (1972).
- K. O. Hever, *ibid.*, Vol. 2, p. 809.
- J. B. Wagner and C. Wagner, *J. Chem. Phys.*, **26**, 1597 (1957).
- D. A. Nissen and R. W. Carlsten, "A Solid Electrolyte Thermal Battery," Sandia Laboratories Report SC-RR-72-0386 (1973).
- P. W. McMillan, *Glass Technol.*, **15**, 5 (1974).
- P. W. McMillan, S. V. Phillips, and G. Partridge, *J. Mater. Sci.*, **1**, 269 (1966).

## Selective Etching of III-V Compounds with Redox Systems

R. P. Tijburg and T. van Dongen

Philips Research Laboratories, Eindhoven, The Netherlands

## ABSTRACT

Redox systems are particularly suitable for use as etching solutions for GaAs and  $\text{Ga}_{1-x}\text{Al}_x\text{As}$ . It is found that solutions with a certain composition and pH selectively etch GaAs with respect to  $\text{Ga}_{1-x}\text{Al}_x\text{As}$  and that other solutions containing the same chemicals but with a different composition and/or pH selectively etch  $\text{Ga}_{1-x}\text{Al}_x\text{As}$  with respect to GaAs. The same behavior is seen on GaP-InGaP and GaP-GaAlAs heterostructures. A survey of the redox systems studied and examples of the applications are given.

In heterojunction laser technology or, more general, in multilayer device technology it may be necessary to etch fine patterns in structures consisting of compounds like, e.g., GaAs and  $\text{Ga}_{1-x}\text{Al}_x\text{As}$ . Important factors determining the choice of a chemical etching agent are generally the etch rate for the materials in question, the degree of undercutting, the chemical aggressiveness of the solution to other materials present, and whether or not the etchant etches one compound selectively with respect to the other. Logan and Reinhart (1) described a very useful bath with which GaAs can be etched selectively with respect to  $\text{Ga}_{1-x}\text{Al}_x\text{As}$ . It is an aqueous solution of

hydrogen peroxide (superoxol 30%) in water to which ammonium hydroxide is added so as to make the pH = 7. Kobayashi and Sugiyama (2) have referred to the selective etching of GaAs with respect to  $\text{Ga}_{1-x}\text{Al}_x\text{As}$  in a solution of superoxol and sodium hydroxide as an undesired behavior of the etchant.

In some of the etching solutions, in addition to the selective etching, one also observes preferential etching of some crystal planes as well. This behavior has been described for GaAs by Marinace and Rutz (3), Gennon and Nuese (4), and Tarui, Komiya, and Harada (5). The present paper draws attention to a new class of etching solutions. Redox solutions are able, depending on their composition and/or pH, to etch GaAs selectively with respect to GaAlAs and con-

Key words: optical waveguides, GaAs laser, preferential etching of III-V compounds.



versely to etch GaAlAs selectively with respect to GaAs. In addition to this some etching solutions preferentially reveal A{111} planes because the etch rate of these planes is slower than that of all other low index planes (5). Other redox solutions show clear differences in etch rate between p- and n-type GaAlAs or p- and n-type GaAs. The selective etching of redox systems is not restricted to GaAs-GaAlAs structures; GaP-InGaP and GaP-GaAlAs structures also display this behavior. Systems which are stable in both acidic and basic environment, such as potassium iodide-iodine, potassium, ferricyanide-potassium ferrocyanide, and quinone-hydroquinone, were studied. Two other etchants which are stable only in an acidic environment, namely, ferrichloride-ferrochloride and cerium (IV) sulfate-cerium (III) nitrate are described.

### Materials and Sample Preparation

The GaAs-GaAlAs heterojunction layers used for etching experiments were laser structures grown onto (100) oriented GaAs substrates by liquid phase epitaxy. While the layer thicknesses varied, typical values used were 0.3-0.7  $\mu\text{m}$  for the GaAs active layer between two Ga<sub>0.7</sub>Al<sub>0.3</sub>As layers which were several microns thick. The carrier concentration of the GaAs p-type top layer was  $2 \cdot 10^{18} \text{ cm}^{-3}$ , the p-type GaAlAs layer was  $4 \cdot 10^{17} \text{ cm}^{-3}$ , and the n-type GaAlAs layer was  $2 \cdot 10^{17} \text{ cm}^{-3}$ . The laser layer was p-type GaAs ( $p = 5 \cdot 10^{17} \text{ cm}^{-3}$ ) while the substrate was n-type GaAs ( $n = 2 \cdot 10^{18} \text{ cm}^{-3}$ ). A cross section of such a slice is given in Fig. 1. To study selective etching, freshly cleaved {110} surfaces were placed in 50 ml of etching solution at room temperature for a time varying between 5 sec and 15 min. The etchant was agitated by a magnetic stirrer. After etching and rinsing, the {110} plane perpendicular to the etched one was cleaved and the sample studied with the scanning electron microscope. The depth of etching was measured with a calibrated microscope using an unetched part of the surface as reference.

### Experimental Results

Two steps that can be distinguished in the etching of semiconductor materials are the oxidation of the semiconductor and the subsequent dissolution of the oxidation products. It is to be expected that the etch rate, i.e., the oxidation rate and/or the dissolution rate, will depend on the composition of the semiconductor compounds. In a redox system the oxidation strength of a solution is influenced by the concentration ratio of the oxidizing agent to the reducing agent. The dissolution of the oxidation products can be influenced by changing the pH of the solution.

Figure 2 illustrates the selective etching behavior of the redox system potassium ferricyanide-potassium ferrocyanide ( $\text{K}_3\text{Fe}(\text{CN})_6$ - $\text{K}_4\text{Fe}(\text{CN})_6$ ). The pH of the redox system is plotted on the ordinate and the molar ratio of the oxidizing and reducing agent along the abscissa. The molar ratio was varied by modifying

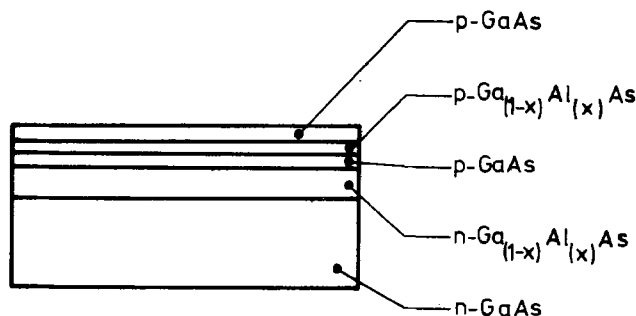


Fig. 1. Cross section of a double heterojunction GaAs-GaAlAs slice. An n-type Ga<sub>1-x</sub>Al<sub>x</sub>As layer, a p-type GaAs layer, a p-type Ga<sub>1-x</sub>Al<sub>x</sub>As layer, and a p-type GaAs layer are successively grown with liquid phase epitaxy on an n-type GaAs substrate.

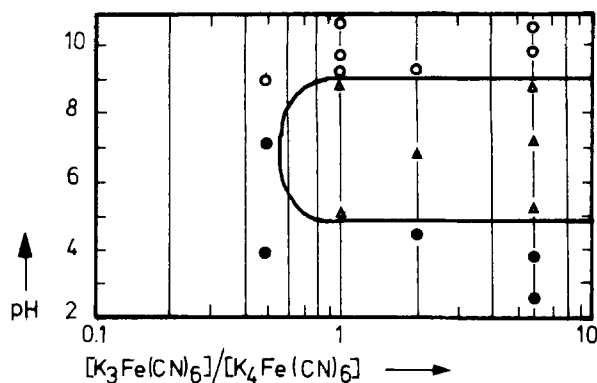


Fig. 2. Diagram of the etching properties of the potassium ferricyanide-potassium ferrocyanide system. The pH of the etching solution is entered on the ordinate and the molar ratio of the redox compounds on the abscissa. The potassium ferricyanide concentration is kept constant at 0.3 mol/liter.  $\circ$ , Selective etching of GaAs;  $\triangle$ , selective etching of Ga<sub>0.7</sub>Al<sub>0.3</sub>As;  $\bullet$ , no selective etching.

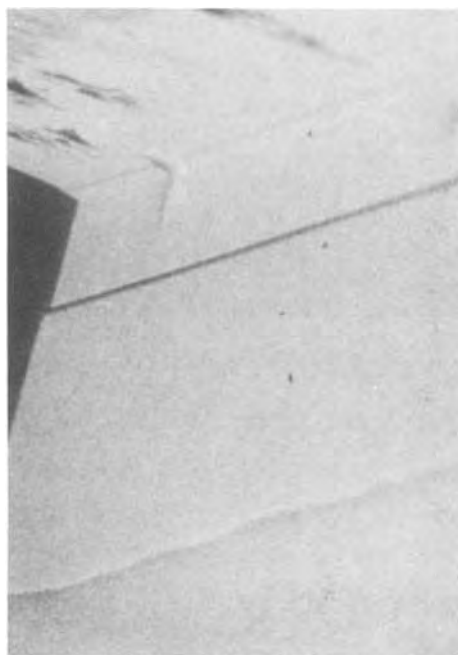


Fig. 3. A secondary emission image of a slice as shown in Fig. 1, etched in a potassium ferricyanide-potassium ferrocyanide solution containing 0.1 mol/liter  $\text{K}_3\text{Fe}(\text{CN})_6$  and 0.1 mol/liter  $\text{K}_4\text{Fe}(\text{CN})_6$ ; pH is 9.7. The three GaAs layers are etched selectively with respect to the GaAlAs layers. The etching time is 3 min.

the concentration of the reducing agent, while the concentration of the oxidizing agent was kept constant at 0.3 mol/liter in all the experiments covered by this graph. The pH was varied by dissolving the chemicals in buffer solutions<sup>1</sup> with the desired pH values or by adding NaOH or HCl to the etchants. Triangles indicate selective etching of Ga<sub>0.7</sub>Al<sub>0.3</sub>As, circles selective etching of GaAs, and dots low selectivity and/or etch rate. Selective etching of GaAs occurs mainly at pH values greater than 9 over a large range of molar ratios, whereas Ga<sub>0.7</sub>Al<sub>0.3</sub>As selective etching was found for pH values between 5 and 9. At pH values lower than these the selectivity is not so clear and possibly depends on the impurity concentration of the compounds. Figure 3 gives an example of selective GaAs etching. The etching solution is given in Table I, No. 1. Figure 4 gives an example of Ga<sub>0.7</sub>Al<sub>0.3</sub>As etching with solution 2 of Table I.

<sup>1</sup> The buffer solutions used are from Ref. (6).



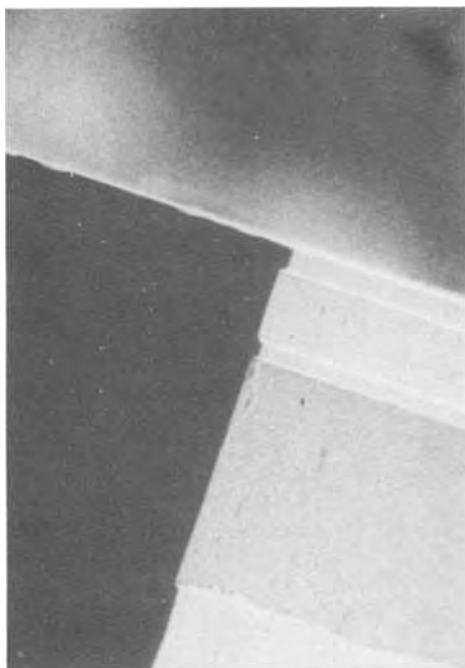


Fig. 4. A secondary emission image of a slice as shown in Fig. 1. The etching solution consists of 0.225 mol/liter  $K_3Fe(CN)_6$  and 0.225 mol/liter  $K_4Fe(CN)_6$ ; the pH is 7. The two GaAlAs layers are etched selectively. The etching time is 10 min.

The organic system quinone-hydroquinone ( $C_6H_4O_2$ - $C_6H_6O_2$ ) forms another redox couple which is stable over a large range of pH values and hence suitable for the selective etching of GaAs and  $Ga_{0.7}Al_{0.3}As$  (Fig. 5). Merely by changing the pH from 1 to 10 a solution of quinone and hydroquinone successively becomes an etchant for GaAlAs and an etchant for GaAs, separated by a region in which hardly any etching occurs. The third redox system which is stable over a large range of pH values is the iodine-potassium iodide ( $I_2$ -KI) solution. This system shows the highest etch rates of all the investigated systems and yet the selectivity for GaAs or GaAlAs is extremely good.

Figure 6 is an SEM photograph of a laser slice with a 0.1  $\mu m$  thick active GaAs layer. The etching solution is given under No. 3 in Table I. In cases where the active layer contains a few per cent of aluminum this solution does not etch at all. Aluminum-containing active layers can be etched with mixture 4 of Table I. With this etchant even a layer with an aluminum content of 15% sandwiched between two  $Ga_{0.7}Al_{0.3}As$  layers can be etched selectively.

Redox systems such as ferrichloride-ferrochloride ( $FeCl_3$ - $FeCl_2$ ) and cerium IV sulfate-cerium III nitrate [ $Ce(SO_4)_2$ - $Ce(NO_3)_3$ ] are stable only in acidic solutions and therefore the dissolution of the oxides

Table I. Preferred etching solutions

Solution No.	Properties	Composition of the etchant	Figure
1	Selective GaAs etching	0.1 mol/liter $K_2Fe(CN)_6$ 0.1 mol/liter $K_4Fe(CN)_6$ pH 9.7	2
2	Selective $Ga_{0.7}Al_{0.3}As$ etching	0.225 mol/liter $K_2Fe(CN)_6$ 0.225 mol/liter $K_4Fe(CN)_6$ pH 7	3
3	Selective etching of GaAs without any aluminum	0.3 mol/liter KI 0.04 mol/liter $I_2$ pH 9.4	6
4	Selective etching of $Ga_{1-x}Al_xAs$ ( $x \leq 0.15$ )	0.3 mol/liter KI 0.1 mol/liter $I_2$ pH 9	—
5	Selective etching of p-type $Ga_{1-x}Al_xAs$	0.0025 mol/liter $Ce(SO_4)_2 \cdot 4H_2O$ 0.0025 mol/liter $Ce(NO_3)_3 \cdot 6H_2O$ pH <2	7

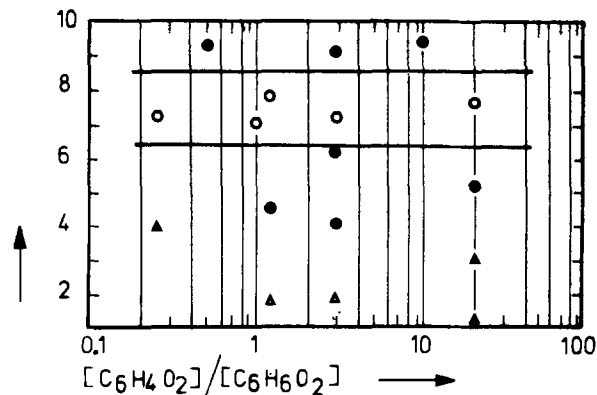


Fig. 5. Diagram of the etching properties of the quinone-hydroquinone system. The pH of the etching solution is entered on the ordinate and the molar ratio of the redox compounds on the abscissa. The total amount of  $C_6H_4O_2$  and  $C_6H_6O_2$  is kept constant at 0.03 mol/liter.  $\circ$ , Selective etching of GaAs;  $\Delta$ , selective etching of GaAlAs.  $\bullet$ , no selective etching.

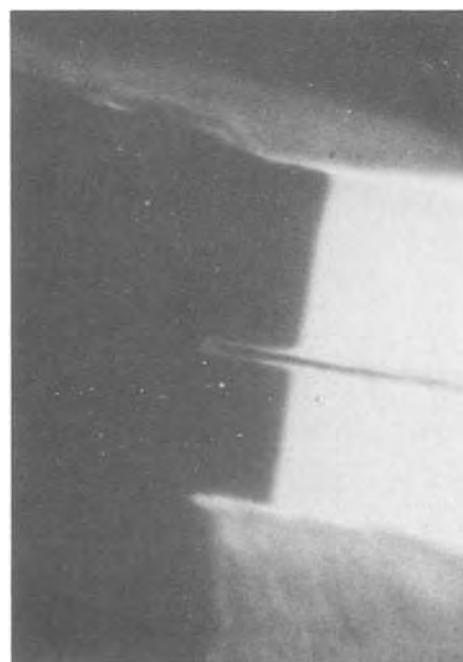


Fig. 6. A secondary emission image of a slice as shown in Fig. 1, etched in an iodine-potassium iodide solution. The solution contains 0.04 mol/liter  $I_2$  and 0.3 mol/liter KI; the pH is 9.4. The GaAs layers are etched selectively. The etching time is 30 sec.

cannot be influenced. Both systems etch only GaAlAs selectively. Apart from the GaAs- $Ga_{1-x}Al_xAs$  selectivity, some of the etching solutions also show a selectivity for a specific type of conductivity. Figure 7 shows an example of selective etching of p-type  $Ga_{1-x}Al_xAs$ . Starting from a high mesa structure (8), p-type as well as n-type  $Ga_{1-x}Al_xAs$  is exposed to a selective etchant. The p-type  $Ga_{1-x}Al_xAs$  is partly removed while the n-type  $Ga_{1-x}Al_xAs$  is hardly etched. This selective etching of p-type  $Ga_{1-x}Al_xAs$  occurs in the cerium (IV)-cerium (III) system as given under No. 5 in Table I.

Preferential etching occurs in many  $I_2$ -KI solutions. In Fig. 8 the left and the right part show both a cleavage perpendicular to the two  $\{110\}$  planes of a double heterojunction GaAs laser slice. The figure demonstrates that the etch rate of the A $\{111\}$  planes is slower than those of other planes. The  $I_2$ -KI solutions can also be used to etch GaP selectively with respect to InGaP or GaAlAs. The composition of the etchant is the same as that used for etching Al-con-

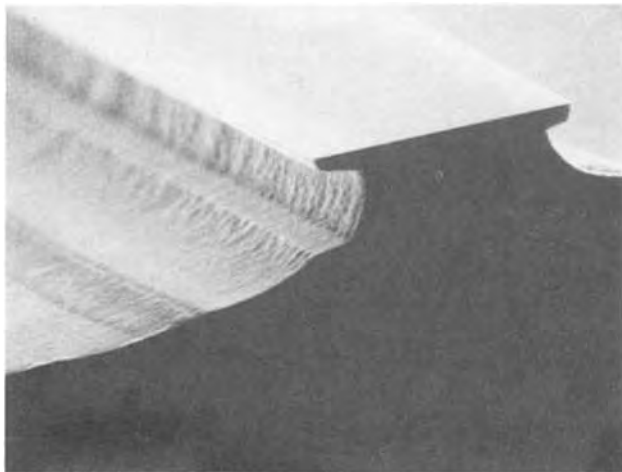


Fig. 7. A secondary emission image of an under-etched mesa structure. The high mesa structure (8) is obtained by etching the slice with a  $\text{H}_2\text{SO}_4:\text{H}_2\text{O}_2:\text{H}_2\text{O}$  (3:1:1) mixture. The p-type as well as the n-type  $\text{Ga}_{1-x}\text{Al}_x\text{As}$  are exposed to the etchant. Only the p-type  $\text{Ga}_{1-x}\text{Al}_x\text{As}$  is etched. The etchant contains 0.0025 mol/liter  $\text{Ce}(\text{SO}_4)_2$  and 0.0025 mol/liter  $\text{Ce}(\text{NO}_3)_3$ ; the  $\text{pH} < 2$ .



Fig. 8. Cross sections of etched heterostructure slices. The etched surface shown in (a, left) is a (011) plane. The etched surface of (b, right) is the (011) plane, which is perpendicular to the (011) plane of (a). The preferential etching is obtained with an etchant consisting of 0.3 mol/liter KI and 0.2 mol/liter  $\text{I}_2$ ; the  $\text{pH}$  is 4. The etching time is 10 sec.

taining GaAs layers (solution No. 4 Table I), the  $\text{pH}$ , however, must be 11 (see Fig. 9).

### Applications

Selective etching is of great assistance in the characterizing of heterostructures and can be of great importance for device technology. Examples of these two aspects are given here. A fast selective etchant as the iodine-potassium iodide system was used successfully for the delineation of the active GaAs layer in GaAs- $\text{Ga}_{1-x}\text{Al}_x\text{As}$  laser structures. A few per cent of aluminum in the GaAs layer is enough to stop the etching. The etch rate is about  $1 \mu/\text{min}$  which is faster than with the superoxol (30%  $\text{H}_2\text{O}_2$ )-ammonia etch used hitherto (1). The  $\text{I}_2$ -KI etchant (solution 3 Table I) is also very useful for the complete removal of the GaAs substrate in order to study the aluminum content of the n-type GaAlAs layer, while no special measures have to be taken to protect this layer as was done by Brown *et al.* (7) removing the GaAs substrate with the superoxol-ammonia etchant (1). The selective  $\text{Ga}_{0.7}\text{Al}_{0.3}\text{As}$  etching with the cerisulfate-cerionitrate system is used to make an "under-etched" mesa structure. Starting from a low mesa structure (8) the active region was narrowed by under-etching

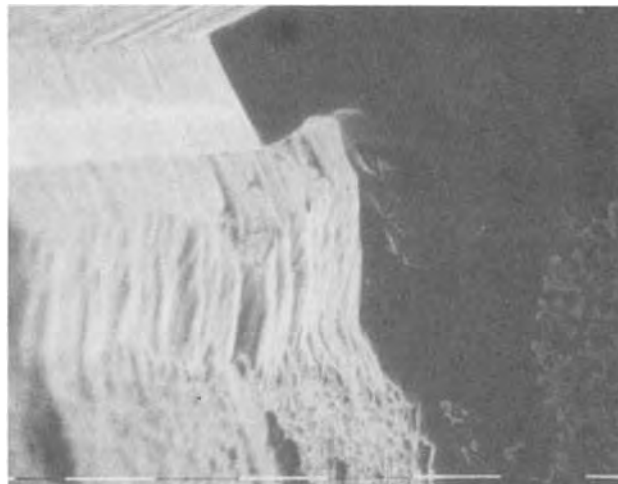


Fig. 9. A secondary emission image of a GaP-InGaP heterostructure. The GaP is selectively etched with a solution consisting of 0.3 mol/liter KI and 0.2 mol/liter  $\text{I}_2$ ; the  $\text{pH}$  is 11. The etching time is 90 min. The temperature of the etching solution is  $45^\circ\text{C}$ .

the p-type  $\text{Ga}_{1-x}\text{Al}_x\text{As}$  layer, which is sandwiched between the top GaAs layer and the active GaAs layer. This structure has the advantage of a larger contact area combined with a narrow active region. The contact resistance and the thermal resistance are found to be superior to those of the classical mesa structure (8) (see Fig. 10). The etch rate of the p-type GaAlAs closely depends on whether the heterojunction between the p-GaAs active layer and the p-type  $\text{Ga}_{0.7}\text{Al}_{0.3}\text{As}$  layer on top of it is exposed to the etching solution or not. An exposed heterojunction increases the etch rate of the GaAlAs by a factor of 3 to 5.

### Conclusions

The etching experiments described have shown conclusively that selective etching in a redox system can be performed successfully. This new approach to obtaining etching solutions gives technologists numerous alternatives. Acidic or basic environment, or even a neutral one, may be chosen if this is required to etch either GaAlAs or GaAs. Dissolving of the photoresist or of the metal contacts, and many other problems, can now be avoided by a suitable choice from numerous etching solutions available.

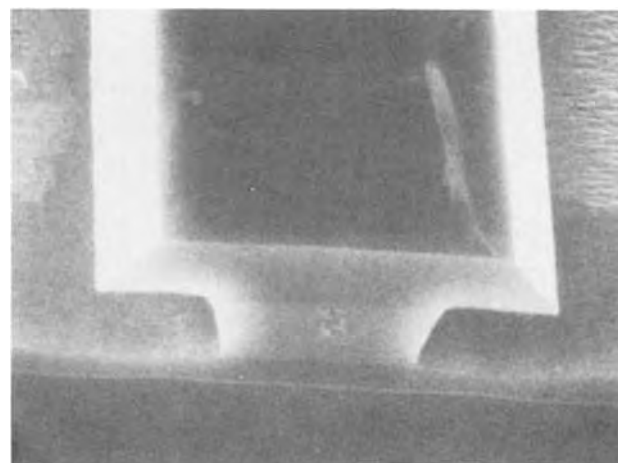


Fig. 10. A secondary emission image of an under-etched mesa-stripe laser. The standard mesa structure is obtained by etching the slice with a  $\text{H}_2\text{SO}_4:\text{H}_2\text{O}_2:\text{H}_2\text{O}$  (3:1:1) mixture. The p-type GaAlAs layer is partly removed by the additional processing step of selective etching. The sharp edges show the high degree of selectivity. The etchant contains 0.0025 mol/liter  $\text{Ce}(\text{SO}_4)_2$  and 0.0025 mol/liter  $\text{Ce}(\text{NO}_3)_3$ ; the  $\text{pH} < 2$ .

This paper is concerned with preliminary experimental results of etching GaAs and GaAlAs with redox systems. The study is being continued in order to achieve a better understanding of the mechanism underlying this kind of etching behavior.

### Acknowledgments

The authors wish to thank Dr. D. de Nobel and Dr. J. Kelly for stimulating discussions and encouragement and Mr. W. Nijman for providing the GaAs-GaAlAs heterostructure material and Miss C. Fisher of Mullard Research Laboratories for providing the GaP-InGaP material. We also thank Mr. C. Geenen, who made the SEM photographs.

Manuscript submitted June 30, 1975; revised manuscript received Dec. 17, 1975.

Any discussion of this paper will appear in a Discussion Section to be published in the December 1976

JOURNAL. All discussions for the December 1976 Discussion Section should be submitted by Aug. 1, 1976.

Publication costs of this article were partially assisted by Philips Research Laboratories.

### REFERENCES

1. R. A. Logan and F. K. Reinhart, *J. Appl. Phys.*, **44**, 4172 (1973).
2. T. Kobayashi and K. Sugiyama, *Japan J. Appl. Phys.*, **12**, 619 (1973).
3. J. C. Marinace and R. F. Rutz, *IBM Tech. Discl. Bull.*, **12**, No. 3, 427 (1969).
4. J. J. Gannon and C. J. Nuese, *This Journal*, **121**, 1215 (1974).
5. Y. Tarui, Y. Komiya, and Y. Harada, *ibid.*, **118**, 118 (1971).
6. The Handbook of Chemistry and Physics, 48th ed., Chemical Rubber Co., Cleveland, Ohio (1967).
7. R. L. Brown and R. G. Soberg, *J. Appl. Phys.*, **45**, 4735 (1974).
8. T. Tsukada, R. Ito, H. Nakashima, and O. Nakada, *IEEE Q.E.*, **9**, 356 (1973).

## Eu<sup>2+</sup> Luminescence in Hexagonal Aluminates Containing Large Divalent or Trivalent Cations

A. L. N. Stevels and A. D. M. Schrama-de Pauw

*Philips Research Laboratories, Eindhoven, The Netherlands*

### ABSTRACT

The Eu<sup>2+</sup> luminescence in hexagonal aluminates containing large divalent or trivalent cations was studied in relation to the crystal structures of the host lattices. It was found that these can be divided into three groups: compounds with the magnetoplumbite structure like MeAl<sub>12</sub>O<sub>19</sub> (Me = Ca, Sr, Eu); the La-containing aluminates (La<sub>1-x</sub>Al<sub>11.2/3+x</sub>O<sub>19</sub> and LaMgAl<sub>11</sub>O<sub>19</sub>) which have a structure quite close to magnetoplumbite; and phases with the β-alumina structure like MeMgAl<sub>10</sub>O<sub>17</sub> (Me = Sr, Eu, Ba) and Ba<sub>1-x</sub>Al<sub>11</sub>O<sub>17.5-x</sub> ("BaAl<sub>12</sub>O<sub>19</sub>"). In the first type of host lattice, the Eu<sup>2+</sup> luminescence is at a relatively short wavelength, in the last group at relatively long wavelength. The La aluminates doped with Eu<sup>2+</sup> take an intermediary position in this respect. The existence of various types of host lattices is also reflected in the shape and the position of the excitation spectra of the Eu<sup>2+</sup> luminescence. Their complicated shapes allow only a qualitative discussion of the position of the excited 5d levels of the Eu<sup>2+</sup> ion. The quantum efficiency of the luminescence was found in most cases to be high. The temperature dependence curves of the intensity of the Eu<sup>2+</sup> luminescence can be divided into two groups: those of the magnetoplumbite (like) phosphors and those of the β-alumina type phosphors. The experimental quenching temperatures are discussed in relation to a model proposed by Blasse and Brill.

Hexagonal aluminates of the general formula MeAl<sub>12</sub>O<sub>19</sub> (Me = Ca, Sr, Ba) have been known for a long time (1). The existence of a La aluminate with a similar composition was found in 1958 (2), while LaMgAl<sub>11</sub>O<sub>19</sub> was reported only quite recently (3).

The luminescence of Eu<sup>2+</sup> ions in hexagonal aluminate host lattices was reported by Blasse and Brill (4) who found differences in the optical properties of CaAl<sub>12</sub>O<sub>19</sub>:Eu<sup>2+</sup>, SrAl<sub>12</sub>O<sub>19</sub>:Eu<sup>2+</sup>, and BaAl<sub>12</sub>O<sub>19</sub>:Eu<sup>2+</sup>. Quite recently many aluminates and gallates have been prepared in our laboratories as host lattices for luminescence (5-9). As far as the hexagonal aluminates are concerned, an important step was taken by Versteegen (9) who prepared Mg-containing aluminate phosphors with compositions derived from MeAl<sub>12</sub>O<sub>19</sub> by analogy with the well-known hexagonal ferrites (10). It was established (6, 9) that most of these Mg-containing aluminate-Eu<sup>2+</sup> phosphors had luminescence properties different from MeAl<sub>12</sub>O<sub>19</sub>:Eu<sup>2+</sup> (Me = Ca, Sr, Ba). Moreover, it was concluded (6) that these compounds also have crystal structures deviating from the magnetoplumbite type which was supposed to be common to the MeAl<sub>12</sub>O<sub>19</sub> compounds. In the same paper (6),

the crystal structure of BaAl<sub>12</sub>O<sub>19</sub> was also said to deviate from the magnetoplumbite type.

The purpose of the present paper is to report in more detail on the luminescence properties of Eu<sup>2+</sup>-activated MeAl<sub>12</sub>O<sub>19</sub> and related Mg-modified aluminate phases. In addition, La aluminate:Eu<sup>2+</sup> and LaMgAl<sub>11</sub>O<sub>19</sub>:Eu<sup>2+</sup> have been included in our discussion of emission and excitation spectra, of quantum efficiencies of the luminescence, and of concentration-quenching or temperature-quenching phenomena.

Parallel to the luminescence investigations, an x-ray diffraction study was carried out in our laboratories in order to establish the crystal structures of the host lattices involved. Not only have magnetoplumbite-type structures been found, but also lattices of a related (β-alumina) type. These differences in crystal structure account for many "anomalies" in the luminescence properties as reported earlier (4, 6, 11).

### Experimental

The samples were prepared by standard ceramic techniques (firing temperatures between 1200° and 1600°C) from highly reactive (γ-) Al<sub>2</sub>O<sub>3</sub>, MgO, and MeCO<sub>3</sub> (Me = Ca, Sr, Ba) or La<sub>2</sub>O<sub>3</sub>. The Eu activator is introduced in the form of Eu<sub>2</sub>O<sub>3</sub>; by heating

in  $N_2$  containing a few per cent  $H_2$ , it is reduced to its divalent state. Introduction of minor amounts of the cations in the form of fluorides ( $MeF_2$  or  $AlF_3$ ) proved to be essential to stimulate host lattice formation and grain growth. Single crystals were obtained from slowly cooled melts or by the Czochralski method. The luminescence measurements were carried out as described in Ref. (12).

### Phase Analysis and Crystal Structures of the Host Lattices

*The  $MeAl_{12}O_{19}$  series ( $Me = Ca, Sr, Ba$ ).—*The hexagonal aluminates  $MeAl_{12}O_{19}$  ( $Me = Ca, Sr, Ba$ ) were studied by Adelskjöld in 1938 (1). The crystal structure of these compounds was said to be of the magnetoplumbite ( $PbFe_{12}O_{19}$ ) type. A projection of the unit cell on the  $[1\bar{1}0]$  plane is shown in Fig. 1(a). It consists of two blocks with the spinel structure separated by layers containing the large cation ( $Me$ ), one small cation ( $Al$ ), and three oxygen ions.

Kato and Saalfeld (13) refined the crystal structure of  $CaAl_{12}O_{19}$  and confirmed its isotypism with  $PbFe_{12}O_{19}$ . For  $SrAl_{12}O_{19}$  and  $BaAl_{12}O_{19}$ , no structure refinements have been published up to now, but it has been generally assumed (4, 14) that these compounds are of the magnetoplumbite type.

However, recent analysis of luminescence and crystallographic data provided evidence that the structure of  $BaAl_{12}O_{19}$  might be of a deviating type. This prompted an extensive x-ray diffraction study at our laboratories on single crystals of this material. Since full details will be published elsewhere (15), we briefly summarize here the results:

(i) The unit cell actually found has a volume threefold that of a magnetoplumbite-type unit cell.

(ii) Two of the three subunits of this large cell have the structure of the  $\beta$ -alumina type and have consequently the formula  $BaAl_{11}O_{17}$ .

(iii) The third subunit has a more complicated structure. It is strongly defective in Ba, but contains extra oxygen atoms.

(iv) As a consequence of ii and iii the approximate composition of Ba aluminate is rather  $Ba_{1-x}Al_{11}O_{17.5-x}$  rather than  $BaAl_{12}O_{19}$ .

The  $\beta$ -alumina structure type is shown in Fig. 1(b). As for magnetoplumbite, the unit cell consists of two spinel blocks separated by intermediate layers. In the  $\beta$ -alumina type only two atoms are positioned in these layers, *viz.*, the large cation  $Me$  and one oxygen ion. Their configuration is such that a relatively large space is available for the  $Me$  cations. It has been concluded earlier (6) that in magnetoplumbites this space is much less and that cation-oxygen distances can become very small with increasing radius of the cations. This possibly explains why Ba aluminate ( $r_{Ba^{2+}} = 1.33\text{\AA}$ ) is of a (distorted)  $\beta$ -alumina type, whereas  $SrAl_{12}O_{19}$  ( $r_{Sr^{2+}} = 1.12\text{\AA}$ ),  $Pb$  ( $r_{Pb^{2+}} = 1.20\text{\AA}$ ), and  $Eu$  ( $r_{Eu^{2+}} = 1.13\text{\AA}$ ) and  $Ca$  ( $r_{Ca^{2+}} = 0.99\text{\AA}$ ) aluminates have the magnetoplumbite structures.

*Mg-substituted aluminates.*—In a recent publication, Verstegen (9) has drawn attention to the fact that a structural relationship exists between ferrites like  $MgFe_2O_4$  (or  $Fe_3O_4 = FeFe_2O_4$ ) and  $BaFe_{12}O_{19}$ , gallates like  $MgGa_2O_4$  and  $MeGa_{12}O_{19}$  ( $Me = Sr, Ba$ ), and aluminates like  $MgAl_2O_4$  and  $MeAl_{12}O_{19}$  ( $Me = Ca, Sr, Ba$ ). On the basis of this analogy, Verstegen has studied aluminate compositions which are counterparts of more complex hexagonal ferrites like  $BaFe_2^{2+}Fe_{16}^{3+}O_{27}$  (the so-called W-type),  $Ba_2Fe_2^{2+}Fe_{12}^{3+}O_{22}$  (Y-type),  $Ba_2Fe_2^{2+}Fe_{28}^{3+}O_{46}$  (X-type), and  $Ba_3Fe_2^{2+}Fe_{24}^{3+}O_{41}$  (Z-type). These compounds have magnetoplumbite structures in which additional  $Fe^{2+}Fe_3^{3+}O_4$  spinel blocks are intercalated or from which  $Fe_3O_4$  has been subtracted.

By substituting  $Al^{3+}$  for  $Fe^{3+}$  and  $Mg^{2+}$  for  $Fe^{2+}$ , Verstegen (9) found aluminate phases which showed very effective activation of luminescence with, *e.g.*,  $Tl^+$ ,  $Eu^{2+}$ , or  $Ce^{3+}$  ions. Although it was concluded that large quantities of  $MgAl_2O_4$  can be taken up in the magnetoplumbite lattice, no indications were found for the existence of phase analogous to the corresponding hexagonal ferrites.

A somewhat different approach (6) leading to samples with similar compositions as discussed above is direct "substitution" of  $Mg^{2+}$  for  $Al^{3+}$  in  $MeAl_{12}O_{19}$  ( $Me = Ca, Sr, Ba$ ) compounds. It was reported in Ref. 6 that for compositions like  $SrMgAl_{11}O_{18.5}$  and  $BaMgAl_{11}O_{18.5}$  both the lattice parameters and also the intensities of several diffraction lines deviate from the nonsubstituted aluminates with magnetoplumbite structure. It was concluded that this type of phases had a close similarity with Ba aluminate.

The combination of the results of the above-mentioned investigations and the fact that Ba aluminate has a pronounced  $\beta$ -alumina character suggested that in  $MgAl_2O_4$ -modified or Mg-substituted aluminates,  $\beta$ -alumina type phases may in fact occur. By analogy with compounds having this structure and containing monovalent metal ions (like  $NaAl_{11}O_{17}$  and  $KAl_{11}O_{17}$ ), the ideal composition of the  $\beta$ -alumina containing large divalent cations and  $Mg^{2+}$  was predicted as  $Me^{2+}MgAl_{10}O_{17}$ . A single crystal study made by Braun *et al.* (15) on  $BaMgAl_{10}O_{17}$  indeed confirmed our conjecture.

By powder diffraction methods, a large number of compounds has been identified as being isostructural to  $BaMgAl_{10}O_{17}$ . Their ideal compositions, lattice parameters, and  $c/a$  ratio of the hexagonal axes are listed in Table I. It can be concluded from this table that  $c/a$  increases with the ionic radius of the large divalent cation. A similar result has also been found for the  $\beta$ -alumina containing monovalent cations.

On studying  $Eu^{2+} \rightarrow Mn^{2+}$  energy transfer in hexagonal aluminates (16), it was found that, apart from

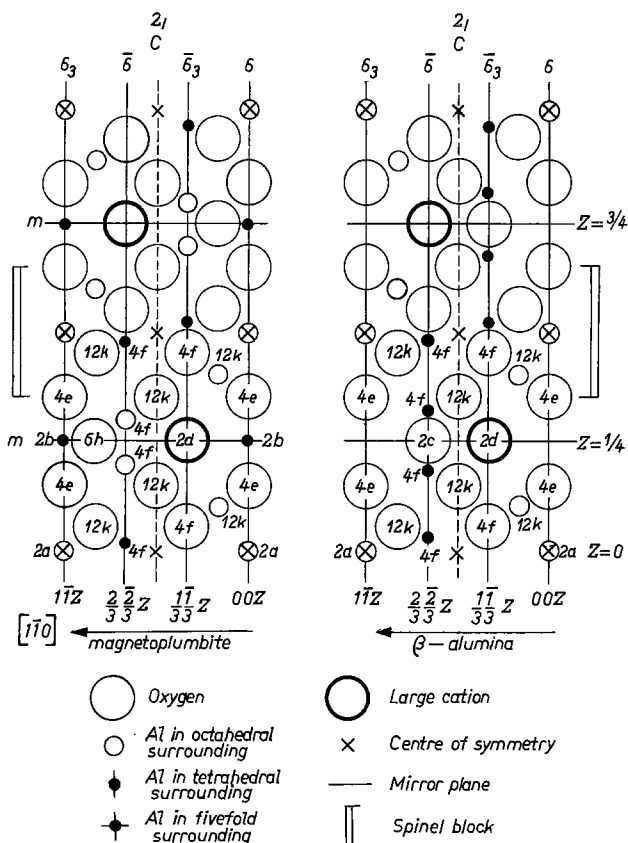


Fig. 1. Projection on the  $[1\bar{1}0]$  plane of unit cells of the (a, left) magnetoplumbite and (b, right)  $\beta$ -alumina crystal structures, Ref. (10).

Table I. Lattice parameters of Me<sup>2+</sup>MgAl<sub>10</sub>O<sub>17</sub> and Me<sup>2+</sup>MnAl<sub>10</sub>O<sub>17</sub> phases

Lattice	a (Å)	c (Å)	c/a	Radius of Me <sup>2+</sup> (Å)
SrMgAl <sub>10</sub> O <sub>17</sub>	5.6255 ± 0.0001	22.3902 ± 0.0006	3.9801	1.12
SrMnAl <sub>10</sub> O <sub>17</sub>	5.6419 ± 0.0002	22.4605 ± 0.014	3.9810	1.12
EuMgAl <sub>10</sub> O <sub>17</sub>	5.609 ± 0.005	22.42 ± 0.01	3.997	1.13
EuMnAl <sub>10</sub> O <sub>17</sub>	5.6448 ± 0.0005	22.472 ± 0.003	3.9809	1.13
PbMgAl <sub>10</sub> O <sub>17</sub>	5.597 ± 0.003	22.52 ± 0.01	4.023	1.20
Ba <sub>1-x</sub> Al <sub>11</sub> O <sub>17.5-x</sub>	5.5910 ± 0.0003	22.720 ± 0.002	4.064	1.33
BaMgAl <sub>10</sub> O <sub>17</sub>	5.6224 ± 0.0001	22.6268 ± 0.0006	4.024	1.33
BaMnAl <sub>10</sub> O <sub>17</sub>	5.593 ± 0.005	22.42 ± 0.03	4.009	1.33

being a luminescence center, Mn<sup>2+</sup> ions can act in a way similar to Mg<sup>2+</sup> ions as a "structure modifier" of magnetoplumbite types. A number of lattice parameters of Mn-containing β-alumina is also listed in Table I.

The homogeneity range of the phases of which the "ideal" composition is listed in Table I could not be established very well. This seems to be due to the slow reaction kinetics in the aluminate systems considered. Even for the fastest reacting qualities of the Al<sub>2</sub>O<sub>3</sub> starting material, only small differences could be established between slowly cooled or rapidly quenched samples.

As can be seen from Table I, no CaMg aluminate with β-alumina type structure could be prepared. In the Al<sub>2</sub>O<sub>3</sub>-rich part of the CaO-MgO-Al<sub>2</sub>O<sub>3</sub> system only a highly defective magnetoplumbite-type phase with possible composition CaMg<sub>x</sub>Al<sub>12-2/3x</sub>O<sub>19</sub> was found; the lattice parameters suggest that Mg indeed enters the lattice. In the same part of the SrO (or EuO or PbO)-MgO-Al<sub>2</sub>O<sub>3</sub> systems, a phase separation between β-alumina and magnetoplumbite phases was found. As far as could be established, the homogeneity range of the magnetoplumbite phases in these ternary systems tends to narrow in the direction of increasing ionic radius of the large cation, that is, in the direction Sr<sup>2+</sup> → Eu<sup>2+</sup> → Pb<sup>2+</sup>.

With the preparation conditions used, there were no indications that in these systems a kind of ordered intermediate phase, e.g., with alternating "β-alumina" and "magnetoplumbite" layers between the spinel blocks of the crystal structure, occurs.

In the Al<sub>2</sub>O<sub>3</sub>-rich part of the BaO-MgO-Al<sub>2</sub>O<sub>3</sub> system, a complete miscibility was found between, e.g., BaMgAl<sub>10</sub>O<sub>17</sub> and Ba<sub>1-x</sub>Al<sub>11</sub>O<sub>17.5-x</sub>. Apparently the distortion of the β-alumina lattice as found for the latter composition can take place in a continuous way.

In Fig. 2 we have summarized the results presented above. This figure suggests that the "β-alumina tendency" increases with increasing ionic radius of the cation and with the addition of Mg, whereas the magnetoplumbite character decreases in the same order.

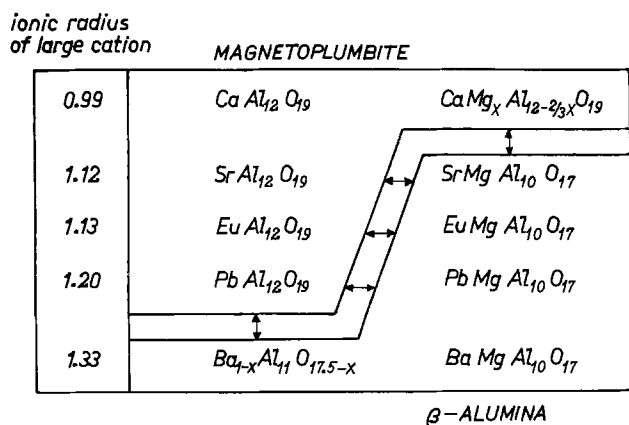


Fig. 2. Schematic drawing of magnetoplumbite-β-alumina relations. The double arrows represent phase separations.

In the systems described above, we have also looked for phases analogous to the complex W, Y, X, and Z ferrites which can be derived from the β-alumina type, similar to the way W, Y, X, and Z ferrites can be derived from magnetoplumbite. Keeping in mind that β-alumina can be derived from magnetoplumbite by subtracting one formula unit Al<sub>2</sub>O<sub>3</sub> and adding one unit MgO for each large cation present in the formula, examples for the BaO-MgO-Al<sub>2</sub>O<sub>3</sub> system are listed in Table II.

With powder synthesis it was not possible to prepare samples containing phases with any of the crystal structures mentioned in Table II. From a melt of MgO-rich Ba aluminates, however, crystals of the β-W phase BaMg<sub>3</sub>Al<sub>14</sub>O<sub>25</sub> were obtained [see also Ref. (15)].

*Hexagonal aluminates containing large trivalent cations.*—By replacing Me<sup>2+</sup> in MeAl<sub>12</sub>O<sub>19</sub> by a trivalent ion of similar ionic radius (e.g., La<sup>3+</sup> or Ce<sup>3+</sup>) and simultaneously substituting Mg<sup>2+</sup> for one of the Al<sup>3+</sup> ions, compounds of the composition LaMgAl<sub>11</sub>O<sub>19</sub> and CeMgAl<sub>11</sub>O<sub>19</sub> can be derived. Such compounds were indeed reported by Verstegen *et al.* (3), who described these phases as being isomorphous to SrAl<sub>12</sub>O<sub>19</sub>, that is, of magnetoplumbite type.

In a similar way as Mg<sup>2+</sup> was substituted for Al<sup>3+</sup> in aluminates containing divalent large cations, we can in the trivalent case substitute Al<sup>3+</sup> for Mg<sup>2+</sup>. In this way La aluminates of approximate composition LaAl<sub>12</sub>O<sub>19.5</sub> are derived. Such a La compound has been reported in the literature by Roth and Hasko (2); its crystal structure was said to be of the β-alumina type. In the patent literature (17) the existence of a possibly isomorphous Ce aluminate is mentioned.

In Table III we have summarized the lattice parameter data of the phases discussed above. We see that the c/a ratios of La<sub>1-x</sub>Al<sub>11 2/3+x</sub>O<sub>19</sub> (3.960) and Ce<sub>1-x</sub>Al<sub>11 2/3+x</sub>O<sub>19</sub> (3.978) are slightly beyond the limits where the magnetoplumbite crystal structure was found [between 3.915 and 3.954, see Ref. (6)]. Preliminary results of x-ray diffraction work at our laboratories show, however, that the La and Ce aluminates have crystal structures at least closely resembling magnetoplumbite. A further indication for this strong similarity may be our observation that a continuous series of solid solutions exists between LaMgAl<sub>11</sub>O<sub>19</sub> and La<sub>1-x</sub>Al<sub>11 2/3+x</sub>O<sub>19</sub> and in the corresponding Ce system.

### Emission and Excitation Spectra

*Emission spectra.*—In Fig. 3 and 4 we plot the emission spectra at 300°K of Eu<sup>2+</sup>-doped magnetoplumbite and β-alumina phases. The wavelengths of the maxima of the bands are summarized in Table IV. In the

Table II. Magnetoplumbite and β-alumina type analogs of ferrites in the BaO-MgO-Al<sub>2</sub>O<sub>3</sub> systems

Ferrite type	Ferrite composition	Magnetoplumbite analog	β-alumina analog
M	BaFe <sub>12</sub> O <sub>19</sub>	BaAl <sub>12</sub> O <sub>19</sub>	BaMgAl <sub>10</sub> O <sub>17</sub>
W	Ba <sub>2</sub> Fe <sub>2</sub> Fe <sub>16</sub> O <sub>27</sub>	BaMg <sub>2</sub> Al <sub>16</sub> O <sub>27</sub>	BaMg <sub>2</sub> Al <sub>14</sub> O <sub>25</sub>
Y	Ba <sub>2</sub> Fe <sub>2</sub> Fe <sub>12</sub> O <sub>23</sub>	Ba <sub>2</sub> Mg <sub>2</sub> Al <sub>12</sub> O <sub>22</sub>	Ba <sub>2</sub> Mg <sub>2</sub> Al <sub>10</sub> O <sub>18</sub>
X	Ba <sub>2</sub> Fe <sub>2</sub> Fe <sub>26</sub> O <sub>36</sub>	Ba <sub>2</sub> Mg <sub>2</sub> Al <sub>26</sub> O <sub>36</sub>	Ba <sub>2</sub> Mg <sub>4</sub> Al <sub>24</sub> O <sub>32</sub>
Z	Ba <sub>2</sub> Fe <sub>2</sub> Fe <sub>24</sub> O <sub>31</sub>	Ba <sub>2</sub> Mg <sub>2</sub> Al <sub>24</sub> O <sub>31</sub>	Ba <sub>2</sub> Mg <sub>2</sub> Al <sub>18</sub> O <sub>25</sub>

Table III. Lattice parameters of hexagonal aluminates containing large trivalent cations

Lattice	a (Å)	c (Å)	c/a	Ref.
LaMgAl <sub>11</sub> O <sub>19</sub>	5.5939 ± 0.0004	21.987 ± 0.002	3.931	6
LaMnAl <sub>11</sub> O <sub>19</sub>	5.593 ± 0.003	21.974 ± 0.01	3.928	This work
La <sub>1-x</sub> Al <sub>11 2/3+x</sub> O <sub>19</sub>	5.5633 ± 0.001	22.031 ± 0.001	3.960	This work
CeMgAl <sub>11</sub> O <sub>19</sub>	5.610 ± 0.004	21.99 ± 0.01	3.920	6
CeMnAl <sub>11</sub> O <sub>19</sub>	5.621 ± 0.005	21.96 ± 0.01	3.907	This work
Ce <sub>1-x</sub> Al <sub>11 2/3+x</sub> O <sub>19</sub>	5.523 ± 0.005	21.96 ± 0.01	3.978	This work

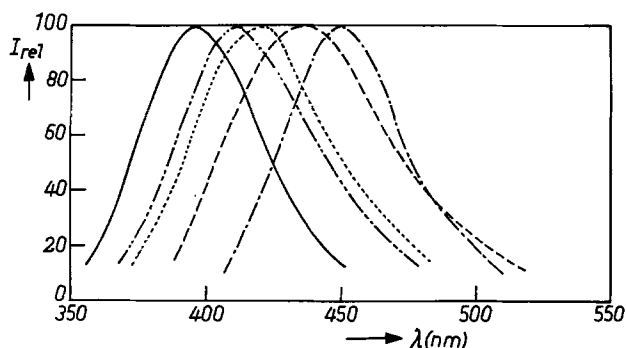


Fig. 3. Spectral energy distribution at 300°K (under 250-270 nm excitation) of the magnetoplumbite  $\text{SrAl}_{12}\text{O}_{19}:\text{Eu}^{2+}$  (—),  $\text{CaAl}_{12}\text{O}_{19}:\text{Eu}^{2+}$  (---),  $\text{EuAl}_{12}\text{O}_{19}$  (· · ·),  $\text{La}_{1-x}\text{Al}_{11\frac{2}{3}+x}\text{O}_{19}:\text{Eu}^{2+}$  (- · - ·), and  $\text{LaMgAl}_{11}\text{O}_{19}:\text{Eu}^{2+}$  (- - -).

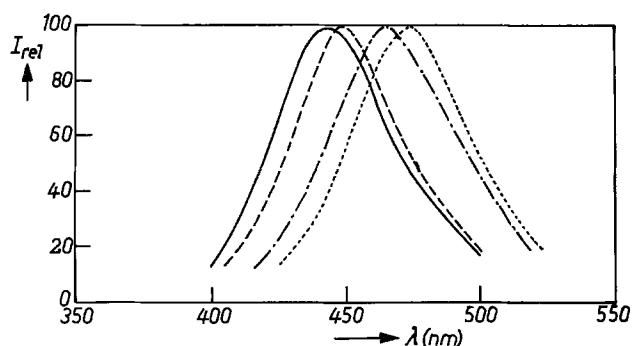


Fig. 4. Spectral energy distribution at 300°K (under 250-270 nm excitation) of the  $\beta$ -alumina  $\text{Ba}_{1-x}\text{Al}_{11}\text{O}_{17.5-x}:\text{Eu}^{2+}$  (—),  $\text{BaMgAl}_{10}\text{O}_{17}:\text{Eu}^{2+}$  (---),  $\text{SrMgAl}_{10}\text{O}_{17}:\text{Eu}^{2+}$  (- · - ·), and  $\text{EuMgAl}_{10}\text{O}_{17}$  (· · ·).

magnetoplumbite group,  $\text{SrAl}_{12}\text{O}_{19}:\text{Eu}^{2+}$  has a maximum at the shortest wavelength (395 nm), the  $\text{CaAl}_{12}\text{O}_{19}:\text{Eu}^{2+}$  band is peaking at 410 nm, and the  $\text{EuAl}_{12}\text{O}_{19}$  band at 420 nm. The luminescence of the La compounds is situated at longer wavelengths: 435 nm for  $\text{La}_{1-x}\text{Al}_{11\frac{2}{3}+x}\text{O}_{19}:\text{Eu}^{2+}$  and 450 nm for  $\text{LaMgAl}_{11}\text{O}_{19}:\text{Eu}^{2+}$ .

Generally, the  $\beta$ -alumina emits at longer wavelengths, the shortest wavelength (of  $\text{Ba}_{1-x}\text{Al}_{11}\text{O}_{17.5-x}:\text{Eu}^{2+}$ ) is found at 440 nm, which is only 10 nm below the longest wavelength emission of the magnetoplumbite ( $\text{LaMgAl}_{11}\text{O}_{19}:\text{Eu}^{2+}$  at 450 nm). The  $\text{BaMgAl}_{10}\text{O}_{17}:\text{Eu}^{2+}$  and  $\text{SrMgAl}_{10}\text{O}_{17}:\text{Eu}^{2+}$  bands peak at 450 and 465 nm, respectively; the  $\text{EuMgAl}_{10}\text{O}_{17}$  at 475 nm.

The above-mentioned maxima of the luminescence band can be shifted to a small extent by changing the amount of  $\text{Eu}^{2+}$  and/or the  $\text{Mg}^{2+}$  present in the samples.

On increasing the Eu content in the host lattices, the maxima of the luminescence bands of the phosphors gradually shift to 420 nm ( $\text{EuAl}_{12}\text{O}_{19}$ ) or to 475

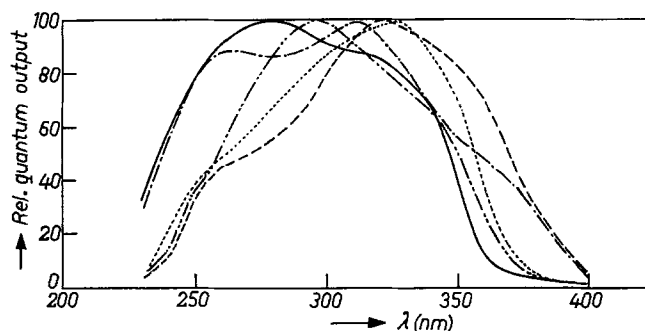


Fig. 5. Excitation spectrum at 300°K of the magnetoplumbite  $\text{SrAl}_{12}\text{O}_{19}:\text{Eu}$  (—),  $\text{CaAl}_{12}\text{O}_{19}:\text{Eu}^{2+}$  (---),  $\text{EuAl}_{12}\text{O}_{19}$  (· · ·),  $\text{La}_{1-x}\text{Al}_{11\frac{2}{3}+x}\text{O}_{19}:\text{Eu}^{2+}$  (- · - ·), and  $\text{LaMgAl}_{11}\text{O}_{19}:\text{Eu}^{2+}$  (- - -).

nm ( $\text{EuMgAl}_{10}\text{O}_{17}$ ). The increase of the Mg content in  $\text{MeMgAl}_{10}\text{O}_{17}:\text{Eu}$  leads to shifts to a longer wavelength of 10-15 nm. This tendency is parallel to what can be seen on comparing the emission maxima of Ca aluminate (410 nm) and Ba aluminate (440 nm), respectively, with Ca-Mg aluminate (425 nm) and Ba-Mg aluminate (450 nm).

Part of the emission spectra shown has been published earlier (4, 6). There is good agreement between the earlier data and those of the present investigation.

In  $\text{Eu}^{2+}$  ions the luminescence usually takes place from excited 5d levels to the 4f ground state. Two factors determine the wavelength of the emission band: on the one hand, the splitting of the 5d levels by the crystal field of the surrounding oxygen ions and, on the other hand, the energy gap between the 4f ground state and the "center of gravity" of 5d excited levels. The latter energy is dependent on the covalent character of the central ion-ligand bonds. More information about the energies involved can be obtained from diffuse reflection and excitation spectra. Due to strong absorption, the reflection spectra are less suitable for obtaining appropriate data. The excitation spectra and their relation to the position of the luminescence bands will be discussed in the next section.

**Excitation spectra.**—Excitation spectra at 300°K for the maxima of the luminescence bands are presented in Fig. 5 and 6. In the magnetoplumbite hosts (Fig. 5) broad, rather superimposed bands in the u.v. region are found. The 2(b) position of the  $\text{Eu}^{2+}$  activator ions (Fig. 1) has a  $D_{3h}$  local symmetry, so that the excited 5d levels of  $\text{Eu}^{2+}$  are expected to split into three levels (A', E', and E'') in the crystal field. Although the form of the excitation curves differs from host to host, the three-band character of each of them can be easily recognized. The spectra suggest further that the center of gravity of the 5d levels remains at about the same wavelength ( $\approx$  around 300 nm). In view of this, we conclude that the crystal field on the  $\text{Eu}^{2+}$  ions is the strongest in  $\text{LaMgAl}_{11}\text{O}_{19}$ , where the lowest excited level can be identified at about 375 nm. In a similar

Table IV. Luminescence data of  $\text{Eu}^{2+}$ -doped aluminates

Magnetoplumbite type	$\lambda_{\text{max}}$ (nm)*	Q.E. (%)**	$T_{50}$ (°K)***	$\beta$ -alumina type	$\lambda_{\text{max}}$ (nm)*	Q.E. (%)**	$T_{50}$ (°K)***
$\text{CaAl}_{12}\text{O}_{19}:\text{Eu}^{2+}$	410	50	380	$\text{SrMgAl}_{10}\text{O}_{17}:\text{Eu}^{2+}$	465	65	575
$\text{CaMg}_x\text{Al}_{12\frac{2}{3}+x}\text{O}_{19}:\text{Eu}^{2+}$	425	40	380	$\text{EuMgAl}_{10}\text{O}_{17}$	475	45	565
$\text{SrAl}_{12}\text{O}_{19}:\text{Eu}^{2+}$	395	55	385	$\text{Ba}_{1-x}\text{Al}_{11}\text{O}_{17.5-x}:\text{Eu}^{2+}$	440	70	535
$\text{EuAl}_{12}\text{O}_{19}$	420	20	370	$\text{BaMgAl}_{10}\text{O}_{17}:\text{Eu}^{2+}$	450	70	610
(Distorted types)							
$\text{La}_{1-x}\text{Al}_{11\frac{2}{3}+x}\text{O}_{19}:\text{Eu}^{2+}$	435	50	400				
$\text{LaMgAl}_{11}\text{O}_{19}:\text{Eu}^{2+}$	450	60	410				

\*  $\lambda_{\text{max}}$  = Position of the maximum of the luminescence band (250-270 nm excitation) 300°K.

\*\* Q.E. = Quantum efficiencies of non-optimized samples doped with 2% Eu at 300°K (250-270 nm excitation).

\*\*\*  $T_{50}$  = Quenching temperature (= temperature at which the intensity of the luminescence is half of that at 77°K) of samples doped with 2% Eu.

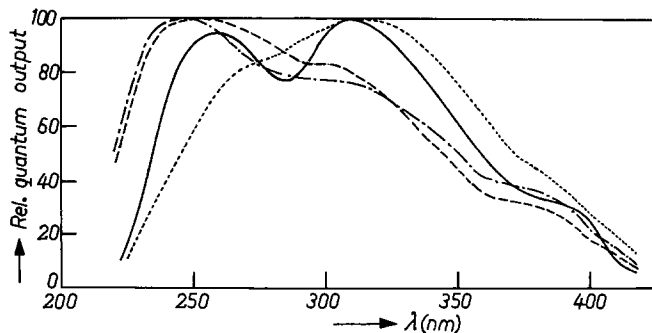


Fig. 6. Excitation spectrum at 300°K of the  $\beta$ -alumina  $\text{Ba}_{1-x}\text{Al}_{11}\text{O}_{17.5-x}:\text{Eu}^{2+}$  (—),  $\text{BaMgAl}_{10}\text{O}_{17}:\text{Eu}^{2+}$  (---),  $\text{SrMgAl}_{10}\text{O}_{17}:\text{Eu}^{2+}$  (- - -) and  $\text{EuMgAl}_{10}\text{O}_{17}$  (· · ·).

way, this level can be situated at about 360 nm for La aluminate:Eu<sup>2+</sup>, at  $\pm 355$  nm for  $\text{EuAl}_{12}\text{O}_{19}$ , at  $\pm 345$  nm for  $\text{CaAl}_{12}\text{O}_{19}:\text{Eu}^{2+}$ , and at about 340 nm for  $\text{SrAl}_{12}\text{O}_{19}:\text{Eu}^{2+}$ . On confrontation with the results of emission measurements we find that a striking parallelism exists: the phosphor with the lowest lying excitation level has also the Eu<sup>2+</sup> emission at the longest wavelength, the Stokes shift between excitation and emission being about 4500 cm<sup>-1</sup> in the whole series.

In the  $\beta$ -alumina host lattices, where the 5d levels are also expected to be split into three bands, the excitation spectra are somewhat better resolved (Fig. 6). Again, the center of gravity of the 5d levels is situated at about the same wavelength for all phosphors considered (300 nm). The lowest lying excitation band is better separated from bands in the 300–350 nm region, but especially in the Mg-containing host lattices some additional splitting of this band seems to occur so that it is difficult to define unequivocally its position. If, however, we extend the parallelism between the position of the lowest lying excitation bands and the position of the emission bands as found for the magnetoplumbites, we conclude that the  $\beta$ -alumina phosphors will emit at longer wavelength than the former group. This is actually observed (see above), with the exception of  $\text{Ba}_{1-x}\text{Al}_{11}\text{O}_{17.5-x}:\text{Eu}^{2+}$ . This may be attributed to the fact that the Stokes shift of the luminescence in Ba aluminate is much smaller ( $\pm 2500$  cm<sup>-1</sup>) than in magnetoplumbites ( $\pm 4500$  cm<sup>-1</sup>). The shape of the excitation spectra (but not the position of the excitation bands) was found to be dependent on the preparation conditions of the samples (raw materials, firing temperature). It may be possible that the slight differences between the excitation spectra of the present investigation, those of Blasse and Brill (4) for  $\text{MeAl}_{12}\text{O}_{19}:\text{Eu}$  (Me = Ca, Sr, Ba), and those of Tamatani (11) for Ba and La aluminate are due to such reasons.

**Eu<sup>2+</sup>-Eu<sup>2+</sup> energy transfer.**—In order to discuss concentration quenching phenomena (see below) and the energy transfer from Eu<sup>2+</sup> to Mn<sup>2+</sup> ions (16) in more detail, we have also considered the Eu<sup>2+</sup>-Eu<sup>2+</sup> energy transfer in hexagonal aluminates. Since the 4f  $\rightarrow$  5d transition in Eu<sup>2+</sup> is an allowed one, the transfer will mainly occur by dipole-dipole interaction (18). The probability,  $P$ , of energy transfer between Eu<sup>2+</sup> ions by this interaction has been given as (18, 19)

$$P_{\text{Eu}^{2+}-\text{Eu}^{2+}} = 3 \cdot 10^{12} \cdot \frac{P_A}{R^6 \tau_{\text{Eu}}} \cdot \frac{1}{E^4} \int f_{\text{Eu}}(E) F_{\text{Eu}}(E) dE \quad [1]$$

where  $P_A$  = the oscillator strength of the 4f  $\rightarrow$  5d transition in Eu<sup>2+</sup>;  $R$  = the distance between the Eu<sup>2+</sup> ions (in Å);  $\tau_{\text{Eu}}$  = the decay time of the luminescence (in sec);  $E$  = the energy transferred (in eV); and  $\int f_{\text{Eu}}(E) F_{\text{Eu}}(E) dE$  = the overlap between emission and excitation bands.  $f_{\text{Eu}}(E)$  and  $F_{\text{Eu}}(E)$  represent the

normalized shape of the emission and the lowest energy absorption (excitation) bands.

For the phosphors under consideration, the problem of determining the overlap integral is to separate a well-defined "lowest excitation level" from the excitation spectra as shown in Fig. 5 and 6. For the  $\beta$ -alumina materials a reasonable estimation can be made; we find for this group an energy overlap of about 0.1 eV<sup>-1</sup>. For the magnetoplumbites the energy overlap can be said to be in the same order of magnitude. Such a figure compares well with energy overlap data of Blasse (19) for Eu<sup>2+</sup> ions in  $\text{BaZrO}_3$  (0.05 eV<sup>-1</sup>) and  $\text{BaBPO}_5$  (0.3 eV<sup>-1</sup>). If we substitute in formula [1]  $P_A = 0.01$  (the usual figure for 4f  $\rightarrow$  5d transitions),  $R = 5.6$  Å (the distance for nearest Eu<sup>2+</sup> neighbors in the lattice), 1  $\mu\text{sec}$  for  $\tau_{\text{Eu}^{2+}}$  (16), and 3 eV for  $E$ , we find  $P_{\text{Eu-Eu}} = 10^9$  sec<sup>-1</sup>. Since the probability of radiative decay ( $P_{\text{rad}}$ ) is about 10<sup>6</sup>, we conclude that efficient energy transfer is found between nearest neighbor Eu<sup>2+</sup> ions in aluminate host lattices.

With the help of Eq. [1], it can also be concluded that the energy transfer between Eu<sup>2+</sup> ions positioned in the same intermediate layer is much more effective than that between Eu<sup>2+</sup> ions in different intermediate layers across the spinel block (Fig. 1). Since, in the latter case, the distance between the ions is about 11 Å, we find for the ratio of the probabilities of transfer between nearest neighbors

$$\frac{P(\text{different layer})}{P(\text{same layers})} \approx \left( \frac{5.6}{11} \right)^6 \approx 0.017$$

#### Quantum Efficiency of the Luminescence

**Quantum efficiency data.**—In Table IV we list typical quantum efficiencies at 300°K for aluminates doped with 2% Eu<sup>2+</sup> ions, using 250–270 nm excitation. In general, we can say that the efficiency of the phosphors is high, especially if we take into account that the maximum of the excitation spectrum is not always situated in the 250–270 nm range. Since the aluminate phosphors were found to have almost flat reflection spectra in the 230–350 nm range, the excitation spectra give directly the quantum efficiency as a function of wavelength. It should be noted that the figures given in Table IV are typical ones. By optimizing the preparation conditions, still higher values can be obtained (9).

**Concentration quenching.**—The usual explanation for the occurrence of concentration quenching, that is, the decrease of the measured quantum efficiency if the activator concentration exceeds a certain level, is that efficient energy transfer from the luminescent centers to, for example, defects in the lattice, which act as radiationless "sinks" takes place. A study by Blasse (19, 20) showed that, as can be expected, the efficiency of the energy transfer between the luminescent centers is in many cases the determining factor for concentration quenching.

As a yardstick for the effectiveness of energy transfer by dipole-dipole interaction, Blasse (19) defined a critical distance,  $R_c$ , between two luminescent centers, S and A, as the distance for which the probability of transfer from S to A equals the probability of radiative emission of S. In terms of Eq. [1] this means that  $P_{\text{Eu-Eu}} \tau_{\text{Eu}} = 1$ . Therefore,  $R_c$  can be found from the equation

$$R_c^6 = 3 \cdot 10^{12} \cdot \frac{P_A}{E^4} \int f_S(E) F_A(E) dE \quad [2]$$

By substituting for the parameters the data given previously, we find for the critical distance of Eu<sup>2+</sup>-Eu<sup>2+</sup> energy transfer in the aluminates figures of about 18 Å.

The distance  $R_c$  can also be estimated from geometrical considerations (19) with help of the formula



$$R_c \approx 2 \left( \frac{3V}{4\pi x_c N} \right)^{1/3} \quad [3]$$

where  $R_c$  = the critical distance (in Å);  $V$  = the volume of the unit cell (in Å<sup>3</sup>);  $x_c$  = the activator atom fraction ("the concentration") at which the quenching starts, the so-called critical concentration; and  $N$  = the number of sites per unit at which the activator atoms enter.

The problem in  $\text{Eu}^{2+}$ -doped aluminates is to establish the critical concentration,  $x_c$ . We can, however, follow the reverse way and estimate  $x_c$  from values of  $R_c$  calculated from Eq. [1]. Since in the aluminates the energy transfer within each intermediate layer is much more efficient than that across the spinel blocks, the volume of the intermediate layers is substituted for  $V$ . We find in this way  $x_c \approx 0.04$  both for magnetoplumbites and  $\beta$ -alumina host lattices.

In Fig. 7 we plot quantum efficiency vs.  $\text{Eu}^{2+}$  concentration for the  $\text{Sr}_{1-x}\text{Eu}_x\text{Al}_{12}\text{O}_{19}$  and  $\text{Ba}_{1-x}\text{Eu}_x\text{MgAl}_{10}\text{O}_{17}$  systems. The solid line refers to the Sr system, the dashed line to the Ba-Mg system. At first sight, the observed  $x_c$  for  $\text{Sr}_{1-x}\text{Eu}_x\text{Al}_{12}\text{O}_{19}$  agrees fairly well with the calculated figure of  $\approx 0.04$ . However, in  $\text{Ba}_{1-x}\text{Eu}_x\text{MgAl}_{10}\text{O}_{17}$ , the measured curve runs almost completely flat. In such a case, it is impossible to estimate a reliable figure for  $x_c$ .

Since in both systems considered the energy transfer between  $\text{Eu}^{2+}$  ions is about equally efficient, this parameter cannot account for the differences in concentration-quenching behavior. This implies, rather, that the defect situation (the "sinks") may influence the form of the concentration-quenching curves. Such a conclusion is supported by experiments in which we have substituted low concentrations of various types of "foreign" atoms (in low concentrations) in, e.g.,  $\text{Sr}_{1-x}\text{Eu}_x\text{Al}_{12}\text{O}_{19}$ . The effect of this substitution is shown in Fig. 7. The quantum efficiency vs. Eu content curve of Sr aluminate:Eu can even take the form of that of BaMg aluminate:Eu. The last-named curve is not changed by the substitution of foreign atoms.

This observation suggests that the agreement between observed and calculated  $x_c$  in Sr aluminates:  $\text{Eu}^{2+}$  is rather accidental. In fact, we do find that, as long as the nature of sinks and the kinetics of radiationless losses of excitation energy are not known, it may be misleading to draw conclusions about energy transfer in phosphors from concentration-quenching data especially if the energy transfer seems to be efficient.

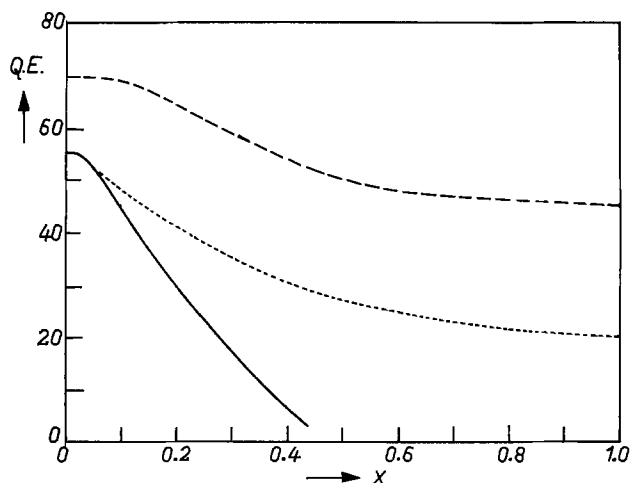


Fig. 7. Concentration-quenching curves. The quantum efficiency (Q.E.) is plotted vs. the  $\text{Eu}^{2+}$  content  $x$ . The solid and the dotted lines represent  $\text{Sr}_{1-x}\text{Eu}_x\text{Al}_{12}\text{O}_{19}$  samples prepared with and without addition of small amounts of foreign atoms, the dashed line represents the  $\text{Ba}_{1-x}\text{Eu}_x\text{MgAl}_{10}\text{O}_{17}$  system.

### Temperature Quenching of the $\text{Eu}^{2+}$ Luminescence

**Temperature-quenching data.**—In Fig. 8 and 9, we present on a relative scale ( $I$  at  $77^\circ\text{K} = 100$ ) temperature-dependence curves of the light output of magnetoplumbite and  $\beta$ -alumina type aluminates doped with 2%  $\text{Eu}^{2+}$  (some data on the effect of the  $\text{Eu}^{2+}$  concentration on temperature quenching are given below) and for the Eu aluminates themselves. On comparing Fig. 8 and 9, a first conclusion is that the quenching of the  $\text{Eu}^{2+}$  luminescence in the  $\beta$ -alumina occurs at much higher temperatures than for the magnetoplumbites. If we take  $T_{50}$ , the temperature at which the intensity of the luminescence is half of that at  $77^\circ\text{K}$ , as an indicator, we find a difference of about  $150^\circ\text{--}200^\circ\text{K}$  (Table IV). Temperature-quenching data for several aluminates  $\text{MeAl}_{12}\text{O}_{19}:\text{Eu}^{2+}$  ( $\text{Me} = \text{Ca}, \text{Sr}, \text{Ba}, \text{La}$ ) have also been published by Blasse and Brill (4, 20) and Tamatani (11). The  $T_{50}$  figures which can be derived from the curves published by these authors agree fairly well with those of the present investigation.

On further consideration of Table IV, it can be seen that within both structural groups the compounds with the largest cations tend to have the highest quenching temperatures. In  $\text{MeAl}_{12}\text{O}_{19}:\text{Eu}^{2+}$ ,  $T_{50}$  for  $\text{Me} = \text{Sr}$  ( $385^\circ\text{K}$ ) is larger than for  $\text{Me} = \text{Ca}$  ( $380^\circ\text{K}$ ); in  $\text{MeMgAl}_{10}\text{O}_{17}:\text{Eu}^{2+}$ ,  $T_{50}$  for  $\text{Me} = \text{Ba}$  ( $610^\circ\text{K}$ ), higher than for  $\text{Me} = \text{Sr}$  ( $575^\circ\text{K}$ ). The Eu aluminates have a more or less special position due to their high activator content. For that reason we cannot compare directly the  $T_{50}$  figures of these materials with the other phosphors.

In the  $\text{Eu}^{2+}$  La aluminates, the divalent Eu is introduced in a  $\text{La}^{3+}$  site without charge compensation, so that these compounds will have quenching properties different from the aluminates with large divalent cations. We note, however, that as for  $\text{Ba}_{1-x}\text{Al}_{11}\text{O}_{17.5-x}:\text{Eu}^{2+}$  and  $\text{BaMgAl}_{10}\text{O}_{17}:\text{Eu}^{2+}$  ( $\Delta T_{50} = 75^\circ\text{K}$ ), the Mg-containing La aluminates have slightly higher quenching temperatures than the La aluminate itself ( $\Delta T_{50} = 10^\circ\text{K}$ ).

Blasse and Brill (20) and Blasse (21) have discussed temperature-quenching phenomena in terms of a con-

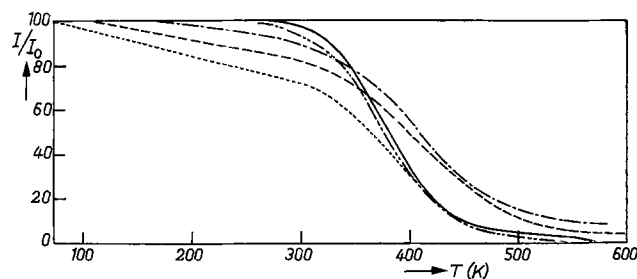


Fig. 8. Temperature dependence of the light output of magnetoplumbite phosphors ( $[\text{Eu}^{2+}] = 0.02$ ).  $\text{SrAl}_{12}\text{O}_{19}:\text{Eu}^{2+}$  (—),  $\text{CaAl}_{12}\text{O}_{19}:\text{Eu}^{2+}$  (---),  $\text{EuAl}_{12}\text{O}_{19}$  (----),  $\text{La}_{1-x}\text{Al}_{11\ 2/3+x}\text{O}_{19}:\text{Eu}^{2+}$  (— · —),  $\text{LaMgAl}_{11}\text{O}_{19}:\text{Eu}^{2+}$  (— · —).

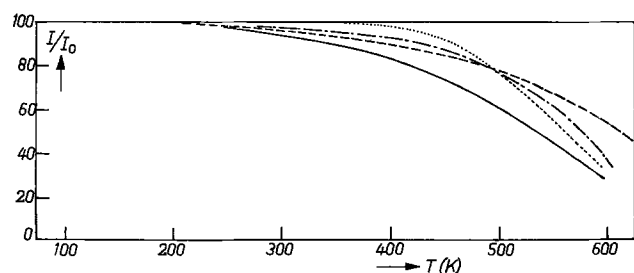


Fig. 9. Temperature dependence of the light output of  $\beta$ -alumina phosphors ( $[\text{Eu}^{2+}] = 0.02$ ).  $\text{Ba}_{1-x}\text{Al}_{11}\text{O}_{17.5-x}:\text{Eu}^{2+}$  (—),  $\text{BaMgAl}_{10}\text{O}_{17}:\text{Eu}^{2+}$  (---),  $\text{SrMgAl}_{10}\text{O}_{17}:\text{Eu}^{2+}$  (— · —),  $\text{EuMgAl}_{10}\text{O}_{17}$  (----).



figuration-coordinate model. For Eu<sup>2+</sup> ions replacing divalent cations, the quenching temperature was said to be relatively high in rigid lattices (the so-called "lattice effect") and in cases where Eu<sup>2+</sup> substitutes for large cations ("size effect"). The data in Table IV indeed confirm these predictions. As far as the lattice effect is concerned, we note that in  $\beta$ -alumina the bonds of the divalent metal ions are strong due to the presence of oxygen ions at a very small distance (in the 2(c) position). This lattice can therefore be considered to be "rigid." In magnetoplumbites the oxygen ions in the intermediate layer are positioned at 6(h) which is much further away. The bond strength is much less so that the lattice can be said to be "weaker." The predicted size effect is also apparent from Table IV (see above), although not so pronounced as for the lattice effect. The replacement of Al<sup>3+</sup> by Mg<sup>2+</sup> results in an increase of the unit cell volume and is therefore equivalent to the introduction of a cation in the 2(c) position (see Fig. 1) of larger size.

If divalent Eu replaces a trivalent cation like La, the luminescent center has formally an effective charge. On considering temperature quenching, Blasse (21) explained that two factors play an important role in such a situation. On the one hand, the lattice is relatively more rigid due to strong La<sup>3+</sup>-O bonds than for the case where Eu<sup>2+</sup> replaces a divalent ion. This will give a higher  $T_{50}$ . On the other hand, the Eu<sup>2+</sup> ground state is more "expanded" due to the presence of lanthanum ions. This results in a lower  $T_{50}$ . The latter can be considered as a kind of a "size effect." Similar to what we have found for the magnetoplumbites with divalent large cations, the lattice effect is supposed to be more important than the size effect so that a higher  $T_{50}$  is expected for the La phosphors. This is indeed the case (410° and 400°K instead of about 380°K).

*Influence of activator concentration on  $T_{50}$ .*—Since concentration quenching is not very effective (see above), no drastic changes in  $T_{50}$  are to be expected if the activator content increases. In Fig 10 we show this for the La<sub>1-x</sub>Al<sub>11/3+x</sub>O<sub>19</sub>:Eu (change in  $T_{50} \approx 10^\circ\text{K}$ )

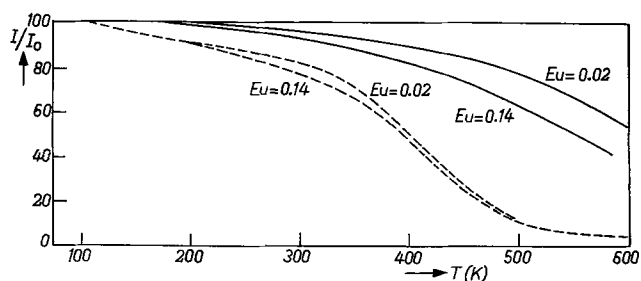


Fig. 10. Concentration effect on the temperature-dependence curves of  $\text{BaMgAl}_{10}\text{O}_{17}:\text{Eu}^{2+}$  (—) and  $\text{La}_{1-x}\text{Al}_{11/3+x}\text{O}_{19}:\text{Eu}^{2+}$  (---).

and  $\text{BaMgAl}_{10}\text{O}_{17}:\text{Eu}^{2+}$  systems (maximum change in  $T_{50} \approx 60^\circ\text{K}$ ). In some of the other aluminate host lattices, more important changes in  $T_{50}$  were observed. X-ray diffraction indicates that a phase separation on introduction of large amounts of  $\text{Eu}^{2+}$  (e.g., in  $\text{Ba}_{1-x}\text{Al}_{11}\text{O}_{17.5-x}:\text{Eu}^{2+}$ ) is responsible for these changes in  $T_{50}$ .

### Acknowledgments

The authors wish to thank Dr. J. L. Sommerdijk and Dr. J. M. P. J. Verstegen for helpful discussions. Dr. P. B. Braun and his research group are thanked for their x-ray diffraction studies and Mr. J. P. M. Damen and G. Verspui for the preparation of the single crystals.

Manuscript submitted Nov. 17, 1975; revised manuscript received Jan. 19, 1976.

Any discussion of this paper will appear in a Discussion Section to be published in the December 1976 JOURNAL. All discussions for the December 1976 Discussion Section should be submitted by Aug. 1, 1976.

Publication costs of this article were partially assisted by Philips Research Laboratories.

### REFERENCES

1. V. Adelskjöld, *Arkiv Kemi, Mineral. Geol.*, **12A**, 1 (1938).
2. R. S. Roth and S. Hasko, *J. Am. Ceram. Soc.*, **41**, 165 (1958).
3. J. M. P. J. Verstegen, J. L. Sommerdijk, and J. G. Verriet, *J. Luminescence*, **6**, 425 (1973).
4. G. Blasse and A. Brill, *Philips Res. Rept.*, **23**, 201 (1968).
5. J. M. P. J. Verstegen, *J. Solid State Chem.*, **7**, 468 (1973).
6. J. M. P. J. Verstegen and A. L. N. Stevels, *J. Luminescence*, **9**, 406 (1974).
7. J. L. Sommerdijk and J. M. P. J. Verstegen, *ibid.*, **9**, 415 (1974).
8. J. L. Sommerdijk, J. M. P. J. Verstegen, and A. Brill, *Philips Res. Rept.*, **29**, 517 (1974).
9. J. M. P. J. Verstegen, *This Journal*, **121**, 1623 (1974).
10. P. B. Braun, *Philips Res. Rept.*, **12**, 491 (1957).
11. M. Tamatani, *Japan. J. Appl. Phys.*, **13**, 950 (1974).
12. A. Brill and W. L. Wanmaker, *This Journal*, **111**, 1363 (1964).
13. K. Kato and H. Saalfeld, *Neues Jahrb. Mineral. Abhand.*, **109**, 192 (1968).
14. R. W. G. Wyckoff, "Crystal Structures," Vol. 4, 2nd ed., Wiley Interscience, New York (1965).
15. P. B. Braun *et al.*, To be published.
16. A. L. N. Stevels and A. D. M. Schrama-de Pauw, *J. Luminescence*, To be published.
17. Brit. Pat. 1,191,014 (1967).
18. D. L. Dexter, *J. Chem. Phys.*, **21**, 836 (1953).
19. G. Blasse, *Philips Res. Rept.*, **24**, 131 (1969).
20. G. Blasse and A. Brill, *Philips Tech. Rev.*, **31**, 304 (1970).
21. G. Blasse, *J. Solid State Chem.*, **9**, 147 (1974).
22. J. M. P. J. Verstegen, J. L. Sommerdijk, and A. Brill, *J. Luminescence*, **9**, 420 (1974).

# Behavior of Impurities during Chemical Vapor Deposition of GaAs

Yu. G. Sidorov, L. F. Vasil'eva, I. V. Sabinina, and S. A. Dvoretzky

*Institute of Semiconductor Physics, Siberian Branch of the USSR Academy, Novosibirsk, USSR*

and A. V. Sidorova

*Electrotechnical Institute, Novosibirsk, USSR*

## ABSTRACT

GaAs doping with Sn, S, Zn, and Cd during growth in an open chloride vapor transport system was studied. The dopant concentration dependences on growth rate, growth temperature, and vapor pressure were measured. Based on an analysis of the results, it follows that the doping depends on both the substrate orientation and on the electrical nature of the impurity. The observed dependence of impurity concentration on vapor pressure can be obtained, assuming that impurity equilibrium is established, but the carrier concentration in the GaAs at the growth temperature is not determined by the impurity concentration. The binding energies and entropies of various impurities in Ge, Si, and GaAs calculated from the solidus curves of the impurity-semiconductor system are reported.

A study of epitaxial layer doping mechanisms is necessary to grow the layers with preset properties and, in particular, to clear up the nature and the sources of uncontrolled impurities. It is necessary to know a number of the kinetic coefficients related to the processes which govern the impurity incorporation in order to determine the absolute doping level.

Impurity incorporation in the growing crystal is a multistage process, which consists of impurity trapping in an adsorption layer, transformation and motion within the adsorption layer, and, finally, transport from the adsorption layer into the crystal. The relationships describing the rates of the different stages are quite different. If the rate of the last process is determining, the over-all incorporation of the electrically active impurity would be sensitive to the electrical nature of the impurity and to the carrier concentration in the semiconductor surface layer. For the other cases the rate would be determined only by the chemical nature of the doping impurity.

If the incorporation of the impurity into the growing layer is limited by the kinetics of one of these stages, an increase in the growth temperature must lead to an increase in impurity concentration, because kinetic rates normally increase with temperature. Furthermore, the concentrations must approach their equilibrium values as the rates increase. In this connection, it would be very useful to compare the experimental concentrations with those calculated on the assumption of complete equilibrium. Certain features of impurity behavior during GaAs growth by the halide chemical vapor transport method used here have already been published (1-3). The present experiments extend these GaAs doping results, notably for doping with sulfur, tin, zinc, and cadmium.

## Experimental

The growth of gallium arsenide epitaxial layers was carried out by an open-tube chloride vapor transport process on semi-insulating GaAs substrates. High purity  $\text{AsCl}_3$  was used as the chloride source. The gallium source was either metallic Ga or GaAs. The growth parameters were: source temperature, 800°-850°C; substrate temperature, 700°-750°C;  $\text{AsCl}_3$  temperature, 0°C; flow rate, 150-300 ml·min<sup>-1</sup>; sub-

strate temperature gradient, 5°C·cm<sup>-1</sup>. It was possible to obtain undoped layers with carrier concentrations  $n \sim 10^4$  cm<sup>-3</sup> and electron mobilities up to 100,000 cm<sup>2</sup>/V·sec at 77°K when grown on (100) substrates by a Ga/AsCl<sub>3</sub>/H<sub>2</sub> system (4). The carrier concentration in undoped layers was 10<sup>15</sup> cm<sup>-3</sup> and the mobility was reduced to 30,000 cm<sup>2</sup>/V·sec at 77°K, when undoped GaAs was used as the source.

The doping sources for Zn and Cd were Zn<sub>3</sub>As<sub>2</sub> and Cd<sub>3</sub>As<sub>2</sub> loaded into quartz ampuls of known volume, which were sealed at one end. The AsCl<sub>3</sub> and the products of its decomposition were allowed to diffuse into the hot ampul and etched the Zn<sub>3</sub>As<sub>2</sub> or Cd<sub>3</sub>As<sub>2</sub> forming gaseous chlorides which diffused out of the ampul. The ampul was placed in a separately controlled temperature zone set at 400°C ahead of the substrate zone. At this temperature neither dissociation of Zn<sub>3</sub>As<sub>2</sub> or Cd<sub>3</sub>As<sub>2</sub> nor condensation of arsenic and chlorides of zinc or cadmium occurs.

The requirements on the precision of maintaining the temperature of the dopant zone are not severe because diffusivity in the gas phase depends only weakly on temperature. Weighing of the ampul before and after the experiment allowed us to determine the total quantity of dopant used. GaAs was used as the Ga source in these experiments because molten elemental gallium could dissolve some of the impurity and lead to errors in calculating the net quantity of impurity in the gas phase.

Doping by tin was carried out either by the introduction of tin into elemental gallium used as the gallium source or by the introduction of tin chloride into the growth zone through a special channel. It was not possible to determine the tin concentration in the gas phase when the first method was used.

Sulfur doping was accomplished by adding hydrogen sulfide to the reactant stream. The hydrogen sulfide, obtained by decomposition of sulfides, was introduced into the reactor through a special inlet. The hydrogen sulfide vapor pressure was controlled by the sulfide temperature.

The resultant carrier concentrations were measured by the Van der Pauw method (precision of determining carrier concentration is ±15%). The electron and hole concentrations allowed us to estimate the electrically active impurity concentrations. This is the core of our investigation. To do this, it was necessary to take into account the degree of compensa-

Key words: chemical vapor deposition, GaAs—growth, impurities, CVD, doping, segregation, facet effects, S, Sn, Zn, Cd.

tion by (unwanted) impurities of opposite electrical type.

The concentrations of Sn and Zn in the grown layers was determined directly by mass spectrometric and emission spectral methods. For these samples, the measured electron and hole concentrations corresponded closely to the Sn and Zn densities, respectively, determined directly. Hence, residual impurity donors and acceptors must be present only at levels below our lowest intentional doping levels. No such conclusions can be drawn for electrically inactive impurities.

The homogeneity of the layers in a direction perpendicular to the face of the substrate was checked by layer-by-layer etching and subsequent measurement of carrier concentration and mobility, and sometimes by mass spectrometry as well. A reduction of carrier concentration near the film-substrate transition was sometimes observed when doping with tin.

### Results and Discussion

A strong variation of dopant concentration with crystallographic orientation has already been established (1-3). However, it was noted that if the carrier concentrations in films grown on substrates of different orientations were plotted against the growth rates on those orientations the results were simple. Although growth rates depend on orientation, dopant densities correlated only with the growth rates (5). Films on different orientations have the same impurity concentrations when their growth rates are equal.

Figure 1 shows the results of films doped by two different Sn concentrations in the gas phase. When polycrystalline GaAs was used as the source (upper curve), the growth rate was changed by varying the amount of gallium arsenide (not exposed surface area) in the source zone. The resultant change of gas phase saturation allowed us to vary the growth rate by two orders of magnitude. The gas phase composition calculated from the net change of source weight during the growth experiment shows that the partial pressures of the components change only a factor of two or three, while the growth rate changes two orders of magnitude. Hence the effect must be kinetic in nature, a departure from equilibrium in the growth zone. When liquid gallium saturated with arsenic was used as the source (lower curve), the growth rate was changed by varying the substrate

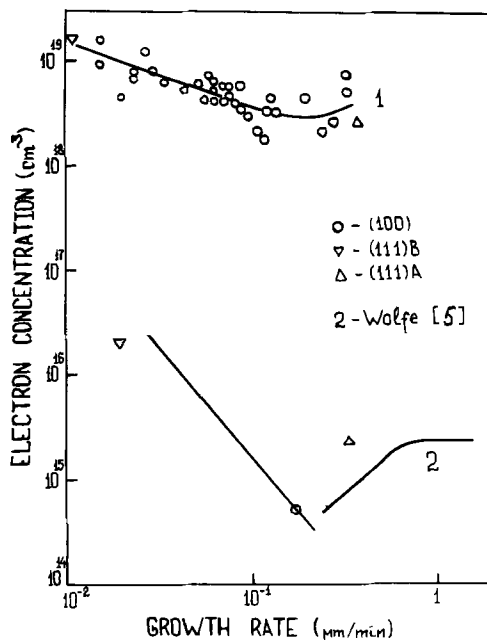


Fig. 1. Dependence of electron concentration on growth rate for Sn doping.

temperature gradient. The mean substrate temperature was held constant. The lower curve was drawn by using the results from Ref. (5). The points on this curve are the results of our present experiments for characteristic growth rates on (100), (111)A, and (111)B planes. The present results agree with the data from Ref. (5).

Note that the curve of carrier concentration *vs.* growth rate has a minimum. This minimum is shallower for the upper curve obtained at higher Sn concentrations in the gas phase (where the doping was carried out by introduction of Sn chlorides through the special channel). This may imply that the orientation dependence reduces as the doping level increases. One can see that the free electron concentrations in films grown on planes (111)B and (100), and also on (111)A and (100), are equal if their growth rates are equal (upper curve). A similar effect was observed during doping with Zn and S (to be published). The calculated equilibrium Sn concentrations corresponding to the upper curve are less than the measured carrier concentrations. (The calculation of impurity equilibrium concentrations is discussed below.)

The dependence of electron concentration on growth rate has a minimum for S doping also. This minimum also occurred for a growth rate  $0.2 \mu\text{m}/\text{min}$  as with Sn doping (Fig. 2).

The dependence of hole concentrations on growth rate for Zn and Cd doping had a maximum at the same growth rates. This is in agreement with the results of another investigation (6). For Zn, the carrier concentrations in films grown on (111)A and (100) planes were equal when their respective growth rates were equal as for the Sn results noted earlier. The growth rates of (111)A and (111)B planes differed by more than one order of magnitude, while the corresponding hole concentrations in films on (111)B ( $7.7 \cdot 10^{17} \text{ cm}^{-3}$ ) were one-half order of magnitude less than on (111)A ( $4.1 \cdot 10^{18} \text{ cm}^{-3}$ ). This is also in agreement with the previous investigations (6). The variations of the growth rates on substrates of different orientations became smaller and, correspondingly, the orientation influence on Zn segregation was reduced at high doping levels ( $\sim 10^{19} \text{ cm}^{-3}$ ).

Orientation dependence during Te doping was observed by Williams (7). If we order his orientations in terms of increasing growth rate, then the associated Te concentrations exhibit a minimum *vs.* growth rate, similar to our donor data.

It is not possible to explain such complicated dependences of doping levels on growth rate with a simple model of material crystallization (1-3). Only

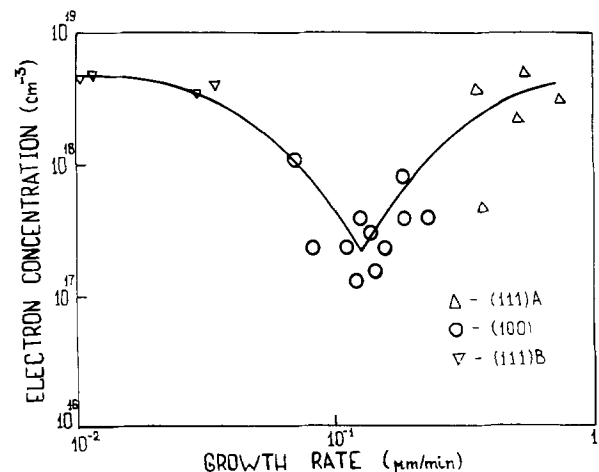


Fig. 2. Dependence of electron concentration on growth rate for S doping.

a monotonic dependence of doping level on growth rate can be predicted (1-3).

However, it is clear that it is primarily the electrical nature of the dopant (donor or acceptor) that determines the observed orientation dependence of the solubility and not the lattice site nor the chemical nature of the dopant nor its molecular form in the gas phase. The donors Sn, S, and Te exhibit a minimum in concentration vs. growth rate, whereas the acceptors Zn and Cd exhibit a maximum. In the reaction zone, Sn is present as  $\text{SnCl}_2$  whereas the other dopants are in elemental form. The donors S and Te occupy As sites, while the acceptors Zn and Cd lie on Ga sites. The donor Sn occupies a Ga site, but its concentration-growth rate behavior is that of the other donors, not that of the other Ga site occupiers. Hence the incorporation of the impurities is sensitive to their electrical nature.

The dependences of Zn and Cd concentrations on the growth temperature for different vapor pressures of these impurities are given in Fig. 3 and 4, respectively. One can see that the Zn concentration hardly depends on the growth temperature. The Cd concentration decreases slowly with temperature at low doping levels and does not depend on growth temperature at high doping levels. The predicted equilibrium Zn (curve 1' in Fig. 3) and Cd concen-

trations decrease very slowly with temperature. (The calculation technique is given below.)

If there are some slowly proceeding kinetic stages during the doping, the concentrations of impurity in the film must be less than the corresponding equilibrium concentrations because the impurity equilibrium has no time to be established. The rates of such kinetic processes usually increase with temperature, and it is natural to expect a decrease in the difference between the equilibrium and the experimental impurity concentrations. However, the small (or even slightly negative) differences observed in the experiments (the experimental concentration, curve 1, is greater than the equilibrium one, curve 1', Fig. 3) and the independence of this difference upon temperature means that the mechanisms determining the impurity segregation cannot be limited by kinetics (in addition, the growth rates of the samples for curve 1 are only weakly dependent on the growth temperature, Fig. 5). Hence, the impurity concentration must be in equilibrium. The differences between the experimental and the theoretical equilibrium impurity concentrations in the films show that some of the assumptions made in the calculations of the equilibrium concentrations are not valid.

The dependence of the impurity concentration in the films on its content in the gas phase (Fig. 6) was studied for Zn and Cd for a growth rate of 12-15  $\mu\text{m/hr}$ . The impurity concentrations in the films increased linearly with the pressure of Zn and Cd. The same dependence was observed for Sn, if the Sn vapor pressure was assumed to be proportional to its content in the Ga source. The observed dependence of the impurity concentration in the film on its vapor pressure could occur only if the carrier concentration in the surface layer of the growing film was not determined by the impurity concentration at the source.

The equilibrium concentration of segregated impurity in the solid can be represented by

$$N_{\text{tot}} = \eta \cdot N_0 = \eta \cdot K \cdot \frac{P_i}{P_{A(B)}} \quad [1]$$

when the degree of ionization  $\eta$  is significant. Here  $N_{\text{tot}}$  is the total impurity concentration in the crystal,  $N_0$  is the neutral impurity concentration,  $K$  is the equilibrium constant, which we shall determine further, and  $P_i$ ,  $P_{A(B)}$  are the pressures of monoatomic vapors of impurity and of the component replaced by impurity, either Ga or As, respectively. The pressures of the component vapors are calculated from their

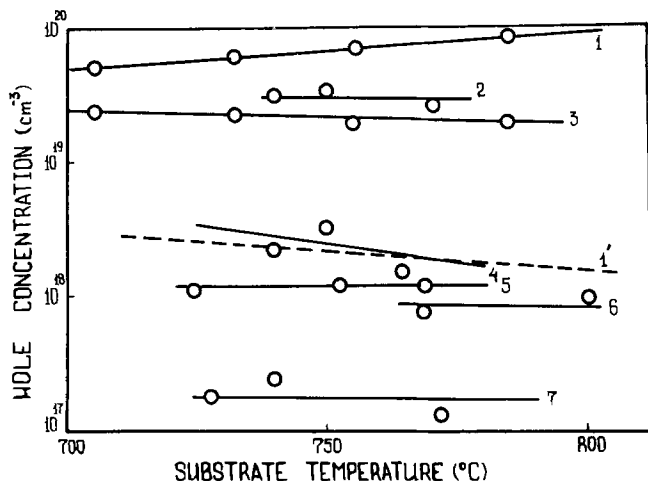


Fig. 3. Dependence of hole concentration on growth temperature for Zn doping, for different vapor pressures  $P^*_{\text{Zn}}$ : curve 1,  $1.12 \cdot 10^{-4}$ ; curve 2,  $1.28 \cdot 10^{-4}$ ; curve 3,  $2.34 \cdot 10^{-5}$ ; curve 4,  $7.87 \cdot 10^{-6}$ ; curve 5,  $5.1 \cdot 10^{-6}$ ; curve 6,  $1.37 \cdot 10^{-6}$ ; curve 7,  $9.75 \cdot 10^{-7}$  (atm). Curve 1', equilibrium concentration of Zn for  $P^* = 1.12 \cdot 10^{-4}$  atm.

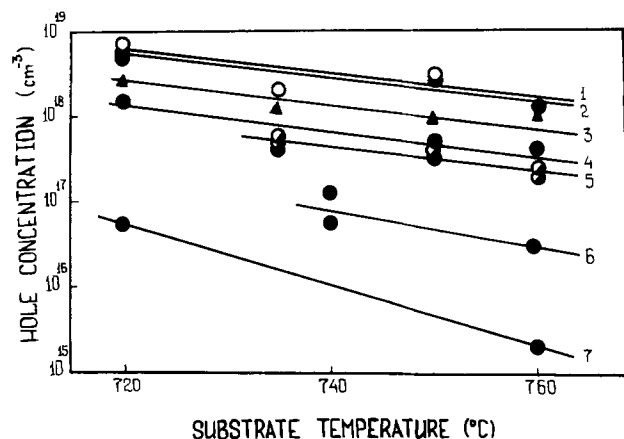


Fig. 4. Dependence of hole concentration on the growth temperature for Cd doping, for different vapor pressures  $P^*_{\text{Cd}}$ : curve 1,  $9.3 \cdot 10^{-3}$ ; curve 2,  $5.2 \cdot 10^{-3}$ ; curve 3,  $3.2 \cdot 10^{-3}$ ; curve 4,  $1.78 \cdot 10^{-3}$ ; curve 5,  $9.5 \cdot 10^{-4}$ ; curve 6,  $1.7 \cdot 10^{-4}$ ; curve 7,  $2.6 \cdot 10^{-5}$  (atm).

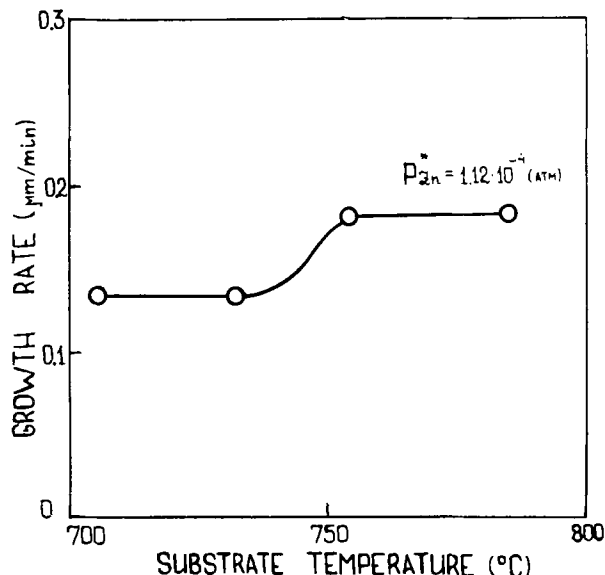


Fig. 5. Dependence of the growth rate on the growth temperature

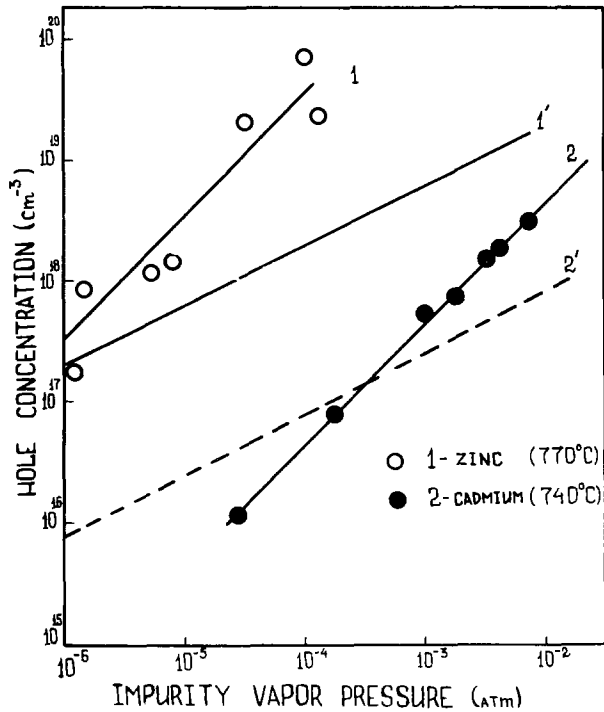


Fig. 6. Dependence of impurity concentration in the layers on its content in the gas phase for Zn and Cd. The experimental concentrations, curves 1 and 2, and the equilibrium concentrations, curves 1' and 2', for Zn and Cd.

gas phase content. The Fermi-Dirac distribution can be approximated by that of Maxwell-Boltzmann in many cases. Then one can obtain a very clear relation:  $\eta = N_{C(V)}/2n(p)$  where  $N_{C(V)}$  is the density of states in the conduction (valence) band and  $n(p)$  is the free electron (hole) concentration. Then we have

$$N_{tot} = \frac{N_{C(V)}}{2n(p)} \cdot K \cdot \frac{P_i}{P_{Ga(As)}} \quad [2]$$

The carrier concentration is equal to the impurity concentration if  $N_{tot} \gg \eta_i$ , where  $\eta_i$  is the intrinsic concentration, i.e.,  $n(p) = N_{tot}$ . (Such a case is shown in Fig. 6 where  $\eta_i \approx 10^{16} \text{ cm}^{-3}$ .) Here

$$N_{tot} = \sqrt{N_{C(V)} \cdot K \cdot \frac{P_i}{P_{Ga(As)}}} \quad [3]$$

and the equilibrium impurity concentration in the film must vary proportionally to the square root of its monoatomic vapor pressure. For Cd it is the total pressure of its vapors. Sn is present in the gas phase in molecular form as  $\text{SnCl}_2$  and the pressure of monoatomic Sn vapor is proportional to the  $\text{SnCl}_2$  vapor pressure. For Zn, the monoatomic vapor pressure differs slightly from the total vapor pressure of the Zn components.

The experimental dependences of the impurity concentrations in the film vs. the pressures of their monoatomic vapors are close to being linear. However, with our assumptions, the equilibrium concentration should be proportional to the square root of the monoatomic vapor pressure. To obtain agreement between the experimental and the theoretical equilibrium concentrations, it is necessary to suppose that the carrier concentrations at the growth temperature (near the surface of the growing crystal, at least) are not determined by the impurity concentration. The actual bulk properties of epitaxial GaAs films at the growth temperatures were determined separately by special measurements (8). It turned out that, at  $1000^\circ\text{K}$ , the free electron concentration was equal to  $10^{18}\text{-}10^{19} \text{ cm}^{-3}$  in films doped with either donor impurities or with acceptors and did not depend on impurity concentra-

tion. In the presence of such a constant free electron concentration, the equilibrium concentration of impurity in the film becomes simply proportional to the pressure of the monoatomic impurity vapors. However, for the acceptor impurities the calculated values of the equilibrium concentrations of impurity were significantly higher than the experimental concentrations; for tin they were lower.

A possible mechanism can explain the independence of carrier concentration in the layer of crystal near the growth surface (where the impurity segregation is determined). It is a surface charge and the "surface quasi-neutrality" connected with it. The influence of surface charge is considered in Ref. (9). To our regret, we cannot see any straightforward ways of determining the carrier concentration in such a layer close to the growing film surface during the film growth. The experimental impurity concentration in the as-grown film is the only information source we have relating to charge carrier concentration. Inserting it in Eq. [2], one can calculate backwards the carrier concentrations which existed during growth. The only way to check the validity of these results is by a comparison of the charge carrier concentrations obtained for different impurities. These have to be connected by the relation  $n \cdot p = n_i^2$ . The accuracy of the equilibrium constant used in Eq. [2] is important in such calculations. An assumption on the invariability of the semiconductor vibration spectrum independent of impurity concentration was made in Ref. (10) when calculating  $K$ . This corresponds to assuming the equality of the doped crystal entropy with that of the pure semiconductor. A treatment of solids of Ge-impurity and Si-impurity systems has shown that in a general case this assumption is not valid. The results of this calculation as a dependence of the excess entropy  $\Delta S_{exc}$  of an impurity in a semiconductor crystal ( $\Delta S_{exc} = S_{i,sol} - S_{semicond.}$ ) on  $E_{Bind}$  are shown in Fig. 7 (10). The excess entropy increases with decreasing  $E_{Bind}$ . The calculated values for Ge and Si give the same dependence. For GaAs, the necessary data turned out to be accessible only for the impurities Zn (11), Sn (11), P, In, Al, and Sb (13). The calculated values of  $E_{Bind}$  and  $\Delta S_{exc}$  for these impurities in GaAs do not fall on the curve for Ge and Si because, for all of them, the excess entropy is close to zero. It is obvious that under sufficiently small binding energies the excess entropy has to increase. It is also possible that  $E_{Bind}$  and  $\Delta S_{exc}$  for impurities in GaAs do not correlate with each other. In any case one can determine the equilibrium constant with satisfactory reliability only for two elements from those considered, and they are Sn and Zn. Similar calculations give for Sn,  $n_s = 4 \cdot 10^{16} \text{ cm}^{-3}$ , and for Zn,  $p_s = 9 \cdot 10^{16} \text{ cm}^{-3}$ . Their product,  $n_s \cdot p_s = 3.6 \cdot 10^{33} \text{ cm}^{-6}$  is close to  $n_i^2$  for GaAs at  $1000^\circ\text{K}$  ( $3.1 \cdot 10^{33} \text{ cm}^{-6}$ ) which says that the suggested model at least is not in contradiction with the experimental

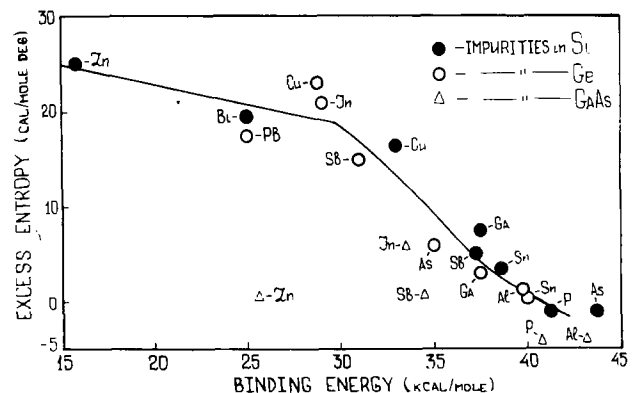


Fig. 7. Dependence of excess entropy on binding energy

results. One can obtain values of  $p_s$  for Cd close to those obtained for Zn, if we assume that  $\Delta S_{exc}$  for Cd is situated in a region between zero and the curve for impurities in Ge and Si.

Thus, the orientation dependence of impurity segregation can be explained (within the framework of these ideas) by the dependence on growth rate and carrier concentration in the crystal layer near the growth surface (and a surface charge of the growing crystal).

Using data from the literature, we can assess the applicability of these ideas for other methods of film growth and for other materials. GaAs doped with Zn (14) and with Cd (15-17) during growth by liquid phase epitaxy also shows a linear dependence between the impurity concentrations in the solid and in the liquid phases. A calculation of the carrier concentrations near the growing surface gives  $n_s \sim 10^{19} \text{ cm}^{-3}$  for Sn and  $p_s \sim 10^{19} \text{ cm}^{-3}$  for Zn. In LPE layers, the incorporation both of donor and acceptor impurities was less than that expected from equilibrium considerations.

The doping of Si epitaxial layers grown by  $\text{SiCl}_4$  pyrolysis by B, As, and P was studied (18). The values  $E_{Bind}$  and  $\Delta S_{exc}$  calculated from the experimental data (15) give points lying higher than the curve for impurities in Ge and Si (Fig. 7). This divergence means that during pyrolysis impurity incorporation exceeds the equilibrium distribution and there is no correlation with the electrophysical nature of the impurity in Si.

### Conclusions

A study of the orientation dependence of doping densities of donor and acceptor impurities in GaAs grown by chloride vapor transport shows that the impurity segregation is sensitive to the electrical nature of the impurities in GaAs. The dependence of impurity concentration on the pressure of its vapors and on temperature can be described in an equilibrium approximation. However, the experimental results require the assumption that the charge carrier concentration in the layer of growing crystal close to the growth surface is not determined by the segregated impurity.

The ideas developed here should be useful in explaining impurity segregation for other growth methods and for other materials.

Manuscript submitted Aug. 30, 1975; revised manuscript received Dec. 1, 1975.

Any discussion of this paper will appear in a Discussion Section to be published in the December 1976 JOURNAL. All discussions for the December 1976 Discussion Section should be submitted by Aug. 1, 1976.

### REFERENCES

1. A. A. Chernov, *Usp. Fiz. Nauk*, **73**, 2, 277 (1961).
2. W. Barton, N. Cabrera, and F. Frank, *Phil. Trans.*, **A243**, 299 (1951).
3. L. G. Lavrent'eva, Sb. "Protsessi rosta crystallov i plenok poluprovodnicov.," Nauka, Novosibirsk, 1970, str. 130.
4. Yu. G. Sidorov, S. A. Dvoretzky, and V. M. Zaletin, *Electronnaia Tekhnica*, Ser. 12, **3**, 21 (1974).
5. C. M. Wolfe, G. E. Stillman, and W. I. Lindley, Proceedings of Second International Symposium, Dallas, 1968, p. 43.
6. L. G. Lavrent'eva, Yu. G. Kataev, L. G. Nesteryuk, and V. V. Skliarenko, Sb. "Arsenid gallia," Tomsky Gosudarstvennyi Universitet, Tomsk, 1969, str. 59.
7. F. V. Williams, *This Journal*, **111**, 886 (1964).
8. V. I. Khokhlov, Yu. G. Sidorov, and S. A. Dvoretzky, *Phys. Status Solidi*, (a), **25**, 311 (1974).
9. K. Lehovc, *Surface Sci.*, **1**, 165 (1964).
10. Yu. G. Sidorov, A. V. Sidorova, and S. A. Dvoretzky, *Izv. Akad. Nauk SSSR, Ser. Neorgan. Materiali*, **8**, 1738 (1972).
11. A. S. Jordan, *This Journal*, **118**, 781 (1971).
12. M. G. Mil'vidsky, O. V. Pelevin, and V. A. Sakhorov, "Fiziko-khi-micheskie osnovi poluchenia razlagayushikhsia poluprovodnicovikh soedineniy," Metallurgia, Moskva, 1974, str. 108.
13. R. F. Brebrick and R. I. Panlener, *This Journal*, **121**, 932 (1974).
14. K. Keller and W. V. Muench, *Solid State Electron.*, **14**, 526 (1971).
15. R. R. Solomon, Proceedings of Second International Symposium, Dallas, 1968, p. 11.
16. I. Kinoshita, W. W. Stein, D. F. Day, and I. B. Money, *ibid.*, pp. 22-27.
17. C. S. Kang and P. E. Greene, *ibid.*, pp. 18-21.
18. R. Rai-Choudhury and Salkovitz, *J. Cryst. Growth* **7**, 353 (1970).

# Electroetching of Platinum in the Titanium-Platinum-Gold Metallization on Silicon Integrated Circuits

R. P. Frankenthal\*

*Bell Laboratories, Incorporated, Murray Hill, New Jersey 07974*

and D. H. Eaton<sup>1</sup>

*Bell Laboratories, Incorporated, Allentown, Pennsylvania 18103*

## ABSTRACT

A new electrochemical technique has been developed for etching platinum in the processing of silicon integrated circuits. A periodically varying potential is applied to a silicon wafer in a room temperature hydrochloric acid solution. The waveform has been designed to overcome problems associated with the passivation of the platinum surface and with the relatively high resistance of the metallization. The process has the following properties: the resolution of electroetched test patterns is good; the process is compatible with both positive and negative photoresists; the etch time is a few minutes for the platinum thicknesses commonly used in integrated circuits; the process lends itself to instrumentation for determination of the completion of platinum removal; the dissolved platinum can be recovered. The electroetching process is also applicable to the etching of other noble metals and to the etching of metallizations on other substrates.

One metallization used in the manufacture of silicon integrated circuits is titanium-platinum-gold. In one method of delineating patterns using this metallization scheme, the titanium and then the platinum are evaporated or sputtered onto the substrate; then the platinum pattern is defined by photoresist and etched. Subsequently, a new layer of photoresist is applied and gold is selectively electroplated. Finally, the exposed titanium is etched. The areas to be etched and the spacings between them may be as narrow as 5-10  $\mu\text{m}$ , while the thicknesses of the platinum and titanium layers are of the order of 2000 and 1000 $\text{\AA}$ , respectively. There are several chemical etches for titanium that can be adequately controlled. The platinum is usually etched in hot aqua regia; however, controlling the etch rate, determining the end point, and preventing undercutting of the photoresist are serious problems.

An electrolytic process is desirable because it offers numerous advantages in the areas of control, automation, and instrumentation. Raub and Buss (1) have etched the noble metals at significant rates using an alternating current in solutions that form complexes with these metals, for example, cyanides and chlorides. Black (2) adapted this technique to the electroetching of platinum metallizations on semiconductor devices. Yahalom (3) used square potential pulses of 1 msec duration in a hydrochloric acid solution at room temperature to etch platinum wires at rates as high as 4000  $\text{\AA}/\text{min}$ . During the anodic pulse at +1.0V (SCE) the platinum dissolves but concurrently the surface is passivated, thereby reducing the rate of dissolution. During the cathodic pulse at -0.3V, the passivating film is reduced. Yahalom showed that platinum would also etch, but at a slower rate, if a triangular potential-controlled waveform between the potential limits of -0.3 and +1.0V were used; the etch rate increased with the frequency of the waveform.

In this paper we report the development of a rapid, reproducible electrolytic method for etching patterns in platinum on semiconductor slices and on other substrates. We describe the method, the theory behind it,

and present some results on its application to integrated circuit test patterns.

## Experimental

The surface of each silicon slice, 1.5 in. (3.8 cm) in diameter, was thermally oxidized. Each slice was then coated with 2000 $\text{\AA}$  of chemical vapor deposited silicon nitride, 1000 $\text{\AA}$  of titanium, and 2000 $\text{\AA}$  of platinum. The thicknesses of the platinum and titanium were controlled no better than  $\pm 10\%$ . A metallization test pattern was defined on the platinum with either a positive (Shipley AZ135OH or AZ135OJ) or a negative (Eastman Kodak KMER or Hunt Chemical WAYCOAT Type III) photoresist. The test pattern contains a continuous metal line meandering from the top to the bottom of each chip. In addition, there are 21 lines adjacent to the meander. The pattern can be tested for shorts between the lines and for opens in the meander.

The etching cell was a 1500  $\text{cm}^3$  beaker in which was placed the slice to be etched (working electrode), a graphite auxiliary electrode, and a saturated calomel reference electrode. The slice was held in a titanium ring by four  $\frac{1}{4}$  in. long titanium knife edges spaced equally around the periphery of the slice. Titanium is inert under the conditions of the test. The electrolyte solution, 3M HCl made from reagent grade acid and distilled water, was not deaerated and was stirred with a magnetic stirrer. All experiments were conducted at room temperature. Potentials are reported relative to the saturated calomel electrode (SCE).

The potential was controlled by a Princeton Applied Research Model 173 potentiostat and the desired waveforms were obtained from a Tektronix Model 114 pulse generator and Tacussel Model GSTP-2 function generator. The waveforms from the two signal generators were superimposed, as described later. The current was monitored on a Tektronix 5103N oscilloscope with a Model 5A13N preamplifier.

At the conclusion of the etch, the sample was removed from the cell with the potential still applied and was quickly rinsed in 3M HCl solution to prevent the redeposition of platinum from the residual solution layer. The sample was then rinsed in distilled water and dried in a stream of nitrogen.

\* Electrochemical Society Active Member.

<sup>1</sup> Present address: Hewlett-Packard, Loveland, Colorado 80537.

Key words: ceramics, etching, noble metals, rhodium.

The quality of the etch was judged by (i) optical or scanning electron microscopy; (ii) electron microprobe analysis for residual platinum; and (iii) etching the exposed titanium; the titanium will etch only if the platinum has been completely removed.

The resistance of the metallization on the slice was measured across a diameter with a volt-ohmmeter by contacting the metallization at the circumference of the slice. The resistance between the titanium holder and a point in the center of the slice was also measured. These resistances are important because of the voltage drop they introduce during electrolytic etching.

### Results

Potential-controlled square wave pulses and a triangular waveform with potential limits of  $-0.3$  and  $1.0V$ , both of which have been used successfully to etch bulk platinum (3), did not etch the platinum metallization on silicon slices. However, a triangular waveform with potential limits of  $-0.3$  and  $1.4V$  and a modified triangular waveform (described below) with the same potential limits were found to etch the platinum metallization and to resolve the patterns completely and distinctly. No significant undercutting of the photoresist occurred during the time required to etch the platinum.

The following discussion is divided into two sections. In the first, we discuss the reasons why the techniques for etching bulk platinum must be modified when etching thin films on semiconductors or on insulators. In the second, we discuss the results of this new method and its application to the processing of integrated circuit slices.

*Modification of electrochemical etch for thin films.*—The difference in etching behavior between the platinum metallization on silicon wafers and bulk platinum was traced to an ohmic potential ( $IR$ ) drop within the silicon-metallization specimen caused by the relatively high resistance of the metallization on the insulating substrate compared to the resistance of bulk platinum. The metallization has a significant resistance that is a function of the film thickness and the resistivities of its components. Figure 1 shows the resistance across the diameter of a Ti(1000Å)-Pt film on a 1.5 in. (3.8 cm) slice as a function of platinum thickness. The resistance varies linearly with reciprocal thickness down to about

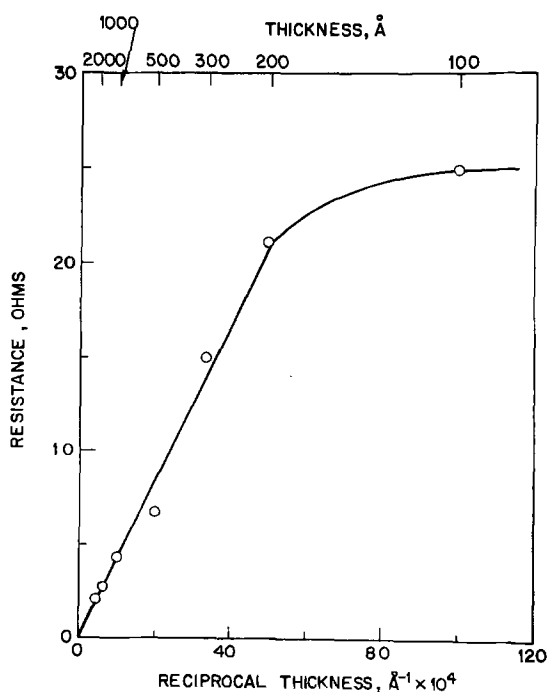


Fig. 1. The effect of platinum film thickness on the resistance of the metallization Ti(1000Å)-Pt across a 1.5 in. (3.8 cm) slice. At low thicknesses the resistance approaches that of the titanium film.

200Å. For thinner films, the resistance approaches that of the underlying titanium layer. It is evident that during platinum etching the resistance, and hence the  $IR$  drop, will increase. However, during pattern etching the resistance never approaches the value corresponding to zero platinum thickness because a pattern of platinum remains; the final value depends on the fractional area etched and the pattern geometry.

When a square wave potential is used to etch a thin platinum film on a silicon slice, the potential for the anodic reaction may initially be great enough to dissolve platinum. However, as the platinum is etched and the  $IR$  drop on the slice increases, the potential available for etching will in time decrease to a value too low for platinum dissolution to occur. The same is true for a triangular waveform with a maximum anodic potential of  $1.0V$ . The lower limit of the anodic potential for etching platinum at an appreciable rate in this solution is approximately  $0.7V$  (3). The upper potential limit appears to be between  $1.0$  and  $1.2V$ . At higher potentials the rate of passivation becomes so great as to decrease the effective rate of dissolution markedly (4).

To compensate for the constantly increasing  $IR$  drop, a triangular waveform with an upper potential limit equal to or greater than  $1.0V$  plus the maximum  $IR$  drop may be used (Fig. 2). With this waveform there will always be a window of approximately  $0.3V$  on the ascending ramp in which etching will occur. Initially this window will be from  $0.7$  to  $1.0V$ . When the  $IR$  drop is  $0.1V$ , the window will be from  $0.8$  to  $1.1V$ , etc. Such a waveform has been used to etch test patterns on metallized silicon slices, and good etching is obtained when the maximum anodic potential is between  $1.4$  and  $1.6V$ . Thus, the maximum  $IR$  drop appears to be approximately  $0.5V$ .

Since most of the etching occurs over a narrow potential band from  $0.7$  to  $1.0V$  on the ascending ramp,<sup>2</sup> only 5-10% of a triangular waveform is utilized for etching. To increase the efficiency, the waveform shown in Fig. 3(a) was used. This waveform is constructed by superimposing a ramp and a square wave, shown in Fig. 3(b). Thus the potential jumps from  $-0.3$  to  $0.7V$  followed by a ramp from  $0.7$  to  $1.4V$ ; then the potential drops instantaneously to that for the cathodic reduction of the passivating film. The time for cathodic reduction in this case has been reduced to  $0.7$  msec, while the anodic ramp is  $1.0$  msec long. With this waveform, etching occurs over approximately 25% of the cycle. The efficiency could probably be increased further by modifying this waveform. However, this course was not pursued because the etch time of approximately 2 min is sufficiently short for practical considerations.

*Application of the electroetching process.*—The process has been applied primarily to the etching of platinum on oxidized silicon wafers for integrated circuits. It can also be used to etch other noble metal

<sup>2</sup> On the descending branch the platinum is passivated and will not dissolve at an appreciable rate.

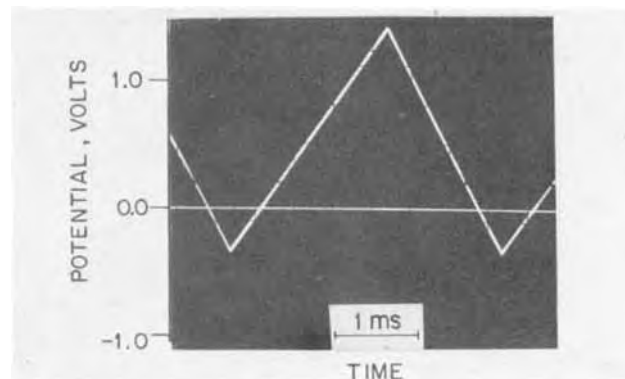


Fig. 2. Triangular waveform that corrects for the increasing  $IR$  drop during etching.



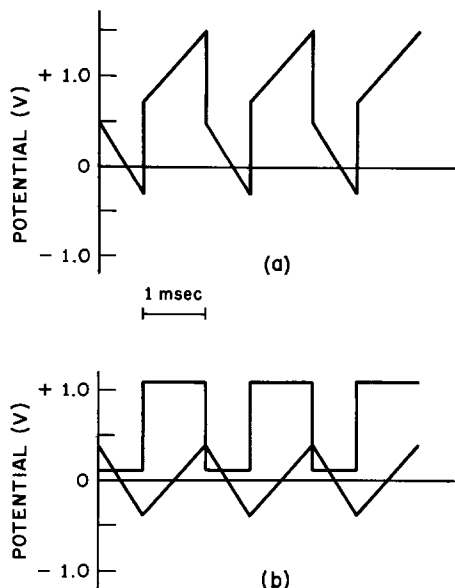


Fig. 3. The composite potential waveform for the electroetching process (a) is the sum of a square wave and a triangular wave (b).

thin films and metal films on high-resistance substrates other than silicon.

For a silicon slice having the metallization Ti(1000Å)-Pt(2000Å), a micrograph of a typical test pattern after electroetching the platinum and chemically etching the titanium is shown in Fig. 4. The dark areas have been etched revealing the silicon nitride layer; tests for the quality of the etch showed no residual platinum on the slice. The light areas are platinum, patterned in this case with a positive photoresist. The results of etching many samples indicate that the etching process is compatible with both positive and negative photoresists. The photoresists are not degraded by the electrolyte solution within the time required for etching, which is nominally 2 min for a 2000Å platinum film. Undercutting is not severe, even for etch times up to 6 min.

The electroetching process has a number of advantages over a hot aqua regia etch. (i) The electroetch is a room temperature process. (ii) The electrolyte solution, 3M HCl, is easier and safer to use. (iii) The etching is more controlled so that a constant etch time can be used. Alternatively, the end point can be determined electrically, as discussed below. (iv) It should be possible to etch a batch of slices at a time. (v) The dissolved platinum can easily be recovered.

The possibility of determining the end point electrically can be seen by comparing the current-time waveforms for the platinum-covered surface (Fig. 5a) and the platinum-free surface (Fig. 5b). The anodic (+) and cathodic (-) currents decrease significantly

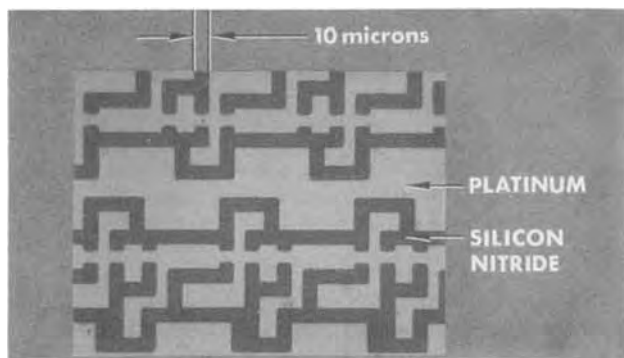


Fig. 4. Micrograph of an electroetched test pattern showing that the process defines the pattern clearly and sharply. The dark areas have had the platinum and titanium etched revealing the silicon nitride layer; the light areas are platinum.

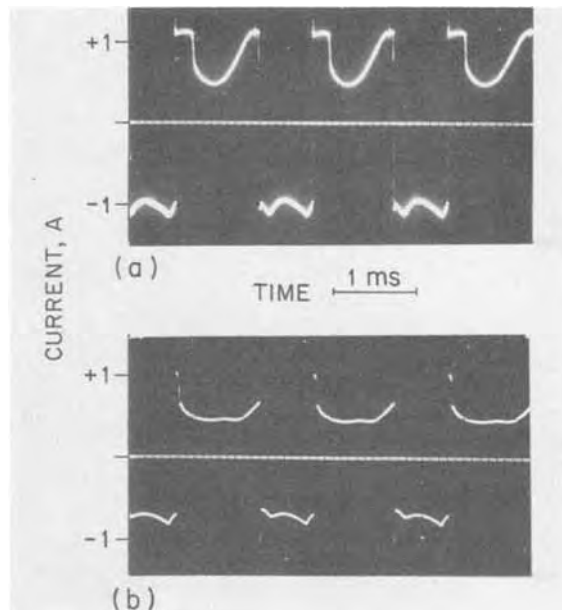


Fig. 5. Current transients (a) on platinum covered surface and (b) on titanium surface from which platinum has been etched. Comparison shows the marked changes that can be used to determine the end point of the etching reaction.

when the platinum has been removed. The residual anodic current is due to the oxidation of chloride ions and water, while the cathodic current is caused by the reduction of hydrogen ions and oxygen. Since the overpotentials for these reactions are greater on titanium than on platinum, the currents are lower on the former metal for a given applied potential. The end point of the etching reaction could therefore be determined by monitoring the anodic waveform<sup>3</sup> and observing the time at which no further change occurs. A safety margin of about 2 min can be added without adverse effects.

The dissolved platinum could easily be recovered. Since it is necessary to agitate the solution to prevent redeposition of the dissolved platinum, the solution could be recirculated through a two-compartment cell, in which etching occurs in one and platinum recovery takes place in the other.

The electroetching process can be applied to the etching of any noble metal provided the resistance of the underlying conductive layer, e.g., titanium, is not too great. We have successfully etched rhodium deposited over 500Å Ti on silicon; line spacings of 1 μm in the test pattern were clearly resolved. Platinum and rhodium over titanium have been etched on ceramic substrates.

One major precaution must be observed when using the electroetching process on thin films: the resistance between the contact point(s) and any point on the substrate must be minimized. For example, with silicon integrated circuits of the type discussed here, contact must be made to the periphery of the slice at several points so that the resistance between the slice holder and any point on the slice, as measured with a volt-ohmmeter, does not exceed one ohm. If the resistance is larger, the resulting IR drop may prevent complete etching.

#### Acknowledgments

We wish to thank Messrs. E. F. Labuda, C. M. Melliar-Smith, and P. C. Milner for helpful discussion.

Manuscript submitted Sept. 29, 1975; revised manuscript received ca. Dec. 23, 1975. This was Paper 161 presented at the Dallas, Texas, Meeting of the Society, Oct. 5-9, 1975.

<sup>3</sup> The changes in the anodic current are greater than those in the cathodic current.

Any discussion of this paper will appear in a Discussion Section to be published in the December 1976 JOURNAL. All discussions for the December 1976 Discussion Section should be submitted by Aug. 1, 1976.

Publication costs of this article were partially assisted by Bell Laboratories.

## REFERENCES

1. E. Raub and G. Buss, *Z. Elektrochem.*, **46**, 195 (1940).
2. J. R. Black, U.S. Pat. 3,560,358 (1971).
3. J. Yahalom, U.S. Pat. 3,798,141 (1974).
4. K. J. Vetter and J. W. Schultze, *J. Electroanal. Chem.*, **34**, 131 (1972).

## Etching of GaN Using Phosphoric Acid

Akira Shintani and Shigekazu Minagawa\*

Hitachi, Limited, Central Research Laboratory, Kokubunji, Tokyo 185, Japan

### ABSTRACT

Hot phosphoric acid is found to be useful for etching and characterizing epitaxial GaN crystals grown on (0001) sapphire substrates. The obtained etch rates are 0.2-1.0  $\mu\text{m}/\text{min}$  and the activation energy is about 4.4 kcal/mole in the temperature region of 50°-200°C. Hydration of Ga ion is considered the rate-determining step of the etching action. The x-ray diffraction and the infrared spectrometric studies indicate that the *ortho* and *meta* phosphoric ions play an important role as attacking ions in etching. This phosphoric acid etching reveals crystal defects in undoped (n), Zn-doped (i), and i-n structure GaN epitaxial crystals. Conical hexagonal pyramid pits and truncated hexagonal pits develop in the undoped layers, and they tend to be arranged along the slip direction and are attributed to certain dislocations. These hexagonal pits are densely generated near the interface of the epitaxial layer and the substrate. The density of the pits decreases exponentially with crystal growth. The pits are apt to increase in density and size when the carrier concentration is high ( $10^{19}$ - $10^{20}$   $\text{cm}^{-3}$ ). The rounded etch figures develop in Zn-doped crystals and sometimes in the undoped crystals with a high carrier concentration ( $10^{19}$   $\text{cm}^{-3}$ ). Etching also indicates that there is a significant difference in growth patterns between the Zn-doped and the undoped crystals even if the Zn-doped layer is continuously deposited on the undoped layer. This implies a difference in the crystal growth mechanism between these crystals.

Gallium nitride is a very promising compound semiconductor for a blue and a violet light emitting diode due to the wide bandgap [3.5 eV (1)] of its direct transition nature. Since Maruska and Tietjen grew epitaxial single crystals of GaN on sapphire substrates by a vapor deposition technique (2), many investigators have studied the preparation techniques and properties of GaN epitaxial layers. However, the crystal characterization has not been as widely investigated as the optical properties, since no appropriate crystal characterization technique has been established for GaN. To date, epitaxial GaN crystals have been characterized by measuring their carrier concentrations and mobilities. They have never been evaluated crystallographically.

Although chemical etching is a useful method for crystal characterization, no suitable etchant for GaN has been found because of its chemical stability against various mineral acids and aqua regia. Heretofore, molten sodium hydroxide, potassium hydroxide, and potassium pyrosulfate at 800°C (3) and a 50% sodium hydroxide aqueous solution (4) were the only known etchants for GaN. The first three etchants are not very useful because they require such a high temperature that GaN decomposes (5). Chu reported that a 50% sodium hydroxide aqueous solution can etch epitaxial GaN grown by the decomposition of  $\text{GaBr}_3 \cdot \text{NH}_3$  and that the activation energy for etching is 18 kcal/mole in the temperature range of 5°-90°C (4). However, Pankove was not able to reproduce this technique for the epitaxial layers prepared by Maruska and Tietjen's technique (6). He attributed this difference to the fact that the epitaxial layers prepared by Chu were possibly more porous than those prepared by himself. It is

also reported by Chu *et al.* that a 40% sodium hydroxide aqueous solution is still useful for etching GaN layers grown by ammonolysis of GaCl, and they showed a triangle etching pattern due to stacking faults which appeared on the  $(\bar{2}110)$  plane (7). Pankove applied the jet electrolytic etching technique to his GaN layers using 0.1N sodium hydroxide aqueous solution as electrolyte, and he freed a Zn-doped i-layer from an i-n structure grown on a sapphire substrate (6). Recently Morimoto reported the etch rate of GaN by phosphoric acid (8), but the details of his experimental procedure and conditions were not clear.

As is described, the previous reports did not make clear whether the above etching technique and the experimental conditions were useful for crystal characterization of GaN or not, nor did they explain the etching mechanism. In this work, we investigated the etching mechanism by means of x-ray diffraction and the infrared absorption of the products grown on GaN powder treated with phosphoric acid, and found the acid is useful for the characterization of crystal defects in GaN crystals.

### Experimental

**Epitaxial layers.**—The GaN epitaxial layers were grown on (0001) sapphires by a chemical vapor deposition technique based on the Maruska and Tietjen method (2). The technique has been described in detail (9). Most of the layers obtained were below 15  $\mu\text{m}$  in thickness and their carrier concentrations were  $10^{18}$ - $10^{20}$   $\text{cm}^{-3}$  in n-type.

As it is difficult to introduce impurity atoms into GaN by thermal diffusion, the Zn-doped growth was performed by admitting the Zn vapor to the reaction chamber. The inlet nozzle for the dopant was placed parallel to other nozzles for introducing reaction gases. The Zn vapor was transported by an Ar or H<sub>2</sub> carrier

\* Electrochemical Society Active Member.

Key words: etching mechanism, etching figures, slip direction, crystal growth mechanism.

flowing over a metallic Zn source heated to 600°C. Because the Zn vapor was partly absorbed into the Ga melt placed downstream to the Zn boat, a higher temperature than that in Pankove's experiments (10) was required in order to compensate for the native donors.

**Etchant and etching method.**—Commercial 85% phosphoric acid was heated to an etching temperature in a 100 cm<sup>3</sup> platinum beaker. The etching temperature was monitored with a Pt-PtRh thermocouple. The sample, held in a platinum basket, was immersed in this etchant during which the etchant was stirred by moving the sample holder. The temperature used for gaining clear etch figures was around 190°C.

**Etch rate.**—Thickness reduction by etching was measured at more than three points on the cleaved edge of each specimen under an optical microscope. The average value per unit etching time was used as the etch rate.

**Qualitative analysis of etchants.**—In order to know component variations of the etchant due to heating, four kinds of etchants (phosphoric acid without heating, one kept at temperatures between 140° and 150°C for 3 hr, one kept at 200°C for 4-5 hr, and one kept at 300°C for 5-7 hr) were analyzed qualitatively employing silver nitrate, zinc acetic acid, and barium chloride, respectively, for *ortho*, *pyro*, and *meta* phosphoric ions.

**X-ray diffraction and infrared absorption spectra measurements.**—In order to clarify the etching mechanism, the reaction products of the phosphoric acid-treated GaN powder surface were investigated. The GaN powder gathered from the wall of the reactor near the substrates was immersed in phosphoric acids at room temperature, 200°, and 300°C for 5-8 hr. These powders, after rinsing in water (not warmed) and drying, were subjected to x-ray diffraction and infrared absorption (KBr disk) analyses.

## Results

**Etching.—Etchant.**—It is well known that heating causes compositional variations in phosphoric acid due to condensation and evaporation of water. With a view to ascertaining the effective chemical species for the etching, commercial phosphoric acid was heated to 150°, 190°, and 300°C for several hours. Then, the composition of each heated acid was qualitatively analyzed. The results of the analysis were that both the original phosphoric acid and the acid heated below 150°C contained three kinds of phosphoric ions: *ortho*, *pyro*, and *meta* types. The phosphoric acid kept at boiling temperature (190°C) for 4-5 hr sometimes showed no evidence of the presence of *ortho* phosphoric ion, and one kept at 300°C did not contain this ion at all but did contain the other two ions.

**Etch rate.**—If phosphoric acid is heated under different temperature conditions, the above compositional variation may produce a different influence on etching even at the same temperature. In fact, the etch rate of Si<sub>3</sub>N<sub>4</sub> film decreases slowly with heating time at a constant temperature, whereas that of SiO<sub>2</sub> film is contrary to this (11). In the case of GaN, however, the etch rate at a constant temperature was almost independent of the heating time (less than 100 min), although the etch rate at etchant boiling temperature was reduced steeply during the first 10 min. The etch rate of GaN was apparently almost constant during heating up to 100 min as long as the etchant does not go through the boiling process. This largely decreases the water concentration.

The temperature dependence of the etch rate was investigated using two kinds of etchants of which the compositions were very different. Etchant "A" was thermally untreated 85% phosphoric acid. While, "B" was made by heating this 85% acid to 320°C for 6 hr, and cooling it to near room temperature. The results obtained are shown in Fig. 1 in the form of an Arrhenius plot. Though the etch rates in etchant A

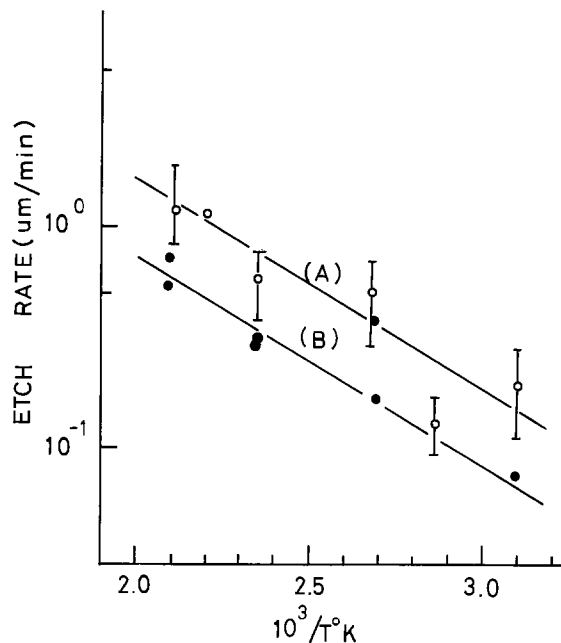


Fig. 1. Temperature dependence of the etch rate. The line (A) —○— and the (B) —●— represent etchant A and B, respectively.

were higher than those in B through all temperatures, the same activation energy, 4.4 kcal/mole, was found for both etchants. This indicates that the rate-determining step of the etching process is the same or similar for both etchants.

**X-ray and infrared measurements.**—Although the same activation energies were found for the above two etchants, the GaN powder immersed in phosphoric acid at three different temperatures (room temperature, 200°, and 300°C) for about 8 hr showed very different x-ray diffraction patterns and infrared absorption spectra. The x-ray diffraction peaks of the powder treated at room temperature were equal to those of the original GaN powder. However, the powder treated at 200°C showed some other medium intense peaks, e.g., at  $2\theta = 26.49, 20.94, 38.89$ , etc. (Bragg angles), besides the diffraction peaks of GaN. These different peaks could be assigned to Fe(PO<sub>4</sub>) by inspecting the ASTM cards, although the nature of a few very weak peaks remained unknown. As Fe ions were not detected in the powder by means of spectrochemical analysis and a sufficient amount of Fe<sup>+3</sup> ion to give the x-ray diffraction cannot be present in this etching system, it is naturally thought that the peaks assigned to Fe(PO<sub>4</sub>) were diffracted from Ga(PO<sub>4</sub>). The diffraction patterns of the powder treated at 300°C became more complicated because of the addition of the peaks due to Ga(PO<sub>3</sub>)<sub>3</sub>. The most intense peak belonged to Ga(PO<sub>3</sub>)<sub>3</sub>, whereas that of the powder treated at 200°C was assigned to GaN. These results were supported by the infrared absorption measurements of GaN powders immersed in phosphoric acid at the above-mentioned temperatures. The absorption peaks are summarized in Table I with those of some phosphates.

**Etch figures.—Etch figures developed on the surfaces of the undoped layers.**—Many hillocks of various sizes were observed on the as-grown surfaces of the epitaxial layers grown at 980°C with a carrier concentration of  $7 \times 10^{19}$  cm<sup>-3</sup> (Fig. 2A). A number of spotlike or linelike figures were developed on these surfaces by etching (Fig. 2B). Observation of these etch figures under a microscope proved that they were pit structures. These etch pits revealed each hillock had a hexagonal structure (Fig. 2A), i.e., the grown surface was of (0001) orientation. The more definite shapes of the etch pits were on the surface of the crystal grown at 1020°C with a carrier concentration of  $1 \times 10^{20}$  cm<sup>-3</sup> (Fig. 3). The basic shapes of the

Table I. The infrared absorption peaks of the GaN powder immersed in phosphoric acid and of some phosphates. The powders A and B were obtained by immersing GaN powder with phosphoric acid at 200°C for 8 hr and at 300°C for 6 hr, respectively.

Powder A	Powder B	PO <sub>4</sub> <sup>a</sup>	KH <sub>2</sub> PO <sub>4</sub> <sup>b</sup>	Na <sub>2</sub> HPO <sub>4</sub> · 12H <sub>2</sub> O <sup>c</sup>	BaHPO <sub>4</sub> <sup>d</sup>	Na <sub>2</sub> P <sub>2</sub> O <sub>6</sub> <sup>e</sup>
492 (vw)	480 (sh)				471 (m)	
501 (vw)	499 (s) 513 (m) 550 (sh)	515 (ν <sub>4</sub> )			498 (m) PO <sub>3</sub> deg. def.	
585 (s)	575 (s) 605 (sh)				591 (m) A PO <sub>3</sub> sym. def.	
	670 (w) 707 (sh) 719 (m) 769 (m)					783 E' ν <sub>s</sub> POP
975 (m.b.)	974 (s)	980 (ν <sub>1</sub> )	960 ⊥ (?)	946 PO str.	977 (m) A PO str.	1015 E' ν <sub>rs</sub> POP
	1023 (w) 1046 (m)		1021 ⊥ (?) 1030 //	1030 PO str. 1068 PO str.		
1058 (sh) 1072 (m)	1055 (m)	} 1082 (ν <sub>3</sub> )			1083 (V <sub>s</sub> ) } E 1110 (V <sub>s</sub> ) } PO <sub>3</sub> deg. def.	} 1098 E' ν <sub>s</sub> PO
	1090 (m) 1110 (sh)					
1150 (s)	1125 (s) 1150 (s)		1160 ⊥ (ν <sub>2</sub> )	1156 PO str.		
	1165 (sh) 1190 (vw)					
1215 (s)	1233 (s)		1250 ⊥ (ν <sub>3</sub> )			
	1250 (s) 1264 (s)			1263 PO str.		1277 A' ν <sub>as</sub> PO
	1290 (sh) 1325 (m)		1295 // 1305 (ν <sub>2</sub> + lat- tice Vib.)			
1425 (m.b.)	1400 (vw)		1437 //			
	1518 (vw)					

<sup>a</sup> G. Herzberg, "Molecular Spectra and Molecular Structure," Chap. II, p. 167, D. Van Nostrand Co. Inc., London (1949).

<sup>b</sup> J. J. Oberly and G. Weiner, *J. Chem. Phys.*, **20**, 740 (1952).

<sup>c</sup> A. Mutchin and K. Maennchen, *Z. Anal. Chem.*, **156**, 241 (1957).

<sup>d</sup> M. Tsuboi, *J. Am. Chem. Soc.*, **79**, 1351 (1957).

<sup>e</sup> Von E. Steger, *Z. Anorg. Allgem. Chem.*, **1958**, 305 (1958).

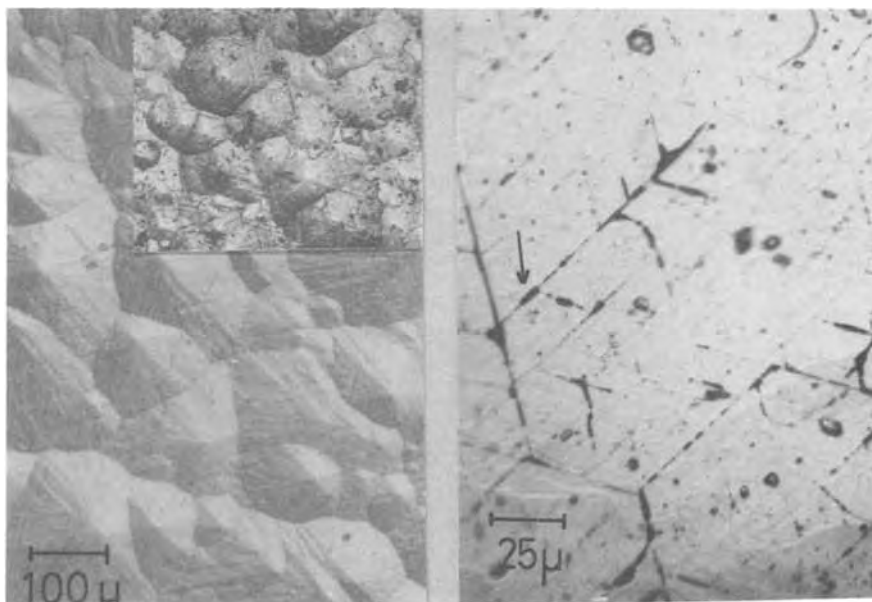
etch pits were hexagonal which reflects the crystal symmetry of GaN. Unclear etch pit shapes could be made definite by re-etching. These etch pits were classified roughly into two types; truncated pyramid pits indicated by the arrows (a) in Fig. 3A and conical pyramid pits by (b), both of which were similar to the etch pits developed on SiC (12-16), CdS (17, 18), and BeO (19). Some irregularly shaped pits (Fig. 3B) were also developed in regions other than the area giving the above clearly shaped pits in the same surface. These irregular pits possibly consisted of some continuous conical pyramid pits, because their bottoms were not as flat as those of truncated pit. The above etch pits were partly arranged in the direction toward

cross-points of crystal growth step lines or parallel to them.

Other-shaped etch figures were sometimes spread all over the surface of the epitaxial layers with a carrier concentration ranging from 10<sup>19</sup> to 10<sup>20</sup> cm<sup>-3</sup> (Fig. 3C). These figures seemed to be prominent, that is, not pits, under a microscope. This surface seemed to be a white muddy color due to light scattering on the rough surface caused by these figures. In the case of such crystal, the figures could be developed even with an etching time of less than 20 sec.

The spiral growth hillocks were observed on the surface of the epitaxial layer with a carrier concentration of 10<sup>18</sup> cm<sup>-3</sup> (Fig. 4A). In this case, the etch pits

Fig. 2. As-grown surface of the undoped GaN and its etched surface. (A, left) As-grown surface (right top figure is its etched surface) and (B, right) the etched surface.



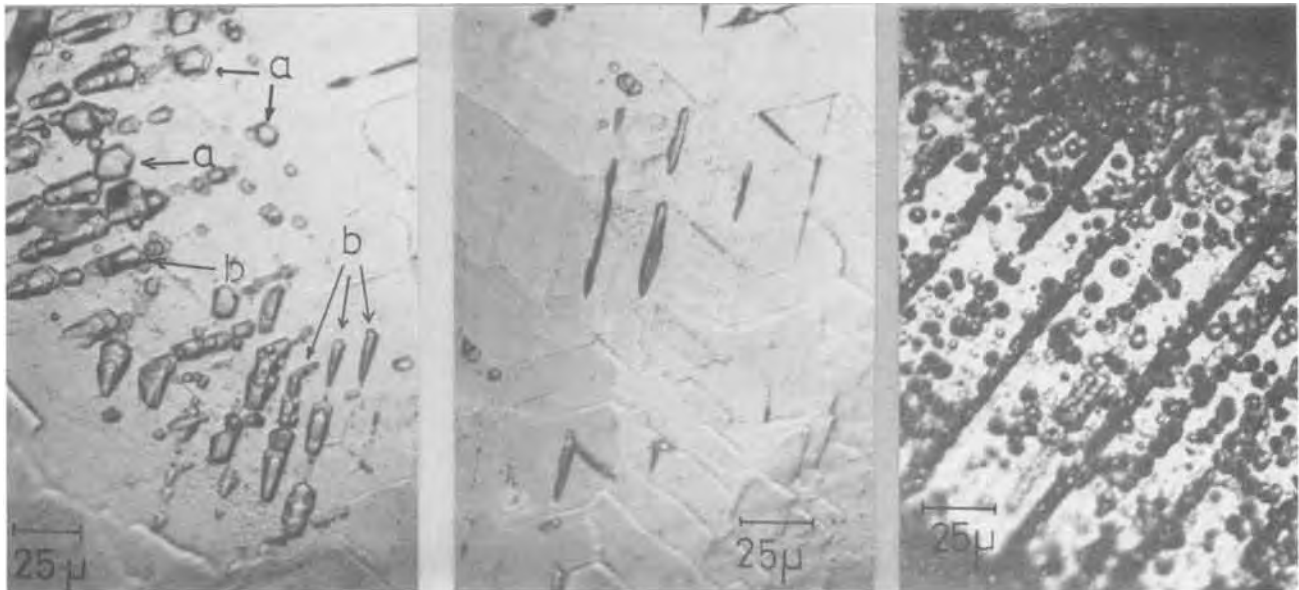


Fig. 3. Two kinds of etch pits developed on the undoped GaN. (A, left) The truncated pit indicated by arrows (a) and the conical pits by (b) can be observed. (B, center) The etch pits are arranged toward the cross-point of the growth step lines. (C, right) The etch figures observed on the surface seemed to be a white muddy color.

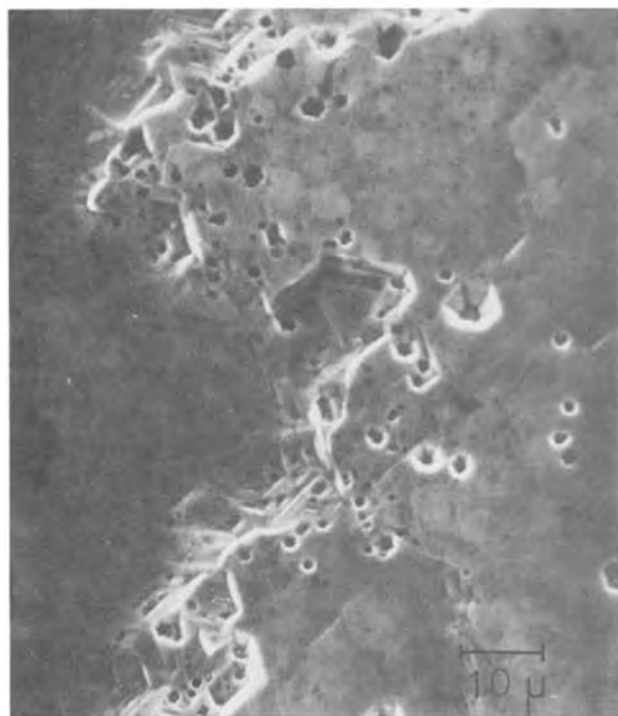
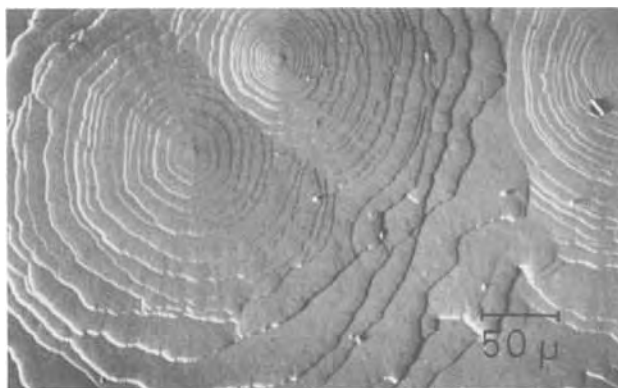


Fig. 4. (A, top) A spiral growth hillock of GaN (SEM image). (B, bottom) SEM image of the etch pits developed on the growth step of the spiral hillocks.

were densely developed at the edges of growth steps of each spiral hillock (Fig. 4B) but were not so well arranged in a fixed direction as shown in Fig. 3B. The etch pits were in the shape of more defined regular hexagons in Fig. 4B than in Fig. 3A, and their size was smaller.

*Etch pits developed on an angle-lapped surface of an undoped epitaxial layer.*—Observation of the etch pits on the angle-lapped surface is useful for gaining some information on the variations of the crystal quality along the crystal growth direction. Figure 5A is an etched 3°-angle-lapped surface of an epitaxial layer of 14  $\mu\text{m}$  in thickness with a carrier concentration of  $3 \times 10^{18} \text{ cm}^{-3}$ . The etch pits appear as dark spots (Fig. 5A). They were most dense in the strip of 40  $\mu\text{m}$  in width (2  $\mu\text{m}$  in epitaxial thickness) at the interface of the epitaxial layer and the substrate, and were reduced steeply along the growth direction. It was also observed that the etch pits were arranged along a direction making angles of 60° or 120° with each other (arrows designated a, b, and c in Fig. 5A). The etch pits were the same in structure as those in Fig. 3A, that is, truncated and conical hexagonal pyramids as seen in Fig. 5B and C. The truncated pits are shallow and flat-bottomed and the conical pyramid pits are deep and circular-bottomed.

In the case of the crystal with a carrier concentration higher than  $10^{19} \text{ cm}^{-3}$ , the etch pit density on the angle-lapped surface was too high for the pits to be clearly observed.

*Etch figures on a Zn-doped and an i-n structural layer.*—A study of the differences in the morphology of the etch figures between the undoped and the Zn-doped or the i-n layers offered some important information on their crystal quality and crystal growth mechanism. The as-grown surfaces of the Zn-doped layers consisted of hexagonal facets or pyramidal hillocks (Fig. 6). The etching made these surfaces a white muddy color due to light scattering on highly dense etch figures. The shape of the figures almost resembled the etch figures shown in Fig. 3C. These figures also were not possibly of pit structure. The morphology of the etch figures on the i-n structural layer varied with etching time (Fig. 7). At the beginning of the etching the etch figures developed only around the bases of the hexagonal pyramidal hillocks (Fig. 7A). The distribution of these figures extended over the faces of the hillocks with increase of etching time (Fig. 7B). Then a larger etch figure was developed at the apex of the

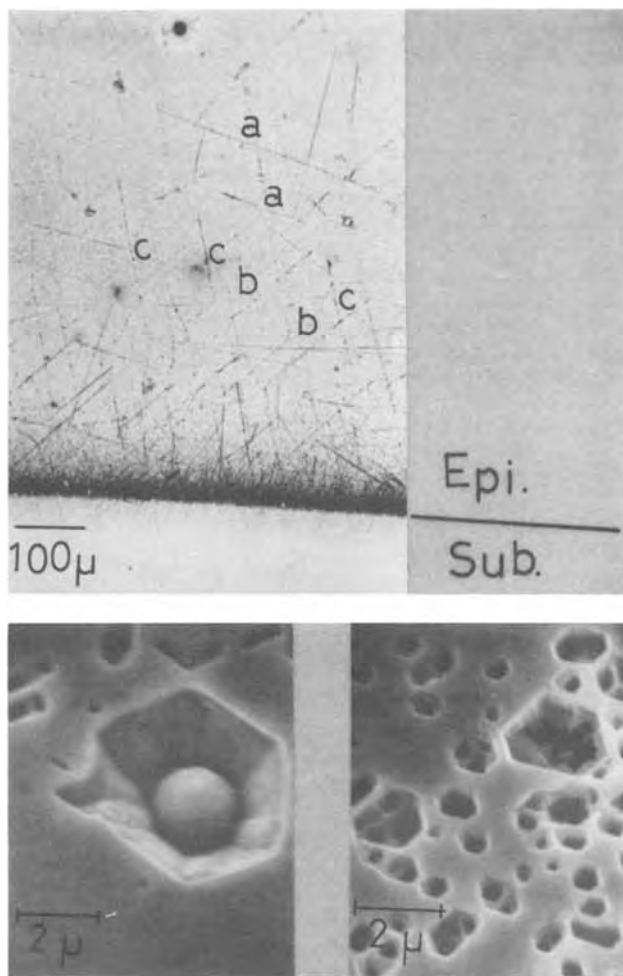


Fig. 5. (A, top) The etched angle-lapped surface. The arrangements of the pits indicated by a and b are crossed with angle of  $60^\circ$  or  $120^\circ$  with each other. (B, bottom left) SEM image of the conical pits. (C, bottom right) SEM image of the truncated pits.

pyramid. Figure 7C shows the surface of the i-n layer when the n-layer came into sight by etching. The dark parts indicated by arrows (a) are the Zn-doped layer hillocks. The etch pits along the spiral growth step of the n-layer, as indicated by arrows (b), displayed some net pattern.

( $\bar{1}102$ ) substrate.—Etching also made the GaN crystal grown on ( $\bar{1}102$ ) sapphire substrates turn a white muddy color due to the rough surface. The developed etch figures were not clear in structure or in shape due to the many growth ridges.

### Discussion

*Etching mechanism.*—Figure 1 reveals that the variation of the etchant composition remarkably affects the etch rate. The constant etch rates, however, were obtained in the etchants heated for less than 100 min at a normal temperature (not boiling temperature). The reason for this is that the evaporation of water at a normal temperature is not so violent as that at boiling temperature. According to this the change in the etchant composition at a normal temperature apparently does not become effective for GaN etching. The etch rates in the etchant preheated for a long time, as seen in Fig. 1, are slower on the average than those in the original etchant. From these experimental facts we can conclude that the etching of GaN in phosphoric acid is inhibited by large condensation of the acid. This is similar to the case of  $\text{Si}_3\text{N}_4$  described previously. However, there is a large difference in the etching activation energy between the two. Gelder and Hausen found an activation energy of 22.8 kcal/mole for  $\text{Si}_3\text{N}_4$ , which has been attributed to the hydrolysis of  $\text{Si}_3\text{N}_4$ (11). This activation energy is close to that of UN hydrolysis, 21 kcal/mole (20). Compared with these energies, the activation energy of GaN etching is considerably smaller. This indicates that such a rate-determining step as hydrolysis in GaN etching does not exist. Enumerating the phenomena of  $\text{Ga}^{+3}$  ions in phosphoric acid of which the activation energy verges comparably upon 4.4 kcal/mole, there are: hydration of Ga ion [6.3 kcal/mole (21)] and the diffusion of a cation in strong phosphoric acid [10 kcal/mole (22)]. If this hydration is the rate-determining step in GaN etching, the etch rate is controlled by the amount of water in the etchant and this qualitatively agrees with the results explained previously. On the other hand, if the diffusion process is the rate-determining step, the activation energy must depend on the chemical composition of the etchant. This is because the diffusion coefficient is not the same for various phosphoric acid compositions. This is not in agreement with the obtained results. Here another process may be considered as the rate-determining step; surface diffusion of ions attacking an active site of the GaN crystal surface, the reaction between Ga ions on surface and attacking species, or desorption of its products from the surface.



Fig. 6. Two kinds of as-grown surfaces of the Zn-doped GaN.



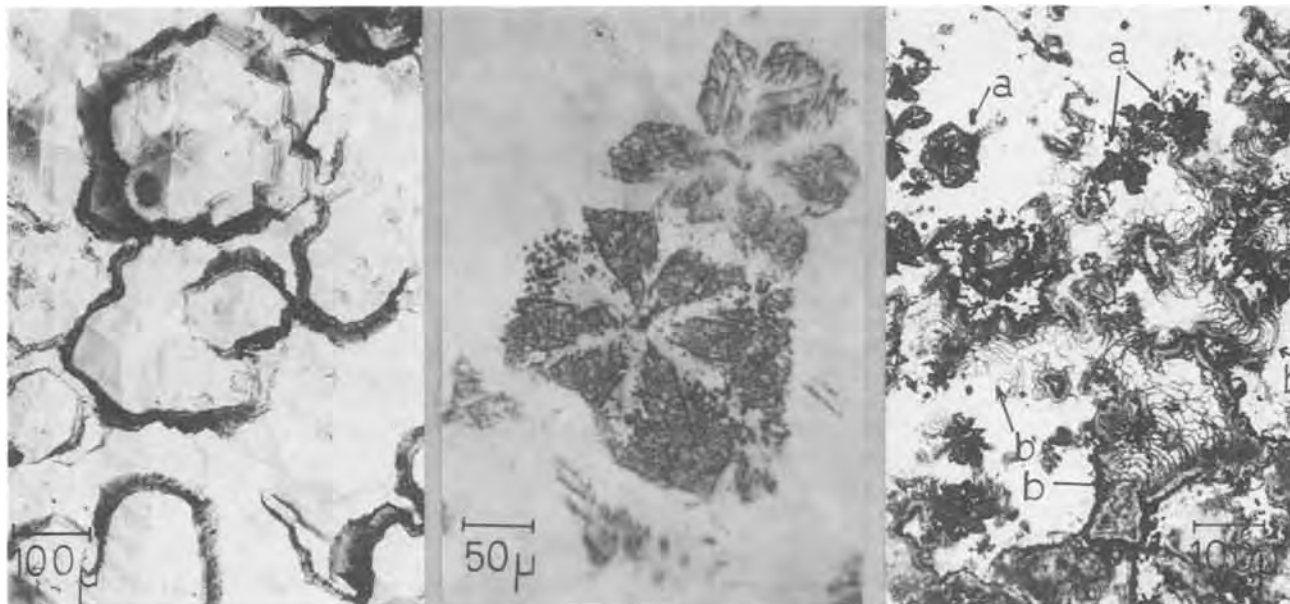


Fig. 7. Variation of the etch patterns developed on the i-n structural GaN with etching time. (A, left) The surface etched for 15 sec, (B, center) 45 sec, and (C, right) 3 min.

The activation energies, however, of these phenomena are not clear.

The above discussion does not give the detailed etching mechanism. The detection of  $\text{GaPO}_4$  in the powder immersed in phosphoric acid at  $200^\circ\text{C}$  suggests the following mechanism:  $\text{PO}_4^{-3}$  ions attack the active sites of the GaN crystal surface to dissociate Ga-N bonds and Ga ions are hydrated, then the hydrated ions are removed from the surface. These hydrated Ga ions react with  $\text{PO}_4^{-3}$  ions to form  $\text{GaPO}_4$  molecules, which are not dissociated in water, during the cooling process. Although the concentration of pyrophosphate ions in this etchant or in the etchant treated at higher temperature is higher than that in the original phosphoric acid as confirmed by qualitative analysis, no gallium pyrophosphate could be found in the powder immersed in phosphoric acid at  $200^\circ$  or  $300^\circ\text{C}$ . This is plausible because Ga ion cannot have a +1 charge and then it can hardly form pyrophosphate. When the temperature of the etchant goes up farther and the resulting concentration of *meta* phosphoric ion increases, the attack on the GaN crystal surface of this ion becomes remarkable similarly to that of *ortho* phosphoric ions at lower temperatures, and  $\text{Ga}(\text{PO}_3)_3$  molecules are formed.

In the case of the  $\text{Si}_3\text{N}_4$  etching, Gelder and Hauser assumed that N atoms could be removed from the crystal surface in the form of an ammonium phosphate. No x-ray diffraction peaks attributed to any ammonium phosphate could be found in the present work. However, it may also be supposed that some ammonium phosphate is formed in one step of GaN etching. Since both powders, as explained already, were sufficiently washed in flowing water before diffraction and infrared measurement in order to extract the viscous phosphoric acid from them, some ammonium phosphate may have been washed away at that time.

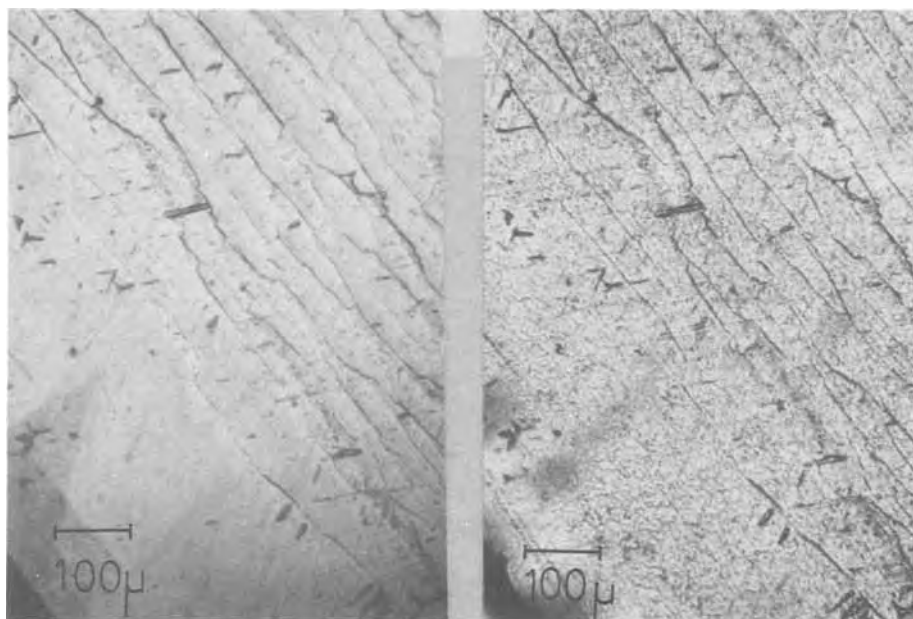
*Etch figures.—Etch figure morphology on the n-layers.*—Conical pyramidlike pits, one of the two kinds of etch pits developed on SiC and CdS, were associated with a dislocation (13, 16, 17). Renolds and Czyzak thought that the movement of the dislocation due to stress in the crystal results in the development of the truncated pits (17). Dislocation trapping impurities can be another plausible cause of these pits. In view of this and the re-etching that made the etch pits clear in shape, it can be said that both the conical and truncated etch pits on the GaN epitaxial layer are associated with dislocations.

The rounded etch figures seen in Fig. 3C have also been reported for Cds (17), SiC (16), and BeO (19). The orientations of these crystal surfaces were all  $(000\bar{1})$  anion surfaces. One mechanism for the development of these was proposed for BeO by Smith *et al.* (19) using Gatos and Warekoi's surface bonding model. The  $(000\bar{1})$  surface has two electrons per atom in the cut bonding orbital, and is more active toward an electrophilic reagent than the  $(0001)$  surface having no electron which is available for bonding. The shapes of the etch figures on the  $(000\bar{1})$  surface resultingly became dull. However, GaN etching was performed by *ortho* and *meta* phosphoric ions. Since these ions are negatively charged in an aqueous solution, they cannot be electrophilic in character. Therefore, in the case of GaN, the surface orientation developing the round etch pits was not confirmed. We do not understand the generation of the rounded etch figures.

Figure 8A is a photograph of the etch pit arrangements developed on the GaN taken only by the reflected light from the etched surface. Figure 8B is a photograph of the same area taken with the addition of transmission light through the surface. In a detailed observation of these photographs, the lines along the etch arrangements can be seen (Fig. 8B) and they are composed of a network pattern. This pattern can be attributed to the crack lines. Clear crack lines in the crystal run parallel to the growth steps of the hexagonal spiral hillocks. Thus, crack lines are in the  $\langle 10\bar{1}0 \rangle$  direction. These crack lines can be ascribed to a slip in the crystal plane. A slip direction of  $\langle 10\bar{1}0 \rangle$  is plausible because the cleaved surfaces in the wurtzite-type crystal are  $\{0001\}$ ,  $\{10\bar{1}0\}$ , and  $\{1\bar{1}20\}$  (23). A simple edge dislocation line is perpendicular to the slip direction and is included in a slip plane. Since edge dislocations are distributed easily along the slip direction, etch pits associated with the dislocation can be set reasonably in an array of  $\langle 10\bar{1}0 \rangle$  direction.

*Variation of etch pit density with crystal growth.*—The relationship between the etch pit density and the distance from the interface between the GaN layer and the substrate was derived from the magnified photograph in Fig. 5A. The result is shown in Fig. 9. The etch pits developed along the slip direction were omitted from the density calculation because the slip lines would be thermally generated after crystal

Fig. 8. The etch pit arrangements and crack lines generated in the undoped layer. (A, left) The photograph taken by the reflected light and (B, right) taken by the reflected and transmission light.



growth as described above. This means that they are not intrinsic characteristics of the GaN crystal growth. The fluctuation of each set of data increases with distance from the interface. This is due to the increasing lack of uniformity of the etch pit distribution with distance. The experimental equation for the density of the etch pits at  $x$   $\mu\text{m}$  from the interface is

$$N = N_0 \exp(-\alpha x) \quad [1]$$

where  $N_0$  is the etch pit density at the interface and  $\alpha$  is a parameter indicating a reduction magnitude of  $0.12 \mu\text{m}^{-1}$ . This exponential reduction of the dislocation has been obtained for GaP grown on GaAs with  $\alpha$  of  $4.1$ – $5.3 \text{ mm}^{-1}$  (24). No theoretical analysis of this relation has been reported. The parameter  $N_0$ , however, will depend both on the differences in lattice constant and crystal structure between a substrate and an epitaxial crystal, and on impurity incorporation from the substrate. Another parameter will depend on the difference in the lattice constant and Young's modulus

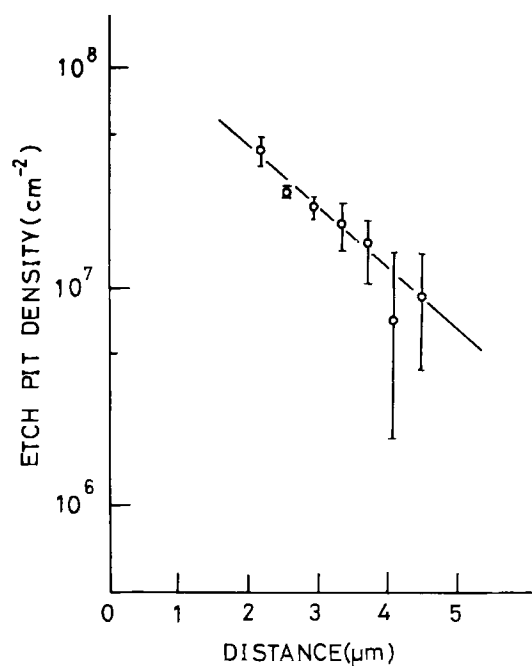


Fig. 9. The relation of the etch pit density to the distance from the interface between the GaN layer and the substrate.

between the nucleus of crystal growth and a strain-free crystal. It further depends on chemical bond strength factors. The number of the dislocations will decrease to that of the bulk crystal with crystal growth.

As the etch pits developed on an epitaxial surface having a spiral growth hillock become more dense at the periphery of the growth step as shown in Fig. 4B, it is difficult to determine the etch pit density. Therefore, from the extrapolation of the line in Fig. 9, an etch pit density is found to be  $3 \times 10^4 \text{ cm}^{-2}$  for the surface of a crystal with a carrier concentration of  $10^{18} \text{ cm}^{-3}$ . The density of the etch pits was estimated at  $10^7 \text{ cm}^{-2}$  at least for a crystal with a  $10^{19}$ – $10^{20} \text{ cm}^{-3}$  carrier concentration. These facts indicate that the etch pit density is closely related to carrier concentration. Since the development of the etch pits is correlated to certain dislocations, it can be said that carrier concentration depends on crystal defects. Growth conditions have some influence on crystal defect formation and etch figure morphology varies with the conditions as described previously.

**Etching of the *i*-layer and the *i-n* structure layer.**—A number of irregularly formed etch figures are developed on the *i*-layer surface as shown previously. These indicate that doped crystals are poorer in crystal quality than undoped crystals, and especially that the base planes and the faces of their pyramidal hillocks are of very low quality (Fig. 7). The etch figures developed on these areas do not arrange themselves in array with a fixed direction. These results imply that the kind and the origin of lattice defects developing the etch figures on the Zn-doped layer are different from those of the undoped ones. These irregular etch figures are attributed to the defects generated by doping a large amount of Zn atoms.

Figure 7C signifies that there exists a difference in the crystal growth mechanism between the undoped and Zn-doped crystals. Though the undoped crystal grows according to the spiral crystal growth mechanism, a lot of doped Zn atoms decorated the spiral steps of the *n*-layer and made them inactive as nuclei for the growth. Even if a Zn-doped crystal grows according to a spiral crystal growth mechanism, the origin of it is different from that of the undoped crystal growth. When  $\text{Zn}^{+2}$  ions with larger ionic radii than that of  $\text{Ga}^{+3}$  ( $\text{Zn}/\text{Ga} = 1.36$ ) are incorporated in the GaN lattice, the crystal deformation or strain in the doped crystal becomes large, generating a number of dislocations, impurity clusters, and vacancies in the crystal.



### Acknowledgments

The authors would like to thank M. Wada for his assistance in the experiments and T. Ishiba for the SEM photos.

Manuscript submitted Sept. 26, 1975; revised manuscript received Jan. 5, 1976.

Any discussion of this paper will appear in a Discussion Section to be published in the December 1976 JOURNAL. All discussions for the December 1976 Discussion Section should be submitted by Aug. 1, 1976.

Publication costs of this article were partially assisted by Hitachi, Limited.

### REFERENCES

1. R. Dingle, D. D. Sell, S. E. Stokwski, and M. Ilegems, *Phys. Rev.*, **B4**, 1211 (1971).
2. H. P. Maruska and J. J. Tietjen, *Appl. Phys. Letters*, **15**, 327 (1969).
3. H. H. Whitaker, Private communication to J. I. Pankove (Ref. 6).
4. T. L. Chu, *This Journal*, **118**, 1200 (1971).
5. M. R. Lorenz and B. B. Vinkowski, *ibid.*, **109**, 24 (1962).
6. J. I. Pankove, *ibid.*, **119**, 1118 (1972).
7. T. L. Chu, K. Ito, R. K. Smeltzer, and S. C. Chu, *ibid.*, **121**, 159 (1974).
8. Y. Morimoto, *ibid.*, **121**, 1382 (1974).
9. A. Shintani and S. Minagawa, *J. Crystal Growth*, **22**, 1 (1974).
10. J. I. Pankove, J. E. Berkeyheiser, and E. Miller, *J. Appl. Phys.*, **45**, 1280 (1974), and their references.
11. W. Van Gelder and V. E. Hauser, *This Journal*, **114**, 869 (1967).
12. V. J. Jennings, *Mater. Res. Bull.*, **4**, S199 (1969).
13. J. W. Fauster, Jr., in "The Surface Chemistry of Metals and Semiconductors," H. C. Gatos, Editor, p. 1964, John Wiley and Sons Inc., New York (1964).
14. S. Amelinckx and G. Strmane, in "Silicon Carbide," J. R. O'Connor and J. Smiltens, Editors, p. 162, Pergamon Press, Oxford, London (1960).
15. J. W. Fauster, *ibid.*, p. 403.
16. T. Gabor and V. J. Jennings, *Electrochem. Technol.*, **3**, 31 (1965).
17. D. C. Renolds and S. J. Czyzask, *J. Appl. Phys.*, **31**, 94 (1960).
18. G. A. Wolff, J. J. Frawley, and J. R. Hietanan, *This Journal*, **111**, 22 (1964).
19. D. K. Smith, H. V. Newkirk, and J. S. Kahn, *ibid.*, **111**, 78 (1964).
20. N. J. Bridger, *Trans. Faraday Soc.*, **63**, 1286 (1967).
21. D. Fiat and R. E. Connik, *J. Am. Chem. Soc.*, **90**, 608 (1968).
22. M. Goto and I. Ishii, CA **71**, 1821W [*Nippon Kagaku Zasshi*, **90**, 376 (1969)], and M. Goto and I. Ishii, CA **75**, 14238U [*ibid.*, **92**, 234 (1971)].
23. W. L. Roth, in "Physics and Chemistry of II-VI Compounds," A. M. Auev and J. S. Prener, Editors, p. 117, North-Holland Publishing Co., Amsterdam (1967).
24. L. C. Luther, *Metal Trans.*, **1**, 594 (1970).

## Anodic Oxidation of GaAs in Mixed Solutions of Glycol and Water

H. Hasegawa<sup>1</sup> and H. L. Hartnagel

Department of Electrical and Electronic Engineering, University of Newcastle upon Tyne, The Merz Laboratories, Newcastle upon Tyne, NE1 7RU, United Kingdom

### ABSTRACT

A native oxidation of GaAs by anodization in mixed solutions of glycol and water (AGW) is described. A detailed comparison between the AGW process and anodization in aqueous solutions (AAS) shows the basic importance of (i) the simultaneous oxide dissolution during growth and (ii) the initial electrochemical active-passive transition of the GaAs anode. The results demonstrate the substantial superiority of the AGW process over various AAS processes. Factors relevant for uniform, stable, and reproducible oxidation are studied which include the effects of illumination, sample edges, and stirring. The dependence of the thickness-voltage rate constant on the current density is established. The AGW process exhibits a high current efficiency.

The usefulness of a semiconductor material depends very much on the availability of a suitable process to form an insulating layer of acceptable qualities on its surface, as has been fully demonstrated by the impressive success of the planar technology of silicon integrated electronic devices. Although it possesses unique features of light emission, of the transferred electron effect, of high electron mobility, of high radiation resistance, etc., which are not readily available in silicon, the use of GaAs material has been limited so far by several factors, particularly by the difficulty of its proper oxidation. However, with the successful demonstration of advanced high-performance microwave and optoelectronic devices using GaAs in recent years, a need exists for a suitable technology to form an insulator on GaAs with good dielectric and inter-

face properties, particularly in view of applications to surface passivation, MOS-type devices and processing steps for planar integration, and fabrication of various devices.

The main difficulty associated with thermal oxidation of GaAs is related first to the volatile component, namely As, which will cause at high temperature, decomposition of GaAs, and second to the even higher volatility of As<sub>2</sub>O<sub>3</sub> which has about 1 atm vapor pressure at about 320°C so that the thermal formation of a native oxide with As properly incorporated would probably only be possible with great technological difficulties. In fact, the thermal oxides grown so far seem to contain only Ga<sub>2</sub>O<sub>3</sub> (1), and little information is available so far on the electrical and chemical properties (such as diffusion of impurities) of this oxide and the oxide-semiconductor interface.

An alternative way of utilizing the deposition of various oxides or nitrides by pyrolysis or other suitable

<sup>1</sup> On leave from Department of Electrical Engineering, Hokkaido University, Sapporo, Japan.

Key words: gallium arsenide, anodization, native oxide, surface passivation.

chemical reactions (2-5), some of which can be carried out at reasonably low temperatures, seems to be of a limited value owing to the formation of porous films, poor adhesion, poor interface properties, a large lateral diffusion of impurity atoms encountered in diffusion-mask applications, etc.

The present paper is concerned with a new and promising electrochemical oxidation process of GaAs which is basically an anodization in a mixed solution of glycol and water (AGW process). It will be shown that the new AGW process is an extremely stable, reliable, and reproducible process leading to the formation of uniform and glassy native oxide films. Thicknesses of up to 7200Å can be grown at room temperature within 10 min of anodization, although the results presented in this paper are based on films of up to 3000-4000Å thickness. A brief first description of the process only was published in a letter form elsewhere (6).

An anodic oxidation of GaAs was first reported by Revesz and Zaininger (7) in 1963 but resulted in a severely pitted surface. Dell'Oca, Yan, and Young (8), and Harvey and Kruger (9) also reported anodization of GaAs in various aqueous electrolytes with limited success. The anodic process on GaAs can also be carried out in a gaseous state by the so-called plasma oxidation process (10, 11). This seems to result in uniform but fairly highly conducting films. Growth of uniform films with low conductivity was first reported in 1973 by Logan, Schwartz, and Sundburg (12) using a constant voltage anodization in an aqueous solution of H<sub>2</sub>O<sub>2</sub>. Various applications have also been suggested and experimentally verified, based on this encouraging success, which include masks for mesa etching (12) and selective Zn-diffusion (13), and controlled wafer thinning (14) for microwave MESFET's.

However, the above H<sub>2</sub>O<sub>2</sub> scheme has unfortunately the following problems (12) which would make its practical exploitation rather difficult: (i) the process is extremely unstable against impurities, (ii) the grown oxide cannot stand the vacuum deposition of Au, (iii) the grown oxide allows leakage currents of  $10^{-5} \sim 10^{-6}$  A/cm<sup>2</sup>, which is still rather high, and (iv) the maximum film thickness available for room temperature electrolytes is limited to about 3000Å whereas the initiation of an anomalous growth by boiling the electrolyte seems to be associated with an electrical breakdown in the oxide (15).

The present AGW process can completely solve the above problems, being extremely stable and producing impervious films with a  $10^3 \sim 10^5$  times higher resistivity and increased dielectric breakdown field-strength. A capacitance-voltage study on MOS devices using such native oxides revealed that interface properties can be dramatically improved by a suitable postgrowth annealing as reported elsewhere (16).

The purpose of the present paper is to establish the optimum conditions for uniform, stable, and reproducible anodic oxidation of GaAs using the AGW process. Most experiments were undertaken with a particular type of AGW electrolyte, namely a mixture of a buffered aqueous solution of tartaric acid and propylene glycol. However, a limited study using either citric acid or phosphoric acid instead of tartaric acid, and ethylene glycol instead of propylene glycol has also shown that each of such combinations works equally well. The results in this paper also indicate that the essential components of the present electrolyte is water and glycol. Therefore, a more generalized formula of the AGW electrolyte will be (i) glycol (diol or more generally polyhydric alcohol), (ii) water, and (iii) a suitable acid, base, or salt. The role of the water is that of the anodic oxidant of GaAs, and the role of component (iii) is to establish a suitable ionic conduction in the electrolyte. A careful choice has to be made for (iii) so that no disastrous

effect on the oxide growth such as strong oxide dissolution etc. is introduced by it.

As for component (i), glycol was used in the past in the anodic oxidation of Al (17), Ta (18), and Si (19). But, the experimental results appeared to indicate that its effect is far more essential in the present case. Therefore, a comparison is presented here of the AGW process with the corresponding anodization process in the aqueous solution without glycol (the AAS process), where the same aqueous solution as in the AGW process was used, but with the glycol omitted.

On the basis of our experimental observations it is concluded that simultaneous dissolution of oxide occurs during the growth and that the classical active-passive transition of the anode (20) plays an important role.

Recently, another successful electrolyte for GaAs (21) has been reported which contains water and N-methylacetamide. This appears to have a similar make-up as the present AGW electrolyte. However, an anomalous growth seems to start at a voltage as low as 45V so that detailed electrical and chemical measurements have to substantiate still the quality of this oxide. Also the bath conditions including the pH adjustment seem to be much more critical.

### Experimental

Slices of p-type bulk material with the carrier concentrations of  $2.2 \times 10^{16}$  cm<sup>-3</sup> and  $1.4 \times 10^{17}$  cm<sup>-3</sup> (both Zn-doped), of n-type bulk material with the carrier concentration of  $1.0 \times 10^{18}$  cm<sup>-3</sup> (Si-doped), of n-type epitaxial material with the carrier concentration  $7.6 \times 10^{14}$  cm<sup>-3</sup> (undoped, mobility = 6600 cm<sup>2</sup>/V·sec, supplied by Monsanto Ltd.) were used in the experiments. In-Ge-Ag or Ag-Sn were used for the ohmic back contacts to n-type material, and In-Ag or In-Zn-Ag for those of p-type material. In all cases, contacts were provided by the deposition of metals in vacuum, followed by a subsequent brief annealing in a hydrogen flow at about 600°C.

The three important low-index planes (100), (111), and ( $\bar{1}\bar{1}\bar{1}$ ) orientations were used. The surfaces to be anodized were chemomechanically polished in an aqueous solution of NaOCl in the case of bulk materials. Wafers were cut into pieces by the use of a wire saw or by cleaving. Various sample surface areas from about 5 to 100 mm<sup>2</sup> were used with typical standard size being  $5 \times 5$  mm. Before the start of anodization, each sample was subjected to a series of "pre-epitaxy" cleaning procedures.

The experimental setup employed for the anodization as reported here is on purpose kept simple by omitting more refined facilities such as a potential probe, because the aim is the development of a reliable production-type technique. It will be shown, however, that this does not prevent the authors from obtaining a good understanding of the basic phenomena involved, and only now a more accurate quantitative study would require the use of a potential probe. The setup is shown in Fig. 1. Pyrex glassware and a cathode of a platinum plate ( $2 \times 2$  cm<sup>2</sup>) were used. The samples were attached to a capillary tube using a high-quality wax, and an electrical contact was made to the back side by a spring through a capillary tube. The generally small sample (Fig. 1 is not to scale, the sample surface area being typically 25 mm<sup>2</sup>) was placed sufficiently deeply into the electrolyte in order to prevent current crowding on that part of the anode surface which is closest to the cathode. In connection with the sample edges, two different cases were studied, namely (i) the side areas and edges being carefully covered by the wax and (ii) the side areas and edges being exposed to the electrolyte. In each case, the values of current density reported here are averaged ones obtained by dividing the total current by the total sample

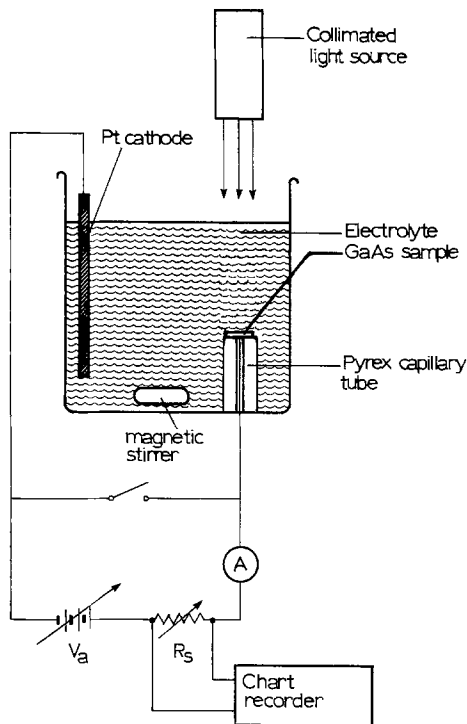


Fig. 1. Experimental setup for anodic oxidation

area exposed to the electrolyte, ignoring the nonuniform current distribution near edges and side areas. For the illumination of the samples during anodization, a collimated light source was used which was a typical microscope lamp with a tungsten bulb.

The circuit for anodization is a simple one where the electrodes are connected to a variable d-c constant-voltage source through a variable resistor  $R_s$ . External circuit conditions are specified by the source voltage  $V_a$  and the short-circuit current density  $j_s = V_a/r_s$ , where  $r_s$  denotes the series resistance per unit area of the sample given by  $R_s S$ , with  $S$  being the area to be anodized. As seen later in Eq. [2],  $r_s$  determines the time constant of the oxide growth. In spite of its simplicity, the present circuit is very flexible and suitable for the analysis of the kinetic behavior of the process, permitting one to change the anodization conditions widely from a nearly constant-voltage condition to a nearly constant-current condition.

For the measurement of thickness of the oxide and GaAs consumed, steps were produced by covering some part of the surface with wax or Shipley photoresist (AZ 1350). Dissolution of the grown oxide layers was undertaken in an HCl solution, followed by a quick but thorough rinse in distilled and deionized water. The thickness was determined by a Zeiss interference microscope and a Dektak profile plotter with both instruments exhibiting an accuracy of about  $\pm 50 \text{ \AA}$  in our cases. Agreement between these two methods was found to be reasonably good.

As already mentioned, a particular type of AGW electrolyte was used throughout the present study. It is produced by first preparing a 3% aqueous solution of tartaric acid if necessary buffered by  $\text{NH}_4\text{OH}$  to obtain a certain pH value (this solution is also referred to regarding our AAS here), and second mixing this with propylene glycol.<sup>2</sup>

Therefore, the pH value of the AGW electrolyte in the present text means the pH value of the buffered aqueous acid solution before mixing with glycol.

As a convenient way to specify the makeup of the electrolyte, the mixing ratio of the electrolyte is defined hereafter as the volume of the glycol divided by

<sup>2</sup> Such mixing tends to result in precipitation of tartrate around a pH = 3 ~ 4, but a complete dissolution can be obtained by treating the system up to around 50°C and cooling down.

that of the acid solution (or water). Thus, an AAS electrolyte has the ratio of null.

## Results and Discussion

**The effect of pH.**—Figure 2 shows the effect of the pH value on the anodic oxide growth for AGW and for its corresponding AAS. Anodization was performed for a fixed time of 10 min and fixed circuit conditions of  $V_a = 150\text{V}$  and  $j_s = 1 \text{ mA/cm}^2$  on p-type samples with covered edges. The mixing ratio of the AGW electrolyte was 2. In both the AAS and the AGW processes, the anodization current drops with time in a roughly exponential way if it does drop, resulting in the growth of an oxide whose thickness is compared in Fig. 2. Clearly, the AGW process is much more immune to pH variations and gives thicker films than the AAS process. Oxidation by the AAS process is restricted to a relatively narrow pH range. Outside this range, a nonuniform anodic dissolution (etching) takes over, and the current stays constant (except for the initial small drop) instead of showing an exponential drop. The transition from the oxide growth takes place in a very abrupt manner with respect to pH.

Another characteristic feature observed in the AAS process is that it is extremely sensitive to contamination and tends to be irreproducible. The data shown in Fig. 2 were taken by using utmost care not to contaminate the bath. It has been experienced very often that the oxidation suddenly turns into etching from one anodization to the next having nominally the same conditions. It is also noted that anodization can be restarted in such a case by increasing the current density  $j_s$  sufficiently. In general, both the pH range for oxidation and the reproducibility of the AAS process increased with the current density.

Even more difficult situations were experienced when a limited study was done at an early stage of the present study on the AAS process using a 30% aqueous solution of  $\text{H}_2\text{O}_2$  of the British arristar grade. With this  $\text{H}_2\text{O}_2$ , which contains more than 1 ppm of HCl, and  $\text{HNO}_3$  when supplied by the manufacturer, oxide growth was impossible in its pure state under all the conditions tried, and after many trials, it was found that the oxide starts to grow only when sufficient  $\text{H}_3\text{PO}_4$  or  $\text{NH}_4\text{OH}$  is added to change the pH toward the acid or base direction (i.e., when the electrolyte conductivity is increased) and when the anodization is done with a small series resistance (nearly constant-voltage condition). Obviously this growth is only possible for very large current densities.

In contrast, the AGW process has been found always very stable and reliable, and the result is always reproducible even after many times of anodization.

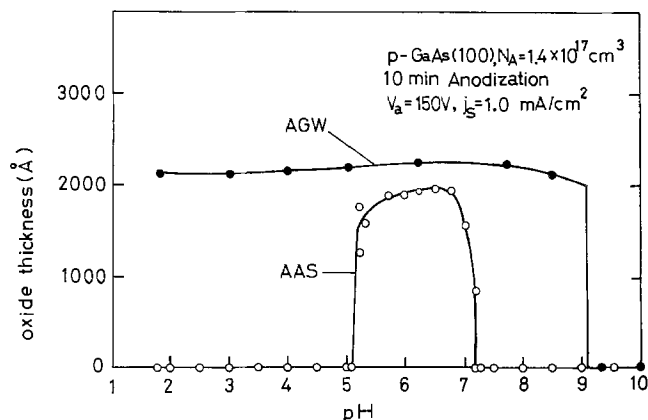


Fig. 2. Effect of pH on anodic oxide growth (AAS: 3% aqueous solution of tartaric acid, buffered by  $\text{NH}_4\text{OH}$  to a certain pH value; AGW: the same as for AAS plus glycol, of the volume ratio 1:2, respectively).

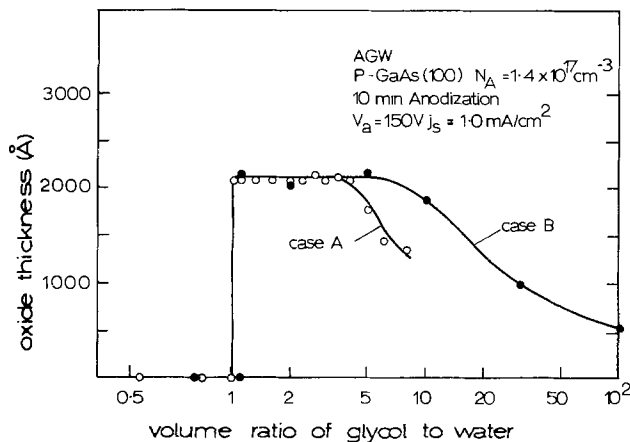


Fig. 3. Effect of mixing ratio of glycol and water on anodic oxide growth.

*The effect of the mixing ratio.*—Figure 3 shows the effect of the mixing ratio of glycol to water of the AGW process on the anodic oxide growth. The GaAs samples and the circuit conditions are the same as with Fig. 2. Two different ways of mixing were employed here. In case A, an unbuffered aqueous solution consisting of 3g of tartaric acid and 100 cm<sup>3</sup> of water (resulting in a pH = 1.8) was prepared at first and glycol was added to the required volume ratio. In case B, the solution consisted of 3g of tartaric acid and 100 cm<sup>3</sup> of glycol<sup>3</sup> at first and water was subsequently added to the required volume ratio. For a given mixing ratio, the actual concentration of the tartaric acid in the mixed solution is therefore quite different for the two cases except in the neighborhood of the volume ratio of unity. Nevertheless, both cases behave in a similar way showing an abrupt transition from anodic dissolution to anodic film formation at about the mixing ratio of unity. In the range of the mixing ratio from 1 to 4, film growth is independent of mixing ratio and concentration of tartaric acid.

The above results concerning pH and mixing ratio indicate that the present AGW bath has a broad empirical optimum at around pH = 6.2 and the mixing ratio of 2 to 4 for stable oxide growth using a moderate anodization current density of the order of 1 mA/cm<sup>2</sup>. Therefore, all further experimental studies of the process have been carried out by standardizing the AGW bath conditions to pH = 6.2 (adjusted by NH<sub>4</sub>OH before mixing) and the mixing ratio of 2. Similarly, for comparison, the AAS bath is standardized to pH = 6.2 which is approximately the center of the pH range in Fig. 2.

*Effect of illumination.*—Another factor which could have a large effect for a uniform and stable growth is the condition concerning illumination. Therefore, some preliminary experiments were carried out using the standard AGW bath and it was found that illumination of the semiconductor surface by a uniform light source has indeed a very large effect on anodic oxidation of n-type samples, particularly when the carrier concentration is low. The difference in the anodization current under illuminated and dark conditions is shown in Fig. 4 for two different carrier concentrations. In both cases the anodization current at a given instant of time increases as the light intensity is increased, and becomes saturated under sufficiently strong illumination. The anodization current behavior and oxide growth under an illumination at saturation level were found to be independent of the carrier concentration as seen in Fig. 4. This also results in a very uniform oxide layer. On the other hand, the anodization current and oxide growth in the dark are strongly

<sup>3</sup> Complete dissolution was attained by heating up to about 50°C and cooling down.

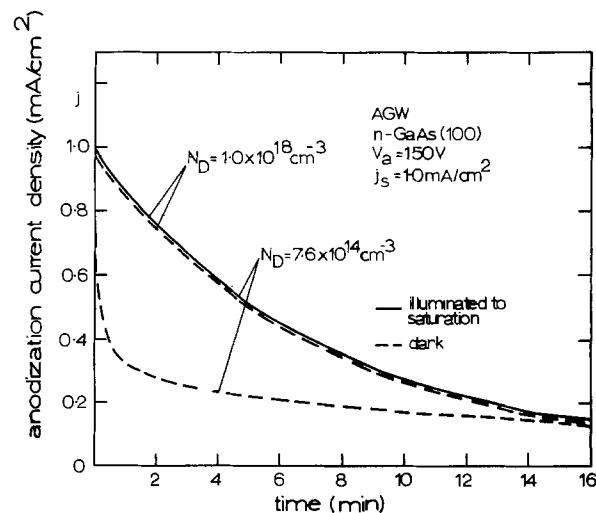


Fig. 4. Effect of illumination on anodic oxide growth on n-type samples.

dependent on the carrier concentration. In the case of the epitaxial sample with a low carrier concentration ( $10^{14}$  cm<sup>-3</sup>), an extremely slow and nonuniform oxide growth resulted, whereas the sample with the higher carrier concentration yielded a very uniform layer. Nonuniform growth can be visibly seen as a nonuniform pattern of oxide interference colors. A repeated careful study of this nonuniform growth has shown that the initial rapid current drop corresponds to a rapid oxidation near the fringe of the sample, and after this slow oxide growth starts from the fringe toward the inner area. It was also noted that anodization reveals several small spots on the surface around which the oxide growth takes place apparently more rapidly. Under a microscope, these spots were identified as defects in the epitaxial layer. The final thickness of the oxide on the sample with the lower concentration after 16 min anodization was about 2600 Å in the case of the sufficiently illuminated surface and about 600 Å on average in the case of the dark surface.

On the other hand, no appreciable effect of light was observed with the anodization of p-type samples, and the anodization current curve coincides with the solid curve in Fig. 4.

A similar marked difference in the behavior between n-type and p-type samples was known for the anodic oxidation of Si (22). It was reported recently that anodic dissolution of n-type GaAs shows an effect of illumination similar to the present case (23). These results indicate that the carriers which are taking part in the anodic reaction at the GaAs anode are holes, irrespective of whether this reaction leads to oxide growth or dissolution. Since the electrolyte-semiconductor interface is basically a Schottky junction, the rate of anodic reaction at the n-type GaAs anode is limited by the thermal generation rate of holes in the reverse biased depletion layer in the semiconductor, unless holes are generated sufficiently by such processes as illumination, thermal generation, or impact ionization.

It is well known that the thermal generation rate of minority carriers decreases as the doping is reduced so that for the lower donor density  $N_D$  of Fig. 4 insufficient holes are provided as long as the applied voltage remains sufficiently small to prevent field or impact ionization. However, it is likely that our results for high  $N_D$  values, when no reduction in the anodization process was found, have to be understood by thermal or impact generation of holes. The latter mechanism is supported by avalanche breakdown results of reverse-biased Schottky junctions.

Similarly, minority carrier generation is likely to be high near the sample fringes and in the neighborhood

of various defects. The effects mentioned here concerning illumination would have a series of interesting applications such as selective anodization, a study of defects on the surface, and delineation of various junctions. However, since uniform and reproducible oxidation is the main purpose of the present paper, further studies on anodization of n-type samples have been done under sufficiently illuminated conditions.

**Behavior of anodization current density.**—The anodization current density is plotted vs. time in Fig. 5 and 6 for the AAS and AGW process, respectively. The current density is normalized for convenience by the short-circuit current density  $j_s$ . By direct comparison,

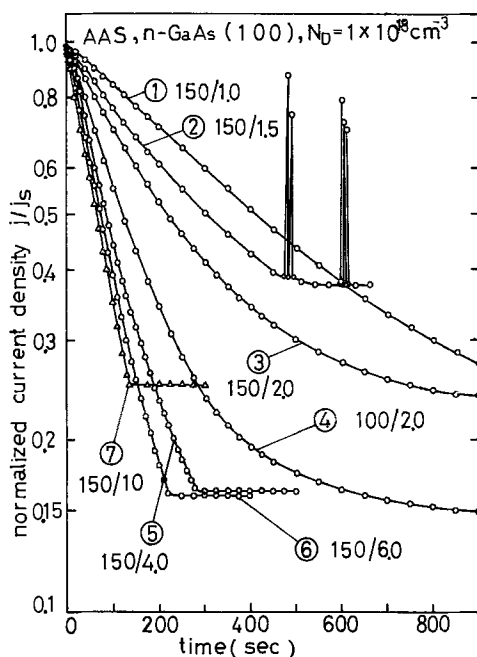


Fig. 5. Normalized anodization current density vs. time for the AAS process. The parameter is  $V_a$  (volt)/ $j_s$  (mA/cm<sup>2</sup>). Curve 7 is taken on a sample with exposed edges.

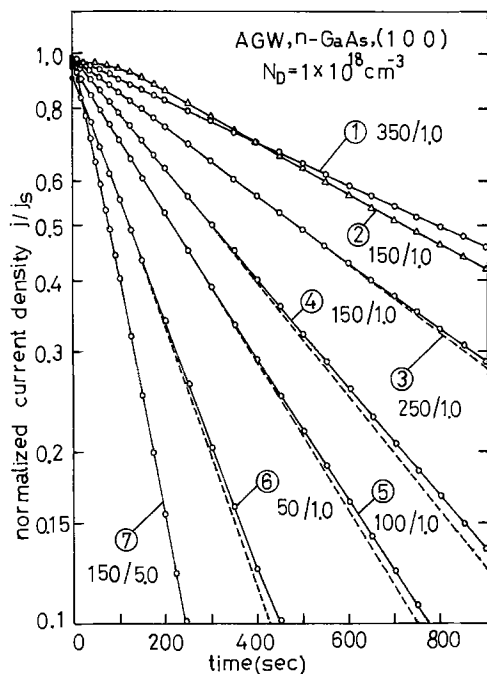


Fig. 6. Normalized anodization current density vs. time for the AGW process. The dashed lines demonstrate when after longer time the experimental curve deviates from an exponential law. The parameter is  $V_a$  (volt)/ $j_s$  (mA/cm<sup>2</sup>). Curve 2 is taken on a sample with exposed edges.

one can see that the AGW process behaves in a much simpler and reproducible way, and that its deviation from an exponential current decrease is only noticeable much later than for the AAS.

The experimental data of these two figures can be understood by an oxide growth rate which is proportional to the anodization current minus an approximately constant dissolution rate. A simultaneous dissolution of oxide into the electrolyte during growth was pointed out by Harvey and Kruger in their analysis of oxide growth based on a potential-sweep method (19). Assuming (a) a constant quasi-steady state field  $E_{ox}$  in the oxide whose dependency on the current density can be ignored, (b) a constant current efficiency, (c) a constant oxide dissolution rate  $f_d$ , and (d) an ohmic bath resistance  $R_b$  leads to the following expression for the normalized anodization current density

$$\frac{j}{j_s} = \frac{j_0 - j_d}{j_s} \exp\left(-\frac{t}{\tau_f}\right) + \frac{j_d}{j_s} \quad [1]$$

where

$$\tau_f = \frac{r_s + r_b}{E_{ox}A} \quad [2]$$

is the time constant of growth, which we call the formation time constant;  $A$  is the formation rate (defined here as the increase in film thickness per unit charge passed through unit area);  $r_s = R_s S = V_a/j_s$  is the external circuit resistance related to anode area (see Fig. 1); and  $r_b = R_b S$  is the bath resistance for unit area of anode

$$j_0 = \frac{V_a - V_r}{r_s + r_b} = j_s \frac{1 - (V_r/V_a)}{1 + (r_b/r_s)} \quad [3]$$

is the initial current density;  $V_r$  is the rest potential of the anodization cell; and

$$j_d = \frac{1}{A} f_d \quad [3a]$$

is the equivalent current density, corresponding to film dissolution.

The corresponding thickness  $x$  is given by

$$x = x_\infty \left[ 1 - \exp\left(-\frac{t}{\tau_f}\right) \right] \quad [4]$$

where  $x_\infty$  is the film thickness in the steady state and is given by

$$x_\infty = \frac{1}{E_{ox}} (V_a - V_r) \left( 1 - \frac{j_d}{j_0} \right) \quad [5]$$

As shown later, assumption (a) does not hold very accurately. However, the deviation is reasonably small and one is still justified to use these simple equations for small variations of current density or for a general description of the process.

In order to exhibit dissolution more clearly also for the AGW process Fig. 7 shows a long-time growth. The value of the film dissolution rate estimated by comparing experimental data with Eq. [1] gives ranges from 1-3 Å/sec for the AAS process and from  $4-6 \times 10^{-2}$  Å/sec for the AGW process, approximately two orders of magnitude a smaller value for the AGW process. For this estimation the experimentally determined values of  $E_{ox}$  and  $E_{ox}A$  were used which is discussed later.

In order to confirm such values of  $f_d$ , a separate etching experiment was carried out where oxide films formed by the AGW process were kept in the AAS or AGW electrolyte without passing a current, and their thickness was measured after constant intervals of time. The result of the experiment is shown in Fig. 8 where thickness dissolved is plotted vs. time. The oxide

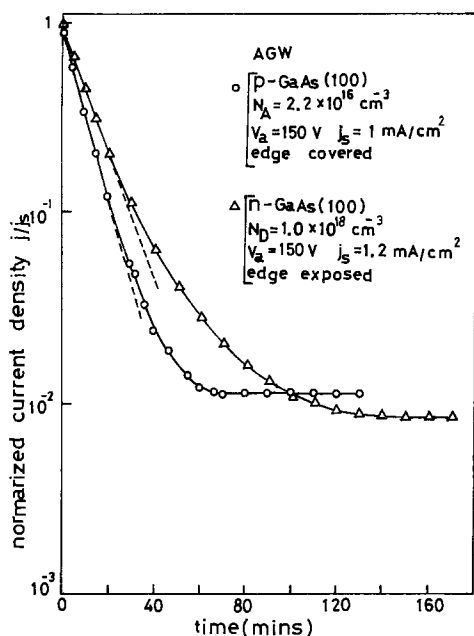


Fig. 7. Current density vs. time for the AGW process for a longer period of anodization.

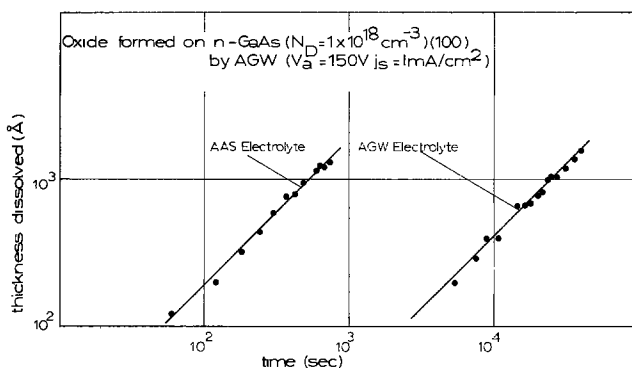


Fig. 8. Etching of oxides in the AAS and AGW electrolyte

dissolution rate  $f_d$  determined by this experiment is  $1.9 \text{ \AA/sec}$  for the AAS electrolyte and  $4.2 \times 10^{-2} \text{ \AA/sec}$  for the AGW electrolyte, and these are indeed in agreement with the previous estimates. This also should be compared with the value of  $f_d = 1.37 \text{ \AA/sec}$  reported by Harvey and Kruger for a different AAS electrolyte (9).

For a given value of the external circuit voltage  $V_a$ , the large effect of oxide dissolution on the growth in the AAS process can be in principle counteracted by passing a larger current through and speeding up the growth. Curves 5, 6, and 7 in Fig. 5, however, show what actually happens in such a case. In addition to the fact that growth proceeds more rapidly with a reduced deviation from the exponential line, as one would expect, the current drop suddenly stops at a certain point and the current stays more or less constant after that with small spiky fluctuations ignored in the drawing. The oxide film grown in such a way shows a whitish granular appearance superimposed on the ordinary interference color, similar to the anomalous growth reported by Logan, Schwartz, and Sundburg (12). A more detailed study showed that the grown oxide is uniform and does not have the anomalous appearance if the growth is stopped before the singular point of the current density is reached, and as soon as this point is reached, the whitish pattern starts to spread from the fringe of the sample toward the inner area and eventually covers the whole surface. A scanning electron micrograph ( $\times 804$ ) of the boundary between the still uniform area and the area with whitish granular

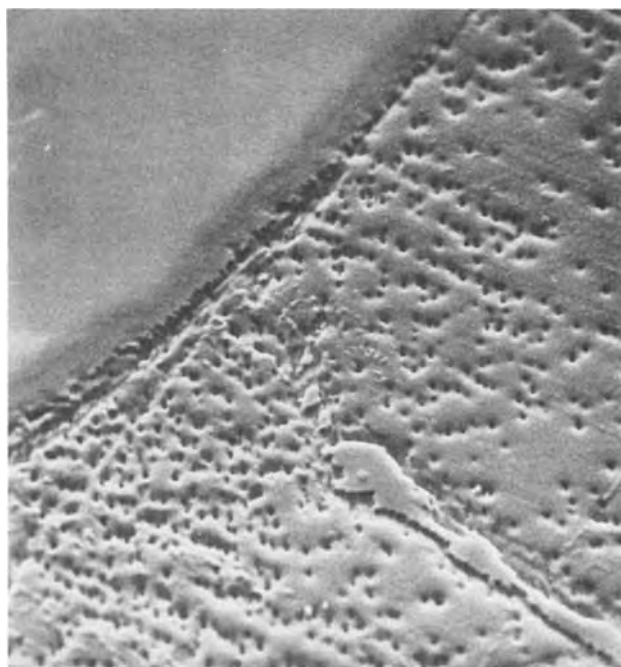


Fig. 9. SEM micrograph of boundary between normal area and anomalous area (804X).

appearance is shown in Fig. 9. The formation of pits is seen in the anomalous region suggesting that serious electrical breakdown took place in the oxide, resulting in the damage of the semiconductor surface. A similar interpretation was given by Spitzer, Schwartz, and Weigle (15). It was indeed found that the whitish granular appearance stays on the surface after the oxide is dissolved away in an HCl solution. In curves 5 and 6 of Fig. 6, both of which are for the samples with covered edges, this breakdown occurred at around 130V, whereas in the curve 7 for the sample with the exposed edges, it took place around 100V.

Curve 2 in Fig. 6 shows yet another anomalous behavior of the AAS process producing current spikes. It has been found that such current spikes correspond again to the formation of pits which are, however, of much larger sizes.

The effect also seems purely local in this case and does not show the tendency of spreading over the entire surface. Except for the pits, the rest of the surface remains uniform. These spikes appear sometimes at very early stages of anodization although they are more frequently observed at later stages, and it looks as if they are caused by a sudden local dissolution of oxide, followed by a rapid regrowth at high current density rather than initiated by breakdown in the oxide. The fact that spikes are more frequently observed in those baths which have been used many times suggests that such a partial dissolution is most probably triggered and enhanced by certain impurities in the electrolyte. In general, the slower the process, or the longer the sample stays in the bath, the higher the probability of producing current spikes. Such an observation was also made by Dell'Oca, Yan, and Young on a different type of AAS electrolyte (8).

*Formation time constant.*—The experimentally determined formation time constant  $\tau_f$  is plotted vs. series resistance per unit area  $r_s$  in Fig. 10 for the various conditions of anodization as indicated in the insert. Most of the data was taken with  $j_s = 1.0 \text{ mA/cm}^2$ , although somewhat larger values were used for the AAS process for the accurate determination of  $\tau_f$  making the effect of oxide dissolution less serious. It is interesting to note that all the data taken on samples with carefully covered edges fall reasonably well on the common straight line with a slope of unity irre-

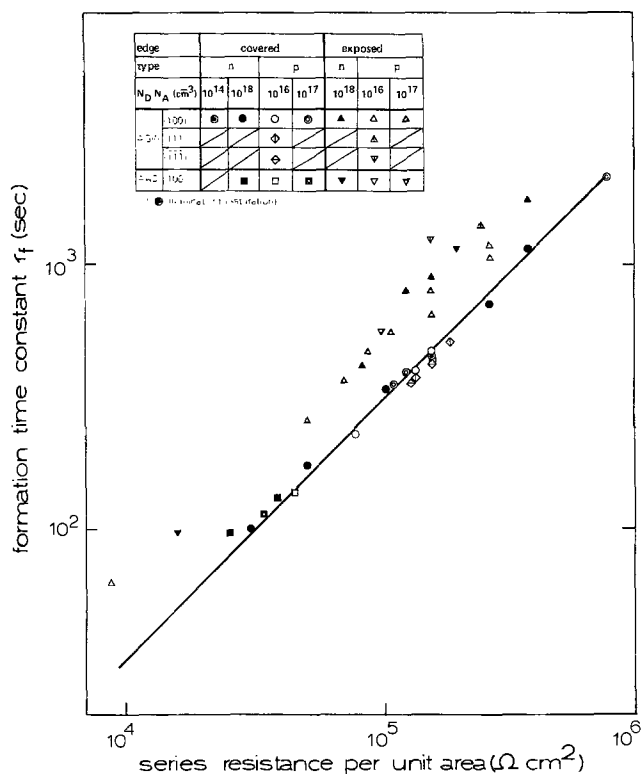


Fig. 10. Measured formation time constant  $\tau_f$  vs. series resistance per unit area,  $r_s$ .

spective of whether it is the AAS or the AGW process and also irrespective of the conduction type, carrier concentration, and crystal orientation. Since all the anodization shown in Fig. 10 was carried out in the situation of  $r_b \ll r_s$ , the result here basically confirms the validity of Eq. [2]. It also strongly suggests that the basic oxide formation process is the same for the AAS and the AGW processes having water as the common anodic oxidant.

As no orientation dependence was observed, it is suggested with reference to the work by Dewald on InSb (24) that, at the field strengths corresponding to the current densities of around 1 mA/cm<sup>2</sup>, the rate-limiting factor of the total process is the ionic transport through the oxide rather than the ionization process at the oxide-semiconductor interface provided that sufficient illumination is given in the case of n-type samples. The straight line of Fig. 10 gives with Eq. [2] and [5] a value for  $AE_{ox}$  of  $3.2 \times 10^2$  cm<sup>2</sup> farad<sup>-1</sup> for a moderate growth rate starting from around 1 mA/cm<sup>2</sup>. This corresponds to a voltage formation rate of 0.32 V/sec for the constant current anodization at 1 mA/cm<sup>2</sup>, which is in agreement with the value of 9.5 V/min reported for a constant-current anodization at 0.5 A/cm<sup>2</sup> in a different electrolyte (21). This agreement demonstrates the similarity of the oxidation processes with various electrolytes containing water, and it shows that our convenient circuit of Fig. 1 also gives growth of a quasi-steady-state nature.

For the anodization at moderate current densities in the standard AAS and AGW baths, the relation of  $r_s \gg r_b$  was almost always satisfied resulting in  $j_s \approx j_0$ . However, when the mixing ratio in the AGW bath exceeded 5, the bath resistance was no longer small as compared with the series resistance which was clearly indicated by the decrease in the initial current density  $j_0$ . Reduction in the thickness of the grown oxides at high mixing ratios seen in Fig. 3 can therefore be explained partly by the increase of bath resistance which leads to a slower growth with an increased time constant according to Eq. [2]. Thus, the reason why case A starts to show slower growth at smaller mixing ratios than case B can be simply understood by the

difference in the amount of tartaric acid which is related to the ionic conduction in the bath.

However, it was found that the actual amount of increase in time constant was found to be too large to be explained quantitatively by the experimentally estimated value of  $r_s$  through Eq. [2]. The anodization curves also showed greatly increased values of  $f_d$  at high values of mixing ratios, with the result that films with reasonable thickness could not be obtained even if one waited for a long time. These two facts show that the whole situation should be explained not only by the increase of bath resistance but also by a marked decrease of the formation rate  $A$  or current efficiency as the mixing ratio becomes high. The latter strongly indicates again that water is the basic anodic oxidant of the process.

*Initial stage of growth.*—The above experimental observation that the formation rate takes more or less the same value for the standard AAS and AGW electrolytes with  $pH = 6.2$  suggests that this rate will also remain more or less constant when the  $pH$  is changed. A careful check has shown that this is indeed the case and that the differences in the thickness of the grown oxides for the AAS and AGW processes in Fig. 2 should therefore be explained primarily by the difference in the oxide dissolution rate  $f_d$ .

However, when the question is considered what the reasons are for the sharp transitions between anodic oxidation and anodic dissolution as observed in both Fig. 2 and 3, an explanation based only on a variation of oxide dissolution rate with bath parameter does not work because one would have expected a more gradual change if such were the case. In fact, an etching experiment of oxide in the unbuffered 3% aqueous solution of tartaric acid has shown that  $f_d$  of such an AAS bath is 5-6 Å/sec which corresponds to  $j_d = 0.7-0.8$  mA/cm<sup>2</sup>. Thus, one should have been able to anodize the sample with the moderate current density of a few milliamperes per square centimeter, which was, however, found always impossible. A further experiment showed the importance of the initial process, in which a sample was anodized in an AGW bath to a few volts corresponding to oxide growth of several ten angstroms, and, after being taken out and subjected to a thorough cleaning and drying, it was immersed into a bath of an unbuffered tartaric acid solution. The result showed that oxide growth can be kept on going in such a case at a moderate current density where oxidation was previously impossible.

Because of this indication of the importance of the initial stage of growth, a more detailed measurement was undertaken using an AGW bath for various current densities. The result is shown in Fig. 11 which clearly shows the presence of a time delay before the initiation of the exponential growth. The length of delay is dependent on the current density rather than the source voltage. The data in Fig. 11 were taken without stirring of the electrolyte. When the electrolyte was stirred, the transition from the flat to the exponential region became more gradual and also the time delay was increased at the same current density.

The observed relationship between time delay and current density is plotted in Fig. 12 for unstirred and moderately stirred conditions. A similar experiment with an AAS bath showed the presence of such a time delay, but no meaningful relationship has been established owing to a large scatter of data and lack of reproducibility which again suggests the extremely sensitive nature of the AAS bath.

All these observations including the abrupt transition from anodic dissolution to anodic oxidation (passivation of the anode), the presence of a minimum threshold current density for oxidation, and the presence of a time delay for oxidation provide strong evidence that the classical active-passive transition of the



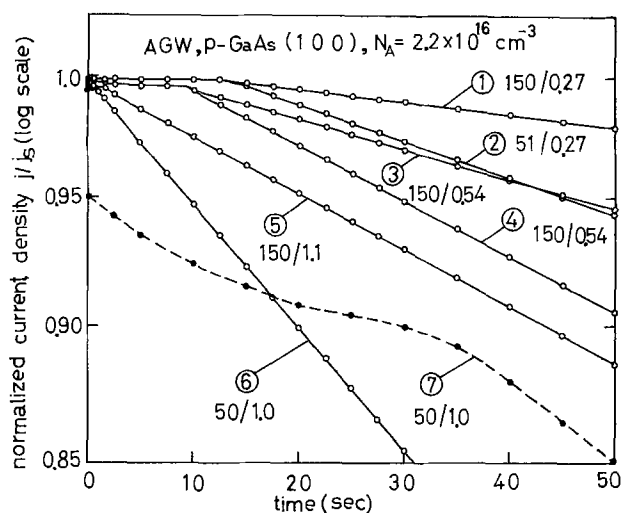


Fig. 11. Initial stage of growth showing passivation time  $t_p$ . The parameter is  $V_a$  (volt)/ $j_s$  ( $\text{mA}/\text{cm}^2$ ). The dashed curve is taken on a sample with exposed edges.

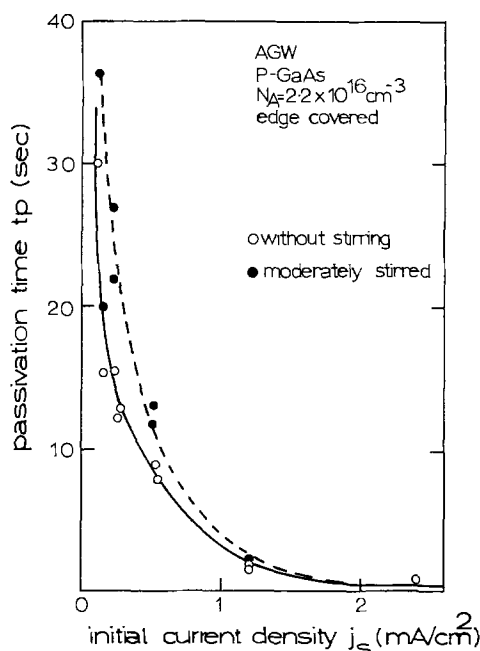


Fig. 12. Passivation time  $t_p$  vs. current density  $j_s$

anode takes place at the initial stage of growth. Such a transition has been known to be very common among certain metals from old times (20), but little practical importance has been attributed to the case of semiconductor materials. Harvey (25) and more recently Harvey and Kruger (9) studied the electron behavior of the GaAs anodes and observed this transition under certain conditions. But, these excellent studies did unfortunately not lead so far to any practical control of such a transition.

The extreme sensitivity of the AAS bath and the observed sharp transitions in Fig. 2 and 3 can be best explained by the fact that the limiting current density  $j_l$  for the active-passive transition is high and it varies very much with the bath parameters and by the introduction of contaminations in the AAS bath. A repeated measurement has shown that the value of  $j_l$  for the present AAS bath at the optimum pH value of 6.2 lies typically in the range of 0.8–5  $\text{mA}/\text{cm}^2$ , and that of the AGW bath is about  $1.0 \times 10^{-1} \text{ mA}/\text{cm}^2$  as seen in Fig. 12.

The observed time delay is obviously the so-called passivation time  $t_p$  of the active-passive transition. The data in Fig. 12 fit better the relation,  $(j - j_l) t_p^{1/2} =$

const, rather than,  $(j - j_l) t_p = \text{const}$ , indicating the establishment of a supersaturated region against the diffusion convection transport (20). A further detailed study seems to be necessary to fully clarify the situation. The reason for the reduction of the limiting current density by the addition of glycol would be either a decrease in the solubility of the initial anodic products, or a reduction in the transport rate of such products, or both, leading to an easier establishment of supersaturation.

The fact that stirring increases the passivation time is obviously consistent with the present picture, and although it thus makes the establishment of the desired situation for growth more difficult, its effect on the AGW process at moderate current density is very small, and, moreover, a continuous stirring at a moderate speed has been found practically very important for uniform growth because, without stirring, any bubbles, accidentally introduced by sample immersion or produced spontaneously, tend to stick on the surface and prevent the initiation of uniform oxidation. Stirring seems also to be important for successful growth of thick films.

The usual anodic film growth takes place thus in the passive region of the GaAs anode after the above transition. Electron diffraction studies confirmed the amorphous glassy nature of such "passive" films for both of AGW and AAS processes in agreement with the previous results on similar films. An electron microprobe analysis has shown the ratio of numbers of Ga and As atoms in the grown films to be unity on average. Other important properties of the AGW oxide films have been described elsewhere (16).

When the current density is below the limiting current, the GaAs anode remains in the active region and the anodic dissolution continues without showing the current drop (or voltage buildup). This dissolution process is a nonuniform one, apparently having higher dissolution rates at mechanically damaged parts and edges, producing sharp ditches at the waxed boundary and leaving characteristic pits and lines on the surfaces. When the anodization current density is just below the limiting current density, it was observed that the entire GaAs surface changes quickly into a brownish, whitish appearance with the current showing no drop. This surface layer could not be removed by HCl, KOH, or  $\text{NH}_4\text{OH}$ , each of which is an etchant of the amorphous passive oxide. It was first thought that this film was similar to the porous, polycrystalline "active" oxide formed in the active region under certain conditions by Harvey and Kruger (9). However, an electron diffraction study showed only the single crystal pattern of GaAs, and a high magnification scanning electron microscope showed a pattern which looks like a roughened surface of GaAs. Thus, the presence of such an active oxide or hydroxide has not been confirmed yet in the present case.

*Effects of bath contamination.*—One of the most important features of the new AGW process is that it is much more immune against contaminations than the AAS process. The present study confirmed that among various commonly used acids and bases, HCl seems to have the strongest effect on the oxide growth. On the other hand the present AGW process exhibits an impressive stability, even up to the level of  $10^{-3}N$  of HCl, as already reported elsewhere (6).

A result of a series of experiments which demonstrate the striking stabilizing effect of glycol is shown in Fig. 13. The final vertical portion of each curve shows the moment of stop of anodization. Curve 1 is the anodization curve for the uncontaminated AAS bath which was taken near the limiting current as indicated by a large passivation time (20 sec). After an artificial introduction of about  $7 \times 10^{-4}N$  of HCl, anodic oxidation stops as shown by curves 2 and 3. At an increased current level by about 2.5 times, it starts



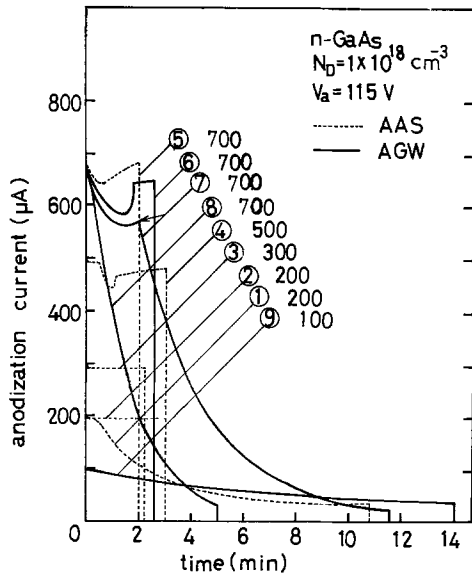


Fig. 13. Action of glycol in the contaminated bath. The parameter is the short-circuit current  $I_s = j_s S$  in  $\mu\text{A}$ . The sample area is  $5 \text{ mm}^2$  with exposed edges.

again after a large passivation time of 30 sec as shown by curve 4, but somehow fails, probably because of a high oxide dissolution rate acting in a nonuniform way. Further increases in the current do not improve the situation very much as shown by curve 5. At this stage, glycol is added with a mixing ratio of 0.5 with an appreciable improvement as shown by curve 6. With a mixing ratio of unity (curve 7), the improvement is remarkable but still insufficient. At the point indicated by an arrow on curve 7, glycol is further added to the ratio of 1.5 and a completely normal anodization is restored, which was repeated from the beginning as shown by curve 8. Curve 9 shows that after the addition of glycol the anodization became possible even at a smaller current density with which the anodization was originally impossible.

**Thickness-voltage rate constant.**—The thickness of the grown oxide layers are plotted vs. voltage across the oxide for various anodization conditions in Fig. 14. Three different ways of growth were employed, i.e., case A: started from  $j_s = 1 \text{ mA/cm}^2$ , and stopped as the predetermined voltage across the oxide is reached with the current density of  $j = 0.1 \sim 0.3 \text{ mA/cm}^2$ ; case B: started either from  $j_s = 1 \text{ mA/cm}^2$  and left until the current density is reduced to more or less the steady state with  $j \approx 1 \times 10^{-2} \text{ mA/cm}^2$ , or started as above, then changed to constant voltage anodization at the predetermined voltage when the voltage across the oxide reaches that value, and left until it reaches the steady state with the current density  $j \approx 1 \times 10^{-2} \text{ mA/cm}^2$ ; case C: rapid growth, started from  $j_s \approx 5 \sim 10 \text{ mA/cm}^2$  and stopped at  $j \approx 2 \sim 3 \text{ mA/cm}^2$ . In each case, the voltage across the oxide was determined simply by  $V = V_a (j_o - j)/j_o$  where the effect of bath resistance is included, but any correction to obtain the exact oxide-producing overpotential is ignored. A separate experiment has shown that such a potential correction is less than 1V, and for the large voltage values ( $> 50\text{V}$ ) employed in the present study with the not so accurate means of thickness determination, such a detailed correction seemed rather insignificant. Figure 14 indicates clearly that the thickness-voltage relationship varies as a function of the current densities employed. This is consistent with the various theories of ionic transport which relate the current density  $j$  with the steady-state oxide field  $E_{ox}$ , generally in the form of  $j = j_o \exp(-W(E_{ox})/kT) \exp(qaE_{ox}/kT)$  (26).

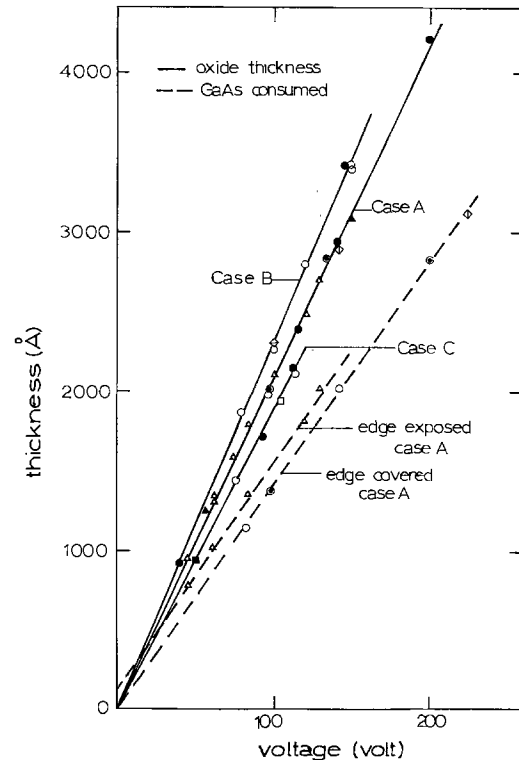


Fig. 14. Oxide thickness and amount of consumed GaAs vs. voltage. Symbols are the same as Fig. 10.

The averaged value of the thickness-voltage constant is  $21 \text{ Å/V}$  for case A,  $23 \text{ Å/V}$  for case B, and  $19 \text{ Å/V}$  for case C. This result explains why different values ranging from 18 to  $22 \text{ Å/V}$  were reported in the past (8, 9, 12, 15, 21) and indicates that the current density must be carefully determined for the accurate control of the process which is, for instance, important for fine thinning of wafers for the purpose of profiling (21) and wafer tailoring for FET's and other devices (14). Within the experimental accuracy no dependence of the rate constants on the carrier concentration or orientation was observed. The amount of GaAs consumed is also shown for case A of growth in Fig. 14 and the average consumption rate is  $14 \text{ Å/V}$  for the samples with carefully covered edges.

On the basis of a more careful study of the rate constants as a function of the final anodization current density  $j_f$ , a plot of this current density vs. the electric field  $E_{ox}$  is obtained as shown in Fig. 15 which shows approximately a simple Mott-Cabrera type exponential dependency on the field (23), given by

$$j_f = 3.75 \times 10^{-15} \exp(6.58 \times 10^{-6} E_{ox}) \quad [6]$$

or

$$\text{rate constant} \equiv \frac{1}{E_{ox}} = \frac{19.8}{1 + 0.069 \log_{10} j_f} \text{ Å/V} \quad [7]$$

where the field and current density have to be expressed in the units of  $\text{V/cm}$  and  $\text{mA/cm}^2$ , respectively. This again confirms the quasi-steady-state nature of our growth. Our results are obviously consistent with the theory of ionic transport (26).

It is not clear at the moment whether the observed small deviations from the exponential line at high fields is due to the experimental error, the transient nature of the experiment, or a more complex dependency on field.

The grown oxides show a regular occurrence of intense interference colors which corresponds to the refractive index of 1.8. Although no detailed ellipsometric measurement has been done, the change of the refractive index with the change of growth conditions

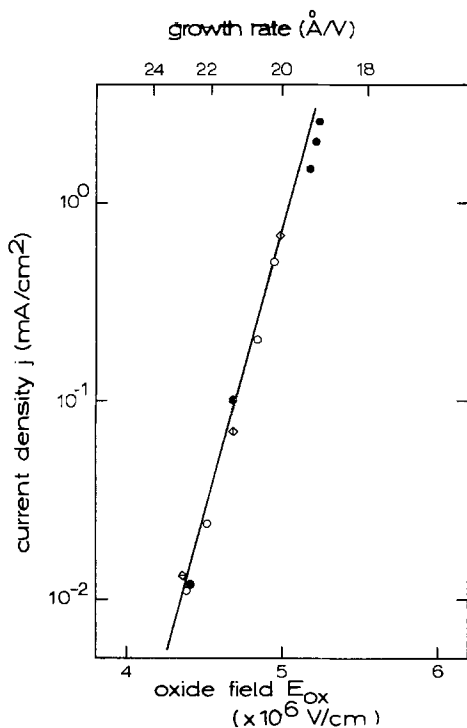


Fig. 15. Current density  $j$  vs. oxide field  $E_{ox}$ . Symbols are the same as Fig. 10.

seems to be very small as compared with the above-mentioned fairly large change in growth rate.

**Effects of exposed edges.**—As already indicated in various figures of the present paper, exposure of sample edges, in particular, mechanically damaged area, has extremely large effects which can become one of the important causes for quantitative irreproducibility of the process. The main effects observed experimentally are as follows: (i) slow down of the process as seen clearly as an increase in formation time constant  $\tau_f$  in Fig. 10, (ii) increase in the passivation time  $t_p$  with a very gradual change in current as shown in Fig. 6 and 11, (iii) increase in the rate of GaAs consumption as shown in Fig. 14, (iv) generation of fluctuations in the anodization current, and (v) lowering of the breakdown voltage in the oxide as shown for the AAS process in Fig. 5.

The effects (i) and (ii) indicate that the exposed mechanically damaged parts (wire sawed for example) behave effectively as if they have a much larger surface than their actual geometrical area. The graded active-passive transition also suggests that the transition does not take place at the same time all over the surface but proceeds nonuniformly, starting perhaps from the edges. The effect (ii) seemed to be particularly large in the anodization of  $(\bar{1}\bar{1}\bar{1})$  faces, sometimes resulting in the impossibility to cause the transition. The effect (iii) is related most probably to (ii) rather than the oxide dissolution because the latter is too small in the AGW baths to account for it. Owing to the delayed and nonuniform proceeding of the transition from the edge, the anodic dissolution continues perhaps for a much longer time on the front surface, resulting in a loss of an appreciable amount of GaAs. Some preliminary results (6) taken on samples with exposed edges thus showed a higher consumption rate of GaAs than for results reported previously. This was originally incorrectly interpreted as a higher density of the oxide.

The data in Fig. 14 indicates that such a loss of GaAs is 100–150Å in case A of growth, and this result shows the vital importance of coverage of the edges in the application of controlled thinning of wafers. The effects (iv) and (v) are most probably related to high

current densities and high fields at the edges causing partial breakdown and partial dissolution of loose oxide.

**Current efficiency.**—Finally, a crude estimate of the current efficiency of the AGW process will be made. From Fig. 15, one obtains  $E_{ox} = 5.05 \times 10^6$  V/cm for  $j_s = 1.0$  mA/cm $^2$ , which gives, combined with the value of  $E_{ox}A$  previously given,  $A = 6.4 \times 10^{-5}$  cm $^3$ /coulomb. Since no direct density measurement has been done so far, a crude estimate is made as follows. From the case B growth in Fig. 14, one obtains the oxide coating ratio (= oxide thickness divided by GaAs consumed) of 1.5, assuming the loss of GaAs at the initial process is negligible for samples with covered edges on the basis of observed good proportionality. Then, if one assumes that the oxide is an amorphous mixture of Ga $_2$ O $_3$  and As $_2$ O $_3$  and ignores the possible effect of hydration on the basis of the detailed analysis of a similar oxide (27), the density of the oxide is estimated as 4.7.

A simple Faradaic analysis based on these data, assuming that each of the Ga and As atoms are ionized to its tripositive state as shown by Harvey and Kruger (9) for a similar oxide growth [Revesz and Zaininger (7) reported the oxide with penta positive As, but it does not seem to be the present case], gives a value of the current efficiency of 90% which is of course due to the small amount of dissolution. The reported anodization of Si has on the other hand a surprisingly low current efficiency of only 1–8% (19, 26).

## Conclusions

By detailed comparisons, certain common features of various AAS processes have become clear, and the essential superiority of the AGW process is established on the basis of the detailed experiments and the theoretical understanding. Factors which affect the uniform and reproducible oxidation have been clarified and relevant process equations and data are given. The AGW process characterized by its easy use, its stability, and reproducibility, seems to be one of the most promising ways of forming insulating layers with acceptable qualities on GaAs. The main conclusions are as follows:

1. Water is a good anodic oxidant of GaAs, and a variety of aqueous solutions can anodize GaAs (AAS process). Anodization in water undergoes the electrochemical active-passive transition at the initial stage, which is characterized by the limiting current density and the passivation time.

2. The limiting current density of the AAS process is high and sensitive to contaminations which make it extremely difficult to anodize at a moderate current density of a few milliamperes per square centimeter in a stable, reliable, and reproducible way.

3. The AAS system is also characterized by a high rate of oxide dissolution which leads to the growth of loose and less impervious oxide films, enhanced partial dissolution of oxide during growth, and premature breakdown in the oxides at fairly low voltages. The oxide dissolution rate is also sensitive to contaminations which provide another cause for unstable and irreproducible results.

4. By the introduction of a fairly large amount of glycol to the AAS system, the limiting current density and oxide dissolution rate is greatly reduced (AGW process), and the process becomes extremely stable, reliable, and reproducible. Optimum bath conditions using tartaric acid and propylene glycol are established.

5. The main factors which affect a uniform and reproducible oxidation are illumination on n-type samples, coverage of sample edges, and a moderate stirring of the electrolyte.

6. The rate thickness-voltage constant shows a fairly large current density dependence.

7. The AGW process has a high current efficiency.

#### Acknowledgments

The authors would like to express their thanks to Dr. B. Schwartz, Bell Laboratories, Murray Hill, New Jersey, and Dr. M. Faktor, Post Office Research Laboratories, Dollis Hill, London, for their useful and stimulating discussions. They would also like to thank Dr. B. Weiss at this department for performing SEM and electron diffraction measurements. Financial assistance is gratefully acknowledged to the U.S. Army European Research Office, London.

Manuscript submitted June 9, 1975; revised manuscript received Oct. 30, 1975. This was Paper 158 presented at the Dallas, Texas, Meeting of the Society, Oct. 5-9, 1975.

Any discussion of this paper will appear in a Discussion Section to be published in the December 1976 JOURNAL. All discussions for the December 1976 Discussion Section should be submitted by Aug. 1, 1976.

#### REFERENCES

1. S. P. Murarka, *Appl. Phys. Letters*, **26**, 180 (1975).
2. J. E. Foster and J. M. Swartz, *This Journal*, **117**, 1410 (1970).
3. J. A. Cooper, E. R. Ward, and R. J. Schwartz, *Solid-State Electron.*, **15**, 1219 (1972).
4. T. Itoh and Y. Sakai, *ibid.*, **17**, 75 (1974).
5. B. J. Baliga and S. K. Ghandhi, *IEEE Trans. Electron Devices*, **ED-21**, 410 (1974).
6. H. Hasegawa, K. Forward, and H. Hartnagel, *Electron. Letters*, **11**, 53 (1975).
7. A. G. Revesz and K. H. Zaininger, *J. Am. Ceram. Soc.*, **16**, 606 (1963).
8. C. J. Dell'Oca, G. Yan, and L. Young, *This Journal*, **118**, 89 (1971).
9. W. W. Harvey and J. Kruger, *Electrochim. Acta*, **16**, 2017 (1971).
10. O. A. Weinreich, *J. Appl. Phys.*, **37**, 2924 (1966).
11. T. Sugano and Y. Mori, *This Journal*, **121**, 113 (1974).
12. R. A. Logan, B. Schwartz, and W. J. Sundburg, *This Journal*, **120**, 1385 (1973).
13. S. M. Spitzer, B. Schwartz, and G. D. Weigle, *ibid.*, **121**, 820 (1974).
14. D. L. Rode, B. Schwartz, and J. V. DiLorenzo, *Solid-State Electron.*, **17**, 1119 (1974).
15. S. M. Spitzer, B. Schwartz, and G. D. Weigle, *This Journal*, **122**, 397 (1975).
16. H. Hasegawa, K. Forward, and H. Hartnagel, *Appl. Phys. Letters*, **26**, 567 (1975).
17. For example, W. J. Bernard and J. W. Cook, *This Journal*, **106**, 643 (1959).
18. For example, D. A. Vermilyea, *Acta Met.*, **1**, 482 (1954).
19. E. F. Duffek, E. A. Benjamini, and C. Mylroie, *Electrochem. Technol.*, **3**, 75 (1965).
20. J. O'M. Bockris, Editor, "Modern Aspects of Electrochemistry," No. 2, p. 262, Butterworths, London (1959).
21. H. Müller, J. Gyulai, J. W. Mayer, F. H. Eisen, and B. Welch, "Proceedings of IVth International Conference on Ion Implantation, Osaka, Japan" (1974); H. Müller, F. H. Eisen and J. W. Mayer, *This Journal*, **122**, 651 (1975).
22. P. F. Schmidt and W. Michel, *This Journal*, **104**, 230 (1957).
23. A. Yamamoto and S. Yano, *ibid.*, **122**, 260 (1975).
24. J. Dewald, *ibid.*, **104**, 244 (1957).
25. W. W. Harvey, *ibid.*, **114**, 472 (1967).
26. J. O'M. Bockris, Editor, "Modern Aspects of Electrochemistry," No. 4, p. 176, Butterworths, London (1966).
27. L. C. Feldman, J. M. Poate, F. Ermanis, and B. Schwartz, "Proceedings of International Conference on Ion Beam Surface Layer Analysis, Yorktown Heights, New York" (1973).

## Quantitative Detection of Oxygen in Silicon Nitride on Silicon

P. H. Holloway and H. J. Stein

Sandia Laboratories, Albuquerque, New Mexico 87115

#### ABSTRACT

The carbon, oxygen, and nitrogen levels in 500-2000Å films of CVD silicon nitride ( $\text{Si}_3\text{N}_4$ ) films have been measured using Auger electron spectroscopy in conjunction with inert gas ion sputtering. The quantitative depth distribution of oxygen throughout the film was determined and interfacial oxides 10Å thick were clearly resolved. Oxygen concentrations in various nitride films were observed to range from 0.4 to 7% (atomic), whereas carbon was below the detection limits. It was shown that bulk oxygen and carbon levels down to 0.05 and 0.2%, respectively, are detectable. The influence of oxygen on the silicon/nitrogen Auger peak height ratio was demonstrated and the presence of oxygen was correlated with changes in the optical index of refraction.

The semiconductor industry has developed thin film silicon nitride both as a barrier for sodium diffusion and as an active element in electrically variable non-volatile MNOS memory devices (1). The properties of silicon nitride can be varied over a wide range depending on the deposition technique and conditions, and these conditions are adjusted to obtain desired characteristics (2). For example, it is known from studies of electrical conductivity vs. deposition conditions that silicon nitride grown by chemical vapor deposition (CVD) at temperatures between 700° and 900°C with a high ammonia to silane ratio yields low

conductivity films suitable for MNOS memory devices (3, 4). However, the quantity and distribution of impurities which are included by a selected growth process have not been fully characterized. A brief study of surface impurities by Auger electron analysis has been reported (5). Variations of optical properties (e.g., refractive index, optical and infrared spectra, etc.) have been used to investigate impurities in silicon nitride (2, 6), but the sensitivity and depth resolution are generally not adequate for complete characterization of supported silicon nitride films.

We will demonstrate that Auger electron spectroscopy (AES) in conjunction with inert gas sputtering is a powerful tool for detecting very thin  $\text{SiO}_2$  layers

at the nitride/silicon interface, for analyzing the quantity and depth distribution of impurities in thin silicon nitride (abbreviated  $\text{Si}_3\text{N}_4$ ) films, and for obtaining a relative measure of the nitrogen to silicon ratio within the films. Oxygen concentrations in excess of 1 atomic per cent (a/o) were observed in the present memory-quality silicon nitride films.

### Experimental

The  $\text{Si}_3\text{N}_4$  films were supplied by Sperry Research Center and were chemically vapor deposited at  $750^\circ\text{C}$  with an ammonia-to-silane ratio of 1000:1. The ratio of silane to total flow (argon carrier gas) was  $2 \times 10^{-4}$  with the total flow rate being 15 liters/min. The ammonia was supplied by Air Products with a purity of 99.999+%. The ultra high purity (UHP) argon was supplied by Matheson Gas Products with a purity of 99.999+%. The semiconductor grade silane was also supplied by Matheson Gas Products at 1% dilution in UHP argon. There was no deliberate contamination of the gases and the observed oxygen content is believed to have entered the process from an improperly capped graphite susceptor.

Gas flow was regulated by flow meters and the nitride reactor was a cold-wall quartz horizontal type with an RF induction-heated graphite susceptor ( $12.7 \times 35.6$  cm). Prior to insertion into the reactor, silicon wafers were cleaned with  $\text{NH}_3\text{-H}_2\text{O}_2$ , rinsed in deionized (DI) water, etched with buffered HF followed by a DI water rinse, the blown dry with nitrogen. The  $\text{Si}_3\text{N}_4$  films were approximately 500-2000Å thick.

Generally, a 10Å thick native oxide film existed at the nitride/silicon wafer interface, but two silicon substrates had thicker  $\text{SiO}_2$  grown before  $\text{Si}_3\text{N}_4$  was deposited. A 30Å  $\text{SiO}_2$  film was formed by heating to  $810^\circ\text{C}$  in 99.999+%  $\text{N}_2\text{O}$ . A 420Å  $\text{SiO}_2$  film was grown in dry oxygen at  $1000^\circ\text{C}$ . The 30Å  $\text{SiO}_2$  film was used to check the resolving power of AES for interfacial oxides, while the 420Å  $\text{SiO}_2$  film was used to standardize AES for quantitative oxygen analysis. A silicon wafer upon which  $\text{SiO}_2$  was formed by heating in air to  $1000^\circ\text{C}$  was also used for AES standardization.

AES (7) was performed with an ion pumped spectrometer from Physical Electronics Industries, Inc., using a cylindrical mirror analyzer and primary electrons from a coaxial gun. The primary electrons had an energy of 5 keV and a beam current of 10  $\mu\text{A}$ . The analyzer modulation was 4 eV peak-to-peak, unless otherwise noted, and the spectra were taken in the derivative mode (7). For sputter profiling, i.e., measuring the Auger electron (AE) derivative peak height while sputter removing surface atoms, a beam of 1 keV argon ions was used. The system argon pressure was  $5 \times 10^{-5}$  Torr, and the sputter rate for  $\text{Si}_3\text{N}_4$  was varied between 0 and 100 Å/min by varying the ion current striking the sample.

Index of refraction data were taken on a Gaertner L119 ellipsometer with a mercury-xenon light source. The light beam was incident at  $60^\circ$  and was monochromatized to the 5461Å mercury line. A two-layer model was used to extract the index from the raw data by a digital computer for the 10 and 30Å interfacial oxides, and simultaneous deposition on a bare substrate was used to verify the index for the nitride deposited on the 420Å oxide.

### Results and Discussion

**Auger electron analysis.**—The silicon AE peaks (near 80 and 1600 eV) and nitrogen AE peak (379 eV) were relatively weak while the carbon AE peak (270 eV) and oxygen AE peak (506 eV) were relatively strong on the as-received  $\text{Si}_3\text{N}_4$  surface (shown in Fig. 1a). This strong oxygen signal probably results from room temperature formation of oxide as shown by the shift of the silicon  $L_{2,3}$  VV peak to 78 eV (8), and the strong

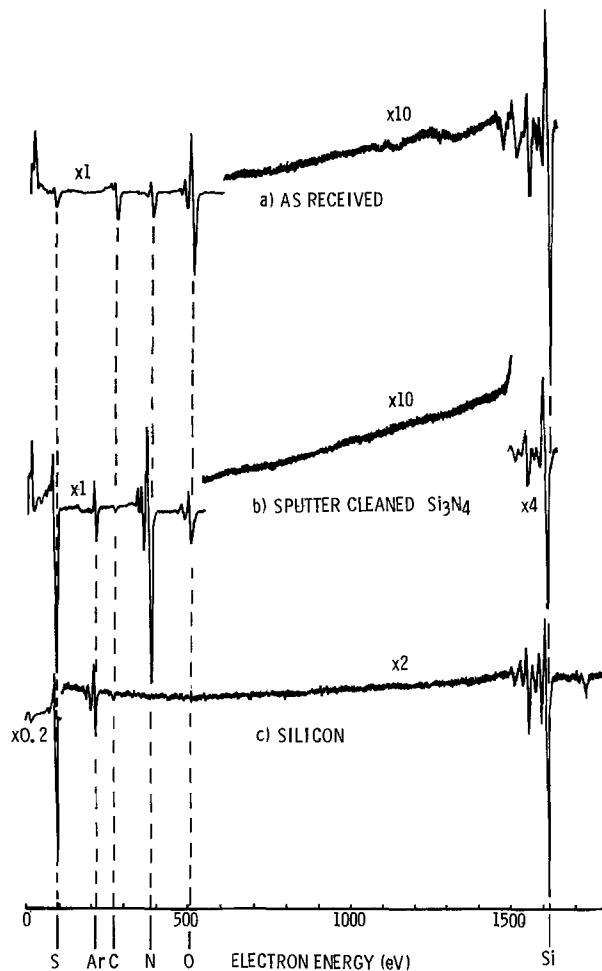


Fig. 1. Spectra from (a) as-received surface, (b) sputter cleaned silicon nitride surface, and (c) silicon surface with  $\text{Si}_3\text{N}_4$  removed. Note the residual carbon and occluded argon in (b) and (c).

carbon signal probably results from the adsorption of carbon-containing atmospheric gases. Sputtering for short times (removing  $\sim 50\text{Å}$ ) was sufficient to remove the high surface concentrations of oxygen and carbon, so that AE signals from silicon and nitrogen are increased in intensity, while those from oxygen and carbon are very weak (Fig. 1b). In addition, new peaks are evident with the strongest transition at 216 eV; these result from argon atoms implanted during sputtering for Auger electron analysis. After sputtering completely through the  $\text{Si}_3\text{N}_4$  film, AE peaks from silicon, argon, and carbon are detected as shown in Fig. 1c. Chemical shifts of the Auger electron peaks from silicon in  $\text{Si}_3\text{N}_4$  make them distinct from Auger electron peaks from elemental silicon or  $\text{SiO}_2$ , as discussed elsewhere (8).

Typical plots of the silicon KLL transition ( $\sim 1615$  eV), oxygen 506 eV, nitrogen 379 eV, and carbon 270 eV AE peak heights vs. depth of material removed by ion sputtering are shown in Fig. 2. In this instance, sputter time was converted to sputter depth by knowledge of the  $\text{Si}_3\text{N}_4$  film thickness. It was assumed that the sputter rate was independent of the presence of surface and interfacial oxides and that the sputter rate was the same in silicon as in  $\text{Si}_3\text{N}_4$ . While these assumptions are probably in error, this is not significant to the discussion below. The sputter profiles show an interfacial oxygen concentration, a significant concentration of oxygen throughout the  $\text{Si}_3\text{N}_4$  film with no detectable concentration in the silicon substrate, and a small concentration of carbon throughout the  $\text{Si}_3\text{N}_4$  and into the Si substrate. The sample shown in Fig. 2a had no intentional oxide grown at the nitride/silicon interface while that in Fig. 2b had 30Å of oxide grown as

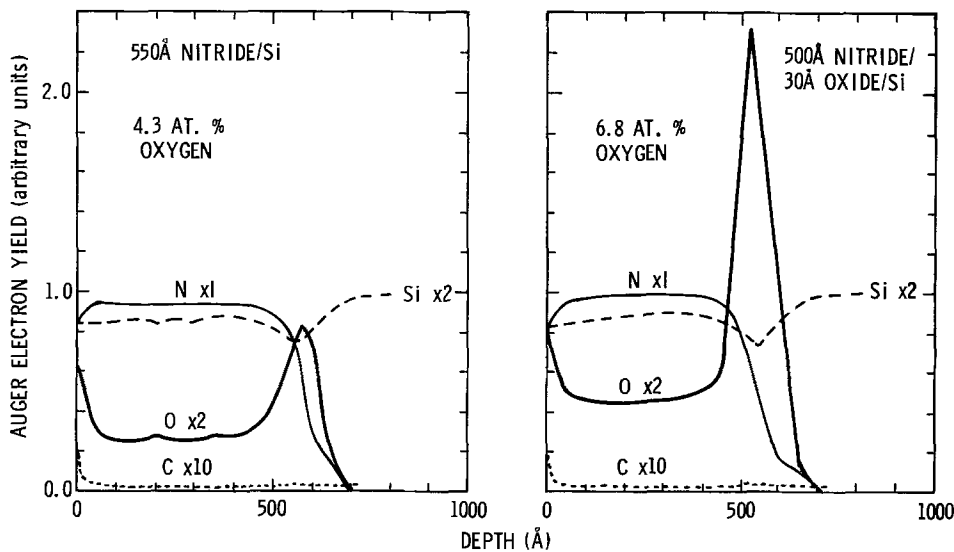


Fig. 2. Auger electron peak heights of silicon, carbon, nitrogen, and oxygen vs. depth for  $\text{Si}_3\text{N}_4$  films with bulk oxygen concentrations of (a, left) 4.3%, and (b, right) 6.8%. The interfacial oxide in (b) is 30 Å thick, while the oxide in (a) is approximately 10 Å thick.

described in the experimental section. The silicon LVV Auger transition peak shape changed consistent with  $\text{SiO}_2$  being present at the nitride/silicon interface. Based on the processing history of silicon substrates prior to  $\text{Si}_3\text{N}_4$  deposition and based on literature data (9), a native oxide film 10 Å thick is expected at the nitride/silicon interface. A relative estimate of interfacial oxide thickness can be made by integrating the area under the oxygen AE peak height vs. time (10). (The thickness cannot be estimated from the abscissa because of nonplanar removal of the  $\text{Si}_3\text{N}_4$ ,  $\text{Si}_3\text{N}_4$  thickness variation, knock-on effects, Auger electron escape depths, etc.) In arbitrary units, the area under the oxygen peak at the interface in Fig. 2a is 54 while the area in Fig. 2b is 144, i.e., a ratio of  $54/144 = 0.37$ . This is quite consistent with the expected ratio of  $10\text{Å}/30\text{Å} = 0.33$ . It is obvious from data in Fig. 2 that 10 Å of oxide under 500 Å of  $\text{Si}_3\text{N}_4$  is easily resolved, and it appears that oxides significantly thinner than 10 Å would be resolvable.

**Quantification of bulk impurity levels.**—Turning our attention to the oxygen and carbon distributed through the bulk of the  $\text{Si}_3\text{N}_4$  films (i.e., the steady-state AE signals observed after removal of the surface contaminants), it is desirable to quantitatively evaluate these impurity concentrations. To accomplish this quantification for oxygen, the AE signal from  $\text{SiO}_2$  formed at 1000°C on silicon and the silicon 1618 eV signal from elemental silicon (after sputter removal of the  $\text{SiO}_2$ ) were measured. In addition, the  $\text{SiO}_2$  oxygen signal and the elemental 1618 eV silicon signal from the substrate of the special nitride sample (prepared with a 750 Å  $\text{Si}_3\text{N}_4$  film on top of a 420 Å  $\text{SiO}_2$  film on a silicon substrate) were measured. The oxygen AE peak height from the bulk of the  $\text{Si}_3\text{N}_4$  film was measured and the bulk oxygen concentration  $C_{\text{O},\text{Si}_3\text{N}_4}$  (a/o) calculated from the equation

$$C_{\text{O},\text{Si}_3\text{N}_4} = 67 \frac{I_{\text{O},\text{Si}_3\text{N}_4}/I_{\text{Si},\text{N}}}{I_{\text{O},\text{SiO}_2}/I_{\text{Si},\text{O}}} \quad [1]$$

where  $I_{\text{O},\text{Si}_3\text{N}_4}$  is the oxygen AE signal from the nitride film,  $I_{\text{O},\text{SiO}_2}$  is the oxygen AE signal from  $\text{SiO}_2$ ,  $I_{\text{Si},\text{N}}$  and  $I_{\text{Si},\text{O}}$  are the silicon 1618 eV signals from the silicon substrate after the nitride or oxide films, respectively, have been completely sputter removed. The factor 67 represents the atomic per cent of oxygen in  $\text{SiO}_2$ . This is essentially the calibration procedure discussed by Chang (7). Here we take oxygen in  $\text{SiO}_2$  as our reference material and assume all other effects such as surface roughness, backscatter factor, escape depth, etc., are all the same for  $\text{SiO}_2$  and  $\text{Si}_3\text{N}_4$ . In addition, the intensity of the elemental silicon 1618 eV AE peak height is used as a standardization to eliminate error

from day-to-day variations in the system gain. The silicon peak from silicon nitride was not used for standardization to avoid error caused by chemical shifts and composition variations. The ratio,  $I_{\text{O},\text{SiO}_2}/I_{\text{Si},\text{O}}$ , was measured over a period of time for both the oxidized silicon wafer and the special nitride sample, and the ratio was found to be  $4.3 \pm 0.3$ . The bulk oxygen levels in the various nitride films were calculated using Eq. [1] and are shown in Table I. As shown, the oxygen concentration was found to vary between 0.4 and 6.8%. However, because of variations in experimental conditions such as surface roughness, film density, electron backscattering, preferential sputtering, matrix chemical effects, etc. (7), the accuracy of the oxygen concentration is estimated to be only  $\pm 40\%$ .

It is important to consider whether the oxygen signal observed through the bulk of the  $\text{Si}_3\text{N}_4$  film is a "true" signal from oxygen impurities or an artifact of the analyzing technique. The possibility of artifact exists since oxygen-containing residual gases (e.g.,  $\text{CO}_2$ ) can readsorb from the vacuum onto the surface during analysis or can be implanted by the ion gun during analysis. The possibility of these effects being large for oxygen is discounted by the facts that (a) all oxygen measurements were made while sputter removing surface atoms, and (b) the oxygen level in the silicon substrate (onto which readsorption or implantation would also occur) was very low. However, the probability seems high that the carbon signal is not a true signal since its intensity is uniform in going from  $\text{Si}_3\text{N}_4$  to silicon and in going from one sample to another.

A finite surface concentration of carbon and oxygen will always exist because of the steady-state balance between adsorption or ion implantation and sputter removal. These effects have been studied experimentally and theoretically as discussed in the Appendix. The conclusions from these considerations are that none of the oxygen levels reported in Table I are influenced by adsorption or implantation, but the re-

Table I. Bulk oxygen concentration, N/Si Auger electron peak height ratio, and index of refraction for various silicon nitride films

Oxygen concentration (a/o)	N/Si AE peak height ratio	Index of refraction
0.4*	2.08	1.96
1.2	2.05	1.93
3.6	1.96	1.91
4.3	1.97	1.885
4.5	—	1.88
6.8	1.85	1.86

\* Special nitride film grown over 420 Å of  $\text{SiO}_2$  on Si substrate.

residual carbon levels shown in Fig. 2 are not true signals but result from adsorbed or implanted carbon which sputtering did not remove. From the Appendix discussion, it is clear that the balance between adsorption/implantation and sputter removal controls the detection limit for oxygen and carbon. Data are presented showing that in the present case, the detection limit for oxygen is 0.05% and for carbon is 0.2% (atomic).

**Comparison of oxygen concentration, refractive index, and nitrogen-to-silicon Auger peak height ratio.**—Oxygen concentration and the corresponding Auger peak height ratio of the nitrogen to silicon 1613 eV peak (from  $\text{Si}_3\text{N}_4$ ) determined for each film is listed in columns 1 and 2 of Table I and plotted in Fig. 3. The correlated decrease in nitrogen with an increase in oxygen concentration indicated in Table I and Fig. 3 is further illustrated in Fig. 4 where a sputter profile has been made through a film in which a peak in the oxygen concentration and a corresponding decrease in the ni-

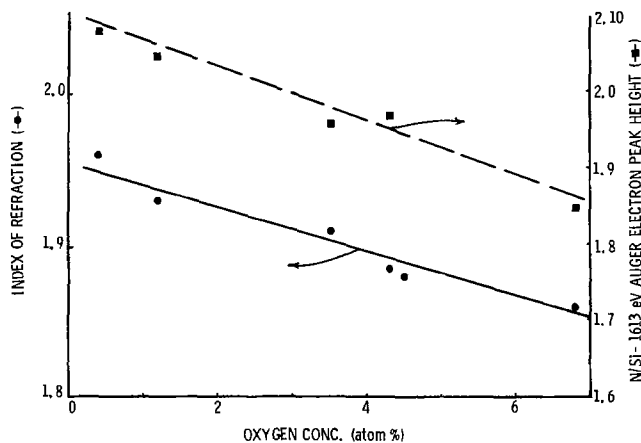


Fig. 3. Correlation between the bulk oxygen concentration and the nitrogen to silicon (1613 eV) Auger electron peak height and the refractive index at 5160Å for  $\text{Si}_3\text{N}_4$ .

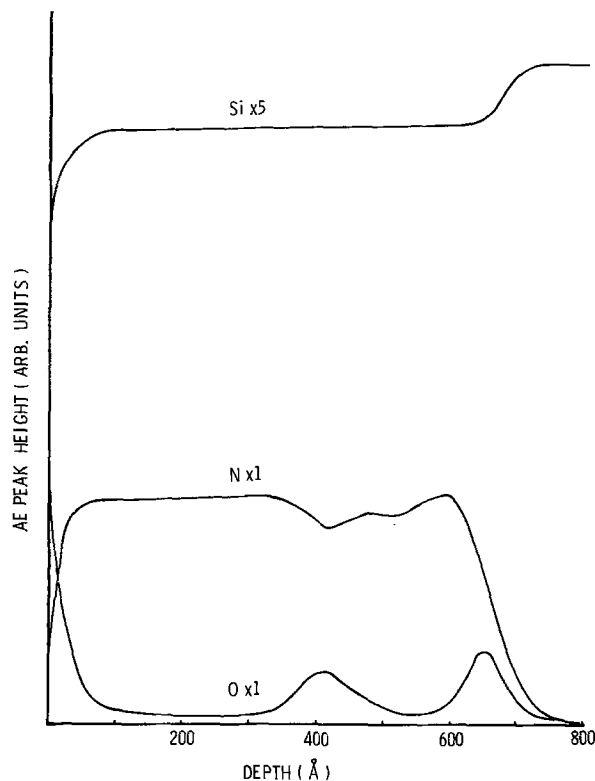


Fig. 4. Auger electron peak heights of silicon, nitrogen, and oxygen vs. depth for a  $\text{Si}_3\text{N}_4$  film showing an increased oxygen concentration in the middle of the film. Note the complementary decrease in nitrogen as oxygen increases.

trogen concentration is observed in the middle of the film. The correlation between the oxygen and nitrogen concentration supports the bonding model of oxygen substitution for nitrogen in the atomic structure (11). The profiling results in Fig. 4, together with those in Fig. 2 demonstrate the detail which can be obtained about the nitride film and the interface region by using the sputter-Auger technique, and this technique is believed to be one of the best available at this time for depth profiling of the film composition.

Refractive indices for the films are also listed in Table I, and the dependence of the index upon the oxygen concentration is further illustrated in Fig. 3. Reduction of the refractive index by the incorporation of oxygen in the film has been demonstrated previously (2, 6, 11), but deposition parameters such as temperature and ammonia-to-silane ratio also affect the refractive index. Auger electron analysis provides a method for quantifying the oxygen concentration and calibrating the refractive index as a measure of the oxygen concentration for a particular growth situation.

### Summary

It has been demonstrated that Auger electron spectroscopy is a powerful technique for measuring the quantity and distribution of impurities in thin  $\text{Si}_3\text{N}_4$  films. Interfacial oxide films thinner than 10Å can be detected. The detection limits in the present system for bulk oxygen and carbon are 0.05 and 0.2%, respectively. For the present memory-quality  $\text{Si}_3\text{N}_4$  films, the actual carbon contamination level was below 0.2%, but oxygen concentrations between 0.4 and 6.8% were observed. Variations in oxygen content between samples were correlated with variations in the refractive index and in the nitrogen-to-silicon ratio.

### Acknowledgment

The authors are grateful to Dr. P. D. Thacher for assistance with the refractive index measurements and to Dr. R. K. Traeger for a critical review of the manuscript. This work was supported by the U. S. Energy Research and Development Administration.

Manuscript submitted Sept. 8, 1975; revised manuscript received Jan 5, 1976.

Any discussion of this paper will appear in a Discussion Section to be published in the December 1976 JOURNAL. All discussions for the December 1976 Discussion Section should be submitted by Aug. 1, 1976.

Publication costs of this article were partially assisted by Sandia Laboratories.

### APPENDIX

#### Steady-State Relationship between Adsorption, Sputter Removal, and Detection Limits

The surface of a solid in a vacuum will always be bombarded with residual gas molecules, and a certain fraction of these molecules will stick (adsorb) onto the solid. If the sample is being sputtered, atoms will be removed from the surface, including adsorbed residual gas molecules, until a steady state is reached where the rate of adsorption equals the rate of sputter removal of residual gas molecules. This can be modeled as follows.

Assume that the adsorption rate of the  $j$ th residual gases,  $\dot{A}_j$ , is independent of the sputter rate, then it may be written as  $\delta_j \dot{I}_j$  where  $\delta_j$  is the sticking coefficient and  $\dot{I}_j$  is the ideal gas impingement rate of the  $j$ th residual gas.  $\dot{I}_j$  is given by

$$\dot{I}_j = \frac{P_j}{(2\pi m_j k T_g)^{1/2}} \quad [\text{A-1}]$$

where  $P_j$  is the pressure of the  $j$ th gas.  $m_j$  is the molecular mass.  $k$  is Boltzmann's constant, and  $T_g$  is the absolute gas temperature. The sputter removal rate of the  $j$ th adsorbed species,  $\dot{S}_j$ , may be written

$$\dot{S}_j = y_j i^+ \frac{\sigma_j}{\sigma_{oj}} \quad [\text{A-2}]$$

where  $y_j$  is the sputter yield (i.e., the number of the  $j$ th atoms sputtered per incident ion),  $i^+$  is the ion current,  $\sigma_j$  is the number of adsorbed  $j$ th molecules per unit area, and  $\sigma_{oj}$  is the number of  $j$ th adsorption sites per unit area (i.e.,  $\sigma_j/\sigma_{oj}$  is the probability that an incident ion will collide with a  $j$ th adsorbed molecule). At the steady state between adsorption and sputtering,  $\dot{A} = \dot{S}$ , therefore

$$\frac{\delta_j P_j}{(2\pi m_j k T_g)^{1/2}} = y_j i^+ \frac{\sigma_j}{\sigma_{oj}} \quad [\text{A-3}]$$

or

$$\sigma_j = \frac{\sigma_{oj} \delta_j P_j}{y_j i^+ (2\pi m_j k T_g)^{1/2}} \quad [\text{A-4}]$$

Thus, for a constant adsorption rate (i.e., constant  $P_j$  in Eq. [A-4]), as the sputter rate decreases (i.e.,  $i^+$  decreases in Eq. [A-4]), the steady-state concentration of adsorbed molecules should increase. Data in Fig. 5 demonstrate that this effect was observed. Figure 5 shows the AE peak heights of oxygen and carbon on either a  $\text{Si}_3\text{N}_4$  or silicon surface as a function of the ion current. As the ion current (and therefore the sputter rate) decreases to  $5 \mu\text{A}$  or less, the AE peak heights increase indicating a significant readsorption effect on oxygen or carbon concentration measurements. Assuming that the sticking coefficient,  $\delta_j$ , and sputter yield,  $y_j$ , is independent of the adsorbed molecule concentration (over the range of interest), then

$$\sigma_j = \frac{K}{i^+} \quad [\text{A-5}]$$

where  $K$  is a constant. Since the AE peak height is proportional to  $\sigma_j$ , Eq. [A-5] has been tested by plotting the AE peak height of oxygen on silicon or  $\text{Si}_3\text{N}_4$  vs.  $1/i^+$  (see Fig. 6). The  $\text{Si}_3\text{N}_4$  data are differences between the measured signal and the signal due to residual bulk oxygen. The straight line indicates that this simple model is a reasonable first approximation, and order of magnitude estimates for  $K$  in Eq. [A-5] supports this conclusion.

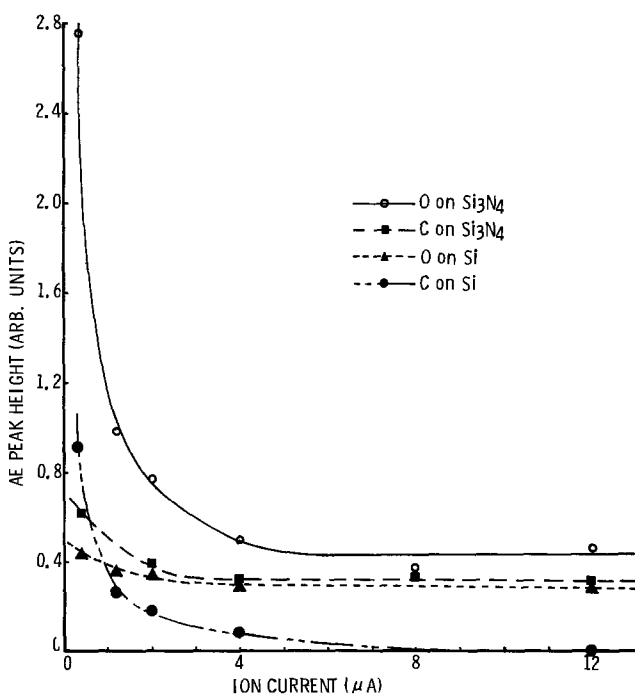


Fig. 5. Auger electron peak heights of carbon and oxygen on silicon or  $\text{Si}_3\text{N}_4$  vs. ion current striking the target. As the sputter rate decreases (i.e., the ion current decreases), adsorption of residual gases from the vacuum occurs, adding to the detected signals. The residual oxygen level shown for  $\text{Si}_3\text{N}_4$  corresponds to a bulk oxygen concentration of 0.4%.

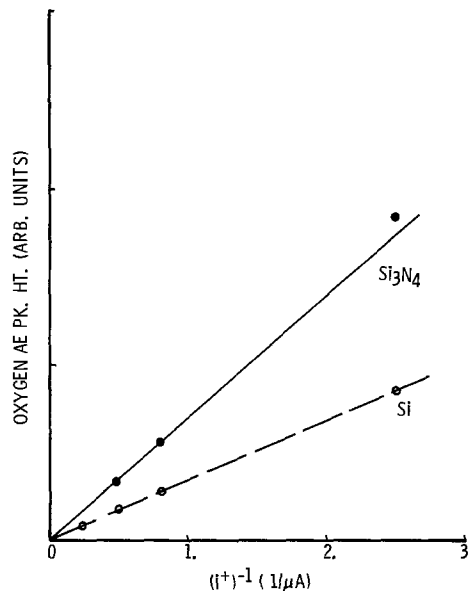


Fig. 6. Oxygen Auger electron peak height on silicon or  $\text{Si}_3\text{N}_4$  vs. the inverse of ion current striking the sample. The straight line agrees with the model discussed in the text.

Obviously then, the detection limits for oxygen or carbon (i.e., the minimum detectable "true" concentrations) are dependent on both the residual gas pressures and the rate of sputter removal of adsorbed residual gases. Using our calibration for oxygen concentrations, at high sputter rates the detection limit for oxygen is approximately 0.05% (atomic). To avoid readsorption artifacts in the oxygen content of  $\text{Si}_3\text{N}_4$ , all measurements were made with more than  $6 \mu\text{A}$  of ion current striking the substrate. Thus it appears that the detection limit for oxygen in silicon nitride is controlled by the balance between gas adsorption and sputter removal.

The straight line fit in Fig. 6 is fortuitous in many respects. We have assumed a steady-state condition both for gas adsorption and for sputtering effects such as "knock-on," defect enhanced diffusion, and ion drift. But perhaps the most serious assumption is that no implantation occurs by ionization of gas phase impurities in the argon. If implantation occurs, it may cause a surface concentration independent of the sputtering rate, and may also cause the detection limit for an element to be high.

A case in point may be carbon which was always detected both on the  $\text{Si}_3\text{N}_4$  films and on the silicon support (see Fig. 1 and 2). The origin is believed to be either residual carbon which cannot be removed by ion sputtering, or a carbon implanted by the ion gun. The residual carbon is not accompanied by an equivalent oxygen peak for the silicon substrate, which suggests that there is no significant oxygen associated with it on the  $\text{Si}_3\text{N}_4$  either. This peak does, however, cause the detection limit for carbon in  $\text{Si}_3\text{N}_4$  to be higher than for oxygen. The carbon concentration was estimated using sensitivity factors reported by Palmberg *et al.* (12), and the residual carbon peak was calculated to be equivalent to a bulk carbon concentration of 0.2%. The actual carbon impurity concentrations in the  $\text{Si}_3\text{N}_4$  films were all less than this detection limit, i.e., all less than 0.2%. If this carbon signal originated from implantation, it must indicate that hydrocarbons (e.g., methane, etc.) were present in the argon. This seems unlikely since a sublimation pump was used to clean the argon. Another explanation for the carbon is that at small residual concentrations, the sputter yield in Eq. [A-2], approaches zero. Such a phenomena has been reported by Tarnag and Wehner (13) for sputter removal of molybdenum from a number of different substrate materials. However, neither the implantation nor the zero yield postulate can be substantiated by the present data.

#### REFERENCES

1. J. T. Milek, "Handbook of Electronic Materials," Vol. 6, Part 2, p. 41, IFI, Plenum Data Corp., New York (1972).

2. J. T. Milek, "Handbook of Electronic Materials," Vol. 3, Part 1, IFI, Plenum Data Corp., New York (1971).
3. P. Balk, "Third European Solid State Device Research Conference, Munich, Germany, September 1973," p. 51.
4. C. T. Naber and G. C. Lockwood, "Second International Symposium on Silicon Materials Science and Technology, Chicago, May 1973," p. 401.
5. H. G. Macguire and P. D. Augustus, *This Journal*, **119**, 791 (1972).
6. E. A. Taft, *ibid.*, **118**, 1341 (1971).
7. C. C. Chang, in "Characterization of Solid Surfaces," P. F. Kane and G. B. Larrabee, Editors, chap. 20, Plenum Press, New York (1974).
8. P. H. Holloway, *Surface Sci.*, **54**, 506 (1976).
9. F. Lukes, *ibid.*, **30**, 91 (1972).
10. J. N. Sweet and P. H. Holloway, *Thin Solid Films*, **27**, 263 (1975).
11. H. R. Philipp, *This Journal*, **120**, 295 (1973).
12. P. W. Palmberg, G. E. Riach, R. E. Weber, and N. C. MacDonald, "Handbook of Auger Electron Spectroscopy," Physical Electronics Industries, Inc., Edina, Minn. (1972).
13. M. L. Tarnag and G. K. Wehner, *J. Appl. Phys.*, **43**, 2268 (1972).

## Oxygen Gettering in Green GaP:N LED's Grown by Overcompensated LPE

P. C. Mürau and R. N. Bhargava

Philips Laboratories, Briarcliff Manor, New York 10510

### ABSTRACT

Improvement in the minority carrier diffusion lengths has been obtained in GaP:N LED's by controlling the oxygen contamination during LPE with getter dopants such as Al, Mg, or Si. Experimental data are presented which show a limited range in which one can achieve oxygen gettering in GaP without reducing the incorporation of nitrogen. Excess Al produces free exciton emission with an external quantum efficiency of 0.02% at 4 A/cm<sup>2</sup>.

Luminescence from the isoelectronic nitrogen center in GaP has been the subject of considerable study (1, 2). Over the years it has been demonstrated that high efficiency green electroluminescence (EL) in GaP:N can be achieved by double liquid phase epitaxy (LPE) (3-8) and vapor phase epitaxy (VPE) (9). The commonly employed acceptor impurity in the p-layer has been Zn, whereas either Te or S has been used as the donor impurity in the n-layer.

At present, one of the problems in the LPE growth of the p-n junction in GaP:N is elimination of the red emission from bound excitons at (Zn-O) complexes which accompanies the green emission. The combination of red and green emission in an LED produces a distinctly yellow green color. Lorimer and Weiner (10) have eliminated the (Zn-O) red component by replacing Zn with another acceptor such as C or Mg, but at the same time a reduction by approximately a factor of five in the EL efficiency was observed.

It has been established (11, 12) that a deep oxygen donor by itself does not act as a nonradiative center in GaP. However, associated complexes of oxygen such as Si-O (13), V<sub>Ga</sub>-O (14), etc., may play a role in the recombination efficiency in both the n- and p-layers of an LED. Evidence to support this hypothesis has been reported by a number of workers (15-18). It is therefore clear that in order to improve the EL and generate purer spectra in green LED's all traces of oxygen must be removed from both the n- and p-layers.

In order to remove the background oxygen impurity, certain precautions can be taken in the LPE process itself. Further reduction in the oxygen level, however, may be achieved by gettering action through intentional codoping of the Ga melt with elements such as Al, Mg, or Si, which are known to form stable oxides.

In this paper we discuss the reaction chemistry between getter dopants with oxygen and nitrogen during LPE, and their effect on N incorporation. We present results which show that O gettering leads to longer minority carrier diffusion lengths. In the case of excess

Al doping, an improvement in the efficiency of free exciton emission has been achieved.

### Chemical Interactions of Getters with Oxygen and Nitrogen

Before considering the gettering action of oxygen by Al, Mg, or Si in a Ga melt, it is helpful to consider some fundamental chemical reactions that can occur during the LPE process. In Table I we list a number of reactions along with their calculated equilibrium constant and free energy of formation at 900°C (19).

Let us first consider LPE performed in an inert atmosphere, such as He or Ar. If the Ga is contained in a

Table I

	900°C K <sub>eq.</sub>	900° ΔF <sub>f</sub> (kcal/mole)
1. Ga(l) + 1/4SiO <sub>2</sub> (s) = 1/2Ga <sub>2</sub> O(g) + 1/4Si(s)	1.0 × 10 <sup>-3</sup>	+ 16.2
2. Ga(l) + 1/2SiO(s) = 1/2Ga <sub>2</sub> O(g) + 1/2Si(s)	1.4	- 0.8
3. Ga(l) + 3/4 O <sub>2</sub> (g) = 1/2Ga <sub>2</sub> O <sub>3</sub> (s)	1.2 × 10 <sup>15</sup>	- 81.2
4. Ga(l) + 3/2H <sub>2</sub> O(g) = 1/2Ga <sub>2</sub> O <sub>3</sub> (s) + 3/2H <sub>2</sub> (g)	7.7 × 10 <sup>2</sup>	- 15.5
5. Ga(l) + 1/2H <sub>2</sub> O(g) = 1/2Ga <sub>2</sub> O(g) + 1/2H <sub>2</sub> (g)	2.2	- 1.9
6. H <sub>2</sub> (g) + 1/2 O <sub>2</sub> (g) = H <sub>2</sub> O(g)	1.3 × 10 <sup>5</sup>	- 43.7
7. SiO <sub>2</sub> (s) + H <sub>2</sub> (g) = SiO(g) + H <sub>2</sub> O(g)	1 × 10 <sup>-13</sup>	+ 70.1
8. SiO <sub>2</sub> (s) + H <sub>2</sub> (g) = Si(s) + 2H <sub>2</sub> O(g)	5.3 × 10 <sup>-6</sup>	+ 36.1
9. Si(s) + 1/3Ga <sub>2</sub> O <sub>3</sub> (s) = SiO(g) + 2/3Ga(l)	1.4 × 10 <sup>8</sup>	- 16.9
10. Si(s) + 2/3Ga <sub>2</sub> O <sub>3</sub> (s) = SiO <sub>2</sub> (s) + 4/3Ga(l)	3.7 × 10 <sup>9</sup>	- 51.4
11. Si(s) + 4/3NH <sub>3</sub> (g) = 1/3Si <sub>3</sub> N <sub>4</sub> (s) + 2H <sub>2</sub> (g)	7.1 × 10 <sup>9</sup>	- 52.9
12. Ga(l) + NH <sub>3</sub> (g) = GaN(s) + 3/2H <sub>2</sub> (g)	1.4 × 10 <sup>3</sup>	- 16.9
13. Mg(l) + 2/3NH <sub>3</sub> (g) = 1/3Mg <sub>3</sub> N <sub>2</sub> (s) + H <sub>2</sub> (g)	4.8 × 10 <sup>3</sup>	- 30.5
14. Mg(l) + 1/3Ga <sub>2</sub> O <sub>3</sub> (s) = MgO(s) + 2/3Ga(l)	6.8 × 10 <sup>10</sup>	- 58.5
15. Mg(l) + 1/2 O <sub>2</sub> (g) = MgO(s)	1.0 × 10 <sup>21</sup>	- 112.5
16. Mg(l) + H <sub>2</sub> O(g) = MgO(s) + H <sub>2</sub> (g)	6.5 × 10 <sup>12</sup>	- 68.8
17. Al(l) + NH <sub>3</sub> (g) = AlN(s) + 3/2H <sub>2</sub> (g)	1.7 × 10 <sup>12</sup>	- 65.7
18. Al(l) + 1/2Ga <sub>2</sub> O <sub>3</sub> (s) = 1/2Al <sub>2</sub> O <sub>3</sub> (s) + Ga(l)	7.1 × 10 <sup>13</sup>	- 74.4
19. Al(l) + 3/4 O <sub>2</sub> (g) = 1/2Al <sub>2</sub> O <sub>3</sub> (s)	8.9 × 10 <sup>28</sup>	- 155.7
20. Al(l) + 3/2H <sub>2</sub> O(g) = 1/2Al <sub>2</sub> O <sub>3</sub> (s) + 3/2H <sub>2</sub> (g)	5.3 × 10 <sup>17</sup>	- 95.2

Key words: GaP light emitting diodes, O gettering in liquid phase epitaxy.



quartz crucible, then we have to consider reactions between the Ga and quartz (reactions 1 and 2) and reactions between the Ga and traces of  $O_2$  and  $H_2O$  in the gas stream (reactions 3-5). According to the values in Table I, reaction 3 is the most favorable, making oxygen contamination of the Ga melt under an inert atmosphere likely.

If, instead of an inert gas, we use  $H_2$  as the carrier gas, we must assume that traces of  $O_2$  in the gas stream react with  $H_2$  at  $900^\circ C$  to form  $H_2O$  (reaction 6), and reactions with traces of  $H_2O$  vapor must also be considered. In addition, as Weiner (20) has shown, Si contamination of the Ga melt via  $H_2$  reduction of the quartz (reactions 7 and 8), must also be considered.

In order to reduce the O and Si contamination level in the Ga melt due to quartz and control the reactions between quartz and the getter dopants, an inert crucible material such as pyrolytic BN or pyrolytic graphite should be considered. Residual traces of oxygen in the Ga melt or oxygen present in the gas stream could be further reduced by using O getters such as Mg, Al, or Si. Reactions between these getter elements and  $O_2$ ,  $H_2O$ , and  $Ga_2O_3$  are also listed in Table I (reactions 9, 10, 14-16, 18-20).

However, LPE for green GaP LED's also requires N doping by addition of ammonia to the  $H_2$  gas stream. This complicates matters since nitrides of O getters are also quite stable. Therefore, competing reactions between the getter dopants, the oxygen bearing species, and the ammonia have to be considered. Lorimor and Weiner (10) have calculated the permissible doping levels of Al, Mg, and Si in Ga at  $900^\circ C$  in the presence of  $NH_3$ . Similar calculations between the getter dopants and dissolved  $Ga_2O_3$  in the Ga melt, at  $900^\circ C$ , show that the oxides are more stable. As will be shown later, oxygen can be effectively removed from the Ga melt before nitride formation limits the incorporation of N into the GaP.

According to the calculations (10), only very small quantities of Al can exist in the melt at reasonable ammonia pressures. However, as we shall see later, in this nonequilibrium LPE process, not all of the unreacted Al precipitates out as the nitride; some unreacted Al gets segregated into the GaP layer (21).

### Experimental

**LPE by overcompensation.**—The LPE layers were grown in an open-flow dipping system described earlier (22). The system (Fig. 1) was slightly modified to accommodate p-n formation by overcompensation (6). With the exception of the crucible and substrate holder, the system is constructed entirely from quartz (GE 204). The crucible and substrate holder are made from either pyrolytic BN or pyrolytic graphite (Union Carbide) to avoid O contamination and prevent attack by the getter dopants (Al, Si, Mg). The substrate holder is constructed to fit the quartz drop tube blowup in Fig. 1) in a lock-and-key arrangement. The whole assembly can be rotated, raised, and lowered within the reaction tube without coming apart. Two substrates fitted back-to-back to the holder rest in angled grooves to prevent them from falling out while simultaneously permitting good melt wipe-off after "dipping." Therefore, with this holder close control of substrate diameter or shape is not essential.

For LPE by overcompensation, the system was prepared as follows. The quartz system along with crucible and holder were first acid cleaned, vacuum dried at  $800^\circ C$  ( $10^{-3}$  mm Hg), and purged and cooled under  $H_2$ . This step is required to remove adsorbed moisture and volatile contaminants. The Ga melt was saturated with GaP, (0.01 mole fraction), vacuum dried at  $200^\circ C$ , and purged with  $H_2$ . Sufficient Te was added to the melt to produce a doping density of  $1-2 \times 10^{17} \text{ cm}^{-3}$  (Fig. 2). The hydrogen atmosphere (UHP Matheson) was passed over a Pd diffuser through stainless

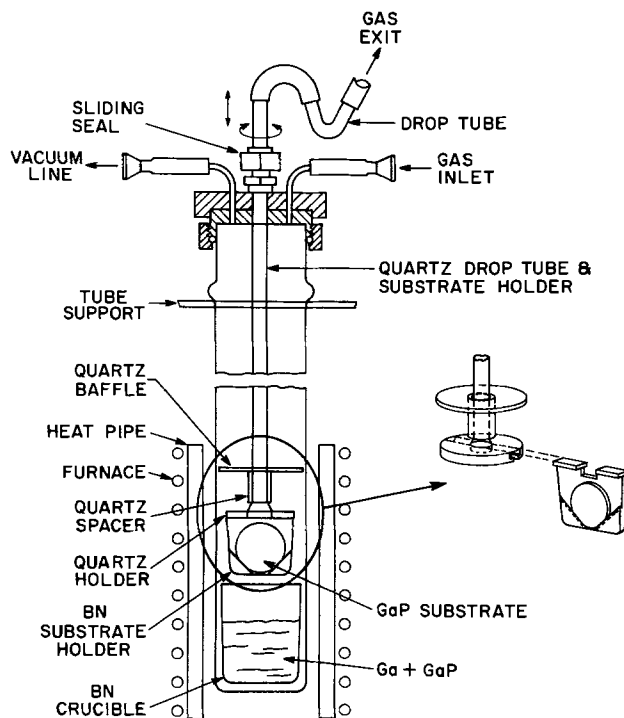


Fig. 1. Vertical dipping system used in the LPE overcompensation technique, with a close-up of the substrate holder arrangement.

steel piping at a flow rate of  $100 \text{ cm}^3/\text{min}$ . The assembly was lowered into a resistance furnace fitted with a heat pipe and heated to  $945^\circ C$  until all GaP is dissolved. The heat pipe provides for improved thermal stability. The temperature was then lowered to  $920^\circ C$ , allowing about  $\frac{1}{2}$  hr for thermal equilibrium to be attained. The substrates were then lowered into the melt. At this point the getter dopant, either Al or Si, was added to the melt via the drop tube. To avoid attack on the quartz drop tube, the Mg getter dopant was added to the melt before heating. The substrates in this case were maintained in the cool zone of the reaction tube to avoid thermal etching of the substrate surface which results in poor surface wetting.

After allowing for some reasonable time ( $\frac{1}{2}$  hr) for the getter dopants to react with the O species and for the substrates to reach thermal equilibrium with the melt, N doping is commenced. This is accomplished by the addition of slightly less than 0.3% by volume of  $NH_3$  from a 1%  $NH_3/H_2$  mixture (UHP Matheson) to the  $H_2$  stream. This is the optimum  $NH_3$  concentration required before GaN precipitates out at  $900^\circ C$  (10).

Before the Ga melt is sufficiently saturated with N, we must assume at this stage that any unreacted O getter dopant left in the melt either precipitates out as the nitride and/or segregates into the epilayer during growth. This will reduce the N incorporation into the epilayer. It is therefore important to add only small quantities of O dopants sufficient to getter the oxygen but not the nitrogen.

The n-LPE was initiated by cooling the melt from  $920^\circ$  to  $890^\circ C$  at a rate of  $0.44^\circ C/\text{min}$ . On conclusion of n-LPE and while the substrates remained immersed in the melt, the furnace was held at constant temperature until the necessary amount of Zn was dropped into the melt through the drop tube to produce a doping density of  $1-2 \times 10^{18} \text{ cm}^{-3}$  ( $X_{Zn}^I = 1.8 \times 10^{-3}$  atomic fraction). After allowing about 15 min for the Zn to dissolve, which was enhanced by oscillatory, circular motion of the substrate holder, p-LPE was initiated by cooling the melt from  $890^\circ$  to  $825^\circ C$  at a rate of  $0.44^\circ C/\text{min}$ . On completion of p-LPE at  $825^\circ C$ , the  $NH_3$  flow was stopped and the substrates pulled out of the melt. The holder was rapidly removed from the furnace and the substrates allowed to cool in hy-

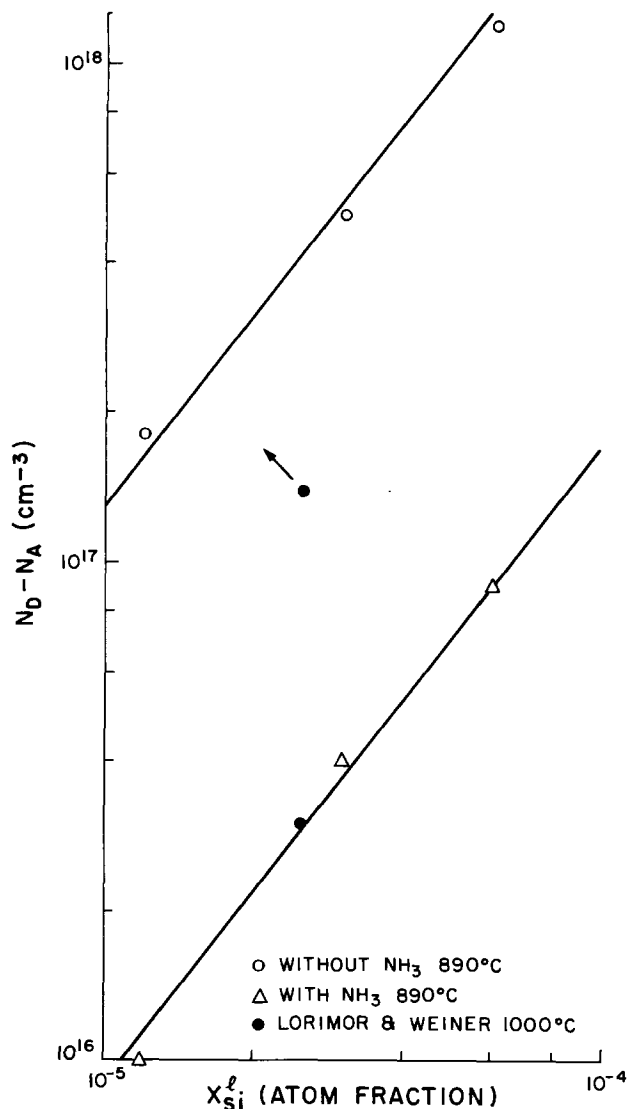


Fig. 2. Net donor concentrations in epitaxially grown GaP in the absence and presence of 0.3%  $\text{NH}_3$  as function of the Si concentration in the Ga melt at  $890^\circ\text{C}$ .

drogen. The wafers were not intentionally annealed. This growth schedule produces a total n- and p-layer thickness of 30-40  $\mu\text{m}$ . The low temperature schedule summarized in Table II provides superior surface morphology and perfection.

For the  $n^+np^+$  structure employed here ( $N_D - N_A = 1-2 \times 10^{17} \text{ cm}^{-3}$ ,  $N_A - N_D = 1-2 \times 10^{18} \text{ cm}^{-3}$ ), LPE by overcompensation provides certain inherent advantages over the normal two-step LPE process (6, 22). It has been our experience as that of Lorimor *et al.* (6) that epilayers grown by overcompensation

Table II. Summary of growth schedule by overcompensation

	n-LPE	p-LPE
Temperature	$920^\circ\text{--}890^\circ\text{C}$	$890^\circ\text{--}825^\circ\text{C}$
Cooling rate	$0.44^\circ\text{C}/\text{min}$	$0.44^\circ\text{C}/\text{min}$
Layer thickness	10-20 $\mu\text{m}$	10-20 $\mu\text{m}$
Dopants	Te, N	Te, N, Zn
O getter dopants	Al, Si, or Mg	Al, Si, or Mg
Net donor or acceptor conc.	$1-2 \times 10^{17} \text{ cm}^{-3}$	$1-2 \times 10^{18} \text{ cm}^{-3}$
$\text{NH}_3$ conc. in gas ambient	0.3%	0.3%

resulted in longer diffusion lengths and higher green efficiencies. This technique in itself leads to a significant decrease in the number of (Zn-O) centers or other O-related complexes in GaP. Oxygen gettering serves as a further refinement of the technique. Oxygen reduction in either or both the epitaxial n-layer and the Ga charge was achieved in part by maintaining the substrate with the n-epilayer submerged within the Ga melt prior to p-LPE. This prevented exposure of the p-n interface to an oxidizing or contaminating ambient. This is normally a problem encountered in a two-step LPE process. The technique has three additional important advantages: (i) maintaining thermal stability near the p-n interface which results in improved junction uniformity, (ii) no meltback and therefore better control of compensation near the interface, and (iii) no surface damage due to thermal etching.

In addition, the oxygen solubility of the melt is obviously reduced by two additional factors: (i) by performing LPE at a lower temperature ( $920^\circ\text{C}$ ) as compared to the higher temperature ( $1100^\circ\text{C}$ ) normally used, and (ii) through the use of inert crucible and substrate holder material such as pyrolytic BN or pyrolytic graphite.

#### Material evaluation.—

**Doping assessment.**—The net donor and acceptor concentration at the epitaxial surface was determined by a standard Schottky barrier diode technique. The net donor carrier density of an unintentionally doped layer grown in pyrolytic BN from  $920^\circ$  to  $890^\circ\text{C}$  was less than  $10^{16} \text{ cm}^{-3}$ . Epitaxy by overcompensation was performed at significantly lower temperatures ( $920^\circ\text{--}825^\circ\text{C}$ ) as compared to the range ( $1050^\circ\text{--}1010^\circ\text{C}$ ) normally employed for double LPE (22). We may therefore assume that the variation in  $N_A - N_D$  between the p-n junction and the surface is small because of the following reasons: (i) the loss of Zn due to volatilization in our dipping system is negligibly small, (ii) the distribution coefficient,  $C_s/C_L$ , at these temperatures is low, and (iii) the grown p-epilayer is thin (6, 23).

The N concentrations in various LPE layers were determined by measuring the absorption of the A line at 2.310 eV at  $77^\circ\text{K}$  (24, 25). The results are listed in Table III.

Table III

Run No.	$X_{\text{Getter}}^1$	$N_A - N_D$ $\times 10^{15} \text{ cm}^{-3}$	$[\text{N}]$ $\times 10^{17} \text{ cm}^{-3}$	Diffusion length ( $\mu\text{m}$ )		Green/red 300°K	$\eta_{\text{green}}^{\text{ext}}$ (%) at 4 A/cm <sup>2</sup>
				$L_e$	$L_h$		
282	—	15	22	1.4	1.5	10	0.1
320-1-Si	$1.2 \times 10^{-5}$	13	17	2.3	2.0	25	0.1
319-1-Si	$2.5 \times 10^{-5}$	18	15	2.0	2.9	—	0.07
323-2-Mg	$3.8 \times 10^{-5}$	14	16	3.1	4.9	15	0.11
314-2-Mg**	$6 \times 10^{-4}$	—	12	—	—	—	—
322-1-Al	$1.3 \times 10^{-5}$	12	20	2.6	3.1	—	0.05
327-1-Al	$3.4 \times 10^{-5}$	12	20	2.4	3.0	>700	0.03
302-1-Al	$6.4 \times 10^{-5}$	5.0	15	2.0	2.8	—	0.03
299-1-Al	$1.9 \times 10^{-4}$	20	1.7	2.5	3.2	>700	0.02*
295-2-Al	$3.9 \times 10^{-4}$	11	0.8	2.0	1.4	—	0.015*
307-1-Al***	$1.9 \times 10^{-4}$	8.0	0.6	1.5	1.7	—	0.02*

\* Free exciton efficiency.

\*\* n-layer only.

\*\*\* No  $\text{NH}_3$  was added in the  $\text{H}_2$  stream.

**Diode efficiency.**—The external EL quantum efficiency of various diodes was determined on fabricated structures which had an evaporated contact similar to the one described by Schumaker *et al.* (26) for red LED's. The  $20 \times 20$  mil die was shaped by laser scribing, mounted on a TO-18 header, and encapsulated in a high refractive index epoxy. Measurements were then performed at  $4 \text{ A/cm}^2$  in an integrating sphere and cross-checked (27, 28).

**Photoluminescence and optical absorption measurements.**—Electroluminescent and photoluminescent spectra were taken using a Spex F/7.8, 0.85 meter Czerny Turner double monochromator in conjunction with a grating blazed at  $1 \mu\text{m}$ . A slit width of  $500 \mu\text{m}$  was used corresponding to a resolution of  $3\text{\AA}$ . Signals were detected by an extended S-20 photomultiplier (EMI9658 AR). This combination provided a spectral response with sensitivity at  $18,000 \text{ cm}^{-1}$ , a factor of five higher than at  $14,000 \text{ cm}^{-1}$ . This correction factor was used when estimates of the ratio of the green and red components in the LED's were made. The intensity of the red emission due to Zn-O complexes was used to monitor the relative amount of oxygen in p-LPE layers. Photoluminescence in the GaP:N samples was generated at  $77^\circ$  and  $300^\circ\text{K}$  using the 4880 or 5145\AA line of an Ar ion laser.

**Diffusion length measurements.**—The minority carrier lifetimes in green LED's were determined by the recombination time through the shunt path (13, 18). A measure of the minority carrier lifetime or the diffusion length thus reflects the concentration of the non-radiative centers. We measured the diffusion length of epitaxial layers near the p-n junction using a scanning electron microscope (SEM) (30-32). A 20 kV electron beam was scanned across a freshly cleaved p-n junction and the beam-induced current was recorded on a logarithmic picoammeter (Keithley Model 26000). The diffusion length in the n-layer and p-layer is determined from the slope of the straight line portion several micrometers from the junction (32).

### Results and Discussion

As discussed earlier, O getters should be able to control the oxygen level in the Ga melt by forming very stable oxides and thereby reducing the number of (Zn-O) centers present in p-type GaP. On the other hand, O getters can also form stable nitrides and, therefore, an excess of them could also seriously limit N incorporation in the GaP and affect the performance of a green LED. In this section we present the results and examine the influence of O getters on such important parameters as: (i) the carrier density in GaP LPE layers, (ii) N incorporation into GaP, (iii) emission spectra, (iv) minority carrier diffusion lengths, (v) electroluminescent efficiency, and (vi) ratio of green-to-red emission.

An important consideration is the influence of O getters on the carrier concentration. Silicon, for example, is an n-type dopant in GaP; its incorporation into GaP in the absence and presence of ammonia is illustrated in Fig. 2. The n-epilayers were grown from  $920^\circ$  to  $890^\circ\text{C}$  in a pyrolytic BN crucible. In the presence of  $\text{NH}_3$ , the Si incorporation in GaP is reduced by an order of magnitude. This implies that, although the  $\text{NH}_3$  vapor above the melt provides for an infinite source of N, insufficient N gets dissolved in the Ga during LPE to consume the unreacted Si and prevent Si from segregating into the LPE layer (16). In other words, LPE is far from being an equilibrium process.

Magnesium on the other hand is a p-type dopant in GaP. However, the Mg concentration range used in our experiments was so low ( $X_{\text{Mg}}^1 = 1-7 \times 10^{-5}$ ) that no noticeable effect on the net donor carrier density ( $N_{\text{D}} - N_{\text{A}} = 1-2 \times 10^{17} \text{ cm}^{-3}$ ) was observed. Aluminum is a neutral dopant in GaP and did not influence the carrier density in our samples.

Absorption measurements on the A line at  $77^\circ\text{K}$  were made to obtain the absolute N concentrations as well as relative variations of N incorporation in GaP. Figure 3 illustrates the influence of the Al concentration in the melt on the relative absorption intensity at the A line. The background absorption peak is a measure of nitrogen in the  $200 \mu\text{m}$  LEC substrate and a  $30 \mu\text{m}$  thick LPE layer not doped intentionally with nitrogen. It should be noted here that the data in Fig. 3 is the relative transmission intensity; the measured values of the epilayer thicknesses were used to calculate absolute [N]. We note that the N incorporation decreases with increasing Al concentration in the melt. Similar results were obtained with Mg and Si dopants. The results on the incorporation of N, as calculated from the absorption data, are tabulated in Table III. It is clear from this table that even small quantities of O getters inhibit N incorporation into the epilayer. Based on the chemical reactions and thermodynamic calculations presented previously, and since oxides of getter dopants are generally more stable than the nitrides, the above results on the N incorporation indicate that the initial oxygen contamination of the LPE system is quite low and that N is being consumed by the excess O getter in the Ga melt. Furthermore, the reduction of N concentration is consistent with the formation of stable nitrides of these O getters. It re-emphasizes the fact that for effective O gettering of the melt and optimum N incorporation in GaP, only very small quantities of getters are required.

Photoluminescence spectra of LPE layers grown from O-gettered melts were taken at  $77^\circ\text{K}$ . The spectra for the Al-gettered case is reproduced in Fig. 4. The N doping level can also be estimated from the relative peak intensities of excitonic recombination at isolated substitutional N atoms (A-O line) and nearest neighbor pairs of N atom ( $\text{NN}_1$  line) (9). The decrease in N incorporation with increasing getter dopants is consistent with the data obtained from the absorption

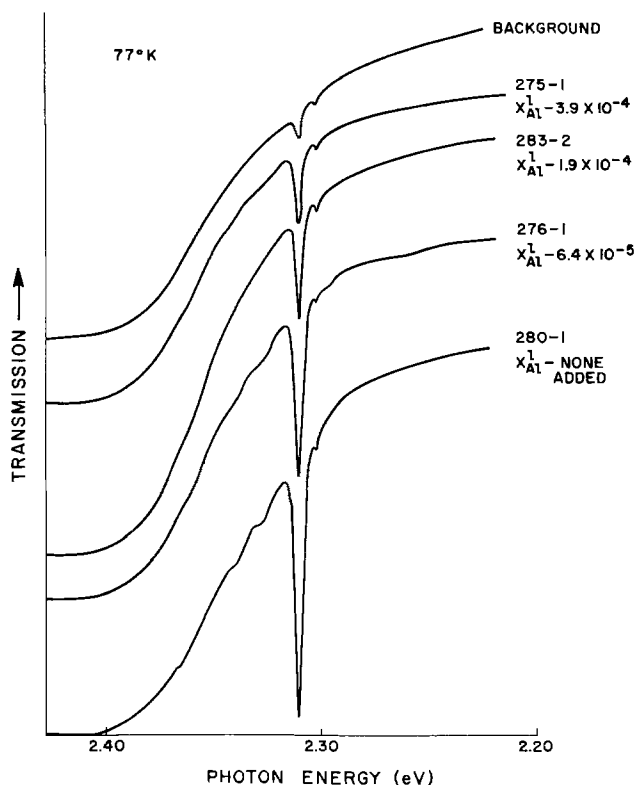


Fig. 3. Transmission spectra of A line (2.31 eV) at  $77^\circ\text{K}$ .  $30-40 \mu\text{m}$  p-n layers on  $200 \mu\text{m}$  LEC substrates (No. 149-34) with Al concentration in melt as indicated.  $\text{NH}_3$  concentration  $\sim 0.3\%$ . The background spectrum is of an undoped epitaxial layer on the LEC substrate.

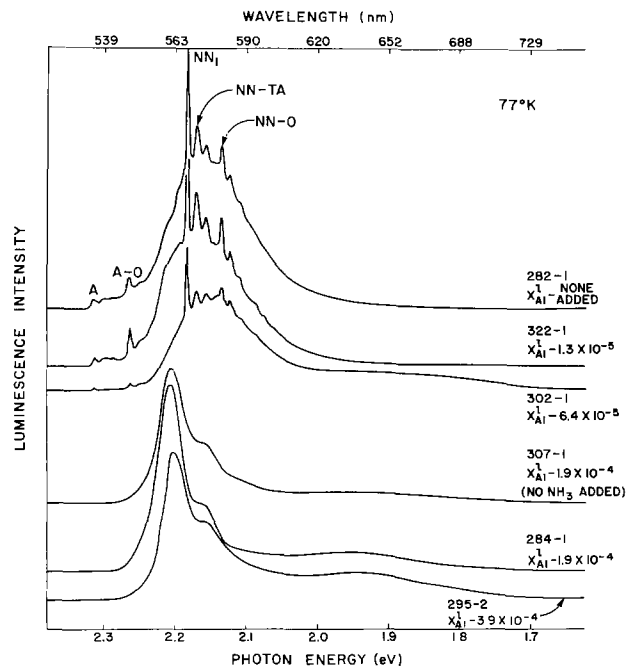


Fig. 4. Photoluminescence spectra at 77°K of p-n layers with Al concentrations in melt as indicated. No. 282-1 was not gettered with Al. With the exception of No. 307-1,  $NH_3$  concentration  $\sim 0.3\%$ , p-layer concentration  $1-2 \times 10^{18} cm^{-3}$ , n-layer concentration  $1-2 \times 10^{17} cm^{-3}$ .

measurements. A similar trend was observed for epilayers which had been grown from Mg- and Si-gettered melts.

Associated with an increase in Al concentration, a general increase is also observed in the free exciton emission around 2.2 eV. Ga melts doped in excess of  $1.9 \times 10^{-4}$  atomic fraction of Al no longer exhibit the normal spectral features of GaP:N. A spectrum of an Al-gettered run (307-1) which was not intentionally doped with N is included for comparison. The emitted radiation is primarily due to free exciton recombination with a peak emission at 2.24 eV (554 nm) (8, 33-35). Free exciton emission is especially dominant in run 299-1-Al (Table III) in which the measured [N] is only  $1.7 \times 10^{17} cm^{-3}$ . This suggests that in order to obtain efficient green LED's with free exciton emission, the N concentration should be maintained below  $\sim 2 \times 10^{17} cm^{-3}$ ; this seems consistent with some earlier data of Bachrach and Lorimor (35). A broad band around 1.9-2.0 eV in Fig. 4 is normally associated with these high Al-gettered runs. The source of this band is not known. The emission peak (Fig. 5) is shifted by 0.05 eV toward higher energies relative to the peak emission of a normal GaP:N diode when operated at room temperature.

Minority carrier diffusion lengths in GaP epilayers are dependent on a number of factors, among which are carrier density, O content, and the LPE process. We observed that the carrier-density dependency is consistent with results reported by Dapkus *et al.* (18, 36). We therefore maintained the following structure throughout our experiments:  $n^+np^+$ , where  $N_D - N_A = 1-2 \times 10^{17} cm^{-3}$  and  $N_A - N_D = 1-2 \times 10^{18} cm^{-3}$ .

We observed, however, a sharp decline in diffusion length values whenever LPE was performed either at a high temperature (1050°C), by a two-step LPE process, or in quartz crucibles. Typical values for  $L_e = 0.5-0.6 \mu m$  and  $L_h = 0.7-0.8 \mu m$  were not uncommon. We associated these low values to high O contamination near the p-n junction since green GaP:N diodes prepared from such material nearly always produced a strong red component due to (Zn-O) centers.

LPE by overcompensation performed at a lower temperature (920°C) and in an inert crucible produced

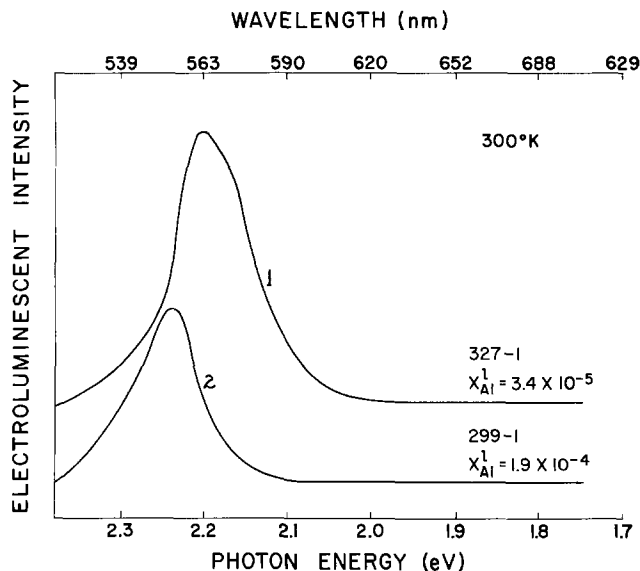


Fig. 5. Electroluminescence spectra at 300°K of two p-n GaP:N LED's with different Al concentrations. At low Al concentration, bound excitonic emission due to N is observed while at the higher Al concentrations free exciton emission is observed.

epilayers with significantly higher diffusion length values:  $L_e = 1.4 \mu m$  and  $L_h = 1.5 \mu m$  (see Table III). The refinement of our LPE technique with O getters increased the diffusion lengths still further. This is consistent with the recent results of Lorimor *et al.* (15) who report that deliberate addition of small amounts of oxygen to the inlet gas produced a pronounced reduction in the quantum efficiency and minority carrier lifetimes.

Recent photocapacitance measurements on red GaP diodes have shown that increased oxygen concentration near the p-n junction decreases the efficiency of red diodes (37). This is interpreted to be due to the presence of oxygen-induced killer centers, which are possibly also effecting the green LED efficiency.

As has been discussed earlier, an excess of O getters in the melt leads to a reduction in the number of N centers in the GaP and to a decrease in the EL efficiency of GaP:N diodes (Table III). Controlled amounts of getter dopants in the melt can, however, lead to optimum N incorporation and an improvement in the EL efficiency. This is evident when we compare the EL efficiency of an ungettered run (282) with lightly gettered runs (320 and 323) in Table III. All three maintain the same efficiency value (0.05% at 4 A/cm<sup>2</sup>). However, diodes which had been fabricated from material grown from highly gettered melts (299) no longer produce the normal GaP:N spectrum. The efficiency values marked with an asterisk in Table III are for free exciton emission. The quantum efficiency of these diodes is typically a factor of five lower than those of optimally N-doped GaP:N LED's. However, the slight downshift in the emitted peak wavelength from 565 to 554 nm in these LED's (Fig. 5) makes these greener free exciton diodes quite attractive. This change in color quality provides a 40% improvement in chromatic discrimination threshold in a 10<sup>4</sup> ft-L illuminated background (38), and which can be filtered to produce improved contrast (39).

The objective of O gettering was to maintain a high N incorporation and a high green EL efficiency while reducing the O concentration in GaP to a level such that it will lead to a decrease in the red emission from the p-epilayer. Such results are reported in Table III as the green-to-red emission ratio in GaP:N LED's. A 1.5-2.5 factor in improvement in green-to-red ratio has been achieved for the gettered runs (320 and 323) over the ungettered run (282), while for Al-gettered runs a

factor in improvement in excess of 70 in green-to-red ratio was realized.

### Conclusions

LPE has been performed by the overcompensation technique at a lower temperature and in inert crucibles. This technique produced epilayers for GaP:N LED's with EL efficiency equal to the present state of the art (0.1% at 4 A/cm<sup>2</sup>).

A problem accompanying all green GaP:N LED's is the red emission associated with the (Zn-O) centers in the p-layer. We have presented experimental data whereby traces of O in the Ga melt can be effectively gettered with either Al, Mg, or Si. We have shown that close control of the getter concentration is required since the getters also form stable nitrides and prevent high N incorporation in GaP, a necessary requirement for high green EL efficiency. Aluminum has an especially strong affinity for N in the melt. Even at very low Al concentrations, N incorporation into the GaP is hindered. As a consequence, diodes from such material produced primarily free exciton emission of superior color contrast, but, so far, of low EL efficiency (0.02% at 5 A/cm<sup>3</sup>). For the n<sup>+</sup>np<sup>+</sup> structure grown by LPE for this study, O gettering produced improved minority diffusion lengths in both n- and p-layers.

### Acknowledgments

We are in debt to J. Jacco for his assistance in the Schottky barrier measurements and LED fabrications, to S. Herko for the optical measurements, to A. Sicignano and C. Michel for the diffusion length measurements, and to W. K. Zwicker and R. L. Bronnes for the growing and polishing of the GaP LEC substrates, respectively. We gratefully acknowledge S. K. Kurtz for his encouragement in this work and for his critical comments on this manuscript.

Manuscript submitted June 26, 1975; revised manuscript received Dec. 5, 1975.

Any discussion of this paper will appear in a Discussion Section to be published in the December 1976 JOURNAL. All discussions for the December 1976 Discussion Section should be submitted by Aug. 1, 1976.

Publication costs of this article were partially assisted by Philips Laboratories.

### REFERENCES

- D. G. Thomas and J. J. Hopfield, *Phys. Rev.*, **150**, 680 (1966).
- R. A. Logan, H. G. White, and W. Wiegmann, *Appl. Phys. Letters*, **13**, 139 (1968).
- R. A. Logan, H. G. White, and W. Wiegmann, *Solid-State Electron.*, **14**, 55 (1971).
- I. Ladany and H. Kressel, *RCA Rev.*, **33**, 517 (1972).
- K. Akita, S. Nakai, T. Kinugasa, T. Kotani, K. Dazai, and O. Ryuzan, *Japan. J. Appl. Phys.*, **12**, 631 (1973).
- O. G. Lorimor, W. H. Hackett, and R. Z. Bachrach, *This Journal*, **120**, 1424 (1973).
- R. H. Saul and D. D. Roccasecca, *ibid.*, **120**, 1128 (1973); see also R. H. Saul and O. G. Lorimor, *J. Cryst. Growth*, **27**, 183 (1974).
- D. R. Wight, J. C. H. Birbeck, J. W. A. Trassler, and M. L. Young, *J. Phys. D: Appl. Phys.*, **6**, 1622 (1973).
- G. B. Stringfellow, M. E. Weiner, and R. A. Burmeister, *J. Electron. Mater.*, **4**, 363 (1975).
- O. G. Lorimor and M. E. Weiner, *This Journal*, **119**, 1576 (1972).
- R. N. Bhargava, *Phys. Rev.*, **B2**, 387 (1970).
- C. H. Henry, *J. Luminescence*, **7**, 127 (1973).
- R. Z. Bachrach, O. G. Lorimor, L. R. Dawson, and K. B. Wolfstirn, *J. Appl. Phys.*, **43**, 5098 (1972).
- R. N. Bhargava, S. K. Kurtz, A. T. Vink, and R. C. Peters, *Phys. Rev. Letters*, **27**, 183 (1971).
- O. G. Lorimor, P. D. Dapkus, and W. H. Hackett, Jr., *This Journal*, **122**, 407 (1975).
- O. G. Lorimor, S. E. Haszko, and P. D. Dapkus, *ibid.*, **122**, 1230 (1975).
- A. S. Jordan, R. Caruso, A. R. von Neida, and M. E. Weiner, *J. Appl. Phys.*, **45**, 3472 (1974).
- P. D. Dapkus, W. H. Hackett, Jr., O. G. Lorimor, and R. Bachrach, *ibid.*, **45**, 4920 (1974).
- "Heat of Formation of Inorganic Oxides," Bulletin 542, U. S. Bureau of Mines (1954); "Chemical Thermodynamic Properties," U. S. Atomic Energy Commission Report ANL 5750, Circular of the National Bureau of Standards, p. 500 (1952).
- M. E. Weiner, *This Journal*, **119**, 496 (1972).
- A. Sicignano and C. Michel, Private communication. In case of Al concentration  $X_{Al} > 5 \times 10^{-4}$ , it is sometimes observed that Al segregated out inhomogeneously in the beginning of LPE growth. This is based on results of microscopic analysis performed on these samples using the energy dispersive analysis system (EDAX) and the scanning electron microscope (SEM).
- R. N. Bhargava and P. C. Müräu, *J. Appl. Phys.*, **45** 3541 (1974).
- A. S. Jordan, *This Journal*, **118**, 781 (1971).
- E. C. Lightowers, J. C. North, and O. G. Lorimor, *J. Appl. Phys.*, **45**, 2191 (1974).
- R. Z. Bachrach, *J. Electron. Mater.*, **3**, 645 (1974).
- N. E. Schumaker and G. A. Rozgonyi, *This Journal*, **119**, 1233 (1972).
- J. M. Ralston, *Rev. Sci. Instr.*, **43**, 876 (1972).
- R. N. Bhargava and R. J. Seymour, Private communication.
- We are indebted to R. H. Saul for the green diodes which we used in this calibration; also to P. D. Dapkus for quantum efficiencies of some of these LED's.
- A. Caverly and D. R. Wight, *Solid-State Electron.*, **13**, 382 (1970).
- W. H. Hackett, Jr., R. H. Saul, R. W. Dixon, and G. W. Kammlott, *J. Appl. Phys.*, **43**, 2857 (1972).
- C. van Opdorp, R. C. Peters, and M. Klerk, *Appl. Phys. Letters*, **24**, 125 (1974).
- M. G. Craford, W. O. Groves, A. H. Herzog, and D. E. Hill, *J. Appl. Phys.*, **42**, 2751 (1971).
- C. D. Mobsby, E. C. Lightowers, and G. Davies, *J. Luminescence*, **4**, 29 (1971).
- R. Z. Bachrach and O. G. Lorimor, *Phys. Rev.*, **B7**, 700 (1973).
- P. D. Dapkus, W. H. Hackett, Jr., G. Lorimor, G. W. Kammlott, and S. E. Haszko, *Appl. Phys. Letters*, **22**, 227 (1973).
- H. Kukimoto, Abstract G7, IEEE Specialists Conference on the Technology of Electroluminescent Diodes, Atlanta, 1974.
- E. E. Loebner, *Proc. IEEE*, **61**, 837 (1973).
- J. M. Ralston, *Proc SID*, **14**, 81 (1973).

# A Comparison of Chemical Etches for Revealing <100> Silicon Crystal Defects

D. G. Schimmel

Bell Laboratories, Reading, Pennsylvania 19604

## ABSTRACT

The Sirtl etch is commonly used for <111> and <100>Si crystal defect evaluation although it is known that misleading results can occur for <100>Si due to lack of etch pit formation. A few of the known factors governing Si etching are presented for a qualitative approach to the understanding of defect etch formulations. In particular, the etch pit results from the Sirtl, Secco, Dash, and an experimental etchant are compared for shallow diffused structures as well as initial starting Si wafers. The best etch pit results were obtained from the Secco etch.

The development of etch pits which denote the emergence of dislocations on Si surfaces by chemical etching is simple and of considerable value in determining the degree of Si crystal perfection (1-5). Various factors which can influence etch pit results are crystal orientation, impurities on the defects, conductivity type, and the various substrate-diffusion combinations which may change the chemical activity of the Si surface with respect to the etching solution.

Historically, the well-known etch formulations of Sirtl and Dash were developed and used principally for evaluating the effects of crystal growing conditions on the resultant crystal perfection. Today, however, chemical etching to produce etch pits at crystal defects has been extended to the evaluation of wafers at various stages of processing. The extended use of chemical etching to Si devices containing p-n junctions creates additional conditions for the etch reaction which, for the most part, enhances the defect etch rate.

### Factors Influencing Etching of Si Defects

The basic reactions in the dissolution of a Si surface are an oxidation of the Si followed by removal of the oxide with HF. In order to delineate a crystal defect as an etch pit, the defect area must be oxidized and removed at a faster rate than the surrounding area. If HF is in excess in the etching solution, the oxide is removed as fast as it forms. Under this condition then, the delineation of the defect will be determined by the oxidation rate differential; *i.e.*, etch rate differential, between the defect and surrounding areas. A logical approach to accentuate this etch rate differential between the defect site and surrounding surface is to slow down the solution etch rate. This is particularly pertinent for (100)Si surfaces which are known to etch at a faster rate than (111)Si surfaces. Since many of the commonly used Si etches consist of various HNO<sub>3</sub>-HF combinations (6, 7), it is of interest to briefly

Key words: dislocations, ion implant, silicon integrated circuits.

review the oxidizing properties of HNO<sub>3</sub>. In solution, HNO<sub>3</sub> can act either as a reducing agent (acid) or an oxidizing agent (base), depending on the solvent system. For example, HNO<sub>3</sub> in water as the solvent is an acid, but it is a strong oxidizing agent in HF as the solvent (8). Thus, even very small quantities of HNO<sub>3</sub> in HF would promote etching of Si. By doing so, preferential etching of the defect may result.

In addition, Brattain and Garrett determined the following relationships between an electrolyte and a semiconductor surface (9): (i) Holes are required for an oxidation process. (ii) Hole-electron pairs are generated by surface illumination. (iii) The effect of light on the majority carrier density is not very great but it is possible for a large relative change in the density of minority carriers to occur. Thus, the effect of light on the electrode potential for a p-type anode (oxidation electrode) is small; but for an n-type anode, it is rather large.

The formulation of an experimental preferential defect etchant was predicated on the factors which influence etching as presented in the preceding paragraphs. The intent was to keep the etch formulation simple, using only HF and HNO<sub>3</sub>, and thereby determine if the approach presented to defect etching was valid. A few survey experiments were performed to determine the HNO<sub>3</sub> concentration necessary to produce etch pits at defects on (100) surfaces. The resultant experimental etch formulation is labeled the "Schimmel" etch and is included in Table I. Because of the lower etch rate, the alternate Secco etch formulation was used for the present comparison. For comparison, the etch formulations in Table I are presented as ratios with the last column listing the mequiv. (milli-equivalents) of oxidizing agent for each etch formulation. This enables a direct comparison of oxidizing agent present in the various etch formulations and will be considered in more detail in the Discussion section.

Table I. Comparison of Sirtl, Secco, Dash, and Schimmel etch formulations

Etch	Formula	Moles/cm <sup>2</sup> oxidizing agent	Mequiv. oxidizing agent	Etch rate
Sirtl	HF:CrO <sub>3</sub> (5M) 1:1	2.5 × 10 <sup>-3</sup>	7.5 × 10 <sup>-3</sup>	Nonlinear ~3.5 μ/min
Secco	HF:K <sub>2</sub> Cr <sub>2</sub> O <sub>7</sub> (0.15M) 2:1	5 × 10 <sup>-5</sup>	3 × 10 <sup>-4</sup>	1.5 μ/min with ultrasonic agitation
Alternate Secco	HF:CrO <sub>3</sub> (0.15M) 2:1	5 × 10 <sup>-5</sup>	1.5 × 10 <sup>-4</sup>	~1 μ/min with ultrasonic agitation
Dash	HF:HNO <sub>3</sub> :HAc* 1:3:10	3.4 × 10 <sup>-3</sup>	3.4 × 10 <sup>-3</sup>	Nonlinear ~0.1 μ/min with light n-substrate
Schimmel	HF:HNO <sub>3</sub> 155:1**	1 × 10 <sup>-4</sup>	1 × 10 <sup>-4</sup>	Nonlinear ~1.8 μ/min with light n-substrate

\* Abbreviation used for CH<sub>3</sub>COOH, acetic acid.

\*\* Ratio is equivalent to 0.1N HNO<sub>3</sub> with HF as the diluent based on conc HNO<sub>3</sub> = 15.6N. HF conc = 28.9N (49%).

### Comparison of Etch Results

*Experimental.*—Whenever possible, test sample substrates were scribed and broken into four pieces (one for each etch solution) to facilitate the comparison of the etch results. Regardless of any test sample processing just prior to etching all samples were immersed in conc HF followed by an overflow deionized water rinse. The etching time for the Sirtl etch was kept constant at 1¼ min while the etching times for the other etches varied from 1 to 10 min, depending on the sample being etched. The times for each etch are noted in the figure captions. In order to minimize surface roughness artifacts due to bubble formation with the Secco etch, ultrasonic agitation was used and resulted in shorter etching times also.

It was found that sample surface illumination, as indicated in the preceding section, did enhance the etching of defects in some instances, but only for the clear (not colored) etching solutions of Dash and Schimmel. However, the combination of etch solution (Dash as well as Schimmel etches) and surface illumination resulted in staining the Si surface. The stain was readily removed with a solution of 1 part conc  $\text{NH}_4\text{OH}$  and 4 parts water in about 1 min which

did not appear to change the Si surface topography. Ultrasonic agitation also aids in the stain removal.

*Etch comparison.*—In general, it is possible to tell from the appearance of the various etch pits if they are shallow or deep defects. Usually by re-etching for a longer time, the shallow defects will slowly disappear. It should be noted that the results shown in the following etch pit comparison photographs have been substantiated by numerous subsequent etching samples.

*n- and p-Type starting wafers.*—For n- and p-type wafers, both the Dash and Schimmel etches were unsatisfactory due to virtually no etch pit formation for short etching times. The effect of extended etch time was not pursued. As seen in Fig. 1, dislocation etch pits denoting dislocations into the bulk were formed by both the Sirtl and Secco etches on n- and p-wafers. It is quite clear from the photographs that the Secco etch pits are larger and easier to distinguish. Also, saucer pits denoting possible nucleation sites for future oxidation-induced stacking faults are evident in the Secco etched samples, both n- and p-type, but not in the Sirtl etched samples. The line type etch results for the Sirtl etched n-type substrate could be

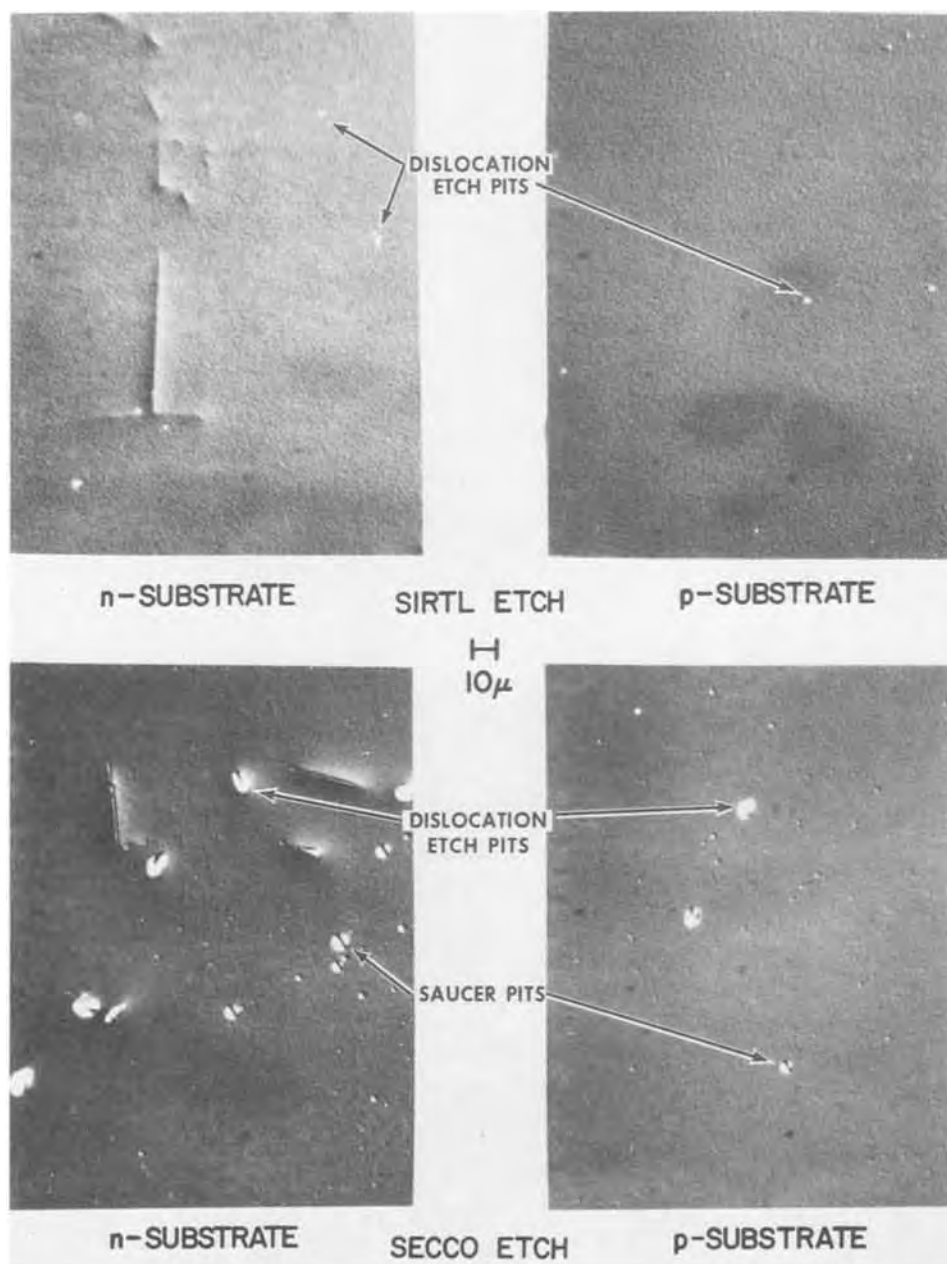


Fig. 1. n- and p-starting wafers with Sirtl etch (1¼ min) and Secco etch (5 min).



either dislocations or etching artifacts while those of the Secco etched sample are probably crystal defects because of the etched surfaces. In addition, the Sirtl etch pit formation on the p-type wafer in particular is less dense than that of the Secco etch. Consequently, the Sirtl etch results imply a lower defect density than is shown to exist by the Secco etch. This is also substantiated by copper decoration and will be described in a later section. Thus for both n- and p-wafers, the Secco etch appears best.

*Oxidized wafers.*—The wafers used in this series of experiments were steam oxidized at 1050°C for 2 hr. Just prior to etching, the oxide was removed in conc HF.

*n-Type.*—The Dash and Schimmel etches again were unsatisfactory for the oxidized n-type wafers due to virtually no etch pit formation. The effect of extended etching time again was not pursued. The Sirtl etch produced stacking fault and dislocation etch pits and some mounds, which were well distributed across the wafer. Well-distributed and somewhat larger stacking fault and dislocation etch pits were produced by the Secco etch. While there is little difference in etch pit distribution between the Sirtl and Secco etches, the

Secco is preferred because of the larger etch pit formation and because the Sirtl etch also produced mounds which may or may not be relevant to crystal defects (1, 4).

*p-Type.*—It was found that for an oxidized p-wafer, surface illumination during the Dash etch apparently inhibited etch pit formation on the Syton-polished surface. The reason for this is not known. Thus, surface illumination was only used for the Schimmel etch and not the Dash etch.

The oxidation-induced stacking fault and dislocation etch pits formed by the Sirtl, Secco, Dash, and Schimmel etches are shown in Fig. 2 for an oxidized p-type substrate. The most well-defined and crystallographic-oriented stacking fault etch pits were produced by the Dash etch. However, these defects were found only in a few small isolated areas across the sample. While the stacking fault and dislocation etch pits formed by the Sirtl and Schimmel etches were easily seen, their density and distribution across the wafer were not equal to those from the Secco etch. Fewer dislocations and oxidation-induced stacking faults were revealed than actually exist as verified by the consistent results of other etch samples. The validity of the Secco etch

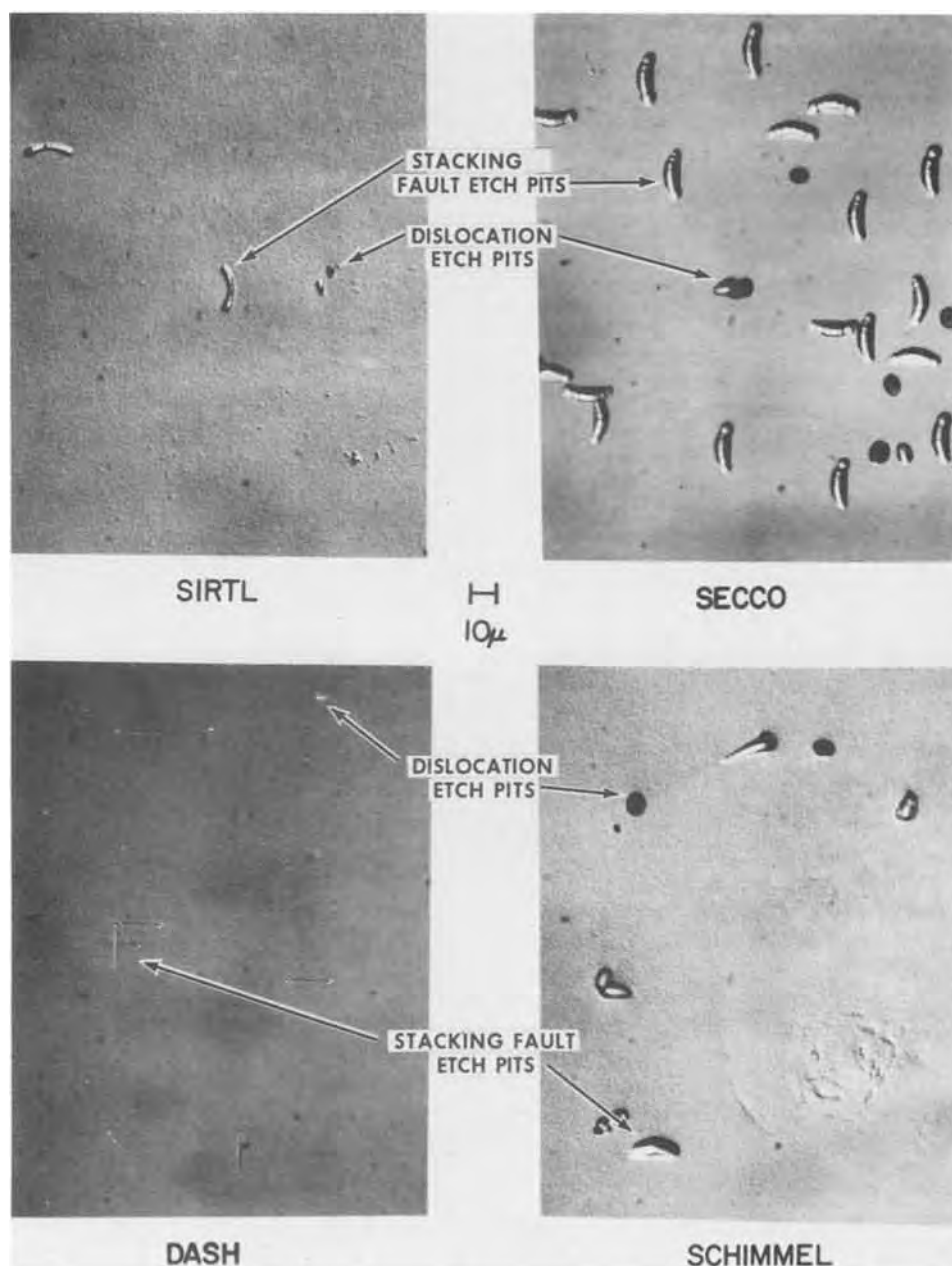


Fig. 2. p-wafer with 2 hr, 1050°C steam oxidation. Sirtl etch, 1¼ min; Secco etch, 5 min; Dash etch, 5 min with no added illumination; Schimmel etch, 1½ min with surface illumination.



pit results was established by the Cu decoration method and shown in the next section.

**Correlation between Secco etch pits and dislocations.**—A simple method for observing defects within the bulk of a Si substrate is by Cu decorating the dislocation and viewing it by infrared transmission (3). Slip dislocations were created in an n-type substrate by a 30 min, 1000°C, Ar atmosphere furnace treatment with a moderate quench (1000° to ~600°C in ~5 sec) withdrawal. The wafer was then Secco-etched to reveal the dislocations generated by the heat-treatment. The front of the wafer was protected and the back side chemically polished to facilitate viewing with the infrared transmission microscope. Immediately after the chemical polish, a thin film of Cu was deposited from dilute HF onto the back side of the wafer. After cleaning the wafer to remove the front protection, the Cu was diffused in at 1000°C in Ar for 30 min.

The top left photograph of Fig. 3 illustrates the etch pits formed originally by the Secco etch after the above furnace quench treatment. The top right-hand side of Fig. 3 shows the picture of infrared transmission through the wafer after Cu diffusion. The Cu decorated dislocations trailing down from the etch pits can be readily seen. The higher magnification photograph at

the bottom of Fig. 3 shows the Cu decorated dislocation in greater detail as well as other near surface line defects. The focus in this picture is essentially at the surface of the wafer. It should be noted that the somewhat mottled background of the lower magnification infrared transmission photograph is due to back surface roughness remaining after the chemical polish.

From the photographs of Fig. 3, it can be seen that the Secco etch pits do form at dislocations, thus the validity of Secco etch pit results is confirmed. Since the Cu was deposited only onto the back side of the wafer, the Cu decorated "tail" was not generated from the etch pit by Cu diffusing from the front.

**Implanted B base and POCl<sub>3</sub> diffused emitter.**—Defects result from the drive-in step following a boron implant. Base dopant introduced by implanting boron which is subsequently driven in at 1150°C in 100% O<sub>2</sub> and then oxidized in steam at 1050°C is an excellent test vehicle to demonstrate the differences in etching results of the various etch formulations. This damage essentially remains unchanged after the emitter diffusion which consists of a POCl<sub>3</sub> deposition and drive-in. Figure 4 illustrates these process-induced defects after both emitter and base operations. Referring to Fig. 4, all four etch formulations result in some degree of etching

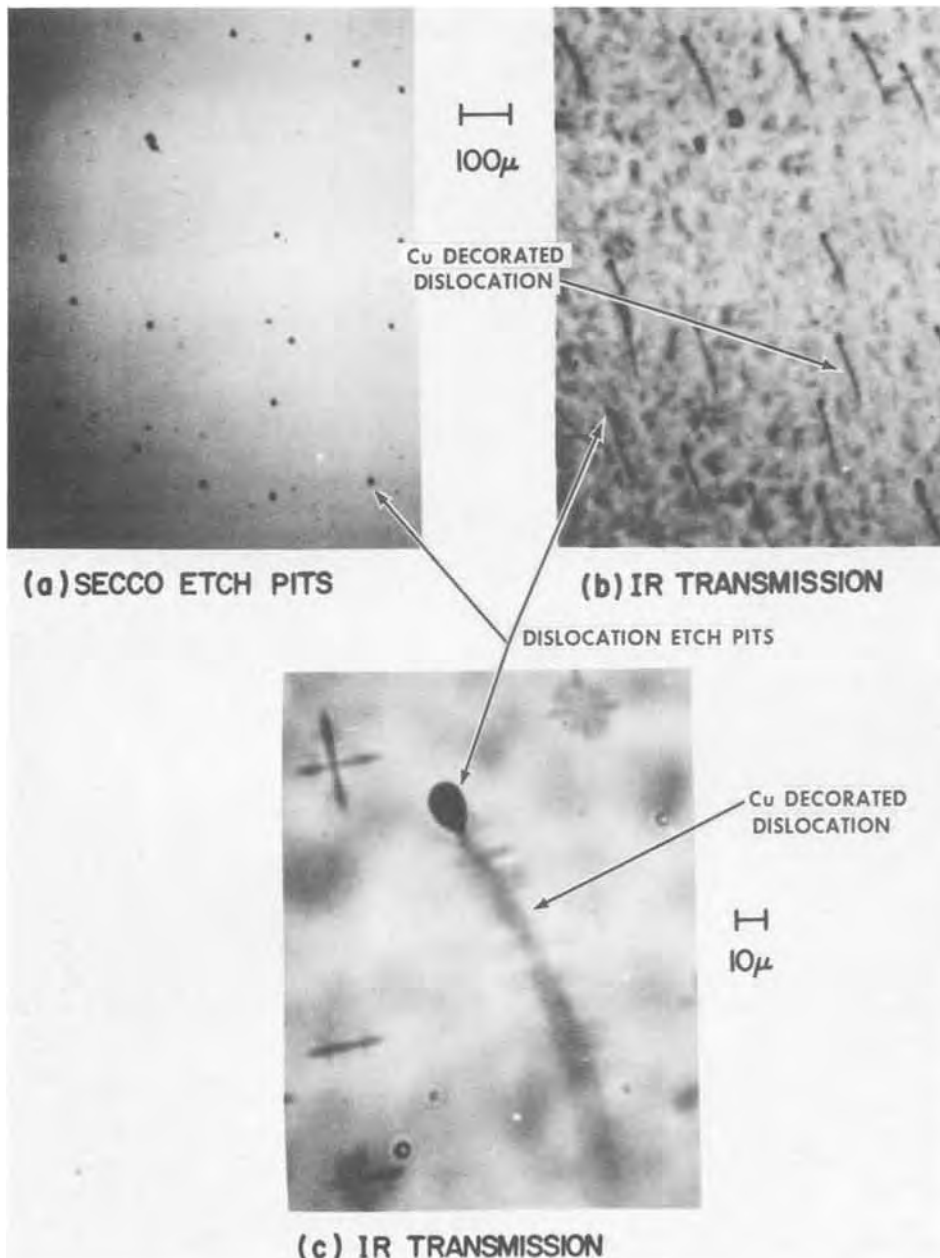


Fig. 3. Top left photograph is of slip dislocation etch pits after Secco etch (10 min). Top right is an infrared transmission photograph of Secco etched sample after Cu decoration. Bottom photograph is a higher magnification infrared transmission photograph of Cu decorated dislocation.

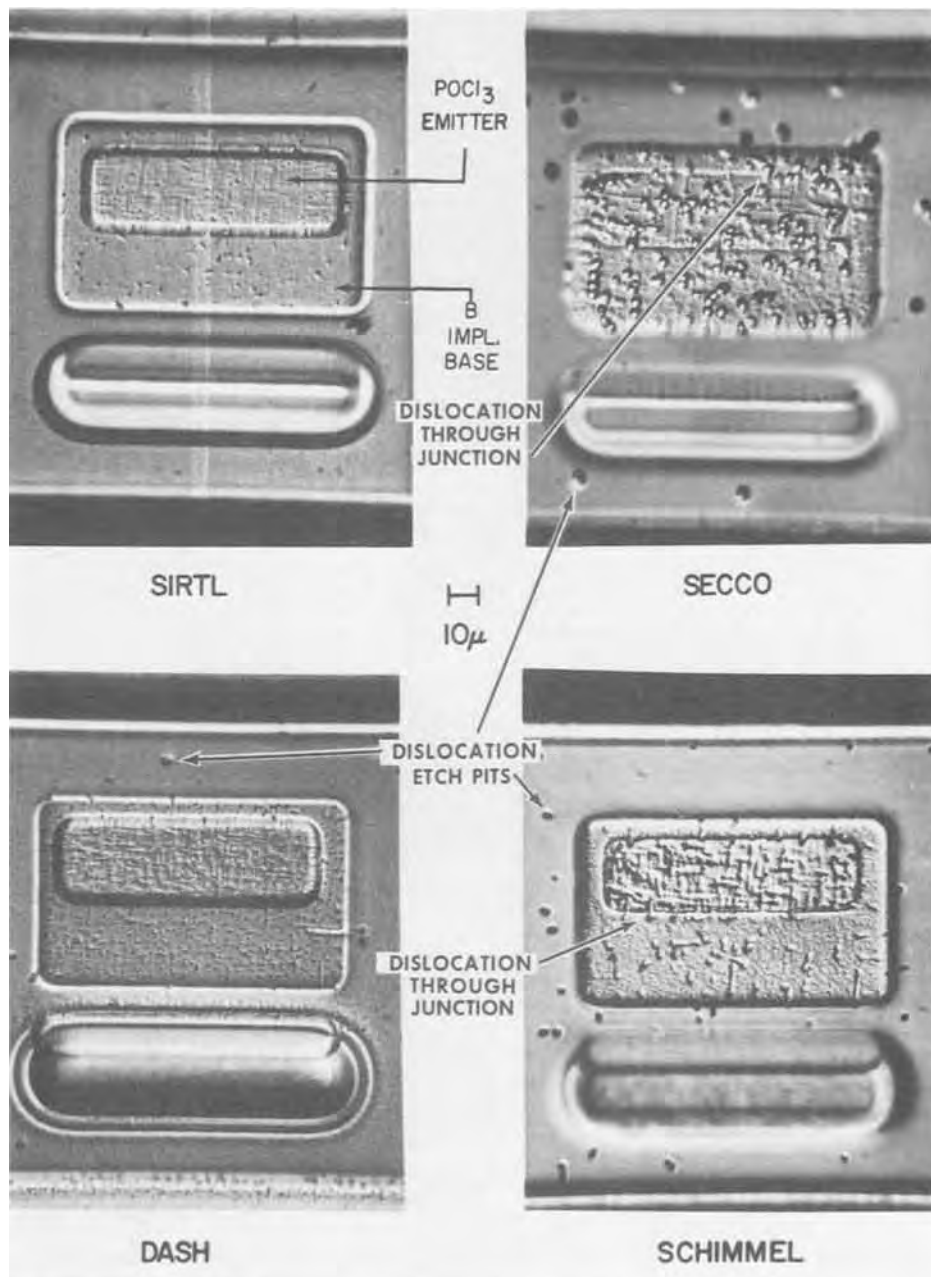


Fig. 4. Etchant comparisons for n-epi with implanted B-base and P ( $\text{POCl}_3$  source) diffused emitter. Sirtl etch,  $1\frac{1}{4}$  min; Secco etch, 2 min; Dash etch, 2 min with surface illumination; Schimmel etch, 1 min with surface illumination.

in both the base and emitter areas. However, the best detail is found in both the Secco etch and Schimmel etch. Line defects (crystallographically oriented) are readily seen on the sample with the Schimmel etch in the base area. Some of these line defects, presumably misfit dislocations, can be seen to extend through the emitter-base junction edges. Also quite visible are dislocation etch pits in the surrounding epi surface. Essentially the same results are evident from the Secco etch with the exception that circular or elliptical etch pit forms are in the B-implanted area rather than the line type probably due to a faster etch rate than the Schimmel etches. The primary difficulty with the Secco etch in this instance is a tendency to overetch in the active areas. This can be compensated for by reducing the etch time from 2 to 1 min. The Dash etch and Sirtl etch both indicate defects in the active regions, but not as distinctly as with the Secco and Schimmel etches. The biggest drawback to the use of the Sirtl etch, as seen in Fig. 4, is the lack of dislocation etch pit formation in the substrate (or epi) areas which leads to a wrong conclusion; i.e., that no dislocations are present in these areas.

**$\text{POCl}_3$  diffused in n-substrates.**—Figure 5 shows the etch pit formation on P diffused from  $\text{POCl}_3$  into an

n-substrate. Again, the absence of dislocation etch pits at the intercepts of the long line defects must be noted for the Sirtl etch. While the Dash etch denotes dislocations at the intercepts of the line defects by virtue of rectangular etch pits, the Secco etch gives more information on the initial direction of the dislocations into the substrate from the etch pit shape and depth. The Secco etch is the first choice in this case with the Dash etch a close second.

**Boron into p-substrate.**—In this section, the sample used for the etching comparison was a p-type substrate with boron implanted-diffused areas. It should be noted that the previous n-substrate and n-epi samples etched with the Dash and Schimmel etches for the etching times used, required sample illumination for etch pits to develop. With p-substrates, however, the Schimmel etch with illumination created excessive etching of the boron implanted areas. Consequently, the use of the Schimmel etch on p-substrates containing p-n junctions is done with room illumination only. Conversely, the Dash etch not only requires sample illumination to promote etch pit formation with p-substrates containing junctions, but an extended etch time as well (increased from 2 to 5 min).

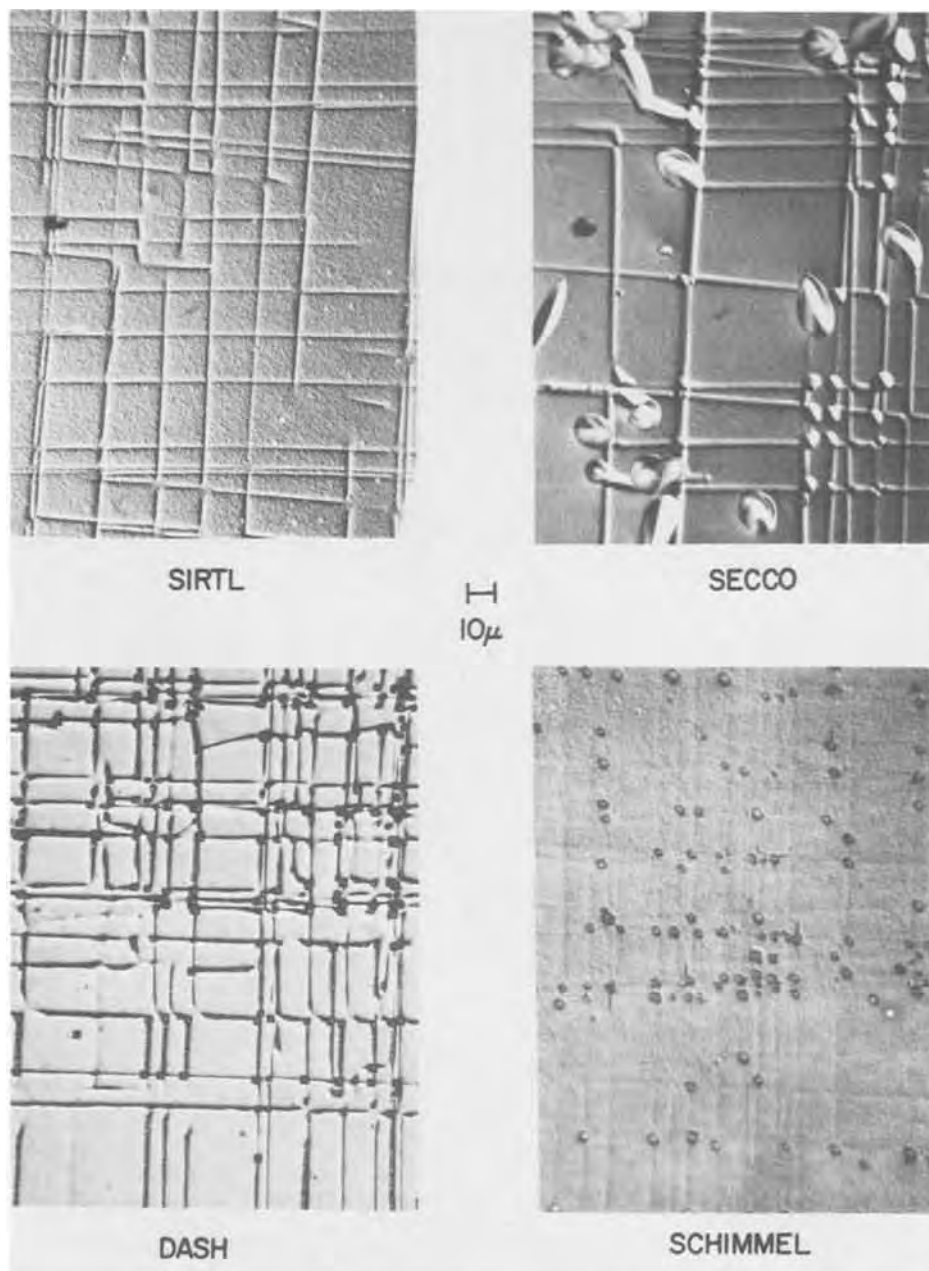


Fig. 5. Etchant comparisons for n-substrate with diffused P ( $\text{POCl}_3$  source). Sirtl etch,  $1\frac{1}{4}$  min; Secco etch, 10 min; Dash etch, 2 min with surface illumination; Schimmel etch, 1 min with surface illumination.

Three of the four pictures in Fig. 6 are typical examples of etch pit formation of probable misfit dislocations for boron implants from the Secco, Dash, and Schimmel etches. The Sirtl etch has the poorest etch figure development. When considering the implanted B, the Secco, Schimmel, and Dash etches are all equivalent in etch results.

An illustration of the large effect that sample illumination can have on the formation of etch pits at defect sites is shown in Fig. 7. The photo on the left shows the etch pit formation with a 5 min Dash etch without sample illumination. The photo on the right is a sample from the same substrate, etched for the same length of time except with the sample illuminated with a microscope light during etching.

#### Discussion

Referring to Table I, it is shown that the Sirtl etch (2) contains the greatest amount of oxidizing agent,  $7.5 \times 10^{-3}$  mequiv. or equiv./ $\text{cm}^3$ . This etchant works best on (111) surfaces which, as noted earlier, have a lower etch rate than (100) surfaces. Two distinct characteristics of this etch solution are: etch pit shapes are mostly determined by crystallographic orientation, and relatively short etching times in the order of 30 sec to 5 min. The Sirtl etch is definitely a preferential

etch which is very widely used to determine dislocations in Si crystals. However, Hallas and Mendel (1) showed that mounds rather than etch pits form at dislocations on (100) surfaces, and difficulties in interpreting etch pit results may occur. These mounds are not necessarily related to dislocations with respect to (100) surfaces. Thus, the Sirtl etch specified as an ASTM test, F47-70, is applicable only to (111) surfaces. As was seen in the etch pit comparison figures, misleading information can result because of a lack of etch pit formation on (100) surfaces.

The Secco etch was formulated by F. Secco d'Aragona and published in 1972 for grown crystal evaluations. It is essentially a modification of the Sirtl etch. The oxidizing agent, chromium (VI), concentration has been significantly reduced with an accompanying increase in HF. The etch pit results differ from the Sirtl etch in two ways. First, it is an isotropic etch in that dislocation etch pits form on surfaces of any orientation; and second, the etch pit shape is not necessarily determined by crystal symmetry alone, but also determined by the direction of the dislocation near the surface. Thus, the pits are principally circular or elliptical.

It is interesting to note that the reduction in oxidizing agent concentration results in a significant decrease

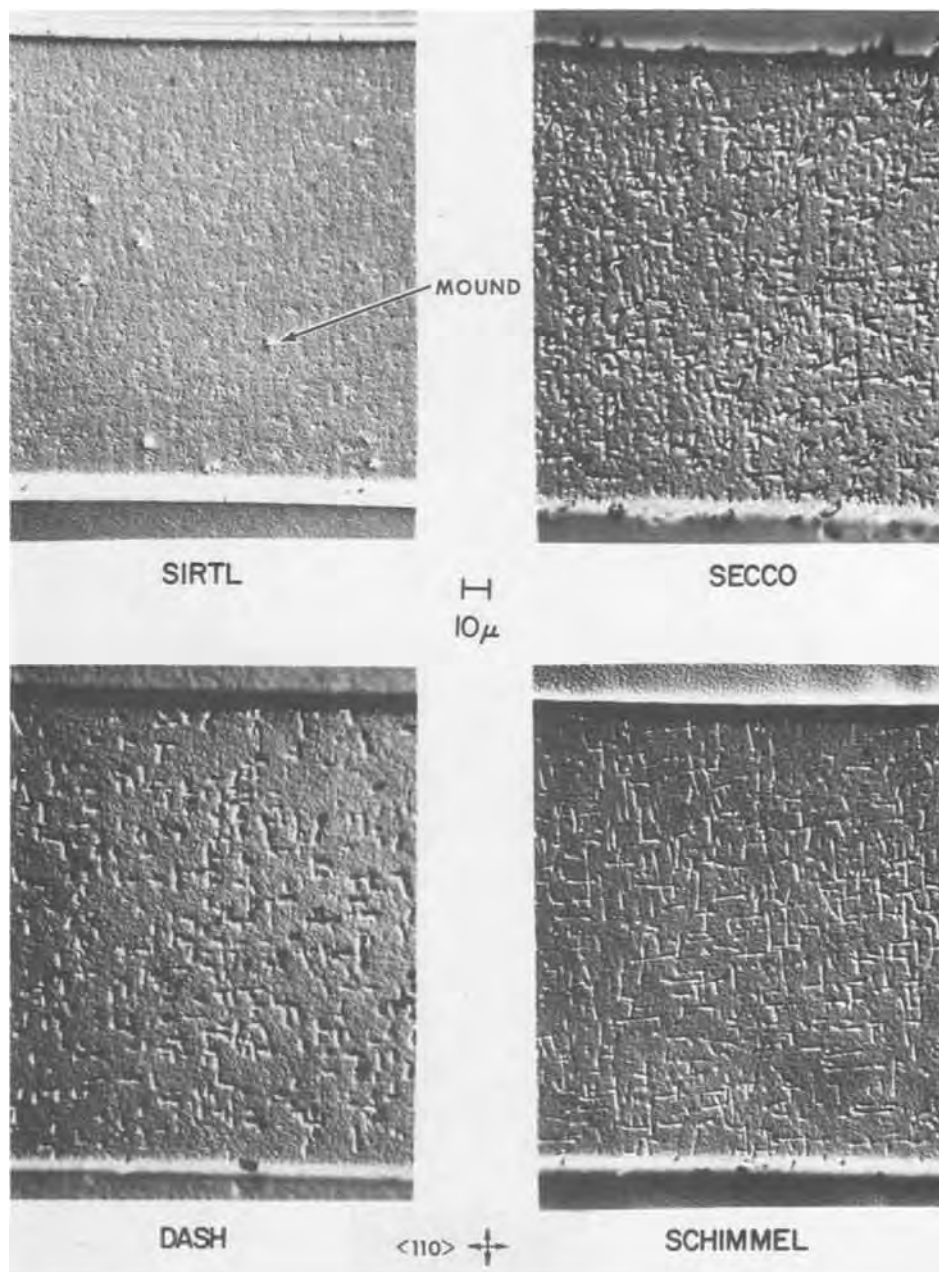


Fig. 6. Etchant comparisons for p-substrate with a B implanted-diffused layer. Sirtl etch, 1¼ min; Secco etch, 2 min; Dash etch, 5 min with surface illumination; Schimmel etch, 1½ min without added surface illumination.

in etch rate. In Table I there are two Secco etch formulations listed. The first formulation is the original published Secco etch and has a  $1.5 \mu/\text{min}$  etch rate when used with ultrasonic agitation. This formulation etches at a slightly higher rate than the alternate formulation using  $0.15\text{M CrO}_3$ . Here the chromium (VI) containing ion concentration is reduced to  $1.5 \times 10^{-4}$  mequiv. with an accompanying reduction in etch rate.

The Dash etch (3), at first glance, appears to contradict the facts as developed thus far. Even though it has an oxidizing agent concentration nearly that of the Sirtl etch,  $3.4 \times 10^{-3}$  mequiv. vs.  $7.5 \times 10^{-3}$  mequiv. for Sirtl, it is considered to be an isotropic etch. Even though the etch rate is lower than would be expected from this concentration of  $\text{HNO}_3$ . Obviously, this anomalous behavior is due to the use of acetic acid as the diluent, which reduces the oxidizing capability of the  $\text{HNO}_3$  to less than that indicated. Because the HF is not in excess, the reaction of HF on the oxide is also probably diffusion limited. While the Dash etch is isotropic, its widespread use has been deterred by reported long etch times (in the order of hours) required for substrate crystals (1, 3). Drum and Van Gelder, however, reported etch pit results on wafers with a 5 min etch

time (10). It was also shown earlier that etch pit development is greatly enhanced for the Dash etch in some instances by strong illumination (focused microscope light) and also by the presence of p-n junctions.

The Schimmel etch formulation was the result of an empirical approach to Si defect etching and it was developed to test the proposed mechanism. It is interesting to note that the  $\text{HNO}_3$  concentration determined experimentally is quite close to the oxidizing agent concentration of the other etches. The etch pit shape appears to be influenced by crystallographic orientation to a greater degree than the Dash or Secco etches. The main drawback of this etch formulation is the rough surface which results from gas bubble formation during etching. The use of ultrasonic agitation to alleviate this condition was not completely satisfactory. While the surface roughness diminishes the aesthetic qualities of appearance, the etch pit figures are readily discernible. It should be noted that the use of surface illumination and the presence of p-n junctions also greatly enhanced etch pit formation by the Schimmel etch.

### Conclusions

Preferential chemical etching of Si surfaces is a fast and reliable method for determining the effects of

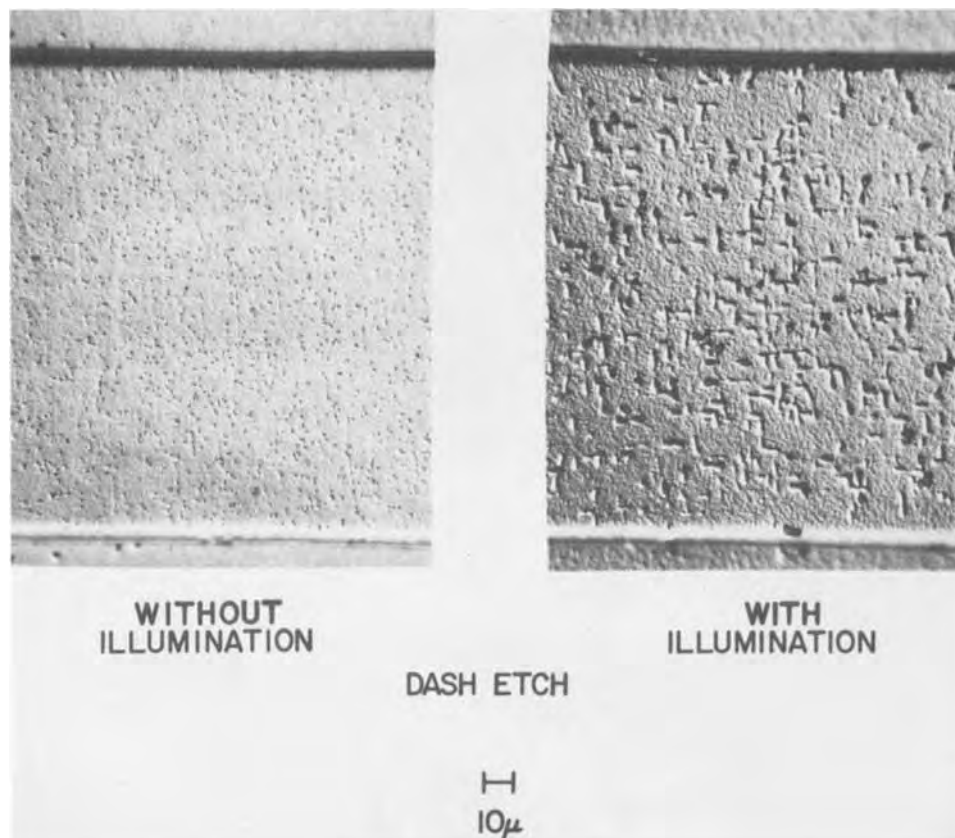


Fig. 7. Same sample as Fig. 6 to demonstrate effect of surface illumination during etching. Left photograph is Dash etch, 5 min without surface illumination. Right photograph is Dash etch, 5 min with surface illumination.

processing on Si crystal perfection. In order to avoid misleading etch results for (100)Si surfaces in particular, the proper choice of etch formulation is important. It has been demonstrated that for the Si sample conditions of interest in SIC, the alternate Secco etch formulation produces acceptable etch pit results for the widest range of <100>Si substrate and shallow junction combinations. In most instances for (100)Si surfaces, the Sirtl etch does not produce the best pos-

sible results and may even result in misleading conclusions in specific instances where etch pits are not formed. The recommended etch formulations for various combinations of <100>Si substrates and junctions are presented in Table II.

Manuscript submitted Aug. 29, 1975; revised manuscript received Dec. 29, 1975. This was Paper 183 presented at the Dallas, Texas, Meeting of the Society, Oct. 5-9, 1975.

Any discussion of this paper will appear in a Discussion Section to be published in the December 1976 JOURNAL. All discussions for the December 1976 Discussion Section should be submitted by Aug. 1, 1976.

Publication costs of this article were partially assisted by Bell Laboratories.

Table II. Recommended etch formulations for <100> Si

Code: 1, Recommended; 2, Acceptable; 3, Marginal; N, Not recommended; (L), Surface illumination.

Test sample	Etch			
	Sirtl	Secco	Dash	Schimmel
Plain substrates (n + p)	2-3	1	N	N
Oxidized n-substrate	2	1	N	N
Oxidized p-substrate	2	1	3-N	2(L)
n-Substrate or n-epi with impl. diffused boron	3	1	2(L)	1-2(L)
n-Substrate or n-epi with P diffused (POCl <sub>3</sub> source)	3	1	2(L)	3(L)
p-Substrate with impl. diffused boron	2-3	1	1(L)	1
	Etch	Formula		
Sirtl		HF:CrO <sub>3</sub> (5M) 1:1		
Alternate Secco		HF:CrO <sub>3</sub> (0.15M) 2:1		
Dash		HF:HNO <sub>3</sub> :HAc (acetic acid) 1:3:10		
Schimmel		HF:HNO <sub>3</sub> 155:1		

#### REFERENCES

1. C. E. Hallas and E. Mendel, *J. Appl. Phys.*, **42**, 477 (1971).
2. E. Sirtl and A. Adler, *Z. Metallk.*, **52**, 529 (1961).
3. W. C. Dash, *J. Appl. Phys.*, **27**, 1193 (1956).
4. F. Secco d'Aragona, *This Journal*, **119**, 948 (1972).
5. P. J. Holmes, "The Electrochemistry of Semiconductors," Academic Press, New York (1962).
6. H. Robbins and B. Schwartz, *This Journal*, **106**, 505 (1959).
7. H. Robbins and B. Schwartz, *ibid.*, **107**, 108 (1960).
8. S. Glasstone, "Textbook of Physical Chemistry," 2nd ed., p. 976, D. Van Nostrand Co., Inc., New York (1951).
9. W. H. Brattain and C. G. Garrett, *Bell System Tech. J.*, **43**, 129 (1955).
10. C. M. Drum and W. Van Gelder, *J. Appl. Phys.*, **43**, 4465 (1972).

# Emitter Dip Effect by Low Temperature Heat-Treatment of Arsenic-Diffused Layer

H. Shibayama, H. Masaki, H. Ishikawa,\* and H. Hashimoto

Fujitsu Laboratories Limited, Nakahara-ku, Kawasaki, Japan

## ABSTRACT

When arsenic is used as the emitter diffusant in a n-p-n silicon transistor, it is well known that the emitter dip effect is not observed. However, it was found that the diffusion of boron underneath the arsenic emitter was accelerated during heat-treatment at 500°-800°C. This phenomenon is related to abnormal behavior of arsenic in silicon. The diffusion of arsenic is enhanced by such treatment. The anomalous diffusion of arsenic depends on treatment time, and is remarkable in the beginning of the treatment. The diffusivity is extremely large in comparison with the normal one extrapolated from high temperature data. It is considered that this anomaly is caused by the generation of excess vacancies during such treatment. The emitter dip effect is also caused by these excess vacancies during heat-treatment at relatively low temperature.

Arsenic is generally used as the emitter diffusant for a microwave n-p-n silicon transistor. The arsenic emitter avoids the emitter dip effect, and the carrier profile is suitable in comparison with phosphorus. The covalent radius of arsenic is nearly equal to that of silicon. Therefore, the lattice strain is considerably reduced as compared to phosphorus.

However, the authors (1) reported that the diffusion of arsenic was accelerated by low temperature heat-treatment and that this caused the emitter dip effect. Such a phenomenon may be due to the excess vacancies formed during these treatments. Large decreases in the conductivity of arsenic-doped silicon during 500°-970°C heat-treatments were reported by Schwenker *et al.* (2). They suggested that the effect was due to the formation of As-As clusters. Miyamoto *et al.* (3) also reported using the x-ray double crystal diffraction technique that the lattice constant of the arsenic-doped silicon was increased after heat-treatment at low temperature. They explained that this lattice expansion and the increase of resistivity were due to arsenic atom precipitation and SiAs formation. Osvenskii *et al.* (4) made an electron microscopic investigation of the structure of silicon single crystals doped with arsenic to a concentration of  $5 \times 10^{20} \text{ cm}^{-3}$  and observed the formation of prismatic dislocation loops during annealing at 800°C. They concluded that the observed dislocation loops were formed by the decrease of a solid solution of arsenic in silicon. Furthermore, Haskell *et al.* (5) investigated the channeling measurements in arsenic-doped silicon using a He<sup>+</sup> ion backscattering technique, and both silicon- and arsenic-aligned yields increased in the arsenic-diffused samples during low temperature annealing. They suggested the model of the formation of the complex on substitutional lattice sites.

Arsenic, which is a relatively normal diffusant in silicon at high temperature, shows the complicated behavior described above by low temperature annealing.

In this paper, the emitter dip effect in a n-p-n transistor using arsenic for the emitter impurity by low temperature heat-treatments is reported. The previous paper (1) suggested that such emitter dip effect was due to the anomalous diffusion of arsenic. First, the anomalous diffusion of arsenic is investigated in detail and the relation between the anomalous diffusion of arsenic and the emitter dip effect is studied. Finally, the influence of such treatments on the electrical char-

acteristic of the silicon devices is examined with the junction field effect transistor (JFET). From these experimental results, the mechanism of this emitter dip effect is discussed.

## Experimental

In the case of singly diffused structures, arsenic was diffused in silicon from an arsenosilicate glass. The glasses were deposited onto p-type 1-2 ohm-cm (111) oriented epitaxial silicon wafers by the reaction of silane, arsine, and oxygen at 450°C. The thickness of the glass was about 1000Å. The diffusion was carried out at 1000°C in an atmosphere of N<sub>2</sub> and O<sub>2</sub> mixture. The arsenic surface concentration was varied by changing the arsenic content in the glasses.

In doubly diffused structures, boron was first diffused into n-type 0.4-0.6 ohm-cm (111) oriented epitaxial silicon wafers with a boron nitride source at 900°C for 30 min and oxidized in wet O<sub>2</sub> at 950°C for 60 min. The silicon dioxide grown during the oxidation was removed by hydrofluoric acid. Then, arsenic was diffused into the boron-diffused layer by the same way described above. The glass was removed by hydrofluoric acid before low temperature heat-treatment. The low temperature heat-treatments were carried out at 500°-800°C in N<sub>2</sub>.

The carrier concentration profiles were determined using the anodic oxidation-resistivity technique and Irvin's data (6). Junction depths were confirmed by the thermal probe method.

The diffusion coefficient of the boron base underneath the arsenic emitter during low temperature heat-treatment was calculated by the following procedure. It is assumed that the diffusivity of the boron-base impurity is not affected by an internal electric field (7, 8) or other interaction between impurity and carrier (9). The base impurity profile is approximated by complementary error function during the heat-treatment. The base-collector junction depth ( $x_j$ ) is given by

$$x_j^2 = 4(D_1 t_1 + D_2 t_2 + D_3 t) \{\text{erfc}^{-1}(C_b/C_s)\}^2 \quad [1]$$

where  $D_1$ ,  $D_2$ , and  $D_3$  are the diffusion coefficient of boron during the base diffusion, the emitter diffusion, and the subsequent low temperature heat-treatment, respectively;  $t_1$  and  $t_2$  are the diffusion times of initial base and emitter;  $t$  is the heat-treatment time, and  $C_b$  and  $C_s$  are the bulk concentration and the surface concentration of the base. The velocity of increase in the junction depth is given by

$$dx_j/dt = 2\{\text{erfc}^{-1}(C_b/C_s)\}^2 x_j^{-1} D_3 \quad [2]$$

\* Electrochemical Society Active Member.  
Key words: emitter dip effect, enhanced diffusion, arsenic diffusion.



When the increase in the junction depth ( $\Delta x_j$ ) during the heat-treatment for  $\Delta T$  is sufficiently smaller than the  $x_j$ ,  $\Delta x_j$  is given by

$$\Delta x_j = 2\{\text{erfc}^{-1}(C_b/C_s)\}^2 x_j^{-1} D_3 \Delta T \quad [3]$$

The similar assumption is used in determining the diffusion coefficient of the amount of dip in the phosphorus-boron system by Nakamura *et al.* (10). The diffusion coefficient can be determined from Eq. [3].

In order to examine the influence of arsenic during low temperature heat-treatment on silicon devices, JFET's were fabricated; gate length and width were 20 and 70  $\mu\text{m}$ , respectively. The current between source and drain in a JFET is restricted to the region beneath the depletion layer boundary. The saturation current at pinch-off on the drain side was measured before and after heat-treatment.

**Results**

*The anomaly of arsenic during low temperature heat-treatment.*—The typical change in carrier profiles in the arsenic-diffused layers by low temperature heat-treatment is shown in Fig. 1. The following phenomena have already been reported in a previous paper (1). The carrier concentration of arsenic decreased during heat-treatment at 700°C, and this decrease occurred at first from the surface. Furthermore, the junction depth increased, and its increase was remarkable in the beginning of the treatment.

In Fig. 1, junction depths are increased considerably even at 500°C. The carrier concentration near the surface decreases, and tails in the low concentration region. The decrease in carrier concentration is not due to the out-diffusion because the recovery of carrier concentration was observed when the sample was

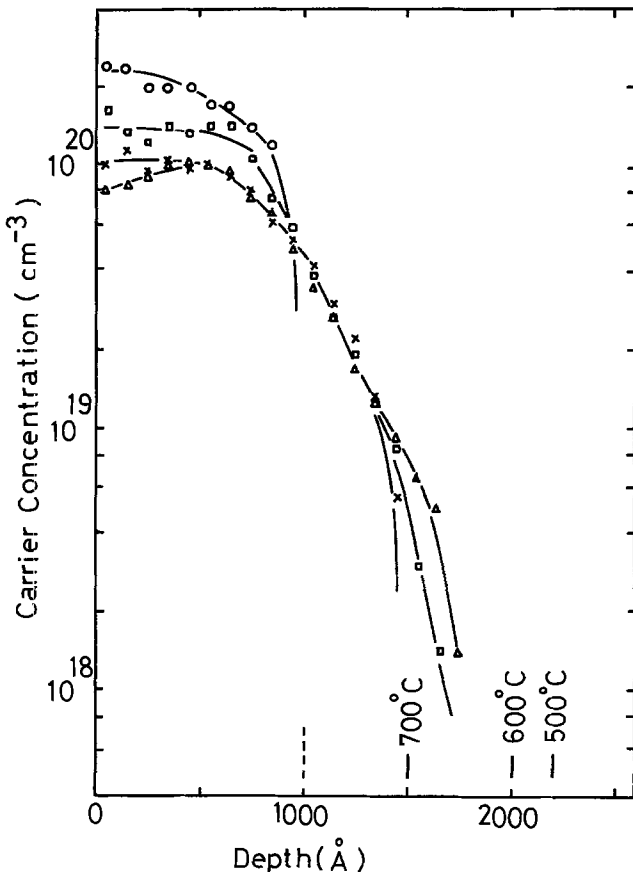


Fig. 1. Effect of heat-treatment at low temperature in N<sub>2</sub> on carrier profiles of the arsenic-diffused layer: ○ before heat-treatment; × heat-treated at 700°C for 24 hr; △ heat-treated at 600°C for 170 hr; □ heat-treated at 500°C for 336 hr. The points marked 500°C, 600°C, and 700°C are the junction depths, which are determined by the thermal probe method.

heated once more at the initial diffusion temperature after low temperature heat-treatment as shown in Fig. 2.

The change in the sheet resistivity is shown in Fig. 3(a) as a function of heat-treatment time and temperature. The sheet resistivity increases rapidly in the

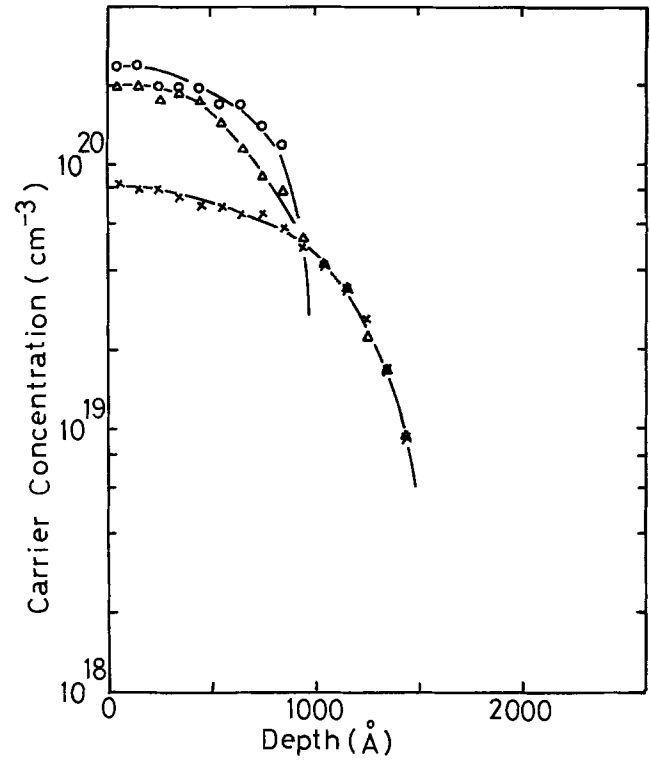


Fig. 2. Effect of the successive high temperature heat-treatment on the arsenic-diffused layer treated at low temperature: ○ before heat-treatment; × heat-treated at 700°C for 170 hr; △ heat-treated at 1000°C for 1 min after heat-treatment at 700°C.

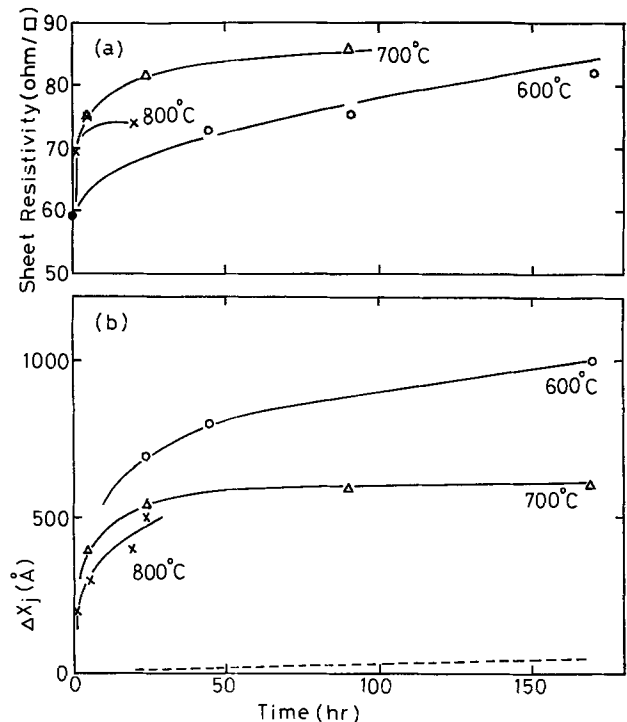


Fig. 3. Variation of sheet resistivity (a) and increase in junction depth (b) of arsenic during low temperature heat-treatment as a function of time and temperature. The dashed line is an increase in junction depth at 700°C, which is determined from high temperature data.

beginning of the heat-treatment and approaches the equilibrium value at long times. As the heat-treatment temperature increases, its equilibrium value decreases. The increase in the sheet resistivity at 600°C is not rapid, and its equilibrium value is not attained in the range of the treatment time in this experiment. This agrees with the result of Schwenker *et al.* (2). On the other hand, the junction depths were increased greatly during such treatment. The increase in the junction depth ( $\Delta x_j$ ) is shown in Fig. 3(b). In the same figure, the calculated values of  $\Delta x_j$ , using the diffusion coefficient of arsenic extrapolated from high temperature data (11) and considering the effect of internal electric field and variation of equilibrium vacancy concentration (12, 13), are also shown. The experimental results are considerably larger than the calculated values.  $\Delta x_j$  increases rapidly in the beginning of the heat-treatment, and increases hardly at all over long times. These changes have the same tendency as that of the sheet resistivity.

In the above experiments, the carrier concentration in the arsenic-diffused layer before low temperature heat-treatment was  $2.4 \times 10^{20} \text{ cm}^{-3}$ . This anomalous diffusion depends on the arsenic concentration. Samples with a varying surface concentration with junction depths 1000-1500Å were treated at 600°C for 45 hr. In Fig. 4, the increase in the junction depth ( $\Delta x_j$ ) is shown as a function of the arsenic surface concentration. The dependence on arsenic concentration is remarkable, and this enhanced diffusion could not be observed for the arsenic surface concentration below  $1 \times 10^{20} \text{ cm}^{-3}$ .

*The emitter dip effect during low temperature heat-treatment.*—In the case of the n-p-n transistor, a study was made to determine whether the abnormal behavior of arsenic mentioned above affected the boron base layer underneath the arsenic emitter. The surface concentration of boron for base impurity before the arsenic diffusion is  $8 \times 10^{18} \text{ cm}^{-3}$ . Typical carrier profiles before and after low temperature heat-treatment are shown in Fig. 5. The emitter-base and base-collector junction depths before heat-treatment were

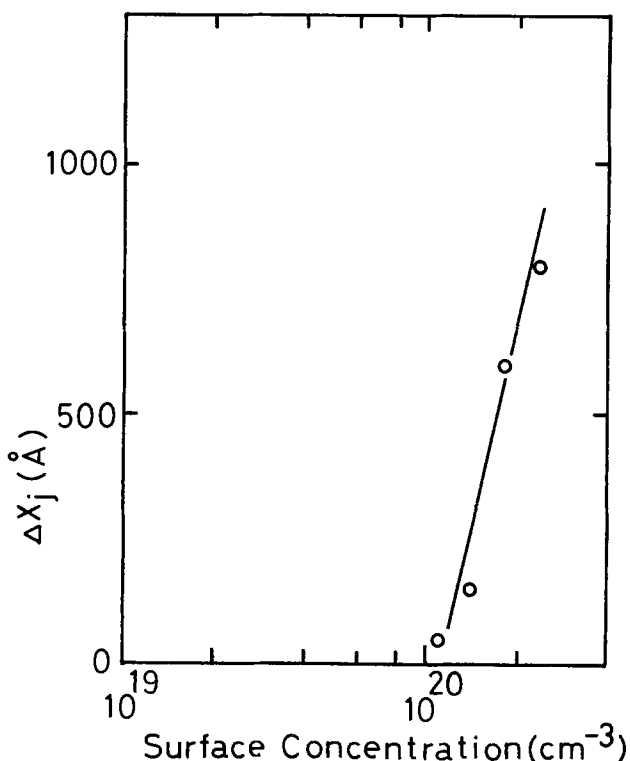


Fig. 4. Dependence on surface concentration of increase in the junction depth. Low temperature heat-treatment is carried out at 600°C for 45 hr.

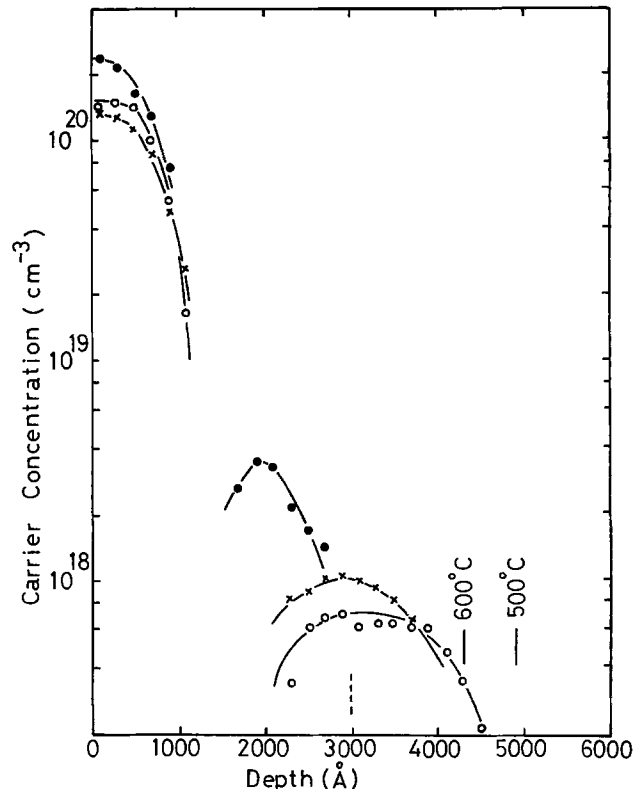


Fig. 5. Effect of heat-treatment at low temperature on carrier profiles of n<sup>+</sup>-p-n structure. Impurities in the n<sup>+</sup>- and p-diffused layer are arsenic and boron: ● before heat-treatment; × heat-treated at 600°C for 45 hr; ○ heat-treated at 500°C for 336 hr. The points marked 500°C and 600°C are the junction depths, which are determined by the thermal probe method.

1000 and 3000Å, respectively. When the boron-diffused layer without the arsenic emitter was treated at such conditions, its carrier profile was not changed. On the other hand, the diffusion of boron underneath the arsenic emitter is extremely enhanced at relatively low temperature. The base-collector junction depth was increased from 3000 to 4900Å by heat-treatment at 500°C for 336 hr. The diffusion of arsenic is enhanced in the low concentration region, as shown in Fig. 1. Therefore, in this structure, the increases in the emitter-base junction depths could be hardly observed because of the compensation with the base impurity.

When the heat-treatments are carried out for 24 hr, the effective diffusion coefficient of boron underneath the arsenic emitter is plotted in Fig. 6 as a function of temperature. The diffusivity of boron during the heat-treatment depends on the time, and therefore, the diffusion coefficient is a function of time. However,  $D_{\text{eff}}$  shown in Fig. 6 was calculated on the assumption that the diffusion coefficient was constant during the heat-treatment for 24 hr. This  $D_{\text{eff}}$ , which is the "average" effective diffusion coefficient, is larger in the beginning of the heat-treatment. In Fig. 6, these values are not changed much by temperature, and are maximum at about 600°C. They are much larger than the normal value extrapolated from the high temperature data (14). This emitter dip effect may be due to the abnormal behavior of arsenic during low temperature heat-treatment. In Fig. 3, the increases in the junction depths of arsenic during the heat-treatment are much larger than the values which are considered the effect of an internal field and equilibrium vacancy concentration (12, 13). Furthermore, their increases occur in the low concentration region, as shown in Fig. 1. Assuming that the arsenic profile is a complementary error function, the "average" effective diffusion coefficients of arsenic in the singly diffused samples were determined from the same procedure as for boron. This



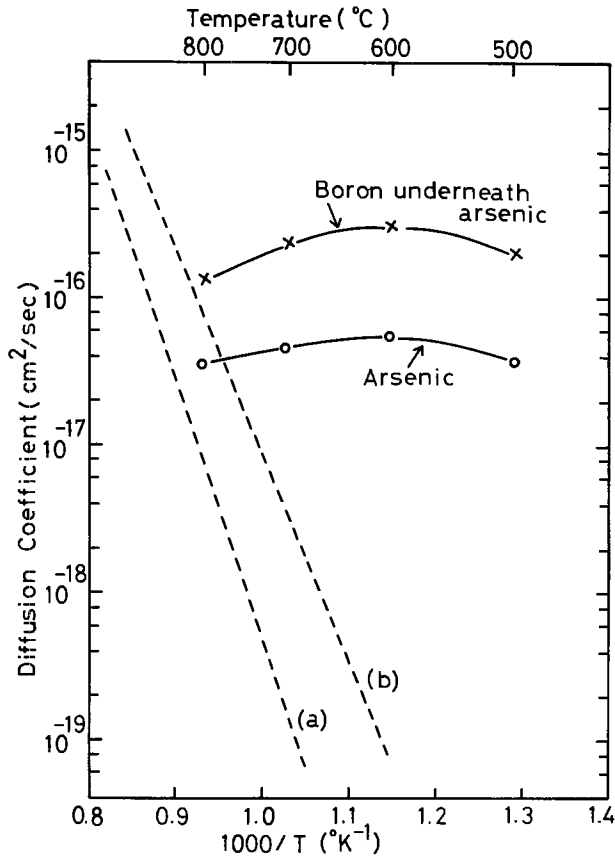


Fig. 6. Effective diffusion coefficient of arsenic and boron underneath the arsenic-diffused layer as a function of temperature. Heat-treatment is carried out for 24 hr in  $N_2$ . Dashed lines are diffusion coefficients extrapolated from high temperature data. (a) and (b) are the diffusion coefficients of arsenic and boron, respectively.

result is also plotted in Fig. 6. The value extrapolated from Fuller's data (15) which were determined by complementary error function is also shown in Fig. 6. The diffusivity of boron underneath the arsenic emitter has the same tendency as that of arsenic.

*The influence of low temperature heat-treatment on the JFET.*—It was clear in the above experiments that the boron diffusion underneath the arsenic-diffused layer was enhanced during low temperature heat-treatment. The influence of this abnormal diffusion on silicon devices was investigated using the JFET shown in Fig. 7. In this JFET, the arsenic- and boron-diffused layers act as the gate and the channel, respectively. Arsenic was diffused into the boron-diffused layer, of which the surface concentration and the junction depth are  $7 \times 10^{18} \text{ cm}^{-3}$  and  $1200\text{\AA}$ ; the values of the arsenic-diffused layer are  $2.4 \times 10^{20} \text{ cm}^{-3}$  and  $800\text{\AA}$ . The equation for current between source and drain in the JFET which had a nonuniform carrier profile in the channel was solved by Bockemuehl (16). The saturation current is a function of the carrier profile, channel height, and device dimensions. In this sample, the saturation current before heat-treatment is  $140\text{--}170 \mu\text{A}$ .

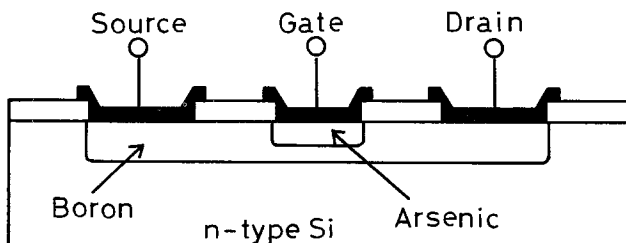


Fig. 7. Schematic cross section of JFET

Heat-treatments were carried out at  $500\text{--}800^\circ\text{C}$  for 24 hr. The results are shown in Fig. 8. The changes in saturation current are very large, and remarkable at  $600^\circ\text{C}$ . This result agrees with the diffusion coefficient in Fig. 6.

The heat-treatment over a long time was not carried out in the ordinary device processing. Therefore, the change in saturation current by heat-treatment for 30 min was measured. The result is shown in Fig. 9 as a function of temperature. The influence of low temperature heat-treatment on saturation current is considerable, and the saturation current is minimum at  $700^\circ\text{C}$ .

The electrical characteristics of the device are considerably changed by heat-treatment even for a short time. As a matter of course, the temperature at which the saturation current is minimum depends on treatment time.

**Discussion**

In a n-p-n transistor using phosphorus for the emitter, the boron base layer underneath the emitter is pushed out during the emitter diffusion. In the arsenic-boron system, a retardation of the boron base layer is generally observed. It is considered that this effect is caused by the internal electric field (7, 8), vacancy clustering, or divacancy formation (17) and ion pairing (18), for example. Recently, Fair (19, 20) suggested that the retardation effect was due to the formation of the vacancy-arsenic complex,  $(V_{Si}As_2)$ , which acted as a vacancy "sink." In the present study, the emitter dip effect was observed in the arsenic-boron system by low temperature heat-treatment. This phenomenon may be due to the abnormal behavior of arsenic during the heat-treatment.

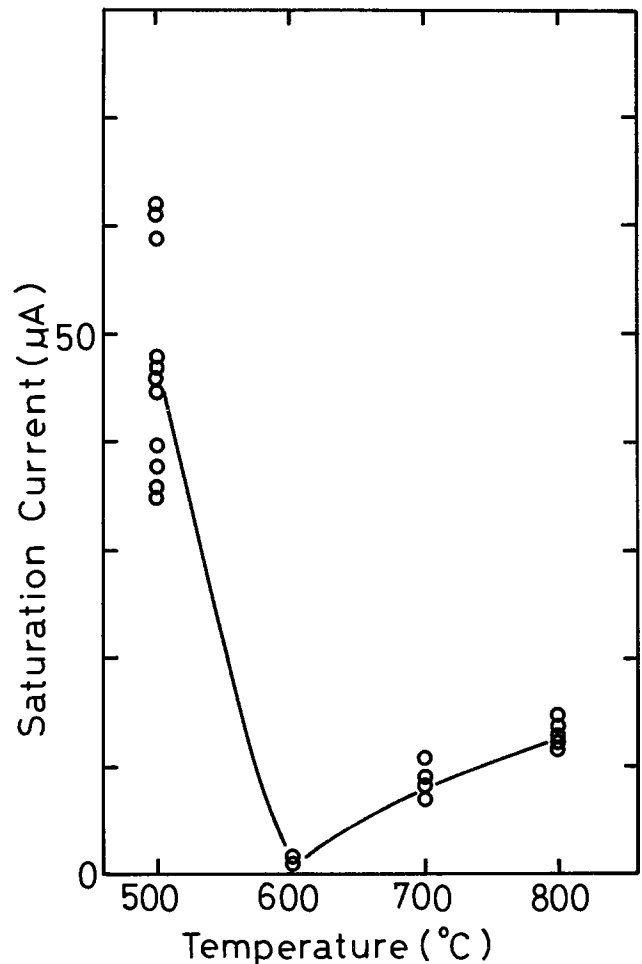


Fig. 8. Changes in saturation current of the JFET by low temperature heat-treatment. Initial saturation current is  $140\text{--}150 \mu\text{A}$ . Low temperature heat-treatment is carried out at  $500\text{--}800^\circ\text{C}$  for 24 hr in  $N_2$ .

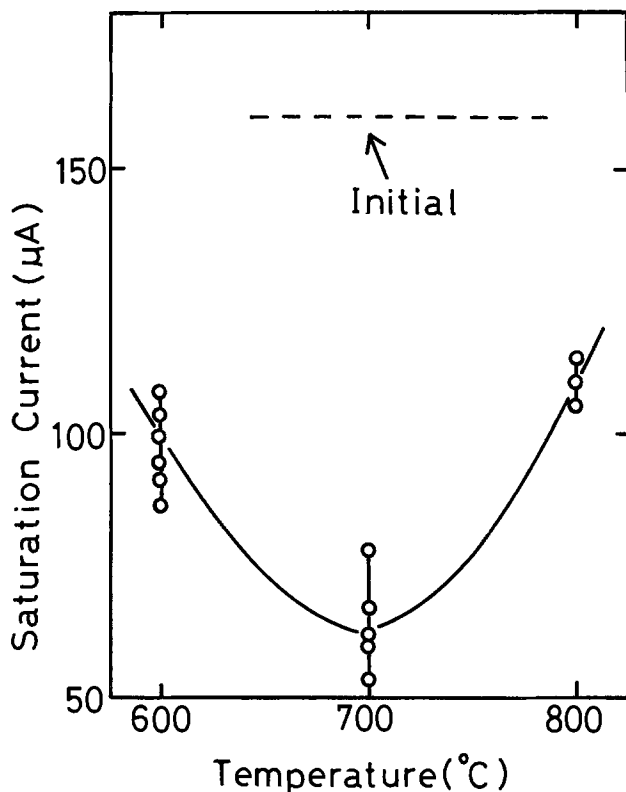


Fig. 9. Changes in saturation current during low temperature heat-treatment. Initial values are 150-170  $\mu\text{A}$ . Heat-treatment time is 30 min.

Various phenomena were observed by low temperature heat-treatment of heavily doped silicon with arsenic. The decreases of conductivity by the heat-treatment were observed, and were explained by a model of substitutional arsenic atoms becoming non-ionized upon clustering together, with one or more vacancies (2). An increase in both silicon- and arsenic-aligned yields during the heat-treatment was investigated by the channeling measurement using  $\text{He}^+$  ion, and this increase in aligned yields was due to the formation of the complex involving substitutional arsenic atoms, as predicted by Schwenker *et al.* (5). In the study using the x-ray double crystal diffraction technique, the lattice expansion due to the arsenic atom precipitation and SiAs formation was observed by the heat-treatment, and could not be observed in the arsenic concentration lower than  $1 \times 10^{20} \text{ cm}^{-3}$  (3). This result agrees with our diffusion data in Fig. 4. The transmission electron microscopic investigation was made on arsenic-doped silicon crystal, and the formation of prismatic dislocation loops during annealing at  $800^\circ\text{C}$  after quenching, which had an interstitial character, was observed (4). Similarly, Dash and Joshi (21, 22) also observed the arsenic precipitation and the interstitial dislocation loop in the arsenic-diffused silicon crystal.

In the present study, the diffusivity of arsenic is enhanced anomalously during low temperature heat-treatment. This effect depends on the treatment time and is extremely large in the beginning of the heat-treatment. This diffusivity is maximum at a particular temperature. As shown in Fig. 8 and 9, this temperature decreases as the heat-treatment time. Supposing the predominant mode of the arsenic diffusion in silicon is via vacancies, it is necessary to generate a large amount of excess vacancies in the beginning of the treatment and to increase excess vacancies with decreasing temperature.

The arsenic concentration in silicon probably exceeds the solid solubility limit during low temperature heat-treatment. The arsenic precipitation or the forma-

tion of the complex which involves arsenic is naturally expected. In this process, excess vacancies may be generated. It is also considered that the excess vacancies are generated when interstitial dislocation loops observed by the transmission electron microscope climb. These excess vacancies enhance the diffusion of arsenic and of boron underneath the arsenic-diffused layer.

The similarly enhanced diffusion of phosphorus during low temperature heat-treatment was observed (23, 24). In the case of phosphorus, the kink in the impurity profile in silicon depends remarkably on the temperature, but this kink is obscure in the case of arsenic. Compared with arsenic, the enhanced diffusion of phosphorus continues well after the decrease of the carrier concentration in the high concentration region stops. These phenomena are different from that of arsenic. Therefore, the mechanism may be a little different from that of arsenic.

### Conclusions

In this work, it was found that the diffusion of arsenic was extremely enhanced during low temperature heat-treatment. This anomalous diffusion is a function of the treatment temperature and time. Under a certain condition, the diffusivity of arsenic increases with decreasing temperature. Such anomaly depends on the arsenic concentration. The enhanced diffusion is hardly observed below  $1 \times 10^{20} \text{ cm}^{-3}$  in the surface concentration.

The abnormal behavior of arsenic by low temperature heat-treatment affects the diffusion of boron underneath the arsenic-diffused layer, and causes the emitter dip effect.

It is considered that this anomaly is caused by the generation of excess vacancies during such treatment. However, this mechanism is difficult to ascertain at this time, and further work is needed.

These phenomena have a bad influence on electrical characteristics such as the microwave transistor which are required to control the base width and concentration precisely.

### Acknowledgments

The authors wish to thank Dr. M. Maeda for useful discussions.

Manuscript submitted Sept. 22, 1975; revised manuscript received Jan. 23, 1976.

Any discussion of this paper will appear in a Discussion Section to be published in the December 1976 JOURNAL. All discussions for the December 1976 Discussion Section should be submitted by Aug. 1, 1976.

Publication costs of this article were partially assisted by Fujitsu Laboratories Limited.

### REFERENCES

1. H. Shibayama, H. Masaki, and H. Hashimoto, *Appl. Phys. Letters*, **27**, 230 (1975).
2. R. O. Schwenker, E. S. Pan, and R. F. Lever, *J. Appl. Phys.*, **42**, 3195 (1971).
3. N. Miyamoto, E. Kuroda, and S. Yoshida, Abstract 408, Proceedings of the 5th Conference (1973 International) on Solid State Devices, Tokyo (1973).
4. V. B. Osvenskii, L. M. Morgulis, S. P. Grishina, and N. M. Klimova, *Sov. Phys. Solid State*, **11**, 1064 (1969).
5. J. Haskell, E. Rimini, and J. W. Mayer, *J. Appl. Phys.*, **43**, 3425 (1972).
6. J. C. Irvin, *Bell Syst. Tech. J.*, **41**, 387 (1962).
7. S. M. Hu and S. Schmidt, *J. Appl. Phys.*, **39**, 4272 (1968).
8. M. Okamura, *Japan. J. Appl. Phys.*, **7**, 1231 (1968).
9. J. F. Ziegler, G. W. Cole, and J.E.E. Baglin, *Appl. Phys. Letters*, **21**, 177 (1972).
10. H. Nakamura, S. Ohyama, and C. Tadachi, *This Journal*, **121**, 1377 (1974).
11. B. J. Masters and J. M. Fairfield, *J. Appl. Phys.*, **40**, 2390 (1969).
12. R. B. Fair, *ibid.*, **43**, 1278 (1972).

13. Y. Nakajima, S. Ohkawa, and Y. Fukukawa, *Japan. J. Appl. Phys.*, **10**, 162 (1971).
14. R. N. Ghoshtagore, *Phys. Rev. B*, **3**, 389 (1971).
15. C. S. Fuller and J. A. Ditzenberger, *J. Appl. Phys.*, **27**, 544 (1956).
16. R. R. Bockemuehl, *IEEE Trans. Electron. Devices*, **ED-10**, 31 (1963).
17. S. M. Hu and T. H. Yeh, *J. Appl. Phys.*, **42**, 2153 (1971).
18. H. Reiss, C. S. Fuller, and F. J. Morin, *Bell Syst. Tech. J.*, **35**, 535 (1956).
19. R. B. Fair, *J. Appl. Phys.*, **44**, 283 (1973).
20. R. B. Fair, *Appl. Phys. Letters*, **22**, 186 (1973).
21. M. L. Joshi and S. Dash, *IBM J. Res. Develop.*, **11**, 271 (1967).
22. S. Dash and M. L. Joshi, *ibid.*, **14**, 453 (1970).
23. F. N. Schwettmann and D. L. Kendall, *Appl. Phys. Letters*, **19**, 218 (1971).
24. F. N. Schwettmann and D. L. Kendall, *ibid.*, **21**, 2 (1972).

## Burning and Extinction of a Laser-Ignited Carbon Particle in Quiescent Mixtures of Oxygen and Nitrogen

Shivadev K. Ubhayakar<sup>1</sup> and Forman A. Williams

*Department of Applied Mechanics and Engineering Sciences,  
University of California, San Diego, La Jolla, California 92093*

### ABSTRACT

Experimental data on the burning mode and lifetime, on the surface temperature, and on the spontaneous extinction of a laser-ignited particle of electrode carbon (50-200 $\mu$ ) in quiescent mixtures of oxygen and nitrogen at room temperature are presented. The test variables were the oxygen mass fraction (0.5-1) and the pressure (0.5-3 atm) of the mixture. High speed cinematography of the burning particle showed that the visible combustion zone was restricted to the surface. Two theoretical models, one neglecting the dissociation of oxygen and the other including it approximately, are developed in order to explain the extinction phenomenon. Comparison of the extinction results computed from these models with the data indicates that the model neglecting dissociation is the preferred one. Based on this model it is shown that the kinetics of oxidation of electrode carbon in the temperature range 2000°-3500°K can be represented by an effective Arrhenius surface oxidation reaction producing CO and having an activation energy of 18 kcal/mole and an order in the range 0.5-1.

The oxidation of carbon has been one of the most widely studied topics in the field of combustion, and yet there remains a paucity of data on the burning of submillimeter particles in quiescent oxidizing atmospheres. About two decades ago Spalding (1, 2) proposed two models for the burning of spherical carbon particles, one of which assumed a CO-O<sub>2</sub> gas-phase reaction producing CO<sub>2</sub> which in turn oxidizes carbon heterogeneously at its surface, while the other assumed a heterogeneous surface reaction of O<sub>2</sub> with carbon producing CO and/or CO<sub>2</sub>. To date, there exist no experimental data to confirm the validity of either of these two models for small carbon particles. Furthermore, there has been much discussion of the fact that large carbon spheres often burn by a mechanism that involves diffusion and reaction within the pores (3, 4). Therefore, an initial objective of the present study was to ascertain whether a gas phase burning mechanism or a surface burning mechanism, possibly accompanied by pore diffusion, occurs for submillimeter particles. An additional objective was to obtain burning duration data of improved accuracy.

High speed cinemicrography soon demonstrated that the burning zone is restricted to the surface and/or interior of the particle. In addition, disagreement of burning duration data with the theory of diffusion-controlled droplet burning led eventually to the discovery of an extinction phenomenon in which the combustion ceases abruptly after the particle burns to a critical size, which depends on the oxygen mass fraction and the total pressure of the ambient mixture. Since the

existence of extinction raised hope of extracting fundamental kinetic data, extinction sizes and burning durations were measured for different ambient conditions.

Attempts to develop theoretical explanations for the extinction data presented here consistently led to predictions of particle temperatures in excess of 2000°K, well above the temperature ranges in which voluminous data (4-11) on the oxidation of various forms of carbon exist. The previous data exhibited activation energies that for the most part tended to decrease with increasing temperature, becoming very near or even less than zero (7, 8, 12) at the highest temperatures. This shed doubt on the particle temperatures inferred theoretically, since the phenomenon of sudden extinction disappears at zero or negative activation energies.

In order to check temperature estimates it was deemed desirable to develop an independent experimental method for measuring the surface temperature of the burning particle. A technique of two-color optical pyrometry was devised and applied to establish that temperatures were in the range 2000°-3500°K, thereby supporting the theoretical estimates. These results along with the extinction data confirmed our original inference (13) of a nonzero positive activation energy of about 21.5 kcal/mole at temperatures exceeding 2000°K. In this respect, it is interesting that the activation energy of soot oxidation recently measured by Park and Appleton (14) at oxygen partial pressures around 0.1-0.5 atm in the temperature range 2200°-4000°K appears to be about 16 kcal/mole, a value near our result on electrode carbon.

The foregoing experimental techniques, data, and theoretical ideas are described in detail in the following sections.

<sup>1</sup>Present address: Avco Everett Research Laboratory, Incorporated, Everett, Massachusetts 02149.

Key words: carbon, heterogeneous oxidation, extinction, activation energy, order of reaction.

### Experiment

The carbon particles for the tests were obtained by grinding in a mortar a rod of electrode carbon manufactured by National Carbon Company and sieving the powder into different sizes in the range 50-200 $\mu$ . The density of the particles was measured as follows. A rod of electrode carbon was weighed, dunked in water to obtain the displaced volume, immediately removed from the water, wiped clean, and reweighed. The initial and final weights differed by less than 3%, the increment resulting from the absorbed water. The weight to displaced volume ratio was 1.5 g/cm<sup>3</sup>. It was assumed that the ground particles have the same density as the rod. This assumption was supported qualitatively by visual observation of the surface of the original carbon rod and one of the ground particles under a microscope; there was no observable structural difference. Since the density of graphite is 2.25 g/cm<sup>3</sup>, the particles were about 33% porous. The composition of the particles was measured with an Ortec Delphi x-ray energy spectrometer. The analysis yielded the following sulfur 0.5%, traces (ppm) of calcium and iron, the rest carbon. Figure 1a shows scanning electron micrographs of a typical particle. Only those particles which were nearly spherical in shape were selected from the size-graded powder. After mounting a particle in the apparatus, its three major dimensions were measured under a stereomicroscope. The cube root of their product was taken to be the diameter of an equivalent sphere.

The experimental apparatus to study the combustion of submillimeter particles has been described by Wilson and Williams (15). Here we briefly point out its essential features. A carbon particle is mounted at the bottom tip of a vertically hanging glass fiber, about 25 $\mu$  in diameter with the aid of a speck of grease

(less than 5% of the volume of the particle) as an adhesive. The particle and the fiber are enclosed in a metal bell jar about 18 cm in diameter, 25 cm high, with 4 quartz windows on the circumference at right angles. The atmosphere within the jar is at room temperature, and its pressure and oxygen mass fraction are preset to desired values. For the tests reported here, industrial grade mixtures of oxygen and nitrogen having less than 30% relative humidity were used. Light from a pulsed ruby laser, with maximum rated energy output of 35 joules, is focused onto the particle through one of the windows. A concave mirror re-focuses the laser energy emerging from the opposite window such that the particle receives approximately equal radiant flux on both sides. The laser pulse ignites the particle, and the particle detaches from the glass fiber and falls downwards, because of gravity, as it burns. It is reasonable to assume that the speck of grease used for mounting the particle ignites and is dispersed before the particle starts burning. The ignition and the burning sequences were observed visually through a green filter having a 0.01  $\mu$ m bandwidth which cut off all harmful light of the laser frequency and were recorded by a high speed "Hycam" 16 mm movie camera. The burning duration is measured with reference to timing marks recorded synchronously on the film edge. Laser-based techniques of this general type were developed independently by a number of investigators, notably Marshall, Nelson, Prentice, and Wilson, all beginning at about the same time (1965); see, for example, Ref. (16-18).

Preliminary tests in air at atmospheric pressure showed that a particle with equivalent sphere diameter in the range 50-200 $\mu$  could not sustain combustion and extinguished a few milliseconds after the ignition pulse. This was verified by collecting the extinguished

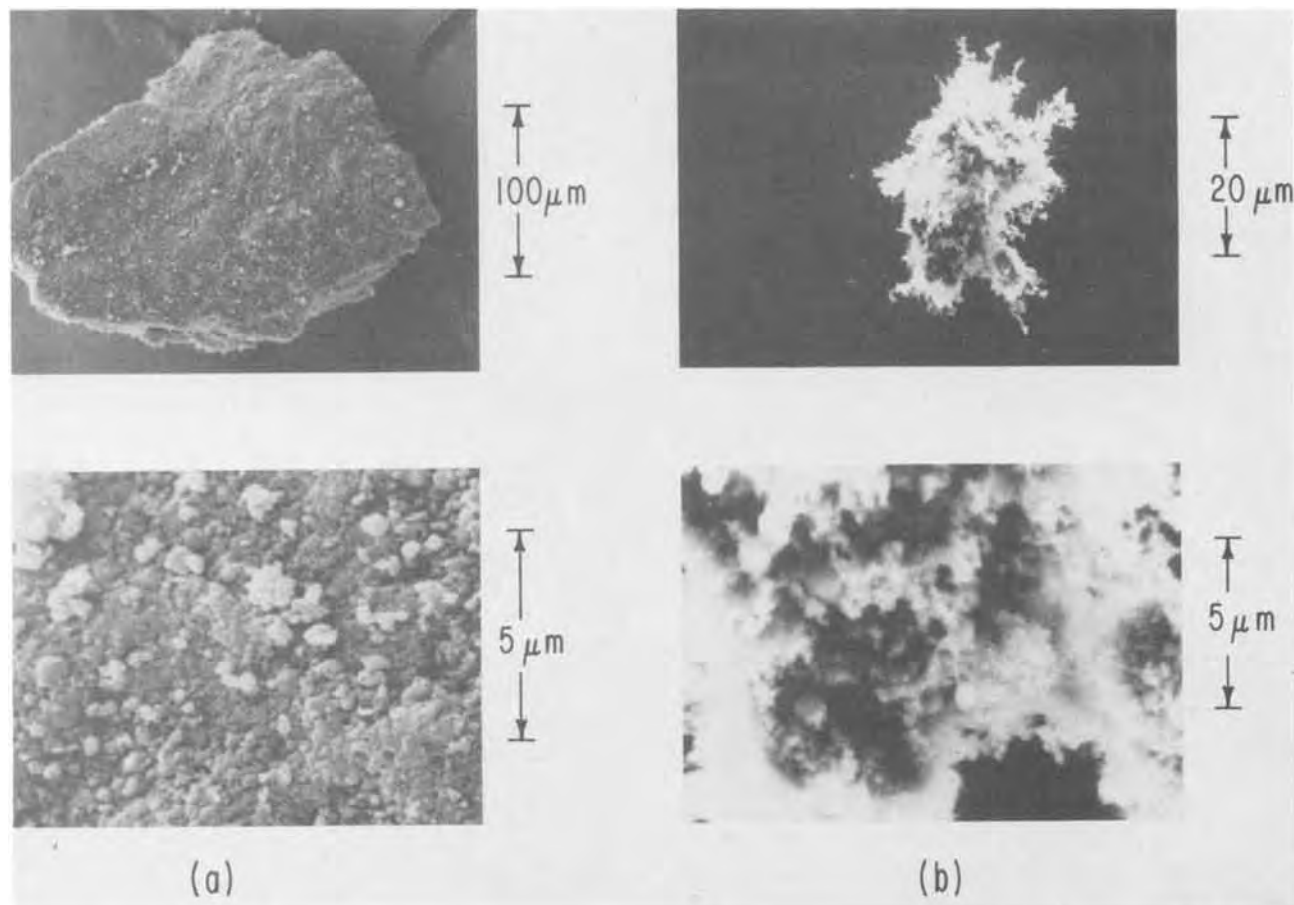


Fig. 1. Scanning electron micrographs of (a) an unburnt particle of electrode carbon and (b) a particle after it extinguished spontaneously while burning in pure oxygen at 0.75 atm.

particle on a large, clean, white sheet of cardboard placed a few inches under the particle. The laser energy could be set high enough to raise the particle temperature to nearly 4500°K, its vaporizing temperature. Despite such high ignition pulses, the particle extinguished without any significant burning. However, tests in oxygen-enriched atmospheres of oxygen mass fraction greater than 0.6 at a pressure of 1 atm displayed sustained combustion as the particle fell downwards. Visual observation of the burning showed that the particle burned intensely, without any noticeable change in the intensity of light emission, until it suddenly disappeared from view. Initially it was thought that the particle burned completely, but careful examination of the cardboard placed under the particle, far below its point of disappearance, revealed a tiny speck about 20 $\mu$  in diameter. Evidently the disappearance of the particle signifies extinction rather than complete consumption.

Further tests showed that the extinction diameter  $d^*$  increased with decreasing oxygen mass fraction  $Y_{O_2}$  and decreasing pressure  $p$ ; for any particular  $Y_{O_2}$  and  $p$ ,  $d^*$  was the same, within a certain scatter band, regardless of the initial size of the particle. Scanning electron micrographs of a typical extinguished residue are shown in Fig. 1b, where a highly porous, flakelike structure is evident. The circles in Fig. 2 show the mea-

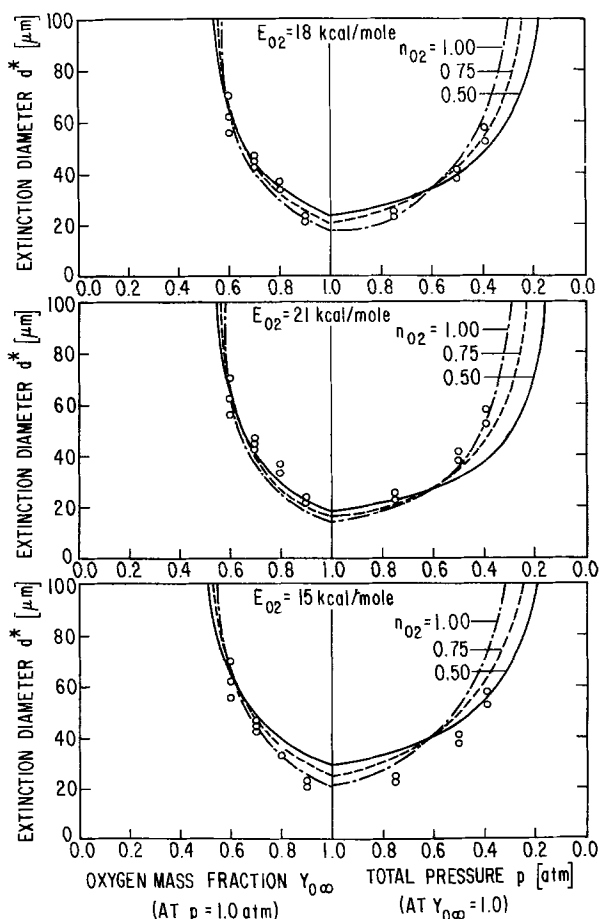


Fig. 2. Extinction diameters shown by the circles. The lines represent extinction diameters computed from Eq. [15], model 1, assuming the activation energies and orders as shown. The values of the preexponential factors (with orders in parentheses) computed to give  $d^* = 65 \mu\text{m}$  at  $Y_{O_2} = 0.6$  and  $p = 1 \text{ atm}$  are the following. Top:  $E_{O_2} = 18 \text{ kcal/mole}$ ,  $k_{O_2}(0.5) = 799 \text{ g}^{0.5}/\text{cm}^{0.5}\text{-sec}$ ,  $k_{O_2}(0.75) = 1.08 \times 10^4 (\text{g-cm})^{0.25}/\text{sec}$ ,  $k_{O_2}(1) = 1.38 \times 10^5 \text{ cm/sec}$ . Middle:  $E_{O_2} = 21 \text{ kcal/mole}$ ,  $k_{O_2}(0.5) = 1561 \text{ g}^{0.5}/\text{cm}^{0.5}\text{-sec}$ ,  $k_{O_2}(0.75) = 2.2 \times 10^4 (\text{g-cm})^{0.25}/\text{sec}$ ,  $k_{O_2}(1) = 2.91 \times 10^5 \text{ cm/sec}$ . Bottom:  $E_{O_2} = 15 \text{ kcal/mole}$ ,  $k_{O_2}(0.5) = 400 \text{ g}^{0.5}/\text{cm}^{0.5}\text{-sec}$ ,  $k_{O_2}(0.75) = 5.12 \times 10^3 (\text{g-cm})^{0.25}/\text{sec}$ ,  $k_{O_2}(1) = 6.18 \times 10^4 \text{ cm/sec}$ .

sured extinction data; here the data are shown repeatedly in three sets in order to avoid clutter of the comparative theoretical results which are derived later. In this figure we note that at 1 atm the extinction diameters increase rapidly with decreasing  $Y_{O_2}$  for  $Y_{O_2}$  less than 0.6. This indicates that air at a pressure of 1 atm is beyond the extinction limit for particles of this size. In pure oxygen at  $p \cong 1 \text{ atm}$ , the extinguished particles could not be detected either because they were too small to be caught or because they burnt completely.

Motion pictures of the burning sequences were taken for various values of  $Y_{O_2}$  and  $p$ . Figure 3 shows an eight-frame sequence of a typical film strip. The time interval between the bright lines on the left margin is 1 msec. The intense flash in the first frame is due to the laser; the top of the hot probe is visible in the second frame. From such films the velocity of fall of each particle was measured to be in the range 5-50 cm/sec. While burning, the particle appears as a bright spot on the film, retaining its original shape, and no gas-phase flame is seen on the film. Gas-phase flames were not registered on the film for any of the various values of  $Y_{O_2}$  and  $p$ . This suggests that the burning zone is restricted to the surface and that a gas-phase reaction between CO and  $O_2$  does not occur outside the particle.

The surface temperature history of the burning particle was measured by two-color optical pyrometry. The technique is well known (19), including its application in situations requiring short time resolution (20-22), the principal potential difficulty being influences of band radiation (19). Based on Wien's approximation for Planck's radiation equation for a thermally radiating surface, the temperature of the surface is uniquely determined by the ratio of intensities at any two wavelengths

$$\frac{J_1}{J_2} = \frac{\epsilon_1}{\epsilon_2} \left( \frac{\lambda_2}{\lambda_1} \right)^5 \exp \left[ \frac{C}{T_s} \left( \frac{1}{\lambda_2} - \frac{1}{\lambda_1} \right) \right] \quad [1]$$

where  $\lambda_{1,2}$  are the two wavelengths,  $\epsilon_{1,2}$  are the spectral emissivities of the surface at  $\lambda_{1,2}$ ,  $T_s$  is the surface temperature,  $C$  is Planck's second radiation constant equal to 14,388 ( $\mu\text{m}^\circ\text{K}$ ), and  $J_{1,2}$  are the intensities at  $\lambda_{1,2}$ . If the emitting surface is gray then  $\epsilon_1/\epsilon_2 = 1$ ; this is a good approximation when the two wavelengths  $\lambda_{1,2}$  are chosen close to each other. With known values of  $\lambda_{1,2}$  and the measured ratio  $J_1/J_2$ , the surface temperature  $T_s$  can be evaluated from Eq. [1]. This method is accurate if only the thermal radiations from the particle surface are metered.

The experimental arrangement using this technique to measure the temperature history of a burning carbon particle is shown schematically in Fig. 4. The particle is located at the center of the chamber. The light emanating from the burning particle is partially focused by a convex lens and split into two beams by a thin glass sheet. These two beams pass through narrow band filters of wavelengths  $\lambda_1$  and  $\lambda_2$  as shown. Each beam of filtered light falls on the active surface of a phototube. By partially focusing the beams, the effect of movement of the burning particle is eliminated since the surface area of the filter is uniformly illuminated irrespective of the position of the particle. One of the phototubes has a variable gain control for calibration purposes. The outputs from the two phototubes are fed to a dual-beam storage oscilloscope set for a single sweep. The laser console switch triggers the ignition pulse as well as the oscilloscope simultaneously. From the stored traces of intensities registered on the oscilloscope the ratio  $J_1/J_2$  is obtained as a function of time. This ratio history is reevaluated in terms of the surface temperature history by using Eq. [1].

The foregoing technique is prone to errors because the intensities measured by the phototubes may in-



Fig. 3. Initial segment of a typical film strip of a carbon particle burning in pure oxygen at 1 atm pressure. Initial size of the particle was about  $100 \times 130 \times 130 \mu\text{m}$ . Magnification on the 1.6 cm wide film is 2.32. Time runs top to bottom. Initial bright region represents the laser pulse. Timing marks on the left edge are spaced 1 msec apart.

clude, in addition to the thermal contribution, the band emissions from any of the gases in the combustion zone. Since the nature of these gases at the surface of the burning carbon particle is not known, an effective way of checking the validity of this technique is to choose two or more pairs of wavelengths. If the

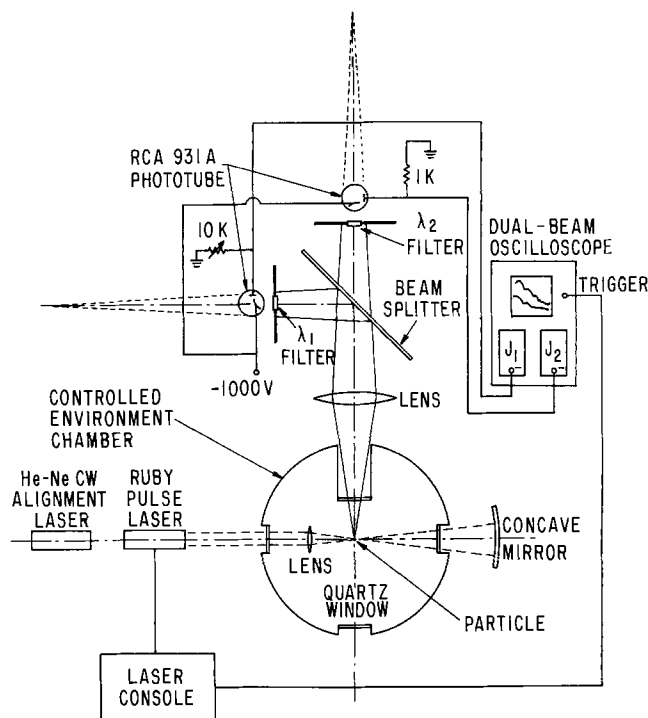


Fig. 4. Schematic diagram for the test arrangement for surface temperature measurement.

temperatures measured for these pairs under the same experimental conditions are the same within the experimental scatterband, then the results can be accepted. Therefore, all the tests were conducted using two pairs of wavelengths:  $\lambda_{1,2} = 0.4393, 0.5203 \mu\text{m}$  and  $0.5203, 0.6000 \mu\text{m}$ , each centered within a bandwidth of  $0.01 \mu\text{m}$ .

A General Electric tungsten ribbon lamp was used for calibration of the test setup. The ribbon was positioned at the same location as the particle, and its intensity was adjusted to any desired level by an auto-transformer input. The brightness temperature of the ribbon was measured by a Leeds and Northrup disappearing filament optical pyrometer. Using the conversion chart given in the report by Rutgers and DeVos (23), the true surface temperature of the ribbon was obtained, and the ratio  $J_1/J_2$  was evaluated from Eq. [1]. Then the gain of the phototube 1 was adjusted such that the ratio of the two intensities registered on the oscilloscope was equal to the evaluated ratio. With the same gain adjustment the temperatures at other ribbon intensities were then checked from the measured intensity ratios. The agreement was within 6% of the temperature measured by the optical pyrometer. The temperature range of calibration was  $1800^\circ\text{--}2700^\circ\text{K}$ .

The spectral emissivity data on carbon given by Touloukian and DeWitt (24) was used to calculate  $\epsilon_1/\epsilon_2$ . This ratio was about 1.04 for the two pairs of wavelengths chosen, thereby justifying the gray surface approximation.

A typical oscilloscope trace is shown in Fig. 5. Here the oscillations in the intensities are caused by the oscillations in the projected area of the randomly rotating nonspherical particle as "seen" by the focusing lens. Were the particle perfectly spherical, there would not have been oscillations. The ratio of the intensities at any instant determines the surface temperature  $T_s$ . It was observed that the temperatures measured by the chosen two pairs of wavelengths were within the experimental scatterband. We therefore infer that the errors in the temperature measurements caused by any band emissions from the gases at the surface of the burning particle were probably negligible. Figure 6 shows the measured surface temperature  $T_s$  as a func-

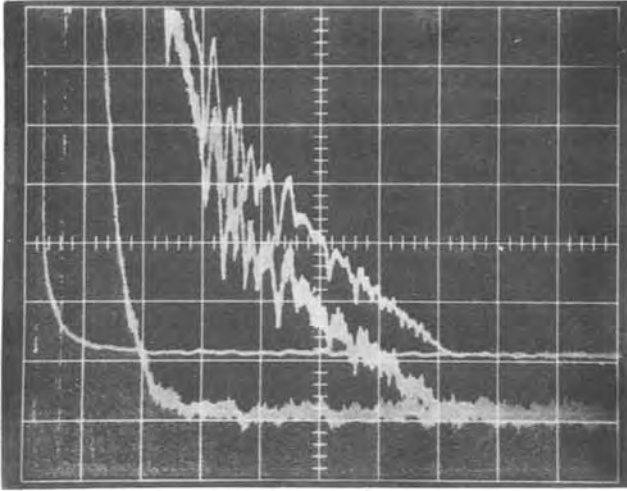


Fig. 5. Oscilloscope traces of the outputs of the two phototubes. The two leftmost curves ending horizontally are the traces of the laser pulse; the horizontal regions serve as base lines for intensity measurements. Horizontal scale is 10 msec per division. Initial size of the particle was  $100 \times 120 \times 120 \mu\text{m}$ . Bottom trace is  $J_1$  and the top trace is  $J_2$ . Actual  $J_1/J_2 = 0.375 \times$  (measured  $J_1/J_2$ ) where 0.375 is the calibration factor.  $\lambda_{1,2} = 0.4393, 0.5203 \mu\text{m}$ .

tion of time  $\tau^*$  prior to extinction. Here despite the scatter we note that in pure oxygen, higher pressure corresponds to higher temperature. Also, all measured temperatures are above  $2000^\circ\text{K}$ .

In Fig. 5 the average intensity is seen to decrease linearly with time. Since the intensity is proportional to the projected area ( $\propto d^2$ ) of the particle, we infer that the square of the diameter decreases approximately linearly with time; this inference is accurate only if the surface temperature does not change with time. Indeed it is seen that this is true within the scatter-band shown in Fig. 6 for each test condition.

Figure 7 shows the burning duration  $\tau^*$  as a function of the initial diameter  $d^0$  of the particle. These data were obtained from the movie film strips by measuring the time interval between the ignition pulse (which lasted about 0.5 msec) and the last frame in which the particle is registered. The oscilloscope traces also yielded the burning durations. In this figure the data points suggest again that the square of the diameter decreases approximately linearly with time. If we compare the data points for  $Y_{O_2}^* = 0.6$  and  $p = 1$  atm with those for  $Y_{O_2}^* = 1$  and  $p = 1$  atm, we observe that the burning duration in pure oxygen is longer than that in lower  $Y_{O_2}$  atmospheres for a fixed initial diameter. This apparent anomaly can be explained by the fact that an

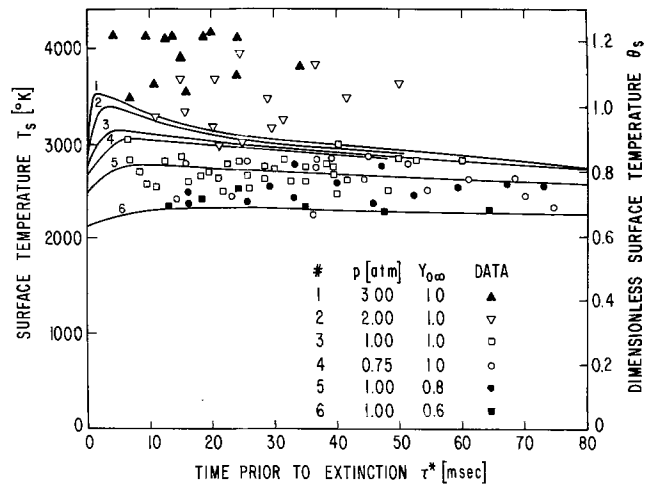


Fig. 6. Surface temperature histories. Full lines computed from Eq. [13]-[15], model 1, for  $n_{O_2} = 0.5$ ,  $E_{O_2} = 18$  kcal/mole,  $k_{O_2} = 799 \text{ g}^{0.5}/\text{cm}^{0.5}\text{-sec}$ , using other data from Table I.

earlier extinction at a larger diameter for a lower  $Y_{O_2}^*$  atmosphere makes the burning duration for the same initial diameter shorter.

The nearly linear decrement of the square of the diameter with time prior to extinguishment suggests a diffusion-controlled burning, whereas the phenomenon of spontaneous extinction must be caused by a slower reaction at the surface. Furthermore, extinction conditions are approached as the size of the particle decreases. Therefore, during the lifetime of a particle the burning mechanism initially is diffusion controlled, but as the size decreases the reaction rate becomes smaller than the diffusion rate, thereby ultimately forcing an extinction.

### Theory

In a recent paper Ubhayakar (25) has analyzed the burning and extinction characteristics of a spherical particle gasified at its surface by oxidant diffusing from the surrounding quiescent gas mixture. Assuming an Arrhenius first-order reaction at the surface with respect to oxygen, he derived theoretically the burning and extinction characteristics. This theory is a segment of a more detailed analysis on carbon particles by Ubhayakar and Williams (13) which includes the dissociation of oxygen as its approaches the hot surface. We present here this analysis and point out the effects of dissociation of oxygen and of the order and activation energy of the surface reaction on the burning and extinction characteristics. The symbols appearing in this section, their definitions and dimensions, are listed

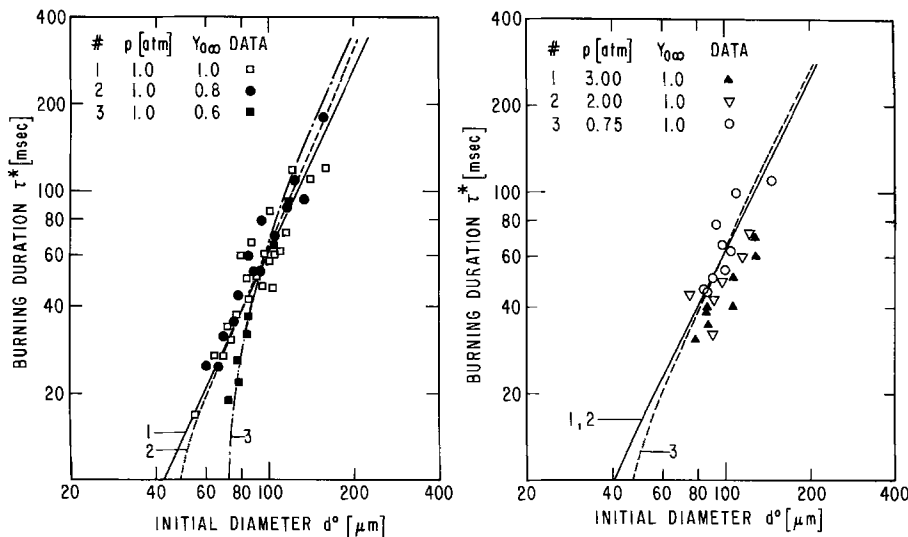


Fig. 7. Burning duration as a function of the initial diameter. Lines computed from Eq. [13]-[15], model 1, for  $n_{O_2} = 0.5$ ,  $E_{O_2} = 18$  kcal/mole,  $k_{O_2} = 799 \text{ g}^{0.5}/\text{cm}^{0.5}\text{-sec}$ , using other data from Table I.



at the end of the paper. While developing the results a number of simplifying assumptions or approximations are made. These are numbered in order to highlight their significance.

(i) The particle is spherical and its velocity of fall (5-50 cm/sec) has little influence on the diffusion flow fields; spherical symmetry is assumed. (ii) For any fixed diameter all flow and reaction conditions are steady, that is, the particle is assumed to burn quasi-steadily. (iii) The particle is isothermal at its surface temperature  $T_s$ . (iv) The ambient mixture of oxygen and nitrogen is at constant temperature  $T_\infty$ , constant oxygen mass fraction  $Y_{O_2}$ , and constant pressure  $p$ . (v) The dissociation of nitrogen is negligible since it is significant only at temperatures exceeding 5000°K (26). (vi) Part of the oxygen diffusing inward may dissociate, in which case the molecular and atomic oxygen equilibrate instantly at any temperature. (vii) The properties  $\rho D$ ,  $\lambda$ , and  $c$  for each species are the same and constant. (viii) The gas mixture and its components behave as ideal gases. (ix) The total emissivity of the particle surface and of the surroundings have an equal and constant value of  $\epsilon$ , and the gases surrounding the particle are radiatively non-participating. (x) The atomic and molecular oxygen arrive stoichiometrically at the surface and react to form CO at a rate per unit area equal to

$$k_O(\rho_s Y_{O_s})^{n_O} \exp(-E_O/RT_s) + k_{O_2}(\rho_s Y_{O_2s})^{n_{O_2}} \exp(-E_{O_2}/RT_s)$$

(xi) These Arrhenius rates are the effective rates in the surface temperature range of the burning particle and include effects of the surface area per unit projected area of the particle (Fig. 1b) as well as any influence of reaction during diffusion within the porous subsurface; nevertheless the effective kinetic parameters  $k_O$ ,  $E_O$ ,  $n_O$ ,  $k_{O_2}$ ,  $E_{O_2}$ , and  $n_{O_2}$  are taken to be constant. (xii)  $CO_2$  production is neglected because it is known (4, 5) that at the measured high temperatures in excess of 2000°K the product of carbon oxidation is primarily CO; the CO produced is assumed to diffuse outwards without further reaction.

Including Fickian diffusion and Stefan flux from the surface, the mass flow rate for each species is

$$m_i = mY_i - 4\pi r^2 \rho D (dY_i/dr) \quad [2]$$

where  $i \equiv O, O_2, CO, \text{ or } N_2$ . The conservation equation for energy is (13, 25)

$$\sum_i m_i [c(T - T_s) - q_i] - 4\pi r^2 \lambda (dT/dr) = -\pi d^2 \epsilon \sigma (T_s^4 - T_\infty^4) \quad [3]$$

The rates of consumption of oxygen atoms and molecules at the surface are equal to their respective rates of arrival at the surface

$$-(m_O + m_{O_2}) = \pi d^2 [k_O(\rho_s Y_{O_s})^{n_O} \exp(-E_O/RT_s) + k_{O_2}(\rho_s Y_{O_2s})^{n_{O_2}} \exp(-E_{O_2}/RT_s)] \quad [4]$$

It is more convenient to write the preceding equations in terms of total oxygen ( $\bar{O}$ ). We therefore define a dissociation fraction  $Z = Y_O/(Y_O + Y_{O_2}) = Y_O/Y_{\bar{O}}$ . Then  $Y_O = ZY_{\bar{O}}$ ,  $Y_{O_2} = (1 - Z)Y_{\bar{O}}$ , and  $Y_{\bar{O}} + Y_{CO} + Y_{N_2} = 1$ . Owing to stoichiometry we have  $m_{\bar{O}} = m_O + m_{O_2} = -(\nu - 1)m$ ,  $m_{CO} = \nu m$ , and  $m_{N_2} = 0$ . Also, by definition heats of formation are  $q_{O_2} = q_{N_2} = 0$ . Using the preceding relations we write Eq. [2]-[4] in the following dimensionless forms

$$\nu M = MY_{CO} - \eta^2 (dY_{CO}/d\eta) \quad [5]$$

$$-(\nu - 1)M = MY_{\bar{O}} - \eta^2 (dY_{\bar{O}}/d\eta) \quad [6]$$

$$M(\theta - \theta_s) - \nu M + Q_0[(\nu - 1)ZM + \eta^2 Y_{\bar{O}}(dZ/d\eta)] - \eta^2 \text{Le}(d\theta/d\eta) = G \text{Le}(\theta_s^4 - \theta_\infty^4) \quad [7]$$

$$(\nu - 1)M = K_O(\alpha Z Y_{\bar{O}}/\theta)^{n_{O_2}} \exp(-\beta_O/\theta_s) + K_{O_2}(\alpha(1 - Z)Y_{\bar{O}}/\theta)^{n_{O_2}} \exp(-\beta_{O_2}/\theta_s) \quad [8]$$

where the equation of state  $p = R\rho T(Y_O/W_O + Y_{O_2}/W_{O_2} + Y_{CO}/W_{CO} + Y_{N_2}/W_{N_2}) = R\rho T/(\alpha W_{O_2})$  has been used in Eq. [4], with  $\alpha = [(W_{O_2}/W_O - 1)ZY_{\bar{O}} + (W_{O_2}/W_{CO} - 1)Y_{CO} + W_{O_2}/W_{N_2}]^{-1}$  and  $(dZ/d\eta) = (\partial Z/\partial \theta)(d\theta/d\eta) + (\partial Z/\partial Y_{\bar{O}})(dY_{\bar{O}}/d\eta) + (\partial Z/\partial Y_{CO})(dY_{CO}/d\eta)$ . Here  $Z$ ,  $(\partial Z/\partial \theta)$ ,  $(\partial Z/\partial Y_{\bar{O}})$ , and  $(\partial Z/\partial Y_{CO})$  are known functions of  $\theta$ ,  $Y_{\bar{O}}$ , and  $Y_{CO}$ , and are derived in the Appendix.

The known boundary conditions at  $\eta \rightarrow \infty$  are  $Y_{CO}(\infty) = 0$ ,  $Y_{\bar{O}}(\infty) = Y_{O_2}$ , and  $\theta(\infty) = \theta_\infty$ . Equations [5] and [6] with the first two boundary conditions are readily integrable, whereas Eq. [7] is not because of the nonlinear terms. The solutions  $Y_{\bar{O}}(\eta)$  and  $Y_{CO}(\eta)$  may be substituted into Eq. [7] to obtain a nonlinear first-order differential equation in  $\theta$  which, in principle, can be solved. However, since  $M$  and  $\theta_s$  are the unknown eigenvalues of the problem, and since they have to be determined from the boundary conditions at infinity and at the surface given by Eq. [8], the problem is too complicated to solve exactly analytically. We shall therefore consider two limiting models to extract useful information from these limiting equations by introducing additional simplifying approximations and assumptions. A reasonable further approximation is (xiii)  $W_{O_2} = 2W_O \simeq W_{CO} = W_{N_2}$ , which produces  $\alpha = (ZY_{\bar{O}} + 1)^{-1}$ .

### Model 1

In this model the effects of dissociation are neglected. This may be reasonable if the surface temperatures are less than about 4000°K (at which  $Z \sim 0.5$ , cf., Appendix) and the reaction of molecular oxygen with carbon is dominant. Then  $Z$  and all its derivatives will be zero,  $\alpha = 1$ , and consequently Eq. [7] becomes integrable. Equations [5]-[7] are solved subject to the boundary conditions at infinity to produce the following relations at surface conditions

$$M = -\ln(1 - Y_{COs}/\nu) \quad [9]$$

$$M = -\ln[(\nu - 1 + Y_{\bar{O}s})/(\nu - 1 + Y_{O_2}^*)] \quad [10]$$

$$M = \text{Le} \ln [1 + \{M(\theta_s - \theta_\infty)/(M\nu - G \text{Le}(\theta_s^4 - \theta_\infty^4))\}] \quad [11]$$

Equation [8] simplifies to

$$M = [K_{O_2}/(\nu - 1)][Y_{\bar{O}s}/\theta_s]^{n_{O_2}} \exp(-\beta_{O_2}/\theta_s) \quad [12]$$

The eigenvalues  $M$ ,  $Y_{COs}$ ,  $Y_{\bar{O}s}$ , and  $\theta_s$  may now be obtained from Eq. [9]-[12] since the following are presumed to be known:  $\text{Le}$  (physical property of the gases),  $\theta_\infty$ ,  $Y_{O_2}^*$  (ambient),  $\nu$ ,  $K_{O_2}$ ,  $\beta_{O_2}$ , and  $n_{O_2}$  (reaction) and  $G$  (radiation). Here the reaction number  $K_{O_2} \propto p^{n_{O_2}d}$  and the radiation number  $G \propto d$ . The solutions therefore depend on the particle size which decreases as the particle burns. The phenomenon of spontaneous extinction brought about by decreasing diameter  $d$  for an order  $n_{O_2} = 1$  has been described by Ubhayakar (25). We shall study here the effect of the order  $n_{O_2}$  on the extinction characteristics. First, Eq. [10] and [11] are written in the linearized forms

$$M = C_Y(Y_{O_2}^* - Y_{\bar{O}s})/(\nu - 1) \quad [13]$$

$$M = C_\theta \text{Le} M(\theta_s - \theta_\infty)/[M\nu - G \text{Le}(\theta_s^4 - \theta_\infty^4)] = (\text{Le}/\nu)[C_\theta(\theta_s - \theta_\infty) + G(\theta_s^4 - \theta_\infty^4)] \quad [14]$$

where  $C_Y$  and  $C_\theta$  are correction factors. Then  $M$  and  $Y_{\bar{O}s}$  are eliminated between Eq. [12]-[14] to obtain the single equation

$$f(\theta_s) = g(\theta_s) \quad [15]$$

where

$$f(\theta_s) = [\text{Le}(\nu - 1)/\nu][C_\theta(\theta_s - \theta_\infty) + G(\theta_s^4 - \theta_\infty^4)]$$

and



$$g(\theta_s) = C_Y Y_{O^*} \left[ 1 + C_Y \theta_s \left\{ \frac{f(\theta_s)^{1-n_{O_2}}}{K_{O_2} \exp(-\beta_{O_2}/\theta_s)} \right\}^{1/n_{O_2}} \right]^{-1}$$

The characteristics of the solutions to this equation have been delineated by Ubhayakar and Williams (13, 25). We summarize the results briefly: (a)  $f(\theta_s)$  represents the heat loss rate while  $g(\theta_s)$  represents the reaction heat release rate; their relative values (which depend on  $d$  through the reaction number  $K_{O_2}$  and the radiation number  $G$ ) determine whether or not there exists a solution  $\theta_s$  significantly greater than  $\theta_a$ . Extinction occurs when  $f(\theta_s)$  becomes tangent to  $g(\theta_s)$ , as illustrated in Fig. 8. (b) Such a tangency is possible only if the activation energy  $E_{O_2}$  is greater than a certain positive nonzero value. (c) For a zero-order reaction the extinction diameters are independent of the pressure  $p$ .

We adopt the following procedure to compare the theoretical extinction results with the data in Fig. 2. Using the constants in Table I and a chosen value of  $d^* = 65 \mu\text{m}$  (at  $Y_{O^*} = 0.6$  and  $p = 1 \text{ atm}$ ), we compute  $G^*$ . Then with  $C_Y = C_\theta = 1$ , Eq. [15] is solved numerically for the tangency condition to get the value of  $K_{O_2}^*$  for certain prechosen values of  $E_{O_2}$  and  $n_{O_2}$ . The numerical solution involved use of a computer for calculating and plotting the functions  $f(\theta_s)$  and  $g(\theta_s)$  for various values of  $K_{O_2}$ . Next  $C_Y$  and  $C_\theta$  are evaluated from Eq. [13] and [14] by use of values of  $M$  and  $Y_{O_s}$  obtained through Eq. [10] and [11], and  $K_{O_2}^*$  is recomputed with these new correction factors. This iterative procedure is continued until the value of  $K_{O_2}^*$  converges. Then the preexponential factor  $k_{O_2}$  is evaluated from the definition of  $K_{O_2}^*$ . Using this value of  $k_{O_2}$  and the chosen values of  $E_{O_2}$  and  $n_{O_2}$  along with the constants in Table I, the extinction diameters  $d^*$  are computed in a similar iterative procedure for the tangency condition for other values of  $Y_{O^*}$  and  $p$ . The results are shown in Fig. 2 for three assumed values of the activation energy  $E_{O_2}$  and three assumed values of the order  $n_{O_2}$ . We notice here that the best agreement of the theory with the data is for  $E_{O_2} = 18 \text{ kcal/mole}$  and  $n_{O_2} = 0.75$ , although the agreement for  $n_{O_2}$  in the range 0.5-1 is favorable, considering the scatter in the data.

**Model 2**

In this model we assume that because of the high reactivity of oxygen atoms, the dissociation fraction  $Z$  is negligible in Eq. [7] but nonnegligible with regard to the surface rate in Eq. [8]. Then Eq. [5]-[7] yield Eq. [9]-[11], as before. Since  $Z$  is assumed small, we put  $\alpha = 1$  and  $Z_s = (a^2/pY_{O_s})^{0.5} \exp(-\Gamma/\theta_s)$ , as derived in the Appendix. For further simplification of

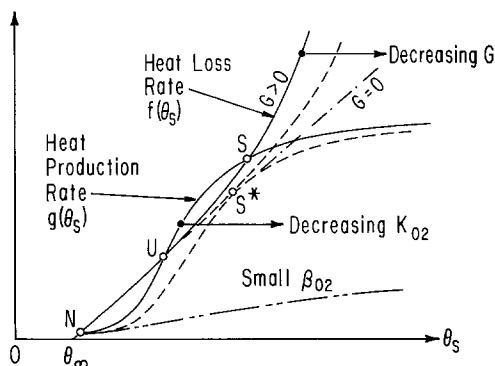


Fig. 8. Schematic diagram of energy balance defined by Eq. [15], illustrating attainment of extinction condition. Solid lines are typical curves having nonburning N, unstable U, and stable burning S solutions. Dashed lines represent extinction conditions with  $S^*$  the tangency point. Also shown are the linear dependence of  $f$  on  $\theta_s$  when  $G = 0$  and the absence of sufficient curvature in  $g(\theta_s)$  to produce multiple intersections when  $\beta_{O_2}$  is small.

Eq. [8] we assume  $n_{O_2} = n_0$ , an approximation expected to have a small effect because of the relative unimportance of  $n_{O_2}$  in model 2. Then Eq. [8] can be written as

$$M = \frac{K_0}{(\nu - 1) \theta_s^{n_0}} [(a^2 Y_{O_s} / p)^{n_0/2} \exp\{- (\Gamma n_0 + \beta_0) / \theta_s\} + \chi Y_{O_s}^{n_0} \exp(-\beta_{O_2} / \theta_s)] \quad [16]$$

where  $\chi = K_{O_2} / K_0 = k_{O_2} / k_0$ .

Experimental results of Rosner and Allendorf (12) and Strickland-Constable and co-workers (7, 8) have proven that at temperatures greater than 2000°K there exists a temperature region in which the activation energy of the reaction between pyrolytic graphite and molecular or atomic oxygen is zero or somewhat negative. To investigate whether this can also be true for our experiments with electrode carbon, we set  $\beta_{O_2} = \beta_0 = 0$  in Eq. [16]. Since the reaction of carbon with molecular oxygen is slow compared to that with atomic oxygen (12), the value of  $\chi$  is small. If  $\chi = 0$ , then comparison of Eq. [16] with Eq. [12] reveals that by including the dissociation of oxygen we have effectively introduced a pseudo-activation energy ( $\gamma n_0$ ) and a pseudo-order ( $n_0/2$ ).

The solutions to Eq. [13], [14], and [16] at the extinction tangency condition were computed in a manner similar to that explained in model 1, and the computed extinction diameters  $d^*$  are shown in Fig. 9 for  $\chi = 0$  and  $\chi = 0.01$  for three assumed values of  $n_0$ . The computations also indicated that for higher values of  $\chi$  the extinction tangency condition could not be satisfied. The interesting feature of this model is that it shows that extinction can occur even if the activation energies of the reactions between carbon and molecular and atomic oxygen are zero provided that the pseudo-activation energy ( $\gamma n_0$ ) arising from the dissociation heat of molecular oxygen is included. How-

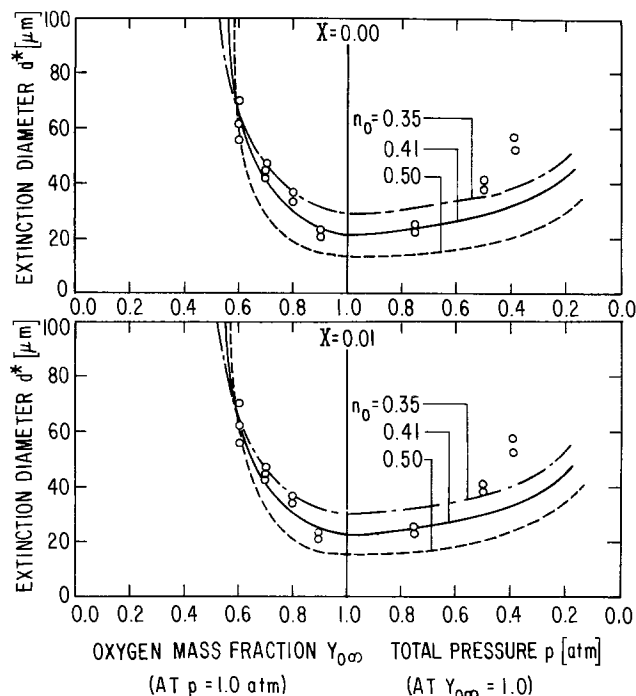


Fig. 9. Extinction diameters computed from Eq. [13], [14], and [16], model 2, using other data from Table I. The circles are the same data shown in Fig. 2. The values of the preexponential factors (with orders in parentheses) computed to give  $d^* = 65 \mu\text{m}$  at  $Y_{O^*} = 0.6$  and  $p = 1 \text{ atm}$  are the following. Top:  $\chi = 0$ ,  $k_0$  (0.35) =  $16.69 \text{ g}^{0.65}/\text{cm}^{0.95}\text{-sec}$ ,  $k_0$  (0.41) =  $41.48 \text{ g}^{0.59}/\text{cm}^{0.77}\text{-sec}$ ,  $k_0$  (0.5) =  $167.4 \text{ g}^{0.5}/\text{cm}^{0.5}\text{-sec}$ . Bottom:  $\chi = 0.01$ ,  $k_0$  (0.35) =  $16.26 \text{ g}^{0.65}/\text{cm}^{0.95}\text{-sec}$ ,  $k_0$  (0.41) =  $39.89 \text{ g}^{0.59}/\text{cm}^{0.77}\text{-sec}$ ,  $k_0$  (0.5) =  $152.72 \text{ g}^{0.5}/\text{cm}^{0.5}\text{-sec}$ .

ever, the agreement between the theory and data is good only for  $n_0 = 0.41$  on the constant- $p$  side and is not good on the constant- $Y_{O^*}$  side in Fig. 9. A value of  $n_0$  as low as 0.41 is difficult to justify theoretically. This model therefore does not appear to be as favorable as model 1. We therefore conclude that model 1 is the preferred model between the two.

### Discussion

The kinetics of oxidation of carbon are known (11) to be distinctly non-Arrhenius in the temperature range 300°-4000°K, and to be dependent on the type of carbon, its impurities, structure, etc. For example, the kinetics of oxidation of pyrolytic graphite measured by Strickland-Constable and co-workers (7, 8) are different from those of electrode carbon measured by Golovina and Khaustovich (9) and Okada and Ikegawa (10). Above 2000°K these differences may arise because of fundamentally different kinetics or because of diffusion-controlled rate limitation. Strickland-Constable and co-workers (7, 8) devised their tests specifically to eliminate the diffusional effects and still found that the reaction rate reaches a maximum and then decreases as the temperature increases. Extrapolation of their rate formula to higher temperatures predicts a minimum rate beyond which the rate begins to rise again. Also, according to their rate formula the rate maximum and minimum disappear at high partial pressures of oxygen. They have explained this behavior by assuming the surface to consist of two types of active sites which are thermally interconvertible. In contrast, Ong (27) has deduced similar results based on fundamental statistical thermodynamics and on only one type of active site. Both schemes appear plausible and yet disagree with each other (11). One of the reasons for this may be the different structures of the carbon studied. According to our preferred model 1, the effective activation energy of the oxidation of electrode carbon in the temperature range 2000°-3500°K has a positive nonzero value of about 18 kcal/mole which is (a) in disagreement with the data of Rosner and Allendorf (12) on pyrolytic graphite at very low  $p_{O_2}$ , (b) in partial agreement with the results of Strickland-Constable and co-workers (7, 8) on pyrolytic graphite at  $p_{O_2} \sim 0.21$  atm (partial because beyond the temperature of minimum rate, their formula predicts an activation energy of 15.2 kcal/mole), and (c) in good agreement with the data of Park and Appleton (14) on soot at  $p_{O_2} \sim 0.1-0.5$  atm. The values of  $p_{O_2}$  at extinction, calculated from Eq. [12]-[14], are of the order of 0.2 atm, which is in the range of this data of Park and Appleton.

The measured kinetics of oxidation are also known (3, 4) to be affected by diffusion and reaction within the porous subsurface. Although the present data are insufficient to differentiate between these effects and the fundamental kinetic details indicated in the last paragraph, the highly porous structure in Fig. 1b suggests that as extinction is approached, the diffusional resistance within pores may become negligible. If this occurs, then the rate constants listed in the caption of Fig. 2 are related to absolute surface rate constants through a roughness factor  $f$ , defined as the ratio of the actual surface area at which reaction occurs to the surface area of the sphere of diameter  $d^*$ . If the previously mentioned surface reaction rates of Park and Appleton (14) are assumed to be correct for the present experiments, and if the aforementioned value of  $p_{O_2}$  is employed along with our measured surface temperatures and rate constants, then values of  $f$  at extinction ranging from 50 to 100 are calculated. Although these values seem to be qualitatively consistent with Fig. 1b, the result cannot be termed definitive. Since the sizes of the soot particles were on the order of 100Å, less than  $10^{-3}$  times the diameter of the present extin-

guished particles, the rough agreement appears encouraging.

Owing to the scatter in the extinction data shown in Fig. 2, it is not possible to ascertain the exact order of the reaction. The theoretical curves for  $n_{O_2}$  in the range 0.5-1 fit the data favorably, although  $n_{O_2} = 0.75$  appears to give the best fit. A convincing fundamental justification for the latter value has not been obtained.

Ong's (27) scheme for carbon oxidation predicts an order of 0.5 at temperatures greater than 2000°K. We shall therefore choose  $n_{O_2} = 0.5$  and the corresponding  $k_{O_2}$  from Fig. 2, and compute the burning durations and temperature histories, the data for which are shown in Fig. 6 and 7. Once  $n_{O_2}$ ,  $E_{O_2}$ , and  $k_{O_2}$  are known, Eq. [13]-[15] are solvable for  $M$ ,  $\theta_s$ , and  $Y_{O_s}$  for any diameter  $d$ . Since  $m = -(d/dt)(\pi\rho c d^3/6) = (2\pi\rho D d)M$ , the burning duration is

$$\tau^* = \int_{t^0}^{t^*} dt = \frac{\rho c}{4\rho D} \int_{d^0}^{d^*} \left( \frac{d}{M} \right) dd$$

which can be computed for any given initial diameter  $d^0$ . Figures 6 and 7 show the computed curves using the constants given in Table I.

In Fig. 6 we note that the theory agrees with the data favorably for all conditions except those in pure oxygen at  $p > 1$  atm. In the diffusion-controlled regime the theory gives the same surface temperature for any fixed diameter and  $Y_{O^*}$  for all pressures; this result depends on the fact that we have assumed the mass diffusivity  $\rho D$  to be independent of pressure and temperature. Since it is known (28) that  $\rho D \propto T^{b-1}$  where  $1.5 \leq b \leq 2$ , the tests at higher pressure, which are seen according to the theory to have higher temperatures as a consequence of the finite-rate chemistry, also correspond to higher  $\rho D$ . This diffusivity effect tends to shift the theoretical high-pressure curves to somewhat higher temperatures. However, the effect does not appear to be sufficiently large, and the greater scatter in the high-pressure tests suggests the possibility of nonnegligible experimental errors brought about by band emissions from the diatomic gases in the combustion zone. Therefore it is unclear whether the discrepancies of temperature at oxygen pressures above atmospheric are attributable primarily to errors in theory or experiment.

In Fig. 7 we observe that the computed lines conform to the "square law" or diffusion-controlled burning for large diameters and that as the diameter decreases toward the extinction value finite-rate chemistry influences the burning duration. Within the accuracy of the data, the agreement between theory and experiment is good in Fig. 7.

### Conclusions

A comparison of the two theoretical models with the extinction data has shown that model 1 is preferred. Based on this model, the kinetics of oxidation of electrode carbon in the temperature range 2000°-3500°K can be effectively represented by an Arrhenius surface reaction having an activation energy of 18 kcal/mole and an order in the range 0.5-1. The burning durations and temperatures computed from this model also agree with experiment, within the accuracy of the data. It

Table I. Constants used in numerical computations

$T_0$	= 295°K
$c$	= $0.3 \times 10^{-3}$ kcal/g-°C, based on 0.3 cal/g-°C for CO and 0.283 cal/g-°C for $O_2$ at 2000°K (29)
$\rho D$	= $6.3 \times 10^{-4}$ g/cm-sec, chosen to fit data in Fig. 7
$Le$	= 1
$W_{CO}$	= $W_{N_2} = 28$ g/mole
$W_{O_2}$	= $2W_O = 32$ g/mole
$\nu$	= $W_{CO}/W_C = 2.3333$ , stoichiometry
$\rho c$	= 1.5 g/cm <sup>3</sup> , measured
$\epsilon$	= 0.83, in the range 1800°-3000°K (24)
$q_{CO}$	= 1.013 kcal/g CO, at 2500°K (29)

therefore appears that the kinetic parameters obtained herein may be suitable for practical use at high temperatures.

### Acknowledgment

The authors acknowledge gratefully the financial support of the Air Force Office of Scientific Research, United States Air Force under Grant No. AFOSR 72-2333.

Manuscript submitted Aug. 29, 1975; revised manuscript received Dec. 1, 1975. This was Paper 197 presented at the Dallas, Texas, Meeting of the Society, Oct. 5-9, 1975.

Any discussion of this paper will appear in a Discussion Section to be published in the December 1976 JOURNAL. All discussions for the December 1976 Discussion Section should be submitted by Aug. 1, 1976.

Publication costs of this article were partially assisted by the University of California.

### APPENDIX

Because of assumption (vi) we have  $p_0 = K_p p_{O_2}^{1/2}$ , where  $K_p = 2a \exp(-\gamma/RT) = 2a \exp(-\Gamma/\theta)$  is the equilibrium constant for the dissociation reaction  $\frac{1}{2} O_2 \rightleftharpoons O$  at temperature  $T$ . Here  $a = 1600 \text{ atm}^{1/2}$  and  $\gamma = 60.5 \text{ kcal/mole O}$  (26). Since all component gases as well as the mixture are assumed to behave ideally, we have  $Y_O = ZY_{O\bar{}} = (p_0 W_O)/(R_p T)$ ,  $Y_{O_2} = (1 - Z)Y_{O_2\bar{}} = (p_{O_2} W_{O_2})/(R_p T)$ . Elimination of  $p_{O_2}$  and  $(R_p T)$  between these equations produces

$$p_0 = K_p^2 (W_O/W_{O_2}) [(1 - Z)/Z] \quad [A-1]$$

The ideal gas law for the mixture is

$$p = \frac{R_p T}{W_O} \left[ \left\{ Z + \frac{W_O}{W_{O_2}} (1 - Z) - \frac{W_O}{W_{O_2}} \right\} Y_{O\bar{}} + \left( \frac{W_O}{W_{CO}} - \frac{W_O}{W_{N_2}} \right) Y_{CO} + \frac{W_O}{W_{N_2}} \right] \quad [A-2]$$

since  $Y_{N_2} = 1 - Y_{CO} - Y_{O\bar{}}$ . Eliminating  $(R_p T)$  between Eq. [A-2] and the relation  $Y_O = (p_0 W_O)/(R_p T)$ , we get an equation for  $p_0$  which may be equated to Eq. [A-1] to obtain a quadratic in  $Z$

$$AZ^2 + BZ + C = 0 \quad [A-3]$$

where

$$A = pY_{O\bar{}} \left( \frac{1}{K_p^2} \right) \left( \frac{W_{O_2}}{W_O} \right) - \left( 1 - \frac{W_O}{W_{O_2}} \right) Y_{O\bar{}}$$

$$B = \left( \frac{2W_O}{W_{O_2}} - 1 - \frac{W_O}{W_{N_2}} \right) Y_{O\bar{}} + \left( \frac{W_O}{W_{CO}} - \frac{W_O}{W_{N_2}} \right) Y_{CO} + \frac{W_O}{W_{N_2}}$$

and

$$-C = \left( \frac{W_O}{W_{O_2}} - \frac{W_O}{W_{N_2}} \right) Y_{O\bar{}} + \left( \frac{W_O}{W_{CO}} - \frac{W_O}{W_{N_2}} \right) Y_{CO} + \frac{W_O}{W_{N_2}}$$

From this equation it is easy to obtain the following

$$Z = [-B + (B^2 - 4AC)^{1/2}]/(2A) \quad [A-4]$$

$$(2ZA + B) \frac{\partial Z}{\partial \theta} = Z^2 p Y_{O\bar{}} \left( \frac{W_{O_2}}{W_O} \right) \left( \frac{1}{K_p^2} \right) \left( \frac{2\Gamma}{\theta} \right) \quad [A-5]$$

$$(2ZA + B) \frac{\partial Z}{\partial Y_{O\bar{}}} = \frac{W_O}{W_{O_2}} - \frac{W_O}{W_{N_2}} - Z^2 \left\{ \frac{W_{O_2}}{W_O} \frac{p}{K_p^2} + 1 - \frac{W_O}{W_{O_2}} \right\} - Z \left( \frac{2W_O}{W_{O_2}} - 1 - \frac{W_O}{W_{N_2}} \right) \quad [A-6]$$

$$(2ZA + B) \frac{\partial Z}{\partial Y_{CO}} = (1 - Z) \left( \frac{W_O}{W_{CO}} - \frac{W_O}{W_{N_2}} \right) \quad [A-7]$$

From Eq. [A-4] we find that  $Z = 0.5$  when  $p = 3 \text{ atm}$ ,  $Y_{O\bar{}} = 1$  and  $T = 4140^\circ \text{K}$  and when  $p = 0.5 \text{ atm}$ ,  $Y_{O\bar{}} = 1$  and  $T = 3660^\circ \text{K}$ . Therefore, in the temperature range of the tests  $Z$  is less than 0.5. It is a good approximation to consider  $Z$  small.

Assumption (xiii) simplifies Eq. [A-4] to

$$Z = \frac{[1 - Y_{O\bar{}}]}{2Y_{O\bar{}} \left( \frac{4p}{K_p^2} + 1 \right)} \left[ \left( 1 + \frac{4Y_{O\bar{}}}{[1 - Y_{O\bar{}}]^2} \left( \frac{4p}{K_p^2} + 1 \right) \right)^{1/2} - 1 \right] \quad [A-8]$$

Since  $Z$  is small when  $K_p$  is small, or when  $T < 4140^\circ \text{K}$ , the 1's in the parentheses in Eq. [A-8] can be neglected in comparison with the other terms, giving for small  $Z$

$$Z \simeq [a/(pY_{O\bar{}})^{1/2}] \exp(-\Gamma/\theta) \quad [A-9]$$

### LIST OF SYMBOLS

$a$	preexponential constant in $K_p$ , $\text{atm}^{0.5}$
$c$	specific heat, $\text{kcal/g} \cdot ^\circ \text{C}$
$C_{Y,\theta}$	correction factors, [-]
$d$	diameter of the particle, $\text{cm}$
$D$	binary diffusion coefficient, $\text{cm}^2/\text{sec}$
$E$	activation energy, $\text{kcal/mole}$
$G$	dimensionless radiation number, $(\epsilon \sigma q_{CO}^3 d)/(2\lambda c^3)$
$k$	preexponential factor $\text{g}^{1-n} \text{cm}^{3n-2}/\text{sec}$
$K$	dimensionless reaction number, $[(kp^n d)/(2\rho D)][(cW_{O_2})/(Rq_{CO})]^n$
$K_p$	equilibrium constant for $O_2$ dissociation, $\text{atm}^{0.5}$
$Le$	Lewis number, $\lambda/(\rho Dc)$
$m$	total outward mass flow rate, $\text{g/sec}$
$M$	dimensionless mass flow rate, $m/(2\pi\rho Dd)$
$n$	order of reaction, [-]
$p$	pressure, $\text{atm}$
$q$	heat of formation at temperature $T_s$ , $\text{kcal/g}$
$Q$	dimensionless heat of formation, $q/q_{CO}$
$r$	radial distance from the center of the particle, $\text{cm}$
$R$	universal gas constant, $1.987 \times 10^{-3} \text{ kcal/mole } ^\circ \text{K}$ or $82.06 \text{ cm}^3 \text{ atm/mole } ^\circ \text{C}$
$t$	time, $\text{sec}$
$T$	temperature, $^\circ \text{K}$
$W$	molecular weight, $\text{g/mole}$
$Y$	mass fraction, [-]
$Z$	dissociation fraction, $Y_O/Y_{O\bar{}}$
$\beta$	dimensionless activation energy, $(E_c)/(Rq_{CO})$
$\epsilon$	total emissivity, [-]
$\gamma$	heat of dissociation of $O_2$ , $\text{kcal/mole O}$
$\Gamma$	dimensionless heat of dissociation of $O_2$ , $(\gamma c)/(Rq_{CO})$
$\eta$	dimensionless distance from the center of the particle, $2r/d$
$\theta$	dimensionless temperature, $cT/q_{CO}$
$\lambda$	thermal conductivity, $\text{kcal/cm} \cdot \text{sec } ^\circ \text{C}$
$\nu$	CO produced/C consumed, $W_{CO}/W_C$
$\rho$	density, $\text{g/cm}^3$
$\sigma$	Stefan-Boltzmann constant, $1.3545 \times 10^{-15} \text{ kcal/cm}^2 \text{ sec } ^\circ \text{K}^4$
$\tau$	burning duration, $\text{sec}$
$\chi$	the ratio, $k_{O_2}/k_O$

### Subscripts

$\bar{c}$	carbon
$\bar{o}$	$O + O_2$
$s$	at the surface of the particle
$\infty$	at large distances from the particle

### Superscripts

$^{\circ}$	initial value
$*$	at extinction

### REFERENCES

1. D. B. Spalding, *Fuel*, **30**, 6, 121 (1951).
2. D. B. Spalding, "Some Fundamentals of Combustion," Vol. 2, pp. 107-109, Academic Press, New York (1955).
3. R. H. Essenhigh and R. W. Froberg, "An Experimental Study of the Oxidation of Suspended Carbon Spheres, *Technical Report FS67-2(U)*, The Pennsylvania State University, University Park, Pennsylvania (1967).
4. M. F. R. Mulcahy and I. W. Smith, *Rev. Pure and Appl. Chem.*, **19**, 81 (1969).
5. P. L. Walker, Jr., F. Rusinko, Jr., and L. G. Austin,

- "Advances in Catalysis," Vol. 11, pp. 133-221, Academic Press, New York (1959).
6. G. Blyholder, J. S. Binford, and H. Eyring, *J. Phys. Chem.*, **62**, 3, 263 (1958).
  7. J. Nagle and R. F. Strickland-Constable, "Proceedings 5th Conference on Carbon," Vol. 1, pp. 154-164, The Macmillan Co., New York (1962).
  8. J. R. Walls and R. F. Strickland-Constable, *Carbon*, **1**, 333 (1964).
  9. E. S. Golovina and G. P. Khaustovich, "8th Symposium (International) on Combustion," pp. 784-792, Williams and Wilkins, Baltimore (1962).
  10. J. Okada and T. Ikegawa *J. Appl. Phys.*, **24**, 1249 (1953).
  11. H. G. Maahs, NASA TN D-6310 (June 1971).
  12. D. E. Rosner and H. D. Allendorf, *Carbon*, **3**, 153 (1965).
  13. S. K. Ubhayakar and F. A. Williams, Fall Meeting Paper No. 15, Eastern States Section, The Combustion Institute, Applied Physics Laboratory of the Johns Hopkins University, Maryland, Nov. 12-13, (1974).
  14. C. Park and J. P. Appleton, *Combust. Flame*, **20**, 369 (1973).
  15. R. P. Wilson and F. A. Williams, "13th Symposium (International) on Combustion," pp. 833-845, The Combustion Institute, Pittsburgh (1971).
  16. R. L. Marshall, Thesis, Virginia Polytechnic Institute (1968).
  17. L. S. Nelson, N. L. Richardson, and J. L. Prentice, *Rev. Sci. Instr.*, **39**, 744 (1968).
  18. R. P. Wilson, Jr., *High Temperature Sci.*, **1**, 367 (1969).
  19. F. P. Bundy and H. M. Strong, in "Physical Measurements in Gas Dynamics and Combustion," R. W. Landenburg, B. Lewis, R. N. Pease, and H. S. Taylor, Editors, High Speed Aerodynamics and Jet Propulsion, Princeton University Press, Vol. IX, pp. 361-364, Princeton, New Jersey (1954).
  20. O. A. Uyehara, P. S. Myers, K. M. Watson, and L. A. Wilson, *Trans. Am. Soc. Mech. Engrs.*, **68**, 17 (1946).
  21. von W. Riezler and L. Hardt, *Z. Angew. Phys.*, **6**, 497 (1954).
  22. D. Rae, *Combust. Flame*, **5**, 341 (1961).
  23. G. A. W. Rutgers and J. C. DeVos, *Physica*, **20**, 715 (1954).
  24. Y. S. Touloukian and D. P. DeWitt, "Thermal Radiative Properties, Non-metallic Solids," Vol. 8, p. 44, IFI/Plenum, New York-Washington (1972).
  25. S. K. Ubhayakar, *Combust. Flame*, **26**, 23 (1976).
  26. *Nat. Bur. Std. Cir. 500* (February 1952).
  27. J. N. Ong, Jr., *Carbon*, **2**, 281 (1964).
  28. F. A. Williams, "Combustion Theory," p. 421, Addison-Wesley, Reading, Massachusetts (1965).
  29. JANAF Thermochemical Tables, Second Edition NSRDS-NBS 37 (1971).

## Flash Desorption as a Surface Ion Spectroscopy for Solid Electrolytes

M. L. Knotek

*Sandia Laboratories, Albuquerque, New Mexico 87115*

### ABSTRACT

An application of flash desorption techniques to solid electrolyte materials which yields a "surface ion spectroscopy" is described. The desorption spectra as a function of surface coverage for Na<sup>+</sup> and K<sup>+</sup> on Na- $\beta$ -alumina are presented as an illustration and show that there are marked differences in their behavior. The kinetics of the desorption process and its dependence on surface coverage are seen to yield abundant detail on the ion-surface interaction.

There are presently available a number of techniques for the study of such surface properties of solids as their elemental makeup, electronic structure, and crystal structure. In addition, various desorption techniques have been used to study the energetics of the adsorption of molecular species on surfaces. The main use of these techniques has been the study of metals and to a lesser extent semiconductors and insulators.

There has emerged in the past few years a particularly intriguing group of materials, the so-called superionic conductors or solid electrolytes (1). These materials are characterized by open cagelike or tunnelike structures with a number of negatively charged sites per unit cell on which cations sit (typically more than one site per cation). The cagelike structures are generally covalent and quite stable and serve as a framework through which the cations can move quite freely owing to the high site density and open structure. This feature gives rise to unique properties. These materials exhibit high cationic conductivities ( $\sim 1$  ohm-cm at 300°K) and show promise of being technologically important as solid ion transport media for various electrochemical applications. At least two of these materials,  $\beta$ -alumina and the zeolites, also have catalytic properties in which (for the case of zeolites) the cations in the structure have recently been shown to play a major role (2-5). In addition, these materials have

unique physical properties which are fundamentally important from the solid-state physics standpoint. A knowledge of the details of the cations interaction with these structures and with each other is needed for a better understanding of their fundamental properties. The surfaces of these materials seem particularly interesting to study since the surface properties should be as complex as the bulk properties, and surfaces can be technologically important. One purpose of this work is to look at the surfaces of these materials with such elemental, electronic, and structural characterization tools as Auger spectroscopy, characteristic loss spectroscopy, depth profiling using ion sputter etching, LEED, and secondary ion mass spectroscopy.

In addition it is important to study the details of the energetics of the ion interaction with the surface, the ionic properties of these materials being their unique feature. We present here the first use of the technique of flash desorption to study ion energetics on these surfaces. The results shown here (which are a representative sample) are interesting from two standpoints. First of all, they provide fundamentally new information on these materials (in essence a "surface ion spectroscopy") which no other technique offers. The results enumerate the spectrum of binding energies of a particular ion on the "surface," and provide data with which to correlate results using other surface characterization techniques. Second, the particular use of the

Key words:  $\beta$ -alumina, surfaces, interfaces, sodium, potassium.

flash desorption technique reported here contains several unique features, and the data show behavior quite unlike that seen in the desorption of neutral species from (say) metals. From both of these viewpoints it would appear that this is an interesting new area for study.

### Experimental Details

The data shown here were taken in an all-metal baked ultra high vacuum system which had the capabilities for Auger spectroscopy, characteristic loss spectroscopy, and quadrupole mass analysis. An array of ion sources, based on the appropriately ion exchanged zeolite such as described by Weber and Cordes (6), and Cuderman (7), was used to deposit ions of Li, Na, K, Cs, Ag, or Cu onto the surface being studied. The type of results reported here have been observed on both single crystal Na- $\beta$ -alumina (both the a-c and a-b planes) and on the Na-zeolite. We report here the results for Na<sup>+</sup> and K<sup>+</sup> on the a-c plane (nominally) of single crystal  $\beta$ -alumina which was the most extensively studied. The a-c plane is perpendicular to the high conductivity plane. The sample surface was prepared by heat cleaning in vacuum at  $\approx 1000^\circ\text{C}$ .

The experiment consisted of depositing controlled amounts of ions onto the surface being studied (incident energy of the ions was  $< 8$  eV to avoid lattice damage) followed by positioning of the sample near a negatively biased collector probe where the sample was heated at a controlled rate. Monitoring of the ion current emitted from the sample surface and collected by the biased probe as a function of time or sample temperature (interrelated) resulted in a spectrum of desorbing ions. Two points should be made about this particular technique as opposed to the classical flash desorption. First, since ions are deposited and ions are desorbed there is no need for an ionizer in the collector assembly and since a biased probe is used, virtually 100% of the desorbed ions are collected. This results in enormously enhanced sensitivity over the standard flash desorption technique ( $< 10^{-5}$  monolayer on an area  $\approx 0.03$  cm<sup>2</sup> can easily be detected during desorption as opposed to the limit of  $\approx 0.1$  monolayer for gases on metals). Second, since the ion collection is line of sight this corresponds to the ideal infinite pumping speed case of flash desorption yielding the highest possible resolution.

### Results

Shown in Fig. 1 and 2 are the results for Na<sup>+</sup> and K<sup>+</sup> on the a-c plane of Na- $\beta$ -alumina as a function of the

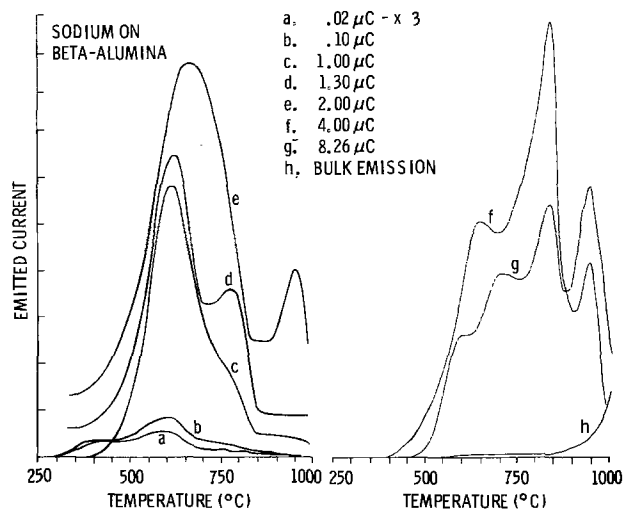


Fig. 1. Emitted sodium ion current vs. sample temperature for a heating rate of  $\approx 100^\circ\text{C}/\text{sec}$ , as a function of ion dose in microcoulombs. Each peak corresponds to a well-defined surface desorption energy. Peak temperatures are not a function of coverage, but the population shifts to higher temperature at higher dose. Current due to bulk Na<sup>+</sup> emission is also shown (curve h).

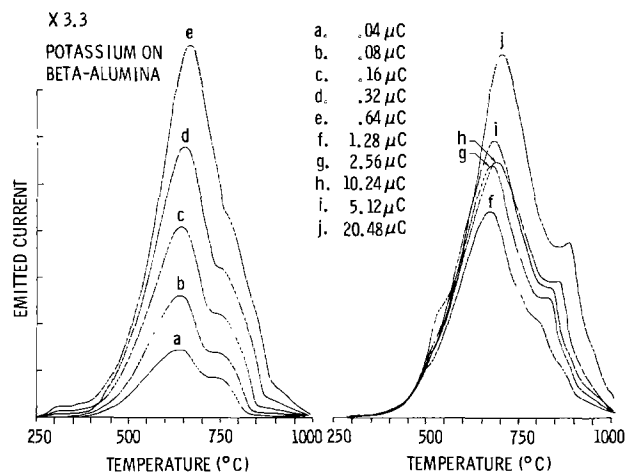


Fig. 2. Emitted potassium ion current vs. sample temperature for a heating rate of  $\approx 100^\circ\text{C}/\text{sec}$ , as a function of ion dose in microcoulombs. Peak temperatures shift with ion dose.

ion dose in microcoulombs ( $\mu\text{C}$ ) to the surface. The data have a large amount of detail both as a function of temperature and coverage indicating a complicated interaction. We briefly discuss the behavior as a function of coverage to point out the major features and to contrast Na and K.

The data are plotted as emitted current vs. sample temperature ( $^\circ\text{C}$ ). For the sample configuration used in taking this data one monolayer corresponds to  $\sim 20 \mu\text{C}$ . The heating rate was approximately linear at  $\sim 100^\circ\text{C}/\text{sec}$ . Using the results of Redhead (8) for first-order processes with a linear heating curve we can approximately relate the temperature of the peak maxima  $T_p(K)$  to the desorption energy  $E$  by  $E = 2.5 \times 10^{-3} T_p^2(\text{eV})$  assuming an attempt frequency  $\nu_1 = 10^{13} \text{ sec}^{-1}$ .

At the lowest dose levels ( $\leq 0.16 \mu\text{C}$ ) Na has three peaks located at  $\sim 425^\circ$ ,  $620^\circ$ , and  $760^\circ\text{C}$  ( $E = 1.74$ ,  $2.23$ , and  $2.58$  eV) while K has two peaks at  $630^\circ$  and  $750^\circ\text{C}$  ( $E = 2.25$  and  $2.56$  eV). In this range both show roughly linear growth of all features with increasing dose. Mass balance, i.e., ions collected during desorption/ions deposited, is close to unity in this range of dosage. We note that this low dose region is the only range of dosages for which K desorbs by what appears to be a first-order process. The assignment of energies using the above discussion is only good under these circumstances.

In the next range of dosage ( $0.2 \mu\text{C} \leq d \leq 1.5 \mu\text{C}$ ) the Na spectra show a loss of the  $425^\circ\text{C}$  peak with initial major growth in the  $620^\circ\text{C}$  peak followed by growth of the  $760^\circ\text{C}$  peak as dose increases. There is no shift in peak temperatures with coverage, indicating a first-order process. K in this range shows a roughly equal growth of the major features and a continuous shift of the peaks to higher temperatures with increasing coverage, indicating a higher order process. Minor features at  $275^\circ$  and  $525^\circ\text{C}$  also appear in this range. A shifting of the K desorption peaks to higher temperatures with increased coverage is quite unlike the usual behavior seen in (say) metals, as illustrated by hydrogen on tungsten (9). Na shows no shifts, but is also unusual in that the least stable states fill first, which is the converse of metals. Thus, both ions tend to be more tightly bound as coverage increases although the details are quite dissimilar. One conclusion is that the ions are immobile on the surface, which is surprising. Another conclusion which seems more likely is that lateral interactions account for the behavior as a function of coverage.

In the remaining range of dosages Na maintains the same type of trend, with major growth at  $760^\circ\text{C}$  and the appearance of another peak at  $950^\circ\text{C}$  ( $3.06$  eV) which eventually becomes the major feature. The  $620^\circ\text{C}$  peak is seen to split into one at  $\approx 600^\circ$  and

700°C at the highest dose. K shows a continued growth and shift to higher  $T_P$  of the two major features and gradual growth of the shoulder at 525°C. Mass balance for both ions is drastically reduced at the highest dose levels.

In all cases studied only the first flash heating of the surface after a deposition was found to yield desorption peaks with subsequent scans (without an intervening deposition) showing no desorption peaks. From this behavior we conclude that the ions coming off are the ones that were deposited and no ion exchange is occurring at the surface. In the case of high dose runs with low mass balance, Auger analysis of the surface after the scan showed that appreciable levels of the species deposited remained on the surface. A more detailed Auger study should determine whether significant diffusion into the bulk is occurring or the deposited species are localized to the surface. It was also found that atoms remaining on the surface significantly affected subsequent runs by altering their spectral shape. Removal of the surface atoms by high temperature anneals returned the spectra to their original shape. This may indicate that some details in the spectra are due to ions interacting with neutrals or clusters of neutrals of the deposited species on the surface (lateral interactions).

Finally, curve h in Fig. 1 is a current due to a continuous bulk emission of Na (no ions were deposited before this scan). This current can be varied over many decades and when plotted on a  $\log I$  vs.  $1/T$  plot displays an activation energy of  $\approx 2.9$  eV.

One striking point is the large amount of charge that we are able to deposit on these surfaces. An ideal insulating surface of this size ( $\approx 0.03$  cm<sup>2</sup>) with microcoulombs of charge deposited on it would be charged to potentials  $\gtrsim 1$  kV, yet we see no large surface charging. This suggests an enormous surface capacitance such as a Helmholtz layer which is a direct consequence of the high ionic conductivity of this material. The point is receiving further study. The possibility of electrons tunneling through such a layer to cause ion neutralization on the surface, leading to the reduced mass balance seen at high dose, would be another consequence of such an interaction.

### Discussion and Conclusions

The results show that there are major differences between the interaction of Na<sup>+</sup> and K<sup>+</sup> with the  $\beta$ -alumina structure. In addition, the general features of ion interactions with these surfaces show major and fundamental differences with that seen for (say) molecules on metals. Both Na and K show a tendency for tighter binding with higher coverage, with the Na desorption appearing first order and that of K of more complex order in that there is a continual change in desorption peak temperatures with coverage. It should be noted that Li<sup>+</sup> and Ag<sup>+</sup> tend to behave like Na<sup>+</sup>, while Cs<sup>+</sup> behaves more like K<sup>+</sup>. K spectra maintain two major features throughout, while those of Na have five features in total throughout the range of coverage. The finding that the ions are immobile on the surface is puzzling, although lateral interactions seem a plausible explanation of the spectral dependence on coverage.

More important than the specific results for Na and K on this particular material is the fact that a method exists to study in detail the energetics of ion interactions with the "surfaces" of this type of material. When the term surface is used here it must be understood that this must include a considerable amount of what could be referred to as "internal surface." This is particularly true of the zeolite materials, which are extremely open structures with large channels. On the nominal a-c plane of  $\beta$ -alumina we expect a considerable density of steps which expose the basal plane, due to the tendency of these materials to cleave along the

a-b plane. The relationship of the interactions with the surface studied here to those in the bulk is an important question, since no method exists to derive the bulk energetics. Walstedt and Remeika (10) also noted distinct differences in the bulk properties of Na<sup>+</sup> and K<sup>+</sup> in  $\beta$ -alumina as did Rees (11) in interdiffusion studies on Na/K zeolite. The bulk as well as the surface energetics are important when studying catalytic reactions involving the cations or the reactions that occur on the surfaces of these materials when they are part of an interface in an electrochemical cell.

While the preliminary results are promising, we feel that due to the complexity of the data the matter of interpretation should be approached cautiously. In the regime of very low dosages to the surface all features behave like classical first-order desorption and thus the simple interpretation given here would seem to suffice. In the region of higher dosages considerable complexity is introduced and more data is needed before the nature of the interaction can be unambiguously determined. The use of Auger spectroscopy and characteristic loss spectroscopy for precise determination of elemental as well as electronic make up of the surface, LEED for determination of surface structure and adsorbate registry, as well as quadrupole mass analysis of both ionic and neutral desorbed species are now being carried out to obtain a more well-defined picture of this complicated process.

In conclusion we have shown that flash desorption provides a "surface ion spectroscopy" for solid electrolyte materials. We expect that the information gained using this and other surface techniques will be of major importance in understanding the electrochemical and catalytic properties of these materials.

### Acknowledgments

I gratefully acknowledge the support of R. J. Baughman who provided the single crystal Na- $\beta$ -alumina used in this study. I also wish to acknowledge many helpful discussions with R. R. Rye and the help of R. A. Jaramillo with the experimental phase of this study. This work was supported by the U. S. Energy Research and Development Administration.

Manuscript submitted Sept. 15, 1975; revised manuscript received Nov. 20, 1975.

Any discussion of this paper will appear in a Discussion Section to be published in the December 1976 JOURNAL. All discussions for the December 1976 Discussion Section should be submitted by Aug. 1, 1976.

Publication costs of this article were partially assisted by Sandia Laboratories.

### REFERENCES

1. See for example, "Fast Ion Transport in Solids, Solid State Batteries and Devices," W. van Gool, Editor, North Holland/American Elsevier, Amsterdam (1973).
2. W. B. Williamson, D. R. Flentge, and J. H. Lundsford, *J. Catal.*, **37**, 258 (1975).
3. J. W. Ward, *ibid.*, **38**, 351 (1975).
4. M. A. Kaliko and M. N. Pervushina, *Kinetics and Catalysis*, **15**, 1064 (1975); (translated from *Kinetika i Kataliz*, **15**, 1198 (1974)).
5. M. Nitta, S. Matsumoto, and K. Aomura, *J. Catal.*, **38**, 498 (1975).
6. R. E. Weber and L. F. Cordes, *Rev. Sci. Instr.*, **37**, 112 (1966).
7. J. F. Cuderman, *Phys. Rev.*, **A5**, 1687 (1972).
8. P. A. Redhead, *Vacuum*, **12**, 203 (1962).
9. For example, R. R. Rye, B. D. Darford, and P. G. Cartier, *J. Chem. Phys.*, **59**, No. 4, 1693 (1973) and references therein.
10. R. E. Walstedt and J. P. Remeika, *Bull. Am. Phys. Soc.*, **20**, No. 3, 331 (1975).
11. L. V. C. Rees, "Fast Ion Transport in Solids, Solid State Batteries and Devices," W. van Gool, Editor, p. 301 North Holland/American Elsevier, Amsterdam (1973).

## In Situ Thickness Monitoring of Silicon Epitaxial Layer

Katsuro Sugawara,\* Takeo Yoshimi, Yukiyoishi Nakazawa, and Katsuhiko Itoh

Hitachi, Limited, Semiconductor and Integrated Circuits Division, Kodaira, Tokyo, Japan

For silicon devices with high performance and large scale integration, precise control of silicon epitaxial layers has been required. One of the control methods is an *in situ* monitoring. The development of in process film thickness monitoring is reviewed in Table I, together with mutual interconnections. In a previous paper (7), the thickness monitoring of thick polycrystalline silicon film was reported wherein an improved infrared radiation method was employed. However, uncertainties remained regarding precise control of the thickness of silicon epitaxial layers. A lack of reproducibility was observed in determining the difference between the deposition rate of polycrystalline films and epitaxial single crystal layers. To solve this problem a novel technique was devised. A silicon substrate, in which a thin "buried" insulating film was formed by ion implantation was used as a test sample and included in a deposition run with other substrates which had not been ion implanted. The thickness of the single crystal deposit on the ion implanted test sample was measured during growth using an optical interference method. Ion implantation of the test sample provides the difference in refractive index between the substrate and the deposit which is required for monitoring the thickness by the optical method. In this note, results using this technique are reported.

The experiment was carried out in the same horizontal epitaxial reactor that was used in a previous investigation (7). The growth temperature was 1220°C [corrected for emissivity according to Allen's data (9)]. The reactant gas ratio was  $\text{SiCl}_4/\text{H}_2 = 0.005$  for this  $\text{SiCl}_4\text{-H}_2$  system. The substrate was Czochralski grown, (111) oriented, and phosphorus doped with a resistivity of 5-10 ohm-cm. Nitrogen implantation of the substrate was performed with fluences of  $1 \times 10^{18}$  ion/cm<sup>2</sup> and by 170 keV energy at room temperature. Cal-

\* Electrochemical Society Active Member.

Key words:  $\text{SiCl}_4\text{-H}_2$  reaction, infrared radiation, nitrogen-implanted silicon substrate, epitaxial growth on implanted substrate, precise control of film thickness.

Table I. Development of in process film thickness monitoring

YEAR	INFRARED RADIATION METHOD	LASER METHOD	ILLUMINATOR METHOD
1967	APPLICATION FOR SiO <sub>2</sub> (1)		
1968			
1969			
1970	APPLICATION FOR Al <sub>2</sub> O <sub>3</sub> (2)		APPLICATION FOR SPUTTER SiO <sub>2</sub> (3)
1971			
1972	APPLICATION FOR POLY Si (4)		
1973		APPLICATION FOR CVD SiO <sub>2</sub> (5) (He-Ne LASER 6328 Å)	
1974		APPLICATION FOR POLY Si (6)	
1975	APPLICATION FOR Si EPI (7,8)	APPLICATION FOR Si EPI (9) (He-Ne IR LASER 1.15 μm)	
1976			

ulation of the nitrogen profile based on LSS theory (10) predicts a Gaussian distribution with a projected range  $R_p = 0.46 \mu\text{m}$ , and a range spread  $\Delta R_p = 0.1 \mu\text{m}$ . The peak of the nitrogen concentration was  $4 \times 10^{22}/\text{cm}^3$ . A  $\text{Si}_3\text{N}_4$  film in the silicon substrate was formed after annealing 30 min at 1200°C in dry nitrogen. The epitaxial layer was grown on the "buried" nitride layer in the substrate (11) by the  $\text{SiCl}_4\text{-H}_2$  reaction as shown in Fig. 1. During the epitaxial growth, infrared radiation emitted from the substrate was received by a PbS cell. All but the 2.0 μm wavelength radiation was excluded with a filter (12). The signal was amplified and recorded as interference waves on the recorder. Since the period of radiation can be related to the thickness of the epitaxial layer, the interference pattern can be used to monitor the thickness during the epitaxial growth.

Figure 2 is the result of monitoring when the epitaxial layer was deposited on the nitrogen-implanted silicon substrate. The abscissa reveals both reaction time and film thickness measured by the Talystep. One cycle of the interference wave was equivalent to approximately 0.28 μm in film thickness when the glancing angle of the photocell was 40°. In this figure, the solid line is an observed value and the broken line represents a calculated one using the following equation

$$T = 1 - \rho \quad [1]$$

where  $T$  is transmissivity and  $\rho$  is reflectivity. The reflectivity equation for the reflection in unpolarized light is

$$\rho = (|R_p|^2 + |R_s|^2)/2 \quad [2]$$

where  $R_p$  and  $R_s$  are reflective coefficients parallel and perpendicular to the plane of incidence in polarized light, respectively. The formula for three layers is (13)

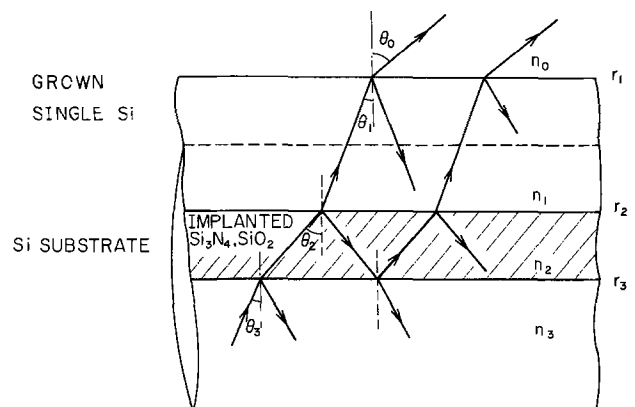


Fig. 1. Schematic model for the occurrence of an interference pattern by a silicon epitaxial single crystal layer on nitrogen-implanted silicon substrate.



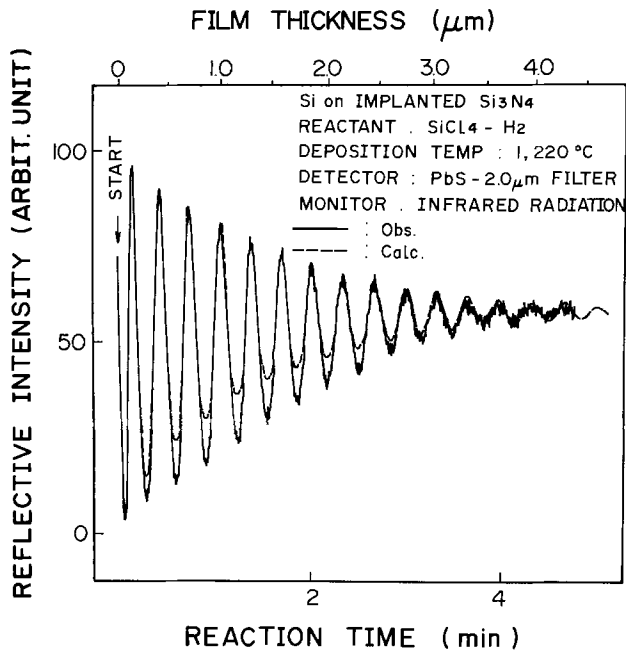


Fig. 2. Interference wave pattern when the silicon epitaxial layer was grown on the nitrogen-implanted silicon substrate.

$$R = \frac{r_{32} + r_{21}e^{-2i\delta_2} + r_{10}e^{-2i(\delta_1 + \delta_2)} + r_{32}r_{21}r_{10}e^{-2i\delta_1}}{1 + r_{21}r_{10}e^{-2i\delta_1} + r_{32}r_{21}e^{-2i\delta_2} + r_{32}r_{10}e^{-2i(\delta_1 + \delta_2)}} \quad [3]$$

where  $r_{ij}$  is the Fresnel reflection coefficient of the interface

$$\delta_1 = \frac{2\pi}{\lambda} n_1^* d_1 \cos \theta_1 \quad [4]$$

$$\delta_2 = \frac{2\pi}{\lambda} n_2^* d_2 \cos \theta_2 \quad [5]$$

$$n_1^* = n_1 - ik \quad [6]$$

$$k = \alpha\lambda/4\pi \quad [7]$$

where  $\delta_i$  = phase retardation in wavelength  $\lambda$  on crossing the layer,  $n$  = refractive index,  $d_i$  = film thickness,  $\theta_i$  = refractive angle in each layer,  $k$  = extinction coefficient, and  $\alpha$  = absorption coefficient at 2.0  $\mu\text{m}$  wavelength. The refractive index of silicon and the extinction coefficient were taken as 3.62 and 0.13, respectively. This refractive index of silicon was obtained from extrapolation to the growth temperature, 1200°C, using the value of  $n = 3.45$  in 2.0  $\mu\text{m}$  wavelength at room temperature (14) and the temperature dependence on the refractive index between 80° and 400°K (15). Improvement was observed in the maximum monitoring thickness,  $d_{\text{max}}$ , compared with the result of the polycrystalline silicon film (7). In the epitaxial case,  $d_{\text{max}}$  increased to approximately 3.9  $\mu\text{m}$ . However, the ef-

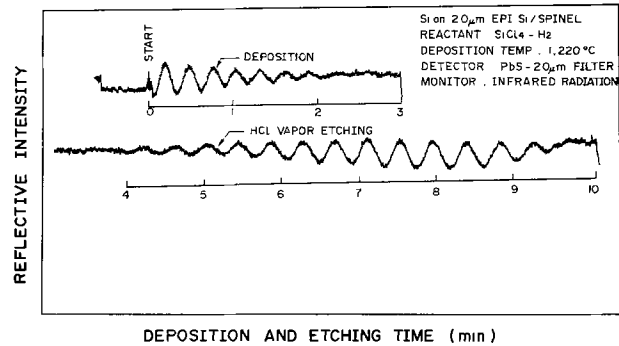


Fig. 3. Interference patterns when the silicon epitaxial layer and then HCl vapor etching were successively formed on the silicon-on-spinel substrate.

fective  $d_{\text{max}}$  of the epitaxial layer was (3.9 - 0.3)  $\mu\text{m} = 3.6 \mu\text{m}$  because of the thin layer (0.3  $\mu\text{m}$  thickness) of silicon on the  $\text{Si}_3\text{N}_4$  layer implanted into silicon substrate. The calculated pattern approximately coincided with the experimental pattern. The crystallinity of the epitaxial layer was not as good as that of the layer grown onto the usual silicon substrate; stacking fault densities were  $10^4 \sim 10^5/\text{cm}^2$  after a Sirtl etch. However, there was no problem in thickness monitoring because the implanted substrate was used only for the test sample.

The above result was confirmed by the next experiment as shown in Fig. 3. The epitaxial growth and HCl vapor etching process were successively carried out on a silicon-on-spinel substrate; the spinel was (111) oriented and the epitaxial layer on the spinel was 2.0  $\mu\text{m}$  in thickness. The maximum monitoring thickness,  $d_{\text{max}}$ , 3.9  $\mu\text{m}$  (total thickness of the spinel-epitaxial and this epitaxial layers) proved to be the same for the layer grown on the spinel and the nitrogen-implanted silicon substrate. In this case, the effective  $d_{\text{max}}$  was (3.9 - 2.0)  $\mu\text{m} = 1.9 \mu\text{m}$ . Autodoping from the spinel substrate caused contamination of the silicon epitaxial layer near the spinel test sample (16). Therefore, the wholly or partially nitrogen-implanted substrate was better in realizing contamination-free epitaxial layers of good quality.

Results of the  $d_{\text{max}}$  are tabulated in Table II. With increase of the growth temperature, the  $d_{\text{max}}$  showed a tendency of increasing to a maximum and then decreasing for the polycrystalline silicon film (7). The same tendency might be expected for the epitaxial layer. Competition between increasing radiation intensity and increasing absorption coefficient of silicon (the latter becoming dominant at higher temperature) may bring about the tendency of increase-maximum-decrease with increase of the deposition temperature. The absorption coefficient at 1200°C may be estimated as  $8 \times 10^5 \text{ cm}^{-1}$  from the observed interference pattern, while that at room temperature is  $5 \times 10^{-2} \text{ cm}^{-1}$  (17).

Table II. Maximum monitoring thickness,  $d_{\text{max}}$ , when the single or polycrystalline silicon film was grown on the various substrates

Grown film		Silicon single crystal		Polycrystalline silicon	
Substrate		Nitrogen-implanted Si substrate	Epitaxial layer on spinel	$\text{Si}_3\text{N}_4$ film on Si substrate	Thermally grown $\text{SiO}_2$ film on Si substrate
Growth condition	Reactants Growth temp	$\text{SiCl}_4\text{-H}_2$ 1220°C	$\text{SiCl}_4\text{-H}_2$ 1220°C	$\text{SiCl}_4\text{-H}_2$ 1220°C	$\text{SiCl}_4\text{-H}_2$ 1220°C
Maximum monitoring thickness, $d_{\text{max}}$		Sub. (3.6 + 0.33) $\mu\text{m}$ = 3.9 $\mu\text{m}$	Sub. (1.9 + 2.0 $\mu\text{m}$ = 3.9 $\mu\text{m}$	2.9 $\mu\text{m}^*$ (3.0 $\mu\text{m})^{**}$	3.1 $\mu\text{m}^*$ (3.3 $\mu\text{m})^{**}$
Control accuracy		$\pm 0.03 \mu\text{m}$	$\pm 0.03 \mu\text{m}$	$\pm 0.03 \mu\text{m}^?$	$\pm 0.03 \mu\text{m}^?$
Remark		Crystallinity—no problem for monitoring	Autodoping $\rightarrow$ contamination	Difference from thickness of single crystal layer	

\* Maximum monitoring thickness for the single crystal silicon film, calibrated by the correlation between thickness of the polycrystalline silicon film and that of the silicon epitaxial layer

\*\* Maximum monitoring thickness for the polycrystalline silicon film.



By further developing the monitoring of the CVD film thickness, in process thickness monitoring of the silicon epitaxial layer was investigated in order to control the thickness precisely. Using the nitrogen-implanted silicon substrate as the test sample, thickness monitoring of the single crystal layer during epitaxial growth was carried out by the improved method. The silicon epitaxial layer, grown at 1220°C by the  $\text{SiCl}_4\text{-H}_2$  reaction, was controlled within  $\pm 0.03 \mu\text{m}$  up to  $3.9 \mu\text{m}$  in thickness, when the filter of  $2.0 \mu\text{m}$  was adapted to detect the infrared radiation emitted from the substrate. The maximum monitoring thickness may be limited by the large absorption coefficient in silicon material, which has a large temperature dependence. The competition between the radiation intensity and the absorption coefficient may bring about the  $d_{\text{max}}$  tendency of increase-maximum-decrease with increase of the growth temperature. The smaller absorption coefficient, approximately  $\frac{1}{2}$  in the single crystal layer compared with that in the polycrystalline silicon film, caused enhancement of the maximum monitoring thickness for the single crystal layer, approximately 30% larger than that for the polycrystalline silicon film.

#### Acknowledgments

The authors express their sincere gratitude to Mr. S. Nishida, Mr. M. Ono, and Dr. Y. Sugita for their valuable discussions and encouragement, to Dr. T. Tsuchimoto for helpful discussion of the ion implantation, and to Mr. Y. Sasaki for his help in the calculation.

Manuscript submitted Sept. 24, 1975; revised manuscript received Dec. 29, 1975. This was Paper 254 RNP presented at the Dallas, Texas, Meeting of the Society, Oct. 5-9, 1975.

Any discussion of this paper will appear in a Discussion Section to be published in the December 1976 JOURNAL. All discussions for the December 1976 Discussion Section should be submitted by Aug. 1, 1976.

Publication costs of this article were partially assisted by Hitachi, Limited.

#### REFERENCES

1. D. J. Dumin, *Rev. Sci. Instr.*, **38**, 1107 (1967).
2. J. F. Roberts, C. A. Clark, and A. C. Dumbi, *ibid.*, **41**, 247 (1970).
3. R. Glang, in "Handbook of Thin Film Technology," L. I. Maissel and R. Glang, Editors, pp. 1-114, McGraw-Hill Book Co., New York (1970).
4. T. I. Kamins and C. J. Dell'Oca, *This Journal*, **119**, 112 (1972).
5. K. Sugawara, T. Yoshimi, H. Okuyama, and T. Shirasu, in "Chemical Vapor Deposition, Fourth International Conference," G. F. Wakefield and J. M. Blocher, Jr., Editors, p. 205, The Electrochemical Society Softbound Symposium Series, Princeton, N. J. (1973); K. Sugawara, T. Yoshimi, H. Okuyama, and T. Shirasu, *This Journal*, **121**, 1233 (1974).
6. K. Sugawara, T. Yoshimi, H. Okuyama, and Y. Homma, *ibid.*, **121**, 1235 (1974).
7. K. Sugawara, Y. Nakazawa, and T. Yoshimi, *ibid.*, **123**, 586 (1976).
8. K. Sugawara, T. Yoshimi, Y. Nakazawa, and K. Itoh, *This work*.
9. F. G. Allen, *J. Appl. Phys.*, **28**, 1510 (1957).
10. J. Lindhard, M. Scharff, H. E. Schiott, and K. Dan, *Vidensk. Selsk. Mat.-Fys. Medd.*, **33**, 1 (1963).
11. R. J. Dexter, S. B. Watelski, and S. T. Picraux, *Appl. Phys. Letters*, **23**, 455 (1973).
12. I. Honda, N. Hashimoto, M. Ashikawa, and S. Muto, Abstract 23, 7th Symposium on Semiconductors and Integrated Circuits Technology of the Electrochemical Society of Japan, Nov. 21-22, 1974 (in Japanese).
13. M. Born and E. Wolf, "Principles of Optics," p. 632, Pergamon Press, Oxford (1970).
14. T. S. Moss, G. J. Burrell, and B. Ellis, "Semiconductor Opto-Electronics," p. 301, Butterworths, London (1973).
15. W. Paul and H. Brooks, "Progress in Semiconductors," Vol. 7, p. 135, John Wiley & Sons Inc., New York (1963).
16. Y. S. Chiang and G. W. Looney, *This Journal*, **120**, 550 (1973).
17. W. R. Runyan, "Silicon Semiconductor Technology," p. 190, McGraw-Hill Book Co., New York (1965).

## Reaction of Anodized GaAs Surfaces in Hydrogen Atmospheres and Their Applications

R. M. Malbon\*

*Hughes Aircraft Company, Torrance Research Center, Torrance, California 90509*

and J. M. Whelan\*

*Materials Science Department, University of Southern California, Los Angeles, California 90007*

The growth of anodic oxides with well-controlled thicknesses from aqueous and nonaqueous solutions has been described (1-5). These oxides with thicknesses between  $\sim 200$  and  $\sim 2500 \text{ \AA}$  are soluble in dilute solutions of nonoxidizing mineral acids. Sequential anodization and oxide dissolution have been used to thin GaAs epitaxial films in a controlled manner (3). Composition of the anodic oxide has been reported to be an amorphous equimolar mixture of  $\text{Ga}_2\text{O}_3$  and  $\text{As}_2\text{O}_3$  with a variation in the mole ratio near the outside surface opposite to the GaAs-oxide interface (6). This paper is concerned with the consequences of heating anodized GaAs in hydrogen under various conditions and their application to ion implantation and epitaxial growth.

\* Electrochemical Society Active Member.

Key words: oxide reduction, oxides of gallium, epitaxial growth.

#### Experimental

The GaAs used in this study was either low resistivity  $n^+$  type Te-doped boat-grown substrate slices or epitaxial films grown on those substrates. Etch pit densities varied from 1000 to 3000  $\text{cm}^{-2}$ . Orientation of the epitaxial film and substrate surfaces were  $3^\circ$  off the  $\langle 100 \rangle$  toward the  $\langle 111 \rangle$ . The substrate slices were chemically polished to remove  $\sim 75 \mu\text{m}$  after mechanical lapping so as to produce a mirrorlike damage-free surface. As-grown surfaces were used for those samples with epitaxial films. The anodizing solution consisted of deionized water acidified to a pH of 2.4 by adding a sufficient amount of a  $\text{H}_3\text{AsO}_4$  solution. The anodic oxides were grown at room temperature to various thicknesses by adjusting the final voltages using a current-limited supply. Platinum foil served as

the cathode. The GaAs anodes were supported by titanium tweezers which had been previously anodized except for a small area about the tips. Care was taken to immerse the GaAs and its supporting tweezer tips in the anodizing solution before applying a bias. After immersion the bias was adjusted to give the desired anodic oxide film thickness as judged by color comparison with a previously prepared group of oxidized GaAs samples. The oxide thickness of these samples had been verified by etching a section of the oxide in aqueous HCl and measuring the oxide step height with a commercial stylus step-height analyzer. It is to be noted that the anodization procedure described above clearly delineated doping inhomogeneities and local surface damage if present.

The anodized samples were annealed under a  $H_2$  atmosphere using a quartz envelope/furnace assembly shown schematically in Fig. 1. The intended purpose was to provide a simple gas-flow pattern with a minimum linear gas velocity of  $10 \text{ cm sec}^{-1}$  at the annealing temperatures.

Inlet  $H_2$  from a liquid  $H_2$  source was preheated by passage through one leg of the horizontal U tube and passed over a small quartz boat containing solid GaAs and a liquid Ga solution saturated with As at the annealing temperature. This source was intended to provide a fraction of the  $As_4$  pressure necessary for equilibrium. Samples to be annealed were mounted on a quartz support assembly attached to a fine quartz rod for easy positioning. The over-all assembly was intended to have a low heat capacity so that it would warm and cool quickly as a resistance furnace on rollers was positioned either for annealing or cooling/loading. Samples cooled typically from the annealing temperatures to  $100^\circ\text{C}$  in  $\sim 5$  min. After loading, the chamber was flushed for a minimum of 1 hr so that the air +  $H_2O$  concentrations were under  $\sim 3$  ppm. Based on prior experience, the  $H_2O$  concentration rises to  $\sim 10$  ppm at the annealing temperatures due to outgassing of the quartz (7). Results of annealing are given below. For a typical sample, chemically polished and anodized to create  $1400\text{\AA}$  of oxide, the result of annealing for 15 min at  $740^\circ\text{C}$  in  $H_2$  is the formation of a high density of small Ga droplets as indicated by Fig. 2. The droplets dissolved preferentially in aqueous HCl or in hot  $H_2$  gas which would be expected for Ga. The resultant GaAs surfaces exposed and under the Ga droplets had height irregularities due to pitting of less than  $1000\text{\AA}$ . Densities of the droplets varied from a value of  $3 \times 10^8 \text{ cm}^{-2}$  in the central 70-80% of the wafer area to near zero at the extreme somewhat rounded edges of the wafer. A feature to be noted is the relatively small spread in the droplet sizes. As indicated in Fig. 2, the average diameter at the interface is approximately  $0.4 \mu\text{m}$ . Based on the estimated volume of an average droplet and their number per  $\text{cm}^2$  of substrate surface, the volume of Ga in the droplets agrees within 20% of the volume expected if the only source of Ga were that resulting from the reduction of the oxide. This agreement is coincidental as is described below.

The sequence of changes upon annealing anodized GaAs surfaces in the  $H_2$  atmospheres is as follows. Provided the temperature is high enough for the re-

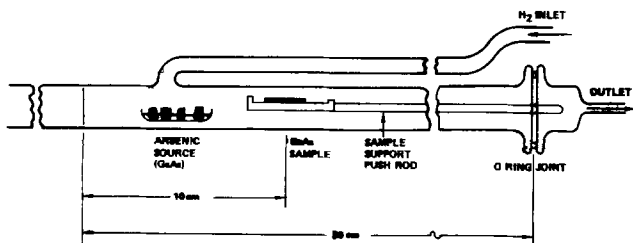


Fig. 1. Quartz annealing assembly for anodized GaAs samples. A 50 cm long resistance furnace on tracks may be centered on the sample or rolled to the left for rapid sample cooling.

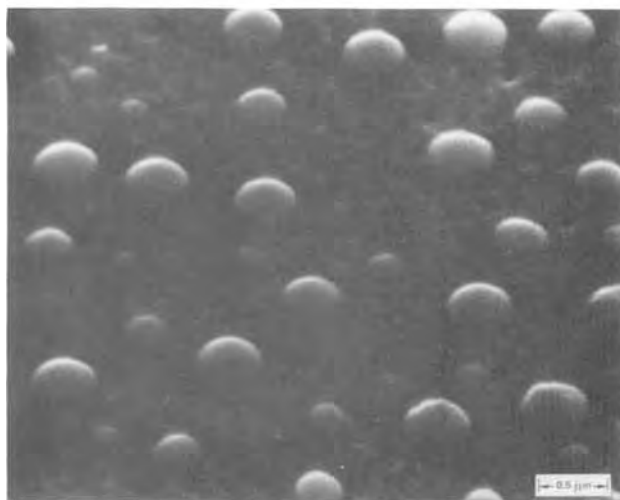
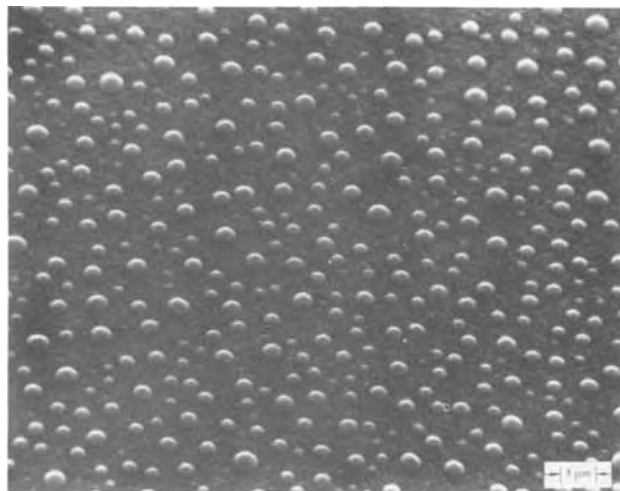


Fig. 2. SEM photographs of an anodized GaAs surface after a 15 min anneal in  $H_2$  at  $740^\circ\text{C}$ . The anodic oxide thickness was  $1400\text{\AA}$ . Top: original magnification 12,500X; bottom: original magnification 50,000X.

duction of the oxide to yield Ga droplets, the droplets form quickly at densities possibly as high as  $10^9$ - $10^{10} \text{ cm}^{-2}$ . The larger droplets initially grow at the expense of the smaller ones. With larger annealing times, the droplet density decreases eventually to zero. Rates for these changes increase with temperature. Figure 3 shows the results of annealing a GaAs surface with a  $1000\text{\AA}$  anodic oxide for 10 min in  $H_2$  at  $800^\circ\text{C}$ . The droplet density is smaller,  $\sim 7 \times 10^7 \text{ cm}^{-2}$ , but the spread in size is somewhat larger than for that shown in Fig. 2. Longer annealing causes the droplet density to decrease, in part, because of droplet migration and coalescence. Evidence for this is shown in Fig. 4. This sample is identical to that represented by Fig. 3 except that the annealing time at  $800^\circ\text{C}$  was 20 min. The smoothed droplet traces or rivulets have moved from left to right. Further evidence for the rivulets was apparent in optical photomicrographs at 700X. The tracks are roughly parallel but do not follow straight-line courses. The consequence of annealing a very thin GaAs anodic film  $\sim 200\text{\AA}$  for 20 min in  $H_2$  is shown in Fig. 5. The average interfacial droplet diameter is  $\sim 0.2 \mu\text{m}$  and the density is  $\sim 3 \times 10^8 \text{ cm}^{-2}$ . Gallium in the droplets is approximately half that in the original oxide. Both the exposed and GaAs droplet-covered surfaces were smoother than that shown in Fig. 4 which was treated identically except that the original oxide was five times thicker.

Control samples of GaAs with chemically polished surfaces did not show the characteristic droplet forma-

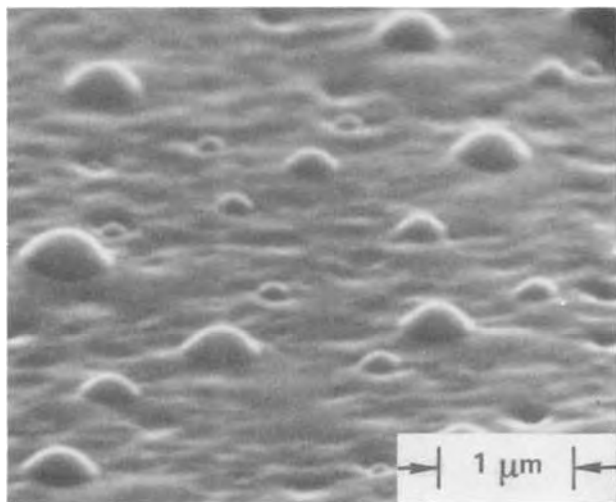


Fig. 3. SEM photograph of an anodized GaAs surface after a 10 min anneal in  $H_2$  at  $800^\circ C$ . The anodic oxide thickness was  $1000\text{\AA}$ . Original magnification 18,000X.

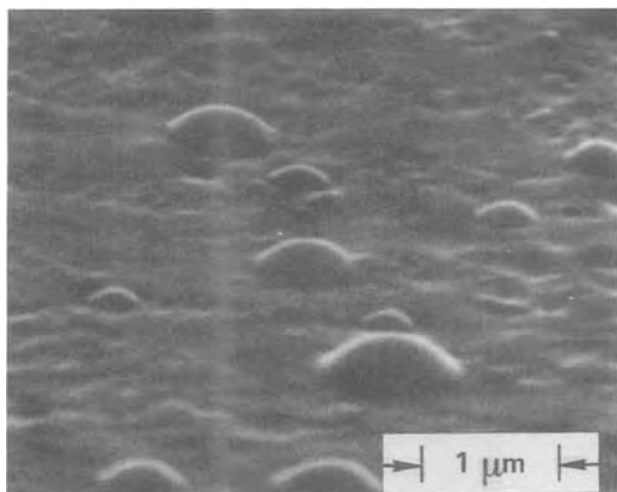


Fig. 4. SEM photograph of an anodized GaAs surface after a 20 min anneal in  $H_2$  at  $800^\circ C$ . The anodic oxide thickness was  $1000\text{\AA}$ . Original magnification 18,000X.

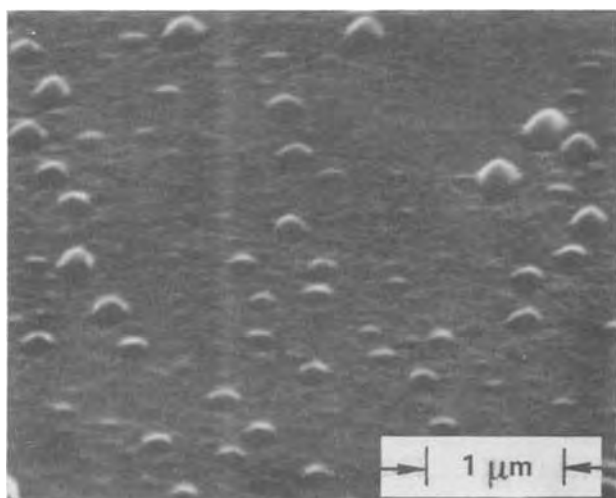


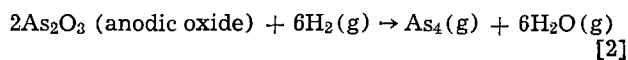
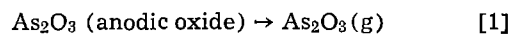
Fig. 5. SEM photograph of an anodized GaAs surface after a 20 min anneal in  $H_2$  at  $800^\circ C$ . The anodic oxide thickness was  $200\text{\AA}$ . Original magnification 18,000X.

tion upon annealing as did those with anodic oxides. The resultant surfaces were, by comparison, featureless except in areas of strain at the edges or near an incompletely removed scratch. As an example, large Ga droplets formed along the original sawed edges of the wafers. This also illustrates the point that arsenic is lost much more rapidly from a saturated Ga solution than from a strain-free GaAs surface.

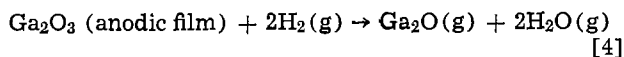
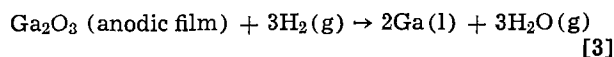
These results and supporting ones may be summarized as follows. The droplet size resulting from short anneals increases with the thicknesses of the original anodic oxides. Surface textures of the GaAs surfaces indicate that the densities of droplets may reach values substantially in excess of the highest noted,  $5 \times 10^8 \text{ cm}^{-2}$ . The initial source of these is the reduction of the Ga species in the oxide which at the reduction temperature must have a gallium-to-arsenic ratio substantially greater than unity. Subsequent to this, the GaAs contributes as an additional source of Ga. As the annealing period is increased, the droplets show signs of migration and eventually they disappear. The latter point requires an eventual loss of Ga to the vapor phase at a greater rate than that for As. Times required for these characteristic changes decrease with increasing annealing temperatures. These features are discussed in the following section in terms of the preliminary loss of As from the anodic oxide, the reduction of the residue to Ga, its dissolution of GaAs, and eventual removal by reaction with  $H_2O$  which is present as an impurity in the  $H_2$ .

#### Discussion

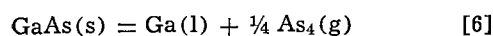
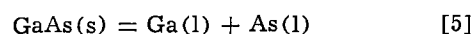
The observations described in the previous section are in accord with the conclusions of Feldman *et al.* (6) regarding the basic composition of the anodic oxide, namely, equimolar amounts of  $As_2O_3$  and  $Ga_2O_3$ . Arsenic oxide is more volatile than  $Ga_2O_3$  and is less stable with respect to reduction by a hydrogen atmosphere buffered with a given amount of water. It is reasonable to assume the selective loss of arsenic from the anodic oxide by these means upon heating in hydrogen at  $700^\circ\text{--}800^\circ\text{C}$  and as summarized by the following reactions



The involvement of Eq. [1] has been previously postulated by Feldman *et al.* upon heating anodic films in oxidizing atmospheres up to  $650^\circ\text{C}$ . Evidence has been summarized to the extensive but incomplete loss of  $As_2O_3$  from the anodic films upon heating in oxidizing atmospheres to  $>700^\circ\text{C}$  and for the formation of  $\beta\text{-Ga}_2O_3 \text{ (s)}$  and  $GaAsO_4 \text{ (s)}$  on the GaAs surface (6). This contrasts with heating in a hydrogen atmosphere. Upon heating a GaAs anodic oxide film in a hydrogen stream, a temperature is reached at which the hydrogen is sufficiently reducing to reduce  $Ga_2O_3$  in the residue of the original film. Possible reactions are represented by Eq. [3] and [4]



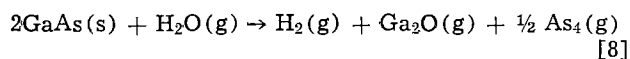
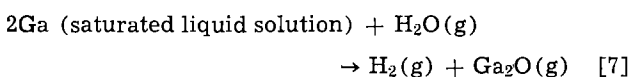
From a thermodynamic point of view one would expect [3] to prevail as the temperature rises towards  $700^\circ\text{C}$  (8-10). The existence of Ga droplets after short heating times indeed suggests that [3] dominates. This liquid droplet formation triggers another concurrent set of reactions. These are represented by Eq. [5], the dissolution of GaAs in the Ga to form a saturated solution and Eq. [6], the evaporation of arsenic from the saturated solution



The effect of Eq. [5] and [6] is to increase the amount of Ga in the saturated liquid phase as the arsenic evaporates. The rate of As evaporation is much faster from the liquid solution than from a solid GaAs surface. Since the vapor pressure of arsenic over the saturated solution and thus the evaporation rate both decrease as the drop size increases, it is to be expected that the drop size distribution will tend to cluster about a given value depending on temperature, flow rate, and the purity of the hydrogen. The mean droplet diameter will also be influenced by the anodic oxide thickness since the drops are initially formed by the reduction of the  $Ga_2O_3$ . For short heating times in very high purity  $H_2$ , the amount of arsenic lost from the GaAs surface is relatively small via dissolution in an evaporation from the liquid phase. Evidence that this is significant for longer heating times is shown by the rivulet path of a migrating droplet as can be seen in Fig. 4. The track of the droplet should depend on relative dissolution rates of GaAs along differing crystallographic directions and the gas-flow patterns.

As indicated in Fig. 2 and 5, the relative drop densities were nearly the same,  $\sim 3 \times 10^8 \text{ cm}^{-2}$ , but the mean drop size was somewhat larger for the sample with the thicker oxide. Detailed conclusions regarding relative drop sizes must be tempered by the disappearance of drops upon longer heating or at higher temperatures. Comparison of Fig. 2 with Fig. 3 illustrates this trend.

As the time of annealing in  $H_2$  is increased, the droplet density decreases and the size initially grows and then decreases. In sufficient time the drops disappear. This behavior is attributed to the reaction of water as an impurity in the  $H_2$  with Ga in the saturated liquid phase with GaAs. Although the chemical potentials of Ga in the liquid phase and in the solid GaAs are identical, the rate of reaction with water is faster at the liquid phase interface. In summary, reaction [7] proceeds faster than [8] until the liquid solution is exhausted. Reaction [8] then becomes the significant one for further surface erosion



It is implied that the consumption of Ga in [7] is accompanied by the vaporization of As from the solution or its precipitation as GaAs so that the liquid solution is saturated until exhausted.

### Applications

**Epitaxial growth.**—We have noted a consistent pattern of smoother films grown on GaAs substrates which were first anodized after chemical polishing relative to ones without chemical polishing. Furthermore, the anodized ones require a minimum of pre-cleaning before insertion in the epitaxy reactor. These are stored in polyethylene bags and simply blown off with  $N_2$  gas. Anodization was done immediately after chemical polishing and water rinsing. Optimum oxide thicknesses are within the range, 400–600Å. The CVD epitaxy system is based on a  $H_2/AsCl_3$  gaseous source which is first passed over a boat containing a Ga solution which has an encrusted surface of GaAs. The pre-growth treatment of the substrates in this process is to flush them in a pure purging  $H_2$  gas stream while the necessary operating temperatures are being established and the separate  $H_2/AsCl_3$  stream is adjusted for normal growth. During the warm-up stage, the anodic oxide on substrates is reduced and leaves a Ga residue as droplets saturated with GaAs. These droplets serve several useful functions. First, etching of the substrates due to traces of  $H_2O$  in the backflushing  $H_2$  is circumvented since the  $H_2O$  reacts preferentially with the liquid droplets. Secondly, the high density ( $\sim 5 \times 10^8 \text{ cm}^{-2}$ ) of freshly etched regions on the substrate

near the Ga droplets is expected to be excellent nucleation sites. Finally, the reaction of Ga droplets with HCl favors the rapid equilibration of  $H_2$ , HCl,  $As_4$ , and GaCl in the gas phase with the substrate. The rate of equilibration is enhanced because of the faster gas-liquid interface reaction than the corresponding gas-solid GaAs reaction. (Note that the chemical potential of Ga is the same in the substrate as it is in the saturated Ga solution.)

**High temperature encapsulant.**—Schwartz *et al.* have noted the satisfactory use of anodic oxides in weakly oxidizing atmospheres as diffusion masks (2). The oxides are currently under evaluation as surface protecting films for post-ion implantation annealing at temperatures between 700°–900°C under slightly oxidizing atmospheres. After heating, the oxides are frequently difficult to dissolve in mineral acids.

They can be reduced and removed during the last few minutes of the annealing period by replacing the slightly oxidizing atmosphere ( $N_2$ ) with a reducing one such as  $H_2$ . The residual Ga droplets can be readily removed with aqueous HCl or by dissolution in Hg. They can be also vapor etched by adjusting the  $H_2O/H_2$  ratio in the inlet  $H_2$  stream and thus be removed *in situ* at the end of the anneal.

### Summary

It has been shown that anodic and thermally grown native oxides on GaAs can be reduced by annealing in  $H_2$  atmospheres to yield GaAs surfaces with upwards of  $10^8$  Ga droplets  $\text{cm}^{-2}$ . These droplets tend to grow in size with decreased densities upon continued annealing in high purity  $H_2$  and are preferentially removed from the GaAs surface by reaction with traces of  $H_2O$  in the  $H_2$ .

Chemically polished GaAs substrates with anodic oxides 400–600Å thick are superior to those without the oxide for the growth of thin epitaxial films from the vapor phase using a  $H_2$ - $AsCl_3$ -Ga system. Advantages are attributed to (i) easier cleaning of the anodic oxide surfaces, (ii) the high density of nucleation sites generated by the preliminary reduction of the oxide, and (iii) the enhanced rate of initial equilibration of the growth atmosphere with the substrate through the rapid reaction of the liquid droplets with the vapor.

Anodic and thermally grown oxides on GaAs used as encapsulants during annealing in oxidizing atmosphere can be removed by annealing in  $H_2$  to form droplets or removed *in situ* by annealing in  $H_2$  containing a controlled amount of  $H_2O$ .

### Acknowledgments

We wish to thank Mrs. C. A. Reamer for sample preparation, H. H. Luckey and S. Hoelke for the SEM photographs, and W. B. Henderson for the epitaxial material.

Manuscript submitted Oct. 14, 1975; revised manuscript received Jan. 14, 1976.

Any discussion of this paper will appear in a Discussion Section to be published in the December 1976 JOURNAL. All discussions for the December 1976 Discussion Section should be submitted by Aug. 1, 1976.

Publication costs of this article were partially assisted by Hughes Aircraft Company.

### REFERENCES

1. R. A. Logan, B. Schwartz, and W. J. Sundburg, *This Journal*, **120**, 1385 (1974).
2. S. M. Spitzer, B. Schwartz, and G. D. Weigle, *ibid.*, **121**, 92C (1974).
3. D. L. Rode, B. Schwartz, and DiLorenzo, *Solid-State Electron.*, **17**, 1119 (1974).
4. H. Hasegawa, K. E. Forward, and H. Hartnagel, *Electron. Letters*, **11**, 53 (1975).
5. H. Hasegawa, K. E. Forward, and H. Hartnagel, *Appl. Phys. Letters*, **26**, 567 (1975).
6. L. C. Feldman, J. M. Poate, F. Ermanis, and

- B. Schwartz, *Thin Solid Films*, **19**, 81 (1973).  
 7. P. S. Vijayakumar, Private communication.  
 8. K. A. Klinedinst and D. A. Stephenson, *J. Chem. Therm.*, **4**, 565 (1972).

9. C. N. Cochran and L. M. Foster, *This Journal*, **109**, 144 (1962).  
 10. C. J. Frosch and C. D. Thurmond, *J. Phys. Chem.*, **66**, 877 (1962).

# Brief Communications



## A Study of the Phosphorus Gettering of Gold in Silicon by Use of Neutron Activation Analysis

S. P. Murarka\*

Bell Laboratories, Murray Hill, New Jersey 07974

Gold is probably the most important impurity acting as a very effective recombination center in both n- and p-type silicon (1-3). Keeping the concentration of gold (and that of other similar impurities) to a minimum is a must for those devices where high minority carrier lifetime is desirable. The reduction in the concentration of such impurities is routinely achieved by introducing a so-called gettering step (4-13) [phosphorus diffusion (1-3, 5, 10-13), mechanical damage (4, 6, 7), or implantation damage (8-10), all on the back surface of the wafers] in the processing sequence. As a result of this treatment, impurities like gold, which have fast diffusivities in silicon, diffuse toward and become trapped in the back surface of the wafer. This phenomenon of trapping impurities in the region away from the active regions of the devices has been called impurity gettering.

A variety of techniques (1-10) has been used to investigate the phenomenon of impurity gettering induced by phosphorus diffusion or mechanical or ion implantation damage. In these investigations the semiconductor was first equilibrated with an external source of impurity (so as to increase the concentration). Subsequently, the gettering was carried out and the bulk and the surface of the semiconductor were analyzed for the impurity content. To the best of the author's knowledge, no attempt other than the diode studies of Meek and Gibbon (5) has been made to study the gettering in as-received silicon wafers where the concentration of the impurities is relatively low. We have used neutron-activation analysis to study the effectiveness of gettering in as-received silicon wafers. Neutron activation analysis provides a very sensitive and generally specific method of analysis. Coupled with autoradiography, this technique offers a very powerful analytical means by which to learn the nature of impurities, and their concentration and spatial distribution in a given material. For the detection of impurities in silicon, this method (14-18) is ideal because of the very low thermal neutron capture cross section of  $^{30}\text{Si}$  and the short half-life of the radioactive product  $^{31}\text{Si}$ . In the present work neutron activation analysis was used to determine the concentration of gold in silicon wafers before and after phosphorus gettering. It may be mentioned that Tasch *et al.* (19) did use neutron activation analysis to look for the gettering of impurities on slip lines, but found that the impurity concentrations were below detection limit.

For each experiment at least two wafers from each crystal were used. To avoid any significant differences arising due to uneven distribution of impurities along the length of the boule, wafers cut adjacent to each other were selected. The slices were degreased, cleaned, and weighed. The degreasing and cleaning were done in accordance with the standard cleaning process used in semiconductor device development. Immediately thereafter, one of the slices was given the standard phosphorus gettering treatment, *i.e.*, 30 min in  $\text{PBr}_3$  at  $1000^\circ\text{C}$  with 1%  $\text{O}_2$ -99%  $\text{N}_2$  as the carrier gas. The slices were then individually placed in specially made and cleaned high purity quartz petri dishes with covers. The covered dishes were then wrapped in aluminum foil and placed in an aluminum container. Irradiations were carried out with thermal neutrons at fluxes  $\approx 1 \times 10^{13} \text{ cm}^{-2} \text{ sec}^{-1}$  for a time period of 5 hr. In a few cases small pieces cut off the silicon slices were used instead of the whole wafers. Such pieces received identical cleaning treatment and were sealed in clean quartz tubes under vacuum ( $\sim 10^{-3}$  Torr). Since the primary interest of this investigation was to determine the concentration of gold in silicon slices, no chemical separation was done prior to counting of the  $\gamma$ -ray activity. The counting of the samples was purposely delayed to let the  $^{31}\text{Si}$  activity (half-life 2.6 hr) decay out so that it made a negligible contribution to the  $\gamma$ -spectrum. The counting was thus done about 40 hr after the irradiation. The samples were counted (in a fixed-reproducible geometry) with a  $\text{Ge}(\text{Li})$  detector attached to a 1024 multichannel analyzer and data printed on a Teletype. The complete detection and counting assembly was calibrated<sup>1</sup> by use of a National Bureau of Standards source of  $\gamma$ -rays of energies varying from 0.0877 MeV of  $\text{Cd}^{109}$  to 1.836 MeV of  $\text{Y}^{88}$ . Attempts were made to identify only the 0.412 MeV peak of  $\text{Au}^{198}$  (half-life 64.7 hr) and in arsenic-doped crystals the 0.56, 0.66, and 1.22 MeV peaks of  $\text{As}^{76}$ .  $\text{As}^{76}$  energies served as the internal standards, since the doping levels of these wafers were known from the electrical measurements. In all cases, calculated concentrations of arsenic compared very well with those obtained by electrical measurements.

The following routine was followed to demonstrate that due to phosphorus gettering of the silicon wafers gold atoms had diffused away from the bulk and were trapped in the phosphorus-rich silicon near the surface.  
 (i) Each of the irradiated samples was ultrasonically

\* Electrochemical Society Active Member.  
 Key words: gettering, activation analysis, gold, phosphorus diffusion.

<sup>1</sup> In another standardization, a solution contained a known amount of Au as a blank and activity thus produced was used to calibrate the counter.

Table I. Effect of phosphorus gettering on the gold concentration in silicon

Sample number	Gold concentration, cm <sup>-3</sup>		
	Ungettered wafer	Gettered wafer	
		After P-glass etched off	After surface Si layer (~2-4 μm) etched off
1	2.9 × 10 <sup>13</sup>	2.0 × 10 <sup>13</sup>	1.2 × 10 <sup>12</sup>
2	0.9 × 10 <sup>14</sup>	2.1 × 10 <sup>14</sup>	3.0 × 10 <sup>12</sup>
3	1.2 × 10 <sup>14</sup>	2.2 × 10 <sup>14</sup>	6.1 × 10 <sup>12</sup>
4	1.4 × 10 <sup>14</sup>	6.6 × 10 <sup>14</sup>	10.7 × 10 <sup>12</sup>
5	3.2 × 10 <sup>13</sup>	5.7 × 10 <sup>13</sup>	5.3 × 10 <sup>11</sup>
6	2.5 × 10 <sup>13</sup>	3.6 × 10 <sup>13</sup>	1.0 × 10 <sup>12</sup>
7	0.9 × 10 <sup>14</sup>	2.6 × 10 <sup>14</sup>	4.2 × 10 <sup>12</sup>
8	0.4-4 × 10 <sup>12**</sup>	1.3 × 10 <sup>12</sup>	BDL*
9	0.9 × 10 <sup>12</sup>	1.0 × 10 <sup>12</sup>	BDL*
10	0.6 × 10 <sup>12</sup>	1.0 × 10 <sup>12</sup>	BDL*

\* BDL = Below detection limit for given irradiation conditions.

\*\* Sample broken.

cleaned in water and in methanol, dried, and counted. (ii) After this first counting, each sample was placed in agitated buffered hydrofluoric acid solution for 2 min to remove any oxide or glass layer on the surface, then washed, dried, and counted. (iii) The wafer was then etched to remove approximately 1 μm of silicon from the surface. The etchant was diluted Sirtl etch which consisted of a 1:1 mixture of CrO<sub>3</sub> [50 weight per cent (w/o) in water] and HF (49%) diluted with equal volume of water. A third counting was carried out. (iv) The sequence of etching and counting was repeated until the count rate of the gold activity per unit mass of silicon did not show any appreciable change. It was found that for the gettered wafers the count rate per unit mass did not show any appreciable change after about 2 μm of silicon had been etched off the surfaces. For the nongettered wafers, the count rate per unit mass was constant.

The amount of gold in the phosphorus glass which was formed on the surface of silicon during phosphorus diffusion and which was etched off in buffered hydrofluoric acid after first counting was determined (i) by counting the etchant solution containing etched-off glass and (ii) from the difference in the gold count rates between first and second countings. But for one exception where the sample was apparently contaminated during the etching sequence, the amount of gold in phosphorus glass was found to be negligible compared to the total in the silicon wafers.

Table I lists the results of this investigation. All concentrations are estimated to be within a factor of two of the true values. Figure 1 shows a plot of the residual gold concentration in the gettered silicon wafers from the surface of which the phosphorus-diffused region of ~2 μm has been etched off vs. the gold concentration in the ungettered ones. It is ap-

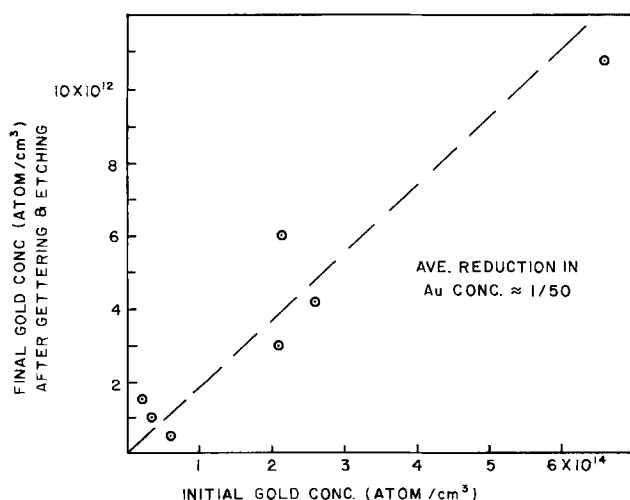


Fig. 1. Effect of phosphorus gettering on the gold concentration in silicon wafers.

parent that the gettering has resulted in an average reduction of the concentration by a factor of 50. Most of the gold initially present was trapped in the approximately 2 μm thick phosphorus-rich region near the surface and was etched off when this layer was removed. It may be mentioned here that no significant amount of gold was detected in the phosphorus glass which demonstrates that the phosphorus glass did not getter gold. Although Lambert and Reese (3) did report the presence of Au in glass, results similar to those reported here were obtained by several workers (4, 10, 20) who have investigated the phosphorus diffusion gettering in intentionally doped silicon wafers or in fabricated devices.

A careful examination of the total gold concentration (Table I) in both gettered, but unetched, and ungettered samples shows that the gold concentration was higher in almost all gettered wafers, although after removal of 2 μm of silicon by etching the concentration goes down considerably. It has been observed (3, 21-24) that during high temperature anneals the impurities from the surroundings diffuse into the semiconductor material. The observed higher amounts of gold on gettered but unetched samples may have thus resulted due to external contamination during the 1000°C/PBr<sub>3</sub> treatment. The possibility of any appreciable gold contamination due to irradiation of samples in quartz containers (22) is ruled out since all samples, gettered or ungettered, were irradiated in identical quartz containers. It may be emphasized that

this increase (by a factor of  $2^{+3}_{-2.6}$ ) in the amount of gold due to external contamination during PBr<sub>3</sub> treatment is relatively insignificant and of secondary importance since the phosphorus gettering has been very effective in leading to a reduction of gold concentration by a factor of  $20^{+40}_{-6}$  (Table I).

Recently, Seidel and Meek (10, 25, 26) have proposed that the gettering mechanism for phosphorus diffusion is solubility enhancement and ion pairing (26) of the substitutional metal ion (acceptor). At lower gold concentrations, such as those in our silicon wafers, essentially all gold could be expected to be paired with phosphorus in the phosphorus-rich (~10<sup>20</sup>-10<sup>21</sup> cm<sup>-3</sup>) silicon surface, resulting in very effective gettering of gold. The good gettering observed in the present case (Fig. 1) thus very well supports the enhanced solubility mechanism.

### Acknowledgments

The author would like to thank J. E. Riley, Jr. and S. S. Voris for their help throughout this investigation. He wishes also to thank W. J. Bertram, H. L. Levinstein, and R. S. Wagner for their help, interest, and encouragement in this work.

Manuscript submitted Oct. 6, 1975; revised manuscript received Jan. 7, 1976.

Any discussion of this paper will appear in a Discussion Section to be published in the December 1976 JOURNAL. All discussions for the December 1976 Discussion Section should be submitted by Aug. 1, 1976.

Publication costs of this article were partially assisted by Bell Laboratories.

### REFERENCES

1. A. Goetzberger and W. Shockley, *J. Appl. Phys.*, **31**, 1821 (1960).
2. S. Ing, R. E. Morrison, L. L. Alt, and R. W. Aldrich, *This Journal*, **110**, 533 (1963).
3. J. L. Lambert and M. Reese, *Solid-State Electron.*, **11**, 1055 (1968).
4. M. Nakamura, T. Kato, and N. Oi, *Japan. J. Appl. Phys.*, **7**, 512 (1968).
5. R. L. Meek and C. F. Gibbon, *This Journal*, **121**, 444 (1974).
6. E. J. Mets, *ibid.*, **112**, 420 (1965).
7. M. Kikuchi and S. Iijima, *J. Phys. Soc. Japan.*, **12**, 824 (1957).



8. T. M. Buck, K. A. Pickar, J. M. Poate, and C. M. Hsieh, *Appl. Phys. Letters*, **21**, 485 (1972).
9. T. M. Buck, J. M. Poate, K. A. Pickar, and C. M. Hsieh, *Surface Sci.*, **35**, 362 (1973).
10. T. E. Seidel and R. L. Meek, in "Proceedings of the 2nd International Conference on Ion Implantation in Semiconductors and Other Materials," B. L. Crowder, Editor, p. 305, Plenum Press, New York (1973).
11. E. Kooi, *This Journal*, **111**, 1383 (1964).
12. W. R. Wilcox, T. J. Lachappelle, and D. H. Forbes, *ibid.*, **111**, 1377 (1964).
13. S. F. Cagnina, *ibid.*, **116**, 498 (1969).
14. J. P. Cali, "Trace Analysis of Semiconductor Materials," The Macmillan Co., New York (1964).
15. K. G. Heinen and G. B. Larrabee, *Anal. Chem.*, **38**, 1853 (1966).
16. W. Gebuhr, J. Martin, and E. Haas, *Z. Anal. Chem.*, **200**, 266 (1964).
17. G. B. Larrabee and J. A. Keenan, *This Journal*, **118**, 1351 (1971).
18. G. B. Larrabee and H. G. Carlson, in "Silicon Device Processing," C. P. Marsden, Editor, p. 375, NBS Special Publication 337, U.S. Gov't. Printing Press, Washington, D. C. (1970).
19. A. F. Tasch, Jr., D. D. Buss, H. R. Huff, T. E. Hartman, and V. R. Porter, in "Semiconductor Silicon 1973," p. 658, H. R. Huff and R. R. Burgess, Editors, The Electrochemical Society Softbound Symposium Series, New York (1973).
20. M. L. Joshi and S. Dash, *J. Appl. Phys.*, **37**, 2454 (1966).
21. I. Fränz and W. Langheinrich, *Telefunkenzeitung*, **39**, 365 (1966).
22. P. F. Schmidt, R. A. Kushner, and D. V. McCaughan, *Proc. IEEE*, **62**, 1220 (1974).
23. J. E. Riley, Unpublished work.
24. S. P. Murarka, To be published.
25. R. L. Meek, T. E. Seidel, and A. G. Cullis, *This Journal*, **122**, 786 (1975).
26. R. L. Meek and T. E. Seidel, *J. Phys. Chem. Solids*, **36**, 731 (1975).

## Effect of Heat-Treatment of GaAs Encapsulated by SiO<sub>2</sub>

B. Molnar\*

Naval Research Laboratory, Washington, D. C. 20375

There is considerable interest in the ion-implantation doping of GaAs, especially in its application to device structures which require submicron-thick doped layers. For most of the applications of ion implantation, it is necessary to heat-treat GaAs at about 800°C in order to remove the irradiation damage (1) and to increase the electrical activity of the implanted ions (2). However, GaAs begins to undergo significant dissociation (3) at temperatures  $\geq 600^\circ\text{C}$ . In addition, there is evidence (4) that implanted GaAs begins to dissociate at an even lower temperature  $< 500^\circ\text{C}$ . In order to prevent the dissociation, coating materials such as SiO<sub>2</sub>, Si<sub>3</sub>N<sub>4</sub>, or AlN have been applied prior to high temperature annealing. However, Ga is relatively fast diffusing in SiO<sub>2</sub> (5), and it has been shown with backscattering measurements (6) that Ga accumulates at the surface of SiO<sub>2</sub> or Si<sub>3</sub>N<sub>4</sub> layers on GaAs substrate following anneals at 700°-800°C. The loss of As or Ga from the surface of GaAs can give rise to large changes in the electrical properties. The affected surface layer may considerably influence the electrical properties of the implanted thin layers.

The purpose of this communication is to report the results of the investigation on the protective quality of rf-sputtered SiO<sub>2</sub> thin films. In order to avoid the complication of implanted layers, the protective quality of SiO<sub>2</sub> on unimplanted GaAs substrates was investigated. The protective quality of the SiO<sub>2</sub> was measured by its ability to maintain the background doping concentration.

The GaAs substrates used were Te doped, n-type with an electron concentration of  $2 \times 10^{17}/\text{cm}^3$ . Prior to loading in the sputtering system, the substrates were etched. An oxide film of about 2000Å thick was deposited on room temperature GaAs substrates by rf sputtering of a SiO<sub>2</sub> target. Etching rates, which indicate the quality of the films, were about 15 Å/sec in P etch. The encapsulated GaAs samples were sealed in a high purity ampul in order to avoid Cu contamination. Vacuum heat-treatment was performed between 500° and 900°C, and after the anneal the ampuls were quickly cooled to room temperature. After heat-treatment, the back side of the samples was etched, and the oxide was removed by HF. For electrical evaluation the back side was provided with a Sn-Au

spot-welded ohmic contact. Schottky barrier metal contacts were sputtered Au delineated by the standard photolithographic technique.

The carrier concentration vs. depth data obtained by using the Schottky barrier technique while successively etching away thin layers are shown in Fig. 1. Before annealing the distribution of carriers was uniform, at the  $2 \times 10^{17}/\text{cm}^3$  level. After heat-treating the GaAs at 800°C for 1 hr, the electron concentration decreased rapidly to around a few times  $10^{15}/\text{cm}^3$  below the surface and then increased to the background doping level at a depth of approximately 1μ. After a 900°C anneal treatment the carrier concentration distribution moved deeper into the sample. The experimental carrier concentration could be regarded as the Te compensation by indiffusing acceptors. The indiffusing acceptors are represented by a complementary error function distribution. The experimental data are, therefore, the superposition of the n-type back-

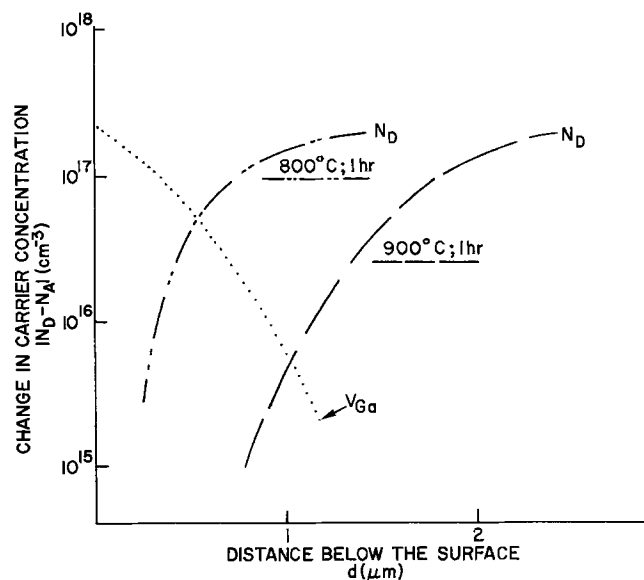


Fig. 1. Change in carrier concentration as a function of depth. Before annealing the distribution is uniform at  $2 \times 10^{17}/\text{cm}^3$ . The distribution of gallium vacancies ( $V_{\text{Ga}}$ ) after 1 hr annealing at 800°C is also indicated.

\* Electrochemical Society Active Member.  
Key words: annealing, GaAs, silicon dioxide, electrical activity, gallium vacancy.

ground doping and a p-type complementary error function distribution. From the appropriate complementary error function, a diffusion coefficient of about  $3 \times 10^{-13}$  cm<sup>2</sup>/sec at 800°C was deduced. By considering the possible out- and in-diffusing species, i.e., Si, O, Te, Ga, and As, it has been found that only Ga vacancies (7) are p-type, have diffusion coefficients in the neighborhood of the deduced one, and an adequate equilibrium concentration for the proposed in-diffusing species. A similar conclusion was reached by S. Y. Chiang and G. L. Pearson by examining heat-treated, but unencapsulated GaAs (7). In conclusion, it has been found that heat-treatment produces significant changes in the surface carrier concentration on the SiO<sub>2</sub> encapsulated GaAs. Furthermore, the results of this experiment present strong evidence that the acceptors formed by the heat-treatment of SiO<sub>2</sub> encapsulated GaAs are due to Ga vacancies.

We are presently carrying out similar type investigation of Si<sub>3</sub>N<sub>4</sub> and AlN films deposited by different methods.

#### Acknowledgment

This work was supported by the Naval Electronic Systems Command.

Manuscript received Dec. 29, 1975. This was Paper 264 RNP presented at the Dallas, Texas, Meeting of the Society, Oct. 5-9, 1975.

Any discussion of this paper will appear in a Discussion Section to be published in the December 1976 JOURNAL. All discussions for the December 1976 Discussion Section should be submitted by Aug. 1, 1976.

Publication costs of this article were partially assisted by the Naval Research Laboratory.

#### REFERENCES

1. L. W. Aukerman, P. W. Davis, R. D. Graft, and T. S. Shillady, *J. Appl. Phys.*, **34**, 3590 (1963).
2. J. D. Sansburg and J. F. Gibbons, *Rad. Effects*, **6**, 269 (1970).
3. C. Y. Lou and G. A. Somorjai, *J. Chem. Phys.*, **55**, 4554 (1971).
4. D. J. Mazey and R. S. Nelson, *Rad. Effects*, **1**, 229 (1969).
5. C. J. Frosch and L. Derick, *This Journal*, **104**, 547 (1957).
6. J. Gyulai, J. W. Mayer, I. V. Mitchell, and V. Rodriguez, *Appl. Phys. Letters*, **17**, 332 (1970).
7. S. Y. Chiang and G. L. Pearson, *J. Appl. Phys.*, **46**, 2986 (1975).

## A New Aqueous Solution for the Anodic Oxidation of GaAs

D. Law and C. A. Lee\*

Department of Electrical Engineering, Cornell University, Ithaca, New York 14850

A number of reports have recently appeared (1, 2) concerning the anodic oxidation of GaAs which utilize nonaqueous solvents. These solutions purport to give higher quality oxide films, in terms of density and resistivity, than previously proposed aqueous solutions (3, 4). The deficiencies of these aqueous solutions variously involved dissolution of the oxide during growth, stability of the solution against impurities, and a tendency to produce a porous oxide of relatively low resistivity and dielectric strength.

In this communication we present a new aqueous solution for the anodic oxidation of GaAs which produces films of equal quality compared to those produced by solutions containing nonaqueous solvents and which is advantageous in a number of other respects (5). This new solution utilizes a common salt that is quite inexpensive compared to solutions containing ethylene glycol, or N-methylacetamide, and is quite safe to handle as opposed to solutions of 30% hydrogen peroxide. Moreover, this new aqueous solution is more versatile in that it has been found to produce high quality anodic oxide films on silicon (6), indium antimonide, and indium phosphide (7). A particular advantage of this new solution applied to silicon is that the anodic oxide films can be made virtually free of alkali ions by treating the solution with ion exchange resins. An assessment of the inversion layers produced by such a treated solution was made by measuring the photoresponse adjacent to a metallurgical junction with a fine light probe. No inversion layers were observed by this light probe technique even for resistivities of a couple of thousand ohm-cm. More conventional steam-grown oxides were limited to resistivities of less than 100 ohm-cm in this context.

The basic electrolyte is a 0.1M solution of dibasic ammonium phosphate in distilled water. Although this solution may be used directly for silicon, InSb, or InP, the pH of the solution is adjusted to a value of 4 by the addition of phosphoric acid when used with GaAs to

prevent dissolution of the oxide film. In a neutral solution, 3600Å of oxide was observed to dissolve in approximately 25 min, whereas there was no detectable dissolution in a buffered solution (pH≈4) for periods up to one day.

The experimental arrangement for preparing the films described below was to immerse an appropriately masked sample into a beaker of the solution and record the breakdown voltage of the film as a function of the time for a specified current. The masking technique employed was to anodize a polished sample of GaAs and mask it with Apiezon wax leaving a window of known area. The window and a contacting area were then cleared of oxide with hydrochloric acid prior to anodizing the area in the window. The GaAs wafers used in these experiments were of heavily doped n-type substrate material. The anodization was carried out with the sample illuminated by a microscope lamp which served to reduce the contact potentials, but was otherwise not deemed necessary to obtaining good anodic films.

The first films were formed in an unbuffered solution (pH≈7) and the cell voltage vs. time for several current densities is shown in Fig. 1. Note that for the lowest current density the cell voltage does not increase linearly with time, indicating a slight dissolution of the oxide.

Buffering the solution to a pH of 4 with phosphoric acid reduces the solubility of the film to a completely negligible value. The cell voltage vs. time for this buffered solution, as shown in Fig. 1 for 0.3 mA/cm<sup>2</sup>, is quite linear down to the lowest measured current densities (~20 μA/cm<sup>2</sup>). Figure 2 shows that the rate at which the oxide film is formed is linearly proportional to the current density and is, in addition, quite reproducible.

Hydrochloric acid was intentionally added to the buffered solution without readjustment of the pH and the stability of the oxide growth process was studied. Uniform oxide films could be grown in a solution with HCl contamination up to  $1 \times 10^{-3}$  N. Further addition of HCl will slowly change the process to etching. As

\* Electrochemical Society Active Member.  
Key words: oxidation, anodization, gallium arsenide, aqueous, buffer.



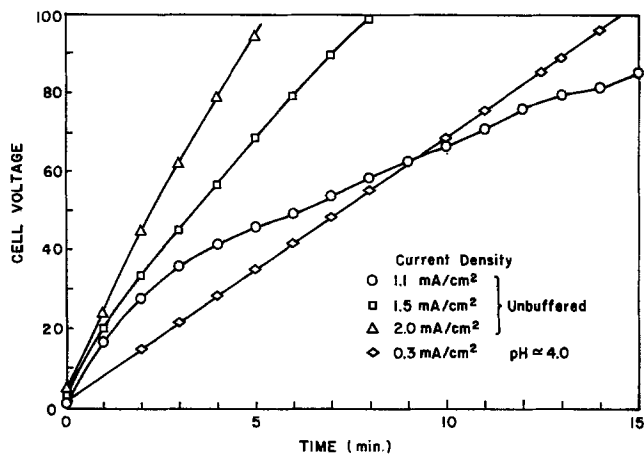


Fig. 1. Cell voltage vs. time as a function of current density for buffered and unbuffered solutions.

compared with the aqueous  $H_2O_2$  solution (3), which was sensitive to a few ppm contamination, this solution is much more stable.

Interference microscope measurements of film thicknesses formed at 60 and 90V agreed within experimental error with published data (1, 3, 8). The breakdown field in these oxide films was observed to be at least  $5 \times 10^6$  V/cm, which is equal in dielectric strength and compactness to that obtained with the best of the other anodizing solutions. Uniform films could be grown to a maximum thickness of 3600Å (180V). Beyond 3600Å, however, the film became uneven in color. Somewhat thicker films could be grown in a boiling solution (4), but again uniformity of the film was a problem. A preliminary estimate of the surface-state density obtained from MOS capacitance indicates a density between  $10^{11}$  and  $10^{12}/cm^2$  for unannealed films.

Manuscript submitted Sept. 19, 1975; revised manuscript received Dec. 22, 1975.

Any discussion of this paper will appear in a Discussion Section to be published in the December 1976

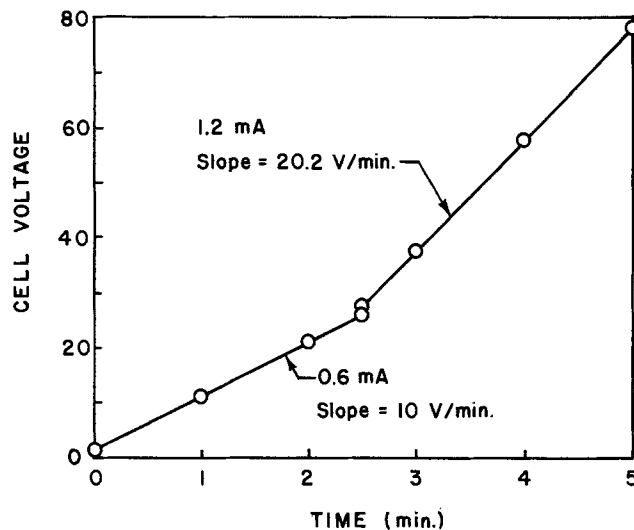


Fig. 2. Cell voltage vs. time showing the direct proportionality of film growth rate to current density for a buffered solution.

JOURNAL. All discussions for the December 1976 Discussion Section should be submitted by Aug. 1, 1976.

#### REFERENCES

1. H. Hasegawa, K. E. Forward, and H. Hartnagel, *Electron Letters*, **11**, 53 (1975).
2. H. Muller, F. H. Eisen, and J. W. Mayer, *This Journal*, **122**, 651 (1975).
3. R. A. Logan, B. Schwartz, and W. J. Sundburg, *ibid.*, **120**, 1386 (1973).
4. S. M. Spitzer, B. Schwartz, and G. D. Weigle, *ibid.*, **122**, 397 (1975).
5. B. Schwartz and F. Ermanis, Paper 21 RNP presented at The Electrochemical Society Meeting, San Francisco, California, May 12-17, 1974.
6. C. A. Lee and R. L. Batdorf, Unpublished data.
7. V. Wrick and J. Berenz, To be published.
8. C. J. Dell'Oca, G. Yan, and L. Young, *This Journal*, **118**, 89 (1971).



## Anodic Behavior of Lithium in Aqueous Electrolytes

### I. Transient Passivation

E. L. Littauer\* and K. C. Tsai\*

*Lockheed Missiles and Space Company, Incorporated,  
 Lockheed Palo Alto Research Laboratories, Palo Alto, California 94304*

#### ABSTRACT

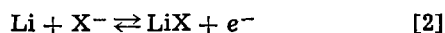
Lithium manifests a transient passivation when it is anodically polarized to  $\sim -2.66$  NHE in LiOH electrolytes. The duration of the passivation ranges from seconds to hours. The occurrence of the passivation is independent of electrolyte concentration, flow velocity, anode-cathode contact pressure, and of the polarization technique used. The duration of the transient is proportional to electrolyte concentration, the more dilute the solution the shorter the time. The passivation is believed due to the formation of an insulating, but unstable aggregate of  $\text{Li}_2\text{O}$  which nucleates at active Li sites at the base of the pores in the protective LiOH film. The recovery of the surface to the active state is due to the conversion of the  $\text{Li}_2\text{O}$  to LiOH in the presence of water at the Li surface.

The recent discovery of ways to electrochemically harness the lithium-water reaction (1) has prompted basic studies of the electrochemical reactions of lithium in aqueous electrolytes. Attempts to minimize polarization effects and to attain high current efficiency have been the subject of an ongoing program. Electrochemical characteristics of the lithium-water cell have been treated in a recent paper (2).

The chemistry of the lithium-water reaction is relatively simple, but the electrochemistry of the system is complex because (i) the reaction rate between lithium and water is very fast and the major portion of the lithium electrode is always covered with thick oxide films



and (ii) the hydrogen evolution at the metal surface always creates pores within the film and this in turn complicates the electrochemical reaction



where  $\text{X}^-$  = anions in the aqueous electrolyte. These simultaneous processes result in a porous electrode comprising randomly formed and moving pores with active reaction sites existing only at the extremity of the pores at the metal-film interface.

The anodic oxide film is of such a form that it permits the inert cathode structure to be pressed against it without shorting. The oxide film acts, in principle, as a battery separator and serves as a conducting medium for the mass transport of ionic species to and from the anode surface. Through control of the anode-cathode applied pressure, exceptionally reproducible anodic polarization curves can be obtained.

In the lithium-water system, the rate-limiting process is the oxidation of lithium rather than the reduction of water at the cathode. It has been found that

under anodic polarization, within certain ranges of hydroxyl ion concentration and electrolyte flow, two types of passivation are manifested. First, transient passivation is observed at a specific electrode potential. As is described in this paper, it is apparently related to the formation of an intermediate oxide. Second, actual mechanical passivation occurs and is presented in Part II of this subject title. Part III deals with the influence of electrolyte flow velocity on the surface coverage of the lithium anode.

#### Experimental

A general setup of the electrochemical cell is shown in Fig. 1. It was designed with the following requirements: rapid assembly, minimum electrical contact resistance between anode holder and the lithium anode, precise control of anode-cathode contact pressures, a

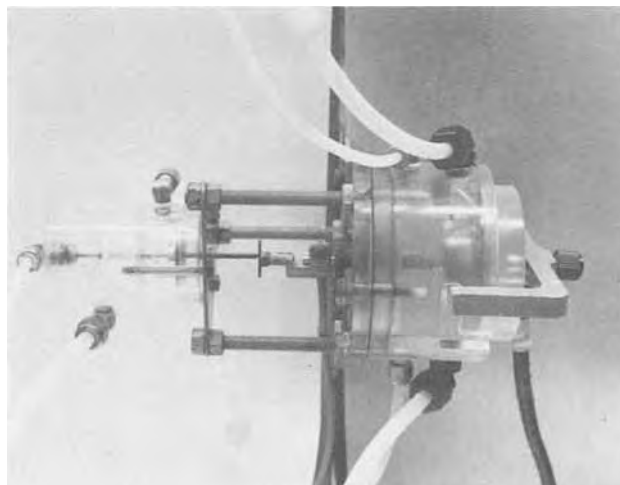


Fig. 1. General setup of the electrochemical cell

\* Electrochemical Society Active Member.  
 Key words: transient passivation, mechanical passivation, lithium, lithium-water cell,  $\eta$ H-potential diagram.

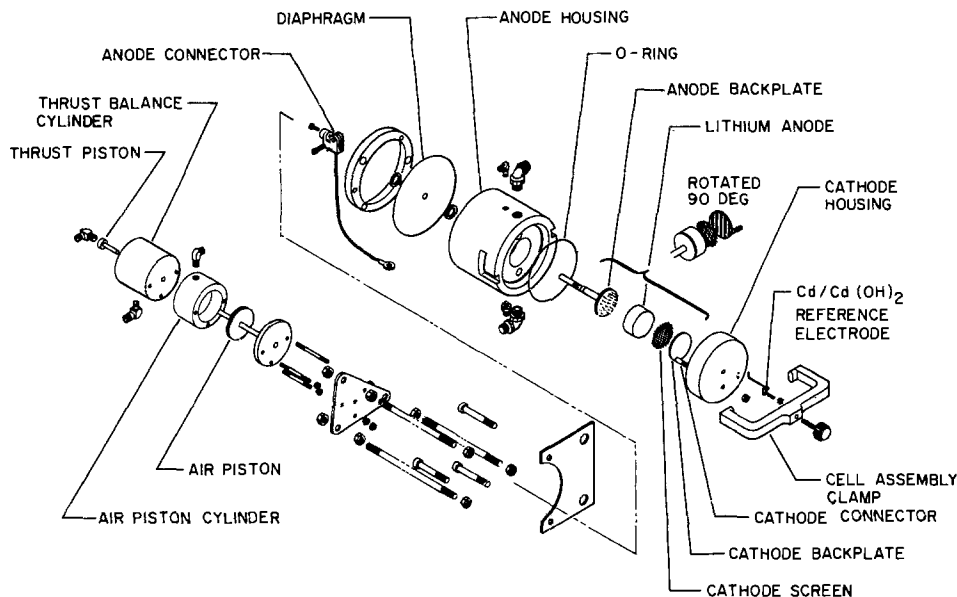


Fig. 2. Exploded view of the 11.4 cm<sup>2</sup> lithium test cell.

wide range of flow rates, and a sealed construction to prevent electrolyte and hydrogen loss.

Figure 2 gives an exploded view of this 11.4 cm<sup>2</sup> (projected electrode area) test cell constructed from Plexiglas and equipped with a fixed cathode and a movable anode.

The anode holder comprised a 0.64 cm diam pushrod, for pressure transference, with an 11.4 cm<sup>2</sup> steel disk affixed. The disk was studded with a large number of steel needles onto which the lithium anode was pressure-bonded.

The lithium anode (99.9% purity) elements were obtained from Foote Mineral Company. Samples were precast into disks 39 mm in diam and 12.7 mm thick. The disks were stored in an argon atmosphere thus eliminating cleaning prior to being pressure-bonded onto the anode holder. The side and back of the assembled anode were insulated with Microflex stop-off lacquer. The electrode was cleaned with methyl ethyl ketone (MEK) and methanol until a bright shiny surface was obtained.

The inert cathode matrix was composed of a wire screen spot-welded to a ribbed iron back plate. This cathode matrix serves at least four functions: (i) it acts as the counterelectrode during the anodic dissolution of lithium, (ii) it provides the reaction path for the mass transport of ionic species to and from the active anode surface, (iii) it serves as a means to control the anodic film thickness because it is actually pressed against the anode, and (iv) it provides a flow path for electrolyte between the ribs in the interelectrode cavity. A circular, rather than a square or rectangular, electrode was used throughout the experiments simply because (i) it was easier to assemble and disassemble, and (ii) it permitted more uniform control of anode-cathode contact pressure. The possible uneven distribution of electrolyte with the flow channels was compensated by positioning the inlet electrolyte nozzle right at the bottom of the middle portion of the cathode matrix. Due to high electrolyte flow rate coupled with short flow distance, the electrolyte concentration gradient along the flow path was minimal. Based on the geometry of the cathode matrix, the Reynolds number was calculated to be from 45 to 270 for the flow velocities, i.e. 6–36 cm·sec<sup>-1</sup>, used in this study. It is expected that the hydrogen gas bubble evolution at the electrode surfaces will alter the values somewhat but is believed that laminar flow maintained in all the experiments.

Anode-cathode contact pressure was precisely controlled by an air pressure cylinder linked to the anode pushrod by an insulator. Elimination of the hydraulic

pressure component was accomplished by a thrust balance cylinder connected to the inlet and outlet lines of the cell. This cylinder has a piston attached to the air piston, thus negating the hydraulic piston effect on the anode. Electrolyte hydraulic pressure could be varied by a control valve on top of the test cell.

Lithium hydroxide electrolytes were prepared using reagent grade chemicals and deionized water. The electrolyte was thoroughly mixed for several hours. A small portion was introduced into the reservoir, thoroughly circulated throughout the system, and then dumped. The remaining electrolyte was introduced into the reservoir and circulated to attain thermal equilibrium within the system while presaturating with hydrogen gas.

During runs, electrolyte was circulated from the reservoir, maintained at a constant temperature within  $\pm 0.1^\circ\text{C}$  through a constant temperature heat exchanger, through the cell and returned to the reservoir by a voltage-controlled Micropump Model 10-41-316. The flow rate was measured with a Brooks Model 1110 250-mm full-view rotameter calibrated for flow rates up to 2.1 liters/min.

Anode polarizations were mostly carried out by the constant load method using a carbon pile resistor. For certain experiments galvanostatic and potentiostatic control was needed and a special fast response high current potentiostat/galvanostat was assembled for this study. The unit had the following capabilities: current capacity, 0–10A; voltage range, 0–10V; response time, 60  $\mu\text{sec}$  (from no load); and input impedance,  $1.5 \times 10^{12}$  ohm (potentiostatic mode). Voltage stability in the potentiostatic mode was 2.5% of the set value. Current stability in the galvanostatic mode was 3.5%.

The unit was built around an integrated circuit voltage regulator. Power to load the cell was provided by a lead-acid battery. The magnitude of the power was controlled by a power Darlington transistor. A metal oxide semiconductor field effect transistor operational amplifier was used to achieve the high input impedance in the potentiostatic mode.

The cell voltage and current were recorded on a Hewlett-Packard Moseley Autograph Model 7001 AM X-Y recorder and also monitored through a pair of Systron Donner Model 7004A digital multimeters. A cadmium/cadmium hydroxide reference electrode ( $E^\circ = -0.809\text{V vs. NHE}$ ) positioned within the interelectrode cavity within 2 mm of anode was used to record the electrode potentials.

## Results

Figure 3 gives polarization curves of Li in 4M LiOH. In the original studies of the system (2), cell perform-

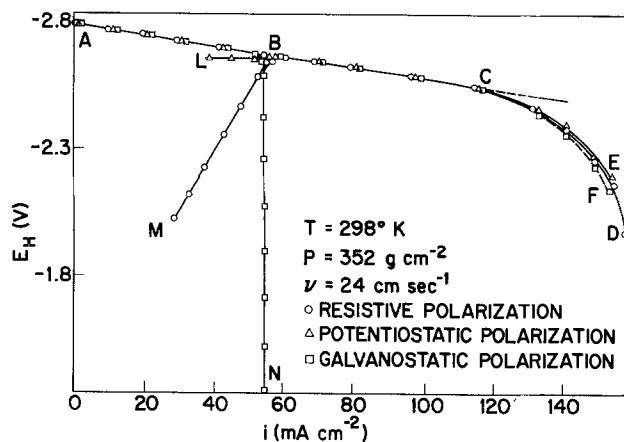


Fig. 3. Transient passivation of lithium in 4M LiOH by various polarization techniques.

ance data were obtained via constant load or resistive polarization. This form of polarization is represented by curve ABCD with the transient passivation phenomenon being shown as BM. The portion of the polarization curve shown as ABC is exclusively resistive and corresponds to transport across the anodic film.

In the region CD the film formation rate exceeds the film dissolution rate and this leads to mechanical passivation. This type of passivation is manifested by many metals when made anodic in aqueous electrolytes (3). It is the result of the formation of sparingly soluble coherent films at the metal surface or the plugging by precipitation or electrocrystallization of imperfections and pores in nonhomogeneous anodic films. In either way, the metal surface tends to become isolated from the electrolyte. Generally Li-H<sub>2</sub>O cells are operated at or near to point C because it has been found in practice that optimum faradaic efficiency is thereby attained. As has been explained previously (*op.cit.*), the cell is adjusted for different operating current densities at more or less constant potential by adjusting the hydroxyl ion concentration of the electrolyte. Thus, for high rate discharge, the electrolyte concentration would be set at 3.5M LiOH and point C would occur at *ca.* 300 mA/cm<sup>2</sup>. To operate at low current densities the polarization curve in, say, 4.8M LiOH would place point C at *ca.* 45 mA/cm<sup>2</sup>.

To characterize the transient passivation effect occurring at point B, and to determine if it could be isolated as a kinetic or thermodynamic phenomenon, galvanostatic and potentiostatic polarization techniques were used. It was postulated that, if the effect had exclusively a kinetic basis, its onset would occur at different potentials according to the experimental conditions. On the other hand, the electrochemical formation of a new phase would be revealed potentiostatically. ABCE in Fig. 3 represents the potentiostatic polarization curve with the transient passivation being shown as BL. Curve ABCF represents the galvanostatic polarization, the transient passivation is BN.

It should be pointed out here that exceptional experimental reproducibility was obtained with this system provided the anode was momentarily placed at OCV prior to performing a polarization. It was necessary to maintain experimental conditions constant, such as anode-cathode contact pressure, electrolyte composition, temperature, and flow rate. Reproducibility from run to run of within 10 mV was easily attained, and generally a steady-state reading at any point was achieved almost instantaneously ( $<10^{-1}$  sec). The exception to this was the sequence of events representing the actual transient passivation.

Under constant load polarization, the carbon pile resistor was adjusted slowly but continuously until point B was reached as indicated by a sudden decrease of current and voltage. At this point, the load was not

altered until the recorder pen returned to B. Polarization was then continued as before. The time for the sequence BMB was about 30 sec under the specified experimental conditions. (At higher flow rates or at lower electrolyte concentration, the time would be less and vice versa.) A similar 30 sec sequence BLB occurred under potentiostatic polarization. Under galvanostatic polarization, the transient passivation became permanent, shown by BN, but on interruption of the current the potential returned to B, and on reimposing current the polarization curve followed BF.

It was observed that the process leading to transient passivation is irreversible since upon reversing the polarization from D, E, or F, toward open circuit, no discontinuity appeared at B or elsewhere on the curve. It should also be noted that for transient passivation to occur the anode did not have to be returned to OCV (2.76 NHE). It was only necessary that it be returned to a point slightly negative to B.

Figure 4 shows the influence of electrolyte flow velocity on transient passivation at constant load. At the lowest flow rate tested, 6 cm-sec<sup>-1</sup>, the sequence took longer than 1 min. At the maximum flow rate, 36 cm-sec<sup>-1</sup>, no passivation was manifested. It was observed that the transient passivation sequence time was more or less inversely proportional to the flow velocity. Exact quantitative data of this was not, however, obtained. The potential for the onset of passivation was found to be virtually independent of flow velocity, *i.e.*, -2.64 NHE at 6 cm-sec<sup>-1</sup> and -2.67 NHE at 27 cm-sec<sup>-1</sup>. Experiments at very low flow rates, *i.e.*,  $<3$  cm-sec<sup>-1</sup>, were not carried out because it became difficult to maintain uniform flow and because at low flow rates, anodic corrosion will be stimulated and concomitant heating occur.

It will also be noted from Fig. 4 that the onset of mechanical passivation at high current densities was significantly influenced by the electrolyte flow rate.

The effect of electrolyte concentration is shown in Fig. 5. It was found that the lowest concentration at which the phenomenon could be observed was 3.8M

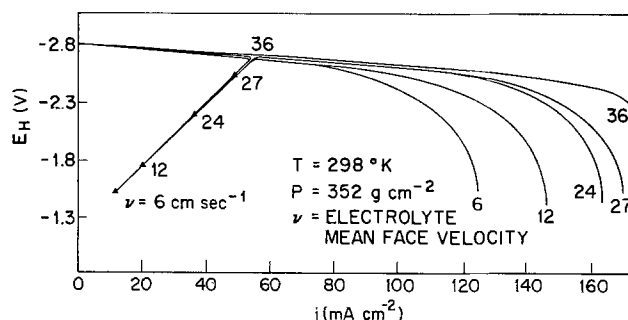


Fig. 4. Influence of electrolyte flow velocity on the transient passivation of lithium in 4M LiOH.

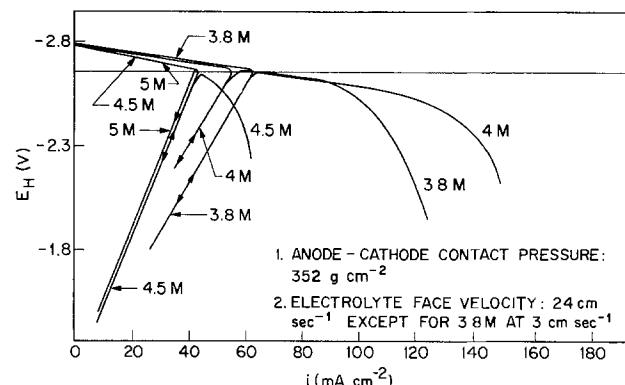


Fig. 5. Effect of electrolyte concentration on the transient passivation of lithium at 25°C.

LiOH, and here it was necessary to reduce the flow rate to 3 cm-sec<sup>-1</sup> for the passivation to appear.

It was also observed that the duration of the passivation sequence was proportional to electrolyte concentration. In fact, in 5M LiOH, the anode required more than 1 hr to recover to the active state. On the other hand, if the anode was in its passive state and the electrolyte was suddenly diluted from, say, 5 to 4M, recovery occurred almost immediately. Alternatively recovery could be accelerated by increasing the flow velocity or raising the electrolyte temperature. In these experiments, the potentials for the onset of transient passivation were virtually independent of electrolyte concentration.

### Discussion

The anodic behavior of Li in aqueous alkaline electrolytes is unlike any other metal. Provided the hydroxyl ion concentration is sufficient, a film forms on the anode which prevents violent direct reaction of Li with H<sub>2</sub>O. In order to harness with good faradaic efficiency the very high potential energy possessed by Li, it is generally necessary to utilize electrolytes in the range 3.5-5M LiOH. In electrolytes such as these, the anodic film tends to act as a barrier. It isolates much of the lithium surface, and reaction of the metal with the electrolyte occurs at the base of pores which permeate the film. High flux rates are supported with little polarization. Because of the reactivity of Li with H<sub>2</sub>O, no activation overvoltage is manifested. Thus the anodic polarization curve is characterized by a straight line which suggests that the polarization is predominantly an IR drop across a constantly forming and dissolving porous film. However, a transient passivation is superimposed upon it at low current densities, and at fairly high current densities mechanical passivation occurs when the rate of film formation exceeds the rate of dissolution. Mechanical passivation similar to this is manifested by many other metals when made anodic in aqueous electrolytes (3). The properties of the mechanically passivating film are very important to the operation of the battery and they are described in Part II. Under normal conditions the transient passivation is not encountered, because the cell is operated within a region of the polarization curve well removed from that where it occurs. It is examined in detail here because if such passivation can be reproducibly controlled, it offers a method to essentially terminate reaction while electrolyte remains in contact with the Li. This, then, could be an effective means to turn off a Li-H<sub>2</sub>O battery without the need to drain the electrolyte.

The transient passivation which may have a duration of many seconds, minutes, or hours depending on the experimental conditions has been shown to occur at an essentially fixed potential. Its duration and extent is influenced by electrolyte concentration, flow rate, and the polarization technique employed.

In the absence of this passivation, the Li is covered with a porous film of LiOH. No doubt, at the base of the pores adjacent to the Li, a complex situation exists because the activity of water is very low. Thus a series of layers of Li compounds of different levels of dehydration would be expected to exist in between the LiOH at the film solution interface and the metal surface. (A treatment of the composition of the anodic film on lithium and of the dominating mass transport processes across it is in preparation.) The fact remains, however, that in order for Li to exhibit extremely low anodic polarization at high current densities (the resistance of the film has been calculated to be 0.136 ohm at an electrolyte face velocity of 24 cm-sec<sup>-1</sup> in 4M LiOH) it is necessary that mass transport occur predominantly through the pores. It was noted above that once the transient passivation sequence has run its course, further polarization is a continuation of the

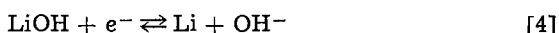
Table I. Calculated pH values

LiOH(M)	$\alpha \pm$	pH
3.8	1.850	14.267
4.0	1.924	14.284
4.5	2.122	14.327
5.0	2.281	14.358

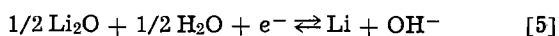
curve which existed prior to passivation. Also, on reversing polarization, it does not reappear. It follows that the phenomenon is caused by the formation of a compound within the pores which can effectively insulate the active metal from the electrolyte for periods ranging from seconds to hours. It has been shown conclusively via three different electrochemical techniques that the onset of transient passivation occurs at a specific potential  $E_{TP} = -2.66$  (NHE) and thus must represent the electrochemical oxidation of Li or a Li-containing species within the pores. This oxidation is presumably independent of the normal formation and dissolution of LiOH for the reasons given above. To obtain an insight into the problem, a pH-potential diagram for the Li-H<sub>2</sub>O system was constructed using thermodynamic (4) and solubility (5) data. The diagram comprises the following elements



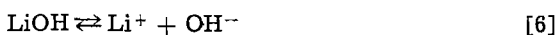
$$E = E^\circ + 0.059 \log [\text{Li}^+]; \quad E^\circ = -3.045\text{V}$$



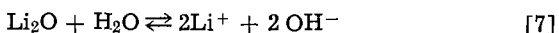
$$E = E^\circ + 0.059 (14 - \text{pH}); \quad E^\circ = -2.95\text{V}$$



$$E = E^\circ + 0.059 (14 - \text{pH}); \quad E^\circ = -2.51\text{V}$$



$$K_{sp} = [\text{Li}^+][\text{OH}^-]; \quad K_{sp} = 0.25$$



$$K_{sp} = [\text{Li}^+]^2 [\text{OH}^-]^2; \quad K_{sp} = 625$$

Mean activities are given in the literature for LiOH at concentrations up to 4M (6). Extrapolation of the data to 5M permits calculation of the pH values, given in Table I, of all the electrolytes of interest in this study.

Inspection of Fig. 6 shows that at the average electrolyte pH, i.e., 14.3, the thermodynamically stable phase is Li<sup>+</sup>. In practice, the Li electrode does initially dissolve rapidly with formation of Li<sup>+</sup>. Then, to retain electrical neutrality, hydroxyl ions migrate to the surface at a rate equal to the rate of ionization of Li

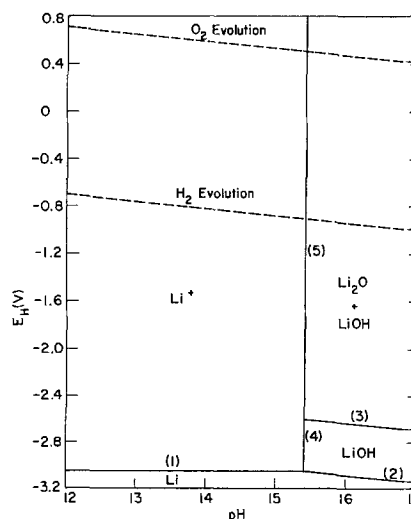


Fig. 6. pH-potential diagram for the Li-H<sub>2</sub>O system ( $[\text{Li}^+] = 1$ )

and, at the same time, water is repelled from the surface. A situation then develops such that the solubility of LiOH is exceeded and the salt precipitates. It follows that directly adjacent to the Li, the water activity will be very low and it is believed that the film actually forms as a series of compounds. These compounds will be proportionately rich in Li at the metal-film interface, and moving away from the metal there will be increasing hydration until LiOH predominates. The film, which is in a state of quasi-equilibrium when the anode is in the active state, dissolves at the film solution interface at the same rate as it forms at the metal surface. The fact that LiOH does form a stable product on Li indicates that the pH within the film at the active surface must exceed ca. 15.5. Of interest to this study is Eq. [3], namely the electrochemical formation of Li<sub>2</sub>O. It is apparent that, as Li is polarized beyond line 3, LiOH and Li<sub>2</sub>O are both thermodynamically stable phases. The observed potential at the onset of passivation  $E_{TP} = -2.66V$  which falls on line 3 at a pH of ca. 16. The chemical significance of such pH values is open to question, the data does however confirm that when dealing with a system as reactive as lithium-water, extreme compositional variations exist.

As was shown in Fig. 4, the extent of passivation and the corresponding time to recovery is directly affected by the electrolyte flow velocity. Analogously, as shown in Fig. 5, electrolyte concentration influences the extent of passivation and the recovery time. The explanation for these related observations is the fact that at higher flow rates and lower hydroxyl ion concentration, the equilibrium for LiOH formation and dissolution is shifted such as to lead to a thinner film. The converse will of course also follow. If the anode surface coverage is assumed essentially constant, as may be inferred from the invariant slope of the prepassivation polarization curves at varying flow rates in Fig. 4, then the mass transport processes across the film will be more rapid as the thickness is reduced.

The variation of  $E_{TP}$  as a function of flow rate from 6-36 cm-sec<sup>-1</sup> was 30 mV. This is ascribed to the slightly lower IR drop across the LiOH films of reduced thickness. Also the measured values of  $E_{TP}$  as a function of M LiOH did not vary significantly which is to be expected since the pH at the reactive metal surface is essentially constant and extremely alkaline.

In the process of transient passivation, the active surface diminishes because of the Li<sub>2</sub>O pore blockage. The active surface potential during transient passivation is described by

$$E = E_{TP} - IR = E_{TP} - \frac{l I}{k A} \quad [8]$$

where  $l$  is the thickness of the porous film,  $k$  the conductivity of electrolyte within the pores, and  $A$  the active surface area.

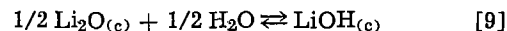
Under the resistive polarization where neither surface current nor potential are controlled both  $E$  and current density  $I/A$  decrease at a constant rate corresponding to the slope  $(-l/k)$ , shown by BM in Fig. 3. During recovery from the transient passive state, the active surface area increases as well as the total anodic current and the surface potential recovers at a constant rate  $(+l/k)$  with respect to the actual current density. This then serves to explain why the line describing transient passivation and the line for recovery are identical but of opposite direction.

Under potentiostatic polarization  $E = E_{TP}$  in Eq. [8] and  $I \rightarrow 0$  which is depicted by BL in Fig. 3. Under galvanostatic polarization the constant current at the surface when  $E_{TP}$  is reached is such as to force the metal to become permanently passivated. The actual active surface area rapidly decreases and based on Eq. [8],  $E$  also decreases rapidly and leads to polarity reversal, BN in Fig. 3.

From the above, the conclusion is reached that the occurrence of transient passivation is an essentially spontaneous, thermodynamically controlled process. Its onset is solely a function of the potential of the Li surface. However, recovery of the anode to an active state from the passivated state is a kinetic phenomenon.

Li<sub>2</sub>O has physical properties dissimilar to LiOH. It is more dense (2.013 vs. 1.46 g-cm<sup>-3</sup>) and it has a cubic structure vs. tetragonal for LiOH. It is hypothesized that, whereas LiOH forms as a porous loose film on the metal, Li<sub>2</sub>O may form as a compact insulating layer at active Li sites. If this is the case, the formation of Li<sub>2</sub>O would cause a sudden shift in the equilibrium for the anodic film formation and dissolution at  $E_{TP}$ . This shift would simultaneously lead to an imbalance between the rates of film formation and film dissolution, such that the former would exceed the latter and lead to passivation.

It is known that Li<sub>2</sub>O is unstable in contact with water



$$K = 2.05 \times 10^6$$

but, as mentioned above, at the location where it initially forms, i.e., at the active Li sites, the water activity is low.

On the other hand, the Li<sub>2</sub>O in contact with alkaline electrolyte at the pore solution interface will be unstable according to reaction [9] and will convert to the final stable reaction product LiOH. LiOH is readily soluble in the electrolyte and this could account for the disappearance of the passivation as the equilibrium between film formation and dissolution once again dominates.

The fact that the transient passivation is observed only when Li is polarized from a potential slightly negative to  $E_{TP}$  suggests that a subtle but permanent change takes place on the anode's surface during the passivation sequence. The slope of the polarization curve is apparently unaltered after passivation which shows that the predominantly changing polarization component is the IR across the film. Thus, any changes which occurred within the anodic layer are obscured making it difficult to examine the phenomenon diagnostically. It may be that once the potential for formation of Li<sub>2</sub>O has been reached, even though this compound dissolves into the electrolyte as discussed above, a certain amount is incorporated into the anodic layers. This then could influence the subsequent formation and dissolution kinetics of the anodic reaction products. On the other hand, at potentials more negative than  $E_{TP}$ , Li<sub>2</sub>O is thermodynamically unstable and the equilibrium which maintains is solely that for the formation and dissolution of LiOH.

It is clear that additional work is needed to fully explain the irreversibility of polarization leading to transient passivation. The present paper has served to introduce the phenomenon, to explain the mechanism of passivation, and to point out the salient features of the Li-H<sub>2</sub>O system.

### Conclusions

Lithium when anodically polarized in aqueous electrolytes forms a protective film of LiOH. In 3.8-5M LiOH this film exists in a state of quasi-equilibrium over an appreciable range of current densities. When the anode is polarized to a fixed potential,  $\sim -2.66V$  vs. NHE, a transient passivation phenomenon of from seconds to hours is manifested. The duration of the transient is proportional to electrolyte concentration, the more dilute solution giving the shorter passivation times. The effect is believed to be associated with the formation of an insulating, but unstable aggregate of Li<sub>2</sub>O which nucleates at active Li sites at the base of the pores in the protective film. Over a period of time,

determined by the rate of transport of water and/or hydroxyl ions through the film, most of the  $\text{Li}_2\text{O}$  reverts to  $\text{LiOH}$  and a state of quasi-equilibrium at the anode surface is recovered. However, as a result of the passivation process, the surface state of the Li is altered.

By understanding the mechanism of the passivation and by defining the ranges of electrolyte concentrations and flow rates within which it occurs, a means may be found to place a lithium-water battery in a standby mode without the need to drain electrolyte from it.

#### Acknowledgments

This study was supported in its entirety by Lockheed Missiles and Space Company.

Manuscript submitted Oct. 30, 1976; revised manuscript received Jan. 26, 1976.

Any discussion of this paper will appear in a Discussion Section to be published in the December 1976

JOURNAL. All discussions for the December 1976 Discussion Section should be submitted by Aug. 1, 1976.

Publication costs of this article were partially assisted by Lockheed Missiles and Space Company, Incorporated.

#### REFERENCES

1. L. Rowley, U.S. Pat. 3,791,871 (1974).
2. E. L. Littauer and K. C. Tsai, "26th Annual Proceedings Power Sources Conference," p. 57 (1974).
3. T. P. Hoar, in "Modern Aspects of Electrochemistry," Vol. II, J. O'M. Bockris, Editor, pp. 262-342, Butterworths Scientific Publishers London (1959).
4. W. M. Latimer, "Oxidation Potentials," 2nd ed., Prentice-Hall, Inc., Englewood Cliffs, New Jersey (1952).
5. "Handbook of Chemistry and Physics," 54th ed., The Chemical Rubber Co. (1973-1974).
6. H. S. Harned and B. B. Owens, "The Physical Chemistry of Electrolytic Solutions," 3rd ed., p. 498, Reinhold Publishing Corp., New York (1963).

## Exhaust Gas Compositions and Fuel Efficiencies of Hydrazine-Air Fuel Cells

Kohki Tamura and Toshiki Kahara

Hitachi, Limited, Hitachi Research Laboratory, Hitachi, Japan

#### ABSTRACT

High fuel efficiency and clean exhaust gas are the two most important requirements in hydrazine-air fuel cells. Four anodes of sintered nickel plaque were studied for these purposes, each one containing either cobalt, nickel, palladium, silver, or platinum as a catalyst. Exhaust gases were determined with a gas chromatograph, the consumption of hydrazine in the anolyte was analyzed chemically, and fuel efficiencies and unreacted product gases were evaluated based on these data. Consequently with the silver catalyzed electrode, 97% fuel efficiency was attained at 50 mA/cm<sup>2</sup> at 25°C.

Hydrazine-air type fuel cells are the ones most promising for special uses such as unmanned stationary electric sources, because they possess advantages over other types, for example, a high current density is obtainable and a liquid fuel which is easier to handle than other formal fuels can be used. But they have disadvantages, that is, fuel is very expensive and their exhaust gas contains nonnatural materials such as hydrogen and ammonia. For this reason, practical applications have been limited.

Thus, the two most important requirements for the wide acceptance of these fuel cells are (i) cleanness of exhaust gas and (ii) high fuel efficiency.

Extensive research and development has been done in the world on hydrazine-air fuel cells, especially their electrodes (1-4). This paper presents the results which were obtained in experiments using a complete cell. The influences of the kinds and amounts of electrode catalysts and the operating conditions were examined for the purpose of attaining the two requirements of clean exhaust gas and high fuel efficiency.

#### Experimental

Figure 1 shows details of experimental cell construction. The cell has one anode and one cathode, each 50 × 50 mm. These two electrodes and three Lucite frames form an anolyte, an electrolyte, and an oxidant chamber. Silicon rubber gaskets are placed between frames. Narrow holes for exhaust gas are opened at the upper walls of the anolyte chamber frame and the

electrolyte chamber frame. The width of each chamber is 10 mm. Four anodes of sintered nickel plaque were constructed, each one containing either cobalt, palladium, silver, or platinum as a catalyst. Cobalt (II) chloride was reduced to cobalt by dipping in 1M sodium bicarbonate and 2M sodium hydroxide solutions, and silver nitrate to silver by 2M sodium formate. Palladium was precipitated in porous plaque from palladium (II) chloride by dipping in a palladium (II) chloride solution, and platinum from chloroplatinic acid. 1-2.5 × 10<sup>-5</sup> mol/cm<sup>2</sup> of catalyst was loaded onto each nickel plaque. The thickness of the anode is about 0.95 mm and the porosity is 67% before adding the catalyst. The cathode is Teflon-bonded catalyzed carbon with a nickel screen.

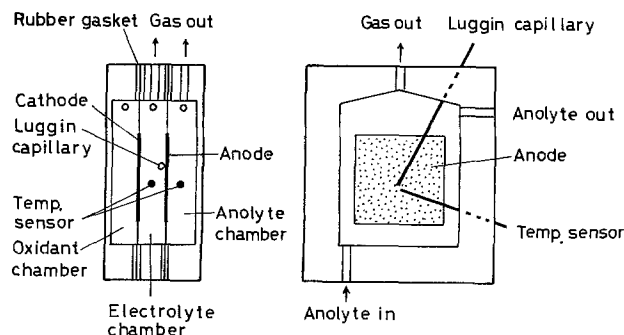


Fig. 1. Experimental cell construction

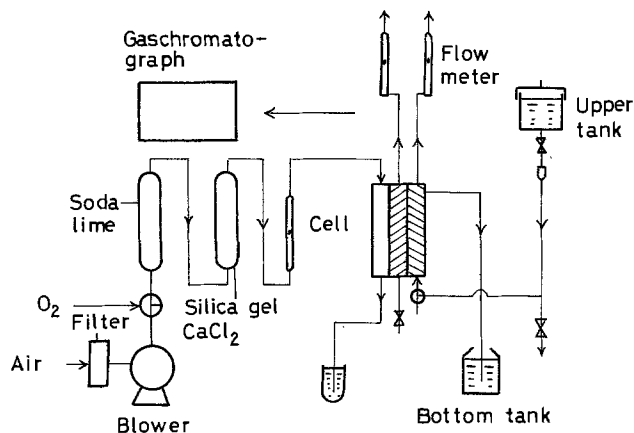


Fig. 2. Layout of the apparatus

A Luggin capillary was inserted in the electrolyte chamber to measure the anode potential. The capillary tip was in contact with the center of the anode surface. The potential of the saturated calomel electrode was used as the standard potential. Temperature sensors were enclosed in the anolyte and the electrolyte chambers.

Figure 2 shows the layout of the apparatus. Anolyte dropped and flowed from the upper tank to the anolyte chamber in the cell, overflowed from the top of the chamber, and was stored in the bottom tank. The flow rate of anolyte was 0.6–0.8 ml/min. Hydrazine concentrations in the anolyte were 0.5, 1, and 3%, and the electrolyte was 30% potassium hydroxide solution. A part of the hydrazine in the anolyte was spent in the anolyte chamber. Air was introduced by a small blower; its flow rate was 1.7 liters/min. About 150 min were expended for each measuring point, and the anolyte and the electrolyte were discharged whenever the measurement of one point was finished.

Hydrazine in the anolyte and the electrolyte was analyzed by the iodine titration method of Eq. [1]



or by the absorption photometric method using *p*-dimethylaminobenzaldehyde as the indicator.

The flow rate of the exhaust gas was measured by a soap bubble flow meter. The exhaust gases were taken out of the exhaust gas holes of the anolyte chamber and the electrolyte chamber separately and determined with a gas chromatograph. The concentration of hydrazine in the anolyte was analyzed chemically. The coulombic fuel efficiency and the cleanness of the gases were evaluated using these data.

### Results and Discussion

*Effect of catalyst.*—The distribution of the catalyst in the anode was examined by surface analysis and line analysis, with an electron probe microanalyzer, as a first step in the experiments.

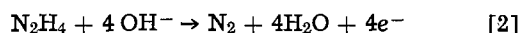
Figure 3 shows the results of analysis of the palladium catalyzed anode. The light areas in Fig. 3 (a)

are the places where the characteristic x-ray of palladium is strong. The dark areas are the places where it is weak or not radiated. But the dark areas do not mean that palladium is absent, because the sintered nickel plaque has an uneven surface, and the characteristic x-ray of palladium is not radiated from concave areas or if it is, it cannot be observed because of its weakness. The peaks pointed toward the bottom of the photograph in Fig. 3 (b) are considered to be the concave areas in the plaque. The same results were obtained for the other catalyzed anodes. Therefore, it is concluded that the catalyst distributes uniformly on and in the sintered nickel plaque.

Figure 4 shows potentials of catalyzed anodes as a function of current density. All potentials are approximately the same except for the silver catalyzed electrode. The difference between the potentials was slight. The potential of the cobalt catalyzed anode was  $-1.2\text{V}$  (*vs.* SCE), palladium  $-1.18\text{V}$ , platinum  $-1.19\text{V}$ , and silver  $-1.12\text{V}$ , at a discharge current density of  $50\text{ mA/cm}^2$ . While it cannot be said that these results will always be obtained, as the potentials vary with the amount and state of the catalyst or with the operating conditions, still it is considered that they describe a relationship that exists among these four catalysts.

The gas evolution rate of each catalyzed electrode was measured as a function of current density; gases from the anolyte and electrolyte chambers were collected separately.

Figure 5 shows the results of analysis of the platinum catalyzed anode. The line of theoretical nitrogen in the figure corresponds to the coulombic amounts calculated by reaction [2]



The gas evolution rate obtained with platinum was higher than that obtained with cobalt, palladium, or silver.

Figure 6 shows the results of analysis of the silver catalyzed anode. The evolution rate of hydrogen and nitrogen from wasted hydrazine is very low, compared with the platinum catalyzed electrodes. The gas evolution rate obtained with silver was lower than that obtained with platinum, cobalt, or palladium.

So, it is clear that (i) the total nitrogen evolution rate increases and the total hydrogen evolution rate decreases linearly with increasing current density, (ii) both nitrogen and hydrogen occur in the largest amounts in the catalyzed platinum, and in the smallest amounts in the catalyzed silver, and (iii) a large amount of gas evolution from the electrolyte chamber can be observed.

The quantities of hydrogen in the exhaust gas were 15.0% with the platinum catalyzed anode, 8.8% with cobalt, 1.8% with palladium, and only 0.2% with silver at a current density of  $50\text{ mA/cm}^2$ .

Attempts were made to detect ammonia in exhaust gases by Nessler's reagent, spectrophotometer, and gas chromatograph, but none could be detected.

Figure 7 shows the coulombic hydrazine efficiency calculated from the results of analysis of hydrazine

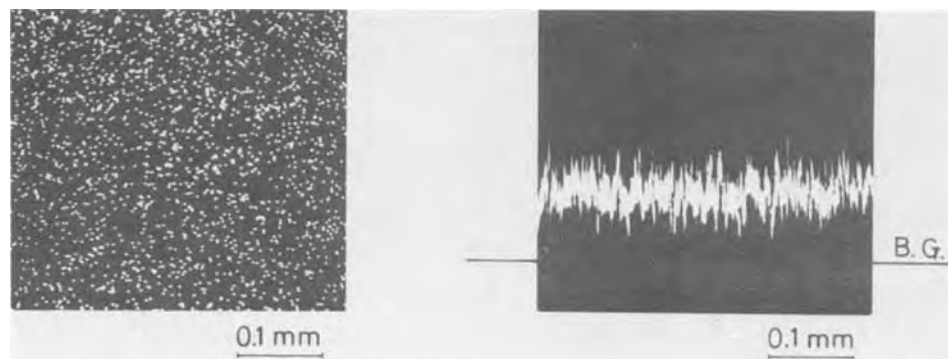


Fig. 3. Analysis of the distribution of palladium catalyst in anode by electron probe microanalyzer: (a, left), surface analysis; (b, right), line analysis.



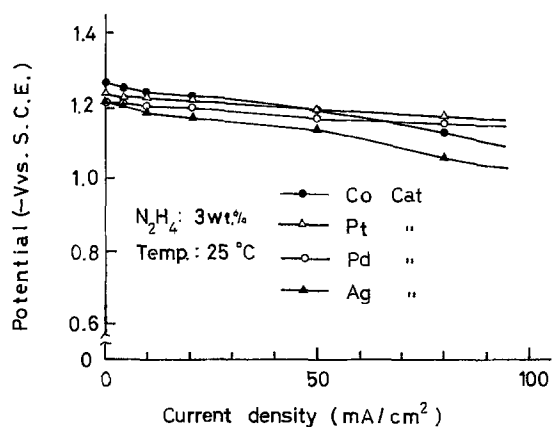


Fig. 4. Polarization curves of anodes with different catalysts

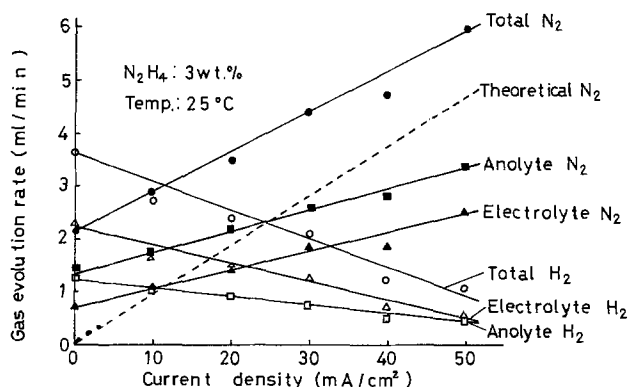


Fig. 5. Effect of current density on gas evolution from a Pt catalyzed anode cell.

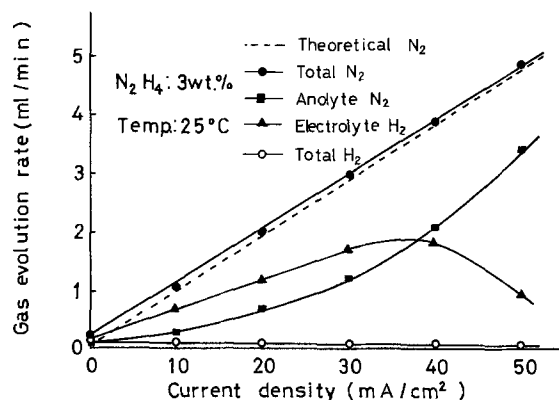


Fig. 6. Effect of current density on gas evolution from an Ag catalyzed anode cell.

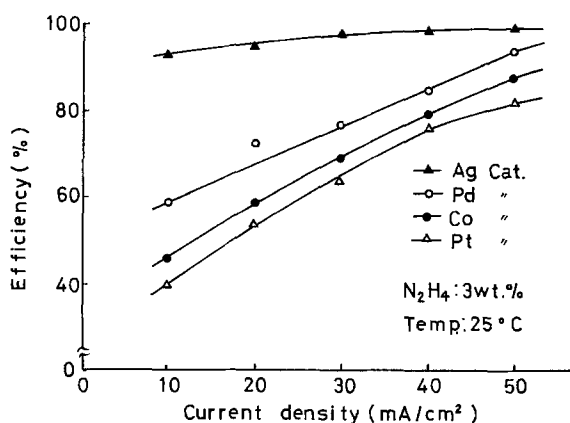


Fig. 7. Coulombic hydrazine efficiency with different catalysts as a function of current density.

concentration in the anolyte and electrolyte chambers after a constant current discharge for 2.5 hr. This is in agreement with the result calculated from the ratio of theoretical to actual nitrogen evolution. The efficiency of the silver catalyzed anode was highest. It was more than 90% even in the low current density area and, for example, was 96% at a current density of 30 mA/cm<sup>2</sup> with a silver catalyzed anode. On the other hand, it was 58% with platinum. The coulombic hydrazine efficiency always increases with increasing current density.

Influences of anode catalyst concentrations,  $1 \times 10^{-4}$ ,  $1 \times 10^{-5}$ , and  $1 \times 10^{-6}$  mol/cm<sup>2</sup>, on polarization curves, gas evolution rate, and efficiency were examined. For polarization curves, no difference existed between anodes with  $1 \times 10^{-4}$  and  $1 \times 10^{-5}$  mol/cm<sup>2</sup>, but the polarization curve was unstable with  $1 \times 10^{-6}$  mol/cm<sup>2</sup>. This might be considered to be because of the characteristics of the sintered nickel plaque. For such low catalyst loading, the techniques used in these experiments could not make the catalyst work effectively.

The effect of palladium catalyst concentration on gas evolution rate is illustrated in Fig. 8. Nitrogen and hydrogen evolution rates are high in high catalyst concentrations. This means that the decomposition of hydrazine which is not used effectively for electrochemical reaction increases with increasing anode catalyst concentration.

When the palladium catalyst concentration was  $1 \times 10^{-5}$  mol/cm<sup>2</sup>, the coulombic efficiency was 93% at a current density of 50 mA/cm<sup>2</sup>, but, when the concentration was  $1 \times 10^{-4}$  mol/cm<sup>2</sup>, it was 73%. Therefore, it is known that excessive catalyst concentrations increase the useless consumption of hydrazine.

*Effect of hydrazine concentration.*—Effects of a hydrazine concentration of 0.5, 1, and 3 weight per cent (w/o) on polarization curves, gas evolution rate, and coulombic hydrazine efficiency were studied. Polarization curves of the hydrazine anode were independent of hydrazine concentration at a current density less than 30 mA/cm<sup>2</sup>, but were influenced at a higher current density, and the potential of the anode became more noble with decreasing hydrazine concentrations because the supply of hydrazine decreased to the point where a reaction could no longer be maintained.

Figure 9 shows the effect of hydrazine concentration on gas evolution rate at a current density of 50 mA/cm<sup>2</sup>. The behavior of gas evolution was similar at other current densities. From this figure it can be seen that the total nitrogen evolution rate increases, but that nitrogen from the anolyte chamber decreases and nitrogen from the electrolyte chamber increases with increasing hydrazine concentrations.

From these results, it is considered that the electrochemical reaction of hydrazine occurs at the anolyte chamber side of the anode in the case of dilute hydra-

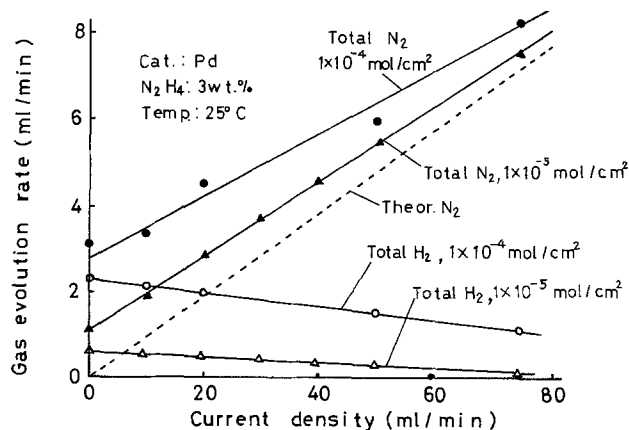


Fig. 8. Effect of catalyst concentration on gas evolution rate

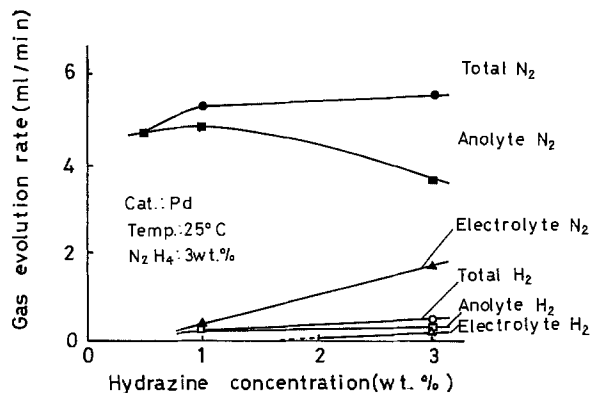


Fig. 9. Effect of hydrazine concentration on gas evolution rate at current density of 50 mA/cm<sup>2</sup>.

zine concentrations and that the reaction area spreads to the electrolyte side of the anode with increasing hydrazine concentrations.

The quantities of hydrogen in the exhaust gas were 0.8% in 0.5 w/o hydrazine, 3.9% in 1 w/o, and 7.9% in 3 w/o, at a current density of 50 mA/cm<sup>2</sup>. It is obvious that hydrogen in the exhaust gas increases with increasing hydrazine concentration.

Coulombic efficiency was about 100% in 0.5 w/o hydrazine, and about 90% in 1 and 3 w/o, at a current density of 50 mA/cm<sup>2</sup>. At a low current density, for example, at 25 mA/cm<sup>2</sup>, the efficiency was 91% in 0.5 w/o hydrazine, 75% in 1 w/o, and 70% in 3 w/o. Therefore, it is obvious that efficiency increases with dilution of the hydrazine and with increasing current density.

**Effect of temperature.**—Effects of temperatures of 25°, 40°, 60°C in the chamber on polarization curves, gas evolution rate, and coulombic hydrazine efficiency were studied.

The potential of the hydrazine anode moved into less noble areas with increasing temperature. For example, the difference of potential was about 15 mV for each 10°C at a current density of 50 mA/cm<sup>2</sup>.

Figure 10 shows the behavior of gas evolution at a current density of 25 mA/cm<sup>2</sup>. Total nitrogen and total hydrogen evolution rates increased with increasing temperature. Especially, total hydrogen increased very rapidly with increasing temperature. Nitrogen from the anolyte chamber was more than that from the electrolyte chamber, but the hydrogen evolution rate was opposite that of the nitrogen evolution rate. Then, at a current density of 25 mA/cm<sup>2</sup>, hydrogen in the exhaust gas was 14% at 25°C, 35% at 40°C, and 49% at 60°C. Only at 60°C, did the exhaust gas make Nessler's reagent turn slightly yellow.

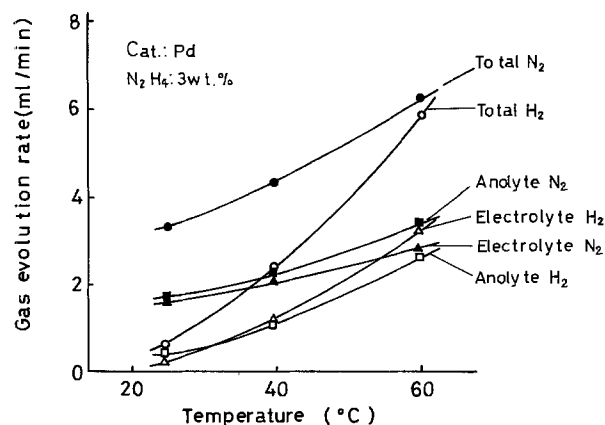


Fig. 10. Effect of operating temperature on gas evolution rate at current density of 25 mA/cm<sup>2</sup>.

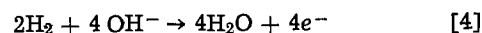
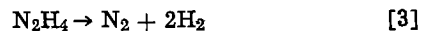
A small amount of ammonia might have existed in the exhaust gas. However, because the amount was negligible, quantitative analysis of it was impossible.

Figure 11 shows the effect of temperature on the coulombic hydrazine efficiency. It is obvious that the efficiency increases with decreasing temperature and with increasing current density.

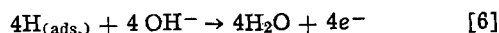
**Anode reaction.**—When reaction [2] occurs, anode potential is about -1.2V (vs. NHE) in 30% potassium hydroxide solution electrolyte. The best value in this paper is -1.03V, namely about 0.2V more noble than the theoretical value.

Many reactions are expected regarding the hydrazine anode:

(i) Hydrazine decomposes to hydrogen and nitrogen, and this hydrogen reacts electrochemically



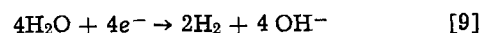
(ii) Hydrogen atoms in hydrazine are absorbed on the electrode surface and react with hydroxyl ions in the electrolyte, or become hydrogen molecules



(iii) Hydrogen in hydrazine reacts gradually with hydroxyl ion in the electrolyte, as reaction [8]



(iv) Reversal reaction occurs and mixed potential is observed



In this paper, because all exhaust gases have hydrogen gas in them either (i), (ii), or (iv) is presumed.

The calculated value of electrochemical potentials of hydrogen reaction [4] is -0.925V in 30% potassium hydroxide solution, but the anode potential in this paper is less noble than this value, not only at open circuit but in the low current density regions. It appears that reaction [2] will occur to a minimum extent, simultaneously with the hydrogen evolution reactions [3], [7], or [9] and their accompanying reactions. In the silver catalyzed electrode reaction the amount of evolved nitrogen is almost the same as the theoretical amount, with very little hydrogen. The reason is the low activity of the catalyst and the efficient use of the small volume of hydrogen.

### Summary

1. The coulombic fuel efficiency is influenced by the kind of catalyst. That of the silver catalyzed anode

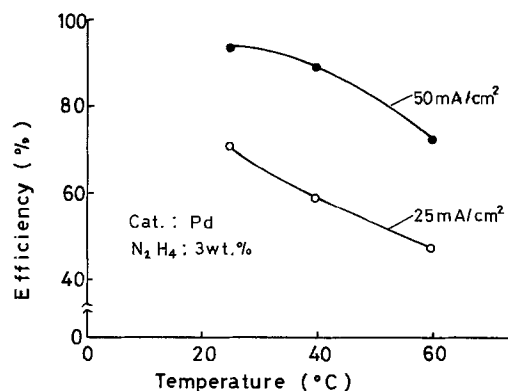


Fig. 11. Effect of operating temperature on coulombic hydrazine efficiency.

cell was the best, and that of the platinum was the worst.

2. The main components of the exhaust gas were nitrogen and hydrogen. A little ammonia was detected when the operating temperature was 60°C.

3. The hydrogen content of the exhaust gas decreases and fuel efficiency increases in accordance with increases in the current density. At a high current density, it is presumed that hydrogen which is produced by side reaction is caught by the anode and is used for further reaction.

4. The hydrogen content of the exhaust gas increases and fuel efficiency decreases with increasing hydrazine concentration. It seems that the decomposition of hydrazine which is not used effectively for electrochemical reaction increases with increasing hydrazine concentrations.

5. The hydrogen in exhaust gas increases and fuel efficiency decreases with increasing cell temperatures.

Manuscript submitted Oct. 2, 1975; revised manuscript received Jan. 27, 1976. This paper was presented in part as Paper 21 at the Boston, Massachusetts, Meeting of the Society, Oct. 7-11, 1973.

Any discussion of this paper will appear in a Discussion Section to be published in the December 1976 JOURNAL. All discussions for the December 1976 Discussion Section should be submitted by Aug. 1, 1976.

Publication costs of this article were partially assisted by Hitachi, Limited.

#### REFERENCES

1. R. Jasinski, *Electrochem. Technol.*, **3**, 129 (1965).
2. H. B. Urbach, D. E. Icenhower, and R. J. Bowen, Proceedings of 25th Power Sources Symposium, p. 182 (1972).
3. J. Heiblum and W. Vielstich, *Electrochim. Acta*, **18**, 501 (1973).
4. S. G. Meibuhr, *This Journal*, **122**, 164 (1975).

## An X-Ray Diffraction, Scanning Electron Microscopy Study of Separator Failure

J. R. Daffler,\* A. A. Garwood, F. W. Wentzel, Jr., Barbara Campbell, and D. L. K. Chu

*ESB Incorporated Technology Center, Yardley, Pennsylvania 19067*

#### ABSTRACT

Resin-bonded paper separators suffer some loss of crystalline material on extended storage in battery grade  $H_2SO_4$ . Similar separators from cycled batteries suffer order of magnitude losses of crystallinity. Scanning electron microscopy has found Pb-salts of two kinds; those grown in regions of high and low supersaturation. The latter often obtain crystal dimensions larger than  $30\mu$ . Comparison with other separator materials used in Pb/acid batteries has led to a model of separator failure based on mechanical abrasion, fluid motion, and crystallization in large pores. The separator matrix is weakened by brittle fracture of the fiber network, accompanied by minor hydrolytic loss of material. These lead in turn to pore enlargement that can enhance the growth of large, well-ordered crystals. A somewhat speculative mechanism for perforation failure of large-pored separators is given.

Paper separators for use in automotive batteries perform beyond ordinary expectation in well-made, well-maintained batteries. Their use yields distinct cost savings when compared to microporous rubber or polymer separators (1). Made by typical paper-forming techniques and impregnated with thermosetting resins, they exhibit exceptional resistance to sulfuric acid (1.25-1.32 sp gr). When subjected to deep cycling at high, steady currents, they regularly exhibit what has come to be called "perforation" failure. Figure 1 shows representative perforation failures found in automotive batteries discharged at high rates.

Perforation spots are generally very rich in Pb-salts. Direct chemical analysis by area has shown these spots to have, frequently, more than twice the total Pb per unit weight as the rest of the matrix. On occasion, direct analysis found 22-23% Pb at a perforation spot, while the rest of the separator had accumulated ~ 10% Pb (analyzed as per cent Pb-metal/unit area). The onset of this particular kind of failure is generally signaled by quite low end-of-charge voltage (ECV) so that perforation spots are regarded as high resistance short circuits.

It was natural to evaluate paper separators for electric and auxiliary vehicle (golf cart) use. The discharge rates are quite high compared to automotive practice, and discharges are much deeper: in the latter cases, ~ 100%. Regular discharge testing of automotive-type batteries using the accepted method (SAE J240a) does little to characterize separators, while the formerly used SAE test (Schedule K) quickly illuminates separator weaknesses. In J-240a testing, resin-bonded paper separators yield excellent results. In testing typically used for golf cart and electric vehicle batteries, paper has proved much less successful.

Paper separators tend to fail after a few hundred cycles if discharged at the 2-5 hr rates. The mechanism of failure has not been defined, but is certainly related to chemical and physical stability. The over-all mode of failure is associated with the physical strength of separators and the average pore size. The failure discussed most in this paper is so-called perforation failure, and this kind of failure is sometimes seen in separators possessing greater chemical and physical stability than resin-bonded paper.

Cellulose matrixes for separators are usually impregnated (phenol formaldehyde resins are common), then die-stamped or roll-died to form a rib structure. The paper is then baked to complete the polymeriza-

\* Electrochemical Society Active Member.

Key words: cellulose, crystallization, hydrolysis, mechanism, porosity, supersaturation.

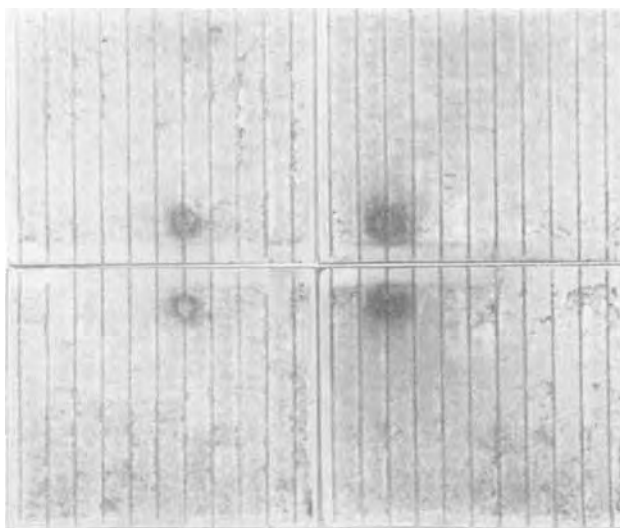


Fig. 1. Perforation failure typically seen in failed cells having low end-of-charge voltage.

tion. In some separators, the ribs are reinforced with polymers such as polyvinyl chloride (PVC). The powdered PVC fuses during the polymerization step, forming a hard surface over the ribs.

Finished separators made in this way have good wicking action, can act as a useful electrolyte reservoir, but fail to provide good retention of positive material; they usually are 60-70% porous. They possess adequate conductivity. The pores in such separators are large. Figure 2 shows scanning electron micrographs of a typical paper separator fiber matrix. The interfiber distances are of the order 20-30 $\mu$ . It is clear, therefore, the average pore size of the fiber matrix is large, compared with the average pore diameters found in many other separators. A summary of typical pore sizes is indicated in Table I. To approach an understanding of the mode of failure we were led to measure the stability of the separator material, *per se*, then to investigate the nature of the Pb-salts present in cycled and failed separators, using scanning electron microscopy (SEM). The key to empirical understanding was cross-characterization of paper with respect to those separators that do not exhibit this particular kind of failure (microporous rubber and polymer).

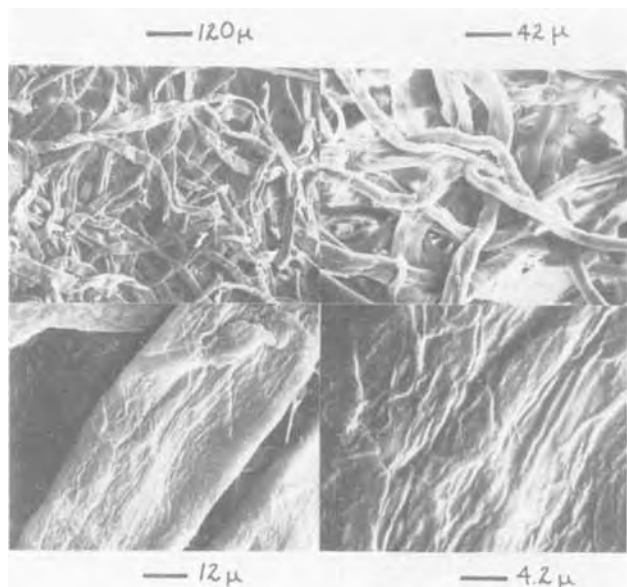


Fig. 2. Scanning electron micrographs of phenol-formaldehyde-bonded cellulose separator matrix.

Table I. Lead/acid separators, "average" pore diameter

Separator	Size ( $\mu$ )
Port Orford cedar	1
Paper	25
Sintered PVC	17
Microporous PVC	5
Hard rubber	0.6
Celgard	<0.05
Microporous polyethylene	0.05
Nonwoven polypropylene	10

*X-ray measurement of crystallinity.*—Our investigation of stability was based on x-ray diffraction measurements of the crystalline cellulose present in the separator matrix, assuming that long-lived crystallinity was to be equated with matrix stability. Hermans and Weidinger have explored the question of crystallinity and recrystallization in a series of papers (2-4). The question of order of crystallinity of cellulose has been discussed at some length (5-8). For the purpose of this study, the term crystallinity serves well.

We did not use the Hermans and Weidinger technique which requires careful fabrication of a compressed plug of sample (2). Instead, following the practice of Venkateswaran (9), we used sheet stocks and have concentrated on direct x-ray comparisons of the crystalline material in unimpregnated paper, finished and used separators. Using typical diffractometer techniques and postsample monochromated Cu-radiation ( $\lambda = 1.543\text{\AA}$ ), we obtained patterns similar to those Hermans and Weidinger (2) obtained with micro-camera, and a carefully compressed plug of sample. As in the case of Hermans and Weidinger and others (2-4, 6, 9), all samples tested gave diffuse peaks in the region,  $8^\circ$ - $15^\circ$   $2\theta$ , and a much taller, less diffuse peak in the neighborhood of  $22^\circ$   $2\theta$ . All samples tested were derived from the same source of  $\alpha$ -cellulose. A representative spectrum can be seen in Fig. 3.

A technique for indexing the amount of crystalline cellulose present in the fiber matrix was developed to serve as a measure of matrix stability as it compared, directly, to the starting material. The important quantity is the number of diffractors present in the target zone. For papers made by the same controlled process, this should be, reasonably, the same. For a standard of comparison, a chip of raw material  $\alpha$ -cellulose (Cellulose-I) before pulping and formulating, is used. A correction is applied to normalize all the samples (papers

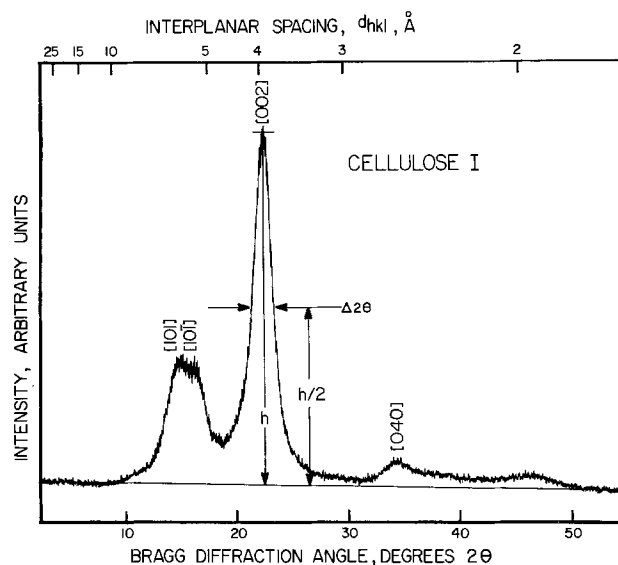


Fig. 3. X-ray diffraction spectrum of Cellulose-I stock used in formulation of separators. The  $I_{std}$  value used in calculating  $J_x$  is calculated by triangulating the [002] diffraction maximum as shown.

and pulp) to the same number of diffractors per unit area. The integrated intensity,  $I_x$ , of the peak measured is given by

$$I_x = An_x \quad [1]$$

where  $n_x$  is the number of diffractors/unit area, and  $A$  is the beam target area. The value of  $n_x$  is proportional to the density,  $\rho_x$ , of species and a constant,  $k_x$  related to their crystalline nature. Therefore, for the comparison standard  $I_{std} = Ak_{std}\rho_{std}$ . Setting target areas equal, and rearranging, the crystallinity index,  $J_x$ , is resolved

$$J_x = (k_x/k_{std}) = (\rho_{std}/\rho_x) (I_x/I_{std}) \quad [2]$$

Figure 3 indicates the way the ratio ( $I_x/I_{std}$ ) is measured. An arbitrary base line is established from  $10^\circ 2\theta$  to  $30^\circ 2\theta$ . The primary  $I_{100}$  peak (10) is then triangulated to arrive at an "integrated" intensity value. This is used to calculate the index of crystallinity of the material after correcting for any differences in density between sample and standard. The density of raw material pulp was 1.352 and the density of the separators was 1.505. Before beginning x-ray procedures, tests to insure "saturation" of the refracted beam were done (9). Single thicknesses of  $\sim 25$  mil back web material yielded the same diffraction maxima as 2-3 thicknesses. Because direct comparisons were made to the source material, no corrections for absorption were used (2).

The index of crystallinity used here and as used in an earlier note (11) differs from the crystallinity index of Segal (6) and others (2-9). This value, the  $J$ -value, is an extensive measure of retained crystallinity where in Segal's case, the measurement was a true degree of crystallinity, that is an intensive measurement. A decrease in  $J$ -value, as used here, represents a measure of the relative degradation of the crystalline cellulose matrix and therefore is a measure of relative stability.

### Experimental Procedures

A large number of separator pieces were stored in  $H_2SO_4$  of varying specific gravities. The acids used were 1.260, 1.280, 1.325, and 1.260 saturated with  $PbSO_4$ .

Forty to sixty 2 in. square chips were made up for each concentration of acid and shuffled before distributing into the acid baths. The samples were put into 1 lb ointment jars of the solutions and these thermostated at  $52^\circ C$  ( $125^\circ F$ ) in an oil bath. At the end of specific storage times, 4-7 samples were taken from each jar and rinsed in tap water and then distilled water until free of sulfate. The chips were vacuum dried at  $40^\circ C$ , examined by x-ray diffraction, and the crystallinity index of each sample calculated. The storage time varied from 690 to 2400 hr.

A set of Group 24 batteries was assembled with single cell covers to facilitate cell-to-cell removal of separators and elements. The cells were tested as part of a separator test program that included removal of separators at regular intervals. Our interest was, principally, in the condition of the separators after known periods of cycling. The discharge scheme, a 25% overcharge program, using the 2 hr rate (formerly SAE Schedule K) was: 20A discharge for 1 hr, 5A charge for 5 hr, and no rest at open circuit.

For indexing the cellulose crystallinity in cycled cells, separators were removed, in order, from cells and immediately washed in running water. After clearing excess acid, the separators were brushed free of loose, active material with a 2 in., soft paint brush and washed 1 hr in cold, running tap water and then soaked repeatedly in distilled water until free of sulfate. After removing excess water, the separators were dried, in vacuo, at  $\sim 40^\circ C$ . Representative pieces were taken for x-ray analysis. Cells that refused to accept charge after a definite number of cycles, characteristically, had "perforation" spots (cf. Fig. 1), and exhibited short-circuit-like behavior.

Samples of cycled separators, prepared as for x-ray studies, were gold coated and examined, using SEM techniques, for types of Pb-salt accumulation.

Reagent grade chemicals were used throughout this program, and acid concentrations were determined by controlled-temperature hydrometry. Separator materials were standard phenol-formaldehyde-impregnated stocks from the Texon Corporation of South Hadley, Massachusetts. The  $\alpha$ -cellulose stocks were also obtained from Texon.

A Philips Electronics Mark II x-ray diffractometer was used to obtain x-ray intensity data. All analyses were done at Cu-target parameters of 35-40 kVA and 15-20 mA x-ray current. Each series of measurements was concluded by analysis of a chip of  $\alpha$ -cellulose at the same current-voltage settings. Scanning electron microscopy was done on a JEOL microscope. Use-time on this instrument was purchased from The Franklin Institute Materials Research Department.

Pore volume measurements were made using an Aminco-Winslow, mercury filled pore volume analyzer.

### Results and Discussion

*X-Ray diffraction.*—There is a decrease in crystallinity upon storage in  $H_2SO_4$ . It is not large, in fact, smaller than the difference between the raw material Cellulose-I and the finished virgin separators. The process of pressing and baking of separators reduces the  $J$ -value of separators to  $59.6 \pm 6.5\%$ , while storage in 1.280 sp gr  $H_2SO_4$  lowers the  $J$ -value to 48% after 2400 hr. The calculated indexes of crystallinity ( $J$ -values) are summarized in Table II.

Dried samples of separators from batteries cycled 5 and 9 weeks were x-rayed and their crystallinity indexes calculated. Some difficulty is experienced in measuring line widths because of interference by Pb-salts in the separator matrix. In the brief summary in Table III, we have indicated the crystallinity indexes of separators analyzed after 5 and 9 weeks of cycling (28 cycles per week).

The use of cellulosic separators in batteries is accompanied by a very large reduction in index of crystallinity, as it is defined in this study. Separators cycled 5-9 weeks suffered a much greater loss of crystallinity than separators stored in battery acid for much longer periods. This loss is not easily explained; however, the x-ray patterns of cycled cellulosic separators are not unlike these found by Segal *et al.* when they subjected Cellulose-I fibers to ball milling and found large losses of crystallinity (6). This suggests that either strenuous physical processes such as stretching and abrading of the fiber matrix, or strong chemical action causes the deep loss of crystallinity of cycled batteries.

The larger losses of crystallinity suffered during storage in acid saturated with  $PbSO_4$  suggest that physical processes such as the abrading and exercising of the matrix no doubt experienced by separators during

Table II. Index of crystallinity: acid-treated separators

$H_2SO_4$ , sp gr	Hours of immersion ( $52^\circ C$ )		
	691	1360	2400
1.260	0.49	0.52	0.49
1.280	0.47	0.55	0.48
1.260 sat'd with $PbSO_4$	0.39	0.39	0.29
1.325	0.48	0.48	0.43

Table III. Crystallinity indexes

Cycle life, weeks	$J$ (index of crystallinity)
5	0.063
9	0.080

cycling lead to increases in crystallinity loss. Segal *et al.* (6) ball milled highly crystalline Cellulose-I powder and found complete loss of crystallinity after 1 hr of milling. Knife-milling has been shown by Segal (6) and others (9) to cause only a slight lowering of crystallinity. Both processes, then lead to a reduction of crystallinity; that caused by compressive (ductile) processes being far greater than caused by tensile (brittle) processes on the fibers. In the environment of the cycling battery, we expect to see both ductile and brittle fracture contributing to loss of crystallinity.

The possible role of oxidative hydrolysis was briefly tested by 100°C extraction of separators with 10% HNO<sub>3</sub>. The index of crystallinity was affected less than by 3500 hr in 1.325 H<sub>2</sub>SO<sub>4</sub>. Ant-Wuorinern and Lehtinen (12) hydrolyzed Cellulose-I in dilute H<sub>2</sub>SO<sub>4</sub> and found material loss, but little change in degree of crystallinity unless the acid was hot and the concentration above 2*N* (sp gr ~ 1.12). At 25°C, Ant-Wuorinen and Visapaa (13) found that neither index of crystallinity nor degree of polymerization of cellulose was affected by hydrolysis with 0.1-2*N* H<sub>2</sub>SO<sub>4</sub> or other mineral acids. In this laboratory, storage of separators in 1.325 H<sub>2</sub>SO<sub>4</sub> did not result in large loss of *J*-value, and the work of McKeown and Lyness (14) and of Gjonnes *et al.* (15) indicate hydrolysis, whether heterogeneous or homogeneous, is not an unequivocal tool for interpreting the intensive degree of crystallinity of cellulose matrixes. In this laboratory, hydrocelluloses were made by hydrolysis in 1.400 H<sub>2</sub>SO<sub>4</sub> at 53°C that had intensive and extensive crystallinities within 10% of that displayed by raw material  $\alpha$ -cellulose.

Other possible causes of the decrease in *J*-value are: (i) thermal effects due to local heating, temperature cycling, and nonuniform spacing between separators and electrodes; and (ii) physical effects due to growth and dissolution of lead salts, a kind of exercising, stretching, and abrading of the fiber matrix by the electrodeposited salts.

Prevailing opinion in this laboratory is that loss of *J*-value is more likely due to thermal effects (hot spots) and simple physical effects (abrading), with hydrolytic losses much smaller than the former. Ruznak and Tanczos (16) found that thermal treatment at

190°C for up to 10 min brought about large increases in the rate constants for acid hydrolysis to occur, but as we have seen, long term storage of separators in quiet battery acid at 52°C led to very little relative loss of crystallinity.

Examination of separators that had so-called perforations, indicates they were all close to the cell tops, where the spacing is confined. Most of the dark spots are centered on ribs and are facing the positive electrode. The most intense darkening, even in the rare cases where the perforation is not centered on a rib, is always on the two raised faces that adjoin the positive plate. The symmetry, or match-up, on the two separator pieces is always very marked. These dark spots are very rich in Pb-salts.

*SEM examination.*—SEM examination found two kinds of salt accumulations: large well-formed crystals and collections of much smaller indistinct growths, rather like handfuls of wet sand in appearance. The well-formed crystals, often, were as large as 30 $\mu$  on their long axis. This is quite large with respect to average pore size of cellulose separators, ~25 $\mu$ . Figure 4 shows both kinds of growth. The poorly defined crystals are quite small and even in SEM pictures, indistinct.

The chemical nature of the crystals imbedded in the paper matrix is not known, since they had been modified by washing and drying procedures to prepare them for SEM analysis. If the material in perforation spots provided a high resistance short-circuit path, then they contained Pb or a form of PbO<sub>2</sub>, both excellent electronic conductors. Their nature surely was changed by experimental treatment. The origin of the crystals, that is, whether seeded by positive material or spontaneously nucleated from supersaturated solution (see next discussion) is not known, but both origins would probably lead to the same species during extended cycling.

Spontaneous nucleation is clearly a possibility. SEM examination of separator chips stored for 2400 hr in 1.260 H<sub>2</sub>SO<sub>4</sub> saturated with PbSO<sub>4</sub>, showed crystals imbedded in the matrix. These solutions were, in all cases quiescent, so that stirring did not provide seeds.

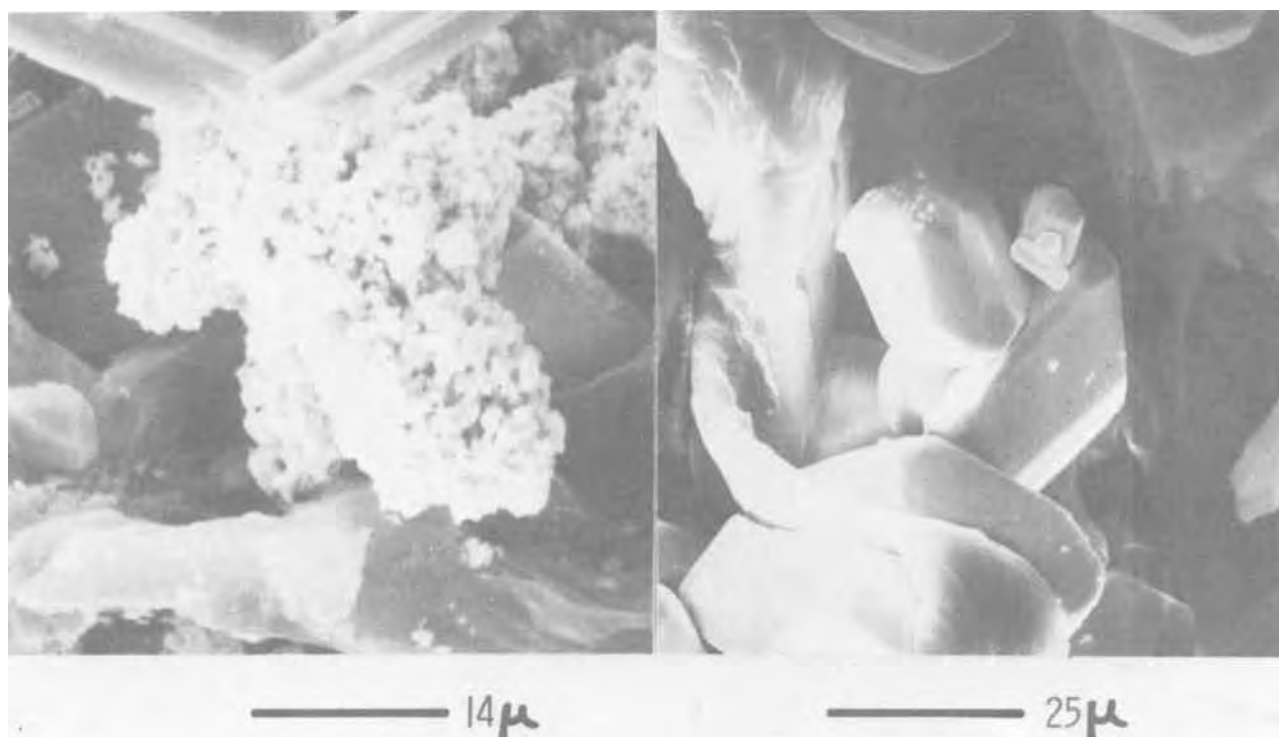


Fig. 4. Scanning electron micrographs of two kinds of crystal growth found in paper separator matrices

The SEM findings are very illuminating. Crystallization and nucleation are very dependent on the degree of supersaturation,  $S$ . The finding of two distinct crystal populations shows the ongoing presence of regions in the separator matrix where the degree of supersaturation is different, despite regular changes in solvated species concentration due to battery cycling. The presence of collections of small "cauliflower-like" growths and faceted, well-defined crystals is dependent on (17-19) what are essentially competing processes, nucleation and crystal growth.

Both processes are dependent on the same driving force, the supersaturation,  $S$  where

$$S \equiv (C_B/C_E) \quad [3]$$

with  $C_B$  the solute concentration in the bulk and  $C_E$  the equilibrium saturation concentration of solute.

The growth rate  $R$ , and nucleation rate  $N$ , are of the form (see Appendix)

$$R = AS^n \quad [4]$$

$$N = BS^m \quad [5]$$

with  $m > n$ . This means that as  $S$  increases in value, what we may call the average crystal size decreases, and the finding of cauliflower clusters indicates we are examining a region of high supersaturation (cf. Fig. 5).

Regions of low supersaturation lead to crystal growth that is slow and orderly, perhaps extending over hundreds of battery cycles (cf. Fig. 6).

Since there is a common electrolyte and soluble Pb-salt species are presumably of the same concentration, the only agency that can create regions of different  $S$ -value is the structure of the pore volume distribution of the separator.

The large pores and pore volumes present in paper separators make it possible for regions of low  $S$ -value to persist, since in large pores, convective mixing is less inhibited by viscosity and diffusivity effects. Convection can be thermally generated whenever the "cell" or pore under consideration is large. For the case of a cell or pore heated from below, Rayleigh showed no

convection could take place if the Rayleigh number  $R$ , were less than a critical value  $R_c$ , where

$$R \equiv g\beta G_L L^4 / \alpha \eta \quad [6]$$

with  $g$ ,  $\beta$ ,  $G_L$ ,  $L$ ,  $\alpha$ , and  $\eta$  the gravitational constant, the volume expansivity, the thermal gradient at the interface inside the cell, the cell dimension, the thermal diffusivity, and the viscosity (20). This means that for values of  $R$  below a critical value ( $R_c \sim 1700$ ), there is no convective mixing.

For battery separators, this indicates that the average pore size plays the crucial role in the mechanism of short-circuit development. In this study, cells which refused charge after some period of cycling invariably had perforation spots and the spots were very rich in total Pb.

This is very suggestive. Hard rubber separators and microporous polyethylene separators do not suffer this kind of failure. Large crystals of Pb-salt were not found in microporous polyethylene separators, while the pores were sometimes occluded with small crystals as shown in Fig. 7.

In an effort to understand these differences, mercury porosimetry was done on separators according to type. The oversize summaries are plotted in Fig. 8. Both paper separators and sintered PVC separators have quite large pores ( $\sim 25\mu$ ) and both have exhibited perforation failure while microporous rubber and microporous polyethylene have not. A visual understanding of pore size differences may be gotten from Fig. 9, a 300X scanning micrograph of four widely used separator matrixes.

Sundberg (21) has related the pore volume distribution of separators to other properties such as resistivity, compressibility when wetted and wettability, and apparent barrier properties for antimony transfer. Since, however, antimony transfer is wholly a diffusion phenomenon (22), the pore size distribution of the separator cannot be a critical factor in preventing antimony transfer, except to the extent convection currents can penetrate the pores or interstices of the separator.

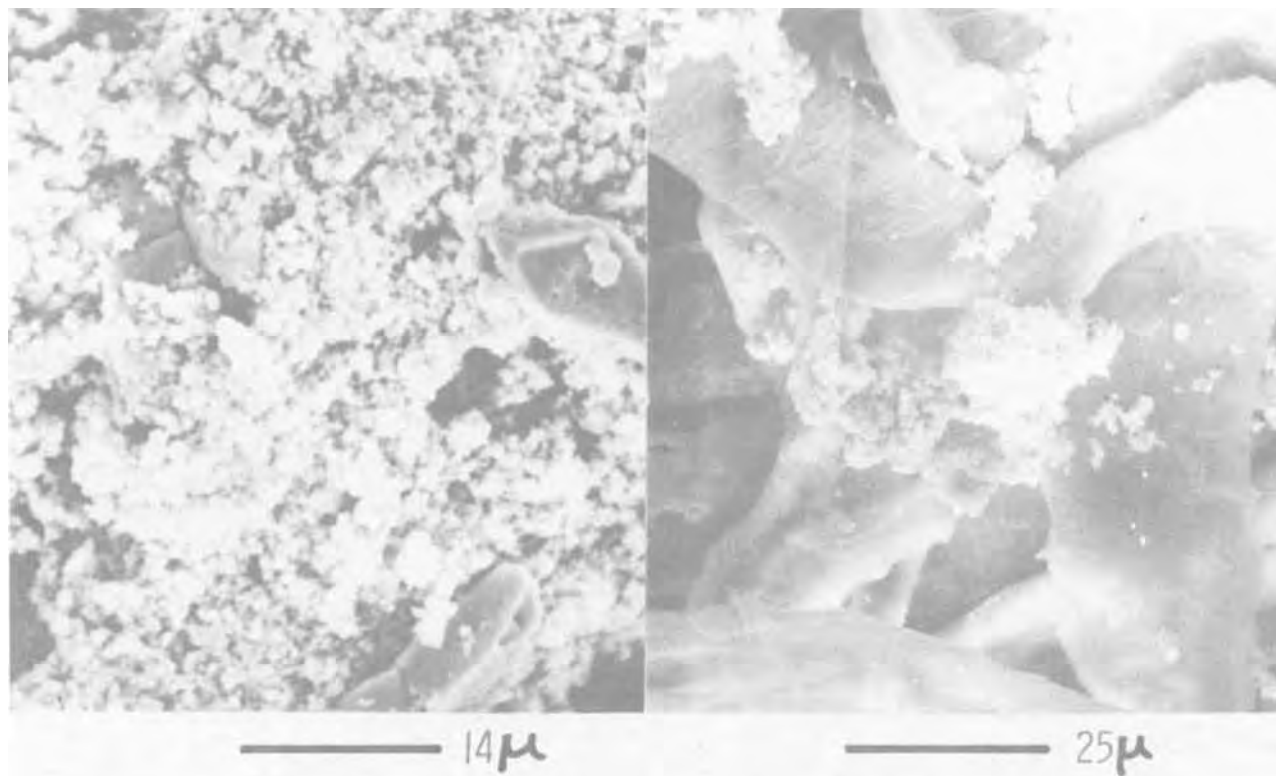


Fig. 5. Scanning electron micrographs of nucleation-controlled growth forms of crystals in paper separator matrix



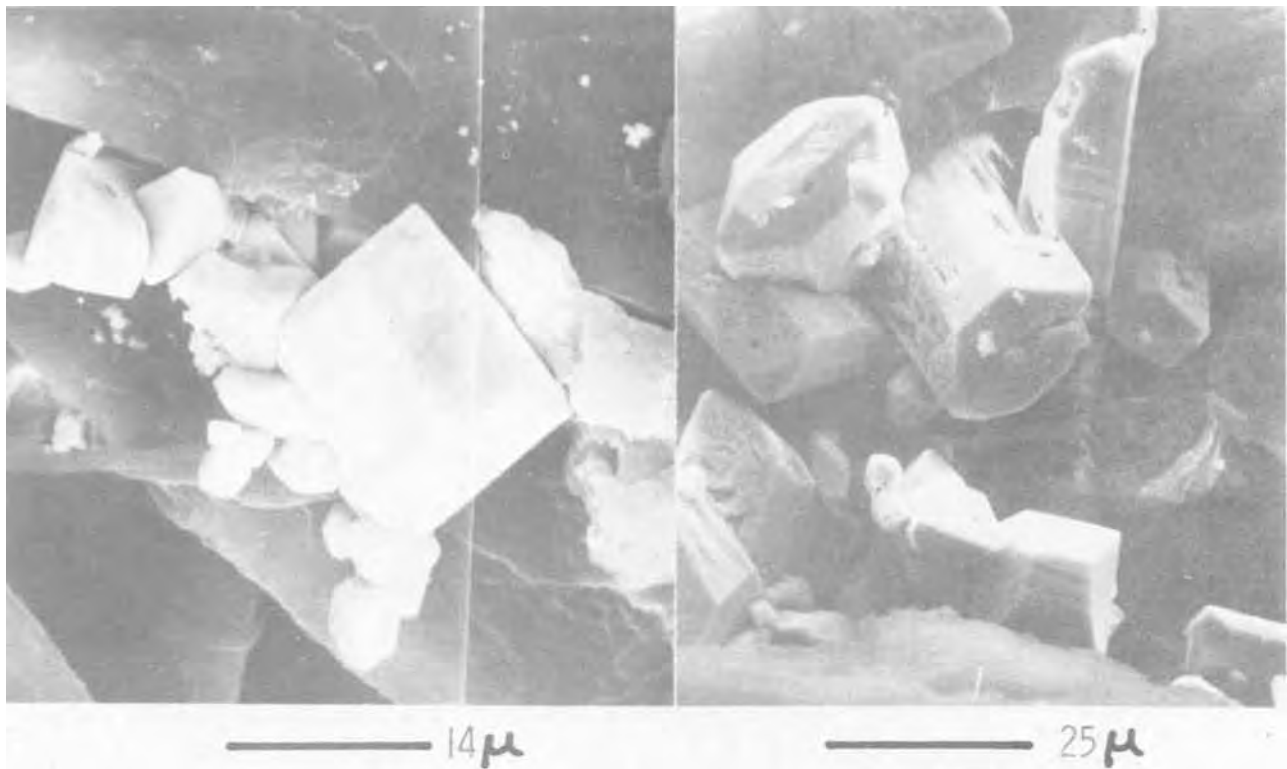


Fig. 6. Scanning electron micrographs of large, faceted diffusion-controlled growth forms of crystals found in paper separator matrix

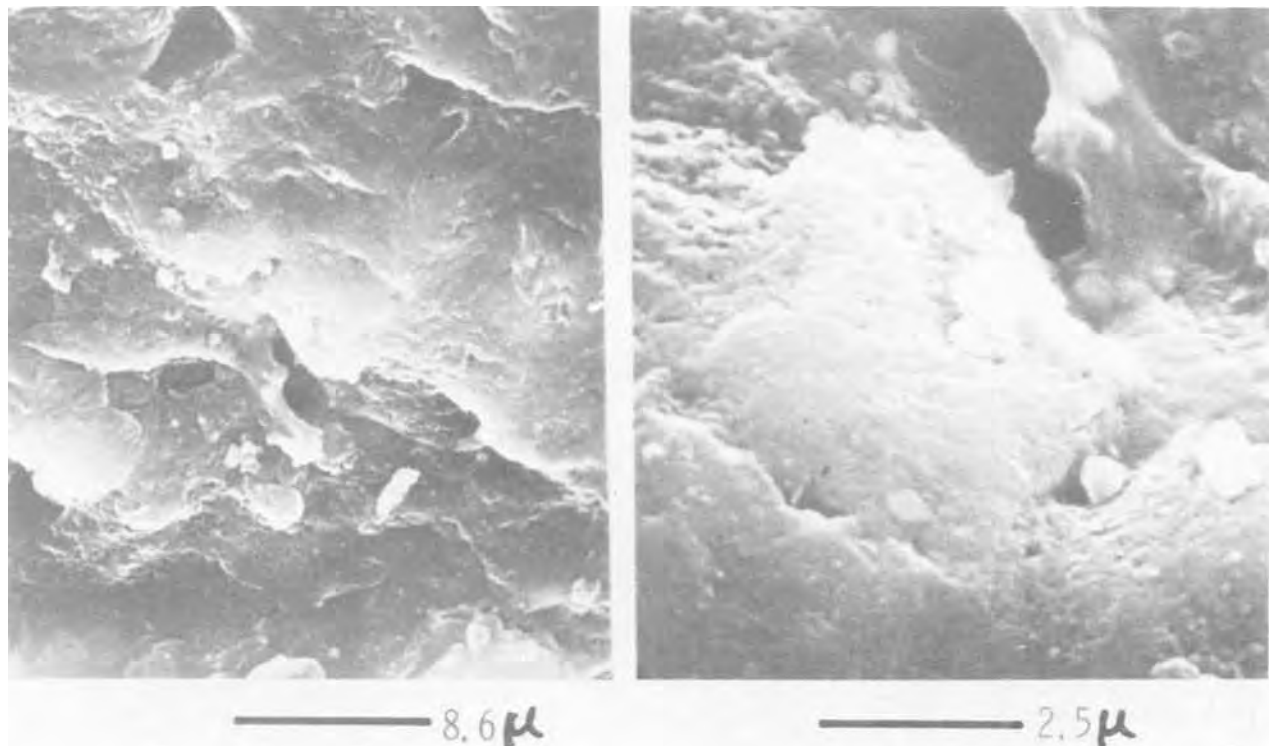


Fig. 7. Scanning electron micrographs of microporous polyethylene separator matrix. Note smallness of pores compared to scattered crystals found in matrix.

*A mechanism for perforation failure.*—The phenomenon of very large crystal growth in large-pore separators had led us to formulate a speculative mechanism for buildup of Pb-salts and subsequent short-circuit failure. Basic to the mechanism is that larger, well-defined crystals have higher conductivities because there are fewer salt/solution interfaces in the short-circuit path. Then, if a crystal has grown in an orderly fashion inside a large pore or cell, it will certainly

provide sites for nucleation-controlled growth when the pore in which it has grown is reduced in size, so that the calculated Rayleigh number is less than the critical value. In Fig. 10 we indicate the basic character of the mechanism: (i) A large, diffusion-controlled crystal forms in a large pore, where, since  $L_{\text{pore}}$  is large, there is convective mixing and the supersaturation is low. (ii) After continued, slow growth, the pore dimension is decreased until  $L_{\text{pore}}$  is small enough. The



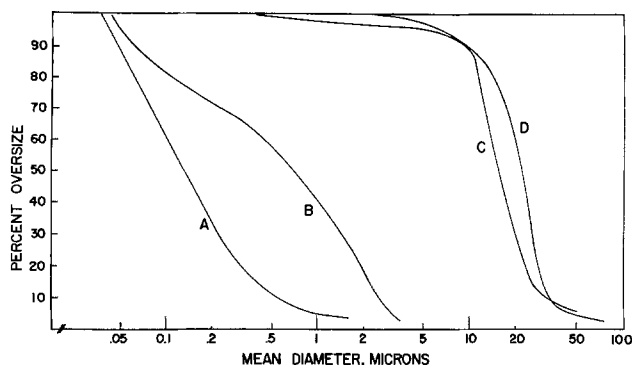


Fig. 8. Pore size distribution curves for four commonly used separator matrices. A, microporous polyethylene; B, hard rubber separator; C, sintered PVC powder separator; and D, resin-bonded paper separator.

Rayleigh number drops below the critical value  $R_c$  and nucleation controlled growth ensues until the boundaries of this pore, or cell, are bridged to a neighboring pore. In this way, a bridge of interconnection of low resistivity is formed through the body of the fiber matrix.

Speculative as this mechanism is, there is evidence in SEM studies for its correctness. Figure 11 shows scanning micrographs of nucleation-controlled growth over large crystals. This means that in these neighborhoods the degree of supersaturation went from a period of low values to a period of high value, suggesting the partial correctness of the speculations above.

SEM investigations also help confirm earlier speculations concerning the decrease in crystallinity of the paper matrix of cycled cells. Study of many SEM photos revealed a large number of brittle fractures of separator fibers in regions where there was large crystal growth, confirming, in part, that growth and dissolution processes stretched, and exercised the matrix to a considerable degree.

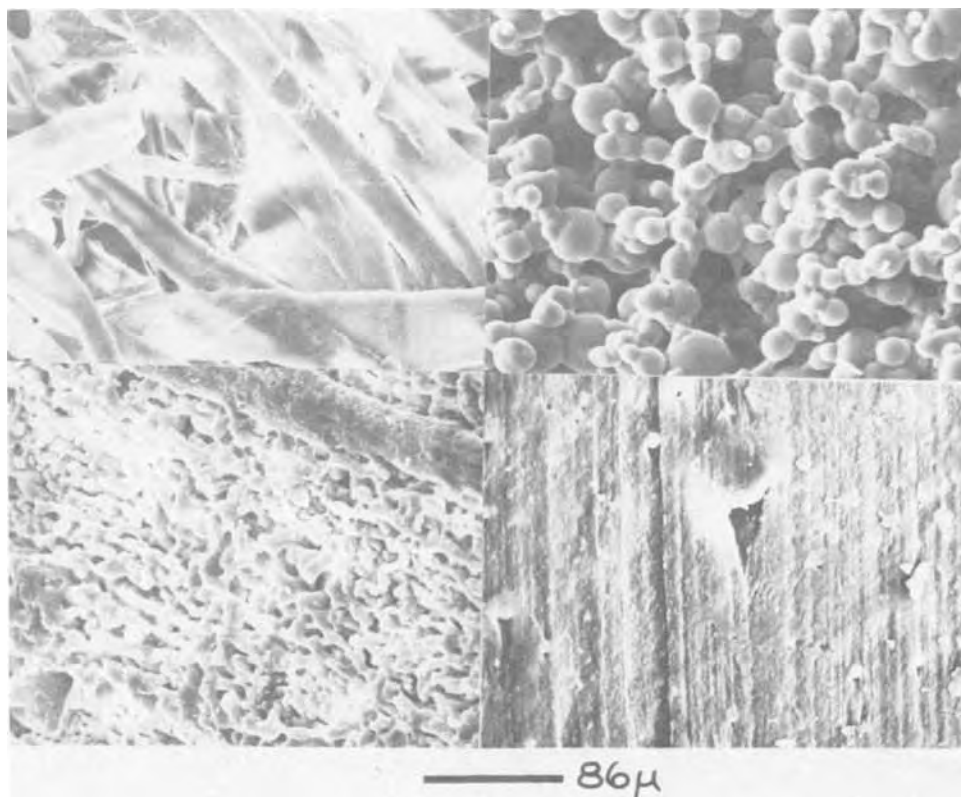
Large scale brittle fracture should result in broadening of the most intense x-ray diffraction peak, the

[002] diffraction maximum. The fiber direction of cellulose coincides with the long axis of the cellulose unit cell (23-25). The main structural element of cellulose, the fibril, has its long axis parallel to the unit cell axis, and as fibers are structured from very large collections of fibrils (8), brittle fracture must reduce crystallite size on the b axis. Fiber rupture, whether brittle fracture across the fibrils or ductile fracture parallel the fibrils, yields an increased accessibility to chemical attack. This is true whether the cellulose model one uses is the crystalline/amorphous model of Clark (23) and others (26, 27), the fringed-micelle model (8), or the protofibril model of St. John Manley (28). As shown by Ant-Wuorinen and his co-workers (12, 13), hydrolysis of knife-milled cellulose leads to limited material loss and some decrease in crystallinity index.

What likely occurs during brittle fracture and knife-milling is creation of end groups with labile hydroxyl groups newly accessible to hydrolytic agents. Rowland, Roberts, and Bose (29) have shown the accessibilities of  $-OH$  groups of cellulose structures are related to the state of order of these groups on the surfaces of crystalline regions, with highly crystalline regions possessing fewer accessible  $-OH$  groups. Microscopic evidence of brittle fracture, therefore, supports physical and physical/chemical mechanisms leading to the large decreases in crystallinity found in cycled separators. Scanning micrographs of brittle fracture are shown in Fig. 12 and 13. It is noteworthy that brittle fracture was found in the neighborhood of large, regular crystal growth. Such crystal growth will cause both brittle fracture, as seen, but will abrade and compress fiber matrixes due to growth and dissolution of crystal bodies. The brittle fracture and ductile fracture will, certainly, lead to depressed values for the crystallinity.

*Other failure mechanisms.*—It was suggested that antimony transfer may contribute to failures evidenced by low end of charge voltage. It is well known that antimony diffusion to the negative grid will lower the hydrogen overpotential and lower end-of-charge voltages (21). It is also understood that in a 25% over-

Fig. 9. Scanning electron micrographs of four commonly used separator matrices. From upper left, clockwise; resin-bonded paper, sintered PVC powder; microporous polyethylene, and hard rubber.



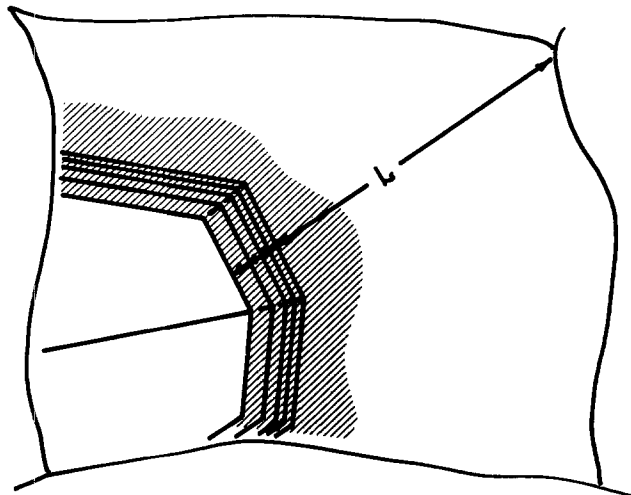


Fig. 10. Diagram of large pore in separator matrix. As the large crystal grows, the pore or cell dimension decreases until nucleation-controlled growth may ensue over the surface of the crystal.

charge program, much of the antimony corrosion capability is removed through stibine evolution during overcharge (30).

In the cycling program used here, starting ECV's were in the neighborhood of 2.85V. Cells with ECV's in the neighborhood of 2.35V invariably had one or more perforation spots (cf. Fig. 1).

In Holland's work (30), older batteries of extremely large capacities ( $\sim 2000$  A-hr) were discharged once a week at the 5 hr rate. They were given a quasi-constant potential charge after overnight, open-circuit stand. The degree of overcharge was 10%, and in this very bad case for antimony transfer, after three years or more of cycling, the ECV fell 0.130V; from 2.60-2.47V. Holland's cells, cycled about 180 times, at high rates, with extensive open-circuit stand had no ECV-drops of the order of 0.5V as seen in our studies. There is, however, no clear-cut manner of measuring the

degree to which antimony transfer did contribute to failure in this program. We chose to disregard the possible contribution of antimony transfer because of the protective effect of the 25% overcharge used, and because of the 1:1 correspondence between low ECV's and perforated separators. In one case, a battery cycled (Schedule K) for 5 weeks (140 cycles) had end-of-charge voltages of 2.42, 2.81, 2.82, 2.79, 2.78, and 2.46V. The two cells with low voltages had perforated separators, while none of the other four cells had such failures.

### Conclusions

The perforation failures of resin-bonded paper separators are high-resistance short circuits, caused, mainly, by a complex mechanism of crystal growth in the large pores of such separators. Resin-bonded paper separators and other separators with large pores ( $\sim 30\mu$ ) can provide sites for the growth of large, faceted crystals, and are the only separators that exhibit this kind of failure under working conditions. The growth of well-formed crystals in such matrices is made possible because the pores are large enough to permit convective mixing which sustains the low degree of supersaturation necessary for well-ordered, large crystal growth.

### Acknowledgments

The authors wish to thank John Brodhacker of ESB's Automotive Group for his support of this work and to give special thanks to W. D. Adams of ESB Canada, who built and discharged the many batteries used in this study.

Manuscript submitted Nov. 6, 1975; revised manuscript received Jan. 12, 1976. This was Paper 18 presented at the Toronto, Canada, Meeting of the Society, May 11-16, 1975.

Any discussion of this paper will appear in a Discussion Section to be published in the December 1976 JOURNAL. All discussions for the December 1976 Discussion Section should be submitted by Aug. 1, 1976.

Publication costs of this article were partially assisted by ESB Incorporated.

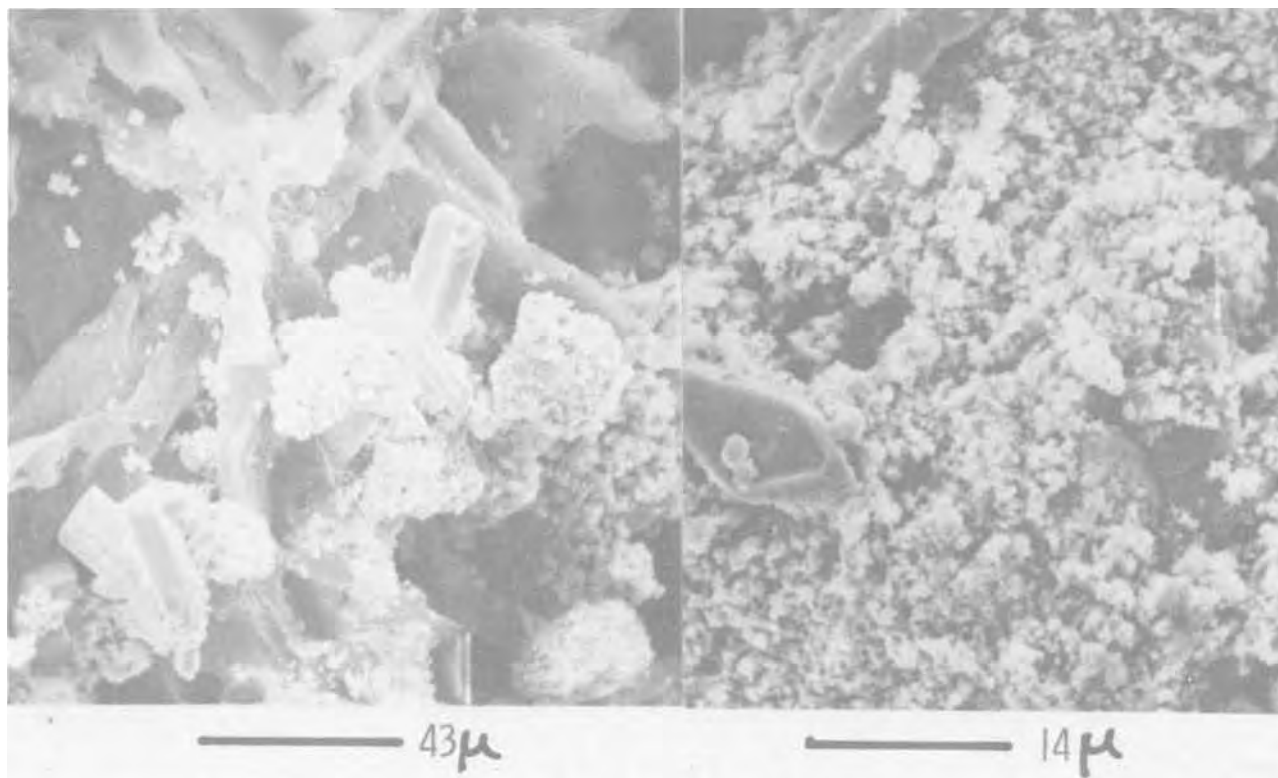


Fig. 11. Examples of nucleation-controlled growth in regions where diffusion-controlled growth had previously occurred. Note that the clusters are all on the examination side of the larger crystals, denoting later deposition.

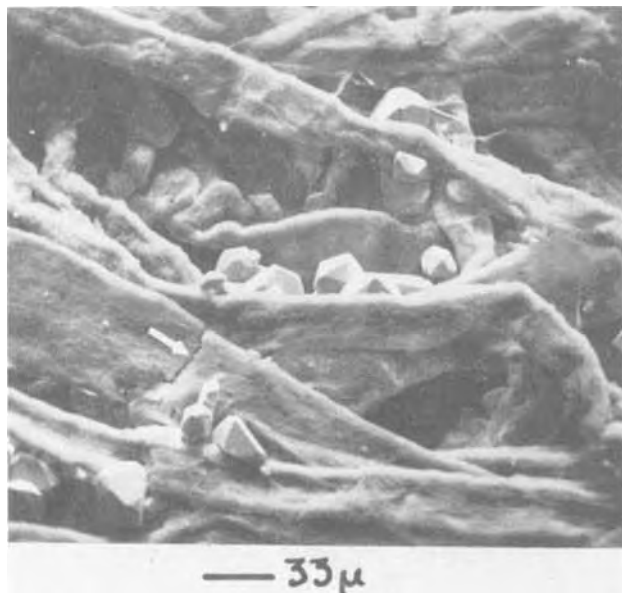


Fig. 12. Scanning electron micrograph of a brittle fracture in a region near well-ordered, diffusion-grown crystals.

#### APPENDIX

If we plot the concentration/temperature relationship for a species crystallizing from solution, we obtain, in general, a simple monotonic curve, with the plane divided into two regions: (i) unsaturated (inactive) region, and (ii) the supersaturated (active) region. What is important is:

There can be no crystallization activity in the unsaturated region,

Spontaneous nucleation can take place, without nuclei or seeds in the active or supersaturated region.

In the active region, in the neighborhood of the curve, nucleation without nuclei is not possible (sometimes called the metastable region).

Growth is possible over the entire active region, and the relationships are summarized in Fig. 14.

The situation is complex, of course, but from a simplified point of view, crystallization is seen as the result of two, competing processes: nucleation and

growth. Growth, in turn, is controlled by the rates of integration and diffusion of crystallizing species.

What follows is a simplified treatment of the processes important to crystallization.

*Nucleation.*—Recalling Eq. [3], we define the degree of supersaturation  $S$  according to

$$S = C_B/C_E \quad [A-1]$$

where  $C_B$  is the concentration of crystallizing species in solution far from the interface, and  $C_E$  is the equilibrium saturation concentration. According to Kelvin (31)

$$\log_e S = 2M\sigma/RT\rho r \quad [A-2]$$

where  $M$ ,  $\sigma$ ,  $\rho$ , and  $r$  are the molecular weight, surface energy, density, and crystal radius.  $R$  and  $T$  are the gas constant and absolute temperature. From simple principles, the Gibbs free energy change for homogeneous nucleation (32) is given by

$$\Delta G = 4\pi r^2\sigma/3 \quad [A-3]$$

and if we eliminate the crystal radius  $r$ , between these two expressions we arrive at

$$\Delta G = 16\pi\sigma^3 M^2/3 (RT \log_e S)^2 \quad [A-4]$$

Clearly, the free energy change for nucleation is profoundly affected by  $S$ . To see the role of nucleation, competing for labile species in the solution phase, we can set up an Arrhenius rate expression of the form  $N = B \exp(-\Delta G/RT)$  where  $N$  is the nucleation rate, and  $B$ , a constant. Substituting from Eq. [A-4], we obtain

$$N = B \exp(-Z/\log_e^2 S) \quad [A-5]$$

with  $Z = 16\pi\sigma^3 M^2/sR^3 T^3 \rho^2$  and the rate of nucleation is seen a very strong function of  $S$  (17).

*Growth.*—It is generally assumed growth depends on the difference in concentration at the crystal interface,  $C_I$ . We have, then, a growth rate  $R$ , given by

$$R = A(C_I - C_E) \quad [A-6]$$

with  $A = A(T, \sigma, \rho)$ .

Recalling Fick's law, we can assume, ignoring, for now, the integration process

$$R = V_M D (dC/dx)_I \quad [A-7]$$

where  $V_M$ ,  $D$ , and  $(dC/dx)_I$  are the molar volume, the



Fig. 13. Electron micrographs of brittle fractures. Because of the nature of the growth, it is clear there are compressive stresses in a direction perpendicular to the plane of the paper.

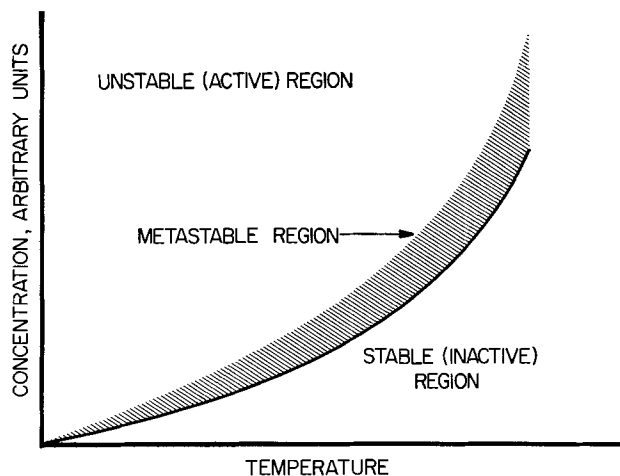


Fig. 14. Concentration/temperature relationship for a dissolved solute crystallizing from solution.

diffusion coefficient, and the concentration gradient for crystallizing species at the interface. We can approximate  $(dC/dx)_I$  by  $(C_B - C_I)\delta$ , where  $\delta$  is a boundary layer thickness at interface. By rearranging and eliminating  $C_I$ , we arrived at the expression

$$R\delta/V_M D + (R/A)^{1/n} = C_B - C_E = (S - 1) \quad [\text{A-8}]$$

The interesting cases of Eq. [A-8] are the well-stirred and the unstirred case. In the well-stirred case,  $\delta/D$  is quite small, and as  $(\delta/D) \rightarrow 0$

$$R = A(S - 1)^n \quad [\text{A-9}]$$

and growth is rapid, competing with the nucleation process itself. This is the situation in industrial crystallizers. In the unstirred case, the boundary layer is thick, and as  $(\delta/D) \rightarrow \infty$

$$R = \frac{V_M D}{\delta} (S - 1) \quad [\text{A-10}]$$

and in the static case, growth is a slower, diffusion-controlled process. A graphic summary of these processes is shown in Fig. 15.

**Integration.**—The over-all rate of growth at the interface depends on two rates: the rate of integration

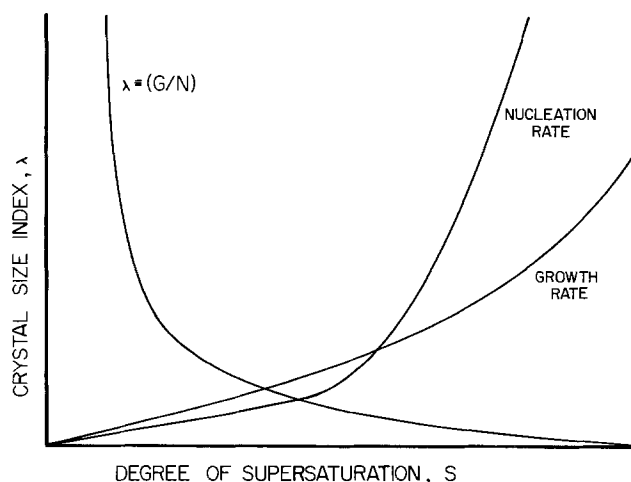


Fig. 15. Crystalline size index as a function of the degree of supersaturation. As the degree of supersaturation increases, growth passes from diffusion control (G), to nucleation control (N). The curves N and G demonstrate the functional dependence of these growth modes on S.

into the crystal and the rate of movement of species to the interface. We can write (17, 32)

$$1/R = 1/r_i + 1/(r_o + bu) \quad [\text{A-11}]$$

with  $r_i$  the rate of integration,  $r_o$  the growth rate if integration is infinitely rapid and  $u = 0$ , and  $u$  is the relative velocity of crystallizing species at the interface. For this study, the unstirred case ( $u = 0$ ) is of interest. As  $u \rightarrow 0$ , we obtain

$$R = kr_i r_o / (r_i + r_o) \quad [\text{A-12}]$$

and this produces two limiting cases ([A-13] and [A-14])

$$r_i \ll r_o, \quad R = k^1 r_i \quad [\text{A-13}]$$

and the rate of integration controls the net growth process

$$r_i \gg r_o, \quad R = k^1 r_o \quad [\text{A-14}]$$

and diffusion controls the process of growth.

## REFERENCES

- J. J. Lander, Proceedings of Symposium on Battery Separators, Columbus, Ohio, Feb. 18-19, 1970, p. 4.
- P. H. Hermans and A. Weidinger, *J. Appl. Phys.*, **19**, 491 (1948).
- P. H. Hermans and A. Weidinger, *J. Polymer Sci.*, **4**, 135 (1949).
- P. H. Hermans and A. Weidinger, *ibid.*, **4**, 709 (1949).
- J. B. Nichols, *J. Appl. Phys.*, **25**, 840 (1954).
- L. Segal, J. J. Creely, A. E. Martin, Jr., and C. M. Conrad, *Textile Research J.*, **29**, 786 (1959).
- L. G. Rodan, F. Rah, and A. R. Peterson, *J. Polymer Sci.*, **C8** 145 (1965).
- W. O. Statton, *ibid.*, **C18**, 33 (1967).
- A. Venkateswaran and J. A. Van Den Akker, *J. App. Polymer Sci.*, **9**, 1167 (1965).
- J. Committee Pwd. Diff. Stds., 3-0289.
- B. A. Campbell and J. R. Dafer, *This Journal*, **122**, 1084 (1975).
- O. Ant-Wuorinen and E. Lehtinen, *Paperi Puu*, **39**, 151 (1957).
- O. Ant-Wuorinen and A. Visapaa, *ibid.*, **39**, 229 (1957).
- J. J. McKeown and W. Z. Lyness, *J. Polymer Soc.*, **41**, 9 (1960).
- J. Gjønnes, N. Norman, and H. Viervoll, *Acta Chem. Scand.*, **12**, 489, 2028 (1958).
- I. Rusznak and I. Tanczos, *J. Polymer Sci.*, **C42**, 1475 (1973).
- H. M. Schoen, *Ind. Eng. Chem.*, **53**, 607 (1961).
- W. A. Tiller, *J. Crystal Growth*, **2**, 69 (1968).
- P. Bennema, *ibid.*, **1**, 287 (1967).
- W. V. R. Malkus, *Proc. Roy. Soc.*, **A225**, 185 (1954).
- E. Sundberg, Proceedings of Symposium on Battery Separators, Columbus, Ohio, Feb. 18-19, 1970, p. 32.
- E. Zehender, W. Herrman, and H. Leibssle, *Electrochim. Acta*, **9**, 55 (1964).
- G. Clark, *Ind. Eng. Chem.*, **22**, 474 (1930).
- K. H. Meyer and L. Misch, *Helv. Chim. Acta*, **20**, 232 (1937).
- A. Viswanathan and S. G. Shenouda, *J. Appl. Polymer Sci.*, **15**, 519 (1971).
- R. F. Nickerson and J. A. Harble, *Ind. Eng. Chem.*, **37**, 1115 (1945).
- A. Sharples, *Trans. Faraday Soc.*, **53**, 1003 (1957).
- R. St. J. Manley, *J. Polymer Sci.*, **9A2**, 1025 (1971).
- S. P. Rowland, E. J. Roberts, and J. L. Bose, *ibid.*, **9A1**, 1431 (1971).
- R. Holland, International Symposium on Batteries, Oct. 21-23, 1958, Paper (i).
- R. C. Evans, "Chemical Crystallography," Cambridge University Press, London (1939).
- J. W. Mullen, "Crystallization," Butterworth and Co., Ltd., London (1961).

# Anodic Oxidation of Copper in Alkaline Solutions

## I. Nucleation and Growth of Cupric Hydroxide Films

D. W. Shoesmith, T. E. Rummery, D. Owen, and W. Lee

Atomic Energy of Canada Limited, Research Chemistry Branch,  
Whiteshell Nuclear Research Establishment, Pinawa, Manitoba, R0E 1L0, Canada

### ABSTRACT

The anodic oxidation of copper in LiOH solution has been investigated by galvanostatic, potentiostatic, and voltammetric sweep techniques. The structure and composition of the films were determined by x-ray and electron diffraction, and by scanning electron microscopy.  $\text{Cu}(\text{OH})_2$  forms in two layers: a base layer grown by a solid-state mechanism and an upper layer of individual crystals nucleated and grown from solution. The size and number of upper layer crystals are dependent on electrode potential. More anodic potentials produce a large number of randomly deposited crystals, whereas less anodic potentials result in fewer, more highly developed crystals. Increased stirring results in a greater loss of material into solution, and in the extreme, nucleation and growth are completely prevented. For sufficiently low crystallization rates, produced galvanostatically, the thermodynamically stable phase,  $\text{CuO}$ , is formed. At higher rates the formation of  $\text{Cu}(\text{OH})_2$  dominates. A nucleation and growth mechanism is given and discussed with reference to other metal systems.

Although the electrochemical behavior of copper metal in alkaline solutions has been extensively studied (1-16), no general agreement has been reached pertaining to the phases formed during anodic polarization in the  $\text{Cu}(\text{II})$  region. Furthermore, disagreement persists as to the mechanism of formation of the major  $\text{Cu}(\text{II})$  passivating phases (12, 15, 16).

Halliday (5) has claimed, on the basis of electron diffraction studies, that galvanostatically formed films at room temperature are on a mixture of  $\text{CuO}$  and  $\text{Cu}(\text{OH})_2$ . This agrees with the results of x-ray diffraction studies of Bouillon *et al.* (6, 7) who also found  $\text{CuO}$  and  $\text{Cu}(\text{OH})_2$  in films formed galvanostatically at 25°C. At low anodic current densities,  $< 0.5 \text{ mA/cm}^2$ , only  $\text{CuO}$  was detected. Between 0.5 and  $0.8 \text{ mA/cm}^2$ , a mixture of  $\text{CuO}$  and  $\text{Cu}(\text{OH})_2$  was observed, while at greater current densities, only the hydroxide was detected.

Macdonald (16) observed fine structure in his cyclic voltammograms in the  $\text{Cu}(\text{II})$  oxidation region, and suggested, based on the work of Bouillon *et al.*, that this is indicative of the formation of both  $\text{CuO}$  and  $\text{Cu}(\text{OH})_2$ . On the other hand, Ambrose *et al.* (14) concluded that the first peak is due to  $\text{Cu}^{2+}$  oxidation, whereas the second peak is due to nucleation and solid-state growth of a passivating layer, thought to be  $\text{Cu}(\text{OH})_2$ .

Two mechanisms have been postulated for the passivation of copper in alkaline solutions. Miller (12), on the basis of rotating split-ring disk experiments, claimed passivation by a dissolution-precipitation mechanism. Ambrose *et al.* (14) claimed passivation by a solid-state nucleation and growth mechanism.

In this work, the identity and mechanism of formation of the passivating film has been extensively investigated by a number of electrochemical techniques, coupled with x-ray and electron diffraction and scanning electron microscopy. A detailed reaction scheme for copper passivation is presented and is discussed with respect to other metals exhibiting similar passivation behavior.

### Experimental

Measurements were made on copper electrodes (99.99% purity) of  $5.0 \text{ cm}^2$  geometric surface area. Rotating disk experiments were made on  $2.5 \text{ cm}^2$  copper disks embedded in Teflon. Samples were polished

with a series of SiC papers and finally with  $1 \mu\text{m}$  diamond paste. Before immersion in the cell, the electrodes were washed in alcohol, acetone, and doubly distilled water. All experiments were performed at  $21.0^\circ \pm 0.2^\circ\text{C}$ , with one exception as noted below, and in  $1 \text{ mol/kg}$  LiOH solution. Solutions were prepared from AR lithium hydroxide monohydrate and doubly distilled water.

The electrochemical cell was of the conventional, three electrode design with the working, counter, and reference electrodes separated into compartments by porous glass frits. Platinum foil was used as a counter-electrode and all potentials were measured against a calomel reference electrode at  $21.0^\circ \pm 0.2^\circ\text{C}$ . The capacity of the cell was  $\approx 400 \text{ ml}$ . This ensured that during the course of an experiment, the buildup of  $\text{Cu}^{2+}$  in the bulk of the solution was insignificant.

Potentiostatic experiments were performed with a Wenking Model 70HC3 potentiostat, programmed with a PAR Model 175 universal programmer. Galvanostatic experiments utilized a Hewlett Packard Model 6186B d-c current source with a Dana Model 5330 digital voltmeter coupled to an analog recorder. Electrodes were rotated with a Pine Instruments Model ASR analytical rotator.

Prior to surface examination, electrodes were removed from the cell, washed with doubly distilled water and acetone, and dried in a stream of nitrogen. The changes which might occur after removal of the electrodes from the cell are dehydration of  $\text{Cu}(\text{OH})_2$  to  $\text{CuO}$ , and interconversion of  $\text{CuO}$  and  $\text{Cu}_2\text{O}$ . However, since both  $\text{Cu}(\text{OH})_2$  and  $\text{Cu}_2\text{O}$  have been identified as single phases on different specimens, and since no oxidation or reduction of specimens has been detected after exposure to air for various lengths of time, it seems unlikely that any significant phase changes occurred after removal from the cell.

X-ray diffractograms were obtained with a Philips vertical goniometer diffractometer and graphite monochromator. Copper  $K_\alpha$  radiation and a scan speed of  $\frac{1}{8}^\circ 2\theta/\text{min}$  were used throughout. Grazing incidence electron diffraction was performed using a Hitachi HU-11A transmission electron microscope at 100 kV. A Cambridge Model 2A stereoscan was used for morphological examination.

### Results

*Potentiostatic oxidation.*—Anodic films grown at potentials between  $-330$  and  $-170 \text{ mV}$ , [Fig. 1(a) and

Key words: corrosion, surface films, crystal growth, dual film formation.

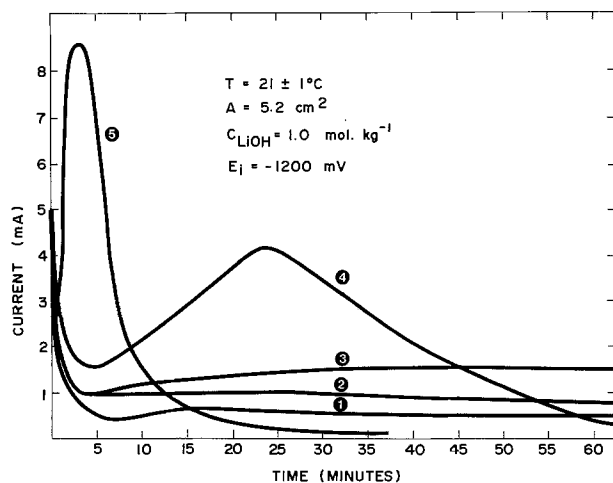


Fig. 1(a). Potentiostatic current-time transients recorded after application of a potential pulse from  $E_i = -1200 \text{ mV}$  to: curve 1,  $-295.0 \text{ mV}$ ; curve 2,  $-282.0 \text{ mV}$ ; curve 3,  $-276.0 \text{ mV}$ ; curve 4,  $-270.5 \text{ mV}$ ; and curve 5,  $-265.0 \text{ mV}$ .

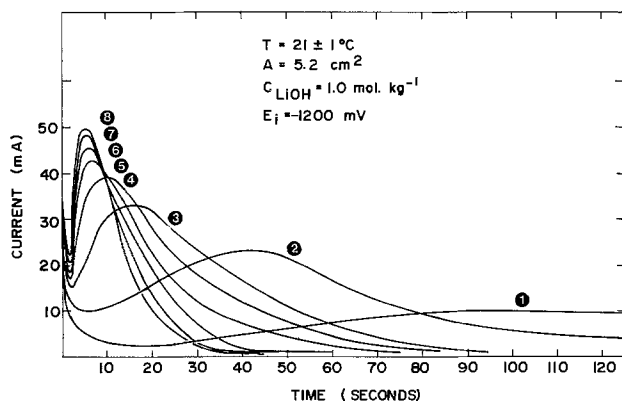


Fig. 1(b). Potentiostatic current-time transients recorded after application of a potential pulse from  $E_i = -1200 \text{ mV}$  to: curve 1,  $-260.2 \text{ mV}$ ; curve 2,  $-250.1 \text{ mV}$ ; curve 3,  $-239.7 \text{ mV}$ ; curve 4,  $-230.0 \text{ mV}$ ; curve 5,  $-220.0 \text{ mV}$ ; curve 6,  $-210.2 \text{ mV}$ ; curve 7,  $-201.0 \text{ mV}$ ; and curve 8,  $-182.1 \text{ mV}$ .

(b)] show the shape of the current-time transient for a series of potentials between  $-295$  and  $-182 \text{ mV}$ . Films grown potentiostatically for up to 8 hr at potentials between  $-330$  and  $-280 \text{ mV}$  contain only  $\text{Cu}_2\text{O}$ ; at  $-276 \text{ mV}$ , the film is mainly  $\text{Cu}_2\text{O}$  with a small amount of  $\text{Cu}(\text{OH})_2$ . For potentials more anodic than  $-265 \text{ mV}$  (up to  $-170 \text{ mV}$ ), only  $\text{Cu}(\text{OH})_2$  could be detected. The appearance of  $\text{Cu}(\text{OH})_2$  corresponds to the appearance of a peak in the transient curve after the initial sharp decrease.

Scanning electron microscope (SEM) photomicrographs show that the final film grown at potentials  $> -276 \text{ mV}$  comprises crystals having a morphology suggestive of nucleation and growth from solution (Fig. 2).

The charge consumed during oxidation,  $Q_A$ , where

$$Q_A = \int_{t=0}^{t=t_p} i_E \cdot dt \quad [1]$$

is independent of potential for  $E \gtrsim -220 \text{ mV}$ . In this potential range, SEM results show that the size and morphology of the surface crystals are independent of potential [Fig. 2(c) and (d)]. For more cathodic potentials, a steep increase in  $Q_A$  was observed (Fig. 3). SEM results show an increase in size and a decrease in surface density, with the acicular morphology remaining essentially the same [Fig. 2(a) and (b)].

The change in surface coverage for various times at constant potential ( $-264.9 \text{ mV}$ ) is shown in the SEM

photomicrographs in Fig. 4(a)-(f). The time in the transient at which electrolysis was terminated, and the sample removed for examination, is shown in Fig. 5. Figures 4(a) and (b) show the development of a continuous, apparently porous base film. The surface shown in Fig. 4(a) was demonstrated by electron diffraction to be  $\text{Cu}(\text{OH})_2$ .

The first appearance of individual surface crystals was observed at the minimum in the current-time transient (point b, Fig. 5) as shown in Fig. 4(b). As the current increases toward the maximum, the population and size of the surface crystals increase such that at the maximum (point e, Fig. 5), the surface is approximately 50% covered [Fig. 4(e)]. Beyond the maximum, crystal growth continues until surface coverage is complete [Fig. 4(f)]. Continued electrolysis for periods up to 2 hr after passivation results in no change in the crystal form, although a small constant residual current persists. It should also be noted that an increased porosity in the base layer occurs around the minimum in the current-time curve [cf. Fig. 4(a), and (b) and (c)].

The effect of stirring on the current-time transient is shown in Fig. 5, and the corresponding effect on the nucleation and growth of surface crystals is illustrated by comparison of Fig. 6 and Fig. 2(b). If stirring is vigorous enough, the solution at the electrode surface does not reach saturation, and nucleation and growth are prevented. This is demonstrated in Fig. 7 for a transient recorded at a rotating disk electrode. For the first 30 min of electrolysis, passivation is prevented by rotation at  $41.7 \text{ Hz}$  (Fig. 7). The absence of upper layer crystal growth on the rotated electrode is obvious even by visual observation. This same effect holds for rotation speeds as low as  $\sim 5 \text{ Hz}$ . As seen in Fig. 7, as soon as rotation is ceased, the current-time transient is of the same form as previously discussed. The greater breadth and smaller value of maximum current shown in Fig. 7, as compared to Fig. 1, are due to residual convection in the solution after rotation is stopped.

If the potentiostatically grown film is reduced at  $-1300 \text{ mV}$ , the charge in the reduction transient,  $Q_C$ , is always less than  $Q_A$ , indicating loss of material by dissolution during anodic oxidation. This loss is not too reproducible, being dependent on the convective conditions at the electrode surface. Figure 8 shows the charge lost by dissolution,  $Q_{\text{diss}} = Q_A - Q_C$ .

*Galvanostatic oxidation.*—Current densities from  $0.10$  to  $0.50 \text{ mA/cm}^2$  were used. The majority of experiments were terminated only after the potential had switched to a value at which oxygen evolution occurred. In order to determine the stages of oxidation, a number of runs were terminated at times prior to the switch to oxygen evolution. Figure 9 shows the potential-time transients recorded.

In the current density range  $0.12$ - $0.50 \text{ mA/cm}^2$ , a mixture of  $\text{Cu}(\text{OH})_2$ ,  $\text{CuO}$ , and  $\text{Cu}_2\text{O}$  was observed when the potential was allowed to progress to the oxygen evolution range. Between  $0.12$  and  $0.20 \text{ mA/cm}^2$ , the predominant phase is  $\text{Cu}_2\text{O}$ . Between  $0.20$  and  $0.50 \text{ mA/cm}^2$ , the proportion of  $\text{Cu}(\text{OH})_2$  and  $\text{CuO}$  increases. At  $0.50 \text{ mA/cm}^2$ ,  $\text{Cu}(\text{OH})_2$  is the major phase. These results can be correlated to the form of the potential-time transient (Fig. 9). The transients all show the same features. On application of the current, the potential rises to the region  $-270 \text{ mV} > E > -280 \text{ mV}$  (region I) and stays in this region for varying lengths of time depending on the current density: the higher the current density, the shorter the time. Subsequently, the potential rises to the region  $-260 \text{ mV} > E > -270 \text{ mV}$  (region II). If oxidation is stopped at any point prior to the end of region II, only  $\text{Cu}_2\text{O}$  is formed. The charge measured coulometrically up to the end of region II shows more extensive  $\text{Cu}_2\text{O}$  growth at lower current densities. This conclusion is borne out by



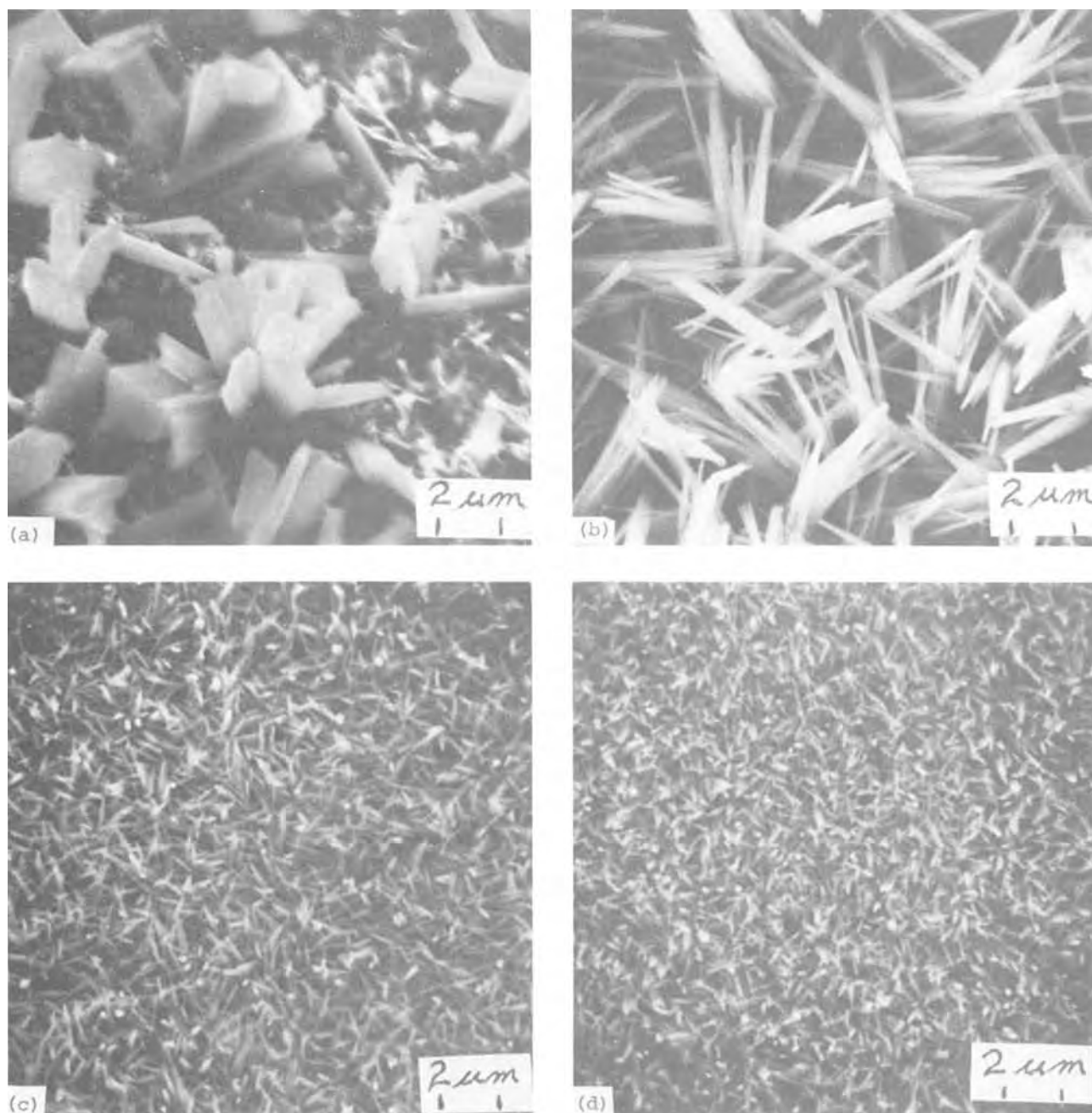


Fig. 2. Surface of copper electrodes potentiostatically oxidized to passivation at (a)  $-276.0$  mV, (b)  $-265.0$  mV, (c)  $-221.3$  mV, and (d)  $-201.0$  mV.

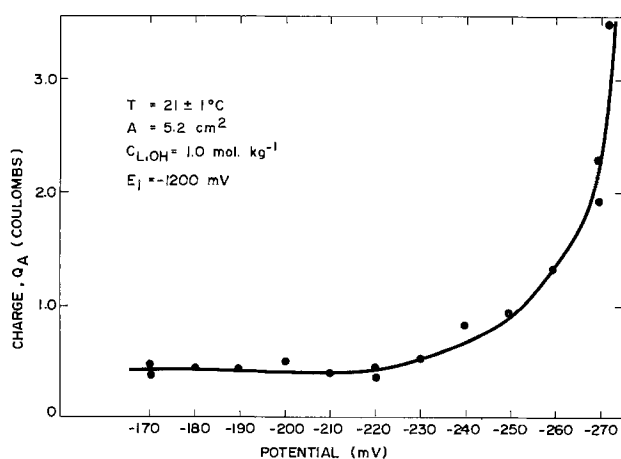


Fig. 3. Anodic charge obtained by integration of the transients in Fig. 1 as a function of applied potential.

x-ray diffraction intensity measurements. The morphology of the  $\text{Cu}_2\text{O}$  film is shown in Fig. 10(a).

Upon entering region III, the potential initially decreases, goes through a minimum, and then increases sharply. This final rise corresponds to passivation and occurs at shorter times for higher current densities. In region III, a mixture of  $\text{Cu}(\text{OH})_2$  and  $\text{CuO}$  crystals form [Fig. 10(b)].

If the temperature is increased from  $21.0^\circ$  to  $25.8^\circ\text{C}$ , for a current density of  $0.16$  mA/cm<sup>2</sup>, the time to passivation increases (Fig. 9) and the potential in region III falls to  $-275$  mV (compared to  $-263$  mV for a similar current density at  $20^\circ\text{C}$ ). In this case, only  $\text{CuO}$  and  $\text{Cu}_2\text{O}$  were detected. The morphology of the film formed at  $25.8^\circ\text{C}$  is shown in Fig. 10(c).

*Voltammetric oxidation.*—Electrodes were oxidized voltammetrically using sweep speeds between 1 and  $8.3 \times 10^{-3}$  mV/sec. Figures 11(a) and (b) show the voltammograms recorded at 1 mV/sec and  $8.3 \times 10^{-3}$  mV/sec, respectively. At slow scanning speeds [Fig.

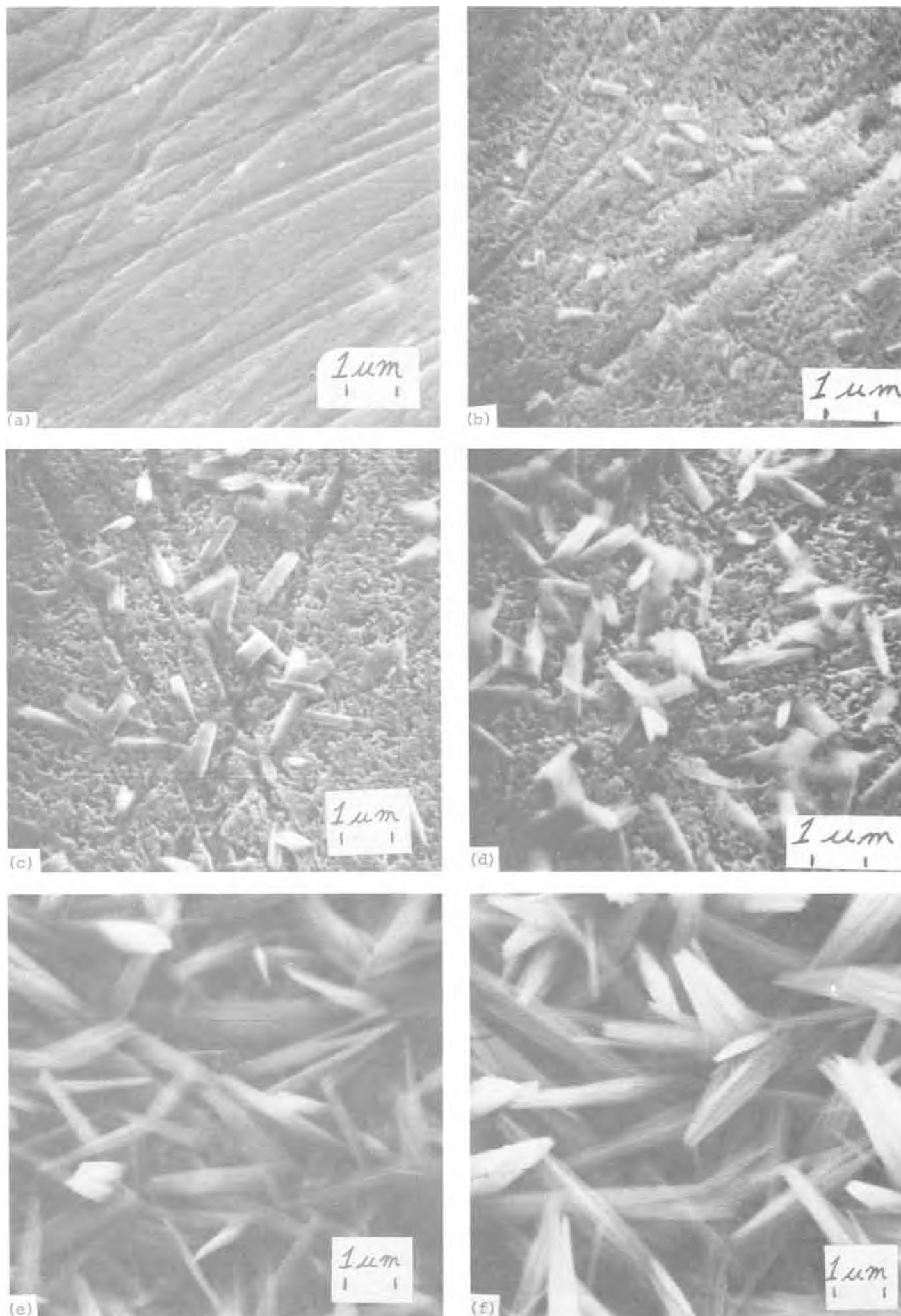


Fig. 4. Surface of copper electrodes potentiostatically oxidized to passivation at  $-264.9$  mV. Sampled at the times indicated in Fig. 5 (solid curve, points (a)-(f)).



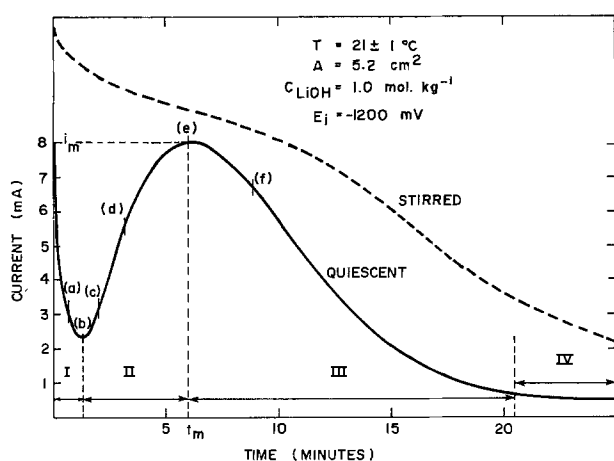


Fig. 5. Solid curve: potentiostatic current-time transient recorded at  $-264.9$  mV; points (a)-(f) correspond to SEM photomicrographs (a)-(f) in Fig. 4. Dashed curve: transient recorded at  $-265.0$  mV with gentle solution stirring using magnetic bar in bottom of cell.

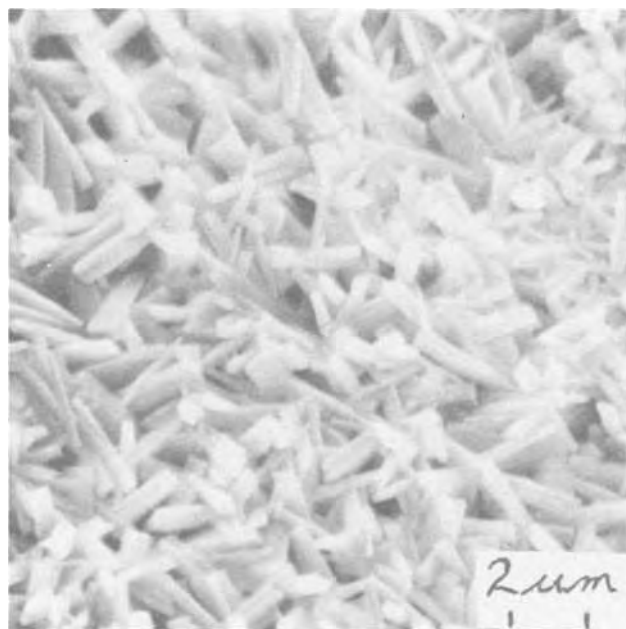


Fig. 6. Surface of copper electrode potentiostatically oxidized to passivation at  $-265.0$  mV in stirred solution; corresponds to dashed curve in Fig. 5.

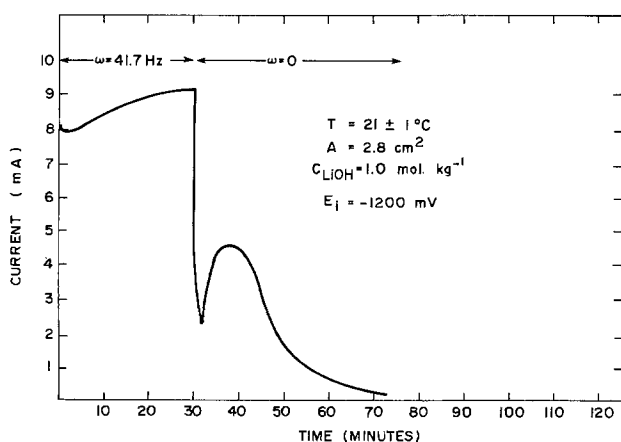


Fig. 7. Potentiostatic transient recorded on a rotating disk electrode; applied potential =  $-264.9$  mV.

11(b)], two peaks were observed in the Cu(II) region. At higher scanning speed [Fig. 11(a)], only a shoulder

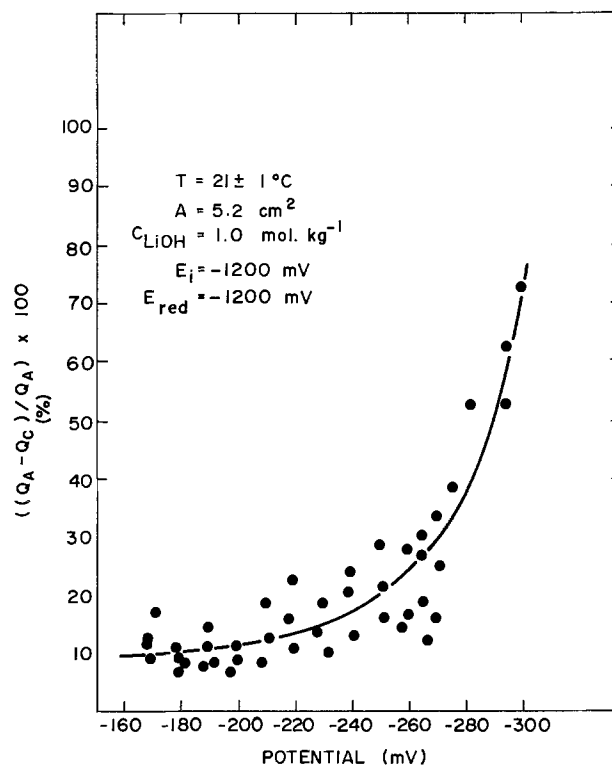


Fig. 8. Percentage charge lost by dissolution during a potentiostatic transient as a function of applied potential.

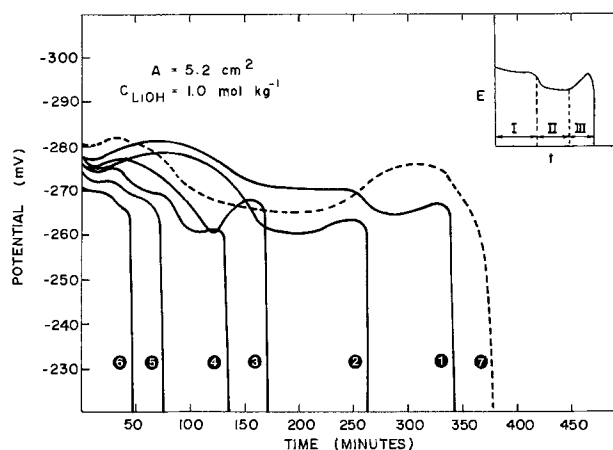


Fig. 9. Galvanostatic potential-time transients recorded for oxidation at constant applied current at: curve 1,  $0.12$  mA/cm<sup>2</sup>,  $T = 21 \pm 1^\circ\text{C}$ ; curve 2,  $0.16$  mA/cm<sup>2</sup>,  $T = 21 \pm 1^\circ\text{C}$ ; curve 3,  $0.20$  mA/cm<sup>2</sup>,  $T = 21 \pm 1^\circ\text{C}$ ; curve 4,  $0.24$  mA/cm<sup>2</sup>,  $T = 21 \pm 1^\circ\text{C}$ ; curve 5,  $0.28$  mA/cm<sup>2</sup>,  $T = 21 \pm 1^\circ\text{C}$ ; curve 6,  $0.50$  mA/cm<sup>2</sup>,  $T = 21 \pm 1^\circ\text{C}$ ; and curve 7,  $0.16$  mA/cm<sup>2</sup>,  $T = 25.8 \pm 0.1^\circ\text{C}$ .

on the cathodic side of peak III was detected. For sweeps which have progressed into the passive region beyond peak III, the amount of Cu<sub>2</sub>O in the film is greater for lower sweep rates and is the predominant phase at  $8.3 \times 10^{-3}$  mV/sec. If the sweep is stopped just beyond the maximum of peak II [Fig. 11(b)], at  $-265$  mV, the major phase is Cu<sub>2</sub>O, with a minor trace of Cu(OH)<sub>2</sub>. At slightly more anodic potentials, around the minimum between the two peaks, the major phase is still Cu<sub>2</sub>O, but the proportion of Cu(OH)<sub>2</sub> has increased. In neither of these two cases are individual upper layer surface crystals observed. Once the sweep progresses into the region of peak II, a progressively increasing proportion of Cu(OH)<sub>2</sub> surface crystals are observed. The passive range, i.e.,  $E > -250$  mV, corresponds to complete coverage of the surface with individual Cu(OH)<sub>2</sub> crystals.

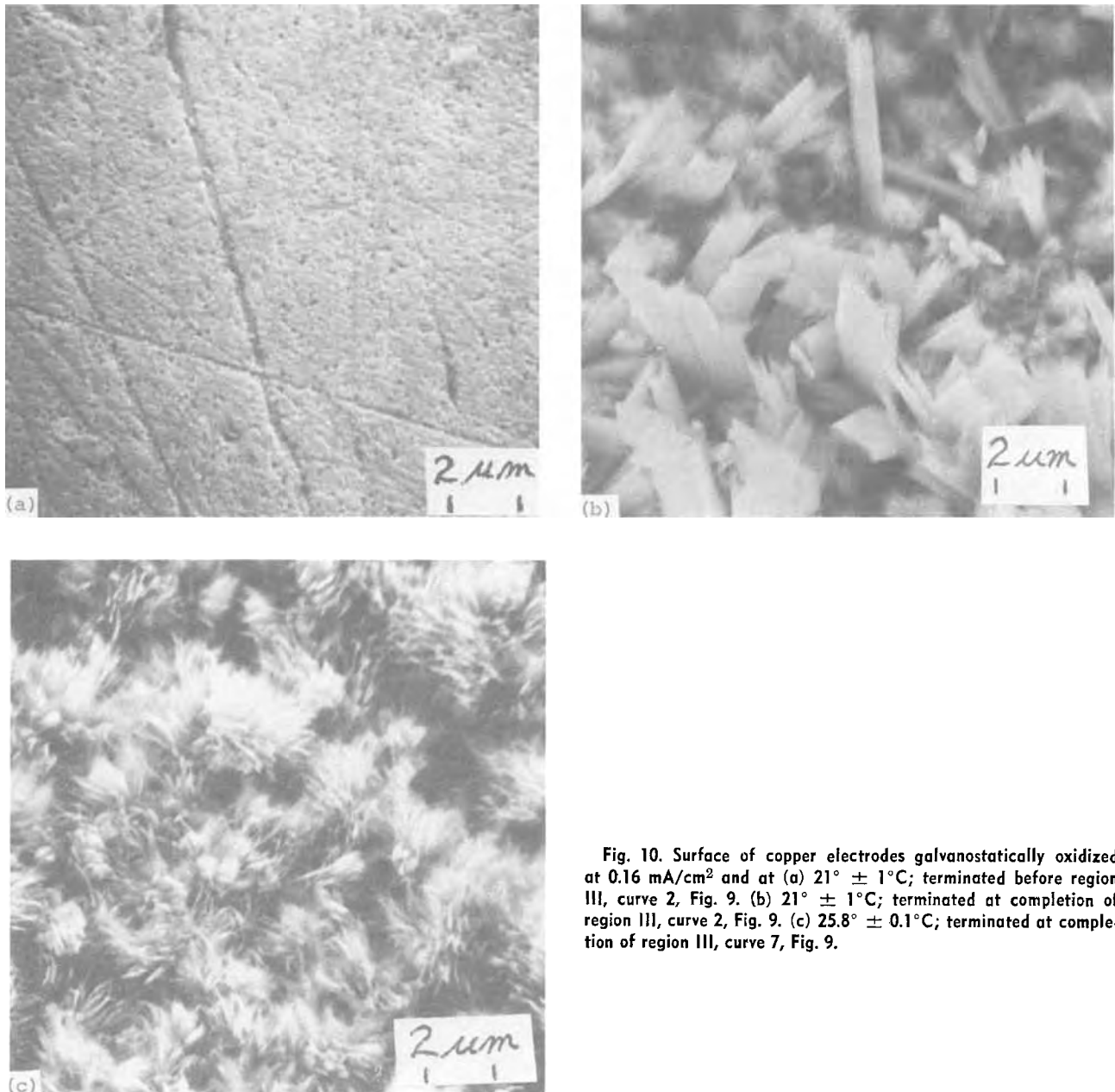


Fig. 10. Surface of copper electrodes galvanostatically oxidized at  $0.16 \text{ mA/cm}^2$  and at (a)  $21^\circ \pm 1^\circ\text{C}$ ; terminated before region III, curve 2, Fig. 9. (b)  $21^\circ \pm 1^\circ\text{C}$ ; terminated at completion of region III, curve 2, Fig. 9. (c)  $25.8^\circ \pm 0.1^\circ\text{C}$ ; terminated at completion of region III, curve 7, Fig. 9.

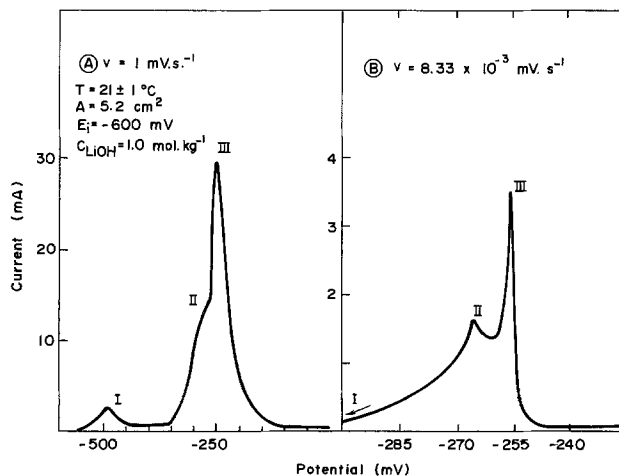


Fig. 11 (a) potential scan at  $1 \text{ mV/sec}$ , (b) potential scan at  $8.33 \times 10^{-3} \text{ mV/sec}$ .

## Discussion

**Dissolution and passivation mechanisms.**—The evidence, both electrochemical and microscopic, shows the nucleation and growth of two different layers of  $\text{Cu}(\text{OH})_2$  in the potential range  $-276$  to  $-170 \text{ mV}$ , as opposed to the simple dissolution and precipitation model proposed by Miller (12).

In region I, Fig. 5, metal dissolution and base layer growth of  $\text{Cu}(\text{OH})_2$  occur. The morphology of this layer indicates that growth is via a solid-state reaction [Fig. 4(a)]. No attempt was made to obtain electrochemical data in region I which would allow an exact time dependence of the current to be calculated. However, the SEM results demonstrate that a film growth mechanism is occurring. Also, since the current is very sensitive to solution agitation, it must contain a major metal dissolution component.

Previous work (14) with a rotating disk electrode showed that dissolution occurs as  $\text{Cu}^{2+}$  and is controlled by the diffusion of  $\text{Cu}^{2+}$  species away from the electrode surface in the range  $-320$  to  $-280 \text{ mV}$ . For

potentials more anodic than  $-280$  mV, dissolution is consistent with the behavior expected for a partially blocked surface (14). This work has shown that the surface blockage is due to the formation of a porous  $\text{Cu}(\text{OH})_2$  base layer [Fig. 4(a)-(d)].

In region II, an upper layer is nucleated and grown [Fig. 4(b)-(e)]. Dissolution in region I eventually leads to local saturation close to the electrode surface. At some degree of supersaturation, nucleation occurs. Depending on conditions close to the surface, nucleation could be initiated on the surface, or at an impurity in the solution close to the surface. In principle, homogeneous nucleation in solution is possible but is unlikely to occur without some degree of heterogeneous nucleation. Once nucleation has occurred, crystals grow from the saturated solution, thereby acting as a sink for soluble  $\text{Cu}^{2+}$ .

The current increase which accompanies this crystal growth can be explained in terms of Eq. [A-7] of the Appendix, which can be written<sup>1</sup>

$$R(t)_{\text{diss}} - R(t)_{\text{depos}} = \frac{i}{nFA} = (j_b)_{o,t} + R(t) \\ = (i_a - i_c)(1 - \theta(t))/nFA \quad [\text{A-7}]$$

As the crystal growth process proceeds,  $R(t)$  increases due to the expanding crystal surface area. This leads to a decrease in the cathodic deposition current,  $i_c$ , and hence an increase in the over-all current,  $i$ . For this to be the case, the electrochemical supply of  $\text{Cu}^{2+}$  [ $R(t)_{\text{diss}}$ ] must be much greater than the rate of incorporation of material at the crystal growth site; i.e., the condition  $i_a \sim i_c \gg i$  must apply, and crystal growth must be the rate-controlling step.

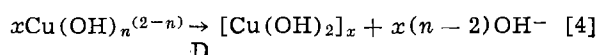
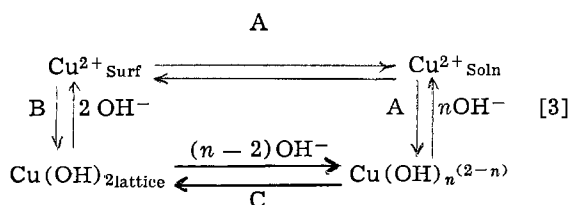
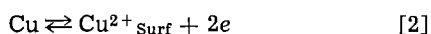
The term  $R(t)_{\text{diss}}$  is the maximum attainable dissolution rate from the base layer. It is the anodic component of the current (neglecting the contribution of the base layer growth).

The over-all dissolution necessary to maintain crystal growth results in an increase of porosity of the base layer (Fig. 4). Whether these pores penetrate to the metal surface, thereby allowing further active metal dissolution, is not known.

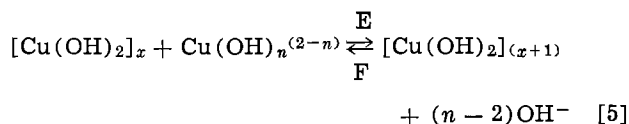
Eventually, the crystals begin to impinge upon one another (Fig. 4), and the dissolution reaction is impeded. This leads to a fall in the current due to surface passivation by the upper layer crystals (Fig. 5, region III).

The current at long times (Fig. 5, region IV) can be attributed to residual dissolution, as demonstrated by comparison of chemical and coulometrical analyses in which it was shown that  $\sim 90\%$  of the charge in region IV has been used to produce soluble copper. The remaining 10% must have been used to produce further base layer growth.

The above description of the behavior observed in the potential range  $-265$  to  $-182$  mV can be summarized in the following equations in which the subscript "Surf" designates a mobile surface species



<sup>1</sup> A list of symbols is given at the end of the article.



where A represents active metal dissolution; B, base layer formation; C, base layer dissolution; D, nucleation; E, crystal growth; and F, crystal dissolution.

In a previous paper (14), the growth of the electrode film was discussed in terms of a model due to Armstrong (17). The process involves the solid-state nucleation, growth, and overlap of conical centers. No account was taken of the dissolution process, and agreement with the predicted current-time form was obtained only around the current maximum where the nucleation and growth processes dominate the current. In the Appendix, a simplified but more realistic model of the present situation is given. This model can be used to describe the observed behavior qualitatively.

*Effect of potential on the crystal growth process.*—The characteristic parameters of the current-time transient ( $i_m$ ,  $t_m$ ,  $Q_A$ ) change very little in the potential range  $-180$  to  $-230$  mV [Fig. 1(a) and Fig. 3]. The form of the crystals and the large number produced [Fig. 2(c) and (d)] indicate extensive nucleation (18). This would require a high degree of supersaturation close to the electrode surface. The major limitation on the crystal growth process is probably the passivation of the electrode, leading to a rapid decrease in the rate of supply of material by anodic dissolution. The random nature in which the crystals are deposited on the electrode would suggest that they were grown in solution and subsequently deposited.

For sufficiently anodic potentials, the maximum dissolution rate ( $i_a/nFA$ ) in Eq. [A-7] will be very large due to its exponential dependence on potential. This maximum rate may be somewhat less than expected due to the presence of the base layer, but must be sufficient to ensure that local supersaturation with soluble copper species is quickly attained, leading to rapid nucleation and growth. The nucleation rate is dependent on the degree of supersaturation attained if initiated in solution, or on the degree of supersaturation and the overpotential if initiated heterogeneously on the electrode surface.

For a rapid nucleation and growth process in quiescent solution, Fig. 8 shows that very little material is lost to solution by diffusion ( $\sim 10-15\%$ ). This corresponds to the condition in Eq. [A-7] where

$$(j_b)_{o,t} \ll R(t) \ll R(t)_{\text{diss}} \quad [6]$$

Figure 1(a) shows that the  $i-t$  profile is becoming independent of potential at the most positive values. Since the growth rate  $R(t)$  determines the current rise, this indicates that a limiting rate of nucleation and growth is attained. This would be expected for both precipitation in solution from very supersaturated solutions and for heterogeneous surface nucleation if all the potentially active sites on the electrode are used for nucleation above  $E \sim -230$  mV.

At less anodic potentials, nucleation and growth are much slower processes [Fig. 1(a) and (b)], implying that the degree of supersaturation attained is much less at these potentials. For  $E < -230$  mV, the transient characteristic parameters [Fig. 1(a), (b), and Fig. 3], show significant changes with potential as do the form and number of crystals (Fig. 2). Figure 4 shows that the rate of appearance of crystals on the electrode surface at  $-265$  mV is relatively low. The crystals at this potential have the form expected from fast crystal growth (18). Their opportunity to grow before passivation is large compared to those grown at  $E > -230$  mV. This leads to an increase in the total charge accumulated on the electrode surface (Fig. 3). The slower passivation of the electrode also allows

greater loss of material by diffusion into solution (Fig. 8); i.e., in Eq. [A-7]

$$(j_b)_{o,t} \sim R(t) < R(t)_{diss} \quad [7]$$

Tapering of the crystals begins once the processes have passed the transient peak and entered region III, Fig. 5 [cf. Fig. 4(e) and (f)]. This is probably due to a limitation on the amount of material reaching the growing crystal faces as the surface coverage increases, i.e., for

$$E = -265 \text{ mV, and } \theta(t) > 0.5$$

$$k_a a_s (1 - \theta(t)) < R(t) \quad [8]$$

at the outer extremities of the crystals.

At anodic potentials between  $-265$  and  $-270$  mV, the current-time transient becomes almost symmetrical about the peak. The analysis of Armstrong (17) shows that this corresponds to centers progressively nucleating at a constant rate. A process of progressive nucleation is maintained by a steady supply of material from the electrode as shown by the appearance of the surfaces in Fig. 4.

At  $E = -276$  mV, the film is mainly  $\text{Cu}_2\text{O}$ , and  $\text{Cu}(\text{OH})_2$  no longer forms the passivating layer [Fig. 2(a)]. Now only a relatively small number of nuclei are formed and crystal growth leads to more tabular crystals, indicating a much slower growth process. Loss of material to solution is  $\approx 30\%$ , i.e.

$$(j_b)_{o,t} \sim R(t) \sim R(t)_{diss} \quad [9]$$

The crystals tend to form in clumps, suggesting that the supply of cupric ions from the electrode surface is now uneven and occurring mainly from faults in the underlying layer of  $\text{Cu}_2\text{O}$ . The change in shape of the crystals in going from condition [7] at  $-265$  mV to condition [9] at  $-276$  mV can be explained in terms of the relative growth rates of individual crystal faces. When the metal dissolution process is fast, growth of crystal faces is unimpeded by material limitations and the crystals grow with an acicular geometry ( $E = -265$  mV). When the supply of material is limited by slower metal dissolution, the supersaturation is not maintained at the surface of the fast growing faces and the growth rate is correspondingly limited. There may also be a change in the order  $p$  in the growth equation (Eq. [A-3], Appendix).

For potentials less than  $-276$  mV, the amount of material lost by diffusion increases markedly, up to 70% at  $E = -298$  mV (Fig. 8). The surface is now only composed of  $\text{Cu}_2\text{O}$ , local supersaturation at the electrode surface with  $\text{Cu}^{2+}$  never being attained.

*Effect of Stirring on the Crystal Growth Process.*—If artificial convection is introduced into the system, a steady-state diffusion layer will be rapidly established. Figure 5 shows that the current increase due to the crystal growth process is now obscured by the current contribution from material flux away from the electrode surface. The crystal form is much more regular (Fig. 6), indicating that the rate of growth on different crystal faces is now approximately equal. The regular form of the crystals indicates that growth is fairly slow, and that the supersaturation at the individual faces is now low.

For the thin diffusion layer obtained at the rotating disk electrode ( $w = 41.7$  Hz,  $\delta = 4.9 \times 10^{-4}$  cm), the concentration of  $\text{Cu}^{2+}$  at the electrode surface is reduced below the solubility limit: i.e.

$$(j_b)_{o,t} \sim R(t)_{diss} - R(t)_{depos} \quad [10]$$

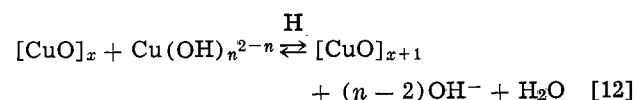
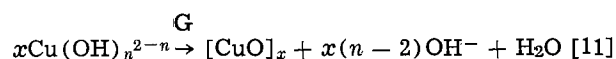
Therefore  $C_{o,t} < (C_{o,t})_{sat}$ , and  $R(t) \rightarrow 0$ . Under these conditions, no crystal growth is observed, and steady-state dissolution of the metal occurs. For large enough rotation speeds,  $C'_{o,t} \rightarrow 0$  and, therefore,  $R(t)_{depos} \rightarrow 0$ , and the limiting rate of surface dissolution is attained.

This condition was investigated previously (14) and dissolution was shown to occur from a blocked surface. This blockage has now been demonstrated to be caused by a base layer of  $\text{Cu}(\text{OH})_2$ . The rise in current when the disk is rotated (Fig. 7) is probably due to the restructuring of the base layer caused by its continuous dissolution and regrowth.

Once the electrode is held stationary again, the current falls as  $\text{Cu}^{2+}$  builds up at the electrode surface and the reverse rate of deposition ( $i_c$ ) begins to increase. Eventually supersaturation is attained and nucleation and growth are again observed.

*Effect of crystallization rate.*—Comparison of free energies of formation of  $\text{CuO}$  and  $\text{Cu}(\text{OH})_2$  shows that  $\text{CuO}$  is more thermodynamically stable than  $\text{Cu}(\text{OH})_2$  under the conditions of our experiments (19). Hence the formation of  $\text{Cu}(\text{OH})_2$  in these experiments must have been kinetically controlled. If the current is controlled by growing films at constant currents  $< 0.3$  mA/cm<sup>2</sup>,  $\text{CuO}$  can be obtained in addition to  $\text{Cu}(\text{OH})_2$  and a large amount of  $\text{Cu}_2\text{O}$ . These currents correspond to low crystallization rates as indicated by the time required for the potential to switch to the oxygen evolution region (Fig. 9, curves 1-4). This is in agreement with the galvanostatic work of other authors (4-7), although Bouillon *et al.* (6, 7) did not report the formation of  $\text{Cu}_2\text{O}$ . The size and morphology of the crystals grown galvanostatically at  $< 0.3$  mA/cm<sup>2</sup> are comparable to those of crystals grown under potentiostatic conditions at  $-276$  mV [cf. Fig. 10(b) and 2(a)] where the maximum current density attained in the growth region [Fig. 1(b), curve 3] was 0.29 mA/cm<sup>2</sup>.

At  $21^\circ\text{C}$ , for low crystallization rates, the rate of dehydration to yield  $\text{CuO}$  is competitive with the rate of crystallization of  $\text{Cu}(\text{OH})_2$  and a mixture is obtained. These processes can be represented by the following equations



where the nucleation and growth steps G and H, respectively, are comparable to the equivalent steps D and E for hydroxide crystallization (Eq. [4] and [5]). At  $25^\circ\text{C}$ , steps G and H predominate, and only  $\text{CuO}$ , with a different morphology, is observed [Fig. 10(c)]. The alternative mechanism of  $\text{CuO}$  formation, by thermal degradation of  $\text{Cu}(\text{OH})_2$  crystals, is judged to be insignificant at this temperature. Further work with respect to the formation of  $\text{CuO}$  as a function of temperature is in progress.

*Identification of peak doublet in Cu(II) region.*—The data of Fig. 11, in combination with the structural and microscopic observations given in the Results section, show that the formation of two peaks in the voltammograms is not due to the formation of a mixture of  $\text{CuO}$  and  $\text{Cu}(\text{OH})_2$ . The observation of small amounts of  $\text{Cu}(\text{OH})_2$  around peak II in Fig. 11(b) and the absence of upper layer crystals on the surface up to this point can be attributed to the formation of a base layer of  $\text{Cu}(\text{OH})_2$ . This leads to the inhibition of the anodic dissolution and the generation of peak II. The presence of upper layer crystals on the surface as the current begins to rise into peak III demonstrates that this peak is due to  $\text{Cu}(\text{OH})_2$  nucleation and growth as previously claimed (14).

*Comparison to other metals.*—A number of other metal systems exhibit potentiostatic current-time transients similar to that observed here for copper. How-

ever, in some cases, the participation of soluble material is negligible.

For cobalt (20), the current-time transient was interpreted in terms of a solid-state nucleation and growth. This conclusion was confirmed using a rotating ring-disk electrode (25) which showed that the participation of soluble material is negligible in the passivation step.

A simple metal dissolution-hydroxide precipitation process was claimed for cadmium (21) on the basis of rotating ring-disk experiments, even though a current-time transient was observed. Armstrong (26) has pointed out that such evidence does not conclusively prove that a dissolution-precipitation mechanism is operative. Since the  $i$ - $t$  transients were recorded at an electrode rotation speed of 35 Hz, it seems unlikely that the formation of the film involved participation of a soluble intermediate. However, under less vigorous stirring conditions, the surface concentration of soluble  $\text{Cd}^{2+}$  could build up sufficiently to produce precipitated material.

The necessity of having accurately controlled convective conditions has been pointed out in the case of zinc in alkaline solution (27-29), and has also been demonstrated previously with copper (14). Potential sweep profiles with zinc under quiescent conditions showed two peaks for very low sweep rates (29) [cf. Fig. 11(b) of this paper], and it is possible that a precipitation and crystal growth process is also involved here. The current-time transient did not show a peak however (28), probably due to the very high metal and hydroxide solubilities.

With aluminum, the rise in current after the early falling transient has been attributed to the nucleation and propagation of pores in a base layer of  $\text{Al}_2\text{O}_3$  (24). These pores gave increased, field-assisted, dissolution of the base layer as  $\text{Al}^{3+}$ , and on saturation, a precipitate of  $\text{Al}(\text{OH})_3$  was formed. This mechanism is based on the claim that the base layer is free of pores during the initial stages. Pore formation is thought to be due to the aggressive action of the proton and the electrolyte anion (22). There is some doubt however, whether such pores are nucleated or are present from very short times in the base layer (23). This behavior could be equally well explained using the arguments presented here for copper. Hence,  $\text{Al}(\text{OH})_3$  could be formed by precipitation from a locally supersaturated solution and the rise in current due to the growth of precipitate. A similar explanation has been given by Vedder and Vermilyea (30) to describe the corrosion of aluminum. One would expect upper layer formation to be more pronounced in electrolytes in which  $\text{Al}^{3+}$  is more soluble, such as oxalic and sulfuric acids, and this is borne out by the experimental evidence (22).

### Acknowledgments

The authors wish to thank A. M. Duclos, E. E. Sexton, and Dr. D. Faulkner for their help in obtaining x-ray and electron diffractograms.

Manuscript submitted Sept. 18, 1975; revised manuscript received Jan. 28, 1976.

Any discussion of this paper will appear in a Discussion Section to be published in the December 1976 JOURNAL. All discussions for the December 1976 Discussion Section should be submitted by Aug. 1, 1976.

Publication costs of this article were partially assisted by Atomic Energy of Canada Limited.

### APPENDIX

#### Mass Balance at the Electrode Surface in the Presence of Crystal Growth

The over-all rate of production of  $\text{Cu}^{2+}$  species at the electrode surface is given by the current,  $i$ , where

$$\frac{i}{nFA} = (k_a a_s - k_c c_{o,t}) (1 - \theta(t)) \quad [\text{A-1}]$$

$$= \frac{(i_a - i_c)}{nFA} \quad [\text{A-2}]$$

$k_a$ ,  $k_c$  are exponentially dependent on potential. In this simplified model, the current due to base layer growth is neglected.

The rate of crystal growth can be expressed, for one crystal face, by the equation

$$R_n = k_n A_n(t) (c_{o,t} - (c_{o,t})_{\text{sat}})^p \quad [\text{A-3}]$$

where  $p$  varies between 1 and 2 depending on the degree of supersaturation (31).

For  $n$  crystal faces and a nucleation rate  $dN/dt$ , the over-all crystal growth rate will be given by

$$R(t) = \int_0^t \left( \frac{dN}{dt} \right)_{t-u} \sum_{i=1}^n R(n) du \quad [\text{A-4}]$$

where  $u$  is the age of a nucleus.

If material used in crystal growth is considered to remain in the plane  $x = 0$ , i.e., close to the electrode compared to the thickness of the time-dependent diffusion layer, then the condition for the material balance at the electrode surface can be written as follows

$$\frac{i}{nFA} = D_{\text{Cu}^{2+}} \left( \frac{\delta C_{o,t}}{\delta x} \right)_{x=0} + \int_0^t \left( \frac{dN}{dt} \right)_{t-u} \sum_{i=1}^n R(n) \cdot du \quad [\text{A-5}]$$

Combining [A-1] and [A-5] yields

$$k_a a_s (1 - \theta(t)) = k_c c_{o,t} (1 - \theta(t)) + D_{\text{Cu}^{2+}} \left( \frac{\delta C_{o,t}}{\delta x} \right)_{x=0} + \int_0^t \left( \frac{dN}{dt} \right)_{t-u} \sum_{i=1}^n R(n) \cdot du \quad [\text{A-6}]$$

In abbreviated terms

$$R(t)_{\text{diss}} = R(t)_{\text{depos}} + (j_b)_{o,t} + R(t) \quad [\text{A-7}]$$

where  $R(t)_{\text{diss}} = k_a a_s (1 - \theta(t))$ ; and  $R(t)_{\text{depos}} = k_c c_{o,t} (1 - \theta(t))$ .

The terms on the right-hand side of Eq. [A-7] are interrelated but the relative rates of each process can be seen to be determined by the parameters  $k_c$ ,  $D_{\text{Cu}^{2+}}$ ,  $\delta$ ,  $dN/dt$ ,  $A_n$ , and  $k_n$ .

This statement represents only one condition in the complicated boundary value problem for the system but can be used to explain the effects of a variety of experimental conditions. A more detailed description of the system will be presented in a later communication.

### LIST OF SYMBOLS

$A$	electrode surface area ( $\text{cm}^2$ )
$A_n$	surface area of the $n$ th crystal face ( $\text{cm}^2$ )
$a_s$	surface activity ( $\text{mol}/\text{cm}^2$ )
$c_{o,t}$	surface concentration of $\text{Cu}^{2+}$ species at time $t$ ( $\text{mol}/\text{cm}^3$ )
$(c_{o,t})_{\text{sat}}$	equilibrium saturation concentration of $\text{Cu}^{2+}$ ( $\text{mol}/\text{cm}^3$ )
$D_{\text{Cu}^{2+}}$	diffusion coefficient of $\text{Cu}(\text{OH})_4^{2-}$ in solution ( $\text{cm}^2/\text{sec}$ )
$E$	electrode potential (V)
$E_i$	initial electrode potential (V)
$F$	Faraday (coulomb)
$i$	current (mA)
$i_m$	current maximum in the potentiostatic transient (mA)
$i_a$	anodic metal dissolution current (mA)
$i_c$	cathodic metal deposition current (mA)
$(j_b)_{o,t}$	flux of $\text{Cu}^{2+}$ species out of the plane of the electrode surface ( $\text{mol}/\text{cm}^2/\text{sec}$ )
$k_a$	potential dependent rate constant for active metal dissolution ( $\text{cm}^2/\text{sec}$ )
$k_c$	potential dependent deposition rate constant ( $\text{cm}^2/\text{sec}$ )
$k_n$	rate constant for the growth of the $n$ th crystal face ( $\text{cm}^2/\text{sec}$ )
$N$	number of nuclei

$n$	number of electrons transferred
$Q_A$	charge consumed during oxidation (coulomb)
$Q_C$	charge consumed during reduction (coulomb)
$Q_{diss}$	charge due to dissolved material (coulomb)
$R_n$	growth rate for the nth crystal face (mol/cm <sup>2</sup> /sec)
$R(t)_{diss}$	time dependent metal dissolution rate (mol/cm <sup>2</sup> /sec)
$R(t)_{depos}$	time dependent metal deposition rate (mol/cm <sup>2</sup> /sec)
$R(t)$	over-all crystal growth rate (mol/cm <sup>2</sup> /sec)
$t$	time (sec)
$t_m$	time of the current maximum in the potentiostatic transient (sec)
$t_p$	passivation time (sec)
$u$	age of a nucleus (sec)
$v$	potential scan rate (mV/sec)
$x$	distance from electrode (cm)
$\delta$	diffusion layer thickness (cm)
$\theta(t)$	degree of electrode coverage
$w$	electrode angular velocity (Hz)

## REFERENCES

1. E. Muller, *Electrochem.*, **13**, 133 (1907).
2. W. Feitknecht and H. W. Linel, *Helv. Chim. Acta*, **27**, 775 (1944).
3. A. Hickling and D. Taylor, *Trans. Faraday Soc.*, **44**, 262 (1948).
4. S. E. S. El Wakkad and S. H. Emara, *J. Chem. Soc.*, **1953**, 3508.
5. J. S. Halliday, *Trans. Faraday Soc.*, **50**, 171 (1954).
6. L. De Brouckere, F. Bouillon, and Y. Bouillon-Nyssen, *Bull. Soc. Chim. Belges*, **60**, 26 (1951).
7. F. Bouillon, J. Piron, and J. Stevens, *ibid.*, **67**, 643 (1958).
8. A. M. Shams El Din and F. M. Abd El Wahab, *Electrochim. Acta*, **9**, 113 (1964).
9. M. J. Dignam and D. B. Gibbs, *Can. J. Chem.*, **48**, 1242 (1970).
10. N. A. Hampson, J. B. Lee, and K. I. MacDonald, *J. Electroanal. Chem.*, **32**, 165 (1971).
11. N. A. Hampson, R. J. Latham, J. B. Lee, and K. I. MacDonald, *ibid.*, **31**, 57 (1971).
12. B. Miller, *This Journal*, **116**, 1675 (1969).
13. H. P. Leckie, *ibid.*, **117**, 1478 (1970).
14. J. Ambrose, R. G. Barradas, and D. W. Shoesmith, *J. Electroanal. Chem.*, **47**, 65 (1973).
15. J. Ambrose, R. G. Barradas, and D. W. Shoesmith, *ibid.*, **47**, 47 (1973).
16. D. D. Macdonald, *This Journal*, **121**, 651 (1974).
17. R. D. Armstrong, M. Fleischmann, and H. R. Thirsk, *J. Electroanal. Chem.*, **11**, 208 (1966).
18. A. G. Walton, "The Formation and Properties of Precipitates," Interscience, New York (1967).
19. W. M. Latimer, "The Oxidation States of the Elements and Their Potentials in Aqueous Solution," 2nd ed. Prentice-Hall, Englewood Cliffs, N. J. (1952).
20. R. D. Cowling and A. C. Riddiford, *Electrochim. Acta*, **14**, 981 (1969).
21. Y. Okinaka, *This Journal*, **117**, 289 (1970).
22. J. W. Diggle, T. C. Downie, and C. W. Goulding, *Chem. Rev.*, **69**, 365 (1969).
23. M. S. Hunter and P. E. Fowle, *This Journal*, **101**, 481 (1954).
24. T. P. Hoar and J. Yahalom, *ibid.*, **110**, 614 (1963).
25. W. K. Behl and J. E. Toni, *J. Electroanal. Chem.*, **31**, 63 (1971).
26. R. D. Armstrong, *Corrosion Sci.*, **11**, 693 (1971).
27. M. Eisenberg, H. F. Bauman, and D. M. Brettner, *This Journal*, **108**, 909 (1961).
28. R. D. Armstrong and G. M. Bulman, *J. Electroanal. Chem.*, **25**, 121 (1970).
29. R. W. Powers and M. W. Breiter, *This Journal*, **116**, 719 (1969).
30. W. Vedder and D. A. Vermilyea, *Trans. Faraday Soc.*, **65**, 561 (1969).
31. C. Y. Liu, H. S. Tsuei, and G. R. Youngquist, *Chem. Eng. Prog. Symp. Ser.*, **67** (110), 43 (1971).

# The Anodic Behavior of Gold in Sulfuric Acid Solutions

## Effect of Chloride and Electrode Potential

R. P. Frankenthal\* and D. E. Thompson

Bell Laboratories, Murray Hill, New Jersey 07974

### ABSTRACT

The anodic behavior of gold has been studied in 1M H<sub>2</sub>SO<sub>4</sub> containing 0, 1, and 10 mM HCl at potentials in the passive and in the transpassive regions. The reaction products are soluble Au(III) and an Au(OH)<sub>3</sub> film. Their rates of formation and the potential dependence of the rates are functions of the chloride concentration. Chloride promotes the dissolution of gold and reduces the rate of film formation. The composition of the film and the mechanism of its formation are not affected by the presence of chloride in solution. Two mechanisms of oxygen evolution exist. At low potentials, oxygen is evolved on the metal surface; at high potentials, the process occurs on the Au(OH)<sub>3</sub> film. At high potentials, the film formation and the oxygen evolution reactions have the same rate-determining steps. The implications of this study to the corrosion of gold conductors on electronic circuits are discussed.

The corrosion of gold is of concern to the electronics industry in the design and manufacture of certain thin film and integrated circuits (1). Although the phenomenology of corrosion failures has been reported, little is known about the basic electrochemical processes that occur. In electronic circuits, the applied voltages between adjacent conductor paths may be greater than 10V. Most of this voltage is dissipated as IR drop across the insulating substrate. The fractions of the applied voltage that appear across the anode/substrate and across the cathode/substrate interfaces

and that are therefore available for the electrochemical reactions are unknown. Thus, it would be helpful to know the reactions that may occur and the conditions of environment, e.g., temperature and relative humidity, and potential under which they do occur.

The electrochemistry of gold in aqueous solutions is a reasonable starting point for obtaining this information. The subject has been studied by many investigators at potentials below the oxygen evolution potential. The literature up to 1972 has been reviewed by Schmid and Curley (2); more recent publications include Ref. (3-10). Studies of the oxygen evolution reaction on gold have been reviewed by Hoare (11).

\* Electrochemical Society Active Member.

Key words: anodic dissolution, chloride, gold, oxide film, oxygen evolution, potential.

In sulfuric acid and in perchloric acid solutions, gold is anodically oxidized between 1.1 and 1.4V (SCE). The passivating film has been estimated to be one to two monolayers in thickness at potentials below the oxygen evolution region (2). At higher potentials, a thicker, poorly adherent film of hydrated  $\text{Au}_2\text{O}_3$  or  $\text{Au}(\text{OH})_3$  grows (12). Barnartt (12) and Whitton and Davies (13) observed a linear rate law for growth of the film at constant current. Whitton and Davies also reported that 1.5% of the oxidized gold appears in the solution, with the remainder appearing in the film. The rate of film growth and the rate of gold dissolution have not been studied as a function of potential.

The addition of chloride ions to sulfuric acid or to perchloric acid solutions enhances the rate of gold dissolution but does not affect the potential of passivation (14, 15). There appear to be no studies on the effects of chloride ions on the composition of the films formed or on the rate of film formation and gold dissolution at potentials in the passive and in the oxygen evolution regions.

The mechanism of the oxygen evolution reaction on oxidized gold surfaces in sulfuric acid and in perchloric acid solutions is not fully understood (11). It has not been studied in the presence of chloride ions.

We report here a study of the composition of the anodic films formed on gold and of their rate and mechanism of formation, as well as the rate of gold dissolution, as a function of potential in sulfuric acid solutions with and without added chloride ions. In addition, the results provide further insight into the mechanism of the oxygen evolution reaction.

### Experimental

The test specimens were gold foils, 2.7 cm long and 1.2 cm wide. To the top of each was spot welded a gold wire lead. The specimen was immersed in the electrolyte solution so that the air/solution interface was on the wire just above the foil. A two-compartment, three-electrode cell was used. The main compartment, 6.7 cm in diameter, housed the test electrode and two gold-plated platinum foil counterelectrodes spaced 3.5 cm apart and parallel to the gold foil surfaces. A Luggin capillary connected the main cell compartment to a saturated calomel reference electrode. The capillary tip was just below the center of the lower edge of the foil. All potentials are reported relative to the saturated calomel electrode (SCE).

Three solutions were used. The basic electrolyte and one of the solutions was 1M  $\text{H}_2\text{SO}_4$  (pH 0.0) made from electronic grade concentrated acid that contains < 50 ppb  $\text{Cl}^-$ . To this was added sufficient HCl to make solutions 1 and 10 mM in HCl. The solutions were stirred with a magnetic stirrer at a reasonably constant rate. They were not deaerated or saturated with any gas, other than those evolved at the electrodes. The solution volume was approximately 250  $\text{cm}^3$ . All experiments were conducted at room temperature.

A PAR Model 173 potentiostat with the PAR Model 176 current-to-voltage converter was used. The latter is equipped with an IR-compensator, which was needed because of the high current densities encountered in the oxygen evolution region. The amount of compensation required is a function of the precise positioning of the gold electrode relative to the tip of the Luggin capillary. In a typical experiment, the compensated resistance was 1 ohm. The resistivity of all the solutions is 2.7 ohm-cm.

A Mettler H54 semimicrobalance with a precision of  $\pm 10 \mu\text{g}$  was used for all weighings. A Marshall tube furnace with a quartz furnace tube and an alumina boat to hold the specimen was used for thermal reduction of the anodic films; nitrogen was passed over the specimen during the reduction process.

The experimental procedure was as follows: The specimen was etched for 15 sec in aqua regia, rinsed with distilled water and then with methanol, and dried in a stream of nitrogen, and its weight,  $W_1$ , was measured. The specimen was inserted into the cell and any adsorbed oxygen or thin oxide film was reduced cathodically at  $-0.5\text{V}^1$ , after which the potential was switched to that to be studied. The time for which each specimen was held at potential ranged from  $10^3$  to  $2 \times 10^4$  sec. The times were chosen to give reasonable weight changes in the intermediate potential range, to avoid thick spalling films at high potentials in pure sulfuric acid solution, to avoid excessive dissolution of the gold at high potentials in the chloride-containing solutions, and to give sufficient time to estimate low corrosion rates at low potentials. It was shown that the corrosion rates were independent of time at potential, as long as spalling was avoided. After anodic polarization, the specimen was rinsed and dried, and its weight,  $W_2$ , was recorded. Alternate specimens were dipped into 5M HCl for 15 sec and weighed,  $W_3$ , or baked at  $570^\circ\text{K}$  and weighed,  $W_4$ . The HCl dip dissolves the anodic film quantitatively but does not attack the gold (12, 13); this was verified by observing no additional weight loss during exposures to the HCl for times up to 1 hr. At temperatures above  $523^\circ\text{K}$ , the anodic film decomposes to metallic gold (16).

### Results

The anodic polarization curves of gold in the three electrolyte solutions are shown in Fig. 1 and 2. The addition of chloride ions increases the anodic dissolution rate up to the passivation potential, 1.35V, which is independent of the chloride ion concentration. In the passive and early transpassive regions, the current is also markedly increased by chloride, but the effect diminishes with increasing potential and above 1.9V the current appears to be independent of solution composition.

The data were analyzed in the following manner: From the weights,  $W_1, \dots, W_4$

$$W_a = W_2 - W_1 = \text{weight change during anodic polarization}$$

$$W_f = W_2 - W_3 = \text{weight of anodic film}$$

$$W_{f^0} = W_2 - W_4 = \text{weight of nongold portion of anodic film}$$

<sup>1</sup> Any weight change due to cathodic reduction was less than the precision of the balance.

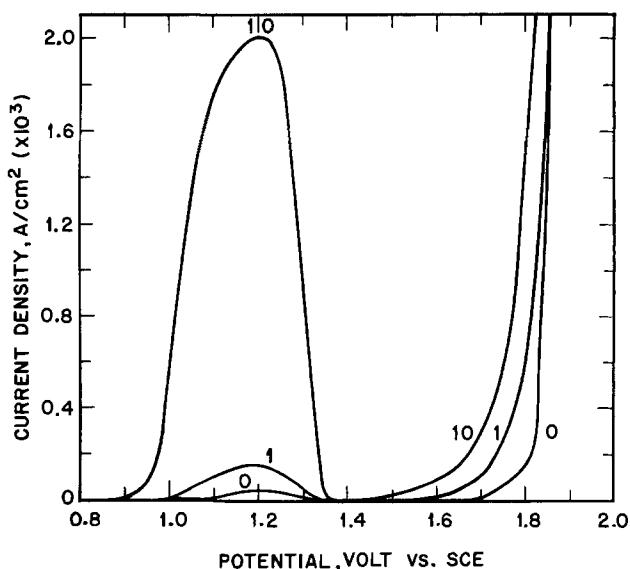


Fig. 1. Anodic polarization curves for Au in 1M  $\text{H}_2\text{SO}_4$  with and without HCl additions. HCl concentrations (mM) shown on each curve.

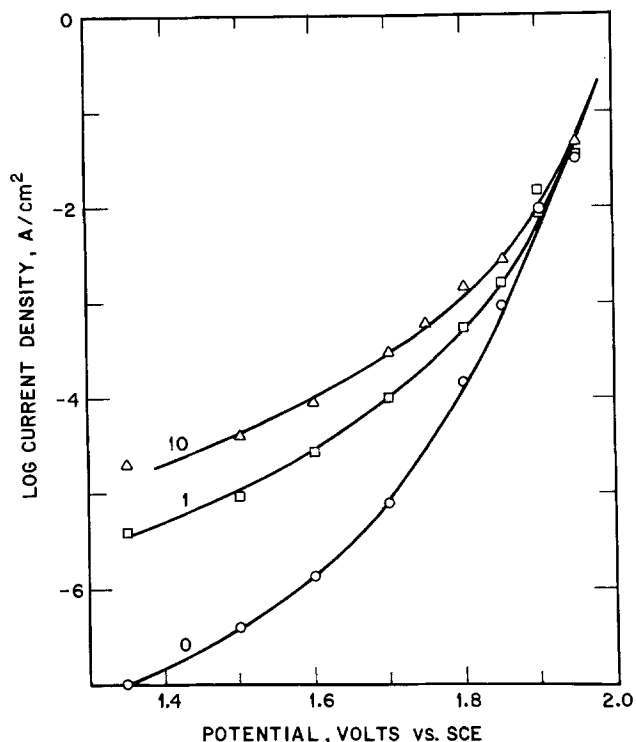


Fig. 2. Anodic polarization curves of Au in 1M H<sub>2</sub>SO<sub>4</sub> with and without addition of HCl at potentials in the passive and transpassive regions. HCl concentrations (mM) shown on each curve.

$W_f - W_f^0 = W_4 - W_3 =$  weight of gold in anodic film  
 $W_a - W_a^0 = W_4 - W_1 =$  weight of anodically dissolved gold.

From  $W_f - W_f^0 = W_a - W_a^0$ , the known polarization times, and assuming Au(III) as the reaction product, the rates of film formation and anodic dissolution were calculated as current densities and plotted as a function of potential (Fig. 3-5). The reproducibility of the

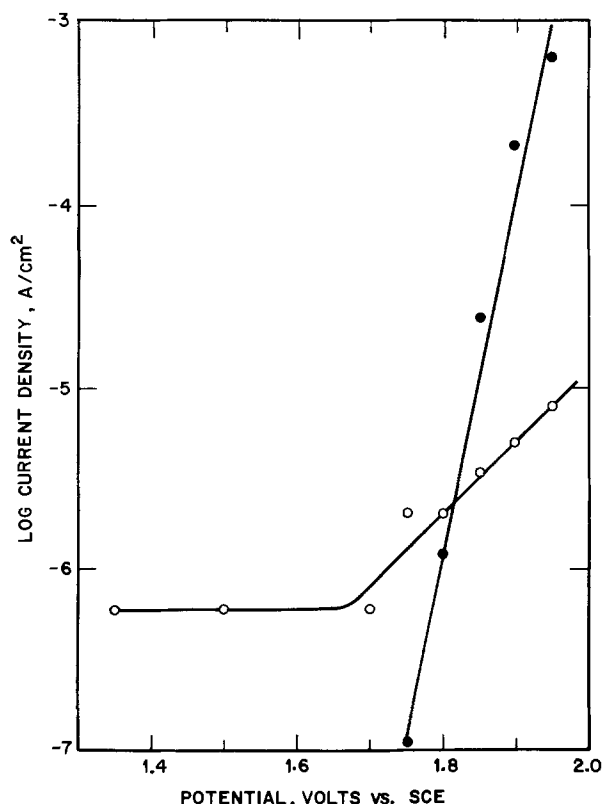


Fig. 3. Anodic oxidation rate of Au in 1M H<sub>2</sub>SO<sub>4</sub> as a function of potential. O, Gold dissolution; ●, film formation.

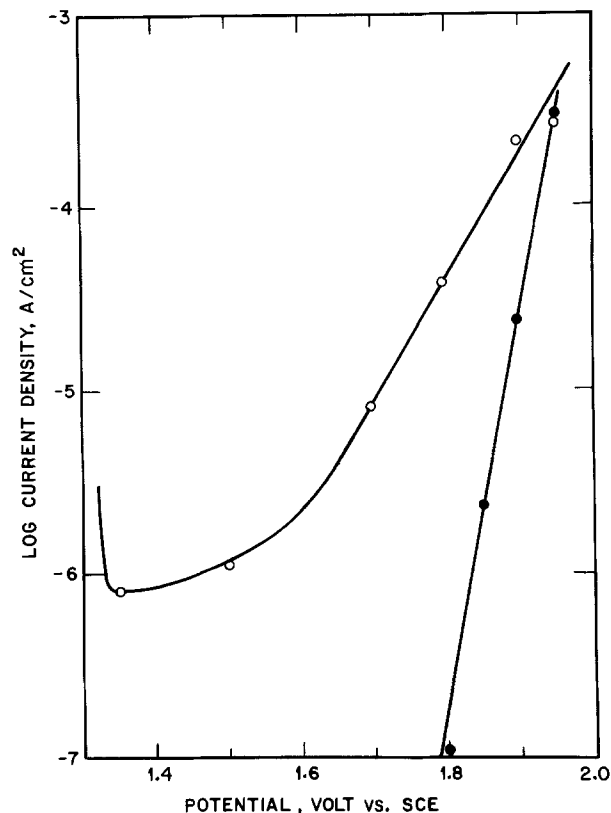


Fig. 4. Anodic oxidation rate of Au in 1M H<sub>2</sub>SO<sub>4</sub> + 1 mM HCl as a function of potential. O, Gold dissolution; ●, film formation.

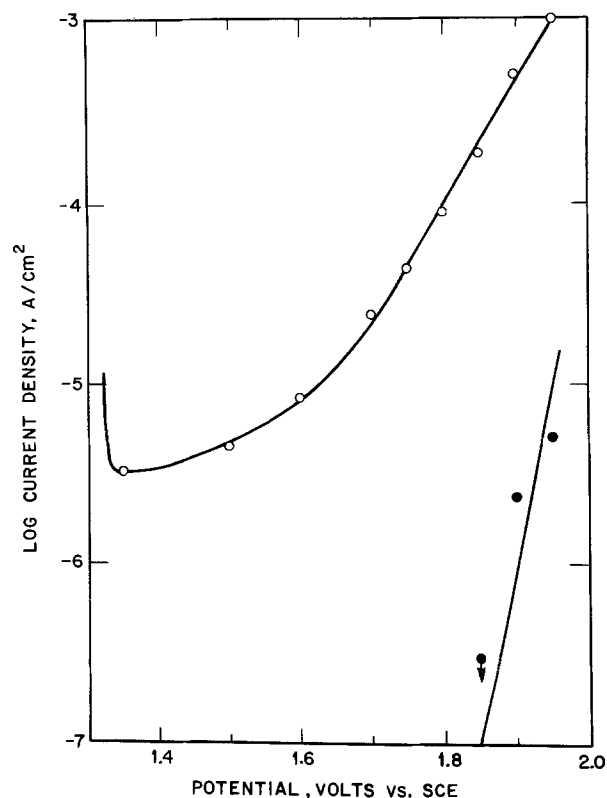


Fig. 5. Anodic oxidation rate of Au in 1M H<sub>2</sub>SO<sub>4</sub> + 10 mM HCl as a function of potential. O, Gold dissolution; ●, film formation. Arrow indicates value less than that shown, which was limit of detection.

data was  $\pm 5\%$  for current densities greater than  $1 \times 10^{-5}$  A/cm<sup>2</sup>, decreased to  $\pm 10-20\%$  at  $1 \times 10^{-6}$  A/cm<sup>2</sup>, and was approximately  $\pm 100\%$  for current densities less than  $4 \times 10^{-7}$  A/cm<sup>2</sup>.



Anodic dissolution is observed in each solution. However, chloride clearly increases the rate of dissolution, the Tafel lines shifting 60 mV with a tenfold change in concentration. The Tafel slopes are 147 mV/decade in the two solutions containing chloride and 245 mV/decade in the solution that does not contain chloride.

Anodic film growth is also observed in each solution. The potential at which it begins appears to increase with increasing chloride concentration. Since a current density of  $10^{-7}$  A/cm<sup>2</sup> flowing for 10 msec corresponds to the oxidation of approximately one monolayer of gold and since the passivating film on gold is one to two monolayers in thickness, it is assumed that a film thicker than the passivating film grows only above a potential  $E_f^\circ$  at which the film growth rate is  $1 \times 10^{-7}$  A/cm<sup>2</sup>. This potential and the slope of the  $E - \log i$  plots for film growth are given in Table I. At 1.85V in the 10 mM chloride ion solution, film growth was not detected, indicating that the growth rate was less than  $3 \times 10^{-7}$  A/cm<sup>2</sup>. The line through the data (Fig. 5) was drawn to intersect 1.85V at  $1 \times 10^{-7}$  A/cm<sup>2</sup>.

Some of the films formed in 0 and 1 mM chloride ion solutions at 1.90V were subjected to evolved gas analysis, in which the specimen is slowly heated (ca. 2°K/min) and the evolved gases are analyzed in a mass spectrometer. For films prepared in either solution, water vapor was evolved continuously at all temperatures from room temperature to about 520°K. Oxygen evolution began at about 410°K; the rate increased greatly above 470°K and peaked at about 530°K. Only traces of SO<sub>4</sub><sup>=</sup> and Cl<sup>-</sup>, measured as H<sub>2</sub>S<sup>+</sup>, HCl<sup>+</sup>, and Cl<sup>+</sup> in the mass spectrometer, were detected. The last two species were detected only on samples exposed to the solution containing chloride ions. From the weight change measurements, the ratio  $(W_f - W_f^0)/W_f^0$ , which is the ratio Au/(O + H<sub>2</sub>O), was calculated for each experimental condition. The median and the average were both 3.4. The ratios for Au<sub>2</sub>O<sub>3</sub> and Au(OH)<sub>3</sub> are 3.21 and 3.86, respectively.

By subtracting the sum of the currents for gold dissolution and film formation from the observed current (Fig. 2), the anodic gas evolution current is obtained (Fig. 6). The data are best fit by two lines, as shown previously by Hoare (17). In the low potential region, the rate is markedly increased by chloride, but the slopes of the plots are the same, 163 mV/decade. Hoare (17) obtained a slope of 158 mV. The difference is attributable to the correction for gold oxidation applied in the present study. At high potentials, the current is independent of chloride ion concentration and the slope is 52 mV/decade. Hoare obtained a slope of 50 mV potentiostatically (17) and 47 mV galvanostatically (18). Barnartt (12) and MacDonald and Conway (19) obtained slopes of 45 mV galvanostatically. These other investigations were performed in sulfuric acid without any chloride additions. The points of intersection of the high and the low potential regions are given in Table II. Hoare's (17) data are given for comparison.

### Discussion

**Gold dissolution.**—Gold dissolution is observed in every solution. However, the rate is a function of chloride ion concentration, as well as potential (Fig. 3-5). In the passive potential region ( $E < 1.7V$ ), dissolution and passivation proceed in parallel, probably due to a competitive adsorption between chloride and

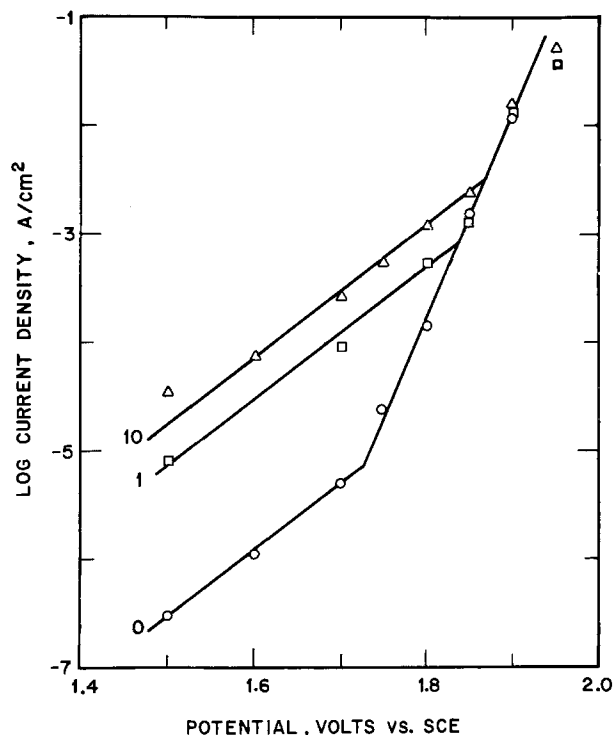


Fig. 6. Anodic gas evolution rate as a function of potential in 1M H<sub>2</sub>SO<sub>4</sub> with and without addition of HCl. HCl concentrations (mM) shown on each curve.

an oxygen species. The former leads to dissolution, the latter produces passivation. In the transpassive region, a pseudo-Tafel behavior is observed, that is,  $\log i$  varies linearly with potential. In the two chloride-containing solutions, the slope is 147 mV/decade, while in the chloride-free solution the slope is 245 mV/decade. The significance of these slopes is not clear. They are probably influenced by at least two factors. First, different reaction products form in the two types of solutions. A chlorogold complex, e.g., AuCl<sub>4</sub><sup>-</sup>, forms in the solutions containing chloride, while an aquogold complex is the principal product in the other solution. Second, the anodic film may influence the rate of dissolution. The thickness and porosity of the film are, most likely, functions of potential and of chloride ion concentration.

**Film formation.**—The evolved-gas analysis decomposition spectra of films formed in both solutions are those of gold oxide or hydroxide (16). The measured ratio Au/(O + H<sub>2</sub>O) indicates the film is Au(OH)<sub>3</sub> with some occluded water, in agreement with Barnartt (12). From these analyses and from the lack of dependence of the Tafel slope on chloride-ion concentration, it is concluded that the film composition and film growth mechanism are unaffected by chloride in solution. However,  $E_f^\circ$ , the potential at which film growth begins, is shifted in the anodic direction by chloride, thereby reducing the rate of film growth at constant potential.

The effect of potential on the film growth rate is consistent with the "blister" mechanism of growth proposed by Barnartt (12). He, as well as Whitton and Davies (13), observed that the films grew linearly with time at constant current density and proposed

Table I. Characteristics of anodic film growth as a function of chloride ion concentration

(Cl <sup>-</sup> ), mM	$E_f^\circ$ , V	$dE/d \log i$ , mV
0	1.75	50
1	1.79	48
10	1.85	50

Table II. Points of intersection of gas evolution plots

(Cl <sup>-</sup> ), mM	$E$ (V)	$i$ (A/cm <sup>2</sup> )
0	1.73	$8 \times 10^{-6}$
0 [Hoare (17)]	1.71	$9 \times 10^{-6}$
1	1.82	$4 \times 10^{-4}$
10	1.86	$3 \times 10^{-4}$

that separation of the film from the substrate occurs locally, permitting access of solution to the film-free surface for further oxidation. Since oxygen evolution should increase the rate of separation, increasing the current density or the potential should increase the rate of film growth (12), as is observed.

**Gas evolution.**—In each solution, the  $E-i$  relation for the gas evolution reaction(s) exhibits two distinct Tafel regions (Fig. 6). In the low potential region, the Tafel slopes are independent of chloride ion concentration; in the high potential region, the current densities are independent of chloride ion concentration. These data are consistent with the measurable evolution (in these experiments) of only one gas, namely oxygen. The simultaneous evolution of chlorine from the 10 mM HCl solution would most likely change the observed  $E-i$  pattern. The absence of an observable chlorine evolution reaction is not surprising since the chloride ion concentration in the 10 mM HCl solution is only  $2 \times 10^{-4}$  of the water concentration.

Hoare (17, 18) suggests that in the low potential region oxygen evolution takes place on a gold surface partially covered with adsorbed oxygen, while in the high potential region it occurs on  $Au_2O_3$ . The present study verified this suggestion because the potential at which film growth begins,  $E^\circ_f$  (Table I), and the potential of intersection (Fig. 6 and Table II) are approximately the same. However, as indicated above, the film is  $Au(OH)_3$ .

The high potential region is characterized by (i) a polarization curve for oxygen evolution that is not affected by the addition of chloride ions to the solution, (ii) the presence of an  $Au(OH)_3$  film that begins to form at the same potential at which this region begins, and (iii) the same Tafel slopes for film formation and oxygen evolution. From (i) it is concluded that chloride ions do not participate in the oxygen evolution reaction, just as they do not participate in the film formation reaction. Observations (ii) and (iii) are consistent with mechanisms for film growth and oxygen evolution that have the same rate-determining step. Further, this step must take place on the film. If it occurred on the film-free surface, the Tafel line should be an extension of the one observed at low potentials and exhibit the same effects of chloride ions.

The most likely rate-determining step, common both to oxygen evolution and to film formation, is the oxidation of water to an intermediate O or OH radical adsorbed on the film. Such radical can react to produce  $O_2$  or  $Au(OH)_3$ . For the latter to occur, the radical must diffuse to the metal/film interface or  $Au(III)$  must diffuse to the film/solution interface. The suggested rate-determining step is similar to the one proposed by MacDonald and Conway (19) for the oxygen evolution reaction without consideration for film formation. They explained the Tafel slope of 45 mV by postulating a dual potential barrier consisting of a film, which was not identified, and the double layer at the film/solution interface.

**Corrosion of electronic circuits.**—Sufficient relative humidity and ionizable impurities on the insulating substrate surface will reduce the insulation resistance between conductors. This will lead to an increase in the current and in the potential available for the anodic and the cathodic reactions. This study shows that an increase in the potential (or current) increases the oxidation rate of gold. Chloride ions increase the quantity of dissolved gold that may migrate to the cathode and be redeposited to form dendrites that can create short circuits (1). In the absence of chloride, a hydroxide film is the main corrosion product. This will not lead to dendrite formation. On the other hand, the film is not self-limiting, and, given sufficient time, much gold could be consumed. Also in the absence of chloride, some gold does dissolve at very high potentials. Given sufficient time, this could also lead to den-

drite formation. Clearly, chloride must be rigorously excluded from electronic circuits with gold metallizations and the insulation resistance must be maintained at a level high enough to prevent the various processes cited above from degrading the gold conductors.

### Conclusions

1. In sulfuric acid solutions, with and without added  $Cl^-$ , gold is oxidized to a soluble  $Au(III)$  species or to a film of  $Au(OH)_3$  at potentials in the passive and transpassive regions. The rates of formation of these reaction products and their potential dependence are a function of  $(Cl^-)$  in the solution.
2. Chloride promotes the dissolution of gold and reduces the rate of film formation. However, both dissolution and film formation occur at sufficiently high potentials in all solutions studied.
3. The potential dependence of the film growth rate is consistent with the "blister" growth mechanism of Barnartt (12). Neither the mechanism of growth nor the composition of the film are affected by the presence of chloride ions in solution.
4. Two potential regions are defined for the oxygen evolution reaction. At low potentials, the reactions occur on a metal surface that is film free or only partially covered by an adsorbed layer. The rate in this region is a strong function of  $(Cl^-)$ . At high potentials, the rate is independent of  $(Cl^-)$  and the reaction occurs on the surface of the  $Au(OH)_3$  film.
5. The formation of  $Au(OH)_3$  and the oxygen evolution reaction appear to have the same rate-determining step. This is postulated to be the oxidation of water to an intermediate O or OH radical.
6. To prevent corrosion of electronic circuits, chlorides must be rigorously excluded and insulation resistance must be maintained at a high level.

### Acknowledgments

We thank Messrs. Barry Miller and P. C. Milner for many fruitful discussions and P. K. Gallagher for the evolved gas analyses. We are grateful to Professor G. M. Schmid of the University of Florida for putting his chapter on the electrochemistry of gold at our disposal before publication.

Manuscript submitted Nov. 26, 1975; revised manuscript received Jan. 29, 1976.

Any discussion of this paper will appear in a Discussion Section to be published in the December 1976 JOURNAL. All discussions for the December 1976 Discussion Section should be submitted by Aug. 1, 1976.

Publication costs of this article were partially assisted by Bell Laboratories.

### REFERENCES

1. R. P. Frankenthal, in "Properties of Electrodeposits: Their Measurement and Significance," R. Sard, H. Leidheiser, Jr., and F. Ogburn, Editors, p. 142, The Electrochemical Society Soft-bound Symposium Series, Princeton, N. J. (1975).
2. G. M. Schmid and M. E. Curley-Fiorino, in "Encyclopedia of Electrochemistry of the Elements," Vol. IV, A. J. Bard, Editor, p. 87, Marcel Dekker, Inc., New York (1975).
3. D. A. J. Rand and R. Woods, *J. Electroanal. Chem.*, **35**, 209 (1972).
4. S. H. Cadle and S. Bruckenstein, *Anal. Chem.*, **44**, 2225 (1972).
5. K. Moslavac, B. Lovrecek, and R. Radeka, *Electrochim. Acta*, **17**, 415 (1972).
6. Y. Y. Vinnikov, V. A. Shepelin, and V. I. Veselovskii, *Soviet Electrochem.*, **8**, 1201 (1972).
7. S. H. Cadle and S. Bruckenstein, *J. Electroanal. Chem.*, **48**, 325 (1973).
8. C. M. Ferro, A. J. Calandra, and A. J. Arvia, *ibid.*, **50**, 403 (1974).
9. C. M. Ferro, A. J. Calandra, and A. J. Arvia, *ibid.*, **55**, 291 (1974).
10. D. Dickertmann, J. W. Schultze, and K. J. Vetter, *ibid.*, **55**, 429 (1974).

11. J. P. Hoare, "The Electrochemistry of Oxygen," Chapters 2 and 3, Interscience Publishers, New York (1968).
12. S. Barnartt, *This Journal*, **106**, 722 (1959).
13. J. L. Whitton and J. A. Davies, *ibid.*, **111**, 1347 (1964).
14. T. Heumann and H. S. Panesar, *Z. Physik. Chem.*, **229**, 84 (1965).
15. J. N. Gaur and G. M. Schmid, *J. Electroanal. Chem.*, **24**, 279 (1970).
16. N. V. Sidgwick, "The Chemical Elements and Their Compounds," pp. 118 and 179, Clarendon Press, Oxford (1950).
17. J. P. Hoare, *Electrochim. Acta*, **11**, 203 (1966).
18. J. P. Hoare, *ibid.*, **11**, 311 (1966).
19. J. J. MacDonald and B. E. Conway, *Proc. Roy. Soc. A*, **269**, 419 (1962).

## Mechanism of Anodic Deposition and Cathodic Stripping of PbO<sub>2</sub> on Conductive Tin Oxide

H. A. Laitinen<sup>\*1</sup> and Noel H. Watkins<sup>2</sup>

*Roger Adams Laboratory, School of Chemical Sciences, University of Illinois, Urbana, Illinois 61801*

### ABSTRACT

Deconvolution of potentiostatic current-time curves during anodic deposition of PbO<sub>2</sub> from nitric acid solutions onto antimony-doped tin oxide electrodes permitted three processes to be delineated, viz., double layer charging, formation of nuclei, and growth of nuclei. The formation and growth laws are similar to those previously observed on platinum. Cathodic stripping voltammetry revealed a sharp peak due to reversible reduction of crystalline PbO<sub>2</sub> followed by a rounded hump or irreversible secondary peak attributed to the first fractional monolayer of PbO<sub>2</sub>. Electron microscopy revealed randomly sized hemispherical deposits at constant and high overpotential, and well-formed crystals upon prenucleation followed by slow growth. Electron spectroscopy (ESCA) revealed a characteristic sharp Pb 4f<sub>7/2</sub> binding energy peak attributable to Pb(IV) attached to SnO<sub>2</sub>, and different from crystalline PbO<sub>2</sub>.

In connection with the study of cathodic stripping coulometry as an analytical method for traces of lead (1), it became important to understand the mechanisms of nucleation, growth, and cathodic stripping of PbO<sub>2</sub> on a substrate of polycrystalline, antimony-doped tin oxide.

Fleischmann and co-workers (2-6) have carried out extensive studies of the kinetics of deposition of  $\alpha$ - and  $\beta$ -PbO<sub>2</sub> onto platinum surfaces from perchloric acid, nitric acid, and acetate solutions. By choosing conditions appropriately, they were able to focus upon the nucleation and growth steps separately. Thus, if random nucleation occurs at a limited number of nucleation sites,  $N_0$ , at a rate proportional to the number of available sites at a given time, the first-order nucleation law is

$$N = N_0[1 - \exp(-At)] \quad [1]$$

where  $N$  is the number of nuclei per unit area at time  $t$  and  $A$  is the potential-dependent nucleation rate constant. For short time intervals at constant potential, this reduces to a linear nucleation law

$$N = N_0At \quad [2]$$

The corresponding growth law for nuclei preformed at a high overpotential and grown at a lower overpotential is of the form

$$i = at^2 \quad [3]$$

It is assumed that no new nuclei are formed and that the preformed nuclei grow nonpreferentially. Such a current-time relationship was verified for the growth of preformed  $\alpha$ -PbO<sub>2</sub> from acetate solutions (2).

If simultaneous nucleation and growth occur at constant overpotential, Eq. [2] and [3] lead to the expect-

tation that the current should be proportional to  $t^3$ . Experimentally, the initial current increased with a power of the time greater than 3, unless an induction period  $t_0$  was subtracted from the elapsed time, in which case the expected third-order dependence was observed for short time intervals. Electron micrographs of the lead dioxide deposited at an overpotential of 300 mV showed the hemispherical shapes expected for nonpreferred growth (5). The rate constants for nucleation and growth were evaluated as a function of potential and pH from the current-time curves, and a stepwise mechanism involving the specific adsorption of hydroxyl radicals and lead (IV) hydroxy species was proposed.

Hampson, Jones, and Phillips (7) used a galvanostatic technique to study the PbO<sub>2</sub>/Pb<sup>2+</sup> mechanism on platinum substrates in perchloric acid and acetate media. They concluded that the charge transfer mechanism changes from a single two-electron step at low overpotential (8,9) to two successive single electron steps at higher overpotentials (7). They regarded the existence of free Pb<sup>4+</sup> ions in solution as unlikely, and postulated an adsorbed Pb(IV) species which accepts an electron to form an adsorbed Pb(III) hydroxy intermediate, [HO-Pb-OH<sup>+</sup>], which rapidly accepts the second electron to form Pb(OH)<sub>2</sub>.

In the present investigation, the use of a tin oxide substrate, with its high oxygen overpotential and low residual current, permitted the deconvolution of the potentiostatic current-time curves into components due to nucleation, growth, and double layer charging. The use of a ring-disk geometry permitted a direct search for soluble intermediates during the formation and stripping steps.

### Experimental

Tin oxide electrodes were prepared by spraying a solution 3M in SnCl<sub>4</sub>, 0.0675M in SbCl<sub>3</sub>, and 1.5M in HCl onto a Pyrex glass substrate heated to 550° (10)

<sup>\*</sup> Electrochemical Society Active Member.

<sup>1</sup> Present address: Department of Chemistry, University of Florida, Gainesville, Florida 32611.

<sup>2</sup> Present address: Monsanto Company, Pensacola, Florida 32501.  
Key words: lead dioxide, anodic deposition, cathodic stripping, tin oxide, ESCA.

to form deposits 0.75–1.0  $\mu\text{m}$  in thickness. Care was taken to avoid excessive cooling of the surface during bursts of spraying. Three different electrode geometries, namely cylindrical, rotating disk, and rotating ring-disk, were used as previously described (1, 11).

Linear potential sweep experiments were performed with a conventional three-electrode polarograph in conjunction with a linear sweep generator (12) and x-y recorder. Apparatus for double pulse potentiostatic experiments, potentiostatic electrodeposition followed by linear voltammetric stripping, integration of coulombic charge between two preselected potentials, and a four-electrode bipotentiostat for use with the ring-disk electrode have been described (1, 11). Special precautions were taken to prevent loss of potentiostatic control in switching between potentiostatic electrodeposition and linear sweep voltammetry, as well as to minimize interaction between ring and disk currents.

Scanning electron microscopy, using Cambridge Stereoscan and JEOLCO instruments, required minimal sample preparation because both the tin oxide substrate and lead dioxide deposit were conductive enough to render vapor deposition of a metal film unnecessary. The samples were air-dried and electrical contact was made to the tin oxide film by means of conductive silver paint.

Electron spectroscopy (ESCA) experiments were carried out by Dr. Nicholas Winograd, of Purdue University, using a Hewlett-Packard 5950 ESCA spectrometer with monochromatic Al  $K\alpha$  x-rays from a quartz crystal disperser. The spectra were deconvoluted using a du Pont 310 curve recorder.

### Results and Discussion

**Soluble intermediates.**—Using the ring-disk electrode, Pb(II) was oxidized to  $\text{PbO}_2$  at the disk while simultaneously holding the ring at +0.2V vs. saturated calomel electrode (SCE) to observe any current due to the reduction of soluble Pb(III) or Pb(IV) species. With 0.25M  $\text{Pb}(\text{NO}_3)_2$  in 0.01–1M nitric acid, no soluble intermediates could be detected. If it is assumed that a soluble intermediate hydrolyzes or oxidizes to form the lead dioxide deposit, a lower limit can be estimated for the homogeneous reaction rate (13, 14). For a soluble intermediate to escape detection at the maximum rotational speed used (211 radians  $\text{sec}^{-1}$ ) we estimate that the first-order reaction rate constant must be greater than  $3 \times 10^2 \text{ sec}^{-1}$ .

In sufficiently acid solution, in the presence of orthophosphate, a soluble intermediate could be detected. With 0.25M  $\text{Pb}(\text{NO}_3)_2$  in 0.08M  $\text{H}_3\text{PO}_4$ , a soluble intermediate was detected using 1M  $\text{HNO}_3$  but not 0.01M  $\text{HNO}_3$ .

These observations are consistent with the findings of Fleischmann and co-workers (2–6) and Hampson, Jones, and Phillips (7), who postulated adsorbed, but not soluble, intermediates of Pb(III) and Pb(IV). They are also consistent with reports of soluble and relatively stable lead (IV)-phosphate species prepared electrochemically in phosphoric acid and sulfuric acid-phosphoric acid mixtures (15–17).

**Kinetics of nucleation and growth.**—To compare tin oxide with platinum as a substrate, preliminary experiments were carried out under conditions comparable to those used by Fleischmann and co-workers (2, 3). Similar results were found: the current is initially limited by an induction period, followed by nucleation and growth, and finally a steady state due to growth alone. For example, using 1M lead acetate in 1M acetic acid–1M sodium acetate, at an overpotential of 302 mV, an induction period of 12 sec was found to give a best fit for a cubic growth law valid from 15 to 50 sec (Fig. 1). When the surface was pre-nucleated at high overpotential, the current increased with the

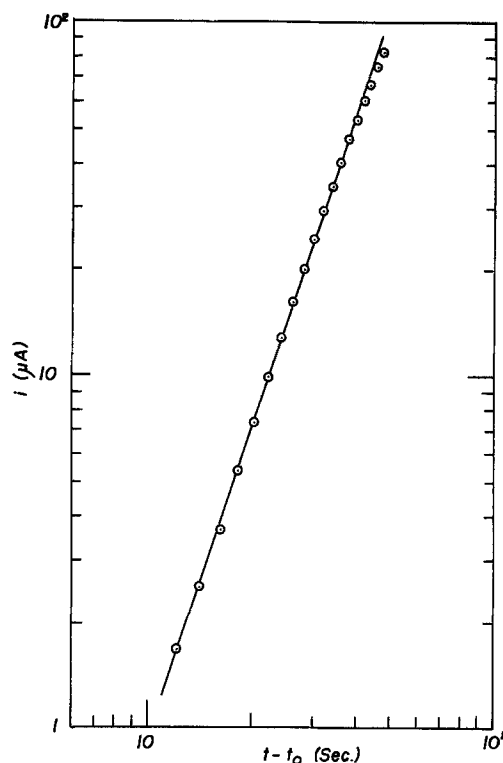


Fig. 1. Variation of  $\log i$  with  $\log (t - t_0)$  for potentiostatic deposition at constant overpotential. 1M  $\text{Pb}(\text{C}_2\text{H}_3\text{O}_2)_2$  in 1M  $\text{NaC}_2\text{H}_3\text{O}_2$ –1M  $\text{C}_2\text{H}_3\text{O}_2\text{H}$ .  $\eta = +0.302\text{V}$  vs.  $\text{PbO}_2/\text{Pb}^{+2}$ ;  $A = 0.2 \text{ cm}^2$ ;  $t_0 = 12 \text{ sec}$ .

square of time. The quantity  $AN_0$  (Eq. [2]) was in reasonable agreement with that reported by Fleischmann and Liler (3). While this does not necessarily prove that the number of nucleation sites  $N_0$  and nucleation rate constant  $A$  are both identical on tin oxide and platinum, the experimentally measured nucleation rates are comparable.

At an overpotential of 600 mV it proved possible to resolve the potentiostatic current-time curve into four distinct regions, corresponding, respectively, to double layer charging, nucleation, crystal growth, and mass transport limited currents. For short time intervals, the mass transport limited current is negligible, as illustrated by the current-time curve for the first 30 msec in Fig. 2.

Neglecting the mass transport limited current, the current-time curve can be represented as the sum of currents due to double layer charging, nucleation, and crystal growth, or

$$i = k_1 \exp(-t/RC) + k_2 N_0 (1 - \exp(-At)) + k_3 B N_0 (t - t_{\text{nuc}})^2 \quad [4]$$

where  $k_1$ ,  $k_2$ , and  $k_3$  are proportionality constants and  $t_{\text{nuc}}$  is the time required for nucleation. It is assumed that double layer charging occurs quickly compared to nucleation and that nucleation is complete before significant crystal growth has occurred.

Deconvolution of the charging and nucleation currents was facilitated by the plot of  $\log i$  vs.  $t$  shown in Fig. 3. The growth current was deconvoluted from the nucleation current by plotting  $i^{1/2}$  vs.  $(t - t_0)$  and selecting  $t_0$  for the best fit. The resulting component currents, when summed, are in reasonably good agreement with the observed current (Fig. 2) except in the region of 11–15 msec probably because nucleation is not complete before growth begins, contrary to the assumption made in curve fitting.

**Voltammetric stripping.**—According to Fig. 2, lead dioxide deposited during the first 10 msec should predominantly exist as crystal nuclei, whereas lead di-

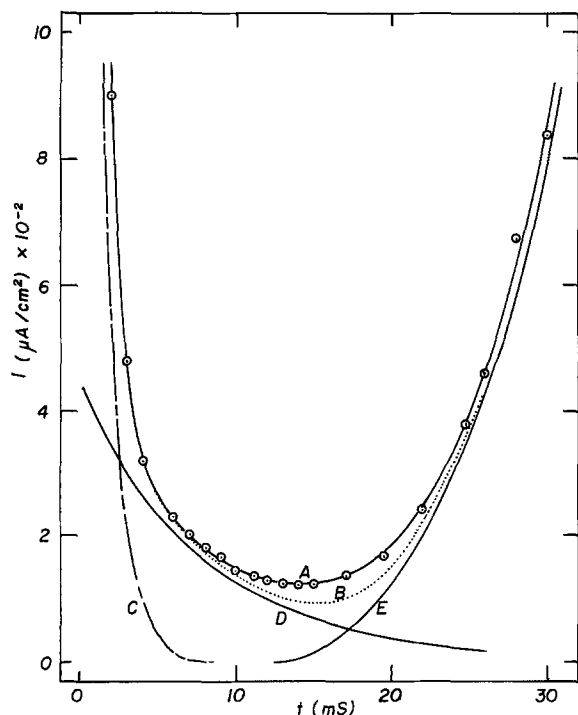


Fig. 2. Current-time curves for potentiostatic deposition of lead dioxide on tin oxide at high overpotential.  $0.25M \text{ Pb}(\text{NO}_3)_2$  in  $1M \text{ HNO}_3$ ,  $\eta = +0.60V$ ;  $A = 1 \text{ cm}^2$ . Curve A, experimental current; B, sum of deconvoluted currents; C, double layer charging current; D, nucleation current; and E, crystal growth current.

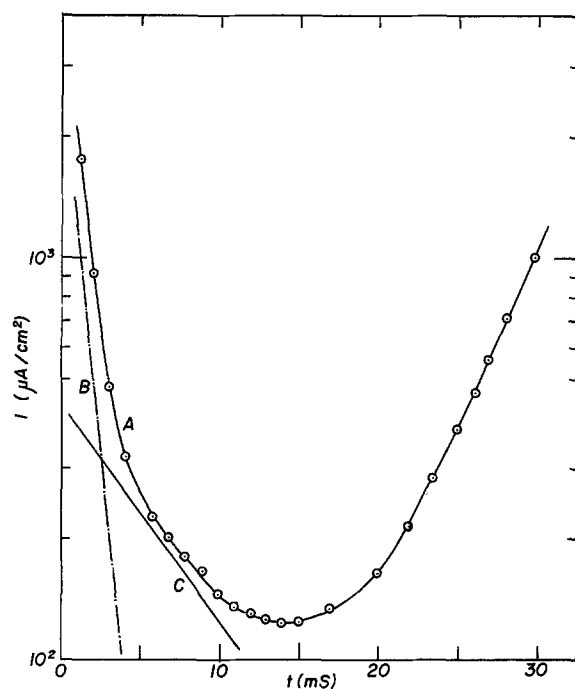


Fig. 3. Variation of  $\log i$  with time for potentiostatic deposition of lead dioxide on tin oxide at high overpotential.  $0.25M \text{ Pb}(\text{NO}_3)_2$  in  $1M \text{ HNO}_3$ ,  $\eta = +0.60V$ ;  $A = 1 \text{ cm}^2$ . Curve A, experimental; B, double layer charging; and C, nucleation.

oxide deposited for 30 msec should include both the crystal nuclei and the developed crystals. This expectation is fully realized in the stripping peaks observed in linear scan voltammetry (Fig. 4). A primary peak occurring near the reversible potential can be ascribed to the developed crystals, whereas the crystal nuclei appear as a broad secondary peak. Evidently a small amount of nucleation has occurred, in addition to crystal growth, in the time interval of 10-30 msec. On a platinum substrate, the reduction of surface

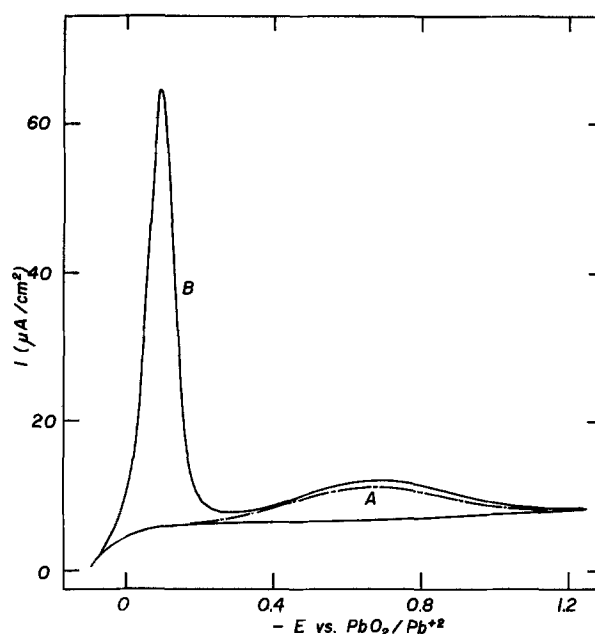


Fig. 4. Voltammetric stripping of lead dioxide deposited at high overpotential.  $0.25M \text{ Pb}(\text{NO}_3)_2$  in  $1M \text{ HNO}_3$ ,  $\eta = +0.60V$ ;  $V = 50 \text{ mV/sec}$ . Curve A, 10 msec; and B, 30 msec.

oxides during the cathodic sweep experiments would completely obscure any observation of secondary reduction peaks such as those observed on tin oxide.

Anodic and cathodic charges are compared in Table I. The anodic charge, obtained by integrating the resolved curves of Fig. 2, was consistently higher than the experimental cathodic stripping charge. This was expected, because the nucleation process is delayed during the double layer charging time, which is not negligible.

To test the nucleation law expressed in Eq. [1], we rewrite it as

$$2.303 \log \left[ 1 - \frac{Q}{Q_0} \right] = -At \quad [5]$$

where the ratio  $N/N_0$  has been replaced by  $Q/Q_0$ , where  $Q$  and  $Q_0$  are the coulombic charges represented by the secondary stripping peak areas observed at time  $t$  and long time intervals. The substitution applies to the condition that all nuclei are of the same age and therefore that the crystallites are of uniform size.

A relatively high overpotential (902 mV) was chosen to facilitate the formation of the maximum number of nuclei, and a high lead concentration ( $0.25M$ ) was used to minimize the anodic current due to oxidation of water and to prevent limiting the deposition by mass transport. A high nitric acid concentration ( $1M$ ) was chosen to achieve a good separation between reversible and secondary peaks. Figure 5 shows a series of linear sweep stripping curves for deposition times from 0.5 to 10 msec. Each deposition experiment was repeated three times to check reproducibility. At the longer deposition times, the crystal growth had become so pronounced that the secondary peak area had to be

Table I. Summary of charge involved in anodic deposition and cathodic stripping

	$Q$ ( $\mu\text{coulomb}$ )	
	10 msec	30 msec
Anodic	2.5	9.0
Cathodic	—	5.9
Reversible	1.9	2.7
Secondary	1.9	8.6
Total	1.9	8.6

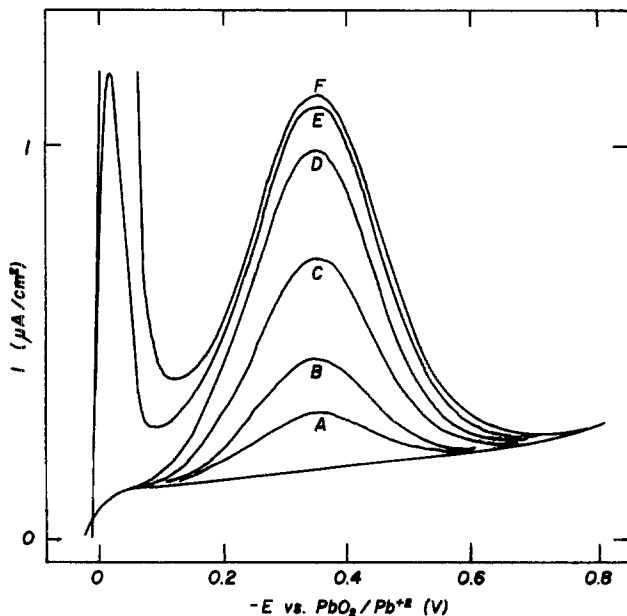


Fig. 5. Voltammetric stripping of lead dioxide deposited at constant overpotential.  $0.25M \text{ Pb}(\text{NO}_3)_2$  in  $1M \text{ HNO}_3$ .  $\eta = +0.902V$ ;  $V = 50 \text{ mV/sec}$ . Time (msec): curve A, 0.5; B, 1; C, 2.5; D, 5; E, 7.5; and F, 10.

estimated by extrapolation, assuming the secondary peak to be symmetrical.

To determine  $Q_0$ , a plot of secondary peak charge density vs. deposition time (Fig. 6) was extrapolated to long time intervals. The maximum charge density  $Q_0 = 8.3 \mu\text{coulomb/cm}^2$ . This corresponds to approximately 3% of monolayer coverage, which is estimated from the unit cell dimensions of  $\text{PbO}_2$  to be 261-315  $\mu\text{coulomb/cm}^2$ , depending upon the crystal orientation, if the roughness factor is taken to be unity. Even a smaller fractional coverage would be estimated if a larger roughness factor were used.

A plot of  $\log(1 - Q/Q_0)$  vs.  $t$  is shown in Fig. 7. The plot is linear with zero intercept, indicating that at this high overpotential the induction period, if it exists, is less than  $50 \mu\text{sec}$ . The nucleation rate constant  $A$ , as determined from the slope, is  $208 \text{ sec}^{-1}$ . This is to be compared with an extrapolated value of approximately  $100 \text{ sec}^{-1}$  from a graph of Fleischmann and Thirsk (3) of  $\log A$  vs.  $1/n^2$  for  $0.25M \text{ Pb}(\text{ClO}_4)_2$  in  $0.1M \text{ HClO}_4$ , in which the highest overpotential used is about  $250 \text{ mV}$ .

Brainina (19), in a review of film stripping voltammetry, considered the stripping of both thick and thin films at stationary and rotating electrodes. For fractional monolayers, the activity was expressed by an empirical equation

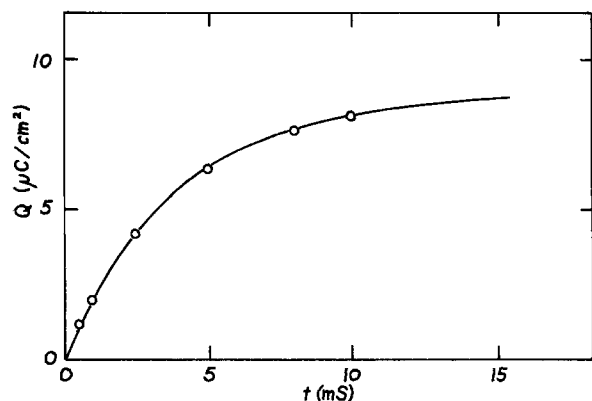


Fig. 6. Variation of secondary peak charge density with deposition time at constant overpotential.  $0.25M \text{ Pb}(\text{NO}_3)_2$  in  $1M \text{ HNO}_3$ .  $\eta = +0.902V$ .

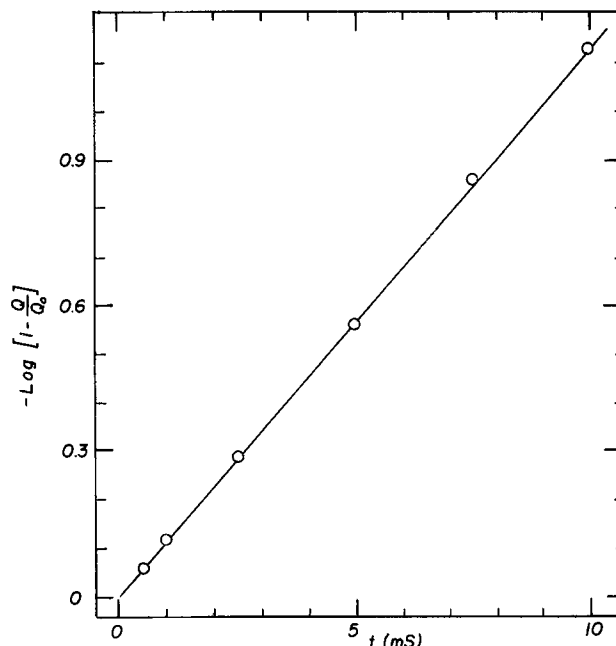


Fig. 7. Variation of  $\log(1 - Q/Q_0)$  with deposition time for the secondary peak deposited at constant overpotential.  $0.25M \text{ Pb}(\text{NO}_3)_2$  in  $1M \text{ HNO}_3$ .  $\eta = +0.902V$ .

$$\alpha = \alpha_s [1 - \exp(-\gamma Q)]$$

where  $\alpha$  is the activity of the pure phase,  $Q$  is the amount of substance deposited, and  $\gamma$  is an empirically determined constant. For the thin film case ( $\gamma Q \ll 1$ ), a convenient diagnostic test for reversibility is a comparison of stripping peaks obtained under stationary and rotating conditions.

For a reversible cathodic film stripping process, rotation of the electrode should shift the stripping peak potential in an anodic direction by an amount

$$\Delta E_m = \frac{RT}{2F} \ln \frac{1}{\delta^2} \frac{DRT}{nFV} \quad [6]$$

where  $\delta_1$  = diffusion layer thickness, cm, and  $V$  = rate of potential change,  $V\text{-sec}^{-1}$ , while the peak current is increased by a factor of about 1.23 for convective mass transport at the rotating electrode as compared with diffusional mass transport at the stationary electrode. For an irreversible process, the back reaction would be negligible and no effect of rotation should be observed.

Experimentally, for the sharp primary reduction peak, the peak current increased by a factor of 1.2 as compared with the theoretical 1.23 and the peak potential shifted anodic by  $25 \text{ mV}$  as compared with the calculated value of  $26.8 \text{ mV}$  for the conditions used ( $\delta = 1.14 \times 10^{-3} \text{ cm}$ ,  $V = 50 \text{ mV/sec}$ ). In contrast, the rounded secondary peak showed no shift in peak potential or peak current upon rotation, even under more extreme conditions ( $\delta = 1.14 \times 10^{-3} \text{ cm}$ ,  $V = 1 \text{ mV/sec}$ ) when a peak voltage shift of  $82.2 \text{ mV}$  would have been expected for reversible stripping.

Other tests of reversibility for the secondary peak (variation of peak current with  $Q$ , peak potential with  $Q$ , peak potential with  $V$ , and peak current with  $V$ ) likewise indicated qualitatively that the reduction process is irreversible (11).

*Scanning electron microscopy.*—A deposit of  $\text{PbO}_2$  on tin oxide formed at a relatively high overpotential ( $240 \text{ mV}$ ) without prenucleation consisted of randomly placed hemispheres of a wide variety of sizes, indicating that nucleation is occurring concurrently with growth, and that growth is nonpreferential (Fig. 8). Preformation of nuclei by a pulse at  $900 \text{ mV}$  followed by growth at  $240 \text{ mV}$  gave rise to hemispherical crys-

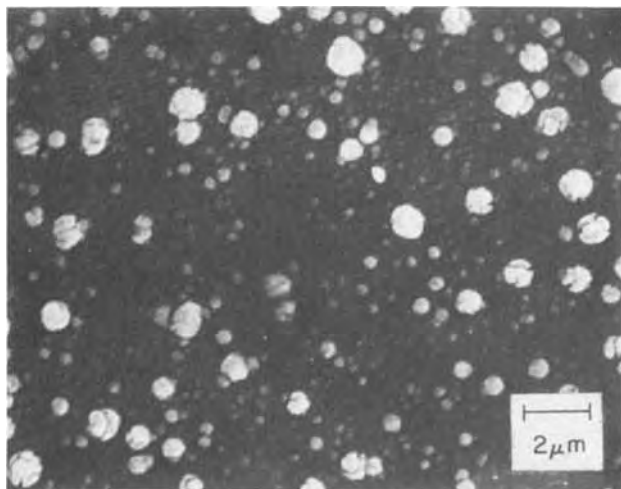


Fig. 8. Scanning electron micrograph of lead dioxide deposited on tin oxide without preformation of nuclei, high magnification.  $0.25M$   $Pb(NO_3)_2$  in  $1M$   $HNO_3$ .  $\eta = +0.24V$ ;  $Q = 3 \times 10^4$   $\mu\text{coulomb}/\text{cm}^2$ .

tallites of uniform size. These observations are similar to those of Fleischmann and Thirsk (5) on platinum.

At low overpotential there was evidence for preferred growth orientation of crystallites. As shown in Fig. 9, a deposit grown at a constant current density of  $1 \mu\text{A}/\text{cm}^2$  upon nuclei preformed at 600 mV overpotential for 50 msec is characterized by clearly discernible crystal faces. This observation is at variance from the statement of Fleischmann and Thirsk (5) that lead dioxide is formed without preferred orientation at high overpotential and also from nitrate solution.

**ESCA studies of lead dioxide.**—The technique of x-ray photoelectron spectroscopy (ESCA) was applied to monolayer deposits of lead dioxide on tin oxide to gain structural information about the  $\text{SnO}_2$ - $\text{PbO}_2$  interaction.

Monolayer deposits were made from two solutions,  $0.25M$   $Pb(NO_3)_2$  in  $1M$   $HNO_3$  and in  $0.08M$   $H_3PO_4$ - $1M$   $HNO_3$ , prepared from reagent grade acids and  $Pb(NO_3)_2$ . Orthophosphate was added to inhibit the formation of reversibly reduced  $\text{PbO}_2$  (1). To minimize the reduction of monolayer deposits, the solutions were pretreated by dispersing  $\text{PbO}_2$  in them, boiling for several minutes, filtering through a fine porosity glass crucible, and storing the solutions in the dark to pre-

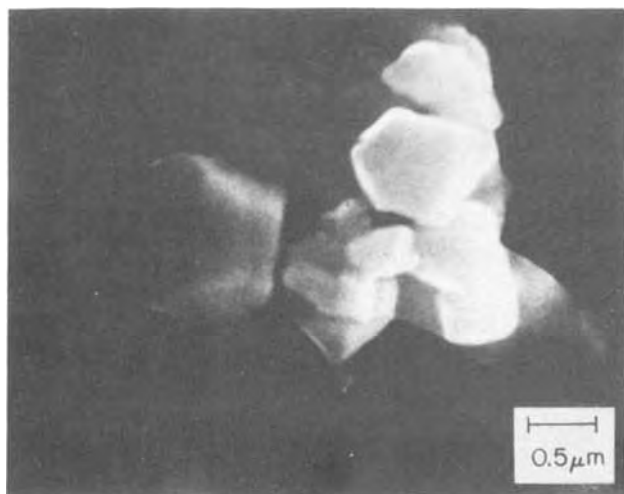


Fig. 9. Scanning electron micrograph of lead dioxide deposit formed at low current density on tin oxide.  $0.25M$   $Pb(NO_3)_2$  in  $1M$   $HNO_3$ . Nuclei preformed at  $\eta = +0.6V$  for 50 msec. Grown with constant current density of  $1 \mu\text{A}/\text{cm}^2$ .

Table II.  $Pb 4f_{7/2}$  spectral assignments

$PbO_2$ type	$Pb 4f_{7/2}$ B.E. (eV)	Assignment
Reversible	137.5	$PbO_2$ , $Pb_3O_4$
	138.7	$Pb_3O_4$
Secondary	138.1*	$PbO_2$ - $\text{SnO}_2$

\* Width at half height is 1.2 eV.

vent photochemical decomposition. The amount of deposit was monitored several times by trial deposition and stripping before the actual sample was prepared. After the deposit was formed and the potentiostat was disconnected, the electrode was rinsed with  $1M$   $HNO_3$  and distilled water and demounted. Within 30 sec from the time of disconnecting the potentiostat the electrode was placed in a vacuum to dry. After drying 20 min the sample was sealed under vacuum in a Pyrex vial. In this manner, samples of one monolayer equivalent could be transferred to vacuum vials with only approximately 20% loss of the original reducible lead. Spectral assignments for  $Pb 4f_{7/2}$  binding energies are listed in Table II.

The spectrum of "reversible" lead dioxide was complicated by the fact that it was especially susceptible to reduction during preparation and may have been present partially as  $PbO$  or  $Pb_3O_4$ . Winograd (18) has pointed out that  $Pb_3O_4$  gives two  $Pb 4f_{7/2}$  lines attributable to a structure such as  $PbO_2 \cdot 2PbO$ . The ratio of the spectral time intensities in the present work varied from one sample to another, due to variation in the amount of  $\text{PbO}_2$  reduced.

The spectrum of "secondary" lead dioxide, *i.e.*, that reduced in the broad secondary cathodic peak, had a single sharp  $4f_{7/2}$  line which was definitely not attributable to bulk phase  $\text{PbO}_2$ . We conclude that the initial monolayer of  $\text{PbO}_2$  bonded directly to  $\text{SnO}_2$  has a perturbed  $Pb$ - $O$  bonding insensitive to the crystal face of cassiterite to which it is bonded, inasmuch as the tin oxide layer is known to have a randomly oriented polycrystalline structure. It should be noted that  $\alpha$ - and  $\beta$ - $\text{PbO}_2$  do not have significantly different  $Pb 4f_{7/2}$  electron binding energies, so that the possibility that the initial layer is  $\alpha$ - $\text{PbO}_2$  and the bulk is  $\beta$ - $\text{PbO}_2$  is excluded on the basis of the ESCA observations.

An incidental observation was that no phosphorus ESCA spectrum was detected in the samples prepared in the presence of phosphate. Thus the initial "secondary"  $\text{PbO}_2$  layer is not a  $Pb(IV)$ -phosphate compound, even though subsequent layers formed under these conditions can be described as a basic phosphate of lead (IV) (1). Another observation was that the tin ESCA spectrum was almost completely obscured by the "secondary" monolayer, whereas the "reversible" lead oxide, present as isolated crystallites showed a tin peak as intense as that exhibited by the original tin oxide surface. This is because ESCA has a sampling depth of only 10-20Å and the "secondary" monolayer is a continuous one.

#### Acknowledgment

This research was supported by the National Science Foundation under grant NSF-RANN 31605.

Manuscript submitted Oct. 30, 1975; revised manuscript received Feb. 3, 1976.

Any discussion of this paper will appear in a Discussion Section to be published in the December 1976 JOURNAL. All discussions for the December 1976 Discussion Section should be submitted by Aug. 1, 1976.

Publication costs of this article were partially assisted by the University of Florida.

#### REFERENCES

- H. A. Laitinen and Noel H. Watkins, *Anal. Chem.*, **47**, 1352 (1975).

2. M. Fleischmann and M. Liler, *Trans. Faraday Soc.*, **54**, 1370 (1958).
3. M. Fleischmann and H. R. Thirsk, *Electrochim. Acta*, **1**, 146 (1959).
4. M. Fleischmann and H. R. Thirsk, "Advances in Electrochemistry and Chemical Engineering," Volume 3, P. Delahay, Editor, pp. 123-210, Interscience, New York (1963).
5. M. Fleischmann and H. R. Thirsk, *Electrochim. Acta*, **2**, 22 (1960).
6. M. Fleischmann, J. R. Mansfield, H. R. Thirsk, H. G. E. Wilson, and L. Wynne-Jones, *ibid.*, **12**, 967 (1967).
7. N. A. Hampson, P. C. Jones, and R. F. Phillips, *Can. J. Chem.*, **46**, 1325 (1968).
8. N. A. Hampson, P. C. Jones, and R. F. Phillips, *ibid.*, **45**, 2039 (1967).
9. N. A. Hampson, P. C. Jones, and R. F. Phillips, *ibid.*, **45**, 2045 (1967).
10. J. M. Mochel, U.S. Pat. 2,564,707 (1951).
11. Noel H. Watkins, Ph.D. Thesis, University of Illinois (1973).
12. R. Bezman and P. S. McKinney, *Anal. Chem.*, **41**, 1560 (1969).
13. W. J. Albery, M. L. Hitchman, and J. Ulstrup, *Trans. Faraday Soc.*, **64**, 2331 (1968).
14. K. B. Prater and A. J. Bard, *This Journal*, **117**, 335 (1970).
15. V. F. Huber and M. S. A. El-Meligy, *Anorg. Allgem. Chem.*, **367**, 154 (1969).
16. R. F. Amlie and T. A. Berger, *J. Electroanal. Chem.*, **36**, 427 (1972).
17. H. Bode and E. Voss, *Electrochim. Acta*, **6**; 11 (1962).
18. K. S. Kim, T. J. O'Leary, and N. Winograd, *Anal. Chem.*, **45**, 2214 (1973).
19. Kh. Z. Brainina, *Talanta*, **18**, 513 (1971).

## Paired Electro-Organic Syntheses

### I. Cathodic Adipate with Anodic Bimalonate

Manuel M. Baizer\* and R. C. Hallcher

Corporate Research Department, Monsanto Company, St. Louis, Missouri 63166

#### ABSTRACT

A procedure is reported for the co-electrolysis of ethyl acrylate and diethyl malonate using  $\text{CH}_3\text{CN}/\text{Bu}_4\text{NI}$  as solvent/electrolyte system to yield diethyl adipate and tetraethyl ethane-1,1,2,2-tetracarboxylate in high (95%) yield and good (60%) current efficiency. A convenient cell which allows experimentation in the 2-5g range was fabricated from a hollowed-out graphite cylinder (optionally lined with lead) which served as one electrode and a graphite rod machined and held so as to be counterelectrode and mechanical stirrer. General aspects of paired organic syntheses are discussed as well as the specific problems that are involved when the paired reactions are hydrodimerization-dehydrodimerization.

It is a truism, of course, that all electrolyses require the simultaneous occurrence of cathodic and anodic reactions. Almost always, however, a synthesis of interest is carried out at only one electrode (the "working" electrode) and a "sacrificial" reaction, without recovery of products, is allowed to proceed at the second (the "secondary," "auxiliary," or "counter") electrode. Ordinarily, in aqueous media, hydrogen or oxygen evolution is used as the respective cathodic or anodic sacrificial reaction. In electro-organic syntheses much ingenuity has been applied in order to assure that the sacrificial reaction produces innocuous products when undivided and even when divided cells are used.

The economic (now including environmental) advantage of devising electrochemical synthetic schemes which employ both electrodes gainfully has often been pointed out (1, 2) along with the difficulties associated with this concept (2). The success of the chlor-alkali industry presents an unending challenge (and frequent taunt) to the organic electrochemist.

Both electrodes are gainfully employed if (i) the sacrificial product may be recovered for sale (1) or preferably for synthesis of the starting material of interest, as, e.g., in the reductive coupling of certain organic halides (3); (ii) reactions at both electrodes<sup>1</sup> are necessary to produce one given product, e.g., propylene  $\rightarrow$  propylene halohydrin (anode)  $\rightarrow$  propylene oxide (cathode) (4); (iii) at least one useful product

is produced at each electrode. We suggest that the latter category be denoted "paired syntheses."<sup>2</sup>

As has already been pointed out (2) there is, in addition to the horrendous technical difficulties involved in devising paired electro-organic syntheses, the question of providing outlets for two products formed in equivalent amounts. Even the chlor-alkali and the cumene  $\rightarrow$  phenol + acetone industries face this problem. However, if one of the products of a paired organic synthesis is sold in huge quantities, e.g., aniline, adipic acid derivatives, terephthalic acid, and can be made advantageously electrochemically, it can be used as a "sink" which allows ad lib adjustment of the scale of production of the coproduct.

We report here a detailed laboratory investigation of a paired synthesis (acrylate  $\rightarrow$  adipate + malonate  $\rightarrow$  bimalonate) which was recently described briefly in the literature (6). In the reported procedure<sup>3</sup> graphite electrodes were used in an undivided cell. The solvent/electrolyte system was acetonitrile/potassium iodide. Methyl acrylate and diethyl malonate were present in 10% concentration. The apparent current density was 0.004 A/cm<sup>2</sup> with an applied voltage of 5-7. The yields of dimethyl adipate and tetraethyl ethane-1,1,2,2-tetracarboxylate<sup>4</sup> were "high."

<sup>2</sup> There has already been occasional reference to this category as "coupled" reactions. Since the latter term has already received widespread use in connection with reactions immediately consequent upon an electron-transfer step (5), we should like to see this practice stopped before it generates confusion.

<sup>3</sup> Supplemented by a personal communication from Professor H. G. Thomas.

<sup>4</sup> The oxidation of malonate to bimalonate by anodically generated iodine but without providing a cathodic organic coproduct had been previously reported (7).

\* Electrochemical Society Active Member.

Key words: paired syntheses, hydrodimerization, oxidative coupling, indirect electrolysis.

<sup>1</sup> This includes both faces of a bipolar electrode.



### Experimental

Two similar cells constructed of graphite were employed in most of the work reported here. A cylinder 12 cm high  $\times$  6 cm in diameter was hollowed out to provide a cylindrical cell 10 cm high  $\times$  3 cm diameter. A small copper screw was machined into the top surface of the wall to permit connection to one of the leads from the power source; a threaded opening in the cell wall 9 cm from the bottom allowed attachment of a threaded polypropylene elbow which held a water-cooled condenser. A threaded Teflon part into the top end of the cell served as a bearing for the counterelectrode; a small copper shim screwed into the Teflon provided for electrical contact with the counterelectrode. The counterelectrode, which also served as a mechanically driven stirrer, was constructed from a graphite rod which was machined down to provide two sets of four vanes 15 mm high, one set at the bottom and the second beginning 3.5 cm from the bottom. The maximum diameter of the rod (at the vanes) was 1.7 cm, the minimum (above the vanes) 1.0 cm. One of the cells was lined with lead, leaving an electrolyte chamber 2.2 cm in diameter. The pores of the all-graphite cell were filled with polyethylene by repeatedly soaking the cell in a hot xylene solution of the polymer and then applying light vacuum to pull the solution through the cell wall. The inside was then carefully reamed out to remove surface polymer. The components of the cell are shown in Fig. 1. Direct current was supplied by Sorensen's Nobatron Model RC 150-7.5. For runs in which current efficiencies were determined a calibrated Lectrocount (Royson Engineering Company, Hatboro, Pennsylvania) was used. Electrode potentials were not controlled.

Analytical glc determinations were made using a Hewlett-Packard 5750 instrument. Two different columns and conditions were employed in the analyses: (i) 6 ft  $\times$   $\frac{1}{8}$  in., 3% OV-17 on Chromosorb W (80-100 mesh), 50°  $\rightarrow$  290° at 20°/min; (ii) 6 ft  $\times$   $\frac{1}{8}$  in., 1%

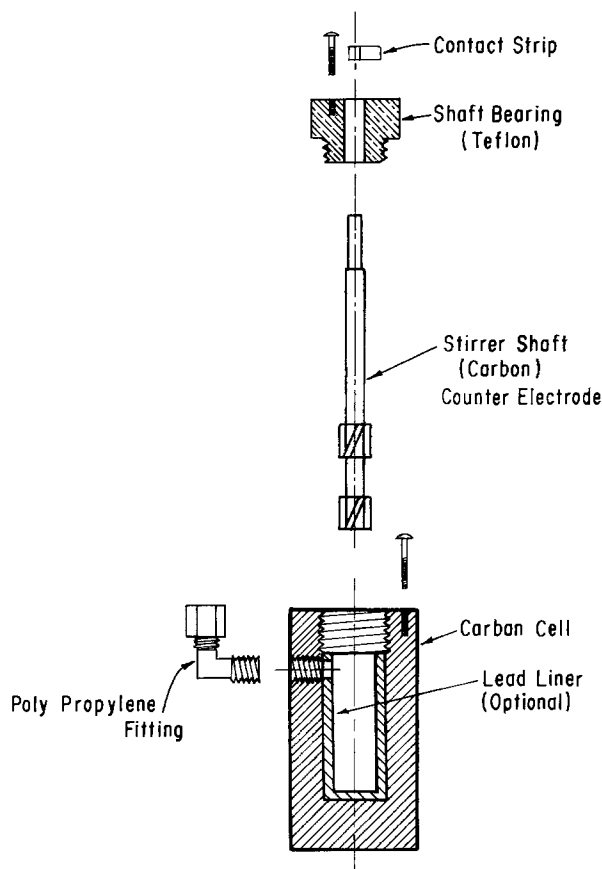


Fig. 1. Cell components

AgNO<sub>3</sub> + 18% Carbowax 20M on Chromosorb W (80-100 mesh), 50° isothermal. Ethyl acrylate and ethyl propionate were determined by method (ii), while method (i) was used for the remainder of the products.

Identification of the products was made by comparison of the glc retention times under identical conditions and always included the peak enhancement method. Diethyl malonate was used as standard in the quantitative analyses. Structures were confirmed by glc-mass spectra analyses.

The experimental data are assembled in abbreviated form in Table I. A typical procedure (runs 29-34) follows. The cell was charged with 1.0g Bu<sub>4</sub>NI and 12 ml of MeCN. The buret for addition of the reagents through the top of the condenser contained diethyl acrylate and diethyl malonate in the quantities indicated together with 5.5 ml of MeCN as solvent. The addition took about 30 min; the electrolysis was continued for 5 min longer. The cell contents were rinsed out quantitatively with MeCN and the solution stored over a trace of hydroquinone.<sup>5</sup> The weighed solution was analyzed by vpc.

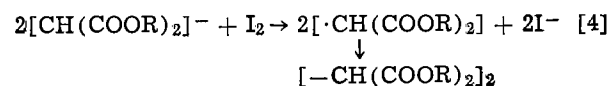
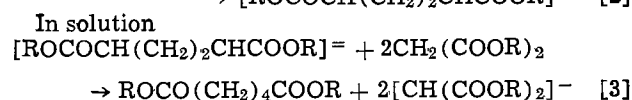
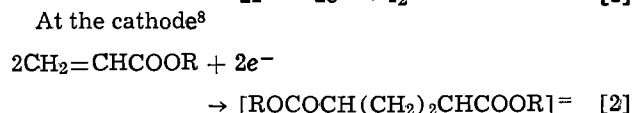
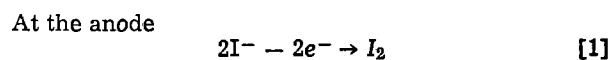
### Results

This study of the co-electrolysis in an undivided cell of ethyl acrylate and diethyl malonate in acetonitrile has resulted in a laboratory procedure for obtaining diethyl adipate and tetraethyl ethane-1,1,2,2-tetracarboxylate in ca. 95% yield at 87-88% conversion and at ca. 60% current efficiency. The only significant by-products were ethyl propionate (3% yield requiring ca. 3% of the current input) and the Michael adduct<sup>6</sup> (1% yield); the latter could be degraded by base catalysis to its components (Eq. [7] below). It was concluded that 40% of the current input was consumed in the wasteful iodine-iodide cycle (Eq. [5]).

The quantitative data obtained by analysis of the product solutions of experiments 33 and 34<sup>7</sup> are given in Table II; the chemical yields and current efficiencies based on these same experiments are given in Table III.

### Discussion

Co-electrolysis in an undivided cell of acrylate and malonate esters in an inert solvent with an iodide supporting electrolyte involves the following major reactions.



In addition, the following principal side reactions occurring at or near the electrode or in the bulk of solution can lead to by-products or decrease of current efficiency



<sup>5</sup> In many "screening" experiments only ratios of products and by-products were determined.

<sup>6</sup> Table I, footnotes P and Q.

<sup>7</sup> Similar results of lesser precision were obtained in experiments 29-32.

<sup>8</sup> We are omitting from this discussion, since it is irrelevant to the results, the still moot question of whether the adipate ester dianion arises by an ec (i.e., dimerization of two acrylate anion radicals) or ece mechanism (i.e., attack of acrylate ester anion radical upon acrylate ester followed by reduction of the dimer ester anion radical).

Table I. Co-electrolyses of ethyl acrylate and diethyl malonate

Expt. No.	Cell <sup>a</sup>	Anode	Cathode	V	mA	mF	Electrolyte (g)	Solvent (ml)	Acrylate (mM)	Malonate (mM)	Product ratios <sup>b</sup>			Other
											Adipate	Bimalonate	Michael adduct <sup>c</sup>	
1	A <sup>c</sup>	Graphite	Graphite	4.5	48	—	KI (0.12)	MeCN (57)	50 <sup>m</sup>	50 <sup>m</sup>	0.51	0.46	1.0	
2	A	Graphite	Graphite	40	200-300	—	KI (0.12)	MeCN (57)	50 <sup>m</sup>	50 <sup>m</sup>	0.19	0.19	1.0	
3	A	Graphite	Graphite	9	300	—	KI (0.25)	MeCN (57) <sup>d</sup>	50 <sup>m</sup>	50 <sup>m</sup>	0.91	1.0	1.0	
4	A	Graphite	Graphite	7	200	48	KI (0.25)	MeCN (50 + 10)	50 <sup>m</sup>	50 <sup>m</sup>	0.86	1.0	1.0	
5	B	Graphite <sup>e</sup>	Graphite	4	270	25	KI (0.2)	MeCN (15 + 5.5)	25 <sup>n</sup>	25 <sup>n</sup>	2.1	2.3	1.0	
6	B	Graphite <sup>e</sup>	Graphite	4	270	30	Bu <sub>4</sub> NI (1.0)	MeCN (15 + 5.5)	25 <sup>n</sup>	25 <sup>n</sup>	0.6	0.6	1.0	Propionate?
7	B	Graphite <sup>f</sup>	Graphite	4	270	30	Bu <sub>4</sub> NI (1.0)	MeCN (15.5 + 5)	25 <sup>n</sup>	25 <sup>n</sup>	5.7	7.0	1.0	Propionate?
8	B	Graphite <sup>f</sup>	Graphite	7.5	3000	32	Bu <sub>4</sub> NI (1.0)	MeCN (15.5 + 5)	25 <sup>n</sup>	25 <sup>n</sup>	>14	14.4	1.0	Propionate?
9	B	Graphite <sup>f</sup>	Graphite	13	3000	41	Bu <sub>4</sub> NI (1.0)	MeCN (15.5 + 5)	25 <sup>n</sup>	25 <sup>n</sup>	6.5	7.9	1.0	Propionate?
10	B	Graphite <sup>f</sup>	Graphite	7.5	1200	37	Bu <sub>4</sub> NI (1.0)	H <sub>2</sub> O (15)	25 <sup>n</sup>	37 <sup>m</sup>	0.73	1.74	1.0	
11	B	Graphite <sup>f</sup>	Lead	10	1000	28	Bu <sub>4</sub> NI (2.0)	MeCN (15 + 5.2)	25 <sup>n</sup>	25 <sup>m</sup>	3.2	5.0	1.0	
12	B	Graphite <sup>f</sup>	Lead	4	250	33	Bu <sub>4</sub> NI (1.0)	MeCN (10 + 5)	25 <sup>n</sup>	25 <sup>m</sup>	1.9	2.1	1.0	
13	B	Graphite <sup>f</sup>	Graphite	8.9	1000	37	Bu <sub>4</sub> NI (1.0)	MeCN (20)	3 <sup>m</sup>	30 <sup>m</sup>	0.54	0.31	1.0	
14	A	Graphite	Graphite	20 <sup>b</sup>	>800	50	Bu <sub>4</sub> NI (1.0)	MeCN (40)	100 <sup>m</sup>	100 <sup>m</sup>	0.74	0.047	1.0	
15	D	Graphite	Graphite	40-60	500	25	KI (satd)	MeCN (60)	100 <sup>m</sup>	100 <sup>m</sup>	1.4	1.4	1.0	
16	D	Graphite	Graphite	35-40	500	50	LiH (0.8)	MeCN (60)	50 <sup>m</sup>	50 <sup>m</sup>	2.3	0.83	1.0	
17	D	Graphite	Graphite	35	300-500	100	Bu <sub>4</sub> NI (2.8)	MeCN (100)	100 <sup>m</sup>	100 <sup>m</sup>	1.3	1.45	1.0	
18	D	Graphite	Graphite	30-37	500	41	Bu <sub>4</sub> NI (3.0)	MeCN (55) + t-BuOH (10)	50 <sup>m</sup>	50 <sup>m</sup>	None	None	None	
19	D	Graphite	Graphite	35-70	500	41	Bu <sub>4</sub> NI (3.0)	t-BuOH (55) <sup>l</sup>	50 <sup>l</sup>	50 <sup>l</sup>	1.0	0	0	Acrylate by-dimer? <sup>g</sup>
20	E	Pt	Hg	105	—	—	Bu <sub>4</sub> NI (1.0) <sup>l</sup>	t-BuOH (55) <sup>l</sup>	50 <sup>l</sup>	50 <sup>l</sup>	2.34	2.57	1.0	No diadduct <sup>h</sup>
21	E	Pt	Hg	—	100-200	—	Bu <sub>4</sub> NI (0.75) <sup>l</sup>	t-BuOH (50) <sup>l</sup>	50 <sup>l</sup>	50 <sup>l</sup>	2.54	2.85	1.0	No diadduct
22	B	Graphite <sup>f</sup>	Graphite	7.5	1000	27.5	Bu <sub>4</sub> NI (1.0)	MeCN (15 + 5.5)	25 <sup>n</sup>	25 <sup>n</sup>	2.20	2.60	1.0	No diadduct
23	B	Graphite <sup>f</sup>	Graphite	7.5	1000	26	Bu <sub>4</sub> NI (1.0)	MeCN (15 + 5.5)	25 <sup>n</sup>	25 <sup>n</sup>	2.20	2.60	1.0	No diadduct
24	B	Graphite <sup>f</sup>	Graphite	7.5	1000	24	Bu <sub>4</sub> NI (1.0)	MeCN (15 + 5.5)	25 <sup>n</sup>	25 <sup>n</sup>	3.62	8.62	1.0	No diadduct; unknown
25	B	Graphite <sup>f</sup>	Graphite	7.5	1000	39	Bu <sub>4</sub> NI (1.0)	MeCN (15 + 5.5)	25 <sup>n</sup>	25 <sup>n</sup>	2.64	4.20	1.0	—
26	B	Graphite <sup>f</sup>	Graphite	7.5	1000	29	Bu <sub>4</sub> NI (1.0)	MeCN (15 + 5.5)	25 <sup>n</sup>	25 <sup>n</sup>	4.33	4.90	1.0	—
27	B	Graphite <sup>f</sup>	Graphite <sup>h</sup>	7.5	1000	27	Bu <sub>4</sub> NI (1.0)	MeCN (12 + 5.5)	25 <sup>n</sup>	25 <sup>n</sup>	15.8	19.1	1.0	Small
28	B	Graphite <sup>f</sup>	Lead	3.75	1000	34	Bu <sub>4</sub> NI (1.0)	MeCN (12 + 5.5)	25 <sup>n</sup>	25 <sup>n</sup>	21.1	26.9	1.0	Unknown
29	C	Graphite <sup>f</sup>	Lead	3.75	1000	34	Bu <sub>4</sub> NI (1.0)	MeCN (12 + 5.5)	25 <sup>n</sup>	25 <sup>n</sup>	22.4	26.0	1.0	—
30	C	Graphite <sup>f</sup>	Lead	3.75	1000	27	Bu <sub>4</sub> NI (1.0)	MeCN (12 + 5.5)	25 <sup>n</sup>	25 <sup>n</sup>	20.0	28.6	1.0	—
31	C	Graphite <sup>f</sup>	Lead	3.75	1500	31	Bu <sub>4</sub> NI (1.0)	MeCN (12 + 5.5)	25 <sup>n</sup>	25 <sup>n</sup>	22.0	30.4	1.0	—
32	C	Graphite <sup>f</sup>	Lead	3.5	1100	31	Bu <sub>4</sub> NI (1.0)	MeCN (12 + 5.5)	25 <sup>n</sup>	25 <sup>n</sup>	22.6	27.1	1.0	—
33	C	Graphite <sup>f</sup>	Lead	7.5	1100	35.6	Bu <sub>4</sub> NI (1.0)	MeCN (12 + 5.5)	25 <sup>n</sup>	25 <sup>n</sup>	23.0	27.0	1.0	—
34	C	Graphite <sup>f</sup>	Lead	6.0	1100	35.6	Bu <sub>4</sub> NI (1.0)	MeCN (12 + 5.5)	25 <sup>n</sup>	25 <sup>n</sup>	2.45	2.51	1.0	—
35	C	Graphite <sup>f</sup>	Lead	7.0	1100	35.6	Bu <sub>4</sub> NI (1.0)	MeCN (12 + 5.5)	25 <sup>m</sup>	25 <sup>m</sup>	0.163	0.0543	1.0	0.072 diadduct
36	C	Graphite <sup>f</sup>	Lead	5	1100	32.6	Bu <sub>4</sub> NBF <sub>4</sub>	MeCN (12 + 5.5)	25 <sup>n</sup>	25 <sup>n</sup>	—	—	—	—

<sup>a</sup> Cell A: large test tube, Cell B: hollowed graphite cylinder as one electrode, graphite rod as other electrode/stirrer; effective areas: cylinder, 50 cm<sup>2</sup>, rod, 22 cm<sup>2</sup>. Cell C: similar to A but cylinder (cathode) is Pb lined. Cell D: three-necked flask. Cell E: divided, sintered disk.

<sup>b</sup> Areas under vpc curves.

<sup>c</sup> Attempt to determine results obtained by H. G. Thomas and E. Lux as reported sketchily in *Tetrahedral Letters*, 965 (1972) and a personal communication.

<sup>d</sup> At reflux.

<sup>e</sup> Cylinder.

<sup>f</sup> Rod.

<sup>g</sup> Redistilled methyl acrylate used.

<sup>h</sup> A-C current.

<sup>i</sup> In anolyte.

<sup>j</sup> Cathode cylinder pores filled with Vydex 525 (by DH).

<sup>k</sup> Cathode area ca. 38 cm<sup>2</sup>, anode area ca. 23 cm<sup>2</sup>.

<sup>l</sup> Added at once.

<sup>m</sup> Added dropwise.

<sup>n</sup> (EtOCO)<sub>2</sub>CHCH<sub>2</sub>COOEt.

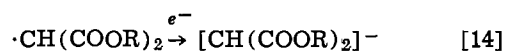
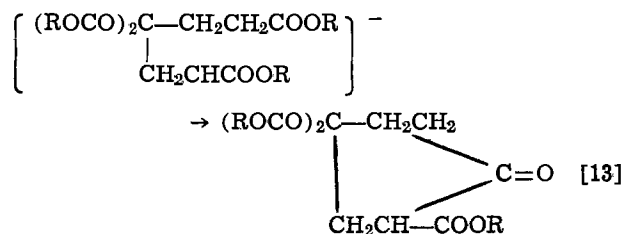
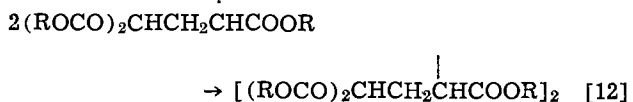
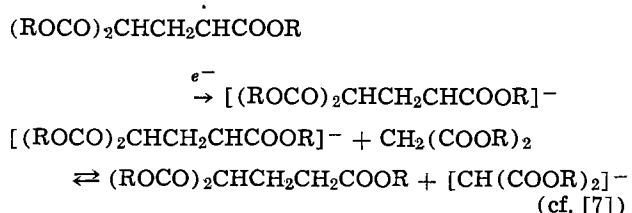
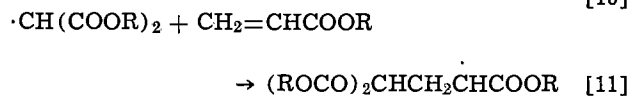
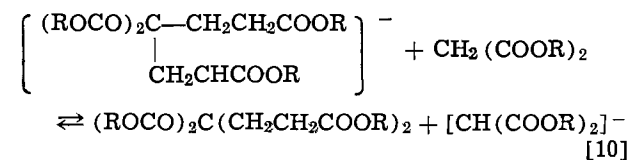
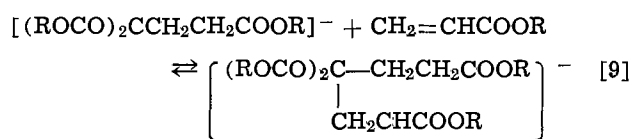
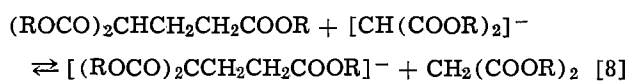
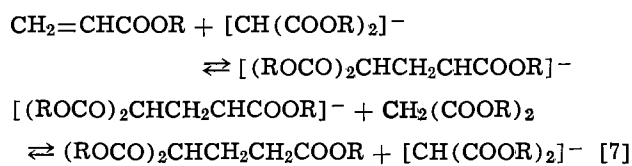
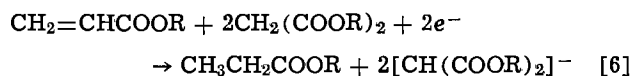
<sup>o</sup> (EtOCO)<sub>2</sub>C(CH<sub>2</sub>CH<sub>2</sub>COOEt)<sub>2</sub>.

Table II. Analyses of products from experiments 33-34

Compound	Experiment 33			Experiment 34		
	G	mM	Equiv. mF <sup>b</sup>	G	mM	Equiv. mF <sup>b</sup>
Et acrylate <sup>a</sup>	0.320	3.20	—	0.341 <sup>a</sup>	3.41	—
Et <sub>2</sub> malonate <sup>d</sup>	0.448	2.80	—	0.469	2.93	—
Et <sub>2</sub> adipate	2.11	10.4	20.8	2.08	10.3	20.6
Et <sub>2</sub> bimalonate	3.50	11.0	22.0	3.25	10.2	20.6
Et propionate	0.0609	0.0597	1.19	0.562	0.546	1.09
Michael adduct	0.0621	0.239	—	0.594	0.228	—

<sup>a</sup> Charged 25.2 mM.<sup>b</sup> Input 35.6 mF.<sup>c</sup> Charged 25.0 mM.<sup>d</sup> Charged 25.0 mM.Table III. Summary of results for experiments 33-34<sup>a</sup>

	Conver- sion (%)	Chemical yield (%)		Current efficiency (%)
		Based on acrylate consumed	Based on malonate consumed	
Ethyl acrylate	86.5-87.5	—	—	—
Diethyl malonate	88.5	—	—	—
Adipate	—	94.5-95.5	—	57.8-58.5
Bimalonate	—	—	92-99	57.3-61.7
Propionate	—	2.5-3.0	—	3.06-3.32
Michael adduct	—	1.0	1.0	—

<sup>a</sup> It will be noted that 99% of the acrylate, 94-100% of the diethyl malonate and ca. 60% of the current used are accounted for.

The challenge of maximizing the yield of and the current efficiency for only two products, adipate, the hydrodimer, and bimalonate, the dehydrodimer, in the midst of a welter of co-existing obnoxious reaction courses requires confrontation by weapons assembled from several fields of current interest to organic electrochemists: reductive coupling (8), oxidative coupling (9), indirect organic electrochemical reactions (10),  $pK_a$ 's of electrogenerated anion radicals and dianions (11) and of carbon acids (12), rates of proton transfer by carbon acids (13), catalysis of the Michael reaction by electrogenerated bases (14), addition of electrogenerated radicals to vinylic compounds (15), and others. In all cases (Eq. [1]-[14]) rate data are of the essence; in most cases these data are lacking, particularly for competitive reactions and in an environment in which intermediate electrophoric molecules can undergo not only chemical reactions but electron transfers with the appropriate electrode or with other intermediate species. These considerations may previously have served as a deterrent to vigorous activity in the area of paired organic electrochemical syntheses.

The following salient points emerge from an examination of the results summarized in Table I:

1. In our hands the procedure of Thomas and Lux yielded about equimolar amounts of adipate and bimalonate but the Michael adduct was a very important by-product (Expt. 1). The situation was improved (Expt. 3) if the reaction was conducted at reflux.

2. Slow addition of the acrylate to the electrolysis mixture (Expt. 5) reduced the relative yield of Michael adduct considerably, even though KI was still used as electrolyte.

3. Changing the electrolyte to Bu<sub>4</sub>NI drastically improved the yield of desired products (Expts. 7-9) provided the rotating rod rather than the cylinder was used as anode. This may be due to less tight ion pairing of R<sub>4</sub>N<sup>+</sup> with the anions or to the greater separation of Bu<sub>4</sub>N<sup>+</sup> discharge (compared to K<sup>+</sup> discharge) from the acrylate reduction potential.

4. There is an optimum current density (Expt. 8 vs. 7 and 9).

5. There is no advantage here in using Pb as cathode instead of graphite (Expt. 12).

6. Other undivided laboratory cells, which do not allow as rapid mixing as Cell B, gave poorer results (Expt. 14-19).

7. A divided cell gave the poorest results of all.

8. Ethyl acrylate gave better results than methyl acrylate (Expt. 8 vs. Expt. 10).

9. Expt. 22-27: None of these gave as good results as were previously obtained (Expt. 8) using the same all-graphite cell. The cathode surface, particularly the porosity, had apparently changed due to gradual removal of the polyethylene filler which had been applied.

10. Expt. 28: Applying a new filler treatment, this time with polytetrafluoroethylene, improved matters somewhat but did not restore the good performance that had been found in Expt. 8. It was concluded that, since the cathode surface (Pb) was less likely to have changed in Cell C than the graphite surface had changed in Cell B, it was desirable to proceed using only Cell C.

11. Expt. 29-32: Very favorable reproducible results were obtained. The  $< 100\%$  current efficiency is, undoubtedly, due to the unproductive reaction  $I^{\cdot-} \rightleftharpoons I^{\circ}$ .

In an undivided cell this can be minimized by control of temperature, rate of stirring, distance between the electrodes, etc., i.e., mass transfer of  $I^{\circ}$  from anode to cathode, charge-transfer from cathode to  $I^{\circ}$ , and rate of reaction of  $I^{\circ}$  with malonate anion must be determined and optimized.

12. Expt. 33-34: These were done under approximately the same conditions as Expt. 29-32, but greater care was taken in measuring the inputs, making quantitative transfers, calibrating the ammeter, etc. The material balances and current efficiencies are shown in Tables II and III.

13. Expt. 35: Reconfirmed that charging all acrylate and malonate before electrolysis gave unfavorable results.

14. Expt. 36: Reconfirmed that direct anodic oxidation of malonate anion (using a  $BF_4^-$  electrolyte) gave much poorer results than indirect oxidation via anodically generated  $I_2$ .

Experiments, not detailed here, on the co-electrolysis of acrylonitrile and diethyl malonate showed that the expected products (adiponitrile and bimalonate tetraester) were, indeed, obtained but that control of by-product formation (propionitrile and Michael adduct) was more difficult. The use of proton donors (e.g., acetylacetone) as precursors of dehydrodimers would also be anticipated to present problems (9).

The extension of hydrodimerization-dehydrodimerization as a class of paired syntheses similar in scope to reductive and oxidative couplings alone would be greatly accelerated when the rate data referred to above become available.

#### Acknowledgment

We wish to thank Dr. John Wagenknecht and Kenneth Koncki for supervising the fabrication of the

graphite cells and David Hemmerly for polymer treatment of these cells.

Manuscript received Oct. 29, 1975. This was Paper 280 presented at the Washington, D.C., Meeting of the Society, May 2-7, 1976.

Any discussion of this paper will appear in a Discussion Section to be published in the December 1976 JOURNAL. All discussions for the December 1976 Discussion Section should be submitted by Aug. 1, 1976.

Publication costs of this article were partially assisted by Monsanto Company.

#### REFERENCES

1. M. Ya. Fioshin, *Khim. Prom. (Moscow)*, **44**, 882 (1968); *Chem. Abstr.*, **70**, 63434k (1969).
2. A. T. Kuhn, "Industrial Electrochemical Processes," p. xii, Elsevier Publishing Co., Amsterdam-London-New York (1971).
3. M. M. Baizer and J. L. Chruma, *J. Org. Chem.*, **37**, 1951 (1972).
4. R. Dietz and H. Lund, in "Organic Electrochemistry," M. M. Baizer, Editor, p. 823, Marcel Dekker, Inc., New York, (1973).
5. G. Cauquis, in Ref. (4), p. 44.
6. H. G. Thomas and E. Lux, *Tetrahedron Letters*, 965 (1972).
7. T. Okubo and S. Tsutsumi, *Bull. Chem. Soc. Japan*, **37**, 1794 (1964).
8. M. M. Baizer, in "Organic Electrochemistry," M. M. Baizer, Editor, Chap. XIX, Marcel Dekker, New York (1973).
9. K. Nyberg, in Ref. (8), Chap. XX.
10. R. Dietz and H. Lund, in Ref. (8), Chap. XXIV; R. Clarke, A. Kuhn, and E. Okoh, *Chem. in Brit.*, **11**, 59 (1975).
11. T. Troll and M. M. Baizer, *Electrochim. Acta*, **20**, 33 (1975).
12. D. W. Earls, J. R. Jones, and T. G. Rumney, *J. Chem. Soc., Perkin II*, 54 (1975).
13. E.g., R. N. Nasirov and S. P. Solodovnikov, *Bull. Acad. Sci. USSR, Div. Chem. Sci.*, **21**, 2047 (1972).
14. M. M. Baizer, J. L. Chruma, and D. A. White, *Tetrahedron Letters*, 5209 (1973).
15. E.g., L. Ebersson, Ref. (8), p. 489.

# Electrogenerated Chemiluminescence

## XXVI. Systems Involving Tetraarylpyrroles, Tetraphenylfuran, and Tetraphenylthiophene

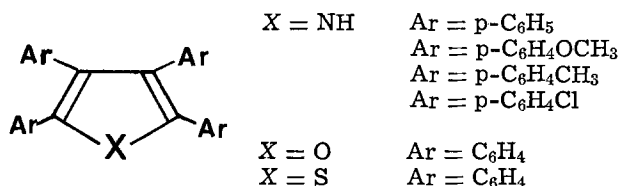
Michel Libert and Allen J. Bard\*

Department of Chemistry, The University of Texas at Austin, Austin, Texas 78712

### ABSTRACT

The production of light upon the electron transfer reaction of electrogenerated radical ions of tetraarylpyrroles [aryl = anisyl (TAP), phenyl (TPP), tolyl (TTP), p-chloro-phenyl (TCPP)], tetraphenylfuran (TPF), and tetraphenylthiophene (TPT) in systems containing these compounds alone in acetonitrile solutions or in mixed systems containing naphthalene, 2,5-diphenyl-1,3,4-oxadiazole, benzophenone, and tri-p-tolylamine is reported. Emission which corresponds to the fluorescence of the TAP, TPP, TTP, TPF, and TPT, as well as longer wavelength emission attributed to exciplex emission for some mixed systems, is observed. The singlet and triplet level energies of the compounds of interest are estimated and their cyclic voltammetric behavior described briefly.

The usual basic requirements for a system which produces light upon the electron transfer reaction of electrogenerated species, e.g.,  $A^{\cdot -}$  and  $D^{\cdot +}$  (electrogenerated chemiluminescence or ECL), include the formation of stable radical ions, the fluorescence of at least one of the parent species (A and D), and sufficient free energy release in the  $A^{\cdot -}/D^{\cdot +}$  reaction to form an excited state. Moreover, efficient ECL systems, such as those involving 9,10-diphenylanthracene and rubrene, involve bulky molecules in which steric effects appear to hinder formation of complexes between the reactant species. Previous studies (1-6) have shown that tetra-aryl substituted five-member ring compounds (pyrroles, furans, and thiophenes)



form stable radical cations upon electrochemical oxidation. Although their luminescent properties and their behavior upon reduction have not been previously investigated, they appeared to be interesting compounds for ECL studies either as the source of both radical ions or as the radical cation source in mixed systems.

### Experimental

The preparation and purification of the pyrrole, furan, and thiophene compounds has been described (1-6). Tri-p-tolylamine (TPTA), naphthalene (NAP), benzophenone (BP), 2,5-diphenyl-1,3,4-oxadiazole (PPD), acetonitrile (ACN), and tetra-n-butylammonium perchlorate (TPAP) were obtained and treated as previously reported (7, 8). The benzene was treated with sodium for 48 hr and then distilled and degassed by four freeze-pump-thaw cycles. All solutions were prepared in an inert atmosphere glove box. Solution preparation, experimental procedures, apparatus, and instrumentation were as previously described (7, 8).

### Results and Discussion

Fluorescence spectra of these compounds have not been previously described. These were obtained for millimolar solutions in acetonitrile and the position of the emission maxima are listed in Table I along with

the u.v. absorbance maxima obtained in previous studies (1-6). The observed emission spectra were not as well defined as those reported for similar, less sterically hindered compounds, such as 4,5-diphenylimidazole (14) so that location of the 0-0 band was not possible. The reported singlet energies ( $E_s$ ) in Table I were obtained by averaging the energies of the emission spectra and absorbance maxima. This method gives  $E_s = 3.45$  eV for TPF as compared to a value of 3.55 eV for 2,5-diphenylfuran as obtained from the well-resolved 0-0 band in the spectrum given by Berlman (14). Cyclic voltammetry (CV) and ECL experiments were generally performed in 2-3 mM solutions of the compound of interest in 0.1M TBAP-ACN. For

tetraphenylpyrrole	(TPP)
tetraanisylpyrrole	(TAP)
tetratolylpyrrole	(TTP)
tetra-p-chlorophenylpyrrole	(TCPP)
tetraphenylfuran	(TPF)
tetraphenylthiophene	(TPT)

TTP and TCPP, which were not soluble in ACN, a 1:1 mixture of ACN-benzene was employed as solvent. A typical cyclic voltammogram, that for TPP, is shown in Fig. 1. The CV results, given in Table I, show that the radical cations of the pyrroles are very stable while those of the furan and thiophene are moderately stable

Table I. Electrochemical and spectroscopic data<sup>a</sup>

	Cyclic voltammetry <sup>b</sup>				Spectroscopy		
	Oxidation		Reduction		u.v. maxm. absorpt (nm)	Fluorescence (nm) maxm.	$E_s$ eV
$+E_{pa}^c$ V vs. SCE	$i_{pa}/i_{pc}$	$-E_{pc}$ V vs. SCE	$i_{pa}/i_{pc}$				
TAP	0.66	1.0	<2.9	0	307	403	3.49
TPP	0.90	1.0	2.78	0	313	397	3.49
TTP	0.81	1.0	≈2.85	0	311	403	3.47
TCPP	1.06	1.0	2.52	0	317	414	3.38
TPF	1.19	0.8	2.47	≈1	324	394	3.45
TPT	1.38	0.9	2.30	≈1	308	407	3.46

<sup>a</sup> For other compounds in this study: Naphthalene:  $E_{pc} = -2.66$  V/SCE (7),  $E_s = 3.99$  eV,  $E_T = 2.63$  eV (10), PPD:  $E_{pc} = -2.17$  V/SCE (8),  $E_s = 3.58$  eV (8), BP:  $E_{pc} = -1.91$  V/SCE (7),  $E_s = 3.22$  eV,  $E_T = 2.97$  eV (11). TPTA:  $E_{pc} = 0.84$  V/SCE (7),  $E_s = 3.51$  eV,  $E_T = 2.96$  eV (12).

<sup>b</sup> For 0.1M TBAP/ACN solutions (except for TTP and TCPP which used 1:1 ACN:benzene); scan rate, 200 mV/sec.  $E_{pa}$  and  $E_{pc}$  are anodic and cathodic peak potentials,  $i_{pa}$  and  $i_{pc}$  anodic and cathodic peak currents.

<sup>c</sup>  $E_{pa}$  vs. (SCE) =  $E_{1/2}$  (vs. Ag-AgCl) - 0.28 (9).

\* Electrochemical Society Active Member.

Key words: electrochemiluminescence, radical ions, fluorescence, nonaqueous solvents, cyclic voltammetry.

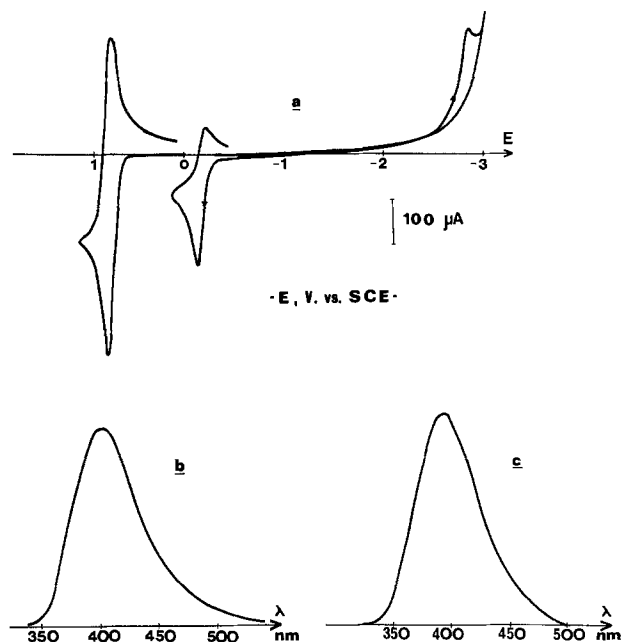


Fig. 1. TPP(-)/TPP(+) system. (a) Cyclic voltammogram of 3.4 mM TPP in 0.1M TBAP-ACN at Pt electrode; scan rate, 200 mV/sec. (b) ECL of the above solution at 500 Hz. (c) Fluorescence spectrum of  $3.4 \times 10^{-5}$  M TPP in ACN;  $\lambda_{exc} = 323$  nm.

during the time scale of the experiment. For the pyrroles the reductions occur close to the background reduction process with no anodic current observed on scan reversal. For TPF and TPT a clear anodic peak is observed in CV, with  $i_{pa} = i_{pc}$  (where  $i_{pa}$  and  $i_{pc}$  are the anodic and cathodic peak currents).

One series of ECL experiments consisted of electro-generation of the radical cations of the compounds of interest ( $R^{\cdot+}$ ) and observing the emission during generation of the radical anion of the same molecule ( $R^{\cdot-}$ ) or of NAP, PPD, or BP ( $A^{\cdot-}$ ) (all of which form relatively stable anion radicals). In another series of experiments, the emission from the reaction of the compound radical anion ( $R^{\cdot-}$ ) with the stable electro-generated radical cation of TPTA (7, 12) ( $D^{\cdot+}$ ) was studied. The ECL results for typical systems are shown in Fig. 1-3, and the results are summarized in Table II. Except for TCPP, the systems involving the pyrrole, TPF, or TPT alone, i.e., as the source of both  $R^{\cdot-}$  and

$R^{\cdot+}$ , showed emission similar to that of the fluorescence of the parent compound. The reaction enthalpy (13),  $\Delta H^{\circ}$ , in these cases was about the same as  $E_s$  so that direct population of the excited singlet state upon electron transfer is possible. In reactions with NAP, PPD, or BP as acceptors or with TPTA as a donor, as well as for TTP, TPF, and TPT alone, emissions at longer wavelengths were also observed. These will be discussed in more detail for a few of the cases investigated.

TPP(-)/TPP(+).—The cyclic voltammogram of TPP in 0.1M TBAP/ACN (Fig. 1) illustrates the stability of TPP $^{\cdot+}$  and the instability of the radical anion. After a cathodic scan in which the radical anion is produced, a reverse scan shows the appearance of a reversible system of  $-0.23$  V vs. SCE. The nature of this system, probably originating from a reaction of the radical anion, was not investigated further, but was observed with all of the pyrroles investigated in this study. The ECL emission observed in this case was quite bright and stable with time for a frequency of pulsing of 500 Hz (Fig. 1).

NAP(-)/TPP(+).—The reaction enthalpy for the reaction of the rather stable NAP radical anion with TPP $^{\cdot+}$  is somewhat less than  $E_s$  of TPP and much less than  $E_s$  of NAP. The observed emission consists of a band at 400 nm, where TPP fluoresces, and a longer wavelength band at 445 nm. The former could originate via triplet-triplet annihilation of  $^3$ TPP while the latter band can be ascribed to a TPP-NAP exciplex. NAP has been shown to form exciplexes with various donors in ECL in ACN solutions with the energy of the exciplex emission,  $E_{ex}$  correlating with the  $E_{pa}$  of the donor according to Eq. [1] [note that the same spectrofluorometer and photomultiplier tube were employed in this study and the previous one (7)]

$$E_{ex} = 1.27E_{pa} + 1.60 \quad [1]$$

The  $E_{pa}$  of TPP of 0.90 V vs. SCE yields an  $E_{ex}$  of 2.73 eV (equivalent to emission at 450 nm) with this equation, which is very close to the experimentally observed value. The longer wavelength emission observed for the PPD(-)/TPP(+) can probably also be ascribed to an exciplex. To examine if TPP-NAP exciplexes could be observed in photoexcitation experiments, the quenching of NAP fluorescence by TPP was investigated. Although TPP was an effective quencher of NAP fluorescence in both ACN and  $CH_2Cl_2$  solutions, no longer wavelength emission was observed. Thus, as has been observed previously (7), formation of the exciplex on direct reaction of the radical ions is

Table II. Summary of ECL results<sup>a</sup>

Compound (R)	System alone R(-)/R(+)			Systems with compound as donor and following acceptors									Compound as acceptor and TPTA as donor R(-)/TPTA(+)		
	$-\Delta H^{\circ}$ eV	$\lambda_{max}$ ECL nm (eV)	$I_{rel}$	Naphthalene NAP(-)/R(+)			PPD PPD(-)/R(+)			Benzophenone BP(-)/R(+)			$-\Delta H^{\circ}$ eV	$\lambda_{max}$ ECL nm (eV)	$I_{rel}$
				$-\Delta H^{\circ}$ eV	$\lambda_{max}$ ECL nm (eV)	$I_{rel}$	$-\Delta H^{\circ}$ eV	$\lambda_{max}$ ECL nm (eV)	$I_{rel}$	$-\Delta H^{\circ}$ eV	$\lambda_{max}$ ECL nm (eV)	$I_{rel}$			
TAP	>3.4	393 (3.15)	1	3.16	No		2.67	395 (3.13)	0.1	2.41	No				
TPP	3.52	397 (3.12)	250	3.40	400 (3.09)	3	2.91	400 (3.09)	1	2.65	No	3.46	412 (3.00)	15	
TTP	$\approx$ 3.5	410 (3.02)	15	3.31	445 (2.78)			515 (2.40)	0.5			$\approx$ 3.5	395 (3.13)	1	
TCPP	3.43	460 (2.69)	0.4	3.56	565 (2.19)	2	2.82	407 (3.04)	0.4	2.56	No	3.20	505 (2.38)		
		No			No		3.07	No		2.81	No	3.20	4.5 (3.0)	Very weak	
TPF	3.50	408 (3.03)	3	3.69	400-500 (3.09-2.47)	0.3	3.20	435 (2.84)	5	2.94	490 (2.53)	2	3.15	415 (2.98)	
		480 (2.58)						485 (2.55)					470 (2.63)	2	
													520 (2.38)		
TPT	3.52	$\approx$ 412 (3.00)	300	3.88	437 (2.83)	90	3.39	437 (2.83)	60	3.13	418 (2.96)	100	2.98	418 (2.96)	
		437 (2.83)									433 (2.86)			520 (2.45)	

<sup>a</sup>  $\Delta H^{\circ}$  is the enthalpy of the radical ion reaction, calculated using the data in Table I and the equation [Ref. 13]):  $-\Delta H^{\circ} = E_{pa} - E_{ps} - 0.16$  (eV);  $I_{rel}$  is the approximate relative intensity of the ECL (dependent also on frequency and solution conditions) with respect to the PPD(-)/thianthrene(+) system, taken as having  $I_{rel} = 100$ ;  $\lambda_{max}$  ECL is position of ECL peak(s), generally with uncertainty of  $\pm 4$  nm.

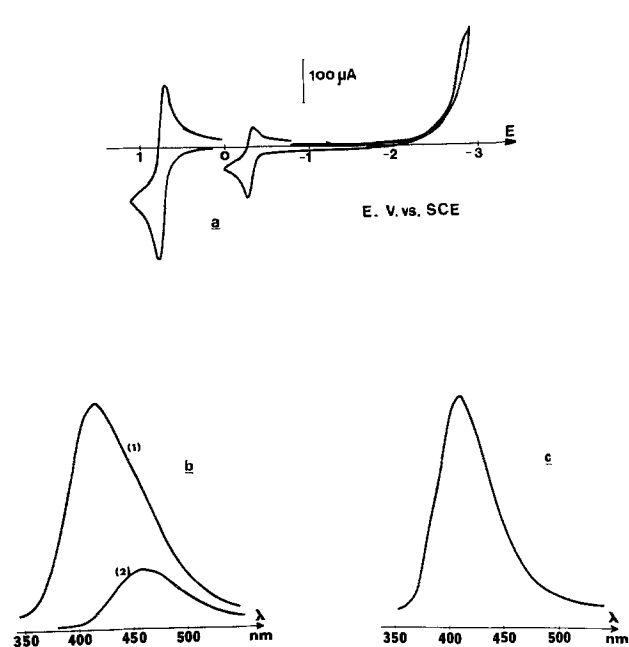


Fig. 2. TTP(-)/TTP(+) system. (a) Cyclic voltammogram of 2.6 mM TTP in 0.1M TBAP in ACN-benzene at Pt electrode; scan rate, 200 mV/sec. (b) ECL of the above solution at (1) 100 Hz and (2) 1 Hz (sensitivity  $\times 8$ ; envelope of individual pulses). (c) Fluorescence spectrum of the above solution;  $\lambda_{exc} = 367$  nm.

a more efficient route than production via photo-excitation. The low intensity of the ECL in this case probably results from dissociation of the exciplex to the ions or to  $^3\text{TTP}$  which undergoes quenching and triplet-triplet annihilation reactions.

**TTP(-)/TTP(+).**—A cyclic voltammogram of TTP (Fig. 2) shows formation of a stable radical cation but the reduction of TTP can hardly be distinguished from the background reduction at *ca.*  $-2.85\text{V}$ , and the TTP radical anion is quite unstable. Just as with TPP, a new reversible system appears during CV at  $-0.26\text{V}$  following a reduction scan. In spite of the instability of the anion, the system shows quite stable ECL consisting of two peaks (Fig. 2). The more intense at 410 nm corresponds to  $^1\text{TTP}^*$  formed directly upon the energy sufficient radical ion reaction; this peak consists of emission during the cathodic pulses and shows maximum intensity at higher frequencies (*ca.* 500 Hz). The second peak consists of emission only on anodic pulses and appears only at low frequencies, showing a maximum intensity at 1 Hz. After about 1 hr of ECL experiments, the CV and the fluorescence spectrum are essentially the same as the starting solution. While the longer wavelength peak could be attributed to an excimer, this doesn't appear to be reasonable since it is only found on anodic pulses, it disappears at higher frequencies, and it is not observed for the structurally similar TPP. A better explanation for this emission invokes the production of a reactant during the cathodic pulse which reacts with radical cation to produce light. At high frequencies the extent of the  $\text{TTP}^-$  decomposition reaction would be small, but at lower frequencies appreciable side-product would be produced. Evidence of this side-product is not obtained by fluorescence measurements after extended ECL, as is usually found for cases in which emission is observed from radical ion decomposition products (15, 16), so that the side-product, if formed, decomposes during or after the electron transfer reaction.

**TPT(-)/TPT(+).**—Both radical cation and anion of TPT are stable on the CV time scale (Fig. 3) and the ECL emission which results from the radical ion electron transfer reaction is rather intense with an emission maximum located between 412 and 438 nm, vary-

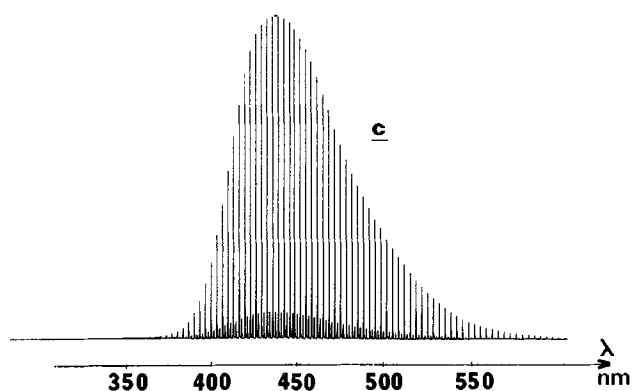
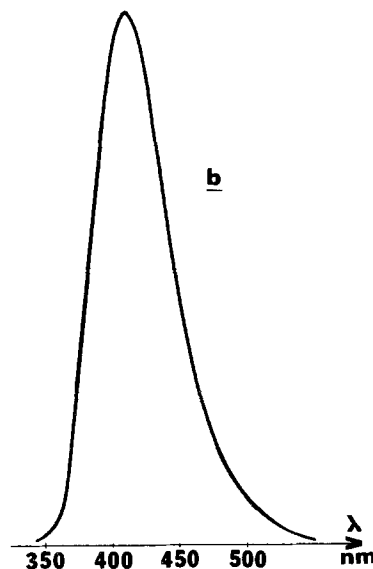
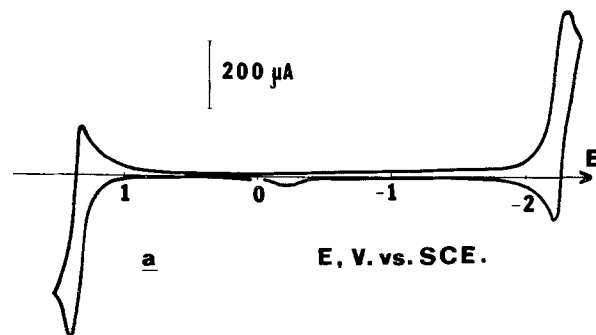


Fig. 3. TPT(-)/TPT(+) system (a) Cyclic voltammogram of 3.4 mM TPT in 0.1M TBAP-ACN at Pt electrode; scan rate, 200 mV/sec. (b) Fluorescence spectrum of 1.8 mM TPT in ACN. (c) ECL of 3 mM TPT in 0.1M TBAP-ACN at 0.25 Hz.

ing from experiment to experiment. Similar results are obtained when NAP, PPD, or BP are the sources of the radical anions. For the BP(-)/TPT(+) system two separate peaks at 418 and 433 nm can be distinguished. In all cases the electrodes are filmed after extended ECL experiments (*ca.* half-hour), resulting in changes in the CV. This filming might account for the lack of reproducibility of the observed emission peak location, if the ECL intensity was changing with time while the spectrum was being recorded. The emission at 410-415 nm is probably that of  $^1\text{TPT}^*$  formed either directly, or for the case of NAP and BP, via triplet-triplet annihilation. The emission at 437 nm could be from a

decomposition product of  $\text{TPT}^+$ . Previous studies (6) have shown that *cis*-dibenzoylstilbene can form from decomposition of the radical cation. A solution of this species, prepared by a previously published procedure (17) did not show fluorescence, however.

**TPT(-)/TPTA(+).**—The ECL in this case shows two distinct peaks: one at 418 nm for anodic pulses and one at 520 nm for cathodic ones. The first peak is again attributable to  $^1\text{TPT}^*$  formed on triplet-triplet annihilation while the longer wavelength emission can be attributed to an exciplex. The emission maximum observed in this case agrees quite well with the relation found for exciplexes formed in ECL resulting from reaction of  $\text{TPTA}^+$  with various acceptors (7)

$$E_{\text{ex}} = -0.65E_{\text{pc}} + 0.86 \quad [2]$$

**Triplet levels.**—Although TPF and TPT show ECL with BP as the source of radical anion, none of the pyrroles do. One possible explanation might be that the enthalpy of the radical ion reaction (2.4–2.6 eV) is insufficient to produce the corresponding pyrrole triplet. To estimate the triplet energies, phosphorescence measurements of TPP and TTP contained in an ethanol glass at 77°K were performed. The triplet energies found for TPP and TTP, 2.48 and 2.46 eV, respectively (with corresponding lifetimes under those conditions of 2.9 and 2.7 sec), demonstrate that the triplets could be formed in the BP(-)/TPP(+) and BP(-)/TTP(+) systems.

A more probable explanation is suggested by the CV of the pyrrole/BP systems. Upon addition of TPP or TTP to a system containing BP, the reverse current following a reductive sweep forming  $\text{BP}^-$  is strongly decreased compared to the behavior of  $\text{BP}^-$  in the absence of these species (Fig. 4). The reversible system centered at  $-0.23\text{V}$  appears when BP is reduced in the presence of TPP (just as it does for the TPP alone system) even when the negative limit of the cathodic sweep is not sufficiently negative to cause TPP reduction. Thus  $\text{BP}^-$  reacts in some way with TPP decreasing its lifetime and preventing ECL. Although we did not investigate the nature of this reaction, a possible one involves abstraction of a proton by the  $\text{BP}^-$ .

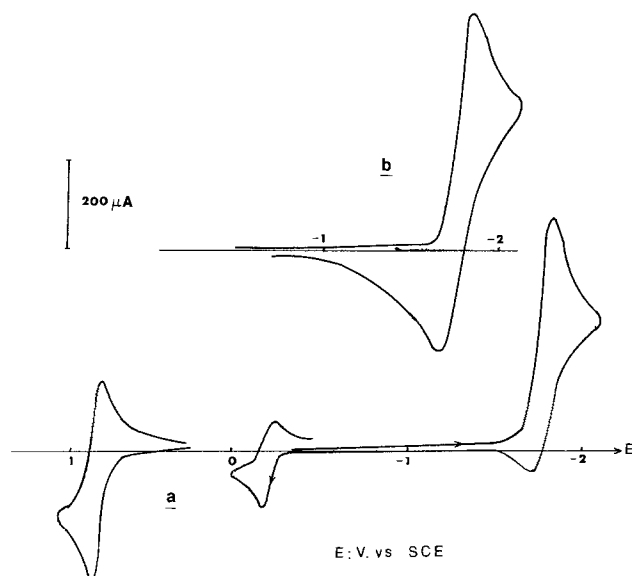
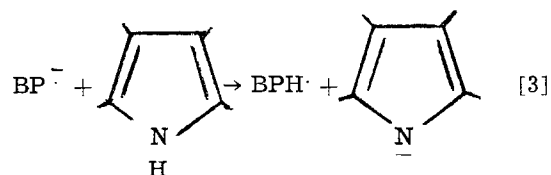
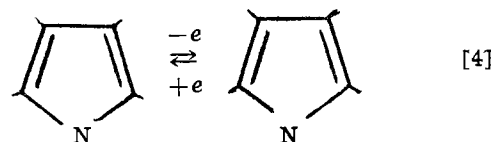


Fig. 4. Cyclic voltammetry of 1.8 mM BP in 0.1M TBAP-ACN at PT electrode with scan rate of 100 mV/sec (a) in presence of 1.7 mM TPP and (b) in absence of TPP.



with the reversible system at  $-0.23\text{V}$  then being



This system could also be formed by reaction of TPP with  $\text{TPP}^-$ , thus explaining the appearance of the reversible systems upon reduction of TPP in the absence of BP. This proton abstraction reaction could not occur, however, with TPF or TPT. Moreover, this explanation is consistent with a previous study (18) which showed that in the presence of a base, e.g., acetate, CV of a TPP solution results in the appearance of a reduction peak at  $-0.3\text{V}$ , attributed to the reduction of the neutral radical.

### Conclusions

A number of systems involving the compounds of interest are capable of producing ECL. While several rather intense systems were found, the lifetime of the systems under the conditions used here were not particularly good and electrode filming frequently occurred. We might note that Zweig *et al.* (19) noticed that the ECL from simple arylfurans was less satisfactory than that obtained from isobenzofuran derivatives. Exciplex formation has been demonstrated on direct radical ion reaction in ACN solutions under conditions where photoexcitation does not produce exciplexes, in agreement with previous results (7, 12). The results here are especially interesting, since the compounds where exciplex emission appears established, TTP and TPT, are rather sterically hindered.

### Acknowledgments

The support of the Army Research Office-Durham as well as NATO for a travel grant to M. L. is gratefully acknowledged. We appreciate the assistance of Professor S. Webber and Mr. Nicholas Pasch in the phosphorescence measurements.

Manuscript submitted Oct. 27, 1975; revised manuscript received Feb. 9, 1976.

Any discussion of this paper will appear in a Discussion Section to be published in the December 1976 JOURNAL. All discussions for the December 1976 Discussion Section should be submitted by Aug. 1, 1976.

Publication costs of this article were partially assisted by The University of Texas at Austin.

### REFERENCES

1. M. Libert and C. Caullet, *Bull. Soc. Chim. France*, **1971**, 1974; *ibid.*, **1971**, 2367.
2. M. Libert, C. Caullet, and J. Huguette, *ibid.*, **1972**, 3639.
3. M. Libert, C. Caullet, and G. Barbey, *ibid.*, **1973**, 536.
4. M. Libert and C. Caullet, *C. R. Acad. Sci. Paris*, **276 C**, 1073 (1973).
5. M. Libert and C. Caullet, *Bull. Soc. Chim. France*, **1974**, 805.
6. M. Libert and C. Caulett, *C. R. Acad. Sci. Paris*, **278 C**, 439 (1974).
7. S.-M. Park and A. J. Bard, *J. Am. Chem. Soc.*, **97**, 2978 (1975).
8. C. P. Keszthelyi, H. Tachikawa, and A. J. Bard, *ibid.*, **94**, 1522 (1972).



9. G. Cauquis and D. Serve, *Bull. Soc. Chim. France*, **1966**, 302.
10. R. S. Becker, "Theory and Interpretation of Fluorescence and Phosphorescence," p. 118, Wiley-Interscience, New York (1969).
11. D. J. Morantz and A. J. C. Wright, *J. Chem. Phys.*, **54**, 692 (1971).
12. K. Zachariess, Ph.D. Thesis, Vrije Universitet te Amsterdam (1972).
13. L. R. Faulkner, H. Tachikawa, and A. J. Bard, *J. Am. Chem. Soc.*, **94**, 691 (1972).
14. I. B. Berlman, "Handbook of Fluorescence Spectra of Aromatic Molecules," Academic Press, New York (1971).
15. L. R. Faulkner and A. J. Bard, *ibid.*, **90**, 6284 (1965).
16. A. J. Bard, K. S. V. Santhanam, S. A. Cruser, and L. R. Faulkner, in "Fluorescence," G. G. Guilbault, Editor, Chap. 14, Marcel Dekker, Inc., New York (1967).
17. R. E. Lutz and D. W. Boykin, *J. Org. Chem.*, **32**, 1149 (1967).
18. M. Libert, Thesis, Université de Rouen (1973) (No. CNRS: A.D. 9047).
19. A. Zweig, G. Metzler, A. Maurer, and B. G. Roberts, *J. Am. Chem. Soc.*, **89**, 4091 (1967).

## Anodic Oxidation of Anhydrous Methanol

G. Bélanger\*

*Hydro-Quebec Institute of Research, Varennes, Quebec, Canada*

### ABSTRACT

The electrooxidation of anhydrous methanol was studied with several electrochemical techniques. The effect of controlled amounts of water in the nonaqueous system was followed. The product analysis confirmed the production of formaldehyde as the predominant reaction product in this nonaqueous system. The addition of controlled quantities of water brings about changes in the polarization curves presumably owing to the formation of oxides on the platinum surface and to the production of formate ions. Strongly adsorbed species are observed at low anodic polarizations in the completely anhydrous system as well as in the presence of water. The exact nature of these species could not be identified but the formation of a polymeric inert film is suspected. The effect of adsorbed sulfur on the platinum working electrode was also examined; the adsorbed sulfur layer is unstable at high anodic potentials and causes an inhibition of the anodic oxidation of methanol or methoxide ion.

Electrooxidation reactions in nonaqueous solvents have been widely studied, in particular with respect to high energy density batteries and electroorganic synthesis. The electrooxidation of methanol in aqueous solutions has been extensively investigated since this material can be a very attractive fuel in a methanol-air fuel cell (1-3). However, relatively few studies have been carried out to elucidate the anodic reactions of pure anhydrous methanol. Recently such work has been published by Sundholm (4) and Iwakura *et al.* (5); the residual water content was rather high (120 ppm) in the work of Iwakura, and also appreciable in the experiments reported by Sundholm. No special procedures seem to have been undertaken to remove the last traces of water and also to work under conditions where the reacting solutions could be kept anhydrous (4,5). In the present work the residual water content was kept as low as possible (below 10 ppm) and the experiments were carried out in a controlled atmosphere enclosure where the anhydrous conditions remained unchanged.

In recent years, attempts have been made to increase the electrochemical activity of electrodes for the electrooxidation by adsorbing sulfur, among other materials, on the working electrode (6-9). Here, the effect of this additive on the electrooxidation of methanol is explored further.

### Experimental

The purification of methanol and the electrochemical polarization experiments were carried out in a controlled atmosphere chamber supplied by Vacuum/Atmospheres Corporation, Model HE454. Under a dynamic flow of argon, the residual water and oxygen content could be maintained in the few ppm range. The methanol was dehydrated according to the following procedure (10): commercial spectro-grade methanol was distilled once after the dissolution of metallic

sodium in it; this distilled methanol was then refluxed for one day over magnesium turnings with traces of iodine; this solution was then distilled and the distillate kept in a glass bottle in the controlled atmosphere chamber. All these procedures were carried out under controlled atmosphere. Determination of the residual water was performed with a modified automatic Karl-Fischer titration apparatus, the Aquatest II; the result of this analysis indicated a residual water content below 10 ppm. The desired concentration of sodium methoxide (the electrolyte solute) was obtained by the dissolution of metallic sodium in the purified methanol.

The steady-state automatic polarization curves were obtained for 20 mV potential steps using electrochemical apparatus and method described previously (11); the electronic apparatus were located outside the controlled atmosphere chamber and the electrical contacts were made via appropriate feedthroughs. A separate electrochemical system was used outside the chamber to carry out the electrode coverage experiments in aqueous solutions. This second electrochemical cell was equipped with a system allowing the electrode to be rinsed thoroughly with deoxygenated 1N Ultrex sulfuric acid. This second aqueous system is required to provide a source of oxygen in the oxidation of the species adsorbed on the electrode in the nonaqueous medium. The transfer of the electrode from the dry box to the aqueous system was performed under argon atmosphere, keeping the exposure of the electrode to the ambient air to a strict minimum.

The description of the instruments and the method used for the determination of the electrode coverage are described elsewhere (12). The integration of the current for the determination of the electrode coverage during anodic or cathodic potential sweeps was performed either by a manual method or electronically as described previously (12).

The analysis of formaldehyde in concentrated methanol requires a method different from the one

\* Electrochemical Society Active Member.

Key words: methanol, nonaqueous, electrooxidation, fuel cells.

used when the product is analyzed in water or air. Due to the presence of concentrated methanol in the solution, gas chromatography proved to be inadequate in the separation of these compounds in the concentration range used (<100 ppm). The only spectrophotometric method that yielded adequate results was based on the use of the Hantzsch reaction with 2,4-pentanedione as the reagent and the procedure described by Yablochkin (13).

In the experiments, when the electrodes were covered by sulfur, the procedures described by Loucka (8,9) for carrying out the adsorption of sulfur on the electrode were used.

All potentials in anhydrous methanol are referred to a reference electrode of Ag/AgCl in KCl-saturated methanol solution. The potential value of this reference electrode vs. the RHE in the same solution was observed at +0.55V. This reference electrode proved to be stable as a function of time and unaffected by the difference in water content of the methanol solutions.

A Beckman Model 188501 platinum disk rotating electrode was used in experiments requiring controlled convection conditions. The disk electrode was polished on a felt with methanol, rinsed in methanol, and dried under vacuum. All electrodes were polarized galvanostatically with a cathodic current in a separate cell to reduce any adsorbed oxygen or oxides, prior to the actual polarization experiments (steady-state, potentiodynamic, or galvanostatic charging curves). The experiments were carried out at room temperature ( $24^\circ \pm 1^\circ\text{C}$ ).

### Results

**Product analysis.**—The constant current polarizations ( $5\text{ mA}\cdot\text{cm}^{-2}$ ) in a small volume cell ( $15\text{ cm}^3$  for the working compartment) were carried out in anhydrous methanol and in solutions with controlled additions of water. The quantitative product analysis was performed only for formaldehyde. No other detectable products could be found by gas chromatography or by mass spectroscopy for the electrolysis time and current density used, typically  $300\mu$  equivalents. No specific tests for formate were carried out.

The results are presented in Table I. It is observed that for the solutions used, the water content as well as the concentration of electrolyte played a very minor role in the over-all product formation. When the water content becomes greater than 10%, the formaldehyde production decreases somewhat; these results are in general agreement with the ones reported previously (4,5). In the above experiments, the solutions were not stirred in any manner.

**Electrode coverage in anhydrous methanol.**—The electrode was polarized potentiostatically at a given potential or was brought to a given potential in a quasi steady-state manner by applying successive potential steps of 20 mV and maintaining each potential step value for 2 min. After this polarization procedure, the electrode was removed from the anhydrous methanol solution and taken out of the controlled atmosphere chamber. It was then transferred rapidly into another cell where the electrode was washed with water and deoxygenated 1N Ultrex sulfuric acid. After several

(five) washings the electrode was polarized potentiostatically at 0.4V (vs. RHE) and was then swept to 0.0V with a potential ramp. The current-voltage curve was recorded and the integration of the resulting curve gave us a measure of the electrode coverage  $\theta$  by the following relationship

$$\theta = \frac{SQ_H - Q_H}{SQ_H}$$

where  $Q_H$  is the charge between 0.4 and 0.04 V (vs. RHE) in the presence of adsorbed species and  $^sQ_H$  is the equivalent hydrogen deposition charge in the absence of such species.

A strongly adsorbed organic entity was observed that could be completely oxidized following an anodic polarization of 1.8V (vs. RHE) for several minutes.

In Fig. 1, we illustrate the adsorption behavior of this strongly adsorbed methanol species as a function of the polarization potential, both in anhydrous methanol and in presence of controlled amounts of water. We note a partial desorption of the strongly adsorbed species as the potential increases and this decrease is concomitant with a change of electrode reaction as is discussed below when the polarization curves for these solutions are presented. We must point out, however, that the absolute values of the coverage are not totally representative of the complete adsorption reactions because it is impossible to perform the coverage experiments *in situ* in the nonaqueous medium since the hydrogen ion adsorption current is not observed in the nonaqueous medium. This hydrogen ion deposition current is clearly resolved only in acidic aqueous solution.

The oxidation of this strongly adsorbed species was also studied. This was done by recording the current during anodic sweeps from 0.4 to 1.6V (vs. RHE) in aqueous solutions. A typical current potential curve is illustrated in Fig. 2 as obtained from oscillographic traces. To oxidize completely the adsorbed species the anodic limit must be raised to at least 1.8V (vs. RHE) and the sweep rate decreased to allow the slow reaction to take place.

**Steady-state polarization data.—Reaction order.**—Steady-state polarization studies were carried out on a rotating platinum disk electrode in anhydrous methanol and in solutions containing controlled amounts of water. An aim of these experiments was to study the order of the reactions with respect to the methoxide concentrations at different potentials. At anodic polarizations of 0.4 and 1.0V (vs. Ag/AgCl), the order of the reaction, ( $\partial \log i / \partial \log c$ )<sub>E</sub>, was found to be 0.90 and 0.82, respectively, as determined by a least square treatment of the data, for methoxide concentrations ranging from 0.05 to 0.5M (in anhydrous methanol). These reaction orders were obtained at an electrode rotation rate of 3000 rpm.

**Effect of rotation.**—No definite relationship between the rate of rotation and the current at different

Table I. Current efficiency for formaldehyde formation

NaOCH <sub>3</sub> conc. and water (ppm) Content in methanol	1	Current density	(mA-cm <sup>-2</sup> )	Current efficiency*	77
		5			
0.05M; anhydrous	73	74			
0.05M; 500 ppm		76			
0.05M; 10 <sup>4</sup> ppm		82			
0.05M; 10 <sup>6</sup> ppm		68			
0.1M; anhydrous		76			

\* Current efficiency calculated from the following reaction:  $2\text{CH}_3\text{O}^- \rightarrow \text{CH}_2\text{O} + \text{CH}_3\text{OH} + 2e$ .

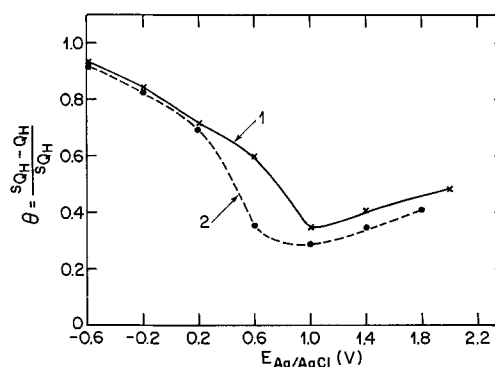


Fig. 1. Surface coverage of a platinum electrode polarized in methanol; electrolyte under mechanical agitation; curve 1, 0.05 NaOCH<sub>3</sub> in anhydrous methanol, and curve 2, 0.05 NaOCH<sub>3</sub> + 1000 ppm H<sub>2</sub>O in methanol.

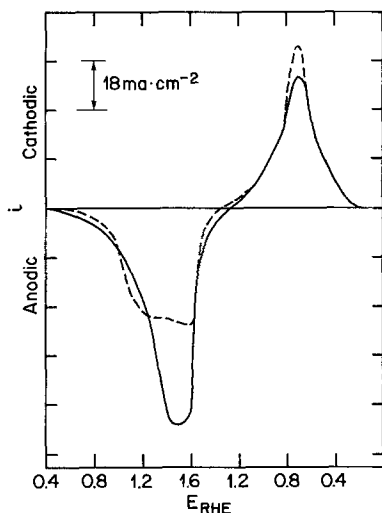


Fig. 2. Potentiodynamic profile on a platinum electrode in 1N  $\text{H}_2\text{SO}_4$ : —, after standing at open circuit in 0.1M  $\text{NaOCH}_3$  solution in methanol; ---, after oxidation of adsorbed species from the nonaqueous solution at 1.8V in 1N  $\text{H}_2\text{SO}_4$ . Voltage sweep rate: 20  $\text{V}\cdot\text{sec}^{-1}$ ; voltage limits 0.4  $\rightarrow$  1.6  $\rightarrow$  0.4  $\text{V}_{\text{RHE}}$ ; electrode, 0.1  $\text{cm}^2$  smooth platinum wire.

potentials could be established for electrode rotation speeds ranging from 600 to 6000 rpm, for several concentrations of methoxide (0.5, 0.1, and 0.5M  $\text{CH}_3\text{ONa}$ ).

This would establish the reaction to be entirely activation controlled as assumed in the current-potential and the reaction order plots.

**Effect of water—Anhydrous methanol.**—In the steady-state polarization curve in anhydrous methanol (0.05M  $\text{CH}_3\text{ONa}$  as electrolyte) shown in Fig. 3, there are several interesting features. At  $-0.35\text{V}$  (*vs.*  $\text{Ag}/\text{AgCl}$ ) an oxidation current commences and a well-defined peak is observed at  $-0.2\text{V}$ . This peak formation is very dependent on the residual water content. The maximum current or limiting current at  $-0.2\text{V}$  is also very much dependent on the rotation speed of the electrode; the current value decreases drastically as the rotation increases. At higher potentials (above 0.1V) a rather long Tafel region is observed with a slope ranging from 110 to 130 mV/decade. Finally, a limiting current potential range from approximately 0.6 to 2.0V is observed. This limiting current value decreases with rotation speed only by a negligibly small extent.

The  $iR$  drop between the tip of the Luggin capillary and the working electrode cannot account for the above limiting current or the curvature observed in the polarization curves, the resistance determined by the interruption technique is of the order of 20–30 ohm and the  $iR$  drop would account for only 50 mV, even at the highest potentials attained.

**Water addition.**—In Fig. 4 we show the steady-state polarization curves for 0.05M methoxide solutions containing 100 and 1000 ppm (0.01 and 0.1%) water.

Fig. 3. Steady-state polarization curve for anhydrous methanol ( $<10$  ppm) with 0.05M  $\text{NaOCH}_3$  as the electrolyte solute; rotating disk platinum electrode of 0.28  $\text{cm}^2$  area at 3000 rpm. Experimental points obtained for 20 mV intervals; each potential was held constant for 2 min before recording the data

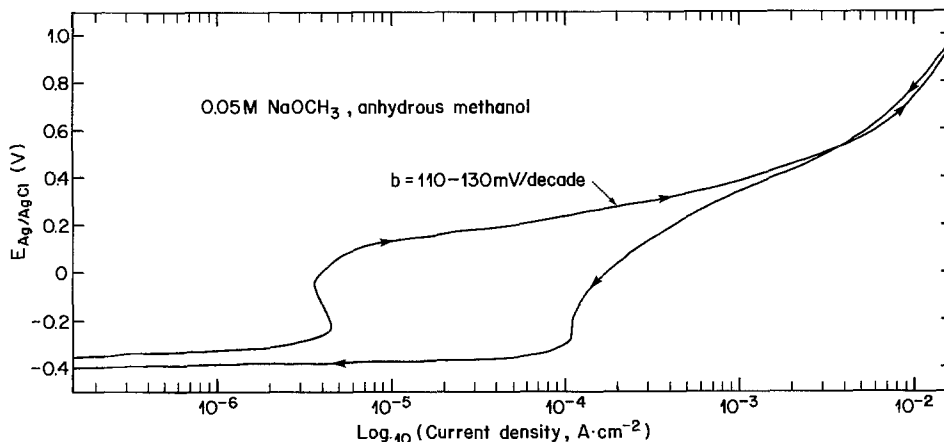
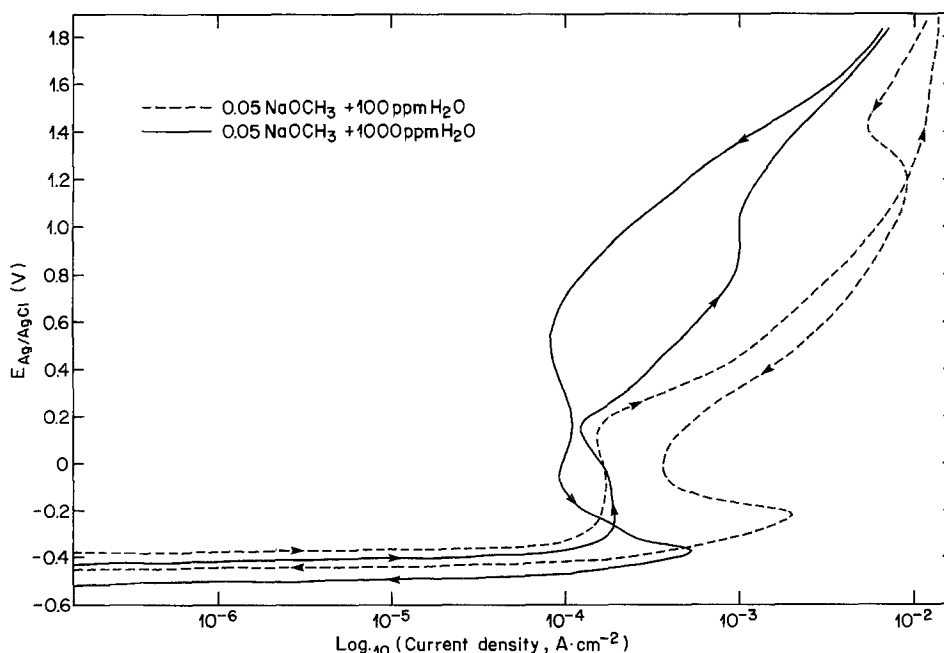


Fig. 4. Steady-state polarization curve for 0.05M  $\text{NaOCH}_3$  solution in methanol with 100 (---) and 1000 (—) ppm  $\text{H}_2\text{O}$ ; rotating disk platinum electrode of 0.28  $\text{cm}^2$  area at 3000 rpm. Same experimental procedure as in Fig. 3.



One can observe at first glance very profound differences between these polarization curves and the ones observed for the anhydrous case (Fig. 3). The main differences are the higher Tafel slopes (200-300 mV/decade) and the limited range where the Tafel relation is obeyed. The qualitative difference in the ascending and descending curves is also more pronounced: very well-defined inhibition peaks are observed and some modification in the current limiting potential range ( $>1V$  vs. Ag/AgCl) behavior is also apparent.

In these solutions the rotation speed of the working electrode had a minimal effect; the effect was in the opposite direction to what is generally observed, *i.e.*, here, the current decreases as the rotation speed increases, presumably owing to the increased concentration of the traces of water (and thence the inhibiting surface oxides) in the vicinity of the electrode at the higher rotation speeds.

The current behavior at relatively high anodic potentials (above 1.0V vs. Ag/AgCl) is quite different in the presence and absence of residual water. In completely anhydrous methanol a true limiting current behavior is observed at or near 1.0V. In the presence of 1000 ppm of water, an inhibition peak is observed at 0.6V, followed by an oxidation current that does not show any definite limiting current up to the highest potentials reached (*i.e.*, 2V vs. Ag/AgCl). The reaction at these high anodic potentials is probably a mixed process involving the methoxide ion and water or the hydroxide ion.

**Galvanostatic charging data.**—In the presence of water some interesting phenomena occur in the cathodic charging curves triggered from anodic potentials. In the completely anhydrous methanol no arrest or structure is observed as a cathodic current is applied to the electrode held at an anodic potential. For a 1000 ppm water content such an arrest appears and a complete analysis of this arrest for a 1% water content (1000 ppm) was carried out because of the better resolution in this solution. A linear relationship between current density and the reciprocal of the arrest period ( $1/\tau$ ) is observed for different rotation speeds and for current densities ranging from  $-0.05$  to  $4 \text{ mA}\cdot\text{cm}^{-2}$ . This arrest is observed at approximately  $-0.5V$  (vs. Ag/AgCl). A typical cathodic charging curve as well as the derivative,  $dE/dt$ , of this curve is shown in Fig. 5. A second arrest is clearly observed as the charging current density reaches values higher than  $2 \text{ mA}\cdot\text{cm}^{-2}$ . The high cathodic potential value for this arrest ( $-1V$  vs. Ag/AgCl) is related to the hydrogen deposition prior to the hydrogen gas evolution reaction.

A similar arrest is also observed in the galvanostatic anodic charging curves. However, the arrest is observed on a different time scale; *i.e.*, this arrest is a much slower phenomenon than the electrode process at  $-0.05V$  (vs. Ag/AgCl). Here again, a linear rela-

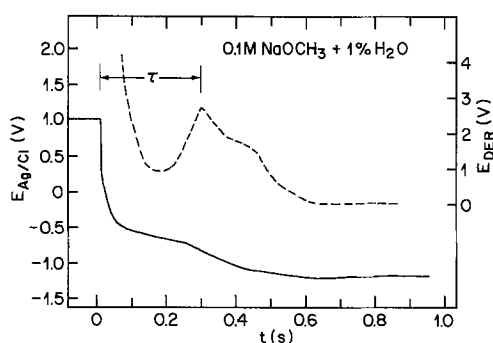


Fig. 5. Cathodic galvanostatic charging curve (—) as well as the derivative of the potential time trace (---); platinum disk electrode at 3000 rpm in 1% water-methanol solution; 1 sec time constant for  $dE/dt$ ;  $\tau$  is the arrest period; charging current density is  $4 \text{ mA}\cdot\text{cm}^{-2}$  from a 2 min potentiostatic polarization at 1.0V.

tionship between the current and the reciprocal of the arrest period is obtained indicating an activation-controlled process. The arrest occurs at 0.8-1.0V (vs. Ag/AgCl) and involves more than the surface oxidation; it lasts several seconds compared to milliseconds in the reduction case for the same current density. For the anodic arrest, the charges involved are of the order of  $940 \text{ mcoulomb}\cdot\text{cm}^{-2}$  for the 1%  $\text{H}_2\text{O}$  solution (at 6000 rpm) and only  $0.8 \text{ mcoulomb}\cdot\text{cm}^{-2}$  for the galvanostatic reduction charge in the same solution.

**Potentiodynamic polarizations in the methanol system.**—Some potentiodynamic profiles were reported by Iwakura *et al.* (5) for sodium methoxide in anhydrous methanol. In the present study, we have extended the potential sweep rates and examined the effect of controlled amounts of water in the anhydrous system.

For anhydrous methanol no structure (peaks) is observed, at all the sweep rates ( $10\text{-}500 \text{ mV}\cdot\text{sec}^{-1}$ ) investigated. A typical potentiodynamic profile is illustrated in Fig. 6A. However, as water is added to the system some structure becomes apparent particularly at low ( $10 \text{ mV}\cdot\text{sec}^{-1}$ ) sweep rates, as shown in Fig. 6B for the 1000 ppm  $\text{H}_2\text{O}$  solution. As the sweep rate increases to  $100 \text{ mV}\cdot\text{sec}^{-1}$ , the peaks are no longer observed and a curve similar to the one for the anhydrous case is obtained.

**Effect of adsorbed sulfur on the anodic oxidation in anhydrous methanol.**—Two main series of experiments were carried out to study the effect of sulfur adsorption on the methanol oxidation reaction. In the first series, the electrode was fully covered by sulfur in an aqueous sulfide solution and the electrode was then taken in the controlled atmosphere chamber where a complete steady-state polarization curve was recorded from the open-circuit potential, *ca.*  $-0.6\text{-}2.0V$  (vs. Ag/AgCl). The electrode coverage was measured before and after these curves. From the latter experiment we noted that the sulfur underwent a desorptive reaction as the electrode was polarized to 2.0V. Also as shown by the steady-state polarization curves in Fig. 7, the descending curve is identical to the one obtained in the absence of sulfur adsorption. Examination of electrode coverage at different points on the polarization curves showed that this desorption occurred above 0.8V (vs. Ag/AgCl).

The main effect brought about by the adsorbed sulfur is the inhibition of the first reaction, *i.e.*, the oxidation of methoxide to formate ions, from open circuit to 0.2-0.4V. This effect was observed more clearly in the next series of experiments where the polarization was carried out from open-circuit potential to only 0.6V (vs. Ag/AgCl). For an electrode on which the coverage by sulfur was near 100%, the inhibition occurs quite clearly, as shown in Fig. 8. In the presence of water, the inhibition is also observed but only for the ascending anodic potentials; for the descending potential, the oxidation reaction (formation of formate) was observed. Coverage experiments have also shown that the sulfur is more readily desorbed in the presence of

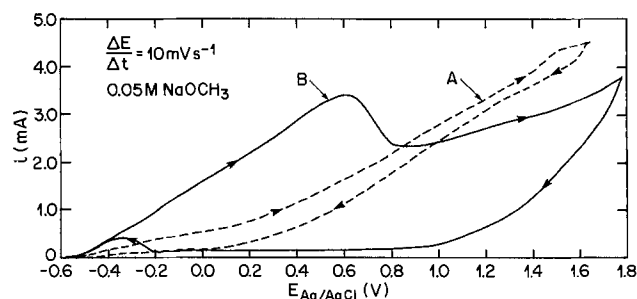


Fig. 6. Potentiodynamic profile on a platinum rotating disk electrode (3000 rpm);  $0.05M \text{ NaOCH}_3$  in methanol, sweep rate  $10 \text{ mV}\cdot\text{sec}^{-1}$ ; curve A, anhydrous methanol; curve B, 1000 ppm  $\text{H}_2\text{O}$  added; first sweep; electrode surface,  $0.28 \text{ cm}^2$ .

Fig. 7. Steady-state polarization curve in 0.1M NaOCH<sub>3</sub> on a platinum wire, 0.1 cm<sup>2</sup>, in anhydrous methanol; —, without any adsorbate present; ---, totally covered by a layer of sulfur atoms.

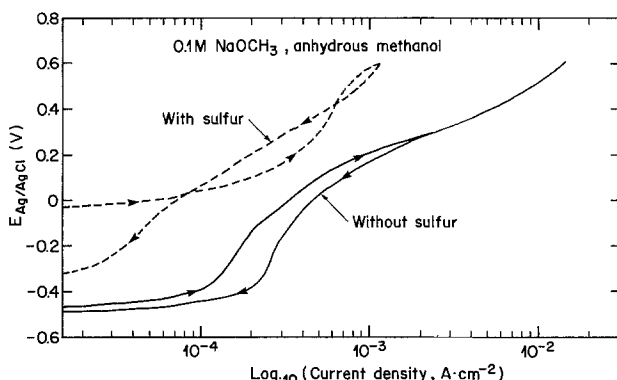
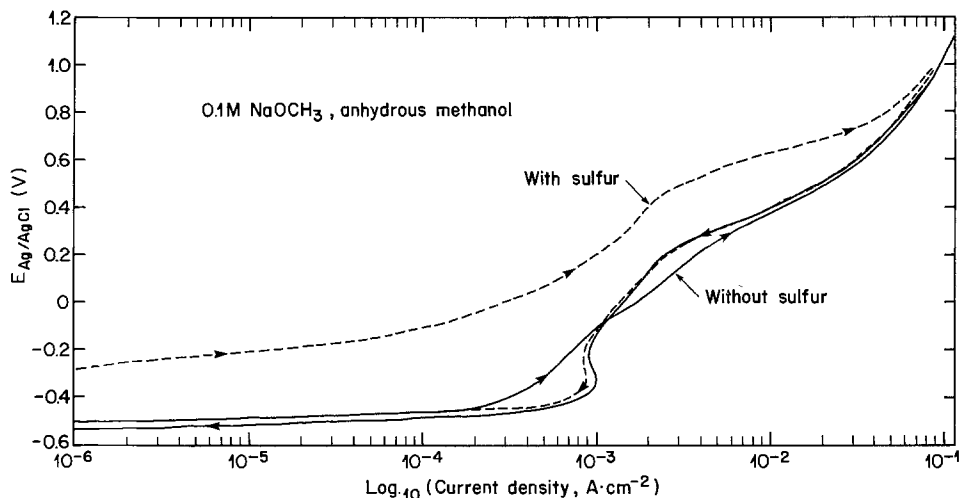


Fig. 8. Steady-state polarization curve in 0.1M NaOCH<sub>3</sub> on a platinum wire, 0.1 cm<sup>2</sup>, in anhydrous methanol; —, without any adsorbate present; ---, totally covered by a layer of sulfur atoms.

water than in the completely anhydrous methanol solution.

### Discussion

**Reaction mechanism.**—From the product analysis data, the effect of water in the methoxide oxidation becomes significant on the current efficiency only at water concentrations higher than 10%. As the water or hydroxide ion concentration increases mixed reactions can proceed according to the following reactions

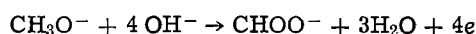
Main reaction



Side reaction

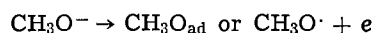


or



However, the over-all reaction equations as well as product analysis bear no direct indication as to the effects of water on the actual kinetics of the reaction.

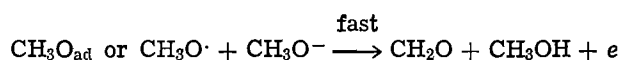
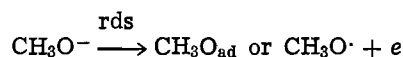
The reaction order of nearly one with respect to the methoxide concentration as well as the Tafel slope of 110–130 mV/decade in the anhydrous methanol tends to indicate a discharge reaction as the rate-determining step (rds), namely



where CH<sub>3</sub>O<sub>ad</sub> is an adsorbed intermediate and CH<sub>3</sub>O<sup>·</sup> a radical near the electrode. For a rds implying a discharge reaction from a reactant in solution, one expects (14) a linear relationship between 1/*i* and 1/√*ω* (where *ω* is the angular rotation speed of a disk electrode). Such correlation is absent for the methoxide-methanol system. In fact the current is invariant

with the rotation speed for potentials 0.4 and 1V (vs. Ag/AgCl). This independence of *i* on *ω* could indicate the formation of an intermediate that is swept away from the electrode as the solution is stirred. This conclusion is corroborated by the observation that the current decreases as the electrode passes from a standstill to any rotation speed.

A proposed reaction mechanism to account for the above fact could be illustrated as

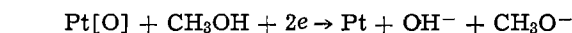


Hysteresis between the ascending and descending potential direction in the anhydrous methanol indicates an irreversible surface electrode phenomenon. This observation can be associated with the formation of an electrochemically inert film as indicated by the higher Tafel slopes observed (300 mV/decade). The occurrence of these higher slope values arising from surface films was discussed previously (15,16). The electrode surface modification could also be deduced from the irreproducibility of the steady-state polarization data; the curves exhibited large differences between successive scanings. The original curve (the first one) was restored by cleaning and polishing the electrode. The results presented above (Fig. 3 and 4) are the data from the first potential scan.

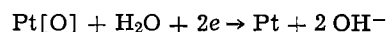
**Oxide effects.**—The presence of water brings about new phenomena. The most important is the formation of an oxide film as indicated by several observations:

1. Inhibition peaks in the steady-state polarization curves as illustrated in Fig. 4 are similar to the ones observed for the methanol oxidation in aqueous medium (1, 2, 17).

2. Arrest in the anodic and cathodic galvanostatic charging curves. The arrest at -0.5V (vs. Ag/AgCl) in the cathodic charging curve can be associated with the reduction of the oxide film formed at high anodic potential. The oxide reduction can proceed according to the following reaction scheme



or



The arrest observed in the anodic charging curve can be associated with the formate formation since it does not occur in absence of water. The following reactions can be involved



or



3. In the potentiodynamic current-potential curves, current peaks are obtained in the presence of water

and a very pronounced hysteresis between the anodic and the cathodic sweep is observed illustrating the inhibitive character of the oxide film formed in the presence of water. The inhibition brought about by the oxide film is similar to the one observed in similar experiments (18, 19) for the electrooxidation of sodium formate or formic acid.

**Sulfur effect.**—The promotion in the anodic oxidation of methanol is not observed in the presence of an adsorbed sulfur film on the electrode. This conclusion is not definite since we could not convert our data to true-platinum-site basis, since in the nonaqueous medium we do not have the hydrogen ion discharge peaks to indicate the true and active surface area. One observation worth noting is the instability of this sulfur film which undergoes a desorptive reaction at high anodic potentials. The steady-state polarization curve (Fig. 7) in the descending potential steps is identical for the electrode that has been covered with a sulfur film and for the bare electrode. This indicates complete desorption of sulfur at potentials of around 1.2V (*vs.* Ag/AgCl). This type of behavior is not observed if the upper anodic potential limit does not exceed 0.8V (*vs.* Ag/AgCl), as illustrated in Fig. 8. The main consequence of sulfur adsorption is a general poisoning effect: the methanol oxidation currents are decreased drastically by the presence of such an adsorbed film.

### Conclusions

The influence of surface oxides on platinum electrodes in the polarization curves of anhydrous methanol containing controlled amounts of water has been investigated. The main effect of these surface oxides (formed in the presence of water at anodic potentials) is to inhibit the oxidation of methoxide to formaldehyde. The other effect of the presence of water is to change the reaction products at low potentials where formate ions can now be produced in presence of water or hydroxide ions. However, at high anodic potentials (above 1V *vs.* Ag/AgCl) the reduction in the formaldehyde production is observed for high water content (1-10% only).

At open circuit a very strongly adsorbed species is formed on the electrode: The removal of this adsorbed film can be brought about by anodic polarization in the nonaqueous medium where the coverage by this adsorbate decreases as the anodic potential increases.

The main effect of a sulfur-covered platinum electrode is to inhibit the reaction: This sulfur adsorbate is unstable at anodic potentials and the sulfur coverage

decreases as the anodic polarization is increased to 2V *vs.* Ag/AgCl in a nonaqueous medium.

### Acknowledgment

The author thanks Mr. G. Trudel for his assistance in the experimental part of this work. Dr. A. K. Vijh's encouragement and advice in course of the study and in the preparation of the manuscript are also acknowledged.

Manuscript submitted May 4, 1975; revised manuscript received Jan. 26, 1976.

Any discussion of this paper will appear in a Discussion Section to be published in the December 1976 JOURNAL. All discussions for the December 1976 Discussion Section should be submitted by Aug. 1, 1976.

Publication costs of this article were partially assisted by Hydro-Quebec Institute of Research.

### REFERENCES

1. E. Gileadi and B. Piersma, in "Modern Aspects of Electrochemistry," Vol. 4, J. O'M. Bockris, Editor, Plenum Co., Ltd., London (1966).
2. V. S. Bagotsky and Yu. B. Vasilyev, *Electrochim. Acta*, **12**, 1323 (1967).
3. L. D. Burke and A. Moynihan, *ibid.*, **16**, 167 (1971).
4. G. Sundholm, *J. Electroanal. Chem.*, **31**, 265 (1971).
5. C. Iwakura, T. Hayashi, S. Kikkawa, and H. Tamura, *Electrochim. Acta*, **17**, 1085 (1972).
6. H. Binder, A. Kohling, and G. Sandstede, *Nature*, **214**, 268 (1967).
7. H. Binder, A. Kohling, and G. Sandstede, *Advan. Energy Conversion*, **7**, 121 (1967).
8. T. Loucka, *J. Electroanal. Chem.*, **36**, 355 (1972).
9. T. Loucka, *ibid.*, **36**, 369 (1972).
10. A. I. Vogel, "Practical Organic Chemistry," Longmans, London (1956).
11. G. Bélanger, *This Journal*, **118**, 583 (1971).
12. G. Bélanger, *J. Chem. Instrum.*, **6**, 55 (1975).
13. V. D. Yablochkin, *Lab. Delo*, 719 (1966); *C. A.*, **66**, 49017 n (1967).
14. A. C. Riddiford, in "Advances in Electrochemistry and Electrochemical Engineering," Vol. 4, P. Delahay, Editor, Interscience Publishers, New York (1966).
15. B. E. Conway and A. K. Vijh, *J. Phys. Chem.*, **71**, 3637 (1967).
16. R. E. Meyer, *This Journal*, **107**, 847 (1960).
17. G. Bélanger, *Can. J. Chem.*, **50**, 1891 (1972).
18. J. Wojtowicz, N. Marincic, and B. E. Conway, *J. Chem. Phys.*, **48**, 4333 (1968).
19. E. Schwarzer, C. H. Hamman, and W. Vielstich, *Electrochim. Acta*, **18**, 561 (1973).

# Slow Potentiodynamic Studies of Porous Alkaline Iron Electrodes

Bo Andersson<sup>1</sup> and Lars Öjefors<sup>1</sup>

Department of Chemical Technology, Royal Institute of Technology, S-100 44 Stockholm 70, Sweden

## ABSTRACT

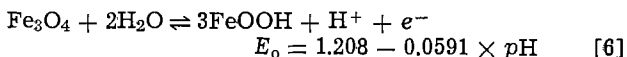
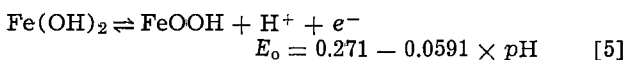
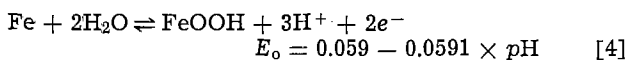
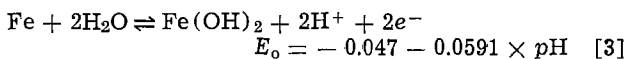
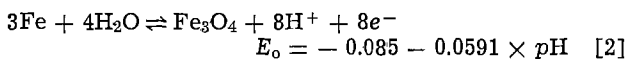
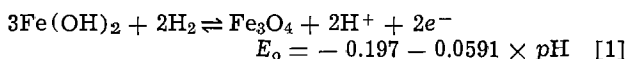
A slow potentiodynamic method where a porous iron electrode is fully discharged and charged has been used to study the reactions of the alkaline iron electrode. Electrode thickness, temperature, average porosity, number of armor nets, electrolyte concentration, and carbonate contents have been varied. The experiments show that high temperature, porosity, and KOH concentration increases the charge efficiency of the electrodes. High KOH concentration promotes the direct oxidation of Fe to FeOOH, and K<sub>2</sub>CO<sub>3</sub> concentrations up to 250 g/liters do not influence the reactions of the electrode considerably.

In spite of high theoretical Ah density, low price, and stability to both mechanical and electrochemical mistreatment, the iron electrode has gradually been replaced by its cadmium counterpart in alkaline accumulators. This change depends mainly on the low hydrogen overvoltage for iron which means poor charge efficiency as hydrogen evolution competes with the charge process. The hydrogen overvoltage also causes comparatively high self-discharge as this process can be characterized as hydrogen-evolving corrosion. Another negative factor is the poor performance at low temperature when compared to its cadmium competitor.

During recent years iron has been the focus as a negative active material in metal-air batteries and, since many of the bad qualities have been overcome, this electrode material is of interest together with nickel oxide positive electrodes to make iron-nickel batteries.

## Theoretical Background

Apart from its cadmium competitor, several discharge reactions can occur at the alkaline iron electrode (1)



The discharge reactions of the iron electrode have been the subject of several investigations (2-6) which show no uniform results according to the products of the discharge processes. The discharged active material has been reported as FeO, Fe(OH)<sub>2</sub>, Fe<sub>3</sub>O<sub>4</sub>, Fe<sub>2</sub>O<sub>3</sub>, FeOOH, and Fe(OH)<sub>3</sub>. Figure 1 shows constant current discharge curves in 4.5M KOH solution at 0°, 25°, 50°, and 70°C. Investigations by x-ray diffraction and SEM techniques (16) show that Fe(OH)<sub>2</sub> is the main discharge product of the first level, while FeOOH is produced on the second discharge level. Consequently, reactions [3] and [5] are dominating.

<sup>1</sup> Present address: Swedish National Development Company, S-103 40 Stockholm 40, Sweden.

Key words: iron electrode, porosity, potentiodynamic curves, sintered electrode.

At temperatures above 50°C a third interposed level appears representing the direct oxidation of Fe to FeOOH in dissolved phases (reaction [4]).

During development work with iron-air batteries at the Royal Institute of Technology and the Swedish National Development Company, the aim has been to find optimal structures of the sintered iron electrode and good separation between the charge and hydrogen evolution reactions. In order to study these variables, a slow potentiodynamic method has been adapted (Fig. 2). The electrode potential is scanned slowly from -1.050 to -400 mV and, as the rate is very slow (5.3 mV/min), the curves thus obtained are actually those of the electrode discharge. Integration of the area under the curves gives the same magnitude of capacity as a constant current discharge during the same time (Fig. 1). In Fig. 2 the different discharge and charge reactions are better separated than in Fig. 1 and it is evident that the interposed direct oxidation to FeOOH is more favored by high temperature than the other reactions. Of particular interest is the separation between the charge reaction and hydrogen evolution which is difficult to study with the constant current technique.

## Experimental

For the experiments a Beckman Electroscan 30 has been used together with an external motor to provide the low scanning rate. Figure 3 shows the test cell in Plexiglas, temperature controlled by a HAAKE thermostat. The electrodes were turn-formed disks (Table I) connected to a platinum wire. For every potentiodynamic discharge and charge, a new electrode disk was used. Before the discharge the electrodes were charged at constant current (100 mA/g) for 1 hr in

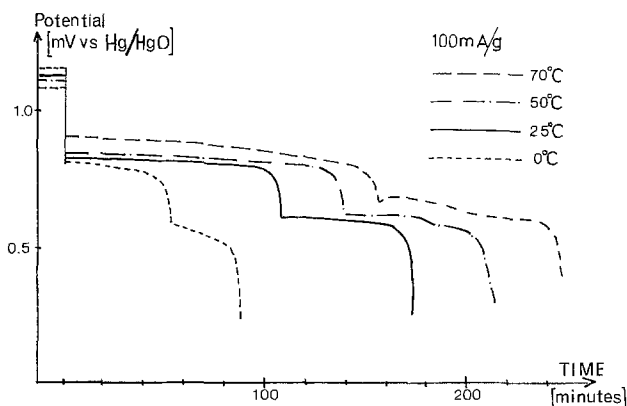


Fig. 1. Constant current discharge curves at different temperatures, 4.5M KOH.

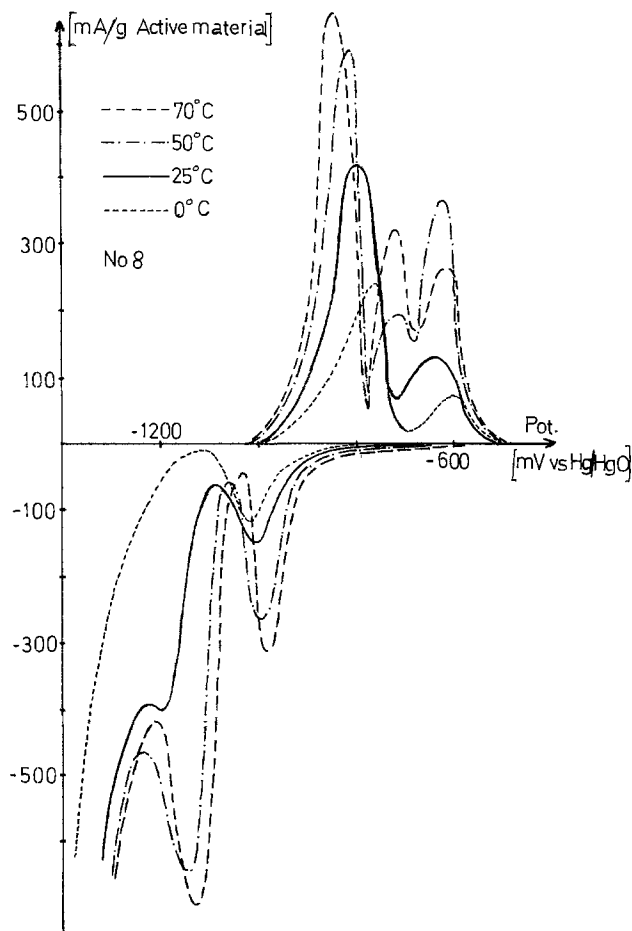


Fig. 2. Potentiodynamic discharge and charge curves at different temperatures (5.3 mV/min, 4.5M KOH).

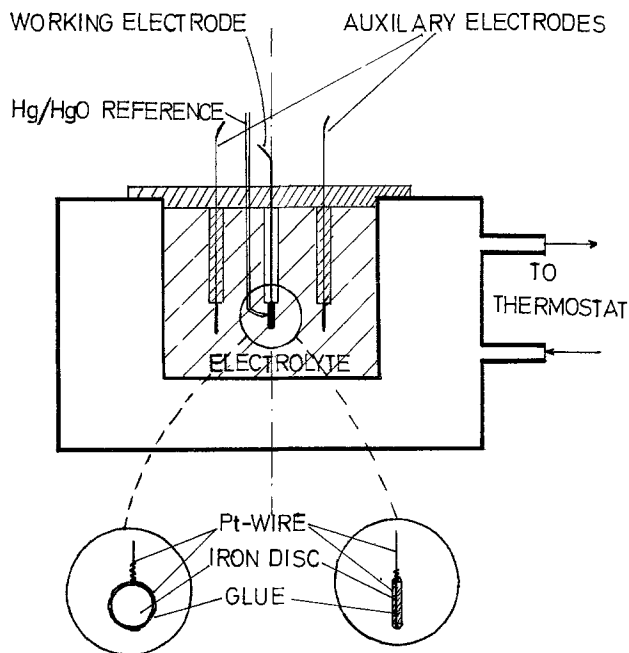


Fig. 3. Test cell

the actual electrolyte. Degassing of the electrodes was not necessary due to the slow discharge rate.

Experiments have shown that a scanning rate of 5.3 mV/min, which should be compared to that generally used (more than 0.5 V/min), for planar electrodes gives good separation of the different reactions at a porous iron electrode while it is charged and discharged to the same degree as in normal battery applications (Fig. 1 and 2). These curves also give

Table I. Physical properties of the electrodes

Electrode number	Thickness (mm)	Diam (mm)	Weight (g)	Surface (mm <sup>2</sup> )	Volume (mm <sup>3</sup> )	Average pore diam (μm)	Number of nets
1	1.2	9.5	0.20	70	84	7	0
2	1.4	9.5	0.24	70	98	7	1
3	1.5	9.5	0.28	70	105	7	2
4	2.2	7.0	0.20	38	76	7	0
5	3.3	5.8	0.21	28	92	7	0
6	1.05	9.0	0.21	64	67	2	0
7	1.15	9.0	0.20	64	74	3.5	0
8	1.25	9.0	0.19	64	80	7	0
9	1.35	9.0	0.20	64	86	10	0

information on current densities for different porosities and thicknesses of the electrode.

Experiments have shown that curves thus obtained are fully representative for the electrodes studied and do not differ from curves of electrodes cycled in the electrolyte considered. A calculation of the capacities in Fig. 1 and 2 shows that the results obtained with potentiodynamic discharge are very close to those of constant current discharge with 100 mA/g.

### Manufacture of the Electrodes

Manufacture of sintered iron anodes is a complex process where many parameters influence the electrochemical behavior of the final electrode. Parameters such as basic material, spacer, compacting pressure, sintering temperature, and time affect the porosity, pore diameter, surface area, mechanical strength, conductivity, and electrochemical performance. In the present work the porosity, thickness, and the number of armor nets are varied to relate these variables to electrochemical behavior. The electrodes presented should not, in terms of capacity per weight and volume, be compared to those of the battery project mentioned, since they have been made from well-defined carbonyl iron with the aim of getting reproducible electrodes suitable for this test.

The manufacture of the test electrodes has, in principle, been made in accordance with Ref. (7). As basic material, a carbonyl iron powder GS 6 from General Aniline & Film Company with the following specifications has been used: average particle diameter, 3-5 μm; apparent density, 1.2-2.2 g/cm<sup>3</sup>; Fe min, 99%; C max, 0.1%; O max, 0.3%; N max, 0.1%.

A homogenous mixture of iron powder and the spacer was obtained by sieving and mixing after which it was compressed to circular plates with 1-3 mm thickness. For some electrodes a 20 mesh iron net was placed in the middle or on top and below the powder bed before compressing. The compressed plates were sintered in a tube furnace under a protective atmosphere. After solving out the spacer with water, the structure with very well-defined porosity was stabilized at another succeeding heat-treatment. The electrodes used in this test are presented in Table I.

### Results

The results are presented in Fig. 2 and 4-8. As expected, the polarization decreases and the maximum current density increases with temperature and porosity for all electrodes and electrolyte concentrations tested.

Figure 2 shows the influence of temperature on charge and discharge processes of the alkaline iron electrode. Both the first and second plateau reactions are favored by higher temperatures, especially between 0° and 25°C. The interposed peak appearing at 50° and 70°C represents the direct oxidation in dissolved phases of iron to FeOOH, which also can be seen from the constant current discharge curves in Fig. 1. At charge no counterpart to this interposed reaction appears. At 50°C there is good separation between the peaks representing reduction of Fe(OH)<sub>2</sub>



and hydrogen evolution which in practice means good charge efficiency in battery applications. At 0°C these reactions, however, seem to overlap each other.

Figure 4 shows clearly that the different reactions are better separated with higher porosity which also favors current density and capacity per weight. Of interest is that high porosity increases the separation between hydrogen evolution and the charge process.

Figure 5 shows the influence of electrode thickness on potentiodynamic curves at 25°C, where the step from 1 to 2 mm seems to be especially important. Experiments show that this effect is more pronounced at lower temperature, while at 50°C the maximum current density per area is the same for all thicknesses. Variations in this dimension do not affect the charge efficiency very much.

The influence of one iron net (20 mesh) in the middle of the electrode and two identical nets on each side of the sintered disk on the potentiodynamic curves is shown in Fig. 6. The two nets have a shielding effect on the active material which is identical to a decrease in porosity. The single net in the middle has a very small effect. It should be pointed out that improvements in conductivity and mechanical stability of the electrode are not registered by the test since small electrode pieces are used.

Decrease in concentration of the electrolyte seems to have the same influence on electrode performance during discharge as a decrease in pore volume (Fig. 7). This probably depends on the fact that lower porosity causes a higher deficit of OH<sup>-</sup> ions during discharge. The charge step is not influenced in the same manner in terms of maximum current for temperatures lower

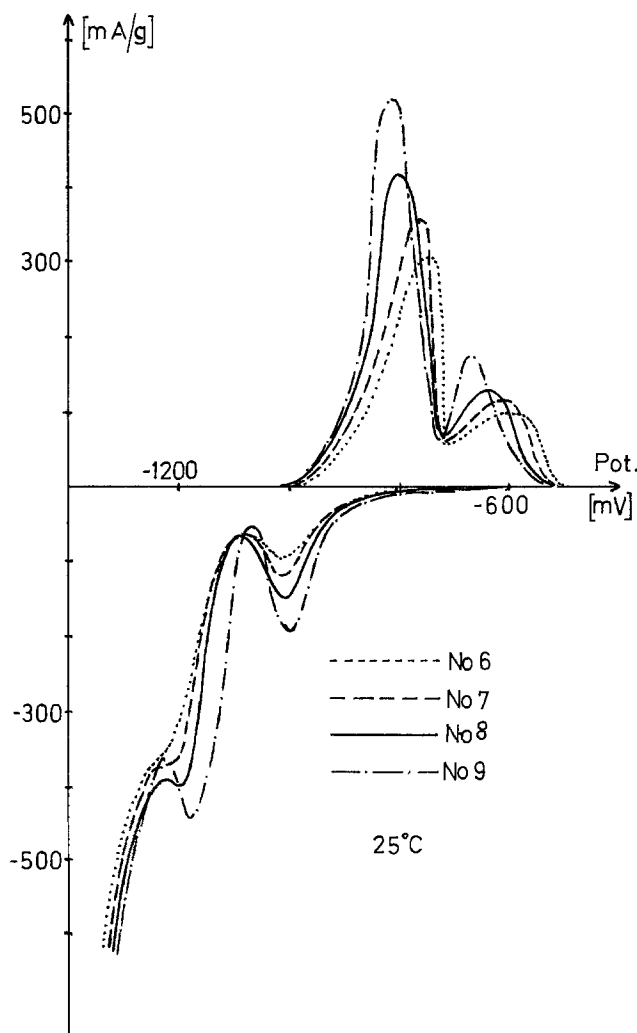


Fig. 4. Influence of different porosities on potentiodynamic discharge and charge at 25°C.

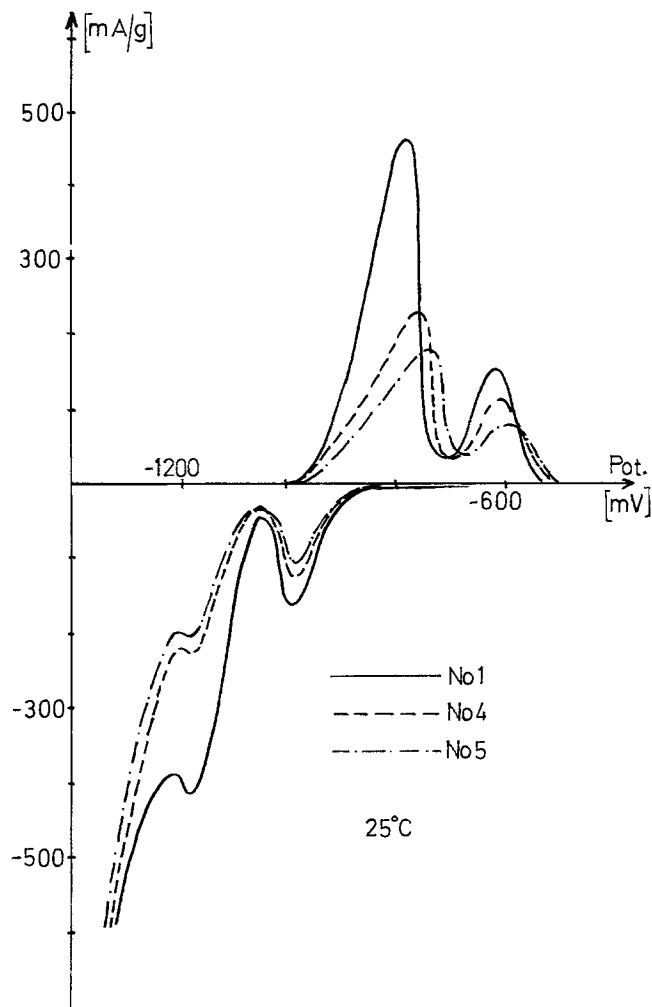


Fig. 5. Influence of thickness on potentiodynamic discharge and charge at 25°C.

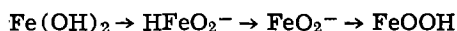
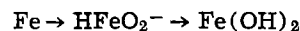
than 25°C. At higher temperatures the negative influence of 3M KOH is pronounced for both the charge and discharge reactions.

High concentration electrolyte (12M) has a negative influence on capacity at 0° and 25°C. For 50°C the capacity does not differ from that of 6M except for the direct oxidation to FeOOH which is favored by this high concentration. The separation between the hydrogen evolution and charge reactions is clearly favored by high molarity.

Carbonization of the electrolyte (Fig. 8) seems to have an identical influence as a decrease in molarity, which probably depends on the lower pH caused by the carbonate. The decrease in conductivity which is important for batteries is not registered in this test. Carbonate has, apart from many other additives to the electrolyte (8, 9), no other influence on the different electrode reactions except for the hydrogen overvoltage which is increased.

#### Discussion

Several investigators have shown that the charge and discharge reactions proceed over dissolved intermediates according to Ref. (4, 6, 11)



Ring-disk studies by Armstrong *et al.* (11) clearly indicate that at high temperatures and in more concentrated electrolytes bivalent iron species are produced in the solution. On the anodic cycle they arise solely from active dissolution of the iron, while on

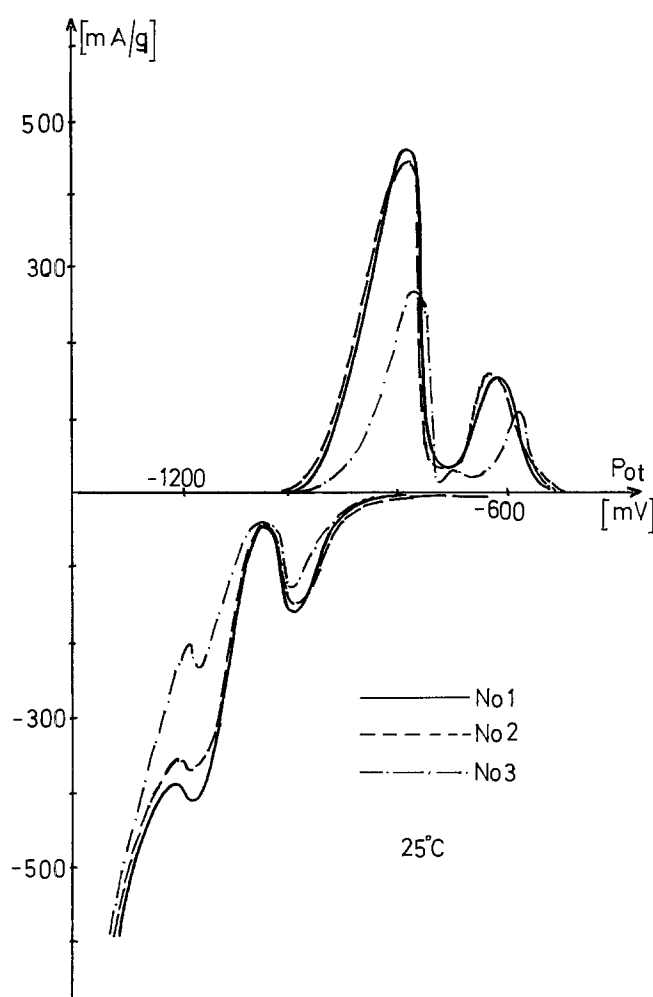


Fig. 6. Influence of 1 and 2 nets on potentiodynamic discharge and charge at 25° and 50°C. No. 1, no net; No. 2, 1 net; No. 3, 2 nets.

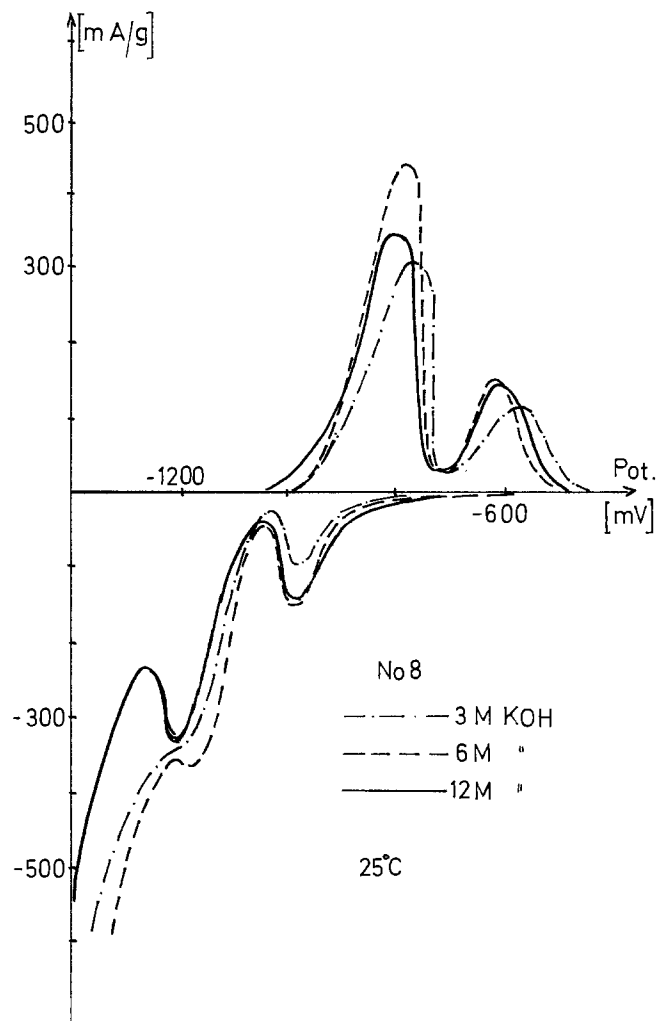


Fig. 7. Influence of electrolyte molarity on potentiodynamic discharge and charge at 25°C.

the cathodic cycle they are formed through the reductive dissolution of the anodic film. The measurements give, however, no evidence for solution soluble Fe(III) intermediates at a concentration above  $10^{-6}$ M.

The strong temperature dependence, especially below 10°C, when compared to the cadmium electrode is explained in Ref. (10) with differences in solubilities of the intermediates. When the solubility surpasses  $\sim 10^{-5}$ M, it is found to have a limiting influence on the reaction rate. Theoretical calculations in Ref. (10) show that the solubility of  $\text{FeO}_2^-$  is more temperature dependent than the other intermediates while it is difficult to determine the exact value.

The second discharge step has been studied in more detail (13, 14). In Ref. (14) the authors state that the absolute and relative extent of the second anodic step at constant current of a porous iron electrode is highly dependent on temperature and current density while electrolyte concentration has relatively little effect. They also notice that when a discharged electrode stands on open circuit it regains some capacity especially on the second step. The observed results are explained with a solid-phase mechanism and an intraelectrode interaction between trivalent and metallic iron.

As shown by Fig. 1 and 2, the relative increase of the second anodic level found by Flerov *et al.* (14) depends probably on the interference of the intermediate reaction appearing above 40°C, where metallic iron via  $\text{HFeO}_2^-$  and  $\text{FeO}_2^-$  goes directly to its trivalent oxide state. The strong influence of temperature on the solubility of the trivalent intermediate explains this phenomena.

Lindström (12) proposes the intermediate reaction to be a combination of the first and second discharge steps caused by an opening of structure at the commencement of the second step. The opening-up procedure should be caused by the trivalent products having a higher density compared to that of bivalent reaction products. The waves in Fig. 2 are too separated to interfere with each other and the increase in porosity observed at the beginning of the second level can be explained with the dissolution of the anodic film.  $\text{Fe}_2\text{O}_3 \cdot n\text{H}_2\text{O}$ , which is supposed to be the trivalent anodic product, has a density of 2.4-3.6 g/cm<sup>3</sup> which should be compared with 3.4 g/cm<sup>3</sup> for  $\text{Fe}(\text{OH})_2$  (15).  $\text{Fe}_3\text{O}_4$ , which has been proposed by some investigators as a discharge product, has a density of 5.2 g/cm<sup>3</sup> but SEM investigations on discharged electrodes show only the gelatinous precipitation characteristic for  $\text{Fe}_2\text{O}_3 \cdot n\text{H}_2\text{O}$  (16).

During charge, the reactions are separated into only two waves which can be explained by a slow dissolution of the Fe(III) discharge products causing a limited conversion to  $\text{Fe}(\text{OH})_2$  since these peaks are comparatively small. The following waves representing temperatures above room temperature are bigger than corresponding ones during discharge which means that direct reduction of Fe(III) species to iron interacts with that of  $\text{Fe}(\text{OH})_2$ .

The solubility of the intermediate species are also highly pH dependent which explains the decrease in performance of charge and discharge reactions with smaller average pore diameter, lower in electrolyte concentration, increasing thickness, and shielding nets. The improved separation between hydrogen evolution

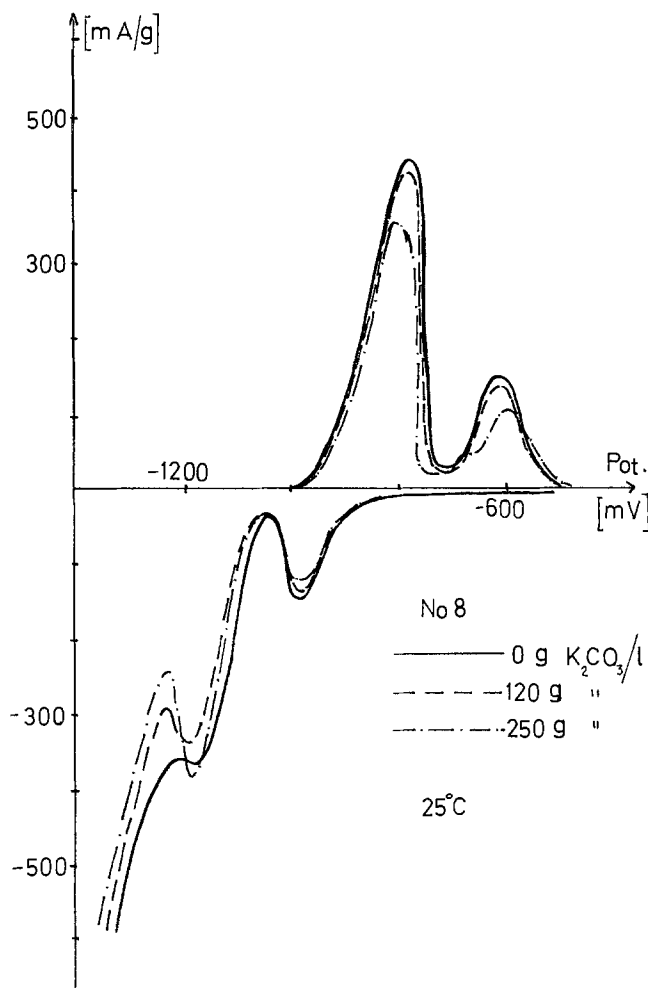


Fig. 8. Influence of carbonization of electrolyte on potentiodynamic discharge and charge at 25°C.

and the charge step with higher porosity depends on easier diffusion of the products of the latter process which is mostly influenced.

A decrease in molarity of the electrolyte has a negative influence on the performance, while a higher concentration changes the hydrogen evolving potential toward more negative values which has a positive effect on charge efficiency and self-discharge (9).

On the effect of carbonate in the electrolyte to the performance of the alkaline iron electrode, very little has been published and the maximum permissible amount of carbonate is considered to be 50 g  $K_2CO_3/l$

liter. The results presented here indicate that performance of the iron electrode is not influenced even at much higher carbonate concentration. However, on repeated cycling and with time, the cells become sluggish with more than 50 g/liter which has a negative influence on the performance.

By slowly discharging and charging a porous electrode, data are obtained which give more information on the processes appearing in the electrode than what is given by constant current techniques. It is, however, necessary to investigate in more detail the relationship between this method of charging and discharging the electrodes to that of normal use in batteries.

#### Acknowledgments

The authors are indebted to Dr. Olle Lindström, Royal Institute of Technology, Stockholm, for valuable discussions and support.

Manuscript submitted June 26, 1975; revised manuscript received Feb. 2, 1976.

Any discussion of this paper will appear in a Discussion Section to be published in the December 1976 JOURNAL. All discussions for the December 1976 Discussion Section should be submitted by Aug. 1, 1976.

Publication costs of this article were partially assisted by the Swedish National Development Company.

#### REFERENCES

1. M. Pourbaix, "Atlas of Electrochemical Equilibria in Aqueous Solutions," Pergamon Press, London (1966).
2. O. Faust, *Z. Elektrochem.*, **13**, 161 (1907).
3. A. K. Salkind, G. J. Venuto, and S. U. Falk, *This Journal*, **111**, 493 (1964).
4. V. S. Flerov and L. T. Pavlova, *Elektrokhim.*, **3**, 621 (1967).
5. H. G. Silver and E. Lekas, *This Journal*, **117**, 5 (1970).
6. J. Labat, J. C. Jarrousseau, and J. F. Laurent, Third Conference on Power Sources, Brighton, England (1970).
7. O. Lindström, U.S. Pat. 3,802,878 (1973).
8. L. Öjefors, Paper presented to the 23rd ISE Meeting, Stockholm, Sweden (1972).
9. L. Öjefors, *Electrochim. Acta*, **21**, 263 (1976).
10. L. Öjefors, *This Journal*, To be published.
11. R. D. Armstrong and I. Baurhoo, *J. Electroanal. Chem.*, **40**, 325 (1972).
12. O. Lindström, Fifth Conference on Power Sources, Brighton, England (1974).
13. I. N. Sherstobikova, B. N. Kabanov, and D. I. Leikis, *Elektrokhim.*, **4**, 1228 (1968).
14. V. N. Flerov, L. I. Pavlova, and L. V. Uziger, *Zh. Prikl. Khim.*, **38**, 569 (1965).
15. "Handbook of Chemistry and Physics," Chemical Rubber Publishing Co., Cleveland, Ohio (1970).
16. L. Öjefors, Submitted to *This Journal*.

# Electrochemical Reduction of Chromate in the Presence of H<sub>2</sub>O in Molten Lithium Chloride-Potassium Chloride Eutectic

I. Uchida\*<sup>1</sup> and H. A. Laitinen\*

Department of Chemistry, University of Florida, Gainesville, Florida 32611

## ABSTRACT

The chronopotentiometric reduction of K<sub>2</sub>CrO<sub>4</sub> was studied in molten LiCl-KCl eutectic at 450°C in the presence of CaCl<sub>2</sub> and/or water. The vapor pressure of H<sub>2</sub>O was varied in the range of 0-22.5 Torr. Under highly dehydrated conditions, a single wave occurs at -1.18V vs. Pt(II), 1M/Pt reference electrode, and Ca(II) ions have no effect on the reduction wave. However, in a moist melt and in the presence of insufficiently dehydrated CaCl<sub>2</sub>, two reduction waves are observed. The first reduction wave occurs at -0.6V and the second at -1.18V. LiCrO<sub>2</sub> is formed as an insoluble product at the first reduction step. The same product is produced chemically by decomposition of synthesized Li<sub>3</sub>CrO<sub>4</sub> in a moist melt. Coulometry and chronopotentiometry revealed that three electrons and two water molecules are consumed per chromate ion and the first step is controlled by H<sub>2</sub>O diffusion. A reduction path consistent with these observations is proposed.

Laitinen and Bankert used chronopotentiometry to study the electrochemical reduction of chromate ions, CrO<sub>4</sub><sup>2-</sup>, in LiCl-KCl eutectic melt in the absence and in the presence of Mg(II) and Ca(II) ions. They showed that the presence of divalent cations lowered the reduction potential of chromate and gave extraordinarily stable deposits (1). In the case of Mg(II) the electrochemical reduction product has been shown to be a single unstoichiometric compound of formula Li<sub>x</sub>Mg<sub>y</sub>CrO<sub>4</sub>, where  $x + 2y = 5$  (2). This empirical formula, Li<sub>x</sub>M(II)<sub>y</sub>CrO<sub>4</sub>, was found to be applicable to other deposits obtained in the melts containing other divalent cations such as Ni(II), Zn(II), and Co(II) (3-5). On the other hand, the reduction of chromate in the presence of Ca(II) ion has been the most irreproducible system encountered. Bankert observed that the addition of CaCl<sub>2</sub> caused a positive shift of reduction potential (1), but Nezu did not obtain a product corresponding to Li<sub>x</sub>Ca<sub>y</sub>CrO<sub>4</sub> (6). Further investigations were unsuccessful in establishing a definite formula and reproducibility of potential shift (7). There were no self-consistent data concerning the Ca(II)-CrO<sub>4</sub><sup>2-</sup> system, although there was a suggestion that the presence of trace quantities of moisture or hydroxide ion in the melt affect the nature of the reduction (5).

Recently Niki and Laitinen have shown that Li<sub>3</sub>CrO<sub>4</sub>, which is believed to be the initial intermediate product in the course of chromate reduction, undergoes a disproportionation reaction in the melt and gives LiCrO<sub>2</sub> (8). This compound was encountered in the early studies (6) when the electrolysis was carried out with a high ratio of Ca<sup>2+</sup>/CrO<sub>4</sub><sup>2-</sup>.

The present investigation was initially undertaken to clarify whether the reduction of chromate is affected by the presence of CaCl<sub>2</sub> in a highly dehydrated condition and to establish the composition of the reduction product. In the course of the investigation it was found that dehydrated Ca(II) ion does not have any special effect on the reduction mechanism but that a trace of water associated with hygroscopic CaCl<sub>2</sub> has quite a remarkable effect. The main purpose of this work was then turned to elucidation of the reduction

mechanism of the H<sub>2</sub>O-CrO<sub>4</sub><sup>2-</sup> system and characterization of the electrode deposit.

## Experimental

**Apparatus.**—A Hevi-Duty MK 3012-S vertical split tube furnace (Hevi-Duty Electric Company, Watertown, Wisconsin) was used. The temperature was regulated with a Wheelco Panel-Mount Capacitrol temperature controller (Wheelco Instrument Company) and a Chromel-Alumel thermocouple. All experiments were performed at 450° ± 1°C. A Sargent Model IV coulometric current source was used in the preparation of electrode deposits and for generation of the Pt(II)/Pt reference electrode. The constant current source employed for chronopotentiometric studies has been described previously (2). A Tektronix 502A oscilloscope served to record the chronopotentiograms.

The procedures employed for cleaning glassware and handling the molten eutectic with special glass devices were described in detail by Johnston (9).

**Electrodes.**—All potentials shown in this work are given with respect to the Pt(II), 1M/Pt reference electrode, construction and properties of which were already described (10). A spectroscopic carbon rod constructed according to the procedure described by Propp (2) was used as the counterelectrode.

The platinum flag electrodes used in the chronopotentiometry and the platinum gauze electrodes used in the preparative work were detachable. The construction of the platinum gauze electrodes and the electrode holders have been described (2). The platinum flag electrodes were constructed by punching a platinum foil (0.06 mm thick) with a paper punch (6.37 mm in diameter) and by spot welding 3 cm of 36 gauge platinum wire to the platinum flag as an electrical lead. The geometric area of each flag was 0.637 cm<sup>2</sup> without correction for the lead wire.

**Reagents.**—Reagent grade CaCl<sub>2</sub> · 2H<sub>2</sub>O (Mallinckrodt) was recrystallized. The resulting CaCl<sub>2</sub> · 6H<sub>2</sub>O was dried to CaCl<sub>2</sub> · 2H<sub>2</sub>O in a vacuum desiccator at room temperature. Then the CaCl<sub>2</sub> · 2H<sub>2</sub>O was further dehydrated by slow heating up to the melting point (772°C) under an HCl atmosphere followed by bubbling the resulting melt with dry HCl for 1 hr. After scrubbing with dry argon gas for 2 hr and filtration through a Vycor glass frit, the purified CaCl<sub>2</sub> was al-

\* Electrochemical Society Active Member.

<sup>1</sup> Present address: Department of Applied Chemistry, Faculty of Engineering, Tohoku University, Sendai, Japan.

Key words: molten salt, chromate reduction, chronopotentiometry, lithium chromite.

lowed to solidify and was sealed in vacuum in a small Vycor vial provided with a break-sensitive tip. The anhydrous  $\text{CaCl}_2$  was introduced into the molten system without moisture contamination from the laboratory atmosphere by breaking the tip in a cell container filled with dry argon. The  $\text{CaCl}_2$  prepared by this method contained 99.9% of the theoretical amount of chloride. Commercially available anhydrous  $\text{CaCl}_2$  (J. T. Baker) and  $\text{CaCl}_2$  dried according to the procedure outlined by Bankert (1) were also used purposely to ascertain the difference between fused-dried  $\text{CaCl}_2$  and vacuum-dried  $\text{CaCl}_2$ .

Anhydrous  $\text{K}_2\text{CrO}_4$  was prepared by drying reagent grade material (J. T. Baker) at  $180^\circ\text{C}$  in vacuum for 24 hr and stored in a vacuum desiccator.

The LiCl-KCl eutectic was supplied from Anderson Physics Laboratories Inc., Champaign, Illinois.

**Experimental techniques.**—Moist argon with various vapor pressures of  $\text{H}_2\text{O}$  was prepared by passing dry argon through a series of two gas washing bottles containing 2 liters of aqueous sulfuric acid of known concentration prepared from 96.4%  $\text{H}_2\text{SO}_4$  (Baker Analyzed Reagent) maintained at a known temperature in a constant-temperature bath. The partial pressures of water in equilibrium with aqueous  $\text{H}_2\text{SO}_4$  are tabulated at various temperatures (11)

Chronopotentiometry of chromate reduction was performed in the absence and presence of  $\text{H}_2\text{O}$ . After the measurements in the dry melt, the moist argon was introduced into two separate compartments containing about 4 ml melt, one of which had chromate and the other no chromate, and the melt was bubbled for at least 30 min. After bubbling was stopped in one of the two compartments, the measurement was carried out within 3 min. A blanket of the moist argon was kept on the melt all the time to maintain the partial pressure of water constant. All measurements were carried out alternately in this way with electrochemical monitoring of the water concentration in the melt.

The samples of the electrode deposit resulting from the reduction of chromate in the presence of water were prepared by constant current electrolysis using platinum gauze electrodes with bubbling of moist argon. Without stirring, the electrode potentials would not have been restricted to the potential range of the first wave.

The procedures of weighing the electrode deposit, dissolving the deposit in hot perchloric acid, and determining chromium and lithium contents have been described in detail (2-4).

The x-ray powder diffraction pattern of the deposit was obtained by using an 11.47 cm Debye-Scherrer camera exposed to Ni-filtered  $\text{Cu-K}\alpha$  radiation from a Norelco x-ray generator. The x-ray powder samples were prepared in the manner mentioned above with platinum coil electrodes (1 mm in diameter and 10 cm length). The spiral was uncoiled over a mortar, and then the electrode deposits were easily peeled off.

## Results and Discussion

**Reduction of  $\text{K}_2\text{CrO}_4$  in the presence of  $\text{CaCl}_2$ .**—The pure melt used here was highly dehydrated as shown in Fig. 1, curve 1, where the initial rising portion is quite linear. Figure 1, curve 2 shows a chronopotentiogram of chromate reduction in the presence of fused-dried  $\text{CaCl}_2$ . There was no difference between the results for chromate reduction in the presence and absence of  $\text{CaCl}_2$ , both cases giving the same  $E_{1/4}$  [ $= -1.19 \pm 0.01\text{V}$  vs. Pt(II),  $1\text{M}/\text{Pt}$ ] and transition time constant ( $= 998 \pm 18 \text{ A}\cdot\text{sec}^{1/2} \text{ cm}/\text{mole}$ ). However, the reduction wave split into two waves in the presence of commercially available  $\text{CaCl}_2$  or the vacuum-dried material as shown in Fig. 2, curve 2. In this case the residual charging curve was no longer the same as that of the dry melt as can be seen in Fig. 2, curve 1.

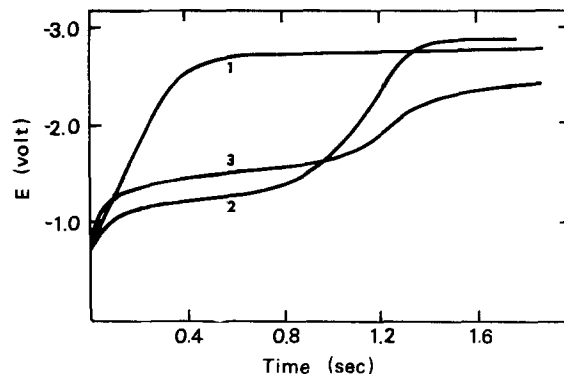


Fig. 1. Potential-time curves for the residual charging in the absence and presence of  $\text{H}_2\text{O}$ , and for the chronopotentiometric reduction of  $\text{K}_2\text{CrO}_4$  in the presence of  $\text{CaCl}_2$ . Curve 1, in a pure dry melt,  $i = 0.755 \text{ mA}/\text{cm}^2$ . Curve 2, in a dry melt containing  $\text{CaCl}_2$ ,  $[\text{CaCl}_2] = 0.19\text{M}$ ,  $[\text{K}_2\text{CrO}_4] = 6.20 \text{ mM}$ ,  $i = 6.04 \text{ mA}/\text{cm}^2$ . Curve 3, in a moist melt,  $P_{\text{H}_2\text{O}} = 15.4 \text{ Torr}$ ,  $i = 1.98 \text{ mA}/\text{cm}^2$ .

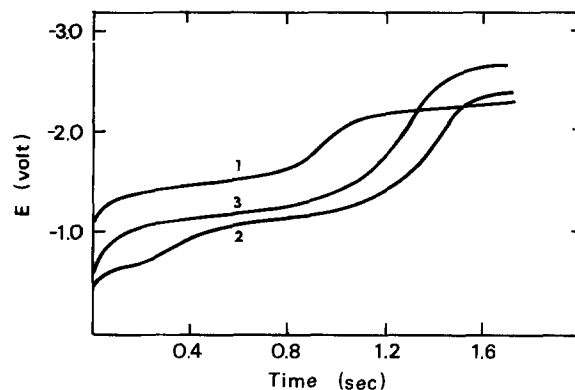


Fig. 2. Potential-time curves for the residual charging and chronopotentiometric reduction of  $\text{K}_2\text{CrO}_4$  in the presence of insufficiently dried  $\text{CaCl}_2$ . Curve 1, in a pure melt containing commercially available  $\text{CaCl}_2$ ,  $[\text{CaCl}_2] = 0.47\text{M}$ ,  $i = 4.94 \text{ mA}/\text{cm}^2$ . Curve 2, taken after addition of  $\text{K}_2\text{CrO}_4$ ,  $[\text{K}_2\text{CrO}_4] = 5.67 \text{ mM}$ ,  $i = 4.88 \text{ mA}/\text{cm}^2$ . Curve 3, taken 30 min after the curve 2.  $i = 4.94 \text{ mA}/\text{cm}^2$ .

Figure 2, curve 1 agreed with the chronopotentiogram of  $\text{H}_2\text{O}$  reduction in Fig. 1, curve 2 ( $E_{1/4} = -1.39\text{V}$ ). The prewave observed in the presence of insufficiently dried  $\text{CaCl}_2$  decreased with elapsed time and seemed to disappear finally. Figure 2, curve 3, which was taken 30 min after curve 2 showed basically the same pattern as Fig. 1, curve 2. This experiment was done under a dry argon atmosphere so that the water introduced with  $\text{CaCl}_2$  was free to escape from the melt. This is the reason why reproducible results were not obtained in  $\text{CrO}_4^{2-}-\text{Ca}^{2+}$  ( $\text{H}_2\text{O}$ ) systems in the previous investigations (6, 7).

**Reduction of  $\text{K}_2\text{CrO}_4$  in the presence of  $\text{H}_2\text{O}$ .**—The effect of  $\text{H}_2\text{O}$  on the reduction of chromate was demonstrated by successively decreasing the concentration of chromate at a constant vapor pressure of  $\text{H}_2\text{O}$ . Figure 3, curve 3 shows that at  $P_{\text{H}_2\text{O}}$  of 15.4 Torr, two transitions were obtained; one, at  $-0.60\text{V}$  and the other at  $-1.18\text{V}$ . With decreased chromate concentration the first wave at  $-0.60\text{V}$  increased and the second wave at  $-1.18\text{V}$  decreased relatively as shown in Fig. 3, curves 2 and 1, while a new wave, which was not well defined, appeared between  $-1.25$  and  $-1.55\text{V}$ . It corresponds to the reduction wave of  $\text{H}_2\text{O}$  in Fig. 1, curve 3. On the other hand, a further increase of chromate concentration simply caused the second wave at  $-1.18\text{V}$  to grow larger and showed no influence on the first reduction step.

The product of  $i$  and  $\tau^{1/2}$ , is shown as a function of chromate concentration in Fig. 4, where  $i$  is current

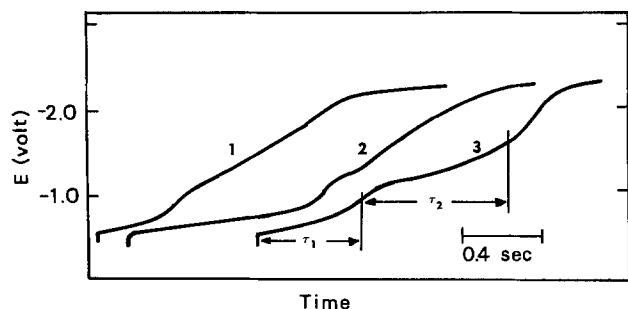


Fig. 3. Effect of  $H_2O$  on the chronopotentiometric reduction of  $K_2CrO_4$  at  $P_{H_2O} = 15.4$  Torr. Curve 1,  $[K_2CrO_4] = 1.10$  mM,  $I = 1.98$  mA/cm $^2$ . Curve 2,  $[K_2CrO_4] = 2.98$  mM,  $I = 2.96$  mA/cm $^2$ . Curve 3,  $[K_2CrO_4] = 4.10$  mM,  $I = 3.94$  mA/cm $^2$ .

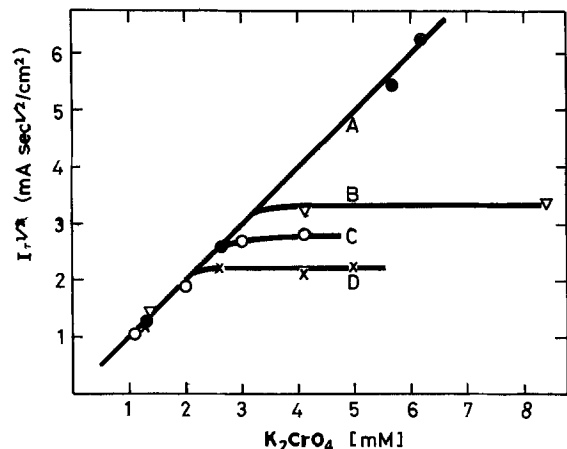


Fig. 4. Dependence of  $I\tau_1^{1/2}$  on chromate concentration at different vapor pressures of  $H_2O$ . Curve A,  $P_{H_2O} = 0$ . Curve B,  $P_{H_2O} = 20.3$  Torr. Curve C,  $P_{H_2O} = 15.4$  Torr. Curve D,  $P_{H_2O} = 11.4$  Torr.

density and  $\tau_1$  is the transition time of the first wave. This relationship confirms the above observation. At a given vapor pressure,  $I\tau_1^{1/2}$  becomes independent of chromate concentration when the latter exceeds a certain value (curves B, C, and D). On the other hand, with the decrease of chromate concentration, presumably when  $[H_2O] > [CrO_4^{2-}]$ ,  $I\tau_1^{1/2}$  follows the zero  $H_2O$  concentration line (curve A), yielding a transition time constant ( $I\tau_1^{1/2}/C$ ) identical with that in the absence of water. Apparently, under water-sufficient conditions the diffusing species is the chromate ion, and all the chromate ions reaching the electrode are reduced in the first reduction step. The limiting values of  $I\tau_1^{1/2}$ , observed under water-deficient conditions, mean that the first reduction step is controlled by the diffusion of water. All the water in the vicinity of the electrode is used up in a time interval ( $\tau_1$ ), and then the second reduction wave develops at the potential observed in the absence of water. Hence the limiting values of  $I\tau_1^{1/2}$  at different vapor pressures are expected to be proportional to the vapor pressure as long as the solubility of water obeys Henry's law.

Data on the solubility of water in molten mixtures of LiCl-KCl are available (12), and the reciprocal Henry's law constant in LiCl-KCl eutectic at  $450^\circ C$  was estimated;  $k^{-1} = 0.26$  mM/Torr where  $[H_2O] = k^{-1} P_{H_2O}$ . For instance, the water concentration in the melt

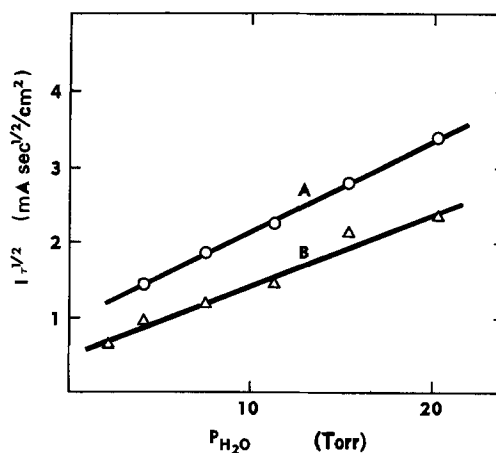


Fig. 5. Comparison of  $I\tau_1^{1/2}$  for  $H_2O$  and first wave of  $CrO_4^{2-}$  in presence of deficiency of  $H_2O$ . Curve A, limiting values of  $I\tau_1^{1/2}$  measured at each  $P_{H_2O}$  in excess of chromate. Curve B,  $I\tau_{H_2O}^{1/2}$  measured at each  $P_{H_2O}$  without chromate.

at  $P_{H_2O} = 15.4$  Torr is  $4.0$  mM. According to the literature (12) Henry's law holds at vapor pressures lower than  $18$  Torr.

The dependence of  $I\tau_1^{1/2}$  on  $I$  was examined for the first reduction step of chromate ( $I\tau_1^{1/2}$ ) and for  $H_2O$  reduction ( $I\tau_{H_2O}^{1/2}$ ). The experiments were carried out only under the condition of low vapor pressures where the concentration of  $H_2O$  in the melt is believed to obey Henry's law. It was found that the Sand equation is applicable to both reductions within the time interval investigated.

Figure 5 shows linear relationships of  $I\tau_1^{1/2}$  and  $I\tau_{H_2O}^{1/2}$  vs.  $P_{H_2O}$ . The linear regression analysis for  $I\tau_{H_2O}^{1/2}$ - $P_{H_2O}$  relation by the least squares method gave a transition time constant of water reduction ( $I\tau_{H_2O}^{1/2} = 0.094 P_{H_2O} + 0.49$ ,  $\gamma = 0.985$ );  $I\tau_{H_2O}^{1/2}/C_{H_2O} = 0.36 \times 10^3$  sec $^{1/2}$  cm/mole using  $k^{-1} = 0.26$  mM/Torr. Assuming  $n = 1$ , the diffusion coefficient of water was calculated as  $D_{H_2O} = 1.77 \times 10^{-5}$  cm $^2$ /sec at  $450^\circ C$ .

Because the first reduction wave is governed by mass transport of  $H_2O$  in excess chromate, the following relation is obtained under water-deficient conditions from the Sand equation

$$I\tau_1^{1/2} = \frac{nF\pi^{1/2}D_{H_2O}^{1/2}C_{H_2O}}{2a} = \frac{n}{a} I\tau_{H_2O}^{1/2} \quad [1]$$

where  $a$  is the number of water molecules required for the reduction of a chromate ion. As can be seen in Fig. 5, the ratio of  $I\tau_1^{1/2}/I\tau_{H_2O}^{1/2}$  is about  $1.5$  at each value of the vapor pressure. Using  $n = 3$  determined from coulometric experiments described later, the number of moles of  $H_2O$  consumed per mole of chromate was found to be  $2$ .

*Characterization of electrode deposit prepared in the presence of  $H_2O$ .*—During the electrolysis the potential of the working electrode was monitored and was never allowed to become more cathodic than  $-0.7V$ . The deposits were insoluble in the melt and adhered to the electrodes. Chemical analysis and coulometric data showed that three electrons are consumed per mole of chromate, and that the empirical formula of the deposit is  $LiCrO_2$ . Typical results are shown in Table I.

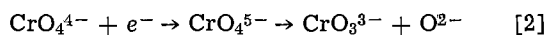
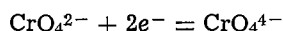
Table I. Analytical results of deposit as a function of current density

$[K_2CrO_4] = 0.0194M$		$P_{H_2O} = 15.4$ Torr			Temperature = $450^\circ C$		
$I$ , mA/cm $^2$	Current passed, $\mu$ equiv.	Deposit obtained, mg	Cr found, $\mu$ moles	$n$	Li found, $\mu$ moles	% wt found (as $LiCrO_2$ )	Empirical formula
1.5	150.04	4.76	49.8	3.01	50.1	95.2	$Li_{1.01}CrO_{2.00}$
3	150.04	4.94	51.1	2.94	54.0	94.9	$Li_{1.06}CrO_{2.00}$
6	150.06	4.82	49.7	3.02	50.1	93.9	$Li_{1.01}CrO_{2.00}$
				$n = 2.99$			$LiCrO_2$

The experiments of Table I were performed in Vycor cells and done in relatively short time. Pyrex glassware was seriously attacked by alkali arising from the electrolysis after prolonged contact with the melt.

*X-ray powder diffraction studies.*—X-ray powder diffraction data are compared in Table II with those of synthesized  $\text{LiCrO}_2$  and a decomposition product of  $\text{Li}_3\text{CrO}_4$  in the moist melt, which is identified as  $\text{LiCrO}_2$  (8).

*Electrochemical reduction mechanism of chromate in the presence of  $\text{H}_2\text{O}$ .*—Electroreduction of chromate in the dry melt was considered to involve consecutive electron transfer steps followed by a chemical reaction (1, 4, 5)

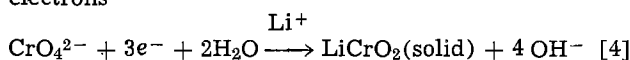


Recently Niki and Laitinen made a potential- $p\text{O}^{2-}$  diagram of chromate based on the stability of  $\text{Li}_3\text{CrO}_4$  and  $\text{Ba}_2\text{CrO}_4$  in  $\text{LiCl-KCl}$  eutectic (8). The diagram predicts that the stability of  $\text{Li}_3\text{CrO}_4$ , which is believed to be the initial product of the reduction, is strongly dependent on the basicity of the melt; if the melt is acidic,  $\text{Li}_3\text{CrO}_4$  decomposes to  $\text{LiCrO}_2$  by a disproportionation reaction



and if it is basic,  $\text{Li}_3\text{CrO}_4$  is stable in the melt. According to this explanation, the presence of acidic species in the melt is expected to promote the disproportionation reaction, and to shift the reduction potential to positive value.

The over-all reduction process in the moist melt was concluded to involve two water molecules and three electrons



and electrochemical measurements showed kinetic complications to be involved. In current-reversal chronopotentiometry, no reoxidation process was found. However, the irreversible type logarithmic plots [ $E$  vs.  $\log(\tau_1^{1/2} - t^{1/2})$ ] were not linear for the reduction process. Therefore this irreversibility must come from an irreversible chemical reaction. The  $E_{1/4}$  depended on current density and chromate concentration, but simple diagnostic criteria (13) were not applicable.

The chemical reaction involved here occurs between  $\text{H}_2\text{O}$  and  $\text{Li}_3\text{CrO}_4$  which is a much stronger base than  $\text{CrO}_4^{2-}$ . The initial electron transfer process,  $\text{CrO}_4^{2-} + e^- = \text{CrO}_4^{3-}$ , seems to be reversible because  $\text{Li}_3\text{CrO}_4$  (solid)/Pt electrodes showed stable equilibrium potentials (14). Hence, the following reaction sequence can be written

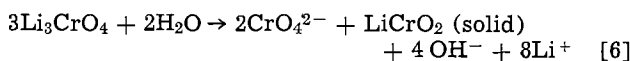
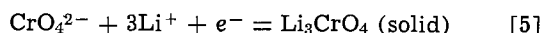


Table II. X-ray data of the electrode deposit prepared in the presence of  $\text{H}_2\text{O}$  ( $P_{\text{H}_2\text{O}} = 15.4$  Torr)

Electrode deposit		Decomposition product of $\text{Li}_3\text{CrO}_4$		Synthesized $\text{LiCrO}_2$	
d, Å	Intensity	d, Å	Intensity	d, Å	Intensity
4.73	m	4.73	90	4.812	100
2.45	w	2.45	50	2.476	28
		2.39	10	2.405	5
2.35	w	2.35	20	2.374	9
2.04	s	2.07	100	2.062	48
		1.88	50	1.895	9
		1.59	60	1.590	12
		1.46	70	1.466	15
1.44	s	1.44	70	1.488	15
1.38	s	1.38	50	1.389	7
		1.20	40	1.198	—

This reaction scheme was confirmed by direct study of the chemical reaction between  $\text{Li}_3\text{CrO}_4$  and  $\text{H}_2\text{O}$  in the melt. Chemical analysis and x-ray diffraction data for the decomposition products of  $\text{Li}_3\text{CrO}_4$  in the moist melt proved that the disproportionation reaction takes place and gives the product  $\text{LiCrO}_2$ . In the dry melt the  $\text{Li}_3\text{CrO}_4/\text{Pt}$  electrodes showed stable equilibrium potentials corresponding to the half-reaction [6] over a few hours, but once  $\text{H}_2\text{O}$  was introduced into the melt, the potential started to decay rapidly. Apparently the presence of  $\text{H}_2\text{O}$  strongly accelerated the decomposition of  $\text{Li}_3\text{CrO}_4$ .  $\text{LiCrO}_2$  was not oxidized electrochemically.

In order to account for the shift of over 600 mV in  $E_{1/4}$  in the moist melt in comparison with the dry melt, we can compare the fate of  $\text{Li}_4\text{CrO}_4$ , which is formed as a primary product in both paths by a reversible electron transfer process. In the moist melt, reaction [6] is so rapid that the surface concentration of  $\text{CrO}_4^{3-}$  is reduced to a vanishingly small value, whereas in the dry melt, the initial decomposition of  $\text{Li}_3\text{CrO}_4$  according to reaction [3] releases  $\text{O}^{2-}$  ions in the vicinity of the electrode surface. Then  $\text{Li}_3\text{CrO}_4$  becomes stable and requires two more electrons to complete the reduction. The decomposition of  $\text{Li}_5\text{CrO}_4$  is so slow that Bankert obtained  $\text{Li}_5\text{CrO}_4$  as a primary product (1). Thus the reaction sequence in the dry melt involves a three electron transfer process with high polarization overvoltage. On the other hand, in the proposed path the initial intermediate is short-circuited to the final product by the rapid disproportionation reaction with a large positive shift of  $E_{1/4}$ , because water has enough buffer action to act as an acid.

### Conclusions

The positive shift of reduction potential reported previously (1) for chromate reduction in the presence of  $\text{CaCl}_2$  is attributed to the effect of water introduced with hygroscopic  $\text{CaCl}_2$ . Addition of water alone produces the same splitting of the reduction wave. Chronopotentiometric and coulometric studies indicated that the first step consumes two water molecules per chromate ion, which is reduced with three electrons in the presence or absence of water.

The diffusion coefficient of water in molten  $\text{LiCl-KCl}$  eutectic was calculated from the transition time constant for the reduction of water alone, as well as from that of the first reduction step of chromate in the presence of a deficiency of water.

The first reduction step in the presence of water produces  $\text{LiCrO}_2$  as an insoluble product. The same product is obtained by the disproportionation reaction of  $\text{Li}_3\text{CrO}_4$ , the initial electron transfer intermediate. This reaction is greatly accelerated by the presence of moisture.

### Acknowledgment

The authors are indebted to Dr. K. Niki for his helpful discussions. This research was supported by a grant from the Army Research Office (Durham).

Manuscript submitted March 24, 1975; revised manuscript received Jan. 15, 1976.

Any discussion of this paper will appear in a Discussion Section to be published in the December 1976 JOURNAL. All discussions for the December 1976 Discussion Section should be submitted by Aug. 1, 1976.

Publication costs of this article were partially assisted by the University of Florida.

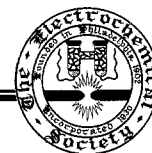
### REFERENCES

- H. A. Laitinen and R. D. Bankert, *Anal. Chem.*, **39**, 1970 (1967).
- J. H. Propp and H. A. Laitinen, *ibid.*, **41**, 644 (1969).
- B. Popov and H. A. Laitinen, *This Journal*, **117**, 482 (1970).
- K. W. Hanck and H. A. Laitinen, *ibid.*, **118**, 1123 (1971).
- H. A. Laitinen and L. R. Lieto, *Croatia Chem.*

- Acta*, **44**, 275 (1972).  
 6. H. Nezu and H. A. Laitinen, Unpublished results.  
 7. K. W. Hanck and E. S. Iracki, Unpublished results.  
 8. K. Niki and H. A. Laitinen, *J. Inorg. Nucl. Chem.*, **37**, 91 (1975).  
 9. R. O. Johnston, Ph.D. Thesis, University of Illinois (1974).

10. W. S. Ferguson, Ph.D. Thesis, University of Illinois (1956).  
 11. "International Critical Table", Vol. 3, p. 303, McGraw-Hill, New York (1928).  
 12. W. J. Burkhard and J. D. Corbett, *J. Am. Chem. Soc.*, **79**, 6361 (1957).  
 13. W. H. Reinmuth, *Anal. Chem.*, **82**, 1514 (1960).

## Brief Communications



### H<sub>2</sub> and H<sub>2</sub>O Oxidation at a Pt/Na<sup>+</sup>-Beta Alumina Interface

Gregory C. Farrington\*

General Electric Company, Research and Development Center, Schenectady, New York 12301

In concept, a Pt/Na<sup>+</sup>-β alumina interface should approximate an ideally polarizable electrode over a potential range limited only by Na<sup>+</sup> reduction at one extreme and O<sup>2-</sup> oxidation at the other. This is a broader range of ideal polarizability than is encountered with typical Pt/liquid electrolyte interfaces.

Both H<sub>3</sub>O<sup>+</sup>-β alumina (1) and H<sup>+</sup>-β alumina (2) have been reported and are prepared by diffusional replacement of the entire Na<sup>+</sup> content of Na<sup>+</sup>-β alumina. It is reasonable, therefore, that adsorbed H<sub>2</sub>O or H<sub>2</sub> should limit the range of ideal polarizability of a Pt/Na<sup>+</sup>-β alumina interface since each can be oxidized to an ion mobile within the β alumina structure. The purpose of this communication is to describe preliminary electrochemical examinations of H<sub>2</sub>O and H<sub>2</sub> oxidation at a Pt/β alumina interface.

#### Experimental

Pt electrodes, 1000Å thick, were sputtered onto both faces of a 1.2 cm diameter, 4 mm thick, polished disk of single phase polycrystalline β alumina of 98% theoretical density, containing approximately 1% MgO and 1% ZrO<sub>2</sub>. A reference electrode hole, 0.6 mm in diameter, was drilled 3 mm into the disk from its edge.

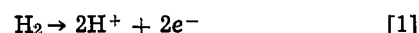
Two series of experiments were carried out: (i) constant potential polarization between each Pt electrode in vacuum and in the presence of trace amounts of H<sub>2</sub> and H<sub>2</sub>O, and (ii) cyclic voltammetry in H<sub>2</sub>O vapor using a Au wire dipped in Tl(Hg) as reference electrode. A small amount of propylene carbonate electrolyte was injected into the reference electrode hole to insure good electrode/β alumina contact. The reference electrode established a potential satisfactorily stable for these measurements. Its specific potential was not determined.

#### Results and Discussion

Figure 1 plots current vs. time during constant 5.00V polarization of a Pt/β alumina/Pt cell at 23°C. Before analysis, the cell was baked at 350°C at 10<sup>-3</sup> Torr for 2 hr. Polarization in vacuum (A) reveals the presence of residual oxidizable species, presumably H<sub>2</sub>O. The supply is rapidly depleted and cell current approaches zero.

When H<sub>2</sub> gas, dried by passage through molecular sieves, is introduced, current increases (B) and then decreases (C) when vacuum is again established. The

most reasonable electrode reaction occurring is



with injection of H<sup>+</sup> into β alumina at the positive electrode. Extended electrolysis for 2-5 min beyond that shown in Fig. 1 produces a gradual decrease in current indicating that exchange of H<sup>+</sup> for Na<sup>+</sup> is accompanied by a decrease in bulk β alumina conductivity.

Introduction of H<sub>2</sub>O vapor produces a response similar to B in Fig. 1 but with a current approximately ten times larger. This may indicate that oxidation of H<sub>2</sub>O at a Pt/β alumina interface is a faster electrochemical process than oxidation of H<sub>2</sub>. The electrochemical reaction of H<sub>2</sub>O adsorbed at a Pt/Na<sup>+</sup>-β alumina interface was examined in greater detail by cyclic voltammetry. Experiments were carried out at 23°C in a flowing stream of N<sub>2</sub> saturated with H<sub>2</sub>O. Results are shown in Fig. 2.

Little cell current is observed upon initial polarization at 0V vs. Tl<sup>+</sup>/Tl. Positive potential sweep encounters several oxidation peaks (A-C) which can be attributed to H<sub>2</sub>O oxidation to H<sub>3</sub>O<sup>+</sup> and O<sub>2</sub>. Sweep reversal produces one significant peak at D which can be associated with reduction of a product, presumably O<sub>2</sub>, formed at A-C.

At potentials less than -0.40V, a second major reduction peak appears (E). The current increases dramatically beyond -0.75V. Sweep reversal reveals peak F, not observed on initial cell polarization. The rapid decay of current in F suggests it corresponds to depletion of a particular species previously produced in peaks D or E.

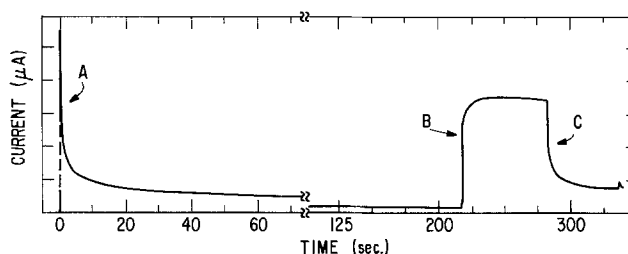


Fig. 1. Controlled potential 5V polarization of Pt/β-alumina/Pt cell. A, initial polarization in vacuum; B, introduction of dry H<sub>2</sub>; C, evacuation of H<sub>2</sub>; 23°C; electrode area = 0.78 cm<sup>2</sup>; current scale is 25 μA/major division.

\* Electrochemical Society Active Member.

Key words: polarization, solid electrolyte, water, β alumina.



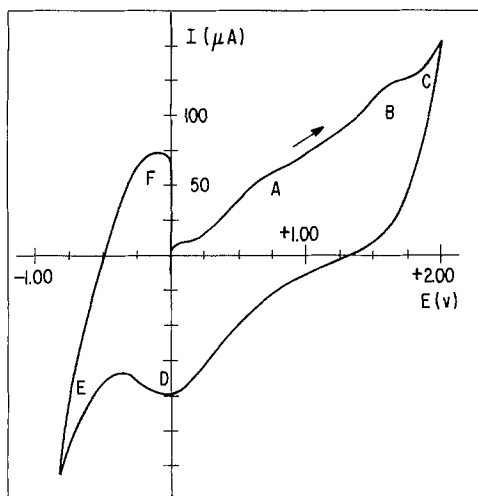
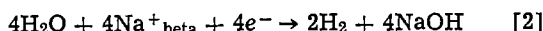


Fig. 2. Cyclic voltammogram of reaction of gaseous  $\text{H}_2\text{O}$  at Pt/ $\beta$  alumina interface. Sweep rate = 200 mV/sec; 23°C; electrode area = 0.78  $\text{cm}^2$ ; peaks A, B, C, and F represent oxidation; peaks D and E reduction.

The characteristics of peaks E and F are consistent with the hypothesis that E corresponds in part to reduction of adsorbed  $\text{H}_2\text{O}$  with simultaneous  $\text{Na}^+$  migration out of the solid electrolyte to the surface. The over-all reaction is



Peak F, then, represents reoxidation of  $\text{H}_2$  and reinjection of  $\text{Na}^+$  into  $\beta$  alumina. Both  $\text{H}_2$  and  $\text{Na}^+$  exist at the interface only as the result of electrochemical production at E.

This illustrates several of the peculiarities of cyclic voltammetry at a  $\beta$  alumina interface. For an electro-

chemical oxidation to occur, it must produce ions mobile within the  $\beta$  alumina structure. An ionic flow substituting new ions in  $\beta$  alumina also produces gradual changes in its bulk resistivity which must be considered in interpretation of any I/V sweep data. Correction for IR drop in cyclic voltammetry, for example, becomes difficult.

### Conclusions

It is clear that  $\text{H}_2\text{O}$  and  $\text{H}_2$  can be oxidized at a Pt/ $\beta$  alumina interface to ionic species mobile within the  $\beta$  alumina structure. Oxidation of  $\text{H}_2\text{O}$ , in particular, must be considered in any experimentation assuming blocking behavior at a Pt/ $\beta$  alumina interface or its equivalent. The presence of trace water is surely responsible for the satisfactory behavior of Pt and Au contacts in low frequency impedance measurements on  $\text{Na}^+$ - $\beta$  alumina (3-5).

Manuscript submitted Dec. 4, 1975; revised manuscript received ca. Feb. 2, 1976.

Any discussion of this paper will appear in a Discussion Section to be published in the December 1976 JOURNAL. All discussions for the December 1976 Discussion Section should be submitted by Aug. 1, 1976.

Publication costs of this article were partially assisted by General Electric Company.

### REFERENCES

1. H. Saalfeld, H. Matthies, and S. K. Datta, *Ber. Deut. Keram. Ges.*, **45**, 212 (1968).
2. G. P. Kummer, *Prog. Solid State Chem.*, **7**, 141 (1972).
3. A. Imai and M. Harata, *Japan. J. Appl. Phys.*, **11**, 180 (1972).
4. J. H. Kennedy and A. F. Sammells, *This Journal*, **119**, 1609 (1972).
5. R. W. Powers and S. P. Mitoff, *ibid.*, **122**, 226 (1975).

## Effect of Water on Beta Alumina Conductivity

F. G. Will\*

General Electric Company, Research and Development Center, Schenectady, New York 12301

Water or its cations have recently been shown by several groups to enter the crystal lattice of sodium  $\beta$  alumina. By repeatedly treating small  $\beta$  alumina crystals in boiling concentrated  $\text{H}_2\text{SO}_4$ , Saalfeld *et al.* (1) could show that most of the 4% sodium was replaced by hydronium ions, accompanied by an increase of the c-axis by 0.125Å. The larger part of the water, associated with the protons, desorbed when heating to between 400° and 700°C and adsorbed reversibly when cooling to 160°C in moist air. A gradual increase of the c-axis, amounting to 0.09Å in 96 hr, was also observed by Roth and Mitoff (2) when exposing  $\beta$  alumina powder to moist air.

Supporting evidence for the penetration of  $\beta$  alumina by protonated species also comes from infrared spectra (3). Beta alumina exposed to moist air for several hours shows a broad absorption band indicative of molecular water. The band disappears when heating to 300°C in dry argon. Furthermore, NMR results on  $\beta$  alumina powder exposed to moist air (4) suggest the presence of both water and mobile protons in the conducting planes, in agreement with Saalfeld's results. The characteristic  $^1\text{H}$  NMR absorption peaks disappear

on heating to 230°C in dry nitrogen, indicating desorption of the water.

While there is clear evidence for the penetration of  $\beta$  alumina by protonated species, no detailed information is available regarding its effects on resistivity. Yet such effects are expected and are significant for the efficient use of  $\beta$  alumina in batteries, in particular, those operating near ambient temperature (5).

The present paper establishes for the case of dense sintered  $\beta$  alumina (a) the role of water *vs.* that of hydronium ions and the mechanism by which these species enter, (b) the magnitude of the resistivity changes, and (c) the effects of water exposure on intragrain and grain boundary conductivity.

### Experimental

Experiments were carried out on sintered sodium  $\beta$  alumina disks of 3 cm diameter and 0.15-0.3 cm thickness. The material has the approximate composition  $\text{Na}_2\text{O} \cdot 8.5 \text{Al}_2\text{O}_3$ , contains 0.5% MgO and 0.5%  $\text{Y}_2\text{O}_3$  by weight and has a density of about 99% of the theoretical value 3.24  $\text{g}/\text{cm}^3$ . It has an average grain size of 10 $\mu$  and is nonpermeable to helium. Details regarding the ceramic processing are published elsewhere (6).

\* Electrochemical Society Active Member.  
Key words: solid electrolyte,  $\beta$  alumina, ionic conductivity, hydronium ion exchange.

The a-c impedance was measured by placing the  $\beta$  alumina disk between two circular platinized platinum electrodes of 2.5 cm<sup>2</sup> area and porous polypropylene spacers of 0.05 cm thickness, saturated with 1N I<sub>2</sub> in a solution of 1N NaI in quartz-distilled propylene carbonate. The contribution of the electrodes and spacers to the impedance was established separately and corrected for. The d-c resistivity was determined from the linear polarization curves between 0 and 10  $\mu$ A/cm<sup>2</sup> and the a-c impedances were obtained either with an a-c impedance bridge or with a setup described elsewhere (7). Determinations of pH were made in N<sub>2</sub>-stirred quartz-distilled water, using a pH meter. Finally, dynamic water vapor absorption was carried out with a thermobalance in flowing nitrogen with a precision of  $\pm 10$   $\mu$ g.

### Results and Discussion

**Occlusion of water.**—Curve 1 in Fig. 1 shows the occlusion of water by a  $\beta$  alumina disk of 0.15 cm thickness during exposure to a stream of water vapor (23 Torr) in N<sub>2</sub> at 25°C. The disk had been previously dried by heating to 900°C in air for 16 hr. The two salient features of this curve are: (i) No straight-line portion is obtained in the  $\sqrt{t}$  plot and (ii) saturation is essentially reached in 30 min to the extent of  $1.5 \cdot 10^{-5}$  moles H<sub>2</sub>O/cm<sup>2</sup>  $\beta$  alumina, equivalent to a weight increase of 0.1%. The same weight increase is observed when exposing the  $\beta$  alumina to liquid water for equivalent lengths of time. Dynamic water absorption at 50°C leads to only half the weight increase. By heating the  $\beta$  alumina to 900°C in air, all the water is removed and the original state regenerated.

The absence of a  $\sqrt{t}$ -relationship (or  $[1 - a \exp(-bt)]$ -relationship for times approaching saturation) shows that the observed fast occlusion of water by  $\beta$  alumina is not determined by a lattice or grain boundary diffusion process. This conclusion is substantiated by the fact that unreasonably large diffusion coefficients for water in  $\beta$  alumina ( $\sim 5 \cdot 10^{-5}$  cm<sup>2</sup>/sec) would have to be assumed to explain the short time to reach saturation. The rapid occlusion of water may be rationalized by the penetration of micropores and cleavage planes, followed by adsorption and possibly capillary condensation. Water-induced cleavage of lattice planes may be an important aspect of this mechanism. We have observed water-induced cleavage on  $\beta$  alumina single crystals, and the phenomenon is also known to occur on other layer structures, such as mica.

**Hydronium ion exchange.**—The pH of water rises distinctly with time when  $\beta$  alumina, previously air-dried at 900°C, is exposed to water. The pH increase is a quantitative and sensitive measure for the exchange of H<sub>3</sub>O<sup>+</sup> in the water against Na<sup>+</sup> ions in the crystal

lattice. This ion exchange should be accompanied by a slight decrease in the weight of  $\beta$  alumina. Actually, this effect is masked by the increase in weight due to the occlusion of water, occurring simultaneously.

Curve 2 in Fig. 1 shows the number of moles H<sub>3</sub>O<sup>+</sup> exchanged for Na<sup>+</sup> in a 3 mm thick  $\beta$  alumina disk during exposure to distilled water at 25°C. In contrast to the penetration of  $\beta$  alumina by water, the penetration by H<sub>3</sub>O<sup>+</sup> ions is proportional to  $\sqrt{t}$ , the rate of penetration is three orders of magnitude smaller ( $1.5 \cdot 10^{-8}$  moles/cm<sup>2</sup> in 1 hr) and no saturation is observed in days.

This behavior is characteristic of a nonsteady-state diffusion process. The slope of the straight line, curve 2 in Fig. 1, is given by  $2c_s \sqrt{D/\pi}$  (8), where  $c_s$  and  $D$  are the solubility and diffusion coefficient of H<sub>3</sub>O<sup>+</sup> in  $\beta$  alumina. Values for  $c_s$  and  $D$  individually are presently not known. An upper limit of  $D_{\max} = 3.5 \cdot 10^{-8}$  cm<sup>2</sup>/sec is established by the absence of saturation in 140 hr. This is a reasonable value as it falls into the range of the known self-diffusion coefficients of Na<sup>+</sup> and K<sup>+</sup> in  $\beta$  alumina at 25°C, namely,  $4.0 \cdot 10^{-7}$  and  $9.6 \cdot 10^{-9}$  cm<sup>2</sup>/sec (9). For uniform H<sub>3</sub>O<sup>+</sup> distribution in the  $\beta$  alumina, the solubility corresponding to  $D_{\max}$  is  $1.8 \cdot 10^{-6}$  moles H<sub>3</sub>O<sup>+</sup>/cm<sup>3</sup>, equivalent to a mole ratio H<sub>3</sub>O<sup>+</sup>:Na<sup>+</sup>  $\sim$  1:4000. The extent of ion exchange in H<sub>2</sub>O at 25°C is thus very small compared to the ratio H<sub>3</sub>O<sup>+</sup>:Na<sup>+</sup> = 1:1 obtained by repeated treatment in boiling H<sub>2</sub>SO<sub>4</sub> (1).

**Resistivity changes.**—The exchange of H<sub>3</sub>O<sup>+</sup> against Na<sup>+</sup> ions is expected to affect the resistivity of  $\beta$  alumina. We have determined the changes in d-c and a-c resistivity (at 1 kHz) that accompany the exposure of dry sintered  $\beta$  alumina to water or water vapor for increasing lengths of time. Curves 3 and 4 in Fig. 1 show that both resistivities increase significantly and proportional to  $\sqrt{t}$  without showing evidence for saturation. This behavior parallels that found for the H<sub>3</sub>O<sup>+</sup> exchange and is radically different from that observed for H<sub>2</sub>O occlusion. For the dry sample ( $t = 0$ ), the d-c resistivity is only slightly larger than the a-c resistivity. However, with increasing exposure to water, the former rises considerably faster, indicating increasing capacitive effects due to H<sub>3</sub>O<sup>+</sup> diffusion. The original low resistivity values can be re-established by air drying at 900°C.

Assuming the resistivity increase to be caused by H<sub>3</sub>O<sup>+</sup> diffusion into the lattice, one arrives at a model of a band of high-resistivity material penetrating into low-resistivity material with the thickness of the latter progressively decreasing. Treatment of this simple model of two resistivities in series yields the expression  $\rho(t) = \rho_\beta + 2\pi\rho_{H\beta} \sqrt{Dt}/d$ , with  $\rho_\beta$  and  $\rho_{H\beta}$  the resistivities of dry and hydrated  $\beta$  alumina and  $d$  the sample thickness. The agreement between observed and predicted behavior indicates that H<sub>3</sub>O<sup>+</sup> diffusion into the lattice, not water occlusion, causes the resistivity increase of  $\beta$  alumina when exposed to water. Since identical effects are observed on exposure to water vapor, it appears that multi-molecular adsorption and capillary condensation [see, for example, Ref. (10)] in micropores and cleavage planes are necessary precursors for H<sub>3</sub>O<sup>+</sup> exchange. Only after liquid water has been formed, can ion exchange proceed with concurrent formation of NaOH in pores and rifts.

The effects of water vapor on resistivity are consistent with the long-term increase of the  $c_0$  lattice parameter (2). This and the fact that complete H<sub>3</sub>O<sup>+</sup> exchange leads to an even larger increase in  $c_0$  (1) is additional evidence that H<sub>3</sub>O<sup>+</sup> exchange causes the observed resistivity increases.

**Grain boundary vs. intragrain effects.**—The mathematical treatment of H<sub>3</sub>O<sup>+</sup> diffusion employs a con-

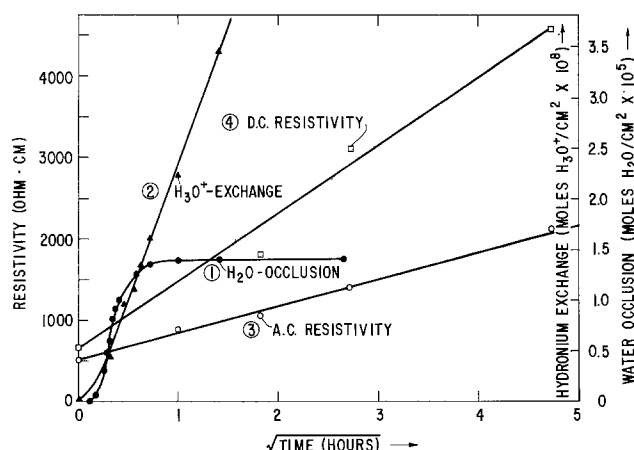


Fig. 1. Water occlusion and hydronium ion exchange (right ordinate) and d-c and a-c resistivity (left ordinate) of sintered dense  $\beta$  alumina as a function of time of exposure to water.

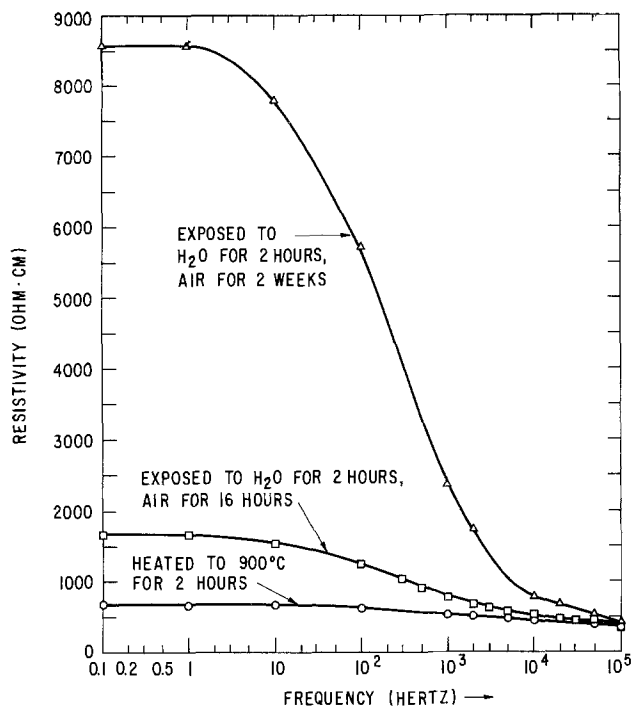


Fig. 2. Specific impedance of dry and moist sintered  $\beta$  alumina as a function of frequency.

tinuum model with effective resistivities. As such it averages over intragrain and grain boundary effects. However, it is of interest to know whether the large resistivity increase is mainly associated with hydronium ions in the lattice of the crystal grains or their boundaries.

The frequency dependence of the  $\beta$  alumina impedance (7, 11) allows a distinction between these two effects. Figure 2 shows the absolute value of the specific impedance plotted against the logarithm of the frequency. All three curves exhibit an upper limit of the impedance at low frequencies, a decrease in a range from 1 to  $10^4$  Hz and a lower impedance limit at frequencies larger than 50 kHz. The impedance limit at high frequencies is relatively insensitive to water exposure of  $\beta$  alumina, increasing from 440 ohm-cm for a dry disk (lower curve) to 530 ohm-cm for the same disk after long-term exposure to water and water vapor (upper curve). On the contrary, the specific impedance at its low-frequency limit is exceedingly sensitive to water exposure: It increases from 675 ohm-cm for the dry disk to 1780 ohm-cm after 2 hr in water and 16 hr in moist air and to 8600 ohm-cm after an additional 2 weeks in moist air.

Powers and Mitoff (7) studied the impedance of sintered  $\beta$  alumina with different grain size. They found that (a) the high-frequency limit is essentially identical to the grain or crystal resistivity,  $\rho_c$ , (b) the low-frequency limit is determined by both the crystal and grain boundary resistivity,  $\rho_b$ , and (c) the crossover frequency is inversely proportional to the grain boundary capacity,  $C_b$ . Due to the random orientation of the crystal grains, the high-frequency limit of the specific impedance is about 30% larger than the crystal resistivity. Hence, we obtain for  $\rho_c$  values of 290 ohm-cm for dry and 350 ohm-cm for moist  $\beta$  alumina. With a measured average grain size of  $10^{-3}$  cm and an assumed grain boundary width of  $5 \cdot 10^{-8}$  cm, we have computed the following values for  $\rho_b$  and  $C_b$ ;  $\rho_b$  increases from  $4.7 \cdot 10^6$  ohm-cm for dry  $\beta$  alumina to  $2.5 \cdot 10^7$  ohm-cm for short-term exposure to moisture and to  $1.6 \cdot 10^8$  ohm-cm for long-term exposure; the grain boundary capacities  $C_b/A$  for the three cases are 460, 160, and  $33 \mu\text{F}/\text{cm}^2$ . The effect of hydronium ions, diffusing into sintered  $\beta$  alumina when exposed to

water, is such as to significantly raise the grain boundary resistivity and lower the grain boundary capacity. The concurrent rise in crystal resistivity is relatively minor, i.e., only 20%.<sup>1</sup> The association of  $\text{H}_3\text{O}^+$  ions with the grain boundaries explains why relatively small amounts ( $\text{H}_3\text{O}^+:\text{Na}^+ = 1:4000$ ) have such significant effect on the resistivity of sintered  $\beta$  alumina.

On  $\beta$  alumina tubes of very much different processing history, Powers and Mitoff obtained typical values of  $\rho_c$  between 80 and 90 ohm-cm,  $\rho_b$  between 1.5 and  $4 \cdot 10^7$  ohm-cm, and  $C_b/A$  between 50 and  $100 \mu\text{F}/\text{cm}^2$ .<sup>2</sup> The agreement with the values of  $\rho_b$  and  $C_b/A$  obtained in this study is good, considering the strong effect of  $\beta$  alumina composition (7) and moisture. However,  $\rho_c$  in this study was found considerably larger (290 ohm-cm) than the above values or the 72 ohm-cm obtained on Monofrax single crystals (12). These discrepancies may be due to the different Na-content of the different samples, i.e., Na:Al = 1:8.5 in the present study vs. 1:7.9 in Ref. (7) and 1:9.4 in Ref. (12).

### Conclusions

When sintered  $\beta$  alumina is exposed to water or water vapor, two processes occur simultaneously: (i) the rapid exothermic occlusion of water, probably by micropores and cleavage planes, reaching saturation within a fraction of an hour and (ii) the slow diffusion of hydronium ions into the crystal lattice, leading to ion exchange with the sodium ions in the conducting planes, with no evidence for saturation within days. A pronounced increase in the  $\beta$  alumina resistivity accompanies the exchange of even a small fraction of the sodium ions. The effect of hydronium ions is such as to raise the resistivity and lower the capacity of the grain boundaries by more than an order of magnitude. The concurrent rise in intragrain resistivity amounts to only 20%.

### Acknowledgments

The author gratefully acknowledges valuable discussions with M. W. Breiter, D. W. McKee, S. P. Mitoff, and R. W. Powers and experimental help from D. W. McKee and E. Szymalak.

Manuscript submitted Dec. 4, 1975; revised manuscript received ca. Feb. 2, 1976.

Any discussion of this paper will appear in a Discussion Section to be published in the December 1976 JOURNAL. All discussions for the December 1976 Discussion Section should be submitted by Aug. 1, 1976.

Publication costs of this article were partially assisted by General Electric Company.

<sup>1</sup> Whittingham and Huggins (12) believe to have evidence for a lowering of the resistivity of Monofrax  $\beta$  alumina crystals due to moisture.

<sup>2</sup> The capacities  $C_b$  reported by Powers and Mitoff (7), i.e.,  $0.012$ – $0.02 \mu\text{F}/\text{cm}$ , pertain to an equivalent circuit and are related to the grain boundary capacity  $C_b$  by  $C_b = C_b' A/d_c$ , where  $d_c =$  average grain size.

### REFERENCES

- H. Saalfeld, H. Matthies, and S. K. Datta, *Ber. Deut. Keram. Ges.*, **45**, 212 (1968).
- W. L. Roth and S. P. Mitoff, General Electric Report No. 71-C-277 (1971).
- M. Bettman, in "Beta-Alumina Electrolytes," by J. T. Kummer, *Progr. Sol. State Chem.*, **7**, 141 (1972).
- D. Kline, H. S. Story, and W. L. Roth, *J. Chem. Phys.*, **57**, 5180 (1972).
- F. G. Will and S. P. Mitoff, *This Journal*, **122**, 457 (1975).
- R. J. Charles, W. J. Dondalski, and S. P. Mitoff, U.S. Pat. 3,607,436 (1971).
- R. W. Powers and S. P. Mitoff, *This Journal*, **122**, 226 (1975).
- D. J. BenDaniel and F. G. Will, *ibid.*, **114**, 909 (1967).
- Y.-F. Yu Yao and J. T. Kummer, *J. Inorg. Nucl. Chem.*, **29**, 2453 (1967).
- J. H. deBoer, "The Dynamical Character of Adsorption," p. 210, Clarendon Press, Oxford (1953).
- G. C. Farrington, *This Journal*, **121**, 120 (1974).
- M. S. Whittingham and R. A. Huggins, *J. Chem. Phys.*, **54**, 414 (1971).

# Dopant Effects on D-C Dynamic Scattering in a Liquid Crystal: Microscopic Pattern Studies

Hong Sup Lim\* and J. David Margerum

Hughes Research Laboratories, Malibu, California 90265

Our studies on the microscopic patterns of d-c dynamic scattering (DS) show that the electrochemical properties of dopants determine the dominant charge injection reaction, direction of liquid crystal (LC) flow, and location of the LC turbulence. This report compares different dopants (an electron acceptor, an electron donor, and a nonreactive salt) in an ester LC. These results differ substantially from earlier microscopic observations (1,2) of d-c DS in other LC's, but are consistent with our studies (3) showing that redox dopants (donors and acceptors which readily undergo reversible electrochemical reactions in the LC) give d-c DS at lower threshold voltages as well as giving higher scattering levels and much longer lifetimes than salt dopants.

A nematic LC (4) designated as HRL-2N10 is used. It has a nematic range of about 18°-55°, a dielectric anisotropy of  $\epsilon_a = -0.12$  (25°C, 500 Hz) and a birefringency of  $\Delta n = 0.14$  (25°, 545 nm). In the undoped state, it is highly resistive ( $\rho_{\perp} = 3.8 \times 10^{11}$  ohm-cm at 100 Hz) and does not show DS effects. The salt dopant used is tetrabutylammonium trifluoromethanesulfonate (TBATMS); the acceptor is (2,4,7-trinitro-9-fluorenylidene)malononitrile (TFM); and the donor is di-*n*-butylferrocene (DBF).

Electrochemical studies (5) in solvents containing 0.1M tetrabutylammonium perchlorate show decomposition potentials (*vs.* saturated calomel electrode) of the LC components at about +1.7V (in acetonitrile) for oxidation and -2.2V (in dimethylformamide) for reduction. The formal reduction potentials (in acetonitrile *vs.* SCE) for the reversible electrode process of the redox dopants are quite low, *e.g.*, 0.03V for TFM and 0.32V for DBF. Thus when the LC contains TFM or DBF, the electrochemical reactions of these dopants should be a dominant factor in the passage of current through the LC (6). This is confirmed by using a polarizing microscope to observe the direction of LC flow between electrodes. Test cells (Fig. 1) are made by sandwiching the LC between a substrate containing two thin-film transparent electrodes and a glass cover plate with a 51  $\mu\text{m}$  thick Mylar spacer. This cell geometry is chosen to allow space for the back flow of the LC outside the area of observation, *i.e.*, in the periphery of the cell where the field is low. The LC is aligned parallel to the surface of the glass and perpendicular to the electric field by a rubbing technique. With TFM added, the LC flow is predominately from the negative to the positive electrode, while with DBF added the predominant LC flow is from positive to negative. When equimolar mixtures are added, the LC flow in each direction is approximately balanced, which is also the case when the salt dopant is used. These flow patterns are observed by the movement of dust particles in the LC. The flow directions are also confirmed by studies in tubular cells with screen electrodes and sidearm capillaries to indicate the pressure effect of the LC flow.

The direction of the LC flow is consistent with a unipolar space charge injection followed by the propagation of the space charge under the influence of the applied electric field, as previously observed (2) or discussed (7) by others. Our results indicate that in the presence of TFM unipolar injection of negative ions

is probably dominant ( $\text{TFM} + e^- = \text{TFM}^-$ ), followed by the reverse reaction at the positive electrode. Similarly with DBF, unipolar injection of positive ions is probably dominant ( $\text{DBF} = \text{DBF}^+ + e^-$ ) followed by the reverse reaction at the negative electrode. A simultaneous bipolar injection occurs when both redox dopants or when the salt is present. However, when the dopant is a nonreactive salt, LC radical ions (8,9) are probably formed at the electrodes.

Scattering patterns with the different dopants at various applied voltages are shown in Fig. 2. (No scattering was observed with the salt dopant at 40V.) With the salt dopant, the scattering pattern has a line structure which contains alternating lines originating from each electrode. Thin flow lines of LC are initiated from each electrode at the same time and propagate toward the opposite electrode. Dust particles move along the lines in the direction of the propagation, indicating that the lines are caused by LC flow. These effects are similar to Williams domains (10), in which the source of the LC hydrodynamic motion has been well analyzed (11-13). However, with a redox dopant the general appearance of the scattering pattern is quite different. Turbulent motions of LC are observed at lower voltages, without formation of a regular line structure. The turbulence is initiated from one electrode and propagates toward the other. Except at very high voltages, the turbulence does not reach the opposite electrode but remains localized near the electrode where it was initiated. The most interesting observation is that the turbulence is initiated from the negative electrode when the dopant is the donor and from the positive when the dopant is the acceptor, while the charge injection and the liquid crystal flow are in the opposite directions. Dust particles move from the rear of the nonturbulent electrode toward the turbulent electrode and travel across it.

When the redox dopant is a balanced mixture of the acceptor and donor, the turbulence occurs more randomly. At low voltages turbulence begins at both

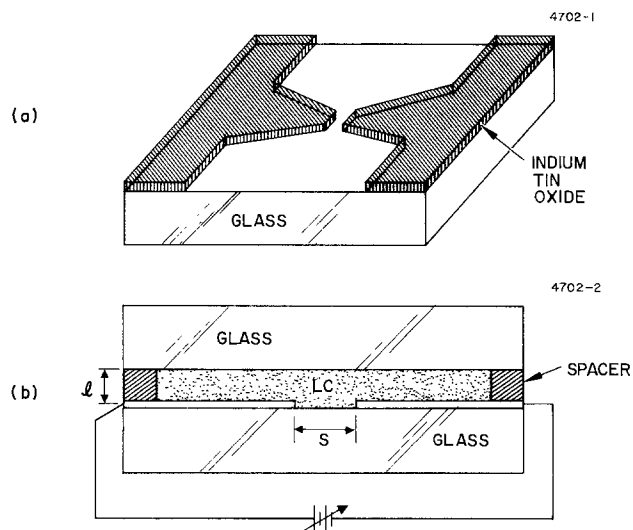
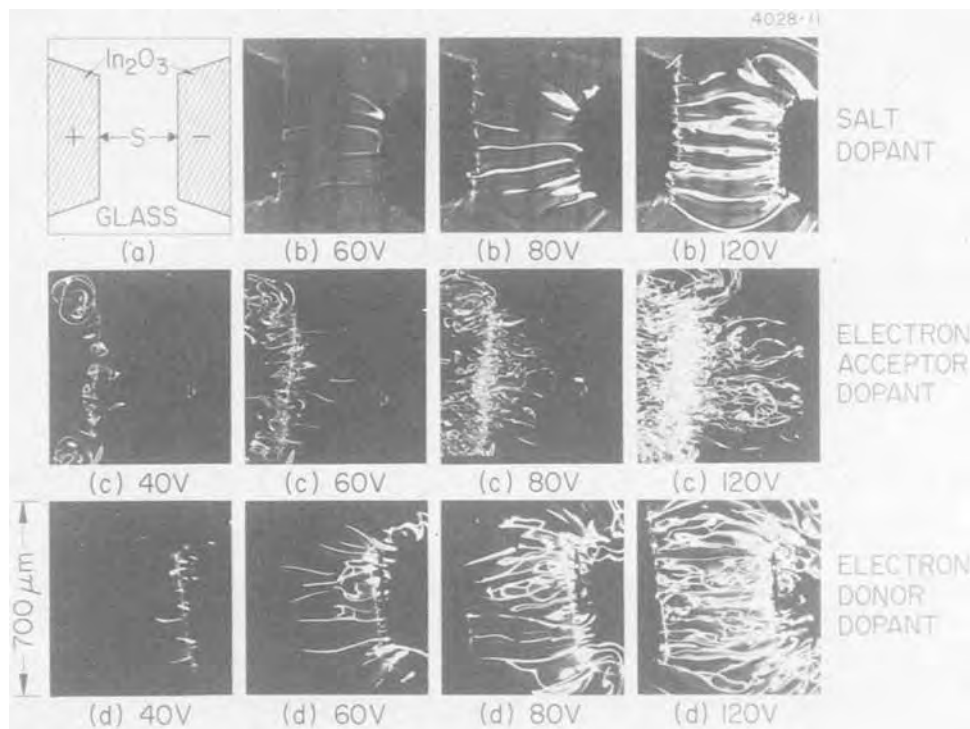


Fig. 1. Test cells for microscopic pattern studies of d-c DS. (a) Substrate with electrodes. (b) Cross section of assembled cell, with  $S \sim 380 \mu\text{m}$  and  $l = 51 \mu\text{m}$ . The microscope view is from the top, perpendicular to the applied field.

\* Electrochemical Society Active Member.  
Key words: redox dopant, salt dopant, charge injection, liquid crystal flow.

Fig. 2. Photographs of the microscopic patterns of DS. (a) Schematic view of the electrodes. (b) 0.0004% TBATMS ( $\rho \sim 5 \times 10^9$  ohm-cm;  $S = 350 \mu\text{m}$ ). (c) 0.5% TFM ( $\rho \sim 5 \times 10^9$  ohm-cm;  $S = 400 \mu\text{m}$ ). (d) 0.5% DBF ( $\rho \sim 3 \times 10^{10}$  ohm-cm;  $S = 375 \mu\text{m}$ ). The polarizers are crossed, with the analyzer perpendicular to the direction of the LC alignment.



electrodes and also between them, although to a lesser extent. Regions of flow may appear, but the over-all effect is more like a combination of pictures from the individual redox dopants than that of the salt dopant finger patterns. The onset of turbulence occurs at lower voltages with redox dopants (single or mixed) than with salt dopants, and the LC turbulence is greater at a given voltage. Similar results are observed with the same LC between transparent electrodes in conventional flat panel cells (3).

#### Acknowledgments

We are indebted to the Directorate of Chemical Sciences, Air Force Office of Scientific Research, contract F44620-72-C-0075 for partial financial support of this research.

Manuscript submitted Jan. 12, 1976; revised manuscript received Feb. 26, 1976.

Any discussion of this paper will appear in a Discussion Section to be published in the December 1976 JOURNAL. All discussions for the December 1976 Discussion Section should be submitted by Aug. 1, 1976.

Publication costs of this article were partially assisted by Hughes Research Laboratories.

#### REFERENCES

1. G. H. Heilmeyer, L. A. Zanoni, and L. A. Barton, *Proc. IEEE*, **56**, 1162 (1968).
2. J. C. Lacroix and R. Tobazeon, *Appl. Phys. Letters*, **20**, 251 (1972).
3. H. S. Lim and J. D. Margerum, *ibid.*, **28**, 478 (1976).
4. A four-component mixture of *p*-butylphenyl *p*-toluate, *p*-butoxyphenyl *p*-butoxybenzoate, *p*-butoxyphenyl *p*-hexyloxybenzoate, and *p*-butoxyphenyl *p*-octyloxybenzoate in a weight ratio of 15:5:9:9, respectively.
5. Authors' unpublished results.
6. The current level in the experiments was much lower than the expected diffusion-limited current of the redox dopants.
7. F. Gaspard and R. Herino, *Appl. Phys. Letters*, **24**, 452 (1974).
8. A. Lomax, R. Hirasawa, and A. J. Bard, *This Journal*, **119**, 1679 (1972).
9. A. Denat and B. Gosse, *Chem. Phys. Letters*, **22**, 91 (1973).
10. R. Williams, *J. Chem. Phys.*, **39**, 384 (1963).
11. E. F. Carr, *Mol. Cryst. Liq. Cryst.*, **7**, 253 (1969).
12. W. Helfrich, *J. Chem. Phys.*, **39**, 384 (1969).
13. P. A. Penz, *Phys. Rev. Letters*, **24**, 1405 (1970).

## DISCUSSION SECTION



This Discussion Section includes discussion of papers appearing in the *Journal of The Electrochemical Society*, Vol. 118, No. 1; January 1971; and Vol. 122, No. 7, 9, 10, 11, and 12; July, September, October, November, and December 1975.

### Electrochemical Properties of $\text{RbAg}_4\text{I}_5$ Solid Electrolyte I. Conductivity Studies

B. Scrosati, G. Germano, and G. Pistoia (pp. 86-89, Vol. 118, No.1)

**K. Shahi:**<sup>1</sup> In the above paper the authors have reported some thorough and systematic investigations

<sup>1</sup> Department of Physics, University of Gorakhpur, Gorakhpur 273001, India.

on a greatly interesting solid electrolyte,  $\text{RbAg}_4\text{I}_5$ . They have reported the specific conductivity also as a function of pellet compression pressure in the range 0-5600 kg/cm<sup>2</sup>. The conductivity increases, as expected, with increasing compression pressure and becomes highest ( $\sigma = 0.243 \pm 3\%$  ohm<sup>-1</sup> cm<sup>-1</sup> at 25°C) at the pressure of 1200 kg/cm<sup>2</sup>. At pressures higher than 1200 kg/cm<sup>2</sup>, they have observed a uniform decrease in conductivity up to the highest pressure (5600 kg/cm<sup>2</sup>) employed, and attribute it to a certain decomposition of the electrolyte or some possible phase changes.

We, in our series of measurements on high conductivity solid electrolytes,<sup>2</sup> have found for all the solid electrolytes including  $\text{RbAg}_4\text{I}_5$ , that the conductivity increases as the compression pressure increases and attains a maximum value ( $0.26 \pm 3\%$  ohm<sup>-1</sup> cm<sup>-1</sup> at 30°C for  $\text{RbAg}_4\text{I}_5$  pellet compressed at 1500 kg/cm<sup>2</sup>) as usual, and remains constant for the higher pressures, examined up to 3900 kg/cm<sup>2</sup>, unlike that observed by Dr. Scrosati.

The conductivity of polycrystalline  $\text{RbAg}_4\text{I}_5$  has also been measured by Dr. Owens<sup>3</sup> and Dr. Raleigh.<sup>4</sup> Owens reports a conductivity of 0.30 ohm<sup>-1</sup> cm<sup>-1</sup> at 30°C for a pellet which was compressed at  $\sim 3600$  kg/cm<sup>2</sup> while Raleigh reports  $0.28 \pm 0.3\%$  ohm<sup>-1</sup> cm<sup>-1</sup> at 25°C for the pellets compressed in the pressure range 1600-3200 kg/cm<sup>2</sup>. Both results are free from any contact resistance and are in excellent agreement if the temperature dependence factor of 1.04% per °C<sup>5</sup> is considered.

If the electrolyte  $\text{RbAg}_4\text{I}_5$  undergoes some phase changes or dissociates to some nonconducting material when compressed at pressures higher than 1200 kg/cm<sup>2</sup>, as observed by Scrosati *et al.*; the latter investigations,<sup>3,4</sup> should seldom give the highest values of conductivity, and, furthermore, which are in excellent agreement, because in these investigations the pellets used are compressed at much higher pressures. As such there appears no evidence of dissociation of  $\text{RbAg}_4\text{I}_5$  at higher pressures, at least up to 3900 kg/cm<sup>2</sup> and, therefore, the observation of Scrosati *et al.* would seem unlikely.

**B. Scrosati:**<sup>5a</sup> I thank Dr. Shahi for having brought my memory back to a paper published in 1971 and work performed in the now-far 1970 when studies on  $\text{RbAg}_4\text{I}_5$  and on solid electrolytes in general were in a very preliminary stage.

In 1976, after the large amount of systematic work which has been carried out on the structural and thermodynamic properties of  $\text{RbAg}_4\text{I}_5$ , it is clear how the hypothesis of a decomposition or of a possible phase change of the electrolyte under moderate pressure appears unrealistic. To anyone just a little familiar with work on solid ionic conductors it is obvious how the slight change in conductivity reported in our paper was probably due to electrode/electrolyte contact effects.

I would like to remark here how a discussion of a paper to be really proficient and scientifically stimulating should be reported within a year of its publication, as, on the other hand, has always, to my knowledge, been the custom of the JOURNAL.

### Catalytic Decomposition of Nitric Oxide on Zirconia by Electrolytic Removal of Oxygen

S. Pancharatnam, R. A. Huggins, and D. M. Mason  
(pp. 869-875, Vol. 122, No. 7)

**K. J. Lim and M. Boudart:**<sup>6</sup> In the paper under discussion, Pancharatnam, Huggins, and Mason compared the rates of nitric oxide decomposition on platinum reported by a number of investigators. They concluded that the agreement between data obtained by very different methods was quite good, except for data of Amirnazmi *et al.*,<sup>7,8</sup> obtained in a flow system, in the absence of oxygen in the feed.

<sup>2</sup> K. Shahi, Ph.D. Thesis, Gorakhpur University (1975).

<sup>3</sup> B. B. Owens and G. R. Argue, *This Journal*, **117**, 898 (1970).

<sup>4</sup> D. O. Raleigh, *J. Appl. Phys.*, **41**, 1876 (1970).

<sup>5</sup> B. B. Owens and G. R. Argue, *Science*, **157**, 308 (1967).

<sup>5a</sup> Istituto di Chimica Fisica e Electrochimica, University of Rome, Italy.

<sup>6</sup> Department of Chemical Engineering, Stanford University, Stanford, California 94305.

<sup>7</sup> A. Amirnazmi and M. Boudart, *J. Catal.*, **39**, 383 (1975).

<sup>8</sup> A. Amirnazmi, J. E. Benson, and M. Boudart, *ibid.*, **30**, 55 (1973); A. Amirnazmi, Ph.D. Thesis, Stanford University (1973).

In fact, the reported discrepancy disappears if the data are correctly extrapolated to the chosen standard comparison condition of 48 Torr NO. A careful analysis of the original papers shows that the data of the batch studies should all be extrapolated using a second-order dependence on NO rather than by the first-order extrapolation of Pancharatnam *et al.* The early data of Green and Hinshelwood,<sup>9</sup> though reported to be first order in NO, were actually fitted better by a second-order expression, as shown by Bachman and Taylor<sup>10</sup> whose own results were also second order. In addition, the recent batch study of Pancharatnam, Lim, and Mason<sup>11</sup> presented evidence for a second-order dependence. When their results at three different NO pressures (400, 800, and 2260 Torr) were extrapolated to 48 Torr using first-order kinetics, three different curves resulted. However, extrapolation using their reported second-order rate expression yielded a single straight line for all the data. Furthermore, Amirnazmi *et al.*<sup>7,8</sup> have shown that NO decomposition on an oxygen-free Pt surface at high temperature follows second-order kinetics.

With the proper extrapolation carried out where needed, all the data summarized in Fig. 11 of the paper under discussion are shown in our Fig. 1. It can

<sup>9</sup> T. E. Green and C. M. Hinshelwood, *J. Chem. Soc.*, **129**, 1709 (1926).

<sup>10</sup> P. W. Bachman and G. B. Taylor, *J. Phys. Chem.*, **33**, 447 (1929).

<sup>11</sup> S. Pancharatnam, K. J. Lim, and D. M. Mason, *Chem. Eng. Sci.*, **30**, 781 (1975).

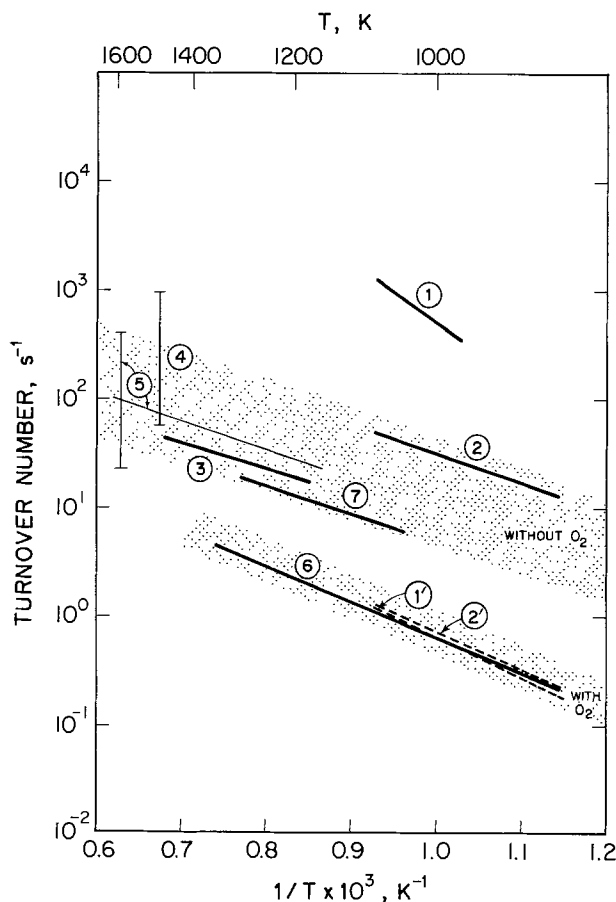


Fig. 1. Comparison of various studies of the decomposition of nitric oxide on platinum, with initial rates expressed as turnover numbers, all data extrapolated to 48 Torr NO. Curve 1': porous Pt, open circuit; 2': nonporous Pt, open circuit (paper under discussion). Curve 1: porous Pt with electrolytic pumping of oxygen (paper under discussion); curve 2: nonporous Pt with electrolytic pumping (paper under discussion); curve 3: heated Pt wire (Ftn<sup>11</sup>); curve 4, heated Pt wire (Ftn<sup>10</sup>); curve 5, heated Pt wire (Ftn<sup>9</sup>); curve 6, supported Pt/Al<sub>2</sub>O<sub>3</sub> and Pt foil with O<sub>2</sub> in feed, extrapolated to zero (O<sub>2</sub>) (Ftn<sup>7,8</sup>); curve 7, Pt foil without O<sub>2</sub> in feed, extrapolated to zero (O<sub>2</sub>) (Ftn<sup>7,8</sup>).

be seen that there is good agreement for the case of oxygen-free platinum between the batch studies (curves 3, 4, and 5), the flow experiments with no added oxygen (curve 7), and the electrochemical results (curve 2). There is excellent accord for the oxygen-covered platinum case, curves 1' and 2' from the electrochemical results, and curve 6 from the flow experiments, but this is expected since Pancharatnam *et al.* chose a reasonable surface-roughness factor to conform their data to that of Amirnazmi *et al.*<sup>7,8</sup>

In conclusion, the agreement in the NO decomposition rates among the various investigators is significantly better than presented by Pancharatnam, Hug-gins, and Mason. Indeed, the agreement is remarkable

considering the widely different NO partial pressures studied (10-2260 Torr), forms of platinum catalyst (platinum wire, platinum foil and platinum crystallites supported on alumina, and sputtered platinum films on zirconia), and methods of analysis (batch pressure drop technique, differential flow reactor analysis using gas chromatography, and electrochemical monitoring using an oxygen pump). More importantly, the agreement between data reinforces the conclusion of Amirnazmi *et al.*<sup>7,8</sup> that oxygen is an inhibitor of the decomposition of NO on platinum, and the conclusion of Pancharatnam *et al.* that this inhibition can be removed by electrochemical pumping.

### Techniques for the Measurement of the Viscosity of a High Vapor Pressure Organic Electrolyte

H. Y. Kang and P. Bro (pp. 1155-1160, Vol. 122, No. 9)

C. R. Schlaikjer and N. Marincic:<sup>12</sup> We would like to call attention to Fig. 5 in the paper under discussion, where the authors present data for the density of electrolytes prepared by mixing liquid sulfur dioxide with various portions of acetonitrile-propylene carbonate-lithium bromide. The measured specific density of pure liquid sulfur dioxide is reported<sup>13-17</sup> in Table I. Somewhere between 90 w/o SO<sub>2</sub> and pure SO<sub>2</sub>, the specific gravity of the electrolyte would have to decrease with increasing SO<sub>2</sub> content in order to correspond with the literature values for the specific gravity of pure liquid SO<sub>2</sub> (see Table II). Based on the reported data of Kang and Bro, we have calculated the partial specific density of liquid sulfur dioxide as a function of the SO<sub>2</sub> content of these mixtures. According to Kang and Bro, the specific gravity of the electrolyte is proportional to the square of the weight fraction of SO<sub>2</sub>

$$\rho = kX^2 + C$$

where  $\rho$  = solution specific gravity, g cm<sup>-3</sup>;  $X$  = weight fraction of SO<sub>2</sub> (0.3-0.9);  $k$  and  $C$  are constants. We wish to find  $\partial V/\partial M$  cm<sup>3</sup> g<sup>-1</sup> where  $V$  = volume,

- <sup>12</sup> GTE Laboratories, Waltham, Massachusetts 02154.  
<sup>13</sup> E. W. Washburn, Editor, "International Critical Tables," McGraw-Hill, New York (1928).  
<sup>14</sup> Andreef, *Ann. Chem.*, 110, 1 (1859).  
<sup>15</sup> Cailletet and Mathias, *J. Phys. Radium*, 5, 549 (1886).  
<sup>16</sup> Cardoso, *Arch. Sci. Phys. Nat.*, 34, 127 (1912).  
<sup>17</sup> Lange, *Z. Angew. Chem.*, 12, 275 (1899).

cm<sup>3</sup> and  $M$  = weight of SO<sub>2</sub>, g for liquid sulfur dioxide based on the data of Fig. 5, and compare the results with the literature values for pure SO<sub>2</sub>. Since

$$X = \frac{M}{S + M} \quad \text{and} \quad M = \frac{SX}{1 - X} \quad [1]$$

where  $S$  = weight of AN, PC, and LiBr, g (LiBr: AN: PC = 3:10:5.13)

$$V = \frac{S + M}{\rho} = \frac{S + M}{kX^2 + C} = \frac{\left(\frac{SX}{1 - X}\right)}{kX^2 + C} = \frac{S}{(1 - X)(kX^2 + C)} \quad [2]$$

$$\frac{\partial V}{\partial M} = \frac{\partial V}{\partial X} \times \frac{\partial X}{\partial M} \quad [3]$$

$$\frac{\partial M}{\partial X} = \frac{S}{(1 - X)^2}; \quad \frac{\partial X}{\partial M} = \frac{(1 - X)^2}{S} \quad [4]$$

$$\frac{\partial V}{\partial X} = \frac{-S(-3kX^2 + 2kX - C)}{(1 - X)^2(kX^2 + C)^2} \quad [5]$$

$$\frac{\partial V}{\partial M} = \frac{3kX^2 - 2kX + C}{(kX^2 + C)^2} \quad [6]$$

Using the data presented in Fig. 5 and  $C = \rho$  when  $X = 0$  and  $k = \Delta\rho/\Delta(X^2)$  we find the results as indicated in Table III.

Table I

Temp °C	-40	-20	0	20	30	50	70
Specific density cm <sup>3</sup> g <sup>-1</sup>	0.6523	0.6739	0.6974	0.7231	0.7375	0.7722	0.8137
Specific gravity g cm <sup>-3</sup>	1.533	1.484	1.434	1.383	1.356	1.295	1.229

Table II

Temp °C	Electrolyte specific gravity at 89.1% SO <sub>2</sub>	Specific gravity of liquid SO <sub>2</sub>	Per cent difference
-40	1.570 g cm <sup>-3</sup>	1.533	-2.4
-20	1.525	1.484	-2.7
0	1.490	1.434	-3.8
20	1.443	1.383	-4.2
30	1.415	1.356	-4.2
50	1.366	1.295	-5.2
70	1.32	1.229	-6.9

Evaluating Eq. [6] for various values of  $X$  and temperature, we find the results in Table IV.

The values of  $\partial V/\partial M$  most nearly match those of pure liquid SO<sub>2</sub> for low values of  $X$ . At higher values of  $X$ ,  $\partial V/\partial M$  becomes smaller than the specific density of the pure solvent ( $1/\rho$ ). If the data in Fig. 5 are correct, they would suggest that the lithium bromide, acetonitrile, and propylene carbonate occupy spaces between the SO<sub>2</sub> molecules in solutions with high SO<sub>2</sub> content.

The reported data are not necessarily inconsistent with the literature values for pure liquid sulfur

Table III

Temp °C	-40	-20	0	20	30	50	70
$C$ (g cm <sup>-3</sup> )	1.12	1.10	1.08	1.065	1.05	1.03	1.01
$k$ (g cm <sup>-3</sup> )	0.513	0.490	0.468	0.425	0.425	0.413	0.375



Table IV

Temp °C	Partial specific density of SO <sub>2</sub> in the electrolyte at various weight fractions of SO <sub>2</sub>							Reported specific density 1/ρSO <sub>2</sub>
	0.3	0.4	0.5	0.6	0.7	0.8	0.9	
-40	0.669	0.661	0.637	0.622	0.615	0.612	0.612	0.6523
-20	0.717	0.679	0.654	0.639	0.632	0.629	0.629	0.6739
0	0.735	0.697	0.672	0.657	0.649	0.646	0.646	0.6974
20	0.760	0.724	0.699	0.684	0.675	0.672	0.671	0.7231
30	0.768	0.731	0.706	0.690	0.682	0.679	0.678	0.7375
50	0.785	0.747	0.722	0.706	0.697	0.694	0.693	0.7722
70	0.814	0.777	0.752	0.736	0.727	0.723	0.722	0.8137

dioxide, but the most interesting part of Fig. 5 has been omitted. Perhaps the authors could have included specific gravity measurements for pure SO<sub>2</sub> along with the rest of their data, if their original purpose made it unnecessary to measure electrolyte specific gravities for values of X above 0.9. With the specific gravities for pure SO<sub>2</sub>, the proposed quadratic function cannot be valid above X = 0.9.

### On the Kinetics of the Breakdown of Passivity of Preanodized Aluminum by Chloride Ions

Z. A. Foroulis and M. I. Thubrikar  
(pp. 1296-1301, Vol. 122, No. 10)

**J. Augustynski and J. Painot:**<sup>18</sup> In the paper under discussion, Foroulis and Thubrikar propose a model of passivity breakdown of aluminum by chloride ions, supported essentially by their investigation of the induction times for pitting nucleation on preanodized aluminum in neutral chloride solutions. The postulated mechanism involves adsorption of Cl<sup>-</sup> ions on the aluminum oxide-solution interface at the critical potential and the subsequent localized dissolution of the oxide film via formation of a soluble, basic aluminum chloride salt. These suggestions, substantially different from models of the passivity breakdown discussed earlier in literature,<sup>19-23</sup> call for comment. The mechanism proposed by Foroulis and Thubrikar implies that at potentials more negative than the critical pitting potential the interaction between chloride ions and the hydrated oxide film is restricted to the oxide-solution interface. However, direct experimental evidence exists that chloride ions become included in the oxide film on aluminum before the critical pitting potential ( $E_{cr}$ ). In our study<sup>24,25</sup> by x-ray photoelectron spectroscopy (XPS or ESCA) of the oxide-covered aluminum exposed to chloride solutions we show that the chlorine content of the aluminum oxide film increases from ca. 3 a/o Al atom at the open-circuit potential ( $E_{st}$ ) to 16 a/o at  $E_{cr} - 0.01V$  (Table I: 0.1N NaCl solution). These XPS analyses were performed on samples prepolarized both in weakly acid (pH 3) and in neutral solutions; the results were similar. The film thickness being, in the former case, less than the XPS effective depth (ca. 20-25Å),<sup>26</sup> the relative Cl concentrations given in Table I are, in fact, the mean Cl concentrations in the whole oxide film covering passive aluminum. Consequently these results should be considered as evidence for chloride ion incorporation into the aluminum oxide film at the potentials more negative than  $E_{cr}$ . Indeed, the mean Cl concentration of 16

Table I. Relative concentrations of Cl species detected in  $\gamma$ -Al<sub>2</sub>O<sub>3</sub> film on aluminum samples pre-exposed to 0.33M Al<sub>2</sub>(SO<sub>4</sub>)<sub>3</sub> + 0.1M NaCl solution at various potentials

Potential (V vs. SCE)	Relative concentration of Cl (a/o)*
-1.20**	3
-0.96	10
-0.73	13
-0.70	16
-0.67***	16

\* Referenced to aluminum.  
\*\* Open-circuit potential.  
\*\*\*  $E_{cr} - 0.010V$ .

Table II. Binding energies of Cl 2p<sup>3/2</sup> electron for some chlorine species

Cl detected in $\gamma$ -Al <sub>2</sub> O <sub>3</sub> film	Binding energy (eV)*
AlCl <sub>3</sub>	203.4
KCl	204.1
KClO <sub>4</sub>	205.45**
	215.0**

\* Referenced to C 1s level at 290 eV.<sup>28</sup>  
\*\* From F<sup>2n</sup>.

a/o is much too high to be assigned to ion adsorption on the hydrated oxide-solution interface, especially if one takes into account that the chloride ion action is localized in certain selected sites in the oxide film. Our XPS results also throw some light on the nature of the Cl bonding inside the oxide film. As shown in Table II, the binding energy of the Cl 2p<sup>3/2</sup> electrons for Cl included in the oxide film is somewhat lower than the corresponding value for AlCl<sub>3</sub>, suggesting that Cl<sup>-</sup> ions entering the aluminum oxide lattice may form an aluminum oxychloride AlOCl. We would like to mention that our XPS results concerning natural, thin, aluminum oxide films go in the same direction as an earlier work of Heine *et al.*<sup>20</sup> who investigated the Cl<sup>-</sup> and SO<sub>4</sub><sup>2-</sup> incorporation into the aluminum oxide film formed by anodization. These authors have observed a marked decrease of the ionic resistance of the oxide film on the aluminum samples exposed to 1N sodium chloride solution. Turning to the paper of Foroulis and Thubrikar, we draw attention to the fact that the different pretreatment (anodization) conditions of aluminum may alter its anodic behavior, not only because of the variation in the film thickness, but also owing to the modifications in the chemical composition of the film. As a matter of fact, the SO<sub>4</sub><sup>2-</sup> anion is incorporated (up to 17%) into porous anodic films formed in sulfuric acid.<sup>27</sup> Thus, the increase of the critical pitting potential reported in the paper under discussion for the aluminum sample preanodized in 15% H<sub>2</sub>SO<sub>4</sub> could be alternatively explained by an inhibiting action of sulfate ions included in the oxide lattice.

**Z. A. Foroulis:**<sup>29</sup> We appreciate the comments by J. Augustynski and J. Painot and the summary of their recent ESCA data on the composition of thin aluminum surface oxide films formed by exposing freshly polished aluminum specimens in electrolytes containing 0.33M Al<sub>2</sub>(SO<sub>4</sub>)<sub>3</sub> + 0.1M NaCl solutions at various potentials.<sup>30</sup> We believe that their results do not contradict our postulated mechanism<sup>31-33</sup> of passivity

<sup>18</sup> Laboratoire de Chimie et d'Electrochimie Appliquées, Université de Genève, Genève, Switzerland.

<sup>19</sup> C. Edeleanu and U. R. Evans, *Trans. Faraday Soc.*, **47**, 1121 (1951).

<sup>20</sup> M. A. Heine, D. S. Keir, and M. J. Pryor, *This Journal*, **112**, 24 (1965).

<sup>21</sup> H. Böhm and H. H. Uhlig, *ibid.*, **116**, 906 (1969).

<sup>22</sup> J. A. Richardson and G. C. Wood, *Corrosion Sci.*, **10**, 313 (1970).

<sup>23</sup> D. A. Vermilyea, *This Journal*, **118**, 525 (1971).

<sup>24</sup> J. Painot and J. Augustynski, *Electrochim. Acta*, **20**, 747 (1975).

<sup>25</sup> J. Painot and J. Augustynski, *J. Electroanal. Chem.*, In press.

<sup>26</sup> This observation is substantiated by the presence of a weak Al<sup>3+</sup> signal (metallic aluminum) in the Al 2p spectrum.

<sup>27</sup> G. C. Wood, in "The Anodic Behavior of Metals and Semiconductors Series," Vol. 2, J. W. Diggle, Editor, pp. 220-222, Marcel Dekker, Inc., New York (1973).

<sup>28</sup> C. K. Jørgensen and H. Berthou, *Mat. fys. Medd. Danske Vid. Selskab*, **38**, No. 15 (1972).

<sup>29</sup> Department of Metallurgy and Materials Science, New York University, New York, New York 10019.

<sup>30</sup> J. Painot and J. Augustynski, *Electrochim. Acta*, **20**, 745 (1975).

<sup>31</sup> Z. A. Foroulis, in "Proceedings of the 5th International Congress on Metal Corrosion," NACE (1975).

<sup>32</sup> Z. A. Foroulis and M. J. Thubrikar, *This Journal*, **122**, 1296 (1975).

<sup>33</sup> Z. A. Foroulis and M. J. Thubrikar, *Werkstoffe Korrosion*, **26**, 350 (1975).



breakdown involving adsorption of chloride ions on the aluminum-oxide solution interface and subsequent localized dissolution of the oxide film via formation of a soluble basic aluminum chloride salt.

Under the experimental conditions used by Augustynski and Painot, it is not surprising as their ESCA data indicate that the oxide surface films formed on aluminum either as a result of natural immersion or by anodic polarization containing chloride ions. In their experiments, the aluminum specimens, prior to being immersed in solutions containing  $\text{Al}_2(\text{SO}_4)_3 + \text{NaCl}$ , were freshly polished with emery paper, and under these conditions, it is reasonable to assume that the aluminum electrodes were covered with a thin (about 25Å) air-formed oxide film which is generally considered to be an amorphous  $\gamma\text{-Al}_2\text{O}_3$ .<sup>34</sup> On exposure to aqueous electrolytes, these thin films are known to thicken at a rate which depends, among other factors, on potential and solution composition.<sup>34-37</sup> It is reasonable to expect that during the film-thickening process, which may initially involve at least partial dissolution of the thin air-formed film,<sup>38</sup> anions including chloride ions from the electrolyte are likely to be incorporated within the oxide lattice formed during the oxide-thickening process. In addition, a higher concentration of chlorides is likely to be incorporated in the oxide film when film thickening occurs at higher potentials.

It is therefore our view that the chloride ions found in the oxide films studied by Augustynski and Painot have their origin not in a passivity breakdown process but in a process of oxide film formation in solutions which contain chloride ions. This explains why chloride ions were found within the oxide film at potentials lower than the critical pitting potentials, at which pitting is not expected to occur.<sup>39,40</sup> The chloride ions, in the case of their experiments, were incorporated during the oxide formation (growth) process, which occurred at potentials lower than the critical pitting potential.

In the case of our experiments,<sup>32,33</sup> the kinetics of the passivity breakdown process was investigated using preanodized aluminum specimens with barrier oxide films of considerable thickness and reasonably well-known structures. The barrier oxide films were formed in solutions which did not contain chloride ions and therefore chloride ions could not be incorporated in the oxide film during formation of these oxide films. In this case, the reasonably thick barrier-type oxide films are likely to be "stable" upon immersion in the test electrolyte during the passivity breakdown experiments, and no further growth of the oxide film is likely to occur. The interaction of such an oxide film with  $\text{Cl}^-$  in solution during passivity breakdown experiments, according to our proposed passivity breakdown mechanism, should be restricted primarily to the oxide solution interface and no significant chloride concentration should be expected within the oxide film material.

This explanation is in accord with the recent findings of G. C. Wood *et al.*,<sup>41</sup> who investigated the interaction of preanodized barrier oxide-covered aluminum surfaces with solutions containing chloride ions at different potentials using secondary ion mass spectrometry. These authors reported that chlorides were abundantly present on the oxide-solution interface, but they found no measurable chloride within the oxide film material, either as a result of natural immersion or by anodic polarization.

It is our view that whether or not chloride ions are likely to be incorporated in the oxide film will very much depend on the thickness and structure of the oxide film pre-existing on the aluminum specimen prior to immersion in aqueous solutions containing chlorides.

When an oxide-covered aluminum specimen is immersed in an aqueous solution, the rate of migration of aluminum ions toward the oxide-solution interface and therefore thickening of the pre-existing oxide film will depend on the over-all potential drop (pd) between the bulk metal and the bulk solution which is controlled either by an external power source (e.g., a potentiostat) or by local action currents. Adsorption of anions such as  $\text{Cl}^-$ ,  $\text{OH}^-$ , etc. from solution on the oxide surface will also create an electrostatic field (due to image charges) which will also tend to accelerate the outward migration of aluminum cations and thus the thickening of the oxide film.

When aluminum covered with thin oxides, such as air-formed films or even thin films formed by anodization,<sup>42</sup> is immersed in an aqueous electrolyte containing  $\text{Cl}^-$ , the electrostatic field strength across the oxide film at constant over-all pd is sufficiently high, the rate of outward migration of aluminum ions through the film is considerable, and film thickening occurs until the oxide film reaches a thickness at which, for the given over-all pd, further migration of aluminum ions through the oxide film becomes negligible. During the surface oxide film thickening process, inclusion of solution anions such as  $\text{Cl}^-$ ,  $\text{SO}_4^{2-}$ , etc. in the oxide lattice is very likely to occur.

However, when aluminum covered with relatively thick oxide films, such as the barrier films used in our work<sup>32-33</sup> as well as those used by G. C. Wood, *et al.*,<sup>41</sup> is immersed in chloride-containing solutions, at constant over-all pd, because of the higher thickness of the pre-existing oxide film the electrostatic field strength across the oxide film is lower and thus the outward migration of aluminum cations is negligible, and thickening of the oxide film does not occur. This mechanism explains the results by Wood and co-workers<sup>41</sup> who found no measurable chloride within a preanodized barrier-type oxide film (of about 720Å) after it was exposed to 1M KCl at different potentials. It also explains the results of Painot and Augustynski<sup>30</sup> and M. A. Heine *et al.*<sup>42</sup> who reportedly found measurable amounts of chloride ions within thin oxide films.

Sulfate ions incorporated in the oxide film during anodization may have some influence on the behavior of oxide films during the passivity breakdown process. However, on the basis of results available to date,<sup>32,33</sup> we feel that the oxide film thickness is likely to be more important as far as the critical pitting potential than the presence of sulfate ions in the film as suggested by Augustynski and Painot.

Finally, it should be stated that the passivity breakdown model proposed in the paper under discussion should be applicable to aluminum whether or not the passive surface oxide film is "contaminated" with chloride ions which may have been incorporated in the oxide lattice during the process of oxide film formation.

### Hydrogen Production under Sunlight with an Electrochemical Photocell

A. Fujishima, K. Kohayakawa, and K. Honda  
(pp. 1487-1489, Vol. 122, No. 11)

**R. Bezman:**<sup>43</sup> The paper under discussion contains what I believe to be a subtle yet important error in the calculation of the energy conversion efficiency of the

<sup>34</sup> H. P. Godard, W. B. Jepson, M. R. Bothwell, and R. L. Kane, "The Corrosion of Light Metals," John Wiley & Sons, Inc., New York (1967).

<sup>35</sup> R. K. Hart, *Trans. Faraday Soc.*, **53**, 1020 (1957).

<sup>36</sup> H. P. Godard and E. G. Torrible, *Corrosion Sci.*, **10**, 135 (1970).

<sup>37</sup> M. J. Pryor, *ibid.*, **11**, 463 (1971).

<sup>38</sup> K. F. Lorking and J. E. O. Mayne, *J. Appl. Chem.*, **11**, 170 (1961).

<sup>39</sup> Z. A. Foroulis and M. J. Thubrikar, *Electrochim. Acta*, in press.

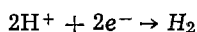
<sup>40</sup> H. Böhm and H. H. Uhlig, *This Journal*, **116**, 906 (1969).

<sup>41</sup> M. F. Abd Rabbo, G. C. Wood, J. A. Richardson, and C. K. Jackson, *Corrosion Sci.*, **14**, 645 (1974).

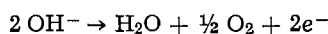
<sup>42</sup> M. A. Heine, D. S. Keir, and M. J. Pryor, *This Journal*, **112**, 24 (1965).

<sup>43</sup> 383 South Lexington Avenue, White Plains, New York 10606.

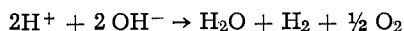
device described. The apparatus produces hydrogen and oxygen via a photoelectrolytic process involving water, and the authors compute its conversion efficiency as the ratio of the heat of combustion of the hydrogen it produces to the time-integrated insolation at its photoanode array. What is overlooked, however, is that the system does not merely electrolyze water. Since the anodes operate in 1.0M NaOH and the cathodes in 0.5M H<sub>2</sub>SO<sub>4</sub>, the electrode reactions are



at the cathode, and



at the anode, from which one finds that the actual cell reaction is



It is clear, therefore, that 1 mole of water is produced per mole of hydrogen, and that the enthalpy of the neutralization, which is essential for spontaneous operation of the cell, is provided not by the sun, but rather by the power plants of the firms that produce the NaOH and H<sub>2</sub>SO<sub>4</sub>.

The heat of combustion of hydrogen to water vapor is -57.8 kcal/mole, while the heat of neutralization of H<sup>+</sup> by OH<sup>-</sup> is approximately -13 kcal/mole. From these values one finds that, at best, the energy conversion efficiency calculated by the authors is overstated by ~25%. This alone is significant, but perhaps more so is the fact that remote energy consumption has not been acknowledged. I feel it is necessary that any new energy production technique be scrutinized to determine to the greatest extent practical not only the amount of energy that is produced, but the amount consumed in hardware fabrication, operation, and maintenance.

#### A. Fujishima,<sup>44</sup> K. Kohayakawa,<sup>45</sup> and K. Honda:<sup>44</sup>

We agree with the comments given by Bezman in relation to the contribution of the neutralization energy to the formation of hydrogen. This contribution was already pointed out in our previous paper<sup>46</sup> where the neutralization energy was expressed in the form of the electromotive force due to the difference in pH between the anolyte and the catholyte. As the electromotive force is 59 mV for unit pH difference in comparison with the thermodynamic decomposition voltage of water of 1.23V, the contribution of neutralization energy to the decomposition of water will be about 5% for each one unit pH difference.

As the integrated incident solar energy was not measured on the day of experiments in the present paper, the reported value of solar energy in Japan of 3000 kcal/m<sup>2</sup>/day was referred to and taking into consideration the above-mentioned contribution and the actual weather conditions of the day of experiments, the rough estimate of the conversion efficiency of 0.4% was given for a simple example.

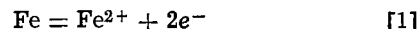
### A Limitation to the Mixed Potential Concept of Metal Corrosion

T. N. Andersen, M. H. Ghandehari, and H. E. Eyring  
(pp. 1580-1585, Vol. 122, No. 12)

**F. M. Donahue:**<sup>47</sup> The paper under discussion is extremely valuable (in my opinion) for two reasons: (i) the authors have correctly identified a mixed po-

tential system where interaction between the partial processes occurs, and (ii) they have supplied sufficient tabular data to allow a quantitative evaluation of their interpretations.

Let us consider the first point in some detail. Both the title of the paper and the text seem to indicate that they have somehow "discovered" something which has not been observed previously. Nearly two decades ago Heusler<sup>48</sup> (and he was probably not the first to note this!) showed that the kinetics of the reaction



in acid solution was dependent upon the hydrogen ion concentration, i.e., the reactant in the cathodic partial process in the corrosion reaction. Since then numerous other authors<sup>49-52</sup> have verified this interaction. This kind of interaction occurs with such frequency in mixed potential systems that this author wrote a paper indicating how the reaction orders for the interacting species (as well as the reaction orders for the "normal" species) could be determined from data at the mixed potential.<sup>53</sup> Therefore, the point the authors of the paper under discussion make that interdependence among the partial processes "does not seem to have been stressed previously" is in error. Admittedly, the interactions were not always indicated in the titles of the papers mentioned above (Ftn<sup>48,53</sup> are exceptions to this), but the text of these papers clearly speaks to such interactions.

The authors are correct in their critical remarks concerning the "superposition" approach. However, they seem to have drawn too much from Vetter's remark concerning the independence of the partial processes (Ftn<sup>54</sup>, p. 732) when the key point in mixed potential theory is "the important principle of additive combination of all partial processes"<sup>54</sup> which Vetter correctly ascribes to Wagner and Traud.<sup>55</sup> Mathematically, this may be written

$$i_{\text{net}}(E) = \sum_j i_j(E) \quad [2]$$

where  $i_{\text{net}}(E)$  is the observed (measured) current density flowing at a polyelectrode at an electrode potential (*vs.* some reference electrode),  $E$ , and  $i_j(E)$  represents the current associated with all electrochemically active species in the solution at that same potential. Equation [2] is merely a statement of the law of conservation of charge; no such law exists for the "conservation of polarization curves for partial processes."

In order to ascertain the presence of interactions, certain experiments are required. The authors have noted that experiments performed somewhat removed from the mixed potential (as in the case of Ftn<sup>48-52</sup>) may be in error due to changes in the "catalytic properties of the surface." This author agrees with this contention and, consequently, developed a scheme for studies at the mixed potential.<sup>53</sup> The authors have chosen a "middle ground" and provided sufficient data to allow an assay of their interpretations.

For the sake of uniformity, the subscripts for current density used by the authors in the paper under discussion will be adopted here. Further, since their reactions [1], [2], and [4] are associated with charge transfer processes (reaction [3], it would seem, is a liquid-phase, homogeneous reaction and cannot have an associated current density as the authors have done), Eq. [2] for the experiments in the presence of oxygen at a fixed electrode potential is

<sup>48</sup> K. E. Heusler, *Z. Elektrochem.*, **62**, 582 (1958).

<sup>49</sup> W. J. Lorenz, H. Yamaoka, and H. Fischer, *Ber. Bunsenges. Physik. Chem.*, **67**, 932 (1963).

<sup>50</sup> J. O'M. Bockris, D. Drazic, and A. R. Despic, *Electrochim. Acta*, **4**, 325 (1961).

<sup>51</sup> E. J. Kelly, *This Journal*, **112**, 124 (1965).

<sup>52</sup> R. J. Chin and K. Nobe, *ibid.*, **119**, 1457 (1972).

<sup>53</sup> F. M. Donahue, *ibid.*, **119**, 72 (1972).

<sup>54</sup> K. J. Vetter, "Electrochemical Kinetics," Academic Press, New York (1967).

<sup>55</sup> C. Wagner and W. Traud, *Z. Elektrochem.*, **44**, 391 (1938).

<sup>44</sup> Department of Industrial Chemistry, University of Tokyo, Tokyo, Japan.

<sup>45</sup> Department of Applied Chemistry, Kanagawa University, Yokohama, Japan.

<sup>46</sup> A. Fujishima, K. Kohayakawa, and K. Honda, *Bull. Chem. Soc. Japan*, **48**, 1041 (1975).

<sup>47</sup> Department of Chemical Engineering, University of Michigan, Ann Arbor, Michigan 48109.

$$i_a(\text{O}_2) = i_1 + i_2 + i_4 \quad [3]$$

A material balance on copper metal yields

$$i(\text{Cu}, \text{O}_2) = i_1 + i_2 \quad [4]$$

Substituting Eq. [4] in Eq. [3] and rearranging

$$i_4 = i_a(\text{O}_2) - i(\text{Cu}, \text{O}_2) \quad [5]$$

Table I shows the values of  $i_4$  computed from the data in Table I of the subject paper. Three points are obvious from this analysis: (i) the numbers are different from those given by the authors, (ii)  $i_4$  is more-or-less constant, and (iii) all of the current densities are negative. Since the reduction of oxygen is a cathodic partial process operating about 1V from its equilibrium potential, one would expect its current density to be constant (at the value of the limiting diffusion current density) and, by convention, negative (see Ftn<sup>54</sup>, p. 8). The analysis given here corroborates that expectation while the authors' analysis does not. The apparent error is their treatment of the material balances (their Eq. [6]-[9]). The computed average value for  $i_4$ , i.e., 1.38 mA/cm<sup>2</sup>, agrees favorably with the authors' limiting diffusion current for oxygen of 1.6 mA/cm<sup>2</sup>.

The magnitude of the interaction can be obtained from

$$i_{\text{inter}} = i(\text{Cu}, \text{O}_2) - i(\text{Cu}, \text{N}_2) \quad [6]$$

Table II shows the values for this interaction as a function of potential. It is not obvious what conclusion(s) can be drawn from this information. If a Tafel line is drawn through these data, one obtains a slope of about 100 mV. If the data at 80 mV are ignored (there seems no justification for this, however), one concludes that the interaction is a constant. If the homogeneous reaction is invoked, i.e., the authors' reaction [3], one anticipates that the rate of this homogeneous reaction would be proportional to the interfacial concentration of cuprous ion. However, one anticipates a Tafel slope for this to be 59 mV at 25°C since (from their model)

$$[\text{Cu}^+] = K \exp \left[ \frac{FE}{RT} \right] \quad [7]$$

where  $[\text{Cu}^+]$  is the concentration of cuprous ion and  $K$  is a constant which includes the standard electrode potential and the "equilibrium" concentration of  $\text{Cu}^+$  at the standard potential. The singular conclusion which does seem evident from the discussion presented here is that the authors' contention that the homogeneous oxidation of cuprous ion as the source of the "interaction" is incorrect. Hopefully, more work in this area will lead to a fuller understanding of the phenomenon.

Table I. Computation of  $i_4$

$E$ (mV)	$i_{\text{net}}(\text{O}_2)$ (mA/cm <sup>2</sup> )	$i(\text{Cu}, \text{O}_2)$ (mA/cm <sup>2</sup> )	$i_4$ (mA/cm <sup>2</sup> )
+10	0.0	1.15	-1.15
+30	0.57	2.14	-1.57
+40	1.37	2.85	-1.48
+50	2.71	4.02	-1.31
+80	14.2	15.6	-1.4
			Avg -1.38

Table II. Computation of  $i_{\text{inter}}$

$E$ (mV)	$i(\text{Cu}, \text{O}_2)$ (mA/cm <sup>2</sup> )	$i(\text{Cu}, \text{N}_2)$ (mA/cm <sup>2</sup> )	$i_{\text{inter}}$ (mA/cm <sup>2</sup> )
30	2.14	0.61	1.53
40	2.85	0.96	1.87
50	4.02	2.19	1.83
80	15.6	11.1	4.5

T. N. Andersen, M. H. Ghandehari, and H. Eyring:<sup>56</sup>

Dr. Donahue's criticism appears to have two points. He believes (i) that the  $\text{Cu}/\text{O}_2\text{-H}_2\text{SO}_4$  system is not unique in the mixed potential sense, as the authors claimed, and (ii) that the authors' theory for the observed results is incorrect. In both cases Donahue missed the point of our paper which careful reading should have made clear. These points shall be rebutted separately, although they are both related to the same misunderstanding.

The first point of our paper was that the corrosion system at hand differs from most in that the anodic and cathodic rates, as determined independently, are not applicable when the reactions are coupled (allowed to occur simultaneously). Thus the reactions are not independent in the mixed potential sense, as defined by Wagner and Traud<sup>55</sup> and reiterated by most other electrochemists (see Ftn<sup>54</sup>). If the reactions were independent, the rate of copper dissolution would be equal in  $\text{N}_2$ - and  $\text{O}_2$ -saturated solutions at the same potential.

In the case of the system referenced by Donahue (Fe in acids), both the isolated anodic (Fe dissolution) and cathodic ( $\text{H}_2$  evolution) reactions have  $\text{H}_3\text{O}^+$  or  $\text{OH}^-$  ions as reactants. Authors who have chosen to couple these reactions in explanation of corrosion phenomena (e.g., see Ftn<sup>51</sup>) have done so successfully using the conventional mixed potential theory, i.e., by adding the rates of the isolated reactions at each potential. In the  $\text{Cu}/\text{O}_2\text{-H}_2\text{SO}_4$  system this could not be done consistent with the observed corrosion rate.

Hence Donahue's references reaffirm the uniqueness of the present system, and his own paper<sup>53</sup> acknowledges agreement with the conventional theory of mixed potentials in the lead-off statement, "Interactions between the anodic and cathodic partial processes in mixed potential systems . . . can be ascertained from extensive studies of the electrode kinetics of the respective partial processes."

The second point of our paper was to provide an explanation for the atypical behavior of the  $\text{Cu}/\text{O}_2\text{-H}_2\text{SO}_4$  system, i.e., for the observation that the copper dissolution rate in  $\text{O}_2$ -saturated solution,  $[i(\text{Cu}, \text{O}_2)]$  is greater than the corresponding rate in  $\text{N}_2$ -saturated solution  $[i(\text{Cu}, \text{N}_2)]$  at the same potential. Our discussion section focuses on developing a suitable theory which is consistent with the various parametric test results obtained as well as with the above observation. Donahue's explanation of our data obliges him to ignore the very point of our paper, that  $[i(\text{Cu}, \text{O}_2)/i(\text{Cu}, \text{N}_2)]_E > 1$ . He passes off this significant observation in his concluding paragraph as unexplainable. Inasmuch as Donahue's theory (his Eq. [3] and [4]) is nothing more than conventional mixed potential theory, it is not surprising that he has no explanation for the above inequality. The first step in our interpretation was to abandon that approach and find a satisfactory one.

Further amplification of the disagreement between our model and Donahue's follows from carrying through the arithmetic of the two differing theories. The discussor's conventional theory of mixed potentials puts all the oxygen consumption into one term,  $i_4$ . The authors' theory obviously deduces the same total rate of  $\text{O}_2$  consumption, which is given by  $i_3 + i_4$  in Table III in the paper under discussion. The reviewer should have noted that there is no sign problem with  $i_4$ , which is defined in its absolute sense by Eq. [7] of the paper.

A final point of misunderstanding on Donahue's part is with regard to the rate of Cu dissolution via the different routes of steps [1], [2], and [3] in the authors' theory. The rate of Cu dissolution is measured as the

<sup>56</sup> Department of Chemistry, University of Utah, Salt Lake City, Utah 84112.

$$i_a(\text{O}_2) = i_1 + i_2 + i_4 \quad [3]$$

A material balance on copper metal yields

$$i(\text{Cu}, \text{O}_2) = i_1 + i_2 \quad [4]$$

Substituting Eq. [4] in Eq. [3] and rearranging

$$i_4 = i_a(\text{O}_2) - i(\text{Cu}, \text{O}_2) \quad [5]$$

Table I shows the values of  $i_4$  computed from the data in Table I of the subject paper. Three points are obvious from this analysis: (i) the numbers are different from those given by the authors, (ii)  $i_4$  is more-or-less constant, and (iii) all of the current densities are negative. Since the reduction of oxygen is a cathodic partial process operating about 1V from its equilibrium potential, one would expect its current density to be constant (at the value of the limiting diffusion current density) and, by convention, negative (see Ftn<sup>54</sup>, p. 8). The analysis given here corroborates that expectation while the authors' analysis does not. The apparent error is their treatment of the material balances (their Eq. [6]-[9]). The computed average value for  $i_4$ , i.e., 1.38 mA/cm<sup>2</sup>, agrees favorably with the authors' limiting diffusion current for oxygen of 1.6 mA/cm<sup>2</sup>.

The magnitude of the interaction can be obtained from

$$i_{\text{inter}} = i(\text{Cu}, \text{O}_2) - i(\text{Cu}, \text{N}_2) \quad [6]$$

Table II shows the values for this interaction as a function of potential. It is not obvious what conclusion(s) can be drawn from this information. If a Tafel line is drawn through these data, one obtains a slope of about 100 mV. If the data at 80 mV are ignored (there seems no justification for this, however), one concludes that the interaction is a constant. If the homogeneous reaction is invoked, i.e., the authors' reaction [3], one anticipates that the rate of this homogeneous reaction would be proportional to the interfacial concentration of cuprous ion. However, one anticipates a Tafel slope for this to be 59 mV at 25°C since (from their model)

$$[\text{Cu}^+] = K \exp \left[ \frac{FE}{RT} \right] \quad [7]$$

where  $[\text{Cu}^+]$  is the concentration of cuprous ion and  $K$  is a constant which includes the standard electrode potential and the "equilibrium" concentration of  $\text{Cu}^+$  at the standard potential. The singular conclusion which does seem evident from the discussion presented here is that the authors' contention that the homogeneous oxidation of cuprous ion as the source of the "interaction" is incorrect. Hopefully, more work in this area will lead to a fuller understanding of the phenomenon.

Table I. Computation of  $i_4$

$E$ (mV)	$i_{\text{net}}(\text{O}_2)$ (mA/cm <sup>2</sup> )	$i(\text{Cu}, \text{O}_2)$ (mA/cm <sup>2</sup> )	$i_4$ (mA/cm <sup>2</sup> )
+10	0.0	1.15	-1.15
+30	0.57	2.14	-1.57
+40	1.37	2.85	-1.48
+50	2.71	4.02	-1.31
+80	14.2	15.6	-1.4
			Avg -1.38

Table II. Computation of  $i_{\text{inter}}$

$E$ (mV)	$i(\text{Cu}, \text{O}_2)$ (mA/cm <sup>2</sup> )	$i(\text{Cu}, \text{N}_2)$ (mA/cm <sup>2</sup> )	$i_{\text{inter}}$ (mA/cm <sup>2</sup> )
30	2.14	0.61	1.53
40	2.85	0.96	1.87
50	4.02	2.19	1.83
80	15.6	11.1	4.5

T. N. Andersen, M. H. Ghandehari, and H. Eyring:<sup>56</sup>

Dr. Donahue's criticism appears to have two points. He believes (i) that the  $\text{Cu}/\text{O}_2\text{-H}_2\text{SO}_4$  system is not unique in the mixed potential sense, as the authors claimed, and (ii) that the authors' theory for the observed results is incorrect. In both cases Donahue missed the point of our paper which careful reading should have made clear. These points shall be rebutted separately, although they are both related to the same misunderstanding.

The first point of our paper was that the corrosion system at hand differs from most in that the anodic and cathodic rates, as determined independently, are not applicable when the reactions are coupled (allowed to occur simultaneously). Thus the reactions are not independent in the mixed potential sense, as defined by Wagner and Traud<sup>55</sup> and reiterated by most other electrochemists (see Ftn<sup>54</sup>). If the reactions were independent, the rate of copper dissolution would be equal in  $\text{N}_2$ - and  $\text{O}_2$ -saturated solutions at the same potential.

In the case of the system referenced by Donahue (Fe in acids), both the isolated anodic (Fe dissolution) and cathodic ( $\text{H}_2$  evolution) reactions have  $\text{H}_3\text{O}^+$  or  $\text{OH}^-$  ions as reactants. Authors who have chosen to couple these reactions in explanation of corrosion phenomena (e.g., see Ftn<sup>51</sup>) have done so successfully using the conventional mixed potential theory, i.e., by adding the rates of the isolated reactions at each potential. In the  $\text{Cu}/\text{O}_2\text{-H}_2\text{SO}_4$  system this could not be done consistent with the observed corrosion rate.

Hence Donahue's references reaffirm the uniqueness of the present system, and his own paper<sup>53</sup> acknowledges agreement with the conventional theory of mixed potentials in the lead-off statement, "Interactions between the anodic and cathodic partial processes in mixed potential systems . . . can be ascertained from extensive studies of the electrode kinetics of the respective partial processes."

The second point of our paper was to provide an explanation for the atypical behavior of the  $\text{Cu}/\text{O}_2\text{-H}_2\text{SO}_4$  system, i.e., for the observation that the copper dissolution rate in  $\text{O}_2$ -saturated solution,  $[i(\text{Cu}, \text{O}_2)]$  is greater than the corresponding rate in  $\text{N}_2$ -saturated solution  $[i(\text{Cu}, \text{N}_2)]$  at the same potential. Our discussion section focuses on developing a suitable theory which is consistent with the various parametric test results obtained as well as with the above observation. Donahue's explanation of our data obliges him to ignore the very point of our paper, that  $[i(\text{Cu}, \text{O}_2)/i(\text{Cu}, \text{N}_2)]_E > 1$ . He passes off this significant observation in his concluding paragraph as unexplainable. Inasmuch as Donahue's theory (his Eq. [3] and [4]) is nothing more than conventional mixed potential theory, it is not surprising that he has no explanation for the above inequality. The first step in our interpretation was to abandon that approach and find a satisfactory one.

Further amplification of the disagreement between our model and Donahue's follows from carrying through the arithmetic of the two differing theories. The discussor's conventional theory of mixed potentials puts all the oxygen consumption into one term,  $i_4$ . The authors' theory obviously deduces the same total rate of  $\text{O}_2$  consumption, which is given by  $i_3 + i_4$  in Table III in the paper under discussion. The reviewer should have noted that there is no sign problem with  $i_4$ , which is defined in its absolute sense by Eq. [7] of the paper.

A final point of misunderstanding on Donahue's part is with regard to the rate of Cu dissolution via the different routes of steps [1], [2], and [3] in the authors' theory. The rate of Cu dissolution is measured as the

<sup>56</sup> Department of Chemistry, University of Utah, Salt Lake City, Utah 84112.

number of  $\text{Cu}^{+2}$  ions dissolved from the metal per unit time, which is the sum of reactions [2] and [3]. Inasmuch as  $i(\text{Cu}, \text{O}_2)$  was defined as this rate multiplied by  $2F$  ( $F$  is Faraday's constant), Eq. [8] follows. The anodic electric current contributed by Eq. [3], which contributes to the total anodic electric current  $i_a(\text{O}_2)$ , is  $i_3$  because reaction [1] precedes  $i_3$  and occurs once for each occurrence of  $i_3$ . Path  $i_2$  contributes 2

electrons, one for its own occurrence and one for the preceding step,  $i_1$ .

The coupling of  $i_1$  and  $i_3$  is the reason the Tafel slope for  $i_3$  is larger than  $2.3 RT/F$  (59 mV). The step  $i_3$  is fed through our step [1] which Donahue takes into account in desiring a Tafel slope of 59 mV;  $i_3$  is also fed by slow-diffusing  $\text{O}_2$  which also adds to the potential dependence and which the discussor has ignored.



## The Erosion of Materials in Molten Silicon

R. E. Chaney\* and C. J. Varker\*

Motorola Incorporated, Semiconductor Products Division, Phoenix, Arizona 85008

### ABSTRACT

The erosion rates and mechanisms are discussed for several materials in contact with molten silicon near its melting point. Vitreous materials, *e.g.*, vitreous carbon and fused silica, behave similarly and erode primarily by dissolution. Pressed-powder materials, *e.g.*, silicon carbide and silicon nitride, degrade by a combination of dissolution and particulate erosion (intergranular corrosion).

The resistance to degradation is an important property to consider when choosing materials for hardware applications with molten silicon. Many materials have been investigated in the past, but the literature is not consistent with respect to experimental conditions or interpretation of results. Here, we are reporting the results of some preliminary work which directly compares some materials and gives insight into criteria which should be applied to future investigations.

**Material selection criteria.**—One of the basic problems in silicon technology to which this project addresses itself is the high concentration of oxygen in crystals grown from crucibles (1, 2). If a material can be found which does not supply high levels of oxygen or any other impurity to the melt, that would be ideal. But the application of a material which supplies an electrically inactive impurity such as carbon or nitrogen in place of oxygen may solve the problem in a satisfactory manner. For this reason a systematic investigation of silicon nitride, silicon carbide, and carbon was undertaken. The nitride and carbide were obtained in the most convenient form available, hot-pressed rods of high purity powder, from Cerac/Pure Incorporated with no binders used in fabrication. A single sample of nitride from Norton Corporation was also tested (NC 350). Vitreous carbon was the carbon form tested because of its ability to take a high polish, the absence of voids in the bulk, and its hardness (6-7 on Mohs scale). The problems associated with porous materials (penetration of the surface by the melt and high surface-to-volume ratio) precluded the use of other forms of carbon in the early stages of this investigation. The vitreous carbon samples were obtained from Beckwith Carbon Corporation.

### Experimental

The procedure used to test the selected materials is simple, but direct. A sample, usually a rod from 0.6 to 1.3 cm in diameter, was prepared by centerless grinding, dry polishing, and cleaning. After its diameter profile was taken, it was mounted in a seed chuck of a standard Czochralski crystal growth furnace. After flushing with helium, a 2 kg charge was melted in a silica crucible. The temperature was adjusted to about 5°C above the melting point so that crystallization on the sample was prevented. The rod is either immersed

about 4 cm into the melt and then withdrawn by stages (termed pulling) or immersed by stages into the melt (termed pushing). Figure 1 shows schematically the process. No difference in results was noted for pushed and pulled samples. After the experimental testing is complete, the sample is removed, adhering silicon is removed with an appropriate etch if necessary, then the diameter measurements are repeated. The difference in diameter gives a measure of the erosion rate. This is translated directly into the rate at which the surface is removed by the melt.

During the experiment the crucible and sample are both rotated slowly so that the effects of any thermal asymmetry are removed. Because one of the proposed

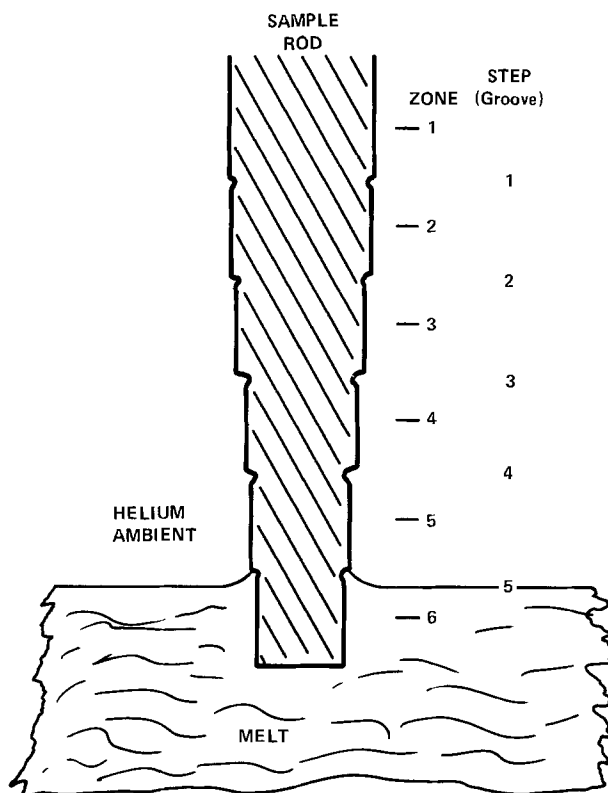


Fig. 1. Schematic diagram of the cross section of samples produced by erosion testing. Note the grooves formed at liquid-solid-ambient interface.

\* Electrochemical Society Active Member.  
 Key words: crystal growth, vitreous carbon, silicon nitride, silicon carbide, silicon.

uses for these materials is for forming dies in ribbon crystal growth processes, the crucible and sample rotation rates are set differently so that the resulting fluid flow on the sample surface approximates the flow conditions in forming dies at a representative growth rate of 5 cm/min (3).

### Results and Discussion

Figure 1 illustrates the type of samples produced. Zone 1 is the area of the rod which was not exposed to the melt. Zones 2-6 were exposed for increasing lengths of time. At the surface of the melt, surface tension-driven flow causes convection currents which accelerate the erosion at the liquid-solid-ambient interface (4). These convection currents are stronger than those caused by stirring or thermal gradients in this region. The accelerated erosion produced grooves which were found in all interface zones of all of the samples tested. All depths were measured with respect to the surface of the same numbered zone, i.e., the depth of groove 1 was measured with respect to the surface of zone 1. Data on the depth of these grooves and their variation with exposure time have been gathered by use of a metallographic microscope. It is presented in this report, but the analysis of this effect is outside the scope of this study.

Table I summarizes the data for all of the samples tested. Results for fused silica are included in the tabulation because it is the currently used crucible material throughout the industry. It is used here as a standard for comparison. For clarity in interpreting the results, the depth of erosion and the grooves is listed for 100 and 60 min, respectively. Thus samples which have erosion curves which do not intersect the axis can be compared in terms of absolute erosion depth.

**Vitreous carbon.**—In this study two sets of experiments with vitreous or glassy carbon were conducted. Samples 1 and 2 were tested in the as-received condition. Samples 3 and 4 were polished prior to testing. Figure 2 shows the results of the erosion testing. The change in sample radius *vs.* exposure time yields the erosion rate or the rate at which the surface recedes with exposure time,  $\Delta r/\Delta t$ .

All samples yield a linear curve, but the results of samples 3 and 4 show that surface polishing yields a surface which erodes less and more reproducibly than the as-received samples. Figure 3 shows an area of a sample after treatment and a light etch. The light area to the left is a fracture surface showing the void-free nature of the bulk. The gray area to the right is the surface which was exposed to the melt for 4 hr. The tiers are very shallow. The grainlike structure suggests a crystalline surface. X-ray diffraction shows no identifiable crystalline SiC structure for the surface. The diffraction spectra for bulk vitreous carbon and the sample surface differed only in relative peak

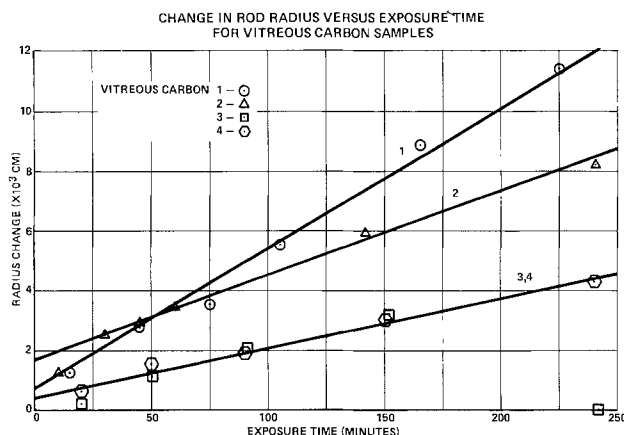


Fig. 2. Graph of radius change with respect to time for various vitreous carbon samples: 1 and 2 were in as-received condition, 3 and 4 were polished prior to treatment.

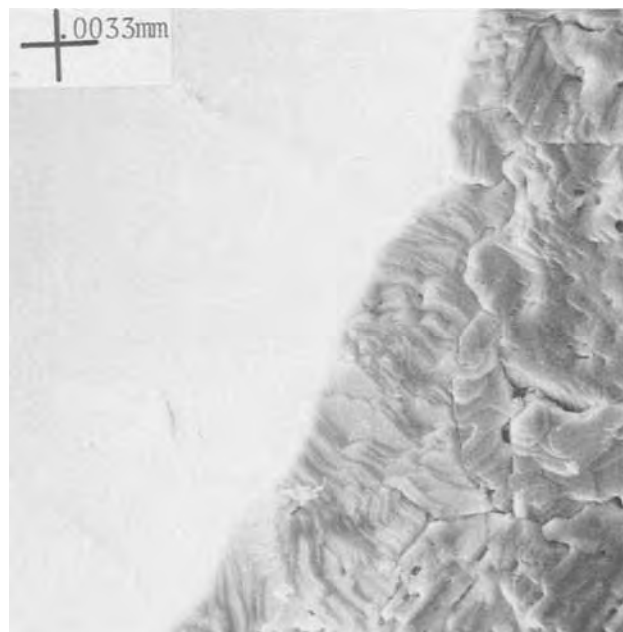


Fig. 3. SEM photo showing the contrast between fracture surface on the left and the treated surface (after etching) on the right of vitreous carbon.

heights and width, but not in peak position or number. Figure 4 shows a cross section of a similar sample. In this case a silicon drop adhered to the bottom of the sample rod. The sample was cut to reveal the vitreous carbon-silicon interface.

Table I. Tabulation of erosion results

Sample	Erosion rate (surface) $\Delta r/\Delta t$	Erosion depth 100 min	Erosion rate (groove) $\Delta x/\Delta t$	Erosion depth 60 min	Comments
SiO <sub>2</sub>	$1.15 \times 10^{-5}$ cm/min	$1.2 \times 10^{-3}$ cm	$8.4 \times 10^{-5}$ cm/min	$6 \times 10^{-3}$ cm	(6)
Vitreous carbon					
1	4.7	5.4	18	11	Pushed
2	2.8	4.5	44	27	Pulled
3	1.7	2.1	6.8	7.3	Pushed
4			0	5	Pulled-flat grooving curve
SiC					
1	5.7	6.8		~16	Pulled
2	7.9	4.1		1.2	Pushed
3	1.1	1.1		5	Pushed
Si <sub>3</sub> N <sub>4</sub>					
1	3.1 (same curve as 5)	1.7	15	9	Pushed
2	1.2	2.0	11	6.6	Pulled
5	3.1	1.7	11	8.0	Pushed
NC350	4.9	4.9	11	7.0	Pulled



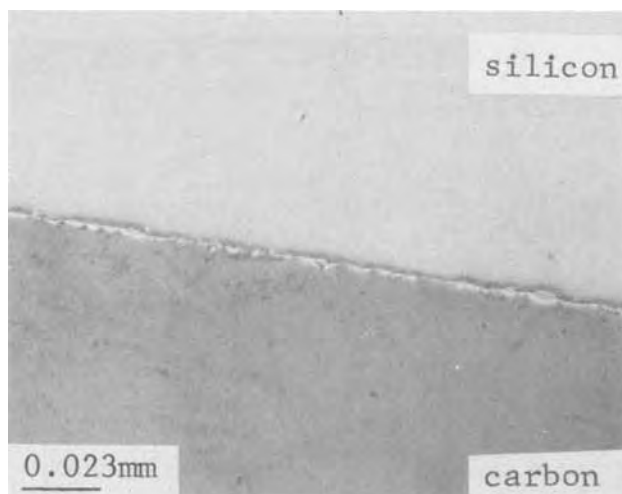


Fig. 4. Optical photomicrograph showing the interface layer formed when molten silicon solidifies on a vitreous carbon surface.

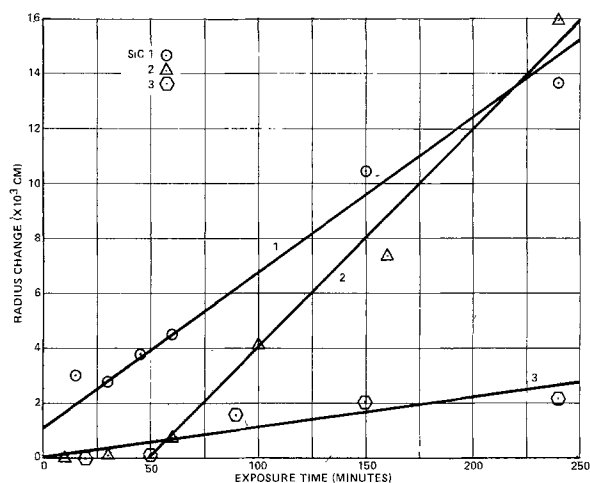


Fig. 5. Radius change vs. exposure time for SiC samples

The transition area is clearly indicated, but very thin ( $2-5 \mu\text{m}$ ) This may in fact be the SiC layer reported in the literature as being a product of the dissolution mechanism (5). Cowland and Lewis report a  $6 \mu\text{m}$

layer formed between a Si melt and carbon crucible which has been identified by x-ray diffraction (6).

The groove formation was not consistent for samples 1 and 2. However, the data were more reproducible for the polished samples 3 and 4 indicating that the surface morphology is important in determining the erosion characteristics of materials.

**Silicon carbide (SiC).**—The SiC sample rods in the as-received condition had a very rough surface and non-circular cross section which necessitated centerless grinding to make reliable samples. The resulting surface was porous and uneven, but sufficient for the purpose of this work.

Figure 5 shows the erosion results plotted for three samples, but severe pitting of the surface leads to some uncertainty in the erosion rates. The very low rate of sample 3 may be due to low melt temperature. Due to heat conduction up the rod, the temperature at the surface may in fact be lower than the melt temperature. This may allow a layer of silicon to freeze onto the sample which protects it from erosion. But in all cases the breakdown of the material was too great to allow its application for hardware such as crucibles and forming dies.

Further evidence of particulate erosion and pitting was obtained from the next two sets of micrographs. Figure 6 shows SEM photos of the interior of a sample rod before treatment. The two samples were obtained by halving a wafer taken from the end of a rod. The section shown in 6(a) was untreated after cutting. The half in 6(b) was etched in  $\text{HF}:\text{HNO}_3$  solution to remove any excess silicon (SiC dissolves much less rapidly in the acid etch). Etching reveals the material to be a loosely packed array of SiC particles which probably breaks down by particulate erosion or intergranular corrosion. The next set of photos in Fig. 7 verifies this conclusion. The sample shown was obtained by cross sectioning the end of sample 2 to which a drop of silicon was frozen. In 7(a) only a very slight coating of Au was deposited on the surface to reduce surface charging in the SEM. It is clearly shown that particles were trapped as they were being lifted out of the sample as indicated by the arrow. Figure 7(b) shows the same sample after a heavier layer of Au was applied. The smooth area to the right is the silicon drop, while the raised areas to the left are the particles of SiC. The arrow shows a particle which has apparently been lifted out of the SiC matrix and lies at the mouth of a long channel penetrating the bulk of the sample rod. Figure 7(c) shows the intricate network of channels

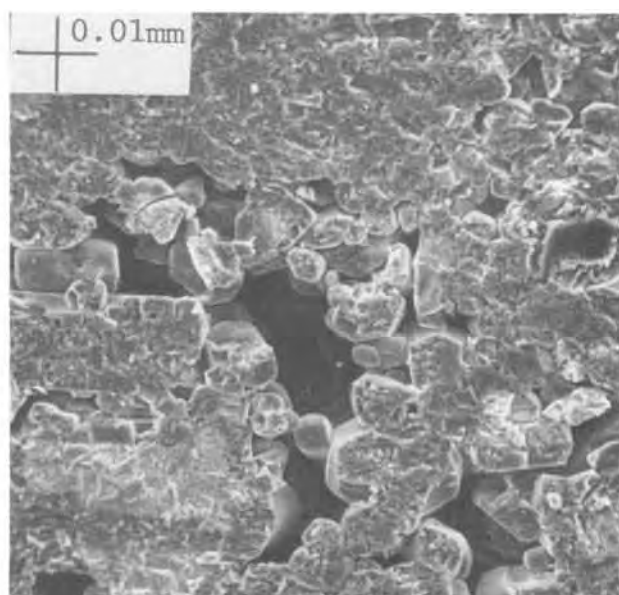
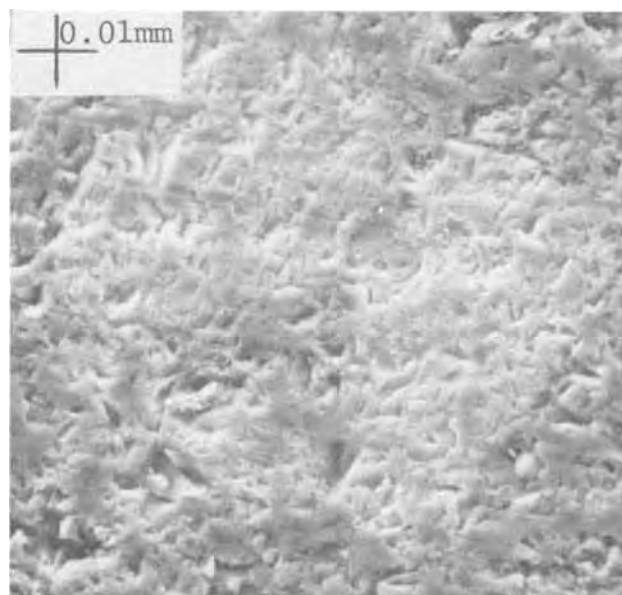


Fig. 6. SEM micrographs of the cross section of SiC sample 4: (a, left) as cut, (b, right) after etching.



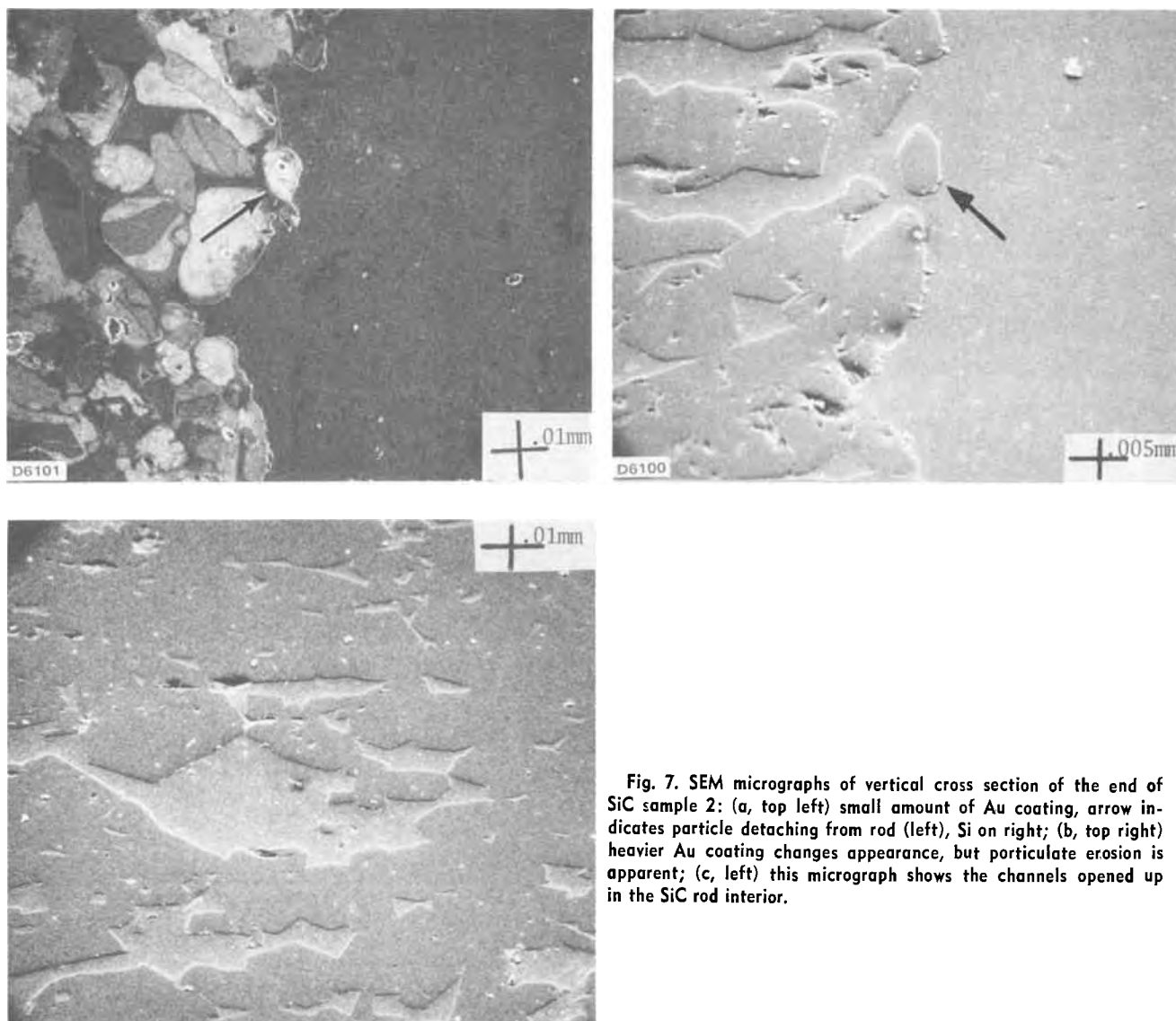


Fig. 7. SEM micrographs of vertical cross section of the end of SiC sample 2: (a, top left) small amount of Au coating, arrow indicates particle detaching from rod (left), Si on right; (b, top right) heavier Au coating changes appearance, but particulate erosion is apparent; (c, left) this micrograph shows the channels opened up in the SiC rod interior.

opened up in the interior of the rod by the molten silicon.

These experiments reveal that the predominant mode of breakdown of pressed powders of SiC in molten silicon is particulate erosion (intergranular corrosion). The ability of the material itself to resist dissolution is not clear. This can be determined by testing other forms of SiC. Sampling the melt after a run may be misleading because the fine particles of SiC may be trapped and lead to an apparently high value for the carbon concentration.

No groove depth rates were calculated for the SiC due to the nonlinear nature of the data points. This may be due to acceleration of particulate erosion caused by the material breakdown process and opening of interior channels. It is clear that the convection currents do cause significant material degradation in silicon carbide pressed-powder materials.

**Silicon nitride ( $\text{Si}_3\text{N}_4$ ).**—The  $\text{Si}_3\text{N}_4$  samples discussed in this section are all formed from powders.  $\text{Si}_3\text{N}_4$  samples 1, 2, and 5 are Cerac hot-pressed rods made from >99.9% pure powders with no binders. NC/350 is a sample of reaction-bonded material from Norton Company in the form of a square rod. Samples were cleaned with TCE and acetone. Figures 8 and 9 show the erosion behavior of these samples. NC/350 has the highest erosion rate of the four samples tested and this material is considered unsuitable for use with molten silicon.  $\text{Si}_3\text{N}_4$  2 shows the lowest erosion rate,

but the curve is offset from the abscissa indicating the rapid removal of a surface layer  $3 \times 10^{-4}$  cm thick. This is difficult to understand because samples 1 and 5 do not exhibit this behavior even though they were received in the same shipment and were treated in the same manner. The erosion of samples 1 and 5 is shown in Fig. 8. Little or no erosion took place up to 50 min exposure, subsequently the erosion rate was linear with time. This again may be due to low melt temperature. The two sets of data appear to curve slightly with time,

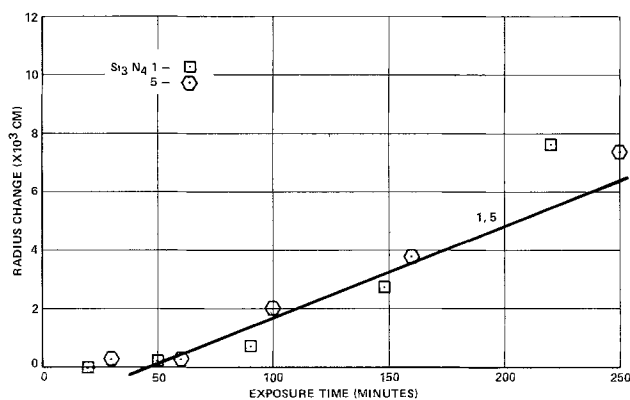


Fig. 8. Radius change vs. exposure time for  $\text{Si}_3\text{N}_4$  samples 1 and 5.

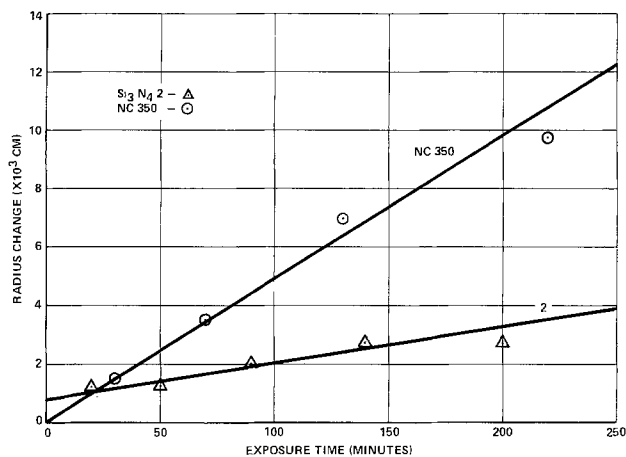


Fig. 9. Radius change vs. exposure time for  $\text{Si}_3\text{N}_4$  samples 2 and NC 350.

however, there is some error in the last two points (time 200 min). The source of this error may be due to a short zone length. These rods were deeply immersed and then withdrawn from the melt. It is often difficult to be precise in setting the zone length. The last zone of samples 1 and 5 is clearly very short. In the experimental setup there is severe turbulence near the surface. This convective flow is responsible for the grooves. Therefore, the measurements of the diameters of the short zones may include not only the normal erosion processes, but also a part due to these convection currents. For this reason, these points were not included in the erosion rates. Without these points there is no justification for concluding anything but a linear erosion rate.

The groove depth data for  $\text{Si}_3\text{N}_4$  samples seemed to be independent of the source. The grooving action was consistent and reproducible from sample to sample.

The mechanism of degradation for these pressed powders appears to be due to both dissolution and

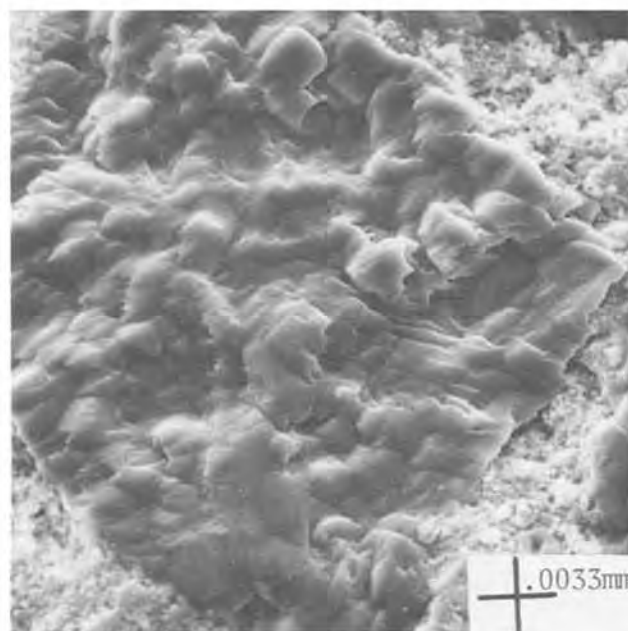
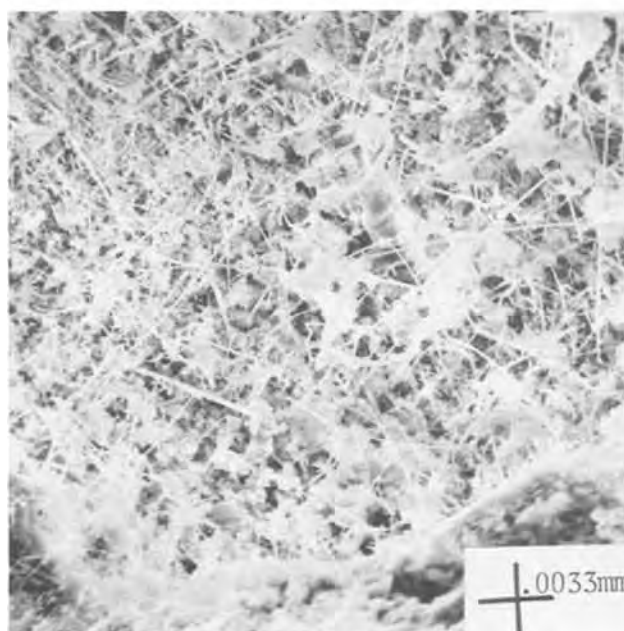
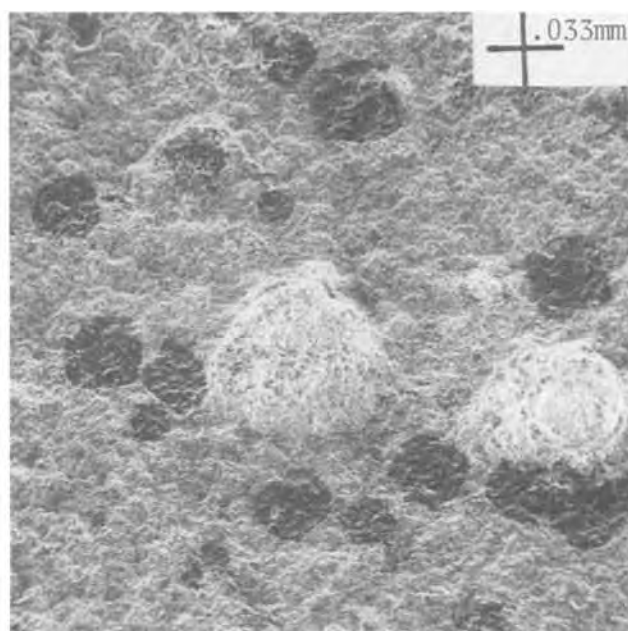
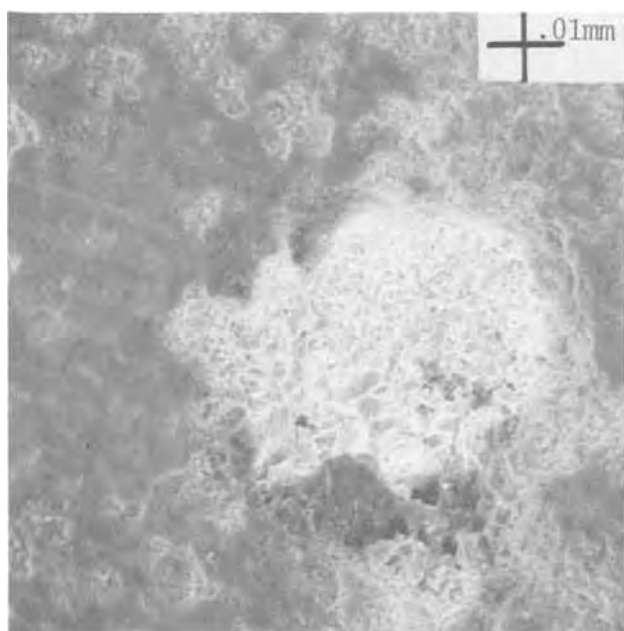


Fig. 10. Cross section of a  $\text{Si}_3\text{N}_4$  rod (as-received) treated to reveal internal structure: (a, top left) untreated after cutting (note the saw marks), the light area is a void; (b, top right) the same material after etching, note the light and dark areas; (c, bottom left) closer view of a light area. The fibers may be formed by the cooling of gas-filled voids after the hot-pressing process; (d, bottom right) closer view of a dark (silicon-rich) area.

particulate erosion processes. Figures 10 and 11 illustrate the structure of the material before and after treatment with molten silicon. Figure 10(a) shows a typical interior revealed by sawing. The white area is a void. Figure 10(b) shows the same area after an HF:HNO<sub>3</sub> etch. The etching process reveals very dark and white regions shown at higher magnification in 10(c) and (d). The dark areas appear to be a silicon-rich phase. The white areas are made up of very loosely packed fibers, which appear white due to the higher yield of secondary electrons in this region. This structure may form upon cooling of gas-filled voids in the material after the hot-pressing process.

Figure 11(a) shows a typical area of a Si<sub>3</sub>N<sub>4</sub> sample which has been exposed to the melt, then etched to remove adhering silicon. Again, light and dark areas are observed. Figures 11(b) and (c) show more detailed views of these areas. The dark regions appear as voids. The relatively large particles on the interior of the holes are the same as shown for the untreated sample [Fig. 10(d)]. No silicon-rich regions were observed. It is evident that the solid crystalline spots melt, dissolve, or erode more rapidly than the bulk material to form these cavities. Figure 11(c) shows a

view of a white area. This appears the same as the untreated bulk material [Fig. 10(c)].

From the photographic evidence it is concluded that these samples of hot-pressed Si<sub>3</sub>N<sub>4</sub> degrade by a combination of particulate erosion and dissolution. The material is quite porous which enables the melt to penetrate the surface, dissolve, or melt away the binding material between the particles or fibers and lift them away from the rod.

### Summary

Based on the results of this study several conclusions can be reached.

1. Many of the materials studied have erosion rates similar to SiO<sub>2</sub> (refer to Table I).

2. The mechanism of the erosion varies according to the type of material. Vitreous materials (SiO<sub>2</sub> and glassy carbon) erode by a single dissolution mechanism. The pressed powders (SiC and Si<sub>3</sub>N<sub>4</sub>) erode by both dissolution and particulate erosion (intergranular corrosion). This combination of mechanisms is due to the particulate nature of the bulk materials which allows penetration of the melt below the sample sur-

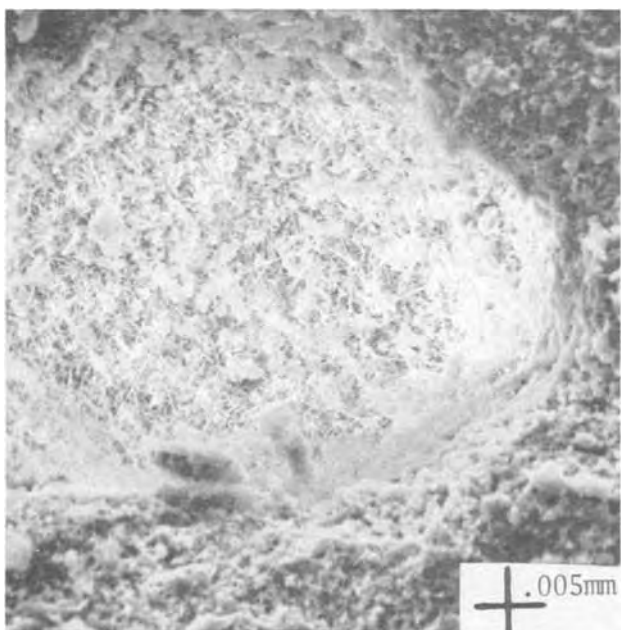
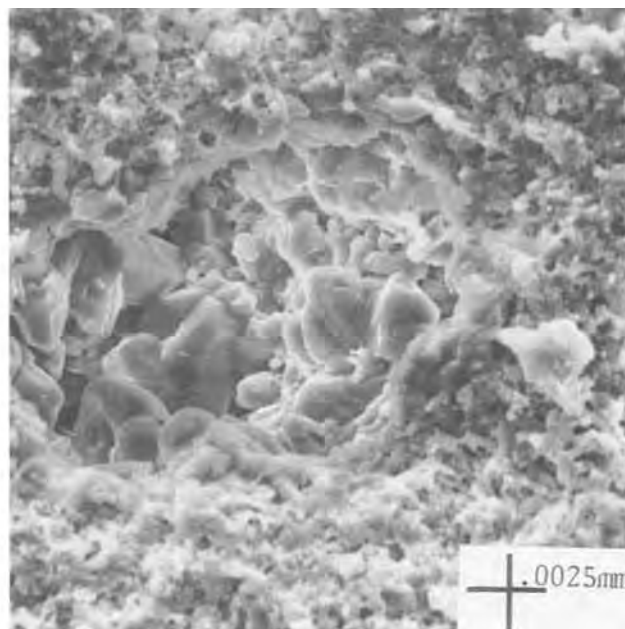
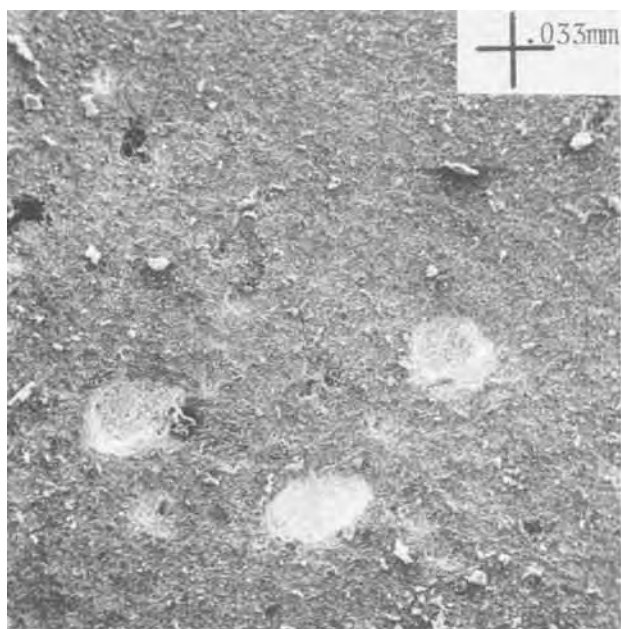


Fig. 11. Si<sub>3</sub>N<sub>4</sub> sample 1 after treatment with molten silicon. These SEM photomicrographs are all of the exposed surface. (a, top left) etched after treatment, note light and dark areas; (b, top right) closer view of dark area, possibly formed by melting or dissolution of silicon-rich phase; (c, left) closer view of a light area, appears the same as for untreated bulk samples.

face or nonstoichiometry which causes voids to open up as unreacted silicon melts.

3. Surface preparation has a strong influence on the erosion levels attained as shown by polishing the vitreous carbon samples. The erosion rates were reproducible and suppressed due to reduction of the surface-to-volume ratio by polishing. This process will allow prediction of the wearing characteristics of materials used in the fabrication of precision components such as forming dies.

### Acknowledgments

The authors wish to thank people of the Semiconductor Analytical Laboratory who helped in this work; included are Bob Fitzpatrick, Lavoie Millican, and Tony Gonzales.

Manuscript submitted Dec. 19, 1975; revised manuscript received Feb. 26, 1976.

Any discussion of this paper will appear in a Discussion Section to be published in the December 1976 JOURNAL. All discussions for the December 1976 Discussion Section should be submitted by Aug. 1, 1976.

Publication costs of this article were partially assisted by Motorola Incorporated.

### REFERENCES

- W. R. Runyan, "Silicon Semiconductor Technology," p. 18, McGraw Hill, New York (1965).
- T. Takano and M. Maki, in "Semiconductor Silicon 1973," H. R. Huff and R. R. Burgess, Editors, p. 469, The Electrochemical Society, Princeton, N.J. (1973).
- T. F. Ciszek, *Mater. Res. Bull.*, **7**, 731 (1972).
- R. A. Laudise, "The Growth of Single Crystals," p. 187, Prentice-Hall, New York (1970).
- R. E. Chaney and C. J. Varker, Submitted to *J. Cryst. Growth*.
- F. C. Cowland and J. C. Lewis, *J. Mater. Sci.*, **2**, 507 (1967).

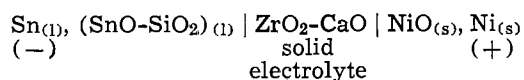
## Activities of SnO in the SnO-SiO<sub>2</sub> System

A. E. Grau and S. N. Flengas\*

Department of Metallurgy and Materials Science, University of Toronto, Toronto, Ontario, Canada

### ABSTRACT

The activities of SnO in the binary melts SnO-SiO<sub>2</sub> have been investigated by emf measurements using the cell

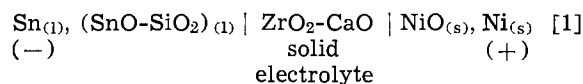


The results indicate positive deviations from an ideal "molecular" model and it is suggested that SnO is one of the more acidic oxides with respect to silica.

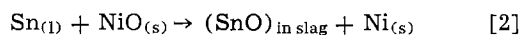
The measurement of the thermodynamic activities of SnO in SnO-SiO<sub>2</sub> liquid solutions has been the subject of several investigations (1-3). The reported results, however, are in total disagreement, thus emphasizing the need of reinvestigating the system.

### Experimental

In the present work, the activities of SnO with respect to the pure liquid oxide as the standard state,  $a_{\text{SnO}}$ , were calculated from the emf's measured in electrochemical cells of the type



The cell reaction is



and the corresponding form of the Nernst equation may be written as

$$E = E^\circ - \frac{RT}{2F} \ln a_{\text{SnO}} \quad [3]$$

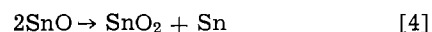
where  $E$  is the cell emf measured at  $T^\circ\text{K}$  and  $E^\circ$  is the emf measured at the same temperature in a cell where the slag phase has been replaced by pure liquid SnO.  $R$  and  $F$  denote the gas constant and the Faraday constant, respectively.

The "closed" cell design employed in the present investigation was identical to that described in a pre-

vious publication from this laboratory (4, 5, 6). The main characteristic of the "closed" cell design is that the two electrode compartments are completely isolated from each other through the use of a CaO-stabilized zirconia tube 24 in. long and closed at one end. In addition, each half-cell compartment containing an electrode is sealed under vacuum at the open end which is located outside the furnace. In this manner, both electrode compartments are operated under the equilibrium partial pressures of oxygen corresponding to the metal-metal oxide system present at the temperature of the measurement. As discussed earlier (5, 6), the "closed" cell design yields emf measurements free of mixed potential effects.

The electrical contact for the Sn/SnO + SiO<sub>2</sub> electrode consisted of a 2 mm diameter iridium wire connected to platinum leads. Thermoelectric emf's due to the Ni-Pt-Ir junctions were measured separately using the same geometric cell arrangement and the same furnace; all reported cell emf values have been corrected for such effects.

The major experimental difficulty found in the SnO system is the instability of this oxide. In a recent investigation, Carbo and Richardson (7) have found that both the solid and liquid SnO are unstable below 1373°K and that they disproportionate according to the reaction



It is clear, then, that the SnO-SiO<sub>2</sub> solutions do not correspond to a truly binary system but rather to a ternary containing SnO, SiO<sub>2</sub>, and variable amounts of SnO<sub>2</sub>. The amount of SnO<sub>2</sub> present in the solution

\* Electrochemical Society Active Member.

Key words: silicate melts, activities in SnO-SiO<sub>2</sub>, emf measurements of SnO.

coexists in equilibrium with SnO and in a closed system it is determined by the temperature and composition of the melt.

Four slag samples of different composition were prepared by thoroughly mixing "Baker Analyzed" SnO powder with SiO<sub>2</sub> obtained by dehydrating silicic acid at 1250°-1300°K for periods of 18-24 hr. The components were always mixed in the amounts corresponding to a total sample of 10g and loaded into a small ZrO<sub>2</sub> crucible provided with a lid of the same material. The ZrO<sub>2</sub> crucible was contained in an Inconel crucible which was placed in a 45 mm bottom-closed quartz tube. Argon gas was continuously flowed during the melting of the slag by means of quartz tubes passed through a rubber stopper at the upper end of the 45 mm quartz tube. The samples were rapidly melted in an induction furnace and kept at temperature for about 15 min. After this time, the power to the induction furnace was shut off, and the samples were allowed to cool while still under argon. The slag obtained was then removed from the zirconia crucible (which had to be destroyed), ground, and stored in a desiccator. There was no indication of chemical interaction between the slag and the crucible, nor visible cracks due to the thermal shock of the zirconia.

The slags were analyzed for both stannous and total tin by the iodimetric method. The total tin was determined by dissolving samples weighing 0.2g in 20 ml conc HCl. The solution was then filtered and the filter paper containing the undissolved silica saved for the SiO<sub>2</sub> determination. 100 ml of distilled water followed by 50 ml of conc HCl were then added to the filtrate. Reduction was affected by the addition of nickel powder and gentle boiling of the solution under an argon atmosphere. After all the nickel had dissolved, the solution was cooled in running water and titrated at once (under A) with 0.1N iodine solution using starch as the indicator.

Stannous tin was determined by dissolving, under an argon atmosphere, 0.2g samples in 20 ml conc HCl, 100 ml distilled water, and 50 ml conc HCl were then added and the solution was immediately titrated as described previously. The amount of Sn<sup>4+</sup> present in the slags was calculated as the difference between total tin and stannous tin.

### Results and Discussion

The results of the chemical analysis are given in Table I together with some information concerning the physical appearance of the slags. In the next to last column, the compositions indicated by the analysis have been proportionally adjusted to 100% in order to provide a basis for the calculation of the molar concentrations. As expected, the amount of stannic oxide found in the slags increases as the silica content decreases. Since the slags were cooled slowly in argon (about 10 min to reach room temperature), it is possible that due to the SnO disproportionation, the concentrations of SnO<sub>2</sub> reported in Table I are somewhat higher than the actual equilibrium values. This is also suggested by the presence of small tin spheres found dispersed in the slag which may have been produced during the cooling of the melts. In any case, it appears that the disproportionation of the SnO dissolved in the slag proceeds fairly slowly as compared to the pure liquid oxide.

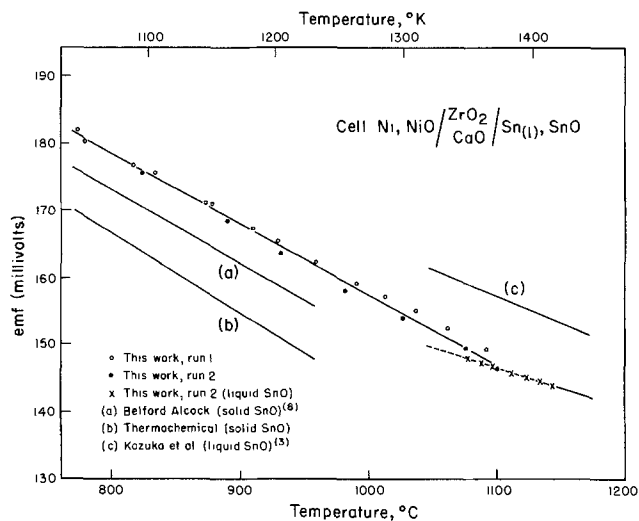


Fig. 1. Temperature dependence of emf for the cell Ni, NiO/ZrO<sub>2</sub>-CaO/SnO, Sn.

The results for pure SnO are shown in Fig. 1, and for the purpose of interpretation may be separated into two groups.

*Results obtained in the temperature range 1050°-1373°K.*—The open and filled circles in Fig. 1 indicate a high degree of reproducibility, as evidenced by the agreement between the results of runs 1 and 2. However, the information available on the stability of SnO indicates that these results should not correspond to the presence of this oxide. The same comments should apply to the tentative electrochemical results of Bedford and Alcock (8) represented by line (a). The thermochemical line (b) has been obtained under the assumption that the heat capacities of SnO are equal to those of SnO<sub>2</sub> (9) and has been included for comparison purposes only.

*Data obtained in the temperature range 1350°-1420°K.*—This is the temperature range (x's in Fig. 1) for which liquid SnO is the stable phase in equilibrium with tin, and, therefore, these data are taken to represent the desired  $E^\circ$  results. Some of the points obtained in the lower part of the temperature interval may correspond to metastable SnO. The results of Kozuka and co-workers (3) for liquid SnO are represented by line (c) in Fig. 1, and are seen to be in poor agreement with the present results. These authors used a galvanic cell employing a solid electrolyte in the shape of a short ZrO<sub>2</sub>-CaO crucible open at the upper end. The crucible contained the Sn<sub>(l)</sub>/SnO<sub>(l)</sub> electrode while the reference electrode consisted of a Ni/NiO pellet pressed against the outer wall of the crucible. In this type of "open cell," due to continuous diffusion in the gaseous phase, the oxygen partial pressures in the two electrode compartments are not at their equilibrium values, and the emf results are incorrect (5, 6).

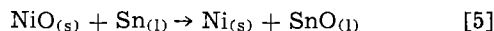
In the present work, errors can also arise, mostly from the presence of small amounts of SnO<sub>2</sub> in SnO. Although the x-ray analysis of samples quenched from 1423°K indicated the presence of SnO only, it is possible that a small amount of SnO<sub>2</sub> dissolved in liquid SnO remained undetected by the x-ray technique.

Table I. Chemical analysis of the SnO-SiO<sub>2</sub> slags

Sample	Calculated composition m/o SiO <sub>2</sub>	Physical appearance	Analysis w/o			Adjusted w/o			Composition m/o		
			SnO	SnO <sub>2</sub>	SiO <sub>2</sub>	SnO	SnO <sub>2</sub>	SiO <sub>2</sub>	SnO	SnO <sub>2</sub>	SiO <sub>2</sub>
1	55	Yellow, transparent glass	59.50	4.27	34.70	60.42	4.34	35.24	42.17	2.71	55.12
2	50	Yellow, transparent glass	62.86	5.20	29.83	64.21	5.31	30.47	43.40	3.20	53.40
3	40	Yellow, transparent glass	68.69	6.50	22.20	70.53	6.67	22.79	55.29	4.67	40.04
4	30	Gray, opaque glass	73.41	8.29	16.60	74.68	8.43	16.89	62.19	6.28	31.53

However the degree of disproportionation of SnO decreases with increasing SiO<sub>2</sub> content, which explains why the present work was limited to the more acidic solutions. Also, some error could arise from the chemical attack of the solid electrolyte by SnO. Although very stable and reproducible measurements were made during the first few hours in the life of the experiments, it is difficult to predict to what extent the behavior of the solid electrolyte is affected by the action of SnO.

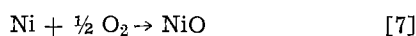
From the experimental results presented in Fig. 1, it is concluded that the temperature dependence of the emf corresponding to the cell reaction



in the temperature range 1350°-1420°K is given by the equation

$$E^\circ = 225.5 - 0.0575T \text{ (mV)} \quad [6]$$

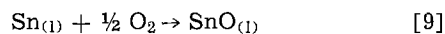
The electrochemical data reported by Charette and Flengas (5) for the cell reaction



are given as

$$E^\circ_{\text{NiO}} = 1210.8 - 0.4399T \text{ (mV)} \quad [8]$$

Since the reaction



is obtained by the addition of reactions [5] and [7], the emf corresponding to the cell reaction [9] in the temperature range 1350°-1420°K is  $E^\circ_{\text{SnO}} = E^\circ + E^\circ_{\text{NiO}}$ . That is

$$E^\circ_{\text{SnO}} = 1436.3 - 0.4974T \text{ (mV)} \quad [10]$$

Thus, the standard free energy of formation of liquid SnO in this temperature range is calculated as

$$\Delta G^\circ_{\text{SnO}(l)} = -66,242 + 22.940T \frac{\text{cal}}{\text{mole}} \quad [11]$$

The emf data obtained for samples 1-4 representing SnO-SiO<sub>2</sub> solutions are shown in Fig. 2. The cells were operated on increasing and decreasing temperature cycles and the emf's were recorded every 20° or 30°K at equilibrium. The time interval between readings usually was 45 min-1 hr. These cells were run for periods of 18-24 hr. Figure 2 also shows the results obtained for pure liquid SnO ( $E^\circ$ ). For this system, because of the instability of SnO, emf results for solid SnO are not shown. The life of the experiments was reduced to a period of 5 or 6 hr after which the emf readings became unstable. This was attributed to the attack of

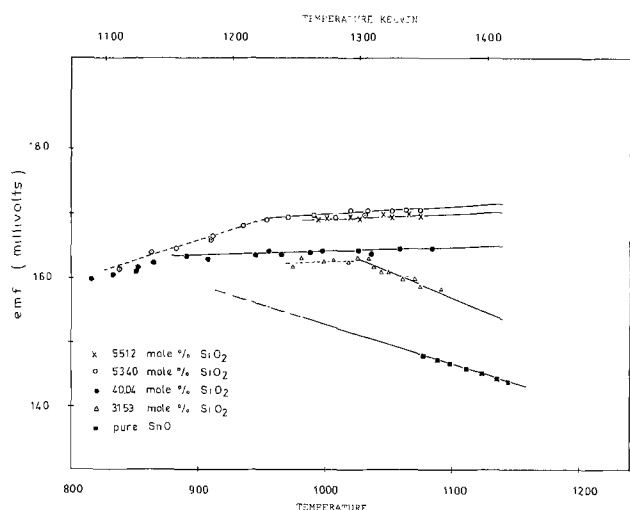


Fig. 2. Temperature dependence of emf for the cell Ni, NiO/ZrO<sub>2</sub>-CaO/Sn, (SnO + SiO<sub>2</sub>).

Table II. Summary of the experimental emf data for the SnO-SiO<sub>2</sub> system

X <sub>SiO<sub>2</sub></sub>	Temp range °K	E = A - BT (mV)		Standard error of estimate (mV)	Maximum deviation (mV)
		A	B		
0.551	1270-1350	169.5	-0.0002	±0.4	0.7
0.534	1230-1350	152.7	-0.0133	0.3	0.5
0.400	1160-1370	154.6	-0.0074	0.3	0.5
0.315	1300-1365	264.5	0.0780	0.6	0.9
"Pure SnO"	1350-1420	225.5	0.0575	0.1	0.2

the solid electrolyte by liquid SnO, as evidenced by the black stains found on the external surface of the ZrO<sub>2</sub>-CaO tube after the cell was cooled and disassembled. The summary of the experimentally obtained emf data and the calculated standard error of estimate and the maximum deviations are presented in Table II.

It may be seen in Fig. 2 that the emf vs. temperature lines show important slope variations at well-defined temperatures. This type of variation is commonly interpreted as accompanying the appearance of either a solid phase or of liquid immiscibility and, when the phase diagram of the system under study is available, it provides a good check of the accuracy of the experimental determinations. Unfortunately, in the case of the SnO-SiO<sub>2</sub> system, the phase diagram is practically unknown, the only information available in the literature being that reported by Keysselitz and Kohlmeyer (9) which is reproduced in Fig. 3. It is very likely that the phase diagram suggested by these authors is an oversimplification of the actual phase relations in the system because of the absence of both the intermediate compounds and the liquid immiscibility region, which are characteristic of the metal oxide-silica systems.

The activities of SnO, referred to the pure liquid oxide as the standard state, were calculated by means of Eq. [3] and the results at 1373°K are shown in Fig. 4.

The activities of silica at 1373°K, referred to the pure solid as the standard state, were calculated from the Gibbs-Duhem equation written in the form

SnO-SiO<sub>2</sub>

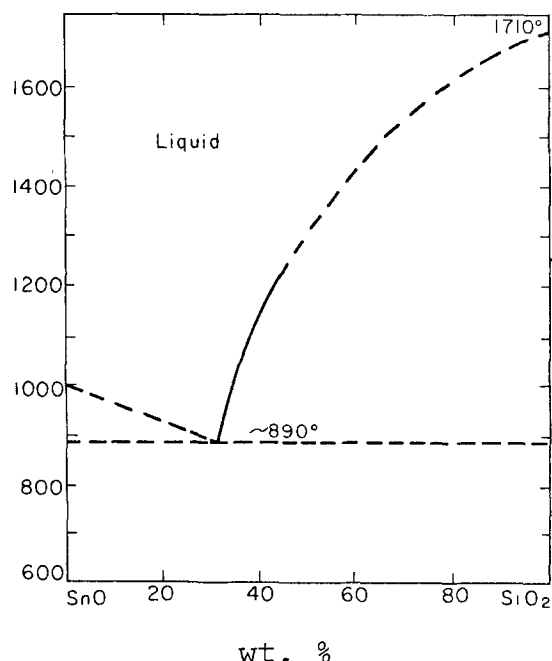


Fig. 3. Phase diagram of the SnO-SiO<sub>2</sub> system, Ref. (9)



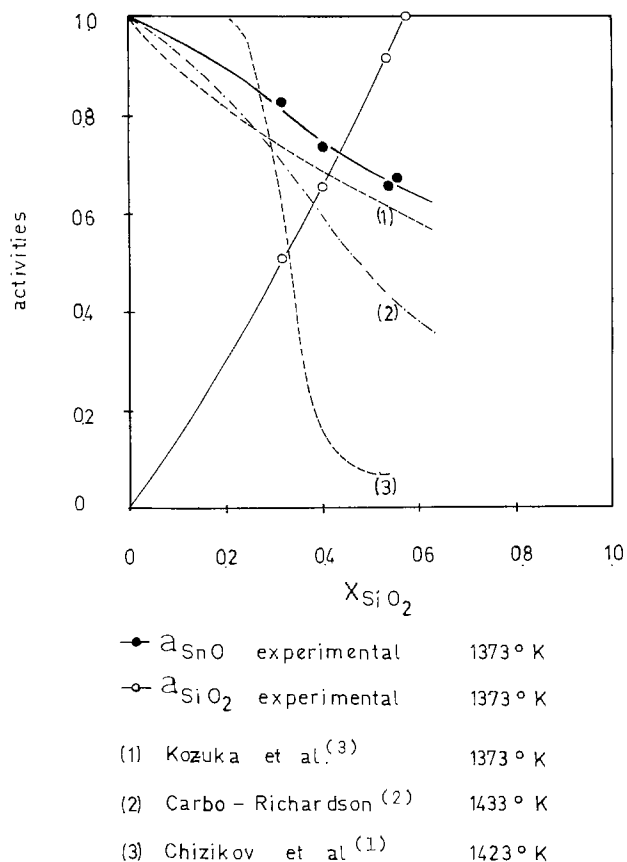


Fig. 4. Activities of SnO and SiO<sub>2</sub> vs. mole fraction of SiO<sub>2</sub> at 1373°K.

$$\int_{\gamma_{\text{SiO}_2} \text{ at } X_{\text{SiO}_2} = 0.565}^{\gamma_{\text{SiO}_2} \text{ at } X_{\text{SiO}_2} = 1.0} d \ln \gamma_{\text{SiO}_2} = - \int_{\gamma_{\text{SnO}} \text{ at } X_{\text{SiO}_2} = 0.565}^{\gamma_{\text{SnO}} \text{ at } X_{\text{SiO}_2} = 1.0} \frac{X_{\text{SnO}}}{X_{\text{SiO}_2}} d \ln \gamma_{\text{SnO}} \quad [12]$$

$$\begin{array}{ll} \gamma_{\text{SiO}_2} \text{ at } & \gamma_{\text{SnO}} \text{ at} \\ \text{SiO}_2 \text{ saturation} & \text{SiO}_2 \text{ saturation at} \\ \text{at } X_{\text{SiO}_2} = 0.565 & X_{\text{SiO}_2} = 0.565 \end{array}$$

In this equation,  $\gamma_{\text{SiO}_2}$  is the activity coefficient of SiO<sub>2</sub> with respect to the pure solid and  $\gamma_{\text{SnO}}$  is the activity coefficient of SnO referred to the pure liquid oxide.

This integration, in order to be accurate, requires precise knowledge of the temperature-composition coordinates at which SiO<sub>2</sub> saturation takes place. In this regard, the only information available is the phase diagram due to Keysseltz and Kohlmeyer (9) (Fig. 3) which, as mentioned earlier, requires further confirmation. Therefore, the activities of silica calculated on this basis which are shown in Fig. 4, should be considered as approximate values only.

It may be readily seen in Fig. 3 that the results of the present work are in disagreement with those reported in previous publications (1, 2, 3).

Chizikov *et al.* (1) used the emf method with cells of the type Sn, SnO/Al<sub>2</sub>O<sub>3</sub>/Sn, (SnO-SiO<sub>2</sub>). However, Al<sub>2</sub>O<sub>3</sub> does not behave as a purely oxide-ion conducting membrane, and therefore, accurate results cannot be expected from cells of this type.

In the work of Carbo and Richardson (2), the activities of SnO were established by measuring the oxygen dissolved in liquid tin brought into equilibrium with the slag through a gas phase. The slag samples contained as much as 10 mole per cent (m/o) Al<sub>2</sub>O<sub>3</sub> which originated from the Al<sub>2</sub>O<sub>3</sub> crucibles used for these experiments. Thus, the activities of SnO determined by this method should correspond to ternary melts containing SnO, SiO<sub>2</sub>, and Al<sub>2</sub>O<sub>3</sub>, and were ob-

tained by extrapolation to the SnO-SiO<sub>2</sub> binary system on the assumption that the Al<sub>2</sub>O<sub>3</sub> had no effect on the activity of SnO in the concentration range covered by the experiments. This last assumption, however, was not experimentally founded, and it should be expected that Al<sub>2</sub>O<sub>3</sub> would behave in a way similar to SiO<sub>2</sub> tending to complex the silicate structure and further decrease the activity of the stannous oxide in the melts.

The electrochemical cells of Kozuka *et al.* (3) may be represented as Sn, SnO /  $\begin{array}{c} \text{ZrO}_2 \\ \text{CaO} \end{array} / \text{Sn}, (\text{SnO-SiO}_2)$  and their characteristic is that of being "open" cells. The problems that are expected in this type of cells have been discussed elsewhere (6). In addition, the Sn, SnO reference electrode, due to both the attack of the SnO on the zirconia and the disproportionation of the oxide at temperatures lower than 1373°K, may have adversely affected the results. It is of interest to note that the activity results of Kozuka *et al.* (3) differ from the present work by about 10% and describe positive deviations with respect to the ideal molecular model.

The comparison between the activities of SnO reported in this work and those of other metal oxides dissolved in silica suggests that SnO is one of the more acidic metal oxides with respect to silica.

The potential  $E$  measured in the cells represented in Eq. [1] could also be interpreted as the potential which accompanies the electrochemical transfer of oxygen between the two-half-cell compartments, and is given as

$$E = - \frac{RT}{2F} \ln \frac{(p_{\text{O}_2})_{\text{Sn}/(\text{SnO-SiO}_2)}}{(p_{\text{O}_2})_{\text{Ni}/\text{NiO}}} \quad [13]$$

where  $(p_{\text{O}_2})_{\text{Sn}/(\text{SnO-SiO}_2)}$  and  $(p_{\text{O}_2})_{\text{Ni}/\text{NiO}}$  represent the partial pressure of oxygen in equilibrium with Sn<sub>(l)</sub>, (SnO/SiO<sub>2</sub>)<sub>(l)</sub>, and Ni, NiO, respectively. Since the temperature dependence of  $(p_{\text{O}_2})_{\text{Ni}/\text{NiO}}$  is well known (6), Eq. [13] may be used to calculate  $(p_{\text{O}_2})_{\text{Sn}/(\text{SnO-SiO}_2)}$  from the experimental emf data reported in Table II. The result of this calculation at 1373°K is shown in Fig. 5.

#### Acknowledgments

The authors are grateful to the National Research Council of Canada for its financial assistance in support of this work.

Manuscript submitted May 27, 1975; revised manuscript received Dec. 29, 1975.

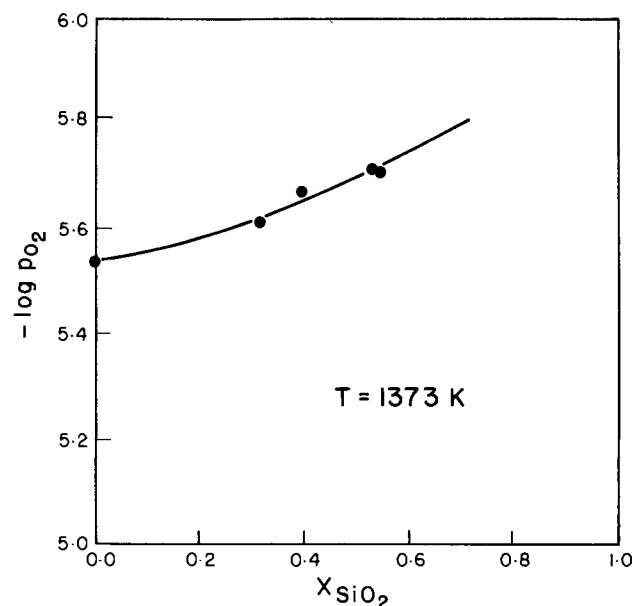


Fig. 5. Partial pressures of oxygen in equilibrium with SnO-SiO<sub>2</sub> slags.

Any discussion of this paper will appear in a Discussion Section to be published in the December 1976 JOURNAL. All discussions for the December 1976 Discussion Section should be submitted by Aug. 1, 1976.

Publication costs of this article were partially assisted by the University of Toronto.

#### REFERENCES

1. D. M. Chizikov, M. E. Volkova, and Yu. V. Isvetkov, *Izv. Akad. Nauk. SSSR Met. Gorn. Delo*, **3**, 82 (1964).
2. J. Carbo and F. D. Richardson, *Trans. Inst. Mining Met.*, **81**, c131 (1972).
3. Z. Kozuka, O. P. Sahaan, and J. Moriyama, *Trans. Japan Inst. Metals*, **9**, 200 (1969).
4. A. E. Grau and S. N. Flengas, *This Journal*, **122**, 352 (1976).
5. G. G. Charette and S. N. Flengas, *ibid.*, **115**, 796 (1968).
6. S. N. Flengas, in "High Temperatures—High Pressures," Vol. 5, pp. 551-566 (1973).
7. J. Carbo and F. D. Richardson, *Trans. Inst. Mining Met.*, **81**, c63 (1972).
8. T. N. Belford and C. B. Alcock, *Trans. Faraday Soc.*, **61**, 443 (1965).
9. B. Keysseltz and E. J. Kohlmeyer, *Metall. u. Erz.*, **30**, 185 (1933).

## Preparation and Properties of Magnetic Garnet Films Containing Divalent and Tetravalent Ions

S. L. Blank, J. W. Nielsen, and W. A. Biolsi

Bell Laboratories, Murray Hill, New Jersey 07974

#### ABSTRACT

The relevant phase equilibrium data necessary to grow garnet films containing divalent and tetravalent ions by liquid phase epitaxy are presented. The effects of melt composition on film magnetic properties and film composition are presented as is the influence of growth kinetics on the film magnetic parameters. Work on the  $(Y,Sm,Ca)_3(Ge,Fe)_5O_{12}$  system is stressed. A coupled distribution coefficient is defined which adequately describes the  $Ca^{2+}$ - $Ge^{4+}$  substitution. The effect of melt depletion on magnetic properties is discussed and data presented to indicate the magnitude of the effect observed in the  $(Y,Sm,Ca)_3(Ge,Fe)_5O_{12}$  system. An example of the propagation characteristics observed in the  $(Y,Sm,Ca)_3(Ge,Fe)_5O_{12}$  system is also shown. A technique for controlling the temperature dependence of the collapse field in LPE films is presented. The use of  $Lu^{3+}$  as both a dodecahedral and octahedral substituent is shown to lead to a system flexible enough to meet most of the present device requirements.

The discovery that some flux-grown magnetic garnet platelets possessed sufficient uniaxial anisotropy to support bubble domains (1, 2) has led to a search for garnet compositions suitable for device use. A large number of magnetic garnet compositions have been suggested for use in bubble domain devices (3-11). Many of these compositions have served well as vehicles for circuit design and prototype device construction, but as the bubble domain memory comes closer to being a practical device for use in a variety of environments, its stability toward temperature changes becomes a major consideration. Along with temperature-stable operation, high operational frequencies are also a requirement. The considerations that lead to high speed materials have been discussed previously (11). To achieve stability toward temperature, the Curie temperature of the garnet film must be as high as possible. Because of the preference of the nonmagnetic tetravalent ions  $Si^{4+}$  and  $Ge^{4+}$  for tetrahedral sites, and partly because of their valence state, substitution of  $Si^{4+}$  or  $Ge^{4+}$  in a magnetic garnet to yield a given  $4\pi M_s$  will exhibit a higher Curie temperature than the same garnet substituted with  $Ga^{3+}$  or  $Al^{3+}$  to achieve the same  $4\pi M_s$ . Although a divalent ion is necessary to charge compensate for the tetravalent substitution, the most convenient-sized ion,  $Ca^{2+}$ , is an S-state ion and has no negative effect on domain mobility. This divalent-tetravalent substitution permits bubble memory operation over a wider temperature range, and propagation margins in excess of 10 oe at 1 MHz and 100°C have been observed on  $Ca^{2+}$ - $Ge^{4+}$  substituted garnets.

In compensation for their higher complexity, the divalent-tetravalent substituted garnets show considerable versatility in meeting a wide range of speed,

temperature, and domain size requirements while at the same time holding to the restriction of matching the lattice parameter of  $Gd_3Ga_5O_{12}$  substrates. For example, the 6  $\mu m$  bubble diameter material,  $Y_{2.62}Sm_{0.38}Ga_{1.2}Fe_{3.8}O_{12}$ , can be adjusted to yield 3  $\mu m$  diameter bubbles in two ways. The decreased nonmagnetic ion substitution, along with the increased anisotropy required, leads to a larger lattice parameter that can be adjusted downward through substitution of either  $Lu^{3+}$  or  $Si^{4+}$ , as in  $Y_{1.46}Lu_{0.34}Sm_{0.28}Ca_{0.92}Ge_{0.92}Fe_{4.08}O_{12}$  or  $Y_{1.68}Sm_{0.38}Ca_{0.94}Ge_{0.84}Si_{0.10}Fe_{4.06}O_{12}$ . Fortunately, the same generalizations applied earlier in the handling of substituted garnets and the melts from which they grow still apply to these more complicated systems. Thus, melts containing magnetic garnet components plus  $Ca^{2+}$ ,  $Ge^{4+}$ , and/or  $Si^{4+}$  behave very much alike from the standpoint of phase equilibrium and kinetics of growth. However, they do differ in some respects from melts containing only trivalent garnet components.

The purpose of this paper is to present some of the relevant phase equilibrium data necessary to grow garnet films containing  $Ca^{2+}$  and  $Ge^{4+}$  by LPE, to show the effects of melt composition on film composition and magnetic properties, to present the growth kinetics observed in the system along with their influence on magnetic properties, and to show the effect of octahedral substitution on the temperature dependence of the bubble collapse field of LPE films. Work on the  $(Y, Sm, Ca)_3(Ge, Fe)_5O_{12}$  systems will be stressed because of a greater tendency for supercooled melts containing  $Si^{4+}$  to nucleate prematurely.

#### Experimental Procedure

All films discussed in this study were grown on  $Gd_3Ga_5O_{12}$  substrates by the dipping technique using supercooled melts (13). Axial rotation was main-



tained constant at approximately 100 rpm during the growth period. The details of the apparatus and growth techniques have been discussed elsewhere (14, 15). Temperatures at saturation were restricted to  $950^\circ \pm 25^\circ\text{C}$  except in specific instances mentioned in the text. Lattice constant measurements were obtained using the HPM method and the 444 and 888 reflections (16). Magnetic property measurements were obtained using the standard techniques (17, 18).

Samples for composition analysis were taken from the uniform region of the LPE films. The analysis was performed on an ETEC Autoscan scanning electron microscope (SEM) using a Kevex-Ray lithium drifted silicon detector and an energy dispersive system. Intensity data were stored in channels 10 eV wide. Resolution is such that peaks separated by  $\sim 150$  eV may be analyzed without significant interference. The x-ray lines used were  $\text{YL}\alpha$ ,  $\text{PbM}\alpha$ ,  $\text{CaK}\alpha$ ,  $\text{SmL}\alpha$ ,  $\text{FeK}\alpha$ , and  $\text{GeK}\alpha$ . The standards used were  $\text{CaF}_2$ ,  $\text{Sm}_3\text{Ga}_5\text{O}_{12}$ ,  $\text{Y}_3\text{Fe}_5\text{O}_{12}$ ,  $\text{Pb}$ , and  $\text{Ge}$ . Electronics stabilization was achieved prior to analysis by allowing the beam (in reduced area mode) to scan the YIG standard for 2 hr. Drift over the analysis time was typically 1.0%. MAGIC IV (19), with appropriate modifications for the specimen geometry, was used to reduce the data.

### Magnetic Properties vs. Composition

The major reason for the substitution of tetravalent ions in bubble garnets is that the Curie temperature per mole of substitution is higher. Geller *et al.* (20) have shown that both the site selectivity and the higher valence will serve to yield higher Curie temperatures over those expected with substitutions by  $\text{Ga}^{3+}$  or  $\text{Al}^{3+}$ . Figure 1 shows the Curie temperatures as a function of nonmagnetic ion substitution for the systems  $\text{Ca}^{2+}:\text{YIG}:\text{V}^{5+}$  (20),  $\text{Ca}^{2+}:\text{YIG}:\text{Si}^{4+}$  (21),  $\text{Ca}^{2+}:\text{YIG}:\text{Ge}^{4+}$  (21),  $\text{YIG}:\text{Ga}^{3+}$  (22), and  $\text{YIG}:\text{Al}^{3+}$

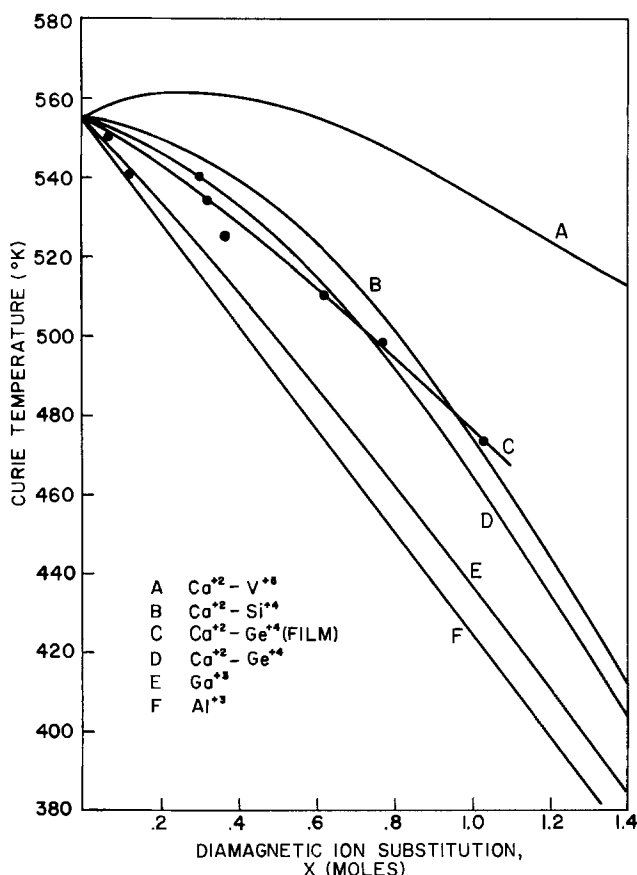


Fig. 1. Curie temperatures as a function of substitution ( $x$ ) in the systems (A)  $\text{Ca}^{2+}:\text{YIG}:\text{V}^{5+}$ ; (B)  $\text{Ca}^{2+}:\text{YIG}:\text{Si}^{4+}$ ; (C)  $\text{Ca}^{2+}:\text{0.15m YIG}:\text{Ge}^{4+}$  (film); (D)  $\text{Ca}^{2+}:\text{YIG}:\text{Ge}^{4+}$ ; (E)  $\text{Ga}^{3+}:\text{YIG}$ ; (F)  $\text{Al}^{3+}:\text{YIG}$ .

(22). For comparison, curve C is from SEM analyses and Curie temperature measurements taken on samples from the  $\{\text{Y}_{2.9}\text{Sm}_{0.1}\text{Ca}_x\}(\text{Fe}_{5-x}\text{Ge}_x)\text{O}_{12}$  system. (All curves are normalized to  $T_c = 555^\circ\text{K}$  at  $x = 0$ .)

It can be seen that the effectiveness in lowering  $T_c$  goes as  $\text{Al}^{3+} > \text{Ga}^{3+} > \text{Ge}^{4+} > \text{Si}^{4+} > \text{V}^{5+}$ . The difference between  $\text{Al}^{3+}$  and  $\text{Ga}^{3+}$  arises mainly from the difference in site selectivity. Aluminum occupies more octahedral sites which are more effective in lowering  $T_c$ . Although site selectivity probably plays a small role in explaining the differences in  $T_c$  seen for  $\text{Ge}^{4+}$ ,  $\text{Si}^{4+}$ , and  $\text{V}^{5+}$  substitution, these ions are highly selective, preferring tetrahedral sites. Therefore, the differences in  $T_c$  seen among  $\text{Ge}^{4+}$ ,  $\text{Si}^{4+}$ , and  $\text{V}^{5+}$  substituted garnets are related mostly to size and charge.

Note that at  $x = 1.0$ , the  $T_c$  for  $\text{Ge}^{4+}$  substitution is  $28^\circ$  higher than for  $\text{Ga}^{3+}$  substitution. The difference between device films is even more striking because of the greater  $\text{Ga}^{3+}$  substitution required to achieve the same moment. For a  $6 \mu\text{m}$  bubble diameter, the substitution level of  $\text{Ga}^{3+}$  in  $\text{YIG}:\text{0.2Sm}$  is about  $x = 1.2$ , and  $T_c = 405^\circ\text{K}$ , while for  $\text{Ca}^{2+}-\text{Ge}^{4+}$ ,  $x = 0.95$  and  $T_c = 480^\circ\text{K}$ , or  $75^\circ$  higher.

The course of curve C is of interest. The curve begins with lower  $T_c$ 's than those exhibited by the polycrystalline samples of Winkler (21), then crosses the plot of his data for the  $\text{Ca}^{2+}-\text{Ge}^{4+}$  substitution. Since the films used to plot the data in curve C were also  $\text{Ca}^{2+}$  and  $\text{Ge}^{4+}$  substituted with the exception of two samples where the compensating ion was lead, the difference in the curves requires some explanation. We suggest that curve C indicates octahedral substitution. Geller (20) has shown similar curves for  $\text{Ca}^{2+}-\text{Si}^{4+}$  and  $\text{Mg}^{2+}-\text{Si}^{4+}$  substituted YIG, where the curve for octahedrally located  $\text{Mg}^{2+}$  compensated by  $\text{Si}^{4+}$  begins below the curve for  $\text{Ca}^{2+}-\text{Si}^{4+}$  substituted samples but then crosses over it, although the effect is more dramatic in that case. Two sources of octahedral substitution are suggested. First, it is possible that under the conditions of temperature and growth rate used for LPE, the substitution of  $\text{Ge}^{4+}$  on octahedral sites may be slightly higher than in the case of ceramic samples. Second, in the case of low and zero substitutions of  $\text{Ca}^{2+}$ , charge compensation occurs through  $\text{Pb}^{2+}$  incorporation. In these samples, lattice parameter measurements suggest  $\text{Y}^{3+}$  may be substituted in octahedral sites in small amounts, probably smaller than the  $\text{Ge}^{4+}$  octahedral substitution.

In Fig. 2 are shown two calculated curves showing room temperature  $4\pi M_s$  vs. Ge substitution over the range  $0.6 < x < 1.4$ . The curves were generated by computer using the method of Dionne (23). In addition to assuming that the molecular field coefficients varied with diamagnetic ion substitution in YIG in the manner assumed by Dionne, an empirically determined factor was applied to account for the small

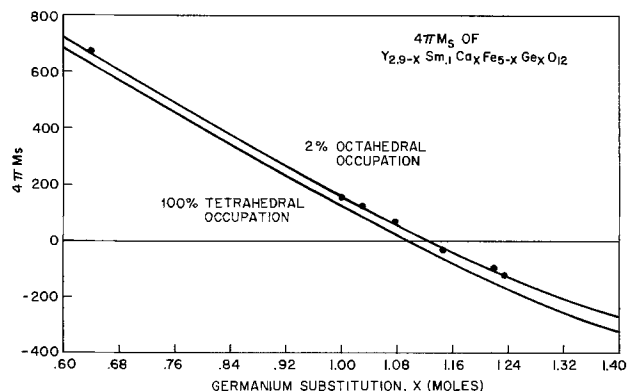


Fig. 2.  $4\pi M_s$  of  $\text{Y}_{2.9-x}\text{Sm}_{0.1}\text{Ca}_x\text{Fe}_{5-x}\text{Ge}_x\text{O}_{12}$  for 0% and 2% octahedral substitution of Ge (— calculated; ● observed).

samarium substitution (24). The lower curve assumes that substitution is entirely tetrahedral, the upper curve assumes 2% of the  $\text{Ge}^{4+}$  is on octahedral sites. The measured values of  $4\pi M_s$ , indicated by the points, fall on or very near the upper curve, strongly suggesting that our samples had about 2%  $\text{Ge}^{4+}$  in octahedral sites. Considering the accuracy of measurements of this type, these data are consistent with Geller's (20) observation that although  $\text{Ge}^{4+}$  is strongly site selective, a small percentage, perhaps 1%, is octahedral at a substitution of  $x = 1$ . The higher substitution observed in the film is probably the result of kinetic effects.

The data are in disagreement with the conclusion of Shimada *et al.* (25) that for  $x = 1$  approximately 14% of the  $\text{Ge}^{4+}$  ions are on octahedral sites. Our magnetic moment, lattice constant, and  $T_c$  data agree closely with the results obtained by Geller (20) and Winkler (21).

Data presented so far have been taken on samples of analyzed compositions from  $\text{PbO-B}_2\text{O}_3$  fluxed melts. Although it is clear that melt compositions must be adjusted to grow varied film compositions, just how the growth parameters of composition and rate are adjusted to yield desired magnetic properties in films is not always obvious, and the establishment of a set of growth parameters that optimize film properties can be tedious. The effect of changing two ratios,  $\text{Fe/Ge}$  and  $\text{Ca/Ge}$  on the germanium content and hence  $T_c$  of  $(\text{YSmCa})_3(\text{Ge, Fe})_5\text{O}_{12}$  films, strongly suggested that in order to make maximum use of the systems containing  $\text{Ge}^{4+}$  and  $\text{Si}^{4+}$  a broad investigation of phase equilibria, distribution coefficients, and kinetic effects was necessary.

### Phase Equilibria Studies

In discussing the  $(\text{YSmCa})_3(\text{FeGe})_5\text{O}_{12}$  system we define six atomic melt ratios

$$R_1 = \frac{\text{Fe}_2\text{O}_3}{\Sigma \text{Ln}_2\text{O}_3} = \frac{\text{Fe}}{\Sigma \text{Ln}}$$

$$R_2 = \frac{2\text{Fe}_2\text{O}_3}{\text{GeO}_2} = \frac{\text{Fe}}{\text{Ge}}$$

$$R_3 = \frac{\text{PbO}}{2\text{B}_2\text{O}_3} = \frac{\text{Pb}}{\text{B}}$$

$$R_4 = \frac{2\Sigma \text{Ln}_2\text{O}_3 + 2\text{Fe}_2\text{O}_3 + \text{GeO}_2 + \text{CaO}}{\text{PbO} + 2\text{B}_2\text{O}_3 + 2\Sigma \text{Ln}_2\text{O}_3 + 2\text{Fe}_2\text{O}_3 + \text{GeO}_2 + \text{CaO}}$$

$$R_5 = \frac{\text{CaO}}{\text{GeO}_2 + \text{CaO}}$$

$$R_6 = \frac{\text{CaO}}{2\Sigma \text{Ln}_2\text{O}_3} = \frac{\text{Ca}}{\Sigma \text{Ln}}$$

where  $\text{Ln}_2\text{O}_3$  refers to the rare earth oxides. These ratios are atomic ratios in contrast to those defined previously (14, 15). In clarification, the ratio  $R_3 = \text{PbO}/2\text{B}_2\text{O}_3$  reads one half the molar ratio of  $\text{PbO}$  to  $\text{B}_2\text{O}_3$ . In the  $\text{Ln}_3\text{Fe}_{5-x}\text{Ga}_x\text{O}_{12}$  systems the ratio  $R_1$  was chosen to place the melt composition within the garnet phase field in the pseudoternary  $\text{Ln}_2\text{O}_3\text{-Fe}_2\text{O}_3\text{-flux}$  somewhere between  $R_1 = 14$  and  $R_1 = 35$ . In the  $(\text{YSmCa})_3(\text{GeFe})_5\text{O}_{12}$  system three ratios are important in delineating the garnet phase field. As in the previous systems,  $\text{Fe}_2\text{O}_3/\Sigma \text{Ln}_2\text{O}_3$  ( $R_1$ ) must still be set to place the melt into the garnet field instead of the orthoferrite or magnetoplumbite fields. However, the ratios  $R_2$  and  $R_5$  must also be adjusted to prevent second-phase precipitation during garnet deposition. Figure 3 shows a portion of the pseudoquaternary  $\text{YIG-Fe}_2\text{O}_3\text{-CaO-GeO}_2$  for  $T_{\text{sat}} \approx 950^\circ\text{C}$ . The ternary represents a plane in the quaternary

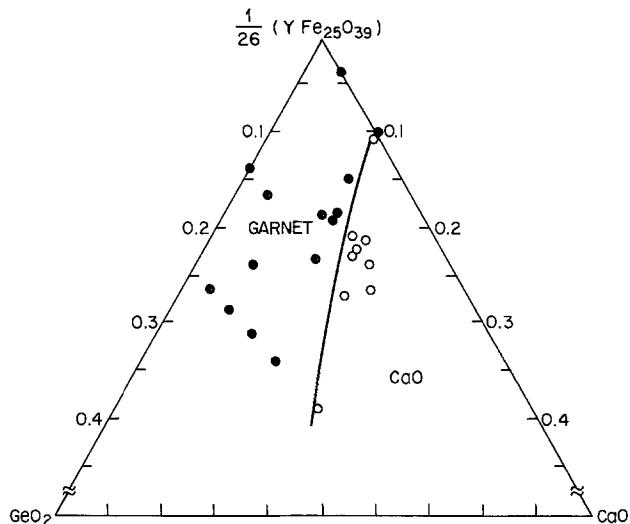


Fig. 3. Section of pseudoquaternary,  $\text{YIG-Fe}_2\text{O}_3\text{-CaO-GeO}_2$  at  $T_{\text{sat}} = 950^\circ\text{C}$ .

having  $R_1 = 25$ , hence the end members are written as  $1/26(\text{YFe}_{25}\text{O}_{39})\text{-GeO}_2\text{-CaO}$ . The  $1/26$  is a scaling factor for the compositional axis used in Fig. 3. The closed circles represent data points where the only phase present was found to be garnet. Open circles represent points where the primary phase was observed to be a colorless parallelepiped which deposited before the iron garnet. Analysis of this colorless phase was performed in an SEM; the only cationic element present was calcium; hence, the phase is almost certainly  $\text{CaO}$ . In order to insure that garnet is the primary phase during crystal growth the ratios  $R_2$  and  $R_5$  must be adjusted to place the melt above the solid line in Fig. 3.

Once the approximate boundary to  $\text{CaO}$  formation was established it was informative to explore the concentration dependencies of  $\text{Ca}$  and  $\text{Ge}$  substitution. As had been done in the case of  $\text{Ga}$ , distribution coefficients between concentrations in the crystal and melt were defined as follows

$$k^{\text{Ge}} = \frac{\left(\frac{\text{Ge}}{\text{Ge} + \text{Fe}}\right)_{\text{crystal}}}{\left(\frac{\text{Ge}}{\text{Ge} + \text{Fe}}\right)_{\text{melt}}}$$

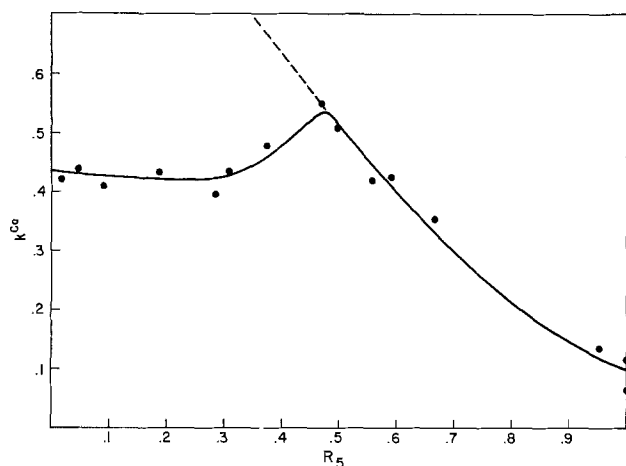
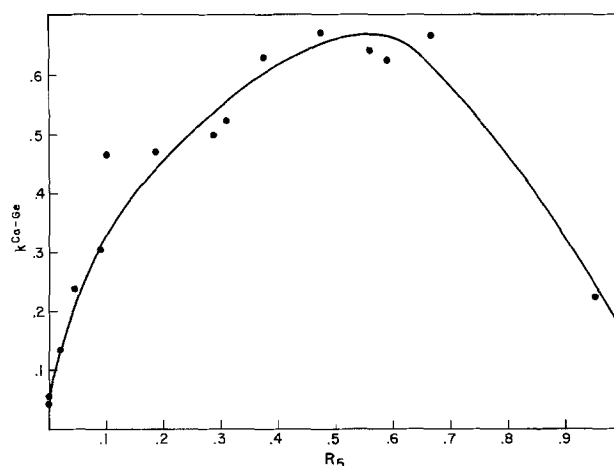
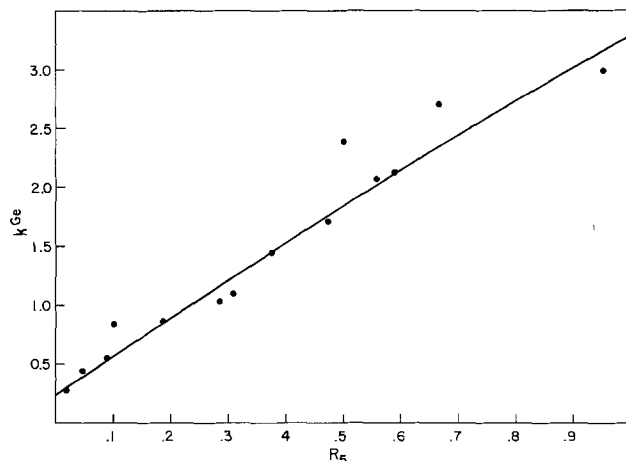
and

$$k^{\text{Ca}} = \frac{\left(\frac{\text{Ca}}{\text{Ca} + \Sigma \text{Ln}}\right)_{\text{crystal}}}{\left(\frac{\text{Ca}}{\text{Ca} + \Sigma \text{Ln}}\right)_{\text{melt}}}$$

where the symbols in the fractions represent the number of moles present.

These distribution coefficients are plotted against  $R_5$  in Fig. 4 and 5 for a series of runs in which the concentrations of  $\text{Ca}$  and  $\text{Ge}$  ranged from zero upward. Note that at zero  $\text{Ca}$  concentration  $k^{\text{Ge}}$  is considerably less than 1,  $\sim 0.24$ , but rises sharply to over 1 as the  $\text{Ca}$  concentration rises. On the other hand,  $k^{\text{Ca}}$  is near 0.1 at high  $\text{Ca}$  and low  $\text{Ge}$  concentrations but rises to  $\sim 0.6$  as the ratio  $R_5$  decreases; *i.e.*, the concentration in the melt of  $\text{Ca}$  relative to  $\text{Ge}$  diminishes. The maximum in  $k^{\text{Ca}}$  at  $R_5$  between 0.4 and 0.5 occurs because of the very large  $\text{Pb}^{2+}$  concentration in the melt which dominates the charge compensation process at low  $\text{Ca}$  concentrations. A comparable break in the  $k^{\text{Ge}}$  does not occur because tetravalent ions other than  $\text{Ge}$ , such as  $\text{Fe}^{4+}$ , have very low concentrations.

Additional details on  $\text{Pb}^{2+}$  incorporation will be presented later; however, the data in Fig. 4 and 5 show the great interdependence of the incorporations

Fig. 4.  $k^{Ca^{2+}}$  vs.  $R_5$ Fig. 6.  $k^{Ca:Ge}$  vs.  $R_5$ Fig. 5.  $k^{Ge^{4+}}$  vs.  $R_5$ 

of Ca and Ge into the crystal. At very low Ge concentrations, the total substitution is strongly influenced by the concentration of Ge and  $k^{Ge}$  is high,  $>1$ , in fact. At very low Ca concentrations the reverse is true; the substitution tends to be Ca controlled, but the presence of lead makes this effect less pronounced than the former case.

We have found it convenient in discussing the substitution of Ca and Ge to define a coupled distribution coefficient as follows

$$k^{Ca:Ge} = \frac{(X_{Ca} + X_{Ge})_{crystal}}{2(X_{Ca} + X_{Ge})_{melt}}$$

where the  $X$ 's are mole fractions based on total garnet ions present.

We can view  $k^{Ca:Ge}$  as a measure of the effectiveness of total substitution in the  $(YSmCa)_3(GeFe)_5O_{12}$  system. In Fig. 6 are plotted values of  $k^{Ca:Ge}$  against  $R_5$ . There it is seen that substitution becomes easier as Ca and Ge concentrations become comparable. It can be seen then, from Fig. 4, 5, and 6, that the incorporations of Ca and Ge are strongly controlled by the concentrations of the ions with valences other than three. In fact, separate experiments revealed that  $k^{Ge}$  and  $k^{Ca}$  are not nearly so sensitive to the temperature of growth as, for example, is  $k^{Ga}$ . Thus while the scatter in the points in Fig. 4, 5, and 6 can perhaps be partially attributed to differences in growth temperatures, it is likely that kinetic factors played a greater role. These will be discussed later.

The incorporation of Pb requires comment. With no Ca in the melt, films grown at the same temperature,  $902^\circ \pm 2^\circ C$ , and at a similar rate contained lead varying from 0.06 to 0.12 in the formula unit as  $R_2$  changed

from 9.4 to 6.0, *i.e.*, as the ratio of Fe to Ge decreased. It was observed, however, that as calcium was added to the melt the lead content was sharply reduced. For example, analysis of films grown from a melt where  $R_1$ ,  $R_2$ , and  $R_5$  were 25, 6, and 0, respectively, yielded the formula  $Y_{2.80}Sm_{0.09}Pb_{0.11}Fe_{4.88}Ge_{0.12}O_{12}$ . Keeping  $R_1$  and  $R_2$  constant and raising  $R_5$  to only 0.3 yielded a composition with Pb 0.01 in the formula unit. We conclude that because of its smaller size, calcium rapidly dominates the charge balancing process in the films even in the presence of large concentrations of divalent lead.

### Growth Kinetics

*Composition vs. growth rate.*—Once the phase equilibria are known and a melt made which has the correct composition to insure that the desired iron garnet is the primary phase, kinetic effects must be considered. There is evidence that at higher temperatures the growth rate is greater for the  $(YSmCa)_3(FeGe)_5O_{12}$  system than it is for the  $(YSm)_3(GaFe)_5O_{12}$  system. For comparison, the growth rate for  $(YSmCa)_3(FeGe)_5O_{12}$  at  $908^\circ$  and  $955^\circ C$  and  $10^\circ$  and  $5^\circ C$  supercooling, respectively, are  $0.30 \mu m/min$  and  $0.97 \mu m/min$  as compared to  $0.26 \mu m/min$  and  $0.25 \mu m/min$  for the Ga system at the same temperatures and degrees of supercooling (26).

Figure 7 shows the  $4\pi M_s$  and Curie temperature as a function of growth rate for samples grown from the melt composition given below

$$\begin{aligned} R_1 &= 25 & R_4 &= 0.236 \\ R_2 &= 9.25 & R_5 &= 0.590 \\ R_3 &= 7.81 & Sm/Y + Sm &= 0.0416 \end{aligned}$$

Note that the  $R_2$ - $R_5$  combination places the melt just inside the garnet field. The compensation temperature moves from below room temperature to above room temperature for growth rates from  $0.80$  to  $2.10 \mu m/min$ . This corresponds to compositions ranging from  $Y_{1.93}Sm_{0.10}Ca_{0.97}Ge_{0.97}Fe_{4.03}O_{12}$ , for the lowest growth rate, to  $Y_{1.75}Sm_{0.10}Ca_{1.15}Ge_{1.15}Fe_{3.85}O_{12}$  for the highest growth rate. Figure 7 predicts that for the melt composition listed above, a growth rate of  $\sim 1.52 \mu m/min$  would result in a material with a compensation temperature at room temperature having the approximate composition  $Y_{1.8}Sm_{0.10}Ca_{1.1}Ge_{1.1}Fe_{3.9}O_{12}$ . By interpolating between the measured lattice constants for samples grown at  $1.06$  and  $1.58 \mu m/min$ , one predicts that the above composition should have a lattice parameter of  $\sim 12.3797 \text{ \AA}$ . Correcting this lattice constant for the approximate Sm and Pb contents, one obtains a lattice constant for  $Y_{1.9}Ca_{1.1}Ge_{1.1}Fe_{3.9}O_{12}$  of  $\sim 12.371 \text{ \AA}$ . This compares well with the lattice constant reported by Winkler (21). We point out that the effect of rate

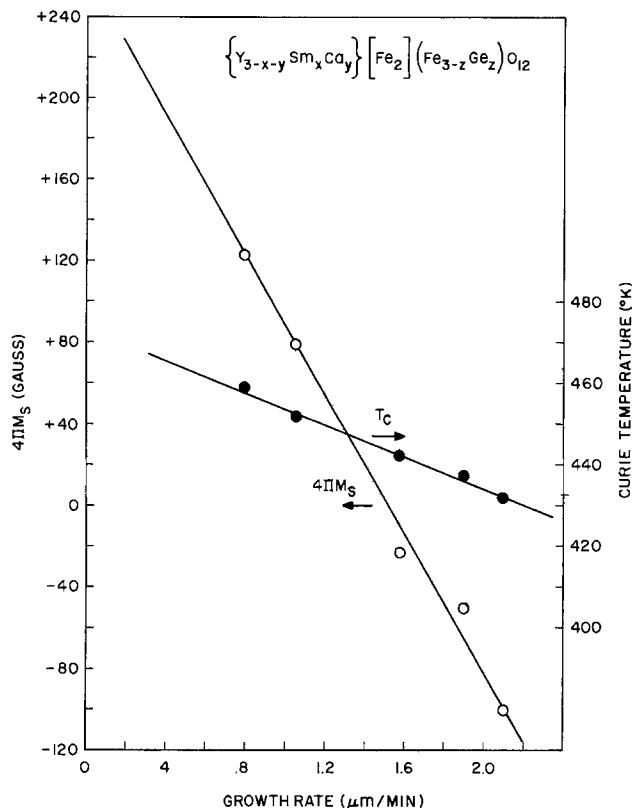


Fig. 7.  $4\pi M_s$  and  $T_c$  vs. growth rate. ● = Curie temperature, ○ =  $4\pi M_s$ .

on  $4\pi M_s$  can be large, and can be greater than in the trivalent substituted systems.

The question arises: Since the sensitivity of  $4\pi M_s$  to growth rate is substantial, does the interdependence of the substitutions of Ca and Ge give a greater flexibility in controlling the rate sensitivity than is observed in the case of a single nonmagnetic ion substituent such as Ga? A series of runs was made to investigate the point.

The sensitivity of the measured  $4\pi M_s$  to growth rate can be expressed by

$$\dot{M} (\text{G}/\mu\text{m}/\text{min}) = \frac{\Delta 4\pi M_s}{\Delta \text{Rate}}$$

For the melt listed above,  $\dot{M} = -170 \text{ G}/\mu\text{m}/\text{min}$ . We show in Fig. 8 the relationship observed between  $\dot{M}$  and  $R_5$  for a fixed  $R_1$  of 25 and for three values of  $R_2$ . Open circles represent  $R_2$  values between 9.0 and 10.0, closed circles represent  $R_2$  values from 6.5 to

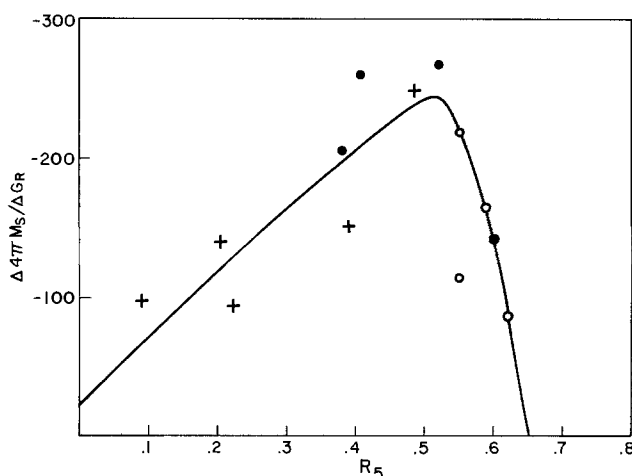


Fig. 8. Growth rate sensitivity vs.  $R_5$

8.0, and crosses represent  $R_2$  values from 5.0 to 6.5. The data show that the growth rate sensitivity of the  $4\pi M_s$  is a maximum at  $R_5$  near 0.5. The values of  $\dot{M}$  range from  $-260 \text{ G}/\mu\text{m}/\text{min}$  for  $R_5 = 0.5$  to approximately  $-90 \text{ G}/\mu\text{m}/\text{min}$  for  $R_5$  or either  $R_5 = 0.167$  or  $0.63$ . For comparison, in the system  $\text{Y}_{2.6}\text{Sm}_{0.4}\text{Ga}_x\text{Fe}_{5-x}\text{O}_{12}$  the average  $\dot{M} = \sim +225$ . Compositions can be used such that the rate sensitivity is at least no greater than it is in gallium-containing systems. Furthermore, the empirically observed growth-rate sensitivity of the  $4\pi M_s$  confirms that the effective distribution coefficient of the  $\text{Ca}^{+2}\text{-Ge}^{+4}$  couple is less than unity. We postulate that, over the useful range of melt compositions studied, calcium is the controlling ion in establishing the effective distribution coefficient for the Ca-Ge couple.

### Melt Depletion Effects

From the data shown in Fig. 4, 5, and 6, one would expect that the effect of melt depletion would be to cause a considerable systematic variation in film composition as garnet is removed from the melt. To investigate this point as well as to establish the effect of temperature on rate sensitivity, a small melt ( $\sim 250\text{g}$ ) was used first to grow films on 12 0.8 in. diameter GGG substrates over the temperature range  $953^\circ \pm 7^\circ\text{C}$ , then flux ( $\text{PbO} + \text{B}_2\text{O}_3$ ) was added to the melt and a second series of 14 samples was grown over a temperature range of  $895^\circ \pm 5^\circ\text{C}$ . The melt ratios were 31.6, 7.38, 0.386, and 2.70 for  $R_1$ ,  $R_2$ ,  $R_5$ , and  $R_6$ , respectively. A second melt, with the same composition as the first except for  $R_4$ , was then used to grow 12 samples over the temperature range  $840^\circ \pm 10^\circ\text{C}$ . Figure 9 shows the measured  $4\pi M_s$  of these three sets of samples as a function of growth rate. Open circles represent the first set of samples, X the second set, and closed circles the third set. Note the large scatter in the points. No attempt is made to indicate the sequential nature of the points.

With a melt as small as 250g, removal of  $1.9 \times 10^{-2}\text{g}$  of garnet ( $\sim 10 \mu\text{m}$  total thickness of film on 0.8 in. diameter substrate) changes the melt ratios significantly. The most important change occurs in  $R_6$ , since Y and Ca are removed from the melt in the ratio of 2/1,  $R_6$  would increase. Increasing  $R_6$  results in increased Ca-Ge substitution in the film. Experimentally, it is found that the  $4\pi M_s$  of films grown from the above-described melt decreases by 4.8G upon removal of a  $10 \mu\text{m}$  thickness of garnet. Correcting the mea-

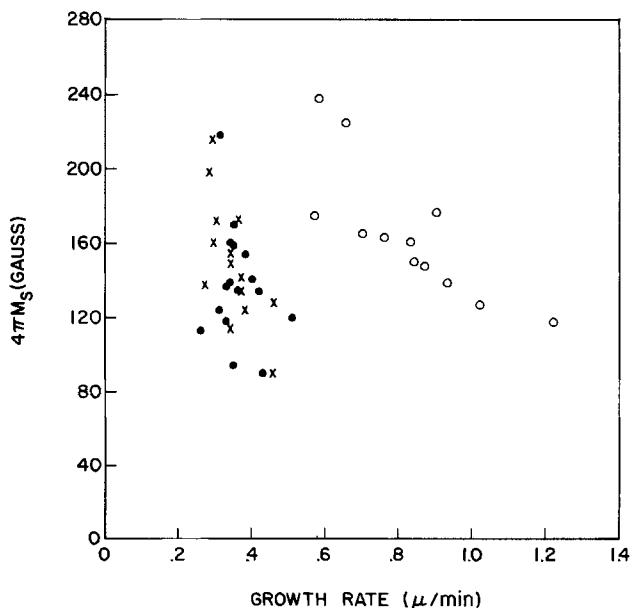


Fig. 9.  $4\pi M_s$  vs. growth rate for  $\text{Y}_{2.9-x}\text{Sm}_{0.1}\text{Ca}_x\text{Fe}_{5-x}\text{Ge}_2\text{O}_{12}$  grown from a 250g melt. ○ =  $953^\circ\text{C}$ , × =  $895^\circ\text{C}$ , ● =  $840^\circ\text{C}$ .

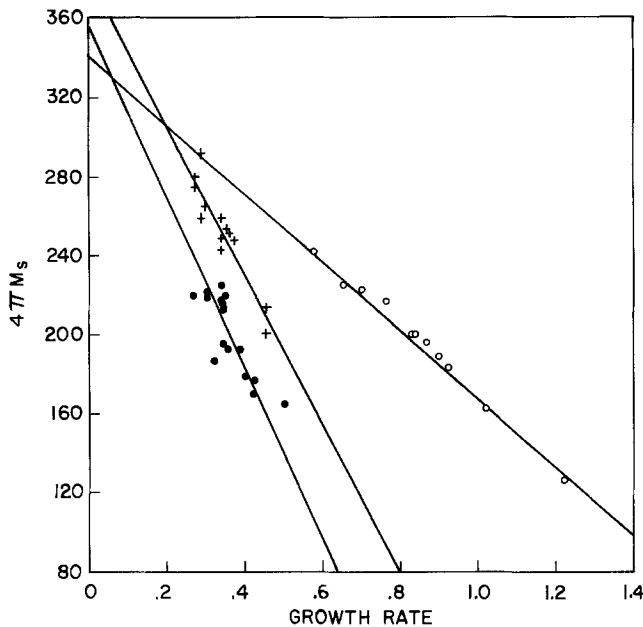


Fig. 10.  $4\pi M_s$  vs. growth rate for  $Y_{2.9-x}Sm_{0.1}Ca_xFe_{5-x}Ge_xO_{12}$  after correction for melt depletion.  $\circ$  =  $953^\circ C$ ,  $+$  =  $895^\circ C$ ,  $\bullet$  =  $840^\circ C$ .

sured  $4\pi M_s$  of each sample by the above factor results in the data shown in Fig. 10. Note the smaller scatter and the trend of decreasing moment with decreasing temperature of growth. The latter effect could result from increased lead content (therefore increased  $Ge^{4+}$  acting as charge compensation) as the growth temperature decreases (15). The growth rate sensitivity of the  $4\pi M_s$  varies from  $-173$  G/ $\mu m/min$  at  $953^\circ C$  to  $-430$  G/ $\mu m/min$  at  $840^\circ C$ . This increased growth rate sensitivity is also thought to be the result of increased lead content. Since the distribution coefficient of Pb is much less than unity, as the concentration in the film is increased the growth rate sensitivity of the  $4\pi M_s$  would also be expected to increase.

#### Temperature Dependence of Magnetic Properties

Samples of  $(YSmCa)_3(GeFe)_5O_{12}$  were grown with net moments parallel to the tetrahedral (positive) and octahedral (negative) iron sublattices. The positive material, with a composition  $Y_{1.92}Sm_{0.10}Ca_{0.98}Ge_{0.98}Fe_{4.02}O_{12}$ , exhibited a normalized slope of the collapse field vs. temperature curve  $(\Delta H_o/H_o\Delta T)_{25^\circ C}$  of  $-0.14\%/^\circ C$ . For the negative material, with a composition  $Y_{1.67}Sm_{0.10}Ca_{1.23}Ge_{1.23}Fe_{3.77}O_{12}$ ,  $(\Delta H_o/H_o\Delta T)_{25^\circ C} = -0.51\%/^\circ C$ . Comparison of the two values on either side of the compositional compensation point indicates that the material with the net moment parallel to the octahedral iron sublattice has a temperature dependence  $\sim 3.5$  times greater than that for the positive material. The change of collapse field with temperature is an important material parameter to consider because it directly affects the temperature sensitivity of circuit performance. To be thermally stable, the bubble garnet chip must be placed in a bias magnet structure where the temperature dependence of the bias field tracks the change in collapse field of the epi material. The most commonly used bias magnets are composed of barium ferrite whose  $(\Delta H_o/H_o\Delta T)_{25^\circ C}$  is  $\sim -0.20\%/^\circ C$  over the  $-10 < T^\circ C < 100$  range. A method by which the  $(\Delta H_o/H_o\Delta T)_{25^\circ C}$  could be varied is therefore of great importance in tailoring a bubble material to a specific application.

It is found experimentally that in the  $(YSmCa)_3(Ge,Fe)_5O_{12}$  system the temperature dependence of the bubble collapse field is a function of growth temperature. Figure 11 shows  $(\Delta H_o/H_o\Delta T)(\%/^\circ C)$  vs. growth temperature ( $^\circ C$ ) for four samples of  $Y_{1.92}Sm_{0.10}Ca_{0.98}Ge_{0.98}Fe_{4.02}O_{12}$ . The increased slope observed as the

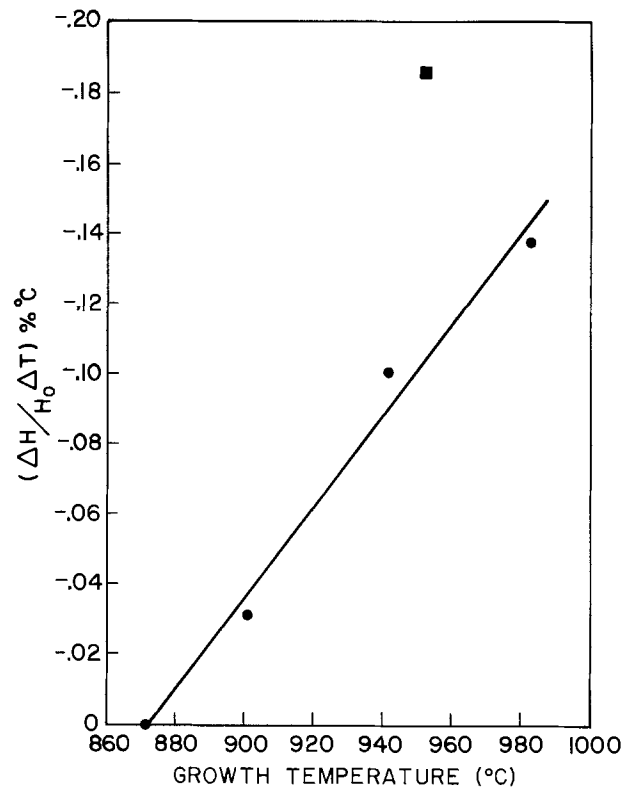


Fig. 11. Normalized collapse field temperature dependence vs. growth temperature.  $\circ$  =  $(YSmCa)_3(Ge,Fe)_5O_{12}$ ,  $\blacksquare$  =  $(LuYSmCa)_3(Ge,Fe)_5O_{12}$ .

growth temperature is increased is thought to be the result of increasing octahedral substitution. A sample of  $Lu_{0.34}Y_{1.44}Sm_{0.28}Ca_{0.94}Ge_{0.94}Fe_{4.06}O_{12}$  was grown at  $952^\circ C$  and the  $(\Delta H_o/H_o\Delta T)_{25^\circ C}$  also plotted in Fig. 11 as the dark square. The increased value for the slope is consistent with the postulation that some small fraction of  $Lu^{3+}$  occupy octahedral sites. Curie temperature measurements confirm some octahedral occupation of  $Lu^{3+}$ . The measured  $T_c$  for the above composition is  $471^\circ K$  with a  $4\pi M_s$  of  $214$  G. The expected value of  $T_c$  is  $\sim 475^\circ K$ . If the decrease in  $T_c$  of  $\sim 185^\circ K$  per mole from octahedral substitution is assumed to be correct, the observed decrease in  $T_c$  of  $4^\circ K$  corresponds to  $\sim 0.022$  moles of  $Lu^{3+}$  on octahedral sites or approximately  $6.5\%$  of the total  $Lu^{3+}$  content. Robertson *et al.* (27) have also reported rare earth ions on octahedral sites.

In order to investigate the effect of octahedral occupation of  $Lu^{3+}$ , a series of samples in the system  $(Y, Sm, Lu, Ca)_3(Fe, Ge)_5O_{12}$  was grown. Figure 12 shows the measured Curie temperature of these samples as a function of the melt ratio  $Fe_2O_3/Lu_2O_3$ . The solid point indicates the measured Curie temperature for a sample grown from a melt where  $Fe_2O_3/Lu_2O_3$  was  $54.5$  but where  $Sc^{3+}$  was added to the melt to incorporate  $0.024 \pm 0.002$  additional moles of  $Sc^{3+}$  on octahedral sites in the epi film. Figure 13 plots the normalized collapse field  $(\Delta H_o)$  defined as the change in collapse field from  $0^\circ$  to  $100^\circ C$  divided by the temperature interval and normalized to the collapse field at  $50^\circ C$  as a function of the octahedral  $Lu^{3+}$  concentration (mole). The substitution on octahedral sites is consistent with the Curie temperature, moment measurement, and film lattice parameter. The solid point again represents the sample containing both  $Lu^{3+}$  and  $Sc^{3+}$ .

#### Propagation Characteristics

In Fig. 14 (28) is shown the longevity plot (29, 30) of a bubble data pattern propagating around a re-entrant loop composed of TX elements. The operating frequency is the parameter, and the limits of the bias

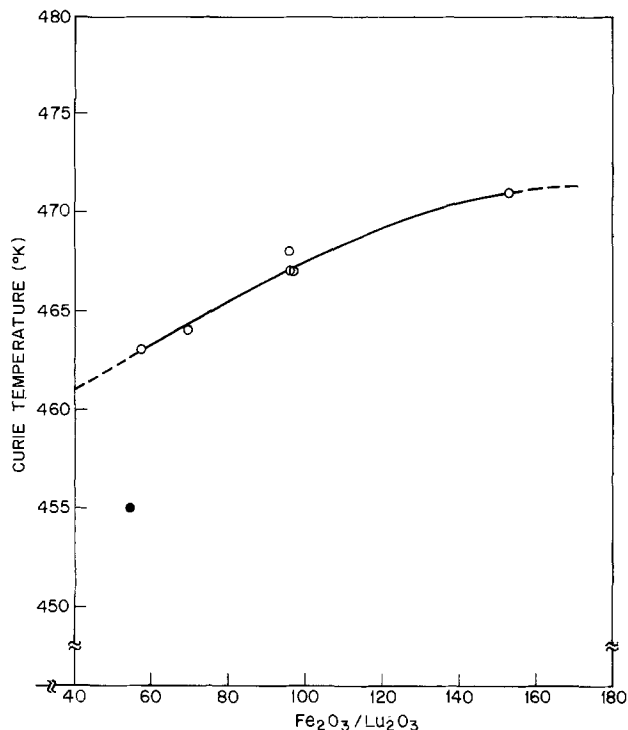


Fig. 12. Curie temperature vs.  $\text{Fe}_2\text{O}_3/\text{Lu}_2\text{O}_3$  (molar ratio)

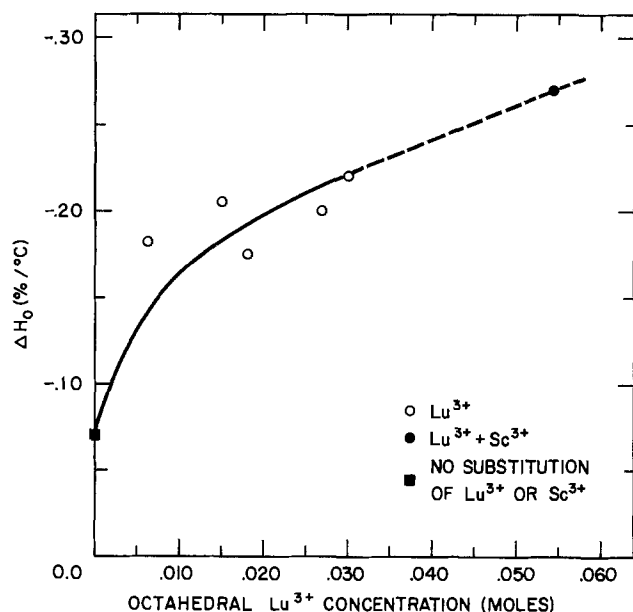


Fig. 13. Normalized collapse field temperature dependence vs. octahedral  $\text{Lu}^{3+}$  concentration.

field operating range are plotted as a function of the number of propagation steps. The circuit period was  $28.8 \mu\text{m}$  and the separation between the epitaxial garnet film and the circuit was from 1.0 to  $1.6 \mu\text{m}$ . The film composition was  $\text{Y}_{1.92}\text{Sm}_{0.10}\text{Ca}_{0.98}\text{Ge}_{0.98}\text{Fe}_{4.02}\text{O}_{12}$ . The magnetic properties of the sample are listed in Table I. It is seen in Fig. 14 that the bias field margins are independent of frequency until 1.1 MHz is reached. At 1.1 MHz, propagation still occurs for a relatively small number of steps but it is not possible to propagate more than  $10^5$  steps and retain the data pattern. At 1.2 MHz, propagation was not possible. Figure 14 illustrates the onset of dynamic conversion and implies that the dynamic conversion failure mechanism is the mechanism operative under the conditions presented.

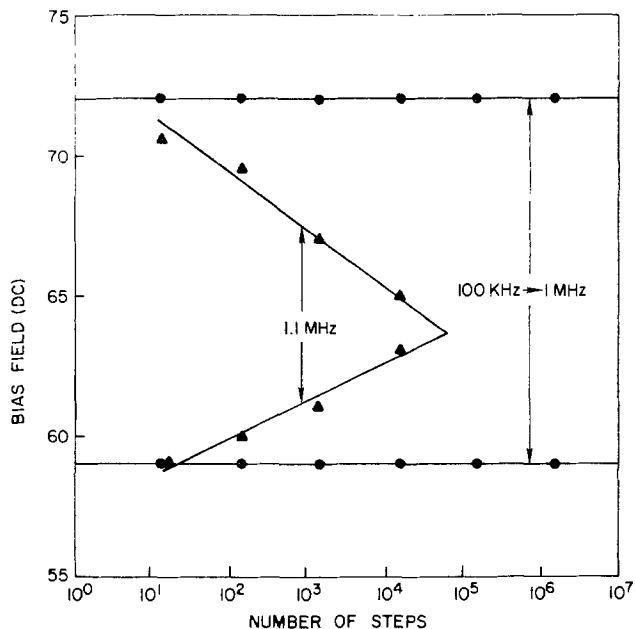


Fig. 14. Bias field operating range limits vs. number of propagation steps.

### Discussion and Summary

Our work on the phase equilibria in the  $\text{Y}_2\text{O}_3\text{-CaO-Sm}_2\text{O}_3\text{-Fe}_2\text{O}_3\text{-GeO}_2\text{-PbO-B}_2\text{O}_3$  system reveals two important differences between it and systems studied earlier (which contained only trivalent ions) that are important to note before depositing garnet films from the system by LPE. First, the distribution coefficients of the diamagnetic ions  $\text{Ca}^{2+}$  and  $\text{Ge}^{4+}$  can be varied over a much wider range by varying the concentration parameters than can the distribution coefficients of  $\text{Ga}^{3+}$  and  $\text{Al}^{3+}$ , i.e., the solutions containing the ions  $\text{Ca}^{2+}$  and  $\text{Ge}^{4+}$  are less "ideal."

Second, the possible crystallization of CaO adds an additional complication to the LPE process. In systems containing trivalent garnet ions the spontaneous crystallization of only garnet, orthoferrite, or magnetoplumbite need be considered, and the elimination of problems with the latter two is a simple matter of controlling  $R_1$ . That is to say, the garnet primary field is readily defined and broad enough to permit a rather wide range of temperature and compositional changes. In the case of the melts containing Ca, the range of compositions available to the film grower is restricted by the formation of CaO within ranges of  $R_2$  and  $R_5$  that are close to the useful values of these ratios. Figure 5 shows that as  $R_5$  increases the melt must become increasingly iron rich to avoid precipitation of CaO.

Returning to the first point, in contrast to Ga and Al, the distribution coefficients of both  $\text{Ca}^{2+}$  and  $\text{Ge}^{4+}$ , as single substituents, are less than unity and vary considerably with concentration. However, that variation is small compared to the change in  $k^{\text{Ca}}$  or  $k^{\text{Ge}}$  observed in melts containing both ions as the concentration of the compensating ion is increased. That is, a small amount of Ca added to a melt containing a substantial quantity of Ge, or a small amount of Ge added to a melt containing a large Ca concentration will sharply increase  $k^{\text{Ca}}$  or  $k^{\text{Ge}}$ , respectively. At low concentrations of Ge, in the presence of large

Table I

$T_{\text{growth}}$	$h$ ( $\mu\text{m}$ )	$SW$ ( $\mu\text{m}$ )	$H_{\text{coll}}$ (oe)	$4\pi M_s$ (G)	$l$ ( $\mu\text{m}$ )	$K_u$ (erg/cm <sup>3</sup> )
947°C	4.0	5.2	70	163	0.66	4400

concentrations of Ca,  $k^{\text{Ge}}$  is over 2. On the other hand, the incorporation of Ca, at low concentrations of Ca in the presence of large concentrations of Ge, is influenced by the presence of Pb and  $k^{\text{Ca}}$  reaches a maximum at a value of  $R_5$  a near 0.45. At that point, and at higher values of  $R_5$  and higher temperatures ( $>925^\circ\text{C}$ ), Ca is substituted to the exclusion of Pb in spite of the large excess of the latter.

The composition of LPE films grown from solutions containing Ca and Ge is more strongly dependent on the rate of growth than the composition of films containing only trivalent ions when  $R_5$  is near 0.5. However, this sensitivity decreases when an excess of either Ca or Ge is present. Apparently, in the presence of large amounts of Ca or Ge, the equivalent of a "buffering action" occurs which stabilizes the rate effect. Of course, high CaO concentrations increase the risk of CaO precipitation.

The temperature dependence of the bubble collapse field can be controlled by adjusting the degree of octahedral substitution, thereby changing the Curie temperature and degree of total diamagnetic ion incorporation. Increased octahedral substitution results in lower Curie temperature and increased values for  $\Delta H_0$ . The use of  $\text{Lu}^{3+}$  as both a dodecahedral and octahedral substituent allows control of the temperature dependence of the bubble collapse field while simultaneously satisfying the other stringent device requirements.

In spite of the increased complexity of the  $\text{Y}_2\text{O}_3\text{-CaO-Sm}_2\text{O}_3\text{-Fe}_2\text{O}_3\text{-GeO}_2\text{-PbO-B}_2\text{O}_3$  system and, perhaps, its high rate sensitivity, the garnets crystallized from it have high potential for use in high speed, temperature-stable, bubble memories. Propagation of 6  $\mu\text{m}$  diameter bubbles at 1 MHz and  $100^\circ\text{C}$  with useful margins has already been demonstrated.

### Acknowledgments

We thank R. D. Pierce and W. B. Venard for magnetic property measurements, R. J. Peirce for propagation data, G. P. Vella-Coleiro for mobility measurements, and R. Caruso for lattice parameter measurements. We thank F. B. Hagedorn, R. Wolfe, J. E. Geusic, and L. J. Varnerin for many useful discussions and for support throughout this investigation.

Manuscript submitted Dec. 2, 1975; revised manuscript received Jan. 27, 1976. This was Paper 223 presented at the Dallas, Texas, Meeting of the Society, Oct. 5-9, 1975.

Any discussion of this paper will appear in a Discussion Section to be published in the December 1976 JOURNAL. All discussions for the December 1976 Discussion Section should be submitted by Aug. 1, 1976.

Publication costs of this article were partially assisted by Bell Laboratories.

### REFERENCES

1. A. H. Bobeck, *IEEE Trans. Magnetics*, **MAG-6**, 445 (1970).
2. A. H. Bobeck, E. G. Spencer, L. G. Van Uitert, S. C. Abrahams, R. L. Barns, W. H. Grodkiewicz, R. C. Sherwood, P. H. Schmidt, D. H. Smith, and E. M. Walters, *Appl. Phys. Letters*, **17**, 131 (1970).
3. L. G. Van Uitert, W. A. Bonner, W. H. Grodkiewicz, L. Pictroski, and G. J. Zydzik, *Mater. Res. Bull.*, **5**, 825 (1970).
4. L. K. Shick, J. W. Nielsen, A. H. Bobeck, A. J. Kurtzig, P. C. Michaelis, and J. P. Reekstin, *Appl. Phys. Letters*, **18**, 89 (1971).
5. E. A. Giess, B. A. Calhoun, E. Klokhholm, T. R. McGuire, and L. L. Rosier, *Mater. Res. Bull.*, **6**, 317 (1971).
6. L. G. Van Uitert, E. M. Gyorgy, W. A. Bonner, W. H. Grodkiewicz, E. J. Heilner, and G. J. Zydzik, *ibid.*, **6**, 1195 (1971).
7. E. A. Giess, B. E. Argyle, D. C. Cronmeyer, E. Klokhholm, T. R. McGuire, D. F. O'Kane, T. S. Plaskett, and V. Sadagopan, *AIP Conf. Proc.*, **5**, 110 (1972).
8. W. A. Bonner, J. E. Geusic, D. H. Smith, F. C. Rossol, L. G. Van Uitert, and G. P. Vella-Coleiro, *J. Appl. Phys.*, **43**, 3226 (1972).
9. E. A. Giess, C. F. Guerci, J. D. Kuptsis, and H. L. Hu, *Mater. Res. Bull.*, **8**, 1061 (1973).
10. W. A. Bonner, *ibid.*, **10**, 15 (1975); W. A. Bonner, *AIP Conf. Proc.*, **18**, 68 (1974).
11. J. W. Nielsen, S. L. Blank, D. H. Smith, G. P. Vella-Coleiro, F. B. Hagedorn, R. L. Barns, and W. A. Biolsi, *J. Electron. Mater.*, **3**, 693 (1974).
12. R. J. Peirce, Private communication.
13. H. J. Levinstein, S. Licht, R. W. Landorf, and S. L. Blank, *Appl. Phys. Letters*, **19**, 486 (1971).
14. S. L. Blank and J. W. Nielsen, *J. Cryst. Growth*, **17**, 302 (1972).
15. S. L. Blank, B. S. Hewitt, L. K. Shick, and J. W. Nielsen, *AIP Conf. Proc.*, **10**, 256 (1973).
16. R. L. Barns, in "Advances in X-Ray Analysis," Vol. 15, K. J. Heinrich, C. F. Barrett, J. D. Newkirk, and C. D. Rund, Editors, p. 330, Plenum Press, New York (1972).
17. D. H. Smith and A. W. Anderson, *AIP CONF. Proc.*, **5**, 120 (1972).
18. G. P. Vella-Coleiro and W. J. Tabor, *Appl. Phys. Letters*, **21**, 7 (1972).
19. J. Colby, Proceedings of the Sixth National Conference on Electron Probe Analysis, Pittsburgh, Pennsylvania, 1971.
20. S. Geller, H. J. Williams, G. P. Espinosa, and R. C. Sherwood, *Bell System Tech. J.*, **18**, 565 (1964).
21. G. Winkler, P. Hansen, and P. Holst, *Philips Res. Rept.*, **27**, 151 (1972).
22. M. A. Gilleo and S. Geller, *Phys. Rev.*, **110**, 1 (1958).
23. G. F. Dionne, *J. Appl. Phys.*, **41**, 4874 (1970).
24. C. D. Brandle and S. L. Blank, *IEEE Trans. Magnetics*, **MAG-12**, 14 (1976).
25. T. M. Shimada, S. Kume, and M. Koizumi, *J. Phys. Chem. Solids*, **31**, 2165 (1970).
26. J. W. Nielsen, S. J. Licht, and C. D. Brandle, *IEEE Trans. Magnetics*, **MAG-10**, 474 (1974).
27. J. M. Robertson, M. J. G. VanHout, J. C. Verplanke, and J. C. Brice, *Mater. Res. Bull.*, **9**, 555 (1974).
28. F. B. Hagedorn, S. L. Blank, and R. J. Peirce, *Appl. Phys. Letters*, **26**, 206 (1975).
29. P. W. Shumate and R. J. Peirce, *ibid.*, **23**, 204 (1973).
30. P. W. Shumate, P. C. Michaelis, and R. J. Peirce, *AIP Conf. Proc.*, **18**, 140 (1974).

# Potential-Induced Impedance Variations in Barrier-Type Aluminum Oxide Films in Aqueous Sodium Sulfate

T. A. Libsch<sup>\*,1</sup> and O. F. Devereux<sup>\*</sup>

Department of Metallurgy and Institute of Materials Science, University of Connecticut, Storrs, Connecticut 06268

## ABSTRACT

Negligible changes occur in the dielectric properties of barrier-layer anodic aluminum oxide films exposed (50 hr) to neutral aqueous sodium sulfate at the open-circuit potential and  $-725$  mV vs. SCE, indicating little film-environment interaction. Transmission electron micrographs of films exposed for this time to the same chemical environment at 10 and 20V show the presence of a deposit on the surface of thinned anodic oxide; this deposit is presumably hydrated aluminum oxide. Significant changes observed in the dielectric properties of films tested at these two potentials have been analyzed by means of an a-c impedance model yielding dielectric constant and resistivity values, and thickness-time profiles for the anodic and hydrated layers.

The oxide film on aluminum acts as a barrier to mass transport between the metal and the environment creating the generally favorable corrosion resistance of aluminum and its alloys. Hence, it is important to determine the manner in which these films are affected by various environmental factors, e.g., anionic constituents, electrolyte pH, and applied potential. Several investigators, e.g., Pryor and co-workers (1-4), Richardson and Wood (5), and Libsch and Devereux (6), have examined the effects of anionic constituents and electrolyte pH upon barrier-layer anodic oxide films on aluminum at the open-circuit potential. Other investigators (7, 8) have studied the formation mechanism of such films. To date, however, few investigations have been directed toward the effect of applied anodic potentials less than the formation potential; these potentials are subsequently referred to as "reduced potentials." The work of O'Sullivan and Wood (9) concerning the effect of reduced potentials on porous anodic aluminum oxide films, and of Renshaw (10) and Libsch and Devereux (11) concerning the effects of reduced potentials on barrier-layer films has been described previously.

In this investigation, the authors chose to examine the effect of reduced potentials upon barrier-layer anodic aluminum oxide films in neutral aqueous sodium sulfate. This chemical environment was chosen for study because of its innocuous effect (4, 5) upon these films at the open-circuit potential, and because of its nonanodizing behavior (12).

## Experimental Procedure

Cylindrical electrodes were machined from aluminum and platinum rods of 99.999 and 99.5% purities, respectively, and successively abraded with 240, 320, 400, and 600 grit metallographic papers. The aluminum surfaces were further prepared by chemical polishing, as outlined previously (11). Electrolytes were prepared from reagent grade chemicals and double-distilled water. The anodizing electrolyte was aqueous 3 weight per cent (w/o) ammonium tartrate adjusted to neutral pH by the addition of several drops of dilute ammonium hydroxide. The testing electrolyte was aqueous 1M sodium sulfate adjusted to neutral pH by the addition of dilute sulfuric acid or sodium hydroxide. The pH of this electrolyte was checked immediately prior to use in each case, and minor adjustments made when necessary.

The electrode assembly was identical to that described previously (6, 11); the electrochemical cell was

also similar except for the introduction of a reference electrode by means of a salt bridge comprised of the testing electrolyte. Barrier-layer anodic films [ $\sim 360\text{\AA}$  thick (3)] were potentiostatically formed at 30V in the manner given previously (11). Cells with anodized electrodes were tested at  $-725$  and  $1000$  mV vs. SCE for 2700 min, and at the open-circuit potential, 10 and 20V for 3000 min. At 2700 min, the potential of cells tested at  $-725$  and  $1000$  mV vs. SCE was abruptly reduced to and maintained at  $-910$  mV vs. SCE (the steady-state open-circuit potential) for 200 min. The potential of cells tested at 10 and 20V was abruptly removed at 3000 min; testing continued, however, for an additional 200 min. In each case, a new electrode was used with testing promptly following anodizing. Cells with platinum electrodes were tested at the open-circuit potential for 4000 min. All cells were maintained at  $30.0^\circ \pm 0.1^\circ\text{C}$  during anodizing and testing by means of a conventional water bath.

The dielectric properties of cells with anodized electrodes were measured at preselected times during the testing period at 0.5, 1, 5, 10, 20, 50, and 100 kHz utilizing the capacitance measuring assembly described previously (6, 11). Cells with platinum electrodes were connected in series with a capacitor (General Radio 1419-B). The dielectric properties of this combination were measured at the above frequencies after a lapse of 4000 min; it had been the authors' previous observation that the properties of these cells do not stabilize for at least 1500 min (6). The dielectric properties of the series capacitor with the same leads were also measured at these frequencies for subsequent correction of these data. This technique was found to be more accurate than that previously employed by the authors (6, 13). The data of cells with platinum electrodes were obtained in order to correct the data of cells with anodized electrodes for the presence of the electrolyte, as discussed below.

Following exposure to the testing electrolyte, the cells were prepared for transmission electron microscopy in the manner given previously (6, 11); in this investigation, however, it was necessary on occasion to sandwich the film between two copper grids to prevent curling upon drying. At 10V, films were tested for 660, 1320, 1980, and 2640 min in order to construct a time sequence of transmission micrographs.

## Experimental Results

*Time dependence of the open-circuit potential.*—The average open-circuit potential value of several cells with anodized electrodes was observed to decrease from approximately  $-400$  mV vs. SCE initially to a nearly constant value of  $-910$  mV vs. SCE after 500 min of testing (14). Cells tested at potentials more

\* Electrochemical Society Active Member.

<sup>1</sup> Present address: Bendix Research Laboratories, Southfield, Michigan 48076.

Key words: aluminum, anodic oxidation, impedance, hydration.



Table I. Average capacitance and resistance values of the neutral aqueous 1M sodium sulfate testing electrolyte\*

A. Determined from cells with platinum electrodes			
f (kHz)	$C_{p2}/A$ ( $\mu\text{f}/\text{cm}^2$ )	$R_{p2} A$ (ohm $\cdot$ cm $^2$ )	$R_{s2} A$ (ohm $\cdot$ cm $^2$ )
0.5	22.2	35.9	4.94
1	18.5	16.4	3.55
5	5.80	3.58	2.51
10	2.23	2.73	2.38
20	0.682	2.41	2.31
50	0.107	2.27	2.26

B. Determined from $R_{s1}$ vs. $\omega^{-1}$ plots	
Specimen potential	$R_{s2} A$ (ohm $\cdot$ cm $^2$ )
Open-circuit	2.16
-725 mV vs. SCE	2.31
1000 mV vs. SCE	2.05
10V	2.03
20V	2.16

\* Parameter definitions can be found in the list of symbols.

positive than the latter value were, therefore, considered to be anodically polarized.

**Calculation of electrolyte and film parameters.**—Electrolyte parameters were determined by two of the methods proposed by Young (15), *i.e.*, by substitution of a dummy electrode of low impedance for the anodized electrode, and by extrapolation of a plot of the initial series resistance of the cell *vs.* reciprocal frequency to infinite frequency. The parallel capacitance ( $C_{p2}$ ) and resistance ( $R_{p2}$ ) of cells with platinum electrodes were calculated from the measured series capacitance ( $C_{s4}$ ) and dissipation factor ( $D_4$ ) of the cell-capacitor combinations, and from the measured series capacitance ( $C_{s5}$ ) and dissipation factor ( $D_5$ ) of the capacitor, as discussed previously, by

$$C_{p2} = C_{s5} C_{s4} (C_{s5} - C_{s4}) / [(C_{s5} - C_{s4})^2 + (C_{s5} D_4 - C_{s4} D_5)^2] \quad [1]$$

$$R_{p2} = [(C_{s5} - C_{s4})^2 + (C_{s5} D_4 - C_{s4} D_5)^2] / \omega C_{s5} C_{s4} (C_{s5} D_4 - C_{s4} D_5) \quad [2]$$

where  $\omega$  represents the angular frequency in rad/sec. The series resistance ( $R_{s2}$ ) of these cells was calculated from  $C_{p2}$  and  $R_{p2}$  by

$$R_{s2} = R_{p2} / [1 + (\omega R_{p2} C_{p2})^2] \quad [3]$$

The average values of  $C_{p2}$ ,  $R_{p2}$ , and  $R_{s2}$  calculated as above from three cells are listed, normalized for the electrode area ( $A$ ), in Table I, part A.<sup>2</sup> These parameters are regarded as characteristic of the electrolyte since the platinum electrodes, in series with the electrolyte, may reasonably be expected to possess negligibly high capacitance and negligibly low resistance. The tabulated values compare favorably with those reported by Heine and Pryor (3) for near-neutral aqueous 1M sodium chromate. The series resistance ( $R_{s2}$ ) of the testing electrolyte was calculated by the latter of the aforementioned methods in the manner outlined previously (11). The average series resistance *vs.* reciprocal frequency plots were linear at each potential reflecting good cell geometry, as suggested by Smyth (16). The average electrolyte resistance values determined in this manner are listed *vs.* potential in Table I, part B. In Table I, the series resistances of the testing electrolyte determined by both methods are observed to be similar, particularly at the higher frequencies.

Cells with anodized electrodes were modeled as a series combination of two parallel RC circuits; one parallel RC circuit representing the electrolyte, the other the anodic film. Utilizing this analog, the bridge

<sup>2</sup> Data at 100 kHz have not been reported throughout this article due to significant errors introduced by the inductance and resistance of the leads and bridge windings (14).

measurements of these cells, *i.e.*, the series capacitance ( $C_{s1}$ ) and dissipation factor ( $D_1$ ), and the electrolyte parameters determined from cells with platinum electrodes (Table I, part A), the series capacitance ( $C_{s3}$ ) and resistance ( $R_{s3}$ ) of the film were calculated by

$$C_{s3} = C_{s1} [1 + (\omega R_{p2} C_{p2})^2] / [1 + C_{p2} (\omega R_{p2})^2 (C_{p2} - C_{s1})] \quad [4]$$

$$R_{s3} = [D_1 + \omega R_{p2} (\omega R_{p2} C_{p2}^2 D_1 - C_{s1})] / \omega C_{s1} [1 + (\omega R_{p2} C_{p2})^2] \quad [5]$$

The cell analog and procedure for calculating film parameters from the data of cells with anodized electrodes and the series resistance of the electrolyte as determined from plots of the initial series resistance of the cell *vs.* reciprocal frequency have been discussed previously (11). In both models, the parallel film capacitance ( $C_{p3}$ ) and resistance ( $R_{p3}$ ) were calculated from  $C_{s3}$  and  $R_{s3}$  by

$$C_{p3} = C_{s3} / [1 + (\omega R_{s3} C_{s3})^2] \quad [6]$$

$$R_{p3} = [1 / (\omega C_{s3})^2 R_{s3}] + R_{s3} \quad [7]$$

Film values calculated by both methods were compared at the 10V potential and found to be negligibly different. The maximum difference in parallel film capacitance ( $\Delta C_{p3}/A$ ) was 0.010  $\mu\text{f}/\text{cm}^2$  (50 kHz, 3000 min), while the maximum difference in parallel film resistance ( $\Delta R_{p3}A$ ) was 10,000 ohm  $\cdot$  cm $^2$  (0.5 kHz; 0 min). Hence, film values at the other testing potentials were calculated only from the data of cells with anodized electrodes.

**Cell and film values.**—The average parallel capacitance ( $C_{p1}$ ) and resistance ( $R_{p1}$ ) of three cells tested at open circuit, -725 and 1000 mV *vs.* SCE, and 10, and 20V are presented, normalized for the electrode area, in Fig. 1-5.  $C_{p1}$  and  $R_{p1}$  values were calculated from the bridge measurements  $C_{s1}$  and  $D_1$  by

$$C_{p1} = C_{s1} / (1 + D_1^2) \quad [8]$$

$$R_{p1} = (1 + D_1^2) / \omega C_{s1} D_1 \quad [9]$$

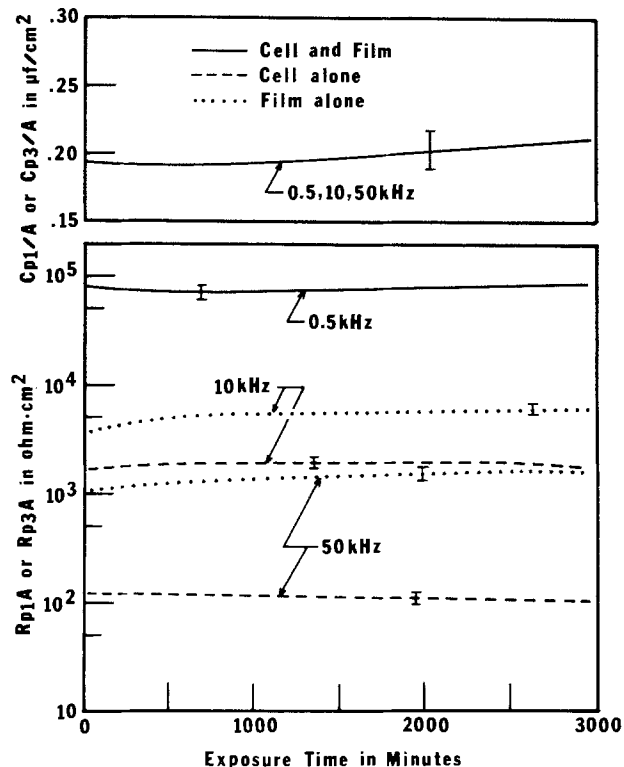


Fig. 1. Time dependence of the average parallel capacitance and resistance of cells having anodized electrodes and of films tested at the open-circuit potential. Error bars typical.

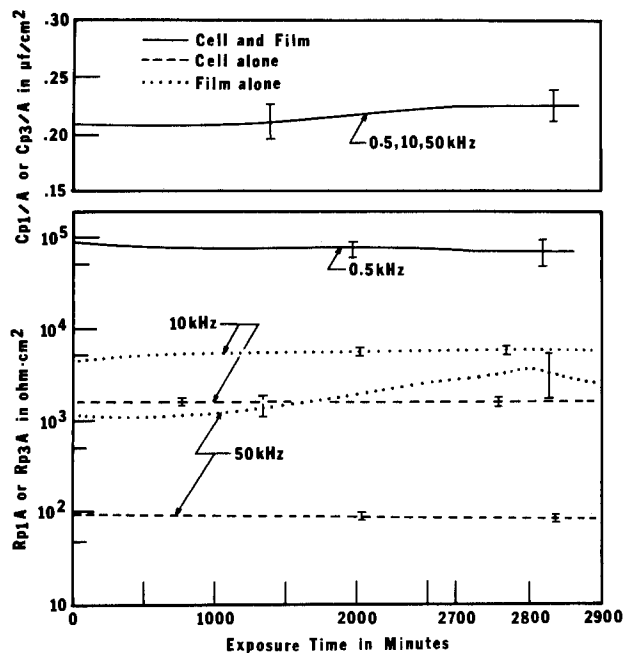


Fig. 2. Time dependence of the average parallel capacitance and resistance of cells and films tested at  $-725$  mV vs. SCE. The potential was reduced to  $-910$  mV vs. SCE at 2700 min, coincident with the expansion in the time scale. Error bars typical.

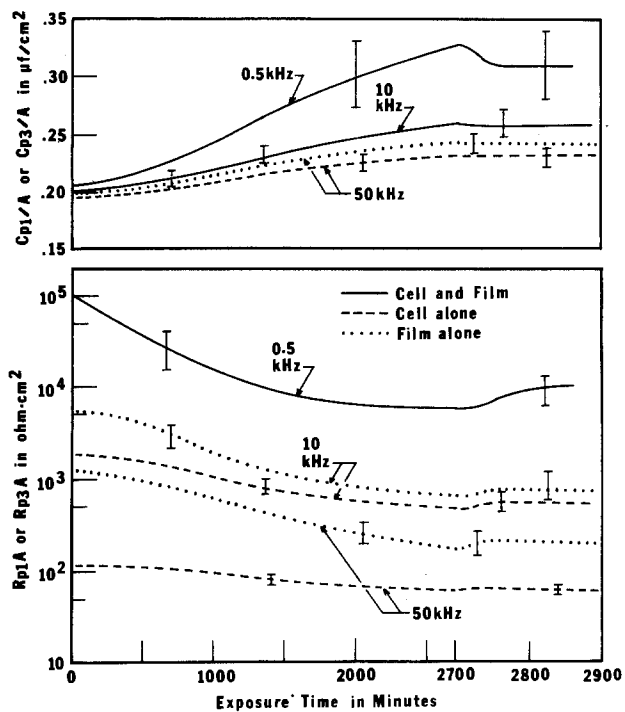


Fig. 3. Time dependence of the average parallel capacitance and resistance of cells and films tested at 1000 mV vs. SCE. The potential was reduced to  $-910$  mV vs. SCE at 2700 min. Error bars typical.

The corresponding film values, calculated as above, are also illustrated in these figures. Data points are not shown in these figures; error brackets have been included solely for the purpose of illustrating typical scatter. The time scale has been expanded by a factor of five at 2700 min in Fig. 2 and 3 and at 3000 min in Fig. 4 and 5 corresponding to the time when the potential was reduced or removed. Significant changes in dielectric parameters are observed only for cells and films tested at 1000 mV vs. SCE and 10 and 20V; a large frequency dispersion of capacitance is also observed at these potentials.

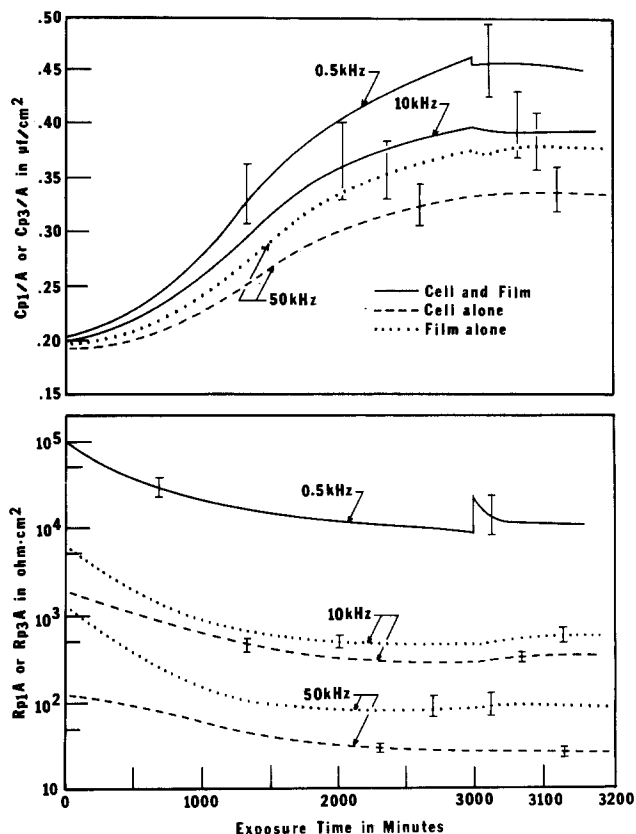


Fig. 4. Time dependence of the average parallel capacitance and resistance of cells and films tested at 10V. The potential was removed at 3000 min, coincident with the expansion in the time scale. Error bars typical.

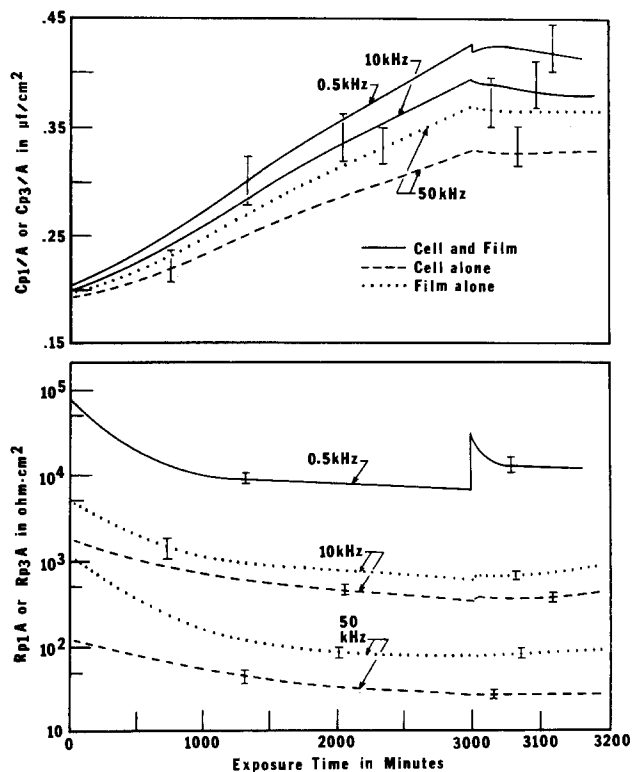


Fig. 5. Time dependence of the average parallel capacitance and resistance of cells and films tested at 20V. The potential was removed at 3000 min. Error bars typical.

*Microscopic examination of films.*—Typical transmission electron micrographs of films tested at each anodic potential are presented in Fig. 6. Films tested at  $-725$  mV vs. SCE appear essentially featureless, except for

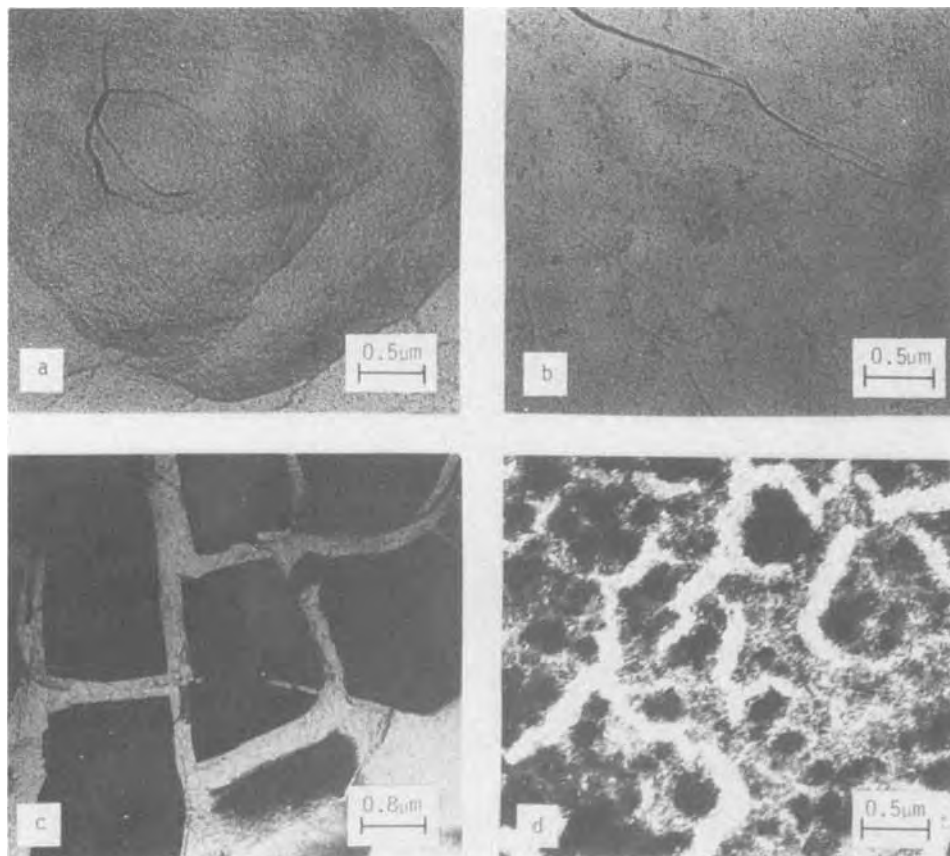


Fig. 6. Transmission electron micrographs of films tested at the anodic potentials: (a)  $-725$  mV vs. SCE, (b)  $1000$  mV vs. SCE, (c)  $10$  V, and (d)  $20$  V. (a) and (b),  $2700$  min; (c) and (d),  $3000$  min.

a scalloped appearance due to the replication of the irregular topography of the substrate, created by the chemical polishing procedure (17). Films tested at  $10$  and  $20$  V show the presence of a deposit on the surface of thinned anodic oxide. This deposit is observed to mask the majority of the anodic oxide, to be considerably thicker than the anodic oxide, and to be permeated by channels. Some tendency toward this behavior is seen in films tested at  $1000$  mV vs. SCE. The appearance of channels in tested films led to the investigation of the development of this phenomenon. Typical transmission electron micrographs of films tested for various times at  $10$  V are presented in Fig. 7; channel development, as observed in these micrographs, is discussed in a subsequent section.

### Discussion

**Film values.**—Heine, Keir, and Pryor (4) and Richardson and Wood (5) have previously reported the dielectric properties of barrier-layer anodic aluminum oxide films tested in near-neutral aqueous sodium sulfate at the open-circuit potential to remain essentially unchanged for a prolonged period. In the current study, the dielectric properties of films tested under similar conditions (Fig. 1) remained nearly constant during  $50$  hr, a result in agreement with that of the aforementioned investigators. The purpose of determining these data was to establish a standard against which the dielectric properties of films subjected to the anodic potentials could be compared. Minor changes in film properties occur at  $-725$  mV vs. SCE (Fig. 2); in view of the micrograph of the film tested at this potential (Fig. 6a), these changes are credited to minor uniform film dissolution.

Significant changes in film dielectric properties were observed at  $1000$  mV vs. SCE and  $10$  and  $20$  V (Fig. 3-5). Micrographs of these films (Fig. 6b-6d) show these changes to result from the thinning of the anodic oxide film and the concurrent thickening of an outer deposit, believed to be hydrated aluminum oxide. The hydrated oxide appears as the dark regions due to its substantial thickness.

Several workers (18-20) have investigated the reaction between boiling water and barrier-layer anodic aluminum oxide films, and reported the simultaneous thinning of the anodic oxide, and thickening of a hydrated oxide. Borate and phosphate ions were found to impede this reaction; sulfate, chromate, and oxalate ions had little effect. The reaction product was identified as pseudoboehmite, a poorly crystallized substance containing considerably more water than stoichiometric aluminum monohydrate (boehmite); it was observed to form in randomly oriented platelets which extended far out into the electrolyte.

The authors believe the hydrated oxide observed in this investigation "cracked" upon drying at the conclusion of the test period. This belief is supported by the following observations: (i) after  $660$  min at  $10$  V (Fig. 7b), the hydrated oxide appears uniform; (ii) the channeled area is relatively small ( $26\%$  in Fig. 6c) and appears to be related to the thickness of the hydrated oxide; and (iii) a model considering the growth of channels *in situ*, described subsequently, proved unrealistic.

Potential-dependent changes were observed in the dielectric properties of films tested at the higher anodic potentials (Fig. 3-5). The authors (11) have previously observed similar changes which were explained by the flow of ionic defects to the oxide/electrolyte interface. The potential-dependent changes in film values in the current investigation can be credited in part to the same phenomenon; the situation is complicated, however, by the presence of the hydrated layer, and these data are presented without further explanation.

**The hydration model.**—The micrographs in Fig. 7 show that the thinned anodic layer is essentially uniform; the film, therefore, was modeled as a series combination of two parallel RC circuits; one circuit representing a uniform (in thickness) anodic layer, the other a uniform hydrated layer. This model was analyzed only for films tested at  $10$  V, and only for the time during which this potential was applied ( $0$ - $3000$  min). The dielectric constants and resistivities of both

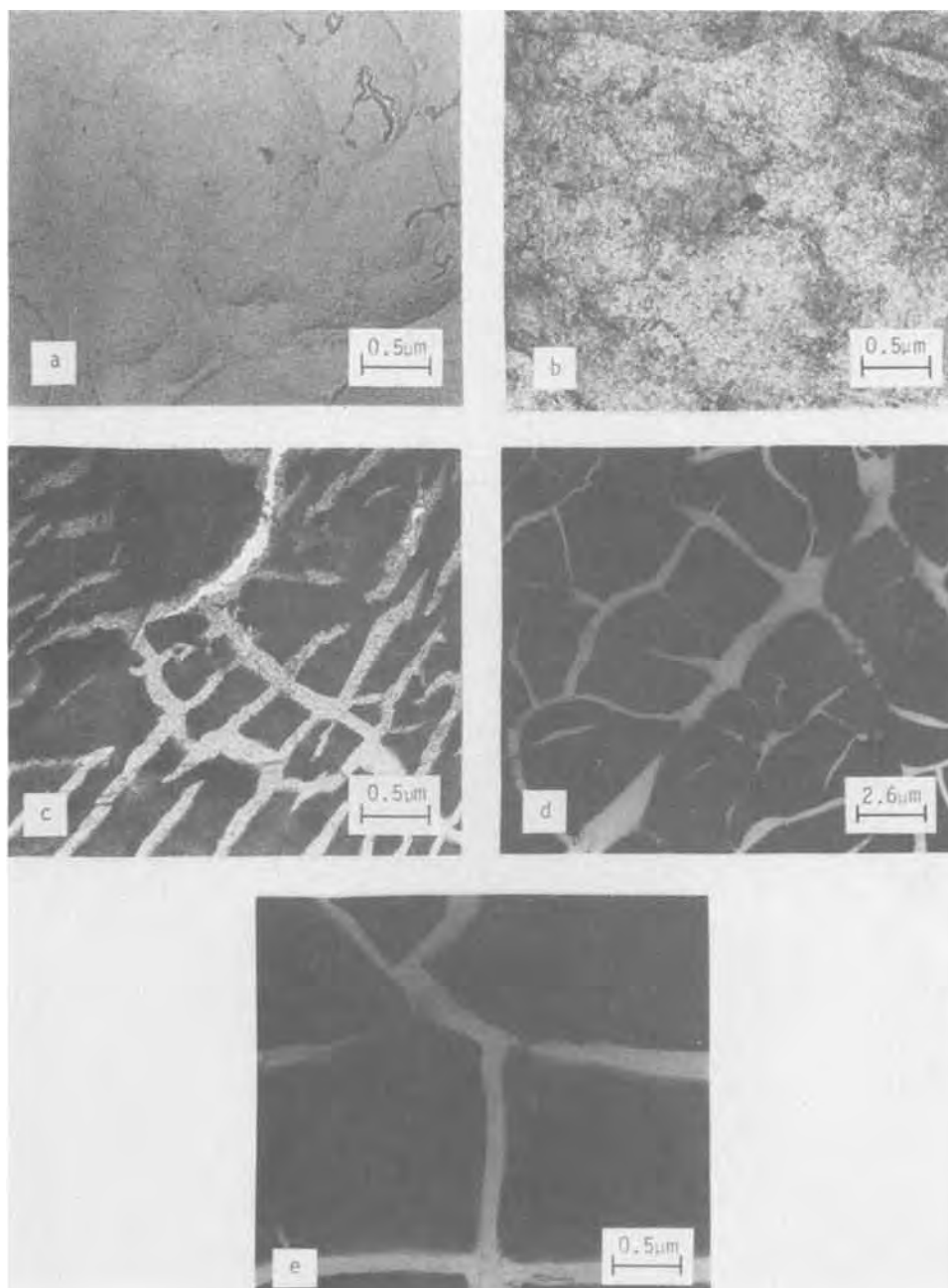


Fig. 7. Transmission electron micrographs of films tested at 10V for: (a) 0, (b) 660, (c) 1320, (d) 1980, and (e) 2640 min.

oxides were assumed independent of layer thickness, and values were assigned for the thickness of each layer at 3000 min. Several final thickness assumptions were examined, each of the form  $d_6:d_7$ , where  $d_6$  and  $d_7$  in this form represent the final thicknesses of the anodic and hydrated layers in angstroms.

The series dielectric constant ( $\kappa s_6$ ) and resistivity ( $\rho s_6$ ) of the anodic oxide were calculated by

$$\kappa s_6 = C s_3 d_0 / \epsilon_0 A \quad [10]$$

$$\rho s_6 = R s_3 A / d_0 \quad [11]$$

where  $d_0$  and  $\epsilon_0$  represent the initial film thickness and the permittivity constant, respectively.  $\kappa s_6$  and  $\rho s_6$  were determined from initial film values since the layer thicknesses are known to be 360 and 0 Å at this time. The values of these parameters are listed *vs.* frequency in Table II, part A.

The series dielectric constant ( $\kappa s_7$ ) and resistivity ( $\rho s_7$ ) of the hydrated layer were calculated by

$$\kappa s_7 = \kappa s_6 C s_3 d_7 / (\kappa s_6 \epsilon_0 A - C s_3 d_6) \quad [12]$$

$$\rho s_7 = (R s_3 A - \rho s_6 d_6) / d_7 \quad [13]$$

A problem was encountered in supplying data for

these expressions since  $d_6$  and  $d_7$  are known only at time zero, which is not useful. Utilizing the dielectric constant and resistivity values of the anodic layer (Table II, part A), and the final values of film capacitance and resistance,  $\kappa s_7$  and  $\rho s_7$  were arbitrarily calculated at 3000 min for each of the following final thickness assumptions: (i) 20:2000, (ii) 20:2500, (iii) 60:2000, and (iv) 60:2500. These values are listed *vs.* frequency in Table II, part B. The dielectric constant and resistivity of the hydrated oxide are observed to be greater and less than, respectively, the same parameters of the anodic oxide. It is also observed both when the assumed hydrated layer thickness is increased at constant anodic layer thickness and when the assumed anodic layer thickness is increased at constant hydrated layer thickness that the dielectric constant increases; at the same time the resistivity of the hydrated oxide decreases.

The thicknesses of the anodic ( $d_6$ ) and hydrated ( $d_7$ ) layers have been determined at any time by

$$d_6 = \kappa s_6 \{ \omega \kappa s_7 \epsilon_0 A R s_3 - [1 + (\omega \kappa s_7 \epsilon_0 \rho s_7)^2]^{1/2} d_7 \cos \theta_2 \} / \kappa s_7 [1 + (\omega \kappa s_7 \epsilon_0 \rho s_6)^2]^{1/2} \cos \theta_1 \quad [14]$$

Table II. Average dielectric constant and resistivity values of the anodic and hydrated layers of films tested at 10V\*

A. Anodic oxide			
Final thickness assumption	f (kHz)	$\kappa S_6$ (unitless)	$\rho S_6$ (ohm · m)
Any	0.5	8.39	$6.75 \times 10^4$
	10	8.12	$3.31 \times 10^3$
	50	8.07	$6.69 \times 10^2$
B. Hydrated oxide			
Final thickness assumption	f (kHz)	$\kappa S_7$ (unitless)	$\rho S_7$ (ohm · m)
20:2000	0.5	119	$2.69 \times 10^4$
	10	101	$1.88 \times 10^3$
	50	95.0	$4.95 \times 10^2$
20:2500	0.5	148	$2.15 \times 10^4$
	10	126	$1.50 \times 10^3$
	50	119	$3.96 \times 10^2$
60:2000	0.5	166	$2.56 \times 10^4$
	10	134	$1.81 \times 10^3$
	50	124	$4.82 \times 10^2$
60:2500	0.5	207	$2.05 \times 10^4$
	10	168	$1.45 \times 10^3$
	50	155	$3.86 \times 10^2$

\* Parameter definitions can be found in the list of symbols.

and

$$d_7 = \kappa S_7 \epsilon_0 A (\cos \theta_1 - \omega C S_3 R S_3 \sin \theta_1) / C S_3 [1 + (\omega \kappa S_7 \epsilon_0 \rho S_7)^2]^{1/2} \sin (\theta_2 - \theta_1) \quad [15]$$

where  $\theta_1$  and  $\theta_2$  are given by

$$\theta_1 = \tan^{-1} (1/\omega \rho S_6 \kappa S_6 \epsilon_0) \quad [16]$$

$$\theta_2 = \tan^{-1} (1/\omega \rho S_7 \kappa S_7 \epsilon_0) \quad [17]$$

Utilizing the dielectric constant and resistivity values of both oxides (Table II) and the capacitance and resistance values of the film at 0.5 kHz,<sup>3</sup>  $d_6$  and  $d_7$  were calculated at several times for each of the aforementioned final thickness assumptions. These thickness profiles are illustrated in Fig. 8; to locate the anodic and hydrated layer profiles for any final thickness assumption, choose the two curves labeled with the values of that assumption. Regardless of the final thickness assumption employed, the anodic layer thins at a nearly constant rate during the initial portion of the

<sup>3</sup> Layer thickness is independent of frequency, hence, film data at 0.5 kHz were arbitrarily chosen.

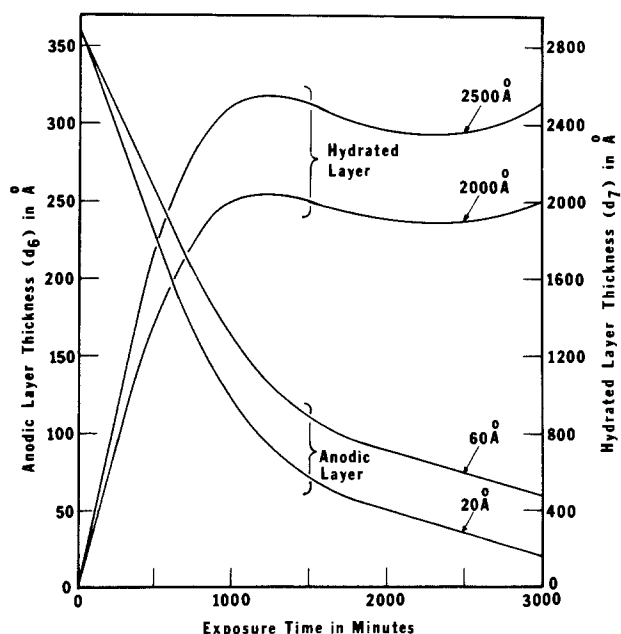


Fig. 8. Average thickness profiles of the anodic and hydrated layers of films tested at 10V as determined by the hydration model.

test; the rate then slows and assumes a nearly constant value of  $\sim 10\%$  of the initial rate. More specifically, for the 20Å curve the initial and final rates are 0.267 and 0.030 Å/min; for the 60Å curve the rates are 0.211 and 0.027 Å/min. This change is attributed to a reduction in the reaction rate at the anodic oxide/hydrated oxide interface due to the thickening of the hydrated layer. Regardless of the assumption, the hydrated layer thickens to approximately its final value during the initial 1000 min of testing, and remains essentially constant after that. The initial growth rate of this layer is 2.85 Å/min for the 2000Å curve and 3.56 Å/min for the 2500Å curve. Using the initial rates cited above, the thickness of hydrated oxide formed per angstrom of anodic oxide consumed is found to be dependent on the final thickness assumption, increasing from 10.7Å for the 20:2000 assumption to 16.9Å for the 60:2500 assumption. These values are greater than that of 2.5Å reported by Hunter, Towner, and Robinson (18) for the reaction between boiling water and nonporous anodic aluminum oxide.

The parallel capacitance and resistance of the anodic and hydrated layers, *i.e.*,  $Cp_6$ ,  $Rp_6$ ,  $Cp_7$ , and  $Rp_7$ , respectively, have been calculated *vs.* time and frequency by

$$Cp_6 = \kappa S_6 \epsilon_0 A / d_6 [1 + (\omega \epsilon_0 \rho S_6 \kappa S_6)^2] \quad [18]$$

$$Rp_6 = d_6 [1 + (\omega \rho S_6 \kappa S_6 \epsilon_0)^2] / (\omega \kappa S_6 \epsilon_0)^2 A \rho S_6 \quad [19]$$

$$Cp_7 = \kappa S_7 \epsilon_0 A / d_7 [1 + (\omega \rho S_7 \kappa S_7 \epsilon_0)^2] \quad [20]$$

$$Rp_7 = d_7 [1 + (\omega \rho S_7 \kappa S_7 \epsilon_0)^2] / (\omega \kappa S_7 \epsilon_0)^2 A \rho S_7 \quad [21]$$

Utilizing the dielectric constant and resistivity values of both layers (Table II) and the thickness profiles (Fig. 8), the capacitance and resistance curves of each layer were determined for each of the aforementioned final thickness assumptions. The capacitance *vs.* time curves are illustrated in Fig. 9; these curves have been condensed into bands for graphical clarity. This figure clearly shows the large increases in film capacitance observed in Fig. 4 to result from the thinning of the anodic oxide, and the large frequency dispersion of capacitance to result from the large frequency dispersion of capacitance of the hydrated oxide. The resist-

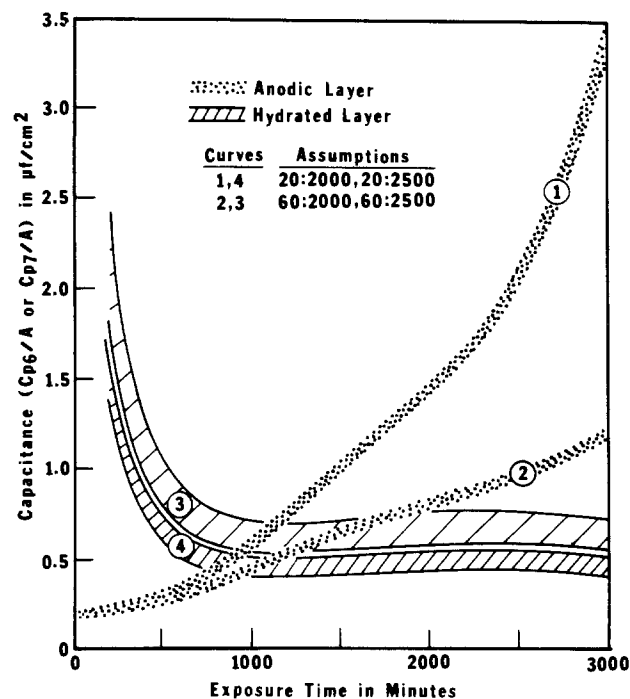


Fig. 9. Time dependence of the average parallel capacitance of the anodic and hydrated layers of films tested at 10V as determined by the hydration model. Each band is constructed from 0.5, 10, and 50 kHz data.

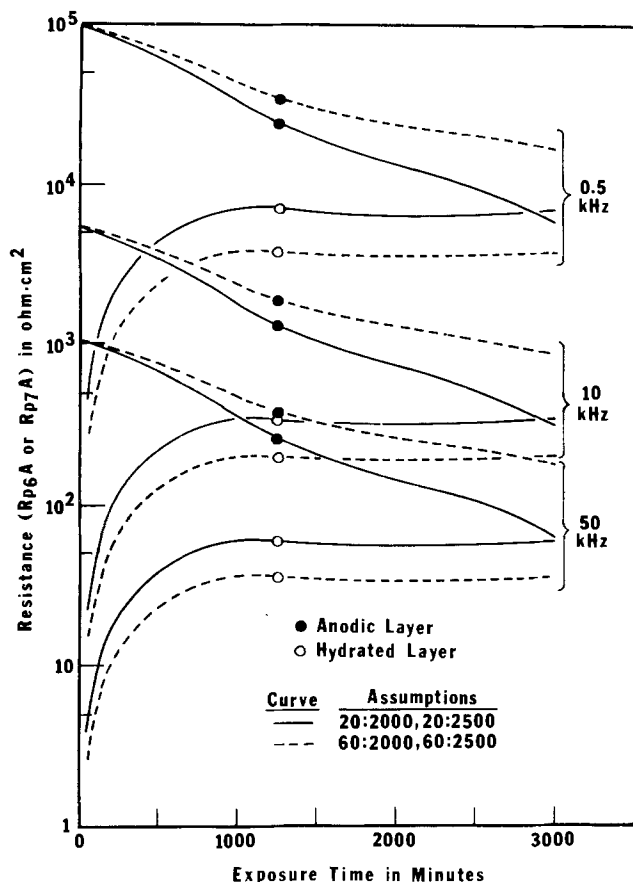


Fig. 10. Time dependence of the average parallel resistance of the anodic and hydrated layers of films tested at 10V as determined from the hydration model.

ance vs. time curves are illustrated in Fig. 10; clearly, the large decreases in film resistance observed in Fig. 4 result from the thinning of the anodic oxide.

*Alternate treatment of the data.*—Using a similar series of steps, the authors have also analyzed the case where the channels are assumed present *in situ* (14). In this analysis, the anodic layer was assumed to thin uniformly, and the channeled area was considered to be a linear function of the thickness of the hydrated layer. Utilizing the film values at 10V and assuming a value of 2000Å for the final thickness of the hydrated layer, it was determined that the final thickness of the anodic layer must necessarily be greater than 115Å. It is apparent from the electron micrograph (Fig. 6c) that the anodic layer is considerably thinner than this at the end of the test, indicating conclusively that the channels are, in fact, an artifact induced during drying of the electrodes.

### Summary and Conclusions

Barrier-layer anodic aluminum oxide films were exposed to neutral aqueous sodium sulfate for 50 hr at the open-circuit potential and at anodic potentials of  $-725$  and  $1000$  mV vs. SCE and 10 and 20V. These films were examined by a-c impedance measurements and transmission electron microscopy. Film dielectric data, calculated from electrochemical cell data by two of the techniques suggested by Young (15), were found to be in excellent agreement.

Significant changes in film dielectric properties were observed only at 1000 mV vs. SCE and 10 and 20V. Transmission electron micrographs of these films show the presence of a deposit, believed to be hydrated aluminum oxide, on the surface of thinned anodic oxide. The authors' belief that the observed "cracked" morphology of the hydrated oxide is not present *in situ*, but rather is an artifact of drying at the conclusion of the test period, is supported by a time sequence of

transmission electron micrographs of films tested at 10V, and by consideration of an a-c impedance model in which channels were assumed present *in situ*.

The average dielectric properties of films tested at 10V have been analyzed by representing the film as a series combination of two parallel RC circuits. The following conclusions have been drawn from this model: (i) the dielectric constant and resistivity of the hydrated oxide are considerably greater and less, respectively, than the same parameters of the anodic oxide; (ii) the anodic oxide thins at a nearly constant rate ( $\sim 0.3$  Å/min) during the initial 1000 min of the test period, but approaches a linear thinning rate of 10% of that value during the final portion of the test; (iii) the hydrated oxide layer thickens (initial rate  $\sim 3$  Å/min) to approximately its final value during the initial 1000 min of the test, and remains essentially constant after that; and (iv) the changes in the film's dielectric properties are primarily attributable to thinning of the anodic oxide layer.

### Acknowledgments

The authors thank the National Science Foundation for its support through grants GK20017 and GH35580. Computations were performed using the facilities of the University of Connecticut Computer Center. The authors also gratefully acknowledge the assistance of Mr. L. McCurdy in operation of the electron microscope.

Manuscript submitted March 26, 1975; revised manuscript received Feb. 4, 1976.

Any discussion of this paper will appear in a Discussion Section to be published in the December 1976 JOURNAL. All discussions for the December 1976 Discussion Section should be submitted by Aug. 1, 1976.

Publication costs of this article were partially assisted by the University of Connecticut.

### LIST OF SYMBOLS

A	film area, m <sup>2</sup>
Cp <sub>1</sub>	parallel capacitance of cells with anodized electrodes, f
Cp <sub>2</sub>	parallel capacitance of the electrolyte, f
Cp <sub>3</sub>	parallel capacitance of the film, f
Cp <sub>6</sub>	parallel capacitance of the anodic oxide layer of the film, f
Cp <sub>7</sub>	parallel capacitance of the hydrated oxide layer of the film, f
Cs <sub>1</sub>	series capacitance of cells with anodized electrodes, f
Cs <sub>3</sub>	series capacitance of the film, f
Cs <sub>4</sub>	series capacitance of cells with platinum electrodes together with the series capacitor, f
Cs <sub>5</sub>	series capacitance of the series capacitor, f
d <sub>0</sub>	initial film thickness, m
d <sub>6</sub>	thickness of the anodic oxide layer of the film, m
d <sub>7</sub>	thickness of the hydrated oxide layer of the film, m
D <sub>1</sub>	dissipation factor of cells having anodized electrodes, unitless
D <sub>4</sub>	dissipation factor of cells having platinum electrodes together with the series capacitor, unitless
D <sub>5</sub>	dissipation factor of the series capacitor, unitless
f	frequency, kHz
Rp <sub>1</sub>	parallel resistance of cells with anodized electrodes, ohm
Rp <sub>2</sub>	parallel resistance of the electrolyte, ohm
Rp <sub>3</sub>	parallel resistance of the film, ohm
Rp <sub>6</sub>	parallel resistance of the anodic oxide layer of the film, ohm
Rp <sub>7</sub>	parallel resistance of the hydrated oxide layer of the film, ohm
Rs <sub>1</sub>	series resistance of cells with anodized electrodes, ohm
Rs <sub>2</sub>	series resistance of the electrolyte, ohm
Rs <sub>3</sub>	series resistance of the film, ohm
ε <sub>0</sub>	permittivity constant, f/m
κ <sub>6</sub>	series dielectric constant of the anodic oxide layer of the film, unitless
κ <sub>7</sub>	series dielectric constant of the hydrated oxide layer of the film, unitless
ρ <sub>6</sub>	series resistivity of the anodic oxide layer of the film, ohm · m

$\rho_{S7}$  series resistivity of the hydrated oxide layer of the film, ohm  $\cdot$  m  
 $\omega$  angular frequency, rad/sec

## REFERENCES

- J. J. McMullen and M. J. Pryor, "Proc. 1st Intern. Congress on Metallic Corrosion," p. 52, Butterworths, London (1961).
- A. F. Beck, M. A. Heine, D. S. Keir, D. van Rooyen, and M. J. Pryor, *Corrosion Sci.*, **2**, 133 (1962).
- M. A. Heine and M. J. Pryor, *This Journal*, **110**, 1205 (1963).
- M. A. Heine, D. S. Keir, and M. J. Pryor, *ibid.*, **112**, 24 (1965).
- J. A. Richardson and G. C. Wood, *ibid.*, **120**, 193 (1973).
- T. A. Libsch and O. F. Devereux, *ibid.*, **121**, 400 (1974).
- S. Anderson, *J. Appl. Phys.*, **15**, 477 (1944).
- G. C. Wood, in "Oxides and Oxide Films," Vol. 2, J. W. Diggle, Editor, Marcel Dekker, Inc., New York (1973).
- J. P. O'Sullivan and G. C. Wood, *Proc. Roy. Soc.*, **A317**, 511 (1970).
- T. A. Renshaw, *This Journal*, **108**, 185 (1961).
- T. A. Libsch and O. F. Devereux, *ibid.*, **122**, 1654 (1975).
- G. C. Wood and J. P. O'Sullivan, *Electrochim. Acta*, **15**, 1865 (1970).
- General Radio Company, "Instruction Manual for Type 1615-A Capacitance Bridge," G. R. Co. (1963).
- T. A. Libsch, Ph.D. Dissertation, University of Connecticut (1975).
- L. Young, "Anodic Oxide Films," Academic Press, New York (1961).
- D. M. Smyth, in "Oxides and Oxide Films," Vol. 2, J. W. Diggle, Editor, Marcel Dekker, Inc., New York (1973).
- J. A. Richardson, G. C. Wood, and A. J. Breen, *Thin Solid Films*, **16**, 81 (1973).
- M. S. Hunter, P. F. Towner, and D. L. Robinson, *Tech. Proc. Am. Electroplaters' Soc.*, **46**, 220 (1959).
- W. J. Bernard and J. J. Randall, *This Journal*, **108**, 822 (1961).
- W. Vedder and D. A. Vermilyea, *Trans. Faraday Soc.*, **65**, 561 (1969).

## Investigation of Magnetic Anisotropy of Electrodeposited Magnetic Films by Measurement of the Magnetoresistance Effects

M. Perakh\*

Graduate School of Applied Science, The Hebrew University of Jerusalem, Jerusalem, Israel

### ABSTRACT

It is suggested that the magnetic texture in films may be estimated by using the characteristic angles azimuthal  $\psi$  and polar  $\beta$ , the first being the integral characteristic of uniaxial texture in a film plane, and the second of "perpendicular" anisotropy. An experimental procedure for determining the characteristic angles on the basis of measurement of galvanomagnetic effects in the film plane is suggested and has been found satisfactory in practice. An algorithm is developed to calculate the constant of perpendicular anisotropy and its components, as well as the demagnetizing factor along the normal of the film plane starting from experimental values of  $\beta$ . The addition of certain materials (saccharin, for instance) to the electrolyte causes a large increase in the perpendicular anisotropy which is found to be due to microstresses and their variations under the influence of the additional organic compounds. According to hysteresis loops and powder domain patterns observed, while the values of the polar angle are  $\beta > 45^\circ$ , the "stripe" film state is achieved.

Magnetic texture is one of the most important properties of ferromagnetic films conditioning their use (1). The concept of texture is meant as a totality of all preferable directions of magnetization regardless of their physical origin. Two especially important kinds of magnetic anisotropy are: first, the uniaxial anisotropy in the film plane and, second, the so-called "perpendicular" anisotropy which appears only in films, the thickness of which exceeds a definite "critical" value. These films are called "transcritical" or "stripe" films. The latter name is due to stripe-shaped domain patterns observed (2) on the film surface while using a powder technique (3).

For investigation of uniaxial texture in the thin film plane, several methods are used although the magnetometer (4) is often most suitable. For measurement of perpendicular anisotropy only a few methods are suggested. The use of a rotation magnetometer, for instance, does not enable one to measure anisotropy, the

constant of which is less than  $10^4$  erg/cm<sup>3</sup>. Furthermore, the value of the anisotropy constant, which is an energetical characteristic, does not give the obvious image about the shape of anisotropy. Finally, use of the magnetometer is connected with experimental difficulties. Therefore, the development of new methods for the investigation of anisotropy, especially in "stripe" films, is still being sought.

### Integral Characteristics of the Magnetic Texture in Films

Let us consider a film (Fig. 1) having a certain distribution of local easy axes in its plane. Let the fraction  $\rho(\alpha)d\alpha$  of local easy axes be contained within the angle from  $\alpha$  to  $\alpha + d\alpha$ . The distribution function  $\rho(\alpha)$  is normalized by the condition

$$\int_0^{\pi/2} \rho(\alpha)d\alpha = 1 \quad [1]$$

If the film has been magnetized to saturation along the x-axis, the magnetic moments lying within the angle  $d\alpha$ , rotate through an angle of  $\alpha$  to the x-axis.

\* Electrochemical Society Active Member (formerly M.Ya. Popereka).

Key words: magnetic films, magnetic anisotropy, galvanomagnetic effects, influence of organic additions on electrodeposition, microstress, demagnetizing factor, domain structure, stripe films.

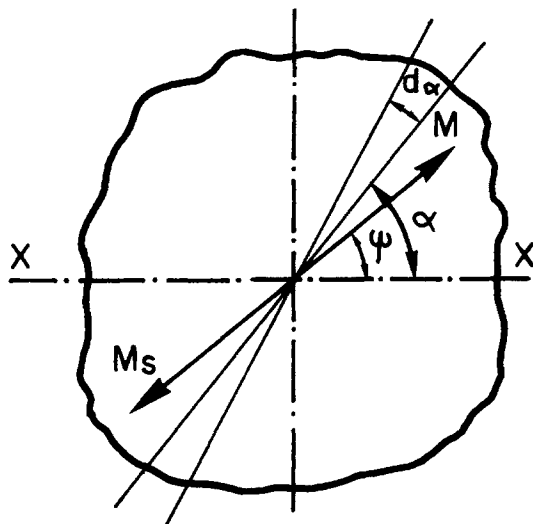


Fig. 1. Diagram showing how the galvanomagnetic effect is calculated with allowance for the dispersion of local easy axes.

It is known (5) that the galvanomagnetic effect (GE), i.e., the change of electroresistance while applying a magnetic field, is proportional to the increment of square magnetization. If the electrical resistance is measured along the x-axis, and the magnetic field acts along the same axis, the contribution of the vectors of magnetic moments, contained before the applying of a field within the angle  $d\alpha$ , to the measured longitudinal GE, will be (neglecting the amplitude dispersion of magnetization)

$$dg^{xx} = [k_{\parallel} M_s^2 - k_{\parallel} (M_s \cos \alpha)^2] \rho(\alpha) d\alpha = k_{\parallel} M_s^2 \sin^2 \alpha \rho(\alpha) d\alpha \quad [2]$$

where  $g^{xx}$  is the value of the longitudinal GE (the first superscript at  $g$  indicates the direction in which the conductivity is measured and the second superscript the direction of magnetic field);  $k_{\parallel}$  is the coefficient of proportionality between longitudinal GE and the square of magnetization,  $M_s^2$ . Hence the total longitudinal GE

$$g^{xx} = k_{\parallel} M_s^2 \int_0^{\pi/2} \sin^2 \alpha \rho(\alpha) d\alpha \quad [3]$$

Now we introduce a characteristic angle  $\psi$  by means of the relation

$$\sin^2 \psi = \int_0^{\pi/2} \sin^2 \alpha \rho(\alpha) d\alpha \quad [4]$$

The physical sense of the angle  $\psi$  is as follows. If all the magnetic moments in the film plane had been at an angle of  $|\psi \pm k \cdot \pi/2|$ , where  $k = 0, 1, 2, \dots$ , to the mean easy axis, then the measured longitudinal GE for this axis would be identical to the one observed at the real distribution of magnetic moments described by the function  $\rho(\alpha)$ . Therefore  $\psi$  could be used as the integral characteristic of uniaxial anisotropy in the film plane. If the distribution of local easy axes in the film plane is isotropic ( $\rho(\alpha) \equiv 2/\pi$ ), then from [4] we obtain  $\psi = \pi/4$ . While a definite degree of anisotropy exists, we have either  $\psi < \pi/4$  (mean easy axis coincides with x-axis) or  $\psi > \pi/4$  (mean easy axis along y); the derivation  $\psi$  from  $\pi/4$  is the measure of anisotropy.

The above consideration relates to the distribution of magnetic moments in the film plane. However, in so-called "transcritical" or "stripe" films, the magnetization vectors "withdraw" from the film plane (5, 7). Carrying out a consideration similar to the one described above, for the distribution of magnetic moments in the plane perpendicular to the film we intro-

duce the characteristic angle  $\beta$

$$\cos^2 \beta = \int_0^{\pi/2} \sin^2 \epsilon \rho_{\perp}(\epsilon) d\epsilon \quad [5]$$

where  $\beta$  is read from the plane of the film, the variable angle  $\epsilon$  is read from the z-axis, being perpendicular to the film plane, and  $\rho_{\perp}(\epsilon)$  is the distribution function of the magnetization vectors in the plane, perpendicular to the film plane, normalized by 1. Hence, the angle  $\beta$  is the angle of inclination of the magnetization vectors to the film plane, averaged over GE; it can be used as the integral characteristic of "perpendicular anisotropy" (PA).

### Determination of the Integral Characteristics of Magnetic Texture from Galvanomagnetic Effects

In Fig. 2 the vector  $M_s$  is a resultant vector of magnetization reduced to a unit of volume and representing the magnetization vectors, directions of which lie within the first octant. The vector  $M_s$  is inclined towards the plane of the film through an angle of  $\beta$ ; the projection of  $M_s$  to the plane xy is at an angle of  $\psi$  to the x-axis.

From geometrical considerations one obtains

$$\sin \gamma = \cos \psi \cos \beta \quad [6]$$

where  $\gamma$  is the angle between vector  $M_s$  and the yz-plane.

Generalizing Eq. [2] to the case of nonplanar distribution of magnetic moments yields for a longitudinal GE

$$g^{xx} = k_{\parallel} M_s^2 (1 - \cos^2 \beta \cdot \cos^2 \psi) \quad [7]$$

The expression [7] was derived by dividing the rotation of vector  $M_s$  to the x-axis in the process of magnetization into two stages: rotation through the angle  $\beta$  to the xy-plane, and afterwards through an angle of  $\psi$  in the xy-plane, to the x-axis.

Now let us consider the transverse GE. The rotation of vector  $M_s$  from its initial position to the y-axis during the process of magnetization along this axis can be divided into two stages: rotation through an angle of  $\gamma$  to plane yz, and then the subsequent rotation through a certain angle in the plane yz to the y-axis. However, while rotating in the yz-plane, the angle between  $M_s$  and the x-axis along which the measuring current is flowing, makes no contribution to the change in conductivity. Hence, the transverse GE  $g^{xy}$  (when magnetization is over y and the conductivity measured over x) is controlled by the angle  $\gamma$ . Taking into ac-

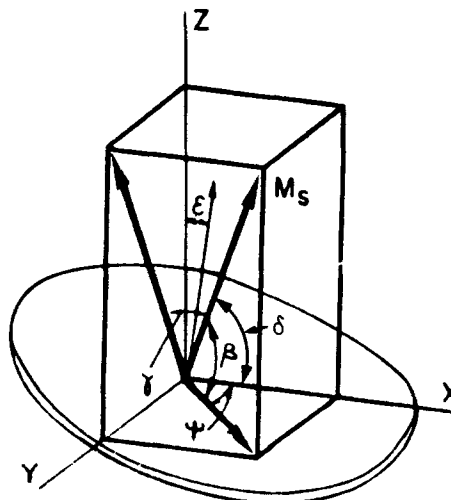


Fig. 2. Diagram illustrating calculation of the relation between the characteristic angles  $\psi$  and  $\beta$  and the magnitudes of longitudinal and transverse galvanomagnetic effects.



count [6], one gets

$$g^{xy} = k_{\perp} M_s^2 \cos^2\psi \cos^2\beta \quad [8]$$

where  $k_{\perp}$  is the coefficient of proportionality between the transverse GE and the square of magnetization.

Analogously, when conductivity is measured along the y-axis, the longitudinal  $g^{yy}$  and transverse  $g^{yx}$  GE are

$$g^{yy} = k_{\parallel} M_s^2 (1 - \cos^2\beta \sin^2\psi); \quad g^{yx} = k_{\perp} M_s^2 \sin^2\psi \cos^2\beta \quad [9]$$

If the magnitudes  $g^{xx}$ ,  $g^{yy}$ ,  $g^{xy}$ , and  $g^{yx}$  are measured experimentally, one gets Eq. [7]-[9] containing the unknown coefficients  $k_{\parallel}$  and  $k_{\perp}$ .

Let us use the II rule of even effects (8), according to which, in the case of isotropic distribution of magnetization

$$g^{xx}_{\text{isotr}} = g^{yy}_{\text{isotr}} = -2g^{xy}_{\text{isotr}} = -2g^{yx}_{\text{isotr}} \quad [10]$$

In the isotropic case, one has simultaneously  $\psi = \beta = \pi/4$ . Thus, we obtain from [8]-[10]

$$\frac{k_{\perp}}{k_{\parallel}} = -\frac{3}{2} \quad [11]$$

Combining Eq. [7]-[11] yields

$$\tan^2\psi = \frac{g^{yx}}{g^{xy}}; \quad \cos^2\beta = \frac{2\eta}{\cos\psi (2\eta - 3)} \quad [12]$$

where

$$\eta = \frac{g^{xy}}{g^{xx}} \quad (13)$$

Formulas [12] and [13] can be used for computing values  $\psi$  and  $\beta$ , the integral characteristics of magnetic texture, from measurement of longitudinal,  $g^{xx}$  and  $g^{yy}$ , and transverse,  $g^{xy}$  and  $g^{yx}$ , GE. The use of the azimuthal angle by itself, as the characteristic of magnetic texture in the film plane, may prove to be a convenient method of estimating uniaxial texture because of comparative simplicity and great accuracy of the GE measurements. Furthermore, separate determination of  $\psi$  may provide a means of verifying information about texture in the film plane obtained by other methods. As regards the polar angle  $\beta$ , one can scarcely find another characteristic of the PA, which combines clarity, ease of determination, and availability regardless of the magnitude of PA as is inherent in  $\beta$ . Finally, as will be subsequently demonstrated, the induced anisotropy actually obtained in films grown in a magnetic field can only be characterized using both characteristic angles  $\psi$  and  $\beta$ .

### Connection Between the Polar Angle $\beta$ and the Constant of Perpendicular Anisotropy

Let us assume (without restricting the generality of the consideration) that the film is isotropic in its own plane. Furthermore, let us divide all the factors influencing the PA into two groups. First, the spontaneous microstresses  $\sigma$  (the GE are measured on films separated from substrates, macrostresses being thus eliminated), and, second, all other possible factors, OF. The OF can be connected, for example, with the conditions of magnetic flux closure (9) with "columnar" structure of film (10), with an axial crystallographic texture (11), etc.

The contribution of microstresses  $\sigma$  to the PA may be represented by the constant

$$K_{\perp\sigma} = -\frac{3}{2}\lambda\sigma \quad [14]$$

where  $\lambda$  is the coefficient of magnetostriction. The contribution of OF to PA is characterized by the constant  $K_{\perp\sigma}$ .

Let us imagine a hypothetical case in which there are neither stresses nor a demagnetizing factor along the normal to the film plane ( $N_z = 0$ ). In this case, the angle of inclination of magnetization vector  $M$  to the film plane is  $\beta_0 < \beta$ , where  $\beta$  is this angle observed experimentally (Fig. 3). In the case in which microstresses act, as well as OF, but, as before  $N_z = 0$ , the angle of inclination is  $\beta^* > \beta$ .

Let us consider an axis  $x_0$  as an effective axis of anisotropy, created by OF, with a corresponding anisotropy constant  $K_0$ . Thus, the free energy of unit volume, for  $N_z = 0$ , is

$$E_0 = K_{\perp\sigma} \cos^2\beta^* + K_0 \sin^2(\beta^* - \beta_0) \quad [15]$$

Minimizing [15] with respect to  $\beta^*$ , we get

$$K_0 = K_{\perp\sigma} \frac{\sin 2\beta^*}{\sin 2(\beta^* - \beta_0)} \quad [16]$$

In a real film vector of magnetization,  $M$  is inclined to the film plane at an angle  $\beta$ , determined experimentally. Allowing for the demagnetizing fields, the free energy of a unit volume equals

$$E = \frac{N_z M^2}{2} \sin^2\beta + K_0 \sin^2(\beta - \beta_0) + K_{\perp\sigma} \cos^2\beta \quad [17]$$

Using the condition of minimum of energy  $E$  yields

$$K_{\perp\sigma} \left(1 - \frac{N_z M^2}{2K_{\perp\sigma}}\right) \sin 2\beta = K_0 \frac{\sin 2(\beta - \beta_0)}{\sin 2(\beta - \beta_0)} \quad [18]$$

Equations [16] and [18] contain three unknowns:  $K_0$ ,  $\beta_0$ , and  $\beta^*$ . A third equation may be obtained, considering an axis  $x^*$  (Fig. 3) as the nominal anisotropy axis with a corresponding anisotropy constant  $K^*$ . The free energy of unit volume in this form is thus

$$E^* = K^* \sin(\beta^* - \beta) + \frac{N_z M^2}{2} \sin^2\beta \quad [19]$$

The magnitude  $K^*$  may be expressed in terms of  $K_{\perp\sigma}$  and  $K_0$ . Let us consider the rotation of  $M$  under the influence of a field  $H$  acting along the axis  $x_i$ , lying at an angle  $\psi$  to the anisotropy axis  $\xi$  (Fig. 3b), and characterized by the anisotropy constant  $K_{\psi}$ . The

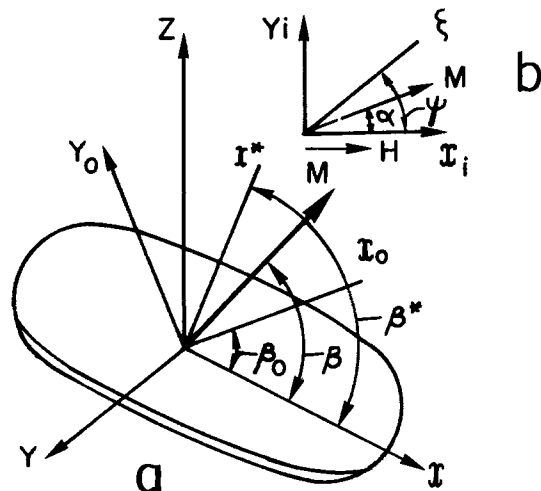


Fig. 3. Diagrams: (a) angles of inclination of magnetization vector  $M$  to film plane and (b) illustrating the calculation of anisotropy constants at magnetization's rotation.

energy of a body magnetized along the axis  $x_1$  in the absence of demagnetizing fields is

$$E_1 = K_\psi \sin^2(\psi - \alpha) - HM \cos \alpha \quad [20]$$

The equilibrium value of  $\alpha$  may be found from the condition for the minimum of  $E_1$

$$H = \frac{K_\psi \sin 2(\psi - \alpha)}{M \sin \alpha} \quad [21]$$

Since  $dM = -M \sin \alpha \, d\alpha$ , the work of magnetizing along the axis  $x_1$  is

$$A_{x_1} = \int_\psi^0 H dM = - \int_\psi^0 \frac{K_\psi \sin 2(\psi - \alpha)}{M \sin \alpha} M \sin \alpha \, d\alpha = K_\psi \sin^2 \psi \quad [22]$$

The anisotropy constant for the new nominal anisotropy axis  $x_1$  equals

$$K_{x_1} = A_{y_1} - A_{x_1} = K_\psi \cos 2\psi \quad [23]$$

Formula [23] relates two anisotropy constants  $K_\psi$  and  $K_{x_1}$ , which are both due to the same source, but which refer to the true and nominal anisotropy axis  $\xi$  and  $x_1$ , respectively, and which are separated by angle  $\psi$ . With regard to  $K^*$ ,  $K_o$ , and  $K_{\perp\sigma}$ , relation [23] enables us to write the following relationship which allows for the additivity of the energy

$$K^* = -K_{\perp\sigma} \cos 2\beta^* - K_o \cos 2(\beta^* - \beta_o) \quad [24]$$

Substituting [24] into [19], and using the condition of minimum energy, yields

$$K_o = -K_{\perp\sigma} \left[ \frac{\cos 2\beta^*}{\cos 2(\beta^* - \beta_o)} + \frac{N_z M^2 \sin 2\beta}{2K_{\perp\sigma} \cos 2(\beta^* - \beta_o) \sin 2(\beta^* - \beta)} \right] \quad [25]$$

To solve the system of Eq. [16], [18], and [25], the following algorithm was developed. From equations [16], [18], and [25] one can get

$$\frac{\sin 2\beta^* \sin 2(\beta - \beta_o)}{\sin 2(\beta^* - \beta_o)} = \left( 1 - \frac{N_z M^2}{2K_{\perp\sigma}} \right) \sin 2\beta \quad [26]$$

$$\frac{\sin 2\beta^* \sin 2(\beta^* - \beta)}{\tan 2(\beta^* - \beta_o)} - \cos 2\beta^* \sin 2(\beta^* - \beta) = \frac{N_z M^2}{2K_{\perp\sigma}} \sin 2\beta \quad [27]$$

The order of computation is as follows:

1. For a film with specific values of  $\beta$  and  $\sigma$  (determined experimentally), one specifies a series of values of  $\beta_{oi} < \beta$ ; for each  $\beta_{oi}$  one plots the left side of Eq. [26] as a function of  $\beta^*$ . On the latter graph the value of  $\beta^*$ , satisfying Eq. [26], is to be found. Thus, the function  $\beta^*(\beta, \beta_o)$  is determined.

2. The left side of Eq. [27] is plotted as a function of  $\beta_o$ ; the values of  $\beta^*$  having been substituted into [27] from the previously constructed  $\beta^*(\beta_o)$  relationship. On the latter graph, the values of  $\beta_o$ , satisfying relationship [27] are to be found.

3. Using the determined values of  $\beta_o$ , one can use any of Eq. [16], [18], or [25] to find  $K_o$ .

The computation described requires a knowledge of  $N_z$ , the demagnetizing factor along the normal to the film plane. It is possible to estimate  $N_z$  as follows. From Eq. [18] one gets for  $\beta = \beta_o$

$$K_{\perp\sigma} = \frac{N_z M^2}{2} \quad [28]$$

Relation [28] has a simple physical meaning: if PA created by the stresses is exactly compensated for by the demagnetizing field, the angle of the departure of  $M$  from the film plane is controlled only by OF, i.e.,  $\beta = \beta_o$ . To use [28] one must substitute into this relation  $K_{\perp\sigma} = -(3/2) \cdot (\lambda\sigma)$  for  $\beta = \beta_o$ . This may be done by successive approximations. As a zero approximation,  $\beta_{oo} = \pi/4$  is to be selected. Extrapolating the experimental data, we find the value of  $\sigma$ , for which  $\beta = \beta_{oo} = \pi/4$ . From Eq. [28] the zero approximation  $N_z = N_{zo}$  is next to be calculated. Furthermore, using the proposed algorithm, which is based on Eq. [26] and [27], the first approximation  $\beta_o = \beta_{o1}$  is to be determined, etc. By using the procedure described, a good convergence was often established without proceeding further than the second approximation ( $(N_{z2} - N_{z1})/N_{z2} \lesssim 0.05$ ).

Hence, the procedure described enables us to determine the constant of perpendicular anisotropy and the demagnetizing factor along the normal to the film plane as well, starting from experimental values of  $\beta$ , determined as proposed above. The total constant  $K_{\perp}$  of PA is to be calculated using the following equation (12)

$$K_{\perp} = K_{\perp o} + K_{\perp\sigma} - \frac{N_z M^2}{2}; \quad (K_{\perp o} = K_o \sin^2 \beta_o) \quad [29]$$

The magnitudes  $K_{\perp}$ ,  $K_{\perp\sigma}$ ,  $K_{\perp o}$ , and  $N_z$  are important characteristics providing useful information about the magnetic structure and areas of use of magnetic films.

#### Verification of the Experimental Procedure

The GE were measured by the potentiometric method (13). The films were deposited on copper substrates, the cell was thermostated ( $\pm 0.5^\circ\text{C}$ ), and the current density was maintained galvanostatically. An electromagnet provided a uniform magnetic field up to  $10^3$  oe in the zone of deposition. Cuts in the shape of the future U-shaped specimens had previously been made on the substrate; one way orientated along the lines of field and the other, across. After deposition the substrate was removed in a 250 g/liter solution of  $\text{GrO}_3$  and 100 g/liter of  $(\text{NH}_4)_2\text{SO}_4$ . The copper was left at the ends of the U-shaped specimen to serve as contacts and at the bridge connecting both branches of the U-shaped specimen. The appearance of uncontrollable internal stress which might have arisen during the cutting of the specimen, was avoided by making the cuts in advance. The final shapes of specimen oriented both (i) along and (ii) across the lines of a magnetic field are schematically presented in Fig. 4. The shape and method of attaching the specimens were such as to avoid error due to magnetostriction and thermo emf. Before measuring, the specimens were demagnetized in a diminishing variable magnetic field. While measuring the conductivity, specimens were

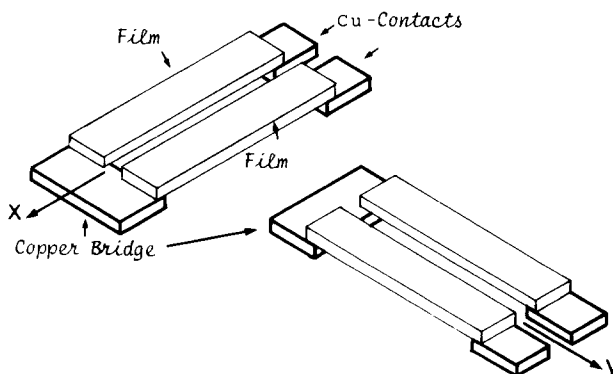


Fig. 4. Schematic representation of U-shaped specimen oriented along x- and y-axes, respectively.

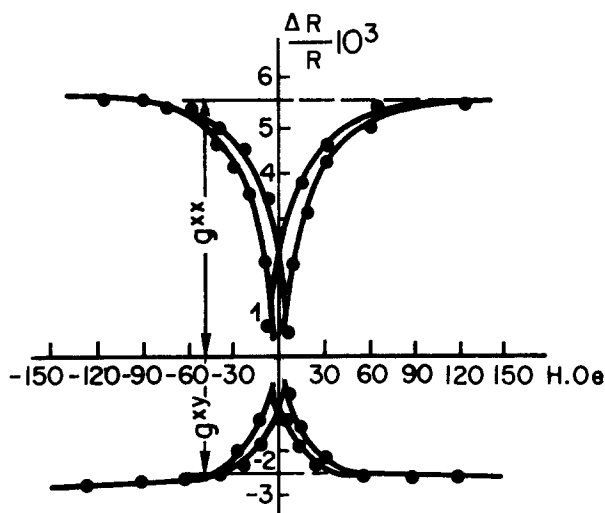


Fig. 5. Examples of the hysteresis loops of the galvanomagnetic effects in film ( $5 \pm 0.2 \mu\text{m}$ ) of an iron-nickel alloy (80% Ni). The values  $g^{xx}$  and  $g^{xy}$  are the measured longitudinal and transverse galvanomagnetic effects at saturation, which are used to calculate the characteristic angles.

fixed with one side in a perspex clamp supplied with current leads and positioned in an oil thermostat between the poles of an electromagnet. The measuring current was 4 mA. The longitudinal and transverse GE were measured at technical saturation (Fig. 5).

The GE were measured and the angles  $\psi$  and  $\beta$  calculated in a rolled plate of nickel (0.5 mm) which had been vacuum annealed at  $10^{-5}$  mm Hg and  $1200^\circ\text{C}$  and cooled for 12 hr. As expected, in this definitely isotropic specimen,  $\psi = \beta = 45 \pm 1.5^\circ$ . Furthermore, the method was verified on electrodeposited nickel film  $5 \mu\text{m}$  thick, vacuum annealed in  $10^{-3}$  mm Hg at  $900^\circ$  for 3 hr and cooled at the rate of  $50^\circ/\text{hr}$ . In this film it was found that  $\psi = 50^\circ \pm 1.5^\circ$  and  $\beta = 38^\circ \pm 1.5^\circ$ . The film was stretched in a special device to a stress of  $\sigma = 3.3 \times 10^8$  N/cm<sup>2</sup>. As a result of the negative magnetostriction of nickel, the uniaxial extension over the x-axis should cause the magnetic moments to rotate towards the perpendiculars to the x-axis (8), that is, towards the y-axis and z-axis. Increases in  $\psi$  and  $\beta$  were to be expected as a result of extension. The experiment showed that in extended state  $\psi = 53^\circ \pm 1.5^\circ$  and  $\beta = 58^\circ \pm 1.5^\circ$ . Thus, our procedure revealed changes in magnetic texture due to the elastic stretching of the film.

The additional verification of the method proposed, based on the use of Crowter's method (14), has been previously described (15). Finally, the method was verified by comparing the values of  $\beta$  with domain patterns and hysteresis loops, as described below.

### Several Experimental Results

*Influence of organic additives on perpendicular anisotropy of Ni-Fe films.*—It was found that the introduction of several organic substances into the electrolyte causes a significant increase of the angle  $\beta$ , i.e., of the PA. In Fig. 6 the corresponding data are presented for nickel films electrodeposited from the solution containing 294 g/liter  $\text{NiSO}_4 \cdot 7\text{H}_2\text{O}$ , 30 g/liter  $\text{H}_3\text{BO}_3$ , 25 g/liter Rochelle salt, and organic compounds, saccharin or sulgin, at 2 A/dm<sup>2</sup>,  $20^\circ\text{C}$ , pH = 2.3. As the concentration of saccharin or sulgin in the electrolyte increased, the angle  $\beta$  increased monotonically up to  $\sim 75^\circ \pm 5^\circ$ ; when the concentration of additives exceeded  $\sim 4 \times 10^{-3}\text{M}$ , a "saturation" was observed, probably connected with the "saturation" of an adsorbed layer on the growing crystals of the film.

The investigation by means of x-rays, electron diffraction, and electron microscopy showed that the increase of  $\beta$  is connected neither with crystallographic texture nor with "columnar" structure of the deposit.

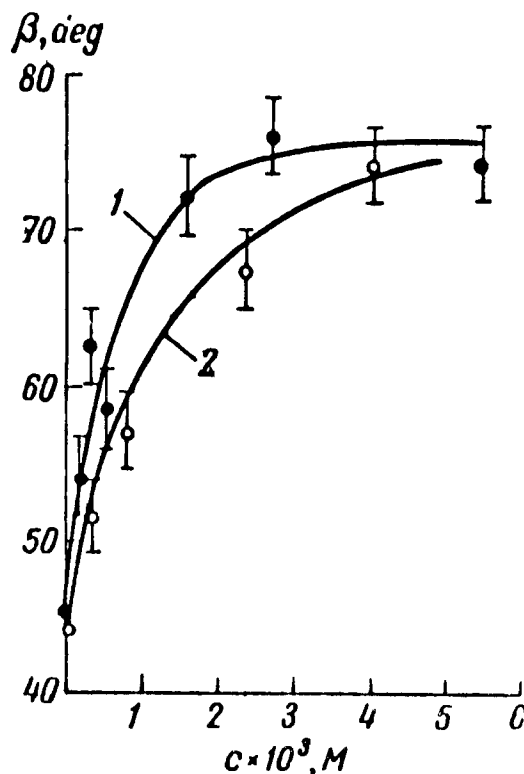


Fig. 6. The angle  $\beta$  in nickel films as a function of concentration of (1) saccharin and (2) sulgin in the electrolyte. Thickness of the film:  $5 \pm 0.2 \mu\text{m}$ . Composition of electrolyte 294 g/liter  $\text{NiSO}_4 \cdot 7\text{H}_2\text{O}$ , 30 g/liter  $\text{H}_3\text{BO}_3$ , 25 g/liter Rochelle salt.  $D_k = 2$  A/dm<sup>2</sup>; pH = 2.3;  $T = 20^\circ\text{C}$ .

Although the macrostresses in films were eliminated while separating the substrate, it was impossible to exclude in advance the existence of an "inherited" anisotropy, caused by planar macrostresses (appearing during the deposition) and "frozen" in the deposit after separation. The macrostresses in deposit were measured using the two-cantilever method, as described in Ref. (16, 17); the absolute values of macrostresses were calculated by means of formulas (18). No connection was found between the macrostresses and angle  $\beta$ . An assumption was proposed that the influence of organic matter on PA is connected with the role of microstresses. In Fig. 7 the characteristic angle  $\beta$  is depicted in its dependence on microstresses in nickel films, determined by means of the x-ray technique. The details of microstress determination were reported elsewhere (19). The various values of microstresses were obtained by adding several organic compounds to the electrolyte. It is seen that between the angle  $\beta$  and the microstresses there is an evident correlation.

In Fig. 8 angle  $\beta$  is presented as a function of film composition (i.e., of nickel content). In the region of negative magnetostriction ( $\geq 80\%$  Ni), the increase of microstresses under the influence of saccharin (19) is accompanied by an increase of angle  $\beta$  (curve 2). In films with 60–80% Ni (positive magnetostriction), saccharin increases the microstresses and simultaneously reduces  $\beta$ . The curves of  $\beta$  vs. composition, obtained with and without saccharin, cross at approximately 80% Ni, i.e., in the range of composition where the sign of magnetostriction is reversed. These facts fall in with the assumption that the increase of PA is due to microstresses.

*Constants of perpendicular anisotropy and the demagnetizing factor of Ni-Fe films.*—In Table I, the values of the effective demagnetizing factor (7) of Ni-Fe films are presented, determined by means of the algorithm described above and based on relations [26]–[28]. The decrease of  $N_z$  along with an increase of Fe

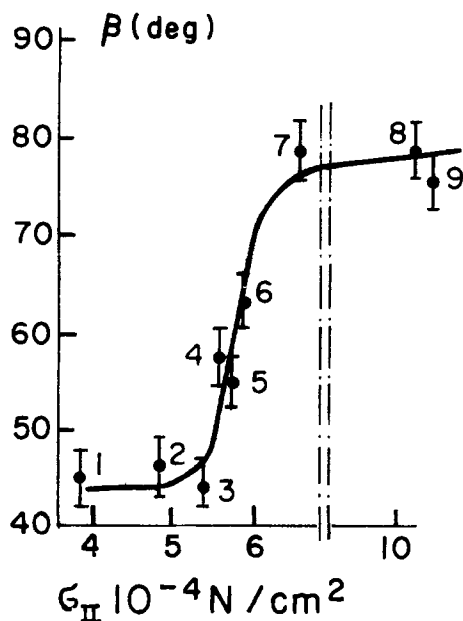


Fig. 7. Characteristic angle  $\beta$  in nickel films as a function of microstresses, determined using x-ray technique. 1, Butine-diol; 2, streptocide; 3, without additive; 4, sulphodimezine; 5, ethanol; 6, sulfacyl; 7, saccharin; 8, benzene sulfamide; 9, sulgin. Thickness of film:  $5 \pm 0.2 \mu\text{m}$ . Conditions of deposition as in Fig. 5.

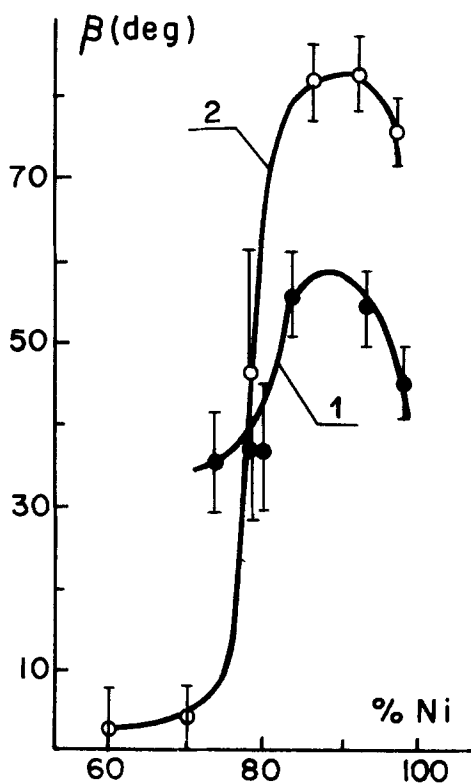


Fig. 8. The angle  $\beta$  in iron-nickel film as a function of their composition. Thickness of films  $5 \pm 0.2 \mu\text{m}$ ; composition of electrolyte: 1, 294 g/liter ( $\text{NiSO}_4 \cdot 7\text{H}_2\text{O} + \text{FeSO}_4 \cdot 7\text{H}_2\text{O}$ ) [the ratio Ni/Fe varies accordingly (23) to get an alloy of required composition]; 2, 30 g/liter  $\text{H}_3\text{BO}_3$ ; 25 g/liter Rochelle salt. The same plus 1 g/liter saccharin.  $D_k = 2 \text{ A/dm}^2$ ;  $\text{pH} = 2.3$ ;  $T = 20^\circ\text{C}$ .

content in alloy is apparently connected with the change in domain structure. In films with  $\sim 83\%$  Ni and especially in Fe films, the values of  $N_z$  are so small that they may be explained only by the appearance of a closed domain structure (9). In such cases, the angle  $\beta$  characterizes the position of  $M$  in internal domains; in surface domains  $M$  lies in a film plane (9).

Table I. Effective demagnetizing factor of iron-nickel films  $5 \pm 0.2 \mu\text{m}$  thick

Composition of film, w/o	$N_z$	Composition of film, w/o	$N_z$
100 Ni	$2 \pm 0.1$	87 Ni-13 Fe	$0.55 \pm 0.05$
95 Ni-5 Fe	$1.6 \pm 0.1$	83 Ni-17 Fe	$0.17 \pm 0.02$
90 Ni-10 Fe	$1 \pm 0.07$	100 Fe	$0.055 \pm 0.001$

In Fig. 9 the anisotropy constants, determined as described above on the basis of Eq. [14] and [26]-[29] are presented. From these curves it is seen that the contribution of OF to PA is small; the main contribution to PA is due to the spontaneous microstresses. The nondependence of  $\beta_0$  and  $K_{\perp 0}$  on  $\beta$  indicates that the division of the total PA constant into the components  $K_{\perp \sigma}$  (depending on microstresses) and  $K_{\perp 0}$  (depending on OF), has a real physical essence.

*Dependence of PA on current density and film thickness.*—It was found that the PA increases in correlation with film thickness increase. In order to explain the phenomenon observed, let us consider once again Eq. [18], which, in combination with [14], can be written as follows

$$\frac{\sin 2(\beta - \beta_0)}{\sin 2\beta} = \frac{3/2 \sigma |\lambda| - E_d}{K_0} \quad [30]$$

where  $E_d = N_z M^2 / 2$  is the energy of the demagnetizing field.

The angle  $\beta_0$ , being controlled by OF, does not depend considerably on the film thickness. On the other hand, in the thickness range of  $1.5\text{--}5 \mu\text{m}$ , in which the increase of  $\beta$  was observed, the microstresses  $\sigma$  are almost constant (20). Thus, the increase of  $\beta$  accompanying the growth of the film may be due only to a change of  $E_d$ . This magnitude, according to theory (7), in the case of a stripe domain structure may be expressed as

$$E_d = \frac{1.7 M^2 d}{t} \quad (\text{erg/cm}^3) \quad [31]$$

where  $t$  is the film thickness and  $d$  the width of domain. The stripe domain structure was disclosed in films under experimental investigation (see below). From theory (7), it is known that the domain width increases proportionally to  $t^{1/2}$ . This theory's prediction has been confirmed experimentally (17). Thus, if at a "critical" thickness  $t^*$ , ensuring the transition from "thin film" state to "stripe film" state, the domain width is  $d^*$ , then at an arbitrary thickness  $t$  the domain width is thus

$$d = d^* \sqrt{\frac{t}{t^*}} \quad [32]$$

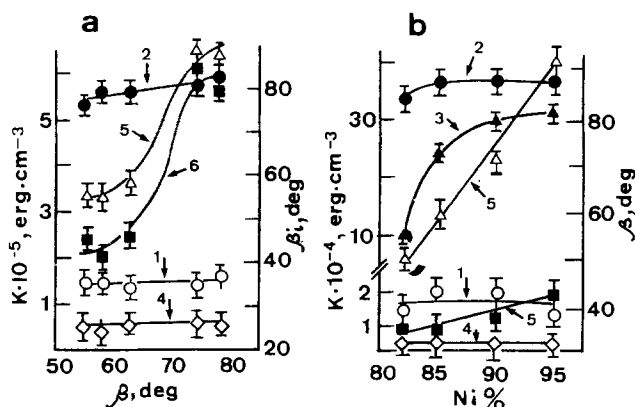


Fig. 9. Angles of inclination of magnetization vector and PA constants for films  $5 \pm 0.2 \mu\text{m}$  thick. (1,  $\beta_0$ ; 2,  $\beta^*$ ; 3,  $\beta$ ; 4,  $K_{\perp 0}$ ; 5,  $K_{\perp \sigma}$ ; 6,  $K_{\perp}$ ). a, For a nickel film; b, for iron-nickel film.

Substituting [31] and [32] into [30] yields

$$\frac{\sin 2(\beta - \beta_0)}{\sin 2\beta} = A - Bt^{-1/2} \quad [33]$$

where

$$A = \frac{3/2 |\lambda| \cdot \sigma}{K_0}; \quad B = \frac{1.7M^2 d_0}{K_0 \sqrt{t^*}} \quad [34]$$

Hence, according to the assumption that the increase of  $\beta$  along with film thickness is due to the decrease of demagnetizing field, the linear dependence of the function  $f(\beta) = \sin 2(\beta - \beta_0)/\sin 2\beta$  on  $t^{-1/2}$  is expected to be observed.

In Fig. 10 the experimental data for Ni film are presented confirming the proposed assumption. From the cutoff segment on the vertical axis, the value of  $K_0$  can be found using Eq. [33] and [34]. In our case  $K_0 = 0.85 \times 10^5$  erg/cm<sup>3</sup>. The average value of  $K_0$  according to data presented in Fig. 8 is  $K_0 \equiv 0.73 \times 10^5$  erg/cm<sup>3</sup>, which means a good agreement.

If the current density increases,  $\beta$  is enlarged as well. The theoretical consideration similar to the one presented above and based on the assumption that the reason for an increase of  $\beta$  in this case is the increase of microstress, predicts that the following dependence is to be observed

$$\sin 2(\beta - \beta_0)/\sin 2\beta \propto \sqrt{\ln D_c}$$

This prediction is also well fulfilled, as is seen from curve 2 in Fig. 10.

*Fluctuations of anisotropy and compensation effect.*—It was found that in a series of film prepared under identical conditions, there was a considerable scatter of  $\beta$  and  $\psi$  from film to film. In Fig. 2 three angles are depicted,  $\psi$ ,  $\beta$ , and  $\delta$ , the latter being the angle between the vector  $M$  of magnetization and mean easy axis  $x$ . The self-explanatory relation

$$\cos \delta = \cos \beta \cos \psi \quad [35]$$

enables us to determine  $\delta$  while  $\psi$  and  $\beta$  are measured. It was discovered that there is a compensation effect. If for random reasons angle  $\psi$  in one film is reduced, then there will be a definite increase in  $\beta$ , while the angle  $\delta$  remains practically unaltered.

Several typical results are presented in Table II.

Fluctuations of  $\psi$  and  $\beta$ , as has been demonstrated (21), are due to the fluctuations in spontaneous internal microstresses. The compensation effect, according to Ref. (21), is due to the demagnetizing field:

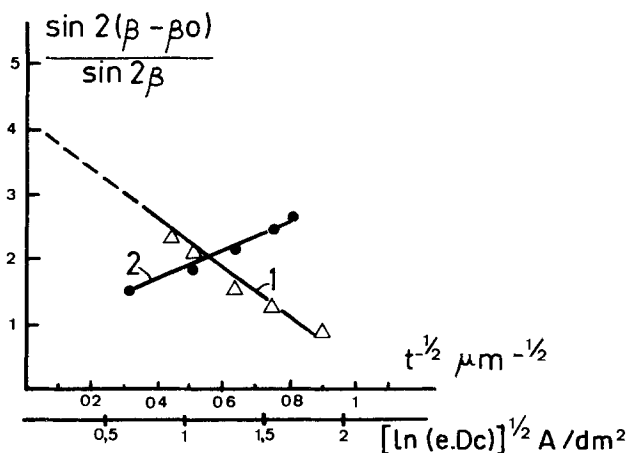


Fig. 10. Dependence of the function  $\sin 2(\beta - \beta_0)/\sin 2\beta$ , obtained from experiments with nickel films, on film thickness (curve 1) and current density (curve 2). For curve 1,  $D_c = 2$  A/dm<sup>2</sup>; for curve 2,  $t = 5 \pm 0.2$   $\mu$ m. Composition of electrolyte: 280 g/liter NiSO<sub>4</sub> · 7H<sub>2</sub>O; 30 g/liter H<sub>3</sub>BO<sub>3</sub>; 25 g/liter Rochelle salt; 1 g/liter saccharin.  $T = 20^\circ$ C.

Table II. Values of the angles  $\psi$ ,  $\beta$  and  $\delta$  in series of nickel films deposited on copper bases with different microrelief

Method of generating base microrelief	Angle	Value, deg		
		max	min	mean
Chemical polishing	$\psi$	46	29	37
	$\beta$	54	46	50
	$\delta$	61	59	60.7
Treatment with emery paper in the direction of the x-axis	$\psi$	60	30	43
	$\beta$	56	18	40
	$\delta$	62	61	61.5
Rolling in direction of x-axis	$\psi$	48	41	43
	$\beta$	48	42	43
	$\delta$	60	60	60
Grooves made by a scalpel in the direction of x-axis	$\psi$	48	40	43
	$\beta$	47	40	43.5
	$\delta$	60	60	60

Note: There is an error of  $\pm 1.5^\circ$  in determination of angles  $\psi$  and  $\beta$  on a specific specimen.

when  $\psi_i$  grows (due to random differences of  $\sigma_{xi}$  and  $\sigma_{yi}$ , for instance), we get a demagnetizing field which reduces  $\beta_i$ , until obtaining again the closed magnetic flux. This keeps  $\delta$  constant.

*Obtaining of "stripe" films.*—In Fig. 11 and 12, the magnetic hysteresis loops and powder diagrams, respectively, are presented. There is an obvious correlation: in films having typical "transcritical" hysteresis loops (b and c in Fig. 11) and a stripe-shaped domain structure, the angle  $\beta \gtrsim 45^\circ$ ; if  $\beta \lesssim 45^\circ$ , we obtain a "thin film" state (a and d in Fig. 11).

The width of domains in the film of  $\sim 82\%$  Ni alloy of thickness  $t = 5$   $\mu$ m was found to be  $D \equiv 1.1$   $\mu$ m, and for the thickness  $t \equiv 10$   $\mu$ m,  $D \equiv 2.3$   $\mu$ m. This shows quantitative agreement with data (22) for vacuum condensates.

### Acknowledgment

The author wishes to express his sincere gratitude to B. S. Zolotkovskii, who took a significant part in the experiments.

Manuscript submitted June 16, 1975; revised manuscript received Jan. 5, 1976. This was Paper 122 presented at the New York, New York, Meeting of the Society, Oct. 14-17, 1974.

Any discussion of this paper will appear in a Discussion Section to be published in the December 1976 JOURNAL. All discussions for the December 1976 Discussion Section should be submitted by Aug. 1, 1976.

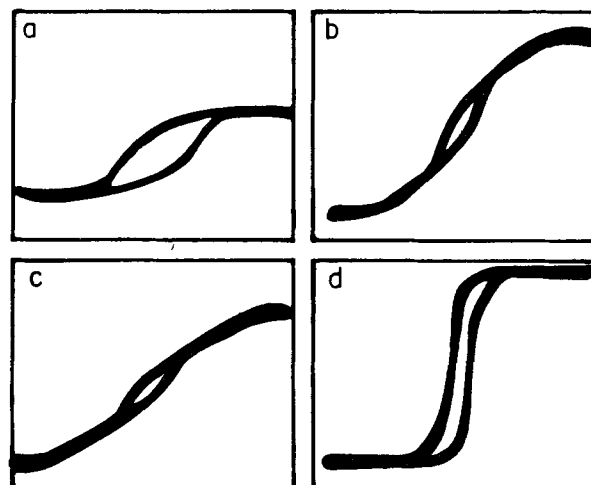


Fig. 11. Hysteresis loops of nickel films deposited from solution (a) without additives and (b-d) with  $4 \cdot 10^{-3}$  M saccharin. a, b, Film on copper substrate; c, detached from substrate; d, annealed in  $10^{-5}$  mm Hg for 1 hr at  $500^\circ$ C. Thickness:  $5 \pm 0.2$   $\mu$ m. Scale of hysteresis loop arbitrary. Frequency: 50 Hz.

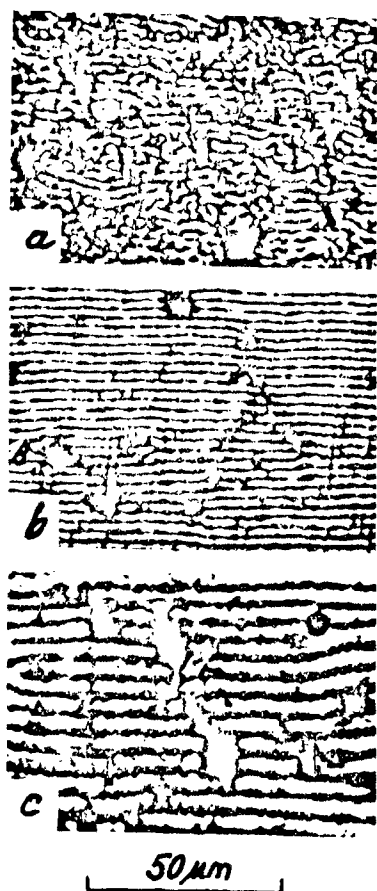


Fig. 12. Powder figures on surface of deposited film of (a) nickel and (b, c) of alloy with  $\sim 82\%$  Ni. Thickness of films: a, b, 5  $\mu\text{m}$ ; c, 10  $\mu\text{m}$ .

#### REFERENCES

1. M. Prutton, "Thin Ferromagnetic Films," Butterworths, London, Washington (1964).
2. R. J. Spain, *Appl. Phys. Letters*, **3**, 208 (1963).
3. E. E. Huber and D. O. Smith, *J. Appl. Phys.*, **30**, 267 (1959).

4. H. Maeda, *J. Appl. Phys. Japan*, **8**, 978 (1969).
5. S. V. Vonsovskii, "Magnetizm," Nauka, Moscow (1971) (Russian).
6. L. D. Landau and E. M. Lifshitz, *Sov. Phys.*, **8**, 153, (1935).
7. C. Kittel, *Phys. Rev.*, **70**, 965 (1946).
8. N. S. Akulov, "Ferromagnetizm," Moscow-Leningrad, GTTI (1939) (Russian).
9. G. S. Krinchik and Ye. Ye. Chepurova, Coll. "Thin Magnetic Films," Proc. of Int. Symposium, Irkutsk (1968).
10. A. A. Glazer, R. I. Tagirov, A. P. Potapova, and Ya. S. Shur, *Trudy IFM, Akad. Nauk SSSR*, **27**, Sverdlovsk (1968) (Russian).
11. S. M. Kochergin, "Textura Elektroosazdennikh Metallov" (Texture of Electro-deposited Metals), Moscow, Metallurgizdat (1964) (Russian).
12. T. Koikeda, S. Fujiwara, and S. Chikazumi, *J. Phys. Soc. Japan*, **21**, 1914 (1966).
13. V. I. Chechernikov, "Magnitnye Izmereniya" (Magnetic Measurements), Moscow Iz. M.G.U. (1963) (Russian).
14. T. Crowter, *J. Appl. Phys.*, **34**, 580 (1963).
15. M. Ya. Popereka and B. S. Zolotkovskii, *Fiz. Met. Metalloved.*, **32**, 1182 (1971) (Russian; Engl. transl., Phys. Met. Metallography).
16. M. Ya. Popereka, in "Elektroosashdeniye plionki" (Electrodeposited films), p. 3, Kalinin Pedagogical Institute, Kalinin, 1970 (Russian).
17. V. M. Bystrov, I. V. Nikitishev, and M. Ya. Popereka, *ibid.*, p. 89.
18. M. Perakh (M. Ya. Popereka), in "Properties of Electrodeposits—Their Measurement and Significance," R. Sard, H. Leidheiser, Jr., and F. Ogburn, Editors, p. 328, The Electrochemical Society Soft-bound Symposium Series, Princeton, N. J. (1975).
19. B. S. Zolotkovskii and M. Ya. Popereka, *Fiz. Met. Metalloved.*, **33**, 268 (1972) (Russian; Engl. transl., Phys. Met. Metallography).
20. L. F. Ilyushenko, "Elektroliticheski osazhdeniye magnitniye plenki" (Electrodeposited magnetic films), Izd. "Nauka i tehnika," Minsk (1972). (Russian).
21. B. S. Zolotkovskiy and M. Ya. Popereka, *Fiz. Met. Metalloved.*, **34**, 217 (1972) (Russian; Engl. transl., Phys. Met. Metallography).
22. L. S. Palatnik, L. I. Lukashenko and A. G. Ravlik, *Fiz. Tverd. Tela.*, **7**, 2829 (1965) (Russian; Engl. transl., Sov. Phys. Solid State).
23. A. Brenner, "Electrodeposition of Alloys," New York (1961).

## Cathodization Luminescence of Silicon

S. Ogura,<sup>1</sup> T. Odajima, and C. R. Viswanathan\*

Electrical Sciences and Engineering Department, School of Engineering and Applied Science, University of California, Los Angeles, California 90024

#### ABSTRACT

Luminescence during the cathodization of silicon and other materials was observed. In the cathodization of silicon in 0.04N  $\text{KNO}_3$ /ethylene glycol, the luminescence was found only when the oxide film was thin. It was observed that the cathodization of silicon resulted in removal of the oxide film. However, in the presence of water, the luminescence occurred without any requirement of an oxide layer.

The galvanoluminescence during anodization has been reported for aluminum by Braun in 1898 (1). Since then, the emission of light on anodization has long been known for other metals such as Ta, Zn, Mg, and W. The luminescence for semiconductors has been reported for silicon by Gee (2) and Waring *et al.* (3). In our study of the anodization process for silicon, the

luminescence was observed not only during the anodization but also during the cathodization of silicon. The luminescence during cathodization was also observed in various metals as Al, Zn, etc.

#### Characteristics of Electroluminescence

0.04  $\text{KNO}_3$ -ethylene glycol solution and silicon wafers were used for the investigation of electroluminescence characteristics in a silicon-electrolyte system. p-and-n-type (111)-orientation silicon wafers, each having a different resistivity, were used.

\* Electrochemical Society Active Member.

<sup>1</sup> Present address: IBM, Raleigh, North Carolina.

Key words: silicon oxidation, reduction, luminescence during cathodization.

After being polished and chemically etched, the silicon samples were held on a Teflon sample holder. The back of the wafer was in contact with mercury, while the front side was in contact with the solution. A platinum wire immersed in the solution formed the counter-electrode. The emission from silicon wafers was picked up by a photomultiplier (EMI 9558B) tube with an S-20 photocathode characteristic.

Two x-y recorders were used; one, in which the output from the PMT was connected to the y-terminal, and the other, in which the cell current was connected to the y-terminal. The cell voltage was fed to the x-terminals of both the x-y recorders. In this manner, the relative light intensity and the cell current are measured simultaneously as a function of light voltage.

When d-c voltage across the cell was swept at a rate of 1 V/sec, the cell current and the luminescent signal shown in Fig. 1 and 2 are obtained. A positive cell voltage corresponds to anodization of silicon, while a negative voltage on the silicon electrode corresponds to cathodization. When the cell voltage is increased as indicated (curve I) in Fig. 1 and 2, the cell current increases and luminescence appears around 10V. It is known that in 0.04N KNO<sub>3</sub>-ethylene glycol solution the thickness of oxide film growth on silicon is proportional to anodization forming voltage and the growth rate of oxide is 4-5 Å/V. Our result indicates almost parabolic increase of luminescence current against forming voltage, which agrees with the data by Waring *et al.* (3). But our experiment was carried out below their breakdown voltage at which the "spark" discharge appeared. The efficiency of forming silicon dioxide is reported to be about 2% (4).

When the cell voltage was reduced at a rate of 1 V/sec from a large positive value, the cell current and the luminescent signal that were obtained as a function of the cell voltage are labeled II in Fig. 1 and 2.

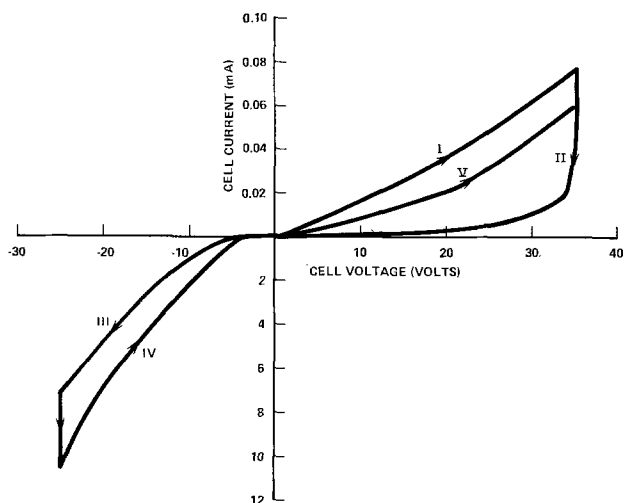


Fig. 1. Cell current vs. cell voltage

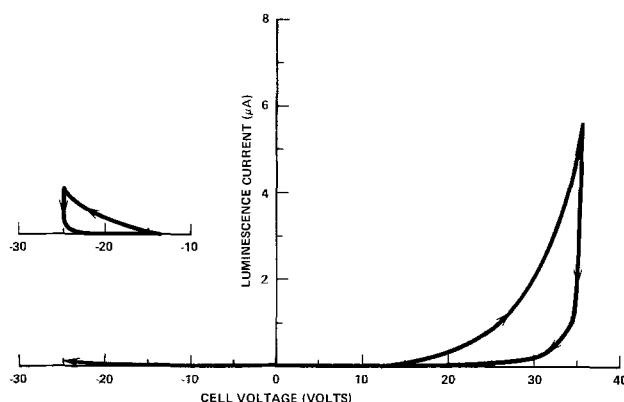


Fig. 2. Luminescence current vs. cell voltage

Next, the polarity of the applied voltage was reversed. When the applied voltage was increased in the negative direction up to -25V at a rate of 1 V/sec, the cell current labeled III in Fig. 1 was obtained. A weak luminescent signal was also obtained beyond -15V as shown by curve in Fig. 2. It was also observed that the cell current characteristics (curve III in Fig. 1) approached another curve (IV in Fig. 1) if at each value of the reverse voltage, sufficiently long time was allowed. The applied voltage was frozen at -25V by stopping the sweep, and if was found that the cell current increased reaching a saturation value. At the same time, the luminescent signal decreased to zero. Then the applied voltage was swept to zero volt at the same rate as before and the cell current dropped to zero as indicated by curve IV in Fig. 1. During this sweepback, no luminescence was observed.

The voltage sweep was next applied in the positive direction (anodization) and the measured cell current followed the curve I in Fig. 1. However, if sufficient time was not allowed for the previous cathodization process at -25V, the cell current during the anodization process will follow a curve intermediate between curves I and II in Fig. 1. This shows that when sufficient time is allowed at -25V during the cathodization, the oxide film on the silicon electrode is completely removed. Since the luminescent signal during cathodization goes to zero when the cell current saturates (corresponding to complete removal of the oxide film), it appears that the weak luminescence occurs only during the process of reduction or dissolution of the oxide film in cathodization. After repeated anodization and cathodization, the silicon surface was observed to be nonuniform and volcanic.

In order to find out more about the cathodization luminescence, an a-c bias voltage was superimposed on the d-c bias as shown in Fig. 3. The amplitude of the a-c bias at a frequency of 70 Hz was varied while the

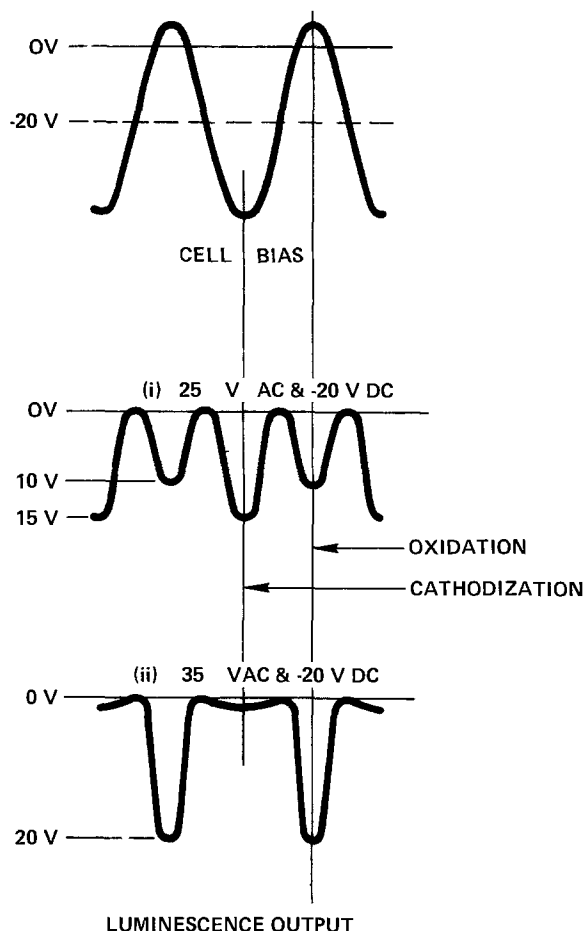


Fig. 3. A-C characteristics of luminescence

d-c bias was kept at  $-20\text{V}$ . The anodization occurs only during that portion of the a-c bias voltage cycle during which the net voltage is positive. On the other hand, cathodization (i.e., reduction or dissolution) occurs during the rest of the a-c bias voltage cycle during which the net voltage is negative. The output of luminescence on oscilloscope as detected by the photomultiplier is also shown in Fig. 3 (i) and (ii). The peak of the luminescence output at the anodization process corresponding to the bias which is above zero was  $10\text{V}$  while that at cathodization was  $15\text{V}$ . It was observed that whenever the luminescence output during the anodization process was smaller than that during the cathodization process, the luminescence output on the oscilloscope was very unstable. When there was a thin oxide film, the luminescence output during cathodization was higher than that during anodization. However, as time went on, and the oxide layer was removed in the cathodization process, the luminescence output of both processes became close to each other. When the a-c bias voltage was increased to  $35\text{V}$  as shown in Fig. 3(ii), the luminescence output of the anodization process increased while that of the cathodization process decreased. When the a-c bias voltage was increased further, the luminescence output of the anodization process became completely dominant.

When the bias voltage in excursion (I) in Fig. 2 is increased up to  $70\text{V}$  or higher, the thick oxide layer is formed. After this process, although reverse cell voltage was increased to  $25\text{V}$  and was maintained at the voltage, cell current did not increase and luminescence was not observed. This indicates that the luminescence during cathodization is observable only when the oxide film is thin and the cathodization of silicon results in removal of the oxide film. The reaction in the cathodization process is suggested to be a reduction of the silicon dioxide layer to silicon by the cations or a dissolving of silicon dioxide to give a compound such as  $\text{K}_2\text{SiO}_3$ , etc.

In order to separate more clearly cathodization luminescence from anodization luminescence, a square wave negative voltage was superimposed on the d-c positive bias as shown in Fig. 4(i). In the figure is shown a value of  $40\text{V}$  for the d-c positive bias with a negative pulse of amplitude  $80\text{V}$ . In the luminescence output corresponding to the cell bias, the cathodization luminescence can be seen as a spike while anodization luminescence is almost negligible compared to cathodization luminescence. Thus cathodization luminescence can easily be separated from anodization luminescence, which is a very useful technique to measure luminescence spectra. The spectral response of the luminescence can be determined by using phase sensitive detector which gives a high  $S/N$  ratio. The luminescence intensity can easily be kept constant while spectrum measurement is carried on. For comparison the anodization luminescence is shown in Fig. 4(ii) corresponding to the bias condition of d-c bias  $-15\text{V}$  and positive pulse height  $80\text{V}$ .

Once water is added into the  $0.04\text{N}$   $\text{KNO}_3$ -ethylene glycol or in  $0.04\text{N}$   $\text{KNO}_3$ - $\text{H}_2\text{O}$ , the luminescence of cathodization was observed without any cycle of anodization. Also, the luminescence intensity for cathodization is much higher for these systems than that for  $0.04\text{N}$   $\text{KNO}_3$ -ethylene glycol. The instability such as observed in the process of removing the oxide in  $\text{KNO}_3$ -ethylene glycol was not observed. Thus the luminescence for the system with water molecules is understood to be different from the previous system. It may be suggested that this luminescence of cathod-

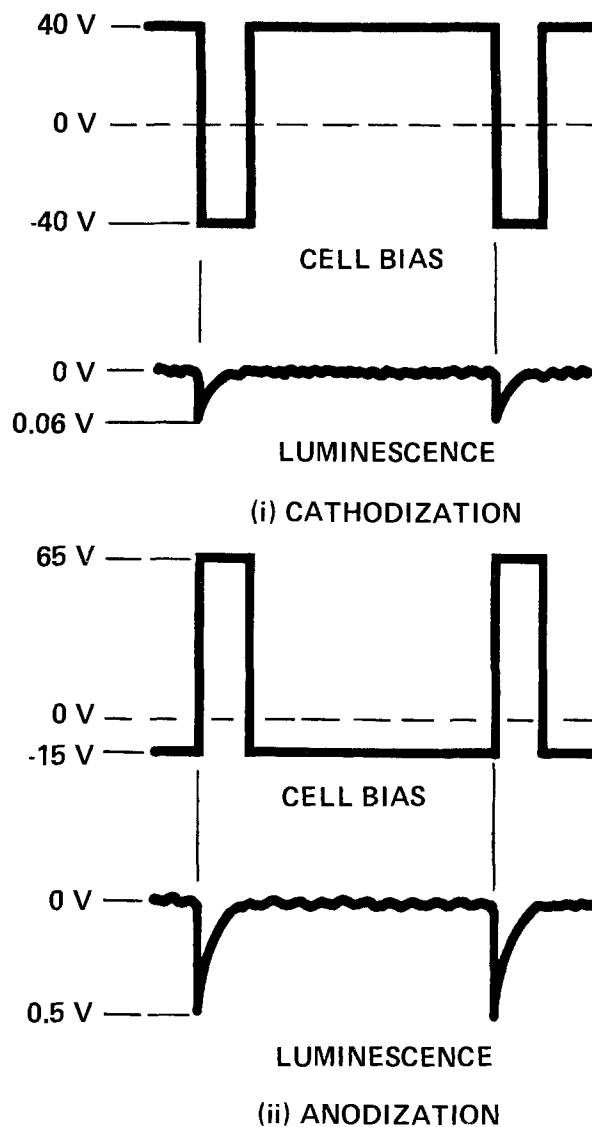


Fig. 4. (i) Cathodization luminescence in  $\text{KNO}_3(0.04\text{N})$ -ethylene glycol. Pulse cycle;  $70\text{ Hz}$  and pulse width,  $1\text{ msec}$  (ii) Anodization luminescence in  $\text{KNO}_3(0.04\text{N})$ -ethylene glycol.

ization with water molecules is associated with the reaction of  $\text{Si}$  and  $\text{H}^+$  or  $\text{H}_3\text{O}^+$ .

Also luminescence for cathodization of such metals as  $\text{Al}$ ,  $\text{Zn}$ ,  $\text{Cu}$ , etc. was observed.

In a subsequent paper, the spectra, resulting from anodization and cathodization luminescence in different solutions, and their interpretation will be given.

Manuscript received Sept. 2, 1975.

Any discussion of this paper will appear in a Discussion Section to be published in the December 1976 JOURNAL. All discussions for the December 1976 Discussion Section should be submitted by Aug. 1, 1976.

#### REFERENCES

1. "The Encyclopedia Britannica," **XIV**, 484 (1963).
2. Allen Gee, *This Journal*, **107**, 787 (1960).
3. W. Warning and E. A. Benjamin, *ibid.*, **111**, 1256 (1965).
4. E. F. Duffek, *et al.*, *Electrochem. Technol.*, **3**, 75 (1965).



# Influence of Precipitating Conditions on the Cathodoluminescence of Zinc Sulfide:Silver Phosphors

R. A. Brown<sup>\*,1</sup> and F. J. Hinnenkamp

RCA Electronic Components, Lancaster, Pennsylvania 17604

## ABSTRACT

A study has been carried out on the properties of zinc sulfide obtained by precipitation from aqueous zinc sulfate solution with gaseous hydrogen sulfide. The influence of three factors, namely H<sub>2</sub>S flow, temperature, and initial concentration of the zinc solution, on (i) the rate of precipitation of zinc sulfide, and (ii) the cathodoluminescent efficiencies of the resultant ZnS:0.015% Ag phosphors has been investigated. Experimental results were interpreted by an empirical method, using a correlation and regression analysis performed by computer procedures. This approach has established quantitative relationships on the behavior of both the rate of formation of ZnS and the phosphor efficiency as changes occur in the three variables which influence the conditions of precipitation.

A study on the preparation and fundamental properties of zinc sulfide is of considerable importance in the technology of the manufacture of luminescent materials. Although there are numerous reports in the literature (1-5) concerning the influence of firing conditions and composition on the properties of zinc sulfide phosphors, there appears to be comparatively little published work on the precipitation of this compound, especially from the viewpoint of the effect of precipitating conditions on the characteristics of the resultant phosphors.

For many years the precipitation of zinc sulfide from acidic, or slightly acidic, solutions of a soluble zinc salt has been used extensively for the analytical separation and determination of zinc (6-8). Hydrogen sulfide (9, 10) appears to be the usual precipitant, although more recently analysis from homogeneous solution by the acid hydrolysis of thioacetamide (11, 12) has been reported. Ortmann and Piwonka (13, 14), Lendvay and coauthors (15), and Brown (16) appear to be among the few investigators to have studied the preparatory conditions of ZnS with the object of obtaining luminescent materials.

Ortmann and Piwonka (13, 14) demonstrated that a slow reaction with rapid stirring at an H<sub>2</sub>S pressure of 1.5 atm yielded crystallites up to 30  $\mu$ m in size. In addition, precipitation at reduced hydrogen sulfide pressures was studied, and produced good phosphors. These investigations (13, 14) showed that the luminescent properties of the materials were dependent largely on the precipitation in the initial stages of the reaction. In all cases, ZnS prepared in strongly acid solution separated in the sphalerite form, the particles being well defined and sufficiently crystalline to give an x-radiogram identical with that obtained from zinc sulfide luminophors recrystallized at 900°C. Lendvay *et al.* (15) prepared ZnS crystals 100-200  $\mu$ m in size by slowly interacting hydrogen sulfide with an acidic solution of a zinc salt. What was more interesting, perhaps, was that phosphors could be obtained directly from solution under ambient conditions without subsequent activation and firing at elevated temperatures. Studies on the particle size and morphology of zinc sulfide precipitates have been reported by Brown (16). This worker demonstrated that preparation of ZnS in strongly acid solution gave irregularly shaped aggregates of the order of 1-5  $\mu$ m, and that the dimensions of these agglomerates influenced the particle size of the final phosphor.

\* Electrochemical Society Active Member.

<sup>1</sup> Present address: Department of Chemistry, The Polytechnic of North London, Holloway, London N7 8DB, England.

Key words: ZnS:Ag phosphors, correlation and regression analysis, Weibull distribution.

Two principal methods have been used for the large-scale manufacture of luminescence-grade zinc sulfide, and these lead to somewhat different products. In the so-called "alkali" process (17), a purified solution of ZnCl<sub>2</sub> is treated with ammonium hydroxide solution until the initial zinc hydroxide precipitate redissolves. Subsequently, ZnS is formed by the addition of hydrogen sulfide or ammonium sulfide. Under these conditions, some hydrolysis of the zinc salt may occur, and this in turn gives rise to oxygen band fluorescence (18) in the ultimate phosphor. Alternatively, the "acid" process (17, 19) may be used. In this method ZnS is synthesized by the interaction of a solution of a zinc salt with hydrogen sulfide in acidic media. This latter procedure was employed in the present study; zinc sulfide precipitates were obtained by the straightforward addition of gaseous hydrogen sulfide to aqueous zinc sulfate solution.

The objective of this work was to carry out a laboratory-scale investigation on the influence of various factors, such as rate and duration of hydrogen sulfide flow; temperature; initial concentration of the zinc solution; on the precipitation of zinc sulfide, from the viewpoint of determining what effect, if any, these variables had on the cathodoluminescent efficiencies of the resultant phosphors. With this object in mind, an attempt was made to determine the important factors affecting (i) the rate of precipitation, and (ii) the peak efficiencies of the various zinc sulfide phosphors under cathodoluminescent excitation. Phosphor preparations were carried out with ZnS:0.015% Ag, 2% sodium chloride as flux, and 1% sulfur as the starting material. Note that these compositions are weight per cent (w/o) values. The results obtained were interpreted with the aid of a regression and correlation analysis carried out by means of an RCA 301 computer program.

## Experimental

*Precipitation of zinc sulfide.*—A detailed description of the starting materials and experimental procedures employed in the preparation of zinc sulfide precipitates has been given previously (16). For the sake of completeness, a brief account of the method used is given below.

The apparatus consisted of a 3 liter glass precipitation flask equipped with necks to provide ports for the gas inlet, gas outlet, and stirrer. A single blade glass paddle was used to agitate the solution; temperature was controlled to within  $\pm 0.5^\circ\text{C}$ . In a typical preparation, 2 liters of 1M zinc sulfate solution were placed in the precipitating vessel and stirred by an electrically driven glass paddle. Hydrogen sulfide at a flow

rate of 0.82 liter/min was passed into the solution through a gas dispersion tube for a period of 3 hr, the flask and its contents being maintained at 25°C. During a precipitation, samples were removed at regular intervals of time, filtered, and the filtrates analyzed for zinc and hydrogen ion contents. Zinc was determined colorimetrically by means of dithizone, using a method which was essentially that of Snell and Snell (20). For the determination of the free acid content, aliquots were titrated against standard sodium carbonate solutions (21) utilizing either methyl orange as indicator, or a potentiometric method to determine the end point. After being left for approximately 18 hr to attain equilibrium, the white precipitate of zinc sulfide was filtered in a Buchner funnel, washed with deionized water until the washings were free from sulfate ions, and dried at 100°C for 6 hr.

Initially, the speed of stirring of the reacting mixture was varied from 50 to 350 rpm. At speeds up to 200 rpm, there was a direct relationship between stirring rate and amount of precipitation. The reaction processes appeared to be independent of agitation for stirring speeds greater than 200 rpm. Consequently, throughout this work a speed of approximately 300 rpm was employed.

Precipitations were carried out with zinc sulfate concentrations from 0.25 to 2.0M, using hydrogen sulfide flows between 0.082 and 5.75 liter/min, and with temperatures in the range 0°-70°C.

*Preparation and measurement of phosphors.*—In order to obtain reproducible results, phosphor samples were prepared by a dry blending process, following the usual procedures. The over-all composition of the starting material was ZnS:0.015% Ag, 2% sodium chloride, with 1% sulfur. A series of experiments to determine the temperature and duration of firing showed that optimum luminescent efficiencies could be attained on heating at 800°C for 1 hr. A brief description of a typical firing cycle is given below.

Test samples of approximately 10g of ZnS:0.015% Ag, 2% NaCl, with 1% sulfur were heated in 10 cm<sup>3</sup> covered "Vitreosil" crucibles for 1 hr at 800°C. Each heating operation involved the firing of six separate specimens. After removal of excess flux by washing with deionized water, the products were dried at 100°C.

Cathodo-luminescent efficiencies and emission spectra were determined with a defocused electron beam having a current density of 1.5  $\mu$ A/cm<sup>2</sup> and an accelerating potential of 8000V, following the procedure of Hardy (22). Peak efficiencies and spectral distribution of energy were measured by means of a recording, grating-type spectroradiometer. An eye-corrected, Weston selenium barrier layer photocell was used for the measurement of visual efficiencies.

## Results

The influence of initial zinc sulfate concentration on the rate of precipitation of zinc sulfide is demonstrated in Fig. 1. In order to make the comparison more straightforward, the results are plotted in the form of w/o zinc remaining in solution as a function of time,  $t$ . Hydrogen sulfide flow was maintained at 0.82 liter/min, temperature at 25°C, and the ZnSO<sub>4</sub> level varied between 0.25 and 2.0M.

A typical set of curves showing the influence of hydrogen sulfide flow on 1M ZnSO<sub>4</sub> solutions at 25°C is presented in Fig. 2, again in the form of w/o zinc vs. time.

In general, a plot of logarithm of the zinc concentration,  $\log [Zn^{2+}]$ , as a function of precipitation time showed a linear dependence over all of the preparative conditions employed in this present study. Thus, the zinc sulfate-hydrogen sulfide reaction follows pseudo-first order kinetics with respect to the zinc ion. At temperatures in the region of 0°C, there was initially a fast precipitation accounting for approximately 40% of the product, followed immediately by a slower process. Both stages of the reaction followed this same

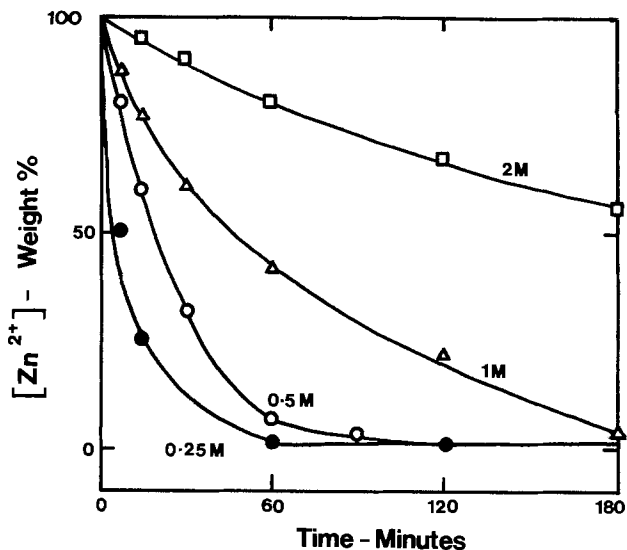


Fig. 1. Influence of initial ZnSO<sub>4</sub> concentration on precipitation of ZnS. 0.82 liter/min H<sub>2</sub>S at 25°C.

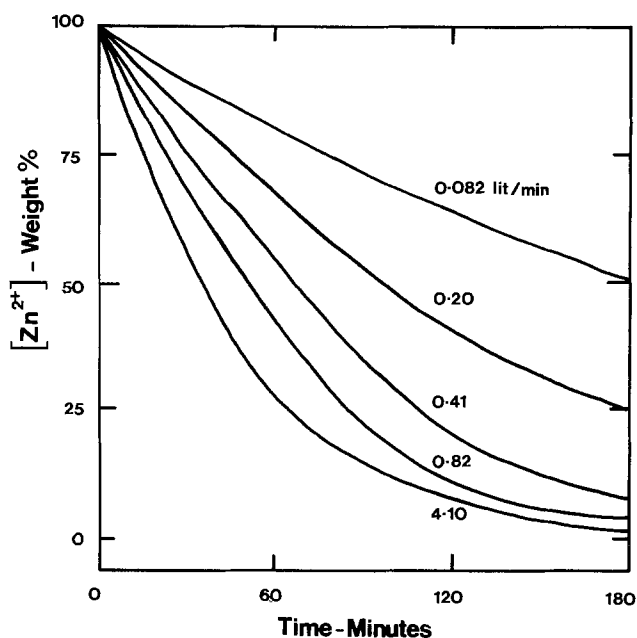


Fig. 2. Influence of H<sub>2</sub>S flow (liter/min) on precipitation of ZnS. 1M ZnSO<sub>4</sub> at 25°C.

straight-line, semilogarithmic behavior. These findings are demonstrated in Fig. 3, which shows the influence of various factors on the relationship between  $\log [Zn^{2+}]$  and precipitation time.

Figure 4 is a typical set of curves in which  $\log [Zn^{2+}]$  is plotted vs.  $t$  for experiments carried out in 1M zinc sulfate solution at 10°-40°C, using a hydrogen sulfide flow of 0.82 liter/min. These data confirm that a linear relationship does, in fact, exist. Measurement of the slopes of these semilogarithmic plots provided the specific rate constants,  $k$ , and these values were used to express the rate of precipitation of ZnS. In practice,  $k$  was calculated by the least squares method, utilizing the computer program which is outlined below.

A plot of  $\log [H^+]$  as a function of  $\log$  (time) for temperatures of 25° and 0°C, in the case of 1M ZnSO<sub>4</sub> at 0.82 liter/min H<sub>2</sub>S, is given in Fig. 5. At 25°C there is a straight-line dependence with a slope of 0.94, whereas the 0°C plot shows a departure from linear behavior.

A summary of the experimental results obtained on the preparation of zinc sulfide precipitates, together with peak efficiencies under cathodo-excitation of the final ZnS:0.015% Ag phosphors, is presented in Table

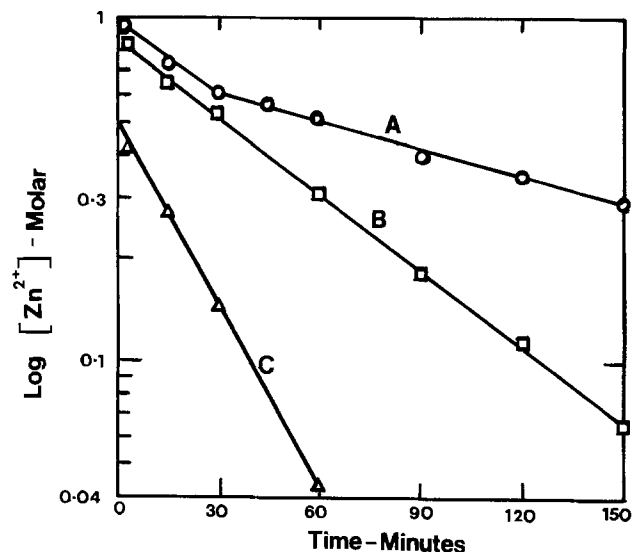


Fig. 3. Log [Zn<sup>2+</sup>] vs. time for ZnS precipitations: (A) 1M ZnSO<sub>4</sub> at 0°C and 0.82 liter/min H<sub>2</sub>S; (B) 1M ZnSO<sub>4</sub> at 25°C and 4.1 liter/min H<sub>2</sub>S; (C) 0.5M ZnSO<sub>4</sub> at 70°C and 0.82 liter/min H<sub>2</sub>S.

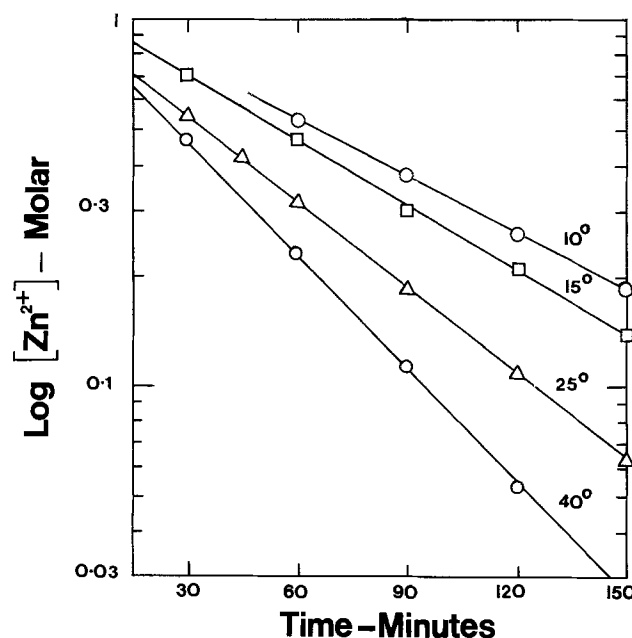


Fig. 4. Log [Zn<sup>2+</sup>] vs. time for ZnS precipitations at 10°-40°C. 1M ZnSO<sub>4</sub> at 0.82 liter/min H<sub>2</sub>S.

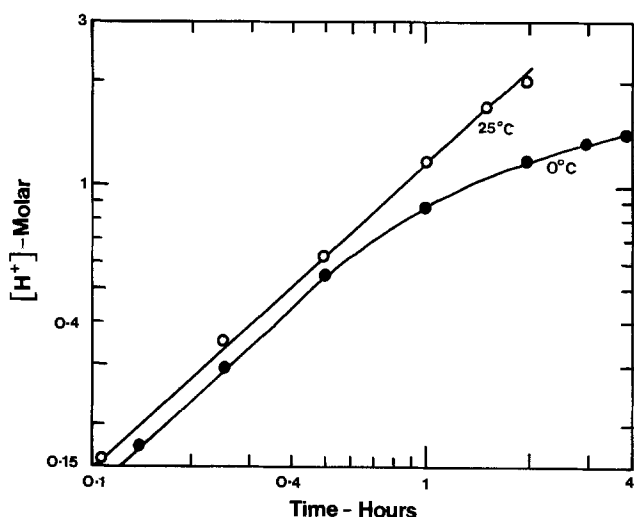


Fig. 5. Relationship between log [H<sup>+</sup>] and log (time) for 1M ZnSO<sub>4</sub> at 0.82 liter/min H<sub>2</sub>S.

I. Table II illustrates the over-all reproducibility of the precipitation stage and phosphor preparation and measurement.

**Discussion**

For convenience, the results obtained are discussed in terms of (i) rate of precipitation, and (ii) cathodoluminescent efficiencies.

(i) *Rate of precipitation.*—Since it was desirable to relate the rate of precipitation of ZnS with the preparative conditions, each of the 36 experimental tests was submitted to analysis by the RCA 301 correlation and regression computer program in a multiple and polynomial regression study. The specific rate constant, *k*, was taken as the dependent variable and various combinations of temperature, duration of precipitation, initial zinc sulfate concentration, and hydrogen sulfide flow as the independent variables. Generally, the mathematical model employed was of the form

$$Y = b_0 + b_1X_1 + b_2X_2 + b_3X_3 + b_4X_4 + b_5X_1^2 + b_6X_2^2 + b_7X_3^2 + b_8X_4^2 + b_9X_1X_2 + b_{10}X_1X_3 + b_{11}X_1X_4 + b_{12}X_2X_3 + b_{13}X_2X_4 + b_{14}X_3X_4 \quad [1]$$

where *Y* is the dependent variable, *X* the independent variable, and *b* is an estimate of the unknown population parameter. In addition to the above terms, the

Table I. Summary of experimental results

Experiment No.	Temperature (°C)	[ZnSO <sub>4</sub> ] (M)	Hydrogen sulfide Flow rate (liter/min)	Duration (hr)	Rate constant ( <i>k</i> × 10 <sup>2</sup> )	Peak efficiency* (P <sub>E</sub> )
1	0	1.0	0.41	3	-0.7183	108
2	0	1.0	0.82	3	-0.7090	108
3	0	1.0	4.10	3	-0.9474	104
4	25	1.0	0.41	3	-1.4391	107
5	25	1.0	0.82	3	-1.6393	104
6	25	1.0	4.10	3	-1.1605	103
7	70	1.0	0.41	3	-1.5366	98
8	70	1.0	0.82	3	-1.5473	103
9	70	1.0	4.10	3	-2.0395	100
10	25	1.0	0.20	7.5	-1.0116	112
11	25	1.0	0.082	8	-0.6518	109
12	25	0.25	0.82	3	-12.2488	66
13	25	0.5	0.82	3	-2.5881	92
14	25	0.5	0.41	3	-2.6658	104
15	25	0.5	0.20	3	-2.6532	114
16	25	0.5	0.082	4	-1.3968	112
17	0	0.5	0.82	3	-1.8283	103
18	70	0.5	0.82	3	-4.0638	84
19	25	2.0	0.82	12	-0.4272	112
20	25	2.0	4.10	12	-0.4622	108
21	0	2.0	0.82	12	-0.1559	118
22	70	2.0	0.82	12	-0.5239	91
23	50	1.5	0.50	6	-1.0163	112
24	10	1.5	0.50	9	-0.4049	108
25	10	0.25	0.50	3	-4.7096	105
26	50	0.25	5.75	1	-29.9573	71
27	10	0.25	5.75	1	-10.4010	80
28	50	0.25	0.5	3	-8.9225	105
29	10	1.5	5.75	6	-0.5380	108
30	50	1.5	5.75	6	-1.3246	108
31	5	1.0	0.82	3	-0.8291	112
32	10	1.0	0.82	3	-1.109	114
33	15	1.0	0.82	3	-1.253	114
34	35	1.0	0.82	3	-2.256	104
35	40	1.0	0.82	3	-2.277	97
36	55	1.0	0.82	3	-1.4575	108

\* Measured against a standard phosphor, JEDEC designation, P22 Sulfide; RCA Phosphor No. 33-Z-265, taken as 100 used as a reference.

Table II. Over-all reproducibility of experimental methods

Runs	Concentration of ZnSO <sub>4</sub> (M)	H <sub>2</sub> S flow (liter/min)	Duration of H <sub>2</sub> S (hr)	Temperature (°C)	Peak efficiency (P <sub>E</sub> )
Runs A-C	1	0.82	3	25	105
	1	0.82	3	25	105
	1	0.82	3	25	104
Runs D-F	1	0.20	7.5	25	112
	1	0.20	7.5	25	112
	1	0.20	7.5	25	112

variables used were expressed as logarithmic, reciprocal, and ratio functions. This analysis showed that the experimental results obtained for the reaction rate could be represented best by the expression

$$\log_{10}k = -2.597 + 0.00575T + 0.000174FT - 1.433 |Zn_0| + 0.303 |Zn_0|^2 \quad [2]$$

where  $k$  = reaction rate constant ( $\text{min}^{-1}$ );  $T$  = temperature ( $^{\circ}\text{K}$ );  $F$  = hydrogen sulfide flow (liter/min); and  $|Zn_0|$  = initial concentration of the zinc sulfate solution (M).

A measure of the fit of a plot to the data it represents is given by the correlation coefficient squared,  $R^2$  (23), which is often expressed as a per cent value. This parameter is defined as the amount of variation of the dependent variable  $Y$ , which can be associated with variations in  $X$ , the independent variable. A perfect fit would give  $R^2 = 100\%$ , whereas a complete nonfit would have  $R^2 = 0\%$ . For Eq. [2], a value of  $R^2 = 91\%$  was calculated. This result indicates that the reaction rate data are represented very well by the given expression.

The type of curve obtained on plotting the three variables, initial zinc concentration, gas flow, and temperature, in accordance with Eq. [2] is given in Fig. 6. This curve is in a hyperbolic form. Note that for purposes of convenience the surface represented in Fig. 6 corresponds to a specific rate constant of  $\log k = -2.0 \times 10^{-2}$ . The advantage of such a plot is that it presents in a relatively straightforward manner a quantitative treatment of the behavior of the precipitation rate as changes occur in the three parameters which influence the preparatory conditions. By setting the first derivative with respect to  $|Zn_0|$  equal to zero, an inflection point is obtained at a concentration level of 2.36M. Since this point is a minimum in the curve, this observation suggests that the slowest reaction rate should be attained with an initial concentration of 2.36M zinc sulfate. Increase in either the temperature, or the hydrogen sulfide flow, or in both of these parameters will give faster rates of reaction.

(ii) *Cathodoluminescent efficiency results.*—A further part of this study was an attempt to relate peak efficiencies of the phosphors obtained from the various precipitates to the conditions of precipitation. These experimental results were less straightforward to analyze than the reaction rate data. A regression and correlation analysis similar to that already described was

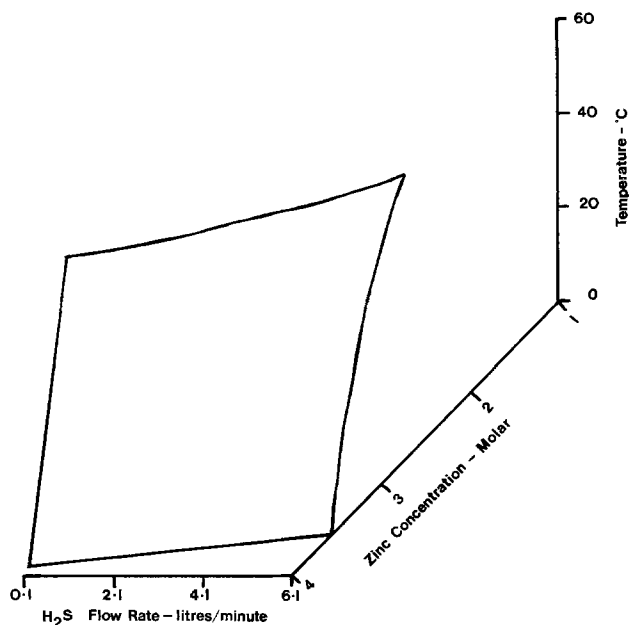


Fig. 6. Reaction rate ( $\log k$ ) as a function of precipitation variables. Surface represents  $\log k = -2.0 \times 10^{-2}$ .

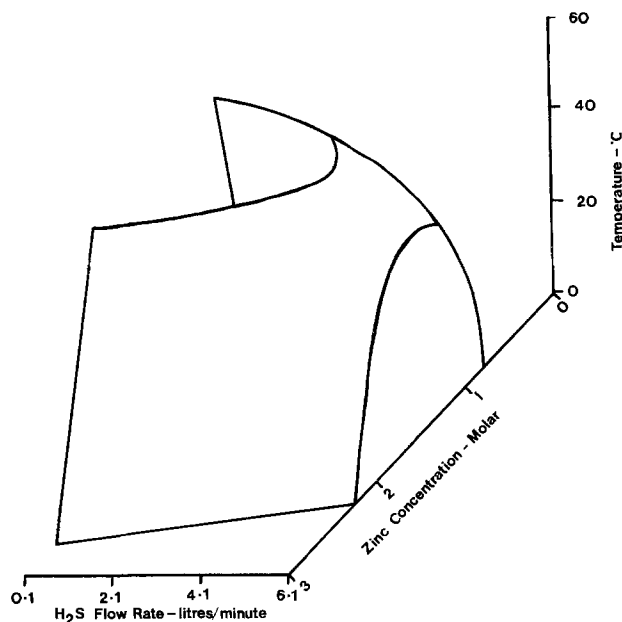


Fig. 7. Phosphor peak efficiency ( $P_E$ ) as a function of precipitation variables. Surface represents  $P_E = 100$ .

carried out for the phosphor brightness results obtained in the 36 experimental tests. In this case, peak efficiency of the phosphor under cathodo-excitation was the dependent variable, and various combinations of reaction temperature, duration and rate of hydrogen sulfide flow, and initial zinc concentration were the independent parameters.

This treatment showed that the experimental data obtained for phosphor efficiency under cathodoluminescence can be described best by the expression

$$P_E = 107 + 46.2 |Zn_0| - 15.2 |Zn_0|^2 - 1.64F - 0.00031T^2 \quad [3]$$

where  $P_E$  is the relative luminescent peak efficiency of a specimen, measured against a standard phosphor<sup>2</sup> sample taken as 100, and the other symbols have the meanings given above. For Eq. [3], a value of  $R^2 = 65\%$  was calculated. This result indicates that the above relationship describes the experimental data reasonably well. The form of curve obtained on plotting the three variables, initial zinc level,  $H_2S$  flow, and temperature in accord with Eq. [3] is illustrated in Fig. 7. The curve describes an elliptical paraboloid. Note that the surface represented in this figure corresponds to a peak efficiency of 100.

On the basis of Eq. [3] and Fig. 7 the following can be deduced:

(a) A decrease in temperature of precipitation and a lower hydrogen sulfide flow both lead to a rise in peak efficiency of the resultant phosphor.

(b) The inflection point occurs at a zinc concentration of 1.52M. This concentration region corresponds to the initial zinc sulfate level which provides the optimum phosphor brightness, on the basis of the experiments actually carried out.

(c) It is interesting to note that the conditions of precipitation which give the fastest rate of formation of  $ZnS$  are those which result in poor phosphor efficiencies. Conversely, those preparatory conditions which give the highest peak efficiencies involve very slow precipitations. This latter finding appears to be in accord with an observation made by Ortmann and Piwonka (13, 14).

It has already been pointed out that this work was undertaken with the object of providing quantitative relationships between the principal factors affecting the rate of precipitation of zinc sulfide, and the cathodoluminescent efficiencies of the final phosphor. The

<sup>2</sup> JEDEC designation, P22 Sulfide; RCA Phosphor No. 33-Z-265.

empirical relationships derived so far, as expressed in Eq. [2] or [3], have gone a long way toward achieving this objective in that these do describe fairly well the behavior of the precipitation rate and phosphor brightness.

It might be worthwhile illustrating the usefulness of this approach by considering a typical application. Rapid precipitations are desirable from an economic viewpoint, since these give maximum utilization of the precipitating vessels. This work has demonstrated that fast reaction rates require elevated temperatures and high  $H_2S$  flows. In addition, the initial zinc sulfate level should be low, for example 0.5M, or high, namely  $>2.36M$ , since a 2.36M solution was shown to provide the slowest rate of reaction. To take one further example, it is well known that optimum phosphor efficiency is a prerequisite for many applications involving luminescent materials so as to obtain desirable product quality. The preparatory conditions required for optimum peak efficiencies are: low precipitation temperatures, a diminished gas flow, and an initial zinc sulfate concentration of 1.52M.

A logical development of this type of approach would be to combine the information obtained from Eq. [2] and [3]. For example, it should be possible to choose precipitating conditions which would give the highest attainable level of phosphor brightness consistent with a practicable rate of reaction. Or, alternatively, to fix conditions for the synthesis of ZnS precipitates which would provide the fastest rates of precipitation consistent with reasonably good luminescent efficiency. Table III illustrates results of some typical calculations involving the combination of Eq. [2] and [3]. These data represent some of the points of intersection of the curves in Fig. 6 and 7. Consequently, the data correspond to a peak efficiency in the region of 100, and a reaction rate of the order of  $\log k = -2.0 \times 10^{-2}$ . Evidently, a fairly wide range of precipitating conditions is available, even within these limitations.

It was pointed out above that the data on phosphor efficiency did not give as good a correlation as those on reaction rate. A possible explanation for this behavior would be that the chosen variables were insufficient to describe completely the phosphor brightness results. For example, it is not unlikely that factors such as the impurities occluded on a precipitate (24), or the particle size and morphology of the zinc sulfide powders (16), may be important in determining the final phosphor brightness. An attempt was made to allow for the sulfate ion content of the precipitates, but this did not improve the correlation coefficient parameter for phosphor efficiency. No direct attempt was made to incorporate the size and habit of the zinc sulfide crystallites in the analysis, although the work of Brown (16) suggests that the precipitation variables chosen should reflect on these parameters. An alternative possibility is that the reproducibility of the precipitation, washing and drying stages, together with that of the phosphor preparation and measurement, may have varied. The results presented in Table II appear to indicate fairly good reproducibility.

As a consequence of this discrepancy, an additional method of analyzing the phosphor brightness results was sought. One procedure employed frequently in the analysis of the statistical distribution of empirical data is that due to Weibull (25). This method is reviewed

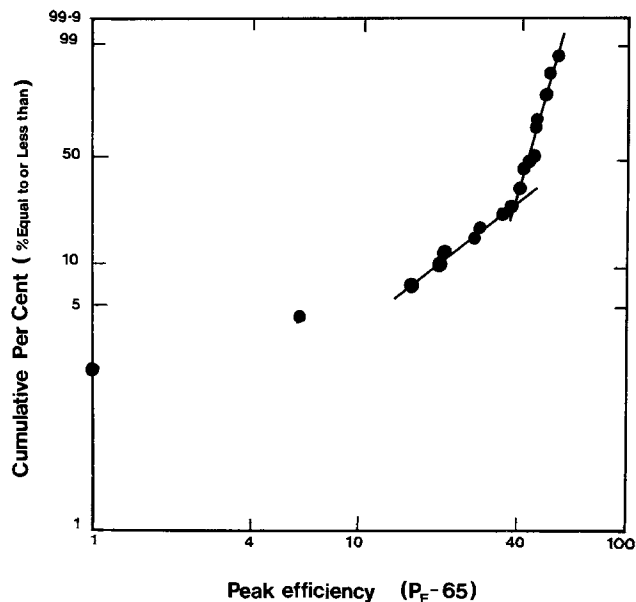


Fig. 8. Weibull distribution plot for phosphor efficiency data. Cumulative per cent vs. peak efficiency ( $P_E - 65$ ).

briefly in the Appendix. Such a technique has proved useful in a wide variety of applications, as pointed out by Berrettoni (26). A Weibull plot of the phosphor efficiency results is given as Fig. 8. The curve shows the relationship between cumulative per cent (i.e., per cent samples less than a given peak efficiency) as the ordinate, and peak efficiency ( $P_E - 65$ ) as the abscissa. Evidently, the slope of the line changes at a peak efficiency of 100. This result indicates the occurrence of a mixed statistical distribution. Thus, samples with a peak efficiency value greater than 100 have a different distribution than those with 100 or less. The occurrence of two distributions suggests that there are probably also two different sets of parameters, or parameter levels, which best describe the two areas. Accordingly, the observed brightness measurements were submitted for correlation and regression analysis in two parts, namely  $P_E \leq 100$  and  $P_E > 100$ . The best-fitting curve, which had an  $R^2$  value of 78%, was obtained for peak efficiencies of 100 or less. This relationship was described by the equation

$$P_E = 62.5 + 58.2 |Zn_0| - 22.1 |Zn_0|^2 \quad [4]$$

This expression indicates that for phosphor efficiencies not greater than 100, the most important factor in the precipitation process is the concentration of the initial zinc sulfate solution.

In summary, this work has shown that numerical relationships can be established between the preparatory conditions used for the zinc sulfide precipitates (especially initial concentration of zinc solution, temperature, and hydrogen sulfide flow), and both the rate of precipitation and the cathodoluminescent efficiency of the final phosphors. As a consequence, precipitating conditions can be specified which would either (i) give very fast reaction rates, such as are economically desirable for maximum utilization of precipitation vessels, or (ii) provide optimum phosphor brightness, in order to improve product quality.

It should be pointed out that these studies have involved a ZnS:Ag phosphor prepared in a particular manner, and with sodium chloride as flux. In addition, only the peak efficiency has been chosen as the phosphor parameter. In fact, many other properties of a zinc sulfide luminophor are important in any given application. For example, utilization in a color kinescope would require such additional features as a given spectral distribution of emitted light, particular size and distribution of the particles of phosphor, and stability during screening operations. It would be of interest to ascertain whether the general method de-

Table III. Relationship between phosphor efficiency and reaction rate

Peak efficiency ( $P_E$ )	Reaction rate ( $\log k$ )	Zinc concentration (M)	Temperature ( $^{\circ}C$ )	$H_2S$ flow (liter/min)
94	$-1.4 \times 10^{-2}$	0.5	0	5.6
100	$-2.0 \times 10^{-2}$	1.7	34	7.5
106	$-1.8 \times 10^{-2}$	0.7	0	1.6
106	$-2.0 \times 10^{-2}$	1.3	13	6.2
112	$-2.4 \times 10^{-2}$	1.7	0	4.0

veloped here is applicable to a variety of luminescent materials, and whether it could be employed to describe other parameters of phosphor systems.

### Acknowledgments

The authors express their gratitude to W. G. Rudy for the measurement of phosphor efficiencies, to Mrs. E. D. Martin, who performed the analyses, and to E. W. Bomgardner for assistance with the preparatory work. For helpful discussions and suggestions, especial thanks are due to Dr. A. L. Smith.

Manuscript submitted Oct. 28, 1975; revised manuscript received Jan. 16, 1976.

Any discussion of this paper will appear in a Discussion Section to be published in the December 1976 JOURNAL. All discussions for the December 1976 Discussion Section should be submitted by Aug. 1, 1976.

### APPENDIX

#### The Weibull Distribution

The cumulative distribution function  $|F(x)|$  of the Weibull distribution is defined as

$$F(x) = 1 - \exp \left| - \frac{(x - \gamma)^\beta}{\alpha} \right|$$

where  $\gamma$  = a location parameter;  $\beta$  = shape parameter (Weibull slope); and  $\alpha$  = scale parameter.

Since the value of  $\gamma$  only determines the position of the curve with respect to the abscissa, it is set to zero for the present purpose. On taking logarithms twice we obtain

$$\ln |1 - F(x)| = - (x/\alpha)^\beta$$

$$\ln \ln |1 - F(x)| = - \beta (\ln x - \ln \alpha)$$

$$\text{or, } \ln \ln |1/\{1 - F(x)\}| = \beta \ln x - \beta \ln \alpha$$

Thus, on plotting  $\ln \ln |1/\{1 - F(x)\}|$  as a function of  $\ln x$ , a straight line of slope  $\beta$  and intercept  $-\beta \ln \alpha$  is obtained. This is the Weibull plot.

For exponential distribution, a value of  $\beta \simeq 1$  is obtained; in the case of normal distribution  $\beta \simeq 3.5$ .

### REFERENCES

1. A. L. Smith, *This Journal*, **93**, 324 (1948).
2. Y. Otomo, *Bull. Chem. Soc. Japan*, **32**, 804 (1959).

3. W. van Gool, *Philips Res. Rept. Suppl.*, **3**, 6 (1961).
4. S. Shionoya, in "Luminescence of Inorganic Solids," P. Goldberg, Editor, pp. 228-230, Academic Press, New York (1966).
5. R. A. Brown, *This Journal*, **118**, 937 (1971).
6. H. A. Fales and G. M. Ware, *J. Am. Chem. Soc.*, **41**, 487 (1919).
7. G. R. Levi and C. G. Fontana, *Atti Accad. Naz. Lincei*, **7**, 502 (1928).
8. W. F. Hillebrand and G. E. F. Lundell, "Applied Inorganic Analysis," p. 331, John Wiley & Sons, New York (1929).
9. I. M. Kolthoff and D. R. Moltzau, *J. Phys. Chem.*, **40**, 779 (1936).
10. H. Sugimoto, T. Hoshi, and H. Kuribayashi, *J. Chem. Soc. Japan, Ind. Chem. Sect.*, **53**, 58 (1950).
11. T. Lipiec, A. Blasozakiewicz, and A. Urbanowska, *Roczniki Chem.*, **28**, 683 (1954); *CA*, **49**, 8729 (1955).
12. D. F. Bowersox, D. M. Swift, and E. H. Swift, *Talanta*, **3**, 282 (1960).
13. H. Ortmann and R. Piwonka, *Z. Physik. Chem. (Leipzig)*, **218**, 64 (1961).
14. H. Ortmann and R. Piwonka, *Monatsber. Deut. Akad. Wiss. Berlin*, **5**, 174 (1963).
15. E. Lendvay, J. Schanda, K. Richter, and M. Somogyi, *Czech. J. Phys.*, **13**, 143 (1963).
16. R. A. Brown, *Electrochem. Technol.*, **6**, 246 (1968); *This Journal*, **116**, 298 (1969).
17. H. W. Leverenz, "An Introduction to Luminescence in Solids," pp. 473-475, John Wiley & Sons, New York (1950).
18. M. I. Tombak, A. V. Popova, O. F. Komar, and A. A. Bundel, *Izv. Akad. Nauk. SSSR, Ser. Fiz.*, **23**, 1363 (1959); *CA*, **54**, 6331g (1960).
19. J. Einig, *Chem. Ztg.*, **55**, 31 (1931); *ibid.*, **56**, 185 (1932).
20. F. D. Snell and C. T. Snell, "Colorimetric Methods of Analysis," Vol. IIA, pp. 315-317, Van Nostrand, Princeton (1959).
21. A. I. Vogel, "A Textbook of Quantitative Inorganic Analysis," 3rd ed., pp. 236 and 949, Longmans, London (1961).
22. A. E. Hardy, *This Journal*, **91**, 221 (1947).
23. W. Volk, "Applied Statistics for Engineers," pp. 229-230, McGraw-Hill, New York (1958).
24. D. T. Palumbo and A. K. Levine, *This Journal*, **102**, 181 (1955).
25. W. Weibull, *J. Appl. Mech.*, **18**, 293 (1951).
26. J. J. Berrettoni, *ASQC Annual Convention Transactions*, 303 (1962).

## Theoretical and Experimental Efficiencies of X-Ray Screens

A. L. N. Stevels and A. D. M. Schrama-de Pauw

Philips Research Laboratories, Eindhoven, The Netherlands

### ABSTRACT

Measured relative light outputs ( $\text{CaWO}_4$  is used as a standard) of the x-ray powder phosphors  $\text{Gd}_2\text{O}_2\text{S:Tb}$ ,  $\text{Y}_2\text{O}_2\text{S:Tb}$ ,  $\text{BaFCl:Eu}^{2+}$ ,  $\text{CsI:Na}$ , and  $\text{CsI:Tl}$  are lower than the figures calculated from CR efficiencies. This might be due to a systematic difference between the radiant efficiencies of phosphors under cathode-ray and x-ray excitation, but probably is related to a large extent to the present sample preparation technology. Comparison of the light outputs under x-ray excitation of powders and screens indicates that the powder screen technology of  $\text{Gd}_2\text{O}_2\text{S:Tb}$  and  $\text{BaFCl:Eu}^{2+}$  is less developed than that of  $\text{CaWO}_4$ . The vapor-deposition technologies of  $\text{CsI:Na}$  and  $\text{CsI:Tl}$  seem to be well established.

In earlier papers (1, 2), we have evaluated the properties of new and traditional x-ray phosphors. The

Key words: luminescence, x-ray phosphors, x-ray screens, efficiency.

potentialities of each material were explored by calculating the x-ray quantum detection efficiencies (QDE) of x-ray screen/detector combinations. In fact these calculated figures do not represent actual realiza-

tions of phosphor screens but rather give an indication what maximum performance will be found under ideal powder- and screen-making conditions.

The purpose of the present paper is to compare some measured data on powders and screens with calculated ones. In this way more insight is gained into the present state of the art of the x-ray screens.

### Results of Calculations

For a given x-ray energy, the x-ray QDE is defined as follows

$$QDE_E = A_E \cdot \eta \cdot \lambda_{Em} \cdot C_E \cdot D_\lambda \quad [1]$$

where  $A_E$  = the x-ray absorption of the screen (in per cent);  $\eta$  = the luminescence radiant efficiency under cathode-ray excitation of the phosphor (in per cent) (in contrast to efficiencies under x-excitation, these are fairly accurately known);  $\lambda_{Em}$  = the mean wavelength of the detected emission;  $C_E$  = a factor representing the energy losses in the screen; and  $D_\lambda$  = the efficiency for detection of the screen luminescence,  $I_\lambda$ , by a detector with response  $R_\lambda$ .  $D_\lambda$  is defined as  $\int_\lambda I_\lambda R_\lambda d\lambda / \int_\lambda I_\lambda d\lambda$ .

In Fig. 1 we show the QDE figures calculated with the above-mentioned equation [for details on the calculations see Ref. (1) and (2)] for powder screens of  $Gd_2O_2S:Tb$ ,  $Y_2O_2S:Tb$ ,  $BaFCl:Eu^{2+}$ ,  $CsI:Na$ , and  $CsI:Tl$  and for vapor-deposited  $CsI:Na$  and  $CsI:Tl$  screens. In order to have a direct comparison of the performance of various phosphors in a particular energy range, a relative scale is used in which the QDE of a reference phosphor is taken as equal to 1, independent of the x-ray energy. In the present case we have chosen  $CaWO_4$  as the reference, since this material is the traditional phosphor in x-ray intensifying screens. In Fig. 1, QDE data are presented for 200  $\mu m$  thick screens. The packing density of the powder screens is put equal to 50%, whereas for screens which can be made by vapor deposition 100% density is assumed. The efficiency,  $D_\lambda$  for the detection of the screen luminescence has been taken equal to 1. This means that the calculated QDE are in fact calculated light outputs.

We conclude from Fig. 1 that as far as calculated data are concerned, the newly developed screen materials considered have higher QDE numbers than  $CaWO_4$ . This conclusion holds for the complete 30-100 keV energy range. Due to their high packing density

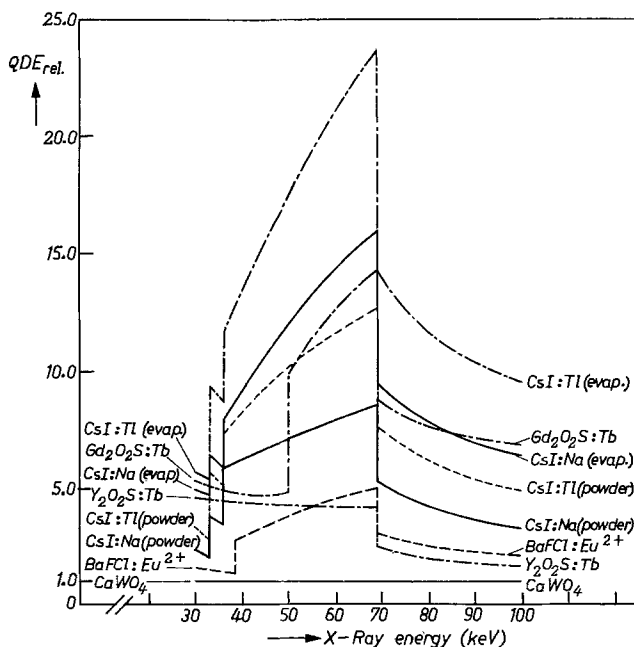


Fig. 1. Calculated relative quantum detection efficiency vs. x-ray energy for 200  $\mu m$  thick phosphor screens ( $CaWO_4 = 1$ ).

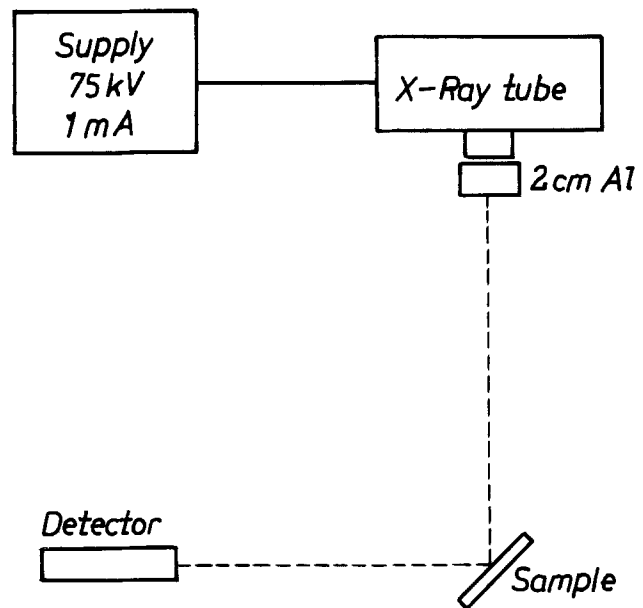


Fig. 2. Schematic diagram of the light output measurement

the vapor-deposited  $CsI:Na$  and  $CsI:Tl$  have the highest QDE figures. This suggests that these materials are very promising for applications. In fact,  $CsI:Na$  is already used on a wide scale as the input screen phosphor of x-ray image intensifier tubes.

### Measurements on Phosphor Powders

Let us now consider how the measured results compare with the calculated ones. The measurements were carried out in the arrangement sketched in Fig. 2. The x-ray source was a Philips Practix tube, operated at a voltage of 75 kV and a tube current of 1 mA. An aluminum filter with a thickness of 2 cm was placed in front of the tube to make the spectral bandwidth narrower. The spectral power distribution of this x-ray source is given in Fig. 2 of Ref. (3).

In order to compare properly with the  $CaWO_4$  reference, it is necessary to correct the results for the spectral sensitivity of the photomultiplier detector, for differences in phosphor layer thicknesses and for differences in the mean grain size. In the last two cases this was done with the aid of Hamaker's formulas (4) for light emission of luminescent screens irradiated by x-rays. The correction factor for the layer thickness was derived by comparing the light output calculated for the sample thickness and that of the standard thickness (200  $\mu m$ ). The samples considered had mean grain sizes ranging between 1 and 5  $\mu m$ . In this range the scattering coefficient is about proportional to  $\sqrt{1/d}$  where  $d$  = mean grain size [see Ref. (5)]. Assuming this proportionality and a standard mean grain size of 3  $\mu m$ , corrections (which did not exceed 15%) can be determined in a similar way as for differences in layer thickness.

Table I gives data corrected in these ways for powders either prepared with our own production facilities or commercially obtained from others. It is concluded that for all new phosphors the measured light output is below the calculated one. This result might be explained by the observation of de Poorter and Bril (3) who found that the actual efficiency of  $CaWO_4$  under x-ray excitation is much higher than under cathode-ray excitation, whereas for all other phosphors considered by these authors the difference was much less. Since we have used for our calculations the fairly accurately known CR radiant efficiencies (rather than the inaccurate x-ray efficiencies), this would imply an underestimation of the calculated light output of

Table I. Measured and calculated relative light outputs of powder phosphors

Phosphor	Measured light output*	Calculated light output
CaWO <sub>4</sub>	1.0	1.0
Gd <sub>2</sub> O <sub>2</sub> S:Tb	4.7-5.6	8.6
Y <sub>2</sub> O <sub>2</sub> S:Tb	3.4-3.7	4.1
BaFCl:Eu <sup>2+</sup>	2.9-3.6	3.8
CsI:Na	4.3-6.3	6.6
CsI:Tl	4.9-7.3	9.8

\* In this column we give the maximum and minimum figures found for the various samples considered.

CaWO<sub>4</sub> and so would introduce a systematic error into our calculations.

However, a few measurements using the well-known (Zn, Cd)S:Ag phosphors as a standard indicated to us that no such systematic error was involved in the discrepancies which are found in Table I. This point of view is supported by data of Ludwig (5) who found, especially for CaWO<sub>4</sub>, a fairly good agreement between the radiant efficiencies of cathode-ray and x-ray excited screens. This makes it probable that the discrepancies in Table I are, to a large part, caused by the fact that, with the present bulk production technology, the performance level of these phosphors under x-ray excitation has not yet reached that of laboratory samples under cathode-ray excitation (the last named figures have been used in the calculations). This may apply more particularly to phosphors that have recently gone into production.

If we consider the phosphors more specifically, the hygroscopic nature of CsI:Na may give rise to lower light outputs of this material. In CsI:Tl the appropriate incorporation of the Tl dope and the avoidance of a yellow body color seem to be the main snags. Due to the hexagonal platelike form of the crystallites, anomalous scattering effects in Tb-doped Gd<sub>2</sub>O<sub>2</sub>S and Y<sub>2</sub>O<sub>2</sub>S may give rise to a lower light output. There are also indications (7) that the control of the grain size of these phosphors is a cumbersome task, which may end in compromising at the cost of the light output. In BaFCl:Eu<sup>2+</sup> the incorporation and reduction of the Eu activator pose the main problem (2).

### Measurements on Screens

In order to get an indication of the present state of the art of screen making we define a relative screen performance (RSP) in the following way

$$\text{RSP} = \frac{\text{light output of phosphor screen/light output of CaWO}_4 \text{ reference screen}}{\text{light output of phosphor powder/light output of CaWO}_4 \text{ reference powder}}$$

In all cases 200 μm thick phosphor layers are considered.

If the RSP of a screen is equal to 1, this means that losses due to screen making are equal to those of CaWO<sub>4</sub> phosphor for which the screen technology was developed decades ago and is well established by now. For recently developed phosphor screens we therefore expect RSP figures below 1.

Due to its high packing density, the RSP of a vapor-deposited screen is significantly higher than that of powder screens; with the present figures, by a factor of 2. Vapor-deposited screens have the additional advantage that no binders have to be used, so that no excitation energy is lost in them and also screen processing may be less harmful to the phosphor efficiency.

Table II. Measured data on relative screen performance (RSP)

Phosphor	RSP	
CaWO <sub>4</sub>	1.00	} powder screens
Gd <sub>2</sub> O <sub>2</sub> S:Tb	0.80	
Y <sub>2</sub> O <sub>2</sub> S:Tb	0.45	
BaFCl:Eu <sup>2+</sup>	0.50	
CsI:Na	2.40	} vapor-deposited screens
CsI:Tl	2.20	

These points combined with the fact that layers can be produced with less scatter (and hence less self-absorption) of the generated light make it possible to find RSP figures even higher than 2.

The measurement of the light outputs of the screens and the grain-size correction of the results in order to put them on a comparable basis were performed in the same way as for the powder phosphors discussed above. In Table II we summarize some data on relative screen performance. For the powder screens of Gd<sub>2</sub>O<sub>2</sub>S:Tb, Y<sub>2</sub>O<sub>2</sub>S:Tb, and BaFCl:Eu<sup>2+</sup>, the RSP figures are clearly below 1, which makes it likely that their screen technologies will be improved. On the other hand, it should be noted that screens produced by methods used in the present state of the art already have given very good application results (2, 8, 9) so that, in fact, our conclusion is that further gains may be expected. For CsI:Na and CsI:Tl screens we find a relative screen performance of more than 2. As we have explained above, this is not unexpected for vapor-deposited layers. A rough estimate of the maximum RSP figure that can be found for vapor-deposited CsI:Na or CsI:Tl is 2.5-2.6. We conclude, therefore that the technology of making these vapor-deposited screens is already well advanced.

### Acknowledgments

The authors wish to thank Mr. F. Pingault of Masiot-Philips, Ailly-le-Haut-Clocher, France, for his contributions to this investigation.

Manuscript received Nov. 17, 1975. This was Paper 207 presented at the Toronto, Canada, Meeting of the Society, May 11-16, 1975.

Any discussion of this paper will appear in a Discussion Section to be published in the December 1976 JOURNAL. All discussions for the December 1976 Discussion Section should be submitted by Aug. 1, 1976.

Publication costs of this article were partially assisted by Philips Research Laboratories.

### REFERENCES

1. A. L. N. Stevels, *Med. Mundi*, **20**, 12 (1975).
2. A. L. N. Stevels and F. Pingault, *Philips Res. Repts.*, **30**, 277 (1975).
3. J. A. de Poorter and A. Bril, *This Journal*, **122**, 1086 (1975).
4. H. A. Klasens, *Philips Res. Rept.*, **2**, 68 (1947).
5. G. Kortüm, "Reflexionsspectroscopie," Springer Verlag, Berlin (1969).
6. G. W. Ludwig, *This Journal*, **118**, 1152 (1971).
7. A. F. Sklensky, R. A. Buchanan, T. G. Maple, and H. N. Bailey, *IEEE Trans. Nucl. Sci.*, **21**, 685 (1974).
8. R. A. Buchanan, S. I. Finkelstein, and K. A. Wickersheim, *Radiology*, **105**, 187 (1972).
9. R. V. Alves and R. A. Buchanan, *IEEE Trans. Nucl. Sci.*, **19**, 415 (1972).



# Optical Properties of Tantalum Oxide Films on Silicon

A. G. Revesz, J. H. Reynolds, and J. F. Allison

COMSAT Laboratories, Clarksburg, Maryland 20734

## ABSTRACT

Tantalum oxide films on silicon were prepared by thermal oxidation of vacuum-deposited Ta films. The optical absorption of these noncrystalline films resembles closely that of crystalline  $Ta_2O_5$ , indicating a strong similarity in their short-range order structures. For given oxidation conditions, the refractive index of the oxide films increases from  $\sim 1.93$  to 2.34 as the thickness increases from 12.5 to 111.7 nm. For a given tantalum film thickness, higher oxidation temperatures result in thicker oxides of lower refractive index. Additional oxide growth occurs during postoxidation heat-treatment in oxygen while the refractive index decreases. The refractive index of a given oxide film increases from the Si/oxide interface toward the outer surface, e.g., from 2.08 to about 2.4. These phenomena are attributed to the incorporation of silicon into the Ta oxide during its growth. However, the estimated amount of silicon in the oxide is not sufficient to explain the observed values if it is assumed that the lowering of the refractive index is due simply to mixing  $Ta_2O_5$  with  $SiO_2$ . Thus, it is concluded that the structure of noncrystalline  $Ta_2O_5$  has a great flexibility which is further enhanced by incorporating silicon; the polarizability of the Ta-O bond is then strongly affected by silicon. This oxide has been applied as antireflection film in recently developed shallow junction silicon solar cells of increased conversion efficiency.

Based on fundamental considerations (noncrystallinity with high degree of short-range order, emphasis on growth rather than deposition techniques, etc.) (1), tantalum and niobium oxides have been developed as antireflection (AR) films (2) for silicon solar cells of increased conversion efficiency (corresponding to a power output  $\geq 18$  mW/cm<sup>2</sup>). These oxides have been prepared by thermal oxidation of vacuum-deposited Ta or Nb films. In the course of that work, we have observed that the refractive index of Ta oxide films on silicon exhibits a gradient (3). This has been attributed to the incorporation of silicon in oxidized form into the oxide during its growth. Rutherford backscattering (RBS) analysis has shown that the Ta oxide films on silicon are, in the first approximation, stoichiometric  $Ta_2O_5$ ; however, the substrate-film interaction has been considered as a possible reason for the increase of their apparent density with thickness (4). The results of gravimetric and secondary ion mass spectroscopy (SIMS) analysis (5) and MOS capacitance measurements (6) also indicate that some interaction takes place in Si/Ta ( $Ta_2O_5$ ) structures.

The purpose of the work presented here was to study in detail the optical properties of  $Ta_2O_5$  films on silicon and, to some extent, on silica substrates. It will be shown in this paper that the optical absorption of noncrystalline thermally grown Ta oxide films on silicon resembles closely that of crystalline  $Ta_2O_5$ , indicating a strong similarity in their short-range order structures. However, the refractive index of these oxide films exhibits a surprisingly large variation that is attributed to the structural flexibility of noncrystalline  $Ta_2O_5$  as well as to modification of the Ta-O bond and/or short-range order by incorporation of silicon from the substrate into the oxide film.

## Experimental

Polycrystalline tantalum films (having the  $\beta$ -tetragonal structure) from  $\sim 10$  to 50 nm thick were deposited at a rate of 0.1-1.0 nm/sec on silicon substrates by electron beam evaporation from a high-purity source. Very smooth silicon surfaces were obtained by the cupric ion polishing technique (7). The vacuum was  $10^{-6}$  Torr. In a few cases, Ta films were also deposited by rf sputtering, but these specimens were not

investigated in detail. Oxidation was performed in oxygen using a resistance heated silica tube furnace. The temperature range was 350°-700°C. Most oxidation experiments were carried out at 525°C. For comparison, a deposition (instead of growth) technique was also used. In this case the oxide film was obtained by vacuum evaporation of high purity  $Ta_2O_5$  using electron beam heating.

The refractive index and thickness of the oxide films were determined with ellipsometry at 546.1 nm wavelength. In the computer evaluation of the  $\Delta$  and  $\psi$  values (8),  $n = 4.06$  and  $k = 0.102$  were used as the optical constants of silicon. These optical constants were determined experimentally. The  $n$  value is close to published values, e.g.,  $n = 4.05$  (9). The published  $k$  values vary significantly, but its actual value has little effect on the refractive index and thickness of dielectric films on silicon. The possibility of having a discrete  $SiO_2$  film between the Si substrate and Ta oxide film has already been eliminated on the basis of ellipsometric measurements performed at two different wavelengths (3). This result has also indicated that the Ta oxide film is nonabsorbing between 435.8 and 546.1 nm wavelengths. Independent absorption increments (see below) also demonstrate that Ta oxide films do not absorb at 546 nm wavelength. Thus, the ellipsometric results for these films are unambiguous. In some cases the ellipsometric measurements were combined with a stepwise etching of the oxide film in HF so that a possible gradient in the refractive index could be revealed.

Optical absorption as a function of wavelength was determined by measuring the reflected and transmitted light using an integrating sphere attached to a spectrometer. For this purpose, the oxide films were produced on fused silica substrates.

## Results

As has been shown previously, the Ta oxide films, even those obtained at 700°C, are noncrystalline and morphologically (as judged by optical and electron microscopy) very uniform (3). They all exhibited bright, continuous interference colors.

The absorption spectra of  $\sim 60$  nm thick thermally grown (curve 1) and vacuum-deposited (curve 2) tantalum oxide films are shown in Fig. 1. It can be seen from this figure that, similarly to a crystalline

Key words: solar cells,  $Ta_2O_5$  on Si,  $Ta_2O_5$  optical properties, antireflection film.

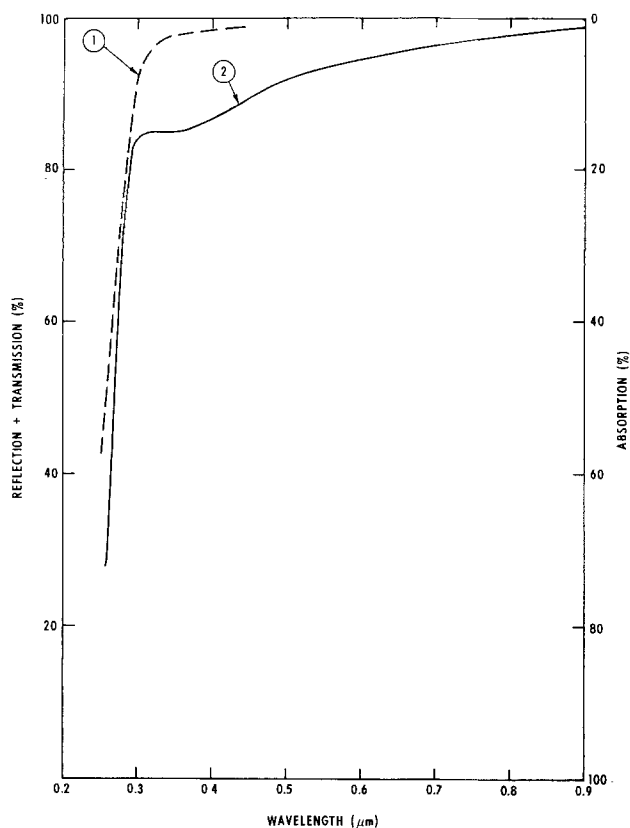


Fig. 1. Absorption of Ta oxide films. The absorption was determined as described in the text. Curve 1: Ta<sub>2</sub>O<sub>5</sub> film obtained by thermal oxidation, Curve 2: Ta oxide obtained by vacuum deposition.

solid, the absorption of the thermally grown noncrystalline Ta oxide film is quite sharp. From this curve, the bandgap can be estimated as 4.1 eV. This value is comparable to 4.2 eV reported for chemically deposited polycrystalline  $\beta$ -Ta<sub>2</sub>O<sub>5</sub> (10) and for noncrystalline Ta<sub>2</sub>O<sub>5</sub> films (11). This result demonstrates that the thermally grown Ta oxide film on silicon can be considered, at least in the first approximation, as stoichiometric Ta<sub>2</sub>O<sub>5</sub>. A similar conclusion has been reached from the RBS analysis (4).

On the other hand, the absorption curve of vacuum-deposited tantalum oxide (curve 2) is distorted; this behavior is typical of noncrystalline solids with large structural disorder. These results demonstrate that, in accordance with the fundamental considerations outlined in Ref. (1), the grown oxide has a higher degree of short-range order and, hence, less unsaturated valences and/or Ta-Ta bonds than the deposited one.

As was already mentioned above, the substrate for the absorption measurement was silica rather than silicon. However, the reflectance spectrum of thermally grown Ta<sub>2</sub>O<sub>5</sub> film on a silicon substrate as well as the characteristics of solar cells fabricated with such an oxide as the AR films shows that the oxide film on a silicon substrate is also essentially nonabsorbing above  $\sim 0.35 \mu\text{m}$  wavelength (2). Thus, from the viewpoint of the optical absorption, there is no significant difference between Ta<sub>2</sub>O<sub>5</sub> films on Si and SiO<sub>2</sub> substrates.

Since the observation of a gradient in the optical index of thermally grown Ta<sub>2</sub>O<sub>5</sub> on silicon was one of the first signs of an unexpected substrate-film interaction (3), the stepwise etching of the oxide film and determination of its refractive index was repeated. The results confirmed those reported previously (3); i.e., the refractive index decreases from the outer surface toward the Si/oxide interface as shown in Fig. 2. In this figure, the open circles along curve 1 indicate the average value of the remaining film after each

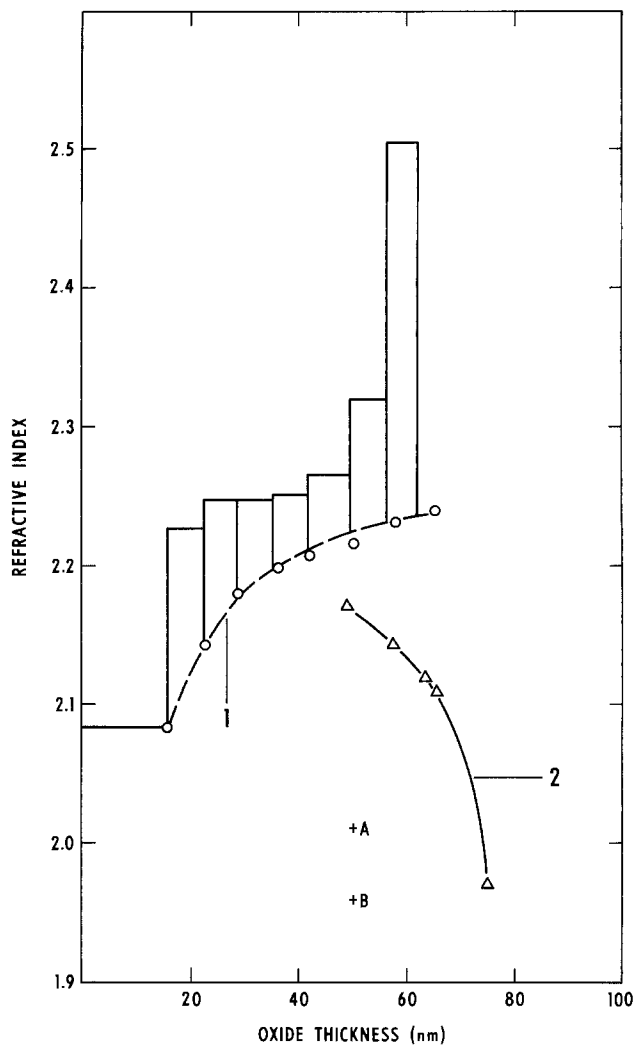


Fig. 2. Refractive index of various Ta oxide films. Curve 1 refers to a Ta oxide film on silicon obtained at 525°C. The film was etched stepwise in HF; the circles indicate the measured refractive index of the remaining film after each step (average refractive index). The superimposed bars give the refractive index of each segment (see text). The refractive index of the outermost segment may be unrealistically high. Curve 2 shows the stepwise etching behavior of a Ta oxide film on GaAs. Points A and B show the refractive indices of two samples for which the Ta film was obtained by sputtering on silicon rather than by vacuum deposition.

etching step, i.e., it was assumed that each segment of the film is homogeneous and that the reflecting surface is silicon. The bars superimposed on curve 1 were obtained by approximating the graded film with a series of discrete homogeneous layers. The lowest average value was taken as the refractive index of the first layer on silicon (assumed to be a homogeneous film 16.0 nm thick), the refractive index and thickness of the second layer were then obtained by reevaluating the ellipsometric data using a multilayer model consisting of the substrate, the first layer, and the unknown second layer. This calculation was repeated for each successive layer; for details of the calculation see Ref. (8).

Since the refractive index change within each layer is small, and the layer thickness ( $\sim 10 \text{ nm}$ ) is a small fraction of the wavelength, this method provides a reasonably accurate approximation of the refractive index profile. It can be seen from Fig. 2 that the greatest inhomogeneity occurs near the two surfaces. We have observed that the refractive index of Ta oxide films obtained by partial oxidation of relatively thick Ta films, i.e., Ta oxide on Ta rather than Si substrate, is higher than 2.4 (this value is, however, somewhat

uncertain due to possible absorption). Thus, Fig. 2 indicates that, with increasing thickness, the Ta oxide film on silicon is becoming more similar to thermally grown oxide film on tantalum.

Another aspect of this behavior is exhibited in Fig. 3, which shows the refractive index values of a series of Ta oxide films on silicon. These samples were obtained by depositing a varying amount of tantalum which was then fully oxidized. It is obvious that the average refractive index of these samples shows a trend which is similar to that seen in Fig. 2, *i.e.*, it increases with increasing oxide thickness. The apparent densities of the oxide films were obtained by using the RBS technique to determine the number of Ta atoms per  $\text{cm}^2$ , then converting this value to the corresponding amount of  $\text{Ta}_2\text{O}_5$  and using the ellipsometric thickness value (4). It has been pointed out in Ref. (4) that the ratio of Ta to O atoms in these films corresponds, to a first approximation, to that of  $\text{Ta}_2\text{O}_5$ ; this justifies the use of this procedure. However, it is very likely that these density values are unrealistically low (hence they are designated as apparent) since some nontantalum constituent, *e.g.*, Si, may not have been detected by the RBS technique.

It is clear from these observations that the refractive index of thermally grown  $\text{Ta}_2\text{O}_5$  films on silicon depends largely on the preparation conditions. If these conditions are properly chosen, then its value as averaged across the film can be very close to 2.3, which is the optimum refractive index for an AR film in a silicon solar cell; also, the film thickness can be adjusted according to the optical matching requirements. In a typical application as AR film, the refractive index of the  $\sim 60$  nm thick  $\text{Ta}_2\text{O}_5$  film is 2.23; the reflection loss from a silicon surface covered with such a film and a fused silica coverslide is about 2% at 540 nm wavelength (primarily due to coverslide reflection). These aspects are discussed in detail in Ref. (2).

It should be mentioned that the behavior of the refractive index, as shown by curve 1 in Fig. 2, is not universally characteristic of thermally grown Ta oxide films. To wit, stepwise etching of a Ta oxide film formed under identical conditions on a GaAs substrate has revealed a gradient which is the opposite of that observed for Ta oxide on silicon (see curve 2 in Fig. 2).

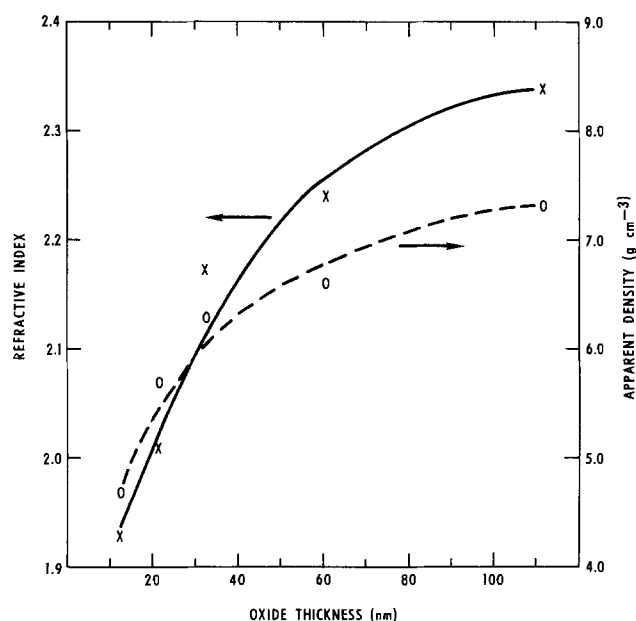


Fig. 3. Average refractive index and apparent density of a series of Ta oxide films on silicon. The thickness of Ta and hence Ta oxide films was varied. The oxidation was done at 525°C for 15 min for each sample. The apparent density was determined from Rutherford backscattering analysis as described in the text.

There is a possibility that the Ta oxide films on GaAs are not completely transparent. Neglecting the absorption in the evaluation of ellipsometric data results in apparent refractive indices that are higher than their true values. Consequently, the true gradient in the refractive index may be lower than that indicated by curve 2 in Fig. 2.

These observations demonstrate that the gradient in the refractive index of Ta oxide films depends largely on the substrate on which the film was formed. This means that, at least in some cases, a significant interaction with the substrate occurs during deposition of the Ta film and/or thermal oxidation. The extent of this interaction apparently depends on various process parameters resulting in a range of refractive index values. This range is much wider than that of the reported values for Ta oxide films produced by anodic oxidation of Ta foils [ $n = 2.22$  (12)] by thermal oxidation of sputtered Ta films on glass or silica [ $n = 2.14$ - $2.25$  (13, 14)], and on Li-tantalate [ $n = 2.21$  (15)] substrates, as well as that obtained by chemical deposition [ $n = 2.3$  (11)], even though these films exhibit a much larger thickness range (80-800 nm) than the films described herein. It is important to note that no gradient in the refractive index has been reported for  $\text{Ta}_2\text{O}_5$  films on glass and similar substrates.

Oxidation of Ta films prepared by sputtering resulted in significantly lower refractive index values than those characteristic of oxides obtained with vacuum-deposited Ta films (see Fig. 2, points A and B). These values are also lower than those quoted above for oxides on insulator substrates although the latter were also obtained by oxidizing sputtered Ta films. It is conceivable that, similar to the reaction resulting in metal-silicide films (16), the film-substrate interaction is easier for sputtered than for vacuum-deposited Ta films. However, it should be mentioned that the vacuum-deposited Ta oxide film also had a relatively low refractive index ( $\sim 2.1$ ).

Another aspect of the effect of process parameters is demonstrated in Fig. 4: the refractive index decreases with oxidation temperature, even though the various Ta oxide films obtained on silicon substrates in the

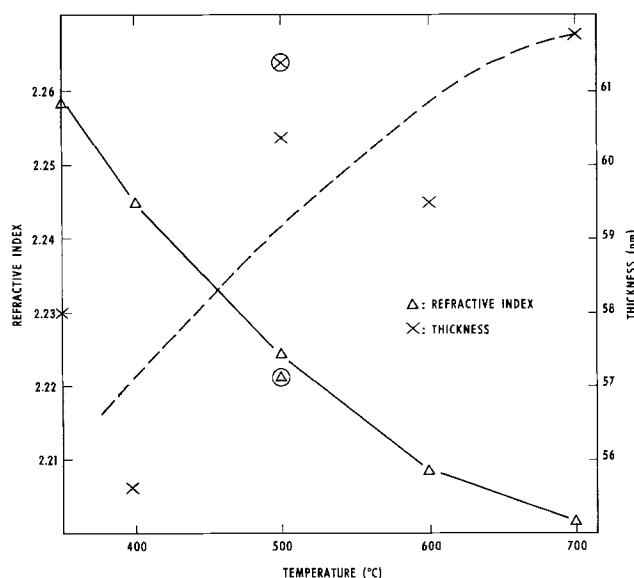


Fig. 4. Refractive index and thickness of Ta oxide films on silicon. The thickness of the Ta film before oxidation was roughly the same for all samples. The oxidation time varied from 5 min at 700°C to 65 hr at 350°C. The Ta film was fully oxidized in each sample. The encircled values refer to an oxide film which was obtained by oxidation at 350°C and then it was heat-treated in oxygen at 500°C for 16 hr.

temperature range 350°-700°C appeared to be morphologically and structurally identical. The increase in the oxide thickness with oxidation temperature was not so well defined, but a trend was discernible. Note that, as demonstrated by the encircled symbols, the refractive index of the oxide film formed at 350°C changed during a subsequent 16 hr heat-treatment in oxygen at 500°C to that characteristic of a film obtained at 500°C in about 15 min and that the thickness also increased significantly. As was pointed out earlier, a similar trend, *i.e.*, increase in thickness and decrease in refractive index, was observed in determining the end point of oxidation of Ta film on silicon (3).

The behavior exhibited in Fig. 4 shows that the oxide composition and/or density depends on the oxidation temperature and subsequent heat-treatment. If it is assumed that the variation in thickness is due to a change in density only, this change is about 9%. The refractive index also decreases as the density decreases and, correspondingly, the mol. polarizability decreases by about 9%. This means that the nature of the Ta-O bond has changed as reflected in the polarizability. Another possibility is, of course, that some chemical change involving a nontantalum component has occurred. Such a chemical change may be, for instance, the incorporation of silicon into the Ta oxide film.

A somewhat similar effect of heat-treatment has also been observed with sputtered Ta films on insulator substrates. Oxidation of 800 nm thick Ta film on glass substrate at 550°C for 16 hr yielded an oxide film with  $n = 2.213$ , whereas a 40 hr treatment resulted in  $n = 2.203$  (13). It has been hypothesized that the change indicates the beginning of crystallization of the non-crystalline oxide. However, the possibility of an interaction with the substrate cannot be excluded. Indeed, discoloration effects in LiTaO<sub>3</sub> were attributed to some interaction with the deposited Ta film during its oxidation (15).

These heat-treatment effects are the opposite to those usually observed with porous films: increase in refractive index and decrease in thickness. The heat-treatment behavior is also opposite to that of anodic Ta<sub>2</sub>O<sub>5</sub> films on Ta substrates for which the dielectric constant increases during heat-treatment in air, but the thickness does not increase (17). The increase in the dielectric constant has been attributed to the creation of an oxygen deficit, *i.e.*, suboxide formation, and to an increase in the long-range order (beginning of crystallization).

The dielectric constant at 1 MHz was determined from MOS capacitance measurement (6) and its value for a ~60 nm thick oxide film was found to be 11.6.

### Discussion

Since the refractive index and mol. polarizability values for these Ta<sub>2</sub>O<sub>5</sub> films on silicon are higher than for SiO<sub>2</sub> and lower than for Ta<sub>2</sub>O<sub>5</sub>, the gradient in the refractive index as well as the effects of oxidation and heat-treatment conditions have been attributed qualitatively to the incorporation of silicon in oxidized form into Ta oxide (3). The results of gravimetric and SIMS analyses have also indicated the presence of silicon in these Ta<sub>2</sub>O<sub>5</sub> films (5), thereby strengthening the above interpretation. In addition, it has been observed that the quantum yield at short wavelengths of shallow junction solar cells using this oxide as AR film is very high. This results from the low surface recombination velocity of minority carriers, indicating that the silicon-oxide interface is reasonably perfect (2). Recent MOS capacitance measurements are also in accordance with this conclusion since they reveal that the interface state density is relatively low, about 10<sup>12</sup> cm<sup>-2</sup> (eV)<sup>-1</sup> (6).

These results indicate that some interaction with the silicon substrate has occurred during the oxidation of the Ta film. It is a general observation that low inter-

face state densities are characteristic of grown rather than deposited oxide (or other insulator) films on semiconductors.

Interpretation of the data shown in Fig. 3 gives some insight into the structure and composition of Ta oxide films on silicon. Since the oxide films can be considered, in the first approximation, to be Ta<sub>2</sub>O<sub>5</sub>, the mol. polarizabilities can be calculated with the Lorentz-Lorenz equation using the molar weight of Ta<sub>2</sub>O<sub>5</sub>. If it is assumed that the apparent density values in Fig. 3 are true, then their mol. polarizability changes from 1.85 × 10<sup>-23</sup> to 1.43 × 10<sup>-23</sup> cm<sup>3</sup> as the thickness increases from 12.5 to 110.7 nm. On the other hand, if it is assumed that the density is constant and equal to 7.9 g/cm<sup>-3</sup> (which is the value for noncrystalline Ta<sub>2</sub>O<sub>5</sub> film obtained by anodic oxidation), then the corresponding change is from 1.05 × 10<sup>-23</sup> to 1.30 × 10<sup>-23</sup> cm<sup>3</sup>. Since the mol. polarizability of anodic Ta<sub>2</sub>O<sub>5</sub> is about 1.262 × 10<sup>-23</sup> cm<sup>3</sup> (using  $n = 2.22$ ), this latter range seems to be more realistic than that calculated from the apparent density values.

Both assumptions concerning the density lead to a large variation (about 25%) in the mol. polarizability. As a comparison, the mol. polarizability of SiO<sub>2</sub> increases by only 5% (from 2.85 × 10<sup>-24</sup> to 2.96 × 10<sup>-24</sup> cm<sup>3</sup>) when its structure changes from coesite ( $d = 2.87$  gcm<sup>-3</sup>,  $n = 1.596$ ) to vitreous [ $d = 2.20$  gcm<sup>-3</sup>,  $n = 1.458$  (18)]. Thus it is very unlikely that the 25% variation can be attributed solely to some small change in the short-range order of noncrystalline Ta<sub>2</sub>O<sub>5</sub>. Some profound change in the polarizability and, hence, in the nature of the Ta-O bond must occur and/or incorporation of silicon into the Ta oxide must be responsible for this effect.

Lowering of the refractive index, albeit to a much lesser extent, was observed for oxide films obtained by anodic oxidation of a sputtered Ta film which contained 23 atom per cent (a/o) aluminum (19). The composition of the oxide film was determined with the Lorentz-Lorenz equation

$$\frac{n_0^2 - 1}{n_0^2 + 2} = \frac{4\pi}{3} (N_1\alpha_1 + N_2\alpha_2)$$

$$= (1 - q) \frac{n_1^2 - 1}{n_1^2 + 2} + q \frac{n_2^2 - 1}{n_2^2 + 2} \quad [1]$$

where  $N$ ,  $\alpha$ , and  $n$  are the number of molecules/cm<sup>3</sup>, molecular polarizability, and refractive index, respectively; and subscripts 0, 1, and 2 refer to the composite film, anodic Ta<sub>2</sub>O<sub>5</sub>, and anodic Al<sub>2</sub>O<sub>3</sub>, respectively. The parameter  $q$  is the volume fraction occupied by anodic Al<sub>2</sub>O<sub>3</sub>. For  $n_0 = 2.12$ ,  $q$  was determined as 14% (using  $n_2 = 1.66$ ) which in turn gave 21 mole per cent (m/o) for Al<sub>2</sub>O<sub>3</sub>, in good agreement with an independent analysis of the composite oxide film. This result demonstrates that the composite oxide can be considered to be a mixture of Ta<sub>2</sub>O<sub>5</sub> and Al<sub>2</sub>O<sub>3</sub> in which no significant interactions between the Ta-O and Al-O bonds occur.

A similar analysis could be also applied to the films described herein, but the refractive indices of oxide films thicker than 32.2 nm are higher than the values reported for anodic Ta<sub>2</sub>O<sub>5</sub> films. Also, as pointed out above, the refractive index of Ta<sub>2</sub>O<sub>5</sub> film grown by thermal oxidation on Ta substrates is somewhat uncertain. Thus, the value of  $n_1$  to be used in Eq. [1] is not quite clear. However, it can be seen from Fig. 5 that the lowest value of the refractive index as extrapolated to infinite thickness is about 2.37. This value is comparable with the mean refractive index (~2.39) calculated from the two indices of the optically biaxial  $\beta$ -Ta<sub>2</sub>O<sub>5</sub> crystal (10).

In order to test the validity of such an analysis, the volume fractions occupied by SiO<sub>2</sub> in the films represented in Fig. 3 and 5 were determined by using 2.37 for  $n_1$  and 1.458 for  $n_2$  in Eq. [1]. The corresponding mole fractions of SiO<sub>2</sub> were calculated by using 7.9

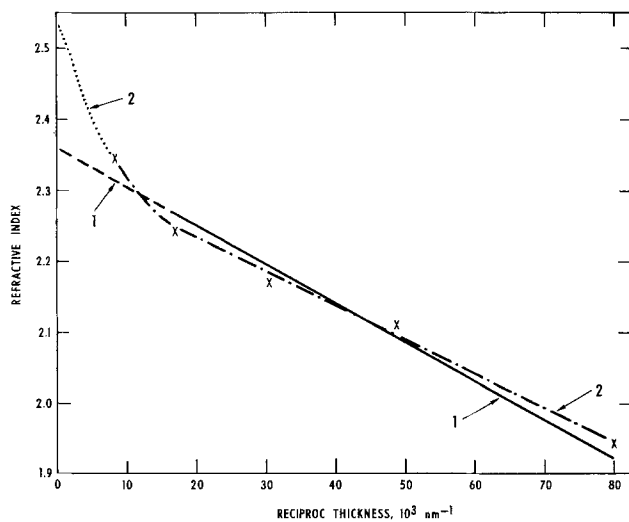


Fig. 5. Refractive index as a function of reciprocal thickness. The samples are the same as in Fig. 4. Curves 1 and 2 represent two possible relationships among the data. The smallest value of the refractive index as extrapolated to zero reciprocal thickness is about 2.37.

and 2.2 g/cm<sup>3</sup> as the densities of Ta<sub>2</sub>O<sub>5</sub> and SiO<sub>2</sub>, respectively. The calculated values are given in Table I. This table indicates that, in general, a substantial amount of SiO<sub>2</sub> is present in the oxide films (using  $n_1 > 2.37$ , this amount would be even larger). However, according to sensitivity estimates of the RBS analyses of these same films, the maximum Si/Ta ratio is 0.16, corresponding to 0.24 mole fraction of SiO<sub>2</sub>. This value is significantly less than most of the values in Table I, indicating that the application of the analysis, as outlined above, is not justified. Accordingly, these films cannot be regarded as simple mixtures of SiO<sub>2</sub> and Ta<sub>2</sub>O<sub>5</sub>, and the values shown in Table I are unrealistic.

Another possibility is that some amount of silicon in the oxide film is present in unoxidized form, *i.e.*, in addition to Ta-O-Si bonds, Ta-Si bonds are also present. However, it is expected that such a structure would absorb light, whereas these films are practically nonabsorbing at 546.1 nm wavelength. Thus, it is very probable that the nature of the Ta-O bonds, and hence their polarizability, varies significantly in the Ta oxide films, and that this variation depends on the amount of silicon incorporated into these films. This is the reason that, as opposed to the composite Ta<sub>2</sub>O<sub>5</sub>-Al<sub>2</sub>O<sub>3</sub> anodic films, these films cannot be considered to be simple mixtures of Ta<sub>2</sub>O<sub>5</sub> and SiO<sub>2</sub>. Consequently, their chemical composition cannot be determined from simple polarizability considerations.

This point is further strengthened by the following argument. The dielectric constant of a ~60 nm thick tantalum oxide film on silicon at 1 MHz is 11.6. The average refractive index of this film is 2.24; this value is almost identical to the refractive index of anodically grown Ta<sub>2</sub>O<sub>5</sub> film even though its dielectric constant is about 27. If  $\epsilon$  is substituted for  $n_2$  in Eq. [1] and  $\epsilon_1 = 27$  and  $\epsilon_2 = 3.8$  (for SiO<sub>2</sub>), then the volume occupied by SiO<sub>2</sub> is 0.28 and the mole fraction of SiO<sub>2</sub> is 0.57. These values are significantly different from

those given in Table I (0.111 and 0.22, respectively). In contrast, it has been found that the mole fraction of Al<sub>2</sub>O<sub>3</sub> in the Ta<sub>2</sub>O<sub>5</sub>-Al<sub>2</sub>O<sub>3</sub> film, as determined from the dielectric constant at 1 kHz, is the same as that determined from the refractive index (19).

The behavior of Ta oxide film on silicon indicates that the frequency dependence of the polarizability is different in these films than in Ta<sub>2</sub>O<sub>5</sub> and SiO<sub>2</sub>. This means that the ionic and dipole contributions to the over-all polarizability and hence the nature of the bonds are also different from those characteristic of anodic Ta<sub>2</sub>O<sub>5</sub> and vitreous SiO<sub>2</sub>.

It is interesting to note that anodic oxidation of a mixed Ta (65 a/o) and Si (35 a/o) sputtered film proceeds under a field of  $5 \times 10^6$  V/cm (20). This field is lower than the field across growing anodic Ta<sub>2</sub>O<sub>5</sub> ( $5.6 \times 10^6$ - $6.2 \times 10^6$  V/cm) and SiO<sub>2</sub> ( $2 \times 10^7$  V/cm). Since the stoichiometry has been reported to be consistent with an oxide composed of Ta<sub>2</sub>O<sub>5</sub> and SiO<sub>2</sub>, the anodization field should be between the two extreme cases. The fact that it is outside of this range is an additional indication that even in the anodically formed mixed oxide the Ta-O and Si-O bonds are different from those present in the pure oxides. Since the refractive index of the mixed anodic oxide is not known, no comparison can be made with the film described herein.

It is concluded from the above discussion that non-crystalline Ta<sub>2</sub>O<sub>5</sub> exhibits a great structural flexibility. Incorporation of silicon (at least partially in oxidized form) during thermal oxidation of Ta film on silicon apparently increases this flexibility as shown by the enhanced stability of the noncrystalline structure. To wit, Ta oxide films on silicon produced even at 700°C are noncrystalline, whereas anodic oxide films usually crystallize at lower temperatures, *e.g.*, at 450°C, at which temperature they also lose their remarkable ductility (21).

## Conclusions

As inferred from the optical absorption spectrum, noncrystalline tantalum oxide films obtained by thermal oxidation of vacuum-deposited tantalum exhibit a great similarity to crystalline Ta<sub>2</sub>O<sub>5</sub> with respect to stoichiometry and short-range order. However, the refractive indices of thermally grown Ta oxide films on silicon vary from  $n = 1.94$  to  $n = 2.34$  as the film thickness increases. Also, the refractive index of a given film has a gradient; the lowest value is in the vicinity of the Si/oxide interface and the highest value is at the outer surface. Since anodic Ta<sub>2</sub>O<sub>5</sub>, chemically deposited Ta<sub>2</sub>O<sub>5</sub>, and Ta oxide film on insulator substrates do not exhibit such a large variation in their refractive indices and no significant gradients have been observed, a substrate-film interaction resulting in the incorporation of silicon into the Ta oxide film is thought to be responsible for these unique effects.

This conclusion is also supported by the heat-treatment behavior which is opposite to that expected for a porous film and that observed with anodic Ta<sub>2</sub>O<sub>5</sub> films on Ta substrate as well as by the results of gravimetric and SIMS analyses. The extent of the film-substrate interaction depends on the thickness of Ta film, oxidation conditions, and postoxidation treatments. Polarizability considerations and Rutherford backscattering analysis of these films indicate that silicon alone cannot account for the observations. Hence, it can be concluded that thermally grown Ta oxide films exhibit a great structural flexibility, resulting in significant variation in the polarizability of the Ta-O bond; this is further enhanced by incorporating Si atoms from the substrate into their noncrystalline structure.

As a result of the flexibility of the noncrystalline structure and the film-substrate interaction, the Si-Ta<sub>2</sub>O<sub>5</sub> interface is reasonably perfect. This interface perfection together with the structural and optical

Table I. Composition of Ta oxide films on silicon as determined from the refractive index

Refractive index	Volume fraction occupied by SiO <sub>2</sub>	Mole fraction of SiO <sub>2</sub>
2.34	0.030	0.06
2.24	0.111	0.22
2.17	0.167	0.34
2.11	0.220	0.45
1.94	0.387	0.79

properties of this Ta<sub>2</sub>O<sub>5</sub> film led to its successful application as antireflection film in shallow junction silicon solar cells.

### Acknowledgments

Thanks are due to B. Free for providing the sputtered Ta samples and to M. Penrose for assistance with the ellipsometric measurements. We also wish to thank Dr. J. Hirvonen (Naval Research Laboratory) for helpful comments on the manuscript. We are indebted to Dr. L. Young (University of British Columbia) for drawing attention to the ductile behavior of anodic Ta<sub>2</sub>O<sub>5</sub>.

This paper is based on work performed in COMSAT Laboratories under the sponsorship of the Communications Satellite Corporation.

Manuscript submitted Oct. 27, 1975; revised manuscript received Jan. 19, 1976.

Any discussion of this paper will appear in a Discussion Section to be published in the December 1976 JOURNAL. All discussions for the December 1976 Discussion Section should be submitted by Aug. 1, 1976.

Publication costs of this article were partially assisted by COMSAT Laboratories.

### REFERENCES

1. A. G. Revesz, *COMSAT Tech. Rev.*, **3**, 449 (1973); also Conference Record of the 10th Photovoltaic Specialists Conference, IEEE, p. 180, Palo Alto, Calif. (1973).
2. A. G. Revesz, J. Allison, and J. Reynolds, *COMSAT Tech. Rev.*, **6**, 57 (1976).
3. A. G. Revesz, J. Allison, T. Kirkendall, and J. Reynolds, *Thin Solid Films*, **23**, S63 (1974).
4. J. Hirvonen, A. G. Revesz, and T. Kirkendall, *ibid.*, **33**, 315 (1976).
5. A. G. Revesz and T. Kirkendall, *This Journal*, To be published.
6. A. G. Revesz and J. Allison, *IEEE Trans. Electron Devices*, In press.
7. E. Mendel and K.-H. Yang, *Proc. IEEE*, **57**, 1476 (1969).
8. F. L. McCrackin, "FORTRAN Program for Analysis of Ellipsometer Measurements," NBS Tech. Note 479 (1969).
9. R. J. Archer, *J. Opt. Soc. Am.*, **52**, 970 (1962).
10. W. H. Knausenberger and R. N. Tauber, *This Journal*, **120**, 927 (1973).
11. C. C. Wang, K. H. Zaininger, and M. T. Duffy, *RCA Rev.*, **31**, 728 (1970).
12. See, for instance, L. Young and F. Zobel, *This Journal*, **113**, 277 (1966).
13. D. H. Hensler, J. D. Cuthbert, R. J. Martin, and D. K. Tien, *Appl. Optics*, **10**, 1037 (1971).
14. M. Fujimori, A. Okamoto, and Y. Nishimura, *Fujitsu Sci. Tech. J.*, **1972**, 177.
15. Y.-K. Lee and S. Wang, *Appl. Phys. Letters*, **25**, 164 (1974).
16. J. W. Mayer and K. N. Tu, *J. Vacuum Sci. Technol.*, **11**, 86 (1974).
17. D. M. Smyth, G. A. Shirn, and T. B. Tripp, *This Journal*, **110**, 1264 (1963).
18. A. G. Revesz, *Phys. Rev. Letters*, **27**, 1578 (1971).
19. D. G. Muth, *J. Vacuum Sci. Technol.*, **6**, 749 (1969).
20. P. J. Silverman and N. Schwartz, *This Journal*, **121**, 550 (1974).
21. S. F. Bubar and D. A. Vermilyea, *ibid.*, **113**, 892 (1966).

## Evolution and Current Status of Aluminum Metallization

Arthur J. Learn\*

Fairchild Camera and Instrument Corporation, Research and Development Laboratory, Palo Alto, California 94304

### ABSTRACT

The requirements which have been placed on metallization for silicon integrated circuits are listed and their origins are traced. Physical models relating to various requirements are discussed. Among these are oxygen activity as a criterion for adherence, slope etching, impurity effects on resistivity, self-shadowing effects on step coverage, and Schottky barrier formation and tunneling as a determinant of contact resistance. The procedures necessary for optimization of some of these properties are considered. Physical vapor deposition methods are reviewed and compared. The more demanding problems of interaction with silicon at contacts, electromigration-induced failure, two-level metallization processing, and corrosion are discussed at length. Approaches designed to allow a basically aluminum metallization to meet all requirements are presented. It is concluded that the use of aluminum alloys is the most generally beneficial technique and that additional effort must be devoted to defining a fully satisfactory method for corrosion protection.

The metallization step in silicon device and integrated circuit processing is one of the last to be performed. Since the value of wafers steadily increases throughout the course of processing, the metallization step is therefore among the more critical ones. The required properties for metallization were relatively simple and few for discrete devices and early integrated circuits. The design of new types of devices and circuits together with processing refinements during the last decade have, however, resulted in increasingly more stringent demands on metallization.

The initial metallization requirements were comfortably met by aluminum and, consequently, it was used for this purpose. Certain problems have sub-

sequently arisen with aluminum, notably those associated with silicon interaction at contacts, electromigration, corrosion, and multilevel metallization. There are essentially two approaches to the solution of such problems. Nonaluminum metallizations which have comparable resistivity such as molybdenum-gold (1), titanium-platinum-gold (2), or titanium-palladium-gold (3) have been developed. Since the preparation of such metallizations is inherently more difficult, and hence more costly, than aluminum they have found only specialized application. The alternative approach is to attempt improvement by techniques which allow retention of basically aluminum metallization. It is activities in the latter area which will be reviewed here.

The paper is organized as outlined below. A list of requirements for metallization will first be presented,

\* Electrochemical Society Active Member.  
Key words: silicon IC metallization, metallization processing, metallization reliability, metallization optimization, aluminum and aluminum alloys.

Each of the requirements will be discussed in turn and in detail. Where it is not obvious, the origins of the requirements will be traced. The properties of aluminum will be compared with this list. Models to explain why good matches are achieved in some cases will be given. Where there is substantial disparity in ideal and actual properties, the methods investigated to more closely approach the ideal will be discussed. Conclusions as to the best over-all approach at this time and areas for further study will be given. It is hoped that the present review will serve to both update and expand other such reviews (4-6). Many volumes or series relating in part to various aspects of metallization are also available (7).

### Metallization Requirements

A list of requirements for metallization on present-day silicon devices and integrated circuits must include the following:

1. Compatible deposition methods
2. Good adherence to dielectrics
3. Selective etchability
4. Low electrical resistivity
5. Complete coverage of surface topography
6. Bondability
7. Low contact resistance
8. Contact stability
9. High electromigration resistance
10. Multilevel capability
11. Resistance to oxidation and corrosion

Requirements 7 and 8 relate specifically to the properties of metallization as a contact material and the remainder primarily to the properties as an interconnection or external connection.

Additional requirements could certainly be considered, such as the ability to solder to or plate onto the metallization and resistance to mechanical abrasion. The latter is readily achieved by deposition of dielectric layers over the metallization (8). Multilayered metal systems have been developed to allow soldering (9) or plating (10, 11) over aluminum metallization. These properties while desirable do not, however, represent basic limitations on the use of aluminum. Accordingly, the above list will be used as a basis for discussion of aluminum metallization.

### Discussion

**Deposition methods.**—The formation of high quality aluminum by chemical vapor deposition has not been achieved, or at least has not been reported. Therefore, physical vapor deposition processes are used. Applicable methods of deposition are listed in Table I and compared with a checklist of desired characteristics when used for providing metallization.

Evaporation of aluminum from tungsten or tantalum filaments is among the earliest techniques used (12, 13). Aluminum will alloy with these materials at evaporation temperatures and filament life is short. Also the deposit thickness is limited by the amount of aluminum which may be loaded on the filament. Perhaps the most serious drawback to filament evaporation is the inability to consistently obtain alkali-free material (14). The consequences as regards MOS

devices are especially grave although bipolar device processing is also developing comparable sensitivity (15) to the various charges in the oxide (16), such as positive fixed surface-state charge or mobile ionic contamination ( $Q_o$ ). Radiation damage effects ( $N_{ot}$ ) are not present with filament evaporation. Porous aluminum carbide rod filaments have been used for aluminum evaporation and reportedly (17) are relatively free of sodium. The development of intermetallics, such as a mixture of boron nitride and titanium diboride, which better resist attack by aluminum also makes evaporation from a boat feasible.

Flash evaporation from a heated bar composed, for example, of the above intermetallic offers several attractive features. Materials can be continuously fed to the bar in the form of pellets (9) or wire (18). The deposition of thick films is therefore intrinsic to this approach and also there is freedom from radiation damage. In addition, the deposition of a variety of aluminum alloys requires only a simple substitution of the appropriate alloy pellets or wire (18).

Inductively heating an aluminum charge held in a crucible of the intermetallic material (19) previously mentioned or boron nitride (20) offers high deposition rates. It should be noted that, with the possible exception of sputtering, the other methods listed yield rates sufficiently high that there is little impact on throughput time for metallization processing. Alloy deposition is possible in a controlled way with inductive heating only by utilizing multiple sources.

Electron beam evaporation (20) has a number of shortcomings. The deposition of thick films or alloys is not inherent in this method and is achieved only at the expense of more complicated and difficult-to-control procedures. Thick films can be considered, just as for other methods, if material is supplied to the molten evaporant pool. This technique (21), heating of a continuously fed rod of material (22-24), or use of multiple sources either operated simultaneously (25) or sequentially can be used for alloy deposition. Consideration must be accorded the possible effects of radiation damage (26).

The boat, flash, and inductive-heating methods typically exhibit flux distribution characteristics approaching a surface (cosine law) source (27). This characteristic is normally assumed in designing rotating or planetary fixturing (28) to yield a deposit of uniform thickness. Unless the deposition conditions are carefully controlled, the distribution from electron beam sources can exhibit beaming or directionality effects (29) and deposits of nonuniform thickness can result.

Although sputtering is listed as useful for thick-film deposition, excessive times may result as a consequence of relatively low deposition rate. In order to sputter aluminum effectively and obtain near-bulk resistivity, d-c bias sputtering (30) or RF sputtering (31, 32) is required. This results in considerably increased cost for the apparatus. The attainment of low  $Q_o$  is somewhat questionable in view of the tendency for the sputtering process to redistribute and activate mobile ionic contamination (33, 34). Likewise, the extent of the effects arising from radiation damage has not been fully defined. Sputtering is, however, attractive for the deposition of alloys and promising new techniques offering increased deposition rates are evolving (35-37).

It may be noted that the limits on  $Q_o$  can be relaxed through the use of layers prior to metallization which inhibit the motion of ionic contaminants or "getter" them. Such layers include silicon dioxide incorporating phosphorus (38) or chlorine (39), silicon nitride (40), and aluminum oxide (41). On the other hand, the presence of nitride restricts the annihilation of fast surface states (16) which normally occurs upon heating in an ambient of hydrogen (42) or with aluminum metallization present (43). This effect must

Table I. Characteristics of metallization deposition techniques

Deposition method	Low cost	High deposition rate	Thick films	Alloy deposition	Low $Q_o$	No $N_{ot}$
Filament	Yes	No	N	N	N	Y
Flash evaporation	Y	N	Y	Y	Y	Y
Inductive heating	N	Y	N	N	Y	Y
Electron beam heating	N	Y	N	N	Y	N
Sputtering	N	N	Y	Y	?	N



then occur by lateral penetration and diffusion of hydrogen under the nitride (44). Such effects are of interest because surface states can appear with those deposition methods for which x-radiation or energetic secondary electrons are prevalent. The preparation of wafers before metallization is also important in minimizing  $Q_0$ . In particular, dilute acid rinses followed by the liberal use of distilled water can remove alkali ion contaminant from the wafer surface (45).

**Adherence to dielectrics.**—The heat of formation for metal oxides has been proposed as a qualitative measure of the adherence of metals to oxide (46-48). If the heat of formation is large and negative, then the tendency of the metal to reduce the oxide onto which it is deposited is pronounced. A strong chemical bond at the interface should therefore result. Bonding of this type was recently reviewed (49, 50).

The oxide heats of formation for aluminum and silicon are  $-399$  and  $-205$  kcal/mole, respectively. Therefore, good adherence of aluminum to silicon dioxide would be expected, as has been universally observed. This inequality in heats of formation also indicates that reduction of residual silicon dioxide in contact windows covered with aluminum would occur upon heating. Such a phenomenon is the basis for the "alloying" or sintering step in silicon device processing where the intent is to promote more intimate metallization contact and thereby lower contact resistance. Rates of silicon dioxide reduction by aluminum have been measured and recorded (52). As an example, a typical 5 min "alloying" period at  $500^\circ\text{C}$  would reduce  $25\text{\AA}$  of oxide.

Silicon nitride is finding more widespread application in device processing, particularly as an oxidation mask in recently developed oxide isolation techniques (53). Frequently the surface of nitride layers is thermally oxidized to provide an etch mask for the nitride delineation. With oxide present, adherence of aluminum metallization should be as discussed above. For deposition directly on nitride it is not certain that an adherence mechanism involving nitride heats of formation can be invoked. The heats of formation for  $\text{AlN}$  (51) and  $\text{Si}_3\text{N}_4$  (54) are  $-131$  and  $-180$  kcal/mole, respectively. In any case, the adherence of aluminum to silicon nitride is found to be completely satisfactory.

**Etching properties.**—Aluminum is readily etched in either basic or acidic solutions. Basic solutions may also etch silicon and their use would necessitate the complete coverage of contacts. In addition, the risk of alkali ion contamination is naturally more pronounced with such solutions. Accordingly, acidic etchants are preferred for aluminum etching. Typically, phosphoric acid is the primary ingredient used. Phosphoric acid will etch underlying nitride layers (55) as well but the etch rate is significant only at temperatures much higher than those employed in etching aluminum.

Normally, the etching is nearly isotropic so that the edge profile of the metallization will be represented by a quarter circle. If the metallization is overetched, i.e., if the etch time exceeds that required to etch through the metallization thickness, then nearly vertical edges will result (56). At least two methods exist for providing a more favorable slope or taper at the metallization edge. If an appropriate ingredient, such as nitric acid, is added to the conventional etchant, loss of adherence of the photoresist will result. If the photoresist lifting is initiated at its edge and increased inward in a controlled manner, suitable profiles can be obtained (57). A second technique utilizes double layers having different etch rates in a given etchant. Both anodic (58) and deposited oxide overlayers (59) were found, in buffered etches, to have larger etch rates than aluminum and therefore to allow attainment of low angle steps.

**Electrical resistivity.**—The resistivity,  $\rho$ , for metallization is normally determined either using a four-point probe (60) or from a resistor pattern of known dimensions. The metallization thickness,  $t$ , is commonly measured by using multiple-beam interferometry (61) or a stylus-type surface profilometer (62). Values of  $\rho$  at room temperature are typically in the  $2.7\text{--}3.0\ \mu\Omega\text{cm}$  range for aluminum of  $1\ \mu$  thickness. This compares quite favorably with the value of  $2.7\ \mu\Omega\text{cm}$  for bulk aluminum. Unless very poor vacuum practices are followed,  $\rho$  is quite tolerant to the conditions of deposition. For example, for work done in our laboratory the ratio of total pressure,  $P$ , to deposition rate,  $R$ , was increased up to a value of about  $3 \times 10^{-6}$  Torr sec/ $\text{\AA}$  in an oil diffusion-pumped vacuum chamber. This would correspond to deposition at a pressure of  $3 \times 10^{-4}$  Torr for a typical rate of  $100\ \text{\AA}/\text{sec}$ . It might be anticipated that  $P/R$  would be a meaningful parameter as regards film properties since it is a measure of the relative impingement rates of impurities and evaporant. As indicated in Fig. 1, there is a substantial effect of  $P/R$  on grain size of the deposits. No correlation of  $\rho$  with  $P/R$  was observed, however, over the range shown in Fig. 1.

More precisely, the effect on  $\rho$  of the reactive gases oxygen and water vapor rather than total pressure should be considered. Table II lists minimum values of  $P/R$  which were found to result in increased  $\rho$  for a number of separate investigations. The relevant deposition parameters also appear including those relating to Fig. 1. In the latter case, the ratio between total pressure and partial pressure of water vapor during deposition was constant at about 30 (63), as indicated in Table II, and no significant effect on  $\rho$  was noted for  $P(\text{H}_2\text{O})/R$  up to  $1 \times 10^{-7}$  Torr sec/ $\text{\AA}$ . In one study (64), the critical value of  $P(\text{H}_2\text{O})$  for water vapor was approximately  $1 \times 10^{-7}$  Torr sec/ $\text{\AA}$  above which resistivity increased significantly. In another case (65), only the total pressure was monitored and the critical  $P/R$  indicated is in the range  $0.5\text{--}5 \times 10^{-8}$  Torr sec/ $\text{\AA}$ . The situation here should be similar to the case for Fig. 1 since filament evaporation was employed. This would imply, however, a greater sens-

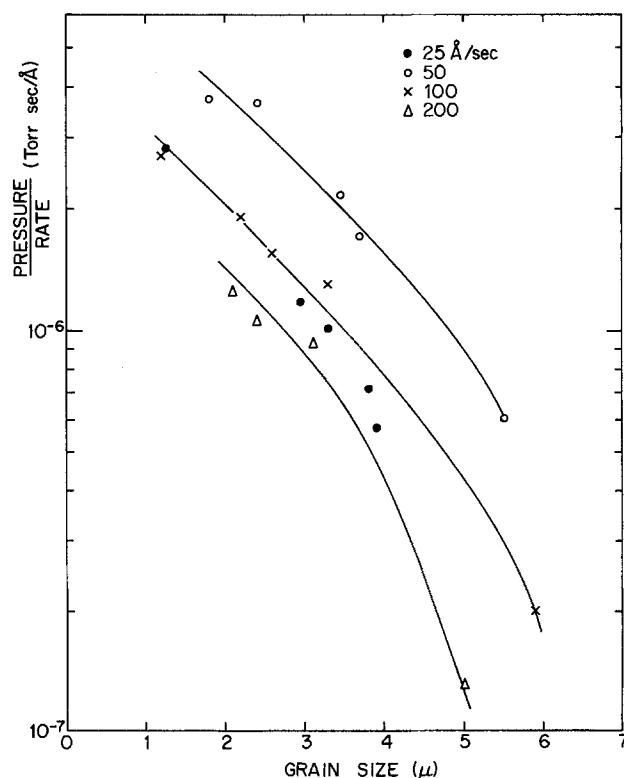


Fig. 1. Aluminum grain size resulting from deposition at different values of  $P/R$  and various rates.



Table II. Deposition parameters for various studies of aluminum film properties

Source	Thick-ness ( $\mu$ )	Temper-ature ( $^{\circ}$ C)	Deposition rate, R ( $\text{\AA}/\text{sec}$ )	P(H <sub>2</sub> O)* (Torr)	P(O <sub>2</sub> )* (Torr)	P(total) (Torr)	Critical P/R (Torr sec/ $\text{\AA}$ )	Reference
Inductively heated BN · TiB <sub>2</sub>	0.5	200	20	$\lesssim 3 \times 10^{-5}$ (M)	$1.2 \times 10^{-7}$ (C)		$0.5\text{--}1 \times 10^{-8}$ (O <sub>2</sub> )	20
W-filament	1	350	100	$\lesssim 1 \times 10^{-5}$ (M)		$\lesssim 3 \times 10^{-4}$		63
Radiatively heated BN	2	$\sim 200$	$\sim 10$	$\sim 1 \times 10^{-6}$ (C)	$\sim 1 \times 10^{-7}$ (C)		$1 \times 10^{-7}$ (H <sub>2</sub> O) $1 \times 10^{-8}$ (O <sub>2</sub> )	64
W-filament	1	Unheated	$\sim 200$			$1\text{--}10 \times 10^{-6}$	$0.5\text{--}5 \times 10^{-8}$	65
W-filament		100					$3 \times 10^{-8}$ (O <sub>2</sub> ?)	66

\* Critical (C) partial pressures or maximum (M) partial pressures investigated.

itivity of  $\rho$  to water vapor partial pressure. It is possible that the pressure monitored was not a true measure of pressure within the deposition chamber. Also the lower deposition temperature may increase sensitivity to water vapor because of an increased sticking coefficient. Consistent with this, an increase in the ratio of room temperature to low temperature resistivity with increasing deposition temperature has been noted (20). In a study (66) with filament evaporation purportedly concerning the effects of oxygen on  $\rho$ , it appears that total pressure was monitored. A critical P/R of  $3 \times 10^{-6}$  Torr sec/ $\text{\AA}$  was found. Assuming the factor of 30 relating total pressure and water vapor partial pressure, the critical P/R would be  $1 \times 10^{-7}$  Torr sec/ $\text{\AA}$ , as above.

Two studies (20, 64) where oxygen was the known residual gas led to a critical P(O<sub>2</sub>)/R of about  $1 \times 10^{-8}$  Torr sec/ $\text{\AA}$ . Thus  $\rho$  is about one order of magnitude more sensitive to oxygen than to water vapor. This is a fortunate happenstance since water vapor is the primary residual gas in oil diffusion-pumped vacuum systems (63).

Geometrical size effects result in increased  $\rho$  for thin aluminum films. Substantial increase is found (65) only for films thinner than approximately 1000 $\text{\AA}$ , even for single crystal aluminum (67). Standard metallization is normally thicker than 0.5 $\mu$ , in order to provide sufficiently low sheet resistance, so that size effects are of little consequence.

**Step coverage.**—The completeness of the metallization coverage at steps or irregularities in the substrate is basically determined by geometrical considerations during the course of deposition. In the case of two sources, the metallization profile near vertical steps may be constructed by considering deposition of thin layers alternately from each source. Even when line of sight is possible from one source to each step, a discontinuity or microcrack will still occur (68). The deposit from each source shadows the deposit from the other source leading to a self-shadowing mechanism for crack formation.

The construction method has been generalized to a larger number of sources (68) and, in the limit, to a distributed or extended source (69, 70). The latter is somewhat analogous (70) to the case where there is substrate movement, such as planetary motion (71), during deposition. It is found (69, 70, 72) that cracks nevertheless occur with an extended source and that (i) the bottom edge contour determines the crack depth with the depth being inversely related to the radius of curvature; (ii) the top edge contour has little effect; and (iii) at an undercut step with a reentrant angle a crack pointing toward the bottom of the undercut portion occurs.

The most straightforward method of avoiding cracks is therefore to control the contour of the step to be covered by maintaining a positive slope and avoiding sharp corners. It has also been found that if the step profile is not too severe, heating of the substrate dur-

ing deposition promotes improved coverage (18, 68). Such an effect is illustrated in Fig. 2 for aluminum deposition onto an undercut step. This type of step results when a composite layer of phosphorus-doped oxide on thermal oxide is etched because of the differing etch rates for the two materials (18). At the lower substrate temperatures, microcracks form with an increasing tendency to seal over the crack with increasing temperature. When a film of the latter type is etched, however, etchant can penetrate into the crack and a tunnel (64, 73), or complete removal of metallization at the step, results. The situation is probably aggravated by the strong capillary forces tending to draw etchant into the crack. Temperatures of approximately two-thirds the melting point temperature are required, or about 300 $^{\circ}$ C for aluminum, to yield acceptable coverage [Fig. 2(c)].

Calculations have indicated that the use of vertical planetary platens and an eccentrically positioned source would minimize crack formation (74). It is not known, however, to what extent this has been verified experimentally. The application of negative bias to the substrate during deposition (75-77) to allow some resputtering has also been employed to obtain coverage on rather severe test steps. There is some question as to the role of substrate heating in this case (78). Calculations for a sputtering source (78) generally indicate the same propensity for crack formation as for evaporation sources.

It is interesting to note that the shadowing effect has been turned to advantage in certain cases. Geometrical shadowing was utilized in the fabrication of closely spaced (submicron) metallization (79, 80) on integrated circuits. Small-dimensioned metal grids were formed by deposition of a thin continuous overlayer on agglomerated films and subsequent etching of the agglomerated material (81). Contrast enhancement in electron microscope replicas is also achieved by shadowed deposition (82).

**Bonding.**—Aluminum wire, usually with small ( $\sim 1\%$ ) silicon additions, may be readily bonded to aluminum metallization by ultrasonic means (83). In this way the surface of the metallization is scrubbed to break up native oxides and the two bonding surfaces are made to conform so that a strong bond results. The failure modes of such bonds have been investigated extensively (84). Generally their reliability is found to be excellent.

With thermocompression wedge or ball bonding (85) of gold wire to aluminum, the potential exists for reduced reliability because of possible intermetallic formation and concomitant void formation (1, 86-88). It was proposed that silicon has the effect of accelerating such interaction and that a black ternary product so formed (89) is more detrimental than the AuAl<sub>2</sub> intermetallic which is purple in color. This effect of silicon was corroborated (90) in another investigation. Recent work (91) has firmly established that reliable gold-aluminum bonds are also achievable.

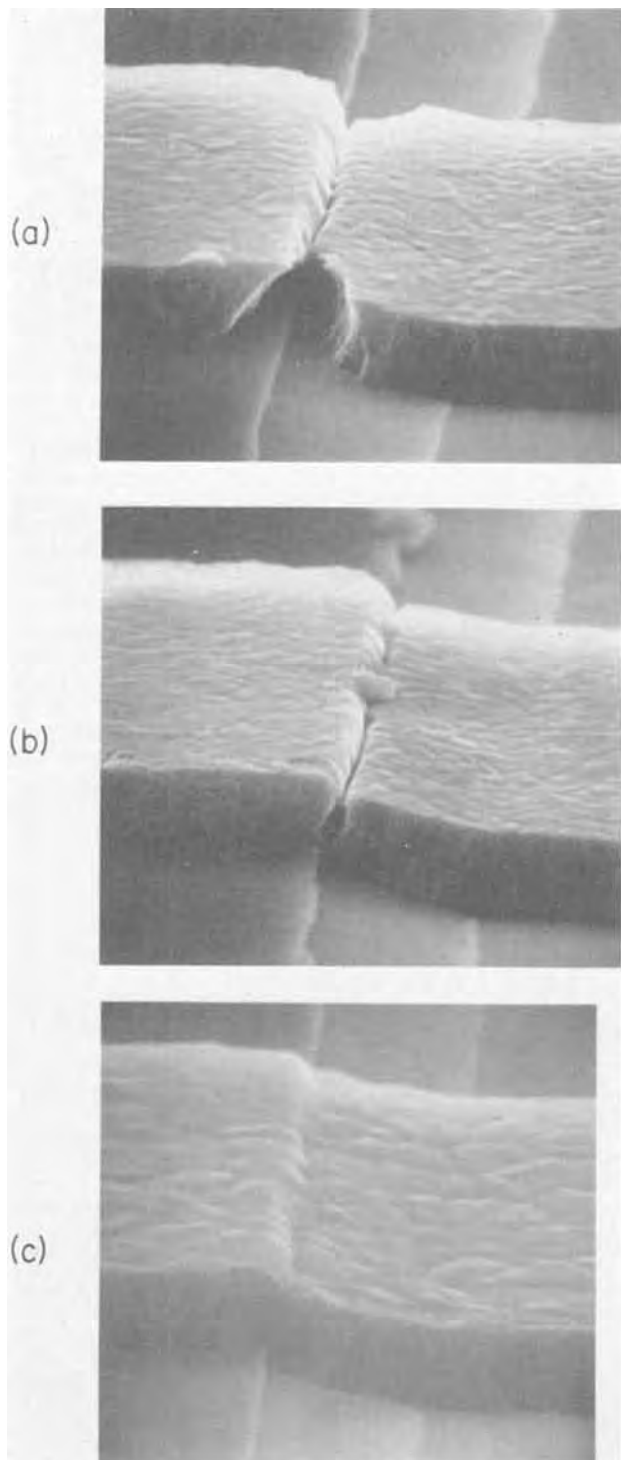


Fig. 2. Metallization coverage and tunnel formation at an undercut step as a function of deposition temperature; (a) 200°C, (b) 250°C, (c) 300°C.

Careful attention must, however, be accorded the amounts of each material available for intermetallic formation, the bonding and postbonding temperatures and the time at temperature.

**Contact resistance.**—When aluminum and n-type silicon having clean surfaces are brought into contact a Schottky barrier occurs (92) of height,  $\phi_{Bn}$ , in the range of 0.68–0.76 eV (93–99). This  $\phi_{Bn}$  is approximately two-thirds of the silicon forbidden gap,  $E_g$ , (100) and is thought to arise from the presence of acceptor states at the silicon surface which fix the Fermi level at the level of the surface states. For silicon, such states occur at an energy of 0.48 eV above

the valence band edge (101). The situation is completely analogous for aluminum to p-type silicon contacts except that the barrier height,  $\phi_{Bp}$ , is then  $E_g - \phi_{Bn}$ . Barrier heights of 0.94 eV (102) and 0.58 eV (103) have been measured, but it is not known to what extent the values were affected by silicon surface conditions.

The mechanism of current flow in a Schottky barrier depends on the width of the barrier, i.e., on the dopant concentration,  $N$ . In the thermionic emission range, with dopant concentrations  $\lesssim 10^{16} \text{ cm}^{-3}$ , barrier width is relatively large and charge carriers must surmount the barrier in order to move between metal and semiconductor. For large dopant concentrations  $\gtrsim 10^{19} \text{ cm}^{-3}$ , barrier width is sufficiently small that quantum mechanical tunneling of charge carriers through the barrier, rather than emission over the barrier, becomes dominant.

The present interest is in metal-semiconductor contacts which exhibit ohmic characteristics. An ohmic contact shall be considered synonymous with a linear current-voltage characteristic. A figure of merit used to describe such contacts is the specific contact resistance (104)

$$R_c \equiv \left. \frac{dV}{dJ} \right]_{V=0} \quad [1]$$

If  $R_c$  is small then a contact can support a large current density,  $J$ , at low voltage,  $V$ .

In the thermionic emission range

$$R_c = \text{const. } e^{q\phi_{Bn}/kT} \quad [2]$$

where  $T$  is absolute temperature,  $q$  is the electronic charge and  $k$  is the Boltzmann constant. Note that  $\phi_{Bn}$  and  $T$  determine the value of  $R_c$  and there is no dependence on  $N$ , as would be expected for emission over the barrier. In the tunneling range

$$R_c = \text{const. } e^{[1/N]^{1/2}} \quad [3]$$

and  $R_c$  is strongly dependent on  $N$  but approximately independent of  $T$ .

Calculation of  $R_c$  in the above ranges, as well as the intermediate one, has been performed (105–107). Experimental values of  $R_c$  for aluminum on n-type silicon are in substantial agreement with the calculated values, both in terms of functional behavior and absolute value (105–109). Somewhat more complete calculations (110), taking into account the penetration of charge carriers into the depletion layer, also yield results coinciding with experiment. Theoretical results are shown in Fig. 3 for [111] silicon and  $\phi_{Bn}$  equal to 0.40 eV, presumably (111) characteristic of aluminum contacts to p-type silicon. An experimental curve of  $R_c$  for contact to p-type silicon (112) is also presented in Fig. 3. The values of  $R_c$  are those obtained subsequent to heat-treatment (“alloying”) at 500°C for 10 min. There is substantial disparity between experimental and calculated values, particularly for smaller  $N$ . A probable explanation involves aluminum doping of the silicon as a consequence of heating. If  $N$  were increased by about  $1 \times 10^{19} \text{ cm}^{-3}$  in this way, the experimental values would coincide more closely with calculation. The solid solubility of aluminum in silicon at 500°C could be of this order of magnitude (113). A similar result regarding doping level is inferred (114) from heat-treatment experiments at 550°C. On [100] rather than [111] silicon,  $R_c$  should be reduced by about one-half (107). It is unlikely that this difference could be readily detected experimentally.

An additional application of the Schottky barrier, other than providing ohmic contact, utilizes the diode properties which arise for contact to lightly doped silicon (104, 115). In particular, such a diode is used in parallel with the collector-base junction of n-p-n transistors in saturated logic circuits to increase switching speed. Ideally, this can be implemented by

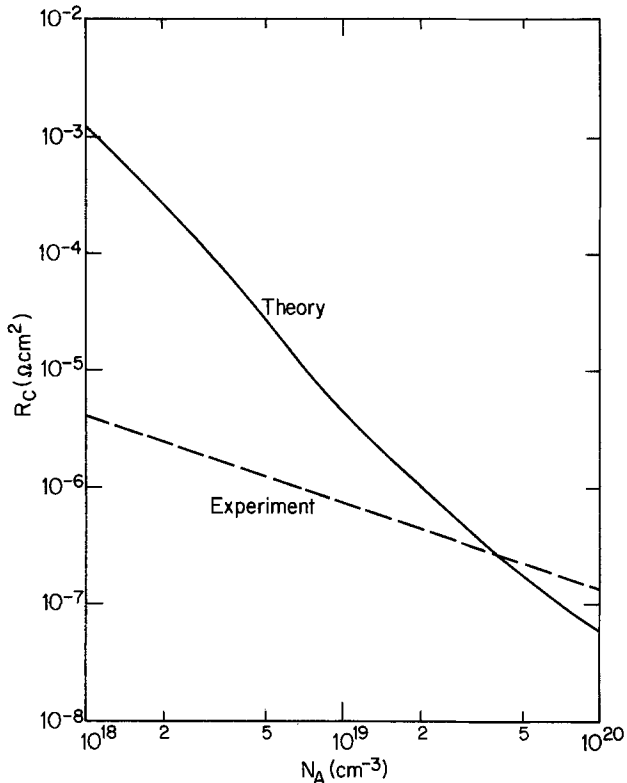


Fig. 3. Specific contact resistance as a function of acceptor concentration. Solid line: theoretical; dotted line: experimental results for contact to p-type silicon following heat-treatment at 500°C for 10 min.

depositing aluminum over the region where the collector-base junction intersects the silicon surface. Such an approach is possible because the aluminum can form ohmic contact to the p-type base and rectifying contact to the n-type collector as discussed above.

Problems were encountered with this simple structure related to effects at the edges of the contact cut in the oxide (104) or to variable  $\phi_B$  upon "alloying" the Schottky diode (96, 97). The latter has been attributed to dissolution and reprecipitation of aluminum-doped silicon in the form of islands or a continuous layer at the metal-silicon interface (97, 99). In order to prevent the silicon dissolution or interaction during "alloying," platinum silicide can be formed in contact areas prior to aluminum metallization (116). The barrier heights  $\phi_{Bn}$  and  $\phi_{Bp}$  for platinum silicide on silicon (116-118) are about 0.15 eV higher and lower, respectively, than for aluminum so that contact properties are similar to those discussed earlier. An additional problem with the platinum silicide-aluminum structure arises as a consequence of an aluminum-platinum intermetallic formation leading to unstable  $\phi_B$  (119, 120). This logically suggests incorporation of a diffusion barrier, such as tungsten (121, 124), between the silicide and aluminum to allow attainment of a stable Schottky diode.

**Contact stability.**—Postmetallization processing such as "alloying," deposition of a scratch protection layer, assembly, and packaging will typically involve temperatures higher than the metallization deposition temperature. During such periods, after breakup of residual oxide at contacts, interdiffusion of the aluminum and silicon will occur. The problem of increased junction leakage or shorting as a consequence of the aluminum-silicon interaction was recognized and the mechanism was elucidated (9). Basically, silicon is dissolved in the aluminum up to the solid solubility limit at a given temperature, e.g., 0.8% at 500°C. Silicon subsequently diffuses out into the aluminum interconnection (125) thus resulting in additional silicon

dissolution at the contact. Consistent with this is the frequent observation that the most pronounced dissolution occurs where the aluminum leads out of the contact (126), i.e., where there is an aluminum sink. At the same time, aluminum diffuses into the silicon or along the silicon-silicon dioxide interface. As shown in Fig. 4, this results in the growth of spikes or shallow spears in these two areas (127-130) for [100] and [111] oriented silicon, respectively. If the process continues for a sufficient period of time, junctions will be shorted by the spikes growing through them or covering them where they intersect the silicon surface. The silicon dissolution in the metallization is further evidenced by enhanced recrystallization of the aluminum and by the presence of silicon precipitates remaining after removal of the aluminum (131).

Junction shorting can be avoided by limiting the temperature and duration of postmetallization processing, but in some cases this is not a feasible approach. In particular, with the advent of shallow junctions, such as occur in devices for emitter coupled logic circuits (132), another solution is required. Three methods have been used to minimize silicon dissolution.

Just as with Schottky diodes, a diffusion-barrier layer such as titanium (133) or nichrome (134) can be interposed between the silicon and aluminum. Consideration must then be given the possible interaction of this material with either or both the aluminum and

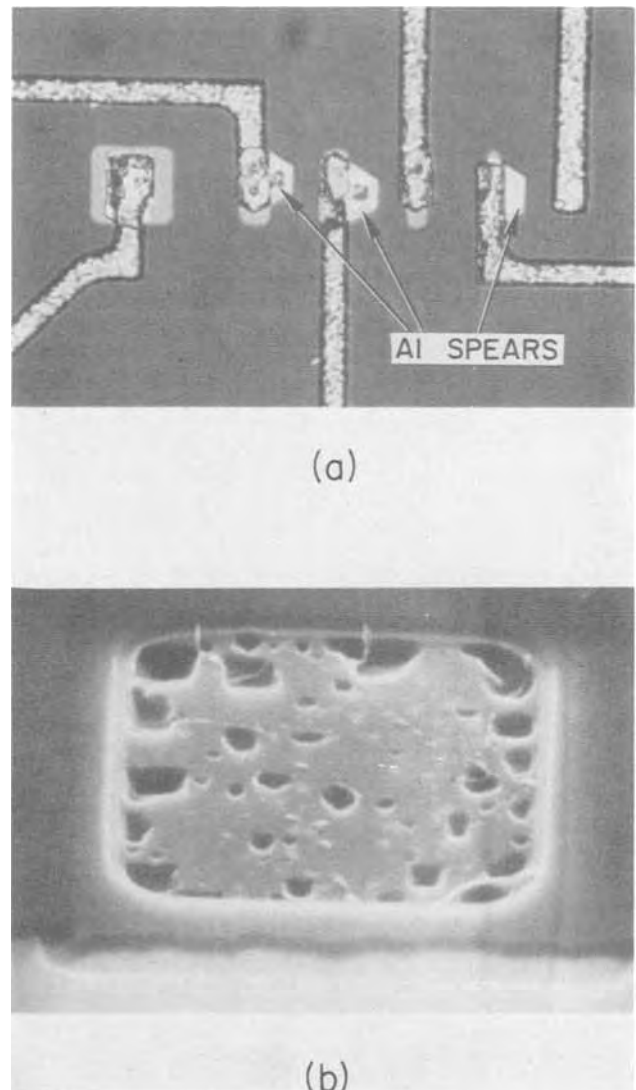


Fig. 4. Structures resulting from overextended heat-treatment of aluminum-silicon contacts; (a) [111] silicon and (b) [100] silicon after metallization removal.

silicon and the contact resistance. As regards the latter, platinum silicide can be utilized. Some care must be exercised in avoiding degradation during the platinum deposition (usually by sputtering) and the sintering to form the silicide. The over-all consequence is, in any case, that a fairly complex structure with more difficult processing results. It should be noted that such a structure is normally present if platinum silicide Schottky diodes are used in the integrated circuits.

Alternatively, a layer of silicon can be deposited prior to the aluminum. The thickness of the silicon film is chosen such that the solid solubility limit is satisfied when the film is fully dissolved in the aluminum (135, 136). For a temperature of 500°C, where the solid solubility is about 0.8 atomic per cent (a/o) and for an aluminum thickness of 1 $\mu$ , the silicon thickness required is approximately 90Å. The silicon thickness, although typically small and difficult to control, is quite critical. If it is too large, then not all of the silicon will be dissolved and  $R_c$  may be increased. If it is too small, the silicon will not fully perform the intended function.

The solid solubility limit can also be satisfied by adding silicon to the aluminum during the course of the metallization deposition (9). As discussed in connection with deposition methods, aluminum-silicon alloy metallization of this type can be prepared by simultaneous evaporation of aluminum and silicon from separate sources, by flash evaporation or sputtering.

**Electromigration.**—For polycrystalline aluminum metallization it has been fairly conclusively established that diffusion occurs primarily in grain boundaries (137). Evidence indicates that as for bulk material (138) a vacancy mechanism is still relevant, at least for copper (139) and silver (140). Consequently, certain grain boundary structures can lead to localized accumulation or depletion of material during electromigration. Examples of such structures are grain boundary triple points (141), with other than 120° angles, and contiguous clusters of large and small grains (142). The net effect of electromigration in an aluminum film is to produce voided areas and hillocks more or less uniformly distributed along the length of the film. If temperature gradients exist in the direction of electron flow, then voids will form in the region of increasing temperature and material accumulation will occur in the region of decreasing temperature (143). Also, at contacts, depletion or accumulation can occur because of the differing diffusion coefficients for silicon and aluminum (144). The depletion of metallization where electrons flow from a contact and the accumulation in the form of whiskers where there is electron flow into a contact are illustrated in Fig. 5.

Of most practical importance is the lifetime,  $\tau$ , before electrical opens occur in interconnections or before electrical contact is lost to silicon. As regards interconnections, it has been assumed (145) that  $\tau$  is inversely proportional to the electromigration flux and directly proportional to the conductor cross-sectional area,  $w$  $t$ , because of the need to remove a certain volume of material before a void reaches across the entire interconnection width. This would imply that

$$\tau = \text{const.} \frac{tw}{J} e^{E_a/kT} \quad [4]$$

where  $J$  is the current density and  $E_a$  is the activation energy for self-diffusion. There has been some discussion as to whether a  $J^{-1}$  or  $J^{-2}$  dependence should result (146, 147). Another treatment of the electromigration-induced failure time indicates (148) a  $J^{-n}$  dependence where  $n$  is 1 with diffusion gradients present, e.g., at contacts, and is 3 with temperature gradients present. Other treatments (149-151) considering self-heating lead to the result that  $n$  should increase, with increased  $J$ , from a value of 1 to large

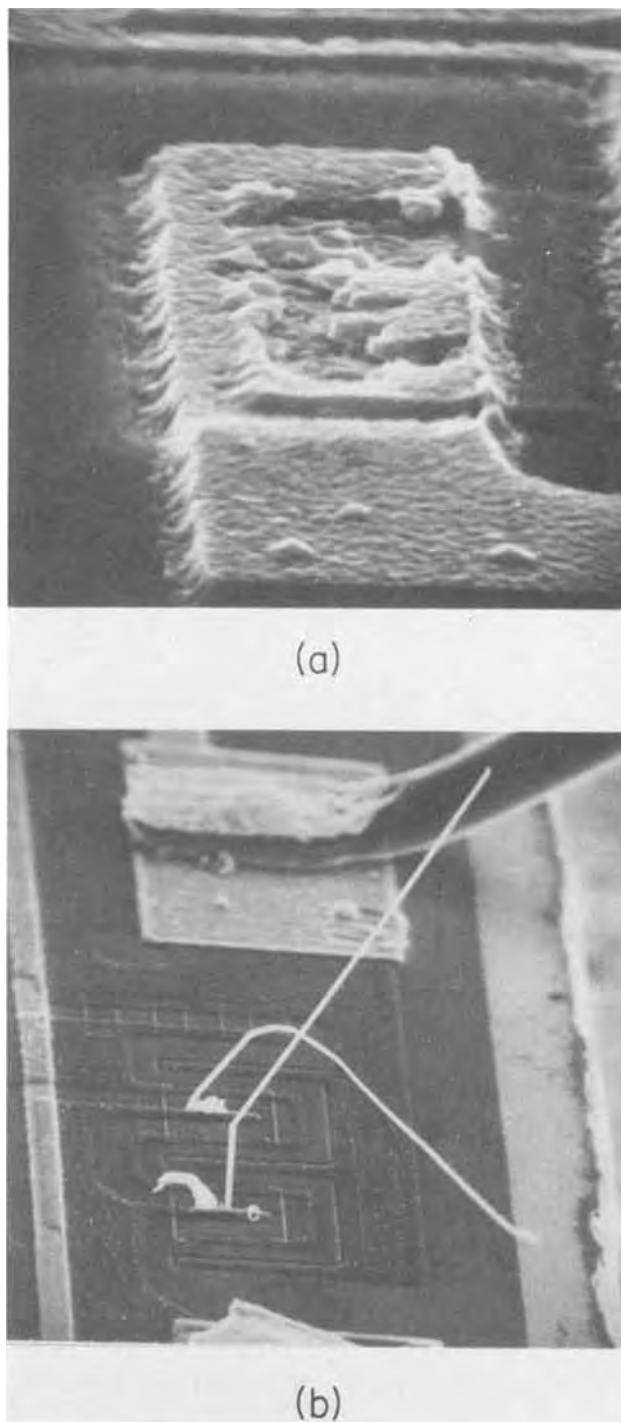


Fig. 5. Electromigration effects at contacts to silicon for electron flow from the contact (a) and electron flow into the contact (b).

values on the order of 10. It has also been suggested (152-153) that current crowding effects are more important than such self-heating. An attempt to unify the dependence on geometrical parameters through a more basic consideration of grain size and grain size distribution leads to (154) approximately the dependency on  $w$  appearing above, an  $e^{\text{const}/L}$  dependence on interconnection length,  $L$ , and an approximately linear dependence on grain size. The length dependence arises because there is a higher probability of finding weak spots, i.e., more severe grain boundary inhomogeneities, for depletion of material with increased length. Similar consideration was given grain characteristics in a discussion of electromigration at rectangular contacts (155). An expression for  $\tau$  in this case is

$$\tau_c = \text{const.} \frac{tw'}{J} e^{E_a/kT} e^{\text{const.}/l} \quad [5]$$

where  $w'$  is the contact dimension parallel to electron flow from the contact,  $l$  is the other contact dimension, and  $J'$  is the average current density over the contact area.

The general features of expressions [4] and [5] are supported by experimental studies. The methods of examination and the potential pitfalls associated with lifetesting and the use of data so generated, in particular, have been thoroughly discussed (156). The early results served primarily to establish the consequences of electromigration in thin films (157-163). A vast store of more quantitative data has been accumulated for aluminum interconnections, in particular. In this case, an exponential dependence on temperature is generally observed. The values of  $E_a$  found are listed in Table III. Many values of  $E_a$  were obtained by lifetesting (142, 144, 164-168). Measurement of transported volumes (141, 169-172) and resistance changes (173, 174) were also used and resultant  $E_a$  values are included. There is considerable spread in the values obtained by different investigators. The generally low values of  $E_a$  are, however, consistent with grain boundary diffusion. In addition, it appears that values, within a given study, are less for aluminum having smaller grain size (142, 144, 167) and significantly large for very large grain size (172). Values of  $n$  (144, 165, 167, 175-177) also appear in Table III. Again, the values exhibit a wide range from 2 to 7. Probably a value of about 2 for  $n$  is most commonly observed and therefore generally used in estimating  $\tau$ . The dependence on interconnection cross-sectional area is approximately supported by an experimental study (144). More specifically, a linear dependence on  $w$  has been observed (178). Decreased  $\tau$  with increased  $L$  was observed in two instances (178, 179). In one case (178), the functional dependence was well represented by  $e^{\text{const.}/L}$ . Other investigations, primarily involving measurement of mass transport, have yielded specific values for diffusivity (141, 169, 171, 180, 181). A Berg-Barrett x-ray topographic technique has also been employed for this purpose (182).

Data are much sparser for electromigration failure at contacts to silicon. The phenomenon has frequently been observed but generally only in a qualitative manner (183-185). In the one exceptional case (186), quantitative lifetime measurements resulted in essentially expression [5] for  $\tau_c$ .

The use of expressions such as [4] and [5] to assess lifetimes under typical operating conditions can sometimes reveal marginal values at best. This is particu-

larly true for aluminum-silicon metallization, in large part due to a low value of  $E_a$  for such material (165, 187). Consideration must therefore be given techniques for extending lifetime. It may be recalled that certain phenomena are necessary to electromigration-induced failure in aluminum. Self-diffusion, via a vacancy mechanism, and grain boundary structures are involved. Vacancies are also necessary in sufficient concentration to allow void formation and growth (188-191).

The relative effect of grain boundaries may be reduced by increasing grain size since this reduces the grain boundary volume per unit cross-sectional area of the conductor. It has already been noted that this results in increased  $E_a$  and, therefore, increased  $\tau$ . If carried to the extreme where no grain boundaries are present, i.e., with a single crystal film, unlimited  $\tau$  is exhibited (192). At the other extreme where grain size is much less than metallization thickness, increased  $\tau$  is also observed (193). It appears that this is a consequence of the multiplicity of diffusion paths through the film thickness rather than any reduction in electrotransport rate. A minimum in  $\tau$  for intermediate grain size has been predicted (194). The increased  $\tau$  observed (195) for low rates of deposition may be explained in this way in light of Fig. 1. The improvement in  $\tau$  obtained through incorporation of aluminum oxide (196) may also be partially attributable to a very small grain size. In another case (197), incorporation of increased amounts of residual gases (presumably actually meaning  $\text{Al}_2\text{O}_3$ ) reduced  $\tau$  which may again be related to decreased grain size.

A second approach is designed to limit the vacancy density and thus inhibit diffusion and void formation. Use of a tightly adherent overcoat to seal the metallization surface and eliminate this source of vacancies is suggested. Somewhat contradictory results have been obtained with silicon dioxide layers deposited by chemical vapor deposition (144, 175). In cases where  $\tau$  was increased, some of the improvement may be attributable to grain growth (176) during oxide deposition and hence the dependence on grain size discussed above. Using anodization at room temperature to provide an alumina overcoat resulted in improved lifetime (167, 179). The increases in  $\tau$  were interpretable on the basis of  $E_a$  increases of up to 0.15 eV. It is of interest that periodic oxidation of aluminum under electrical stress also prolonged  $\tau$  (198). Increases in  $\tau$  as a consequence of dielectric overcoating have also been interpreted as a consequence of pressure-inhibiting effects on diffusion (199).

Another approach involves the addition of small concentrations of metals to aluminum which can segregate to grain boundaries and inhibit diffusion of solvent atoms (166, 200). Very substantial increases in  $\tau$  were attained through copper (166, 201-205), nickel (206), magnesium (206-209), chromium (206, 210), or titanium (211) additions. It appears that copper has won the most widespread application for this purpose. Difficulties can arise using the other additives. For example, for magnesium, low temperature reactions with silicon dioxide and resistivity increases render such metallization less useful (208). Resistivity increases are also quite substantial with chromium additions (210). Ternary and quaternary alloy metallizations such as aluminum-copper-magnesium and aluminum-copper-nickel-magnesium have also been investigated (212). Lifetime improvements, however, would not appear to be sufficiently greater than with copper to merit full consideration, particularly in view of side effects such as those with magnesium. As with pure aluminum, many qualitative studies of the effects of electromigration in aluminum-copper have been performed. It is found that the copper is a more rapid diffuser and that failure frequently occurs in regions depleted of copper (166, 202, 213, 214). The film struc-

Table III. Electromigration parameters resulting from the referenced investigations

$E_a$ (eV)	$n$	Grain size ( $\mu$ )	Method	Reference
0.74 ± 0.08		4	Transported volume	141
0.51 ± 0.10		2	Lifetest	142
0.73 ± 0.05		8	Lifetest	142
0.48	2	1.2	Lifetest	144
0.84		8	Lifetest	144
0.3-1.2*			Lifetest	164
0.55	~2		Lifetest	165
0.51 ± 0.10			Lifetest	166
0.34		~1	Lifetest	167
0.46	2-3	~5	Lifetest	167
0.41		~1	Lifetest	168
0.7 ± 0.2		0.5-several	Transported volume	169
0.63			Transported volume	170
0.7			Transported volume	171
1.22		Single crystal	Transported volume	172
0.5-0.6			Resistance	173
0.5-0.6		1-2	Resistance	174
	~3		Lifetest	175
	~7	0.35-1.5	Lifetest	176
	~7		Lifetest	177

\* Thickness dependent.

ture per se and distribution of second-phase precipitates are also found to be important (166, 203, 205, 214-217). Increases in  $E_a$  up to approximately 0.3 eV have been measured (166) for aluminum-copper metallization and these are sufficient to account for the increased  $\tau$ . Values of the exponent  $n$  in the range of 2 to 3 were determined (201, 202). Lifetime is found to reach a minimum when the film width is about twice the grain size (218). For larger ratios of width-to-grain size,  $\tau$  varies approximately linearly with  $w$ . Other fundamental quantities such as copper ion velocity (219) or effective charge and diffusivity parameter for copper (220-224) were also measured for aluminum-copper. The addition of copper to aluminum-silicon metallization results (187) in  $\tau$  increases comparable to those with aluminum-copper. Consequently, the use of aluminum-copper-silicon metallization simultaneously protects against junction shorting and premature electromigration-induced failure.

**Multilevel capability.**—In order to exploit fully the sophisticated device structures and processing which have resulted in substantial reductions in device size, it is frequently necessary to employ at least two levels of metallization (225). The two levels are in contact through vias in the insulator which electrically isolates the levels in all other regions. Several dielectrics have been utilized including anodized aluminum (226), silicon nitride (227), sputtered quartz (228, 229), and polyimide (230). By far, the most widely used (231) is a phosphosilicate glass ( $\text{SiO}_2 \cdot \text{P}_2\text{O}_5$ ) obtained by the simultaneous oxidation of silane and phosphine (232, 233) at temperatures in the vicinity of 400°C. The addition of phosphorus serves to reduce stress and to yield a more compatible thermal expansion coefficient (175, 234), both of which aid in limiting cracking or crazing of such layers.

The presence of a second level of metallization requires careful attention to the vias and to crossover areas for the two levels. The via must be free of foreign layers and relatively free of oxide in order to achieve intimate contact between metallization levels and yield acceptably low resistance (235). As with contact to silicon, some small thickness of silicon dioxide can be reduced by heating. With proper processing of vias, a specific via resistance of less than  $1 \times 10^{-7} \Omega\text{cm}^2$  is readily obtained.

The electrical integrity of the insulator at metallization crossovers is determined primarily by the uniformity of the coverage of edges or irregularities, such as hillocks, occurring in the first level of metallization. Deposited phosphosilicate glass tends to grow preferentially at sharp corners and nodule formation can result (18, 175, 236). Nodules formed over hillocks are difficult to cover with photoresist and may therefore be removed during via etching. In addition, such nodules may be broken off when a mask is brought into contact with wafers. In either case, the net result is shorting between levels when the second level of metallization is deposited. The occurrence of nodular growth at metallization edges both thins the insulator along the vertical surface and renders more difficult the deposition of continuous second-level metallization. The problems associated with edges can be avoided by slope etching of the first level. Insulator coverage is then of reasonably uniform thickness. It is also desirable to slope etch the vias (237-239) thereby promoting better second-level metallization coverage at the vias. The phenomenon of hillock growth bears some analogy to electromigration in that both involve movement of material by diffusion. The driving force in hillock growth is compressive stress (240, 241) rather than forces exerted by charge carriers, as in electromigration. Consistent with this analogy, it is found that those approaches leading to increased lifetime are also applicable to limiting hillock growth. The density of annealing hillocks in aluminum

is reduced for larger grained films (242-243). In addition, anodization (243) or copper (244, 245) and other (246) additions were demonstrated to be very effective in minimizing hillock growth. It is of interest that no electromigration effects were noted with second-level metallization present which were not predictable on the basis of measurements with a single level of metallization (229).

**Oxidation and corrosion.**—The oxidation of aluminum is normally a self-limiting process and is therefore not a cause for concern. For example, in room temperature air the maximum oxide thickness formed is less than 50Å (247). Moreover, in a water-free ambient, corrosion of aluminum is not observed. Consequently, corrosion of aluminum metallization on silicon devices placed in hermetically sealed packages is virtually nonexistent. In plastic encapsulation which water vapor can penetrate, however, corrosion of an electrochemical nature is frequently prevalent (248).

In addition to water vapor, an impurity which will combine with the water to form an electrolyte is required. Finally, an electric field larger than some threshold value is necessary between adjacent conductors. A common impurity, in the above sense (249), which is frequently present is phosphorus or phosphorus oxide. This can arise from a scratch-protection layer over the metallization, from the insulating layer between two levels of metallization, or from films under the metallization, such as are formed in silicon dioxide masking layers during phosphorus diffusion. Corrosion in this type of environment has been thoroughly investigated (250) and it is found that the corrosion rate is increased with increased relative humidity, phosphorus content, electric field, and temperature. Rather than failure at the anode, as with ordinary anodic dissolution, it occurs initially at the cathode. This is a consequence of the formation of aluminum hydroxide. Other impurities such as chlorine or sodium (251) have been demonstrated to cause similar corrosion effects. The corrosion rate for aluminum-alloy metallization is found to be no greater than that of pure aluminum (252). Such behavior is entirely unexpected on the basis of results for bulk specimens (253) of aluminum-copper or aluminum-copper-silicon. Since it has been observed (254) that corrosion of aluminum metallization occurs preferentially at grain boundaries, the improved corrosion properties of the alloys, as for electromigration, may be related to the altered structure of the boundaries.

### Summary and Conclusions

The properties of aluminum as they relate to the requirements for metallization on silicon devices were discussed. It was found that in most instances there is a suitable match between properties and requirements. In those cases where it is an aid to the full understanding of a property, suitable physical models exist. Examples of such properties are adherence, step coverage, and contact resistance.

Pure aluminum was found lacking in some aspects of contact stability, electromigration resistance, multilevel capability, and corrosion resistance. Although more than one alternative is available to improve performance in the first three areas, the use of aluminum alloy metallization is beneficial for all. The conversion from aluminum to aluminum-copper or aluminum-copper-silicon metallization involves little change in processing or design. Versatile deposition methods, such as flash evaporation, are available which are equally simple for aluminum or aluminum alloys. In addition, the adherence, etching, step coverage, bonding, and contact resistance properties for the above alloys remain essentially the same as for aluminum while resistivity is increased only about 15%. Care must be exercised in postmetallization heat-treatments because of the reduced eutectic temperatures of the



alloys (255). With one possible exception, it may therefore be stated that the employment of aluminum alloy metallization has allowed the requirements for metallization on silicon to be met and has greatly extended the usefulness of a basically aluminum process.

The most notable area in which additional work remains to be done is in providing more effective corrosion protection for aluminum metallization. The solution may again lie in the use of aluminum alloys. For example, it is known that the corrosion resistance of aluminum-chromium alloys is superior (256) to that of aluminum, at least in bulk form. Alternatively, a satisfactory approach may involve the use of hermetic deposited overlayers such as silicon nitride, aluminum oxide, or a combination of nitride and aluminum oxide (257). Low temperature deposition processes for silicon nitride and aluminum oxide are being investigated and characterized (258-262). It appears highly probable that a suitable solution will be forthcoming and that aluminum metallization will long remain the standard of the semiconductor integrated circuit industry.

Finally, it may be noted that, as in other semiconductor processing steps, the move toward more complete automation of metallization would be highly desirable. Among the deposition methods included in Table I, sputtering is perhaps most amenable to such an approach. As mentioned earlier, new sputtering techniques (35-37) are being investigated in order to increase deposition rates and minimize radiation damage. It is hoped that these types of development will continue and will be expanded in scope and effort. Complete characterization of the metallization obtained by the various deposition methods must, in any case, be performed. This becomes necessary since many properties are structure sensitive and structure is in turn dependent on the details of the deposition process.

#### Acknowledgments

The author wishes to thank Dr. Bruce E. Deal for his encouragement in the organization of material for and writing of this review.

Manuscript submitted Dec. 9, 1975; revised manuscript received Jan. 28, 1976. This was Paper 190 presented at the Toronto, Canada, Meeting of the Society, May 11-16, 1975.

Any discussion of this paper will appear in a Discussion Section to be published in the December 1976 JOURNAL. All discussions for the December 1976 Discussion Section should be submitted by Aug. 1, 1976.

Publication costs of this article were partially assisted by Fairchild Camera and Instrument Corporation.

#### REFERENCES

- J. A. Cunningham, *Solid-State Electron.*, **8**, 735 (1965).
- M. P. Lepselter, *Bell Syst. Tech. J.*, **45**, 233 (1966).
- L. A. Murray and B. W. Richards, *Wescon Record*, **15**, 20/3 (1971).
- H. Sello, in "Ohmic Contacts to Semiconductors," B. Schwartz, Editor, p. 277, The Electrochemical Society Softbound Symposium Series, New York (1969).
- J. C. Blair and P. B. Ghate, *Wescon Tech. Papers*, **5**, Session 2, Paper 1 (1971).
- B. H. Vromen, Proc. Semiconductor/IC Processing and Production Conf., p. 84, Industrial and Scientific Conf. Management, Chicago (1971).
- G. Hass et al., Editors, "Physics of Thin Films," Academic Press, New York; L. I. Maissel and R. Glang, Editors, "Handbook of Thin Film Technology," McGraw-Hill, New York (1970); K. Chopra, "Thin Film Phenomena," McGraw-Hill, New York (1969).
- G. L. Schnable and R. S. Keen, *Proc. IEEE*, **57**, 1570 (1969).
- P. A. Totta and R. P. Sopher, *IBM J. Res. Develop.*, **13**, 226 (1969).
- R. T. Eynon and R. C. Grace, Abstract 97, p. 245, The Electrochemical Society Extended Abstracts, Spring Meeting, Boston, Massachusetts, May 5-9, 1968.
- S. E. Grossman, Editor, *Electronics*, **47**, 89 (1974).
- D. M. Rynne, *Solid State Technol.*, **11**, 48 (1968).
- R. H. Dudley, in "Integrated Circuit Technology," T. A. Longo, Editor, p. 215, Boston Technical Publishers, Cambridge, Mass. (1970).
- J. W. Guthrie, V. A. Wells, and G. F. Derbenwick, Abstract 136, p. 349, The Electrochemical Society Extended Abstracts, Fall Meeting, Dallas, Texas, Oct. 5-9, 1975.
- W. M. Werner, Abstract 24, p. 71, The Electrochemical Society Extended Abstracts, Spring Meeting, San Francisco, California, May 12-17, 1974.
- B. E. Deal, *This Journal*, **121**, 198C (1974).
- J. J. A. Ploos van Amstel and E. Kooi, *ibid.*, **120**, 840 (1973).
- A. Learn, *Thin Solid Films*, **20**, 261 (1974).
- I. Ames, L. H. Kaplan, and P. A. Roland, *Rev. Sci. Instr.*, **37**, 1737 (1966).
- F. d'Heurle, L. Berenbaum, and R. Rosenberg, *TMS-AIME*, **242**, 502 (1968).
- T. Santala and C. M. Adams, Jr., *J. Vacuum Sci. Technol.*, **7**, S22 (1970).
- H. R. Smith, Jr., K. Kennedy, and F. S. Boericke, *ibid.*, **7**, S48 (1970).
- J. S. Foster and W. H. Pfeifer, *ibid.*, **9**, 1379 (1972).
- R. Nimmagadda, A. C. Raghuram, and R. F. Bunschah, *ibid.*, **9**, 1406 (1972).
- Circuits Mfg.*, p. 65 (April 1973).
- E. H. Snow, A. S. Grove, and D. J. Fitzgerald, *Proc. IEEE*, **55**, 1168 (1967).
- M. Knudsen, "The Kinetic Theory of Gases," p. 26, Methuen and Co., London (1934).
- L. Holland, "Vacuum Deposition of Thin Films," p. 146, John Wiley & Sons, New York (1960).
- E. B. Graper, *J. Vacuum Sci. Technol.*, **10**, 100 (1973).
- A. G. Blachman, *ibid.*, **10**, 299 (1973).
- F. d'Heurle, *Met. Trans.*, **1**, 725 (1970).
- J. J. Cuomo, R. J. Gambino, and R. Rosenberg, *J. Vacuum Sci. Technol.*, **11**, 34 (1974).
- D. V. McCaughan and R. A. Kushner, *Thin Solid Films*, **22**, 359 (1974).
- D. V. McCaughan, R. A. Kushner, and V. T. Murphy, *Phys. Rev. Letters*, **30**, 614 (1973).
- R. P. Riegert and P. Clarke, *Electron. Packaging Prod.*, **13**, 85 (1973).
- J. S. Chapin, *Res./Dev.*, **25**, 37 (1974).
- F. A. Green and B. N. Chapman, *Appl. Phys. Letters*, **27**, 189 (1975).
- D. R. Kerr, J. S. Logan, P. J. Burkhardt, and W. A. Pliskin, *IBM J. Res. Develop.*, **8**, 376 (1964).
- R. J. Kriegler, Y. C. Cheng, and D. R. Colton, *This Journal*, **119**, 388 (1972).
- M. J. Grieco, F. L. Worthing, and B. Schwartz, *ibid.*, **115**, 525 (1968).
- S. K. Tung and R. E. Caffrey, in "Thin Film Dielectrics," F. Vratny, Editor, p. 286, The Electrochemical Society Softbound Symposium Series, New York (1969).
- P. Balk, Abstract 109, p. 237, The Electrochemical Society Extended Abstracts, Spring Meeting, San Francisco, California, May 9-13, 1965.
- P. Balk, Abstract 111, p. 29, The Electrochemical Society Extended Abstracts, Fall Meeting, Buffalo, New York, October 10-14, 1965.
- R. C. Dockerty and M. D. Cowan, Abstract 51, p. 136, The Electrochemical Society Extended Abstracts, Spring Meeting, San Francisco, California, May 12-17, 1974.
- W. R. Knolle and T. F. Retajczyk, Jr., *This Journal*, **120**, 1106 (1973).
- S. Bateson, *Vacuum*, **2**, 365 (1952).
- M. Humenick, Jr. and W. D. Kingery, *J. Am. Ceram. Soc.*, **37**, 18 (1954).
- J. E. McDonald and J. G. Eberhart, *TMS-AIME*, **233**, 512 (1965).
- D. M. Mattox, *Thin Solid Films*, **18**, 173 (1973).
- B. N. Chapman, *J. Vacuum Sci. Technol.*, **11**, 106 (1974).
- "Handbook of Chemistry and Physics," Chemical Rubber Publishing Co., Cleveland, Ohio (1957).
- J. R. Black, in "Silicon Device Processing," NBS

- Special Publication 337, p. 398, U.S. G.P.O., Washington, D.C. (1970).
53. D. Peltzer and B. Herndon, *Electronics*, **44**, 52 (1971).
  54. "Selected Values of Chemical Thermodynamic Properties," NBS Circular 500, U.S. G.P.O., Washington, D.C. (1952).
  55. E. L. MacKenna, Proc. Semiconductor/IC Processing and Production Conf., p. 71, Industrial and Scientific Conf. Management, Chicago (1971).
  56. R. G. Brandes and R. H. Dudley, *This Journal*, **120**, 140 (1973).
  57. L. R. Johnson and R. M. Whelton, U.S. Pat. 3,586,922 (1971).
  58. T. Agatsuma, A. Kikuchi, K. Nakada, and A. Tomozawa, *This Journal*, **122**, 825 (1975).
  59. G. L. Schnable and R. S. Keen, in "Advances in Electronics and Electron Physics," Vol. 30, p. 79, Academic Press, New York (1971).
  60. L. B. Valdes, *Proc. IRE*, **42**, 420 (1954).
  61. S. Tolansky, "Multiple Beam Interferometry of Surface and Films," Oxford University Press, London (1949).
  62. H. L. Eschback and F. Verheyen, *Thin Solid Films*, **21**, 237 (1974).
  63. A. J. Learn, *This Journal*, **122**, 1127 (1975).
  64. R. K. Dheer, Proc. Twentieth Electronics Components Conf., p. 76, IEEE, New York (1970).
  65. P. Lloyd, *Brit. J. Appl. Phys.*, **15**, 1349 (1964).
  66. J. Fridrich, *Thin Solid Films*, **7**, 277 (1971).
  67. L. R. Kirkland and R. L. Chaplin, *J. Appl. Phys.*, **42**, 3054 (1971).
  68. I. A. Blech, J. F. Campbell, and W. H. Shepherd, Proc. Eighth Reliability Physics Symp., p. 144, IEEE, New York (1970).
  69. I. A. Blech, *Thin Solid Films*, **6**, 113 (1970).
  70. T. C. Tisone and J. B. Bindell, *J. Vacuum Sci. Technol.*, **11**, 72 (1974).
  71. G. O. B. Mahl, *Res./Dev.*, **21**, 46 (1970).
  72. I. A. Blech, *Thin Solid Films*, **13**, 117 (1972).
  73. S. N. Lee and R. A. Kjar, Proc. Thirteenth Reliability Physics Symp., p. 34, IEEE, New York (1975).
  74. K. H. Behrndt, *J. Vacuum Sci. Technol.*, **9**, 995 (1972).
  75. J. L. Vossen and J. J. O'Neill, Jr., *RCA Rev.*, **31**, 276 (1970).
  76. J. L. Vossen and J. J. O'Neill, Jr., *ibid.*, **29**, 566 (1968).
  77. J. L. Vossen, *J. Vacuum Sci. Technol.*, **8**, S12 (1971).
  78. J. B. Bindell and T. C. Tisone, *Thin Solid Films*, **23**, 31 (1974).
  79. C. N. Berglund, J. T. Clemens, and E. H. Nicollian, *This Journal*, **120**, 1255 (1973).
  80. J. D. E. Beynon, R. A. Haken, and I. M. Baker, *ibid.*, **121**, 1124 (1974).
  81. R. S. Spriggs and A. J. Learn, *Solid-State Electron.*, **10**, 353 (1967).
  82. G. Thomas, "Transmission Electron Microscopy of Metals," p. 134, John Wiley & Sons, New York (1962).
  83. J. M. Peterson, H. L. McKaig, and C. F. DePrisco, *IRE Intern. Conv. Record*, **10**, 3 (1962).
  84. For a recent review, see G. C. Harman, Proc. Twelfth Reliability Physics Symp. IEEE, p. 131, New York (1974).
  85. O. L. Anderson, H. Christensen, and P. Andreatch, *J. Appl. Phys.*, **28**, 923 (1957).
  86. C. V. Browning, L. E. Colteryahn, and D. G. Cummings, *Phys. Failure Electron.*, **4**, 428 (1965).
  87. I. A. Blech and H. Sello, *This Journal*, **113**, 1052 (1966).
  88. B. Selikson, *Proc. IEEE*, **57**, 1594 (1969).
  89. B. Selikson and T. A. Longo, *ibid.*, **52**, 1638 (1964).
  90. E. Philofsky, *Solid-State Electron.*, **13**, 1391 (1970).
  91. E. Philofsky, Proc. Ninth Reliability Physics Symp., p. 114, IEEE, New York (1971).
  92. S. M. Sze, "Physics of Semiconductor Devices," Chap. 8, Wiley-Interscience, New York (1969).
  93. M. J. Turner and E. H. Rhoderick, *Solid-State Electron.*, **11**, 291 (1968).
  94. A. Y. C. Yu and C. E. Mead, *ibid.*, **13**, 97 (1970).
  95. P. Gutknecht and M. J. O. Strutt, *Appl. Phys. Letters*, **21**, 405 (1972).
  96. K. Chino, *Solid-State Electron.*, **16**, 119 (1973).
  97. T. M. Reith and J. D. Schick, *Appl. Phys. Letters*, **25**, 524 (1974).
  98. A. Thanailakis, *J. Phys. C*, **8**, 655 (1975).
  99. J. Basterfield, J. M. Shannon, and A. Gill, *Solid-State Electron.*, **18**, 290 (1975).
  100. T. C. McGill and C. A. Mead, *J. Vacuum Sci. Technol.*, **11**, 122 (1974).
  101. A. Lewis, *Solid-State Commun.*, **13**, 547 (1973).
  102. T. Itoh, I. Matsuda, and K. Hasegawa, *J. Appl. Phys.*, **41**, 1945 (1970).
  103. B. L. Smith and E. H. Rhoderick, *Solid-State Electron.*, **14**, 71 (1971).
  104. A. Y. C. Yu, *IEEE Spectrum*, **7**, 83 (1970).
  105. J. Vilms and L. Wandinger, in "Ohmic Contacts to Semiconductors," B. Schwartz, Editor, p. 31, The Electrochemical Society Softbound Symposium Series, New York (1969).
  106. A. Y. C. Yu, *Solid-State Electron.*, **13**, 239 (1970).
  107. C. Y. Chang, Y. K. Fang, and S. M. Sze, *ibid.*, **14**, 541 (1970).
  108. H. H. Berger, *This Journal*, **119**, 507 (1972).
  109. A. Shepela, *Solid-State Electron.*, **16**, 477 (1973).
  110. P. Pellegrini and G. Salardi, *ibid.*, **18**, 791 (1975).
  111. E. J. Charlson and J. C. Lien, *J. Appl. Phys.*, **46**, 3882 (1975).
  112. J. Archer, Private communication.
  113. F. A. Trumbore, *Bell Syst. Tech. J.*, **39**, 205 (1960).
  114. H. C. Card and K. E. Singer, *Thin Solid Films*, **28**, 265 (1975).
  115. J. M. Andrews, *J. Vacuum Sci. Technol.*, **11**, 972 (1974).
  116. D. Kahng and M. P. Lepselter, *Bell Syst. Tech. J.*, **44**, 1525 (1965).
  117. J. Saltich, in "Ohmic Contacts to Semiconductors," B. Schwartz, Editor, p. 187, The Electrochemical Society Softbound Symposium Series, New York (1969).
  118. J. M. Andrews and M. P. Lepselter, *Solid-State Electron.*, **13**, 1011 (1970).
  119. H. H. Hosack, *Appl. Phys. Letters*, **21**, 256 (1972).
  120. H. H. Hosack, *J. Appl. Phys.*, **44**, 3476 (1973).
  121. A. K. Sinha and T. E. Smith, *ibid.*, **44**, 3465 (1973).
  122. A. K. Sinha, *This Journal*, **120**, 1767 (1973).
  123. A. K. Sinha, M. H. Read, and T. E. Smith, *ibid.*, **120**, 1775 (1973).
  124. R. W. Wilson, *J. Vacuum Sci. Technol.*, **12**, 26 (1975).
  125. J. O. McCaldin and H. Sankur, *Appl. Phys. Letters*, **19**, 524 (1971).
  126. R. J. Anstead and S. R. Floyd, *IEEE Trans. Electron Devices*, **ED-16**, 381 (1969).
  127. J. McCarthy, *Microelectron. Reliab.*, **9**, 187 (1970).
  128. J. A. Cunningham and R. H. Wakefield, *ibid.*, **9**, 515 (1970).
  129. T. E. Price and L. A. Berthoud, *Solid-State Electron.*, **16**, 1303 (1973).
  130. J. S. Best and J. O. McCaldin, *J. Appl. Phys.*, **46**, 4071 (1975).
  131. J. O. McCaldin and H. Sankur, *Appl. Phys. Letters*, **20**, 171 (1972).
  132. V. A. Dhaka, J. Muschinske, and W. K. Owens, *IEEE J. Solid-State Circuits*, **SC-8**, 368 (1973).
  133. R. W. Bower, *Appl. Phys. Letters*, **23**, 99 (1973).
  134. A. K. Hochberg, Trans. Electronic Materials Processing Conf.-School, p. 81, Materials Research Corp., Orangeburg, New York (1973).
  135. D. M. Duncan, U.S. Pat. 3,740,835 (1973).
  136. S. P. Bellier and L. B. Ehlert, Abstract 125, p. 316, The Electrochemical Society Extended Abstracts, Spring Meeting, Chicago, Illinois, May 13-18 (1973).
  137. See, for example, F. M. d'Heurle, *Proc. IEEE*, **59**, 1409 (1971).
  138. C. J. Smithells, "Metals Reference Book," Vol. 2, p. 643, Plenum Press, New York (1967).
  139. F. M. d'Heurle and A. Gangulee, *Thin Solid Films*, **25**, 531 (1975).
  140. J. T. Robinson and N. L. Peterson, *Surface Sci.*, **31**, 586 (1972).
  141. L. Berenbaum, *J. Appl. Phys.*, **42**, 880 (1971).
  142. M. J. Attardo and R. Rosenberg, *ibid.*, **41**, 2381 (1970).
  143. I. A. Blech and E. S. Meieran, Proc. Symp. Reliability, p. 243, IEEE, New York (1970).
  144. J. R. Black, *Proc. IEEE*, **57**, 1587 (1969).
  145. J. R. Black, *IEEE Trans. Electron Devices*, **ED-16**, 338 (1969).
  146. G. L. Hofman and H. M. Breitling, *Proc. IEEE*, **58**, 833 (1970).



147. J. C. Blair, P. B. Ghate, and C. T. Haywood, *ibid.*, **59**, 1023 (1971).
148. D. S. Chhabra and N. G. Ainslie, IBM Tech. Report TR. 22.419 (July 1967).
149. J. D. Venables and R. G. Lye, Proc. Tenth Reliability Physics Symp., p. 159, IEEE, New York (1972).
150. R. A. Sigsbee, Proc. Eleventh Reliability Physics Symp., p. 301, IEEE, New York (1973).
151. R. A. Sigsbee, *J. Appl. Phys.*, **44**, 2533 (1973).
152. Yi-S. Chang and H-Li. Huang, *Japan. J. Appl. Phys.*, **14**, 267 (1975).
153. Yi-S. Chang and H-Li. Huang, *ibid.*, **14**, 431 (1975).
154. M. J. Attardo, R. Rutledge, and R. C. Jack, *J. Appl. Phys.*, **42**, 4343 (1971).
155. G. S. Prokop and G. Liang, *J. Electron Mater.*, **1**, 474 (1972).
156. L. Braun, *Microelectron. Reliab.*, **13**, 215 (1974).
157. I. A. Blech and H. Sello, *Phys. Failure Electron.*, **5**, 496 (1967).
158. P. B. Ghate, *Appl. Phys. Letters*, **11**, 14 (1967).
159. J. K. Howard and R. F. Ross, *ibid.*, **11**, 85 (1967).
160. I. A. Blech and E. S. Meieran, *ibid.*, **11**, 263 (1967).
161. J. R. Devaney, Proc. Eighth Reliability Physics Symp., p. 127, IEEE, New York (1970).
162. P. S. Ho and L. D. Glowinski, *Z. Naturforsch.*, **26**, 32 (1971).
163. J. K. Howard and R. F. Ross, *J. Appl. Phys.*, **42**, 2996 (1971).
164. S. M. Spitzer and S. Schwartz, *This Journal*, **116**, 1368 (1969).
165. G. J. van Gorp, *Appl. Phys. Letters*, **19**, 476 (1971).
166. F. M. d'Heurle, N. G. Ainslie, A. Gangulee, and M. C. Shine, *J. Vacuum Sci. Technol.*, **9**, 289 (1972).
167. A. Learn, *J. Appl. Phys.*, **44**, 1251 (1973).
168. T. Satake, K. Yokoyama, S. Shirakawa, and K. Sawaguchi, *Japan. J. Appl. Phys.*, **12**, 518 (1973).
169. I. A. Blech and E. S. Meieran, *J. Appl. Phys.*, **40**, 485 (1969).
170. S. J. Horowitz and I. A. Blech, *Mater. Sci. Eng.*, **10**, 169 (1972).
171. J. Weise, *Thin Solid Films*, **13**, 169 (1972).
172. A. Gangulee and F. M. d'Heurle, *ibid.*, **16**, 227 (1973).
173. R. Rosenberg and L. Berenbaum, *Appl. Phys. Letters*, **12**, 201 (1968).
174. M. C. Shine and F. M. d'Heurle, *IBM J. Res. Develop.*, **15**, 378 (1971).
175. M. M. Schlacter, E. S. Schlegel, R. S. Keen, Jr., R. A. Lathlaen, and G. L. Schnable, *IEEE Trans. Electron Devices*, **ED-17**, 1077 (1970).
176. J. C. Blair, P. B. Ghate, and C. T. Haywood, *Appl. Phys. Letters*, **17**, 281 (1970).
177. J. C. Blair, C. R. Fuller, P. B. Ghate, and C. T. Haywood, *J. Appl. Phys.*, **43**, 307 (1972).
178. B. N. Agarwala, M. J. Attardo, and A. P. Ingraham, *ibid.*, **41**, 3954 (1970).
179. A. Learn and W. H. Shepherd, Proc. Ninth Reliability Physics Symp., p. 129, IEEE, New York (1971).
180. L. Berenbaum and R. Rosenberg, *Thin Solid Films*, **4**, 187 (1969).
181. R. Rosenberg, *Appl. Phys. Letters*, **16**, 27 (1970).
182. J. C. Pieri, J. Bagnol, E. Berger, and R. Jouty, *J. Mater. Sci.*, **6**, 1192 (1971).
183. C. B. Oliver, Proc. Sixth Reliability Physics Symp., p. 209, IEEE, New York (1968).
184. J. R. Black, *IEEE Trans. Electron Devices*, **ED-17**, 800 (1970).
185. G. S. Prokop, C. Y. Ting, and R. R. Joseph, Proc. Eighth Reliability Physics Symp., p. 121, IEEE, New York (1971).
186. G. S. Prokop and R. R. Joseph, *J. Appl. Phys.*, **43**, 2595 (1972).
187. A. Learn, *J. Electron. Mater.*, **3**, 531 (1974).
188. M. Ohring, *Mater. Sci. Eng.*, **7**, 158 (1971).
189. M. Ohring, *J. Appl. Phys.*, **42**, 2653 (1971).
190. R. Rosenberg and M. Ohring, *ibid.*, **42**, 5671 (1971).
191. H. Suhl and P. A. Turner, *ibid.*, **44**, 4891 (1973).
192. F. d'Heurle and I. Ames, *Appl. Phys. Letters*, **16**, 80 (1970).
193. A. Learn, *ibid.*, **19**, 292 (1971).
194. C. B. Oliver and D. E. Bower, Proc. Eighth Reliability Physics Symp., p. 116, IEEE, New York (1970).
195. R. Shield and T. H. Ramsey, Proc. Electron. Comp. Conf., p. 424, IEEE, New York (1969).
196. H. J. Bhatt, *Appl. Phys. Letters*, **19**, 30 (1971).
197. P. M. Austin and A. F. Mayadas, *J. Vacuum Sci. Technol.*, **8**, 606 (1971).
198. L. Berenbaum, *Appl. Phys. Letters*, **20**, 434 (1972).
199. N. G. Ainslie, F. M. d'Heurle, and O. C. Wells, *ibid.*, **20**, 173 (1972).
200. R. Rosenberg, *J. Vacuum Sci. Technol.*, **9**, 263 (1972).
201. I. Ames, F. M. d'Heurle, and R. E. Horstmann, *IBM J. Res. Develop.*, **14**, 461 (1970).
202. F. M. d'Heurle, *Met. Trans.*, **2**, 683 (1971).
203. B. N. Agarwala, B. Patnaik, and R. Schnitzel, *J. Appl. Phys.*, **43**, 1487 (1972).
204. A. K. Kakar, *Solid State Technol.*, **16**, 47 (1973).
205. B. N. Agarwala, L. Berenbaum, and P. Peressini, *J. Electron. Mater.*, **3**, 137 (1974).
206. A. Gangulee and F. M. d'Heurle, *Appl. Phys. Letters*, **19**, 76 (1971).
207. R. Rosenberg, A. F. Mayadas, and D. Gupta, *Surface Sci.*, **31**, 566 (1972).
208. F. M. d'Heurle, A. Gangulee, C. F. Aliotta, and V. A. Ranieri, *J. Electron. Mater.*, **4**, 497 (1975).
209. A. Gangulee and F. M. d'Heurle, *Thin Solid Films*, **25**, 317 (1975).
210. F. M. d'Heurle and A. Gangulee, in "The Nature and Behavior of Grain Boundaries," H. Hu, Editor, p. 339, Plenum Press, New York (1973).
211. J. C. Anderson, *Thin Solid Films*, **12**, 1 (1972).
212. F. M. d'Heurle and A. Gangulee, Proc. Tenth Reliability Physics Symp., p. 165, IEEE, New York (1972).
213. J. J. Gajda and V. C. Marcotte, Proc. Int. Microelectron. Symp., p. 5-5-1 (1971).
214. L. Berenbaum and R. Rosenberg, Proc. Ninth Reliability Physics Symp., p. 136, IEEE, New York (1971).
215. L. Berenbaum and B. Patnaik, *Appl. Phys. Letters*, **18**, 284 (1971).
216. E. Hall, E. Philofsky, and A. Gonzales, *J. Electron. Mater.*, **1**, 333 (1972).
217. G. A. Walker and C. C. Goldsmith, *J. Appl. Phys.*, **44**, 2452 (1973).
218. G. A. Scoggin, B. N. Agarwala, P. P. Peressini, and A. Brouillard, Proc. Thirteenth Reliability Physics Symp., p. 151, IEEE, New York (1975).
219. J. K. Howard and R. F. Ross, *Appl. Phys. Letters*, **18**, 344 (1971).
220. P. S. Ho and J. K. Howard, *J. Appl. Phys.*, **45**, 3229 (1974).
221. P. S. Ho and J. E. Lewis, *Thin Solid Films*, **25**, 301 (1975).
222. H. S. Wildman, J. K. Howard, and P. S. Ho, *J. Vacuum Sci. Technol.*, **12**, 75 (1975).
223. Y. Limoge, *Solid-State Commun.*, **12**, 1141 (1973).
224. P. S. Ho and J. K. Howard, *Appl. Phys. Letters*, **27**, 261 (1975).
225. J. L. Vossen, G. L. Schnable, and W. Kern, *J. Vacuum Sci. Technol.*, **11**, 60 (1974).
226. D. R. Collins, S. R. Shortes, W. R. McMahon, R. C. Bracken, and T. C. Penn, *This Journal*, **120**, 521 (1973).
227. R. Heinecke, P. G. Eldridge, and M. Pion, Proc. International Conf. on Microelectronics, Eastbourne, June 1969, p. 27, IEE, London (1969).
228. R. Birk, *TMS-AIME*, **242**, 523 (1968).
229. P. B. Ghate, W. R. Gardner, and D. L. Crosthwait, *IEEE Trans. Reliability*, **R-22**, 186 (1973).
230. K. Sato, S. Harada, A. Saiki, T. Kimura, T. Okubo, and K. Mukai, Proc. Electron. Comp. Conf., p. 15, IEEE, New York (1973).
231. For a general reference see, G. L. Schnable, W. Kern, and R. B. Comizzoli, *This Journal*, **122**, 1092 (1975).
232. D. L. Tolliver and D. L. Elgan, Abstract 183, p. 51, The Electrochemical Society Extended Abstracts, Fall Meeting, Philadelphia, Pa., Oct. 9-14, 1966.
233. M. L. Barry and P. Olofsen, *Solid State Technol.*, **11**, 39 (1968).
234. H. Sunami, Y. Itoh, and K. Sato, *J. Appl. Phys.*, **41**, 5115 (1970).
235. J. P. Rioult and G. Hurst, *Thin Solid Films*, **10**, 283 (1972).
236. C. J. Santoro and D. L. Tolliver, *Proc. IEEE*, **59**, 1403 (1971).
237. L. H. Hall and D. L. Crosthwait, *Thin Solid Films*,

- 9, 447 (1972).
238. R. A. Haken, I. M. Baker, and J. D. E. Beynon, *ibid.*, **18**, S3 (1973).
239. R. A. Moline, R. R. Buckley, S. E. Haszko, and A. U. MacRae, *IEEE Trans. Electron Devices*, **ED-20**, 840 (1973).
240. P. Chaudhari, *J. Appl. Phys.*, **45**, 4339 (1974).
241. P. L. Castro and J. F. Campbell, in "Ohmic Contacts to Semiconductors," B. Schwartz, Editor, p. 332, The Electrochemical Society Softbound Symposium Series, New York (1969).
242. C. J. Santoro, *This Journal*, **116**, 361 (1969).
243. C. J. Dell'Oca and A. J. Learn, *Thin Solid Films*, **8**, R47 (1971).
244. E. Philofsky, K. Ravi, E. Hall, and J. Black, Proc. Ninth Reliability Physics Symp., p. 120, IEEE, New York (1971).
245. D. S. Herman, M. A. Schuster, and R. M. Gerber, *J. Vacuum Sci. Technol.*, **9**, 515 (1972).
246. K. Sato, T. Oi, H. Matsumaru, T. Okubo, and T. Nishimura, *Met. Trans.*, **2**, 691 (1971).
247. D. L. Kinosh and D. L. Belitskus, *This Journal*, **118**, 1375 (1971).
248. For a recent reference see, H. Khajezadeh and A. S. Rose, Proc. Thirteenth Reliability Physics Symp., p. 87, IEEE, New York (1975).
249. N. Nagasima, H. Suzucki, T. Tanaka, and S. Nishida, *This Journal*, **121**, 434 (1974).
250. W. M. Paulson and R. W. Kirk, Proc. Twelfth Reliability Physics Symp., p. 172, IEEE, New York (1974).
251. H. Koelmans, *ibid.*, p.168.
252. M. L. Barry, Private communication.
253. K. R. Van Horn, Editor "Aluminum. Vol. I. Properties, Physical Metallurgy and Phase Diagrams," p. 238, American Society for Metals, Metals Park, Ohio (1967).
254. R. C. Olberg, Private communication.
255. A. J. Learn, *Proc. IEEE*, **61**, 476 (1973).
256. Ref. (253), p. 206.
257. C. J. Dell'Oca and M. L. Barry, *Solid-State Electron.*, **15**, 659 (1972).
258. H. F. Sterling and R. C. G. Swann, *ibid.*, **8**, 653 (1965).
259. S. M. Hu and L. V. Gregor, *This Journal*, **114**, 826 (1967).
260. C. J. Mogab, P. M. Petroff, and T. T. Sheng, *ibid.*, **122**, 815 (1975).
261. T. M. Kennedy, *Electron. Packaging Prod.*, **14**, 136 (1974).
262. P. C. Munro and H. W. Thompson, Jr., *This Journal*, **122**, 127 (1975).

## The Growth of Uniform Submicron GaAs Layers by Liquid Phase Epitaxy

Hadis Morkoc and L. F. Eastman

School of Electrical Engineering, Cornell University, Ithaca, New York 14853

### ABSTRACT

Very close agreement between theory and experiment in the growth of submicron layers has been achieved. Difficulties in obtaining uniform wetting have been overcome by growing a porous and amorphous oxide layer on the substrate and stripping it off in 50% aqueous HCl immediately before it is loaded into the reactor. By the introduction of a source-seed crystal, precise saturation of the melt has been obtained. It has been observed that slow growth rates (800 Å/min) and lower growth temperatures yield nearly featureless FET layers.

Early successful use of liquid phase epitaxy (LPE) in the preparation of GaAs laser diodes stimulated a very intense research program to provide a wide variety of microwave and optical materials and devices. Since the original application of LPE to compound semiconductor technology using a tilting boat by Nelson (1), dipping and slider boats have been developed to generate material for high performance devices. In particular, the bottom-of-the-melt method in which the growth is initiated from the bottom and the melt is saturated from the top surface has met stringent tolerances required by state-of-the-art devices. This technique has been widely applied specifically to generate materials for such complete and complicated devices as Read structures, double heterostructure lasers, Gunn logic devices, and microwave field effect transistors.

Small and Barnes (2) reported on the diffusion-limited LPE growth model and on the solution of the diffusion equation involved for a set of simplified boundary conditions. Later, Crossley and Small (3) presented a numerical calculation method to compute the precise As profile, with somewhat more accurate boundary conditions at the growth interface, which advances into the solution as the growth progresses. Minden (4) reported on a closed form solution of the diffusion equation with the semi-infinite melt approximation. Finally, Rode (5) gave a series solution of the

LPE diffusion in a bounded melt including the temperature dependence of the diffusion coefficient of As in a Ga solution.

Little is present in the literature concerning the LPE growth of the submicron layers required for microwave FET's. It is therefore the intention of this paper to discuss the particular difficulties involved in the growth of such layers by LPE. The dominant problems associated with submicron-thick epitaxial layers are thickness uniformity and reproducibility, which are common to both LPE and vapor phase epitaxy (VPE) techniques. We will show that in the case of LPE these problems are predominantly caused by nonuniform wetting, which can be overcome by techniques to be described. Nonsimultaneous wetting, in the very beginning moments of growth, which is, in general, caused by a residual or deposited oxide layer on the surface of the substrate, results in nonuniform layer thickness. In our experiments oxide layer formation is prevented by making the system vacuum tight and limiting the water vapor content in the reactor. Any native oxide and surface impurities present are imbedded in an intentionally grown porous oxide layer and are removed when it is stripped off with 50% aqueous HCl. Stripping just prior to placing the substrate into the boat allows us to start with an oxide-free surface. A source-seed crystal is located on the slider forward of the main substrate to assure precise saturation of the melt; only such saturation

\* Key words: liquid phase epitaxy, submicron, GaAs.

permits a uniform growth rate over the total surface of the substrate. By following the above techniques, sub-micron FET layers can be grown by LPE with as good thickness uniformity as by VPE and with significantly better reproducibility. Wetting, thickness control, reproducibility, and the surface morphology will be discussed in detail in following sections. In addition, the predictions of computer calculations which include a temperature dependent As diffusion coefficient will be compared with experimental results.

### The System

The reactor consists of a horizontal sliding boat inside a 64 mm OD quartz tube heated by a three-zone resistive furnace. The fused quartz tube is cleaned in aqua regia approximately every 50 runs in a negative pressure tube cleaning hood (Air Control, Incorporated, Norristown, Pennsylvania). Hydrogen is purified by passing it through a Matheson Model 8361 Pd diffuser. The high purity hydrogen is introduced into the vacuum-tight reactor via high purity stainless tubing and fittings. On the output end, the hydrogen passes through a Panametrics  $\text{Al}_2\text{O}_3$  water vapor sensor to monitor quartz dissociation and any leaks. The exhaust end is located in a laminar flow loading station where positive pressure is maintained to eliminate particle migration from the room into the reactor during loading and unloading. The reactor is purged with high purity gaseous nitrogen before and after loading to prevent explosive gas mixtures. In addition, the gaseous nitrogen flow was maintained during loading to inhibit particle diffusion into the reactor. Before the first growth attempt made, the fused quartz reactor is baked at an elevated temperature, such as  $1000^\circ\text{C}$  for 5-6 hr before the graphite boat is inserted. This boat has previously been out-gassed at  $1400^\circ\text{C}$  in a vacuum chamber with an rf induction heater down to  $10^{-7}$  Torr. A second bakeout at  $850^\circ\text{C}$  in hydrogen atmosphere with the boat wells filled with Ga lasts 10 hr and in the end this Ga is discarded. Skipping the outgassing step and the last bakeout causes a  $10^{17} \text{ cm}^{-3}$  impurity level, particularly for a freshly fabricated boat.

Figure 1 is a 3-D diagram of the graphite boat used in the experiment. The slider boat setup has been chosen because the only objective of this work was to grow material for high performance devices. It is similar to that described by Rode (5) except that the body of this boat consists of two pieces held together with precision graphite pins, with the upper part resting on the slider with the force of gravity. This configuration allows practically negligible clearance between the bottom surface of the upper half and the

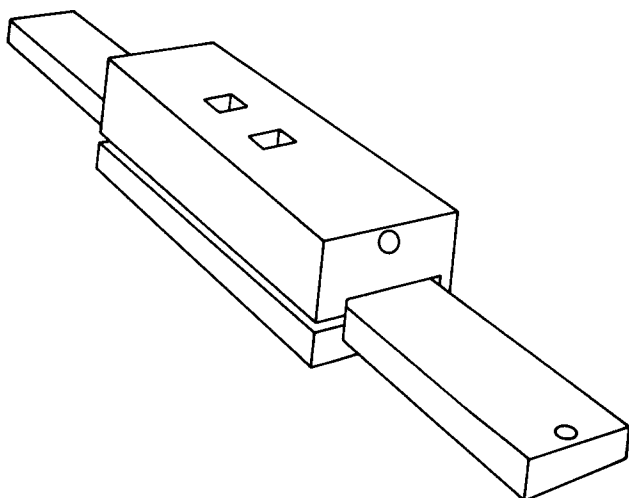


Fig. 1. Diagram of the double-bin gravity-type boat. The area of wells is  $1 \times 1 \text{ cm}$ , the height is 15 mm, the spacing between the wells is 20 mm, the wall thickness at the wells is 15 mm.

substrate. The resultant wiping action upon removal of the substrate after growth eliminates localized GaAs deposition from Ga-rich melt droplets on the grown layers. This feature is of great importance in obtaining uniform thicknesses and a sharp, flat interface between successive layers, in the case where a buffer layer is to be grown.

A hydrogen flow rate of  $600 \text{ cm}^3/\text{min}$  (quartz tube bore is 60 mm ID) has been found to be the minimum adequate level for uniform wetting and has been standardized upon. Measured water vapor content is less than 0.2 ppm when the furnace is hot. The furnace (Lindberg Model 54357) has three separately controlled zones which keep the temperature uniform within  $\pm 1^\circ\text{C}$  over a length of 50 cm.

### Substrate Qualification and Preparation

The substrate material has been obtained from three different suppliers within the United States (Laser Diode, Crystal Specialties, and Texas Materials). Both (100) and  $3^\circ$  off (100) toward (110) oriented Cr-doped substrates have been used and our experiments with submicron and 5- $10\mu$  thick layers showed no apparent disadvantage of using  $3^\circ$  off (100) substrates (made available to us by Wright Patterson Air Force Base Laboratories, Ohio). A small piece from each shipment is subjected to a qualification process similar to that described by Barrera (6) with the aid of evaporated Al Schottky barriers. Since there are very few qualifiable Cr-doped substrates available, work on growing a  $5\mu$  thick buffer layer underneath the active layer is already underway. To date, we have achieved high purity layers with repeatable levels of mobility of  $170,000 \text{ cm}^2/\text{V}\cdot\text{sec}$  at liquid nitrogen temperature and a total ionized impurity density of  $1.9 \times 10^{14} \text{ cm}^{-3}$ , with a net donor density of less than  $1 \times 10^{14} \text{ cm}^{-3}$ ; the details of this project will be reported elsewhere.

In processing microwave FET's, the pattern geometry is created by electron beam lithographic or photolithographic exposure techniques. In any case, it is necessary to have an extremely flat surface to be able to achieve sharp geometry and high yield. This in a sense puts strong requirements on the preparation of the substrates. We should therefore examine the details of substrate preparation in light of two main requirements: cleanliness and planar surface achievement.

To obtain a planar layer requires an initial planar substrate surface because any corrugations on the substrate are closely replicated on the epilayer. The substrate thickness uniformity should also be within reasonable tolerances. Thus the polishing and etching techniques should be optimized to result in flat and parallel surfaces.

To achieve a flat surface, we removed the saw damage by lapping on both sides with  $5 \mu\text{m}$  grit and then mechanical-chemical polishing both sides down to  $250\mu$  final thickness. The pressure and chemical flow rate during polishing are adjusted to obtain the best resulting surface. The chemical etch before the substrate is loaded into the reactor is done in  $\text{H}_2\text{SO}_4$ :  $\text{H}_2\text{O}_2$ :  $\text{H}_2\text{O}$  (5:1:1) at room temperature for 4 min; note that  $\text{H}_2\text{SO}_4$  must be added slowly to prevent boiling, and thus turbulence in the liquid, which may be responsible for corrugations on the substrate surface.

### Wetting

As stressed earlier, wetting is the single most dominant factor in achieving uniform submicron epitaxial layers. Once simultaneous wetting on the surface is achieved, it is then only a question of parameter selection and control (growth rate, growth temperature, and saturation technique) to accomplish not only a repeatable thickness but also close agreement with the predicted thickness values from the diffusion-limited growth theory we have mentioned. Any irregularities in the wetting during the early part of the growth will have a magnified effect in the thick-

ness, because the locally wetted areas of the melt will be deficient in As concentration relative to the non-wetted areas (where deposition does not take place). This in turn allows a relatively longer growth time and larger growth rate on the nucleation centers, with a transverse surface diffusion of As to the deposition sites near the interface.

Barrera (7) has indicated that he achieved better wetting when the reactor was leak tight. He also urged that high hydrogen flow rates improve the wetting. He then concluded that in a leaky reactor, oxide deposition on the substrate surface prior to epilayer deposition has the prime responsibility in preventing uniform wetting. Clearly, higher hydrogen flow rates reduce the amount of oxygen in the reactor, among other benefits. One then concludes that the oxide deposition must be avoided by vacuum sealing the reactor. The second important aspect related to the oxide layer is that the native oxide and the remaining organic impurities should be removed from the surface of the substrate. The etch in 5:1:1 for 4 min removes approximately  $5\mu$  of material from each side to assure that minor work damage from polishing is eliminated. We have observed that this etch leaves a thin oxide layer (about 30-50Å) and does not remove some organic based impurities. Experiments at 735°, 750°, and 780°C have been carried out to investigate the initial growth phase and the degree of wetting. Shown in Fig. 2 is a layer grown at 735°C on a substrate which had undergone a standard cleaning process. Supercooling of  $1/4^\circ\text{C}$  was applied to initiate a downward temperature ramp and the substrate was quickly slid under the melt, being kept there for 5 sec while the slope of the ramp cooling was maintained at  $1^\circ\text{C}/\text{min}$ . It is clear that the growth was only initiated on small islands; moreover, this photograph is of the region of highest density of these nucleation centers. There was no growth at all on most of the substrate. Similar experiments (at 750° and 780°C) indicated that the wetting becomes better as the growth temperature increases. This indicates that the residual oxide layer is removed during the relatively high temperature bakeout period and the transverse expansion of the nucleation centers is aided by the faster growth rate.

Shaw (8) has found that an oxide layer on Ga and GaAs remains below approximately 700°-750°C and disappears above this critical temperature, in strong agreement with our observations.

Dawson (9) mentioned that his substrates were cleaned in HCl without giving any particular reason.

Spitzer *et al.* (10) and Rode *et al.* (11) reported that aqueous HCl is used to remove the oxide layer after it has been grown by anodic oxidation and, especially in the former paper, it is pointed out that HCl would not remove the oxide layer after it had gone through a heat-treatment in dry nitrogen atmosphere. Cho (12) has also indicated that employing a combination of amorphous oxide layer growth followed by removal in aqueous HCl helps achieve flatter layers. Schwartz (13) presented the results he achieved concerning the oxidation of GaAs and GaP during various types of chemical etching. For instance, on a (100) surface he found that in room temperature water  $\text{Ga}_2\text{O}_3$ , and in warm water (60°C) GaO, growth takes place.

In light of all this background, we began to look into improving the technique of removing oxide layers (including the native oxide) during the preparation phase. We have found that the best results are achieved by growing an approximately 150Å amorphous and porous oxide layer in room temperature DI water for 20 min. The thickness of such an oxide layer has been measured using a Talystep which also demonstrated the spongy nature of the surface. The same thickness can be obtained in warm water in a shorter period of time. However, precaution must be taken as the oxide layer tends to become polycrystalline at higher temperatures and cannot be easily and uniformly removed in HCl.

The stripping process, which uses 50% aqueous HCl for a minimum of 5 min, not only removes the freshly grown porous oxide layer but also removes any residual native oxide along with much of the organic impurities on the outer surface. A very quick DI water rinse is applied and the substrate is loaded into the reactor after the water is blown off with high purity gaseous nitrogen. The substrate is not exposed to free air for more than about 20 sec (gaseous nitrogen flow in the reactor is maintained during loading as well).

Experiments similar to those described earlier have been carried out to study the early growth phase and therefore the effect of HCl treatment. In Fig. 3 a photomicrograph of a layer grown at 735°C on a substrate which had gone through porous oxide-HCl treatment is shown. Growth was initiated after a supercooling of  $1/4^\circ\text{C}$  and 5 sec growth time at a cooling rate of  $1^\circ\text{C}/\text{min}$  was allowed. Notice the remarkable improvement in the wetting; it is very uniform and the layer is nearly featureless. The layer thickness is estimated to be below 150Å. The same experiment has been repeated at 750° and 780°C.

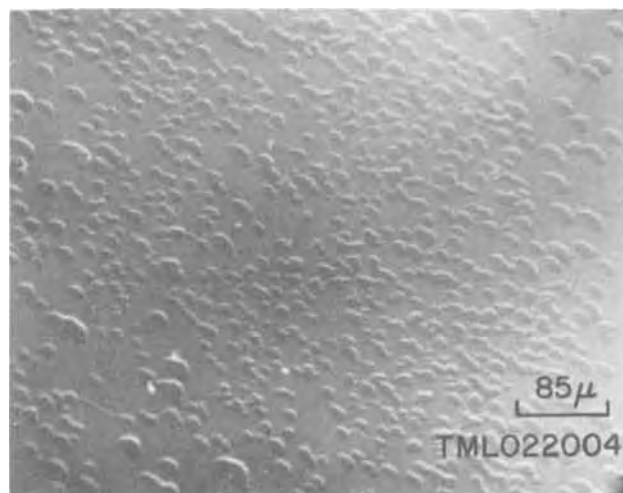


Fig. 2. Photomicrograph (Nomarski phase contrast) of a layer grown at 735°C on a substrate which had undergone only a standard cleaning procedure. The growth time  $t = 5$  sec; linear cooling  $\alpha = 1^\circ\text{C}/\text{min}$ , supercooling  $1/4^\circ\text{C}$ . Notice the formation of nucleated growth centers and nonuniform wetting.



Fig. 3. Photomicrograph (Nomarski phase contrast) of a layer grown at 735°C on a substrate that had undergone a porous oxide-HCl treatment in addition to standard cleaning. Growth parameters were unchanged from that shown in Fig. 2. The improvement in the wetting is remarkable.

It can be concluded that to achieve uniform sub-micron epilayers for FET's, the crucial "wetting" parameter can be controlled with the porous oxide-50% HCl process.

### As Profile, Growth Rate, and Layer Thickness

We have pointed out earlier that once the wetting is controlled, the other important parameters are the perfect saturation of the melt solution and the growth rate. We now examine the effect of these parameters and compare the experimental results with theoretical predictions.

In the growth of thick layers such as Gunn diode layers, a deviation of about  $\pm 1^\circ\text{-}2^\circ\text{C}$  in the saturation of the melt with As will have a small effect on the final layer thickness since a total temperature drop of around  $20^\circ\text{C}$  takes place. By contrast, for the growth of submicron ( $0.2\mu$ ) epilayers, the total temperature drop can be as low as  $1.5^\circ\text{C}$  ( $780^\circ\text{C}$ , with cooling rate  $\alpha = 1^\circ\text{C}/\text{min}$ , supercooling  $\Delta T = 0$ ). Therefore, it is clear that one cannot afford any under- or oversaturation of the melt. Our observations show that the wetting is best when the melt is saturated from the top. Experimentally we have found that bakeout times about twice as long as the diffusion time are not necessarily long enough to establish equilibrium. (To check this point, a GaAs source 10 mg heavier than that found from Rubenstein's data (14) was weighed and added to the melt.) The saturation was studied by placing a polished source-seed crystal beneath the melt after a bakeout time of  $2 \times (\text{melt height})^2/\text{diffusion coefficient}$  during which the temperature was kept practically constant. The source seed was removed after 10 min and examination showed that a very nonuniform backdissolving occurred. Non-uniformity can be caused by strains and imperfections in the bulk material but, nevertheless, it is very likely that the bottom of the melt was undersaturated and in a nonuniform manner. Therefore, we find that it is necessary to have a source-seed crystal [first used by Dawson; see Ref. (5) and (9)] preceding the main substrate to trim out the As concentration of the melt at the bottom. Only then can one achieve repeatable thicknesses by controlling the growth rate on oxide-free substrates. The layers grown without a source-seed crystal have thicknesses ranging from negative values (backdissolving) up to the intended values.

The growth rate is the third mechanism that is of vital consequence to the parameters of the grown layer. Submicron layers with thicknesses of about  $0.2\mu$  have been grown at temperatures of  $780^\circ$ ,  $750^\circ$ ,  $735^\circ$ , and  $700^\circ\text{C}$ . The ramp cooling rate was in all cases  $\alpha = 1^\circ\text{C}/\text{min}$  and in certain cases supercooling of  $\Delta T = 3^\circ\text{C}$  was applied. Our experiments show that with high growth rate, control over the thickness repeatability becomes poorer. Moreover, surface imperfections, such as cusps and undulations become more pronounced in contrast to Crossley and Small (15) and Hsieh (16). Illustrated in Fig. 4 is a layer grown at  $780^\circ\text{C}$  for 15 sec after a supercooling of  $3^\circ\text{C}$ . The wetting is adequate but the surface features make such a layer useless. In this case no source-seed crystal was used. The growth rate in the early moments of the growth is fairly high and decreases with time. The growth rate has been calculated at  $780^\circ\text{C}$  from the numerical analysis including the temperature dependence of As diffusion coefficient and is shown in Fig. 5, both with and without a supercooling of  $3^\circ\text{C}$ . It is very clear that the difference between the two conditions is very large. The much higher growth rates associated with supercooling place nearly impossible requirements on the actual growth time, especially for submicron layers. For example, a small hesitation of 2 sec pushing the slider will mean about 2 sec of traveling time under the melt and 13 sec of actual stationary contact time (at  $780^\circ\text{C}$  with  $\Delta T = 3^\circ\text{C}$ ). During this 2 sec, about 15% of the total growth



Fig. 4. Steps caused by a fast growth rate. This particular layer is about  $0.2\mu$  thick and grown at  $780^\circ\text{C}$ . The growth parameters are: supercooling  $\Delta T = 3^\circ\text{C}$ , linear cooling rate  $\alpha = 1^\circ\text{C}/\text{min}$ , and the growth time  $t = 15$  sec.

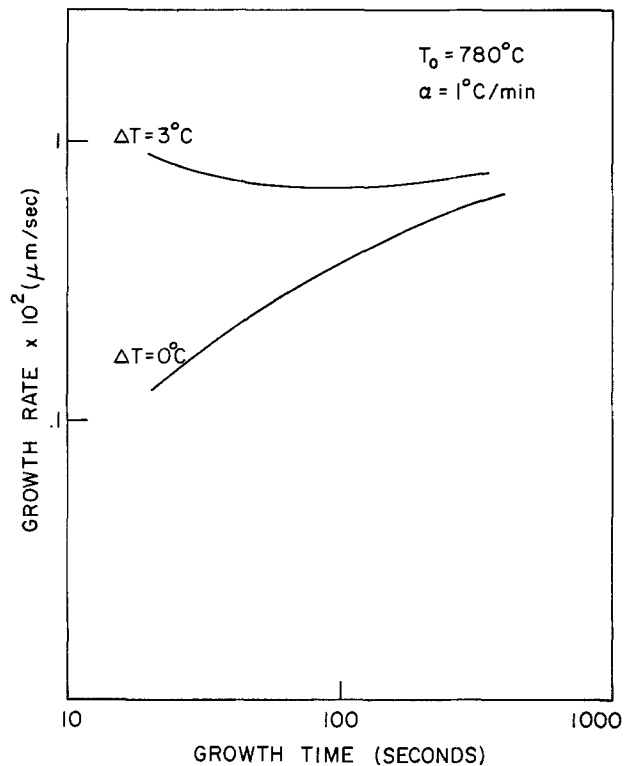


Fig. 5. Plots of growth rate at  $780^\circ\text{C}$  as a function of growth time both with and without a supercooling of  $3^\circ\text{C}$ .

would take place causing steps in the thickness similar to meniscus lines to form [first observed by Crossley and Small (15)]. In addition, a faster growth rate may cause steps.

We have done experiments at  $780^\circ\text{C}$  with only ramp cooling ( $\alpha = 1^\circ\text{C}/\text{min}$ ) and observed considerable improvement in thickness control and surface morphology. A further improvement in both occurs when a  $0.2\mu$  (or less)-thick layer is grown on the source seed and subsequently a  $0.2\mu$  layer is grown on the main substrate.

These phenomena can be explained by examining the As concentration profile, the slope of which at the substrate-solution interface determines the growth rate. Shown in Fig. 6 is a set of calculated As profiles vs. segment number at  $780^\circ\text{C}$ . Segment number 0 corresponds to the substrate-liquid interface at  $t = 0$  and segment number 50 corresponds to the opposite surface

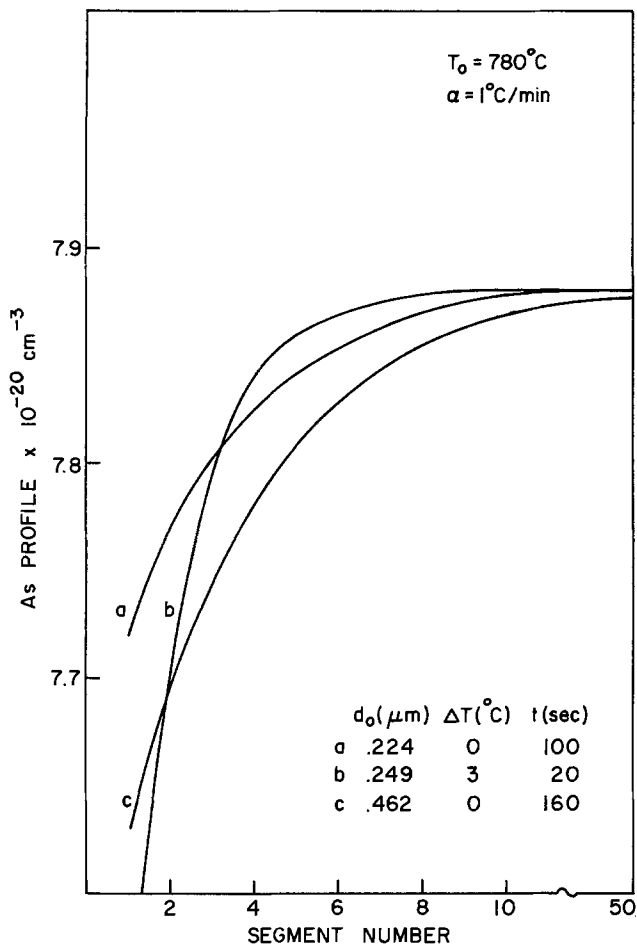


Fig. 6. Predicted As profile in Ga melt at the end of growth with various growth parameters at 780°C.  $d_0$  represents the grown layer thickness after a time interval  $t$  at a cooling rate of 1 °C/min with and without a supercooling of  $\Delta T$ .

of the solution (the melt height = 1 cm); As profile is calculated for each segment every 2 sec of growth time. Figure 6b shows the As profile at the end of a 0.25 $\mu$  layer growth when a supercooling of 3°C was applied. The As profile at the beginning of the growth is much steeper than at the end; even then, the profile is very steep, making the thickness very hard to control. Shown in Fig. 6a is the As profile at the end of the growth of the 0.22 $\mu$  thick layer on the source seed with no supercooling. The profile is not steep even during early growth because there are no sudden excess As concentrations. Shown in Fig. 6c is As profile at the end of the 0.24 $\mu$  layer grown on the main substrate (as opposed to the beginning profile in Fig. 6a). It is clear that the As profile follows a very nice and controllable variation from the beginning to the end. To still further decrease the growth rate (and hence improve controllability), the growth temperature was dropped from 780°C which had been the normal growth temperature, down first to 750°C, later 735°C, and presently to 700°C. We are able to lower the growth temperature so much because with the HCl treatment the substrates wet very uniformly even at 700°C.

Preliminary studies show that the layers can be grown more repeatably at 700°C than at higher growth temperatures. The optimum average growth rate to achieve minimum cusp density has been experimentally determined to be about 800 Å/min. The density of the cusps decreased considerably [ $10^5 \text{ cm}^{-2}$  at 780°C and  $10^2 \text{ cm}^{-2}$  or less at 700°C (17)], as well as timing errors, because the growth rate is slower (it now takes almost 3 min to grow 0.2 $\mu$  thick layers).

Thickness and doping profiles have been deduced from C-V measurements done with the aid of a phase-locked amplifier and by using an automatic profiler. To

do this, Al Schottky barriers of 3000Å thick and 250 $\mu$  in diameter have been evaporated through a mask under high vacuum ( $\sim 6 \times 10^{-8}$  Torr). Lehovc and Zuleeg (18) have argued that the C-V method of determining impurity concentration and distribution becomes less accurate as the depletion layer expands toward the substrate interface. Near pinch-off conditions, the channel resistivity becomes so high that the resistivity between the two back-to-back biased Schottky barrier diodes becomes very large. To reduce the effect of the forward-bias resistance, a large-area Al pad has been evaporated and biased. This diode is forward biased during the measurement. Wiley and Miller (19) have reported on the effect of series resistance in C-V profiling, how to reduce it, and how to interpret the measurement when a large series resistance is present. It is clear that one can only be specific about the thickness of submicron epitaxial layers deduced from C-V plots after the errors associated with the measurements have been analyzed. An alternative way would be to actually fabricate FET's to evaluate the layers, which is time consuming and uneconomical.

Nevertheless, illustrated in Fig. 7 is the measured doping profile of a layer grown at 735°C using a source-seed crystal. Notice that the doping profile is flat and the total thickness variation is small.

Layers with thicknesses ranging from 2 to 5 $\mu$  have been grown at 700°, 735°, 750°, and 780°C. The experimental thickness data have been compared against numerical calculations, which included the temperature dependence of As diffusion coefficient determined by Rode (5), and close agreement within measurement errors has been achieved. Therefore, we completely agree about not only the diffusion-limited growth model, but the diffusion coefficient of As as a function of temperature in Ga solution as presented by Rode. Moon and Long (20) have recently used the solution of the diffusion equation reported by Small and Barnes (2) in 1969. In the 1969 article  $C_0$  appears (equilibrium As concentration in the melt) in the denominator of the thickness equation. This was changed correctly to  $C_s$  (As concentration in the solid) in the article by Crossley and Small (3) in 1971. Hsieh (16) has reported on the growth relations from supercooled, linearly cooled, and a combination of both types, which was a restatement

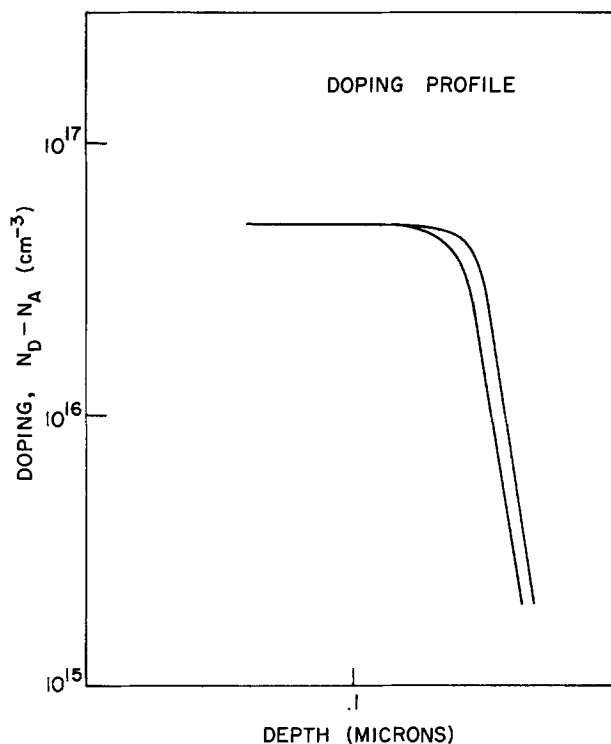


Fig. 7. Doping profile of a layer grown at 735°C using a source-seed crystal with no supercooling.

ment of those originally reported by Small and Barnes (2) and Crossley and Small (3). The main point made by Moon and Long (20) was that the diffusion coefficient appears to be relatively constant for the large temperature drop of  $30^\circ$  used by them. This result is in complete contrast with our work and that of Rode's for smaller temperature drops. It is clear that the simplified theory they used is only realistic for short growth times and small temperature drops; these limits vary with the growth temperature due to the solubility curve. Therefore, since their theory predicts thicker layers than actually grown, and since a  $30^\circ$  temperature drop, at  $1^\circ\text{C}/\text{min}$ , exceeds the realistic range, the semi-infinite melt approximation becomes a questionable assumption. It is possible that minute crystallites as shown by Hsieh (16) and Crossley and Small (3) competed for As during growth in their experiments to yield their results.

The layers grown at  $780^\circ$  and  $750^\circ\text{C}$  with and without a supercooling and at  $735^\circ\text{C}$  with a supercooling have been selected out to have C-V measurements performed on them. Thus the data points for these cases do not show much spread in the thickness vs. growth time curves to be described. But the measurements on layers grown at  $735^\circ\text{C}$  preceded by a seed crystal have been done with no selection. Therefore the displayed spread in data points for this case is much greater even though it is actually almost the same as the others. In Fig. 8, the calculated thickness vs. growth time at  $780^\circ\text{C}$  is shown. Four data points with and without a supercooling are also shown. Two distinct methods of numerical calculations were used to predict the thickness. The technique reported by Rode (5) with temperature-dependent As diffusion coefficient has been primarily used. The boundary conditions are identical to those reported by him (zero excess As concentration at the interface and zero spatial derivative of excess As concentration at the top of melt). The melt height in our experiments is 10 mm. The alternate calculation uses Crossley and Small's (3) model modified to include Rode's As diffusion coefficient. In the latter case, the semi-infinite melt approximation was made. For growth periods negligible compared to diffusion time across the melt, which is true for all the

experiments reported here, both techniques have agreed quite closely. However, the semi-infinite melt approximation cannot be relied upon for longer growth intervals.

In Fig. 9 and 10 the same curves as those shown in Fig. 7 are repeated for  $750^\circ$  and  $735^\circ\text{C}$ , respectively. We believe that a thickness reproducibility from layer to layer of  $\pm 0.015\mu$ , and a thickness uniformity as low as  $\pm 4\%$  over a portion of the layer that excludes the edge lip, can be achieved with these techniques whereas at higher temperatures these figures must at least be doubled.

We are now concentrating on growing these layers at  $700^\circ\text{C}$  with no supercooling. We reduced the cooling rate, in an attempt to lower the growth rate and the edge growth, which should enable us to make use of more of the area and achieve better thickness uniformity. But, much slower growth rates increased the density of cusps remarkably. Preliminary results at  $700^\circ\text{C}$  show that about  $\pm 4\%$  thickness uniformity can be achieved repeatably. It has also been demonstrated that with slower growth rate (about  $800 \text{ \AA}/\text{min}$ ) at lower growth temperature, one can achieve reproducible submicron layers when any oxide layer present is removed with aqueous HCl and the melt saturation is trimmed with a source-seed crystal.

### Summary and Conclusions

The controlled-growth mechanism and the factors affecting it, along with the necessary countermeasures, have been examined in detail for the growth of submicron FET layers. Remarkably good agreement between theory and experiments has been achieved. The temperature dependence of the As diffusion coefficient determined by Rode has been reaffirmed. It has also been demonstrated that with slower growth rate (about  $800 \text{ \AA}/\text{min}$ ), at lower growth temperature, one can achieve reproducible submicron layers when any oxide layer present is removed with aqueous HCl and the melt saturation is trimmed with a source-seed crystal.

### Acknowledgments

The authors wish to extend their sincere thanks to Dr. A. Immorlica of Rockwell Science Center for sur-

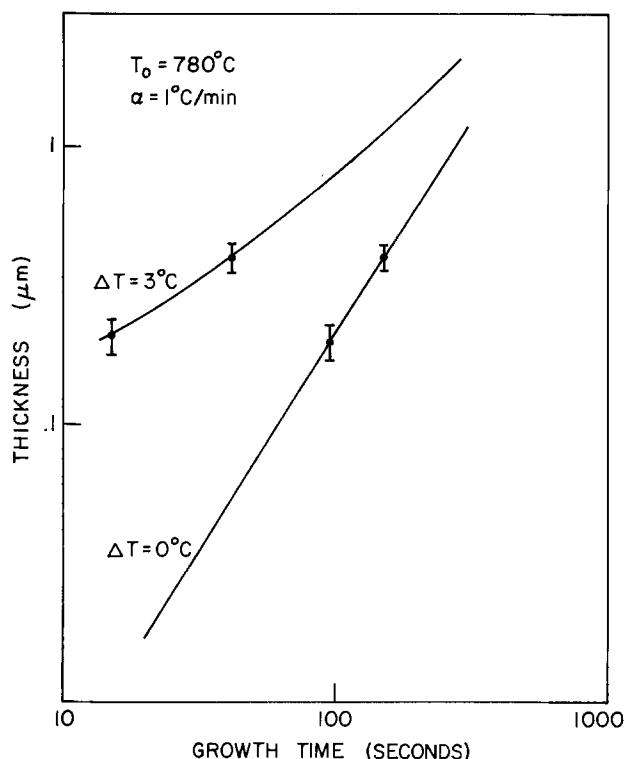


Fig. 8. Thickness vs. growth time at  $780^\circ\text{C}$ . Calculated (solid lines) and experimental.

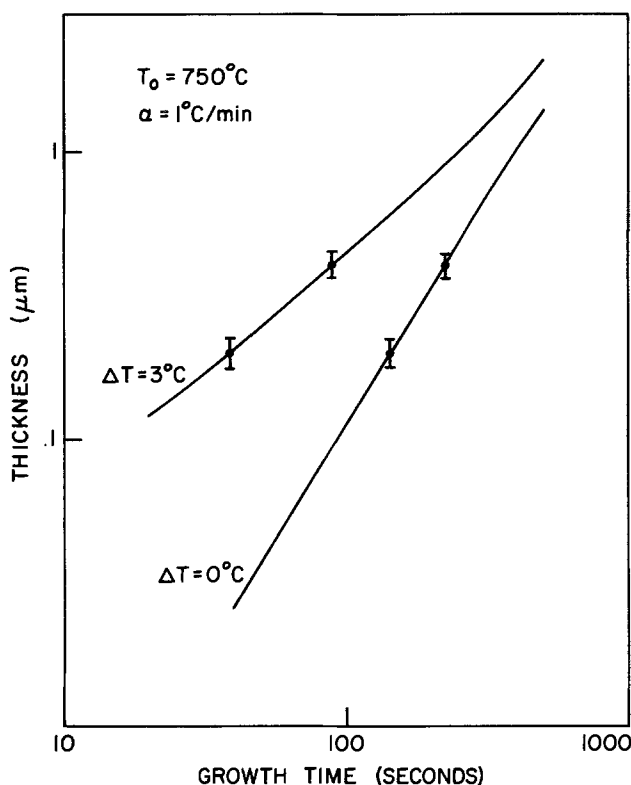


Fig. 9. Thickness vs. growth time at  $750^\circ\text{C}$ . Calculated (solid lines) and experimental.

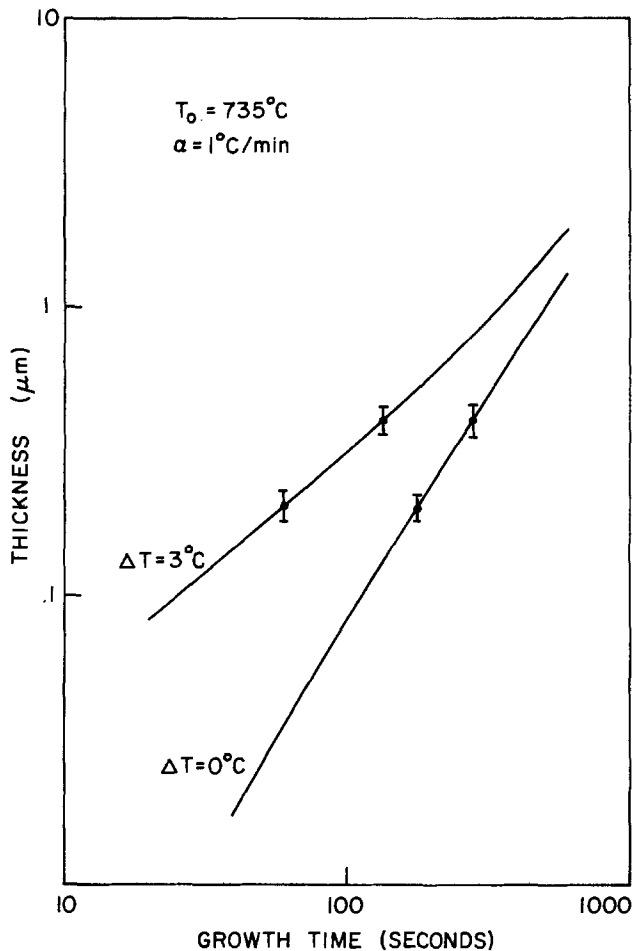


Fig. 10. Thickness vs. growth time at  $735^\circ\text{C}$ . Calculated (solid lines) and experimental.

face morphology analysis. They are also indebted to Dr. D. Woodard for advice and encouragement, to Prof. C. A. Lee for his invaluable discussions through-

out this work, and to R. Gurney for his careful review of this paper.

This work was supported in part by the Air Force Systems Command, Rome Air Development Center, Griffiss Air Force Base, New York, under contract F30602-74-C-0001 and by Advanced Research Project Agency under contract AFCRL-TR-74-0172 through Rockwell Science Center under contract INTL-75-52378.

Manuscript submitted Oct. 14, 1975; revised manuscript received Feb. 2, 1976.

Any discussion of this paper will appear in a Discussion Section to be published in the December 1976 JOURNAL. All discussions for the December 1976 Discussion Section should be submitted by Aug. 1, 1976.

Publication costs of this article were partially assisted by Cornell University.

#### REFERENCES

1. H. Nelson, *RCA Rev.*, **24**, 603 (1963).
2. M. B. Small and J. F. Barnes, *J. Cryst. Growth*, **5**, 9 (1969).
3. J. Crossley and M. B. Small, *ibid.*, **11**, 157 (1971).
4. H. Minden, *ibid.*, **6**, 228 (1970).
5. D. L. Rode, *ibid.*, **20**, 13 (1973).
6. J. Barrera, Proceedings of Fifth Biennial Cornell Electrical Engineering Conference, p. 135 (1975).
7. J. Barrera, Private communication.
8. D. Shaw, *J. Cryst. Growth*, **8**, 118 (1971).
9. L. R. Dawson, *ibid.*, **27**, 86 (1974).
10. M. Spitzer, B. Schwartz, and G. D. Weigle, *This Journal*, **122**, 397 (1975).
11. D. L. Rode, B. Schwartz, and J. V. DiLorenzo, *Solid-State Electron.*, **17**, 1119 (1974).
12. A. Cho, Private communication.
13. B. Schwartz, *This Journal*, **118**, 657 (1971).
14. M. Rubenstein, *ibid.*, **113**, 752 (1966).
15. J. Crossley and M. B. Small, *J. Cryst. Growth*, **15**, 275 (1972).
16. J. J. Hsieh, *ibid.*, **27**, 49 (1974).
17. A. Immorlica, Private communication.
18. K. Lehovc and R. Zuleeg, Symposium on GaAs and Related Compounds, Inst. Phys. Conf. Ser. No. 24, pp. 292-306 (1975).
19. J. D. Wiley and G. L. Miller, *IEEE Trans. Electron Devices*, **ED-22**, 265 (1975).
20. R. L. Moon and S. I. Long, *J. Cryst. Growth*, To be published.



# Characteristics of p-Doped Polysilicon with B<sub>2</sub>H<sub>6</sub> Used as In Situ Dopant Source

R. E. Chappelow

IBM System Products Division, Essex Junction, Vermont 05452

and P. T. Lin\*<sup>1</sup>

IBM System Products Division, East Fishkill Facility, Hopewell Junction, New York 12533

## ABSTRACT

Unusual effects are seen when heavily p-doped polycrystalline Si is deposited via the H<sub>2</sub>/B<sub>2</sub>H<sub>6</sub>/SiH<sub>4</sub> system. For example, material resistivity does not diminish monotonically as B<sub>2</sub>H<sub>6</sub> abundance is increased; also, resistivity variation due to subsequent layer oxidation is not monotonic. Manipulation of these and associated effects, such as variation in the volumetric conversion ratio to the oxide, can result in product improvements.

There are many cases in current semiconductor technology in which doped polysilicon layers find utility, such as gate electrodes and device field shields (1, 2). In general, applications make demands on poly-Si properties, such as etch characteristics, material resistivity, and material response to oxidation cycles. Since satisfying these requirements is not always possible with a standard material, several compromises are usually necessary.

In this paper, we describe some unusual effects that are present when B<sub>2</sub>H<sub>6</sub> is used to heavily dope the poly-Si layer during deposition. By properly manipulating these effects, one can effectively gain several distinct processing advantages.

## Description of Experiments

The poly-Si layers were deposited on 2¼ in. p-type, 2 ohm-cm substrates, upon which about 300Å of Si<sub>3</sub>N<sub>4</sub> had been previously deposited. SiH<sub>4</sub>, diluted to 5% in N<sub>2</sub>, was the silicon source used. In general, poly-Si layer thickness was intended to be near to 4500Å; however, tests in other thickness ranges gave similar results.

Poly-Si thickness measurements were most often made by mechanical methods, although some data were taken using reflectance spectra techniques. Resistivity data were calculated from four-point probe measurements. Oxide thickness over the poly-Si was generally derived from reflectance spectra.

Most experiments consisted of several runs, with B<sub>2</sub>H<sub>6</sub> flow rate as the variable between runs; dummy runs were made, as needed, to stabilize the reactor background doping levels. The samples thus generated were then subjected to a variety of tests (e.g., thickness, R<sub>s</sub> and etch rate determinations) as well as to several additional processing sequences, such as oxidation under various conditions and pattern etching.

Experimental sets were processed over the temperature range of 750°C to about 1000°C, using different carrier gases (N<sub>2</sub> or H<sub>2</sub>), and in different reactor types. While the effects to be discussed showed some sensitivity to such processing changes, these influences were relatively minor compared to the effects described below.

## Discussion

*Preliminary experiments: as-deposited material resistivity.*—Assuming that the fraction of electrically active B incorporated into the growing poly-Si film is

\* Electrochemical Society Active Member.

<sup>1</sup> Present address: Cambridge Memories Inc., Poughkeepsie, New York 12603.

Key words: polysilicon, B<sub>2</sub>H<sub>6</sub> (diborane), silicon boride, boron silicide, poly-Si oxide.

reasonably independent of boron availability, one expects that the boron concentration in the film will be approximately linearly dependent on B<sub>2</sub>H<sub>6</sub> input flow rate, at least insofar as the flow rate is much less than the total rate of flow in the reactor

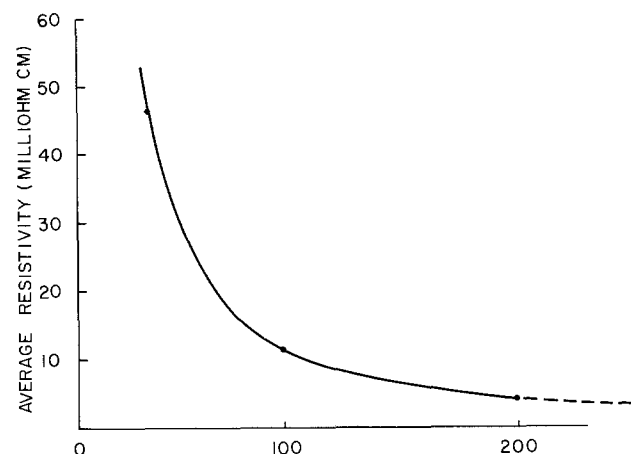
$$N_a \sim K|B_2H_6| \quad [1]$$

where  $K$  is some constant and  $|B_2H_6|$  is the flow rate of the dopant. If this were true, one should be able to plot the (average) material resistivity against  $|B_2H_6|$  (and thus  $N_a$ , by virtue of [1]) and achieve a functional dependence similar to published data (3). This type of functional dependence is approximately given by

$$\bar{\rho} \simeq A|B_2H_6|^{-B} \quad [2]$$

in which  $\bar{\rho}$  is the average poly-Si resistivity, and where  $A$  and  $B$  are positive constants over some range of  $|B_2H_6|$ . This approximation had previously been shown to be reasonable in the range of  $\bar{\rho} \sim 1$  ohm-cm for n-type dopants. In this study, the first several runs also showed  $\bar{\rho}$  to depend on  $|B_2H_6|$  in approximately this manner, as shown in Fig. 1.

Certainly,  $\bar{\rho}$  is expected to be a monotonically decreasing function of  $|B_2H_6|$ ; the fact that this assumption fails at high values of  $|B_2H_6|$  is shown in Fig. 2. The anomalous increase in  $\bar{\rho}$  at high B<sub>2</sub>H<sub>6</sub> flow rates is



05% B<sub>2</sub>H<sub>6</sub> IN H<sub>2</sub> FLOW RATE (cc/min)

Fig. 1. Expected behavior of  $\bar{\rho}$  on  $|B_2H_6|$

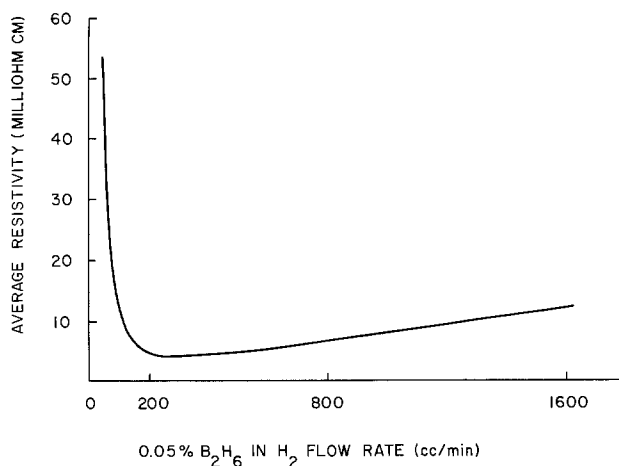


Fig. 2. As-deposited resistivity as a function of  $B_2H_6$  flow rate

attributed to the formation of a new phase, possibly one of the silicides of boron.

The anomaly noted above was the first of several which appeared over the course of additional study. In general, these effects were somewhat responsive to changes in processing conditions and reactor type, but not extremely so. The process reported in Table I was chosen as the vehicle for additional experiments. Table II displays  $B_2H_6$  flow rate values for a typical four-run experimental set.

**Poly-Si deposit rate.**—Typical material deposit rates are also shown in Table II. In some experiments, qualitative agreement with published data was noted (4). In other cases, the growth rate showed a complicated, nonmonotonic dependence on  $B_2H_6$  flow rate and other process variables. Since the range of variation from run to run in an experimental set was generally less than  $\pm 15\%$ , extensive study of deposit rate phenomena was not undertaken.

**Poly-Si oxidation rate.**—Wafers from one experimental set were subjected to oxidation in steam at  $1050^\circ C$ . These samples were prepared as noted in Tables I and II.

After initial characterization, the wafers were oxidized for 7.5 min, cooled, and halved. One half was retained for measurements and the other half was processed further. This procedure was repeated twice, the second oxidation being for 7.5 min, and the final cycle having 15 min of oxidation.

Poly-Si thickness was measured on each sample. The most convenient plot of poly-Si thickness over oxidation time is on semilog scales, as illustrated in Fig. 3. The same information is displayed in Fig. 4, in which the amount of poly-Si consumed by the oxidation step is plotted against oxidation time. The data show the following features: (i) heavily doped samples oxidize somewhat faster than lightly doped samples; (ii) the

Table I. Process for boron-doped poly-Si experiments

$H_2$	65 S.L./min
$SiH_4$ (5% in $N_2$ )	500 S.C.C./min
$B_2H_6$ (0.05% in $H_2$ )	0-2000 S.C.C./min
Temperature	$930^\circ C$

Table II.  $B_2H_6$  flow rate and poly-Si deposit rate, typical experimental set

Run number	$B_2H_6$ flow rate (S.C.C./min) (0.05% $B_2H_6$ in $N_2$ )	Poly-Si deposit rate ( $\text{\AA}/\text{min}$ )
1	200	160
2	800	152
3	1600	134
4	30	173

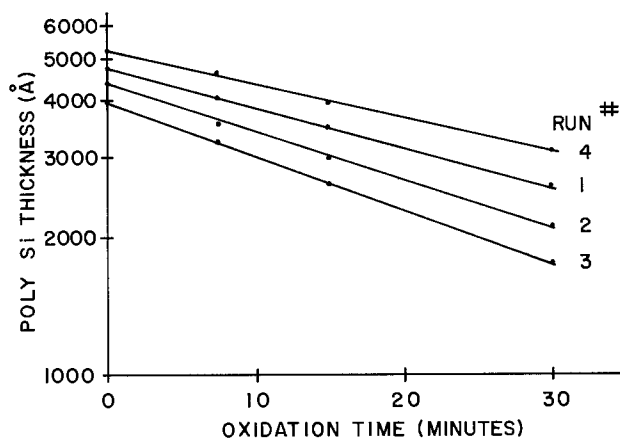


Fig. 3. Poly-Si thickness as a function of oxidation time for several values of  $|B_2H_6|$ .

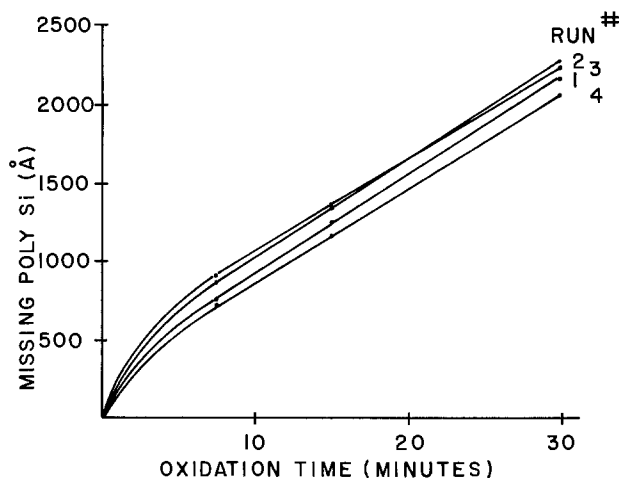


Fig. 4. Amount of poly-Si removed as a function of oxidation time for several values of  $|B_2H_6|$ .

variation in oxidation rate is about  $\pm 15\%$ ; and (iii) the per cent variation in material removal rate diminishes as oxidation time increases.

These data can be summarized with the statement that poly-Si oxidation rate (under the aforementioned conditions) is not very dependent on the  $B_2H_6$  flow rate during deposition. While this conclusion does not seem unusual, it is quite important in regard to the results of the next section.

**Poly-Si to  $SiO_2$  volume conversion factor.**—Another parameter of interest is the amount of oxide generated when a unit thickness of the deposited poly-Si layer is consumed during oxidation. We define the characteristic quantity, conversion ratio (C.R.), as

$$C. R. = \frac{T_{ox}}{\Delta T_{poly-Si}} \quad [3]$$

where  $T_{ox}$  is the oxide thickness measured over the the poly-Si, and where  $\Delta T_{poly-Si}$  is the amount of deposited material consumed by the oxidation process. Since we are dealing with a very boron-rich material, we should expect that the C.R. observed is not equal to that obtained from pure silicon. If the material has average stoichiometry given by  $Si_xB_y$ , then the expected value for C.R. would be

$$C.R.(\text{expected}) = \frac{x}{x+y} \cdot C.R._{Si} + \frac{y}{x+y} \cdot C.R._{B} \quad [4]$$

where  $C.R._{Si}$  and  $C.R._{B}$  are the respective C.R. values for Si and B.  $C.R._{Si}$  is about 2.1, and  $C.R._{B}$  is expected to be between about 3.0 and 5.0. The observed value of

C.R. for the composite material should then asymptote to about 2.1, for small values of  $|B_2H_6|$  during deposition, and should approach 4.0 or greater for samples deposited with high diborane flow rates. Measurements of sample C.R. show exactly this type of behavior, as shown in Fig. 5 and 6. The data suggest an effective C. R. for the boron component of about 4.5. Extending the analysis a bit further allows an expression to be generated for the ratio  $x/y$ , in terms of the observed sample C.R.

$$\frac{x}{y} = \frac{4.5 - \text{C.R. (sample)}}{\text{C.R. (sample)} - 2.1} \quad [5]$$

**Material resistivity after oxidation.**—Another effect noted during these experiments dealt with the response of  $\bar{\rho}$ , in samples prepared as described above, to oxidation cycles. It is a well-known fact that boron tends to segregate into the  $SiO_2$  layers formed on the silicon during oxidation. Since less dopant then remains in the silicon, this effect is generally evidenced by an increase in  $\bar{\rho}$ . As illustrated in Fig. 7, the expected response is, in fact, observed on lightly doped samples: resistivity increases markedly as a function of oxidation time. Heavily doped samples, however, exhibit anomalous behavior, as illustrated in Fig. 8. On these samples, it can be observed that  $\bar{\rho}$  actually diminished as oxidation time increased. In Fig. 9,  $\bar{\rho}$  is plotted against  $B_2H_6$  flow rate, with oxidation time as a parameter. Note that if the poly-Si deposition is performed with  $|B_2H_6|$  value near about 550 S.C.C./min, the material resistivity is almost insensitive to oxidation time, at least over the range of variation explored.

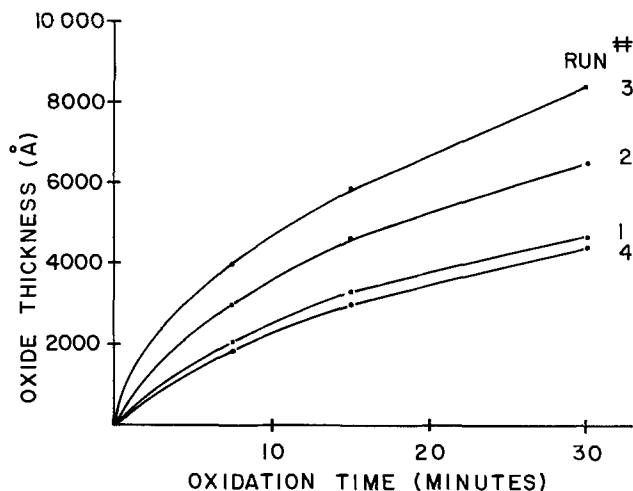


Fig. 5. Amount of oxide grown from the poly-Si as a function of oxidation time for several values of  $|B_2H_6|$ .

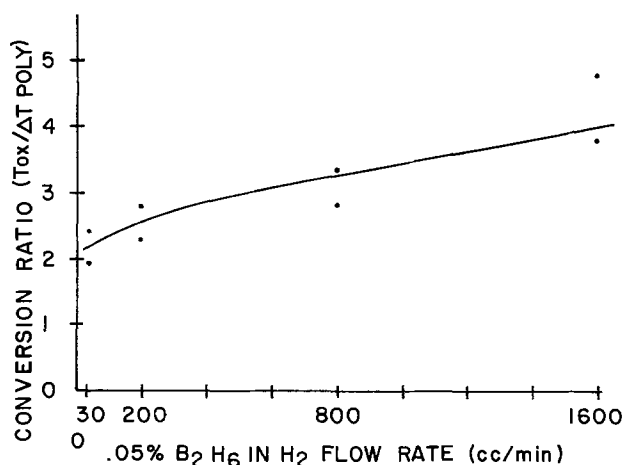


Fig. 6. Poly-Si to oxide conversion ratio as a function of  $|B_2H_6|$

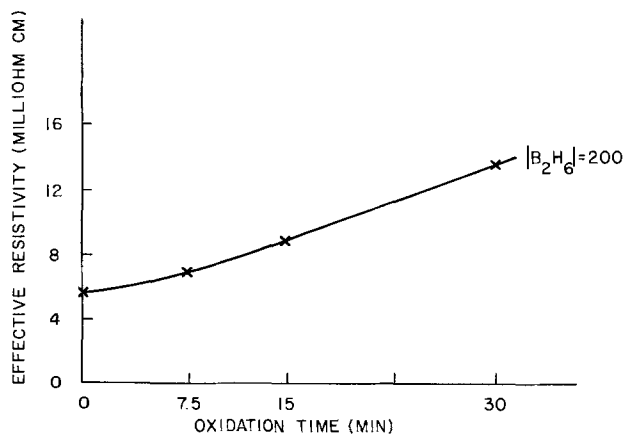


Fig. 7. Average resistivity as a function of oxidation time for a lightly doped sample.

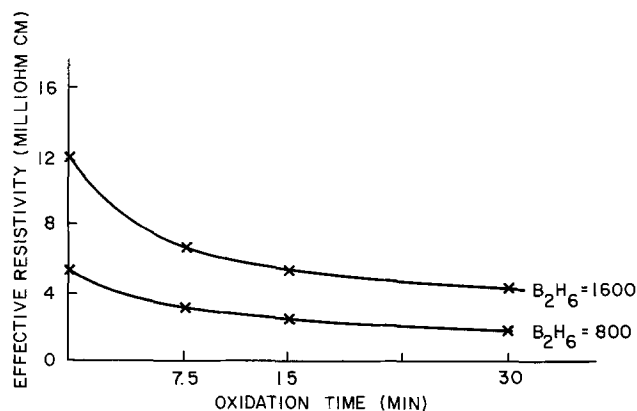


Fig. 8. Average resistivity as a function of oxidation time for heavily doped samples.

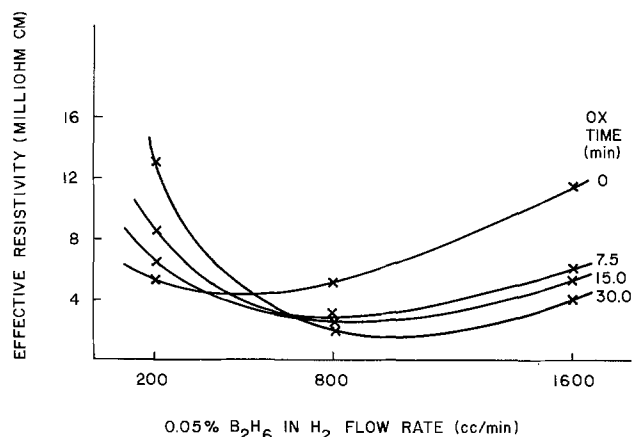


Fig. 9. Dependence of  $\bar{\rho}$  on  $B_2H_6$  flow rate for several oxidation times.

This phenomenon is apparently due to at least the following three simultaneous effects: (i) grain growth in the poly-Si; (ii) depletion of the boron into the already boron-rich oxide; and (iii) decomposition of the hypothesized new phase in such a manner as to keep the B concentration in the poly-Si layer near the solubility limit. In contrast, simple heat-treatment of similar samples caused little, if any, change in average resistivity. In such cases, the phase decomposition can apparently occur only to the extent that grain growth also occurs; the phase must continue to exist unless a "sink," such as oxide, is available to accumulate excess boron.

**Poly-Si etch rate.**—Poly-Si etch rate as a function of  $|B_2H_6|$  was also investigated. The etchant used here

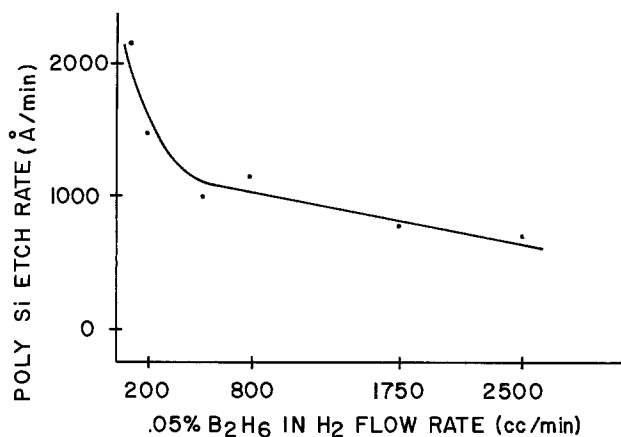


Fig. 10. Poly-Si etch rate as a function of  $|B_2H_6|$

was composed of HF, HNO<sub>3</sub>, and acetic acid in proportions 1:26:33. The etch rate of undoped poly-Si in this solution is generally near 1500 Å/min, increasing slightly with p-doping near the 0.05 ohm-cm range of resistivity.

When the poly-Si is boron doped into the low 10<sup>-3</sup> ohm-cm region, however, the etch rate decreases rapidly, as shown in Fig. 10. This behavior is also attributed to the hypothesized silicide phase within the composite material.

### Conclusion

The various types of anomalous behavior discussed above were found to be fairly reproducible, and the

existence of such effects is now quite well established. Similar tests made with AsH<sub>3</sub> and PH<sub>3</sub> showed no anomalies, at least in the resistivity regions of interest here. To this time, no attempt has been made to more precisely identify the apparent new phase in the B<sub>2</sub>H<sub>6</sub> case.

It is not difficult to imagine many cases in which proper manipulation of such effects can result in significant processing advantages. In the cases attempted to date, results have followed expectations rather well.

### Acknowledgments

The authors wish to acknowledge J. Doulin and D. Doney for much of the experimental work. Also, I. Dolgov, T. Litz, and C. Liu performed many of the etch rate experiments.

Manuscript submitted Sept. 16, 1975; revised manuscript received Feb. 17, 1976.

Any discussion of this paper will appear in a Discussion Section to be published in the December 1976 JOURNAL. All discussions for the December 1976 Discussion Section should be submitted by Aug. 1, 1976.

Publication costs of this article were partially assisted by IBM Corporation.

### REFERENCES

1. F. Faggin and D. Klein, *Solid-State Electron.*, **13**, 1125 (1968).
2. D. C. Hoefler, *Electronic News*, (January 18, 1971).
3. J. C. Irvin, *Bell System Tech. J.*, **41**, 387 (1962).
4. F. C. Eversteyn and B. H. Put, *This Journal*, **120**, 106 (1973).

## Effect of III/V Ratio on the Properties of Vapor Phase Epitaxial GaP

G. B. Stringfellow\* and H. T. Hall, Jr.

Hewlett-Packard, Palo Alto, California 94304

### ABSTRACT

The effect of III/V ratio in the gas stream on the properties of GaP grown by the vapor phase epitaxial (VPE) technique has been studied. At the substrate temperature of 840°C, the nitrogen distribution coefficient is found to increase strongly with increasing III/V ratio. Equilibrium thermodynamic calculations explain the dependence well. On the other hand, the residual doping level, believed to be due to S, has the opposite dependence on III/V ratio which is not understood. The minority carrier lifetime and diode efficacy are observed to increase with III/V ratio. An analysis of this behavior indicates the dominant nonradiative recombination center in this material may be a deep acceptor residing on the Ga sublattice, such as Cu or Fe.

The family of III-V compounds is generally very stoichiometric because of the strong covalent bonding. This characteristic is important for many of the properties of these semiconductors, including the ability to be doped both n- and p-type and the very slow substitutional diffusion observed in them.

There are few reliable studies on the actual degree of nonstoichiometry, but recent studies on the Ga compounds have indicated that the stability range is largely on the Ga-rich side of perfect stoichiometry (1-4), the dominant defect probably being vacancies on the Group V sublattice which may exist with con-

centrations of up to 10<sup>19</sup> cm<sup>-3</sup> (1-4). In GaAs and GaP, these vacancies are apparently electrically and optically inactive, but in GaN they render the material always n-type (5, 6). The Ga vacancy, although present in smaller numbers, appears to be a deep acceptor, and there are many reports that it acts either alone or paired with various donor impurities as a nonradiative recombination center which reduces the minority carrier lifetime and recombination efficiency (7-11). Photoluminescence and absorption peaks in the infrared are sometimes ascribed to such defects (12-14). Arsenic interstitials rather than Ga vacancies have also been implicated in these effects (15, 16).

The experiments usually considered to give the most reliable indication of the effect of Ga vacancies on ma-

\* Electrochemical Society Active Member.

Key words: GaP, stoichiometry, light emitting diodes, vapor phase epitaxy.

terials properties are those in which the activity of Ga,  $a_{\text{Ga}}$ , is changed systematically in a series of growth runs while monitoring the change in some property which depends on the gallium vacancy concentration. In LPE experiments, this requires changing from the V-rich to the Ga-rich side of the liquidus at a fixed temperature (8) or changing the temperature. In VPE, the III/V ratio, which is defined as the ratio of HCl to  $\text{PH}_3$  in the input gas stream, is simply changed. However, as discussed later,  $a_{\text{Ga}}$ , the quantity which will be used to specify the gas phase stoichiometry at the solid-vapor interface, is not linearly proportional to the III/V ratio as is normally assumed (14, 17-19). The problem with this type of experiment is that the results are always ambiguous. The defect responsible for changes in the property being monitored cannot be identified with certainty because changes in  $a_{\text{Ga}}$  affect the distribution coefficients for Ga site impurities and  $V_{\text{Ga}}$  in the same way (20).

In VPE GaP similar to that to be described in the present study, the major residual donor impurities have been identified and the donor and acceptor concentrations were found to be  $<10^{16} \text{ cm}^{-3}$  for nitrogen-doped material (21). In this study, we have systematically varied the III/V ratio during a series of VPE runs and observed the effects on  $N_{\text{D}}$ ,  $N_{\text{A}}$ ,  $E_{\text{D}}$ , and the nitrogen doping level. Taking these effects into account, we have then attempted to understand the influence of vapor phase stoichiometry on the minority carrier lifetime and diode efficiency.

### Experimental

The  $\text{PH}_3$ -HCl-Ga- $\text{H}_2$  system was used to grow the GaP layers. The details have been presented elsewhere (22), but the important feature is that the system is rf heated so all the hot elements which the gases contact are high purity graphite. The LEC GaP substrate, either  $n^+$  sulfur doped or semi-insulating Cr doped, was oriented  $4^\circ$  off the (100) plane. The substrate temperature was  $840^\circ\text{C}$  for all experiments.

The GaP doped only with N was characterized by measuring: (i) the photoluminescent spectrum which yields the nitrogen concentration (22) and information about deep levels in the material; (ii) the minority carrier lifetime by photoluminescent decay measurements (23); and (iii) the diode efficacy,  $B/J$ . All of these measurements are standard and have been described in previous publications. The efficacy measurements were made on diodes with absorbing back contacts without epoxy encapsulation. The electrical properties of this material, which is always observed to be  $n$ -type under the conditions described, were measured by making van der Pauw measurements *vs.* temperature, which can be interpreted to yield  $N_{\text{D}}$ ,  $N_{\text{A}}$ , and  $E_{\text{D}}$  (21).

### Results

The growth conditions used for the series of runs are listed in Table I. For runs 611-618, an attempt was made to keep as many parameters, including growth

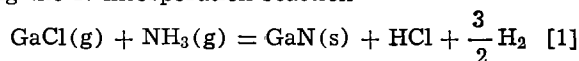
Table I. Growth conditions for runs with varying III/V ratio. All runs were carried out with a substrate temperature of  $840^\circ\text{C}$ .

Run No.	$f_{\text{PH}_3}$ (sccm)	$f_{\text{HCl}}$ (sccm)	$f_{\text{H}_2}$ (sccm)	$f_{\text{NH}_3}$ (sccm)	$f_{\text{HCl}}/f_{\text{PH}_3}$ (III/V ratio)	Growth rate ( $\mu/\text{min}$ )	$a_{\text{Ga}}$
604	3.3	16.7	613	0.9	5.1	0.93	0.068
605	3.3	15.5	613	30.0	4.7	0.95	0.062
606	3.3	14.6	613	50.0	4.4	0.90	0.059
611	6.6	17.8	775	30.0	2.7	1.07	0.032
612	6.6	16.0	775	30.0	2.7	0.97	0.032
613	6.6	34.8	775	15.3	5.3	1.01	0.071
614	6.6	66.4	775	7.75	10.1	1.07	0.14
615	6.6	71.2	775	5.4	10.8	0.99	0.15
616	6.6	5.4	775	47.8	0.82	0.40	0.018
617	13.2	5.9	1100	57.3	0.45	0.35	0.015
618	18.8	5.4	1369	61.2	0.29	0.37	0.014
619	6.6	68.0	1100	23.0	5.20	1.8	0.067

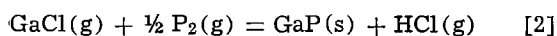
rate and nitrogen concentration in the solid, as constant as possible. Thus for high III/V ratios, where the  $\text{PH}_3$  flow rate controls growth rate, the  $\text{PH}_3$  flow rate was held at a value giving a growth rate of  $\sim 1 \mu\text{m}/\text{min}$ . At low III/V ratios, the HCl flow rate was held at this value and the  $\text{PH}_3$  flow rate increased, to again maintain  $\sim 1 \mu\text{m}/\text{min}$  growth rates. The  $\text{NH}_3$  flow rates were varied to give what was calculated to be an approximately constant nitrogen concentration.

One problem with trying to cover such a wide range of III/V ratios is that the morphology becomes bad at both high (pyramids) and low (pits) III/V ratios (24). However, the morphology was sufficiently good to allow fabrication of van der Pauw samples and LED's over the entire range of III/V ratios from 0.3 to 10.

*Nitrogen incorporation.*—The most easily interpreted parameter found to vary with III/V ratio is the nitrogen distribution coefficient. As reported previously (22), at  $840^\circ\text{C}$  the experimental solid/vapor distribution coefficient agrees with an equilibrium thermodynamic calculation. The calculation basically consists of using the N incorporation reaction



to calculate  $X_{\text{GaN}}/p_{\text{NH}_3}$  using the data of Thurmond and Logan (25) for  $\Delta G_{\text{f}}^\circ(\text{GaN})$ , a value of 23,000 cal/mole for  $\Omega^{\text{s}}$  used to calculate the activity coefficient of GaN in the GaP-rich solid (26-28) and values of  $p_{\text{GaCl}}$  and  $p_{\text{HCl}}$  at the solid-vapor interface which must be calculated. The mass action relations for the two reactions



and



are used with the conservation conditions

$$p_{\text{PH}_3}^\circ - 2p_{\text{P}_2} - 4p_{\text{P}_4} = p_{\text{GaCl}}^\circ - p_{\text{GaCl}} \quad [4]$$

$$p_{\text{HCl}}^\circ = p_{\text{HCl}} + p_{\text{GaCl}} \quad [5]$$

to determine the four parameters  $p_{\text{GaCl}}$ ,  $p_{\text{HCl}}$ ,  $p_{\text{P}_2}$ , and  $p_{\text{P}_4}$  given the input conditions  $p_{\text{PH}_3}^\circ$  and  $p_{\text{HCl}}^\circ$  and the substrate temperature. The experimental data are compared with the calculated distribution coefficient *vs.* III/V ratio in Fig. 1. The calculation describes the re-

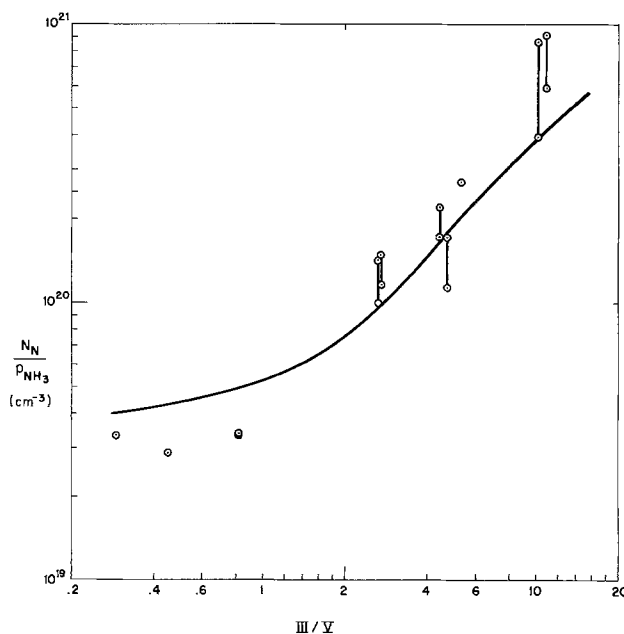


Fig. 1. Distribution coefficient of nitrogen,  $N_{\text{N}}/p_{\text{NH}_3}$ , *vs.* III/V ratio in the input gas stream,  $p_{\text{HCl}}^\circ/p_{\text{PH}_3}^\circ$ . The solid line was calculated assuming thermal equilibrium at the growth interface as described in the text.

sults very well. Notice that the distribution coefficient does not vary linearly with III/V ratio. This is because the actual III/V ratio at the growing interface  $p_{\text{GaCl}}/2p_{\text{P}_2} + 4p_{\text{P}_4}$  is of course not equal to the "III/V ratio" defined as  $p_{\text{RCl}}^0/p_{\text{PH}_3}^0$ . For a linear relationship between dopant concentrations and III/V ratio, the III/V ratio at the gas-solid interface must be used. This is an important point generally ignored by many papers dealing with the III/V ratio effects on VPE materials (14, 17-19). In fact, a very convenient quantity for expressing stoichiometry is  $a_{\text{Ga}}$  defined as  $p_{\text{Ga}}^{(g)}/p_{\text{Ga}}^{(l)}(T)$ . This can be used to compare the stoichiometry of the solid with that obtained by LPE. For the high III/V ratios used in this work,  $a_{\text{Ga}}$  is nearly equal to that for LPE. The equilibrium values calculated for  $a_{\text{Ga}}$  are listed in Table I along with the III/V ratio to give an idea of the relationship between the two. In applying these thermodynamic calculations to N incorporation, it must be acknowledged that the incorporation need not be thermodynamically controlled, as is the case for S doping to be discussed below. In fact, at 820°C the N concentration in the solid is substantially higher than the solid solubility limit (26). However, the success achieved in calculating the absolute magnitude of the distribution coefficient and its dependence on III/V ratio at 840°C, all with no adjustable parameters, indicates that the solid-vapor equilibrium is the determining factor in this case.

**Doping level.**—Since the residual donor in nitrogen-doped GaP has been identified as S in previous investigations (21), one would expect a relationship between  $N_D$  and III/V ratio similar to that for nitrogen, since both reside on the P sublattice so both should be proportional to  $a_{\text{Ga}}$ . However, the results have the opposite dependence. As seen in Fig. 2,  $N_D$ ,  $N_A$ , and  $N_D - N_A$  decrease as the III/V ratio and  $a_{\text{Ga}}$  increase. This is similar to the results of Enstrom *et al.* (29) on GaAs, which they attributed to kinetic effects, namely the change in the sticking coefficient with III/V ratio. If the residual donor were a Group IV impurity, rather than S, we could understand the effect thermodynamically,

but the ionization energy and previous optical absorption experiments seem to rule out all donors except S. Because of the dependence of  $N_A$  on  $a_{\text{Ga}}$ , one might conclude that the acceptor resides on the Ga site, but this is uncertain in light of the results for the donor. An interesting observation is that the ratio  $N_D/N_A$  remains nearly constant. Similar results have been reported by Okamoto *et al.* (17) and Ashten *et al.* (30) for VPE GaAs. A similar trend is also observed in the data for VPE GaP of Craford *et al.* (31).

**Minority carrier lifetime and quantum efficiency.**—A very significant effect of the III/V ratio is on the minority carrier lifetime. In Fig. 3, the reciprocal of the photoluminescent decay time is plotted vs. III/V ratio. A trend to longer lifetime at high III/V ratio is observed, similar to the results reported by Wessels (19) for charge storage times measured in VPE GaP over a much narrower range of III/V ratio. For comparison, we include the solid line given by the expression

$$1/\tau = A/a_{\text{Ga}} \quad [6]$$

where  $a_{\text{Ga}}$  is the activity of Ga calculated at the growing interface and the parameter  $A$  is adjusted to give the best fit to the data.

A number of studies of deep nonradiative recombination centers (NRC's) have been performed recently. Hamilton *et al.* (32) observed that in undoped LPE GaP the lifetime is inversely proportional to the concentration of a NRC observed at 0.75 eV above the valence band. Other workers have presented evidence attempting to identify specifically the point defect responsible for determining the lifetime. In heavily n-type samples, the complex  $V_{\text{Ga}}-(D_P)_3$  (11, 14) is believed to dominate. Other complexes, such as  $\text{Si}_{\text{Ga}}-\text{O}_P$ ,  $\text{C}_{\text{Ga}}-\text{O}_P$  (34),  $V_{\text{Ga}}-\text{Te}_2$  (35), and  $V_{\text{Ga}}P_{\text{Ga}}V_{\text{Ga}}$  (36) have also been suggested to be NRC's. Smith and Abbott (37) found in undoped LPE GaP that  $L_P$  was proportional to  $n^{-1/2}$  and implied from this that  $\text{Si}_P$  was the dominant NRC. In fact, any deep center binding two carriers such that it can produce Auger recombination is a possible NRC (38). A number of possible NRC's are tabulated in Table II for convenience.

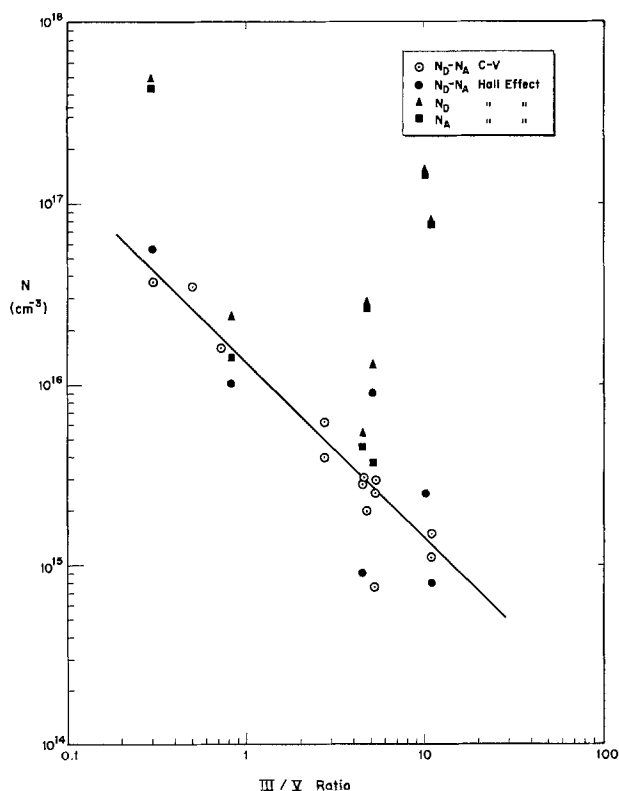


Fig. 2.  $N_D$  ( $\blacktriangle$ ),  $N_A$  ( $\blacksquare$ ) and  $N_D - N_A$  ( $\circ$ ) plotted vs. III/V ratio in the input gas stream.

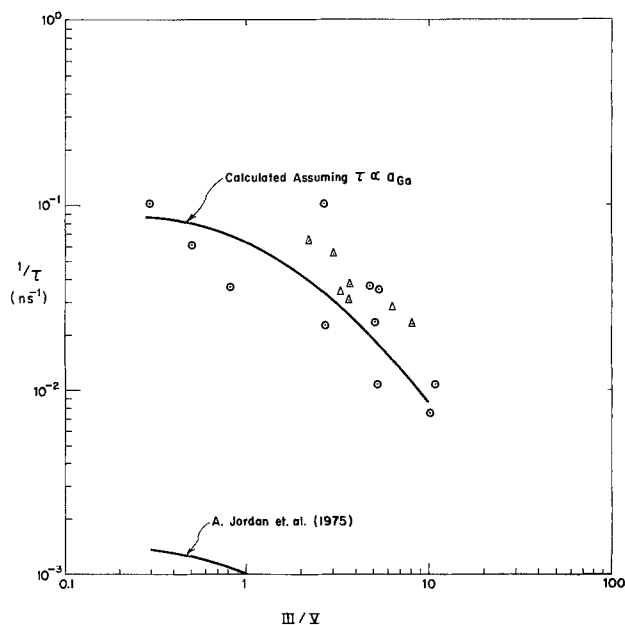


Fig. 3. Reciprocal minority carrier lifetime obtained from photoluminescent decay measurements vs. III/V ratio in the input gas stream. The solid line was calculated assuming  $1/\tau \propto V_{\text{Ga}}$  with  $V_{\text{Ga}}$  assumed proportional to  $a_{\text{Ga}}^{-1}$  and the proportionality constant adjusted to fit the experimental data. The lower curve is the calculated result using the proportionality constant from Ref. (10). The data are from the present work ( $\circ$ ) and for charge storage times in VPE samples reported by Wessels (19) ( $\triangle$ ).

Table II. Behavior of several postulated NRC's as a function of III/V ratio. In the table  $n = d(\log[\text{NRC}])/d(a_{\text{Ga}})$ . Experimentally  $n = -1$ .

NRC	Reference	n	Comparison with experiment	Possible NRC
Si <sub>P</sub>	(37)	+1		
V <sub>Ga</sub>	(10)	-1	τ 100X too small	
D <sub>P</sub> (Group VI)		-1*	Shallow, not NRC	
D <sub>Ga</sub> (Group IV)		-1	Shallow, not NRC	
A <sub>Ga</sub> (Group II)		-1	Group II—not NRC	
Cu or Fe	(40)	-1	Good	X
V <sub>Ga</sub> -O <sub>P</sub>	(34)	0		
Si <sub>Ga</sub> -O <sub>P</sub>	(33, 34)	0		
C <sub>Ga</sub> -O <sub>P</sub>	(34)	0		
V <sub>Ga</sub> -Te <sub>2</sub>	(35)	1(-3*)		
V <sub>Ga</sub> -(D <sub>P</sub> ) <sub>3</sub>	(11, 14)	2(-4*)		
(V <sub>Ga</sub> ) <sub>2</sub> -P <sub>Ga</sub>	(36)	-4		

\* If D<sub>P</sub> incorporation is kinetically controlled as described in the text.

For our system, several possible NRC's can be eliminated immediately, based on the dependence of τ on stoichiometry. Since the concentration of the NRC is apparently proportional to 1/a<sub>Ga</sub>, if the defect is an isolated point defect, it must reside on the Ga site. This assumes equilibrium incorporation, of course, and thus the Group VI P-site donors are an exception and must also be considered; however, they are common shallow donors and hence have not been reported to act as NRC's. Since the NRC must reside on the Ga sublattice, all Group IV acceptors, including Si<sub>P</sub> must be eliminated. Furthermore, none of the complexes listed in Table II have the proper dependence on a<sub>Ga</sub>. For example, the V<sub>Ga</sub>-(D<sub>P</sub>)<sub>3</sub> complex should have a concentration proportional to (a<sub>Ga</sub>)<sup>2</sup> for equilibrium incorporation, or (a<sub>Ga</sub>)<sup>-4</sup> for kinetically limited incorporation of D<sub>P</sub>. Similarly, the V<sub>Ga</sub>-Te<sub>2</sub> complex can be eliminated. The concentrations of Si<sub>Ga</sub>-O<sub>P</sub>, C<sub>Ga</sub>-O<sub>P</sub>, and V<sub>Ga</sub>-O<sub>P</sub> should be independent of stoichiometry. This leaves V<sub>Ga</sub>, D<sub>Ga</sub>, and A<sub>Ga</sub> as the remaining possibilities. The lifetime associated with Ga vacancies can be predicted from the results of Jordan *et al* (10). The resultant lifetimes are 100 times longer than observed in this study.

The Group IV elements are the major Ga-site donors. They are well established to form shallow levels and are not believed to be NRC's. In our present system, in fact, the concentration of Si in the GaP epilayer can be reduced by adding NH<sub>3</sub> (21) with little change in lifetime. This indicates the Si<sub>Ga</sub> at the 10<sup>17</sup> cm<sup>-3</sup> level is not the dominant NCR. Similar results were reported by Wessels (19). The effect of Sn doping is not clearly established but preliminary results indicate that at a concentration of 10<sup>17</sup> cm<sup>-3</sup> Sn does not affect the lifetime in N-doped GaP (39).

The Group II and IIB acceptors, Mg, Cd, and Zn, are common dopants in III-V compounds and at the concentrations considered here do not decrease the lifetime. This leaves the transition metals, such as Fe or Cu, which are deep acceptors and are believed the most logical choice. However, one possible inconsistency observed is that the Cu acceptor level has been determined to be 0.55 eV (40) above the valence band while Hamilton *et al*. (32) found the ionization energy of the dominant NRC to be 0.75 eV for LPE GaP. However, it is possible that the dominant NRC is different for the present VPE GaP than for the LPE material used by Hamilton. The results of this analysis are summarized in Table II.

One other possibility which could make the simple thermodynamic analysis invalid would be the redistribution of point defects during cooling. This situation is impossible to analyze but, as suggested by Van Vechten (36), it could result in the concentration of V<sub>Ga</sub>P<sub>Ga</sub>V<sub>Ga</sub> centers being proportional to a<sub>Ga</sub><sup>-1</sup>, as observed experimentally. If indeed the association reaction con-

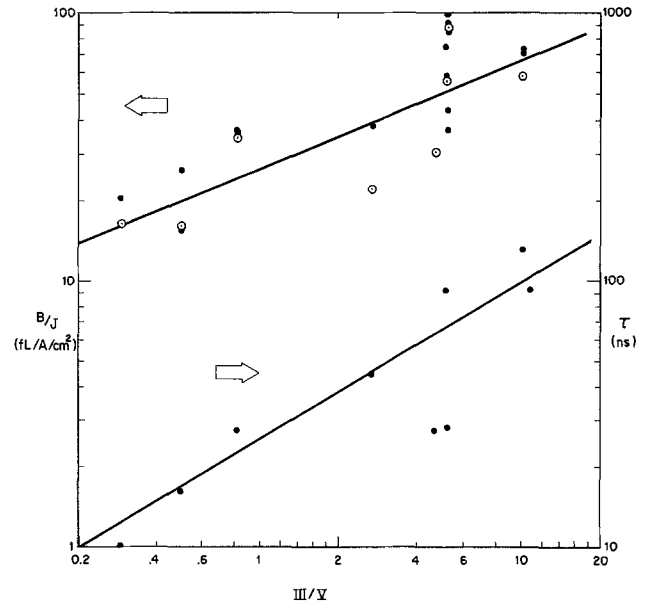


Fig. 4. Diode efficacy (fL/A/cm<sup>2</sup>) measured at  $J = 10$  A/cm<sup>2</sup> and minority carrier lifetime (nsec) vs. III/V ratio in the gas stream.

tinues until all Ga vacancies are used up, any of the defects involving one Ga vacancy are possibilities.

The change in minority carrier lifetime is also manifest as a change in the efficacy of LED's fabricated in this material. The efficacy is plotted along with the lifetime vs. III/V ratio in Fig. 4. In spite of the scatter, a clear trend to increasing efficiency for samples grown at high III/V ratios is observed. More scatter is observed for efficacy than lifetime measurements partly because the nitrogen concentration, an important factor in the determination of efficacy (22), is not completely constant.

Stewart (14) reported in GaAs,P with  $N_D - N_A > 10^{17}$  cm<sup>-3</sup> the presence of a photoluminescent peak at ~ 9500Å the intensity of which was observed to vary with III/V ratio. In the VPE GaP samples used in the present study, the only photoluminescent peak observed in the infrared (out to 12,000Å) was a small peak at ~ 7000Å. The intensity of this peak was small, about 1% of the green peak and independent of III/V ratio.

### Conclusions

A carefully controlled set of experiments was performed where the III/V ratio in the input gas phase was varied systematically from 0.3 to 10. In these experiments, the flow rates were varied in such a way as to keep the growth rate and nitrogen concentration in the solid as nearly constant as possible. The samples were then characterized by measuring  $N_D$  and  $N_A$ , the nitrogen concentration, the majority carrier lifetime (photoluminescent decay time), and the efficacy of LED's fabricated by Zn diffusion in the material.

The nitrogen incorporation is found to increase with increasing III/V ratio and to be well described by thermochemical calculations. The donor and acceptor concentrations and  $N_D - N_A$  are found to decrease as the III/V ratio is increased. The lifetime and diode efficacy are both found to increase with increasing III/V ratio. This is thought to indicate that a deep impurity, probably a transition metal acceptor residing on the Ga sublattice, is responsible for the nonradiative recombination in this material.

### Acknowledgments

The authors are pleased to acknowledge the many useful discussions held with R. A. Burmeister and P. E. Greene of Hewlett-Packard Laboratories.

Manuscript submitted Nov. 10, 1975; revised manuscript received Feb. 13, 1976.

Any discussion of this paper will appear in a Discussion Section to be published in the December 1976 JOURNAL. All discussions for the December 1976 Discussion Section should be submitted by Aug. 1, 1976.

Publication costs of this article were partially assisted by Hewlett-Packard.

#### REFERENCES

1. R. K. Hester, A. Sher, and J. F. Soest, *Phys. Rev. B*, **10**, 4262 (1974).
2. R. M. Logan and D. T. J. Hurle, *J. Phys. Chem. Solids*, **32**, 1739 (1971).
3. A. F. W. Willoughby, C. M. H. Driscoll, and B. A. Bellamy, *J. Mater. Sci.*, **6**, 1389 (1971).
4. A. S. Jordan, A. R. VonNeida, R. Caruso, and C. K. Kim, *This Journal*, **121**, 153 (1974).
5. H. P. Maruska and J. J. Tietjen, *Appl. Phys. Letters*, **15**, 327 (1969).
6. M. Ilegems and H. C. Montgomery, *J. Phys. Chem. Solids*, **34**, 885 (1973).
7. B. Tuck, *Phys. Status Solidi*, **29**, 793 (1968).
8. M. B. Panish, *J. Phys. Chem. Solids*, **29**, 409 (1968).
9. A. S. Jordan, A. R. VonNeida, R. Caruso, and M. DiDomenico, Jr., *Appl. Phys. Letters*, **19**, 394 (1971).
10. A. S. Jordan, R. Caruso, A. R. VonNeida, and M. E. Weiner, *J. Appl. Phys.*, **45**, 3472 (1974).
11. H. Kressel and I. Ladany, *Solid-State Electron.*, **11**, 647 (1968).
12. L. J. Vieland and I. Kudman, *J. Phys. Chem. Solids*, **24**, 437 (1963).
13. E. W. Williams, *Brit. J. Appl. Phys.*, **18**, 253 (1967).
14. C. E. E. Stewart, *J. Cryst. Growth*, **8**, 259 (1971).
15. H. Kressel, J. U. Dunse, H. Nelson, and F. Z. Hawrylo, *J. Appl. Phys.*, **39**, 2006 (1968).
16. C. M. H. Driscoll, A. F. W. Willoughby, and E. W. Williams, *J. Mater. Sci.*, **9**, 1615 (1974).
17. H. Okamoto, S. Sukata, and K. Sakai, *J. Appl. Phys.*, **44**, 1316 (1973).
18. P. Merenda, *J. Cryst. Growth*, **13/14**, 1331 (1972).
19. B. W. Wessels, *This Journal*, **122**, 402 (1975).
20. F. A. Kroeger, "The Chemistry of Imperfect Crystals," North Holland Pub. Co., Amsterdam (1964).
21. G. B. Stringfellow, H. T. Hall, Jr., and R. A. Burmeister, *J. Appl. Phys.*, **46**, 3006 (1975).
22. G. B. Stringfellow, M. E. Weiner, and R. A. Burmeister, *J. Electron. Mater.*, **4**, 363 (1975).
23. G. B. Stringfellow and D. Kerps, *Solid-State Electron.*, **18**, 1019 (1975).
24. T. Y. Wu, *J. Cryst. Growth*, **21**, 85 (1974).
25. C. D. Thurmond and R. A. Logan, *This Journal*, **119**, 622 (1972).
26. G. B. Stringfellow, *J. Cryst. Growth*, **27**, 21 (1974).
27. G. B. Stringfellow, *This Journal*, **119**, 1780 (1972).
28. D. D. Manchon, Jr., B. J. Gross, and B. A. Reese, *ibid.*, **121**, 996 (1974).
29. R. E. Enstrom, C. J. Nuese, J. R. Appert, and J. J. Gannon, *ibid.*, **121**, 1516 (1974).
30. D. J. Ashen, P. J. Dean, D. T. J. Hurle, J. B. Mullin, A. Royle, and A. M. White, "GaAs and Related Compounds 1974," p. 229, Institute of Physics, London (1975).
31. M. G. Craford, W. O. Groves, A. H. Herzog, and D. E. Hill, *J. Appl. Phys.*, **42**, 2751 (1971).
32. B. Hamilton, A. R. Peaker, S. Bramwell, W. Harding, and D. R. Wight, *Appl. Phys. Letters*, **26**, 702 (1975).
33. R. Z. Bachrach, O. G. Lorimor, L. R. Dawson, and K. B. Wolfstirn, *J. Appl. Phys.*, **43**, 5098 (1972).
34. R. N. Bhargava, *Philips Tech. Rpt.*, **32**, 261 (1971).
35. E. Fabre, R. N. Bhargava, and W. K. Zwicker, *J. Electron. Mater.*, **3**, 409 (1974).
36. J. A. Van Vechten, *This Journal*, **122**, 423 (1975).
37. B. L. Smith and M. Abbott, *Solid-State Electron.*, **15**, 361 (1972).
38. J. S. Jayson, *Phys. Rev. B*, **6**, 6 (1972).
39. G. B. Stringfellow, Unpublished results.
40. E. Fabre and R. N. Bhargava, *Appl. Phys. Letters*, **24**, 322 (1974).

## Epitaxial Deposition of $Pb_xSn_{1-x}Te$ on $Pb_xSn_{1-x}Te$ Substrates in a Closed System

Sidney G. Parker\*

Texas Instruments Incorporated, Dallas, Texas 75222

#### ABSTRACT

Epitaxial films of  $Pb_{0.79}Sn_{0.21}Te$ , which were p-type with carrier concentrations in the  $10^{17}/cm^3$  range were deposited on  $Pb_{0.79}Sn_{0.21}Te$  (100) substrates in a closed system at a rate of 1.5-3.0  $\mu m/hr$ . The epitaxial films were deposited from stoichiometric or slightly metal-rich charges at 425°-525°C. Those films which were deposited n-type contained metal inclusions. The morphology of the films was influenced by defects in the substrates, substrate temperature, and charge composition. Films up to 100  $\mu m$  in thickness were obtained. Infrared detector arrays with blackbody detectivities of  $10^{10}$  cm  $Hz^{1/2}/W$  at 77°K were made on the epitaxial films using a Schottky barrier technique.

Epitaxial films of  $PbTe$  and  $Pb_xSn_{1-x}Te$  have been deposited for fabrication of infrared detectors, which are used for various thermal imagery applications. These films have been grown by vacuum evaporation techniques, vapor transport in flow reactors, and from liquid phases (1-12). Films deposited by vacuum evaporation may vary in composition because of the nonequilibrium conditions which are inherent in this process. Vapor transport in a flow system has given good quality films but with film thickness limited to 10-20  $\mu m$  (8). Epitaxial growth from liquid phases can

give elemental inclusions unless great care is taken. The substrates used for epitaxial deposits have included  $BaF_2$ ,  $NaCl$ ,  $PbSe$ ,  $PbTe$ , and  $Pb_xSn_{1-x}Te$ . Most of the epitaxial films have been made on  $NaCl$  or  $BaF_2$  substrates because of the unavailability of good quality  $PbTe$  or  $Pb_xSn_{1-x}Te$  substrates. Use of  $BaF_2$  and  $NaCl$  as substrates causes cracks and strains to develop in the epitaxial films because of differences in thermal coefficients of expansion of the substrate and the epitaxial layers.

In an effort to avoid some of these problems, epitaxial growth of  $Pb_xSn_{1-x}Te$  films on single crystal substrates of  $Pb_xSn_{1-x}Te$  by vapor transport in a closed system was studied. This approach was taken

\* Electrochemical Society Active Member.  
Key words: IV-VI compounds, infrared detectors, carrier control, vapor phase epitaxial growth.



because of our success in growing large single crystals of  $PbTe$  and  $Pb_xSn_{1-x}Te$  by vapor transport in a closed tube (13). Further, it was hoped that epitaxial growth in a small quartz tube sealed under vacuum would give films under more equilibrium conditions than those existing in dynamic vacuum evaporations or in flow systems. The large, single crystals were grown at temperatures  $800^{\circ}$ - $895^{\circ}C$  while the epitaxial films were to be made at substrate temperatures of  $425^{\circ}$ - $525^{\circ}C$ . The lower substrate temperatures were selected in an attempt to obtain low carrier concentrations in the epitaxial films which was not always possible using other vacuum evaporation methods. Further, it was hoped that deposition conditions could be established such that epitaxial films of  $\geq 30 \mu m$  thickness could be laid down in a few hours with a carrier concentration of  $10^{17}/cm^3$ . To avoid the Burstein shift with subsequent decrease in the wavelength cutoff and efficiency of  $Pb_xSn_{1-x}Te$  infrared detectors, the carrier concentration must be  $\leq 10^{17}/cm^3$ . Slices from bulk crystals of  $Pb_xSn_{1-x}Te$  as-grown have carrier concentrations of  $3 \times 10^{19}/cm^3$  and require one month of metal-rich annealing to bring the carrier concentration down to the low  $10^{17}/cm^3$  range.

### Experimental

The quartz reactor that was used for the growth of epi films is illustrated in Fig. 1. The apparatus was similar to that used in crystal growth with the exception that a constant diameter, larger opening to the seed was utilized (13). The quartz tubes were made in various diameters to accommodate substrates from 1 to 2.5 cm in length.

The substrates, which were {100}, were cut from single crystals of  $Pb_{0.79}Sn_{0.21}Te$  with a string saw. Surface irregularities from the sawing operation were removed from the substrates by lapping with a slurry of 600 mesh SiC. The substrates were then polished on a Pellon pad with concentrated HBr solution containing 5 volume per cent (v/o)  $Br_2$  until about  $400 \mu m$  had been removed; removal of this amount of material was necessary to insure removal of saw damage. The substrates were then removed from the polishing block and etched in HBr- $Br_2$  solution for 2 min to remove small scratches introduced on the polishing pad. The substrates were then electrolytically etched for 1 min to reveal damage. If no scratches were still present and if the number of dislocations was less than  $10^5/cm$ , the substrates were used for the growth studies. The substrates were etched in HBr- $Br_2$  solution again by swirling for 1-2 min following the electrolytic etch. The substrates were 9-29 mm in length, 5-15 mm in width, and approximately 1.5 mm thick.

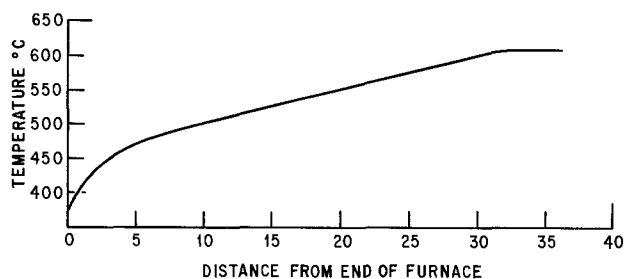
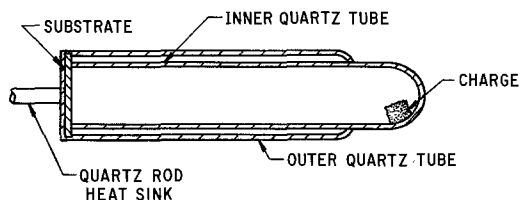


Fig. 1. Diagram of quartz apparatus used for epitaxial growth and a temperature profile used in one growth run.

The charges varied in composition from those which were stoichiometric to those containing 0.1 mole per cent (m/o) excess metals; these charges were compounded as described for crystal growth (13). Pieces weighing 2-3g were used as charges for the epitaxial growth experiments. After placing the charge in the growth tube, the system was sealed off at  $10^{-6}$  Torr.

Figure 1 also gives a temperature profile with respect to the growth tube which was used during an epitaxial growth experiment. Although the temperature of the substrate for the experiment in Fig. 1 was  $500^{\circ}C$  with the charge at  $610^{\circ}C$ , substrate temperatures of  $425^{\circ}$ - $525^{\circ}C$  were used with temperature differences between the substrate and charge of  $15^{\circ}$ - $200^{\circ}C$ . To initiate epitaxial growth, the growth tube was inserted into a vertical, resistance heater already at the desired growth temperature and with the necessary thermal difference between the substrate and the charge. The length of a growth run was from 4 to 100 hr. At the conclusion of a run the growth tube was removed from the furnace and air quenched. The substrates were removed from the growth tubes by sawing the quartz.

Microscopic examination and x-ray diffraction were used to evaluate the crystalline quality of the epitaxial deposits. Electron microprobe was used to determine the composition of the films and their uniformity. The carrier type was determined by thermal probe. Schottky barriers were used to determine the carrier concentration of the epitaxial films.

### Results and Discussion

The morphology of the deposits was greatly influenced by the substrate temperature. With a substrate temperature  $\geq 520^{\circ}C$  the deposits had blocklike features as shown in Fig. 2(a). Figure 2(b) illustrates the surface of a continuous, smooth deposit approximately  $50 \mu m$  thick which was laid down with the substrate at  $490^{\circ}C$ . Both deposits were made from charges of  $Pb_{0.791}Sn_{0.211}Te$  at  $590^{\circ}C$  over a period of 24 hr. All deposits laid down at  $425^{\circ}$ - $490^{\circ}C$  from a charge of  $Pb_{0.791}Sn_{0.211}Te$  were similar in appearance to that shown in Fig. 2(b). At the higher temperature  $\geq 520^{\circ}C$  nucleation and growth probably occur at fewer sites than at lower temperatures. Thus, at the lower temperature the increased number of nucleation sites for growth probably leads to continuous deposits. It is also possible that more two-dimensional growth occurs at lower temperatures. Changes in morphology with temperature have been observed for many substances (14-16), and it has been the general conclusion that different growth mechanisms predominate at different temperatures. Deposition periods  $\geq 72$  hr with substrate temperatures of  $520^{\circ}$ - $525^{\circ}C$  also gave continuous deposits but the surfaces were still covered with blocklike structures. For epitaxial growth at  $800^{\circ}$ - $850^{\circ}C$ , which is the temperature range used for growth of large single crystals (13), the deposit surfaces were smooth and featureless. Nearly all deposits had regular-shaped crystallites or blocklike structures on their surface when removed from the growth tube. However, these were loosely adhering crystallites which

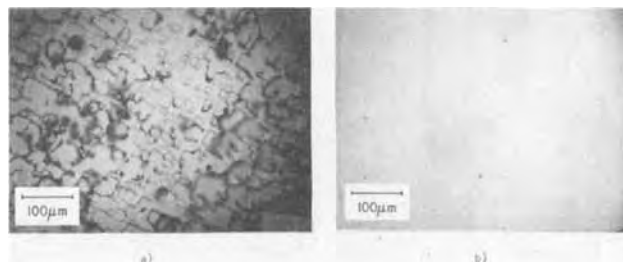


Fig. 2. Deposit surfaces at different substrate temperatures. (a) Substrate at  $525^{\circ}C$ , (b) substrate at  $490^{\circ}C$ . 350X magnification.

formed by rapid condensation of vapors during cool-down and were easily wiped off with a wet swab.

The surface quality of the substrate together with internal crystalline perfection affected the morphology of the epitaxial film as has been observed with numerous systems. Scratches and areas containing dislocations  $\geq 10^6/\text{cm}^2$  lead to irregular or blocklike features on the deposit surface. Figure 3 shows the surface of an epitaxial film with blocklike structures growing from scratches on the substrate. These structures extend about  $20\ \mu\text{m}$  above the epitaxial surface and demonstrate the effect of more rapid growth at dislocations or damaged regions. Usually these damaged regions could not be seen on the polished surfaces even under high magnification, however, the polished substrates were electrolytically etched to bring out these damaged areas. The presence of small angle grain boundaries and dislocations  $\leq 10^5/\text{cm}^2$  seemed to have no effect on the quality of the epitaxial film. The epitaxial films contained 3-10 times fewer dislocations than the substrates on which they were deposited.

The composition of the charge also had an influence on the morphology of the deposits. Charges ranging in composition from  $\text{Pb}_{0.790}\text{Sn}_{0.210}\text{Te}$  to  $\text{Pb}_{0.791}\text{Sn}_{0.211}\text{Te}$  gave smooth deposits while charges containing more excess metal gave irregular growth surfaces with needlelike projections. The needlelike projections were found to be metal rich by microprobe and metal-rich inclusions were found in the interior of the epitaxial layers deposited from these metal-rich sources. Chemical polishing of these epitaxial films with  $\text{HBr}-\text{Br}_2$  resulted in holes being formed at the metal-rich inclusions. Similar growth features have been observed by others when using metal-rich charges in other growth methods (20-24). The tops of the needlelike projections are rounded and suggest that a vapor-liquid-solid type growth mechanism is involved when excess metal is present. These metal inclusions cause electrical shorts in the epitaxial films. The use of Te-rich charges gave irregular deposits which contained Te inclusions that were etched out during processing to leave holes.

Good quality epitaxial films were grown by proper control of charge stoichiometry, substrate surface preparation, and deposition temperature. A scanning x-ray topograph of a good quality epitaxial film is illustrated in Fig. 4. Topographs of the substrates before and after deposition of epitaxial films showed no changes in crystalline perfection. That the deposits were single crystal was also shown by x-ray diffraction using the large area Laue technique. The x-ray topograph in Fig. 4 shows the epitaxial film to be rather uniform in texture and free of strains. The white areas correspond

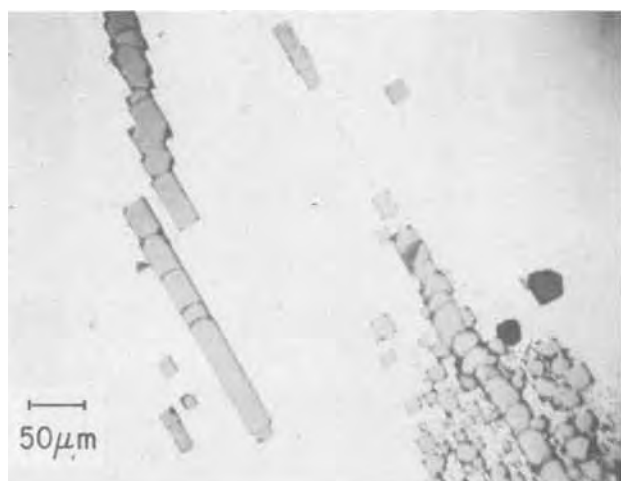


Fig. 3. Buildinglike growth caused by scratches and dislocations in the substrate. Source temperature  $\approx 590^\circ\text{C}$ , 24 hr run, feed of  $\text{Pb}_{0.79}\text{Sn}_{0.21}\text{Te}$ . 80X magnification.

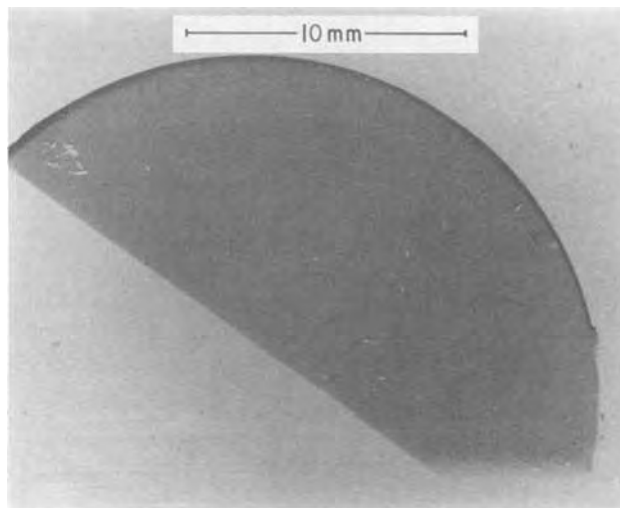


Fig. 4. Scanning x-ray topograph of an epitaxial film. 4.5X magnification.

to scratches and small holes introduced during the handling operations. This epitaxial layer was deposited with the substrate at  $490^\circ\text{C}$  and with the  $\text{Pb}_{0.791}\text{Sn}_{0.211}\text{Te}$  charge at  $590^\circ\text{C}$ . The epitaxial layer shown in Fig. 4 was  $60\ \mu\text{m}$  thick and was deposited over a 24 hr period.

The epitaxial growth rate was varied by changing the temperature of the substrate and the composition of the charge. The deposition rate with the substrate at  $420^\circ\text{C}$  and the charge of  $\text{Pb}_{0.790}\text{Sn}_{0.210}\text{Te}$  at  $590^\circ\text{C}$  was  $1.5\ \mu\text{m}/\text{hr}$ . With the substrate at  $480^\circ\text{C}$  and the charge at  $590^\circ\text{C}$  the deposition rate was  $2.6\ \mu\text{m}/\text{hr}$ . Figure 5 shows a photomicrograph of a cleaved substrate with the epitaxial layer deposited under these conditions. The epitaxial layer is clearly defined. The pits in the surface of the epitaxial layer were caused by material breaking away during the cleaving operation. Material also condensed on the walls of the growth tube and grew into small crystals but this material was not analyzed for its composition. This condensation occurred over about half the length of the growth tube but represented only a few per cent of the total charge weight. With stoichiometric charges the deposition rates were 30-50% less than for the slightly metal-rich charges used above. This suggests that uncombined metal may be involved in the growth mechanism and influences the growth rate.

The composition of the epitaxial films at their surfaces was rather uniform as determined by electron



Fig. 5. Cleaved substrate showing epitaxial layer grown at  $480^\circ\text{C}$  from a charge of  $\text{Pb}_{0.791}\text{Sn}_{0.211}\text{Te}$  at  $590^\circ\text{C}$ . 160X magnification.

Table I. Composition by electron microprobe of an epitaxial film and the charge used in making the epitaxial film

Material	Mean chemical composition with 2 sigma limits		
	a/o Sn	a/o Pb	a/o Te
Epitaxial* film	11.49 ± 0.10	38.95 ± 0.36	49.55 ± 0.40
Charge**	10.53 ± 0.09	38.73 ± 0.80	50.75 ± 0.79

\* Substrate at 425°C with the charge at 590°C. Run period of 48 hr with an epitaxial film, ~60 μm thick. Six random spots/cm<sup>2</sup> were used for analysis.

\*\* Analysis on the charge after the epitaxial run.

microprobe analysis. Typical results are shown in Table I. The initial charge, which was used in the run described in Table I, was weighed out to give a stoichiometric charge of  $Pb_{0.79}Sn_{0.21}Te$  or 10.5 atomic per cent (a/o) Sn, 39.5 a/o Pb, and 50 a/o Te. The composition of the charge after the deposition run was the same as that of the initial charge within the limits of experimental error. There was enrichment of SnTe in the epitaxial film which has also been observed in regular crystal growth at 850°C. This enrichment of SnTe is caused by the slightly greater vapor pressure of SnTe over that of PbTe (25). No microprobe measurements were made to determine if the compositions of the epitaxial films were uniform throughout their entire depth.

The type of dominant carrier in the epitaxial films was determined by thermal probe both at 77° and 300°K. The carrier concentration in the epitaxial films was determined by the Schottky barrier technique (26). Both carrier type and concentration showed variations with deposition temperature and with the feed composition as shown in Table II. It is doubtful that useful n-type films could be made because the n-type or mixed type material contained metal inclusions, which resulted in nonuniform etching during device fabrication and electrical shorts. It was necessary to use stoichiometric charges to obtain p-type deposits free of metal inclusions for substrate temperatures below 480°C. No deposition runs were made with stoichiometric charges for substrates below 425°C. The p-type carrier concentration decreased as the substrate deposition temperature decreased as expected based on annealing studies for  $Pb_{0.79}Sn_{0.21}Te$  (27). Usually 10 μm were lapped and etched from the epitaxial layers before fabrication of the Schottky barriers so surface effects were eliminated.

A Schottky barrier infrared detector array was made on a 50 μm thick film deposited at 510°C from a charge of  $Pb_{0.791}Sn_{0.211}Te$  at 600°C. The 22 element detector array had an average blackbody detectivity of  $1 \times 10^{10}$  cm Hz<sup>1/2</sup>/W at 77°K and varied by no more than ±10% from the average detectivity. The responsivity was about 10<sup>4</sup> V/W with a spectral cutoff at 12 μm. The properties of this array were very similar to those of Schottky barrier arrays made on annealed, bulk material (28). Only a few hours were required to obtain these epitaxial films while annealing the bulk material required a minimum of three weeks.

Depositions of PbTe on  $Pb_xSn_{1-x}Te$  substrates as well as  $Pb_xSn_{1-x}Te$  on PbTe substrates were also

made using the closed-tube method. However, the deposition temperatures and the charges used were different from the ones described here and will not be further discussed.

### Summary

Epitaxial films of  $Pb_xSn_{1-x}Te$  were deposited on  $Pb_{0.79}Sn_{0.21}Te$  substrates at 425°-525°C in a closed system at 10<sup>-6</sup> Torr. Good quality, p-type films with carrier concentrations in 10<sup>17</sup>/cm<sup>3</sup> range were obtained. The n-type films produced contained metallic inclusions. The quality of the deposits was greatly influenced by the charge composition, substrate temperature, and defects in the substrate. Deposition rates ranged from 1.5 to 3.0 μm/hr.

### Acknowledgments

The author gratefully acknowledges the help of Jack E. Pinnel in the experimental work. Appreciation is expressed to Henry Morris for making the Schottky barrier for determining carrier concentration and for fabrication of detector arrays. The discussions with Rowland E. Johnson and Richard A. Chapman were very helpful.

Manuscript submitted Nov. 17, 1975; revised manuscript received Feb. 20, 1976. This was Paper 163 presented at the Dallas, Texas, Meeting of the Society, Oct. 5-9, 1975.

Any discussion of this paper will appear in a Discussion Section to be published in the December 1976 JOURNAL. All discussions for the December 1976 Discussion Section should be submitted by Aug. 1, 1976.

Publication costs of this article were partially assisted by Texas Instruments Incorporated.

### REFERENCES

1. K. Yogi, K. Takayanagi, K. Kobayashi, and G. Honjo, *J. Cryst. Growth*, **9**, 84 (1971).
2. B. Lewis and D. J. Stirling, *ibid.*, **3**, 4, 200 (1968).
3. H. Holloway and E. M. Logothetis, *J. Appl. Phys.*, **41**, 3543 (1970).
4. H. Holloway and E. M. Logothetis, *ibid.*, **42**, 4522 (1971).
5. W. Rolls, R. Lee, and R. J. Eddington, *Solid-State Electron.*, **13**, 75 (1970).
6. S. E. R. Hiscocks, *J. Cryst. Growth*, **17**, 222 (1972).
7. J. R. Lowney and D. A. Cammack, *Mater. Res. Bull.*, **9**, 1639 (1974).
8. D. W. Bellavance, *J. Electron. Mater.*, To be published.
9. A. M. Andrews, J. A. Higgins, J. F. Longo, E. R. Gertner, and J. G. Pasko, *Appl. Phys. Letters*, **21**, 295 (1972).
10. J. F. Longo, J. S. Harris, Jr., E. R. Gertner, and J. C. Chu, *J. Cryst. Growth*, **15**, 107 (1972).
11. A. Laugier, J. Cadoz, M. Faure, and M. Moulin, *ibid.*, **21**, 235 (1974).
12. J. F. Longo, E. R. Gertner, and A. S. Joseph, *Appl. Phys. Letters*, **19**, 202 (1971).
13. S. G. Parker, J. E. Pinnel, and R. E. Johnson, *J. Electron. Mater.*, **3**, 731 (1974).
14. S. G. Parker and J. E. Pinnel, *J. Cryst. Growth*, **3**, 4, 490 (1968).
15. E. I. Givargizov and N. N. Sheftal, in "Crystal Growth," H. S. Peiser, Editor, p. 277, Pergamon Press, Oxford (1967).
16. M. Weinstein and G. A. Wolff, in *ibid.*, p. 537.
17. H. Aharoni, A. Bar-Lev, and S. Margolit, *J. Cryst. Growth*, **17**, 254 (1972).
18. J. L. Kenty, *J. Electron. Mater.*, **2**, 239 (1973).

Table II. Carrier type and concentration in epitaxial films

Run No.	Composition of charge	Charge temp, °C	Substrate temp, °C	Film thickness, μm	Deposition rate, μm/hr	Carrier type	Carrier conc, No./cm <sup>3</sup>
532	$Pb_{0.791}Sn_{0.211}Te$	591	515	65	2.7	p	$2 \times 10^{18}$
456	$Pb_{0.791}Sn_{0.211}Te$	600	510	15	2.0	p	$7 \times 10^{17}$
500	$Pb_{0.791}Sn_{0.211}Te$	600	500	75	3.0	p	$2.5 \times 10^{17}$
687	$Pb_{0.795}Sn_{0.210}Te$	590	480	50	2.6	p	$1 \times 10^{18}$
655	$Pb_{0.795}Sn_{0.210}Te$	590	425	30	1.5	p	$1 \times 10^{17}$
614	$Pb_{0.791}Sn_{0.211}Te$	590	425	40	1.7	n & p	—
656	$Pb_{0.792}Sn_{0.212}Te$	590	425	50	2.0	n & p	—

19. R. Ueda and F. Inuzuka, *J. Cryst. Growth*, **9**, 79 (1971).
20. M. Paic and V. Paic, *J. Mater. Sci.*, **7**, 1260 (1972).
21. I. Kasai and D. W. Bassett, *J. Cryst. Growth*, **27**, 215 (1974).
22. J. N. Walpole, A. R. Colowa, R. W. Ralston, and F. C. Harman, *Appl. Phys. Letters*, **23**, 620 (1973).
23. G. F. McLane and K. J. Sleger, Paper presented at 16th Electronic Materials Conference, Boston, Massachusetts, Sept. 9-11, 1974.
24. I. Kasai, J. Hornung, and J. Boors, Paper presented at 16th Electronic Materials Conference, Boston, Massachusetts, Sept. 9-11, 1974.
25. D. A. Northrop, *J. Phys. Chem.*, **75**, 118 (1971).
26. C. A. Mead, *Solid-State Electron.*, **9**, 1023 (1966).
27. C. R. Hewes, M. S. Adler, and S. D. Senturia, *J. Appl. Phys.*, **44**, 1327 (1973).
28. H. B. Morris, R. A. Chapman, R. L. Guldi, and S. G. Parker, Proceedings of 1975 IRIS Detector Specialties Meeting, Fort Monmouth, New Jersey, March 1975.

## Structure and Strength Effects in CVD Titanium Carbide and Titanium Nitride Coatings

W. Schintlmeister, O. Pacher, and K. Pfaffinger

*Metallwerk Plansee AG & Company KG, 6600 Reutte, Austria*

and T. Raine

*Cutanit Limited, Grappenhall, Warrington, England*

### ABSTRACT

The first part of the study deals with the influence of CVD titanium carbide and titanium nitride coatings on the transverse rupture strength of M10 and P40 cemented carbide. The rupture strength is noticeably reduced by the coating, the extent of this decrease depending on coating thickness, coating structure, and the presence of a decarburization or brittle phase in the surface zone of the substrate material. Furthermore, it was found that a thin intermediate nickel layer does not have any positive effect on the rupture strength. The second part deals with investigations on the effect of substrate composition on the structure of the TiC and TiN coatings. In presence of nickel-containing substrates, the TiN forms dendritic structures, the TiC coarse-grained structures. Nickel is also incorporated into the coating. Increasing the reactant concentration in the gas phase intensifies these effects. Finally, the mechanisms underlying these effects are briefly discussed.

Titanium carbide, titanium nitride, and titanium carbonitride are currently widely employed in the form of homogeneous coatings and as multiple coatings to improve the wear resistance of cemented carbide tools and also to achieve decorative effects (1). The increase in wear resistance caused by these coatings is of particular importance in machining. The excellent stability and hardness as well as the attractive colors of some hard materials are gaining importance for decorative purposes.

Materials used in machining must have adequate toughness in addition to maximum wear resistance. For coated materials the adhesion to the substrate is another important factor. The wear resistance and toughness requirements of cemented carbides are mutually contradictory so that a compromise must be sought in each particular application.

If, for example, a cemented carbide grade with great wear resistance but insufficient toughness is employed in a certain machining application, fracture may occur. If, on the other hand, the toughness is greater than required, the cutting speed must be reduced in order to prevent softening or plastic deformation of the cutting edge.

The optimum utilization of coated materials thus requires a knowledge of their toughness behavior. In cemented carbide technology, the transverse rupture strength is taken as a measure of toughness and we have carried out a number of experimental studies on the effect of hard coatings on the transverse rupture strength.

Key words: transverse rupture strength, thickness of coatings, structure of coatings, composition of base material.

Coated TiC cemented carbide with Ni-Mo binder is of interest for wear parts as well as for decorative purposes. In decorative applications, the coating should not only exhibit good adhesion and corrosion resistance but should also be smooth so that a bright polish can be achieved. Coating experiments have shown, however, that the TiC-Ni-Mo grades, in contrast to the WC-Co grades, tend to form rough coating structures. This different behavior of the substrate material has induced us to carry out an investigation on the effect of the substrate on the coating structure.

### Investigations on the Effect of the Coating on the Transverse Rupture Strength

A study carried out by Lee and Richman (2) has shown that a TiC coating on C2 and C4 cemented carbide reduces the transverse rupture strength by approximately 45%. The authors suppose that this decrease is due to the columnar coating structure; an equiaxed structure would presumably eliminate this deficiency.

We have first carried out preliminary studies on the effect of TiC and TiN coatings on two different grades of cemented carbide. The effect of a thin metallic intermediate layer was also investigated. This led to the necessity to investigate the dependence of the transverse rupture strength on the coating thickness, the effect of a decarburization zone between substrate and coating, and the behavior of coatings with different structures.

*Test procedure and evaluation of results.*—Transverse rupture strength rods of ISO groups M10 and P40 were coated with TiN and TiC by CVD (M10: 6%

Co, 10% TiC + Ta(Nb)C, remainder WC; P40: 13% Co, 10% TiC + Ta(Nb)C, remainder WC). Two lots of M10 rods were sintered. The rods cut from presintered blocks were sintered and then tumbled in a barrel with a boron carbide containing slurry for edge rounding and removal of the sintering skin and were then sand blasted. This preparation was essential in order to have the same conditions as with normal disposable tips.

The coating was carried out in a medium frequency induction furnace with graphite susceptor which was coated on the inside and had an internal diameter of 120 mm. The nickel-containing TiC coating was obtained by first depositing the TiC, then applying a nickel layer by electrolytic deposition and then again a layer of TiC. The coating conditions are summarized in Table I.

Figure 1 shows the arrangement for the measurement of the transverse rupture strength in accordance with ASTM B 405-70 standard (3) (corresponds to ISO standard DIS 3327, Type B) with the only difference that the specimen thickness was reduced. The specimen dimensions were  $6.5 \times 3.6 \times 20$  mm with a distance between supports of 14.5 mm. In accordance with the above standards, the supports consisted of cemented carbide rolls having a diameter of 6 mm and the load was applied in the center of the specimen by means of a 10 mm diameter cemented carbide sphere.

In transverse rupture testing, a considerable scatter is normal (the Swedish standard SIS 112618 considers a standard deviation of 12% of the mean value with 10 specimens as normal) so that a statistically significant result requires a correspondingly large number of specimens. Hence, 19-20 specimens were used for each test; some supplementary tests were carried out on only 14 or 15 specimens. The arithmetic means and the 95% confidence limits were determined for each test series. In order to permit conclusions on the effect of the coating structure, we prepared SEM (scanning electron microscope) micrographs at 3300X magnification at the specimen bottom where the material is subjected to tensile stress. Additionally, optical micrographs at 1500X magnification were also prepared.

**Results.**—Table II contains the results on the rods of lot 1 and Table III those of lot 2. In addition to the number of rods tested for each variant, the tables indicate the variation of the transverse rupture strength with the coating. The arithmetic mean of the uncoated rods was defined to 100%. The individual values fit fairly well into a normal distribution. Figure 2 shows as an example the distribution of the individual values for different coating thicknesses in the probability grid. Figure 3 (a-d) shows the coating structures at the fracture surface for the TiC, TiN, and TiC-Ni-TiC coating on M10 and for the TiN coating on P40 cemented carbide; Fig. 3 (e-g) the corresponding optical micrographs.

Further coating structures of fracture surfaces are shown in Fig. 5(a) and 5(b) for a thin and a thick TiC

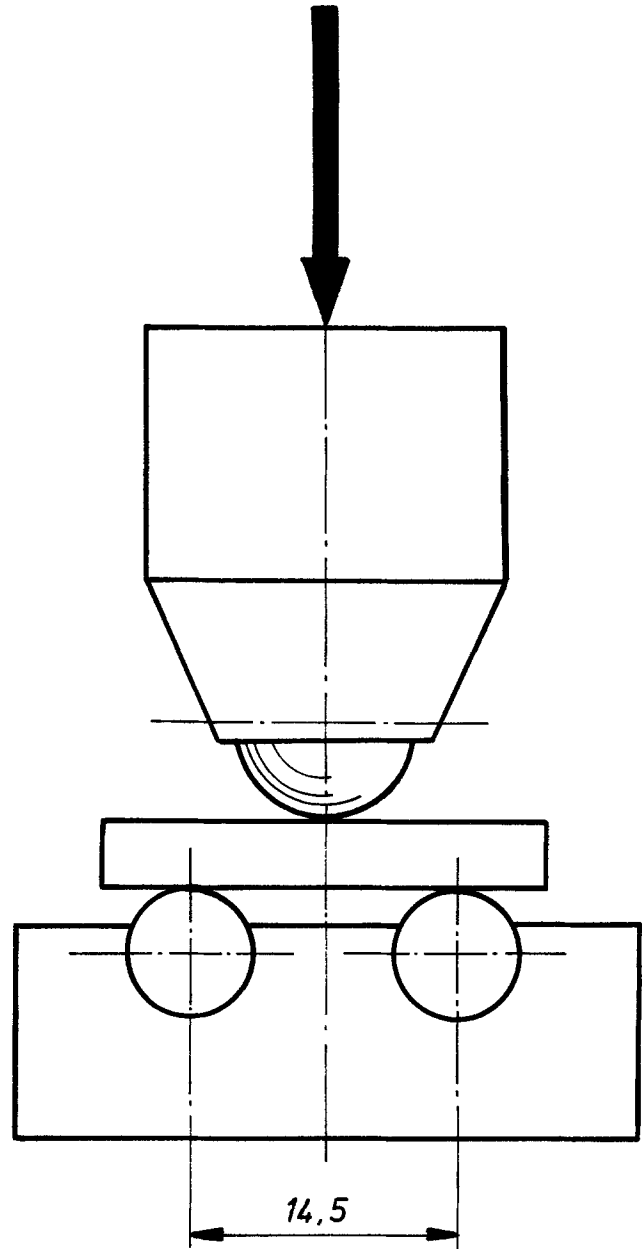


Fig. 1. Arrangement for the TRS measurement

layer, Fig. 6(a) and 6(c) for 6-7 $\mu$  thick TiC layers with and without decarburized phase, and Fig. 6(b) for a TiC layer with grainy structure. A comparison of the results permits the following conclusions.

**Effect of TiC and TiN layers on M10 and P40 cemented carbide.**—TiC and TiN layers over 10 $\mu$  thick lower the transverse rupture strength of M10 and P40 grades by approximately one-third. These layers have a columnar structure [SEM micrographs Fig. 3(a-c)]; although this structure is thicker and more pronounced in the TiN coating, there is no difference in their effects.

Table I. Coating conditions

Coating	Temp °C	Time min	TiCl <sub>4</sub> *	Liter/hr N <sub>2</sub>	C <sub>6</sub> H <sub>6</sub> **	Liter/hr H <sub>2</sub>
9 $\mu$ m TiC	915	75	200	—	110	815
12 $\mu$ m TiN	915	105	200	200	—	575
TiC/Ni/TiC	915	38	200	—	110	815
	915	37	200	—	110	815
1.2 $\mu$ m TiC	915	10	200	—	110	815
2.5 $\mu$ m TiC	915	20	200	—	110	815
7 $\mu$ m TiC	915	65	200	—	110	815
11.5 $\mu$ m TiC	915	135	200	—	110	815
2 $\mu$ m TiC with 2.5 $\mu$ m <sub>11</sub> eta layer	915	20	200	—	110	815
6.5 $\mu$ m TiC with 3 $\mu$ m eta layer	915	60	200	—	110	815

\* Liter/hr H<sub>2</sub> saturated with TiCl<sub>4</sub> at 37°C.

\*\* Liter/hr H<sub>2</sub> saturated with C<sub>6</sub>H<sub>6</sub> at 15°C.

Table II. Transverse rupture strength (TRS) of the rods of lot 1

Coating	Base material	No. of specimen	TRS kp/mm <sup>2</sup>	%
Uncoated	M10	20	182.4 $\pm$ 7.6	100
9 $\mu$ m TiC	M10	18	126.1 $\pm$ 9.8	69.1 $\pm$ 5.4
12 $\mu$ m TiN	M10	19	126.1 $\pm$ 4.6	69.1 $\pm$ 2.5
Uncoated	P40	20	256.0 $\pm$ 7.2	100
12 $\mu$ m TiN	P40	19	169.1 $\pm$ 6.2	66.0 $\pm$ 2.4
4.5 $\mu$ m TiC/ 0.5 $\mu$ m Ni/ 3.5 $\mu$ m TiC	M10	19	118.3 $\pm$ 3.7	64.9 $\pm$ 2.0

Table III. Transverse rupture strength (TRS) of the rods of lot 2\*

Coating	No. of specimen	TRS kp/mm <sup>2</sup>	%
Uncoated	17	188.7 ± 7.7	100
1.2 μm TiC	17	180.1 ± 8.0	95.4 ± 4.2
2.5 μm TiC	19	169.4 ± 5.0	89.8 ± 2.6
7 μm TiC	19	135.1 ± 6.2	71.6 ± 3.3
11.5 μm TiC	19	123.1 ± 5.4	65.2 ± 2.9
Uncoated and 3 μm eta layer	15	180.9 ± 7.6	95.9 ± 4.0
2 μm TiC with 2.5 μm eta layer	15	152.4 ± 8.9	80.8 ± 4.7
6.5 μm TiC with 3 μm eta layer	15	127.7 ± 5.1	67.7 ± 2.7
7 μm TiC grainy structure	15	147.9 ± 6.5	78.4 ± 3.4

\* Base material M10 hardmetal.

**Effect of coating thickness.**—The transverse rupture strength as a function of the TiC coating thickness is shown in Fig. 4. With thin layers (up to 5μ), the coating thickness has a great influence. With increasing coating thickness, this influence is less pronounced. The fracture micrographs Fig. 5(a) and (b) show that in the thicker coatings, a very fine-grained structure is present near the substrate, with a transition to a columnar structure. The latter seems to be absent in the thin coatings.

**Effect of the decarburization zone (eta layer).**—Figure 4 also gives values for two different TiC layer thicknesses combined with an approximately 3μ thick decarburization zone (W<sub>6</sub>Co<sub>6</sub>C etc.). The curve showing the influence of the coating thickness is slightly shifted to lower rupture strengths, i.e., the decarburization zone has the same effect as a thicker coating.

**Influence of the coating structure.**—By variation of the coating parameters it was possible to produce a grainy (equiaxed) structure [see Fig. 6(b)]. This structure gives a higher rupture strength but at 7μ coating thickness, the decrease still amounts to about 22%.

**Incorporation of a thin nickel layer in a TiC coating.**—It was found that the incorporation of an intermediate nickel layer alters the structure of the TiC coating and causes a further decrease in rupture strength [Fig. 3(d)]. Thus, an intermediate layer does not act as a crack barrier.

**Fracture mechanism.**—Cemented carbide and TiC differ considerably in Young's modulus and transverse

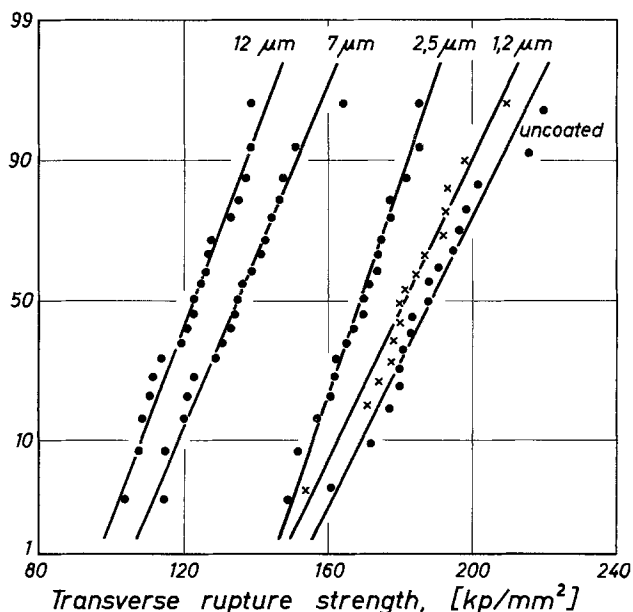


Fig. 2. Distribution of individual TRS values for different coating thicknesses in the probability grid. Ordinate: cumulative per cent of frequency.

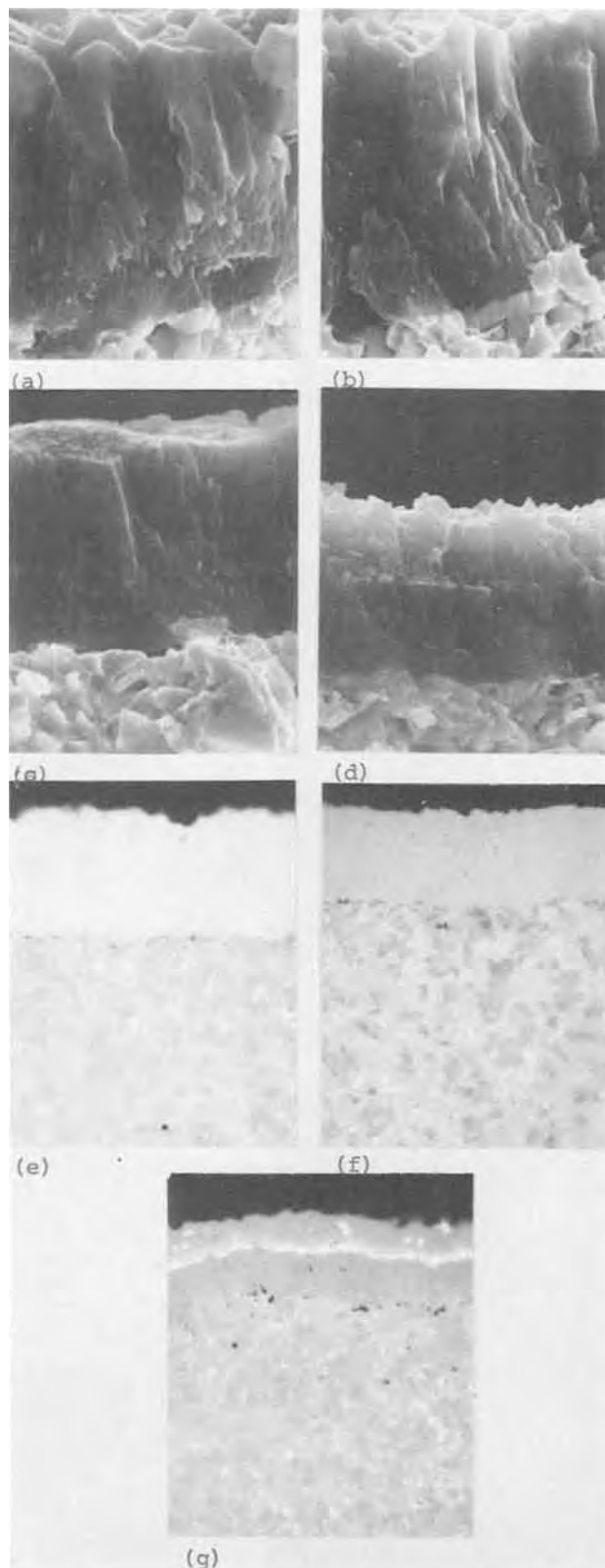


Fig. 3. SEM of the fracture surface of TiN and TiC coatings as well as TiC-Ni-TiC coatings deposited on M10 and P40 cemented carbides (a-d). Magnification X3000. Optical micrographs of TiN and TiC coatings as well as TiC-Ni-TiC coatings (e-g). Magnification X1300.

rupture strength.

	M10 cemented carbide	P 40	TiC
Young's modulus, kg/mm <sup>2</sup>	62,000 <sup>1</sup>	56,000 <sup>1</sup>	32,200 <sup>2</sup>
Transverse rupture strength, kg/mm <sup>2</sup>	185 <sup>1</sup>	256 <sup>1</sup>	40 <sup>2</sup>

<sup>1</sup> Own measurements.

<sup>2</sup> Values according to Ref. (4).

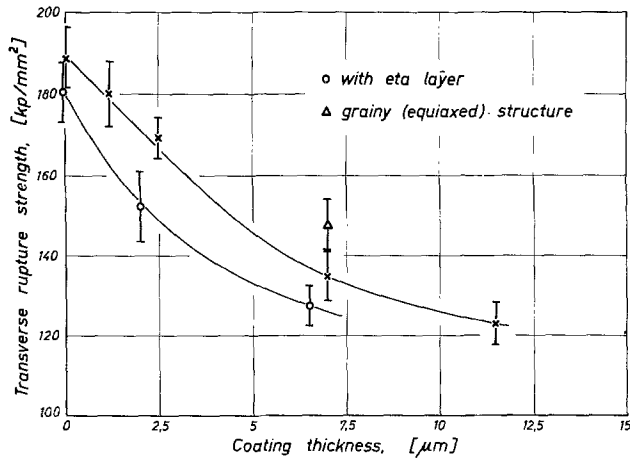


Fig. 4. TRS in dependence of the TiC coating thickness

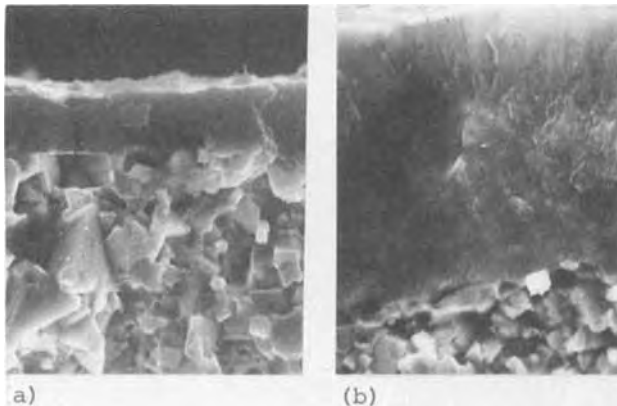


Fig. 5. SEM of the fracture surface for two different TiC coating thicknesses on M10 cemented carbide.

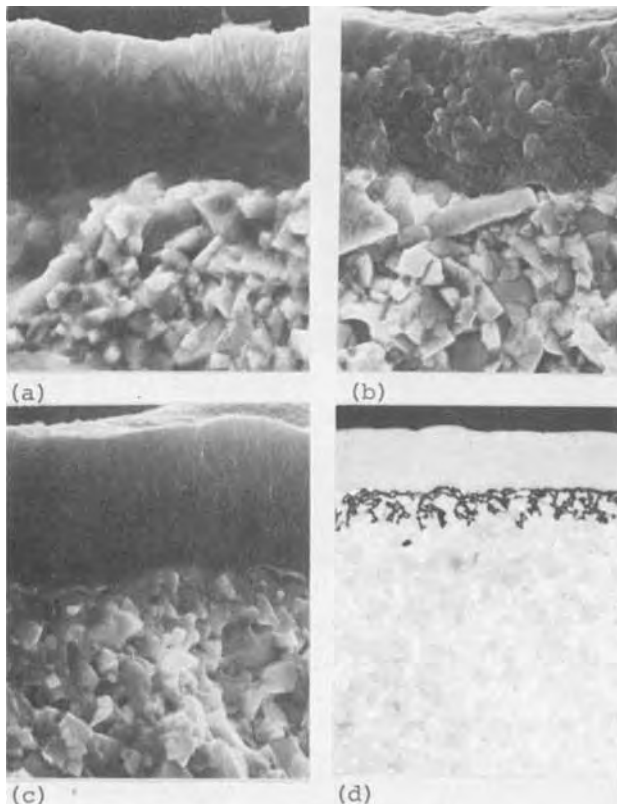


Fig. 6. Structure and cross section of various TiC coatings with columnar and grainy structure as well as an eta layer under the coating.

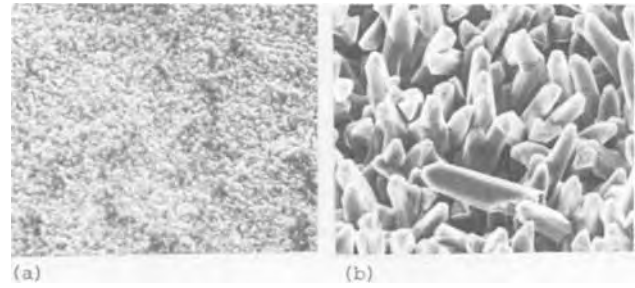


Fig. 7. SEM of the surface of (a) P40 and (b) TiC-Ni-Mo cemented carbide coated simultaneously with TiN.

On the basis of these values one would expect that the coating cracks on the side subjected to tension in the transverse rupture test without the crack propagating immediately into the cemented carbide. This crack could act as a notch. Coatings of different thickness would have to give notches of different depth. Further investigations are underway and will show whether this model adequately accounts for the dependence of the transverse rupture strength on the coating thickness and for the effects of different coating structures.

**Conclusions.**—The following inferences can be derived from the above results. The transverse rupture strength of cemented carbide is noticeably lowered by coating with tightly adhering hard materials, with the following factors being of importance: (i) the coating thickness, particularly with very thin coatings; (ii) the coating structure, with grainy structures being preferable to columnar structures; and (iii) a decarburization or brittle phase in the surface zone of the substrate. Hence, these factors must be included in any investigation on the strength of coated materials. A thin, electrolytically deposited nickel layer does not have any positive effect on crack propagation.

#### Influence of the Substrate on the Coating Structure

Hintermann, Gass, and Lindström (5) have shown that in TiC coating of cemented carbide, the composition of the substrate has an important effect on the coating structure. As mentioned above, we obtained dendritic structures in coating of TiC cemented carbide with Ni-Mo binder under certain conditions, whereas on WC-Co cemented carbide, finely crystalline, smooth coatings resulted. Figure 7 shows the surfaces of a 10μ thick TiN layer on P40 and on TiC-Ni-Mo hard metal, which were coated simultaneously. As it was not clear at first whether these structure effects were produced by the TiC or the Ni binder, we have coated P40 hard metal with 5-7μ thick TiC and then nickel-plated them electrolytically. We have carried out structure investigations on TiC and TiN coatings at normal and double reactant concentration.

**Experimental conditions and results.**—The coating conditions are given in Table IV. Figure 8 shows surface textures of TiN coatings deposited at normal and double concentration. The TiN deposition on TiC, i.e., a nickel-free substrate, always gives finely crystalline coatings such as are obtained on WC-Co hard metals. Doubling of the concentration does not affect the structure. Conversely, the nickel-plated specimens ex-

Table IV. Coating conditions

	Temp °C	Time min	TiCl <sub>4</sub> *	Liter/hr N <sub>2</sub>	C <sub>6</sub> H <sub>6</sub> **	Liter/hr H <sub>2</sub>
TiC	915	90	200	0	110	815
	915	45	400	0	220	815
TiN	915	85	200	200	0	575
	915	42 or 12	400	380	0	575

\* Liter/hr H<sub>2</sub> with TiCl<sub>4</sub> at 37°C.

\*\* Liter/hr H<sub>2</sub> saturated with C<sub>6</sub>H<sub>6</sub> at 15°C.



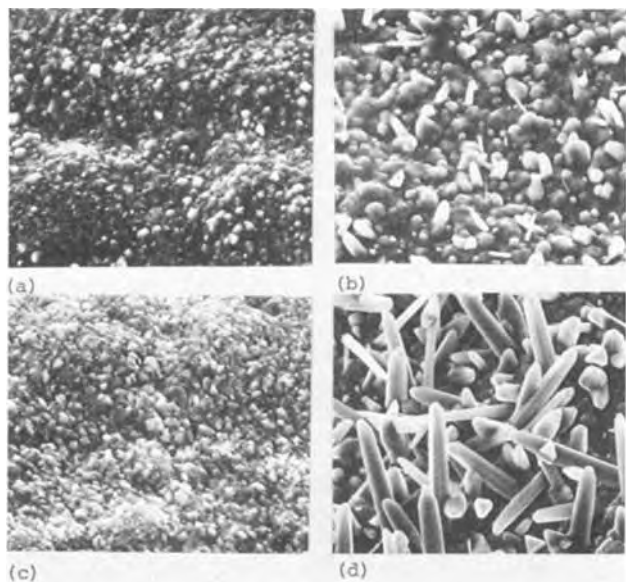


Fig. 8. SEM of the surface of TiN coatings deposited simultaneously on TiC [(a) and (c)] and on Ni [(b) and (d)] at two different coating runs with normal concentration (top) and double concentration (bottom).

hibit a pronounced dendritic crystal growth, particularly so at double reactant concentration. In the TiC deposits made under the same conditions, pronounced dendritic structures are absent, but the coating is more coarse grained in presence of nickel.

Figure 9 shows TiC deposits obtained at double reactant concentration. On the nickel-plated specimen, a new phase is observed in the form of inclusions, particularly at higher concentrations. These inclusions were identified by EDAX as finely divided nickel.

Figure 10 shows polished sections of TiC and TiN coatings on nickel-plated substrates with finely divided nickel inclusions in the coating; a Ni and Ti analysis by means of EDAX and a fracture structure. The latter shows the typical dendritic crystal growth. As it appeared logical that this crystal habit is due to heterogeneous nucleation at the Ni surface, we have carried out short-time coating tests in order to observe the processes taking place during the initial coating phase. Figure 11 provides a comparison of the surface structures obtained in short-time and normal coating. With the nickel-plated specimen, a greatly inhibited nucleation can be observed, resulting in a columnar to dendritic structure with longer coating durations. In contrast, specimens not nickel plated exhibit intense nucleation at the surface during the initial coating stage, thus yielding finely crystalline, smooth coatings.

**Discussion.**—The following inferences can be drawn with regard to the influence of different substrate compositions on the coating structure. TiC and WC-Co cemented carbide substrates always give smooth coatings under our coating conditions. Nickel-plated or

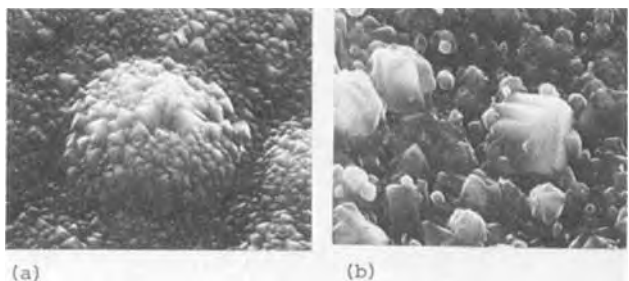


Fig. 9. TiC coating on TiC substrate (a) and on Ni substrate (b) deposited simultaneously.

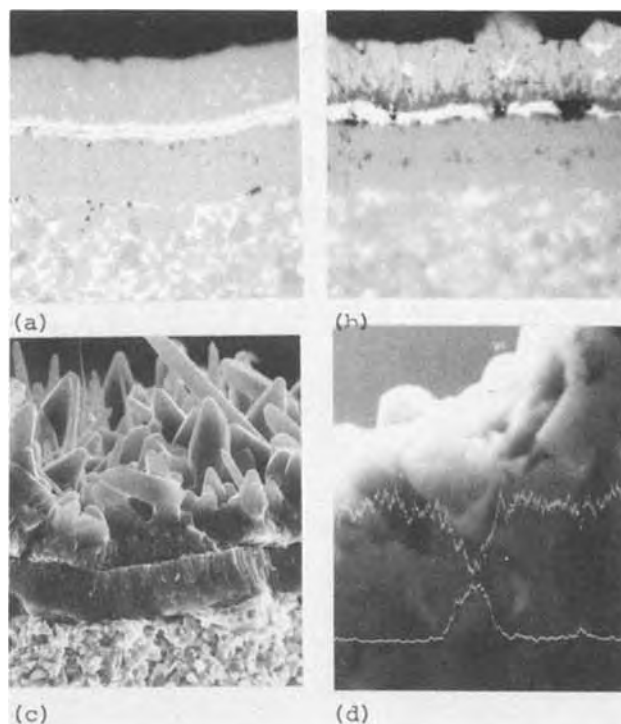


Fig. 10. Top: cross section of a TiC coating on Ni (a) and a TiN coating on Ni (b) deposited with double concentration. Bottom: fracture of a TiN coating deposited on Ni. (c) SEM; (d) EDAX of Ni and Ti.

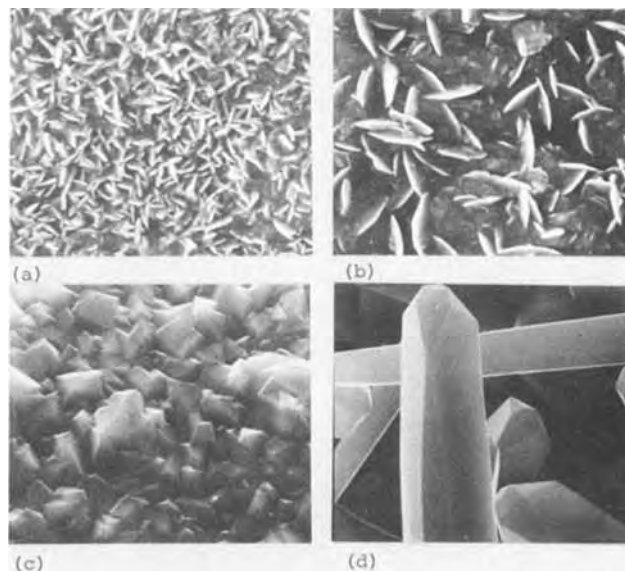


Fig. 11. SEM of the surface of a TiC substrate [(a) and (c)] and a Ni substrate [(b) and (d)] coated simultaneously with TiN. Top: after 12 min coating time; Bottom: after 42 min coating time.

nickel-containing substrates, on the other hand, particularly when TiN is deposited, exhibit intense dendritic crystal growth. Doubling the concentration in this case has a much greater effect than in TiC coating, when the Ni merely causes a slight coarsening of the structure. It is possible, however, that under different coating conditions this effect will be more intense even for the TiC deposition. Nickel incorporation into the coating can be observed in TiC and TiN coating; in TiN coating, the effect of the nickel probably consists in a reduction of the number of nuclei in the initial stage. Thus, coarser coatings will result. At the same time, preferred growth directions develop. The coating conditions probably also affect



the result; for example, in our case, a higher concentration results in faster growth in one direction and thus also in an intensification of dendritic growth.

Concerning the Ni incorporation, the following transport mechanisms may be assumed: (i) a gas phase transport via nickel chlorides resulting in a constant nickel chloride concentration in the deposition zone and in continuous nickel deposition at certain points; (ii) surface diffusion of the nickel during the growth of the TiC or TiN crystallites; and, (iii) formation of a liquid phase which penetrates cavities formed during deposition.

In the system Ti-Ni, the lowest temperature of the liquid phase is about 950°C, representing an eutectic containing 70 weight per cent titanium. Which of these theoretically possible transport mechanisms is actually operative, cannot be decided at this time.

Manuscript submitted May 27, 1975; revised manuscript received ca. Dec. 19, 1975.

Any discussion of this paper will appear in a Discussion Section to be published in the December 1976 JOURNAL. All discussions for the December 1976 Discussion Section should be submitted by Aug. 1, 1976.

Publication costs of this article were partially assisted by Metallwerk Plansee AG & Company KG.

#### REFERENCES

1. W. Schintlmeister and O. Pacher, *Metall.*, **28**, 690 (1974).
2. M. Lee and M. H. Richman, *Metals Technol.*, **December**, 538 (1974).
3. Annual Book of ASTM Standards, Part 9 (1974).
4. R. Kieffer and F. Benesovsky, "Hartstoffe," p. 97, Springer Verlag Wien, Austria (1963).
5. H. E. Hintermann, H. Gass, and J. N. Lindström, in "Chemical Vapor Deposition, Third International Conference," p. 352, Salt Lake City, Utah, April 24-27, 1972.

## Oxidation of Fe-29Ni-17Co Alloy

R. A. Piscitelli\*

*Bendix Corporation, Electrical Components Division, Sidney, New York 13838*

and S. K. Rhee and F. N. Bradley

*Bendix Corporation, Research Laboratories, Southfield, Michigan 48076*

#### ABSTRACT

The effect of composition, microstructure, and preferred orientation upon the oxidation of iron-nickel-cobalt alloy was investigated. Decarburized samples were oxidized at various temperatures and times. Decarburization at 1100°C in wet hydrogen enhances the (200) orientation. The oxidation rate depends on the alloy grain size and minor alloy constituents and is enhanced at the grain boundaries. The oxide is predominantly spinel with increased amounts of  $\alpha$ -Fe<sub>2</sub>O<sub>3</sub> appearing in fine-grain alloy oxidized at lower temperatures and longer times.

Variations in the oxidation behavior of iron-nickel-cobalt alloy under constant production conditions have been observed from heat to heat and from vendor to vendor. These variations cause processing difficulties in the production of components requiring glass-to-metal seals, consequently lowering the production yield. The problem is especially severe (i) where close process control is used to achieve a standard oxide weight gain on the parts prior to the glass fusing operation and/or (ii) where continuous processing is desired.

The purpose of the present investigation was to determine the causes of the differences in the oxidation characteristics of the ASTM F-15 glass-sealing alloy so that its oxidation behavior could be predicted.

Very little work has been done on the oxidation characteristics of the ternary alloy, iron-nickel-cobalt. Abendroth (1) studied the oxidation of the iron-nickel-cobalt alloy having a chemical composition similar to ASTM F-15 at 700°-900°C and concluded that the oxidation product is predominantly Fe<sub>3</sub>O<sub>4</sub> with some cobalt and nickel present. He attributed oxidation below 800°C to iron ion diffusion through Fe<sub>3</sub>O<sub>4</sub> and above 800° to iron ion diffusion through FeO. However, the wustite phase (FeO) was not detected by x-ray diffraction.

Abendroth's work is inconclusive pertaining to the mechanisms of oxidation of the iron-nickel-cobalt alloy and provides no information on the variation of oxidation characteristics with respect to inherent mate-

rial variables. Therefore, it was decided to investigate the effects of the composition, microstructure, and preferred orientation on the oxidation rate, oxide composition, and structure as a function of temperature and time.

#### Materials and Experimental Procedures

Materials for this investigation were chosen from three vendors referred to as I, II, and III. Two heats of the alloy were chosen from each supplier according to their chemistry, microstructure, and texture. All materials were stamped into rectangular coupons 2.54 × 2.39 cm with an average thickness from 0.015 to 0.041 cm. The chemical compositions as provided by the manufacturers of the materials (unless otherwise noted) are given in Table I.

The materials were oxidized in dry air (dew point at -70°C) at 787°, 850°, and 900°C for periods of 4-20 min. These oxidation conditions were chosen because previous experimental work indicated that the optimum production conditions for oxidizing parts to be glass sealed fell within this time and temperature range.

Prior to decarburization and oxidation, the metal coupons were chemically cleaned by hydrochloric acid and degreased. After the cleaning operation, groups of ten coupons of each material were weighed on a Mettler analytical balance to ±0.1 mg. They were then loaded in a sand-sealed retort which was placed in a Lindberg box furnace for decarburization and oxidation. A total of six materials was arranged in groups of

\* Electrochemical Society Active Member.

Key words: Fe-Ni-Co alloy, oxidation, grain boundary, decarburization, spinel.

Table I. Material properties and oxidation data

Material	Bulk composition							Grain dimensions		Oxidation rate			Activation energy (kcal/mole)	Arrhenius pre-exponential constant $10^6$ (mg <sup>2</sup> /cm <sup>4</sup> min)
	Fe	Ni†	Co	Cr	Mn	Si	Al	D ( $\mu$ )	D <sup>-1</sup> × 10 <sup>3</sup> ( $\mu^{-1}$ )	k × 10 <sup>2</sup> (mg <sup>2</sup> /cm <sup>4</sup> min)				
	787°C			850°C			900°C							
Vendor IA	Bal.	28.5	17.3	0.15	0.23	0.11	—	11	91	0.50	2.32	5.26	52.4	324.7
Vendor IB	Bal.	28.4	17.4	0.11†	0.23	0.11	—	15	67	0.52	2.05	6.24	54.8	982.9
Vendor IIC	Bal.	28.4	17.2	0.01	0.42	<0.05	<0.05	78	13	0.32	1.19	2.66	46.7	13.7
Vendor IID	Bal.	28.5	17.1	<0.01	0.40	0.03	<0.05	132	8	0.28	1.00	2.28	46.6	11.0
Vendor IIIE	Bal.	29.2	17.0	0.03	0.32	0.11	0.04	9	111	1.18	3.77	8.25	43.1	8.8
Vendor IIIF	Bal.	28.4	17.0	0.06†	0.26	0.03	0.05	50	20	0.32	1.05	2.54	45.7	8.3

Material	% Oxide composition															
	787°C				850°C				900°C							
	8 min		20 min		4 min		8 min		20 min		4 min		8 min		20 min	
$\alpha^*$	S**	$\alpha$	S	$\alpha$	S	$\alpha$	S	$\alpha$	S	S	$\alpha$	$\alpha$	S	$\alpha$	S	
IA	18.6	81.4	29.0	71	0	100	25.7	74.3	11.8	88.2	0	100	0	100	7.8	92.2
IB	0	100	32.6	67.4	0	100	0	100	0	100	0	100	0	100	0	100
IIC	0	100	0	100	0	100	0	100	10.5	89.5	0	100	5.6	94.4	5.5	94.5
IID	0	100	0	100	0	100	0	100	0	100	0	100	0	100	0	100
IIIE	21.7	78.3	33.5	66.5	0	100	0	100	20.3	79.7	0	100	0	100	7.5	92.5
IIIF	8.8	91.2	8.5	91.5	0	100	0	100	0	100	0	100	0	100	7.9	92.1

† Analyzed at Bendix.

\*  $\alpha$ -Fe<sub>2</sub>O<sub>3</sub>.\*\* Spinel (Fe, Ni, Co)<sub>3</sub>O<sub>4</sub>.

ten coupons in the retort. Platinel thermocouples were placed at the front and rear of the retort to monitor the temperature. The reported temperatures are accurate to better than  $\pm 5^\circ\text{C}$ . The materials were decarburized at  $1100^\circ\text{C}$  for 25 min in wet hydrogen (dew point at room temperature). They were then cooled to the desired oxidation temperature under a dry argon blanket (dew point at  $-72^\circ\text{C}$ ). The furnace temperature was stabilized, and dry air was introduced into the system at a flow rate of  $1600\text{ cm}^3/\text{min}$ . The chamber volume was  $2122\text{ cm}^3$ . When oxidation had taken place for the desired time, the air was switched off and the samples were cooled to room temperature under an argon blanket. After cooling, each material was then weighed in groups of ten coupons on the analytical balance to obtain the group oxide weight gain. The average surface area of each material was determined from the coupon dimensions, and, subsequently, weight gain in  $\text{mg}/\text{cm}^2$  was obtained.

The oxides were characterized by x-ray diffractometry and spectroscopy. Calibration samples having predetermined ratios of Fe<sub>2</sub>O<sub>3</sub> to Fe<sub>3</sub>O<sub>4</sub> were used to prepare a calibration curve for quantitatively determining the oxide phases formed. Selected decarburized samples and oxidized samples were also examined with a Cambridge scanning electron microscope. The iron, cobalt, and nickel concentrations in the oxide were obtained with an energy dispersive x-ray analyzer attachment on the SEM. The microstructure of the oxide/metal interface was studied by examining tapered sections under a metallurgical microscope.

The preferred orientation of the material was determined by comparing the relative intensities of the x-ray diffraction peaks for the (111), (200), and (220) planes of face-centered cubic (fcc) alloy. A Phillips diffractometer was employed with copper K $\alpha$  radiation as the source. Preferred orientation was determined on both the as-received materials and on samples which had been decarburized.

## Results and Discussions

It is known that oxidation behavior is dependent on substrate orientation (2-5). For this reason, the preferred orientation of each material was determined.

The results of the metal preferred orientation measurements are summarized in Table II. As-received material showed preferred orientation of the (111), (200), and (220) planes for different heats of material, but the decarburization treatment at  $1100^\circ\text{C}$  strongly enhanced the (200) cube face orientation in the roll plane. Thus, the decarburization process eliminates the

orientation variable, i.e., the effect of substrate crystal plane orientation on the oxidation characteristics of the six materials should be the same. No significant evidence of oxide orientation or residual stress was detected within the limits of experimental error. This is probably due to the thickness of the oxide formed.

The average grain size of the materials after decarburization at  $1100^\circ\text{C}$  was found to vary from 9 to  $132\ \mu$  as shown in Table I. The grain size was determined by the line intercept method.

For fixed time and temperature, the oxide weight gain varied as much as 54% among the six materials. The weight gain is plotted as a function of the oxidation time in Fig. 1. The calculated rate constants are shown in Table I. The oxide weight gain is found to increase parabolically.

High temperature parabolic oxidation indicates that the rate-determining step is a thermal diffusion process (6). Abendroth (1) also observed parabolic oxidation rates for iron-nickel-cobalt alloy in the range  $700^\circ\text{C}$ - $900^\circ\text{C}$ .

Logarithms of the rate constants are plotted as an inverse function of temperature in Fig. 2. The activation energies for oxidation were obtained from a least squares fit to the Arrhenius plots in Fig. 2.

The activation energies observed for oxidation of materials IA and IB are close to the value of 54-55 kcal/mole obtained for iron diffusion in Fe<sub>3</sub>O<sub>4</sub> (7). The activation energies obtained for materials IIC, IID, IIIE, and IIIF are approximately 46 kcal/mole. The difference in activation energy between the two groups appears to be related to chromium content (Table I). These two values are found to be substantially greater than the activation energy (30.9 kcal/mole) reported by Abendroth (1).

The x-ray diffraction results are summarized in Table I. The spinel form predominated in all cases. Nickel and cobalt were detected in the oxide by x-ray

Table II. Preferred orientation

Material	Relative x-ray intensities					
	As received			Decarburized		
	(111)	(200)	(220)	(111)	(200)	(220)
Vendor IA	28	100	32	15	100	12
Vendor IB	100	60	50	—	100	—
Vendor IIC	35	85	100	9	100	—
Vendor IID	100	64	32	—	100	—
Vendor IIIE	19	100	16	20	100	10
Vendor IIIF	100	58	24	—	100	—

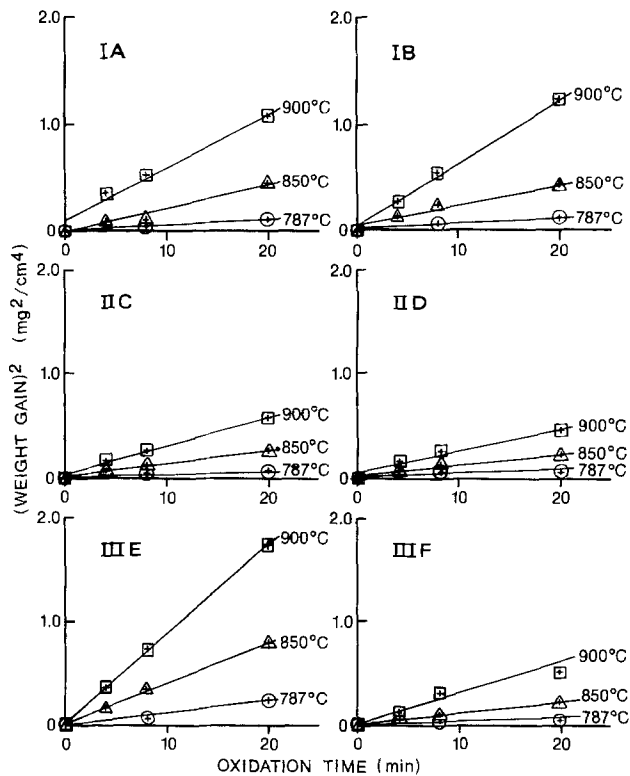


Fig. 1. Oxide weight gain

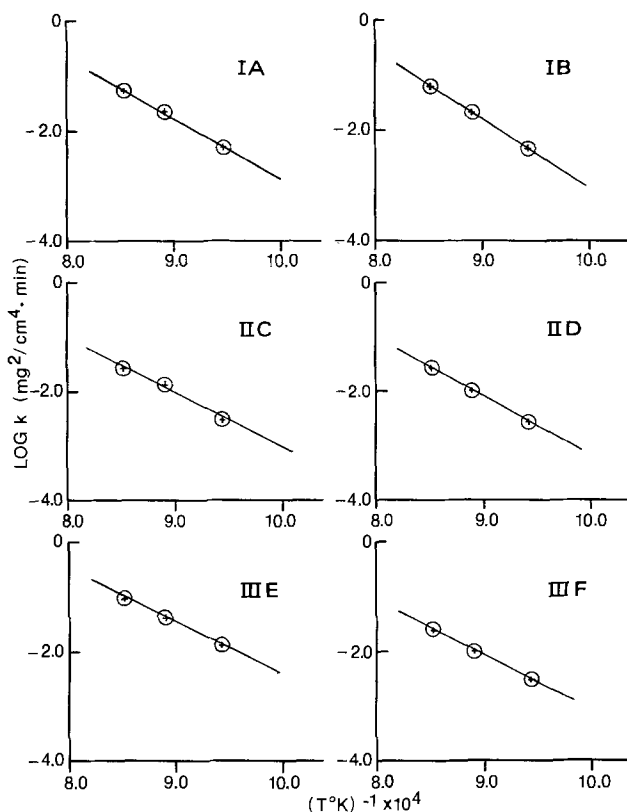


Fig. 2. Arrhenius plots

spectroscopy. Hematite ( $\alpha\text{-Fe}_2\text{O}_3$ ) was present in some cases. The percentage of  $\alpha\text{-Fe}_2\text{O}_3$  in the oxide was found to increase at lower oxidation temperatures and longer times. Graham and Cohen (8) also observed the formation of  $\alpha\text{-Fe}_2\text{O}_3$  after the oxidation of pure iron at longer periods of time, but not after short-time oxidation.

This can be explained in terms of the diffusion of iron, cobalt, and nickel. The oxide scale formed on the iron-nickel-cobalt alloy is basically a diffusion couple

with the alloy on one side and oxygen on the other side. The separate monoxides ( $\text{FeO}$ ,  $\text{NiO}$ ,  $\text{CoO}$ ) will immediately react on the surface to form the spinel  $[(\text{Fe}, \text{Co}, \text{Ni})_2\text{O}_4]$ . This spinel is stable over a wide range of cation and oxygen anion concentrations. The diffusivities of iron, cobalt, and nickel cations vary considerably so that the cation ratios will change with the oxide film thickness. Mayer and Smeltzer (9) and Dalvi and Smeltzer (10) have shown that  $D_{\text{Fe}} = 1.6 D_{\text{Co}}$  at  $1200^\circ\text{C}$  and  $D_{\text{Fe}} = 3D_{\text{Ni}}$  at  $1000^\circ\text{C}$  in  $(\text{Co}, \text{Fe})\text{O}$  and  $(\text{Ni}, \text{Fe})\text{O}$  scales, respectively. Similar trends were observed in spinel layers by Abendroth (1). His measurements of oxide chemical composition of iron-nickel-cobalt alloy indicated that iron diffused more rapidly than cobalt which also diffused more rapidly than nickel in the temperature range  $750^\circ\text{C}$ - $900^\circ\text{C}$ . His measurements also indicated that the difference in relative diffusivities decreased as the oxidation temperature increased. Therefore, longer times at lower temperatures will result in the formation of more  $\alpha\text{-Fe}_2\text{O}_3$  with the iron cation concentration building up at the oxide/air interface. The tendency for iron ion to diffuse faster than nickel ion in iron-nickel-cobalt alloys was also noted by Ikeda and Sameshima (11). Thus, at suitably long times, the diffusion couple will consist of alloy/spinel/ $\alpha\text{-Fe}_2\text{O}_3$ / $\text{O}_2$  (air). The  $\alpha\text{-Fe}_2\text{O}_3$  is also found to form in thicker oxide scales which are favored by smaller grained alloy substrates. The smaller grained substrates appear to be related to higher silicon content. SEM x-ray analysis was performed on some of the materials decarburized at  $1100^\circ\text{C}$ . The analysis showed that the over-all silicon concentration was greater on the surface of the decarburized material than on the as-received material. Silicon-rich precipitates were observed along the grain boundary and in the grain matrix of the decarburized alloy. These silicon-rich precipitates appear to be oxides and may be inhibiting grain growth of the alloy. They are easily seen in Fig. 3, a SEM photomicrograph of a smaller grained alloy, material 1B ( $15\ \mu$ ). Douglas (12) also observed these silicon-rich precipitates after heat-treating the Fe-51 weight per cent (w/o) Ni alloy which contained up to 0.10 w/o silicon at  $1150^\circ\text{C}$  for 30 min in hydrogen.

Figure 4 shows the effect of the grain boundary area on the parabolic rate constant, pointing out the strong contribution of grain boundary oxidation to the formation of oxide scale. The total grain boundary surface area per unit volume of metal is inversely proportional to the average grain diameter,  $D$  (13). From a least squares fit to the plot of the parabolic rate constant of the materials containing less than 0.11 w/o chromium vs,  $1/D$ , the oxidation rate constants at  $787^\circ$ ,  $850^\circ$ , and  $900^\circ\text{C}$  were obtained; (i) the oxidation rate at the grain surface only,  $k_{\text{gs}}$ , which is the value of  $k$  at

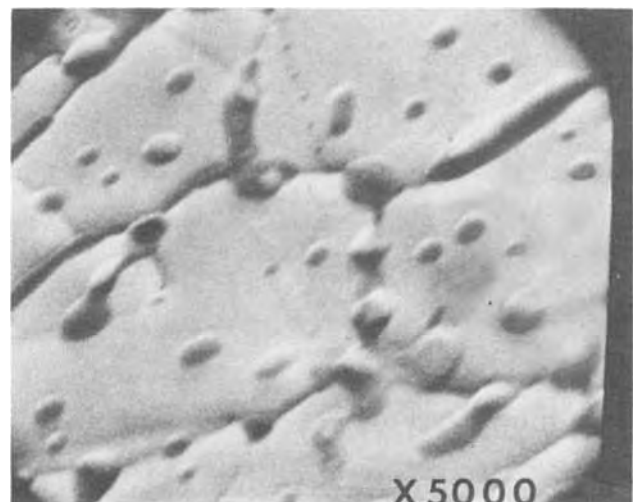


Fig. 3. SEM photograph of decarburized alloy surface (X5000)

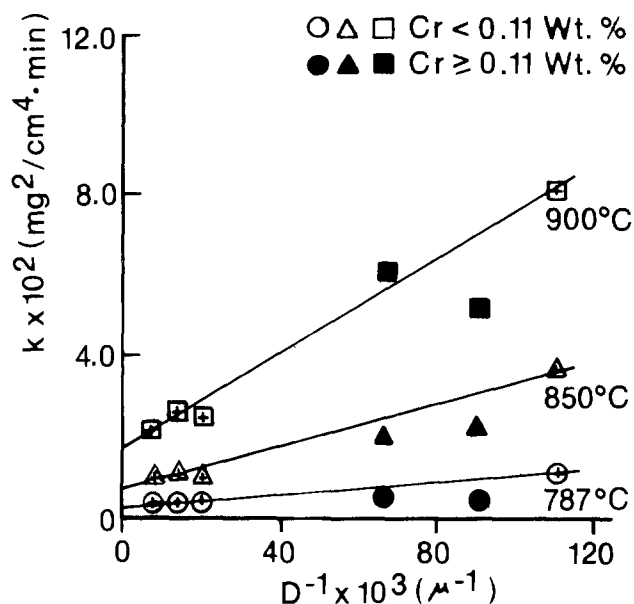


Fig. 4. Oxidation rate as a function of grain boundary area

$1/D$  equal to zero (grain boundary area is zero) and (ii) the oxidation rate per unit grain boundary area,  $k_{gb}$  which is obtained from the slope of the plot. These values are given in Table III.

The effect of chromium ( $\approx 0.11$  w/o) on the oxidation rate is also shown in Fig. 4. The oxidation rates of the materials with higher chromium concentrations are lower as is indicated by the points falling below the line (with one exception at  $900^\circ\text{C}$  which may be due to experimental error). This would indicate that a chromium content of less than  $0.06$  w/o will not substantially affect the oxidation rate; whereas, chromium greater than  $0.11$  w/o will inhibit it.

Logarithms of the rate constants are plotted as an inverse function of temperature in Fig. 5. A least squares analysis of the plots shows the activation energy for oxidation on the grain surface to be  $48.5$  kcal/mole and for oxidation on the grain boundary to be  $41.3$  kcal/mole, a decrease of  $7.2$  kcal/mole.

Thus, for material III E (Table I) where the grain size is small ( $9\mu$ ), the activation energy for oxidation,  $43.1$  kcal/mole, is close to the value obtained for pure grain boundary oxidation ( $41.3$  kcal/mole). As the grain size is increased, the activation energy increases to  $46.6$  kcal/mole where it levels off (Fig. 6). This value is approaching that for pure grain surface oxidation ( $48.5$  kcal/mole). As shown in Fig. 6, the leveling begins at approximately  $50\mu$  grain diameter indicating the smaller contribution of the grain boundary to the oxidation of the larger grained alloys.

The taper sections which were prepared indicate a major contribution of the metal grain boundaries to oxidation as illustrated in Fig. 7 (material IIC, grain size,  $78\mu$ ). Oxide grain boundaries extend from the metal grain boundaries. The oxide grain boundaries are of different composition than the oxide formed on the metal grain surfaces. SEM x-ray analysis shows that the surface of the grain boundary oxide is richer in iron and depleted in nickel as compared to the oxide formed on the metal grain surface (Table IV). Thus it appears that iron is being preferentially oxidized at the grain boundary compared with the grain surface. Preferential oxidation of iron has been observed in

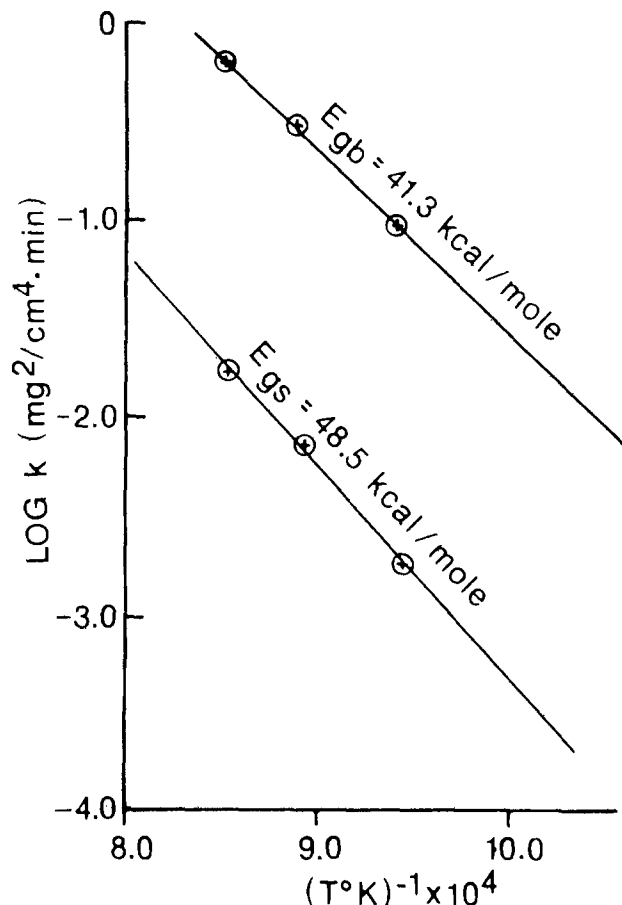


Fig. 5. Activation energy for grain boundary and grain surface oxidation.

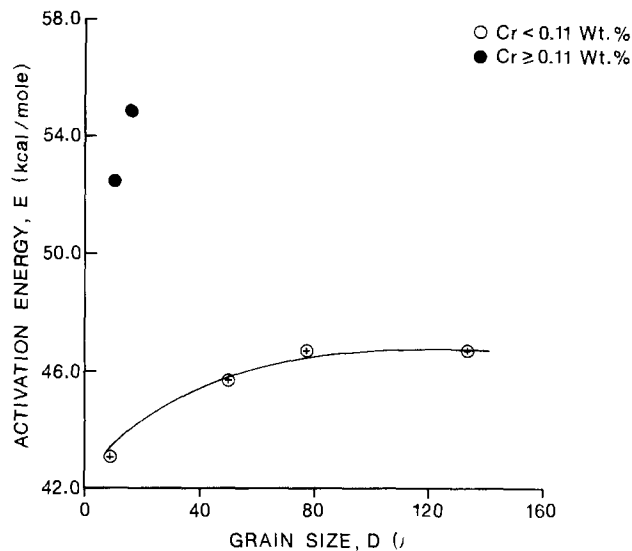


Fig. 6. Activation energy as a function of grain size

iron-nickel alloys (14). This in turn results in a gradual enrichment of nickel at the alloy/oxide interface. The SEM micrograph of material in Fig. 8 also illustrates the more rapid oxide growth (sometimes described as extrusion of oxide at metal grain boundaries) occurring at the grain boundary.

### Conclusions

The six as-received materials had different preferred orientations, either (111), (200), or (220). Decarburization at  $1100^\circ\text{C}$  in wet hydrogen produces the (200) preferred orientation in all the materials.

The rate of oxidation of the iron-nickel-cobalt alloy follows parabolic kinetics. The grain size of the alloys strongly affects the oxidation rate; the smaller the

Table III. Parabolic rate constants

$T^\circ\text{C}$	Oxidation rate at grain surface, $k_{gs} \times 10^2$ ( $\text{mg}^2/\text{cm}^4 \cdot \text{min}$ )	Oxidation rate per unit grain boundary area $k_{gb} \times 10^2$ ( $\text{mg}^2/\text{cm}^4 \cdot \text{min}$ )
787	0.189	8.881
850	0.719	27.281
900	1.716	58.523

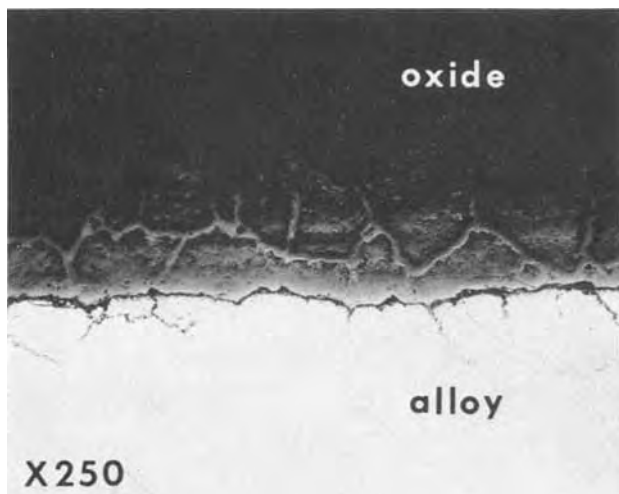


Fig. 7. Taper section of oxide/alloy interface

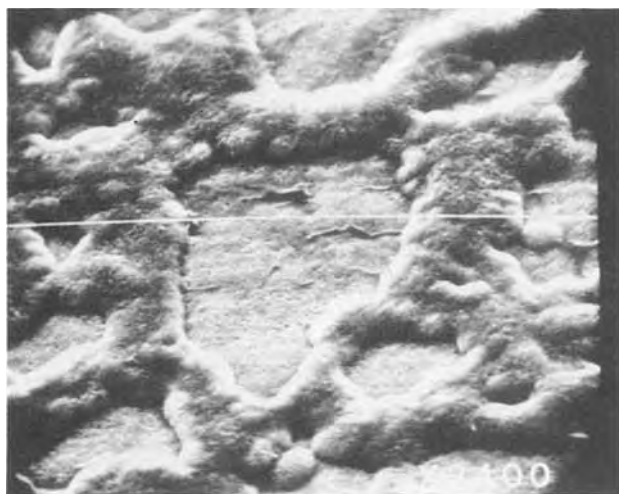


Fig. 8. SEM photograph of oxide/air interface

grain size, the higher the oxidation rate. The activation energy for the oxidation of the material having the smallest grain size ( $9\mu$ ) is 43.1 kcal/mole close to the value, 41.3 kcal/mole, calculated for grain boundary oxidation. As the grain size increases, the activation energy for oxidation increases to 46.6 kcal/mole becoming constant for materials having an average grain size greater than  $50\mu$ . The value is approaching that calculated for grain surface oxidation (48.5 kcal/mole). Thus, the effect of grain size becomes less pronounced when the grain diameter is greater than  $50\mu$ .

Higher silicon content appears to inhibit grain growth and hence produces a higher oxidation rate. Where the grain size is similar, high concentrations of chromium (0.11 w/o) retard the oxidation rate and increase the activation energy for oxidation from 46 to 55 kcal/mole. It appears that a chromium content of less than 0.06 w/o will not substantially affect the oxidation rate or the activation energy for oxidation.

A mixed spinel containing iron, nickel, and cobalt  $[(Fe, Ni, Co)_3 O_4]$  is initially formed at the metal/

Table IV. SEM analysis of oxide formed at 787°C at 8 min

Area	Material	% Metal content		
		Fe	Co	Ni
Grain boundary	IA	69.13	16.29	6.21
	IIIE	69.83	16.73	4.33
Grain surface	IA	56.10	17.45	25.11
	IIIE	57.00	19.60	19.89

oxide interface. The formation of  $\alpha\text{-Fe}_2\text{O}_3$  at the oxide/air interface is favored by low oxidation temperatures and long times because iron ions diffuse faster than nickel or cobalt ions, particularly at lower temperatures. Higher concentrations of  $\alpha\text{-Fe}_2\text{O}_3$  are formed on the fine-grained alloy due to its higher oxidation rate (thicker scale).

The oxide forms more rapidly on the alloy grain boundary and has a different chemical composition from that of the oxide formed on the grain surfaces. The grain boundary oxide is more enriched in iron and depleted in nickel with respect to the oxide formed on the grain surface.

### Acknowledgments

The authors wish to thank C. A. Johnson, J. Cook, and C. T. Young for technical assistance; Bendix Electrical Components Division and Bendix Research Laboratories for permission and assistance in publishing this paper.

Manuscript submitted Oct. 6, 1975; revised manuscript received Feb. 6, 1976. This was Paper 264 presented at the Toronto, Canada, Meeting of the Society, May 11-16, 1975.

Any discussion of this paper will appear in a Discussion Section to be published in the December 1976 JOURNAL. All discussions for the December 1976 Discussion Section should be submitted by Aug. 1, 1976.

Publication costs of this article were partially assisted by the Bendix Corporation.

### REFERENCES

1. R. P. Abendroth, *Mater. Res. Std.*, **5**, 459 (1965).
2. P. Kofstad, "High-Temperature Oxidation of Metals," pp. 23, 25, 38-41, John Wiley & Sons, Inc., New York (1966).
3. J. Benard, in "Oxidation of Metals and Alloys," p. 15, American Society for Metals, Cleveland (1970).
4. J. V. Cathcart, *ibid.*, pp. 31, 34-35.
5. F. P. Fehlner and N. F. Mott, *ibid.*, p. 50.
6. P. Kofstad, "High-Temperature Oxidation of Metals," p. 12, John Wiley & Sons, Inc., New York (1966).
7. O. Kubaschewski and B. E. Hopkins, "Oxidation of Metals and Alloys," p. 33, Butterworths, London (1962).
8. M. J. Graham and M. Cohen, *This Journal*, **116**, 1431 (1969).
9. P. Mayer and W. W. Smeltzer, *ibid.*, **121**, 538 (1974).
10. A. D. Dalvi and W. W. Smeltzer, *ibid.*, **121**, 386 (1974).
11. Y. Ikeda and Y. Sameshima, Proc. 6th Japanese Congress on Testing Materials, p. 127 (1963).
12. P. Douglas, *J. Mater. Sci.*, **8**, 1647 (1973).
13. P. A. Beck, J. C. Kremer, L. J. Demer, and M. L. Holzworth, *Trans. AIME*, **175**, 372 (1948).
14. R. T. Foley, *This Journal*, **109**, 1202 (1962).

# Structural Principles of $\alpha$ -AgI and Related Double Salts

J. C. Phillips

Bell Laboratories, Murray Hill, New Jersey 07974

## ABSTRACT

The structures of  $\text{RbAg}_4\text{I}_5$  and related superionic conductors are discussed, and quantitative measures of chemical bonding are proposed which explain the formation of double salt compounds. Alternative diffusing cation candidates are proposed.

The  $\alpha$ -phases of AgI, CuI, and CuBr are perhaps the most remarkable binary solids known. Although the anions form a bcc lattice, the cations are distributed among many nearly equivalent sites; the distribution is so nearly uniform that the cations may be said to form a liquid (1-3). The temperatures,  $T_\alpha$  for the  $\beta$  (wurtzite)  $\rightarrow \alpha$  transition and the melting points,  $T_m$ , for these three crystals are listed in Table I. For CuI and CuBr,  $T_\alpha$  and  $T_m$  are close enough together (especially for CuBr) that one might say that the cation sublattice has merely melted (or premelted) just before the anion sublattice. However, no other single phase compounds are known to melt in stages, and general theories of first order phase transitions do not suggest that such phenomena should occur. Moreover, the  $\alpha$ -phase of AgI is stable over a very wide range of temperature (Table I).

A second explanation for these extraordinary phases is that they are in some way peculiar to Ag and Cu salts. Apart from its alchemical character, this explanation is not satisfactory because AgCl and AgBr do not form  $\alpha$ -phases. However, Tubandt and co-workers showed long ago that  $\text{Cu}_2\text{S}$ ,  $\text{Ag}_2\text{S}$ ,  $\text{Ag}_2\text{Se}$ , and  $\text{Ag}_2\text{Te}$  all have ionic conductivities much higher than in ordinary salts. A particularly interesting case, studied by Ketelaar (4), is  $(\text{Ag}, \text{Cu})_2\text{HgI}_4$ . This compound has essentially the zinc blende structure, but only three of the four cation sites in cubic unit cell are occupied. In principle, this may give rise to a tetragonal structure, and in the Cu case it does ( $c/a - 1 = 0.010$ ), but in the Ag case the structure remains cubic ( $c/a - 1 = 0.000$ ). The disordering temperature,  $T_d$ , for  $\text{Ag}_2\text{HgI}_4$  is  $50^\circ\text{C}$ , considerably lower than  $T_\alpha = 146^\circ\text{C}$  in AgI.

## Double Salts

One may regard  $\text{Ag}_2\text{HgI}_4$  as a double salt, i.e.,  $(\text{AgI})_2\text{HgI}_2$ . One may also hypothesize, as Bradley and Greene (5) and Owens and Argue (6) apparently did independently, that forming double salts has a eutectic effect on  $T_\alpha$ , and that a more judicious choice of the second salt to be combined with AgI might lower  $T_\alpha$  further. Of course, such qualitative reasoning may not be rigorously justified, but, in fact, new double salts were discovered (5, 6), such as  $\text{RbAg}_4\text{I}_5$ , which have an ionic conductivity of  $0.27 \text{ ohm}^{-1} \text{ cm}^{-1}$  at ambient temperatures.

The discovery of  $\text{RbAg}_4\text{I}_5$  has stimulated further investigations which have shown that there are many compounds with the majority of the cations exhibiting high mobility. All of the highly mobile majority cations in compounds prepared so far are Ag or Cu. However, it seems possible that alternative cations may exhibit similar behavior. Moreover, the crystal structures of many of the new compounds can be said to be as novel as  $\alpha$ -AgI, or perhaps even more novel.

To see why the structure of  $\text{RbAg}_4\text{I}_5$  is extraordinary, it is instructive to compare it with  $\text{Ag}_2\text{HgI}_4$ . The latter structure is a superstructure of sphalerite, with a unit cell four times as large, analogously to the chalcopyrite compounds which have a unit cell twice

as large as the sphalerite cell. Both structures may have the cations ordered by a tetragonal distortion, or remain cubic with disordered cations. In the chalcopyrite structure the tetragonal distortion can be explained (7) in terms of dielectric electronegativities (for II-IV-V<sub>2</sub> compounds such as  $\text{ZnSnAs}_2$ ), but no simple pattern has been established for the tetragonal distortions in (Ag, Cu)-III-VI<sub>2</sub> compounds because of the complications introduced by the (Cu, Ag) d electrons.

## Exotic Structures

The mechanism of ionic conductivity in  $\text{Ag}_2\text{HgI}_4$  is easy to understand. When the cations are disordered the cation defect sites (created by replacement of two  $\text{Ag}^+$  ions in  $\text{Ag}_4\text{I}_4$  by a  $\text{Hg}^{++}$  ion and a neutral vacancy) can form conducting paths through the lattice, the ions passing from one tetrahedral site to the next by means of shared tetrahedral faces. This nomenclature has been adopted to describe conductivity in  $\text{RbAg}_4\text{I}_5$  and many other of the new and novel double salts synthesized in the last decade. However, here I argue that while this description is not incorrect, it does not really exhibit the remarkable structural character of these compounds, which in my opinion is closely related to that of the single salt prototype,  $\alpha$ -AgI. In fact, unlike  $\text{Ag}_2\text{HgI}_4$ , the new double salts have exotic crystal structures which are not variants or superstructures of any known single salt. Thus the most basic question regarding these materials is the nature of the microscopic interactions responsible for their exotic structures.

An argument can be made at the outset that these interactions cannot be analyzed or explained. Many of these ternary structures are stable over narrow temperature ranges; the compounds readily disproportionate. The unit cells often are large, containing several formula units and dozens of atoms. Certainly from quantum mechanics it is not possible to calculate free energies accurately enough to deduce these structures.

## Crystal Chemistry

The answer to this argument, and the theoretical basis for this paper, lies in the emerging science of crystal chemistry which has successfully accounted for the systematics of phase transitions, heats of formation, dielectric properties, and interatomic forces in many binary compounds. Many of the basic ideas in this field are old and can be traced back to Goldschmit, Pauling, and earlier workers, but their de-

Table I\*

Compound	$T_\alpha$ ( $^\circ\text{C}$ )	$T_m$ ( $^\circ\text{C}$ )
AgI	146	555
CuI	440	602
CuBr	470	488

\* The low temperature ( $\beta$ ) phases of these binary salts are tetrahedrally coordinated, while they undergo a transition at  $T_\alpha$  to the  $\alpha$ -phase where the cations are in a "liquid" state. Also listed are the melting temperatures  $T_m$ .

Key words: solid electrolytes, soft lattices, addition compounds, double salts.

velopment in quantitative form has been more rapid recently with the acquisition of a vast amount of experimental data.

More specifically, we can hope to identify (at least semiquantitatively) the interactions which stabilize exotic double-salt structures just because there are so many of them. In the double-salt formula  $MX(\text{AgI})_p$  ( $4 \lesssim p \lesssim 7$ ),  $M$  may be Ag, an alkali ion, or any one of many organic cations with very large molecular weights (8-12). Also  $X$  may be S (8) or a radical such as CN (13) or  $(\text{P}_2\text{O}_7)_{1/4}$  (14). An increasing number of double salts  $MX(\text{CuX})_p$  with  $X = \text{Cl}, \text{Br}, \text{or I}$  and  $M$  an even larger organic cation have been reported (14, 15).

### Preview

Our discussion is divided into four parts. First, we consider macroscopic changes in density which show that  $\text{RbAg}_4\text{I}_5$  is more closely related to  $\alpha$ -AgI than are defect compounds such as  $\text{Ag}_2\text{HgI}_4$ . Second, we indicate the degree of covalent-ionic mixed bonding which makes it possible to form the  $\alpha$ -AgI and related exotic double salt structures. Third, we connect the lattice dynamics of the parent single salts AgI and CuX with the general theory of soft lattices, which applies not only to insulators but also to intermetallic compounds, many of which are high temperature superconductors. Fourth, we discuss the role played by vibrational entropy in stabilizing exotic structures near their Debye temperatures but well below their melting points.

### Covalent Melting

The transformation of  $\text{Ag}_2\text{HgI}_4$  from the  $\beta$ -phase (ordered cations in a slightly tetragonally distorted sphalerite superstructure) to the cubic  $\alpha$ -phase at  $50^\circ\text{C}$  is accompanied by negligible volume change (16), but in AgI the  $\beta \rightarrow \alpha$  transition gives (3)

$$\frac{\Delta V_t(\text{AgI})}{V_t} = -0.05 \quad [1]$$

with the sign corresponding to a reduction in molar volume. A typical value for the reduction in molar volume of all tetrahedrally coordinated partially covalent semiconductors upon melting is (17)

$$\frac{\Delta V_m(\text{ANB}^{8-N})}{V_m} = -0.15 \quad [2]$$

Comparison of [1] and [2] shows that the picture of  $\alpha$ -AgI as "half-melted" is qualitatively satisfactory.

We can now compare the molar volume of  $\text{RbAg}_4\text{I}_5$  with the volumes of RbI and 4AgI with (18)  $\Omega(4\text{RbAg}_4\text{I}_5) = (11.24)$  (3) and (19)  $a_{\text{AgI}} = 6.473 \text{ \AA}$  and  $a_{\text{RbI}} = 7.342 \text{ \AA}$  we find a contraction  $\Delta V_{\text{ds}}$  for the double salt

$$\Delta V_{\text{ds}} = \frac{V(\text{RbAg}_4\text{I}_5) - V(\text{RbI}) - 4V(\text{AgI})}{V(\text{RbAg}_4\text{I}_5)} = -0.04 \quad [3]$$

Note that in  $\alpha$ -AgI all the cations are liquid, whereas in  $\text{RbAg}_4\text{I}_5$  only four-fifths of them are liquid. Correspondingly

$$\frac{\Delta V_{\text{ds}}}{V_{\text{ds}}} = \frac{4}{5} \frac{\Delta V_t(\text{AgI})}{V_t(\text{AgI})} \quad [4]$$

which shows the close macroscopic relationship between  $\alpha$ -AgI and  $\text{RbAg}_4\text{I}_5$ . Note that in  $\text{RbAg}_4\text{I}_5$  each cation complex has the same coordination configuration as in the single salt, i.e., each Rb minority cation is octahedrally coordinated with six I anions, while each "liquid" Ag majority cation is tetrahedrally coordinated with four I anions. In the large cubic unit cell for  $\alpha$ -AgI it was suggested (3) that there were 30 possible sites for  $4\text{Ag}^+$  ions (none of them tetrahedrally coordinated, as the I anions form a bcc lattice). For  $\text{RbAg}_4\text{I}_5$  there are 52 possible quasi-tetrahedrally coordinated Ag sites per unit cell containing 16 Ag ions (15). The question of whether the Ag sites are strictly

tetrahedral is probably of secondary importance because as we shall see the Ag coordination complexes are soft; of more importance are the density changes [1]-[4], which are characteristic of the melting of fourfold coordinated complexes.

### Microscopic Models

Macroscopic density changes  $\Delta V_m/V_m$  upon melting are nearly constant (17) for all tetrahedrally coordinated binary compounds  $\text{ANB}^{8-N}$ . We therefore ask next what is special about AgI, CuCl, CuBr, and CuI that leads to the formation of exotic double salts. We note that each of these compounds is tetrahedrally coordinated, and that octahedrally coordinated AgCl and AgBr do not form exotic double salts. This can be explained by the density argument discussed above; for octahedrally coordinated halides  $\Delta V_m > 0$  and therefore formation of an exotic, liquid majority cation structure with  $\Delta V_{\text{ds}} < 0$  is excluded.

A simple explanation for the proclivity of AgI, CuCl, CuBr, and CuI to form double salts is the presence of easily polarized d electrons on Ag and Cu atoms, which make the atoms "soft" and therefore can more easily accommodate the changes  $\Delta V_m$  (or  $\Delta V_{\text{ds}}$ ) needed to form exotic double salts. The weakness in this explanation is that the Cu d electrons are much more easily polarized than the Ag d electrons. Indeed the color of Cu stems from the d absorption threshold at 2 eV, while the color of Ag is related to the fact that the d absorption threshold at 4 eV is well outside the visible part of the spectrum. Yet the exotic structures are much more easily formed from AgI than from the Cu halides, and the  $\alpha$ -modification of AgI is stable (Table I) at much lower temperatures than the  $\alpha$ -modifications of the Cu halides.

A macroscopically accurate explanation of the relative softness of AgI and the Cu halides can be obtained from the general theory of noncentral (bond-bending) interatomic forces. The idea was stated originally (20) before the synthesis of most of the double salts based on the Cu halides, and it permits one to draw distinctions between them in accord with more recent experiments and also in contradiction with the qualitative trends between CuBr and CuI shown in Table I. Thus it may be said that the interatomic force criteria have already demonstrated some predictive value.

### Binary Phase Transitions

The microscopic criteria have evolved from the study of phase transitions of homologous binary compounds. For primarily intermetallic compounds the balance between metallic and ionic energies often determines phase transitions between competing structures (21). For the fairly polarizable bonds of insulators and semiconductors pertinent to the present compounds, the energies to be balanced are covalent and ionic. These energies can be determined spectroscopically with almost no adjustable parameters (20), and they provide a quantitative basis (see Fig. 1) for understanding the free energy differences between fourfold and sixfold coordinated  $\text{ANB}^{8-N}$  binary octet compounds (22). (A less precise but more general discussion of phase transitions in this family has recently been given (23) in terms of atomic parameters only.) The emerging science of crystal chemistry has thus provided us, with its theory of the effect of chemical bonding on crystal structure, with a quantitative basis for the following discussion.

### Scaffolded Structures

The characteristic feature of double salts



where NY may be AgI, CuCl, CuBr, or CuI, is the large value of  $p$  which occurs in spite of the fact that  $N$  is the diffusing cation. Thus the structure is stabilized by the minority cation  $M$  (which is 10-20% as numerous as  $N$ ). This is the structural feature that distin-

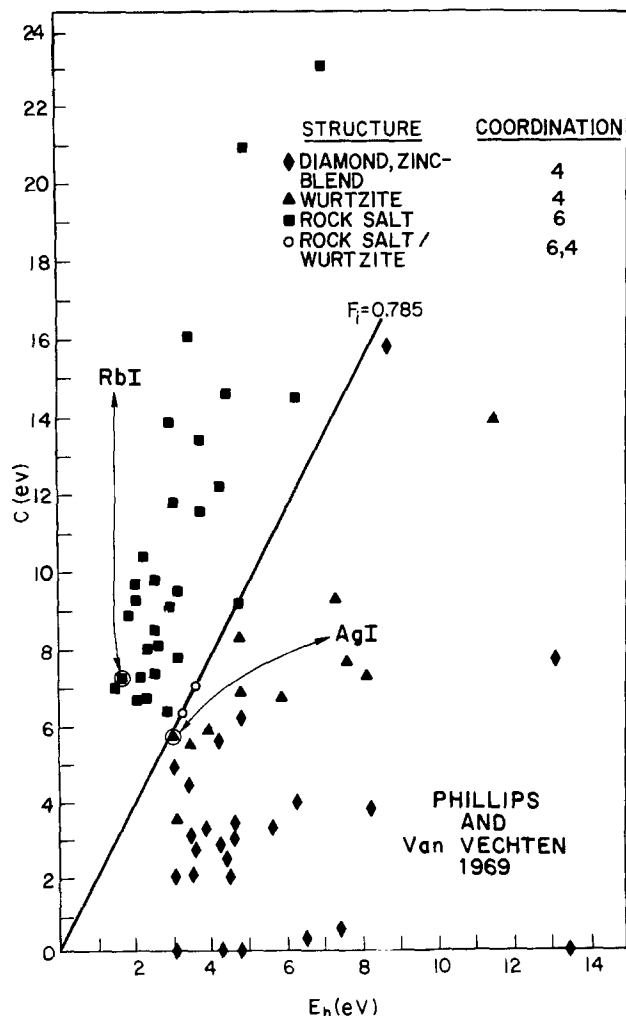


Fig. 1. Distribution of  $A^N B^{8-N}$  compounds in the  $E_h$  (covalent energy)  $C$  (ionic energy) plane. The line  $F_i = E_h^2 / (E_h^2 + C^2) = 0.785$  successfully separates compounds with fourfold and sixfold coordination. Of particular interest are the locations of  $AgI$  and  $RbI$ , which are indicated in the figure.

guishes these double salts from, for example, sodium  $\beta$ -alumina, which contains (24) about eleven stabilizing Al cations for every diffusing Na ion. Because of the large value of  $p$ , the entropy associated with disorder among the diffusing cations is large, and this entropy may play an important role in stabilizing these double salts. This leads to the picture of a compound which has compromised between two coordination configurations by forming a scaffolded structure, with a skeletal framework of minority cation complexes. The framework is decorated by loosely bound, quasi-interstitial majority cations which supply a neutralizing charge sheath enveloping the over-all structure.

This structural description can be visualized more easily in the case (19) of the layer compound  $(C_5H_6N)Ag_5I_6$ . The organic minority cation, pyridinium, has a planar structure which gives rise to the layered skeletal framework, again illustrating the determinative role played by the minority cation. The pyridinium ion is at the center of the unit cell, and it is sandwiched between staggered hexagonal rings of iodine ions. Outside the iodine rings and coplanar with the minority pyridinium ions, are Ag dodecadons, with every site occupied. At  $-30^\circ C$  no Ag was found in planes halfway between sandwiches, although these sites may be occupied temporarily when ion transport takes place. In contrast to  $RbAg_4I_5$ , the Ag ions occupy both smaller tetrahedral sites (where two rings contact) and larger octahedral sites (in the free volume between three rings). Here the principle of alternating charge sheaths is more easily visualized, as the struc-

ture consists of an hexagonal array of coaxial capacitative cylinders, with Ag ions making up the outer cylinder, iodine ions the inner cylinder, and pyridinium ions forming the skeletal axes. Also, the near equality in energy of octahedrally and tetrahedrally coordinated Ag ions clearly helps to stabilize the structure.

### Chemical Bonding

We can now identify the characteristic properties of the NY chemical bonds which produce scaffolded structures. While the minority cation complexes  $MX_6$  must form stable units (such as  $RbI_6$ ), the  $NY_s$  complexes must be "soft" in the sense that the bond-bending energy differences which determine whether  $s$  is four or six (or some intermediate value) are small. This is the case most dramatically for  $AgI$ , where the difference in energy (22) of the two configurations is  $\lesssim 0.5$  kcal/mole, but it also holds for the Cu halides (see Fig. 2). Bond-bending energies can also be analyzed quantitatively by comparing the noncentral force constant,  $\beta$ , with the central force constant,  $\alpha$ , (see Fig. 3). The appropriate values of these quantities, together with the spectroscopic ionicity  $f_i$ , are collected in Table II. Both the free energy differences and  $\beta/\alpha$  tend to zero as  $f_i \rightarrow F_i = 0.785$ , the characteristic ionicity of the bond in  $A^N B^{8-N}$  compounds associated with the transition from fourfold to sixfold coordination (20).

We have also listed in Table II the transition temperatures,  $T_\alpha$ , for cation "melting" (the  $\beta \rightarrow \alpha$   $AgI$  transition) in  $CuBr$  and  $CuI$ . Note that the disordering temperature,  $T_\alpha$ , for  $CuI$  is lower than for  $CuBr$ , although the ionic conductivity (14) of the organic double salt based on the former is 20 times less than that of the latter, indicating that the reaction to produce a scaffolded structure is much more complete at  $150^\circ C$  in the latter. This ordering is consistent, however, with the chemical bonding parameters  $f_i$  and  $\beta/\alpha$  quoted in Table II. This shows that it is these bonding parameters (and not the disordering temperature,  $T_\alpha$ ) which are relevant to the realization of new scaffolded structures.

We are not in a position at present to calculate the absolute energies of  $A^N B^{8-N}$  compounds in either four-

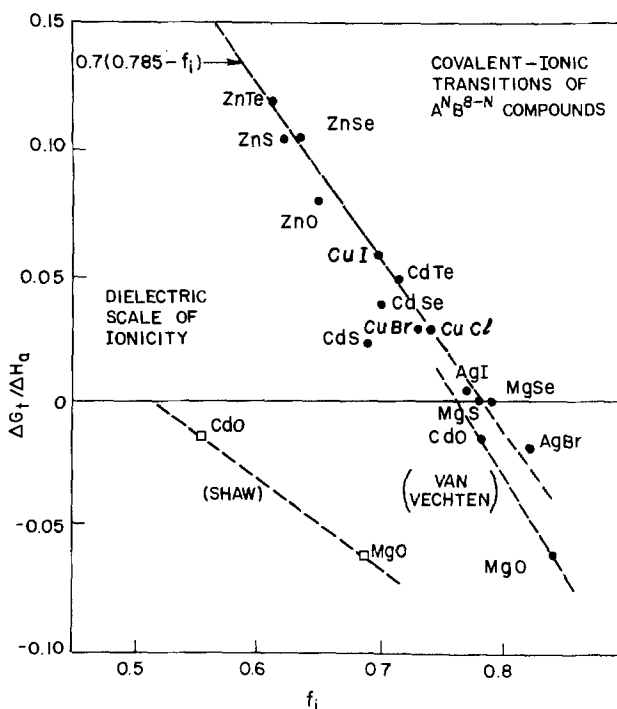


Fig. 2. Differences,  $\Delta G_L$ , in Gibbs free energy between  $A^N B^{8-N}$  compounds in fourfold and sixfold coordinated structures. For normalization reasons the ratio  $\Delta G_L/\Delta H_a$  is plotted where  $\Delta H_a$  is the enthalpy of atomization of the compound.



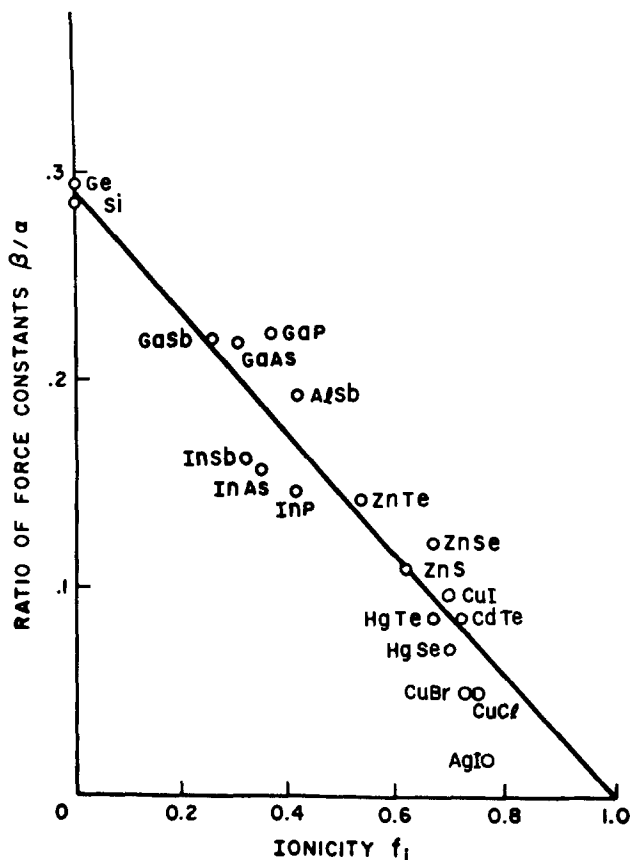


Fig. 3. Ratio of noncentral bond-bending force constant,  $\beta$ , to central bond-stretching force constant,  $\alpha$ , as a function of spectroscopic ionicity,  $f_i$ . As  $\beta \rightarrow 0$  the transverse acoustic frequencies  $\rightarrow 0$ .

fold or sixfold coordinated structures with sufficient accuracy near  $f_i = 0.8$  to locate the critical ionicity  $F_i$  at which the covalent-ionic phase transition takes place (20), but there is an interesting electrostatic explanation for the value of  $F_i$  as the one at which the bond charge is centered on the anion (22, 25). Thus one can understand in balancing internal energies,  $U$ , how the macroscopic electrostatic sheath energies can be competitive with microscopic coordination energies when  $f_i$  ( $NY$ ) is near  $F_i$ , but not otherwise. The balance is very delicate, for at low temperatures disproportionation may take place, e.g., in  $RbAg_4I_5$  (10), which may be contrasted with the stable condensation of Ag ions in layered AgI double salts (19). Evidently the entropy associated with fractional occupancy of Ag sites is essential to the stability of  $RbAg_4I_5$ , this stabiliza-

Table II. Structural parameters of cation instabilities in binary octet salts

ANBS-N compound	$(0.79 - f_i)^a$	$\Delta G_i$ (kcal/mole)	$\beta/\alpha$	$T_a$ ( $^{\circ}C$ )	$T_m$ ( $^{\circ}C$ )
AgI	0.02	0.5 <sup>b</sup>	0.02 <sup>1</sup>	146 <sup>d</sup>	
CuCl	0.05	4.5 <sup>b</sup>	0.05 <sup>c</sup>	(525)	430
CuBr	0.05	4.5 <sup>b</sup>	0.05 <sup>c</sup>	469 <sup>e</sup>	492
CuI	0.10	8.5 <sup>b</sup>	0.10 <sup>c</sup>	407 <sup>e</sup>	605
MgS	0.00	$\sim -0.1$			
MgSe	0.00	$\sim -0.1$			
CdSe	0.11	4.0 <sup>b</sup>	0.15 <sup>c</sup>		
HgSe	0.11	1.9 <sup>g</sup>			800 <sup>f</sup>
HgTe	0.14	2.8 <sup>h</sup>			670 <sup>f</sup>

<sup>a</sup> Ref. (13).

<sup>b</sup> Ref. (14).

<sup>c</sup> R. C. Hanson, J. R. Halberg, and C. Schwab, *Appl. Phys. Letters*, 21, 490 (1972).

<sup>d</sup> L. W. Strock, *Z. Physik. Chem.*, B31, 157 (1936).

<sup>e</sup> J. B. Wagner and C. Wagner, *J. Chem. Phys.*, 26, 1597 (1957).

<sup>f</sup> J. A. Van Vechten, *Phys. Rev.*, 7B 1479 (1973), Table VI.

<sup>g</sup> J. A. Kafalas, H. C. Gatos, and M. C. Lavine, *J. Phys. Chem. Solids*, 23, 1541 (1962).

<sup>h</sup> J. Blair and A. C. Smith, *Phys. Rev. Letters*, 7, 124 (1961).

<sup>1</sup> Ref. (22).

tion arising from the distribution of the Ag ions among the available sites. One has here an ionic realization of Pauling's concept of resonating bonds: the resonating ions stabilize the structure when the minority cation is a single alkali ion.

### Organic Minority Cations

The obvious defect of a sheath structure is that the attractive interactions between oppositely charged sheaths may tend, in general, to be smaller than the repulsive interactions between ions belonging to the same sheath. However, it appears that with the cations on the outer sheath the two energies nearly cancel, leaving the determination of the structure to the small coordination energies and the resonating ion entropies. One way to shift the balance in favor of the scaffolded structure is to increase the size of the minority cation, e.g., by replacing Rb by tetramethylammonium, an almost spherical ion (10). This increases the distance from the common axis to the outer majority cation and inner anion sheaths, thereby reducing the repulsive interactions within the sheaths, without substantially altering the spacing or the capacitance attraction between the other oppositely charged sheaths. It also predicts an increase in  $p$ , and this is usually observed [ $Rb$ ,  $p = 4$ ; tetraalkylammonium (26),  $p = 6.5$ ; N-alkyl hexamethylenetetramine (14),  $p = 7$ ; but for organic ions with planar substituents or containing sheath-warping N-H dipoles no consistent pattern for  $p$  has been found (12)].

As the radius of the central minority cation increases, the stability of the (larger circumference) sheaths against wavelike (spinodal) decomposition (buckling) is reduced, and one would expect to find a maximum radius,  $R_{max}$ , beyond which the scaffolded structure becomes unstable. For the nearly spherical tetraalkylammonium ions this discontinuity (which can also be correlated with molecular weight) is particularly striking (10), but if one allows for nonhomologous differences between cubic and layer structures there appears to be (12) a  $R_{max}$  for all AgI-based double salts, which occurs near a molecular weight of 110 for the spherical ions and 290 for the planar ions.

If we now consider the Cu halide-based double salts, then in addition to balancing the ionic resonance and residual sheath energies, we have a much larger coordination energy difference to deal with (about ten times larger in CuBr than in AgI, see Table II). This means that we may expect to find a  $R_{min}$  as well as a  $R_{max}$  and that  $R_{max}$  should be much larger than in AgI; moreover, we expect both  $R_{min}$  and  $R_{max}$ , respectively, to be larger for double salts based on CuI than for double salts based on CuBr. The lowest molecular weight for the nearly spherical tetraamine [adamantane family (27)]-based cations which form conducting double salts with CuBr is about 140, i.e., slightly larger than 110. Thus it appears that  $R_{min}$  (CuBr)  $>$   $R_{max}$  (AgI), but studies of more cases are needed to confirm this point.

In addition to the electrostatic contribution to the enthalpy, the entropy contribution of the partially ordered diffusing majority cations may be changed when the size of the minority cation is increased. Naively, one would expect there to be more sites available to the majority cation with increasing radius of the minority cation, which would tend to stabilize the double salts with large minority cations. This is also a plausible explanation for the existence of a  $R_{min} > 0$  in the Cu-halide-based double salts.

The coordination configuration plays a vital role for the stabilizing minority cations just as much as it does for the "soft" majority cations. On a gross level this is obvious from the fact that  $(C_5H_5NH)Ag_5I_6$  has a layer structure whereas  $RbAg_4I_5$  is cubic. However, that the balance of energies associated with the stabilizing majority cation is just as delicate as for the minority cations is evident from the ions  $M$  which form  $MAg_4I_5$ : these are (6) K and Rb, but not Li, Na, or

Cs, although  $M = \text{Cs}$  does form solid solutions with  $M = \text{K}$  or  $\text{Rb}$ . Originally this was explained (6) merely as a size effect, *i.e.*,  $R(\text{Cs}) > R_{\text{max}}$  and (presumably)  $R(\text{Li}) < R(\text{Na}) < R_{\text{min}}$ . With the later discovery (10, 12), however, of stabilization of scaffolded structures by giant organic cations, the nonexistence of  $\text{CsAg}_4\text{I}_5$  became puzzling. The most likely explanation is that  $\text{CsI}$  is normally eightfold coordinated, but is unstable toward a rearrangement toward sixfold coordination. The volume change,  $\Delta V_t$ , between eightfold and sixfold coordination is only a few per cent, however, and thus  $\text{CsI}$  cannot fill a stabilizing role.

### Connection with Lattice Dynamics

Because of the open, low density nature of tetrahedrally coordinated  $\text{ANB}^{8-N}$  salts with zinc blende and wurtzite structures, the lattice vibration frequencies in short wavelength transverse acoustic (shear) modes are anomalously low even in Si and Ge. With increasing ionicity the noncentral, bond-bending force constant  $\beta$  decreases compared to the nearest neighbor (central) bond-stretching force constant  $\alpha$ . This decrease, which is shown in Fig. 3, becomes catastrophic in the Cu halides and  $\text{AgI}$ . While  $\beta/\alpha$  measures the softening of the shear elastic constants, the effect at short wavelengths (Brillouin zone boundary phonons) is even greater. In zinc blende compounds the transverse acoustic mode frequencies are low at the centers of the  $L = (111)$  and  $X = (100)$  Brillouin zone faces; in wurtzite structures the doubling of the unit cell (in effect) folds back the former to  $k = 0$ , where it is observable by Raman scattering.

In Table III the frequencies  $\nu(E_2^1)$  are shown, together with their pressure derivatives where known. (By  $E_2^1$  we mean the low frequency transverse optic phonon at  $k = 0$  in wurtzite structures, or its transverse acoustic analogue at  $k = L$  in zinc blende structures.) The most noteworthy feature of Table III is the low value of  $\nu(E_2^1)$  in  $\beta$ - $\text{AgI}$ . The significance of this result has been discussed elegantly (28) from the present point of view, with emphasis on the  $\beta \rightarrow \alpha$  transition in  $\text{AgI}$ . In particular, the connection of the low frequency with low values of  $\beta/\alpha$  and with the proximity of  $f_1(\text{AgI})$  to  $F_1$  has been stressed (28). Also, the character of the iodide ion motion and its relation to a transformation from hcp to bcc is noted for the first time (28).

The success of the lattice dynamical interpretation (28) of the  $\beta \rightarrow \alpha$  phase transition in  $\text{AgI}$  increases our interest in  $\nu(E_2^1)$  as a possible configuration coordinate for describing the formation of scaffolded double salts. We therefore show in Table III these frequencies for the Cu halides and  $\text{ZnO}$  and  $\text{CdS}$ . Clearly, the Cu halides are next most favorable after  $\text{AgI}$ , while  $\text{CdS}$  is a better candidate than  $\text{ZnO}$ . Also,  $\text{CuBr}$  is significantly better than  $\text{CuI}$ . (The same conclusion was reached on the basis of Table II, in agreement with experiment, but in contradiction with the overly simple  $T_\alpha$  trends in Table I.)

Table III. Soft phonon frequencies and their shifts with pressure in some  $\text{ANB}^{8-N}$  compounds

Compound	$\nu(E_2^1)$ ( $\text{cm}^{-1}$ )	$\Delta\nu$ (10 kbar) ( $\text{cm}^{-1}$ )
Si	150 <sup>a</sup>	-0.7 <sup>a</sup>
ZnO	99 <sup>b</sup>	-1.3 <sup>b</sup>
CdS	42 <sup>b</sup>	-2.0 <sup>b</sup>
CuBr	31 <sup>c</sup>	
CuI	34 <sup>d</sup>	
$\text{AgI} (\beta)$	15 <sup>e</sup>	

<sup>a</sup> W. Richter, J. B. Renucci, and M. Cardona, *Solid-State Commun.*, **16**, 131 (1975).

<sup>b</sup> S. Mitra *et al.*, *Phys. Rev.*, **186**, 942 (1969).

<sup>c</sup> B. Frevot *et al.*, *Solid-State Commun.*, **13**, 1275 (1973).

<sup>d</sup> B. Hennion *et al.*, *Phys. Rev. Letters*, **28**, 964 (1972).

<sup>e</sup> R. C. Hanson, T. A. Fjeldy, and H. D. Hochheimer, *Phys. Status Solidi*, **B70**, 567 (1975).

### Vibrational Entropy

The low lying frequencies  $\nu(E_2^1)$  listed in Table III give rise to very large (strongly anharmonic) vibrations at ambient temperatures, primarily of iodine ions in  $\text{AgI}$ , which correspond to a mean phonon occupation number  $\bar{n}(E_2^1) \sim 12$  in  $\text{AgI}$ . [This explains, incidentally, the very large Debye-Waller damping for the iodine ions which puzzled Hoshino (16).] Such large phonon occupation numbers increase the vibrational entropy of  $\text{AgI}_4$  complexes, thereby helping to stabilize  $\text{RbAg}_4\text{I}_5$  against disproportionation (20) down to 27°C. As  $\nu(E_2^1)$  increases, the vibrational amplitudes decrease, which tends to destabilize the  $\text{CuX}$  double salts compared to the  $\text{AgI}$  ones. The same effect may explain the tetragonal distortion which is present in  $\text{Cu}_2\text{HgI}_4$  but absent in  $\text{Ag}_2\text{HgI}_4$ : in the latter case the motional Jahn-Teller effect has "averaged out" the tetragonal distortion.

### Synthesis at High Pressures?

The pressure derivatives in Table II are interesting. One can ask, is it not possible, by applying pressure, to bring the spectroscopic ionicity,  $f_1$ , of the Cu halides or  $\text{CdS}$  close enough to  $f_1(\text{AgI})$  so that one could form scaffolded structures involving the former? But one must be careful in interpreting Fig. 2, for the effect of pressure is to change both  $f_1$  (AB) and the critical ionicity,  $F_1$ , *i.e.*, both  $\partial f_1/\partial p$  and  $\partial F_1/\partial p$  must be considered. To make this distinction, consider  $\text{CuBr}$ , which transforms to the rock salt structure (14) at 43 kbar. Assume that  $\partial\nu/\partial p$  is about the same in  $\text{CuBr}$  as it is in  $\text{CdS}$ ; then  $\nu(\text{CuBr}, 40 \text{ kbar}) \cong 31 - 8 = 23 \text{ cm}^{-1}$ . Thus about half of the difference between  $\nu(\text{CuBr})$  and  $\nu(\text{AgI})$  can be removed by application of pressure, but half cannot. An even less favorable case is  $\text{CdS}$ , where the transition pressure is (14) anomalously low (25 kbar); thus  $\nu(\text{CdS}, 20 \text{ kbar}) = 38 \text{ cm}^{-1}$ , which is more than twice the  $\text{AgI}$  value.

### Two-Phase Behavior

Highly conductive single crystals with mole ratios near the optimum value have been grown from several double salts (18, 19) based on  $\text{AgI}$ . However, Takahashi, Yamamoto, and Ikeda (14) usually were unable to prepare single phase double salts based on Cu halides, and do not report the structure of their "single phase" samples. Sannels, Gougoutas, and Owens have similarly reported (15) that while the optimum  $\text{Cu}_p/\text{organic NH}_4$  halide mole ratios for high ionic conductivity ranged from  $p = 4$  to  $p = 7$ , the only single crystals which they have grown correspond to  $p = 2.5$ . While the latter is reported to be conductive, it seems unlikely that it has high ionic conductivity comparable to that achieved for the larger optimal values of  $p$ . Our model for formation of scaffolded structures suggests that two-phase behavior may be intrinsic to all but the  $\text{AgI}$ -based double salts. The two-phase behavior may correspond to intrinsic disproportionation, for example, into a phase with high ionic conductivity ( $\alpha$ ) and one with much lower ionic conductivity ( $\alpha'$ ). The fraction of the  $\alpha$ -phase may be unity in  $\text{AgI}$ -based salts, near 0.5 for  $\text{CuX}$ -based salts (and somewhat larger for  $X = \text{Br}$  than for  $X = \text{I}$ ) and may be near zero, *e.g.*, in  $\text{CdS}$ -based salts.

Two-phase behavior is especially common in soft lattices; Ketelaar, in his early work (4), mentions that the surface of  $\text{AgI}$  undergoes the  $\beta \rightarrow \alpha$  transition (with an accompanying change in color) before the interior does. This behavior can occur because of the strain field at the sample surface. Ferroelastic crystals are especially sensitive to strain fields, and it seems that many soft lattices may be equally sensitive to shape and surface effects. In some cases, such as quasi-one-dimensional molecular crystals, the coexistence of two phases may be necessary to relieve internal strain fields (30), and in the case of KCP such

coexistence has been observed by neutron scattering (30).

The basic factor limiting the formation of double salts may well be internal strain fields. In the case of quasi-one-dimensional materials this is obvious because of the problem of lattice-constant mismatch between the two chains (30). For the Cu-halide based double salts the presence of the second salt apparently tends to produce a uniaxial (quasi-tetragonal) distortion of  $\text{CuX}_4$  complexes. On the other hand, the symmetry (and lattice constants) of the minority scaffolded structure may not be consistent with slightly tetragonally distorted majority cation complexes. This produces internal strain which can be relieved by two-phase behavior. In the quasi-one-dimensional materials at low temperatures the two phases may be replaced by a single phase with a much larger unit cell; the low temperature phases (31) of  $\text{RbAg}_4\text{I}_5$  may arise in this way. However, in other crystals the two phases may coexist in practice without ordering at low temperatures.

### Alternative Majority Cations

The discovery (14) of the solid-solid reaction between  $[\dots]\text{X}$  and  $\text{CuX}$  (instead of  $\text{AgI}$ ) raises the possibility of forming double salts based on  $\text{A}^{\text{N}}\text{B}^{8-\text{N}}$  compounds with  $\text{N} = 2$ . Two candidates, Mg and Cd, are considered in Table II.

Considering only  $\Delta G_{\text{t}}$ , we are tempted to choose  $\text{MgS}$  or  $\text{MgSe}$ . However, strictly speaking, at room temperature  $\Delta G_{\text{t}}$  is probably slightly negative (as indicated in the table), so that the fourfold coordinated form is only metastable. Under compaction to form a double salt these two compounds transform to the denser rock salt structure, which will probably block the reaction to form the scaffolded structure.

We must therefore consider the Cu salts and the Cd salts. From the discussion given above, the configuration coordinates  $\Delta G_{\text{t}}$ ,  $\beta/\alpha$ , and  $\nu(E_{1/2}^{\text{t}})$  of the Cu salts are substantially more favorable than those of the Cd salts, with or without pressure. However, it may still be possible to prepare double salts based on  $\text{CdS}$ ,  $\text{CdSe}$ , or  $\text{CdTe}$ .

A more remote possibility is to combine a tetrahedral  $\text{A}^{\text{N}}\text{B}^{8-\text{N}}$  binary compound (such as  $\text{CdS}$ ) with an octahedral  $\text{C}^{\text{N}}\text{B}^{10-\text{N}}$  compound (such as  $\text{PbS}$ ). This appears unlikely, because Pb, for example, usually would be tetravalent rather than divalent. However, some early work indicated (32) the existence of  $\text{Cd}_4\text{Ge}(\text{S or Se})_6$ , with a nearly cubic unit cell containing four formula units, in strong similarity to  $\text{RbAg}_4\text{I}_5$ . However, later work on  $\text{Cd-Ge-S}$  (33) and  $\text{A}^2\text{-C}^4\text{-S}$  [with  $\text{C} = \text{Si or Ge}$  and  $\text{A} = \text{Cd or Hg}$  (34)] showed that the correct formula is  $\text{A}_4^2\text{C}_4^4\text{S}_6$ , i.e., with  $\text{C} = \text{Si or Ge}$  the C atoms are indeed tetravalent. In general, the ability to form divalent states increases with increasing atomic weight in the fourth column, so it still might be possible to prepare  $\text{Cd}_4\text{PbS}_6$ . The existence of a number of compounds of formula  $\text{A}_4^2\text{C}_4^4\text{B}_6^6$  (i.e., the proper ratio, 4:1, of tetrahedral to possibly octahedral cations) suggests that this is an interesting possibility, but so far no such compounds have been reported.

### Alternative Anions

The principles that govern anion substitution are less clear-cut than those that govern cation substitution. Early work (8, 9) showed that  $\text{Ag}_3\text{SI}$  transformed to a cation-disordered perovskite structure at  $T_c = 235^\circ\text{C}$ , while  $\text{Ag}_3\text{SBr}$  transformed (35) at  $430^\circ\text{C}$ . It is interesting that Pauling's table of elemental electronegativities (36) gives  $X(\text{S}) = X(\text{I}) = 2.5$ , while  $X(\text{Br}) = 2.8$ ; this may explain the lower value of  $T_c$  in the iodide. The heats of formation ( $-\Delta H_f$  in kcal/mole) are (37) 7.8 ( $\text{Ag}_2\text{S}$ ), 15 ( $\text{AgI}$ ), and 24 ( $\text{AgBr}$ ), and this, together with (20)  $f_1(\text{AgBr}) = 0.79 + 0.06$  ( $\text{AgBr}$  has the  $\text{NaCl}$  structure) also supports the

higher value of  $T_c$  in the bromide compared to the iodide. Again we see that strongly ionic interactions hinder cation disorder, primarily because they favor octahedral sites over tetrahedral ones, whereas nearly equal site energies make possible cation disorder at low values of  $T_c$ .

### Microscopic Models

Most theoretical models of superionic conductors have emphasized the activation energy,  $\Delta H_a$ , for ionic diffusion as derived from an Arrhenius plot of  $\sigma(T)$ . Such a discussion is appropriate, e.g., for ionic conduction in sodium  $\beta$ -alumina (24). However, in cation-disordered salts such as  $\alpha$ -AgI, and equally in scaffolded double salts such as  $\text{RbAg}_4\text{I}_5$ , this hopping model appears to be irrelevant to understanding the very high ionic conductivities (small values of  $\Delta H_a$ ) that are actually observed. With a number of sites available to the diffusing cations, all in closer proximity than cation sites in the majority cation single salt, it is clear that the nature of the structure (cation-disordered or scaffolded, as the case may be) is such that the near equality in energy of inequivalent sites is accompanied by a very substantial anharmonic softening or lowering of barrier heights  $\Delta H_a$  from what one would calculate from the uncorrelated hopping ion picture. This is the essential common feature of both cation-disordered and scaffolded structures. It can be pictured as lopping off the barrier between two equivalent sites and putting between them an inequivalent site with only a slightly higher energy than that of the lowest site. This picture has been implicit in the experimental discussions for some time (6), but it seems to have been omitted from most microscopic models. The present discussion takes this model for granted and utilizes the data for the copper-ion conductors (14, 15) to elucidate differences between ionic conduction in the cation-disordered and scaffolded salts. In particular, our model shows why scaffolded  $\text{CuBr}$  double salts can be more conducting than scaffolded  $\text{CuI}$  double salts, although the latter have the lower cation disordering temperature,  $T_c$ .

An amusing example of an oversimplified hopping model has been presented in terms of small polaron theory (38). These authors do not discuss scaffolded structures at all, but they do assert that  $\Delta H_a$  does not change much upon cation disordering, thereby ignoring the change in conductivity of several orders of magnitude at  $T_c$  and ignoring what most experimentalists use to distinguish ordinary ionic conductivity from superionic conductivity. They also claim to explain "for the first time" why  $\text{CuCl}$  is not a good superionic conductor. (The hopping energy in  $\text{CuCl}$  is calculated to be 2.5 times that of  $\text{CuBr}$ , which in turn is twice that of  $\text{CuI}$ .) But, as we have seen, scaffolded  $\text{CuBr}$  double salts are better ionic conductors than scaffolded  $\text{CuI}$  double salts. Moreover, one does not need many-body theory to explain why  $\text{CuCl}$  is not a superionic conductor. From the values of  $T_c$  in  $\text{CuI}$  and  $\text{CuBr}$ , it is clear that  $T_c$  increases with the Debye temperature, and a reasonable guess for  $T_c$  in  $\text{CuCl}$  is  $530^\circ\text{C}$ , or about  $100^\circ\text{C}$  above the melting point,  $T_m$  (see Table II).

The reason why the polaron coupling constant  $\lambda = (1/\epsilon_{\infty} - 1/\epsilon_0)$  is not a relevant configurational coordinate for superionic conductors is that it measures the longitudinal ionic forces responsible for the difference in frequency of longitudinal and transverse optic modes at  $k = 0$ . However, as we have seen, it is the frequencies of the  $E_{1/2}^{\text{t}}$  modes (essentially transverse acoustic zone-boundary phonons) that measure the softness against shear that is the characteristic feature of  $\text{AgI}$  and the Cu halides. Indeed, of all the configuration coordinates, the polaron coupling parameter is the one that is least relevant to cation disordering and to the formation of superionic structures.

### Conclusions

The structural principles which make possible the formation of scaffolded superionic conductors were discussed. Primary emphasis was laid on the necessity for "soft" majority and "rigid" minority cation coordination configurations, which were shown to be of greater structural significance for the scaffolded double salt than the possibility of cation disorder in the majority cation salt, although the latter is also, of course, related to the "soft" majority cation configuration. Alternative majority cation salts were discussed.

*Postscript.*—Studies of ionic conductivity in (Zn, Cd, Hg, Cu, and Pb)<sub>2</sub>S have been reported (39) that indicate mixed ionic and electronic conductivity, possibly caused by the presence of stacking faults in (Zn and Cd)<sub>2</sub>S.

*Second postscript.*—An elegant and convincing demonstration of the transferability of the 4-6 coordination isomerism discussed here (and illustrated by the abscissa intercepts of Fig. 2 and 3) has been obtained recently by Teo and Calabrese (40) and Churchill and co-workers (41). They have studied the structural variations in metal clusters (R<sub>3</sub>Y)<sub>4</sub>M<sub>4</sub>X<sub>4</sub> where R is C<sub>6</sub>H<sub>5</sub> or C<sub>2</sub>H<sub>5</sub>, Y is P or As, and the metal core salt atoms M are Cu or Ag while X is a halide. In crystals the M<sub>4</sub>X<sub>4</sub> core may have either a cubane structure (right-angle M bonds, analogous to sixfold coordination in MX salts) or a chair structure (distorted tetrahedral M bonds, as in fourfold coordinated MX salts). Only with M = Ag and X = I is an unprecedented isomerism present. However, with M = Cu conversion from the cubane form with X = Cl to the chairlike configuration with X = Br and I is established. Considering that each cluster has a large surface area, the general similarity of these isomeric transformations to the quantitative "softness" criteria discussed in this paper is striking.

Manuscript submitted May 15, 1975; revised manuscript received Feb. 4, 1976.

Any discussion of this paper will appear in a Discussion Section to be published in the December 1976 JOURNAL. All discussions for the December 1976 Discussion Section should be submitted by Aug. 1, 1976.

Publication costs of this article were partially assisted by Bell Laboratories.

### REFERENCES

1. C. Tubandt, H. Reinhold, and W. Jost, *Z. Anorg. Chem.*, **177**, 269 (1929).
2. G. V. Hevesey and W. Seith, *ibid.*, **180**, 150 (1929).
3. L. W. Strock, *Z. Physik. Chem.*, **B25**, 441 (1934).
4. J. A. A. Ketelaar, *ibid.*, **B26**, 327 (1934); *ibid.*, **B30**, 53 (1935).
5. J. N. Bradley and P. D. Greene, *Trans. Faraday Soc.*, **63**, 424 (1967).
6. B. B. Owens and R. G. Argue, *Science*, **157**, 308 (1967).
7. J. C. Phillips, *J. Phys. Chem. Solids*, **35**, 1205 (1974).
8. B. Reuter and K. Hardel, *Naturwiss.*, **48**, 161 (1961).
9. T. Takahashi and O. Yamamoto, *Electrochim. Acta*, **11**, 779 (1966).
10. B. B. Owens, *This Journal*, **117**, 1536 (1970).
11. M. L. Beradelli, C. Biondi, M. DeRossi, G. Fonseca, and M. Giomini, *ibid.*, **119**, 114 (1972).
12. B. B. Owens, J. H. Christie, and G. T. Tiedeman, *ibid.*, **118**, 1144 (1971).
13. G. W. Mellors and D. V. Louzos, *ibid.*, **118**, 846 (1971).
14. T. Takahashi, S. Ikeda, and O. Yamamoto, *ibid.*, **119**, 477 (1972); T. Takahashi, O. Yamamoto, and S. Ikeda, *ibid.*, **120**, 1431 (1973); *ibid.*, **122**, 83 (1975).
15. A. F. Sammells, J. Z. Gougoutas, and B. B. Owens, *ibid.*, **122**, 1291 (1975).
16. S. Hoshino, *J. Phys. Soc. Japan*, **10**, 197 (1955).
17. J. A. Van Vechten, in "Phase Transitions and Their Applications in Materials Science," L. E. Cross, Editor, p. 139, Pergamon Press, New York (1973).
18. S. Geller, *Science*, **157**, 310 (1967).
19. S. Geller, *ibid.*, **176**, 1016 (1972); S. Geller and B. B. Owens, *J. Phys. Chem. Solids*, **33**, 1241 (1972).
20. J. C. Phillips, *Rev. Mod. Phys.*, **42**, 317 (1970); "Bonds and Bands in Semiconductors," Fig. 3.6 and p. 46, Academic Press, New York (1973).
21. E. Mooser and W. B. Pearson, *Acta Cryst.*, **12**, 1015 (1959); W. B. Pearson, *J. Phys. Chem. Solids*, **23**, 103 (1962).
22. J. C. Phillips, *Phys. Rev. Letters*, **27**, 1197 (1971); A. Navrotsky and J. C. Phillips, *Phys. Rev.*, **11B**, 1583 (1975).
23. J. St. John and A. Bloch, *Phys. Rev. Letters*, **33**, 1095 (1974).
24. C. R. Peters, M. Bettman, J. W. Moore, and M. D. Glick, *Acta Cryst.*, **B27**, 1826 (1971).
25. Y. Tsang and M. L. Cohen, *Phys. Rev.*, **B9**, 3541 (1974).
26. S. Geller and M. D. Lind, *J. Chem. Phys.*, **52**, 5854 (1970).
27. H. Stetter, *Angew. Chem.*, **66**, 217 (1954).
28. W. Bührer and P. Brüesch, *Solid-State Commun.*, **16**, 155 (1975).
29. L. E. Topol and B. B. Owens, *J. Phys. Chem.*, **72**, 2106 (1968).
30. J. C. Phillips, To be published.
31. W. V. Johnston, H. Wiedersich, and G. W. Lingberg, *J. Chem. Phys.*, **51**, 3739 (1969).
32. R. Nitsche, *Z. Krist.*, **120**, 229 (1964).
33. E. Kaldis and R. Widmer, *J. Phys. Chem. Solids*, **26**, 1697 (1965).
34. J. Serment, G. Perez, and P. Hagenmuller, *Bull. Soc. Chim. France*, **1968**, 561.
35. B. Reuter and K. Hardel, *Z. Anorg. Allgem. Chem.*, **340**, 158 (1965).
36. L. Pauling, "Nature of the Chemical Bond," p. 93, Cornell University Press, Ithaca, New York (1960).
37. D. D. Wagman et al., NBS Tech. Note 270-4, Washington (1969).
38. G. D. Mahan and W. J. Pardee, *Phys. Letters*, **49A**, 325 (1974).
39. R. Galli and F. Garbassi, *Nature*, **253**, 720 (1975).
40. B. K. Teo and J. C. Calabrese, *J. Am. Chem. Soc.*, **97**, 1256 (1975); To be published.
41. M. R. Churchill and K. L. Kalra, *Inorg. Chem.*, **13**, 1899 (1974); M. R. Churchill and B. G. Deboer, *ibid.*, **14**, 2502 (1975).

# The Preparation and Properties of Tin Oxide Films Formed by Oxidation of Tetramethyltin

B. Jayant Baliga\*<sup>1</sup> and Sorab K. Ghandhi\*

Electrical and Systems Engineering Department, Rensselaer Polytechnic Institute, Troy, New York 12181

## ABSTRACT

A new technique is described for the deposition of SnO<sub>2</sub> films based upon the pyrolysis of tetramethyltin (TMT) in oxygen at relatively low temperatures ( $\approx 450^\circ\text{C}$ ). As a tin source, TMT has the advantages of being stable in air and moisture and of being a liquid with a relatively high vapor pressure at room temperature. Thus, a simple bubbler system is used to transport its vapors to the reaction chamber. The deposition technique is characterized by (i) high and controllable growth rates (more than 300 Å/min), (ii) high conductivity layers [more than  $30(\text{ohm-cm})^{-1}$  undoped], and (iii) highly transparent layers in the visible range (more than 95% transmission for 1500Å layers). In addition, the films can be doped to achieve conductivities as high as  $200(\text{ohm-cm})^{-1}$  without loss in transmission. Finally, fast, low temperature anneals with forming gas in an open-tube system can be effectively used to result in an additional twofold increase in conductivity.

Tin oxide has the unusual properties of high transparency in the visible spectrum, combined with a high conductivity. These properties are shared with only a few other materials, and many techniques for its deposition have therefore been developed. Among these, the most commonly used are reactive sputtering (1, 2) and chemical vapor deposition using SnCl<sub>4</sub> (3-7). Substrate temperatures ranging from 500° to 750°C are necessary in the SnCl<sub>4</sub> process. Although lower temperatures are used in reactive sputtering, the properties of the resulting films are difficult to control in spite of elaborate target preparation procedures (1). In this paper, a new technique is described for the chemical vapor deposition of SnO<sub>2</sub> films based on the oxidation of tetramethyltin (TMT) at relatively low temperatures (450°-550°C).

The growth of electronic materials using organometallic compounds as sources was pioneered by Manasevit and co-workers, who have used TMT to obtain films of SnTe, SnS, and PbSnTe chalcogenide glasses (8). TMT has the advantages of being stable in air and moisture which allows its handling in glass containers with no hazard to the user, of being a liquid at room temperature, and of having a relatively high vapor pressure at room temperature (100 mm of Hg). The last two properties readily allow vapor transport to the reaction zone by bubbling an inert gas through liquid TMT.

Undoped SnO<sub>2</sub> films have high conductivity; nevertheless, the conductivity can be improved by doping with Sb<sub>2</sub>O<sub>5</sub> (4, 7) and by annealing in a vacuum (3, 6). In this paper we report the results of doping SnO<sub>2</sub> films with P<sub>2</sub>O<sub>5</sub> and the effects of forming gas anneals in an open-tube system. These techniques are substantial simplifications on the previously available methods for increasing the conductivity of the SnO<sub>2</sub> films.

## Experimental Conditions

**Apparatus.**—The deposition of SnO<sub>2</sub> films was performed in an open-tube reactor similar to that described by Goldsmith and Kern (9). In this reactor, a stainless steel susceptor was maintained at the deposition temperature (to within  $\pm 5^\circ\text{C}$ ) by conventional resistance heating. UHP argon gas was bubbled through the TMT<sup>2</sup> at 30°C to transport its vapors to the heated substrate. All depositions were conducted using an argon carrier gas flow of 2.0 liter/min.

\* Electrochemical Society Active Member.

<sup>1</sup> Present address: General Electric Company, Research and Development Center, Schenectady, New York 12301.

<sup>2</sup> 5N electronic grade, Alpha Organometallics, Danvers Massachusetts.

Key words: pyrolysis, thin films, tetramethyltin, CVD.

**Deposition procedure.**—Deposition of SnO<sub>2</sub> films was simultaneously conducted on 8 mil glass slides (Corning Cover Glass No. 1½) and silicon wafers. These substrates were degreased in a 1:1:1 solution of isopropyl alcohol, trichloroethylene, and acetone, cleaned in Caro's etch [1:1 solution of H<sub>2</sub>SO<sub>4</sub> (97%) and H<sub>2</sub>O<sub>2</sub> (47%)], and given a final rinse in methanol prior to loading into the reactor. After the substrate reached the deposition temperature in the argon ambient, silane<sup>3</sup> and oxygen<sup>4</sup> were introduced to obtain a 2000Å layer of SiO<sub>2</sub> on the substrate surface. All SnO<sub>2</sub> layers were deposited on this freshly prepared SiO<sub>2</sub> layer.

A Dektak thickness gauge was used to measure the film thickness. Since layer thickness was found to increase linearly with time, the deposition rate was calculated by dividing film thickness by deposition time. A film thickness of 1600Å was used to characterize the growth rate and to obtain the conductivity of the resulting films.

## Deposition Characteristics

**Temperature.**—The temperature dependence of the growth rate of SnO<sub>2</sub> films was studied using an argon flow of 15 ml/min through the TMT bubbler and an oxygen flow of 48 ml/min. As shown in Fig. 1, the growth process was reaction-rate controlled over the temperature range used in this study and had an activation energy of 1.64 eV/molecule (37.8 kcal/mole). The effect of decreasing the TMT transported to the chamber by reducing the argon flow through the TMT bubbler to 0.75 ml/min is also shown in Fig. 1. The growth rate is still reaction-rate controlled at lower temperatures, but the effects of mass-transport limited kinetics begin to appear at 530°C.

**Oxygen flow.**—The effect of changing the oxygen flow on deposition rate was measured at 500°C using an argon flow of 15 ml/min through the TMT bubbler. The growth rate was seen to increase linearly with oxygen flow, over the range from 0 to 48 ml/min. It was found that sufficient air was present in the open-chamber arrangement in our apparatus to produce deposition rates of 55 Å/min of SnO<sub>2</sub> in the absence of oxygen flow.

**TMT flow.**—Experiments were also conducted at 500°C to determine the effect of changing the TMT concentration in the chamber while maintaining an oxygen flow of 48 ml/min. Figure 2 shows the results

<sup>3</sup> Semiconductor grade, Matheson Gas Products, East Rutherford, Massachusetts.

<sup>4</sup> Research purity 99.99%, Matheson Gas Products, East Rutherford, Massachusetts.

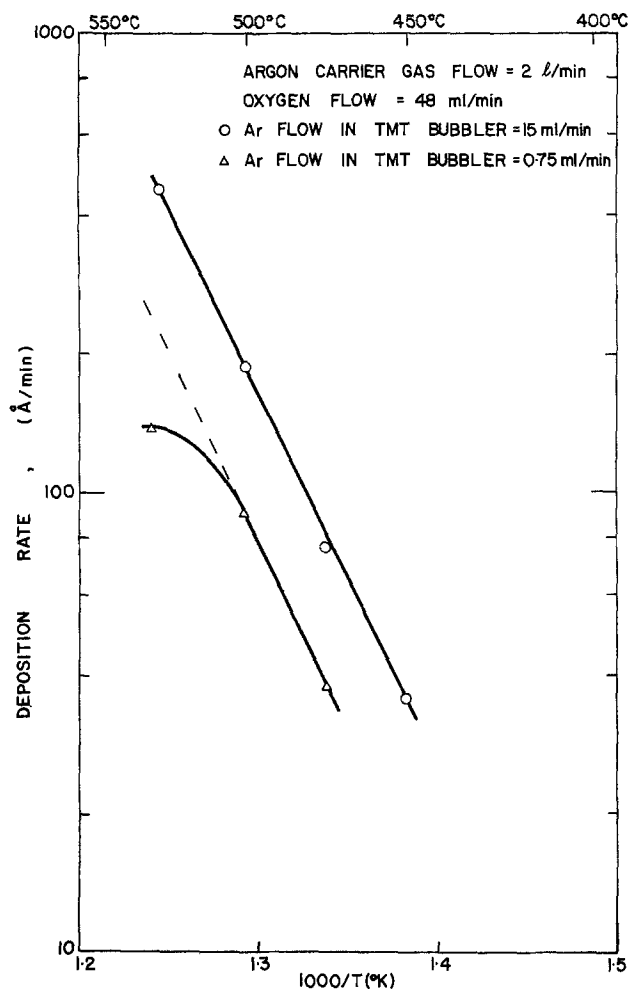


Fig. 1. Variation of tin oxide deposition rate with substrate temperature.

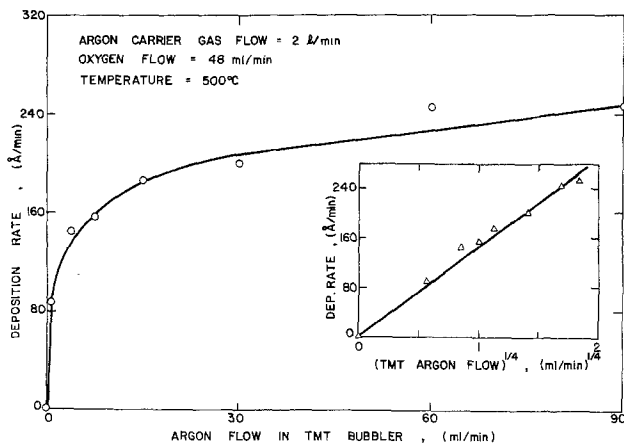


Fig. 2. Variation of tin oxide deposition rate with TMT concentration.

of increasing the argon flow through the TMT bubbler from 0 to 90 ml/min. The growth rate increases rapidly as argon flow is increased from 0 to 7.5 ml/min but is not a strong function of the TMT concentration at higher flows. The variation of growth rate with temperature (Fig. 1) at argon flows of 15 and 0.75 ml/min through the TMT bubbler shows that the kinetics of the growth are reaction-rate controlled and have the same activation energy over the entire range of TMT concentrations studied in Fig. 2 at a substrate temperature of 500°C. The observed variation cannot, therefore, be ascribed to a change in reaction kinetics. Indeed, the insert in this figure shows that the observed growth rate behavior can be explained if the reaction

is assumed to be of one-quarter order with respect to TMT concentration.

These results show that, using the TMT-O<sub>2</sub> system, SnO<sub>2</sub> films can be deposited at rates in excess of 300 Å/min. These rates compare well with those observed by CVD using SnCl<sub>4</sub> and exceed those normally observed in reactive sputtering. In comparison with these methods, the system described here has the advantage of requiring lower substrate temperatures and the capability of depositing uniform layers over a large area. Furthermore, repeated deposition of films under standardized conditions (substrate temperature = 500°C, argon flow in TMT bubbler = 15 ml/min, oxygen flow = 48 ml/min) results in less than ±5% variation in growth rate.

### Electrical Properties

SnO<sub>2</sub> is a wide bandgap (> 3.5 eV) semiconductor with predominantly n-type conductivity (3). The electron concentration in the conduction band primarily arises from lack of stoichiometry produced by an oxygen deficiency (4, 5). It is, therefore, important to examine the effect of the TMT/O<sub>2</sub> mole ratio upon conductivity. Further, the addition of antimony oxide has been found to enhance the conductivity of SnO<sub>2</sub> films (4, 7). In this section, we examine the effect of the addition of phosphorus pentoxide to these films.

*Undoped films.*—As expected, increasing the oxygen flow while maintaining a constant concentration of TMT resulted in layers with decreasing conductivity. On the other hand, SnO<sub>2</sub> films grown using increasing TMT flow while maintaining a fixed oxygen flow had increasing conductivities. The conductivity of SnO<sub>2</sub> films grown in this study was, therefore, controlled by an oxygen deficiency. The proportionality between conductivity and the TMT/O<sub>2</sub> flow ratio is shown in Fig. 3 for TMT/O<sub>2</sub> mole ratios up to 0.25. An oxygen excess was used in all these experiments.

Changing the deposition temperature was found to have a strong influence on the conductivity of the layers. Under fixed TMT and oxygen flows, the conductivity was found to decrease rapidly as the deposition temperature was increased. As seen from Fig. 1, this decrease in conductivity is accompanied by a rapid increase in growth rate. We, therefore, conclude that increasing substrate temperature results in the oxidation reaction proceeding further to completion, and leads to a fall in the conductivity.

*Doped films.*—Since SnO<sub>2</sub> is a semiconductor in which the conductivity is derived from lack of stoichiometry, its conductivity can be enhanced by the addition of oxides of Group V elements. We have studied the effect of the addition of P<sub>2</sub>O<sub>5</sub>, using phosphine gas<sup>5</sup> as a source. Phosphine is readily available in a wide range of concentrations due to its common usage

<sup>5</sup> Electronic grade 99.999% purity, Matheson Gas Products, East Rutherford, Massachusetts.

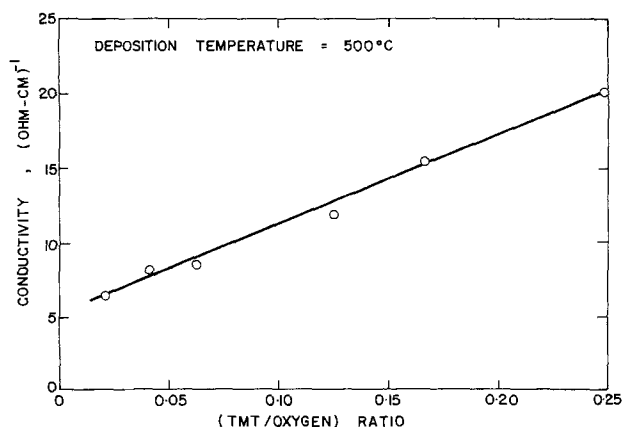


Fig. 3. Variation of the conductivity of tin oxide films with (TMT/oxygen) mole ratio.

as a n-type dopant for silicon, and its oxidation at low temperatures has been well studied (10, 11).

The effect of the addition of  $P_2O_5$  to  $SnO_2$  layers was studied at a deposition temperature of  $500^\circ C$ , using an argon flow of 15 ml/min through the TMT bubbler and an oxygen flow of 48 ml/min. A source of 460 ppm of phosphine in argon was used to obtain a wide range of low phosphine concentrations in the reactor. Figure 4 shows the change in conductivity as a function of the  $PH_3/TMT$  mole ratio over a range of three decades. The TMT concentration was computed using a vapor pressure of 100 mm of Hg at room temperature and assuming equilibrium transport from the bubbler. As seen from Fig. 4, the addition of phosphine increases the conductivity of the  $SnO_2$  layers by more than a factor of twenty. The highest conductivities were observed in our system for a  $PH_3/TMT$  ratio of 0.01. Increasing the phosphine concentration beyond this value produced a rapid decrease in conductivity. All of these layers exhibited a transmission coefficient of greater than 95% over the visible spectrum.

**Annealing behavior.**—The conductivity of  $SnO_2$  films has been increased by annealing the films in a vacuum (3, 6). In this work, we present results of annealing studies, performed on both doped and undoped samples, in a reducing ambient. Annealing the films in forming gas (20% hydrogen, 80% nitrogen) for relatively short periods (5 min) was found to produce a twofold increase in conductivity. This technique allowed fast, effective annealing in a simple open-tube apparatus as compared to the more complex vacuum annealing processes.

Typical results of isochronal anneals (5 min time intervals) are shown for both a doped and an undoped sample in Fig. 5. Little change in conductivity occurred below  $200^\circ C$ . The highest conductivity after annealing occurred for temperatures between  $300^\circ C$  and  $350^\circ C$ . At higher temperatures the conductivity decreased until visible signs of the reduction of  $SnO_2$  to Sn were observed at  $500^\circ C$  and above. Extended anneals at  $500^\circ C$  resulted in complete reduction of the  $SnO_2$ , as evidenced by the appearance of tiny balls of Sn on the sample. These results indicate an optimum anneal temperature of  $300^\circ C$ . Isothermal anneals performed at this temperature showed that the anneal is complete within 5-10 min (12).

The depositions in our study were performed by the pyrolysis of tetramethyltin in oxygen. Consequently, conductivity changes caused by the presence of incorporated methyl groups during annealing have also been considered. Annealing in a dry nitrogen atmosphere at  $300^\circ C$  showed no conductivity change. Hence, we conclude that the reducing effect of these groups, if incorporated into the films, is negligible.

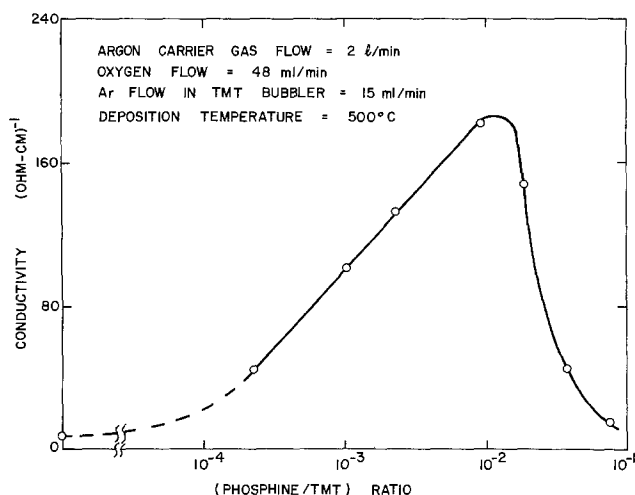


Fig. 4. Effect of the addition of phosphine during deposition upon conductivity of tin oxide films.

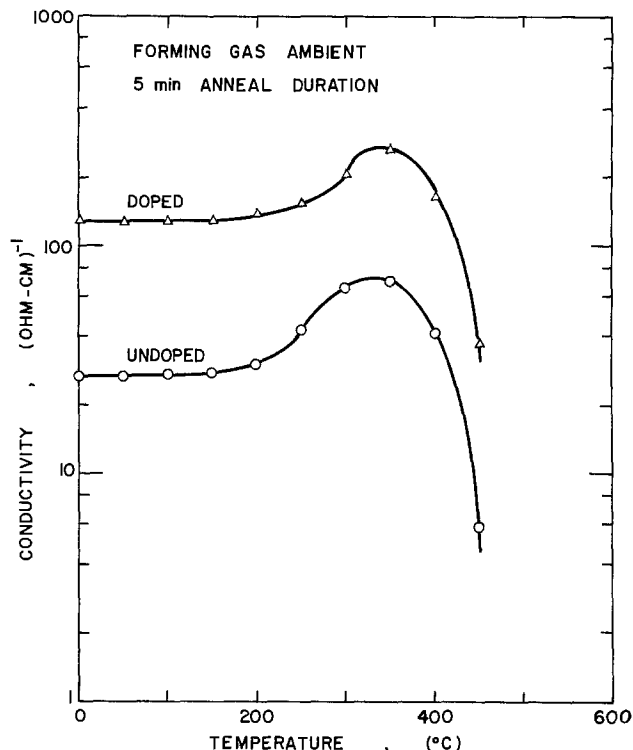


Fig. 5. Effect of isochronal annealing in forming gas upon the conductivity of tin oxide films.

## Discussion and Conclusions

Repetitive deposition of  $SnO_2$  films under standard conditions (deposition temperature =  $500^\circ C$ , argon flow in TMT bubbler = 15 ml/min, oxygen flow = 48 ml/min) produced layers whose conductivities varied by less than  $\pm 10\%$ . This reproducibility partially stems from the deposition of the  $SnO_2$  layers on the freshly deposited  $SiO_2$  layers, which makes the properties of the  $SnO_2$  films insensitive to the substrate cleaning procedure.

In our experiments, undoped layers could be grown with conductivities as high as  $30 (\text{ohm-cm})^{-1}$ . The conductivity is found to increase with increasing TMT/ $O_2$  ratio and is also increased by annealing the layers in a reducing ambient. This confirms that the conductivity arises predominantly from an oxygen deficiency and not from the presence of impurities in the TMT source.

The addition of  $P_2O_5$  to the  $SnO_2$  increases the conductivity of our films from  $8 (\text{ohm-cm})^{-1}$  for undoped films to as high as  $180 (\text{ohm-cm})^{-1}$  for films grown under an optimum  $PH_3/TMT$  mole ratio of 0.01, and the conductivity falls rapidly at higher ratios. A similar behavior, observed in the doping of  $SnO_2$  films with  $Sb_2O_3$  (7), has been attributed to a measured decrease in electron mobility. It is likely that the decrease in conductivity of our films for  $PH_3/TMT$  ratios above 0.01 is also due to this effect.

Annealing these films in forming gas at  $300^\circ C$  for 5 min produces a twofold increase in conductivity for both undoped and  $P_2O_5$ -doped films. In this study the highest conductivity observed after annealing was  $320 (\text{ohm-cm})^{-1}$ . Annealing at higher temperatures can result in sample destruction by reduction of  $SnO_2$  to Sn.

In conclusion, this paper introduces a new CVD process for the deposition of high conductivity  $SnO_2$  films based on the oxidation of tetramethyltin. Growth rates exceeding 300 Å/min are achievable, with film quality comparable to that obtained by either reactive sputtering or chemical vapor deposition using  $SnCl_4$ . This new deposition technique, however, offers the advantages of simplicity of apparatus, low deposition temperatures, and good reproducibility.



### Acknowledgments

The authors are indebted to R. Bhat for technical assistance and to R. Rafun for assistance in manuscript preparation.

Manuscript submitted Nov. 6, 1975; revised manuscript received Feb. 9, 1976.

Any discussion of this paper will appear in a Discussion Section to be published in the December 1976 JOURNAL. All discussions for the December 1976 Discussion Section should be submitted by Aug. 1, 1976.

Publication costs of this article were partially assisted by Rensselaer Polytechnic Institute.

### REFERENCES

1. W. R. Sinclair, F. G. Peters, D. W. Stillinger, and S. E. Koonce, *This Journal*, **112**, 1096 (1965).
2. J. L. Vossen and E. S. Poliniak, *Thin Solid Films*, **13**, 281 (1972).

3. K. Ishiguro, T. Sasaki, T. Arai, and I. Imai, *J. Phys. Soc. Japan*, **13**, 296 (1958).
4. R. E. Aitchison, *Australian J. Appl. Sci.*, **5**, 10 (1954).
5. J. A. Aboaf, V. C. Marcotte, and N. J. Chou, *This Journal*, **120**, 701 (1973).
6. V. K. Miloslavskii, *Opt. Spectr.*, **7**, 154 (1959).
7. R. Muto and S. Furuuchi, *Rept. Res. Lab. Asahi Glass Co.*, **23**, 27 (1973).
8. H. M. Manasevit and W. I. Simpson, *This Journal*, **122**, 444 (1975).
9. N. Goldsmith and W. Kern, *RCA Rev.*, **28**, 153 (1967).
10. B. J. Baliga and S. K. Ghandhi, *J. Appl. Phys.*, **44**, 990 (1973).
11. M. Shibata and K. Sugawara, *This Journal*, **122**, 155 (1975).
12. B. J. Baliga and S. K. Ghandhi, Paper 5.6, International Electron Devices Meeting, December (1975).

# Technical Note



## Particle Morphology and Lamp Maintenance of $(1-x)\text{YPO}_4 \cdot x\text{YVO}_4$ Phosphors Containing $\text{Eu}^{3+}$

R. C. Ropp and B. Carroll

Department of Chemistry, Rutgers University, Newark, New Jersey 07102

In a prior paper (1), a study of solid solution formation between  $\text{YPO}_4$  and  $\text{YVO}_4$  was presented. Complete solid solution was observed only if the two were coprecipitated or if the salt,  $\text{YPO}_4 \cdot 5/3 \text{H}_2\text{O}$  was employed as a reaction base. The use of any other phosphate resulted in an apparent deviation from Vegard's law due to incomplete solid-solution formation caused by competing side reactions. These side reactions were shown to result in the formation of polyvanadates [e.g.,  $\text{Y}(\text{VO}_3)_3$ ] in the high phosphate region, or polyphosphates [e.g.,  $\text{Y}(\text{PO}_3)_3$ ] in the high vanadate region. It was further demonstrated that the salt,  $\text{YPO}_4 \cdot 5/3 \text{H}_2\text{O}$ , exhibits an acicular crystal habit, and if used in a solid-state reaction, produced solid-solution particles of  $(1-x)\text{YPO}_4 \cdot x\text{YVO}_4$  which were also acicular (pseudomorphism). A similar circumstance was noted (2) several years ago for the case of  $\text{CaHPO}_4 \cdot 2\text{H}_2\text{O}$  where the original particle morphology was carried through to form pseudomorphic calcium halophosphate phosphor.

If  $\text{Eu}^{3+}$  is included as a coprecipitate in either of the two (or both) salts,  $\text{YPO}_4 \cdot 5/3 \text{H}_2\text{O}$  and  $\text{YVO}_4$ , a phosphor results with an acicular crystal habit. This phosphor exhibits a marked improvement in light output and light maintenance when incorporated into a 400W high pressure mercury vapor lamp, as shown by the data in Table I. Whether this improvement in light

Key words: morphology, phosphors, yttrium, phosphate-vanadate.

Table I.

Moles $\text{PO}_4$	Moles $\text{VO}_4$	Particle habit	Lumens			
			0 hr lamp	Red (due to phosphor)		
			0 hr	100 hr	%M	
0.60	0.40	acicular	26,294	3837	3792	98.8
0.60	0.40	normal*	25,510	3672	2872	78.2

\* The "normal" particle habit is a sort of irregular dodecahedron.

output is due to improved packing of the acicular particles in the phosphor coating as in the case of halophosphate, or is due to a greater resistance to surface degradation of the particles under the influence of the photon flux as a function of time is not fully understood at this time.

Manuscript received Feb. 19, 1976.

Any discussion of this paper will appear in a Discussion Section to be published in the December 1976 JOURNAL. All discussions for the December 1976 Discussion Section should be submitted by Aug. 1, 1976.

### REFERENCES

1. R. C. Ropp and B. Carroll, *Inorg. Chem.*, **14**, 2199 (1975).
2. R. C. Ropp, Unpublished data.



## Elimination of Stacking Faults in Silicon by Trichloroethylene Oxidation

Takeshi Hattori

Sony Corporation Research Center, Hodogaya-ku, Yokohama 240, Japan

There has been an increasing interest in recent years in the advantages of SiO<sub>2</sub> films thermally grown in the presence of small amounts of a chlorine-bearing species in a dry oxygen atmosphere (1). Until recently, most procedures have introduced chlorine into the oxidizing ambient in the form of HCl or Cl<sub>2</sub> (2-9), while a more manageable chlorine source has been sought to avoid its corrosive and deleterious effects (10-12). The author and co-workers reported in a previous paper (11) that the use of trichloroethylene (C<sub>2</sub>HCl<sub>3</sub>), which is far less corrosive and much easier to handle, results in the excellent characteristics of MOS devices.

Thermal oxidation of silicon at high temperatures is well known to result in the generation of extrinsic stacking faults in the surface layers of the crystal (13-19). These stacking fault defects frequently increase the reverse current of planar p-n junctions (19-20) and/or give rise to bright spots or lines in the image of silicon vidicons (21), charge coupled imagers (22), and related image-sensing devices. Very recent reports (23-24) indicate that both standard oxidation at extremely high temperatures above 1200°C (or 1300°C in steam) and HCl oxidation at 1200°C cause stacking faults to vanish from the surface of silicon. The purpose of this article is to present the effects of trichloroethylene (TCE) oxidation on the elimination and shrinkage of stacking faults in silicon wafers.

For the present studies, dislocation-free silicon wafers [grown by the Czochralski method, chem-mechanically polished, (100) oriented, 40 mm in diameter, n-type, 2-3 ohm-cm] were used. These were cleaned by a standard process for MOS LSI's and oxidized at temperatures ranging from 1000° to 1200°C in a dry oxygen flow of 1500 cm<sup>3</sup>/min (constant) in a quartz furnace. TCE oxides were grown under the same condition, but with varying flows of dry nitrogen through a quartz bubbler filled with purified liquid C<sub>2</sub>HCl<sub>3</sub>. The temperature of the bubbler was controlled constantly at 27°C.

Virtually no difference between standard and TCE oxide films was observed in refractive index, dielectric constant, maximum dielectric strength, etch rate in buffered HF, and wavelength of infrared absorption peak, but the oxidation rate of silicon (11) was considerably increased in the presence of C<sub>2</sub>HCl<sub>3</sub>. Both Auger electron spectroscopy (AES) and ion microprobe mass analysis (IMMA) showed that the chlorine profile in the TCE oxide was sharply peaked near the Si-SiO<sub>2</sub> interface (12) as well as in the HCl oxide (4-6).

After these oxide films were removed in hydrofluoric acid, oxidation-induced stacking faults contained in the silicon wafers were revealed by Secco etching (25). Stacking faults were extrinsic in character and consist of an extra plane of silicon atoms on the (111) plane. The defect size, taken as the largest length on the

wafer surface, was measured by optical microscopy. Stacking fault densities were about 10<sup>2</sup> defects/cm<sup>2</sup> through these experiments, except for the case of the complete elimination.

Figure 1 shows the dependence of stacking fault length on the oxidation conditions. The size was plotted as a function of the flow rates of nitrogen through a bubbler filled with TCE. No oxidation-induced stacking faults appeared at the flow rate of more than 15 and 200 cm<sup>3</sup>/min for 1200° and 1100°C, respectively, while 10-20 μm long stacking faults were generated by standard oxidation without TCE-N<sub>2</sub> flow. The relationship between temperatures and the minimum C<sub>2</sub>HCl<sub>3</sub>/O<sub>2</sub> ratio at which stacking faults could be completely eliminated is shown in Fig. 2. This ratio increased considerably with decrease of oxidation temperature, and, at 1000°C and below, elimination was virtually not observed, though the oxidation-induced stacking fault length was very short due to comparatively low temperatures.

Elimination or shrinkage of existing stacking faults could also be obtained by using TCE oxidation. Wafers having oxidation-induced 34 μm long stacking faults generated by standard oxidation in dry O<sub>2</sub> for 2 hr at 1200°C were subjected, with the initial oxides left intact, to additional oxidation containing TCE vapor for various times. As shown in Fig. 3, the existing stacking faults shrank and were finally eliminated within 2 hr at 1200°C. The defects shrank gradually after slight expansion at 1100°C. Significant shrinkage phenomena could not be observed below 1100°C. Almost the same elimination phenomena have been reported for the use of HCl (24), and were observed also when the initial oxides were revealed prior to TCE oxidation.

The exact mechanism by which the TCE vapor acts to eliminate or shrink the stacking faults is not known. Generation of vacancies at the surface of silicon and their flow to the fault might occur under the influence

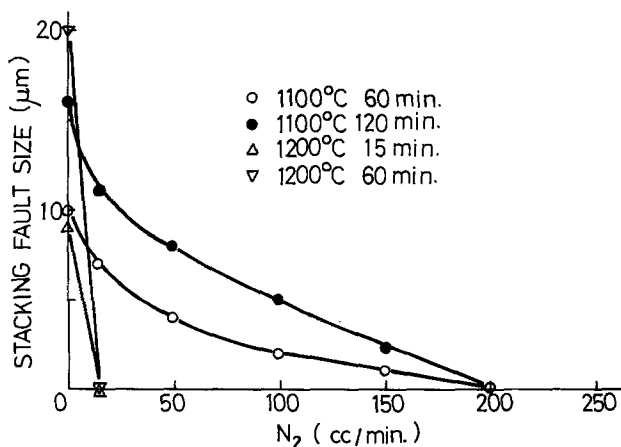


Fig. 1. Stacking fault size vs. C<sub>2</sub>HCl<sub>3</sub>-N<sub>2</sub> flow during oxidation

Key words: silicon processing, chlorine incorporation, thermal oxidation, lattice defect, C<sub>2</sub>HCl<sub>3</sub>.

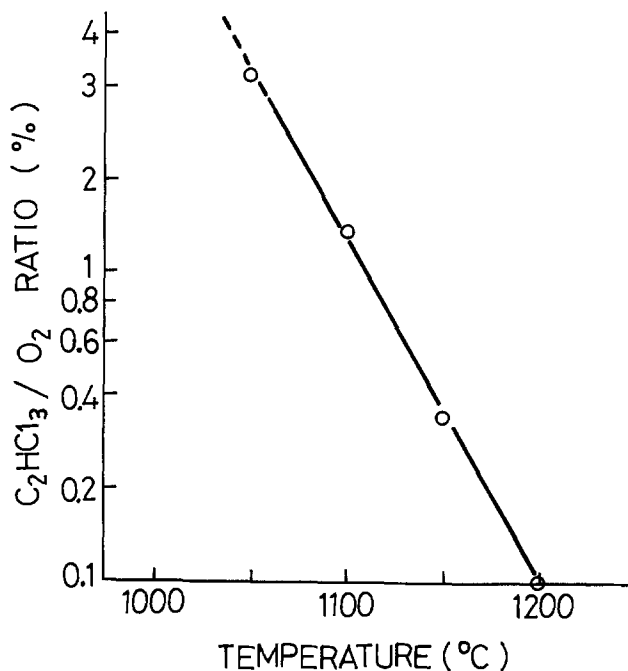


Fig. 2. Oxidation temperature vs.  $C_2HCl_3/O_2$  ratio whereby stacking faults could be completely eliminated.

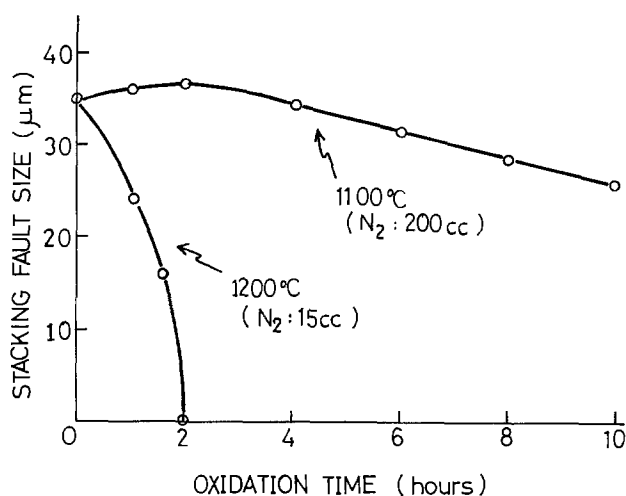


Fig. 3. Shrinkage of existing stacking faults during additional oxidation in the presence of  $C_2HCl_3$ .

of the pyrolytic product of  $C_2HCl_3$ , chlorine, and it will therefore result in the elimination or shrinkage of

these defects. Further experiments are required to establish the validity of the inference.

It may be expected that TCE oxidation has great potential for silicon devices, particularly image-sensing devices like charge coupled imagers requiring very high quality oxides and crystals.

Manuscript submitted Dec. 2, 1975; revised manuscript received Feb. 2, 1976.

Any discussion of this paper will appear in a Discussion Section to be published in the December 1976 JOURNAL. All discussions for the December 1976 Discussion Section should be submitted by Aug. 1, 1976.

Publication costs of this article were partially assisted by Sony Corporation.

#### REFERENCES

1. R. J. Kriegler, *IEEE Intl. Solid State Circuits Conf. Digest of Technical Papers*, **18**, 56 (1975).
2. R. J. Kriegler, *This Journal*, **119**, 388 (1972).
3. R. J. Kriegler, in "Semiconductor Silicon 1973," H. R. Huff and R. R. Burgess, Editors, p. 363, The Electrochemical Society Softbound Symposium Series, Princeton (1973).
4. R. J. Kriegler, *Denki Kagaku*, **41**, 466 (1973).
5. R. J. Kriegler, Proc. of the 1973 Intl. Conf. on Solid State Devices, p. 341, Tokyo (1973).
6. Y. J. Van der Meuler, C. M. Osburn, and J. F. Ziegler, *This Journal*, **122**, 284 (1975).
7. M. Severi and G. Soncini, *Electron. Letters*, **8**, 403 (1972).
8. K. Kobayashi, K. Tanabashi, K. Ohta, and T. Kubota, *Denki Kagaku*, **42**, 294 (1974).
9. Y. C. Cheng, J. W. Haslett, E. Kendall, R. J. Kriegler, and F. J. Scholz, *Proc. IEEE*, **62**, 859 (1974).
10. M. C. Chen and J. W. Hile, *This Journal*, **119**, 223 (1972).
11. G. J. Declerck, T. Hattori, G. A. May, J. Beaudouin, and J. D. Meindl, *ibid.*, **122**, 436 (1975).
12. T. Hattori, The 8th Symposium on Semiconductors and IC Technology Extended Abstracts, p. 19, Tokyo (1975).
13. H. J. Quisser and P. G. G. Van Loon, *J. Appl. Phys.*, **35**, 3066 (1964).
14. G. R. Booker and R. Stickler, *Phil. Mag.*, **11**, 1303 (1965).
15. G. R. Booker and W. J. Tunstall, *ibid.*, **13**, 71 (1966).
16. J. E. Lawrence, *J. Appl. Phys.*, **40**, 360 (1969).
17. A. J. R. de Kock, *Appl. Phys. Letters*, **16**, 100 (1970).
18. H. Shiraki, *Japan. J. Appl. Phys.*, **13**, 1514 (1974).
19. R. V. Ravi and C. J. Varker, *J. Appl. Phys.*, **45**, 263 (1974); *ibid.*, **45**, 272 (1974).
20. K. V. Ravi, C. J. Varker, and C. E. Volk, *This Journal*, **120**, 533 (1973).
21. H. Shiraki, Proc. of the 2nd Conference on Solid State Devices, p. 61, Tokyo (1971).
22. T. Hattori, Unpublished data.
23. S. M. Hu, *Appl. Phys. Letters*, **27**, 165 (1975).
24. H. Shiraki, *Japan. J. Appl. Phys.*, **14**, 747 (1975).
25. F. Secco D'Aragna, *This Journal*, **119**, 948 (1972).

## DISCUSSION SECTION



This Discussion Section includes discussion of papers appearing in the *Journal of The Electrochemical Society*, Vol. 122, No. 8, 10, and 11; August, October, and November 1975.

### A Note on the Chemistry of Lead Sulfide Sensitization for Infrared Detection

G. M. Wolten (pp. 1149-1150, Vol. 122, No. 8)

**O. A. Kunze:**<sup>1</sup> In the technical note under discussion it is proposed that the effect of oxidants on the deposi-

<sup>1</sup> C.S.I.R., National Physical Research Laboratory, Pretoria 0001, South Africa.

tion of photoconductive lead sulfide films is the formation of a solid solution of  $PbSO_4$  in  $PbS$ . The initial presence of sulfate is regarded as being responsible for the observed sensitizing effect. In support of this the author has presented chemical arguments which differ substantially from the results obtained in our laboratory.

The general acceptance of the role of oxygen and oxygen compounds in the photoconduction of lead sulfide is based on electrical measurements. Attempts to

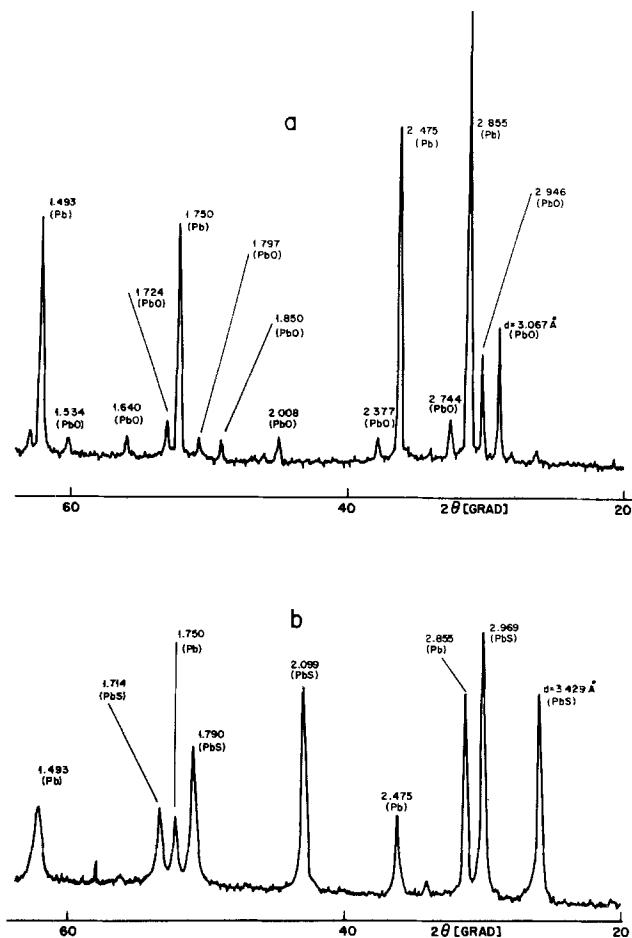


Fig. 1. Powder diffractograms, copper  $K\alpha$  radiation: (a) plumbite + AIMSA, (b) plumbite + AIMSA + thiourea.

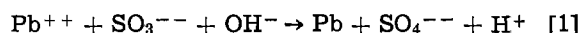
relate the sensitizing action of oxidants (or reducing agents) directly to the actual oxygen concentration in the layers have failed so far. For example, we have found that mass spectrographic analyses of PbS layers formed with and without hydroxylamine<sup>2</sup> show the same low oxygen concentration for both cases. Another example is the data by Blount *et al.*<sup>3</sup> which show the lowest oxygen value for the sample formed with the highest amount of oxidant.

From our results given below we consider reduction rather than oxidation as the crucial step involved in sensitization. Further we conclude that the initial formation of lead sulfate can be excluded.

Thiourea is oxidized easily in aqueous alkaline solution of the type used in the deposition of PbS films. We have determined polarographically that the half-wave potential for thiourea in 0.3N sodium hydroxide solution is close to 0V. We have also found that in place of oxidants, aminoiminomethanesulfinic acid (AIMSA) and several other reducing agents have a pronounced sensitizing effect on PbS layers.

In a strongly alkaline medium AIMSA reduces plumbite to elemental lead in a slow reaction. This is shown in Fig. 1(a), which is part of a powder diffractogram of the reaction product of an aqueous solution 0.03N in  $Pb(NO_3)_2$ , 0.3N in NaOH, and 0.009N in AIMSA. The diffractogram shows the presence of lead and lead(II) oxide. Figure 1(b) is the diffractogram of the reaction product of a similar solution which in addition was 0.013N in thiourea. In this case the precipitate was found to consist of lead sulfide and lead. In both cases formation of lead sulfate did not take place. This is in agreement with Bennett and Dur-

rant who give sulfite as the oxidation product of sulfoxylate in an alkaline medium.<sup>4</sup> This also excludes the possibility that added sulfite is responsible for the formation of sulfate according to



(completed reaction [4] in the discussed note). As expected, no formation of sulfate in a plumbite solution containing sodium sulfite was observed in an experiment designed to test reaction [1]. On the contrary, sulfite was found to induce the photochemical oxidation of plumbite to lead(IV) by dissolved oxygen, as reported by Kunze *et al.*<sup>5</sup>

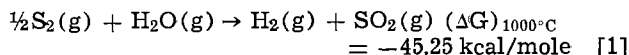
Finally, it should be pointed out that the easy substitution of sulfate for sulfide in the PbS lattice as suggested by Wolten appears to be doubtful. The effective ionic radius of  $[SO_4]^{--}$  is not 1.49Å as quoted but of the order of 2.2Å.<sup>6</sup>

Instead of allowing the formation of excess lead in the layers, which has thus far been supposed, the action of those reducing agents which are effective sensitizers might well be to inhibit the oxidation of sulfide to sulfur due to the presence of dissolved oxygen. Lead sulfide formed by the plumbite thiourea reaction is known to contain an excess of sulfur.<sup>7</sup> The presence of reducing agents would thus result in the formation of deposits with improved stoichiometry. This reasoning is supported by our finding that PbS layers deposited without a reducing additive show very little if any photoconductivity. Their photoconductive response can, however, be enhanced if the deposition is conducted in an inert atmosphere using chemicals and solvent from which the adsorbed and dissolved oxygen have carefully been removed.

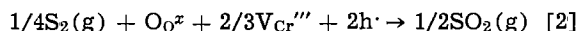
### The Transport of Chromium in $Cr_2O_3$ Scales in Sulfidizing Environments

G. Romeo, H. S. Spacil, and W. J. Pasko  
(pp. 1329-1333, Vol. 122, No. 10)

**F. A. Kröger:**<sup>8</sup> This paper explains the marked effect of sulfur on the diffusivity of Cr in  $Cr_2O_3$  scales by donor action of sulfur dissolved in the  $Cr_2O_3$ . The donor is supposed to be sulfur at an oxygen site. Such a donor would have a donor level  $S_0^x$  somewhat above the valence band of  $Cr_2O_3$ . Although such a center may trap a hole, it will not do so very efficiently. It seems more likely that sulfur acts as a reducing agent by reacting with oxygen with the formation of  $SO_2$ . The same reaction has been proposed to explain the reducing effect of sulfur on  $ZnO$ <sup>9</sup> and of oxygen on  $ZnS$ <sup>9</sup> and  $CdS$ .<sup>10</sup> Owing to the large negative Gibbs free energy of the reaction



this reaction is even effective in reducing the low oxygen activities established by  $H_2$ - $H_2O$  mixtures. Reaction with  $Cr_2O_3$  can be formulated



and thus leads to a reduction in the concentrations of holes and Cr vacancies. The increased mobility of chromium in the scale can be explained by the increase of interstitial Cr caused by the decrease of the Cr vacancy concentration. This is seen from Eq. [I-A] of the paper under discussion which represents a modi-

<sup>4</sup> H. Bassett and R. G. Durrant, *J. Chem. Soc.*, 1927, 1401.

<sup>5</sup> O. A. Kunze, O. G. Malan, P. A. Büger, and W. Fink, *Z. Naturforsch.*, 26b, 8 (1971).

<sup>6</sup> O. W. Flörke, *Naturwiss.*, 39, 478 (1952).

<sup>7</sup> B. Reuter and R. Stein, *Z. Elektrochem.*, 61, 440 (1957).

<sup>8</sup> Department of Materials Science, University of Southern California, Los Angeles, California 90007.

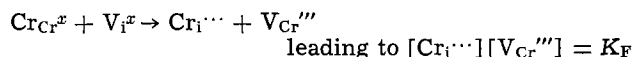
<sup>9</sup> F. A. Kröger and J. A. M. Dikhoff, *This Journal*, 99, 144 (1952).

<sup>10</sup> H. H. Woodbury, *J. Phys. Chem. Solids*, 27, 1257 (1956).

<sup>2</sup> O. A. Kunze, O. G. Malan, and P. A. Büger, *J. S. African Chem. Inst.*, 25, 60 (1972).

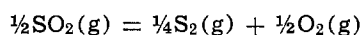
<sup>3</sup> G. H. Blount, P. J. Schreiber, D. K. Smith, and R. T. Yamada, *J. Appl. Phys.*, 44, 978 (1973).

fied Frenkel disorder reaction. It can also be explained by normal Frenkel disorder of chromium

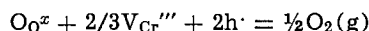


Formation of CrS at the interface  $\text{Cr}_2\text{O}_3$ -Cr metal indicates that sulfur penetrates the oxide layer. This must occur either by bulk diffusion or by grain boundary diffusion. In the former case, some sulfur must be dissolved in the  $\text{Cr}_2\text{O}_3$ , either at oxygen sites ( $\text{S}_{\text{O}}^x$ ) or at interstitial sites ( $\text{S}_{\text{I}}$ ). It is known for the chalcogenides of lead, cadmium, and zinc that chalcogen diffusion occurs by neutral interstitials at low metal activities but by a nonmetal vacancy mechanism at high metal activities. If the bulk diffusion of S is involved in the present case, it is probably of the latter type.

**G. Romeo,<sup>11</sup> H. S. Spacil,<sup>12</sup> and W. J. Pasko:<sup>12</sup>** Kröger has suggested that our experimental results may be due to the reducing action of sulfur, in the gas phase, rather than sulfur actually dissolved in the oxide. His reaction [2], however, can be combined with the dissociation of gaseous  $\text{SO}_2$



to yield, using Kröger-Vink notation



which is identical to, though reversed in direction from, our reaction [I-B]. Whether modified or normal Frenkel defects are also considered to exist, the Cr defect concentration would depend only on oxygen activity, and be independent of sulfur activity. Sulfur could then influence chromium transport under our experimental conditions only by changing the oxygen activity or by acting as a sink for chromium moving across the scale.

While sulfur does act as a reductant in the systems cited by Kröger, its effect as a reductant in our system is best considered in terms of the relative effects of sulfur and hydrogen on the oxygen potential of a hydrogen-sulfur-oxygen gas containing a fixed amount of oxygen. Table I gives the oxygen potential in such a gas as a function of the atomic sulfur to hydrogen plus sulfur ratio, for an atomic fraction of oxygen equal to  $10^{-5}$ , at  $900^\circ\text{C}$  and 1 bar.<sup>13</sup>

Thus the addition of sulfur to a gas initially containing only hydrogen and oxygen can only increase the oxygen potential and activity, and could not increase chromium mobility through an increase in interstitial concentration as proposed by Kröger.

Prior investigators [see Ref. (13) and (14), in the paper under discussion] have shown that oxidation rates of chromium in oxygen-containing gases have either increased or remained relatively constant with oxygen activity. Such results imply that chromium mobility in  $\text{Cr}_2\text{O}_3$  would show a similar dependence on oxygen activity. Our Fig. 2, however, illustrates the

<sup>11</sup> General Electric Company, Vallecitos Nuclear Center, Pleasanton, California 94566.

<sup>12</sup> General Electric Company, Research and Development Center, Schenectady, New York 12301.

<sup>13</sup> The oxygen potential was obtained by determining the equilibrium composition, under the stated conditions of the gaseous species  $\text{H}_2$ ,  $\text{O}_2$ ,  $\text{S}_2$ ,  $\text{H}_2\text{O}$ ,  $\text{H}_2\text{S}$ ,  $\text{SO}_2$ , and  $\text{H}_2\text{SO}_4$ .

Table I

S/(H + S)	$\mu_{\text{O}}$ (kcal/g-atom O)
0	-68.9
0.2	-66.8
0.4	-61.8
0.6	-59.7
0.8	-57.6
1.0	-46.4

increase in chromium transport through the oxide in going from an  $\text{O}_2$  atmosphere to a  $\text{H}_2$ -10%  $\text{H}_2\text{S}$  mixture. If the oxygen activity were the only controlling factor of chromium mobility in  $\text{Cr}_2\text{O}_3$ , this quantity should remain the same or decrease as a consequence of changing the atmosphere from  $\text{O}_2$  to  $\text{H}_2$ -10%  $\text{H}_2\text{S}$ . Since actually an increase is observed, sulfur does not appear to function only as a sink for chromium, but can also be a factor of enhancement of the chromium mobility by affecting the defect equilibria in the  $\text{Cr}_2\text{O}_3$ .

We do not advance any mechanism by which sulfur penetrates  $\text{Cr}_2\text{O}_3$  to form the internal sulfide layer observed in our experiments. While we have proposed that sulfur enters the oxide as an electron donor on oxygen sites, with subsequent effects on chromium mobility, simultaneous sulfur transport through the oxide may occur as a result of gaseous transport in cracks or the mechanism mentioned by Kröger.

### Doping of Silicon by Neutron Irradiation

H. A. Herrmann and H. Herzer (pp. 1568-1569, Vol. 122, No. 11)

**J. Burtscher:<sup>14</sup>** Herrmann and Herzer write about the chances of neutron-irradiated silicon perhaps somewhat too cautiously, finishing their paper with the statement, "Further work must be undertaken to establish whether transmutation doping will play a dominant role in addition to the standard methods for growing silicon crystals."

The use of neutron-irradiated silicon for manufacturing large-area devices (especially high power devices) is by no means a question of the future. In 1973, Schnöller<sup>15,16</sup> had already presented rectifiers and thyristors which were made from Siemens silicon irradiated in the swimming pool reactor FRJ1 in Jülich (Germany). By observation of the avalanche radiation<sup>17</sup> it was shown in Schnöller's work that the breakdown in these structures was much more homogeneous than in devices made from conventional doped crystals. In addition to the homogeneity of the resistivity across the area, it is also important that the desired mean value of the resistivity can be reached more exactly by neutron irradiation than by any conventional doping method, at least in the range 10-200 ohm-cm n-type which is currently the most important one for high power, high voltage devices. This finer fitting of the resistivity value made it possible to improve the always necessary compromises between breakdown voltage, current capability, and dynamic properties.<sup>18,19</sup> This point has been discussed somewhat more exactly in the meantime.<sup>20</sup>

Details about the reached resistivity tolerances when using different reactors were reported in Ftn<sup>21,24</sup>. Also, the safety questions connected with the storing and handling of bigger quantities of irradiated material have been examined; the required waiting times for the radioactivity to decay are of the order of days.<sup>25</sup> The use of neutron-irradiated silicon for the production of high voltage, high power devices has become standard in the meantime.

<sup>14</sup> Siemens AG, D-8000 Munich, Germany.

<sup>15</sup> M. Schnöller, 2nd DFG Colloquium on Power Devices, Freiburg (1973).

<sup>16</sup> M. Schnöller, *IEEE Trans. Electron Devices*, ED-21, 313 (1974).

<sup>17</sup> P. Voss, *ibid.*, ED-20, 299 (1973).

<sup>18</sup> H. Patalong, 3rd DFG Colloquium on Power Devices, Freiburg (1974).

<sup>19</sup> B. Voss, *ibid.*

<sup>20</sup> K. Platzöder and K. H. Loch, 4th DFG Colloquium on Power Devices, Freiburg (1975); Submitted to *IEEE Trans. Electron Devices*.

<sup>21</sup> W. Haas and M. Schnöller, *J. Electron. Mater.*, 5 (1976).

<sup>22</sup> W. Haas and M. Schnöller, *Siemens Z.*, 1, 2 (1976).

<sup>23</sup> W. Haas and M. Schnöller, Submitted to *IEEE Trans. Electron Devices*.

<sup>24</sup> M. Schnöller, Symposium Leistungselektronik, Elektrotechnicki Institut Nikola Tesla, Belgrad (1975).

<sup>25</sup> J. A. Martin, E. Haas, and M. Schnöller, "Dotierung von Halbleitermaterial durch Kernumwandlung," GDCH Hauptversammlung, Fachgruppe Kern-, Radio-, and Strahlenchemie, Köln (1975).

**H. A. Herrmann and H. Herzer:**<sup>26</sup> Neutron-irradiated silicon, we agree, is not only a question of the future, but has grown up to be a very important technique for high power device technology since writing our publication in *This Journal*. The interest in this material now overflows nearly all applications in the resistivity range above 20 ohm-cm n-type.

The meantime from our first publication<sup>27</sup> up to now can be characterized by three typical features: (i) the rapid increase in fundamental work,<sup>28-34</sup> (ii) the rapid increase in R&D work,<sup>35</sup> and (iii) the rapid increase in demand for production quantities.<sup>36</sup> The latter point

<sup>26</sup> Wacker-Chemitronic, 8263 Burghausen, Germany.

<sup>27</sup> H. A. Herrmann and E. Mücke, 2nd DFG Colloquium on Power Devices, Freiburg (1973).

<sup>28</sup> H. A. Herrmann and H. Herzer, *This Journal*, 122, 1568 (1975).

<sup>29</sup> A. Sonntag, 3rd DFG Colloquium on Power Devices, Freiburg (1974).

<sup>30</sup> H. A. Herrmann, H. Herzer, and E. Sirtl, in "Advances in Solid State Physics," Vol. XV, H. J. Queisser, Editor, pp. 279-318, Pergamon, London (1975).

<sup>31</sup> H. Herzer, 4th DFG Colloquium on Power Devices, Freiburg (1975).

<sup>32</sup> H. Sonntag, *ibid.*

<sup>33</sup> M. J. Hill, P. M. Van Iseghem, and W. Zimmermann, Submitted to *IEEE Trans. Electron Devices*.

<sup>34</sup> Literature cited by Dr. Burtscher.

<sup>35</sup> Private communications from a number of customers.

<sup>36</sup> Wacker-Chemitronic sales meeting, Burghausen (1975).

always judges whether a technological progress has been received or not. The cautious question which we put up in the communication regarding whether transmutation doping will play a dominant role can only be answered by both scientific-technical arguments and economic facts. From the point of view of a silicon supplier with a leading position in polysilicon quality and floating-zone technique as well, this question can be answered positively also under economical aspects. Many important power device producers have published exciting, good results. Therefore the list references cited by J. Burtscher has to be completed.

So neutron transmutation-doped silicon, which we call Waso-ND, seems to give us a nice example for the mutual stimulation between nuclear and semiconductor physics, in spite of a delay of several years, we have seen: (i) a nearly closed understanding on a physical process,<sup>37</sup> (ii) material in education books,<sup>38</sup> (iii) rediscovery as a doping-technique, and (iv) rapid turnover of a section of semiconducting applications.

<sup>37</sup> M. Tanenbaum and A. D. Mills, *This Journal*, 108, 171 (1961).

<sup>38</sup> G. Dearnaley and D. C. Northrop, "Semiconductor Counters for Nuclear Radiations," Spon Limited, London (1966).



## The Reduction of Manganese Dioxide in Leclanché-Type Dry Cells as Displayed by Derivative Discharge Functions

C. R. A. Clauss and H. E. L. G. Schweigart

Council for Scientific and Industrial Research, Chemical Engineering Research Group, Pretoria, South Africa

### ABSTRACT

The derivative discharge curves for  $\beta$ - and  $\gamma$ - $MnO_2$  down to  $\sim 0.7V$  open cell voltage were resolved into one characteristic set of four normal distribution functions (peaks). Only peak positions shift to lower voltages for  $\beta$ - compared to  $\gamma$ - $MnO_2$ . When the ratio of electrolyte to  $MnO_2$  is increased, the first peak increases while the other peaks decrease (the second passes through a maximum) and at a mass ratio above 14 only the first peak remains. The first peak represents direct reduction of  $Mn^{4+}$  to soluble  $Mn^{2+}$  which ends at pH 7.5, the second is attributed to the formation of  $Mn(OH)_2$ , and the third to the formation of  $MnOOH$ . Each reaction takes place throughout the depolarizer pellet before the next becomes significant. Electrochemical tests for the evaluation of the dry cell activity of  $MnO_2$  samples should be performed at the same mass ratio of electrolyte to  $MnO_2$  as used in commercial dry cells. Higher ratios lead to an overestimation of samples with low activity.

The complex reaction mechanism in a Leclanché-type dry cell manifests itself in the mode of potential drop during cell discharge. Brenet (1) proposed considering the derivative of the function coulombs produced per gram of  $MnO_2$  vs. cell voltage for characterization and interpretation of the reactions in the manganese dioxide cathode. This paper presents the results obtained by this method from a large number of discharge curves measured as open-circuit potential during short current interruption. Different types of manganese dioxide were tested varying the ratio of electrolyte to manganese dioxide in the depolarizer mixes, the length of the depolarizer pellet formed therefrom, the mass current density, and the superficial current density.

### Experimental

**Manganese dioxide samples.**—Three different types of manganese dioxide were used in the experiments. Their properties are given in Table I. The two ores were of South African origin: the  $\beta$ - $MnO_2$  had an activity which was too low for use in commercial dry cells, whereas the Nsutite ore showed an acceptable activity. X-ray diffraction analysis indicated that the Nsutite ore consisted mainly of Nsutite 1.65, following the classification given by Sorem and Cameron (2), and a small amount of  $\beta$ - $MnO_2$ .

The samples were crushed in a jaw crusher and dry ground in a sintered corundum mortar until the whole material would pass a 100 BSM sieve and 85% of it a 200 BSM sieve on a ROTAP sieve shaker.

**X-ray diffraction analyses.**—A Philips x-ray diffractometer Model PW 1310 with unfiltered Cu radiation was used. The diffracted beam was monochromatized

by a curved carbon crystal (AMR focusing monochromator E 202) and measured with a pulse height discriminator. This device gave very low background values so that lines of low intensity could easily be detected.

**Preparation of black mixes (depolarizers).**—The black mix compositions used in tests with  $\beta$ - $MnO_2$  are given in Table II. Mixes containing the other types of  $MnO_2$  had similar compositions.

The indicated proportions of the dry components were mixed by hand. The required amount of electrolyte solution was sprayed over the dry mixture which was then kneaded by hand to give a homogeneous black mix (3).

**Discharge tests.**—The cell used in all tests with black mixes is shown schematically in Fig. 1. The cylindrical pellets of the black mixes were discharged at constant current. After each 199 msec the current was interrupted for 1 msec and the voltage between the zinc reference electrode and the cathode was measured during the last 200  $\mu$ sec of the interruption period using a

Table I. Properties of the manganese dioxide samples used in the experiments

Type of manganese dioxide	$x$ in $MnO_x$	Content of $MnO_x$ in sample, % of mass	Dry cell activity,* sec
$\beta$ - $MnO_2$ (ore)	1.984	93.2	5,900
$\gamma$ - $MnO_2$ (electrolytic)	1.955	93.5	24,000
Nsutite (ore)	1.964	73.9	7,500

\* Measured with the pulse galvanostatic analyzer under standard conditions, discharged to 1.00V.

Table II. Black mix compositions used in the discharge tests with  $\beta$ -MnO<sub>2</sub>

Mass ratio electrolyte: MnO <sub>2</sub> ††	Composition in % of mass				Electrolyte†
	MnO <sub>2</sub> ore	Carbon black*	Aerosil**	NH <sub>4</sub> Cl	
0.64	58.3	7.3	—	8.7	25.7
2.7	22.4	22.3	—	3.3	52.0
4.7	13.7	27.5	—	2.0	56.8
6.5	10.3	28.5	—	1.5	59.7
12.3	5.9	16.6	9.5	0.9	67.1
12.5	5.5	30.9	—	0.8	62.8
24	3.1	17.4	9.7	0.5	69.3
25	2.8	32.1	—	0.4	64.7

\* Carbon black: Shawinigan.

\*\* Aerosil: Aerosil 380, DEGUSSA.

† Electrolyte composition: 20% mass NH<sub>4</sub>Cl, 10% mass ZnCl<sub>2</sub>, 70% mass H<sub>2</sub>O.

†† Electrolyte including solid NH<sub>4</sub>Cl, MnO<sub>2</sub> as active oxygen.

pulse galvanostatic analyzer (4, 5). These voltages were recorded as a function of time and the discharge curves obtained are virtually identical to those obtained under continuous discharge conditions, excluding ohmic resistances, since the recovery potentials during interruption periods up to 1 msec do not exceed 10 mV (5).

**Conducting-foil tests (1, 6).**—A strip of carbon-filled conducting plastic foil, 10 × 20 mm (Nikolaus Branz, Berlin, Germany) was glued with hexane on to the end of an equally wide but longer strip of gold foil and kept for 30 min at 70°C. After cooling, the composite strip was weighed and a certain amount of manganese dioxide particles (85 BSM > size > 100 BSM) spread evenly over the plastic foil. The particles were hydraulically pressed into the foil which was warmed underneath to 110°C by a preheated support. Any loose particles were washed off with a jet of water. After drying for 30 min at 70°C and cooling the strip was reweighed.

The cathode thus prepared was placed into a beaker containing 50-200 ml of electrolyte solution. At the low discharge current applied (1 mA) polarization of the zinc anode can be neglected and this electrode can be used also as reference electrode. The electrolyte solution was stirred magnetically. For discharging this cell was connected to the pulse galvanostatic analyzer.

**Evaluation of the discharge curves (7).**—The discharge period of time was read off the recorder chart in 0.02V steps of decreasing cell voltage and converted to specific capacity  $Q$  given as coulomb/gram MnO<sub>2</sub> (MnO<sub>2</sub> determined as active oxygen) taking black mix composition and discharge current into account.

The numerical resolution of the discharge curve entailed the finding of a stable derivative of the em-

pirically defined function and the separation of a sum of Gaussian peak functions into components.

For a given set of readings ( $Q_i, V_i$ ) an estimate  $\sigma_i$  of the expected error in  $Q_i$  is made that is proportional to the tangent of the graph at the given point. The graph is now approximated by a spline function which passes through the points ( $\hat{Q}_i, V_i$ ) where  $\hat{Q}_i$  is the smoothed value for  $Q_i$ . The  $\hat{Q}_i$  are determined such that the approximation is the smoothest for which the restriction

$$\sum_{i=1}^{i=n} \left[ \frac{Q_i - \hat{Q}_i}{\sigma_i} \right]^2 \leq n$$

is satisfied.

Since the spline function is mathematically given by a formula of the form

$$Q(V) = Q_i + a_i(V - V_i) + b_i(V - V_i)^2 + C_i(V - V_i)^3$$

for  $V_i \leq V \leq V_{i+1}$  the derivative at  $V_i$  is simply  $a_i$ .

For the separation of the peaks, a nonlinear least squares fit is now used on the obtained values of the derivative at  $V_i$ .

**Calculation of pH in the electrolyte solution.**—For interpretation of the results knowledge of the pH changes in the electrolyte solutions during the initial discharge period was desired.

For these computations the molar concentrations of NH<sub>4</sub>Cl and ZnCl<sub>2</sub> in the electrolyte before the discharge tests were calculated from the black mix compositions taking the amount of solid ammonium chloride, being part of the mixture of the dry components, as dissolved in the electrolyte. The coulomb/gram MnO<sub>2</sub> values were converted to Faraday/liter electrolyte (F/l) based on the known black mix compositions.

Protons are consumed in the reduction of manganese dioxide as well as in the dissolution of the reduction products. For the range of peak A it is assumed that manganese dioxide is reduced to manganous ions which are dissolved in the electrolyte. According to reaction [1] (see below) 2M protons are used per F/l. Until the end of peak A ammonium ions are considered to be the only proton donors. Any quantity of protons consumed produces therefore an equivalent amount of ammonia, most of which will be bound by zinc ions according to Eq. [3] and [4] as long as enough zinc ions are available.

Some of the derivative discharge curves show a small peak, O, at cell voltages higher than peak A. As it is assumed that this peak is related to adsorbed oxygen, only one equivalent of protons is consumed per F/l in this range.

The ammonium ion concentration in the cathode mix decreases due to the discharge reactions and increases by migration and normal diffusion from the free electrolyte adjacent to the black mix pellet. Changes due to this diffusion were neglected in the calculations. The electrolyte in the black mix contains during the initial discharge period, besides water, essentially the following seven species: ZnCl<sub>4</sub><sup>2-</sup>, Cl<sup>-</sup>, NH<sub>4</sub><sup>+</sup>, Zn<sup>2+</sup>, NH<sub>3</sub>, Zn(NH<sub>3</sub>)<sub>2</sub><sup>2+</sup>, and Zn(NH<sub>3</sub>)<sub>4</sub><sup>2+</sup>.

Of these the last three do not exist in the free electrolyte and only the first three species must be considered for ion migration through the free electrolyte-black mix interface. Since the concentration of Zn<sup>2+</sup> ions in the free electrolyte is always low due to formation of the ZnCl<sub>4</sub><sup>2-</sup> complex at high chloride concentrations (8), Zn<sup>2+</sup> ion transport can be neglected. The Zn(NH<sub>3</sub>)<sub>2</sub><sup>2+</sup> and Zn(NH<sub>3</sub>)<sub>4</sub><sup>2+</sup> ions being formed only in the black mix do not migrate toward the zinc anode.

## Results and Discussion

**Mass ratio of electrolyte to manganese dioxide.**—Derivatives of discharge curves for the  $\beta$ -MnO<sub>2</sub> are shown in Fig. 2a-f. Figure 2a represents the curve ob-

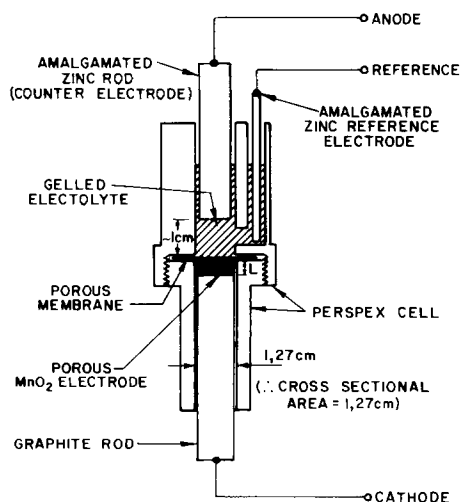


Fig. 1. Cross section of test cell

tained from a black mix composition normally used in commercial Leclanché-type dry cells. The curve can be described essentially as the sum of four normal distribution functions (peaks A, B, C, and D). These peaks appear at different cell voltages and they differ in half-maximum width and surface areas.

Comparison between Fig. 2a and b shows that the areas of peaks A and B increase while that of peak C decreases with increasing mass ratio of electrolyte to manganese dioxide. Furthermore a slight shift in the position of the four peaks can be observed. Peak B shifts, e.g., about 0.04V toward lower and peak C 0.01V toward higher cell voltages when the mass ratio in-

creases from 0.64 to 2.7 (Table III). At the next higher mass ratio examined (Fig. 2c) only three peaks appear. Taking into account the observed shifts one can assume that the middle peak consists of peaks B and C, the upper and lower peaks being A and D, respectively. Figures 2a-f show that with increasing mass ratio of electrolyte to manganese dioxide peak A increases, peak C and D decrease and tend to disappear at a certain mass ratio, whereas peak B increases at first and then also decreases at the higher mass ratios studied. At a mass ratio of about 24 all peaks but A have become insignificant.

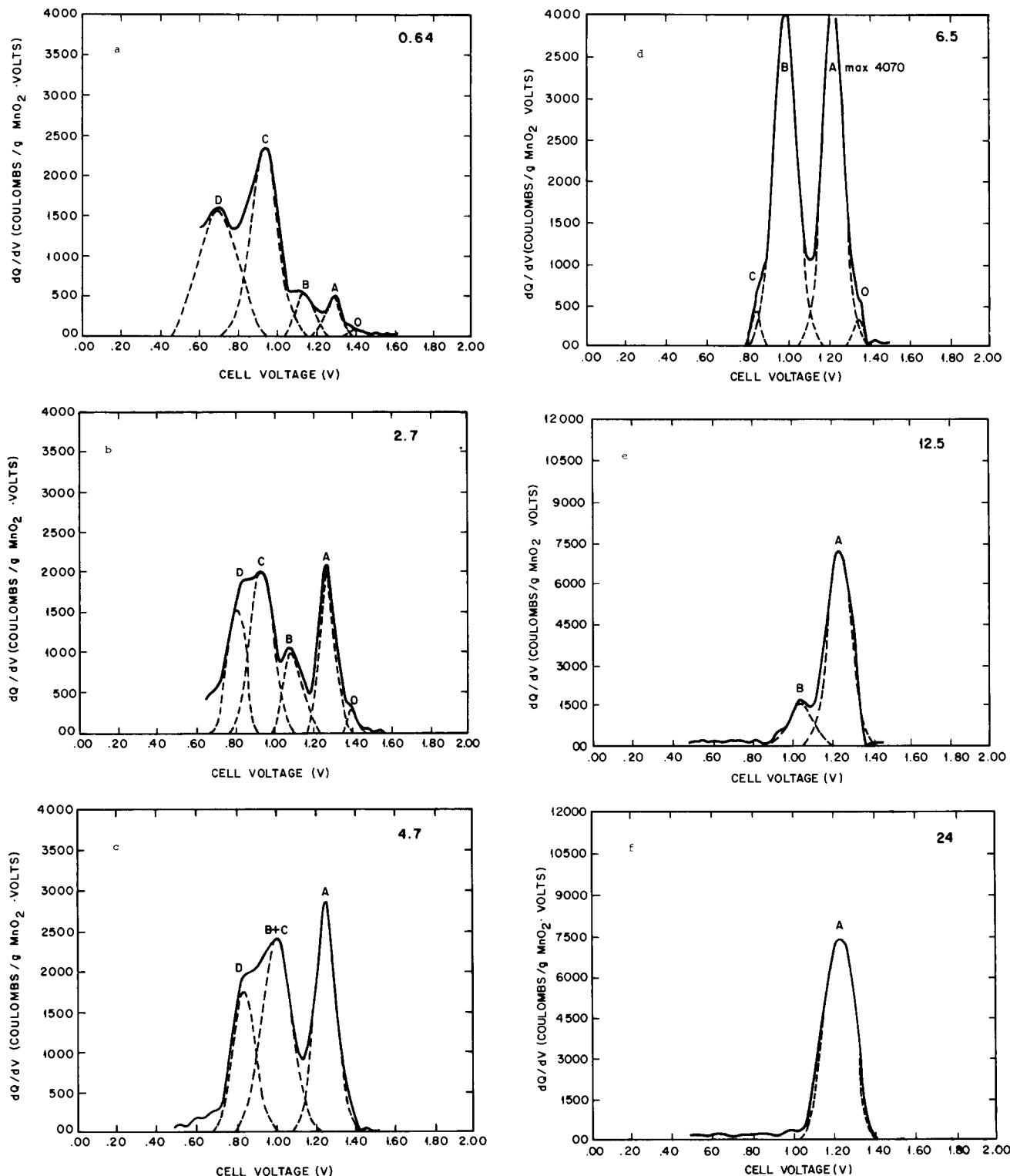


Fig. 2 a-f. Derivative discharge curves obtained with  $\beta$ - $\text{MnO}_2$  in black mixes of increasing mass ratio of electrolyte to manganese dioxide. Values in figures indicate the mass ratios of electrolyte to manganese dioxide in pellets. The corresponding black mix compositions are given in Table II.



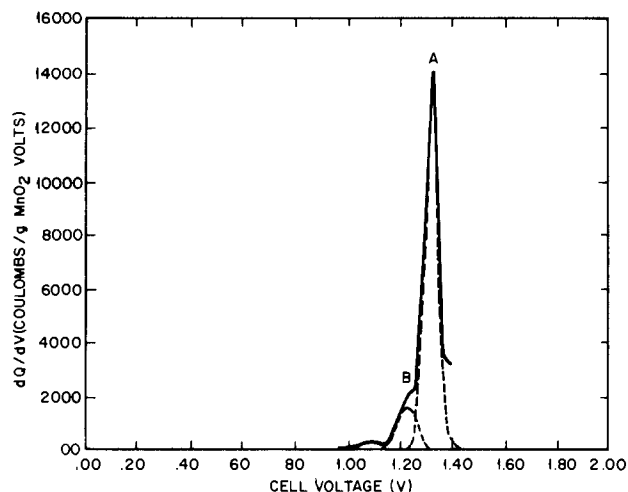


Fig. 2g. Derivative discharge curve of  $\beta$ - $\text{MnO}_2$  obtained by cathodic reduction (1.03 mA) of a thin layer of 25.6 mg manganese dioxide impressed on a conducting plastic foil immersed in well-aerated electrolyte solution.

This finding was confirmed by discharge experiments in which a thin layer of manganese dioxide was cathodically reduced in the presence of a large excess of well-stirred electrolyte solution. Figure 2g shows that under these conditions essentially one sharp peak at 1.30V is obtained. A minor peak at somewhat lower cell voltages may be assigned to peak B and/or C.

The observed increase of peak A with increasing mass ratio of electrolyte to manganese dioxide could also be due to the simultaneous increase in the carbon black to manganese dioxide mass ratio of the mixes used in the discharge tests. The carbon black content had to be increased in the mixes in order to achieve the desired uptake of electrolyte. The conducting-foil tests (6) did not exclude a possible influence of carbon because the  $\text{MnO}_2$  particles were in contact with the carbon filler of the plastic foil. To distinguish between the influence of carbon black and of electrolyte, two mixes were prepared in which about half of the carbon black was replaced by Aerosil 380 as electrolyte carrier. The shapes of the derivative discharge curves obtained in these experiments (Fig. 3a-b) are similar to those of equal mass ratio of electrolyte to manganese dioxide where only carbon black is used as carrier for the available electrolyte (Fig. 2e-f). Curves for equal ratios of carbon black to manganese dioxide but different electrolyte to manganese dioxide mass ratios differ significantly (Fig. 2d and 3a). This indicates that the mass ratio of carbon black to manganese dioxide in

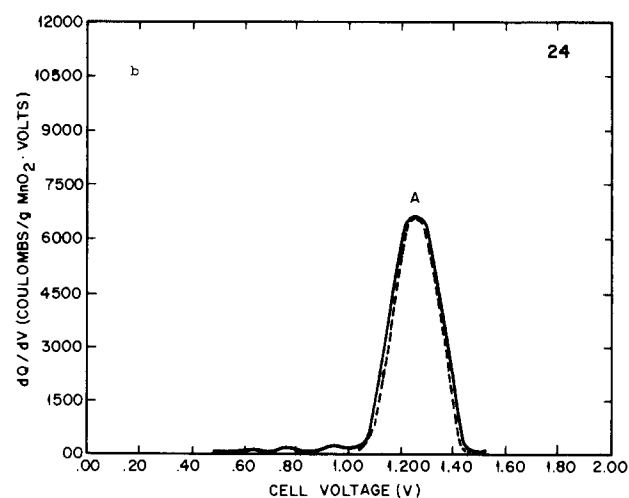
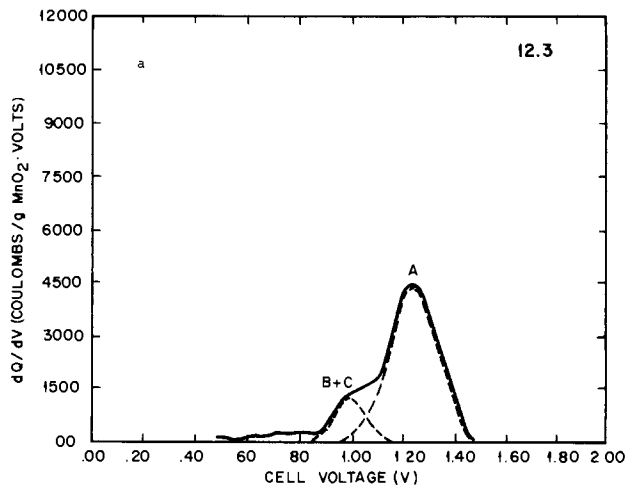


Fig. 3 a-b. Derivative discharge curves of  $\beta$ - $\text{MnO}_2$  in black mixes where part of the carbon black is substituted by Aerosil 380. Values in figures indicate the mass ratios of electrolyte to manganese dioxide in the pellets.

the black mix composition is not the shape-determining factor in the range examined.

The areas under the derivative discharge curves as well as those of the peaks represent the electrical charge in coulomb/gram of manganese dioxide exchanged within the ranges of the cell potentials considered. The size of the peaks obtained under various discharge conditions, presented as coulomb/gram  $\text{MnO}_2$ , and the positions of the peak maxima for the curves

Table III. Positions of maxima [cell voltage (volt)] and surface areas (coulomb/gram  $\text{MnO}_2$ ) of the peaks forming the derivative discharge curves of  $\beta$ - $\text{MnO}_2$  obtained for various mass ratios of electrolyte to manganese dioxide. Discharge current 12 mA; 2.00g black mix.

Fig.	Mass ratio electrolyte: $\text{MnO}_2$	Mass current density, mA/g $\text{MnO}_2$	Peak A V	Peak A coulomb/g $\text{MnO}_2$	Peak B V	Peak B coulomb/g $\text{MnO}_2$	Peak C V	Peak C coulomb/g $\text{MnO}_2$	Peak D V	Peak D coulomb/g $\text{MnO}_2$	Sum of peak areas, coulomb/g $\text{MnO}_2$
2a	0.64	11	1.29	49	1.13	63	0.92	374	0.68	430	916
2b	2.7	29	1.26	208	1.09	137	0.93	313	0.80	188	846
						Peak (B + C)					
					V	coulomb/g $\text{MnO}_2$					
2c	4.7	48	1.25	387	1.00	449	0.81	258	—	—	1094
2d	6.5	63	1.22	542	0.99	586	0.85	26	—	—	1154
3a	12.3*	73	1.24	1078	1.00	210	—	—	—	—	1288
2e	12.5	118	1.24	1117	1.04	249	—	—	—	—	1366
3b	24*	140	1.25	1558	—	—	—	—	—	—	1558
2f	25	152	1.22	1450	—	—	—	—	—	—	1450
2g	$\infty$ **	40	1.31	1074	1.22	120	—	—	—	—	1194

\* The black mix contained Aerosil 380 and carbon black, 3.00g black mix were discharged.  
\*\* Conducting-foil test.

shown in Fig. 2a-g and 3a-b are listed in Table III. The values in Table III clearly show the increasing predominance of peak A as the mass ratio of electrolyte to manganese dioxide increases. The last column shows the over-all increase in discharge capacities, expressed as sum of peak areas, with increasing mass ratio of electrolyte to manganese dioxide. Above a ratio of about 6.5 the discharge capacities are higher than the theoretical value for complete reduction to the trivalent state. The results, therefore, indicate that above a certain mass ratio the reduction proceeds beyond the trivalent state of the manganese ions. Complete reduction to the bivalent state, however, has never been observed in our experiments. The values obtained in conducting foil tests were surprisingly lower than the highest values found in the discharge tests of long pellets. The reason for this discrepancy may be ex-

plained either by insufficient contact between some of the manganese dioxide particles and the electron-conducting plastic foil or by inaccessibility of electrolyte solution to some of the imbedded manganese dioxide particles.

*Electrolytic MnO<sub>2</sub>.*—Figures 4a-e and the values compiled in Table IV show the corresponding results obtained from discharge tests of electrolytic  $\gamma$ -MnO<sub>2</sub>. Again it is possible to interpret the derivative discharge curves essentially as sums of four or less peaks. The peak positioned at the highest cell voltage behind the small peak O increases with increasing mass ratio of electrolyte to manganese dioxide and remains practically the only one at and above a mass ratio of 7. For  $\gamma$ -MnO<sub>2</sub> the peak maxima A, B, and C occur at higher cell voltages than for  $\beta$ -MnO<sub>2</sub>. Peak D cannot be lo-

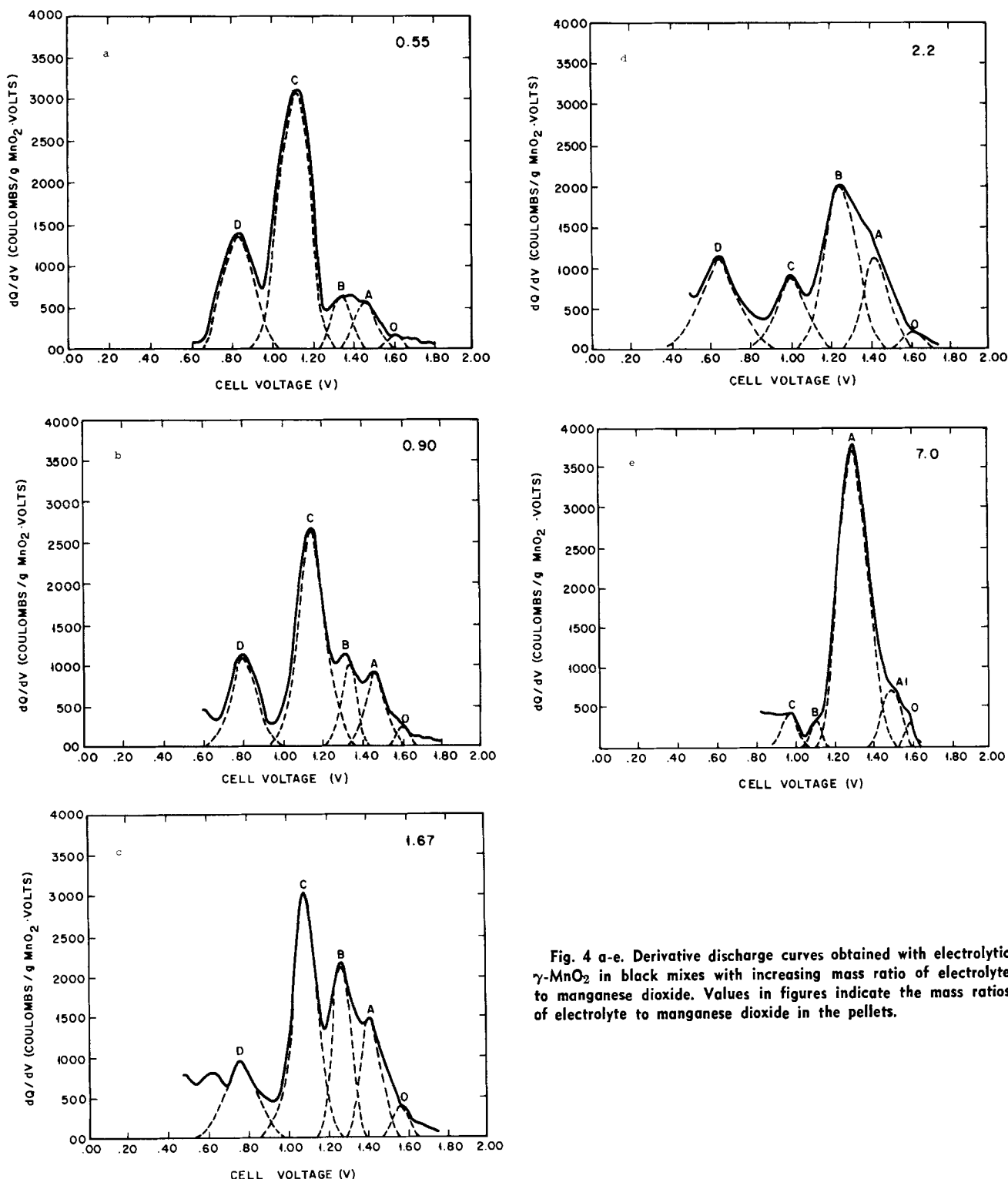


Fig. 4 a-e. Derivative discharge curves obtained with electrolytic  $\gamma$ -MnO<sub>2</sub> in black mixes with increasing mass ratio of electrolyte to manganese dioxide. Values in figures indicate the mass ratios of electrolyte to manganese dioxide in the pellets.

Table IV. Positions of maxima [cell voltage (volt)] and surface areas (coulomb/gram  $MnO_2$ ) of the peaks forming the derivative discharge curves of electrolytic  $\gamma$ - $MnO_2$  obtained for various mass ratios of electrolyte to manganese dioxide. Discharge current 12 mA.

Fig.	Mass ratio electrolyte: $MnO_2$	Mass of black mix, g	Mass current density, mA/g $MnO_2$	Peak A V	Peak A coulomb/ g $MnO_2$	Peak B V	Peak B coulomb/ g $MnO_2$	Peak C V	Peak C coulomb/ g $MnO_2$	Peak D V	Peak D coulomb/ g $MnO_2$	Sum of peak areas, coulomb/ g $MnO_2$
4a	0.55	0.744	29	1.46	68	1.35	77	1.12	631	0.84	280	1056
4b	0.90	0.744	37	1.46	123	1.33	104	1.14	499	0.80	195	921
4c	1.67	2.00	21	1.42	193	1.27	316	1.09	441	0.77	200	1150
4d	2.20	2.00	25	1.42	189	1.24	436	0.99	168	(0.69)	(272)	1065
—	3.4	0.744	96	{ 1.54 1.30 1.51 1.30	{ 54 500 75 737	1.11	83	n.d.	n.d.	—	—	—
4e	7.0	2.27	59	{ 1.51 1.30 1.41	{ 75 737 1211	1.10	27	0.98	43	—	—	882
—	$\infty^*$	—	28	1.41	1211	1.36	288	—	—	—	—	1499

\* Conducting-foil test with 38.2 mg  $MnO_2$ .

Table V. Positions of maxima [cell voltage (volt)] and surface areas (coulomb/gram  $MnO_2$ ) of the peaks forming the derivative discharge curves of Nsutite obtained for various mass ratios of electrolyte to manganese dioxide. Discharge current 12 mA.

Mass ratio electrolyte: $MnO_2$	Mass of black mix, g	Mass current density, mA/g $MnO_2$	Peak A1 V	Peak A1 coulomb/ g $MnO_2$	Peak A V	Peak A coulomb/ g $MnO_2$	Peak B V	Peak B coulomb/ g $MnO_2$	Peak C V	Peak C coulomb/ g $MnO_2$	Peak D V	Peak D coulomb/ g $MnO_2$	Sum of peak areas, coulomb/ g $MnO_2$
0.73	0.744	37	1.40	24	1.31	62	1.20	55	0.97	472	0.76	88	701
2.18	2.00	26	1.40	37	1.27	210	1.13	131	0.95	325	0.84	124	827
Peak (B + C)													
V													
3.50	2.00	38	1.39	43	1.24	258	1.02	190	0.93	36	(0.66)	(38)	822
6.3	2.00	60	1.40	29	1.24	599	1.03	190	—	358	—	—	986
9.0	2.00	86	1.40	57	1.22	639	1.07	190	0.93	36	—	—	922
16.1	2.00	152	1.38	46	1.22	982	1.04	56	—	—	—	—	1084
32	3.00	194	—	—	1.22	1164	0.99	80	—	—	—	—	1244
$\infty^*$	—	32	—	—	{ 1.38 1.32	{ 876 229	1.26	201	—	—	—	—	1306

\* Conducting-foil test. Discharge current: 1.0 mA, 30.9 mg  $MnO_2$ .

cated accurately and it is therefore not possible to decide whether the position of its maximum is related to the type of  $MnO_2$  or to the black mix compositions. The sums of the peak areas are about the same for both types of manganese dioxide.

*Nsutite*.—Table V presents the results of an analogous series of experiments using a Nsutite-type manganese dioxide ore which showed a relatively high activity in dry cell tests. The over-all picture compares fairly well with the results of the other series with the exception of the existence of another peak (designated as A1) which is situated at about the same cell voltages as peak A of the  $\gamma$ - $MnO_2$ . With regard to its position and behavior the following peak A can be compared to the peak A of  $\beta$ - $MnO_2$ . The area of peak A1 is quite independent of the mass ratio of electrolyte to manganese dioxide. These observations can be explained by assuming that the Nsutite-type ore contains a small amount of a more active component.

In performing the conducting foil test with the Nsutite-type ore it was found that virtually all (96%) of the coulombs exchanged were used to produce  $Mn^{2+}$  going into solution.

*Discharge current densities and length of the black mix pellet*.—The influence of the discharge conditions on the shape of the derivative discharge curves was studied for one black mix composition close to those used in Leclanché-type dry cells. Under the prevailing test conditions the following parameters were varied: (i) length (millimeters) of the cylindrical black mix pellet; (ii) superficial current density (milliampere/square centimeter), i.e., the discharge current divided by the basal area of the black mix pellet; and (iii) mass current density (milliampere/gram  $MnO_2$ ) which is the quotient of the discharge current and the mass of manganese dioxide (calculated as active oxygen) in the black mix pellet.

These three parameters are interdependent and in a series of experiments with one black mix composition only one parameter can be kept constant while the others vary.

Derivative discharge curves obtained by discharging pellets of various lengths, containing  $\gamma$ - $MnO_2$  as an example, are shown in Fig. 5. The positions and areas of the peaks forming these curves and those obtained at higher current densities are given in Table VI. From the results of a large number of experiments the following general rules can be deduced: (i) The shorter the black mix pellet and the lower the discharge current the greater is the resemblance of the derivative discharge curves to those obtained from experiments with higher mass ratios of electrolyte to manganese dioxide. The sum of the peak areas increases in the same manner as observed for increasing electrolyte to  $MnO_2$  mass ratios. (ii) The longer the pellet the better are the peaks resolved. (iii) The mass current density has little influence on the shape of the derivative discharge curves within the examined range from 1.8 to about 70 mA/g  $MnO_2$  as long as diffusion does not interfere [rule (i)].

If one expects that each peak is related to a specific reaction in the black mix it can be concluded that the peaks A and B belong to reactions related to the electrolyte composition while peak C and possibly peak D are linked to reactions which become significant only after certain changes of electrolyte composition. The observation that the resolution of the peaks improves with increasing length of the black mix pellet [rule (ii)] leads to the conclusion that each type of reaction proceeds essentially through the whole length of the black mix pellet before the next type of reaction starts. The resolution decreases under conditions where diffusion becomes significant and only then different types of reactions may take place simultaneously at different depths in the black mix pellet.

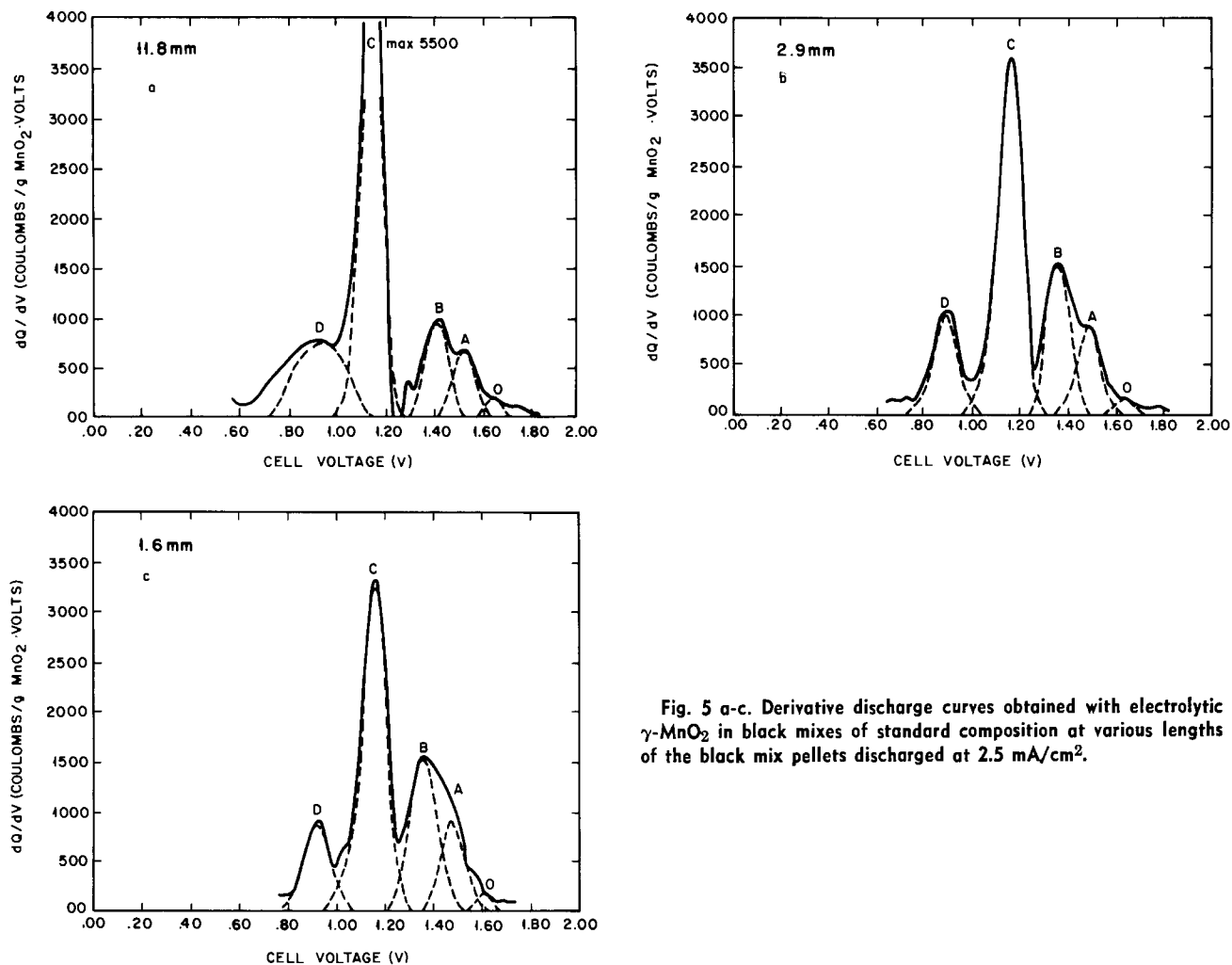


Fig. 5 a-c. Derivative discharge curves obtained with electrolytic  $\gamma$ - $\text{MnO}_2$  in black mixes of standard composition at various lengths of the black mix pellets discharged at  $2.5 \text{ mA/cm}^2$ .

*Consequences with respect to test methods.*—The type of manganese dioxide seems to have little influence on the shape of the derivative discharge curves when black mix compositions, geometry of the black mix pellet, mass, and superficial current densities are comparable. The same peaks appear, however, at different cell voltages. For active types of manganese dioxide the peaks are positioned at somewhat higher cell voltages than for the less active types and for this reason the energy available from a dry cell down to a certain cell voltage is higher if it contains the active material.

It has been stated by several authors that under certain conditions battery-inactive types of manganese dioxide, e.g.,  $\beta$ - $\text{MnO}_2$ , can become as active as the most active types (9, 10). Our work shows that this happened at high electrolyte to manganese dioxide mass ratios when only the electrolyte-dependent reaction (peak A) exists. Tests where high mass ratios of elec-

trolyte to manganese dioxide are used such as conducting-foil tests (1, 6) or the Kornfeil test (11) cannot give reliable values because in these tests the reaction of type A is overemphasized and a material of low dry cell activity would be judged too favorably. The same argument is valid for conditions where diffusion of reaction products from the black mix into adjacent electrolyte and of  $\text{NH}_4^+$  ions in the opposite direction is significant. It follows that in activity tests the electrolyte volume between the black mix and the zinc counterelectrode should be kept as small as in commercial dry cells and the black mix composition should be the same as used in batteries in order to get the best relation between the fast laboratory tests and the behavior of  $\text{MnO}_2$  in batteries.

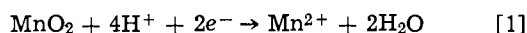
*Assignment of peaks.*—As it is likely that each of the observed peaks belongs to a specific reaction taking place in the black mix during the cathodic reduction

Table VI. Positions of maxima [cell voltage (volt)] and surface areas (coulomb/gram  $\text{MnO}_2$ ) of the peaks forming the derivative discharge curves of electrolytic  $\gamma$ - $\text{MnO}_2$  obtained from black mix pellets of different lengths for discharge currents of 3 and 12 mA. (Standard black mix composition: 62.3%  $\text{MnO}_2$  sample, 7.7% carbon black, 13.4%  $\text{NH}_4\text{Cl}$ , 2.1%  $\text{ZnCl}_2$ , 14.5%  $\text{H}_2\text{O}$ ; mass ratio of electrolyte to manganese dioxide: 0.53.)

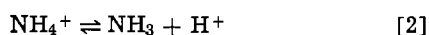
Length of pellet (calculated), mm	Superficial discharge current density, $\text{mA/cm}^2$	Mass current density, $\text{mA/g MnO}_2$	Peak A		Peak B		Peak C		Peak D		Sum of peak areas, coulomb/g $\text{MnO}_2$
			V	coulomb/g $\text{MnO}_2$	V	coulomb/g $\text{MnO}_2$	V	coulomb/g $\text{MnO}_2$	V	coulomb/g $\text{MnO}_2$	
11.8	2.5	1.8	1.52	78	1.40	111	1.15	557	0.90	213	957
2.9	2.5	7.2	1.49	112	1.36	193	1.15	484	0.89	158	947
2.6	2.5	8.3	1.47	139	1.34	185	1.16	499	0.91	104	927
1.6	2.5	13.4	1.47	118	1.35	229	1.15	443	0.92	123	911
11.8	10	7.2	1.48	55	1.35	105	1.14	614	0.80	175	949
10.4	10	8.3	1.50	48	1.37	99	1.15	550	0.80	192	889
2.9	10	29	1.46	82	1.35	56	1.11	645	0.83	273	1056
1.6	10	54	1.46	91	1.36	59	1.16	574	0.80	114	838

of the manganese dioxide the following assignments are proposed.

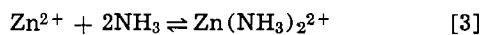
The relative predominance of peak A depends mainly on the quantity of electrolyte available per mass unit of manganese dioxide. Conducting-foil tests at low discharge current densities give essentially only one peak (1) situated at about the same cell voltage at which peak A appears in the pulse galvanostatic analyzer tests. Under conditions of the conducting-foil tests a stoichiometric cathodic dissolution of the manganese dioxide has been found by us in agreement with the results obtained by Chreitzberg, Allenson, and Vosburgh (12) under comparable conditions at somewhat higher superficial current densities. The conditions in Cahoon's "utilization test" (13) agree with those in our tests at highest mass ratios of electrolyte to manganese dioxide, i.e., with excess electrolyte. In the example quoted in this paper the stoichiometrical amount of  $Mn^{2+}$ , as expected from Eq. [1], has been found in solution when discharging manganese dioxide to  $MnO_{1.6}$  in an electrolyte of 33%  $ZnCl_2$ , 20%  $NH_4Cl$ , and 47% water. Therefore peak A can be related to the cathodic dissolution of manganese dioxide following the over-all equation



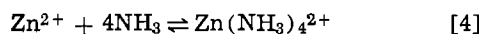
This reaction predominates in acid electrolyte (14-17) but is also observed in neutral electrolytes up to about pH 8, (12, 18-20). It was assumed that in neutral electrolyte (pH 6-8) the dissolution reaction and solid-state diffusion occur simultaneously (17), while in alkaline electrolyte only a solid-state diffusion mechanism is envisaged (9, 17, 21-24). Under conditions where peak A prevails the ammonium ion should, directly or indirectly, be the proton donor (17) for reaction [1]



The ammonia formed in this way is bound to the zinc ions to form di- and tetrammine complexes (25) following the equations



and



In this way, the system acts as a buffer solution and the pH only starts to increase rapidly after practically all the available  $Zn^{2+}$  ions are used up by reactions [3] and [4].

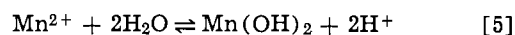
As reaction [1] is dependent on the pH of the electrolyte in the black mix it is to be expected that the reaction is practically terminated when the pH has reached a specific value. The pH values of the electrolytes were therefore calculated using Eq. [1], the equilibrium constants (26, 27) corresponding to Eq. [3] and [4], and also considering the electric transport of  $NH_4^+$  ions into and  $ZnCl_4^{2-}$  ions out of the electrolyte of the black mix. For nearly all discharge experiments for which a diffusional exchange with the electrolyte paste adjacent to the black mix was negligibly small, a pH value of about 7.5 was computed for the intersection points of the outlines of peaks A and B. For electrolytic  $\gamma$ - $MnO_2$  and Nsutite at relatively low mass ratios of electrolyte to manganese dioxide, pH values between 8 and 9 were computed. Under all conditions in which the derivative discharge curve contains only peak A the calculated pH does not reach 7.5 during the entire discharge test.

Curves obtained in correlating pH and cell voltage (28) show a sharp kink at this particular pH. This is the point where 0.12 V/pH intersects with 0.06 V/pH indicating that the two-electron four-proton process changes into the one-electron one-proton process.

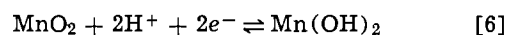
Cahoon *et al.* (18) pointed out that the primary (electrochemical) reaction consumes protons (Eq. [1]), consequently increasing the pH, and the secondary

(chemical) reaction ( $MnO_2 + Mn^{2+} + 2OH^- \rightarrow 2MnOOH$ ) consumes  $OH^-$ , thus increasing acidity in the electrolyte at the surface of the depolarizer and that this increase will be faster for the more active types of  $MnO_2$ . This could explain why for the end of peak A of electrolytic  $MnO_2$  and Nsutite the calculated pH is higher than would be expected and that the actual surface pH of the active  $MnO_2$  particles is, in fact, similar to that found in tests with less active material or with excess electrolyte.

Peak B increases at first with increasing mass ratio of electrolyte to manganese dioxide and decreases again at the higher mass ratios examined. This points to this peak being related also to the composition of the electrolyte. Since peak B starts at a pH where peak A ends, the chemical reaction corresponding to peak B should become predominant at and above pH 7.5. The precipitation of manganous hydroxide could be a possible reaction



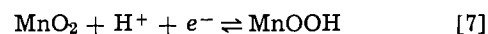
and can act as a proton-donating buffered system for a possible electrochemical reaction



which may be related to peak B. Under these conditions the area of peak B should approximate that of peak A since all manganous ions produced in the chemical reaction related to peak A would be consumed by the reaction related to peak B. Diffusion of  $NH_3$  into, and electrical transport of  $NH_4^+$  ions from, the adjacent paste electrolyte into the depleted black mix can explain the relatively larger surface areas of peak B observed in some cases. Furthermore, it is not necessary to assume that reaction [6] is terminated when most of the manganous ions are consumed.

If the manganous hydroxide formed by reaction [6] would be attached to the surface of the manganese dioxide particles as a dense monolayer of manganous hydroxide so that reaction [6] could not proceed further, much lower areas of peak B are to be expected. In order to explain the observed larger capacities one has to accept that the manganous hydroxide precipitation forms a separate detached phase in such a way that the manganese dioxide surface remains accessible to further reaction.

Peak C may be attributed to the well-known solid-state reduction of manganese dioxide (9, 17, 21-24) represented by the equation



This reaction starts only once the electrolyte composition prevents continuation of the reactions ascribed to peaks A and B, i.e., at higher pH values than normally described in literature.

Peak D is often difficult to separate from peak C and its surface areas cannot be clearly defined so that its dependence on the experimental conditions is uncertain. Attempts to relate the occurrence of peak D to the formation of hetaerolite, which has been described as the most significant reaction product in battery discharge (28-30), failed. Practically no hetaerolite could be detected by x-ray diffraction in black mixes which had been discharged slightly below the cell voltage which indicates the end of peak D. Hetaerolite could be identified only in black mixes after discharging to 0.0V cell voltage. The formation of hetaerolite appears to be a secondary (chemical) reaction (25, 31) and is found mainly in black mixes exposed to low current, long term discharge conditions (32).

The sequence of peaks into which the area under the derivative discharge curve can be resolved follows the scheme laid out for the depolarization of manganese dioxide implied from magnetic susceptibility measure-

ments by Ghosh and Brenet (33, 34). These authors found that during the first stage of discharge no  $Mn^{3+}$  was formed but that the  $Mn^{4+}$  lattice remained while reduction proceeded to  $Mn^{2+}$  (peaks A and B). On further reduction  $MnOOH$  (peak C) and finally  $Mn_3O_4$  (peak D) could be identified.

### Conclusion

Consideration of the derivative discharge curves shows that the discharge mechanism of the cathode of Leclanché-type dry cells is more complicated than implied by the models previously proposed. From the experimental results presented in this work it follows conclusively that composition and quantity of electrolyte and changes in the electrolyte during discharge have a pronounced influence on the form of the discharge curves. The discharge curve obtained under the conditions of commercial Leclanché-type dry cells represents a variety of different reactions and it is not possible to consider only one type of reaction, as for instance the solid-state diffusion model.

The dissolution reaction and manganous hydroxide formation occur first before the solid-state diffusion reaction becomes predominant. Resolution of the peaks of the derivative contour line increases as diffusional exchange of reaction products and salts between the electrolyte in the black mix and the electrolyte in the compartment diminishes. This indicates that each type of reaction proceeds throughout the length of the black mix pellet before the next reaction becomes significant.

For these reasons electrochemical tests for the evaluation of dry cell activity of manganese dioxide should be carried out at the same mass ratios of total electrolyte quantity to manganese dioxide as used in commercial dry cells. In particular the activities of manganese dioxide ores with low depolarization capacity are overestimated if the values obtained from tests with excess electrolyte, terminated at a predetermined cell voltage, are taken as criteria for the activity, because the values of the areas of peaks A and B which occur at higher cell voltages are higher in the presence of more electrolyte.

### Acknowledgment

The authors wish to express their appreciation to Mr. D. P. Laurie and Dr. R. Rösel of the National Research Institute for Mathematical Sciences-CSIR for establishing computer programs for the evaluation of the discharge curves and the pH calculations.

Manuscript submitted Aug. 4, 1975; revised manuscript received ca. Feb. 2, 1976.

Any discussion of this paper will appear in a Discussion Section to be published in the June 1977 Journal.

All discussions for the June 1977 Discussion Section should be submitted by Feb. 1, 1977.

Publication costs of this article were partially assisted by the Council for Scientific and Industrial Research.

### REFERENCES

1. L. Balewski and J. P. Brenet, *Electrochem. Technol.*, **5**, 527 (1967).
2. R. K. Sorem and E. N. Cameron, *Econ. Geol.*, **55**, 278 (1960).
3. H. Schweigart, CSIR Special Report CHEM 74 (1969).
4. H. Schweigart and I. Olivier, *Coal, Gold, Base Minerals of S.A.*, **19**, 43 (1971).
5. I. Olivier, CSIR Special Report CENG 12 (1973).
6. R. Huber and J. Kändler, *Electrochim. Acta*, **8**, 265 (1963).
7. D. P. Laurie, CSIR Special Report WISK 148 (1974).
8. T. Takahashi and K. Sasaki, *J. Electrochem. Soc. Japan*, **24**, 221 (1956).
9. A. Kozawa and R. A. Powers, *Electrochem. Technol.*, **5**, 535 (1967).
10. C. Drotschmann, *Batterien*, **18**, 651 (1964).
11. F. Kornfeil, *This Journal*, **106**, 1062 (1959).
12. A. M. Chreitzberg, D. R. Allenson, and W. C. Vosburgh, *ibid.*, **102**, 557 (1955).
13. N. C. Cahoon, *ibid.*, **99**, 343 (1952).
14. B. M. Thompson, *J. Ind. Eng. Chem.*, **20**, 476 (1928).
15. A. Keller, *Z. Elektrochem.*, **37**, 342 (1931).
16. S. Yoshizawa and W. C. Vosburgh, *This Journal*, **104**, 399 (1957).
17. A. Era, Z. Takehara, and S. Yoshizawa, *Electrochim. Acta*, **12**, 1199 (1967).
18. N. C. Cahoon, R. S. Johnson, and M. P. Korver, *This Journal*, **105**, 296 (1958).
19. K. Neumann and W. Fink, *Z. Elektrochem.*, **62**, 114 (1958).
20. W. C. Vosburgh, M. J. Pribble, A. Kozawa, and A. Sam, *This Journal*, **105**, 1 (1958).
21. J. J. Coleman, *Trans. Electrochem. Soc.*, **90**, 545 (1946).
22. A. B. Scott, *This Journal*, **107**, 941 (1960).
23. F. Kornfeil, *ibid.*, **109**, 349 (1962).
24. A. Kozawa and R. A. Powers, *ibid.*, **113**, 870 (1966).
25. N. C. Cahoon and G. W. Heise, *ibid.*, **94**, 214 (1948).
26. J. Bjerrum, "Metal Ammine Formation in Aqueous Solution," Thesis (1941), p. 163, reprinted by P. Haase & Son, Copenhagen (1957).
27. Y. Wormser, *Bull. Soc. Chim. France*, 387 (1954).
28. H. F. McMurdie, D. N. Craig, and G. W. Vinal, *Trans. Electrochem. Soc.*, **90**, 509 (1946).
29. L. C. Copeland and F. S. Griffith, *ibid.*, **89**, 495 (1946).
30. J. F. Laurent and B. Morignat, "Batteries," D. H. Collins, Editor, p. 309, Pergamon Press (1963).
31. F. Griffith, *Trans. Electrochem. Soc.*, **92**, 172 (1947).
32. F. L. Tye, Private communication.
33. S. Ghosh and J. P. Brenet, *Electrochim. Acta*, **7**, 449 (1962).
34. S. Ghosh and J. P. Brenet, *Ber. Bunsenges. Physik. Chem.*, **67**, 723 (1963).

# The Chemistry of $\text{TiS}_3$ and $\text{NbSe}_3$ Cathodes

Donald W. Murphy\* and Forrest A. Trumbore\*

Bell Laboratories, Murray Hill, New Jersey 07974

## ABSTRACT

The cell discharge reactions of  $\text{NbSe}_3$  and  $\text{TiS}_3$  cathodes in nonaqueous lithium cells have been shown to involve three lithiums per  $\text{MX}_3$ . Using reaction with  $n\text{-BuLi}$  as a model for cell discharge we show that cell discharge involves topochemical reactions in which the basic structure of the  $\text{MX}_3$  is maintained. Both  $\text{NbSe}_3$  and  $\text{TiS}_3$  are chain structures containing X-X bonds. The  $(\text{X}_2)^{2-}$  groups are reducible as well as the  $\text{M}^{4+}$  ion, accounting for the stoichiometry. The cell reaction is reversible for  $\text{NbSe}_3$ , but only partially reversible for  $\text{TiS}_3$ . Irreversibility in  $\text{TiS}_3$  is suggested to be due to a change in coordination geometry of  $\text{Ti}^{4+}$  from trigonal prismatic to octahedral.

Recent reports have described the use of  $\text{MX}_3$  ( $\text{M} = \text{Ti, Nb, Ta}$ ;  $\text{X} = \text{S, Se}$ ) compounds as cathodes in secondary nonaqueous lithium batteries (1-5). The reversibility of these cathodes, especially  $\text{NbSe}_3$ , led us to embark on a study of the chemistry of cell discharge in the hope that an understanding of the chemistry would lead to improved performance and suggest other potential secondary cathode materials.

The trichalcogenides of the groups IVB and VB transition metals have similar structures. The group IVB compounds are typified by  $\text{ZrSe}_3$  (6) with which  $\text{TiS}_3$  is isostructural (Fig. 1). The structure is monoclinic and may be thought of as consisting of chains of trigonal prismatic  $[\text{TiS}_6]$  units sharing opposite faces. The sulfur atoms are not equidistant from each other, but two of the three are closer to each other and form a disulfide linkage. A more informative formula than is  $\text{TiS}(\text{S}_2)$ , a compound of  $\text{Ti}^{4+}$ . The sulfide sulfur of one chain is also loosely coordinated to titanium ions of two adjacent chains to give a bicapped trigonal

prismatic coordination about titanium and making the compound pseudo two-dimensional rather than one-dimensional. The group IVB compounds have a  $d^0$  configuration and are semiconductors (7).

The group VB compounds  $\text{NbSe}_3$  (8) (Fig. 2) and  $\text{TaSe}_3$  (9) have structures similar to the group IVB compounds, but slightly different. The planes of connected chains are somewhat puckered, apparently due to some Se-Se bonding between chains as well as intrachain diselenide formation. The puckering is slightly different in the two compounds. The compounds are formally  $d^1$  and are metallic (10). All of the  $\text{MX}_3$  compounds grow in a fibrous morphology elongated in the  $b$  direction (the direction of the metal chains). It is very difficult indeed to obtain crystals of  $\text{NbSe}_3$  more than a few microns in the  $a$  and  $c$  directions while over a centimeter in the  $b$  direction.

## Experimental

The starting  $\text{TiS}_3$  and  $\text{NbSe}_3$  were prepared by reaction of the elements in sealed quartz tubes. Excess sulfur ( $\text{S}:\text{Ti} = 3.5:1$ ) was used with titanium powder (325 mesh, 3N pure) at  $500^\circ\text{C}$ , and stoichiometric amounts of niobium powder ( $30\mu$ , 3N5 pure) and selenium shot (5N pure) were reacted at  $680^\circ\text{C}$  (8). Crystals of  $\text{TiS}_3$  were grown by  $\text{I}_2$  vapor transport at  $500^\circ\text{--}550^\circ\text{C}$ .

The thin needlelike crystals of  $\text{TiS}_3$  tend to aggregate at one point much like a fan, while  $\text{NbSe}_3$  forms long hairlike fibers which intertwine to form physically connected (electrically conductive) mats much like miniature steel wool pads, as illustrated in Fig. 3.

Simple cells were constructed with lithium foil anodes ( $15 \text{ mil} \times 0.5 \text{ cm} \times 1.5 \text{ cm}$ ), a  $1.0\text{M}$   $\text{LiClO}_4$  in propylene carbonate (PC) electrolyte ( $\sim 3 \text{ mil}$ ), and

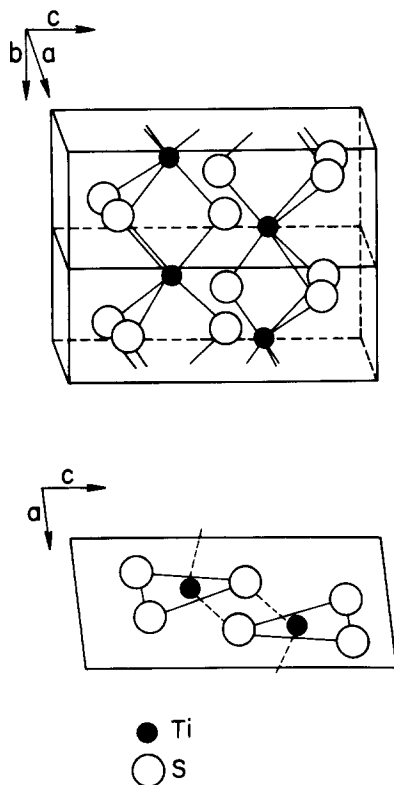


Fig. 1. The monoclinic structure of  $\text{TiS}_3$  (6)

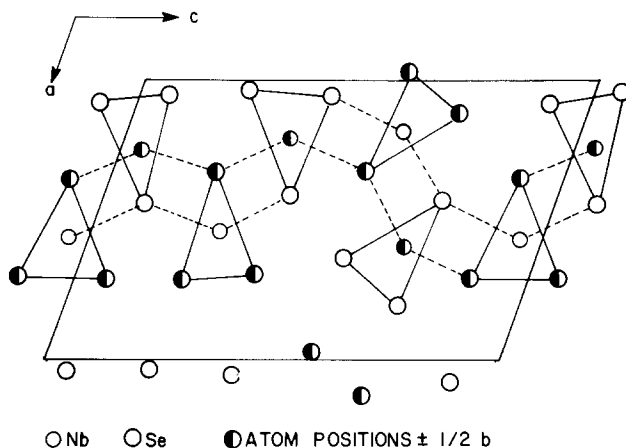


Fig. 2. The monoclinic structure of  $\text{NbSe}_3$  (8)

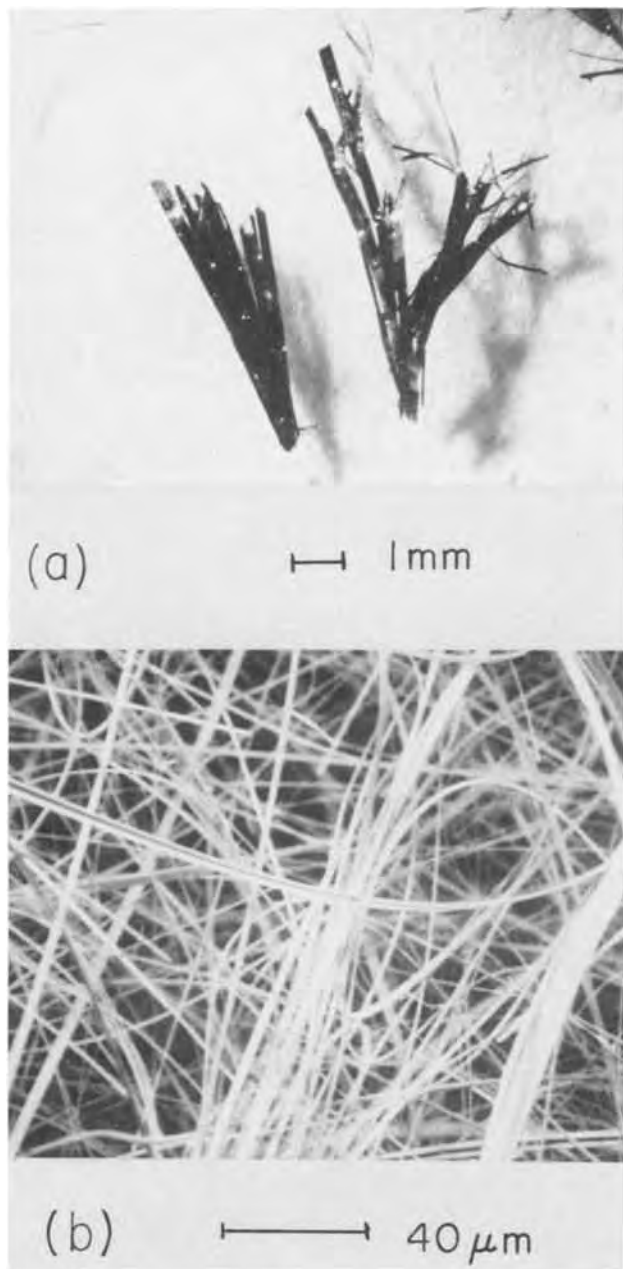


Fig. 3. (a) Fanlike aggregates of  $TiS_3$  crystals formed by iodine transport. (b) Typical fibrous nature of  $NbSe_3$ .

cathodes prepared by crimping gold wire onto either a fan of  $TiS_3$  crystals or a mat of  $NbSe_3$ . Cathode sizes varied from 0.05 to 10.0 mg for  $TiS_3$  and 0.1 to 200 mg for  $NbSe_3$ . The anodes and cathodes were suspended via gold wires into the electrolyte so that they were approximately 0.5 cm apart. The cells were discharged under a constant load and the area under the voltage vs. time curve allowed determination of the number of coulombs. Then, knowing the weight of pure cathode material, the number of lithium atoms involved per  $MX_3$  unit could be calculated. Representative initial discharge curves are shown in Fig. 4 ( $TiS_3$ ) and Fig. 5 ( $NbSe_3$ ). Some cells were set up with a reference and a working lithium electrode to determine the part played by anodic processes on the discharge behavior. In each case the potentials of the working and reference electrodes were the same.

Cells were recharged by applying a 3V battery across the cell. The total charge was found by measuring the voltage across a known resistor in the circuit and integrating the voltage-time curve.

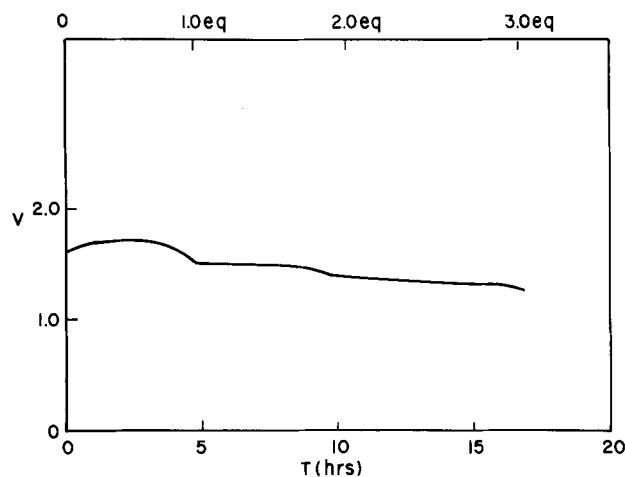


Fig. 4. Initial discharge curve for an aggregate of pure  $TiS_3$  (0.63 mg) crystals in PC with 1M  $LiClO_4$  and a load of 68 kohms ( $i = 0.02$  mA at 1.5V).

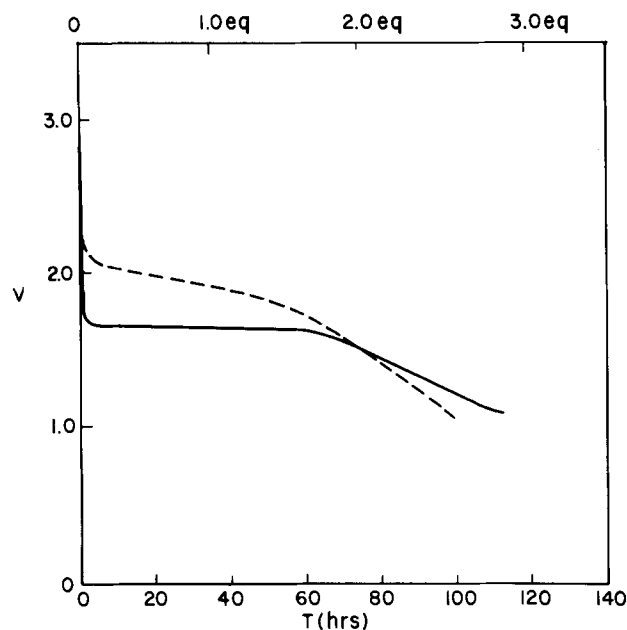


Fig. 5. Initial discharge curve for a fibrous mat of pure  $NbSe_3$  (10.4 mg) in PC with 1M  $LiClO_4$  and a load of 68 kohms, ——— ( $i = 0.02$  mA at 1.5V). Second discharge, - - - -.

Reactions of  $TiS_3$  and  $NbSe_3$  were also run with sodium and lithium in liquid ammonia and with *n*-butyl lithium (*n*-BuLi) as a model for the cell reaction. All such reactions were run under anhydrous conditions in argon. Completion of reactions with stoichiometric amounts of *n*-BuLi was verified by observation of no color change when a drop of the solution was added to 1,10-phenanthroline. Excess *n*-BuLi could be determined by titration of the *n*-BuLi (after filtration) with butyl alcohol in xylene using 1,10-phenanthroline as indicator (11). All transfers of discharged products were carried out in an inert atmosphere box.

Powder x-ray photographs were taken on a Debye-Scherrer camera with  $CuK\alpha$  radiation. Debye-Scherrer capillaries were loaded inside the dry box, sealed with wax, then with a flame outside the box.

### Results and Discussion

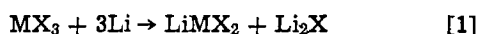
Cells discharged with known amounts of pure  $TiS_3$  (Fig. 4) and  $NbSe_3$  (Fig. 5) indicate that approximately three lithiums per formula unit are used on discharge to approximately 1V. The discharge curve



for NbSe<sub>3</sub> shows a definite break at two equivalents while TiS<sub>3</sub> shows breaks at one and two equivalents.

Cells discharged with pure NbSe<sub>3</sub> cathodes maintained fibrous morphology and could be recharged to over 90% of capacity for several cycles [four is the maximum we have tried with pure NbSe<sub>3</sub> in this study, while thin film cathodes have been cycled several hundred times (12)]. Cells using pure TiS<sub>3</sub>, however, readily exfoliate (splinter), and only about a third of the charge is regained on regeneration.

Several chemical schemes are possible to account for the observed reaction with three lithiums. First, a decomposition to the MX<sub>2</sub> compound followed by intercalation of lithium into the MX<sub>2</sub> compound as in Eq. [1]



Decomposition to the MX<sub>2</sub> was originally proposed as the cell reaction (1).

Second, ternary compounds similar to the known BaTaS<sub>3</sub> (13) (Fig. 6) could be formed. These compounds have the same kind of chain structures as the MX<sub>3</sub> compounds except that the Ta is octahedrally coordinated and the chains are isolated from adjacent chains by Ba ions. The Ta ions are formally 4+ in BaTaS<sub>3</sub>. Lithium ions could occupy sites between chains as do the barium ions, and the third lithium could be thought of as reducing the metal ions to the 3+ state with the same structure. The switch from trigonal prismatic to octahedral coordination could be accomplished by a simple twist without any gross atomic rearrangement. Whittingham (14, 15) has suggested that such topochemical reactions with retention of the main structural features leads to reversibility in a number of systems including the MX<sub>3</sub>'s.

A third possibility suggested by the two-dimensional nature of the compounds is a simple two-dimensional insertion similar to that of graphite and the layered MX<sub>2</sub> compounds (16). Three lithiums could be accommodated by reduction of the dichalcogenide linkage (2Li) and reduction of the 4+ ion to the 3+ ion (1Li). The dichalcogenide linkages form the surface of the van der Waals gap between layers. Intercalation has been suggested by Holleck *et al.* (5) as the possible cell reaction.

The first of these possibilities, decomposition to MX<sub>2</sub> and intercalation of lithium, seems untenable in view of the maintenance of the fibrous morphology of the cathode on discharge. In addition, the formation of MX<sub>2</sub> would require severe atomic reorganization, and it is difficult to imagine such a process being reversible at room temperature.

We had hoped that examination of x-ray powder patterns of the discharged cathodes would distinguish between the various possible discharge products. How-

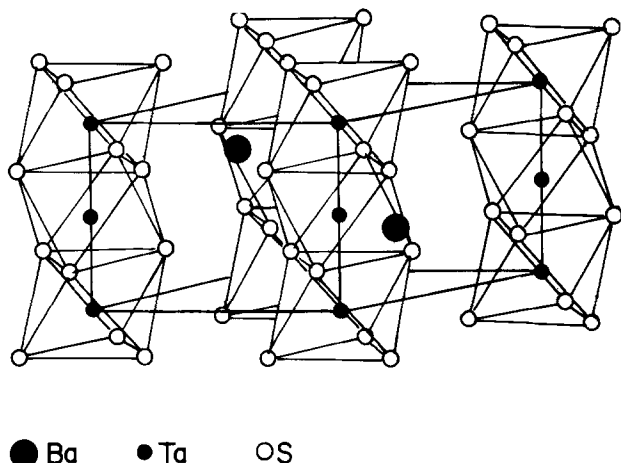


Fig. 6. Crystal structure of BaTaS<sub>3</sub> (13)

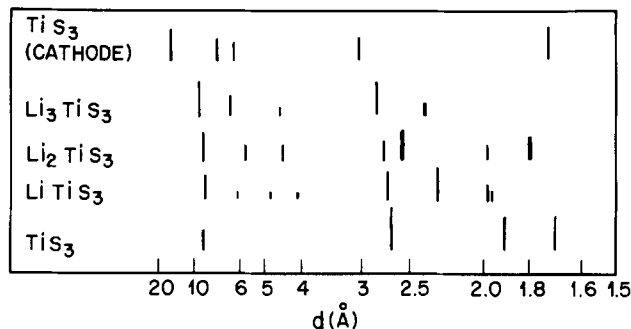


Fig. 7. Diagram of x-ray powder pattern of TiS<sub>3</sub> cathode discharged in PC (top), and products of TiS<sub>3</sub> treated with n-butyl lithium.

ever, the discharged TiS<sub>3</sub> gave a powder pattern with very large d spacings (top of Fig. 7) unlike any of the expected products, and the discharged NbSe<sub>3</sub> gave only a very weak pattern containing only a few broad lines. Poor quality x-ray powder patterns are often found in solids formed near ambient temperature even if the compound is crystalline. The large d spacings for the discharged TiS<sub>3</sub> suggested the possibility of solvent incorporation on discharge and, indeed, combustion analysis of the discharged TiS<sub>3</sub> and NbSe<sub>3</sub>, after washing with PC and ether then vacuum drying, showed 17 and 12% C, respectively. This solvent incorporation does not appear to be detrimental to cycle behavior, but may change the cell voltage slightly, and could cause swelling problems in a real battery.

To avoid complications from solvent incorporation we investigated model reactions for cell discharge. The simplest model reaction is the treatment of the cathode compound with a solution of the alkali metal in liquid ammonia. Analysis of x-ray powder patterns (Fig. 8) of TiS<sub>3</sub> treated with sodium in liquid ammonia are consistent with a two-dimensional topochemical addition of sodium (and ammonia) into the TiS<sub>3</sub> structure. Addition of one sodium (two ammonia molecules are also incorporated as determined by weight gain) increases the c axis by ~ 4.3Å. The b axis remains unchanged [(020) at 1.70Å] and the strong (012) peak shifts appropriately from 2.68 to 2.74Å. No lines associated with the a axis were observed. Addition of a second sodium causes only a slight increase in c while the (020) peak becomes weak and broad. The third sodium gave a product with no powder pattern.

Treatment of NbSe<sub>3</sub> with sodium in liquid ammonia gave Na<sub>2</sub>Se as the only product giving an x-ray powder pattern. With lithium in liquid ammonia Li<sub>2</sub>Se was the only product observable in the x-ray powder pattern. When this NbSe<sub>3</sub> treated with lithium in liquid ammonia, which was hoped would correspond to the discharged NbSe<sub>3</sub>, was placed in a cell it recharged only slightly (about 0.1 of expected); thus it is unlikely that these products correspond to those of cell discharge.

We suspected that the ammonia might be responsible for the decomposition of NbSe<sub>3</sub> with lithium. This could occur by catalytic formation of LiNH<sub>2</sub> which might displace Se in the compound as in Eq. [2] below,

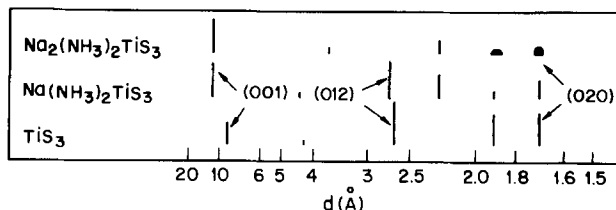
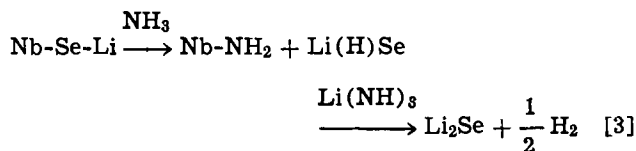
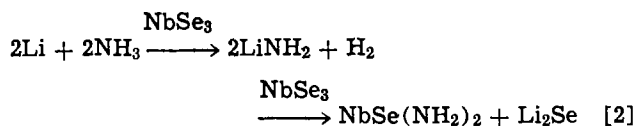


Fig. 8. Diagram of x-ray powder patterns of TiS<sub>3</sub> cathode discharged with sodium in liquid ammonia.

or by aminolyses of Nb-Se-Li linkages to form  $\text{Li(H)Se}$  which could then react with another lithium in solution to give  $\text{Li}_2\text{Se}$  as shown in Eq. [3]



In order to eliminate complications from ammonia we used reaction with *n*-butyl lithium in hexane as a model reaction for cell discharge. This reaction has been described in detail elsewhere (17, 18) and has been suggested as a model for cell discharge (19-21). Reaction of  $3n\text{-BuLi}$  with  $\text{NbSe}_3$  gave a product ( $\text{Li}_3\text{NbSe}_3$ ) whose x-ray powder pattern (Debye-Scherrer photographs) showed no  $\text{Li}_2\text{Se}$ , but also showed very little else (Fig. 9). When this  $\text{Li}_3\text{NbSe}_3$  (the product maintained fibrous morphology) was placed in a cell the potential was  $\sim 1\text{V}$  vs. lithium, the same as the discharged  $\text{NbSe}_3$ . Furthermore, recharging to 3V required the charge expected for three lithium atoms per niobium, evidence that this  $\text{Li}_3\text{NbSe}_3$  is analogous to the cell discharge product. Reaction with one and two equivalents of *n*-BuLi gave more discernible products. Powder patterns of the one and two lithium products (Fig. 9) are very similar to  $\text{NbSe}_3$  itself and demonstrate that the cell reaction (at least for the first two lithiums) is a topochemical reaction. The x-ray powder pattern for  $\text{LiNbSe}_3$  is very similar to  $\text{NbSe}_3$ , while in  $\text{Li}_2\text{NbSe}_3$  a number of small peaks are missing, those that remain are broadened and the intensities of corresponding peaks have changed, as well as some small changes in the *d* spacings. The third lithium causes the diffraction pattern to be almost totally obliterated. Only three very weak, broad peaks are observed which are not obviously related to any peaks in  $\text{NbSe}_3$ . Chianelli and Dines (22) have obtained similar data for lithiated  $\text{NbSe}_3$ , but also report a distinct pattern for  $\text{Li}_3\text{NbSe}_3$  very similar to  $\text{NbSe}_3$ , which they were able to index. This discrepancy may be due to a slight difference in reaction conditions. Addition of  $\text{NH}_3$  to  $\text{Li}_3\text{NbSe}_3$  did indeed cause decomposition with  $\text{Li}_2\text{Se}$  being observed in the x-ray powder pattern.

After recharging  $\text{Li}_3\text{NbSe}_3$  the resulting "NbSe<sub>3</sub>" also shows only a weak diffuse x-ray diffraction pattern, indicating a high degree of disorder, conceivably a different or a random arrangement of the  $\text{NbSe}_3$  chains. In line with this observation, discharged cathodes do not track the original discharge curve on subsequent

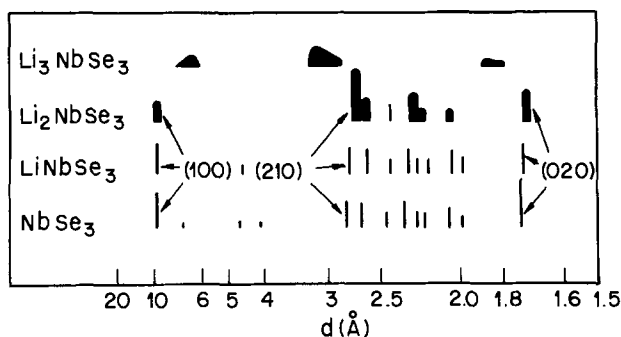


Fig. 9. Diagram of x-ray powder patterns of  $\text{NbSe}_3$  treated with *n*-butyl lithium.

cycles, but higher, gradually decreasing voltages are observed (Fig. 5).

Lithiation of  $\text{TiS}_3$  with *n*-BuLi gives rise to a phase of higher symmetry (possibly hexagonal) as indicated by the x-ray powder pattern (Fig. 7) and also observed by Chianelli (22). Lengthwise splitting of  $\text{TiS}_3$  crystals occurs during reaction with *n*-BuLi. This change in crystal symmetry implies a more drastic change in the local coordination as well, compared to  $\text{NbSe}_3$ .

We have also measured d-c conductivities of the lithiated  $\text{NbSe}_3$  and  $\text{TiS}_3$  compounds by a four-probe method on pressed powders. The conductivity of  $\text{NbSe}_3$  is progressively lowered from about 300 to  $10^{-1}$  ( $\text{ohm-cm}^{-1}$ ) for  $\text{Li}_3\text{NbSe}_3$ , while  $\text{TiS}_3$  and all the  $\text{Li}_i\text{TiS}_3$  have conductivities near about 0.2 ( $\text{ohm-cm}^{-1}$ ) (7). Formation of a nonconducting discharge product cannot be the cause of irreversibility in  $\text{TiS}_3$ . The larger *d* spacings in the powder pattern of the discharged  $\text{TiS}_3$  cathode are due to the inclusion of PC coordinated to the lithium ions.

Comparing and contrasting the lithiated compounds of  $\text{TiS}_3$  and  $\text{NbSe}_3$  provides a rationale for the differences in reversibility. For  $\text{NbSe}_3$  the structure remains virtually unchanged on going to  $\text{Li}_2\text{NbSe}_3$ . Such maintenance of structure allows for easy reversibility of the cell reaction as suggested in other systems (14, 15). With  $\text{TiS}_3$  a higher crystal symmetry is likely indicative of a greater structure change. The most likely change is the simple twist to octahedral coordination noted earlier for  $\text{BaTaSe}_3$ . Octahedral coordination is expected to be favored for  $[\text{TiS}_6]$  units as it is in  $\text{TiS}_2$  (23). The trigonal prismatic coordination of  $\text{TiS}_3$  is stabilized by the short S-S bonds and the coordination of sulfides from adjacent chains to give an eight coordinate  $\text{Ti}^{4+}$ . When the S-S bonds are broken and the interchain bonding disrupted the  $\text{Ti}^{4+}$  is free to assume its favored coordination. This change is irreversible. By contrast  $[\text{NbSe}_6]$  units prefer trigonal prismatic coordination in  $\text{NbSe}_2$ . Thus when  $\text{NbSe}_3$  chains separate they need not change coordination geometry, but if they do, such a change could be reversible at room temperature. The weak x-ray powder pattern of  $\text{Li}_3\text{NbSe}_3$  can be explained as a highly disordered aggregation of chains.

## Conclusions

Both  $\text{TiS}_3$  and  $\text{NbSe}_3$  undergo topochemical reactions with lithium on discharge in nonaqueous cells to form compounds of the formula  $\text{Li}_3\text{MX}_3$ . This cell reaction is completely reversible for  $\text{NbSe}_3$ , but only partially reversible with  $\text{TiS}_3$ . The basic chain structure of both compounds is maintained on lithiation. Reversibility has been equated with maintenance of microstructure. We suggest that  $\text{TiS}_3$  changes from trigonal prismatic to octahedral coordination on lithiation and that this change is irreversible. Perhaps the investigation of other structures capable of remaining basically the same following lithiation will lead to new secondary cathode materials.

## Acknowledgments

We would like to thank Professor J. Rouxel for communication of the structure of  $\text{NbSe}_3$  prior to publication, J. Broadhead, F. J. Di Salvo, and D. O. Feder for helpful discussions, and T. M. Putvinski for technical assistance.

Manuscript submitted Dec. 5, 1975; revised manuscript received Feb. 20, 1976. This was Paper 26 presented at the Toronto, Canada, Meeting of the Society, May 11-16, 1975.

Any discussion of this paper will appear in a Discussion Section to be published in the June 1977 JOURNAL. All discussions for the June 1977 Discussion Section should be submitted by Feb. 1, 1977.

Publication costs of this article were partially assisted by Bell Laboratories.

## REFERENCES

1. J. Broadhead and F. A. Trumbore, Paper 178 presented at The Electrochemical Society Meeting, Chicago, Illinois, May 13-18, 1973.
2. J. Broadhead, F. J. Di Salvo, and F. A. Trumbore, U.S. Pat. 3,864,167 (1975).
3. F. A. Trumbore and J. Broadhead, Paper 179 presented at The Electrochemical Society Meeting, Chicago, Illinois, May 13-18, 1973.
4. F. A. Trumbore, J. Broadhead, and T. M. Putvinski, Paper 61 presented at The Electrochemical Society Meeting, Boston, Massachusetts, Oct. 7-11, 1973.
5. G. L. Holleck, F. S. Shuker, and S. B. Brummer, Paper 52 presented at The Electrochemical Society Meeting, New York, New York, Oct. 13-17, 1974.
6. W. Kronert and K. Plieth, *Z. Anorg. Allgem. Chem.* **336**, 207 (1965).
7. H. G. Grimmeiss, A. Rabenau, H. Hahn, and P. Ness, *Z. Elektrochem.*, **65**, 776 (1961).
8. A. Meerschaut and J. Rouxel, *J. Less-Common Metals*, **39**, 197 (1975).
9. E. Bjerkelund, J. H. Fermor, and A. Kjekshus, *Acta Chem. Scand.*, **20**, 1836 (1966).
10. P. Haen, P. Monceau, and B. Tissier, in "Low Temperature Physics," Vols. M. Krusius and M. Vuorio, Editors, p. 445, North Holland/American Elsevier, Amsterdam (1975).
11. S. C. Watson and J. F. Eastham, *J. Organomet. Chem.*, **9**, 165 (1967).
12. F. A. Trumbore, J. Broadhead, and T. Putvinski, Unpublished results.
13. P. A. Gardner, M. Vlasse, and A. Wold, *Inorg. Chem.*, **8**, 2784 (1969).
14. M. S. Whittingham, *This Journal*, **122**, 526 (1975).
15. M. S. Whittingham, *ibid.*, **123**, 315 (1976).
16. F. R. Gamble and T. H. Geballe, in "Treatise on Solid State Chemistry," N. B. Hannay, Editor, Vol. 3 (1975).
17. M. B. Dines, *Mat. Res. Bull.*, **10**, 287 (1975).
18. D. W. Murphy, F. J. Di Salvo, G. W. Hull, and J. V. Waszczak, *Inorg. Chem.*, **15**, 17 (1976).
19. M. B. Armand, in "Fast Ion Transport in Solids," W. van Gool, Editor, North Holland Press (1973).
20. D. W. Murphy and F. A. Trumbore, Paper 26 presented at The Electrochemical Society Meeting, Toronto, Canada, May 11-16, 1975.
21. M. S. Whittingham, R. R. Chianelli, and M. B. Dines, Paper 35 presented at The Electrochemical Society Meeting, Dallas, Texas, Oct. 5-9, 1975.
22. R. R. Chianelli and M. B. Dines, *Inorg. Chem.* **14**, 2417 (1975).
23. F. R. Gamble, *J. Solid State Chem.*, **9**, 358 (1974).

# Anodic Behavior of Lithium in Aqueous Electrolytes

## II. Mechanical Passivation

E. L. Littauer\* and K. C. Tsai\*

Lockheed Palo Alto Research Laboratories, Lockheed Missiles and Space Company, Incorporated, Palo Alto, California 94304

### ABSTRACT

The anodic passivation of lithium in flowing alkaline electrolytes was studied chronopotentiometrically. The experimental results reveal that the passivation follows the classical diffusion-limited process. An empirical relationship similar to the Sand equation, but including a term for the critical current,  $i_c$ , is observed

$$(i - i_c) = kt_p^{-1/2}$$

A theoretical model of the dissolving lithium anode has been formulated to explain the dependence of the time to passivation,  $t_p$ , on the experimental variables. This model involves the diffusion of the soluble species through a fixed porous solid layer on the electrode surface and through the electrolyte diffusion layer. The assumption made for the initial boundary condition requires the existence at OCV of a concentration gradient within the porous oxide layer. It has led to an analytical solution which can successfully represent the  $i - t_p$  relationship for metals in highly corrosive media.

Lithium, when in a strongly alkaline aqueous electrolyte at open circuit or under anodic polarization, is always covered with a fairly thick film. It is believed that the film has a complex structure comprising a thin, coherent lithium oxide layer of unknown stoichiometry directly adjacent to the metal surface which is overlaid by a pored oxide/hydroxide layer. At the film-solution interface, gray anhydrous LiOH has been identified by x-ray, intermixed together with white LiOH · H<sub>2</sub>O. Under anodic dissolution, high flux rates are supported across the film with little polarization.

A previous paper (1) showed that in a Li-H<sub>2</sub>O battery the anode-to-cathode contact pressure, electrolyte concentration, flow rate, and polarization level have to be controlled for the Li to dissolve with near to 100% faradaic efficiency. This paper indicates that if the Li is polarized beyond a critical C.D. it becomes

passivated. A passivated anode in a multicell battery may require considerable time (ca. 1-5 min) to return to the active state. It is therefore important to understand the processes which lead to passivation in order to prevent its occurrence as power demands from the battery are changed.

It is believed that in the process of passivation, Li conforms to the classical theory (2) which postulates that pores and imperfections in an anodic film become blocked. This blocking effect occurs when a critical concentration of reacting species is exceeded within the film and/or at the metal-film interface or the film-solution interface. The passivation is then a reflection of the increase in overvoltage for cation transport from the metal surface into the bulk solution.

Electrochemically, Li has features similar to other reactive metals, e.g., Zn and Cd, which form insulating films when under anodic polarization in alkaline solution. It also has certain unique characteristics. The protective oxide film has been found to be considerably

\* Electrochemical Society Active Member.

Key words: mechanical passivation, lithium, diffusion, porous oxide layer, diffusion layer, Sand equation.

thicker (ca. 0.3 mm) than is usually observed on reactive metals, and the corrosion rate at OCV is far higher (i.e.,  $>10$  kA/m<sup>2</sup> in 3M LiOH and  $\approx 2.5$  kA/m<sup>2</sup> in 4.5M LiOH).

Frequently studies of passivation are hampered by difficulties in achieving an identical electrode surface condition from one experiment to the next. However, in this system, the high corrosion rate of Li at OCV causes the electrode to return always to the same state without surface preparation (provided electrolyte composition and temperature remain constant) and excellent experimental reproducibility results.

This paper examines the processes leading to and controlling mechanical passivation at various electrolyte flow velocities and concentrations keeping anode-cathode contact pressure constant.

### Experimental

The experimental arrangement described in the previous paper (1) was used. This comprised  $1.14 \times 10^{-3}$  m<sup>2</sup> electrode area cell with means to control anode to cathode contact pressure, electrolyte temperature, flow rate, and concentration. Experiments were performed to determine (i) the critical C.D.'s at three electrolyte concentrations and (ii) the influence of electrolyte flow velocity on the time to passivation in the same electrolytes.

The three concentrations were 3.1, 4.1, and 4.6M LiOH. For the critical current density experiments, the flow rates were controlled at 0.24 and 0.6 m/sec, and for the time to passivation studies, flow rates ranging from 0.12 to 0.72 m/sec were used.

Initially, a series of resistive polarization runs were made in the three electrolytes. The point at which the  $E-i$  curve changed slope to indicate the onset of the passivation region was taken to be the critical C.D. These C.D.'s are depicted by point b in Fig. 1. In this figure, line b-c represents the mechanical passivation region. Point c which corresponds to 1.95V polarization was arbitrarily selected as the cutoff level. A minimum of five C.D.'s were chosen between b and c for the passivation experiments. These experiments were performed chronopotentiometrically. The time to passivation,  $t_p$ , was measured from the  $E-t$  curves using a Tektronix No. 549 storage oscilloscope. In an analogous way,  $t_p$  values were obtained as a function of electrolyte flow rate at a C.D. intermediate between b and c for the three electrolytes of interest.

Experiments were performed in triplicate. The reproducibility of the  $E-i$  curves was within 2% and the reproducibility of  $t_p$  was within 5%. During each run, the temperature and anode-cathode contact pressure were maintained constant.

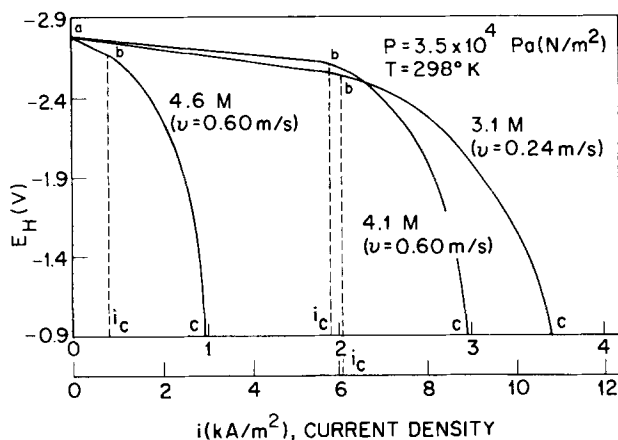


Fig. 1. Anodic polarization of lithium in LiOH showing the critical current density  $i_c$ .

### Results

The  $E-i$  plots of Fig. 1 indicate that for the electrolytes of interest, a critical C.D.  $i_c$  shown as point b has to be exceeded before passivation will occur. The values for  $i_c$  taken from the curves are approximately 0.25, 2, and 6 kA/m<sup>2</sup> in 4.6, 4.1, and 3.1M LiOH, respectively. It was found that in the most dilute electrolyte, the flow rate had to be reduced from 0.60 to 0.24 m/sec for passivation to appear within a reasonable C.D. range. The relationship between C.D. and time to anodic passivation for electrochemical systems which follow the classical diffusion limited process is

$$i = k't_p^{-1/2} \quad (1)$$

where  $k'$  is a constant. Plots of  $i$  vs.  $t_p^{-1/2}$  are given in Fig. 2.

It is evident that the curves do not pass through the origin which would have been the case if Eq. [1] was implicitly obeyed. Extrapolation of the linear plots to  $t_p^{-1/2} = 0$  gives intercepts of 0.20, 1.92, and 5.90 kA/m<sup>2</sup>. It will be noted that these values are very close to those obtained for  $i_c$  in Fig. 1. Accordingly, for the Li-H<sub>2</sub>O system an empirical equation may be written

$$(i - i_c) = k't_p^{-1/2} \quad (2)$$

Figure 3 shows that a linear relationship exists between mean electrolyte face velocity  $v$  and  $t_p^{-1/2}$ . This would be expected since the experimental conditions maintained the anode-cathode contact pressure and film thickness constant for each value of  $v$ .

### Discussion

#### Passivation Time-Current Density Relationship

The classical Sand equation (3)

$$i = k't_p^{-1/2} \quad (1)$$

where  $k' = \frac{1}{2} nFA(\pi D)^{1/2} \Delta C$ ,  $A$  is the active surface

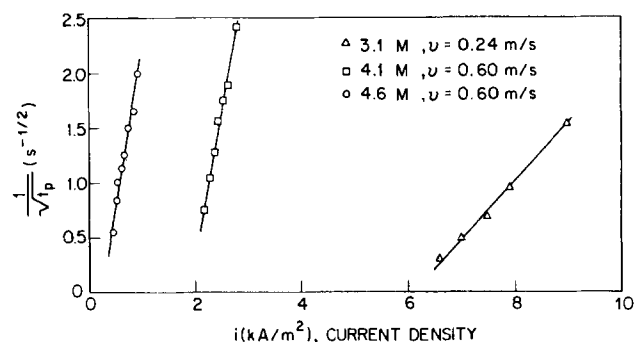


Fig. 2. Variation of time to passivation with current density at various LiOH concentrations.

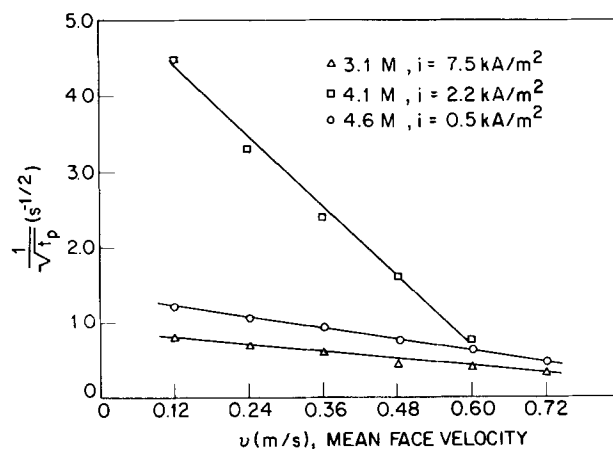


Fig. 3. Relationship between time to passivation and electrolyte flow velocity  $v$  at various LiOH concentrations.

area and  $\Delta C$  is the concentration difference between reactive species at the metal surface and the bulk solution, satisfactorily describes the response of metals which form sparingly soluble and thin protective films. Examples are Fe, Ni, Au, Cr, and Cr-Fe alloys (4). Here, the basic assumption is that the passivation C.D.  $i_p$  is equivalent to the limiting diffusion C.D.  $i_d$  at  $t_p$ . This assumption generally requires an initial boundary condition such as  $C(x,0) = C^*$  or  $C(x,0) = 0$ , where  $C(x,0)$  is the initial concentration of the corroding metal cations within the transport medium and  $C^*$  is the bulk concentration. However, for a metal which forms a protective film in a strongly corroding medium, such as Li or Zn in alkaline solution or Ni in acid solution (5),  $C(x,0) \neq C^*$  and a concentration gradient will exist even at OCV. In this situation the Sand equation will not hold. To resolve this, it is necessary to include an additional term  $\gamma$  in Eq. [1] to account for the initial concentration gradient across the film. Obviously, the OCV corrosion rate will influence the value of  $\gamma$ .

An empirical equation

$$(i - \gamma) = k't_p^{-1/2} \quad [3]$$

where  $\gamma$  is a constant, was first proposed to account for the passivation behavior of Zn in flowing (11) and tranquil (6-10) electrolytes. The previous investigators attributed the constant  $\gamma$  to either nondiffusional mass transport (predominantly convection) or to varying rates of film growth (11). These explanations do not offer an analytical solution to the existence of the critical current density  $i_c$ .

Lithium unlike Zn does not form complex ions in alkaline solution. It is much more reactive than Zn and forms considerably thicker films at the metal surface. An analysis of the controlling processes between the Li surface and the electrolyte may therefore be undertaken. Figure 4 represents a one-dimensional model for a filmed Li anode surface in a flowing electrolyte. In this model it is assumed that mass transport of  $\text{Li}^+$  occurs exclusively via diffusion across a porous oxide layer of constant thickness ( $x_0$ ) and through an adjacent diffusion layer of electrolyte of thickness  $\delta$ . In a flowing electrolyte system operating under laminar flow, mass transport can be assumed to occur exclusively across these two layers. The transport of  $\text{Li}^+$  away from the diffusion layer is controlled by convection (12).

The diffusion equation for the oxide layer can be described as

$$D_1 \frac{\partial^2 C(x,t)}{\partial x^2} = \frac{\partial C(x,t)}{\partial t} \quad [4]$$

where  $D_1$  is the diffusion coefficient of  $\text{Li}^+$  in the porous oxide medium and  $C(x,t)$  the concentration of  $\text{Li}^+$  within the medium. It is subject to the following boundary conditions

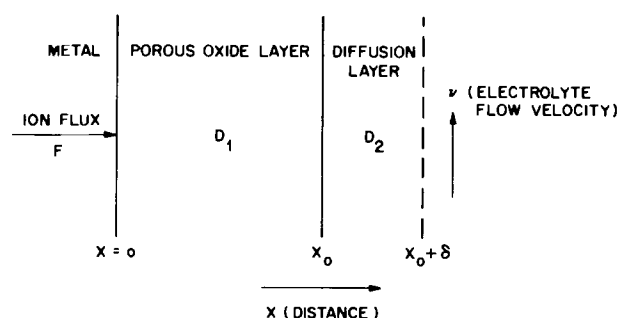


Fig. 4. One-dimensional model of the electrode/porous oxide layer/diffusion layer (electrolyte) system  $D_1$  = diffusion coefficient of  $\text{Li}^+$ .

$$C(0,0) = C^*_1, \text{ (the initial concentration of } \text{Li}^+ \text{ at the metal surface at OCV)} \quad [5]$$

$$C(x,0) = C^*_1 e^{-\rho_1 x}, \text{ (the initial concentration gradient at OCV)} \quad [6]$$

where  $\rho_1$  is a constant

$$D_1 \left( \frac{\partial C(x,t)}{\partial x} \right)_{x=0} = \frac{-i(t)}{nFA} \text{ (the ion flux at the metal surface)} \quad [7]$$

Using the Laplace transform technique and considering galvanostatic polarization, i.e.,  $i(t) = i$  (constant), Eq. [4] can be solved for  $C(x,t)$ .<sup>1</sup>

$$\begin{aligned} C(x,t) = & C^*_1 [\exp(-\rho_1 x + \rho_1^2 D_1 t) \\ & - \frac{1}{2} \exp(-\rho_1 x + \rho_1^2 D_1 t) \operatorname{erfc}(x/2\sqrt{D_1 t} - \rho_1 \sqrt{D_1 t}) \\ & + \frac{1}{2} \exp(\rho_1 x + \rho_1^2 D_1 t) \operatorname{erfc}(x/2\sqrt{D_1 t} + \rho_1 \sqrt{D_1 t})] \\ & - \frac{i}{nFA D_1} [x \operatorname{erfc}(x/2\sqrt{D_1 t}) \\ & - 2\sqrt{D_1 t/\pi} \exp(-x^2/4D_1 t)] \quad [8] \end{aligned}$$

Equation [8] represents the concentration profile of  $\text{Li}^+$  within the porous oxide medium and satisfies all the boundary conditions given under [5], [6], and [7].

It can be shown that, when  $t = t_p$ , the active Li surface is passivated due to the precipitation of  $\text{LiOH}$  on the electrode; thus the surface concentration of  $\text{LiOH}$  reaches its saturation. Therefore, at  $t = t_p$

$$C(0, t_p) = C_s \quad [9]$$

Equation [8] can then be written in terms of  $i$

$$\begin{aligned} i = & \frac{nFA(\pi D_1)^{1/2}}{2} (C_s) t_p^{-1/2} - \frac{nFA(\pi D_1)^{1/2}}{2} C^*_1 \\ & \exp(\rho_1^2 D_1 t_p) \{1 - \frac{1}{2} [\operatorname{erf}\{\rho_1 (D_1 t_p)^{1/2}\} \\ & - \operatorname{erf}\{-\rho_1 (D_1 t_p)^{1/2}\}]\} t_p^{-1/2} \quad [10] \end{aligned}$$

For small  $t_p$ , the error function and exponential function can be approximated by a series expansion

$$\operatorname{erf}(\pm x) = \pm \frac{2}{\sqrt{\pi}} \left( x - \frac{x^3}{3} + \frac{x^5}{5.2!} - \frac{x^7}{7.3!} + \dots \right)$$

and

$$e^y = 1 + y + \frac{y^2}{2!} + \frac{y^3}{3!} + \dots$$

Since in actual practice

$$x = \rho_1 (D_1 t_p)^{1/2} \ll 1$$

and

$$y = x^2 = \rho_1^2 D_1 t_p \ll \ll 1$$

then

$$\operatorname{erf}(\pm x) \simeq \pm \frac{2}{\sqrt{\pi}} x$$

and

$$e^y \simeq 1$$

Therefore, [10] can be further simplified as follows

$$\begin{aligned} i - (nFA D_1 \rho_1) C^*_1 \\ = \left\{ \frac{nFA(\pi D_1)^{1/2}}{2} (C_s - C^*_1) \right\} t_p^{-1/2} \quad [11] \end{aligned}$$

Let

$$i_c = (nFA D_1 \rho_1) C^*_1 \quad [12]$$

and let

$$k' = \frac{nFA(\pi D_1)^{1/2}}{2} (C_s - C^*_1) \quad [13]$$

Then [11] may be expressed

<sup>1</sup> A detailed treatment of the following mathematical development is given in the Appendix.

$$i - i_c = k't_p^{-1/2} \quad [14]$$

Equation [14] derived here theoretically, is identical to [2] which empirically satisfied the experimental results obtained in the investigation. It is obvious from [12] that the magnitude of the critical C.D. is proportional to the product of surface concentration (at OCV) and the concentration gradient,  $\rho_1$ , within the oxide film which in turn is determined by the corrosion rate of Li. Unlike other metals such as Fe, Au, Cr etc., Li corrodes rapidly in aqueous media. Therefore, a distinct  $i_c$  is observed at various concentrations of LiOH. The reason that the term  $i_c$  is not observed with Fe, Au, Cr, etc., is that their corrosion rates at OCV (more specifically, their exchange current densities) are small in comparison to the applied current density. Then within experimental error, Eq. [1] rather than [14] is observed. In the case of Zn, the corrosion rate at OCV is generally enhanced by complex formation. Thus, as with Li, there is a significant critical current density. The slopes of the  $i - t_p^{-1/2}$  curves shown in Fig. 3 may be predicted from [13]; at higher bulk electrolyte concentration, the surface concentration would be anticipated to be higher, and the difference between  $C_s$  and  $C^*_1$  would be smaller. Therefore, a smaller  $k'$  value would result.

The concentration at the active metal surface,  $C^*_1$ , is related to the bulk electrolyte concentration,  $C^*$ , in the following manner. At OCV ( $t = 0$ ), the concentration gradient within the diffusion layer,  $x_0 \leq x \leq x_0 + \delta$ , can be described as

$$C(x, 0) = C^*_2 e^{-\rho_2(x-x_0)} \quad [15]$$

where

$$C^*_2 = C(x_0, 0) = C^*_1 e^{-\rho_1 x_0} \quad [16]$$

Equation [16] describes the boundary condition for the concentration continuity across the oxide/electrolyte interface when  $x \cong x_0 + \delta$  and  $C(x_0 + \delta, 0) = C^*$ . Then, from [16]

$$C^*_1 = C^* e^{(\rho_1 x_0 + \rho_2 \delta)} \quad [17]$$

For the simplest case in which  $\rho_1 = \rho_2 = \rho$ , [17] becomes

$$C^*_1 = C^* e^{\rho(x_0 + \delta)} \quad [18]$$

with

$$0 \leq \rho \leq \frac{\ln(C_s/C^*)}{(x_0 + \delta)}$$

Equation [18] indicates the relationship between surface concentration and bulk concentration under any experimental condition where the film thickness and diffusion layer thickness can be determined. This equation also demonstrates that the initial surface concentration can be ascertained without knowledge of the details of the concentration profile within the diffusion layer. A comprehensive analytical treatment of the mass transport of  $\text{Li}^+$  through a finite region of oxide film and diffusion layer is in preparation.

#### Electrolyte Flow Velocity-Passivation Time Relationship

The anodic polarization is predominantly an IR drop across the porous film and it is considered reasonable to suppose that the film resistance and the film thickness are linearly related. Inspection of the  $E-i$  curves as a function of flow rate in the active polarization region (1), and subsequent experiments to examine this aspect in more detail, show that the resistance and hence the film thickness are linearly related to the electrolyte flow velocity. If  $x_0$  is the film thickness and  $v$  the flow velocity then

$$x_0 = x_0^0 - \xi v \quad [19]$$

where  $x_0^0$  is the film thickness at  $v = 0$  and  $\xi$  is a constant. In this system,  $x_0 \gg \delta$  (i.e., the film thickness is ca. 0.3 mm and the diffusion layer thickness is assumed to be ca 0.01 mm) then since  $\rho(x_0 + \delta) \ll 1$ ,

[18] becomes

$$C^*_1 = C^* [1 + \rho x_0^0 - \rho \xi v] \quad [20]$$

In practice, and as is shown in a subsequent paper (13), the parasitic reaction is fairly independent of  $v$  within the range of conditions of interest in this study. Hence

$$C_s - C^*_1 \cong \text{constant}$$

Then [14] can be written as

$$x - \psi v = k't_p^{-1/2} \quad [21]$$

with

$$x = i + (nFA D_1 \rho C^*) [1 + \rho x_0^0]$$

and

$$\psi = nFA D_1 \rho^2 \xi C^*$$

Equation [21] gives the relationship between the electrolyte face velocity and the passivation time. Figure 3 shows that the experimental results confirm this relationship. It is apparent that increasing face velocity shortens the distance for the mass transport of  $\text{Li}^+$  from the anode surface, and thus makes it more difficult for the electrode surface to become passivated. The practice of increasing the electrolyte face velocity to prevent Li passivation during cell operation can therefore be understood.

#### Conclusions

When Li is anodically polarized to a level just prior to the critical current density, the film existing on its surface is in a state of dynamic equilibrium with the electrolyte. The thickness of the film is fixed by the electrolyte flow rate, anode to cathode contact pressure, and molarity. At the critical polarization level, the direct parasitic reaction is essentially zero while the electrochemical reaction rate is near to its maximum. (At open circuit the converse holds.)

As the C.D. exceeds the critical level, the dynamic equilibrium is disturbed as precipitation of reactive species occurs within the film and the active sites diminish and eventually disappear entirely. It is not known where the precipitation occurs within the film. It could be adjacent to the oxide film at the base of the pores, within the matrix comprising the overlaying film(s), or both. The diminution of active sites is reflected as a sudden increase in polarization and within a short period the cell potential decreases to zero at constant load or, under galvanostatic conditions, polarity reversal occurs.

The onset of passivation can be controlled by either altering the rate of mass transfer of the cations into the bulk electrolyte via adjustment of the electrolyte concentration or temperature, or by changing the thickness of the mass transfer medium, i.e., changing the film thickness.

An analytical solution for the passivation phenomenon has been predicted on the mass transport of  $\text{Li}^+$  through the anodic oxide film and through the diffusion layer. The experimental data support the model which is based on the assumption that at OCV there exists a concentration gradient of  $\text{Li}^+$  across the film. It is this premise which differs from the classical basis of the Sand equation. This leads to Eq. [14] which relates C.D. and passivation time and includes a term for the critical current  $i_c$ . It is believed that [14] will apply to the passivation of other metals which have a high OCV corrosion rate, e.g., Zn. The analytical solution permits calculation of  $i_c$  and of the slope of the current density-time to passivation curve at any concentration.

Further, the fact that the anode-cathode contact pressure is held constant has led to the development of an analytical treatment to describe the effect of electrolyte flow velocity on time to passivation. This information, coupled with the ability to calculate  $i_c$ , may be used to guide the selection of control parameters for the Li- $\text{H}_2\text{O}$  battery.

### Acknowledgments

This study was supported in their entirety by Lockheed Missiles and Space Company.

Manuscript submitted Oct. 30, 1975; revised manuscript received Feb. 28, 1976.

Any discussion of this paper will appear in a Discussion Section to be published in the June 1977 JOURNAL. All discussions for the June 1977 Discussion Section should be submitted by Feb. 1, 1977.

Publication costs of this article were partially assisted by the Lockheed Missiles and Space Company.

### APPENDIX

$$D_1 \frac{\partial^2 C(x, t)}{\partial x^2} = \frac{\partial C(x, t)}{\partial t} \quad [\text{A-1}]$$

is to be solved for  $C(x, t)$ , subject to the following boundary conditions (B.C.'s)

$$C(0, 0) = C^*_1 \quad [\text{A-2}]$$

$$C(x, 0) = C^*_1 e^{-\rho_1 x} \quad [\text{A-3}]$$

and

$$D_1 \left( \frac{\partial C(x, t)}{\partial x} \right)_{x=0} = \frac{-i(t)}{nFA} \quad [\text{A-4}]$$

First, taking the Laplace transform (L.P.T.) of [1] with respect to  $t$ , yields

$$D_1 \frac{\partial^2 \bar{C}(x, s)}{\partial x^2} = s\bar{C}(x, s) - C(x, 0) \quad [\text{A-5}]$$

where

$$\bar{C}(x, s) = L_t[C(x, t)] = \int_0^\infty e^{-st} C(x, t) dt \quad [\text{A-6}]$$

Rearranging [5] and using the B.C. given by [3] yields

$$\frac{\partial^2 \bar{C}(x, s)}{\partial x^2} - a^2 \bar{C}(x, s) = -b e^{-\rho_1 x} \quad [\text{A-7}]$$

in which  $a = \sqrt{s/D_1}$  and  $b = C^*_1/D_1$ . For simplicity, the variable  $s$  is temporarily dropped and [7] reads

$$\frac{\partial^2 \bar{C}(x)}{\partial x^2} - a^2 \bar{C}(x) = -b e^{-\rho_1 x} \quad [\text{A-8}]$$

Taking the L.P.T. of [8] with respect to  $x$ , gives

$$P^2 \bar{C}(p) - pA - B - a^2 \bar{C}(p) = \frac{-b}{p + \rho_1} \quad [\text{A-9}]$$

where  $A$  and  $B$  are arbitrary constants with respect to  $P$  and

$$\bar{C}(p) = L_x[\bar{C}(x, s)] = \int_0^\infty e^{-px} \bar{C}(x, s) dx \quad [\text{A-10}]$$

Rearranging [9] and using partial fractions yields

$$\bar{C}(p) = \frac{b/(a^2 - \rho_1^2)}{p + \rho_1} + \frac{A'}{p + a} - \frac{B'}{p - a} \quad [\text{A-11}]$$

where  $A'$  and  $B'$  are constants with respect to  $p$ .

Taking the inverse L.P.T. of [11] gives an expression for  $\bar{C}(x)$

$$\bar{C}(x, s) = \frac{b}{a^2 - \rho_1^2} e^{-\rho_1 x} + A'(s) e^{-ax} + B'(s) e^{ax} \quad [\text{A-12}]$$

Since the boundary condition requires that  $\bar{C}(x, s)$  remains bounded as  $x \rightarrow \infty$ ,  $B'(s) = 0$ , and [12] becomes

$$\bar{C}(x, s) = \frac{b}{a^2 - \rho_1^2} e^{-\rho_1 x} + A'(s) e^{-ax} \quad [\text{A-13}]$$

$A'(s)$  can be evaluated by differentiating [A-13] with respect to  $x$ , setting  $x = 0$ , and substituting the result

into the transform with respect to  $t$  of boundary condition [A-4]. When this is done and the values of  $a$  and  $b$  are inserted, [A-13] becomes

$$\bar{C}(x, s) = \frac{C^*_1}{s - D_1 \rho_1^2} e^{-\rho_1 x} - \left[ \frac{\rho_1 D_1^{1/2} C^*_1}{s^{1/2} (s - D_1 \rho_1^2)} - \frac{\bar{i}(s)}{nFA D_1^{1/2} \cdot s^{1/2}} \right] \cdot e^{-\sqrt{s/D_1} x} \quad [\text{A-14}]$$

Under galvanostatic polarization,  $i(t) = i$  (a constant), thus  $\bar{i}(s) = i/s$  and [A-14] becomes

$$\bar{C}(x, s) = \frac{C^*_1}{s - D_1 \rho_1^2} e^{-\rho_1 x} - \left[ \frac{\rho_1 D_1^{1/2} C^*_1}{s^{1/2} (s - D_1 \rho_1^2)} - \frac{i}{nFA D_1^{1/2} s^{3/2}} \right] e^{-\sqrt{s/D_1} x} \quad [\text{A-15}]$$

Finally, the concentration profile  $C(x, t)$  can be obtained by taking the inverse L.P.T. of [A-15]. The inverse L.P.T.'s of the first term and of the second term in the bracket of the right hand side of [A-15] can be obtained readily from a table.<sup>2</sup> The inverse L.P.T. of the first term in the bracket of the right hand side of [A-15] was obtained as follows

Let

$$J(t) = L_s^{-1} \left( \frac{e^{-ns^{1/2}}}{s^{1/2} (s - m^2)} \right) \quad [\text{A-16}]$$

with

$$m = \rho_1 D_1^{1/2} \text{ and } n = x D_1^{-1/2}$$

Since

$$f(t) = L_s^{-1} \left( \frac{e^{-ns^{1/2}}}{s^{1/2}} \right) = \frac{1}{\sqrt{\pi t}} e^{-n^2/4t}$$

$$h(t) = L_s^{-1} \left( \frac{1}{s - m^2} \right) = e^{m^2 t}$$

we have by the Law of Convolution

$$J(t) = \frac{e^{m^2 t}}{\sqrt{\pi}} \int_0^t \exp[-m^2 \tau - n^2/4\tau] \frac{d\tau}{\sqrt{\tau}} \\ = \frac{1}{2m} \exp(m^2 t - mn) \operatorname{erfc}(n/2\sqrt{t} - m\sqrt{t}) \\ - \frac{1}{2m} \exp(m^2 t + mn) \operatorname{erfc}(n/2\sqrt{t} + m\sqrt{t}) \quad [\text{A-17}]$$

Therefore

$$c(x, t) = C^*_1 [\exp(-\rho_1 x + \rho_1^2 D_1 t) \\ - \frac{1}{2} \exp(-\rho_1 x + \rho_1^2 D_1 t) \operatorname{erfc}(x/2\sqrt{D_1 t} - \rho_1 \sqrt{D_1 t}) \\ + \frac{1}{2} \exp(\rho_1 x + \rho_1^2 D_1 t) \operatorname{erfc}(x/2\sqrt{D_1 t} + \rho_1 \sqrt{D_1 t})] \\ - \frac{i}{nFA D_1} \left[ x \operatorname{erfc}(x/2\sqrt{D_1 t}) \right. \\ \left. - 2\sqrt{D_1 t/\pi} \exp\left(-\frac{x^2}{4D_1 t}\right) \right] \quad [\text{A-18}]$$

<sup>2</sup> G. E. Roberts and H. Kaufman, "Table of Laplace Transforms," W. B. Saunders Co., London (1966).

### REFERENCES

1. E. L. Littauer and K. C. Tsai, *This Journal*, **123**, 771 (1976).
2. H. J. Müller, "Die Bedeckungstheorie der Passivität der Metalle und ihre experimentelle," Begründung Verlag Chemie, Berlin (1933).
3. H. J. S. Sand, *Phil. Mag.*, **1**, 45 (1901).
4. K. J. Vetter, "Electrochemical Kinetics," pp. 773-778, Academic Press, New York (1967).
5. R. Landsberg and M. Hollnagel, *Z. Elektrochem.*, **58**, 680 (1954); *ibid.*, **60**, 1098 (1956).
6. M. Eisenberg, H. F. Bauman, and D. M. Brettner, *This Journal*, **108**, 909 (1961).
7. H. Bartelt and R. Landsberg, *Z. Physik. Chem.*,

- 222, 217 (1962).
8. N. A. Hampson, M. J. Tarbox, J. T. Lilley, and J. P. G. Farr, *Electrochem. Technol.*, **2**, 309 (1964).
  9. N. A. Hampson and M. J. Tarbox, *This Journal*, **110**, 95 (1963).
  10. N. A. Hampson, P. E. Shaw, and R. Taylor, *Brit. Corr. J.*, **4**, 207 (1969).
  11. E. D. Farmer and A. H. Webb, *J. Appl. Electrochem.*, **2**, 123 (1972).
  12. V. G. Levich, "Physicochemical Hydrodynamics," Prentice-Hall, Englewood Cliffs, N. J. (1962).
  13. D. N. Bennion and E. L. Littauer, Submitted to *This Journal*.

## Pore Volume and Density of Unformed Pastes of Lead-Acid Battery Plates

C. W. Fleischmann\* and W. J. Schlotter

*C&D Batteries, an Eltra Corporation, Plymouth Meeting, Pennsylvania 19462*

### ABSTRACT

The specific pore volume,  $v$ , and solids' density,  $d$ , were determined for the pastes of unformed lead-acid battery plates by a simple laboratory technique.  $v$  was found to vary linearly with the apparent density of the dry paste,  $D$ , according to  $v = 0.356 - 0.0569D$  for pastes cured to develop  $4\text{PbO} \cdot \text{PbSO}_4$  and  $v = 0.271 - 0.0415D$  for pastes otherwise cured.  $d$  was determined from the relationship  $d^{-1} = D^{-1} - v$ .  $d$  decreased continually with decreasing  $D$  for all plates except those cured to develop  $4\text{PbO} \cdot \text{PbSO}_4$ . For the latter plates  $d$  went through a maximum as  $D$  decreased. This maximum is explained in terms of the differing crystalline perfections of the  $4\text{PbO} \cdot \text{PbSO}_4$  crystals in the plates.

The method of preparing lead-acid battery plates from pastes of acidified lead oxides is well known (1, 2) and good practical instructions for making the pastes are available (3). The commercial oxides which are employed to make such pastes may contain, in addition to PbO, various amounts of Pb or  $\text{Pb}_3\text{O}_4$  (4). In brief, to prepare an unformed battery plate, the paste is pressed into a lead alloy grid, and the plate is then allowed to stand or "cure" to oxidize most of the free lead and to develop various basic sulfates. The chemistry of basic sulfates has received considerable attention. The thermodynamics of these compounds were discussed by Barnes and Mathieson (5), and the phase changes and the chemistry of the curing processes were reviewed by Ritchie and co-workers (2), and have been discussed and reviewed by others (1, 6, 7). Specific curing techniques and practical instructions are available (1, 2, 6) and it has been generally summarized (1, 2, 6, 7) that plates cured by drying at ambient conditions or at slightly elevated temperatures and humidities develop  $\text{PbO} \cdot \text{PbSO}_4$  and  $3\text{PbO} \cdot \text{PbSO}_4 \cdot \text{H}_2\text{O}$  as the principal basic sulfates while those cured at higher temperatures (above  $70^\circ\text{C}$ ) and humidities principally develop  $4\text{PbO} \cdot \text{PbSO}_4$ . After curing, the plates are electrochemically "formed" to produce positive plates, composed of  $\text{PbO}_2$ , or negative plates, composed of Pb (1). Because the porosity of the plates ultimately affects battery performance (1, 8), it is an important parameter of battery production.

### Experimental

Pastes were made using three different commercial oxides: a leady oxide (26% free Pb) made by a ball-milling process; a leady oxide (19% free Pb) made by a Barton process; and a nonleady oxide, made by a Barton process followed by a mechanical furnace. The latter contained 9.5%  $\text{Pb}_3\text{O}_4$ . The procedure for preparing the paste mix was to blend together 9.07 kg of commercial oxide with 1-1.3 liters of water and then to add, slowly, 460-960 ml of 7.02M  $\text{H}_2\text{SO}_4$ . The wet

paste density decreased, as expected (2, 3), with the total fluids, principally with the amount of acid. Since it is well known that variations in the method of grid pasting affect the relationship between the density of the dry paste obtained from a given wet density (3), all the pasting was done by hand and by the same operator. The plates ranged in thickness since four different grid thicknesses were employed, 0.18, 0.41, 0.68, and 0.79 cm.

After pasting, some of the plates of the different oxides and grid thicknesses were selectively cured in order to develop or not to develop  $4\text{PbO} \cdot \text{PbSO}_4$ . The predominance of  $4\text{PbO} \cdot \text{PbSO}_4$  in certain pastes was confirmed by x-ray analysis. The pastes of the other plates contained  $3\text{PbO} \cdot \text{PbSO}_4 \cdot \text{H}_2\text{O}$ ,  $\text{PbO} \cdot \text{PbSO}_4$ , but no  $4\text{PbO} \cdot \text{PbSO}_4$  as the principal sulfated species.

For each dry, cured plate, the dry paste density,  $D$ , (gram/cubic centimeter) and the specific pore volume,  $v$ , (cubic centimeter/gram) of the paste were determined. The fractional porosity, a frequently used parameter, is the product of  $D$  and  $v$ .

The specific pore volume was determined from the mass of water that the plate absorbed under low vacuum. The pore volumes so obtained were found to agree within 2% with those using an hydraulic oil as the absorbed medium and within 15% with pore volumes obtained by mercury intrusion. The range of pore diameters for samples tested by mercury intrusion was  $2.5 \times 10^{-5}$ - $5 \times 10^{-4}$  cm. Mercury intrusion measurements and the measurements of solids' density by gas pycnometry were services purchased from Micromeritics Instrument Corporation, Norcross, Georgia.

The volume of the paste on a plate was determined from the total volume of the plate minus the grid volume. The volume of each plate was obtained, using Archimedes principle, from the difference in mass of the water-impregnated plates when weighed in air and in water. The volume of each grid was obtained from the density of the alloy and an estimate of the mass. This estimate was obtained from the measured mass of cast twins which were subsequently separated. The uncertainty in the single grid mass due to this

\* Electrochemical Society Active Member.

Key words: battery plates, electrode porosity, basic lead sulfates, electrode density.



estimate led to an uncertainty of less than 1% in the final calculated value of the dry paste density.

The wet paste density,  $W$ , or "wet cube" of the paste, in gram/cubic centimeter, was taken to be the mass of paste which could be pressed flush into a cup of known volume (3).

Optical examinations were by metallographic techniques similar to those described by Simon (7,9). Crystal volume estimates were from photographs of the paste structure at magnifications at 600X.

Linear fits to the data points were obtained using the program routines in the Texas Instruments Calculator, Model SR-51A.

### Results and Discussion

Relationships between wet paste density, dry paste density, void volume, and solids' density were derived from the experimental data.

*Wet paste density vs. dry paste density.*—The density of the dry paste,  $D$ , varied with the density of the wet paste  $W$ . The following relationship was observed

$$D = 1.23W - b \quad [1]$$

where  $b$  was between 0.34 and 1.07. Low magnitudes of the intercept,  $b$ , generally correspond to the data for the thinner plates and to the data for the pastes which did not contain  $4\text{PbO} \cdot \text{PbSO}_4$ .

*Specific void volume vs. dry paste density.*—The specific void volume,  $v$ , measured for each paste is plotted against the value of the dry paste density in Fig. 1. The data fell into two groups: those for pastes in which  $4\text{PbO} \cdot \text{PbSO}_4$  was developed, and those for the other pastes. Each set of data define a different linear relationship between  $v$  and  $D$ . The pastes in which  $4\text{PbO} \cdot \text{PbSO}_4$  was developed had greater specific void volumes than the other pastes at the same dry paste density. The data points are not identified according to oxide or plate thickness because correlations to these parameters were not observed. The data for the pastes containing  $4\text{PbO} \cdot \text{PbSO}_4$  were fitted by Eq. [2] (with a correlation constant of 0.995) while the data for the other pastes were fitted by Eq. [3] (with a correlation constant of 0.959)

$$v = 0.356 - 0.0569D \quad [2]$$

$$v = 0.271 - 0.0415D \quad [3]$$

*The solids' density vs. the dry paste density.*—The relationship between  $v$  and  $D$  in terms of the density

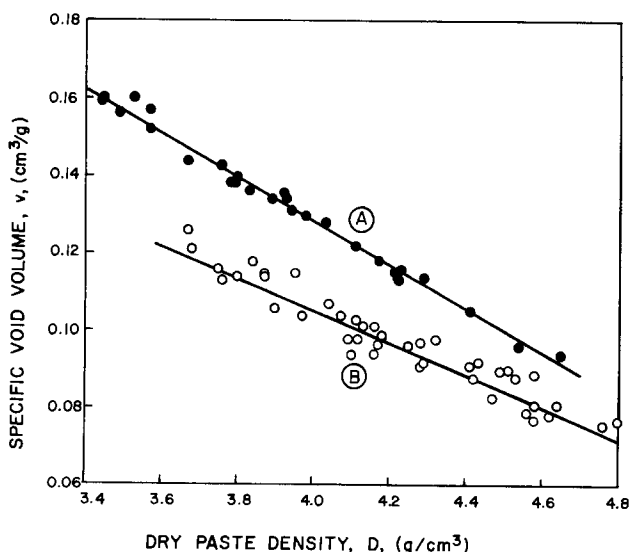


Fig. 1. Specific void volume of cured pastes plotted against the dry paste density. Curve A for plates which were treated to develop  $4\text{PbO} \cdot \text{PbSO}_4$ ; curve B for plates in which  $4\text{PbO} \cdot \text{PbSO}_4$  was not developed.

of the solids in the paste,  $d$ , is given by Eq. [4]. This equation simply states that for one gram of paste, the total paste volume,  $D^{-1}$ , must be the sum of the void volume,  $v$ , and the volume  $d^{-1}$ , occupied by the solids

$$D^{-1} = d^{-1} + v \quad [4]$$

Expressing Eq. [2] and [3] by the general form of Eq. [5], in which  $g$  and  $p$  are the slope and intercept constants, respectively

$$v = p - gD \quad [5]$$

and solving in terms of  $d$  from Eq. [4], Eq. [6] is obtained

$$d = D(gD^2 - pD + 1)^{-1} \quad [6]$$

This function is plotted in Fig. 2 for each of the two sets of data given in Fig. 1. The function goes through a maximum value of  $d$  when the value of  $D$  is equal to  $g^{-1/2}$ . For the data for the pastes in which  $4\text{PbO} \cdot \text{PbSO}_4$  was developed, the maximum occurs at  $D = 4.19 \text{ g/cm}^3$  as shown in Fig. 2. The data for the other pastes do not exhibit a maximum in Fig. 2, because it would be calculated to occur beyond the experimental range at  $D = 4.93 \text{ g/cm}^3$ . The solids' density of some pastes were independently measured by gas pycnometry. Samples containing  $4\text{PbO} \cdot \text{PbSO}_4$  were specifically chosen to range about the maximum. The values obtained by gas pycnometry were all in agreement within  $\pm 6\%$  of those obtained by the method described above.

The density of each and every element or compound that is present in the lead oxides is greater than each and every element or compound that is expected to occur in the sulfated pastes, e.g., see the list of densities given by Burbank (10). Because of that difference in the densities, it would be expected that  $d$  would decrease with increased sulfation. Increased sulfation corresponds to decreased values of the wet ( $W$ ) and corresponding dry ( $D$ ) paste densities because, as

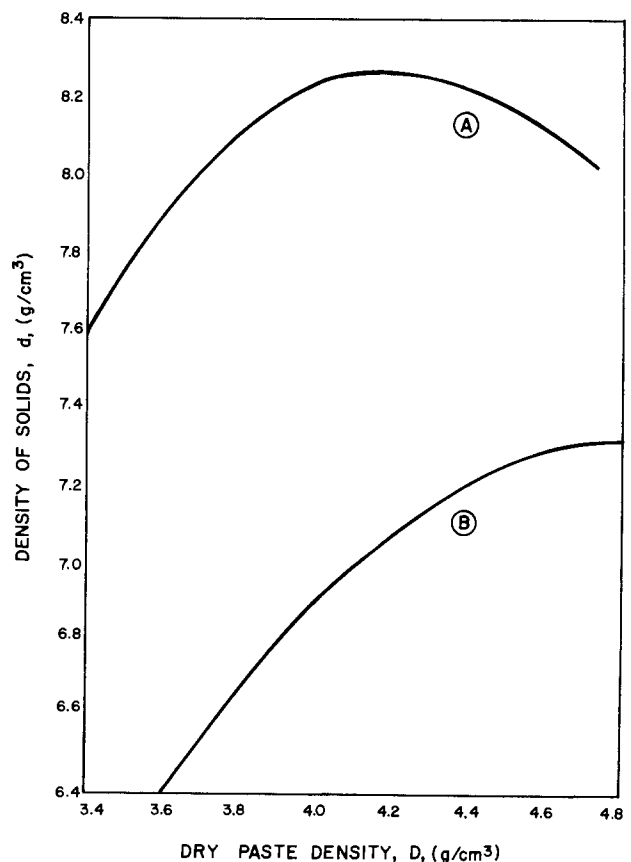


Fig. 2. Density of the solids in the dry paste plotted against the dry paste density. Curve A for plates cured to develop  $4\text{PbO} \cdot \text{PbSO}_4$ ; curve B for plates in which  $4\text{PbO} \cdot \text{PbSO}_4$  was not developed.

pointed out above, these parameters are experimentally adjusted principally by the acid addition. Therefore a general decrease in  $d$  with a decrease in  $D$  would also be expected. In this study, sufficient acid was added to sulfate 8-17 mole per cent of the  $PbO$ . Such sulfations may be calculated to produce solids' densities for the pastes containing  $4PbO \cdot PbSO_4$  within the range 8.33-8.88  $g/cm^3$ . Similarly the solids' densities of the other pastes would be expected to range within 7.90-8.98  $g/cm^3$ . Specific calculated densities were not determined for each paste because quantitative analyses were not obtained for the constituents. The density values generated according to Eq. [6] (see Fig. 2) generally fell below the predicted ranges. Such lower values may be expected if the crystals of the starting materials and products are imperfect, i.e., they contain occluded voids whose volumes are not included in  $v$ . However, from the known composition of the starting oxides and the solids' density values of these oxides as determined by gas pycnometry, it was estimated that the density of the starting oxides was high, about 95% of the theoretical values. Therefore, it is assumed that the deviations of the crystalline densities of the products from their theoretical values caused the observed lower solids' densities. As an aid to interpret the particularly unexpected behavior of the pastes containing  $4PbO \cdot PbSO_4$ , these pastes were subjected to optical examinations.

*Optical examinations.*—From the optical examinations, it was found that the largest crystals of  $4PbO \cdot PbSO_4$  were developed in those pastes in which the sulfate concentration was low (high values of  $D$ ). On the other hand, a larger number of smaller crystals developed when the sulfate concentration in the pastes was high (low values of  $D$ ). Figure 3 illustrates the relative volumes of the crystals of  $4PbO \cdot PbSO_4$  developed in pastes of three different densities.

Presumably, the larger crystals of  $4PbO \cdot PbSO_4$  which formed at the lowest sulfate concentrations occluded significantly more voids than the smaller crystals which formed at the highest sulfate concentrations. This difference in crystalline perfection is believed to be responsible for the maximum observed in the relationship between  $d$  and  $D$  for plates containing  $4PbO \cdot PbSO_4$ .

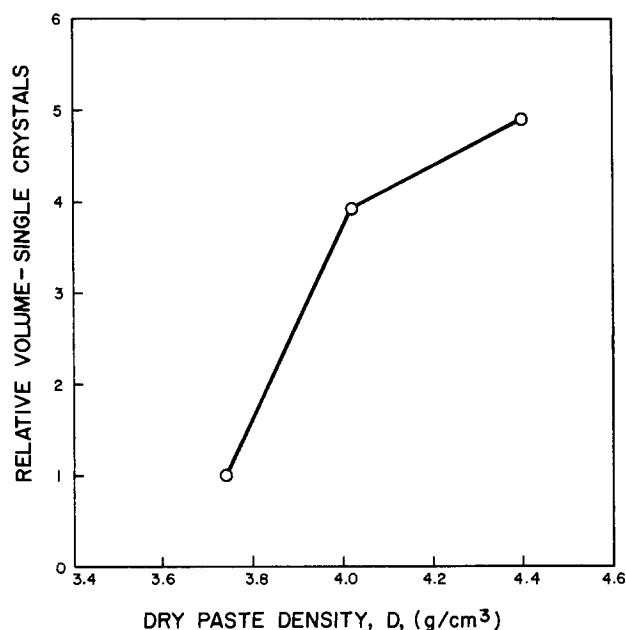


Fig. 3. Relative volumes of  $4PbO \cdot PbSO_4$  crystals in cured pastes plotted against the dry paste density.

## Conclusions

A simple laboratory method has been used to determine the specific void volumes and the dry paste densities of battery pastes, and to permit calculations of the densities of the solids within the paste. The void volumes were greater for pastes cured to develop  $4PbO \cdot PbSO_4$  than for the other pastes. A linear relationship was found between the void volumes and the dry paste densities. Different linear relationships were found for the pastes cured to develop  $4PbO \cdot PbSO_4$  and for the pastes cured otherwise. These relationships were not affected by the type of oxide nor the thickness of the plate but only by the method of cure. The degree of sulfation affected the size of  $4PbO \cdot PbSO_4$  crystals in plates cured to develop that species with the largest crystals formed at the lowest sulfations and, correspondingly, the highest dry paste densities.

An unexpected result was that the calculated density of the solids' portion of the dry paste went through a maximum value within the experimental range of dry paste densities for those pastes which contained  $4PbO \cdot PbSO_4$ . In contrast, the solids' densities of the other pastes fell off smoothly as the dry paste density was reduced. The maximum was interpreted to be a result of the difference in the crystalline perfections of the  $4PbO \cdot PbSO_4$  within the pastes of different dry paste densities.

## Acknowledgments

This work was supported, in part, by the Prestolite Battery Division, an Eltra Company, and the authors are grateful to Mr. John P. Badger, of that Division, for useful technical discussions. In addition, the authors are anxious to acknowledge their gratitude to Mr. D. Kemble Bauman, of C&D Batteries, who conducted much of the experimental work.

Manuscript received Jan. 23, 1976.

Any discussion of this paper will appear in a Discussion Section to be published in the June 1977 JOURNAL. All discussions for the June 1977 Discussion Section should be submitted by Feb. 1, 1977.

Publication costs of this article were partially assisted by C&D Batteries.

## LIST OF SYMBOLS

- $b$  intercept constant of the linear relationship between  $D$  and  $W$ ,  $g/cm^3$
- $d$  density of the solids in the dry, cured paste,  $g/cm^3$
- $D$  density of the total dry, cured paste,  $g/cm^3$
- $g$  slope constant of the linear relationship between  $v$  and  $D$ ,  $cm^6/g^2$
- $p$  intercept constant of the linear relationship between  $v$  and  $D$ ,  $cm^3/g$
- $v$  specific void volume of dry, cured, paste,  $cm^3/g$
- $W$  density of wet paste mix,  $g/cm^3$

## REFERENCES

1. G. W. Vinal, "Storage Batteries," 4th Ed., John Wiley & Sons, Inc., New York (1967).
2. H. B. Stephensen, C. L. Hixon, H. S. Long, J. S. Bryson, J. D. Purdum, and E. J. Ritchie, "Final Report on ILZRO Combined Projects LE-82 and LE-84, Pastes and Grids for the Lead-Acid Battery 1971," International Lead Zinc Research Organization, New York.
3. J. F. Dittman and H. R. Harner, "Paste Preparation and Plate Control, Starting and Lighting Batteries, Starting and Lighting Batteries, No. 7 in a Series," Eagle-Picher Co., Cincinnati, Ohio (1956).
4. N. E. Hehner (Section I) and E. J. Ritchie (Section II), "Lead Oxides," Independent Battery Manufacturers Associates Inc., Largo, Florida (1974).
5. S. C. Barnes and R. T. Mathieson, "Batteries 2," D. H. Collins, Editor, p. 41, Pergamon Press, New York (1965).
6. J. Armstrong, I. Dugdale, and W. J. McCusker, "Power Sources 1966," D. H. Collins, Editor, p. 163, Pergamon Press, New York (1967).

7. A. C. Simon "Batteries 2," D. H. Collins, Editor, p. 63, Pergamon Press, New York (1965).
8. H. R. Harner and M. F. Chubb, "Data for Storage Battery Design, Starting and Lighting Batteries, Number 6 in a Series," Eagle-Picher Co., Cincinnati, Ohio (1946).
9. A. C. Simon and E. L. Jones, *This Journal*, **102**, 279 (1955).
10. J. Burbank, *ibid.*, **113**, 10 (1966).

## Effect of Base Lead Composition on Metallurgical Properties of Maintenance-Free Battery Alloys

T. W. Caldwell and U.S. Sokolov\*

NL Industries, Incorporated, Central Research Laboratory, Hightstown, New Jersey 08520

### ABSTRACT

The effects of trace element additions on the microstructure and age-hardening properties of Pb-Ca and Pb-Ca-Sn alloys for maintenance-free batteries are reported. A specific laboratory casting procedure duplicating grid solidification conditions and the solidification-cast property relationships upon which it is based are discussed. It was found that bismuth, antimony, copper, and silver in amounts typical of high bismuth primary and refined secondary base leads have little or no influence on microstructure in Pb-0.085Ca and Pb-0.085Ca-0.8Sn. The addition of trace elements increased the early hardness of Pb-0.085Ca-0.8Sn but had no effect in Pb-0.085Ca.

Maintenance-free batteries are designed to be sealed and require no periodic addition of water. This restriction requires new, low gassing, grid alloy compositions, as the conventional Pb-Sb alloys contribute heavily to hydrogen evolution (1). The Pb-Ca system has been employed for many years in float service (2). Consequently, grid alloy development for SLI maintenance-free applications has focused on the Pb-Ca and Pb-Ca-Sn systems.

It has been reported that "the presence of bismuth is assumed to be disturbing" (3), and that bismuth and other common trace elements decrease strength and castability (4). In the latter study, it was postulated that bismuth or other trace elements interacted with calcium, reducing the effective calcium content. Other studies have indicated no interaction between bismuth and calcium (5), or interaction only at high bismuth levels (6). Davey found that below 0.034 weight per cent (w/o) bismuth, no interaction with calcium could occur, based on the Pb-Ca-Bi phase diagram (7). This level is above that found in typical commercial base leads. This study reports the effects of trace elements on the metallurgical properties of lead, Pb-Ca, and Pb-Ca-Sn alloys for maintenance-free applications.

Certain important properties of grid alloys are best measured under controlled conditions in the laboratory, and in some cases, on samples different in shape and size from cast grids. Laboratory tests also enable the screening of a large number of alloys without the difficulties of preparing alloys in grid form. Certain metallurgical aspects must be considered when measuring material properties of laboratory samples and relating results to actual cast grids. These aspects are discussed as applied to the alloy properties of interest. A technique is presented for preparing laboratory samples having properties equal to cast grids.

### Cast Structure—Property Relationships

Figure 1(a) illustrates the typical microstructure of a Pb-Ca-Sn grid. A rodlike morphology is evident within each grain, with the rodlike structure having a single orientation within a given grain. Occasionally, these structures "break down" into branched structures. This branched structure is termed a dendrite,

and the rodlike or unbranched morphology is termed fibrous dendritic. These well-known structural morphologies of alloys are discussed elsewhere in detail (8). The fibrous dendritic structure is similar to another morphology which is termed cellular (9). Cells grow in the heat flow direction while dendrites grow at some small angle to it. The importance of the distinction between cells and fibrous dendrites is that segregation of alloying and trace elements is generally more severe in dendritic solidification.

The cellular and fibrous dendritic morphologies are typically found in alloys of low solute content, such as the Pb-Ca and Pb-Ca-Sn compositions studied herein. Alloys of higher solute content, e.g., antimonial lead grid alloys, typically exhibit more fully developed dendritic structures as shown in Fig. 1(b). A fully developed dendrite is seen clearly in the center of the photograph. Around the periphery, only portions of dendrite arms are visible as the plane of polish intersects those dendrite axes at an angle. These peripheral areas are actually portions of other grains, as dendrite orientation is constant within a given grain. The dendrite is single phase solid solution surrounded by material of essentially eutectic composition.

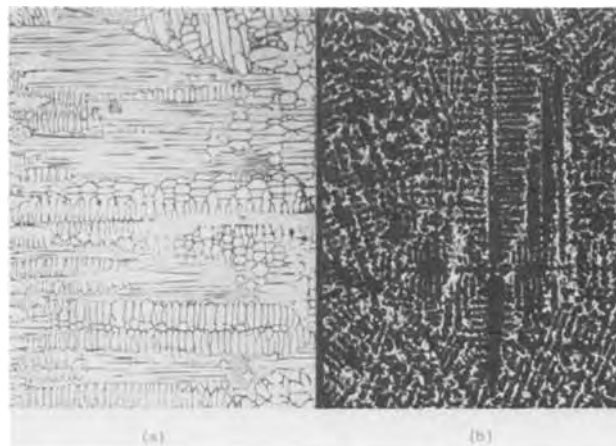


Fig. 1. Typical microstructure of Pb-Ca-Sn and Pb-Sb grids; (a) Pb-0.07Ca-0.75Sn, 80X, (b) Pb-6Sb-0.5As-0.5Sn, 150X.

\* Electrochemical Society Active Member.

Key words: lead-acid battery, lead-calcium alloys, grid casting, microstructure, mechanical properties.

The dominant feature of the intragranular microstructure of many alloys is the spacing between dendrite arms. In most cases, properties have been related to the spacing of secondary dendrite arms, *i.e.*, arms branching directly from the main or primary dendrite stalk or axis. At constant composition, tensile strength, fatigue strength, and elongation increase as dendrite arm spacing decreases (10, 11). It has been shown that antimonial lead corrosion is influenced by dendrite arm spacing (12). Furthermore, the rate of solidification of Pb-Ca alloys, and the rate of cooling through the single phase region of the Pb-Ca phase diagram were found to significantly affect tensile strength (13). It has also been determined that microstructure has a considerable influence on the rate of hydrogen evolution on a number of lead alloys (14).

Dendrite arm spacing and solidification rate are directly related as shown in Fig. 2. Data are shown for a number of alloys in different alloy systems. The relationship is usually expressed as secondary dendrite arm spacing *vs.* local solidification time, defined as the time between passage of the start-of-freezing and end-of-freezing isotherms at a given point in a casting (16). On a log-log scale, the relationship is linear, only the slope and ordinate intercept differing with alloy composition. Because of the manner in which local solidification time is defined, the relationship is independent of the amount of undercooling occurring before solidification is initiated. The relationship applies to all alloy systems as it is a characteristic of the mechanism of dendritic solidification.

For a given alloy, two castings having identical local solidification times at a given location will exhibit identical dendrite arm spacings. All the properties influenced by either of these two parameters (alternate expressions of the same phenomenon) will be equal at the given location in the two castings. With this concept, it is observed that duplicating the properties of a cast grid in laboratory samples requires the reproduction of conditions in the solidifying metal. Any combination of mold and metal temperatures, mold coat, and section size can be employed, as long as the combination yields the same local solidification time as found in the cast grid. The dendrite arm spacing provides a means of comparing solidification rates of laboratory samples and cast grids.

### Alloy Composition

Laboratory castings of lead, Pb-0.085Ca and Pb-0.085Ca-0.8Sn were prepared from three commercial base leads. Calcium and tin compositions were chosen as typical of those which may ultimately be employed in maintenance-free battery grids. The base lead compositions were determined by spark source mass spec-

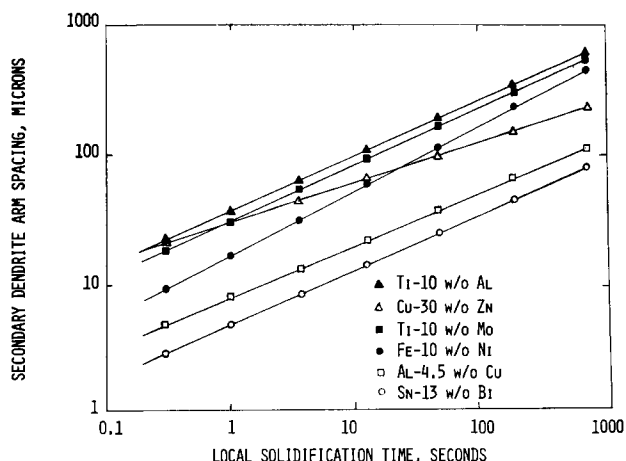


Fig. 2. Relationship between dendrite arm spacing and local solidification time for a number of alloy systems (15).

Table I. Base lead composition, ppm(wt)

	Bi	Sb	Cu	Ag
LOW Bi PRIMARY	<10	<.03	.3	6
HIGH Bi PRIMARY	180	<.03	5	5
REFINED SECONDARY	160	10	10	10

trometry and are shown in Table I. Only those elements which differed in concentration among the three base leads are shown, with all other elements < 0.001 w/o each. Comparison of the two primary base leads essentially measures the effect of bismuth, with a small increase in copper. Comparison of the high bismuth primary and the refined secondary lead essentially measures the effect of small combined additions of antimony, copper, and silver. A comparison of the low bismuth primary and the refined secondary lead measures the combined effect of all four trace elements, the major element being bismuth. It is recognized that after addition of calcium, the antimony content will decrease due to the interaction of these two elements (17). The compound  $\text{Ca}_3\text{Sb}_2$  is 33 w/o calcium. It is obvious that the 5 ppm loss of calcium due to compound formation with 10 ppm antimony is negligible for a Pb-0.085Ca alloy (850 ppm Ca), even if the reaction went to completion.

### Sample Preparation

A technique for casting lead alloy samples under solidification conditions identical to those encountered in actual grid casting was developed. Figure 3 illustrates an eight-cavity carbon steel mold. The mold was preheated to 365°C, and the molten alloy, also at 365°C, was poured into each of the eight 2.54 cm diam  $\times$  0.65 cm deep cavities. The alloy, of course, remained molten at this mold temperature. A signal was sent to a solenoid valve on a high pressure water line, allowing water to enter the mold through the water lines shown, rapidly cooling the mold, and solidifying the alloy samples. Approximately 600g, twice the weight of the eight cast samples, was melted in a resistance-heated, graphite-coated Armco iron crucible for each experiment. A new crucible was used in each experiment. The molten metal surface was covered with powdered charcoal during melting and alloying. The mold was coated with Chemco J-500, a graphite mold spray. Conditions and button geometry were chosen so that the start-of-freezing and end-of-freezing isotherm velocities were constant and essentially equal as the iso-

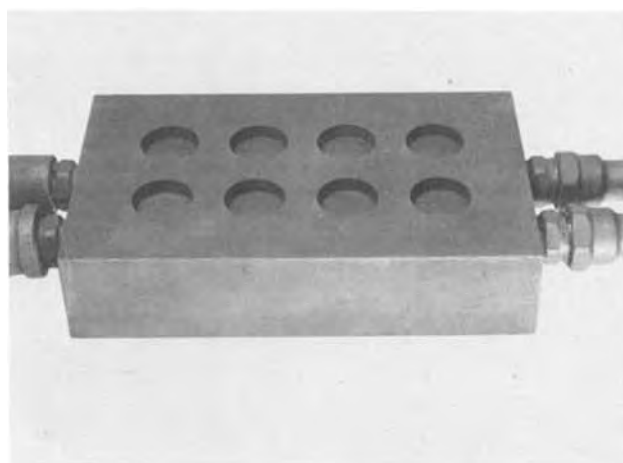


Fig. 3. Eight-cavity mold with solenoid-controlled water lines

Table II. Average tertiary dendrite arm spacing of Pb-6Sb-0.5As-0.5Sn

AVERAGE SPACING, $\mu$	
GRID WIRE	12.3
BUTTON	11.1
BUTTON/CORK MOLD COAT	15.4

therms moved across the thickness of each button during solidification. From the definition given previously, it is clear that under these conditions, local solidification time and hence dendrite arm spacing will be constant throughout the buttons. The heat flow condition resulting in constant isotherm velocity near a mold surface is often termed "*h*-controlled" heat flow, where *h* is the interface heat transfer coefficient. The mold coat then becomes the major barrier to heat flow in the system. These conditions apply when casting thin sections in metal molds, as in grid casting.

The chill surface of each sample was flat and free of cold shuts and porosity. The cast samples, called buttons, solidified in a substantially unidirectional manner perpendicular to the mold/metal interface.

#### Alloy Microstructures

The microstructures of the eight buttons simultaneously cast of each alloy were identical, and were reproducible in subsequent castings of the same alloy. To verify that the castings were produced under the conditions present in solidifying grids, the average tertiary dendrite arm spacings of a Pb-6Sb-0.25As-0.25Sn button and grid were compared, as shown in Table II. The average dendrite arm spacings of the grid and the button cast in the manner previously described were identical, within the accuracy of the measurement technique. These structural comparisons were performed on a Pb-Sb alloy as Pb-Ca and Pb-Ca-Sn alloys do not exhibit well-defined dendrite arms.

To illustrate the sensitivity of the dendrite arm spacing to changes in solidification conditions, the use

of a cork spray in place of the graphite mold coat normally employed in the button mold resulted in a proportionally large difference in dendrite arm spacing, as shown. In other words, when the bottom mold was coated with the graphite spray, dendrite arm spacings were identical to those found in cork-sprayed grid casting molds. When the button mold was coated with a cork spray, however, dendrite arm spacings increased. This illustrates that it is the combination of mold and metal temperatures, mold coat, and section size which determines the resultant structure.

The specially prepared alloy and base lead samples were examined metallographically to determine the influence of both alloy additions and trace elements on cast structure. The bottom face of each button examined was polished and etched to reveal the microstructure. An acetic acid-hydrogen peroxide attack polish and an ammonium molybdate etchant were employed. In many cases, the samples required overetching, with resultant pitting, to provide enough contrast for photographic reproduction.

Figure 4 shows the structure of the three base leads employed. A grain boundary is observed in Fig. 4(a), while the other photographs show portions of a single grain. The fine structure is the fibrous dendritic morphology. Although not shown, the grain size was approximately equal in all three base leads. Areas of elongated cells were occasionally observed, but the structure consisted mostly of "regular" cells, with some breakdown into true branched dendrites. In some areas the distinction between structures was not clear. The growth conditions in the castings were therefore in the range of the cellular-dendritic transition for these alloys, where local thermal perturbations or slight differences in over-all cooling rates between castings can alter the shape and size of cells (18). Figure 5 presents a side view of the structure in Fig. 4(a). The rodlike fibrous dendritic morphology is readily apparent. The dendritic segments are actually much longer than observed, as the dendrite axes intersect the sample surface at an angle, giving a shortened appearance.

Figure 6 illustrates the structure of Pb-0.085Ca alloys prepared with each base lead. The addition of calcium to the base leads has decreased the grain size in all cases. Figures 6(a) and (b) illustrate that the addition of bismuth does not measurably affect grain size. However, the addition of the other trace elements de-

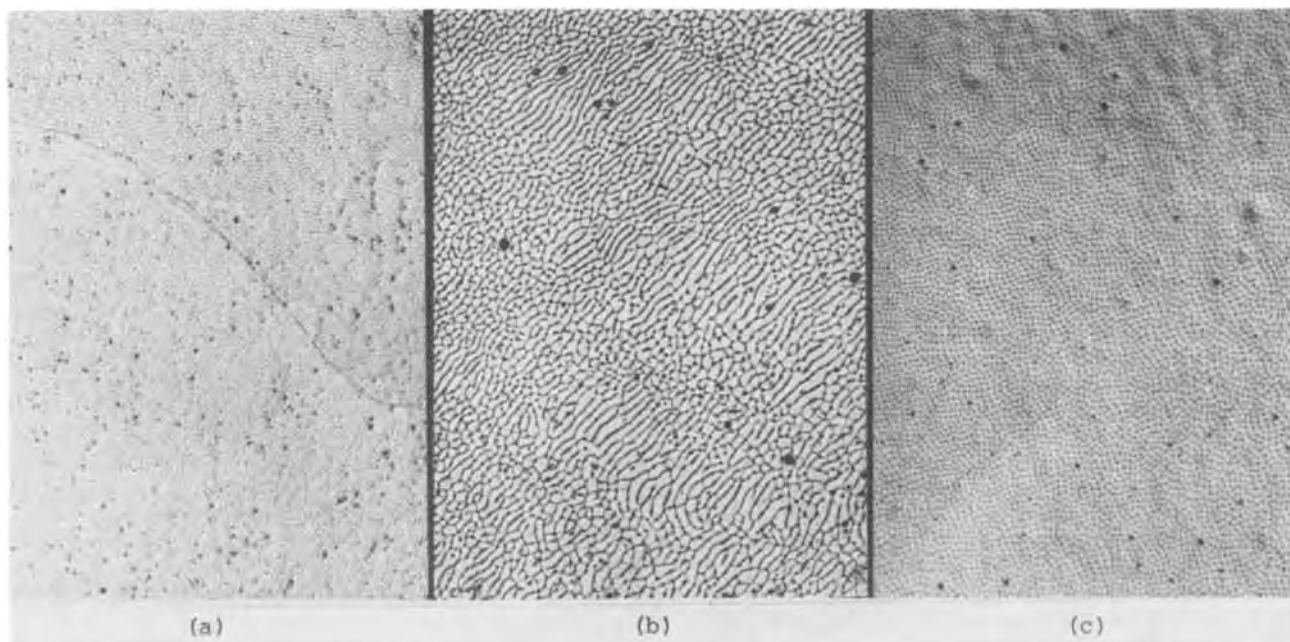


Fig. 4. Cast microstructure of the three base leads; (a) low Bi primary, (b) high Bi primary, and (c) refined secondary lead, 52X

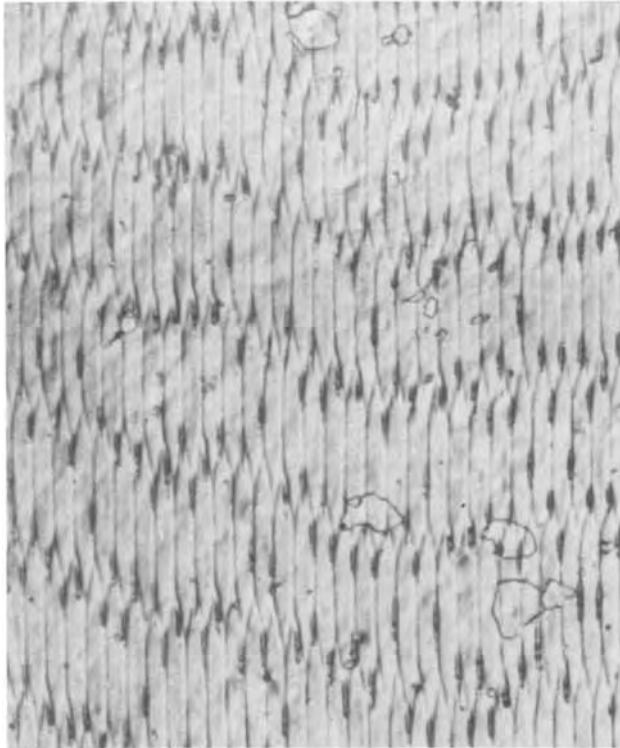


Fig. 5. Side view of casting in Fig. 4(a) showing fibrous dendritic morphology, 120X.

creases grain size slightly, comparing Fig. 6(b) and (c). The underlying fibrous dendritic structure is still visible. Some of the small grainlike features observed on the surface are remnants of the deformed surface layer produced during sample preparation. This can be demonstrated by successively polishing and photographing the same area. When a particular grain is initially absent, then appears, and finally disappears from within an underlying grain without touching a third grain, while the underlying structure remains the same, Euler's law (19) for polyhedral bodies in a space-filling aggregate is violated. The disappearing

grain is an artifact. Artifact grains cut across fibrous dendrites in Fig. 5.

The addition of 0.8Sn to form Pb-0.085Ca-0.8Sn modifies the structure as shown in Fig. 7. The structure closely resembles that found in the base leads shown in Fig. 4, *i.e.*, a larger grain size and pronounced fibrous dendritic morphology are again evident. Local variations in cell size are again evident in all three alloys. Comparison of the three alloys indicates that the structure is unaffected by the addition of bismuth, or combined additions of bismuth, antimony, copper, and silver.

### Age Hardening

The hardness of the cast buttons was measured as a function of time after casting. While hardness is only an indirect measure of mechanical properties, reasonably good correlation between hardness and tensile strength in Pb-Ca alloys has been obtained (13). A crossplot of yield strength *vs.* hardness from data in this reference also indicates a reasonable correlation. Hardness was measured on the Rockwell Superficial 15Y scale. Cast buttons were given a minor surface preparation consisting of filing the surface smooth on a fine file. This treatment did not affect the hardness measurement, as a button prepared in this manner every day before testing for three days was identical in hardness to a button of the same composition filed and tested for the first time at three days after casting, *i.e.*, after substantial age hardening. Five hardness readings were averaged to determine the hardness at each time of measurement.

As further verification of the sample preparation technique, Pb-Ca-Sn alloy buttons cast of metal taken from the melting pot of a grid casting machine exhibited a hardness close to that of grids from the same alloy, shown in Fig. 8. Hardness was measured with a Barber-Coleman 936 Impressor, a device suitable for measuring the hardness of small sections such as found in cast grids (20).

Figure 9 illustrates the age-hardening behavior of the Pb-Ca and Pb-Ca-Sn alloys studied. For the Pb-Ca alloys, age hardening is observed in the first 24 hr after casting. Hardness continues to increase at a very low rate as evidenced by the increased hardness at 60 days after casting. The differences between alloys of differ-

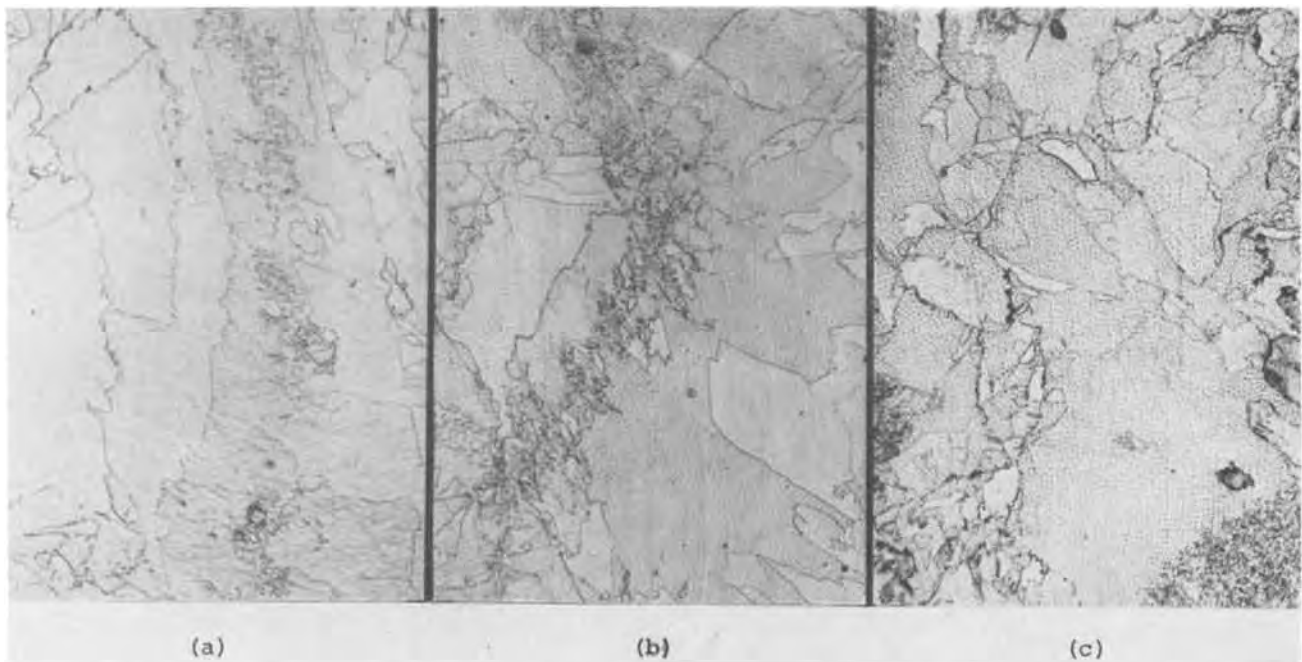


Fig. 6. Cast microstructure of Pb 0.085Ca with three base leads; (a) low Bi primary, (b) high Bi primary, and (c) refined secondary, 52X



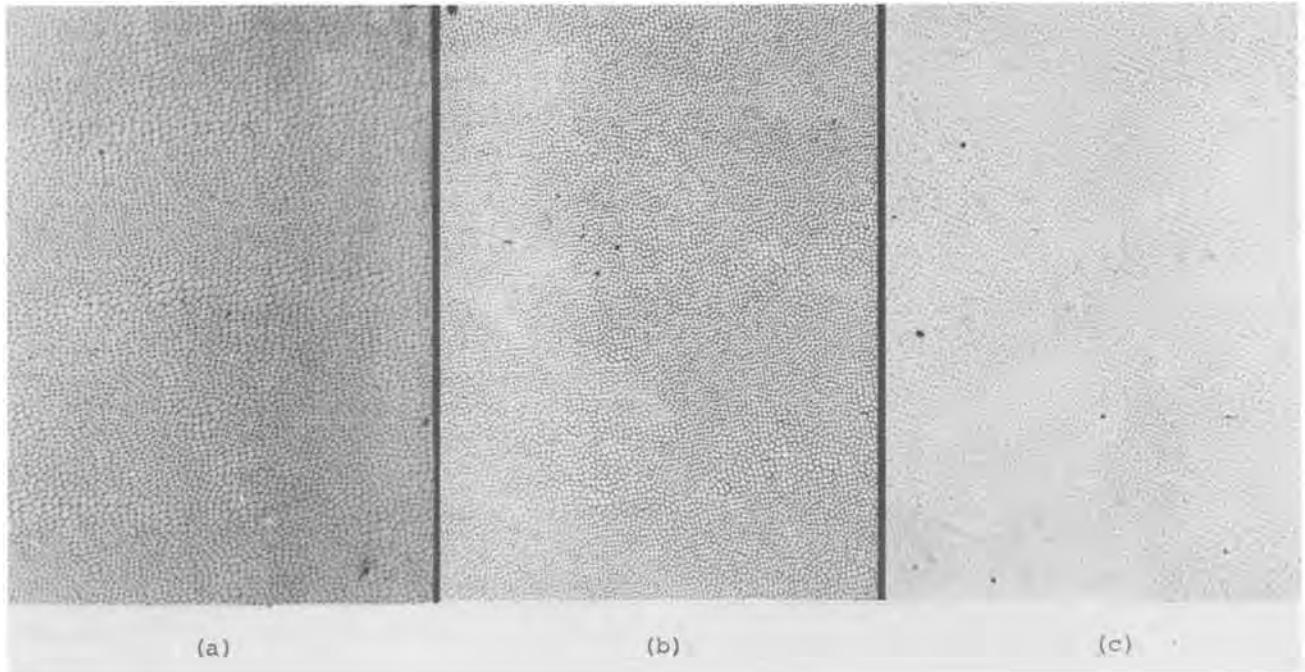


Fig. 7. Cast microstructure of Pb-0.085Ca-0.8Sn with three base leads; (a) low Bi primary, (b) high Bi primary, and (c) refined secondary, 52X.

ent base leads are not considered statistically significant, as the range of individual hardness readings at each time are as large as the differences between alloys.

The hardness curves of the Pb-Ca-Sn alloys indicate a very large age-hardening effect shortly after casting, compared to the Pb-Ca alloys. The hardness is initially much lower in Pb-Ca-Sn than in Pb-Ca alloys,

but it increases rapidly, approaching the Pb-Ca hardness after 2 days. Thereafter, age hardening continues at a slow rate. At 60 days after casting, the hardness has increased to the level found in the Pb-Ca alloys. It appears from the slopes of the curves that the Pb-Ca-Sn alloy hardness will surpass that of the Pb-Ca alloys. This has been observed previously (21, 22). Significant differences in hardness are observed as a function of base lead composition, for up to 2 days after casting. In the initial 2 day period, hardness increases with the addition of bismuth, and increases further

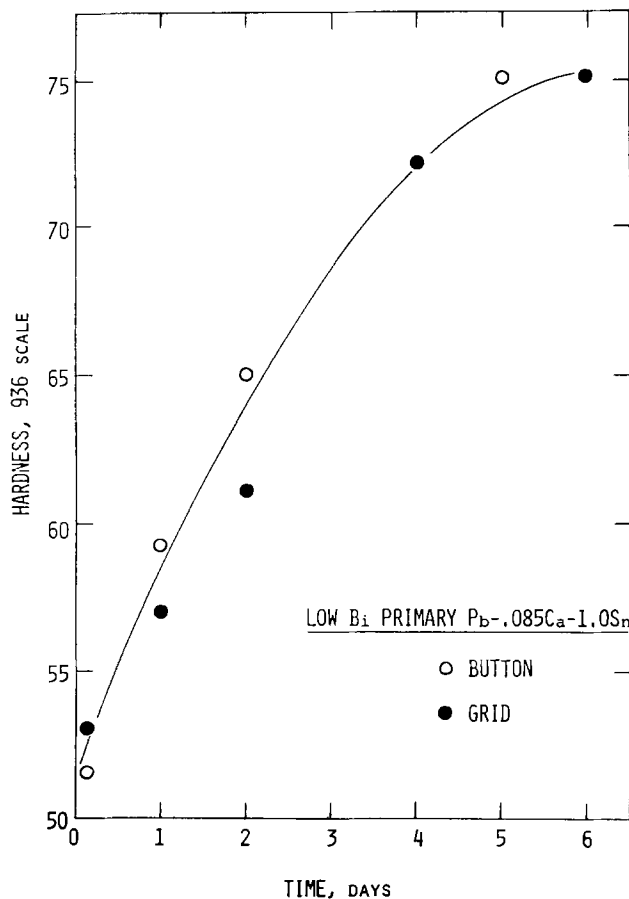


Fig. 8. Comparison of grid and button hardness

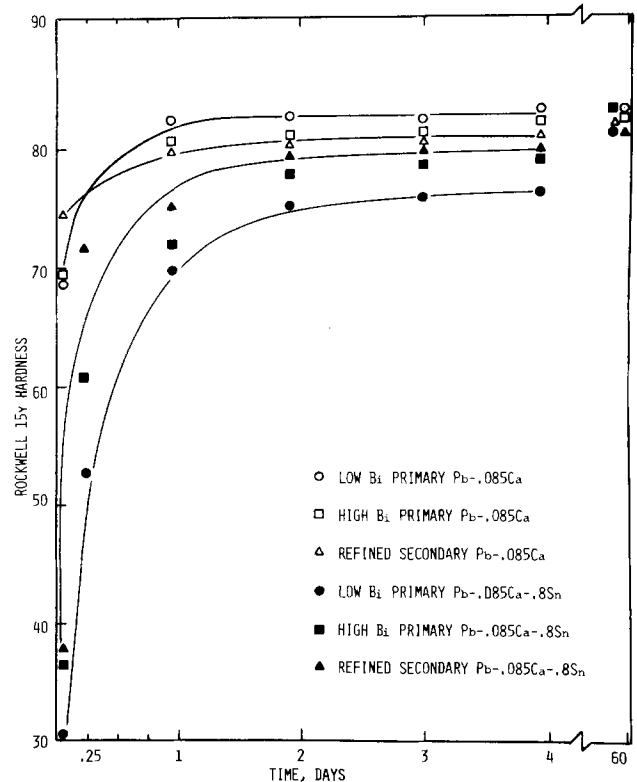


Fig. 9. Hardness vs. time after casting for three Pb-Ca and Pb-Ca-Sn alloys.

with combined additions of bismuth, antimony, copper, and silver. After 2 days, differences between alloys are not statistically significant with the measurement technique used.

### Discussion

General relationships between solidification parameters and resultant microstructural features have been presented. When studying laboratory specimens for the purpose of screening potential grid alloys, or even for quality control of established grid alloys, it is evident that the duplication of actual cast grid properties requires the duplication of conditions in the solidifying metal. A special casting technique has been presented for this purpose. The procedures employed to evaluate the accuracy of this technique can be employed to design casting procedures for other sample configurations as well.

Metallographic examination of Pb-0.085Ca and Pb-0.085Ca-0.8Sn alloys made from the three base leads has shown that bismuth, in the range studied, does not alter grain size or the fibrous dendritic morphology. In Pb-0.085Ca, the combined addition of antimony, copper, and silver does promote some grain refinement, but no grain refinement is observed when these additions are made to Pb-0.085Ca-0.8Sn. The grain-refining agent is most likely copper. These observations are in qualitative agreement with previous work on the effect of calcium, tin, and bismuth at similar levels (23).

The addition of tin, at the level studied, masks the microstructural effects of both calcium and trace element additions, as the microstructure of Pb-0.085Ca-0.8Sn is essentially indistinguishable from the base leads. The masking effect of tin on metallurgical and electrochemical properties is discussed in detail elsewhere (20). Some of the effects observed when tin is added to Pb-Ca alloys can be understood as calcium being added to Pb-Sn alloys, as the tin content is usually many times greater than the calcium content.

The effects of additions of bismuth, antimony, copper, and silver on hardness are observable only at relatively low hardness values, only during the initial 2 day aging interval in Pb-0.085Ca-0.8Sn, and not at all in Pb-0.085Ca. At the higher hardness levels, the influence of these trace elements on hardness presumably still exists, but the net effect is not measurable on the Rockwell 15Y scale and may be of no significance. The contribution of calcium to the hardness overshadows the effect of these trace element additions at these high hardness levels.

Recently, it has been shown (23) that bismuth additions greater than 220 ppm increase the initial age hardening rate of Pb-0.06Ca but have no effect on Pb-0.09Ca, a composition close to that used herein. In the same study it was observed that the additions of 0.5 and 1.0% tin delayed the onset of age hardening regardless of bismuth content. The hardening mechanism was shown to be at least partly due to grain refinement by calcium and bismuth in the absence of tin. However, it is not clear from the microstructures observed and the trace element levels used in this study what the hardening mechanism is that distinguishes alloys of differing trace element levels at less than 2 days of aging in Pb-0.85Ca-0.8Sn. Trace elements may contribute to solid solution hardening and/or change the precipitation kinetics of age hardening.

### Conclusions

The conclusions of this study are summarized as follows:

1. A specific sample preparation technique has been developed to duplicate solidification conditions in cast grids. Castings so produced exhibit cast grid microstructures and hardness values.

2. Addition of 180 ppm bismuth does not influence the microstructure of Pb-0.085Ca or Pb-0.085Ca-0.8Sn.

3. Combined additions of 160 ppm bismuth, 10 ppm antimony, 10 ppm copper, and 4 ppm silver to Pb-0.085Ca have a slight grain-refining effect.

4. In Pb-0.085Ca-0.8Sn, the combined additions of 160 ppm bismuth, 10 ppm antimony, 10 ppm copper, and 4 ppm silver have no visible effect on microstructure.

5. Additions of bismuth, and combined additions of bismuth, antimony, copper, and silver in the above contents do not influence the age hardening behavior of Pb-0.085Ca. Significant increases in hardness and the rate of hardening of Pb-0.085Ca-0.8Sn in the period 0-2 days after casting are found with the above element additions.

### Acknowledgments

The authors would like to thank D. Goodmacher for the metallographic work and E. R. Hein and G. R. Kotler for helpful discussions throughout the course of the study. The authors also thank NL Industries for permission to publish this work.

Manuscript submitted Jan. 7, 1975; revised manuscript received March 4, 1976. This was Paper 34 presented at the Boston, Massachusetts, Meeting of the Society, Oct. 7-11, 1973.

Any discussion of this paper will appear in a Discussion Section to be published in the June 1977 JOURNAL. All discussions for the June 1977 Discussion Section should be submitted by Feb. 1, 1977.

Publication costs of this article were partially assisted by NL Industries, Incorporated.

### REFERENCES

1. J. T. Crennel and A. G. Milligan, *Trans. Faraday Soc.*, **27**, 103 (1931).
2. H. F. Haring and U. B. Thomas, *Trans. Electrochem. Soc.*, **68**, 293 (1935).
3. C. Drotschmann, *Batterien*, **19**, 851 (1966).
4. ILZRO Combined Report LE-82 and LE-84 (1971).
5. E. E. Schumacher and G. M. Bouton, *Metals Alloys*, **14**, 865 (1941).
6. V. Goler, *Giesserei*, **25**, 262 (1938).
7. T. R. A. Davey, *Trans. AIME*, **206**, 341 (1956).
8. M. C. Flemings, "Solidification Processing," McGraw-Hill Book Co., New York (1974).
9. D. Walton, W. A. Tiller, J. W. Rutter, and W. C. Winegard, *J. Metals*, **7**, 1023 (1955).
10. E. M. Passmore, M. C. Flemings, and H. F. Taylor, *Trans. AFS*, **66**, 96 (1958).
11. R. F. Polich and M. C. Flemings, *ibid.*, **73**, 28 (1965).
12. S. Feliu, L. Galan, and J. A. Gonzalez, ILZRO Report LE-130 (1970).
13. A. B. Townsend, USAEC Report Y-1307 (1960).
14. T. W. Caldwell and U. S. Sokolov, in "Power Sources 5," D. H. Collins, Editor, p. 73, Academic Press, New York (1975).
15. H. D. Brody, in "Solidification Technology," J. J. Burke, M. C. Flemings, and A. E. Gorum, Editors, Brook Hill Publishing Co., Chestnut Hill, Mass. (1974).
16. T. F. Bower, H. D. Brody, and M. C. Flemings, *Trans. AIME*, **236**, 624 (1966).
17. G. M. Bouton and G. S. Phipps, *Trans. Electrochem. Soc.*, **92**, 305 (1947).
18. L. R. Morris and W. C. Winegard, *J. Cryst. Growth*, **6**, 61 (1969).
19. C. S. Smith, *Met. Rev.*, **9**, 1 (1964).
20. T. W. Caldwell, U. S. Sokolov, and L. M. Bocciairelli, Paper 36 presented at the Electrochemical Society Meeting Boston, Massachusetts, Oct. 7-11, 1973; To be published.
21. N. L. Parr, A. Muscott, and A. J. Crocker, *J. Inst. Met.*, **87**, 321, (1958/59).
22. E. R. Hein, Unpublished research.
23. M. Myers, H. R. Van Handle, and C. R. DiMartini, *This Journal*, **121**, 1526 (1974).



# Electrochemical Properties of Sodium Beta-Alumina in $\text{ZnCl}_2$ -NaCl Melts

David R. Flinn\*<sup>1</sup> and Kurt H. Stern\*

Naval Research Laboratory, Chemistry Division, Washington, D.C. 20375

## ABSTRACT

On the basis of membrane potential measurements, sodium  $\beta$ -alumina is shown to be almost completely selective for sodium ions in  $\text{NaCl}$ - $\text{ZnCl}_2$  melts. However, the continuous electrolysis of  $\beta$ -alumina in these melts decreases its conductivity. These results are interpreted in terms of the movement of mobile sodium ions becoming impeded by nearly immobile zinc ions introduced into the ceramic under the applied electric field. Beta-alumina is therefore not useful in battery applications where ions other than sodium are present. It can, however, be used in the construction of sodium ion specific membrane electrodes.

In recent years an enormous amount of work has been done on sodium  $\beta$ -alumina (SBA), primarily because of its potential applicability as a sodium-ion-conducting ceramic separator in the sodium-sulfur battery. Other possible uses of the material have been much less explored. For example, it was conceivable that the material might be useful for selectively passing sodium from one compartment to another in a molten salt battery containing a mixture of molten salts, and in the construction of ion-selective electrodes. The present work was undertaken with these applications in mind.

Several years ago Yao and Kummer (1) reported ion exchange equilibrium constants for single crystals of SBA in a variety of molten salts. They found that the exchange was particularly unfavorable for divalent cations, *i.e.*, in some cases no exchange of these cations for sodium ions in SBA could be detected by weight change methods when diffusion, *i.e.*, a chemical potential gradient, was the only driving force.

We therefore chose a representative melt,  $\text{ZnCl}_2$ -NaCl, for this study. It has a sufficiently wide liquid range at temperatures low enough for the vapor pressure of  $\text{ZnCl}_2$  not to be prohibitively high, and zinc electrodes are reversible to zinc ions in these melts. Thermodynamic activity data for these melts are available, although they are not as accurate as is desirable.

The major object of this study was to find out whether sodium would continue to be the only current-carrying species in SBA as current was passed through it from one  $\text{ZnCl}_2$ -NaCl melt to another, and whether the composition of the SBA remained constant as evidenced, for example, by the electrical conductivity.

## Experimental

Commercially prepared SBA tubes from two sources were examined. Tubes purchased from GEC Power Engineering, Ltd., London, England, (GEC) were 8 mm ID, 10 mm OD, and 17 cm in length. Other tubes examined were manufactured by Tokyo Shibaura Electric Co., Ltd. (TSE), and were provided to us by Mr. Roy Rice of the Naval Research Laboratory. These tubes were 13 mm ID, 15 mm OD, and 15 cm in length. X-ray analysis of the tubes showed the presence of  $\sim 8$  volume per cent  $\alpha$ - $\text{Al}_2\text{O}_3$  in the GEC tubes, with none detectable in the TSE tubes. The GEC tubes were found to contain more than 0.5% Zr and several per cent Si by emission spectrographic analysis; the TSE tubes contained several per cent Si and Mg.

\* Electrochemical Society Active Member.

<sup>1</sup> Present address: U.S. Bureau of Mines Metallurgy Research Center, College Park, Maryland 20740.

Key words: electrolysis,  $\beta$ -alumina, molten salts, galvanic cells, conductivity.

The zinc metal used was NBS freezing point standard 43e. Reagent grade NaCl was vacuum dried at 300°C. Reagent grade  $\text{ZnCl}_2$  was purified by bubbling HCl gas through the molten salt followed by helium.

All experiments were carried out in a helium-filled Vacuum Atmospheres Corporation dry box, with water and oxygen content maintained at less than 1 ppm by a recirculating purification system. High purity alumina crucibles, McDanel 998, were used to contain the molten salts. Molten zinc electrodes were held in small silica cups, suspended in the melt by small silica tubes, through which tantalum wires contacted the molten zinc.

Potentials were measured with an Orion Model 801 digital pH meter or a Corning Model 12 pH meter, used in the millivolt mode. Current was integrated with a Koslow Scientific Coulometer, Model 541. Current was maintained approximately constant by manual adjustment of the power supply voltage. Resistance of the SBA was measured either by a General Radio Type 1608A impedance bridge at 1 kHz or at d.c., or by measuring the potential drop across the cell for a given current. The resistance, rather than the resistivity, is reported, since the area of melt contact with the tubes was not known accurately.

The first experiment, illustrated in Fig. 1, was carried out to determine the ion selectivity of SBA in  $\text{ZnCl}_2$ -NaCl mixtures. In this experiment a GEC tube was used to separate a known, constant composition  $\text{ZnCl}_2$ -NaCl mixture from a variable mixture, initially concentrated in  $\text{ZnCl}_2$ . Zinc electrodes, contained in Pyrex tubes, with tantalum contact wires, were used as reference electrodes in each melt mixture. A zinc electrode was also used in direct contact with the variable melt mixture. Open-circuit potentials were re-

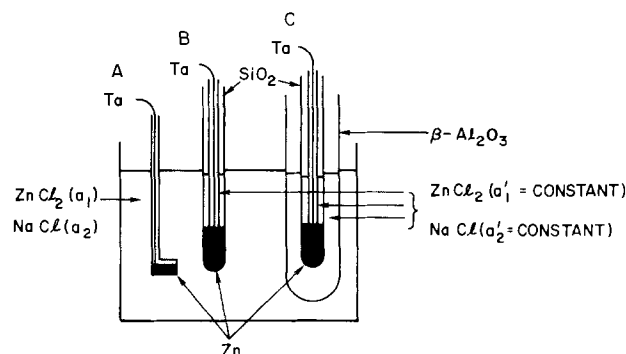


Fig. 1. Galvanic cell used to determine ion selectivity of SBA. For a description of the method see text.

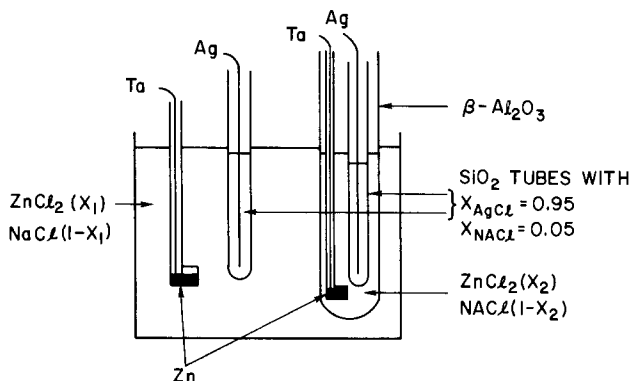


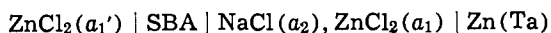
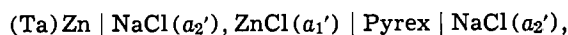
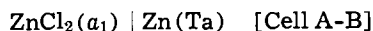
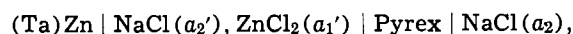
Fig. 2. Galvanic cell used for electrolysis of SBA. For a description of the method see text.

corded following NaCl additions to the variable mixture side.

In the other experiments (Fig. 2), a potential was applied across the SBA tube separating two ZnCl<sub>2</sub>-NaCl mixtures. Zinc electrodes were in direct contact with the melt mixture on each side of the SBA. Also, a Ag/AgCl-NaCl reference electrode inside a Pyrex membrane was used as a reference electrode in the outer compartment when the smaller GEC tube was used, and on each side when the larger TSE tubes were used. From the amount of charge which passed through the SBA the amount of sodium transferred from one compartment to the other was calculated, assuming that sodium ion carried all of the charge. This assumption was tested by comparing the melt composition thus calculated with the composition obtained potentiometrically. All measurements were carried out at 500°C.

### Results

The cell illustrated in Fig. 1 is actually a double cell in which two glass reference electrodes, one in the inner, the other in the outer compartment, can be measured against a zinc electrode in the melt of variable composition. For clarity we write the two cells separately



[Cell A-C]

where  $a_2' = 0.301$ ,  $a_1' = 0.699$ , and  $a_1$  and  $a_2$  are variable. (Sources of activity data for ZnCl<sub>2</sub>-NaCl melts are discussed below.)

The chief function of the Pyrex membrane inside the SBA tube (cell A-C) is to prevent direct contact between metallic zinc and SBA. Since the inside and outside of this Pyrex tube are in contact with melts of the same composition (this is also the composition in electrode B), no net membrane potential is developed across this glass, and the inner zinc electrode thus behaves as if the Pyrex were absent. Since Pyrex is highly selective for sodium ion in NaCl-ZnCl<sub>2</sub> melts (2), the emf expected for cell A-B is (3)

$$E_{A-B} = \frac{RT}{2F} \ln \left[ \left( \frac{a_1'}{a_1} \right) \left( \frac{a_2}{a_2'} \right)^2 \right] \quad [1]$$

If SBA were also highly selective for sodium ion compared to zinc ion, Eq. [1] should also be the emf of cell A-C, and  $E_{B-C}$  should be zero for all ZnCl<sub>2</sub>-NaCl compositions in the outer compartment.

Figure 3 shows a plot of the observed potentials  $E_{A-B}$  (□) and  $E_{A-C}$  (○) vs. the potentials predicted from Eq. [1]. The line shown is drawn through the 0,0 origin with a slope of unity. Activity coefficients were

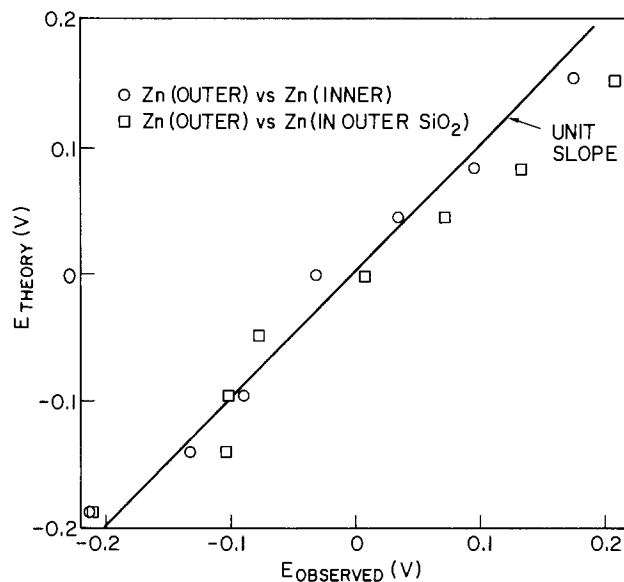
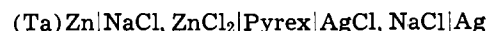


Fig. 3. Experimental test of Eq. [1], using the cell in Fig. 1. □  $E_{A-B}$ , ○  $E_{A-C}$ .

taken from Bloom *et al.* (4), and were determined by a transpiration technique. The results shown in Fig. 3 indicate that SBA shows nearly the same selectivity for sodium ion over zinc ion as that shown by Pyrex.

The experimental cell used in the second set of experiments is shown in Fig. 2. This cell consists of two complete cells of the form



with the NaCl-ZnCl<sub>2</sub> melts separated by a SBA membrane.

The predicted potentials between the zinc electrodes are the same as those given by Eq. [1], assuming a high sodium ion selectivity for the Pyrex and β-alumina. The emf expected between the zinc electrode and silver electrode pair on each side of the SBA may be expressed by the equation

$$E_{Zn/Ag} = E^{\circ}_{ZnCl_2/AgCl} - \frac{RT}{2F} \ln \frac{a_{AgCl}^2}{a_{ZnCl_2}} - \frac{a_{NaCl} \text{ (in AgCl)}}{a_{NaCl} \text{ (in ZnCl}_2)} \quad [2]$$

where  $E^{\circ}_{ZnCl_2/AgCl}$  is that for the reaction:  $2Ag + ZnCl_2 = 2AgCl + Zn$ , and is  $-0.707V$  at 500°C (5).

A potential was applied between the two zinc electrodes of the cell shown in Fig. 2 and the current was continuously integrated. At selected times the applied potential was disconnected and the SBA resistance and the open-circuit potentials were measured as a function of charge passed. Occasionally a weighed amount of NaCl was added to the outer melt compartment to maintain a reasonable concentration of NaCl in the melt.

The concentrations and activities of NaCl and ZnCl<sub>2</sub> were calculated for both compartments for each potential measurement by assuming that all of the charge passed through the SBA was carried by sodium ions. Figure 4 shows a comparison of the emf measured (for both GEC and TSE tubes) between the zinc electrodes and the emf predicted by Eq. [1]. Both dashed lines are drawn through the respective sets of points with unit slope, and with best visual fit, to illustrate the asymmetry between the measured and predicted cell potentials. This asymmetry is in the same direction as the applied potential (▼), even though the potentials were measured at open circuit. For the TSE tube, two emf's were also measured after electrolysis in the opposite direction, and the resulting values are shown

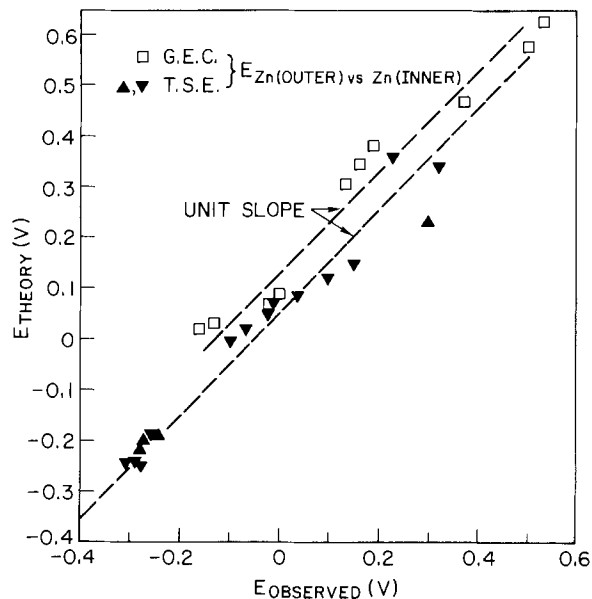


Fig. 4. Experimental test of Eq. [1] using the cell in Fig. 2

in Fig. 4 by the symbol  $\blacktriangle$ . Although only one potential was recorded for a long reverse electrolysis period (upper right-hand portion of the figure), its value suggests that the asymmetry potential in the SBA is reversible.

For the TSE tube cells, other potentials were also recorded. The potential between the two silver electrodes was observed to be nearly zero for all concentrations, as would be expected for analogous reasons that  $E_{B-C}$  is zero for the cell in Fig. 1. This result can easily be calculated from Eq. [1] and [2] by computing

$$E_{Zn(I)/Zn(II)} - E_{Zn(I)/Ag(I)} - E_{Zn(II)/Ag(II)} \equiv E_{Ag(I)/Ag(II)} = 0$$

The emf's observed between the pairs of zinc and silver electrodes on each side of the SBA were also measured for most concentrations. These results are compared in Fig. 5 to those predicted from Eq. [2]. The observed potentials are about 100 mV more positive than those predicted.

The resistance across an effective area of  $4.7 \text{ cm}^2$  of the TSE tube observed during the electrolysis is shown in Fig. 6. The number to the right of each point is the mole fraction of the NaCl in the side of the cell which is supplying sodium ions to the membrane. Dur-

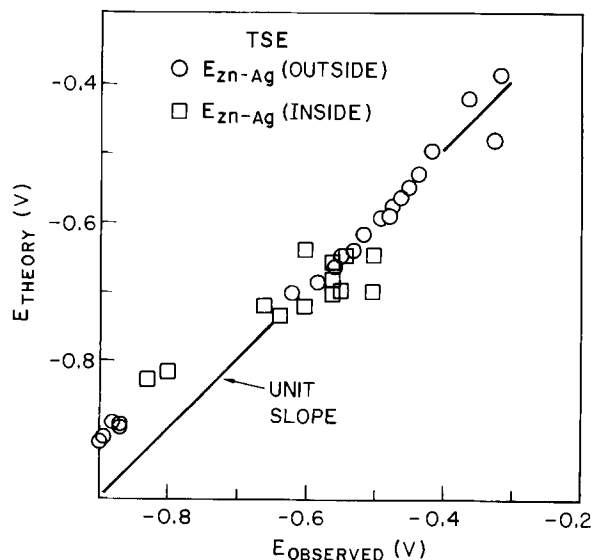


Fig. 5. Experimental test of Eq. [2] using the cell in Fig. 2

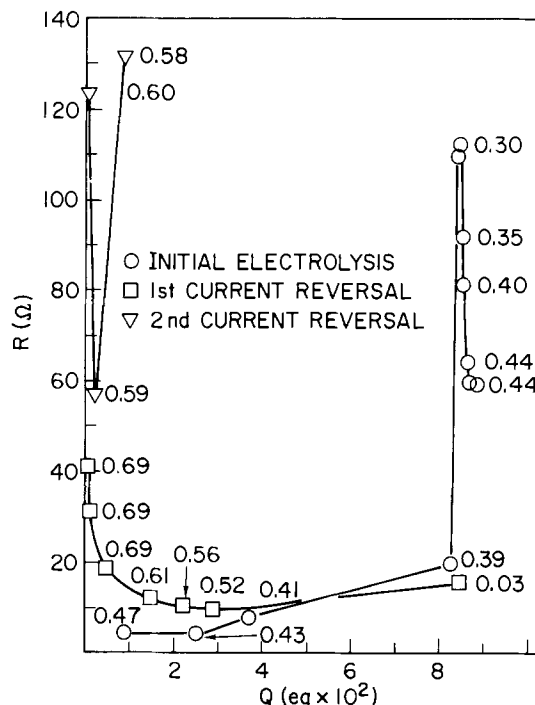


Fig. 6. Resistance of TSE tube as a function of charge passed during electrolysis. For details see text.

ing the initial electrolysis (at  $42.6 \text{ mA}\cdot\text{cm}^{-2}$ ) the cell resistance increased rapidly after the passage of  $\sim 18.5 \text{ mequiv}\cdot\text{cm}^{-2}$ . Additional sodium chloride was added to the side from which sodium was being electrolyzed. Although these additions did result in a lower resistance, the original low resistance value for the same mole fraction was not regained.

When the current was reversed, the resistance fell to a value which was approximately twice that originally observed, and slowly rose with increasing charge passed. The resistance did not rise to the high value observed in the initial electrolysis direction, even at low NaCl mole fractions. The current was then again reversed to the original direction and after a short-lived decrease, the resistance increased again, rising to approximately 500 ohms in a very short time. Further additions of zinc,  $\text{ZnCl}_2$ , and NaCl to the cell did not lower the membrane resistance.

When the GEC tube was electrolyzed, high resistances were noted for both electrolysis directions after about the same amount of charge (per unit area) was passed as in the TSE tube case.

### Discussion

Equation [1] is a simplified form of the Eisenman equation (6) which holds when the membrane is highly selective for a given cation in a mixture of two different cations, and includes the Nernst potential arising from the electrode reactions. A complete discussion and development of Eq. [1] is given in Ref. (3).

The results of the open-circuit experiments shown in Fig. 3 indicate that SBA is highly selective for sodium ion in the presence of zinc ion in the mixed chloride melt. The selectivity constant of the Eisenman equation (6) includes a thermodynamic equilibrium constant of ion exchange at the membrane surface and the mobility ratio of the two exchanging ions in the membrane. The selectivity constant may thus be large because the equilibrium constant is large, the mobility ratio is large, or because both are large. Unfortunately, the open-circuit experiment does not discriminate between the two possibilities.

The results shown in Fig. 4 suggest that the SBA ceramic itself may be polarized as a result of an electric field applied across it, and that this polarization

may be reversed by reversing the field. However, some doubt is cast on this interpretation by the apparent asymmetry exhibited by the separate pairs of Zn-Ag electrodes for which SBA is not in the circuit being measured. An alternate explanation may lie in the poor activity data available for ZnCl<sub>2</sub>-NaCl melts. This system deviates highly negatively from Raoult's law and calculated emf's are thus quite dependent on activities. The data used (4), the only ones available at 500°C, were obtained from transpiration experiments and disagree with data obtained by other methods at higher temperatures (7). Nevertheless, the data in Fig. 3-5 show clearly that SBA acts as a sodium-selective membrane in ZnCl<sub>2</sub>-NaCl melts.

The question of ion mobility in SBA is apparently answered by the electrolysis experiments. Figure 6 shows that continued electrolysis through the SBA in a given direction results in increasing cell resistance. Reversal of the electrolysis direction is unable to remove the cause of the increased resistance, since when the current was again reversed, the high resistance persisted. Apparently the zinc ion, which is present to some extent at the melt/SBA interface due to the ion exchange equilibrium at the interface, becomes trapped in the SBA structure as it is transported by the applied electric field and inhibits sodium ion migration. Current reversal is not effective in removing the zinc ion from the SBA in any reasonable time period.

An attempt was made to test the above hypothesis by direct Auger analysis of an SBA tube that had been electrolyzed in a ZnCl<sub>2</sub>-NaCl melt. Over a depth of ~3000Å the Zn concentration decreased progressively by at least a factor of four from its value at the surface. Because of surface inhomogeneities and sputtering angles, this value represents an upper limit and the actual concentration in the bulk SBA may have decreased more. Since the concentration of sodium in SBA is low to begin with, meaningful changes of the sodium concentration with sputtering distance could not be obtained. The Auger results are, however, at least qualitatively, consistent with our interpretation.

Even though the resistance of the SBA increased with the amount of charge passed through it, the zinc ion within the SBA did not affect the ability of the material to continue to function as a sodium ion selective electrode. The high mobility of sodium ion in the SBA continues to control the potential.

The conductivity was noticeably affected only after an amount of charge was passed through the SBA equivalent to the total amount of sodium initially in the material. This observation indicates that the ion

exchange equilibrium constant also apparently favors sodium ion over zinc ion exchange from the chloride melt into SBA, just as the mobility of sodium is greater than that of zinc in SBA. Both these factors cause SBA to exhibit high sodium selectivity in the presence of zinc ions in a chloride melt.

### Conclusions

We have shown that sodium is favored over zinc in the SBA structure. However, when zinc ion moves into the structure under the influence of an applied electric field, it has such a low mobility that the over-all conductivity of the SBA is greatly impaired. Current reversal is apparently not effective in removing the zinc ion once it has entered the structure. The presence of zinc ion in the SBA does not alter the high selectivity for sodium ion, so that even though SBA would not be a good separator in battery applications using molten NaCl-ZnCl<sub>2</sub> mixtures, it could be used as an accurate monitor of sodium ion activity in such melts over a wide range of sodium ion activity. Most likely, the sodium ion selectivity of SBA would hold in any mixture of a sodium salt with salts of higher valent cations.

### Acknowledgment

We would like to thank Dr. James Murday and Mrs. Elaine Shafrin for carrying out the Auger analysis.

Manuscript submitted Oct. 16, 1975; revised manuscript received Feb. 5, 1976. This was Paper 3 presented at the Toronto, Canada, Meeting of the Society, May 11-16, 1975.

Any discussion of this paper will appear in a Discussion Section to be published in the June 1977 JOURNAL. All discussions for the June 1977 Discussion Section should be submitted by Feb. 1, 1977.

Publication costs of this article were partially assisted by the Naval Research Laboratory.

### REFERENCES

1. Y. Yu Yao and J. T. Kummer, *J. Inorg. Nucl. Chem.*, **29**, 2453 (1967).
2. C. G. M. Dijkhuis and J. A. A. Ketelaar, *Electrochim. Acta*, **12**, 795 (1967).
3. K. H. Stern and D. R. Flinn, *Phys. Chem. Glasses*, **15**, 18 (1974).
4. H. Bloom, T. H. Spurling, and J. Wong, *Australian J. Chem.*, **23**, 501 (1970).
5. W. J. Hamer, M. S. Malmberg, and B. Ruben, *This Journal*, **103**, 8 (1956).
6. G. Eisenman, in "Advances in Analytical Chemistry and Instrumentation," Vol. 4, C. N. Reilly, Editor, p. 219, Interscience, New York (1965).
7. M. F. Lantranov and A. F. Alabyshev, *J. Appl. Chem. USSR*, **27**, 685 (1954).

# The Electrical Properties of Protective Polymer Coatings as Related to Corrosion of the Substrate

Martin W. Kendig and Henry Leidheiser, Jr.\*

Center for Surface and Coatings Research, Lehigh University, Bethlehem, Pennsylvania 18015

## ABSTRACT

The effective electrical permittivity of polymer-coated steel was measured between 200 Hz and 100 kHz as a function of time of exposure to 0.52M NaCl. The real and imaginary parts of the permittivity increased over the entire frequency range as a consequence of electrolyte penetration. The development of a  $-1$  slope on the log loss vs. log frequency curve suggested localized penetration of the dielectric coating by a conducting phase. This behavior correlated with the onset of visible localized corrosion. Results were discussed in terms of a metal/metal oxide/penetrated-coating model.

The mechanism by which a polymer coating protects a metal substrate against corrosion is of great interest. The coating serves as a mass transport barrier to reactants, but this role does not describe completely the phenomena that are observed in some systems (1). This study was undertaken with the recognition from previous work that the electrical properties of the electrolyte/coating/substrate composite can be correlated with corrosion behavior. In this communication the electrical response and a parallel observation of the corrosion potential of polymer-coated steel exposed to a model 0.52M NaCl corrosive medium will be presented. Particular attention is given to the ability of these measurements to elucidate the mechanism of corrosion of polymer-coated steel. Of subsidiary interest is the applicability of the measurements to provide a means for appraising the corrosion protection properties of the coating.

Many studies of the electrical properties of protective polymer coatings reported in the past include measurements of the current response of an isolated film or a coated metal to an applied potential. Mayne and co-workers have extensively investigated the d-c conductivity of free polymer films (2, 3) while the a-c response has been treated and discussed recently by several workers in terms of equivalent resistances and capacitances (4-6). In this laboratory, polybutadiene coatings on steel substrates have been observed to show a decrease in both in-phase and out-of-phase impedance after exposure to a NaCl solution. There is a rapid change at the point where the coating fails completely (5). Under the assumption that it is only the "dielectric" coating which is probed by the a-c measurement, and that the penetrating aqueous phase is distributed within the coating as random aggregates, the per cent water uptake may be determined from the equivalent parallel capacitance (4, 5, 7). While these estimates of water uptake may be valid for the early stages of coating exposure to an aqueous environment and for relatively thick coatings, the estimates have limitations. Indeed, porous penetration of conducting phase (8, 9), interfacial impedance (10), and Maxwell-Wagner and/or Debye losses within the polymer and interface may all contribute to the observed electrical response of a polymer/substrate system (11). In a theoretical discussion, Shmirev and Egorov (12) consider the coating to be represented by a three-element network which may be experimentally determined by a measurement of the impedance at three different frequencies. Likewise, Tomashov *et al.* (10) suggest that a frequency dependence of the impedance may illuminate the nature of coating break-

down. Preliminary results in this laboratory suggest that the frequency-dependent response of a coating is related to its corrosion protective properties (8).

To explore further the nature of the electrical response which develops temporally during exposure of the coating to 0.52M NaCl, the coating impedance between 0.2 and 100 kHz has been followed as a function of time and of coating thickness.

The second electrical property of polymer-coated substrates which provides useful information germane to the mechanism of corrosion is the corrosion potential. Since the potential of a corroding substrate is determined by the relative importance of the separate cathodic and anodic rates, changes in this measured quantity with time provide significant insights into the rate-determining steps. Recently, a review of the corrosion potential as applied to painted steels has appeared (13).

## Experimental

**Substrate preparation.**—Common blackplate 0.026 cm thick, in 10 by 15 cm pieces, was obtained from Bethlehem Steel Corporation. The samples were cleaned by soaking in mineral spirits and rubbing dry with a lint-free cloth prior to application of the coating (5). Confirmation that macroscopic dust particles were removed was obtained by sighting the steel plate at a low angle while whisking the plate with a lint-free cloth. Immediately following this procedure, the coating was applied to the samples, and cured as described below. Chromated steel substrates were produced using the procedure of Bancroft, Mayne, and Ridgway (14).

**Coating preparation.**—The coating which was primarily used in this study was a polybutadiene denoted PB (15). An epoxy (16), denoted EX, a methylmethacrylate copolymer, denoted AB (17), and a polybutadiene stabilized acrylic copolymer nonaqueous dispersion, denoted CLX (18) were also used. The solutions, PB, EX, AB, were passed through a 5  $\mu$ m millipore filter prior to application. The nonaqueous dispersion was used as received. AB was used as a polymer solution; the other coatings were fully formulated.

The coatings were drawn onto the substrate with wire bars. The thickness of the cured coatings was controlled by use of wire coating bars of different gauge. Freshly coated samples were immediately placed in a hot, covered ceramic container and maintained in an oven for the appropriate cure time. The cover of the container was positioned so as to allow solvent vapors to escape. Information about the samples is presented in Table I. The temperature represents the average temperature of the atmosphere in the oven during curing. The oven temperature rose slightly after closing the door. Optimum cure for the polybutadiene was considered to be obtained when the

\* Electrochemical Society Active Member.

Key words: polymer coatings, electrical permittivity, underfilm corrosion, corrosion, polymer coated steel.

Table I. Description of samples used

Sample	Thickness ( $\mu\text{m}$ )	Time (min)	Cure	Temp ( $^{\circ}\text{C}$ )
PB25-1	25.0 $\pm$ 2.0	26		190
PB37				
PB39	3.5 $\pm$ 0.5	19		192
PB40	5.0 $\pm$ 1.0	19		192
PB41	9.0 $\pm$ 1.0	18		192
PB42	11.0 $\pm$ 1.0	18		194
PB43	15.0 $\pm$ 1.0	18		194
PB44	18.0 $\pm$ 2.0	18		194
PB45	24.0 $\pm$ 3.0	19		193
AB3-3	24.0 $\pm$ 2.0	30		130
AB3-2	20.0 $\pm$ 2.0	30		130
CLX1-1	27.0 $\pm$ 2.0	10		203
CLX1-2	26.0 $\pm$ 2.0	10		203
EX18-2	29.0 $\pm$ 3.0	23		166
PB785-8-8	13.0 $\pm$ 2.0	20		230
PB785-12-10	28.0 $\pm$ 3.0	20		200
PB785-7-8	12.0 $\pm$ 2.0	20		205
PB785-11-10	11.0 $\pm$ 1.0	20		205
	Chromated steel			
PB785-22-15	10.0 $\pm$ 1.0	20		200
PB785-17-13	11.0 $\pm$ 1.0	20		205
PB785-19-14	15.0 $\pm$ 2.0	20		210
PB785-24-16	24.0 $\pm$ 2.0	20		208

samples exhibited a slightly green hue, an overbake leading to a yellow color and the underbake leading to a gray color.

The coating thicknesses were determined by micrometer measurements of the panels before and after coating. Results are expressed as an average of eight or more measurements. Typical scatter in these measurements was 10% (see Table I).

*Cell description.*—Experimental cells were constructed from the coated sample by cementing the ground end of 17-18 mm ID tubes onto the coating surface with epoxy cement. A guard ring surrounded the cell to minimize stray capacitances. Mercury was placed in the cell and the equivalent parallel capacitance and loss tangent measurement was made between 200 Hz and 100 kHz prior to any exposure to the corrosive medium. The cell was then filled with 1 ml of air-saturated aqueous 0.52M NaCl solution and allowed to stand for the desired period of time. The sodium chloride was decanted and clinging drops were wiped free of the surface with an absorbent, lint-free tissue. The mercury electrode was again placed over the coating and the equivalent parallel capacitance and loss tangent were measured across the mercury/electrolyte penetrated coating/substrate interface. The mercury was removed and the sodium chloride electrolyte was reintroduced for an additional period of time.

Cells used for the potential measurements were constructed as described by Leidheiser and Touhsaent (5). The potential was measured between the metal substrate and a saturated calomel reference (SCE) electrode.

*Electrical measurements.*—Capacitance and loss tangent measurements across the substrate/coating/mercury interface were accomplished with a General Radio 716C Shering Bridge and 716-P4 guard circuit. The bridge was driven by a variable frequency Rhode and Schwartz oscillator at 1V peak-to-peak between 200 Hz and 100 kHz. The signal to be nulled was detected by a Rhode and Schwartz tuned indicating amplifier or a PAR Model 129 lock-in amplifier. The response of the coating to an applied oscillating field,  $V_0 e^{i\omega t}$  was determined by bridge balancing of the response to that of an equivalent parallel resistor and capacitor. The bridge elements were linear and the detector was tuned only to the fundamental frequency, so it is the first-order response which is observed by this method. These data may be represented in a variety of ways: (i) real and imaginary conductivity, (ii) equivalent parallel resistance and capacitance, (iii) effective in-phase and out-of-phase permittivity, (iv) capacitance and loss tangent. For this discussion, the in-phase and out-of-phase effective permittivity

will be used to account for the current response across the coating/metal interface. The real and imaginary components of the permittivity ( $\epsilon''$ ,  $\epsilon'$ ) are related to the equivalent parallel resistance and capacitance by the following

$$\epsilon'' = \frac{d}{A\epsilon_0\omega R_{xp}}$$

$$\epsilon' = \frac{d}{A\epsilon_0} C_{xp}$$

where  $\epsilon_0$  = absolute permittivity of free space,  $A$  = apparent coating area,  $d$  = coating thickness,  $\omega$  = frequency in radians,  $R_{xp}$  = equivalent parallel resistance, and  $C_{xp}$  = equivalent parallel capacitance. The equivalent parallel resistance and capacitance of a complex element may be calculated from bridge balances. Then, by the above equation and the film and cell dimensions, the effective complex permittivity ( $\epsilon''$ ,  $\epsilon'$ ) of the coating may be determined.

*Potential measurement.*—The corrosion potential was measured between the coated substrate and the SCE reference electrode using a Keithley 600A electrometer and a cell, 50 mm ID. Since the electrometer input impedance was significantly greater than the impedance of the coated interface, virtually no current was drawn on the system under observation. The potential was measured at intervals over a period of about 40 days. Every time the potential was measured the 25 ml of 0.52M NaCl was renewed.

Visible underfilm corrosion was assessed via ASTM Standard D610 (19) in two ways. First, by observing the area covered by dark spots of corrosion product, and second by estimating the surface area that was delaminated. The appropriate ASTM D610 designation was assigned to these two types of areas. These designations run from 1, representing 50% destruction, to 10, representing no change. As an example, Fig. 1 shows a photograph of a sample which was treated with 0.52M NaCl and had commenced to corrode. The two types of areas are readily apparent with the delaminated areas well outlined around the dark corrosion spots.

*Inflicted defect.*—One sample, PB44, was purposely damaged, and the damaged spot was exposed to the 0.52M NaCl solution. The damage was accomplished by pressing the coating with a tapered 0.7 mm OD stainless steel syringe needle. Approximately 0.3 ml of 0.52M NaCl was placed on this spot for 1 hr after which

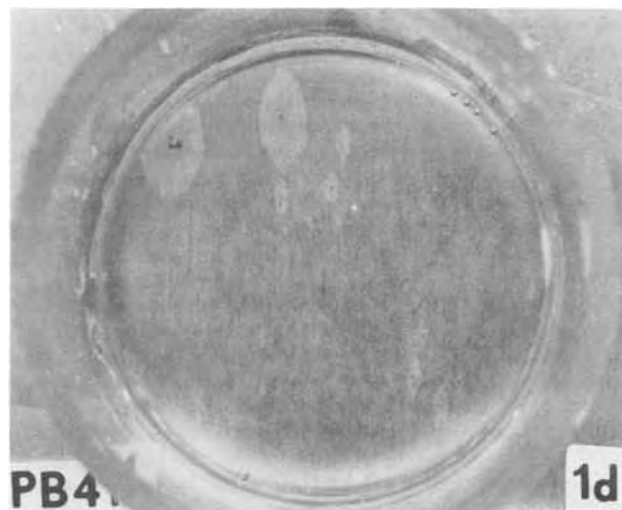


Fig. 1. Photograph of a polybutadiene-coated steel sample after exposure to 0.52M NaCl for one day. Corrosion appears in upper left as dark spots surrounded by a light region.

it was wiped off and the electrical response of the sample was measured in the manner previously described.

*Inert atmosphere.*—An inert atmosphere of dry nitrogen purified by passage over hot copper wire was produced within a polyethylene glove bag by maintaining a positive pressure of nitrogen in the system. The electrometer cables were fed through a bulkhead sealed to the polyethylene bag. The 0.52M NaCl electrolyte was flushed with nitrogen for 20 min, stoppered, and placed within the nitrogen-flushed bag. The sealed bag containing cells, SCE reference, electrometer cable and electrolyte was allowed to equilibrate for 3 hr with nitrogen. The electrolyte was then introduced into the cells and the potential measurements were commenced.

### Results

Figures 2-5 illustrate the log loss vs. log frequency results for several polymer coatings (20-30  $\mu\text{m}$ ) on steel at different times of treatment in 0.52M NaCl. The onset of corrosion coincided with the development of the  $-1$  slope at low frequencies in the log  $\epsilon''$  vs. log  $f$  plots. The sample which showed no low frequency slope, Fig. 5, showed no corrosion on exposure time of 30 days.

In a second set of experiments a series of polybutadiene-coated steel samples, having a range of coating thicknesses between 5 and 24  $\mu\text{m}$ , was treated with 0.52M NaCl and the effective complex permittivities

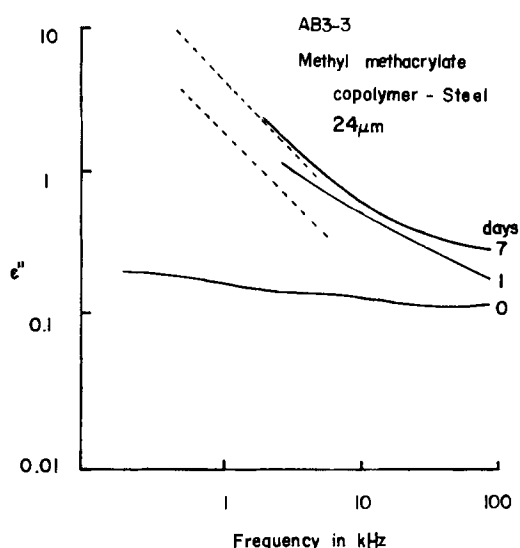


Fig. 2. Log loss vs. log frequency for a methylmethacrylate copolymer-coated steel exposed for 0, 1, and 7 days to 0.52M NaCl.

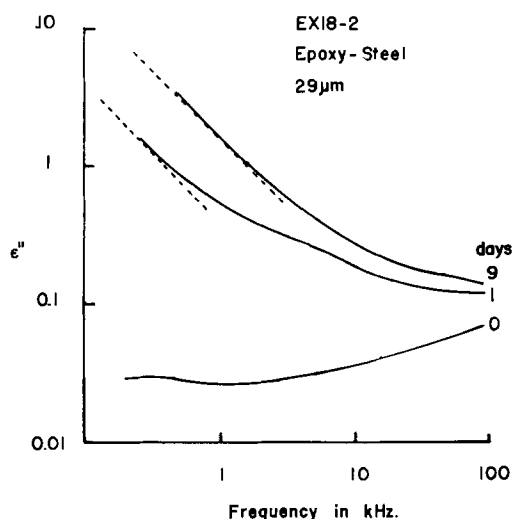


Fig. 3. Log loss vs. log frequency for an epoxy-coated steel exposed for 0, 1, and 9 days to 0.52M NaCl.

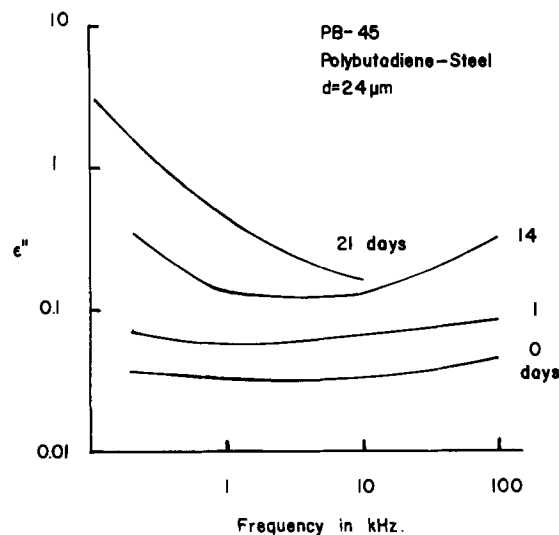


Fig. 4. Log loss vs. log frequency for a polybutadiene-coated steel exposed for 0, 1, 14, and 21 days to 0.52M NaCl.

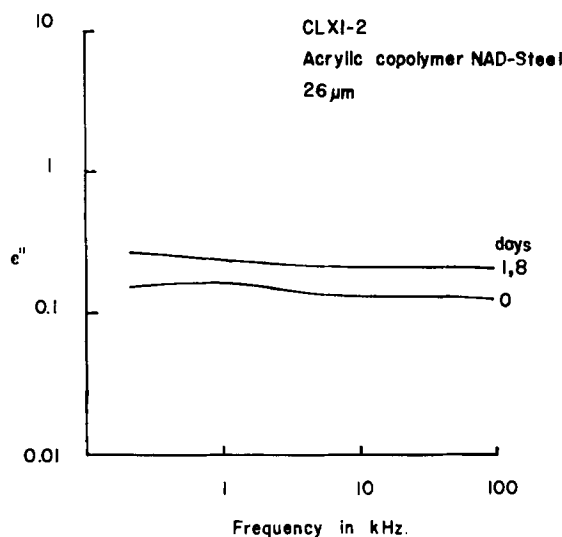


Fig. 5. Log loss vs. log frequency for acrylic copolymer NAD-coated steel exposed for 0, 1, and 8 days to 0.52M NaCl.

over the 200 Hz to 100 kHz range were measured periodically. The thin coatings did not achieve the  $-1$  slope in the frequency range studied as may be seen in Fig. 6 where the 21 day result for this series of

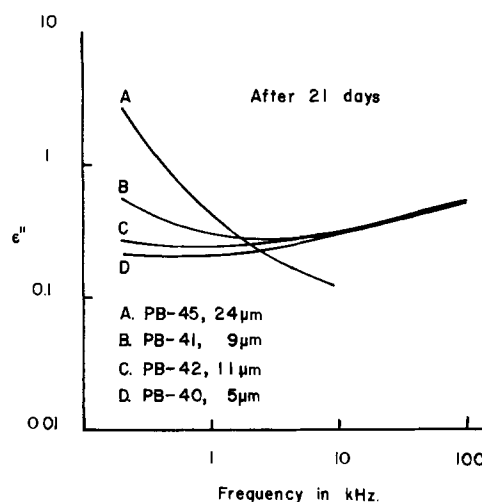


Fig. 6. Log loss vs. log frequency for several samples of polybutadiene-coated steel exposed for 21 days to 0.52M NaCl.

Table II. The relationship between the slope of the  $\epsilon''$  vs.  $\log f$  plots at low frequency and the rate of corrosion of polybutadiene-coated steel in 0.52M NaCl

Ranking on basis of corrosion rate	Sample designation	Low frequency slope	
		After 7 days	After 20-22 days
1 (greatest)	PB39	-1.0	Totally corroded
2	PB41	-0.37	-0.44
3	PB45	0	-1.0
4	PB42	-0.48	0
5	PB40	0	0
6 (least)	PB43	0	-0.18

Table III. The slope of the  $\log \epsilon''$  vs.  $\log f$  plots at low frequency for chromated steel samples coated with polybutadiene and exposed to 0.52M NaCl

Sample	Low frequency slope after two weeks	% Surface corroded after two weeks
785-19-14	-1.0	35
785-28-15	-0.1	5
785-22-15	-0.1	1
785-17-13	0	0

samples is recorded. There is nonetheless, a correlation of the low frequency slope with corrosion as illustrated by Table II. Similarly the correlation of the low frequency data is also indicated for chromated samples in Table III.

That the onset of a  $-1$  low frequency  $\log \epsilon''$  vs.  $\log$  frequency slope may be associated with a path of continuous conductivity through the coating is illustrated by the results depicted in Fig. 7 which shows the  $\log \epsilon''$  vs.  $\log$  frequency results for a polybutadiene-coated steel sample in which the coating was punctured with a needle and allowed to equilibrate with 0.52M NaCl solution for 1 hr. The  $-1$  slope at low frequencies of the  $\log \epsilon''$  vs.  $\log$  frequency plot is seen.

The out-of-phase component of the effective complex permittivity does not vary as rapidly with frequency. If one were to assume that the out-of-phase effective permittivity were a true permittivity of the composite coating and dispersed aqueous phase, its value would be a function of the volume fraction of the dispersed phase (5, 7). The assumption neglects the fact that there may be a contribution from the substrate/polymer interface. Nevertheless, it is important to note the increase of this effective permittivity with time of exposure. Barring interfacial effects and for small volume fraction of the dispersed phase, the function  $(\epsilon'_t/\epsilon'_{t,0} - 1)$  is proportional to the volume fraction of the dis-

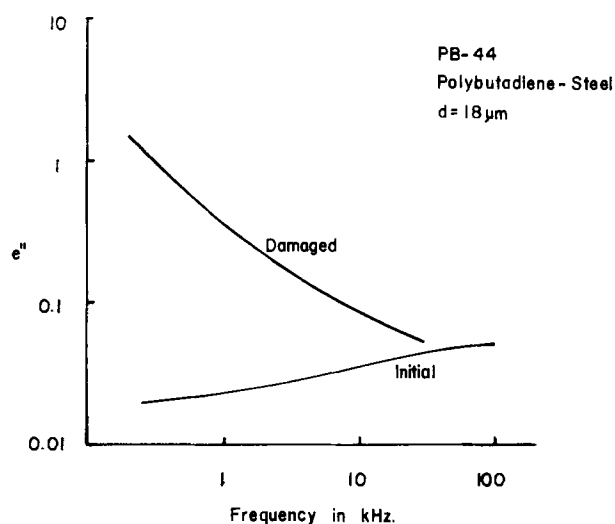


Fig. 7. Log loss vs. log frequency for an intentionally damaged polybutadiene-coated sample.

Table IV. Values of the function  $(\epsilon'_t/\epsilon'_{t,0} - 1)$  as a function of frequency

	After one week				After two weeks			
	200	1000	10k	100k	200	1000	10k	100k
PB25-1	0.346	0.189	0.137	0.140				
PB39	Very large				Totally destroyed			
PB40	0.283	0.259	0.253	0.166	0.810	0.772	0.742	0.592
PB41	0.291	0.273	0.261	0.235	0.651	0.631	0.580	0.405
PB42	0.600	0.610	0.555	0.464	0.713	0.690	0.657	0.599
PB43	0.554	0.551	0.507	0.294	0.678	0.652	0.571	0.471
PB45	0.195	0.197	0.162	0.127	0.468	0.578	0.508	0.347

persed phase.<sup>1</sup> The proportionality constant is dependent upon the particular geometry of the dispersed phase (11). This quantity,  $(\epsilon'_t/\epsilon'_{t,0} - 1)$ , is tabulated for the series of polybutadiene coated steel samples in Table IV. Using the treatment of Leidheiser and Touhsaent (5) and previous work where a random distribution of aqueous phase is assumed, the "calculated per cent water uptake" after two weeks is between 10 and 13% and with minor dependence upon coating thickness.

Figures 8-10 give results of the substrate potential vs. time for three samples of polybutadiene-coated

<sup>1</sup> Here  $\epsilon'_t$  is the permittivity at time  $t$ ,  $\epsilon'_{t,0}$  is the initial permittivity.

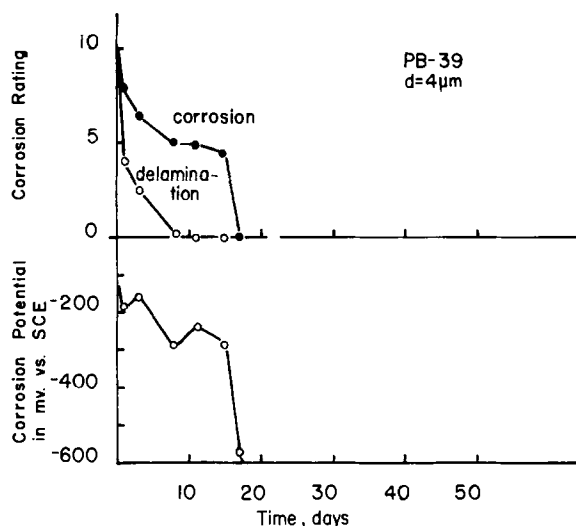


Fig. 8. Upper curves, ASTM D610 rating of corrosion and delamination vs. time of exposure to 0.52M NaCl. Lower curve, corrosion potential of steel substrate as a function of time of exposure to 0.52M NaCl. Results for 4  $\mu$ m coating of polybutadiene on steel.

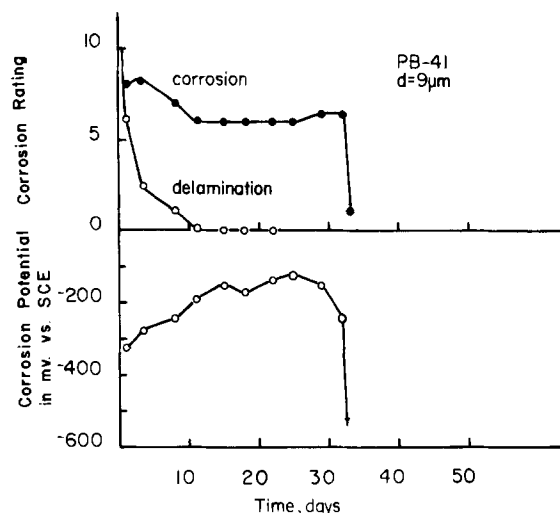


Fig. 9. Upper curves, ASTM D610 rating of corrosion and delamination vs. time of exposure to 0.52M NaCl. Lower curves, corrosion potential of steel substrate as a function of time of exposure to 0.52M NaCl. Results for a 9  $\mu$ m coating of polybutadiene on steel.



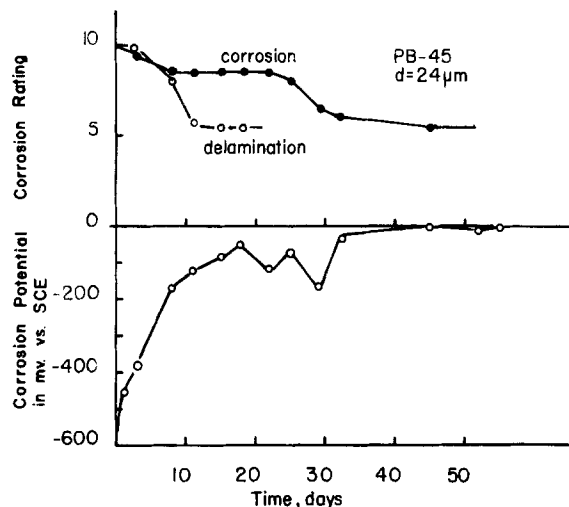


Fig. 10. Upper curves, ASTM D610 rating of corrosion and delamination vs. time of exposure to 0.52M NaCl. Lower curves, corrosion potential of steel substrate vs. time of exposure to 0.52M NaCl. Results for a 24  $\mu\text{m}$  coating of polybutadiene on steel.

steel. The potential is anodic initially and moves to more cathodic potentials with time. This movement to more cathodic potentials correlates with the increase in the delaminated area which occurs around the dark corrosion spots (Fig. 1). After a length of time depending upon the thickness of the sample, there is complete failure of the coating as observed by the formation of a black to orange corrosion film over the entire surface. The transition occurs quite rapidly, usually within one day, and is followed by an equally fast plunge of the substrate potential to the vicinity of  $-650$  mV, a potential approximating that at which mild steel actively corrodes in aerated NaCl.

The initial corrosion potentials were more cathodic with decreasing coating thickness as illustrated in Fig. 11. This relationship suggests that it is the cathodic half-reaction which is rate controlling in active under-film corrosion in the polybutadiene-steel system. The relative rate of oxygen penetration of coatings of different thickness explains the greater degree of cathodic depolarization in the thinner samples than in the thicker samples.

Further evidence for the importance of the cathodic half-reaction is provided by the results of corrosion potential measurements carried out in an oxygen-free environment. Neither significant corrosion nor delamination occurred for samples held under nitrogen. Ac-

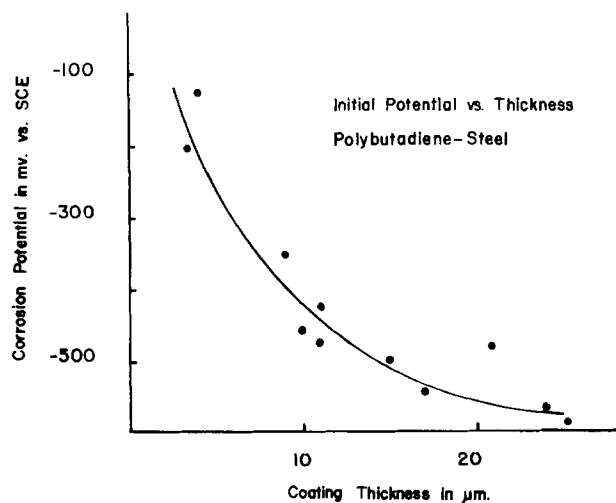


Fig. 11. Extrapolated initial corrosion potential of polybutadiene-coated steel substrate vs. coating thickness.

cordingly, the corrosion potential of the metal substrate remained near  $-650$  mV, not trending toward more positive potentials as the aerated delaminating samples did. A comparison is shown in Fig. 12. Curve A is the typical behavior of an aerated sample in which the positive movement of the potential follows the delamination. The samples held in an oxygen-free environment yield an approximately constant potential of  $-600$  to  $-650$  mV as shown by the lower two curves. Upon exposure of the samples to air, the thinner samples remained at  $-600$  to  $-700$  mV, but the 24  $\mu\text{m}$  sample equilibrated at  $-250$  mV. Many small corrosion spots became visible soon after exposure to the air.

### Discussion

In discussing the electrical properties of a polymer coating, it is convenient to describe the coating/metal oxide interface/metal in terms of a circuit analog having an equivalent frequency response.

The frequency dependent response of a coating impedance which is electrically equivalent to a parallel resistor and capacitor yields a  $-1$  slope for the variation of  $\log \epsilon''$  vs.  $\log$  frequency. While this slope has been observed for many samples in which corrosion processes have become visible under the coating, it is not by any means general for a polybutadiene-coated steel treated with aqueous 0.52M NaCl. Specifically, Fig. 2-5 show that prior to exposure to the electrolyte,  $\log \epsilon''$  does not change greatly with frequency, but after exposure for several days there is an increase in the low frequency loss. Shmirev and Egorov (12) suggest an equivalence of the coating to a parallel resistor and capacitor circuit which itself is connected in series with a capacitor representing the interface. This equivalent circuit cannot generally represent the coating impedance since for this network, the expected response would have a  $-1 \log \epsilon''$  vs.  $\log$  frequency slope at frequencies below this characteristic frequency. Clearly, in the initial stages and for several of the observed samples presented in Fig. 5, this is not the case. As mentioned above, the loss is rather flat over the measured frequencies. It does not reach a sharp maximum.

A general equivalent circuit may be represented by a distribution of series resistors and capacitors in parallel as illustrated schematically in Fig. 13. Physically, this picture represents what will be referred to as a heterogeneous assembly of electrolytically conducting paths. The heterogeneous nature of the electrical properties of several polymer films has been previously noted by Mayne (2).

There are two types of behavior. In some localized areas, the coating does not behave as a dielectric, but

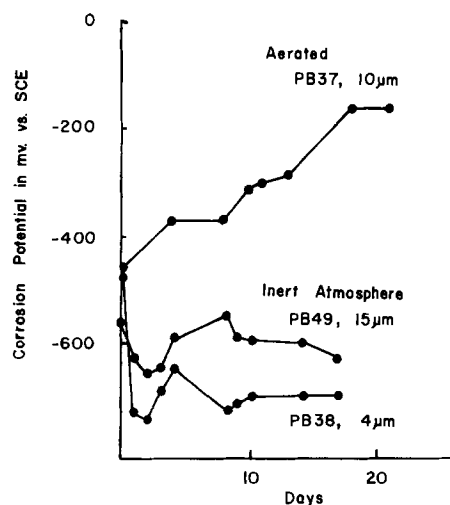


Fig. 12. Comparison of typical corrosion potential vs. time curves of polybutadiene-coated steel in a deaerated and aerated environment.

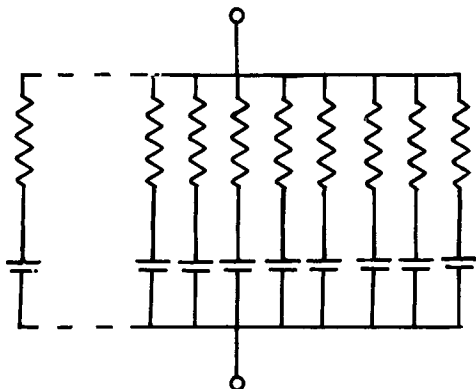


Fig. 13. The electrical analog of a polymer coating heterogeneously penetrated by a conducting phase.

exhibits electrolytic conductivity as a consequence of polymer breakdown such that electrolyte is dissolved within a hydrolyzed region, or because of penetration by the electrolyte through pores. In other localized areas, the coating remains a highly cross-linked, relatively inert, dielectric material. The entire coating/metal oxide/metal system may be considered to consist of electrolytically activated, conducting regions penetrating the coating randomly over the surface with respect to depth. In terms of Fig. 13, each parallel path is a resistor in series with a lossy capacitor. The lossy capacitor is a series connection of the dielectric polymer and the very lossy metal oxide interface. From this model, the effective permittivity of the whole coating may be formulated (see Appendix). The coating is divided into regions having a given conductive length,  $l$ , which is related to an effective dielectric thickness  $d_i$

$$d_i = d_o - l$$

$d_o$  = the macroscopically determined coating thickness

The observed effective complex permittivity of the whole coating will be a weighted sum of the complex permittivities of each region defined by a particular  $d_i$

$$\epsilon_{\text{obs}} = \sum_i P(d_i) \epsilon(d_i)$$

Here  $P(d_i)$  is the fraction of the surface where the coating has an effective dielectric thickness  $d_i$ , and effective dielectric permittivity  $\epsilon(d_i)$ .

In order to make a test of the above concept, the following assumptions are made:

1. The fraction of the surface having an effective dielectric thickness  $d_i$  is a function of the effective thickness,  $P(d_i)$ , and decreases exponentially with differences ( $d_i - d_o$ )

$$P(d_i) = N e^{(d_i - d_o)/D}$$

$N$  = normalization factor  
 $d_i$  = the effective dielectric thickness  
 $d_o$  = apparent coating thickness  
 $D$  = penetration factor

2. An oxide with an electrical response similar to  $\alpha\text{-Fe}_2\text{O}_3$  is considered to represent the interfacial phase. An oxide reported by Hilborn (20) and certain modifications thereof (Table V) are also considered. These are the only iron oxides of interest for which data are available.

3. The conductivity of the penetrating phase is considered to be equivalent to that of bulk electrolyte. In the case of 0.52M NaCl the specific conductance is 0.047 mho/cm.

4. The oxide thickness at the interface is considered to be 50Å.

The model, as formulated in the Appendix, is calculated by computer with the above parameters, and

Table V.

	$K_1^*$	$K_s^*$	$10^{-5}$ sec, $\tau$	$\gamma^*$	$\sigma_{a-c}$ , mho/cm
Oxide #1	30	670	1.2	0.22	$5.39(10)^{-10**}$
Oxide #2	30	670	1.2	0.22	$5.39(10)^{-9}$
Oxide #3	30	670	1.2	0.22	$5.39(10)^{-8}$

\* The parameters may be defined as follows from (20):  $\epsilon'' = (K_s - K_1)(\cos \phi) \gamma \sin \gamma \phi + C/\omega$ ;  $\epsilon' = K_s - (K_s - K_1)(\cos \phi) \gamma \cos \gamma \phi$ ;  $\cot \phi = \omega$ ;  $\tau$  is a characteristic time related to the distribution of the oxide resistivity and  $\gamma$  is related to the breadth of the distribution of the oxide resistivity;  $C = \sigma_{a-c}/\epsilon_0$ .

\*\* An oxide observed by (20).

for several penetration factors. Factors between 1.4 and 2.5  $\mu\text{m}$  yield both in-phase and out-of-phase permittivities which are qualitatively similar to experimentally determined frequency response for the early stages of treatment with electrolyte. Figure 14 shows  $\log \epsilon''$  vs.  $\log$  frequency for the two penetration factors, 1.4  $\mu\text{m}$  and 2.0  $\mu\text{m}$ . They are also values which yield experimentally reconcilable values of  $(\epsilon'/\epsilon'_{t,0} - 1)$  in Fig. 15. Furthermore, for these penetration factors, the permittivity  $\epsilon'$  remains relatively constant with frequency.

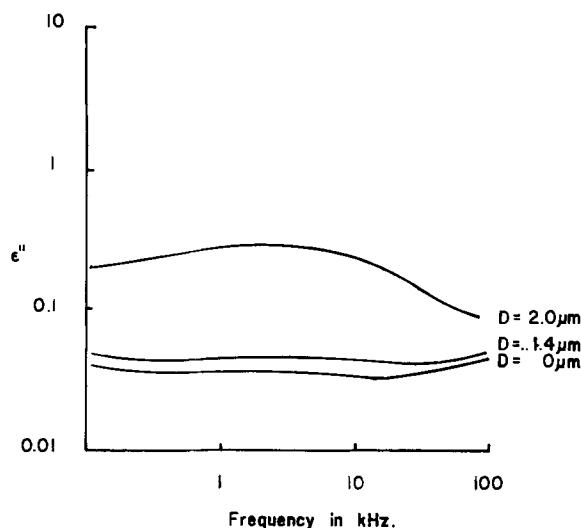


Fig. 14. The calculated log loss vs. log frequency for a polybutadiene coating on a 50Å  $\alpha\text{-Fe}_2\text{O}_3$  oxide. The coating is penetrated by a conducting phase of conductivity 0.047 mho/cm to various depths characterized by the penetration factor  $D$ .

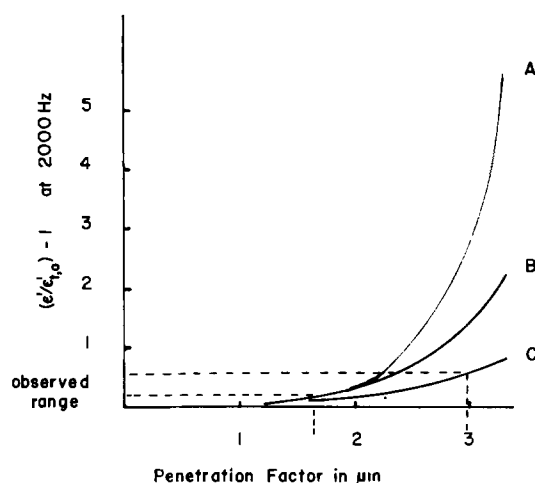


Fig. 15. The change in the complex permittivity, expressed as  $(\epsilon'/\epsilon'_{t,0} - 1)$  at 2000 Hz as a function of penetration factor for conducting phases of: A, 0.047 mho/cm; B, 0.0047 mho/cm; and C, 0.00047 mho/cm conductivities.

In this model, the loss,  $\epsilon''$ , is very sensitive to the structure and nature of the oxide interface. The oxide may become either thinned or it may become more conductive. In either case, the value of  $\log \epsilon''$  increases toward lower frequencies as either of these changes occur in the oxide. Figure 16 illustrates this point for the case where the oxide described by (20) is thinned, while in Fig. 17, the oxide is modified with respect to its d-c conductivity (Table V) to yield also a loss that increases at low frequency.

There are two basic stages in the development of the electrical response of the electrolyte-impregnated, coated steel. First, the coating is heterogeneously penetrated by the conducting electrolyte phase. At a statistical number of points, this phase is in contact with the metal oxide interface whose properties will largely determine the low frequency in-phase electrical response of the coating/metal oxide/substrate couple. A metal oxide that becomes conductive will result in the development of a  $-1$  slope of the  $\log \epsilon''$  vs.  $\log$  fre-

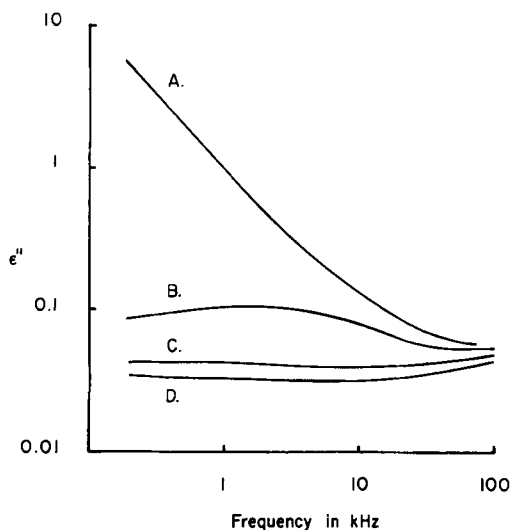


Fig. 16. Calculated log loss vs. log frequency for a 20  $\mu\text{m}$  polybutadiene coating on a steel substrate. A, No oxide interface; penetration factor of 1.43  $\mu\text{m}$ . B, Penetration factor 1.43  $\mu\text{m}$ ; 0.5 nm  $\alpha\text{-Fe}_2\text{O}_3$  (19) oxide interface. C, Penetration factor 1.43  $\mu\text{m}$ ; 5 nm  $\alpha\text{-Fe}_2\text{O}_3$  (19) oxide interface. D, No penetration of electrolyte.

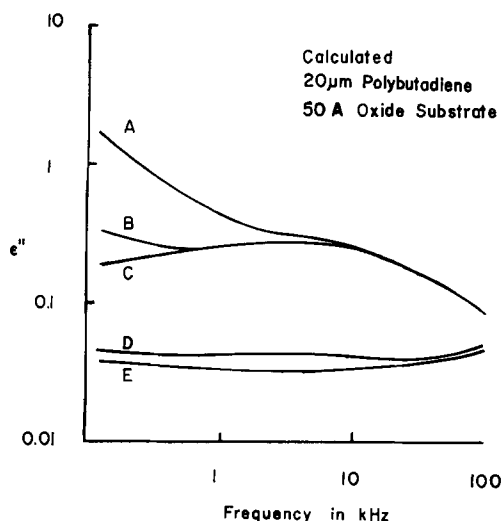


Fig. 17. Calculated complex permittivity for 20  $\mu\text{m}$  polybutadiene on steel with 5 nm oxide interface. Shown is the effect of penetration of electrolyte and change in oxide properties. A, 2.00  $\mu\text{m}$  penetration factor, oxide #3 (Table IV). B, 2.00  $\mu\text{m}$  penetration factor, oxide #2. C, 2.00  $\mu\text{m}$  penetration factor, oxide #1. D, 1.43  $\mu\text{m}$  penetration factor, oxide #1. E, Initial, no penetration.

quency curve corresponding to an effectively short-circuited coating, while an insulating oxide will present a rather flat  $\log \epsilon''$  vs.  $\log f$  curve. In spite of the fact that there is significant uncertainty in the precise electrical nature of the metal oxide interface and the precise bulk conductivity of the conducting phase within an electrolyte treated polymer, there is qualitative agreement of typical behavior of the polymer-coated steel to that modeled by this treatment.

The model qualitatively interprets the behavior of the coating whose electrical response as a function of time is shown in Fig. 4. First, there is a frequency-independent increase of the loss as seen for the 1 day exposure. This increase corresponds to the random penetration of the conducting electrolyte phase into the polymer coating. After 14 days, penetration of the conducting electrolyte to the interface becomes apparent with the initiation of the  $-1 \log \epsilon''$  vs.  $\log$  frequency slope at low frequencies.

### Relation of the Electrical Response to the Mechanism of Corrosion (22)

Initially, the electrolyte penetrates the coating and sets up conducting paths to random depths over the coating surface. The initial stages of exposure of PB45, as shown in Fig. 4, are representative of the resultant electrical response. Both the in-phase and out-of-phase permittivity increase in a similar manner more or less uniformly over the frequency range observed. Paths of complete penetration develop with time, however, which allow the electrolyte phase to meet the metal oxide interface and a corrosion cell is activated. The first visual signs of corrosion are green-gray to black spots around which regions of delamination subsequently grow. The growth of the delaminated region correlates with an increase in corrosion potential. The spots represent points of anodic attack electrochemically coupled to the oxygen depolarized cathodic delamination region. For the thicker films, the local dissolution reaction increases the conductivity of the interfacial oxide and the coating, and the  $-1$  slope of the  $\log \epsilon''$  vs.  $\log$  frequency plot is observed.

It is to be pointed out that the cathodic half-reaction is self propagating in the sense that the alkaline products formed at the interface aid in the hydrolysis of the interface and cause further delamination. It has been observed that delamination of an externally polarized defect occurs only for cathodic currents (23).

At the point of final breakdown, the cathodic region becomes active because deterioration of the film in the presence of alkali occurs in the cathodic region. Further support for this point is found in the previous observation that increased alkalinity has an accelerating effect upon the degradation of the polybutadiene film (6).

Manuscript received Feb. 4, 1976.

Any discussion of this paper will appear in a Discussion Section to be published in the June 1977 JOURNAL. All discussions for the June 1977 Discussion Section should be submitted by Feb. 1, 1977.

Publication costs of this article were partially assisted by Lehigh University.

### APPENDIX

#### Model for Coating Impedance

The region at the base of a pore is electrically represented by the impedance  $Z_1$ , which is a series combination of the impedances of the respective polymer and oxide phases

$$Z_1 = Z_{\text{poly},1} + Z_{\text{oxide},1} \quad [\text{A-1}]$$

Referring to Fig. A-1,

$d_i$  = unpenetrated polymer dimension

$A^1$  = area of the pore

$d_{\text{ox}}$  = oxide thickness

$r_1 = d_{\text{ox}}/d_o$ ,  $d_o$  = total polymer thickness

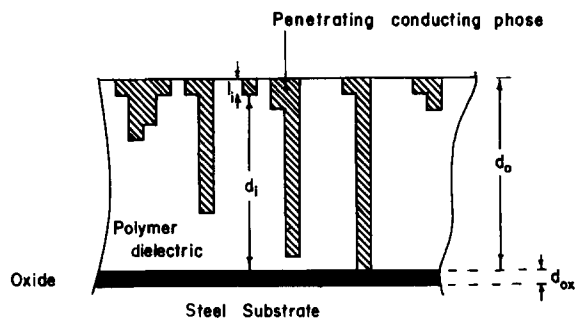


Fig. A-1. Schematic of polymer coating heterogeneously penetrated by a conducting phase.

considering the following definitions [A-2]

$\epsilon_p', \epsilon_p''$  = bulk polymer permittivity  
 $\epsilon_{ox}', \epsilon_{ox}''$  = oxide permittivity  
 $den = (\epsilon''^2 + (\epsilon')^2)$  of respective oxide and polymer  
 $Z_I$  may be more explicitly stated

$$Z_I = \frac{d_i}{\omega A' \epsilon_o} \left( \frac{\epsilon_p''}{den(p)} + \frac{r_1 \epsilon_{ox}''}{den(ox)} + j \left\{ \frac{\epsilon_p'}{den(p)} + r_1 \frac{\epsilon_{ox}'}{den(ox)} \right\} \right) \quad [A-3]$$

The impedance of the penetrating conducting phase,  $Z_p$ , is

$$Z_p = \frac{d_o - d_i}{A' \sigma^*} \quad [A-4]$$

where  $\sigma^*$  is the conductivity of the porous phase. Since the pore impedance is in series with that of the interface, the total impedance,  $Z_T$ , will be the sum

$$Z_T = Z_p + Z_I \quad [A-5]$$

Therefore the respective real and imaginary components of  $Z_T$  are

$$Re(Z_T) = \frac{d_i}{\omega A' \epsilon_o} \left\{ \frac{d_o - d_i}{d_i} \cdot \frac{\omega \epsilon_o}{\sigma^*} + \frac{\epsilon_p''}{den(p)} + r_1 \frac{\epsilon_{ox}''}{den(ox)} \right\}$$

$$Im(Z_T) = \frac{d_i}{\omega A' \epsilon_o} \left\{ \frac{\epsilon_p'}{den(p)} + r_1 \frac{\epsilon_{ox}'}{den(ox)} \right\} \quad [A-6]$$

Defining the complex quantity

$$Z_x = \frac{\omega A' \epsilon_o}{d_i} Z_T \quad [A-7]$$

The effective permittivity of the region having a penetration  $d_i$  is

$$\epsilon(d_i) = \frac{1}{X \cdot Z_x} \quad [A-8]$$

where  $X = \frac{d_i}{d_o + d_{ox}}$  = unpenetrated fraction. Since the coating may be thought of as a parallel combination of such regions, the observed complex permittivity,  $\epsilon_{obs.} = P(0)\epsilon(0) \sum_{i=1}^n P(d_i)\epsilon(d_i)$  where  $P(d_i)$  is the fraction of the coating area which is conductively penetrated to within  $d_i$  of the oxide.

The total penetration term  $P(0)\epsilon(0)$  must be treated separately since terms in  $1/d_i$  in the above formulations are undefined. Furthermore, thinning of the oxide and delamination (effective increase in oxide area) must also be considered for  $d_i = 0$ .

#### REFERENCES

1. J. E. O. Mayne, *Research (London)*, **5**, 278 (1952).
2. J. E. O. Mayne, *Brit. Corrosion J.*, **5**, 106 (1970).
3. E. M. Kinsella and J. E. O. Mayne, *Brit. Polym. J.*, **1**, 173 (1969).
4. K. A. Holtzman, *J. Paint Technol.*, **43**, 47 (1971).
5. H. Leidheiser, Jr. and R. Touhsaent, *Corrosion*, **28**, 435 (1972).
6. H. Leidheiser, Jr. and D. Wallace, *This Journal*, **120**, 230C (1973).
7. D. M. Brasher and A. H. Kingsbury, *J. Appl. Chem.*, **4**, 62 (1954).
8. M. W. Kendig and H. Leidheiser, Jr., *This Journal*, **121**, 275C (1974).
9. B. V. Hamon, *Australian J. Phys.*, **16**, 304 (1953).
10. N. D. Tomashov, Yu N. Milhailovskii, and V. V. Leonov., *Corrosion*, **20**, 125t (1964).
11. L. K. H. Van Beek, *Prog. Dielectrics*, **7**, 69 (1967).
12. V. V. Shmirev and B. N. Egorov, *Lakokrasochnye Materialy ikh. Primeneniya*, **1973**, 63.
13. J. Wolstenholme, *Corrosion Sci.*, **13**, 521 (1973).
14. G. M. Bancroft, J. E. O. Mayne, and P. Ridgway, *Brit. Corrosion J.*, **6**, 119 (1971).
15. E. I. du Pont de Nemours Co., RK-662 Budium (TM) Polybutadiene Can Coating.
16. G. W. Gerhardt, Private communication.
17. Rohm and Haas, Technical Manual—Acrylic B-48N.
18. Celanese, Tech. Data Sheet X1197 and Darrell D. Hicks, U.S. Pat. 3,779,977.
19. American Society for Testing and Materials 'Standard Method of Evaluating Degree of Rusting on Painted Steel Surfaces,' ASTM Annual Standards, 1972, Part 21, 99.
20. R. B. Hilborn, Jr., *J. Appl. Phys.*, **36**, 1553 (1965).
21. O. P. Gonzalez, P. H. Josephic, and R. A. Oriani, *This Journal*, **121**, 29 (1974).
22. M. Kendig and H. Leidheiser, Jr., *Corrosion*, **32**, 69 (1976).
23. M. Kendig and H. Leidheiser, Jr., To be published.

# A Model for Copper Electroplating of Multilayer Printed Wiring Boards

Thomas Kessler<sup>\*,1</sup>

Bell Laboratories, Whippany, New Jersey 07981

and Richard Alkire\*

Department of Chemical Engineering, University of Illinois, Urbana, Illinois 61801

## ABSTRACT

An analytical model is developed for predicting electroplated copper thickness distributions on multilayer printed wiring boards. Plated copper thickness distributions are predicted within a plated-through hole (PTH) by coupled solutions of the potential, kinetics, and mass diffusion equations. The model establishes: (a) correlation parameters including geometric, charge transfer, mass transfer, and ohmic solution effects, and (b) the minimum electrolyte convection required in a PTH to avoid rough or powdery deposits. Predictions are compared with experimental data obtained over a wide range of operating scales from breakers to full-scale production tanks.

The production of reliable multilayer printed wiring boards (MLB's) containing plated-through holes (PTH's) requires many carefully controlled process steps. One of the most important steps is the electroplating of copper in holes drilled through the board (PTH's) in order to provide electrical connections among the various circuit layers. MLB's are electroplated with copper in large multiple-cell tanks with cell geometries typified by the schematic in Fig. 1. The electrolyte used in these tanks is a high conductivity acid-copper sulfate bath containing proprietary organic additives. The electrolyte is stirred by air, sparging pipes being located in the bottom of the tank. The air bubbles rising from the spargers are intended to minimize electrolyte concentration gradients and provide some electrolyte convection in the PTH's.

MLB's are manufactured in panels which are physically larger than the final MLB product. Diagonally opposite corners of these panels contain test coupons which are, hopefully, representative of the MLB or MLB's closer to the center of the panel. Some of these test coupons are destructively tested to assure reliability of the MLB product in each panel. In order that the test coupons properly represent the rest of the panel, it is important to obtain uniformly plated copper throughout the panels. In addition the plated copper must be sufficiently uniform and ductile within each individual PTH to enable the PTH to withstand the strains encountered in a forty year design life. For coupons to be truly representative of panels, the copper plated in the coupon PTH's and in any PTH in the panel must have identical thickness distributions and mechanical properties.

The purpose of the investigation is to develop the analytical models to provide scaling information for predicting PTH copper thickness distributions. These models, supported by experimental data, can be used to establish necessary operating conditions for producing uniformly plated MLB's.

The characteristics of electroplated metals in plated-through holes have been determined experimentally by several authors. A brief summary of the results for electroplated copper is contained in Ref. (1). Several experiments by Dini (2) indicate the difficulty of plating into deep plated-through holes. Dini also observed that additives in a fluoborate bath refine the grain

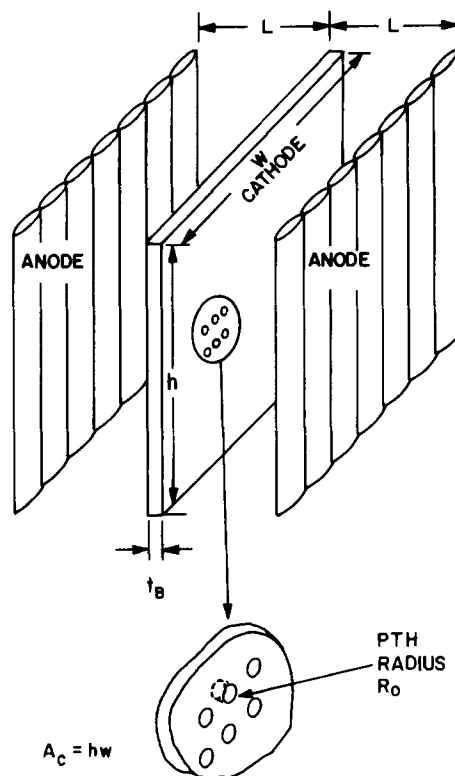


Fig. 1. Schematic of a typical MLB electroplating cell

structure in the deposit, but they do not affect the thickness distribution in the hole. An extensive set of experiments with several plating baths by Rothschild (3) have shown that the plated thickness distribution becomes more nonuniform as the ratio of the board thickness ( $t_B$ ) to the hole radius ( $R_0$ ) increases. For each plating bath Rothschild found the resulting plated thickness on the board surface for a specified minimum thickness in a hole to be a function only of  $t_B/R_0$ . A simple qualitative calculation by Irvine (4) has shown that some electrolyte agitation is required for satisfactory plating of through-holes. This is the only modeling, prior to the present work, that the authors are aware of regarding this problem. Saubestre and Khera (5) plated circuit boards in several copper plating baths including standard and high-throw cop-

\* Electrochemical Society Active Member.

<sup>1</sup> Present address: Xerox Corporation, Rochester, New York 14644.  
Key words: current distribution, multilayer circuit board, mathematical model, copper deposition.

per sulfate baths with additives. Jawitz (6) has presented results for printed circuit board plating with various copper plating baths including a standard copper sulfate bath. The phenomenon of skip plating, *i.e.*, locally thin plating near the outer corner of a PTH, which sometimes occurs when plating with additives has been discussed by Luke (7). Experiments by Dini, Johnson, and Brown (8) with copper pyrophosphate solutions show that such skip plating can be eliminated by increasing either the current density or the agitation.

Several auxiliary experimental studies, not directly related to the PTH geometry, were essential to the development of the present analytical models. Rotating disk electrode kinetics experiments by Rudy (9) established that the Cubath® M and Cubath® I additives in use do not cause significant changes in either the copper kinetics or the diffusion coefficient of the copper ions in solution. Similar results were obtained by Turner and Johnson (10, 11) for copper sulfate solutions with several different additives; although their work shows that some additives can affect kinetics. These results are consistent with the review papers by Kardos (12-14) which discuss the effects of additives in several plating systems. In many cases, additives only affect the deposit morphology and what Kardos calls "microleveling" over small roughnesses the order of 5 mils or less in size. It is recognized that additive baths sometimes cause dishing or skip plating (thin plating) near the outer edges of the holes (8). These observed effects basically do not affect the plated copper distribution down in a smooth hole which is of primary interest here.

The theoretical model developed in the following section characterizes the region in and close to a PTH. Current distributions in this region are obtained by a solution of the coupled equations for conservation of charge and species, along with a reaction rate law. Additive effects have been neglected in this model. Details of the model and comparisons with experimental results are included in the next two sections.

### Theoretical Model

Many salient features of the PTH system are similar to the tubular electrode (TE) system for which a fundamental investigation has recently been conducted (17). Figure 2 shows, in the upper portion, a schematic diagram of a single PTH; the lower portion illustrates a TE for which the analysis is available. A comparison of the two drawings indicates that the TE is geometrically similar to the PTH except insofar as the characterization of the external surface is concerned. The PTH has a sharp exterior edge at the mouth along

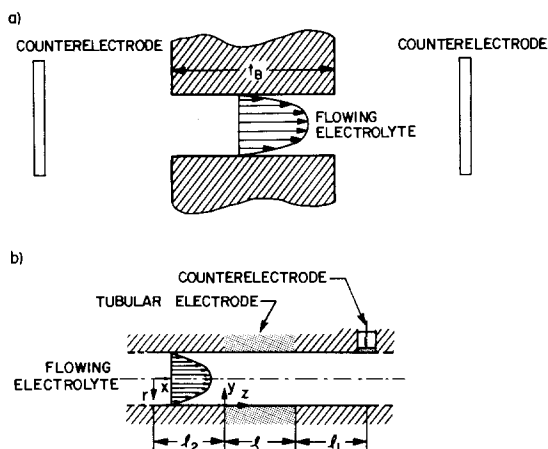


Fig. 2. Schematic diagram of a PTH and the model tubular electrode. (a) PTH, (b) tubular electrode; counter-electrode downstream.

with a cathodic conductor on the external MLB surface, whereas the TE does not. The PTH has counter-electrodes on both sides whereas the TE has but one counter-electrode. Within the TE, steady laminar flow will prevail provided that  $Re < 2100$ , while the L  v  que approximation will be valid provided that  $lD_s/2\bar{v}R_0^2 \ll 0.01$ . The hydrodynamic flow pattern in the two systems will be somewhat different owing to end effects in the PTH. However, for the particular system at hand these effects are negligible since the foregoing restrictions on flow rates correspond to the range of  $0.2 < \bar{v} < 180$  cm/sec, which is the range of practical interest in the PTH problem. For plating with the acid copper system, the effect of cupric ion migration is negligible owing to the high acid concentration; the system is also characterized by a large value of the Schmidt number.

Plated copper thickness distributions in the vicinity of a PTH are complex to predict because there are many different effects which control electrode behavior. The above brief comparison of the PTH system and the TE system has shown that the two systems are similar in many ways with respect to geometric, mass transfer, hydrodynamic, and kinetic characteristics. On this basis, the TE model has been used in order to estimate behavior in the PTH system. The analysis predicts the current distribution dependence on geometry, electrolyte conductivity, charge transfer characteristics, electrolyte convection, and electrolyte composition. To be sure, a detailed comparison of TE theory with experimental data may reveal differences, but it is to be expected that the qualitative trends and intuitive feeling gained by study of the TE system will be helpful in understanding the PTH system.

The tubular electrode system, depicted in Fig. 2(b), consists of an electrode of length,  $l$ , positioned between two long cylindrical sections of insulating material. Electrolytic solution flows through the assembly in fully developed laminar flow. The counter-electrode may be either downstream, as shown, or upstream; in either case, the counter-electrode is sufficiently far away that its precise position does not affect TE behavior. At the electrode surface, the TE model (17) assumes that the rate of electrochemical reaction obeys the Butler-Volmer kinetic rate expression (24). Mass transfer limitations should they arise, are assumed to be confined to a thin shell near the tube periphery. Because concentration differences are confined near the electrode surface, two distinct regions may be identified within the electrolytic solution flowing through the electrode: (a) the diffusion layer region within which concentrations vary, and (b) the bulk region which fills the central region of the tube. The TE model employs separate equations for these two regions and develops a procedure for solving them simultaneously. Details of the mathematical treatment may be found in Ref. (17).

It is worthwhile to review the dimensionless parameters which arise from the TE analysis. There are four parameters:  $\Phi_A$ ,  $\gamma_0$ ,  $\xi$ , and  $N$ .  $\Phi_A$  is the dimensionless applied potential, and  $\gamma_0$  is the aspect ratio. The interpretation of  $\xi$  and  $N$  is more complex. The quantity

$$\xi_k = \frac{2nFl^2}{R_g TR_0 \kappa} i_0 \quad [1]$$

is essentially the linear form of the polarization parameter in that it denotes the relative importance of ohmic to charge-transfer resistances in the linear region of polarization. Provided that mass transfer effects are absent, the value of  $\xi_k$  indicates whether the current distribution within the TE is uniform or not. Qualitatively, values of  $\xi_k > 1$  indicate that the ohmic resistance is greater than the charge-transfer resistance so that the portions of the TE nearest the counter-

electrode will have a greater deposition rate than portions farther from the counterelectrode. Values of  $\xi_\kappa$  less than unity indicate that the current distribution will be uniform along the surface. For application to the PTH system, it is more convenient to use a different form of  $\xi$  which is applicable to the Tafel (18) charge-transfer rate equation

$$\xi_{TK} = \frac{2\alpha_c F l^2 \bar{j}}{R_g T R_o \kappa} \quad [2]$$

$\xi_{TK}$  contains kinetic information about the Tafel slope whereas  $\xi_\kappa$  contains information about the exchange current density.  $\xi_{TK}$  is also related to the dimensionless average current density in the TE

$$\beta_a = 4\xi_{TK} \quad [3]$$

Note that the only kinetic parameter contained in  $\xi_{TK}$  is  $\alpha_c$ , the cathodic transfer coefficient, which has been shown to be independent of the presence of plating additives.  $\xi_{TK} \ll 1$  implies that charge transfer resistance predominates and a uniform current density distribution results.  $\xi_{TK} \gg 1$  implies that solution ohmic resistance dominates in the hole, and nonuniform primary current distributions are expected.

The parameter  $N$  is the dimensionless average limiting current density;  $N$  also contains the ratio  $D_j c_o / \kappa$  and thereby indicates the relative importance of concentration overpotential to ohmic overpotentials

$$N = \frac{3n^2 F^2 l^2 D_j c_o}{s_j R_g T R_o \kappa \Gamma(4/3)} \left( \frac{2v_{max}}{9D_j R_o l} \right)^{1/3} \quad [4]$$

A large value of  $N$  indicates that the limiting current is high so that mass transfer proceeds with relative ease with respect to ohmic resistance effects. For small values of  $N$ , the concentration overpotential tends to be the largest overpotential so that limiting current behavior is approached. The lowest value which  $N$  can take on is the dimensionless average limiting current density

$$\beta_{a,lim} = N \quad [5]$$

Two additional quantities are useful;  $J$  the dimensionless current

$$J = \frac{j}{\bar{j}} \quad [6]$$

and the average current density divided by the average limiting current density

$$\frac{\bar{j}}{\bar{j}_{lim}} = \frac{\beta_a}{N} \quad [7]$$

### Theoretical Results and Discussion

MLB's are typically electroplated with copper at average current densities from 26.9 to 32.2 mA/cm<sup>2</sup> (25-30 A/ft<sup>2</sup>) in high-throw acid copper sulfate solutions. These solutions, which contain 0.27M CuSO<sub>4</sub>, 1.76M H<sub>2</sub>SO<sub>4</sub>, 30 ppm of Cl<sup>-</sup> and proprietary additives, are assumed to consist of the following major ionic concentrations:  $c_j = (\text{Cu}^{+2}) = 0.27\text{M}$ ,  $(\text{H}^+) = 1.49\text{M}$ ,  $(\text{HSO}_4^-) = 2.03\text{M}$ .

The PTH system for which calculations have been made is defined by the parameters in Table I (15, 16, 24). Two sets of calculations will be presented in order to arrive at tentative criteria by which boards may be

Table I.

$c_j$	$= 0.27 \times 10^{-3} \text{ g-mol/cm}^3$
$\kappa$	$= 0.55 \text{ (ohm-cm)}^{-1}$
$i_o$	$= 10^{-3} \text{ A/cm}^2$
$R_o$	$= 0.058 \text{ cm (23 mils)}$
$t_B$	$= 0.305 \text{ cm (120 mils)}$
$D_1$	$= 0.55 \times 10^{-5} \text{ cm}^2/\text{sec}$
$n$	$= 2 \text{ g-equiv./g-mol}$
$\nu$	$= 1.22 \times 10^{-2} \text{ cm}^3/\text{sec}$

designed to assure uniform deposits of high quality. These criteria have been tested against experimental data as discussed in subsequent sections.

In the absence of mass transfer limitations ( $N = \infty$ ), the effect of  $\xi_{TK}$  on the TE current distribution is shown in Fig. 3. These calculations are based on a one-dimensional approximation to Laplace's equation (17). Because a PTH has counterelectrodes on both sides of the board, the current distribution will be symmetric about the centerline (that is,  $l = t_B/2$ ). Consistent with the comments above, acceptably uniform current distributions will be obtained provided that

$$\xi_{TK} < 1 \quad [8]$$

The numbers given in parenthesis in Fig. 3 indicate the plating rates (milliamperes/square centimeter) in the PTH system; it is seen that the common plating rate of 25-30 mA/cm<sup>2</sup> is in a crucial region where the current distribution within the holes is very sensitive to seemingly minor variations in applied current.

It is known that the acceptable morphology of copper deposits depends strongly on maintaining sufficient electrolyte agitation to insure that mass transfer effects do not arise. Therefore, the TE model has been used to estimate the importance of electrolyte convection in a PTH. For this purpose the electrolyte length  $l$  was chosen to be board thickness  $t_B$ ; since the TE system has but one counterelectrode, the predicted current distributions will represent the extreme case. Figure 4 illustrates how the total overpotential within the TE varies with  $N$  (flow rate) for a given value of  $\beta_a$  (applied current density of 25 mA/cm<sup>2</sup>). The quantity  $\Phi_m^*$  is the potential in the solution at the mouth of the electrode nearest the counterelectrode; this quantity is a sensitive indicator of concentration overpotential. Recall that for  $N = \infty$ , the convection rate is so large that concentration overpotential effects are negligible. As the flow velocity is decreased, the total overpotential increases because of the onset of concentration overpotentials which arise in the electrolyte. As  $N$  approaches the lowermost limiting value of  $\beta_{a,lim} = 12$ ,

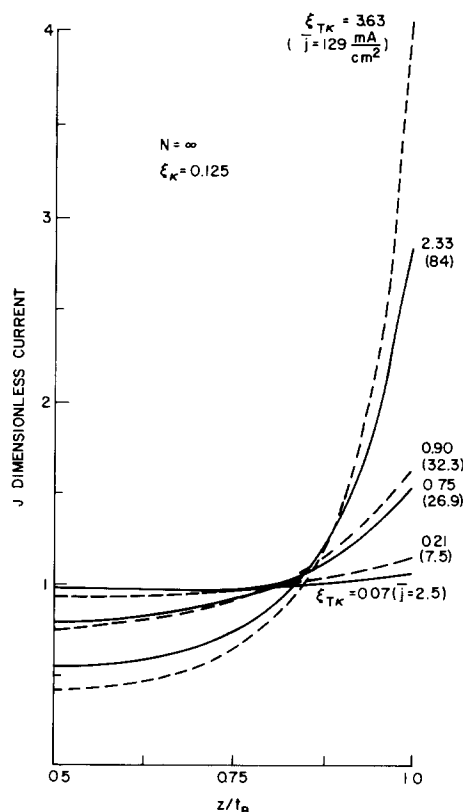


Fig. 3. Current distributions in a PTH for various  $\xi_{TK}$

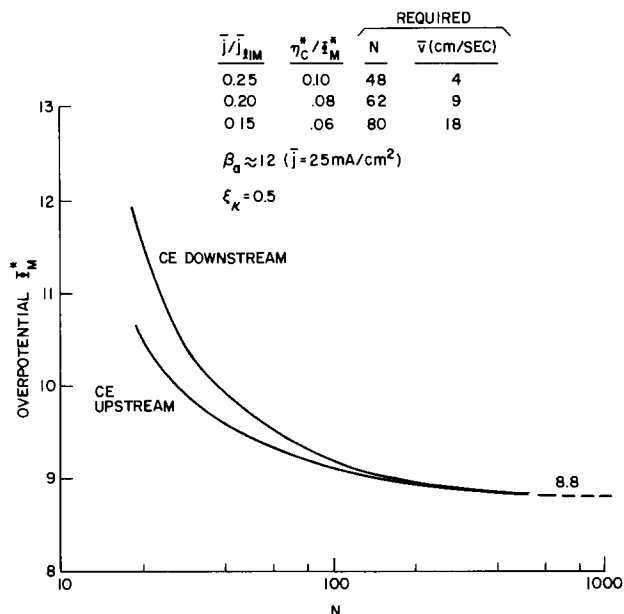


Fig. 4. Effect of average limiting current density on overpotential

the limiting current distribution is obtained and the total overpotential increases sharply. Figure 4 contains two curves, one for an upstream counterelectrode and one for a downstream counterelectrode. Although they differ slightly, it is seen that convective mass transfer does not significantly influence electrode behavior for values of  $N$  greater than 50. As indicated in the inset in Fig. 4, the concentration overpotential comprises only 10% of the total overpotential at a value of  $N = 48$  (25% of the average limiting current density).

For the PTH system parameters at 30 mA/cm<sup>2</sup> ( $\beta_{a,lim} = 14.5$ ), current distributions have been estimated for several values of  $N$  as shown in Fig. 5. It is seen that for  $N = 14.5$ , the limiting current distri-

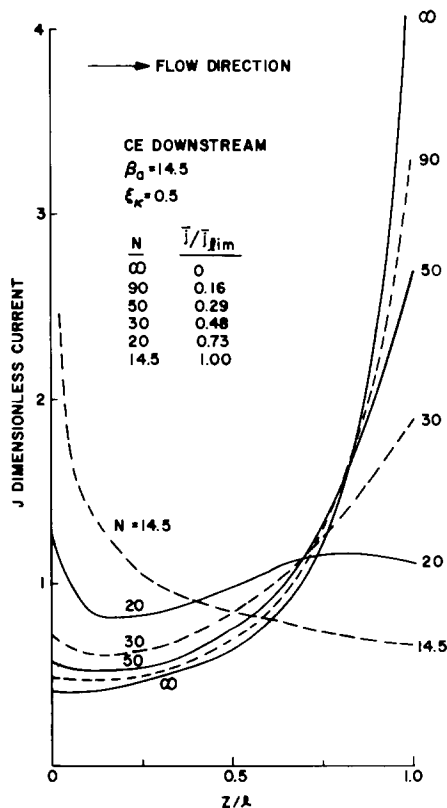


Fig. 5. Current distributions for various fractions of the limiting current density.

bution is obtained whereby upstream portions of the electrode are most reactive; for  $N = \infty$ , the downstream portion of the electrode, nearest the counterelectrode, is most reactive. For this particular system, the current distribution for  $N = 50$  is for the most part within 20% of the current distribution for  $N = \infty$ . Therefore, as a rough estimate of the conditions under which concentration overpotentials are relatively un-influential in controlling electrode behavior, one has  $N > 50$  for the system at hand, or

$$N > 4\beta_{a,lim} \quad [9]$$

MLB's are typically copper plated at average currents between 25-30 mA/cm<sup>2</sup>. It is clear from Fig. 3 that the present systems therefore operate in the critical region where the current distributions within the holes are very sensitive to seemingly minor increases in current. For example, it is known that nonuniform plating current distributions on MLB's can cause the test coupons near the outer edges of panels to receive current densities that are a factor of two to three larger than the current densities near the panel center. Therefore, the current distribution in a coupon PTH may look something like the curve labeled 78 mA/cm<sup>2</sup> while the PTH's near the panel center might exhibit current distributions which are similar to the curve labeled 25 mA/cm<sup>2</sup>. The copper thickness in the coupon PTH will always be greater than in interior panel PTH's since the  $J$  in Fig. 3 is made dimensionless with the local average current density. In order that the electrodeposited copper in coupon PTH's be representative of the copper plated in the interior PTH's, one of two situations is necessary: Either (i)  $\xi_{TK} < 1$  and  $N > 4\beta_{a,lim}$ , or (ii)  $\xi_{TK}$  and  $N$  must have constant values over the entire panel.

### Comparison Between Predictions and Experimental Results

Experiments have been conducted by several investigators to determine the electroplated copper thickness distributions in and around PTH's in MLB's. In all cases, the inside of the holes and the outer copper planes received a thin coating of approximately 20  $\mu$ in. of electroless copper prior to electroplating. Table II gives a summary of the experimental conditions for each investigation. Comparisons between model predictions and results from these experiments indicate that the model provides good qualitative agreement with the experiments for the wide range of conditions tested.

Effects of the CuSO<sub>4</sub>/H<sub>2</sub>SO<sub>4</sub> ratio on the electroplating of PTH's have been determined experimentally in a systematic study by Turner and Havens (20). The experiments were conducted in a 1500 ml beaker with air agitation provided by a sparger located under the cathode. The CuSO<sub>4</sub>/H<sub>2</sub>SO<sub>4</sub> ratio was varied by keeping the total concentration of CuSO<sub>4</sub> · 5H<sub>2</sub>O and H<sub>2</sub>SO<sub>4</sub>

Table II. Range of parameters for PTH plating experiments

No.	Ref.	Parameters
1	20	$t_B$ (mils) = 108 $R_o$ (mils) = 15.5, 23, 44.5, 82 $\bar{j}$ (mA/cm <sup>2</sup> ) = 16.1, 26.9, 37.7 $c_j$ (M) = 0.14, 0.28, 0.52, 0.8 Agitation: air sparged
2	20	$t_B$ (mils) = 108; $R_o$ (mils) = 23 $\bar{j}$ (mA/cm <sup>2</sup> ) = 16.1, 26.9, 53.8, 80.7, 107.6 $c_j$ (M) = 0.27 Agitation: forced flow ( $24 \leq \bar{v}$ (cm/sec) $\leq 83$ )
3	21	$t_B$ (mils) = 111, 187; $R_o$ (mils) = 23 $\bar{j}$ (mA/cm <sup>2</sup> ) = 10.8, 14, 21.5, 43.1, 86.1 $c_j$ (M) = 0.27 Agitation: air sparged, transverse MLB motion, or forced flow
4	21	$t_B$ (mils) = 93, 123; $R_o$ (mils) = 23 $\bar{j}$ (mA/cm <sup>2</sup> ) = 5, 25, 40, 100 $c_j$ (M) = 0.34 Agitation: forced flow ( $\bar{v}$ (cm/sec) = 0.16, 25, 87)
5	MLB product	$t_B$ (mils) = 160; $R_o$ (mils) = 23 $\bar{j}$ (mA/cm <sup>2</sup> ) = 25; $c_j$ (M) = 0.27 Agitation: air sparged



constant at 250 g/liter. For easy comparison of results, the total number of coulombs transferred was identical for each experiment. PTH resistances were determined with a commercially available four-point probe system (Caviderm® by Unit Process Assemblies, Incorporated). Figure 6, which has been taken from Ref. (20), shows that the PTH resistances are near a minimum for typical high-throw solutions at about 70 g/liter  $\text{CuSO}_4 \cdot 5\text{H}_2\text{O}$ . The experimental results shown are for additive-free solutions; however, additional experiments (20) conducted with proprietary additives produced negligible changes in resistance. Turner and Havens report (20) that the high PTH resistances for high copper concentrations are caused by poor copper thickness distributions in the holes. At low copper concentrations they found that the high resistances were due to the poor quality of the plated copper in the hole. The present model supports the view that poor distributions result from large ohmic effects ( $\xi_{TK} > 1$ ) and poor deposit quality is a consequence of inadequate mass transport ( $N < 4\beta_a$ ). The following paragraphs outline three experimental methods which were used to establish this interpretation.

### High Copper Concentrations

An explanation for the observations in Ref. (20) is found by recasting the data in terms of the dimensionless parameters defined by the foregoing model. For the moment, let us focus discussion on copper concentrations above 70 g/liter of  $\text{CuSO}_4 \cdot 5\text{H}_2\text{O}$ . Since the PTH resistance is inversely proportional to the hole radius  $R_0$ , it is convenient to define an equivalent PTH resistance as  $R_H[R_0(\text{mils})/23]$ . A plot of equivalent PTH resistance vs. the parameter  $\xi_{TK}$  is shown in Fig. 7. The average PTH resistance for the center 5 holes in the flow cell experiments (20) are also included on this plot. The good correlation shown for the wide range of parameters studied confirms the utility of the parameter  $\xi_{TK}$ . Higher resistances occur for larger values of  $\xi_{TK}$  because the ohmic solution resistance in the hole is large; leading to more nonuniform current distributions in the holes.

A second useful measure of the uniformity of the plated copper in a hole is the throwing power,  $t_s/t_H$ ;

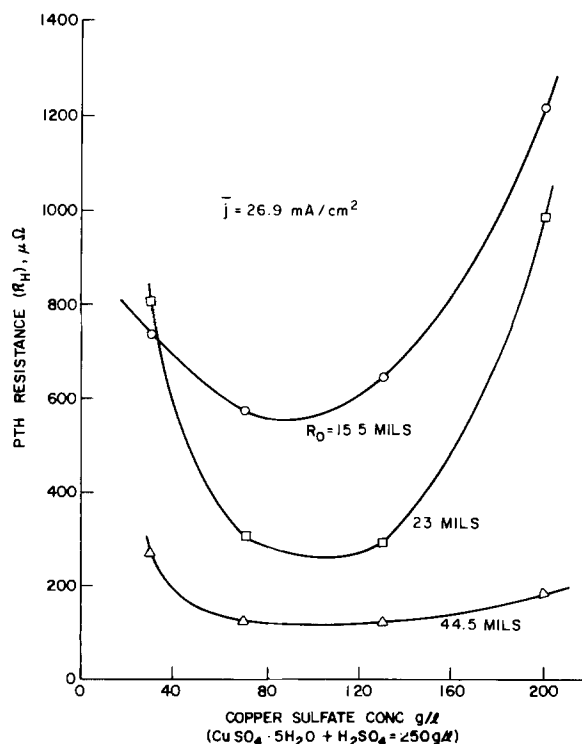


Fig. 6. Effect of copper-acid ratio on PTH resistance [Figure supplied by Turner and Havens (20)].

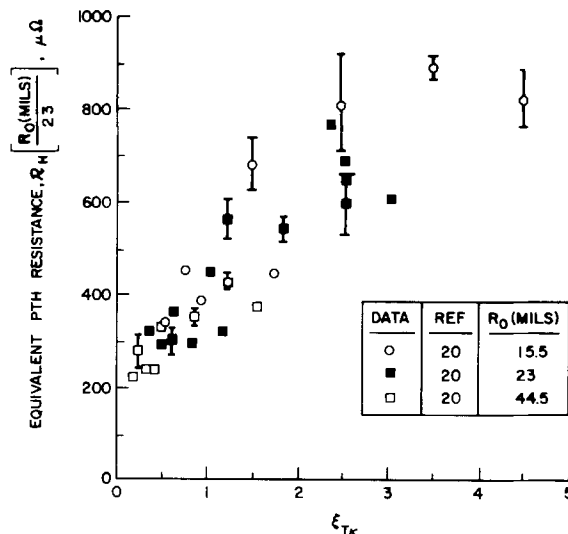


Fig. 7. Dependence of the equivalent plated-through hole resistance on the parameter  $\xi_{TK}$ .

where  $t_s$  is the plated copper thickness at the outer edge ( $z = 0$  or  $t_B$ ) of the hole and  $t_H$  is the plated thickness in the center ( $z = t_B/2$ ) of the hole. This ratio has been determined from microscopic examination of PTH cross sections. A plot of the throwing power vs. the parameter  $\xi_{TK}$  is presented in Fig. 8. Turner and Havens (20) actually measured the plated copper thickness on the outer surface of the MLB next to the PTH; however, these thicknesses are close enough to  $t_s$  values for the purpose at hand. Note the agreement, considering the scatter in the data, among the experiments conducted at widely different scales. The data in Fig. 8 are representative of the following wide range of experimental conditions: (i) Experiments were conducted with and without additives. (ii) Experiments were conducted in full size production plating tanks, small beakers (1 and 4 liters) (20, 21) and 77 liter flow cells (21). (iii) Experiments were conducted with air sparger agitation, transverse agitation of the MLB's, and with forced electrolyte convection through the holes.

The predicted throwing power agrees with the data for  $\xi_{TK} < 1.5$ . For values of  $\xi_{TK} > 1.5$ , the applicability of the simplified model for the potential distribution breaks down most likely because the geometry of the PTH "mouth," where the reaction rate is largest, is not taken into account. Nevertheless, the qualitative features of the model continue to be valid even for

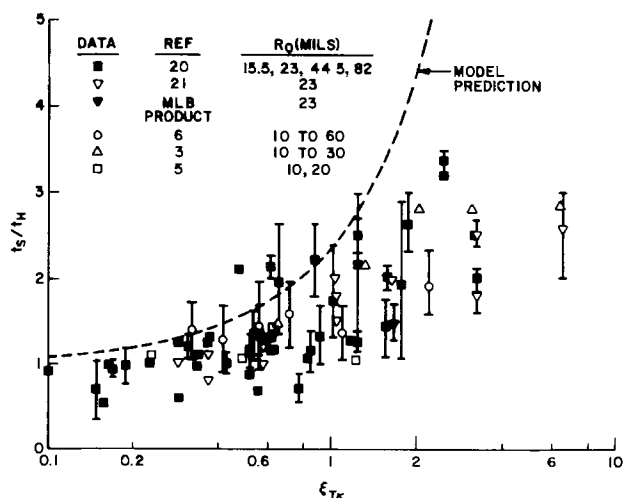


Fig. 8. Dependence of the throwing power ( $t_s/t_H$ ) on the parameter  $\xi_{TK}$ .

Table III. Specific experimental conditions for the data presented in Fig. 9-13, and 15

$\xi_{TK}$	Ref.	$t_B$ (mils)	$R_o$ (mils)	$c_1$ (molarity)	[H <sub>2</sub> SO <sub>4</sub> ] (molarity)	Additives	$\bar{v}$ (cm/sec)	$\bar{j}$ (mA/cm <sup>2</sup> )	Plating time (min)
0.15	21	123	23	0.34	1.76	None	87	5	480
0.57	21	111	23	0.375	1.76	Proprietary organic	82	21.5	150
0.62	20	108	23	0.27	1.84	None	24.4	26.9	69
1.24	20	108	23	0.27	1.84	None	24.4	53.8	34
1.62	MLB product	160	23	0.27	1.76	Proprietary organic	Unknown	26.9	90
1.86	20	108	23	0.27	1.84	None	24.4	80.7	23
2.48(1)	20	108	23	0.27	1.84	None	49	107.6	17
2.48(2)	20	108	23	0.27	1.84	None	83	107.6	17
2.48(3)	20	108	23	0.27	1.84	None	63	107.6	17
2.97	21	123	23	0.34	1.76	None	87	100	24
2.97	21	123	23	0.34	1.76	None	25	100	24

large values of  $\xi_{TK}$ . The model provides a conservative estimate of conditions under which satisfactory distributions may be obtained. The data show that increasingly poor distributions are obtained as  $\xi_{TK}$  increases above unity. It is clearly desirable to maintain  $\xi_{TK} < 1$  to assure uniform copper distributions in the holes.

The correlation of throwing power with  $\xi_{TK}$  has important implications regarding the relevance of the copper plated in test coupon PTH's to the copper plated in the PTH's nearer to the center of the panel. The higher current densities that frequently exist near panel edges, where the coupons are located, will cause larger  $\xi_{TK}$  values at the coupons than near the panel centers (19). Consequently, the copper thickness distributions in coupon PTH's can be expected to be less uniform than corresponding distributions in PTH's near the panel center. For this reason, the current density throughout panels should be made more uniform, and board thicknesses and/or average current densities should be decreased to reduce  $\xi_{TK}$ .

The third and most direct method is to compare distributions with actual copper thickness distributions determined from PTH cross sections. Such comparisons are shown in Fig. 9 through 11. It should be emphasized that the model contains no unknown parameters which may be arbitrarily adjusted to force agreement with experimental data. The agreement between predictions and the measurements (20, 21) is good for  $0.57 \leq \xi_{TK} < 2.48$ . Details of the experimental conditions for the data used in Fig. 9 through 14 are contained in Table III. Figure 9 shows that small values of  $\xi_{TK}$  produce relatively uniform deposits. The experimental curves for  $\xi_{TK} = 0.57$  in Fig. 9 are for two different holes from a single plating experiment; these curves illustrate typical reproducibility for rough hole walls. The results in

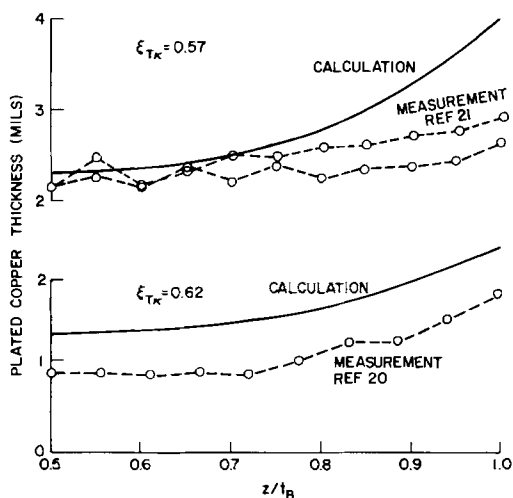


Fig. 9. Comparison between predicted copper thickness distributions in a PTH and measurements for  $\xi_{TK} < 1$ .

Fig. 10 show that at intermediate values of  $\xi_{TK}$  the distributions become nonuniform. This nonuniformity increases with  $\xi_{TK}$ , but the agreement between measurements and predictions is still excellent. Figure 11 shows a highly nonuniform deposit distribution for  $\xi_{TK} = 2.48$  which is typical of large values of  $\xi_{TK}$ . Measured thickness distributions from three separate additive-free experiments are shown to indicate experimental reproducibility. As discussed previously, the analysis is conservative in the sense that larger nonuniformities are

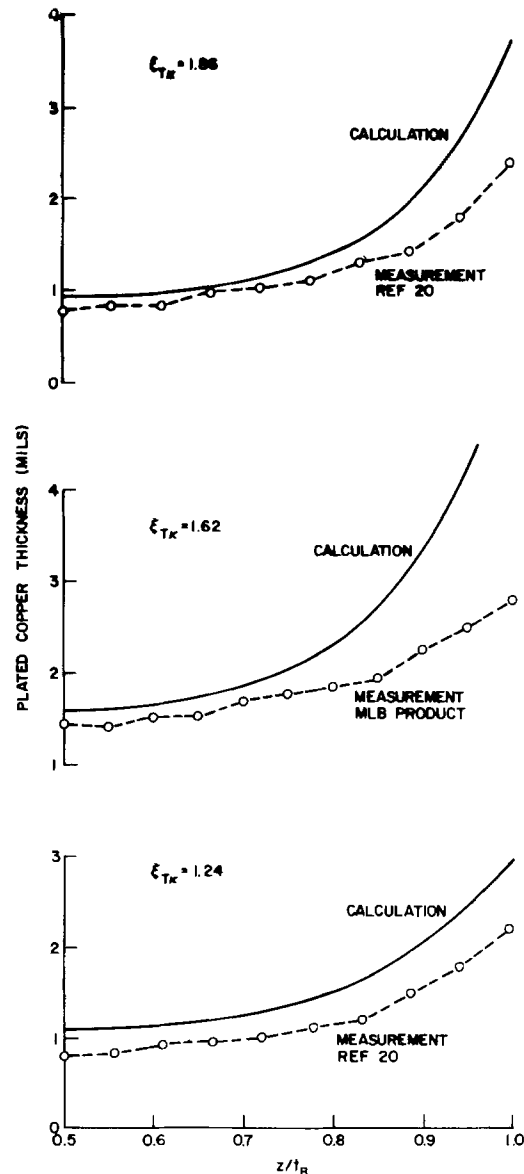


Fig. 10. Comparison between predicted copper thickness distributions in a PTH and measurements for  $1 < \xi_{TK} < 2$ .

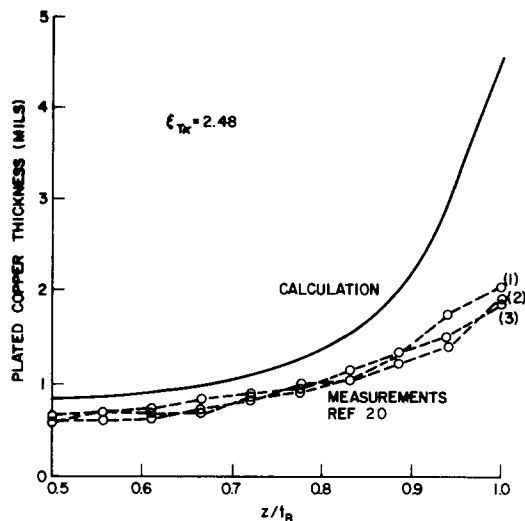


Fig. 11. Comparison between predicted copper thickness distribution in a PTH and measurements for  $\xi_{TK} = 2.48$ .

predicted than are found experimentally. Nevertheless, the over-all agreement between experiments and predictions confirms the salient features of the model.

The experimental results from Ref. (20) in Fig. 9 through 11 were conducted with electrolyte pumped through the seven holes in a small MLB to provide controlled and uniform agitation in the holes. The results in Fig. 11 show little difference in plated copper thickness distributions for average convection velocities in the holes from 49 to 83 cm/sec. The parameter  $\beta_a$  is approximately 39 for these experiments, and the calculated value of  $N$  is between 110 and 131. As shown in Fig. 4, the model predicts the observed insensitivity for values of  $N$  several times larger than  $\beta_a$ .

The foregoing threefold comparison of data and predictions supports the view that nonuniform deposit thickness distributions are the consequence of large ohmic effects ( $\xi_{TK} > 1$ ). Further evidence of this is shown in the photographs of PTH cross sections in Fig. 12 and 13 for  $\xi_{TK} = 0.15$  and 2.96, respectively. As can be seen in Table III, both of these PTH's were plated with the same average number of coulombs in an additive-free solution with controlled agitation in the holes (21). The symmetry of the copper thickness distributions in the holes indicates that flow direction and development effects in the holes are not important. The desirability of  $\xi_{TK} < 1$  for uniform thickness distributions in PTH's is apparent.

#### Low Copper Concentrations

Let us now turn to a discussion of the data in Fig. 6 for low copper concentrations. Turner and Havens (20) report that the higher PTH resistances at 35 g/liter of  $\text{CuSO}_4 \cdot 5\text{H}_2\text{O}$  were caused by excessively rough copper deposits in the holes. Since the electrolyte velocity in the holes was neither measured nor controlled for these air sparged experiments, the ratio of  $\bar{j}/\bar{j}_{lim}$  can only be crudely estimated. Such an estimate indicates that  $\bar{j}/\bar{j}_{lim}$  exceeds 0.35 for all cases where rough copper was deposited in the holes.

The importance of adequate electrolyte convection in the through-holes during plating has been established by experiments (20, 21). Figure 14 presents PTH resistance data (21) as a function of average plating current density and average electrolyte velocity in the PTH's. The error bars indicate the resistance range for at least ten PTH's plated in an additive-free bath at the conditions shown. For  $\bar{j} \leq 40$  mA/cm<sup>2</sup>, the resistances are insensitive to variations in solution velocity from 25 to 87 cm/sec. Nevertheless, convection effects are significant at  $\bar{j} = 100$  mA/cm<sup>2</sup>. For  $\bar{j} = 100$

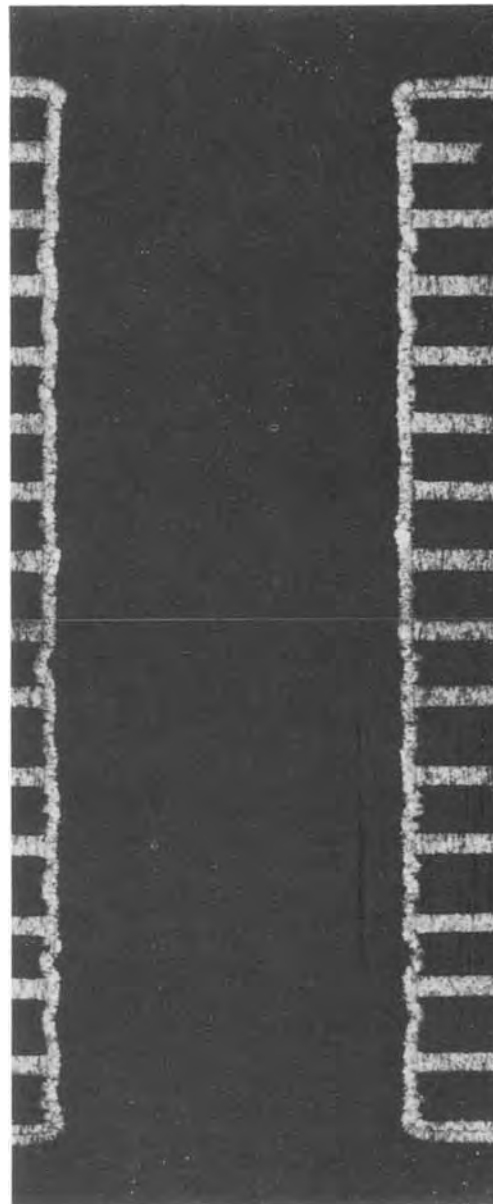


Fig. 12. Cross section of a plated-through hole in a multilayer board. Plating parameters:  $\xi_{TK} = 0.15$ ,  $\bar{v} = 87$  cm/sec,  $\bar{j}/\bar{j}_{lim} = 0.015$ .

mA/cm<sup>2</sup> and  $\bar{v} = 87$  cm/sec, which results in a ratio  $\bar{j}/\bar{j}_{lim}$  of approximately 0.28, convection is sufficient to produce good quality copper in the holes as shown in Fig. 13. However, for  $\bar{v} = 25$  cm/sec,  $\bar{j} = 100$  mA/cm<sup>2</sup>, and  $\bar{j}/\bar{j}_{lim} = 0.43$ , the higher resistance in Fig. 14 is indicative of poor quality copper in the hole (or on the board surface). The cross section shown in Fig. 15 shows that the copper quality is indeed poor at these plating conditions. Similar results have been obtained with additive-free baths (20). Plating at  $0.3 \leq \bar{j}/\bar{j}_{lim} \leq 0.36$  produced good quality copper, whereas plating at  $\bar{j}/\bar{j}_{lim} = 0.45$  produced significantly rougher coarse grained copper. Since rough deposits are usually encountered under limiting current conditions, these data suggest that the current density  $\bar{j}$  was too close to the average limiting current density  $\bar{j}_{lim}$ .

The observations that poor quality copper deposits for plating at  $\bar{j} > 0.35 \bar{j}_{lim}$  are also in agreement with observations in the literature (22, 23). Rotating cylindrical cathode studies by Gabe and Robinson (22) suggest that rough copper deposits may occur above  $\bar{j}/\bar{j}_{lim}$

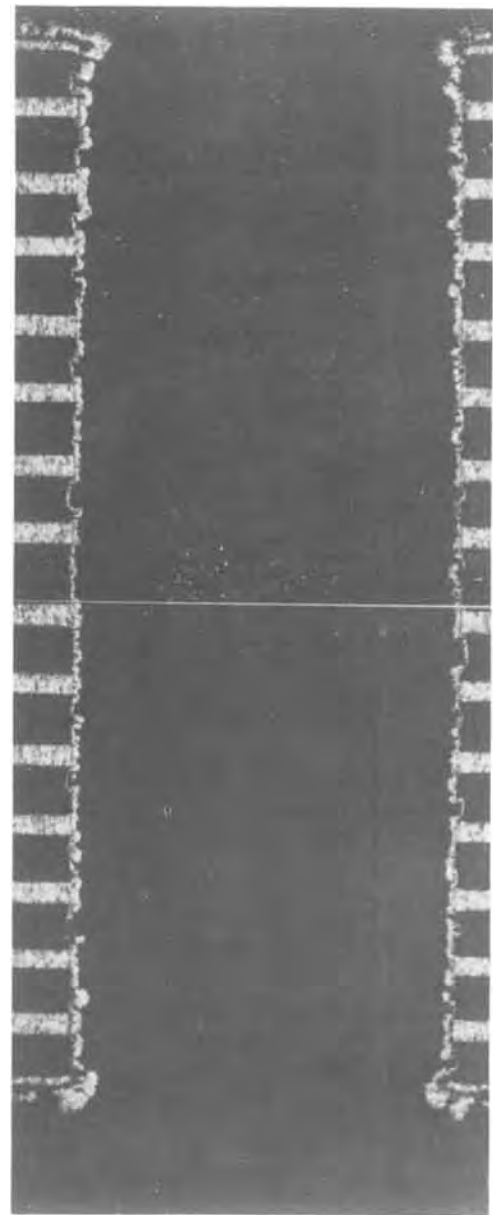
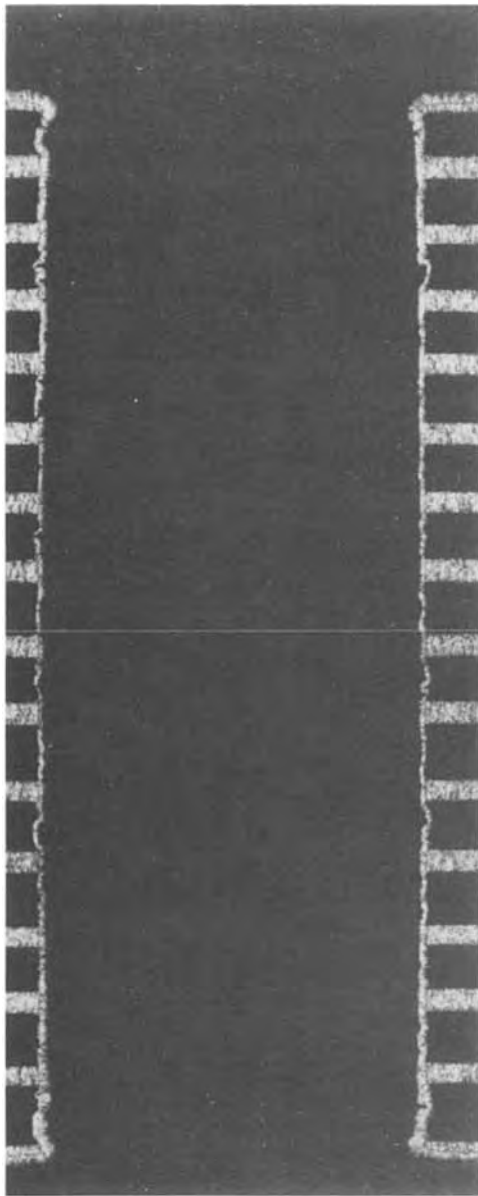


Fig. 13. Cross section of a plated-through hole in a multilayer board. Plating parameters:  $\xi_{TK} = 2.96$ ,  $\bar{v} = 87$  cm/sec,  $\bar{j}/\bar{j}_{lim} = 0.28$ .

Fig. 15. Cross section of a plated-through hole in a multilayer board. Plating parameters:  $\xi_{TK} = 2.96$ ,  $\bar{v} = 25$  cm/sec,  $\bar{j}/\bar{j}_{lim} = 0.43$ .

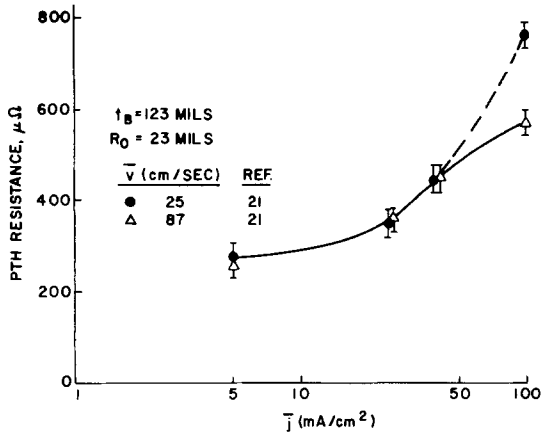


Fig. 14. Dependence of PTH resistances on average current density and convection in the PTH's.

$\bar{j}/\bar{j}_{lim} = 0.4$ ; in practice they found very rough copper above  $\bar{j}/\bar{j}_{lim} = 0.7$ . Measurements of deposit surface roughness from acid-sulfate baths by Ibl and Braun (23) indicate

that rough deposits occur for  $\bar{j}/\bar{j}_{lim}$  exceeding 0.7. In the plating experiments of Ref. (20) and (21), it is possible that the initiation of rough copper actually occurred because  $\bar{j}/\bar{j}_{lim}$  was too large on the board surface outside of the hole. Since the convection on this outer surface is unknown, no quantitative estimates of this ratio for the outer surface are possible.

The above interpretation of the experiments in Ref. (20) and (21) may now be used to make a rational choice for the required minimum electrolyte convection in a PTH. Figure 4 has shown that the overpotential  $\Phi^*_m$  asymptotically approaches a limiting value of  $N$ , but a criterion is needed for choosing a minimum acceptable value for  $N$ . Since poor plating quality has been found at values of  $\bar{j}/\bar{j}_{lim}$  exceeding 0.35, a recommended maximum value for operating conditions is  $\bar{j}/\bar{j}_{lim} = 0.25$ . This value of  $\bar{j}/\bar{j}_{lim}$  requires a minimum  $N$  value of  $4\beta_a$  and implies (see Fig. 4) that  $\eta_c$  contributes no more than 10% of  $\Phi^*_m$ . Note also that this value of  $N$  is sufficient to eliminate convective effects on copper distribution as shown in Fig. 5.

For the system at hand (Table I) where  $\beta_a \simeq 12$ , the requirement  $N > 50$  implies a minimum average solution velocity of 4 cm/sec in the holes. Further agitation experiments are required to determine if such convection velocities exist uniformly throughout production plating tanks. To guarantee uniform copper plating on panels, the minimum convection velocity in PTH's as well as the primary current distribution across the panel must be controlled.

### Summary and Conclusions

A program of experimental and theoretical studies has provided a consistent interpretation of the processes which control copper electroplating of PTH's. The studies have clarified how ohmic resistance, charge transport, cell geometry, plating additives, and mass transport effects can all contribute toward determining the electrochemical behavior during PTH deposition. Engineering design of a plating system for MLB's is complex because the relative importance of these several phenomena may vary widely from place to place along the MLB surface. The following paragraphs summarize the over-all picture which has emerged from this program of engineering analysis. The analysis provides design criteria for assuring uniform high quality plating.

The model establishes the importance of two dimensionless parameters ( $\xi_{TK}$  and  $N$ ), which are essentially independent of additive effects, for characterizing current distribution effects in and close to a PTH.  $\xi_{TK}$  is shown to control the copper thickness distribution within PTH's for sufficient agitation.  $\xi_{TK}$  is proportional to  $l^2/R_o$ ; that is, the geometrical scale-up is not  $l/R_o$  as might have been anticipated.  $N$  determines the effectiveness of the electrolyte convection in the holes. It is important to recognize that both of these parameters can be obtained without solving the equations of the model. Furthermore, only a minimum amount of theoretical calculations were needed to establish the following desirable ranges for these parameters:

1.  $\xi_{TK} < 1$  or else uniform  $\xi_{TK}$  throughout a panel. The uniformity of  $\xi_{TK}$  may be controlled by adjusting the cell geometry to provide a more uniform primary current distribution throughout a panel.

2.  $N > 4\beta_a$ . This minimum value for  $N$  is needed to assure the elimination of concentration overpotential effects on either the deposit morphology or the thickness distributions. This criterion implies a minimum average electrolyte convection of 4 cm/sec in each PTH. This minimum convection is required in all PTH's in the panel to assure that test coupons are representative of the panel interior.

For these conditions of  $\xi_{TK}$  and  $N$ , a test coupon from the panel edge will accurately represent the state of electrodeposition in the panel interior.

The criterion that  $\bar{j}/j_{lim}$  not exceed 0.35 should be regarded as a preliminary result. A more refined determination of this ratio, both with and without additives in the electrolyte, could be made with the use of rotating disk and/or rotating cylinder electrodes for which the current ratio can be determined precisely. In addition, at various predetermined ratios, optical observations of deposit quality could be made.

### Acknowledgment

The authors are grateful to D. R. Turner and B. R. Havens for the use of previously unpublished data; to A. A. Mirarefi for some of the model calculations; and to A. J. Colucci for the experimental measurements.

Manuscript submitted Aug. 4, 1975; revised manuscript received Feb. 6, 1976. This was Paper 151 presented at the Dallas, Texas, Meeting of the Society, Oct. 5-9, 1975.

Any discussion of this paper will appear in a Discussion Section to be published in the June 1977 JOURNAL.

All discussions for the June 1977 Discussion Section should be submitted by Feb. 1, 1977.

Publication costs of this article were partially assisted by Bell Laboratories.

### LIST OF SYMBOLS

$c_j$	cupric ion concentration, g-mole/cm <sup>2</sup>
$D_j$	diffusion coefficient of species j, cm <sup>2</sup> /sec
$F$	Faraday's constant, 96,500 coulombs/g-equiv.
$h$	cathode (panel) height, cm
$i_o$	exchange current density, A/cm <sup>2</sup>
$\bar{j}$	current density, A/cm <sup>2</sup>
$\bar{j}$	average current density, A/cm <sup>2</sup>
$j_{lim}$	limiting current density, A/cm <sup>2</sup>
$\bar{j}_{lim}$	average limiting current density, A/cm <sup>2</sup>
$J$	$\bar{j}/\bar{j}_{lim}$ normalized local current density, dimensionless
$l$	length of tubular electrode, cm
$l_1$	distance from counterelectrode to edge of tubular electrode, cm
$l_2$	distance from rear edge of tubular electrode to rear plane of equipotential, cm
$L$	anode to cathode spacing, cm
$n$	number of electrons taking part in electrode reaction
$N$	$\frac{3n^2F^2l^2D_jc_a}{s_jR_gTR_o\kappa\Gamma(4/3)} \left( \frac{2v_{max}}{9D_jR_o l} \right)^{1/3}$ average limiting current density, dimensionless
$r$	spatial variable in radial direction, cm
$R$	resistance, $\mu\text{ohm}$
$Re$	Reynolds number, $2R_o\bar{v}/\nu$
$R_g$	gas constant, 8.31 joules/g-mole deg
$R_o$	through-hole radius, cm
$s_j$	stoichiometric coefficient of the reaction species
$Sc$	Schmidt number $= \nu/D_j$
$t_B$	MLB panel thickness, cm
$t_H$	plated copper thickness at the center ( $z = t_B/2$ ) of the hole, cm
$t_s$	plated copper thickness at outer edge ( $z = 0$ or $t_B$ ) of hole, cm
$T$	temperature
$v_{max}$	electrolyte velocity along tube axis, cm/sec
$\bar{v}$	average electrolyte velocity in tube, cm/sec
$w$	cathode (panel) width, cm
$x$	spatial variable in axial direction, cm
$y$	spatial variable normal to electrode surface, cm
$z$	spatial variable in axial direction, cm
$Z$	$z/l$ , spatial variable along electrode surface, dimensionless
$\alpha_c$	cathodic transfer coefficient in reaction rate expression
$\beta_a$	average current density, Eq. [3], dimensionless
$\gamma_o$	aspect ratio: $l/R_o$
$\Gamma(4/3)$	Gamma function
$\eta_c$	concentration overpotential, V
$\eta^*$	$(nF/R_gT)\eta$ overpotential, dimensionless
$\kappa$	electrolyte conductivity, $\text{ohm}^{-1}\text{-cm}^{-1}$
$\nu$	electrolyte kinematic viscosity, cm <sup>2</sup> /sec
$\xi_{TK}$	$2nFl^2i_o/R_gTR_o\kappa$ , ratio of ohmic resistance to linear charge transfer resistance, dimensionless
$\xi_{TK}$	$2\alpha_cFl^2\bar{j}/R_gTR_o\kappa$ , ratio of ohmic resistance to Tafel charge transfer resistance dimensionless
$\phi$	potential in electrolyte phase, V
$\phi_A$	potential applied across cell, V
$\Phi^*_{m}$	average overpotential at the mouth of the hole nearest the counterelectrode, dimensionless
$\Phi^*$	$(nF/R_gT)\phi$ potential in electrolyte phase, dimensionless

### REFERENCES

1. F. A. Lowenheim, "Modern Electroplating," 3rd ed, pp. 215-223, John Wiley & Sons, Inc., New York (1974).
2. J. W. Dini, *Plating*, **51**, 119 (1964).
3. R. F. Rothschild, *ibid.*, **53**, 437 (1966).
4. T. H. Irvine, *Metal Finishing*, **65**, 85 (January 1967).
5. E. B. Saubestre and R. P. Khara, in "3rd Symposium on Plating in the Electronics Industry," American Electroplaters Society, pp. 230-242 (1971).
6. M. W. Jawitz, *Metal Finishing*, **71**, 31 (July 1973).

7. D. A. Luke, *Trans. Inst. Metal Finishing*, **47**, 36 (1969).
8. J. W. Dini, H. R. Johnson, and D. E. Brown, *Photochem. Mach.-Photochem. Etching*, **7**, (March-April 1972).
9. D. A. Rudy, Bell Laboratories, To be published.
10. D. R. Turner and G. R. Johnson, *This Journal*, **109**, 798 (1962).
11. G. R. Johnson and D. R. Turner, *ibid.*, **109**, 918 (1962).
12. O. Kardos, *Plating*, **61**, 129 (1974).
13. O. Kardos, *ibid.*, **61**, (1974).
14. O. Kardos, *ibid.*, **61**, 316 (1974).
15. J. Newman, "Electrochemical Systems," pp. 364-365, Prentice-Hall, Inc., Englewood Cliffs, New Jersey (1973).
16. C. R. Wilke, M. Eisenberg, and C. W. Tobias, *This Journal*, **100**, 513 (1953).
17. R. Alkire and A. A. Mirarefi, *ibid.*, **120**, 1507 (1973).
18. T. P. Hoar, *Plating*, **61**, 35 (1974).
19. H. L. Pinkerton, in "Electroplating Engineering Handbook," 3rd ed. A. K. Graham, Editor, Chap. 16, Van Nostrand Reinhold Co., New York (1971).
20. D. R. Turner and B. R. Havens, Paper 154 presented at The Electrochemical Society Meeting, Dallas, Texas, Oct. 5-9, 1975.
21. W. Engelmaier, T. J. Kessler, and A. J. Colucci, Paper 150 presented at The Electrochemical Society Meeting, Dallas, Texas, Oct. 5-9, 1975.
22. D. R. Gabe and D. J. Robinson, *Trans. Inst. Metal Finishing*, **49**, 17 (1971).
23. N. Ibl and M. Braun, *Chem.-Ing.-Tech.*, **45**(4), 182 (1973).
24. J. Newman, "Electrochemical Systems," p. 177, Prentice-Hall, Inc., Englewood Cliffs, New Jersey (1973).

## Investigations of an Electrodeposited Tin-Nickel Alloy

### I. Thermal Stability by Differential Thermal Analysis and X-Ray Diffraction

J. E. Bennett and H. G. Tompkins

Bell Laboratories, Columbus, Ohio 43213

#### ABSTRACT

The equiatomic (65 weight per cent Sn) tin-nickel alloy, which can only be produced by electrodeposition, has found various practical applications. This plated alloy is a nonequilibrium metastable phase since the equilibrium configuration of such an alloy should be a mixture of the two compounds  $Ni_3Sn_2$  and  $Ni_3Sn_4$ . Previous investigations have reported that the alloy decomposed at temperatures ranging from 250° to 500°C. This work was conducted to better define the transition point since it can be a deciding factor for many applications. By means of differential thermal analysis it was found on heating at a rate of 5°C/min the alloy decomposed exothermally over the range 350°-380°C with a maximum at 365°C. This was confirmed by x-ray diffraction analyses (powder and diffractometer methods) of samples heated to just below and just over the transition range. From additional isothermal heat-treatments and x-ray diffraction analyses it was concluded that caution should be taken when applications with service temperatures over 300°C are expected.

The electrodeposited equiatomic [65 weight per cent (w/o) Sn-35 w/o Ni] tin-nickel alloy<sup>1</sup> continues to be of considerable scientific and technological interest. A commercially usable technique for plating this equiatomic alloy was first demonstrated by Parkinson (1) and colleagues (2). Electrolytically formed binary alloys may or may not be identical in phase constitution with alloys of identical chemical composition formed by conventional metallurgical processes (3). Tin-nickel electrodeposit is a case in point as Rooksby originally found it to be a single-phase, intermetallic compound, with a NiAs-type unit cell (4). However, the published equilibrium diagram (Fig. 1) of the binary nickel-tin system, based upon metallurgically prepared alloys, shows that an alloy of equiatomic chemical composition is composed of a mixture of the two intermetallic compounds  $Ni_3Sn_2$  and  $Ni_3Sn_4$  (5, 6). Thus, the electrodeposited equiatomic single-phase alloy can be considered a nonequilibrium metastable phase (4). However, on the basis of their x-ray (7) and calorimetric results (8), Dutta and Clarke argue that the alloy is in fact a new compound which is a stable phase at its usual temperature of formation (70°C).

The 65/35 tin-nickel alloy plating has found various practical applications, e.g., coating of automotive ignition components and pistons in thermostatic and

shower mixing valves (9). It has also been recommended as a substitute, or as an underplating for gold on copper printed circuit boards (9-11). Certain fundamental characteristics of the alloy which have technological importance are its corrosion resistance or passivity, and its thermal stability. Although several studies of these properties have been conducted in the past, there is still uncertainty as to the temperature at which the alloy becomes unstable and transforms to the equilibrium phases, and as to what is the nature of the surface which leads to the exceptional passivity of this alloy. This paper reports on a study to clarify some of these matters using differential thermal analysis (DTA), x-ray diffraction, and the electron microprobe. A companion paper (12) by the authors deals with the surface passivity of the alloy.

#### Alloy Preparation

Material for this investigation was prepared from the plating bath formulation in Table I. The electro-

Table I. Tin-nickel plating bath composition

Stannous chloride ( $SnCl_2 \cdot 2H_2O$ )	20 g/liter
Nickel chloride ( $NiCl_2 \cdot 6H_2O$ )	250 g/liter
Ammonium bifluoride ( $NH_4HF_2$ )	40 g/liter
Ammonium hydroxide ( $NH_4OH$ )*	35 ml/liter of bath

Key words: metastable, passivity, plating.  
<sup>1</sup>International Standard ISO 2179: 1972.

\* Utilized with HF to maintain bath at  $2.5 < pH < 3.0$ .

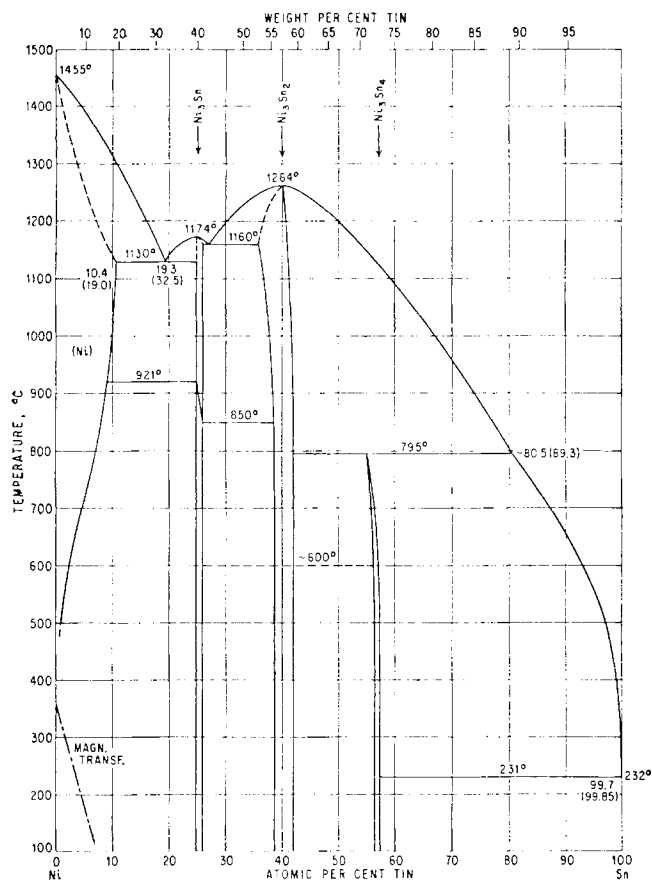


Fig. 1. Equilibrium diagram for the binary nickel-tin system (5). (From "Constitution of Binary Alloys" by M. Hansen and K. Anderko. Copyright 1958, McGraw-Hill, New York. Used with permission of McGraw-Hill Book Company.)

lyte was continuously filtered and maintained at  $72^\circ \pm 2^\circ\text{C}$ . Separate anodes of 2 nickel to 1 tin were used on a common anode rail. Anodes were bagged to prevent sludge formation in the bath and the anodes were removed from the bath when not in use. Current density during plating was  $0.0215\text{ A/cm}^2$  ( $20\text{ A/ft}^2$ ). The freshly prepared bath was initially operated using a nickel screen cathode to remove impurities from the bath. Strips of type 301 stainless steel were used as cathodes for obtaining experimental samples. By severe flexing of the plated cathodes, large flakes of the alloy plating were obtained for subsequent evaluations. The plating was analyzed with a scanning electron microscope-microprobe using pure elements as standards and found to contain 34.97 w/o Ni. An independent gravimetric analysis using dimethyl glyoxime found 34.41 w/o Ni.<sup>2</sup>

### Background

Since this alloy should not be single phase according to the equilibrium diagram (5), it is understandable that its as-plated stability should be a matter of concern for practical applications. Several investigations (2, 4, 7, 13) have dealt with this matter. The procedure used in all these investigations has been the same, i.e., isothermal heat-treatments of the alloy plating with x-ray diffraction analysis of the samples before and after treatment. In his original work (4) Rooksby stated that "up to about  $350^\circ\text{C}$  no appreciable change was observed but heating at  $400^\circ\text{C}$  for one hour in either air or vacuo was sufficient to effect substantial decomposition." It was subsequently reported by Rooksby and co-workers (2) that heat-treatments up to temperatures of about  $300^\circ\text{C}$  (for an unspecified

length of time) produce no detectable change, but above this temperature decomposition begins and various mixtures of the normal  $\gamma\text{-Ni}_3\text{Sn}_2$  phase and the  $\text{Ni}_3\text{Sn}_4$  phase form, depending upon the chemical composition of the electrodeposit. By heat-treating in air for 1 hr at various temperatures, Smart and Robins (13) found their deposits to be "structurally stable at temperatures up to at least  $500^\circ\text{C}$  but at  $700^\circ\text{C}$  and above decomposition into a mixture of two phases,  $\text{Ni}_3\text{Sn}_2$  and  $\text{Ni}_3\text{Sn}_4$ , takes place." They attribute the difference in their results from those of Rooksby to differences in plating conditions. In metallographic sections they found no evidence of compound formation at the interface between plating and substrate even after heat-treatment at these elevated temperatures and suggest that this further indicates the high stability of the tin-nickel compounds. A similar lack of interaction at  $50^\circ\text{C}$  has been previously reported by Thwaites (14). Finally, Dutta and Clarke (7) annealed electrodeposit samples covering the composition range from 24.41 to 42.90 w/o Ni for periods of 150 hr at  $250^\circ$ ,  $300^\circ$ ,  $350^\circ$ , and  $450^\circ\text{C}$ . They found the appearance of additional lines in the x-ray patterns of all their alloys at all the temperatures, indicating that the alloys were unstable even at  $250^\circ\text{C}$ . They reported that the decomposition increased sharply above  $300^\circ\text{C}$ , as judged by the number of new lines which appeared.

### Results

As mentioned above, all previous studies have employed heat-treatments at specific temperatures thereby permitting estimates of the temperature at which transition of the alloy plating to the stable equilibrium compounds occurs. This investigation utilized the technique of DTA which consists of recording the difference in temperature between a substance and a reference material against temperature as the two specimens are subjected to identical temperature regimes in an environment heated or cooled at a controlled rate. Thus, the temperature of the alloy plating could be monitored continuously and that temperature at which the transition to the equilibrium compounds occurs could be observed by virtue of the enthalpy or heat change associated with the reaction. The equipment used was a CSI-R. L. Stone DTA System with a palladium cell employing ring-type differential thermocouples and a monitoring thermocouple of Pt/Pt-10% Rh. Samples and reference material, pure  $\alpha\text{-Al}_2\text{O}_3$ , were contained in small aluminum pans which fit inside the ring-type differential thermocouples. The temperature axis was calibrated using the peak points for the transitions of National Bureau of Standards DTA Standards of Sn ( $237^\circ\text{C}$ ),  $\text{KClO}_4$  ( $309^\circ\text{C}$ ), and  $\text{Ag}_2\text{SO}_4$  ( $433^\circ\text{C}$ ). A cover gas of flowing (0.075 SCFH) argon (99.999%) was used for all experiments.

In Fig. 2 are representative DTA curves for heating of the NBS calibration materials through their transition points and for heating of the alloy plating up to  $460^\circ\text{C}$ , at a rate of  $5^\circ\text{C/min}$ . Duplicate runs of plating samples exhibited the same broad exothermic peak ranging from  $350\text{--}380^\circ\text{C}$  with maximum at  $365^\circ\text{C}$ . Exothermic effects upon heating correspond to the liberation of energy during the decomposition of energy-rich substances which are metastable at lower temperatures (14).

Further confirmation and explanation of the decomposition peak was made from x-ray diffraction analyses of the following: (a) as-plated material, (b) DTA sample heated only to  $340^\circ\text{C}$ , (c) DTA sample heated only to  $390^\circ\text{C}$ , (d) DTA sample heated to  $460^\circ\text{C}$ , and (e) sample encapsulated in an argon-filled quartz container and heated at  $500^\circ\text{C}$  for 1 hr in a muffle furnace. All DTA:x-ray samples were cooled rapidly from the indicated temperature by removing the furnace from around the DTA cell; x-ray sample (e) was cooled rapidly by withdrawing it from the muffle furnace.

<sup>2</sup> Ledoux & Company, Teaneck, New Jersey 07666.

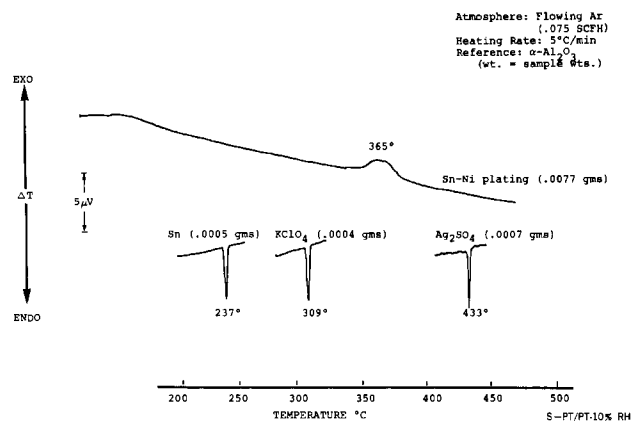


Fig. 2. DTA curves for heating of electrodeposited tin-nickel and NBS calibration materials Sn,  $\text{KClO}_4$ , and  $\text{Ag}_2\text{SO}_4$ .

The x-ray analyses were made by the Debye-Scherrer powder method and by the diffractometer method. Samples for the powder method were the actual DTA pan samples whereas those for the diffractometer were large flakes of the plating which had been placed separately in the bottom of the DTA cell and heated simultaneously with the actual DTA samples. X-ray results are listed in Table II and representative diffractometer patterns are illustrated in Fig. 3-6. Although diffractometer patterns were run from  $2\theta = 30^\circ$  to  $2\theta = 100^\circ$  for all samples, the reduced region ( $30^\circ$ - $55^\circ$ ) in Fig. 3-6 is sufficient to show the significant difference among the samples.

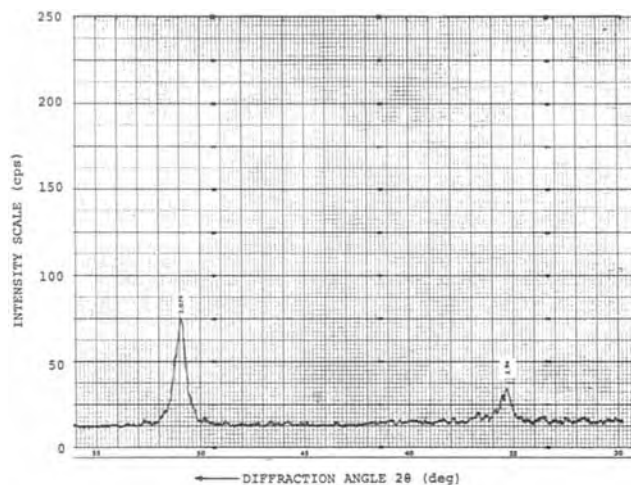


Fig. 3. X-ray diffraction pattern of electrodeposited tin-nickel flake. Filtered cobalt radiation 50 kV, 12 mA. Observed d spacings (angstroms) indicated at peaks.

It can be seen from Fig. 3 and 4 or Table II that heating the plating to  $340^\circ\text{C}$ , i.e., just below where the exothermic DTA peak is observed, resulted in no significant structural change. It has the same diffraction pattern as that for as-deposited plating corresponding to ASTM X-ray Diffraction File Card 7-256. However, the pattern in Fig. 5 for the sample heated to  $390^\circ\text{C}$  is distinctly different from Fig. 3 and confirms that the gradual exothermic reaction observed by DTA at  $350^\circ$ -

Table II. X-ray diffraction results [d spacings (angstroms)]

ASTM 7-256 Sn-Ni	(a) As-plated		(b) DTA to $340^\circ\text{C}$		ASTM 6-0414 $\text{Ni}_3\text{Sn}_2$	ASTM 4-0845 $\text{Ni}_3\text{Sn}_4$	(c) DTA to $390^\circ\text{C}$		(d) DTA to $460^\circ\text{C}$ Film	(e) 1 hr at $500^\circ\text{C}$ Chart
	Chart	Film	Chart	Film			Chart	Film		
2.94*	2.94x	2.95x	2.93x	2.93x	2.903*	2.95*	2.96	2.96	2.96	2.98 2.92 2.90x
						2.89 2.84 2.68	2.89x	2.89x	2.90x	2.70
					2.576		2.70	2.69	2.70	
2.56						2.55 2.51 2.33 2.31 2.20 2.14	2.56	2.555	2.55	2.56 2.54 2.375 2.347 2.208 2.093 2.080
					2.077*		2.068x	2.070x	2.070x	2.195 2.100 2.070x
2.076*	2.079x	2.08x	2.065x	2.075x	2.036*	2.06*	2.040x	2.020x	2.050	2.068x 2.046x 2.022x
						2.03* 1.73	2.022x	2.020x	2.020x	
1.687	1.699	1.70	1.687	1.685	1.667	1.66	1.653	1.658	1.660	1.675 1.656
1.601					1.597	1.58	1.583	1.585	1.590	1.593 1.587 1.535
					1.544	1.53	1.535	1.538	1.540	
1.528						1.49			1.495	1.503
1.470	1.47	1.465	1.470		1.455*	1.47	1.442	1.446	1.450	1.445
						1.45 1.43 1.42 1.35				
1.314			1.304	1.290	1.289		1.277	1.282	1.304 1.285	1.300 1.280
1.280					1.226			1.223	1.226	
1.198	1.198	1.20	1.192	1.195	1.184*	1.19			1.192 1.180	1.186
					1.178	1.18	1.173	1.172	1.170	1.175 1.167
						1.17	1.167			

Diffractometer chart:  $\text{CoK}\alpha$  radiation 50 kV, 12 mA, iron oxide filters.  
Debye-Scherrer film:  $\text{CuK}\alpha$  radiation 50 kV, 30 mA, nickel filters.

\* ASTM Card intensities  $I/I_1 \geq 75$ .

x Strong observed peaks.



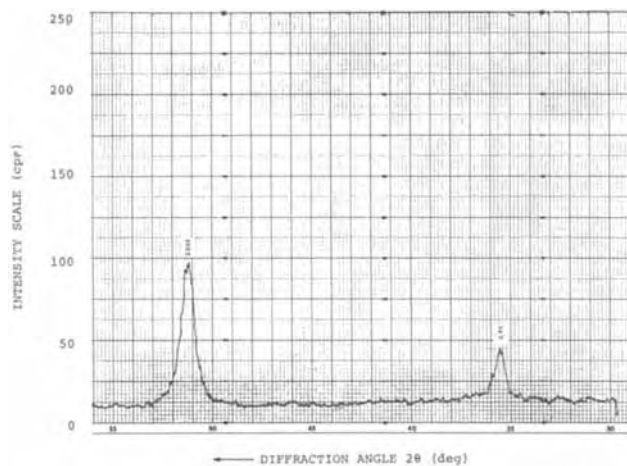


Fig. 4. X-ray diffraction pattern of electrodeposited tin-nickel flake heated only to 340°C in DTA cell. Filtered cobalt radiation 50 kV, 12 mA. Observed d spacings (angstroms) indicated at peaks.

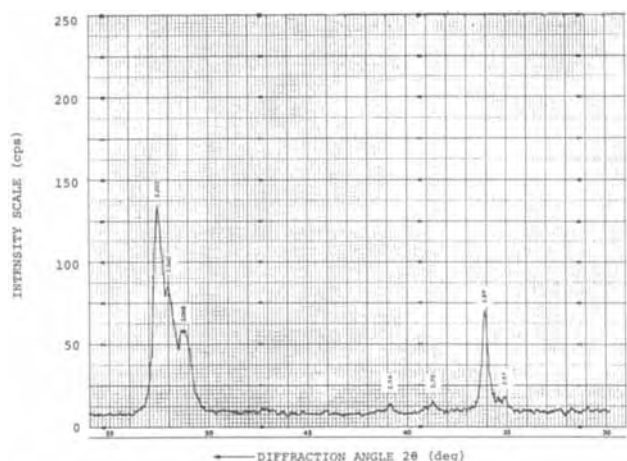


Fig. 5. X-ray diffraction pattern of electrodeposited tin-nickel flake heated only to 390°C in DTA cell. Filtered cobalt radiation 50 kV, 12 mA. Observed d spacings (angstroms) indicated at peaks.

380°C corresponds to the transition of the metastable as-deposited structure to the equilibrium compounds  $\text{Ni}_3\text{Sn}_2$  (ASTM Card 6-0141) and  $\text{Ni}_3\text{Sn}_4$  (ASTM Card 4-0845). The encapsulated flake sample heated at 500°C for 1 hr yielded the pattern in Fig. 6, which is also that for the equilibrium compounds except that the peaks

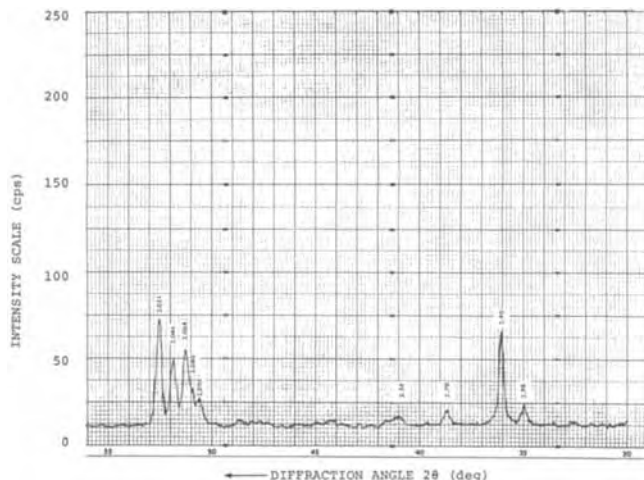


Fig. 6. X-ray diffraction pattern of electrodeposited tin-nickel flake encapsulated in quartz and heated at 500°C for 1 hr. Filtered cobalt radiation 50 kV, 12 mA. Observed d spacings (angstroms) indicated at peaks.

are sharper and better defined due to grain growth and/or more complete transformation from extended heating at a more elevated temperature.

For further confirmation of the transition, experiments similar to those of other investigators (4, 7, 13) were also carried out. Samples of the plating were ground into powder and heated in air at various temperatures. As could be expected, a sample heated for 1 hr at 360°C was completely transformed to the equilibrium compounds. However, samples heated at 340° and 330°C for 1 hr were also completely transformed and at 320°C some faint new lines appeared. After 1 hr at 280°C or 100 hr at 200°C the pattern was still that of the as-plated alloy.

All of the results thus show that the electrodeposited tin-nickel alloy is indeed metastable. Heating at a slow rate of 5°C/min does cause the decomposition to occur at 365°C but the transition can be brought about at lower temperatures by holding for extended times. The DTA results indicate that under a constant heating rate there is a specific although broad range over which the reaction occurs. Under different heating rates this range may change in size or shift. The results from heating samples at the lower temperatures support the results of Rooksby *et al.* (2). The results of Smart and Robins (13) are in complete disagreement with those of this study and the other previous investigations. The results of this study and those of Dutta and Clarke (7) suggest that a study of the kinetics of the transition at various temperatures, particularly below 340°C, is needed. As Fig. 3-6 illustrate, appropriate heat-treatments of the plated alloy followed by x-ray analyses with the diffractometer could be used to study kinetics by following the behavior of the 2.076 line of the as-plated material since it splits into 3-5 different lines as decomposition occurs.

### Summary

Electrodeposited tin-nickel alloy has been investigated with differential thermal analysis and x-ray diffraction. DTA and x-ray diffraction have shown that transformation from the metastable to the equilibrium structure for the equiatomic composition occurs as an exothermic reaction over a range of temperature centered at 365°C upon heating at a rate of 5°C/min. It has also been shown that extended heating at fixed temperatures between 300° and 365° can result in partial or complete transformation. Kinetic studies are needed for further elucidation of the transition at these lower temperatures.

From the standpoint of thermal stability, it is advisable that tin-nickel plating not be used if service temperatures are expected to exceed 300°C, for any period of time, and some caution should be taken if long periods (>100 hr) over 250°C are anticipated (7).

### Acknowledgments

The authors wish to express their appreciation to the following individuals for their considerable assistance in this investigation: G. V. McIlhargie for preparing the alloy, D. E. Heath for microprobe and x-ray diffraction analyses, and T. M. Paskowski for differential thermal analyses. Also the encouragement and critical review of the manuscript by M. R. Pinnel and K. F. Bradford is appreciated.

Manuscript submitted Dec. 12, 1975; revised manuscript received ca. Feb. 1, 1976.

Any discussion of this paper will appear in a Discussion Section to be published in the June 1977 JOURNAL. All discussions for the June 1977 Discussion Section should be submitted by Feb. 1, 1977.

Publication costs of this article were partially assisted by Bell Laboratories.

## REFERENCES

1. N. Parkinson, *J. Electrodep. Tech. Soc.*, **27**, 129 (1951).
2. J. W. Cuthbertson, N. Parkinson, and H. P. Rooksby, *This Journal*, **100**, 107 (1953).
3. N. P. Fedotev and P. M. Vyacheslavov, *Plating*, **57**, 700 (1970).
4. H. P. Rooksby, *J. Electrodep. Tech. Soc.*, **27**, 153 (1951).
5. M. Hansen, "Constitution of Binary Alloys," p. 1042, McGraw-Hill Book Co., New York (1958).
6. F. Shunk, "Constitution of Binary Alloys, Second Supplement," p. 555, McGraw-Hill Book Co., New York (1969).
7. P. K. Dutta and M. Clarke, *Trans. Inst. Metal Finishing*, **46**, 20 (1968).
8. M. Clarke and P. K. Dutta, *J. Phys. D: Appl. Phys.*, **4**, 1652 (1971).
9. International Nickel Co., *Nickel Topics*, **27**, 11 (1974).
10. G. C. Wilson, *Trans. Inst. Metal Finishing*, **50**, 109 (1972).
11. M. Rao, M. Mitchell, and R. Anderson, *Solid State Technol.*, **17**, 47 (1974).
12. H. G. Tompkins and J. E. Bennett, *This Journal*, **123**, 1003 (1976).
13. R. F. Smart and D. A. Robins, *Trans. Inst. Metal Finishing*, **37**, 108 (1960).
14. C. J. Thwaites, *ibid.*, **36**, 203 (1959).

# Investigations of an Electrodeposited Tin-Nickel Alloy

## II. Surface Passivity Studied with Auger Electron Spectroscopy

H. G. Tompkins and J. E. Bennett

Bell Laboratories, Columbus, Ohio 43213

### ABSTRACT

The electrodeposited equiatomic tin-nickel alloy exhibits a strong corrosion passivity. There has been some conjecture as to why this alloy exhibits this passivity and as to the nature of the passive surface film. This work investigates the surface film which is formed in air, using Auger electron spectroscopy and depth profiling. The surface film appears to be primarily a tin-rich oxide which is several atoms thick. The passive film which forms may not depend on the metastable nature of the alloy.

The electrodeposited equiatomic [65 weight per cent (w/o) Sn-35 w/o Ni] tin-nickel alloy continues to be of considerable scientific and technological interest and has found various practical applications, e.g., coating of automotive ignition components and pistons in thermostatic and shower mixing valves (1). It has also been recommended as a substitute, or as an underplating, for gold on copper printed circuit boards (1-3). Certain fundamental characteristics of the alloy which have technological importance are its corrosion resistance or passivity, and its thermal stability. Although several studies of these properties have been conducted in the past, there is still uncertainty as to the temperature at which the alloy becomes unstable and transforms to the equilibrium phases, and as to what is the nature of the surface which leads to the exceptional passivity of this alloy. A companion paper (4) deals with the thermal stability and the metastable nature of the alloy. This paper deals with the surface passivity which is studied with Auger electron spectroscopy.

### Background

The alloy has found considerable use as a protective and decorative coating for less corrosion resistant materials. Such applications stem from the studies of Parkinson, Britton, and Angles (5, 6). They found that the electroplated alloy resists serious attack from many liquid and vapor reagents, including those which rapidly attack the component metals. It was suggested (6) that the exceptional corrosion resistance of the alloy was due to a protective film of oxide containing both metal components.

Clarke and Britton (7) reported that, in aqueous solutions, the alloy forms an oxide film of a special nature, that the film is remarkably stable over a wide range of pH and potential in the presence of many different anions, and that for solutions open to air three oxidation states of the film are observable. From electrochemical measurements of the passivation potential for the alloy, Clarke and Elbourne (8, 9) relate that it is considerably lower than those for the

parent metals, which implies that the oxide formed on the alloy is more stable than either of the two lowest oxides of nickel or tin.

From a reassessment of the results of Clarke and co-workers, Hoar (10) concluded that the three oxidation states which had been observed correspond to three different passive films and that the films should be nickel stannite and stannates with nickel and tin in the same ratio as in the alloy.

More recently, Hoar, Talerman, and Trad (11) examined oxide films on the electrodeposited tin-nickel alloy by Auger spectroscopy where the films were formed either naturally in air or by potentiostatic anodic polarization in phosphate solutions of various pH values. For comparison, they chemically prepared nickel-tin hydrous oxides as precipitates from aqueous solutions. They conclude that their data strongly suggest that the oxide film which confers corrosion resistance on tin-nickel alloy is a glassy nickel polystannate containing water and hydroxyl ions. This extrapolation from observations on precipitates found in aqueous solutions to the natural film is questionable. In addition, in contrast to their conclusions, their calculated atomic ratio data indicate that the natural film and one of the three films formed electrochemically have a 3 to 1 tin to nickel ratio rather than an equal amount of tin and nickel, as would be expected in a nickel stannate. Thus, their conclusion that the natural film is a glassy nickel polystannate is questionable and inconsistent with their data.

The conclusions in these and earlier studies regarding the nature of the air-formed film were reached essentially by comparison or analogy to the nature of films or precipitates formed in aqueous solutions. The investigation reported herein was intended to utilize the more recently developed Auger technique of depth profile analysis to clarify the nature of the passive air-formed film by direct measurements.

### Results

The sample preparation has been described (4) previously. It is essentially a metastable alloy of equal

mole fractions of tin and nickel. The samples were made by electroplating onto a stainless steel substrate. When the substrate was then severely flexed, large flakes (1-5 mm) of the alloy were obtained for subsequent evaluations.

The Auger analysis (12) was made with a Physical Electronics Industries commercial instrument using a beam voltage of 3 kV and current of 15  $\mu$ A (elliptical beam dimensions of 0.1 and 0.4 mm). Depth profiles were obtained by analyzing while sputtering with argon ions (gaussian beam with half-width of the order of 3 mm). The argon pressure during sputtering was  $5 \times 10^{-5}$  Torr with a titanium sublimation pump operating. A typical spectrum is shown in Fig. 1. This is the surface approximately four days after plating. The peaks observed are Sn, Ni, O, and C. Some carbon is typically seen on all samples exposed to the atmosphere for any significant length of time where the exposure occurs in an unprotected manner (dust, hydrocarbons, etc). A depth profile was then obtained and is shown in Fig. 2. The peak to peak height ( $dN/dE$ ) is plotted vs. sputtering time. The sputtering rate (1.3 A/min) for tin-nickel was calibrated by sputtering through a sample of known thickness. The initial rise of the Sn signal is probably due to the removal of the atmospheric carbonaceous material. The most notable part of this profile is the fact that the surface is Sn rich. After the surface region was removed exposing a new surface, the sample was exposed to the atmosphere for four days in a protected (clean) manner. A spectrum and a profile were again obtained. This surface was essentially bulk material exposed to air with all evidence of the as-plated surface removed. The profile is shown in Fig. 3 and is somewhat different from the profile in Fig. 2. (Other samples exposed for considerably less than four days showed basically the same results. This surface condition seems to be formed in less than 1 hr.)

The measured intensity profiles shown in Fig. 2 and 3 do not quite represent the actual concentrations of the various species present, for the following reason: Auger electrons escaping from the sensed volume are attenuated in an exponential manner (13). Characteristic depths of escape have been determined and published (12) and range from 4 to 50 Å (the escape depth is the thickness of material which attenuates the escaping electrons by a factor of  $1/e$ ). If the distance over which the concentration varies is large compared to the escape depth, the measured intensity profile corresponds closely to the actual concentration profile. If, on the other hand, the concentration varies significantly over distances on the order of the escape depth, the measured intensity profile must be deconvoluted to obtain the actual concentration profile. One result of this phenomenon is that a nonzero value for the peak height of nickel at the surface (time zero) in Fig. 3 does not necessarily imply nickel on the surface since the escape depth for nickel Auger electrons (840 eV) is 11 Å.

Examination of both Fig. 2 and Fig. 3 shows that the tin concentration in the vicinity of the surface (the first couple of minutes of sputtering) is obviously higher than the nickel concentration.

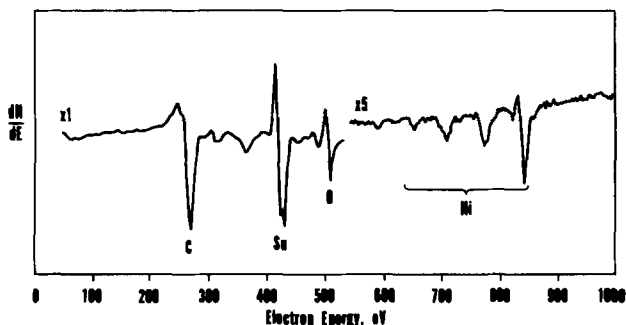


Fig. 1. Typical Auger spectrum of tin-nickel surface as-plated

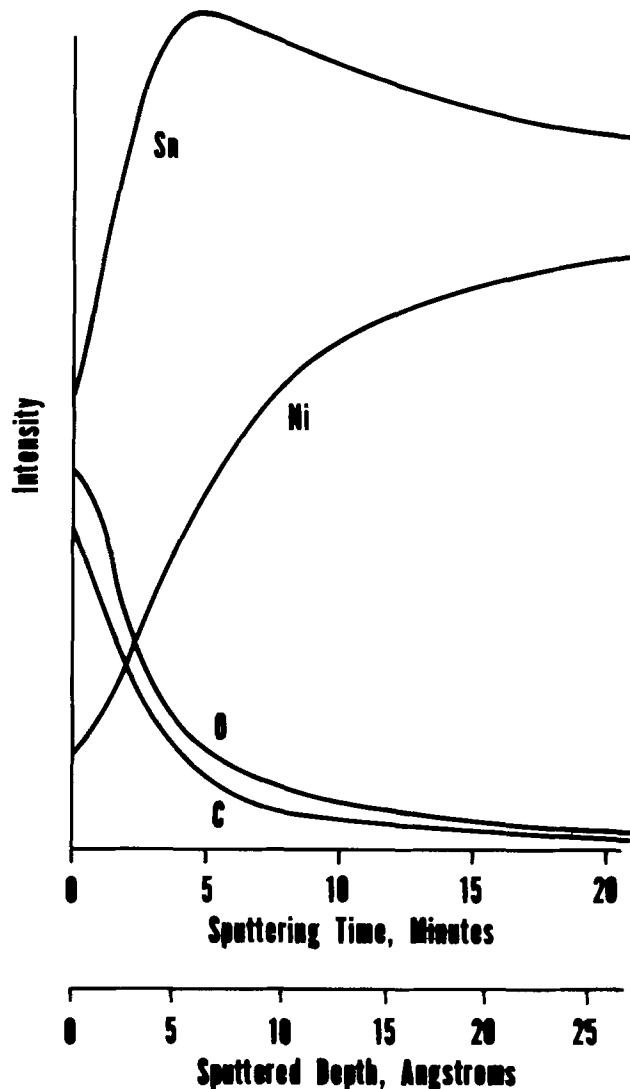


Fig. 2. Intensity profile of as-plated surface

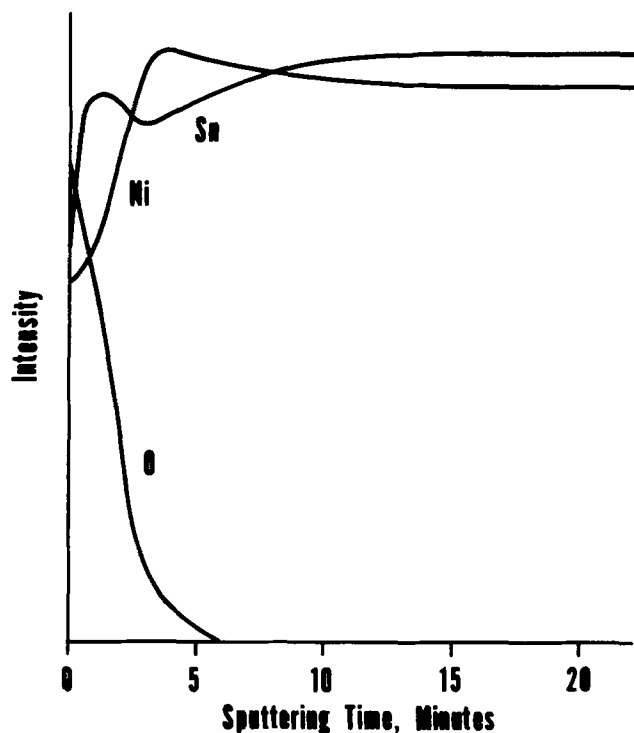


Fig. 3. Intensity profile of sputter-generated surface after oxidation.

A different method (14) of obtaining information about the homogeneity of a material and/or film thickness is by investigating the ratio of the high (840 eV) and low (60 eV) energy peaks of Ni. Electrons involved in these two transitions have escape depths of 11 and 4Å, respectively (12). The ratio of the peak heights in a homogeneous material (concentration does not vary with depth) will be different than in a layered (nonhomogeneous) material where the layer thickness is of the order of the escape depths. The ratio of the low peak to the high peak for any homogeneous nickel-containing material was determined to be about 1.6 on the instrument used. The homogeneous material used for this determination was pure nickel. This ratio measured from a spectrum taken immediately prior to obtaining the profile in Fig. 3 was about 0.8, indicating that the low energy peak (with escape depth 4Å) was attenuated more than the high energy peak (with escape depth 11Å). This indicates a deficit of nickel at and near the surface. Using an exponential attenuation factor, it was calculated that a 4Å film of tin oxide (or anything else not containing nickel) would give the observed change in the ratio. The expression used is

$$\frac{I_l}{I_h} = \frac{I_l}{I_h} \Big]_H \frac{e^{-t/4}}{e^{-t/11}}$$

where  $I_l/I_h$  is the ratio of the low and high energy peak heights, the "H" refers to a homogeneous material, and  $t$  is the thickness of the film. This calculation, of course, assumes no tin in the film and cannot be used to conclude that there is no tin in the film. The 4Å value calculated in this manner is, however, consistent with the changes in the profile in Fig. 3. Most of the changes occur in the first 4 min (or 5Å since the sputtering rate is 1.3 Å/min).

Since the size of a tin atom is about 3Å, we clearly are dealing with one or two atomic layers. The film is, however, different from simply a chemisorbed layer of oxygen since the tin is extracted from the tin-nickel to form a layer of oxide on top of the tin-nickel. It must be kept in mind that AES cannot detect hydrogen so the layer may be a hydroxide rather than an oxide. It is clear, however, that the surface layer contains significantly more tin and oxygen than nickel and it appears to be on the order of 4Å thick.

Figure 2 was obtained from the as-plated surface. Using the calibrated sputtering rate, a distance axis has been added to Fig. 2. There is a tin-rich surface, oxygen which appears to extend deeper in the sample than in Fig. 3, and nickel which appears to rise gradually rather than abruptly to its bulk values. One significant difference in the profiles shown in Fig. 2 and 3 is the presence of carbon in Fig. 2. Some sputtering time is required to remove the carbonaceous material and if there is a range of thickness (i.e., part of the carbonaceous material is thicker than another part), the thin underlying layer will not all be exposed at the same time. Features on a profile which would be sharp if there were no carbonaceous material will tend to be smeared out when the thin layer is covered with a carbonaceous material with a range of thicknesses. This might be one of the reasons that the profiles are different in the two figures. The possibilities are that there is either (i) a phase which contains tin, nickel, and oxygen, (ii) grains of tin oxide along with grains of tin-nickel, or (iii) a tin oxide film on top of tin-nickel.

Thus, in this work, methods not previously applied to the tin-nickel system were used to obtain additional information about the nature of the passive film. When the previously proposed model (7-11) is examined in light of the new data, it becomes clear that that model, of equal amounts of tin and nickel in the film, is contradictory to these results. There are, however, several models all involving a tin-rich oxide which are consistent with these data. The least complex of these is a simple tin oxide containing no nickel.

A sample annealed at 500°C for 1 hr in argon was analyzed in the same way as the previously described samples. The initial profile obtained after annealing was identical with Fig. 2. The sputtered surface was then oxidized as described previously (exposed to air for 4 days at room temperature) and the resulting profile was identical to Fig. 3. It would appear that the initial surface film does not significantly change or deteriorate with such treatment even though the alloy undergoes a transition from the metastable form to a mixture of the equilibrium compounds (4). By comparing oxidation behavior of freshly sputtered surfaces, it can be seen that the oxide formed on the as-plated material and on the annealed material is essentially the same. This suggests that the transformed material may be as passive in air as the metastable material and that the passivity of the as-plated alloy may depend not on its metastable nature but primarily on the presence of the two elements.

The true test of this possibility will be the comparison of passive films on  $\text{Ni}_3\text{Sn}_2$ , on  $\text{Ni}_3\text{Sn}_4$ , and on the metastable alloy described herein. These investigations are in progress. It should be emphasized that these studies deal with the air-formed film and do not deal with corrosion in aqueous solutions.

### Summary

The passive film formed in air on the electrodeposited tin-nickel alloy has been investigated with Auger electron spectroscopy, and a concentration profile of the surface layer which is responsible for the alloy passivity has been displayed. An approximate thickness of the passive film was determined (approximately 4Å) and it was shown that the nickel content of the film is significantly less than the tin content. Previous investigators have proposed that the film is a nickel stannate of some kind. Their model seems to be based on analogy rather than observation and on the assumption that the film formed on an alloy "must contain the different metal cations in the same proportion as they exist in the metal" (9). Surface segregation (15-17) and selective reaction (17-18) have been shown to occur frequently, however. It has been proposed that components which segregate to the surface are those which are more readily oxidized (19). Observation in this work that the surface of electroplated tin-nickel is enriched in tin is consistent with that proposal since tin is more readily oxidized than nickel as can be seen from free energy/temperature diagrams for oxides (20). Thus it is concluded that the passivating film forms via a selective reaction with the oxygen in the atmosphere to form an oxide. The previous model (7-11) of equal amounts of tin and nickel in the film is contradicted by the results of the present work. There are several models, all involving a tin-rich oxide, which are consistent with these results. The least complex of these is a simple tin oxide containing no nickel.

The passive film which forms in air on the metastable plated material was found to be essentially unchanged after heating the alloy in argon at 500°C to produce the equilibrium structure. It was also found that the film formed on this equilibrium structure by oxidation after sputter cleaning was the same as that formed on a sputter-generated surface of the metastable alloy. This would suggest that from a corrosion standpoint the alloy could be used to at least 500°C. However, the metastable structure was shown (4) to have definitely transformed by 365°C with DTA; since the alloy could have concomitant changes in physical, chemical, mechanical, and electrical properties it is advisable that such possibilities be recognized when the alloy is used.

### Acknowledgments

The authors wish to express their appreciation to the following individuals for their considerable assistance in this investigation. G. V. McIlhargie for preparing the alloy, and R. Schroeder for Auger analyses. Also, the encouragement and critical review of the manu-

script by M. R. Pinnel and K. F. Bradford is appreciated.

Manuscript submitted Dec. 12, 1975; revised manuscript received Feb. 18, 1976.

Any discussion of this paper will appear in a Discussion Section to be published in the June 1977 JOURNAL. All discussions for the June 1977 Discussion Section should be submitted by Feb. 1, 1977.

Publication costs of this article were partially assisted by Bell Laboratories.

#### REFERENCES

- International Nickel Co., *Nickel Topics*, **27**, 11 (1974).
- G. C. Wilson, *Trans. Inst. Metal Finishing*, **50**, 109 (1972).
- M. Rao, M. Mitchell, and R. Anderson, *Solid State Technol.*, **17**, 47 (1974).
- J. E. Bennett and H. G. Tompkins, *This Journal*, **123**, 999 (1976).
- N. Parkinson, S. Britton, and R. Angles, *Sheet Metal Ind.*, **28**, 1 (1951).
- S. Britton and R. Angles, *J. Electrodep. Tech. Soc.*, **27**, 293 (1951).
- M. Clarke and S. Britton, *Corrosion Sci.*, **3**, 207 (1963).
- M. Clarke and R. Elbourne, *ibid.*, **8**, 29 (1968).
- M. Clarke and R. Elbourne, *Electrochim. Acta*, **16**, 1949 (1971).
- T. P. Hoar, *This Journal*, **117**, 17C (1970).
- T. Hoar, M. Talerman, and E. Trad, *Nature Phys. Sci.*, **244**, 41 (1971).
- P. W. Palmberg, *Anal. Chem.*, **45**, 549A (1973).
- M. L. Tarnag and G. K. Wehner, *J. Appl. Phys.*, **44**, 1539 (1973).
- M. P. Seah, *J. Phys. F: Metal Phys.*, **3**, 1538 (1973).
- C. A. Haque, Proceedings Holm Seminar 1972, p. 287, Illinois Institute of Technology.
- H. P. Bonzel and H. B. Aaron, *Scripta Met.*, **5**, 1057 (1971).
- F. L. Williams, and M. Boudart, *J. Catalysis*, **30**, 438 (1973).
- C. T. H. Stoddart and E. D. Hondros, *Nature Phys. Sci.*, **237**, 90 (1972).
- F. L. Williams and D. Nason, *Surface Sci.*, **45**, 377 (1974).
- J. Mackowiak, "Physical Chemistry for Metallurgists," p. 158, American Elsevier Pub. Co., New York (1966).

## Conductivity and Other Transport Parameters in Ammonium Citrate Gold Baths

B. Miller\* and S. Menezes Affonso

Bell Laboratories, Murray Hill, New Jersey 07974

#### ABSTRACT

Specific conductivity and the transport parameters of solution kinematic viscosity and gold species diffusion coefficient have been measured in ammonium citrate-potassium gold cyanide systems over the temperature range 25°-70°C. Diffusion coefficients were derived from rotating disk electrode limiting current results with lead ion catalysis of gold reduction. The dissociation constant of  $\text{HAu}(\text{CN})_2$  was also measured and found to be greater than  $10^{-1}$ .

To support studies of the mechanistic and throwing properties of commonly applied gold plating systems, conductivity and transport parameters of some citrate baths and component solutions have been measured over the range 25°-70°C. Specific conductivity ( $\kappa$ ) and kinematic viscosity ( $\nu$ ) were determined directly and diffusion coefficients ( $D$ ) were calculated from rotating disk electrode (RDE) limiting current data. Schmidt numbers,  $\text{Sc} = \nu/D$ , are also given.

In addition, the dissociation constant,  $K_a$ , of  $\text{HAu}(\text{CN})_2$  was investigated with pH and conductometric analyses. The value of this  $pK_a$  is necessary to interpret the behavior of acid gold baths, and we have found the literature value underestimates the strength of the acid by several orders of magnitude.

#### Theoretical

The limiting current to an electrode of area  $A$  for the  $n$ -electron deposition of a species of bulk concentration  $C$  is written from a Nernst layer model as

$$i_D = nFAi_D C / \delta \quad [1]$$

with  $\delta$  the diffusion layer thickness. For the convective-diffusion limiting current at a disk rotating at speed  $\omega$ , Levich's equation [1] for  $\delta$  yields

$$i_D = 0.62nFACD^{2/3}\nu^{-1/6}\omega^{1/2} \quad [2]$$

This is numerically accurate to about 3% for  $\text{Sc} = 1000$ . A more exact analytical expression for  $i_D$  as  $f(\text{Sc})$  has been written by Newman (2). A convenient form for calculating  $D$  from the Newman computations and the experimental data for  $i_D$  and  $\nu$  is given by Bruckenstein (3) as

$$D = \nu[(J^{-1} - 0.122939)^{1/2} - 0.1490]^{-3} \quad [3]$$

where

$$J^{-1} = \frac{0.62048nFA(\omega\nu)^{1/2}C}{i_D} = \frac{K_L n(\omega\nu)^{1/2}C}{i_D} \quad [4]$$

Equations [3] and [4] have been used to obtain  $D$  values in this work.

However, this use of the Levich equation presumes that sufficiently concentrated additional electrolyte is present to suppress ionic migration contributions to transport of the electroactive species so that the measured limiting current,  $i_L$ , is equal to  $i_D$ . Another means of describing this "supporting electrolyte" case is to say that the transport number (fraction of the current carried) of the electroactive species (gold entity) is zero. This will, of course, also be accomplished if the transported electroactive species is neutral and carries no charge, e.g.,  $\text{HAu}(\text{CN})_2$ .

Supporting electrolyte conditions are usually achieved in typical "strike" gold baths, exemplified by solution VI below where  $C_{\text{KAu}(\text{CN})_2} = 0.0045M$  and  $C_{(\text{NH}_4)_2\text{HCitrate}} = 0.22M$ , nearly a fiftyfold concentra-

\* Electrochemical Society Active Member.

Key words: rotating disk electrodes, diffusion coefficients, kinematic viscosity, plating.

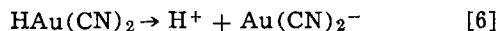
tion ratio. However, ionic migration possibilities must be considered in the typical formulation with  $C_{\text{KAu}(\text{CN})_2} = 0.07M$  in the same citrate electrolyte, a concentration ratio of only about 3.

The calculation of such migration effects is much more complex (4, 5) than the classical models (6) indicate. In simplest form, these latter suggest that the contributions are separable and that the transport of an anion (as  $\text{Au}(\text{CN})_2^-$ ) to a cathode against the field reduces the limiting current,  $i_L$ , ratio to the pure convective diffusion value,  $i_D$ , by

$$\frac{i_L}{i_D} = \frac{1}{1 + t_-} \quad [5]$$

where  $t_-$  is the transport number of  $\text{Au}(\text{CN})_2^-$ . Newman (4) has shown that a simultaneous solution considering transport by all means, diffusion, convection, and migration, is necessary in the general case. The resulting differential equations require that the products of the reaction and their charge must also be considered so that the ionic conductivities of all species are needed.

In citrate gold baths a further complication exists in identifying the migrating gold species. Maja (7), from the pH of  $\text{KAu}(\text{CN})_2$  solutions, obtained a  $K_a$  for



of  $\approx 10^{-5}$ . Since the pH of citrate baths is about 5, a  $pK_a$  of 5 suggests that comparable amounts of charged and neutral gold species exist. The determination of this  $pK_a$  and an estimate of the  $t_-$  of  $\text{Au}(\text{CN})_2^-$  are necessary for qualitatively assessing the contribution of migration and thus the significance of the apparent  $D$  value, when calculated from the Levich equation with its assumption of convective diffusion.

### Experimental

Kinematic viscosity and conductivity vessel temperatures were controlled to  $\pm 0.1^\circ\text{C}$  in a water thermostated bath. RDE limiting current data were obtained with a jacketed cell and circulation from the same bath.

The following solutions were prepared with triply distilled water and reagent grade chemicals, and will be identified below by number:

- I. 20 g/liter  $\text{KAu}(\text{CN})_2$
- II. 50 g/liter  $(\text{NH}_4)_2\text{SO}_4$
- III. 50 g/liter  $(\text{NH}_4)_2\text{HC}_6\text{H}_5\text{O}_7$ , diammonium citrate
- IV. 20 g/liter  $\text{KAu}(\text{CN})_2$  + 50 g/liter  $(\text{NH}_4)_2\text{HC}_6\text{H}_5\text{O}_7$  + 1 ppm Pb
- V. 20 g/liter  $\text{KAu}(\text{CN})_2$  + 50 g/liter  $(\text{NH}_4)_2\text{HC}_6\text{H}_5\text{O}_7$  + 50 g/liter  $(\text{NH}_4)_2\text{SO}_4$  + 1 ppm Pb
- VI. 1.3 g/liter  $\text{KAu}(\text{CN})_2$  + 50 g/liter  $(\text{NH}_4)_2\text{HC}_6\text{H}_5\text{O}_7$  + 1 ppm Pb

In solutions IV, V, and VI the final concentration of 1 ppm Pb was obtained by the addition of a stock solution of Pb as  $\text{PbO}$  dissolved in the lead-free electrolyte of the final composition.

**Kinematic viscosity,  $\nu$ .**—A Cannon-Fenske viscometer of size 25 calibrated against water over the temperature range of  $25^\circ\text{--}70^\circ\text{C}$  was employed for kinematic viscosity measurements. The viscometer constant of  $1.871 \times 10^{-2}$  centistokes/sec was found to be independent of temperature over the range investigated. It is assumed for both  $\nu$  and  $\kappa$  that the 1 ppm of Pb contained in solutions III, IV, and V does not affect these quantities.

**Conductivity,  $\kappa$ .**—A Beckman Conductivity Bridge RC-19 (accuracy  $\pm 0.25\%$ ) and Beckman H-100 cell were used. The cell was calibrated with  $0.0100M$  KCl over the range of  $15^\circ\text{--}30^\circ\text{C}$  for which detailed conductance data were available (8), and the cell constant of

$100.0 \text{ cm}^{-1}$  did not vary outside the accuracy of the bridge. Hence it was assumed constant over the full range (to  $70^\circ\text{C}$ ) investigated, as claimed by the manufacturer.

**Limiting current,  $i_L$ , and diffusion coefficient,  $D$ .**—The electrode was a gold disk of  $0.0615 \text{ cm}^2$  area in an epoxy insulated mantle. The cell (9), motor (10), and circuitry (11) have been described earlier. Limiting currents were obtained for the RDE from recorded current-potential curves with linear potential scans.

Solutions IV, V, and VI, which all contain 1 ppm Pb, were studied in this manner. The catalytic behavior of lead toward this deposition, discovered by Reinheimer (12), makes it generally possible to obtain a limiting current region for all solutions and temperatures. Without added Pb the current-potential curves vary in appearance from being virtually indistinguishable from the pure citrate electrolyte (blank) trace to exhibiting well-defined steps for gold reduction. Studies of this current-potential behavior are described elsewhere (13). The curves in 1 ppm Pb(II) containing solution have variable shapes and inflections before the limiting current is reached. These are partly due to the fact that the Pb(II) catalysis is time and coverage dependent. The region of limiting current may be poorly resolved from the supporting electrolyte reaction and be highly sloped. Thus a graphic procedure was followed to determine the limiting current. This consisted of simply extrapolating tangents to the current-potential plot from beyond the limiting current and at the upper part of the pre-limiting current region and taking their point of intersection as the limiting current estimate for that value of  $\omega^{1/2}$ .

The graphic method biases the current towards higher values. To compensate for this and other systematic errors, such as area uncertainties for the small disk [ $D$  depends on (disk radius)<sup>3</sup>], the value of  $K_L$  in Eq. [4] was calibrated with  $i_L - \omega^{1/2}$  data for ferrocyanide ion, employing a similar graphic technique. For these purposes  $4.00 \text{ mM K}_4\text{Fe}(\text{CN})_6$  in  $1M$  KCl was run at  $25^\circ\text{C}$ , applying the accepted value (15) of  $D_{\text{Fe}(\text{CN})_6^{-4}} = 6.32 \times 10^{-6} \text{ cm}^2/\text{sec}$  and solving Eq. [3] and [4] for  $K_L$ . Solution VI, for which Cheh (14) found  $D = 1.67 \times 10^{-5} \text{ cm}^2/\text{sec}$  at  $60^\circ\text{C}$  for the gold species in lead-free solutions by weighing a RDE deposit obtained at  $i > i_D$ , was run for comparison. This solution gives no definable current step in the Pb-free version.

Solution volumes of 150 ml maintained under nitrogen were employed. The electrode surface was repolished for each of the scans from which limiting current data were obtained, and at least two scans were used at each temperature. Scan rates of  $10 \text{ mV}/\text{sec}$  were employed and the rotation speed range of  $400\text{--}6400 \text{ rpm}$  was covered, where feasible. Lower ranges, such as  $400\text{--}1600 \text{ rpm}$ , were used whenever the catalyzed waves became insufficiently separated from supporting electrolyte reduction reactions at the higher currents (speeds) to apply the graphic technique.

### Results and Discussion

Kinematic viscosity data for solutions III, IV, and V at five temperatures are given in Table I and plotted logarithmically vs. reciprocal temperature in Fig. 1. The values for solutions III and IV are very similar and

Table I. Kinematic viscosity in  $\text{cm}^2 \text{ sec}^{-1}$  as a function of temperature

$T^\circ\text{C}$	Solution		
	III	IV	V
25	0.00970	0.00957	0.01019
35	0.00785	0.00775	0.00830
50	0.00600	0.00597	0.00639
60	0.00514	0.00511	0.00550
70	0.00446	0.00444	0.00479

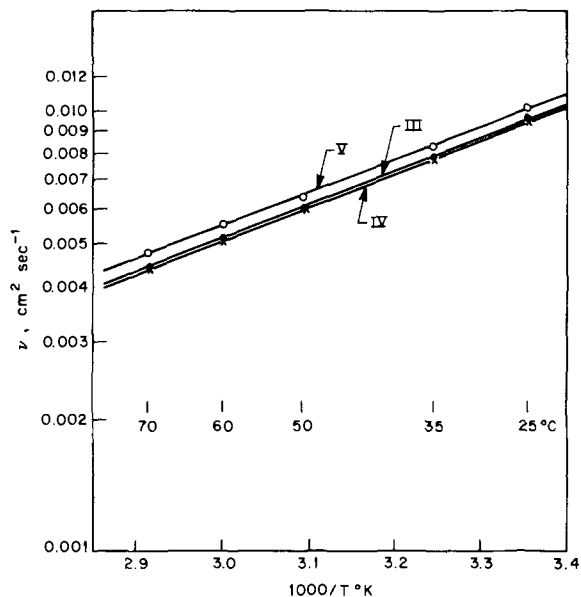


Fig. 1. Data of Table I plotted on log scale ( $\nu$ ,  $\text{cm}^2\text{sec}^{-1}$ ) vs. reciprocal absolute temperature. Solutions as indicated.

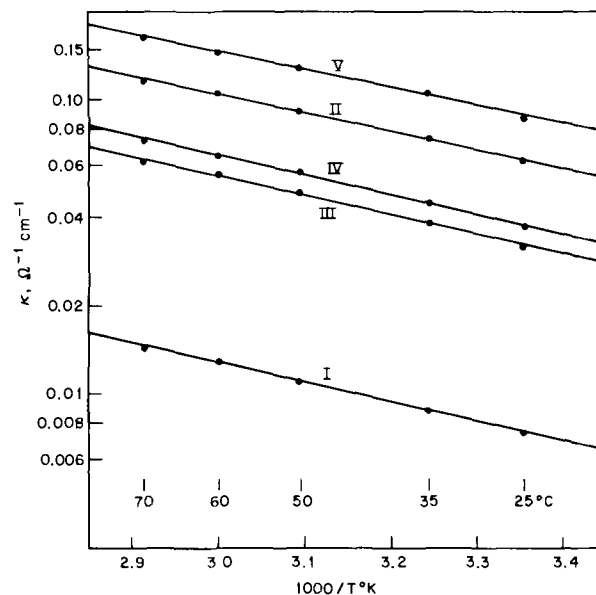


Fig. 2. Data of Table II plotted on log scale ( $\kappa$ ,  $\text{ohm}^{-1}\text{cm}^{-1}$ ) vs. reciprocal absolute temperature. Solutions as indicated.

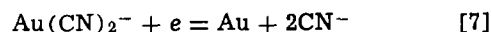
in fact show a small decrease in  $\nu$  with the added  $\text{KAu}(\text{CN})_2$ . When expressed as the  $\nu^{-1/8}$  factor in the Levich equation, the change in kinematic viscosity from the addition of 20 g/liter  $\text{KAu}(\text{CN})_2$  to the citrate electrolyte amounts to only a maximum of 0.2% at 25°C and <0.1% at 70°C in RDE limiting currents. The increase in  $\nu$  produced by the addition of 50 g/liter  $(\text{NH}_4)_2\text{SO}_4$  (solution V) to the standard gold bath IV corresponds to approximately a 1% decrease in limiting current at a RDE over this temperature range. The activation energy calculated from the linear  $\log \nu$  vs. reciprocal temperature plot is 3-3.5 kcal and the corresponding variation of  $\nu^{-1/6}$  from 25°-75°C is less than 14% for any of the solutions measured.

The conductivity results for solutions I-V are given in Table II and are plotted as  $\log \kappa$  vs. reciprocal temperature in Fig. 2. Some numerical relationships can be gained by considering the  $\kappa$  values at one temperature, e.g., 60°C, a normal operating level for gold baths such as IV and V. Taking the  $\kappa$  value for solution I as unity, the normalized figures from Table II are

	I	II	III	IV	V
$\kappa$	1	8.08	4.30	5.00	11.3

Pure additivity of components implies  $\kappa_{\text{I}} + \kappa_{\text{III}} = \kappa_{\text{IV}}$  (found 5.30 and 5.00),  $\kappa_{\text{I}} + \kappa_{\text{II}} + \kappa_{\text{III}} = \kappa_{\text{V}}$  (found 13.38 and 11.3), and  $\kappa_{\text{II}} + \kappa_{\text{IV}} = \kappa_{\text{V}}$  (found 13.08 and 11.3). None of these comparisons contravenes usual concentration effects on equivalent conductivity. Addition of the conductivity salt,  $(\text{NH}_4)_2\text{SO}_4$ , more than doubles the bath conductivity at all temperatures.

The ratio  $\kappa_{\text{III}}/\kappa_{\text{I}}$  is 4.3 and, with an assumption that  $\text{Au}(\text{CN})_2^-$  is the gold species and that this anion and  $\text{K}^+$  are equally mobile,  $t_-$  for  $\text{Au}(\text{CN})_2^-$  in bath IV can be approximated by 0.5/5.3 or 0.09. In the higher conductivity bath V, a comparable estimate of  $t_-$  is 0.04. If the electrode reaction is written as



it resembles a redox reaction such as  $\text{Fe}(\text{CN})_6^{3-} + e = \text{Fe}(\text{CN})_6^{4-}$  with anion reactants and products in the sense of ionic migration effects. The ferri-ferrocyanide reduction appears to be the only such anion reduction for which  $i_{\text{L}}/i_{\text{D}}$  values as a function of an added electrolyte (with one common ion) have been theoretically calculated (4). In the extreme case, pure  $\text{K}_3\text{Fe}(\text{CN})_6$  (no added salt), the minimum value of  $i_{\text{L}}/i_{\text{D}} = 0.87$ . In an equimolar  $\text{K}_4\text{Fe}(\text{CN})_6 - \text{K}_3\text{Fe}(\text{CN})_6$  solution, doubling the  $\text{K}^+$  concentration (with  $\text{KOH}$ ) suffices to increase the  $i_{\text{L}}/i_{\text{D}}$  ratio to 0.97 from the zero added electrolyte ratio of 0.94.

These values suggest that, with the  $t_-$  estimates for the gold baths IV and V, the decrease in the limiting current due to transport against the electric field (anion reduction at a cathode) is at most a few per cent in IV and negligible in V.<sup>1</sup> Any effect of  $i_{\text{L}} < i_{\text{D}}$  is amplified by the  $i_{\text{D}}^{3/2} \propto D$  relation in calculating diffusion coefficients. However, from the experimental values of  $i_{\text{L}}$  that follow, other effects of the addition of the  $(\text{NH}_4)_2\text{SO}_4$  apparently dominate any tendency for  $i_{\text{L}}$  to increase with electrolyte concentration. The  $D$  values calculated from the Levich equation with  $S_{\text{c}}$  corrections ought to be reasonable estimates of this parameter for the gold species in these baths even where the supporting electrolyte case is less than ideal.

The determination of  $D$  for the 4 mM ferrocyanide in 1M  $\text{KCl}$  solution at 25°C by the graphic method, gave a value of  $7.67 \times 10^{-6} \text{ cm}^2/\text{sec}$ . Von Stackelberg *et al.* (15) obtained  $6.32 \times 10^{-6} \text{ cm}^2/\text{sec}$ . As noted, the ratio of these values calibrates the system  $K_{\text{L}}$  to reduce graphic bias and the effect of other errors, e.g., in area measurement at the 0.06  $\text{cm}^2$  level. A  $\pm 3\%$  error in  $D$  corresponds to  $\pm 14\mu$  error in disk radius. Since the kinematic viscosities of solutions III and IV were nearly identical, their average value was used for  $D$  and  $S_{\text{c}}$  calculations for solution VI.<sup>2</sup> Applying the calibrated  $K_{\text{L}}$ , the value then obtained for  $D$  at 60°C in solution VI was  $1.72 \times 10^{-5} \text{ cm}^2/\text{sec}$ , in good agreement with Cheh's value (14) of  $1.67 \times 10^{-5} \text{ cm}^2/\text{sec}$  for a weighed deposit.

Log plots of  $i_{\text{L}}/AC\omega^{1/2}$  and of  $D$  and  $S_{\text{c}}$  vs. reciprocal temperature, are given in Fig. 3 and 4, respectively. The  $D$  values and  $S_{\text{c}}$  numbers are summarized in

Table II. Specific conductivity in  $\text{ohm}^{-1} \text{cm}^{-1}$  as a function of temperature

T°C	Solution				
	I	II	III	IV	V
25	0.00744	0.0623	0.0316	0.0370	0.0857
35	0.00896	0.0740	0.0382	0.0445	0.103
50	0.0114	0.0921	0.0486	0.0567	0.129
60	0.0130	0.105	0.0557	0.0648	0.146
70	0.0146	0.117	0.0626	0.0729	0.163

<sup>1</sup> A reviewer has calculated the decrease, from Newman's theory, to be 0.8% in IV, the more sensitive case.

<sup>2</sup> The value used for  $\nu$  at 60°C is within 1% of that measured directly by Cheh (14).



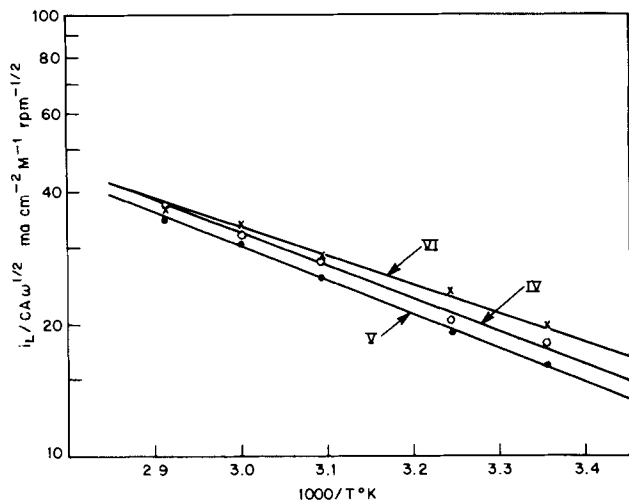


Fig. 3.  $i_L/CA\omega^{1/2}$  plotted on log scale vs. reciprocal absolute temperature. Solutions as indicated.

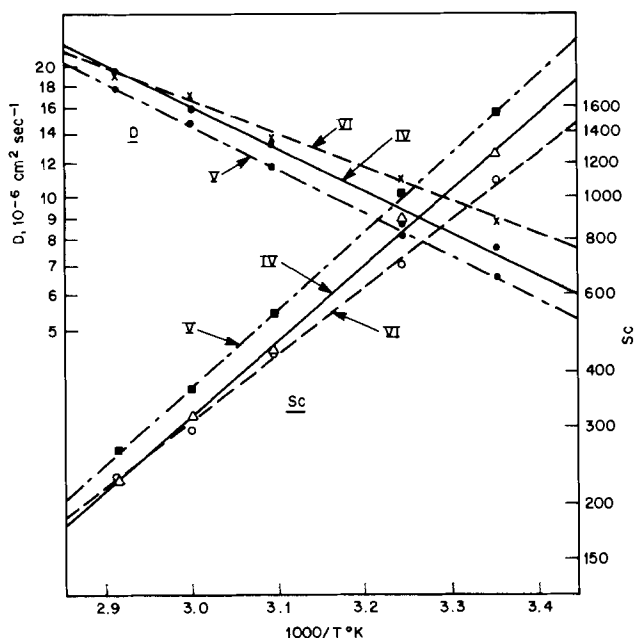
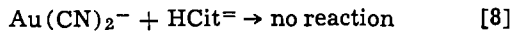


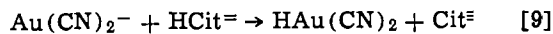
Fig. 4. Calculated  $D$  and  $S_c$  from Tables III and IV plotted on log scale vs. reciprocal absolute temperature.

Tables III and IV, respectively. The apparent activation energy for diffusion is  $4 \pm 1$  kcal for gold baths IV, V, and VI.

The approximate additivities of the conductivity data above are not inconsistent with the  $pK_a$  of 5 for  $HAu(CN)_2$  given by Maja (7). For example, the alternatives



or



probably would not produce easily detectable conductivity differences. Accordingly, to establish the  $pK_a$ ,  $KAu(CN)_2$  was titrated with HCl in separate experi-

Table III. Diffusion coefficient in  $10^{-6} \text{ cm}^2 \text{ sec}^{-1}$  as a function of temperature

T°C	Solution		
	IV	V	VI
25	7.68	6.56	8.80
35	8.71	8.12	11.0
50	13.3	11.7	13.5
60	15.9	15.0	17.2
70	19.5	17.8	19.1

Table IV. Schmidt number as a function of temperature

T°C	Solution		
	IV	V	VI
25	1250	1552	1097
35	890	1022	708
50	449	544	444
60	321	368	298
70	228	270	232

ments with a glass electrode pH meter and conductometric monitoring. A known system, acetic acid with  $pK_a$  of 4.75, was treated in parallel experiments by titrating  $KOOCCH_3$  solutions.

The pH titrations are shown in Fig. 5. The pH at half-equivalence ( $f = 0.5$ ) of 4.7 for the acetate titration agrees with the  $pK_a$ ; the behavior of  $KAu(CN)_2$  is that expected of the salt of an acid with  $pK_a < 2$ . Similarly the conductometric titrations in Fig. 6 show

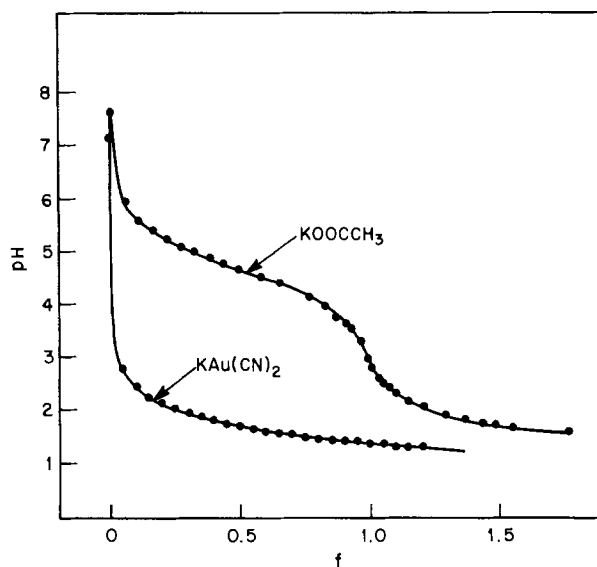


Fig. 5. pH titrations of  $KAu(CN)_2$  and  $KOOCCH_3$ . Plotted as pH vs.  $f$  where  $f = \text{volume/volume to calculated equivalence point}$ . Titrant is 1.045M HCl.

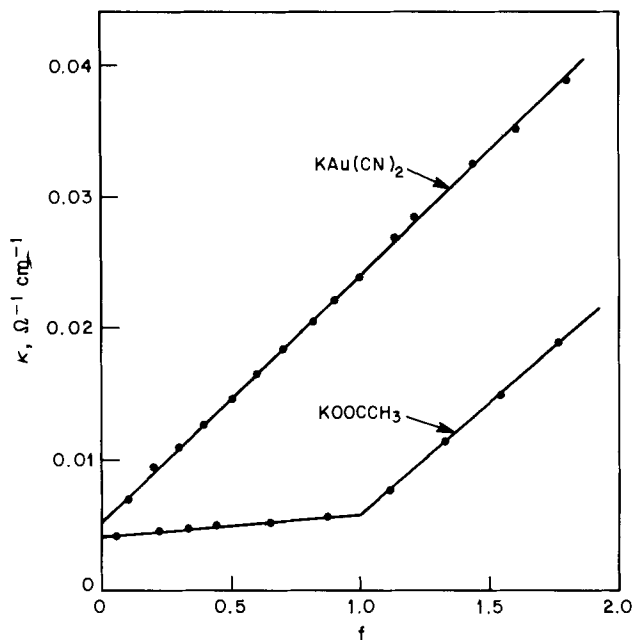


Fig. 6. Conductometric titrations of  $KAu(CN)_2$  and  $KOOCCH_3$ . Plotted as specific conductivity vs.  $f$ . Titrant is 1.045M HCl and conductivity is corrected for titrant dilution.



Table V.  $pK_a$  of  $\text{HAu}(\text{CN})_2$  from pH of half-neutralized  $\text{KAu}(\text{CN})_2^*$ 

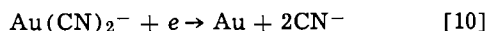
	Solution	pH	$pK_a$ (calc)
1.	0.100M $\text{KAu}(\text{CN})_2$	1.12	0.26
	0.100M $\text{HAu}(\text{CN})_2$		
	0.100M KCl		
2.	0.05M $\text{KAu}(\text{CN})_2$	1.42	0.55
	0.05M $\text{HAu}(\text{CN})_2$		
	0.05M KCl		

Solutions prepared from  $\text{KAu}(\text{CN})_2$  and HCl.

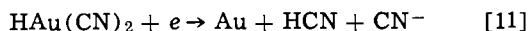
\*  $\text{KAu}(\text{CN})_2$  is considered as essentially fully dissociated as  $\text{K}^+$  and  $[\text{Au}(\text{CN})_2]^-$  in view of its conductivity shown in Table II.

the expected shape for  $\text{KOOCCCH}_3$  ( $\text{Cl}^-$  for  $-\text{OOCCH}_3$  substitution at  $f < 1$ ,  $\text{H}^+ + \text{Cl}^-$  dilution at  $f > 1$ ), but no evidence of reaction for  $\text{KAu}(\text{CN})_2$  ( $\text{H}^+ + \text{Cl}^-$  dilution for all  $f$ ).

pH measurements on nominal  $f = 0.5$  solutions of two different Au(I) concentrations are summarized in Table V with calculations of the  $pK_a$ , corrected for  $\text{HAu}(\text{CN})_2$  dissociation. The fraction dissociated is so high as to preclude accurate measurement of the  $pK_a$ , but a  $pK_a < 1$  value is established. The significance of this acidity is that, in all practical gold baths including the hard gold usually deposited from lower pH, cobalt containing citrate formulations, gold is transported as the ion  $\text{Au}(\text{CN})_2^-$  and the pH change at the electrode is due to



rather than



Since  $\text{CN}^-$  is a strong base ( $pK_{\text{HCN}} = 9.2$ ), the effect of [10] as opposed to [11] is to produce  $2\text{OH}^-/e$  rather than  $1\text{OH}^-/e$ .

In Maja's work only  $\text{KAu}(\text{CN})_2$  solution pH measurements are cited. When such measurements are made with the pure  $\text{KAu}(\text{CN})_2$  grade used in this work, drifting pH values of 7.5-8.3 are obtained at 0.1M concentration, corresponding to a calculated  $pK_a$  2-3.6. Addition of only  $2 \times 10^{-4}\text{M}$  KCN corresponding to a 0.04 weight per cent (w/o) impurity in the original

$\text{KAu}(\text{CN})_2$  salt raises the pH to 9.6 and the apparent  $pK_a$  to 6.2. The use of  $\text{KAu}(\text{CN})_2$  solutions only is obviously deceptive, as would be true for any strong acid salt.

The data presented in this work can be used to predict limiting current through Eq. [1] in any system for which  $\delta$  can be estimated. Cheh's data (14) indicated that the value of  $D$  for  $\text{Au}(\text{CN})_2^-$  was similar in citrate, phosphate, and alkaline baths at  $60^\circ\text{C}$ . As a first approximation, the range of  $D$  values given here as a function of temperature can probably be applied to most gold baths in present use.

Manuscript submitted Nov. 17, 1975; revised manuscript received March 22, 1976.

Any discussion of this paper will appear in a Discussion Section to be published in the June 1977 JOURNAL. All discussions for the June 1977 Discussion Section should be submitted by Feb. 1, 1977.

Publication costs of this article were partially assisted by Bell Laboratories.

#### REFERENCES

- V. G. Levich, *Acta Physicochimica, USSR*, **17**, 257 (1942).
- J. S. Newman, *J. Phys. Chem.*, **70**, 1327 (1966).
- S. Bruckenstein, *This Journal*, **122**, 1215 (1975).
- J. S. Newman, *Ind. Eng. Chem. Fundamentals*, **5**, 525 (1966).
- J. S. Newman, "Electrochemical Systems," Chap. 19, Prentice-Hall, Inc., Englewood Cliffs, N. J. (1973).
- I. M. Kolthoff and J. J. Lingane, "Polarography," Chap. VII, Interscience Publishers, New York (1952).
- M. Maja, *Atti. Accad. Sci. Torino*, **99**, 1111 (1965).
- Manual for Model RC-19 Conductivity Bridge, Beckman Instruments, Inc., Cedar Grove, N. J.
- R. H. Sonner, B. Miller, and R. E. Visco, *Anal. Chem.*, **41**, 1498 (1969).
- B. Miller and S. Bruckenstein, *ibid.*, **46**, 2026 (1974).
- B. Miller, *This Journal*, **116**, 1117 (1969).
- H. Reinheimer, U.S. Pat. 3,833,487 (1974).
- B. Miller and S. Menezes Affonso, To be published.
- H. Y. Cheh, *This Journal*, **118**, 551 (1971).
- M. von Stackelberg, M. Pilgram, and V. Toome, *Z. Elektrochem.*, **57**, 342 (1953).

## Aging Effects in Single Crystal Reduced Rutile Anodes

L. A. Harris and R. H. Wilson\*

General Electric Company, Research and Development Center, Schenectady, New York 12301

#### ABSTRACT

Single crystal samples of reduced rutile used as anodes in a photoelectrochemical cell with  $1.0\text{N}$   $\text{H}_2\text{SO}_4$  show significant changes with use. Saturated photocurrent as a function of illumination wavelength and differential capacitance as a function of anode half-cell voltage were measured before and after varying periods of operation under intense illumination. Shifts in the photoresponse and capacitance are observed only when the illuminating photon energy exceeds the bandgap energy of rutile and when a field exists in the crystal. The changes, possibly indicating a motion of donors toward the crystal surface, are also accompanied by an eventual loss in quantum efficiency and striking alterations in surface morphology. Reduced rutile may not have sufficient stability for prolonged use as the anode in electrochemical cells.

The properties of reduced rutile ( $\text{TiO}_2$ ) and its behavior as an anode in an electrochemical cell have received increasing attention recently (1-8). This interest stems from the work of Fujishima and Honda (9, 10) who suggested rutile as an agent for electrolyzing water with photons (sunlight) supplying the necessary

energy. If rutile or some similar plentiful oxide in the polycrystalline state could be so employed successfully, it would greatly enhance the prospects for the economic utilization of solar energy.

Although the bandgap of rutile is fairly large [3.05 eV (11)] allowing it to usefully capture only a small fraction of the energy available in sunlight, it is one of very few semiconducting materials considered suf-

\* Electrochemical Society Active Member.

Key words: photoelectrochemistry,  $\text{TiO}_2$ , rutile, hydrogen, aging.

ficiently stable to resist corrosion when used as an illuminated anode in an aqueous electrochemical cell (7, 9). Previous investigators have been able to detect no change in weight of the material after considerable use (2) or evidence of Ti ions in the electrolyte (9).

We report here observations of changes in electrical behavior and surface structure of single crystal rutile anodes under the influence of light and electric field conditions that obtain when water is dissociated in an electrochemical cell of this type. These aging effects result in an eventual loss of quantum efficiency which seriously reduces the effective life of the material as a water-splitting agent, even though no obvious chemical dissolution occurs.

### Experimental Procedures

**Measurements.**—The tests to be described were carried out in an electrochemical cell similar to those described by other workers (2, 10). The anode was a rutile crystal, about 0.5 cm<sup>2</sup> in area, and the cathode was a blackened platinum foil, about 14 cm<sup>2</sup> measured area. Two saturated calomel reference electrodes (SCE) were connected through appropriately placed Luggin capillaries to measure the half-cell voltages at each electrode. Hydrogen could be bubbled over the platinum black cathode to avoid depolarization effects, particularly when hydrogen was not being liberated there by the action of the cell.

All the electrodes were placed in a 400 ml Vycor beaker containing 250 ml of 1.0N H<sub>2</sub>SO<sub>4</sub>. The electrolyte was not stirred during the experiments, after earlier tests had shown the current and half-cell voltages to be independent of stirring.

The rutile anode could be illuminated, by either of two 150W Bausch and Lomb xenon light sources, by simply rotating the beaker appropriately as indicated in Fig. 1. The light from source 1 was separated into its components by a small Bausch and Lomb grating monochromator and focused to a spot 2 cm in diameter at the sample by a quartz lens. The light from source 2 was focused directly by another quartz lens to about the same size spot. The total power density at the sample from source 2 was about 1.4 W/cm<sup>2</sup>.

Figure 1 also shows the circuit used to measure the volt-ampere relations of the two half-cells or the photoresponse of the anode half-cell; and the polarities of the voltages and currents are defined there. Capacitance of the cell was measured without illumination using the bridge circuit shown in Fig. 2. This bridge design assumes a series RC equivalent circuit for the cell, in which the capacitive reactance is associated primarily with a depletion layer in the semiconductor electrode (12-15). Differential capacitance as a function of anode half-cell d-c potential,  $V_1$ , was measured using an approximately 3 kHz square or

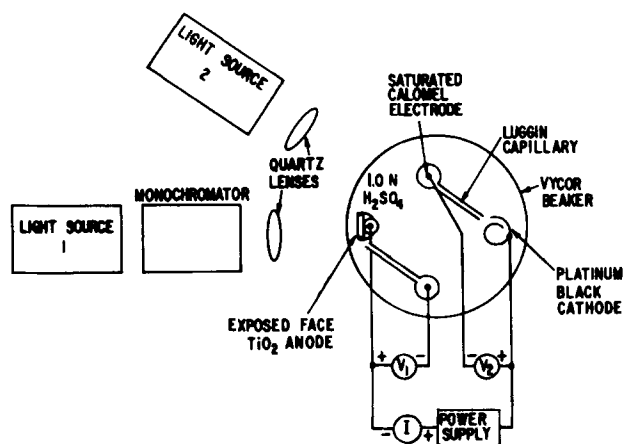


Fig. 1. Schematic of experimental arrangement for photocurrent measurements and aging.

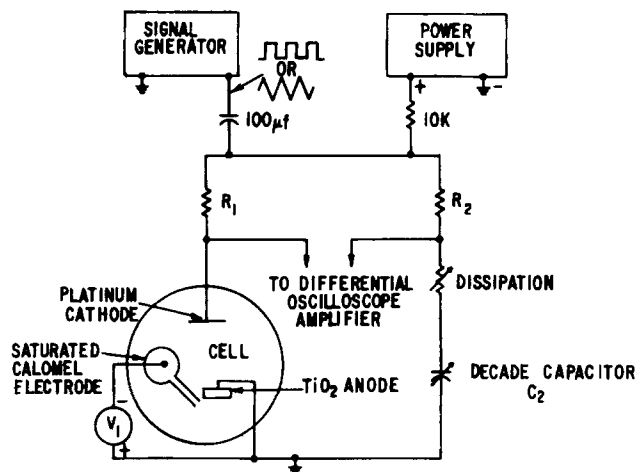


Fig. 2. Schematic of circuit for measuring differential capacitance vs. half-cell voltage.

triangular wave to excite the bridge and an oscilloscope as the balance detector. Even when perfect nulls could not be obtained because the RC circuit in the reference arm inadequately represents the cell (15), an unambiguous balance could be detected by the amplitude and symmetry of the detector wave form.

**Sample preparation.**—All samples were sliced from a single crystal boule of rutile purchased from the National Lead Company. The most detailed tests were done on samples cut normal to the C axis of the crystal, exposing a (001) face, though some measurements were made on (100) and (110) faces. The slices were approximately 1 mm thick and were polished on one side with 0.3 $\mu$  abrasive.

The crystals were insulating as prepared and were heated in a reducing atmosphere to make them conducting (11, 16). This treatment makes the crystals n-type. The usual reduction procedure was heating the polished slices in 1 atm of H<sub>2</sub> at 650°C for 15 min, a treatment we found to give about the optimum quantum efficiency. We shall indicate where results pertain to samples with other than (001) orientation or prepared with other reduction processes.

Ohmic contact was made on the rough, unpolished face of the crystal slice with a Ga-In or Ga-Ag alloy, and a wire was soldered to this face with a drop of In-Sn solder. The sample was then sealed to a glass tube and coated with epoxy cement so that only the polished face was exposed to the electrolyte. As noted earlier, sample areas were typically about 0.5 cm<sup>2</sup>.

### Results

A typical  $V$ - $I$  curve for the illuminated anode (TiO<sub>2</sub>) half-cell resembles those reported elsewhere (9, 10). For convenience the curve is shown in Fig. 3, along

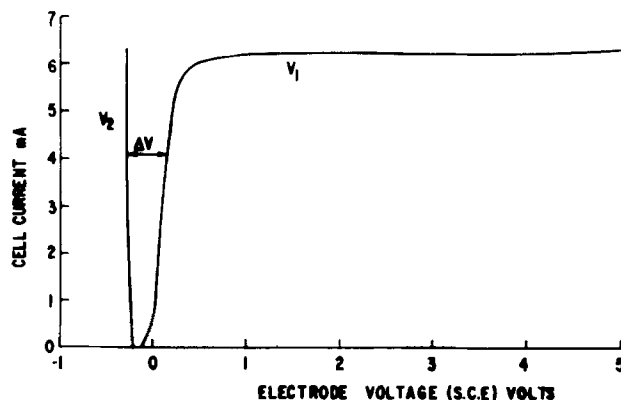


Fig. 3. Current vs. half-cell voltages ( $V_1 \rightarrow \text{TiO}_2$ ;  $V_2 \rightarrow \text{Pt}$ )

with that for the platinum black cathode after it is saturated with hydrogen. These curves verify the conclusion of Wrighton *et al.* (2) that the short-circuited cell will not support an appreciable current, even when illuminated, unless the voltage deficiency indicated between the two half-cell characteristics is supplied from an external source.

The height of the current plateau at any given time is proportional to the intensity of the illumination (10), as determined with a set of calibrated neutral density filters, but the response was observed to vary with the sample history. Systematic measurements were made to clarify the nature of these changes with sample "age."

**Standard reduction, (001) orientation.**—Immediately after preparation and before any exposure to light from source 2, the cell capacitance as a function of  $V_1$  and the saturated photocurrent at constant  $V_1 = 2V$  were measured. Then, with  $V_1$  held at the same constant value to draw the saturated current, the rutile anode was exposed to light from source 2 for a period of time, after which the  $C-V_1$  and spectral response measurements were repeated. This sequence of exposure and measurement was continued for a number of aging intervals, all with exposure to the same light intensity, about 10 times that of unconcentrated sunlight. Although this high intensity undoubtedly accelerated the aging effects reported here, the rate of aging with different light intensities was not investigated.

The results of one such sequence of measurements on sample number 9b2 are summarized in Fig. 4, 5, and 6, in which age represents the total time the sample was illuminated by source 2 prior to the measurement indicated. Figure 4 shows the results of capacitance measurements plotted as  $A^2/C^2$  vs.  $V_1$ , where  $A$  is the geometric area of the sample. The slope of this Schottky plot gives a measure of the net donor density for a flat surface if the changes in capacitance all occur in the semiconductor as is usually the case (12-14). Under these assumptions the initial donor density is about  $7 \times 10^{19}$  per  $\text{cm}^3$ . The calculated depletion widths using these assumptions are also shown in Fig. 4.

Figure 5 shows the photocurrent as a function of wavelength from source 1 for different ages. These curves are uncorrected for the spectral intensity dis-

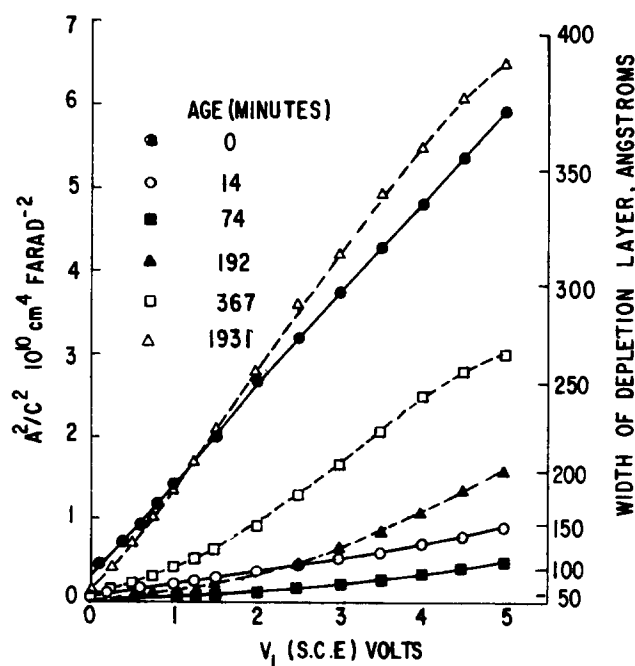


Fig. 4. Schottky plot of reciprocal of capacitance squared vs. half-cell voltage. Flat surface area assumed to calculate width of depletion layer. Sample number 9b2.

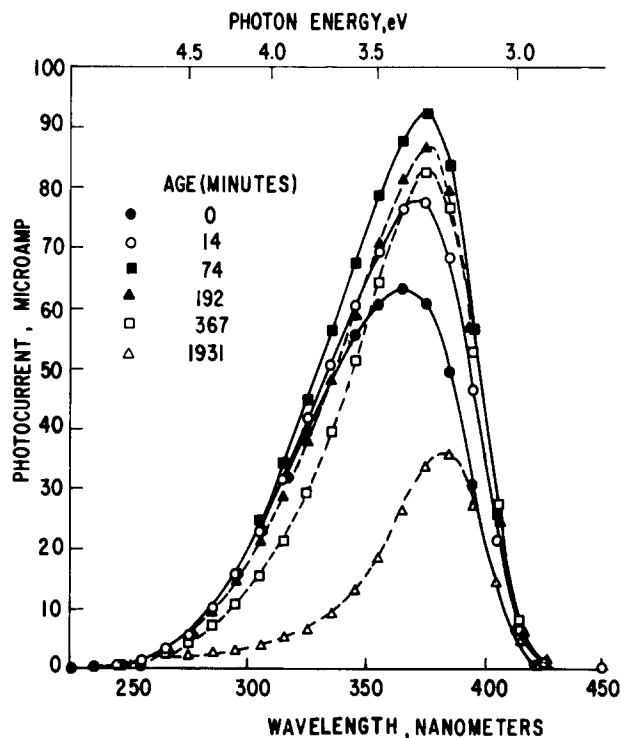


Fig. 5. Spectral dependence of photocurrent at different stages of aging for strongly reduced sample number 9b2.

tributed at the monochromator output. The wavelength resolution is quite broad because the monochromator slits were wide (4 mm) to give adequate intensity for measurement. (In an earlier test of a similarly prepared sample, correction of the spectral response curve for monochromator output distribution and absorption in the cell wall and electrolyte, but not for reflection at the sample surface, showed a quantum efficiency of about 0.74 electrons per photon with energy exceeding the bandgap of  $\text{TiO}_2$ .) The uncorrected curves adequately show the shift with age of the spectral response toward the longer wavelengths and the initial rise and subsequent fall of the peak current.

The rise and fall of current with age is also evident in the graph of saturation current (Fig. 6) under full illumination from light source 2. During the course of the experiment there were many interruptions when the sample remained inactive in the electrolyte. The capacitance and spectral response were always checked after such intervals and found to vary little from their values before the interruptions. Values of the saturation current taken immediately after resumption of the aging schedule tended to be lower than their previous values but came back to the value shown in the

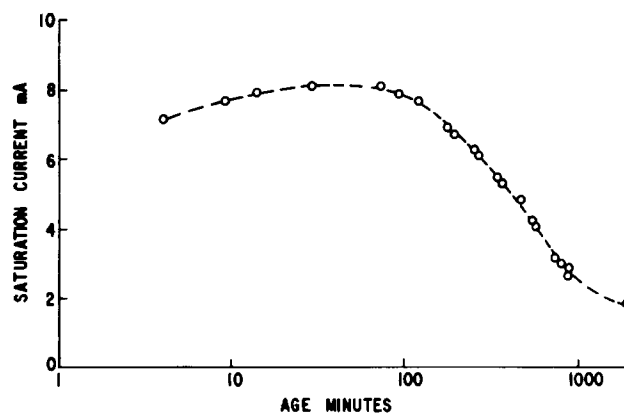


Fig. 6. Change in photocurrent with age. Sample number 9b2, full light from source 2.

figure within a few minutes. The age, defined as the total time of exposure to full illumination, appears to be the principal determinant of the changes in electrical properties reported here.

The aging effects just described for a reduced rutile crystal with the (001) face exposed raise questions regarding the conditions necessary for them to occur; in particular, the influence of crystal orientation, amount and method of reduction, light, and electric field. A number of additional experiments were done to answer some of these questions.

*Other orientations and reductions.*—Repetition of the aging experiments with crystals reduced in hydrogen at 650°C for 15 min but with the (100) and (110) faces exposed showed similar initial increases in capacitance and shifts of the spectral response toward long wavelengths. The capacitance increased for the full duration of the experiments and rose to higher values than in the (001) case, particularly with the (110) face exposed. Otherwise the behavior was qualitatively similar.

Figure 7 shows the photoresponse of an unreduced rutile crystal with the (001) face exposed. Although there is some growth of the peak current with age, its value is about three orders of magnitude below that measured in reduced crystals, and the response remains confined to a narrow region near the low energy absorption edge of  $\text{TiO}_2$  (16-18). The sample capacitance was very small and independent of  $V_1$  or age.

Another sample, number 9c, with (001) orientation was reduced by heating to approximately 580°C for 15 min in an ultrahigh vacuum system where the pressure was  $3 \times 10^{-9}$  Torr before heating and  $5 \times 10^{-7}$  Torr during heating. This treatment resulted in a very lightly reduced crystal (about  $2 \times 10^{16}$  donors/cm<sup>3</sup> based on the slope of an  $A^2/C^2$  plot) which was subjected to the same sequence of aging experiments described earlier. It showed an increase in capacitance with aging similar to sample number 9b2.

The changes in photoresponse for sample 9c are shown in Fig. 8. Initially, this response peaks at about 325 nm but with age a second peak develops at about 375 nm while the shorter wavelength response de-

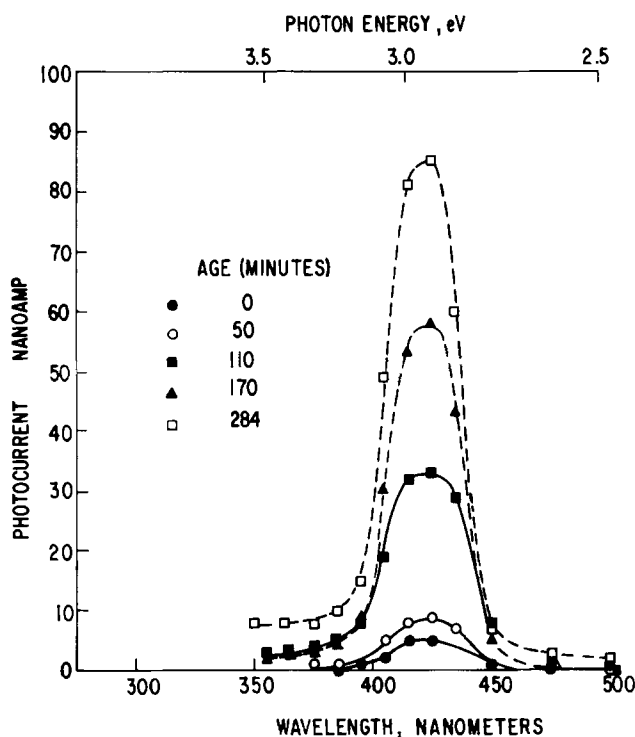


Fig. 7. Spectral dependence of photocurrent at different stages of aging for unreduced sample.

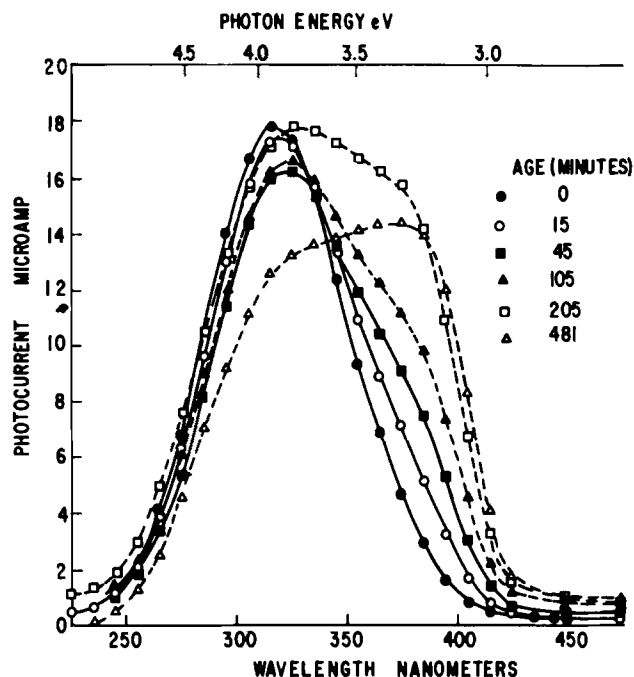


Fig. 8. Spectral dependence of photocurrent at different stages of aging for lightly reduced sample number 9c.

creases somewhat. These shifts are consistent with those of Fig. 5 but are much more obvious in the present case. It should be noted that the curves of current shown in Fig. 8, if plotted on the same scale as those of Fig. 5, would lie below the latter curves.

*Influence of field and illumination.*—After having examined the effects of aging on a variety of samples, we then examined the effects of varying the aging parameters, the illumination and applied voltage.

Sample number 12a was reduced in the standard way. It was then subjected to the sequence of aging tests already described, except that  $V_1$  was held at 0.2V instead of the usual 2V. The results were similar in all respects to those of sample 9b2 except possibly for a lower rate of change with sample 12a, though differences in the initial level of reduction make this rate change uncertain.

The final sample to be discussed, number 12b, was reduced in the same process as sample 12a and underwent a series of aging tests. In the first of these the cell was short circuited, which set  $V_1$  at about -0.27V. As can be seen from the intercepts of the  $A^2/C^2$  curves (Fig. 4) this approximates the flatband condition in which there is no depletion region in the semiconductor. The aging tests, with the sample illuminated as usual by the full light from source 2, showed no significant changes in photoresponse or capacitance.

Since the sample was apparently unchanged, another aging test was made with  $V_1 = 2V$  but with no illumination. Again no significant changes in the crystal were observed.

A third test was made on the same specimen with  $V_1 = 2.0V$  and with illumination by filtered light from source 2. The light was passed through a Corning CS 3-37 filter which has a sharp cutoff for light of wavelengths less than about 430 nm. Since the transmitted light consisted of photons with insufficient energy to excite hole-electron pairs in the  $\text{TiO}_2$ , no change in current was observed with the light on or off. Once again, aging had no significant effect on the photoresponse or the capacitance.

As a final check, to ensure that this sample was a representative one, it was aged for 15 min with  $V_1 = 2V$  and with full illumination. After this brief aging the striking increases in capacitance observed with other samples were evident.

**Surface structure changes.**—It was observed that the exposed surfaces of aged samples changed their visual appearances, usually from a shiny dark gray or black to a velvety matte surface. Some of these surfaces have been examined with the aid of a scanning electron microscope. At present, the information is too preliminary to report in detail, but striking changes in surface morphology do indeed occur with aging. Figure 9 shows some of the changes which occur on the (001) surface of rutile when it is reduced, and then the nature of subsequent changes when the surfaces were aged in the photoelectrochemical cell. The difference between Fig. 9a and 9b shows that some surface change occurs on reduction with hydrogen. Figure 9c shows the surface of sample 12b, the last to be discussed above, which, though in the electrolyte for a whole series of tests, underwent active aging for only 15 min. Figure 9d is a comparable micrograph of the surface of sample 12a which had been actively aged for a total of 360 min with  $V_1 = 0.2V$ . Micrographs of aged (100) and (110) crystal faces also show the development of considerable porosity but differ in detail from those shown in Fig. 9c and d.

### Discussion

We have presented data which show changes in a reduced rutile crystal when it is used as an anode in a photoelectrochemical cell. Three major effects were observed: (i) the quantum efficiency decreases for high energy (greater than 3.6 eV) photons and increases for intermediate energy (3.0–3.6 eV) photons; (ii) the capacitance of the electrolyte-crystal junction changes; and (iii) the surface structure of the crystal changes. Whether these effects are independent or merely different aspects of a single process is not entirely clear at present.

One possible interpretation of the capacitance changes involves the accumulation of donors near the surface as a result of the combined action of bandgap radiation and applied field. This increased concentration at the surface would narrow the depletion region and increase the observed capacitance. The changes in

spectral response, however, are not adequately accounted for on this basis without resorting to a number of other improbable assumptions.

Another possible explanation for the observations is a change in surface roughness giving rise to an increased contact area between electrolyte and crystal. A factor of three increase in area in the first 14 min of aging would explain the observations in Fig. 4, but such an increase is more than would be predicted from the appearance of surface roughness in Fig. 9c. This model could also explain increased quantum efficiency for intermediate energy photons by assuming the development of pores in the surface that provide collection surface deep in the crystal where the photons are absorbed. The model, however, does not provide an explanation for the large difference between the quantum efficiencies for the heavily and lightly doped crystals.

By the time the crystal is aged to the point corresponding to Fig. 9d, the quantum efficiency has begun decreasing. This decrease can be explained if the restructured surface is composed of an electrically inert layer that absorbs photons without contributing to the current. The layer could also affect the capacitance measurement by decreasing the contact area between the electrolyte and electrically active surface. The restructuring itself is possibly due to a current-driven migration of surface atoms. Only about one atom rearranged per thousand electrons through the circuit is necessary to cause the observed effects. This process may be related to that discussed by Vermilyea (19) for anodized  $Ta_2O_5$  films.

### Conclusions

We have shown that the quantum efficiency of a reduced rutile crystal used as an electrode for photoelectrolysis depends on the process used to reduce it. This quantum efficiency is subsequently changed in use. The long term result is a decrease in quantum efficiency apparently related to rearrangement of  $TiO_2$  at the surface. Experiments have shown that both bandgap excitation and a strong field are necessary for these aging effects to occur. The influence of processing and experimental history on the behavior of this material could lead to the discrepancies in quantum efficiencies reported by different workers.

Aside from its too-wide bandgap,  $TiO_2$  may prove to be unsuitable as a photochemical solar energy collector because of the instabilities reported here. Although these instabilities were demonstrated only for  $TiO_2$  and only in a 1.0N  $H_2SO_4$  electrolyte, they may well occur under a wider variety of operating conditions and with other semiconductor electrodes, particularly those made semiconducting by the introduction of lattice defects.

Further effort is necessary to clarify the fundamental nature of the instabilities so that their effects may be minimized or avoided by proper choice of material and operating conditions.

### Acknowledgments

We would like to acknowledge helpful discussions with M. W. Breiter, G. C. Farrington, S. D. Silverstein, D. A. Vermilyea, K.-L. Wang, J. L. Weininger, and F. G. Will.

Manuscript submitted Sept. 15, 1975; revised manuscript received Nov. 10, 1975. This was Paper 221 presented at the Washington, D. C., Meeting of the Society, May 2–7, 1976.

Any discussion of this paper will appear in a Discussion Section to be published in the June 1977 JOURNAL. All discussions for the June 1977 Discussion Section should be submitted by Feb. 1, 1977.

Publication costs of this article were partially assisted by the General Electric Company.

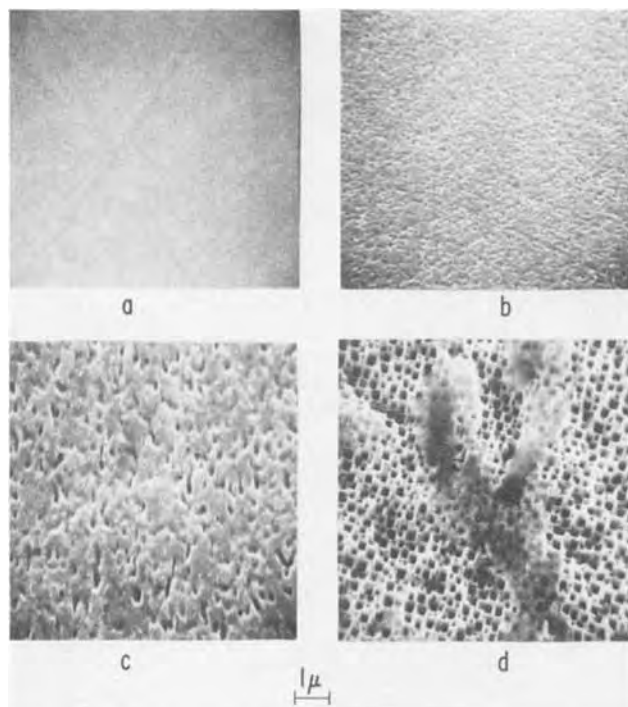


Fig. 9. Scanning electron micrographs of polished (001) rutile electrode surfaces at 10,000X. a: As polished; b: after reducing 15 min at 650°C in  $H_2$ ; c: after 15 min aging  $V_1 = 2V$  sample number 12b; d: after 360 min aging  $V_1 = 0.2V$  sample number 12a.

## REFERENCES

1. J. Keeney, D. H. Weinstein, and G. M. Haas, *Nature*, **253**, 720 (1975).
2. M. S. Wrighton, D. S. Ginley, P. T. Wolczanski, A. B. Ellis, D. L. Morse, and A. Linz, *Proc. Nat. Acad. Sci. U.S.A.*, **72**, 1518 (1975).
3. H. Yoneyama, H. Sakamoto, and H. Tamura, *Electrochim. Acta*, **20**, 341 (1975).
4. K. L. Hardee and A. J. Bard, *This Journal*, **122**, 739 (1975).
5. W. Gissler, P. L. Lensi, and S. Pizzini, *J. Appl. Electrochem.*, **6**, 9 (1976).
6. S. N. Paleocrassas, *Solar Energy*, **16**, 45 (1974).
7. H. Gerischer, *J. Electroanal. Chem. Interfacial Electrochem.*, **58**, 263 (1975).
8. M. D. Archer, *J. Appl. Electrochem.*, **5**, 17 (1975).
9. A. Fujishima and K. Honda, *Bull. Chem. Soc. Japan*, **14**, 1148 (1971).
10. A. Fujishima and K. Honda, *Nature*, **238**, 37 (1972).
11. R. G. Breckenridge and W. R. Hosler, *Phys. Rev.*, **91**, 793 (1953).
12. P. J. Boddy, *Progr. Solid State Chem.*, **4**, 81 (1967).
13. P. J. Boddy, *This Journal*, **115**, 199 (1968).
14. R. DeGryse, W. P. Gomes, F. Cardon, and J. Vennik, *ibid.*, **122**, 711 (1975).
15. S. Toshima, *Progress in Surface and Membrane Science*, Ed. J. F. Danilli, M. D. Rosenberg and D. A. Cadenhead, **4**, 231 (1971).
16. D. C. Cronmeyer, *Phys. Rev.*, **87**, 876 (1952).
17. P. Moch, M. Balkanski, and P. Aigrain, *Compt. Rend.*, **251**, 1373 (1960).
18. M. Cardona and G. Harbeke, *Phys. Rev.*, **137**, A1467 (1965).
19. D. A. Vermilyea, *ibid.*, **104**, 212 (1957).

## The Membrane Transport Matrix: Analytical and Experimental Techniques for Complete Characterization

A. Zelman\* and R. Tankersley

Center for Bio-Medical Engineering, Rensselaer Polytechnic Institute, Troy, New York 12181

A. Ford

Meharry Medical College, Nashville, Tennessee 37208

H. Wayt

Department of Electrical Engineering, Tennessee State University, Nashville, Tennessee 37209

and A. Schindler

Research Triangle Institute, Research Triangle Park, North Carolina 27709

### ABSTRACT

This report describes experimental and analytical methods of resolving frequently encountered problems of linearity, accuracy, reproducibility, reliability, and concentration polarization in characterization of membrane transport coefficients. An apparatus has been constructed for nonsteady-state characterization of membrane transport. This apparatus employs simultaneous monitoring of salt and volume transport in each half-cell, independently, to provide internal checks on accuracy. Sufficient data are generated from a single experiment to evaluate a complete matrix of coefficients ( $L_p$ ,  $\sigma$ ,  $\omega$ ). Ambiguities resulting from combining data from different experimental conditions in a single coefficient matrix are completely eliminated. Two analytical-experimental methods are employed: the zero volume flux method (ZVFM) and the linearization of the flux equations leading to the least squares straight line method (LSM). Average reproducibility of a coefficient matrix, using ZVFM or LSM, is about 5%. Average accuracies for the LSM coefficients  $L_p$ ,  $\omega$ , and  $\sigma$  are 2.9, 0.5, and 4.8%, respectively. A quantitative measure is introduced for the over-all reliability of a coefficient matrix. The "reliability coefficient,"  $R_J$ , demonstrates how well the experimental fluxes can be reproduced by the transport coefficient matrix over the range of thermodynamic forces. For these experiments  $R_{J_v} \approx 3 \times 10^{-8}$  cm-sec<sup>-1</sup> and  $R_{J_s} \approx 2 \times 10^{-10}$  mole-cm<sup>-2</sup>-sec<sup>-1</sup>. The problems of linearity and concentration polarization are nearly solved, as evidenced by the reliability with which the experimental fluxes can be predicted by the transport coefficients.

The first complete characterization of membrane transport phenomena was achieved by Staverman, who demonstrated the inequality of osmotic and hydrostatic transmembrane pressures in producing volume flux (1, 2). By a simple application of the principles of nonequilibrium thermodynamics developed by

Onsager (3, 4), Staverman showed that, in addition to water and solute permeabilities, a third transport coefficient is necessary for complete characterization of membrane transport. He named this additional term the "reflection coefficient" and described its physical significance.

Since Staverman's efforts, interest in elaborating the theoretical principles underlying membrane transport phenomena, and the choice of reference frames for

\* Electrochemical Society Active Member.

Key words: reflection coefficient, hydraulic conductivity, membrane permeability, concentration polarization, irreversible thermodynamics.

membrane characterization, has resulted in voluminous literature contributions. Distinguished reviews of membrane biophysics have been published (5-7). Staverman's original concept of the reflection coefficient has been generalized by Zelman (8). Several research groups have developed specific apparatus and techniques for evaluating three or more transport coefficients for membrane-solution systems [true steady state, (9, 10); quasi-steady state, (11-18); nonsteady state, (19-21)].

In all of the methods thus far developed for complete characterization of membrane transport, both theoretical and experimental anomalies are introduced which place severe limitations on the evaluated coefficients. There are basically five problems thwarting complete characterization of a matrix of coefficients.

I. The linear form of the transport equations can be developed from either macroscopic or microscopic considerations (22). The two basic forms for the transport equations are

$$\vec{J}_i = - \sum_{j=1}^N L_{ij} \nabla \mu_j \quad [1]$$

and

$$J_i = - \sum_{j=1}^N L'_{ij} \Delta \mu_j \quad [2]$$

The transport coefficients,  $L_{ij}$ , are in principle functions of hydrostatic pressure, solute concentration, and voltage. However, if the differential form, Eq. [1], is linear, then the difference form, Eq. [2], obtained by integration of Eq. [1], will be intrinsically nonlinear (23). Use of the macroscopic transport Eq. [2] must therefore be restricted to narrow regions of electrochemical potential difference where linearity is found experimentally to exist.

II. For a three component system consisting of a membrane, solute, and solvent, there are two independent flux equations and three independent transport coefficients. These three coefficients cannot be evaluated from a single state of the membrane-solution system. Consider two chemical species, denoted by subscripts 1 and 2, in a membrane-solution system whose state is denoted by a superscript prime

$$-J_1' = L_{11} \Delta \mu_1' + L_{12} \Delta \mu_2' \quad [3]$$

$$-J_2' = L_{21} \Delta \mu_1' + L_{22} \Delta \mu_2' \quad [4]$$

where, according to the principle of Onsager reciprocity,  $L_{12} = L_{21}$ . To generate a third equation and solve the system, one must alter some chemical potential and, thus, the mass fluxes which occur. The second state of the system is denoted by superscript double primes

$$-J_1'' = L_{11} \Delta \mu_1'' + L_{12} \Delta \mu_2'' \quad [5]$$

$$-J_2'' = L_{21} \Delta \mu_1'' + L_{22} \Delta \mu_2'' \quad [6]$$

Any three equations from [3]-[6] can be used to evaluate the independent coefficients. The important aspect, however, is that a second state of the chemical system, developed by altering the chemical potentials, was necessary to generate sufficient data to determine the complete matrix of coefficients. The transport coefficients, then, are not derived experimentally from a single state of the membrane-solution system, but they are functions of at least two different states. The magnitude of the coefficients will depend on the method of averaging the coefficients over these different thermodynamic states. Theoretical attempts at deriving the transport coefficients by integrating the differential flux equations across a single state of the membrane-solution system encounter intrinsic difficulties.

III. Concentration polarization is the nemesis of the membranologist. The boundary layer is, of course,

impossible to eliminate completely (24). For systems with three or more transport coefficients, it becomes a monumental task to develop sufficient data to use the Wilson plot method of eliminating the boundary layer by extrapolation to infinite solution agitation. There are two alternatives. One can either manufacture a test cell with mathematically well-defined boundary layers, or one can design a stirring apparatus which makes the boundary layer an insignificant contribution to the transmembrane mass transfer resistance.

IV. From the standpoint of absolute accuracy, the transport coefficients can be evaluated most easily by performing separate experiments in different transport cells and even with different membrane samples. A set of experiments can thus be used to evaluate a single matrix of coefficients. This procedure introduces into a single matrix, however, coefficients which reflect different boundary layer conditions and inhomogeneity in the different membrane samples. They do not rigorously reflect the same membrane-solution system. Ideally, data should be collected from one experimental cell, and, if possible, during one experimental trial.

V. As discussed previously, transport coefficients are obtained from at least two different states of the membrane-solution system. However, in practice one uses the set of coefficients to generate the fluxes expected for a single state. Thus, it is essential for every report to examine the validity of the reported transport coefficients by including a comparison between the fluxes generated by the experimental transport coefficients and the actual measured experimental fluxes. This aspect of membrane characterization has been sorely neglected in the literature.

This discussion leads to the conclusion that the optimal characterization of a solution-membrane system requires a single matrix of coefficients evaluated from experiments which maintain a constant, negligibly small boundary layer. All measurements should be performed in the same transport cell with the same adequate stirring conditions. The apparatus should incorporate as many double checks on each measurement as possible to ensure accuracy and reproducibility. The coefficients should be "properly" averaged over the various states of the membrane-solution system used to evaluate the transport coefficients. Finally, the validity of the calculated transport coefficients should be demonstrated by reproducing the measured fluxes within experimental accuracy.

The purpose of this report is to describe a nonsteady-state system designed for complete membrane characterization for a membrane-aqueous salt solution system. In addition, we demonstrate the appropriate analytical methods necessary for evaluation of the transport coefficients from rigorously valid experimental data. The calculated transport coefficients can be used to reproduce the experimental fluxes over an extended range of solute concentrations.

### Analytical Method

An apparatus has been constructed for nonsteady-state characterization of membrane transport phenomena. This system is unique in that every necessary experimental parameter can be determined, with precision, in each half-cell simultaneously. Thus, an entire matrix of transport coefficients can be obtained from a single experiment.

Temperature, solution concentration, and solution volume were monitored continuously in each half-cell. Experiments were designed such that the solute concentration in each half-cell varied with time while the solution temperatures and transmembrane hydrostatic pressure difference were maintained constant.

Figure 1 shows a hypothetical transport cell used to define the sign notations applicable to the thermodynamic forces and fluxes involved. Differences in the thermodynamic variables are taken right minus left.

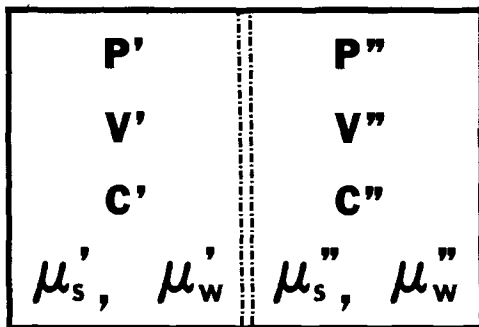


Fig. 1. Hypothetical cell for transport of salt and water across a permeable membrane.

Fluxes are taken to be positive when transport is from the left to the right half-cell.

The solute and volume fluxes are written as time derivatives of the experimentally accessible parameters; half-cell volume,  $V(t)$ , and solute transport,  $n_T(t)$ . Osmotic pressure and chemical potential are developed as time-dependent functions of concentration,  $c(t)$ .  $V(t)$ ,  $c(t)$ , and  $n_T(t)$  are developed as polynomial expressions in time using the Crout reduction method. The time-dependent equations for half-cell volume, solute concentration, and solute transport are

$$V(t) = \sum_{i=1}^m a_i t^i \quad [7]$$

$$c(t) = \sum_{i=1}^n b_i t^i \quad [8]$$

and

$$n_T(t) = \sum_{i=1}^p d_i t^i \quad [9]$$

Data points can in general be fitted to a polynomial with a vanishingly small standard deviation by increasing the degree of the polynomial. To gain a realistic function for these polynomials, however, we decreased  $m$ ,  $n$ , and  $p$  until the standard deviation for the polynomial was about equal to the experimental imprecision ( $m, n, p \approx 4$ , usually). Thus, the higher order terms which forced the polynomial to fit the data points were eliminated. Smooth, experimentally reasonable curves for  $V'(t)$ ,  $V''(t)$ ,  $c'(t)$ ,  $c''(t)$ ,  $n_T'(t)$ , and  $n_T''(t)$  were obtained in this manner.

The volume flux,  $J_v(t)$ , is given by

$$J_v(t) = -(1/A) (dV'(t)/dt) = (1/A) (dV''(t)/dt) \quad [10]$$

where  $A$  is the exposed membrane area. The solute flux,  $J_s(t)$ , is given by

$$J_s(t) = -(1/A) (dn_T'(t)/dt) = (1/A) (dn_T''(t)/dt) \quad [11]$$

The time-dependent transport equations were written, for a single solute, as (2, 5, 8)

$$J_v(t) = -L_p(\Delta P - \sigma \Delta \Pi(t)) \quad [12]$$

and

$$J_s(t) = \bar{c}(t) (1 - \sigma) J_v(t) - \omega \Delta \Pi(t) \quad [13]$$

where  $\bar{c}(t)$  is a logarithmic average solute concentration defined by

$$\bar{c}(t) = \Delta \Pi(t) / \Delta \mu_s^c(t) \quad [14]$$

For a uni-univalent salt, the osmotic pressure and  $\mu_s^c$  can be written

$$\mu_s^c(t) = 2RT \ln (\gamma_{\pm}(t) m_s(t))$$

$$\text{and } \pi(t) = \frac{18.016RT}{1000 \bar{v}_w(t)} (2\Phi_s(t) m_s(t)) \quad [15]$$

This particular form of the transport equations was chosen because the coefficients  $L_p$ , the hydraulic conductivity,  $\sigma$ , the reflection coefficient, and  $\omega$ , the solute permeability at zero net volume flux are reasonably independent of solute concentration (25). In Eq. [12] and [13], these coefficients may be treated as constants so long as  $\Delta \Pi(t)$  is not "too large."

Two methods were used to evaluate the transport coefficients. The "zero volume flux" method uses relationships from Eq. [12] and [13] to evaluate the coefficients

$$\omega = -(J_s(t) / \Delta \Pi(t))_{J_v=0} \quad [16]$$

$$\sigma = (\Delta P / \Delta \Pi(t))_{J_v=0} \quad [17]$$

$$L_p = -(1/N) \sum_{i=1}^N (J_v(t_i) / (\Delta P - \sigma \Delta \Pi(t_i))) \quad [18]$$

In Eq. [18], the hydraulic conductivity is determined as an average over the number of experimental data points,  $N$ , collected at the times  $t_i$  during an experiment. In this analytical method, the per cent standard deviations of  $\omega$  and  $\sigma$  are the sums of the per cent standard deviations of the terms which contribute to their calculation. The standard deviation of  $L_p$  was determined from

$$\text{s.d. } (L_p) = \left( \sum_{i=1}^N (L_p(t_i) - L_p)^2 / (N - 1) \right)^{1/2} \quad [19]$$

In this method, the coefficients  $\omega$  and  $\sigma$  are determined for the single state of the membrane-solution system when the net volume flux is zero. The hydraulic conductivity is an average over the range of thermodynamic states produced in each experiment.

The second method of data reduction, the least squares straight line method, uses a linearization of the volume and salt flux expressions as follows. From Eq. [12], one obtains

$$J_v(t) = -L_p \Delta P + L_p \sigma \Delta \Pi(t) \quad [20]$$

which can be written as

$$Y(t) = Y_0 + S X(t) \quad [21]$$

The salt flux expression Eq. [13] can be rearranged to obtain

$$J_s(t) / (\bar{c}(t) J_v(t)) = (1 - \sigma) + (-\omega) (\Delta \Pi(t) / (\bar{c}(t) J_v(t))) \quad [22]$$

or

$$Y'(t) = Y'_0 + S' X'(t) \quad [23]$$

Least square straight lines are determined for  $Y(t)$  and  $Y'(t)$ . Since  $\Delta P$  is an experimentally determined constant, the transport coefficients are obtained from

$$L_p = -Y_0 / \Delta P \quad [24]$$

$$\sigma = -S / L_p = 1 - Y'_0 \quad [25]$$

$$\omega = -S' \quad [26]$$

The correlation coefficient,  $r$ , and the level of significance,  $p$ , were determined for all experimental data fit to a linear equation. The standard deviations of the slopes and intercepts of the straight lines were also determined (26).

Coefficients determined using the least squares straight line method are average values over all states of the membrane. Thus, these coefficients are unambiguously developed to characterize transport phenomena over a specified range of thermodynamic states.



### Experimental Method

Figure 2 contains an illustration of the transport cell utilized in these experiments. The cell consisted of two 3 in. ID conical end Kimax glass pipe elbows connected with aluminum flanges (Kimax, Owens-Illinois Incorporated, Fluid Process Systems, Vineland, New Jersey). The membrane was supported between the glass elbows by two pieces of  $0.062 \pm 0.001$  in. thick Plexiglas. Holes of diameter  $0.250 \pm 0.001$  in. were arranged in a circular array to provide an exposed membrane area of  $16.64 \pm 0.07$  cm<sup>2</sup>. These holes were aligned using two stainless steel pins placed eccentrically in the plastic sheets and external to the half-cell solutions. Neoprene gaskets were used between connected parts.

The half-cells were closed at their outer ends with  $\frac{1}{2}$  in. thick Plexiglas fastened to the glass using aluminum flanges and Neoprene gaskets. Connections to the half-cells were either nylon "Swagelok" or "Ultra-torr" fittings (Crawford Fitting Company, Solon, Ohio). Combinations of "Tygon" and polyethylene tubing (Norton Plastics and Synthetics, Akron, Ohio) were used to connect conductivity cells, pumps, and devices for volume measurement to the half-cells.

Thermometers accurate to  $\pm 0.01^\circ\text{C}$  were placed in each half-cell (Model No. 41235, Brooklyn Thermometer Company, Farmingdale, New York). Temperature regulation was accomplished in two steps. First, the entire transport assembly was enclosed in a plywood box with the temperature maintained to  $\pm 0.1^\circ\text{C}$  using an air temperature controller (Yellow Springs Instrument Company, Yellow Springs, Ohio). Second, the glass transport cell was placed inside a water bath. The bath temperature was regulated to  $\pm 0.02^\circ\text{C}$  by a water

circulator-temperature controller (Model K-2/RD, Brinkmann Instrument Company, Westbury, New York). In all experiments, the temperature in each half-cell was maintained to  $\pm 0.04^\circ\text{C}$ .

Concentration polarization at each membrane-solution interface was mitigated by two means. First, internal  $\frac{1}{2}$  in. egg shaped Teflon coated magnets (Bel Art, Pequannock, New Jersey), directly next to each side of the membrane, were driven at 500 rpm by two external magnets directly under the cell. The external magnets were controlled by an a.c.-d.c. series motor (Model 2M057, Dayton Electric Manufacturing Company, Chicago, Illinois) run off of a variable voltage regulator (Superior Electric Company, Bristol, Connecticut) and synchronized using a gear train assembly. The second means of stirring the solution in each half-cell was provided by aiming the output of each circulating pump (Micropump Corporation, Concord, California) directly at the center of the membrane. The circulating pumps were magnet drive gear pumps. Pump heads were specially manufactured entirely from plastic components. The circulation rate of each pump, about 1 liter/min was controlled by a "Variac" voltage regulator (General Radio Company, Concord, Massachusetts).

Solution salt concentrations of NaCl were monitored using conductivity cells (Model JD20, Beckman Instruments Company, Cedar Grove, New York). The solution resistance in each half-cell was measured using an impedance comparator (Model 1654, General Radio Company, Concord, Massachusetts) and a standard decade resistance box (Model 1433-G, General Radio Company, Concord, Massachusetts). Conductivity cell constants were determined to  $\pm 0.1\%$  using 0.1000M NaCl placed in the transport cell. In this manner, salt concentrations were measured in each half-cell with an accuracy of  $\pm 0.1\%$ , reproducibility of  $\pm 0.04\%$ , and sensitivity of 0.003% change in concentration.

Corrections for resistance changes due to temperature variations within the transport cell were obtained by establishing  $25^\circ\text{C}$  as a reference temperature. All resistance readings were corrected to  $25^\circ\text{C}$  using the expression

$$R_{25^\circ\text{C}} = R_T(1 + \beta(T - 25^\circ\text{C})) \quad [27]$$

where  $R_T$  was the actual resistance reading at temperature  $T$ . The temperature coefficient  $\beta$  was determined with data from the International Critical Tables (27). Concentration changes in the course of an experiment were calculated by linear extrapolation of conductivity-concentration data (27).

Volume measurement in the low pressure half-cell was made by allowing overflow into a stoppered glass weighing bottle. The weighing bottle was vented using a hypodermic needle to relieve pressure due to volume changes in the bottle and to prevent evaporation of the solution in the bottle. Weight changes measured to  $\pm 0.2$  mg were converted to volume changes in the half-cell using the known density of the solutions (27). On the high pressure side, volume changes were measured with a 10 ml Mohr pipette graduated in intervals of 0.1 ml and calibrated to  $\pm 0.01$  ml.

An estimate of the rate of solution loss of each half-cell was made prior to each experiment. Typical leak rates were  $3 \mu\text{l/hr}$ . The measured leak rates were used to correct the experimental volume and salt transport measurements.

Hydrostatic pressures were measured by a Bourdon tube-type pressure gauge with 2000 Torr full scale deflection (Model CMM-8 1/2, Dresser Industries, Newtown, Connecticut) with an accuracy of  $\pm 2$  Torr, reproducibility of  $\pm 0.4$  Torr, and sensitivity of 0.2 Torr. An empty 5 liter gas storage bottle attached to the pressure system served as ballast. The pressure system

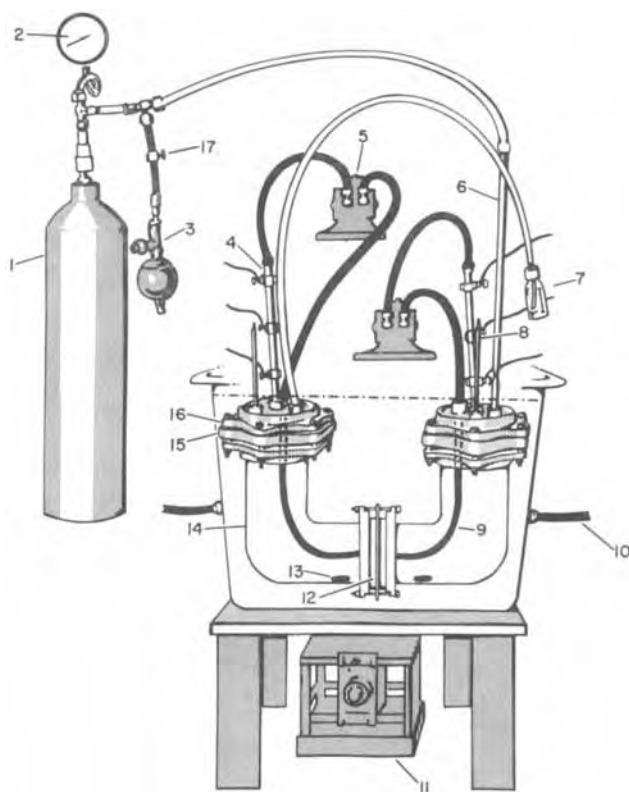


Fig. 2. Schematic of the experimental transport apparatus. 1, pressure ballast tank; 2, pressure gauge; 3, pressure relief port; 4, conductivity cell; 5, circulating pump; 6, Mohr pipette; 7, weighing bottle; 8, mercury thermometer; 9,  $\frac{1}{8}$  in. ID polyethylene tubing-to pump outlet; 10, connection to bath circulator-temperature controller; 11, motor driving internal magnets; 12, membrane support; 13, internal Teflon-coated magnets; 14, 3 in. conical end glass elbows-cell body; 15,  $\frac{1}{2}$  in. Plexiglas-cell top; 16, aluminum flanges; 17, shut-off valve for pressure system.

was attached to the pipette used for volume measurement in the high pressure half-cell.

An injection port was designed for each half-cell using an "Ultra-torr" fitting made for  $\frac{3}{8}$  in. OD tubing. The O-ring normally used in the fitting was replaced by a disk of soft natural rubber through which a hypodermic needle could be inserted to add or remove solution.

Each experiment is initiated by measuring conductivity cell constants and solution leak rates. Appropriate amounts of solutions are added to each half-cell to obtain starting solute concentrations. With the desired hydrostatic pressure applied, the system is allowed to come to mechanical equilibrium for 24 hr before taking the first readings of the experiment. Each data point taken requires reading temperature, volume, and solution resistance of each half-cell. These readings are accomplished without physically disturbing the conditions of the experiment.

### Results

In each experimental trial, initial osmotic (NaCl) and hydrostatic pressure differences were first established across the membrane. As each experiment proceeded, the hydrostatic pressure was maintained constant while the osmotic pressure difference decreased with time. The experiments were primarily designed such that the net volume flux was initially in the opposite direction to the salt flux, then zero, and finally in the same direction as the salt flux. This sequence was a result of the decaying transmembrane concentration difference.

The low pressure half-cell, in which volume measurements were obtained using the weighing bottle, gave the most precise volume measurements. Volume fluxes were calculated from data taken from this half-cell. The volume data on the high pressure side was used as an internal check on the volume data taken from the low pressure half-cell. Experiments are not reported where the solute and solvent mass balances are not within 3%. Less than 20% of the experimental trials were discarded.

Figures 3 through 7 depict results from a single, typical experiment. Data were collected over a time span of almost eight days. Figure 3 shows the time-dependent half-cell concentrations and their polynomial fit. The data points shown are significantly larger than the actual experimental imprecision. For this transport apparatus, the half-cell volumes are approximately equal ( $\approx 1200$  ml); thus, the concentration curves produced are very nearly mirror images of each other. This experimental design was developed to hold  $\bar{c}$  as constant as possible, as shown in Fig. 3. In this manner, the concentration-dependent character of the transport coefficients should be kept to a minimum during a single experiment, but concentration dependence may be examined by choosing a series of average concentrations over which to evaluate the coefficients.

Figure 4 contains experimental data and polynomial fits for the time-dependent salt and volume transport in a single experiment. The slopes of these curves are equal to the fluxes through the membrane at any time  $t$  during the experiment. From the volume transport curve in Fig. 4 and the sign conventions previously assumed for chemical fluxes in the transport system, the net volume flux is first into the high pressure half-cell ( $J_v > 0$ ), then zero, and finally into the low pressure half-cell ( $J_v < 0$ ). From these data, individual sets of transport coefficients can be obtained from the zero volume flux method (ZVFM) and from the least squares method (LSM) of data analysis. Transport coefficients for the experiment shown in Fig. 3 through 7 are given in Table I under experiment 128.

The reflection coefficient from the solute flux expression was not calculated for these experiments. The sensitivity in concentration measurement necessary to

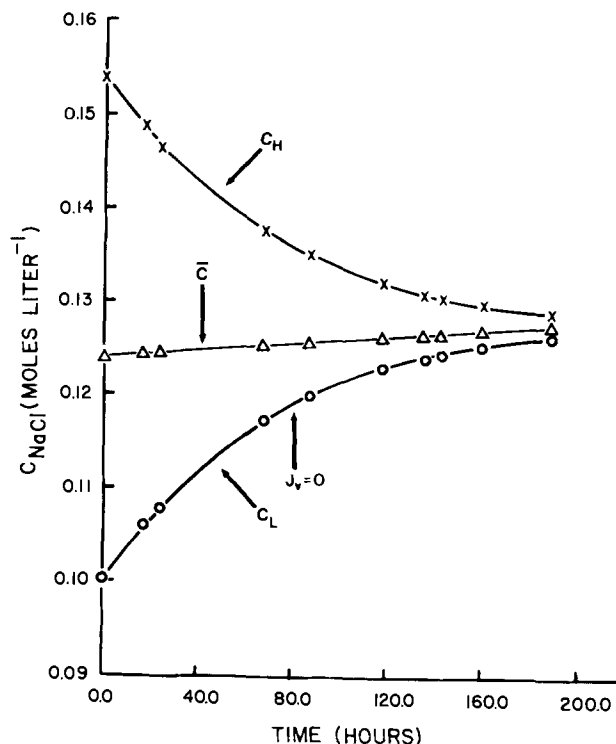


Fig. 3. Experimental half-cell salt concentrations, logarithmic average salt concentration, and polynomial curve fit of salt concentration in each half-cell. Data points are shown significantly larger than experimental imprecision for reasons of clarity. Not all experimental points shown. Experiment 128.

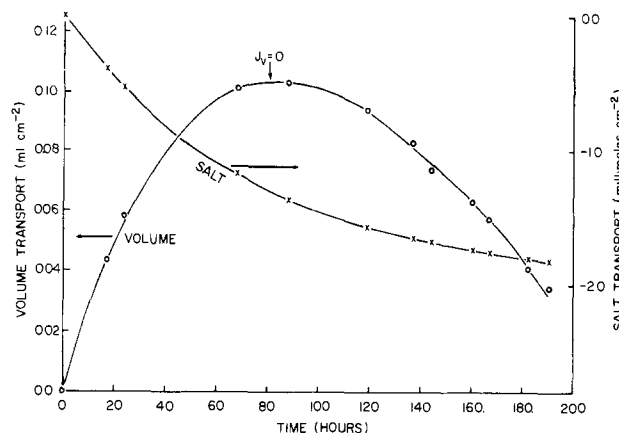


Fig. 4. Experimental salt and volume transport profiles and polynomial curve fits to these data. Not all experimental points shown. Experiment 128.

determine  $\sigma$ , from Eq. [13], accurately is 0.002% change in salt concentration per hour. The smallest sensitivity obtainable with our experimental apparatus was determined to be near 0.04% change in salt concentration per hour. Consequently, the reflection coefficients reported for the least squares method were obtained solely from the volume flux equation.

**Linearity.**—Figures 5 and 6 are plots of the linear forms of the transport Eq. [20] and [22]. The correlation coefficients,  $r$ , for the linearized solute and volume fluxes are always greater than 0.9909 in absolute magnitude. This high degree of linearity demonstrates the validity of assuming the transport coefficients to be independent of solution concentration during each experiment, at least so long as  $\bar{c}$  is maintained nearly constant.

**Accuracy.**—Reporting the accuracy of the transport coefficient matrix is complicated by the fact that the

Table I. Results of experiments performed using the transport apparatus described

Expt. No.	$\bar{c}(t) \times 10^4$ (mole-cm <sup>-3</sup> )	$L_p \times 10^6$ (cm-sec <sup>-1</sup> -atm <sup>-1</sup> )		$\omega \times 10^8$ (mole-cm <sup>-2</sup> -sec <sup>-1</sup> -atm <sup>-1</sup> )		$\sigma$ (dimensionless)		$\Delta P$ (Torr)	Initial $\Delta c = c^* - c'$		Membrane sample No.
		ZVFM	LSM	ZVFM	LSM	ZVFM	LSM		$c^*$ (M)	$c'$ (M)	
137	0.0		1.18 ± 0.01		3.24 ± 0.13		0.043 ± 0.002	125	0.0	0.0	(2) cellophane
133	0.22	1.25 ± 0.25	1.24 ± 0.05	2.97 ± 0.12	2.97 ± 0.01	0.039 ± 0.002	0.042 ± 0.003	25	0.0351	0.0086	(1) cellophane
132	0.45	1.31 ± 0.22	1.35 ± 0.05	3.04 ± 0.04	3.04 ± 0.01	0.045 ± 0.002	0.042 ± 0.003	25	0.0589	0.0321	(1) cellophane
134	0.53		1.28 ± 0.05	3.30 ± 0.01	3.30 ± 0.01	0.046 ± 0.001	0.046 ± 0.001	25	0.0298	0.0780	(1) cellophane
128	1.26	1.04 ± 0.06	1.08 ± 0.02	3.46 ± 0.14	3.46 ± 0.01	0.040 ± 0.002	0.044 ± 0.001	25	0.1540	0.1002	(1) cellophane
140	3.18	1.03 ± 0.07	1.06 ± 0.02	3.16 ± 0.13	3.16 ± 0.01	0.037 ± 0.002	0.038 ± 0.002	125	0.4359	0.2002	(3) cellophane
130	3.30	1.09 ± 0.15	1.15 ± 0.04	2.78 ± 0.11	2.78 ± 0.01	0.040 ± 0.002	0.037 ± 0.002	25	0.345	0.3167	(1) cellophane
139	3.58	1.18 ± 0.06	1.13 ± 0.03	1.54 ± 0.06	1.54 ± 0.01	0.47 ± 0.02	0.47 ± 0.01	125	0.6054	0.1024	(3) cellophane
146	1.20	0.31 ± 0.01	0.30 ± 0.01					250	0.1575	0.0868	(2999) mosaic

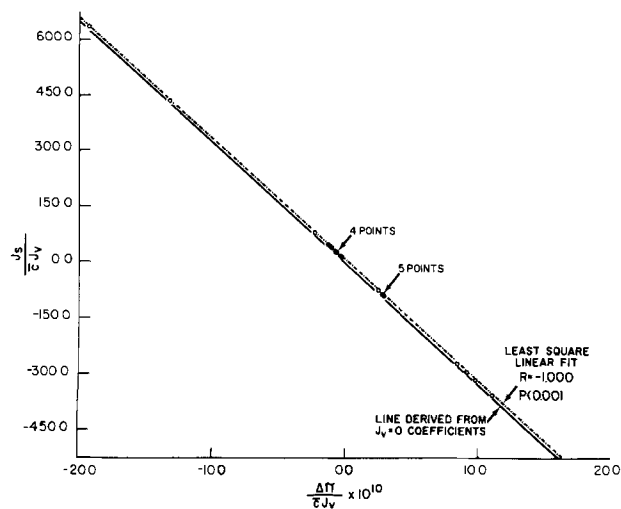


Fig. 5. Linearization of the solute flux equation. Experimental data are fit to a least squares straight line to produce the LSM transport coefficients. ZVFM produces coefficients which can reproduce the linear curve within experimental accuracy. Separation between lines is larger than actual for clarity. Experiment 128.

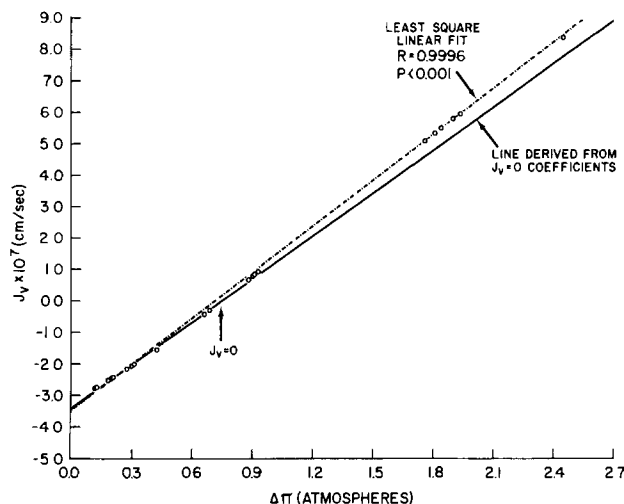


Fig. 6. Linearization of the volume flux equation. Experimental data are fit to a least squares straight line to produce the LSM transport coefficients. ZVFM produces coefficients which are less accurate at high  $\Delta\Pi$  as a result of concentration polarization. Experiment 128.

coefficients are arrived at through an averaging process. In these experiments, accuracy is a composite of experimental imprecision and standard deviation over a set of experimental points. In the discussion, we shall propose a method of reporting coefficients which will alleviate this problem. The method of obtaining the standard deviation of the transport coefficients was outlined under analytical methods and the results are reported in Table I.

Theoretically, the LSM is intrinsically more accurate than the ZVFM. In order to determine the zero volume flux point, several data points must be included in the region near  $J_v = 0$ . However, as  $J_v \rightarrow 0$ , the precision of the volume flux measurement goes to zero. In the ZVFM, this greater imprecision in the volume flux is transmitted to the coefficients, calculation of two of which are directly based on determination of the time when  $J_v = 0$ . LSM avoids this problem by averaging the transport coefficients over all experimental points. As indicated in Table I, the standard deviations for  $\omega$  and  $L_p$  obtained from the least squares method are significantly less than those calculated for the zero

Table II. Reproducibility of the transport coefficient matrix.  
Each series of experiments has nearly the same value of  $\bar{c}$ .

Expt. No.	$L_p(\text{cm-sec}^{-1}\text{-atm}^{-1}) \times 10^5$		$\omega(\text{moles-cm}^{-2}\text{-sec}^{-1}\text{-atm}^{-1}) \times 10^9$		$\sigma(\text{dimensionless})$	
	ZVFM	LSM	ZVFM	LSM	ZVFM	LSM
132, 133, 134	$1.28 \pm 0.04$ ( $\pm 3.3\%$ )	$1.29 \pm 0.06$ ( $\pm 4.3\%$ )	$3.11 \pm 0.13$ ( $\pm 6.1\%$ )	$3.08 \pm 0.14$ ( $\pm 4.6\%$ )	$0.041 \pm 0.003$ ( $\pm 6.9\%$ )	$0.043 \pm 0.002$ ( $\pm 5.3\%$ )
Average over-all values	$1.29 \pm 0.05$ ( $\pm 4.0\%$ )		$3.09 \pm 0.14$ ( $\pm 4.4\%$ )		$0.042 \pm 0.003$ ( $\pm 5.9\%$ )	
Average reproducibility for a coefficient matrix is 4.8%.						
128, 130	$1.07 \pm 0.04$ ( $\pm 3.3\%$ )	$1.11 \pm 0.06$ ( $\pm 5.3\%$ )	$3.23 \pm 0.10$ ( $\pm 3.1\%$ )	$3.23 \pm 0.10$ ( $\pm 3.1\%$ )	$0.043 \pm 0.004$ ( $\pm 8.3\%$ )	$0.042 \pm 0.006$ ( $\pm 13.5\%$ )
Average over-all values	$1.09 \pm 0.05$ ( $\pm 4.4\%$ )		$3.23 \pm 0.08$ ( $\pm 2.5\%$ )		$0.042 \pm 0.004$ ( $\pm 9.1\%$ )	
Average reproducibility for a coefficient matrix is 5.3%.						

volume flux method. These methods apparently have about equal accuracy for determining  $\sigma$ .

**Reproducibility.**—To determine reproducibility, sets of experiments were run without altering  $\bar{c}$  significantly. In Table II, two groups of experiments are shown. For each group,  $\bar{c}$  differs by nearly an order of magnitude. All of the experiments in Table II used the same membrane, without removing it from the membrane holder.

Reproducibility of the transport coefficients is slightly larger than experimental imprecision. The larger deviation for  $\sigma$  in experiments 128 and 130 was compensated for in later experiments by employing a more precise pressure gauge, as listed in experimental methods. For each average solute concentration, the set of coefficients has an average reproducibility of about 5%. It appears that both analytical methods, ZVFM and LSM, have about equal average reproducibility.

**Reliability.**—The experimental solute and volume fluxes, as well as curves calculated from the transport coefficients determined by both analytical methods, are shown in Fig. 6 and 7. It is not surprising that the LSM develops a line which follows the volume flux more closely than the ZVFM does, since the least squares coefficients are obtained directly from the  $J_v$  vs.  $\Delta\Pi$  graph. Any effect of concentration polarization on  $L_p$  and  $\sigma$  is incorporated directly into the LSM coefficients. For the zero volume flux method,  $J_v$  tapers off at large values of  $\Delta\Pi$  because the effect of concentration polarization is to decrease the actual osmotic pressure difference across the membrane. When  $\Delta\Pi$  is small, the two analytical methods give essentially equal values of  $J_v$ . Even when  $\Delta\Pi$  is at its maximum,

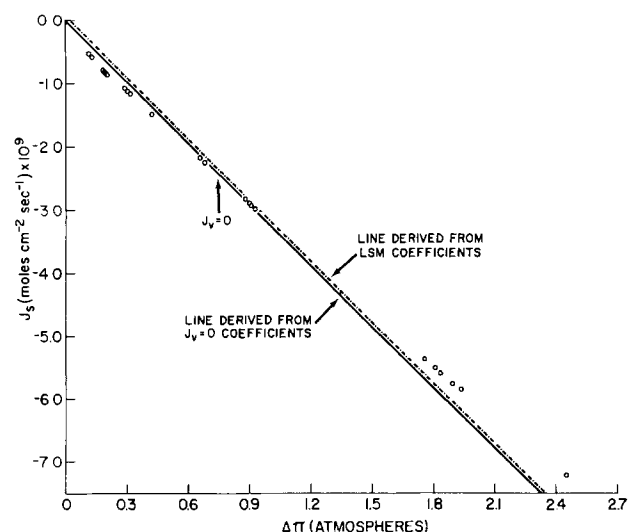


Fig. 7. Experimental data and predicted solute fluxes for both analytical methods. Separation between calculated curves is larger than actual for clarity. Experiment 128.

there is at most a 6% difference between the two calculated fluxes.

Figure 7 shows the experimental and calculated solute fluxes over the range of osmotic pressures in a single experiment. Initially,  $J_s$  and  $J_v$  are in opposite directions, in which case concentration polarization would tend to decrease  $\Delta\Pi$  across the membrane and  $J_s$  is smaller than expected. The data points and calculated fluxes cross in the region where  $J_v = 0$ , where concentration polarization is minimized. Toward the end of the experiment, the net volume and solute fluxes are in the same direction. At this point, the effect of concentration polarization depends on the concentration of solution permeating the membrane, given by  $J_s/J_v$ . In these experiments,  $J_v$  was small and the solution concentration was higher than that of either half-cell solution. The boundary layer next to the membrane on the high hydrostatic pressure, high concentration side decreased in salt concentration whereas the boundary layer on the low hydrostatic pressure, low concentration side increased in concentration. The transmembrane osmotic pressure difference, induced solely by concentration polarization, tends to drive water in the same direction as the hydrostatic pressure difference and the volume flux is increased over that expected from  $\Delta P$  and  $\Delta\Pi$  alone. In turn, the experimental solute flux will be larger than predicted from the experimental data.

Since the least squares method averages the coefficients over both positive and negative  $J_v$ , the effect of concentration polarization is cancelled out to some extent. This is indicated by the fact that the zero volume flux method, where concentration polarization is least, develops essentially the same value transport coefficients as the least squares method of analysis.

**Ranges of experimental variables and membrane types.**—The apparatus was designed to measure, within 0.04%, a range of concentrations from  $2 \times 10^{-4}$  to 3M NaCl. The hydrostatic pressure difference across the membrane can be varied from 0 to 2.6 atm. Thus, a range of thermodynamic forces can be produced which is sufficiently large that any type of flat sheet membrane sample can be characterized.

Table I lists the transport coefficients for two extremes in membrane composition and osmotic pressures. Experiments 128-140 characterized a hydrophilic, nonionic cellophane membrane (No. 70160-3, 3-7/16 flat cellophane tubing, Central Scientific Company, Chicago, Illinois) with osmotic pressures from 0 to 22.5 atm. Experiment 146 characterizes a sample of a hydrophobic, ionic mosaic membrane. This particular membrane is a mosaic of anionic and cationic patches; however, the anionic regions dominate the over-all character of the membrane (28), with  $t_+ \approx 0.1$ , and the reflection coefficient is positive.

## Discussion

This paper has presented a rather complete methodology for obtaining very reliable and complete

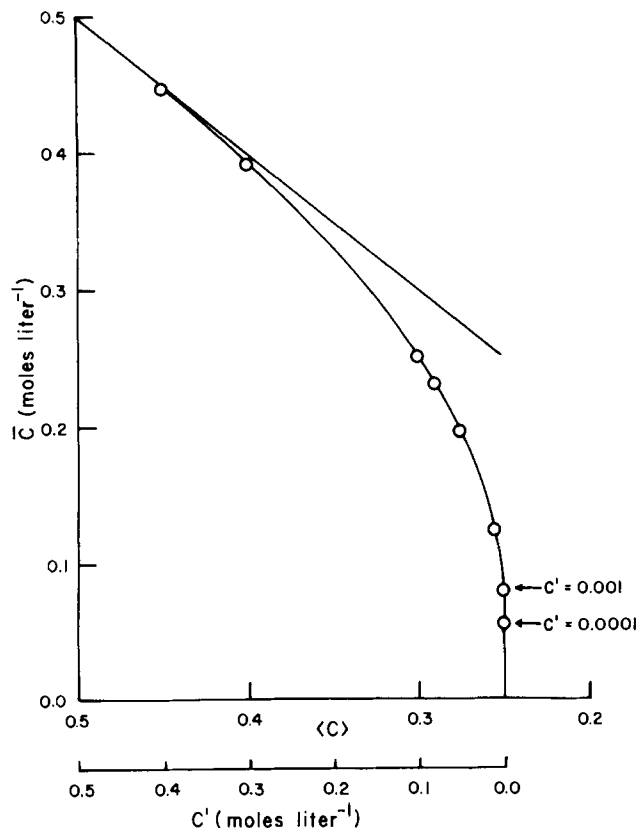


Fig. 8. Logarithmic and arithmetic average salt concentrations as the concentration in one half-cell approaches zero. Logarithmic average,  $\bar{c}$ , and arithmetic average,  $\langle c \rangle = (c' + c'')/2$ .  $c'' = 0.5M$ . Upper line indicates  $\bar{c}$  plotted numerically equal to  $\langle c \rangle$ .

characterization of transport coefficients where a single solute and solvent permeate a synthetic membrane. It is now appropriate to address ourselves to the five problems stated in the beginning.

It is clear that the problem of linearity of the macroscopic flux equations is nearly resolved, not by methodology but by happenstance. The coefficient matrix proposed by Staverman produced a set of coefficients which are nearly independent of concentration so long as the average concentration,  $\bar{c}$ , is maintained constant. However, the transport coefficients are very dependent on hydrostatic pressure differences due to stretching of the membrane matrix (29, 30). The transformation of the practical coefficients ( $L_p$ ,  $\sigma$ ,  $\omega$ ) into the conductance coefficients ( $L_{11}$ ,  $L_{12}$ ,  $L_{22}$ ) involves  $\bar{c}$ . To the extent that  $\bar{c}$  changes during the course of an experiment, so must the transport coefficients be concentration dependent. Since the conductance coefficients are simply linear combinations of  $L_p$ ,  $\sigma$ , and  $\omega$  with  $\bar{c}$ , constructing experiments such that  $\bar{c}$  is constant ensures that the conductance coefficient matrix will not be concentration dependent.

There is an irregularity in  $\bar{c}$  that should not be overlooked.  $\bar{c}$  is close to the arithmetic mean of the half-cell solution concentrations only when  $\Delta c$  is small.

Figure 8 is a plot of  $\bar{c}$  vs. the arithmetic mean concentration,  $\langle c \rangle$ . As the concentration on one side of the membrane becomes small, the chemical potential tends toward infinity and  $\bar{c}$  goes to zero. This would indicate, from Eq. [13], that convective transport would go to zero also. Zelman's derivation (8) of  $\sigma$  in terms of the conductance coefficients shows that  $\sigma$  contains a  $\bar{c}$  term which cancels  $\bar{c}$  in the solute flux equation. The complete term  $\bar{c}(1 - \sigma)J_v$  is really independent of  $\bar{c}$  except for indirect dependence of the  $L$  coefficients on concentration. Values of  $\sigma$  should not be tabulated without recognizing this special variance of  $\sigma$  with  $\bar{c}$ .

Another problem involved proper averaging of the coefficients over the various states of the membrane-solution system necessarily produced to obtain sufficient data to evaluate the transport coefficients. Both of the analytical methods, linearization of the transport equations leading to the least squares straight line method and the zero volume flux method, are "natural" extensions of the mathematical representation of the flux equations. If further justification be necessary, it must be noted that the coefficients obtained from these methods can be used to reproduce the measured fluxes within experimental reproducibility.

The problem of ambiguities resulting from data obtained from separate experiments or multiple experimental cells was resolved by engineering a single apparatus from which sufficient data would be obtained to determine all of the coefficients from a single experiment.

The final, and perhaps most difficult, problem was that of concentration polarization and the ubiquitous boundary layer. In as much as no experimental means can remove the boundary layer, and the solute concentration within the boundary layer is a strong function of  $J_s/J_v$ , and the purpose of developing transport coefficients is to be able to evaluate  $J_s$  and  $J_v$  over extended ranges of thermodynamic forces, it should be clear that a more meaningful system for reporting uncertainties in the transport coefficients would be desirable. What is important to an engineer is how accurately a coefficient matrix can predict the solute and volume fluxes over a particular range of thermodynamic forces. A simple, yet adequate representation of accuracy is the standard deviation of the experimental fluxes from the calculated values. This quantity can be called the "reliability coefficient,"  $R_J$ , and is given by

$$R_J = \left( \sum_{i=1}^N (J_{ic} - J_{ie})^2 / (N - 1) \right)^{1/2} \quad [28]$$

where  $J_{ic}$  is the calculated flux of species  $i$  and  $J_{ie}$  is the experimental flux. If each report would characterize its coefficients both in experimental accuracy (Table I) and the reliability in reproducing the measured fluxes over a range of thermodynamic variables (Table III), the usefulness of reported values would be enhanced. Note that the reliability index,  $R_J$ , in Table III indicates that the uncertainty in the calculated solute flux can be much greater than that indicated from the accuracy of the transport coefficients as given in Table I, depending on the magnitude of the flux

Table III. Reliability coefficients,  $R_J$ , for typical experimental trials from Table I

Expt. No.	$L_p$ (cm-sec <sup>-1</sup> -atm <sup>-1</sup> )	$\omega$ (moles-cm <sup>-2</sup> -sec <sup>-1</sup> -atm <sup>-1</sup> )	$\sigma$	$\Delta c = c''(M) - c'(M)$	$\Delta P$ (Torr)	$R_J$	
						$J_v$ (cm-sec <sup>-1</sup> )	$J_s$ (moles-cm <sup>-2</sup> -sec <sup>-1</sup> )
128	$1.06 \times 10^{-5}$	$3.30 \times 10^{-9}$	0.046	$\Delta c_{1n} = 0.1540 - 0.1002$ $\Delta c_{1r} = 0.1285 - 0.1260$	25	$1.0 \times 10^{-9}$	$2.5 \times 10^{-10}$
146	$3.01 \times 10^{-9}$	$1.54 \times 10^{-9}$	0.47	$\Delta c_{1n} = 0.1571 - 0.0868$ $\Delta c_{1r} = 0.1235 - 0.1210$	250	$6.6 \times 10^{-9}$	$1.0 \times 10^{-10}$

involved. This reliability coefficient takes into account all the errors of evaluation, both experimental and analytical, whereas the accuracy of each coefficient represents errors specific to that coefficient.

Accurate representation of the experimental characterization of membrane transport coefficients requires several types of indices by which to judge the value of the reported coefficient matrix. Essential parameters are accuracy and reproducibility, but more importantly the newly defined reliability.

### Acknowledgment

This research was supported by Public Health Service Grant AM 16802 and AM 19198. One of the authors (A. Z.) acknowledges support from MBS grant No. 5506 RRO 8037. Services rendered by Mr. George Braun, Mrs. Nan Braun, and the Meharry Medical College Computer Center, Nashville, Tennessee are appreciated. Mosaic membranes were prepared under U.S. Department of Interior, Office of Water Research and Technology, Contract No. 14-30-2747. Illustrations were prepared by Mr. George Card, Medical Illustrator, Meharry Medical College.

Manuscript submitted July 23, 1975; revised manuscript received ca. Feb. 6, 1976. This was Paper 342 presented at the Toronto, Canada, Meeting of the Society, May 11-16, 1975.

Any discussion of this paper will appear in a Discussion Section to be published in the June 1977 JOURNAL. All discussions for the June 1977 Discussion Section should be submitted by Feb. 1, 1977.

Publication costs of this article were partially assisted by Rensselaer Polytechnic Institute.

### LIST OF SYMBOLS

$A$	exposed membrane area, $\text{cm}^2$
$\bar{c}$	solute concentration, $\text{mole}\cdot\text{cm}^{-3}$
$\bar{c}$	logarithmic average solute concentration across the membrane, $\text{mole}\cdot\text{cm}^{-3}$
$\rightarrow$	
$J_i$	the vector molar flux of component $i$ , $\text{mole}\cdot\text{cm}^{-2}\cdot\text{sec}^{-1}$
$J_s$	the scalar molar salt flux, $\text{mole}\cdot\text{cm}^{-2}\cdot\text{sec}^{-1}$
$J_v$	the volume flux, $\text{cm}\cdot\text{sec}^{-1}$
$L_p$	hydraulic conductivity coefficient, $\text{cm}\cdot\text{sec}^{-1}\cdot\text{atm}^{-1}$
$L_{ik}$	linear phenomenological coefficient, general units of flux per unit thermodynamic force
$n_T', n_T''$	moles of salt transported across the membrane in an experiment, mole
$m$	molality, mole/kg water
$N$	number of experimental data points
$p$	level of significance of a linear fit of experimental data, dimensionless
$r$	correlation coefficient for linear regression analysis, dimensionless
$R$	molar gas constant, $\text{cm}^3\cdot\text{atm}\cdot\text{mole}^{-1}\cdot\text{K}^{-1}$
$R_j$	reliability coefficient; general units of flux, Eq. [28]
$R_T$	solution resistance recorded at temperature $T$ , ohms
$R_{25^\circ\text{C}}$	solution resistance corrected to $25^\circ\text{C}$ , ohms
$S, S'$	slopes of general linear equations, Eq. [21] and [23]
$t$	time sec
$T$	temperature, $^\circ\text{C}$
$v_w$	partial molal volume of water, $\text{cm}^3/\text{mole}$
$V$	solution volume in one half-cell, $\text{cm}^3$
$X, X'$	independent variables for general linear equations, Eq. [21] and [23]
$Y, Y'$	dependent variables for general linear equations, Eq. [21] and [23]
$Y_0, Y'_0$	intercepts of general linear equations, Eq. [21] and [23]

$\beta$	fractional change in solution resistance with temperature, $^\circ\text{C}^{-1}$
$\Delta$	denotes difference, taken right minus left
$\gamma_{\pm}$	mean molal activity coefficient, dimensionless
$\mu_j$	total chemical potential of species $j$ , $\text{cm}^3\cdot\text{atm}\cdot\text{mole}^{-1}$
$\mu_j^c$	concentration part of the electrochemical potential, $\text{cm}^3\cdot\text{atm}\cdot\text{mole}^{-1}$
$\Pi$	osmotic pressure, atm
$\sigma$	reflection coefficient, dimensionless
$\omega$	solute permeability at zero net volume flux, $\text{mole}\cdot\text{cm}^{-2}\cdot\text{sec}^{-1}\cdot\text{atm}^{-1}$
$\Phi$	molal osmotic coefficient, dimensionless

### REFERENCES

1. A. J. Staverman, *Rec. Trav. Chim. Pays-Bas*, **70**, 344 (1951).
2. A. J. Staverman, *Trans. Faraday Soc.*, **48**, 176 (1952).
3. L. Onsager, *Phys. Rev.*, **37**, 405 (1931).
4. L. Onsager, *ibid.*, **38**, 2265 (1931).
5. A. Katchalsky and P. Curran, "Nonequilibrium Thermodynamics in Biophysics," Harvard University Press, Cambridge, Mass. (1965).
6. K. S. Cole, "Membranes, Ions, and Impulses," University of California Press, Berkeley, Calif. (1968).
7. N. Lakshminarayanaiah, "Transport Phenomena in Membranes," Academic Press, New York (1969).
8. A. Zelman, *Biophysical J.*, **12**, 414 (1972).
9. A. Zelman, J. C. T. Kwak, J. Liebovitz, and K. S. Spiegler, *Experientia Suppl.*, **18**, 679 (1971).
10. M. Demarty and E. Selegny, *Compt. Rend.*, **C276**, 1549 (1973).
11. T. G. Kaufman and E. F. Leonard, *Am. Inst. Chem. Engrs. J.*, **14**, 110 (1968).
12. P. Meares and A. H. Sutton, *J. Colloid Interface Sci.*, **28**, 118 (1968).
13. W. J. McHardy, P. Meares, A. H. Sutton, and J. F. Thain, *ibid.*, **29**, 116 (1969).
14. H. Kramer and P. Meares, *Biophysical J.*, **9**, 1006 (1969).
15. P. Meares, "Permeability and Function of Biological Membranes," North Holland Publishing Co., Amsterdam (1970).
16. D. G. Dawson and P. Meares, *J. Colloid Interface Sci.*, **33**, 117 (1970).
17. P. Meares, J. F. Thain, and D. G. Dawson, "Membranes," Vol. 1, chap. 2, Dekker Publishing Co., New York (1972).
18. T. Foley, J. Klinowski, and P. Meares, *Proc. Royal Soc. London*, **A336**, 327 (1974).
19. R. E. L. Farmer and R. I. Macey, *Biochim. Biophys. Acta.*, **196**, 53 (1970).
20. R. E. L. Farmer and R. I. Macey, *ibid.*, **290**, 290 (1972).
21. R. E. L. Farmer and R. I. Macey, *ibid.*, **255**, 502 (1972).
22. S. R. deGroot and P. Mazur, "Nonequilibrium Thermodynamics," North Holland Publishing Co., Amsterdam (1962).
23. R. Schogl, *Discussions Faraday Soc.*, **21**, (1956).
24. H. L. Evans, "Luminal Boundary-Layer Theory," Addison-Wesley Publishing Co., Reading, Mass. (1968).
25. K. S. Spiegler and O. Kedem, *Desalination*, **1**, 311 (1966).
26. T. Welch, E. J. Potchen, and M. Welch, "Fundamentals of the Tracer Method," W. B. Saunders Co., Philadelphia (1972).
27. "International Critical Tables of Numerical Data, Physics, Chemistry and Technology," McGraw-Hill Book Co., Inc., New York (1933).
28. Jan C. T. Kwak, Dept. of Chemistry, Dalhousie University, Nova Scotia. Transport numbers are the courtesy of precision experiments by Dr. Kwak.
29. A. Zelman, Ph.D. Dissertation, University of California, Department of Physics, Biophysics Group, Berkeley, California (1971).
30. Richmond Tankersley, M.Sc. Thesis, University of New Orleans, Department of Chemistry, New Orleans, Louisiana (1974).

# Semiconductor Electrodes

## V. The Application of Chemically Vapor Deposited Iron Oxide Films to Photosensitized Electrolysis

Kenneth L. Hardee\* and Allen J. Bard\*\*

Department of Chemistry, The University of Texas at Austin, Austin, Texas 78712

### ABSTRACT

The preparation of polycrystalline n-type  $\text{Fe}_2\text{O}_3$  electrodes by the chemical vapor deposition (CVD) of iron oxide onto Ti and Pt substrates is reported. The behavior of these electrodes in aqueous solutions of different pH in the absence and presence of illumination is shown. Photoassisted electrolysis of water occurs at wavelengths longer than 400 nm and the current *vs.* wavelength curve for this process is compared to that of a CVD  $\text{TiO}_2$  electrode.

Recently there has been much interest in the utilization of semiconductor electrodes for solar energy conversion by the photoassisted electrolysis of water (1-4). By illuminating an n-type electrode with light energy greater than the bandgap energy, holes are produced in the valence band which, under anodic polarization, migrate to the surface where they can react with a species in solution. Thus with a suitable semiconductor electrode it is possible to oxidize water to oxygen utilizing solar energy. However, only  $\text{TiO}_2$  (1, 2, 4),  $\text{SnO}_2$  (5, 6), and  $\text{SrTiO}_3$  (7) have been shown to be capable of oxygen generation without decomposition of the electrode material. All of these materials have a large bandgap (greater than 3 eV) and thus require u.v. illumination for the reaction. Other semiconducting materials with smaller bandgaps (*e.g.*, GaAs, CdS, Si) decompose under anodic polarization and/or illumination. A nonreactive electrode which shows appreciable photocurrents at wavelengths longer than 415 nm (3.0 eV) has not been reported. Since the bulk of the solar radiation on the surface of the earth is found at longer wavelengths [only about 3% occurs in the 315-400 nm range (3, 8)], a practically useful material for solar energy conversion must be able to utilize this lower energy radiation.

We recently reported the preparation of n-type  $\text{TiO}_2$  electrodes by chemical vapor deposition (CVD) (9). We report here the preparation of iron oxide ( $\text{Fe}_2\text{O}_3$ ) electrodes by CVD and their use in the photoassisted oxidation of water at potentials less positive than those at platinum and at wavelengths longer than 400 nm. The unavailability of a single crystal of iron oxide prevented comparison of its characteristics with the CVD material, but based on our findings with CVD *vs.* single crystal  $\text{TiO}_2$ , we would expect generally similar behavior.

### Experimental

The basic experimental setup for CVD has been described (9). The vapor source was iron acetylacetonate ( $\text{Fe}(\text{C}_5\text{H}_7\text{O}_2)_3$ ) obtained from Alfa/Ventron. This was placed in a flask heated with a heating mantle. Purified nitrogen, the carrier gas, was passed over the heated compound, then through a glass tube situated approximately 1 cm above the substrate. A second line containing nitrogen which had been bubbled through heated water was attached to a side-arm on the inverted funnel over the substrate to provide a reactive atmosphere. Both Ti and Pt metal served as substrates. The Ti was cut into  $1 \times 1$  cm squares after being polished to a mirror finish. The Pt was 0.002 in. thick foil cut into suitable squares. All substrates were

cleaned in distilled water and ethanol prior to use. The substrate temperature was maintained at about 400°C, with a hot plate during CVD. The procedure used in depositing the iron oxide was as follows. A glass slide was placed on the hot plate and the nitrogen flow rate adjusted to give the desired film growth rate, determined by observing the change in interference colors. The rate of deposition did not appear to be critical and therefore no attempt was made to control this rate precisely. Typically a rate showing the formation of three sets of interference colors in 2 min was used. After the flow rate was adjusted, the desired substrate was positioned under the nozzle. When a suitable layer was deposited (usually in about 2 min), the substrate was placed in the flame of a Meeker burner for about 1 min. The substrate became almost white hot during this treatment and upon removal from the flame it was observed that the interference colors had disappeared. When cool the surface of the coated Pt had a reddish purple color, while with Ti the color was mostly gray, with some reddish patches. Several layers (between 3 and 7) were thus deposited on each substrate. With the Ti substrate some of the film flaked off of the electrode after the heat-treatment. In this case the affected portions were wiped off and deposition continued. Deposition on Pt produced no flaking problems. In fact, the best performing electrodes were made by continuing the deposition on Pt until no interference color change could be observed, indicating a fairly thick layer. The surface had a uniform steel-blue appearance. Heating produced a uniform red-purple coating. This was repeated 3-4 times. All films deposited on platinum exhibited a very low resistance, so that no vacuum treatment following CVD was used, as was necessary in the case of the  $\text{TiO}_2$  electrodes. A copper wire was attached to the back of the substrate with silver epoxy (Epoxy Products Company, New Haven, Connecticut). The electrode was then mounted in a glass tube with Apiezon wax, exposing only the oxide-coated surface to the solution.

All electrochemical measurements were performed with a PAR Model 173 potentiostat (Princeton Applied Research Corporation, Princeton, New Jersey) controlled by a PAR Model 175 universal programmer. Current-potential curves were recorded on a Model 2000 X-Y recorder (Houston Instruments, Austin, Texas). A simple H-cell with a glass frit separating working and auxiliary compartments was used. A Pyrex window allowed illumination of the working electrode. Platinum wire served as the counterelectrode and a saturated calomel electrode (SCE) was the reference electrode. All potentials are reported *vs.* SCE.

The illumination system consisted of a 450 Watt Xenon lamp (Oriental Corporation, Stamford, Connecticut).

\* Electrochemical Society Student Member.

\*\* Electrochemical Society Active Member.

Key words: photoelectrochemistry, semiconductor electrodes, solar energy, oxygen evolution.

cut) in an Oriel Model 6140 housing with an Oriel Model 6242 power supply. For current-wavelength curves, an Oriel Model 7242 grating monochromator with 12 nm band pass slits was used. The intensity of the incident light from the monochromator (in microwatts/square centimeter) was measured with a Model 550 radiometer (EG & G, Salem, Massachusetts). The intensity was normalized to the intensity at 470 nm and then used to correct the photocurrent *vs.* wavelength curves for variations in intensity with wavelength.

### Results and Discussion

Current-potential curves for  $\text{Fe}_2\text{O}_3$  films on Ti and Pt substrates in neutral unbuffered media (0.5M KCl for Ti and 0.5M  $\text{Na}_2\text{SO}_4$  for Pt) are shown in Fig. 1. Qualitatively the two curves are similar. The dark current is slightly larger with the Ti substrate electrode, possibly because of some reaction at bare Ti, since the surface had a very patchy appearance. The cathodic currents in the dark can be attributed to the reduction of dissolved oxygen and of the  $\text{Fe}_2\text{O}_3$ . When nitrogen was bubbled through the solution, the current at potentials more positive than  $-0.4\text{V}$  markedly decreased; however the currents at more negative potentials were not affected appreciably. Continued scans to potentials negative of  $-0.4\text{V}$  gradually reduced the photoresponse of the electrode. The surface became lighter in color until the coating was virtually gone.

Under illumination there is a large rise in anodic current commencing at about  $+0.2\text{V}$  *vs.* SCE, with both Pt and Ti substrates. Gas evolution appears promptly with the anodic current and is quite noticeable on the electrode surface, implying that the reaction is the photoassisted oxidation of water to produce oxygen. Prolonged illumination in an unbuffered solution at  $E = +0.800\text{V}$  results in a decrease in pH. The current rise continues with increasing positive potentials to at least  $+1.5\text{V}$  without showing the current plateau characteristic of  $\text{TiO}_2$  electrodes. However, even in the dark at *ca.*  $+1.2\text{V}$  (shifting to more negative potentials with increasing pH), the  $\text{Fe}_2\text{O}_3$ -coated

substrates exhibit a large current rise with simultaneous gas evolution. This probably represents the direct oxidation of water at these potentials as a result of tunneling through the film. A similar gas evolution and current rise is observed in the dark on CVD  $\text{TiO}_2$  electrodes, but at more positive potentials (*ca.*  $+2\text{V}$ ). Thus at  $\text{Fe}_2\text{O}_3$  the nonphotoassisted oxidation current at large positive potentials adds to the photoassisted current and thus masks the appearance of the photocurrent plateau.

There appears to be a small photocurrent beginning at about  $-0.4\text{V}$  *vs.* SCE under white light illumination with the Ti substrate. The current continues to rise gradually until the onset of the large photocurrent at  $+0.2\text{V}$ . This small photocurrent is probably due to the presence of some  $\text{TiO}_2$  formed during the heat-treatment. Evidence of this is the gray color of the surface and the flaking problems encountered during preparation. This photocurrent appears at about the same potentials as those observed with CVD  $\text{TiO}_2$  electrodes. On scan reversal from positive potentials with a Pt substrate electrode, a cathodic peak appears at about  $+0.20\text{V}$  (the shape and location of this peak vary somewhat with different electrodes). The peak shifts to negative potentials with increasing pH and does not appear on Ti substrates. This peak probably represents the reduction of adsorbed oxygen produced during the anodic scan under illumination. It does not appear in dark scans to potentials less positive than  $+1.2\text{V}$ , but is seen if an anodic scan is made to more positive potentials. It is also observed when the anodic scan is made under illumination and the light turned off during the cathodic scan. The cathodic current negative of  $0.0\text{V}$  is also increased after anodic scans with light, representing an increase in the concentration of dissolved oxygen.

The potential for the onset of the photocurrent ( $E_L$ ) shifts to more negative values with increasing pH. The current-potential curves for an  $\text{Fe}_2\text{O}_3$ -coated Pt electrode in solutions of several different pH values are shown in Fig. 2. The value of  $E_L$  varied somewhat (about  $200\text{ mV}$ ) for different electrodes.

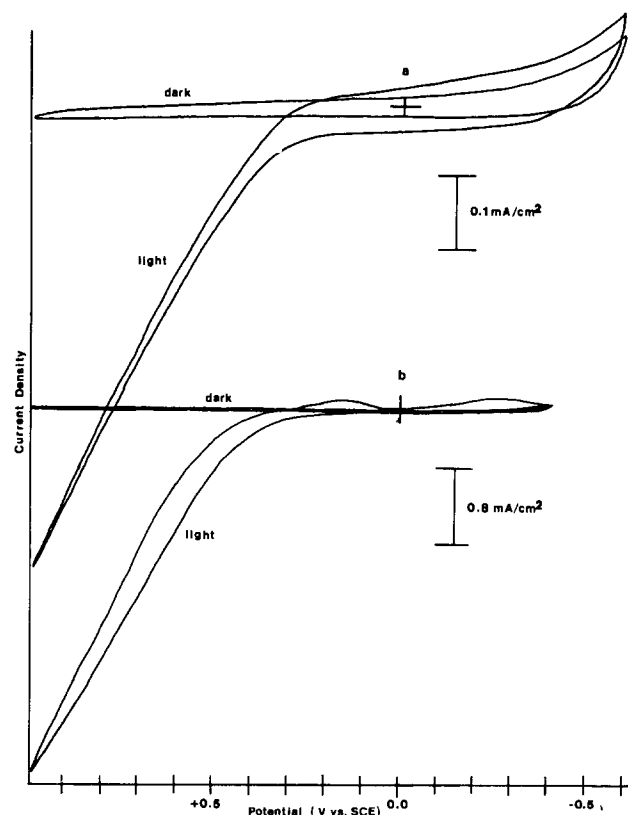


Fig. 1. Current density vs. potential for  $\text{Fe}_2\text{O}_3$  films on (a) Ti, in 0.5M KCl, and (b) Pt, 0.5M  $\text{Na}_2\text{SO}_4$ .

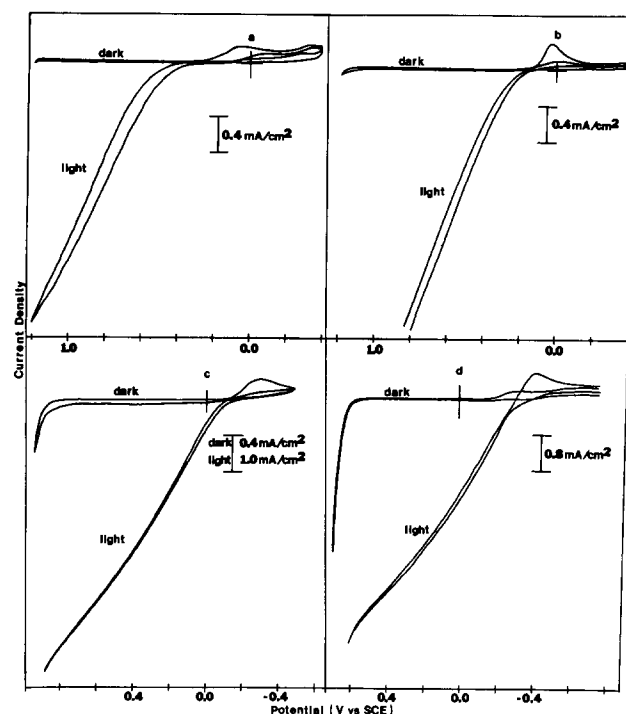


Fig. 2. Current density vs. potential for  $\text{Fe}_2\text{O}_3$ -coated Pt electrodes in 0.25M  $\text{Na}_2\text{SO}_4$  solutions buffered to pH (a) 4.50, acetate, (b) 6.70, acetate, and (c) 10.36, ammonia. Curve (d) is for 1M NaOH.



The iron oxide electrodes appeared stable at open circuit in alkaline solutions up to 1M NaOH. Acid solutions (pH less than 4) slowly dissolved the oxide coating. Continuous potential scans between +1.0 and -0.6V in alkaline solutions produced no noticeable changes in surface appearance or  $i$ - $E$  characteristics, although holding the electrode at potentials negative of -0.6V could possibly damage the electrode. There was no detectable change in behavior after holding the electrode at +0.600V at a pH of 10.4 ( $\text{NH}_4\text{Cl-NH}_3$  buffer containing 0.25M  $\text{Na}_2\text{SO}_4$ ) for 1 hr (current density, 4.7 mA/cm<sup>2</sup>); under these conditions the electrode was covered with gas bubbles. In pH 4.5 acetate buffer the  $\text{Fe}_2\text{O}_3$  film gradually dissolved during a series of scans between +1.2 and -0.6V. However if the electrode was held at +0.600V in this buffer under illumination no decrease in photocurrent was observed.

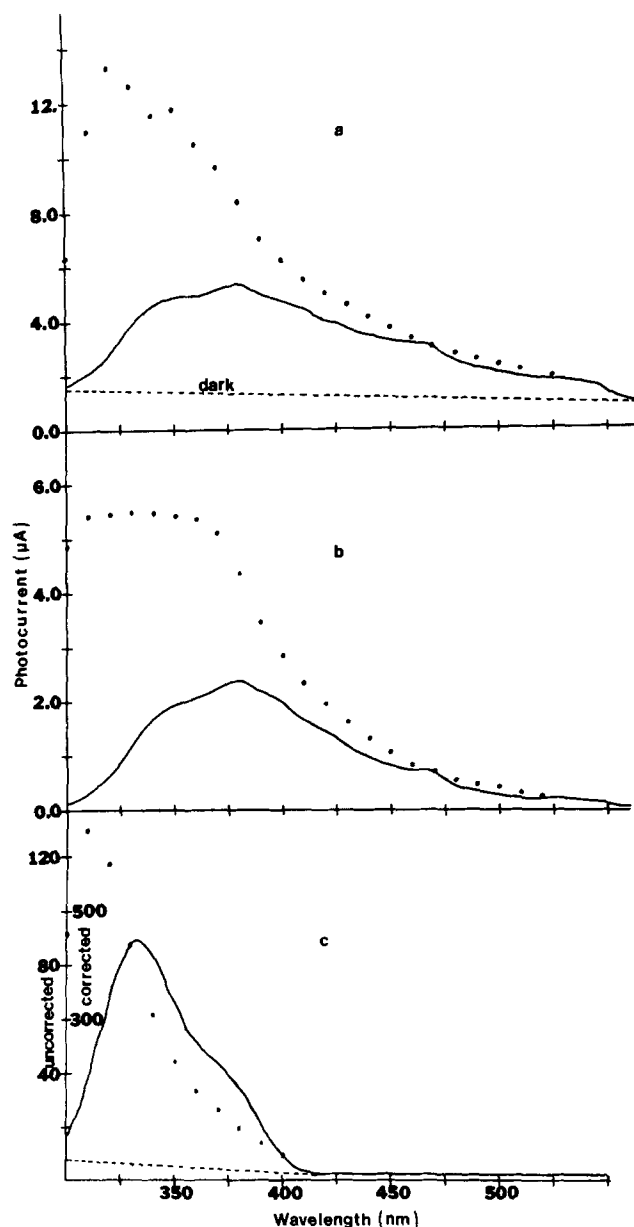


Fig. 3. Photocurrent vs. wavelength at a potential of  $E = +0.800\text{V}$  (vs. SCE) for  $\text{Fe}_2\text{O}_3$  films on (a) Ti, in 0.5M KCl, (b) Pt, in 0.5M  $\text{Na}_2\text{SO}_4$ , and (c) CVD  $\text{TiO}_2$  electrode in 0.5M KCl. Solid line is uncorrected for intensity variations; circles are the corrected curve.

On the other hand, holding it at -0.5V under the same conditions caused a rapid dissolution of the coating.

The spectral response of the  $\text{Fe}_2\text{O}_3$  electrodes at  $E = +0.800\text{V}$  is shown in Fig. 3a (Ti substrate) and 3b (Pt substrate). Figure 3c is a spectral curve of CVD  $\text{TiO}_2$  on Ti shown for comparison. Curves are given with and without corrections for lamp/monochromator output variations. The dark current for the Ti substrate decayed slowly during measurement resulting in a sloping base line. The spectral response curves for all of the  $\text{Fe}_2\text{O}_3$ -coated substrates were virtually identical in shape, indicating that the photoeffect is due to the  $\text{Fe}_2\text{O}_3$  itself. A significant portion of the total photocurrent under the curve shown (approximately 20% of corrected curve) is at wavelengths longer than 400 nm, compared to virtually zero for  $\text{TiO}_2$ . Thus the  $\text{Fe}_2\text{O}_3$  electrode could be operated at +0.400V in 1M NaOH with a yellow filter having <0.1% transmittance below 450 nm, yielding a current density of 700  $\mu\text{A}/\text{cm}^2$  with gas bubbles being observed on the surface.

The photocurrent for the iron oxide begins at about 550 nm which would correspond to the reported bandgap of  $\text{Fe}_2\text{O}_3$ , i.e., 2.2 eV (10). A coating of the iron oxide was deposited on a quartz slide and heated in flame. Although the coating was quite adherent, it showed a high resistance. An absorbance vs. wavelength curve (taken with a Cary 14 spectrophotometer) of the  $\text{Fe}_2\text{O}_3$  on quartz sample showed a steep rise in absorbance beginning at about 580 nm, with absorbance above 1.0 at 550 nm, again agreeing with the bandgap energy of  $\text{Fe}_2\text{O}_3$ .

The spectral response and reasonable stability of the iron oxide film electrode makes it suitable for use in photoelectrochemical experiments at longer wavelengths, as well as a possible electrode for the photo-assisted electrolysis of water and in photoelectrochemical solar cells (3, 11).

#### Acknowledgment

The support of this research by the National Science Foundation (MPS 74-23210) is gratefully acknowledged.

Manuscript submitted Oct. 27, 1975; revised manuscript received Feb. 9, 1976.

Any discussion of this paper will appear in a Discussion Section to be published in the June 1977 JOURNAL. All discussions for the June 1977 Discussion Section should be submitted by Feb. 1, 1977.

Publication costs of this article were partially assisted by The University of Texas at Austin.

#### REFERENCES

1. A. Fujishima, K. Honda, and S. Kikuchi, *J. Chem. Soc. Japan (Ind. Chem. Sec.)*, **72**, 108 (1969).
2. A. Fujishima, K. Kohayakawa, and K. Honda, *Bull. Chem. Soc. Japan*, **48**, 1041 (1975).
3. M. D. Archer, *J. Appl. Electrochem.*, **5**, 17 (1975).
4. M. S. Wrighton, D. S. Ginley, P. T. Wolczanski, A. B. Ellis, D. L. Morse, and A. Linz, *Proc Nat. Acad. Sci. USA*, **72**, 1518 (1975).
5. F. Möllers and R. Memming, *Ber. Bunsenges. Physik. Chem.*, **76**, 469 (1972).
6. H. Kim and H. A. Laitinen, *This Journal*, **122**, 53 (1975).
7. M. S. Wrighton, Private communication.
8. P. Moon, *J. Franklin Inst.*, **230**, 583 (1940).
9. K. L. Hardee and A. J. Bard, *This Journal*, **122**, 739 (1975).
10. W. H. Strehlow and E. L. Cook, *J. Phys. Chem. Ref. Data*, **2**, 163 (1973).
11. D. Laser and A. J. Bard, *This Journal*, **123**, 1027 (1976).

# Semiconductor Electrodes

## VI. A Photoelectrochemical Solar Cell Employing a $\text{TiO}_2$ Anode and Oxygen Cathode

Daniel Laser and Allen J. Bard\*

Department of Chemistry, The University of Texas at Austin, Austin, Texas 78712

### ABSTRACT

A photoelectrochemical cell for conversion of light to electrical energy based on the photosensitized oxidation of water at a chemically vapor deposited, thin film, n-type  $\text{TiO}_2$  anode and the reduction of oxygen at a fuel cell-type cathode is described. The effect of load resistance on the current, cell voltage, and power was studied, and quantum and power efficiencies under short-circuit conditions for monochromatic light of about 365 nm was estimated as 26% and 1-2%, respectively. Open-circuit cell voltages of 0.89V were obtained. The cell is simple to construct and is capable of continuous operation with no apparent deterioration in performance.

Photoeffects at semiconductor electrodes received renewed attention when these materials were recognized as potential candidates for use in the conversion of light to electrical and chemical energy via some electrochemical process; this subject has been reviewed and discussed recently (1, 2). Of special interest are semiconductor electrodes which do not decompose or corrode during the photoelectrochemical process (e.g., n-type  $\text{TiO}_2$ ), so that the light exclusively induces charge transfer to selected species in solution. We describe here the construction and behavior of an electrochemical photocell which produces electrical power under illumination by light of suitable spectral characteristics. Although this electrochemical cell differs in operating mechanism from the familiar solid-state solar cell, the result, conversion of light to electrical energy, is the same. The cell is based on the photosensitized oxidation of water to oxygen at a chemically vapor deposited n-type  $\text{TiO}_2$  anode and the reduction of oxygen at a fuel cell-type cathode and offers good quantum efficiency, simple construction, and continuous operation without renewal of electrolyte or electrode decomposition. Its major limitation for utilization of solar energy is its response only to the short wavelength (below 400 nm) portion of the spectrum.

### Experimental

The cell, shown schematically in Fig. 1, consisted of an aqueous solution (acidic or basic) confined between a quartz window and the cathode. The cathode was the type employed in hydrogen-oxygen fuel cells (American Cyanamid experimental fuel cell electrode, 2.5 mg Pt/cm<sup>2</sup>, deposited on a nickel-gold screen with Teflon backing). In parallel and spaced 12 cm away was fixed a bright Pt foil (0.2 mm thick) which was perforated by numerous pinholes (about 6 holes/cm<sup>2</sup>) which reduced its geometric area only slightly and which was covered on both sides with a  $\text{TiO}_2$  film produced by chemical vapor deposition (CVD) (3). The side facing the window served as the photoactive  $\text{TiO}_2$  anode with ionic conductivity from this part of solution to the oxygen electrode being accomplished through the pinholes in the foil. The  $\text{TiO}_2$  film on the other side of the membrane (facing the  $\text{O}_2$  electrode) eliminated contact between solution and bare Pt surface. The procedure for the CVD of the  $\text{TiO}_2$  film described by Hardee and Bard (3) was followed. The Pt substrate, after being punched, was cleaned in a 3:1 HCl:HNO<sub>3</sub> mixture; the film was then deposited and annealed. After about four successive coatings, each of them at the maximum thickness possible without

causing the film to peel off, the resulting film was quite thick. It had a hazy gray appearance and interference fringes could no longer be observed; the adhesion of this film to the Pt was excellent. After the CVD the  $\text{TiO}_2$  film was vacuum treated for 8 hr (750°C, 10<sup>-4</sup> Torr). This procedure converted the dielectric  $\text{TiO}_2$  film into a conductive n-type material.

Two inlets to the cell allowed the immersion of a saturated calomel reference electrode (SCE) and another Pt electrode into the cell for potentiostatic measurements. For these a Princeton Applied Research (PAR) Model 173 potentiostat was used. While operating as a galvanic cell, the voltage and current were determined with a standard resistance load connected across the cell terminals. A 450W Xenon lamp (Oriental Corporation, Stamford, Connecticut) was the light source. For spectral response and efficiency determinations an Oriel Model 7242 high intensity grating monochromator and a Model 550 (EG & G, Salem, Massachusetts) calibrated radiometer assembly were used.

### Results and Discussion

Electrochemical photocells can be classified as two distinct types (1, 2). In the first, radiation is converted into chemical energy, i.e., under illumination a normally endothermic chemical reaction will take place spontaneously or with an electrical energy input less than the reversible value for this reaction. In the second type, which is the one of interest here, no over-all chemical change occurs in the system and the absorption of light results in the generation of electrical power. Both electrochemical half-cell reactions which were

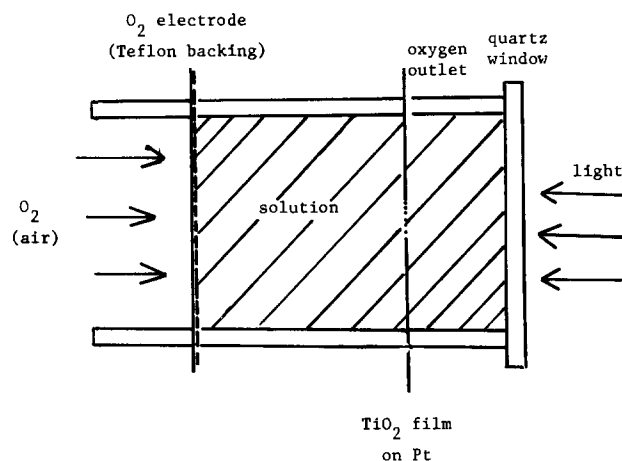
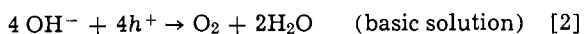
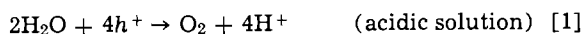


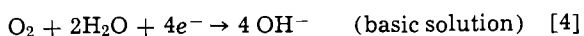
Fig. 1. Schematic representation of the n- $\text{TiO}_2$ /Pt( $\text{O}_2$ ) photoelectrochemical solar cell.

\* Electrochemical Society Active Member.  
Key words: photoelectrochemistry, semiconductors, solar cells, galvanic cells.

employed have been the subject of separate previous studies and so are not dealt with here in detail. The anode reaction was the evolution of oxygen at an illuminated n-type  $\text{TiO}_2$  electrode. This reaction has been studied at both single crystal (4-7) and thin film (3) materials. With the omission of mechanistic details oxygen evolution from aqueous solution at an illuminated  $\text{TiO}_2$  electrode can be represented as



The holes ( $h^+$ ) are produced by the appropriate band-gap illumination and the efficiency of the process depends on the electrical state of the semiconductor electrode. A sufficiently positive bias will result in an extended space charge region in which the recombination of the photogenerated holes with electrons ( $e^-$ ) (the majority carrier) is minimized and an efficient separation of the photoproduced  $h^+/e^-$  pairs occurs, with the holes drifting to the electrode surface. The photo-oxidation of water takes place at a "negative overpotential" (8), i.e., at a less positive electrode potential than the reversible one (thermodynamically independent of electrode composition), thereby allowing the utilization of the light energy. The cathode reaction, the well-known reduction of oxygen at a Pt catalyst fuel cell electrode



is just the reverse of the anodic reaction, except that electrons participate in it instead of holes.

The behavior of the complete cell can be predicted from the individual current-potential curves for each electrode measured potentiostatically against a reference electrode; typical results for 5M NaOH and 5M  $\text{HClO}_4$  solutions are given in Fig. 2. If the electrodes are shorted together (load resistance  $R_L$ , of 0) and solution resistive drop is negligible, they attain the same potential, at which the current at each is of the same magnitude and opposite in polarity (dashed line, Fig. 2). The less favorable situation in the acidic solu-

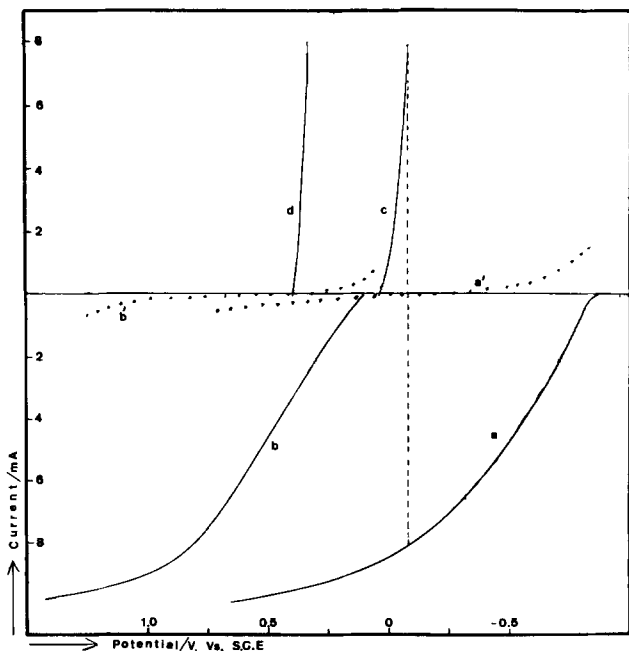


Fig. 2. Current-potential curves of the cell electrodes. (a)  $\text{TiO}_2$  film electrode, 5M NaOH, under illumination and (a') in dark; (b)  $\text{TiO}_2$  film electrode, 5M  $\text{HClO}_4$ , under illumination and (b') in dark; (c) oxygen cathode in 5M NaOH; (d) oxygen cathode in 5M  $\text{HClO}_4$ . Electrode areas,  $20\text{ cm}^2$ . White (Xe) light illumination.

tion results from the less reversible behavior of the oxygen cathode, i.e., its failure to shift to more positive potentials with decreasing pH by an amount equivalent to the anode shift (for a reversible reaction a shift of 60 mV/pH unit is expected). The open-circuit potential in alkaline solution is about 900 mV under illumination. The maximum current ( $R_L = 0$ ) is about 85% of the saturation (plateau) current which represents the maximum current obtainable at a given light level for the photooxidation process at the  $\text{TiO}_2$  electrode. Thus, even if the cathode could be shifted to more positive potentials [e.g., at a silver/silver oxide cathode (9)] the maximum cell current would only increase by a small amount; the cell power would increase, however, because of the greater cell voltage. During operation oxygen is evolved at the  $\text{TiO}_2$  electrode and the same amount of oxygen is incorporated from outside of the cell at the oxygen electrode. Because of the high concentration of reactant employed (water,  $\text{OH}^-$ ,  $\text{O}_2$ ), concentration polarization is negligible. A small outlet near the upper part of the  $\text{TiO}_2$  electrode allowed escape of the electrogenerated oxygen. The solution on the dark side of the Pt/ $\text{TiO}_2$  electrode was held at a pressure slightly greater than atmospheric so that the solution level remained constant throughout the cell.

The voltage, current, and power curves of the cell for different  $R_L$  values at the same light levels as in Fig. 2 are given in Fig. 3. In bright sunlight about one-half to one-third of the power shown in Fig. 3 was obtained. The internal resistance of the cell was mainly due to that of the  $\text{TiO}_2$  film, estimated to be 5-10 ohms. At the current density employed, little power dissipation due to internal cell resistance was observed. The spectral response of the  $\text{TiO}_2$  film agreed with that of previous reports (3, 7, 10) with a maximum at about 365 nm (uncorrected for lamp output). The quantum or photon efficiency,  $\eta_\phi$  (1), defined as the current density at the  $\text{TiO}_2$  electrode divided by the flux of light at the wavelength of maximum response (or electrons flowing per photon impinging on electrode), determined under potentiostatic conditions for the saturation current, was  $30 \pm 5\%$ . This figure should be regarded only as a representative one, since different  $\text{TiO}_2$  films differ in their photoresponse depending on the method and conditions of preparation. A single crystal of  $\text{TiO}_2$  was found to have an efficiency of  $80 \pm 10\%$ , under similar conditions. Thus, if the film was sufficiently thick for the absorption of all the light, some other factors, such as enhanced surface  $e^-/h^+$  recombination, may contribute to the lower efficiency of the  $\text{TiO}_2$  films. In the operation as a galvanic cell with  $R_L = 0$  about 85% of the saturation current is obtained for the same illumination condi-

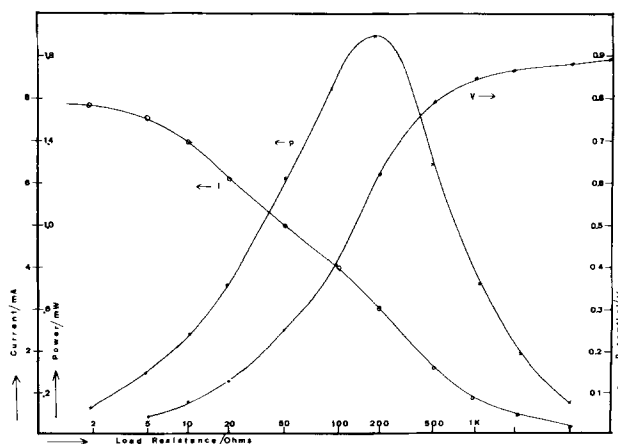


Fig. 3. Voltage (V), current (I), and power (P) of the cell as a function of the load resistance. Under same white (Xe) light intensity as in Fig. 2.

tions. Thus the quantum efficiency under short-circuit conditions is about 26% for this cell. The maximum power efficiency takes into account the energy of the incident photons as well as their flux and depends on  $R_L$ . It will be defined as the maximum cell power per square centimeter electrode area over the light intensity at the wavelength which corresponds to the maximum response. This quantity could not be measured directly, because of the low intensity of the monochromatic light (produced using a slit width of about 2 mm to give a bandwidth of about 2 nm) resulting in an electrical power of less than  $1 \mu\text{W}$ . Moreover, this power efficiency depended on the illumination intensity and  $R_L$ . If the white light intensity was varied, using neutral density filters in the ratio of 1:0.62:0.40:0.12, an over-all (polychromatic) maximum electrical power with a ratio of 1:0.6:0.46:0.15 at loads of 150, 200, 500, and 1000 ohm, respectively, was obtained. The corresponding saturation currents at the  $\text{TiO}_2$  measured potentiostatically were, as expected, linear with white light intensity and were 10, 6.1, 4.1, and 1.2 mA for the intensity ratios given above. These observations are consistent with the fact that in general the current at the  $\text{TiO}_2$  electrode is not exactly proportional to the light intensity at all potentials on the rising portion of the wave as it is for the saturation current. The maximum (monochromatic) power efficiency was estimated as follows. The cell power ( $0.22 \text{ mW/cm}^2$ ) and the  $\text{TiO}_2$  potentiostatic saturation current ( $1.5 \text{ mA/cm}^2$ ) were measured under the same intensity white light concentrated on the center  $1 \text{ cm}^2$  of the electrode. Then, using monochromatic light, the light intensity ( $96.4 \mu\text{W/cm}^2$ ) and saturation current for the  $\text{TiO}_2$  ( $9 \mu\text{A/cm}^2$ ) were determined. Thus, for monochromatic light (367 nm) a saturation current of  $0.093 \mu\text{A}/\mu\text{W}$  is produced. The saturation current found with the white light is thus equivalent to a monochromatic light intensity of  $16 \text{ mW/cm}^2$ . Thus the maximum power efficiency for monochromatic light is 1-2%. The efficiency for solar energy conversion is much lower, of course, because only about 3% of the solar spectrum would be utilizable at a  $\text{TiO}_2$  electrode (1).

The cell appeared capable of operation either continuously or in on/off cycles with no deterioration in performance (e.g., Fig. 4). The cell also could operate without a separate oxygen feed to the cathode (on the oxygen dissolving at the anode) or with air fed to the cathode. In the latter case the cell, besides producing energy, serves to separate oxygen from the air.

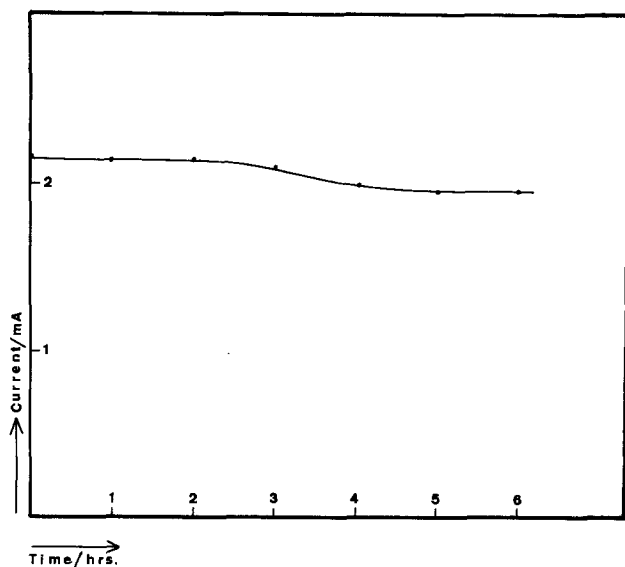


Fig. 4. Cell operation under white light illumination with time; load resistance, 100 ohms.

Although the described cell arrangement appeared satisfactory, *i.e.*, allowed full illumination of the photosensitive surface with a reasonable current density distribution and internal ohmic losses, some other cell configurations were also tried. Among these was a thin sandwich cell employing the same oxygen cathode and electrolyte solution but with the  $\text{TiO}_2$  film deposited on a transparent  $\text{SnO}_2$  film-on-glass substrate. Memming (10) previously showed that such  $\text{TiO}_2$  films show light-induced electrochemical activity and that the  $\text{SnO}_2$  is transparent to the wavelengths which generate photocurrents at the  $\text{TiO}_2$  film. In this arrangement the  $\text{TiO}_2$  film faces the cathode and is illuminated from the rear through the glass plate and the  $\text{SnO}_2$  film. In this way the cell geometry is optimized and the distance between the electrodes, volume of solution, and its internal resistance are minimized. However, this cell performance was inferior to that of the previously described one; we attribute this mainly to the poorer efficiency of the  $\text{TiO}_2$  film deposited on the  $\text{SnO}_2$  substrate. We found it difficult to prepare a  $\text{TiO}_2$  film which was thick enough to give good photosensitized electrochemical behavior and show good conductivity and at the same time obtain good light transmittance through the glass/ $\text{SnO}_2$ / $\text{TiO}_2$  system. The major problem was that the glass substrate system could not be subjected to the high temperatures needed in the CVD-coating procedure without deterioration of the  $\text{SnO}_2$  film. The conversion of the  $\text{TiO}_2$  to an n-type material in this case was accomplished by heating to  $450^\circ$  in a hydrogen atmosphere, since heating to high temperatures under vacuum was not possible.

We might also note that a recent paper by Mavroides *et al.* (11) utilized a platinized-Pt cathode of geometric area 50 times that of the anode operating on the reduction of dissolved oxygen to evaluate the performance of various semiconducting  $\text{TiO}_2$  anodes. High quantum efficiencies were also obtained in that study for operation in a photogalvanic mode. Similarly Keeny *et al.* (6) effectively used a Pt-oxygen cathode in their laboratory cell.

While the photoelectrochemical cell here operates on the water-oxygen system, similar cells for conversion of light to electrical energy without a net chemical change in the system could operate with other redox couples (represented by  $\text{Ox} + ne \rightleftharpoons \text{Red}$ ). The potential range of the  $\text{TiO}_2$  anode would be limited to values near the flatband potential where sufficient band bending occurs to cause efficient separation of the  $h^+/e^-$  pairs. Thus for any redox couple the anodic  $i$ - $E$  curve will probably be close to the one given for water oxidation. The cathode curve for reduction of  $\text{Ox}$  to  $\text{Red}$  will depend on the  $E^\circ$  and the reversibility of the reduction reaction. The more positive the values at which the  $i$ - $E$  curve lies the greater will be the power of the cell at a given illumination level. Thus redox couples with more positive  $E^\circ$  values should lead to higher power efficiencies with the constraint that for couples with  $E^\circ$  values larger than that of the oxygen/water couple (adjusted to the appropriate pH value), species  $\text{Ox}$  will tend to be unstable in aqueous solutions. Moreover the work of Fujishima and Honda (12, 13), as well as our own recent studies (14) suggest that as the  $E^\circ$  of the redox couple becomes more positive water may compete more successfully with  $\text{Red}$  for the photogenerated holes, leading to an over-all irreversibility in the cell reaction. If one abandons an aqueous system, however, and uses a solvent with a wider available potential range, such as acetonitrile, for example (15), then even more positive redox couples can be employed. The most positive  $E^\circ$  value for a couple used in a solvent which participates in neither the anodic nor cathodic reaction is one located at about the position of the valence band of the n-type semiconductor, where  $\text{Red}$  is still capable of combining with holes at the electrode surface. Under

these conditions the maximum utilization of the energy of the incident photons should occur.

#### Acknowledgment

The support of this research by the National Science Foundation (MPS 74-23210) is gratefully acknowledged.

Manuscript submitted Oct. 31, 1975; revised manuscript received Feb. 16, 1976.

Any discussion of this paper will appear in a Discussion Section to be published in the June 1977 JOURNAL. All discussions for the June 1977 Discussion Section should be submitted by Feb. 1, 1977.

Publication costs of this article were partially assisted by The University of Texas at Austin.

#### REFERENCES

1. M. D. Archer, *J. Appl. Electrochem.*, **5**, 17 (1975).
2. H. Gerischer, *J. Electroanal. Chem.*, **58**, 263 (1975).
3. K. L. Hardee and A. J. Bard, *This Journal*, **122**, 739 (1975).
4. P. J. Boddy, *ibid.*, **115**, 199 (1968).
5. A. Fujishima and K. Honda, *Nature*, **238**, 37 (1972); *Bull. Chem. Soc. Japan*, **44**, 1148 (1971).
6. J. Keeney, D. H. Weinstein, and G. M. Haas, *Nature*, **253**, 719 (1975).
7. M. S. Wrighton, D. S. Ginley, P. T. Wolczanski, A. B. Ellis, D. L. Morse, and A. Linz, *Proc. Natl. Acad. Sci. USA*, **72**, 1518 (1975).
8. D. Laser and A. J. Bard, *Chem. Phys. Letters*, **34**, 605 (1975).
9. James P. Hoare, in "Encyclopedia of Electrochemistry of the Elements," A. J. Bard, Editor, Vol. II, Chap. 5, (and references therein), Marcel Dekker, Inc., New York (1974).
10. R. Memming, *This Journal*, **121**, 1160 (1974).
11. J. G. Mavroides, D. I. Tchernev, J. A. Kafalas, and D. F. Kolesar, *Mat. Res. Bull.*, **10**, 1023 (1975).
12. A. Fujishima and K. Honda, *J. Chem. Soc. Japan (Ind. Chem. Soc.)*, **74**, 355 (1971).
13. A. Fujishima and K. Honda, *Production Research (Japan)*, **22**, 478 (1970).
14. A. J. Bard and S. N. Frank, Paper 294 presented at The Electrochemical Society Meeting, Washington, D. C. May 2-7, 1976.
15. S. N. Frank and A. J. Bard, *J. Am. Chem. Soc.*, **97**, 7427 (1975).

## Primary Resistances for Ring-Disk Electrodes

Joseph J. Miskis, Jr., and John Newman\*

*Inorganic Materials Research Division, Lawrence Berkeley Laboratory, and  
Department of Chemical Engineering, University of California, Berkeley, California 94720*

#### ABSTRACT

A system consisting of a disk electrode, a concentric ring electrode, and a large counterelectrode at infinity has three independent resistance values describing the primary potential difference between any two electrodes when current is passed between any two electrodes. These resistance values are calculated and presented as dimensionless correlations as functions of the ratios of radii of the disk and ring.

A common electrode geometry in electroanalytical and research applications involves a disk electrode and a concentric ring electrode both embedded in an insulating plane and rotated about the axis of the disk. Species produced by an electrochemical reaction at the disk can frequently be detected quantitatively by electrochemical reaction at the ring (1-3). In some of these applications it is desirable to assess the ohmic potential drop in the solution. For example, to have a controlled electrode potential for the reaction at the disk one needs to know how a current to the disk and a current to the ring separately influence the potential in the solution in the neighborhood of the disk (4, 5). To ensure that a limiting current is maintained on the ring involves a similar question (6).

Experimental efforts to answer these questions involve abrupt changes in the current to either the ring or the disk followed by a measurement of the change in potential of both the ring and the disk as shortly thereafter as possible (4, 5, 7). Such rapid changes in potential and current are associated with the primary distributions of potential and current (8).

Consequently, we can define a mathematical problem in which the potential obeys Laplace's equation

$$\nabla^2\Phi = 0 \quad [1]$$

the potential is zero at infinity, and has a uniform value in the solution adjacent to each electrode. Corresponding to a zero current density, the normal component of

the potential gradient is zero on the insulating annulus between the disk and the ring and on the plane surrounding the ring. This problem excludes consideration of the variation of conductivity within the thin diffusion layer adjacent to the electrodes and effectively regards the change in potential drop to be determined by the bulk of the solution. Also excluded from consideration is the effect of electrode kinetics, it being assumed that the double-layer capacity is sufficiently large that the potential difference across it does not change during the time of the measurement (8). [The course of events involving the change of the charge of the double-layer capacity has been examined by Nişancioğlu and Newman (9-11).]

The problem thus defined is limited in scope since it involves only the geometry of the system, the conductivity of the solution, and the potentials and currents themselves. The principal result of the model is the expression of the disk and ring potentials in terms of the disk and ring currents

$$V_d = R_{dd}I_d + R_{dr}I_r \quad [2]$$

$$V_r = R_{rd}I_d + R_{rr}I_r \quad [3]$$

where  $I_d$  and  $I_r$  are the total currents to the disk and ring electrodes, respectively, and  $V_d$  and  $V_r$  are the potentials, presumed uniform, in the solution adjacent to the two electrodes. In the absence of concentration and surface overpotentials,  $V_d$  and  $V_r$  can be regarded to be the potentials of the electrodes themselves, and this is the usual manner of speaking when discussing primary-distribution problems. Bear in mind that in

\* Electrochemical Society Active Member.

Key words: current distribution, potential distribution, Laplace's equation, interrupter techniques.

the applications discussed above these quantities  $I_d$ ,  $I_r$ ,  $V_d$ , and  $V_r$  probably represent instantaneous changes in the electrode currents and the corresponding instantaneous changes in the electrode potentials.

Equations [2] and [3] follow directly from the mathematical problem and the linearity of Eq. [1]. By the principle of superposition, the potential  $\Phi$  in the solution can be expressed as the sum of two functions, one proportional to  $V_d$  and the other proportional to  $V_r$ . Since the current to an electrode is obtained from the integral over the area of the normal component of the potential gradient at the electrode, it is clear that both  $I_d$  and  $I_r$  are sums of two terms, one proportional to  $V_d$  and the other proportional to  $V_r$ . Inversion of these relations then leads to Eq. [2] and [3] and the corresponding definition of the resistances.

$R_{dd}$ ,  $R_{dr}$ ,  $R_{rd}$ , and  $R_{rr}$  are the primary resistances defined by Eq. [2] and [3] for this ring-disk system. We can attach a physical meaning to them by the following considerations. When there is no ring current,  $I_r = 0$ , we see that  $R_{dd}$  represents the resistance between the disk electrode and a counterelectrode at infinity. This resistance will be lower in the presence of the ring than for the disk alone because current can find a path through the ring electrode to the disk, bypassing some of the resistance of the solution. This is true even though there is no net current to the ring. Under these circumstances, the potential of the ring will take on a definite, uniform value to satisfy the condition of no net current to the ring. This value is determined by  $R_{rd}$  in Eq. [3]. Thus,  $R_{rd}$  is a quantity having the dimensions of a resistance but which yields the potential on the ring due to a current on the disk.

In a similar manner, we see that when there is no disk current,  $R_{rr}$  is the resistance between the ring and a counterelectrode at infinity while  $R_{dr}$  reproduces the uniform potential on the disk due to a current on the ring. As shown below,  $R_{dr} = R_{rd}$ .

The geometry of the ring-disk system is defined adequately by the ratio  $r_0/r_1$  of the disk radius to the inner radius of the ring and the ratio  $r_1/r_2$  of the inner and outer radii of the ring. The resistances can be made dimensionless with the conductivity  $\kappa$  of the solution and a characteristic length, which we choose to be the outer radius  $r_2$  of the ring. Therefore, the results of this study can be presented simply by correlating three dimensionless resistances ( $R_D^D = \kappa r_2 R_{dd}$ ,  $R_D^R = R_R^D = \kappa r_2 R_{dr}$ , and  $R_R^R = \kappa r_2 R_{rr}$ ) as functions of two geometric ratios ( $r_0/r_1$  and  $r_1/r_2$ ). This simplicity and generality is a further justification for restricting the problem to the primary resistances.

In a subsequent paper from this laboratory (12), we shall discuss some more complicated behavior of the ring-disk system in which concentration variations and electrode kinetics are considered in order to assess the current distribution on a sectioned electrode (composed of the ring and disk at the same potential) below the limiting current, the collection efficiency of the system when the current distribution on the disk is nonuniform due to the ohmic potential drop in the solution, and the anomalous diffusion coefficient for a redox couple measured by means of the limiting current to a ring electrode with zero current to the disk.

### Symmetry of Resistances

Let us consider two cases: case 1 where  $I_d = 0$  and case 2 where  $I_r = 0$ . For any two functions  $\Phi_1$  and  $\Phi_2$ , Green's theorem says (13)

$$\int (\Phi_1 \nabla^2 \Phi_2 - \Phi_2 \nabla^2 \Phi_1) dV_0 = \oint (\Phi_1 \nabla \Phi_2 - \Phi_2 \nabla \Phi_1) \cdot dS \quad [4]$$

The integral over the volume  $V_0$  is zero here because both  $\Phi_1$  and  $\Phi_2$  obey Laplace's equation. The surface integral is over the entire area enclosing the volume

$V_0$ , which we shall take to be the entire half-space between the plane of the disk and the counterelectrode at infinity. The integral over the insulating surfaces is zero because the normal component of the potential gradient is zero there. The integral over a hemisphere at infinity is zero because each potential is inversely proportional to the radius, the potential gradient is inversely proportional to the square of the radius, and  $dS$  is proportional to the square of the radius.

This leaves us with integrals over only the surfaces of the electrodes

$$\int_d (\Phi_1 \nabla \Phi_2 - \Phi_2 \nabla \Phi_1) \cdot dS = - \int_r (\Phi_1 \nabla \Phi_2 - \Phi_2 \nabla \Phi_1) \cdot dS \quad [5]$$

Now, by the definition of the primary distributions, the potential adjacent to each electrode is uniform and can be removed from the integral, with the result

$$\begin{aligned} V_{d1} \int_d \nabla \Phi_2 \cdot dS - V_{d2} \int_d \nabla \Phi_1 \cdot dS \\ = - V_{r1} \int_r \nabla \Phi_2 \cdot dS + V_{r2} \int_r \nabla \Phi_1 \cdot dS \end{aligned} \quad [6]$$

Furthermore, the integral of the normal component of the potential gradient over the surface of an electrode is proportional to the total current to the electrode. Equation [6] becomes

$$V_{d1} I_{d2} - V_{d2} I_{d1} = - V_{r1} I_{r2} + V_{r2} I_{r1} \quad [7]$$

For the cases chosen here,  $I_{d1} = 0$  and  $I_{r2} = 0$ , and this reduces to

$$V_{d1} I_{d2} = V_{r2} I_{r1} \quad [8]$$

Substitution of Eq. [2] and [3] for the electrode potentials, with  $I_{d1} = I_{r2} = 0$ , yields

$$R_{dr} I_{r1} I_{d2} = R_{rd} I_{d2} I_{r1} \quad [9]$$

or

$$R_{dr} = R_{rd} \quad [10]$$

Gabrielli *et al.* (7) state this result and provide supporting experimental results. Equation [10] could be considered to be an example of the Onsager reciprocal relation.

It should be emphasized that this demonstration of reciprocity is valid for an arbitrary geometry of the electrodes and insulators. For example, the presence of the Luggin capillary from a reference electrode can modify the values of the resistances but still  $R_{dr} = R_{rd}$ . Also, the counterelectrode does not need to be a hemisphere at infinity. By taking the third electrode to be the zero of potential, one can still reduce Eq. [4] to Eq. [5] and obtain the reciprocal relation for the primary resistances.

### Analysis

Newman (14) reviewed methods of calculating current and potential distributions in ring or disk geometries. At first we thought that we could treat the ring-disk system as a composite disk of radius  $r_2$  and use the method of separation of variables in rotational elliptic coordinates. Then the current density would be zero on the insulating annulus while the potentials would be specified on the ring and disk, and the coefficients of the series would be determined by trial and error or by matrix inversion so as to satisfy these boundary conditions. However, such a series is inadequate to represent the distributions of potential and current in this system because the current density approaches infinity at the inner edge of the ring and at the edge of the disk. [The coordinate system does allow treatment in a natural way of the infinite current density near the outer edge of the ring, just as it does for the primary distribution near the edge of a disk without a ring (15).]

As an alternative, the currents due to the ring and the disk were treated separately by different methods. First a series of ten cases was defined with prescribed current distributions on the ring. For cases 1 and 3, these current distributions were

$$i_{r1} = \frac{2}{\sqrt{1-x^2}} \quad [11]$$

and

$$i_{r3} = \sqrt{\frac{2}{1+x}} \quad [12]$$

where

$$x = \frac{2r - r_1 - r_2}{r_2 - r_1} \quad [13]$$

Case 2 has a zero current density everywhere on the ring but will have a current assigned to the disk as described below. Cases 4 through 10 (denoted by values of  $k$  from 4 through 10) were assigned the following current distributions on the ring

$$i_{r,k} = P_{k-4}(x) \quad [14]$$

where  $P_k(x)$  is the Legendre polynomial.

It was felt that these cases would represent a complete set which could be superposed to reproduce any primary current distribution on the ring electrode. In particular, case 1 has an infinite current density at both the inner and the outer edge of the ring, and the current density approaches infinity in the manner required when an electrode is embedded in an insulating plane, namely, by being inversely proportional to the square root of the distance from the edge.<sup>1</sup> Case 3 involves an infinite current density only at the inner edge of the ring. A superposition of cases 1 and 3 should be able to match the way in which any primary current distribution goes to infinity at the inner and outer edges of the ring. The residual current distribution should be finite over the ring and adequately represented by a superposition of the remaining cases 4 through 10. For some values of  $r_0/r_1$  and  $r_1/r_2$  where the accuracy of the results was questionable, the number of cases was extended from 10 to 20.

<sup>1</sup>This means that the product of the current density and the square root of distance from the edge has a finite, nonzero limit as the edge is approached.

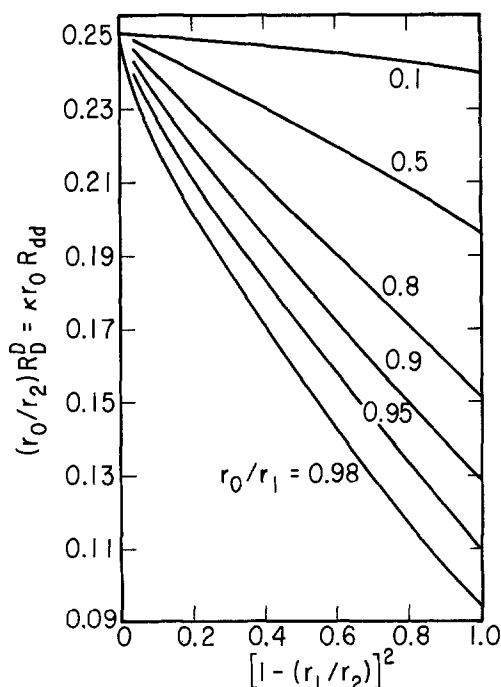


Fig. 1. Correlation of the disk resistance

The next step in the procedure is to evaluate the potential distribution on both the disk and the ring due to the current distribution on the ring for each of the cases described above. For this purpose, we use the formula for the potential in the plane of the disk (14)

$$\Phi_0(r) = \frac{2}{\pi\kappa} \int_{r_1}^{r_2} \frac{i(r')K(m)r'dr'}{r+r'} \quad [15]$$

where

$$m = \frac{4rr'}{(r+r')^2} \quad [16]$$

and  $K(m)$  is the complete elliptic integral of the first kind

$$K(m) = \int_0^{\pi/2} \frac{d\alpha}{\sqrt{1-m\sin^2\alpha}} \quad [16a]$$

The potential due to a uniform ring current source of radius  $r'$ , located in the plane  $z=0$  and of strength  $2idr'$  (ampere per unit length), is

$$\begin{aligned} d\Phi &= \frac{2ir'dr'}{4\pi\kappa} \int_0^{2\pi} \frac{d\theta}{[z^2 + (r-r'\cos\theta)^2 + (r'\sin\theta)^2]^{1/2}} \\ &= \frac{ir'dr'}{2\pi\kappa} \frac{2}{\sqrt{z^2 + (r+r')^2}} \int_0^\pi \frac{d\theta}{\left[1 - \frac{2rr'}{z^2 + (r+r')^2} \frac{1+\cos\theta}{2}\right]^{1/2}} \\ &= \frac{ir'dr'}{2\pi\kappa} \frac{4}{\sqrt{z^2 + (r+r')^2}} \int_0^{\pi/2} \frac{d\alpha}{\left[1 - \frac{4rr'}{z^2 + (r+r')^2} \sin^2\alpha\right]^{1/2}} \end{aligned} \quad [16b]$$

where  $\alpha = (\pi - \theta)/2$ . Integration for current rings between  $r_1$  and  $r_2$  and evaluation for  $z=0$  yield Eq. [15].

The evaluation of the integral in Eq. [15] for the potential distribution on the ring requires care, first of all, because the elliptic integral approaches infinity when  $r' = r$ , corresponding to the infinite potential at the ring itself produced by a ring of nonzero current but infinitesimal width. Additional difficulties are introduced for cases 1 and 3 where the current distribution approaches infinity at the inner or outer edge of the ring.

The potential distributions obtained above will be nonuniform on both the ring and the disk. For each case, the potential can be made uniform on the disk by superposing the potential distribution due to a current distribution introduced on the disk. Here we use rotational elliptic coordinates  $\eta$  and  $\xi$  based on the radius  $r_0$  of the disk. The coordinate transformation reads

$$z = r_0\xi\eta \quad \text{and} \quad r = r_0\sqrt{(1+\xi^2)(1-\eta^2)} \quad [17]$$

and the solution of Laplace's equation by separation of variables in this coordinate system is (14, 16)

$$\Phi = \sum_{n=0}^{\infty} B_n P_{2n}(\eta) M_{2n}(\xi) \quad [18]$$

where  $B_n$  represents arbitrary coefficients,  $P_{2n}(\eta)$  is again the Legendre polynomial, and  $M_{2n}(\xi)$  [called  $M_n(\xi)$  in Ref. (14)] is a Legendre function of imaginary argument having properties described earlier. Selection of even Legendre polynomials in Eq. [18] ensures that the corresponding current distribution is zero in the plane outside the disk; hence, the current distribution is not modified on the ring by superposing a potential distribution of the type in Eq. [18].

In practice, Eq. [18] is truncated after a finite number of terms, say 20. For each case the  $B$  values are

then chosen so that the potential (including that due to the ring current) will be zero on the surface of the disk. Up to this point, case 2 has not been defined or modified. We now require that the potential  $\phi_0$  be equal to unity on the surface of the disk, for case 2, which is equivalent to setting  $B_0 = 1$ . The superposition of the disk potential function in Eq. [18] will generate a nonzero net current and a uniform potential for the disk for each case.

Next, for each case, we should calculate the potential distribution on the ring due to the current distribution on the disk, and we should add this to the potential distribution previously obtained from the current distribution on the ring. This step involves the use of Eq. [18] with values of  $\xi$  greater than zero since

$$\phi_0 = \sum_{n=0}^{\infty} B_n P_{2n}(0) M_{2n}(\xi) \quad [19]$$

in the plane for  $r$  greater than  $r_0$ . The evaluation of  $M_{2n}(\xi)$  has been necessary in earlier work (6), and we have introduced refinements here (17) to permit accurate calculation for large values of  $\xi$  and  $n$ .

The several cases that have been treated now each have prescribed current distributions on the ring and disk, known total currents, a uniform potential on the disk, and a nonuniform but finite potential distribution on the ring. The final step of the procedure is to superpose cases 3 through 10 onto cases 1 and 2, in turn, in such a way that the potential distribution on the ring is made uniform. More cases can be used to attain a higher degree of uniformity.

Cases 1 and 2 now satisfy all the requirements of a primary distribution: They have uniform potentials on the ring and the disk, and they satisfy Laplace's equation and all the other boundary conditions. Analysis of cases 1 and 2 according to Eq. [2] and [3] yields values of the resistances  $R_{dd}$ ,  $R_{dr}$ ,  $R_{rd}$ , and  $R_{rr}$ .

This solution for the primary potential and current distributions by superposition may seem involved and complicated, but it is economical and accurate, and it avoids any trial-and-error calculations. The functions chosen for superposition make special allowance for the geometry of the system and can treat the infinite current densities at the edges of the electrodes even when the insulating annulus is quite thin.

**Results**

In the computed results,  $R_{dr}$  and  $R_{rd}$  usually agreed to within 0.01%. Certain limiting situations could also be checked to ensure the validity of the results.

Figures 1, 2, and 3 show the values of the three independent resistances as functions of the geometric ratios  $r_0/r_1$  and  $r_1/r_2$ . These results are also given in Table I. For a very thin ring,  $R_{rr}$  becomes infinite in a

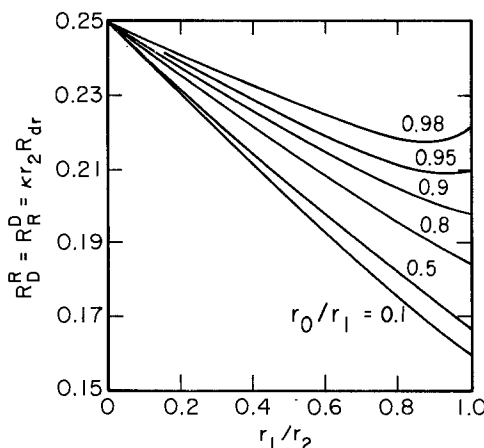


Fig. 2. Correlation of the interaction resistance

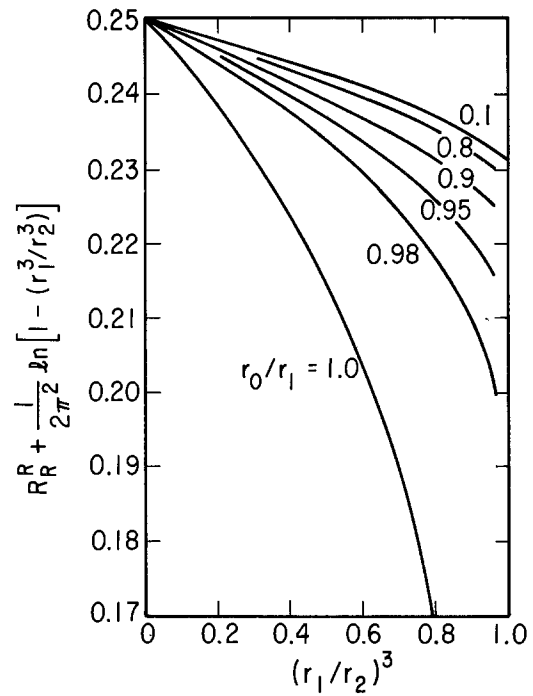


Fig. 3. Correlation of the ring resistance

manner which is discussed in the Appendix. Consequently, on Fig. 3 we have added a term which compensates for this and produces a finite limit as  $r_1$  approaches  $r_2$ . An exception is the (unrealistic) limit of a zero gap distance. As  $r_0$  approaches  $r_1$ , the value of  $\kappa r_2 R_{rr}$  approaches 0.25, independent of the value of  $r_1/r_2$ .

**Discussion**

The results for  $R_{dd}$  can be comprehended in relation to the value  $1/4\kappa r_0$  for the primary resistance (15) for a single disk in an insulating plane. The values for the disk resistance, as plotted in Fig. 1, therefore approach the value 0.25 as the influence of the ring becomes negligible, either for thin rings ( $r_1 \rightarrow r_2$ ) or for wide gaps between the rings and the disk ( $r_0 \ll r_1$ ). The influence of the ring is always to lower the resistance value  $\kappa r_0 R_{dd}$  below the value 0.25 because the ring provides an alternative current path which can help the current get from infinity to the neighborhood of the disk. Figure 1 shows how this effect becomes more pronounced for wide rings and narrow gaps.

There are several ways of thinking about the coupling resistances  $R_{dr} = R_{rd}$ . First imagine a current to the disk with no current to the ring. Then the potential distribution will bear some resemblance to that for a single disk in an insulating plane, and the similarity will become exact in the limit of a thin ring. The ring, in addition to distorting this potential field, will acquire a potential corresponding to the single disk at some radial position  $r_*$  which lies between  $r_1$  and  $r_2$ . Since

$$(r/r_0)^2 = 1 + \xi^2 \quad [20]$$

on the ring and since

$$M_0(\xi) = \frac{2}{\pi} \text{ctn}^{-1}(\xi) \quad [21]$$

the potential in the plane at a radial position  $r_*$  due to the primary distribution on a single disk is

$$V_r = V_d \text{ctn}^{-1}(\xi) = \frac{I_d}{2\pi\kappa r_0} \sin^{-1}\left(\frac{r_0}{r_*}\right) \quad [22]$$

This leads to the resistance value

$$\kappa r_2 R_{rd} = \frac{r_2}{2\pi r_0} \sin^{-1}\left(\frac{r_0}{r_*}\right) \quad [23]$$



Table I. Computed values of resistances as functions of the geometry of the ring-disk system

$r_0/r_1$	$r_1/r_2$	$\kappa r_2 R_{dd}$	$\kappa r_2 R_{dr}$	$\kappa r_2 R_{rr}$
0.10	0.99	2.5252	0.1602	0.4107
	0.98	2.5510	0.1610	0.3770
	0.95	2.6314	0.1634	0.3343
	0.90	2.7770	0.1674	0.3045
	0.80	3.1215	0.1755	0.2785
	0.60	4.1463	0.1925	0.2590
	0.40	6.1743	0.2107	0.2523
	0.20	12.2038	0.2299	0.2503
	0.10	24.2128	0.2399	0.2500
	0.05	48.2077	0.2449	0.2500
0.50	0.99	0.5050	0.1674	0.4106
	0.98	0.5102	0.1682	0.3769
	0.95	0.5261	0.1704	0.3342
	0.90	0.5546	0.1741	0.3044
	0.80	0.6207	0.1816	0.2785
	0.60	0.8092	0.1973	0.2590
	0.40	1.1641	0.2140	0.2523
	0.20	2.1759	0.2317	0.2503
	0.10	4.1523	0.2408	0.2500
	0.05	8.0844	0.2454	0.2500
0.80	0.99	0.3156	0.1850	0.4084
	0.98	0.3188	0.1855	0.3748
	0.95	0.3285	0.1871	0.3323
	0.90	0.3455	0.1897	0.3029
	0.80	0.3834	0.1954	0.2774
	0.60	0.4855	0.2076	0.2586
	0.40	0.6677	0.2209	0.2522
	0.20	1.1664	0.2352	0.2503
	0.10	2.1252	0.2425	0.2500
	0.05	4.0225	0.2463	0.2500
0.90	0.99	0.2806	0.1982	0.4031
	0.98	0.2833	0.1984	0.3698
	0.95	0.2917	0.1991	0.3282
	0.90	0.3059	0.2006	0.2997
	0.80	0.3367	0.2045	0.2756
	0.60	0.4172	0.2142	0.2580
	0.40	0.5572	0.2253	0.2520
	0.20	0.9345	0.2374	0.2502
	0.10	1.6590	0.2436	0.2500
	0.05	3.0794	0.2468	0.2500
0.95	0.99	0.2658	0.2096	0.3941
	0.98	0.2683	0.2093	0.3617
	0.95	0.2758	0.2090	0.3219
	0.90	0.2882	0.2093	0.2954
	0.80	0.3145	0.2117	0.2732
	0.60	0.3820	0.2194	0.2572
	0.40	0.4977	0.2287	0.2518
	0.20	0.8068	0.2391	0.2502
	0.10	1.3948	0.2445	0.2500
	0.05	2.5572	0.2472	0.2500
0.98	0.99	0.2575	0.2211	0.3773
	0.98	0.2599	0.2201	0.3474
	0.95	0.2664	0.2185	0.3121
	0.90	0.2770	0.2177	0.2891
	0.80	0.2991	0.2187	0.2700
	0.60	0.3550	0.2245	0.2562
	0.40	0.4500	0.2322	0.2516
	0.20	0.7021	0.2409	0.2502
	0.10	1.1823	0.2454	0.2500
	0.05	2.1447	0.2477	0.2500

This formula becomes rigorous for thin rings when we set  $r_*$  equal to  $r_2$ . Thus, the intercept on the right side of Fig. 2 is known with certainty. The limit for the ordinate is 0.25 for narrow gaps ( $r_0 \rightarrow r_1$ ) and  $\frac{1}{2}\pi = 0.1592$  for wide gaps ( $r_0 \ll r_1$ ).

For thick rings, it is convenient to think of a zero current on the disk. Then the ring itself will look like a disk, with a small imperfection at the center, and the potential distribution will be nearly that for a disk of radius  $r_2$  in an insulating plane. The small disk of radius  $r_0$  can then sense only one potential, that approximately equal to the potential of the ring  $V_r = I_r/4\kappa r_2$ . This leads to the limit

$$\kappa r_2 R_{dr} \rightarrow 0.25 \text{ as } r_2/r_1 \rightarrow \infty \quad [24]$$

independent of the value of  $r_0/r_1$ .

By an analysis of the current deflected from the insulating region for  $r < r_1$ , one can find a correction to Eq. [24] for small disks

$$\kappa r_2 R_{dr} = \frac{1}{4} - \frac{1}{\pi^2} \frac{r_1}{r_2} \quad [25]$$

for  $r_1 \ll r_2$  and  $r_0 \ll r_1$ . This limiting slope is verified in Fig. 2.

For rings which are neither thick nor thin, we can use the results in Fig. 2 to calculate the value of  $r_*$  according to Eq. [23]. It turns out that  $r_*$  varies from the arithmetic average of  $r_1$  and  $r_2$  for thin rings to a value of  $2r_2/\pi$  for thick rings (in order to reproduce the limit in Eq. [24]). This suggests the method of correlation of  $R_{dr}$  shown in Fig. 4. Here a value of  $r_*$  is calculated *a priori*, and the ratio of the left and right sides of Eq. [23] represents a deviation function which is close to unity. The only advantage of Fig. 4 over Fig. 2 is that the scale can be expanded because the minimum and maximum values now differ by a factor of 1.05 instead of a factor of 1.57.

Let us next turn our attention to the ring resistance  $R_{rr}$ . For wide rings, it is clear that the resistance value is given by

$$\kappa r_2 R_{rr} = 0.25 \quad [26]$$

the value for a single disk of radius  $r_2$ . In the other extreme

$$\kappa r_2 R_{rr} + \frac{1}{2\pi^2} \ln \left( 1 - \frac{r_1^3}{r_2^3} \right) = \frac{\ln 96}{2\pi^2} = 0.2312 \quad [27]$$

for thin rings ( $r_1 \rightarrow r_2$ ) and small disks ( $r_0 \ll r_1$ ), a result which is developed in the Appendix.

Figure 3 was plotted so that the small disk case ( $r_0 \ll r_1$ ) would show these limits clearly. According to this figure, the effect of a nonzero disk is always to lower the ring resistance, because an alternative path is provided between the counterelectrode at infinity and the ring electrode. The correction to Eq. [27] for small disks is very small,  $-(r_0/r_2)^5/45\pi^2$ . Thus, we see that the curve for  $r_0/r_1 = 0.8$  is already very close to the curve for  $r_0/r_1 = 0.1$ .

Gabrielli *et al.* (7) have measured resistances for four ring-disk geometries. They verified the coupling relationship between  $R_{rd}$  and  $R_{dr}$ . A comparison between their measurements and our calculated values is made in Table II. For this purpose,  $1/\kappa$  was given the value 2.25 ohms-cm for a 2N  $H_2SO_4$  solution. The comparison cannot be regarded as satisfactory. Two experimental values of  $\kappa r_0 R_{dd}$  are greater than 0.25, which should not be possible under any circumstances. The other two values of  $\kappa r_0 R_{dd}$  show good agreement. Measured values of the coupling resistance are consistently lower than those calculated. One value of  $\kappa r_2 R_{rr}$  is lower than 0.25, which again should not be possible

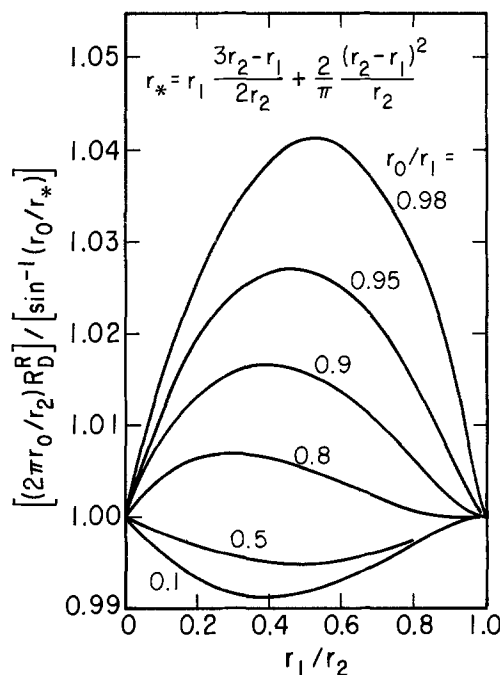


Fig. 4. Correlation of interaction resistance

Table II. Comparison of calculated resistances with those measured by Gabrielli *et al.* (7) for four ring-disk geometries

$r_0/r_1$	$r_1/r_2$	$\kappa r_2 R_{rr}$		$\kappa r_2 R_{dr}$		$\kappa r_0 R_{dd}$	
		Meas.	Calc.	Meas.	Calc.	Meas.	Calc.
0.952	0.42	0.244	0.252	0.211	0.228	0.307	0.192
0.968	0.62	0.272	0.261	0.194	0.22	0.217	0.215
0.976	0.82	0.311	0.273	0.189	0.218	0.231	0.238
0.976	0.976	1.213	0.342	0.177	0.219	0.262	0.2495

under any circumstances. The other measured values of  $\kappa r_2 R_{rr}$  are significantly higher than the calculated values. It seems that some new experimental measurements are in order.

Shabrang and Bruckenstein (5) analyze their results in terms of equations of the form

$$V_d - V_T = R_D I_d + (I_d + I_r) R_C \quad [28]$$

and

$$V_r - V_T = R_R I_r + (I_d + I_r) R_C' \quad [29]$$

where  $R_D$ ,  $R_R$ ,  $R_C$ , and  $R_C'$  are resistances and  $V_T$  is the potential of the reference electrode and can be expressed as

$$V_T = R_{Aux} I_d + R_{Aux}' I_r \quad [30]$$

Comparison with Eq. [2] and [3] shows that we can make the associations

$$R_{dd} = R_D + R_C + R_{Aux} \quad [31]$$

$$R_{dr} = R_C + R_{Aux}' \quad [32]$$

$$R_{rd} = R_C' + R_{Aux} \quad [33]$$

and

$$R_{rr} = R_R + R_C' + R_{Aux}' \quad [34]$$

In view of Eq. [10], we can write

$$R_C - R_C' = R_{Aux} - R_{Aux}' \quad [35]$$

Shabrang and Bruckenstein take these differences to be zero. Indeed, if the counterelectrode is far away and the reference electrode is moderately far away from the ring-disk system, we can estimate (15)

$$R_{Aux} = R_{Aux}' = \frac{1}{2\pi\kappa\rho} \quad [36]$$

where  $\rho$  is the radial position of the reference electrode in spherical coordinates. However, the currents  $I_d$  and  $I_r$  do not, in general, need to have the same influence on the potential  $V_T$  in Eq. [30]; the difference will become accentuated the closer the reference electrode probe is to the ring-disk system.

In the extreme case, place the reference electrode adjacent to one of the working electrodes say the ring. Then  $V_T = V_r$  and  $R_{Aux} = R_{rd}$  and  $R_{Aux}' = R_{rr}$ . It is unlikely that  $R_{rd} = R_{rr}$ .

From Fig. 1, 2, and 3, we find  $\kappa r_0 R_{dd} = 0.249$ ,  $\kappa r_2 R_{rd} = 0.209$ , and  $\kappa r_2 R_{rr} = 0.3238$  for the geometry of Shabrang and Bruckenstein ( $r_0/r_1 = 0.95$  and  $r_1/r_2 = 8/8.4$ ).  $R_D$  corresponds approximately to  $R_{dd} - R_{dr}$ , and  $R_R$  corresponds approximately to  $R_{rr} - R_{rd}$ , whereas Shabrang and Bruckenstein came to the conclusion that  $R_R$  and  $R_D$  correspond to  $R_{rr}$  and  $R_{dd}$ , respectively. For the ratio  $R_D/(R_D + R_R)$ , they find values of 0.37, 0.35, 0.34, 0.39, 0.36, 0.34, and 0.31, whereas we calculate 0.366 for the corresponding ratio. (Here, we assume that the labels  $V_o/V_D$  and  $V_o/V_R$  are interchanged in their Table III.)

Because of uncertainties in the position of the reference electrode and the conductivity of the solution, we refrain from further comparisons with their data.

From the results of Miller and Bellavance (4) we deduce an experimental value of  $\kappa r_2 R_{rd} = 0.192$ . The corresponding value from Fig. 2 is  $\kappa r_2 R_{rd} = 0.206$  for  $r_0/r_1 = 0.909$  and  $r_1/r_2 = 0.812$ .

## Conclusion

Computed values of the primary resistances for a ring-disk system, as presented here, should permit estimation of the uncompensated resistances when an attempt is made to control the potentials of the electrodes. There are few geometries for which this information is available.

Discrepancies between calculated and experimental values may lead to refined experiments or to considerations beyond the scope of the primary resistances.

## Acknowledgment

This work was supported by the United States Energy Research and Development Administration.

Manuscript submitted Aug. 8, 1975; revised manuscript received Feb. 3, 1976.

Any discussion of this paper will appear in a Discussion Section to be published in the June 1977 JOURNAL. All discussions for the June 1977 Discussion Section should be submitted by Feb. 1, 1977.

Publication costs of this article were partially assisted by the University of California.

## APPENDIX

### Thin Rings

The limiting resistance behavior for a thin ring (in the presence of only a small disk) can be obtained by application of Eq. [15] to case 1, where the current-density distribution is given by Eq. [11]. First note that the ring current for case 1 is given by  $I_r = \pi^2 r_2^2 - r_1^2$ . To evaluate the potential on the ring, we thus write

$$\begin{aligned} \Phi_0(r) &= \frac{2}{\pi\kappa} \int_{r_1}^{r_2} \frac{2}{\sqrt{1-x^2}} \frac{K(m)r'dr'}{r+r'} \\ &= \frac{r_2 - r_1}{\pi\kappa} \int_{-1}^1 \frac{K(m)}{\sqrt{1-x^2}} \frac{1+2\epsilon x'}{1+\epsilon(x+x')} dx' \quad [A-1] \end{aligned}$$

where  $x$  has been introduced according to Eq. [13] and

$$\epsilon = \frac{1}{2} \frac{r_2 - r_1}{r_2 + r_1} \quad [A-2]$$

is a small quantity for a thin ring.

Now,  $m$  is close to 1. In fact

$$1 - m = \frac{\epsilon^2(x-x')^2}{[1+\epsilon(x+x')]^2} \quad [A-3]$$

and

$$K(m) \rightarrow -\frac{1}{2} \ln \frac{1-m}{16} + O(\epsilon^2 \ln \epsilon) \quad [A-4]$$

Equation [A-1] simplifies to

$$\begin{aligned} \Phi_0 &= \frac{r_2 - r_1}{\pi\kappa} \left[ -\frac{\pi}{2} \ln \frac{\epsilon^2}{16} - \frac{1}{2} \int_{-1}^1 \frac{\ln(x-x')^2}{\sqrt{1-x^2}} dx' \right. \\ &\quad \left. + \pi\kappa\epsilon \ln \epsilon + O(\epsilon) \right] \quad [A-5] \end{aligned}$$

The integral in this equation has the remarkable property that it is a constant if  $-1 < x < 1$ . Then

$$\int_{-1}^1 \frac{\ln(x-x')^2}{\sqrt{1-x^2}} dx' = -2\pi \ln 2 \quad [A-6]$$

This property manifests itself, for example, in the primary current and potential distributions (18) for a strip electrode embedded in an insulating plane. Then the primary current distribution on the electrode is like case 1, treated here, and the constancy of the integral in Eq. [A-6] is required to produce a constant potential on the electrode.

By the introduction of Eq. [A-6], the ring current for case 1, and approximations valid for thin rings, Eq. [A-5] becomes

$$\Phi_0 = \frac{I_r}{2\kappa r_2 \pi^2} \left[ \ln 32 - \ln \left( 1 - \frac{r_1}{r_2} \right) - \epsilon(2-x) \ln \epsilon + O(\epsilon) \right] \quad [A-7]$$

This potential distribution is nearly constant, and we see that case 1 alone provides an approximation to the primary current and potential distributions for thin rings. Equation [A-7] thus gives the basis for the limiting behavior of  $\kappa r_2 R_{rr}$  (see Eq. [27] and Fig. 3).

#### LIST OF SYMBOLS

$B_n$	coefficients in series 18 for the potential
$I_d$	disk current, A
$I_r$	ring current, A
$K$	complete elliptic integral of the first kind
$m$	see Eq. [16]
$M_{2n}$	Legendre function of imaginary argument
$P_k$	Legendre polynomial
$r$	radial position in cylindrical coordinates, cm
$r_0$	radius of disk, cm
$r_1$	inner radius of ring, cm
$r_2$	outer radius of ring, cm
$r^*$	position on ring electrode, cm
$R_{dd}, R_{dr}, R_{rd}, R_{rr}$	resistances defined by Eq. [2] and [3], ohm
$R_D, R_R, R_C, R_C'$	resistances defined by Eq. [28] and [29], ohm
$R_{Aux}, R_{Aux}'$	resistances defined by Eq. 30, ohm
$R_D^D, R_D^R, R_R^D, R_R^R$	dimensionless resistances
$S$	surface area, $\text{cm}^2$
$V_d$	disk potential, V
$V_r$	ring potential, V
$V_T$	potential at the reference electrode, V
$V_0$	volume, $\text{cm}^3$
$x$	see Eq. [13]

$z$	distance from the plane of the disk, cm
$\eta$	rotational elliptic coordinate
$\kappa$	conductivity of the solution, $\text{ohm}^{-1}\text{-cm}^{-1}$
$\xi$	rotational elliptic coordinate
$\rho$	radial position in spherical coordinates, cm
$\Phi$	potential in the solution, V

#### REFERENCES

1. A. Frumkin, L. Nekrasov, B. Levich, and Ju. Ivanov, *J. Electroanal. Chem.*, **1**, 84 (1959).
2. W. J. Albery and S. Bruckenstein, *Trans. Faraday Soc.*, **62**, 1920 (1966).
3. W. H. Smyrl and J. Newman, *This Journal*, **119**, 212 (1972).
4. B. Miller and M. I. Bellavance, *ibid.*, **120**, 42 (1973).
5. M. Shabrang and S. Bruckenstein, *ibid.*, **121**, 1439 (1974).
6. W. H. Smyrl and J. Newman, *ibid.*, **119**, 208 (1972).
7. C. Gabrielli, M. Keddani, and H. Takenouti, *J. Chim. Phys.*, **69**, 737 (1972).
8. J. Newman, *This Journal*, **117**, 507 (1970).
9. K. Nisancioglu and J. Newman, *ibid.*, **120**, 1339 (1973).
10. K. Nisancioglu and J. Newman, *ibid.*, **120**, 1356 (1973).
11. K. Nisancioglu and J. Newman, *ibid.*, **121**, 523 (1974).
12. P. Pierini and J. Newman, In preparation.
13. F. B. Hildebrand, "Advanced Calculus for Applications," p. 293, Prentice-Hall, Inc., Englewood Cliffs, New Jersey (1962).
14. J. Newman, in "Electroanalytical Chemistry," A. J. Bard, Editor, pp. 321-334, Marcel Dekker, Inc., New York (1973).
15. J. Newman, *This Journal*, **113**, 501 (1966).
16. J. Newman, *ibid.*, **113**, 1235 (1966).
17. J. J. Miksis, Jr., M.S. Thesis, University of California, Berkeley, In preparation.
18. C. Wagner, *This Journal*, **98**, 116 (1951).

## Rapid Computation of Current Distribution by Orthogonal Collocation

Reinaldo Cabán and Thomas W. Chapman\*

Department of Chemical Engineering, University of Wisconsin, Madison, Wisconsin 53706

#### ABSTRACT

Current distributions on two plane, parallel electrodes embedded in the walls of a flow channel have been computed by orthogonal collocation. Although the calculation includes the effects of mass transfer, electrode spacing, and complete Butler-Volmer kinetics, accurate computation of current density distribution requires only 2 sec of computing time. Cell polarization curves are readily generated with applied potential as the independent variable. It is suggested that the speed and efficiency of the collocation method can make possible the analysis of more complicated problems such as mixed-potential processes and can also facilitate the interpretation of experimental polarization data.

The design of electrolysis cells is primarily an empirical experimental endeavor because of the complex phenomena involved in electrochemical systems. Development and optimization of new industrial processes is a difficult and expensive task because of the multitude of parameters to be considered in cell design. The measurement of basic electrochemical properties such as kinetic parameters is also difficult for the same reason.

The application of systematic analysis to these problems requires that one be able to characterize current distribution and polarization behavior of a cell given a knowledge of the hydrodynamics and physical

chemistry of the system. Newman (1) has outlined the basic problem of computing current distribution below the limiting current when both concentration and potential variations as well as electrode kinetics are important. Newman and others (2-7) have in recent years analyzed a number of geometries to show the effect of various parameters on the uniformity of the current distribution. Each one of the problems treated has required significant computational effort on a high speed digital computer. In this paper we present an alternative procedure for solving such problems. Although the method presented here yields only an approximation to the complete solution, it can be made quite accurate. Furthermore, since it generally requires relatively little computation time, it may be extended to more complicated problems such as the cal-

\* Electrochemical Society Active Member.

Key words: current distribution, electrochemical mass transfer, electrode kinetics, cell polarization, orthogonal collocation.

ulation of current efficiency or corrosion rates where multiple electrochemical reactions occur. It may also be useful for repetitive calculations in the statistical estimation of system parameters from experimental data.

Probably the most comprehensive treatment of a current distribution problem accomplished so far is the work of Parrish and Newman (4) on two plane, parallel electrodes in channel flow. Accordingly, we choose this example to illustrate our method as it provides a measure of the relative computational effort required to obtain current distributions and polarization curves.

### Mathematical Formulation of the Problem

Parrish and Newman (4) have presented the mathematical formulation of the current distribution problem for two planar electrodes of equal length  $L$  which are located opposite one another in the walls of a channel of width  $h$ . The flow through the channel is laminar, and the Peclet number is large so that a thin diffusion layer approximation is valid.

The potential in the bulk solution can be written for this geometry (7) as

$$\begin{aligned} \phi(x,y) = \bar{\phi} - \frac{1}{2\pi\kappa_s} \int_0^L i_{\text{cath}}(\bar{x}) \ln \left\{ \sinh^2 \frac{\pi}{2h} (x - \bar{x}) \right. \\ \left. + \sin^2 \frac{\pi}{2h} (y - h) \right\} d\bar{x} - \frac{1}{2\pi\kappa_s} \int_0^L i_{\text{an}}(\bar{x}) \\ \ln \left\{ \cosh^2 \frac{\pi}{2h} (x - \bar{x}) + \sin^2 \frac{\pi y}{2h} \right\} d\bar{x} \quad [1] \end{aligned}$$

where  $x$  is distance downstream from the leading edges of the electrodes,  $y$  is distance normal from the anode towards the cathode, and  $i_{\text{cath}}(x)$  and  $i_{\text{an}}(x)$  are the local current densities on the cathode and anode. The latter are taken to be negative and positive, respectively. The constant  $\bar{\phi}$  represents the potential of the solution in the absence of current, relative to ground.

Parrish and Newman express the current distribution on the electrodes as an integral over the limiting current distribution and the actual surface concentration distribution. Stewart (8) has shown that the surface concentration can similarly be written as an integral of the current distribution on the electrode and the uniform-flux concentration distribution. This form is more convenient for our purposes so we write the surface concentration of a reactive solute on each electrode as

$$\begin{aligned} \frac{c_0}{c_\infty} = \frac{c_{\text{an};\text{cath}}(x)}{c_\infty} = 1 - \left( \frac{Dh}{18\langle v \rangle} \right)^{1/3} \frac{s_R(1-t_R)}{\Gamma\left(\frac{2}{3}\right)nFDc_\infty} \\ \times \int_0^x \frac{i_{\text{an};\text{cath}}(\bar{x})}{[x-\bar{x}]^{2/3}} d\bar{x} \quad [2] \end{aligned}$$

For convenience we consider the same reaction to occur at each electrode, metal dissolution at the anode and deposition at the cathode ( $s_R = 1$ ) with kinetics of the form

$$i(x) = i_0(c_\infty) \left[ \frac{c_0}{c_\infty} \right]^\gamma \left[ e^{\frac{\alpha_A F \eta_s}{RT}} - e^{-\frac{\alpha_C F \eta_s}{RT}} \right] \quad [3]$$

where  $c_0$  is the surface concentration,  $c_{\text{an}}(x)$  or  $c_{\text{cath}}(x)$ , on each electrode, and  $\eta_s$  is the surface overpotential of the electrode.

The applied cell potential  $V$  is the difference between the anode potential  $V_{\text{an}}$  and the cathode potential  $V_{\text{cath}}$

$$V = V_{\text{an}} - V_{\text{cath}} \quad [4]$$

where

$$V_{\text{an}} = \phi_{0,\text{an}}(x) + \eta_{s,\text{an}}(x) + \eta_{c,\text{an}}(x) \quad [5a]$$

and

$$V_{\text{cath}} = \phi_{0,\text{cath}}(x) + \eta_{s,\text{cath}}(x) + \eta_{c,\text{cath}}(x) \quad [5b]$$

The electrostatic potential  $\phi_0(x)$  is obtained by extrapolating the solution potential  $\phi(x,y)$ , given by Eq. [1] to the electrode surfaces,  $y = 0$  or  $h$ . The concentration overpotential at each electrode is given by

$$\eta_c = \frac{RT}{\lambda F} \left[ \ln \frac{c_0}{c_\infty} + t_+ \left( 1 - \frac{c_0}{c_\infty} \right) \right] \quad [6]$$

where

$$\lambda \equiv -n \quad [7a]$$

for a well-supported electrolyte and

$$\lambda = \frac{-z_+ z_-}{z_+ - z_-} \quad [7b]$$

for a solution of a binary electrolyte.

Finally, the currents passing through the two electrodes must be equal so that

$$\int_0^L i_{\text{cath}}(x) dx + \int_0^L i_{\text{an}}(x) dx = 0 \quad [8]$$

In order to reduce the number of parameters in the problem we define the following dimensionless groups and variables

$$\tau = - \frac{n\lambda F^2 D c_\infty}{4\pi\Gamma\left(\frac{4}{3}\right)(1-t_+)RT\kappa_s} \left( \frac{18\langle v \rangle L^2}{hD} \right)^{1/3} \quad [19]$$

$$\xi = x/L \quad [10]$$

$$\alpha = \alpha_A/\lambda \quad [11a]$$

$$\beta = \alpha_C/\lambda \quad [11b]$$

$$\psi = \pi L/2h \quad [12]$$

$$c^* = c_0/c_\infty \quad [13]$$

$$V^* = \frac{\lambda F}{RT} V \quad [14]$$

$$\eta_c^* = \eta_c \frac{\lambda F}{RT} \quad [15]$$

$$\eta_s^* = \eta_s \frac{\lambda F}{RT} \quad [16]$$

$$\phi_0^* = \frac{\lambda F}{RT} \phi_0 \quad [17]$$

$$\bar{\phi}^* = \frac{\lambda F}{RT} \bar{\phi} \quad [18]$$

$$i_0^* = \frac{i_0(c_\infty)}{|i_{\text{lim}}|} \quad [19]$$

and

$$i^*(\xi) = \frac{i(x)}{|i_{\text{lim}}|} \quad [20]$$

In these calculations we assume that the cathodic reaction is the reduction of a cationic solute species so that  $i_{\text{lim}}$  is taken to be the limiting current at the cathode

$$i_{\text{lim}} = \frac{nFDc_\infty}{(1-t_+)\Gamma\left(\frac{4}{3}\right)} \left( \frac{2\langle v \rangle}{3Dhx} \right)^{1/3} \quad [21]$$

where  $(-n)$  is the number of electrons required to reduce a cation. Therefore, the average limiting current used in the above definitions is

$$\langle i_{\text{lim}} \rangle = -\frac{3}{2} \frac{nFDc_{\infty}}{(1-t_+) \Gamma\left(\frac{4}{3}\right)} \left(\frac{2\langle v \rangle}{3DhL}\right)^{1/3} \quad [22]$$

With these definitions the basic equations become

$$\phi_{0,\text{cath}}^*(\zeta) = \bar{\phi}^* - T \left\{ \int_0^1 i_{\text{cath}}^*(\bar{\zeta}) \ln [\sinh^2 \psi(\zeta - \bar{\zeta})] d\bar{\zeta} + \int_0^1 i_{\text{an}}^*(\bar{\zeta}) \ln [\cosh^2 \psi(\zeta - \bar{\zeta})] d\bar{\zeta} \right\} \quad [23]$$

$$\phi_{0,\text{an}}^*(\zeta) = \bar{\phi}^* - T \left\{ \int_0^1 i_{\text{cath}}^*(\bar{\zeta}) \ln [\cosh^2 \psi(\zeta - \bar{\zeta})] d\bar{\zeta} + \int_0^1 i_{\text{an}}^*(\bar{\zeta}) \ln [\sinh^2 \psi(\zeta - \bar{\zeta})] d\bar{\zeta} \right\} \quad [24]$$

$$c_{\text{cath}}^*(\zeta) = 1 + \frac{3\sqrt{3}}{4\pi} \int_0^{\zeta} \frac{i_{\text{cath}}^*(\bar{\zeta})}{[\zeta - \bar{\zeta}]^{2/3}} d\bar{\zeta} \quad [25]$$

$$c_{\text{an}}^*(\zeta) = 1 + \frac{3\sqrt{3}}{4\pi} \int_0^{\zeta} \frac{i_{\text{an}}^*(\bar{\zeta})}{[\zeta - \bar{\zeta}]^{2/3}} d\bar{\zeta} \quad [26]$$

$$\eta_{\text{c,cath}}^*(\zeta) = \ln c_{\text{cath}}^*(\zeta) + t_+ (1 - c_{\text{cath}}^*(\zeta)) \quad [27]$$

$$\eta_{\text{c,an}}^*(\zeta) = \ln c_{\text{an}}^*(\zeta) + t_+ (1 - c_{\text{an}}^*(\zeta)) \quad [28]$$

$$V_{\text{cath}}^* = \phi_{0,\text{cath}}^*(\zeta) + \eta_{\text{s,cath}}^*(\zeta) + \eta_{\text{c,cath}}^*(\zeta) \quad [29]$$

$$V_{\text{an}}^* = \phi_{0,\text{an}}^*(\zeta) + \eta_{\text{s,an}}^*(\zeta) + \eta_{\text{c,an}}^*(\zeta) \quad [30]$$

$$V^* = V_{\text{an}}^* - V_{\text{cath}}^* \quad [31]$$

$$i_{\text{cath}}^*(\zeta) = i_0^* [c_{\text{cath}}^*(\zeta)]^{\gamma} [e^{\alpha\eta_{\text{s,cath}}^*(\zeta)} - e^{-\beta\eta_{\text{s,cath}}^*(\zeta)}] \quad [32]$$

$$i_{\text{an}}^*(\zeta) = i_0^* [c_{\text{an}}^*(\zeta)]^{\gamma} [e^{\alpha\eta_{\text{s,an}}^*(\zeta)} - e^{-\beta\eta_{\text{s,an}}^*(\zeta)}] \quad [33]$$

and

$$\int_0^1 i_{\text{cath}}^*(\zeta) d\zeta = -\int_0^1 i_{\text{an}}^*(\zeta) d\zeta \quad [34]$$

The problem then is to solve Eq. [23]-[34] for  $i_{\text{cath}}^*$ ,  $i_{\text{an}}^*$ ,  $c_{\text{cath}}^*$ , and  $c_{\text{an}}^*$  as functions of  $\zeta$ , the parameters  $\alpha$ ,  $\beta$ ,  $\gamma$ ,  $t_+$ ,  $i_0^*$ ,  $T$ , and  $\psi$ , and the applied voltage  $V^*$ .

### Solution by Orthogonal Collocation

Parrish and Newman (4) solved the problem stated above by a numerical procedure which involved iterations within iterations. That is, for an assumed overpotential distribution the total applied potential was varied until the total current matched a specified level. Then the detailed overpotential distributions were adjusted until all equations were satisfied. Three to eight iterations were required for convergence in each inner loop, and up to 70 iterations on the overpotential distribution were required to obtain the complete solution. Numerical values of the functions at 100 to 180 points on an electrode were used, and the integrals were evaluated numerically. Note that two integrals must be evaluated at each mesh point on each iteration of the computation. Accordingly, the calculation was time consuming and expensive. Furthermore, it does not seem very feasible to extend the method to more complicated problems or to use it for routine, repetitive design or data-processing calculations.

An approximate numerical method suited to efficient calculation of complex problems is orthogonal collocation. Stewart has described collocation and its application to transport problems (9), and a variety of problems have been solved by the method (10,11).

The basic idea of collocation is that a trial solution is postulated as a finite series of orthogonal polynomials. The  $N$  coefficients of this series are determined by making the trial solution satisfy the basic equations of the problem at  $N$  particular collocation points, where  $N$  is a small number. The collocation points are chosen according to some optimality criterion, such as the requirement that the trial solution should give the best possible quadrature estimate of the solution for a given  $N$ .

In electrochemical design problems, the most important characteristic of the system is probably the polarization curve. Therefore, we may not be as interested in the detailed structure of the current distribution or the current density at a given point as in the total current for a given applied potential. Accordingly, we seek here the best estimate of the total current, expressed as the dimensionless average current density  $\langle i^* \rangle$  where

$$\langle i^* \rangle \equiv \frac{i_{\text{avg}}}{|\langle i_{\text{lim}} \rangle|} = \int_0^1 |i_{\text{cath}}^*| d\zeta = \int_0^1 i_{\text{an}}^* d\zeta \quad [35]$$

We implement a collocation procedure by postulating current distribution functions of the form

$$i_{\text{cath}}^{*(N)}(\zeta) = \sum_{j=0}^{N-1} A_j \zeta^j \quad [36]$$

and

$$i_{\text{an}}^{*(N)}(\zeta) = \sum_{j=0}^{N-1} B_j \zeta^j \quad [37]$$

where  $N$  is the order of the approximation and the  $2N$  coefficients  $A_j$  and  $B_j$  are to be determined. We obtain an optimal estimate of  $\langle i^* \rangle$  by Gauss-Legendre quadrature (12,13) for a given  $N$  by requiring that Eq. [36] and [37] satisfy Eq. [23] to [34] exactly at  $N$  collocation points  $\zeta_i$  on each electrode. The collocation points  $\zeta_i$  are chosen as the roots of  $P_N^*(\zeta)$ , the Legendre polynomial of degree  $N$  shifted to be orthogonal over the interval  $[0, 1]$  (13). After the coefficients  $A_j$  and  $B_j$  have been determined in this way, the average current may be estimated by the quadrature formula (12, 13)

$$\langle i^* \rangle \doteq \frac{1}{2} \sum_{i=1}^N w_i |i_{\text{cath}}^{*(N)}(\zeta_i)| \quad [38]$$

where  $w_i$  are the quadrature weights and  $i_{\text{cath}}^{*(N)}(\zeta_i)$  are the cathodic current densities at the points  $\zeta_i$  as computed from Eq. (36). According to the proper choice of the  $\zeta_i$ , this Gauss-Legendre quadrature formula would be exact if  $i_{\text{cath}}^*$  could be represented exactly by a polynomial of degree  $(2N - 1)$  or less. Thus, the estimate of the average current can be considerably more accurate than a local current density at any given order of approximation. Roots and quadrature weights for the shifted Legendre polynomials with  $N = 6, 7, \text{ and } 8$  are given in Table I.

Although Eq. [36] and [37] are written as truncated power series, they may be viewed as rearranged linear combinations of Legendre polynomials. Working in terms of the powers of  $\zeta$  is equivalent to using a set of explicit polynomials but is easier computationally. Identification of these power series as the linear combination of orthogonal polynomials permits the use of Eq. [38] and determines the proper collocation points for the computation.

We proceed by substituting Eq. [36] and [37] into Eq. [23] to [34]. For example, Eq. [25] and [26] for the surface concentrations become

$$c_{\text{cath}}^*(\zeta) = 1 + \frac{3\sqrt{3}}{4\pi} \sum_{j=0}^{N-1} A_j E_j(\zeta) \quad [39]$$

Table I. Collocation points  $\xi_i$  as roots of shifted Legendre polynomials of degree  $N$ , and the associated Gauss-Legendre quadrature weights  $w_i$  [derived from Ref. (13)]

Degree $N$	$i$	Collocation points $\xi_i$	Quadrature weights $w_i$
6	1	0.0337652429	0.1713244924
	2	0.1693953068	0.3607615730
	3	0.3806904070	0.4679139346
	4	0.6193095930	0.4679139346
	5	0.8306046932	0.3607615730
	6	0.9662347571	0.1713244924
7	1	0.0254460438	0.1294849662
	2	0.1292344072	0.2797053915
	3	0.2970774243	0.3818300505
	4	0.5000000000	0.4179591837
	5	0.7029225757	0.3818300505
	6	0.8707655928	0.2797053915
8	1	0.0198550718	0.1294849662
	2	0.1016667613	0.2223810345
	3	0.2372337950	0.3137066459
	4	0.4082826788	0.3626837834
	5	0.5917173212	0.3626837834
	6	0.7627662050	0.3137066459
	7	0.8983332387	0.2223810345
	8	0.9801449262	0.1012285363

and

$$c_{an}^*(\xi) = 1 + \frac{3\sqrt{3}}{4\pi} \sum_{j=0}^{N-1} B_j E_j(\xi) \quad [40]$$

where

$$E_j(\xi) = \int_0^\xi \frac{\bar{\xi}^j d\bar{\xi}}{[\xi - \bar{\xi}]^{2/3}} = 3^{j+1/3} \sum_{k=0}^j \frac{(-1)^{j-1} \binom{j}{k}}{3j - 3k + 1} \quad [41]$$

Note that the assumed form has allowed analytic evaluation of the superposition integral.

Similarly, Eq. [23] and [24] for the potential may be rewritten

$$\phi_{0,cath}^*(\xi) = \bar{\phi}^* - \tau \sum_{j=0}^{N-1} [A_j R_j(\xi) + B_j S_j(\xi)] \quad [42]$$

and

$$\phi_{0,an}^*(\xi) = \bar{\phi}^* - \tau \sum_{j=0}^{N-1} [A_j S_j(\xi) + B_j R_j(\xi)] \quad [43]$$

where

$$R_j(\xi) = \int_0^{\xi-1} \bar{\xi}^j \ln [\sinh^2 \psi(\xi - \bar{\xi})] d\bar{\xi} \quad [44]$$

and

$$S_j(\xi) = \int_0^{\xi-1} \bar{\xi}^j \ln [\cosh^2 \psi(\xi - \bar{\xi})] d\bar{\xi} \quad [45]$$

Although these integrals cannot be determined analytically, we note that they need to be evaluated only at the  $N$  collocation points  $\xi_i$  and that for a given value of  $N$  the two  $N \times N$  matrices,  $R_j(\xi_i)$  and  $S_j(\xi_i)$ , need to be evaluated only once and not repeatedly.

If all the system equations were linear, it would be a straightforward procedure to determine  $A$  and  $B$  by requiring that Eq. [29] and [30] be satisfied at each of the  $N$  collocation points on each electrode. Because of the nonlinear nature of the current-potential relationships, however, an iterative procedure is required. Fortunately the collocation formulation lends itself to a more systematic iterative scheme than is possible with a brute-force numerical method.

### Computational Procedure

To obtain the coefficients  $A$  and  $B$  we must satisfy

$$f(\xi_i) = i_0^* c_{cath}^{*\gamma}(\xi_i) [e^{\alpha\eta_{s,cath}^*(\xi_i)} - e^{-\beta\eta_{s,cath}^*(\xi_i)}] - \sum_{j=0}^{N-1} A_j \xi_i^j = 0 \quad [46]$$

at each collocation point  $\xi_i$  on the cathode and similarly

$$g(\xi_i) = i_0^* c_{an}^{*\gamma}(\xi_i) [e^{\alpha\eta_{s,an}^*(\xi_i)} - e^{-\beta\eta_{s,an}^*(\xi_i)}] - \sum_{j=0}^{N-1} B_j \xi_i^j = 0 \quad [47]$$

on the anode, where the concentrations are given by Eq. [39] and [40] and the overpotentials are obtained from a combination of Eq. [27]-[31], [42], and [43].

At this point we recognize that in addition to the  $2N$  coefficients  $A_j$  and  $B_j$  we must also evaluate  $\bar{\phi}^*$ . This can be done by including Eq. [34] with the  $2N$  Eq. [46] and [47]. Equation [34] may be rewritten as

$$\int_0^1 \sum_{k=0}^{N-1} (A_k \xi^{2k} + B_k \xi^k) d\xi = \sum_{k=0}^{N-1} \left( \frac{A_k + B_k}{k+1} \right) = 0 \quad [48]$$

This relationship completes the necessary set of  $2N + 1$  equations.

We solve these nonlinear algebraic equations by Newton's method (12) by writing  $f(\xi_i)$  and  $g(\xi_i)$  as truncated (linear) Taylor series in the variables  $A_0, A_1, \dots, A_{N-1}, B_0, B_1, \dots, B_{N-2}$ , and  $\bar{\phi}^*$  around trial values of these unknowns. The last coefficient  $B_{N-1}$  is determined by Eq. [48].

The computational algorithm proceeds as follows:

1. The applied potential  $V^*$  is specified. The value of  $V_{an}^*$  or  $V_{cath}^*$  is fixed arbitrarily and the other obtained from Eq. [31].

2. The degree of approximation  $N$  is chosen, and the collocation points  $\xi_i$  are obtained as the roots of  $P_N^*(\xi)$ .

3. The coefficients  $E_j(\xi_i), S_j(\xi_i)$ , and  $R_j(\xi_i)$  are computed for  $j = 1, 2, \dots, N$  and  $i = 1, 2, \dots, N$  from Eq. [41], [44], and [45]. These arrays need to be determined only once for a given  $N$ .

4. Initial values of  $A_j$  and  $B_j$  are obtained by guessing a realistic current distribution and inverting the matrix Eq. [36] and [37] as written at the collocation points.  $\bar{\phi}^*$  is set to zero, and  $B_{N-1}$  made consistent by use of Eq. [48].

5. The surface concentrations are calculated at the collocation points by Eq. [39] and [40].

6. The concentration overpotentials  $\eta_c^*$  are computed at the collocation points by Eq. [27] and [28].

7. The surface potentials  $\phi_0^*$  at the collocation points are computed by Eq. [42] and [43].

8. The surface overpotentials  $\eta_s^*$  at the collocation points are computed from Eq. [29] and [30].

9. The current densities  $i_{cath; an}^{*(N)}$  at the collocation points are computed from Eq. [32] and [33].

10. The local current densities are tested for convergence with respect to the previous values of the  $A$  and  $B$  coefficients. Specifically, the rms of the changes of the current densities at all collocation points relative to the values of the initial guess or the previous calculation is computed. The convergence criterion used here was a rms change less than  $10^{-4}$ , where the current densities have been normalized by  $\langle i^* \rangle$ .

11. If the convergence criterion is not satisfied, the partial derivatives  $\frac{\partial g(\xi_i)}{\partial A_j}$  and  $\frac{\partial f(\xi_i)}{\partial A_j}$  for  $j = 0, 1, \dots$

$N - 1, \frac{\partial g(\xi_i)}{\partial B_j}$  and  $\frac{\partial f(\xi_i)}{\partial B_j}$  for  $j = 0, 1, \dots, N - 2$ , and

$\frac{\partial f(\xi_i)}{\partial \bar{\phi}^*}$  and  $\frac{\partial g(\xi_i)}{\partial \bar{\phi}^*}$  are computed at each of the collocation points.

The equations for these derivatives can be obtained by differentiating Eq. [46] and [47] after the necessary substitutions have been made. Newton's method is applied to Eq. [46] and [47] to obtain new estimates of  $A_k, B_k$ , and  $\bar{\phi}^*$ ; the algorithm then cycles back to step 5 and iterates until convergence is attained.

12. The foregoing procedure is repeated with increasing  $N$  until some characteristic quantity, say  $\langle i^* \rangle$  as obtained from Eq. [38], converges to a steady value within specified limits, taken here to be 0.01%. This criterion tests the accuracy of the polynomial approximation.

### Results

Calculations have been done for a variety of parameter values. For total currents near the limiting current where the most nonuniform distributions are observed, as few as seven collocation points ( $N = 7$ ) give satisfactory results for  $\langle i_{an}^* \rangle$  and  $\langle i_{cath}^* \rangle$ , and 11 iterations on the polynomial coefficients give convergence within the specified limits. For small values of  $\tau$ , where the current distribution is fairly symmetrical, only four iterations were required. A typical problem required no more than 2 sec of computing time on a Univac 1110 computer to obtain current distribution curves.

In particular, calculations were done for  $\tau = 3$  and 15, and for  $i_0^* = 0.05$  and 0.5; the other parameters  $\alpha$ ,  $\beta$ ,  $\gamma$ ,  $t_+$ , and  $h/L$  were set at 0.5. The applied potential  $V$  was varied from zero to more than 1V. These values were chosen to correspond to results published by Parrish and Newman (4).

Convergence was always obtained even for currents very near the limiting current ( $\langle i^* \rangle = 0.99$ ) although double precision computation (20-place accuracy) was required there. Figure 1 shows current distributions on the cathode at selected fractions of the limiting current for  $\tau = 15$  and  $i_0^* = 0.05$  as computed with  $N = 7$ . The distributions at limiting current and at  $\langle i^* \rangle = 0.79$  for  $h/L = \infty$  are also shown.

Figure 2 shows the reactant concentration distributions on the cathode surface corresponding to the curves in Fig. 1.

Figure 3 shows cell polarization curves at various combinations of  $\tau$  and  $i_0^*$ .

### Discussion of Results

The parameters used to obtain Fig. 1 and 2 were chosen to correspond roughly with those represented by Fig. 7 and 9 in Parrish and Newman (4). Compari-

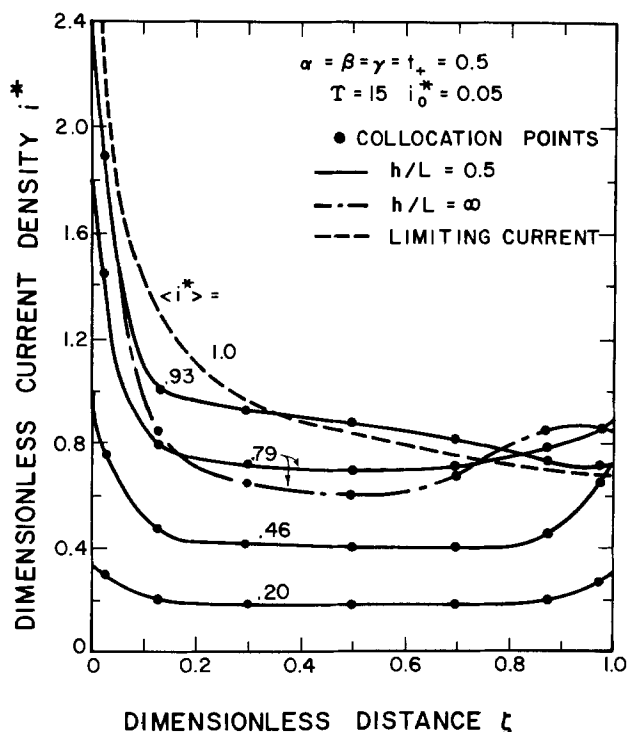


Fig. 1. Current density distributions on the cathode at various fractions of limiting current.

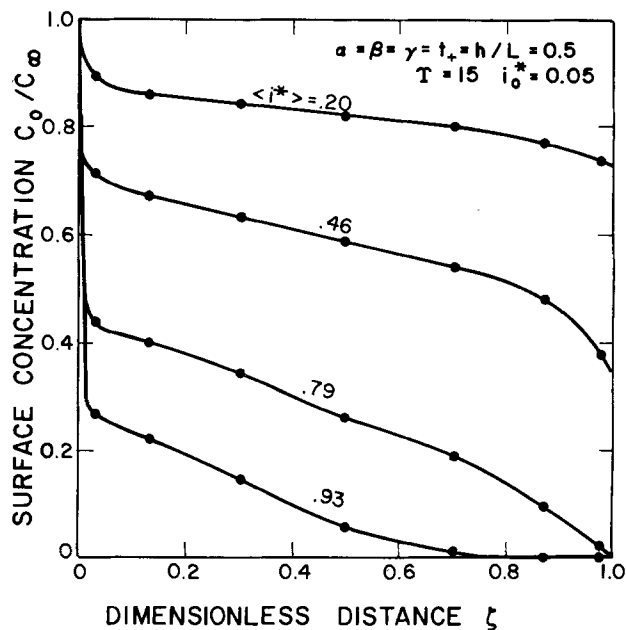


Fig. 2. Reactant concentration distribution on the cathode surface at various fractions of limiting current.

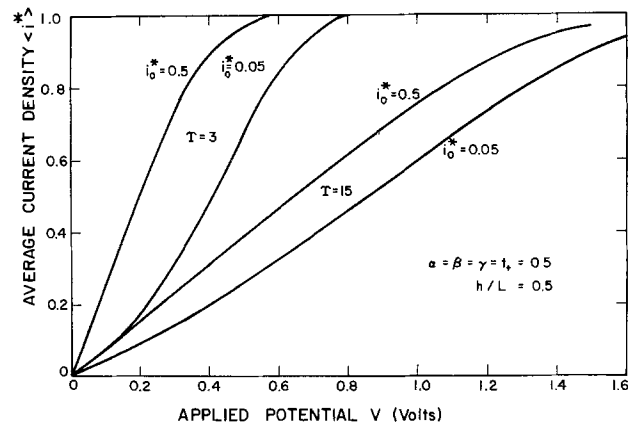


Fig. 3. Polarization curves plotted as average current density, relative to limiting current, vs. applied potential for various parameter values.

son with their work shows that our results for both anodic and cathodic current distribution and surface concentration are quite similar to the more detailed numerical computations. In fact, our calculations with seven points are even capable of reproducing the maximum in the local current density observed by Parrish and Newman (3) at currents near the limiting current with large  $h/L$ . (A similar but slight maximum is also observed around  $\langle i^* \rangle = 0.85$  for  $h/L = 0.5$ .)

The results for large  $h/L$  were obtained by reproducing the earlier calculations (3) for the case where a plane cathode could be considered separately from polarization behavior on the anode. In that case we obtained results in 1 sec of computing time and within four to seven iterations except at currents very near (99%) the limiting current where 15 iterations were required. This effort can be compared with Parrish and Newman's procedure which took 50 to 140 mesh points on the electrode and as many as 35 iterations. In their method the integral equations must be evaluated at each mesh point in each iteration so that almost 5000 numerical integrations might be required.

It should be noted that Parrish and Newman generally simplify the complete kinetics expression, Eq. [3], to either the linear or the Tafel form. Because the collocation method can handle any general kinetics

expression, there is no particular advantage to making such simplifying assumptions.

Parrish and Newman have already commented on the physical significance of the current distribution curves. We shall mention here only that we have chosen a slightly different nondimensionalization of the problem. We have defined  $\tau$  in Eq. [9] to represent the ratio of electrical resistance to mass transfer resistance in the solution; it is proportional to the parameter  $N$  used by Parrish and Newman. On the other hand, we have chosen  $i_o^*$  rather than  $J$  of Parrish and Newman to represent the importance of kinetic effects. Their parameter  $\delta$  has no counterpart in our formulation because we specify  $V$  and compute the current. Their procedure is to specify  $\delta$ , that is, the total current, as the independent variable.

The critical parameters in our calculations then are  $\tau$  and  $i_o^*$ . At large  $\tau$  the current distribution is determined by potential effects and approaches the secondary or primary current distribution according to  $i_o^*$ . At low values of  $\tau$  the current distribution approaches the limiting current distribution provided that  $i_o^*$  is large. At intermediate values of  $\tau$  and at small  $i_o^*$  the current distribution is more uniform than in either limiting case.

The important point of this work is that current distribution problems can be solved with good accuracy but nominal computational effort by means of orthogonal collocation. Because of the facility and speed with which the method converges we are encouraged to extend it to even more difficult problems. An obvious possibility is the treatment of mixed-potential processes where several electrode reactions occur on the same electrode.

The problem treated here was simplified considerably by the thin diffusion layer approximations. Thus, it was possible to satisfy the relevant differential equations for  $c_0$  and  $\phi$  by the integral Eq. [1] and [2]. The collocation procedure used here is required only to satisfy boundary conditions on the electrodes. This might be called boundary collocation (10). In the more general case one must solve coupled, nonlinear partial differential equations in the solution as well as to satisfy the nonlinear, coupled boundary conditions on the electrodes. Such a problem would be extremely difficult to solve by conventional finite difference methods. It may be reasonably tractable, however, by the method of mixed collocation (10) where collocation points are chosen both on the boundaries as well as at selected points in the interior of the electrolytic solution.

### Acknowledgments

The authors acknowledge helpful discussions with Professor Warren E. Stewart concerning the use of orthogonal collocation. Reinaldo Cabán is on supported leave from the Department of Chemical Engineering of the University of Puerto Rico at Mayaguez. This work has been funded in part by the National Oceanic and Atmospheric Administration's Office of Sea Grant, Department of Commerce, through an institutional grant to the University of Wisconsin.

Manuscript received July 16, 1975; revised manuscript received March 22, 1976.

Any discussion of this paper will appear in a Discussion Section to be published in the June 1977 JOURNAL. All discussions for the June 1977 Discussion Section should be submitted by Feb. 1, 1977.

### LIST OF SYMBOLS

$A, A_j$	coefficients defined by Eq. [36]
$B, B_j$	coefficients defined by Eq. [37]
$c$	concentration, mole/m <sup>3</sup> , or dimensionless surface concentration
$D$	diffusion coefficient, m <sup>2</sup> /sec
$E_j$	coefficient defined by Eq. [41]
$F$	Faraday's constant, 96,487 C/equiv

$f$	function defined by Eq. [46]
$g$	function defined by Eq. [47]
$h$	distance between electrodes, m
$i$	current density, A/m <sup>2</sup>
$i_o$	exchange current density, A/m <sup>2</sup>
$i_{lim}$	limiting current density at cathode, A/m <sup>2</sup>
$i^*$	dimensionless current density, normal component
$L$	length of electrodes, m
$N$	number of collocation points on an electrode
$n$	number of electrons produced by electrode reaction when written as an oxidation. $n = -z_+$ for reaction considered here
$P_i^*$	shifted Legendre polynomial of degree $i$
$R$	universal gas constant, 8.3143 J/mole K
$R_j$	coefficient defined by Eq. [44]
$S_j$	coefficient defined by Eq. [45]
$s_R$	stoichiometric coefficient of the solute species, which is the reactant in the cathodic reaction
$Sc$	Schmidt number
$T$	temperature, °K
$t_R, t_+$	transference number of reactive solute, taken here to be a cation
$\langle v \rangle$	average flow velocity, m/sec
$V$	voltage or electrode potential, V
$w_i$	quadrature weight at collocation point $\xi_i$
$x$	distance along electrode $m$
$z_i$	charge number of species $i$

### Greek Letters

$\alpha_A$	anodic transfer coefficient
$\alpha$	dimensionless anodic transfer coefficient
$\alpha_C$	cathodic transfer coefficient
$\beta$	dimensionless cathodic transfer coefficient
$\gamma$	a dimensionless kinetic parameter, the order of the reaction
$\kappa$	conductivity, mho/cm
$\Gamma(x)$	gamma function of $x$
$\xi$	dimensionless distance, $x/L$
$\eta_s$	surface overpotential, V
$\eta_c$	concentration overpotential, V
$\lambda$	parameter defined by Eq. [7]
$\tau$	dimensionless parameter defined by Eq. [9]
$\phi$	electric potential, V
$\phi$	reference potential in solution, V
$\psi$	dimensionless electrode length, $\pi L/2h$

### Common Subscripts

an	refers to the anode
cath	refers to the cathode
an; cath	applies to either anode or cathode
$i$	of species $i$ or index of collocation points
0	evaluated at the electrode surface
$\infty$	refers to bulk solution

### Common Superscripts

*	dimensionless variable
(N)	refers to the Nth approximation

### REFERENCES

1. J. Newman, "Electrochemical Systems," Prentice-Hall, Inc., Englewood Cliffs, New Jersey (1973).
2. J. Newman, *This Journal*, **113**, 1235 (1966).
3. W. R. Parrish and J. Newman, *This Journal*, **116**, 169 (1969).
4. W. R. Parrish and J. Newman, *ibid.*, **117**, 43 (1970).
5. W. Smyrl and J. Newman, *ibid.*, **119**, 212 (1972).
6. K. Nisancioglu and J. Newman, *ibid.*, **121**, 241 (1974).
7. C. Wagner, *ibid.*, **98**, 116 (1951).
8. W. E. Stewart, *A.I.Ch.E. J.*, **9**, 528 (1963).
9. W. E. Stewart, in "Lectures in Transport Phenomena," No. 4 in A.I.Ch.E. Continuing Education Series, Bird, Stewart, Lightfoot, and Chapman, Editors, Chap. 4, A.I.Ch.E., New York (1969).
10. J. V. Villadsen and W. E. Stewart, *Chem. Eng. Sci.*, **22**, 1483 (1967).
11. J. P. Sørensen and W. E. Stewart, *ibid.*, **29**, 811 (1974).
12. F. B. Hildebrand, "Numerical Analysis," 2nd ed., McGraw-Hill Book Company, New York (1974).
13. M. Abramowitz and I. Stegun, Editors, "Handbook of Mathematical Functions," pp. 773, 887 (entry 25.4.30), and 916, National Bureau of Standards, Washington, D. C. (1964).



# The Behavior of an Oscillating Solid Microelectrode for Voltammetric Studies in Aqueous and Molten Salt Solutions

P. Pint<sup>1</sup> and S. N. Flengas\*

Department of Metallurgy and Materials Science, University of Toronto, Toronto 181, Ontario, Canada

## ABSTRACT

An oscillating planar solid indicator microelectrode was developed for voltammetric investigations. An investigation of the variables which affect the limiting current using this particular microelectrode was conducted. The electrode was successfully used in aqueous electrolytes, in molten nitrate electrolytes up to 330°C, and in molten equimolar sodium and potassium chlorides at 700°C.

The dropping mercury electrode has proven to be useful and convenient in aqueous polarography and also in low melting molten salt systems. However, it cannot be used at temperatures higher than 200°C due to the volatility of mercury.

Several high temperature polarizable indicator microelectrodes have been proposed, namely, the dropping molten metal electrodes (1, 2), the stationary wire electrode (3, 4), gas flushed electrodes (5), mechanically rotated wire (6), and rotated disk electrodes (7). The rotating disk electrode has been extensively and successfully studied, and the fluid flow characteristics have been understood particularly after the rigorous treatment by Levich (8). In high temperature liquids the convection currents are unpredictable and the electroreducible species do not migrate to the indicator electrode solely by diffusion. In the forementioned techniques controlled convection in the electrolyte was a necessary requirement for the attainment of reproducible limiting currents. Similarly, mention should be made of Lindsey's high frequency vibrated platinum wire microelectrode (9-11), and of the various vibrating dropping mercury electrodes (12, 13).

The electrode developed in this laboratory consists of a planar solid microelectrode, oscillated at low frequencies in a direction perpendicular to the surface of the electrolytic solution. The behavior of this electrode was studied in aqueous electrolytes where it could readily be compared to the dropping mercury electrode (DME), in molten nitrate melts at temperatures up to 330°C and in molten chlorides containing as the solvent the equimolar mixture of KCl and NaCl at 700°C. This electrode is particularly suited for fused salt systems because of its simplicity, the well-defined surface area, and its ability to operate in totally enclosed cells under a protective atmosphere and to yield reproducible and time-independent limiting currents.

## Experimental

The experimental assembly shown in Fig. 1 consists of the solid indicator microelectrode dipping into the electrolyte and a calomel (Hg, Hg<sub>2</sub>Cl<sub>2</sub>, KCl saturated) electrode as a nonpolarizable reference. The solutions in the two sections of the Pyrex cell are separated from each other by means of a low resistance agar plug.

The indicator microelectrode was made out of platinum or tungsten wires, about 0.5 mm diameter sealed into Pyrex glass tubing having a diameter of approximately 0.5 cm. The tip of the electrode was polished flat so that the electrode was in effect a flat tungsten or platinum disk encased in glass sheathing. The wire protruding from the top of the glass sheath was connected to the negative terminal of the polaro-

graph. The potentials to the cell were applied by means of the Fisher electropode (Model No. 65) and the resulting currents were recorded on the Fisher recorder (No. 66) which was coupled to the electropode. The potentials could be applied either automatically or manually. During the automatic operation the potential was applied at a rate of 200 mV/min corresponding to a chart speed of 10 divisions/in./min.

The mechanical oscillator consisted of a piston driven by a rotating off center disk. This arrangement imposed a harmonic vibrating motion on the electrode and the frequency of oscillation could be changed from zero to a maximum of about 350 oscillations/min. The amplitude of the stroke was constant at 0.5 cm.

For the experiments the cell assembly was immersed in a constant temperature water bath at 25°C. Prior to determining any I-V curves the solutions were flushed with argon gas which was bubbled through the side arm shown in Fig. 1 for approximately 10 min.

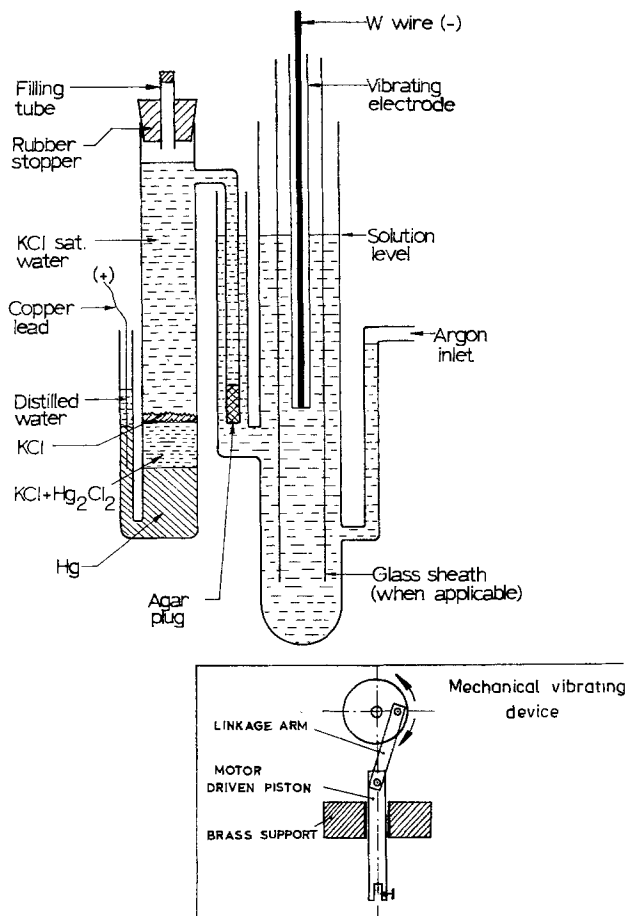


Fig. 1. Experimental cell assembly for aqueous voltammetry

\* Electrochemical Society Active Member.

<sup>1</sup> Present address: INCO Research Laboratories, Sheridan Park, Mississauga, Ontario, Canada.

Key words: polarography, molten salt systems, vibrating microelectrode.

Lead, copper, and cadmium salts were used in the aqueous investigations with the bulk of the experiments being conducted with  $\text{Pb}(\text{NO}_3)_2$  dissolved in 1N  $\text{NaNO}_3$  supporting electrolyte. The limiting currents ( $i_L$ ) in aqueous solutions were investigated as functions of the oscillation frequency  $\nu$ , the concentration of the solution  $C$ , the temperature, and of the viscosity of the solution. In addition the dependence of  $i_L$  on geometric factors such as the ratio of the exposed cross-section area of the metal wire electrode to the total cross-section area of the indicator electrode, the diameter of the electrolyte container, and the positioning of the electrode in the electrolyte container were investigated, as well as the macroscopic appearance of the flow patterns around the electrode due to its motion.

The limiting currents were obtained from the experimental I-V traces by the standard graphical technique.

The high temperature cell employing molten nitrates shown in Fig. 2, had an indicator electrode of platinum wire 0.508 mm in diameter sealed into a 5.64 mm diameter Pyrex capillary, as opposed to tungsten wire which was used in aqueous voltammetry. Tungsten was found to be unacceptable in these oxidizing melts since very high erratic diffusion currents were produced. In all cases the seal between the platinum and Pyrex appeared to be adequate.

The electrode could be introduced into the melt by sliding it through a "Sargent Teflon Seal," which also served as a gas seal during oscillation. A ground glass joint made possible the removal of the electrode assembly from the cell.

A large platinum disk (1.54  $\text{cm}^2$ ) served as the depolarized reference electrode. Argon could be bubbled over this electrode in order to stir or flush the electrolyte if so desired. Another large platinum foil electrode was incorporated into the system which was used for electropolishing the indicator electrode. Thus the electrode did not have to be removed for cleaning and the possibility of introducing impurities into the melt was minimized.

The potential of the reference electrode is stable under these conditions, as indicated by the reproduc-

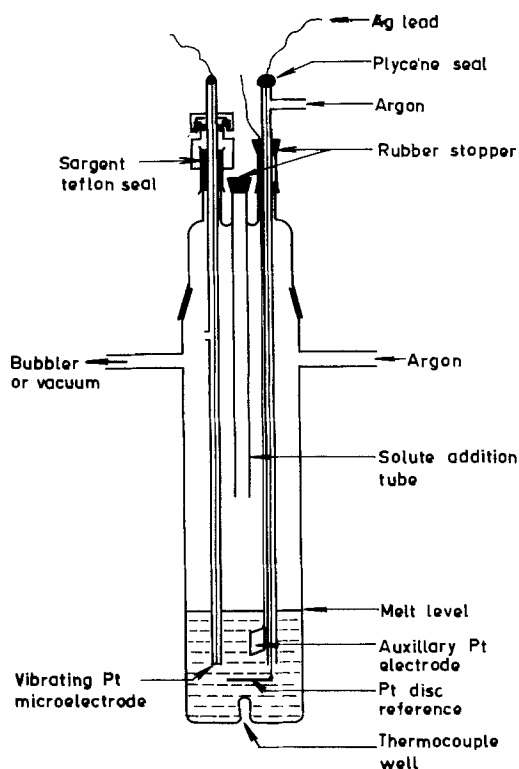


Fig. 2. Experimental cell assembly for high temperature voltammetry.

ibility of the decomposition potentials shown by the I-V curves. Although the complete anodic reaction cannot be defined from such data, it is expected that platinum immersed in a melt containing  $\text{NO}_3^-$  species should behave like an oxygen electrode.

Solute additions could be made to the melt through a glass tube located at the top of the cell.

With molten nitrates, the supporting electrolyte was a low melting mixture containing 54 mole per cent (m/o)  $\text{KNO}_3$  and 46 m/o  $\text{NaNO}_3$  (mp  $222^\circ\text{C}$ ). The electroactive species for all of these investigations was  $\text{AgNO}_3$ . The certified standard (A.C.S.) sodium nitrate and potassium nitrate, obtained from Fisher Scientific, were premixed and dried in air at about  $120^\circ\text{C}$ . These nitrates were loaded into a Pyrex cell and were vacuum dried and melted under argon. The silver nitrate (A.C.S.) from Johnson, Matthey, and Mallory was melted under vacuum and solidified under argon.

The cell containing about 250g of solvent electrolyte was heated in a resistance-type furnace, the temperature of which was kept constant to within  $\pm 3^\circ$  by means of a Thermovolt controller. The furnace was partially lined with a heavy grounded Inconel sheath in order to minimize temperature gradients in the melt and eliminate external electrical interference.

All experiments were conducted under an argon gas atmosphere.

The variables investigated were the effect of temperature on the background current in the supporting electrolyte, the dependence of  $i_L$  on the concentration of  $\text{AgNO}_3$ , the dependence of  $i_L$  on temperature at constant concentration of  $\text{AgNO}_3$ , and the dependence of  $i_L$  on the frequency of oscillation.

The 1:1 molar  $\text{NaCl-KCl}$  (mp  $660^\circ\text{C}$ ) was chosen as the solvent for high temperature voltammetric investigations. The electroactive  $\text{Ag}^+$  species was added as  $\text{AgCl}$ . The reagent grade sodium and potassium chlorides containing less than 0.01% total impurities, obtained from Fisher Chemical Company, were premixed and dried under vacuum at about  $100^\circ\text{C}$  for 48 hr. The temperature was then slowly raised to the melting point while anhydrous  $\text{HCl}$  gas was passed through the salts. The salts were then alternately purged with argon and evacuated, and then finally solidified under vacuum. The reagent grade silver chloride was obtained from Fisher Chemical Company and was treated at  $400^\circ\text{C}$  with anhydrous  $\text{HCl}$  gas.

The high temperature cell employing molten alkali metal chlorides was similar to that shown in Fig. 2, with the main difference being that the tungsten wire electrode was sealed into quartz glass by using Corning GSC-1 and GSC-3 glass which gave leakproof glass to metal seals. Also instead of the Teflon seal structure a brass bellows was used for the oscillating electrode assembly. The cell was of silica glass.

The reference, depolarized electrode was a high purity graphite rod (16.5  $\text{cm}^2$  surface area) around which argon gas could be bubbled.

The cell containing 250g of the prepared solvent was heated in a furnace containing a heavy grounded Inconel sheath which was controlled by a Thermovolt temperature controller at  $700^\circ \pm 3^\circ\text{C}$ .

## Results and Discussion

A typical I-V curve obtained for the reduction of divalent lead in a 1N  $\text{NaNO}_3$  supporting aqueous electrolyte solution can be seen in Fig. 3(a). The sharp increase in current at about  $-0.75\text{V}$  is due to the low overvoltage of hydrogen on tungsten. Figure 3(b) indicates the trace obtained employing the DME. The trace from the oscillating electrode (OE) is well defined and does not indicate the maximum shown on the DME polarogram.

Figure 4 illustrates the dependence of the limiting current on frequency. It can be seen that the limiting current decreases linearly with a decreasing frequency.

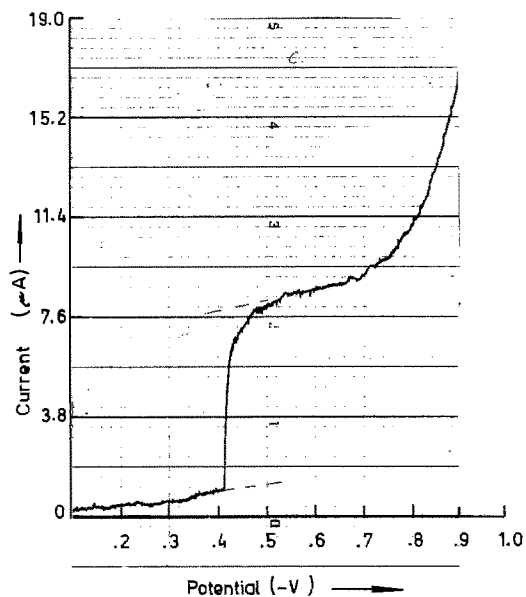


Fig. 3. (a) Typical I-V curve for the electroreduction of  $\text{Pb}^{2+}$  ions at the solid microelectrode at  $25^\circ\text{C}$ .

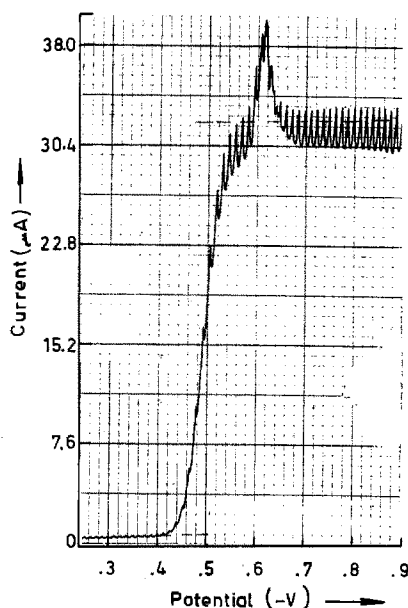


Fig. 3. (b) DME polarogram of  $\text{Pb}(\text{NO}_3)_2$  in  $\text{NaNO}_3$  at  $25^\circ\text{C}$

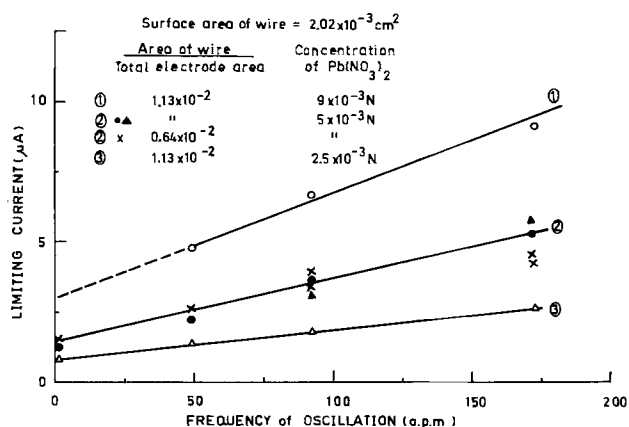


Fig. 4. The dependence of the limiting current on the oscillation frequency at  $25^\circ\text{C}$ .

The limiting current at zero frequency was determined from a single continuous I-V run. Generally the I-V

curves at zero frequency were poorly defined, indicated a time dependence, and had irregular plateaus. The dependence of  $i_L$  on the surface area of the microelectrode is shown in Fig. 5(a) and it is seen that the limiting current is proportional to the surface area of the metal. It is also important to note that the ratio ( $R$ ) of the cross-sectional area of the surface of the metal electrode to the total cross-sectional area of the entire electrode is an important variable, as is illustrated in Fig. 5b. This plot shows that  $i_L$  becomes independent of  $R$  at all concentrations when  $R$  exceeds about  $1/100$ . Furthermore, the bulk concentration of  $\text{Pb}(\text{NO}_3)_2$  and the limiting current are directly proportional as illustrated in Fig. 6.

The dependence of  $i_L$  on the temperature of the electrolyte appears to be linear. The ratio of  $i_L$  at  $25^\circ\text{C}$  to  $i_L$  at  $20^\circ\text{C}$  is 1.1 which is the value found for  $\text{Pb}^{2+}$  ions when employing the DME.

To increase the viscosity of the electrolyte, glycerin was added to aqueous solutions containing  $\text{Pb}(\text{NO}_3)_2$ . The limiting current decreases linearly with an increasing glycerin content and increasing viscosity as expected. Furthermore, it was found that the limiting current is independent of the dimensions of the container containing the electrolyte, providing that the oscillating electrode is not placed within a distance of about 3 cm from the bottom and the walls of the container.

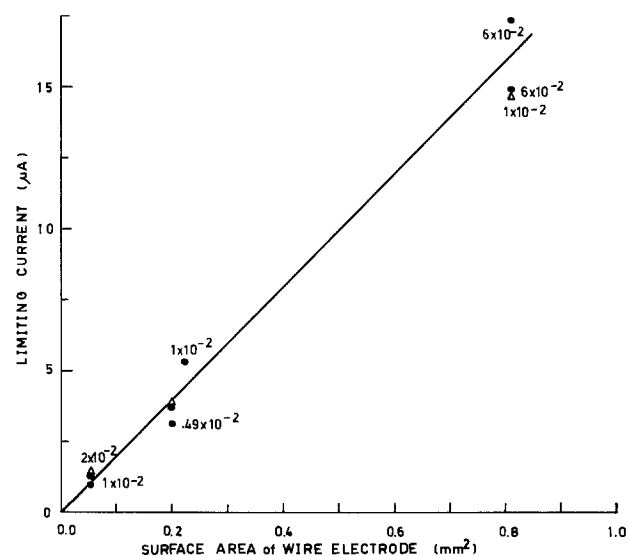


Fig. 5. (a) The dependence of the limiting current on the microelectrode surface area. Numbers along curve refer to the ratio  $R = \text{area of wire electrode} / \text{total surface area}$ .

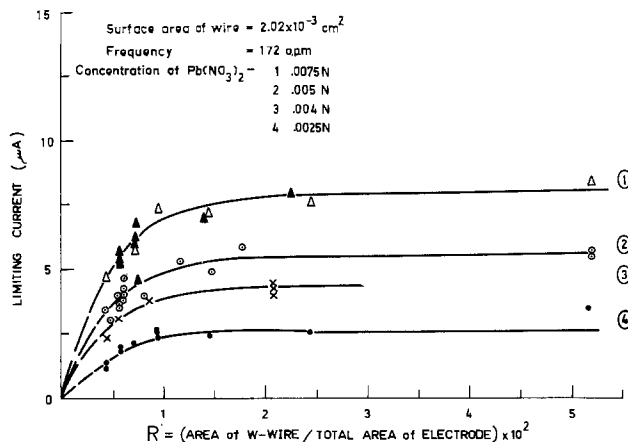


Fig. 5. (b) The dependence of the limiting current on the ratio of the area of tungsten wire to the total area of the electrode face, including glass sheathing at various concentrations of  $\text{Pb}(\text{NO}_3)_2$  in solution.

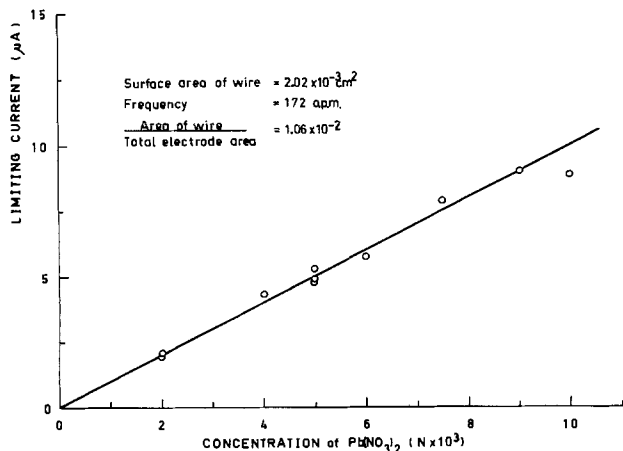


Fig. 6. The dependence of the limiting current on the concentration of  $\text{Pb}(\text{NO}_3)_2$  at  $25^\circ\text{C}$ .

The results conducted in aqueous solutions of  $\text{CuSO}_4$  in  $1\text{N NaNO}_3$  verified the relationships observed with  $\text{Pb}^{2+}$  as the electroactive species.

Figures 7(a) and (b) illustrate current plateaus for multiple reduction steps in aqueous solutions containing both  $\text{Cu}^{2+}$  and  $\text{Pb}^{2+}$  ions and  $\text{Cu}^{2+}$ ,  $\text{Pb}^{2+}$  and  $\text{Cd}^{2+}$  ions, respectively. The approximate half-wave potential against the Pt-disk reference electrode for the deposition of  $\text{Cu}^{2+}$ ,  $\text{Pb}^{2+}$ , and  $\text{Cd}^{2+}$  in aqueous solutions are  $-0.10$ ,  $-0.45$ , and  $-0.6\text{V}$ , respectively.

The macroscopic flow patterns about the vibrating microelectrode in the present study were qualitatively determined by adding red dye to the proximity of the electrode and observing the resulting patterns on the upward and downward strokes of the electrode. On the upward stroke a suction is imposed on the fluid and fresh electrolyte is brought from the sides to the proximity of the electrode surface. The electrolyte at the center of the electrode remains relatively undisturbed with a stagnant layer appearing at the face of the electrode. This flow pattern appears to be laminar. During the instant of reversal of motion turbulent flow appears to be taking place at the electrode-electrolyte interface. However, during the downward motion the laminar flow appears to be established again and the solution behaves like an incompressible fluid. The linear dependence of the limiting currents on concentration indicates the establishment of a steady state in the electroreduction process at the electrode-electrolyte interface. The observed flow pat-

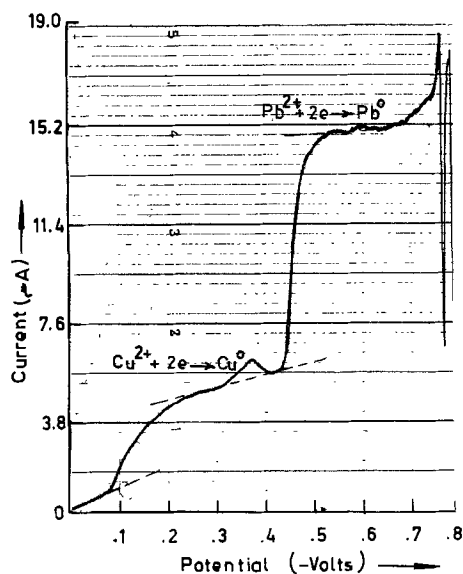


Fig. 7. (a) Limiting current plateaus for the electroreduction of  $\text{Cu}^{2+}$  and  $\text{Pb}^{2+}$  ions at  $25^\circ\text{C}$ .

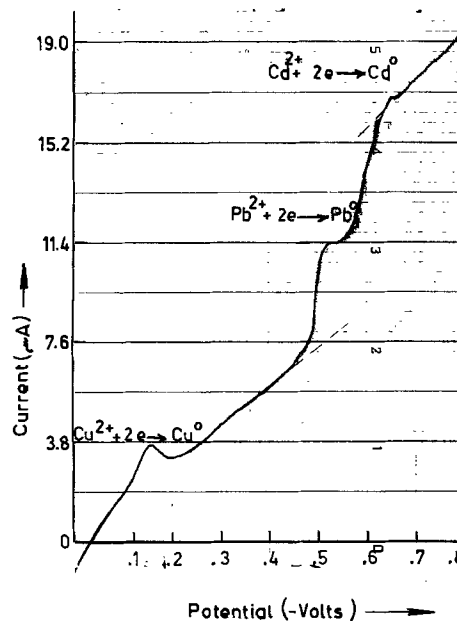


Fig. 7. (b) Limiting current plateaus for the electroreduction of  $\text{Cu}^{2+}$ ,  $\text{Pb}^{2+}$ , and  $\text{Cd}^{2+}$  ions in aqueous solutions at  $25^\circ\text{C}$ .

terns indicate that both diffusive and convective processes are taking place. Because of this complicated behavior a rigorous solution of the over-all transport process has not been obtained and the theoretical treatment of diffusion and mass transport control under these conditions has not been found in the literature. In a recent paper by Podesta *et al.* (14) an expression for ionic mass transfer at horizontal disk electrodes under longitudinal vibrations has been derived.

The vibrating electrode in the above study consisted of a rather large bright platinum disk having a diameter between 0.3 and 1.5 cm, mounted on the end of an inverted, hollow, truncated cone made of insulating material. The entire electrode was connected to a 7 in. commercial loudspeaker and could be vibrated in the frequency range 20-200 Hz. Its optimum frequency was found to be about 50 Hz. The I-V curves obtained in aqueous solutions only, indicated a linear dependence of the current on the concentration of the electroreducible species in solution, a dependence on the  $3/4$  power of the frequency, and a dependence on the  $1/2$  power of the electrode surface area.

The steady-state limiting currents obtained represented a mixed convective- and diffusion-type control mechanism and were dependent on the amplitude of the vibrations and possibly on the angle of the supporting hollow cone. The type of flow pattern prevailing at frequencies about 50 Hz indicated the establishment of an almost immobile cylindrical zone attached to the disk surface.

The vibrating microelectrode developed in the present study differs significantly from that investigated by Podesta *et al.* (14) in its over-all geometry, its current dependence on frequency and on electrode surface area, and on the over-all pattern of the fluid flow established at the electrode solution interface during the vibrations. It is evident that at the lower frequencies of about 3 Hz used in the present study, and for a geometry represented by a small metal disk surrounded by a large glass surface, the electrode solution interface is forced to follow the relatively slow vibrations of the electrode and the steady-state current is again the result of a mixed convective and diffusion-type control mechanism. However, the theoretical treatment of the mass transport problem for the two electrodes should be different.

The linear dependence of the limiting currents on oscillation frequency, concentration of solute species, and electrode surface area indicate that the empirical

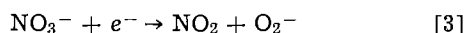
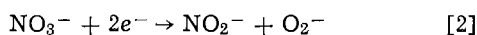
expression for the limiting current should be given as

$$i_L = (K_1 + K_2\nu)AC \quad [1]$$

where  $K_1$  and  $K_2$  are constants,  $\nu$  is the oscillation frequency,  $A$  is the area of the microelectrode, and  $C$  is the concentration of the electroactive species in the bulk phase.

A typical I-V curve obtained for the electroreduction of  $\text{Ag}^+$  added as  $\text{AgNO}_3$  to the equimolar melt of  $\text{KNO}_3$ - $\text{NaNO}_3$  is shown in Fig. 8.

From experiments it became apparent that the residual currents due to the  $\text{NaNO}_3$ - $\text{KNO}_3$  solvent were dependent on the temperature of the melt, increasing rapidly at temperature higher than  $340^\circ\text{C}$ . Hills (15) has investigated this problem in detail and has proposed that this sharp increase in currents is due to the irreversible cathodic reduction of nitrate ions to nitrite ions or nitrogen peroxide according to



At higher temperatures these reactions are expected to be favored, and especially with a platinum electrode which is serving as a catalyst.

Thus the appearance of such high residual currents restricts the use of the platinum microelectrode in nitrate solvent melts to metallic cations which can be reduced at voltages below  $-0.5\text{V}$ .

It is of interest that I-V curves obtained in the  $\text{NaNO}_3$ - $\text{KNO}_3$  electrolyte employing a milliammeter as the current detection instrument, and two large stationary electrodes,  $2.5\text{ cm}^2$  in surface area, show a decomposition potential of  $2.4\text{V}$ . This unusual behavior has been verified in several experiments and seems to indicate that reactions [2] and [3] are rather slow and can only appear as a residual current on a microelectrolysis experiment. The over-all decomposition reaction for the  $\text{KNO}_3$ - $\text{NaNO}_3$  molten electrolyte occurs at  $2.4\text{V}$  and probably involves the reduction of the alkali metal ions to metal.

From the results in Fig. 9, it is seen that the limiting current is directly proportional to the concentration of the electroreducible silver ions. Furthermore, it was observed that the limiting current for the electroreduction of  $\text{Ag}^+$  ions at the microelectrode increases by  $0.058\ \mu\text{A}/^\circ\text{C}$  in the temperature range between  $200^\circ$  and  $300^\circ\text{C}$ . The limiting current for the reduction of  $\text{Ag}^+$  ions in a nitrate melt also decreases with de-

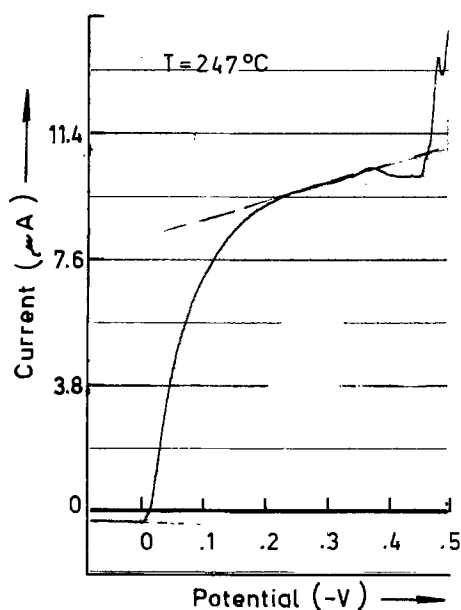


Fig. 8. A typical I-V curve for the electroreduction of  $\text{Ag}^+$  ions in solution in the equimolar melt  $\text{KNO}_3 + \text{NaNO}_3$  at  $247^\circ\text{C}$ .

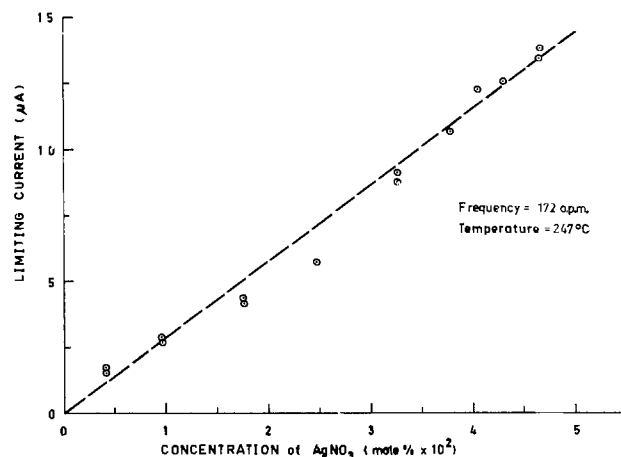


Fig. 9. The dependence of the limiting current on the concentration of  $\text{AgNO}_3$  at  $247^\circ\text{C}$ . The solvent melt is an equimolar mixture of  $\text{KNO}_3 + \text{NaNO}_3$ .

creasing frequency of electrode oscillation as observed in the aqueous solutions.

For the electroreduction of  $\text{Pb}^{2+}$  ions in aqueous electrolytes plots of the well-known Heyrovsky-Ikovic (16) and Kolthoff-Lingane (17) relationships give a straight line but the slopes differ from the theoretical expected slope of 0.0296 for a two-electron electrode process.

Even though the slope of the Heyrovsky-Ikovic relationship is closer to the predicted slope for a two-electron reduction step, the Kolthoff-Lingane (17) equation should be the valid relationship for a reversible reaction. It is unlikely that at  $25^\circ\text{C}$  lead would alloy with tungsten at the indicator electrode. Hence, the deviation from the predicted slope of 0.0296 is probably due to irreversibility.

For the reduction of  $\text{Ag}^+$  in the nitrate melts it was found that the reduction of  $\text{Ag}^+$  ions obeyed the Kolthoff-Lingane relationship. This indicates that the deposit of silver must quickly reach unit activity and that the silver does not diffuse into platinum at least during the time of the experiment.

At more negative voltages the experimental points deviate from the linearity predicted by the Kolthoff equation.

From the results it appears that the half-wave potential for the silver deposition is about  $-0.05\text{V}$  with respect to the platinum disk reference electrode.

Typical I-V curves for the electroreduction of  $\text{Ag}^+$  added as  $\text{AgCl}$  in the equimolar melt of  $\text{KCl}$ - $\text{NaCl}$  are shown in Fig. 10. These curves are not as well defined as with the nitrate melts, but illustrate the dependence of the limiting current on the concentration of  $\text{AgCl}$ .

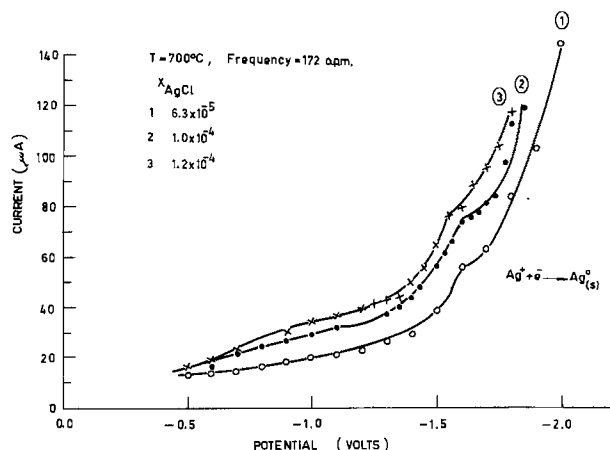


Fig. 10. I-V curves for the electroreduction of  $\text{Ag}^+$  ions in solution in the equimolar melt at  $\text{KCl} + \text{NaCl}$  at  $700^\circ\text{C}$  at various concentrations of  $\text{AgCl}$ .

The half-wave potential for silver deposition in the chloride electrolytes is about  $-1.6\text{V}$  with respect to the graphite reference electrode. This is close to the theoretical values of  $-1.605$  and  $-1.660\text{V}$  for the reversible decomposition potential of  $\text{AgCl}$  (18) in solutions containing  $1.2 \times 10^{-4}$  and  $6.3 \times 10^{-5}$  mole fraction of  $\text{AgCl}$ , respectively.

### Conclusions

A low frequency vibrating solid planar indicator microelectrode was developed for voltammetric investigations in aqueous electrolytes and low temperatures nitrate melts. The electrode behaved well in aqueous electrolytes giving excellent voltammetric curves. The limiting current during electroreduction was related to the concentration of the electroreducible species, the area of the microelectrode, its geometric characteristics, the frequency of oscillation of the microelectrode, the viscosity of the electrolyte, and its temperature. The electroreduction of  $\text{Pb}^{2+}$  ions in aqueous electrolytes at  $25^\circ\text{C}$  was found to be irreversible.

This electrode also produced good voltammograms in nitrate melts and behaved predictably with respect to variables which define the limiting current. For the electroreduction of  $\text{Ag}^+$  ions in nitrate melts the Kolthoff-Lingane equation is obeyed.

Reasonably good voltammograms were also obtained for the electroreduction of  $\text{Ag}^+$  ions in the equimolar  $\text{NaCl-KCl}$  supporting electrolyte.

Manuscript submitted April 21, 1975; revised manuscript received Feb. 19, 1976.

Any discussion of this paper will appear in a Discussion Section to be published in the June 1977 JOURNAL. All discussions for the June 1977 Discussion Section should be submitted by Feb. 1, 1977.

Publication costs of this article were partially assisted by the University of Toronto.

### REFERENCES

1. H. Hoff, *Electrochim. Acta*, **16**, 1059 (1971).
2. R. J. Heus and J. J. Egan, *This Journal*, **107**, 824 (1968).
3. H. A. Laitinen, C. H. Liu, and W. S. Ferguson, *Anal. Chem.*, **30**, 1266 (1958).
4. V. K. Val'tsev and N. F. Dibora, *Siber. Chem. J.*, **2**, 374 (1968).
5. S. N. Flengas, *J. Chem. Soc.*, **1956**, 109, 354.
6. S. Okada, M. Kawane, and T. Hashind, *Z. Electrochem.*, **62**, 437 (1958).
7. Yu. K. Delimarskii, B. F. Markov, and L. S. Berenblum, *Zh. Fiz. Khim.*, **27**, 1848 (1953).
8. V. G. Levich, "Physicochemical Hydrodynamics," Prentice Hall, Englewood Cliffs, New Jersey (1962).
9. A. J. Lindsey, *J. Phys. Chem.*, **56**, 439 (1952).
10. E. D. Harris and A. J. Lindsey, *Analyst*, **76**, 647 (1951).
11. E. D. Harris and A. J. Lindsey, *ibid.*, **76**, 650 (1951).
12. R. E. Corer and J. G. Connery, *Analyt. Chem.*, **41**, 13, 1797 (1969).
13. J. Connery and R. E. Corer, *ibid.*, **41**, 10, 1191 (1969).
14. J. J. Podesta, G. F. Pans, and A. J. Arvia, *Electrochim. Acta*, **19**, 583 (1974).
15. G. J. Hills and K. E. Johnson, "Advances in Polarography," Vol. 3, p. 974, Pergamon Press, London (1960).
16. Yu. K. Delimarskii and B. F. Markov, "Electrochemistry of Fused Salts," Sigma Press, Washington, D.C. (1961).
17. I. M. Kolthoff and J. J. Lingane, "Polarography," Vol. 1 and 2, Interscience Publishers, New York (1952).
18. "The Encyclopedia of Electrochemistry," G. A. Hampel, Editor, p. 648, Reinhold Publishing Corp., New York (1964).

## Recording Characteristics of Anodic Oxide Films on Aluminum Containing Electrodeposited Ferromagnetic Metals and Alloys

Satoshi Kawai and Ikuo Ishiguro

*The Pilot Pen Company, Limited, Hiratsuka Works, Kanagawa, Japan*

### ABSTRACT

Fe, Co, Ni, Co-Ni, Fe-Ni, and Fe-Co were electrodeposited into the micropores of oxide films on aluminum anodized in a sulfuric acid bath. The coercive force of the Fe deposit reached about 2300 oe and the maximum value of 3200 oe was obtained by the Fe-Co alloy. Good squareness ratios were observed in the Fe, Ni, and their alloys. The magnetic recording characteristics were studied by measuring the frequency response. It was found that the films having vertical anisotropy showed better results than the films of horizontal ones. The recording density was calculated to be about 14,000 BPI in the Fe-Ni alloy at about  $3 \mu\text{m}$  in thickness.

In a previous paper (1), it was revealed that anodic oxide films containing electrodeposited Co and/or Ni show very characteristic magnetic properties. The micropores of oxide film in which Co or Ni was precipitated showed magnetic anisotropy perpendicular to the substrate. In the Co-Ni (50%) alloy, the anisotropy turned to the horizontal direction of the surface. The coercivities ranged from about 500 to 1100 oe in the oxide films anodized under various kinds of electrolytes. A more recent report (2) disclosed that the electrodeposited metals were densely packed at the bottom of micropores and grew to the surface. In the

oxide films obtained by a sulfuric acid bath, the deposits were observed as needlelike crystals of about  $100\text{\AA}$  in diameter. As the porosity of micropores was estimated to be about 10% of whole film, the strength of magnetization which depends on the amount of deposition indicated the lower value compared to a conventional thin film. However, when the thickness of oxide films was mechanically thinned by polishing, the densities of residual magnetization of the films containing Co and Ni reached about 1700 and 600G, respectively.

Since the fine particles of magnetic metals have been known to show a high coercive force, the evaluation stimulated an application for magnetic recording

Key words: anodic oxide film, coercive force, magnetic disk, frequency response.

Table I. Bath conditions

(a) Anodizing condition	
Procedures	Remarks
Degreasing	5% NaOH, 60°C, 1 min
Desmut	5% HNO <sub>3</sub> , 20°C, 1 min
Anodizing	15% H <sub>2</sub> SO <sub>4</sub> , 0.1% Al, 1.5 A/dm <sup>2</sup> , 20°C, 20 min
Electrodeposition	15V (a.c. 50 Hz), 30°C bath compositions are indicated as follows*
Sealing	1% Ni(CH <sub>3</sub> COO) <sub>2</sub> · 4H <sub>2</sub> O, 90°C, 20 min

(b) Electrodeposition composition						
*Component (g/liter)	Fe	Co	Ni	Co-Ni	Fe-Ni	Fe-Co
FeSO <sub>4</sub> · 7H <sub>2</sub> O	50				25	30
CoSO <sub>4</sub> · 7H <sub>2</sub> O		50		20		20
NiSO <sub>4</sub> · 7H <sub>2</sub> O			50	80	250	
H <sub>2</sub> BO <sub>3</sub>	25	25	25	25	25	25
Glycerine	20	20	20	20	20	20
pH	4	5	5	5	4	4

devices (3), and the thin films of magnetic metals which are obtained by platings or evaporations are promising as a high density recording medium. In the study of digital recording, Bonyhard *et al.* (4) pointed out that the width of an isolated flux transition is proportional to the value of  $Br \cdot t/2\pi \cdot Hc$ , where  $t$  is the thickness of coating,  $Br$  is the retentivity of the medium, and  $Hc$  indicates the coercivity. Dudson (5) compared the iron oxide coating with the Co thin film, and explained that the Co plating gives an output which is at least three times greater than that of the iron oxide. Talke *et al.* (6) investigated the interface between a transducer and a magnetic disk, and reported that the readback pulse width can be reduced by decreasing the flying height of the magnetic head and the thickness of the film. The magnetic tapes and disks have been developed extensively for the last decade; according to the study of Mallinson (7), the ultimate density given by an information theory is demonstrated to be in the range of  $10^8$ - $10^9$  bits per square inch.

Anodic oxide films containing magnetic metals have been considered as retaining the properties of either the fine particles or the thin films. The present paper studies the magnetic recording characteristics of the oxide films containing electrodeposited ferromagnetic metals and alloys.

## Experimental Procedures

Specimens used for the experiment were prepared in two types. At the outset, for the measurement of magnetometer, rolled aluminum sheets ( $100 \times 50 \times 0.5$  mm<sup>3</sup>) 99.99% in purity were used with no particular mechanical surface treatment. Then, aluminum disks ( $150\phi \times 5$  mm) of the same purity, which had been previously stress relieved by a thermal treatment of ca. 250°C for about 500 min, were supermachined by a diamond bit in a lathe. After the disks were anodized in a sulfuric acid bath and electrodeposited in metal sulfate solutions, mirrorlike finishings were obtained by using a lapping machine with an abrasive of aluminum oxide powder in a size of about 0.1  $\mu$ m. The surface flatness and roughness were checked at each step of polishing by an optical flatness meter and a stylus contact roughness meter. With a microscopic observation, the hardness of the anodic oxide films was measured along the depth on the cross sections.

As shown in Table I (a), a standard condition of electrolytic anodizing was introduced, and the thickness of films controlled to about 10  $\mu$ m. Then, Fe, Co, and Ni metals and various ratios of Co-Ni, Fe-Ni, and Fe-Co alloys were electrodeposited into the micropores to be fully filled with arranging the electrolysis time. Table I(b) indicates the typical conditions of electrodeposition to the specimens for measuring the magnetic hysteresis loops which are shown in Fig. 1. The pH of electrolytes was adjusted by adding dilute solutions of ammonium hydroxide and sulfuric acid, and, in the case of baths containing ferrous sulfate, electrolytes were slightly acidified to prevent precipitation. The amount of deposited metals was determined with an atomic absorption spectroscopy. Magnetic hysteresis loops were recorded with a sample vibrating magnetometer which has been explained in a previous paper (1).

In order to find the recording property of the oxide films, frequency responses were measured between rotating disks and a magnetic head. The aluminum disks turned around at a speed of 9.5 m/sec (3600 rpm), while a flying head was positioned over the disk surface in a floating distance of 0.3  $\mu$ m. The magnetic head was made from a ferrite core (Ni-Zn alloy) having 1.5  $\mu$ m gap length and 16 turns in coiling. Square pulse of NRZ all-one signals were written into the magnetic film of disks, and readback responses in the most optimum voltage were recorded with varying the writing currents in the head.

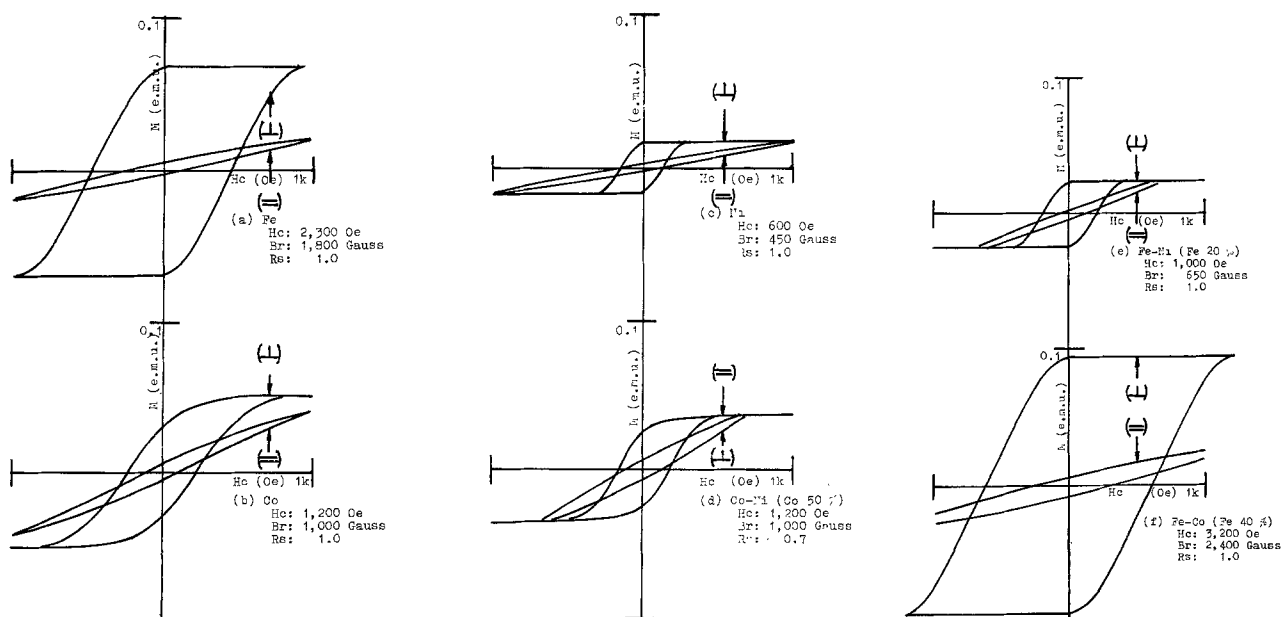


Fig. 1. (a)-(f) M-H hysteresis curves of anodic oxide films electrodeposited with ferromagnetic metals

**Experimental Results**

The hysteresis loops of the magnetic films containing Fe, Co, Ni, Co-Ni, Fe-Ni, and FeCo alloys are described in Fig. 1 (a), (b), (c), (d), (e), and (f), respectively. Strong magnetic anisotropies in the vertical direction to the substrate were observed; however, the anisotropy in the horizontal direction appeared in the Co-Ni (50%) alloy. Squareness ratios of  $M_r/M_s$  reached about 1.0, except Co and its alloy deposits which were calculated to be in the range of about 0.6-0.7.

In the Fe-Ni alloy, the coercivities increased almost linearly with enlarging the Fe content from about 700 oe of Ni to 2300 oe of Fe. On the other hand, in the Fe-Co alloy, the coercivities varied from about 1100 oe of Co to 2300 oe of Fe, while at the Fe content of about 20%, the coercivity peaked at about 3200 oe. The results are shown in Fig. 2 and 3.

The strength of residual magnetizations of Fe, Co, and Ni was measured to be about 200, 150, and 50 emu/g, respectively, and these values were nearly equal to the values of magnetic moments of the bulk metals.

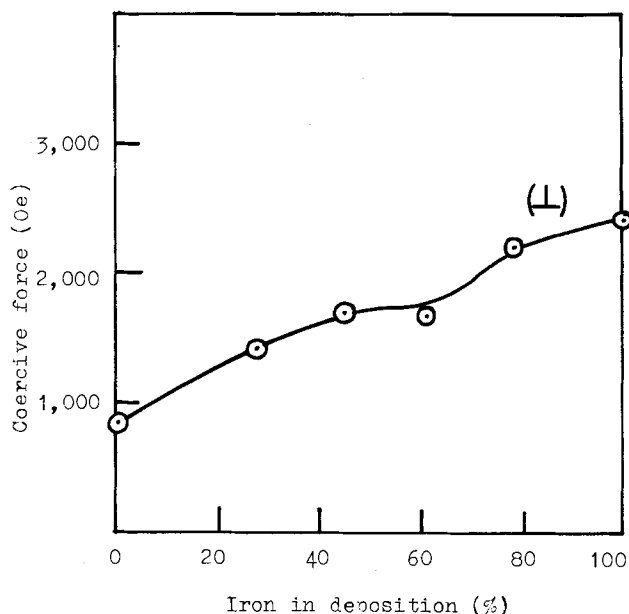


Fig. 2. Coercive forces of anodic oxide films electrodeposited with Fe-Ni.

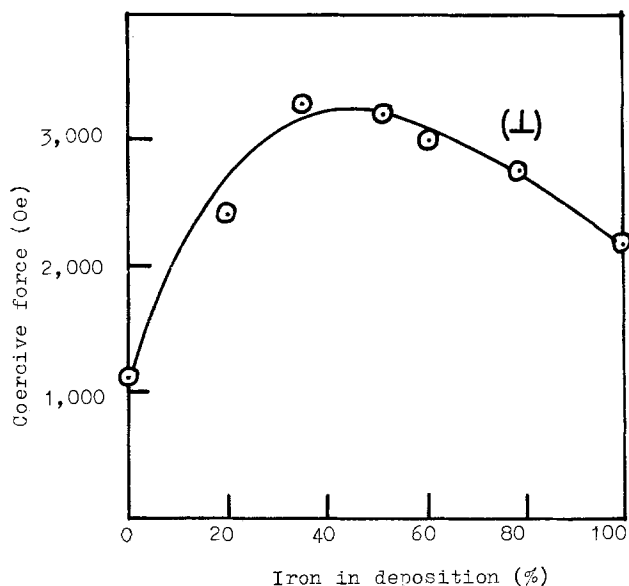


Fig. 3. Coercive forces of anodic oxide films electrodeposited with Fe-Co.

As a result of mechanical finishing, the surface roughness of the base metals became about  $0.2 \mu\text{m}$ , and that of the oxide films after the superpolishing reached about  $0.02 \mu\text{m}$  as shown in Fig. 4(a) and (b). The final flatness of the surface observed by an interference fringe was about  $2.0 \mu\text{m}$  per 100 mm. An excellent roughness of the disk surface can be obtained because of the brittleness of the oxide film. Figure 5 depicts the microhardness of the film which increased by degrees as approaching closer to the inner layer, and reached approximately 500 Hv ( $\text{kg}/\text{mm}^2$ ) at about  $2 \mu\text{m}$  distance from the aluminum substrate. A schematic view of the cross section of the anodic oxide film containing metals is shown in Fig. 6.

On the measurement of frequency response, the relationship between writing currents of the head and reading voltages of the same head was recorded, while keeping the frequency constant at 2 MHz. The saturation currents attained 55 mA in the Ni and 100 mA in the Co-Ni and Fe-Ni deposits, respectively, as shown in Fig. 7. The wave forms of response pulse observed through an oscilloscope are shown in Fig. 8 in which (a) shows a typical form obtained from the films having horizontal anisotropy and (b) indicates a form of

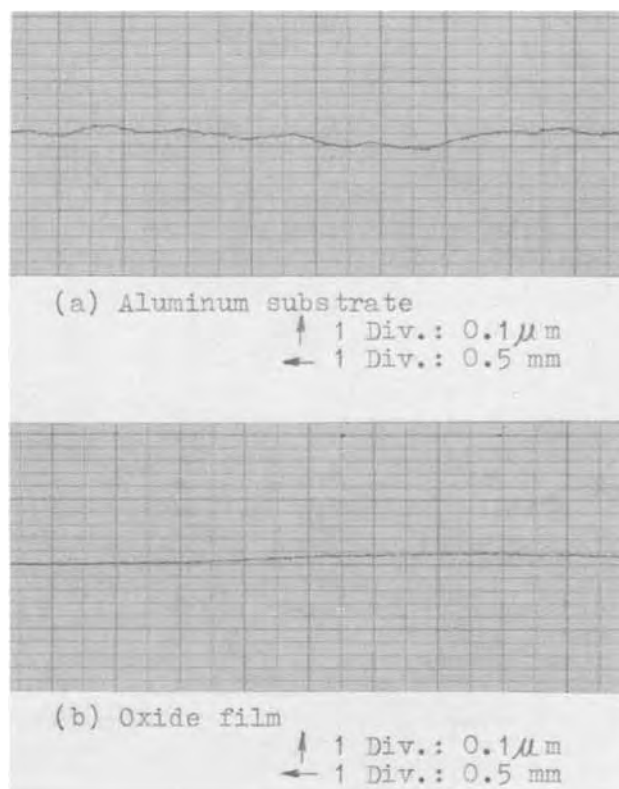


Fig. 4. Mechanically finished surface roughness

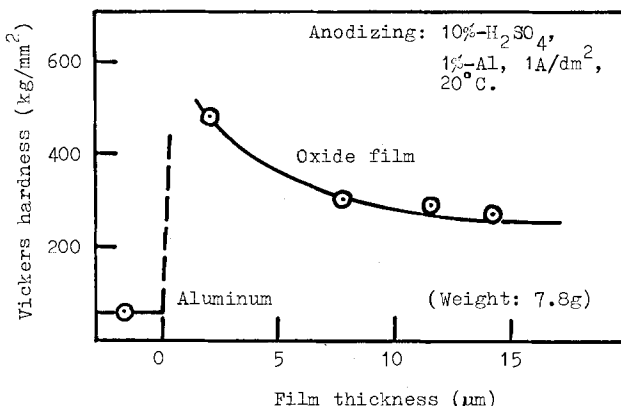


Fig. 5. Hardness of oxide film on cross section



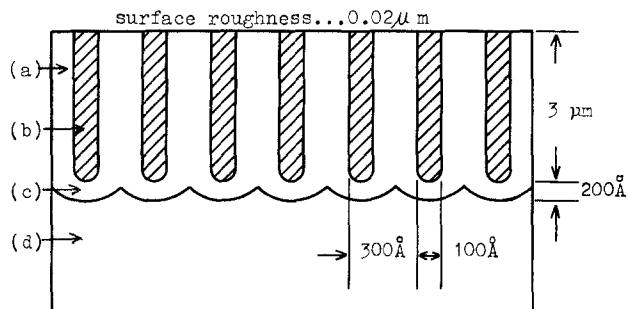


Fig. 6. Schematic model on cross section of oxide film containing electrodeposited metal; (a) aluminum oxide film, (b) electrodeposited metal, (c) barrier layer, (d) aluminum substrate.

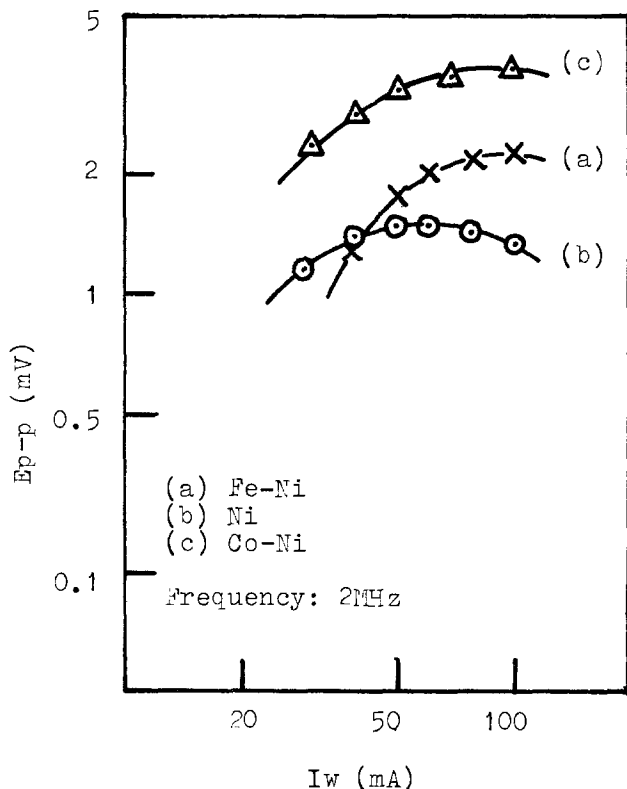


Fig. 7. Writing currents vs. reading voltages

the vertical one at a low frequency range. These forms, however, became a normal sine curve pulse (c) with increasing the frequency to 3 MHz. Then readback voltages from the stored disks under different frequencies were measured as shown in Fig. 9. The films containing Ni and Fe-Ni alloy deposits indicated better frequency response than the film of Co-Ni deposit Table II elucidates the comparison between the magnetic properties of the films and the estimated recording densities.

**Coercivities of Oxide Films**

In this experiment, the coercive forces varied from about 700 to 3200 oe. Luborsky (8) has shown that the

Table II. Recording characteristics of oxide films

Magnetic film	Ni	Ni-Co	Ni-Fe
Hc (=)		700	
Br (=)		750	
Rs (=)		0.7	
Hc (L)	600	600	1050
Br (L)	450	350	350
Rs (L)	1.0	0.3	1.0
t (μm)	3	3	3
Iw (mA)	55	100	100
Ep-p (mV)	1.5	3.7	2.2
BPI	12,200	5400	13,800

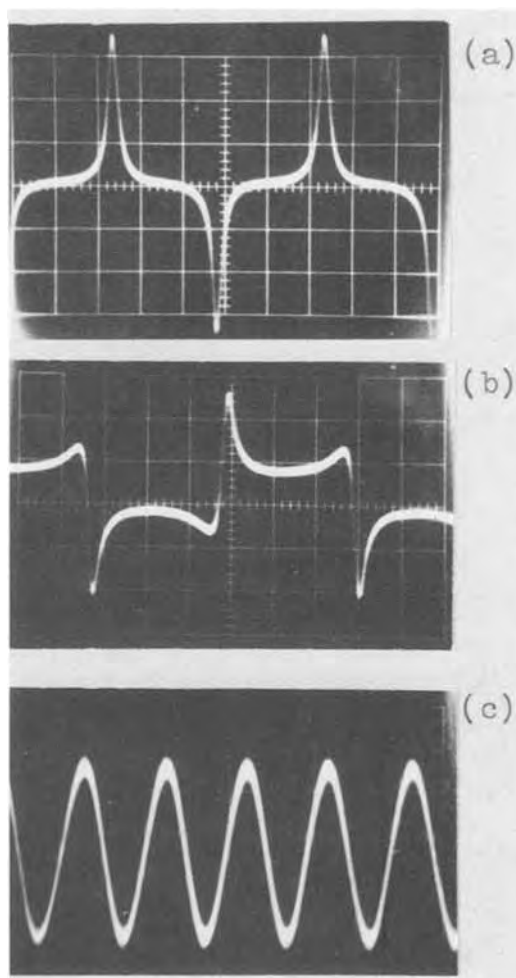


Fig. 8. Wave forms of readback pulse, (a) Co-Ni: frequency 0.2 MHz; (b) Fe-Ni: frequency 0.3 MHz; (c) Co-Ni, Fe-Ni: frequency 5.0 MHz.

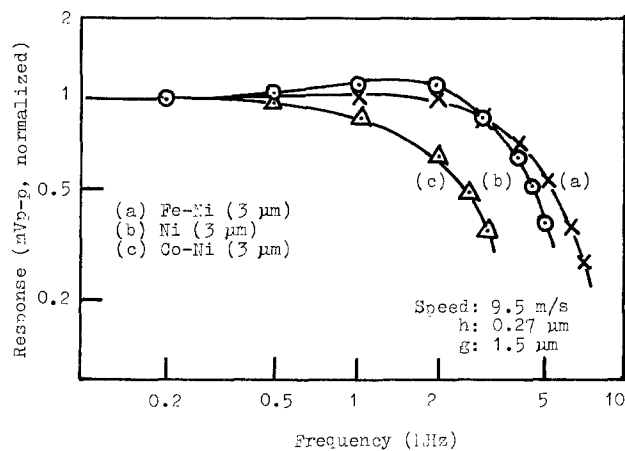


Fig. 9. Frequency response of various kinds of metals

coercive forces of fine particles of Fe and Co metals depend upon their particle diameters, and the maximum coercivity of about 1000 oe is obtained by the size of about 100-200 Å. The deposits in the micropores of oxide films anodized in a sulfuric acid bath have a similar diameter to that of the particles, therefore, it is considered that the high coercivities of precipitations may be caused by the size of crystallization.

The magnetic anisotropies were dominated in the vertical direction and the excellent squareness ratios were recorded in the Fe and Ni deposits. In the single crystal of Fe, the easier magnetization axis has been reported to lie parallel to the cube edge and the same axis of Ni crystal orients to the cube diagonal (9), and,

frequently, these axes have been studied to coincide with the axes of crystal growing. In hexagonal Co, however, the variation of magnetizability with crystallographic direction is even greater than the Fe or Ni, and the c axis of crystal growth direction was reported to show harder magnetization than the other main axes. This may have a relation to the squareness inferiority in the hysteresis loop of the Co deposit.

### Recording Characteristics

On the magnetic recording experiments, good output responses were recognized in the high frequency zone. From the values of rotation speed and frequencies at 0.5 mV of output voltage, the recording densities can be calculated to be 6000, 12,000, and 14,000 BPI with the deposits of Co-Ni, Ni, and Fe-Ni, respectively. The density obtained from the Co-Ni alloy seems to be almost equal to the values of iron oxide coatings in current use. On the other hand, the densities of the Ni and Fe-Ni deposits are considered much the same as the values of thin films which are now in trial use under experiment (10).

The highest readback voltage was measured in the Co-Ni deposit, and this might be due to the fact that this kind of magnetic head is designed to write and read the signals which are oriented in the lateral direction more effectively than those lined in the normal direction. In spite of the micropores being arranged perpendicular to the substrate, the oxide films of Co-Ni (50%) deposit indicate the magnetic anisotropy lying in the horizontal direction, and this proves the phenomenon of crystal anisotropy in which the easier magnetization axis progressed in the lateral direction. It has been known that this composition of deposit showed a lamellar structure and the axis of crystal growth was identical to the horizontal direction (1).

In the Ni and Fe-Ni (Fe 20%) deposits, the good responses lasted even in the range of high frequency, and it is assumed that the magnetic leakage flux developed in the normal direction may have the influence to more easily induce a current to the flying magnetic head.

Although the thickness of oxide films used in this experiment was somewhat greater than the films prepared by platings or evaporations, there are possibilities for obtaining the much higher recording

density when the thickness could be reduced to very thin and flat. Also, the oxide films produced by a hard anodizing process have a practical application for the film of disks without any protective coatings.

The oxide films anodized in a sulfuric acid bath have been assumed to be a transparent medium, with the magnetic particles dispersed very uniformly into the film. This colloidal layer may have possible application for the magneto-optical Kerr or Faraday effect when a laser beam reflects or passes through the layer.

It may be concluded that the oxide films containing electrodeposited magnetic metals and alloys can be used for the magnetic memories of high bit density recording.

### Acknowledgments

The authors thank Messrs. Y. Ikeda and H. Yoshimoto of the Pilot Pen Company, Limited, and express their sincere appreciation to Messrs. K. Yasuda and T. Sato of Nippon Telegram and Telephone Public Corporation for their experimental help.

Manuscript submitted Dec. 31, 1975; revised manuscript received March 19, 1976.

Any discussion of this paper will appear in a Discussion Section to be published in the June 1977 JOURNAL. All discussions for the June 1977 Discussion Section should be submitted by Feb. 1, 1977.

Publication costs of this article were partially assisted by The Pilot Pen Company, Limited.

### REFERENCES

1. S. Kawai and R. Ueda, *This Journal*, **122**, 32 (1975).
2. S. Kawai, *ibid.*, **122**, 1026 (1975).
3. A. Berkowitz and E. Kneller, "Magnetism and Metallurgy," Vol. 1, p. 370, Academic Press, New York (1969).
4. P. I. Bonyhard, A. V. Davis, and B. K. Middleton, *IEEE Trans. Mag.*, **MAG-2**, 1 (1969).
5. M. F. Dudson, *Radio Electron. Eng.*, **38**, 225 (1969).
6. F. E. Talke and R. C. Tseng, *IEEE Trans. Mag.*, **MAG-9**, 133 (1973).
7. J. C. Mallinson, *ibid.*, **MAG-10**, 368 (1974).
8. F. E. Luborsky, *J. Appl. Phys. Suppl.*, **32**, 171 (1961).
9. R. Bozorth, "Ferro-Magnetism," pp. 555, D. Van Nostrand Co., Inc., Princeton, N. J. (1968).
10. K. Koyama, K. Ito, S. Nakagawa, and R. Tsunoi, *IEEE Digest of Intermag. Conf.*, 27-4 (1972).

# Conduction Mechanisms in Alkali Metal Vapor Electrolysis Cells

W. Y. Shiu, S. L. Ezer, D. J. Young,\* M. J. Dignam,\* and B. Rao

Department of Chemistry, University of Toronto, Toronto, Ontario, Canada M5S 1A1

## ABSTRACT

The operating characteristics of an alkali metal vapor plasma electrolysis cell, designed for ultrahigh vacuum vapor deposition of alkali metals, have been studied. The metal ions are generated at a tungsten anode in a gaseous plasma, following which they migrate through a glass envelope, on the far side of which they are discharged at a gold or platinum evaporated metal cathode, and thence enter the vacuum chamber. Many of the operating characteristics of the cells are explained in terms of the known behavior of gas discharge tubes. Some unexplained behavior remains, however, which appears to relate to nonlinear conduction behavior in the glass. Specifically, the units display voltage-time transients under constant current conditions, and certain units show a switching phenomenon, during which the current drops abruptly and spontaneously from  $\sim 10$  mA to  $\sim 10$   $\mu$ A in  $\lesssim 1$  sec. No irreversible changes accompany these phenomena.

The vacuum evaporation of many metals is now a routine procedure, and commonly employed in the deposition of thin films of high purity. Alkali metals, because of their low melting points, are not suited to this technique.

A standard technique for the deposition of alkali metals involves electrolysis of the cation from a molten salt, through glass (1, 2). We have developed a procedure which is suitable for ultrahigh vacuum systems (3). In this procedure, metal ions are generated within the gaseous plasma. These migrate through the glass envelope, are then discharged at a gold or a platinum film cathode deposited on the far side of the envelope, and enter the vacuum space as a gas. A useful feature of this process is the purity of the metal passed through the glass, free ( $< 2$  ppm) of hydrogen and hydrocarbons (4). This purification is due primarily to the fact most impurities are in general very much less mobile in appropriately chosen glass than the desired metal cation (5).

In this paper we are concerned primarily with the conduction mechanism operating in these plasma electrolysis units. A number of surprising operating characteristics have been observed and some tentative explanations offered.

## Construction

A standard deposition unit (Fig. 1) consists of a glass envelope containing a tungsten electrode, alkali metal vapor, and argon. For purposes of comparison some units were investigated in which no argon was present, others in which the gas plasma was replaced by a molten salt electrolyte  $\text{NaNO}_3$ . The envelope was made of appropriate glass, according to whether sodium or potassium was to be evaporated. This envelope was

\* Electrochemical Society Active Member.

Key words: gas plasma electrolysis, ionic conduction in glasses, alkali metal vapor deposition.

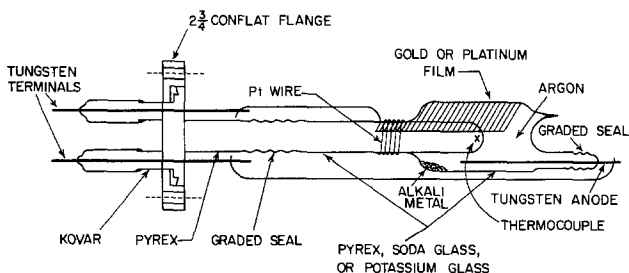


Fig. 1. Design of a typical plasma electrolysis unit

sealed to a central tube of the same glass which in turn was sealed to an ultrahigh vacuum flange. The central tube carried a small heating unit and thermocouple. Specifically, in the case of the unit containing the molten salt, the central tube was in direct contact with the electrolyte. Thus the cell temperatures measured in the case of the molten salt system closely represent the electrolyte temperature. The unit was activated by applying a potential difference between the tungsten anode and a metal film cathode deposited on the external surface. Additional details are given elsewhere (3).

## Operating Characteristics

In all, five different evaporation systems were studied. These were sodium in Pyrex (Na/Pyrex), sodium plus 0.1-1 Torr argon in Pyrex (Ar-Na/Pyrex), molten sodium nitrate in Pyrex ( $\text{NaNO}_3$ /Pyrex), sodium plus 0.1-1 Torr argon in soda glass (Ar-Na/soda glass), and potassium plus argon in potassium glass (Ar-K/potassium glass). The behavior of each of these units is presented in turn.

*Na/Pyrex unit.*—These units display close-to-ohmic behavior on increasing the voltage in small steps from 0 to 1200V over the temperature range 375°-500°C (Fig. 2) and settle rapidly to the new current ( $< 2$  sec). The current-voltage (C-V) curves are both reversible and reproducible as long as the voltage is changed in small steps. However, transient behavior occurs when a unit is subjected suddenly to a high applied voltage.

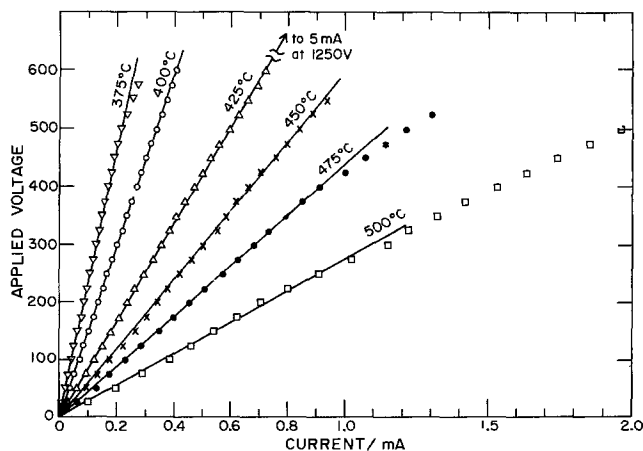


Fig. 2. Steady-state conduction data for a Na/Pyrex unit

The current increases over a period of about 10-20 sec to a value substantially larger than that obtained upon applying the voltage slowly, and is accompanied by a visible discharge; this situation may persist for a number of seconds, but ultimately the current falls off to  $\sim 10 \mu\text{A}$  in a period  $\sim 1$  sec, and the visible discharge ceases. The transient can be repeated after holding the unit for a short period at zero applied voltage. Typical transients are shown in Fig. 3.

No difference in operating characteristics is observed for units constructed so that the tungsten anode makes contact with the molten sodium. However, if in addition the molten sodium is in contact with a portion of the Pyrex envelope which is coated with gold or platinum, much higher currents are obtained (50 mA for  $\sim 200\text{V}$ ) and rapid puncture of the envelope results.

**Ar-Na/Pyrex unit.**—Addition of argon at a pressure from 0.1 to 1 Torr completely alters the C-V characteristics of the Na/Pyrex (Fig. 4 and 5). For such units, an intense discharge is observed which can be struck by the application of less than 200V. For voltages less than that required to sustain the discharge, these units displayed close-to-reversible ohmic behavior. Following the onset of the discharge, the current rises over a period of from 3 to 10 min to a value 10-100 times larger than the predischARGE value. In the discharge region, the steady-state C-V relation is far from ohmic (Fig. 5). However, for a rapid change in the applied current, the instantaneous voltage change is approximately proportional to the current change, following which the voltage approaches its new steady-state value in a time which is of the order of 10-100 sec (Fig. 6).

On initiation of the discharge, the discharge is purple, and centered on the anode, changing over the few minutes required to establish steady-state conditions to the bright yellow characteristic of the sodium D lines. The spectrum of the emitted light contained in addition to the sodium D lines, three lines which appear to be due to Ar [568  $m\mu$  (strong), 514  $m\mu$  (intermediate), 499  $m\mu$  (weak)].

Units containing argon and constructed so that the tungsten anode makes contact with the molten sodium

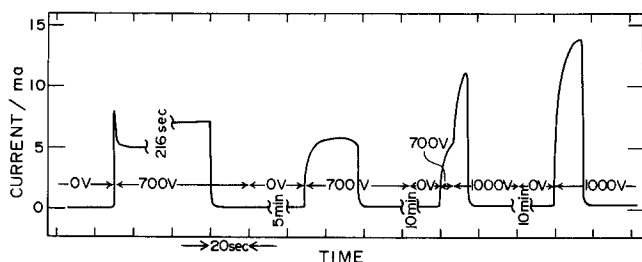


Fig. 3. Transient response for a Na/Pyrex unit

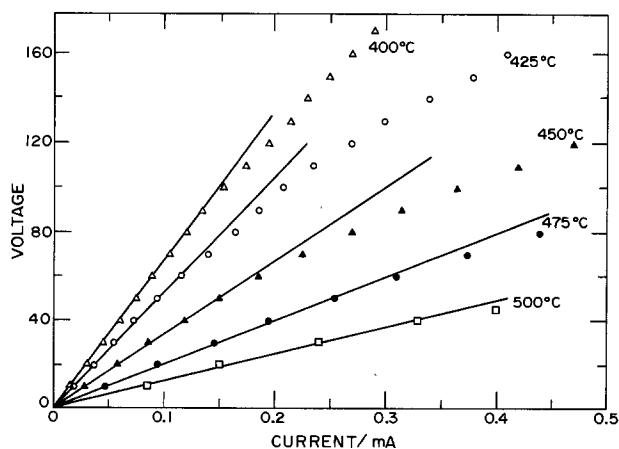


Fig. 4. Conduction data for an Ar-Na/Pyrex unit in the pre-discharge region.

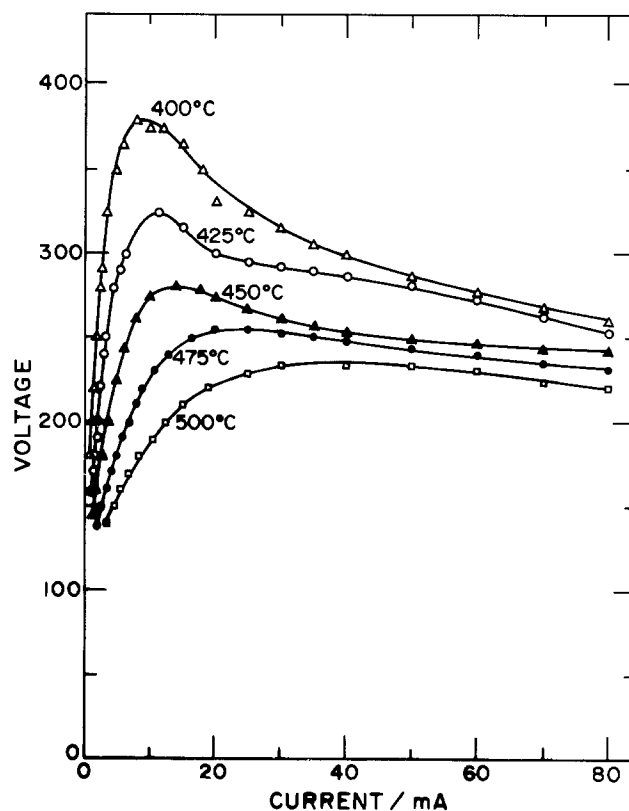


Fig. 5. Steady-state conduction data for an Ar-Na/Pyrex unit in the discharge region.

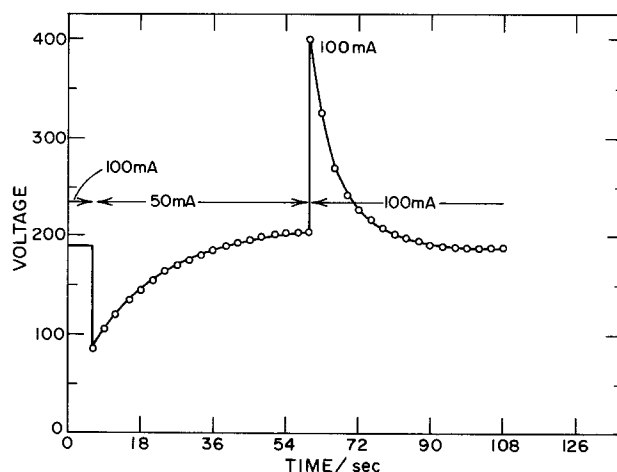


Fig. 6. Transient response for an Ar-Na/Pyrex unit in the discharge region.

generally give little or no visible discharge at any voltage, the current increasing smoothly as the potential is increased from zero to several hundred volts (Fig. 7).

At the higher voltage, the C-V behavior differs from that for units without anode-sodium contact (Fig. 5) mainly in that the curves are displaced to lower voltages.

**NaNO<sub>3</sub>/Pyrex unit.**—These units were constructed somewhat differently from that depicted in Fig. 1. The envelope possesses a side arm to the atmosphere through which the molten salt is introduced, the anode inserted, and from which the oxides of nitrogen produced in the electrolysis are released. The portion of the Pyrex envelope which is coated with the gold or platinum film is in contact with the molten salt, which is in turn in contact with the anode.

The steady-state C-V behavior for these units (Fig. 8) is similar to the Ar-Na/Pyrex units with

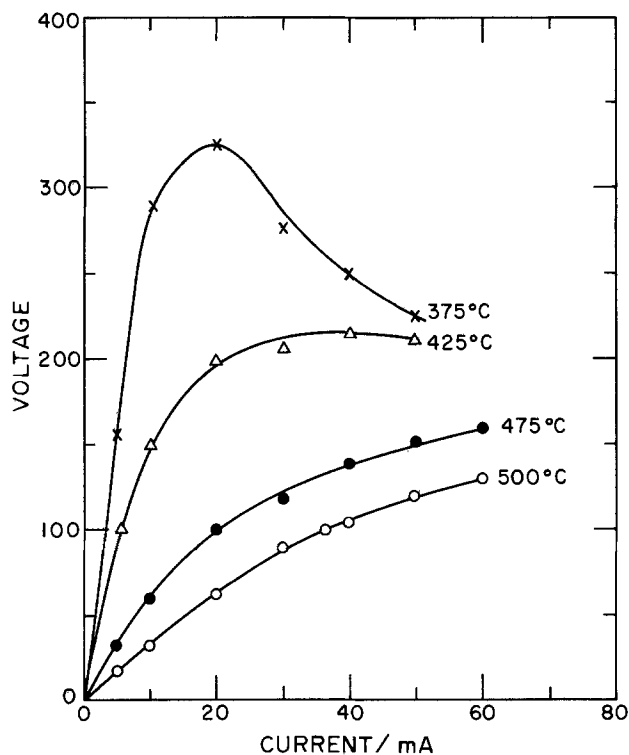


Fig. 7. Steady-state conduction data for an Ar-Na/Pyrex unit with Na-anode contact.

anode-sodium contact (Fig. 7) and to the standard Ar-Na/Pyrex units in the discharge region (Fig. 5). Their response to a sudden change in current is also similar (Fig. 9).

*Ar-Na/Na glass units.*—These units perform in a manner similar to the Ar-Na/Pyrex units except that they operate satisfactorily at a substantially lower temperature, and the conductances calculated from the slopes in the predischARGE regions are very much larger.

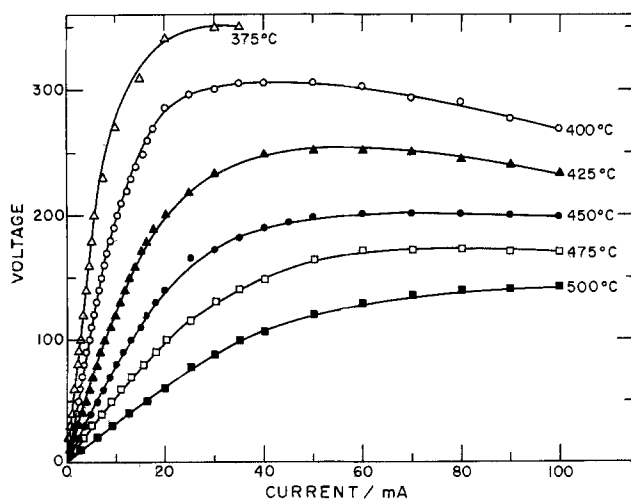


Fig. 8. Steady-state conduction data for a NaNO<sub>3</sub>/Pyrex unit

### Discussion

As most of the data obtained relate to units which involve sodium ion migration through Pyrex, we shall restrict discussion mainly to these units.

In Fig. 10, conductance data obtained from the initial Ohmic regions for the various Pyrex units are presented in the form of Arrhenius plots of approximately the same slope, corresponding to an activation energy of about 19 kcal/mole. Conductivity data for Pyrex (6) lead to a value of 19.8 kcal/mole.

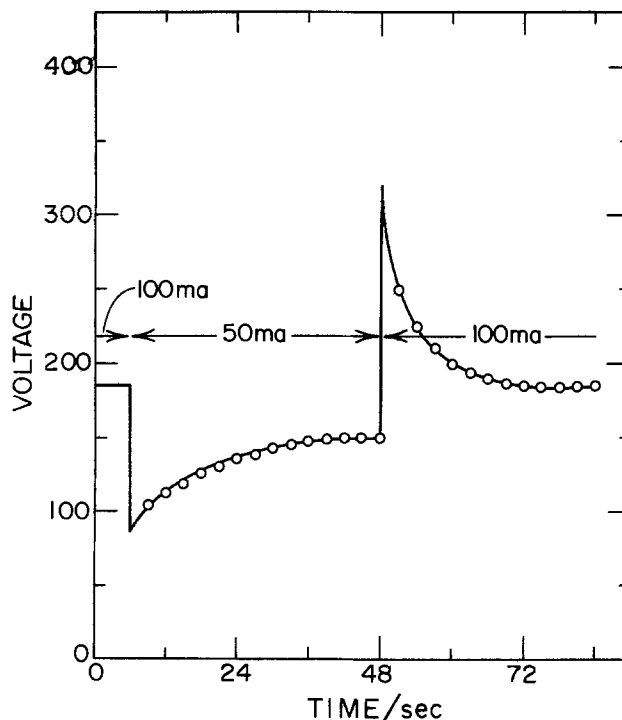


Fig. 9. Transient response for a NaNO<sub>3</sub>/Pyrex unit in the region of high differential conduction.

Although the activation energies for the four units are nearly the same, the conductances themselves are not. The conductances of the units NaNO<sub>3</sub>/Pyrex and Ar-Na/Pyrex with Na-anode contact are essentially the same, as are those of the Na/Pyrex, and Ar-Na/Pyrex without Na-anode contact, but the former have conductances about 50 times larger than the latter.

On the basis of the data presented, and the known properties of gas discharges, we offer the following account of the operating behavior of the various Pyrex units.

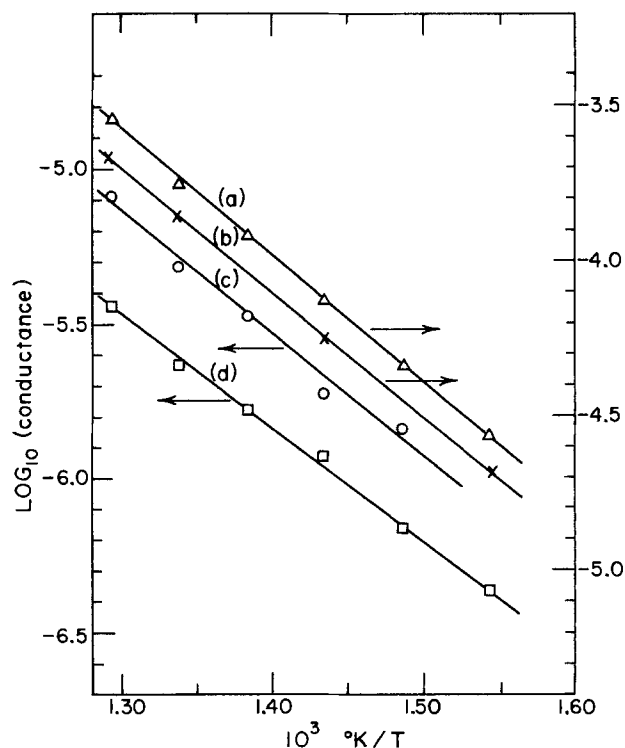


Fig. 10. Arrhenius activation energy plots of the conductance for the various Pyrex units; (a) NaNO<sub>3</sub>/Pyrex units, (b) Ar-Na/Pyrex unit with Na-anode contact, (c) Ar-Na/Pyrex unit without Na-anode contact, (d) Na/Pyrex unit.

*Na/Pyrex unit.*—A comparison between the steady-state behavior of this unit and that of the  $\text{NaNO}_3/\text{Pyrex}$  unit will now be made. It may be presumed that  $\text{Na}^+$  migration through Pyrex determines the  $i$ - $V$  relationship for the latter unit. We assume here that the only charged particles present in significant numbers in the gas phase of the  $\text{Na}/\text{Pyrex}$  unit are sodium cations (when there is no discharge), the cations being generated on the tungsten anode via an adsorption-desorption process. For currents in the  $\mu\text{A}$  range, this anodic process is apparently not rate controlling, so that a positive space charge region is established close to the anode to equalize the net current at the anode with that at the cathode. Assuming now that the cathodic current is controlled by the field strength in the Pyrex glass, then on neglecting the thickness of the positive space charge region, and assuming no net surface or volume charge associated with the glass, one obtains for an ideal, one-dimensional current flow, the relation

$$i = (\sigma V/l)/[1 + KL/l] \quad [1]$$

where  $i$  is the current density,  $V$  the total applied voltage,  $\sigma$  the glass conductivity,  $l$  and  $L$  the thicknesses of the glass and gas column, respectively, and  $K$  the dielectric constant of the glass. As the corresponding relationship for the  $\text{NaNO}_3/\text{Pyrex}$  unit is

$$i = \sigma V/l \quad [2]$$

Eq. [1] predicts the conductance of the  $\text{Na}/\text{Pyrex}$  unit to be less than that of the  $\text{NaNO}_3/\text{Pyrex}$  unit by a factor of  $(1 + KL/l)$ , which for  $K = 4.8$  (6),  $l = 0.1$  cm, and  $L \sim 1$  cm is about 50, in satisfactory agreement with observation. The results of the Arrhenius plots (Fig. 10) are also in agreement with Eq. [1] and [2]. The agreement obtained justifies the assumption that only sodium cations contribute to the current in the gas phase of the  $\text{Na}/\text{Pyrex}$  unit.

If a high voltage is applied suddenly to a  $\text{Na}/\text{Pyrex}$  unit, breakdown occurs in the gas and a discharge is established which leads to higher currents as described in the following section on the  $\text{Ar-Na}/\text{Pyrex}$  unit. This discharge is not stable, however, and is ultimately extinguished (see Fig. 3). It seems likely that as the discharge develops, more and more of the applied voltage appears across the glass until finally the discharge is extinguished. The details of the process, however, remain obscure. Thus, it appears necessary to assume that during this process the conductivity of the glass is reduced dramatically so that following extinction of the discharge the conductance of the unit is about 100 times less than it is for the same unit when the voltage is applied slowly.

*Ar-Na/Pyrex unit.*—In the predischARGE region, the operating characteristics are indistinguishable from those of the  $\text{Na}/\text{Pyrex}$  unit, the two mechanisms being therefore presumably the same.

Above the breakdown voltage, a situation analogous to that in a normal glow discharge appears to be established, in which positive ions and electrons are generated by collision in the region of the cathode fall. The role of the argon is undoubtedly to increase the probability of ionization by collision, possibly through a Penning effect. Neglecting the voltage drop within the positive column, and assuming no surface or volume charge associated with the glass, we obtain

$$i = [\sigma(V - V_a)/l]/[1 + Kd_c/l] \quad [3]$$

where  $d_c$  is the effective length of the region of cathode fall and  $V_a$  the anode fall.

On comparing the behavior of  $\text{Ar-Na}/\text{Pyrex}$  units with and without  $\text{Na-anode}$  contact, it is apparent that the voltages required to sustain given currents are much less in the former. On the other hand, the conduction behavior of the  $\text{Ar-Na}/\text{Pyrex}$  unit with  $\text{Na-anode}$  contact is nearly the same as that of the  $\text{NaNO}_3/\text{Pyrex}$  unit over the entire range of currents studied. The most obvious explanation for these observa-

tions is that  $Kd_c/l$  is small compared to unity and  $V_a$  is essentially zero for the unit with  $\text{Na-anode}$  contact, while  $\sim 100\text{V}$  for the unit without  $\text{Na-anode}$  contact. It appears, therefore, that in the absence of  $\text{Na-anode}$  contact, direct ionization of sodium at the tungsten anode cannot accommodate currents in the  $\text{mA}$  range, so that an anode fall is established in which positive ions, required for the positive column, are generated by collision. On this basis, one expects  $V_a$  to decrease with increasing current. On comparing Fig. 5 and 7,  $V_a$  appears to be about  $100\text{V}$  at low currents, increasing to a maximum  $\sim 180\text{V}$  at from 4 to 17  $\text{mA}$ , depending on the temperature, then falling off rapidly to well below  $100\text{V}$  at higher currents. Perhaps the initial increase in  $V_a$  with increasing current is due to a contribution to the generation of positive ions at the anode by field emission of sodium adsorbed on the tungsten anode. Thus  $\text{Na}^+$  ion generation passes with increasing current through an equilibrium regime ( $V_a$  independent of  $i$ ), a field emission regime ( $V_a$  increasing with  $i$ ), and finally a collision ionization regime ( $V_a$  decreasing with increasing  $i$ ).

If this explanation for the operating behavior of the two types of  $\text{Ar-Na}/\text{Pyrex}$  units is accepted, then we must conclude that most of the visible emission of light is associated with processes occurring close to the anode, since the units with  $\text{Na-anode}$  contact show little if any visible emission.

The transient behavior exhibited by both the  $\text{Ar-Na}/\text{Pyrex}$  unit (Fig. 6) and the  $\text{NaNO}_3/\text{Pyrex}$  unit (Fig. 9) must be due to a time dependence of the conductance of the glass, as the relaxation times are much too large to be associated with any likely gas phase phenomenon. The transients are very similar for the two units, as expected, since under constant current conditions,  $V_a$  should be constant, and is in any event substantially smaller than the voltage drop across the glass in the current range 50-100  $\text{mA}$ .

The possibility that the nonlinear conduction behavior of the units, as well as the voltage transients (Fig. 6 and 9), is due to temperature nonuniformities is now considered. Both effects are of the correct general form to be accounted for by a temperature differential between the conducting glass and the thermocouple, the difference increasing with increasing power dissipation in the unit. To explain in this way the voltage value required to sustain a 100  $\text{mA}$  current in the  $\text{NaNO}_3/\text{Pyrex}$  unit at a nominal temperature of  $400^\circ\text{C}$  would require assuming that the conducting part of the glass envelope was at a temperature about  $125^\circ\text{C}$  higher than that of the thermocouple.

The energy dissipation of this unit under the above conditions is about 30W. The thermocouple is situated inside a well which is immersed in the molten salt, and less than 1 cm from the conducting portion of the envelope which is also in contact with the molten salt. At the operating temperature for these units, the principle mechanism for heat loss to the surroundings is by radiation, rather than conduction, so that a substantial temperature gradient from the outside to the interior of the cell cannot be maintained as a consequence of power dissipation in the outer region. On the other hand, the conducting portion of the glass envelope is coated with metal, a material of low emissivity compared to glass.

It is difficult to rule out the possibility that a  $125^\circ\text{C}$  temperature differential could be maintained within the deposition unit under operating conditions, although such a large differential seems improbable. Perhaps the most convincing evidence against such a large thermal effect is provided by the very similar behavior of the  $\text{NaNO}_3/\text{Pyrex}$  and  $\text{Ar-Na}/\text{Pyrex}$  units, despite the great difference in conductivity between molten  $\text{NaNO}_3$  and a low pressure gas. Finally, we note that the transients depicted in Fig. 3 are clearly not explicable solely in terms of nonuniformity of temperature. We believe that both transients, as well as the nonlinear conduction behavior, are due to nonlinear processes with the glass.

Representing the current density in the glass by the relationship

$$i = envE \quad [4]$$

where  $e$  is the charge on the proton,  $v$  the mobility and  $n$  the concentration of the current carriers (sodium ions), and  $E$  the electric field strength in the glass, then if the constant current transients are due to a time dependence of  $n$ ,  $1/V$  should display the same time dependence as does  $n$ . It is found from appropriate plots that within experimental scatter,  $1/V$  decays according to first order kinetics, the relaxation times for a number of different runs being recorded in Table I. They are seen to be about the same for the two units, Ar-Na/Pyrex and NaNO<sub>3</sub>/Pyrex, and essentially independent of temperature.

The observed kinetics are consistent with a conduction mechanism in which conducting ions are produced in the glass by an avalanche mechanism, and are destroyed by a first order process. Thus assuming that

$$\frac{dn}{dt} = ki - n/\tau \quad [5]$$

we obtain with Eq. [4]

$$\log_e \left| \frac{E_s/E - 1}{E_s/E_0 - 1} \right| = -t/\tau \quad [6]$$

$$E_s = k\tau/ev \quad [7]$$

where  $E_0$  is the field strength at time zero and  $E_s$  the final steady-state field strength, which is seen to be independent of  $i$ , in accord with the observed behavior in the limit of large  $i$ . For sufficiently small  $i$ ,  $n$  is presumably constant and no longer varies according to Eq. [5].

Perhaps the main objection to this mechanism is that the precise nature of the first order process is obscure, and the lack of a significant temperature dependence for  $\tau$  surprising. Additionally, it does not predict  $\tau$  to be dependent on  $i$ .

A mechanism which eliminates both these objections can be formulated if one assumes generation of ion pairs by a "second order avalanche process," as proposed by Young (7) for ionic conduction in anodically formed Ta<sub>2</sub>O<sub>5</sub>, with ion recombination controlled by the current flow, a situation that could obtain if conduction in a glass were similar to the movement of charged bodies in a viscous fluid. This mechanism gives

Table I. Relaxation times for  $1/V$  ( $i$  constant)

Temp °K	Relaxation time in sec			
	Ar-Na/Pyrex unit		NaNO <sub>3</sub> /Pyrex unit	
	At 50 mA	At 100 mA	At 50 mA	At 100 mA
375	25	—		
400	23	14	25	23
425	29	15		
430	24	22		
435			26	21
440	27	18		
450	39	17	22	16
475	28	15	18	11

$$\frac{dn}{dt} = k_1 i^2 - k_2 ni \quad [8]$$

with  $k_2$  essentially temperature independent, which again leads to Eq. [6] with  $\tau = 1/k_2 i$  and  $E_s = k_1/k_2 ev$ . An objection to this mechanism is the lack of direct experimental or theoretical justification for a process of ion-pair generation which is proportional to  $i^2$ . Other mechanisms have been proposed to account for high field ionic conduction in anodically formed oxide films (8), however none of these appear to apply to the present systems.

*Ar-Na/Na glass and Ar-K/K glass units.*—In all important respects, these units behave as do the corresponding Pyrex units. Thus in the predischARGE region, the Arrhenius activation energies for conduction in each of the units agree with those calculated from published data (6, 9). Not all of the experiments performed on the Pyrex units, however, were carried out for these units.

### Summary

The process of plasma electrolysis of alkali metal vapor, using a glass cathode and metal anode, has been studied over a range of temperatures and plasma conditions. The results are compared with the electrolysis of NaNO<sub>3</sub>, also using a glass cathode.

At low currents, sodium ions are generated at a tungsten anode by a dischargeless process, which is not rate controlling. At high currents, they are generated by collision ionization in the anode fall region, the process being accompanied by the emission of light. If liquid sodium is used for the anode, sodium ions are generated by a dischargeless process at all currents studied.

The voltage-time transient under constant current conditions, and the switching phenomenon observed for Na/Pyrex units are probably due to nonlinear conduction processes within the glass cathode.

Manuscript submitted May 9, 1974; revised manuscript received Jan. 13, 1976.

Any discussion of this paper will appear in a Discussion Section to be published in the June 1977 JOURNAL. All discussions for the June 1977 Discussion Section should be submitted by Feb. 1, 1977.

Publication costs of this article were partially assisted by the University of Toronto.

### REFERENCES

1. E. Warburg, *Wied. Ann.*, **40**, 1 (1890).
2. C. Stuber, *Z. Physik. Chem.*, **A172**, 401 (1935).
3. W. Y. Shiu, S. L. Ezer, D. J. Young, B. Rao, and M. J. Dignam, *J. Vacuum Sci. Technol.*, **11**, 1131 (1974).
4. R. C. Burt, *J. Opt. Soc. Am.*, **11**, 87 (1925).
5. M. Sitting, "Sodium, Its Manufacture, Properties and Uses," Reinhold Publishing Corp., New York (1956).
6. "Properties of Selected Glasses," Corning Glass Works, New York (1965).
7. L. Young, *Can. J. Chem.*, **50**, 574 (1972).
8. M. J. Dignam, in "Oxides and Oxide Films," Vol. 1, J. W. Diggle, Editor, Chap. 2, Section VIII, Marcel Dekker, New York (1972).
9. V. I. Danilkin, L. A. Kadryavtsev, and V. A. Ivanov, "The Structure of Glasses," Vol. IV, Consultants Bureau, New York (1965).

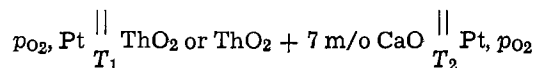
# Thermoelectric Power in Pure and CaO-Doped ThO<sub>2</sub> Electrolytes

H. S. Maiti<sup>1</sup> and E. C. Subbarao

Department of Metallurgical Engineering, Indian Institute of Technology, Kanpur 208016, India

## ABSTRACT

The Seebeck coefficient of the thermocells of the type



was measured in the temperature range 600°-1000°C with  $p_{O_2} = 10^{-0.7}$  (air),  $10^{-5}$ , and  $10^{-23}$  atm. Electron holes are the charge carriers in the mixed-conduction region. The temperature dependence of the total Seebeck coefficient is accounted for by the variation of transference numbers and  $\alpha_h$  (Seebeck coefficient due to electron holes) with temperature.

Recent studies (1) have shown that the electrical conductivity of ThO<sub>2</sub>-CaO electrolytes is predominantly due to electron holes at oxygen partial pressures greater than about  $10^{-6}$  atm and due to oxygen ions at lower  $p_{O_2}$  values, similar to the case of ThO<sub>2</sub>-Y<sub>2</sub>O<sub>3</sub> electrolytes. As a supplement to the electrical conductivity data, thermoelectric power measurements have been carried out over the temperature range of 600°-1000°C on sintered disks of nominally pure ThO<sub>2</sub> and ThO<sub>2</sub> doped with 7 mole per cent (m/o) CaO. The latter composition has a much higher conductivity than the former throughout the oxygen partial pressure range. These results are compared with those of Tallan and Bransky (2, 3) on pure ThO<sub>2</sub>.

## Experimental

The alumina tube sample holder, used earlier for electrical conductivity measurements (4), was utilized for the Seebeck coefficient measurements with the following modifications. The cylindrical sample used here (9 mm in diameter and 1 cm in length) was longer than that used for electrical conductivity study. The necessary temperature gradients up to 15°C were created across the specimen by supplying a d-c voltage to a platinum wire wound over the alumina pressing rod just above the specimen surface. The Seebeck coefficient was estimated from the slope of the straight line of the emf vs. the temperature gradient plot. The sign of the Seebeck coefficient, as determined from the polarity of the cold end of the specimen, was positive, indicating that the electron holes are the charge carriers. The experimental considerations in the measurement of Seebeck coefficient are discussed by Blumenthal and Seitz (5). The measurements were made at three oxygen partial pressures [ $p_{O_2} = 10^{-0.7}$  (air),  $10^{-5}$ , and  $10^{-23}$  atm]. The desired low oxygen partial pressures were generated by using an electrochemical oxygen pump based on CaO-stabilized zirconia tube (1).

## Results and Discussion

The total Seebeck coefficient ( $\alpha_T$ ) for the two samples in air and at  $p_{O_2} = 10^{-5}$  atm is plotted in Fig. 1 as a function of temperature, together with the temperature variation of  $t_{ion}$ .

The Seebeck coefficient of pure ThO<sub>2</sub> increases with temperature reaching a maximum between 800° and 900°C in air and between 900° and 1000°C at  $p_{O_2} = 10^{-5}$  atm. The  $\alpha_T$  value at 1000°C in air is 1.25 mV/°K and is close to the  $1.2 \pm 0.1$  mV/°K reported by Bransky and Tallan (2) at  $p_{O_2} = 10^{-1}$  atm at 1000°C. The Seebeck coefficient at any fixed temperature is lower at

the lower oxygen partial pressure. This is contrary to the slight increase in  $\alpha_T$  reported by Bransky and Tallan (2) as the oxygen partial pressure is lowered to  $10^{-5}$  at 1000°C. The reason for this discrepancy is not clear.

The total Seebeck coefficient ( $\alpha_T$ ) of a mixed (partially ionic and partially electron hole) conductor is given by

$$\alpha_T = t_i \alpha_i + t_{hah} \alpha_h \quad [1]$$

where  $t_i$  and  $t_h$  are the transference numbers for ions and electron holes and  $\alpha_i$  and  $\alpha_h$  are the corresponding Seebeck coefficients. The temperature coefficient of  $\alpha_T$  depends on the temperature dependence of the four terms on the right-hand side of Eq. [1]. In air,  $t_i$  of pure ThO<sub>2</sub> decreases from 0.2 at 600°C to 0.05 at 700°C and remains constant at higher temperatures. The value at 1000°C is smaller than the 0.15 observed by

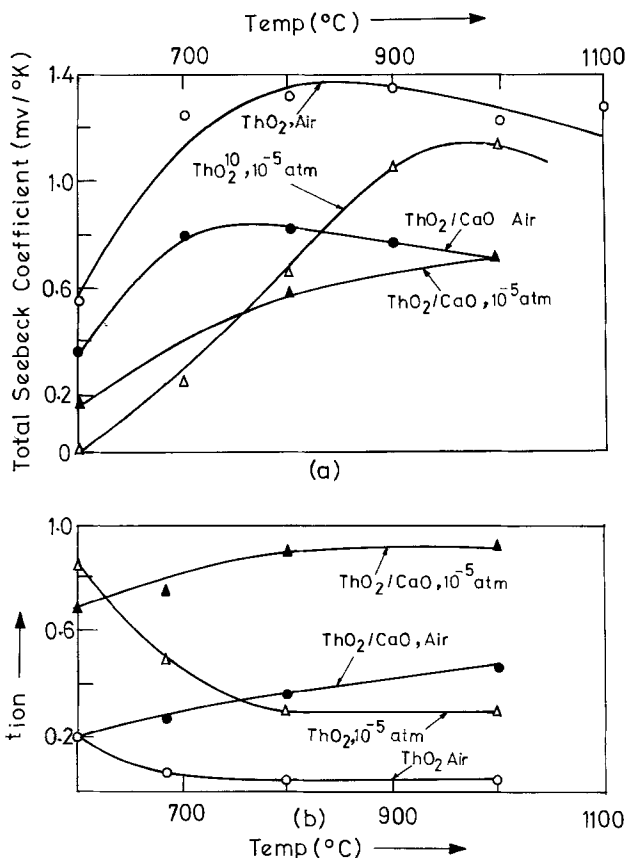


Fig. 1. (a) Seebeck coefficient and (b)  $t_{ion}$  of pure and 7 m/o CaO-doped ThO<sub>2</sub> specimens in air and at  $p_{O_2} = 10^{-5}$  atm.

<sup>1</sup> Present address: Materials Science Center, Indian Institute of Technology, Kharagpur 721302, India.

Key words: Seebeck coefficient, temperature dependence, mixed conduction.



Bransky and Tallan (2) for their ThO<sub>2</sub> which is purer than the present sample. Thus  $t_i \ll t_h$ . Besides,  $\alpha_i$  (0.45 mV/°K) is reported (2) to be less than  $\alpha_h$  (1.4 mV/°K) at  $p_{O_2} = 10^{-1}$  atm at 1000°C. As a result, the contribution of  $t_i\alpha_i$  to  $\alpha_T$  is negligible. The temperature coefficient of  $\alpha_h$  was shown to be

$$\frac{d(\alpha_h)}{dT} = \frac{-K}{e} \frac{d(\ln p)}{dT} \quad [2]$$

for a p-type semiconductor; here  $K$  is the Boltzmann constant,  $e$  is the electronic charge, and  $p$  is the electron hole concentration. Therefore,  $\alpha_h$  decreases slightly with increasing temperature. Since  $t_h$  increases from 0.8 to 0.95 as the temperature is varied from 600° to 800°C,  $\alpha_h t_h$ , and correspondingly  $\alpha_T$ , increases with temperature in this range. On the other hand,  $t_h$  remains constant beyond 800°C and therefore  $\alpha_h t_h$  and  $\alpha_T$  decrease slightly with temperature above 800°C. Bransky and Tallan (2) have reported a similar decrease in  $\alpha_T$  as the temperature rises from 900° to 1400°C.

Similar considerations explain the temperature variation of  $\alpha_T$  of pure ThO<sub>2</sub> at  $p_{O_2} = 10^{-5}$  atm. The large increase in  $t_h$  from 0.15 at 600°C to 0.7 at 800°C is reflected in the steep rise of  $\alpha_T$  with temperature below about 900°C. At all temperatures,  $t_h$  is less at  $p_{O_2} = 10^{-5}$  atm than in air. As a result,  $\alpha_T$  is lower at  $p_{O_2} = 10^{-5}$  atm than in air. In fact, at a very low oxygen partial pressure ( $p_{O_2} \approx 10^{-23}$  atm) when the "pure" ThO<sub>2</sub> is exclusively an ionic conductor and the total conductivity was extremely low, the Seebeck coefficient was too small to be measured with certainty. This may be compared with a value of  $0 \pm 0.1$  mV/°K observed by Tallan and Bransky (2) on pure ThO<sub>2</sub> at 1000°C and at  $p_{O_2}$  in the range of  $10^{-11}$ - $10^{-19}$  atm.

The  $t_h$  is considerably smaller for 7 m/o CaO sample than for pure ThO<sub>2</sub> in air and at  $p_{O_2} = 10^{-5}$  atm at all temperatures (Fig. 1). Therefore,  $t_h\alpha_h$ , and conse-

quently  $\alpha_T$ , is smaller for the doped sample than for pure ThO<sub>2</sub>, even though  $\alpha_h > \alpha_i$ . This was indeed the case in air at all temperatures and at  $p_{O_2} = 10^{-5}$  atm above 800°C. The increase of  $\alpha_T$  with temperature at lower temperatures must be due to the increase of  $t_i$  and slightly of  $\alpha_i$  with temperature. At higher temperatures,  $t_i$  remains constant and therefore the influence of the negative temperature coefficient of  $\alpha_h$  is seen in the decrease of  $\alpha_T$  with temperature above 800°C in air. However, such a trend was not detected at  $10^{-5}$  atm, since  $t_h$  is very small ( $\approx 0.1$ ) in this case. A Seebeck coefficient of 0.25 mV/°K was measured in this sample at 1000°C at  $p_{O_2} \approx 10^{-23}$  atm, where the sample is a purely ionic conductor.

### Acknowledgments

This work was supported, in part by the Aerospace Research Laboratories under contract AFOSR 71-2136, for which the authors are grateful. We are thankful to C. B. Choudhary for his assistance.

Manuscript submitted Oct. 24, 1975; revised manuscript received Feb. 16, 1976. This was Paper 47 presented at the Toronto, Canada, Meeting of the Society, May 11-16, 1975.

Any discussion of this paper will appear in a Discussion Section to be published in the June 1977 JOURNAL. All discussions for the June 1977 Discussion Section should be submitted by Feb. 1, 1977.

### REFERENCES

1. H. S. Maiti and E. C. Subbarao, To be published.
2. I. Bransky and N. M. Tallan, *J. Am. Ceram. Soc.*, **53**, 625 (1970).
3. N. M. Tallan and I. Bransky, *This Journal*, **118**, 345 (1971).
4. A. K. Mehrotra, H. S. Maiti, and E. C. Subbarao, *Met. Res. Bull.*, **8**, 899 (1973).
5. R. N. Blumenthal and M. A. Seitz, in "Electrical Conductivity in Ceramics and Glass," Part A, N. M. Tallan, Editor, p. 143, Marcel Dekker, Inc., New York (1974).

## Technical Notes



### Surface Analysis of 2024 Aluminum after Treatment with Sulfuric-Chromic Acid Solutions

Neil T. McDevitt and William L. Baun

*Air Force Materials Laboratory, Mechanics and Surface Interactions Branch,  
Wright Patterson Air Force Base, Ohio 45433*

and James S. Solomon

*University of Dayton Research Institute, Dayton, Ohio 45469*

Adhesive bonding of aluminum alloys for use as primary structures of aircraft is becoming an important method of assembly. Present adhesive technology has increased the cohesive strength of bonding resins to the point where the adhesive-oxide interface now plays the major role in the durability of the bonded structure. This requires the oxide layer to play two important roles; (i) it must be a clean active sur-

face that is suitable for bonding and (ii) it must be an adherent protective film for the metal. Therefore, the surface preparation of the metal becomes an important step in the procedure to obtain optimum bond strength, durability, and reproducibility. The fracture strength of the oxide layer is also an important property, however; a thin alumina layer ( $< 5000\text{\AA}$ ) should not limit joint strength.

Fulfilling the requirements stated in i and ii above is made difficult by the complex nature of the aluminum

alloy surface. The elements added for alloying purposes may appear in solid solution, as microparticles of the elements or be present as particles of intermetallic compounds. The stoichiometry of the oxide layer of a material as received from the manufacturer is usually dictated by the particular heat-treatment the alloy has received. In the case of 2024-T3, this surface layer has been shown to consist of a magnesium-rich layer (1). Minford (2) in his work on surface preparations has shown that 6061-T6 aluminum when only vapor degreased before bonding has reasonable initial strength but no durability when exposed to an aggressive environment. Smith (3) has reported that this alloy has a magnesium-rich surface after a heat-treatment. Vapor degreasing has little chemical effect on the surface of an alloy, therefore, it remains the same as that generated by the heat-treatment process. Some preliminary studies in our laboratory show that 2024-T3 bare aluminum has poor durability when only vapor degreased before bonding. These data indicate that a magnesium-rich surface on aluminum lends no durability to a bonded joint. In our studies we have observed that the aluminum alloys 7075, 6061, and 7050 all tend to have a magnesium-rich layer in their as-received state from the manufacturer. It is apparent from the literature that no correlation has been made between the surface chemistry of a vapor-degreased surface and its poor durability. The literature states only that the "old oxide" layer must be removed, so indirectly a magnesium-rich layer is avoided.

With aluminum alloys an acid cleaner (deoxidizer) is invariably used to remove the old oxide surface layer. After deoxidizing, another surface layer will be generated and in our opinion the surface chemistry of this layer is also important and needs to be analyzed. The chemical surface treatment for aluminum alloys usually consists of an acid-bath etch. The acid bath used worldwide, with a few exceptions, is a mixture of sulfuric-chromic acid (or sodium dichromate) solutions. In spite of this large usage, very few surface studies have been performed (4-6) on materials treated in these solutions. To a large extent these few studies have dealt mainly with the physical properties of the surface.

A number of instrumental techniques are now available that allow us to chemically analyze the surfaces of these treated materials. Particular to this study are ion scattering spectroscopy (ISS), secondary ion mass spectroscopy (SIMS), and Auger electron spectroscopy (AES).

This paper reports on the types of elements found in the surface layer of 2024-T3 aluminum after treatment by several acid cleaners. These data represent the initial phase in our program to correlate the surface chemistry of aluminum alloys to adhesive bond durability.

### Experimental

**Instrumentation.**—Standard instrumental parameters were employed for the ISS, SIMS, and AES studies and have been reported previously (1). ISS and SIMS were obtained simultaneously. They are capable of uniquely identifying the elements in the first monolayer of a surface when using  $^4\text{He}$  as the probe ion. AES probes somewhat deeper ( $\sim 20\text{-}30\text{\AA}$ ), however, it is capable of sputtering through a film and recording a depth profile of the elements present. Each technique by itself suffers from some deficiency in sensitivity for various elements, however, the three instruments form a fine complementary technology base for surface analysis.

**Chemical treatments.**—All of the 2024-T3 samples were pretreated with an acetone wash, carbon tetrachloride ultrasonic cleaning, and a room temperature etch in 0.1N sodium hydroxide for 2 min.

Three acid solutions were used in this study: Solution 1. 300g sulfuric acid, 30g sodium dichromate per liter of solution (commonly known as FPL etch). Time and temperature were varied. Solution 2. 100g sulfuric acid, 30g chromic acid per liter of solution. Temperature was maintained at 50°C while time varied. Solution 3. 300g sulfuric acid, 40g chromic acid per liter of solution. Temperature was maintained at 60°C while time varied.

All samples were rinsed in tap water for 15 min and wiped dry.

### Results and Discussion

2024-T3 aluminum is a high copper (4.5%)-magnesium (1.5%) alloy and in all cases a surface layer will be formed by the chemical interaction of the acid bath and the aluminum metal. The corrosion resistance of the metal will depend on the tenacity and chemical nature of the hydrated oxide layer placed on the surface. These two characteristics will depend on the nature of the alloy and the chemical treatment that is responsible for the film.

The artificial aging of this alloy causes the compound  $\text{CuAl}_2$  to precipitate along the grain boundaries. This compound is highly cathodic if brought into contact with an aggressive environment. As mentioned previously, a magnesium-rich oxide layer does not appear to provide a durable surface (2) for bonding. Sulfate and chromate anions can both become part of the treated surface due to their presence in the acid etch solutions. Any sulfate left in the oxide layer could, under the proper conditions, form a white powdery product (6), namely  $\text{Al}_2(\text{SO}_4)_3 \cdot 18\text{H}_2\text{O}$ . The positive or negative effects of the chromate anion on the oxide layer-adhesive interface have not been studied in any detail.

The data presented in this paper are primarily concerned with the chemical nature of each surface film and the comparative results are based on the presence of copper, magnesium, chromium, sulfur, and the relative thickness of each film. We propose that the desired surface should contain a minimum amount of the elements presented above.

Figure 1 shows the intensity data for oxygen, copper and aluminum (1396 eV) obtained from an Auger profile. It is a typical example of the profile data obtained for this study. The intensity profile for each element was normalized and plotted through the use of a computer program. The oxide thickness was arbitrarily determined by extending the profile slope of oxygen directly to the baseline. The copper concentra-

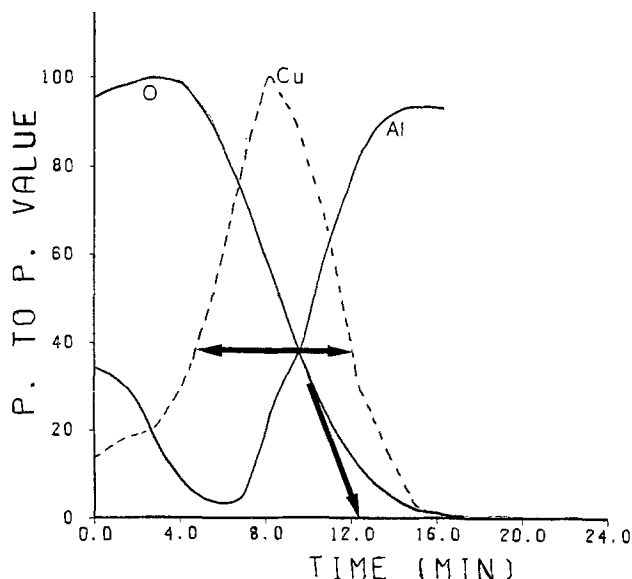


Fig. 1. AES intensity profile of oxygen, copper, and aluminum

tion was arbitrarily determined by measuring the width of the copper intensity profile curve at the oxygen-aluminum crossover. Both of these data points were left in the unit of time. Since copper is part of the bulk alloy its concentration can be greater than the thickness of the oxide layer.

Figure 2 shows the comparative oxide film thickness and copper concentration of the 2024-T3 aluminum surface for various time and temperature treatments in the FPL etch (solution 1). An etch temperature of 65°C leaves a relatively constant oxide layer and copper concentration regardless of the time in bath. At 55°C these values increase and at 45°C they are approximately double that of the 65°C etch.

Figure 3 shows the data obtained from the straight acid etches. The 100-30 mixture (solution 2) at 50°C averages almost 17 min sputter time in both film thickness and copper concentration. The 300-40 mixture (solution 3) at 60°C averages approximately 13 min for oxide layer thickness and 11 min for copper concentration.

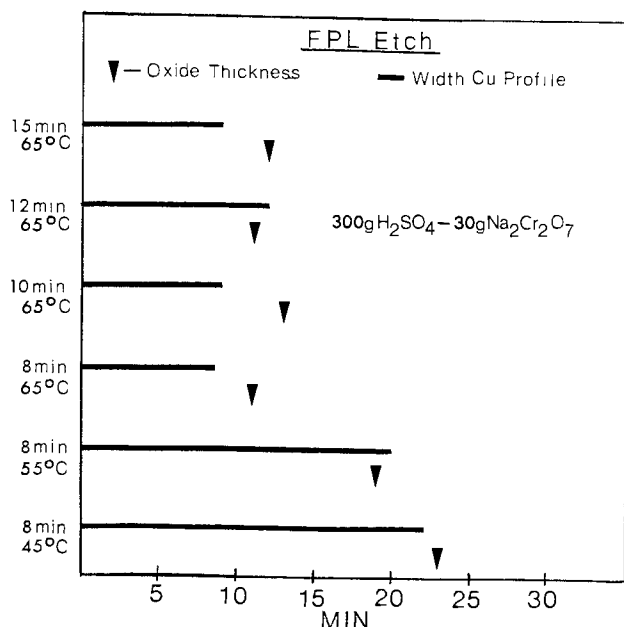


Fig. 2. Variations of oxide thickness and copper concentration on 2024-T3 generated by an FPL etch solution.

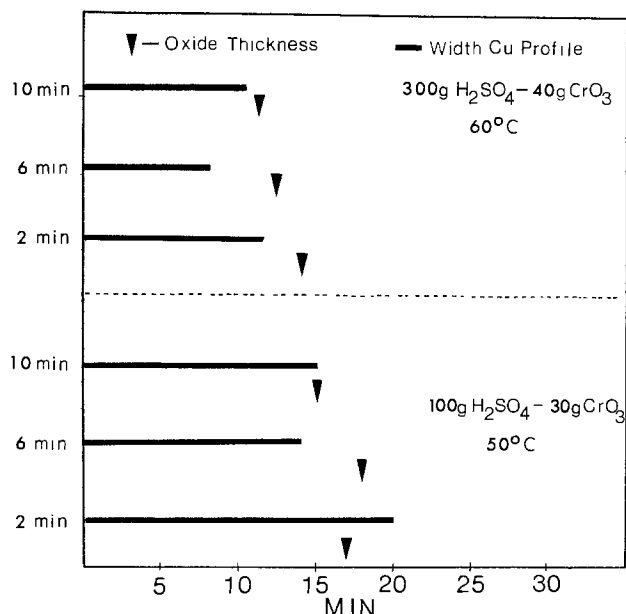


Fig. 3. Variations of oxide thickness and copper concentration on 2024-T3 generated by sulfuric-chromic acid solutions.

Magnesium was reduced to a minimum by these solutions and due to its low sensitivity by the Auger technique could not be profiled with any accuracy. Figures 4 and 5 show typical ISS-SIMS and Auger spectrograms, respectively. These curves were obtained from a sample treated for 6 min in solution 2. Oxygen, 510 eV, usually masks the chromium energy peaks at 489 and 529 eV (Fig. 5) making it impossible to obtain an intensity profile curve for this element.

Sulfur is observed in all of the Auger spectra at approximately 8% of the peak-to-peak intensity of oxygen. The Auger technique is sensitive to sulfur while the ISS and SIMS techniques are not. Several intensity profiles indicate sulfur is only part of the outer surface layer with its intensity falling almost to zero after 2 min. This is based on a sputtering rate of 10-15 Å/min. Carbon seems to be always present and follows the same discussion as that for sulfur, however, it should not have been placed there directly by our preparation techniques.

Since magnesium, chromium and sulfur are difficult to profile by Auger for this particular investigation, they are reported in Tables I and II as detected elements.

Copper was observed by ISS, SIMS, and AES for all of the solutions studied and is not reported in these tables. Magnesium will be masked by aluminum in the ISS technique but can be observed by SIMS (Fig. 4). Table I shows magnesium is detected on the metal surface for all of the FPL etch solutions by SIMS, how-

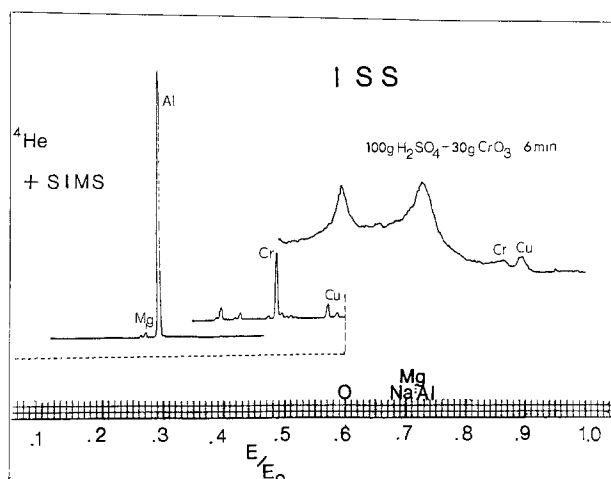


Fig. 4. ISS-SIMS spectra of a surface prepared from a 6 min etch in a 100-30 sulfuric-chromic acid solution.

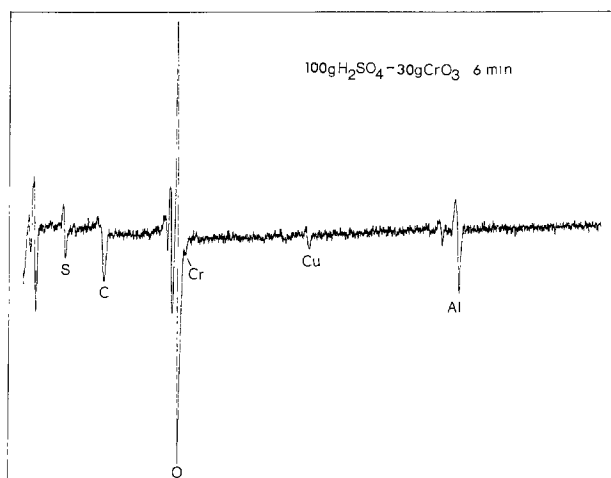


Fig. 5. AES spectrum of a surface prepared from a 6 min etch in a 100-30 sulfuric-chromic acid solution.

Table I. Sulfuric-sodium dichromate solution. Detection of magnesium, chromium, and sulfur by ISS (I), SIMS (S), and AES (A)

Time (min)	Temp (°C)	Mg	Cr	S
8	45	S		A
8	55	S	S	A
8	65	S	S	A
10	65	S	S	A
12	65	S	S	A
15	65	S	S	A

Table II. Sulfuric-chromic acid solutions. Detection of magnesium, chromium, and sulfur by ISS (I), SIMS (S), and AES (A)

Time (min)	100g H <sub>2</sub> SO <sub>4</sub> -30g CrO <sub>3</sub>			300g H <sub>2</sub> SO <sub>4</sub> -40g CrO <sub>3</sub>		
	Mg	50°C Cr	S	Mg	60°C Cr	S
2	S, A	I, S, A	A	S		A
4	S, A	I, S, A	A		S	A
6	S	I, S, A	A		S	A
8	S	I, S, A	A		S	A
10	S	I, S, A	A		I, S	A

ever, it must be remembered that the concentration at the surface has to be small since it was not observed in the Auger spectra. Chromium is detected by SIMS in most of the studies but not only by ISS or AES, indicating only a small amount is present.

Table II shows that the 100-30 mixture leaves the metal surface relatively chromium rich as it is detected by all three instrumental techniques. Magnesium is detected by SIMS and AES for the 2, 4, and 6 min etch times and SIMS for the 8 and 10 min periods. The 300-40 mixture removes all of the magnesium below detectable limits in the 4 through 10 min etch periods, while chromium is detected only by SIMS in the 4-10 min period and by ISS in only the latter.

### Conclusions

In any electrochemical reaction the most negative or active half-cell will be oxidized. In order to help

protect the aluminum surface from corrosion, the electrochemical potential of the surface oxide layer should be as small as possible. This can be achieved by maintaining an oxide layer just thick enough to do its job, and by keeping all other metal elements and anions in the oxide layer at a minimum.

All of the solutions studied form a thin oxide layer (200-300Å) on 2024-T3 aluminum. The 300-40 mixture (solution 3), with a time in bath of 6-8 min, gives a surface with the minimum amount of detectable elements for this study. From the electrochemistry viewpoint this oxide layer should form a good surface film. In order to determine the influence of the surface on the long-term properties of an adhesive joint, the authors propose that sufficient chemical data must be obtained not only on the surface of each alloy but on different lots of the same alloy as well. Using this data base all of these surfaces must then be correlated with environmental studies.

Manuscript submitted Dec. 19, 1975; revised manuscript received March 3, 1976.

Any discussion of this paper will appear in a Discussion Section to be published in the June 1977 JOURNAL. All discussions for the June 1977 Discussion Section should be submitted by Feb. 1, 1977.

Publication costs of this article were partially assisted by the Air Force Materials Laboratory.

### REFERENCES

1. N. T. McDevitt, W. L. Baun, and J. S. Solomon, AFML-TR-75-122, Wright Patterson AFB, Ohio 45433.
2. J. D. Minford, *Adhesives Age*, **17**, 24 (1974).
3. J. A. Smith and W. E. Martinsen, *Am. Ceram. Soc. Bull.*, **52**, 855 (1973).
4. R. E. Herfert, Private communication.
5. P. Bijlmer and R. Schliekelmann, *SAMPLE Quarterly*, October, 13 (1973).
6. A. W. Smith, *This Journal*, **120**, 1551 (1973).
7. P. M. Aziz and H. P. Godard, *Corrosion*, **15**, 529t (1959).

## The Electrochemical Response of Nickel Electrodes in Aqueous Sulfuric Acid Solutions

J. R. Vilche<sup>1</sup> and A. J. Arvía\*

*Instituto de Investigaciones Fisicoquímicas Teóricas y Aplicadas, División Electroquímica, Universidad Nacional de La Plata, La Plata, Argentina*

Two or more current peaks are associated with the potentiodynamic anodic dissolution of nickel in aqueous sulfuric acid solutions. Different explanations have been proposed to account for the occurrence of those current peaks which are related to the  $\text{Ni} = \text{Ni}^{2+} + 2e$  reaction (1-6). But most of them are not fully consistent since the potentiodynamic response of nickel electrode depends on a large number of variables which usually are not systematically changed under comparable conditions. This is immediately concluded after a critical revision of the published results.

The aim of this report is precisely to call attention to the complexity of kinetic results related to nickel corrosion and passivity in acid aqueous media and the difficulty of deriving from them prompt mechanistic interpretations which are not fully substantiated.

When a polycrystalline nickel wire electrode is polarized in a 1N NiSO<sub>4</sub> + 0.05N H<sub>2</sub>SO<sub>4</sub> solution at 25°C, under a triangular potential sweep, the E/I profile depends upon the anodic as well as the cathodic potential limits reached, on the potential sweep rate, and on the number of repetitive potential cycles.

A freshly electropolished nickel electrode immersed in this solution exhibits a rest potential of -0.240V (vs. a SCE). When the electrode is polarized at 0.5 V/min from  $E_i = -0.260\text{V}$  up to 0.505V (anodic scan) the E/I contour (Fig. 1) presents a well-defined anodic current peak (I) at 0.065V which corresponds to metal passivation. This is revealed by the reverse cathodic potential scan where practically no current is recorded. The following successive potential scans confirm the onset of the passive state on the electrode. The current peak associated with passivity entails an anodic charge which largely exceeds that of a monolayer and its contour is appreciably asymmetric in shape. The latter

\* Electrochemical Society Active Member.

<sup>1</sup> Present address: División de Investigación y Desarrollo, Fate Electrónica, San Fernando, Buenos Aires, Argentina.

Key words: nickel, corrosion, passivation.

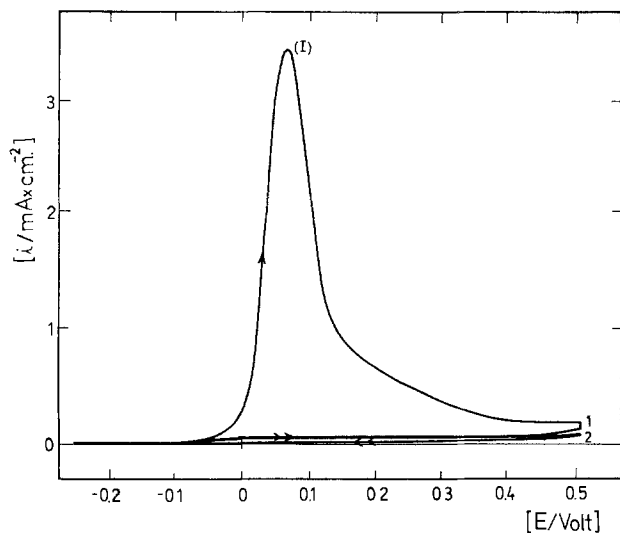


Fig. 1.  $E/I$  display obtained with a symmetric triangular potential sweep at 0.5 V/min in a 1N  $\text{NiSO}_4 + 0.05\text{N H}_2\text{SO}_4$  solution. First scans 1 and 2 are shown. Arrows indicate the direction of the potential scan.

is due to the occurrence of at least two additional current peaks at the anodic side of current peak I. This is confirmed (Fig. 2) by carrying on the same experiment with an electrode previously potential cycled within the same potential range and left in contact with the solution until it attained the rest potential. Now the  $E/I$  profile shows a marked decrease in the height of current peak I and a better definition of the new current peaks located at ca. 0.15 and at ca. 0.35V, respectively.

The potentiodynamic  $E/I$  profile change during the initial cycles (Fig. 3) and the relative change of the  $E/I$  contours with the number of cycles strongly depends on the anodic potential limit reached. In the case of Fig. 3, both the height of the anodic current peak I and the amount of anodic charge involved decrease with the number of successive cycles, while the corresponding current peak potential becomes more negative.

During the cathodic scan an appreciable anodic current is also observed, which approaches a limiting value during the successive potential scans. At relatively low potential sweep rates (Fig. 4), the  $E/I$  characteristics recorded within a potential range which is anodic with respect to the hydrogen electrode potential exhibit during the first anodic scan the anodic current peak I together with a shoulder at ca. 0.1V, and the returning cathodic scan reveals another anodic current peak (II) at a potential very close to the nickel rest potential. Under these circumstances the potential

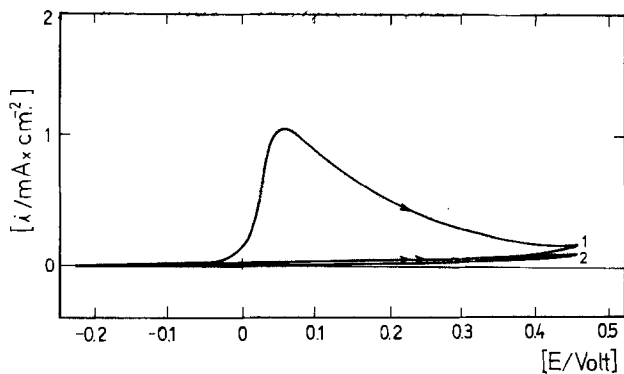


Fig. 2.  $E/I$  display obtained as indicated in Fig. 1, but with an electrode previously potential cycled and left in contact with the solution until attaining the rest potential.

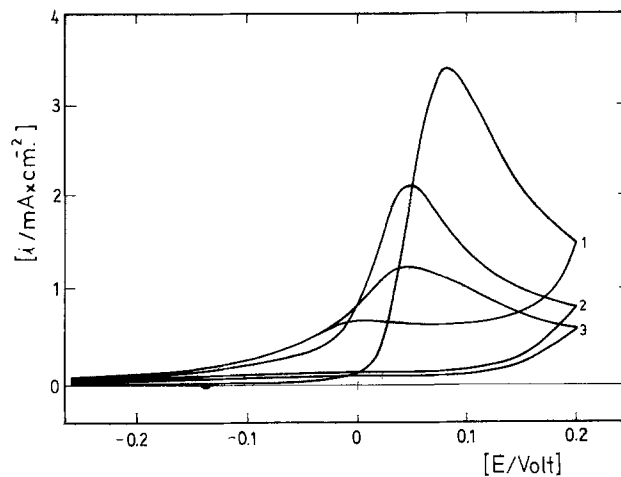


Fig. 3.  $E/I$  display obtained with symmetric repetitive triangular potential scans under the experimental conditions indicated in Fig. 1.

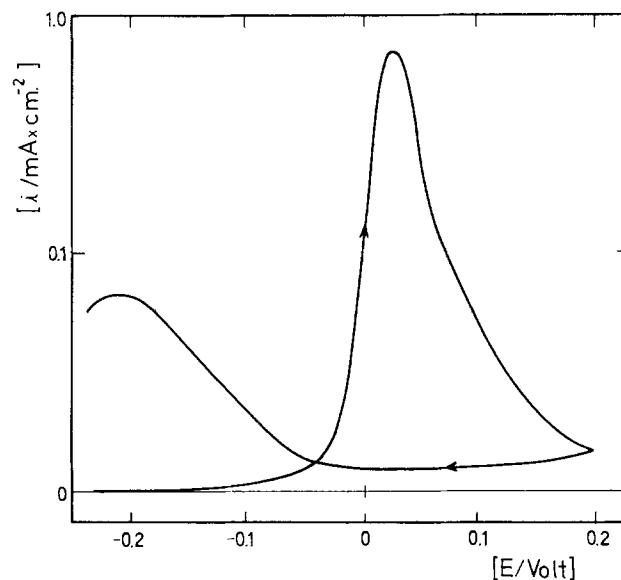


Fig. 4.  $E/I$  display recorded with a single symmetric triangular potential sweep at 0.05 V/min in 1N  $\text{NiSO}_4 + 0.05\text{N H}_2\text{SO}_4$  solution.

of current peak I lies close to the potential attained at larger potential sweep rates after  $n$  cycles (Fig. 3).

A similar effect is observed (Fig. 5) when the cathodic potential limit extends towards the hydrogen evolution region. The potentiodynamic sweep starts

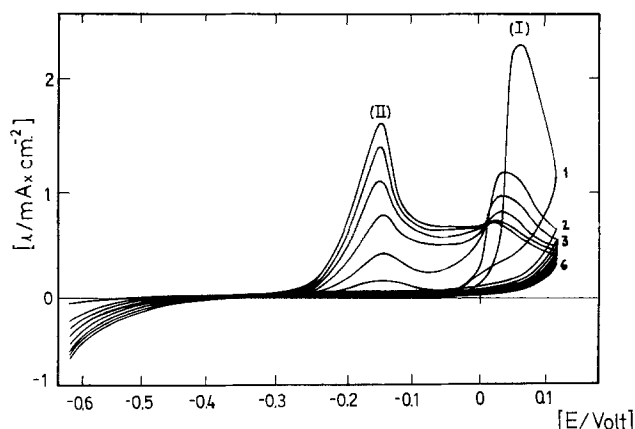


Fig. 5. Repetitive  $E/I$  displays at 0.5 V/min covering the hydrogen evolution region with the same electrolytic solution.

from the rest potential ( $-0.240\text{V}$ ) going toward the cathodic potential region (down to  $-0.630\text{V}$ ) and the following repetitive cycles run between  $-0.630$  and  $0.120\text{V}$ . Now, the first anodic sweep exhibits only the anodic current peak I at  $0.080\text{V}$ , while no cathodic current is found during the returning half-cycle. The second anodic scan exhibits a well-defined anodic current peak II at  $-0.150\text{V}$ . The height of the latter increases during the successive cycles without an appreciable change of the corresponding potential.

Simultaneously, both the height and the potential of current peak I decrease. A well-defined limiting current region is also found between  $-0.1$  and  $0\text{V}$ , which increases during the repetitive potential cycling. The whole voltammogram attains a stable contour after a relatively large number of cycles ( $n \geq 20$ ).

At  $0.010\text{V}$ , the  $E/I$  profiles exhibit a crossing point which probably corresponds to an isopotential point. Furthermore, the relative peak height distribution depends also on the potential sweep rate and the difference of the current peak potentials decreases as the potential sweep rate increases.

The multiplicity of current peaks depicted in Fig. 5 coincides with those recently reported (6) which were assigned to the effect of cathodic treatment of nickel and the bubbling rate of different gases (6).

The effect of stirring was determined with a nickel rotating disk electrode. For this purpose the electrode was first cycled until the  $E/I$  display attained a stable contour. A stable  $E/I$  profile run at  $6\text{ V/min}$ , when the stirring rate is changed stepwise from  $0$  up to  $2500\text{ rpm}$ , shows a net increase of the limiting current peak located between the anodic current and no appreciable influence of stirring on current peak I.

From this brief phenomenological description of the electrochemical behavior of nickel in sulfuric acid-containing solutions, one concludes that their potentiodynamic  $E/I$  characteristics depend both on the conditions of the potential perturbation and stirring. Their influence on the kinetic parameters of the process is probably more marked than that resulting from the crystallographic characteristics of the base metal (7).

The kinetics of nickel electrodisolution in  $\text{H}_2\text{SO}_4$  solutions outstandingly depends on the state of the

electrode surface either before or during anodic polarization, which must include the participation of the  $\text{SO}_4^-$  anion adsorption process (8). The dependence of the kinetic characteristics of nickel in aqueous solutions on ionic composition should be correlated with the anion adsorption free energy. The latter will also explain the different behavior of nickel in electrolytes such as  $\text{H}_2\text{SO}_4$  or  $\text{HCl}$  (9) or a mixture of both electrolytes (10).

#### Acknowledgments

This work is part of the research program of the ECOMAR project sponsored by the SENID (Office for Research and Development, Argentine Navy) and the Consejo Nacional de Investigaciones Científicas y Técnicas of Argentina.

Manuscript received Nov. 19, 1975.

Any discussion of this paper will appear in a Discussion Section to be published in the June 1977 JOURNAL. All discussions for the June 1977 Discussion Section should be submitted by Feb. 1, 1977.

#### REFERENCES

1. J. L. Weininger and M. W. Breiter, *This Journal*, **110**, 484 (1963).
2. Y. M. Kolotyркин, *Zash. Metal.*, **3**, 131 (1967).
3. C. J. Chatfield and L. L. Shreir, *Corrosion Sci.*, **12**, 563 (1972).
4. H. J. Ratzler-Scheibe and H. G. Feller, *Electrochim. Acta*, **18**, 175 (1973).
5. I. A. Gindin, L. N. Jagupolskaja, W. K. Aksenov, and Ja. D. Starodubow, *Corrosion Sci.*, **13**, 967 (1973).
6. B. MacDougall and M. Cohen, *This Journal*, **122**, 383 (1975).
7. R. Piontelli, G. Poli, and G. Serravalle, in "Trans-action of Symposium of Electrode Processes," E. Yeager, Editor, p. 67, John Wiley & Sons, New York (1961).
8. N. A. Balaskova, N. T. Gorokhova, and S. A. Lilin, *Soviet Electrochem.*, **9**, 666 (1973).
9. J. R. Vilche and A. J. Arvia, *Corrosion Sci.*, **15**, 419 (1975).
10. Z. Szklarska-Smialowska, *ibid.*, **11**, 209 (1971); *ibid.*, **12**, 527 (1972).

## Brief Communication



### Cathodic Instability in Solid Copper Ion Battery Electrolytes: A Suggested General Mechanism

Douglas O. Raleigh\*

Rockwell International, Science Center, Thousand Oaks, California 91360

There have now been reports of a number of solid room temperature copper ion conductors based on double salts of polar organic halides and  $\text{CuI}$ . Takahashi *et al.* reported copper ion conductivity in the N-alkyl (or hydro)-hexamethylenetetramine halide-copper halide system (1) and later in the N,N'-dialkyl (or dihydro)-triethylenediamine dihalide-copper halide system (2). Recently, Sammells *et al.* have reported

room temperature copper ion conductivity in some nine substituted organic ammonium halide-copper halide compounds (3).

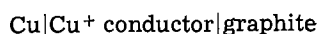
In each case, an interest in solid-state battery applicability presumably led to attempts to construct cells involving copper and a solid-state oxidant as electrodes. Indications to date, however, are that these compounds are all chemically unstable in contact with oxidant materials. Sammells and co-workers reported electrolyte deterioration in such cells for all electrolyte

\* Electrochemical Society Active Member.

Key words: solid electrolyte, copper battery, instability.

compositions, whether or not a current was drawn from the cell, for both oxide ( $V_2O_5$ ,  $MoO_3$ ) and organic polybromide cathode materials. No specific mechanism was offered. Takahashi and co-workers reported conductivities, but no galvanic cell results. The purpose of this communication is to suggest a general instability mechanism for a solid copper-ion conductor in contact with a solid oxidant.

Copper ion conductors are unique among solid electrolytes in that the current-carrying ion may be oxidized to a higher valence state by most common oxidants. In crystal ionic compounds, the presence of such a higher valence state in the crystal bulk should generally give rise to hole conduction, either of the hopping or valence band type, depending on whether the most energetic filled electronic states are localized or form energy bands (4). A third possibility is that the electron holes thus produced are immobilized by being in deep potential wells. This does not appear likely, however, for the copper ion conductors under consideration. Takahashi and co-workers (1, 2) found that in polarization cells of the type

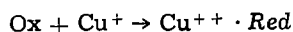


an observed low level electronic conductivity showed the exponential increase with voltage characteristic of hole conductivity. Thus, it appears that holes in these compounds are mobile.

The mobility of both  $\text{Cu}^+$  ions and holes in these compositions suggests a general transport mechanism by which deterioration of electrolyte properties should occur in contact with practically any solid oxidant material. The polarization cell results of Takahashi *et al.* suggest that the electron energetics in these compounds may be represented by a straightforward energy band picture, with a bandgap  $\gg kT$ . Figure 1(a) shows a schematic energy level diagram for a  $\text{Cu}^+$  conductor as it is about to be brought in contact with a solid oxidant. The midbandgap position of Fermi level  $E_F$  corresponds to assuming exact cation-anion stoichiometry (effective Cu valence 1.00). A stoichiometric Cu excess would give rise to conduction electrons and a Cu deficit to valence band holes, in accordance with the usual Wagner picture (5). The Fermi level in the oxidant corresponds to the electron affinity in the equilibrium system  $\text{Ox} + ne \rightleftharpoons \text{Red}$  appropriate for this oxidant. It is shown to lie deeper with respect to the vacuum level than the top of the valence band in the  $\text{Cu}^+$  conductor, to indicate that the oxidant is more oxidizing than the  $\text{Cu}^+$ ,  $\text{Cu}^{++}$  couple in the conductor.

In this picture, when electrolyte-oxidant contact is established,  $\text{Cu}^+$  ions on the electrolyte surface should be oxidized to  $\text{Cu}^{++}$ . In addition, the greater electron affinity in the oxidant should cause an incipient influx of electrons from the electrolyte. In the absence of any mass transport, this would result in an interfacial electronic equilibrium with a local accumulation of holes in the electrolyte valence band, electrons in the oxidant phase, and an equilibrium interface potential that prevents further charge transfer. This situation, with the resultant band bending, is shown in Fig. 1(b).

In the presence of mobile  $\text{Cu}^+$  ions, however, this situation is not time invariant. These ions should now move towards the oxidant phase under the influence of the interface potential,  $V(x)$ . On reaching the interface, they can be oxidized by the oxidant:



where  $\text{Cu}^{++} \cdot \text{Red}$  is the reaction product. This motion of  $\text{Cu}^+$  ions, however, reduces the diffuse space charge in the electrolyte, and thus draws more electrons into the oxidant phase to maintain the interfacial Fermi level equilibration. The net result should be matching countercurrent flows of valence band holes into the

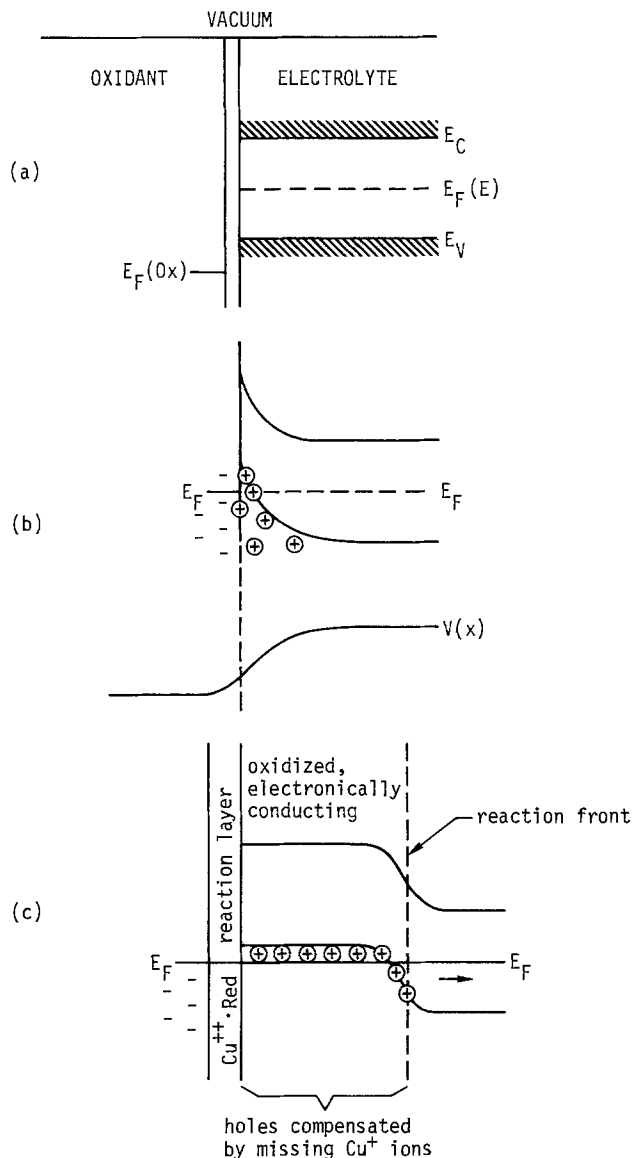


Fig. 1. Schematic of energy band structure of  $\text{Cu}^+$  ion conductor in contact with solid oxidant: (a) prior to contact, (b) initial electronic equilibrium and interface voltage profile, (c) during subsequent bulk oxidation.

electrolyte and  $\text{Cu}^+$  ions to the interface, with a small fraction of the bulk  $\text{Cu}^+$  ions being replaced by holes in a "front" of the electrolyte that moves continually into the crystal bulk. Concurrent with this would be the buildup of a  $\text{Cu}^{++} \cdot \text{Red}$  reaction layer at the interface. This is the situation shown in Fig. 1(c).

Note that this is simply the thermodynamically favored chemical oxidation of the electrolyte, which is enabled to occur in  $\text{Cu}^+$  conductors by the existence of mobile electronic charge corresponding to the +2 valence state. In  $\text{Ag}^+$  and alkali ion conductors, the absence of a higher cation valence state renders the electrolyte stable toward a number of oxidants.

We might ask whether electrolyte deterioration could be avoided by suitable ionic and electronic transport properties of the reaction layer or a suitable choice of the battery oxidant material. With respect to the former, low polarization in a battery requires that  $\text{Cu}^+$  ions be mobile in this reaction layer, since this layer is the product of drawing current from a  $\text{Cu}|\text{Cu}^+$  conductor|oxidant cell. The mobility of  $\text{Cu}^+$  ions therein is the mechanism by which current could continue to be drawn. Since, in addition, the simultaneous presence of  $\text{Cu}^+$  and  $\text{Cu}^{++}$  ions in this layer should insure significant hole conductivity, its transport properties would appear adequate to support the suggested de-

terioration mechanism. If the oxidant chosen is too weak to oxidize  $\text{Cu}^+$ , it must lie between the  $\text{Cu}^0$ ,  $\text{Cu}^+$  and  $\text{Cu}^+$ ,  $\text{Cu}^{++}$  couples in oxidizing strength, resulting in a maximum cell emf of only  $\sim 0.35\text{V}$  (6). For oxidants strong enough to be of interest in battery applications, the oxidizability of  $\text{Cu}^+$  appears to insure a general anodic self-discharge mechanism that propagates across the electrolyte a compositional change resulting in electronic conduction.

The specific deterioration mechanism suggested is obviously the simplest of a number of possibilities. Sammells *et al.* reported that the use of oxide oxidants such as  $\text{V}_2\text{O}_5$  and  $\text{MoO}_3$  gave no electrolyte color change, while halide oxidants resulted in blackening as well as cell voltage loss. The blackening may reflect either a greater degree of oxidation within the original structure or actual chemical decomposition. The purpose of the present communication is not to "prove" a particular deterioration mechanism or even to prove that a copper ion electrolyte battery cannot be made. It is rather to suggest that the lack of success thus far is the result of something other than an unfortunate

choice of the cathode material or an anomalous property of the particular copper electrolyte.

Manuscript submitted Dec. 29, 1975; revised manuscript received March 29, 1976.

Any discussion of this paper will appear in a Discussion Section to be published in the June 1977 JOURNAL. All discussions for the June 1977 Discussion Section should be submitted by Feb. 1, 1977.

Publication costs of this article were partially assisted by Rockwell International.

#### REFERENCES

1. T. Takahashi, O. Yamamoto, and S. Ikeda, *This Journal*, **120**, 1431 (1973).
2. T. Takahashi and O. Yamamoto, *ibid.*, **122**, 83 (1975).
3. A. F. Sammells, J. Z. Gougoutas, and B. B. Owens, *ibid.*, **122**, 1291 (1975).
4. See, for instance, N. F. Mott and R. W. Gurney, "Electronic Processes in Ionic Crystals," Oxford University Press, London (1948).
5. C. Wagner, *Z. Elektrochem.*, **60**, 4 (1956).
6. J. F. Hunsberger, in "Handbook of Chemistry and Physics," 54th ed., p. D-120, CRC Press, Cleveland (1973).

### Errata

In the paper "Computer-Controlled Differential Capacitance Measurements" by David M. Mohilner, Joyce C. Kreuser, Hisamitsu Nakadomari, and Patricia M. Mohilner which appeared on pp. 359-366 in the March 1976 JOURNAL, Vol. 123, No. 3, Eq. [5] should read as follows:

$$\gamma = - \int_{E_x}^E \int_{E_x}^E C_d E dE + \gamma_{\max}$$

In the paper "Cathodic Characteristics of a CuS Electrode in Liquid Ammonia" by Yoshiharu Matsuda, Hiroaki Ueyama, and Yoshio Takasu which appeared

on pp. 220-222 in the February 1976 JOURNAL, Vol. 123, No. 2, the captions to Fig. 2 and 4 should read as follows:

Fig. 2. Relations between specific conductivity and temperature for liquid ammonia with thiocyanates. Solute: ● = 4 mole/l  $\text{NH}_4\text{SCN}$ , ○ = 4 mole/l  $\text{KSCN}$ , ⊙ = 4 mole/l  $\text{NaSCN}$ .

Fig. 4. Cathodic polarization curves for a CuS electrode. Electrode composition: CuS 80%, polyethylene 5%, graphite 15%. Solute: 4 mole/l  $\text{NH}_4\text{SCN}$  + 0.5 mole/l  $\text{NH}_4\text{Cl}$ . Temperature: ● = 25°C, ○ = 0°C, △ = -65°C, ⊙ = -75°C.





## The Active Oxidation of Si and SiC in the Viscous Gas-Flow Regime

J. W. Hinze\*<sup>1</sup>

*Systems Research Laboratories, Incorporated, Dayton, Ohio 45440*

and H. C. Graham

*Air Force Materials Laboratory, Wright Patterson Air Force Base, Ohio 45433*

### ABSTRACT

The active oxidation of Si and SiC was investigated in the viscous gas-flow regime. Kinetics were measured as a function of temperature and oxygen partial pressure using thermogravimetric techniques. Active oxidation was initiated by exposing oxide-free samples to low oxygen partial pressures in O<sub>2</sub>/Ar gas mixtures. Oxidation rates were found to be controlled by oxygen transport through the gaseous boundary layer. Active oxidation of Si was found to occur in two distinct stages rather than in only one as expected. Linear sample weight losses were observed during the first stage; however, in the second stage unusual and destructive behavior was observed in the form of extremely rapid sample weight gains. This phenomenon was interpreted in terms of a simultaneous SiO vaporization and SiO<sub>2</sub> condensation process. No such behavior was observed during SiC active oxidation.

Si-base materials such as Si<sub>3</sub>N<sub>4</sub>, SiC, and their composites have been proposed for a number of applications because of their exceptional high temperature properties, in particular, strength, oxidation resistance, and thermal-shock resistance. A number of investigators have studied the oxidation of these materials in environments where protective silica scales are formed on the substrate. Although the details of the oxidation mechanisms are still not well understood (1-8), the activation energies for oxidation and the extremely low oxidation rates found by various investigators are in reasonable agreement. An important limitation of Si-base materials is their tendency to form gaseous products during oxidation in reduced oxygen pressures at high temperatures. Instead of a protective SiO<sub>2</sub> scale being formed, the substrate surface either remains bare or, as we shall see later, nonprotective SiO<sub>2</sub> in the form of whiskers is grown. Under these conditions extremely rapid rates of material loss occur.

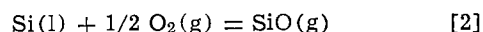
Active oxidation can be initiated at high temperatures by exposing the material to either pure oxygen at low total pressure (molecular gas-flow regime) or dilute oxygen/inert gas mixtures at or near atmospheric pressure (viscous gas-flow regime). Results from several investigations involving the active oxidation of Si and SiC in the molecular gas-flow regime have been reported (9-14), and the mechanisms of active oxidation are well understood. Solid SiO<sub>2</sub> was stable in the oxygen pressure and temperature environments used; however, active oxidation was initiated by decreasing the ambient oxygen pressure ( $P_{O_2} = P_T$ ) below the equilibrium SiO pressure at the Si-SiO<sub>2</sub> or SiC-SiO<sub>2</sub>

interface. Rapid attack ensued when the SiO<sub>2</sub> scale mechanically ruptured causing the escape of SiO(g) through pores and fissures in the scale (9, 12, 14). The steady-state rate of material loss by SiO evaporation was calculated by using the Hertz-Knudsen equation and by equating the rates of oxygen arrival and SiO removal (14) as follows

$$J_{SiO} = J_O = 2\alpha P^{\circ}O_2 / (2\pi M_{O_2} RT)^{1/2} \quad [1]$$

where  $J_{SiO}$  and  $J_O$  are, respectively, the fluxes of SiO and oxygen,  $P^{\circ}O_2$  is the ambient oxygen pressure,  $M_{O_2}$  is the molecular weight of oxygen, and  $\alpha$  is the collision efficiency.

Unlike the molecular-flow regime, the active-oxidation mechanisms of Si and SiC in the viscous-flow regime are not well understood. Wagner (15) has offered a theory of active oxidation based on the experimental results of Kaiser and co-workers (16-17) who exposed liquid Si to an oxygen/inert-gas mixture of low  $P_{O_2}$  at high temperature. The Si getters oxygen in such a way that diffusion gradients for the oxygen and the inert gas become established. The oxygen partial pressure at the Si surface,  $P^*O_2$ , is reduced below the stability limit for SiO<sub>2</sub> shown as a vertical line in Fig. 1 ( $P^*O_2 \approx 10^{-20}$  atm at 1600°K). Because only gaseous oxides are stable below this  $P_{O_2}$ , the surface of the Si will remain free of solid oxidation products so long as  $P^*O_2$ , the ambient  $P_{O_2}$ , is maintained at a sufficiently low value. Active oxidation then proceeds according to the reaction



$$P^*_{SiO} = K_2 P^{*1/2}O_2 \quad [2a]$$

The steady-state rate of active oxidation is controlled solely by the rate of oxygen impingement at the Si

\* Electrochemical Society Active Member.

<sup>1</sup> Present address: Owens-Corning Fiberglas Technical Center, Granville, Ohio 43023.

Key words: viscous gas flow, vaporization, mass-transfer coefficient, passive oxidation.

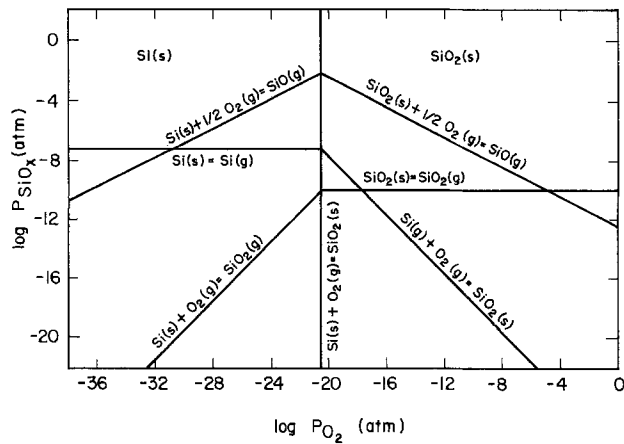


Fig. 1. Thermodynamics of the Si-O system at 1600°K using data of Zmbov *et al.* (21) and JANAF (23).

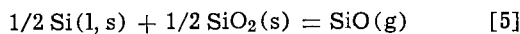
surface which, in the viscous-flow regime, is given by Fick's law of diffusion, whence

$$J_{SiO} = J_O = 2D_{O_2} P^{\circ}_{O_2} / \delta_{O_2} RT = 2h_{O_2} P^{\circ}_{O_2} / RT \quad [3]$$

where  $h_{O_2}$  is the average boundary-layer mass-transfer coefficient,  $P^{\circ}_{O_2}$  is the ambient oxygen partial pressure,  $D_{O_2}$  is the oxygen/inert gas interdiffusivity, and  $\delta_{O_2}$  is the effective thickness of the oxygen boundary layer. As  $P^{\circ}_{O_2}$  is increased,  $P^*_{O_2}$  increases until it reaches the critical value (vertical line in Fig. 1) corresponding to incipient  $SiO_2$  formation. The Si surface becomes covered with a coherent, protective layer of  $SiO_2$ , and passive oxidation occurs. In Wagner's notation the ambient  $P_{O_2}$  corresponding to the transition from active-to-passive oxidation is given by

$$P^{\circ}_{O_2}(\max) = 1/2(D_{SiO}/D_{O_2})(\delta_{O_2}/\delta_{SiO}) P^{eq}_{SiO} \quad [4]$$

where  $D_{SiO}$  and  $D_{O_2}$  are, respectively, the SiO- and  $O_2$ -inert gas interdiffusivities,  $\delta_{SiO}$  is the effective thickness of the SiO-boundary layer, and  $P^{eq}_{SiO}$  is the equilibrium SiO partial pressure calculated from the equation



If the boundary layer is laminar, it can be shown that

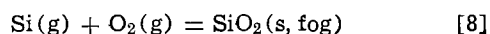
$$(\delta_{SiO}/\delta_{O_2}) \approx (D_{SiO}/D_{O_2})^{1/2} \quad [6]$$

and Eq. [4] becomes

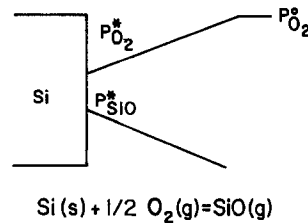
$$P^{\circ}_{O_2}(\max) = 1/2(D_{SiO}/D_{O_2})^{1/2} P^{eq}_{SiO} \quad [7]$$

The ratio  $D_{SiO}/D_{O_2}$  can be determined from well-known gas-kinetics equations. Because this ratio is virtually temperature and gas-flow velocity independent, a plot of  $\log P^{\circ}_{O_2}(\max)$  vs.  $1/T$  is expected to give the enthalpy of formation of SiO according to Eq. [5].

While the Wagner model of active oxidation has been used to rationalize the experimental observations of Kaiser *et al.* (16-17) for the active oxidation of liquid Si, the model proposed by Turkdogan, Grieveson, and Darken (18) for the oxidation-enhanced vaporization of metals could be valid for the case of Si for certain temperatures and gas-flow characteristics. This model is compared to that proposed by Wagner in Fig. 2. In the Turkdogan *et al.* model metal atoms vaporize by desorption and diffuse through the diluent gas away from the surface. The metal vapor reacts with oxygen in the gas phase to give solid metal-oxide "fog." The metal-vaporization process is enhanced because the oxidation reaction increases the gradient for metal-atom diffusion. Turkdogan *et al.* have successfully applied this model to the oxidation-enhanced vaporization of such metals as Cr, Fe, Cu, and Co. As applied to the case of Si, the fog-formation reaction is



### WAGNER MODEL



### TURKDOGAN, GRIEVESON, AND DARKEN MODEL

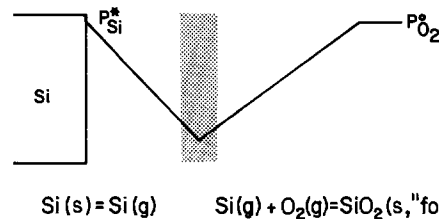


Fig. 2. Comparison between the Wagner model and the Turkdogan, Grieveson, and Darkin model applied to the active oxidation of Si.

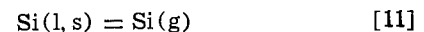
The rate of Si removal is controlled by oxygen diffusion through the boundary layer in advance of the fog-formation front according to the equation

$$J_{Si} = J_{O_2} = h_{O_2} P^{\circ}_{O_2} / RT \quad [9]$$

The rate of Si consumption predicted by the Turkdogan *et al.* model (Eq. [9]) is one-half of that predicted by the Wagner model (Eq. [3]) for a given  $P^{\circ}_{O_2}$  and  $h_{O_2}$ . As  $P^{\circ}_{O_2}$  is increased, the fog-formation front approaches the Si surface. An abrupt transition from active-to-passive oxidation occurs when the front reaches the surface. The  $P^{\circ}_{O_2}$  at the transition is given by (18)

$$P^{\circ}_{O_2}(\max) = \frac{P^*_{Si}}{h_{O_2}} \left( \frac{RT}{2\pi M_{Si}} \right)^{1/2} \quad [10]$$

where  $P^*_{Si}$  is the vapor pressure of Si according to the equation



The mass-transfer coefficient for oxygen in both models is given by (18, 19)

$$h_{O_2} = 0.664 (D_{O_2}^4/\nu_{O_2})^{1/6} (v_g/l)^{1/2} \text{ (cm/sec)} \quad [12]$$

where  $D_{O_2}$  is as defined earlier,  $\nu_{O_2}$  is the kinematic viscosity,  $v_g$  is the gas velocity in the vicinity of the sample, and  $l$  is the sample length in the direction of the gas flow. Both  $D_{O_2}$  and  $\nu_{O_2}$  may be calculated from first principles (20), and vary as  $T^{3/2}$ . According to Eq. [12], at constant gas velocity  $h_{O_2} \propto T^{3/4}$  and  $\sqrt{T}/h$  in Eq. [10] is only weakly temperature dependent ( $\sim T^{-1/4}$ ). Therefore, a plot of  $\log P^{\circ}_{O_2}(\max)$  as a function of  $1/T$  is expected to give the enthalpy of vaporization or sublimation of Si according to Eq. [11]. Furthermore, because  $h_{O_2} \propto v_g^{1/2}$ ,  $P^{\circ}_{O_2}(\max)$  in Eq. [10] is expected to be strongly dependent upon gas-flow velocity in contrast to the Wagner model where no such dependence is expected.

The evidence presented by Kaiser *et al.* (16, 17), suggests that the Wagner model is valid for their experimental temperatures and gas-flow characteristics. Large concentrations of oxygen were found to be dissolved in the Si upon active oxidation; the concentration of dissolved oxygen being proportional to  $P^{\circ}_{O_2}$ . This could occur only if oxygen had access to the Si surface. In the Turkdogan *et al.* model the oxidant is consumed in advance of the Si surface, therefore, if this model were valid, the Si should remain free of dissolved oxygen.

For the Wagner model, a question remains concerning the stability of the liberated SiO molecule as it diffuses through the gaseous boundary layer away from the Si surface. In principle, the SiO should react with oxygen in the boundary layer to form SiO<sub>2</sub> when the  $P_{O_2}$  in the boundary layer reaches that value given by the vertical line shown in Fig. 1. Therefore, some of the oxygen should be consumed in advance of the Si surface in a manner similar to that proposed by Turkdogan *et al.* except that now SiO rather than Si would react with O<sub>2</sub> to give SiO<sub>2</sub> fog.

The purpose of this investigation is to determine the mechanism of Si and SiC active oxidation in the viscous-gas-flow regime (i) by studying the dependence of reaction rates upon time and  $P_{O_2}$ , and (ii) by locating  $P_{O_2}(\max)$ , i.e., the  $P_{O_2}$  corresponding to the transition from active-to-passive oxidation, as a function of temperature. For Si a plot of  $\log P_{O_2}(\max)$  as a function of  $1/T$  is expected to have a slope corresponding to the enthalpy of formation of SiO [ $\Delta H_f(\text{SiO})$ ] according to Eq. [5] if the Wagner model applies. On the other hand, a slope corresponding to the enthalpy of vaporization or sublimation of Si [ $\Delta H_{v,s}(\text{Si})$ ] according to Eq. [11] is expected if the Turkdogan *et al.* model applies. Because  $\Delta H_{v,s}(\text{Si})$  is greater than  $\Delta H_f(\text{SiO})$  by  $\sim 27$  kcal/mole (21) [ $\Delta H_{v,s}(\text{Si}) \approx 110$  kcal/mole and  $\Delta H_f(\text{SiO}) \approx 83$  kcal/mole] such a plot should indicate whether Si or SiO is the desorbed species at the Si surface during active oxidation.

For SiC a Turkdogan *et al.* mechanism seems unlikely in view of the very low vapor pressure of SiC (9). Therefore, active oxidation should obey a Wagner-type mechanism where both SiO and CO are desorbed at the SiC surface. A plot of  $P_{O_2}(\max)$  as a function of  $1/T$  is expected to yield the thermodynamic equilibrium describing the transition from active to passive oxidation and, therefore, an indication of whether SiO or CO is the important desorbed species at the transition.

### Experimental

High purity n-type Si having a resistivity of 3-8 ohm-cm was purchased from Crysteco (Wilmington, Ohio) in the form of single crystal disks having (111) faces. Polycrystalline  $\beta$ -SiC was provided by General Electric Company in the form of a hot-pressed billet, major impurities being B (1500 ppmw) and W (500 ppmw). Coupons ( $\sim 1.5 \times 0.6 \times 0.1$  cm) were cut from the larger pieces. The Si coupons were polished with  $1\mu$  diamond paste, and the SiC was ground with 220 mesh diamond abrasive. The coupons were cleaned ultrasonically in acetone and in methanol before each oxidation experiment. Undried commercial grade Ar and O<sub>2</sub>/Ar mixtures were used.

Active oxidation kinetics were determined by monitoring sample weight changes continuously with a Cahn RH electrobalance having a sensitivity of  $\pm 2$   $\mu$ g. Details of the furnace-balance system were given previously (22). The temperature of the furnace was controlled to within  $\pm 0.5^\circ\text{C}$ . Sample temperature was measured with a Pt 6 Rh-Pt 30 Rh thermocouple located within  $\sim 1$  cm of the sample. The specimen was situated in the center of a  $\sim 4$  cm long hot zone within the reaction tube. The lateral temperature gradient in the hot zone was no greater than  $2^\circ\text{C}$ . Experiments were initiated by lowering the Si or SiC coupon into Ar ( $P_{O_2} \approx 10^{-8}$  atm) at the desired temperature. In early experiments an H<sub>2</sub> pretreatment was used to remove any oxide film initially present on the surface; however, this treatment was found to be unnecessary. An O<sub>2</sub>/Ar gas mixture of low  $P_{O_2}$  was introduced into the reaction tube (inside diameter = 3.81 cm) to begin active oxidation. The  $P_{O_2}$  was varied by combining two different O<sub>2</sub>/Ar mixtures with calibrated flow meters. To avoid cooling of the sample by the flowing gas, very low flow rates [ $\sim 85$  cm<sup>3</sup>/min (STP)] were used. In all cases the total system pressure was maintained at 150 Torr. Because the room

temperature flow rates were constant, linear gas-flow velocities in the sample region were linearly dependent upon the sample temperature.

### Results

*Si active oxidation.*—The active oxidation of Si was investigated in the temperature range  $1400^\circ\text{--}1650^\circ\text{K}$ . Results for a typical experiment are shown in Fig. 3 where sample weight change is plotted as a function of time. In this experiment  $P_{O_2}$  was increased in small increments, from  $5.4 \times 10^{-5}$  to  $9.2 \times 10^{-3}$  atm. Although the curve in Fig. 3 appears to be smooth, oxidation kinetics at each  $P_{O_2}$  were linear except in the transition regions. The most striking feature of this plot is the appearance of two distinct regions of active oxidation instead of the one expected on the basis of the Wagner (15) and the Turkdogan *et al.* (18) models. In the first region (stage I), the Si surface was found to be completely free of oxidation products. However, when the ambient  $P_{O_2}$  was increased to a critical value [ $P_{O_2}(\max)_I$ ], instead of passive oxidation occurring a transition from stage I to the second stage of active oxidation (stage II) occurred. In this stage active oxidation was characterized by extremely rapid, linear sample weight gains. When the ambient  $P_{O_2}$  was increased, stage II active oxidation continued until a second critical  $P_{O_2}$  [ $P_{O_2}(\max)_{II}$ ] was reached. At this point passive oxidation was initiated, resulting in low reaction rates (indicated by the horizontal line in the figure) governed by diffusion through a protective SiO<sub>2</sub> layer.

Figure 4 reveals the morphology of the oxide scale which formed in the Si specimen oxidized at  $1500^\circ\text{K}$  in the stage II active oxidation regime. The unusual whiskerlike oxide structure suggests that a vaporization-condensation process occurred. The whiskers were identified as SiO<sub>2</sub> by the energy shift of the Si peak upon microprobe analysis. X-ray analysis indicated that the SiO<sub>2</sub> was amorphous. Figure 5 illustrates the temperature dependence of the scale morphologies. Figure 5a is an SEM micrograph of the fractured cross section, whereas Fig. 5(b-d) are SEM micrographs of the sample surface. At the lowest temperature, Fig. 5(a), the scales consisted of extremely fine whiskers; at the highest temperature, Fig. 5(b-d), a thick spongy SiO<sub>2</sub> layer was formed (A) in addition to the whiskerlike structure (B). In the stage II oxidation mode, neither type of oxide structure was protective; i.e., the oxygen had direct access to a significant area of the Si surface.

In order to determine whether the transition from stage I to stage II active oxidation is reversible, a Si coupon was oxidized in the stage II mode after which  $P_{O_2}$  was decreased. The chronology of this experiment is shown in Fig. 6 where a distinct hysteresis effect is

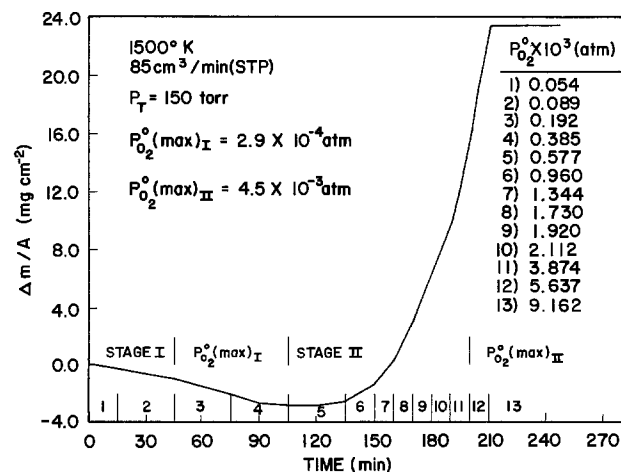


Fig. 3. Chronology of Si active oxidation at  $1500^\circ\text{K}$ . Vertical lines at figure base indicate an increase in  $P_{O_2}$ .

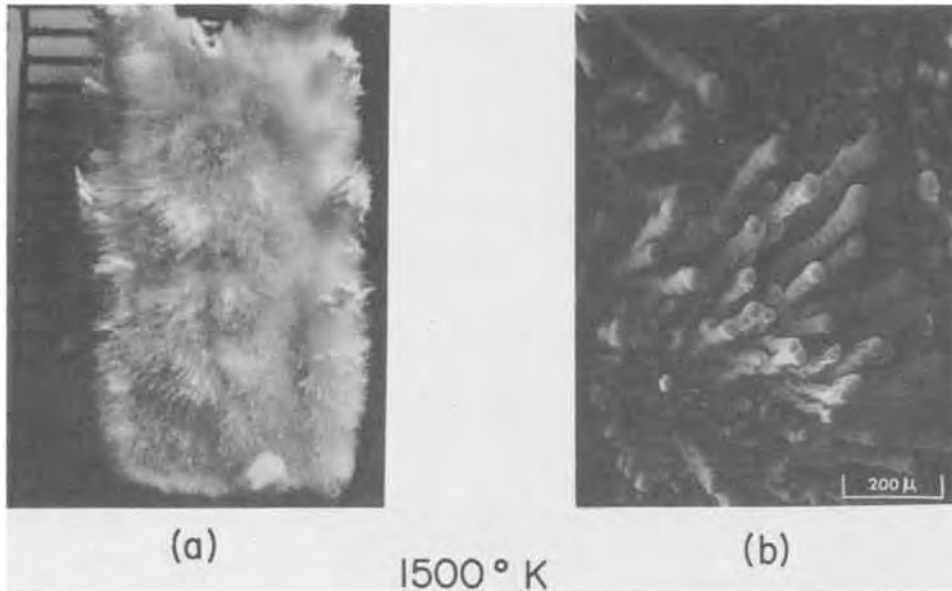


Fig. 4. Macrograph (a) and SEM micrograph (b) of a Si specimen oxidized at 1500°K in the stage II active oxidation regime.

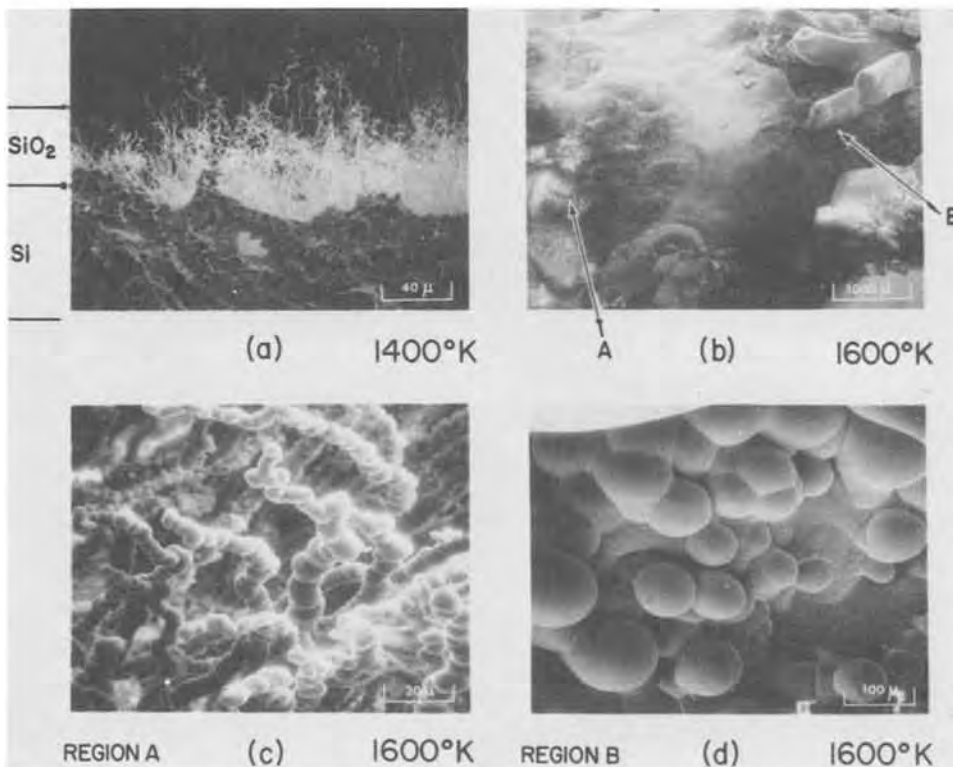


Fig. 5. SEM micrograph showing temperature dependence of the oxide morphologies for Si oxidized in the stage II regime: (a) cross section, 1400°K; (b)-(d) surface, 1600°K.

exhibited; stage II active oxidation, once established, continues even when  $P^{\circ}O_2$  is lowered into the range where stage I active oxidation had occurred previously [see, for example,  $P^{\circ}O_2$  steps 2-4 (15-120 min) and  $P^{\circ}O_2$  steps 4-2 (240-280 min)]. Because Si is removed (as SiO) during stage I oxidation, and  $O_2$  is gained (as  $SiO_2$ ) during stage II oxidation, for a given  $P^{\circ}O_2$

$$k_a(\text{stage I}) = - (M_{Si}/M_{O_2}) k_a(\text{stage II}) \text{ (mg-cm}^{-2}\text{-min}^{-1}) \quad [13]$$

where  $k_a$  is the linear rate constant for active oxidation. Figure 7 is a plot of the absolute magnitude of the rate constants [ $k_a$ ] obtained from the slopes of the curves shown in Fig. 3 and 6 as a function of  $P^{\circ}O_2$ . The vertical line on the graph denotes the transition  $P^{\circ}O_2$  from stage I to stage II active oxidation [ $P^{\circ}O_2(\text{max})_I$ ]. The linearity of the data indicates that the reaction is controlled by oxygen diffusion through the gaseous boundary layer in both regimes. Since no discontinuity in the curve is exhibited at  $P^{\circ}O_2(\text{max})_I$ ,

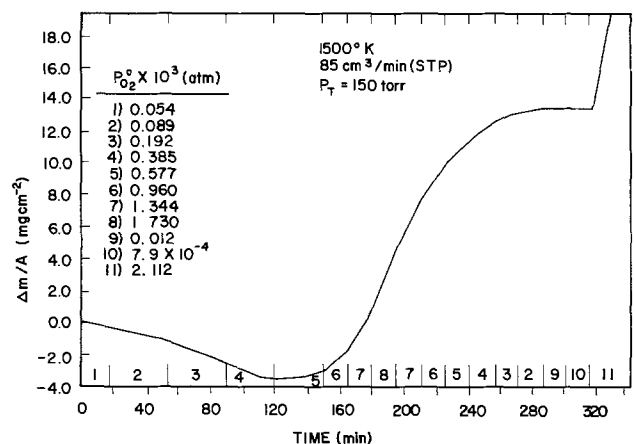


Fig. 6. Chronology of Si active oxidation at 1500°K showing irreversibility of the stage I to stage II transition.

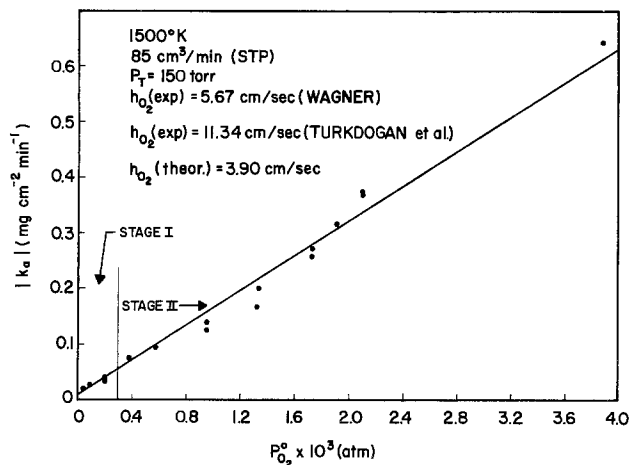


Fig. 7. Oxygen partial pressure dependence of the rate constant for Si active oxidation at 1500°K.

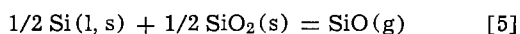
$h_{O_2}$  is independent of the active oxidation mode. The slope of the curve is related to the boundary layer mass-transfer coefficient,  $h_{O_2}$ , by the equation

$$d|k_a|/dP_{O_2}^0 = nh_{O_2}/RT \quad [14]$$

where  $n = 1$  or  $2$ , depending upon which model [i.e., the Turkdogan *et al.* (18) model ( $n = 1$ ) or the Wagner (15) model ( $n = 2$ )] applies. The  $h_{O_2}$  calculated on the basis of the Turkdogan *et al.* model is a factor of three larger than the theoretical value calculated from Eq. [12], whereas  $h_{O_2}$  calculated on the basis of the Wagner model is less than a factor of two larger. Because of the low gas-flow rates used, the boundary layer thickness is greater than the radius of the furnace tube ( $\sim 2$  cm); therefore, slight deviations from the theoretical  $h_{O_2}$  were anticipated.

It is important to note that the curves which appear in Fig. 7 and later in Fig. 11 are linear, even in the low  $P_{O_2}$  regions. This implies that concentrations of impurities such as  $H_2O$  in the gas phase do not influence the oxidation kinetics. If the reactions had been impurity sensitive, the plots of  $|k_a|$  as function of  $P_{O_2}$  would have exhibited upward curvature at low  $P_{O_2}$  until a lower limiting value of  $|k_a|$  corresponding to  $P_{H_2O}$  in the gas was reached. No such curvature or limiting value of  $|k_a|$  was seen.

Data of the type shown in Fig. 3 and 7 were obtained at six temperatures in the range 1400°–1650°K. Active oxidation was found to occur in two stages at each temperature. One experiment was conducted on polycrystalline Si; the behavior was identical to that of the single crystal material. The experimental  $P_{O_2}^0(\max)_I$  and  $P_{O_2}^0(\max)_{II}$  values are plotted in Fig. 8 and compared with predictions based on the Wagner and Turkdogan *et al.* models. Because these models predict only a single stage of active oxidation, only one  $P_{O_2}^0(\max)$  value was calculated. The predictions were made by inserting the recent thermodynamic data of Zmbov *et al.* (21) for  $P_{Si}^*$  and  $P_{SiO}^{eq}$  together with the calculated diffusivity ratio  $D_{SiO}/D_{O_2} \approx 0.8$  into Eq. [7] and [10]. Values for  $P_{O_2}^0(\max)_I$  are in fair agreement with predictions from Wagner's theory for the transition from active to passive oxidation. A relatively large uncertainty in the value of  $P_{O_2}^0(\max)_I$  exists because the transition takes place gradually over several increments in  $P_{O_2}^0$ , whereas a rapid transition from stage II to passive oxidation occurs. The activation energy for  $P_{O_2}^0(\max)_{II}$  is  $\sim 83$  kcal/mole which agrees with the 83 kcal/mole obtained by Zmbov *et al.* for the enthalpy of the reaction



indicating that  $SiO(g)$  is the important desorbed species at the transition. The  $P_{O_2}^0(\max)$  predicted by the Turkdogan *et al.* model falls below the experimental

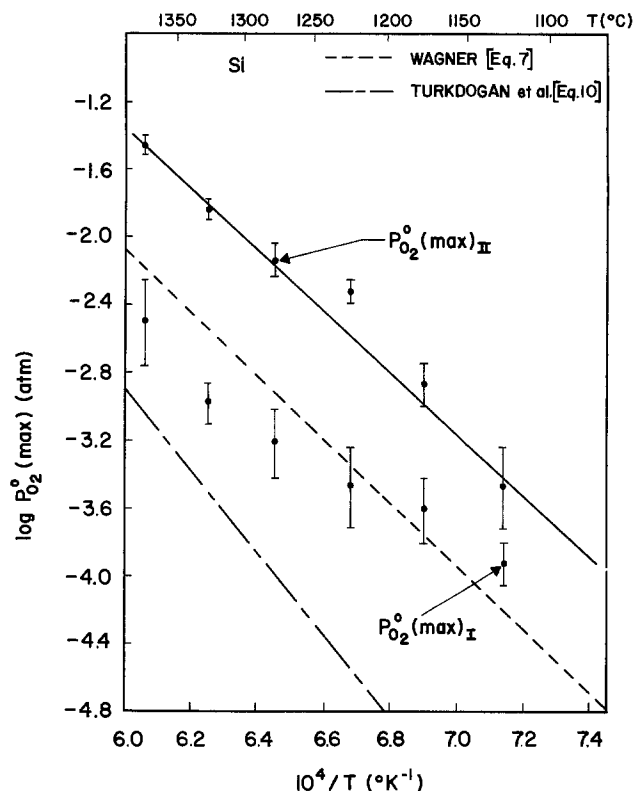
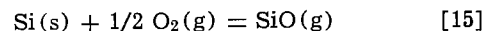


Fig. 8. Temperature dependence of  $P_{O_2}^0(\max)_I$  and  $P_{O_2}^0(\max)_{II}$  for Si active oxidation in the viscous gas-flow regime compared with predictions based on the Wagner model (15) and the Turkdogan *et al.* model (18).

data for  $P_{O_2}^0(\max)_I$  and has a much larger activation energy, suggesting that Si desorption from the surface during active oxidation is unimportant.

**Mechanism of Si active oxidation.**—The above results indicate that neither the Wagner model nor the Turkdogan *et al.* model completely describes the mechanism of Si active oxidation. Although the Wagner model correctly identifies the nature of the gaseous species as  $SiO$  at the Si surface, the existence of the stage II active oxidation mode was not suggested. The Wagner model predicts that once  $P_{O_2}^0(\max)_I$  is exceeded, the inward flux of oxygen (as  $O_2$ ) at the Si surface will exceed the outward flux of oxygen [as  $SiO(g)$ ] and that  $SiO_2(s)$  will form and grow laterally on the surface. The first part of this prediction was found to be correct; however, lateral growth was not exhibited. Instead  $SiO_2$  whiskers grew perpendicular to the Si surface, and only after a second critical  $P_{O_2}^0$  was exceeded did the  $SiO_2$  grow laterally to form a protective layer.

In order to determine the conditions under which the stage II mode of active oxidation can become stable, consider the schematic representation of attack shown in Fig. 9. When  $P_{O_2}^0 < P_{O_2}^0(\max)_I$  [Fig. 9(a)], stage I active oxidation occurs and the Si surface remains bare in agreement with the Wagner model. The  $\delta_{SiO}$  and  $\delta_{O_2}$  are nearly equal because the ratio  $D_{SiO}/D_{O_2}$  in Eq. [6]  $\approx 0.8$ . As  $P_{O_2}^0$  is increased,  $P_{SiO}^*$  increases according to the reaction



with

$$P_{SiO}^* \propto P_{O_2}^{*1/2} \quad [16]$$

When  $P_{O_2}^0$  is increased to  $P_{O_2}^0(\max)_I$ ,  $P_{SiO}^*$  reaches the equilibrium value  $P_{SiO}^{eq}$  given by Eq. [5] and incipient  $SiO_2$  formation takes place. Initially the  $SiO_2$  forms as tiny islands [see Fig. 9(b)], with most of the surface remaining bare. From thermodynamic considerations, the tendency for  $SiO_2$  and  $SiO$  formation is equal;  $SiO$  removal from the surface will continue as

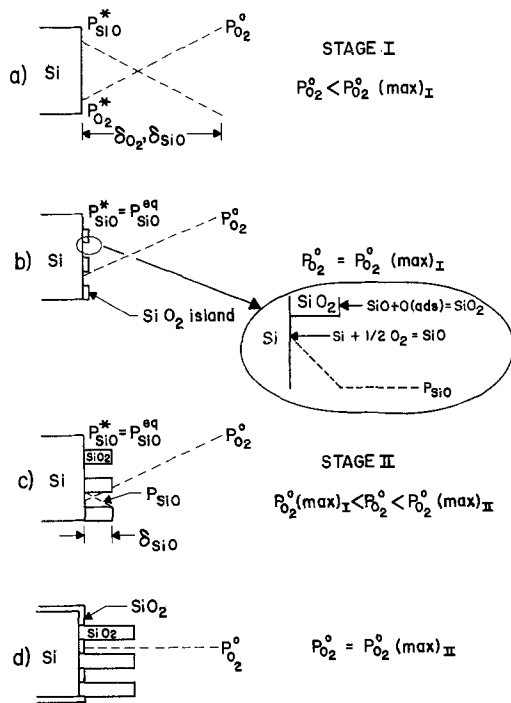
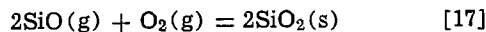
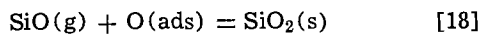


Fig. 9. Schematic representation of the mechanism of active oxidation of Si in the viscous gas-flow regime.

SiO<sub>2</sub> attempts to grow lateral to the surface. The SiO molecules will be exposed to as ever-increasing P<sub>O<sub>2</sub></sub> as they diffuse away from the surface. Therefore, these molecules have a tendency to oxidize forming SiO<sub>2</sub> according to the reaction



This homogeneous reaction is relatively unfavorable because it requires a trimolecular collision of two SiO molecules and one O<sub>2</sub> molecule in the gas phase. However, the SiO<sub>2</sub> islands can serve as nucleation sites for heterogeneous reaction. Since the tip of the island is at a higher P<sub>O<sub>2</sub></sub> than the edges, the availability of oxygen is greatest there. If oxygen is adsorbed at the tip, the islands will grow perpendicular to the Si surface to form the observed SiO<sub>2</sub> whiskers according to the heterogeneous reaction



According to the Wagner model when P<sup>o</sup><sub>O<sub>2</sub></sub> exceeds P<sup>o</sup><sub>O<sub>2</sub></sub>(max)<sub>I</sub>, the inward flux of oxygen will be greater than the outward flux of SiO and the surface becomes covered with a protective layer of SiO<sub>2</sub>. In the present investigation, no such layer was observed, instead active oxidation was found to continue independent of time with rates being linearly dependent upon P<sup>o</sup><sub>O<sub>2</sub></sub>. The rates agreed well with those predicted from gas kinetic equations implying that oxygen transport through the boundary layer is rate controlling and that oxygen has direct access to the Si surface. In order for this to occur, either P\*<sub>SiO</sub> must increase or δ<sub>SiO</sub> must decrease in order to increase the removal rate of SiO given by the equation

$$J_{\text{SiO}} = D_{\text{SiO}} P^*_{\text{SiO}} / \delta_{\text{SiO}} RT \quad [19]$$

Once SiO<sub>2</sub> is formed at the surface, P\*<sub>SiO</sub> is fixed at its equilibrium value P<sup>eq</sup><sub>SiO</sub> given by Eq. [5]. Therefore, δ<sub>SiO</sub> must decrease in order that J<sub>SiO</sub> be maintained at a level which is sufficiently high to accommodate the inward flux of oxygen. Figure 9(c) shows the manner in which heterogeneous reaction at the tip of the whiskers reduces δ<sub>SiO</sub>. This mechanism bears some resemblance to the Turkdogan *et al.* model in that some oxygen is consumed in advance of the Si surface, thereby increasing the diffusion gradient for the de-

sorbed species. However, in this case the reaction occurs at the tip of the SiO<sub>2</sub> whiskers and enables their growth. By decreasing δ<sub>O<sub>2</sub></sub>, J<sub>SiO</sub> becomes increased according to Eq. [19]. This allows active oxidation to continue until P<sup>o</sup><sub>O<sub>2</sub></sub> reaches P<sup>o</sup><sub>O<sub>2</sub></sub>(max) according to Eq. [4], where P<sup>o</sup><sub>O<sub>2</sub></sub>(max) is the experimentally observed P<sup>o</sup><sub>O<sub>2</sub></sub>(max)<sub>II</sub>. When P<sup>o</sup><sub>O<sub>2</sub></sub> = P<sup>o</sup><sub>O<sub>2</sub></sub>(max)<sub>II</sub>, SiO cannot be removed at a sufficiently rapid rate and the Si surface becomes covered with a coherent, protective layer of SiO<sub>2</sub> [Fig. 9(d)].

**SiC active oxidation.**—The active oxidation of SiC was investigated to determine whether a stage II mode would be characteristic of other Si-base materials. Results of a typical experiment are shown in Fig. 10. Unlike the behavior of Si, no stage II active oxidation was observed for SiC. Instead, rates of weight loss increased with incremental increases in P<sup>o</sup><sub>O<sub>2</sub></sub> until P<sup>o</sup><sub>O<sub>2</sub></sub>(max) was reached after which extremely low rates of oxidation were observed, indicative of diffusion control through a protective SiO<sub>2</sub> layer. Subsequent increases in P<sup>o</sup><sub>O<sub>2</sub></sub> did not cause the onset of stage II active oxidation. Lower ambient oxygen partial pressures or higher temperatures were required to establish the active oxidation process for SiC. Weight losses were linear with time, in agreement with stage I Si active oxidation.

The rate of active oxidation, |k<sub>a</sub>|, is plotted linearly against P<sup>o</sup><sub>O<sub>2</sub></sub> in Fig. 11, indicating that the reaction for SiC is also controlled by oxygen diffusion through the boundary layer. As with Si active oxidation, boundary layer mass-transfer coefficients, h<sub>O<sub>2</sub></sub> (assum-

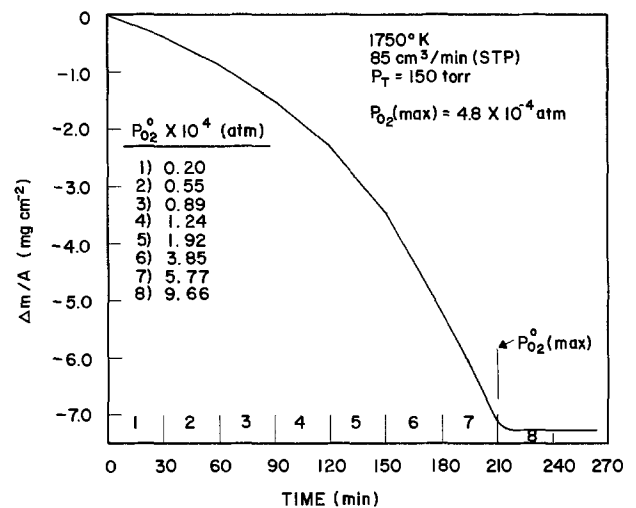


Fig. 10. Chronology of SiC active oxidation at 1750°K. Note the absence of stage II active oxidation behavior.

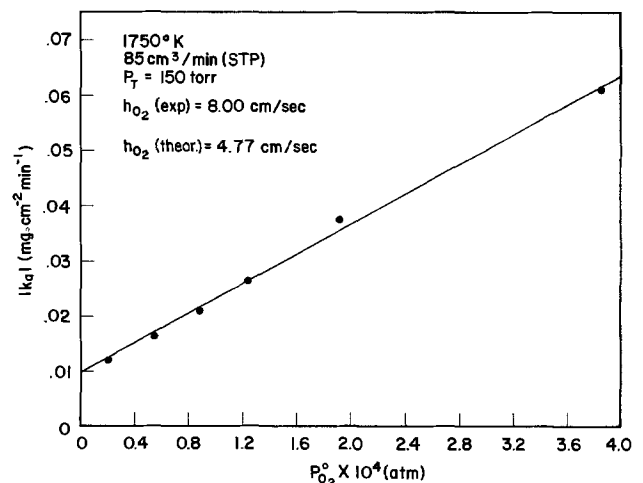
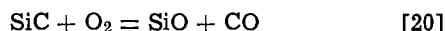


Fig. 11. Oxygen partial pressure dependence of the rate constant for SiC active oxidation at 1750°K.

ing SiO and CO to be the desorbed species), are  $\sim 1.5$  times larger than the theoretical values calculated from Eq. [12].

**Mechanism of SiC active oxidation.**—The active oxidation process in SiC is believed to occur according to the reaction



where CO rather than CO<sub>2</sub> is desorbed at the SiC surface because of the low  $P_{\text{O}_2}$  which is established there. The rate of oxygen impingement at the SiC surface controls the reaction, the rate being given by the equation

$$J_{\text{O}_2} = D_{\text{O}_2} P^{\circ}_{\text{O}_2} / \delta_{\text{O}_2} RT \quad [21]$$

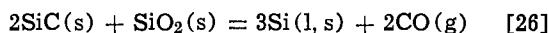
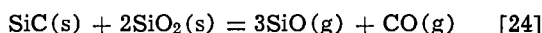
If it is assumed that the reaction proceeds stoichiometrically, then

$$J_{\text{SiO}} = J_{\text{CO}} = J_{\text{O}_2} \quad [22]$$

where  $J_{\text{SiO}}$  is given by Eq. [19] and  $J_{\text{CO}}$  is given by

$$J_{\text{CO}} = D_{\text{CO}} P^{\circ}_{\text{CO}} / \delta_{\text{CO}} RT \quad [23]$$

The thermodynamics describing the conditions for the transition from active to passive behavior are not so straightforward as those for Si oxidation where Eq. [5] is the only pertinent relation to be considered. A number of equilibria must be considered in the case of SiC, the most likely being



Combining Eq. [21], [22], and [23]

$$P^{\circ}_{\text{O}_2} = (D_{\text{CO}}/D_{\text{O}_2}) (\delta_{\text{O}_2}/\delta_{\text{CO}}) P^{\circ}_{\text{CO}} \quad [27]$$

and combining Eq. [21], [22], and [19]

$$P^{\circ}_{\text{O}_2} = (D_{\text{SiO}}/D_{\text{O}_2}) (\delta_{\text{O}_2}/\delta_{\text{SiO}}) P^{\circ}_{\text{SiO}} \quad [28]$$

If it is assumed that

$$(\delta_{\text{CO}}/\delta_{\text{O}_2}) = (D_{\text{CO}}/D_{\text{O}_2})^{1/2} \quad [29]$$

and

$$(\delta_{\text{SiO}}/\delta_{\text{O}_2}) = (D_{\text{SiO}}/D_{\text{O}_2})^{1/2} \quad [6]$$

Then Eq. [27] and [28] become

$$P^{\circ}_{\text{O}_2} = (D_{\text{CO}}/D_{\text{O}_2})^{1/2} P^{\circ}_{\text{CO}} \quad [27a]$$

and

$$P^{\circ}_{\text{O}_2} = (D_{\text{SiO}}/D_{\text{O}_2})^{1/2} P^{\circ}_{\text{SiO}} \quad [28a]$$

Depending on the thermodynamics of the transition,  $P^{\circ}_{\text{O}_2}(\text{max})$  will be given either by

$$P^{\circ}_{\text{O}_2}(\text{max}) = (D_{\text{CO}}/D_{\text{O}_2})^{1/2} P^{\text{eq}}_{\text{CO}} \quad [30]$$

or

$$P^{\circ}_{\text{O}_2}(\text{max}) = (D_{\text{SiO}}/D_{\text{O}_2})^{1/2} P^{\text{eq}}_{\text{SiO}} \quad [31]$$

where  $P^{\text{eq}}_{\text{CO}}$  and  $P^{\text{eq}}_{\text{SiO}}$  can be calculated from Eq. [24-26].

In Fig. 12 the experimental  $P^{\circ}_{\text{O}_2}(\text{max})$  values are compared with predictions based on Eq. [30] and [31], assuming that  $D_{\text{SiO}}/D_{\text{O}_2} = 0.8$  and  $D_{\text{CO}}/D_{\text{O}_2} = 1.02$  (20). Although only fair agreement was found, Eq. [26] and [30] best describe the transition behavior. This implies that CO rather than SiO is the important gaseous species in determining  $P^{\circ}_{\text{O}_2}(\text{max})$ . The thermodynamics of the transition are in agreement with those found by Gulbransen and Jansson (9) for SiC under molecular gas-flow conditions. These results allow the following physical interpretation of the active oxidation of SiC to be made: When  $P^{\circ}_{\text{O}_2} < P^{\circ}_{\text{O}_2}(\text{max})$ , the rates of both CO and SiO removal from the SiC surface are sufficiently large to accommodate the inward flux of oxygen, as evidenced by the linear  $P^{\circ}_{\text{O}_2}$  dependence of the reaction rate. However, when  $P^{\circ}_{\text{O}_2} = P^{\circ}_{\text{O}_2}(\text{max})$ , CO (rather than SiO) cannot be removed at a sufficiently rapid rate and passive oxidation occurs. Unlike the case for Si where  $\delta_{\text{SiO}}$  was reduced

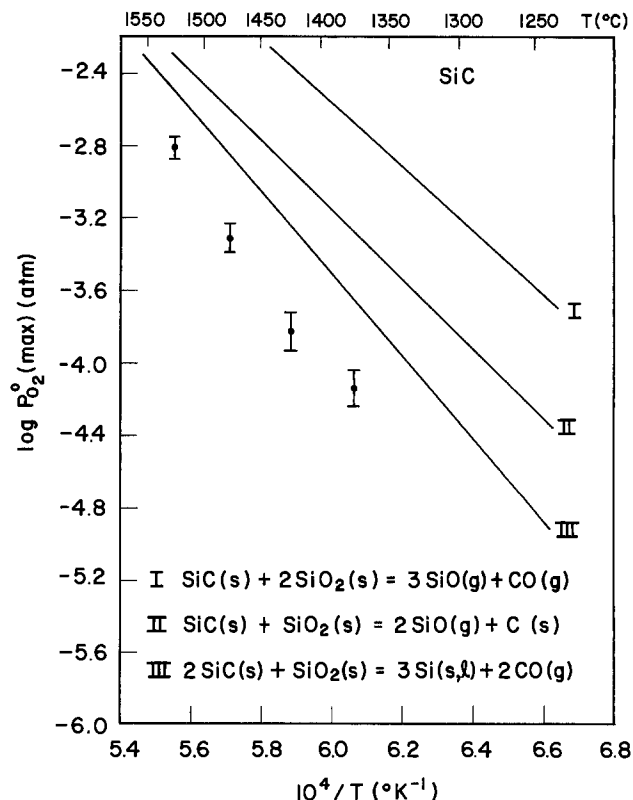


Fig. 12. Temperature dependence of  $P^{\circ}_{\text{O}_2}(\text{max})$  for SiC active oxidation in the viscous gas-flow regime.

via a heterogeneous reaction [Fig. 9(c)] causing the onset of stage II active oxidation, the  $P_{\text{CO}}$  gradient adjacent to the surface cannot be increased by reducing  $\delta_{\text{CO}}$ . Therefore, stage II active oxidation in SiC is impossible.

### Acknowledgments

The authors wish to thank Dr. R. A. Rapp for his helpful suggestions during the course of this research. This work was partially supported by U. S. Air Force Contract F33615-71-C-1841.

Manuscript submitted Nov. 5, 1975; revised manuscript received Feb. 27, 1976.

Any discussion of this paper will appear in a Discussion Section to be published in the June 1977 JOURNAL. All discussions for the June 1977 Discussion Section should be submitted by Feb. 1, 1977.

Publication costs of this article were partially assisted by the Air Force Materials Laboratory.

### LIST OF SYMBOLS

$J_i$	flux of species i
$\alpha$	collision efficiency
$P^{\circ}_i$	partial pressure of species i in the ambient
$P^*_i$	partial pressure of species i at the surface
$D_i$	interdiffusivity of species i and inert gas
$\delta_i$	boundary layer thickness for species i
$h_i$	average boundary layer mass-transfer coefficient for species i
$\nu_i$	kinematic viscosity of species i
$v_g$	gas velocity
$l$	sample length in direction of gas flow
$P^{\circ}_{\text{O}_2}(\text{max})$	ambient $P_{\text{O}_2}$ corresponding to the transition from active-to-passive oxidation
$P^{\circ}_{\text{O}_2}(\text{max})_I$	ambient $P_{\text{O}_2}$ corresponding to the transition from stage I active oxidation to stage II active oxidation
$P^{\circ}_{\text{O}_2}(\text{max})_{II}$	ambient $P_{\text{O}_2}$ corresponding to the transition from stage II active oxidation to passive oxidation
$k_a$	linear rate constant for active oxidation

## REFERENCES

1. B. E. Deal and A. S. Grove, *J. Appl. Phys.*, **36**, 3770 (1965).
2. A. G. Revesz and R. J. Evans, *J. Phys. Chem. Solids*, **36**, 551 (1969).
3. R. Brückner, *J. Non-Crystalline Solids*, **5**, 177 (1971).
4. R. L. Meek, *J. Am. Ceram. Soc.*, **56**, 341 (1973).
5. E. A. Irene, *This Journal*, **121**, 1613 (1974).
6. J. W. Hinze, W. C. Tripp, and H. C. Graham, *ibid.*, **122**, 1249 (1975).
7. S. C. Singhal, in "Ceramics for High Performance Applications," by J. J. Burke, A. E. Gorum, and R. N. Katz, Editors, p. 533, Brook Hill Publishing Co., Chestnut Hill, Mass. (1974).
8. W. C. Tripp, H. C. Graham, and H. H. Davis, *Bull. Am. Ceram. Soc.*, **52**, 612 (1973).
9. E. A. Gulbransen and S. A. Jansson, *Oxid. Metals*, **4**, 181 (1972).
10. E. A. Gulbransen, K. F. Andrew, and F. A. Bras-sart, *This Journal*, **113**, 834 (1966).
11. E. A. Gulbransen, K. F. Andrew, and F. A. Bras-sart, *ibid.*, **113**, 1311 (1966).
12. J. E. Antill and J. B. Warburton, *Corrosion Sci.*, **11**, 337 (1971).
13. D. E. Rosner and H. D. Allendorf, *J. Phys. Chem.*, **74**, 1829 (1970).
14. C. Gelain, A. Cassuto, and P. De Goff, *Oxid. Metals*, **3**, 139 (1971).
15. C. Wagner, *J. Appl. Phys.*, **29**, 1295 (1958).
16. W. Kaiser and P. H. Keck, *ibid.*, **28**, 882 (1957).
17. W. Kaiser and J. Breslin, *ibid.*, **29**, 1292 (1958).
18. E. T. Turkdogan, P. Grieveson, and L. S. Darken, *J. Phys. Chem.*, **67**, 1647 (1963).
19. C. O. Bennett and J. E. Myers, "Momentum, Heat, and Mass Transfer," McGraw-Hill Book Co., Inc., New York (1962).
20. J. O. Hirschfelder, C. F. Curtiss, and R. B. Bird, "Molecular Theory of Gases and Liquids," John Wiley & Sons, Inc., New York (1954).
21. K. F. Zmbov, L. L. Ames, and J. L. Margrave, *High Temp. Sci.*, **5**, 235 (1973).
22. W. C. Tripp and H. C. Graham, *This Journal*, **118**, 1195 (1971).
23. JANAF Thermochemical Tables, 2nd Ed., D. R. Stull and H. Prophet, Editors, NSRDS-NBS 37, (1971).

## The Criterion for Stability of a Planar Alloy-Oxide Interface upon Oxidation of Binary Alloys

D. P. Whittle,<sup>1</sup> D. J. Young,<sup>\*2</sup> and W. W. Smeltzer\*

Department of Metallurgy and Materials Science, McMaster University, Hamilton, Ontario, Canada, L8S 4M1

### ABSTRACT

Linear perturbation theory is used to analyze the stability of a moving planar alloy-oxide interface when oxidation of a binary solid solution alloy leads to growth of a superficial metal conducting oxide scale. The transport equations for metal and oxygen in the alloy and oxide phases are analyzed under limiting approximations consistent with ternary diffusion theory. If oxygen diffusion in the alloy occurs predominantly down its own gradient the stability criterion for a planar interface is

$$\frac{N_A^{I*}D_{OoI} + 2(N_A^{Io} - N_A^{I*})\sqrt{D_{AA^I}D_{OoI}}}{N_A^{I*}D_{AA^I} + N_A^{II*}D_{A^{II*}V^I/V^{II}}} > 1$$

This criterion becomes in the case of oxygen diffusion in the alloy occurring predominantly from its interaction with the metal gradient

$$\frac{N_A^{I*}V^{II}D_{AA^I}}{N_A^{II*}V^ID_{A^{II*}}} \left\{ 1 - N_A^{I*}\epsilon_O^A \frac{D_{OoI}}{D_{AA^I}} \right\} > 1$$

In these expressions,  $D$ ,  $N$ , and  $V$  represent self-diffusion coefficients, mole fractions, and molar volumes of the alloy and oxide phases denoted by superscript I and II, respectively. Asterisks on these parameters refer to values at a planar alloy-oxide interface. A and O refer to the selectively oxidized metal component and oxygen.  $N_A^{Io}$  is the initial concentration of A, and  $\epsilon_O^A$  is the Wagner interaction coefficient between oxygen and A in the alloy.

The diffusion controlled oxidation of a binary alloy to form a superficial single-phase scale is characterized by the development of a planar or nonplanar interface between alloy and oxide. Wagner (1) has developed an equation defining a limiting criterion for planar interface stability under the assumptions that the solubilities of oxygen in the alloy and of the more noble alloy component in the oxide are negligible. More recently, Coates and Kirkaldy (2) have analyzed the conditions for the stability of planar phase interfaces in isothermal ternary systems making no assumptions about phase constitution with the alloy-oxide interface as a

special case. The purpose of this paper is to examine the effects of removing the two solubility restraints introduced by Wagner on the criterion for planar interface stability. Although it is necessary to consider two limiting approximations of the ternary diffusion equations in order to obtain tractable mathematical solutions, we demonstrate that oxygen dissolution into the alloy with or without diffusional interactions leads to a less restrictive criterion for planar interface stability.

### Planar Interface Stability Criterion

The ternary diffusion model employed in this analysis is shown schematically in Fig. 1. We consider the diffusional controlled growth by metal transport of the oxide  $(AB)_rO$ , in which  $r$  represents the atoms of metal per atom of oxygen, on alloy A-B with concurrent oxy-

\* Electrochemical Society Active Member.

<sup>1</sup> Department of Metallurgy and Materials Science, The University of Liverpool, Liverpool, England, L69 3BX.

<sup>2</sup> Division of Chemistry, National Research Council of Canada, Ottawa, Ontario, Canada, K1A 0R9.

Key words: oxidation, binary alloys, alloy-oxide planar stability.



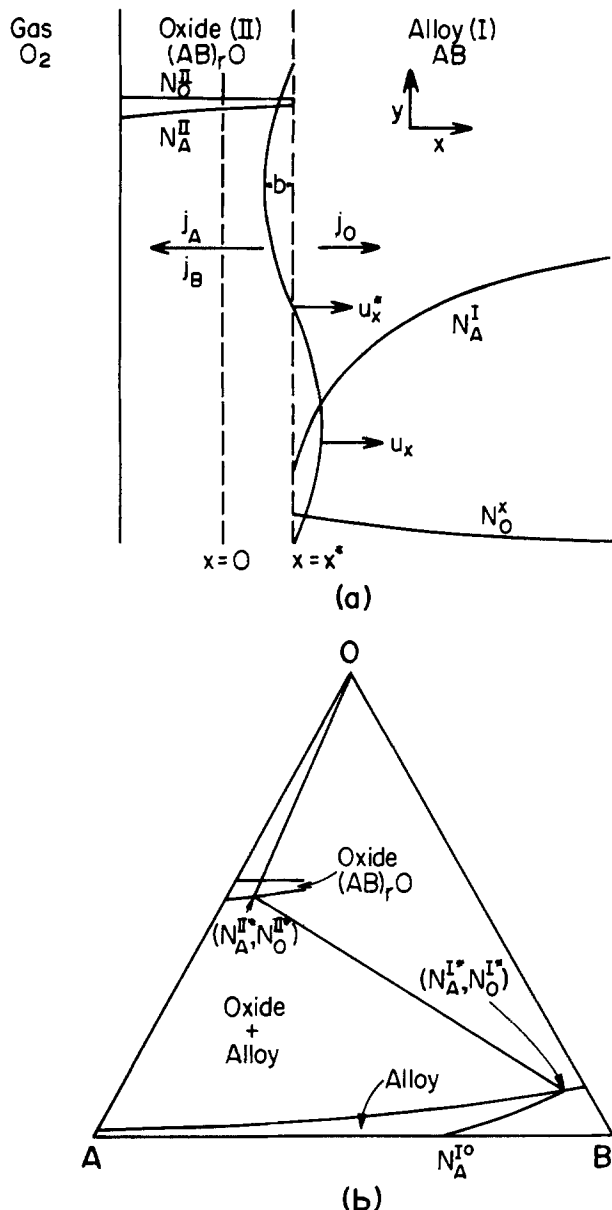


Fig. 1. The oxide scale-alloy model with symbols corresponding to those in text: (a) Cross-section of  $(AB)_rO$  scale and  $AB$  alloy showing planar interface at  $x = x^*$  moving at velocity  $u_{x^*}$ , sinusoidal interface  $x = x^* + b \sin(\omega y)$  moving at velocity  $u_x$ , and the gradients of metal A and oxygen O in the alloy (I) and oxide (II). (b) The diffusion path for metal A and oxygen O in the alloy (I) and oxide (II), superimposed on the ternary A-B-O isotherm in the case of a planar oxide scale-alloy interface. The interfacial compositions of A in the alloy and B in the oxide are assumed to be very dilute.

gen diffusion into the alloy. Metal A which is preferentially oxidized and oxygen are chosen as the independent diffusing components. The composition path corresponding to the diffusion profiles is also shown superimposed on the ternary A-B-O isotherm in Fig. 1 to emphasize that we consider the case corresponding to small solubilities of metal B in the oxide and oxygen in the alloy. These latter restrictions are required in order to obtain a tractable mathematical analysis.

The instantaneous velocity of a planar alloy-oxide interface,  $u_{x^*}$ , is related to the mass boundary condition for either A or oxygen

$$u_{x^*} \left[ \frac{N_{II}^{II*}}{V_{II}} - \frac{N_{I}^{I*}}{V_I} \right] = j_{II}^{II(x^*)} - j_{II}^{I(x^*)} \quad [1]$$

where  $j$  is a component flux,  $N$  represents a mole fraction, and  $V^I$ ,  $V^{II}$  are the molar volumes of alloy (I) and

oxide (II). To investigate the stability of this planar interface, we follow Wagner (1) in impressing a sinusoidal perturbation of infinitesimal amplitude  $b$  on the metal surface such that the locus of the interface is given by

$$x = x^* + b \sin(\omega y) \quad [2]$$

where  $\omega = 2\pi/\lambda$  and  $\lambda$  is the wavelength satisfying  $b \ll \lambda \ll x^*$ . The instantaneous velocity of the perturbed interface,  $u_x$ , is described by an equation identical to [1] although the fluxes and concentrations now depend on  $y$ , the position along the interface. These quantities will be denoted by the absence of asterisks. One can conclude upon examining Fig. 1 that the perturbation decays if at points where the local oxide thickness exceeds the average value the local velocity of the interface is smaller than the average value, and if at points where the local oxide thickness is less than the average value the local velocity exceeds the average value. Thus the planar interface stability criterion is

$$(u_x - u_{x^*})/\sin(\omega y) < 0 \quad [3]$$

In order to define this criterion as a function of diffusivities and concentrations, we must seek solutions for the diffusion equations coupled to the alloy and oxide phases and solve for the interfacial fluxes, compositions, and material balances.

### Diffusion Equations

*Diffusion in the alloy.*—In the region  $x > x^* + b \sin(\omega y)$ , the diffusion equations for metal and oxygen can be written

$$j_A^{I(x)} = -\frac{D_{AA}^I}{V^I} \frac{\partial N_A^I}{\partial x} - \frac{D_{AO}^I}{V^I} \frac{\partial N_O^I}{\partial x} \quad [4a]$$

$$j_O^{I(x)} = -\frac{D_{OA}^I}{V^I} \frac{\partial N_A^I}{\partial x} - \frac{D_{OO}^I}{V^I} \frac{\partial N_O^I}{\partial x} \quad [4b]$$

Analogous equations hold for the  $y$  direction. These equations, with [4a] and [4b] and the continuity condition

$$\frac{\partial N_A^I}{\partial t} = \frac{\partial j_A^{I(x)}}{\partial x} + \frac{\partial j_A^{I(y)}}{\partial y} \quad [5a]$$

$$\frac{\partial N_O^I}{\partial t} = \frac{\partial j_O^{I(x)}}{\partial x} + \frac{\partial j_O^{I(y)}}{\partial y} \quad [5b]$$

may in principle be solved to yield  $N_O^I$ ,  $N_A^I$  as spatial functions. In view of the nontrivial nature of the problem, limiting approximations are sought. We use those introduced by Wagner (1) who has demonstrated that the steady-state approximation  $\partial N_A^I/\partial t \approx \partial N_O^I/\partial t \approx 0$  can be used when  $b \ll 2\pi/\omega \ll x^*$ . Solutions of the coupled equations in [5] even with the above approximations still remain complex, particularly when  $D_{AO}^I$  and  $D_{OA}^I$  have to be treated as functions of composition.

We first consider the limiting case where  $D_{AA}^I$  and  $D_{OO}^I$  are approximately concentration independent and the cross diffusional effects are negligible. Under these assumptions, the solution of Eq. [4] and [5] are

$$N_A^I = N_A^{I*} + G_A^I \{ (x - x^*) + \beta_A^I b \sin(\omega y) \exp - \omega(x - x^*) \} \quad [6a]$$

$$N_O^I = N_O^{I*} + G_O^I \{ (x - x^*) + \beta_O^I b \sin(\omega y) \exp - \omega(x - x^*) \} \quad [6b]$$

where  $G_A^I$  and  $G_O^I$  are the gradients of A and oxygen at the planar interface,  $\beta_A^I$  and  $\beta_O^I$  are constants to be evaluated later. The exponentials in [6] may be approximated to unity at the perturbed interface  $x = x^* + b \sin(\omega y)$  since  $b$  is small. Consequently, [6] leads to

$$N_A^{I,i} = N_A^{I*} + G_A^I b \sin(\omega y) \{ 1 + \beta_A^I \} \quad [7a]$$

$$N_{O^{I,i}} = N_{O^{I,*}} + G_O^I b \sin(w y) \{1 + \beta_{O^I}\} \quad [7b]$$

A second limiting case occurs when cross diffusional effects prevail. Oxygen diffusion in alloys is commonly interstitial with  $D_{OO^I} \gg D_{AA^I}$  implying that  $|\partial N_{O^I}/\partial x| \ll \partial N_{A^I}/\partial x$ . If this solid solution is sufficiently dilute in A and oxygen, the diffusional cross term is (3)

$$D_{OA^I} = D_{OO^I} \epsilon_{O^I} N_{O^I} \quad [8]$$

where  $\epsilon_{O^I} = (\partial \ln \gamma_{O^I} / \partial N_A)_{N_B \rightarrow 1}$  is the Wagner interaction coefficient (4). Thus [4a] and [4b] approximate to

$$j_{A^I(x)} = \frac{-D_{AA^I}}{V^I} \frac{\partial N_{A^I}}{\partial x} \quad [9a]$$

$$j_{O^I(x)} = \frac{-D_{OA^I}}{V^I} \frac{\partial N_{A^I}}{\partial x} \quad [9b]$$

whence

$$j_{O^I(x)} = \left( \frac{D_{OO^I} \epsilon_{O^I} N_{O^I}}{D_{AA^I}} \right) j_{A^I(x)} \quad [10]$$

The solution of [9a] is given by [7a] which together with [10] yields an evaluation of the oxygen flux.

*Diffusion in the oxide.*—A small degree of nonstoichiometry in the ternary metal conducting oxide phase  $(AB)_rO$  is assumed such that the mole fractions of the components approximate to

$$N_{A^{II}} + N_{B^{II}} + N_{O^{II}} \simeq 1 \quad [11]$$

Following Wagner (5) and Coates and Dalvi (6), the flux equations for the oxide constituents relative to the  $x$ -coordinate in Fig. 1 may be written as

$$j_{i^{II}(x)} = -D_{i^{II}} \frac{N_{i^{II}}}{V^{II}} \frac{\partial \ln a_i}{\partial x} + u_x \frac{N_{i^{II}}}{V^{II}} \quad [12a]$$

$$j_{O^{II}(x)} = u_x \frac{N_{O^{II}}}{V^{II}} \quad [12b]$$

where  $i$  refers to metal A or B. From the Gibbs-Duhem equation, assuming ideal or Henrian behavior

$$d \ln a_i^{II} = d \ln N_i^{II} - d \ln a_{O^{II}} \quad [13]$$

Substitution of [13] in [12a] yields

$$j_{i^{II}(x)} = \frac{-D_{i^{II}}}{V^{II}} \left\{ \frac{\partial N_{i^{II}}}{\partial x} - N_{i^{II}} \frac{\partial \ln a_{O^{II}}}{\partial x} \right\} + u_x \frac{N_{i^{II}}}{V^{II}} \quad [14]$$

An approximation must be sought to [14] since an analytical solution for  $N_{i^{II}}$  and  $a_{O^{II}}$  is not available. Frequently  $D_{A^{II}}$  and  $D_{B^{II}}$  in a ternary p-type oxide are of the same order of magnitude and near the interface (7)

$$\frac{\partial N_{A^{II}}}{\partial x} \simeq \frac{\partial N_{B^{II}}}{\partial x} \simeq 0 \quad [15]$$

whence [14] becomes

$$j_{i^{II}} = \frac{D_{i^{II}}}{V^{II}} N_{i^{II,i}} \frac{\partial \ln a_{O^{II}}}{\partial x} + u_x \frac{N_{i^{II,i}}}{V^{II}} \quad [16]$$

where  $N_{i^{II,i}}$  is the mole fraction of A or B in the oxide at the alloy/scale interface. In order to use Eq. [16], one requires the functional relationship between  $D_{i^{II}}$  and  $a_{O^{II}}$ . An analytical form which has found application to the rock-salt structured  $(AB)O$  p-type oxides is (8)

$$D_{i^{II}} = D_{i^{II}(o)} \gamma^{(N_{A^{II}}-1)} (a_{O^{II}})^n \quad [17]$$

where  $D_{i^{II}(o)}$  is the metal self-diffusion coefficient in pure AO or BO and  $\gamma$  is the ratio of the mole fraction of vacant cation sites in pure AO to that in pure BO. Equation [16] becomes upon substitution of [17]

$$j_{A^{II}(x)} = \frac{D_{A^{II}(o)}}{V^{II}} \gamma^{(N_{A^{II}}-1)} \frac{N_{A^{II,i}}}{n} \frac{\partial (a_{O^{II}})^n}{\partial x} + u_x \frac{N_{A^{II,i}}}{V^{II}} \quad [18]$$

An expression similar to [18] is found for the flux of A in the  $y$ -direction. Assuming that the oxide has a constant molar volume and that it deforms plastically, the velocity of the alloy-oxide interface is divergence free

$$\frac{\partial u_x}{\partial x} + \frac{\partial u_y}{\partial y} = 0 \quad [19]$$

Solution of [19] for  $x < x^* + b \sin(w y)$  recalling that  $\partial N_{A^{II}}/\partial t = 0$  is similar to the equivalent equations for the alloy and gives

$$(a_{O^{II}})^n = (a_{O^{II}^*})^n + G_{O^{II}} \{ (x - x^*) - \beta_{O^{II}} b \exp w(x - x^*) \sin(w y) \} \quad [20]$$

where  $G_{O^{II}}$  is the gradient  $\partial (a_{O^{II}})^n / \partial x$  at the mean or planar interface and  $\beta_{O^{II}}$  is a constant to be evaluated. Knowing  $a_O = F(x, y)$  the flux  $j_{A^{II}}$  can be computed from [18].

### Boundary Conditions

*Interfacial compositions.*—Neglecting any capillarity effects, application of the Gibbs-Duhem equation to the local equilibrium concentrations in the alloy and oxide phases at their common interface gives

$$(N_{A^{II}} - N_{A^I}) (d \ln a_A - d \ln a_B) + (N_{O^{II}} - N_{O^I}) (d \ln a_O - d \ln a_B) = 0 \quad [21]$$

Since the oxygen solubility and the residual interfacial concentration of the element A in the alloy are very small, they are regarded as being sufficiently dilute to meet Henrian solution behavior. Accordingly

$$d \ln a_A = \frac{d N_{A^I}}{N_{A^I}}; \quad d \ln a_O = \frac{d N_{O^I}}{N_{O^I}};$$

$$d \ln a_B = -d N_{A^I} - d N_{O^I} \quad [22]$$

Substitution of [22] into [21] followed by integration yields

$$N_{A^{II}} \ln N_{A^I} + N_{O^{II}} \ln N_{O^I} = \text{constant} \quad [23]$$

where  $N_{O^I}$ ,  $N_{A^I} \ll 1$  is assumed throughout the calculation. Letting the standard states of the solute components be defined at infinite dilution and the oxide be considered as near stoichiometric,  $N_{A^{II}}$ ,  $N_{O^{II}} \simeq 1$ , [23] yields

$$N_{A^I} N_{O^I} = a_{A^I} a_{O^I} = K \quad [24]$$

where  $K$  is an equilibrium constant.

$a_{O^{II}}$  is evaluated from Eq. [20] by setting  $x = x^* + b \sin(w y)$  and approximately the exponential to unity

$$(a_{O^{II,i}})^n = (a_{O^{II}^*})^n + b G_{O^{II}} (1 - \beta_{O^{II}}) \sin(w y) \quad [25]$$

Since only small deviations from a planar interface are considered,  $a_{O^{II,i}} \simeq a_{O^{II}^*}$  and  $b G_{O^{II}} (1 - \beta_{O^{II}}) \sin(w y) \ll 1$ . Equations [25] is expanded as a binomial series and truncated after two terms to yield

$$a_{O^{II,i}} = a_{O^{II}^*} \left\{ 1 + \frac{b G_{O^{II}}}{n (a_{O^{II}^*})^n} (1 - \beta_{O^{II}}) \sin(w y) \right\} \quad [26]$$

*Fluxes at the interface.*—The flux of A in the oxide is found by substituting the derivative of [20] into [18] and approximating the exponential to obtain

$$j_{A^{II,i}} = \frac{D_{A^{II}(o)}}{V^{II}} \gamma^{(N_{A^{II}}-1)} \frac{N_{A^{II,i}}}{n} G_{O^{II}} \{ 1 - w b \beta_{O^{II}} \sin(w y) \} + u_x \frac{N_{A^{II,i}}}{V^{II}} \quad [27]$$

The oxygen flux is given simply by Eq. [12b] for the recession rate of the alloy.

On the alloy side of the interface, the distribution of A and its interfacial value,  $N_A^{I,i}$ , are given by Eq. [6a] and [7a], respectively. Differentiation of [6a] and substitution for  $\partial N_A^I/\partial x$  in [9a] yields after approximating the exponential

$$j_{A^{I,i}} = \frac{-D_{AA}^I}{V^I} G_A^I (1 - w b \beta_A^I \sin(w y)) \quad [28]$$

The interfacial oxygen concentration,  $N_{O^{I,i}}$ , is found from Eq. [24]. The two previously given limiting cases are employed to describe the oxygen flux. In the situation where oxygen diffusion is controlled solely by the oxygen gradient, the oxygen profile is described by Eq. [6b], the interfacial concentration by [7b] and the oxygen flux by

$$j_{O^{I,i}} = \frac{-D_{OO}^I}{V^I} \frac{\partial N_{O^I}}{\partial x} = \frac{-D_{OO}^I G_{O^I}}{V^I (1 - w b \beta_{O^I} \sin(w y))} \quad [29]$$

For the case of dominant diffusional interaction on oxygen transport, the oxygen flux at the interface is evaluated from Eq. [10] and [28]

$$j_{O^{I,i}} = \frac{-D_{OO}^I}{V^I} \epsilon_0^A N_{O^{I,i}} G_A^I (1 - w b \beta_A^I \sin(w y)) \quad [30]$$

*Interfacial material balance.*—This mass balance for element A is found from [1], [27], and [28]

$$u_x \left\{ \frac{N_A^{II,i}}{V^{II}} - \frac{N_A^{I,i}}{V^I} \right\}$$

$$\beta_{O^I} = \frac{N_A^{I*} D_{OO}^I - N_A^{I*} D_{AA}^I - 2N_{O^{I,i}} D_{AA}^I G_A^I / G_{O^I} - N_A^{II,i} D_A^{II*} V^I / V^{II}}{N_A^{I*} D_{OO}^I + N_A^{I*} D_{AA}^I + N_A^{II,i} D_A^{II*} V^I / V^{II}} \quad [39]$$

$$= \frac{D_A^{II(o)}}{V^{II}} \gamma^{(N_A^{II,i}-1)} \frac{N_A^{II,i}}{n} G_{O^{II}} \{1 - w b \beta_{O^{II}} \sin(w y)\} + u_x \frac{N_A^{II}}{V^{II}} + \frac{D_{AA}}{V^I} G_A^I (1 - w b \beta_A^I \sin(w y)) \quad [31]$$

Also, the interface velocity can be found from [1] by considering the oxygen flux in the oxide and alloy. In the first limiting case where diffusional interaction in the alloy was neglected, substitution of [12b] and [29] into [1] gives

$$u_x \left[ \frac{N_{O^{II,i}}}{V^{II}} - \frac{N_{O^{I,i}}}{V^I} \right] = u_x \frac{N_{O^{II,i}}}{V^{II}} + \frac{D_{OO}^I}{V^I} G_{O^I} (1 - w b \beta_{O^I} \sin(w y)) \quad [32]$$

or

$$u_x = \frac{-D_{OO}^I G_{O^I}}{N_{O^{I,i}}} (1 - w b \beta_{O^I} \sin(w y)) \quad [33]$$

Substitution of [33] into [31] using [7a] and [7b] to evaluate  $N_A^{I,i}$  and  $N_{O^{I,i}}$ , respectively, gives

$$\{N_A^{I*} + G_A^I (1 + \beta_A^I) b \sin(w y)\} \left\{ \frac{D_{OO}^I G_{O^I}}{V^I} (1 - w b \beta_{O^I} \sin(w y)) \right\} = \{N_{O^{I*}} + G_{O^I} (1 + \beta_{O^I}) b \sin(w y)\} \left\{ \frac{D_A^{II(o)}}{V^{II}} \gamma^{(N_A^{II,i}-1)} \frac{N_A^{II,i}}{n} G_{O^{II}} (1 - w b \beta_{O^{II}} \sin(w y)) + \frac{D_A^I}{V^I} G_A^I (1 - w b \beta_A^I \sin(w y)) \right\} \quad [34]$$

Equating coefficients, neglecting terms in  $b^2$  and those not involving  $w$  since as indicated earlier  $w \gg 1$  leads to

$$\frac{N_A^{I*} D_{OO}^I G_{O^I}}{V^I} = \frac{N_{O^{I*}} D_A^{II(o)} \gamma^{(N_A^{II,i}-1)} N_A^{II,i} G_{O^{II}}}{n V^{II}} + \frac{N_{O^{I*}} D_{AA}^I G_A^I}{V^I} \quad [35]$$

and

$$\frac{N_A^{I*} D_{OO}^I G_{O^I} \beta_{O^I}}{V^I} = \frac{N_{O^{I*}} D_A^{II(o)} \gamma^{(N_A^{II,i}-1)} N_A^{II,i} G_{O^{II}} \beta_{O^{II}}}{n V^{II}} + \frac{N_{O^{I*}} D_{AA}^I G_A^I \beta_A^I}{V^I} \quad [36]$$

Equation [7] giving the concentration of element A and oxygen at the perturbed interface when substituted into expression [24] for the local equilibrium values yields upon noting that  $N_A^{I*} N_{O^{I*}} = K$

$$\frac{1 + \beta_A^I}{1 + \beta_{O^I}} = - \frac{N_A^{I*}}{N_{O^{I*}}} \frac{G_{O^I}}{G_A^I} \quad [37]$$

when terms involving  $b^2$  are ignored. From the equilibrium statement,  $N_{O^{I,i}} \sim a_{O^{I,i}} = a_{O^{II,i}}$ , and upon equating [7b] and [26] we obtain

$$\frac{1 + \beta_{O^I}}{1 - \beta_{O^{II}}} = \frac{G_{O^{II}}}{G_{O^I}} \frac{N_{O^{I*}}}{n (a_{O^{II*}})^n} \quad [38]$$

Using Eq. [17] to define  $D_A^{II*}$  and combining [37], [38] with [35], [36] yields

We now consider the second limiting case where diffusional interaction of oxygen with the metal gradient is dominant,  $D_{OA} \partial N_A / \partial x \gg D_{OO} |\partial N_{O^I} / \partial x|$ . Substitution of [12b] and [30] into [1] gives

$$u_x \left[ \frac{N_{O^{II,i}}}{V^{II}} - \frac{N_{O^{I,i}}}{V^I} \right] = u_x \frac{N_{O^{II,i}}}{V^{II}} + \frac{D_{OO}^I}{V^I} \epsilon_0^A N_{O^{I,i}} G_A^I (1 - w b \beta_A^I \sin(w y)) \quad [40]$$

Dividing [31] by [40] and substituting [7a] for  $N_A^{I,i}$  yields upon rearrangement

$$\{N_A^{I*} + G_A^I b \sin(w y) (1 + \beta_A^I) - D_A^I / D_{O^I} \epsilon_0^A\} \left\{ \frac{D_{OO}^I}{V^I} \epsilon_0^A G_A^I (1 - w b \beta_A^I \sin(w y)) \right\} = \frac{D_A^{II(o)}}{V^{II}} \gamma^{(N_A^{II,i}-1)} \frac{N_A^{II,i}}{n} G_{O^{II}} (1 - w b \beta_{O^{II}} \sin(w y)) \quad [41]$$

For Eq. [41] to be satisfied, the coefficients of  $\sin w y$  must be equal as must the constants. If terms involving  $b^2$  are ignored

$$\left\{ N_A^{I*} - \frac{D_{AA}^I}{D_{OO^I} \epsilon_0^A} \right\} \frac{D_{OO}^I}{V^I} \epsilon_0^A G_A^I = \frac{D_A^{II(o)}}{V^{II}} \gamma^{(N_A^{II,i}-1)} \frac{N_A^{II,i}}{n} G_{O^{II}} \quad [42]$$

$$\begin{aligned}
& - \left\{ N_A^{I*} - \frac{D_{AA}}{D_{Oo^I} \epsilon_O^A} \right\} \frac{D_{Oo^I}}{V^I} \epsilon_O^A G_A^I w \beta_A^I \\
& \quad + \frac{D_{Oo^I}}{V^I} \epsilon_O^A G_A^I G_A^I (1 + \beta_A^I) \\
& = \frac{-D_{AA}^{II(o)}}{V^{II}} \gamma^{(N_A^{II,1}-1)} \frac{N_A^{II,i}}{n} G_O^{II} \beta_O^{II} w \quad [43]
\end{aligned}$$

Recalling that  $w \gg 1$ , the second term on the LHS of [43] is neglected. The comparison of [42] and [43] gives the result

$$\beta_A^I = \beta_O^{II} \quad [44]$$

Substitution of [7a] into the equilibrium statement [24] yields

$$N_O^{I,i} = \frac{K}{N_A^{I*} + G_A^{Ib} \sin(wy) (1 + \beta_A^I)} \quad [45]$$

Since  $N_O^{I,i} \simeq a_O^I = a_O^{II}$ , substitution of [26] into [45] gives

$$\begin{aligned}
a_O^{II*} \left\{ 1 + \frac{bG_O^{II}}{n(a_O^{II*})^n} (1 - \beta_O^{II}) \sin(wy) \right\} \\
= \frac{K}{N_A^{I*} \left\{ 1 + \frac{G_A^{Ib}}{N_A^{I*}} (1 + \beta_A^I) \sin(wy) \right\}} \quad [46]
\end{aligned}$$

Since  $G_A^{Ib} (1 + \beta_A^I) \sin(wy) / N_A^{I*} \ll 1$  by definition, the RHS of [46] may be approximated by a truncated binomial expansion and

$$\begin{aligned}
a_O^{II*} \left\{ 1 + \frac{bG_O^{II}}{n(a_O^{II*})^n} (1 - \beta_O^{II}) \sin(wy) \right\} \\
= \frac{K}{N_A^{I*}} \left\{ 1 - \frac{bG_A^I}{N_A^{I*}} (1 + \beta_A^I) \sin(wy) \right\} \quad [47]
\end{aligned}$$

Since  $K/N_A^{I*} = N_O^{I*} = a_O^{I*} = a_O^{II*}$ , [47] yields

$$\frac{1 + \beta_A^I}{1 - \beta_O^{II}} = \frac{-G_O^{II} N_A^{I*}}{n G_A^I (a_O^{II*})^n} \quad [48]$$

Substitution of [44] into [48] gives

$$\beta_A^I = - \left\{ 1 + \frac{G_O^{II} N_A^{I*}}{n G_A^I (a_O^{II*})^n} \right\} \left/ \left\{ 1 - \frac{G_O^{II} N_A^{I*}}{n G_A^I (a_O^{II*})^n} \right\} \right. \quad [49]$$

### Equations for Planar Interface Stability

We are now in position to consider the stability criterion for a planar interface under the two limiting cases where oxygen migration in the alloy is controlled by: (i) oxygen diffusion down its own gradient and (ii) oxygen diffusion by its interaction with the metal gradient. The interface stability criterion is given by Eq. [3] using Eq. [1] to define the interface velocity.

*Stability criterion: oxygen diffusion down its own gradient.*—We have shown that

$$u_x = - \frac{D_{Oo^I} G_O^I}{N_O^{I,i}} (1 - w b \beta_O^I \sin(wy)) \quad [33]$$

Substituting from Eq. [7b] for  $N_O^{I,i}$ , approximating the denominator by the first two terms of a series expansion and neglecting second order terms in  $b$  gives

$$\begin{aligned}
u_x = - \frac{D_{Oo^I} G_O^I}{N_O^{I*}} \left[ 1 - \left\{ w \beta_O^I - \frac{G_O^I}{N_O^{I*}} (1 + \beta_O^I) \right\} \right. \\
\left. b \sin(wy) \right] \quad [50a]
\end{aligned}$$

Clearly at a planar interface  $b \sin(wy) = 0$  this re-

sult becomes

$$u_x^* = - D_{Oo^I} G_O^I / N_O^{I*} \quad [50b]$$

and thus

$$u_x - u_x^* = - u_x^* w b \beta_O^I \sin(wy) \quad [51]$$

Thus, the criterion for stability is found from [3] to be

$$\beta_O^I > 0 \quad [52]$$

Therefore, using the expression  $\beta_O^I$  from [39] and equating  $N_A^{II,i} \simeq N_A^{II*}$ , the stability criterion is

$$\begin{aligned}
N_A^{I*} D_{Oo^I} - N_A^{I*} D_{AA} - 2 N_O^{I*} D_{AA}^I G_A^I / G_O^I \\
- N_A^{II,i} D_{AA}^{II*} V^I / V^{II} > 0 \quad [53]
\end{aligned}$$

Approximating

$$G_A^I \simeq (N_A^{Io} - N_A^{I*}) / \sqrt{D_{AA}^I} \quad [54]$$

$$G_O^I \simeq - N_O^{I*} / \sqrt{D_{Oo^I}}$$

where  $N_A^{Io}$  is the bulk alloy atom fraction of A, we obtain from [53]

$$\frac{N_A^{I*} D_{Oo^I} + 2(N_A^{Io} - N_A^{I*}) \sqrt{D_{AA}^I D_{Oo^I}}}{N_A^{I*} D_{AA}^I + N_A^{II*} D_{AA}^{II*} V^I / V^{II}} > 1 \text{ (stable)} \quad [55]$$

*Stability criterion: oxygen diffusion on metal gradient.*—Equation [40] upon rearrangement gives the interfacial velocity

$$u_x = - D_{Oo^I} \epsilon_O^A G_A^I (1 - w b \beta_A^I \sin(wy)) \quad [56]$$

and for the planar interface

$$u_x^* = - D_{Oo^I} \epsilon_O^A G_A^I \quad [57]$$

Thus

$$u_x - u_x^* = - u_x^* w b \beta_A^I \sin(wy) \quad [58]$$

and the stability criterion is found from [3] to be

$$\beta_A^I > 0 \quad [59]$$

where  $\beta_A^I$  is defined by [49]. Evaluating  $G_{Oo^I} / G_A^I$  from [42] and using [17] to define  $D_{AA}^{II} = D_{AA}^{II*}$  at an oxygen activity  $a_O^*$ , Eq. [49] becomes

$$\beta_A^I = \frac{q - 1}{q + 1} \quad [60]$$

where

$$q = \frac{N_A^{I*} V^{II} D_{AA}^I}{N_A^{II*} V^I D_{AA}^{II*}} \left\{ 1 - N_A^{I*} \epsilon_O^A \frac{D_{Oo^I}}{D_{AA}^I} \right\} > 1 \text{ (stable)} \quad [61]$$

This criterion can be seen to result by comparing [59] and [60] to [61] knowing that the interaction coefficient  $\epsilon_O^A$  must be of negative magnitude for oxygen diffusion into the alloy on the gradient of element A.

### Discussion

The criterion for the stability of the planar alloy-oxide interface is given by Eq. [55] or [61] when oxygen diffusion into the alloy is taken into account according to ternary diffusion theory. These equations can be compared to the expression developed for the pseudobinary limit—no oxygen solution in the alloy and an oxide consisting entirely of the selectively oxidized metallic component. We then consider the validity of the limiting equations used in the present analysis to describe the oxygen flux in the alloy. Finally, some remarks are directed to the applicability of the stability criterion to the oxidation properties of transition metal alloys.

The expression derived by Wagner (1) under the pseudobinary limit using the present nomenclature reads

$$\frac{N_A^{I*} D_{AA}^I V^{II}}{(1 - N_A^{I*}) D_{AA}^{II*} V^I} > 1 \text{ (stable)} \quad [62]$$

It is clear, however, that [62] represents an extreme case: a planar interface is not stable if  $N_A^{I*} \rightarrow 0$ . In this case, Eq. [55], describing oxygen diffusion down its own gradient leads to

$$\frac{2N_A^{I0}\sqrt{D_A^I D_{O0}^I} V^{II}}{N_A^{II*} D_A^{II} V^I} > 1 \text{ (stable)} \quad [63]$$

For  $D_A^I/D_A^{II} \ll 1$ ,  $N_A^{I*} \rightarrow 0$ . However, in [63] the relevant ratio of diffusion coefficients is  $\sqrt{D_A^I D_{O0}^I}/D_A^{II}$  which is not necessarily less than unity because  $D_{O0}^I \gg D_{AA}^I$ . Hence the diffusion of oxygen into the alloy reduces the stability criterion. A similar effect is apparent when oxygen diffuses via interaction with the metal gradient as seen in Eq. [61] since  $\epsilon_0^A \ll 0$  is often found (Table I). Under this restriction, Eq. [61] can lead to

$$-\frac{(N_A^{I*})^2 V^{II} \epsilon_0^A D_{O0}^I}{N_A^{II*} V^I D_A^{II*}} > 1 \text{ (stable)} \quad [64]$$

which is a less stringent criterion insofar as  $D_{O0}^I \gg D_A^{II}$ . It is also interesting to note that [61] under the pseudobinary approximation of no oxygen diffusion into the alloy,  $\epsilon_0^A = 0$ , becomes

$$\frac{N_A^{I*} D_{AA}^{IVII}}{N_A^{II*} D_A^{II*} V^I} > 1 \text{ (stable)} \quad [65]$$

in close similarity to the Wagner expression. The mole fraction  $N_A^{II*}$  rather than  $1 - N_A^{I*}$  has arisen due to the present analysis incorporating ternary properties of the oxide phase.

The validity of the limiting approximations for oxygen flux in the alloy is now examined. For ideal or Henrian solution of oxygen in the alloy,  $\epsilon_0^A = 0$  and oxygen diffusion is to be regarded as occurring solely on its own gradient (Eq. [4]). In the case of more complicated oxygen solution behavior in the alloy, the limiting ratio of the oxygen flux for diffusion on its gradient (Eq. [4] and [54]) to that for diffusion dependent upon oxygen interaction with the metal gradient (Eq. [10] and [54]) is

$$\begin{aligned} & \frac{j_0 \text{ (oxygen gradient)}}{j_0 \text{ (metal gradient)}} \\ &= -\frac{D_{O0}^I N_{O0}^{I*} / \sqrt{D_{O0}^I}}{D_{O0}^I \epsilon_0^A N_{O0}^{I*} (N_A^{I0} - N_A^{I*}) / \sqrt{D_{AA}^I}} \\ &= -\frac{1}{\epsilon_0^A \Delta N_A^I} \sqrt{\frac{D_{AA}^I}{D_{O0}^I}} \quad [66] \end{aligned}$$

Although it was necessary to assume in our analysis that the alloy was a relatively dilute solution of oxygen and the second metallic component, the paramount importance of oxygen diffusion by interaction with the metal gradient in transition metal alloys resulting from selective oxidation of a metal component can be qualitatively assessed. At 1000°C, the diffusivities of oxygen and metal in the fcc transition metals are of the order

$10^{-7}$  and  $10^{-12}$  cm<sup>2</sup>/sec, respectively. Thus the ratio in [66] becomes  $-3 \times 10^{-2}/\epsilon_0^A$  for an alloy depletion of A of 0.1 atom fraction at the interface. Hence for  $\epsilon_0^A = -1$ , a very small interaction coefficient, the oxygen flux results predominately from the presence of the metal gradient. Interaction coefficients for oxygen with alloying elements which are selectively oxidized from transition metal alloys are in the range  $-5$  to  $-50$  and as high as  $\sim -10^3$  (Table I). It is thus seen that the oxygen flux being considered in the criterion for planar interface stability can readily arise from either the oxygen or metal gradients dependent upon the thermodynamic properties of the alloy solid solution.

These qualitative remarks aptly demonstrate that an oxygen flux relaxes the interface stability criterion based simply on the pseudobinary model of metal diffusion in the oxide and alloy phases. This magnitude of the oxygen flux is dependent upon the thermodynamic properties of the alloy, a large interaction of oxygen with the metallic element which is selectively oxidized greatly increasing the magnitude of oxygen diffusion. Unfortunately, we cannot give a more quantitative analysis directed to specific cases since oxygen interaction parameters are known only for molten alloys and mainly at the very high temperatures in the range of 1600°C for molten steel. Extrapolation of the known values demonstrate that they increase with decreasing temperature (9). Accordingly one expects that oxygen diffusion, which leads to a less stringent condition for interface stability in comparison to the pseudobinary model, occurs predominantly by interaction with the transient metal gradient set up in the alloy during the very early intervals of oxidation (Eq. [61]).

Equations [55] and [61] must be regarded as necessary but not a sufficient condition for describing the stability of a planar alloy-oxide interface. When  $D_A^{II} \simeq D_B^{II} \leq D_{AA}^I$ , these equations describe planar stability when a compact scale grows under the influence of chemical diffusion insofar as structural imperfections such as line defects do not influence the nucleation of oxide and the subsequent atomistics of diffusion. However, an essentially planar interface can occur even when  $D_A^{II} \simeq D_B^{II} \gg D_{AA}^I$  under two commonly observed situations. In the first case, the solubility of B in (AB)<sub>r</sub>O can be of sufficient magnitude to invalidate an approximation of this analysis,  $N_B^{II} \ll N_A^{II}$ , which will cause only a very small gradient of A in the alloy beneath the scale. In this situation a model for growth of a ternary oxide scale with a planar interface at the A-B alloy surface is applicable (5). In the second case, the inward flux of oxygen described by [55] and [61] may lead to internal oxidation and subsequent relaxation of gradients which is not taken into account in the present model. Thus oxide precipitation internally would give only a small transient period for interface instability which would be of little ultimate dimensional consequence.

These above considerations can be exemplified by referring to the oxidation properties of binary alloys composed of metals in the first transition series ranging from chromium to nickel. The stabilities of the isotopic oxides decrease from chromium to nickel: a metal on the left (A) tends to be selectively oxidized from an alloy matrix of the metal to the right (B). On the binary alloys where a rhombohedral oxide (AB)<sub>2</sub>O<sub>3</sub> is formed, e.g., Cr<sub>2</sub>O<sub>3</sub> on Fe-Cr and Co-Cr alloys,  $D_{Cr}^{II} < D_{Cr}^{I}$  and a stable interface results. Likewise a planar interface is found upon formation of spinel oxide scales (AB)<sub>3</sub>O<sub>4</sub> as a consequence of two properties: first,  $D_A^{II} \simeq D_B^{II} \simeq D_{AA}^I$  and, second, these oxides exhibit a relatively large solubility of B which minimizes metal gradients in the alloy ( $N_A^{I*} \gg 0$ ). Conversely, several of the rock-salt structured divalent MO oxides show large metal diffusivi-

Table I. Values of the Wagner first-order oxygen interaction coefficient with several alloying elements,  $\epsilon_0^A = \left( \frac{\partial \ln \gamma_O}{\partial N_A} \right)_{N_B \rightarrow 1}$ , in molten dilute iron and copper alloys at 1600°C (9, 10).

Base alloy	Element	$\epsilon_0^A$	Base alloy	Element	$\epsilon_0^A$
Iron	Al	$-3.3 \times 10^8$	Copper	Co	$-1.3 \times 10^1$
Iron	La	$-4.2 \times 10^8$	Copper	Fe	$-4.4 \times 10^1$
Iron	Cr	$-3.4 \times 10^1$	Copper	Ni	-5.2
Iron	Ni	$-1.9 \times 10^1$	Copper	Ag	-3.1
Iron	Ti	$-5.1 \times 10^2$			
Iron	V	$-2.5 \times 10^2$			

ties. As examples, the ratio  $D_{A^{II}}/D_{AA^I}$  is of the order  $10^6$  and  $10^8$  for the FeO-Fe and CoO-Co systems, respectively. However, a planar alloy interface is maintained upon oxidation of Co-Ni, Co-Fe, and Fe-Mn alloys. In these cases the oxides form a complete homogeneous (AB)O solid solution negating the interface stability criterion. Consequently a diffusional analysis based on growth of uniformly thick ternary oxide scales has been found to describe the oxidation properties of these alloys (11-13). FeO exhibits a negligible solubility for nickel (14). Nevertheless, a planar interface results upon formation of an (FeNi)O scale on Fe-Ni alloys due to the removal of the stability restraint as a consequence of inward diffusion of oxygen and copious internal oxidation resulting in formation of a distinct subscale (15).

### Acknowledgments

The authors gratefully acknowledge helpful discussions with J. S. Kirkaldy and the financial support for this work by The National Research Council of Canada.

Manuscript submitted Nov. 3, 1975; revised manuscript received ca. March 11, 1976.

Any discussion of this paper will appear in a Discussion Section to be published in the June 1977 JOURNAL.

All discussions for the June 1977 Discussion Section should be submitted by Feb. 1, 1977.

Publication costs of this article were partially assisted by McMaster University.

### REFERENCES

1. C. Wagner, *This Journal*, **103**, 571 (1956).
2. D. E. Coates and J. S. Kirkaldy, *Trans. ASM*, **62**, 426 (1969).
3. J. S. Kirkaldy and G. R. Purdy, *Can. J. Phys.*, **40**, 208 (1962).
4. C. Wagner, "Thermodynamics of Alloys," p. 51, Addison-Wesley Publishing Co. Inc., Reading, Mass. (1952).
5. C. Wagner, *Corrosion Sci.*, **9**, 91 (1969).
6. D. E. Coates and A. D. Dalvi, *Oxidation Metals*, **2**, 331 (1970).
7. D. P. Whittle, B. D. Bastow, and G. C. Wood, *ibid.*, **7**, 225 (1973).
8. A. D. Dalvi and D. E. Coates, *ibid.*, **3**, 203 (1971).
9. G. K. Sigworth and J. F. Elliott, *Metal Science*, **8**, 298 (1974).
10. E. S. Tankins, *Can. Met. Quart.*, **9**, 353 (1970).
11. B. D. Bastow, D. P. Whittle, and G. C. Wood, *Corros. Sci.*, In press.
12. P. Mayer and W. W. Smeltzer, *This Journal*, **119**, 626 (1972).
13. P. Mayer and W. W. Smeltzer, *ibid.*, **121**, 538 (1974).
14. A. D. Dalvi and W. W. Smeltzer, *ibid.*, **117**, 1431 (1970).
15. W. W. Smeltzer, L. A. Morris, and R. C. Logani, Proc. IVth Int. Congress Metallic Corrosion, p. 221, N.A.C.E. (1969).

## Codeposition of Glassy Silica and Germania Inside a Tube by Plasma-Activated CVD

D. Küppers, J. Koenings, and H. Wilson

Philips GmbH Forschungslaboratorium Aachen, 5100 Aachen, West Germany

### ABSTRACT

Codeposition of glassy silica and germania inside a tube reactor has been studied with the aid of a microwave discharge. The plasma enhances the reaction rate of the reactions  $\text{SiCl}_4 + \text{O}_2 \rightarrow \text{SiO}_2 + 2\text{Cl}_2$  and  $\text{GeCl}_4 + \text{O}_2 \rightarrow \text{GeO}_2 + 2\text{Cl}_2$  which are negligibly small at the applied wall temperature of  $\sim 1000^\circ\text{C}$ . With an excess of oxygen, both reactions result in complete conversion to  $\text{SiO}_2$  and  $\text{GeO}_2$ , respectively. A SEM analysis of the codeposit of both oxides shows that their deposition kinetics are different. This has a marked effect on the distribution of the refractive index within a single layer. However, when the layer is formed by building up some thousands of individual layers, on an average scale the deposit no longer reflects the deposition kinetics but only the gas phase composition.

In the development of glass fibers for optical communication, methods of producing fibers with well-defined index profiles are of interest. At present, the best results are obtained by successive deposition of layers with differing refractive index onto the inner wall of a quartz tube reactor.

In the flame hydrolysis process (1), silicon dioxide soot doped with other oxides is formed inside the quartz tube by gas phase reactions and is deposited onto the walls. In the modified chemical vapor deposition process the soot is simultaneously deposited and fused (2-3). Here, normally about 50 layers with varying dope concentrations are deposited to approach a given index profile. In both processes the tube is subsequently collapsed to a rod and a fiber is drawn.

In this paper we present the results of a method where the hot zone is replaced by a nonisothermal

plasma zone. In this plasma-activated CVD process, soot is avoided and thin film growth is obtained by surface reactions. Normally between 500 and 2000 layers are deposited without increase of the total deposition time.

### Experimental

The experimental setup is shown in Fig. 1. The gases  $\text{SiCl}_4$ ,  $\text{GeCl}_4$ , and  $\text{O}_2$  are metered from a typical supply system using mass flow controllers for regulation of the gas flow  $Q$ . In the experiments which are reported here, typical values are  $30 \text{ sccm} \leq Q_{\text{O}_2} \leq 50 \text{ sccm}$ ,  $2 \text{ sccm} \leq Q_{\text{SiCl}_4} \leq 3.2 \text{ sccm}$ , and  $0.2 \text{ sccm} \leq Q_{\text{GeCl}_4} \leq 0.3 \text{ sccm}$ . The reaction zone is a short section of an approximately 1m long quartz glass tube of 8 mm outer diameter and 1 mm wall thickness surrounded by a microwave cavity connected to a 2.450 GHz generator with a maximum power,  $E$ , of 200W. The temperature,  $T_f$ , of the substrate tube can

Key words: optical fiber communication, microwave discharge, chemical reactions.

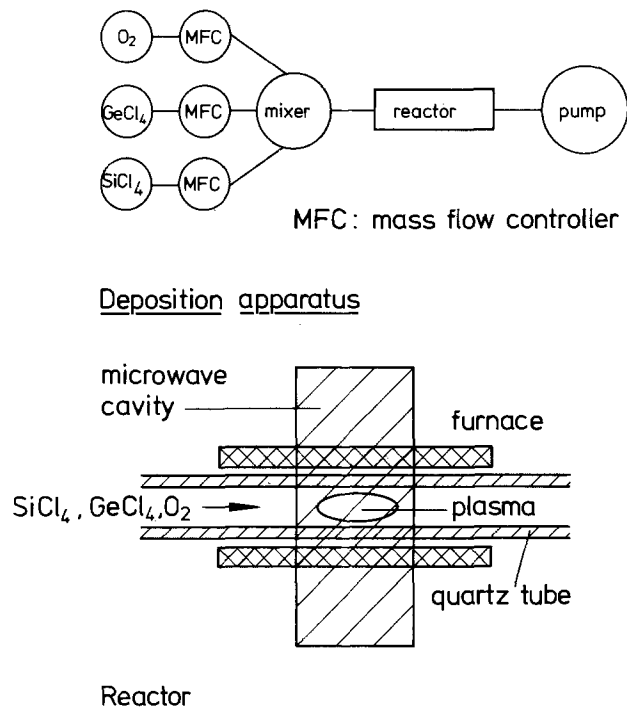


Fig. 1. Experimental setup

be controlled with an additional furnace between room temperature and 1100°C. A sorption pump is used to maintain an oil-free and water-free atmosphere. The pressure,  $p$ , inside the tube is selected between 1 and 20 Torr.

### Results and Discussion

**Local deposition of pure quartz glass.**—The reaction  $\text{SiCl}_4 + \text{O}_2 \rightarrow \text{SiO}_2 + 2\text{Cl}_2$  when initiated by a non-isothermal plasma proceeds with the substrate at room temperature. However, the layers are found to be of high chlorine content and to peel off if the thickness is greater than about 1000Å. When substrate temperatures of 800°–1000°C are used, the chlorine content in the deposited layer is reduced to 0.1% and no cracks appear within the layers (4). The plasma-aided deposition always takes place by surface reaction. Under the applied experimental conditions, soot particles, which might originate from gas phase reactions, are not observed under the microscope.

In order to analyze the deposition profile, the cavity was held in a fixed position and the deposition process was followed over a length of time. A typical result is shown in Fig. 2 for three different deposition periods up to 35 min. The photographs show a section along the tube axis in which the maximum thickness of the deposit is 2 mm. Nearly all  $\text{SiCl}_4$  fed into the tube reacts to  $\text{SiO}_2$  and is deposited onto the walls. In these and the following experiments the gas flow enters from the left. The evaluation of these deposition profiles gives that the time-dependence of the deposited mass can be written (5)

$$m_L(z, t) = m_L^0(z) \cdot t \quad [1]$$

where  $m_L(z, t)$  is the total deposited mass per unit length after time,  $t$ , and where  $z$  is the length coordinate in the direction of the tube axis.

Equation [1] means that the mass deposited per unit length and unit time,  $m_L^0(z)$ , is not affected by the narrowing of the tube. For convenience,  $m_L^0(z)$  will be called the deposition profile. The deposition kinetics are consistent with a diffusion model where it is assumed that on entering the plasma region the  $\text{SiCl}_4$  and  $\text{O}_2$  molecules are dissociated and  $\text{SiO}_2$  deposition occurs on striking of the tube walls by Si species (5).

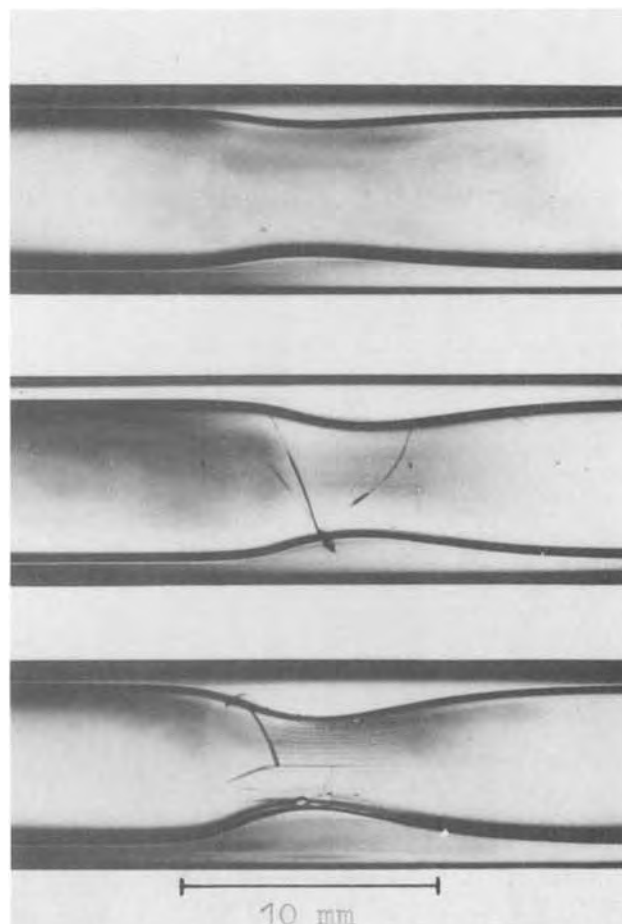


Fig. 2. Deposition of pure quartz glass with stationary plasma (top, 15 min; middle, 25 min; bottom, 35 min).  $T_f = 970^\circ\text{C}$ ,  $Q_{\text{O}_2} = 30$  sccm,  $Q_{\text{SiCl}_4} = 3.2$  sccm,  $p = 8$  Torr,  $E = 75\text{W}$ .

**Local deposition of doped quartz glass.**—In the experiments described in this section, the cavity was at a fixed position. A constant ratio of  $\text{SiCl}_4$  and  $\text{GeCl}_4$  flow, normally between 10 and 100, is maintained for codeposition of  $\text{SiO}_2$  and  $\text{GeO}_2$ . A deposition profile similar to that shown in Fig. 2 is obtained and is given in the lower curve of Fig. 3, where  $\ln(m_L(z, t)/R_T^2\pi\rho)$  is plotted as a function of the length coordinate  $z$ .  $R_T$  is the starting inner radius of the tube,  $\rho$  the density of the deposit. By definition  $0 \leq m_L(z, t)/R_T^2\pi\rho \leq 1$ .

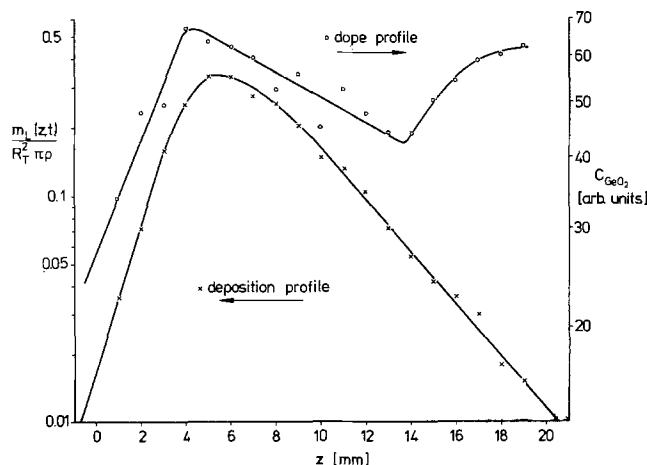


Fig. 3. Simultaneous deposition of  $\text{SiO}_2$  and  $\text{GeO}_2$ .  $T_f = 900^\circ\text{C}$ ,  $Q_{\text{O}_2} = 50$  sccm,  $Q_{\text{SiCl}_4} = 2.7$  sccm,  $Q_{\text{GeCl}_4} = 0.14$  sccm,  $p = 6$  Torr,  $E = 65\text{W}$ .

Microprobe analysis of the deposited profile revealed a constant value for the concentration,  $C_{\text{GeO}_2}$  of  $\text{GeO}_2$  normal to the tube axis and a change in concentration parallel to the tube axis. In the upper curve of Fig. 3,  $C_{\text{GeO}_2}$  (in arbitrary units) is given as a function of  $z$ . From Fig. 3 it is obvious that the deposition profiles  $^S m_L^o(z)$  and  $^G m_L^o(z)$  where S and G stand for  $\text{SiO}_2$  and  $\text{GeO}_2$ , respectively, are different. This result is to be expected since each reaction gives its own deposition profile,  $m_L^o(z)$ .

Interestingly, one observes an increase of the dope concentration at the tail end of the deposit. Though the measurements become difficult when the layer is thinner than  $\sim 10 \mu\text{m}$ , there is evidence that we have a further large increase in germanium concentration beyond the region given in Fig. 3. This reflects the fact that the  $\text{GeO}_2$  deposition profile is more elongated than the  $\text{SiO}_2$  profile. The larger deposition area has been confirmed in separate experiments where only  $\text{GeO}_2$  was deposited.

*Deposition of a single quartz layer doped with  $\text{GeO}_2$ .*—When the plasma reactor is moved with constant velocity in one direction a layer of uniform thickness is deposited.

*Moving the reactor in the direction of the gas flow.*—If the plasma, and therefore the dope profile of Fig. 3, is moved with constant velocity,  $v$ , in the same direction as the gas flows through the tube, the consequence is a radial variation of the germanium dioxide concentration in the deposit as illustrated in Fig. 4a.  $D$  is the inner diameter of the starting tube,  $\Delta d$  the thickness of the layer, and  $r$  is the radial coordinate within the core of the collapsed preform. The resulting germanium distribution in the preform core of Fig. 4a can of course be calculated exactly if  $^S m_L^o(z)$  and  $^G m_L^o(z)$  are known.

For this purpose, one considers that the mass which is deposited between  $z$  and  $z + \Delta z$  in the stationary case corresponds to the mass between  $r$  and  $r + \Delta r$  in the case where a layer is deposited by the moving reactor and a preform produced. Therefore the problem is to find the relationship between  $r$  and  $z$ .

If  $z'$  gives the coordinate of the microwave resonator, then the generalization of Eq. [1] for a moving resonator leads to

$$m'_L(z, t) = \int_{t_0}^t m_L^o(z, z'(t)) dt \quad [2]$$

In the case of constant velocity we have  $z' = v \cdot t$  and therefore

$$m'_L(z, t) = \frac{1}{v} \int_{v \cdot t_0}^{v \cdot t} m_L^o(z, z') dz' \quad [3]$$

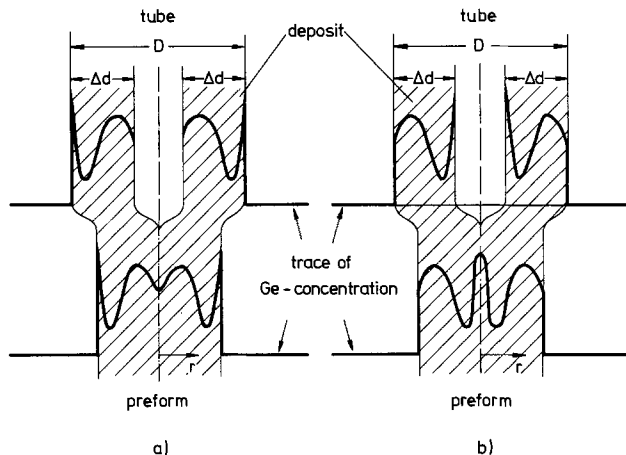


Fig. 4. Variation of dope concentration over layer thickness in single layer deposition (schematic): a. moving the reactor with the gas flow, b. moving the reactor toward the gas flow.

If  $t_e$  determines the end of the deposition, we get

$$r^2 \pi = \frac{1}{v} \int_{vt}^{vt_e} \frac{m_L^o(z, z')}{\rho} dz' \quad t_0 \leq t \leq t_e \quad [4]$$

By assuming  $m_L^o(z, z') = m_L^o(z - z')$ , which means that the deposition profile does not depend on the position  $z'$  of the resonator, we obtain

$$r^2 \pi = \frac{1}{v} \int_{vt-z}^{vt_e-z} \frac{m_L^o(-\omega)}{\rho} d\omega \quad [5]$$

with the abbreviation  $\omega = z' - z$ . Because the deposition profile has a width of about 10 mm and because the length of the total deposition layer is about 200 mm we can neglect the end effects and can replace  $t_e$  by  $-\infty$ . Thus we get

$$r^2 \pi = \frac{1}{v} \int_{-\infty}^{-vt+z} \frac{m_L^o(\omega)}{\rho} d\omega \quad [6]$$

Dividing by  $R_c^2 \pi$  where  $R_c$  is the radius of the core and by inserting Eq. [1] we find

$$\left(\frac{r}{R_c}\right)^2 = \left(\frac{R_T}{R_c}\right)^2 \frac{1}{v \cdot \tau} \int_{-\infty}^{-\omega_t} \frac{m_L(\omega, \tau)}{R_T^2 \pi \rho} d\omega \quad [7]$$

with the abbreviation  $\omega_t = v \cdot t - z$ . In our case  $m_L(\omega, \tau)/R_T^2 \pi \rho$  is given by Fig. 3. If  $N$  is the normalization constant

$$\left(\frac{R_c}{R_T}\right)^2 \cdot v \cdot \tau = \int_{-\infty}^{+\infty} \frac{m_L(\omega, \tau)}{R_T^2 \pi \rho} d\omega = N \quad [8]$$

must obviously hold. Therefore we obtain as the final result

$$\frac{r}{R_c} = \left[ \frac{1}{N} \int_{-\infty}^{-\omega_t} \frac{m_L(\omega, t)}{R_T^2 \pi \rho} d\omega \right]^{1/2} \quad [9]$$

Equation [9] gives  $r/R_c$  as a function of  $\omega_t$  or vice

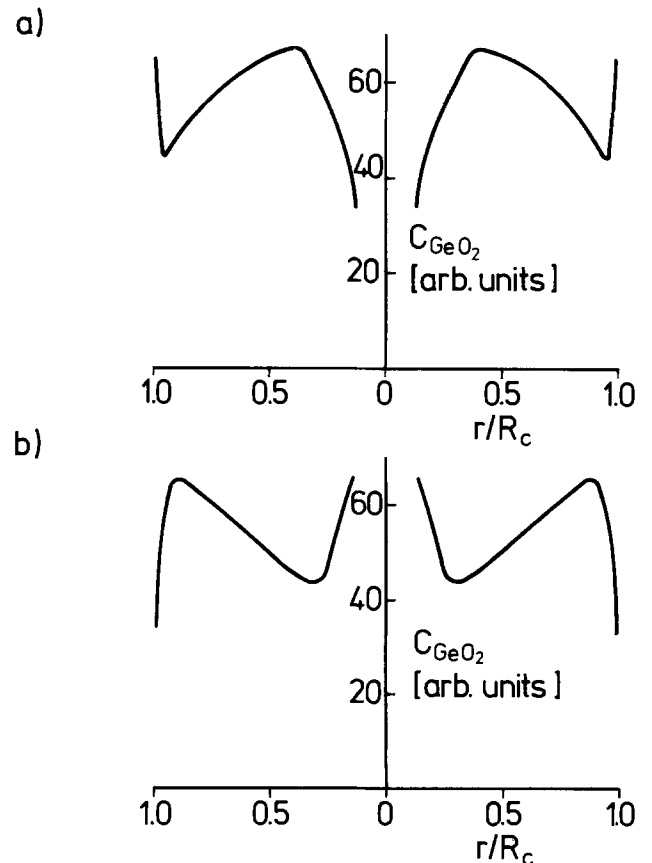


Fig. 5. Variation of the dope concentration over the layer thickness (calculated from Fig. 3): a. moving the reactor with the gas flow, b. moving the reactor toward the gas flow.



versa. Thus from the knowledge of  $C_{\text{GeO}_2}$  as a function of  $z$  in the stationary case, we now find  $C_{\text{GeO}_2}$  as a function of  $r/R_c$  in the case where a layer is deposited. The integral of Eq. [9] has been computed and the resulting  $C_{\text{GeO}_2}(r/R_c)$  is plotted in Fig. 5a.

We have confirmed these conclusions experimentally by depositing a layer with the reactor moving in the gas flow direction. Figure 6a shows a SEM picture of the collapsed preform core together with the germanium microprobe analysis signal. The bright base line gives the position of the microprobe trace. The form of the signal agrees qualitatively with the calculated concentration shown in Fig. 5a. Regions of higher germanium concentration appear brighter in the picture because of the greater secondary electron emission of germanium compared to that of silicon.

*Moving the reactor against the gas flow direction.*—If the reactor is moved in the opposite direction to the gas flow, then a dope variation as illustrated in Fig. 4b must result. We have confirmed this by calculation and by experiment. Because of the change in the direction of the reactor movement, Eq. [9] is changed to

$$\frac{r}{R_c} = \left[ \frac{1}{N} \int_{\omega_i}^{\infty} \frac{m_L(\omega, \tau) d\omega}{R_T^2 \pi \rho} \right]^{1/2} \quad [10]$$

The results are given in Fig. 5b and 6b, respectively. In contrast to predictions based on Fig. 5b, a deep dip in the germanium concentration occurs in the

center of Fig. 6b. This is due to the depletion of germanium dioxide by evaporation from the inner surface of the tube during the collapsing process. This effect also occurs in Fig. 6a of course, but coincides with the dip expected from Fig. 5a.

Though the general features are predicted very well by Fig. 5a and 5b, respectively, one fails to get quantitative agreement between Fig. 5 and 6. The reason may be that the experimental conditions are different in different experiments. It turns out that  $S_{m_L}$  and  $G_{m_L}$  depend very strongly on the plasma energy, the furnace temperature, and the total gas flow.

*Deposition of doped multilayer structure.*—The above-described variation of  $\text{GeO}_2$  content and thus of refractive index in radial direction is undesirable if well-defined index profiles are wanted, as in the case of optical fibers with low pulse dispersion. Therefore, we have made preforms in which the core was built up of many layers. After deposition of 46 layers, the variation in the dope concentration still could clearly be detected. Figure 7a shows a double beam interference picture of the corresponding preform. Because the core was made by passes both from right to left and from left to right, the periodicity of Fig. 7a is only 23-fold. In another experiment, about 2000 layers were deposited with linearly increasing  $\text{GeO}_2$  concentration, each layer with a thickness of about 1100 Å. In Fig. 7b these layers can no longer be individually detected because of their thinness. Though in both examples the deposited layers were of nearly equal thickness inside the tube for each pass, this is not true at all for the rod as a consequence of geometrical considerations of the collapsing process.

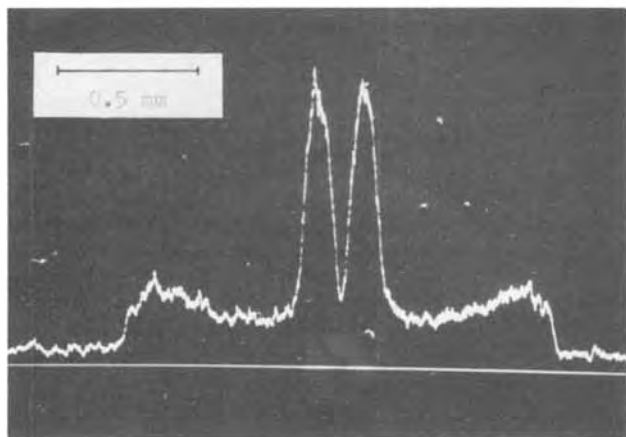
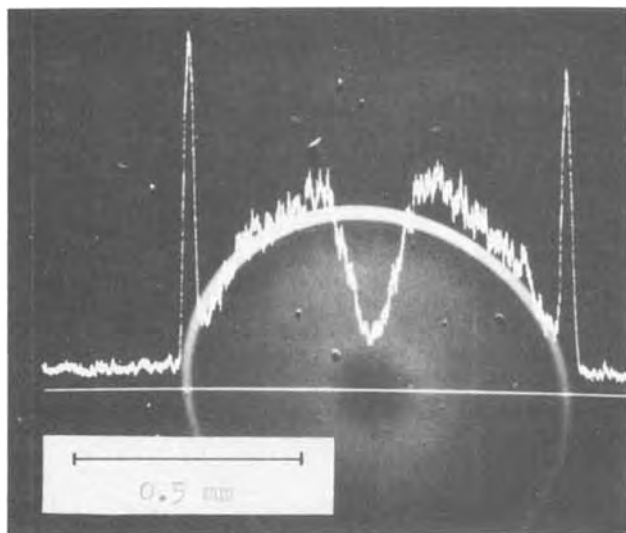


Fig. 6. Microprobe analysis of preform cores. a (top):  $T_f = 800^\circ\text{C}$ ,  $Q_{\text{O}_2} = 50$  sccm,  $Q_{\text{SiCl}_4} = 2.8$  sccm,  $Q_{\text{GeCl}_4} = 0.3$  sccm,  $p = 8$  Torr,  $E = 150\text{W}$ . b (bottom):  $T_f = 1040^\circ\text{C}$ ,  $Q_{\text{O}_2} = 55$  sccm,  $Q_{\text{SiCl}_4} = 2$  sccm,  $Q_{\text{GeCl}_4} = 0.2$  sccm,  $p = 7$  Torr,  $E = 90\text{W}$ .

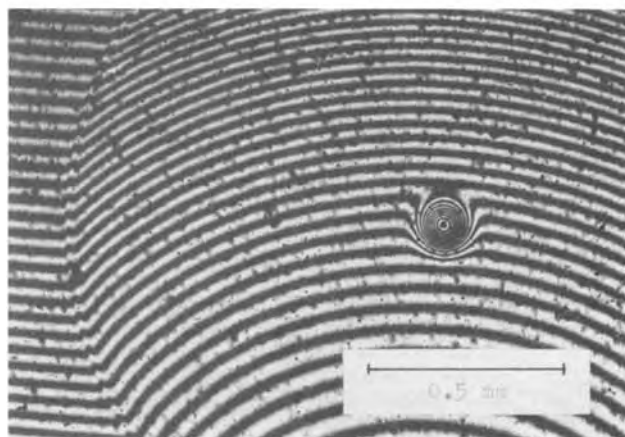
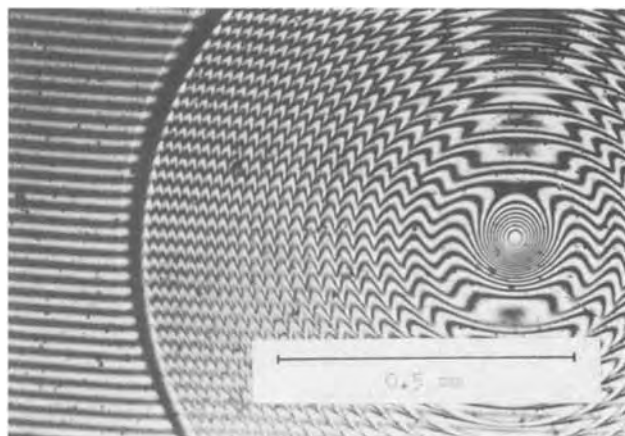


Fig. 7. Interference micrograph of the core of a preform with a (top): 45 successive layers,  $T_f = 900^\circ\text{C}$ ,  $Q_{\text{O}_2} = 50$  sccm,  $Q_{\text{SiCl}_4} = 2.8$  sccm,  $Q_{\text{GeCl}_4} = 0.3$  sccm,  $p = 10$  Torr,  $E = 100\text{W}$ . b (bottom): 2000 successive layers,  $T_f = 1000^\circ\text{C}$ ,  $Q_{\text{O}_2} = 50$  sccm,  $Q_{\text{SiCl}_4} = 2.5$  sccm,  $Q_{\text{GeCl}_4} = 0.3$  sccm,  $p = 15$  Torr,  $E = 100\text{W}$ .

This, in particular, leads to the quadratic index profile of Fig. 7b.

Other arbitrary dope profiles can obviously be obtained by proper variation of the dopant concentration in the reacting gases. Fibers drawn from preforms produced by the process described above give minimum attenuation of 1.4 dB/km at  $1.05\mu$  (6).

### Summary

$\text{SiO}_2$  and  $\text{GeO}_2$  were deposited simultaneously onto the inner wall of a quartz tube reactor with the aid of a nonisothermal plasma. It was found that the deposition profiles of the two oxides do not coincide. This has a marked effect on the radial dope concentration in multilayer structures with a single layer thickness of some micrometers. If the layer thickness gets very small, however, the short range variations are smeared out during collapsing and the radial dope profile is no longer influenced by deposition kinetics but solely by the gas phase composition.

### Acknowledgments

The authors wish to thank Dr. F. Meijer, Philips Research Laboratories, Eindhoven, The Netherlands,

for helpful suggestions and Mrs. B. Krafczyk for the SEM and microprobe pictures.

Manuscript submitted Jan. 16, 1976; revised manuscript received March 22, 1976.

Any discussion of this paper will appear in a Discussion Section to be published in the June 1977 JOURNAL. All discussions for the June 1977 Discussion Section should be submitted by Feb. 1, 1977.

Publication costs of this article were partially assisted by Philips GmbH Forschungslaboratorium.

### REFERENCES

1. P. C. Schultz, *Bull. Am. Ceram. Soc.*, **52**, 383 (1973).
2. J. B. McChesney *et al.*, Proc. of the 10th Int. Glass Congress 6/40-45 (1974).
3. D. N. Payne and W. A. Gambling, *Opt. Commun.*, **13**, 422 (1975).
4. D. Küppers, H. Lydtin, and L. Rehder, Patent submitted.
5. J. Koenings, D. Küppers, H. Lydtin, and H. Wilson, in "Chemical Vapor Deposition, Fifth International Conference," J. M. Blocher, Jr., H. E. Hintermann, and L. H. Hall, Editors, p. 270, The Electrochemical Society Softbound Symposium Series, Princeton (1975).
6. P. Geittner, D. Küppers, and H. Lydtin, *Appl. Phys. Letters*, **28**, 645 (1976).

## The Solid Solubility of Bi in GaP

A. S. Jordan,\* F. A. Trumbore,\* D. L. Nash, and M. Kowalchik

Bell Laboratories, Murray Hill, New Jersey 07974

### ABSTRACT

The solid solubility of Bi (an isoelectronic center) in GaP crystals, grown by a thermal gradient transport technique from Bi-Ga alloys at  $\sim 1050^\circ\text{C}$ , has been determined by emission spectroscopic analysis. These results, together with earlier data on solution-grown platelets, are thermodynamically analyzed by means of liquidus isotherms and activities calculated from a recent theory of regular associated liquid solutions applicable to the Ga-P-Bi system, permitting the evaluation of the equilibrium constant for Bi incorporation according to  $\text{Bi}(1) + \text{Ga}(1) = \text{Bi}_\text{P} + \text{Ga}_\text{Ga}$ . This leads to the calculation of the solid solubility isotherms for Bi in GaP over a wide temperature range. It is shown that in equilibrium Bi is incorporated on phosphorus sites. Furthermore, the GaP-Bi pseudo-binary solidus curve is retrograde and compares favorably with the results of an estimate based on the solubility of Bi in Ge and Si. The solubility of Bi in GaP increases with increasing temperature. Although the measured values at  $\sim 1050^\circ\text{C}$  are low ( $\sim 10^{17}$  atoms  $\text{cm}^{-3}$ ), it is predicted that doping levels as high as  $\sim 10^{19}$  atoms  $\text{cm}^{-3}$  should be possible by a suitable high temperature crystal growth technique.

The technologically important ternary solid solutions obtained by the addition of a third element from Group III or V of the periodic system to binary III-V semiconducting compounds occur as both continuous series and terminal (primary) solid solutions. For example, the red and infrared light-emitting materials  $\text{GaAs}_x\text{P}_{1-x}$  and  $\text{Ga}_x\text{Al}_{1-x}\text{As}$  both form continuous series of solid solutions since the differences in the tetrahedral covalent radii of As and P and of Ga and Al are small (1). In contrast, when either N or Bi substitutes for P in GaP, terminal solid solution behavior is exhibited because of the large size difference between N and P or Bi and P.<sup>1</sup> The properties of the isoelectronic impurity N occupying P-sites have been thoroughly investigated and this center is responsible for efficient room temperature green lu-

minescence in commercially available GaP light-emitting diodes (2). The isoelectronic impurity Bi in GaP also produces a deep trap which is a very efficient emitter of yellow-orange light at low temperatures ( $20^\circ\text{K}$ ) (3). There is recent evidence that the addition of Bi to N-doped GaP leads to yellow instead of green light emission at room temperature (4). However, the doping levels of Bi in GaP achieved in all those studies were only in the low  $10^{17}$  atoms/ $\text{cm}^3$  range whereas, depending on the growth technique, N-doping levels one to two orders of magnitude higher have been attained.

Future crystal growth experiments directed toward exploiting light generation of a desirable wavelength by increasing the contribution of the Bi center require a detailed knowledge of solid-liquid equilibria in the Ga-P-Bi ternary system. Therefore, the major goal of this study is to construct the solid solubility isotherms for Bi in GaP over a wide range of compositions and temperatures. First, we present the solid solubility of Bi in GaP as determined by emission

\* Electrochemical Society Active Member.

Key words: crystal growth, semiconductors, impurity incorporation, phase diagrams, thermodynamics.

<sup>1</sup> The tetrahedral covalent radii of Ga and Al are 1.26Å for both atoms, while the radii of N, P, As, Sb, and Bi are 0.70, 1.10, 1.18, 1.36, and 1.46Å, respectively (1).

spectroscopic analysis on crystals grown from Bi-Ga solutions at  $\sim 1050^\circ\text{C}$  by means of thermal gradient transport (TGT) over a very small temperature difference. Second, these results, together with previously reported Bi solubility data on solution-grown GaP platelets (3), are treated thermodynamically in order to evaluate the temperature dependence of the equilibrium constant for Bi incorporation. The Ga-P-Bi ternary liquidus isotherms and activities needed to perform a self-consistent analysis are obtained from a recent study based on a regular associated solution model (5). Third, it is shown that the calculations are consistent with the expected preference of Bi for P-sites and the findings are discussed in relation to the major modes of substitutional impurity incorporation (equilibrium and surface controlled) in GaP. Finally, in view of the retrograde nature of the GaP-Bi pseudo-binary solidus curve, the results are compared with the similarly retrograde solubility of Bi in the elemental semiconductors Ge and Si.

### Experimental Procedure

Bi-doped GaP crystals were grown by a thermal gradient transport technique (TGT) used previously for solid solubility studies in GaP (6). Excess GaP (Monsanto boat-grown ingot material), together with known amounts of Ga and Bi (both of 99.9999% nominal purity) were sealed under vacuum in a tapered vitreous silica tube. Several such tubes, containing varying amounts of Ga and Bi, were placed in a furnace for 45 days in a thermal gradient of  $\sim 12^\circ\text{C}/\text{cm}$  at  $\sim 1050^\circ\text{C}$ . The resulting Bi-doped GaP crystals were separated from the Ga-Bi solutions by digesting in  $\text{HNO}_3$ .

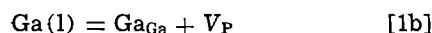
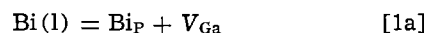
The procedure used to prepare the crystals for emission spectroscopic analysis is described here in some detail to emphasize the care needed to obtain consistent results for doping levels of  $\sim 5 \times 10^{17}$  atoms/cm<sup>3</sup>. The critical requirement is that all occluded bismuth must be eliminated prior to analysis. In fact, in a number of crystals inclusions were visible to the naked eye. The samples were crushed and powdered using a boron carbide mortar and pestle, yielding a brownish powder. After digesting for about 1 min in conc  $\text{HNO}_3$  to which a few drops of conc  $\text{HCl}$  were added, the powder turned a bright yellow or orange color characteristic of GaP. This color change apparently results from solution of the "damaged" GaP, discussed by Rubenstein (7). It should be noted that if the few drops of  $\text{HCl}$  were not added to the  $\text{HNO}_3$  the damaged material was not dissolved and, although  $\text{HNO}_3$  dissolves bismuth, higher and more erratic values of the bismuth concentration were obtained spectroscopically. In addition, it was found that the analytical results were erratic if the  $\text{HNO}_3$ - $\text{HCl}$  solution (containing any dissolved bismuth) was separated simply by washing in deionized water. These erratic results are thought to have been caused by hydrolysis of the soluble bismuth salt to form an insoluble compound. When portions of the same GaP powder sample were treated the same way but were washed with dilute  $\text{HNO}_3$  prior to the final washing with deionized water, the bismuth concentrations obtained were lower and more consistent. In Table I we list the Bi concentrations,  $C_{\text{Bi}}^{\text{s}}$  (atoms/cm<sup>3</sup>), determined in a number of GaP crystals grown by TGT as a function of initial Bi atom fraction in the Ga-Bi alloy.

### Analysis of the Data

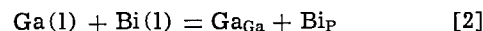
Substitutional isoelectronic impurities such as N or Bi in GaP are considered to be electrically neutral. Therefore, assuming that at the crystal growth temperature equilibrium between the solid and liquid phases prevails, the incorporation of Bi in GaP can be represented by the following defect chemical reactions

Table I. Emission spectroscopic analysis of Bi-doped GaP crystals grown by thermal gradient transport at  $\sim 1050^\circ\text{C}$

Sample number	Atom fraction Bi in Ga-Bi alloy prior to dissolution of GaP	Atom fraction Bi in Ga-P-Bi ternary solution	Atom fraction Ga in ternary solution	Atoms/cm <sup>3</sup> Bi in GaP $\times 10^{17}$
KG99-1	0.05	0.046	0.93	1.1
KG99-3	0.25	0.24	0.75	3.0
KG99-4	0.40	0.39	0.60	2.7
KG99-5	0.60	0.59	0.40	3.4
KG99-8	0.95	0.94	0.053	3.4
KG99-9	1.00	0.96	0.025	1.9



where Eq. [1c] is the reaction of the Schottky pair. The sum of these three reactions yields the over-all incorporation of Bi in GaP according to



At any growth temperature,  $T$ , the equilibrium constant,  $K$ , for reaction [2] can be written as

$$K = \frac{x_{\text{Bi}}^{\text{s}}}{a_{\text{Ga}} a_{\text{Bi}}} \quad [3]$$

where  $a_{\text{Ga}}$  and  $a_{\text{Bi}}$  are the thermodynamic activities of Ga and Bi, respectively, at some composition along the ternary liquidus isotherm of the Ga-P-Bi system, and  $x_{\text{Bi}}^{\text{s}}$  is the corresponding equilibrium Bi concentration in the solid in site fraction units. In Eq. [3], it is assumed that the site fraction of Ga atoms on their own sites is unity and that Henry's law applies for Bi in the dilute solid solutions. Thus, the activity coefficient of Bi in GaP (i.e., Henry's law constant) has been absorbed in  $K$ .

To evaluate  $K$  at  $\sim 1050^\circ\text{C}$  from the solubility data in Table I (listed as  $2.47 \times 10^{22} x_{\text{Bi}}^{\text{s}}$ ), the activities  $a_{\text{Ga}}$  and  $a_{\text{Bi}}$  along the liquidus isotherm, as well as the actual ternary liquid compositions, corresponding to the initial binary Ga-Bi alloy compositions were taken from Ref. (5). In Ref. (5) a new theory of regular associated solutions was formulated to provide a consistent representation of the ternary liquidus surface and the participating binaries in the Ga-P-Bi system. It was assumed that the ternary liquid solution is comprised of Ga, P, and Bi atoms and  $\text{Bi}_2$  dimeric molecules. The activities derived for a ternary system are given by

$$RT \ln a_{\text{Ga}} = RT \ln x_{\text{Ga}} + \alpha_{\text{Ga-Bi}} x_{\text{Bi}}^2 + \alpha_{\text{Ga-P}} x_{\text{P}}^2 + x_{\text{Bi}} x_{\text{P}} (\alpha_{\text{Ga-Bi}} + \alpha_{\text{Ga-P}} - \alpha_{\text{Bi-P}}) + RT \ln \frac{2(x_{\text{s}} + Q_{\text{s}})}{(1 + x_{\text{s}})(1 + Q_{\text{s}})} \quad [4a]$$

$$RT \ln a_{\text{Bi}} = RT \ln x_{\text{Bi}} + \alpha_{\text{Ga-Bi}} x_{\text{Ga}}^2 + \alpha_{\text{Bi-P}} x_{\text{P}}^2 + x_{\text{Ga}} x_{\text{P}} (\alpha_{\text{Ga-Bi}} + \alpha_{\text{Bi-P}} - \alpha_{\text{Ga-P}}) + RT \ln \frac{1 + Q^{\circ}}{1 + Q_{\text{s}}} \quad [4b]$$

$$RT \ln a_{\text{P}} = RT \ln x_{\text{P}} + \alpha_{\text{Ga-P}} x_{\text{Ga}}^2 + \alpha_{\text{Bi-P}} x_{\text{Bi}}^2 + x_{\text{Ga}} x_{\text{Bi}} (\alpha_{\text{Ga-P}} + \alpha_{\text{Bi-P}} - \alpha_{\text{Ga-Bi}}) + RT \ln \frac{2(x_{\text{s}} + Q_{\text{s}})}{(1 + x_{\text{s}})(1 + Q_{\text{s}})} \quad [4c]$$

where

$$x_{\text{s}} = x_{\text{Ga}} + x_{\text{P}}, Q_{\text{s}} = \sqrt{1 + \frac{4}{K_{\text{d}}}(1 - x_{\text{s}}^2)} \quad \text{and} \quad Q^{\circ} = \sqrt{1 + \frac{4}{K_{\text{d}}}}$$

The quantities  $x_{Ga}$ ,  $x_{Bi}$ , and  $x_P$  are the atom fractions of the designated components in the liquid solution. The quantities  $\alpha_{Ga-P}$ ,  $\alpha_{Ga-Bi}$ , and  $\alpha_{Bi-P}$  are ternary interchange energies and  $K_d$  is the equilibrium constant for the dissociation reaction  $[Bi_2(l) = 2Bi(l)]$ . Substituting Eq. [4a] and [4c] into the general thermodynamic equation for the liquidus surface of a binary compound containing a small amount of an impurity yields

$$\begin{aligned} \Delta H_{GaP}^F - T\Delta S_{GaP}^F + RT \ln 4x_{Ga}x_P \\ = \alpha_{Ga-P}[0.5 - x_P(1 - x_{Ga}) - x_{Ga}(1 - x_P)] \\ + \alpha_{Ga-Bi}x_{Bi}(2x_{Ga} - 1) + \alpha_{Bi-P}x_{Bi}(2x_P - 1) \\ - 2RT \ln \frac{2(x_s + Q_s)}{(1 + x_s)(1 + Q_s)} \end{aligned} \quad [5]$$

where  $\Delta H_{GaP}^F$  and  $\Delta S_{GaP}^F$  are the molar enthalpy and entropy of fusion of GaP, respectively. In Ref. (5)  $\alpha_{Ga-Bi}$  and the enthalpy and entropy changes related to  $K_d$ ,  $\Delta H_d$ , and  $\Delta S_d$ , were evaluated from binary activity data for the Ga-Bi system. In addition, the interchange energy,  $\alpha_{Bi-P}$ , was estimated by fitting the pseudo-binary liquidus data to a simplified form of Eq. [5] valid along the pseudo-binary ( $x_{Ga} = x_P$ ). All the relevant parameters required to calculate the activities and liquidus isotherms for the Ga-P-Bi system are summarized in Table II.

Once the liquidus isotherm at 1050°C is known, the determination of the actual ternary liquid composition corresponding to the initial binary (Ga-Bi) alloy composition is quite simple. From stoichiometric relationships and the properties of an equilateral composition triangle, routinely used to represent ternary isothermal data, it can be proven that the final equilibrium concentration attained when an excess of an AC compound (e.g., GaP) is heated in contact with a binary liquid alloy (e.g., Ga-Bi) lies on a straight line connecting the initial binary composition on the A-B axis with the compound composition on the A-C axis. The ternary liquid compositions obtained by intersecting the straight lines with the 1050°C liquidus isotherm are also listed in Table I. It can be seen that the difference between the binary and ternary compositions is quite small since the ternary liquid solution is very dilute in P.

Substituting the ternary compositions into Eq. [4a] and [4c] yields the Ga and Bi activities for the liquid phase which are necessary to calculate  $K$  according to Eq. [3]. Excluding from the analysis the two samples grown from alloys with extremely high Bi concentration ( $x_{Bi} = 0.94$  and  $0.96$ ) because the measured impurity levels may reflect some inadvertently present occluded Bi, the logarithmic least square (8) value of  $K$  at  $\sim 1050^\circ\text{C}$  becomes  $K = 5.51 \pm 0.40 \times 10^{-5}$ . In Fig. 1 the solid solubility of Bi in GaP in equilibrium with solutions along the 1050°C Ga-P-Bi

Table II. Interchange energies\*

Interaction	a (cal)	b (cal °K <sup>-1</sup> )
Ga-Bi	3,350	-3.68
Ga-P	5,080	-5.75
Bi-P	23,300	-11.18

\*  $\alpha = a + bT$ .

Required enthalpies and entropies  
Reaction

$\Delta H_d = 8,180$ cal/mole	} $Bi_2(l) = 2Bi(l)$
$\Delta S_d = 1.06$ cal/mole °K	
$\Delta H_{GaP}^F = 27,600$ cal/mole	} $Ga(l) + Bi(l) = BiP + GaGa$
$\Delta S_{GaP}^F = 15.9$ cal/mole °K	
$\Delta H = 43,100$ cal/mole	}
$\Delta S = 16.9$ cal/mole °K	

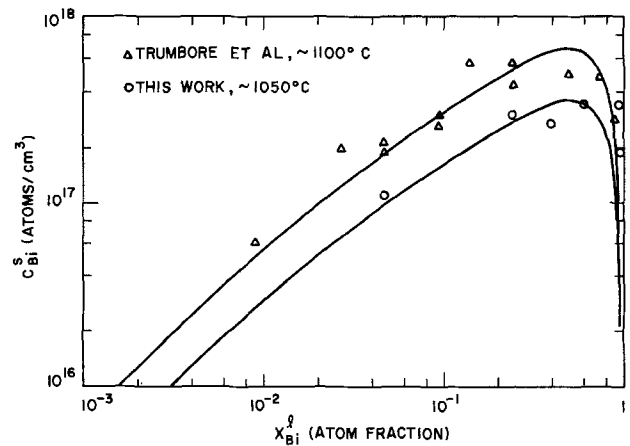


Fig. 1. Solubility data for Bi in GaP as a function of Bi concentrations along the 1050° and 1100°C ternary liquidus isotherms in the Ga-P-Bi system. The lines — were calculated from Eq. [3], [4], and [5] in combination with the parameters listed in Table II.

ternary liquidus isotherm, calculated from Eq. [3], [4], and [5], is superimposed on the experimental data. Apart from the previously mentioned high Bi concentrations, the theoretical and experimental values are in good agreement.

To evaluate the temperature dependence of  $K$ , we must use solubility data obtained at a different crystal growth temperature in the analysis. Previously, Trumbore *et al.* (3) determined the solubility of Bi in GaP platelets by emission spectroscopic analysis. The crystals were prepared by the slow cooling of saturated unseeded solutions of GaP in Ga-Bi alloys (SG) from an initial growth temperature of  $\sim 1160^\circ$  to  $\sim 900^\circ\text{C}$ .<sup>2</sup> The average growth temperature is estimated to be  $\sim 1100^\circ\text{C}$  since the platelets grown by SG are nearly fully developed upon reaching this temperature. The approximate temperature assignment is also supported by the fact that the Zn solubility in GaP crystals grown from solutions with a wide range of Zn additions (a factor of 40) is well represented by the theoretical 1100°C solid solubility isotherm (9).

After deleting the two measurements with erratically high Bi solubility at  $x_{Bi} > 0.9$ , we reproduce the solubility data on SG platelets from Ref. (3) in Fig. 1. Following the procedure discussed with respect to the TGT crystals, the ternary compositions have been located along the 1100°C liquidus isotherm. A combination of the ternary compositions and appropriate values of  $a_{Ga}$  and  $a_{Bi}$  with  $x_{Bi}$  via Eq. [3] leads to a set of discrete  $K$  values which when treated by the logarithmic least square technique yield  $K = 10.70 \pm 0.60 \times 10^{-5}$ . In Fig. 1 we further present the solid solubility of Bi in GaP in equilibrium with ternary solutions along the 1100°C Ga-P-Bi liquidus isotherm, calculated from Eq. [3], [4], and [5] and the constants in Table II. The theoretical curve provides a reasonably good over-all representation of the experimental results.

Having evaluated the equilibrium constant for Bi incorporation in GaP according to Eq. [3] at two temperatures, we can derive the temperature dependence of  $K$  by applying to the data the thermodynamic relation

$$-RT \ln K = \Delta H - T\Delta S \quad [6]$$

where  $\Delta H$  and  $\Delta S$  are the enthalpy and entropy change associated with reaction [2]. From the  $K$  values at 1050° and 1100°C, the two constants are determined to be

$$\Delta H = 48.1 \text{ kcal/mole}, \quad \Delta S = 16.9 \text{ cal/mole}^\circ\text{K}$$

<sup>2</sup> The subtleties involved in Bi analysis, as given in the section on experimental procedure, were not fully appreciated in Ref. (3). Hence, the effect of occluded Bi on the analysis cannot be completely ruled out.

The knowledge of the liquidus isotherms, activities (Eq. [4]), and the temperature dependence of the incorporation equilibrium constant permits the calculation of the solid solubility isotherms of Bi in GaP over a wide range of compositions and temperatures. In Fig. 2 the solid solubility isotherms are shown between 900° and 1400°C in 100°C intervals. The 1100°, 1200°, and 1300°C isotherms are terminated on the P-rich side at compositions where phase separation occurs in the liquid (5) (Bi-doped GaP and two immiscible liquid solutions). In Fig. 3 we present the pseudo-binary liquidus curve together with the published data (10, 11) and the corresponding pseudo-binary solidus curve in temperature *vs.*  $x_{\text{Bi}}$  and temperature *vs.*  $\log x_{\text{Bi}}$  projections, respectively. Note that the calculated pseudo-binary solidus curve exhibits retrograde behavior.

### Discussion

**Modes of incorporation and site preference for Bi in GaP.**—Two major modes of impurity incorporation have been observed in III-V compounds. Rapidly diffusing ionized impurities (*e.g.*, Zn-acceptors in GaP and GaAs) follow defect chemical relations appropriate for bulk equilibrium (6, 8, 12). In contrast, slowly diffusing ionized impurities [*e.g.*, Te-donors in GaAs (15) and Te (13) and O-donors (13, 14) in GaP] exhibit surface-controlled incorporation behav-

ior.<sup>3</sup> Furthermore, it appears that the incorporation of isoelectronic impurities such N or Bi in GaP is also a bulk equilibrium process. For a liquid solution dilute in Bi ( $a_{\text{Ga}} \approx 1$ ), Eq. [3] immediately suggests a linear relation between Bi concentration in the solid and in the liquid as long as this solute obeys Henry's law in both phases. In Fig. 1 and 2,  $C_{\text{Bi}}^{\text{s}}$  is linear in  $x_{\text{Bi}}$  up to  $x_{\text{Bi}} \approx 0.01$ ; above this value departure from linearity is observed because of the deviation of  $a_{\text{Ga}}$  from unity and  $a_{\text{Bi}}$  from Henry's law. The good agreement seen in Fig. 1 between the thermodynamically calculated solid solubility isotherms and the experimental data at  $\sim 1050^\circ$  and  $\sim 1100^\circ\text{C}$  may be taken as evidence that the incorporation of Bi in GaP follows a bulk equilibrium process. It is very likely that the incorporation of N is also an equilibrium process, at least when crystals are grown by liquid-phase epitaxy, on account of the linear variation of N solubility on the partial pressure of  $\text{NH}_3$  up to the pressure corresponding to the formation of GaN (16).

The maximum followed by a downturn exhibited by the experimental data<sup>4</sup> and the calculated solubility curves are consistent with the expectation that Bi occupies P-sites (3). If Bi were incorporated on Ga-sites, then at a fixed  $T$   $C_{\text{Bi}}^{\text{s}}$  would be proportional to the product  $a_{\text{Bi}}a_{\text{P}}$  and not to  $a_{\text{Bi}}a_{\text{Ga}}$ . But both  $a_{\text{Bi}}$  and  $a_{\text{P}}$  increase along the Ga-rich branch of the ternary liquidus isotherm. Hence, unlike the product  $a_{\text{Bi}}a_{\text{Ga}}$  that shows a maximum before the downturn,  $a_{\text{Bi}}a_{\text{P}}$  governing the supposed incorporation on Ga-sites increases continuously along the Ga-rich isotherm followed by a rapid upturn as the P-rich side is reached, which is contradicted by the experimental information. Of course, the calculated maximum would occur even if the liquid solution were ideal, as assumed in Ref. (3). However, the solubility isotherms calculated on the basis of the ideal solution model would be located about a factor of two below the data for low Bi levels, both at 1050° and 1100°C. In contrast, in the same region, the solubility isotherms based on the regular associated liquid solution model agree well with the data. It was pointed out earlier that for ternary solution compositions containing  $x_{\text{Bi}} > 0.90$ , the measured Bi concentrations are above the predicted values. It is reasonable to assume that entrapped Bi is responsible for the large apparent Bi levels. However, this explanation is complicated by the emergence of a ternary miscibility gap near these liquid solution compositions (5).

A key feature of the complete solubility isotherms in Fig. 2 is the increase in Bi-doping levels with increasing  $T$  at a constant Bi concentration in the liquid solution. It appears that at elevated temperatures Bi additions between  $10^{18}$  and  $10^{19}$  atoms/cm<sup>3</sup> in GaP are feasible. Therefore, if it is assumed that when GaP is simultaneously doped with Bi and N (4), the yellow light generation is limited by the relatively small Bi solubility set by the conventional liquid-phase epitaxial and SG techniques, the efficiency might be increased by high temperature growth [*e.g.*, the liquid-encapsulation Czochralski method from nonstoichiometric melts at, say,  $\sim 1400^\circ\text{C}$  (17)].

**Relation between terminal and continuous series solid solutions.**—The solid solubility isotherms for Bi in GaP calculated from the combination of the defect chemical equilibrium constant (Eq. [3] and [6]) and the Ga-P-Bi liquidus isotherms (Eq. [15]) and illustrated in Fig. 2 show terminal solid solution behavior.

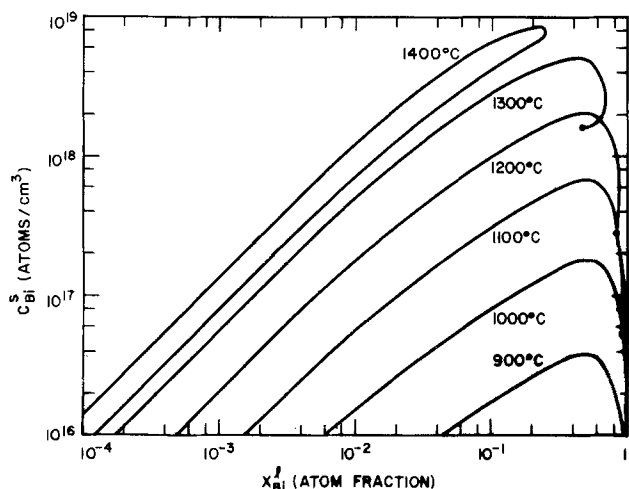


Fig. 2. Calculated solid solubility isotherms for Bi in GaP along the 900°, 1000°, 1100°, 1200°, 1300°, and 1400°C liquidus isotherms in the Ga-P-Bi system. The 1100°, 1200°, and 1300°C isotherms are terminated by solid dots at the liquid compositions where phase separation occurs in the liquid phase.

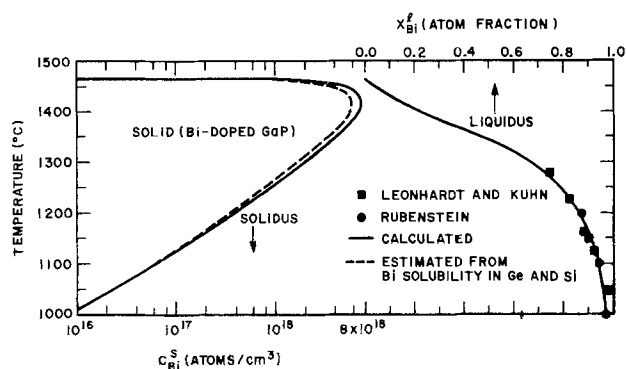


Fig. 3. Solid-liquid equilibria along the pseudo-binary liquidus curve ( $x_{\text{Ga}} = x_{\text{P}}$ ) of the Ga-P-Bi ternary system. The liquidus and solidus curves (solid lines) are based on Eq. [3] and Eq. [4], and [5], respectively, in combination with the parameters listed in Table II. The solidus curve (dashed line) is estimated from the average enthalpy and entropy of Bi incorporation in Si and Ge (see text).

<sup>3</sup> If, at the growth rates employed, equilibrium can be reached between an impurity in the external phase and the bulk of the crystal, we refer to bulk equilibrium incorporation. If, however, equilibrium is established only between the external phase and the semiconductor surface but not between this surface and the bulk, we speak of surface-controlled incorporation.

<sup>4</sup> Even at the highest Bi concentration in the liquid where occlusions of Bi would be expected to give high values of  $C_{\text{Bi}}^{\text{s}}$  the data indicate a maximum in the solid solubility.

It is of course well known that replacing P with As in GaP leads to a continuous series of solid solutions  $\text{GaAs}_u\text{P}_{1-u}$ . For such solid solutions the thermodynamic description of solid-liquid equilibria is well established. Accordingly, at any  $T$  the solid-liquid phase relations are given by the roots of a pair of transcendental "heat of fusion" equations of the form (18, 19)

$$\Delta H_{\text{GaZ}}^{\text{F}} - T\Delta S_{\text{GaZ}}^{\text{F}} = RT \ln \frac{a_{\text{GaZ}}^{\text{Ga}}(0.5)a_{\text{GaZ}}^{\text{Z}}(0.5)}{a_{\text{GaZ}}} + RT \ln a_{\text{GaZ}}^{\text{s}} \quad [7]$$

where  $Z = \text{P}$  and, say,  $\text{As}$ ;  $a_{\text{GaZ}}^{\text{s}}$  is the activity of GaZ in the solid solution, and  $a_{\text{GaZ}}^{\text{Ga}}(0.5)$  and  $a_{\text{GaZ}}^{\text{Z}}(0.5)$  are the Ga and Z activities in the liquid solution at  $T$  and at the compound composition  $x_{\text{Ga}} = x_{\text{Z}} = 0.5$ . A question of importance is whether Eq. [3] and [5] for terminal solid solutions are related in any manner to Eq. [7] for a continuous series of solid solutions.

In the particular case of Bi dissolved in GaP, we have  $a_{\text{GaP}}^{\text{s}} = 1$  (GaP is almost pure) and in the dilute (henrian) limit of the regular solution approximation  $RT \ln a_{\text{GaBi}}^{\text{s}} = RT \ln u + \alpha_{\text{Bi-P}}^{\text{s}}$ . In this relation  $u (\ll 1)$  is the site-fraction of Bi atoms on P-sites and  $\alpha_{\text{Bi-P}}^{\text{s}}$  is the Bi-P interchange energy in the crystal. Under these conditions Eq. [7] reduce to

$$\Delta H_{\text{GaP}}^{\text{F}} - T\Delta S_{\text{GaP}}^{\text{F}} = RT \ln \frac{a_{\text{GaP}}^{\text{Ga}}(0.5)a_{\text{GaP}}^{\text{P}}(0.5)}{a_{\text{GaP}}} \quad [8a]$$

and

$$\Delta H_{\text{GaBi}}^{\text{F}} - T\Delta S_{\text{GaBi}}^{\text{F}} = RT \ln \frac{a_{\text{GaBi}}^{\text{Ga}}(0.5)a_{\text{GaBi}}^{\text{Bi}}(0.5)u}{a_{\text{Ga}}a_{\text{Bi}}} + \alpha_{\text{Bi-P}}^{\text{s}} \quad [8b]$$

where  $\Delta H_{\text{GaBi}}^{\text{F}}$  refers to the hypothetical III-V compound "GaBi." Equation [8a] is identical with the thermodynamic liquidus equation from which the Ga-P-Bi liquidus surface was derived (Eq. [5]). A simple thermodynamic identity<sup>5</sup> transforms Eq. [8b] into

$$-RT \ln \frac{u}{a_{\text{Ga}}a_{\text{Bi}}} = \Delta H_{\text{GaBi}}^{\text{o}} - T\Delta S_{\text{GaBi}}^{\text{o}} + \alpha_{\text{Bi-P}}^{\text{s}} \quad [9]$$

where  $\Delta H_{\text{GaBi}}^{\text{o}}$  and  $\Delta S_{\text{GaBi}}^{\text{o}}$  are the enthalpy and entropy of formation of GaBi from pure liquid components.

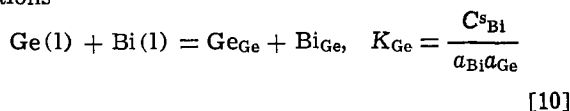
It can be readily observed that Eq. [9] is identical with Eq. [3] and [6] because  $u \equiv x_{\text{Bi}}$  and  $u/a_{\text{Ga}}a_{\text{Bi}} = K$ . Accordingly, the pair of simultaneous equations describing solid-liquid equilibria for a continuous series of solid solutions (Eq [7]) decouple in the limit of  $a_{\text{GaP}}^{\text{s}} \approx 1$  to the thermodynamic equation of the ternary liquidus surface (Eq. [8a]) and an equation providing the solubility of the isoelectronic impurity in the ternary solid solution in equilibrium with the liquid phase (Eq. [9]).

In order to contrast the behavior of Bi and N in GaP we estimate the free-energy of formation of GaBi. Comparing Eq. [9] and [6] and assuming that  $\alpha_{\text{Bi-P}}^{\text{s}}$  is as large as  $\alpha_{\text{Bi-P}}$ , we obtain from the values in Table II +17,400 cal at 1300°K for the free-energy of formation from pure liquid components. Adding the free energy of condensation for 1/2  $\text{Bi}_2(\text{g})$  (21) yields 8600 cal at 1300°K for the free-energy of formation of GaBi from  $\text{Ga}(\text{l}) + 1/2 \text{Bi}_2(\text{g})$ . That this quantity is positive agrees with the fact that no compound exists in the Ga-Bi system.<sup>6</sup> In contrast, the

free-energy of formation of GaN from  $\text{Ga}(\text{l}) + 1/2 \text{N}_2(\text{g})$  is negative below 1100°K (23). Likewise, the enthalpy of formation of GaN is negative, whereas that of GaBi is positive. This difference in the sign of the enthalpies of formation is consistent with the opposite heat effects accompanying N and Bi incorporation in GaP. Accordingly, the distribution coefficient-related ratio  $C_{\text{N}}^{\text{s}}/\sqrt{p_{\text{N}_2}}$  increases with decreasing  $T$ , while the distribution coefficient  $C_{\text{Bi}}^{\text{s}}/x_{\text{Bi}}$  increases with increasing  $T$ .

*Comparison with Bi solubility in Si and Ge.*—As seen in Fig. 3, Bi-doped GaP crystals in equilibrium with liquid solutions along the GaP-Bi pseudo-binary liquidus curve exhibit retrograde behavior. Retrograde solid solubility is a common occurrence for a variety of impurities, including Bi, in the elemental semiconductors Ge and Si (24). In view of the notable similarities between compound and elemental semiconductors in their thermodynamic properties (25), it would be of interest to estimate the GaP-Bi pseudo-binary solidus on the basis of data for Si and Ge.

To meet this objective, we construct the pseudo-equilibrium constants  $K_{\text{Ge}}$  and  $K_{\text{Si}}$ , in analogy with reactions [2] and Eq. [3] for the over-all incorporation reactions<sup>7</sup>



and a similar expression for Si and  $K_{\text{Si}}$ , obtained by replacing the subscript Ge by Si in Eq. [10].

Combining the solubility data of Trumbore (24) and Trumbore *et al.* (26) for the Si-Bi and Ge-Bi systems, respectively, with the activities along the appropriate liquidus curves evaluated from the work of Thurmond and Kowalchik (27),  $K_{\text{Ge}}$  and  $K_{\text{Si}}$  were determined as a function of  $T$ . Treating the temperature dependences as in Eq. [6],  $\Delta H_{\text{Ge}}$ ,  $\Delta S_{\text{Ge}}$ ,  $\Delta H_{\text{Si}}$ , and  $\Delta S_{\text{Si}}$  were obtained for the above over-all incorporation reactions. In line with Thurmond's study on the thermodynamic properties of GaP and GaAs (25), we estimate the enthalpy and entropy changes for the over-all incorporation of Bi in GaP (reaction [2]) by forming the average of these quantities in Ge and Si. Then, we find for Bi in GaP  $\Delta H = 45.8$  kcal/mole,  $\Delta S = 15.1$  cal/mole°K which compare favorably with the values derived from the solubility of Bi in GaP (viz., Table II). In Fig. 3, we show the GaP-Bi pseudo-binary solidus (dashed curve) calculated on the basis of these estimated quantities. It can be seen that the solidus derived from information for the elemental semiconductors closely parallels the actual solidus.

Finally, it is worth mentioning that the GaP-Bi pseudo-binary liquidus curve also possesses some features in common with the Ge-Bi and Si-Bi binary liquidus curves. As seen in Fig. 3, the GaP-Bi pseudo-binary liquidus curve is concave for small values of  $x_{\text{Bi}}$ . Since  $\Delta S_{\text{GaP}}^{\text{F}}$  is not unduly small, the concavity is a consequence of a strong positive deviation from ideality in the liquid solution which may be a symptom of imminent phase separation in the liquid. Like the GaP-Bi pseudo-binary, the Ge-Bi binary liquidus curve is concave, while a miscibility gap has been observed in the Si-Bi system (22, 27). Considering GaP dissolved in the liquid solution along the GaP-Bi pseudo-binary as an equimolar mixture of Ge and Si, one could argue if no other information were available, that the GaP-Bi system approaches demixing. Extending the reasoning, one would expect that by moving from the pseudo-binary toward more P-rich compositions liquid immiscibility must

<sup>5</sup> The identity (20) is

$$\Delta H_{\text{GaBi}}^{\text{F}} - T\Delta S_{\text{GaBi}}^{\text{F}} - RT \ln a_{\text{GaBi}}^{\text{Ga}}(0.5)a_{\text{GaBi}}^{\text{Bi}}(0.5) = -\Delta H_{\text{GaBi}}^{\text{o}} + T\Delta S_{\text{GaBi}}^{\text{o}}$$

<sup>6</sup> InBi is the only known III-V compound involving Bi (22).

<sup>7</sup> The actual equilibrium constant here would be for the reaction  $\text{Bi}(\text{l}) = \text{Bi}_{\text{Ge}}^+ + e^-$ . Since Bi in GaP is neutral, for purposes of comparison, the ionization of Bi in Ge and Si has been ignored.

occur because this corresponds to adding more Si to the solution. In fact, the regular associated solution treatment of the complete Ga-P-Bi liquidus surface leads to a ternary miscibility gap on the P-rich side of the system (5).

### Acknowledgments

The authors are grateful to C. D. Thurmond for helpful discussions and critical comments on the manuscript. Useful suggestions on the paper by R. H. Saul are also appreciated.

Manuscript submitted Sept. 26, 1975; revised manuscript received Jan. 26, 1976.

Any discussion of this paper will appear in a Discussion Section to be published in the June 1977 JOURNAL. All discussions for the June 1977 Discussion Section should be submitted by Feb. 1, 1977.

Publication costs of this article were partially assisted by Bell Laboratories.

### REFERENCES

1. L. Pauling, "The Nature of the Chemical Bond," 3rd ed., Cornell University Press, Ithaca, N.Y. (1960).
2. See, for example, A. A. Bergh and P. J. Dean, *Proc. IEEE*, **60**, 156 (1972); H. Kressel and H. Nelson, in "Physics of Thin Films," Vol. 7, G. Hess, M. H. Francombe, and R. W. Hoffman, Editors, Academic Press, Inc., New York and London (1973).
3. F. A. Trumbore, M. Gershenson, and D. G. Thomas, *Appl. Phys. Letters*, **9**, 4 (1966).
4. C. H. Henry and C. D. Thurmond, Unpublished work.
5. A. S. Jordan, *Met. Trans.*, **7B**, 191 (1976).
6. F. A. Trumbore, H. G. White, M. Kowalchik, R. A. Logan, and C. L. Luke, *This Journal*, **112**, 782 (1965).
7. M. Rubenstein, *ibid.*, **112**, 426 (1965).
8. A. S. Jordan, *ibid.*, **118**, 781 (1971).
9. A. S. Jordan, L. Derick, R. Caruso, and M. Kowalchik, *ibid.*, **119**, 1585 (1972).
10. M. Rubenstein, Abstract 65, p. 129, The Electrochemical Society Extended Abstracts of the Electronics Division, Spring Meeting, Los Angeles, California, May 6-10, 1962.
11. A. Leonhardt and G. Kuhn, *Kristall Technik*, **9**, 77 (1974).
12. M. B. Panish and H. C. Casey, Jr., *J. Phys. Chem. Solids*, **28**, 1673 (1967).
13. A. S. Jordan, F. A. Trumbore, K. B. Wolfstirn, M. Kowalchik, and D. D. Roccasecca, *This Journal*, **120**, 791 (1973).
14. R. C. Peters and A. T. Vink, "Proceedings of the Fifth International Symposium on GaAs and Related Compounds, Deauville (1974)," Institute of Physics, London (1975).
15. H. C. Casey, Jr., M. B. Panish, and K. B. Wolfstirn, *J. Phys. Chem. Solids*, **32**, 571 (1971).
16. D. D. Manchon, Jr., B. J. Gross, and B. A. Reese, Abstract 141, p. 344, The Electrochemical Society Extended Abstracts, Spring Meeting, San Francisco, California, May 12-17, 1974.
17. A. R. Von Neida, L. J. Oster, and J. W. Nielsen, *J. Cryst. Growth*, **13/14**, 647 (1972).
18. A. S. Jordan, *Met. Trans.*, **2**, 1959 (1970).
19. M. B. Panish and M. Ilegems, in "Progress in Solid State Chemistry," H. Reiss and J. O. McCaldin, Editors, Pergamon Press, Elmsford, N.Y. (1972).
20. A. S. Jordan and M. Ilegems, *J. Phys. Chem. Solids*, **36**, 329 (1975).
21. D. R. Stull and G. C. Sinke, "Thermodynamic Properties of the Elements," Advances in Chemistry Series, No. 18, American Chemical Society, Washington, D.C. (1956).
22. M. Hansen, "Constitution of the Binary Alloys," McGraw-Hill Book Co., New York (1958), and supplementary volumes edited by R. P. Elliott (1965) and F. A. Shunk (1969).
23. C. D. Thurmond and R. A. Logan, *This Journal*, **119**, 622 (1972).
24. F. A. Trumbore, *Bell System Tech. J.*, **39**, 205 (1960).
25. C. D. Thurmond, *J. Phys. Chem. Solids*, **26**, 785 (1965).
26. F. A. Trumbore, W. G. Spitzer, R. A. Logan, and C. L. Luke, *This Journal*, **109**, 734 (1962).
27. C. D. Thurmond and M. Kowalchik, *Bell System Tech. J.*, **39**, 169 (1960).



# The Anodization of GaAs and GaP in Aqueous Solutions

B. Schwartz,\* F. Ermanis, and M. H. Brastad

Bell Laboratories, Murray Hill, New Jersey 07974

## ABSTRACT

The anodic oxidation of GaAs and GaP in properly conductivity- and/or pH-adjusted water has been successfully demonstrated under both constant voltage and constant current conditions. With  $\text{H}_3\text{PO}_4$  as the acidic conductivity/pH modifier, uniform, well-controlled oxides have been grown in the pH range 2.5-3.5. The oxide thickness-voltage relationships for both GaAs and GaP are linear, with slopes of approximately 20 and 12 Å/V, respectively. At room temperature, oxides as thick as 3600 and 2000 Å can reproducibly be grown on GaAs and GaP, respectively; at 100°C, an oxide as thick as 5000 Å has been grown on GaAs. Under basic conditions, with  $\text{NH}_4\text{OH}$  as the conductivity/pH modifier, oxides have been grown in the pH range of 10-11, but dissolution of the oxide in the bath results in much poorer control than in the acidic system; this dissolution effect can be utilized more in the line of electroetching than in simple oxide formation. Anodic oxidation, with relatively little oxide dissolution, has also been accomplished in near neutral-pH water (*i.e.*, ~7) with  $(\text{NH}_4)_2\text{HPO}_4$  as the conductivity/pH modifier. Restricted-area oxidation and/or etching has been demonstrated whereby a pre-fabricated photoresist pattern is used to define restricted areas for anodization; lines as narrow as 5 μ wide are readily delineated. Anodization in aqueous solutions containing either  $\text{Cl}^-$  or  $\text{NO}_3^-$  ions is shown to result in simple electroetching, and current densities in the range 10-20 mA/cm<sup>2</sup> are demonstrated to be most effective for controlled electroetching. The grown oxides are soluble, in HCl,  $\text{HNO}_3$ , and  $\text{H}_2\text{SO}_4$ , and are affected by prolonged contact with water. If properly baked, however, the oxide grown on GaAs shows no evidence of change in months of storage in laboratory air; the oxide grown on GaP does show evidence of moisture absorption after 1 month of equivalent storage. A preliminary analysis of some of the controlling electrical factors during anodization shows that under constant voltage conditions, the current (*I*) varies as

$$I = \sqrt{\frac{A}{Bt + C}}$$

and under constant current conditions, the time derivative of the voltage is a constant.

The growth of native oxides on GaAs and GaP by galvanic and anodic techniques (1-4) using 30% aqueous solutions of  $\text{H}_2\text{O}_2$  as the electrolyte has been shown to be a useful new technology for passivation of semiconductor device surfaces (5, 6), as a diffusion mask (7), and for selective area etching (2). The use of a buffered aqueous solution for the growth of an anodic oxide on GaP has recently been described (8). This paper describes the successful results of growing anodic oxides on GaAs and GaP using water as the electrolyte, under the proper conductivity and/or pH conditions. For both materials, the oxide thicknesses are approximately linear with applied voltage, but the complication of rapid film dissolution at the oxide-electrolyte interface can be an appreciable correction factor to be considered. In fact, it is shown that the entire range, from anodic oxidation with minimal oxide etching to total anodic etching with minimal residual surface oxide, can be controllably achieved by proper choice of anion, pH, and conductivity control.

The choice of anion in the pH/conductivity modifier can be a very important factor, and conditions where simple anodic etching is achieved are described.

Finally, the feasibility of combining photoresist technology and oxidation in water to make restricted area oxide patterns directly on the surface of the semiconductor are shown; under the proper solution conditions, electrolytic etching through these photoresist masks can also be accomplished readily.

\* Electrochemical Society Active Member.

Key words: native oxides, compound semiconductors, anodic oxidation.

## Experimental Procedure

The electrolytic cell used for this study was almost identical to that previously described (1), except that either a constant voltage or a constant current supply could be used as the power source. Because the reagent was water instead of  $\text{H}_2\text{O}_2$ , the lack of reaction between the platinum cathode and the electrolyte eliminated the need for a baffle in the system, and a simple quartz beaker was, therefore, used as the bath container. The semiconductor samples were either partly or fully immersed in the bath while held in an aluminum clamp since the aluminum also anodized in water (3). The water used in these studies was 15 megohm-cm at the resin bed and 6 megohm-cm at the point of use; the pH of the starting water was approximately 6.5. When anodization was attempted in this water directly, it was found that the conductivity was so low that almost the entire voltage drop occurred across the solution (2) and very little appeared at the semiconductor-electrolyte interface, so that no oxide growth was achieved. The pH of the water was adjusted downward with  $\text{H}_3\text{PO}_4$  or upward with  $\text{NH}_4\text{OH}$ ; in one series of anodizations, the pH was made nearly neutral (*i.e.*, 7.8) with  $(\text{NH}_4)_2\text{HPO}_4$  as the conductivity modifier.

The GaAs slices were all n-type, (100)-oriented, Si- or Te-doped at about  $1 \times 10^{18}/\text{cm}^3$ . Most of the GaP used was n-type, (111)-oriented, Se-doped with  $|\text{N}_D - \text{N}_A|$  between 0.1 and  $1 \times 10^{18}$ . A few experiments were performed on p-type, Zn-doped GaP with  $|\text{N}_A - \text{N}_D| = 0.5$  to  $5 \times 10^{18}$ . All samples were chem-



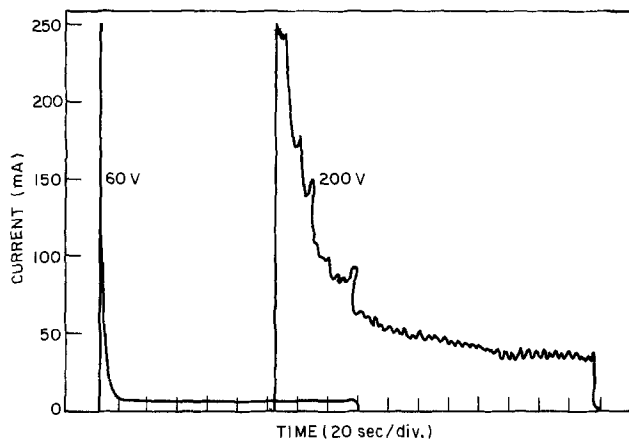


Fig. 1. Current vs. time during anodization of n-type GaAs at constant voltage of 60 and 200V in acidic ( $\text{pH} = 2.5$ ) water.

mechanically polished directly from the saw-cut condition in a 0.075% bromine-in-methanol solution, on a PAN-W polishing cloth. Following this step, the slices were given at least 12 cycles of acetone wash in a Soxhlet extractor, then air dried and stored until used.

After anodization, the samples were either water-rinsed and air-dried, or water-rinsed and bake-dried in a nitrogen-purged oven for 1 hr at  $95^\circ\text{C}$  and 2 hr at  $250^\circ\text{C}$ ; then the thickness and index of refraction were determined on a Rudolph ellipsometer<sup>1</sup> at  $6328\text{\AA}$  radiation.

### Experimental Results

**Anodic oxidation in acidic [ $\text{H}_3\text{PO}_4$ ] water: GaAs.**—A monitoring of the current as a function of time, for constant voltage anodizations and with the room temperature water adjusted to a pH of 2.5, yielded the data presented in Fig. 1. At voltages up to and including 170V, all of the results appeared similar to the 60V curve; the entire surface area of the grown film was uniform in color and specular. However, at biases in the range 180–200V, the data shown as the 200V  $I-t$  curve resulted. The films were still uniform in color, but were slightly hazy in appearance; above 200V, the samples took on a nonuniform mottled look (1).

A monitoring of the voltage as a function of time, for constant current anodization, with the room temperature water adjusted to a pH of 2.5, yielded the data shown in Fig. 2.<sup>2</sup> The conclusions to be drawn from these data are: (i) the apparent critical current density necessary to start the oxide growth, and (ii) the apparent linear relationship between voltage and time, which is to be compared with the very nonlinear current-time curve determined for constant voltage anodization (see Fig. 1). In the case of constant voltage, if the anodization is allowed to proceed long enough for the asymptotic current level to be approached, or in the case of constant current a predetermined voltage level is reached,<sup>3</sup> a plot of the resulting oxide thickness against applied voltage yields a straight line, as shown in Fig. 3. Note that this curve extrapolates back through the origin and has a slope of about 20  $\text{\AA}/\text{V}$ .

In order that the influence of temperature on the thickness-voltage curve might be determined, a series of samples were anodized in water at  $100^\circ\text{C}$  (i.e., the water was adjusted to a pH of 2.5 at room temperature and then brought to its boiling point). The data obtained are shown in Fig. 4; note that the lower por-

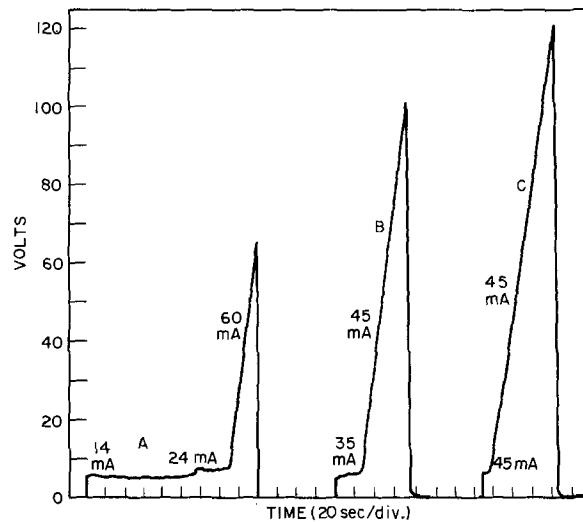


Fig. 2. Voltage vs. time during anodization of n-type GaAs in the constant current mode in acidic ( $\text{pH} = 2.5$ ) water.

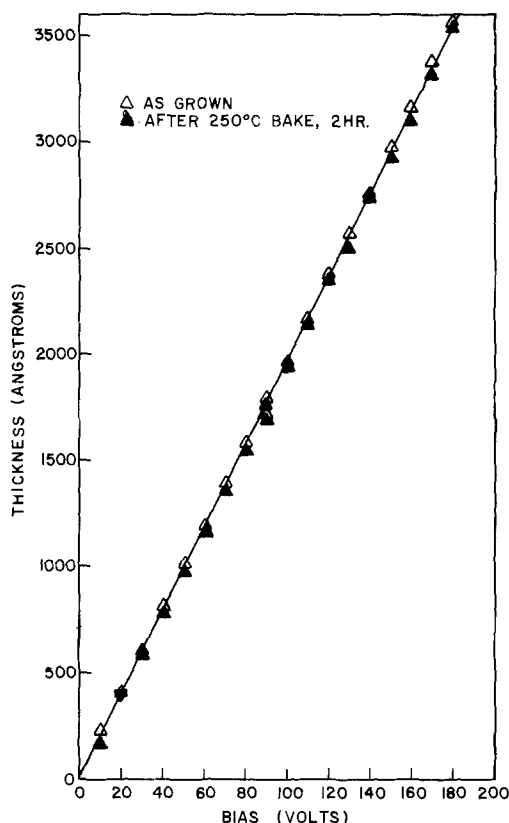


Fig. 3. Oxide thickness vs. bias voltage for n-type GaAs anodized at constant voltage in acidic ( $\text{pH} = 2.6$ ) water.

tion of this curve is linear with a slope of approximately 25  $\text{\AA}/\text{V}$ , but that as the voltage increases the thickness dependence rises superlinearly, approaching almost 50  $\text{\AA}/\text{V}$  at the upper end before the "limiting" voltage is reached. This higher order dependence is similar to that observed in the anodization of GaAs in boiling  $\text{H}_2\text{O}_2$  (3).

The effect of varying the pH on the growth of an oxide at a fixed bias (i.e., 45V) is shown in Fig. 5; note the falloff in growth rate below a pH of 2.5 and above a pH of 3.5.

As was observed in the anodization of GaAs in  $\text{H}_2\text{O}_2$  (3), a bake in dry nitrogen at about  $250^\circ\text{C}$  has been found suitable for stabilizing the grown oxide. Thickness changes of less than 10% and refractive index shifts (i.e., from  $n = 1.80$ ) of less than  $\pm 0.01$  have been observed during this drying procedure. The stabilized oxide has been found to be soluble in

<sup>1</sup> A few measurements were also made on a Gaertner ellipsometer with 5461 $\text{\AA}$  light.

<sup>2</sup> Although the area of the exposed surfaces was held relatively constant at about  $1\text{ cm}^2$ , there was enough unmeasured variation to indicate that the currents listed do not necessarily reflect the absolute current densities.

<sup>3</sup> Assuming the time to be long enough for the achievement of a steady-state condition, and the voltage to be near neither the breakdown limit of the oxide nor the saturation limit of the power supply.

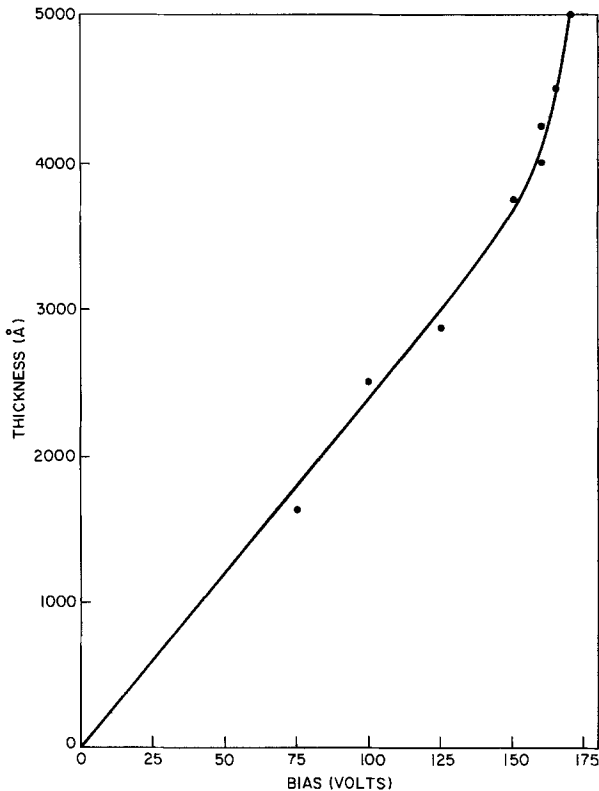


Fig. 4. Oxide thickness vs. bias voltage for n-type GaAs anodized at constant voltage in acidic ( $\text{pH} = 2.6$ ) water at  $100^\circ\text{C}$ .

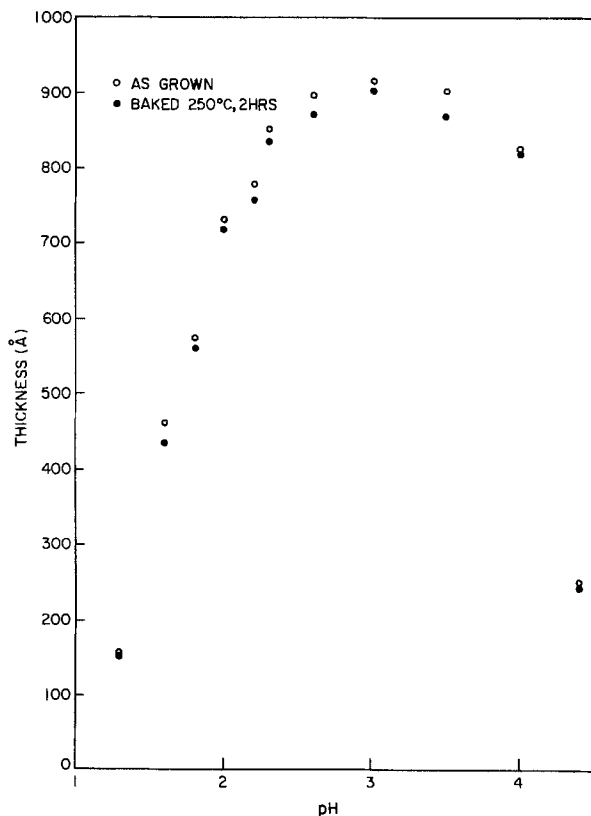


Fig. 5. Variation of oxide thickness as a function of  $\text{pH}$  for n-type GaAs anodized at constant 45V.

aqueous solutions of  $\text{NH}_4\text{OH}$  and  $\text{HCl}$ , both in the concentrated forms (15 and 12M, respectively) and diluted 10 parts water to 1 part concentrated base or acid. Again, as was found with the anodic oxide grown in  $\text{H}_2\text{O}_2$ , the oxide grown in water was insoluble in  $\text{Br}_2\text{-CH}_3\text{OH}$  whether it was baked or not. Exposed to room air, the baked oxides showed no ob-

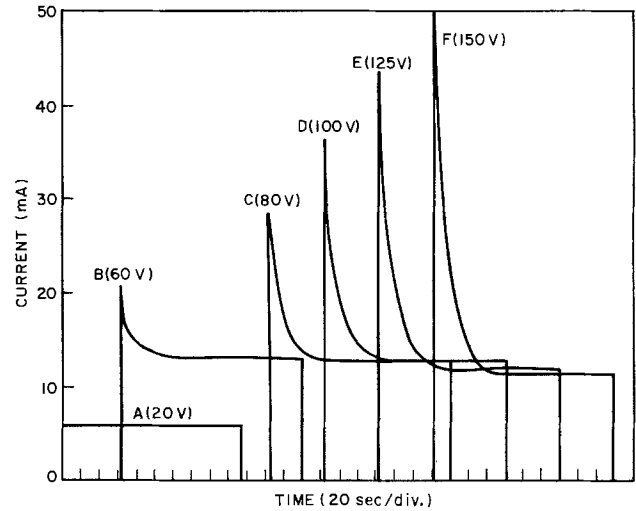


Fig. 6. Current vs. anodization time for n-type GaAs in basic water ( $\text{pH} = 10$ ) at constant voltage.

servable changes over a period of 10 months. In direct contact with deionized water, however, both the as-grown and the baked oxides developed localized pin-hole-type defects and nonuniform thickness changes.

Optically levered laser-beam measurements (9) on 10 mil thick GaAs slices anodized in acidic water indicated that there is no measurable stress<sup>4</sup> induced in the samples after anodization, after baking at  $250^\circ\text{C}$ , or after annealing at  $650^\circ\text{C}$  in dry nitrogen for  $\frac{1}{2}$  hr.

*Anodic oxidation in basic  $[\text{NH}_4\text{OH}]$  water: GaAs.*—Figure 6 shows the results of attempting anodization of GaAs, in room temperature water adjusted to a  $\text{pH}$  of 10, under various constant voltage conditions. The most obvious result is that at 20V no oxide of any appreciable thickness grew and only etching was achieved. Secondly, even where oxide growth was evident (i.e., by current falloff with time), the ultimate leakage current was relatively high (i.e., 2 to 3 times as high as in the acidic case shown in Fig. 1), again indicating rapid dissolution of the oxide under steady-state conditions. Further evidence for this rapid dissolution of the native oxide in basic water is shown in Fig. 7. In this case, an initial bias of 120V was applied to the sample for 40 sec, after which time the voltage was dropped to only 20V; this lower bias was then maintained for approximately 60 sec. The sequence was then repeated twice before the power supply was turned off. On examination of any complete cycle in Fig. 7, it becomes quite obvious that during the second part of the cycle, where the bias on the sample was maintained at the lower voltage (i.e., 20V), the resistance of the cell was changing with time. This resistance change was the result of a thinning of the oxide layer by dissolution, until the very thin, steady-state oxide thickness for the 20V was achieved.

Anodization under constant current conditions in water at a  $\text{pH}$  of about 10 also yielded data indicative of excessive etching of the oxide (see Fig. 8). In addition, whereas constant current anodization in acidic water yielded a linear dependence of the voltage on time, there is evidence that deviation from linearity occurred in a number of cases for the basic system.

The nonreproducibility of oxide thickness for basic-water oxidation was also illustrated when a plot of thickness vs. voltage was attempted; the scatter of the points was so large as to make this kind of plot essentially meaningless, thus indicating the poor control for growing oxides in high  $\text{pH}$  solutions. However, the potential for use of this  $\text{pH}$  range as an electrolytic etching region becomes attractive.

*Anodic oxidation in acidic  $[\text{H}_3\text{PO}_4]$  water: GaP.*—When GaP was anodized in room temperature water

<sup>4</sup> Minimum measurable stress level in GaAs is  $1\text{-}2 \times 10^9$  dynes/cm (2).

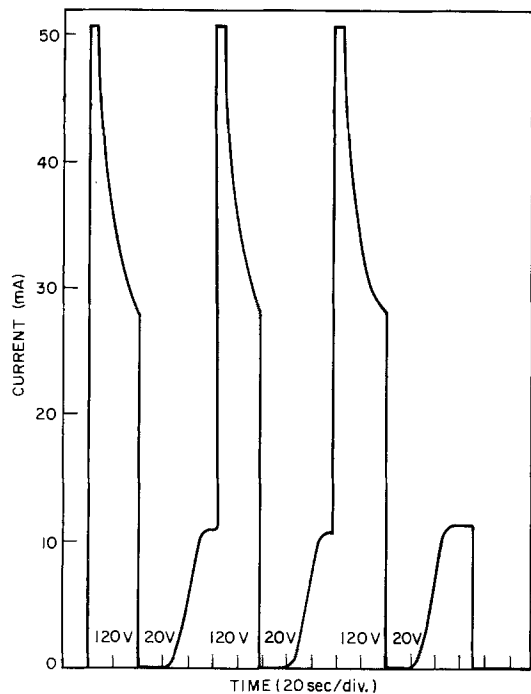


Fig. 7. Behavior of anodization current as a function of time during anodization of n-type GaAs in basic ( $\text{pH} = 11$ ) water at cycled biases of 120V and 20V. The current maximum of 52 mA was due to a current limiter on the powder supply used.

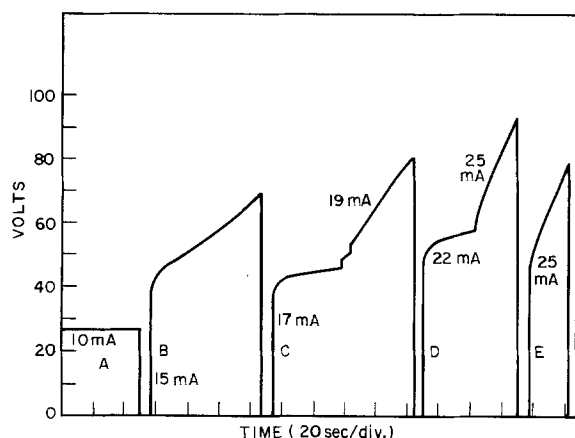


Fig. 8. Voltage vs. time during anodization of n-type GaAs in the constant current mode in basic ( $\text{pH} = 10$ ) water.

adjusted to a  $\text{pH}$  of 2.8, at either constant voltage or constant current, curves similar to those shown in Fig. 1 and 2 were obtained. Figure 9 is a plot of thickness vs. voltage for both p- and n-type GaP anodized at constant voltage. The plot also shows the negligible effect of drying on the film thickness. The slopes of the straight lines through both sets of data are approximately  $12 \text{ \AA/V}$ . The one for n-type GaP, however, is shifted toward higher voltages, thus showing that n-type material anodized at identical voltages grows an oxide approximately  $100 \text{ \AA}$  thinner than p-type material. This voltage shift is believed to be due to the different (*i.e.*, lower) doping level of the n-type samples (10). In any case, the ultimate oxide thickness achievable in the anodization of GaP is lower than that for GaAs which can be anodized under similar conditions at about  $20 \text{ \AA/V}$ .

Another effect that is delineated in the data of Fig. 9 is the nonlinearity of the apparent film thickness in both the low and the high voltage ranges. A probable reason for the scatter in the low voltage range is the relatively large uncertainty in the assignment of thickness values from the ellipsometrically measured parameters,  $\Delta$  and  $\Psi$ , in this, the thin film re-

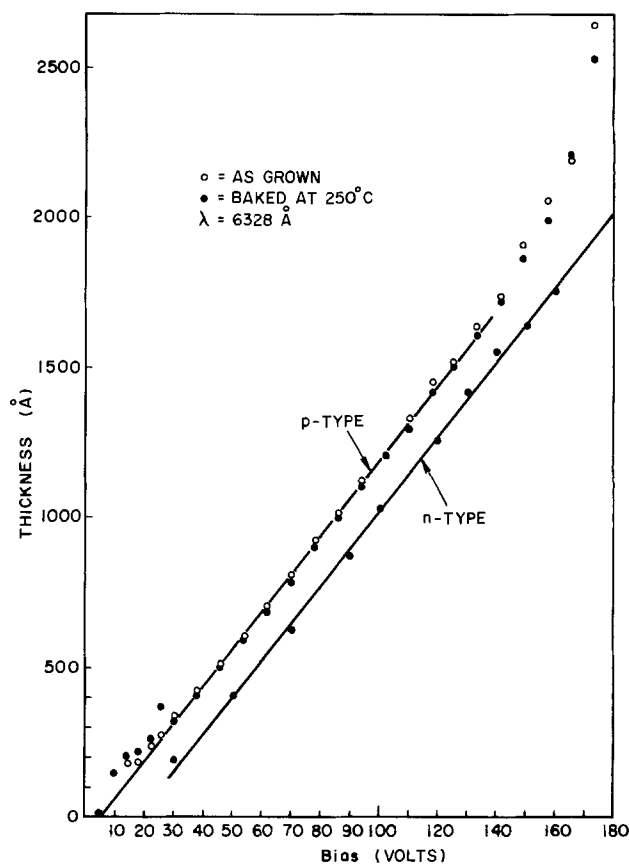


Fig. 9. Ellipsometrically determined oxide thickness vs. applied voltage for p- and n-type GaP anodized in acidic ( $\text{pH} = 2.7$ ) water. The wavelength of the measuring light source was  $6328 \text{ \AA}$ .

gion (11). It is believed that in the thick oxide region of the curve, the deviation from linearity is only an artifact of the measurement; evaluation of the film thickness on a rotating-analyzer ellipsometer (12) yields data to indicate that the thickness extrapolates linearly to about 200V. The fact that the refractive index appears to vary as a function of the oxide-forming voltage (see Fig. 10), and that the variation seems to be measurement wavelength dependent are thought to be due to an anomalous reflectivity effect at the oxide-semiconductor interface (4). An attempt is under way at this time to achieve an understanding of this anomaly.

When the effect of  $\text{pH}$  on the growth of the GaP-oxides in acidic media was examined, the data shown in Fig. 11 were obtained. Again, a falloff in oxide thickness was observed below a  $\text{pH}$  of about 2 and above about 3.5. As noted in Fig. 9, baking the oxidized samples at  $250^\circ\text{C}$  for 2 hr in a nitrogen-purged oven had very little effect on the oxide thickness. However, anodization at a  $\text{pH}$  less than 2 yielded some very startling results in the aging characteristics of the formed oxide. Whereas an oxide grown on GaP at  $\text{pH} = 2.7$  and not stabilized can sit in a flat-pack on the shelf for about 2 weeks with no apparent change in thickness or refractive index, a film grown at a  $\text{pH}$  of 1.9 or less will show drastic color changes when allowed to sit unstabilized for less than 1 day under identical conditions. The instability of the oxide becomes evident on the baked samples as well after storage of about 1 month, when localized color changes can be observed. The new color spots are those of oxides thicker than those originally grown, thus indicating a swelling of the oxide, possibly due to absorption of moisture from the atmosphere. This relative instability is to be compared to the case of a galvanic oxide grown on GaP which was bake-dried and showed no change in thickness or refractive index after storage in room air for 2.5 years.

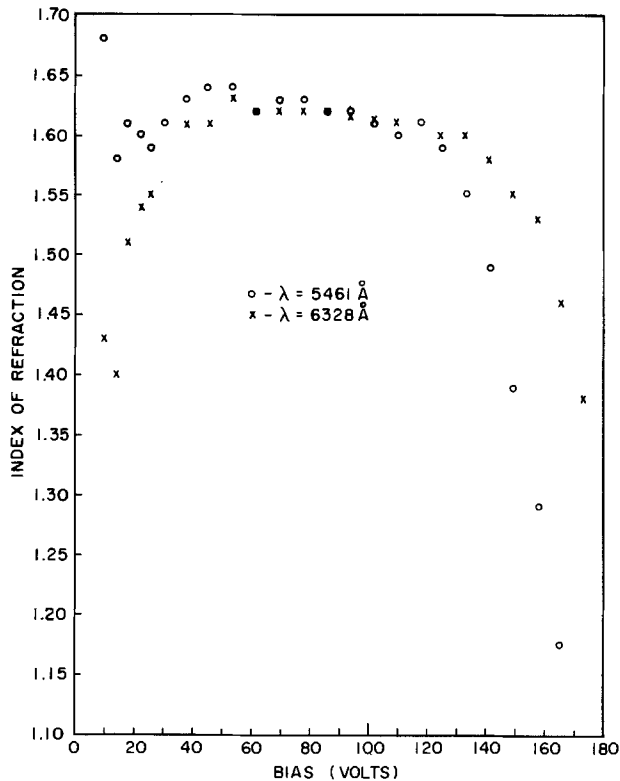


Fig. 10. Index of refraction of GaP-oxide films as a function of anodization voltage, in acidic ( $\text{pH} = 2.8$ ) water determined ellipsometrically on the same sample with 2 different wavelengths of light:  $5401\text{\AA}$  (○) and  $6328\text{\AA}$  (×).

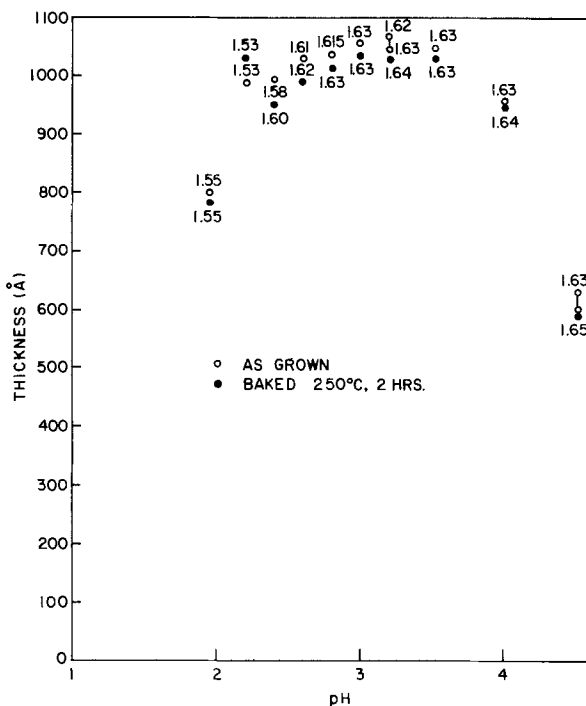


Fig. 11. Thickness of GaP-oxide films grown at a constant bias of 100V, as a function of the pH of the acidified water electrolyte. The figures near the symbols denote the index of refraction before (○) and after (●) a 2 hr,  $250^\circ\text{C}$  bake.

In order that the effects of water on anodized and baked GaP might be observed, 2 samples with oxides 750 and  $2000\text{\AA}$  thick were immersed in deionized water for a period of 4 weeks. After an initial loss of about  $20\text{\AA}$  during the first 2 or 3 days, the sample remained covered with an oxide which showed a tendency toward increasing thickness. Owing to its nonuniform

appearance, however, no exact thickness measurements were obtainable.

**Anodic oxidation in basic  $[\text{NH}_4\text{OH}]$  water: GaP.**—As was found with GaAs, anodization of GaP in water at pH of 10-11 can yield relatively thick surface oxides as an end product. However, again as with GaAs, the high solubility of the oxide in the high pH electrolyte causes large errors when attempts are made to reproduce an oxide thickness-voltage plot (i.e., very short delays in removing the sample from the solution and rinsing it can introduce large errors due to the severe etching of the formed oxide). It is therefore recommended that this pH range be considered more for its electroetching potential than for its oxide growth capability.

**Anodic oxidation in near neutral  $[(\text{NH}_4)_2\text{HPO}_4]$  water: GaAs.**—Because deionized water (i.e., 16 megohm-cm) has extremely low conductivity, it is very difficult to achieve an anodization of GaAs or GaP at moderate voltages. It was therefore decided to attempt to modify the conductivity of the deionized water without going very far in either the acidic or the basic direction. This is easily accomplished by the use of the ammonium acid phosphate salts, and we chose to examine  $(\text{NH}_4)_2\text{HPO}_4$  as the additive; a  $0.1N$  aqueous solution of this reagent will automatically adjust to a pH of 7.8. When a constant voltage anodization at 100V was attempted, the classic rapid current falloff was observed and a gold-colored oxide (i.e.,  $2000\text{\AA}$ ) was found on the sample. Adjusting the pH of the solution to 7.15 by the addition of  $\text{H}_3\text{PO}_4$  also yielded good oxidation. It appeared that some slight etching of the oxide occurred in the original pH 7.8 solution, and less in the 7.15 pH solution. A further discussion of the potential of this system appears in the next section which deals with masked anodization.

**Restricted-area anodic oxidation: GaAs and GaP.**—All anodizations described thus far were performed by immersing the samples in the electrolyte and anodizing the entire exposed surface area. Subsequent to anodization photolithographic processing has been utilized to define specifically required oxidized and nonoxidized regions of the surface for further device fabrication needs (13). Thus certain implied restrictions were placed on the condition of the sample to allow for this processing approach (e.g., no nonoxidizable ohmic contacts were to be exposed). In addition, it had been noted (13) that in the development of the photoresist (i.e., AZ-111) the developing solution was caustic enough that both the exposed photoresist and the underlying grown oxide were removed simultaneously. Although this single develop-etch process simplifies the operation of oxide pattern generation, it provides for a less controlled geometry in that undercutting of the oxide is a severe problem when one attempts to achieve fine line definition. When a negative resist was used with a nonalkaline developer, the single develop-etch step was eliminated. However, it was difficult to control the amount of oxide undercutting during the oxide etch step.

As an alternative to using oxidation first and then photolithography, an experiment in reversing the order (i.e., first photolithography and then anodization) was attempted. When this was performed in the  $30\% \text{H}_2\text{O}_2$  electrolytic system, it was found that the photoresist could survive only for seconds because of the strong oxidizing action of the  $\text{H}_2\text{O}_2$  on the organic polymer. However, when the same experiment was tried on some n-type GaAs in acidic water ( $\text{pH} = 2.05$ , 55V bias, 60 sec anodization time) with the Ealing test pattern as the geometry system, localized oxidation was observed. The sample was then placed in an acetone-containing Soxhlet extractor (after being blot-dried but not baked) and the photoresist was stripped from the sample. Subsequent baking in a nitrogen-purged oven at  $95^\circ\text{C}$  for 1 hr and then at  $250^\circ\text{C}$  for 2 hr yielded the sample shown in Fig. 12 (i.e., the dark



Fig. 12. A GaAs sample with deposited Ealing test pattern after anodization at 55V in water of pH = 2.5 and after removal of the photoresist. The oxidized areas are dark; original magnification was approximately 30X.

regions are the oxidized areas). On careful examination of the generated oxide pattern, it was determined that oxide stripes  $5\mu$  wide were well delineated on the surface of the GaAs.

When a similar experiment was attempted in basic water (i.e., pH = 10,  $\text{NH}_4\text{OH}$ ), similar oxidation results were obtained. However, when the sample was allowed to sit in the electrolyte after the voltage was turned off, the oxide redissolved. A restricted-area etching experiment was then performed whereby a photoresisted sample was anodized in basic water under conditions similar to those shown in Fig. 7; 120V for 40 sec and then 20V for 60 sec for a total of 3 complete cycles. Subsequent Talystep scanning of the sample surface (after removal of the AZ-111 with acetone) showed that the 3 cycles of oxidation and dissolution produced steps about  $6000\text{\AA}$  deep. The delineation of the Ealing pattern was only fair, however, because the AZ-111 had obviously been attacked by the alkaline water.

In either case (i.e., acidic or basic water), after a few minutes exposure of the photoresist to the electrolytic solution, deterioration of the resist was observed. However, when a similar experiment was performed in water with  $(\text{NH}_4)_2\text{HPO}_4$  as the conductivity modifier, oxidation was observed; and negligible attack occurred on the photoresist even after 10 min exposure.

**Anodic etching: GaAs and GaP.**—Up to this point, the discussion has centered about the anodization of GaAs and GaP in phosphate or hydroxide solutions. Previous observations revealed that a change in the anion used for pH modification to  $\text{NO}_3^-$  or  $\text{Cl}^-$  resulted in severe inhibition of oxide growth (2). A more detailed examination of this effect indicates that electrolytic etching takes place in the presence of these two anions (i.e., the oxide never really grows very thick before it is dissolved in the electrolyte). The contamination level required before an anion will cause the system to shift from oxide growth to etching has been determined. The approach used was to take concentrated HCl and  $\text{HNO}_3$  and dilute, 1 ml acid to 99 ml water. One drop of this diluted acid<sup>5</sup> was then added each time to about 400 ml of  $\text{H}_3\text{PO}_4$ -acidified water, preset at a pH of 3. An anodization

<sup>5</sup> It was found that 40 drops were equivalent to  $1\frac{1}{2}$  ml.

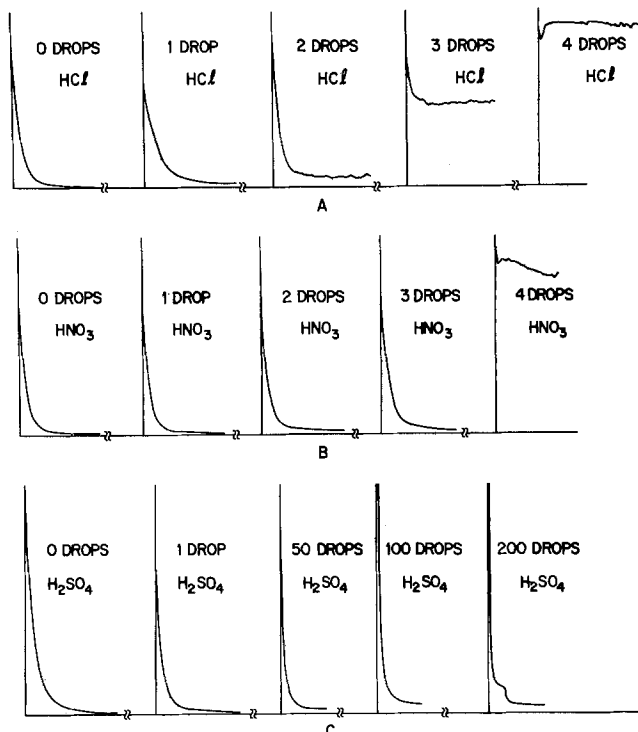


Fig. 13. Current-time curves for a constant voltage (50V) anodization of n-type ( $N_D - N_A \approx 1 \times 10^{18} \text{ cm}^{-2}$ ) GaAs in acidic (pH = 3) water. (A) Contamination with dilute HCl where each drop of additive provided  $4.4 \times 10^{-6}$  moles of HCl. (B) Contaminated with dilute  $\text{HNO}_3$  where each drop of additive provided  $6.2 \times 10^{-6}$  moles of  $\text{HNO}_3$ . (C) Contaminated with dilute  $\text{H}_2\text{SO}_4$  where each drop of additive provided  $6.8 \times 10^{-6}$  moles of  $\text{H}_2\text{SO}_4$ .

curve (constant voltage) was then generated using a new piece of standard n-type, silicon-doped GaAs with  $[N_D - N_A] \approx 1 \times 10^{18}$ , at a fixed 50V bias. Figure 13 A and B are the current-time curves of the samples after zero to four drops of diluted acid were added to the electrolytic solution. Note, in Fig. 13A, that there was a very gradual increase in the saturation current for the HCl-contaminated solution from almost the first drop, but that there was a large shift on the addition of the third and fourth drops of contaminant. The  $\text{HNO}_3$ -contaminated system did not appear to respond until at least the third drop, but by the fourth drop it reacted severely. Considering that one drop of added dilute solution caused an impurity level of about 0.2-0.3 parts per million, it appears that at approximately one part per million of either  $\text{NO}_3^-$  or  $\text{Cl}^-$ , radical effects are observed.

Because not all acidic anions are deleterious to oxide growth (e.g., phosphate, tartrate, citrate), it was decided to examine  $\text{H}_2\text{SO}_4$  to determine the effect of the sulfate anion. Figure 13C shows that very little effect on the anodization curves was observed up to about 100 drops of diluted  $\text{H}_2\text{SO}_4$  and that at 200 drops, a moderate effect was beginning to emerge. Clearly, the system can tolerate almost two orders of magnitude more sulfate ion than it can either chloride or nitrate ion.

Going one step further, the conditions for straightforward electrolytic etching of GaAs and GaP in dilute solutions of HCl and  $\text{HNO}_3$  have been studied. Table I is a summary of the etching characteristics of both GaAs and GaP in these reagents as a function of acid concentrations and current densities. An analysis of these data combined with impressions obtained on visual examination of the surface after etching can be summarized as follows: (i) A current density of  $40 \text{ mA/cm}^2$  and above "pulverizes" the surface, leaving a black-appearing residue on the surface. (ii) A current density of  $2 \text{ mA/cm}^2$  barely attacks the surface, only

Table I.

Run number	Acid	Sample*	Concentration (normality)	Sample surface area (cm <sup>2</sup> )	Orientation	Current** (mA)	Voltage (V)	Amount removed (Å)	Electron conversion efficiency (%)
1	HNO <sub>3</sub>	GaAs	1	0.5	(100)	5.0	1.6	3,750	12.5
2	HNO <sub>3</sub>	GaAs	1	0.5	(100)	10.0	2.5	5,000	8.3
3	HNO <sub>3</sub>	GaAs	1	0.5	(100)	50.0	2.3	100,000	—
4	HNO <sub>3</sub>	GaAs	1	0.5	(100)	1.0	1.2	750	—
5	HNO <sub>3</sub>	GaAs	0.1	0.5	(100)	5.0	2.4	6,000	20.0
6	HNO <sub>3</sub>	GaAs	0.1	0.5	(100)	10.0	3.2	7,125	13.8
7	HNO <sub>3</sub>	GaAs	0.1	0.5	(100)	20.0	3.4	64,000	—
8	HNO <sub>3</sub>	GaAs	0.1	0.5	(100)	1.0	1.0	2,000	—
9	HNO <sub>3</sub>	GaAs	0.01	0.4	(100)	5.0	3.8	675	1.7
10	HNO <sub>3</sub>	GaAs	0.01	0.4	(100)	10.0	6.2	1,300	1.6
11	HNO <sub>3</sub>	GaAs	0.01	0.4	(100)	1.0	2.0	750	9.5
12	HCl	GaAs	0.1	0.5	(100)	1.0	1.0	700	11.0
13	HCl	GaAs	0.1	0.5	(100)	5.0	2.0	10,000	33.3
14	HNO <sub>3</sub>	GaP	0.1	0.5	(111)	5.0	—	80	—
15	HNO <sub>3</sub>	GaP	0.1	0.5	(111)	10.0	—	1,250	—

\* All samples were n-type.

\*\* All samples anodized for 300 sec.

delineating some of the residual polishing scratches. (iii) The most efficient current density for good electrolytic etching is between 10 and 20 mA/cm<sup>2</sup>.

### Discussion

*Analysis of electrical control parameters.*—Until this point only the phenomenological observations made during the anodization of GaAs and GaP have been described. In this section an attempt is made to obtain better understanding of the anodization processes by developing a set of current-voltage-time equations based on a very simple linearized equivalent circuit, shown in Fig. 14. In this circuit the oxide resistance is represented by a variable resistance,  $r$ , which during anodic oxidation varies from essentially zero to extremely large values while during anodic etching remains very small.

From the two basic equations:

Ohm's law

$$V = I(r + R) \quad [1]$$

where  $r$  and  $R$  are the resistances of the oxide and of the solution, respectively, and

Faraday's law

$$r = K \int_0^t I(t) dt \quad [2]$$

where the constant  $K$  includes all parameters assumed to be constant, such as the geometrical factors, the oxide composition, resistivity, and electron-to-oxide conversion efficiency, etc. The time-dependent form of Ohm's law which results is

$$\frac{\partial V}{\partial t} = \left( R + K \int_0^t I(t) dt \right) \frac{\partial I}{\partial t} + KI^2 \quad [3]$$

For the case of constant current,  $I = I_a$ , the solution of

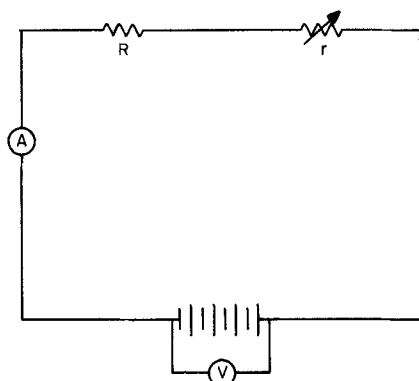


Fig. 14. Simplified circuit diagram of the anodizing system:  $R$ , resistance of the electrolyte;  $r$ , resistance of the oxide layer;  $V$ , applied bias;  $A$ , current following.

Eq. [3] is

$$V = KI_a^2 t + I_a R \quad [4]$$

For the case of constant voltage,  $V = V_a$ , Eq. [3] reduces to

$$(r + R) \frac{\partial I}{\partial t} + KI^2 = 0 \quad [5]$$

which has a solution

$$I = \sqrt{\frac{V_a^2}{R^2 + 2V_a K t}} \quad [6]$$

or with proper substitutions

$$r = \sqrt{R^2 + 2V_a K t} - R \quad [7]$$

The voltage drop across the oxide,  $V_o$ , is then

$$V_o = V_a \left( 1 - \frac{R}{r + R} \right) \quad [8]$$

One can now readily see, that by taking the derivative of Eq. [4], the time variation of voltage at constant current is a constant, which is exactly what was observed in the data of Fig. 2. Since in this analysis it was assumed that the resistivity, among other factors, was held constant in order to yield the linear voltage-time dependence, the experimental verification of this linear dependence implies that the resistivity of the growing film is constant under the constant-current anodization conditions studied here.

Also note, from Eq. [6], that the current-time relationship, at constant voltage, is a relatively complicated expression. Whereas previously an exponential dependence of current on time had been assumed (2), one can now see that an inverse square root form of dependence on time could be governing the situation. The extremely rapid current falloff in the initial stages of anodization is now recognized to be due to the operation of the parameter  $K$  (which has a value of about  $10^5$  ohms-coulombs<sup>-1</sup>) on  $t$  in Eq. [6].

In utilizing the equivalent circuit shown in Fig. 14, the situation has been drastically oversimplified. The assumption is made for example, that  $R$  is a simple constant, that there is no voltage drop in the semiconductor, and that there is no charge storage in the oxide. These simplifications have allowed a working basis from which to start. These corrections may now be incorporated into the equations just developed.

Since the simple properties of concentrated acids and bases are well known (15), one can easily determine that the reagent concentrations for the anodic oxidation systems under study are approximately 0.002M for H<sub>3</sub>PO<sub>4</sub> and 0.02M for NH<sub>4</sub>OH. In Tables II and III are listed the resistivity, equivalent conductance, and pH as functions of molarity of H<sub>3</sub>PO<sub>4</sub> and NH<sub>4</sub>OH solutions, respectively (only values up to about 10M are listed). On the basis of these data, one might

Table II.

Concentration (equiv./liter)	Resistivity* (ohm-cm)	Equivalent (19, 20) conductance (mho-cm <sup>2</sup> /g-equiv.)	pH (21, 15)
Pure water	2.5 × 10 <sup>7</sup>	—	7
0.0 (infinite dilution)	—	376	—
0.002 (H <sub>3</sub> PO <sub>4</sub> )	0.64	311.9	—
0.01	4.50	222.0	~2.15
0.05	37.74	132.0	—
0.1	86.15	104.0	1.5
0.43	71.44	32.55	—
0.89	39.48	28.46	—
1.66	23.55	25.57	—
5.37	12.40	15.01	—
7.96	9.98	12.59	—
11.20	7.80	11.44	—

\* Calculated.

Table III.

Concentration (equiv./liter)	Resistivity* (ohm-cm)	Equivalent (22) conductance (mho-cm <sup>2</sup> /g-equiv.)	pH (14)
Pure water	2.5 × 10 <sup>7</sup>	—	7
0.0 (infinite dilution)	—	242	—
0.0001 (NH <sub>4</sub> OH)	15.2 × 10 <sup>4</sup>	(66)**	—
0.0005	52.6 × 10 <sup>3</sup>	38	—
0.001	35.7 × 10 <sup>3</sup>	28	—
0.005	15.2 × 10 <sup>3</sup>	13.2	—
0.01	10.4 × 10 <sup>3</sup>	9.6	10.6
0.05	43.5 × 10 <sup>2</sup>	4.6	—
0.1	30.3 × 10 <sup>2</sup>	3.3	11.1
0.5	14.8 × 10 <sup>2</sup>	1.35	—
1.0	11.2 × 10 <sup>2</sup>	0.89	11.6
5.0	9.9 × 10 <sup>2</sup>	0.202	—
10.0	18.5 × 10 <sup>2</sup>	0.054	—

\* Calculated.

\*\* Estimated.

postulate that: (i) The simple solution resistance for the caustic system should be about 5 orders of magnitude higher than for the acid system used, and (ii) because the minimum in the acid system resistivity is close to the  $2 \times 10^{-3}$ M determined for the electrolyte concentration used, this should be the governing factor in the shape of Fig. 5.

Unfortunately, the data indicate a factor of only about 10 difference in our anode-to-cathode electrical resistance (i.e., approximately 30-3 kohms for base and acid, respectively) and not the factor of  $10^5$  predicted. This higher resistance in the caustic system could also be involved in the very rapid voltage increases noted in Fig. 8. Note that whereas Table II predicts a factor of 20 increase in resistance between pH = 2.15 and 1.5, the data in Fig. 5 show that there is a drop in ultimate thickness of about a factor of 3. Unquestionably, the resistance of the solution is an important factor in the control of oxide formation, but it is not the total answer.

Examining the question of field distribution in going from the solution into the solid anode, one finds that at least five "resistances" must be taken into account: the depletion region at the liquid-oxide interface, the oxide itself, the depletion width in the semiconductor, the resistance in the bulk of the semiconductor, and the contact resistance between the semiconductor and the aluminum-tipped tweezers. One can dispense with the bulk and contact resistances by assuming that they are constant and can be included in  $R$  of Fig. 14. It must be kept in mind, however, that a large change in the free carrier concentration in the semiconductor could introduce an appreciable amount of bulk series resistance, thereby altering the field distribution available for oxidation at the surface. For this reason one should expect moderate effects on the position of the thickness-voltage curve (such as that shown in Fig. 9) for samples with lower or higher free

carrier density than was used to generate any of the voltage thickness curves in this paper.

The three remaining resistances to be considered are the two depletion regions at the liquid-oxide and oxide-semiconductor interfaces and the oxide resistance itself. It was shown recently (16) that when an n-type electrode is used as the anode in either of these electrolytes, a reverse biased Schottky diode situation is achieved. One can therefore expect that the additional voltage drop across the depletion layer in the semiconductor will also cause variation in the position of voltage vs. thickness plots as the doping density of the semiconductor varies. Therefore, in order to be more thorough, one would have to account for this additional voltage drop ( $V_b$ ) in Eq. [8] by subtracting it from  $V_a$  thus

$$V_o(t) = (V_a - V_b)(r(t)) \quad [9]$$

One possible way to minimize this doping level effect is to generate free carriers optically, with high intensity light of the proper energy.

Similarly, if one examines the solutions being used for these oxidations one finds that there are  $1.1 \times 10^{18}$  and  $5 \times 10^{17}$  ionized molecules/cm<sup>3</sup> for the H<sub>3</sub>PO<sub>4</sub> and NH<sub>4</sub>OH solutions, respectively. Again, depletion regions are formed on the solution side of the electrolyte-oxide interface because of the higher dielectric constant of water [80 for pure H<sub>2</sub>O as against 11 and 10 for GaAs and GaP, respectively (15, 17)]. Also, the caustic solution will have a larger voltage drop than the acid solution because of the lower free charge density in the former solution. Consideration of the voltage drop,  $V_s$ , across the depletion region on the electrolyte side of the solution-oxide interface results in an additional modification to Eq. [8] shown as

$$V_o = (V_a - V_b - V_s)(r(t)) \quad [10]$$

Earlier in this section we concluded that the resistivity of the oxide was a constant because of the linearity of the voltage-time plot of Fig. 2. This does not necessarily mean, however, that the oxide is absolutely uniform in the lack of distributed charge. On the contrary, some recent results (18) concerning the conduction mechanism for oxides indicate the presence of large quantities of trapped charges in the oxide. If this is so, then on the average, the resistivity of the oxide can be a constant, but the local field in the oxide does not necessarily have to be constant. Therefore, as the oxide becomes thicker, the field nonuniformities can become appreciable; and a stage is finally reached where nonuniform oxide growth will occur. The authors realize, however, that this is not the full explanation of the nonuniform coloration on the 200V samples. As was mentioned earlier, films grown at applied biases up to about 180V for GaAs and 125V for GaP in acidic baths had constant refractive indexes (1.81 and 1.60, respectively), but above this voltage range the apparent refractive index began to deviate markedly from these values (see Fig. 10). We believe this deviation is due to the formation of a peculiar interface region, which is neither well defined nor well understood, but which interferes with a good specular reflection from the oxide-semiconductor interface.

In the analysis presented here, all of the charge carriers in the anodization system have been treated identically, and differentiating between electronic and ionic current has been avoided. Obviously, simplification has been employed again in order to make the problem tractable. Because the specific ionic species moving in and through the oxides are not known (from either the semiconductor or the electrolyte side), it would be foolhardy to attempt an in-depth analysis of the drift effects that most assuredly play a role in the anodic oxidation of these materials. However, the following can be done as a first attempt in this direction. The field across the oxide that causes ionic drift of the oxidant is

$$E_o = \frac{V_o}{d} \quad [11]$$

where  $d$  is the thickness of the oxide. Note that the slope of the thickness vs. applied bias curves (see Fig. 3 and 9) is  $d/V_a$ , the slopes being 20 and 12 Å/V for GaAs and GaP, respectively. In obtaining the data for Fig. 3 and 9, heavily doped material (i.e.,  $\sim 1 \times 10^{18} \text{ cm}^{-3}$ ) was used and therefore  $V_B$  was approximately  $\leq 10\text{V}$  (17). Because high-conductivity solutions were used,  $V_s$  can be expected to be negligibly small. Therefore, at  $t = \infty$  under constant voltage conditions

$$V_o = V_A - 10 \quad [12]$$

but at high applied voltages

$$V_o \approx V_A \quad [13]$$

and one can therefore write

$$E_o = \frac{1}{\frac{d}{V_o}} \cong (\text{slope})^{-1} \quad [14]$$

This means, then, that for GaAs and GaP,  $E_o \cong 5 \times 10^6$  and  $8 \times 10^7 \text{ V/cm}$ , respectively, and one might consider these to be the critical fields necessary for oxide growth to take place.

It is hoped that some future studies will help to elaborate the details of the mechanisms interactive in this area.

### Conclusions

Information is reported regarding the anodization of GaAs and GaP in aqueous solutions, whereby one can obtain either controlled oxide growth or controlled electrolytic etching. By replacing the older (i.e., aqueous  $\text{H}_2\text{O}_2$ ) approach with the simpler, cheaper water system, one eliminates the problems of spontaneous electrolyte decomposition at the platinum cathode. Also, because of the absence of gas generation, the need for the baffle between the anode and the cathode has disappeared and apparatus requirements have been simplified still further. In addition, since one no longer need purchase a commercial product (i.e.,  $\text{H}_2\text{O}_2$ ) from an outside vendor, it is now possible to have total control of all aspects of the electrolyte preparation.

The influence of a graded region at the semiconductor oxide interface is seen in the anomalous ellipsometry values obtained on samples grown at high voltages. More work will have to be done in order to explain these effects.

### Acknowledgments

The authors would like to extend sincere thanks to the many colleagues whose discussions and comments

were helpful to us. We especially wish to thank D. L. Rode for his analysis that led to the development of the  $I$ - $V$ - $t$  equations, D. E. Aspnes for his assistance with ellipsometry problems, E. H. Nicollian for discussions on the charge in the oxide, F. K. Reinhart and W. C. Niehaus for discussions regarding the depletion layers at the two oxide interfaces, D. L. Deppen for his preparation of the photoresist pattern used in restricted-area oxidations, and A. P. Pisarchik for his general help on this project.

Manuscript submitted Sept 29, 1975; revised manuscript received Feb. 9, 1976. This was Paper 282 presented at the Miami Beach, Florida, Meeting of the Society, Oct. 8-13, 1972.

Any discussion of this paper will appear in a Discussion Section to be published in the June 1977 JOURNAL. All discussions for the June 1977 Discussion Section should be submitted by Feb. 1, 1977.

Publication costs of this article were partially assisted by Bell Laboratories.

### REFERENCES

1. B. Schwartz and W. J. Sundburg *This Journal*, **120**, 576 (1973).
2. R. A. Logan, B. Schwartz, and W. J. Sundburg, *ibid.*, **120**, 385 (1973).
3. S. M. Spitzer, B. Schwartz, and G. D. Weigle, *ibid.*, **122**, 397 (1975).
4. F. Ermanis and B. Schwartz, *ibid.*, **121**, 1665 (1974).
5. R. L. Hartman, B. Schwartz, and M. Kuhn, *Appl. Phys. Letters*, **18**, 304 (1971).
6. B. Schwartz, J. C. Dymont, and S. E. Haszko, "Gallium Arsenide and Related Compounds 1972," p. 187, The Institute of Physics, London (1973).
7. S. M. Spitzer, B. Schwartz, and G. D. Weigle, *This Journal*, **121**, 820 (1974).
8. J. M. Poate, P. J. Silverman, and J. Yahalom, *J. Phys. Chem. Solids*, **34**, 1847 (1973).
9. N. N. Axelrod, H. J. Levinstein, and W. Royer, Private communication.
10. W. C. Niehaus and B. Schwartz, Submitted to *Solid State Electron.*
11. R. J. Archer, *J. Opt. Soc. Am.*, **52**, 970 (1962).
12. D. E. Aspnes, *Opt. Comm.*, **8**, 222 (1973).
13. R. L. Field, Jr., Private communication.
14. H. Gerischer, *Ber. Bunsenges*, **69**, 578 (1965).
15. "Handbook of Chemistry and Physics," 50th ed., R. C. Weast, Editor, Chemical Rubber Co., Cleveland (1969).
16. D. L. Rode, J. V. DiLorenzo, and B. Schwartz, *Solid State Electron.*, **17**, 1119 (1974).
17. S. M. Sze, "Physics of Semiconductor Devices," p. 24, John Wiley & Sons, Inc., New York (1969).
18. E. H. Nicollian and B. Schwartz, To be published.
19. H. E. Phillips, *J. Chem. Soc., London*, **95**, 59 (1909).
20. A. A. Noyes, *J. Am. Chem. Soc.*, **30**, 335 (1908).
21. H. T. S. Britton, *J. Chem. Soc.*, 614 (1927).
22. H. Falkenhagen, "Electrolytes," Clarendon Press, Oxford (1934).



# A Mechanism for Generation of Pulsating Growth and Nonrotational Striations during Initial Transient of Solidification

H. U. Walter

Department of Physics, University of Alabama, Huntsville, Alabama 35807

## ABSTRACT

A system of on-facet and off-facet striations was observed in selenium-doped ( $10^{19}/\text{cm}^3$ ) InSb that was prepared at  $g$ -levels of  $10^{-4}$ - $10^{-6}$  during Skylab mission SL-4. The off-facet striations could not be explained in terms of existing theory. A new concept is derived that considers the decrease of liquidus temperature in the initial transient region due to buildup of a diffusion layer. This model not only explains off-facet striations in space-grown InSb, but may also be the basis of certain nonrotational striations that are observed in crystals processed on the ground.

Redistribution of solute resulting from directional solidification of a binary solution under conditions of complete mixing has been treated mathematically by Gulliver (1), Scheuer (2), Hayes and Chipman (3) for normal freezing, and by Pfann (4) for zone melting. Both normal freezing and zone melting have been analyzed by Tiller *et al.* (5) with the assumption that convection in the liquid is negligible. Further treatment of this subject was given by Smith *et al.* (6). Effects of natural and forced convection on macrosegregation have been calculated by Wagner (7) and others.

Constant rate of solidification and/or constant segregation coefficient throughout the process of solidification is assumed with these theories. An additional difficulty associated with their application is due to the fact that both of the extreme cases, complete mixing and solely diffusion-controlled conditions, are difficult to verify in practice. Complete mixing can only be approximated due to the difficulty of effectively stirring the diffusion layer; whereas some convective mixing is observed even with crystal growth under stabilizing thermal gradients, solidification of conductive melts in transverse magnetic fields, and with growth at low Rayleigh numbers. The latter includes the use of baffles and growth in capillaries.

This transient fluid flow, which we are unable to control on earth, is one of the major causes of compositional microinhomogeneities (striations) that we observe in virtually all material prepared by directional solidification of multicomponent systems. Aside from inhomogeneities that are due to constitutional supercooling, grain boundary segregation, solid-liquid interface facet formation, solid-state diffusion of impurities to defect clusters, changes of melt composition, inclusions and cavities, microinhomogeneities are generally attributed to growth rate variations and changes of diffusion layer thickness. Such changes may be caused by the following effects: (i) thermal effects such as thermal instabilities, Joule and Peltier heating and Peltier cooling of interfaces, thermal asymmetry in conjunction with crystal rotation (rotational striations), (ii) mechanical effects, *e.g.*, vibrations, mechanical instabilities due to imperfect pulling mechanisms, (iii) pressure effects due to variations of isostatic pressure in confined geometries and also vibrations, (iv) electrical effects such as electromigration, and, most importantly, (v) fluid flow effects. Fluid flow may be due to stirring, both thermally and compositionally induced gravity-driven convection, surface tension gradients (Marangoni-flow), volume changes upon solidification, Coriolis forces, instabilities of liquid meniscus both at seed and crucible walls ("meniscus jumps").

Key words: macro- and microsegregation, indium antimonide, nonrotational striations, space processing.

Owing to their transient nature, most of the impurity striations caused by these effects have been described qualitatively only. Quantitative models are available for a few specific cases. For diffusion-controlled conditions step function changes of solidification rate have been treated by Tiller *et al.* (5) and Smith *et al.* (6). Sinusoidal growth rate oscillations have been analyzed by Lewis (8) and Carruthers (9) and the effect of sinusoidal temperature fluctuations by Hurler *et al.* (10, 11). Variations of melt composition and changes of diffusion layer thickness during steady-state crystallization were treated by Prim (12) and Burton, Prim, and Slichter (13), respectively. Reviews are given by Carruthers and Witt (14) and Slichter and Burton (8).

Other theories on impurity striations consider adsorption of dopant impurities at the solid-liquid interface (15); theories by Landau (16) and Milevski (17) postulate periodic buildup and solidification of constitutionally supercooled layers. The latter theories are, however, in disagreement with the experimental finding that interfaces become corrugated as soon as constitutional supercooling develops. In addition, diffusion layer thickness is of the order of microns only, larger spaced striations could not be considered on the basis of this mechanism.

As a result of the space program of the National Aeronautics and Space Administration, theories on solidification of quiescent melts could be tested by performing normal freezing experiments on board of orbiting space stations such as Skylab and ASTP. With the exclusion of gravity-driven convection, it was expected that macrosegregation would closely follow profiles as predicted by Tiller *et al.* (5) and Smith *et al.* (6); microsegregation was expected to be minimal. Ideal, diffusion-controlled, steady-state segregation was indeed observed with InSb doped with tellurium to  $10^{18}/\text{cm}^3$  (18) whereas considerable microinhomogeneities were present in germanium crystals doped with gallium to  $8 \cdot 10^{16}$  atoms/ $\text{cm}^3$  (19); both experiments were conducted on board Skylab.

A systematic set of impurity striations was observed in InSb doped with  $10^{19}$  atoms of selenium per cubic centimeter melt. This sample was also prepared on board Skylab during Skylab mission SL-4 at  $g$ -levels of  $10^{-4}$ - $10^{-6}$ . Since the observed striations could not be understood in terms of existing theory, an attempt is made in the following to explain these segregation effects in terms of a new model.

## Experimental Observations

The selenium-doped InSb crystal described in the following was prepared on board Skylab by seeded, directional solidification of a pendant drop. Experimental details are described elsewhere (20, 21). Growth direction was approximately [110]; length of

space-grown sample was about 2 cm, maximum diameter 1 cm. Interface shape was convex throughout solidification. Average selenium concentration in the starting material (seed) was  $10^{19}/\text{cm}^3$  as determined by resistivity and Hall measurements.

High resolution differential etching (22) of longitudinal sections reveals a system of very distinct impurity striations in the first half of the crystal as shown in Fig. 1 and 2. Orientation of the section shown in Fig. 1 is (111)A. Usually (211) cuts are investigated, the major reason being that differential etching of (111)A surfaces also reveals crystal defects such as grain and twin boundaries, dislocations, and vacancy clusters. In our case this was not a severe limitation since no grain boundaries were present; dislocation density was of the order of  $100/\text{cm}^2$  in the first part of the crystal and decreased to virtually zero in the last half of the sample.

Three types of striations can be discerned in the crystal section shown in Fig. 1. Rotational striations in the Czochralski-grown seed in the lower half, and in the space-grown section (upper half) off-facet striations at right and striations associated with the formation of a peripheral (111)B solid-liquid interface facet at left. Etch pits decorating the outcrops of dislocations are also visible. Off-facet striations are again shown at larger magnification in Fig. 2. Only off-facet striations are considered in the following.

Off-facet striations extend 5-7 mm into the crystal. The very first off-facet striations observed within 0.5 mm of regrown material are most distinct. Beginning in the center of the crystal, they become increasingly shallow and degenerate slowly into multiple oscillatory-type impurity bands until they disappear completely. This striated section is followed by a homogeneously doped region of about 5-8 mm after which increasingly sharp striations reappear towards the end of the sample.



Fig. 1. Etched (111)A longitudinal section of InSb(Se) single crystal (sample E3-SL4). Arrow indicates demarcation between Czochralski-grown seed at bottom with rotational striations and space-grown section. (111)B solid-liquid interface facet striations at upper left, off-facet striations at upper right. Etch pits due to In-dislocations. Magnification approximately 17X. Inset (b) Melt-back interface, 125X.

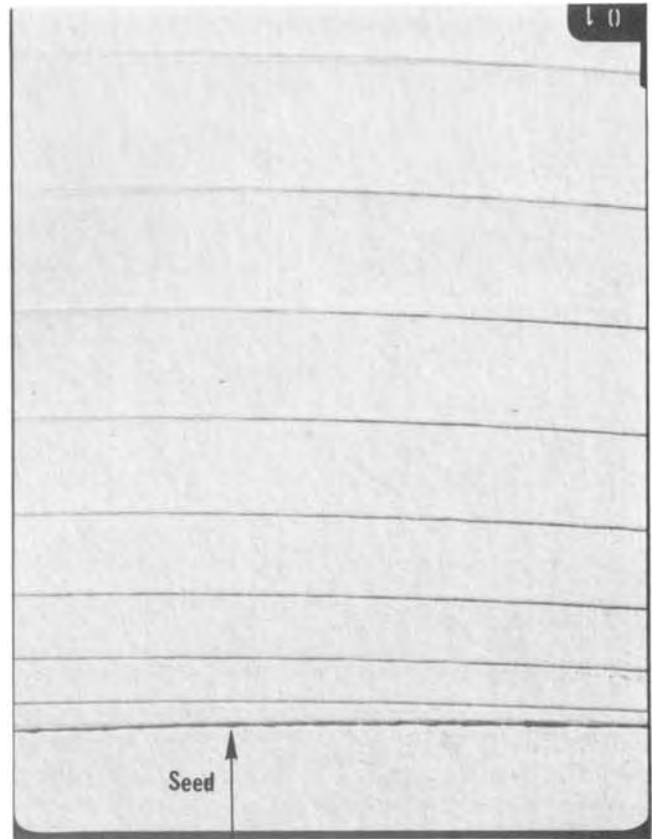


Fig. 2. Striations in off-facet region of space-grown crystal. Multiple striations begin to appear at  $N = 4$  on left side toward center of sample, on right side toward periphery at  $N = 5$ . Magnification 53X.

Tolanski multiple beam microscopy reveals the relief of the surface associated with the first off-facet striations (Fig. 3); 0 denominates the interface between seed and space-grown crystal. Surface depressions that mark striae become increasingly shallow as one proceeds along the direction of growth. A similar area as in Fig. 3 is shown in the dual beam interferogram in Fig. 4. Higher contrast and much more defined interference fringes that are due to reflection from the space-grown material indicate much improved chemical microhomogeneity as compared to the Czochralski-grown seed material. In addition, we observe, especially for the first striations, that the shape of fringes between striae is asymmetrical and S-shaped, rather than U-shaped. Spacing of striations is plotted in Fig. 5; only the very first, singular ones are included.

Since the melt was completely uncontained during solidification, additional information concerning variation of dopant concentration in the bulk could be obtained from surface features. The termination of bulk striations on the surface of the sample is marked by annular grooves for sharp striations and smooth surface undulations for shallow and oscillatory striations as they occur later in the sample. Discontinuous meniscus rearrangements during solidification, meniscus jumps, a possible mechanism for growth discontinuities could be ruled out on the basis of this observation since meniscus jumps would always result in sharp surface grooves and not undulations. In addition, no orientation dependence of surface features could be observed; steps on surface facets and grooves on the cylindrical portions coincide. Wetting instabilities would not occur simultaneously for faceted and cylindrical regions and it can, therefore, be concluded that these features result from discontinuities in bulk solidification and not vice versa.



Fig. 3. Off-facet striations in space-grown InSb(Se); Tolanski multiple beam interferogram of etched, longitudinal section. Note the decreasing fringe deflection-peak sharpness with increasing order number of striations. Dark streak is fault in Fizeau plate. Magnification 100X.



Fig. 4. Off-facet striations in space-grown InSb(Se); dual beam interferogram of etched, longitudinal section. Fringe contrast in space-grown section is much enhanced due to improved microhomogeneity. Magnification 140X.

Further causes of off-facet striations to be considered are mechanical instabilities, thermal instabilities, and surface tension gradient-driven convection (Marangoni flow). Both gyro and temperature data that were obtained for the period of solidification were analyzed; no events that could possibly account for the growth discontinuities could be detected. An average solidification rate of  $6.9\text{--}2.9 \mu\text{/sec}$  could be calculated from cooldown rate ( $0.6^\circ\text{C}/\text{min}$ ) and gradients in the melt (min,  $14.5^\circ\text{C}/\text{cm}$ ; max,  $35^\circ\text{C}/\text{cm}$ ) that were obtained experimentally and by computer analysis of the system. To account for the first striae, sudden heating or cooling of the interface would have to take place at the following times after solidification is initiated. For  $R = 6.9 \mu\text{/sec}$ : 4 sec, 15 sec, 31 sec, 52 sec, 75 sec, 103 sec, 134 sec, etc.; for  $R = 2.9 \mu\text{/sec}$ : 10 sec, 35 sec, 73 sec, 124 sec, 179 sec, 245 sec, 320 sec, etc. Fluid flow cycles that take minutes for each cycle

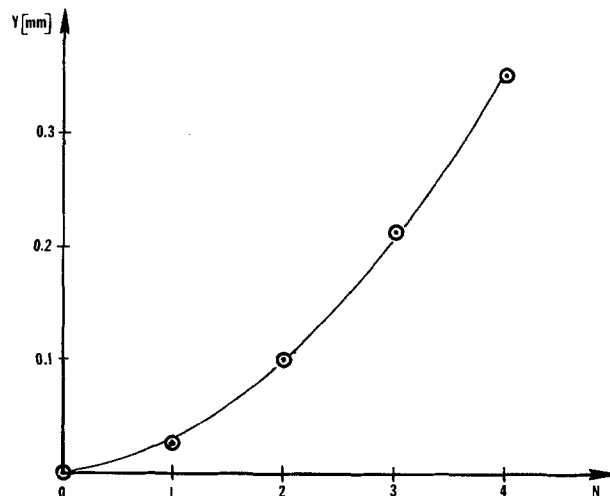


Fig. 5. Distance of singular striations from meltback interface vs. order number  $N$  (measured at periphery of crystal).

with a distinct thermal discontinuity preserved are very unlikely especially with a melt that is a good thermal conductor. A fluid flow pattern of this type would also be reflected in the interface morphology (depressions where hot melt descends) and in radial intensity variations of striations. Since none of these features is observed, fluid flow, including Marangoni flow, can be ruled out as the cause of striations.

The systematics of the observed striation pattern implies a basic underlying mechanism. It comes to mind that earth-grown samples also exhibit features that we do not thoroughly understand. Dickhoff (23), for example, reports what he terms "fundamental" striations in germanium crystals. Possible known causes, such as pulling, vibrations, rotation, etc., were excluded in this experiment and he concludes that "some striations may be due to some fundamental property of the growth process." A multitude of small amplitude, periodic compositional variations with periodicity of 5 to several hundred microns is always observed in doped crystals grown from the melt. In crystals grown by the Czochralski technique without rotation, they are referred to as "nonrotational" striations (e.g., 24-26). An example of such striations is shown in Fig. 6 for a nonrotated ground-based control sample of InSb(Se). They are presently attributed to convective flow mainly (e.g., 27-31). However, a one

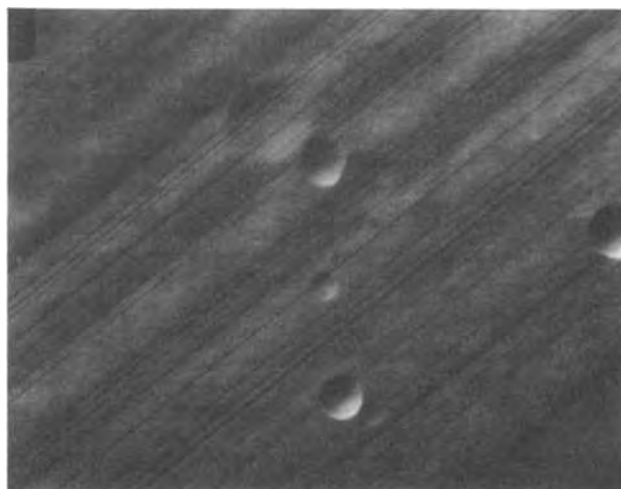


Fig. 6. "Nonrotational striations" in the off-core region of a single crystal of InSb doped with selenium (35 mg Se/85g charge). (211) longitudinal section of crystal pulled without rotation, growth axis [111]B. Numarski interference contrast micrograph of polished and etched surface. Magnification 224X.

to one correlation could not always be shown (e.g., 23, 32-36). Additional underlying basic principles cannot be excluded.

Presuming that fluid flow was negligible, meaning that the diffusion layer was undisturbed, the off-facet striations observed in the space-grown InSb(Se) sample cannot be explained in terms of existing theory. A concept is presented in the following that satisfies both the occurrence as well as the sequence and intensity of these striations.

### Theory

The effective distribution coefficient  $k_{\text{eff}}$  is defined as follows

$$k_{\text{eff}} = \frac{C_{s(\text{act})}}{C_{l(\text{act})}} \quad [1]$$

where  $C_{l(\text{act})}$  is the bulk concentration in the liquid far enough from the growing interface so that concentration gradients are negligible,  $C_{s(\text{act})}$  is the concentration in the solid. Values reported for the effective off-facet segregation coefficient for Se in InSb range from 0.17 to 0.35 (37).  $k_{\text{eff}}$  is affected by experimental conditions such as the rate of stirring, the rate of solidification, crystallographic orientation, and concentration of solute and impurities in the melt.

The equilibrium distribution constant  $k_0$  is given by

$$k_0 = \frac{a_{s(\text{eq})}}{a_{l(\text{eq})}} \quad [2]$$

where  $a_{l(\text{eq})}$  is the equilibrium activity in the liquid and  $a_{s(\text{eq})}$  is the equilibrium activity of the solute in the solid. For solidification of dilute solutions at slow rates,  $k_0$  may be defined as follows

$$k_0 = \frac{C_{s(\text{eq})}}{C_{l(\text{eq})}} = \frac{C_s}{C_T} = k_T \quad [3]$$

$C_T$  is the concentration in the liquid directly at the interface,  $k_T$  is the interface segregation coefficient. Since  $k_0 = k_T \leq k_{\text{eff}} \leq 1$ , the interface segregation coefficient  $k_T$  of Se in InSb may be of the order of 0.2.

During initial transient, the buildup of solute concentration at the interface as a function of interface location  $x$  at constant solidification rate  $R$  is described by the following equation (5)

$$C_T = \frac{C_s}{k_0} = C_0 \left\{ \frac{1 - k_0}{k_0} \left[ 1 - \exp\left(-k_0 \frac{R}{D} x\right) \right] + 1 \right\} \quad [4]$$

where  $C_s$  is the solute concentration in the solid at the interface,  $D$  is the diffusion constant in the liquid. In deriving this equation, the assumptions were made that mass transport in the melt is due to diffusion only and diffusion in the solid is negligible.

After the initial transient, when steady-state solidification has been established, the concentration of solute in the liquid at the interface  $C_T$  is equal to  $C_0/k_T$ , where  $C_0$  is the initial concentration in the liquid. In our case with  $C_0 = 10^{19}/\text{cm}^3$ ,  $k_0 = 0.2$ ,  $C_T$  will reach a steady-state value of  $5 \cdot 10^{19}/\text{cm}^3$ . The growth distance  $x$  required to reach steady state depends on the growth rate. An estimate can be obtained from  $x \approx 2D/(k_0 R)$ . Initial transient rise of solute as a function of interface location for the system InSb(Se) is shown in Fig. 7 for various growth rates.

This variation of solute concentration corresponds to a variation of liquidus temperature of the liquid adjacent to the interface. According to the equilibrium phase diagram of a binary system A,B, the equilibrium liquidus temperature is given by

$$T_E = T_0 - m C_T \quad [5]$$

where  $T_0$  is the melting temperature of pure phase A

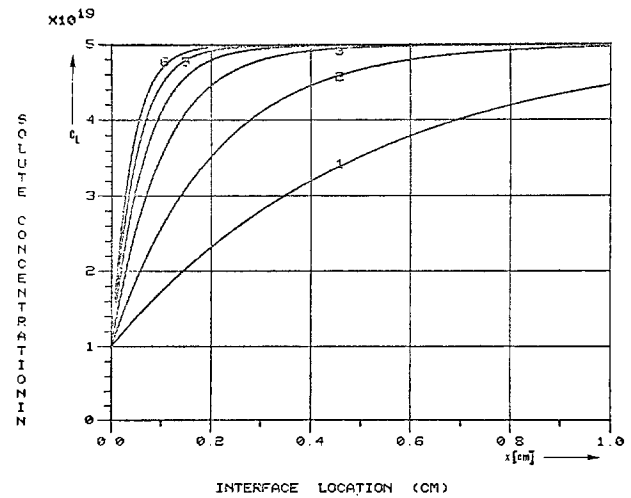


Fig. 7. Dopant concentration in liquid adjacent to solid-liquid interface as a function of interface position. System: InSb(Se); parameters,  $C_0 = 10^{19}/\text{cm}^3$ ,  $D = 10^{-5} \text{ cm}^2/\text{sec}$ ,  $k_0 = 0.2$ ,  $R_1 = 1 \mu/\text{sec}$ ,  $R_2 = 2.5 \mu/\text{sec}$ ,  $R_3 = 5 \mu/\text{sec}$ ,  $R_4 = 7.5 \mu/\text{sec}$ ,  $R_5 = 10 \mu/\text{sec}$ ,  $R_6 = 12.5 \mu/\text{sec}$ .

and  $m$  is the slope of the liquidus curve. As usual, this slope is assumed to be constant.

The liquidus temperature  $T_E$  as a function of  $x$  can be described, using Eq. [4] and [5], by the following expression

$$T_E = T_0 - m C_0 \left\{ \frac{1 - k_0}{k_0} \left[ 1 - \exp\left(-k_0 \frac{R}{D} x\right) \right] + 1 \right\} \quad [6]$$

Melting and solidification curves (temperature vs. time with linear cool down or heating) were determined to estimate liquidus and solidus temperature changes. Excluding supercooling required for nucleation, solidification of InSb doped with selenium to  $10^{20}/\text{cm}^3$  extends over a temperature range of approximately  $20^\circ\text{C}$ . The shape of the curves indicates partial mixing; temperature change associated with the initial period was  $5^\circ\text{--}10^\circ\text{C}$ . Since the phase diagram InSb-Se is not available, a more conservative value of  $0.21^\circ\text{C}/(10^{19}\text{Se}/\text{cm}^3)$  as determined by linear interpolation of melting temperatures is used in the following. Using Eq. [6] and this value, liquidus temperature changes as a function of interface position were computed as shown in Fig. 8. In our experiment, solidification was

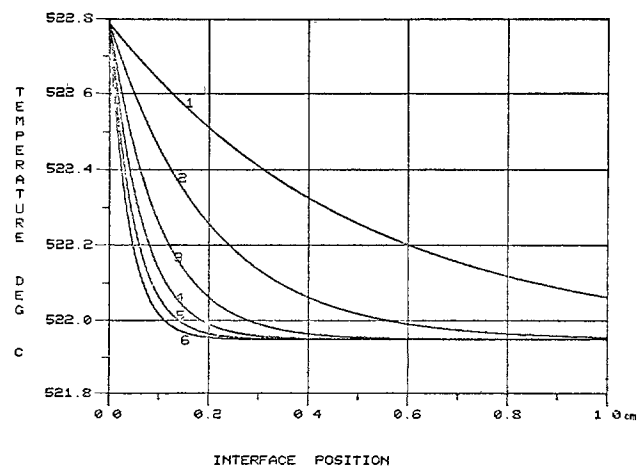
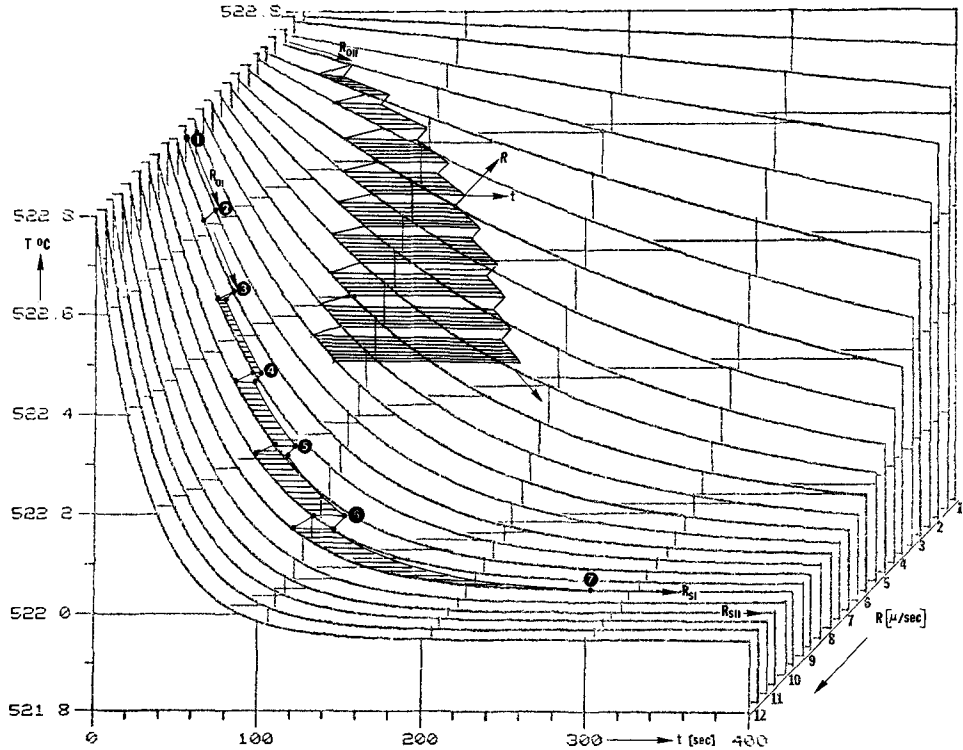


Fig. 8. Decrease of liquidus temperature due to increase of solute concentration in liquid adjacent to advancing solid-liquid interface as a function of interface position. System: InSb(Se);  $T_m = 523.0^\circ\text{C}$ ;  $\Delta T/(10^{19}\text{Se}/\text{cm}^3) = 0.21^\circ\text{C}$ . Growth rates and other parameters as listed in Fig. 7.

Fig. 9. Decrease of liquidus temperature in the system InSb(Se) as a function of time and growth rate  $R$  with each plot computed for constant  $R$  (Eq. [6]). Three dimensional step-by-step procedure used to determine  $T$  vs.  $x$  and  $R$  vs.  $x$  (see Fig. 10) is indicated for two cases I and II.



initiated by programmed cooldown of 0.6°C/min after a 1 hr soak period. Consequently, the rate of solidification has to be modified during initial transient of solidification owing to a decrease of liquidus temperature of 0.84°C, which corresponds to a time lag of 1.4 min.

In the following, possible cases as to how this can be accomplished are examined. Parameters for InSb(Se) are used. However, the considerations are applicable to multicomponent solidification systems with  $k < 1$  in general, and, analogously to systems with  $k > 1$ .

Aside from shifts of the time axis that need to be considered, solidification has to proceed along the surface shown in the liquidus temperature-time-growth rate diagram in Fig. 9. Steady-state solidification rate  $R_s$  is determined by the cooldown rate  $dT/dt$  and the gradient in the melt at the interface

$$R_s = \frac{dT/dt}{\text{grad } T} \quad [7]$$

Assuming that virtually no supercooling is required to drive growth and assuming immediate response of the growth rate to alterations of the thermal situation, the growth rate  $R_s$  is modified by changes of the liquidus temperature as follows

$$R = R_s - \frac{(dT_E/dt)_R}{\text{grad } T} \quad [8]$$

Neglecting thermal inertia so that  $dT_{\text{cool}}/dt = \text{const}$  throughout solidification, the rate  $R_o$  at which growth is initiated at  $t = 0$  is determined by

$$\left( \frac{dT_E}{dt} \right)_{R_o} = \frac{dT}{dt} \quad [9]$$

$$R_o \leq R_s \quad [10]$$

Slower rate would result in increasing supercooling, faster rate is not permissible. With the assumption that virtually no supercooling is required for growth, growth rate will increase from  $R_o$  to  $R_s$  according to the condition

$$\frac{dT_E}{dR} = \text{const} \quad [11]$$

Using Eq. [6], [7], [9], and [11], variation of  $R$  with time or interface position and, consequently, variation of  $T_{\text{liq}}$ ,  $C_T$ , and  $C_s$  can be determined numerically by a three-dimensional step-by-step procedure. This procedure is indicated in Fig. 9 for two cases,  $R_I$  with small  $\Delta R = R_{sI} - R_{oI}$  and  $R_{II}$  with larger  $\Delta R$ .

Variation of  $R_I$ ,  $T_I$ , and  $R_{II}$ ,  $T_{II}$  with interface location determined in this manner is shown in Fig. 10. With increasing  $\Delta R$ , the curves deviate more and more from exponential functions; note the inflection points in the  $R_{II}$  and  $T_{II}$  curves. Resulting concentration profiles in the solid are given in Fig. 13, for comparison, a profile that would be obtained with  $R = \text{const}$  is included.

Even though the assumptions made concerning supercooling and response may not be realistic as will be shown in the following, experimental findings may still be in good agreement with data derived by this approach. Best agreement would be expected for dopant levels and systems where the decrease of liquidus temperature is small and the cooldown rapid and where, in addition, growth interfaces are diffuse. These conditions are closely met with the InSb(Te) Skylab experiment mentioned in the introduction (18). Decrease of liquidus temperature due to  $10^{18}\text{Se/cm}^3$  is of the order of 0.05°C only; a relatively

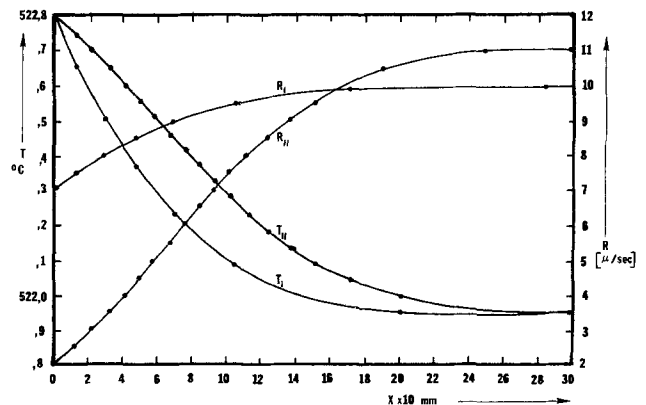


Fig. 10. Liquidus temperature and growth rate  $R$  vs. solid-liquid interface location  $x$  as determined by step-by-step procedure indicated in Fig. 9 for the system InSb(Se).

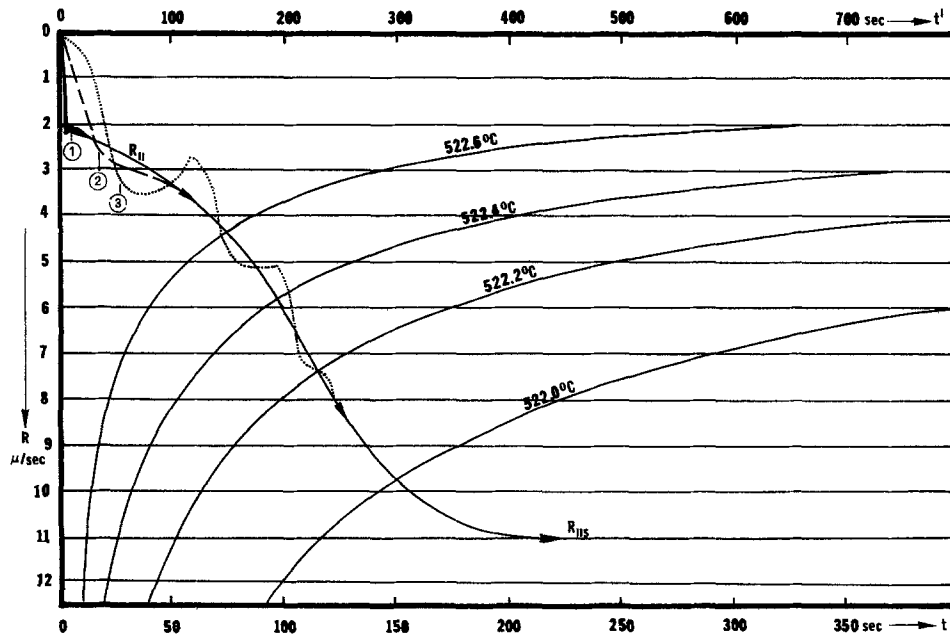


Fig. 11. Top view of  $T-R-t$  block diagram shown in Fig. 9 with isotherm lines indicating times after which the respective liquidus temperatures are established at constant solidification rates. Different cases of growth rate variations with time  $t'$  ( $t'$  scale compressed to have correct relation with isotherms) are as follows: (A): Curve  $R_{II}$ , continuous variation of  $R$  due to decrease of liquidus temperature, step function change from  $R = 0$  at  $t = 0$  to  $R_{II}$ . (B): Curve ①, small undercooling required for growth. (C): Curve ②,  $R$  proportional to undercooling. (D): Curve ③, growth rate hysteresis. (See also Fig. 12.)

rapid cooldown of  $2.4^{\circ}\text{C}/\text{min}$  was employed; growth axis was  $[111]B$ ; the interface was, however, concave. Details close to the meltback interface could not be resolved and the dopant profile agrees within experimental errors with an exponential profile.

As already mentioned, the assumption of a step-function change from  $R = 0$  to  $R_0$  is not realistic. More realistically, this increase will require finite time. Consequently,  $R$  will increase from zero to the balance curve (e.g.,  $R_{II}$ ) in a manner indicated in the  $R-t$  diagram (top view of Fig. 9) shown in Fig. 11 (curve 1, heavy line). Since growth at  $R < R_{II}$  equals increasing supercooling, an overshoot into the region  $R > R_{II}$  will result. Due to this overshoot, the thermal imbalance is reversed and one or several high frequency, rapidly decaying growth rate oscillations may result in this region. Finally, growth will proceed according to the  $R_{II}$  curve. Even though attributed to drifting of the interface during thermal soak due to thermal instabilities, similar features were observed with antimony ( $10^{17}/\text{cm}^3$ ) and gallium ( $10^{19}/\text{cm}^3$ )-doped germanium solidified during ASTP-mission (38).

Considering the various theories describing molecular kinetic mechanisms for solidification, two basic cases can be discerned for our purpose: (i) Growth rate  $R$  is proportional to the degree of undercooling  $\Delta T$ . (ii) Growth rate  $R$  is not proportional to the degree of undercooling  $\Delta T$ . Proportionality is generally expected for diffuse interfaces, where the interface advances continuously without lateral spreading. The same interdependence is predicted for growth with screw dislocations. Growth of a perfect crystallographic flat is expected to follow an exponential law (nucleation-limited growth), the dislocation law predicts a growth rate that is approximately proportional to  $(\Delta T)^2$ , whereas BCF theory allows for both linear and parabolic laws. Reviews are, for example, given by Jackson (39), Bennema and Gilmer (40), and Cahn *et al.* (41). Cahn lines out that mock-lateral growth, a continuous mechanism based on lateral growth on interface terrace steps, may be most common especially when growth rate anisotropy is large. Examining both theory and experimental evidence, Cahn concludes that stepwise growth prevails at low undercooling and continuous growth at high undercooling. If different growth mechanisms are operable at different growth rates, growth rate minima and associated striations may be accentuated by enhanced entrapment of solute due to lateral spreading. Information on supercooling required to drive solidification of InSb is available only for  $\{111\}$  facet growth (42). Supercooling up to  $6^{\circ}\text{C}$  has been measured during growth. Systematic changes

of interface characteristics with growth rate due to the tendency to approach diffuse interfaces under conditions of rapid growth and singular interfaces at slow growth may, in addition, lead to hysteresis. In this context, growth rate dependent adsorption of impurities that decrease the interfacial free energy may also be of importance.

Growth rate and concomitant liquidus temperature variations resulting from linear interdependence of  $R$  and  $\Delta T$  (Fig. 12b) are indicated in Fig. 11 and 12, dashed curves ②. In analogy to minimal supercooling (Fig. 11, curve ①), one or several lower frequency sinusoidal oscillations of  $R_{(2)}$  about  $R_{II}$  should be expected (Fig. 11, curve ②). In terms of liquidus temperature (Fig. 12), oscillations will be about  $T_{II(2)}$  (dashed curve) and not  $T_{II}$  (solid curve) since supercooling is required for growth in this case. So far, this type of behavior has not been observed in space-grown crystals.

Nonlinear interdependence of  $R$  and  $\Delta T$  (Fig. 12c) results in more initial delay (Fig. 11). Consequently, there is more overshoot into the region  $R > R_{II}$ . The

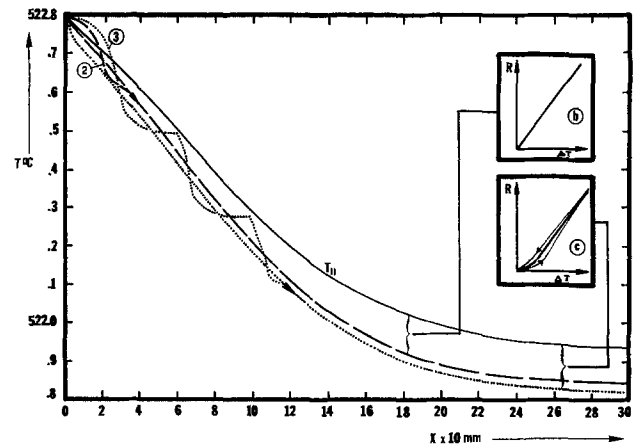


Fig. 12. Decrease of liquidus temperature as a function of interface location. (A), Continuous decrease,  $T_{II}$ , as in Fig. 10, zero undercooling. (B),  $R$  proportional  $\Delta T$  as indicated in upper right; dashed curve parallel  $T_{II}$  indicates the temperature at which growth would proceed according to  $R_{II}$  (Fig. 10). Initial oscillations due to initial time lag, dashed curve ②. (C), Discontinuities (curve ③) due to nonlinear dependence of  $R$  and  $\Delta T$  and eventually hysteresis as indicated in  $R - \Delta T$  diagram at lower right. Dotted curve parallel  $T_{II}$  shows temperature variation required to grow according to  $R_{II}$ .



balance is reversed and the growth rate decreases to  $R < R_{II}$ . This process again continues until the oscillations are damped out and growth proceeds along  $R_{II}$ . Due to the relation of  $R$  and  $\Delta T$ , oscillations are non-sinusoidal as long as  $R$  decreases into the nonlinear region of the  $R - \Delta T$  curve.

Hysteresis (Fig. 12c), which should be more pronounced in the low growth rate region, results in pronounced growth rate discontinuities for minima of  $R$  and eventually discontinuities at maxima. This is shown schematically in Fig. 11 and 12, dotted curve (3).

Figure 1b shows the solid-liquid interface that has developed during soak (1 hr) at large magnification. Clearly this interface is not diffuse but rather composed of a multitude of crystallographic flats. Similar features indicating that interfaces did not simply reflect isotherm shape during solidification are observed with the interfaces marked by the first striae. This observation implies the possibility of growth rate hysteresis that decreases as growth proceeds and overall growth rate increases. Jackson's  $\alpha$ -factor predicts diffuse interfaces for  $\alpha < 2$  and an increasing tendency for singular interfaces for larger  $\alpha$ . It is defined as follows:  $\alpha = \zeta L/RT$ , where  $\zeta < 1$  is a geometric coefficient equal to the ratio of the nearest neighbor coordination number in the surface to that in the bulk,  $L$  is the latent heat of fusion. Not considering  $\zeta$ ,  $\alpha = 7.7$  for InSb, which also indicates that growth interfaces tend to be nondiffuse, and, consequently nonlinear growth laws are applicable. Similarly, surface profiles of etched sections as viewed by dual beam interferometry (Fig. 4) indicate nonlinear growth at slow growth rates and growth rate hysteresis. Interference fringes are most asymmetrical and S-shaped close to the melt-back interface; minima are increasingly less pronounced, as growth proceeds fringes become less asymmetrical and more and more U-shaped (Fig. 3).

Possible dopant profiles resulting from above mechanisms are shown in Fig. 13. Additional complications would be due to variation of distribution coefficients with melt composition, concentration, and growth rate. The effective off-facet segregation coefficient of selenium and InSb increases from 0.3 to 0.6 as the growth rate increases from 0.8 to 25  $\mu$ /sec (43). Also, effects due to evolution of latent heat of fusion ( $\approx 12$  kcal/mol for InSb), which should mostly result in damping of oscillations were not considered.

### Conclusions

Experimental evidence has been presented that strongly suggests that growth rate oscillations and

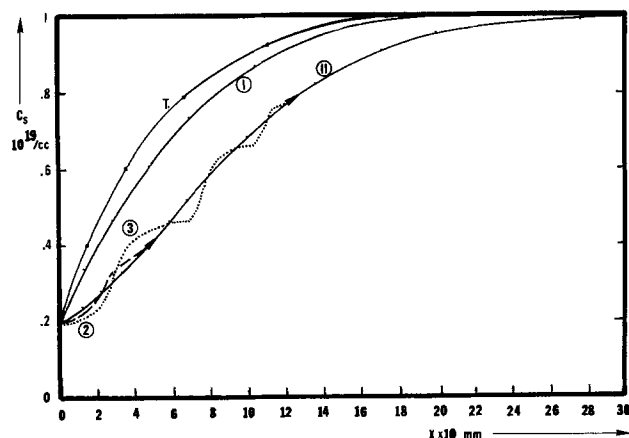


Fig. 13. Possible cases of initial transient dopant profiles when sample is prepared from a quiescent melt. Curve T,  $R = \text{constant}$  throughout solidification [computed according to Tiller *et al.* (5)],  $C_0 = 10^{19}/\text{cm}^3$ ,  $k_0 = 0.2$ ,  $R = 10 \mu/\text{sec}$ . Curves (1) and (II), supercooling not considered; modulation of  $R$  due to decrease of liquidus temperature (Fig. 9). Curve (2), linear interdependence of  $R$  and supercooling. Curve (3), growth rate hysteresis.

growth rate pulsations may result from kinetic supercooling during initial transient. This has been analyzed for quiescent melts and impurities with segregation coefficient  $k_0 < 1$ . According to different models on kinetics of crystal growth, the following cases could be distinguished:

1. Supercooling is neglected; immediate response of growth to the thermal situation is assumed. Growth rate is continuously modified due to decrease of liquidus temperature during initial transient of solidification. Data were obtained for growth rate, liquidus temperature, and concentration of solute in the solid as a function of interface location by three-dimensional step-by-step numerical analysis. These data were used as baseline for the following cases.

2. Growth rate increase from  $R = 0$  at  $t = 0$  to  $R_{\text{baseline}}$  is not a step function change. Assuming linear interdependence of growth rate  $R$  and supercooling  $\Delta T$ , sinusoidal oscillations of growth rate (frequency depending on slope of  $R$  vs.  $\Delta T$ ) result in the initial region.

3. Nonlinear interdependence of  $R$  and  $\Delta T$  similarly results in oscillations; oscillations are, however, non-sinusoidal.

4. Growth rate hysteresis causes growth rate discontinuities (distinct striations) in the initial transient region of solidification.

To minimize effects of liquidus temperature changes during solidification in practice, rapid cool down (rapid growth) is advantageous.

Similar considerations apply for systems with impurities that have segregation coefficients  $k_0 > 1$ , and also for terminal transient conditions. It has been observed by Bardsley *et al.* (44) for Czochralski-pulling of gallium-doped germanium that "in the later stage of growth, the diameter of the crystal steadily decreases if the power supplied to the melt is held constant." He reasons that "the rejection of gallium into the melt continually lowers the liquidus temperature of the melt, thus making the melt too hot for growth at constant diameter." This observation indicates (continuous) growth rate modulation during terminal transient or throughout solidification under conditions of partial mixing.

Oscillatory or pulsating growth may result during terminal transient as well. Growth rate variations with reversed sequence (oscillatory in the beginning and increasingly distinct towards the end) are observed within the last 2 mm in our crystal. These terminal transient variations may be explained on the basis of the same principles as for initial transient.

Clearly defined growth discontinuities of the kind observed with space-grown crystals could not be observed on earth because of gross convective disturbances. However, the same basic mechanisms are present and, therefore, "nonrotational striations" observed in earth-grown crystals may, in many instances, have to be attributed to kinetic effects.

### Acknowledgment

The author is grateful to Drs. J. H. Bredt, NASA headquarters, J. R. Carruthers, Bell Laboratories, and R. S. Snyder, NASA, MSFC, for stimulating discussions and helpful comments. This work was supported by a NASA contract.

Manuscript submitted April 22, 1975; revised manuscript received Jan. 19, 1976.

Any discussion of this paper will appear in a Discussion Section to be published in the June 1977 JOURNAL. All discussions for the June 1977 Discussion Section should be submitted by Feb. 1, 1977.

Publication costs of this article were partially assisted by the University of Alabama in Huntsville.

### REFERENCES

1. G. H. Gulliver, "Metallic Alloys (Appendix)," Chas. Griffin & Co., London (1922).

2. E. Scheuer, *Z. Metallkunde*, **23**, 237 (1933).
3. A. Hayes and J. Chipman, *Trans. AIME*, **135**, 85 (1939).
4. W. G. Pfann, *J. Metals*, **4**, 747 (1952).
5. W. A. Tiller, K. A. Jackson, J. W. Rutter, and B. Chalmers, *Acta Met.*, **1**, 428 (1953).
6. V. G. Smith, W. A. Tiller, and J. W. Rutter, *Can. J. Phys.*, **33**, 723 (1955).
7. C. Wagner, *J. Metals*, **6**, 154 (1954).
8. W. P. Slichter and J. A. Burton, in "Transistor Technology," H. E. Bridges, J. H. Scaff, and J. N. Shive, Editors, Chap. 6, pp. 108, 109, Van Nostrand, Princeton, N.J. (1958).
9. J. R. Carruthers, *Can. Met. Quart.*, **5**, 55 (1966).
10. D. T. J. Hurle, E. Jakeman, and E. R. Pike, *J. Crystal Growth*, **3**, 4, 633 (1968).
11. D. T. J. Hurle and E. Jakeman, *ibid.*, **5**, 227 (1969).
12. See Ref. (8), p. 107.
13. J. A. Burton, R. C. Prim, and W. P. Slichter, *J. Chem. Phys.*, **21**, 1987 (1953).
14. J. R. Carruthers and A. F. Witt, in "Proceedings of the 2nd International Spring School on Crystal Growth," J. B. Mullin and R. Veda, Editors, North Holland Publishing Co., Amsterdam, (1975).
15. R. N. Hall, *J. Phys. Chem.*, **57**, 836 (1953).
16. A. I. Landau, *Fiz. Metal. i Metalloved.*, **6**, 148 (1958).
17. L. S. Milevskii, *Soviet Phys.—Crystallography*, **6**, 193 (1961).
18. A. F. Witt, H. C. Gatos, M. Lichtensteiger, M. C. Lavine, and C. J. Herman, *This Journal*, **122**, 276 (1975).
19. J. T. Yue and F. W. Voltmer, *J. Crystal Growth*, **29**, 329 (1975).
20. H. U. Walter, Proc. Third Space Processing Symp.—Skylab Results, NASA Report No. M-74-5, June 1974.
21. H. U. Walter, American Inst. Aeron. Astron., Paper No. 74-1241 (1974).
22. A. F. Witt, *This Journal*, **114**, 298 (1967).
23. J. A. M. Dickhoff, *Philips Tech. Rev.*, **25**, 195 (1963).
24. K. Morizane, A. F. Witt, and H. C. Gatos, *This Journal*, **113**, 51 (1966).
25. A. F. Witt and H. C. Gatos, *ibid.*, **113**, 808 (1966).
26. J. R. Burke, J. D. Jensen, and B. Houston, *ibid.*, **120**, 431 (1972).
27. A. Murgai, A. F. Witt, and H. C. Gatos, *ibid.*, **122**, 1276 (1975).
28. A. Müller and W. Wilhelm, *Z. Naturforschung*, **20a**, 1190 (1965).
29. H. P. Utech and M. C. Flemings, in "Crystal Growth," H. S. Peiser, Editor, p. 651, Pergamon, London (1967).
30. D. T. J. Hurle, in "Crystal Growth," H. S. Peiser, Editor, p. 659, Pergamon, London (1967).
31. D. T. J. Hurle, *Phil. Mag.*, **13**, 305 (1966).
32. H. C. Gatos, A. J. Strauss, M. C. Lavine, and T. C. Harmon, *J. Appl. Phys.*, **32**, 2057 (1961).
33. C. Brehm, J.-Y. Boniort, and P. Margotin, *J. Crystal Growth*, **18**, 191 (1973).
34. R. R. Zupp, J. W. Nielsen, and P. V. Vittorio, *ibid.*, **5**, 269 (1969).
35. H. F. John, J. W. Faust, and R. Stickler, *IEEE Trans. Parts, Materials, Packing*, **PMP-3**, 51 (1966).
36. M. E. Drougard, *J. Appl. Phys.*, **37**, 1858 (1966).
37. A. J. Strauss, *ibid.*, **30**, 559 (1959).
38. A. F. Witt, Paper presented at "Tutorial Conference on Materials Processing in a Microgravity Environment" Lehigh Univ., Bethlehem, Pa. Oct. 1975.
39. K. A. Jackson, "Solidification," Chap. 5, Am. Soc. Met. (1971).
40. P. Bennema and G. H. Gilmer, in "Crystal Growth," P. Hartman, Editor, Chap. 10, p. 263, North-Holland Publishing Co., Amsterdam, (1973).
41. J. W. Cahn, W. B. Billig, and G. W. Sears, *Acta Met.*, **12**, 1421 (1964).
42. E. A. Demyanov, *Soviet Phys.—Crystallography*, **15**, 690 (1971).
43. U. Merten, K. D. Vos, and A. P. Hatcher, *J. Phys. Chem. Solids*, **30**, 627 (1969).
44. W. Bardsley, J. S. Boulton, and D. T. J. Hurle, *Solid-State Electron.*, **5**, 395 (1962).

## Poly(Methyl Methacrylate-Isobutylene) Copolymers as Highly Sensitive Electron Beam Resists

Edward Gipstein, Wayne Moreau,<sup>1</sup> and Omar Need

IBM Research Laboratory, San Jose, California 95193

### ABSTRACT

Methyl methacrylate-isobutylene P(MMA-IB) copolymers have been synthesized and investigated as positive electron beam resists. A 75/25 composition P(MMA-IB) copolymer had a sensitivity of  $4.5 \times 10^{-6}$  C/cm<sup>2</sup> at an accelerating voltage of 15 kV. The high sensitivity is attributed to the isobutylene "weak links" in the polymer chain. The incorporation of elastomeric isobutylene groups in the copolymers was also found to improve their adhesion on siloxane substrates. The improvement of the resist performance of PMMA represents an application of polymer tailoring wherein certain deficiencies in one polymer system (PMMA) may be overcome by copolymerization with another monomer (IB) which has good radiation sensitivity, but has limited resist applicability.

The fabrication of very small component circuit elements using current photolithographic technology is limited to linewidths of about  $1\mu$  (1). Electron beams, both in theory and practice, have resolution capabilities of the order of  $0.1\mu$  or less and are being used increasingly for fabricating microelectronic devices (2-4).

The general use of electron beam fabrication techniques requires polymeric resist materials which have been designed for this process and are optimized with respect to sensitivity, resolution, and processing. While many of the present electron beam systems make use

of homopolymers as resists, recent developments suggest that copolymer and terpolymer resists should provide more significant processing advantages because of improved physical and chemical properties (5-6).

Several investigators have used copolymerization and terpolymerization techniques to improve the properties of poly(methyl methacrylate), PMMA, a widely used positive electron beam resist (3, 7). Harris (8) has found that the adhesive properties of PMMA can be improved significantly when it is hydrolyzed with base to form a methyl methacrylate-methacrylic acid copolymer. Roberts (9, 10) has improved the vertical wall profile of PMMA through copolymerization with methacrylic acid and conversion of the acid groups to poly(methacrylic anhydride) sequences by heating at 200°C. Sensitivities comparable to those obtained by

<sup>1</sup> Present address: IBM System Products Division, East Fishkill Facility, Hopewell Junction, New York 12533.

Key words: electron beam lithography, positive resists, methyl methacrylate-isobutylene copolymers, polymer resists, electron resists.



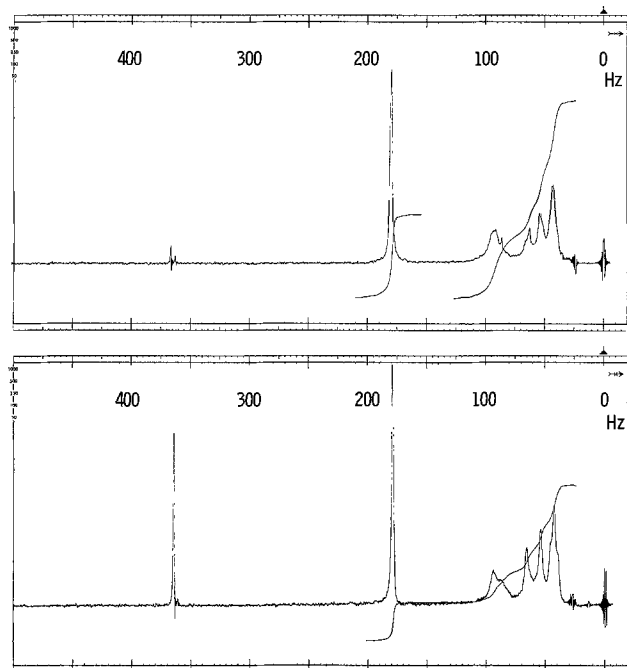


Fig. 1. NMR spectra of P(MMA-IB) in *o*-dichlorobenzene at 148°C; (top) 90/10 composition, (bottom) 75/25 composition.

Roberts have been reported for copolymers of methyl methacrylate and methyl isopropenyl ketone (11).

For the PMMA copolymers to meet the engineering requirements for economical processing, minimum sensitivities of  $3 \times 10^{-6}$  C/cm<sup>2</sup> or better would be needed. At the present time, sensitivities of this order of magnitude have been observed only with the poly (olefin sulfones), a new family of positive resists (12-14), and with several copolymers and terpolymers which function as negative resists (15). The lower sensitivities observed for many positive type polymeric resists have been attributed to their low  $G$ (scission), which is about 1.7 for PMMA (16).

To obtain the higher sensitivities desired in PMMA, copolymers containing the high radiation susceptible isobutylene group [ $G$ (scission) of about 5.4 (17)] were synthesized and evaluated. The maximum isobutylene content in these copolymers was evaluated as a function of resist performance. Additionally, the effect of the elastomeric isobutylene groups on the adhesive properties of the copolymers was evaluated on silanol and siloxane substrates. The sensitivity and etch performance of the copolymers were compared to a polymethylmethacrylate resist of similar molecular weight.

### Experimental

The P(MMA/IB) copolymers were prepared in a sealed Parr pressure reactor. Methyl methacrylate was complexed with ethyl aluminum sesquihalide ( $\text{AlEt}_{1.5}\text{Cl}_{1.5}$ ) (MX) at  $-20^\circ$  to  $-30^\circ\text{C}$  for 30 min inside a helium-purged dry box. Isobutylene and benzoyl per-

oxide catalyst were introduced, the reactor was sealed, and the polymerization was carried out at  $0^\circ\text{C}$  for 24 hr. The polymerization was terminated by adding the reaction mixture slowly to a large excess of cold methyl alcohol containing dilute hydrochloric acid. The copolymer was dissolved in benzene, precipitated in methyl alcohol, and extracted with hexane.

The copolymer structures were confirmed from their NMR spectra (Fig. 1) obtained in *o*-dichlorobenzene at  $148^\circ\text{C}$  with a Varian HA-100 spectrometer using tetramethylsilane as an internal standard. The methylene protons of the MMA units appeared as three peaks centered at 1.10, 1.26, and 1.44 $\delta$ , assigned to the cotactic configuration. The methylene protons belonging to both MMA and IB appeared together as a broad peak in the range 1.79-2.22 $\delta$ . The methoxy protons appeared as a single peak at 3.62 $\delta$ . The gem dimethyl protons of the isobutylene segments appeared as an unresolved single peak centered at 1.00 $\delta$ . Integration of the peak areas indicated that the ratios of methoxy protons to isobutylene methyl protons were correct for the proposed copolymer structures.

Elemental analyses for these copolymers confirmed the chemical compositions. Analysis calculated for a 90/10 P(MMA/IB) copolymer: C, 62.54; H, 8.69; O, 28.76. Found: C, 62.73; H, 8.59; O, 28.73. Analysis calculated for a 75/25 P(MMA/IB) copolymer: C, 66.40; H, 9.63; O, 23.97. Found: C, 66.76; H, 9.20; O, 24.15.

Molecular weight distribution and molecular weight averages (number and weight averages compared to polystyrene) were obtained with a modified Waters Associates GPC 200 chromatograph in THF solvent. Molecular weight averages ranged from 20,000 to > 100,000 (Table I).

Glass transition temperatures were determined with a du Pont TMA 900 differential thermal analyzer (Table I).

**Resist evaluation.**—The oxidized silicon surfaces were of two types, siloxane and silanol. The surfaces were prepared by the oxidation method described by Lusow (18). Resist films (1.0 $\mu$  thick) were spin coated from 7% solutions in chlorobenzene using a Headway Research Model EC-101 spinner. The films were pre-baked for 1 hr in air at  $145^\circ\text{C}$ . The thickness of the resist and oxide films (0.7 $\mu$ ) was measured on a Rank Talystep instrument. The resist films were exposed to measure doses of 15 kV electrons with a scanning raster type electron beam. The developed films were post-baked at  $100^\circ\text{C}$  for 30 min. The oxide films were etched with buffered HF at  $22^\circ\text{C}$ . The etch ratio of undercut (19) was measured by scanning electron microscopy.

### Results and Discussion

The isobutylene/MMA mole ratio in the monomer feed was an important factor in obtaining an alternating-type copolymer. In the presence of a large excess of isobutylene, an alternating copolymer was formed. When less isobutylene was used, the copolymer was rich in MMA (Table I). Similar results have been observed in the copolymerization of vinyl chloride and MMA (20). When  $\text{ZnCl}_2$  was used as the metal halide,

Table I. Copolymerization of methyl methacrylate and isobutylene<sup>a</sup>

Polymer composition, m/o, MMA/IB	MMA/MX, mole	IB/MMA, mole	Conversion, %	Molecular weight <sup>b</sup>		Glass transition temp $T_g$ , °C
				$M_w$	$M_n$	
90	10	1	14	28,750	18,940	60
75	25	4.5	34	115,700	41,250	43-47
Block <sup>c</sup>	1 <sup>d</sup>	1.5	5	43,800	24,400	77
50	50	25	°	—	—	—
100	0 (PMMA control)	—	—	107,420	42,175	105
0	100 (PIB control)	—	—	—	—	-73

<sup>a</sup> Benzoyl peroxide catalyst; monomer/catalyst = 500/1.

<sup>b</sup> Relative to polystyrene in THF by GPC.

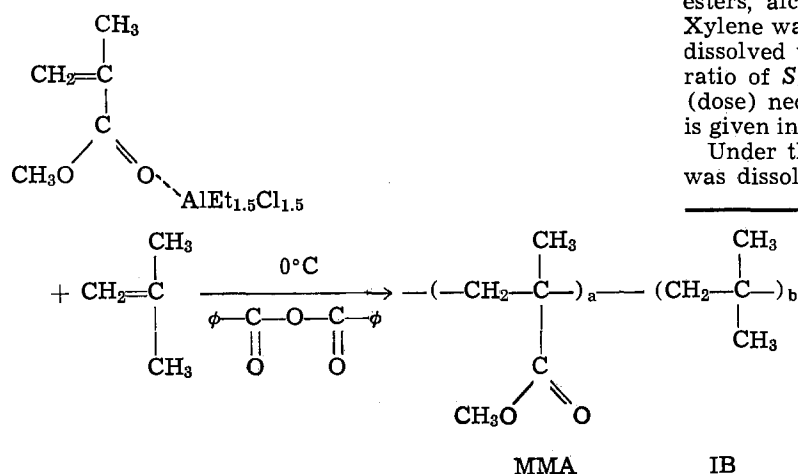
<sup>c</sup> Polymerization in ethyl acetate solvent at  $25^\circ\text{C}$ , no ratio determined.

<sup>d</sup> MX =  $\text{ZnCl}_2$ .

<sup>e</sup> Workup of polymer was difficult; the polymer was a solid at  $0^\circ\text{C}$ , but became a liquid at ambient temperature. The polymer molecular weight must be presumed to be low because of the dilution effect of the large excess of isobutylene.

a block-type copolymer was formed. These polymers were not of high molecular weight and all efforts to increase the molecular weight by changing the IB/MMA ratio and by use of different radical catalysts were unsuccessful.

The use of benzoyl peroxide, a free radical catalyst, in the presence of ethyl aluminum sesquichloride, increased the rate of polymerization with a concurrent decrease in the copolymer molecular weight. It has been demonstrated that the catalyst reacts with the charge transfer complex, that the radical initiated polymerization occurs concurrently with the spontaneous polymerization, and that the propagation reaction is the same irrespective of the initiation mechanism (20, 21), that is



The alternating- and block-type structures of the copolymers were established by pyrolysis studies in a gas chromatograph. The experimental polymers and a PMMA homopolymer were pyrolyzed into a gas chromatograph and the products were fractionated on a 15 ft  $\times$   $\frac{1}{8}$  in. chromosorb G column. PMMA depolymerized 95% to monomer, a portion of the chain undergoing dehydration and decarboxylation to leave a polyene residue. The block copolymer gave polyene fragments and isobutylene indicative of extensive sequences of PMMA uninterrupted by isobutylene sequences. The alternating copolymers gave products characteristic of isobutylene and branched isobutylene structures. Very little of the typical polyene backbone fragments, characteristic of PMMA, were observed, indicating that the PMMA sequences had been extensively interrupted.

The glass transition temperatures ( $T_g$ ) of the alternating- and block-type copolymers were found to depend on the isobutylene content of the copolymer and on the polymer structure (Table I). Increasing the isobutylene content of the alternating polymers reduced the  $T_g$ . The  $T_g$  of the block copolymer were higher than those of the alternating polymers. These copolymers and PMMA and PIB homopolymer controls having comparable molecular weights (Table I) were evaluated as electron beam resists.

The copolymers were soluble in many organic solvents and were spin coated from chlorobenzene solutions to thicknesses of several microns. The copolymer films, prebaked at 145°C, were sufficiently melted to allow the casting solvents to evaporate and to provide solid-phase wetting of the oxide substrate. PMMA (8) required a higher prebake of 180°C to remove solvents and to prevent excessive thinning of the unexposed region in the developer. Heating PMMA or the copolymers above 190°C resulted in chain scissioning to lower molecular weights and to the chain unzipping to monomer fragments. Polyisobutylene was a poor resist which had limited resolution because of a low glass transition temperature. Above the glass temperature, this polymer exhibited cold-flow properties and deformed under solvent developer stress (22).

Table II. Sensitivities of P(MMA-IB) copolymers at 15 kV

Polymer	Sensitivity, $\mu\text{C}/\text{cm}^2$
90/10	7.0
Block	6.0
75/25	4.5
PMMA	28.5

The resist sensitivities were determined by systematic stepped exposures ranging from  $1 \times 10^{-6}$  to  $1 \times 10^{-4}$  C/cm<sup>2</sup> at 15 kV. The choice of developers was evaluated by solubility mapping of the rate of dissolution of the unexposed ( $S_0$ ) area of copolymer films in various classes of organic solvents such as ketones, esters, alcohols, alkanes, and aromatic hydrocarbons. Xylene was found to be a representative solvent which dissolved the exposed region at rate  $S$ . The solubility ratio of  $S/S_0$  was fixed at 5 to 1, and the sensitivity (dose) necessary to achieve the differential dissolution is given in Table II.

Under these conditions, only 20% of a 1 $\mu$  thick film was dissolved after development. The processed films

could be used either in a lift-off scheme of metal patterns, or as an etch resist. The resists are readily stripped in solvents such as benzene or acetone.

The sensitivity of the copolymers increased with isobutylene content (Table II). The 75/25 copolymer required a low dose of  $5 \times 10^{-6}$  C/cm<sup>2</sup> compared to  $3 \times 10^{-5}$  C/cm<sup>2</sup> for the PMMA control. A comparable dose of  $4 \times 10^{-5}$  C/cm<sup>2</sup> has been noted (23) for PMMA when developed in optimum solvents to a  $S/S_0$  of 5.

The incorporation of isobutylene links in the PMMA chain whether in the form of alternating or blocky sequences enhanced the chain scissioning. Since higher initial molecular weights can also enhance the sensitivity of a positive resist (24), we attempted to increase the molecular weight of the copolymers but were not successful with other catalysts or reaction conditions.

The resist exhibited good resolution capable of producing fine dots of 1.25  $\mu$  geometry in 7000Å thick films of oxidized silicon (Fig. 2). Doses as low as  $3 \times 10^{-6}$  C/cm<sup>2</sup> could be used but the unexposed resist thinned about 40%.

The P(MMA-IB) copolymers were unaffected by cold flow because of their higher glass transition tem-

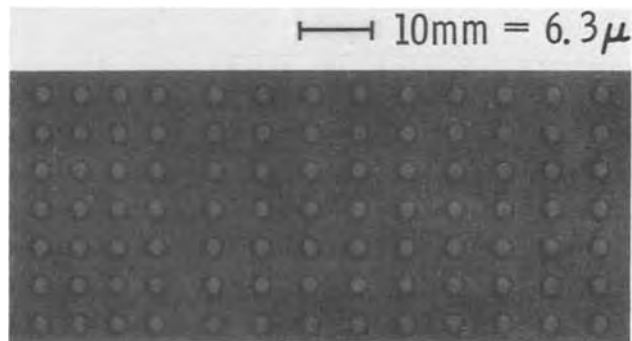


Fig. 2. Images (1.25 $\mu$ ) etched with P(MMA-IB) resist in 7000Å thermal SiO<sub>2</sub>.

peratures (Table I). However, for optimum processing, the isobutylene content of the copolymer should not exceed 25 mole per cent (m/o) because the glass transition temperature will be significantly lowered. If the glass transition temperature is too low, images in the polymer melt during thermal processing above 100°C. The glass transition of the block copolymer was higher than those of the alternating copolymer. The block form would offer higher processing temperatures.

The adhesion and etch resistance of PMMA and the P(MMA-IB) copolymers on silanol (Si-OH) and

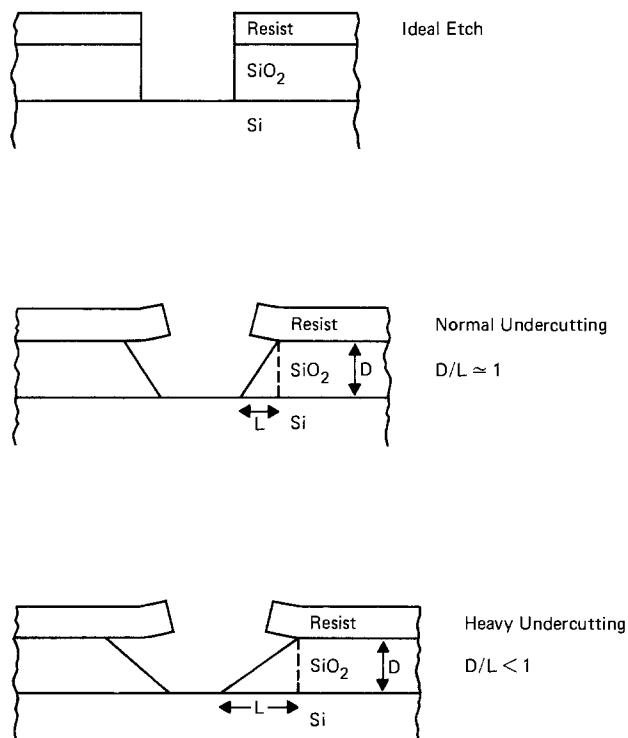


Fig. 3. Resist pattern adhesion and undercutting

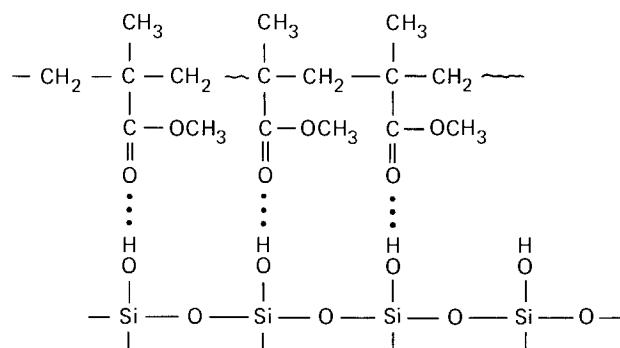


Fig. 4. H bonding of PMMA to silanol surface

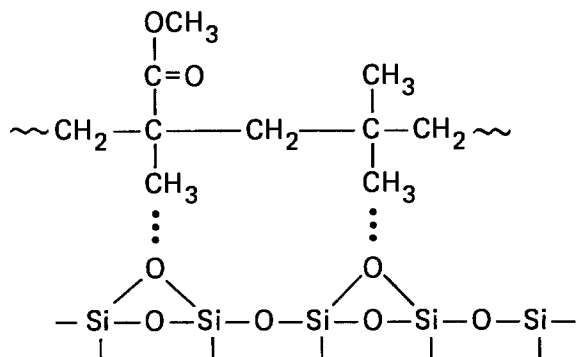


Fig. 5. Van Der Waals bonding of MMA-IB copolymers to siloxane surfaces.

Table III. Adhesion of P(MMA-IB) copolymers on siloxane surfaces

Polymer	Adhesion, $D/L$
PMMA	$0.4 \pm 0.1$
90/10	$0.7 \pm 0.1$
75/25	$0.9 \pm 0.1$
Block	$0.6 \pm 0.1$

siloxane (SiO) surfaces were evaluated by measurement of an undercut factor,  $D/L$ . Films of resist (1.0 $\mu$  thick) were used to etch 7000Å films of silicon dioxide. The undercut factor,  $D/L$ , assesses the depth,  $D$ , to lateral width,  $L$ , of a normalized line at the bottom of the etched substrate (19). A  $D/L$  factor less than one implies heavy undercutting (large  $L$ ) underneath the resist edge (Fig. 3).

On silanol surfaces, PMMA adhered very well and exhibited a normal undercut of  $D/L$  of  $0.9 \pm 0.1$ . The adhesion of PMMA and other methacrylate polymers on silica surfaces has also been measured by absorption isotherms and infrared spectroscopy (25, 26). Adhesion was attributed to the hydrogen bonding of the carbonyl group (C=O) (Fig. 4) of the ester to the surface hydroxyl (OH) groups of silanol. The isobutylene segments in the P(MMA-IB) copolymers did not alter the adhesion on the silanol surfaces ( $D/L = 0.9 \pm 0.1$ ) since there are sufficient ester groups remaining for hydrogen bonding.

When PMMA was coated on siloxane surfaces, the etched images were badly undercut with a  $D/L$  value of  $0.4 \pm 0.15$ . The poor adhesion is attributed to the loss of hydrogen bonding since the silanol groups have been converted to siloxane bridges. However, the adhesion of the P(MMA-IB) copolymers on the siloxane surfaces improved with increasing isobutylene content (Table III). The enhanced adhesion is attributed to the increased Van der Waals type bonding with the increasing number of alkyl groups in the polymer chain (Fig. 5).

## Summary

PMMA copolymers containing isobutylene groups are very sensitive to electron beam radiation. The high sensitivities are attributed to the isobutylene "weak links" in the polymer chain.

The adhesion of PMMA type resists can also be improved on siloxane surfaces by incorporation of elastomeric isobutylene groups.

The improvement of the resist performance of PMMA represents an application of polymer tailoring wherein certain deficiencies in one polymer system (PMMA) may be overcome by copolymerization with another monomer (IB) which has good radiation sensitivity, but has limited applicability.

## Acknowledgments

Analytical and instrumental measurements and assistance are gratefully acknowledged: The GPC measurements by A. Ouano and A. Gregges, the NMR analyses by T. Horikawa, the chromatographic and DTA analysis by E. Barrall and J. Logan, and the sensitivity measurements by B. Zingerman.

Manuscript submitted Oct. 14, 1975; revised manuscript received March 5, 1976.

Any discussion of this paper will appear in a Discussion Section to be published in the June 1977 JOURNAL. All discussions for the June 1977 Discussion Section should be submitted by Feb. 1, 1977.

Publication costs of this article were partially assisted by IBM Corporation.

## REFERENCES

- M. Hatzakis, Applied Polymer Symposium, **23**, 73 (1974).
- G. Brewer, IEEE Spectrum, **8**, 23 (1971).
- M. Hatzakis, This Journal, **116**, 1033 (1969).
- A. Broers and M. Hatzakis, Sci. Am., **33**, 37 (1973).

5. L. Thompson, *Solid State Technol.*, **17**, 7 (1974).
6. L. Thompson, *ibid.*, **17**, 8 (1974).
7. I. Haller, M. Hatzakis, and R. Srinivasan, *IBM J. Res. Develop.*, **12**, 251 (1968).
8. R. Harris, *The Journal*, **120**, 270 (1973).
9. E. Roberts, *Applied Polymer Symposium*, **23**, 87 (1974).
10. E. Roberts, *ACS Organic Coating and Plastic Chemistry Preprints*, **35**, 281 (1975).
11. A. Levine, M. Kaplan, and E. Poliniak, *Poly. Eng. Sci.*, **14**, 518 (1974).
12. L. Thompson and M. Bowden, *This Journal*, **120**, 1722 (1973).
13. M. Bowden and L. Thompson, *J. Appl. Poly. Sci.*, **17**, 3211 (1973).
14. M. Bowden and L. Thompson, *Applied Polymer Symposium*, **23**, 99 (1974).
15. L. Thompson, E. Feit, M. Bowden, P. Lenzo, and E. Spencer, *This Journal*, **121**, 1500 (1974).
16. A. Charlesby, "Atomic Radiation and Polymers," p. 338 Pergamon Press, New York (1960).
17. *ibid.*, p. 326.
18. R. Lussow, *This Journal*, **115**, 660 (1968).
19. L. Maissel and R. Glang, "Handbook of Thin Film Technology," pp. 7-44, McGraw-Hill, New York (1970).
20. B. Patnaik and N. Gaylord, *Poly. Letters*, **9**, 347 (1971).
21. N. Gaylord, *J. Poly. Sci.*, **31**, 247 (1970).
22. H. Ku and L. Scala, *This Journal*, **116**, 980 (1969).
23. J. S. Greeneich, *ibid.*, **122**, 970 (1975).
24. M. Hatzakis, C. Ting, and N. Viswanathan, Editors "Electron and Ion Beam Science and Technology, Sixth International Conference," p. 63, San Francisco Press, San Francisco (1975).
25. B. Fontana and J. Thomas, *J. Phys. Chem.*, **65**, 480 (1961).
26. B. Fontana, *ibid.*, **68**, 2360 (1963).

## Variation of Solid Composition and Thickness during LPE Growth of $\text{Al}_x\text{Ga}_{1-x}\text{As}$

Hachiro Ijuin<sup>1</sup> and Shun-ichi Gonda

*Electrotechnical Laboratory, Tanashi, Tokyo, Japan*

### ABSTRACT

The variations of the solid composition and of the layer thickness with the growth time in the LPE  $\text{Al}_x\text{Ga}_{1-x}\text{As}$  were measured by utilizing luminescence, x-ray analysis, and microscopy by means of an electron microprobe. The variations determined by the experiments are in good agreement with the calculations based on the diffusion-limited growth theory including the effects of nucleation in the ternary solution.

Liquid phase epitaxy (LPE) has been widely used for such applications as electronic and optoelectronic devices which require high quality in crystallographic nature and variety in structure. The LPE layer is normally grown on the substrate from a saturated solution and occasionally from an undersaturated or a supersaturated solution. Variables such as the solid composition and the thickness of the crystal grown by LPE are of great importance in practical application. The variation of the solid composition of  $\text{Al}_x\text{Ga}_{1-x}\text{As}$  with the growth temperature reflects the growth process and growth conditions. Theoretically, the variation of the solid composition with the growth temperature has been investigated on the basis of the phase diagram for the growth from a saturated solution by Ilegems and Pearson (1) and from a supersaturated solution by Thompson and Kirkby (2). Experimentally, the variation has been investigated by Rado and Crawley (3) and Thompson and Kirkby (2). The results of Rado and Crawley have been compared with the theoretical ones of Ilegems and Pearson. The variation of the solid composition with the growth temperature is regarded as independent of the cooling rate of the growth in the above investigations.

Since LPE growth is not an equilibrium process, the variations of the composition and the thickness of the grown layer are affected by the diffusion rate of the solutes in the solution. Crossley and Small (4) have analyzed the diffusion-limited process by means of a numerical method with which complicated growth conditions are easily taken into account. Nucleation in the solution is considered to affect the process in the LPE growth. We have analyzed the diffusion-limited process taking into account the effects of nucleation in the

ternary solution (5, 6). A consistent argument about the experiment and theory has not been made except for the very low cooling-rate process.

In this paper, by the LPE growth of  $\text{Al}_x\text{Ga}_{1-x}\text{As}$  under different growth conditions, the phase diagram of  $\text{Al}_x\text{Ga}_{1-x}\text{As}$  generated using the phase data by Ilegems and Panish (7) is discussed. Furthermore, the variations of the solid composition and the thickness of  $\text{Al}_x\text{Ga}_{1-x}\text{As}$  are measured in detail and the experimental results are compared with the calculations based on the diffusion-limited growth theory including the effects of nucleation in the solution.

### Experimental

The  $\text{Al}_x\text{Ga}_{1-x}\text{As}$  with various solid compositions  $x = 0.35, 0.40, 0.45,$  and  $0.55$  was grown by LPE at  $850^\circ\text{C}$  on (100) GaAs substrate using a horizontal sliding-type LPE apparatus. The solution was prepared from 3g of Ga and sufficient amounts of GaAs and Al to produce a LPE layer with appropriate solid composition. Equilibrium liquid compositions were calculated from the phase data reported by Ilegems and Panish (7). The errors in measuring weights of source materials were less than 0.5 mg for GaAs and Al and 5 mg for Ga. The loaded boat was heated in a resistance furnace up to the maximum temperature,  $900^\circ\text{C}$ , and was held there for 30 min. Then it was cooled to a growth temperature of  $850^\circ\text{C}$  and held again for about 30 min to ensure a uniform temperature profile around the boat. The substrate had been tipped in the solution for 20 min before it was cooled at a rate of  $0.5^\circ$  or  $1^\circ\text{C}/\text{min}$ . The solution was pushed off after the temperature was lowered to  $840^\circ$  or  $830^\circ\text{C}$ . In order to make a consistent argument of the phase diagram and growth mechanisms, the optimum temperature program was used so as to dissolve the source materials completely and to minimize vaporization of the con-

<sup>1</sup> On leave of absence from Waseda University, Shinjuku, Tokyo, Japan.

Key words: compositional variation, nucleation in ternary solution, constitutional supercooling, equilibrium liquidus temperature.

stituents. Clear and flat surfaces from which the growth solutions were wiped off were obtained in a leak-tight system.

After cleaving the crystal, layer thickness was measured using photo and scanning electron microscopy. Solid compositions were measured by electron probe x-ray microanalysis (EPMA) on the cleaved surfaces along the direction of growth in  $2\ \mu\text{m}$  steps. Radius of the electron beam was smaller than  $200\text{\AA}$ . Emission wavelength of cathodoluminescence was measured in order to check the results obtained by EPMA. In this case the solid composition,  $x$ , was determined by the empirical formula of Onton *et al.* (8). The errors in these measurements were estimated to be less than 3%.

### Experimental Results

The variations of the solid composition in the grown layer determined using EPMA for various LPE  $\text{Al}_x\text{Ga}_{1-x}\text{As}$  are shown by circles in Fig. 1. Closed and open circles correspond to the results of the growth at  $0.5$  and  $1.0\ ^\circ\text{C}/\text{min}$ , respectively. The solid composition decreases with increasing thickness in the composition range shown here. The variations of the layer thickness with growth time are shown in Fig. 2. As in Fig. 1, closed and open circles indicate the different cooling rates  $0.5^\circ$  and  $1.0^\circ\text{C}/\text{min}$ , respectively. The measured initial compositions of the layers range from about  $0.35$  to  $0.55$ . The difference in growth rate of the layers with different initial solid compositions is small.

Once the solid composition,  $x$ , and the growth temperature are determined, sufficient amounts of source materials can be calculated by using the phase diagram. The relation between the weights of Al and GaAs for  $3\text{g}$  of solvent Ga are shown in Fig. 3 by those contours of equilibrium temperature and solid

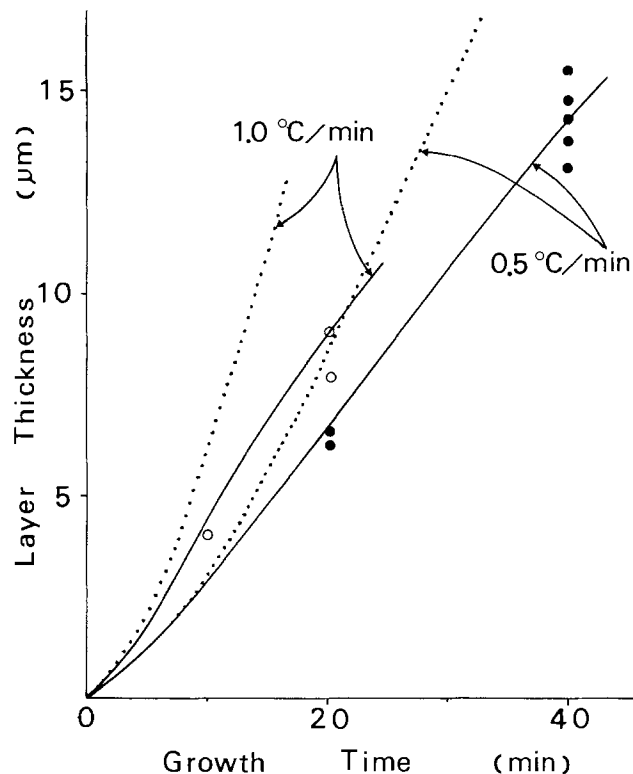


Fig. 2. The variation of the layer thickness with the growth time in LPE  $\text{Al}_x\text{Ga}_{1-x}\text{As}$ . Solid and dotted lines indicate the curves for  $x = 0.40$  calculated using the diffusion-limited growth theory with and without nucleation in the solution, respectively.

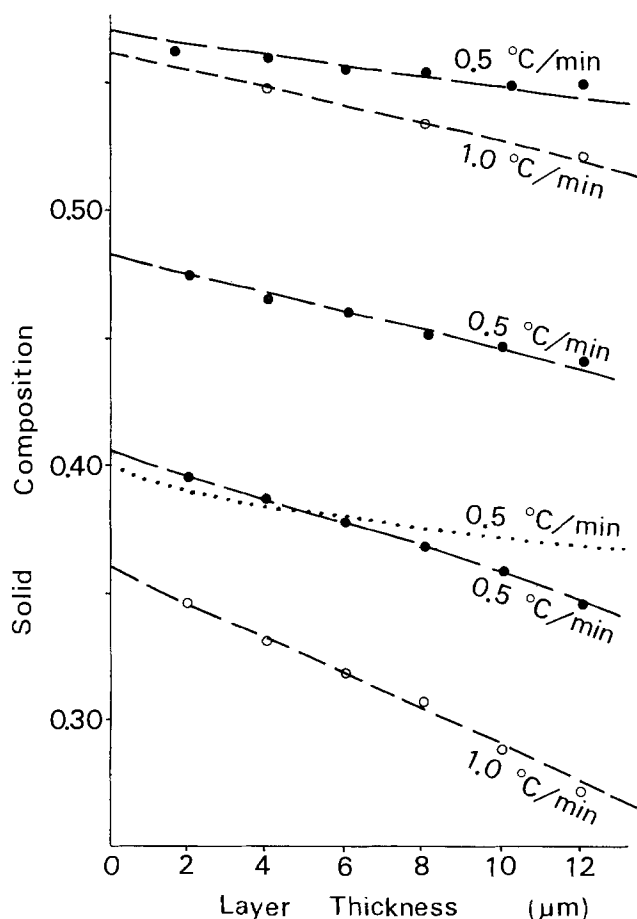


Fig. 1. The variation of the solid composition in the  $\text{Al}_x\text{Ga}_{1-x}\text{As}$  LPE layers with layer thickness. Dashed and dotted lines are the results calculated using the diffusion-limited growth theory with and without nucleation in the solution.

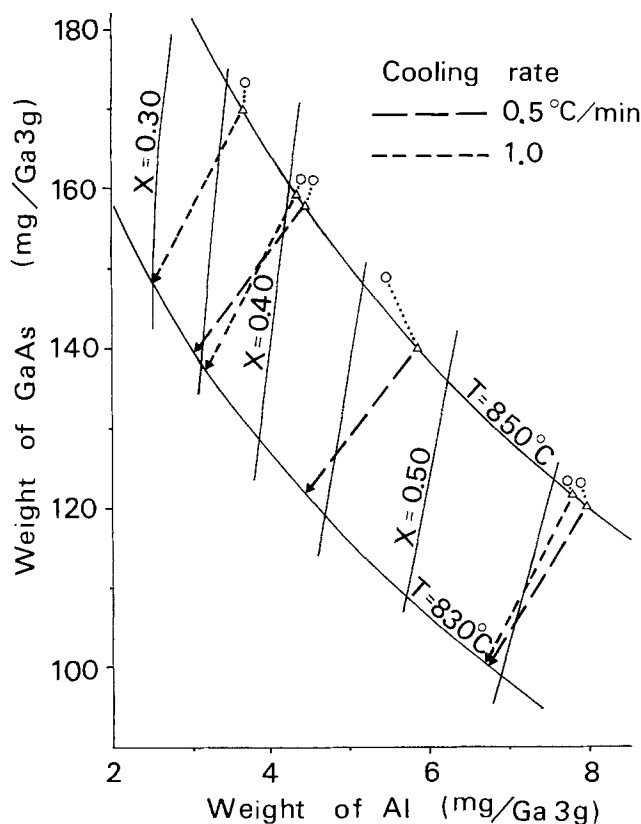


Fig. 3. Contours of the equilibrium temperature and the solid composition (solid lines) on the weight axes of Al and GaAs. Explanation of the various marks is given in the text.

composition which are calculated by using the phase data of the Al-Ga-As system reported by Ilegems and Panish (7). Circles indicate the measured weights of the source materials, Al and GaAs. Triangles indicate

the starting growth temperature and the initial solid compositions determined from the experiments. Arrows in Fig. 3 show the variation of the solid composition converted from Fig. 1 using the thickness vs. temperature relation which can be easily derived from Fig. 2.

### Discussion

Compositional profiles in the grown layer are monotonically decreasing ones toward the direction of growth in the composition range concerned, as shown in Fig. 1. This tendency is mainly the result of the large distribution coefficient of solute Al. When nucleation in the liquid cannot be neglected in the LPE growth, the variation of the solid composition tends to be large because the growth rate decreases due to less compositional gradient of solutes in the solution. Since the growth rate of  $\text{Al}_x\text{Ga}_{1-x}\text{As}$  is limited by an arrival rate of As to the growing interface, the growth rate is expected to be lowered for crystals of larger solid composition (of Al) which grow from solutions with a lesser atomic fraction of As. As shown in Fig. 2, a significant difference in the variation of growth rate for different solid compositions was not recognized by experiments in the presented composition range. If the LPE growth process is analyzed taking into account nucleation in the solution, the experimental results can be well explained.

We have newly introduced the effects of nucleation in the ternary solution into analysis of the growth mechanism (5, 6). As the growth proceeds at higher cooling rate, the compositions of solutes in the liquid decrease more at the growing interface but the composition does not change so much at the solution surface. The equilibrium liquidus temperature of the solution calculated from the phase data and the compositions of solutes are highest at the solution surface because of constitutional supercooling. Effects of nucleation are taken into account by considering that the equilibrium liquidus temperature of the solution cannot be higher than  $T + \Delta T_c$ , where  $T$  is the real temperature of the solution and  $\Delta T_c$  is a certain critical value of supercooling. The compositional profiles of solutes are flattened at the solution surface at first due to nucleation in the solution when the equilibrium liquidus temperature becomes higher than  $T + \Delta T_c$ . Therefore, an additional boundary condition to satisfy a criterion of nucleation is applied to the numerical analysis of LPE growth process made by Crossley and Small (4) for the growth of  $\text{Al}_x\text{Ga}_{1-x}\text{As}$  from a nucleation-free solution. In numerical calculation we assumed solution thickness of 5 mm for Ga solution of 3g in the solution reservoir of the boat with area of  $1 \times 1 \text{ cm}^2$ . The diffusion coefficient of As was adopted from the data of Rode (9), while the coefficient of Al was adjusted to be 75% of the value in Sn solution reported by Ma and Swalin (10) so as to fit the theoretical curves to the experimental data (6). By adopting  $2.5^\circ\text{C}$  as  $\Delta T_c$ , good agreement between the experimental and theoretical results is obtained, concerning the growth of the LPE layer grown at different cooling rates as shown by solid lines in Fig. 2 as well as dashed lines in Fig. 1 concerning the variation of the solid composition in the grown layer. Theoretical calculations indicate that the growth rate shows almost the same variations in the presented composition range, although the growth rate largely deviates in the

smaller composition range. The critical value of supercooling may be thought to be different for different cooling rates, growth temperatures, or solid compositions. However, the difference is hardly recognized in the critical value of supercooling in the ranges concerned. For comparison, the results for  $\text{Al}_x\text{Ga}_{1-x}\text{As}$  ( $x = 0.40$ ) calculated without taking account of nucleation in the solution are shown by dotted lines in Fig. 1 and 2.

The phase diagram based on the phase data by Ilegems and Panish (7) is experimentally checked, as shown in Fig. 3. The solid compositions of AlAs at the starting growth temperature nearly coincide with the values expected from the contours of constant AlAs in the solid, but these appear to be slightly larger in the large solid composition region. This is presumably due to vaporization of the solute As from the solution.

### Conclusions

The variation of solid composition in the grown  $\text{Al}_x\text{Ga}_{1-x}\text{As}$  layer and the variation of the layer thickness with growth time were investigated experimentally and were compared with the growth theory. Good agreement was obtained when a critical supercooling of the ternary solution is assumed to be  $2.5^\circ\text{C}$ . A sort of phase diagram, the relations among the weights of source materials, of the Al-Ga-As system generated by using the reported phase data was checked experimentally. Rather good agreement was obtained, although there was some tendency to deviate in the large solid composition range.

### Acknowledgments

The authors are grateful to Y. Matsushima and Y. Makita for their helpful discussions and to T. Okumura and T. Ikeno for the EPMA measurements. They also thank S. Mukai, J. Shimada, K. Sakurai, and Y. Mita for their continued interest.

Manuscript submitted Dec. 31, 1975; revised manuscript received Feb. 26, 1976.

Any discussion of this paper will appear in a Discussion Section to be published in the June 1977 JOURNAL. All discussions for the June 1977 Discussion Section should be submitted by Feb. 1, 1977.

Publication costs of this article were partially assisted by Electrotechnical Laboratory.

### REFERENCES

1. M. Ilegems and G. L. Pearson, "1968 Symposium on GaAs," p. 3, Institute of Physics and the Physical Society London (1968).
2. G. H. B. Thompson and P. A. Kirkby, *J. Cryst. Growth*, **27**, 70 (1974).
3. W. G. Rado and R. L. Crawley, *This Journal*, **119**, 1779 (1972).
4. I. Crossley and M. B. Small, *J. Cryst. Growth*, **15**, 268 (1972).
5. S. Gonda and H. Ijuin, *Bull. Electrotech. Lab.*, **39**, 490 (1975).
6. H. Ijuin and S. Gonda, *J. Cryst. Growth*, **33**, 215 (1976).
7. M. Ilegems and M. B. Panish, *J. Phys. Chem. Solids*, **35**, 409 (1974).
8. A. Onton, M. R. Lorentz, and J. M. Woodall, *Bull. Am. Phys. Soc.*, **16**, 371 (1971).
9. D. L. Rode, *J. Cryst. Growth*, **20**, 13 (1973).
10. C. H. Ma and R. A. Swalin, *Acta Met.*, **8**, 390 (1960).



## Particle Growth in Zinc Sulfide Phosphor Containing Halide Fluxes

R. A. Brown\*<sup>1</sup>

RCA Electronic Components, Lancaster, Pennsylvania 17604

The mechanisms by which zinc sulfide powders grow under the action of heat and in the presence of a fluxing agent have been the subject of considerable discussion and speculation (1). Common fluxes employed in ZnS type phosphors include the halogen salts of ammonium and the alkali or alkaline earth metals, although compounds such as barium thiozincate (2) have been recommended also. According to the classical concept of flux action (3), the function of the additive is to provide a liquid phase in which the zinc sulfide is soluble, so that transport of material can occur readily. Apparently, no experimental evidence has been offered in support of this hypothesis. Indeed, the data of Gashurov and Levine (4) show that at 880°C ZnS has a very limited solubility of 0.0152 mole/1000g solvent in the common fluxing agent NaCl. More recent work (5-7) has emphasized the importance of diffusion phenomena in thermal recrystallization and sintering experiments on zinc sulfide powders.

Thus, McQueen and Kuczynski (5) carried out work on the sintering of polycrystalline ZnS as a function of temperature and atmosphere of firing, and interpreted the results obtained in terms of material transport by diffusion mechanisms. Studies on the kinetics of hexagonal-cubic phase transformation in ZnS at 800°-900°C in zinc vapor (6) suggested a diffusion-controlled transition having an activation energy of 67 kcal. Brown (7) investigated the mechanism of flux action in ZnS:Ag phosphors containing either 2 or 10% NaCl. In these systems, and also for zinc sulfide without additives, the rate of increase in particle diameter,  $D$ , at a firing time,  $t$ , followed the expression  $D^3 = kt$ , where  $k$  is a constant. Two distinct regions of growth were noted. Below about 1000°C an activation energy of 29 kcal was obtained, corresponding to movement of zinc through interstitial channels. At higher temperatures the measured activation energy was 59 kcal, suggesting bulk diffusion of zinc. This change in mechanism corresponded to the onset of the cubic-hexagonal phase transformation.

The objective of the present work was to extend the particle growth experiments reported previously (7) to include other fluxes, with the aim of obtaining a better understanding and control of the particle size characteristics of zinc sulfide phosphors. With this object in mind, measurements were carried out on the rate of increase in particle diameters, as a function of duration and temperature of heating, for the following systems: ZnS:0.015% Ag with either 2% ZnCl<sub>2</sub>, 2% NH<sub>4</sub>Cl, or 2% CaCl<sub>2</sub>. Note that these values correspond to weight per cent (w/o) compositions. Particle dimensions were obtained by Coulter Counter techniques;

the numbers quoted represent median point by weight of particles.

### Experimental and Results

Details of the precipitation of zinc sulfide (8) and the preparation and measurement of phosphors (7) have been given previously. A brief account will suffice here.

Batches of about 200g of zinc sulfide were obtained from 2 liters of 1M zinc sulfate solution at 25°C, using a hydrogen sulfide flow of 0.82 liter/min. After filtration through a Buchner funnel and washing with deionized water, the precipitate was subsequently dried for 6 hr at 100°C.

Compositions studied included ZnS:0.015% Ag with 2% ZnCl<sub>2</sub>, 2% NH<sub>4</sub>Cl, or 2% CaCl<sub>2</sub>. Zinc chloride was added as the hexahydrated salt and calcium chloride as the dihydrate. In order to avoid oxidation of the zinc sulfide and maintain a stoichiometric composition during heating, the following experimental procedure was employed. Test samples of 10g were placed in covered Vitreosil crucibles, located in a larger crucible, surrounded by ZnS powder, and covered with a lid. Kremheller (9) employed a somewhat similar technique during heating of ZnS single crystals and found no sublimation of the crystals, even at 1200°C. Specimens were fired at temperatures in the range 750°-1250°C, for periods of 1-10 hr. Subsequently, the materials were washed with deionized water to remove excess flux, dried at 100°C, and examined by Coulter Counter methods to determine particle sizes.

Figure 1 shows a typical set of curves in which  $\log D$  is plotted as a function of  $\log t$  (7) for ZnS:0.015% Ag with 2% zinc chloride. Between 750° and 1100°C the curves are linear with a slope of 0.33. Thus particle growth follows a  $D^3 = kt$  dependence. An Arrhenius activation energy was derived from the data of Fig. 1, using a plot of  $-\log t'$  against  $1/T$  (7) where  $t'$  is the time required to reach an arbitrarily chosen particle size of 10  $\mu\text{m}$ . This plot is shown in Fig. 2, which gave an activation energy of  $29 \pm 2$  kcal for the growth processes. Activation energies were calculated by means of a regression and correlation analysis carried out by G. M. Ehemann of this laboratory with the use of an RCA Spectra 70 computer program. At 1200° and 1250°C in this system the relationship between  $\log D$  and  $\log t$  was again linear, but in this case with a slope of 0.66 as demonstrated in Fig. 1.

Particle size results for ZnS:Ag containing 2% NH<sub>4</sub>Cl are given in Fig. 3. Up to 1000°C there was a gradual, slow rise in particle diameter with increase in the temperature and duration of firing, although no accurate activation energy could be obtained in this range. Between 1100° and 1200°C the relationship between  $\log D$  and  $\log t$  was linear with a slope of 0.66, i.e., a  $D^{1.5} = kt$  law was followed. Figure 4 gives the

\* Electrochemical Society Active Member.

<sup>1</sup> Present address: Department of Chemistry, The Polytechnic of North London, Holloway, London N7 8DB, England.

Key words: thermal recrystallization, ZnS-ZnCl<sub>2</sub>, ZnS-NH<sub>4</sub>Cl, ZnS-CaCl<sub>2</sub>.

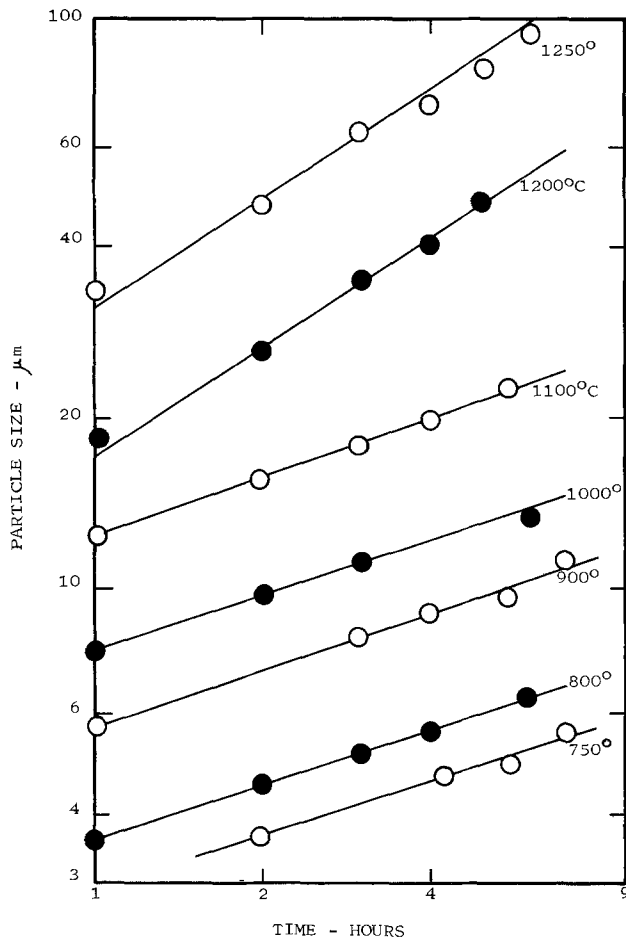


Fig. 1. Rate of particle growth in ZnS:Ag, 2% ZnCl<sub>2</sub>

corresponding Arrhenius plot, from which the energy of activation was calculated to be  $48 \pm 3$  kcal.

Results obtained in the particle growth experiments for ZnS:Ag, 2% CaCl<sub>2</sub> are presented in Fig. 5. At 750° or 800°C the slope of the lines was 0.33, whereas from 850° to 1250°C a slope of 0.5 was obtained. Figure 6 gives the Arrhenius plot for particle growth in ZnS:0.015% Ag with 2% calcium chloride. From this plot an activation energy of  $36 \pm 2$  kcal was calculated for temperatures in the region 850°-1250°C.

Table I summarizes reported work concerning activation energies and particle size dependences obtained for various zinc sulfide systems. Since the results obtained are a function of factors such as sample size, configuration of the firing vessel, duration of heating, rate of cooling, and atmosphere of firing, an exact correspondence is not to be expected. However, the overall time dependence and activation energies obtained

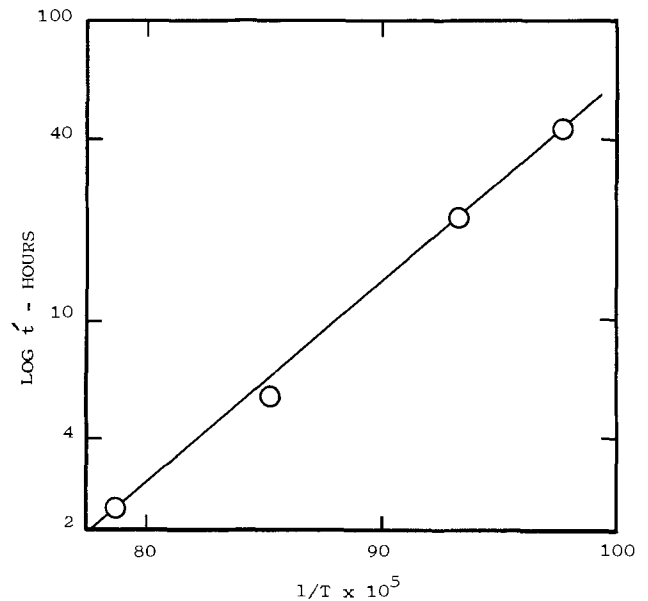


Fig. 2. Arrhenius plot for ZnS:Ag, 2% ZnCl<sub>2</sub>

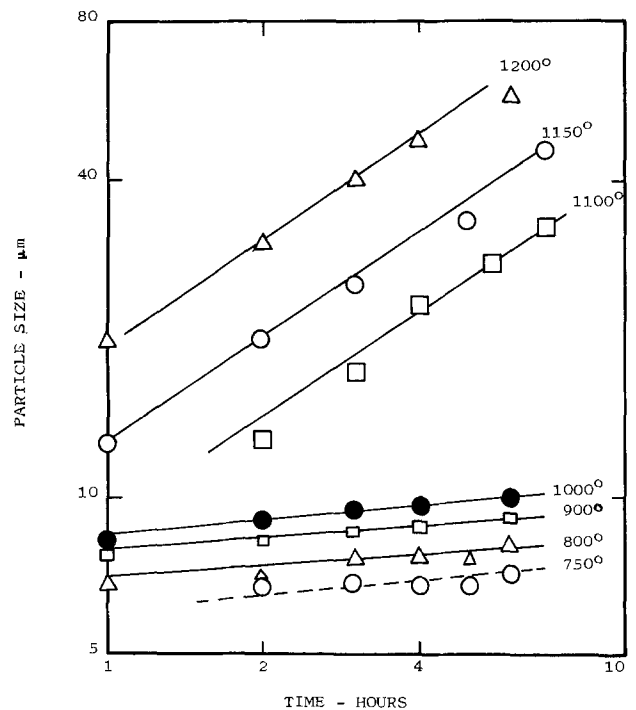


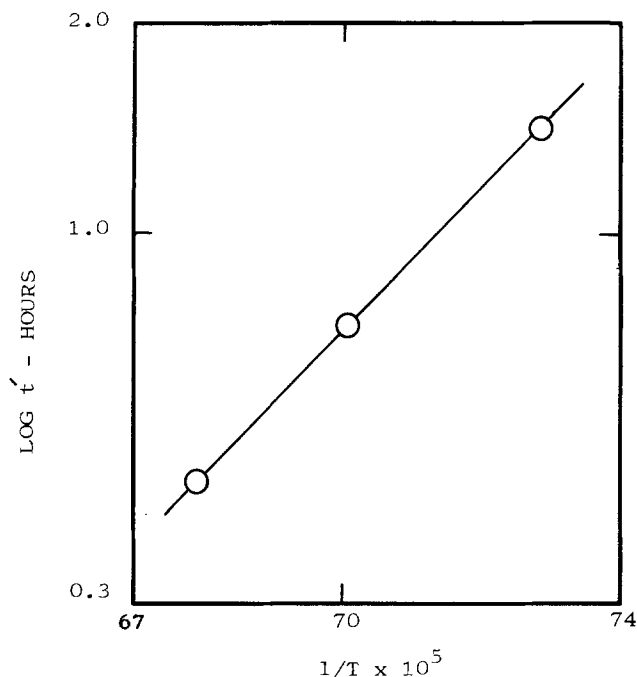
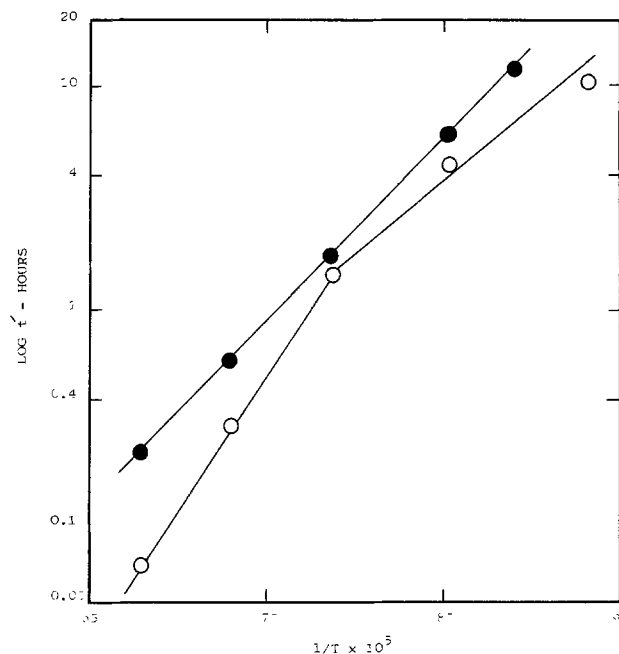
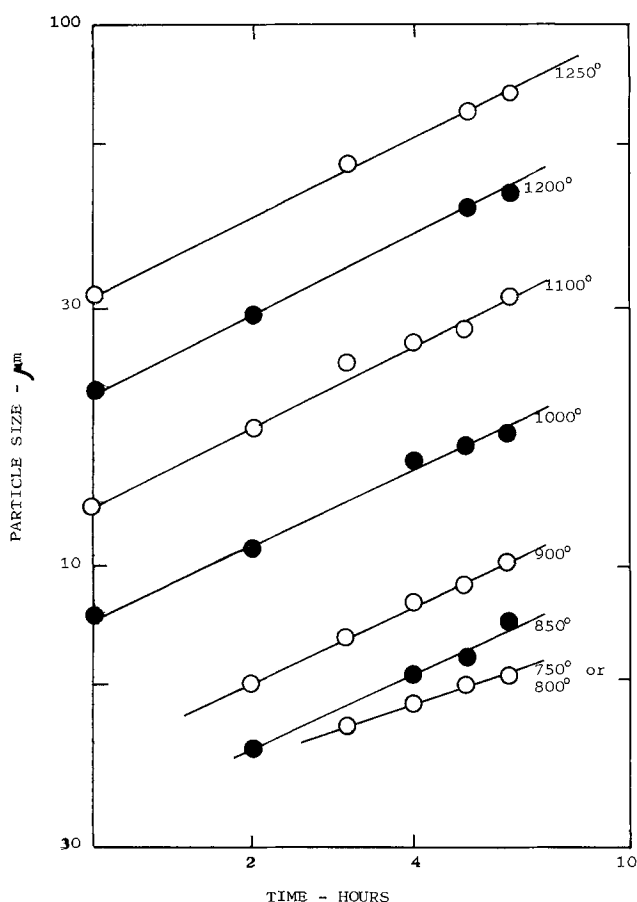
Fig. 3. Rate of particle growth in ZnS:Ag, 2% NH<sub>4</sub>Cl

should be comparable, provided the experimental conditions are not radically different.

Table I. Summary of particle growth data obtained by various workers for ZnS systems

System	Temperature (°C)	Activation energy (kcal)	D <sub>n</sub>	Reference	Comments
1. ZnS:Ag, 2% NaCl	700-1100	13	D <sub>4/5</sub>	(7b)	Initial recrystallization
2. ZnS, 2% NaCl	750-1200	14	D <sub>2</sub>	(11)	
3. ZnS:Ag, 2% or 10% NaCl	750-1000	29	D <sub>3</sub>	(7a)	Possibly initial recrystallization?
4. ZnS:Ag, 2% ZnCl <sub>2</sub>	750-1000	29	D <sub>3</sub>	Present	
5. ZnS:Cu, 4% or 10% NaCl	1000-1150	30	D <sub>3</sub>	(13)	Diffusion-controlled mechanism suggested
6. ZnS	900-1350	30	D <sub>3</sub>	(12)	
7. ZnS	800-1200	28	D <sub>2</sub>	(11)	
8. ZnS, 2% NaCl	1250		D <sub>3</sub>	(14)	
9. Interstitial Zn diffusion in ZnS		29		(10)	Bulk Zn diffusion
10. ZnS:Cu	1000-1150	80	D <sub>3</sub>	(13)	
11. ZnS:Ag, 2% or 4% NaCl	1000-1250	58	D <sub>3</sub>	(7a)	
12. ZnS	1100-1250	61	D <sub>3</sub>	(7a)	
13. Bulk diffusion of Zn in ZnS		61.5		(10)	Evaporation-condensation
14. ZnS:Ag, 2% NH <sub>4</sub> Cl	1100-1200	48	D <sub>1.5</sub>	Present	
15. ZnS:Ag, 2% ZnCl <sub>2</sub>	1200 and 1250		D <sub>1.5</sub>	Present	Diffusion-controlled precipitation
16. ZnS:Ag, 2% CaCl <sub>2</sub>	850-1250	36	D <sub>3</sub>	Present	



Fig. 4. Arrhenius plot for ZnS:Ag, 2% NH<sub>4</sub>ClFig. 6. Arrhenius plots for particle growth: ● ZnS:Ag, 2% CaCl<sub>2</sub>; ○ ZnS:Ag, 2% NaCl—data of Brown, Ref. (7a).Fig. 5. Rate of particle growth in ZnS:Ag, 2% CaCl<sub>2</sub>

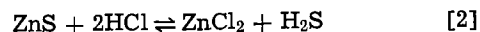
### Discussion

On the basis of these results, the following sequences are suggested to occur during thermal recrystallization in zinc sulfide containing the various fluxes.

In the presence of 2% zinc chloride, particle growth at 750°-1000°C followed a  $t^{1/3}$  law with an activation energy of 29 kcal. These same results were obtained by Brown (7a) for thermal recrystallization in ZnS containing 2 or 10% NaCl in this temperature range, and

these findings are in accord with the value of 29 kcal given by Secco (10) for interstitial zinc diffusion. It is interesting to compare the data obtained in the present study with those given by other authors, as reported in Table I. Thus, Kremheller and Faria (11) fired zinc sulfide, and ZnS with different additives, for 2 hr at 750°-1250°C in open boats using a flowing helium atmosphere, and measured particle sizes by a gas adsorption method. For ZnS without additives these workers (11) derived an activation energy for particle growth of 28 kcal,<sup>2</sup> together with a time dependence of 0.5. This same value of 30 kcal was quoted by Bube (12) on the basis of a diffusion model. Shionoya and Amano (13) obtained a  $(\text{time})^{1/3}$  dependence and an activation energy of 30 kcal for thermal recrystallization in zinc sulfide:Cu containing either 4 or 10% NaCl. The data of Leverenz (14) for ZnS, 2% NaCl at 1250°C also follow a  $t^{1/3}$  expression. Consequently, the time dependence and activation energy are the same in zinc sulfide without flux as for ZnS containing either NaCl or ZnCl<sub>2</sub>, which suggests that the same mechanism operates in these systems. In addition, the process does not appear dependent on the activator. These results appear to support the findings of Brown (7a) who proposed material transport by diffusion of zinc through interstitial channels.

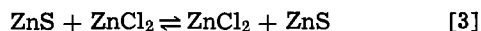
At temperatures above about 1050°C, ZnS:Ag containing 2% ammonium chloride followed a  $t^{2/3}$  dependence with an activation energy of 48 kcal. Since these results are not in accord with the diffusion mechanism outlined above, an alternative process was sought. A well-known procedure (15, 16) for obtaining single crystals of zinc sulfide involves vapor transport in a closed system under reduced pressure, with NH<sub>4</sub>Cl as a transfer agent. The processes occurring may be represented by the reactions



This sequence seems likely to occur during the growth of polycrystalline ZnS containing NH<sub>4</sub>Cl as flux, in keeping with an observation made by Smith (17). Although an evaporation-condensation reaction can take place at least as low as 700°C under appropriate con-

<sup>2</sup> For convenience, results quoted elsewhere in eV are expressed in kcal, on the basis that 1 eV = 23.05 kcal.

ditions, it was observed only at higher firing temperatures in the present work. One possibility is that the experimental procedures employed, and especially protection of the vessel by a stagnant zinc sulfide atmosphere, may delay the onset of the vapor transport process. Note that at 1200° and 1250°C the ZnS-ZnCl<sub>2</sub> system also obeyed a  $t^{2/3}$  relationship. Zinc chloride has a boiling point of 732°C (18) and should have an appreciable vapor pressure above 1000°C. Consequently, it is possible that at higher temperatures an evaporation-condensation mechanism may operate, according to an exchange reaction of the type



In ZnS:Ag containing 2% calcium chloride a  $t^{1/3}$  relationship was followed at 750° and 800°C, in keeping with the ZnCl<sub>2</sub> or NaCl additives, which might indicate a diffusion process, although there is insufficient evidence to make this more than a suggestion. Between 850° and 1250°C a different mode of material transport must be in effect. This change in mechanism became evident at about 800°-850°C, which is close to the normal melting point of 773°C (19) given for the calcium chloride flux. Particle growth in this temperature region was characterized by a time dependence of 0.5 and an activation energy of 36 kcal. Note also that, in contrast to all of the other fluxes examined so far, there was no change in mechanism as the system underwent the cubic-hexagonal phase transition at approximately 1020°C. This point is illustrated in Fig. 6, which demonstrates the Arrhenius curves obtained with ZnS:Ag containing either 2% CaCl<sub>2</sub> or 2% NaCl flux. A  $t^{1/2}$ , parabolic rate law (20) has been observed in many systems involving diffusion-controlled growth processes at an interface. Typical examples include the tarnishing, oxidation, or nitridation of metals (21). The theoretical basis for such processes has been derived by various authors (22). Kremheller and Faria (11) and Gashurov and Banks (23) have applied these concepts to zinc sulfide phosphors, thus it is not proposed to reiterate the discussion here. In the ZnS-CaCl<sub>2</sub> system it appears that, at temperatures above the normal melting point of calcium chloride, interaction between host material and flux takes place on the surface of the particles. Subsequently, growth proceeds by a dissolution-precipitation process, limited by diffusion of the solute atoms into the moving interface. Such a mechanism would require only a limited solubility of CaCl<sub>2</sub> in ZnS.

In summary, these studies have demonstrated that the mechanisms of particle growth in zinc sulfide phosphors are dependent on the nature of the flux used. Thus far, interstitial or bulk diffusion of zinc, diffusion limited dissolution-precipitation, and evaporation-condensation means of material transport have been suggested to occur. Sizes obtained have varied from 3-4 to almost 100  $\mu\text{m}$ . A clearer insight has been gained

into the understanding and control of the particle size characteristics of this important class of luminescent materials.

#### Acknowledgments

The author expresses his gratitude to E. W. Bomgardner for assistance with the preparatory work, and thanks Mrs. J. N. Shenk and Mrs. E. M. Rineer for providing the Coulter Counter measurements.

Manuscript received Feb. 10, 1976.

Any discussion of this paper will appear in a Discussion Section to be published in the June 1977 JOURNAL. All discussions for the June 1977 Discussion Section should be submitted by Feb. 1, 1977.

#### REFERENCES

1. P. Goldberg and A. K. Levine, Abstract 31, p. 22, The Electrochemical Society Extended Abstracts, Spring Meeting, Chicago, Illinois, May 2-6, 1954.
2. J. Malur, *Z. Chem.*, **5**, 399 (1965).
3. A. Schleede and H. Gantzkow, *Z. Physik. Chem.*, **106**, 37 (1923).
4. G. Gashurov and A. K. Levine, *J. Chem. Eng. Data*, **5**, 517 (1960).
5. H. J. McQueen and G. C. Kuczynski, *J. Am. Ceram. Soc.*, **45**, 343 (1962).
6. T. Bansagi, E. A. Secco, O. K. Srivastava, and R. R. Martin, *Can. J. Chem.*, **46**, 2881 (1968).
7. R. A. Brown, (a) *This Journal*, **118**, 937 (1971); (b) *ibid.*, **116**, 298 (1969).
8. R. A. Brown, *Electrochem. Technol.*, **6**, 246 (1968).
9. A. Kremheller, *Sylvania Technologist*, **8**, 11 (1955).
10. E. A. Secco, *Can. J. Chem.*, **42**, 1396 (1964).
11. A. Kremheller and S. Faria, *This Journal*, **107**, 891 (1960).
12. R. H. Bube, *J. Chem. Phys.*, **20**, 716 (1952).
13. S. Shionoya and K. Amano, *J. Chem. Soc. Japan, Pure Chem. Sect.*, **77**, 303 (1953).
14. H. W. Leverenz, "An Introduction to Luminescence of Solids" p. 50, Dover Publications Inc., New York (1968).
15. I. Bertoti, M. Farkas-Jahnke, E. Lendvay, and T. Nemeth, *J. Mater. Sci.*, **4**, 699 (1969).
16. E. Lendvay, *J. Cryst. Growth*, **10**, 77 (1971).
17. A. L. Smith, *This Journal*, **96**, 75 (1949).
18. R. C. Weast, Editor, "Handbook of Chemistry and Physics," 50th ed., p. B-174, The Chemical Rubber Co., Cleveland (1969).
19. E. D. Eastman, D. D. Cubicciotti, and C. D. Thurmond, in "Chemistry and Metallurgy of Miscellaneous Materials," L. L. Quill, Editor, p. 10, McGraw-Hill Book Co., New York (1950).
20. F. S. Stone, in "Reactivity of Solids," J. H. de Boer, Editor, pp. 12-14, Elsevier Publishing Co., Amsterdam (1961).
21. G. Tammann, *Z. Anorg. Chem.*, **111**, 78 (1927), G. Romeo, H. S. Spacil, and W. J. Pasko, *This Journal*, **122**, 1329 (1975); S. K. Iyer and W. L. Worrell, in "Reactivity of Solids," J. S. Anderson, Editor, pp. 294-302, Chapman and Hall, London (1972).
22. C. Zener, *J. Appl. Phys.*, **20**, 950 (1949).
23. G. Gashurov and E. Banks, *This Journal*, **114**, 1143 (1967).

# Ion Implantation Gettering of Gold in Silicon

T. W. Sigmon

Hewlett-Packard Laboratories, Palo Alto, California 94304

and L. Csepregi<sup>1</sup> and J. W. Mayer\*

California Institute of Technology, Pasadena, California 91125

Numerous studies have demonstrated the feasibility of using ion implantation damage to getter metal impurities in silicon (1-5). Since metallic contaminants are known to degrade the electrical characteristics of a p-n junction, leading to high reverse leakage currents and soft breakdown voltages, this technique is of technological interest (6). The study of Seidel *et al.* (5) showed that the gettering efficiency of the ion-damaged layers is related to the residual disorder present after annealing at elevated temperatures (850°-1150°C). They also show in that work that the amount of residual disorder depends on the implanted ion species. They correlate this effect with the atomic size of the bombarding ion. We note that the implantation doses reported in this work were more than sufficient ( $10^{16}/\text{cm}^2$ ) to form an amorphous layer (except for the B-implanted samples) and that  $\langle 111 \rangle$  oriented Si wafers were used.

We would like to point out that factors other than ion size can have a comparable or equal influence on the amount of disorder remaining after anneal. Previous studies on the annealing behavior of high dose implants have indicated that the thermal history of the annealing process (7), the orientation of the crystal substrate (8), and the implantation condition (dose, ion energy) (9) can have a pronounced effect. For example, it has been shown that for amorphous layers, formed by either B or As implants on  $\langle 111 \rangle$  Si, the amount of disorder remaining after anneal is dependent on the procedure used in annealing: samples annealed at 550°C and then at 950°C exhibit significantly less disorder than samples annealed directly to 950°C (7). We show in this note that the orientation of the substrate used for the gettering can have a pronounced influence on the amount of Au that is gotten.

In this work,  $\langle 100 \rangle$  and  $\langle 111 \rangle$  oriented 2-10 ohm-cm resistivity, n-type, low dislocation density wafers were equilibrated with Au at 1100°C in N<sub>2</sub> following the procedures given by Seidel and Meek (3). After lapping away the piled-up Au at the surfaces and polishing the samples, Si ions were implanted with the substrate held near LN<sub>2</sub> temperature at energies (dose) of 200 ( $2 \times 10^{15} \text{ cm}^{-2}$ ), 150 ( $10^{15} \text{ cm}^{-2}$ ), 100 ( $8 \times 10^{14} \text{ cm}^{-2}$ ), and 50 ( $4 \times 10^{14} \text{ cm}^{-2}$ ) keV to form an approximately 4000Å thick amorphous layer (10). After implantation the samples were annealed together in dry N<sub>2</sub> at 1000°C for 1 hr. Due to a slight amount of oxygen present in the N<sub>2</sub>, approximately 50Å of SiO<sub>2</sub> is grown on the surface of the wafer during this anneal.

This differs slightly from the procedures used by Seidel and Meek as there was no heat-treatment at 375°C before going to the higher anneal temperature. However, it is known that relatively little or no recrystallization of amorphous layers occurs at this temperature (11). Backscattering and channeling of 2 MeV He ions were used to study the residual disorder and the amount of gotten Au impurities.

The substrate orientation dependence of the amount of residual disorder after anneal can be seen in the random and aligned spectra shown in Fig. 1. Also, the thin oxide layer can be seen in the aligned spectra. For the  $\langle 100 \rangle$  sample, the aligned spectra are close to

that for an unimplanted sample (minimum yield is less than 5%). This low amount of residual disorder was also found in  $\langle 100 \rangle$  Si implanted to amorphous condition by B and As ions (rather than Si ions) and annealed directly to temperatures of 950°C (7, 8). However, for the  $\langle 111 \rangle$  samples the spectra show that the amount of residual disorder is quite high. The height of the aligned spectra shown in Fig. 1 over the thickness of 4000Å is about 65% of the random yield. These high levels of disorder were also found in B- and As-implanted  $\langle 111 \rangle$  samples that were annealed directly to 950°C (7).

The aligned spectra shown for samples used by Seidel *et al.* (3, 12) in their gettering studies also exhibit a high level of disorder. It is to be noted that these wafers were all of  $\langle 111 \rangle$  orientation. Also, the As spectra show considerably less residual damage than the other atoms used in their experiments. This effect has been reported before (9) and can be partly attributed to substrate temperature rise during implantation.

Since the amount of Au gotten is influenced by the amount of residual disorder, it is much higher (a factor of 10) in the  $\langle 111 \rangle$  than in the  $\langle 100 \rangle$  oriented sample. The gotten Au peak in Fig. 1 appearing at energies greater than 1.6 MeV in the spectra for the  $\langle 111 \rangle$  oriented sample extends over a depth which correlates well with the thickness of the disorder

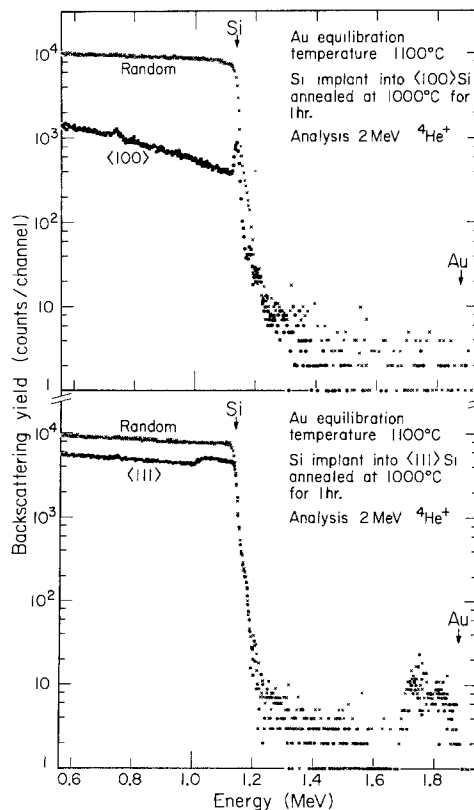


Fig. 1. Random and aligned 2 MeV  $^4\text{He}^+$  backscattering spectra for  $\langle 100 \rangle$  and  $\langle 111 \rangle$  Si equilibrated with Au at 1100°C and implanted with Si at LN<sub>2</sub> temperature. Samples were annealed at 1000°C for 1 hr in N<sub>2</sub>. The channeling axis coincides with the surface normal.

\* Electrochemical Society Active Member.

<sup>1</sup> Present address: Central Research Institute for Physics, Budapest, Hungary.

Key words: ion implantation, silicon, gettering.

layer; the amount of Au gettered in this layer is about  $5 \times 10^{13}$  atom/cm<sup>2</sup>. These observations for the <111> oriented Si are consistent with the results presented in the previous gettering studies referenced.

In conclusion, we point out: (i) the results of gettering studies on implant-damaged <111> Si should be applied with caution to Si substrates of other orientations; (ii) the residual disorder in <111> oriented Si depends strongly on the thermal history of the sample both during and after the implantation. Hence, the amount of gettered impurities may also depend upon these factors.

### Acknowledgments

Work supported in part by the National Science Foundation and the Institute of Cultural Relations, Budapest, and ONR (L. Cooper).

Manuscript submitted Dec. 24, 1975; revised manuscript received March 11, 1976.

Any discussion of this paper will appear in a Discussion Section to be published in the June 1977 JOURNAL. All discussions for the June 1977 Discussion Section should be submitted by Feb. 1, 1977.

Publication costs of this article were partially assisted by Hewlett-Packard Laboratories.

### REFERENCES

1. T. M. Buck, K. A. Pickar, J. M. Poate, and C. M. Hsieh, *Appl. Phys. Letters*, **21**, 485 (1972).
2. C. M. Hsieh, J. R. Mathews, H. D. Seidel, K. A. Pickar, and C. M. Drum, *ibid.*, **22**, 238 (1973).
3. T. E. Seidel and R. L. Meek, in "Ion Implantation in Semiconductors and Other Materials," B. L. Crowder, Editor, p. 305, Plenum Press, New York (1973).
4. J. M. Poate and T. E. Seidel, *ibid.*, p. 317.
5. T. E. Seidel, R. L. Meek, and A. G. Cullis, in "Lattice Defects in Semiconductors 1974," F. A. Huntley, Editor, p. 494, The Institute of Physics, London (1975).
6. A. Goetzberger and W. Shockley, *J. Appl. Phys.*, **31**, 1821 (1960).
7. L. Csepregi, W. K. Chu, H. Müller, J. W. Mayer, and T. W. Sigmon, *Radiation Effects*, **28**, 277 (1976).
8. H. Müller, W. K. Chu, J. Gyulai, J. W. Mayer, T. W. Sigmon, and T. R. Cass, *Appl. Phys. Letters*, **26**, 292 (1975).
9. W. K. Chu, H. Müller, J. W. Mayer, and T. W. Sigmon, in "Ion Implantation in Semiconductors," S. Namba, Editor, p. 177, Plenum Press, New York (1975).
10. L. Csepregi, J. W. Mayer, and T. W. Sigmon, *Phys. Letters*, **A54**, 157 (1975).
11. J. W. Mayer, L. Eriksson, S. T. Picraux, and J. A. Davies, *Can. J. Phys.*, **46**, 663 (1968).
12. T. E. Seidel, R. L. Meek, and A. G. Cullis, *J. Appl. Phys.*, **46**, 600 (1975).

## Formation of Silicon Nitride at a Si-SiO<sub>2</sub> Interface during Local Oxidation of Silicon and during Heat-Treatment of Oxidized Silicon in NH<sub>3</sub> Gas

E. Kooij,\* J. G. van Lierop, and J. A. Appels

Philips Research Laboratories, Eindhoven, The Netherlands

This paper is primarily based on an observation which we made during the preparation of MOS integrated circuits using local oxidation of the silicon (LOCOS) to prepare the thick field oxide. In certain cases the effect may also play a role in the preparation of other LOCOS devices, as has been described in previous publications (1-4).

### Preparation of a LOCOS Field Oxide in MOS Circuits

A sketch of part of a possible method of preparing LOCOS MOS devices is given in Fig. 1. A layer of silicon nitride (1500Å in our experiments) is used as the oxidation mask. The silicon nitride is separated from the silicon by a thin layer (500Å) of silicon oxide. The presence of this oxide prevents the formation of dislocations which might be induced in the silicon if the latter were heated in direct contact with the nitride layer (1). The presence of the oxide layer also influences the shape of the sunk-oxide pattern (2, 4). Due to some lateral oxidation effect, the oxide acquires a smooth beak shape at the edges where the nitride mask is lifted up. In our experiments the LOCOS process was carried out by 16 hr oxidation in wet O<sub>2</sub> (dew point 95°C) at 1000°C. The nitride mask and the underlying oxide were then removed and a gate oxide grown (45 min oxidation at 1100°C, yielding 1000Å SiO<sub>2</sub>). The further processing of the MOS devices has not been indicated in Fig. 1. If used, a silicon gate process would include the deposition of a polycrystalline silicon film, and definition of gate, source, and drain areas, etc. (4).

\* Electrochemical Society Active Member.

Key words: silicon nitride, local oxidation, silicon surfaces, ammonia.

### A "White Ribbon" Effect in LOCOS Structures

In the final stage indicated in Fig. 1, we observed occasionally a peculiar effect at the LOCOS edges. Through an optical microscope it would look like a "white ribbon" with a width of about 1 μm, following precisely the LOCOS pattern (Fig. 2). The effect was observed for both (111) and (100) oriented substrates, although the photographs presented in this paper all refer to (100) material. A scanning electron microscope picture of a cross section, as indicated in Fig. 3, shows that this ribbon is due to a narrow region of nonoxidized silicon present at a small distance from the beak-shaped LOCOS edge. To explain the effect, we have to assume that the silicon in the ribbon area is covered by a very thin oxidation-masking material. The best oxidation-masking material known is silicon nitride and the most probable assumption is, therefore, that in the ribbon area some silicon nitride is formed at the Si-SiO<sub>2</sub> interface during the local oxidation process. Of course this nitride may not consist of pure Si<sub>3</sub>N<sub>4</sub>, but for simplicity we will indicate it as such. The question is, of course, how such an effect can occur. The model we propose is indicated in Fig. 4. It is based on the transfer of nitrogen from the nitride oxidation mask to the Si-SiO<sub>2</sub> interface. The figure indicates that during the LOCOS process H<sub>2</sub>O diffuses through the growing oxide film. There is also a lateral diffusion and subsequent oxidation of silicon under the edge of the nitride oxidation mask, causing the ultimate beak-shaped pattern to be formed. Some oxidation of the silicon nitride will also occur, not only at the top side but also at the lower side of the nitride edges. In a simple chemical reaction equation as indicated in Fig.

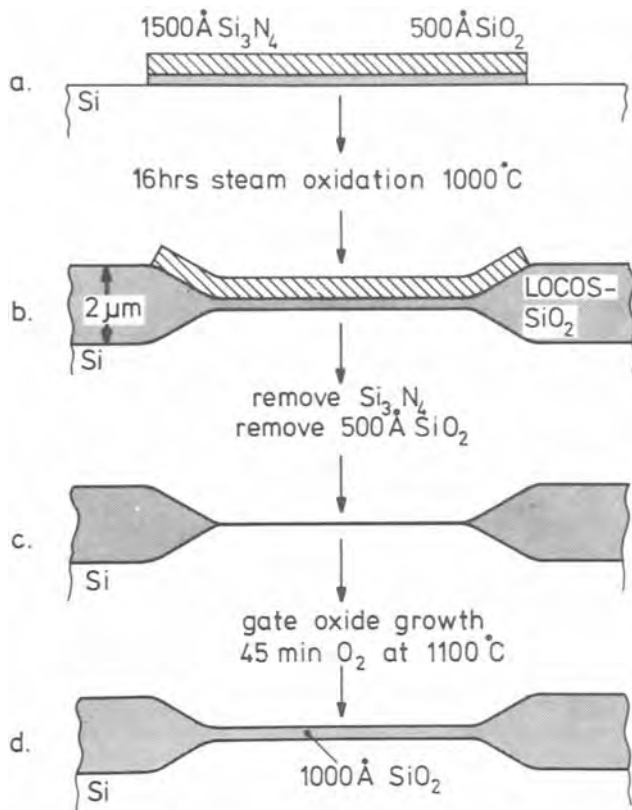


Fig. 1. Part of a LOCOS MOS process. After gate oxide growth (d) the phenomenon indicated in Fig. 2 and 3 may be observed.

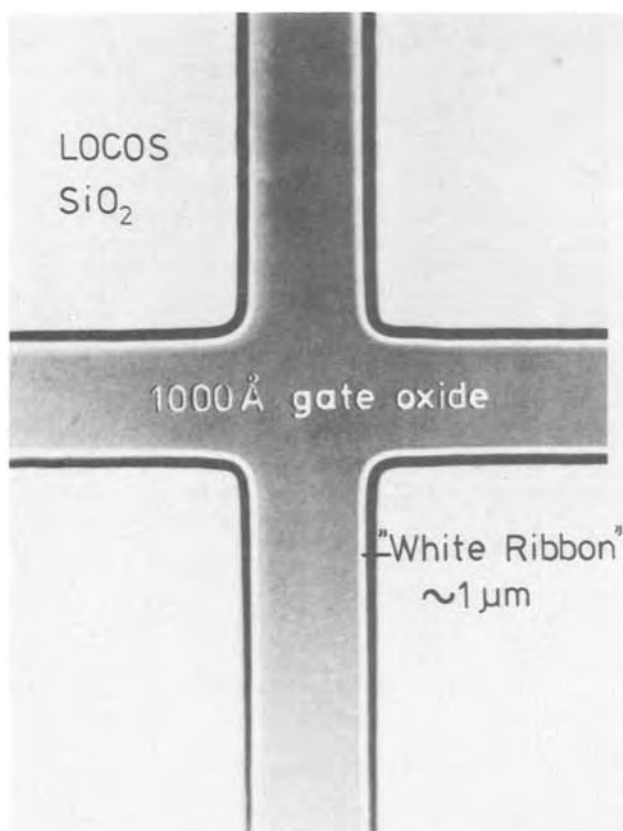


Fig. 2. Top view of a LOCOS structure with a "white ribbon" effect.

4, one can assume that the oxidation results in the formation of  $\text{SiO}_2$  and  $\text{NH}_3$ . It is more probable that instead of  $\text{NH}_3$ , the formation of nitrogen atoms or some other  $\text{NH}$  compound will occur. What has to be

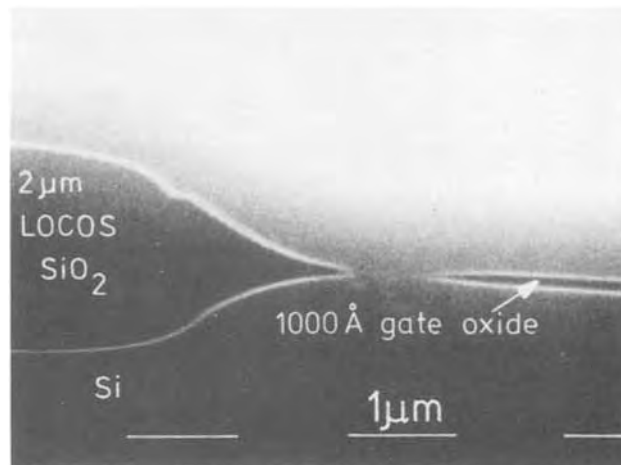


Fig. 3. Scanning electron microscope picture of a cross section of a LOCOS structure with a "white ribbon" effect. (The cross sections shown in this paper were made after a layer of polycrystalline silicon had been deposited on the specimen. This helps to give a good contrast in the SEM picture).

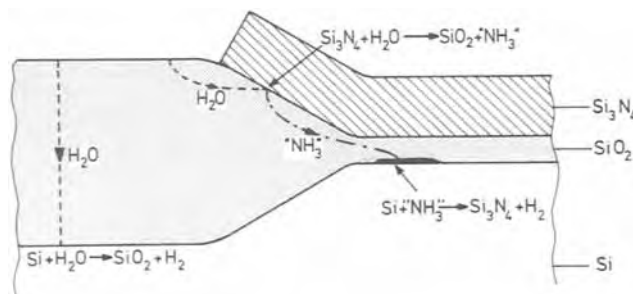


Fig. 4. Proposed model to explain silicon nitride formation at the Si- $\text{SiO}_2$  interface at some distance from the LOCOS edge.

assumed is that the reactive nitrogen can diffuse relatively easily through  $\text{SiO}_2$ . It can reach the Si- $\text{SiO}_2$  interface. But under the LOCOS and also at the beak this does not result in an effective reaction product because of the competition of the oxidation reaction of Si with  $\text{H}_2\text{O}$ . However, at some distance from the LOCOS edge, under the nitride mask, the concentration of  $\text{H}_2\text{O}$  becomes low enough to allow a reaction of silicon with " $\text{NH}_3$ " to form  $\text{Si}_3\text{N}_4$ . Again, it is quite possible that stoichiometric  $\text{Si}_3\text{N}_4$  is not really formed but rather a mixed compound of silicon, nitrogen, oxygen, and, possibly, hydrogen.

When, as in Fig. 1, the nitride oxidation mask and the underlying thin oxide film are removed, the nitride ribbon may remain present. Consequently, the gate oxidation will not be effective in that area and the results shown in Fig. 2 and 3 are to be expected. The fact that this effect is often not observed can be explained by removal of the nitride ribbon due to some overetching applied when the oxide film is removed. Nitridation experiments, to be described later on in this paper, lead us to believe that the nitride formed at the silicon surface is probably not more than 10-20 Å thick.

#### Further Evidence for the Occurrence of the "White Ribbon" Effect

We have argued that, if the given explanation is true, the effect indicated in Fig. 4 will always take place (in the given process conditions). This can readily be checked by doing experiments as indicated in Fig. 5. In this case the nitride oxidation mask is removed after the LOCOS process carried out by oxidation in wet  $\text{O}_2$  (water at  $95^\circ\text{C}$  through which oxygen is bubbled, the same result is obtained with nitrogen as carrier gas), but the thin oxide film under it is kept

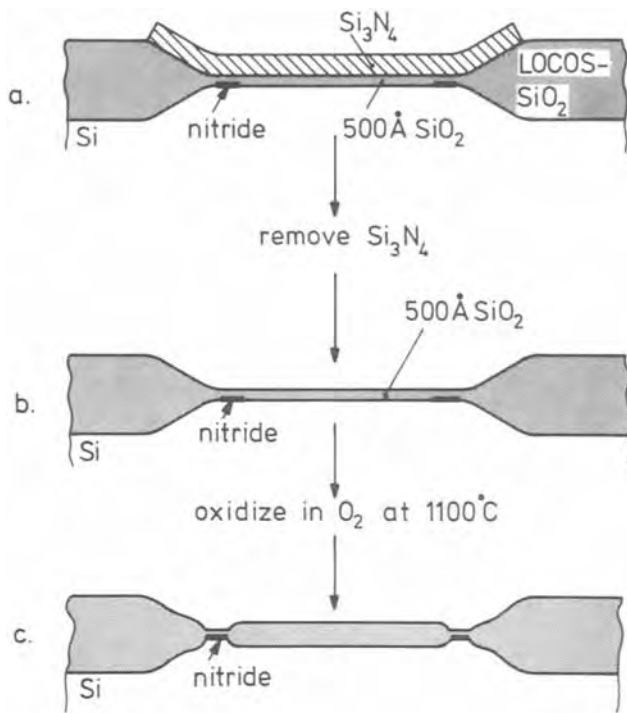


Fig. 5. Experimental procedure to show that the nitride formation along a LOCOS edge always takes place (under the given conditions of local oxidation: 16 hr steam at  $1000^\circ\text{C}$ ).

in place. This means that any nitride formed under it cannot be attacked either. A subsequent oxidation treatment would then cause no (or retarded) oxide growth in the "ribbon areas." A cross section like that indicated in Fig. 5c would then be the result.

The cross section in Fig. 6 shows that the expected result is obtained. In this case the oxidation after nitride removal was carried out for 2 hr in dry oxygen at  $1100^\circ\text{C}$ . The  $500\text{Å}$   $\text{SiO}_2$  already present has increased in thickness to  $1800\text{Å}$ , but in a ribbon-type region along the LOCOS edge the oxide has remained  $500\text{Å}$  thick.

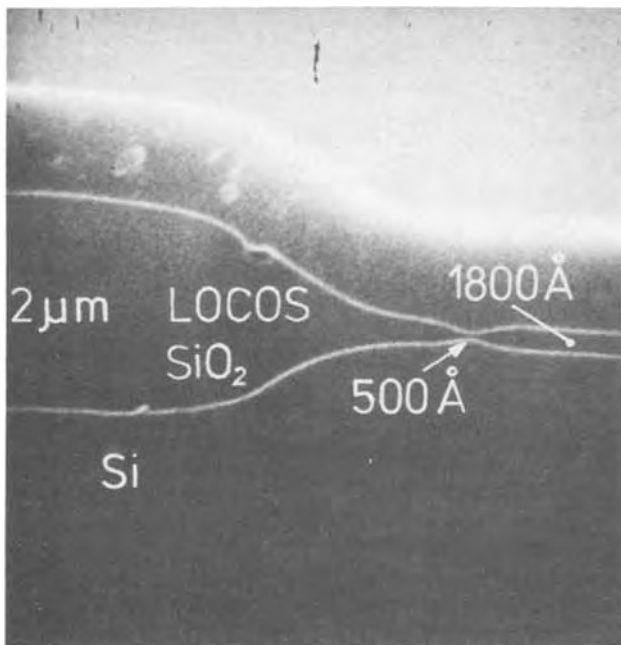


Fig. 6. Cross section of a silicon sample which had been subjected to a procedure as shown in Fig. 5. Experimental conditions: LOCOS by steam oxidation, 16 hr at  $1000^\circ\text{C}$ ; oxidation after nitride mask removal, 2 hr  $\text{O}_2$  at  $1100^\circ\text{C}$ .

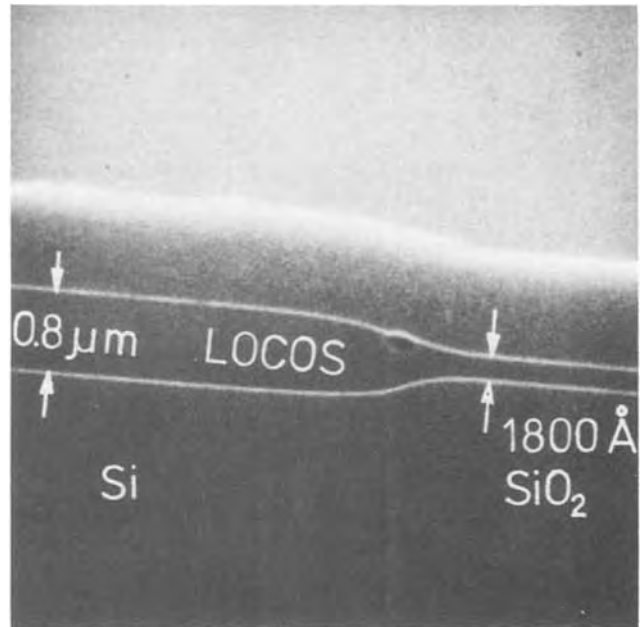


Fig. 7. Cross section of a silicon sample which had been subjected to a procedure as shown in Fig. 5. Experimental conditions: LOCOS by oxidation in dry  $\text{O}_2$ , 64 hr at  $1000^\circ\text{C}$ ; oxidation after nitride mask removal, 2 hr at  $1100^\circ\text{C}$ . In contrast with Fig. 6, no oxidation retardation along the LOCOS edge is observed.

Figure 7 shows a cross section of a sample subjected to the same reoxidation treatment of 2 hr dry oxygen at  $1100^\circ\text{C}$ . In this case, however, the LOCOS pattern was grown in dry  $\text{O}_2$  (64 hr at  $1000^\circ\text{C}$ , yielding  $0.8\mu\text{m}$   $\text{SiO}_2$ ). In contrast with the wet oxidation case, no indication of a ribbon-type oxidation masking effect along the LOCOS edge is observed. This means either that during dry oxidation the formation of nitrogen due to oxidation of silicon nitride is much less effective, or that the nitrogen formed diffuses less rapidly through  $\text{SiO}_2$ , or that the nitrogen species formed in this case are not very reactive with the silicon surface.

#### Nitride Formation during Heat-Treatment of Oxidized Silicon in $\text{NH}_3$ Gas

The foregoing results and their probable explanation brought us to the idea that a similar effect might be obtained by heating oxidized silicon in  $\text{NH}_3$  gas.  $\text{NH}_3$  molecules or reactive dissociation products of it such as nitrogen atoms might be expected to diffuse through  $\text{SiO}_2$  and cause nitride formation at the Si- $\text{SiO}_2$  interface. The easiest way to check such nitride formation is to subject the samples afterwards to a thermal oxidation treatment. The oxide will not increase in thickness as long as oxidation-masking silicon nitride has not been converted to silicon oxide.

Table I gives some results for a nitridation treatment at  $900^\circ\text{C}$ . One sample had a very thick ( $20,000\text{Å}$ ) ox-

Table I. Oxidation resistance of (111) oriented oxidized silicon slices after nitridation. Nitridation: 16 hr at  $900^\circ\text{C}$  in  $\text{N}_2$  with 3%  $\text{NH}_3$ .

First oxidation treatment	Oxide thickness	Oxidation resistance at $900^\circ\text{C}$ in $\text{O}_2$ after nitridation	$\text{SiO}_2$ thickness which can be grown on bare Si during time of oxidation resistance
Bovling nitric acid	20Å	10 hr	1300Å
15 min dry $\text{O}_2$ at $1100^\circ\text{C}$	500Å	7 hr	1100Å
16 hr steam at $1000^\circ\text{C}$	20,000Å the oxide was then thinned by etching to 500Å	3 hr	650Å

ide. As such a thick oxide increases very slowly in thickness during further oxidation, we etched it down to 500Å after the nitridation cycle and then measured the oxidation resistance. The table shows that even for the thick oxide a considerable oxidation resistance effect is found, although less than for the thinner oxides. This indicates that, although the diffusion of the nitrogen through the SiO<sub>2</sub> has influence on the nitridation, the presence of oxide does not prevent the effect at all. The fact that the sample with the 20,000Å thick oxide shows resistance against oxidation even after the major part of the oxide has been etched off proves that nitridation occurs at or near the Si-SiO<sub>2</sub> interface. This does not exclude, of course, that some nitridation effect may occur throughout the oxide, but we have no indications that this is an appreciable effect. Assuming that the nitridation treatment does not change the SiO<sub>2</sub> properties but rather adds a nitride surface film, some nitride thicknesses were calculated from ellipsometric measurements. Table II presents results as a function of temperature and (at 1000°C) as a function of time. The initial oxide was 20Å in this case and made by oxidation in boiling nitric acid. Using samples with 500Å thermal oxide, we obtained in this manner a nitride thickness of 10Å after nitridation for 16 hr at 1000°C (to be compared with 18Å for a sample with 20Å initial oxide). Material removal by sputtering combined with Auger electron spectroscopy was carried out on samples with 20Å initial oxide, treated with N<sub>2</sub>-3% NH<sub>3</sub> for 16 hr at 1000°C. The results revealed the presence of oxygen at the top and nitrogen at the silicon side of the surface film(s).

A few experiments were carried out with hydrogen instead of nitrogen as the carrier gas for the NH<sub>3</sub>. Oxidation resistance appeared to be of the same order of magnitude. It has recently been shown by Raider, Gdula, and Petrak (5) that nitrogen gas as such has a nitridation effect, even when a (thin) silicon oxide film is present on the silicon. These authors heated silicon samples for several days at 1000°C in N<sub>2</sub> and found an oxidation resistance time (in O<sub>2</sub> at 1000°C) of the order of a couple of hours. Table III indicates clearly that NH<sub>3</sub> is indeed much more effective than N<sub>2</sub>. Although we found oxidation retardation after 16 hr treatment at 1150°C in N<sub>2</sub> of a silicon slice covered with 500Å SiO<sub>2</sub>, heating of a similar sample for 16 hr at 1000°C did not result in a measurable effect. For comparison, a result has been given of a treatment for 16 hr at 1000°C in N<sub>2</sub> with 3% NH<sub>3</sub> added. In this case an oxidation resistance time of 10 hr was measured.

Although the nitride films formed in the described manner are rather thin, we think that they may have a number of interesting device applications; for ex-

Table II. Nitride thickness after treatment of Si (with 20Å SiO<sub>2</sub>) in N<sub>2</sub> + 3% NH<sub>3</sub>. The given values are based on ellipsometric measurements and the assumption that a nitride film with index of refraction  $n = 2.0$  is formed in addition to the SiO<sub>2</sub> film ( $n = 1.47$ ) already present.

	900°C	1000°C	1100°C
1 hr	—	15Å	—
4 hr	—	17Å	—
16 hr	11Å	18Å	27Å

Table III. Comparison of nitridation of oxidized silicon with NH<sub>3</sub> and with N<sub>2</sub>

Initial oxide	Nitridation treatment	Time of oxidation resistance in O <sub>2</sub> at 1000°C	SiO <sub>2</sub> thickness which can be grown on bare Si during time of oxidation resistance
500Å	16 hr N <sub>2</sub> + 3% NH <sub>3</sub> 1000°C	10 hr	2600Å
500Å	16 hr N <sub>2</sub> 1000°C	0	0
500Å	16 hr N <sub>2</sub> 1150°C	2 hr	1150Å

ample, as masking layers. In Tables I and III we have indicated how much oxide can be grown on bare silicon during the time that a nitridized surface can withstand oxidation. The figures indicate that employment for local oxidation of silicon (the substrate or, if present, poly-Si lines) is possible, although not when thick LOCOS patterns are desired. For that purpose thicker nitride films would be needed. Table II indicates that the nitride film thickness is limited. Diffusion of either nitrogen or silicon through the film may be the limiting factor for further growth. We would like to emphasize, however, that the present paper presents preliminary results. As long as the nitridation mechanism is not fully clear, one may think, for example, that thicker nitride films may be possible when the NH<sub>3</sub> pressure is increased. Further, it may be that traces of H<sub>2</sub>O have an effect on the nitridation and that the results presented need to be reconsidered in the light of more precisely defined experimental conditions.

A very interesting aspect of nitridation is that a new type of silicon surface is formed. Measurements made so far show that the number of fixed oxide charges and fast surface states can be low [ $2 \cdot 10^{10}$  per cm<sup>2</sup> for (100) surfaces] and that the nitridation causes an improvement of MOS structures with respect to charge trapping at the silicon surface under negative gate-bias conditions. The behavior of the new interface during annealing in various ambient gases can be different from the usual Si-SiO<sub>2</sub> interface and deserves further study.

### Conclusions

The experimental results presented in this paper indicate that at elevated temperatures nitrogen can diffuse relatively easily through SiO<sub>2</sub> films on silicon so that silicon nitride can form at the Si-SiO<sub>2</sub> boundary. Ammonia gas has considerably more effect than molecular nitrogen. A specific case of production and subsequent diffusion of active nitrogen through SiO<sub>2</sub> was found in the case of preparation of LOCOS structures by steam oxidation. This can result in the formation of some nitride at the silicon surface along the LOCOS edge. It has a masking action against oxidation and consequently the gate oxide of MOS structures may become too thin near the LOCOS edge, resulting in low gate-breakdown voltages. In practice the effect can readily be overcome by removal of the nitride ribbon by etching. The nitridation effects may find use in the preparation of stable silicon surfaces and/or the preparation of special device structures.

### Acknowledgments

The ellipsometry mentioned in this paper was carried out by A. Kroes and F. Meyer, and the Auger electron spectroscopy by J. J. A. M. Vrakking, to whom we are most grateful. We also wish to thank D. J. Breed for his stimulating interest and for the surface state measurements.

Manuscript submitted Jan. 15, 1976; revised manuscript received March 23, 1976. This was Paper 275 RNP presented at the Dallas, Texas, Meeting of the Society, Oct. 5-9, 1975.

Any discussion of this paper will appear in a Discussion Section to be published in the June 1977 JOURNAL. All discussions for the June 1977 Discussion Section should be submitted by Feb. 1, 1977.

Publication costs of this article were partially assisted by Philips Research Laboratories.

### REFERENCES

1. J. A. Appels, E. Kooi, M. M. Paffen, J. J. H. Schatorjé, and W. H. C. G. Verkuylén, *Philips Res. Rept.*, **25**, 118 (1970).
2. J. A. Appels and M. M. Paffen, *ibid.*, **26**, 157 (1971).
3. E. Kooi, J. G. van Lierop, W. H. C. G. Verkuylén, and R. de Werdt, *ibid.*, **26**, 166 (1971).
4. E. Kooi and J. A. Appels, in "Semiconductor Silicon 1973," H. R. Huff and R. R. Burgess, Editors, p. 860, The Electrochemical Society Softbound Symposium Series, Princeton, N. J. (1973).
5. S. I. Raider, R. A. Gdula, and J. R. Petrak, *Appl. Phys. Letters*, **27**, 150 (1975).



## Electromigration in Current-Controlled LPE

L. Jastrzebski, H. C. Gatos,\* and A. F. Witt\*

Department of Materials Science and Engineering,  
Massachusetts Institute of Technology, Cambridge, Massachusetts 02139

It was shown experimentally that current-controlled LPE (1) of III-V compounds (*e.g.*, GaAs and InSb) is brought about by electromigration of the group III and group V charged atoms in the liquid phase. The mobility of these charged atoms was estimated; the growth rate calculated from the mobility values was found to be in good agreement with measured growth rate. Peltier cooling at the growth interface makes no appreciable contribution to current-controlled LPE.

It has been reported (1) that LPE could be initiated and sustained by passing electric current across the growth interface while the temperature of the over-all growth system is maintained constant; growth has been attributed to Peltier cooling associated with current flow. InSb (1), GaAs (2), and GaAlAs (3) layers have been successfully grown by this method. In the present note experimental results are reported showing that electromigration leads to the observed LPE. Electromigration has been extensively studied in metallic melts (4); its occurrence in semiconductor solutions has also been proposed (3, 5).

Current-controlled LPE layers of GaAs were grown in a commonly employed apparatus described elsewhere (1). Using a 96.3 a/o Ga-3.7 a/o As solution doped with Cd and Sn and a current density of 8 A/cm<sup>2</sup> [with the (100) substrate having a positive polarity], an n-type GaAs layer ( $n = 2.5 \times 10^{18}/\text{cm}^3$ ) 1 cm<sup>2</sup> was obtained, in 90 min at 850°C, having a thickness of 60 μm. On the basis of the Ga-As phase diagram, the amount of the epitaxially deposited GaAs would necessitate a temperature decrease of about 20°C, assuming that GaAs was nucleated only on the substrate (nucleation in the melt or elsewhere would necessitate even greater decrease in temperature). Yet, a total temperature decrease of only 0.2°C was measured with a thermocouple at a distance of about 200 μm from the growth interface. In a conventional cooling experiment using the same experimental arrangement (but no electric current), an epitaxial layer of about 0.5 μm was obtained upon a temperature decrease of 0.2°C.

These results indicate that Peltier cooling is not the primary driving force in current-controlled LPE; rather electromigration of As to the growth interface causes supersaturation of the melt and consequently nucleation and growth of GaAs at a virtually constant temperature. Consistent with this conclusion a p-type ( $p = 2 \times 10^{19}/\text{cm}^3$ ), Ge-doped layer of GaAs was grown at 800°C at a current density of 7 A/cm<sup>2</sup> (with the substrate having a positive polarity); the rate of growth in this case, as determined by interface demarcation (6), was approximately the same as for n-type material, *i.e.*, 0.35 μm/min. In the case of the p-type GaAs, the sign of the Peltier coefficient (as determined experimentally) was opposite to that of the n-type GaAs and slight heating took place at the

growth interface. It should also be pointed out that upon reversing the direction of the current, dissolution of the substrate took place, regardless of the sign of the Peltier coefficient, apparently due to electromigration of Ga to the growth interface and of As away from the interface.

To demonstrate the electromigration of As and Ga, the following experiment was performed. A GaAs wafer was brought into contact with Ga-As melt, in equilibrium at 850°C, contained in two wells as shown schematically in Fig. 1. The system was allowed to equilibrate for 30 min and then current was passed. The result obtained with a p-type (Zn-doped  $2 \times 10^{18}/\text{cm}^3$ ) GaAs wafer ( $1 \times 0.18 \times 0.03$  cm) after passing current (0.5 A/cm<sup>2</sup>) for 40 sec in a hydrogen atmosphere is shown in Fig. 2. The solidified melts are attached to the ends of the wafer. It is seen that migration of the solution took place along the surface of the wafer up to regions B and B' in the figure. Elec-

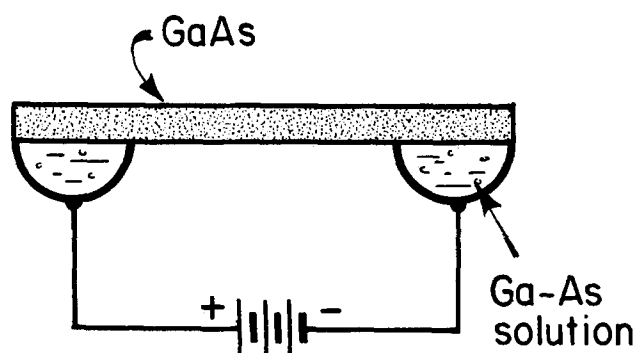


Fig. 1. Schematic diagram of experimental arrangement for observing electromigration in solutions of III-V compounds.

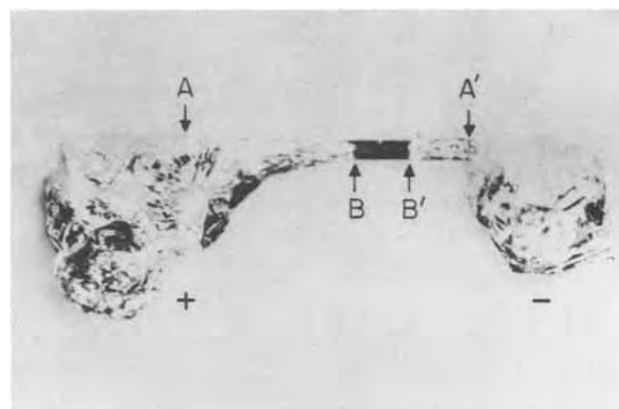


Fig. 2. Electromigration of Ga and As (see text). A and A' are starting points of electromigration of Ga and As, respectively. At B and B' electromigration was terminated.

\* Electrochemical Society Active Member.

Key words: electromigration, liquid phase epitaxy, gallium arsenide.



tron microprobe analysis showed that the concentration of As in the solution on the wafer near B' was more than 50% higher than on the surface near B. Apparently electromigration of charged As and Ga species caused the observed migration of the solution (4); no solution migration was obtained in the absence of an electric current. The distance of migration on the wafer was found to increase linearly with time and with electric field. Accordingly, effective mobilities for Ga (migrating to the negative end of the wafer) and for As (migrating to the positive end) were calculated to be  $2 \times 10^{-2}$  and  $7 \times 10^{-3}$  cm<sup>2</sup>/V sec, respectively. These mobility values are believed to be smaller than in the LPE process, since surface tension is acting against solution migration in the experimental arrangement of Fig. 1.

On the basis of the Verhoeven (4) analysis for electromigration in metallic melts, the growth rate during current-controlled LPE was estimated. Since the contribution of diffusion and the movement of the growth interface can be neglected, the flux of As toward the interface is (6)

$$J_{As} = C_{As} C_{Ga} \bar{V}_{Ga} U E$$

where  $C_{As}$  is the concentration of As in the melt (0.0235),  $C_{Ga}$  is the concentration of Ga,  $\bar{V}_{Ga}$  is the partial molar volume of Ga (in the present case  $C_{Ga} \bar{V}_{Ga} \approx 1$ ),  $U$  is the difference in mobilities  $v_{Ga} - v_{As}$  (taken from the present experiments  $\approx 2.7 \times 10^{-2}$  cm<sup>2</sup>/V sec), and  $E$  is the electric field (10<sup>-3</sup> V/cm);  $E$  was calculated from the current density (10 A/cm<sup>2</sup>), the dimensions of the solution, and the resistivity of the solution which was taken as 10<sup>-4</sup> ohm-cm assuming a linear increase with temperature from its value of  $2.6 \times 10^{-5}$  ohm-cm at 30°C (7). On the basis of the above relationship, and assuming no nucleation of GaAs in the melt, a growth rate of  $\sim 8 \times 10^{-1}$  μm/min is obtained; this value is in good agreement with the experimentally determined values of  $4-7 \times 10^{-1}$  μm/min.

The above experiments were also carried out employing In-Sb solutions (25 a/o Sb) and InSb substrates at 450°C. The results were consistent with those obtained for the GaAs system. (The mobilities of In and Sb were estimated to be  $3 \times 10^{-3}$  and  $0.6 \times 10^{-3}$  cm<sup>2</sup>/V sec, respectively.)

In summary, it was shown that electromigration rather than Peltier cooling is the controlling factor in current-induced LPE. The implications of the present finding to the refinement of the growth and doping of III-V compound liquid-phase epitaxial layers are being pursued.

#### Acknowledgments

The authors are grateful to the National Science Foundation for financial support.

Manuscript received March 1, 1976.

Any discussion of this paper will appear in a Discussion Section to be published in the June 1977 JOURNAL. All discussions for the June 1977 Discussion Section should be submitted by Feb. 1, 1977.

Publication costs of this article were partially assisted by the Massachusetts Institute of Technology.

#### REFERENCES

1. M. Kumagawa, A. F. Witt, M. Lichtensteiger, and H. C. Gatos, *This Journal*, **120**, 583 (1973).
2. D. J. Lawrence and L. F. Eastman, *J. Cryst. Growth*, **30**, 267 (1975).
3. J. J. Daniele and C. Michel, Proc. 5th International Symposium of GaAs and Related Compounds, Deauville, France, p. 155, Institute of Physics, London (1974); J. J. Daniele, *Appl. Phys. Letters*, **27**, 373 (1975).
4. See, for example, S. E. Epstein, *Advan. Phys.*, **16**, 325 (1967); J. D. Verhoeven, *Trans. Met. Soc. AIME*, **233**, 1156 (1965).
5. D. T. J. Hurle, J. B. Mullin, and E. R. Pike, *Phil. Mag.*, **9**, 423 (1964).
6. M. Lichtensteiger, A. F. Witt, and H. C. Gatos, *This Journal*, **118**, 1013 (1971).
7. A. R. Williams and M. Appapillai, *J. Phys.*, **F3**, 772 (1973).



## Cathodic Reduction Mechanisms of Manganese Dioxide from Derivative Discharge Curves

H. E. L. G. Schweigart and C. R. A. Clauss

Chemical Engineering Research Group, Council for Scientific and Industrial Research, Pretoria 0001, South Africa

1558

### ABSTRACT

Derivative discharge curves of  $\alpha$ -,  $\beta$ -, or  $\gamma$ - $\text{MnO}_2$  can be resolved into a set of six normal distribution functions, designated as peaks O, A, B, C, D, and E, which can each be attributed to a specific reaction. Peak O situated at the highest cell voltages is attributed to the reduction of adsorbed oxygen. The following peak A which is linked to the formation of dissolved  $\text{Mn}^{++}$ -ions ends when the solubility product of  $\text{Mn}(\text{OH})_2$  is attained in the electrolyte. For peak B the over-all reaction  $\text{MnO}_2 + \text{Mn}^{++} + 2\text{H}_2\text{O} + 2e^- \rightarrow 2\text{Mn}(\text{OH})_2$  is proposed. In 9M KOH the electrochemical reduction of  $\beta$ - $\text{MnO}_2$  proceeds in one step to  $\text{Mn}(\text{OH})_2$ ,  $\alpha$ - $\text{MnO}_2$  is at first (peak C) reduced to  $\text{Mn}_3\text{O}_4$  and then (peak D) to  $\text{Mn}(\text{OH})_2$ , and  $\gamma$ - $\text{MnO}_2$  reduces in three successive steps to an amorphous substance,  $\text{Mn}_3\text{O}_4$  and  $\text{Mn}(\text{OH})_2$ . As in practically all cases the presence of  $\text{Mn}(\text{OH})_2$  has been observed, it is proposed that bivalent manganese is the primary reduction product which reacts in alkaline electrolyte with unreduced  $\text{MnO}_2$  to give secondary reduction products the kind of which depends on the type of  $\text{MnO}_2$  involved, the electrolyte, and time of contact. Mixing  $\text{MnO}_2$  with appropriate amounts of  $\text{Mn}(\text{OH})_2$  gives, under comparable conditions, the same products as obtained in electrochemical reduction.

Following the proposition of Balewski and Brenet (1) the first derivatives of discharge curves obtained during cathodic reduction of manganese dioxides under Leclanché-type dry cell conditions have been examined with a pulse galvanostatic analyzer (2, 3). The derivative discharge curves obtained can be resolved into a set of up to six normal distribution functions: peaks O, A, B, C, D, and E. Their relative importance is mainly governed by the mass ratios of electrolyte to manganese dioxide in the depolarizer mix pills (3). This observation and especially the changes of the peak areas with increasing mass ratios suggest that each peak may be attributable to a specific chemical reaction taking place in the depolarizer mixes during the cathodic reduction.

It is the purpose of the present communication to make proposals for this attribution. In order to obtain further evidence, discharge reactions of  $\alpha$ -,  $\beta$ -, and  $\gamma$ - $\text{MnO}_2$  in 9M KOH and in modified Leclanché-type dry cell electrolytes have been investigated and the various reduction products formed in alkaline electrolyte have been examined by x-ray diffraction.

### Experimental

**Samples and discharge procedure.**—The properties of the manganese dioxides used in the experiments are compiled in Table I and the compositions of the depolarizer mixes are presented in Table II. The pulse galvanostatic analyzer, preparation of the depolarizer mixes, and discharge tests together with their evaluation are described in foregoing publications (2, 3).

Key words: reduction, manganese dioxide, Leclanché, dry cell, potassium hydroxide, discharge curves, derivative, mechanism, reaction.

**Examination of reduction products.**—For the x-ray diffraction analysis of the reduction products, the discharge tests were interrupted at the desired reduction states, the depolarizer mix transferred from the test cells into the sample holder as quickly as possible and analyzed immediately. Part of the mix was washed with distilled water on a filter until the wash water was neutral, dried in a vacuum desiccator, and analyzed soon after. In some cases samples were stored unwashed and washed and investigated after a period of several days to determine the effect of washing.

The x-ray diffraction tests were carried out using a Philips x-ray diffractometer with unfiltered Cu radiation. The diffracted beam was monochromatized by a curved carbon crystal (AMR focusing monochromator E202) and measured with a pulse height discriminator.

Table I. Characterization of manganese dioxide samples used in experiments

Type of manganese dioxide	$x$ in $\text{MnO}_x$	Content of $\text{MnO}_2$ in sample (mass %)	Dry cell activity,* coulombs/g $\text{MnO}_2^{**}$	
			Leclanché	Alkali
$\alpha$ - $\text{MnO}_2$ (Wad-ore)	1.992	87.0	450	1200
$\beta$ - $\text{MnO}_2$ (Merck)	1.936	86.5	177	850
$\beta$ - $\text{MnO}_2$ (II)***	1.970	95.2	519	773
$\gamma$ - $\text{MnO}_2$ (electrolytic)	1.955	92.5	750	950
$\alpha$ - $\beta$ - $\text{MnO}_2$ (26% $\alpha$ ; 74% $\beta$ - $\text{MnO}_2$ )	1.968	93.6	153	242

\* Measured with pulse galvanostatic analyzer standard condition cut off voltage: 1.00V.

\*\*  $\text{MnO}_2$  determined as active oxygen.

\*\*\* Kozawa and Powers (8).

Table II. Composition of depolarizer mixtures

Designation of depolarizer mixture	Type of manganese dioxide	Composition of depolarizer mixture in mass %							
		MnO <sub>2</sub> sample	Carbon black	ZnCl <sub>2</sub>	NH <sub>4</sub> Cl	MnCl <sub>2</sub>	NH <sub>3</sub>	KOH	H <sub>2</sub> O
1	Electrolytic ( $\gamma$ -MnO <sub>2</sub> )	61.9	7.7	2.1	13.5	—	—	—	14.8
2	Electrolytic ( $\gamma$ -MnO <sub>2</sub> )	48.6	12.1	3.1	14.3	—	—	—	21.9
3	Electrolytic ( $\gamma$ -MnO <sub>2</sub> )	32.4	18.9	4.4	13.6	—	—	—	30.7
4	Electrolytic ( $\gamma$ -MnO <sub>2</sub> )	26.4	21.3	4.8	13.6	—	—	—	33.9
5	Electrolytic ( $\gamma$ -MnO <sub>2</sub> )	47.8	12.1	2.9	8.0	4.2	1.9	—	23.1
6	Electrolytic ( $\gamma$ -MnO <sub>2</sub> )	32.3	18.9	4.1	6.4	5.5	2.7	—	30.1
7	Electrolytic ( $\gamma$ -MnO <sub>2</sub> )	26.4	21.4	4.5	7.4	4.8	2.4	—	33.1
8	Electrolytic ( $\gamma$ -MnO <sub>2</sub> )	47.9	12.1	3.1	6.3	—	2.1	—	28.5
9	Electrolytic ( $\gamma$ -MnO <sub>2</sub> )	32.1	18.8	4.5	7.0	—	3.0	—	34.6
10	Electrolytic ( $\gamma$ -MnO <sub>2</sub> )	26.4	21.3	4.9	8.0	—	2.6	—	36.8
11	Electrolytic ( $\gamma$ -MnO <sub>2</sub> )	16.4	24.6	—	—	—	—	21.8	37.2
12	Ore ( $\beta$ -MnO <sub>2</sub> )	59.2	7.4	2.5	13.7	—	—	—	17.2
13	Ore ( $\beta$ -MnO <sub>2</sub> )	16.4	24.6	—	—	—	—	21.8	37.2
14	Ore ( $\alpha$ -MnO <sub>2</sub> )	31.9	8.0	5.5	15.8	—	—	—	38.8
15	Ore ( $\alpha$ -MnO <sub>2</sub> )	14.1	21.1	—	—	—	—	24.0	40.8
16	$\beta$ -MnO <sub>2</sub> (II)	59.0	7.3	2.5	13.8	—	—	—	17.4
17	$\beta$ -MnO <sub>2</sub> (II)	15.4	23.1	—	—	—	—	22.7	38.8
18	Ore ( $\alpha$ - $\beta$ -MnO <sub>2</sub> )	63.6	7.6	2.2	11.5	—	—	—	15.1
19	Ore ( $\alpha$ - $\beta$ -MnO <sub>2</sub> )	16.4	24.6	—	—	—	—	21.7	37.3
20	Ore mixture (26% $\alpha$ -MnO <sub>2</sub> , 74% $\beta$ -MnO <sub>2</sub> )	14.3	21.4	—	—	—	—	23.7	40.6

This device gives very low background values so that lines of low intensity can easily be detected. In most cases the range of  $2\theta$  between  $6^\circ$  and  $70^\circ$  was examined.

*Reactions between manganese dioxide and manganous hydroxide.*—2g of MnO<sub>2</sub> sample (grain size < 76  $\mu$ m) were suspended in a solution of 23.4g KOH in 32 ml H<sub>2</sub>O stirred magnetically in a beaker which was placed into a closed vessel flushed by oxygen-free nitrogen. That an oxygen-free atmosphere was obtained under these conditions was ascertained by the observation that a suspension of freshly precipitated manganous hydroxide did not darken within 20 hr. Manganous chloride solution 4.6g MnCl<sub>2</sub> · 4H<sub>2</sub>O in 6.3 ml H<sub>2</sub>O (a) or 3.1g MnCl<sub>2</sub> · 4H<sub>2</sub>O in 15 ml H<sub>2</sub>O (b) was added dropwise from a separating funnel fixed in the lid of the vessel. The mole ratios of MnO<sub>2</sub> to Mn(OH)<sub>2</sub> being formed in the process were chosen such as to result in an oxidation state of MnO<sub>1.5</sub> (a) or MnO<sub>1.6</sub> (b) on complete reaction. The reaction mixture was stirred for 3 hr after which the precipitate was allowed to settle. The supernatant solution was sucked off, the remaining precipitate dried by pressing between filter paper and examined by x-ray diffraction.

### Results and Discussion

*Discharge in zinc-ammonium chloride electrolytes.*—The derivative discharge curves of  $\alpha$ -,  $\beta$ -, or  $\gamma$ -MnO<sub>2</sub> from reduction reactions in ammonium-zinc chloride can be resolved into about six peaks designated as O, A, B, C, D, and E as shown in Fig. 1 for  $\gamma$ -MnO<sub>2</sub>. Among these peaks A and B depend on the electrolyte composition. Their areas increase with the mass ratio of electrolyte to manganese dioxide in the depolarizer mixtures (3) indicated for  $\gamma$ -MnO<sub>2</sub> in Fig. 2 and Table

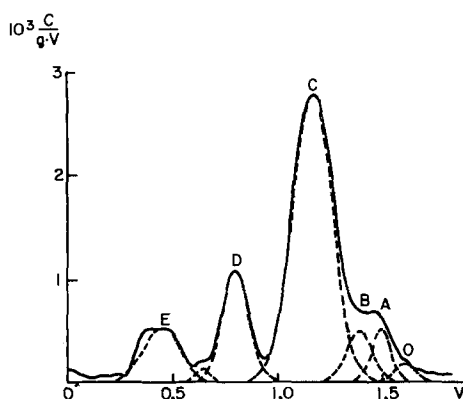
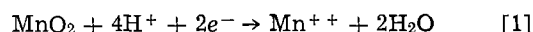


Fig. 1. Derivative discharge curve of  $\gamma$ -MnO<sub>2</sub> in ammonium-zinc chloride electrolyte [ $dQ/dV$  (coulombs/g MnO<sub>2</sub> · V) vs. cell voltage (V)].

II (mixes 2, 3, and 4). At very high mass ratios in the mixes or in foil tests (1, 4) peak A predominates and it was shown that during the latter test stoichiometric dissolution of manganese dioxide occurs (3, 5) following the over-all equation



It has therefore been proposed that this reaction is related to the occurrence of peak A. Evaluation of numerous discharge experiments made under various conditions, combined with calculations of changes in electrolyte composition during the initial part of the discharge, showed that the reaction related to peak A ends when the pH of the electrolyte reaches 7.5 or 8.5

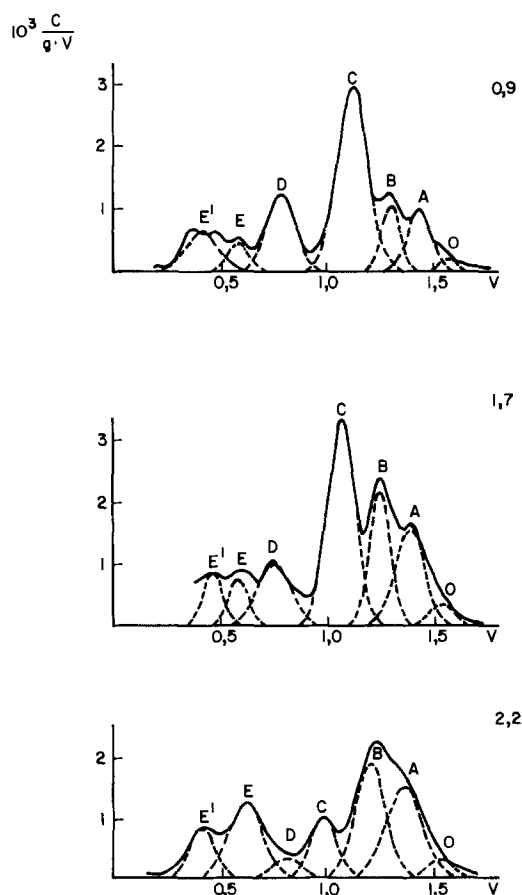


Fig. 2. Derivative discharge curves of  $\gamma$ -MnO<sub>2</sub> [ $dQ/dV$  (coulombs/g MnO<sub>2</sub> · V) vs. cell voltage (V)] and effect of electrolyte content in depolarizer mixture (ratios of electrolyte to MnO<sub>2</sub> indicated on drawing).

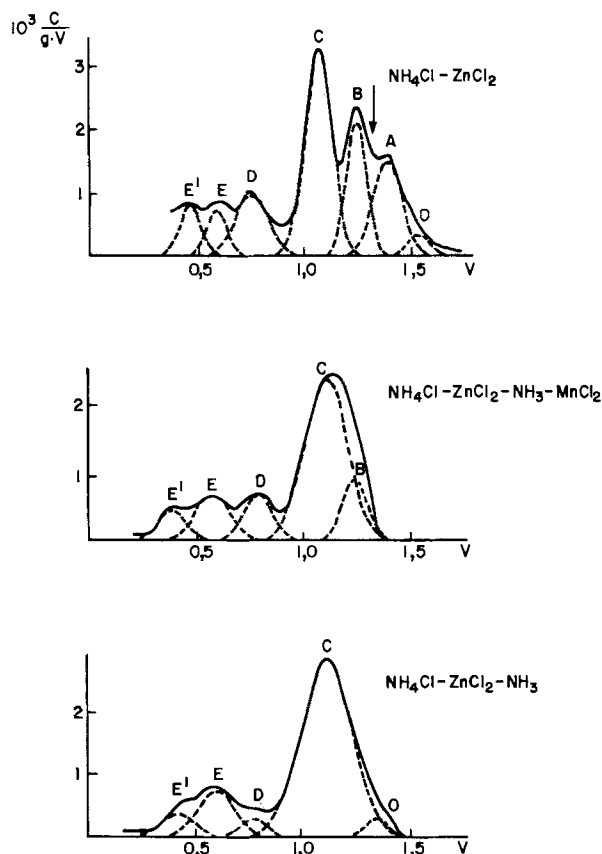
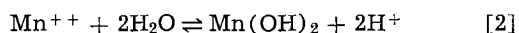
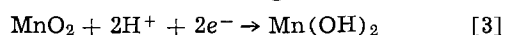


Fig. 3. Derivative discharge curves of  $\gamma$ -MnO<sub>2</sub> in electrolyte compositions simulating partial discharge conditions [ $dQ/dV$  (coulombs/g MnO<sub>2</sub> · V) vs. cell voltage (V)]. (a, top; b, center; c, bottom.)

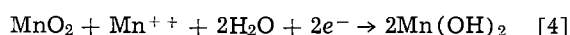
during the discharge of  $\beta$ - or  $\gamma$ -MnO<sub>2</sub>, respectively (3). In the range of these pH values precipitation of manganous ions, formed during the initial discharge following Eq. [1], as hydroxide is to be expected



Protons liberated in this reaction may thus be available for further reduction of manganese dioxide



Combination of Eq. [2] and [3] leads to the over-all equation



to which peak B may be attributed.

In order to obtain further experimental evidence for these attributions depolarizer mixes corresponding to the calculated compositions for the end of peak A with

and without addition of the calculated amounts of manganous ions have been discharged. If peak B is linked to a reaction where manganous ions, or their reaction products with manganese dioxide, are involved it should be observed only for mixtures to which manganous chloride has been added. Figure 3 shows as an example the derivative discharge curves of  $\gamma$ -MnO<sub>2</sub> discharged (a) in normal zinc-ammonium chloride electrolyte, (b) in an electrolyte of the composition calculated for the intersection point between peak A and B near the end of peak A as indicated by the arrow in the upper diagram of Fig. 3, and (c) in an electrolyte similar to the composition used in (b) but without addition of manganous chloride. The curves clearly show that in case (b) peak A has disappeared, peak B is present, although somewhat reduced in comparison to (a) while in case (c) peaks A and B can no longer be observed. The actual values together with those obtained for other mass ratios of electrolyte to manganese dioxide presented in Table III confirm the observations from Fig. 3. When the reactions related to peak A and B are inhibited more manganese dioxide is available for subsequent reactions. This explains the increase of the areas of peak C in cases (b) and (c).

*Reduction of adsorbed oxygen.*—A small peak O positioned at the highest values of the cell voltage scale of the derivative discharge curves is observed in the reduction of all manganese dioxides examined in zinc-ammonium chloride as well as in alkaline electrolytes. This peak may be attributed to the reduction of adsorbed oxygen as proposed by Drucker (6). The coulombic efficiency above 100% found by Boden *et al.* (7) during the initial discharge of  $\gamma$ -MnO<sub>2</sub> in alkaline electrolyte can also be interpreted as reduction of adsorbed oxygen.

*Discharge in 9M KOH electrolyte.*—The shapes of the derivative discharge curves of  $\alpha$ - and  $\gamma$ -MnO<sub>2</sub> in 9M KOH (Fig. 4) are similar to those of the corresponding curves observed in zinc-ammonium chloride electrolyte with the exceptions of peaks A and B being absent and peak O shifted toward peak C. For  $\beta$ -MnO<sub>2</sub> peaks D and E, which are well developed in zinc-ammonium electrolyte, are not observed in 9M KOH. Peaks are much sharper in alkaline than in zinc-ammonium chloride electrolyte. This fact corresponds, course, to the pronounced steps in the discharge curves which have been observed before (8, 9).

Attribution of the peaks C, D, and E to specific reactions requires identification of reduction products obtained by discharging the depolarizer mix to the end and, when considered necessary, to the center of the respective peaks. The different positions of comparable peaks on the cell voltage scale already suggest that the reduction products obtained after discharging to the end of peaks C and D, formed either directly or

Table III. Position (cell voltage) and surface area (coulombs/g MnO<sub>2</sub>) of peaks forming the derivative discharge curves of  $\gamma$ -MnO<sub>2</sub> in electrolytes of compositions (Table II) simulating various states of discharge

Depolarizer mix (No. according to Table II)	Electrolyte components	pH	Peaks											
			O		A		B		C		D		E	
			V	C/g	V	C/g	V	C/g	V	C/g	V	C/g	V	C/g
1	NH <sub>4</sub> Cl-ZnCl <sub>2</sub>	4.95	1.60	23	1.49	58	1.39	75	1.17	646	0.80	171	0.44	122
2	NH <sub>4</sub> Cl-ZnCl <sub>2</sub>	4.95	1.59	20	1.46	147	1.32	111	1.14	532	0.80	200	0.60	62
5	NH <sub>4</sub> Cl-ZnCl <sub>2</sub> -NH <sub>3</sub> -MnCl <sub>2</sub>	7.8	—	0	—	0	1.32	76	1.14	640	0.78	182	0.51	95
8	NH <sub>4</sub> Cl-ZnCl <sub>2</sub> -NH <sub>3</sub>	9.0	—	0	—	0	—	0	1.14	782	0.81	112	0.52	99
3*	NH <sub>4</sub> Cl-ZnCl <sub>2</sub>	4.95	1.56	51	1.41	268	1.27	263	1.09	538	0.77	203	0.61	93
6*	NH <sub>4</sub> Cl-ZnCl <sub>2</sub> -NH <sub>3</sub> -MnCl <sub>2</sub>	7.8	—	0	—	0	1.28	193	1.12	518	0.81	122	0.59	146
9*	NH <sub>4</sub> Cl-ZnCl <sub>2</sub> -NH <sub>3</sub>	9.0	1.36**	37	—	0	—	0	1.13	777	0.79	51	0.62	168
4	NH <sub>4</sub> Cl-ZnCl <sub>2</sub>	4.35	1.55	49	1.38	327	1.22	339	1.00	159	0.82	54	0.64	251
7	NH <sub>4</sub> Cl-ZnCl <sub>2</sub> -NH <sub>3</sub> -MnCl <sub>2</sub>	7.5	—	0	—	0	1.26	190	1.09	698	0.83	149	0.54	154
10	NH <sub>4</sub> Cl-ZnCl <sub>2</sub> -NH <sub>3</sub>	8.2	1.36**	41	—	0	—	0	1.13	766	0.82	264	0.63	201

\* Depicted in Fig. 3.

\*\* Attribution of this peak is uncertain.

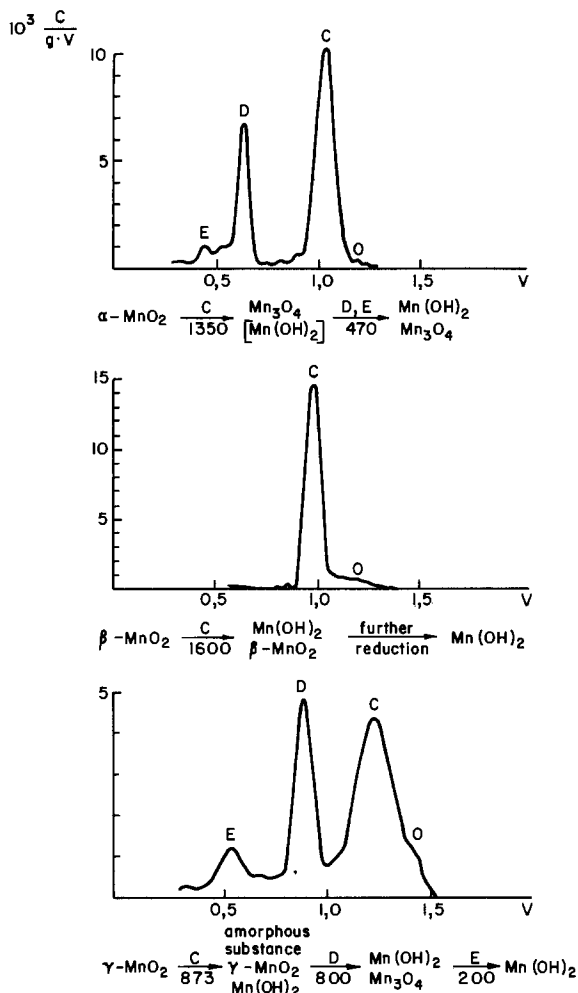


Fig. 4. Derivative discharge curves [ $dQ/dV$  (coulombs/g  $\text{MnO}_2 \cdot \text{V}$ ) vs. cell voltage (V)] and reduction products of  $\alpha$ -,  $\beta$ -, and  $\gamma$ - $\text{MnO}_2$  in 9M KOH electrolyte (figures under arrows: coulombs/g  $\text{MnO}_2$ ).

during secondary chemical reactions taking place within the time available during discharge, cannot be the same for the different types of manganese dioxide examined. The corresponding schemes and products of reduction identified by x-ray diffraction analysis of fresh unwashed samples taken directly after the relevant steps are shown below the graphs of the derivative discharge curves of  $\alpha$ -,  $\beta$ - and  $\gamma$ - $\text{MnO}_2$  obtained in 9M KOH (Fig. 4).

Since the x-ray diffraction patterns of  $\gamma$ - $\text{Mn}_2\text{O}_3$  and  $\text{Mn}_3\text{O}_4$  are very similar, it is difficult to decide which of the two substances was present in the reduction products. According to the data presented by Bricker (10) the most important differences between these patterns are the intensities of the  $d = 1.82\text{\AA}$  lattice spacings with a relative intensity of 10% for  $\gamma$ - $\text{Mn}_2\text{O}_3$  and 50% for  $\text{Mn}_3\text{O}_4$  and the absence of lines at  $d = 1.030$  and  $0.985\text{\AA}$  for  $\gamma$ - $\text{Mn}_2\text{O}_3$ . Contrary to this the patterns presented by Ramdohr (11) and by Moore *et al.* (12) for  $\text{Mn}_3\text{O}_4$  indicate a low intensity of the line corresponding to  $d = 1.82\text{\AA}$ . In the diffraction diagrams of the reduction products the line at  $d = 1.82\text{\AA}$  had a low intensity and the lines corresponding to  $d = 1.030$  and  $0.985\text{\AA}$  were present. The criteria derived from Bricker's work contradict these findings and do not allow any decisions to be made. If one accepts the work of Ramdohr and Moore *et al.* the observed reduction products are  $\text{Mn}_3\text{O}_4$  and not  $\gamma$ - $\text{Mn}_2\text{O}_3$ . We therefore, in agreement with McBreen (18), assume that the reduction product is  $\text{Mn}_3\text{O}_4$ ; the conclusions derived from our observations would, however, not be affected if the wrong choice had been made.

Washing and drying normally causes  $\text{Mn}(\text{OH})_2$  to disappear if present in smaller amounts, and leads further to the formation of secondary products. Among these  $\alpha$ -,  $\beta$ -,  $\gamma$ - $\text{MnOOH}$ , hydrohausmannite (13, 14), manganous manganite (15), and todorokite (16) were identified. The cathodic reduction of the samples was normally terminated within 3 hr. After storing the discharged depolarizer mixes for 24 hr or after slow discharges during the same time interval, other products such as  $\beta$ - or  $\gamma$ - $\text{MnOOH}$  and hydrohausmannite could be identified. Our observations lead to the conclusion that these compounds were formed in secondary reactions from primary reduction products.

Reduction of two, well-crystallized  $\beta$ - $\text{MnO}_2$  samples of different origin and with an x-ray pattern similar to that given by Byström (17) showed only one peak with an area of 1600 coulombs/g  $\text{MnO}_2$ , which is well above the 1033 coulombs/g necessary to reduce  $\text{MnO}_{1.936}$  to the trivalent state. At the end of this peak only  $\text{Mn}(\text{OH})_2$  together with some unreduced  $\beta$ - $\text{MnO}_2$  were identified. Therefore  $\text{Mn}(\text{OH})_2$  seems to be the only significant reduction product to occur. Another  $\beta$ - $\text{MnO}_2$  ore sample, with x-ray diagram differing somewhat from the previous samples, showed the presence of a small peak D after peak C. In agreement with McBreen (18), no lattice dilation of  $\beta$ - $\text{MnO}_2$  during reduction was observed.

Kozawa and Powers (8) observed a two-step discharge curve for their  $\beta$ - $\text{MnO}_2$  (II and III) in 9M KOH which had been prepared by heating electrolytic  $\gamma$ - $\text{MnO}_2$  for 10 days at  $400^\circ \pm 10^\circ\text{C}$ , followed by sulfuric acid treatment. Discharge of a sample prepared by us in the same manner confirmed this observation. The x-ray diagram of this sample has fewer and broader lines than those of the above-mentioned  $\beta$ - $\text{MnO}_2$  samples. It may be concluded that the  $\beta$ - $\text{MnO}_2$  obtained by the method of Kozawa and Powers is less crystallized and does not fully represent the pyrolusite phase. In agreement with McBreen (18), who prepared samples in the same way,  $\text{Mn}(\text{OH})_2$  and  $\text{Mn}_3\text{O}_4$  are observed on reduction to the end of peak C.

During the reduction of  $\alpha$ - $\text{MnO}_2$  mainly  $\text{Mn}_3\text{O}_4$  together with a small amount of  $\text{Mn}(\text{OH})_2$  is found after the first step at the end of peak C. On further reduction during the second step, peak D, part of the  $\text{Mn}_3\text{O}_4$  is converted to  $\text{Mn}(\text{OH})_2$ . On further reduction more  $\text{Mn}(\text{OH})_2$  is formed but some  $\text{Mn}_3\text{O}_4$  can still be observed in discharge products sampled at cell voltages indicating the end of peak E.

The derivative discharge curve of  $\gamma$ - $\text{MnO}_2$  in 9M KOH clearly shows three major peaks C, D, and E. After discharging to a voltage indicating the end of peak C some weak lines of  $\gamma$ - $\text{MnO}_2$  are still observed. The shift of their positions indicates that lattice dilation has taken place confirming the findings of Brenet (1), Bell and Huber (19), and Boden *et al.* (7). Some lines of minor intensity indicate the presence of  $\text{Mn}(\text{OH})_2$ . The higher background of the spectra may be explained, in agreement with Boden *et al.* (7), by the presence of an amorphous substance which seems to be the major reduction product after discharge to the end of peak C. On further discharge to the end of peak D  $\text{Mn}(\text{OH})_2$  and a smaller amount of  $\text{Mn}_3\text{O}_4$  are found. These may have been formed by the reduction of the amorphous substance and the residual  $\gamma$ - $\text{MnO}_2$ . The following peak E is related to the reduction of  $\text{Mn}_3\text{O}_4$  to  $\text{Mn}(\text{OH})_2$ . Its position on the cell voltage scale is equal to that of peak D observed during the reduction of  $\alpha$ - $\text{MnO}_2$  to which the same reaction is attributed.

*Discharge of a mixed  $\alpha$ ,  $\beta$ - $\text{MnO}_2$  ore.*—The reduction of an ore sample, which by x-ray analysis proved to be a mixture of 26%  $\alpha$ - and 74%  $\beta$ - $\text{MnO}_2$  resulted in a derivative discharge curve (Fig. 5) of a shape very similar to that obtained for pure  $\alpha$ - $\text{MnO}_2$  with the exception of peak C being shifted downward by 0.07V.

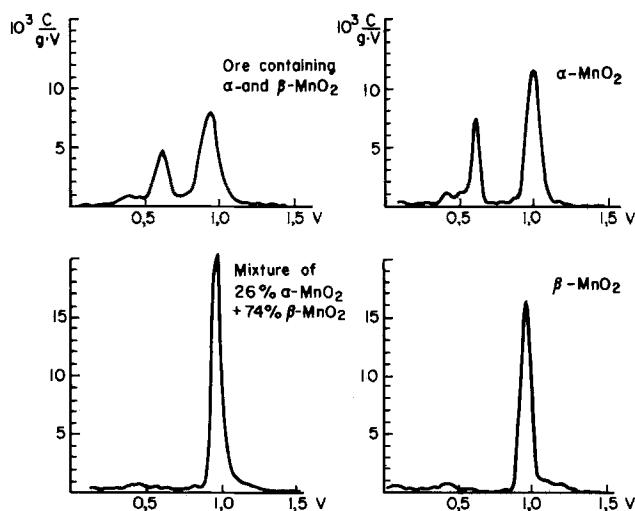
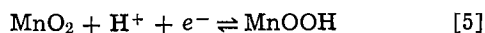


Fig. 5. Derivative discharge curves of an  $\alpha$ ,  $\beta$ -MnO<sub>2</sub> ore, an artificial mixture of  $\alpha$ - and  $\beta$ -MnO<sub>2</sub> and of the single components,  $\alpha$ -MnO<sub>2</sub> and  $\beta$ -MnO<sub>2</sub>, in 9M KOH electrolyte [ $dQ/dV$  (coulombs/g MnO<sub>2</sub> · V) vs. cell voltage (V)].

Discharging an artificial mixture of the same composition prepared from pure  $\alpha$ - and  $\beta$ -MnO<sub>2</sub> gave a derivative discharge curve with only one peak situated at a cell voltage approximately 0.02V higher than peak C of  $\beta$ -MnO<sub>2</sub>. On account of this observation it may be assumed that an intercrystalline mixture of two MnO<sub>2</sub> phases can behave differently from the corresponding interparticle mixture.

*A general model for the discharge mechanism.*—Hitherto the reaction corresponding to peak C in the derivative discharge curves was attributed by various authors (8, 20-24) to the solid-state reduction of manganese dioxide following the equation



However, no indication of the presence of any one of the three known phases of MnOOH at the end of peak C has been found in the fresh samples. Only after washing, drying, or storage of reduced manganese dioxide samples  $\alpha$ -,  $\beta$ -, and  $\gamma$ -MnOOH could be identified. Therefore these compounds appear not to be the primary reaction products corresponding to peak C and it is therefore unlikely that a reaction corresponding to Eq. [5] takes place, particularly so during the reduction of  $\alpha$ - and  $\beta$ -MnO<sub>2</sub>. The amorphous substance observed after peak C during the reduction of  $\gamma$ -MnO<sub>2</sub> cannot be ruled out to be a noncrystalline form of MnOOH so that reaction [5] could be valid for this case. The lattice dilation observed only during reduction of  $\gamma$ -MnO<sub>2</sub> may well support this view.

All our observations point to bivalent manganese always being the primary reduction product, either in the form of manganous ions or as hydroxide depending on the pH of the electrolyte in the depolarizer mixture. In alkaline electrolyte the manganous hydroxide reacts with the remaining  $\alpha$ -MnO<sub>2</sub> to yield Mn<sub>3</sub>O<sub>4</sub> or with  $\gamma$ -MnO<sub>2</sub> to give the amorphous substance. There is no appreciable reaction between  $\beta$ -MnO<sub>2</sub> and manganous

hydroxide in 9M KOH within the time required for the discharge experiment.

In order to obtain further evidence manganous hydroxide was prepared *in situ* in suspensions of either  $\alpha$ -,  $\beta$ -, or  $\gamma$ -MnO<sub>2</sub> powders in strong KOH solutions by addition of appropriate amounts of manganous chloride solutions. After stirring the suspensions in an oxygen-free atmosphere for durations comparable to the discharge times applied in the pulse galvanostatic analyzer discharge test the solids were filtered off and, without further treatment, examined by x-ray diffraction. In the case of  $\beta$ -MnO<sub>2</sub> no reaction with manganous hydroxide was observed under these conditions. Practically identical x-ray diagrams were obtained for  $\alpha$ - and  $\gamma$ -MnO<sub>2</sub> reduced either electrochemically to the middle or end of peak C or by reaction with the corresponding amounts of Mn(OH)<sub>2</sub>.

Manuscript received Dec. 30, 1975. This was Paper 9 presented at the Dallas, Texas, Meeting of the Society, Oct. 5-9, 1975.

Any discussion of this paper will appear in a Discussion Section to be published in the June 1977 JOURNAL. All discussions for the June 1977 Discussion Section should be submitted by Feb. 1, 1977.

Publication costs of this article were assisted by the Chemical Engineering Research Group, CSIR.

#### REFERENCES

1. L. Balewski and J. P. Brenet, *Electrochem. Technol.*, **5**, 527 (1967).
2. H. E. L. G. Schweigart, Paper presented at International Symposium on Manganese Dioxide, Cleveland, Oct. 1-2, 1975.
3. C. R. A. Clauss and H. E. L. G. Schweigart, *This Journal*, **123**, 951 (1976).
4. R. Huber and J. Kändler, *Electrochim. Acta*, **8**, 265 (1963).
5. A. M. Chreitzberg, D. R. Allenson, and W. C. Vosburgh, *This Journal*, **102**, 557 (1955).
6. C. Drucker, *Z. Physik. Chem. Bodensteinfestband*, **912** (1931).
7. David Boden, C. J. Venuto, D. Wisler, and R. B. Wylie, *This Journal*, **114**, 415 (1967).
8. A. Kozawa and R. A. Powers, *Electrochem. Technol.*, **5**, 535 (1967).
9. A. Kozawa, "Electrochemistry of Manganese Dioxide and Manganese Dioxide Batteries in Japan," The U.S. Branch Office of the Electrochemical Society of Japan, Vol. 12, p. 39, Cleveland (1971).
10. O. Bricker, *Am. Mineralogist*, **50**, 1296 (1965).
11. P. Ramdohr, Paper presented at the 20th Intern. Geol. Cong. Symp. Mangan., **1**, 19 (1956).
12. T. E. Moore, M. Ellis, and P. W. Selwood, *J. Am. Chem. Soc.*, **72**, 856 (1950).
13. W. Feitknecht, P. Brunner, and H. R. Oswald, *Z. Anorg. Allgem. Chem.*, **316**, 154 (1962).
14. W. Feitknecht and W. Marti, *Helv. Chim. Acta*, **28**, 129 (1945).
15. M. Pierre Dubois, *Ann. Chim., Ser. 11*, **5**, 411 (1936).
16. L. J. Lawrence, P. Bayliss, and P. Tonkin, *Mineral. Mag.*, **36**, 757 (1968).
17. A. M. Byström, *Acta Chem. Scand.*, **3**, 163 (1949).
18. James McBreen, *Electrochim. Acta*, **20**, 221 (1975).
19. G. S. Bell and R. Huber, *This Journal*, **111**, 1 (1964).
20. A. Era, Z. Takehara, and S. Yoshizawa, *Electrochim. Acta*, **12**, 1199 (1967).
21. J. J. Coleman, *Trans. Electrochem. Soc.*, **90**, 545 (1946).
22. A. B. Scott, *This Journal*, **107**, 941 (1960).
23. F. Kornfeil, *ibid.*, **109**, 349 (1962).
24. A. Kozawa and R. A. Powers, *ibid.*, **113**, 870 (1966).

# Electrochemical Behavior of Sulfur and Sulfide in Molten Sodium Tetrachloroaluminate Saturated with NaCl

R. Marassi,<sup>1</sup> G. Mamantov,\* and J. Q. Chambers

Department of Chemistry, University of Tennessee, Knoxville, Tennessee 37916

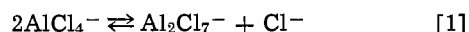
## ABSTRACT

The electrochemical behavior of sulfur and sulfide in molten NaAlCl<sub>4</sub> saturated with NaCl has been investigated at different temperatures and with different electrode materials. In melts containing sulfur one reduction and one oxidation wave are seen at tungsten and glassy carbon electrodes. At platinum two reduction waves are observed. The oxidation waves are similar for all three electrode materials. Reduction of sulfur leads to the formation of sulfide; the oxidation leads to S(I) or S(II) depending on the temperature, the higher oxidation state being formed at higher temperatures. The data obtained in sulfur solutions have been confirmed by the results obtained in melts containing Na<sub>2</sub>S. The mechanism for the electrochemical oxidation of sulfur apparently involves a complex set of charge transfer and chemical steps.

The chemistry and electrochemistry of sulfur in molten salts have received considerable attention in recent years because of the possible use of sulfur as a cathode material in a secondary battery using molten chlorides as solvents and lithium or its alloys as anodes (1-3). A closely related application involves the development of the high temperature sodium-sulfur battery using  $\beta$ -alumina as a solid electrolyte (1-3). The interest has been focused mainly on the electrochemical characterization of the couple S/S<sup>2-</sup> in molten chlorides (4-8) and thiocyanates (8-10). Some papers have been concerned with the spectroscopic characterization of the sulfur species responsible for the blue or green solutions that result from the interaction of sulfur and sulfide in both melts (11-15). Electrochemical oxidation of sulfur in the molten LiCl-KCl eutectic has also been briefly explored (4, 5).

In a recently published note (16) we reported some preliminary results on the electrooxidation and electroreduction of sulfur in molten chloroaluminates (AlCl<sub>3</sub>-NaCl mixtures) of different compositions. The electrochemistry of this system is markedly dependent on the melt composition.

It is now well established (17-21) that the acid-base properties of molten chloroaluminates near the 1:1 AlCl<sub>3</sub>/NaCl mole ratio can be described by the equilibrium



The Lewis acidity can be expressed in terms of  $p\text{Cl}$  ( $p\text{Cl} = -\log [\text{Cl}^-]$ ); the most basic system corresponds to a NaCl-saturated melt in which the  $p\text{Cl}$  is constant in the presence of solid NaCl, and at 175°C is equal to 1.1 (22).

In this paper we report the results obtained in chloroaluminate melts saturated with NaCl; in these melts the electrochemistry of the sulfur system is simpler than in the more acidic melts. The effect of the melt acidity on the oxidation wave of sulfur has been briefly reported in Ref. (16) and will be the subject of a later communication.

## Experimental

The melt preparation and other experimental procedures have been reported previously (23, 24).

Sulfur was introduced in the melt after purification by repeated crystallizations from benzene and vacuum

\* Electrochemical Society Active Member.

<sup>1</sup> Present address: Istituto Chimico, Università di Camerino, 62032 Camerino (MC), Italy.

Key words: chloroaluminates, AlCl<sub>3</sub>-NaCl melts, sulfur electrochemistry, sulfide, NaAlCl<sub>4</sub>.

sublimation; anhydrous Na<sub>2</sub>S (Alfa Products) was used as received.

## Results and Discussion

**Voltammetry of sulfur and Na<sub>2</sub>S solutions.**—Sulfur solutions in the AlCl<sub>3</sub>-NaCl<sub>sat</sub> melt in the temperature range 175°-300°C are pale yellow in the presence and absence of Na<sub>2</sub>S. This is indicative of the absence of equilibria that can generate anionic species such as S<sub>3</sub><sup>-</sup> or S<sub>2</sub><sup>-</sup> that are responsible for the blue or green solutions of polysulfides in molten chlorides and thiocyanates (11-15).

Sulfur itself is not very soluble in the melt. The concentration of the sulfur electroactive species cannot be quoted since the aggregation state of sulfur is not known. In the temperature range of interest for basic chloroaluminates (> 160°C) sulfur (S<sub>8</sub>) undergoes marked structural changes to form open chains and polymers (25). For the sake of comparison and in order to have a reference point, all concentrations in this paper are referred to a hypothetical sulfur monomer. From visual observations the solubility of sulfur (as S) in AlCl<sub>3</sub>-NaCl<sub>sat</sub> melt at 175°C is less than  $2.1 \times 10^{-2}$  molal.

In Fig. 1 and 2 voltammograms are presented for sulfur at a glassy carbon electrode at 175°C. The voltammogram in Fig. 1 was obtained by recording the current at 5 sec after the application of potential steps

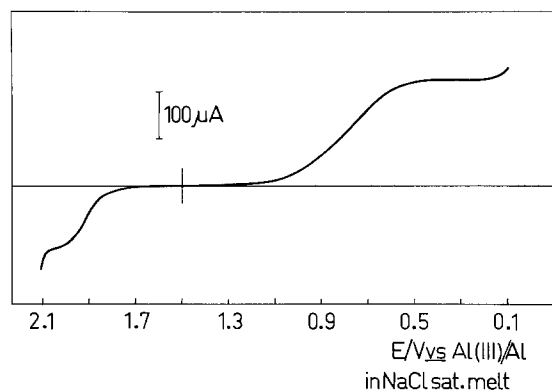


Fig. 1. Voltammogram obtained from current-time curves (current measured 5 sec after the application of the potential step) in a  $1.8 \times 10^{-2}$  molal sulfur (as sulfur monomer) solution in NaCl saturated melt at 175°C. Glassy carbon electrode area: 0.07 cm<sup>2</sup>. Potentials vs. Al(III)/Al reference electrode in NaCl-saturated melt.

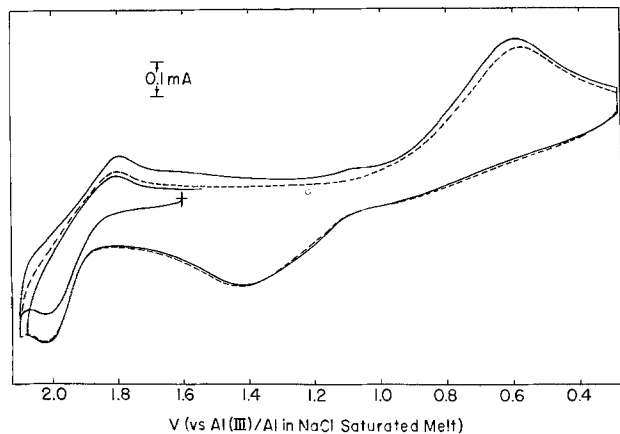


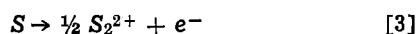
Fig. 2. Cyclic voltammogram at a glassy carbon electrode (area  $0.07 \text{ cm}^2$ ) in a  $1.8 \times 10^{-2}$  molal sulfur solution in NaCl-saturated melt at  $175^\circ\text{C}$ . Scan rate  $0.1 \text{ V}\cdot\text{sec}^{-1}$ . Potentials vs. Al(III)/Al reference electrode in NaCl-saturated melt.

of different amplitude to the electrode (23). Similar current-potential curves can be obtained on tungsten electrodes. For both cyclic and pulse voltammograms, the peak or limiting current ratios of the oxidation wave to the reduction wave are *ca.* 0.5.

A different behavior is observed for the reduction wave if platinum is used as the electrode material. The reduction process occurs in two approximately equal steps. At longer times, *e.g.*, 5 sec as in Fig. 1, the constructed voltammograms have the same general shape except that the first reduction wave is larger than the second. The total limiting current measured on the second plateau is, however, twice the limiting current for the oxidation step. The different reduction behavior of the sulfur system at various electrode materials is evident also in the cyclic voltammograms which show that the reduction process takes place in one drawn-out irreversible step at glassy carbon and tungsten, while two waves are again seen at platinum. The nature of the second wave at platinum has not been studied in detail except to note that it depends greatly on the previous history of the electrode and on the number of cycles in the voltammograms.

The shape of the oxidation wave is not, on the contrary, dependent on the electrode materials. Similar oxidation waves were obtained on glassy carbon, tungsten, and platinum working electrodes.

The results for elemental sulfur are complemented by the experiments on  $\text{Na}_2\text{S}$  solutions in the same melt at the same temperature. Sodium sulfide dissolves very slowly in the melt and does not seem to be very soluble; however, the sulfide concentration that can be realized is sufficiently high to allow its electrochemical detection. The oxidation of  $\text{S}^{2-}$  occurs in two steps as is seen in the pulse voltammogram obtained at a tungsten electrode (Fig. 3). The voltammograms for the sulfide solutions are similar to those of elemental sulfur except for the shift of the zero current line. This correspondence and the limiting current data suggest that sulfur is reduced to a negative two-oxidation state and oxidized to a positive one-oxidation state in these melts. A reaction sequence consistent with these results is shown in Eq. [2] and [3]



in which  $\text{S}_2^{2+}$  is proposed as the oxidation product. In these equations elemental sulfur is written as S for convenience, although its aggregation state is unknown. Paulsen and Osteryoung have also suggested  $\text{S}_2\text{Cl}_2$  as the oxidation product of sulfur in basic  $\text{NaAlCl}_4$  melts (26).

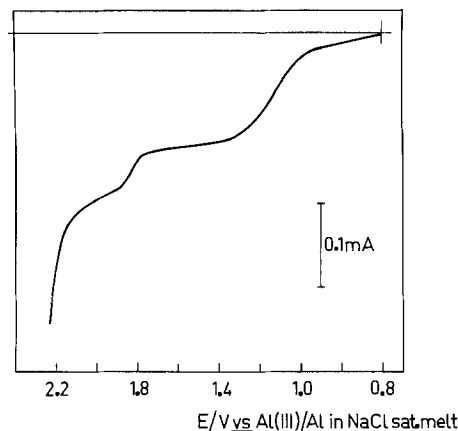


Fig. 3. Normal pulse voltammogram for a  $1.04 \times 10^{-2}$  molal  $\text{Na}_2\text{S}$  solution (assuming that the salt is completely dissolved) in NaCl-saturated melt at  $175^\circ\text{C}$ . W electrode area  $0.07 \text{ cm}^2$ . Scan rate  $5 \text{ mV}\cdot\text{sec}^{-1}$ ; 57 msec pulse. Potentials vs. Al(III)/Al reference electrode in NaCl-saturated melt.

The electrochemical behavior changes at higher temperatures both in the  $\text{Na}_2\text{S}$  and sulfur solutions. The  $\text{S}/\text{S}^{2-}$  couple becomes more reversible on tungsten and platinum electrodes (Fig. 4) and the oxidation wave assumes the shape of an irreversible system at low scan rates. When the scan is initiated in the positive direction, a prewave that is not seen at lower temperatures appears before the main reduction wave. In addition, the limiting current ratio of the oxidation to the reduction wave increases and approaches a value of unity as the temperature is raised. This behavior is evident in Fig. 5 (compared to Fig. 3) and suggests the sequence in Eq. [4] and [5] for the high temperature oxidation



This hypothesis is consistent with spectroscopic evidence in more acidic chloroaluminate melts which indicates that  $[\text{S}_2^{2+}]$ ,  $\text{S}_4^{2+}$ ,  $\text{S}_8^{2+}$ , and  $\text{S}_{16}^{2+}$  are stable at low temperatures and that  $\text{S}^{2+}$  can be formed at high temperatures (27, 28). It is also consistent with the general observation that higher oxidation states are more stable in more basic melts which is the case at higher temperatures both due to the increased solubility of NaCl in  $\text{NaAlCl}_4$  and the greater dissociation of  $\text{AlCl}_4^-$  (18, 23).

*Sulfur oxidation mechanism.*—Considerable experimental effort has been expended on mechanistic studies

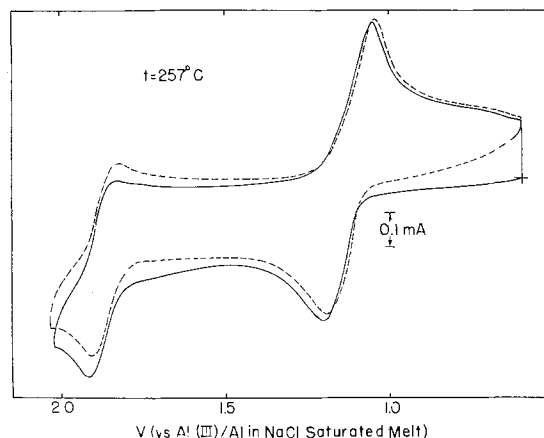


Fig. 4. Cyclic voltammogram for a  $1.04 \times 10^{-2}$  molal  $\text{Na}_2\text{S}$  solution in NaCl-saturated melt at  $257^\circ\text{C}$ . W electrode area  $0.07 \text{ cm}^2$ . Scan rate  $0.1 \text{ V}\cdot\text{sec}^{-1}$ . Potentials vs. Al(III)/Al reference electrode in NaCl-saturated melt.



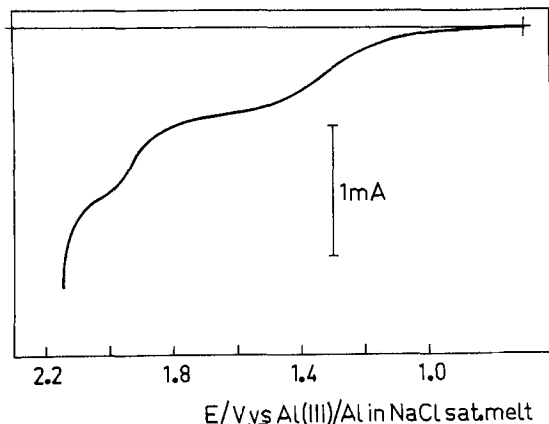


Fig. 5. Normal pulse voltammogram for a  $1.04 \times 10^{-2}$  molal  $\text{Na}_2\text{S}$  solution in NaCl-saturated met. at  $230^\circ\text{C}$ . W electrode area  $0.07 \text{ cm}^2$ . Scan rate  $5 \text{ mV}\cdot\text{sec}^{-1}$ ; 57 msec pulse. Potentials vs. Al(III)/Al reference electrode in NaCl-saturated melt.

of the sulfur oxidation wave with only partially satisfactory results. The proximity of the oxidation wave to the anodic background discharge of the chloroaluminate melt and the uncertainty in the actual sulfur concentration made these measurements difficult. However, several observations can be made on the basis of the cyclic voltammetric and chronoamperometric measurements.

The cyclic voltammetric data at platinum are given in Tables I-III (similar results were obtained at glassy carbon and tungsten electrodes). At all temperatures the peak width, the peak separation, and the ratio of the cathodic to the anodic peak current are dependent

on sweep rate. At the fastest sweep rates at all temperatures the ratio of peak currents is unity which indicates that the direct product of the oxidation is relatively stable. At these sweep rates the peak separation is considerably larger than that expected for a one-electron (or greater) process, while the peak width of the anodic wave is less than the value for a one-electron process (29, 30). Significantly, the current function,  $i_p/v^{1/2}$ , is independent of sweep rate within experimental error over a wide sweep rate range. These results suggest that fragmentation of the sulfur molecules in the oxidation process is fast on the voltammetric time scale and that the charge transfer is quasi-reversible. The decrease of the ratio  $i_p^{\text{cath}}/i_p^{\text{an}}$  at lower scan rates becoming more pronounced at higher temperatures (Fig. 6) is indicative of a following chemical reaction.

These results may be (at least partially) rationalized in terms of a generalized model given in Eq. [6] and [7] for the oxidation process. This model involves anodic fragmentation of the sulfur rings which may be initiated thermally or by electron transfer. The overall process leads to formation of sulfur in the +1 oxidation state which is indicated by the limiting current ratios observed for the sulfur and sulfide voltammograms

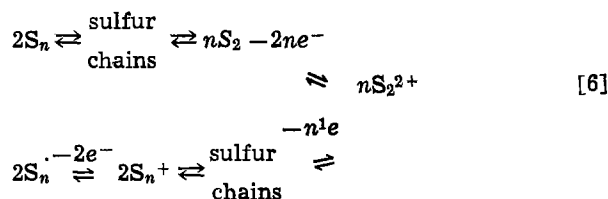


Table I. Cyclic voltammetric parameters for the oxidation of sulfur in  $\text{AlCl}_3\text{-NaCl}_{\text{sat}}$  melt at  $175^\circ\text{C}$ . Sulfur concentration  $1.8 \times 10^{-2}$  molal (as sulfur monomer). Platinum electrode area  $0.08 \text{ cm}^2$ . Potentials vs. Al(III)/Al in NaCl saturated melt.

Scan rate (V-sec <sup>-1</sup> )	$i_p$ ( $\mu\text{A}$ )	$E_p$ (V)	$(E_p - E_{p/2})$ (mV)	$(E_p^a - E_p^c)$ (mV)	$i_p v^{-1/2}$ ( $\mu\text{A}\cdot\text{sec}^{1/2} \text{ V}^{-1/2}$ )	$i_p^{\text{cath}}/i_p^{\text{an}}$
0.020	110	1.98	55	95	778	0.66
0.050	173	1.99	57	107	774	0.76
0.100	250	1.99	65	110	791	0.82
0.200	338	2.00	70	142	756	0.94
0.500	578	2.00	75	150	817	0.97

1.000: at this scan rate the oxidation wave is no longer peak shaped.

$$\bar{X} = 783 \pm 23$$

Table II. Cyclic voltammetric parameters for the oxidation of sulfur in  $\text{AlCl}_3\text{-NaCl}_{\text{sat}}$  melt at  $210^\circ\text{C}$ . Sulfur concentration  $7.7 \times 10^{-3}$  molal (as sulfur monomer). Platinum electrode area  $0.08 \text{ cm}^2$ . Potentials vs. Al(III)/Al in NaCl-saturated melt.

Scan rate (V-sec <sup>-1</sup> )	$i_p$ ( $\mu\text{A}$ )	$E_p$ (mV)	$(E_p - E_{p/2})$ (mV)	$(E_p^a - E_p^c)$ (mV)	$i_p v^{-1/2}$ ( $\mu\text{A}\cdot\text{sec}^{1/2} \text{ V}^{-1/2}$ )	$i_p^{\text{cath}}/i_p^{\text{an}}$
0.090	213	1.94	55	105	710	0.79
0.164	272	1.94	60	115	672	0.84
0.460	446	1.98	70	145	656	0.92
1.000	664	1.99	75	165	664	0.95
2.000	1000	2.01	82	210	707	1.02
3.000	1264	2.02	94	235	730	1.03

$$\bar{X} = 690 \pm 30$$

Table III. Cyclic voltammetric parameters for the oxidation of sulfur in  $\text{AlCl}_3\text{-NaCl}_{\text{sat}}$  melt at  $262^\circ\text{C}$ . Sulfur concentration  $7.7 \times 10^{-3}$  molal (as sulfur monomer). Platinum electrode area  $0.07 \text{ cm}^2$ . Potentials vs. Al(III)/Al in NaCl-saturated melt.

Scan rate (V-sec <sup>-1</sup> )	$i_p$ ( $\mu\text{A}$ )	$E_p$ (V)	$(E_p - E_{p/2})$ (mV)	$(E_p^a - E_p^c)$ (mV)	$i_p v^{-1/2}$ ( $\mu\text{A}\cdot\text{sec}^{1/2} \text{ V}^{-1/2}$ )	$i_p^{\text{cath}}/i_p^{\text{an}}$
0.084	276	1.92	45	85	952	0.63
0.168	362	1.93	53	90	883	0.70
0.420	540	1.94	50	90	833	0.79
0.840	760	1.95	65	100	829	0.90
1.840	1140	1.97	75	135	840	0.99
4.400	1745	1.99	80	160	832	1.01

$$\bar{X} = 862 \pm 49$$

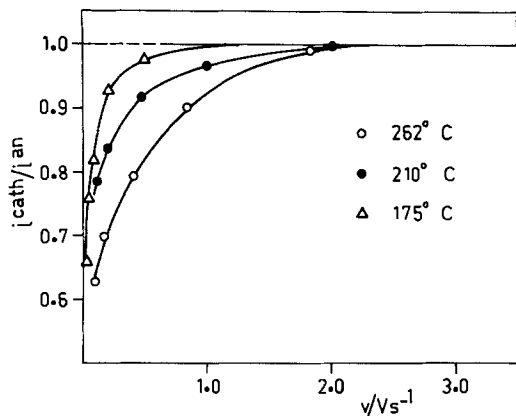
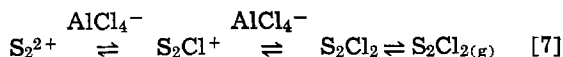


Fig. 6. Variation of the ratio  $i_p^{\text{cath}}/i_p^{\text{an}}$  with the scan rate at different temperatures.



Actually a complex set of electron transfer and sulfur-sulfur bond fragmentation reactions may be envisioned between the  $\text{S}_n$  rings and the  $\text{S}_2^{2+}$  dications. The quasi-reversible nature of the oxidation wave could be due to oxidation of the fragments over the potential range encompassed by the oxidation wave.

The slopes of the  $\log [i/(i_d - i)]$  vs.  $E$  plots for the pulse voltammograms are dependent on the time at which the current is measured. Figure 7 shows two voltammograms obtained at 57 msec (curve A) and 5 sec (curve B). The latter curve is more "reversible" and the slope approaches a value for a two-electron transfer (45 mV at 175°C). The plots are shown in Fig. 8. This behavior is consistent with the above

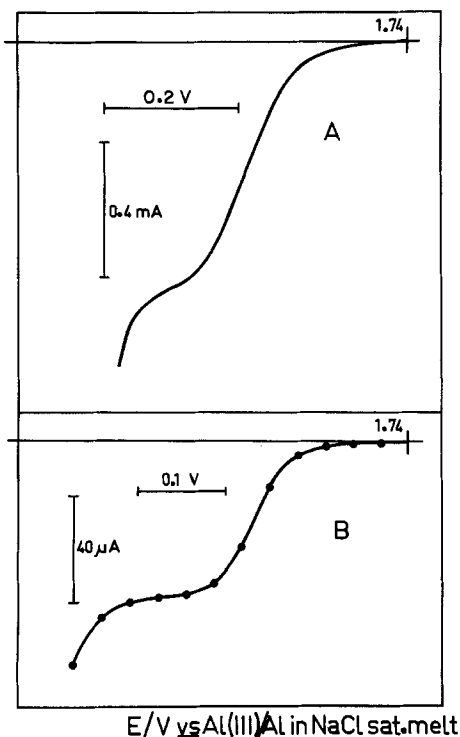


Fig. 7. (A) Normal pulse voltammogram for the oxidation of sulfur in NaCl-saturated melt at 175°C. Sulfur concentration  $1.8 \times 10^{-2}$  molal. Platinum electrode area  $0.06 \text{ cm}^2$ . Scan rate  $2 \text{ mV}\cdot\text{sec}^{-1}$ ; 57 msec pulse. Potentials vs. Al(III)/Al reference electrode in NaCl-saturated melt. (B) Voltammogram constructed from current-time curves (current measured at 5 sec) for the oxidation of sulfur in NaCl-saturated melt at 175°C. Sulfur concentration  $7.7 \times 10^{-3}$  molal. Potentials vs. Al(III)/Al reference electrode in NaCl-saturated melt.

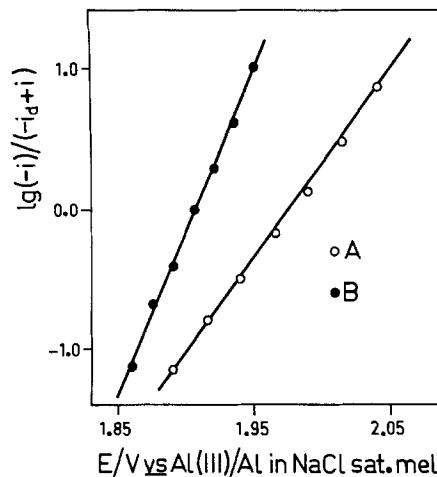


Fig. 8. Plots of  $\log(-i)/(-i_d + i)$  vs.  $E$  for the voltammograms in Fig. 7. A corresponds to Fig. 7A (reciprocal slope 74 mV); B corresponds to Fig. 7B (reciprocal slope 44 mV).

scheme in that it suggests a two-electron oxidation of the  $\text{S}_2$  molecules at long times. At short times (57 msec pulse) the experimental slope is reasonably close to the expected value for a one-electron reversible charge transfer.

Additional support for the further oxidation at the same potential of the partially oxidized product following one or more chemical steps is provided by the increase of the chronoamperometric  $it^{1/2}$  value from 98 to  $127 \mu\text{A}\cdot\text{sec}^{1/2}$  with a variation of  $t$  from 1.25 to 5 sec (these results were obtained at the tungsten electrode,  $A = 0.07 \text{ cm}^2$ , at 175°C at a potential corresponding to the diffusion plateau of the oxidation wave; S molality  $7.7 \times 10^{-3}$ ).

The behavior of the ratio  $i_p^{\text{cath}}/i_p^{\text{an}}$  as a function of sweep rate and temperature indicates that the oxidation product is more rapidly removed from the diffusion layer at the higher temperatures. The nature of this reaction is not fully understood, but complexation of  $\text{S}_2^{2+}$  by the basic melt is likely. This is shown in Eq. [7] as successive formation of  $\text{S}_2\text{Cl}^+$  and  $\text{S}_2\text{Cl}_2$  moieties. A slow step in the complexation of  $\text{S}_2^{2+}$  or a slow loss of gaseous  $\text{S}_2\text{Cl}_2$  from the diffusion layer would explain the EC behavior of the sulfur oxidation process.

A better understanding of the oxidation of sulfur in basic chloroaluminate melts should result from spectroscopic and spectroelectrochemical studies. Such studies are in progress in this laboratory as well as elsewhere (27).

#### Acknowledgments

Part of this research was supported by contract No. DAAB 07-73-7-0060, U.S. Army Electronics Command, Fort Monmouth, New Jersey.

Manuscript submitted Dec. 16, 1975; revised manuscript received March 25, 1976.

Any discussion of this paper will appear in a Discussion Section to be published in the June 1977 JOURNAL. All discussions for the June 1977 Discussion Section should be submitted by Feb. 1, 1977.

Publication costs of this article were assisted by the University of Tennessee.

#### REFERENCES

1. D. A. J. Swinkels, in "Advances in Molten Salt Chemistry," Vol. 1, J. Braunstein, G. Mamantov, and G. P. Smith, Editors, pp. 165-223, Plenum Press, New York (1971).
2. E. J. Cairns and R. Steunenbergh, in "Progress in High Temperature Physics and Chemistry," Vol. 5, C. A. Rouse, Editor, pp. 63-124, Pergamon Press, Elmsford, N. Y. (1973).
3. K. V. Kordesh, in "Modern Aspects of Electrochemistry," No. 10, J. O'M. Bockris and B. E.

- Conway, Editors, pp. 339-443, Plenum Press, New York (1975).
4. G. Delarue, *Bull. Soc. Chim. France*, **1960**, 1654.
  5. F. G. Bodewig and J. A. Plambeck, *This Journal*, **116**, 607 (1969).
  6. C. H. Liu, A. J. Zielen, and D. M. Gruen, *ibid.*, **120**, 67 (1973).
  7. J. H. Kennedy and F. Adamo, *ibid.*, **119**, 1518 (1972).
  8. B. Cleaver, A. J. Davies, and D. J. Schiffrin, *Electrochim. Acta*, **18**, 747 (1973).
  9. R. E. Panzer and M. J. Schaer, *This Journal*, **112**, 1136 (1965).
  10. P. Cescon, M. Drago, F. Pucciarelli, and R. Marassi, *J. Electroanal. Chem.*, **59**, 155 (1975).
  11. F. G. Bodewig and J. A. Plambeck, *This Journal*, **117**, 904 (1970).
  12. H. Lux and H. Anslinger, *Chem. Ber.*, **94**, 1161 (1961).
  13. J. Greenberg, B. R. Sundheim, and D. M. Gruen, *J. Chem. Phys.*, **29**, 461 (1958).
  14. W. Giggenbach, *Inorg. Chem.*, **10**, 1308 (1971).
  15. D. M. Gruen, R. L. McBeth, and A. J. Zielen, *J. Am. Chem. Soc.*, **93**, 6691 (1971).
  16. R. Marassi, G. Mamantov, and J. Q. Chambers, *Inorg. Nucl. Chem. Letters*, **11**, 245 (1975).
  17. B. Tremillon and G. Letisse, *J. Electroanal. Chem.*, **17**, 371 (1968).
  18. G. Torsi and G. Mamantov, *Inorg. Chem.*, **10**, 1900 (1971).
  19. G. Torsi and G. Mamantov, *ibid.*, **11**, 1439 (1972).
  20. A. A. Fannin, L. A. King, and T. W. Seegmiller, *This Journal*, **119**, 801 (1972).
  21. L. G. Boxall, H. L. Jones, and R. A. Osteryoung, *ibid.*, **120**, 223 (1973).
  22. D. E. Bartak and R. A. Osteryoung, *ibid.*, **122**, 600 (1975).
  23. G. Torsi, K. W. Fung, G. M. Begun, and G. Mamantov, *Inorg. Chem.*, **10**, 2285 (1971).
  24. R. Marassi, J. Q. Chambers, and G. Mamantov, *J. Electroanal. Chem.*, **69**, 345 (1976).
  25. M. Schmidt and W. Siebert, in "Comprehensive Inorganic Chemistry," Vol. 2, J. C. Bailar, H. J. Emeleus, R. Nyholm, and A. F. Trotman-Dickenson, Editors, pp. 802-813, Pergamon Press, Elmsford, N. Y. (1973).
  26. K. A. Paulsen and R. A. Osteryoung, 170th National Meeting, American Chemical Society, Chicago, Illinois, August 1975.
  27. N. J. Bjerrum, Private communication.
  28. Sulfur polycations have been recently discussed by R. J. Gillespie and J. Passmore, in "Advances in Inorganic Chemistry and Radiochemistry," Vol. 17, H. J. Emeleus and A. G. Sharpe, Editors, pp. 49-87, Academic Press, New York (1975).
  29. R. S. Nicholson and I. Shain, *Anal. Chem.*, **36**, 706 (1964).
  30. R. S. Nicholson, *ibid.*, **38**, 1406 (1966).

## Compatibility of Aluminum Nitride in Environments Representative of High Temperature Cells

Ram A. Sharma,\* Richard A. Murie, and Elton J. Cairns\*

*General Motors Corporation, Electrochemistry Department, Research Laboratories, Warren, Michigan 48090*

### ABSTRACT

Compatibility tests of hot-pressed, high purity AlN of 90-99% of theoretical density were carried out in molten lithium, lithium-saturated LiCl-KCl, lithium saturated LiF-LiCl-KCl, molten 30 weight per cent (w/o) Li<sub>2</sub>S-S and molten S at 400°C for up to 10,000 hr, and lithium-saturated LiCl and chlorine-saturated LiCl at 650°C for up to 1430 hr. At 400°C, the AlN was not attacked to any significant extent (<0.5 w/o), whereas at 650°C, AlN experienced intergranular attack by lithium and reacted at a rate of 1% per 100 hr in Cl<sub>2</sub>-LiCl.

One of the main problems in the development of high temperature molten salt cells is the identification of a suitable electrical insulating material for use in the cells. This problem occurs because of the very corrosive nature of the materials in such systems (e.g., Li/Cl<sub>2</sub> with LiCl as electrolyte, and Li/S with an alkali halide mixture as the electrolyte). The problem is especially difficult because of the high operating temperatures, i.e., about 650°C for the Li/Cl<sub>2</sub> cell and about 400°C for the Li/S cell (1, 2).

Based on the standard free energy of formation and availability, oxides such as Li<sub>2</sub>O, BeO, MgO, Y<sub>2</sub>O<sub>3</sub>, La<sub>2</sub>O<sub>3</sub>, ThO<sub>2</sub>, and CaO may be considered to be prospective insulators in these corrosive environments. The unsuitability of Li<sub>2</sub>O, MgO, La<sub>2</sub>O<sub>3</sub>, ThO<sub>2</sub>, and CaO has been pointed out (3-5), and it has also been reported that Y<sub>2</sub>O<sub>3</sub> did not show any appreciable change when tested in 20 atom per cent (a/o) Li-80 a/o S at 375°C for 331 hr. In the case of BeO, the results of compatibility tests varied depending on the type and the quality of BeO used; for example, in early tests, BeO in the form of a porous crucible disintegrated when tested in lithium for 25 hr at 350°C (3, 4). In later

tests, high purity, hot-pressed BeO proved to be the most corrosion-resistant material with a corrosion rate near 0.02 mm/yr in lithium at 375°C for 1000-1200 hr (5).

Cairns *et al.* (6) reported that some double oxide compounds, particularly LiAlO<sub>2</sub>, MgAl<sub>2</sub>O<sub>4</sub>, and CaZrO<sub>3</sub>, show promise as insulating materials. Fishwick and Yeh (7) investigated the compounds Li<sub>2</sub>O · Al<sub>2</sub>O<sub>3</sub>, Li<sub>2</sub>O · 5Al<sub>2</sub>O<sub>3</sub>, Li<sub>2</sub>O · ZrO<sub>2</sub>, CaO · Al<sub>2</sub>O<sub>3</sub>, CaO · 5Al<sub>2</sub>O<sub>3</sub>, CaO · 2.5Al<sub>2</sub>O<sub>3</sub>, and CaO · ZrO<sub>2</sub>, and reported only CaO · ZrO<sub>2</sub> to be compatible in lithium as a result of a test in lithium at 580°C for 92 hr.

At General Motors Research Laboratories, earlier material compatibility studies indicated AlN to be a promising material, since only minor degradation of AlN was found after being in contact with lithium at 700°C for about 575 hr (8). Therefore, the present investigation was conducted to test AlN under conditions similar to those existing in the Li/Cl<sub>2</sub> or Li/S cells. The present AlN tests were further warranted because a better quality of material with respect to purity and density has become available (9).

### Experimental

Aluminum nitride specimens of 97-99% of theoretical density (but in one case, 90% of theoretical density)

\* Electrochemical Society Active Member.

Key words aluminum nitride, insulators, corrosion, lithium, sulfur, high temperature.

were prepared by hot-pressing high purity AlN powder (0.06 weight per cent (w/o) oxygen, 0.35 w/o carbon) in a dense graphite die. Pressures in the range of 17.0-20.5 MPa were applied during gradual heating to about 1700°C to yield samples of ~97% theoretical density; and pressures of 35-41 MPa with heating to 2000°C were used for 99% theoretical density. The pressure and temperature were maintained for 20-60 min, after which the die was cooled slowly to room temperature, while maintaining the pressure. The AlN samples were diamond-ground to remove adherent graphite. After grinding, the color was gray to black. All of the longer term corrosion samples were sliced from the same cylindrical samples with a diamond wafering saw in an attempt to have uniformity of sample properties. A scanning electron micrograph (SEM) of a typical high density sample, Fig. 1, shows this AlN to be well sintered and dense.

The slices of AlN used in the corrosion tests were in various disk shapes (circular, semicircular, rectangular, circular disks with holes, etc.) having dimensions of about 12.7 mm, with a thickness of about 3 mm. (When a number of samples were placed in a single container, the positions of the holes in the samples were used for identification.) The samples were cleaned ultrasonically in methanol or acetone for 15 min, and were baked at 400°-650°C overnight under vacuum before being weighed and placed in the corrosion capsules in a pure helium atmosphere.

Lithium chloride of 99.6% purity and potassium chloride of 99.9% purity were used to prepare the eutectic mixture (59 mole per cent (m/o) LiCl-41 m/o KCl, mp = 352°C). This mixture was purified by bubbling chlorine through the melt at about 500°C for 2-4 hr and subsequently removing the chlorine by bubbling with helium for 1 hr. High purity, optical grade lithium fluoride (used for preparing u.v. filters) was used in the preparation of the ternary LiF-LiCl-KCl eutectic (3.5 m/o LiF-56.0 m/o LiCl-40.5 m/o KCl, mp = 346°C).

Lithium metal of 99.97% purity was used as received, after cutting away the surface metal from the ingot in a high purity helium atmosphere. Sulfur of 99.999% purity was used as received. Lithium sulfide with an analysis of 29.8 w/o Li (*vs.* 30.26 w/o theoretical for Li<sub>2</sub>S) was used. The chlorine was 99.8% pure, and the helium had a total impurity level of less than 40 ppm.

The test cells used for the experiments involving lithium were constructed of Type 304 stainless steel and had cooling coils around the top to keep the gasket



Fig. 1. SEM photograph of a fractured surface of a typical pre-test AlN sample.

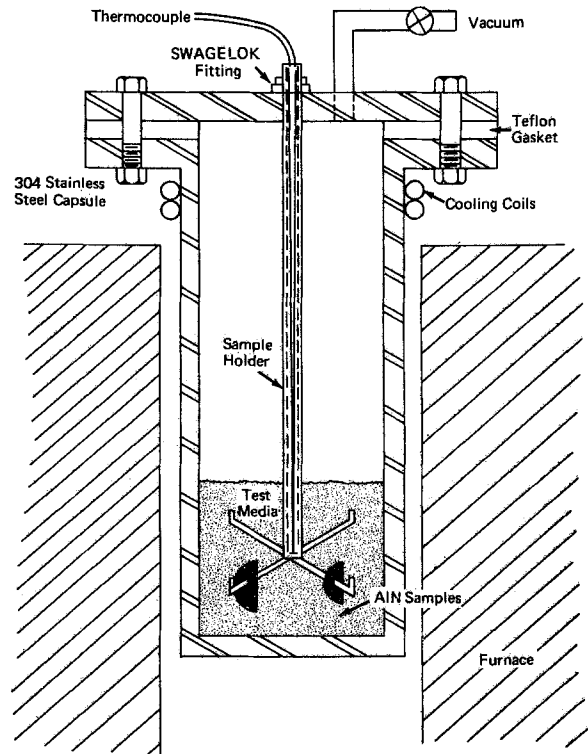


Fig. 2. Stainless steel test capsule containing test media at 400°C. Samples were suspended from "crow's-foot" in melt.

cool. Figure 2 shows the test cell (300 mm high  $\times$  70 mm ID) used for multiple-sample experiments. The samples were suspended from a crow's-foot on a closed-end tube which passed through a Swagelok fitting in the lid. The closed-end tube served as a thermocouple well for monitoring and controlling purposes. Figure 3 shows the arrangement used for experiments involving single AlN samples. This cell also had an inlet and outlet for the passage of helium during the test period. Each test cell was cleaned by washing in distilled water, rinsing in methanol, and hydrogen firing at 1000°C. When cool, the cells were placed in a helium atmosphere glove box for loading of the samples.

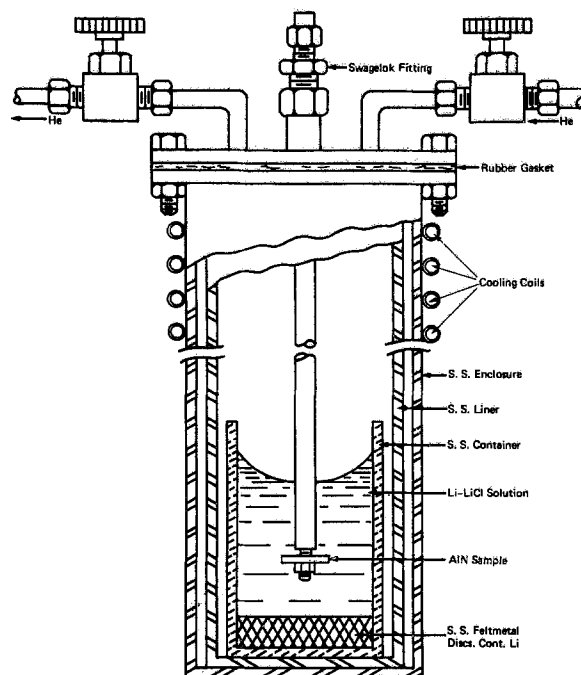


Fig. 3. Schematic diagram of the apparatus for compatibility tests in Li-LiCl solutions.

To load the stainless steel test cells, enough lithium was added to the cell to insure that the AlN sample(s) would be covered when melting occurred. The PTFE gasket was fitted to the cell flange, the tube with the sample(s) was fitted through the Swagelok fitting and adjusted to the proper length to insure that the samples would be totally immersed in the molten lithium. The test cell was then bolted shut, removed from the helium atmosphere, and mounted in a furnace.

The stainless steel test cells used with the molten salts (LiCl-KCl eutectic and LiF-LiCl-KCl eutectic) saturated with lithium were loaded in the same manner as above; however, stainless steel feltmetal disks (40.5 mm diam  $\times$  1.27 mm thick) impregnated with lithium were placed in the bottom of the test cell, Fig. 3, prior to adding the salt, providing a lithium source for impregnating the salt.

When a sample from a test cell containing multiple samples (on the crow's-foot) was to be removed, the furnace was turned off and the test cell was cooled to room temperature. The cell was taken into the helium glove box, placed in a furnace well, and heated. When the test medium was molten, the cell cover was removed and a sample was removed from the crow's-foot. The cover was then replaced, the cell was cooled, removed from the dry box, and again placed in the test furnace. The sample was then removed from the dry box, ultrasonically washed in distilled water, methanol, and acetone followed by a 3-4 hr vacuum bakeout at 400°C. When cool, the samples were weighed and sectioned on a diamond wafering saw for microscopic examination.

When a cell contained only a single AlN sample, entry into the dry box for sample removal was not necessary. The Swagelok fitting was loosened, and the sample was raised until clear of the molten test medium. The cell was then cooled and opened for sample removal and cleansing as described above.

The Li<sub>2</sub>S-S and sulfur tests were carried out in quartz or Vycor test cells. The design of these test cells is shown in Fig. 4. The AlN and test medium were loaded into the cell in the helium atmosphere. After loading, a small amount of high vacuum stopcock grease was used to lubricate the standard taper joint

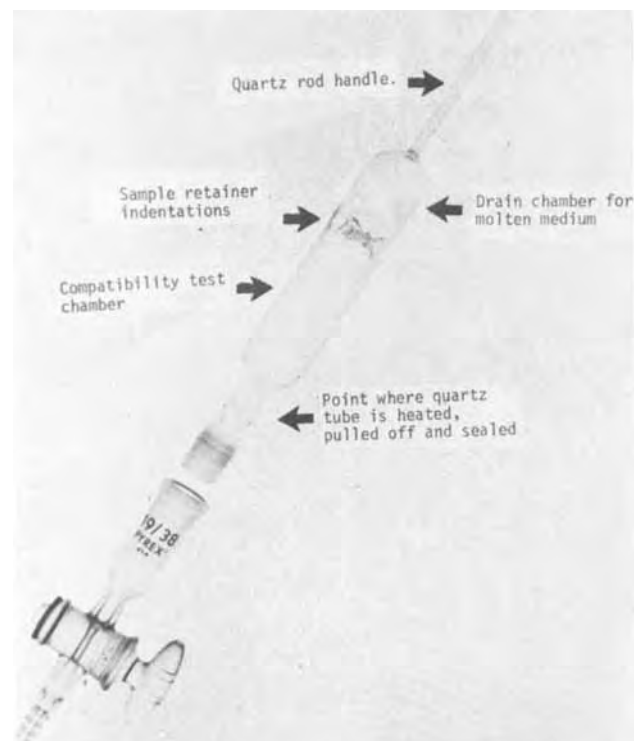


Fig. 4. Quartz test capsules used to contain Li<sub>2</sub>S-S test media

and the stopcock cap was attached. The cell was evacuated, removed from the helium atmosphere, and sealed, with removal of the standard taper and stopcock cap. The test cell was then inserted into a sand bath which was suspended in a stainless steel container in a furnace, Fig. 5. The sand completely covered the cell and aided in maintaining a uniform temperature. When the test was terminated, the furnace was turned off and the test cell was removed while the test medium was still molten. Holding the cell by the long quartz handle, Fig. 4, and inverting it caused the molten test medium to run into the bottom chamber while the AlN test sample was held on the indentation. When cool, the quartz or Vycor cell was opened, the sample was removed and cleaned in an ultrasonic cleaner using distilled water, methanol, and acetone. Finally, the sample was vacuum dried at 400°C for 4 hr, cooled, and weighed. The vacuum drying also removed any remaining free sulfur adhering to the sample.

Compatibility testing in LiCl through which chlorine gas was bubbled was carried out in the apparatus shown in Fig. 6. To load the sample, a clean dry Vycor enclosure (350 mm long  $\times$  65 mm diam) with a Vycor

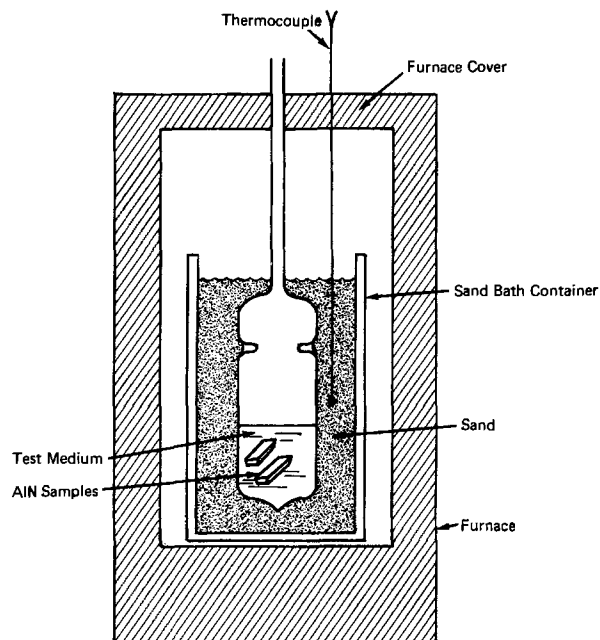


Fig. 5. Quartz test capsule in furnace

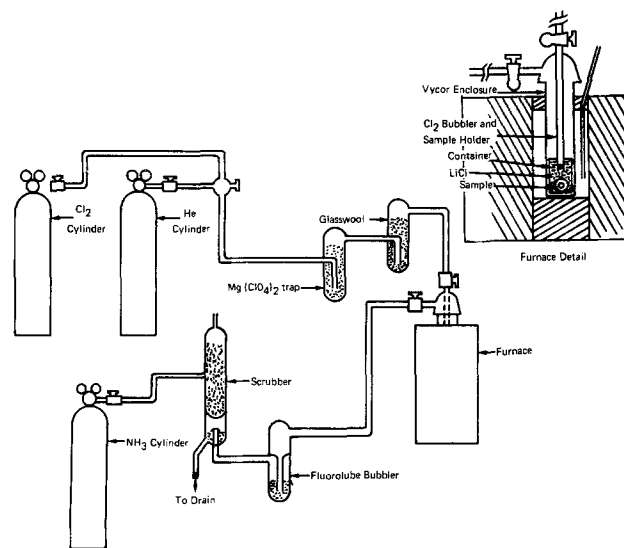


Fig. 6. Schematic diagram of the apparatus for compatibility tests in LiCl through which Cl<sub>2</sub> was bubbling.

container (80 mm long  $\times$  55 mm diam) and sample holder was taken into the helium atmosphere. The sample holder was fixed in position in the standard taper joint at the top of the enclosure. The sample was then placed on the hook of the sample holder, which was then placed into the Vycor container. Lithium chloride (about 175g) was placed into the container to cover the sample and to keep it in position on the hook. The container was then carefully slipped into the enclosure without disturbing either the salt or the sample, and the top of the enclosure was set into place. The gas inlet and outlet were closed and the enclosure was removed from the helium atmosphere and placed in the furnace. Helium was passed through the enclosure, and the furnace was heated to 650°C. The helium was then replaced by chlorine gas and the sample was kept under these conditions for the duration of the test. At the end of the exposure period, the chlorine was replaced by helium and the sample was taken out of the melt to cool. The sample was cleaned in methanol, dried, and weighed.

### Results and Discussion

The results of all of the compatibility tests are summarized in Table I. The extent of attack is reported in terms of percentage weight change. The samples with numbers having an alphabetic suffix were cut from the same cylinder of hot-pressed AlN. For example, samples 1a, 1b, 1c, and 1d all came from a single cylinder of AlN, having a density of 99.3% of theoretical (3.26 g/cm<sup>3</sup>). In addition, samples having this type of number were all exposed to a given melt in

the same container and are called multiple-sample tests. The last sample in each of these sets was placed in the container only for the final 1000 hr of the test in order to determine if the corrosiveness of the melt had changed from that of the initial 1000 hr.

*Molten lithium at 400°C.*—The results of the multiple-sample tests of AlN in molten lithium at 400°C are presented in the upper part of Table I. A total of 12 samples, 4 in each of 3 stainless steel containers, were exposed for periods of 1000–10,000 hr. Examination of the samples by optical microscopy and by SEM up to 3000 $\times$  revealed no visible attack. The weight change values indicate some loss, about 3% in 6000–7000 hr. The losses of this magnitude are associated with sample breakage, samples 1b and 1c, and crystal pullouts from surface cracks in samples 2b and 2c. Therefore, the weight loss due to nonmechanical causes is probably significantly less than 3% in several thousand hours.

Some SEM photographs of the surface and fracture surfaces of sample 3c are shown in Fig. 7. The fracture surface-exposed edge interface in Fig. 7b and c reveals no lithium penetration and shows the presence of a very thin surface film. This is a typical result. Part d of the figure is typical of the interior of the high density ( $\sim$ 99% theoretical) samples.

The small weight losses shown by samples 1d, 2d, and 3d indicate that the corrosiveness of the lithium used in these exposures did not increase noticeably during the experiments. The small weight gains of samples 3b and 3c may be taken as an indication of the precision of these experiments and the difficulties of cleaning the samples after exposure.

Table I. Results of AlN compatibility tests in various media at 400° and 650°C

Sample No.	Environment	Temperature, °C	Exposure time, hr	Theoretical density, %	Initial weight,** g	Weight change, %	Remarks
1a	Molten lithium	400	1,000	99.3	1.6700	0.00	Samples 1b and 1c were broken during removal from the cell. No visible attack; no surface conductance
1b	Molten lithium	400	6,000	99.3	1.5455	-3.25	
1c	Molten lithium	400	7,000	99.3	2.1424	-1.19	
1d	Molten lithium	400	1,000*	99.3	1.2825	-0.08	
2a	Molten lithium	400	1,000	99.0	1.9295	-0.04	Sample intact; no visible attack or surface conductance
2b	Molten lithium	400	6,000	99.0	1.7901	-3.44	
2c	Molten lithium	400	7,000	99.0	1.8560	-3.02	
2d	Molten lithium	400	1,000*	99.0	1.5417	-0.18	
3a	Molten lithium	400	1,000	98.8	0.9958	-0.05	Sample intact; no visible attack or surface conductance
3b	Molten lithium	400	9,000	98.8	1.3138	+0.02	
3c	Molten lithium	400	10,000	98.8	1.8171	+0.06	
3d	Molten lithium	400	1,000	98.8	0.7365	-0.01	
4	Molten LiCl-KCl saturated with Li	400	2,600	>97	2.293	-0.06	Sample intact; no visible attack or surface conductance
5	Molten LiCl-KCl saturated with Li	400	2,600	>97	2.396	-<0.1	
6a	Molten LiF-LiCl-KCl saturated with Li	400	1,000	98.8	1.3952	0.00	
6b	Molten LiF-LiCl-KCl saturated with Li	400	6,000	98.8	1.4080	+0.25	
6c	Molten LiF-LiCl-KCl saturated with Li	400	7,000	98.8	1.4086	+0.56	Sample intact; no visible attack or surface conductance
6d	Molten LiF-LiCl-KCl saturated with Li	400	1,000*	98.8	1.0003	-0.43	
7	Molten LiCl saturated with Li	650	425	>97	2.972	-6.0	
8	Molten LiCl saturated with Li	650	400	>97	2.900	—	
9	Molten LiCl saturated with Li	650	570	>97	1.570	-3.0	Intergranular attack No visible attack
10	Molten LiCl saturated with Li	650	1,430	>97	1.524	-10.0	
11a	Molten 30 w/o Li <sub>2</sub> S-70 w/o S	400	1,000	98.7	1.9112	-0.19	Numerous cracks Sample intact, no visible attack
11b	Molten 30 w/o Li <sub>2</sub> S-70 w/o S	400	4,128	98.7	1.4654	-0.13	
11c	Molten 30 w/o Li <sub>2</sub> S-70 w/o S	400	6,528	98.7	1.2251	-0.28	
11d	Molten 30 w/o Li <sub>2</sub> S-70 w/o S	400	1,000*	98.7	1.5872	+0.02	
12a	Molten 30 w/o Li <sub>2</sub> S-70 w/o S	400	1,000	90.0	0.9148	+1.85	
12b	Molten 30 w/o Li <sub>2</sub> S-70 w/o S	400	9,000	90.0	0.8147	+0.52	
12c	Molten 30 w/o Li <sub>2</sub> S-70 w/o S	400	10,000	90.0	0.8117	+0.11	
12d	Molten 30 w/o Li <sub>2</sub> S-70 w/o S	400	1,000*	90.0	0.8037	+1.00	
13	Molten sulfur	400	2,420	>97	1.554	0.0	
14	Molten LiCl with Cl <sub>2</sub> bubbling	650	185	>97	0.984	-1.0	
15	Molten LiCl with Cl <sub>2</sub> bubbling	650	565	>97	0.945	-7.0	
16	Molten LiCl with Cl <sub>2</sub> bubbling	650	1,155	>97	0.973	-9.0	

\* Sample placed in corrodant for final 1000 hr of test.

\*\* Weighted on semimicrobalance to nearest 0.01 mg.

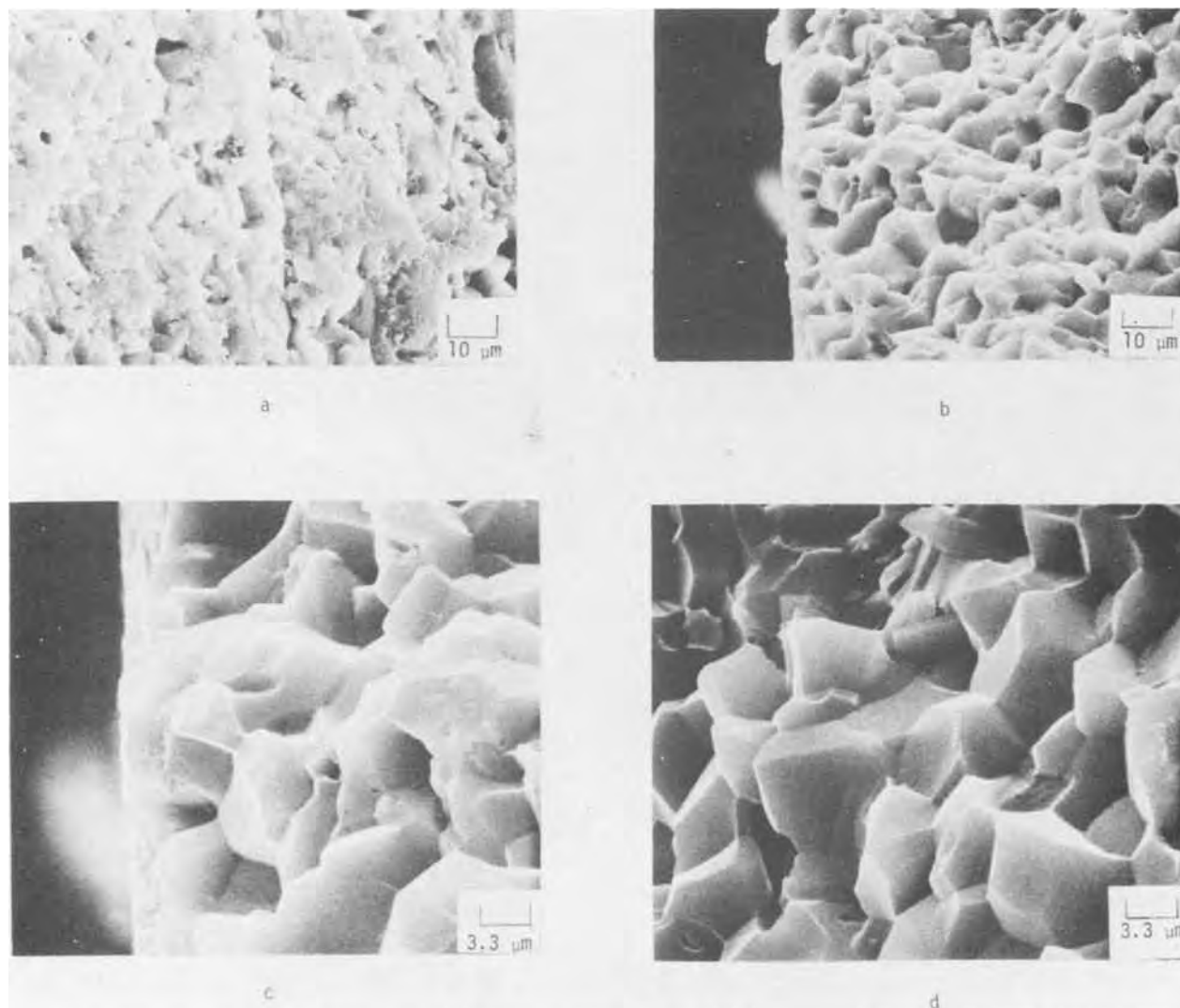


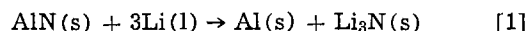
Fig. 7. SEM photographs of sample 3c after 10,000 hr in 400°C lithium. (a) AlN surface after exposure to lithium, (b) fracture surface and edge showing tightly bound crystals of AlN with no penetration of lithium, (c) higher magnification of fracture surface shown in (b), (d) interior fracture surface.

*Molten LiCl-KCl saturated with lithium at 400°C.*—Aluminum nitride samples 4 and 5 of Table I showed weight loss rates similar to those for AlN in lithium at 400°C. The values are in the range of less than 0.1% for 2600 hr. The samples were intact, with no visible signs of corrosion. All edges remained sharp.

*Molten LiF-LiCl-KCl saturated with lithium at 400°C.*—The results of this multiple-sample test are consistent with those for lithium and LiCl-KCl saturated with lithium. The weight change was small; the samples looked as they did at the beginning of exposure. The small diamond-saw marks on the surfaces of the samples remained. Figure 8 shows SEM views of samples 6b and 6c, indicating very little attack.

*Molten LiCl saturated with lithium at 650°C.*—The results of exposure of four samples of AlN (numbers 7 through 10) to lithium-saturated LiCl at 650°C (characteristic of the Li/LiCl/Cl<sub>2</sub> cell) are shown in Table I. At this higher temperature, attack on the samples is clearly evident, predominantly intergranular in nature. Weight losses as large as 10% after 1430 hr were observed. Figure 9 shows low-magnification (4.5×) views of the surface of sample 8 before and after 400 hr of exposure. Note the clear evidence of intergranular attack. In Fig. 10b, it can be observed that little coherency among the AlN grains remains.

The thermodynamic stability of AlN with regard to lithium is expected to be very good, based on the reaction



The free energy of this reaction ranges from about +150 kJ/mole AlN at 400°C to about +160 kJ/mole AlN at 650°C (10). The possibility of excess lithium reacting with the aluminum produced by reaction [1] would yield a lower free energy, as would the dissolution of Li<sub>3</sub>N in the molten salt mixture. It appears unlikely that these two effects would result in such a high rate of attack (e.g., 10 w/o in 1400 hr). It is conceivable that the intergranular attack of samples 7 through 10 is associated with either an impurity effect or poor sintering, or both.

*Molten 30 w/o Li<sub>2</sub>S-70 w/o S at 400°C.*—This melt represents a relatively strongly oxidizing environment, in contrast to the strongly reducing conditions represented by the melts discussed above, and was intended to be related to the conditions found in the positive electrode of a lithium/sulfur cell. Two multiple-sample tests of AlN in Li<sub>2</sub>S-S were carried out, the results of which are summarized in Table I. The weight losses observed were all less than 0.3%, however some weight gains were also found in the 90% dense samples. This weight gain for samples 12a-12d is probably a reflection



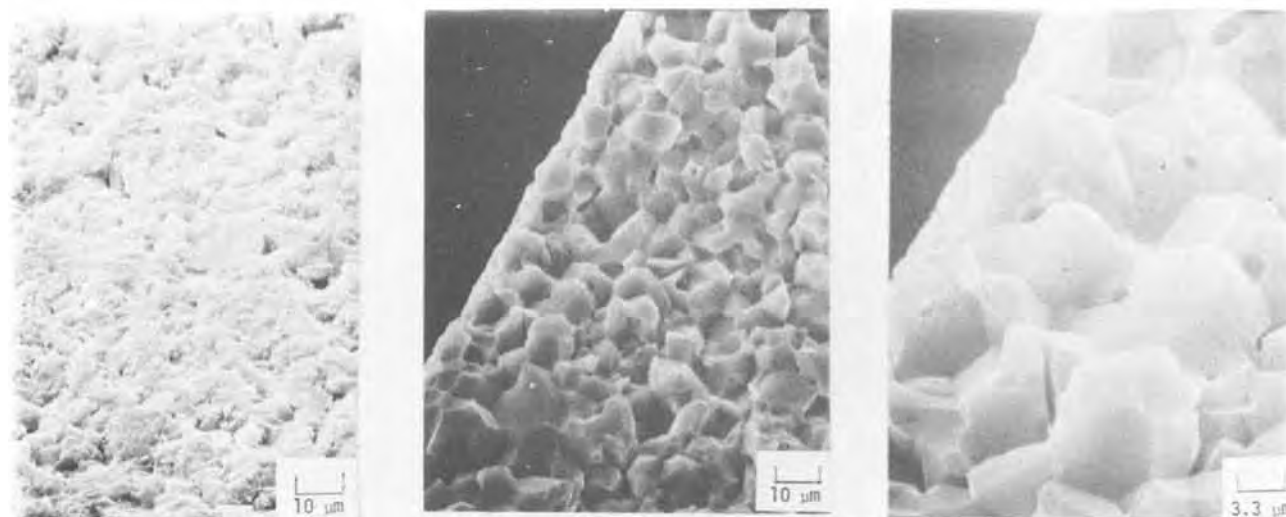


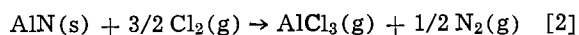
Fig. 8. SEM photographs of AlN samples 6b and 6c after 6000 and 7000 hr, respectively, in LiF-LiCl-KCl eutectic saturated with lithium at 400°C. (a) Surface of AlN sample 6b after exposure for 6000 hr. This surface is typical of AlN samples 6b and 6c. (b) Fracture surface and edge of AlN sample 6b. The grain boundaries are sharp and no evidence of penetration by the test media. (c) Higher magnification of fracture surface shown in (b).

of the difficulty of removing all of the  $\text{Li}_2\text{S-S}$  from the pores of the samples. Examination of the samples by optical microscopy and SEM revealed negligible attack at the sample surfaces, and no penetration, except into occasional pores. Figure 11 shows SEM photographs of samples 11b and 11c, which indicate no attack after as much as 6528 hr.

**Molten sulfur at 400°C.**—One AlN sample was exposed to molten sulfur at 400°C for 2420 hr. No weight change was found, and no attack on the sample could be observed by optical microscopy or SEM.

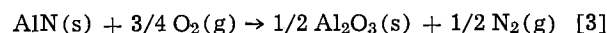
**Molten LiCl with  $\text{Cl}_2$  bubbling at 650°C.**—These test conditions were intended to represent the environment at the chlorine electrode of a Li/LiCl/ $\text{Cl}_2$  cell, which usually operates in the vicinity of 650°C. The AlN samples, numbers 14-16, experienced significant weight loss rates, in the vicinity of 1%/100 hr of exposure. The samples also changed color from gray to white, and the surfaces became chalky.

Considering the thermodynamics of the situation for AlN in contact with  $\text{Cl}_2$ , the candidate reaction



has a free energy of reaction at 627°C of  $-315 \text{ kJ/mole AlN}$  (10). It is to be expected, then, that  $\text{AlCl}_3$  and  $\text{N}_2$  would form, resulting in a weight loss. The above re-

action has been reported to occur at 600°-700°C (11). In addition to reaction [2], it is possible for other reactions to take place, modifying the rate at which reaction [2] would proceed. Two possibilities are



$$\Delta G_{627^\circ\text{C}} = -473 \text{ kJ/mole (10)}$$



$$\Delta G_{627^\circ\text{C}} = -252 \text{ kJ/mole (10)}$$

These reactions are consistent with the observation of a white film on the surface of the AlN. Furthermore, exposure of AlN powder to ambient air results in an ammonia odor.

### Conclusions

1. High density AlN ( $\sim 99\%$  theoretical) experiences negligible attack (about 0.5 w/o or less) in the strongly reducing environments of molten lithium, or lithium dissolved in LiCl-KCl, or LiF-LiCl-KCl, at 400°C for periods of 1000-10,000 hr.

2. At 650°C, in Li-saturated LiCl, intergranular attack of AlN was observed after 400-1430 hr on samples less dense than those used in the lower temperature work. Further investigation with higher density samples is in order.

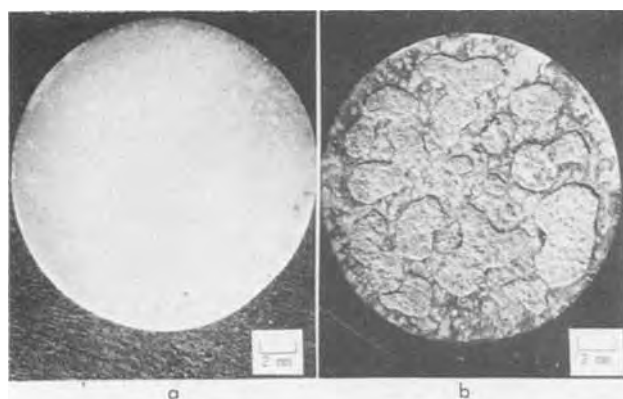


Fig. 9. Photographs of AlN sample. (a) Original sample surface, and (b) sample surface after exposure in Li-LiCl solution for 400 hr at 650°C.

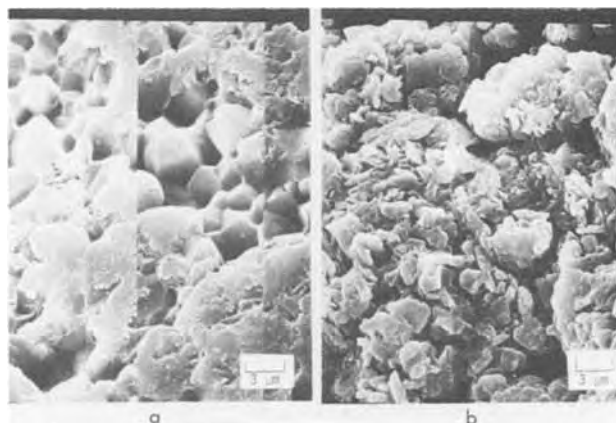


Fig. 10. SEM pictures of AlN sample. (a) Before the test, and (b) after exposure in Li-LiCl solution for 400 hr at 650°C.



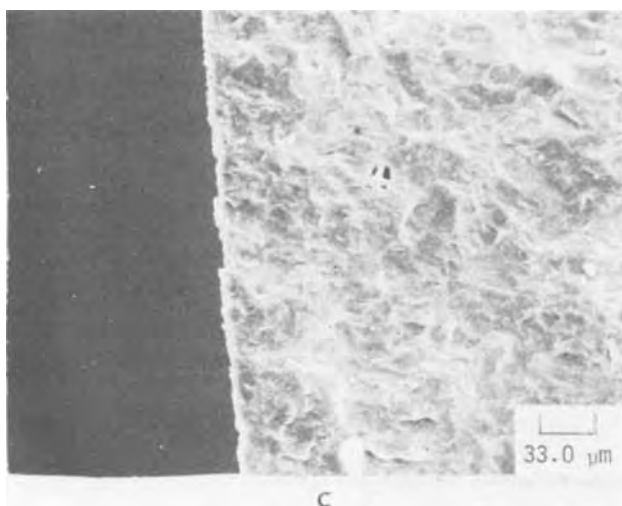
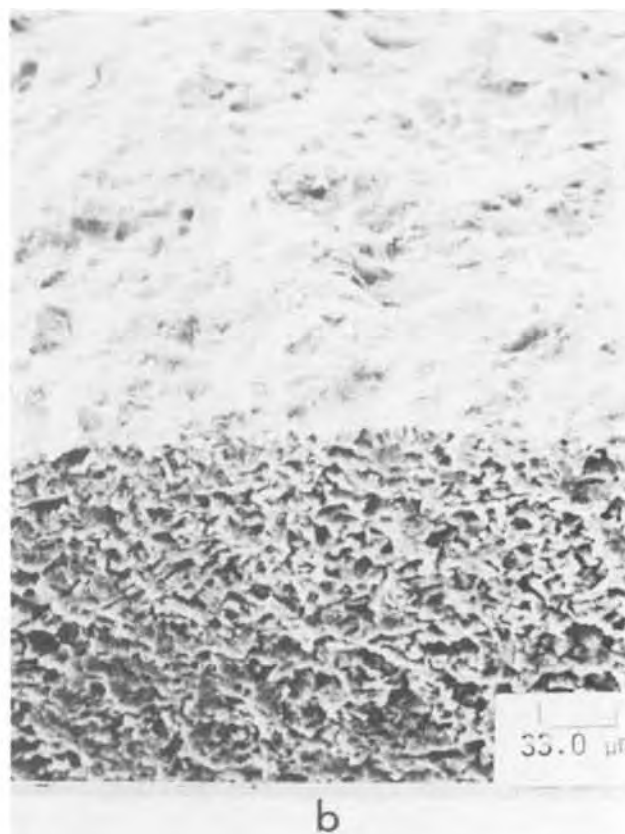


Fig. 11. SEM photographs of AlN samples 11b and 11c after 4128 and 6528 hr, respectively, in  $\text{Li}_2\text{S-S}$ . (a) Exposed test surface of AlN sample 11c. This surface is typical of both samples. (b) AlN sample 11c showing both the exposed test surface and fracture surface. (c) Fracture surface and edge of AlN sample 11c. No penetration is present.

3. No attack (weight loss  $\leq 0.28$  w/o) was observed on AlN exposed to S or 30 w/o  $\text{Li}_2\text{S-S}$  at  $400^\circ\text{C}$  for 1000-10,000 hr.

4. Aluminum nitride is attacked by  $\text{Cl}_2$  in  $\text{LiCl}$  at  $650^\circ\text{C}$ , resulting in a weight loss rate of about 1%/100 hr, for periods of 185-1155 hr.

5. Aluminum nitride appears to be a suitable insulator for use in  $\text{Li/S}$  cells at  $400^\circ\text{C}$ .

6. Aluminum nitride is not acceptable at the chlorine electrode and may or may not be acceptable at the lithium electrode in  $\text{Li/Cl}_2$  cells at  $650^\circ\text{C}$ .

#### Acknowledgments

The authors thank D. W. Buttram and W. J. Wright for assistance in the experimental work, T. P. Schreiber for SEM work, and T. G. Bradley and J. S. Dunning for helpful discussions and suggestions.

Manuscript received Feb. 3, 1976. This was Paper 16 presented at the Washington, D. C., Meeting of the Society, May 2-7, 1976.

Any discussion of this paper will appear in a Discussion Section to be published in the June 1977 JOURNAL. All discussions for the June 1977 Discussion Section should be submitted by Feb. 1, 1977.

Publication costs of this article were assisted by General Motors Corporation.

#### REFERENCES

1. E. J. Cairns and R. K. Steunenberg, in "Progress in High Temperature Physics and Chemistry," Vol. 5, C. A. Rouse, Editor, p. 63, Pergamon Press, New York (1973).
2. T. G. Bradley and R. A. Sharma, Proceedings of 26th Annual Power Sources Conference, pp. 60-64, Atlantic City, N. J. (1974).
3. Chemical Engineering Division, Semiannual Report, Jan.-June, 1967, Argonne National Laboratory, Argonne, Illinois, Report No. ANL-7375, Oct. 1967, p. 174.
4. E. J. Cairns *et al.*, Progress Report for the Period Feb. 1969-June 1970, Chemical Engineering Division, Argonne National Laboratory, Argonne,

- Illinois, July 1970, pp. 39-43.
5. M. L. Kyle *et al.*, Proceedings of 1971 Intersociety Energy Conversion Engineering Conference, Society Automotive Engineers, New York, 1971, p. 80.
  6. E. J. Cairns *et al.*, Progress Report for the Period Feb.-July, 1972, Argonne National Laboratory, Argonne, Illinois, Report No. ANL-7953, Sept. 1972; Report No. ANL 7998, Jan. 1973.
  7. J. H. Fishwick and W. C. T. Yeh, *Bull. Am. Ceram. Soc.*, **51**, 633 (1972).
  8. C. M. Little, R. A. Murie, N. T. Mills, and T. G. Bradley, Private communication.
  9. E. J. Cairns and R. A. Murie, in "Corrosion Problems in Energy Conversion and Generation," C. S. Tedman, Jr., Editor, The Electrochemical Society Softbound Symposium Series, Princeton, N. J. (1974).
  10. JANAF Thermochemical Tables, 2nd edition, NSRDS-NBS, p. 37 (June 1971).
  11. K. M. Taylor and C. Lenie, *This Journal*, **107**, 308 (1960).

## Temperature Dependence of Iron and Cadmium Alkaline Electrodes

Lars Öjefors

Swedish National Development Company, 103 40 Stockholm 40, Sweden

### ABSTRACT

The charge and discharge reactions of the alkaline iron and cadmium electrodes go over the soluble intermediates  $\text{HFeO}_2^-$ ,  $\text{FeO}_2^-$ , and  $\text{Cd}(\text{OH})_4^{2-}$ , respectively. The saturation concentrations for these ionic species are rate determining as they directly influence the rates of diffusion and crystallization. By calculating the temperature coefficients for the reactions involved, it is shown that the saturation concentrations for  $\text{HFeO}_2^-$  and  $\text{FeO}_2^-$  are highly temperature dependent while this is not the case for the cadmium intermediate. This explains the bad performance of the iron electrode at low temperatures.

The alkaline iron electrode has been used since the beginning of this century, and interest in this electrode material has been maintained due to its high ampere-hour contents (0.96 A-hr/g on the first discharge level), low price, and long life. Other advantages are inexhaustible supply of iron and its energy reserve on the second discharge level.

In spite of these advantages iron has continuously been substituted by cadmium in commercially produced batteries. This depends mainly on three properties: bad performance at low temperature, extensive self-discharge on open circuit, and hydrogen evolution competing with the charge process. The latter two problems depend on an electrode potential more cathodic than what is required for hydrogen evolution and a low hydrogen overvoltage.

Attention is presently again being focused on the alkaline iron electrode as a part of a metal air system for vehicle propulsion. As cadmium active material is expensive, scarce, and causes pollution problems, there are also obvious advantages to replace it with iron in the nickel-cadmium systems. Since 1969 an iron-air battery system has been under development in Sweden jointly carried out by the Swedish National Development Company and Department of Chemical Technology of Royal Institute of Technology, both located in Stockholm.

### Previous Works

*Iron electrode.*—The discharge reactions of the alkaline iron electrode has been the subject of several previous investigations (1-5). These works which have been done with analytical, chemical, and crystallographical techniques show, however, no uniform results according to the products of the discharge processes. The discharged active material has been reported as  $\text{FeO}$ ,  $\text{Fe}(\text{OH})_2$ ,  $\text{Fe}_2\text{O}_3$ ,  $\text{Fe}_3\text{O}_4$ ,  $\text{FeOOH}$ , and  $\text{Fe}(\text{OH})_3$ .

A voltametric study by Flerov and Pavlova (3) considered the possibility of reactions in dissolved phases, and this has recently been investigated further by

Labat *et al.* (5). They explain the discharge reaction by the intervention of the dissolved forms of the divalent and trivalent hydroxides ( $\text{HFeO}_2^-$  respectively  $\text{FeO}_2^-$ ) which are supposed to be responsible for the slow rate of the electrochemical process. The products are according to x-ray diffraction analysis  $\text{Fe}(\text{OH})_2$  at the first level,  $\text{FeOOH}$  and  $\text{Fe}_3\text{O}_4$  at the second. In normal battery operation only the first "plateau" is being used while the second is not utilized because of its less negative potential although a deep discharge sometimes has a positive effect on the capacity of the electrode.

Recent experimental work using rotating disk electrodes (6) also gives evidence for soluble Fe-intermediates both during the charge and discharge processes.

*Cadmium electrode.*—Two radically different mechanisms have been proposed in the literature for the anodic oxidation of cadmium: the dissolution-precipitation mechanism (7-13) and the solid-state oxidation mechanism involving ionic transport through a  $\text{Cd}(\text{OH})_2$ -film (14-15). The mechanism of cathodic reduction of  $\text{Cd}(\text{OH})_2$  has been studied to a much less degree than its anodic counterpart in spite of its importance in the charge process of the battery cadmium electrode (14, 16, 17).

During the last three years the discharge mechanism has been thoroughly studied by Armstrong *et al.* (18) in sintered electrodes and at rotating electrodes by Okinaka (19) and Armstrong *et al.* (20). These investigations give evidence for dissolution-precipitation mechanism which goes over soluble  $\text{Cd}(\text{OH})_4^{2-}$ .

These recent investigations on alkaline iron and cadmium electrodes show that the discharge mechanisms are quite similar and go over soluble intermediates which are precipitated.

*Thermodynamic background.*—Potential-pH (Pourbaix) diagrams, which present thermodynamic data for metal-water-oxide systems are generally used to interpret results of corrosion experiments (21). They

Key words: iron electrode, solubility of intermediates, temperature dependence.

also give information of the discharge and charge processes of the electrodes. As these alkaline electrodes work in 3-7N KOH solutions which have a pH of more than 14, it can clearly be seen that the electrodes work in the alkaline corrosion areas which are identical to the solubility regions of  $\text{HFeO}_2^-$  and  $\text{Cd}(\text{OH})_4^{2-}$  which are supposed to be the soluble species in the Pourbaix diagrams of Fig. 1-4.

Unfortunately the published potential-pH diagrams have been restricted to 25°C, which depends on a lack of thermodynamic data relevant to other temperatures. In order to better define the chemistry of metals and corrosion products in water, thermodynamic studies have been done (22-27) on metals, metal oxides and ions at other temperatures, mainly elevated.

There are two ways of calculating which are in quantitative agreement. One is based on the methods of irreversible thermodynamics, by deBethune *et al.* (22, 28) for calculating the temperature coefficients of the reactions from the ionic entropies of the species involved. The other method uses the "correspondence principle" by Criss and Cobble (29-31) which relates the ionic entropies at 25°C to those at higher temperatures.

The technique used here is determining  $\Delta G^\circ$  for a reaction at a temperature  $T$  and insert this value in the Nernst equation which gives the half-cell reaction potential for a general chemical reaction in an aqueous system

$$E = E_0 - \frac{RT}{z \cdot F} \cdot \ln \left[ \frac{(a_B)^b \cdot (a_{\text{H}_2\text{O}})^c}{(a_A)^a \cdot (a_{\text{H}^+})^d} \right] \quad [1]$$

Since  $-\log a_{\text{H}^+} = \text{pH}$ ,  $a_{\text{H}_2\text{O}} = 1$  and  $\Delta G^\circ = -z \cdot F \cdot E_0$  Eq. [1] will be reduced to Eq. [2]

$$E = -\frac{\Delta G^\circ}{n \cdot F} - \frac{2.303 \cdot R \cdot T}{z \cdot F} \cdot b \cdot \log a_B - a \log a_A - \frac{2.303 \cdot R \cdot T}{z \cdot F} \cdot \text{pH} \quad [2]$$

The standard free energy change for a reaction at a temperature  $T$  is calculated according to Eq. [3]

$$\Delta G^\circ_T = \sum \gamma_p \cdot G^\circ_{T,p} - \sum \gamma_r \cdot G^\circ_{T,r} \quad [3]$$

where  $\gamma_p$  and  $\gamma_r$  are the corresponding stoichiometric coefficients.

If heat capacity data are available the free energy of formation of a substance can be calculated by using Eq. [4]

$$G^\circ_T = G^\circ_{25} - S^\circ_{25} [T - 298.15] - T \int_{298.15}^T \frac{(C_p^\circ)}{T} \cdot dT + \int_{298.15}^T C_p^\circ \cdot dT \quad [4]$$

Some investigators have assumed that  $\Delta C_p = \nu_i G_{T1} = 0$  in the temperature interval here considered, which essentially simplifies the calculations. Townsend (32) has shown, however, that these calculations are not in as good agreement with experimental data as those when  $C_p$  has been estimated. For nonionic substances heat capacity functions are available in literature (Table I), but for ionic ones this is unfortunately not the case. According to MacDonald and Butler (26) Eq. [4] can be transformed into Eq. [5] with an error below 1%

$$G^\circ_T = G^\circ_{25} - [T \cdot S^\circ_T - 298.15 \cdot S^\circ_{25}] + \frac{T - 298.15}{\ln \left( \frac{T}{298.15} \right)} \cdot [S^\circ_T - S^\circ_{25}] \quad [5]$$

The "absolute" entropies  $S^\circ_T$  of the ions are estimated by using the "correspondence principle" by Criss and Cobble (30).

Table I. Numerical data for the iron-water and cadmium-water systems

Substance	$G^\circ_{25}$ (34) kcal/mole	$S^\circ_{25}$ (34) cal/mole, deg.	$S^\circ_{25(\text{abs})}^{***}$ cal/mole, deg.	$C_p$ , cal/mole, deg.
$\text{Fe(s)}$	0	6.49 (35)		$3.37 + 7.10 \cdot 10^{-3} T + 0.43 \cdot 10^{-5} T^{-2}$
$\text{Fe}^{2+}$	-18.85	-32.9	-42.9	
$\text{Fe}(\text{OH})_2$	-116.3	21.0		$19.05 + 20.0 \cdot 10^{-3} T$
$\text{HFeO}_2^-$	-90.60		6.7	
$\text{FeO}_2^-$	-84.82		30.0	
$\text{FeO}_2^{2-}$	-108.80		-40.3	
$\text{Cd(s)}$	0	12.37		$5.31 + 2.94 \cdot 10^{-3} T$
$\text{Cd}^{2+}$	-18.58	-17.5	-27.5	
$\text{Cd}(\text{OH})_2$	-112.4	23.0		$15.98 + 20.20 \cdot 10^{-3} T$
$\text{Cd}(\text{OH})_3^-$	-143.60		22.3	
$\text{Cd}(\text{OH})_4^{2-}$	-180.16****		11.1	
$\text{H}^+$	0	0	-5	
$\text{H}_2$	0	31.208		$6.52 + 7.80 \cdot 10^{-3} T + 0.120 \cdot 10^{-5} T^{-2}$
$\text{O}_2$	0	49.003		$7.16 + 1.0 \cdot 10^{-3} T - 0.40 \cdot 10^{-5} T^{-2}$
$\text{H}_2\text{O}$	-56.678	16.71		17.99

\* Calculated from  $C_p(\text{FeO})$   $C_p(\text{Ca}(\text{OH})_2)/C_p(\text{CaO})$ .  
 \*\* Calculated from  $C_p(\text{Fe}_2\text{O}_3)$   $C_p(\text{Al}_2\text{O}_3 \cdot \text{H}_2\text{O})/C_p(\text{Al}_2\text{O}_3)$ .  
 \*\*\* Calculated via  $S^\circ_{25(\text{abs})} = S^\circ_{25(\text{conv})} - 5.0 \cdot Z$ .  
 \*\*\*\* Calculated by assuming  $\log[\text{Cd}(\text{OH})_4^{2-}] = -4.5$  at 25°C.

*The iron-water system.*—For iron there are two systems (21) where alternatively  $\text{Fe}-\text{Fe}_3\text{O}_4-\text{Fe}_2\text{O}_3$  or  $\text{Fe}-\text{Fe}(\text{OH})_2-\text{Fe}(\text{OH})_3$  are considered as the only solid substances. At temperatures above 90°C,  $\text{Fe}(\text{OH})_3$  will convert into well-defined crystals of  $\text{Fe}(\text{OH})$  which on further heating decomposes to  $\text{Fe}_2\text{O}_3$ . The dihydroxide  $\text{Fe}(\text{OH})_2$  starts decomposing to  $\text{Fe}_3\text{O}_4$  at 60°C (the Schikorr reaction). As the electrodes used in this investigation are supposed to work in the temperature interval 0°-60°C the latter of these systems is better suited for studying the charge, discharge, and self-discharge processes.

The chemical species involved in this system are listed in Table I together with thermodynamical data necessary for the calculations.

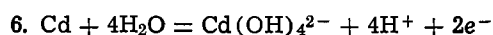
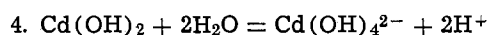
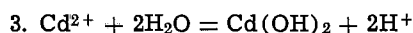
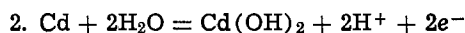
The following set of equations is used to derive potential-pH diagrams for the iron-water system. Reaction numbers are in accordance with those of Pourbaix (21):

12.  $\text{Fe} + 2\text{H}_2\text{O} = \text{Fe}(\text{OH})_2 + 2\text{H}^+ + 2e^-$
16.  $2\text{Fe}(\text{OH})_2 + 2\text{H}_2\text{O} = 2\text{Fe}(\text{OH})_3 + 2\text{H}^+ + 2e^-$
18.  $\text{Fe}^{2+} + 2\text{H}_2\text{O} = \text{Fe}(\text{OH})_2 + 2\text{H}^+$
19.  $\text{Fe}(\text{OH})_2 = \text{HFeO}_2^- + \text{H}^+$
23.  $\text{Fe} = \text{Fe}^{2+} + 2e^-$
24.  $\text{Fe} + 2\text{H}_2\text{O} = \text{HFeO}_2^- + 3\text{H}^+ + 2e^-$
28.  $\text{Fe}^{2+} + 3\text{H}_2\text{O} = \text{Fe}(\text{OH})_3 + 3\text{H}^+ + e^-$
29.  $\text{HFeO}_2^- + \text{H}_2\text{O} = \text{Fe}(\text{OH})_3 + e^-$
- $\text{Fe}(\text{OH})_3 = \text{FeO}_2^- + \text{H}^+ + \text{H}_2\text{O}$
- $\text{HFeO}_2^- = \text{FeO}_2^- + \text{H}^+ + e^-$
- a  $\text{H}_2 = 2\text{H}^+ + 2e^-$
- b  $4\text{OH}^- = \text{O}_2 + 2\text{H}_2\text{O} + 4e^-$

*The cadmium-water system.*—For cadmium there are three different oxidation products, namely,  $\text{CdO}$ , "active"  $\text{Cd}(\text{OH})_2$ , and "inactive"  $\text{Cd}(\text{OH})_2$ . By oxidation in alkaline media "active"  $\text{Cd}(\text{OH})_2$  is produced which turns into inactive hydroxide by the process of aging (21). Consequently  $\text{Cd}$  and "active"  $\text{Cd}(\text{OH})_2$  are considered as the only solid substances.  $\text{Cd}^{2+}$  and  $\text{Cd}(\text{OH})_4^{2-}$  are considered as dissolved substances.

Numerical data for the components are listed in Table I.

The following set of equations are used for cadmium-water system:



$S_{25}^{\circ}$  for soluble intermediates.—Entropy data  $S_{25}^{\circ}$  can be found in literature (33, 34) for all components except  $\text{HFeO}_2^-$ ,  $\text{FeO}_2^-$ ,  $\text{FeO}_2^{2-}$ ,  $\text{Cd}(\text{OH})_3^-$ , and  $\text{Cd}(\text{OH})_4^{2-}$ . For these oxyanions there are two empirical relations available

$$S_{25}^{\circ}(\text{abs}) = 43.5 - 46.5 \cdot (Z - 0.28n) \quad [6]$$

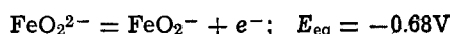
$$S_{25}^{\circ}(\text{abs}) = 40.2 + 3/2 \cdot R \cdot \ln M - 108.8 \frac{Z^2}{n \cdot r} \quad [7]$$

In the first one by Connick and Powell (35)  $Z$  is the number of unit charges carried by the ion and  $n$  is the number of oxygen atoms excluding those of the hydroxyl groups. By using this relationship  $S_{25}^{\circ}$  for both  $\text{HFeO}_2^-$  and  $\text{Cd}(\text{OH})_3^-$  will be 10.0 cal/mole, °C. The corresponding value for  $\text{FeO}_2^-$  will be 23.1 cal/mole, °C. The average discrepancy to experimental data is  $\pm 3.7$  cal/mole, °C according to the authors.

In the second relationship by Coture and Laidler (36)  $R$  is the gas constant and  $r$  is the effective iron radius in angstroms,  $n$  and  $Z$  being the same as before. For the ions considered the value on  $r$  is unknown. These radii can be considered as the sum of  $r_{12}$  which is the distance between the center of atom and the center of the surrounding oxygen atoms plus 1.40Å, which is the van der Waal radius of oxygen. Consequently  $r_{12} + 1.40\text{Å}$  represents the radius of a sphere that completely circumscribes the anion. The values on  $r_{12}$  can be calculated from the single bond distances Fe-Fe, Cd-Cd, and O-O according to Pauling (37).

Bond length data in (38) give  $r_{\text{HFeO}_2^-} = r_{\text{FeO}_2^-} = 2.32\text{Å}$  and  $r_{\text{Cd}(\text{OH})_4^{2-}} = 2.88\text{Å}$ , which inserted in the second relationship give  $S_{25}^{\circ}(\text{abs})$  data in Table I. The mean deviation against experimental data is declared to be 3.6 eu. For the calculations values from the second relation have been used because it considers the difference in molecular weight.

For all components but  $\text{FeO}_2^-$ ,  $G_{25}^{\circ}$  data are available in the literature. According to Latimer (43) ferric hydroxide is quite soluble in concentrated alkali with the formation of ferrite ion  $\text{FeO}_2^-$ . Grube and Gmelin (44) have found in 40% sodium hydroxide solution at 80°C that



By using the techniques here described for calculating  $G_{25}^{\circ}$  for this equilibrium  $G_{25}^{\circ}$  for  $\text{FeO}_2^-$  is found to be  $-84.82$  kcal/mole. Thermodynamic data for all components are listed in Table I.

**Calculations.**—Potential-pH diagrams for 5° and 70°C were calculated on a CompuCorp 322 G Scientists by using Eq. [2], [4], and [5].  $S_{25}^{\circ}$  values for ionic species calculated by the correspondence principle (30) are listed in Table II and free energy data for all the components can be found in Table III.

When using the Pourbaix diagrams at different temperatures, consideration must be taken to the change in the dissociation constant of water which strongly influences the pH. The ionic product is exactly  $1 \cdot 10^{-14}$  at 24°C and is defined as  $k_w = a_{\text{H}^+} \cdot a_{\text{OH}^-}$ . If pH is defined as  $-\log(a_{\text{H}^+})$  the neutral point will be given by  $\text{p}k_w/2$ .

Table II.  $S_{25}^{\circ}$  values for ionic components at different temperatures (cal/mole, deg.)

Substance	278°K	298°K	323°K	343°K	353°K
$\text{Fe}^{2+}$	-47.9	-42.9	-38.4	-34.2	—
$\text{HFeO}_2^-$	13.7	6.7	-1.6	-7.9	—
$\text{FeO}_2^-$	24.1	30.0	24.8	20.1	17.9
$\text{FeO}_2^{2-}$	-27.1	-40.3	-56.7	-69.9	-76.8
$\text{Cd}^{2+}$	-31.7	-27.5	-23.5	-19.8	—
$\text{Cd}(\text{OH})_3^-$	25.3	22.3	19.7	15.1	—
$\text{Cd}(\text{OH})_4^{2-}$	16.6	11.1	5.4	-1.8	—
$\text{H}^+_{\text{aq}}$	-5.6	-5.0	-3.3	-1.8	—

Table III. Free energies of iron species at different temperatures  $G_{25}^{\circ}$  (kcal/mole)

Substance	278°K	298°K	323°K	343°K	353°K
$\text{Fe}_{(s)}$	0.106	0.0	0.144	-0.258	—
$\text{Fe}^{2+}$	-19.75	-18.85	-17.83	-17.08	—
$\text{Fe}(\text{OH})_2$	-115.9	-116.3	-116.8	-117.3	—
$\text{Fe}(\text{OH})_3$	-166.1	-166.5	-167.3	-168.3	—
$\text{HFeO}_2^-$	-90.40	-90.60	-90.66	-90.65	—
$\text{FeO}_2^-$	-84.18	-84.82	-85.50	-85.94	-86.13
$\text{FeO}_2^{2-}$	-109.49	-108.80	-107.58	-106.29	-105.55
$\text{Cd}_{(s)}$	0.240	0.0	-0.286	-0.574	—
$\text{Cd}^{2+}$	-19.18	-18.58	-17.95	-17.53	—
$\text{Cd}(\text{OH})_2$	-112.0	-112.4	-113.0	-113.5	—
$\text{Cd}(\text{OH})_3^-$	-143.13	-143.60	-144.12	-144.44	—
$\text{Cd}(\text{OH})_4^{2-}$	-179.89	-180.16	-180.36	-180.37	—
$\text{H}^+$	-0.103	0.0	0.123	0.218	—
$\text{H}_2$	0.596	0.0	0.757	-1.371	—
$\text{O}_2$	0.972	0.0	-1.226	-2.223	—
$\text{H}_2\text{O}$	-56.35	-56.68	-57.11	-57.49	—

For the temperature levels here considered the following values on the ionic product is given:

Temperature	5°C	25°C	50°C	70°C	80°C
$\text{p}k_w$	14.72	14.00	13.26	12.83	12.65
pH of neutral point	7.36	7.0	6.63	6.41	6.32

In Fig. 1-4 it can clearly be seen that the changes of the diagrams are mainly concentrated to the solubility regions of  $\text{HFeO}_2^-$  and  $\text{Cd}(\text{OH})_4^{2-}$ .

The saturation concentration in the different cases is given by inserting the pH of 5M KOH at the different temperatures in the log C-pH-relationship where pH for 5N KOH solutions has been calculated from the formulas

$$\text{pOH} = -\log [(\gamma_{\text{OH}^-}) \cdot 5]$$

$$\text{pH} + \text{pOH} = \text{p}k_w, T$$

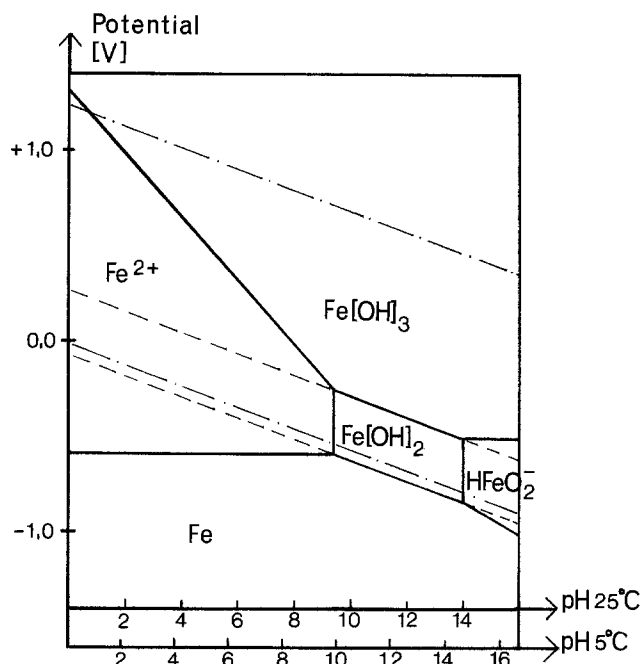


Fig. 1. Potential-pH diagram for iron at 5°C

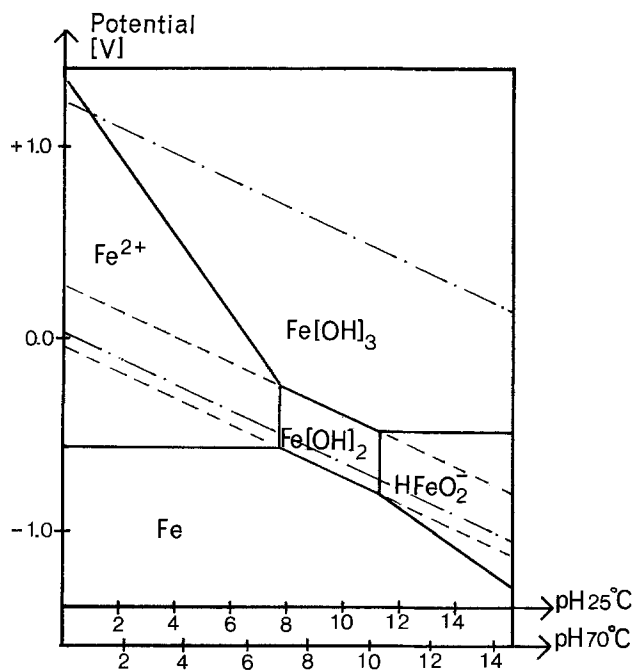


Fig. 2. Potential-pH diagram for iron at 70°C

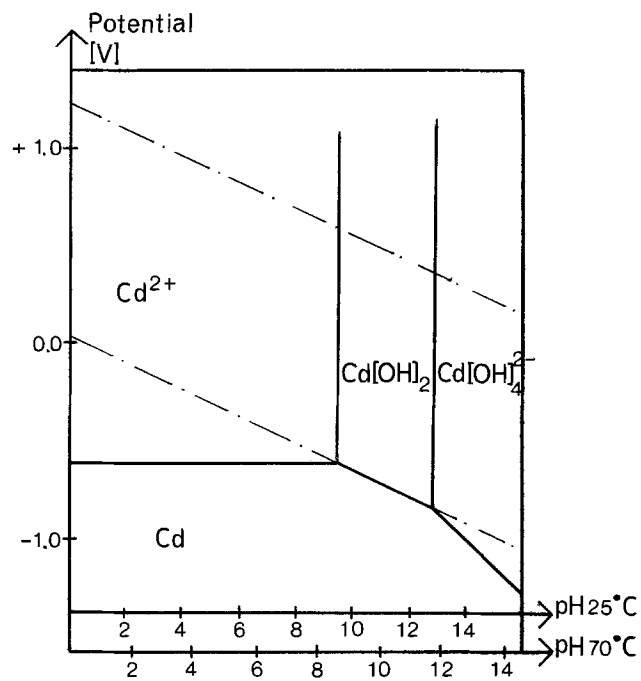


Fig. 4. Potential-pH diagram for cadmium at 70°C

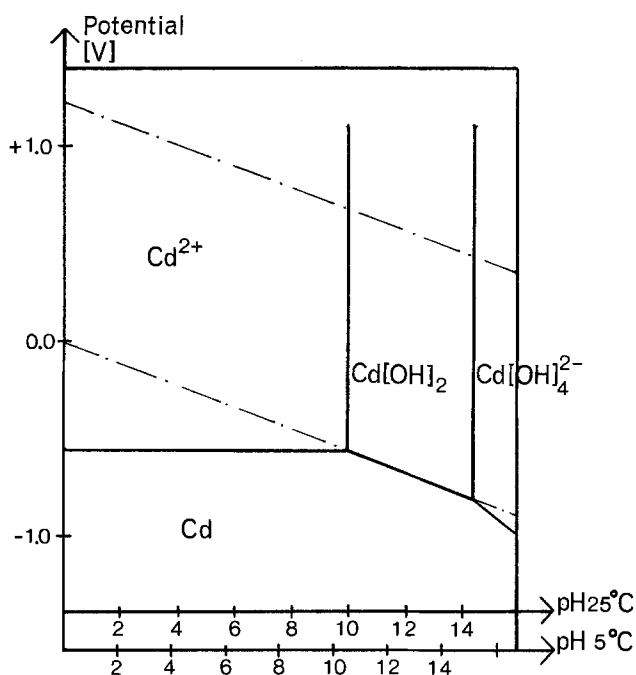


Fig. 3. Potential-pH diagram for cadmium at 5°C

where  $\gamma_{\text{OH}^-}$  is the active coefficient at the temperature level considered (41). Figure 5 shows that the solubility of  $\text{HFeO}_2^-$  and  $\text{FeO}_2^-$  in 5N KOH is highly temperature dependent while this is not the case for  $\text{Cd(OH)}_4^{2-}$ .

*Relationship between solubility of intermediate and kinetics of porous electrodes.*—During discharge the metal will dissolve as  $\text{HFeO}_2^-$  or  $\text{Cd(OH)}_4^{2-}$ , diffuse through the layers of the discharge products and then precipitate from the supersaturated electrolyte. Vetter (40) has shown for the charge process

$$C_0 > C = K \cdot \frac{I}{D}$$

where  $K$  is a constant depending on porosity, average pore diameter, and BET-surface of the electrode,  $D$  is the diffusion constant in the electrolyte, and  $I$  is cur-

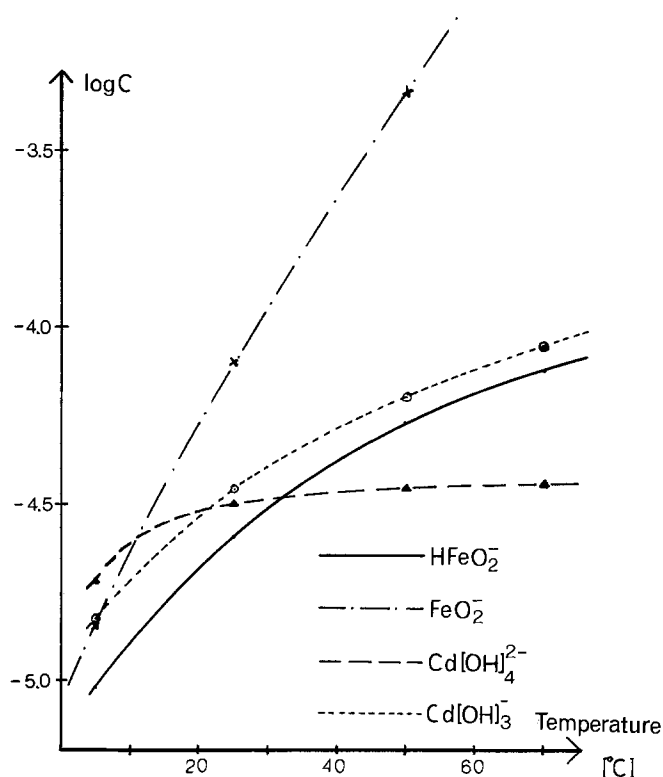


Fig. 5. Calculated solubilities in 5M KOH of Fe and Cd ions at different temperatures.

rent density. Figure 6 gives the concentration symbols. For both processes an increase in  $C_0$  means faster diffusion of the soluble intermediates and less risk for precipitation close to the dissolving center. Also the rate of precipitation increases with  $C_0$ . Consequently the value on  $C_0$  directly influences the maximum current density for both the charge and discharge processes.

### Experimental

The influence of temperature on current density and capacity of the discharge processes of cadmium and iron electrodes has been investigated by scanning the potential slowly from  $-1.050$  to  $-400$  mV vs. Hg/HgO. As the scanning rate is very slow (5.3 mV/min) the

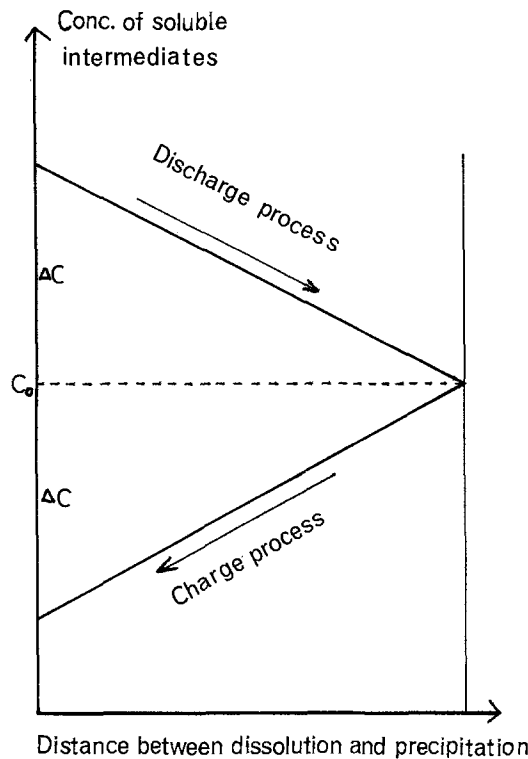


Fig. 6. Concentration of soluble intermediates during charge and discharge.

curves thus obtained are actually those of electrode discharge (Fig. 7-9). If the area under the curve is integrated, it will give the same magnitude of capacity as from constant current discharge during the same time.

As active anode material Jungner Cd and Fe material for pocket electrodes as well as carbonyl iron electrodes from the project mentioned have been used. The latter electrodes were sintered in hydrogen atmosphere (46), 8 mm in diameter, 2.4 mm thick, and weighing 0.32g. As basic material carbonyl iron powder GS 6 from General Aniline & Film Company was used. Two iron nets were incorporated in order to increase mechanical stability and conductivity. The pockets for the Jungner material were 8 mm in diameter and 1

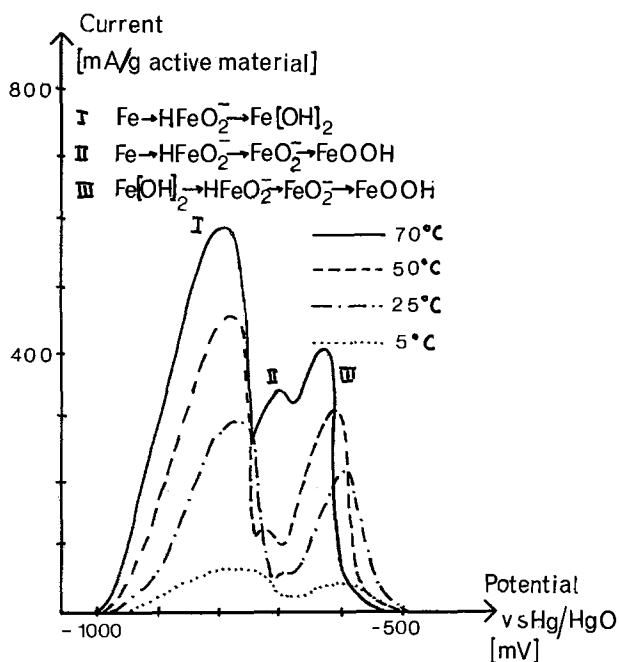


Fig. 7. Potentiodynamic discharge of sintered iron electrode

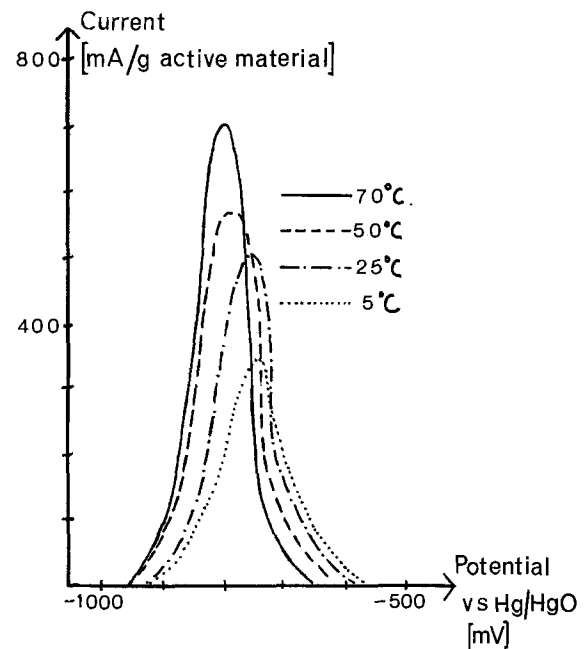


Fig. 8. Potentiodynamic discharge of active Jungner cadmium material.

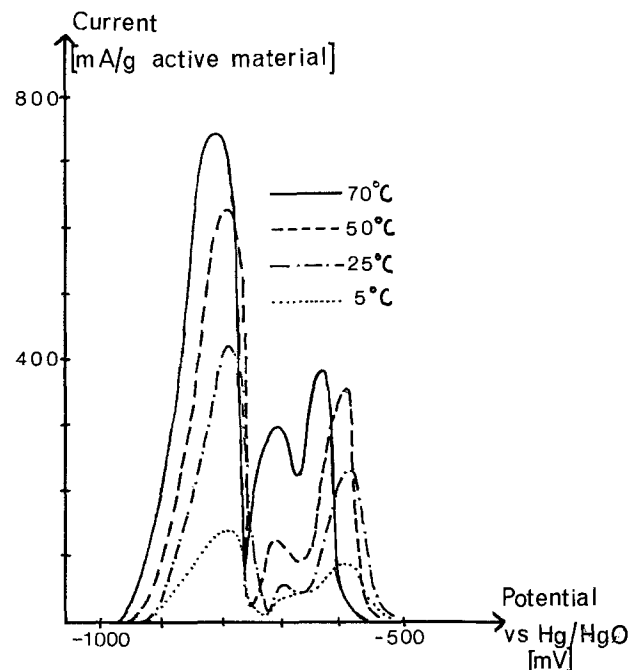


Fig. 9. Potentiodynamic discharge of active Jungner iron material

mm in inner thickness. Before each discharge the electrodes had been discharged and charged to 150% under constant current conditions.

### Results

In Fig. 7, 8, and 9 it can clearly be seen that the discharge reactions are favored by higher temperatures and that current densities of the iron electrode are more influenced than those of the cadmium electrode. Especially below 5°C the current density of the iron electrode is very depressed which agrees well with the results of Cnobloch *et al.* (42). It is also evident that the intermediate hump representing direct oxidation of Fe to FeOOH is favored more by temperature than the other reactions.

### Discussion

This decrease in capacity and current density for the iron electrode compared to its cadmium competitor

depends evidently on the reported difference in temperature sensitivity for the soluble intermediates. At  $C_0 < 2 \cdot 10^{-5}N$  this effect seems to have an essential influence on the electrode performance, a fact that is in good agreement with (40). The increased rate for the direct oxidation with temperature can also be explained with Fig. 5 since the saturation concentration for  $FeO_2^-$  is probably so low that the reaction of the second anodic step must mainly go via migration of ions and electrons in the solid phase. The rapid increase for this concentration with temperature makes it possible to directly oxidate Fe to  $FeOOH$  in dissolved phases. The absolute level for the  $FeO_2^-$  line in Fig. 5 might be too high due to uncertainty in the free energy value but this does not influence the actual temperature dependence which is the important factor for these discussions.

The solubility of  $Cd(OH)_2$  as a function of KOH concentration and temperature has been investigated by Lake and Goodings (39). These results show, however, higher solubilities at temperatures above 25°C in comparison with our calculations for  $Cd(OH)_4^{2-}$ , but are in good agreement at lower temperatures. As shown in Fig. 5 the solubility of  $Cd(OH)_3^-$ , which probably is the more stable intermediate at higher temperatures, is much higher compared to  $Cd(OH)_4^{2-}$  in this region. This explains the experimental results of (39) which, according to Armstrong *et al.* (45), are difficult to interpret rigorously due to the possibility of large errors in estimating liquid-junction potentials.

The only published data on the solubility of ferrous hydroxide in alkali is that 1.375N NaOH will dissolve  $7 \cdot 10^{-5}$  g-equiv.  $Fe(OH)_2$  per liter at 20°C (43). At 80°C in 40% NaOH-solution the solubility of  $FeO_2^-$  is determined by (44) to 1.5 g/liter which is equal to 2.7 g-equiv./liter. This corresponds well to the values calculated for  $FeO_2^-$ .

These calculations also show that the solubility of the intermediates is highly pH dependent. In (47) it is shown that capacity decreases at room temperature when the electrolyte concentration is lowered from 6 to 3N. This means a decrease in pH with about 0.25 units corresponding to a change in  $\log HF_2O_2^-$  from -4.5 to -4.75 at 25°C. Also smaller average pore diameter, increasing thickness, and shielding armor nets have a negative effect on the discharge process due to a higher deficit of  $OH^-$ .

These experiments (47) also show that 250g of  $K_2CO_3$  must be added to every liter electrolyte to get a noticeable decrease in capacity during the first cycle. This effect depends on decrease in pH. However on continued cycling the electrodes become sluggish and capacity decreases also at lower carbonate concentrations.

#### Acknowledgment

The author is indebted to Professor, Dr. Olle Lindström, Royal Institute of Technology, Stockholm for valuable discussions and support.

Manuscript received March 31, 1976.

Any discussion of this paper will appear in a Discussion Section to be published in the June 1977 JOURNAL. All discussions for the June 1977 Discussion Section should be submitted by Feb. 1, 1977.

Publication costs of this article were assisted by the Swedish National Development Company.

#### REFERENCES

- O. Faust, *Z. Electrochem.*, **13**, 161 (1907).
- A. K. Salkind, G. J. Vanuto, and S. U. Falk, *This Journal*, **111**, 493 (1964).
- V. S. Flerov and L. T. Pavlova, *Electrokhimija*, **3**, 621 (1967).
- H. G. Silver and E. Lekas, *This Journal*, **117**, 5 (1970).
- J. Labat, J. C. Jarrousseau, and J. F. Laurent, *Power Sources* **3**, Brighton 1970.
- R. D. Armstrong and I. Baurhoo, *J. Electroanal. Chem.*, **40**, 325 (1972).
- S. A. Rozentsveig *et al.*, *Trudy Soveshemaniva Elektrokim. Akad. Nauk. SSSR, Otdel. Khim. Nauk*, **1950**, 571 (1953).
- R. Huber, *This Journal*, **100**, 376 (1953).
- R. Huber and H. Stucki, *Helv. Chim. Acta*, **51**, 1343 (1968).
- R. E. Lake and E. J. Casey, *This Journal*, **105**, 52 (1958).
- I. Sanghi, E. Visvanathan, O. Anantmanarayanan, *Electrochim. Acta*, **3**, 65 (1960).
- S. Yosmizawa and Z. Takemara, *ibid.*, **5**, 240 (1961).
- M. A. V. Devanathan and S. Laksmanan, *ibid.*, **13**, 667 (1968).
- G. T. Croft, *This Journal*, **106**, 278 (1959).
- G. T. Croft and D. Tuomi, *ibid.*, **108**, 915 (1961).
- M. W. Breiter and J. L. Weininger, *ibid.*, **113**, 651 (1966).
- M. W. Breiter, *et al.*, *Trans. Faraday Soc.*, **63**, 1042 (1967).
- R. D. Armstrong, A. D. Sperrin, L. F. Tye, and G. D. West, *J. Appl. Electrochem.*, **2**, 265 (1972).
- Y. Okinaka, *This Journal*, **117**, 289 (1970).
- R. D. Armstrong and G. D. West, *J. Electroanal. Chem.*, **30**, 385 (1971).
- M. Pourbaix, "Atlas of Electrochemical Equilibria in Aqueous Solution," Pergamon Press, Oxford (1966).
- A. J. de Bethune, T. S. Licht, and N. Swendeman, *This Journal*, **106**, 616 (1959).
- V. Ashworth and P. J. Boden, *Corrosion Sci.*, **10**, 709 (1970).
- R. J. Biernat and R. G. Robins, *Electrochim. Acta*, **17**, 1261 (1972).
- P. A. Brook, *Corrosion Sci.*, **12**, 279 (1972).
- D. D. MacDonald and P. Butler, *ibid.*, **13**, 259 (1973).
- H. E. Townsend, *ibid.*, **10**, 343 (1970).
- A. J. deBethune, *This Journal*, **107**, 829 (1960).
- C. M. Criss and J. W. Cobble, *J. Am. Chem. Soc.*, **86**, 5390 (1964).
- C. M. Criss and J. W. Cobble, *ibid.*, **86**, 5385 (1964).
- J. W. Cobble, *ibid.*, **86**, 5394 (1964).
- H. E. Townsend, *Corrosion Sci.*, **13**, 311 (1973).
- K. K. Kelley, Bulletin 592, U.S. Bureau of Mines, Washington (1961).
- D. D. Wagman, NBS Technical Note 270-3, 270-4, Washington (1968, 1969).
- R. E. Connick and R. E. Powell, *J. Chem. Phys.*, **21**, 2206 (1953).
- A. M. Coture and K. J. Laidler, *Can. J. Chem.*, **35**, 202 (1957).
- L. Pauling, "The Nature of the Chemical Bond," New York (1960).
- "Handbook of Chemistry and Physics," 53rd ed. (1973).
- P. E. Lake and J. M. Goodings, *Can. J. Chem.*, **36**, 1089 (1958).
- K. J. Vetter, *Chemie Ingr.-Tech.*, **45**, 4, 213 (1973).
- C. G. Akerlof and A. Bender, *J. Am. Chem. Soc.*, **70**, 2366 (1948).
- H. Cnobloch *et al.*, *Chem. Ingr.-Tech.*, **45**, 203 (1973).
- W. H. Latimer, "Oxidation Potentials," New York (1952).
- G. Grube and H. Gmelin, *Z. Electrochem.*, **26**, 459 (1920).
- R. D. Armstrong, K. Edmonson, and G. D. West, *Electrochemistry*, **4**, 18 (1974).
- O. Lindström, U.S. Pat 3,802,878, (1972).
- B. Andersson and L. Öjefors, *This Journal*, **123**, 824 (1976).

# Surface Stress Curves for Gold

K. F. Lin\* and T. R. Beck\*\*

Department of Chemical Engineering, University of Washington, Seattle, Washington 98195

## ABSTRACT

Changes in surface stress of gold ribbon electrodes as a function of potential were measured in various electrolytes with an extensometer instrument. Electrocapillary-type curves were obtained for which the change in surface stress can be equated to change in surface tension. As for mercury, the potential of the surface stress maximum for gold is independent of pH. The observed anion adsorption order on gold was  $I^- > Br^- > Cl^- > OH^-, ClO_4^-, NO_3^- > SO_4^{2-}$ . Experimental surface stress data and charge passed gave approximate agreement with the Lippmann equation in the electric double layer region. Formation of oxide film significantly lowered the surface stress.

Much of what is known about the metal-electrolyte interface derives from measurements made with mercury. A number of review papers have been published describing this work (1-5). One of the important measurements is change in interfacial tension with potential using the Lippmann capillary electrometer. The curve of the interfacial tension against the applied potential is called the electrocapillary curve. For an ideal polarized electrode, the slope of the electrocapillary curve is equal to the charge density on the electrode with the sign reversed. It follows that the charge is zero at the electrocapillary maximum. Potential of zero charge can be determined in several ways: by electrocapillary methods, capacitance methods, mechanical properties, adsorption, etc. (6). Recently methods have been developed to measure electrocapillary-type curves for solid metals (7-10).

Important differences between mercury and solid metals relevant to measurement of changes in interfacial tension are: (i) Mercury is a liquid at room temperature and absolute values of its interfacial tension can readily be measured by means of the pressure required to force it through a capillary of given diameter. (ii) The rigidity of a solid metal lattice resists changes in surface stress requiring an extremely sensitive measurement with a specimen of small cross section. (iii) Mercury is atomically smooth while solid metals have grain boundaries and surface roughness. (iv) Clean new surfaces can be easily generated for mercury while unrenovable surfaces with increasing contamination is a severe problem with solid metals. (v) Mercury has a wide potential range with ideal polarization, i.e., a region free of faradaic reactions. Many of the solid metals are complicated by formation of oxide, hydride, or other compounds.

## Extensometer Instrument

An extensometer instrument (7,11) provided a promising new means to measure change in surface stress. The change in surface stress with potential causes a change in length of a ribbon, working electrode, which is determined with a sensitive extensometer head. A diagram of the instrument is given in Ref. (7). In the present case, thin gold ribbons were used as both working electrode and counterelectrode. The working electrode is held under slight tension by attachment to a spring-loaded quartz rod in the extensometer head. Both electrodes and electrolyte were contained in a cell of 1.3 cm ID by 58 cm length glass tube.

The relationship between change in surface stress and change in ribbon length is given by<sup>1</sup>

\* Electrochemical Society Student Member.

\*\* Electrochemical Society Active Member.

Key words: electric double layer, Lippmann equation, adsorption, oxide film, electrocapillary curves.

<sup>1</sup> The list of symbols is given at the end of paper.

$$\Delta\sigma_s = - (AE/PL)\Delta L \quad [1]$$

The derivation of Eq. [1] is given in Appendix A.

Surface stress is related to surface free energy (surface tension) by the Shuttleworth equation (12,13)

$$\sigma_s = \gamma + \frac{d\gamma}{d\epsilon_s} \quad [2]$$

For liquids, surface stress is equal to surface free energy, i.e., the second term on the right-hand side of Eq. [2] is zero. For solids, surface stress is not generally equal to surface free energy. It can be shown, however, that the design of the extensometer gives a constant second term on the right. The change in surface stress is therefore equal to the change in surface free energy (see Appendix B)

$$\Delta\sigma_s = \Delta\gamma \quad [3]$$

The instrument measures only the change in surface stress, not the absolute value.

The extensometer head measures the change in ribbon length by comparing a pair of differential capacitors formed between a grounded aluminum bobbin attached to the quartz rod and two axially mounted annular aluminum plates insulated from the head frame with Teflon holders. The capacitors are balanced by vernier screw adjustment of the annular Teflon holders. The pair of differential capacitors is connected to the input of a Decker Model 906 Delta unit. This instrument develops a d-c potential, across the terminals of a radio-frequency excited neon tube, that is directly proportional to the position of the bobbin (14). The output voltage is thus a measure of change in ribbon length. The length calibration relating voltage to change in surface stress of the ribbon has been described (7). The Decker instrument was modified by placing a quieter, solid-state, Analog 40A operational amplifier in place of the original tube-type amplifier between the neon tube and the plotter.

The extensometer produces an output voltage  $V_{\Delta L}$  proportional to the length change  $\Delta L$  by a capacitance sensor connected to two capacitances  $c_1$  and  $c_2$  (15)

$$V_{\Delta L} = K_1 \left( \frac{1}{c_1} - \frac{1}{c_2} \right) = K_2 \Delta L \quad [4]$$

This linear relationship between output voltage and incremental extension was confirmed by hanging known weights on the bottom of the glass tube, which was supported by its upper end, and measuring the voltage output corresponding to the stretch. The stretch is given by

$$\Delta L_t = L_t W / A_t E_t \quad [5]$$

The stretch is transmitted through the ribbon to the capacitance sensor which reads out a potential.



A typical calibration curve is shown in Fig. 1. The sensitivity of the extensometer was found to be dependent on the average spacing  $d = (d_1 + d_2)/2$ , where  $d_1$  and  $d_2$  are, respectively, the spacing of the upper and lower capacitors. This dependence is shown in Fig. 2.

### Experimental

Electrolyte solutions prepared from ACS specification, reagent-grade chemicals and reverse-osmosis purified water were used in most of the experiments of this paper.

A continuous circulating-electrolyte purification system, as diagrammed in Fig. 3, was used for final cleanup of  $K_2SO_4$  solutions used in the experiments relating to tests with the Lippmann equation. The electrolyte, stored in a 3000 ml three-neck flask, was

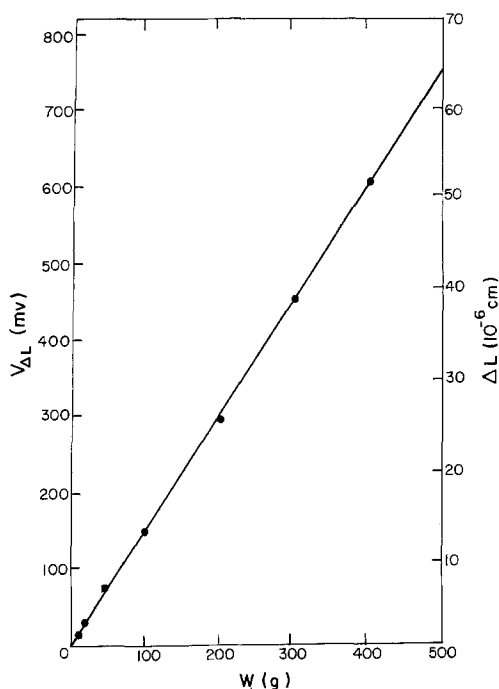


Fig. 1. Typical calibration curve of the extensometer

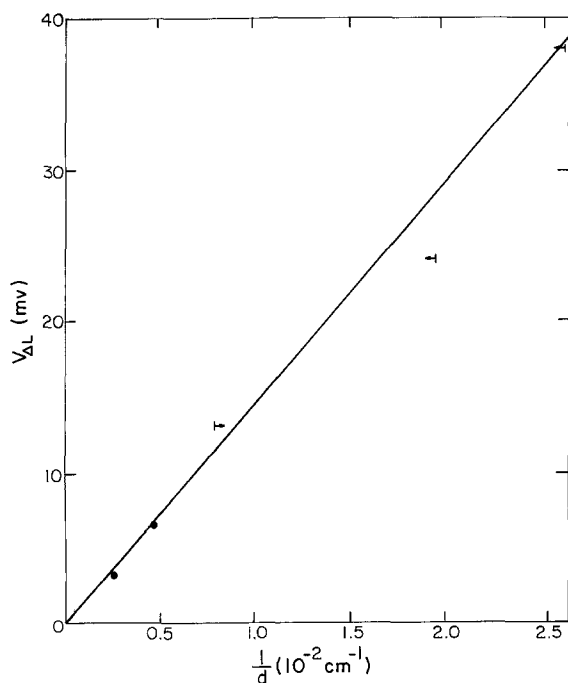


Fig. 2. Sensitivity of the extensometer as a function of average capacitor spacing  $d = (d_1 + d_2)/2$ ,  $W = 50g$ .

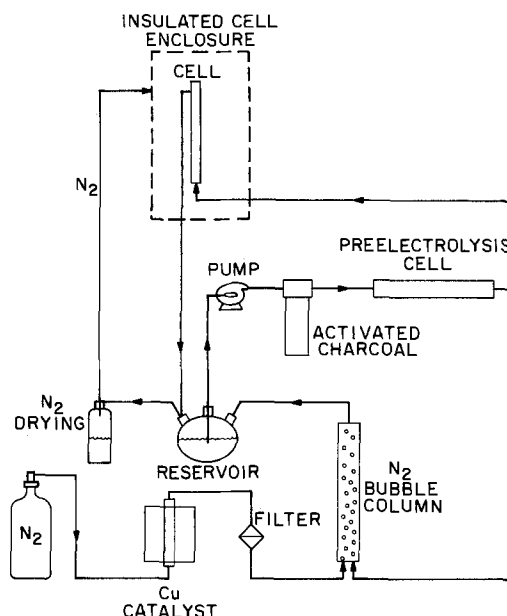


Fig. 3. Electrolyte purification system

pumped by a Teflon pump (Saturn Model SP4000) through a commercially available Millipore carbon bed to adsorb organic impurities from solution. The solution then passed through a (2 cm ID, 55 cm length) pre-electrolysis cell, which was employed to remove heavy metal ions. Some organic material could also be oxidized on the anode surface. Gold ribbon electrodes were used to avoid contamination by metals other than gold. The solution was deaerated by bubbling oxygen-free nitrogen through a 5 cm ID by 60 cm length glass tube. All of the tubing in the system was either glass or Teflon. The solution was circulated for at least 5 days before using in the experiment.

Effluent nitrogen from the purification system was passed over concentrated sulfuric acid in a drying bottle to decrease its dew point. This nitrogen was used as inert atmosphere in the insulated box surrounding the extensometer instrument.

The equation for change in concentration of ions deposited in the preelectrolysis cell is

$$C = C_0 \exp \left[ -\frac{\tau a D}{V \delta} \right] \quad [6]$$

The diffusion layer thickness was estimated to be  $6.0 \times 10^{-3}$  cm from decay of current after an impulse input of  $Cu^{++}$  ion. A constant 1.7V was applied to the cell. This was a maximum potential that could be used yet avoid significant hydrogen and oxygen contamination.

The electrolyte purification has been applied to the 0.1M  $K_2SO_4$  solution only in the presently reported experiments. Prior to installation in the extensometer, gold ribbons were washed with acetone to remove organic material on the surface. Before the extensometer was filled with electrolyte, it was cleaned with concentrated nitric acid and thoroughly rinsed in reverse osmosis water. Experimental data were taken after approximate steady-state temperature was reached in the experimental box. At least half an hour was required so that the expansion due to thermal drift became negligible.

A saturated calomel reference electrode was used in the experiments. All potentials were converted to standard hydrogen electrode ( $V_{SHE}$ ) by adding 0.24V.

### Results and Discussion

Gold has a wide range of potential for its electric double layer region as for mercury. It is therefore an appropriate solid metal for initial electrocapillary studies.

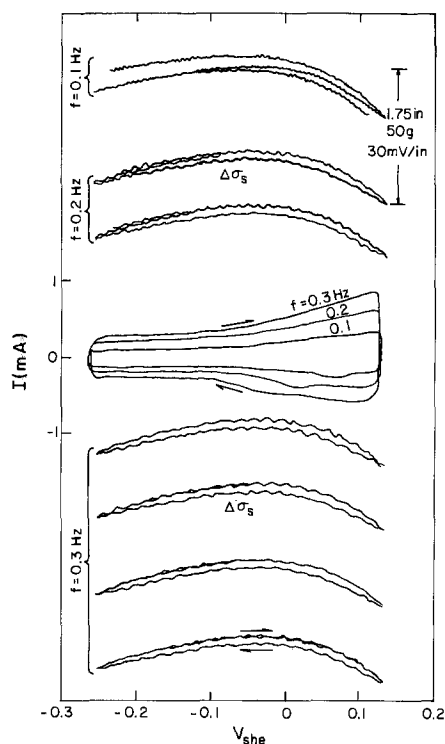


Fig. 4. Surface stress curves (with oscillations) and cyclic voltammograms in  $0.1M$   $K_2SO_4$  with various sweeping frequencies.

**Electrocapillary curve.**—Figure 4 shows current and surface-stress data at three sweep frequencies ( $f = 0.1$ ,  $0.2$ , and  $0.3$  Hz).<sup>2</sup> The potential was limited to the vicinity of surface stress maximum. The oscillations in surface stress curves were due to vibration in the system (11). For  $f = 0.1$  Hz, the first run, steady-state temperature had not been reached in the experimental cell so that the surface stress curve did not close after one complete cycle. For  $f = 0.2$  and  $0.3$  Hz, run subsequently, thermal drift became negligible and surface stress curves closed. The source of surface stress hysteresis in the electric double layer region is not known.<sup>3</sup> The procedure of data processing was to take 4 to 6 curves at a given frequency and average to minimize noise. A least squares polynomial was then fitted to the average data.

The stretch of the glass tube due to hanging a 50g weight is seen to give an average 1.75 in. deflection at the scale of 30 mV/in. at the right of Fig. 4. This stretch, calculated from Eq. [5] with  $L_t = 46.5$  cm,  $W = 50$ g,  $A_t = 0.55$  cm<sup>2</sup>, and  $E_t = 6.4 \times 10^8$  g/cm<sup>2</sup>, was  $6.6 \times 10^{-6}$  cm. A 1-in. deflection in Fig. 4 would therefore correspond to an actual differential length change of  $3.77 \times 10^{-6}$  cm. With  $A = 4.8 \times 10^{-4}$  cm<sup>2</sup>,  $E = 7.93 \times 10^{11}$  dyne/cm<sup>2</sup>,  $P = 0.635$  cm, and  $L = 56.5$  cm for the gold ribbon, Eq. [1] gives the magnitude of surface stress change as  $\Delta\sigma_s = 40$  dyne/cm/in. deflection in Fig. 4.

**Oxide film effect.**—Figure 5 shows the surface stress curve and the cyclic voltammogram with  $0.1M$   $K_2SO_4$  solution of pH 3.6. In the potential range shown, three regions were covered, i.e., hydrogen evolution, electric double layer (EDL), and oxide formation. No hysteresis or change in slope of the surface-stress curve was observed in the hydrogen region. Hydrogen is reported to be neither absorbed on nor dissolved in gold to an appreciable extent (17, 18). The surface stress hystere-

<sup>2</sup> The convention of plotting increasing positive potentials to the right as is common for electrode kinetics data (16) is used instead of the usual convention for electrocapillary data for mercury (3).

<sup>3</sup> Irreversible adsorption or surface penetration by some species and change of the surface elastic modules,  $E_s$  in Eq. [A-7] are possible causes.

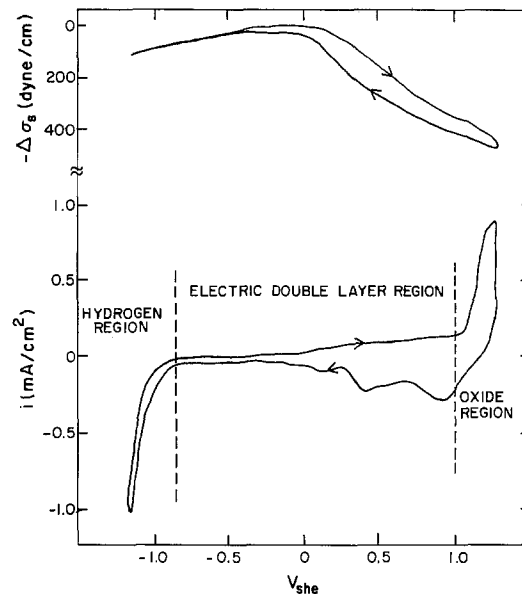


Fig. 5. Surface stress curve and cyclic voltammogram in  $0.1M$   $K_2SO_4 + 10^{-4}N$   $H_2SO_4$ , pH = 3.6,  $f = 0.1$  Hz.

sis observed on the anodic side was mainly due to the formation and dissolution of oxide film. The oxidation process has been reported as highly irreversible (19, 20).

The effect of formation of oxide film can be studied by limiting the span to the EDL and the oxide regions. Figure 6 for  $1M$   $HClO_4$  shows that where anodic oxidation started at I, there was a corresponding increase in surface stress deflection. The ratio of charge under the anodic to the cathodic curve is close to unity. The flat plateau anodic current without peaks prior to I, indicates good purity of the electrolyte (19).

A charge density of  $0.45$  mcoulombs/cm<sup>2</sup> corresponds to a monolayer of oxide on a gold surface (20). Oxide coverage, calculated from the areas under the current curves is shown in Fig. 7 for both sweep directions. Almost complete removal of oxide is seen on the cathodic sweep. At a fixed potential, hysteresis in surface stress

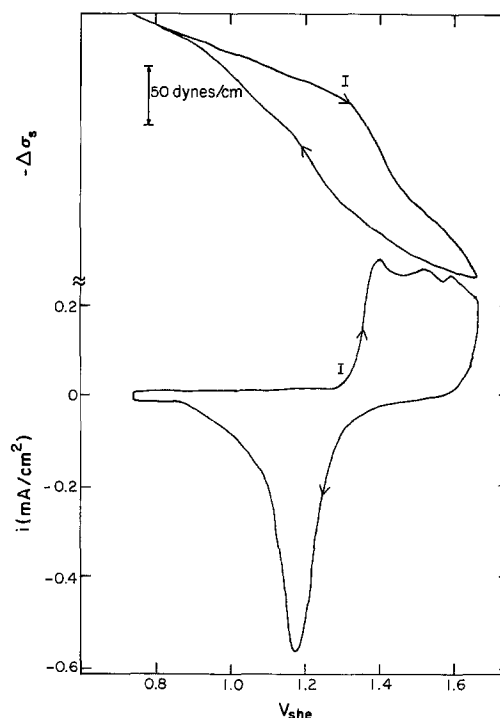


Fig. 6. Surface stress curve and cyclic voltammogram in  $1M$   $HClO_4$ ,  $f = 0.1$  Hz.

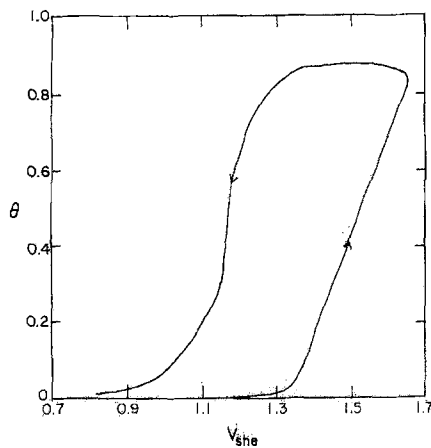


Fig. 7. Oxide coverage in anodic and cathodic sweeps as a function of potential in 1M HClO<sub>4</sub>,  $f = 0.1$  Hz.

and oxide coverage between anodic and cathodic sweeps could be read from Fig. 6 and 7. The maximum difference in oxide coverage occurred at 1.34V<sub>SHE</sub> and corresponded to a maximum difference in surface stress between anodic and cathodic sweeps in Fig. 6.

**Effect of pH.**—The potential of surface stress maximum  $\phi_m$  as a function of pH is shown in Fig. 8. It is seen that  $\phi_m$  is independent of pH as it is for mercury. Noniski and Lazarova (21) using a scraping technique on gold observed the same behavior for the point of zero charge (pzc), but at high pH, they found that the pzc became linearly dependent on pH.

**Effect of surface active anions.**—Figure 9 shows plots of surface stress in the anodic sweep with potassium salt solutions of various anions. All curves were made coincident at the negative branch by sliding them along the surface stress axis. The slopes of the curves were identical where they overlapped as for mercury (1).

Table I gives data of  $\phi_m$  and  $\phi_{pzc}$  with solutions of different anions. For mercury the order of adsorption according to increasing pzc and decreasing amount of adsorbed ions is (22-25) I<sup>-</sup> > Br<sup>-</sup> > ClO<sub>4</sub><sup>-</sup> > Cl<sup>-</sup> > OH<sup>-</sup> > SO<sub>4</sub><sup>=</sup> > F<sup>-</sup> while for gold it appears that

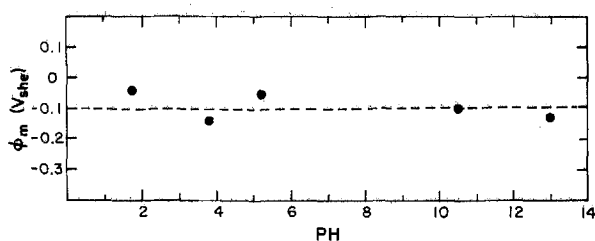


Fig. 8. Effect of pH on the potential of surface stress maximum in 0.1N K<sub>2</sub>SO<sub>4</sub>.

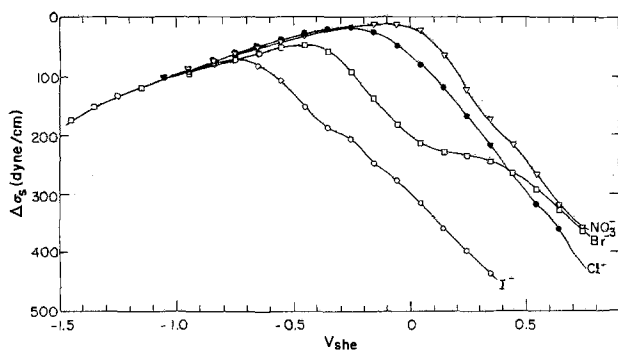


Fig. 9. Surface stress curves for different ions in 0.1N potassium salt, gold electrode anodic sweep.

Table I. Potential of surface stress maximum and point of zero charge for gold

Anions	(a) $\phi_m$ (V <sub>SHE</sub> ) 10 <sup>-3</sup> N K <sup>+</sup> salt	(b) $\phi_{pzc}$ (V <sub>SHE</sub> ) 10 <sup>-3</sup> N Na <sup>+</sup> salt Ref. (26)	(c) $\phi_{pzc}$ (V <sub>SHE</sub> ) 10 <sup>-3</sup> N K <sup>+</sup> salt Ref. (27)	(d) $\phi_{pzc}$ (V <sub>SHE</sub> ) 10 <sup>-2</sup> N K <sup>+</sup> salt Ref. (28)
SO <sub>4</sub> <sup>=</sup>	-0.06	0.14	0.06	—
ClO <sub>4</sub> <sup>-</sup>	-0.16	0.14	-0.18	—
NO <sub>3</sub> <sup>-</sup>	-0.16	—	-0.04	—
OH <sup>-</sup>	-0.16	—	—	—
SCN <sup>-</sup>	—	—	-0.44	—
F <sup>-</sup>	—	0.19	-0.06	0.18
Cl <sup>-</sup>	-0.21	-0.07	-0.11	0.06
Br <sup>-</sup>	-0.46	-0.24	-0.26	-0.18
I <sup>-</sup>	-0.74	-0.53	-0.47	-0.46

(a) Present method.  
(b), (c) Scraping method.  
(d) From integration of capacity data.

I<sup>-</sup> > Br<sup>-</sup> > Cl<sup>-</sup> > OH<sup>-</sup>, ClO<sub>4</sub><sup>-</sup>, NO<sub>3</sub><sup>-</sup> > SO<sub>4</sub><sup>=</sup>. The following adsorption orders were reported for gold in literature (21, 26) I<sup>-</sup> > Br<sup>-</sup> > OH<sup>-</sup> > Cl<sup>-</sup> > SO<sub>4</sub><sup>=</sup> > ClO<sub>4</sub><sup>-</sup> > F<sup>-</sup> and (29) Br<sup>-</sup> > Cl<sup>-</sup> > SO<sub>4</sub><sup>=</sup> > ClO<sub>4</sub><sup>-</sup>. The reason for the generally more negative values of  $\phi_m$  compared to other reported values of  $\phi_{pzc}$  in Table I remains to be determined. After careful solution purification,  $\phi_m$  did not change with anodic or cathodic pre-polarization.

For the strongly adsorbed ions, I<sup>-</sup> and Br<sup>-</sup>, plateaus in surface stress curves are seen at about -0.36 and 0.14V<sub>SHE</sub>, respectively, in Fig. 9. The plateau corresponded to a region of potential associated with a peak at II in the current curve shown in Fig. 10 for I<sup>-</sup>. This peak was reversible, as can be seen from the near coincidence in the anodic and cathodic sweeps. The increase in current at III could be due to the reactions 2I<sup>-</sup> = I<sub>2</sub> + 2e<sup>-</sup>, or I<sup>-</sup> + Au = AuI + e<sup>-</sup> (30).

**Lippmann equation.**—For an ideal polarized electrode, the interfacial tension is related to potential by the Lippmann equation (1)

$$\left[ \frac{\partial \gamma}{\partial \phi} \right]_{\mu, T, p} = -q \quad [7]$$

where  $q$  is charge density on the electrode.

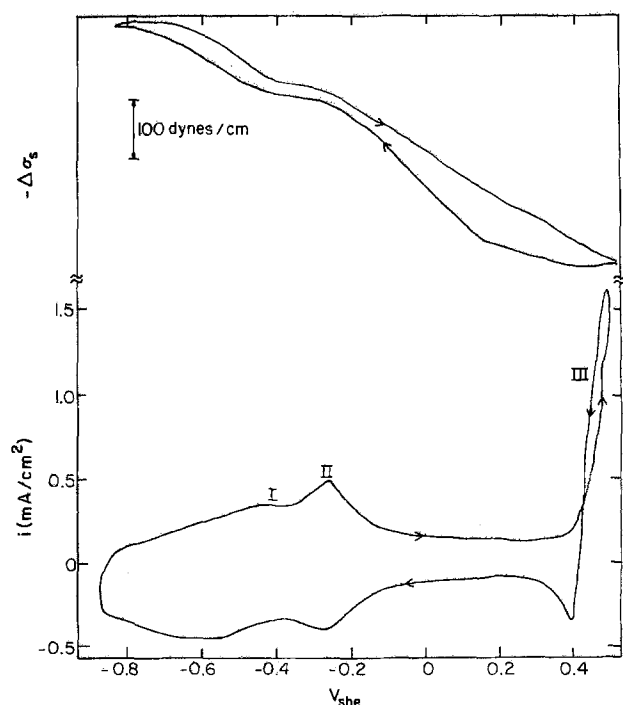


Fig. 10. Surface stress curve and cyclic voltammogram in 0.1N KI,  $f = 0.2$  Hz.

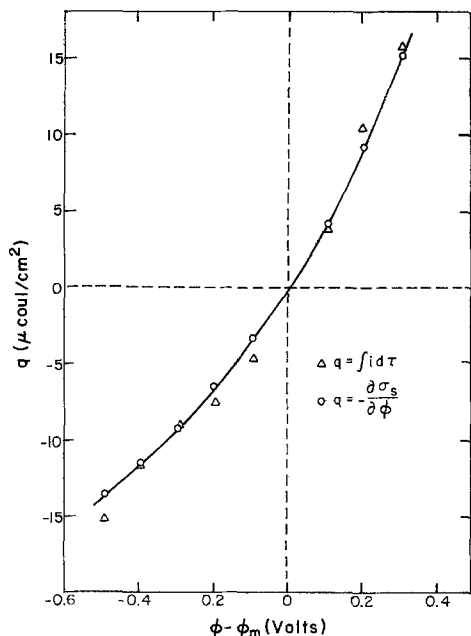


Fig. 11. Charge density as a function of potential in 0.1M K<sub>2</sub>SO<sub>4</sub> in electric double layer region.

At the surface stress maximum, charge density is equal to zero. Figure 11 shows the comparison of charge density for a fresh gold electrode in 0.1M K<sub>2</sub>SO<sub>4</sub> purified in the system of Fig. 3. One of the charge density curves was obtained from the numerical integration of current data in Fig. 12, starting from potential of surface stress maximum. The other was through Eq. [7] and numerical differentiation of a least squares fitted polynomial of eighth degree to the surface stress data in Fig. 12. Figure 11 shows remarkable check of the Lippmann equation in the electric double layer region for gold, despite more experimental difficulties associated with gold than with mercury. Thus for a first approximation, for gold, the assumptions made in the derivation in Appendix A appear to be justified. The experimental data also agreed with the Lippmann equation in the cathodic sweep. The Lippmann equation had been confirmed with mercury-electrolyte interface by Grahame (1). Surface roughness was assumed to be unity. A SEM photo of gold ribbon at magnification factor of 6000 showed a smooth surface.

Deviation from the Lippmann equation occurs after a number of runs, probably due to the "cycling" effect for the gold electrode (31, 32) or adsorption of impurities. Deviation from the Lippmann equation would also be expected for oxide film or hydrogen evolution and other faradaic reactions. The general Lippmann equation has been derived for a reversible redox system (33). However, there has not been any theoretical relationship for an irreversible system.

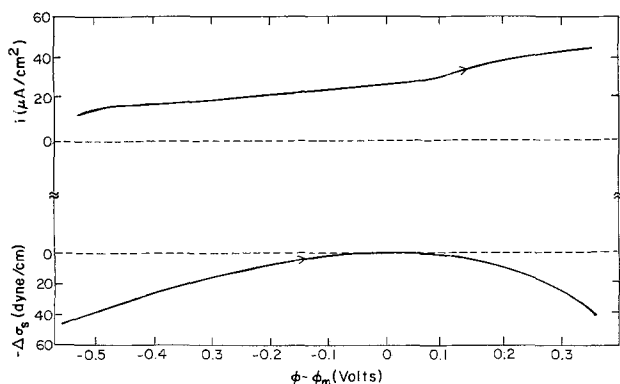


Fig. 12. Surface stress and current data in 0.1M K<sub>2</sub>SO<sub>4</sub>

**Conclusions**

The following conclusions can be reached from the study of surface stress of gold.

1. The measured change in surface stress can be shown to be equal to the change in surface free energy.
2. The observed adsorption order of anions based on the potential of the surface stress maximum is I<sup>-</sup> > Br<sup>-</sup> > Cl<sup>-</sup> > OH<sup>-</sup>, ClO<sub>4</sub><sup>-</sup>, NO<sub>3</sub><sup>-</sup> > SO<sub>4</sub><sup>=</sup>.
3. Formation of a gold oxide (or hydroxide) film tends to lower the surface stress.
4. For weakly adsorbed ions the potential of the surface stress maximum is independent of pH.
5. Measured change in surface stress and integrated charge density are in agreement with the Lippmann equation in electric double layer region for a new ribbon in a carefully purified system.

**Acknowledgment**

The authors wish to express their thanks to National Science Foundation for the Grant GK 43993.

Manuscript submitted Jan. 9, 1976; revised manuscript received March 15, 1976.

Any discussion of this paper will appear in a Discussion Section to be published in the June 1977 JOURNAL. All discussions for the June 1977 Discussion Section should be submitted by Feb. 1, 1977.

Publication costs of this article were assisted by the University of Washington.

**APPENDIX A**

*Derivation of Eq. [1]*

Suppose an unstressed metal ribbon and a spring are each attached to respective ends of a tube such that there is a gap  $\Delta L_0$  between them, as shown in Fig. 13, initial condition 1. Assume the tube is very stiff so that it does not change dimension. The ribbon and spring are stretched to connect their free ends, stretched condition 1. The ribbon is stretched by  $\Delta X_1$  and the force on the ribbon and spring is then

$$F_1 = m_r \Delta X_1 = m_s (\Delta L_0 - \Delta X_1)$$

in which  $m_r = EA/L$ . Eliminating  $\Delta X_1$ , gives

$$F_1 = \frac{m_r m_s \Delta L_0}{m_r + m_s}$$

Going back to the original unstretched condition (Fig. 13) the ribbon is increased in length by an amount  $\Delta L$  due to a change of the applied potential in the experiment, initial condition 2. This decreases the gap by  $\Delta L$ . Suppose the ribbon and spring are again stretched to connect their free ends, stretched condition 2. The ribbon is stretched by  $\Delta X_2$  and the new force on the ribbon and spring is

$$F_2 = m_r \Delta X_2 = m_s (\Delta L_0 - \Delta L - \Delta X_2)$$

(Since  $\Delta L$  is very small, the spring constant of the

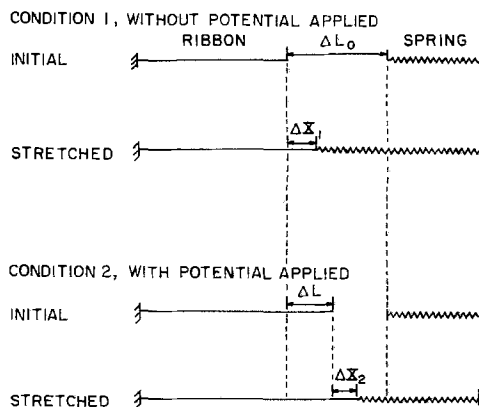


Fig. 13. Schematic diagram of the spring and ribbon system

ribbon is assumed to remain constant after the change in length,  $\Delta L$ .) Eliminating  $\Delta X_2$  gives

$$F_2 = \frac{m_r m_s (\Delta L_0 - \Delta L)}{m_r + m_s}$$

The change in force due to the increase in length,  $\Delta L$ , is then

$$\Delta F = F_2 - F_1 = \frac{-m_r m_s \Delta L}{m_r + m_s}$$

The instrument is designed so that  $m_r \gg m_s$ , giving

$$\Delta F \approx -m_s \Delta L \quad [\text{A-1}]$$

The force balance between the ribbon and spring is shown in Fig. 14. The length of the abscissa is  $\Delta L_0$  for the initial condition 1 in Fig. 13.

The assumption will be made that the force on the ribbon is resisted by separable bulk and surface stresses,  $\sigma$  and  $\sigma_s$ , respectively. The surface stress is assumed to be in a region of atomic thickness on the surface of the metal. Therefore

$$F = \sigma A + \sigma_s P$$

and

$$\Delta F = \sigma \Delta A + A \Delta \sigma + \sigma_s \Delta P + P \Delta \sigma_s \quad [\text{A-2}]$$

By Hooke's law

$$\Delta \sigma = E \frac{\Delta L}{L} \quad [\text{A-3}]$$

It is assumed that the bulk elastic modulus,  $E$ , is unchanged by potential applied to the ribbon, i.e., no lattice penetration occurs.

The change in area is

$$\Delta A = (t + \Delta t)(w + \Delta w) - tw$$

By Poisson's law

$$\frac{\Delta t}{t} = -b \frac{\Delta L}{L}$$

and

$$\frac{\Delta w}{w} = -b \frac{\Delta L}{L} \quad [\text{A-4}]$$

Therefore

$$\frac{\Delta A}{A} = \left(1 - b \frac{\Delta L}{L}\right)^2 - 1 \approx -2b \frac{\Delta L}{L} \quad (\text{neglecting the square term}) \quad [\text{A-5}]$$

From Eq. [A-3] and [A-5]

$$\left| \frac{\sigma \Delta A}{A \Delta \sigma} \right| = \frac{2b\sigma}{E} \rightarrow 0$$

(since the bulk strain  $\sigma/E$  is very small), or

$$A \Delta \sigma \gg \sigma \Delta A \quad [\text{A-6}]$$

An elastic modulus,  $E_s$ , is assumed for the atomic layer on the surface of the ribbon. It is assumed to be constant although it may be affected by adsorbed atoms or ions on the surface and penetration of atoms into the surface layer. Then

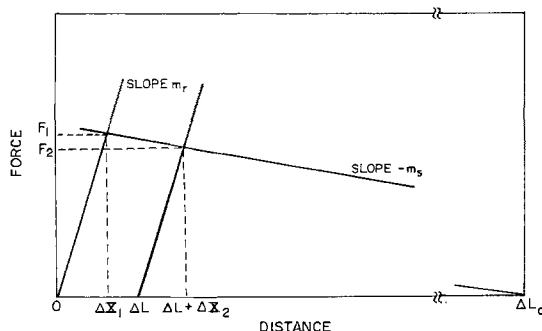


Fig. 14. Force equilibrium in the ribbon and spring system

$$\Delta \sigma_s = E_s \frac{\Delta L}{L} \quad [\text{A-7}]$$

and

$$P \approx 2w (w \gg t)$$

Therefore

$$\frac{\Delta P}{P} = \frac{\Delta w}{w} = -b \frac{\Delta L}{L} \quad [\text{A-8}]$$

From Eq. [A-7] and [A-8]

$$\left| \frac{\sigma_s \Delta P}{P \Delta \sigma_s} \right| = \frac{b \sigma_s}{E_s} \rightarrow 0$$

(since the surface linear strain  $\sigma_s/E_s$  is very small), or

$$P \Delta \sigma_s \gg \sigma_s \Delta P \quad [\text{A-9}]$$

From Eq. [A-1], [A-2], [A-6], and [A-9]

$$\Delta F \approx A \Delta \sigma + P \Delta \sigma_s \approx -m_s \Delta L$$

But

$$A \Delta \sigma = AE \frac{\Delta L}{L} = m_r \Delta L \text{ and } m_r \gg m_s$$

$$\therefore A \Delta \sigma + P \Delta \sigma_s \approx 0$$

and

$$\Delta \sigma_s \approx -\frac{AE}{PL} \Delta L \quad [\text{A-10}]$$

which is Eq. [1] in the text.

## APPENDIX B

### Derivation of Eq. [3]

Write Eq. [1] in differential form

$$d\sigma_s = -\frac{AE}{P} d\epsilon \quad [\text{B-1}]$$

where  $d\epsilon$  is the differential linear strain ( $dL/L$ ). Integrating Eq. [B-1]

$$\sigma_s = c_1 - \frac{AE}{P} \epsilon \quad [\text{B-2}]$$

where  $c_1$  is an integration constant.

For a long, thin ribbon, the total surface area  $S$  is approximated by

$$S \approx 2wL \quad [\text{B-3}]$$

From Eq. [A-4] and [B-3], the differential surface strain is given by

$$d\epsilon_s = \frac{dS}{S} \approx (1-b) d\epsilon \quad [\text{B-4}]$$

From Eq. [2], [B-2], and [B-4]

$$\frac{d\gamma}{d\epsilon} + (1-b)\gamma - (1-b) \left( c_1 - \frac{AE}{P} \epsilon \right) = 0 \quad [\text{B-5}]$$

The solution is

$$\begin{aligned} \gamma &= c_1 + \frac{AE}{P(1-b)} - \frac{AE}{P} \epsilon + c_2 e^{-(1-b)\epsilon} \\ &= \sigma_s + \frac{AE}{P(1-b)} + c_2 e^{-(1-b)\epsilon} \end{aligned}$$

where  $c_2$  is an integration constant

For  $\epsilon \rightarrow 0$

$$\gamma = \sigma_s + \frac{AE}{P(1-b)} + c_2$$

Then

$$\Delta \gamma = \Delta \sigma_s \quad [\text{B-6}]$$

which is Eq. [3] in the text.

## LIST OF SYMBOLS

- $A$  cross-sectional area of the gold ribbon in the extensometer,  $\text{cm}^2$   
 $A_t$  cross-sectional area of the glass tube in the extensometer,  $\text{cm}^2$

$a$	surface area of gold ribbon cathode (or anode) in the preelectrolysis cell, $\text{cm}^2$
$b$	Poisson's ratio, usually between 1/3 and 1/4
$C$	concentration of reducible (or oxidizable) impurity, $\text{mole}/\text{cm}^3$
$C_0$	initial concentration of reducible (or oxidizable) impurity, $\text{mole}/\text{cm}^3$
$c_1$	capacitance of the upper capacitor, farad, or an integration constant
$c_2$	capacitance of the lower capacitor, farad, or an integration constant
$D$	diffusion coefficient, $\text{cm}^2/\text{sec}$
$d$	average spacing of the upper and lower capacitors, $\text{cm}$
$d_1$	spacing of the upper capacitor, $\text{cm}$
$d_2$	spacing of the lower capacitor, $\text{cm}$
$E$	bulk elastic modulus of gold ribbon, $\text{dyne}/\text{cm}^2$
$E_s$	surface elastic modulus of gold ribbon, $\text{dyne}/\text{cm}$
$E_t$	elastic modulus of glass tube, $\text{g}/\text{cm}^2$
$F$	force in the gold ribbon, $\text{dyne}$
$F_1$	force in the spring (or gold ribbon) without applied potential, $\text{dyne}$
$F_2$	force in the spring (or gold ribbon) with applied potential, $\text{dyne}$
$f$	sweeping frequency of the triangular wave, $1/\text{sec}$
$I$	current, $\text{mA}$
$i$	current density, $\text{mA}/\text{cm}^2$
$K_1$	proportional constant, coulomb
$K_2$	proportional constant, $\text{V}/\text{cm}$
$L$	immersed length of gold ribbon in the extensometer, $\text{cm}$
$L_t$	length of glass tube from a support point near the upper end to the weight hanger near the lower end, $\text{cm}$
$m_r$	spring constant of gold ribbon, $\text{dyne}/\text{cm}$
$m_s$	spring constant of the spring, $\text{dyne}/\text{cm}$
$P$	periphery of the cross section of gold ribbon, $\text{cm}$
$p$	pressure, $\text{dyne}/\text{cm}^2$
$q$	charge density, $\mu\text{coulomb}/\text{cm}^2$
$S$	total surface area of gold ribbon in the extensometer, $\text{cm}^2$
$t$	thickness of gold ribbon in the extensometer, $\text{cm}$
$T$	temperature, $^\circ\text{C}$
$V$	volume of electrolyte in the purification system, $\text{cm}^3$
$V_{\text{SHE}}$	potential relative to saturated hydrogen electrode, $\text{V}$
$V_{\Delta L}$	voltage output from the capacitance sensor, $\text{V}$
$W$	hanging weight, $\text{g}$
$w$	width of gold ribbon in the extensometer, $\text{cm}$
$\Delta L_0$	gap between the unstretched spring and gold ribbon without applied potential, $\text{cm}$
$\Delta X_1$	length stretched in gold ribbon without applied potential, $\text{cm}$
$\Delta X_2$	length stretched in gold ribbon with applied potential, $\text{cm}$
$\tau$	time, $\text{sec}$
$\delta$	diffusion thickness, $\text{cm}$
$\gamma$	surface free energy, $\text{erg}/\text{cm}^2$
$\mu$	chemical potential, $\text{erg}/\text{mole}$
$\epsilon$	linear surface strain of gold ribbon ( $\Delta L/L$ )
$\epsilon_s$	surface strain of gold ribbon ( $\Delta S/S$ )
$\sigma$	bulk surface stress, $\text{dyne}/\text{cm}^2$
$\sigma_s$	surface stress, $\text{dyne}/\text{cm}$
$\phi$	potential, $\text{V}$
$\phi_m$	potential of surface stress maximum, $\text{V}$
$\phi_{pzc}$	potential of zero charge, $\text{V}$

## REFERENCES

1. D. C. Grahame, *Chem. Rev.*, **41**, 441 (1947).
2. R. Parsons, in "Advances in Electrochemistry and Electrochemical Engineering," Vol. 1, P. Delahay, Editor, Interscience Publishers, New York (1961).
3. P. Delahay, "Double Layer and Electrode Kinetics," Interscience Publishers, New York (1965).
4. D. M. Mohilner, in "Electroanalytical Chemistry," Vol. 1, A. J. Bard, Editor, Marcel Dekker, Inc., New York (1966).
5. R. Payne, in "Techniques of Electrochemistry," Vol. 1, E. Yeager and A. J. Salkind, Editors, Wiley-Interscience, New York (1972).
6. R. S. Perkins and T. N. Andersen, in "Modern Aspects of Electrochemistry," No. 5, J. O'M. Bockris and B. E. Conway, Editors, Plenum Press, New York (1969).
7. T. R. Beck, *J. Phys. Chem.*, **73**, 466 (1969).
8. A. Y. Gokhstein, *Electrochim. Acta*, **15**, 219 (1970); USSR Certificate of Authorship 178,161 and 179,043, Translated by Associated Technical Services, Inc.
9. R. A. Fredlein, A. Damjanovic, and J. O'M. Bockris, *Surface Sci.*, **25**, 261 (1971).
10. R. A. Fredlein and J. O'M. Bockris, *ibid.*, **46**, 641 (1974).
11. T. R. Beck and K. W. Beach, in "Proceedings of the Symposium on Electrocatalysis," M. W. Breiter, Editor, pp. 357-364, The Electrochemical Society Softbound Symposium Series, Princeton, N. J. (1974).
12. R. A. Oriani and G. A. Johnson, in "Modern Aspects of Electrochemistry," No. 5, J. O'M. Bockris and B. E. Conway, Editors, Plenum Press, New York (1969).
13. R. Shuttleworth, *Proc. Phys. Soc. (London)*, **A63**, 444 (1950).
14. K. S. Lion, U.S. Pat. 2,800,622 (1959).
15. Instruction Manual Decker Delta Unit Model 906, The Decker Corporation Bala-Cynwyd, Pennsylvania.
16. K. J. Vetter, "Electrochemical Kinetics," Academic Press, New York (1967).
17. A. Hickling, *Trans. Faraday Soc.*, **42**, 518 (1946).
18. F. Bauman and I. Shain, *Anal. Chem.*, **29**, 303 (1957).
19. C. M. Ferro, A. J. Calandra, and A. J. Arvia, *J. Electroanal. Chem.*, **59**, 239 (1975).
20. H. A. Laitinen and M. S. Chao, *This Journal*, **108**, 726 (1961).
21. K. I. Noniski and E. M. Lazarova, *Soviet Electrochem.*, **9**, 648 (1973).
22. D. C. Grahame, E. M. Coffin, J. I. Cummings, and M. A. Poth, *J. Am. Chem. Soc.*, **74**, 1207 (1952).
23. D. C. Grahame and B. A. Soderberg, *J. Chem. Phys.*, **22**, 449 (1954).
24. W. Wroblowa, Z. Kovac, and J. O'M. Bockris, *Trans. Faraday Soc.*, **61**, 1523 (1965).
25. D. C. Grahame, *J. Am. Chem. Soc.*, **80**, 4201 (1958).
26. D. D. Bodé, Jr., T. N. Andersen, and H. Eyring, *J. Phys. Chem.*, **71**, 792 (1967).
27. R. S. Perkins, R. C. Livingston, T. N. Anderson, and H. Eyring, *ibid.*, **69**, 3329 (1965).
28. J. Clavilier and N. Van Huong, *J. Electroanal. Chem.*, **41**, 193 (1973).
29. W. K. Paik, M. A. Genshaw, and J. O'M. Bockris, *J. Phys. Chem.*, **74**, 4266 (1970).
30. W. M. Latimer, "The Oxidation States of the Elements and Their Potentials in Aqueous Solutions," 2nd edition, Prentice-Hall, Inc., New York (1952).
31. K. Kinoshita, J. T. Lundquist, and P. Stonehart, *J. Electroanal. Chem.*, **48**, 157 (1973).
32. J. M. Otten and W. Visscher, *ibid.*, **55**, 1 (1974).
33. A. Frumkin, O. Petry, and B. Damaskin, *ibid.*, **27**, 81 (1970).

# Stress Corrosion Cracking of Stainless Steel and Nickel Alloys at Controlled Potentials in 10% Caustic Soda Solutions at 550°F

J. R. Cels\*

The Babcock & Wilcox Company, Alliance Research Center, Alliance, Ohio 44601

## ABSTRACT

Potentiodynamic polarization curves were obtained in deaerated 10% NaOH solution at 550°F for nickel, Inconel 600,<sup>1</sup> Incoloy 800,<sup>1</sup> and Type 304 stainless steel. The curves for the first three materials exhibited narrow current density peaks at the same value of potential, indicating that these peaks were caused by nickel corrosion or by the oxidation of a lower oxide of nickel. Multiple stress corrosion cracking tests were performed on spring-loaded bent-beam specimens in deaerated 10% sodium hydroxide solution at 550°F at controlled potentials and at open-circuit conditions. A well-defined critical potential range was observed for the stress corrosion cracking of Inconel 600 specimens. Cracking of Incoloy 800 specimens at controlled potentials was difficult to reproduce. However, cracking could be reproduced under open-circuit conditions with a nitrogen cover gas.

Type 304 stainless steel was originally selected for the fabrication of heat-exchanger tubing for pressurized water reactors in order to reduce corrosion to a minimum. However, stress corrosion cracks can be formed in this alloy as a result of accidental entry of chlorides into the boiler water. Accordingly, it has now been generally replaced by the nickel alloys, Incoloy 800 and Inconel 600, which are very resistant to chloride attack. They are, nevertheless, susceptible to stress corrosion cracking in solutions of strong alkalis

The heat flux through the steam generator tube can provide a concentrating mechanism for impurities in the boiler water. In regions where the water circulation is restricted, and particularly under conditions of high heat transfer, a steam blanket can form at the tube surface. The thermal insulating effects of the steam then permit the surface to be superheated with respect to the boiler water. This superheat allows impurities to be concentrated by factors which have been estimated to exceed 10<sup>4</sup> so that a few parts per million of free NaOH can build up locally to several weight per cent. This is particularly likely to occur in the hot leg of the U-tube steam generator where the temperature differential between the primary and secondary coolants is greatest (1).

Several investigations of the stress corrosion behavior of stainless steels and nickel alloys in caustic soda solutions at high temperatures have been reported (2-4) but without control of the specimen potential. However, Mazille and Uhlig (5) and Parkins (6) have pointed out the importance of specimen potential on both the occurrence and the rate of caustic stress corrosion cracking. The purpose of this paper is to demonstrate the importance of electrical potential on the stress corrosion cracking behavior of Type 304 stainless steel and the nickel alloys, Inconel 600

and Incoloy 800, in deaerated 10% by weight NaOH solution at 550°F. An attempt is also made to determine the specimen potentials for maximum rates of cracking for each material. The results reported here are a representative selection taken from a larger study made on four heats of Inconel 600, two heats of Incoloy 800, and two heats of Type 304 stainless steel.

## Experimental Procedures

**Materials.**—The chemical compositions supplied by the manufacturers for the commercial alloys used in this study are presented in Table I. Caustic soda solutions were made up to a concentration of 10% by weight using reagent grade NaOH and distilled deionized water.

**Specimens.**—Cylindrical specimens, 0.250 in. diameter × 0.600 in. long with an internal threaded hole, were used for polarization experiments. For stress corrosion cracking experiments, strip specimens were machined to the dimensions 1¾ in. long × 3/16 in. wide × 0.040 in. thick. Both sides of the strips were ground in the long direction in order to adjust the final thickness to a value of 0.040 in.

**Polarization experiments.**—Potentiodynamic polarization experiments were performed in deaerated 10% NaOH solutions in autoclaves at 550°F using standard electrical equipment. The potential scanning rate used was 2 V/hr. The cylindrical test specimens were mechanically polished through 600 grit SiC metallographic paper. They were then mounted on threaded stainless steel rods which passed out of the autoclave head through Conax pressure fittings as shown in Fig. 1. The stainless steel rods were coated with shrinkable Teflon tubing for electrical insulation and were surrounded by ¼ in. diameter stainless steel sleeves. The sleeves were compressed against Teflon gaskets at both ends in order to seal out the test electrolyte from the stainless steel center rods. A set of six equally spaced test specimens encircled a central nickel cyli-

\* Electrochemical Society Active Member.

<sup>1</sup> Registered trademarks of the International Nickel Company.

Key words: potentiostat, autoclave, intergranular.

Table I. Chemical composition of the test alloys

Alloy	C	Mn	S	P	Si	Cr	Ni	Fe	Cu	Other
Inconel 600	0.04	0.38	0.006	0.007	0.11	15.71	74.42	8.60	0.03	Al 0.28, Ti 0.24, Co 0.049
Incoloy 800	0.06	0.81	0.007	—	0.30	20.36	32.45	44.95	0.27	Al 0.39, Ti 0.38
Type 304 SS	0.07	1.09	0.008	0.03	0.52	18.55	9.45	bal.	0.44	—

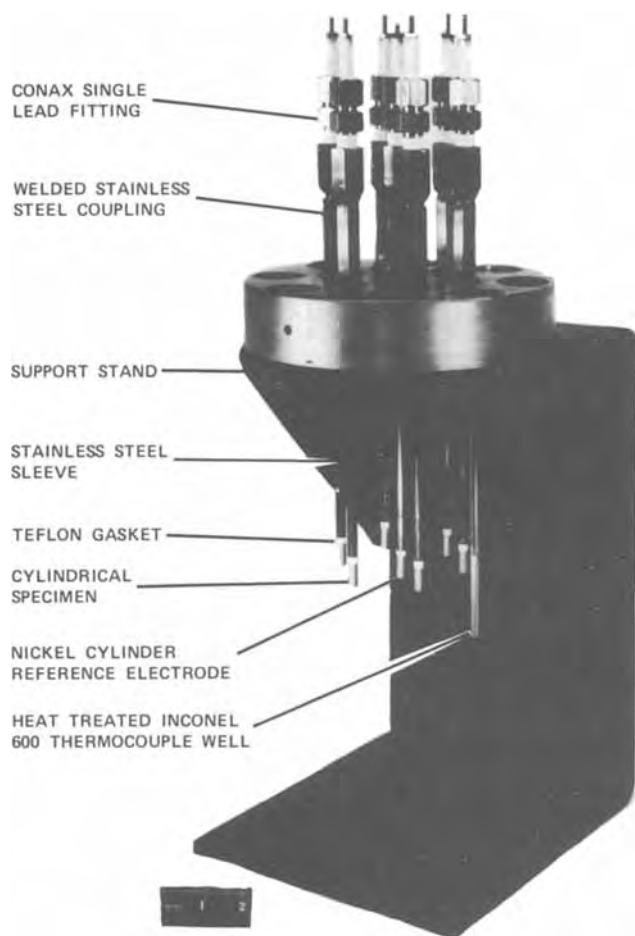


Fig. 1. Head of 1 gal autoclave for anodic polarization experiments.

inder specimen which was used as a hydrogen reference electrode. Some experiments were also conducted in a 1 liter stress-relieved Inconel 600 autoclave using a platinized platinum wire as the reference electrode.

The deaerated 10% NaOH test solution was contained in a nickel liner inside a 1 gal Type 316 autoclave. Water occupied the space between the liner and the autoclave and served as a heat transfer medium. A cover gas of 5% hydrogen in nitrogen at an overpressure of 200 psi at room temperature was used for experiments in this autoclave. A similar procedure was followed with the 1 liter autoclave using cover gases of either purified nitrogen or 5% hydrogen in nitrogen.

**Stress corrosion cracking experiments.**—The surface of the strip specimens was hand abraded through 600 grit SiC metallographic paper. A length of Teflon-coated 0.025 in. diameter Inconel 600 wire was spot welded to one end of the specimen to provide an electrical connection. The specimen was cleaned ultrasonically in 1% Alconox solution, rinsed with distilled water, and dried with Kimwipe tissue. It was then positioned in a special vise and bent to a radius of 1 in. The ends of the bent specimens were gripped between the Inconel 600 washers in the spring-loaded bending fixture shown in Fig. 2, and the Inconel spring was compressed until the specimen could be removed from the fixture without springback. At this point, the span of the bent specimen was 1-9/16 in. The Inconel spring was then further compressed to reduce the span to a final value of 1-7/16 in. as described by Uhlig and White (7).

The stressing fixtures with mounted bent-beam specimens were attached to support brackets bolted to Inconel vanes as shown in Fig. 3. The brackets were

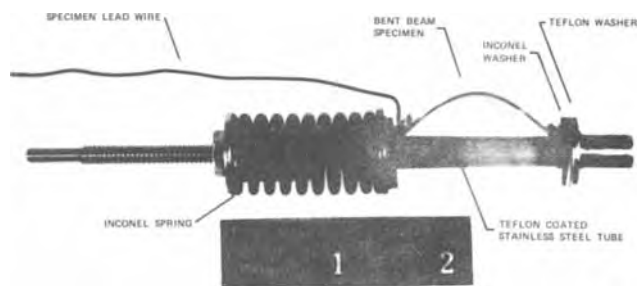


Fig. 2. Stressing fixture with mounted bent-beam specimen

electrically insulated from the Inconel vanes by Teflon sleeves and washers. Individual hydrogen reference electrodes fabricated from 0.040 in. diameter nickel wires were used for each stressed specimen. Each wire was coated with shrinkable Teflon tubing except for a 1 in. length at the end which was positioned close to the apex of a stressed bent-beam specimen. The wires passed out of the autoclave through a Conax six-lead pressure fitting mounted on an air-cooled stainless steel column.

The deaerated 10% NaOH test solution was contained in a nickel liner in the same manner as for the anodic polarization experiments. Its volume was selected so that the solution level at the operating temperature was just below the spot weld on the lead wire. Specimen potentials were independently controlled by individual potentiostats using the autoclave as a common counterelectrode. This necessitated the use of isolation transformers between the potentiostats and the grounded a-c supply. The specimen potentials were either controlled at fixed values with respect to the nickel reference electrodes, or were increased at a slow constant rate over a selected potential range. Both techniques were used simultaneously in some experiments.

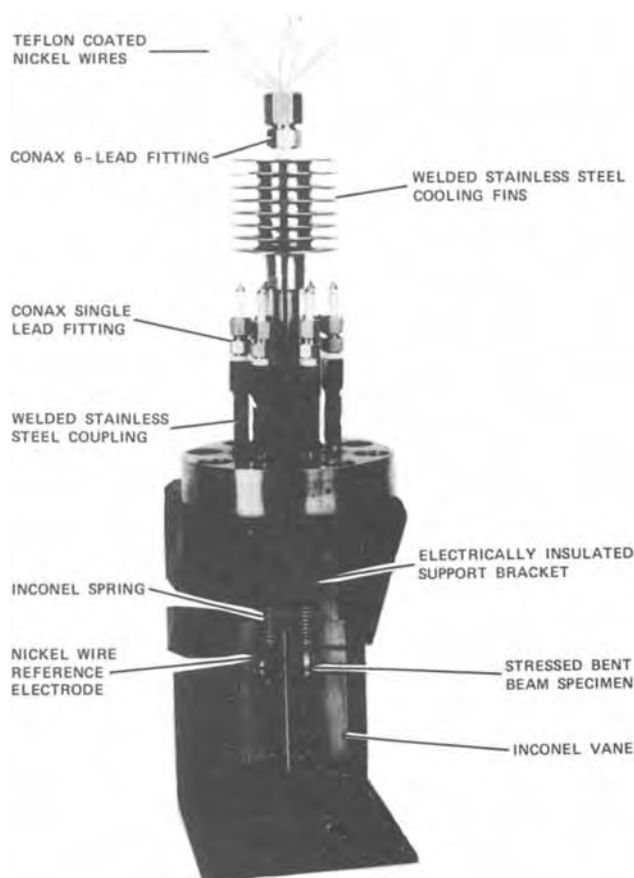


Fig. 3. Head of 1 gal autoclave for stress corrosion experiments



After each stress corrosion cracking experiment, the strip specimen was removed from the stressing fixture, bent slightly, and examined under a metallurgical microscope for the presence of cracks. Polaroid photomicrographs were taken of the surface of all specimens not cracked completely through in order to compare the extent of cracking among the different specimens of a set. Polished and etched metallographic cross sections were also prepared from some specimens to check the mode of cracking.

### Results

**Anodic polarization curves.**—Potentiodynamic polarization curves obtained on cylindrical specimens of nickel, Inconel 600, Incoloy 800, and Type 304 stainless steel in 10% deaerated NaOH solutions at 550°F are presented in Fig. 4. A central nickel cylinder was used as a reference for each curve, and the cover gas was a mixture of 5% hydrogen in nitrogen at an initial overpressure of 200 psi at room temperature. Figure 4 reveals that the potentials of the specimens are all equal to that of the nickel reference electrode at low values of applied current. While the anodic current peak of Type 304 stainless steel is relatively broad, those of nickel, Inconel 600, and Incoloy 800 are very narrow with the current density maximum falling at a potential close to +140 mV in each case. Measurements were repeated on successive days with only a slight change in the potentials of these narrow current density peaks. However, this was not the case for experiments performed using a cover gas of purified nitrogen instead of 5% hydrogen in nitrogen. The results of such measurements made on a cylindrical Inconel 600 specimen in deaerated 10% NaOH solution at 550°F are presented in Table II. These measurements were made in a 1 liter autoclave using a platinized platinum wire as the reference electrode. The open-circuit corrosion potential of the Inconel 600 specimen was equal to that of the platinum wire with a cover gas of 5% H<sub>2</sub> and was about -2 mV in the case of a nitrogen cover gas. With a cover gas of 5% H<sub>2</sub> in N<sub>2</sub>, the potential of the current density peak was +144 mV after 22 hr at temperature and it increased to +148 mV in successive runs. However, with a nitrogen cover gas the initial potential of the current density peak was +67 mV and this value increased progressively on successive runs and attained a value of +127 mV after 140 hr at temperature.

**Specimen corrosion potentials vs. time.**—The results of a series of measurements of the open-circuit cor-

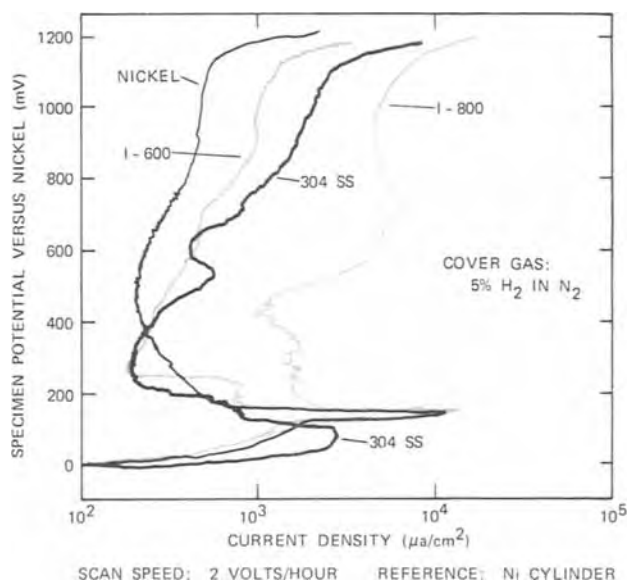


Fig. 4. Anodic polarization curves in deaerated 10% NaOH solution at 550°F.

rosion potentials of unstressed specimens in deaerated 10% NaOH solution at 550°F with a cover gas of 5% H<sub>2</sub> in N<sub>2</sub> are presented in Table III. It can be seen that the potentials of the cylinders of Inconel 600 and of nickel were identical to that of the platinized platinum reference cylinder throughout the test. The nickel wire, which was used as a reference for the stress corrosion cracking experiments, maintained a potential of about -4 mV whereas that of the autoclave itself was about +3 mV.

**Stress corrosion cracking at controlled potential.**—Stress corrosion cracking results on spring-loaded bent-beam specimens of Inconel 600 in the mill-annealed and heat-treated condition are presented in Table IV. The relative extent of cracking is indicated qualitatively in the last column of the table.

The mill-annealed specimen maintained at a potential of +200 mV cracked completely through in a 72 hr period. The extent of the cracking decreased progressively at lower values of specimen potential and no cracking was observed in the specimen which was allowed to stand under open-circuit conditions. A slow

Table II. Time dependence of the potential of the current density peak in the anodic polarization curves of an Inconel 600 specimen\*

Time (hr)	Potential of current density peak (mV vs. Pt)	
	Cover gas 5% H <sub>2</sub> in N <sub>2</sub>	Cover gas N <sub>2</sub>
1	—	+67
22	+144	+78
44	—	+92
68	—	+108
118	+148	—
140	—	+127
214	+148	—

\* Solution: deaerated 10% NaOH, temperature: 550°F.

Table III. Time dependence of specimen corrosion potentials\*

Time at 550°F (hr)	Corrosion potential vs. platinum (mV)			
	I-600 cyl	Ni cyl	Ni wire	Autoclave
0**	0	0	-4	+4
2	0	0	-4	+4
19	0	0	-4	+3
43	0	0	-4	+2
67	0	0	-6	+3
91	0	0	-5	+2
115	0	0	-4	+3
139	0	0	-4	+3
163	0	0	-4	+3
187	0	0	-4	+3
235	0	0	-4	+3

\* Solution deaerated 10% NaOH, temperature: 550°F, cover gas: 5% H<sub>2</sub> in N<sub>2</sub>.

\*\*5½ hr after switching power to autoclave heater.

Table IV. SCC results on specimens of mill-annealed and heat-treated Inconel 600\*

Metallographic conditions	Specimen potential (mV)	Time (hr) or scan rate	Results
Mill annealed	+125	72	Numerous fine cracks
	+150	72	Few small cracks
	+175	72	Numerous large cracks
	+200	72	Specimen cracked through
18 hr at 1150°F	+185 to +233 Open circuit	1 mV/hr	Numerous large cracks
		72	No cracking
	+175 to +250	175	Numerous fine cracks
		175	Numerous small cracks
		175	Few fine cracks
		175	General corrosion
	+150 to +200 to +250	1 mV/hr	Numerous fine cracks
		1 mV/hr	General corrosion

\* Solution: deaerated 10% NaOH, temperature: 550°F, cover gas: 5% H<sub>2</sub> in N<sub>2</sub>.

potential scan at the rate of 1 mV/hr over the potential range +185 to +233 mV was also employed. This specimen was part of the same set as the others and exhibited numerous large cracks.

A similar experiment was conducted with the heat-treated Inconel 600 specimens but the test duration was extended to 175 hr. It is apparent that the extent of cracking was very much reduced compared with the first set in spite of the longer test period. The potential for maximum rate of cracking was in the neighborhood of +200 mV. The results of the potential scan tests showed numerous fine cracks over the potential range +150 to +200 mV and general corrosion with no cracking over the range +200 to +250 mV.

The caustic stress corrosion cracking results for Inconel 600 were quite reproducible. The mode of cracking for this material was intergranular for all specimens examined.

Similar experiments with specimens of Incoloy 800 and Type 304 stainless steel are presented in Table V. The first set represents some early measurements made in the 1 gal autoclave before it was subdivided so that the constant potential tests had to be run in sequence rather than simultaneously. No cracking was observed after a period of 355 hr at open circuit or after 96 hr at a potential of +20 mV. Some small cracks were present in the specimen held at +40 mV but the specimen held at +60 mV was cracked three-quarters of the way through.

The second set of experiments with Incoloy 800 specimens was run simultaneously. A wider range of fixed potentials was selected as well as slow voltage scans over two ranges of potential. According to these results, the potential for maximum cracking was now in the vicinity of +80 mV but the extent of cracking was much less than in the first set. More extensive cracking was observed in the slow voltage scan experiments. Experiments with the heat-treated alloy were conducted under open-circuit conditions with a nitrogen cover gas where the cracking of Incoloy 800 was more reproducible (Table VI).

In the last experiment in Table V, spring-loaded specimens of Type 304 stainless steel were tested for a 72 hr period. One specimen was allowed to stand at open circuit and the other was maintained at a potential of +80 mV. The one at open circuit cracked completely through whereas only a few small cracks were observed in the other at a potential of +80 mV. These results show that the potential for the maximum rate of crack growth lies in the neighborhood of the open-circuit potential for this material.

Photomicrographs were prepared from a number of specimens which cracked in deaerated 10% NaOH solution at 550°F. The crack mode was transgranular for both Incoloy 800 and Type 304 stainless steel.

Table V. SCC results on specimens of mill-annealed Incoloy 800 and Type 304 stainless steel\*

Material	Specimen potential (mV)	Time (hr) or scan rate	Results
Incoloy 800	+20	96	No cracking
	+40	96	Few small cracks
	+60	96	Crack ¾ way through
Open circuit		355	No cracking
		355	No cracking
Incoloy 800	+40	72	No cracking
	+60	72	Few very small cracks
	+80	72	Numerous small cracks
	+100	72	Few very small cracks
	+40 to +80	1 mV/hr	Relatively large, deep cracks
	+50 to +71	0.5 mV/hr	Relatively large, deep cracks
Type 304 SS	Open circuit	72	Specimen cracked through
	+80	72	Few small cracks

\* Solution: deaerated 10% NaOH, temperature: 550°F, cover gas: 5% H<sub>2</sub> in N<sub>2</sub>.

*Stress corrosion cracking at open circuit.*—The results of stress corrosion cracking experiments on spring-loaded bent-beam specimens in deaerated 10% NaOH solution at 550°F with a cover gas of purified nitrogen are presented in Table VI. Inconel 600, Incoloy 800, and Type 304 stainless steel were compared before and after a heat-treatment for 18 hr at 1150°F. No cracking was observed with the Inconel 600 specimens in either the mill-annealed or the heat-treated condition. On the other hand, cracks formed in the Incoloy 800 specimens in both the mill-annealed and the heat-treated condition. Cracking was somewhat less severe in heat-treated alloy. The specimen of mill-annealed Type 304 stainless steel showed no cracking, but numerous small cracks were present in the heat-treated alloy.

## Discussion

*Reference electrodes.*—The electrical potential of a test specimen is of crucial importance to properly define the conditions of metal corrosion. Unfortunately, a reliable reference electrode for temperatures as high as 550°F is not yet available. The narrow current density peaks observed in the anodic polarization curve of Inconel 600 in deaerated 10% NaOH solution at 550°F are sufficiently sharp and reproducible to be used as a potential reference. They are associated with the nickel component of the alloy and represent either nickel corrosion or the oxidation of nickel corrosion products. It follows that they should not be dependent on the hydrogen partial pressure within the autoclave.

We can now interpret the results presented in Table II in terms of this potential reference. For the experiment with a cover gas of 5% H<sub>2</sub> in N<sub>2</sub>, the potential of the hydrogen electrode was -144 mV after 22 hr at temperature. It was -148 mV after 118 hr and remained unchanged after 214 hr. In the experiment starting with a cover gas of purified nitrogen, the potential of the hydrogen electrode was initially -67 mV. Its potential drifted relatively rapidly in the negative direction and attained a value of -127 mV after 140 hr at temperature. This potential decrease was undoubtedly caused by the slow accumulation of hydrogen in the autoclave due to metal corrosion. These results show that the hydrogen electrode maintained an almost constant potential for experiments in deaerated 10% NaOH solution at 550°F starting with a partial pressure of hydrogen. From the results in Table III, the hydrogen electrode can be fabricated from platinized platinum, Inconel 600, or nickel with identical results. For this reason, a nickel reference electrode was used instead of platinum for most of the experiments described in this paper.

*Stressing procedure.*—To accelerate the rate of stress corrosion cracking, we have adopted the severe stressing procedure developed by Uhlig and White. This allows measurements to be made on specimens of convenient size which are maintained at levels of stress beyond the yield point. It is also a straightforward matter to control the electrical potentials of these stressed specimens.

Table VI. SCC results on specimens of mill-annealed and heat-treated Inconel 600, Incoloy 800, and Type 304 stainless steel\*

Material	Metallurgical condition	Time (hr)	Results
Inconel 600	Mill annealed	123	No cracking
	1150°F/18 hr	120	No cracking
Incoloy 800	Mill annealed	123	Numerous large cracks
	1150°F/18 hr	120	Numerous small cracks
Type 304 SS	Mill annealed	123	No cracking
	1150°F/18 hr	123	Numerous small cracks

\* Solution: deaerated 10% NaOH, temperature: 550°F, cover gas: N<sub>2</sub>.

**Rate of stress corrosion cracking.**—Accurate measurements of the rates of cracking require the techniques of fracture mechanics. However, an estimate of cracking rates can be made by comparing the extent of cracking in different specimens under identical test conditions except for electrical potential. Crack initiation times are presumed to be of short duration for highly stressed specimens in an aggressive medium such as 10% NaOH solution at a temperature of 550°F.

**Effect of potential on rate of cracking.**—From the results presented in Table IV, specimens of Inconel 600 crack most rapidly at a potential around +200 mV in deaerated 10% NaOH solution at 550°F with a cover gas of 5% H<sub>2</sub> in N<sub>2</sub>. General corrosion tends to predominate over stress corrosion cracking at higher values of specimen potential. On the other hand, it can be seen from the results in Table V that mill-annealed Type 304 stainless steel specimens cracked much more rapidly at open circuit than at a potential of +80 mV. The dependence of the cracking rate of Incoloy 800 specimens on electrical potential is not clear because of the difficulty of reproducing caustic cracking of this material. However, Incoloy 800 specimens do crack reproducibly in deaerated 10% NaOH solution at 550°F with a cover gas of purified nitrogen. With this cover gas, the specimen open-circuit corrosion potential is only about 36-77 mV more positive than that in an autoclave with a cover gas of 5% H<sub>2</sub> and N<sub>2</sub> where no cracking was observed after a test period of 355 hr.

According to Staehle (8), stress corrosion cracking may take place at values of specimen potential corresponding to the potentials for passive film instability at the upper and lower boundaries of the region of passivity in the anodic polarization curve. It is difficult to see how concepts relating to passive film instability could be applied to an alloy where each constituent would have a different anodic polarization curve. The caustic cracking behavior of Inconel 600 and Incoloy 800 is quite different in spite of the similarity of the anodic polarization curves of these two alloys at potentials up to the current density peak at about +145 mV.

**Effect of heat-treatment on rate of SCC.**—The results presented in Table IV show that the rate of caustic stress corrosion cracking of Inconel 600 was greatly reduced after a heat-treatment for 18 hr at 1150°F. At a potential of +200 mV, which is close to the value for the maximum rate of cracking, the mill-annealed specimen cracked completely through in a period of 72 hr whereas the heat-treated specimen exhibited only numerous small cracks after the longer test period of 175 hr. A smaller effect was also shown for specimens of Incoloy 800 tested in deaerated 10%

NaOH solution at 550°F under open-circuit conditions for a period of about 120 hr as shown in Table VI. Wilson and Aspden (9) also observed a marked increase in the resistance of Inconel 600 to stress corrosion cracking in deoxygenated 10% NaOH solution at 630°F after a sensitizing heat-treatment. A similar result was reported by Blanchet *et al.* (10) for the stress corrosion cracking of Inconel 600 in deoxygenated pure water at 350°C (662°F).

### Acknowledgments

The author thanks Mr. J. V. Monter for technical assistance, the Metallurgical Laboratory for specimen examination, and The Babcock & Wilcox Company for permission to publish these results.

Manuscript submitted Oct. 27, 1975; revised manuscript received April 19, 1976. This was Paper 68 presented at the Dallas, Texas, Meeting of the Society, Oct. 5-9, 1975.

Any discussion of this paper will appear in a Discussion Section to be published in the June 1977 JOURNAL. All discussions for the June 1977 Discussion Section should be submitted by Feb. 1, 1977.

Publication costs of this article were assisted by The Babcock & Wilcox Company.

### REFERENCES

1. J. R. Weeks, in "Corrosion Problems in Energy Conversion and Generation," C. S. Tedmon, Editor, The Electrochemical Society Softbound Symposium Series, Princeton (1974).
2. I. L. W. Wilson, F. W. Pement, and R. G. Aspden, *Corrosion*, **30**, 139 (1974).
3. I. L. W. Wilson and R. G. Aspden, Paper presented at the Corrosion Research Conference, NACE Corrosion/75, Ontario, Canada, April 1975.
4. P. P. Snowdon, *J. Iron Steel Inst.*, **194**, 181 (1960).
5. H. Mazille and H. H. Uhlig, *Corrosion*, **28**, 427 (1972).
6. R. N. Parkins, in "The Theory of Stress Corrosion Cracking in Alloys," J. Scully, Editor, pp. 449-468, NATO, Brussels (1971).
7. H. H. Uhlig and R. A. White, *Trans. Am. Soc. Metals*, **52**, 830 (1960).
8. R. W. Staehle, in "The Theory of Stress Corrosion Cracking in Alloys," J. Scully, Editor, pp. 223-288, NATO, Brussels (1971).
9. I. L. W. Wilson and R. G. Aspden, Paper presented at The International Conference on Stress Corrosion Cracking and Hydrogen Embrittlement of Iron Base Alloys, Unieuz-Firminy, France, June 12-16, 1973.
10. J. Blanchet, H. Coriou, L. Grall, C. Mahieu, C. Otter, and G. Turluer, Paper presented at the International Conference on Stress Corrosion Cracking and Hydrogen Embrittlement of Iron Base Alloys, Unieuz-Firminy, France, June 12-16, 1973.

# Relationship Between the Electrochemical and Corrosion Behavior and the Structure of Stainless Steels Subjected to Cold Plastic Deformation

B. Mazza,\* P. Pedefferri, D. Sinigaglia, A. Cigada, L. Lazzari, G. Re, and D. Wenger<sup>1</sup>

Centro di Studio del C.N.R. sui Processi Elettrodici, Politecnico di Milano, 20133 Milano, Italy

## ABSTRACT

The present investigation forms part of a systematic study about the influence of cold plastic deformation on the electrochemical and corrosion behavior of metallic materials, with the aim of determining and elucidating such aspects of their behavior and correlating them with the microstructural effects of the deformation, these being analyzed by metallographic and x-ray techniques and by transmission electron microscopy. In this respect, the influence of cold plastic deformation on the electrochemical and corrosion behavior of two stainless steels (AISI 304 L and 316 L) in different aggressive media (with and without chloride ions) has been studied with reference to the following points: (i) deformation type, *i.e.*, tensile stress, cold drawing, or cold rolling, and conditions, *i.e.*, at room temperature and at  $-196^{\circ}\text{C}$ ; (ii) relative orientation of the exposed surface with the deformation direction, *i.e.*, parallel and perpendicular; (iii) texture, defects, and martensite transformation.

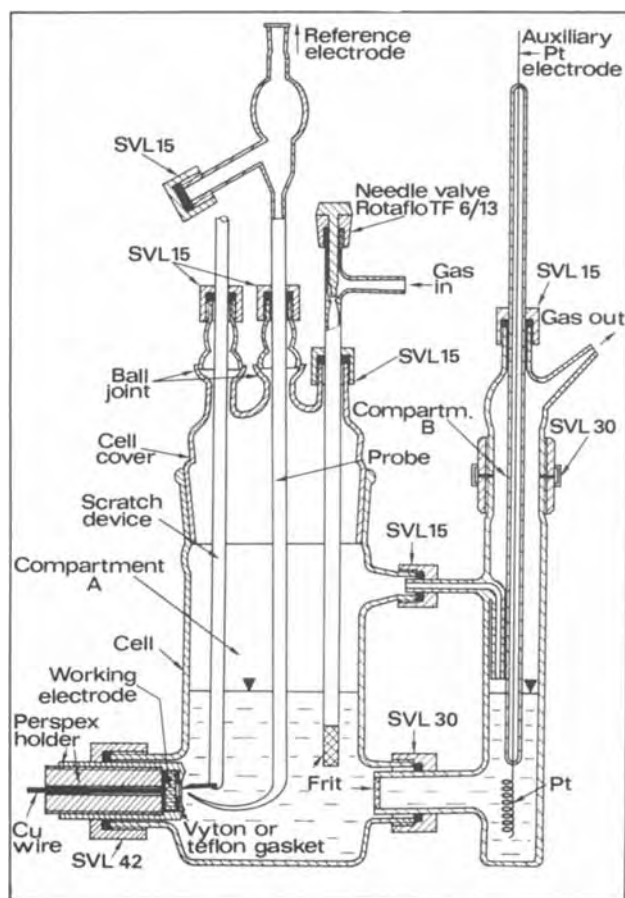


Fig. 1. Test cell (cross section)

The study of the influence of cold plastic deformation on the electrochemical and corrosion behavior of austenitic stainless steels was carried out in our Institute mainly because of the need for a systematic collection of data as a basis for a more reliable utilization

\* Electrochemical Society Active Member.

<sup>1</sup> Present address: Centro Informazioni Studi Esperienze (CISE), Milano, Italy.

Key words: corrosion, austenitic stainless steels, cold plastic deformation, martensite transformation, passivity, pitting, surgical plants.

of these materials which are often used in the work-hardened state. The correlation between the electrochemical behavior and the structural effects produced by cold plastic deformation, *i.e.*, texture, surface

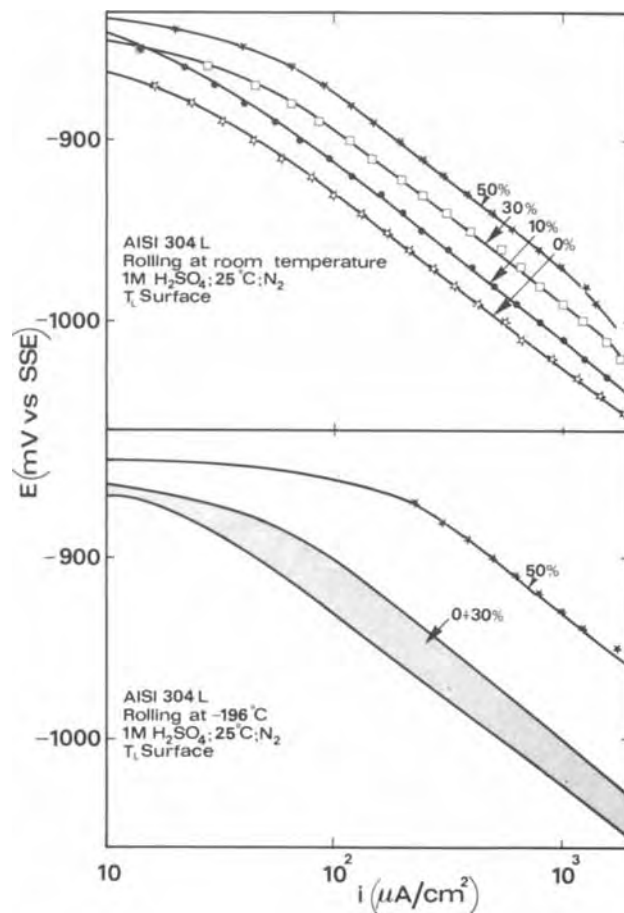


Fig. 2. Cathodic polarization curves for hydrogen evolution on AISI 304 L steel in deaerated  $1\text{M H}_2\text{SO}_4$  solution at  $25^{\circ}\text{C}$  for different values of the deformation degree (indicated as a percentage). Deformation by rolling at both room and liquid  $\text{N}_2$  temperature; long transversal ( $T_L$ ) section. Potential values are relative to a standard mercury sulfate electrode (SSE).

Table I. Chemical composition and some structure characteristics of the studied stainless steels (in the as-received state, i.e., after solution heat-treatment)

Austenitic stainless steel	Subsequent cold working	Weight percent composition									ASTM micrograin size number	$M_{d50}^a$ ( $^{\circ}\text{C}$ )	$M_s^b$ ( $^{\circ}\text{C}$ )	$\delta$ -ferrite (%)	Dislocation density ( $10^8 \text{ cm/cm}^2$ )
		C	Si	Mn	P	S	Cr	Ni	Mo	N					
AISI 304 L	Tension	0.025	0.45	1.39	0.023	0.021	18.60	8.75	0.50	0.036	6 $\div$ 6.5	+22	< -196	0.1 $\div$ 0.2	1.30 $\pm$ 0.63
	Rolling	0.020	0.41	1.40	0.032	0.013	18.10	10.30	0.32	0.038	4 $\div$ 4.5	+18	< -196	0	0.96 $\pm$ 0.21
AISI 316 L	Tension	0.022	0.43	1.51	0.033	0.023	16.80	10.65	2.90	0.033	5	-14	< -196	0	1.17 $\pm$ 0.65
	Drawing	0.023	0.40	1.45	0.034	0.023	16.60	10.90	3.00	0.037	5.5	-17	< -196	0	1.02 $\pm$ 0.28
	Rolling	0.026	0.41	1.24	0.008	0.011	16.10	10.90	2.20	0.034	4 $\div$ 4.5	+7	< -196	0	1.59 $\pm$ 0.76

<sup>a</sup>  $M_{d50}$  = temperature at which 50% of martensite is formed in tension after a true strain of 0.30 [calculated Ref. (3)].

<sup>b</sup>  $M_s$  = martensite starting temperature.

defectiveness, phase transitions, is undoubtedly important from a basic standpoint as well.

For each material in every state of cold work the main aspects of the electrochemical and corrosion behavior are delineated by the corrosion rates vs. time curves (determined, for example, by the Stern-Geary method), by the polarization curves of anodic dissolution and cathodic hydrogen evolution, and by the passivation and passivity parameters. Each state of cold work is characterized by the type of the deformation process and by the rate, temperature and degree of the deformation itself. The effect of the orientation of the specimen surface under study with respect to the deformation direction must be taken into account as

well. The development lines of our research and the principal results successively obtained are explained below (1).

Regarding the phenomenological aspects of the electrochemical and corrosion behavior in deaerated sulfuric acid solution of the austenitic stainless steels AISI 304 L, 304, and 316 deformed by application of a tensile stress (AISI 304 L steel was deformed also by cold drawing), the following points came to light.

(i) The cold working of the material leads to an increase in the generalized and uniform corrosion rate in the active region. This influence was observed on the surfaces orientated perpendicularly or at  $45^{\circ}$  to the deformation direction, above a critical threshold of the deformation degree of roughly 15% for all the steels studied. The susceptibility to the effect of the

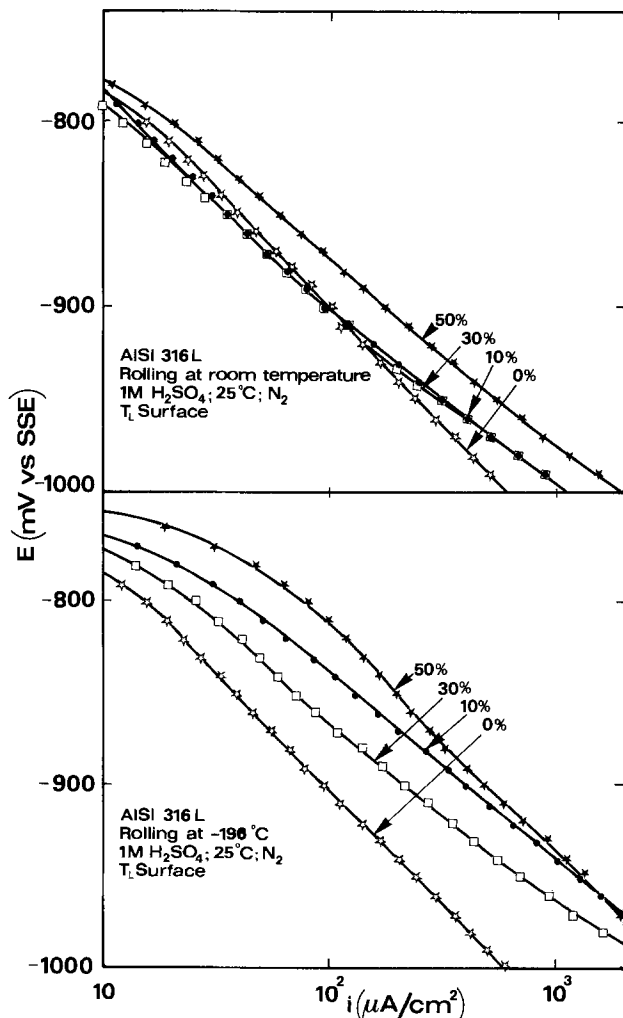


Fig. 3. Cathodic polarization curves for hydrogen evolution on AISI 316 L steel in deaerated 1M  $\text{H}_2\text{SO}_4$  solution at  $25^{\circ}\text{C}$  for different values of the deformation degree (indicated as a percentage). Deformation by rolling at both room and liquid  $\text{N}_2$  temperature; long transversal ( $T_L$ ) section. Potential values are relative to SSE.

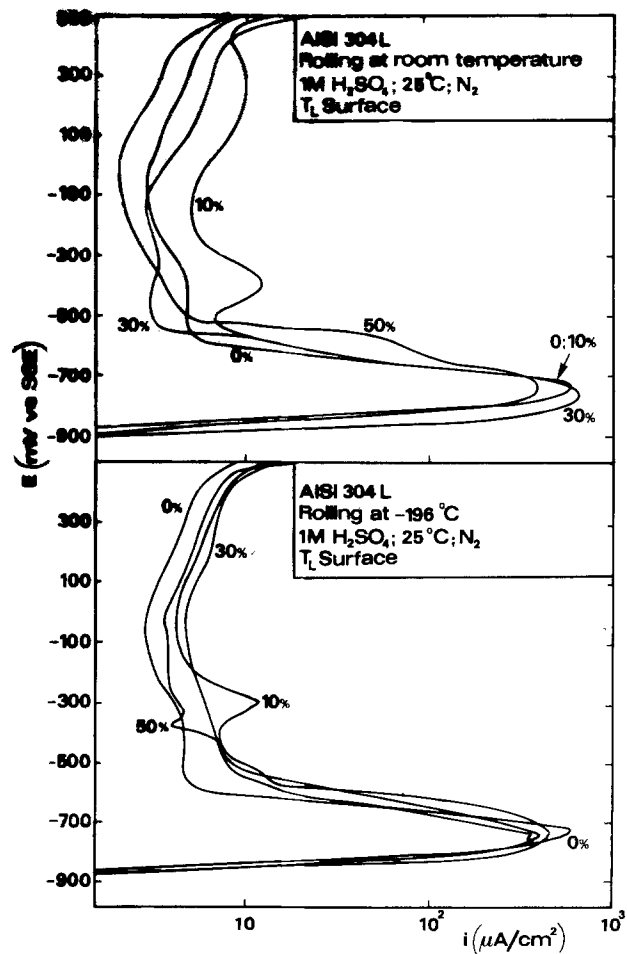


Fig. 4. Potentiodynamic (30 mV/min) anodic polarization curves of AISI 304 L steel in deaerated 1M  $\text{H}_2\text{SO}_4$  solution at  $25^{\circ}\text{C}$  for different values of the deformation degree (indicated as a percentage). Deformation by rolling at both room and liquid  $\text{N}_2$  temperature; long transversal ( $T_L$ ) section. Potential values are relative to SSE.

cold working increases in the sequence AISI 316 < AISI 304 < AISI 304 L.

(ii) A decrease in the overvoltage of the cathodic hydrogen evolution always corresponds to an increase

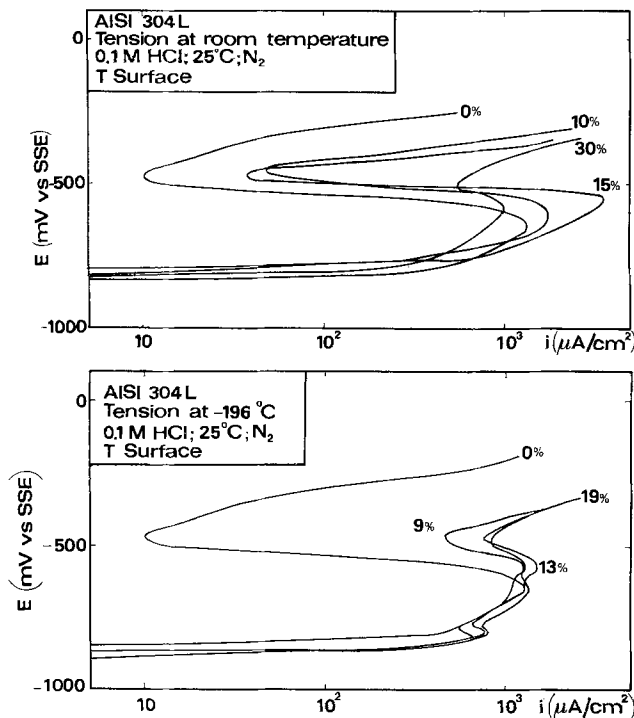


Fig. 5. Potentiodynamic (25 mV/min) anodic polarization curves of AISI 304 L steel in deaerated 0.1M HCl solution at 25°C for different values of the deformation degree (indicated as a percentage). Deformation by tension at both room and liquid N<sub>2</sub> temperature; transversal (T) section. Potential values are relative to SSE.

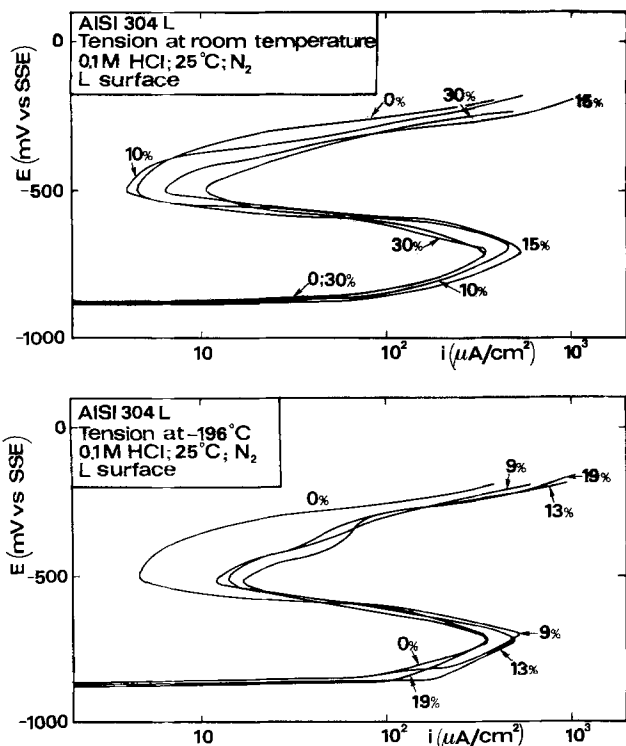


Fig. 6. Potentiodynamic (25 mV/min) anodic polarization curves of AISI 304 L steel in deaerated 0.1M HCl solution at 25°C for different values of the deformation degree (indicated as a percentage). Deformation by tension at both room and liquid N<sub>2</sub> temperature; longitudinal (L) section. Potential values are relative to SSE.

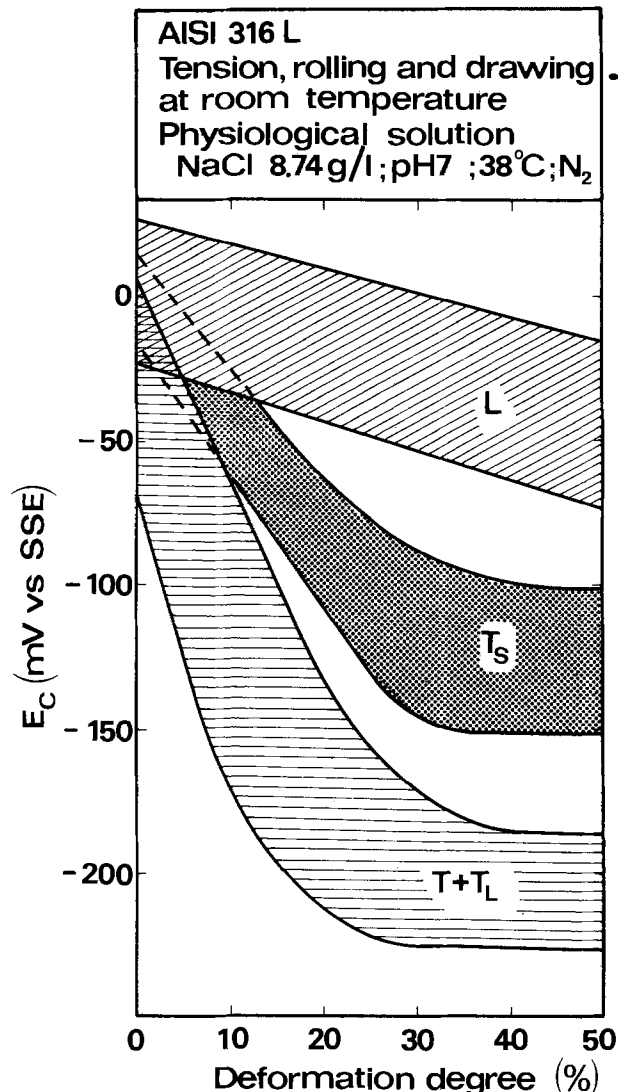


Fig. 7. Critical pitting potential of AISI 316 L steel in the artificial physiological solution of the composition given below, as a function of the deformation degree and the orientation of the exposed surface to the deformation direction, for the different types of cold working (at room temperature). Solution of 8.74 g/liter NaCl, 0.35 g/liter NaHCO<sub>3</sub>, 0.06 g/liter Na<sub>2</sub>HPO<sub>4</sub>, 0.06 g/liter NaH<sub>2</sub>PO<sub>4</sub>, pH 7, in atmosphere of N<sub>2</sub> gas, at 38°C. L, T, T<sub>s</sub>, and T<sub>L</sub> correspond to longitudinal, transversal, short or long transversal sections, respectively. Potential values are relative to SSE.

in the corrosion rate with the deformation degree, whereas the anodic behavior in the active region of the considered materials is not appreciably affected.

(iii) Extending the investigation beyond the active region, a larger work hardening of the material results in an unfavorable effect, which is enhanced by the addition of chlorides, on the formation of the passivating films and sometimes on their protective characteristics as well. The surfaces parallel to the deformation direction generally exhibit a more stable passivity.

Regarding the structural effect of the cold plastic deformation, i.e., texture, surface defectiveness, phase transitions, to which the decreases in the hydrogen overvoltage (and the corresponding increases in the corrosion rate) can be ascribed, the following points may be underlined.

(i) In the case of deformation by application of a tensile stress, the preferred orientation of the crystal grains is negligible. On the other hand, the drawn steel AISI 304 L assumes a certain degree of fibrous texture in the [111] direction. The measurements performed in our Institute on the various faces of single crystals of

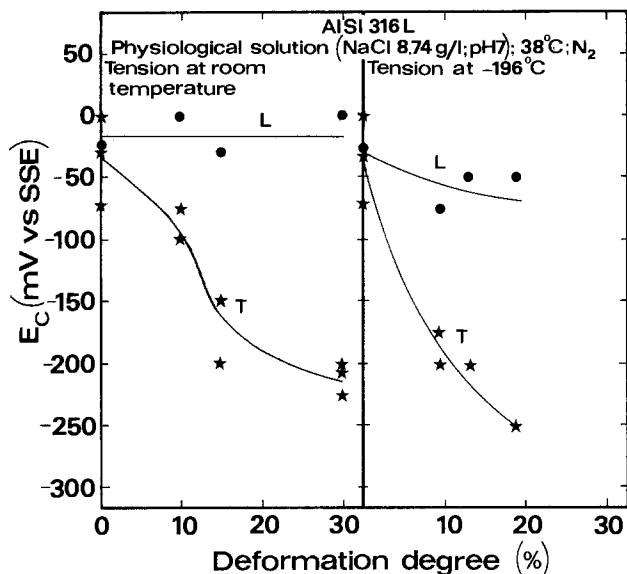


Fig. 8. Critical pitting potential of AISI 316 L steel in the artificial physiological solution of the composition given in Fig. 7 as a function of the deformation degree and the orientation of the exposed surface to the deformation direction. Deformation by tension at both room and liquid N<sub>2</sub> temperature. Potential values are relative to SSE.

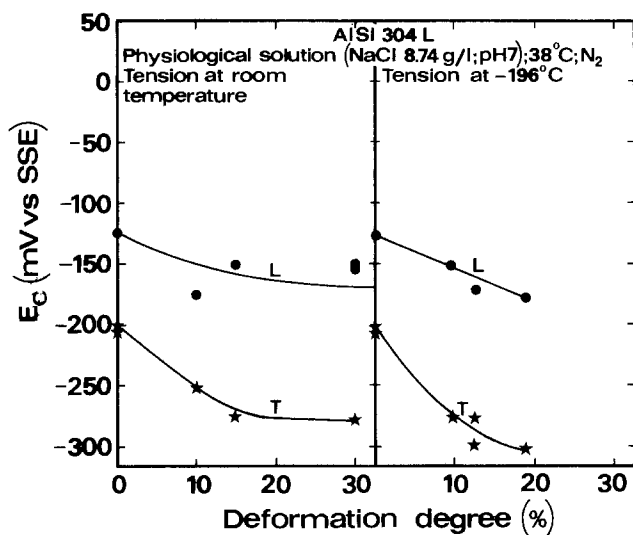


Fig. 9. Critical pitting potential of AISI 304 L steel in the artificial physiological solution of the composition given in Fig. 7 as a function of the deformation degree and the orientation of the exposed surface to the deformation direction. Deformation by tension at both room and liquid N<sub>2</sub> temperature. Potential values are relative to SSE.

austenitic stainless alloy have shown, moreover, that the highest hydrogen overvoltage values correspond exactly to this direction (2).

The cold plastic deformation which, as already seen, causes the hydrogen overvoltage to decrease must therefore act through the other structural effects (that is, through the increase in structural defects emerging on the specimen surface and/or the occurrence of phase transitions).

(ii) The density of the structural defects does not increase progressively with the deformation degree, but shows a steep rise for a deformation value of about 15%. Above this value, the density of the observed deformation bands increases according to the sequence AISI 316 < AISI 304 L < AISI 304. It was found that these bands are also composed of deformation twins, while in the case of the strongly deformed steel 304 L the presence of  $\alpha'$ -martensite generated by the phase

transformation of austenite to martensite as a consequence of the deformation itself was detected.

The inversion noted between the AISI 304 and AISI 304 L in the relationship between the "structure" (density of the deformation bands higher in the AISI 304) and the electrochemical and corrosion behavior (susceptibility to the effect of cold plastic deformation higher for AISI 304 L) must, in our opinion, be ascribed to the presence of  $\alpha'$ -martensite in the AISI 304 L. The research subsequently developed toward isolating the effect exerted on the electrochemical and corrosion behavior of the AISI 304 L and 316 L steels by the phase transformation of austenite to martensite from the one due to the presence of defects.

The choice of these steels was determined not only by their intrinsic structural instability which makes them particularly suitable for the purpose, but also by their importance in technologically advanced fields. In particular, the AISI 316 L is practically unsusceptible to intergranular corrosion and is resistant to pitting; its behavior in the work-hardened state is especially interesting in view of its application as a material for surgical plants in the human body.

### Experimental

In order to separate and compare the effect of both the martensite and that due to the defects, cold plastic deformation of the AISI 304 L and 316 L steels<sup>2</sup> was carried out by either tension, drawing, or rolling at room temperature as well as at liquid nitrogen temperature (-196°C) so as to obtain significant amounts of martensite.

Details of the material working schedule (solution heat-treatment, deformation,<sup>3</sup> cutting, surface preparation), of the microstructural analysis, and of the electrochemical experimental techniques, polarization cell, and electrode assembly have already been described elsewhere (1, 4).

Cathodic polarization curves relative to the hydrogen evolution on the considered steels were recorded

<sup>2</sup> Chemical compositions and some structure characteristics of the considered steels are given in Table I.

<sup>3</sup> Reductions in the cross-sectional area were always adopted to express the deformation degree.

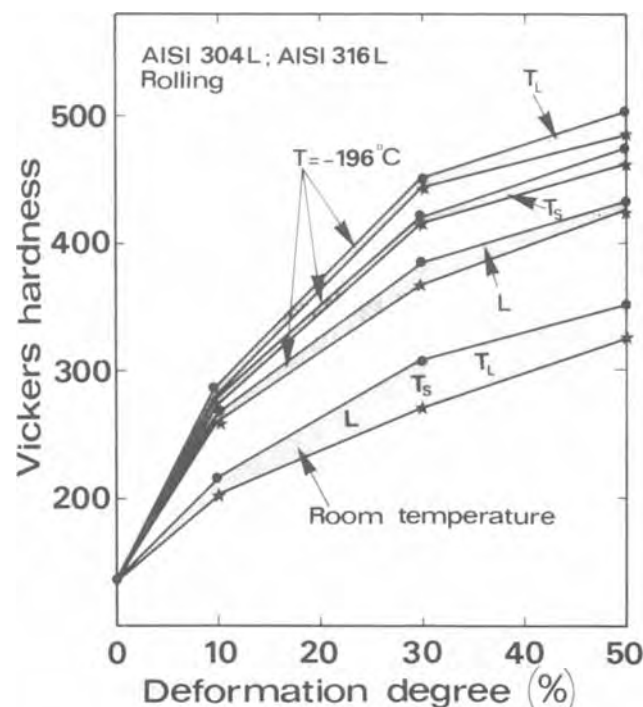


Fig. 10. Vickers hardness of AISI 304 L and 316 L steels as a function of the deformation degree and the orientation of the specimen surface to the deformation direction. Deformation by rolling at both room and liquid N<sub>2</sub> temperature.

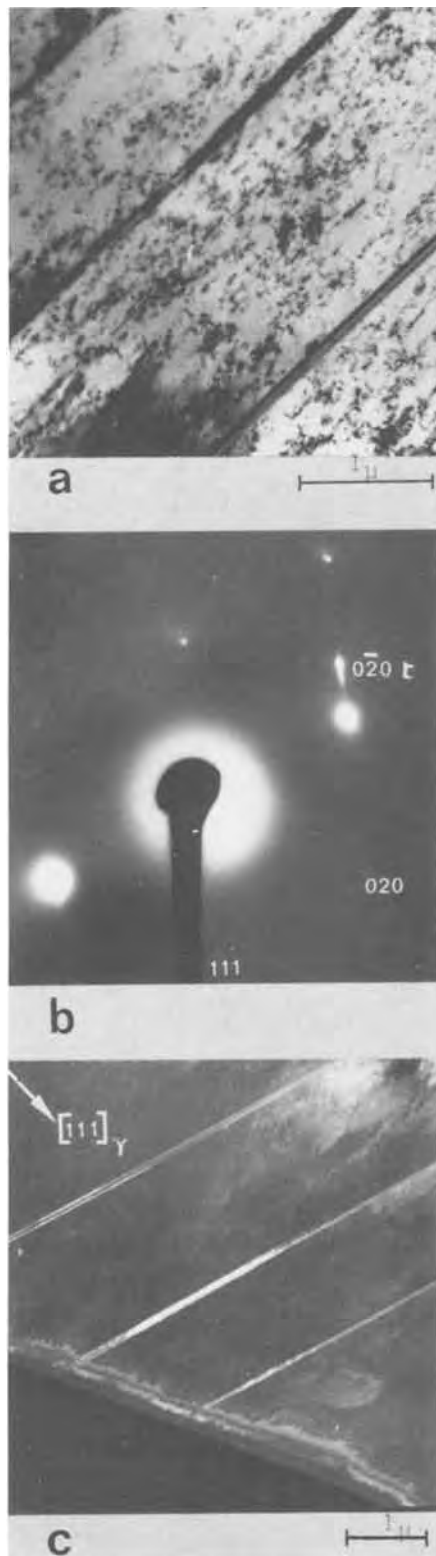


Fig. 11. Deformation twins in AISI 316 L steel deformed 15% by tensile stress at room temperature: (a) bright-field image; (b) electron diffraction pattern,  $[101]_{\gamma}$  zone axis; (c) dark-field image obtained by  $020_{\gamma}$ -twin reflection.

in a 1M  $H_2SO_4$  solution, deaerated and stirred by circulation of  $N_2$  gas, at a temperature of 25°C. Anodic polarization curves were recorded in both a 1M  $H_2SO_4$  and a 0.1M HCl (5) solution in an atmosphere of  $N_2$  gas at 25°C.

Critical pitting potentials of the considered steels<sup>4</sup> were determined in an artificial "physiological" solu-

<sup>4</sup>A passivation pretreatment was carried out by dipping the specimens in 30%  $HNO_3$  solution at 55°C for 30 min.



Fig. 12.  $\epsilon$ -hexagonal martensite bands in AISI 304 L steel deformed 15% by tensile stress at room temperature: (a) bright-field image; (b) electron diffraction pattern,  $[011]_{\gamma}$  and  $[1011]_{\epsilon}$  zone axes; (c) dark-field image obtained by  $1011_{\epsilon}$ -reflection.

tion, simulating the aggressiveness of the human body, of the following composition: 8.74 g/liter NaCl, 0.35 g/liter  $NaHCO_3$ , 0.06 g/liter  $Na_2HPO_4$ , 0.06 g/liter  $NaH_2PO_4$ , pH 7, in atmosphere of  $N_2$  gas, at 38°C (4). These measurements were performed by applying the "scratching" technique introduced by Pessall and Liu (6). The electrode potential was maintained constant with the potentiostat at a selected value below the ex-



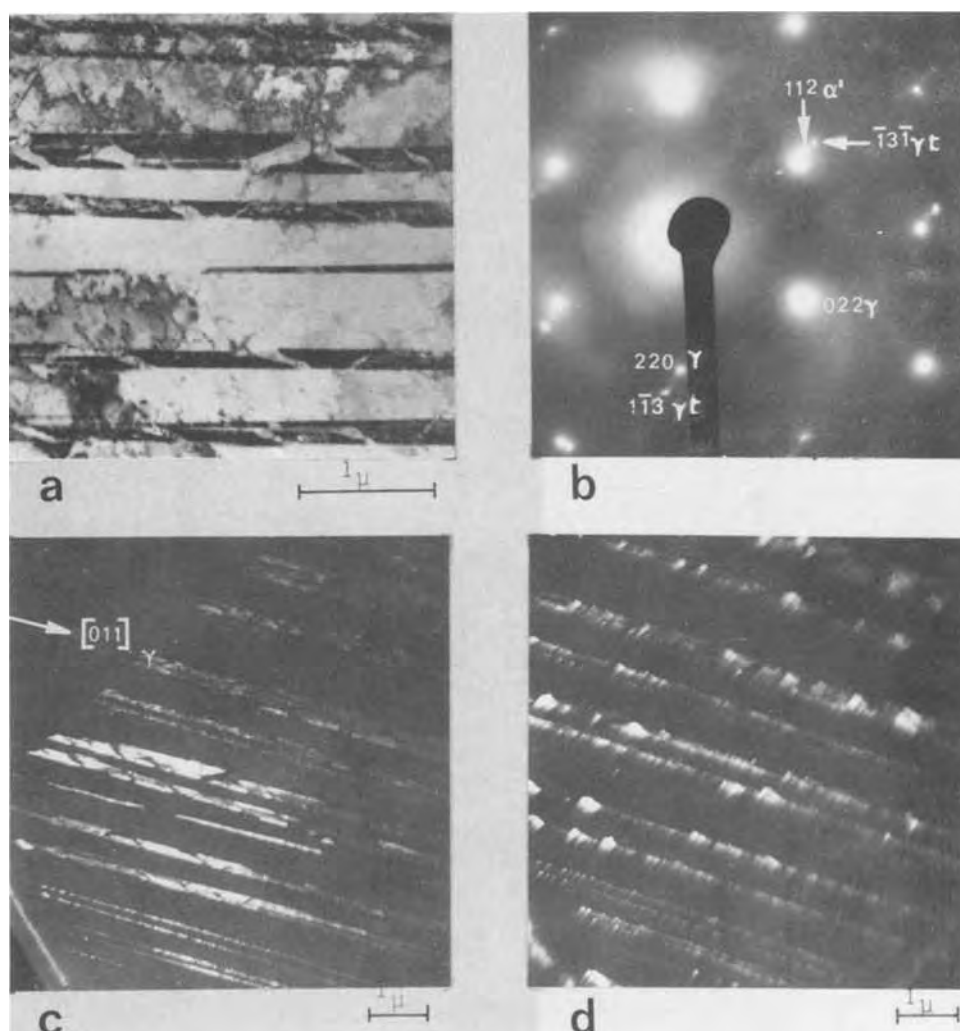


Fig. 13.  $\alpha'$ -cubic martensite plates in deformation twins in AISI 304 L steel deformed 15% by tensile stress at room temperature: (a) bright-field image; (b) electron diffraction pattern,  $[\bar{1}\bar{1}\bar{1}]_{\gamma}$  and  $[4\bar{1}\bar{1}]_{\gamma}$ -twin zone axes; (c) dark-field image obtained by  $\bar{1}\bar{1}\bar{3}$   $\gamma$ -twin reflection; (d) dark-field image obtained by  $112$   $\alpha'$ -reflection.

pected pitting potential and then the specimen surface was scratched with a tungsten point (Fig. 1). The current/time relationship was recorded for a few minutes until the specimen repassivated. This procedure was continued with the electrode potential adjusted by 25 mV steps to more and more noble values, until the scratch failed to repassivate, a failure which was indicated by a gradual current rise in time; the presence of pits developed at the scratched site was verified microscopically. The electrode potentials were always referred to the Hg,  $\text{Hg}_2\text{SO}_4/\text{K}_2\text{SO}_4$  (saturated) electrode (SSE) whose potential relative to the standard hydrogen electrode at 25°C is +642 mV.

### Results and Discussion

Some results of the electrochemical measurements are given in Fig. 2 to 9. The lowering effect on the hydrogen overvoltage produced by increasing the deformation degree is higher when the cold working of the considered steels is carried out at the liquid nitrogen temperature; at room temperature the influence of the cold plastic deformation is much more notable for the AISI 304 L than for the AISI 316 L steel (Fig. 2 and 3).

On the anodic side, the change from sulfuric acid (Fig. 4) to hydrochloric acid (Fig. 5 and 6) solution magnifies the unfavorable effects of the degree of work hardening on the occurrence of the passivation phenomena and on the protective characteristics of the passivating films to an extent which depends on the orientation of the specimen surface with respect to the deformation direction and on the temperature at which the cold plastic deformation is carried out.

All the types of cold plastic deformation—by either tension, drawing, or rolling—cause the critical pitting potential of the considered steels to diminish as shown in Fig. 7-9. Again, a considerable anisotropy of this property was observed; for example, for the rolling the critical pitting potential decreases, the degree of work hardening remaining unchanged, from the longitudinal (L) section to the short transversal ( $T_s$ ) one and from the latter to the long transversal ( $T_L$ ) section. An influence of the cold working temperature again came to light (Fig. 8). For the AISI 304 L steel (Fig. 9) the susceptibility to the pitting corrosion is greater (as is well known), but it appears to be less affected by the deformation degree than for the AISI 316 L steel.

The relationship between the previously described aspects of the electrochemical behavior of the considered steels and the structural effects of the cold plastic deformation would need a complete, systematic, and quantitative study of these latter, whereas only some qualitative "flashes" will be shown here. All the same, we think they are already sufficiently meaningful.

First of all, a general idea of the work-hardening effects of the materials is given by the Vickers hardness diagrams of the type in Fig. 10, which, at least in the case of cold rolling at the liquid nitrogen temperature, exhibits an anisotropy of this property.

Investigations by transmission electron microscopy, electron diffraction, and x-ray diffraction enabled us to get a qualitative picture of the structure of the AISI 304 L and 316 L steels deformed by tension at both room and liquid nitrogen temperature. This picture includes dislocations density, presence and nature of the deformation bands [*i.e.*, deformation twins (Fig.

Table II. Results of the observation under the electron microscope of AISI 304 L and 316 L steels deformed by tensile stress

Austenitic stainless steel	Deformation Temperature	Degree (%)	Dislocations density (cm/cm <sup>2</sup> )	Deformation bands	Bands nature			Austenite
					Twins	$\epsilon$ -martensite	$\alpha'$ -martensite	
AISI 304 L	Room temperature	0	$1.3 \times 10^9$	No	No	No	No	$\approx 100\%$
		10	$\approx 1.5 \times 10^{10}$	Few	Yes	Not observed	No	$\approx 100\%$
		15	$> 2 \times 10^{10}$	Medium quantity	Yes	Yes	Little	Largely prevailing
	Liquid N <sub>2</sub> temperature	30	$> 2 \times 10^{10}$	Many	Yes	Not observed	Medium amount	Prevailing
		9	—	Many	Yes	Not observed	Much	Much
AISI 316 L	Room temperature	13	—	Largely prevailing	—	—	Very much	Little
		19	—	Scarcely discernible	—	—	Largely prevailing	Not observed
		0	$1.17 \times 10^9$	No	—	—	—	—
	Liquid N <sub>2</sub> temperature	10	$\approx 1 \times 10^{10}$	Probably not present	No	No	No	100%
		15	$\approx 2 \times 10^{10}$	Few	No	No	No	100%
		30	$> 2 \times 10^{10}$	Medium quantity	Yes	Not observed	No	$\approx 100\%$
		9	—	Many	Yes	Not observed	Not observed	Largely prevailing
13	—	Prevailing	Not observed	Yes	Medium amount	Prevailing		
19	—	Yet discernible	—	—	Much Prevailing	Medium amount Little		

Table III. Qualitative results of the x-ray diffraction measurements for AISI 304 L and 316 L steels deformed by tensile stress

Deformation Temperature	Degree (%)	AISI 304 L			AISI 316 L		
		(111) $\gamma$	(110) $\alpha'$	(10 $\bar{1}$ ) $\epsilon$	(111) $\gamma$	(110) $\alpha'$	(10 $\bar{1}$ ) $\epsilon$
Room temperature	10	S	VW	—	S	—	—
	15	SS	VW	—	SS	—	—
	30	SS	W	—	SS	—	—
Liquid N <sub>2</sub> temperature	9	S	W + M	VW	S	W	VW
	13	M	M	VW	M + S	W	VW
	19	W	M + S	VW	M	M	VW

S = strong; M = medium; W = weak; VW = very weak.

11),  $\epsilon$ -hexagonal martensite (Fig. 12), or slip bands which cannot be morphologically distinguished from each other], presence of  $\alpha'$ -cubic martensite (Fig. 13), and residual austenite. The results are summarized in Tables II and III.

In the case of deformation at room temperature, the behavior of the considered steels is quite different; the dislocations density as well as the density of the deformation bands is always higher in the AISI 304 L than in the 316 L steel. Moreover, in the strongly deformed 304 L steel,  $\alpha'$ -martensite is present in amounts increasing with the deformation degree, whereas the 316 L steel does not exhibit any phase transition even in the state of maximum deformation (in accordance with the  $M_{d30}$  values given in Table I).

In the case of deformation at the liquid nitrogen temperature, the behavior of the considered steels becomes essentially the same for both of them in that the phase transition of austenite to martensite is always notable or even prevailing; nevertheless a greater structural instability of the AISI 304 L steel compared with the 316 L is confirmed.

Much more research work must be carried out on the structural aspects, also as regards the spatial distribution and orientation of the formed martensite and the influence on the passivating films, in order to explain

the previously described anisotropy effects on the electrochemical behavior of the deformed steels.

Manuscript submitted Feb. 17, 1976; revised manuscript received March 31, 1976.

Any discussion of this paper will appear in a Discussion Section to be published in the June 1977 JOURNAL. All discussions for the June 1977 Discussion Section should be submitted by Feb. 1, 1977.

Publication costs of this article were assisted by the Politecnico di Milano.

#### REFERENCES

- W. Nicodemi, P. Pedferri, and D. Sinigaglia, *Met. Ital.*, **63**, 23 (1971); D. Sinigaglia, P. Pedferri, B. Mazza, G. P. Galliani, and L. Lazzari, *ibid.*, **65**, 77 (1973); B. Mazza, P. Pedferri, D. Sinigaglia, U. Della Sala, and L. Lazzari, *Werkstoffe Korrosion*, **25**, 239 (1974).
- A. La Vecchia, L. Peraldo Bicelli, and C. Romagnani, *Ann. Chim.*, **62**, 489 (1972).
- T. Angel, *J. Iron Steel Inst.*, **168**, 165 (1954); F. C. Hull, *Welding J. (Res. Suppl.)*, **52**, 193s (1973).
- A. Cigada and P. Pedferri, *Ann. Chim.*, **65**, 509 (1975).
- M. Da Cunha *et al.*, *Mem. Sci. Rev. Met.*, **70**, 725 (1973).
- N. Pessall and C. Liu, *Electrochim. Acta*, **16**, 1987 (1971).

# X-Ray Photoelectron Spectroscopic Study of the Aqueous Oxidation of Monel-400

N. S. McIntyre, T. E. Rummery, M. G. Cook, and D. Owen

Atomic Energy of Canada Limited, Whiteshell Nuclear Research Establishment, Pinawa, Manitoba, Canada

## ABSTRACT

The surface of Monel-400 alloy was exposed to high pH, aqueous corrosion at 285°C, under both oxidizing and reducing conditions. After exposures lasting from 0.3 to 335 hr the surfaces were examined by x-ray photoelectron spectroscopy, scanning electron microscopy, and other techniques. Under reducing conditions, no corrosion film forms on the metal surface, but under oxidizing conditions, the first corrosion layer which forms at the solution interface is entirely Ni(OH)<sub>2</sub>. This hydroxide, which persists for long times at pH ~ 10 but which rapidly converts to NiO at pH ~ 14, is shown to result from a precipitation process. The composition of the corrosion film is determined by the relative solubilities of nickel and copper at the interface. A composition profile of the corrosion layer beneath the outermost film shows a gradual increase in cuprous ion concentration with increasing depth, probably due to solid-state migration. This suggests that the aqueous corrosion of Monel-400 involves both solid-state oxide growth and an ionic dissolution and precipitation mechanism.

Monel-400<sup>1</sup> (66% Ni, 32% Cu) is one of the alloys used as heat-exchanger tubing in CANDU-PHW<sup>2</sup> power reactors. As part of a study of the transport of radionuclides in reactor coolant systems, we have investigated the aqueous corrosion behavior of Monel-400 under conditions of high temperature and pressure which simulate those found in the coolant of a power reactor.

Most aqueous corrosion studies of nickel-copper alloys have concentrated on film growth rates (1-10) or on the composition and structure of oxide films which were formed over lengthy periods of corrosion (11-13). One study used electron diffraction to identify the corrosion products Ni(OH)<sub>2</sub>, NiOOH, and NiO which had formed on some copper-nickel alloys after several hours of aqueous corrosion (14). With the development of other analytical techniques sensitive to surface films no thicker than a few atomic layers, both composition and structure can be determined qualitatively and quantitatively following very brief exposures to corrosion conditions.

In this work, corroded surfaces were studied by x-ray photoelectron spectroscopy (XPS or ESCA) as well as scanning electron microscopy, and, where possible, by x-ray diffraction. In XPS, photoelectrons produced by an impinging x-ray beam emerge from the top 1-2 nm of a surface and their kinetic energies are analyzed (15). The exact kinetic energy of the photoelectron reflects not only the atomic number of the originating element, but also the chemical environment of this element. If this technique is combined with ion sputtering to remove successive layers of surface film, it is possible to obtain a profile of the elemental distribution through the corrosion layer.

XPS provides an average analysis of the elements on several square millimeters of surface. Complementary information about the distribution of crystallites within this area can be obtained using scanning electron microscopy. Also, where a film of sufficient thickness (~0.1-1 μm) has formed, x-ray diffraction can be used to confirm the XPS analysis.

In two previous XPS studies, corroded copper-nickel surfaces have been examined. Hullet and co-workers (16) examined films on a 70:30 cupronickel alloy which had been anodized in sodium chloride solutions. Above

the passivation potential, the surface was found to consist primarily of a nickel-oxygen species whose identity could not be absolutely established. The XPS core line spectra of the nickel-rich surface did not, however, correspond to stoichiometric NiO. Castle (17), however, examined 70:30 copper-nickel alloy surfaces heated in oxygen and in this case was able to identify the nickel phase as NiO. The surface of the oxidized alloy was enriched in nickel compared with the bulk metallic phase. Both cuprous and cupric oxide phases were identified under different oxidizing conditions.

In this work, the corrosion films formed on Monel-400 were studied following brief exposures of the alloy to alkaline (pH = ~10-14), high temperature (285°C) solutions saturated with respect to either hydrogen or oxygen. In each case the XPS spectra of the corrosion products could be clearly identified with the spectra of known nickel or copper species. From the analysis of the surface corrosion products and the elemental depth profile, a mechanism for the aqueous corrosion of Monel-400 is proposed.

## Experimental

Mechanically abraded Monel-400 coupons of 3 cm<sup>2</sup> surface area were exposed to 0.1 liter of 1.0 mol/kg and 1 × 10<sup>-4</sup> mol/kg Li(OH) solutions at 285°C in a Teflon-lined titanium autoclave. The autoclave was initially purged and filled to a pressure of 0.1 MPa at 25°C with reagent grade hydrogen or oxygen. The inner surfaces of the autoclave, in contact with solution, were lined with Teflon since it was found that even after thorough cleaning microquantities of metallic contaminants remained on the titania surfaces and were readily transported to the Monel-400 surfaces during exposure. The Teflon liner was pretreated under reaction conditions for over 50 hr to eliminate any significant contribution of fluoride and chloride ion to the solution and the absence of these impurities on the Monel-400 surface after treatment was confirmed by photoelectron spectroscopy. Photoelectron spectroscopy also confirmed the absence of elemental impurities, other than adsorbed oxygen and minor quantities of hydrocarbon, on the Monel surfaces prior to exposure.

Effective exposure periods varied from 0.3 to 335 hr. The effective period was taken to be the time at which the surface was corroded at temperatures between 225° and 285°C, and allowed for the time of additional corrosion during heating-up and cooling-down. Following

Key words: Monel, nickel hydroxide, aqueous oxidation, photoelectron spectroscopy, corrosion.

<sup>1</sup> Trade name of the International Nickel Company of Canada Limited.

<sup>2</sup> CANDU-PHW = Canada deuterium uranium-pressurized heavy water.

exposure, coupons were cooled *in situ*, washed with distilled water, and transferred to the spectrometer. When the effects of dissolved hydrogen were studied, particular care was required to prevent possible oxidation of the surfaces after exposure, and the transfer to the spectrometer was done under an argon atmosphere. The total quantities of copper and nickel products in solution from each corrosion reaction of Monel were determined using flame or flameless atomic absorption spectroscopy.

A McPherson ESCA-36 XPS spectrometer with a cryogenically pumped sample chamber was used. The excitation radiation used was either the Mg  $K_{\alpha}$  or Al  $K_{\alpha}$  line. The instrument work function (3.8-4.2 eV) was set so that the Au(4f 7/2) peak was at 84.00 eV for a gold metal surface. Rather large charging shifts (1-3 eV) were encountered for all Monel surfaces exposed to aqueous oxidation. The surface charging was corrected by measuring the shift of the background carbon C(1s) line, which normally occurs at  $285.0 \pm 0.2$  eV. In some cases a gold film was evaporated onto the surface and its equivalent charging shift was measured (18). In general, agreement between the two measurements, however, was within  $\pm 0.2$  eV. Such corrections, however, substantially affect the precision of the peak assignment and the errors quoted result from ten determinations of the peak position.

Appropriate relativistic energy corrections were made to all binding energies reported. A 10 keV argon ion gun was used for depth profile studies. Ion flux on these surfaces was limited to  $5 \mu\text{A cm}^{-2}$  to minimize effects of chemical decomposition and preferential sputtering. Surface morphology was determined with a Cambridge "Stereoscan" Mark 2A scanning electron microscope. X-ray diffractometry was carried out using a Philips vertical goniometer with monochromated Cu  $K_{\alpha}$  radiation.

### XPS Spectra

The x-ray photoelectron spectra of a number of oxides and hydroxides of copper and nickel have been studied in this (19) and other (20-22) laboratories. The binding energies associated with the more prominent metal and oxygen core lines as well as the energy of the major metal LMM Auger transition are given in Table I. In Fig. 1 and 2 the M(2p) and M(3s) spectra for some oxides and hydroxides of copper and nickel are shown. Cuprous oxide is distinguishable from copper metal only by the shift of the Cu Auger LMM line. Cupric oxide and hydroxide are characterized by their differing metal and oxygen core binding energies as well as by the metal "shake-up" satellite spectra located on the high binding energy side of most cupric compounds (23). In the case of the nickel-oxygen system, NiO and Ni(OH)<sub>2</sub> can be clearly distinguished using similar criteria as in the copper spectra. Spectra of another nickel-oxygen species have been reported by Kim and Winograd (22) following the low pressure oxidation of polycrystalline nickel surfaces. They suggest that this species is a defect structure containing Ni<sup>3+</sup>. Similar spectra have been observed in this laboratory (24) during room temperature oxidation of nickel surfaces. Although this oxide has metal and oxygen core line energies rather close to those for nickel hydroxide, the separation is still adequate to provide characterization of either species,

Table I. Some metal and oxygen core binding energies of copper and nickel oxygen compounds

Compound	M(2p 3/2) eV	M(3p 3/2) eV	O(1s) eV	M(L <sub>4,5</sub> M <sub>4,5</sub> ) eV
Cu metal	932.4 ± 0.1	75.1 ± 0.1	—	919.0 ± 0.2
Cu <sub>2</sub> O	932.4 ± 0.1	75.1 ± 0.1	530.5 ± 0.2	917.4 ± 0.3
CuO	933.7 ± 0.2	76.6 ± 0.25	529.6 ± 0.15	917.7 ± 0.3
Cu(OH) <sub>2</sub>	934.2 ± 0.25	77.0 ± 0.25	531.2 ± 0.2	—
Ni metal	852.5 ± 0.1	66.3 ± 0.15	—	842.3 ± 0.3
NiO	854.0 ± 0.2	67.4 ± 0.2	529.6 ± 0.15	839.5 ± 0.4
Ni(OH) <sub>2</sub>	855.9 ± 0.3	68.1 ± 0.2	531.4 ± 0.3	838.4 ± 0.3

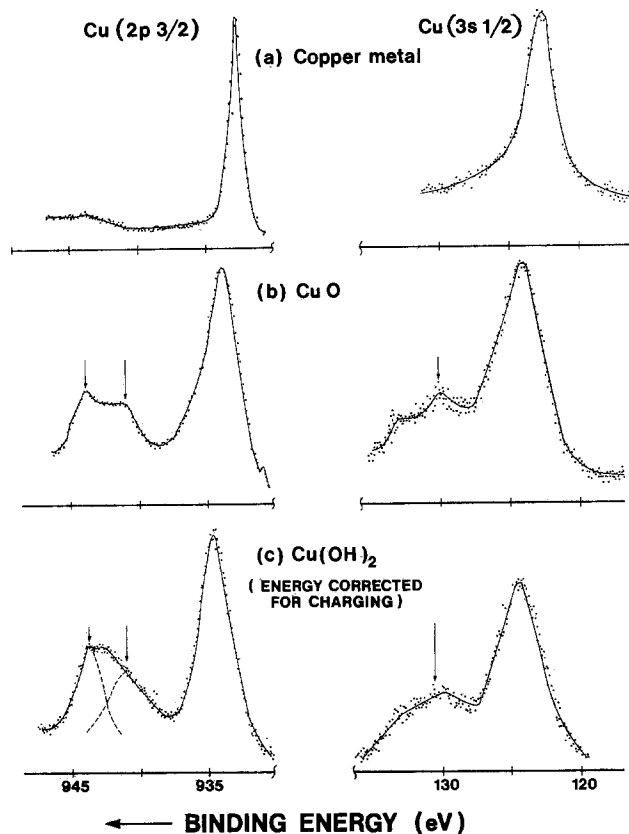


Fig. 1. XPS Cu(2p 3/2) and Cu(3s) core line spectra for Cu metal, CuO, and Cu(OH)<sub>2</sub>. The arrows indicate satellite peaks due to multi-electron excitation (shake-up) or multiplet interaction processes.

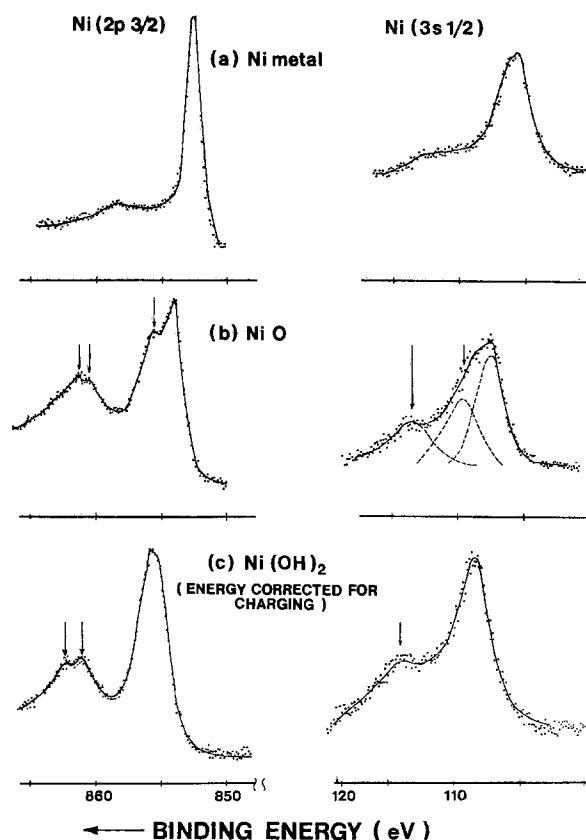


Fig. 2. XPS Ni(2p 3/2) and Ni(3s) core line spectra for Ni metal, NiO, and Ni(OH)<sub>2</sub>. The arrows indicate satellite peaks due to multi-electron excitation (shake-up) or multiplet interaction processes.

particularly when combined with the quite different satellite and Auger spectra produced by each. The "surface nickel oxide" species of Kim and Vinograd (22) was not observed during the present work.

### Results

**Exposure in  $10^{-4}$  mol/kg Li(OH)—0.1 MPa  $H_2$  overpressure.**—After exposure of a Monel coupon in 285°C solutions (pH  $\sim$ 10) under hydrogen for periods up to 335 hr, no evidence of any significant oxidation product on the surface was seen using XPS. Spectra of the Cu(2p 3/2) and Ni(2p 3/2) lines for a Monel surface were the same as those for pure metal surfaces [Fig. 3(a)]. As little as 0.3 of a monolayer of NiO or Ni(OH)<sub>2</sub> could be detected using these lines. The O(1s) spectrum of the Monel surface [Fig. 3(a)] shows a small peak at 531.7 eV due to minor concentrations of a surface oxygen species. Such complexes are normally observed on metal surfaces not treated under vacuum prior to examination. The copper-nickel ratio of the surface was determined from both M(2p) and M(3p) integrated line intensities using prepared copper-nickel alloys of known composition as intensity standards (25). Using the M(2p) line ratios a nickel:copper atom ratio of  $75:25 \pm 10\%$  ( $2\sigma$ ) was determined while an atom ratio of  $65:35 \pm 7\%$  ( $2\sigma$ ) was found using the M(3p) line ratios. The M(3p) photoelectrons with kinetic energies of 1200 eV have a mean escape depth (1–2 nm) around three times larger than the M(2p) photoelectrons which have kinetic energies of 300–400 eV (26). Although the more deeply sampled surface layer has, within experimental error, copper-nickel ratio equivalent to that in bulk of Monel-400, the extreme outer surface appears to be depleted in copper. This could be due to a preferential dissolution of copper or surface segregation as discussed below.

The absence of any oxide is consistent with thermodynamic calculations. Comparison of calculated equilibrium partial pressures for hydrogen reduction of NiO, Cu<sub>2</sub>O, and CuO (27) with the hydrogen overpressure of 0.1 MPa used in these experiments indicates that the metallic phase is thermodynamically stable for both nickel and copper.

**Exposure in  $10^{-4}$  mol/kg Li(OH)—0.1 MPa  $O_2$  overpressure.**—The exposure of Monel-400 under conditions

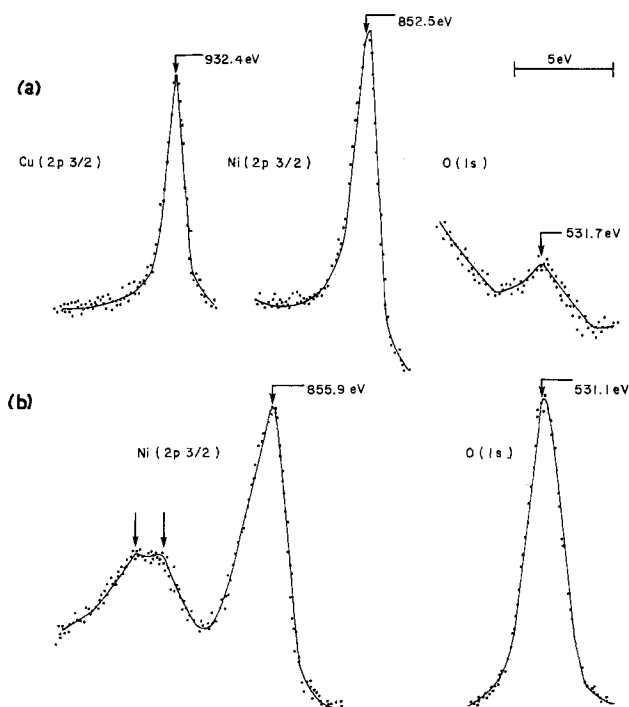


Fig. 3. XPS Cu(2p 3/2), Ni(2p 3/2), and O(1s) core line spectra for Monel-400 surface exposed to  $1 \times 10^{-4}$ M Li(OH) at 285° for 0.3 hr; (a) hydrogen overpressure, (b) oxygen overpressure.

as described above except for an oxygen overpressure resulted in rapid growth of a corrosion film. After an effective exposure of 0.3 hr, a scanning electron micrograph of the surface [Fig. 4(b)] indicated a layer of acicular crystals 0.1  $\mu$ m in diameter. A micrograph of the reduced surface [Fig. 4(a)] is included for comparison. The needlelike morphology of the crystals suggests that they were formed by precipitation from solution rather than by a solid-state growth process.

Only a nickel phase was detected on the outer surface using XPS. If copper was present at all, it constituted less than 5 atomic per cent (a/o) of the corrosion layer (expressed as CuO). Spectra of the Ni(2p 3/2), Cu(2p 3/2), and O(1s) line regions are shown in Fig. 3(b). The binding energies of the principal lines

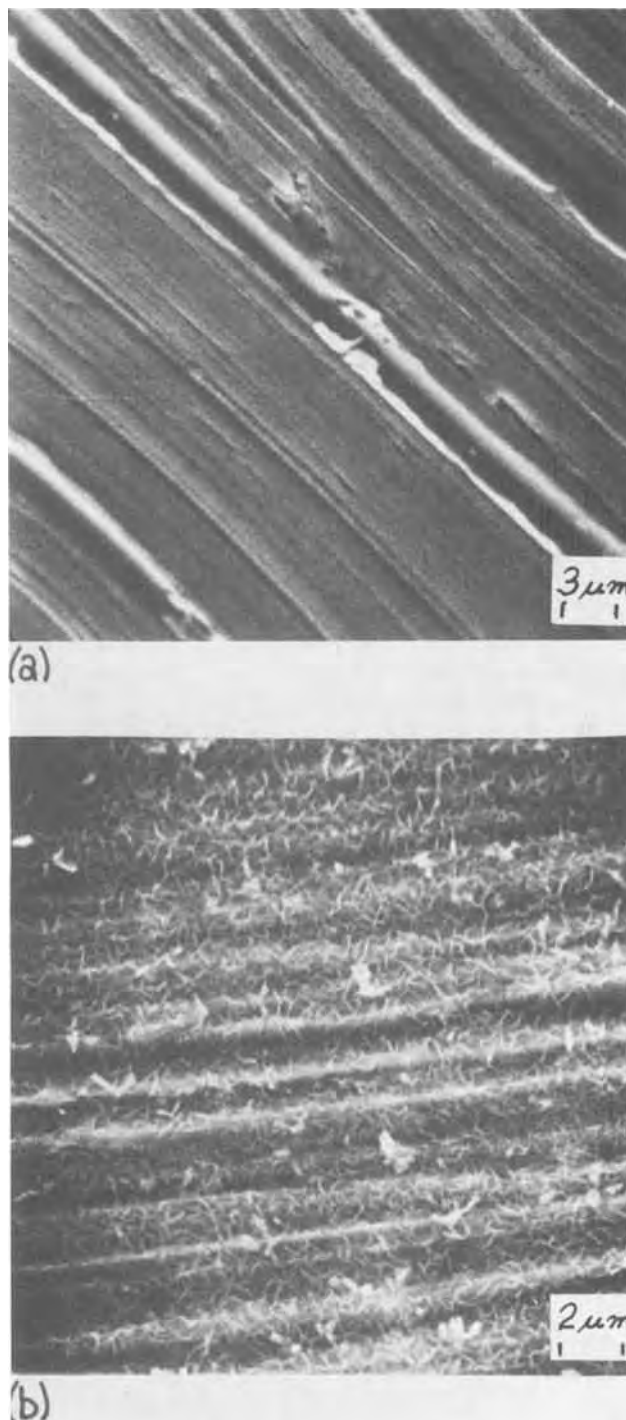


Fig. 4. Scanning electron micrograph of a Monel-400 surface exposed to  $1 \times 10^{-4}$ M Li(OH) at 285°C for 0.3 hr, (a) hydrogen overpressure, (b) oxygen overpressure.

correspond within 0.2 eV to those given for bulk  $\text{Ni}(\text{OH})_2$  in Table I. Moreover, the characteristics of the  $\text{Ni}(2p\ 3/2)$  shake-up spectrum (twin peaks at 5.1 and 6.8 eV above the principal line) and  $\text{Ni}(3s)$  spectrum (strong satellite at 5.1 eV) are the same as those observed for  $\text{Ni}(\text{OH})_2$ . Confirmation of this assignment of  $\text{Ni}(\text{OH})_2$  as the outer layer was not possible by x-ray diffraction because of the very thin surface film developed, but diffraction analysis of Monel surfaces exposed for periods of 48 hr indicated the presence of  $\text{Ni}(\text{OH})_2$  as the sole detectable corrosion product phase.

Several possible mechanisms for  $\text{Ni}(\text{OH})_2$  formation were considered: (i) hydration at high temperature or during cool-down of a predominantly  $\text{NiO}$  surface phase could yield an external film of  $\text{Ni}(\text{OH})_2$ ; (ii)  $\text{Ni}(\text{OH})_2$  is known to be unstable in a nonaqueous environment at 285°C (28). Thus the  $\text{Ni}(\text{OH})_2$  observed could have formed during cooling of the autoclave; (iii)  $\text{Ni}(\text{OH})_2$  could form at high temperature by direct precipitation of an excess of nickel at the solid-liquid interface.

The first premise was tested by exposing a suspension of stoichiometric  $\text{NiO}$  under similar autoclave conditions for 48 hr, with oxygen or hydrogen overpressures. Under neither condition was there any indication of a significant quantity of surface  $\text{Ni}(\text{OH})_2$ , although when  $\text{NiO}$  was exposed to oxygen-saturated solutions, evidence of some change in the oxide structure was seen. Production of  $\text{Ni}(\text{OH})_2$  on Monel surfaces by hydration of  $\text{NiO}$  is thus not considered likely.

Significant precipitation of  $\text{Ni}(\text{OH})_2$  during cooling of the autoclave is also considered unlikely. Solubilities of  $\text{Ni}(\text{OH})_2$  in  $10^{-4}$  mol/kg  $\text{Li}(\text{OH})$  solutions have recently been determined experimentally in the temperature range 25°-300°C (29). From these, it is estimated that the change in solubility of  $\text{Ni}(\text{OH})_2$  in cooling down from 300°C is less than  $10^{-6}$  mol/kg. Precipitation of this magnitude would result in a coverage of the sample surface no greater than 0.1 monolayers which is three to four orders of magnitude below the thickness of the  $\text{Ni}(\text{OH})_2$  films observed in this work.

If  $\text{Ni}(\text{OH})_2$  is the major corrosion product at 285°C, its stability under such hydrothermal conditions is surprising considering the known instability in nonaqueous conditions at these temperatures (28). Recently, Swaddle (30) has measured the stability of bulk  $\text{Ni}(\text{OH})_2$  under hydrothermal conditions similar to those above. It was found that, although the  $\text{Ni}(\text{OH})_2$  phase did indeed decompose to  $\text{NiO}$  at 280°-300°C, the rate was quite slow, typical half-lives being of the order of several hours. Thus, with continual precipitation on the Monel-400 surface it is possible to rationalize the existence of a significant layer of  $\text{Ni}(\text{OH})_2$  at these temperatures.

The aqueous oxidation of Monel was also carried out for periods considerably longer than 0.3 hr. In all cases, XPS studies of the outermost surface showed the major product to be  $\text{Ni}(\text{OH})_2$ , although small quantities of copper in cupric form were sometimes observed. X-ray diffraction of samples exposed for these periods indicated the presence of  $\text{Ni}(\text{OH})_2$ , but no other copper or nickel corrosion products were detected. Scanning electron microscopy coupled with energy dispersive x-ray spectrometry showed that a second crystallite phase develops on the surface at these longer exposure times. This phase, indicated with an arrow in Fig. 5, contains both copper and nickel and is quite localized, covering no more than 10% of the surface area.

The effect of increased concentration of copper ion in solution on the surface composition was studied by adding a 300  $\text{cm}^2$  copper foil to the autoclave. The surface composition was largely unaffected by the addition except that the surface concentration of cuprous oxide increased to 10-15 a/o compared to <5 a/o observed with no copper source present. SEM photomicrographs (Fig. 6) showed that the morphology of the

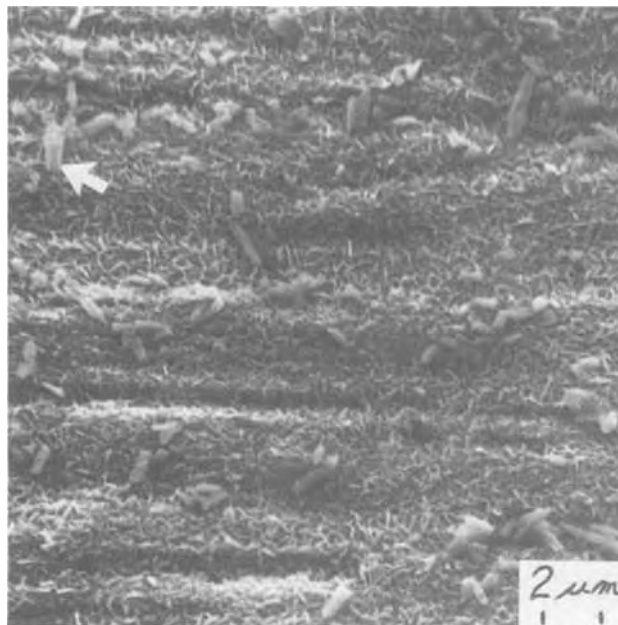


Fig. 5. Scanning electron micrograph of a Monel-400 surface exposed as in Fig. 4(b) for a period of 48 hr. A cupronickel phase is indicated by the arrow.

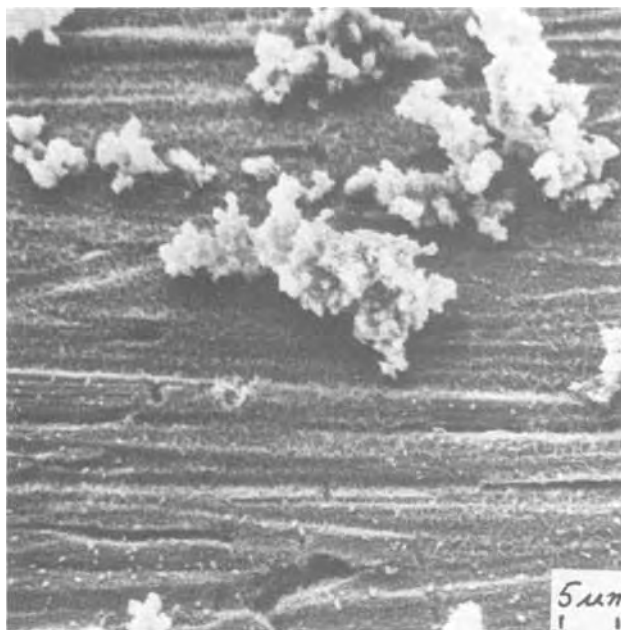


Fig. 6. Scanning electron micrograph of a Monel-400 surface exposed as in Fig. 5 with an additional copper source present in the autoclave.

deposited copper phase is much different from the film observed on a Monel surface with no copper source present (Fig. 5). The addition of an external source of copper causes, at saturation, the formation of relatively pure, localized, large crystallites of a copper phase on the film, leaving the major surface area as  $\text{Ni}(\text{OH})_2$ .

Elemental intensity profiles of the Monel-400 corrosion films were obtained using argon ion bombardment and a typical one is shown in Fig. 7. Of particular note is the copper phase, undetectable or barely detectable at the original outer surface, but which increases in concentration until it reaches a value about 25% of the nickel concentration [pure  $\text{Cu}_2\text{O}$  and  $\text{Ni}(\text{OH})_2$  used as intensity standards]. The depth attained in this and in similar profiles was estimated to be 20-100 nm.



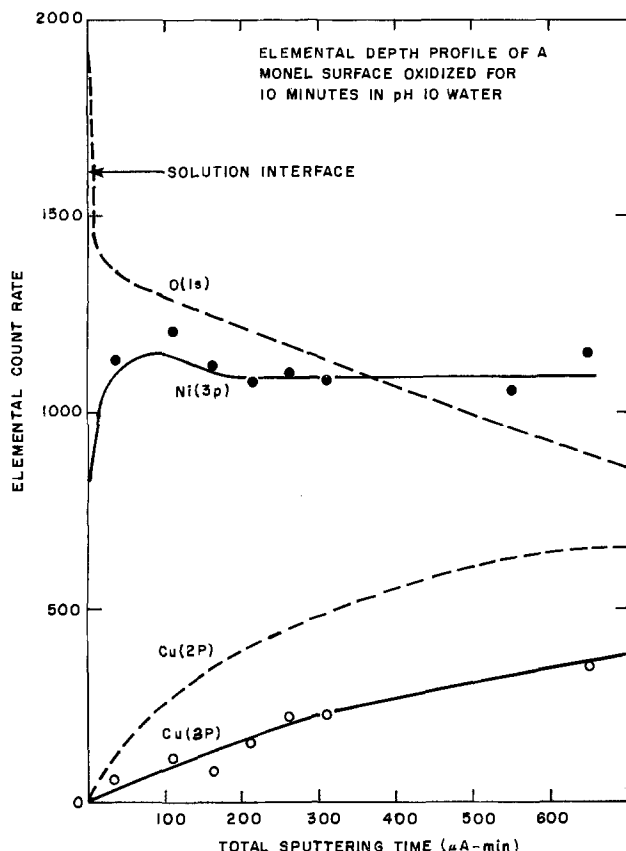


Fig. 7. Elemental intensity profile as a function of integrated sputtering current for a Monel-400 surface exposed to  $1 \times 10^{-4} M$  Li(OH) at  $285^\circ C$  for 0.3 hr under oxygen.

The Cu(2p 3/2), (3p 3/2) and Auger LMM energies indicated the presence of only cuprous oxide. Although 10 keV ion bombardment of cupric oxide has been found to result in some reduction to cuprous oxide, some contribution due to CuO usually remains, particularly in the Cu(3p) spectrum. The Cu(3p) line, because of its higher kinetic energy, samples the surface to a greater depth than the Cu(2p) line and thus minimizes the effect of sputtering damage which occurs largely, but not completely, in the outer 1 nm of surface remaining.

As each film was initially sputtered (0-10  $\mu A$ -min), rapid changes in metal and oxygen binding energies indicated a partial dehydration of Ni(OH)<sub>2</sub> to NiO. This can also be seen from the sharp change in slope of the O(1s) intensity in Fig. 7. The presence of at least some of the NiO is almost certainly due to sputtering-induced decomposition, for it is likely that such a major amount of NiO distributed throughout the film would have been detected by x-ray diffraction. During the remainder of the sputtering profile the ratio NiO/Ni(OH)<sub>2</sub> gradually increased, and it is not clear whether this represents the appearance of an NiO phase which was actually present in the original film during formation, or whether it is due to additional ion bombardment damage.

The effect of exposing an oxidized Monel-400 surface for a second period in the autoclave with a hydrogen overpressure was studied. The coupon initially was exposed for 0.3 hr in 0.1 MPa oxygen followed by replacement with a hydrogen atmosphere and continued exposure for 335 hr. SEM photomicrographs showed that features of the surface film were basically unchanged from those seen in Fig. 4(b). XPS analysis of the outer surface indicated that both NiO and Ni(OH)<sub>2</sub> were present in comparable quantities, but that no metallic nickel was present on the surface. Thus, aside from some decomposition of Ni(OH)<sub>2</sub> to NiO, the surface film was not greatly affected by long exposure to

hydrogen, indicating that the reduction of Ni(OH)<sub>2</sub> (and NiO) to elemental nickel is very slow under these aqueous conditions.

Attempts to estimate solution concentrations of copper and nickel during the high temperature exposures gave unreproducible results ranging from 10-100  $\mu g$ /liter for both elements.

*Exposure in 1.0 mol/kg Li(OH)—0.1 MPa O<sub>2</sub> overpressure.*—To further understand the role played by solution phenomena in the corrosion of Monel-400, experiments were also carried out at  $285^\circ C$  in 1.0 mol/kg Li(OH) (pH  $\sim 14$ ). At this pH, solubilities of both copper and nickel were found to be much higher than at pH 10, and autoclave solution concentrations could be estimated and correlated with film surface composition. After a 48 hr autoclave exposure, a film several micrometers in thickness had developed with a morphology much different from the acicular crystals found at pH  $\sim 10$ . A SEM photomicrograph of a typical region is seen in Fig. 8. XPS showed that the surface consisted entirely of NiO. No Ni(OH)<sub>2</sub> or copper phases were identified on the surface nor was any copper phase revealed when the surface was sputtered to a depth of several nanometers. The film was sufficiently thick that strong x-ray diffraction lines were obtained showing the bulk corrosion film to be entirely NiO. The detection limit of additional oxide phases such as Ni(OH)<sub>2</sub>, Cu<sub>2</sub>O, or Cu(OH)<sub>2</sub> was  $\sim 5\%$  in this case.

The observation of NiO rather than Ni(OH)<sub>2</sub> is still consistent with a precipitation-based mechanism for film formation. The rate of decomposition of Ni(OH)<sub>2</sub> at this pH and temperature has been shown by Swadlow (30) to be very high, and is around two orders of magnitude faster at pH  $\sim 14$  than at pH  $\sim 10$ .

Solution analyses following Monel exposure at pH  $\sim 14$  showed the copper concentration to be about 75 times higher than that of nickel (30,000  $\mu g$ /liter of copper vs. 400  $\mu g$ /liter of nickel).

*Exposure in gaseous oxygen.*—The compositions of corrosion films formed on Monel-400 under aqueous conditions were compared with those formed under gaseous oxidation at the same temperature. Abraded Monel-400 surfaces were exposed at  $250^\circ$ - $300^\circ C$  to 0.1 volume per cent (v/o) dry oxygen in argon for 0.3 hr. The resultant XPS spectrum, shown in Fig. 9(a), indicated that NiO and Cu<sub>2</sub>O were present on the outer

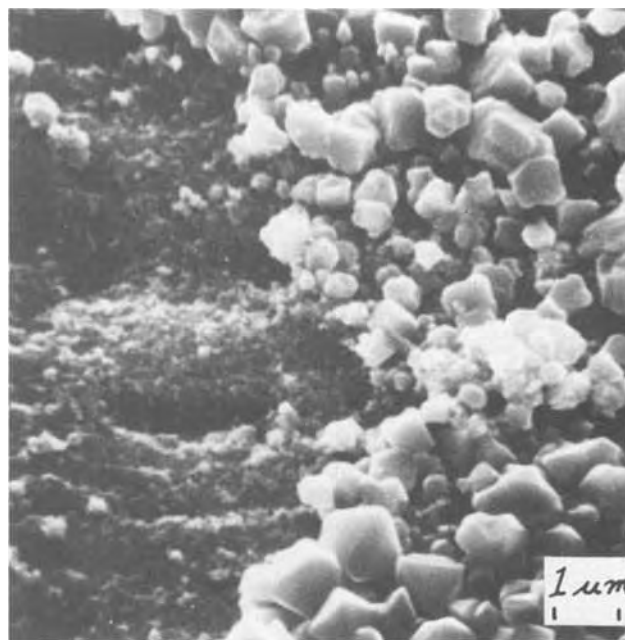


Fig. 8. Scanning electron micrograph of a Monel-400 surface exposed to 1.0M Li(OH) at  $285^\circ C$  for 48 hr.

surface in approximately the 2:1 atomic ratio expected from the alloy composition.

No attempt was made to determine whether the cuprous oxide and nickel oxide formed by gaseous corrosion of Monel-400 are in solid solution or are present as separate oxides, i.e., NiO and Cu<sub>2</sub>O. According to Schnal and Muller (31) these oxides are mutually insoluble, and hence one would expect a mixture to form. However, XPS spectra show only one prominent O(1s) line. Since the oxygen binding energy in Cu<sub>2</sub>O is different from that in NiO by 0.8 eV (19), one would have expected to see a contribution from both oxygen in Cu<sub>2</sub>O and NiO, if separate phases were present. Thus at least on the surface, a mixed cupronickel oxide may be formed.

### Discussion

This work shows that, under the experimental conditions used, the aqueous oxidation of Monel-400 is at least partly controlled by a dissolution-precipitation mechanism. At pH ~10, the nickel-rich outer corrosion film is believed to be a result of Ni(OH)<sub>2</sub> precipitation from a solution not yet saturated with respect to any copper species. When the copper does eventually reach saturation in the closed system, it nucleates in localized areas on the hydroxide surface, leaving the major surface coverage as Ni(OH)<sub>2</sub>. At pH ~14, the copper-nickel solubility difference is much larger and the resultant corrosion film is composed entirely of a nickel phase (NiO) after 48 hr. Longer exposures would eventually result in saturation with respect to copper species, and again a copper phase would be expected to nucleate and grow at the nickel phase-water interface.

The possibility was considered that nickel enrichment in the surface phase could also arise from a higher outward diffusion rate of nickel ions in the solid lattice. However, the oxide film produced by solid diffusion in the gaseous oxidation experiments on Monel-400 contains copper and nickel in quantities proportional to their concentrations in the alloy. Thus, under these time and temperature conditions, it appears that the relative diffusion rates of copper and nickel are approximately the same and are unlikely to result in surface nickel enrichment. Castle (17) previously studied the oxidation layer of a 50:50 Cu/Ni alloy and after heating the specimen in 13 kPa of oxygen for 0.5 hr at 500°C, the surface layer was found to be somewhat richer in copper than in nickel.

One other possibility which might lead to only a nickel oxidation product on the surface is the prior enrichment of one component of the alloy due to phase separation. Copper-nickel alloys are known to exhibit phase separation in this temperature range (32); however, the analyses of Monel-400 surfaces exposed under hydrogen at 285°C show that if separation does take place its extent is clearly insufficient to explain the major compositional change observed here during oxidation.

Under the oxygen partial pressure and temperature used in the aqueous corrosion experiments, film growth must occur by both solid-state diffusion and by dissolution-precipitation. An oxide of copper appears rapidly as the outermost layers of corrosion films formed at pH ~10 are removed by sputtering. It is believed that this copper is present in the film by virtue of a diffusion process since, as shown above, copper precipitation has not been found to occur in significant quantities even after lengthy exposure. The rising concentration of copper in the composition profile shown in Fig. 7 is likely controlled by the diffusion rate of the ion and possibly by the rate of leaching of copper by the unsaturated solution. On the other hand, while the presence of a significant diffusion process is based on the observation of copper in the underlying oxide layer, the evidence for a dissolution-precipitation process is based on the identification of Ni(OH)<sub>2</sub>, a phase which can only form by this mechanism. The occurrence of Ni(OH)<sub>2</sub> in a film thick enough to be measured by x-ray diffraction helps to establish that the precipitated layer is not just a negligibly thin layer formed on top of a layer formed largely by solid diffusion, but rather that it constitutes an appreciable portion of the total corrosion product. At pH ~14, it is clear that the major corrosion process is dissolution precipitation since no copper phases are detected by any means in the film.

Since the composition of the surface products depends at any time on the solution concentrations of copper and nickel, the effects of exposing Monel-400 in a "once-through" autoclave system are expected to be different from those observed for the "closed" system in the present study.

Manuscript submitted Dec. 8, 1975; revised manuscript received March 29, 1976. This was Paper 75 presented at the Toronto, Canada, Meeting of the Society, May 11-16, 1975.

Any discussion of this paper will appear in a Discussion Section to be published in the June 1977 JOURNAL. All discussions for the June 1977 Discussion Section should be submitted by Feb. 1, 1977.

Publication costs of this article were assisted by Atomic Energy of Canada Limited.

### REFERENCES

1. S. C. Datsko and C. R. Breden, USAEC, Report ANL-5354 (1954).
2. W. E. Berry and F. W. Fink, Rept. NP-8425, Battelle Memorial Institute, Columbus, Ohio (1958).
3. J. McGrew, S. Frank, and T. Page, Report MND-E-2655, Martin Company Nuclear Division (1961).
4. H. Urata, N. Kawashima, and O. Asai, *Hitachi Rev.*, **10**, 19 (1962); *CA*, **61**, 11707a (1964).
5. G. C. Wiedersum, *ASME Trans.*, **87**, 324 (1965).
6. J. E. LeSurr, P. E. C. Bryant, and M. G. Tanner, *Corrosion*, **23**, 57 (1967).
7. E. G. Brush and W. L. Pearl, *ibid.*, **25**, 99 (1969).
8. J. E. LeSurr, Report AECL-3778, Atomic Energy of Canada Limited (1970).
9. P. J. Boden, *Corrosion Sci.*, **11**, 363 (1971).
10. D. W. Rahoi, R. C. Scarberry, J. R. Crum, and P. E. Morris, *ASME Trans.*, **95**, 27 (1973).
11. B. E. Hopkinson, Report 62-WA-274, ASME (1962).
12. J. E. Castle, J. T. Harrison, and H. G. Masterson, in "Proceedings of the Second International Congress on Metallic Corrosion," NACE, p. 822, New York (1963).
13. A. van der Linde, Report RCN-194, Stichting Reactor Centrum (1973).
14. Y. Arai, *Kogyo Kagaku Zasshi*, **64**, 600 (1961); *CA*, **57**, 5701E (1962).

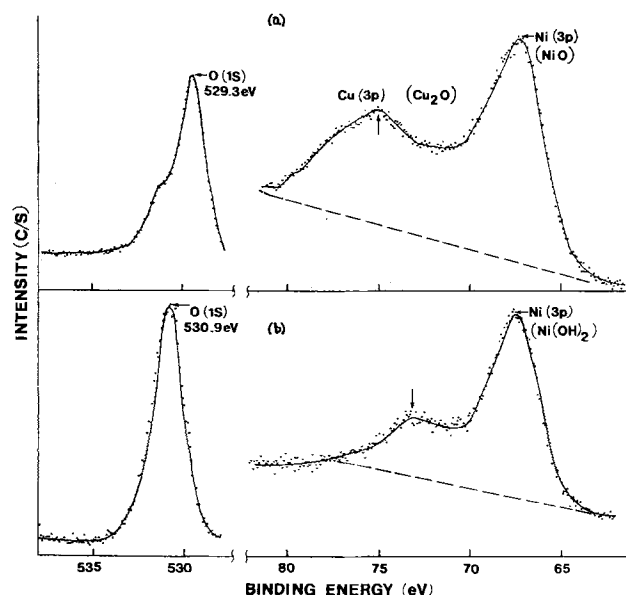


Fig. 9. Comparative XPS spectra of a Monel-400 surface exposed in (a) oxygen and (b)  $1 \times 10^{-4} M$  Li(OH) with an oxygen overpressure. In (b) the shoulder on the Ni(3p) peak indicated by the arrow results from a multi-electron excitation.



15. K. Siegbahn, C. Nordling, A. Fahlman, R. Nordberg, K. Hamrin, J. Hedman, G. Johansson, T. Bergmark, S. Karlsson, I. Lindgren, and B. Lindberg, "ESCA—Atomic Molecular and Solid State Structure Studied by Means of Electron Spectroscopy," Almquist and Wiksells, Uppsala (1967).
16. L. D. Hulett, A. L. Bararella, L. L. Donnic, and J. C. Griess, *J. Electron Spectry.*, **1**, 169 (1972).
17. J. E. Castle, *Nature*, **234**, 93 (1971).
18. D. J. Hnatowich, J. Hudis, M. L. Perlman, and R. C. Ragaini, *J. Appl. Phys.*, **42**, 4883 (1971).
19. N. S. McIntyre and M. G. Cook, *Anal. Chem.*, **47**, 2208 (1975).
20. G. Schoen, *Surface Sci.*, **35**, 96 (1973).
21. K. S. Kim and R. E. Davis, *J. Electron Spectry.*, **2**, 251 (1973).
22. K. S. Kim and N. Winograd, *Surface Sci.*, **43**, 625 (1973).
23. T. Robert and G. Offergeld, *Phys. Status Solidi*, **14**, 277 (1972).
24. N. S. McIntyre, Unpublished results.
25. N. S. McIntyre and M. G. Cook, "Surface Analysis Techniques for Metallurgical Applications," STP 596, ASTM (1976).
26. C. J. Powell, *Surface Sci.*, **44**, 29 (1974).
27. T. E. Rummery and D. D. Macdonald, *J. Nucl. Mater.*, **55**, 23 (1975).
28. S. Le Bihan and M. Figlarz, *Thermochim. Acta*, **6**, 319 (1973).
29. P. H. Tewari, Private communication (1975).
30. T. W. Swaddle, Private communication (1974).
31. N. G. Schmahl and F. Mueller, *Z. Anorg. Allgem. Chem.*, **332**, 217 (1964).
32. W. M. H. Sachtler and R. Jongepier, *J. Catalysis*, **4**, 665 (1965).

## Studies in Derivative Chronopotentiometry

### IV. Chemical Reactions Preceding Reversible Charge Transfer

R. H. Gibson\*

Department of Chemistry, University of North Carolina at Charlotte, Charlotte, North Carolina 28223

and P. E. Sturrock\*

School of Chemistry, Georgia Institute of Technology, Atlanta, Georgia 30332

#### ABSTRACT

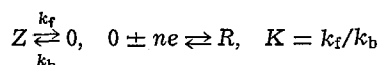
The derivative technique for the measurement of chronopotentiometric transition times is applied to systems complicated by homogeneous chemical reactions preceding charge transfer. The manner in which the technique may be applied is discussed, and kinetic parameters for two complex systems, cadmium/cyanide and cadmium/nitritoltriacetic acid, are presented. Close agreement between experimental results (derivative and conventional chronopotentiometry) and theoretical predictions is observed; corrected conventional results agree with derivative results where overlap is possible.

Previous papers in this series have dealt with instrumentation and diffusion-controlled systems, analytical applications, and sub-millisecond transition times (1). Material dealing with correction and compensation of charging currents and with details of instrumentation, presented in earlier papers, is not repeated here.

Relationships dealing with the kinetics of homogeneous chemical steps preceding chronopotentiometric charge transfer have been presented by others (2, 3) and have been applied in a recent study (4). Our purpose is to present the theory and model systems illustrating the application of derivative chronopotentiometry in studies of systems complicated by a chemical step preceding reversible charge transfer.

#### Derivative of the Potential-Time Curve

In order to apply the derivative technique to a system such as



it is first necessary to obtain relationships for the potential-time ( $E-t$ ) curve and for the derivative of the  $E-t$  curve, and to relate the transition time,  $\tau$ , to the value of  $(dE/dt)_{\min}$ , as was done for diffusion-controlled systems (5).

For systems with reversible charge transfer, the expressions for the surface concentrations of the oxidized ( $C_O$ ) and reduced ( $C_R$ ) forms can be substituted into the Nernst equation to obtain the appropriate  $E-t$  expression. Previously, Delahay and Berzins (3) determined the expression for  $C_O$  to be

$$C_O = \frac{K}{1+K} \left[ C^* - \frac{2i_0 t^{1/2}}{nF(\pi D)^{1/2}} - \frac{i_0}{nFD^{1/2}} \left( \frac{\operatorname{erf} [t^{1/2}(k_f + k_b)^{1/2}]}{K(k_f + k_b)^{1/2}} \right) \right] \quad [1]$$

where  $C^* = C_{O(t=0)} + C_{Z(t=0)}$ . The appropriate expression for  $C_R$  is determined from the flux of this substance at the electrode surface and by application of Duhamel's theorem (3)

$$C_R = 2i_0 t^{1/2} / nF(\pi D)^{1/2} \quad [2]$$

$C_O$  and  $C_R$  are valid at the electrode surface, and  $D$  is the diffusion coefficient assumed to be equal for  $O$  and  $R$ . All symbols have their usual significance, as defined in Ref. (3). The expressions for  $C_O$  and  $C_R$  are substituted into the Nernst equation

$$E = E_{1/2} + (RT/nF) \ln(C_O/C_R) \quad [3]$$

After substituting for  $C^*$  (using the condition that, at  $C_O = 0$ ,  $t = \tau$  in Eq. [1]), the following is obtained for the  $E-t$  curve

\* Electrochemical Society Active Member.

Key words: chronopotentiometry, complexes, kinetics.

$$E = E_{1/2} + (RT/nF)\ln[K/(1 + K)] \\ + (RT/nF)\ln\{(\tau/t)^{1/2} - 1 + [\pi^{1/2}/2K(k_f + k_b)]^{1/2}\} \\ \times [\operatorname{erf} \tau^{1/2}(k_f + k_b)^{1/2} - \operatorname{erf} t^{1/2}(k_f + k_b)^{1/2}]/t^{1/2} \quad [4]$$

A solution for Eq. [4], relating  $(dE/dt)_{\min}$  to  $\tau$ , requires differentiating the expression twice and setting  $(d^2E/dt^2)$  equal to zero. The resulting expression is used to relate  $t$  at the minimum to  $\tau$ , and this relationship is then substituted into the  $(dE/dt)_{\min}$  expression. Such a process was attempted for all values of  $K$ ,  $t$ , and  $\tau$  but yielded intractable expressions of little utility. More useful information was obtained by considering limiting behavior similar to that considered by Delahay and Berzins (3).

When the argument of the error function is small ( $< 0.1$ ), the function is virtually equal to  $(2/\pi^{1/2})$  times the argument [Ref. (6), p. 200]. Applying the conditions

$$\tau^{1/2}(k_f + k_b)^{1/2} < 0.1 > t^{1/2}(k_f + k_b)^{1/2}$$

to Eq. [4] yields

$$E = E_{1/2} + (RT/nF)\ln[(\tau^{1/2} - t^{1/2})/t^{1/2}] \quad [5]$$

which is identical to that for purely diffusion-controlled systems. Thus, as derived in Ref. (5), the differentiation of [5] gives

$$(dE/dt)_{\min} = -(27RT)/(8nF\tau) \quad [6]$$

When the argument of the error function is large ( $> 2$ ), the function is virtually equal to unity [Ref. (6), p. 199]. Applying these conditions

$$\operatorname{erf} \tau^{1/2}(k_f + k_b)^{1/2} > 2 < \operatorname{erf} t^{1/2}(k_f + k_b)^{1/2}$$

to Eq. [4] yields

$$E = E_{1/2} + (RT/nF)\ln[K/(1 + K)] \\ + (RT/nF)\ln[(\tau^{1/2} - t^{1/2})/t^{1/2}] \quad [7]$$

It is obvious that differentiation of Eq. [7] will lead to Eq. [6] which is therefore valid for this limit also.

Thus, for both the upper and lower limits of the argument of the error function, the expressions for  $(dE/dt)_{\min}$  are identical to that for diffusion-controlled systems. The transition time can be calculated from the value of  $(dE/dt)_{\min}$  within these limits, in a fashion identical to that used for diffusion-controlled systems (1, 5). Although the  $dE/dt$  expressions are identical, it is interesting to note that the  $E-t$  curves are not; the kinetic  $E-t$  curve for the case where the argument of the error function is  $> 2$  contains the additional term  $(RT/nF)\ln[K/(1 + K)]$ .

The procedure to be followed then is to calculate the kinetically influenced  $\tau$  by use of Eq. [6]. The  $\tau$ 's thus calculated are used in the manner suggested by Delahay (6). It should be noted that the only information lost in using the limiting forms of the derivative technique is identical to that lost in using the limiting forms suggested for the conventional technique; the information lost is the nonlinear section of the  $i_o\tau^{1/2}$  vs.  $i_o$  plot [see Fig. 8-10, p. 201, Ref. (6)]. The disadvantage in using the derivative technique with the procedures described above is that irreversible charge-transfer systems must be excluded from consideration. If such systems are to be considered, equations already available (3) for obtaining the appropriate  $E-t$  curve must be used.

### Experimental

Chronopotentiometric and derivative chronopotentiometric data were taken using the instrument and read-out systems described earlier (1). For the cadmium cyanide experiments, solutions were 10 mM in  $\text{Cd}(\text{NO}_3)_2$  and 1.0M in KCN. For the cadmium nitrilotriacetate (NTA) experiments, four solutions were used. The solutions were 1.0 mM in  $\text{Cd}(\text{NO}_3)_2$ , 40 mM in nitrilotriacetic acid, 1.0M in  $\text{KNO}_3$ , and 0.1M total

in acetic acid/sodium acetate buffer, with NaOH added to achieve the desired pH's. The pH's of the solutions were measured and found to be 2.92, 3.37, 3.73, and 4.00. All experiments were performed at ambient temperatures.

### Results and Discussions

**Cadmium cyanide system.**—In these experiments, current densities ranging from 3.91 to 5.71 mA/cm<sup>2</sup> were utilized in obtaining conventional transition times ranging from 90 to 2.7 msec. Derivative transition times ranged from 75 msec to 80  $\mu\text{sec}$  at current densities of 3.82-14.26 mA/cm<sup>2</sup>. The current densities were corrected for the double layer charging current by use of the equation

$$i_{o(\text{corr})} = (i_o\tau - B)/t \quad [8]$$

where  $B$  is the intercept of the Bard plot (1, 7) for the derivative data corresponding to short transition times. For the conventional data,  $B$  was calculated from the initial slope of the  $E-t$  curve, as suggested by Noonan (4). The corrected current densities ranged from 3.88 to 4.60 mA/cm<sup>2</sup> for the conventional data and 3.82-8.04 mA/cm<sup>2</sup> for the derivative data.

The data were treated in the manner suggested by Delahay and Berzins (3) for conventional data; their suggestion is based upon their Eq. [22] as follows

$$i_o\tau^{1/2} = (\pi D)^{1/2}nFC^*/2 \\ - \pi^{1/2}i_o \operatorname{erf}[(k_f + k_b)^{1/2}\tau^{1/2}]/2K(k_f + k_b)^{1/2} \\ \text{[Eq. [22] Ref. (3)]}$$

This approach leads to two expressions, [9] and [10]

$$i_o\tau^{1/2} = [nF(\pi D)^{1/2}C^*]/2 - i_o\pi^{1/2}/[2K(k_f + k_b)^{1/2}] \quad [9]$$

Equation [9] is derived from Eq. [22] of Ref. (3) for the case where the argument of the error function is  $> 2$ . It is, therefore, applicable at low current densities (long transition times). It indicates that a plot of  $i_o\tau^{1/2}$  vs.  $i_o$  should be a straight line with an intercept at  $i_o = 0$  equal to the product of  $C^*$  and the chronopotentiometric constant. The quantity  $K(k_f + k_b)^{1/2}$  can be obtained from the slope. At high current densities, the argument of the error function in Eq. [22] of Ref. (3) is  $< 0.1$  and the equation reduces to

$$i_o\tau^{1/2} = [nF(\pi D)^{1/2}C^*]/[2(1 + 1/K)] \quad [10]$$

If sufficiently short transition times are experimentally accessible, the value of  $K$  may be calculated from the intercept of Eq. [9] and the experimental quantity  $i_o\tau^{1/2}$  in Eq. [10].

Data for the cadmium cyanide system are plotted in Fig. 1. The increased range of the derivative data is obvious. The least squares slope and intercept of the derivative data at long transition times (first 10 points) are  $-1.149 \pm 0.045$  and  $5.43 \pm 0.18$ , respectively. The corresponding values for the conventional data are  $-1.123 \pm 0.040$  and  $5.52 \pm 0.17$ . Careful examination of the derivative data for short transition times shows that the region of constant  $i_o\tau^{1/2}$  values has not been reached. Equations [9] and [10] were solved simultaneously, using the derivative data, to obtain a first approximation for  $K$ , and then Eq. [9] was employed to calculate  $(k_f + k_b)$ . Then Eq. [22] of Ref. (3) was used to obtain an improved estimate of  $K$  and this cycle repeated until successive approximations of  $(k_f + k_b)$  were constant within 0.1.

The values calculated were  $1.20 \times 10^{-2}$  for  $K$  and  $4.2 \times 10^3$  for  $(k_f + k_b)$ . These constants were substituted into Eq. [22] of Ref. (3) and theoretical values of  $i_o\tau^{1/2}$  and  $i_o$  calculated for a number of values of  $\tau^{1/2}$ . These theoretical points are plotted also in Fig. 1.

Recently, Reinmuth (8) advocated plotting  $1/\tau^{1/2}$  vs.  $1/i_o\tau^{1/2}$ . Figure 2 is such a plot of the same data shown in Fig. 1. A least squares calculation of the first 10 points (long transition times) of the derivative data

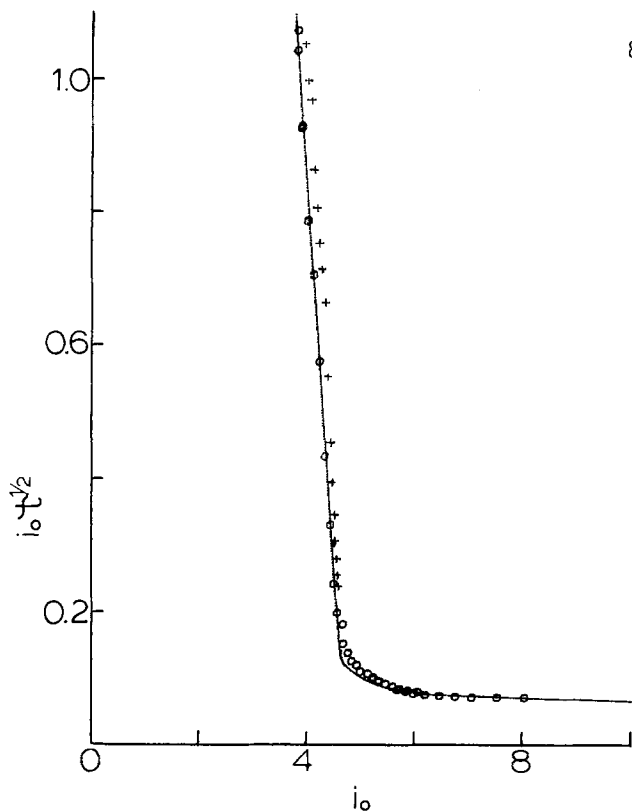


Fig. 1. Delahay (6) plot of chronopotentiometric data for solution 10 mM  $\text{Cd}(\text{NO}_3)_2$ , 1M  $\text{KNO}_3$ .  $i_0$  units are  $\text{mA}/\text{cm}^2$ ;  $i_0 t^{1/2}$  units are  $\text{mA}\cdot\text{sec}^{1/2}/\text{cm}^2$ .  $\circ$ , Derivative chronopotentiometry;  $+$ , conventional chronopotentiometry; and —, theoretical line for calculated kinetic parameters.

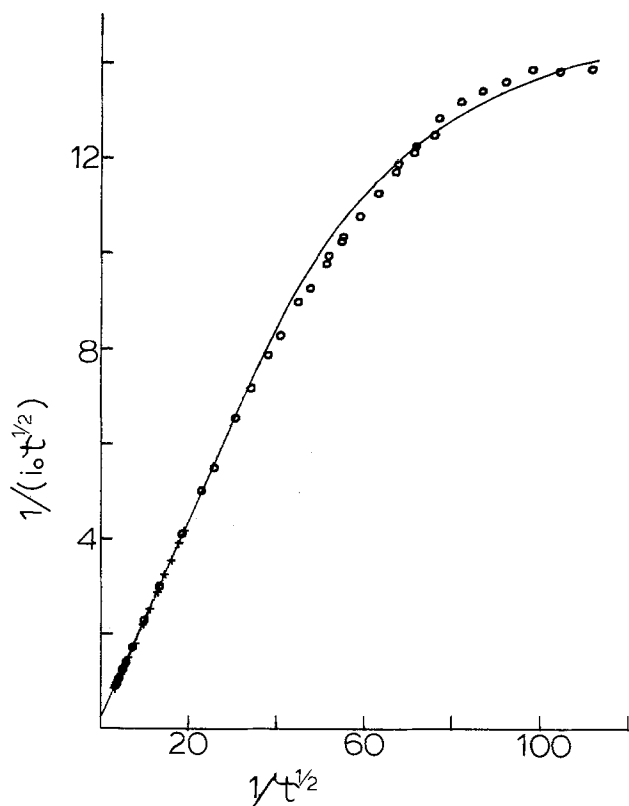


Fig. 2. Reinmuth (8) plot of same data as in Fig. 1

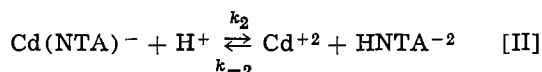
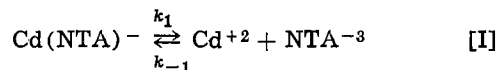
gives  $0.212 \pm 0.001$  for the slope and  $0.182 \pm 0.003$  for the intercept. The corresponding calculations for the conventional data give  $0.204 \pm 0.001$  and  $0.177 \pm 0.006$ . The inverse of the intercepts (5.49 and 5.64) compare

8

well with the intercepts of Fig. 1. However, if points in addition to the first 10 are used in the least squares calculations, the calculated values change significantly and the standard deviations increase markedly. Thus, although the Reinmuth plot (Fig. 2) compresses the data for long transition times so that they appear smoother, no significant advantage was found over the Delahay plot (Fig. 1) in the mathematical analysis of these data.

These results indicate that the derivative technique yields data superior to those obtainable using conventional chronopotentiometry since the derivative data are significantly less distorted by double layer effects. Questions, however, now must be asked about the system. The system has been studied by Gierst and Juliard (2), Delahay and Berzins (3), Noonan (4), Gerischer (9), and Flengas (10). Most agree that the species reduced is not  $\text{Cd}(\text{CN})_4^{2-}$ , but rather one of the less highly coordinated complexes. Gerischer and Noonan have suggested that  $\text{Cd}(\text{CN})_3^-$  is the species reduced. This suggestion is based upon the nature of the electrode reaction (9) and upon the value of  $K$  calculated from an estimate of the value of  $i_0 t^{1/2}$  at high  $i_0$  (4). However, the derivative results presented here indicate a larger value of  $K$  than reported previously (4, 11-13). The reasons for the discrepancy are not clear, though possibilities are noncoincidence of ionic strengths, concentration of complexes, and a possible (though not likely) residual double layer effect. Still another possibility is that the reducible species is an ion pair, perhaps  $\text{K}[\text{Cd}(\text{CN})_4]^-$  or  $\text{K}_2[\text{Cd}(\text{CN})_4]$ . In addition, Gerischer (9, 14) has attributed some degree of irreversibility to the reduction of  $\text{Cd}(\text{CN})_3^-$  and  $\text{Cd}(\text{CN})_2$ . His experiments, however, employed solutions markedly different from ours, the solutions containing substantial amounts of chloride ion.

*Cadmium-nitilotriacetic acid system.*—This system has been studied in detail (15-17 and references therein). The system shows two only slightly separated polarographic waves in acetate buffers ( $\leq \text{pH } 5$ ), the second wave being the direct, irreversible reduction of the complex. The wave at more positive potentials is the reversible reduction of cadmium ion to the metal. Two parallel reactions precede this first reduction



Reaction [II] is much faster than reaction [I]. The results reported here refer to the first reduction wave and are composite rate and equilibrium parameters for [I] and [II].

The system provides a formidable challenge if one is limited to the use of conventional chronopotentiometry. The two waves occur close in potential and merge at high current densities, as ohmic ( $IR$ ) problems become severe. We chose not to rely upon the conventional technique, and the results in Table I are calculated from derivative chronopotentiometric data exclusively. Results for  $\text{pH } 2.92$  (curve a) and  $4.00$  (curve b) are shown in Fig. 3. The common intercept of 0.502

Table I. Rate and equilibrium parameters for Cd-NTA. Solutions: 1.0 mM  $\text{Cd}(\text{NO}_3)_2$ , 40 mM NTA, 1.0 M  $\text{KNO}_3$  and 0.1M in acetate buffers at the indicated pH's.

pH	—Slope	$1/K(k_f + k_b)^{1/2}$	K	$k_f$
2.92	0.14	0.15	—	—
3.37	0.63	0.71	0.026	72
3.73	1.9	2.1	0.016	13
4.00	2.6	2.9	0.014	7.8

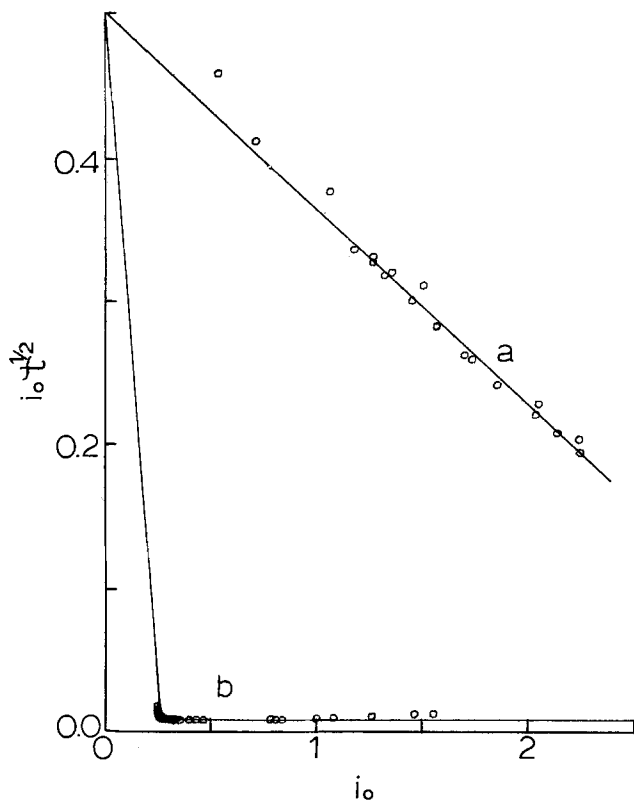


Fig. 3. Derivative chronopotentiometry for Cd-NTA solutions (see Experimental Section). Units same as Fig. 1.  $\circ$ , Curve a: pH = 2.92.  $\circ$ , Curve b: pH = 4.00. Solid lines: theoretical lines for calculated kinetic parameters.

on the  $i_0\tau^{1/2}$  axis in the figure is the value obtained for the data at pH 2.92; sufficient data for independent determinations of the intercept value for the other pH's were experimentally inaccessible.

The results in Table I compare favorably with measurements reported earlier by Shuman and Shain (15) and by Carney (16). Discrepancies between ours and the two earlier studies are not so large as the discrepancies between the two earlier sets. Since our primary goal is the introduction of the derivative chronopotentiometric technique, its theory and methodology, we prefer not to speculate either concerning the sources of the discrepancies or concerning the detailed chemistry of the system. We note, however, that our results generally fall between those of the earlier two studies despite the fact that our technique is dif-

ferent from the similar techniques used in those studies.

### Conclusions

These combined results confirm the utility of derivative chronopotentiometry in kinetics studies. The technique is obviously superior to conventional chronopotentiometry (and, perhaps, to other techniques) where applicable. The chief disadvantage and limiting feature of the technique is its restriction to systems involving reversible charge transfer following the chemical step.

Manuscript submitted Jan. 19, 1976; revised manuscript received April 1, 1976.

Any discussion of this paper will appear in a Discussion Section to be published in the June 1977 JOURNAL. All discussions for the June 1977 Discussion Section should be submitted by Feb. 1, 1977.

Publication costs of this article were assisted by the University of North Carolina at Charlotte.

### REFERENCES

- (a) P. E. Sturrock, J. Hughey, B. Vaudreil, G. O'Brien, and R. H. Gibson, *This Journal*, **122**, 1195 (1975); (b) P. E. Sturrock, B. Vaudreil, and R. H. Gibson, *ibid.*, **122**, 1311 (1975); (c) P. E. Sturrock and R. H. Gibson, *ibid.*, **123**, 629 (1976).
- L. Gierst and A. Juliard, Proc. Intern. Comm. Electrochem., Thermodynam. and Kinet., 2nd Meeting, pp. 117, 279, Milan (1950).
- P. Delahay and T. Berzins, *J. Am. Chem. Soc.*, **75**, 2486 (1953).
- D. C. Noonan, Ph.D. Dissertation, Columbia University (1967).
- D. G. Peters and S. L. Burden, *Anal. Chem.*, **38**, 530 (1966); S. L. Burden, Jr., Ph.D. Dissertation, Indiana University (1966).
- P. Delahay, "New Instrumental Methods in Electrochemistry," Chap. 8, Interscience Publishers, New York (1954).
- A. J. Bard, *Anal. Chem.*, **35**, 340 (1963).
- W. H. Reinmuth, *J. Electroanal. Chem.*, **38**, 95 (1972).
- H. Gerischer, *Anal. Chem.*, **31**, 33 (1959).
- S. N. Flengas, *Trans. Faraday Soc.*, **51**, 62 (1955).
- L. G. Sillen and A. E. Martell, "Stability Constants of Metal Ion Complexes," The Chemical Society (Special Publication 17), London (1964).
- J. Bjerrum, *Chem. Rev.*, **46**, 381 (1950).
- K. B. ĪAfsimirkii and V. P. Vasilev, "Instability Constants of Complex Compounds," Consultants Bureau, New York (1960).
- H. Gerischer, *Z. Elektrochem.*, **57**, 604 (1953); *Z. Physik. Chem., N.F.*, **2**, 79 (1955).
- M. S. Shuman and I. Shain, *Anal. Chem.*, **41**, 1818 (1969).
- J. H. Carney, *ibid.*, **47**, 2267 (1975).
- B. Raspor and M. Branica, *J. Electroanal. Chem.*, **59**, 99 (1975).

# Effect of Temperature on the Electrochemical Kinetics of Gadolinium in the Curie Region

David W. DeBerry\*

Radian Corporation, Austin, Texas 78766

and Norman Hackerman\*\*

Department of Chemistry, Rice University, Houston, Texas 77001

## ABSTRACT

Anodic dissolution and hydrogen evolution kinetics of Gd were investigated over the range 5°-30°C. Reaction orders with respect to pH for the HER and for anodic dissolution of Gd are temperature independent, as are the transfer coefficients. The apparent activation energy of anodic dissolution changes at the Curie temperature with that above 17°C being smaller. The change for the HER is almost the same but in the opposite direction. For both reactions there is a simultaneous change in the preexponential factor, yielding a practically smooth over-all  $\ln i$  vs.  $1/T$  curve. This behavior can be rationalized by addition of a ferromagnetic energy term to the activation energies. A model is proposed based on the existence of paramagnetic surface layers below the Curie temperature and the consequent introduction of an energy gradient for the transport of electrons to and from the metal surface.

The influence of the metal of an electrode on electrochemical reaction rates is of interest both to electrochemical kinetics and practical applications. Comparison of results for different metals is complicated by simultaneous changes in properties which might influence rates, and occasionally by changes in reaction mechanisms. Similar problems exist with alloys where unknown variations may exist between surface and bulk compositions. This research determined rates of electrochemical reactions involving Gd in the paramagnetic (Pm) and ferromagnetic (Fm) states.

Changes in reactivity of metals and alloys at their Curie temperatures ( $T_C$ ) have been observed, mainly for gas/solid catalysis. Variation in temperature coefficients at  $T_C$  is known as the magnetocatalytic or Hedvall effect (1-3). For example, decomposition of formic acid on Co-Pd shows a 30% increase in activation energy ( $E_A$ ) and a thousandfold increase in pre-exponential factor ( $\xi$ ) above  $T_C$  (4). Similar results were obtained for the oxidation of Fe-Cr in oxygen (5). In general both  $E_A$  and  $\xi$  change so as to give a practically smooth over-all Arrhenius curve. The effect is usually explained by qualitative discussions of changes in electronic states, orientation of electron spins, d-band holes, and work function (6, 7).

A related area involves the study of reactions at a series of alloys with compositions changing from Fm to Pm at constant temperature. Conway (8) determined the electrochemical rates and  $E_A$  of the HER at a series of Cu-Ni alloys. The apparent  $E_A$ 's and exchange current densities ( $i_0$ ) decrease from pure Ni to pure Cu, but beyond 60% Cu the changes were much smaller. The results could only partially be explained by changes in the metal-H bond energy caused by changes in the number of d-holes per atom of Ni. Anodic passivation studies of Ni alloys indicate anomalous changes at critical alloy compositions (9, 10), also attributed to d-electron configuration changes. Recently doubt has been expressed regarding correlation between d-band character and M-H bond energy (11). Surface composition may be quite different from the bulk composition (12).

Gadolinium was chosen for this research since its  $T_C$  (17°C) is accessible. Electrochemical measurements at a Gd electrode are complicated by the thermodynamic instability of the metal in the presence of water (13). The mixed potential of Gd in aqueous solutions (pH 5-6) has been measured at temperatures including  $T_C$  by Prall (14) and Daire (15). Below  $T_C$  they observed an increase in mixed potential to more active values with increasing temperature. Prall ascribed the changes to the effects on the work function or sublimation energy while Daire suggested either an abnormal increase in anodic dissolution rate or electronic surface states different from those in bulk metal. He also indicated that it was difficult to explain the changes in terms of classical thermodynamics. Daire found no abnormal changes in the heat of solution of Gd in 1N HCl from 3° to 40°C (16).

## Experimental

The Gd (Material Research Corporation) was obtained as 0.25 in. diameter cast rods, prepared from the distilled metal. The typical emission spectrographic analysis supplied with the sample lists the following impurities: 0.005% Eu, Dy, and Y; 0.01% Sm, Tb, Ca, Mg, Si, Fe, and Al. A Beckman rotating electrode assembly was used to drive a rotating disk electrode (RDE) consisting of a Gd cylinder fitted very tightly in a cylindrical Teflon sheath. A rotation rate of 50 rps was used for the results given here. Electrodes were degreased, stored in trichlorethylene, and polished on 3M 600 grit and Buehler 4/0 grit emery paper before use.

Teflon standard taper adapters were used to fit the reference electrode, precision thermometer, and rotating electrode body to the cell. The main body of the cell was jacketed to allow circulation of water from a constant temperature ( $\pm 0.03^\circ\text{C}$ ) bath. A large area Pt gauze auxiliary electrode was contained in a tube separated from the main cell solution by a fine glass frit. The reference compartment containing a normal calomel electrode at 25°C and bridge were filled with cell solution but were separated from the main compartment by a coarse frit. Test solutions were de-aerated with high purity He after removing trace oxygen with Ridox oxygen scavenger (Fisher Scientific

\* Electrochemical Society Active Member.

\*\* Electrochemical Society Honorary Member.

Key words: hydrogen evolution, anodic dissolution, ferromagnetism, activation energy.

Company) and presaturating with test solution. Water was purified with a two-stage quartz still fed with laboratory deionized water. Suitability of this water for electrochemical measurements was tested by reproducing the accepted current-potential curves at a Pt RDE in 0.5M  $H_2SO_4$ . Reagent grade chemicals were used in all solutions.

A scanning potentiostat of conventional design (18) was used to obtain current-potential curves. Ohmic potential drop in the solution was compensated by positive  $IR_s$  feedback obtained by galvanostatic pulse measurements. A scan rate of 0.050 V/min was used for the results given here. The cathodic scan was always made first. Equivalent results were obtained for the anodic scan if it was done first, but the subsequent cathodic scan results were erratic. Experimental procedures are described in more detail elsewhere (17).

### Results

**Selection of electrolyte system.**—In acidic aqueous solutions (0.2M  $NaClO_4$  +  $HClO_4$  to pH 1-3) Gd undergoes rapid attack with vigorous hydrogen evolution. The polarization curves show mass transfer control. In pH 12, 0.5M  $Na_2SO_4$  a fine white precipitate [probably  $Gd(OH)_3$ ] forms on part of the electrode surface. The corrosion rate is substantially decreased in slightly acidic or neutral (pH 5-7) aqueous salt solutions. In this category, solutions of  $NaClO_4$ ,  $Na_2SO_4$ ,  $(NH_4)_2SO_4$ ,  $GdCl_3$ , and  $Gd(ClO_4)_3$  were used. Reproducible and kinetically useful results are unobtainable in these unbuffered solutions. This is probably due to change in pH, especially near the electrode surface during polarization. In addition, localized corrosion and pitting of the electrode were usually evident, especially in solutions containing  $Cl^-$ .

Attempts to study the  $Gd^{3+}/Gd$  reaction in acetonitrile and in dimethylformamide were unsuccessful. The open-circuit potential was not reproducible, was more positive (noble) than that expected for this couple, and at times oscillated slowly. The electrode was readily polarized at small current densities (e.g.,  $\Delta V = 0.5V$  for  $i = 10 \mu A/cm^2$ ). This behavior is probably caused by oxidation of the metal surface by impurity water to form a stable film. The procedure for the purification of DMF is said to reduce the water to less than 20 ppm (19).

These results indicated that it was desirable to use a buffered, slightly acidic, aqueous electrolyte solution. The acetic acid/sodium acetate buffer system proved satisfactory. There is no apparent localized corrosion or pitting in these solutions. Mixed potential ( $V_M$ ) values obtained after about 25 min were reproducible to  $\pm 0.011V$ .

**Polarization curves and transfer coefficients.**—Polarization curves were recorded at each temperature and pH. Some of the results obtained are given in Fig. 1 and 2, where  $i$  is the current density and  $\pi = V - V_M$ . The most linear curves were obtained in the higher pH solutions (pH 5.94 and 6.46) since, in these, the open-circuit corrosion current density is low compared to those at which mass transfer becomes important. The linear Tafel slopes obtained in these solutions were used to obtain the transfer coefficients presented in Table I. The same slopes apply to the lower pH results at moderate current densities. The lower limit is at about pH 5.06, however, since results obtained at pH 4.70 did not show any appreciable linear region. The transfer coefficients are independent of temperature within experimental error ( $\pm 0.03$  in  $\alpha$ ). A cathodic Tafel slope of 0.170V ( $\alpha_c = 0.35$ ) was obtained by Greene (20) in phosphate buffered solutions at 25°C. He did not obtain linear anodic Tafel slopes in these solutions.

**Reaction orders.**—The effect of solution pH at 1.00M sodium acetate on the rates of both the cathodic and

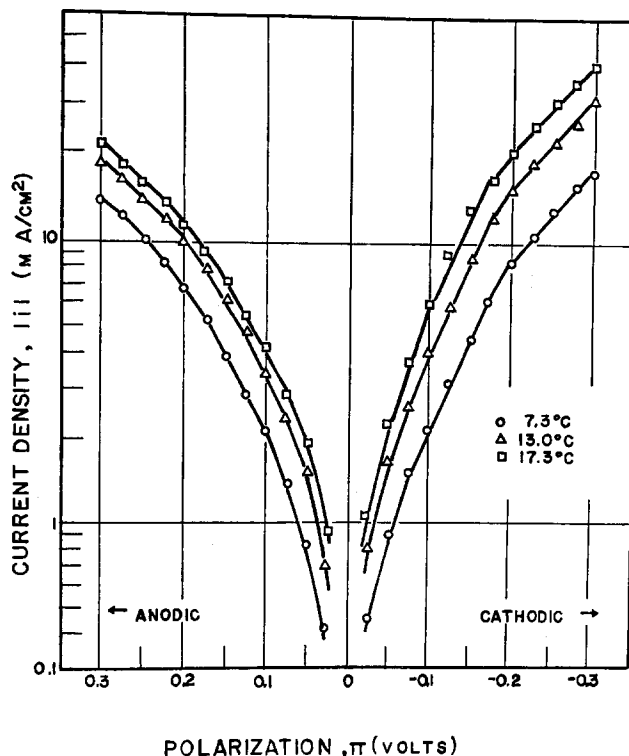


Fig. 1. Polarization curves for Gd in pH 5.45 acetate buffer at 7.3°, 13.0°, and 21.2°C.

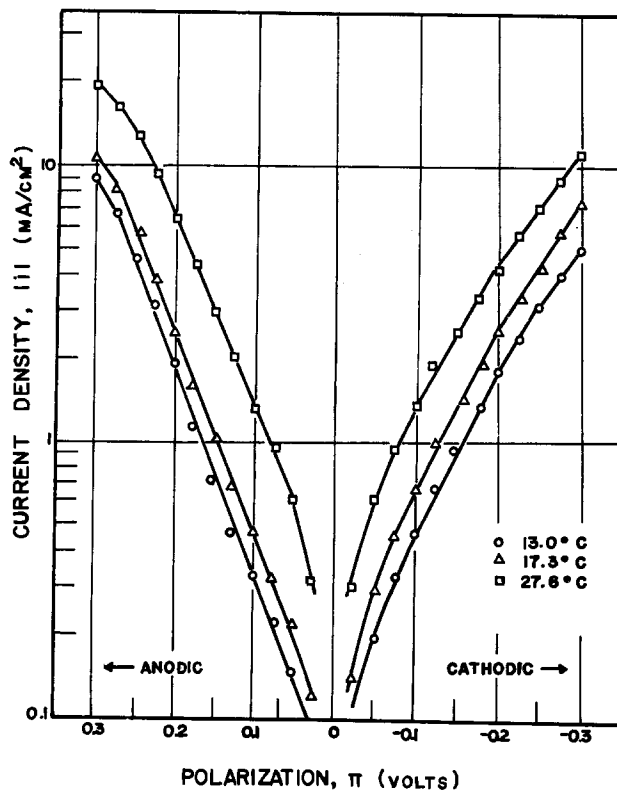


Fig. 2. Polarization curves for Gd in pH 6.46 acetate buffer at 13.0°, 17.3°, and 27.6°C.

anodic reactions is shown in Fig. 3-5. The maximum pH-temperature variation estimated from thermodynamic data (21) is about the same as the uncertainty of pH values measured at 25°C ( $\pm 0.03$  pH units); no correction was attempted. The effect of acetate ion concentration on anodic reaction rate at pH 5.45 is shown in Fig. 6. A constant ionic strength ( $I = 1.00M$ ) was maintained by addition of  $NaClO_4$ .

Table I. Experimental transfer coefficients

T (°C)	$\alpha_c$	$\alpha_a$
5.6	0.31	0.38
7.3	0.33	0.41
10.1	0.30	0.41
13.0	0.33	0.40
16.2	0.34	0.40
17.3	0.35	0.40
19.0	0.34	0.39
21.2	0.36	0.40
23.3	0.34	0.38
25.6	0.33	0.41
27.6	0.35	0.38
29.7	0.32	0.37
Average	0.33	0.40

For the HER the average reaction order is  $-1.11 \pm 0.06$  (95% confidence limits). As summarized in Table II, the Gd dissolution reaction orders with respect to both pH and acetate ion are zero within experimental error. In all cases there is no apparent temperature dependence.

**Temperature dependence.**—The temperature dependence of each reaction rate was determined at a constant cell potential with respect to a reference electrode at room temperature. The thermal liquid junction potential (TLJP) developed in the solution (1.00M NaAc/HAc) salt bridge was estimated from published data (22) and found to be negligible (0.02 mV/deg) over the temperature range used. Most other electrochemical  $E_A$  determinations have been made for acidic or alkaline solutions in which the TLJP's are large and not accurately known. This has led to use of isothermal working and reference electrodes which introduces additional uncertainties since the temperature dependence of the reference electrode-solution potential difference is unknown.

Current densities for the HER at  $-1.220V$  vs. SHE (25°C) were obtained from the experimental polarization curves for all temperatures and pH values. This cell potential was chosen so that  $i$  for each run would

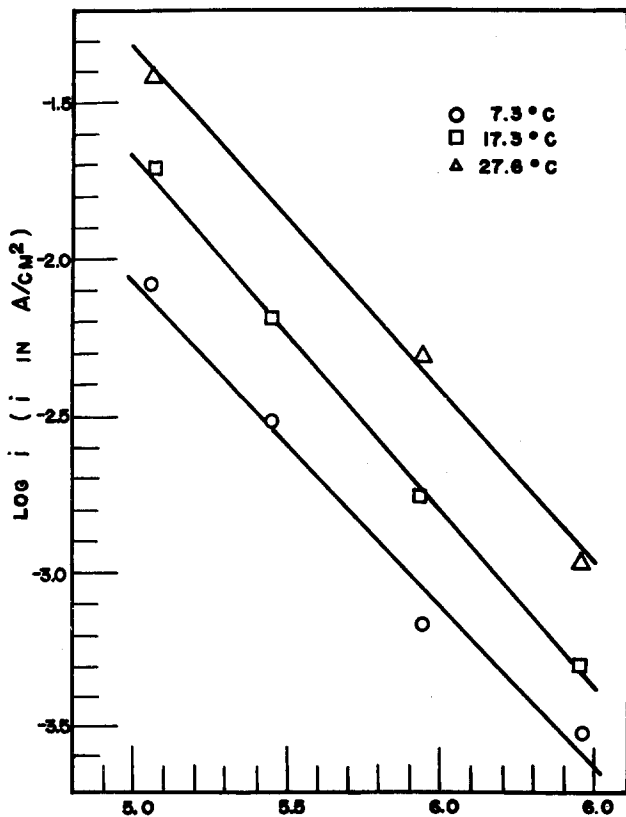


Fig. 3. Cathodic  $\log i$  vs. pH at 7.3°, 17.3°, and 27.6°C ( $i$  measured at  $-1.220V$  vs. SHE).

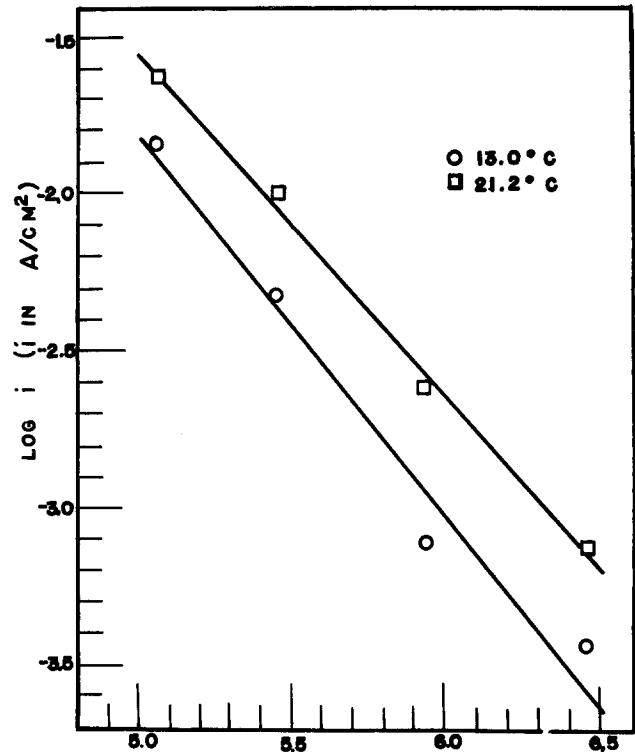


Fig. 4. Cathodic  $\log i$  vs. pH 13.0° and 21.2°C ( $i$  measured at  $-1.220V$  vs. SHE).

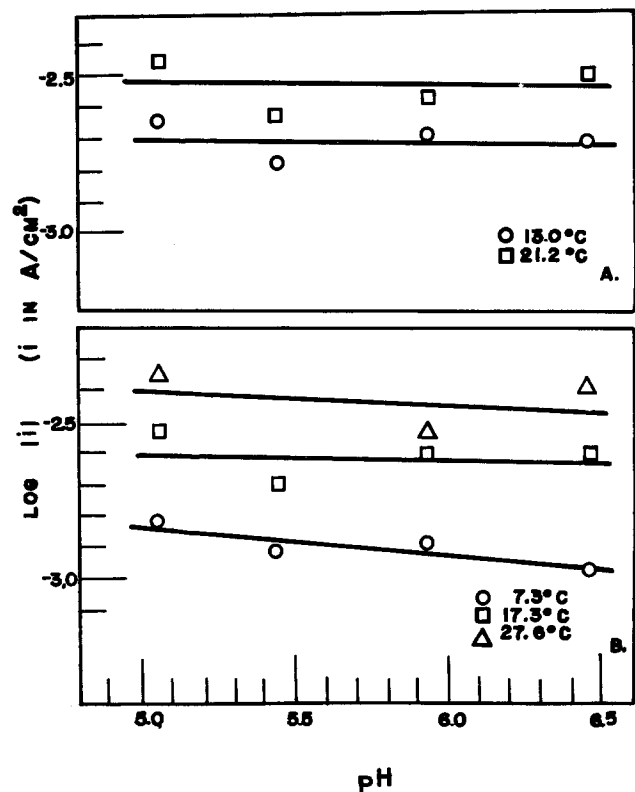
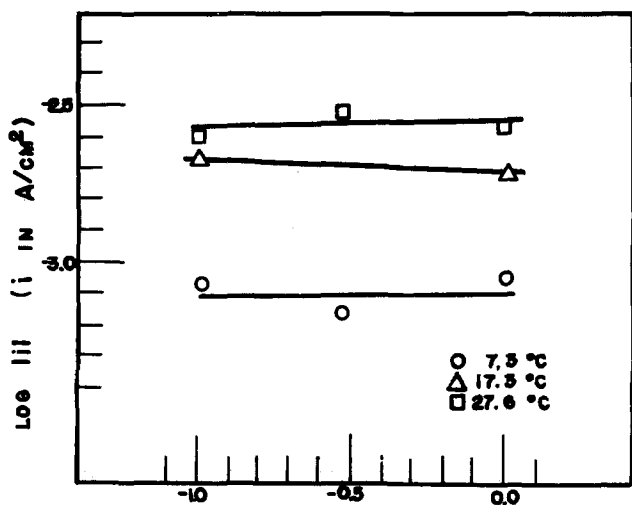


Fig. 5. Anodic  $\log |i|$  vs. pH ( $i$  measured at  $-0.920V$  vs. SHE).

be in the linear region of the  $\ln i$  vs.  $\pi$  plot. The  $\ln i$  values for pH 5.06, 5.45, and 6.46 were then converted to the corresponding values for pH 5.94. Results representing 63 runs at 12 temperatures are shown in Fig. 7 with mean deviations. Values of the  $E$ 's, intercepts (B), and standard deviations calculated for the over-all curve and indicated high and low temperature intervals using replicated data linear least squares method are given in Table III. An analysis of variance of re-



LOG C<sub>Ac<sup>-</sup></sub> (C<sub>Ac<sup>-</sup></sub> IN MOLE/L)  
 Fig. 6. Anodic log |i| vs. log (acetate concentration)

gression was carried out (23). The amount of deviation using the two individual lines is significantly reduced compared to the over-all regression line (ratio of mean squares = 4.13;  $F_{0.05,2/59} = 3.15$ ). The difference between the slopes of the individual lines is significant at the  $F_{0.01}$  level.

The data treatment for the Gd dissolution reaction was analogous to the HER except that no pH normalization was necessary. The  $i$ 's were measured at  $-0.920V$  vs. SHE (25°C). Results from 65 runs at 12 temperatures are shown in Fig. 8. Calculated values are given in Table III. A highly significant reduction in the amount of deviation is obtained by using the high and low temperature intervals as compared to the over-all regression line (ratio of mean squares = 10.41;  $F_{0.01,2/61} = 4.98$ ). This is due primarily to the significant difference in the two individual slopes for which ratio = 19.20;  $F_{0.01,1/61} = 7.08$ .

Standard  $E_A$  values were not necessary for this study which is concerned only with such changes at a given potential. For completeness the approximate  $E_A$ 's at the standard potentials,  $V^{\circ}_j$ , of the  $H^+/H_2$ , and  $Gd^{3+}/Gd$  electrodes were calculated by adding

Table II. Reaction orders

T (°C)	Cathodic		Anodic	
	$p(H^+)$	$p(H^+)$	$p(H^+)$	$p(Ac^-)$
7.3	1.04 ± 0.13	0.10 ± 0.15	0.01 ± 0.14	—
13.0	1.20 ± 0.20	0.01 ± 0.08	—	—
17.3	1.13 ± 0.13	0.02 ± 0.12	-0.03 ± 0.19	—
21.2	1.08 ± 0.13	0.01 ± 0.12	—	—
27.6	1.11 ± 0.11	0.05 ± 0.15	—	—
25.6	—	—	0.04 ± 0.12	—

Table III. Activation energies and preexponential factors

	Cathodic temperature range, (°C)			Anodic temperature range, (°C)		
	(5.6-16.2)	(17.3-29.7)	(5.6-29.7)	(5.6-16.2)	(17.3-29.7)	(5.6-29.7)
$E_A$ (kcal/mole)	8.9 ± 2.4	16.2 ± 2.9	14.5 ± 1.4	12.1 ± 2.0	4.9 ± 2.3	8.3 ± 0.9
$\ln B$	8.9 ± 8.8	21.8 ± 4.9	18.9 ± 2.4	15.0 ± 3.6	2.6 ± 4.0	8.3 ± 1.6
No. of runs	29	34	63	30	35	65
OSS <sup>a</sup>	1.93627667	1.39671461	3.7997982	0.36008640	0.98830610	1.8085222
$E^{\circ}$ (kcal/mole) <sup>b</sup>	18	26	24	25	18	21

95% confidence limits shown.  
<sup>a</sup> Over-all sum of squares of deviations.  
<sup>b</sup>  $E_A$  referenced to standard potentials.

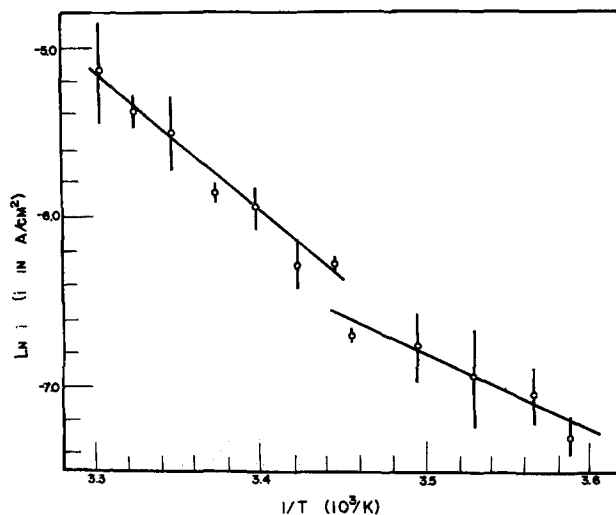


Fig. 7. Cathodic  $\ln i$  at  $-1.220V$  (vs. SHE) vs.  $1/T$

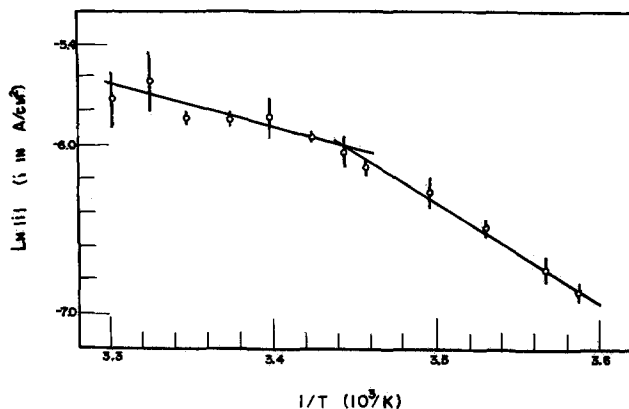


Fig. 8. Anodic  $\ln |i|$  at  $-0.920V$  (vs. SHE) vs.  $1/T$

$\alpha_j F(V - V^{\circ}_j)$  to the experimental  $E_A$ 's and are given in Table III.<sup>1</sup>

Discussion

The results can be divided into two groups: (i) transfer coefficients and reaction orders relating to HER at Gd and the anodic dissolution of Gd, and (ii) the rates of these reactions as a function of temperature. There is no detectable change in the quantities of the first group over the temperature range studied. This indicates that the mechanisms of these reactions are the same for paramagnetic and ferromagnetic gadolinium. Both reactions are charge-transfer controlled under the conditions of interest; possible mech-

<sup>1</sup> The  $V^{\circ}$  value of the Gd/Gd<sup>3+</sup> electrode, taken as  $-2.29V$  vs. SHE for these calculations, is based on the heat of solution of Gd measurements given by Spedding (24) and by Daire (16). The  $V^{\circ}$  value usually quoted ( $-2.40V$ ) is based on the heat of solution measurements by Bommer (25) which have been criticized by Spedding. Experimental values at 25°C for  $S^{\circ}_{Gd}$  (16.267 eu) (26) and  $S^{\circ}_{Gd^{3+}}$  ( $-48.0$  eu) (27) were used in the calculation of the  $V^{\circ}$  proposed here.



anisms have been analyzed (17). Aspects of the experimental temperature dependence are examined first. Deficiencies of a model based solely on changes in bulk energy of the electrode to explain the temperature dependence are then discussed. A model based on changes in electronic structure of Gd on magnetic ordering as well as changes in this structure near the metal surface is proposed.

Two observations of the  $\ln i$  vs.  $1/T$  curves are especially pertinent. (i) The magnitudes of the apparent changes in  $E_A$  of the HER and the Gd dissolution reaction at  $T_C$  are almost the same (but in opposite directions). (ii) For both reactions there is a simultaneous change in the preexponential factor in such a way as to give a practically smooth over-all  $\ln i$  vs.  $1/T$  curve. These observations can be rationalized if it is recognized that any possible contribution to  $E_A$  due to "magnetic" order in the ferromagnetic state will decrease as  $T_C$  is approached. It is reasonable to assume that such contributions are absent in the paramagnetic state and take that as "normal." Then the ferromagnetic contribution to the over-all activation energy below  $T_C$  can be written in the form

$$E_F = \kappa f(T/T_C) E^{\circ}_F \quad [1]$$

where  $f(T/T_C) \rightarrow 0$  as  $T \rightarrow T_C$ ,  $\kappa$  is a constant, and  $E^{\circ}_F$  is the energy contribution at  $T = 0$ . The assumed form of Eq. [1] implies that  $\kappa$  can be identified with the symmetry factor or Bronsted coefficient appearing in linear free energy relationships. To this approximation,  $\kappa$  is a constant for reactions of similar type and can take on the values  $0 < \kappa < 1$ . It is often found that  $\kappa \simeq 1/2$ .

The magnitude of  $E_F$  is apparently the same for the HER and Gd dissolution reaction, but the contribution is such that the over-all  $E_A$  of the HER is decreased while that of the anodic reaction is increased in the ferromagnetic state. The cathodic and anodic current densities can then be expressed as

$$i_c = B_c \exp [-(E_{c,p} - E_F)/RT] \exp [-\alpha_c FV/RT] \quad [2a]$$

$$-i_a = B_a \exp [-(E_{a,p} + E_F)/RT] \exp [\alpha_a FV/RT] \quad [2b]$$

in which temperature-independent terms are contained in the  $B$  factors and  $E_{c,p}$  and  $E_{a,p}$  are the "paramagnetic" cathodic and anodic activation energies. Rearrangement yields Eq. [3]

$$\ln i_c - E_F/RT = -1/RT(E_{c,p} + \alpha_c FV) + \ln B_c \quad [3a]$$

$$\ln |i_a| + E_F/RT = -1/RT(E_{a,p} - \alpha_a FV) + \ln B_a \quad [3b]$$

Application of these equations to the experimental data with suitably chosen values of  $\kappa$ ,  $E^{\circ}_F$ , and the function  $f(T/T_C)$  should result in  $(\ln i \pm E_F/RT)$  vs.  $1/T$  plots linear over the entire temperature range. Further discrimination of mechanisms is based on the estimation of  $E_F$  and prediction whether the over-all  $E_A$ 's should be increased or decreased by its application.

At a given potential vs. a reference electrode the electronic energy levels in different metal electrodes are considered to be equal. Under this condition, there is essentially no explicit dependence of the rates of an electrode reaction on the work functions of different metals (28). For reactions in which there is strong interaction with the electrode, differences in these rates from one metal to another are thought to be due primarily to differences in the adsorption energy of reactant on the metal (28, 29). The HER, involving the adsorption of hydrogen atoms, is the best known example of this type of dependence. For metal deposition and dissolution reactions, the free energies of ionic solvation, ionization of the metal atom, and cohesion of different metals must also be taken into account.

The results for Gd might be considered to be those for two "different" metals, paramagnetic Gd and ferro-

magnetic Gd. Therefore, the HER results might be interpreted as being due to changes in the energy of adsorption of hydrogen atoms. For Gd dissolution, the metal cohesion energy and the energy of adsorption of intermediate adatoms or adions might be affected by the degree of magnetic order.

It would be difficult to calculate the energies of adsorption and cohesion in detail. They can be estimated, however, if it is assumed that they are due solely to the bulk exchange energy of the metal. The Weiss molecular field theory is the simplest model that can be expected to give a reasonable estimate of the over-all exchange energy of Gd. Calculations based on this theory are given in the Appendix. The calculated contributions to  $\ln i$  are quite small even with  $\kappa = 1$ . At the lowest temperature (5.6°C)  $E_F/RT$  is 0.10, and decreases rapidly at higher temperatures. There is little effect on the experimental  $\ln i$  vs.  $1/T$  plots, and there is still a significant difference between the high and low temperature slopes. Since these calculations represent an expected upper limit, a model based solely on over-all changes in the bulk metal energy as influencing the energies of adsorption and cohesion appears to be inadequate.

Consideration of the probable surface properties of a ferromagnetic substance also leads to difficulties in the interpretation given above. Although little is known about these properties, the collective nature of ferromagnetism alone leads to an expected decrease in the degree of magnetic order near the surface of a ferromagnet. A recent analysis based on a molecular field model indicates that near the Curie temperature the relative magnetization near the surface is (30)

$$\delta \propto (1 - T/T_C) \quad [4]$$

while the bulk value is

$$\delta \propto (1 - T/T_C)^{1/2} \quad [5]$$

Therefore near  $T_C$  the molecular field quantity  $U_M$  should be much smaller near the surface than in the bulk. Observations of the magnetic properties of thin evaporated films of nickel indicate that the apparent  $T_C$  decreases with decreasing film thickness (31). A 20Å Ni film has no spontaneous magnetization at room temperature, and the magnetization vs.  $T$  curves are considerably flatter than those of the bulk metal. A similar decrease in magnetization with decreasing film thickness has been reported for electroplated Ni, Fe, and Co. These observations indicate that very near the surface the electronic structure of a ferromagnetic metal must change more or less abruptly to the corresponding paramagnetic structure. This is expected to be especially true near the  $T_C$  of the bulk material.

The magnetic ordering in rare earth metals is thought to occur through an indirect exchange mechanism between the highly localized magnetic 4f electrons via spin polarized conduction electrons. Gadolinium, one of the simpler examples, shows only ferromagnetic behavior below the Curie point. Conduction band and Fermi surface calculations have been made for Gd (32, 33). The calculated conduction bands are quite different from those of the free-electron model and resemble those of the transition metals. There is a high density of states near the Fermi level. Ordering of the 4f moments introduces energy gaps in the conduction bands at or near the Fermi surface and "destroys" large segments of the surface (34). These gaps are about the same magnitude as the exchange coupling,  $j_{sf}$ , between the 4f and conduction electrons. There is then an exchange splitting of the conduction bands. This splitting has been used to explain an experimentally observed infrared absorption peak of ferromagnetic Gd (35-37). This peak occurs at about 0.70 eV at low temperature, shifts to longer wavelengths as the temperature is increased, and disappears above  $T_C$ .

The shift correlates with the spontaneous magnetization-temperature curve of Gd within the accuracy limits of the measurements (37). The value of  $j_{sf}$  estimated from the "excess" moment of Gd (i.e.,  $7.55 \mu_B$  instead of  $7.0 \mu_B$ ) and the calculated density of states at the Fermi level is  $0.087 \text{ eV}$  (34). The value calculated from the absorption peak at  $0.70 \text{ eV}$  is  $0.10 \text{ eV}$ .

It is proposed that the existence of such energy gaps at or near the Fermi level of the ferromagnetic bulk metal, relative to the paramagnetic surface layers, introduces an energy gradient for the transport of electrons near the metal surface. The qualitative features of the experimental results could be explained if this gradient favors the transport of electrons to the electrode surface (as in the HER) below the Curie temperature while the transport of electrons to the bulk metal (as in Gd dissolution) is simultaneously retarded. The magnitude of the effect should be the same for the two reactions, in accordance with the results. Furthermore, if it is assumed that  $E_F$  can be identified with  $j_{sf}$  and  $f(T/T_C)$  with  $\delta$ , Eq. [1] becomes, with  $\kappa = 1/2$

$$E_F = 1/2 \delta j_{sf} \quad [6]$$

The application of this equation with  $j_{sf} = 0.10 \text{ eV}$  to the experimental points using Eq. [3] is shown in Fig. 9 and 10. There is no significant difference between the slopes of the paramagnetic and ferromagnetic curves. The lines drawn in Fig. 9 and 10 correspond to the pooled high and low temperature slopes and intercepts. Although the pooled slopes fit the data quite well, there appears to be small residual changes in the intercepts ( $\ln B_j$ ) at the Curie point. Due to the approximate nature of the model it is not at present possible to comment on the reality of these changes.

An expression for the mixed potential of the electrode can be obtained from Eq. [2] by setting  $i_c$  equal to  $|i_a|$ . Using  $E_F$  from Eq. [6],  $V_M$  is given by

$$V_M = \frac{1}{(\alpha_a + \alpha_c)F} \left[ j_{sf}\delta + E_{a,p} - E_{c,p} + RT \ln \frac{B_c}{B_a} \right] \quad [7]$$

In terms of the pooled  $E_A$ 's (both referenced to the SHE) and pooled intercepts,  $V_M$  can be evaluated as

$$V_M = 0.1378 - 1.663 + 2.025 \times 10^{-3}T \quad (\text{volts}) \quad [8]$$

Calculated values of  $V_M$  as a function of temperature are shown in Fig. 11. The magnitude of the changes and shape of the curve agrees well with the experimental curve (17). Good agreement is also obtained with Daire's (15) data in  $0.1M \text{ GdCl}$ , after fitting the second and third terms of Eq. [8] to the "paramagnetic" part of his data.

The deduction of Eq. [6] is admittedly rough and intuitive. One of the major assumptions concerns the direction of the proposed energy gap gradient. Photoemission results (38) for Gd indicate that the energy

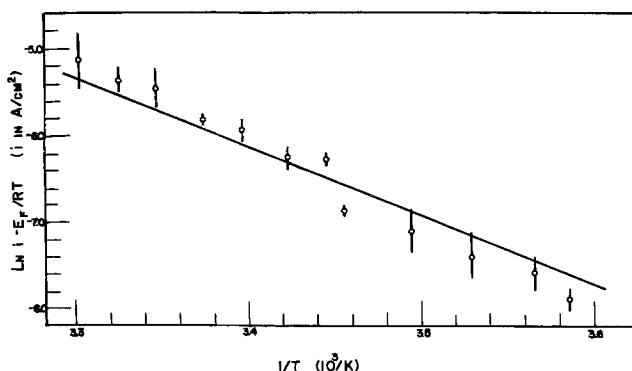


Fig. 9. Cathodic  $\ln |i| - E_f/RT$  vs.  $1/T$

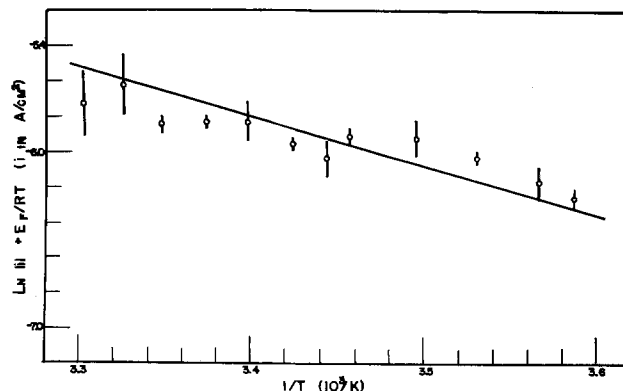


Fig. 10. Anodic  $\ln |i| + E_f/RT$  vs.  $1/T$

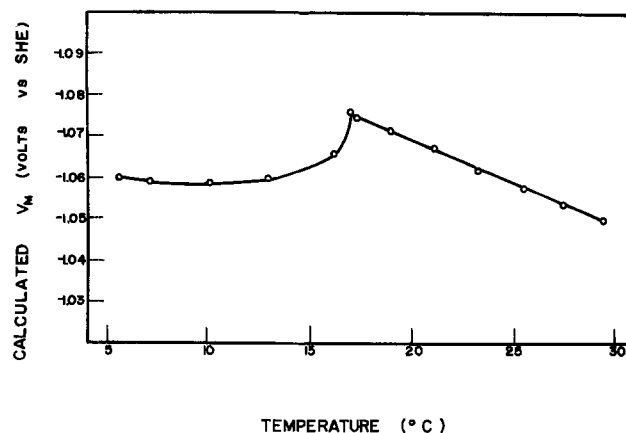


Fig. 11. Calculated mixed potential vs. temperature

distribution curves at  $-80^\circ$  and  $25^\circ\text{C}$  are identical in shape (the resolution was  $0.1 \text{ eV}$ ). The curve at  $-80^\circ\text{C}$  is shifted to higher energies by about  $0.03 \text{ eV}$  from the  $25^\circ\text{C}$  curve. Intermediate temperature results lie between these two curves. This gives a rough indication that the Fermi level is higher in the ferromagnetic state than in the paramagnetic state and supports the proposed direction of the energy gradient. Although the identification of  $j_{sf}$  as the over-all energy change may be an oversimplification, the experimental results are adequately represented by the magnitude and temperature dependence of this quantity.

### Conclusions and Implications

The proposition given above is an attempt to explain the experimental results in terms of the magnetic properties of gadolinium. It is, in part, contrary to most of the commonly accepted notions of the role of a metal electrode in electrochemical reactions. It is difficult to rationalize all of the observations in terms of accepted theories. Although Gd may represent a special case, it is felt that attempts to apply free-electron models to real metals and ignoring possible changes in electron structure very near the metal surface cannot be expected to yield a quantitative description of the electrochemical behavior of a metal electrode.

Acceptance of the proposed model implies that similar considerations may also apply to Fe, Co, and Ni. All are ferromagnetic at temperatures normally encountered in electrochemical measurements, and thermal behavior similar to that considered here is not expected. Although speculative, it is possible that some peculiarities of their electrochemical behavior may be partially explained in terms of the model given here. It is known that chemisorption of some species can alter the magnetization of very small "superparamagnetic" particles (39). Chemisorption on Fe, Co, and Ni electrodes might also modify the "magnetic" properties of

the surface relative to the bulk metal and influence any existing gradient. It is likely that the initial stage of anodic passivation of these metals is accompanied by the adsorption of an oxygen anion (40). This adsorption may result in an increase in the gradient (and increase in activation energy) for metal dissolution. The consequent "electronic inhibition" could be partially responsible for the abrupt and pronounced onset of passivity for these metals when only a very thin "film" is present.

#### Acknowledgments

The authors gratefully acknowledge the financial support of the Robert A. Welch Foundation of Houston, Texas. D.W.D. would also like to thank the Phillips Petroleum Company for financial assistance.

Manuscript submitted June 4, 1975; revised manuscript received ca. March 23, 1976.

Any discussion of this paper will appear in a Discussion Section to be published in the June 1977 JOURNAL. All discussions for the June 1977 Discussion Section should be submitted by Feb. 1, 1977.

Publication costs of this article were assisted by Rice University.

#### APPENDIX

In the Weiss molecular field theory the total exchange energy contribution to the internal energy of the solid is (41)

$$U_M = -\frac{1}{2}\gamma M_s(O)2\delta^2 \quad [A-1a]$$

where  $\gamma$  is molecular field constant,  $\delta = M_s(T)/M_s(O)$ , and  $M_s(T)$  is the saturation magnetization at the temperature  $T$ . Using  $\gamma$  calculated from the  $T_C$  and the experimental value of  $M_s(O)$  (42),  $U_M$  can be estimated as

$$U_M \simeq -7.0 \times 10^2 \delta^2 \quad (\text{cal/mole}) \quad [A-1b]$$

The experimental temperature variation of  $\delta$  near the  $T_C$  of Gd can be represented by the Brillouin function with  $J = 7/2$

$$\delta = \frac{2J+1}{2J} \coth \frac{2J+1}{J} x - 1/2J \coth(x/2J) \quad [A-2a]$$

where

$$x = (3J/J+1)(T_C/T)\delta \quad [A-2b]$$

For the experimental temperature range discussed here,  $T \rightarrow T_C$  and a series expansion of the coth  $y$  terms of Eq. [A-2a] can be used to obtain an explicit expression for  $\delta$  in terms of  $T/T_C$ .

Using the above assumptions and Eq. [A-1a] and [A-1b] the magnitude of the exchange contribution to the  $E_A$ 's can be expressed as

$$E_F = (\kappa\gamma/2)M_s(O)2\delta^2 \quad [A-3a]$$

$$E_F \simeq 7.0 \times 10^2 \kappa\delta^2 \quad (\text{cal/mole}) \quad [A-3b]$$

where  $f(T/T_C)$  is identified as  $\delta^2$ .

#### REFERENCES

- J. A. Hedvall, "Solid State Chemistry," pp. 78-93, Elsevier Publishing Co., Amsterdam (1966).
- P. W. Selwood, "Magnetochemistry," 2nd ed., pp. 404-407, Interscience, New York (1956).
- F. F. Roca, *Ann. Chim.*, **2**, 255 (1967).
- G. Cohn and J. A. Hedvall, *J. Phys. Chem.*, **46**, 841 (1942).
- H. H. Uhlig and A. de S. Brasunas, *Trans. Electrochem. Soc.*, **97**, 448 (1950).
- D. A. Dowden, *J. Chem. Soc.*, **1950**, 242.
- J. Lielmezs and J. P. Morgan, *Chem. Eng. Sci.*, **22**, 781 (1967).
- B. E. Conway, E. M. Beatty, and P. A. D. DeMaine, *Electrochim. Acta*, **7**, 39 (1962).
- P. Borggrafe and H. G. Feller, *Corrosion Sci.*, **7**, 265 (1965).
- J. Osterwald and H. H. Uhlig, *This Journal*, **108**, 515 (1961).
- A. K. Vijh and A. Belanger, *Z. Physik Chem. Neue Folge*, **83**, 173 (1973).
- Alfred Clark, "The Theory of Adsorption and Catalysis," p. 338, Academic Press, New York (1970).
- M. Pourbaix, "Atlas of Electrochemical Equilibria," p. 185, Pergamon Press, London (1966).
- J. K. Prall and P. R. Doidge, *Nature*, **199**, 800 (1963).
- M. Daire, *Electrochim. Acta*, **15**, 211 (1970).
- M. Daire, *C. R. Acad. Sci. Paris*, **266** (Ser. C), 1111 (1968).
- D. W. DeBerry, Ph.D. Thesis, Rice University, May 1974.
- E. R. Brown, T. G. McCord, D. E. Smith, and D. D. DeFord, *Anal. Chem.*, **38**, 1119 (1966).
- R. L. Ritchie, *J. Am. Chem. Soc.*, **89**, 1447 (1967).
- S. L. Morse and N. D. Greene, *Electrochim. Acta*, **12**, 179 (1967).
- H. S. Harned and B. B. Owen, "The Physical Chemistry of Electrolytic Solutions," 2nd ed., Reinhold, New York (1950).
- A. J. de Bethune, *This Journal*, **107**, 829 (1960).
- P. D. Lark, B. R. Craven, and R. C. L. Bosworth, "The Handling of Chemical Data," p. 170, Pergamon Press, Oxford (1968).
- F. H. Spedding and J. P. Flynn, *J. Am. Chem. Soc.*, **76**, 1474 (1954).
- H. Bommer and E. Hohmann, *Z. Anorg. Allgem. Chem.*, **248**, 357 (1941).
- F. J. Jelinek, B. C. Gerstein, M. Griffel, R. E. Shochdople, and F. H. Spedding, *Phys. Rev.*, **149**, 489 (1966).
- S. L. Bertha and G. R. Choppin, *J. Inorg. Chem.*, **8**, 613 (1969).
- A. N. Frumkin, *J. Electroanal. Chem.*, **9**, 173 (1965).
- R. Parsons, *Surface Sci.*, **2**, 418 (1964).
- T. Wolfram and R. D. Dewames, *Prog. Surface Sci.*, **2**, 234 (1972).
- E. C. Crittenden, Jr. and R. W. Hoffman, *Rev. Mod. Phys.*, **25**, 310 (1953).
- J. O. Dimmock and A. J. Freeman, *Phys. Rev. Letters*, **13**, 750 (1964).
- S. C. Keeton and T. L. Loucks, *Phys. Rev.*, **168**, 672 (1968).
- R. E. Watson, A. J. Freeman, and J. P. Dimmock, *Phys. Rev.*, **167**, 497 (1968).
- C. C. Schuler, "Optical Properties and Electronic Structure of Metals and Alloys," F. Abeles, Editor, p. 221, North-Holland, Amsterdam (1965).
- J. N. Hodgson and B. Cleyet, *Proc. Phys. Soc., London, Solid St. Phys., Ser. 2*, **2**, 97 (1969).
- Yu. V. Knyazev and M. M. Noskov, *Phys. Metals, Metallog.*, **31**, 211 (1971).
- A. J. Blodgett, Jr., W. E. Spicer, and A. Y-C. Yu, *Rev. Mod. Phys.*, **25**, 256 (1953).
- P. W. Selwood, "Adsorption and Collective Paramagnetism," Academic Press, New York (1962).
- Norman Hackerman, *Z. Elektrochem.*, **62**, 632 (1958).
- D. H. Martin, "Magnetism in Solids," p. 225, Iliffe, London (1967).
- H. E. Nigh, S. Levgold, and F. H. Spedding, *Phys. Rev.*, **132**, 1092 (1963).

# The Conductance of Heptyl Viologen Dibromide in Water and Methanol

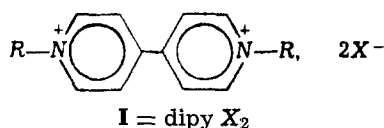
H. T. van Dam

Philips Research Laboratories, Eindhoven, The Netherlands

## ABSTRACT

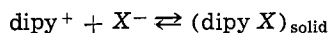
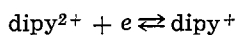
The conductance of heptyl viologen dibromide in water and methanol has been measured. The data have been treated according to the theory of Murphy and Cohen, extended to account for incomplete dissociation. In water, heptyl viologen dibromide is completely dissociated; in methanol, the dissociation of the second bromide ion is incomplete with a dissociation constant  $K = 5.5 \times 10^2$ . The heptyl viologen ion obeys the Walden rule in these two solvents.

The 4,4'-dipyridinium compounds (I) known as the viologens form a group of 2-1 electrolytes, which are interesting because of their ability to form stable, colored radical ions on reduction. This property proves to be very useful since it provides the basis of a feasible electrochemical display (1)

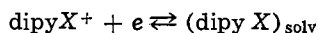


We found that with a proper choice of the substituent  $R$  and the anion  $X^-$  in (I) the reduced form is insoluble in water. This is not the case in organic solvents such as acetonitrile, acetone, or methanol. We also observed that the reduction potentials depend on the anion concentration only for the case of water. We have explained these differences in behavior as follows (2). In water the electroactive species is the completely dissociated ion  $\text{dipy}^{2+}$  but in organic solvents one  $X^-$  remains attached and  $\text{dipy } X^+$  is reduced instead, i.e., we have the following reaction scheme

in water



in organic solvent



In order to check the above hypotheses, we have measured both in water and in methanol the ionic conductivity of heptyl viologen dibromide as a much-used representative of the viologen. In this way one should be able to obtain information on the presupposed degree of dissociation. Methanol was selected as the organic solvent because accurate measurements of transference numbers in that solvent are available and from these the equivalent conductance of some anions.

## Experimental

**Materials.**—Heptyl viologen dibromide was prepared using the Menschutkin reaction as described previously (2). The product was recrystallized twice from ethanol, the first time with norit. Benzene was added and the ethanol distilled off azeotropically. After filtration the remaining benzene was removed *in vacuo* until constant weight was attained. The analysis of  $\text{Br}^-$  gave the theoretical value; the optical density of a 0.1 mole liter<sup>-1</sup> solution in water at 400 nm was less than 0.07.

The water used was obtained by distilling deionized water to which some NaOH pellets and some  $\text{KMnO}_4$  crystals had been added. The resultant liquid was distilled twice under nitrogen in a quartz still. Con-

Key words: viologen, conductivity, electrochromic, display.

ductivity was better than  $0.4 \times 10^{-6} \text{ ohm}^{-1} \text{ cm}^{-1}$ . Methanol *p.a.* from Merck was used as received. Conductivity was  $0.6 \times 10^{-6} \text{ ohm}^{-1} \text{ cm}^{-1}$ . Potassium chloride suprapure from Merck was dried to constant weight.

**Measurements.**—All solutions were prepared by weighing. Cell constants were determined according to Lind *et al.* (3). Cell resistances were measured with a Jones conductivity bridge 4666 from Leeds and Northrop using  $0.4 V_{\text{rms}}$  at 1 kHz as input signal. The output signal was fed to a Phillips PM 7835 synchronous amplifier. The two d-c outputs of this amplifier were made to vanish by the adjustment of the bridge. A series of measurements was done at different frequencies of 1, 2, 5, and 10 kHz. Extrapolation to infinite frequencies showed a polarization error of 0.04%. The cells were immersed in a 70 liter oil bath kept at  $25^\circ \pm 0.02^\circ\text{C}$ .

**Equations for the conductivity.**—For the analysis of the conductivity data we have used the theory of Murphy and Cohen (4), which is an improvement of the Fuoss-Onsager theory and applicable to asymmetric electrolytes. This means that for any electrolyte a distance of closest approach can be calculated from conductance data. It also means that deviations from the theory expected for what we call weak electrolytes can be detected on the same basis for asymmetric electrolytes as for symmetric ones. These deviations are accounted for in the usual way (5); we start from the expression for the equivalent conductance  $\Lambda_{\text{th}}$  given by Murphy and Cohen's theory (see Appendix)

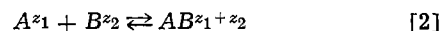
$$\Lambda_{\text{th}} \equiv \Lambda_0 + \Lambda_1 \beta \kappa + \Lambda_2^1 (\beta \kappa)^2 \ln \beta \kappa + \Lambda_2 (\beta \kappa)^2 \quad [1]$$

where

$$\beta \kappa = 8.4042 \times 10^6 \times |z_+ z_-| \frac{I^{1/2}}{(DT)^{3/2}}$$

and  $I$  = ionic strength =  $\frac{1}{2} \sum_i z_i^2 c_i$ ;  $c_i$  = concentration of ion  $i$  in mole liter<sup>-1</sup>;  $D$  = relative dielectric constant of the solvent;  $T$  = temperature in  $^\circ\text{K}$ ;  $z_i$  = valency of ion  $i$ . This equation is used to fit conductivity data with a least squares method;  $\Lambda_1$  and  $\Lambda_2^1$  are given by the theory while  $\Lambda_0$  and  $\Lambda_2$  are adjustable parameters.  $\Lambda_0$  is the conductance at infinite dilution and  $\Lambda_2$  is a function of the distance of closest approach,  $a$ , between the ions. Once  $\Lambda_2$  is determined experimentally  $a$  can be calculated from the expression for  $\Lambda_2$  given by Murphy and Cohen.

If the electrolyte  $A_{z_1}B_{z_2}$  is not completely dissociated the following equilibrium exists



with equilibrium constant

$$K_1 = \frac{[AB^{z_1+z_2}]}{[A^{z_1}][B^{z_2}]} \quad [3]$$

When the electrolyte is asymmetric the species  $AB^{z_1+z_2}$  is charged and contributes to the conductivity. This means that we now have a mixture whose conductivity can be calculated using the "mixture rule" (6). If a fraction  $\alpha_1$  of  $A^{z_1}$  is present this rule states that the specific conductance of the mixture is given by

$$\rho^{-1}_{\text{mixt}} = \alpha_1 \rho^{-1}(A^{z_1}, B^{z_2}) + (1 - \alpha_1) \rho^{-1}(AB^{z_1+z_2}, B^{z_2}) \quad [4]$$

where  $\rho^{-1}(A^{z_1}, B^{z_2})$  is the specific conductivity of  $A_{z_2}B_{z_1}$  at the total ionic strength. Let us now suppose that the only difference between  $A^{z_1}$  and  $AB^{z_1+z_2}$  is the electric charge. In that case they have the same mobility and distance of closest approach towards  $B^{z_2}$  and their equivalent conductances can be calculated from [1]. Now  $\Lambda = 1/\rho c$  where  $c$  is the equivalent concentration according to  $c = |z_i|c_i$ . The equivalent concentration of the complex electrolyte  $AB^{z_1+z_2}, B^{z_2}$  is therefore given by  $|z_1| - |z_2| |c_1|$  or  $|z_2| |c_1 - c_2|$  and we have

$$\Lambda_{\text{mixt}} \equiv \frac{1}{\rho_{\text{mixt}} c} = \alpha_1 \Lambda(A^{z_1}, B^{z_2}) + \frac{|z_1| - |z_2|}{|z_1|} (1 - \alpha_1) \times \Lambda(AB^{z_1+z_2}, B^{z_2}) \quad [5]$$

from which

$$\alpha_1 = \frac{\Lambda_{\text{mixt}} - \Lambda(AB^{z_1+z_2}, B^{z_2}) \frac{|z_1| - |z_2|}{|z_1|}}{\Lambda(A^{z_1}, B^{z_2}) - \Lambda(AB^{z_1+z_2}, B^{z_2}) \frac{|z_1| - |z_2|}{|z_1|}} \quad [6]$$

Introducing  $\alpha_1$  into [3] we have

$$K_1 = \frac{(1 - \alpha_1) c_1 f_{\pm}(AB^{z_1+z_2}, B^{z_2})}{\alpha_1 c_1 \{c_2 - (1 - \alpha_1) c_1\} f_{\pm}(A^{z_1}, B^{z_2})} \quad [7]$$

where  $\ln f_{\pm} = -\frac{1}{2} \beta \kappa$  different for the different species because of  $\beta$ .

Introducing a constant  $\gamma$  defined by

$$\gamma c \equiv |z_1| \alpha_1 c_1 + |z_1| - |z_2| | (1 - \alpha_1) c_1 \quad [8]$$

we can rewrite [7] as

$$\alpha_1 = 1 - \frac{\alpha_1 c}{|z_2|} K_1 \gamma \frac{f_{\pm}(A^{z_1}, B^{z_2})}{f_{\pm}(AB^{z_1+z_2}, B^{z_2})} \quad [9]$$

which becomes with the help of [6]

$$\Lambda_{\text{mixt}} = \Lambda(A^{z_1}, B^{z_2}) - \frac{1}{|z_2|} K_1 c \gamma \frac{f_{\pm}(A^{z_1}, B^{z_2})}{f_{\pm}(AB^{z_1+z_2}, B^{z_2})} \times \left\{ \Lambda_{\text{mixt}} - \Lambda(AB^{z_1+z_2}, B^{z_2}) \left( 1 - \left| \frac{z_2}{z_1} \right| \right) \right\} \quad [10]$$

While checking the calculations with measurements taken from the literature, it was found that in solvents with a small dielectric constant negative values for  $\alpha_1$  are obtained. This points to the following equilibrium



with corresponding constant  $K_2$  given by

$$K_2 = \frac{[AB^{z_1+2z_2}]}{[AB^{z_1+z_2}][B^{z_2}]} \quad [12]$$

With  $\gamma$  defined by

$$\gamma c \equiv \alpha_1 c_1 + |z_1| - |z_2| | (1 - \alpha_1) \alpha_2 c_1 + |z_1| - 2|z_2| | (1 - \alpha_1) (1 - \alpha_2) c_1 \quad [13]$$

we have similar to [7]

$$\frac{(1 - \alpha_1) \alpha_2}{\alpha_1} = \frac{1}{|z_2|} K_1 c \gamma \frac{f_{\pm}(A^{z_1}, B^{z_2})}{f_{\pm}(AB^{z_1+z_2}, B^{z_2})} \quad [14a]$$

and

$$\frac{1 - \alpha_2}{\alpha_2} = \frac{1}{|z_2|} K_2 c \gamma \frac{f_{\pm}(AB^{z_1+z_2}, B^{z_2})}{f_{\pm}(AB^{z_1+2z_2}, B^{z_2})} \quad [14b]$$

From the mixture rule we find  $\alpha_1$  in terms of the equivalent conductances of the different species in the mixture as in [6]. Combining, we obtain finally

$$\Lambda_{\text{mixt}} = \Lambda(A^{z_1}, B^{z_2}) - \frac{1}{|z_2|} \left\{ K_1 c \gamma \frac{f_{\pm}(A^{z_1}, B^{z_2})}{f_{\pm}(AB^{z_1+z_2}, B^{z_2})} + \frac{1}{|z_2|} K_1 K_2 (c \gamma)^2 \frac{f_{\pm}(A^{z_1}, B^{z_2})}{f_{\pm}(AB^{z_1+2z_2}, B^{z_2})} \right\} \times \left\{ \Lambda_{\text{mixt}} - \alpha_2 \left( 1 - \left| \frac{z_2}{z_1} \right| \right) \Lambda(AB^{z_1+z_2}, B^{z_2}) - (1 - \alpha_2) \left( 1 - 2 \left| \frac{z_2}{z_1} \right| \right) \Lambda(AB^{z_1+2z_2}, B^{z_2}) \right\} \quad [15]$$

The calculation proceeds as follows: with some assumed value for the equivalent conductance at infinite dilution  $\Lambda_0$ ,  $\Lambda_{\text{mixt}}$  is approximated and using Eq. [6] and [8] a set of values for  $\gamma$  is obtained. With these the  $\Lambda_{\text{mixt}}$  is corrected and a new set of  $\gamma$ 's is obtained. This process is repeated until it is internally consistent. With a least squares method, values for  $\Lambda_2$  of Eq. [1],  $K_1$  and  $K_1 K_2$  are calculated. In this run  $\alpha_2$  is taken to be equal to 1, from  $K_2$  a set of  $\alpha_2$  values is obtained, and the whole procedure is repeated. If  $K_2 < 0$ , then  $K_2$  is put equal to 0, the calculation starts again; if now  $K_1 < 20$ ,  $K_1$  is also assumed to vanish. The reason for rejecting small positive  $K_1$  values is that the  $\Lambda_2$  and the  $K_1$  terms in [14] or rather [9] then show almost the same concentration dependence and discrimination between them becomes difficult. With the values for the parameters obtained in this way, the whole procedure is again repeated until consistent. From  $\Lambda_2$  a value for the distance of closest approach,  $a$ , is determined, which provides a check for the acceptability of the procedure:  $\Lambda_2$  is a sensitive function of  $a$  and only a small range, different for different electrolytes, corresponds with physically reasonable values.

As an example, we have analyzed the precision data (7) of the conductivity of KCl and NaCl in methanol (Table I). The discrepancy between Gordon's results and those of Evers and of Frazer remains and is worse in fact since Gordon used 31.52 for the dielectric constant of methanol. Evers and Frazer's results agree to 0.02% when treated in the same way, but are still inconsistent with the transference numbers of Gordon (8),  $\Lambda_0$  for KCl being too large and for NaCl too small.

Frazer's data for  $\text{AgNO}_3$  were also treated because this was the one electrolyte that did not give the correct slope at infinite dilution; it does when a slight association is taken into account.

Table I. Parameters for some salts in methanol at 25°C

Substance	Source	$\Lambda_0$ (lit.)	$\Lambda_0$	$-\Lambda_1$	$\Lambda_2^1$	$\Lambda_2$	$a$ (Å)	Remarks
KCl	Gordon	104.78	104.62	27.77	4.330	3.17	3.76	
KCl	Frazer	105.95	104.94	27.80	4.357	0.02	3.42	
KCl	Evers	104.93	104.90	27.80	4.353	1.93	3.59	
NaCl	Gordon	97.61	97.45	27.07	3.732	4.44	4.31	
NaCl	Frazer	96.95	97.17	27.04	3.709	4.56	4.34	
NaCl	Evers	97.25	97.23	27.05	3.714	4.27	4.28	
$\text{AgNO}_3$	Frazer	112.95	110.77	28.37	4.842	-4.22	3.02	$K_1 = 42$

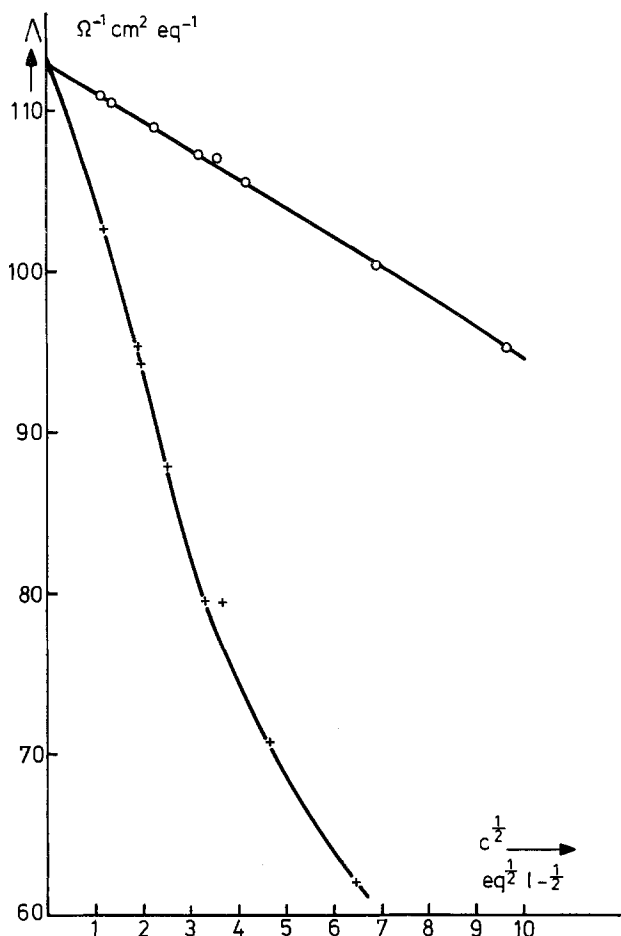


Fig. 1. Equivalent conductance of heptyl viologen dibromide, ○ in water, + in methanol.

### Results and Discussion

In Table II the equivalent conductance of heptyl viologen dibromide in water and in methanol is given. In Table III and Fig. 1 the results of the analysis for this compound are given. It is seen that in water this compound behaves as a strong electrolyte and that therefore the species  $\text{dipy}^{2+}$  occurs exclusively. In methanol however, a finite  $K_1$  value is needed to fit the results, corresponding to a degree of dissociation  $\alpha_1 = 0.34$  at a concentration of  $0.004 \text{ mole liter}^{-1}$ . Here  $(\text{dipy X})^+$  is the predominant species. These conclusions support the reaction scheme of the reduction of viologen given in the introduction. The similarity be-

Table II. Equivalent conductance of heptyl viologen dibromide at 25°C

In water		In methanol	
$c \times 10^4$ equiv. $\text{l}^{-1}$	$\text{ohm}^{-1} \text{cm}^2$ equiv. $\text{l}^{-1}$	$c \times 10^4$ equiv. $\text{l}^{-1}$	$\text{ohm}^{-1} \text{cm}^2$ equiv. $\text{l}^{-1}$
1.274	110.90	1.459	102.73
1.897	110.46	3.676	95.36
5.198	108.92	3.789	94.19
10.185	107.34	6.326	87.85
12.646	106.99	10.964	79.47
17.380	105.57	13.290	79.53
48.325	100.34	21.816	70.75
93.123	95.21	41.970	62.08

Table III. Conductance parameters of heptyl viologen dibromide

Solvent	$\Lambda_0$	$-\Delta_1$	$\Delta_2'$	$\Delta_2$	$a(\text{\AA})$	$K_1$	Remarks
Water	112.73	28.38	-1.223	-6.78	3.74	0	$\alpha_1 = 0.34$
Methanol	112.48	23.15	2.105	-9.69	4.15	546	At $c = 0.002$ equiv. $\text{l}^{-1}$

tween the  $\Lambda_0$  values in the two solvents is remarkable; this is also observed for some other bis-quaternary ammonium or pyridinium compounds (9). The Walden product of these compounds for the positive ion mobilities only is found to be constant, for heptyl viologen 0.309 in water and 0.305 in methanol. This ion obeys Stokes' law and this implies that it moves freely and is not solvated. Because of this a comparison of reduction potentials in different solvents is meaningful.

Lastly, we note that the distance of closest approach,  $a$ , is about 4Å. The same order of magnitude is found, when analyzed in the same way, for Fuoss' bolaform electrolytes (9), which have a charge distribution similar to the viologens. The magnitude of the molecule as a whole is immaterial, the anions seek the locations of the positive charge. Fuoss *et al.* obtained larger values (about 7Å) from their dissociation constant. This constant, however, describes more than the known electrostatic interactions in contrast to Murphy and Cohen's  $\Delta_2$  function.

Manuscript submitted June 13, 1975; revised manuscript received Sept. 22, 1975.

Any discussion of this paper will appear in a Discussion Section to be published in the June 1977 JOURNAL. All discussions for the June 1977 Discussion Section should be submitted by Feb 1, 1977.

Publication costs of this article were assisted by Philips Research Laboratories.

### APPENDIX

For convenience, the expressions for the different coefficients in Murphy and Cohen's equation are given

$$\Lambda_1 = -\frac{q^2 \Lambda_0}{3(1+q)} + (z_1 + z_2) \frac{eF}{6\pi\eta\beta}$$

(the Onsager slope)

$$\Delta_2' = \frac{q^2 \Lambda_0}{6} - (z_1 + z_2) \frac{eF}{6\pi\eta\beta} \left( \frac{q^2}{2} - \frac{(z_1 + z_2)^2}{2z_1 z_2} \right)$$

where  $\eta$  = the viscosity of the solvent;  $F$  = the Faraday constant;  $e$  = elementary charge

$$q = \frac{|z_1 z_2|}{|z_1| + |z_2|} \frac{\Lambda_0}{|z_1| \Lambda_0^{(1)} + |z_2| \Lambda_0^{(2)}}$$

where  $\Lambda_0^{(i)}$  is the equivalent conductance of ion  $i$  at infinite dilution.

$$\begin{aligned} \Delta_2 = & -\frac{q^2 \Lambda_0}{6} \left[ -1.154430 \right. \\ & + \frac{6q + 15q^2 + 21q^3 - 13q^4 - 35q^5 + 6q^6}{12q^2(1+q)(1-q^2)} \\ & - \frac{2 - q^2(1-q^2)}{2(1-q^2)} \ln(2+q) - \frac{1-2q^2}{1-q^2} \ln(1+2q) \\ & - \frac{(1-q^2)^2}{2q^2} \ln(1+q) + Ei(b) - [e^b(23b^2 + 9b + 12) \\ & \quad \left. - 6b^3 - 8b^2 - 9b - 12](18b^3)^{-1} \right. \\ & \left. - \frac{(z_1 + z_2)^2}{2z_1 z_2(1-q^2)} \left( \frac{1}{3} - \frac{2q^2}{1-q^2} \ln \frac{3}{2+q} \right) \right] \\ & + \frac{eF(|z_1| + |z_2|)}{6\pi\eta\beta} \left[ \frac{18q + 61q^2 + 21q^3 - 6q^4}{48q^2(1+q)} \right. \\ & \quad + [(1-2q+q^2+q^3-q^5) \ln(1+q) \\ & \quad \left. - (1+q^2)(1-q) \ln(1-q) \right. \\ & \quad \left. - (2+q+q^2+5q^3-q^5) \ln(2+q) + (1+q^2) \right. \\ & \quad \left. \times (2-q) \ln(2-q) \right] (8q^3)^{-1} + (q^2 b)^{-1} \end{aligned}$$

$$\begin{aligned}
& + \frac{1}{2} [Ei(b) - 1.154430] \\
& + [e^b(-5b^5 - 36b^4 + 30b^3 + 30b^2 - 18b - 36) \\
& + 6b^4 - 45b^3 + 6b^2 + 54b + 36](108b^5)^{-1} \\
& - (q^2 z_1 z_2)^{-1} \sum_{n=3}^{\infty} \frac{(b/z_1 z_2)^{n-2}}{n!(n-2)} \left( \frac{z_1^n - z_2^n}{z_1 - z_2} \right)^2 \\
& + \frac{(z_1 + z_2)^2}{2q^2 z_1 z_2} \left( 0.577215 + \ln 3 - \ln b + \frac{1}{6} \right) \\
& - \frac{eF(|z_1| + |z_2|)}{72\pi\eta\beta\Lambda_0 b^4} \left[ e^b(b^4 + 5b^3 + 3b^2 - 12b + 6) \right. \\
& \quad \left. - \frac{9}{2} b^4 - 3b^3 + 6b^2 + 6b - 6 \right]
\end{aligned}$$

Murphy and Cohen define the exponential integral  $Ei(-x)$  only for  $x > 0$ . For  $x < 0$  we have used in our calculations the principal value of this integral. It is easily shown that for  $x > 0$

$$\begin{aligned}
Ei(x) & \equiv -PP \int_{-x}^{\infty} \frac{e^{-t}}{t} dt \\
& = Ei(-x) + \sum_{k=0}^{\infty} \frac{2x^{2k+1}}{(2k+1)(2k+1)!}
\end{aligned}$$

## REFERENCES

1. C. J. Schoot, J. J. Ponjeé, H. T. van Dam, R. A. van Doorn, and P. T. Bolwijn, *Appl. Phys. Letters*, **23**, 64 (1973); with S. van Houten, SID International Symposium, p. 146, (1973).
2. H. T. van Dam and J. J. Ponjeé, *This Journal*, **121**, 1555 (1974).
3. J. E. Lind, J. J. Zwolenik, and R. M. Fuoss, *J. Am. Chem. Soc.*, **81**, 1557 (1959).
4. T. J. Murphy and E. G. D. Cohen, *J. Chem. Phys.*, **53**, 2173 (1970); *ibid.*, **56**, 3734 (1972).
5. H. Falkenhagen, W. Ebeling, and W. D. Kraeft, "Ionic Interactions," Vol. I, S. Petrucci, Editor Chap. 2 (1970).
6. D. G. Miller, *J. Phys. Chem.*, **71**, 616 (1967).
7. J. P. Butler, H. I. Schiff, and A. R. Gordon, *ibid.*, **19**, 752 (1951); E. C. Evers and A. G. Knox, *J. Am. Chem. Soc.*, **73**, 1739 (1951); J. E. Frazer and H. Hartley, *Proc. Roy. Soc. (London)*, **A109**, 351 (1925).
8. J. A. Davies, R. L. Kay, and A. R. Gordon, *J. Chem. Phys.*, **19**, 749 (1951).
9. O. V. Brody and R. M. Fuoss, *J. Am. Chem. Soc.*, **79**, 1530 (1957).

## Concentration Profile of $\text{CuSO}_4$ in the Cathodic Diffusion Layer

Yasuhiro Awakura and Yoshio Kondo

Department of Metallurgy, Kyoto University, Sakyo-ku, Kyoto 606, Japan

## ABSTRACT

The concentration profile of  $\text{CuSO}_4$  in the cathodic diffusion layer which is accompanied by the upward natural convection along the plane vertical cathode was measured by holographic interferometry in aqueous solutions containing 0.05 and 0.1 mol/liter  $\text{CuSO}_4$ . The measurement was conducted at various heights from the lower edge of cathode. The cathodic current density was also varied. The theoretical expressions of the concentration difference between the cathode surface and the bulk electrolyte and the thickness of the diffusion layer were derived under the assumption of uniform cathodic current density distribution. Experimental results obtained at the current densities far lower than the limiting value were in good agreement with the theoretical value.

Since it was recognized (1-3) that the natural convection along the surface of a plane vertical electrode plays an important role in the electrolysis of an unstirred aqueous solution, many theoretical and experimental studies have been carried out on the velocity profile of vertical convective flow in the hydrodynamic boundary layer (4-7), the concentration profile in the diffusion layer (8-10), and the resultant distribution of local current densities on the electrode surface (11-13). This convective flow is caused by the density difference between the solution in the diffusion layer and the bulk electrolyte: the direction of convective flow is upward or downward depending on whether the density in the diffusion layer is lower or higher than in the bulk electrolyte.

Wagner (2) studied the vertical distribution of the limiting current density on the surface of a copper plane cathode which is solely determined by the transfer rate of  $\text{Cu}^{2+}$  ion through the diffusion layer. He also measured the average limiting current density on

the copper plane vertical cathode of different heights and demonstrated that the experimental results were in excellent agreement with the theory.

Industrial electrolytic refining and plating are usually conducted below the limiting current density. In this region of lower cathodic current densities, Asada *et al.* (13) proposed a theoretical procedure of calculating the distribution of current density on a plane vertical cathode immersed in an unstirred electrolyte. In order to verify the theoretical current density distribution, Asada weighed the electrodeposited copper after cutting the cathode plate into slices in the horizontal direction.

A few experimental studies have been made, on the other hand, to measure the concentration profile of  $\text{CuSO}_4$  in the diffusion layer near the cathode surface. However, the thickness of this diffusion layer is about 0.1 cm or less, and the measurements were difficult. The measuring precision of the freezing method conducted by Brenner (8, 9) is supposed to be insufficient. An optical measurement using the technique of Jamin interferometry was proposed by Ibl (10). In this mea-

Key words: vertical electrode, holographic interferometry, natural convection, ionic diffusion.

surement, however, the optical precision imposed on the electrolytic cell is so strict that only cells of smaller size can be used because of the difficulty in the preparation. Thus Ibl measured the concentration profile of CuSO<sub>4</sub> at a height of only 0.9 cm from the lower edge of cathode.

Holographic interferometry (14-16) is employed in the present work to measure the concentration profile of CuSO<sub>4</sub> in the cathodic diffusion layer. One major experimental advantage of this technique is the employment of common path interference, which is different from the two-beam interference used in the above-mentioned Jamin interferometry. Because of this advantage, it becomes possible to measure the concentration profile along the surface of a taller plane cathode installed in a large electrolytic cell of lower optical precision.

**Theoretical**

In the hydrodynamic boundary layer, a volume element of (*d* × *l* × *dx*) is presumed at a height *x* from the lower edge of cathode. The integrated Navier-Stokes equation (5) concerning this volume element is expressed as

$$\frac{d}{dx} \int_0^l u^2 dy = \alpha g \int_0^l \theta dy - \nu \left( \frac{du}{dy} \right)_{y=0} \quad [1]$$

The mass balance equation of Cu<sup>2+</sup> ion is

$$\frac{d}{dx} \int_0^l u \theta dy = \frac{i(1 - t_1)}{z_1 F} \quad [2]$$

In order to integrate Eq. [1] and [2], it is presumed according to Ibl (5) that the concentration profile of CuSO<sub>4</sub> in the diffusion layer and the velocity profile of upward convective flow in the hydrodynamic boundary layer are expressed by the following equations

$$\theta = \theta \left( 1 - \frac{y}{\delta} \right)^\omega \quad [3]$$

$$\left. \begin{aligned} u &= \frac{u_m}{\lambda - 1} \left[ \lambda \frac{y}{\tau} - \left( \frac{y}{\tau} \right)^\lambda \right] && \text{for } 0 \leq y \leq \tau \\ u &= u_m \left[ 1 - \frac{y - \tau}{\epsilon \tau} \right] && \text{for } \tau \leq y \leq (\epsilon + 1)\tau \end{aligned} \right\} \quad [4]$$

respectively. In these equations,  $\delta = \eta\tau$  and  $l = (\epsilon + 1)\tau$ . Substitution of Eq. [3] and [4] in Eq. [1] and [2] yields upon integration

$$0 = \left( \frac{\alpha g}{\omega + 1} \right) \delta \theta - \left( \frac{\nu \eta \lambda}{\lambda - 1} \right) \frac{u_m}{\delta} \quad [5]$$

and

$$\frac{\Phi}{\eta(\lambda - 1)} \frac{d}{dx} (u_m \theta \delta) = \frac{i(1 - t_1)}{z_1 F} \quad [6]$$

respectively. The term on the left-hand side of Eq. [1] is much smaller than each term on the right-hand side of the same equation (2), and it was omitted in Eq. [5]. The symbol  $\Phi$  in Eq. [6] is

$$\begin{aligned} \Phi &= \frac{\lambda(\eta - 1)\omega + 2}{\eta^\omega(\omega + 1)(\omega + 2)} \left[ \left( \frac{\eta}{\eta - 1} \right)^{\omega + 2} \right. \\ &\quad \left. - \frac{\lambda - 1}{\epsilon \lambda} - \frac{\omega + 2}{\lambda(\eta - 1)} - 1 \right] - \eta^{\lambda + 1} B_{1/\eta}(\lambda + 1, \omega + 1) \end{aligned} \quad [7]$$

and

$$B_a(b, c) = \int_0^a t^{b-1} (1 - t)^{c-1} dt \quad [8]$$

By eliminating *u<sub>m</sub>* from Eq. [5] and [6], we have

$$\frac{\Phi}{(\omega + 1)\eta^{2\lambda}} \frac{\alpha g}{\nu} \frac{d}{dx} (\delta^3 \theta^2) = \frac{i(1 - t_1)}{z_1 F} \quad [9]$$

On the other hand, the mass transfer equation of cation and anion on the cathode surface are written as (3)

$$\frac{i}{z_1 F} = k_1 \left( \frac{dc}{dy} \right)_{y=0} + cU_1 \left( \frac{d\phi}{dy} \right)_{y=0} \quad [10]$$

and

$$0 = k_2 \left( \frac{dc}{dy} \right)_{y=0} - cU_2 \left( \frac{d\phi}{dy} \right)_{y=0} \quad [11]$$

respectively. The first and second terms on the right-hand side of Eq. [10] and [11] represent the rate of mass transfer due to diffusion and migration, respectively. After eliminating the term  $(d\phi/dy)_{y=0}$  in Eq. [10] and [11] which represents the potential gradient on the cathode surface, we have

$$\frac{i^* t_2}{z_1 F} = D \left( \frac{dc}{dy} \right)_{y=0} \quad [12]$$

where

$$t_2 = 1 - t_1 = \frac{U_2}{U_1 + U_2}$$

$$D = \frac{k_2 U_1 + k_1 U_2}{U_1 + U_2}$$

Substitution of Eq. [3] in Eq. [12] yields

$$\frac{\omega D \theta}{\delta} = \frac{i^* t_2}{z_1 F} \quad [13]$$

It is noted that Eq. [9] and [13] are the basic equations of mass transfer in the cathodic diffusion layer which is accompanied by upward natural convection. The solution of simultaneous Eq. [9] and [13] under the assumption that  $\theta = c$ , for example, reveals the distribution of the local current densities and the thickness of the diffusion layer at the limiting current density. Furthermore, by combining Eq. [9] and [13] with the Laplace equation in the form of  $\Delta\phi = 0$ , which determines the potential distribution within the electrolytic cell and the rate equation of electrode reactions, it is possible to obtain the general solution which holds below the limiting current density.

When the current density is lower than about one-half of the limiting value, it was shown (12, 17) that the local current density is regarded as being equal from bottom to top of the cathode surface. Under this condition of  $i = \text{const}$ , the following expressions of concentration difference and diffusion layer thickness are obtained from Eq. [9] and [13]

$$\Delta c = \theta = \frac{\eta E}{\omega} \frac{t_2}{z_1 F D} \left( \frac{z_1 F \nu D^2}{g \alpha^* t_2} \right)^{1/5} i^{4/5} x^{1/5} \quad [14]$$

$$\delta = \eta E \left( \frac{z_1 F \nu D^2}{g \alpha^* t_2} \right)^{1/5} i^{-1/5} x^{1/5} \quad [15]$$

where

$$E = \left[ \frac{\omega^2 (\omega + 1) \lambda}{\Phi \eta^3} \right]^{1/5}$$

Furthermore, the modified Grashof number of

$$Gr^* = \frac{g \alpha^* t_2 i x^4}{z_1 F \nu^2 D} \quad [16]$$

and the Sherwood number in the form of

$$Sh_x = \frac{k_x x}{D} \quad [17]$$

where the mass transfer coefficient *k<sub>x</sub>* is defined as

$$\frac{i^* t_2}{z_1 F} = k_x \Delta c \quad [18]$$

are employed together with the Schmidt number



$$Sc = \frac{v}{D} \quad [19]$$

Equations [14] and [15] are then rewritten as

$$Sh_x = \frac{\omega}{\eta E} (Sc \cdot Gr^*)^{1/5} \quad [20]$$

and

$$\frac{\delta}{x} = \eta E (Sc \cdot Gr^*)^{-1/5} \quad [21]$$

respectively.

### Experimental

The experimental arrangement employed in the present work is schematically illustrated in Fig. 1. A helium-neon gas laser emitter L of 10 mW output was used as the light source. The laser beam was split into two beams by a half-mirror B. A reference beam was reflected on the mirrors  $M_1$  and  $M_4$  and expanded by a lens  $E_2$ , and the beam intensity was adjusted by an attenuation polarizer A. Then it was transmitted to a photographic plate H. Another beam was collimated to a diameter of 1.2 cm by the lenses  $E_1$  and  $L_1$ . After passing through the vicinity of the cathode surface in the electrolytic cell C, it was joined with the reference beam on the same photographic plate: the image of the vicinity of the cathode surface was magnified about fifteen diameters and the back edge of the cathode surface facing the camera was focused on the screen SC by a lens  $L_2$ . After the photographic plate was developed, the hologram was reset at the same position in the frame of the plate holder. With the reference beam incident upon this hologram, the wave front of the beam which was passed through the electrolytic cell was reconstructed. By superposition with the beam which was passed through the electrolytic cell, a parallel interference fringe was easily obtained on the screen. Then the position of the cathode surface of the reconstructed image and the real image was finely adjusted by a rack and pinion mechanism within an error of  $10\mu$ . When the electrolysis was started, this fringe was shifted due to the concentration gradient formed in the diffusion layer. Then the real silhouette of the cathode surface on the screen SC appears to be advanced into the solution side of the interface due to the gradient of the refractive index. However, the position of the cathode surface of the reconstructed image does not change during the electrolysis, and this position was taken as the origin of horizontal distance from the cathode surface.

The electrolytic cell is illustrated in Fig. 2. The inner dimensions of the cell were 0.7 cm thick, 13 cm wide, and 10 cm high. The copper electrodes were 0.47 cm square and 16 cm long, and the effective electrode area was  $0.47 \times 9.0 \text{ cm}^2$ . The distance between both electrodes was maintained at 10 cm. As mentioned

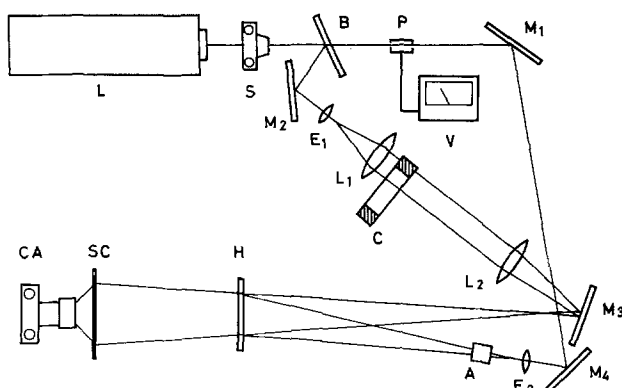


Fig. 1. Experimental arrangement. L, laser emitter; S, shutter; B, beam splitter; P, photometer; V, voltmeter; C, electrolytic cell; CA, camera;  $M_1$ ,  $M_2$ ,  $M_3$ ,  $M_4$ , mirrors;  $E_1$ ,  $E_2$ , expanders;  $L_1$ ,  $L_2$ , lenses; A, attenuation polarizer, H, hologram; SC, screen.

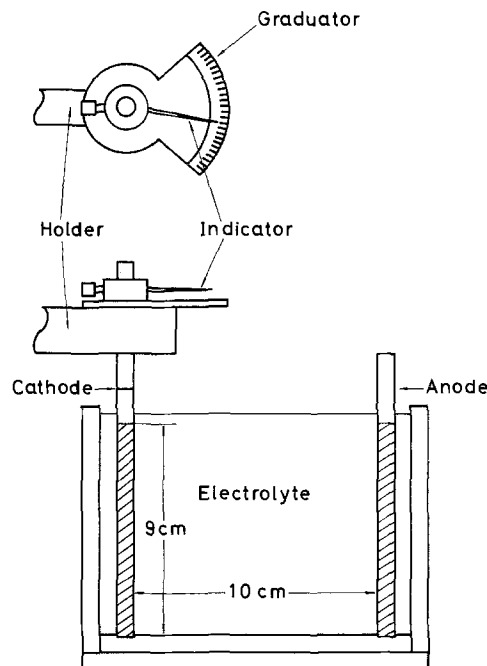


Fig. 2. Electrolytic cell

above, the thickness of the cathodic diffusion layer is less than about 0.1 cm, and it was essential to install the cathode surface parallel to the incident beam. In order to realize this, a revoluble cathode holder was employed, and after the cell wall on the light-entrance side was adjusted to be at right angles to the incident beam, the cathode was gently revolved and maintained at a position where the enlarged silhouette of the cathode surface on the screen SC recedes farthest.

Analytical reagent grade  $\text{CuSO}_4$  and deionized water were used, and the aqueous  $\text{CuSO}_4$  solution was prepared. The experimental conditions are summarized in Table I. The measurement was conducted at  $23^\circ \pm 1^\circ\text{C}$ .

The current-potential curves were measured with the electrolytes shown in Table I, and they are demonstrated in Fig. 3. The average cathodic current densities at which the concentration profile was measured are also shown in the figure. It is seen that the applied current densities ranged up to the limiting value in the solution containing 0.05 mol/liter  $\text{CuSO}_4$  and were below one-half of the limiting value in the solution of 0.1 mol/liter  $\text{CuSO}_4$ .

A few examples of holographic interferograms are shown in Fig. 4. A holographic interferogram near the cathode surface before the start of electrolysis is shown in Fig. 4(a). The horizontal interference fringe in this figure was employed as the reference for measuring the concentration profile. Figures 4(b) through (d) demonstrate the interferograms of 0.05 mol/liter  $\text{CuSO}_4$  solution at an average cathodic current density of 1.84  $\text{mA}/\text{cm}^2$ . The measuring height was varied at 1, 4, and 8 cm from the lower edge of the cathode, respectively. They were filmed after 10 min had elapsed from the start of electrolysis: it was confirmed that the diffusion layer is maintained at the steady state. As seen in Fig. 4(b) through (d), the thickness of diffusion layer increases in the upper portion of cathode. This is due to the upward flow caused by natural convection.

The relationship between the change of the refractive index of the solution and the fringe shift is given

Table I. Experimental conditions

Concentration of $\text{CuSO}_4$ (mol/liter)	0.05, 0.1
Distance from lower edge of cathode (cm)	1.0, 2.0, 4.0, 8.0
Average cathodic current density ( $\text{mA}/\text{cm}^2$ )	0.473, 0.946, 1.42, 1.84, 2.29, 2.76, 3.65, 4.60

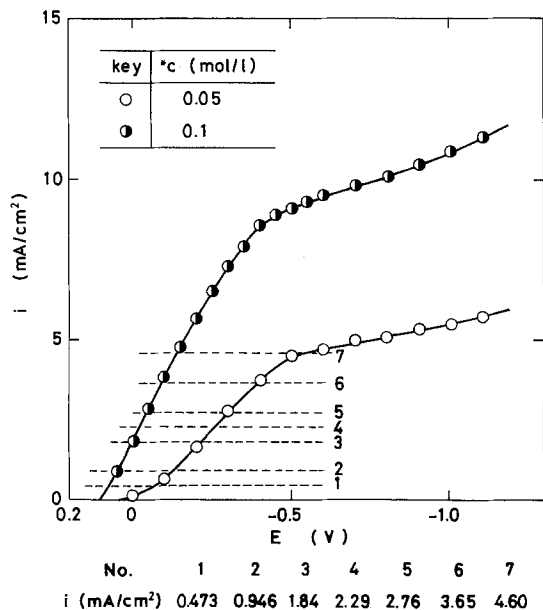


Fig. 3. Current potential curve

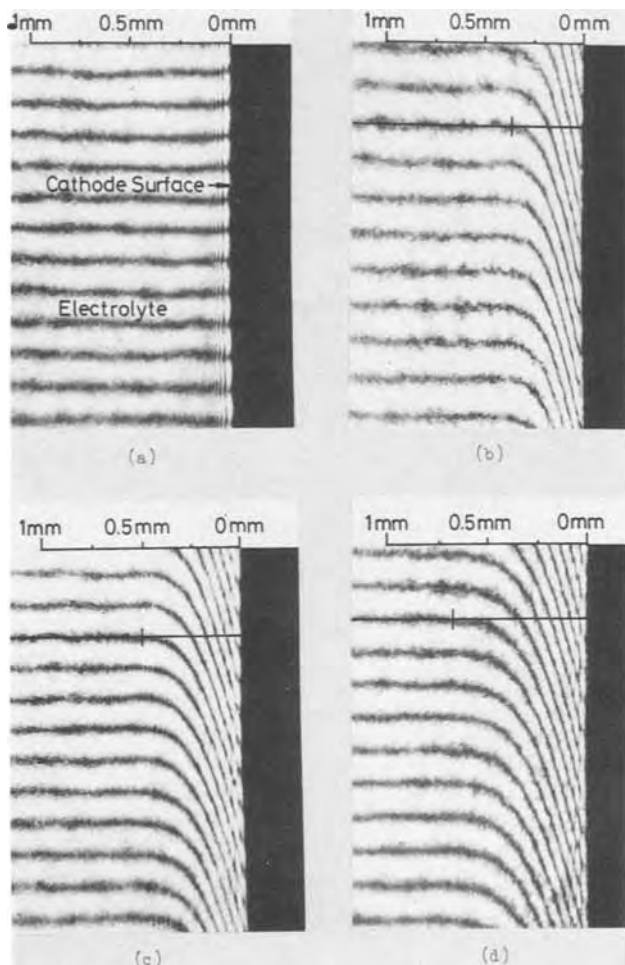


Fig. 4. Holographic interferograms of cathodic diffusion layer: (a) before the start of electrolysis, (b)  $x = 1$  cm, (c)  $x = 4$  cm, and (d)  $x = 8$  cm during the electrolysis of 0.05 mol/liter CuSO<sub>4</sub> solution at  $i = 1.84$  mA/cm<sup>2</sup>.

by (10)

$$\frac{(*n - n)d}{\lambda'} = N \quad [22]$$

When the incident beam is transmitted into a solution

with a varying refractive index, however, the valid profile of the refractive index is not obtained from Eq. [22] (18, 19). This is because the incident beam in the diffusion layer is deflected toward the direction of higher refractive index as shown in Fig. 5 (20).

The corrected profile of the refractive index in the diffusion layer was obtained as follows. The optical path length  $p$  along this deflected trajectory in the solution is obtained from the holographic interferogram as

$$p = *nd - \lambda'N \quad [23]$$

Assuming that the direction of incident beam is at right angles to the inner wall of the electrolytic cell, the beam trajectory in the solution is obtained by the following differential equation (21)

$$\frac{d^2y}{dz^2} = \frac{1}{2n_1^2} \frac{dn^2}{dy} \quad [24]$$

When the change of refractive index is linear in the solution, we have

$$n = n_1 + ky \quad [25]$$

By substituting Eq. [25] in Eq. [24], the maximal difference between the length of this beam trajectory and the electrode width ( $s - d$ ) and the maximal deflection  $\Delta y$  of the incident beam within the solution were calculated along the cathode surface to be 0.42 and 55 $\mu$ , respectively, at the average cathodic current density of 4.6 mA/cm<sup>2</sup> in the solution containing 0.05 mol/liter CuSO<sub>4</sub>. As shown later,  $n_1 = 1.3344$  and  $k = 6.6 \times 10^{-2}$  under these experimental conditions. Since ( $s - d$ ) is very trivial and  $\Delta y$  is far lower than the electrode width, it can be assumed that the refractive index expressed by  $p/d$  represents the mean value along the beam trajectory and that the trajectory is linear. The refractive index obtained corresponds to the value at the middle point M shown in Fig. 5.

The position of point M was calculated in the whole diffusion layer as follows. Provided that the local profile of the refractive index in any small portion of the diffusion layer is expressed as

$$n^2 = b + ay \quad [26]$$

the solution of Eq. [24] is obtained under the following boundary conditions.

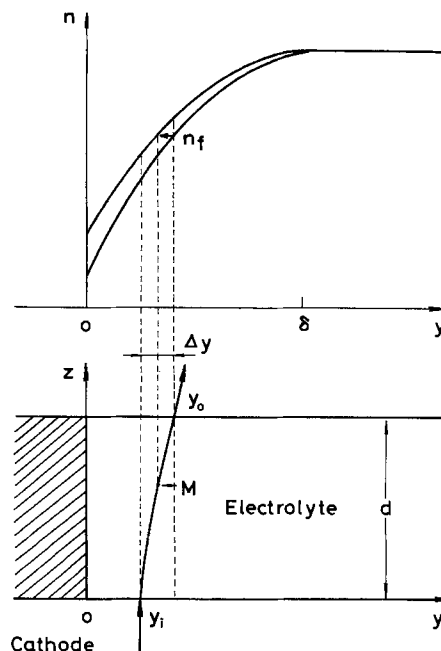


Fig. 5. Schematic illustration of beam deflection and correction of refractive index.

When

$$\left. \begin{aligned} z = 0, & \quad y = y_i \\ z = d, & \quad y = y_o \end{aligned} \right\} \quad [27]$$

$$\begin{aligned} \Delta y &= y_o - y_i \\ &= \frac{ad^2}{4n_i^2} \end{aligned} \quad [28]$$

Then the position of point M is obtained as

$$y_o - \frac{\Delta y}{2} = y_o - \frac{ad^2}{8n_i^2} \quad [29]$$

The constant  $a$  and the refractive index  $n_i$  in this equation were estimated from the holographic interferogram: the refractive indices obtained near point  $y_o$  were substituted in Eq. [26] and  $a$  was estimated by the least squares method. The difference between  $n_i$  and the mean refractive index obtained from the interferogram was minor and the latter index was used in the calculation. Thus the corrected profile of the refractive index in the solution was obtained.

From the regression of the refractive index upon  $\text{CuSO}_4$  concentration in the solution, the concentration was calculated. The regression was expressed as

$$n = 1.3330 + 28.44c \quad [30]$$

in the aqueous  $\text{CuSO}_4$  solution below 0.5 mol/liter at 23°C.

A few examples of the corrected concentration profile are demonstrated in Fig. 6, which was obtained in the 0.05 mol/liter  $\text{CuSO}_4$  solution at a height of 4 cm. The uncorrected concentration profiles at each current density are also shown. It is seen in this figure that  $\text{CuSO}_4$  concentration on the cathode surface is lowered and the thickness of the diffusion layer is decreased when the average cathodic current density is raised. It is furthermore seen that the above-mentioned correction becomes significant when the concentration profile is steeper.

### Discussion

Although the calculating procedure of the profile of the refractive index from the obtained holographic in-

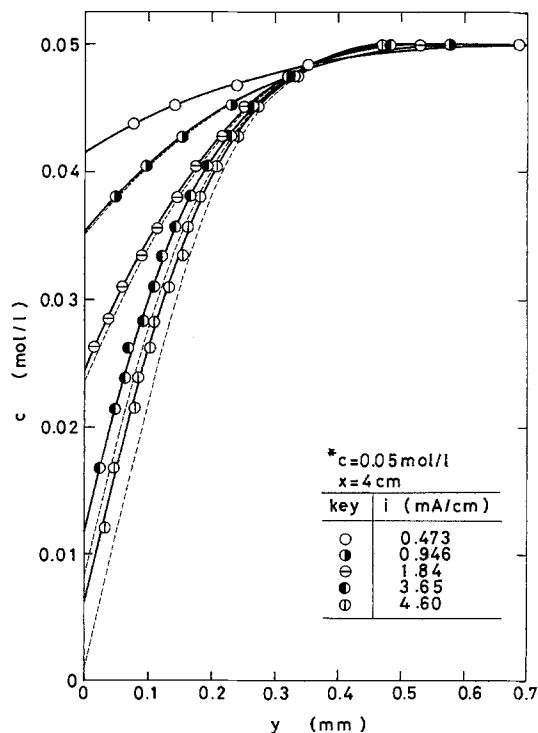


Fig. 6. Concentration profile of  $\text{CuSO}_4$  in the cathodic diffusion layer (broken lines show the uncorrected concentration profile).

terferogram employed in this work is an approximation, it is thought to be satisfactory for calculating the concentration profile in the diffusion layer with a relatively small concentration gradient. Assuming that the variation of the refractive index in the vicinity of the cathode surface is linear as shown in Eq. [25], the deviation of concentration due to the approximation was estimated. In this calculation, the effect of refraction within the back wall of the electrolytic cell was neglected (18).

When the direction of the incident beam is at right angles to the direction of the refractive index gradient in the solution, the optical path length  $p$  along the beam trajectory and the deflection  $\Delta y$  of the incident beam are derived from Eq. [24] (18) as

$$p = \frac{n_i d}{2} + \frac{n_i^2}{4k} \sinh\left(\frac{2kd}{n_i}\right) \quad [31]$$

$$\Delta y = -\frac{n_i}{k} + \frac{n_i}{k} \cosh\left(\frac{kd}{n_i}\right) \quad [32]$$

respectively. From Eq. [31] and [32], the difference between the refractive index  $p/d$  obtained in the preceding section and the refractive index at  $\Delta y/2$  is obtained as

$$\begin{aligned} \Delta n &= \frac{p}{d} - \left( n_i + k \frac{\Delta y}{2} \right) \\ &= \frac{n_i}{2} \cosh\left(\frac{kd}{n_i}\right) \left[ \frac{n_i}{kd} \sinh\left(\frac{kd}{n_i}\right) - 1 \right] \end{aligned} \quad [33]$$

From Eq. [30], on the other hand, the concentration difference  $\Delta c_e$  which corresponds to  $\Delta n$  is

$$\Delta c_e = \frac{\Delta n}{28} \quad [34]$$

The  $\Delta c_e$ -value represents the deviation due to the approximation in estimating the concentration mentioned in the preceding section. From Eq. [34], the maximal  $\Delta c_e$  on the cathode surface was calculated at several cathodic current densities in the solution containing 0.05 mole/liter  $\text{CuSO}_4$  and demonstrated in Table II. The refractive index gradient  $k$  on the cathode surface was calculated by using Eq. [12] and [30] together with the property constants (10, 22, 23) shown in Table III. Furthermore, the average concentration difference  $\bar{\Delta c}$  between the bulk electrolyte and the cathode surface in the vertical direction was obtained from the interferogram and shown in Table II. The relative deviation  $(\Delta c_e / \bar{\Delta c}) \times 100$  is also demonstrated.

Table II. Error due to approximation in 0.05 mol/liter  $\text{CuSO}_4$  solution

$i$ (mA/cm <sup>2</sup> )	$k$ (cm <sup>-1</sup> )	$\Delta y$ ( $\mu$ )	$\Delta c_e$ (mol/liter)	$\bar{\Delta c}$ (mol/liter)	$[\Delta c_e / \bar{\Delta c}]$ $\times 100$ (%)
0.473	$6.79 \times 10^{-3}$	5.6	0.0000164	0.0084	0.195
0.946	$1.36 \times 10^{-2}$	11.3	0.0000862	0.0145	0.594
1.84	$2.04 \times 10^{-2}$	16.9	0.000204	0.0198	1.03
1.84	$2.64 \times 10^{-2}$	21.9	0.000340	0.0234	1.45
2.29	$3.29 \times 10^{-2}$	27.2	0.000532	0.0265	2.01
2.76	$3.96 \times 10^{-2}$	37.8	0.000771	0.0307	2.51
3.65	$5.24 \times 10^{-2}$	43.4	0.00121	0.0353	3.43
4.60	$6.60 \times 10^{-2}$	54.6	0.00215	0.0439	4.90

Table III. Property constants used in the calculation

Concentration of $\text{CuSO}_4$ in solution (mol/liter)	0.05	0.1
$z_1$ (—)	2	2
$D_1$ (cm <sup>2</sup> /sec) (22)	$6.5 \times 10^{-9}$	$6.0 \times 10^{-9}$
$\nu$ (cm <sup>2</sup> /sec) (23)	$1.043 \times 10^{-2}$	$1.902 \times 10^{-2}$
$\alpha_1$ (cm <sup>3</sup> /mol) (10)	151.5	151.5
$t_2$ (—) (10)	0.643	0.643

As seen in this table, the deviation of concentration on the cathode surface is minor when the average cathodic current density is lower. At higher current densities of 3.65 and 4.60 mA/cm<sup>2</sup>, the relative deviation increases to 3.43 and 4.90%, respectively. It is thought, however, that this has only a minor effect on the variation of  $\Delta c$  in the vertical direction, because the deviation is of the same order of magnitude at various heights when the applied cathodic current density is constant.

In order to calculate the concentration difference and the thickness of the diffusion layer by Eq. [14] and [15], respectively, it is necessary to obtain the numerical values of the parameters involved in these equations. The parameter  $\omega$  which influences the concentration profile of CuSO<sub>4</sub> was determined as follows. The logarithm of  $(\theta/\theta)$  in the 0.05 mol/liter CuSO<sub>4</sub> solution was plotted against  $\log(1 - y/\delta)$  in Fig. 7 according to Eq. [3]. As seen in this figure, almost all of the experimental data are scattered within the region between the slopes of 2.0 and 3.0, and  $\omega$  was determined as 2.39 by the least squares method. From a similar plot obtained for the 0.1 mol/liter CuSO<sub>4</sub> solution, the parameter  $\omega$  was estimated to be 2.31: Ibl (5) obtained the numerical value of 2.3 from the interferometric measurement in the 0.6 mol/liter CuSO<sub>4</sub> solution at a height of 0.9 cm. The other parameters  $\lambda$ ,  $\epsilon$ , and  $\eta$  involved in Eq. [4], which influence the velocity profile of natural convection, were presumed to be 1.7, 10, and 2.1, respectively, from the experimental results obtained by Awakura *et al.* (6).

In order to examine the validity of Eq. [14] and [15], the logarithmic concentration difference between the bulk electrolyte and the cathode surface,  $\log \Delta c$ , was plotted against the logarithmic average cathodic current density, and Fig. 8 and 9 were obtained for the solutions of 0.05 and 0.1 mol/liter CuSO<sub>4</sub>, respectively. As seen in these figures, the slope of all straight lines is 4/5 which is equal to the theoretical value derived from Eq. [14].

The dependence of  $\log \Delta c$  on the logarithmic height from the lower edge of cathode was also examined:  $\log \Delta c$  in the solutions of 0.05 and 0.1 mol/liter CuSO<sub>4</sub> was plotted against  $\log x$  in Fig. 10 and 11, respectively. By comparing the experimental slopes with the theoretical value of 1/5 from Eq. [14], it is seen that the measured slopes in Fig. 10 are equal to 1/5 when the

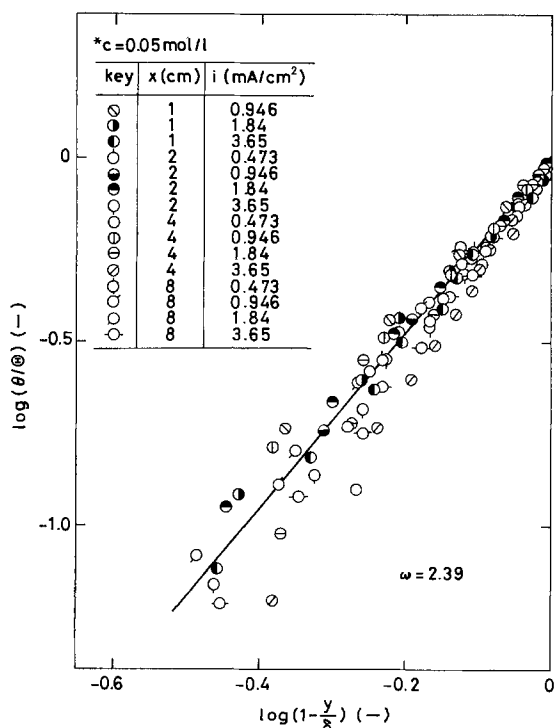


Fig. 7. Plot of  $\log(\theta/\theta)$  vs.  $\log(1 - \gamma/\delta)$

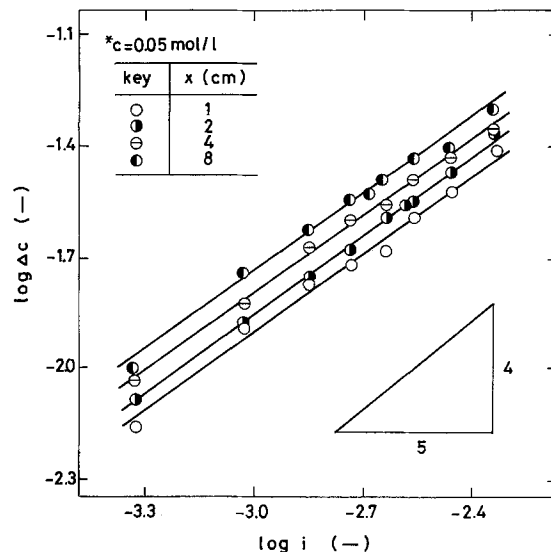


Fig. 8. Relationship between concentration difference and average cathodic current density (\*c = 0.05 mol/liter).

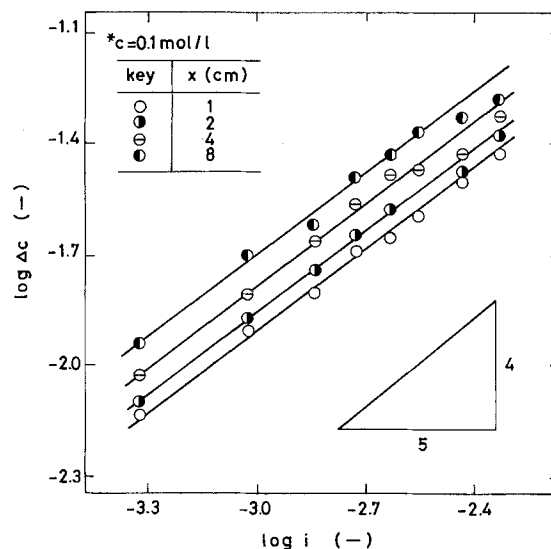


Fig. 9. Relationship between concentration difference and average cathodic current density (\*c = 0.1 mol/liter).

average current density is below 2.76 mA/cm<sup>2</sup> and the slope decreases when the average current density becomes higher than 3.65 mA/cm<sup>2</sup>. This may suggest that the local cathodic current density varies in the vertical direction above 3.65 mA/cm<sup>2</sup>. By comparing Fig. 11 with Fig. 10, it was also revealed that the slopes in Fig. 11 are nearly equal to the theoretical value of 1/5 up to the current density of 4.6 mA/cm<sup>2</sup>. This is due to the relatively lower current densities rather than the limiting value.

The dimensionless numbers of  $Sh_x$ ,  $Gr^*$ , and  $Sc$  were calculated by using the experimental data in addition to the property constants shown in Table III, and  $\log(Sh_x)$  was plotted against  $\log(Sc \cdot Gr^*)$  in Fig. 12. The theoretical value was calculated from Eq. [20] and is shown in this figure. It is seen that the experimental results obtained at lower current densities are in fairly good agreement with the theoretical value.

Next, the theoretical relationship demonstrated in Eq. [15] was examined. The logarithmic thickness of the diffusion layer in both electrolytes is plotted against the logarithmic average current density in Fig. 13 and 14. As seen in these figures, the slopes in the region of the lower current densities are in fairly good agreement with the theoretical value of  $-1/5$ , and the slopes decrease at higher current densities.

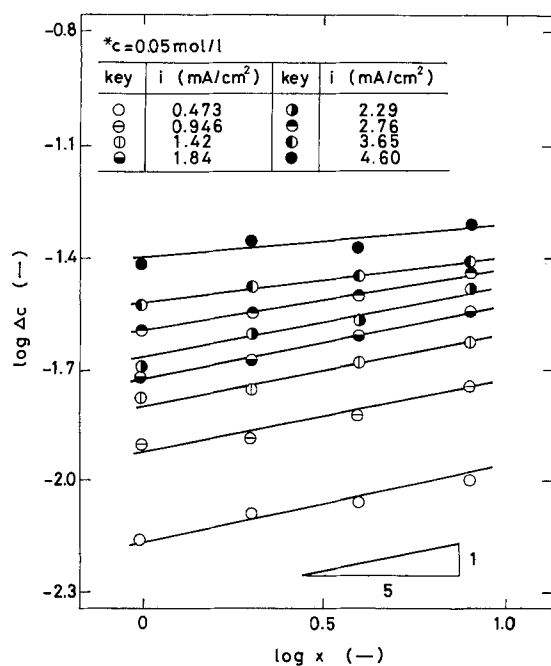


Fig. 10. Relationship between concentration difference and height from lower edge of cathode (\*c = 0.05 mol/liter).

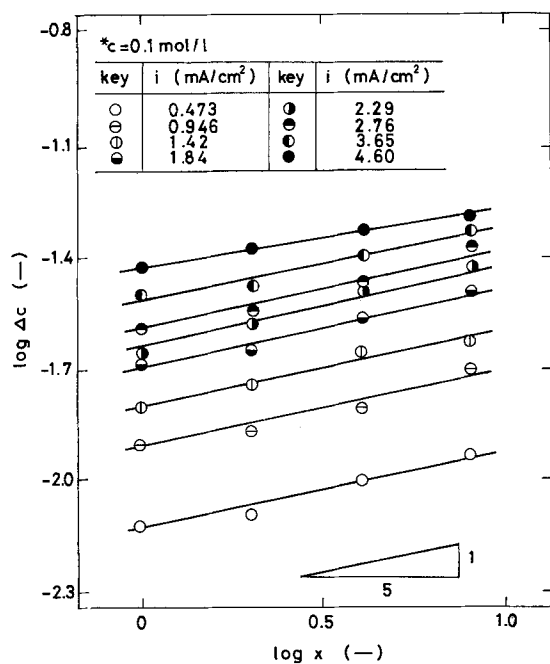


Fig. 11. Relationship between concentration difference and height from lower edge of cathode (\*c = 0.1 mol/liter).

From a theoretical calculation of the diffusion layer thickness under the boundary condition that  $c = \text{const}$  which is valid at the limiting current density, it was revealed (3) that  $\delta$ 's are constant at various current densities. Furthermore, a comparison of Fig. 14 with Fig. 13 reveals that the theoretical slope of  $-1/5$  is maintained up to the higher current densities in the 0.1 mol/liter  $\text{CuSO}_4$ .

In order to determine the dependence of the diffusion layer thickness on the height from the lower edge of the cathode surface, the logarithmic thickness measured in both solutions of 0.05 and 0.1 mol/liter  $\text{CuSO}_4$  were plotted against  $\log x$ , and Fig. 15 and 16 were obtained. The theoretical slope of the straight line is  $1/5$  from Eq. [15]. As seen in these figures, this linear relationship is reasonably well confirmed. The scatter of  $\delta$  values is thought to be related to the lower preci-

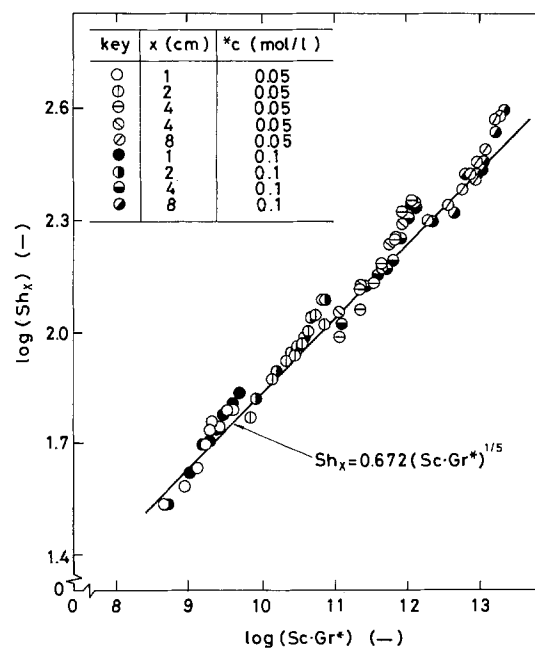


Fig. 12. Plot of  $\log (Sh_x)$  vs.  $\log (Sc \cdot Gr^*)$

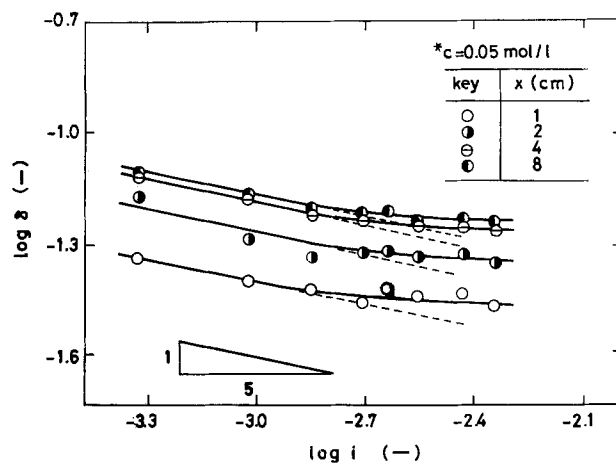


Fig. 13. Relationship between thickness of cathodic diffusion layer and average current density (\*c = 0.05 mol/liter).

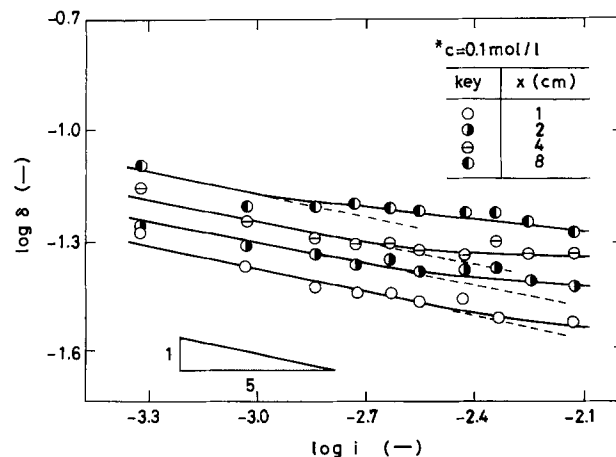


Fig. 14. Relationship between thickness of cathodic diffusion layer and average current density (\*c = 0.1 mol/liter).

sion in the measurement of the diffusion layer thickness.

For the comparison of the measured and theoretical thickness of the diffusion layer, the experimental  $\log(\delta/x)$  was plotted against  $\log(Sc \cdot Gr^*)$  in Fig. 17.

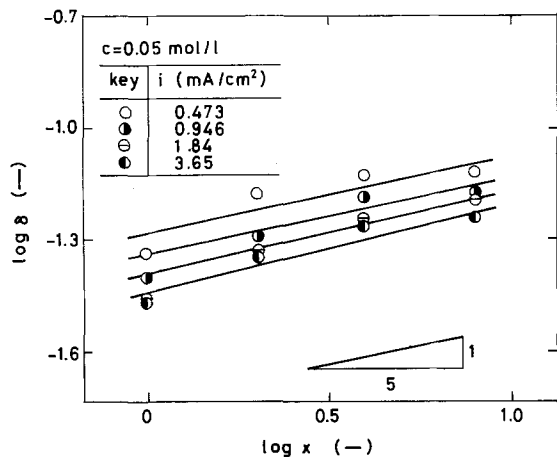


Fig. 15. Relationship between thickness of cathodic diffusion layer and height from lower edge of cathode ( $c = 0.05$  mol/liter).

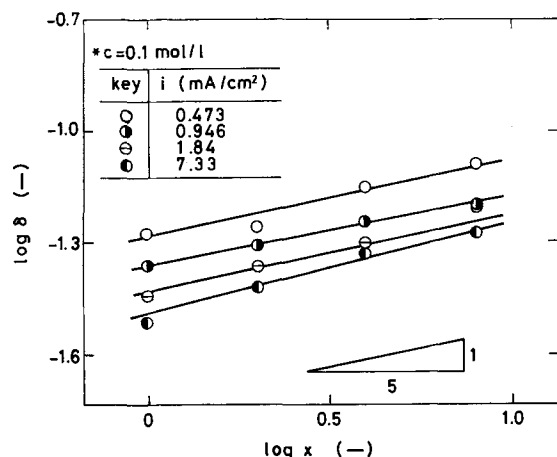


Fig. 16. Relationship between thickness of cathodic diffusion layer and height from lower edge of cathode ( $c = 0.1$  mol/liter).

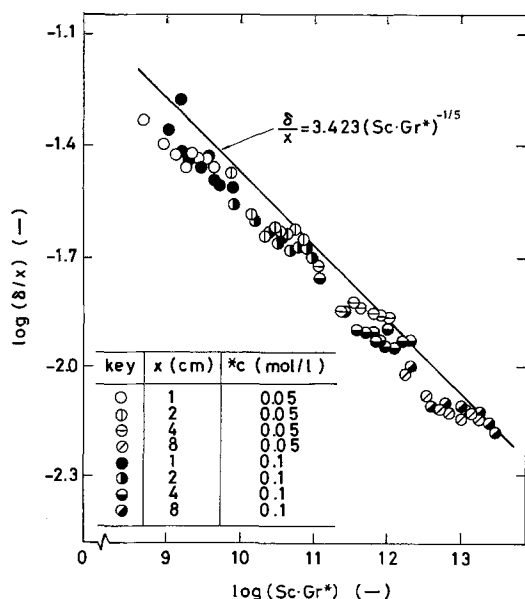


Fig. 17. Plot of  $\log(\delta/x)$  vs.  $\log(\text{Sc} \cdot \text{Gr}^*)$

In addition, the parameters and property constants were substituted in Eq. [21], and the theoretical line is also demonstrated in the same figure. It is seen in this figure that the experimental results may be explained by Eq. [21], although the experimental data in this figure are somewhat lower than the corresponding theoretical values.

## Summary

The measurement of the concentration profile of  $\text{CuSO}_4$  in the cathodic diffusion layer which is accompanied by the upward natural convection is indispensable for studying the rate of mass transfer of cation through this layer. By using the technique of holographic interferometry, it becomes feasible to measure the concentration profile because of the principle of common path interferometry employed in this technique.

The concentration profile in the aqueous 0.05 and 0.1 mol/liter  $\text{CuSO}_4$  solutions was measured at various cathodic current densities below the limiting value and at various heights from the lower edge of cathode. In the derivation of the concentration profile from the holographic interferogram, the effects of beam refraction in the diffusion layer were considered and an approximation was employed to interpret the holographic interferogram. Furthermore, the deviation due to the approximation was estimated at several current densities. It was found that the approximation was appropriate under the experimental conditions employed in this work. It was disclosed then from the experimental results that the concentration of  $\text{CuSO}_4$  on the cathode surface is lowered and the thickness of the diffusion layer is decreased when the average current density is increased. It was also revealed that the thickness of the diffusion layer is increased in the upper part of the plane vertical cathode at a constant cathodic current density.

From the integrated Navier-Stokes equation and the mass balance equation of  $\text{Cu}^{2+}$  ion with regard to the hydrodynamic boundary layer together with the assumed concentration and velocity profiles in the generalized form and the mass transfer equations of  $\text{Cu}^{2+}$  and  $\text{SO}_4^{2-}$  ions at the cathode surface, the basic equations of mass transfer in the cathodic diffusion layer were derived. When the cathodic current density is lower than about one-half of the limiting value, the local current densities remain equal in the vertical direction. Under this condition, the concentration difference and the thickness of the diffusion layer are expressed by Eq. [14] and [15], respectively.

In order to examine the validity of these theoretical expressions, the dependences of measured  $\log \Delta c$  and  $\log \delta$  on the logarithm of the current density and the height were evaluated. At the cathodic current densities far lower than the limiting value, the above dependences were confirmed. At higher current densities, on the other hand, the experimental results start to deviate from the theoretical value. This is supposed to be caused by the unequal local current densities in the vertical direction. The following dimensionless equations were derived from Eq. [14] and [15]

$$\text{Sh}_x = \frac{\omega}{\eta} \left( \frac{\Phi \eta^3}{\omega^2 (\omega + 1) \lambda} \right)^{1/5} (\text{Sc} \cdot \text{Gr}^*)^{1/5}$$

and

$$\frac{\delta}{x} = \eta \left( \frac{\omega^2 (\omega + 1)}{\Phi \eta^3} \right)^{1/5} (\text{Sc} \cdot \text{Gr}^*)^{-1/5}$$

The first equation concerns the concentration difference. In order to further confirm the theoretical relationship, the experimental parameters which influence the concentration difference and the diffusion layer thickness and the property constants were substituted in the above dimensionless equations, and the theoretical values were compared with the experimental results. It is shown that both theoretical and experimental values are in good agreement with each other in the region of the lower current densities.

Manuscript submitted June 23, 1975; revised manuscript received April 1, 1976.

Any discussion of this paper will appear in a Discussion Section to be published in the June 1977 JOURNAL. All discussions for the June 1977 Discussion Section should be submitted by Feb. 1, 1977.

Publication costs of this article were assisted by Kyoto University.

## LIST OF SYMBOLS

$a$	constant (liter/cm)	$z$	distance perpendicular to x- and y-directions (cm)
$b$	constant (—)	$z_1$	valency of $\text{Cu}^{2+}$ ion (= 2 g-equiv./mol)
$c$	concentration of $\text{CuSO}_4$ at a distance $y$ from cathode surface (mol/cm <sup>3</sup> )	$\alpha$	densification coefficient of $\text{CuSO}_4$ , $1/\rho(\partial\rho/\partial c)$ (cm <sup>3</sup> /mol)
${}^{\circ}c$	concentration of $\text{CuSO}_4$ on the cathode surface (mol/cm <sup>3</sup> )	$\delta$	thickness of diffusion layer (cm)
$*c$	concentration of $\text{CuSO}_4$ in the bulk electrolyte (mol/cm <sup>3</sup> )	$\epsilon, \eta, \lambda, \omega$	numerical parameter (—)
$\frac{\Delta c}{\Delta c}$	= ( $*c - {}^{\circ}c$ ) (mol/cm <sup>3</sup> )	$\theta$	= ( $*c - c$ ) (mol/cm <sup>3</sup> )
$\frac{\Delta c}{\Delta c}$	average value of $\Delta c$ in vertical direction (mol/cm <sup>3</sup> )	$\Theta$	= ( $*c - {}^{\circ}c$ ) (mol/cm <sup>3</sup> )
$\Delta c_e$	deviation due to approximation in estimating the concentration (mol/cm <sup>3</sup> )	$\lambda'$	wavelength (cm)
$d$	width of cathode (cm)	$\nu$	kinematic viscosity (cm <sup>2</sup> /sec)
$D$	diffusivity of $\text{CuSO}_4$ (cm <sup>2</sup> /sec)	$\tau$	distance between cathode surface and the position of maximal velocity of natural convection (cm)
$E$	constant (—)	$\phi$	potential (V)
$F$	Faraday constant (=96,500 coulombs/g-equiv)		
$g$	gravitational acceleration (=980 cm <sup>2</sup> /sec)		
$\text{Gr}^*$	modified Grashof number, $g\alpha^*t_2ix^2/z_1Fv^2D$ (—)		
$h$	constant (—)		
$i$	current density (A/cm <sup>2</sup> )		
$k$	constant (liter/cm)		
$k_1$	diffusivity of $\text{Cu}^{2+}$ ion (cm <sup>2</sup> /sec)		
$k_2$	diffusivity of $\text{SO}_4^{2-}$ ion (cm <sup>2</sup> /sec)		
$k_x$	mass transfer coefficient at a vertical distance $x$ (cm/sec)		
$l$	thickness of hydrodynamic boundary layer (cm)		
$n$	refractive index of solution at a distance $y$ (—)		
$*n$	refractive index of solution in the bulk electrolyte (—)		
$n_1$	refractive index of solution at a distance $y_1$ (—)		
$\Delta n$	deviation due to approximation in estimating refractive index (—)		
$N$	number of fringe shift (—)		
$p$	optical path length along the beam trajectory (cm)		
$s$	length of beam trajectory, $(n_1/k) \sinh(kx/n_1)$ (cm)		
$\text{Sc}$	Schmidt number, $\nu/D$ (—)		
$\text{Sh}_x$	Sherwood number, $k_x x/D$ (—)		
$*t_1$	transference number of $\text{Cu}^{2+}$ ion in the bulk electrolyte (—)		
$*t_2$	transference number of $\text{SO}_4^{2-}$ ion in the bulk electrolyte (—)		
$u$	velocity of natural convective flow (cm/sec)		
$u_m$	maximal velocity of natural convective flow (cm/sec)		
$U_1$	mobility of $\text{Cu}^{2+}$ ion (cm <sup>2</sup> /sec · V)		
$U_2$	mobility of $\text{SO}_4^{2-}$ ion (cm <sup>2</sup> /sec · V)		
$x$	height from lower edge of cathode (cm)		
$y$	horizontal distance from cathode surface (cm)		
$y_1$	distance between the incident point of beam and the cathode surface (cm)		
$y_0$	distance between the exit point of beam and the cathode surface (cm)		
$\Delta y$	= ( $y_0 - y_1$ ) (cm)		

## REFERENCES

1. J. N. Agar, *Discussions Faraday Soc.*, **1**, 26 (1947).
2. C. Wagner, *This Journal*, **95**, 161 (1949).
3. G. H. Keulegan, *J. Res. Nat. Bur. Std.*, **47**, 2240 (1951).
4. N. Ibl and R. H. Müller, *Z. Elektrochem.*, **59**, 671 (1955).
5. N. Ibl and R. H. Müller, *This Journal*, **105**, 346 (1958).
6. Y. Awakura, Y. Takenaka, and Y. Kondo, *Electrochim Acta*, **21** (1975).
7. J. Selman and J. Newman, *This Journal*, **118**, 1070 (1971).
8. A. Brenner, *Proc. Am. Electroplater's Soc.*, **1940** 95; *ibid.*, **1941**, 28.
9. T. Yannakopoulos and A. Brenner, *This Journal*, **105**, 521 (1958).
10. N. Ibl, Y. Barrada, and G. Trümpler, *Helv. Chim. Acta*, **37**, 583 (1954).
11. C. R. Wilke, M. Eisenberg, and C. W. Tobias, *This Journal*, **100**, 513 (1953).
12. N. Ibl, W. Rüegg, and G. Trümpler, *Helv. Chim. Acta*, **36**, 1624 (1953).
13. K. Asada, F. Hine, S. Yoshizawa, and S. Okada, *This Journal*, **107**, 242 (1960).
14. C. Knox, R. R. Sayano, E. T. Seo, and H. P. Silverman, *J. Phys. Chem.*, **71**, 3102 (1967).
15. L. O. Hefinger, R. F. Werker, and R. E. Brooks, *J. Appl. Phys.*, **37**, 642 (1966).
16. E. Yeager and A. J. Salkind, "Techniques of Electrochemistry," Vol. 2, p. 144, John Wiley & Sons, Inc., New York (1973).
17. C. Wagner, *This Journal*, **104**, 129 (1957).
18. R. H. Müller, "Advances in Electrochemistry and Electrochemical Engineering," Vol. 9, p. 281, John Wiley & Sons, Inc., New York (1973).
19. K. W. Beach, R. H. Müller, and C. W. Tobias, *J. Opt. Soc. Am.*, **63**, 559 (1973).
20. A. Tvarusko and L. S. Watkins, *This Journal*, **118**, 248 (1971).
21. B. Rossi, "Optics," p. 55, Addison-Wesley Publishing Co., London (1967).
22. Y. Awakura, A. Ebata, M. Morita, and Y. Kondo, *Denki Kagaku*, **43**, 10 (1975).
23. "International Critical Tables of Numerical Data, Physics, Chemistry and Technology," E. W. Washburn, Editor Vol. 3, p. 67, McGraw-Hill Book Co., New York (1928); *ibid.*, Vol. 5, p. 14 (1929).

## Hydrogen Gas Absorber Made of Manganese Dioxide

Akiya Kozawa\*

Union Carbide Corporation, Battery Products Division, Cleveland, Ohio 44101

Manganese dioxide catalyzed with palladium (1) or silver was found to be a good hydrogen absorber. Manganese dioxide alone (without a catalyst) has practically no ability to absorb hydrogen gas at room temperature (2). This note describes the preparation conditions and the properties of the hydrogen absorber and also a few possible applications.

### Experimental

A typical method for preparing the hydrogen gas absorber is as follows. The components listed in Table I are mixed thoroughly. An appropriate amount of water (for example, 300g of water per 1000g of the dry mix) is added, and the mixture is well blended to produce a moldable paste. The paste is extruded or molded into various shapes (rod, pellet, sheet, etc.) depending on the application. Then it is dried at 75°-80°C overnight. The shaped body becomes rigid because the cement sets during the drying process. The stainless steel wool is not necessary but makes the porous body strong, particularly in the case of sheets. The solid body is porous and most of the water added in the blending step is removed in the drying process.

The rate of hydrogen absorption was tested with the apparatus shown in Fig. 1 and 2 for fast adsorption and slow absorption, respectively. The absorption is a chemical reaction between H<sub>2</sub> gas and MnO<sub>2</sub>. The apparatus shown in Fig. 1 is used to test the initial absorption rate employing a 1 ~ 2g sample. The apparatus shown in Fig. 2 is used to measure the total absorption capacity employing a 100-200 mg sample.

To operate the apparatus (Fig. 2) first the air in the test tube (B) was replaced by N<sub>2</sub> gas by purging while the mouth of the test tube was maintained slightly above the oil level (H). Then the oil level in the test tube was raised to around (I) by applying a vacuum. Finally H<sub>2</sub> gas was introduced and the oil level was brought down to (H). All the fine plastic tubes (D) were then removed. The oil level was read from time to time to measure the hydrogen gas uptake by the sample. This was not a very accurate measurement ( $\pm 0.5$  cm<sup>3</sup>), but satisfactory for the present purpose.

\* Electrochemical Society Life Member.

Key words: hydrogen, manganese dioxide, palladium, gas absorber.

Table I. Components of the hydrogen gas absorber

	Typical example	Range
1. Manganese dioxide*	73.7% (by wt)	50-80% (by wt)
2. Binder (Portland cement)**	18.5	10-40
3. Pd-catalyzed carbon*** (or Ag <sub>2</sub> O or AgO)	4.6 (3.0)	0.4-20 (1-10)
4. Chopped steel wool	2.3	0-5
5. Acetylene black	0.9	0-5

\* Electrolytic manganese dioxide for dry cell such as I.C. MnO<sub>2</sub> No. 1, 2, and 3 (6).

\*\* Eliminate Portland cement in the case of Ag<sub>2</sub>O or AgO catalyst.

\*\*\* Obtained from Engelhard Industries, Incorporated. This material contained 5% Pd, 45% carbon, and 50% H<sub>2</sub>O.

### Results and Discussion

**Absorption capacity.**—When 100 mg of the absorber having the composition shown in Table I was tested in the apparatus shown in Fig. 2, the material absorbed about 17.5 cm<sup>3</sup> of H<sub>2</sub> gas in 5 days as shown in Fig. 3. According to the reaction (MnO<sub>2</sub> + H<sub>2</sub> → MnO + H<sub>2</sub>O), the MnO<sub>2</sub> contained in the absorber should absorb about 19 cm<sup>3</sup> of H<sub>2</sub> gas. This result (Fig. 3) indicates that MnO<sub>2</sub> is reduced almost to MnO. In the case of Ag<sub>2</sub>O or AgO catalyst, MnO<sub>2</sub> was reduced to only MnOOH or slightly more than MnOOH.

**Absorption rate.**—The absorption rate is fast initially and becomes slower and steady after 1 hr. The steady rate depends on the amount of the catalyst as well as binder as shown in Table II for Pd-catalyzed absorbers and Fig. 4 for silver-catalyzed absorbers. The test temperature and particle size of manganese

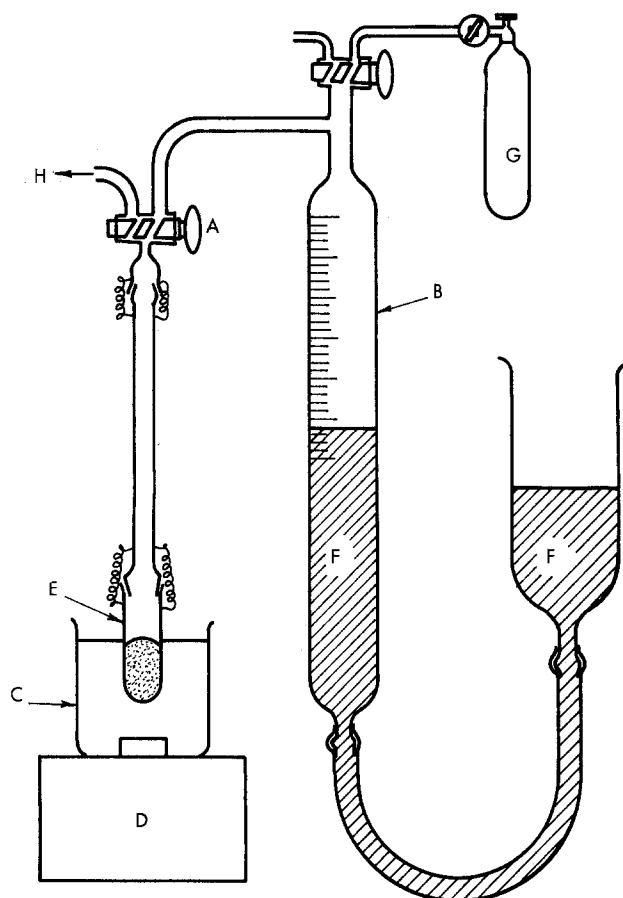


Fig. 1. Apparatus for measuring the hydrogen gas absorption rate. After evacuation of the sample tube, the sample tube was connected to the main gas burette by opening stopcock A. A: Stopcock, B: gas burette (100 cm<sup>3</sup>), C: liquid paraffin bath, D: magnetic stirrer and hot plate with temperature control, E: sample tube, F: mercury, G: hydrogen gas cylinder, H: vacuum pump.



Table II. Effect of the catalyst content on the H<sub>2</sub> absorption rate  
(data given in this table are the average of two experiments)

Catalyst content* (%)	Actual sample tested (g)	Amount of MnO <sub>2</sub> in the sample (g)	Maximum H <sub>2</sub> to be absorbed (cm <sup>3</sup> )	H <sub>2</sub> absorbed in 2 hr at 45°C (cm <sup>3</sup> )	H <sub>2</sub> absorbed in first 30 min (cm <sup>3</sup> )	Absorption rate after 1 hr (cm <sup>3</sup> /hr)
0.8	1.51	0.97	200	9.0 ± 0.5	3.0 ± 0.5	4.5 ± 0.5
2.0	1.47	0.95	195	23.0	10.0	7.0
4.0	1.45	0.90	187	32.0	15.0	11.0
9.2	1.35	0.76	162	48.0	27.0	11.0
16.8	1.38	0.73	151	54.0	32.0	13.5

\* The basic composition is as follows, the catalyst content being varied: MnO<sub>2</sub>: 160g, Pd-carbon: 0.4-16.8%, acetylene black: 2g, binder (Portland cement): 80g, steel wool: 5g.

dioxide influence the absorption rate as seen in Fig. 5 and 6.

*Use of H<sub>2</sub> gas permeable film.*—If the hydrogen gas to be absorbed coexists with a solution, e.g., in the alkaline manganese dioxide-zinc cell, this porous hydrogen absorber may be wrapped with a thin polyethylene film through which H<sub>2</sub> gas is permeable at a sufficient rate but which prevents the solution from going into the porous body. A 1 mil thick polyethylene film (such as Zedel made by Union Carbide Corporation) has a sufficient hydrogen gas permeability for most applications.

*Other catalysts.*—The catalyst can be platinum black or other noble metals; palladium dispersed on carbon is satisfactory and inexpensive compared to other noble metal catalysts. The function of the palladium would be the dissociation of hydrogen molecules to atomic hydrogen.

*Bonding agent.*—Among various bonding agents including organic plastics dissolved in organic solvents, a few inorganic binders, water, glass, and cement were found to be most convenient. Organic plastics

(polyethylene, polysulfone, etc.) sometimes deactivate the catalyst, probably because the polymer covers the active centers of the palladium.

*CO adsorption.*—It was found in a preliminary test of this Pd-catalyzed hydrogen absorber for CO adsorption that this material does have a relatively good capability for CO adsorption.

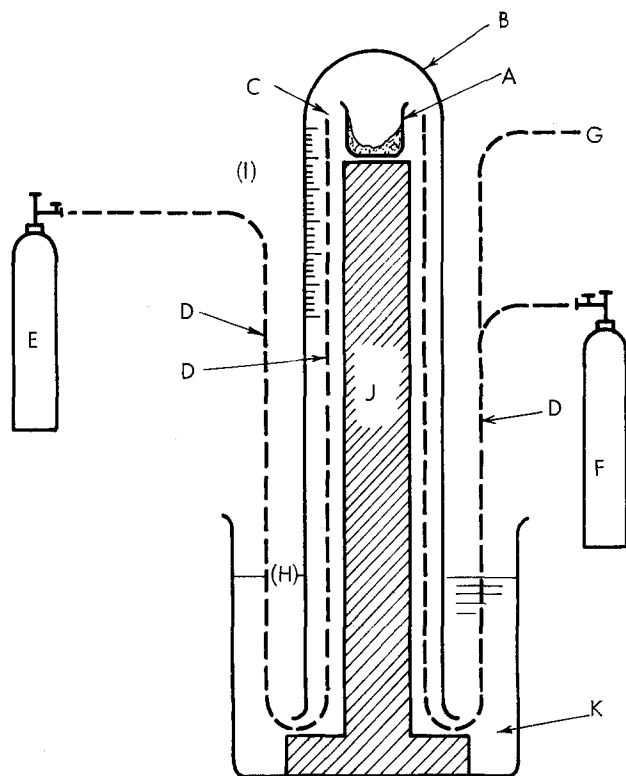


Fig. 2. Apparatus for measuring hydrogen gas absorption (see text for operation). A: 10 cm<sup>3</sup> beaker containing sample, B: an inverted test tube (3.5 cm in diameter, 30 cm long), C: hydrogen gas, D: fine plastic tubes, E: hydrogen cylinder, F: nitrogen cylinder, G: vacuum, H: oil level, I: top of the plastic rod, J: plastic rod, K: vacuum pump oil in 250 cm<sup>3</sup> beaker.

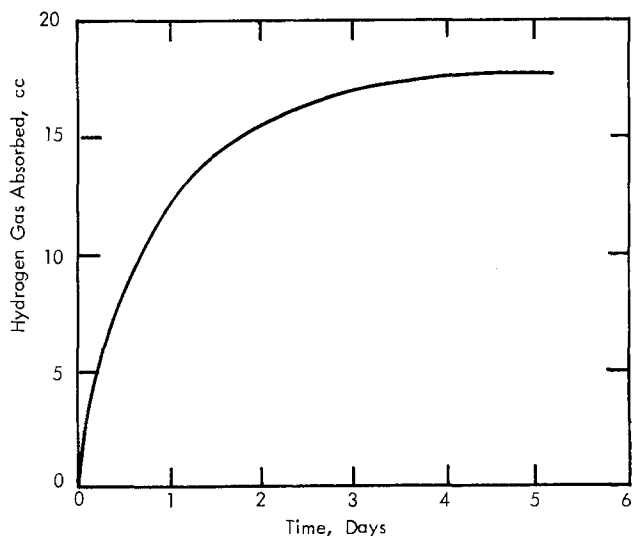


Fig. 3. Hydrogen gas absorption by a 100 mg crushed sample having a formula shown in Table I.

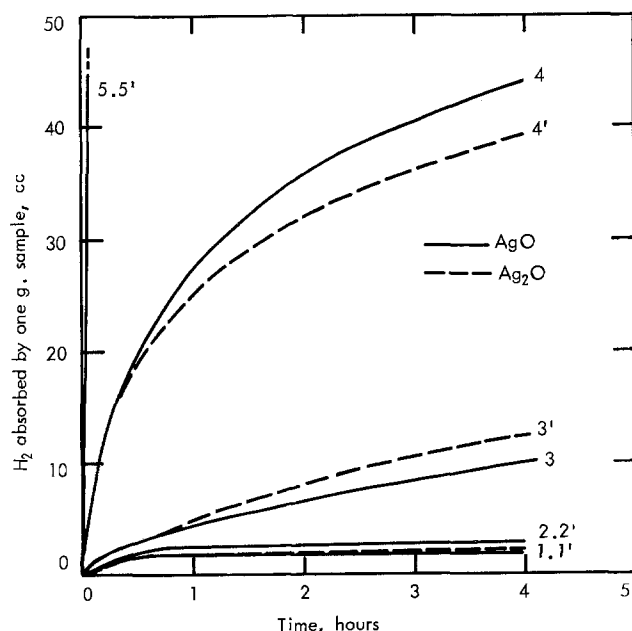


Fig. 4. Hydrogen gas absorption by 1g sample (MnO<sub>2</sub> + Ag<sub>2</sub>O or AgO). Ag<sub>2</sub>O or AgO content was as follows: 1.1':0.1%, 2.2':0.3%, 3.3':1%, 4.4':3%, 5.5':10%.

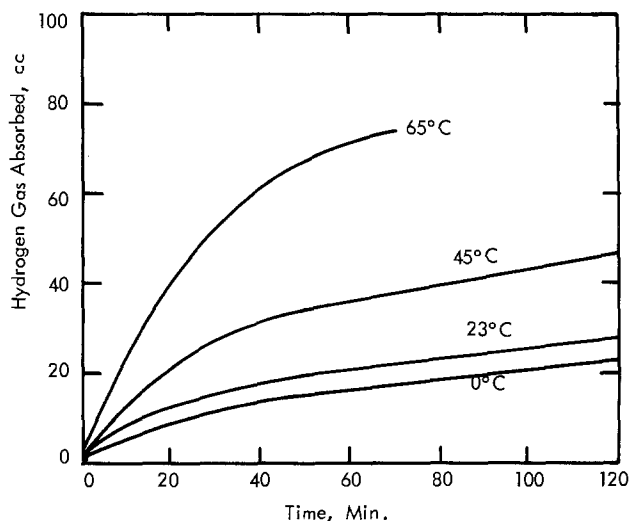


Fig. 5. Effect of temperature of the hydrogen gas absorption rate. The composition of the absorber was as follows:  $\text{MnO}_2$ : 160g, Pd-catalyzed carbon: 25g, cement: 80 g, acetylene black: 2g, steel wool: 5g. The sample of each test had about 1.5g in a crushed powder form.

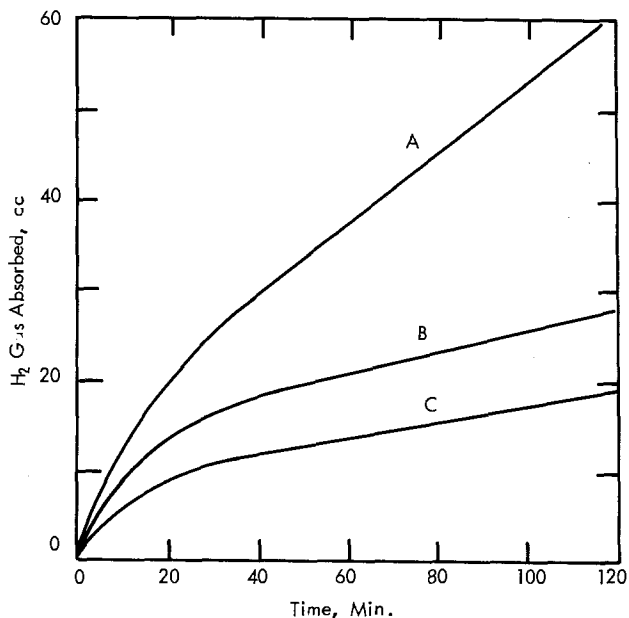
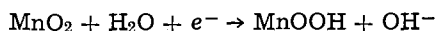


Fig. 6. Effect of particle size of manganese dioxide used in the adsorber having a formula as follows:  $\text{MnO}_2$ : 160g, Pd-catalyzed carbon: 10g, acetylene black: 2g, cement: 40g, steel wool: 5g. Particle size of  $\text{MnO}_2$ : A: less than  $40\mu$ , B:  $50-100\mu$ , C:  $150-300\mu$ .

**Mechanism of  $\text{MnO}_2$  reduction.**—The reduction of  $\text{MnO}_2$  in dry cells has been extensively studied (3-5). According to the studies, the electrochemical reduction process is a proton injection into the  $\text{MnO}_2$  lattice at least up to  $\text{MnO}_{1.5}$ , as shown below



The reduction of  $\text{MnO}_2$  by  $\text{H}_2$  gas would involve the same mechanism, although the source of protons is  $\text{H}_2$  ( $= 2\text{H}$ ) instead of  $\text{H}_2\text{O}$  ( $= \text{H}^+ + \text{OH}^-$ ).

**Stability in air.**—A hydrogen absorber was prepared with 0.4% palladium-carbon catalyst, stored in air for 5 years and tested. Although the absorber contained only 0.4% of the catalyst, it was possible to maintain almost the same absorption rate as the fresh sample. The total absorption capacity, however, decreased to 70% of the initial capacity during the 5 year storage in air at  $23^\circ\text{C}$ . The reduced  $\text{MnO}_2$  in the hydrogen absorber by the reaction with hydrogen gas is reoxidized up to about 30-60% by oxygen in air. The regeneration feature of this material is important for certain applications.

### Applications

One application of the hydrogen absorber is the removal of hydrogen gas in sealed cells (1). In sealed cells such as alkaline  $\text{MnO}_2$ -Zn cells,  $\text{H}_2$  gas evolved from the zinc anode by corrosion accumulates, and this hydrogen must be removed before the internal pressure becomes too high. A rod or pellet form of this hydrogen absorber, which is wrapped with a thin polyethylene film, can be used for this purpose.

Another application is the removal of accumulated hydrogen gas in confined areas or compartments, since any possible explosion hazard must be eliminated for safety. Such confined areas include underwater vessels or closed rooms in which hydrogen gas may be leaked from a pipeline or generated by various chemical or radiochemical reactions or from lead-acid batteries.

Another application is the removal of hydrogen gas generated from a battery power pack which operates adjacent to electronic equipment. Hydrogen gas is often generated from dry batteries and rechargeable batteries and alters the characteristics of the capacitors and resistors in the electronic circuit. This type of problem can be easily eliminated by using the present hydrogen absorber at the top of the battery pack.

### Acknowledgments

The author wishes to thank Mrs. H. M. Joseph for her assistance in preparation of the manuscript.

Manuscript submitted Jan. 29, 1976; revised manuscript received March 10, 1976. This was Paper 219 presented at the Chicago, Illinois, Meeting of the Society, May 13-18, 1973.

Any discussion of this paper will appear in a Discussion Section to be published in the June 1977 JOURNAL. All discussions for the June 1977 Discussion Section should be submitted by Feb. 1, 1977.

Publication costs of this article were assisted by Union Carbide Corporation.

### REFERENCES

1. A. Kozawa, U. S. Pat. 3,893,870 (1975) and 3,939,006 (1976); Brit. Pat. 1,321,853 (1975); Austrian Pat. 302,436 (1972); Belgian Pat. 755,337 (1971); German Pat. DT 2,042,266 (1971).
2. C. S. Brooks, *J. Catalysis*, **4**, 535 (1965).
3. A. Kozawa and J. F. Yeager, *This Journal*, **112**, 959 (1965).
4. A. Kozawa and R. A. Powers, *ibid.*, **113**, 870 (1966).
5. A. Kozawa and R. A. Powers, *J. Chem. Education*, **49**, 587 (1972).
6. International common sample of manganese dioxide, *This Journal*, **119**, 152C (1972). The  $\text{MnO}_2$  samples are available from the I. C. Sample Office, sponsored by the Cleveland Section of the Electrochemical Society, P. O. Box 6116, Cleveland, Ohio 44101.

## Solid Lithium-Silicon Electrode

San-Cheng Lai\*

Rockwell International, Atomics International Division Canoga Park, California 91304

Lithium-metal sulfide high energy density batteries are being developed at the Atomics International Division of Rockwell International and at Argonne National Laboratory for use in load leveling and electric vehicles (1-3). The battery system is operated with an electrolyte of LiCl-KCl eutectic salt at temperatures of 400°-450°C. Iron sulfide compounds are employed as the active material for the positive electrode with either elemental lithium or a solid lithium alloy as the anode.

Two approaches to the lithium anode have been studied. A porous lithium-aluminum alloy, suitably supported, can retain up to 20 weight percent (w/o) of lithium as a solid (3-5). One disadvantage in using this electrode is the loss of 0.3V *vs.* pure lithium, thus reducing the theoretical energy density attainable when coupled with the various metal sulfide electrodes. An alternative approach is retention of liquid lithium metal in a porous metal substrate which avoids the voltage loss associated with the alloy. However, retaining lithium on metallic substrates in molten lithium-potassium halide salt mixtures saturated with Li<sub>2</sub>S has been difficult (1).

Other binary lithium alloys electrochemically formed by depositing lithium from a LiCl-KCl fused salt electrolyte, such as Li-Bi, Li-Pb, and Li-Sn, have been reported (6). These binary lithium alloys have lower potentials *vs.* lithium than does Li-Al and the lithium content in the alloy is low. Lead and tin, for example, form alloys containing lesser amounts of lithium than does aluminum, and the high molecular weight of these elements would thus reduce the energy capacity of a lithium electrode. None of these alloys were found to be practical for the application to the secondary batteries. Possibly a need still exists for a lithium electrode which upon continued cycling will retain its capacity and will operate at a potential nearer that of liquid lithium. This paper presents the result of the preliminary investigation of a solid lithium-silicon electrode.

### Experimental

All experiments reported in the paper were performed in a helium-atmosphere dry box where the concentrations of oxygen, nitrogen, and water were removed to below the parts per million level to avoid reactions with lithium.

Lithium metal from Foote Mineral Division of Newmont Mining Company was used in all experiments. Silicon, 97% pure, purchased from MC/B, Manufacturing Chemists, was used in the preparation of the alloys. Highly prepurified electrolyte salts were purchased from Anderson Laboratories for the tests described here. A titanium fiber mat was purchased from Gould Laboratory, Cleveland, Ohio. It had fibers approximately 100 $\mu$  diameter, having an apparent density of 19%.

A laboratory cell design shown in Fig. 1 was used during the course of this investigation. The cell consists

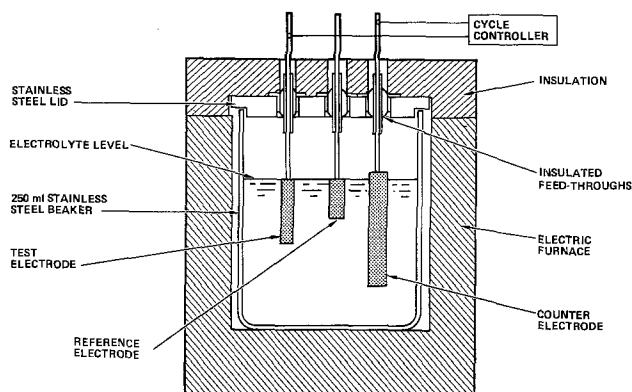


Fig. 1. Laboratory investigation cell

of a stainless steel beaker (250 ml) where a eutectic electrolyte, 59 mole percent (m/o) LiCl-41 m/o KCl, was retained. A lithium-silicon electrode was prepared by impregnating the titanium fiber mat with a molten alloy containing 60 w/o of lithium and 40 w/o of silicon at 700°C. Titanium was chosen for the supporting structure because the solubility of this metal in lithium is low and it therefore resists attack by the molten alloy during the impregnation process. A copper Feltmetal panel impregnated with pure lithium metal was used as the counterelectrode. A nickel Feltmetal panel impregnated with pure lithium was used as the reference electrode. The electrode leads were mounted through insulated feed-throughs brazed to a close-fitted cover for a beaker containing the KCl, LiCl eutectic salt electrolyte. A thermocouple permitted the temperature of the electrolyte to be monitored accurately.

A series of measurements was made to characterize the voltage plateaus and to identify the alloy compositions corresponding to each. Entropy calculations were also made by measuring the variations in the potential, *E*, of the alloy electrode *vs.* pure liquid lithium at each plateau at different temperatures ranging from 360° to 440°C.

The electrode was discharged through the successive voltage plateaus, disregarding the first plateau which had essentially the same potential as liquid lithium. From the known weight of the alloy in the electrode and the quantity of lithium discharged past each transition point, it was possible to calculate the alloy compositions.

### Results and Discussion

Figure 2 shows the experimental result of the discharge of a lithium-silicon electrode having an initial composition of 60 w/o of lithium and 40 w/o of silicon [86 atom percent (a/o) lithium] five distinct voltage plateaus *vs.* pure lithium were observed. For comparison, the lithium-silicon alloys described in the available literature (7, 8) are also shown in Fig. 2. The compositions, Li<sub>5</sub>Si and Li<sub>2</sub>Si, have been established with some certainty. The empirical formula, Li<sub>4.1</sub>Si, may

\* Electrochemical Society Active Member.

Key words: lithium-silicon alloy, molten salt, high temperature secondary battery.

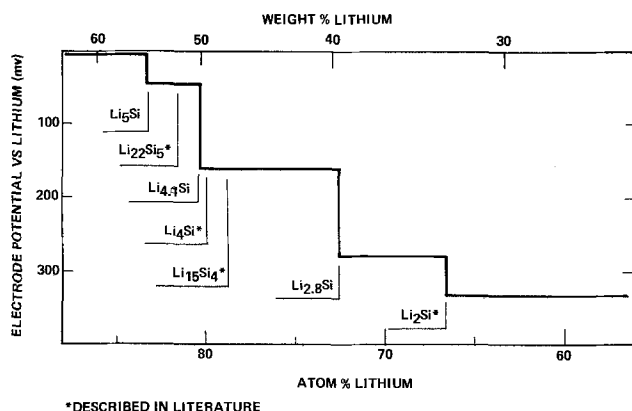


Fig. 2. Discharge voltage plateaus of 60Li-40Si (w/o) electrode in LiCl-KCl eutectic electrolyte at 400°C.

actually represent  $\text{Li}_4\text{Si}$ . More precise tests will be required to establish the exact stoichiometric ratio. No reference has yet been found to a composition even approximating that of  $\text{Li}_{2.8}\text{Si}$ . It is planned in the near future to identify the compositions corresponding to each voltage plateau by chemical and/or metallurgical methods.

The average potential over the four plateaus corresponding to solid alloy is 228 mV positive to lithium as contrasted to 300 mV for lithium-aluminum alloy. The total capacity of the solid alloy regions is 2.12 A-hr/g.

The variation of potential with temperature was sufficiently linear so that a straight line formula could be written for each plateau using the least squares method. The voltage-temperature relationship derived in this manner is shown in Table I.

These measurements permitted calculation of  $\Delta S^\circ_f$ ,  $\Delta H^\circ_f$ , and  $\Delta G^\circ_f$  for each alloy composition from the well-known thermodynamic functions

$$\Delta S = nF(\Delta E/\Delta T)_p$$

where  $\Delta S$  = entropy change,  $F$  = Faraday constant,  $\Delta E$  = change in cell voltage,  $\Delta T$  = change in cell temperature,  $n$  = number of electrons, and  $p$  signifies a constant pressure.

The free energy and enthalpy functions could then be calculated from the following relationships

Table I. Temperature dependence of emf of lithium-silicon alloys vs. lithium metal at 400°C

Voltage plateau at 400°C	Temperature dependence (mV vs. °K)
+48	137.7-0.1336T
+158	276.5-0.1761T
+280	332.1-0.0771T
+336	430.7-0.1402T

Table II. Thermodynamic data for lithium-silicon alloys at 400°C

Alloy	$\Delta G^\circ_f$ (kcal/mole)	$\Delta S^\circ_f$ (eu)	$\Delta H^\circ_f$ (kcal/mole)
$\text{Li}_5\text{Si}$	-26.4	-15.9	-37.1
$\text{Li}_{4.1}\text{Si}$	-25.4	-13.2	-34.3
$\text{Li}_{4.8}\text{Si}$	-20.7	-7.9	-26.0
$\text{Li}_3\text{Si}$	-15.5	-6.5	-19.9

$$\Delta G = -nFE$$

$$\Delta H = \Delta G + T\Delta S$$

where  $\Delta G$  = change in Gibbs free energy and  $\Delta H$  = change in enthalpy. The results of these calculations appear in Table II.

This preliminary investigation has shown that lithium-silicon alloy contains substantially higher usable lithium content in the alloy (~83 a/o) and has less potential penalty than the other alloys mentioned above. It is therefore promising as an excellent anode material for high energy density batteries. Further work is under way to incorporate lithium-silicon alloy anodes with metal sulfide cathodes to achieve high specific power and energy density batteries for load leveling and electric vehicle propulsion applications.

Manuscript submitted Feb. 23, 1976; revised manuscript received May 10, 1976.

Any discussion of this paper will appear in a Discussion Section to be published in the June 1977 JOURNAL. All discussions for the June 1977 Discussion Section should be submitted by Feb. 1, 1977.

Publication costs of this article were assisted by Rockwell International.

#### REFERENCES

- L. R. McCoy, S. Lai, R. C. Saunders, and L. A. Heredy, Paper presented at 26th Power Sources Conference, Atlantic City, New Jersey, April 29-May 2, 1974.
- Laszlo A. Heredy, San-Cheng Lai, Lowell R. McCoy, and Richard C. Saunders, in "New Uses of Sulfur," Advances in Chemistry Series 140, American Chemical Society, Washington, D. C. (1975).
- P. A. Nelson, *et al.*, "High-Performance Batteries for Off-Peak Energy Storage and Electric-Vehicle Propulsion," ANL 75-1 Progress Report (1975).
- E. S. Buzzelli, U.S. Pat. 3,445,288 (1969).
- N. P. Yao, L. A. Heredy, and R. C. Saunders, *This Journal*, **118**, 1039 (1971).
- E. S. Buzzelli, Abstract 14, Extended Abstracts, Fall Meeting, p. 40, The Electrochemical Society, Miami Beach, Florida, Oct. 8-13, 1972.
- F. A. Shunk, "Constitution of Binary Alloys, Second Supplement," p. 481, McGraw-Hill, New York (1969).
- B. W. Mott, "Intermetallic Compounds and Alloys of the Alkali Metals," Special Publication No. 22, p. 92, The Chemical Society, London (1967).

## Stochastic Process of Chloride Pit Generation in Passive Stainless Steel

Norio Sato\*

Corrosion Research Group, Faculty of Engineering, Hokkaido University, Sapporo, Japan

Pitting corrosion of passivated metals takes place in two apparently different stages, pit nucleation and growth. Pit generation is frequently characterized by a

\* Electrochemical Society Active Member.  
Key words: pitting frequency histogram, pit generation probability, pitting potential.

critical pitting potential, defined as the least noble potential at which pits can be generated, and by an induction time for pit initiation after introduction of aggressive ions at constant potential.

The generation of pits on stainless steel is a random phenomenon discrete in time and location on the sur-

face, and therefore may be regarded as a stochastic process. It has recently been suggested that probability theory can be applied to the induction time for pit generation in stainless steel (1); the induction time has often been equated, though approximately (2), to the inverse of the pit generation rate (3, 4).

The present paper describes an application of the theory of the Markov process to potentiostatic pit generation in a rotating stainless steel electrode in an acid solution containing sulfate and chloride ions.

### Pit Generation Intensity

If pit generation takes place in the restriction of the Markov property that the future probability of pit nucleation is uniquely determined once the state of the system at the present stage is given, the probability,  $P(\Delta t)$ , of another pit breaking out in a time interval larger than  $\Delta t$  after the preceding pit has opened is given by (5)

$$dP(\Delta t)/P(\Delta t) = -\lambda(\Delta t)dt \quad [1]$$

where  $\lambda(\Delta t)$  is the pit generation intensity or relative pit generation rate, equivalent to the pit generation probability for unit time at time interval  $\Delta t$ . Consequently, the following equation is obtained

$$\lambda(\Delta t) = -2.3026 \{d \log P(\Delta t)/dt\} \quad [2]$$

### Frequency Histogram of Pit Generation

In a previous paper (2), a number of potentiostatic pit generation experiments with 18Cr-8Ni stainless steel have been carried out to measure the time interval,  $\Delta t$ , for pits successively breaking out at constant potential in a solution containing chloride ions. A rotating stainless steel electrode of surface area 3.54 cm<sup>2</sup>, potentiostatically passivated for 1 hr in 0.1M Na<sub>2</sub>SO<sub>4</sub> of pH 3 prior to introduction of chloride ions, was used, and the solution was 0.2M NaCl containing 0.1M Na<sub>2</sub>SO<sub>4</sub> at 25°C. The classical induction time for the first pit to appear was excluded from  $\Delta t$  because of different physical meaning (2).

Figure 1 shows the relative frequency histogram of the pit generation at three different potentials. The relative frequency which is given by  $N_{\Delta t \sim \Delta t + \delta t} / N_T$ , with  $N_T$  the total number of measurements and

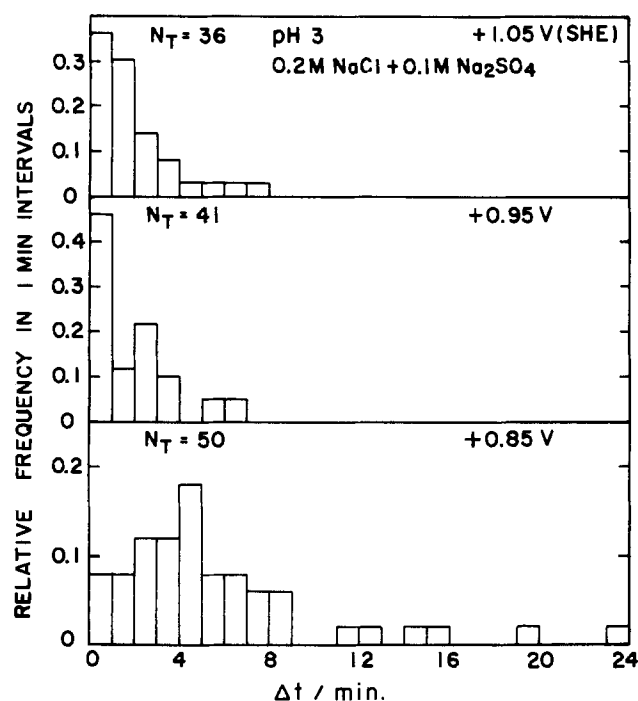


Fig. 1. Frequency histogram of potentiostatic pit generation on a rotating 18Cr-8Ni stainless steel electrode.

$N_{\Delta t \sim \Delta t + \delta t}$  the number of measurements in which the pit generation time interval is in the range  $\Delta t \sim \delta t$ , is related to the probability  $P(\Delta t)$  in Eq. [1] as follows

$$P(\Delta t) = \frac{\sum_{\delta t=0}^{\infty} N_{\Delta t \sim \Delta t + \delta t}}{N_T} \quad [3]$$

Figure 2 shows the logarithm of  $P(\Delta t)$  as a function of pit generation time interval  $\Delta t$ . It is observed that there is essentially a linear relationship between  $\log P(\Delta t)$  and  $\Delta t$ , giving an integral function of Eq. [1]

$$2.3026 \log P(\Delta t) = -\lambda \cdot \Delta t \quad [4]$$

where  $\lambda$ , the pit generation intensity, is independent of  $\Delta t$ , and is given by  $\lambda = 0.175 \text{ min}^{-1}$  at +0.85V (SHE),  $\lambda = 0.500 \text{ min}^{-1}$  at +0.95V, and  $\lambda = 0.614 \text{ min}^{-1}$  at +1.05V. For unit area of the surface, therefore,  $\lambda_0 = 0.0494 \text{ min}^{-1} \text{ cm}^{-2}$  at +0.85V (SCE),  $\lambda_0 = 0.141 \text{ min}^{-1} \text{ cm}^{-2}$  at +0.95V, and  $\lambda_0 = 0.173 \text{ min}^{-1} \text{ cm}^{-2}$  at +1.05V.

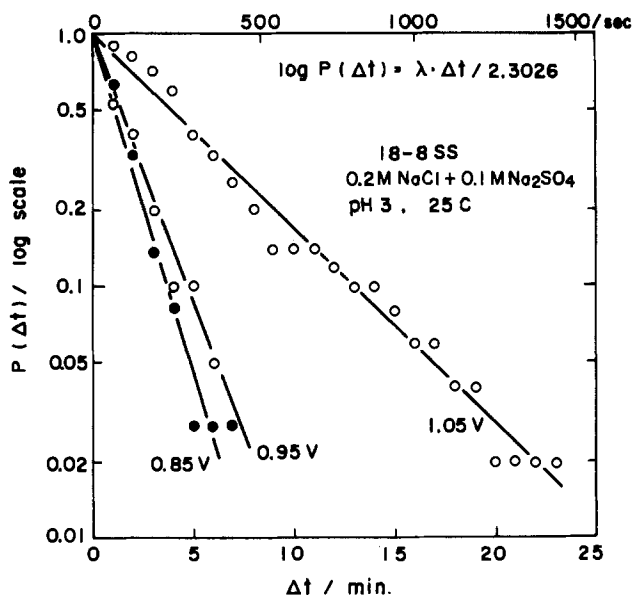


Fig. 2. Cumulative relative frequency curve for pit generation time interval at three different potentials.

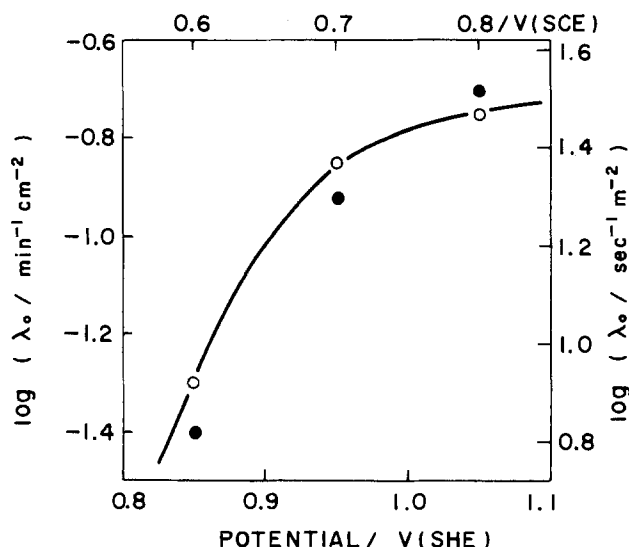


Fig. 3. Pit generation intensity for unit surface area as a function of potential; ○ = present calculation by the stochastic method, ● = previous calculation by the least squares method (2).

In Fig. 3, the pit generation intensity,  $\lambda_0$ , for unit area of the surface is plotted against the potential at which pits are generated; the pit generation rate estimated by the least squares method is also shown for comparison. The pit generation probability increases and appears to approach a ceiling asymptotically as the potential becomes more noble.

In view of stochastic process, the critical potential for pit generation may be defined as the least noble potential at which the pit generation probability is practically recognizable. Notice that the pit generation probability depends on the area of the metal surface.

Manuscript submitted March 22, 1976; revised manuscript received April 19, 1976.

Any discussion of this paper will appear in a Discussion Section to be published in the June 1977 JOURNAL.

All discussions for the June 1977 Discussion Section should be submitted by Feb. 1, 1977.

Publication costs of this article were assisted by Hokkaido University.

#### REFERENCES

1. T. Shibata and T. Takeyama, *Nature*, **260**, 315 (1976).
2. N. Sato, T. Nakagawa, K. Kudo, and M. Sakashita, in "Localized Corrosion," International Corrosion Conference Series NACE-3, p. 447, NACE, Houston (1974); *Trans. Japan Inst. Metals*, **13**, 103 (1972).
3. H. J. Engell and N. D. Stolice, *Z. Physik. Chem. (N.F.)*, **20**, 113 (1959).
4. N. D. Stolice, *Corrosion Sci.*, **9**, 205, 455 (1969).
5. A. T. Bharucha-Reid, "Elements of the Theory of Markov Processes and Their Applications," p. 295, McGraw-Hill Book Co. Inc., London (1960).

## Evaluation of Electrochemical Information Transfer System

### I. Effect of Electric Fields on Living Organisms

Andrew A. Marino, Thomas J. Berger, B. Peter Austin, and Robert O. Becker

Veterans Administration Hospital and Upstate Medical Center, Syracuse, New York 13210

and Francis X. Hart

University of the South, Sewanee, Tennessee 37375

The concepts of electrochemical information transfer occurring at membrane interfaces in biological systems (1,2) imply that exposure of living organisms or cells to electromagnetic fields will produce nonthermal effects. In view of the widespread alteration of the electrical environment produced by electrical power transmission facilities, the question of a resultant biological effect becomes significant. A preliminary study involving chronic exposure of rats to 60 Hz, 150 V/cm, electric fields is reported herein. Our object was to determine whether such exposure would; (i) act as a body stressor, i.e., direct glandular (cell) effect, (ii) affect the blood proteins, i.e., the cells which produce them, (iii) affect the growth rate of immature animals. To these ends we measured the concentration of serum corticoids, the relative distribution of serum proteins, and body weight.

#### Methods

Twenty-one day old male Sprague-Dawley rats, fed and watered *ad libitum*, were exposed continuously for one month to a 60 Hz electric field generated between the plates of a capacitor which was oriented to produce an electric field vertical to the earth's surface (3).

Each experimental and control group consisted of a minimum of 11 rats. In the first three experiments, the rats were weighed at the end of the exposure period, decapitated, and the sera from each group was pooled and analyzed. In the fourth experiment, the rats were subjected to a cold stress ( $-13^{\circ}\text{C}$  for 1 hr) at the end of the exposure period, after weighing and prior to sacrifice. All experiments were performed consecutively.

The relative percentages of the four major groups of serum proteins were determined by electrophoresis on cellulose acetate with planimetric integration (3). The concentration of 11-hydroxycorticosterone in the pooled sera (serum corticoids) was measured fluorometrically by Mattingly's method (4) as modified by Purves and Sirett (5).

#### Results

The final weight of all four experimental groups was lower than that of the corresponding control group, significantly so ( $P < 0.05$ ) in two experiments (Table I). In the three experiments in which they were measured, a statistically significant elevation in albumin percentage and a statistically significant decrease in gamma globulin percentage was noted, compared to the corresponding control group (Table II). In the first three experiments, the serum corticoids were consistently lower in the experimental group as compared to the corresponding control group (Table I). All experimental and control animals were autopsied at sacrifice and no gross pathology was observed.

Experiment 4 was performed to determine whether the observed disturbances in the adrenal-pituitary system (control system for serum corticoids) would prevent the exposed rats from responding to a known stress. When subjected to a cold stress, the serum corticoids in both groups rose markedly (Table I), indicating that the exposed rats remained capable of responding to a known stress in the predictable fashion.

All the observed metabolic alterations are consistent with the effect of chronic exposure to a non-

Table I. Effects of continuous exposure to 60 Hz electric fields on body weight and serum corticoids of rats

Experiment No.	No. of rats	Final body weight (g)	Serum corticoids ( $\mu\text{g}/100\text{ ml}$ )
1	Experimental (14)	244.0* $\pm$ 12.6	14.6
	Control (19)	273.1 $\pm$ 16.7	22.0
2	Experimental (14)	276.5 $\pm$ 24.1	12.4
	Control (22)	290.8 $\pm$ 27.9	18.0
3	Experimental (14)	270.4 $\pm$ 14.3	10.4
	Control (18)	277.8 $\pm$ 15.8	14.5
4	Experimental (14)	228.7* $\pm$ 26.1	56.8
	Control (11)	251.0 $\pm$ 11.3	53.4

Table II. Electrophoretically determined serum protein relative percentages of rats exposed continuously to 60 Hz electric field for one month. For each group, the listed values are averages and standard deviations of 10 determinations (5 strips/pool, 2 scans/strip).

Experiment No.		Serum proteins (%)			
		Albumin	$\alpha$ -globulin	$\beta$ -globulin	$\gamma$ -globulin
1	Experimental	59.1 $\pm$ 1.7*	22.3 $\pm$ 1.0*	12.2 $\pm$ 0.9	6.4 $\pm$ 1.4*
	Control	53.8 $\pm$ 1.6	24.1 $\pm$ 0.9	13.6 $\pm$ 0.9	8.6 $\pm$ 1.2
2	Experimental	52.4 $\pm$ 2.8*	25.7 $\pm$ 1.0	14.6 $\pm$ 1.1	7.5 $\pm$ 0.8*
	Control	49.2 $\pm$ 1.0	26.9 $\pm$ 1.0	14.7 $\pm$ 0.6	9.2 $\pm$ 0.7
3	Experimental	52.7 $\pm$ 1.4*	25.9 $\pm$ 2.1	14.8 $\pm$ 0.9	7.3 $\pm$ 0.9*
	Control	49.1 $\pm$ 3.3	27.2 $\pm$ 2.4	14.0 $\pm$ 0.6	9.6 $\pm$ 1.2

\*  $P < 0.05$ .

specific environmental stressor (6-8), with the development of the general adaptation syndrome as described by Selye (6). Since data were obtained only at the termination of one month's exposure, the initial stages of this reaction were not documented.

In summary, the results support the concept of electrochemical information transfer in biological systems, and indicate that it involves at a minimum, direct cellular and glandular responses quite distinct from that due to Joule heating.

#### Acknowledgments

This work was supported by the Veterans Administration Research Service, Project No. 0865-01.

Manuscript received April 19, 1976.

Any discussion of this paper will appear in a Discussion Section to be published in the June 1977 JOURNAL.

All discussions for the June 1977 Discussion Section should be submitted by Feb. 1, 1977.

Publication costs of this article were assisted by the Veterans Administration Hospital.

#### REFERENCES

1. A. A. Pilla, *Ann. N.Y. Acad. Sci.*, **238**, 149 (1974).
2. R. O. Becker and A. A. Pilla, in "Modern Aspects of Electrochemistry No. 10," J. O'M. Bockris, Editor, Plenum Press, New York (1975).
3. A. A. Marino, T. J. Berger, J. T. Mitchell, R. A. Duhacek, and R. O. Becker, *Ann. N.Y. Acad. Sci.*, **238**, 436 (1974).
4. D. Mattingly, *J. Clin. Path.*, **15**, 374 (1962).
5. H. D. Purves and N. E. Stirett, *J. Exp. Biol. Med. Sci.*, **47**, 589 (1969).
6. H. Selye, "Stress," Acta Inc., Montreal (1950).
7. A. Daniels-Severs, L. C. Keil, and J. Vernikos-Danellis, *Pharmacology*, **9**, 348 (1973).
8. B. F. Brain and N. W. Nowell, *Gen. Comp. Endocrinol.*, **16**, 149 (1971).



## Kinetics of the Reactive Sputter Deposition of Titanium Oxides

K. G. Geraghty<sup>1</sup>

*Inorganic Materials Research Division, Lawrence Berkeley Laboratory, Berkeley, California 94720*

and L. F. Donaghey\*

*Department of Chemical Engineering, University of California, Berkeley, California 94720*

### ABSTRACT

The reactive sputtering of titanium was studied in an rf plasma containing argon and oxygen. The kinetics of the reactive sputtering process and the properties of deposited titanium oxide films were studied as a function of the oxygen partial pressure in the plasma, bias voltage, and rf power. Models for the transient oxidation of titanium were explored in relation to oxidation mechanisms. Model parameters were determined from experimental studies. The sputter etch rate of the titanium target reached a maximum at an oxygen mole fraction of 0.002. The sputter deposition rate was found to decrease sharply at a critical oxygen mole fraction equal to 0.007, corresponding to the onset of target oxidation. The time dependence of the target oxidation process was found to be in qualitative agreement with a reactive sputter-oxidation model.

Titanium dioxide is an important dielectric material for refractory, optical, and electronic applications. In optical and microelectronics applications, TiO<sub>2</sub> thin films can be sputter deposited by the rf sputtering of titania, or by the reactive sputtering of titanium in a plasma containing a partial pressure of oxygen (1-3). The optical properties of TiO<sub>2</sub>, particularly its high refractive index, have proven invaluable to the optics industry for over 25 years, and much thin film research in this industry has been carried out in the preparation of TiO<sub>2</sub> lens coatings (4, 5). Titania can also be deposited as a protective coating (6). In addition to the practical importance of titanium dioxide, the Ti-O system is of theoretical interest because of the large number of phases in this system, and because the kinetics of reactive sputter deposition of these phases have not been established. Bailey has reported that essentially all film physical properties of sputtered films are strongly dependent on deposition parameters such as time, deposit rate, argon pressure, cathode-anode distance, and substrate temperature (7). The establishment of kinetic rates and conditions for the deposition of TiO, of the Magneli phases Ti<sub>n</sub>O<sub>2n-1</sub> where n ≥ 2, and of TiO<sub>2</sub> by reactive sputtering is the subject of the present study.

### The Ti-O System

There is considerable literature on the condensed phases of the Ti-O system. Several investigators have determined the phase diagram of this system during the last 20 years (8-10). The low temperature portion of the phase diagram for the Ti-O system after Roy

and White is reproduced in Fig. 1 (10). This diagram indicates that temperatures above 800°C are required to produce rutile crystals under equilibrium conditions. Below this temperature, anatase is the stable phase. Thus, in order to obtain rutile, it is necessary to insure that the effective deposition temperature be maintained

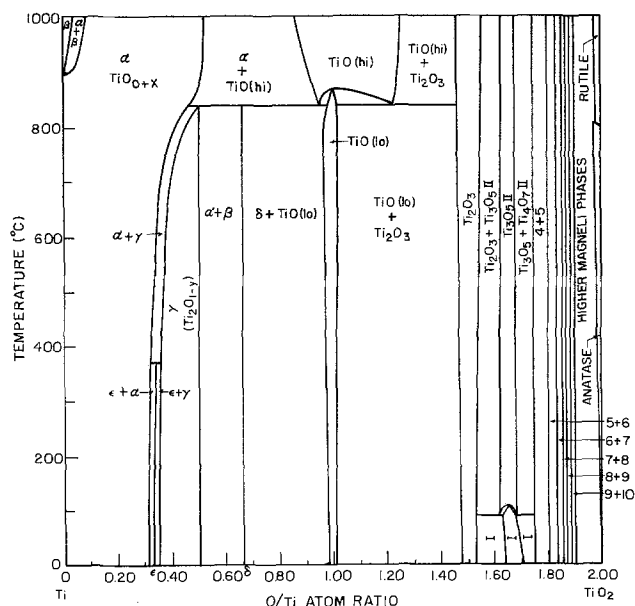


Fig. 1. Low temperature condensed phase diagram for the Ti-O system. The Magneli phases have the form Ti<sub>n</sub>O<sub>2n-1</sub> where n = 4,5,6, . . . , ∞.

\* Electrochemical Society Active Member.

<sup>1</sup> Present address: General Dynamics, Pomona Division, Pomona, California 91766.

Key words: sputtering, reactive sputtering, oxidation, titanium oxides, thin films.



above 800°C, either by heat generated from the impacting atoms themselves or through external heating of the substrate.

The stability range of  $Ti_3O_5$  and the Magneli phases with regard to temperature and oxygen fugacity was determined by Porter (11). These studies confirmed the existence of an indeterminate number of intermediate oxide phases between  $TiO$  and  $TiO_2$ . Of these,  $Ti_2O_3$  and  $Ti_3O_5$  are distinct phases, while the Magneli phases form a closely related series of shear-defect compounds with the homologous formula  $Ti_nO_{2n-1}$  where  $4 \leq n \leq \infty$  (12).

Figure 2 summarizes the stability ranges of these phases as a function of the reciprocal temperature and oxygen fugacity. The figure shows that  $TiO_{2-x}$  (anatase) is the stable oxide phase at an estimated target surface temperature of 400°C and an oxygen fugacity near unity. For substrate temperatures below 800°C,  $TiO_{2-x}$  (anatase) should be the thermodynamically stable, but not necessarily the kinetically favored, phase deposited by reactive sputtering with  $Ar/O_2$  over a range of oxygen fugacity.

### Theories of Target Oxidation

The sputtering process consists of accelerating positively charged plasma ions into a target material under the influence of a bias electric field. The incident ions eject atoms of the target material from the target surface by initiating a chain-collision energy transfer process through the crystal lattice. Reactive gaseous components in the plasma can react with the target causing oxidation of the target surface, and energetic ions have sufficient energy to be implanted into the target to cause internal oxidation.

While a d-c bias voltage suffices for sputtering conducting materials, an rf field is required for sputtering of dielectrics in order to remove the negative charge buildup at the target surface by highly mobile plasma electrons. In addition, rf power can also cause sputtering of conducting materials.

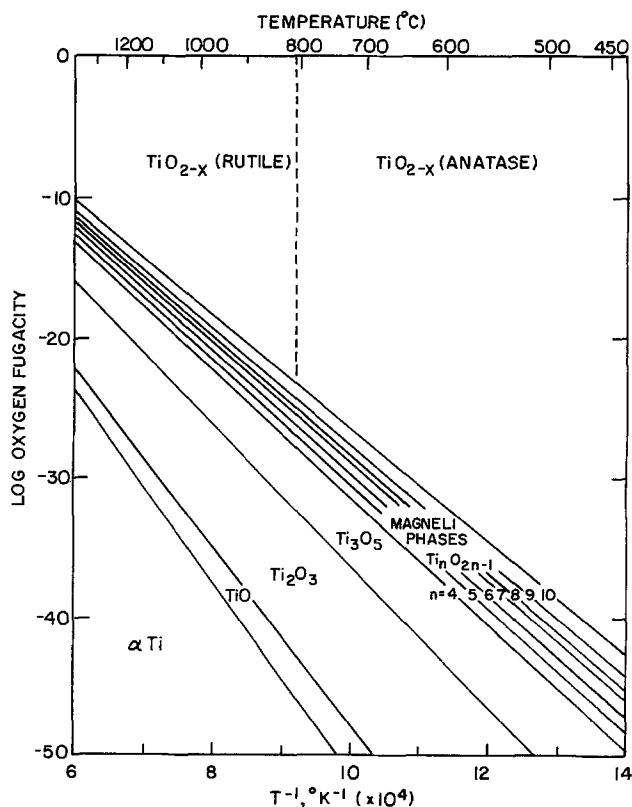


Fig. 2. Stability ranges of titanium oxides as a function of reciprocal temperature and oxygen fugacity.

The plasma gas for the sputtering process is normally an inert gas, typically argon. Introducing a reactive gas with the argon allows reactive sputtering, wherein the sputtered target atoms react with the active gas, and the products are collected on the substrate. The mechanism of this reaction is not clearly understood, as the precise time of reaction has not been determined. The oxidation reaction could occur at the target surface, on collision with the substrate, or by diffusion and reaction following deposition on the substrate. Oxidation reactions in the gas phase are negligible because of the low collision cross sections and low pressures involved.

The subject of target oxidation has received even less attention than the reaction-chemistry mechanism of reactive sputtering, perhaps because commercial applications are primarily concerned with the materials deposited during sputtering and not with the target condition or rate kinetics. However, new contributions to the mechanisms of target oxidation are available from recent developments in the analogous field of plasma anodization and oxidation (13-15).

*The plasma anodization model.*—Plasma anodization is the process of growing an oxide film on a metallic substrate by immersing the substrate in an oxygen plasma and applying an electric field (14). Plasma oxidation is virtually the same technique lacking only the externally applied bias voltage. The current interest in these technologies stems from their application to the fabrication of oxide tunnel barriers for thin film Josephson junction devices.

The pioneering work of Miles and Smith offered the first indication of the potential uses of plasma anodization for both tunneling barriers and thin film dielectrics (13). They offered a qualitative explanation of the oxidation process, and concluded that positive metal ions dissolve into the surface oxide layer under the influence of the electric field. The ions, under a combination of drift and diffusion, move to the oxide-plasma interface, and react chemically with gaseous oxygen, thereby initiating oxide growth. They further observed that for a constant bias potential, the oxide growth reaches a certain thickness and then ceases. Thickness control can be exercised by varying the applied field strength.

A few years after this work, Schroen looked at the physics of the oxidation process and presented a molecular model for the reaction (14). The initially neutral substrate is raised to a negative potential by the mobile plasma electrons. This negative potential attracts  $O^+$  and  $O_2^+$  positively charged oxygen molecules to the target surface. These ions enter the target as  $O_2$  neutrals, diffuse into the metal lattice, and react to form an oxide. The model is still tentative, and lacks any quantifying formulae.

O'Hanlon (15) reviewed plasma anodization, and presented a model very similar to Schroen's for the plasma anodization process in terms of two distinct mechanisms. One mechanism is that of Schroen, whereby  $O_2^+$  ions dissociate upon impact and diffuse into the target. A second mechanism is that  $O^+$  and  $O_2^+$  ions originating in the plasma are implanted directly into the oxide. This model is supported by Whitlock and Bounden (16) and by Thompson (17), who were unable to detect any measurable negative ion current density in the negative glow of an oxygen discharge.

Miles and Smith have studied oxide growth rates on aluminum by plasma anodization (13). An essential requirement for oxide growth by this method is the formation of a "priming oxide layer" by exposing the aluminum to an  $O_2$  plasma for a period of 600 sec before applying a bias potential. Without the priming period, no oxide was formed. The thin oxide layer (<20Å) formed after the priming period by plasma anodization without external bias potentials was shown by O'Hanlon (15) to have a logarithmic dependence on

time given by

$$x = x_0 + k \ln t \quad [1]$$

where  $t > 1$  min. Using the same data, however, one can show that a parabolic growth law is followed during the same time period

$$x = k'\sqrt{t} \quad [2]$$

where  $t > 0$ . Thus, it appears that a diffusional mechanism could drive the plasma anodization process at zero bias.

The oxidation rate of Ti metal in pure  $O_2$  at 1 atm pressure has been measured by Kubaschewski and Hopkins (18). The oxidation time dependence can be described by the parabolic dependence of oxide thickness on time with a rate constant given by

$$K_p = 0.16 \exp(-45,050/RT) \quad [3]$$

(550°-850°C) where  $K_p$  has the units  $[g^2 \text{ cm}^{-4} \text{ sec}^{-1}]$ ,  $R = 1.98719 \text{ cal}_{\text{th}} \text{ mole}^{-1} \text{ }^\circ\text{K}^{-1}$ , and  $T$  is in  $^\circ\text{K}$ . Thus, the  $TiO_2$  oxide thickness  $x$  in centimeters has the time dependence

$$x = \{10^{-1.027 - 4923T^{-1}}\}t^{1/2} \quad [4]$$

where time  $t$  is in seconds. This equation indicates that temperatures of  $\sim 1000^\circ\text{C}$  are needed to form a  $1 \mu\text{m}$  thick oxide layer in  $10^3$  sec, whereas an oxide layer of  $10\text{\AA}$  forms at only  $385^\circ\text{C}$  in the same time. Although a water-cooled sputtering target remains within a few degrees of the coolant temperature during sputtering, the temperature at the sputtering collision site can reach a significant fraction of the melting point. Therefore, it can be anticipated that the oxidation rate in an oxygen-containing plasma is partly diffusion controlled, in spite of the finite sputtering process.

*The reactive sputter-oxidation models.*—The first quantitative analysis of the oxidation phenomena was advanced by Greiner, who investigated rf sputter etching in oxygen (19). The basis of Greiner's theory is the assumption that the sputtering and oxidation rates are independent and concurrent. The rate of change of oxide thickness on the target,  $dx/dt$ , is then

$$\frac{dx}{dt} = R_{\text{ox}} - R_{\text{sp}} \quad [5]$$

where  $R_{\text{ox}}$  is the oxidation rate and  $R_{\text{sp}}$  is the sputter rate of the target phase. In this model, Greiner invokes two assumptions. First, the oxide thickness follows a logarithmic time dependence given by  $x = x_0 + k \ln t$ , and, second, the sputter each rate,  $R_{\text{sp}}$ , is constant. Consequently

$$R_{\text{ox}} = Ke^{-x/x_0} \quad [6]$$

Using Greiner's assumption, the total rate of change of oxide thickness becomes

$$\left(\frac{dx}{dt}\right)_{\text{total}} = Ke^{-x/x_0} - R_{\text{sp}} \quad [7]$$

This differential equation has the integral form

$$x = x_0 \ln \left[ \frac{K}{R_{\text{sp}}} - \left( \frac{K}{R_{\text{sp}}} - e^{x_1/x_0} \right) e^{-R_{\text{sp}}t/x_0} \right] \quad [8]$$

where  $x_1$  is the oxide thickness at time  $t = 0$ . This equation has a transient time constant  $x_0/R_{\text{sp}}$  and a steady-state limit given by

$$\lim_{t \rightarrow \infty} x = x_0 \ln (K/R_{\text{sp}}) \quad [9]$$

The steady-state limit can also be obtained by setting  $dx/dt = 0$  in Eq. [7]. Note that this theory predicts that a finite thickness of oxide is present on the target only if  $K > R_{\text{sp}}$ , and that the time constant for transient oxidation is  $x_0/R_{\text{sp}}$ .

In a more recent model, Heller presented an analysis of the results of his work on reactively sputtering

metals in oxidizing atmospheres (20). Heller found the existence of a critical oxygen partial pressure in the plasma,  $p_{O_2}^*$ , below which no oxidation of the target takes place. For  $p_{O_2} < p_{O_2}^*$ , the sputter rate exceeded the oxidation rate and no oxide layer formed on the target. For  $p_{O_2} > p_{O_2}^*$ , an oxide layer of finite thickness formed. These experimental results are not inconsistent with Greiner's study in that Greiner never explored the range of  $p_{O_2}$  values below which no oxide formed.

Heller improved Greiner's assumption concerning  $R_{\text{ox}}$  and  $R_{\text{sp}}$  by introducing the following oxidation equation. He defined

$$R_{\text{ox}} = \frac{A(P)}{\rho} e^{-x/x_0} \quad [10]$$

where the parameter  $A(P)$  is a pressure-dependent function and  $\rho$  is the density of the sputtered target phase. The target oxide density will vary with composition from  $4.5 \text{ g/cm}^3$  for Ti to  $4.26 \text{ g/cm}^3$  for  $TiO_2$ . Heller assumes that  $R_{\text{sp}}$  is a monotonically decreasing function which yields the correct sputtering rates at  $x = 0$  and  $x \rightarrow \infty$ , i.e.

$$\left(\frac{dx}{dt}\right)_{\text{sp}} = R_{\text{sp}} = R_{\text{sp},0} + (R_{\text{sp},m} - R_{\text{sp},0})e^{-x/x_0} \quad [11]$$

where  $R_{\text{sp},0}$  and  $R_{\text{sp},m}$  are the sputtering rates of target oxide and metallic Ti, respectively. This model was tested in a second paper by Greiner who obtained sufficient data to determine the unknown parameters of the model (21).

Notwithstanding the previous efforts to arrive at a quantitative analysis of the oxidation phenomenon, Leslie and Knorr have concluded, from their investigation of the plasma oxidation of tantalum, that the complex interrelation of system parameters and the present dearth of experimental work prohibit the formulation of any complete model (22).

## Experimental

*Sputtering apparatus.*—The experimental equipment consisted of modular diode-sputtering system together with a 1 kW rf power supply. The sputtering system was attached to a vacuum system consisting of an NRC series VHS, 6 in. (15.2 cm) diffusion pump with a pumping speed of 2400 liter-air/sec, a Welch liquid nitrogen cold trap, and a 7 liter-air/sec centrifugal roughing pump. This system, shown in Fig. 3, could achieve an ultimate pressure below  $10^{-7}$  Torr<sup>2</sup> ( $1.3 \times 10^{-5}$  Pa).

Chamber pressure was monitored simultaneously by a Pirani GP-310 gauge for pressures below 0.1 Torr and an Autovac Type 3294-B gauge for pressures in the range from 1 mTorr to 1000 Torr. The main purpose of

<sup>2</sup> 1 Torr = 133.3224 Pa.

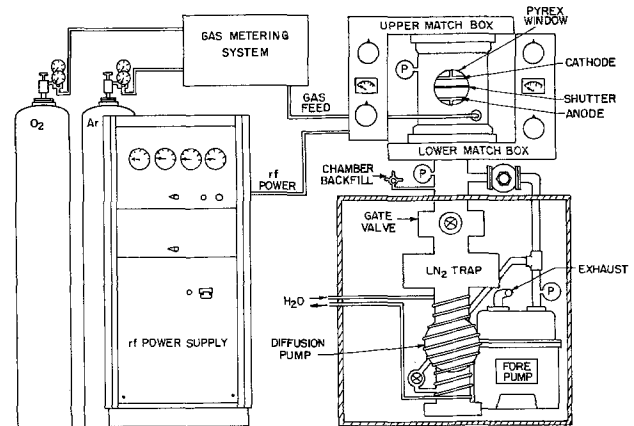


Fig. 3. RF sputtering system and ancillary apparatus

the dual meter system was to eliminate errors due to meter fluctuations after calibration.

The O<sub>2</sub> flow was controlled and monitored by means of a microflowmeter capable of measuring flow rates between 0.2 and 15 ml/min. The oxygen was mixed with Ti-getter purified argon stream and passed through a Hastings-Raydist mass flowmeter, where the total gas flow, and, by difference, the argon flow rate were measured.

The maximum volumetric gas flow through the chamber was determined by the limitations of the diffusion pump. The maximum foreline pressure was chosen as a conservative 200 mTorr. At this pressure, the argon flow rate reached an upper limit of 150 ml/min. Since the microflowmeter could resolve as low as 0.2 ml/min, the minimum measurable O<sub>2</sub> volume fraction attainable was 0.0013. The volume fraction of O<sub>2</sub> is identical to the mole fraction at the low chamber pressures involved (25 mTorr).

A calculation of the amount of O<sub>2</sub> removed from the plasma during the deposition of stoichiometric TiO<sub>2</sub> film indicates that negligible oxygen partial pressure change occurs by the deposition reaction. Only 1.3% of the total gaseous O<sub>2</sub> would be entrained at an oxygen plasma mole fraction of 0.007 provided that the maximum gas flow rate is maintained.

**Materials.**—Titanium targets 6 in. (15.2 cm) in diameter were fashioned from 0.032 in. (0.081 cm) thick sheet metal.<sup>3</sup> The purity was assayed at 99.9% and the results of a spectrographic analysis indicated that iron was the only significant impurity (0.1%). Several targets were used to ensure oxide-free surfaces for each phase of the research. The anode was covered with a Ti disk to minimize film impurities due to backsputtering.

Three different substrates were used: microscope slides for thickness measurements, microscope cover slides for weight change measurements, and type 10 quartz plate for electron diffraction, optical, and electrical measurements. The quartz plates were precut into 1.3 × 1.3 cm squares for electron microscopy and spectrophotometric analyses. High optical quality substrates were essential in order to obtain reliable u.v. spectra.

**Procedure.**—Sputtering was performed in the range of oxygen mole fraction  $y$  ranging from 0 to 0.15. Titanium was sputtered in pure Ar ( $y = 0$ ) as a standard for comparison in assessing the effects of O<sub>2</sub> on sputtering parameters. A minimum deposition time of 30 min was chosen for this series to generate films sufficiently thick for characterization purposes.

A sputtering pressure of 24 mTorr, determined by mean free path considerations, produced the optimum initial power match. Forward and reflected power settings were normally 500 and 90W, respectively, delivering a d-c bias voltage of about 1.9 kV. These values were not constant throughout a run, however, and provided an early indication of change in the target surface state, which was subsequently interpreted as oxidation. The chamber pressure remained constant during all experiments.

Following reactive sputtering, substrate specimens were examined by reflection electron microscopy to determine their structure. Spectral absorbance of the samples was measured in the ultraviolet, visible, and infrared regions of the optical spectrum. The u.v. and visible absorbances were obtained on a Cary Model 118 spectrophotometer, while the Perkin-Elmer Model 421 spectrophotometer was used for the infrared spectra. A four-point conductivity apparatus was constructed to measure the conductivity of metallic and semimetallic films.

The target oxidation phenomenon was studied by the following procedure. The target was first sputter etched

of all surface oxide in Ar. Then O<sub>2</sub> and Ar were simultaneously admitted at a given oxygen mole fraction  $y$  for a measured time interval. The O<sub>2</sub> flow was then shut off and the target again sputter etched in Ar. The etch time was recorded.

Possible contamination of the system by atmospheric oxygen was minimized by completely evacuating the system for 30 min before each run. After each opening of the system to air, a complete sputter cleaning was required before a new run was possible. A minimum of 10 min was necessary to remove the chemisorbed oxide layer which formed on the target surface. The *in situ* determination of the target oxidation state was made from measurements of reflected power bias potential and plasma color.

## Results

The titanium oxide films deposited under various conditions were characterized to determine the effects of reactive sputtering variables on the physical, optical, and electrical properties of deposited films and to determine reactive sputtering rate kinetics.

**Deposition rates.**—A significant transition in density and deposition rate was observed at an oxygen mole fraction  $y^* = 0.007$ , as shown in Fig. 4. Deposition rates and film densities were independent of  $y$  for  $y > y^*$ . Deposition rate data showed a sharp decrease by an order of magnitude as  $y$  increased above  $y^*$ , as shown in Fig. 4. The significance of these results becomes apparent when one contemplates the conditions needed to deposit films of constant and reproducible properties. For  $y > y^*$ , the data indicate film properties are invariant with  $y$ , which allows for easy control of film parameters, particularly in large volume commercial applications. However, the low deposition rate for  $y > y^*$  represents a drawback for operations requiring rapid processing rates.

**Physical properties.**—Films were found to etch rapidly in concentrated HNO<sub>3</sub>. The rapid etching characteristics of reactively sputtered TiO<sub>x</sub> films with  $x < 2$  suggest that the films are amorphous. This assumption was borne out by electron microscopy studies, using a Hitachi HU-125 operated at 100 keV. Figure 5 shows the radial dependence of the photodensity of a typical film which demonstrates the amorphous structure of the films. The Au coating was applied by evaporation on the films to prevent electrostatic charging, but too thick a layer interfered with the reflection pattern. The photodensitometric effect of the 50Å Au film was subtracted from the composite pattern to yield the TiO<sub>x</sub> diffraction pattern alone.

The density of reactively sputter-deposited films was determined from weight change and thickness measurements. The results are shown in Table I. A significant increase in film density occurred for  $y$  near  $y^*$ . All

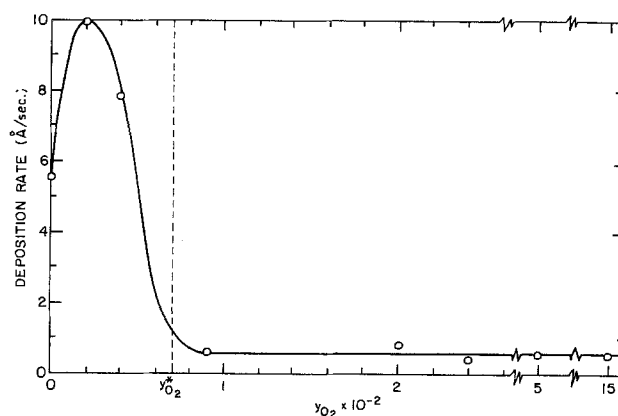


Fig. 4. TiO<sub>x</sub> film deposition rate vs. O<sub>2</sub> mole fraction in the plasma.

<sup>3</sup> Continental Metals, North Hollywood, California.

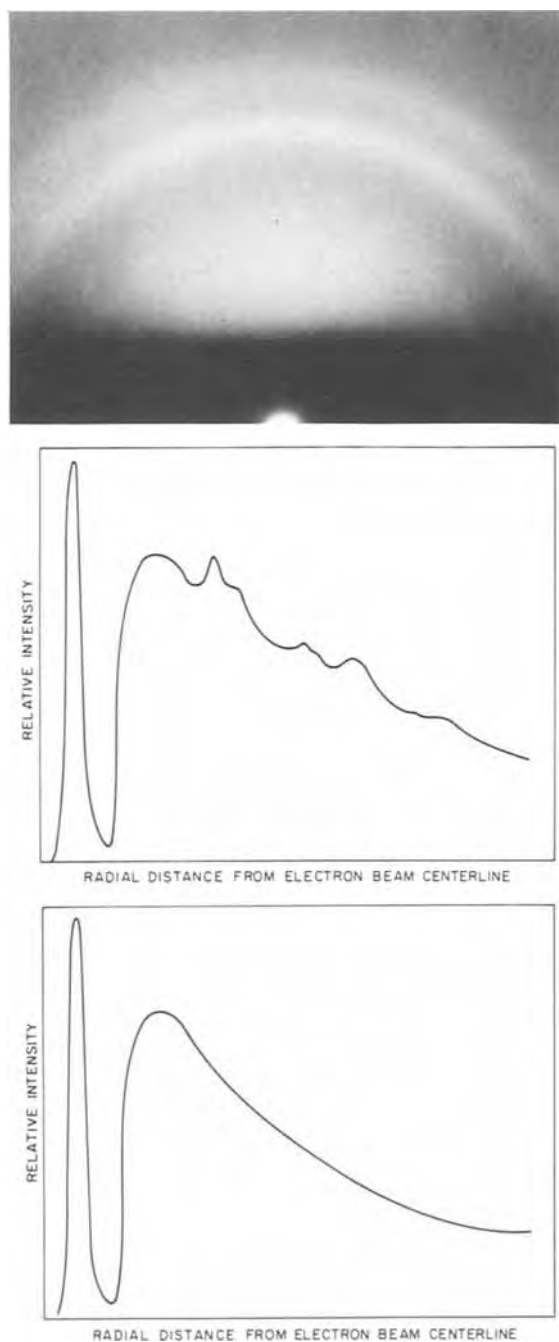


Fig. 5. Reflection electron diffraction of a  $\text{TiO}_2$  film. (Top) Reflection electron diffraction pattern from reactively sputtered  $\text{TiO}_2$ . (Middle) Photodensitometer trace for a Au-coated  $\text{TiO}_2$  film. (Bottom) Photodensitometer trace calculated for the  $\text{TiO}_2$  film without the Au reflections.

films deposited at  $y > 0.035$  showed essentially no absorption in the visible range, and were in fact transparent to the eye. Films deposited at very low  $y$  ( $\leq 0.002$ ) were metallic and showed some visible absorbance while films deposited at  $y = 0.02$  possessed a slight gold tint. From optical data it was inferred that the yellow-gold colored samples were  $\text{TiO}$ .

Table I. Reactively sputter-deposited titanium oxide film densities

Film phase	Plasma composition	$\rho$ (g/cm <sup>3</sup> )
Ti	$y = 0$	2.05
TiO	$y \lesssim y^*$	~5
$\text{TiO}_x$ ( $x \sim 2$ )	$y > y^*$	3.9

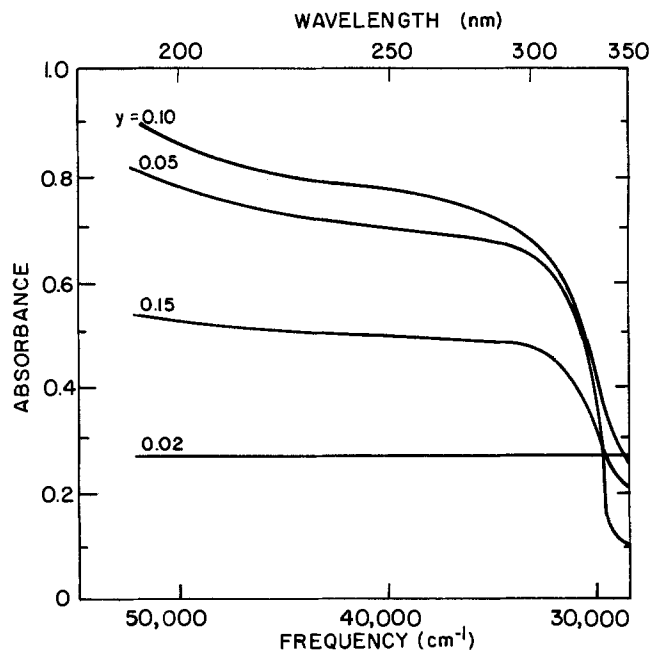


Fig. 6. U.V. spectrograph of  $\text{TiO}_x$  thin films deposited at several oxygen plasma conditions.

The u.v. spectra of deposited films show an absorption edge at about 330 nm. These spectra are shown in Fig. 6 and correspond to a bandgap of 3.76 eV for  $\text{TiO}_2$ .

**Target oxidation-etch rates.**—Target oxidation at different oxygen partial pressures was studied by exposing the target to the reactive gas mixture for a fixed time, then measuring the etching time to remove the oxide. The experimentally measured oxidation and etch times are shown in Table II.

### Discussion

The phase diagram for the Ti-O system shown in Fig. 1 indicates that the anatase phase of  $\text{TiO}_2$  would be expected for low temperature deposition. Presumably the amorphous phase persists because of the high impact energy of the depositing atoms, which destroys any crystalline lattice which would otherwise form. A heat transfer calculation showed that the substrate surface temperature was 20.3°C. In order to deposit a crystalline phase, it will be necessary to provide an external heating source capable of maintaining the substrate several hundred degrees above its unheated tem-

Table II. Experimentally measured plasma oxidation and etch times and power settings at different plasma  $\text{O}_2$  concentrations

$y$ (mole fraction)	$\text{O}_2$ exposure time (sec)	Time to start of color change (sec)	Time to etch target (sec)
0.007	180	105	182
0.007	300	138	178
0.008	80	55	468
0.008	100	37	465
0.008	150	55	416
0.014	80	35	245
0.014	100	25	364
0.014	120	22	320
0.014	120	20	321
0.014	150	20	390
0.014	200	18	360
0.014	250	22	400
0.022	100	20	174
0.022	150	12	162
0.022	200	12	164
0.040	82	5	284
0.040	100	5	250
0.064	15	3	170
0.064	60	3	211
0.064	100	3	235
0.175	80	15	112
0.175	80	13	180
0.175	100	18	216
0.175	150	15	288
0.027	100	10	199
0.033	100	10	199

perature. This will provide sufficient kinetic energy to the already deposited material for annealing.

Film physical properties exhibited a strong dependence on the state of target oxidation. In particular, film density followed the trend shown by the deposition rate with increasing  $y$ . An obvious transition at  $y^*$  was again found, with film density remaining constant for  $y$  above this value. The invariance of both deposition rate and density for  $y$  above  $y^*$  can be taken as an indication that film stoichiometry no longer changes, and that the target oxide here in fact is stoichiometric  $\text{TiO}_2$ .

Lakshmanan reports spectra for  $\text{TiO}_2$  reactively deposited in pure  $\text{O}_2$  remarkably similar both in shape and value to that shown in Fig. 6. The bandgap energy of 3.65 eV which he reports agrees quite closely with the value of 3.76 eV obtained in this study for amorphous  $\text{TiO}_2$  (23).

The spectrum for the sample deposited at  $y = 0.02$  shows low absorption throughout the u.v. range, probably for  $\text{TiO}$ . The films deposited at 0.05, 0.10, and 0.15 mole fraction of  $\text{O}_2$  in the plasma all absorb strongly below 300 nm and are probably amorphous Magneli phases. The species deposited at  $y = 0.15$  represents an anomaly in that it absorbs less below 330 nm than the oxide films formed with lower  $y$ .

The films deposited with  $y = 0.035$  were found to give less u.v. absorbance than did films deposited at  $y = 0.05$  or 0.10. Because no target etching was performed before each successive deposition of these samples, the oxidation state of the target should have affected the amount of oxygen incorporated into successively deposited films. This hysteresis effect is evident in experimental data.

The effects of exposing a clean titanium target to an oxidizing plasma were studied as a function of exposure time and oxygen concentration. The steady-state target oxide thickness was formed by oxidation in an  $\text{Ar}/\text{O}_2$  plasma for a time sufficiently long to achieve steady state. The dependence of the steady-state oxide thickness developed on the target at different oxygen molar concentrations in the plasma was measured indirectly by the time required to etch the target clean of oxide in an  $\text{Ar}$  plasma. Figure 7 shows the dependence of the etch time on the plasma oxygen mole fraction. In this figure, the end of the etching period was determined from the color change of the plasma. The etch times shown are the average of several experiments for each value of  $y$ . Since the  $\text{Ar}$ -plasma etch time is the product of sputter yield times the oxide thickness, the proportionality between oxide thickness and etch time holds only if the oxide properties are independent of  $y$ . It is possible that the sputter yield for films deposited for  $0.01 < y < 0.02$  is lower than for  $y > 0.02$  to give the peak observed in Fig. 7. A low sputter yield is expected for the highly stable phases  $\text{Ti}_2\text{O}_3$  and  $\text{Ti}_3\text{O}_4$ .

Figure 7 shows that no oxide formed on the target for  $y < y^* = 0.007$ . There was an increase in etch time at  $y^*$ , then a drop and a gradual rise with increasing  $y$ . The initial increase can be attributed to the formation of a highly stable phase such as  $\text{Ti}_2\text{O}_3$  or  $\text{Ti}_3\text{O}_4$  on the target surface. The dashed line tangent to the curve for  $y > 0.03$  delineates the approximate increase in  $\text{O}_2^+$  ions resulting from a rise in  $y$  and indicates that target oxide thickness is proportional to  $y$  in that range. This result is somewhat in contradiction to models for the reactive sputter-oxidation process which predicts that the oxide thickness is proportional to  $\ln(KR_{\text{sp}}^{-1})$ , unless different phases form on the target, each with different values of  $K$  and  $R_{\text{sp}}$ .

The dependence of the deposition rate on  $y$  was found to exhibit an order-of-magnitude decrease if the deposition rate occurs near  $y^*$ . Part of the rise in target oxide etch time depicted in Fig. 7 is probably due to an increasing oxygen incorporation in the deposited

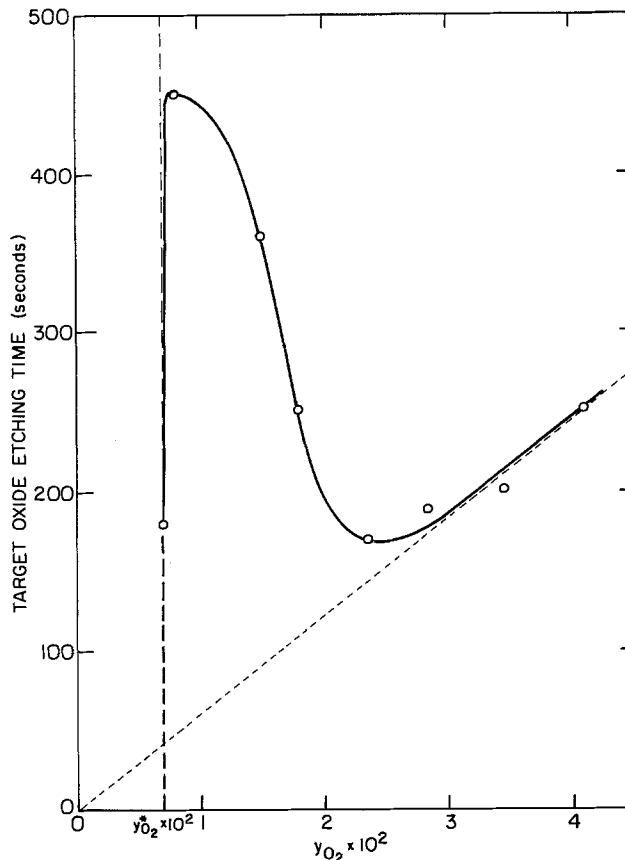


Fig. 7. Target etch time following target oxidation as a function of  $y_{\text{O}_2}$ .

film provided by  $\text{O}_2$  in the plasma, and, to a lesser extent, to an increasing sputter etch rate due to  $\text{O}_2^+$  ions superimposed on a constant  $\text{Ar}$  sputter etch rate. The nonreactive  $\text{Ti}$  sputtering rate of 5.6  $\text{\AA}/\text{sec}$  is an order of magnitude higher than the extrapolated sputtering rate of 0.48 obtained for  $y \gg y^*$ , indicating that titanium metal has a much higher sputter yield than does  $\text{TiO}_2$ . This disparity is larger than would be expected if the sputtering process removed individual atoms from the target, since the  $\text{Ti-Ti}$  bond energy is 112.6 kcal/mole compared to a  $\text{Ti-O}$  bond energy of 157 kcal/mole (24) and since the sputter yield should vary with the square root of the atom binding energy. Thus, molecular groups such as  $\text{TiO}$  and  $\text{TiO}_2$  are probably removed from the target during reactive sputtering at high values of  $y_{\text{O}_2}$ .

The transient growth of oxide on the  $\text{Ti}$  target in an  $\text{Ar}/\text{O}_2$  plasma for which  $y_{\text{O}_2} = 0.014 = 2y^*$  was also studied by measurement of  $\text{Ar}$  plasma sputter etching times needed to remove the oxide films. Again, the oxide thickness was assumed proportional to the  $\text{Ar}$  plasma etch time provided that the sputter yield of the oxide is independent of oxide thickness. The oxide thickness increased monotonically with time. If the steady-state oxide thickness corresponds to a target oxide sputter etch time of 400 sec, then the time constant for transient oxidation can be found by comparing the data with Eq. [4] and [8]. The experimental data were found not to show a parabolic oxidation rate as would be required by diffusion-controlled kinetics. On the other hand, the time constant for the exponential time dependence of the reactive sputter-oxidation model, Eq. [8], was found to be (20)

$$KR_{\text{sp}}^{-1} = 67 \pm 11$$

Since the oxide sputtering rate at a bias voltage of 1.9 kV was independently measured experimentally to be 0.48  $\text{\AA}/\text{sec}$ , the apparent oxidation constant for the anodic oxidation theory was  $x_0 = 32\text{\AA}$ . This data is in

qualitative agreement with the reactive sputter-oxidation model, with significant deviations at short sputter-oxidation times.

### Conclusion

This study of the reactive sputter deposition rates of titanium oxides showed that amorphous films were deposited at room temperature over the entire range of oxygen mole fractions studied. Deposited films were generally metallic  $\alpha$ Ti for oxygen mole fractions  $y < 0.002$ , and dielectric TiO<sub>2</sub> for  $y > 0.035$ . A sharp transition in deposition rate took place at  $y^* = 0.007$ , where TiO is deposited, and corresponded to the onset of oxidation of the titanium target.

Models describing the target oxidation phenomenon were tested against experimental data. The dependence of the target oxidation rate on oxygen mole fraction indicated that the target oxidation process is influenced by oxygen-atom incorporation in the target and by sputter etching of the target oxide by oxygen ions. The time dependence of the target oxidation process cannot be described by a parabolic time dependence. The reactive sputter-oxidation model is in qualitative agreement with the experimental data.

### Acknowledgment

The support of the U.S. Energy Research and Development Administration in the current project is gratefully acknowledged.

Manuscript submitted July 7, 1975; revised manuscript received March 22, 1976.

Any discussion of this paper will appear in a Discussion Section to be published in the June 1977 JOURNAL. All discussions for the June 1977 Discussion Section should be submitted by Feb. 1, 1977.

### REFERENCES

1. K. Wasa and S. Hayakawa, *Microelectron. Reliabil.*, **6**, 213 (1967).
2. T. K. Lakshmanan, C. A. Wysocki, and W. J. Slegesky, *IEEE Trans. Component Parts*, **CP-11**, 14 (1964).
3. F. Huber, *ibid.*, **CP-11**, 38 (1964).
4. G. Haas, *Vacuum*, **2**, (1952).
5. G. Haas and A. P. Bradford, *J. Opt. Soc. Am.*, **47**, 125 (1957).
6. G. V. Samsonov and A. P. Epik, in "Coatings on High Temperature Materials," H. H. Hausner, Editor, Chap. 5, Pt. 1, Plenum Press, New York (1966).
7. R. F. Bailey, Transaction of the Conference on Sputtering Technology, Pebble Beach, California June 1973.
8. R. C. Devries and R. Roy, *Ceram. Bull.*, **33**, 370 (1954).
9. P. G. Wahlbeck and P. W. Gilles, *J. Am. Ceram. Soc.*, **49**, 180 (1966).
10. R. Roy and W. B. White, *J. Cryst. Growth*, **13/14**, 78 (1972).
11. V. R. Porter, Ph.D. Thesis, Pennsylvania State University (1965).
12. S. Andersson and L. Jahnberg, *Arkiv Kemi*, **21**, 413 (1963).
13. J. L. Miles and P. H. Smith, *Electrochem. Technol.*, **110**, 1240 (1963).
14. W. Schroen, *J. Appl. Phys.*, **39**, 2671 (1968).
15. J. F. O'Hanlon, *J. Vacuum Sci. Technol.*, **7**, 330 (1970).
16. W. S. Whitlock and J. E. Bounden, *Proc. Phys. Soc. (London)*, **77**, 845 (1961).
17. J. B. Thompson, *Proc. Roy. Soc. (London)*, *Ser. A*, **262**, 503 (1961).
18. O. Kubaschewski and B. Hopkins, "Oxidation of Metals," Pergamon Press, New York (1958).
19. J. H. Greiner, *J. Appl. Phys.*, **42**, 5151 (1971).
20. J. Heller, *Thin Solid Films*, **17**, 163 (1973).
21. J. H. Greiner, *J. Appl. Phys.*, **45**, 32 (1974).
22. J. D. Leslie and K. Knorr, *This Journal*, **121**, 263 (1974).
23. T. K. Lakshmanan and J. M. Mitchell, Chemical Formation of Microcircuit Elements, AD 613563, March 1965.
24. "Handbook of Chemistry and Physics," Chemical Rubber Co., Cleveland, Ohio (1966).

## On the Behavior of Mobile Ions in Dielectric Layers of MOS Structures

W. Marciniak and H. M. Przewlocki

*Nauk. Prod. Centrum Polprzewodnikow, 02-675 Warszawa, Komarowa 5, Poland*

### ABSTRACT

Equilibrium and nonequilibrium behavior of mobile charges in dielectric layers of MOS structures have been investigated. A variety of MOS structures has been studied using the TVS method, and a newly developed technique of quasi-continuous registration of the C-V characteristic shifts (ACVS method). Basic models are considered, and an image force trapping model is proposed to interpret the measurement results.

The existence of mobile charges in dielectric layers of MOS structures may cause instability of MOS device parameters. Due to this fact, the behavior of mobile ions in thermally grown SiO<sub>2</sub> layers on Si substrates has been extensively studied in recent years. A concise summary of current understanding of the nature and properties of these and other charges in the thermally oxidized silicon structures has been given by Deal (1). Some of the properties of mobile charges in SiO<sub>2</sub> layers have been explained already, while other properties are not fully understood. It was, for example, demonstrated experimentally that mobile ions have a tendency to accumulate in the neighbor-

hood of the electrodes (metal or silicon) rather than in the bulk of the SiO<sub>2</sub> layer. It was also observed that the activation energy for ion motion in SiO<sub>2</sub> from the metal to the silicon electrode is higher than for the motion in the opposite direction. These properties of mobile charges in SiO<sub>2</sub> have not been fully explained as yet.

In the present work, equilibrium and nonequilibrium behavior of mobile ions has been studied experimentally. Several models have been considered which may explain the observed phenomena. Triangular voltage sweep (TVS) method has been used in experimental studies of equilibrium behavior of mobile ions, while a newly developed method of automatic registration

of C-V characteristics shifts (ACVS) has been used for nonequilibrium measurements. A variety of MOS capacitors was measured, with both n- and p-type silicon substrates of various resistivities and with different metal electrode materials. Based on the models considered, certain characteristics of MOS structures have been calculated and compared with the experimentally observed ones. Conclusions are drawn as to the validity of these models.

### Experimental Procedure

**Sample preparation.**—Metal-SiO<sub>2</sub>-Si capacitors were prepared on 250  $\mu\text{m}$  thick,  $\langle 111 \rangle$  oriented silicon substrates with chemically-mechanically polished surfaces. Silicon wafers were oxidized in dry oxygen at 1200°C to obtain the 1300Å thick SiO<sub>2</sub> layer. Metal electrodes, 800  $\mu\text{m}$  in diameter and 0.3  $\mu\text{m}$  thick, were evaporated on the SiO<sub>2</sub> layer through mask holes. A variety of samples was prepared with n- and p-type silicon substrates of different resistivities, and with different metal electrode materials such as Al, Au, Cr, Mn, W, Ti, Pt, which were evaporated using either the tungsten filament source, or the E-gun heated source.

**Measurement methods.**—Properties of mobile ions were investigated using two principal methods: the triangular voltage sweep (TVS) method, and the automatic registration of the C-V curve shifts (ACVS) method.

(i) **The TVS method.**—Theoretical foundations of this method were given by Chou (2) and were modified and extended to a more general form by the authors of this work (3). The experimental setup for TVS measurements was similar to the ones described in Ref. (2) and (4). Triangular wave function generator was used to provide sweep rates in the range of from 2 mV/sec to 2 V/sec. The shielded probe set contained six movable probes and a resistance-heated pedestal, which allowed measurements in the temperature range of up to 500°C. MOS capacitors were measured at different temperatures and with different sweep rates. It was demonstrated that at a temperature  $T = 250^\circ\text{C}$  the normalized TVS current-voltage characteristic,  $I_G/\delta = f(V_G)$ , does not depend on the sweep rate  $\delta$ , if  $\delta \leq 5$  mV/sec, which means that quasi-equilibrium conditions (2) are fulfilled for  $\delta \leq 5$  mV/sec at  $T \cong 250^\circ\text{C}$  (see Fig. 4). It was also shown that with very few exceptions the electrodes are blocking up to the temperature of about 300°C. At higher temperatures, double-peaked TVS curves were usually obtained, indicating the onset of electrode reactions (2) (see Fig. 3). The voltage ramp amplitude of  $\pm 3.5\text{V}$  was found sufficient to obtain meaningful results (*i.e.*, application of higher ramp amplitudes did not result in any changes of shapes and heights of the TVS current peak). Densities of mobile charges  $Q_j$  (in C/cm<sup>2</sup>) were calculated by finding the area under the reduced TVS current peak (2), and by measuring the reduced TVS current peak height (3). The agreement between the results obtained was used as a self-consistency criterion for the proper choice of measurement conditions.

(ii) **The ACVS method.**—The principal method widely used to investigate redistribution of mobile charges in the dielectric layer was based on measurement of high frequency CV characteristic shifts under bias-temperature (BT) stresses. Usually point-by-point measurements were made subsequent to cycles of heating and cooling the MOS structure under test. In this work, a new method was developed which allows quasi-continuous automatic registration of the C-V characteristic shifts. This method makes use of the pulsed MOS capacitor deep-depletion characteristics, which are just as sensitive to changes in flatband voltage ( $\Delta V_{\text{FB}}$ ) as the high frequency C-V characteristics, and are easily measured at elevated temperatures. As in the case of the classic high frequency C-V method,  $\Delta V_{\text{FB}}$  can be detected as changes in the gate voltage

value,  $V_1$ , which corresponds with a given value of capacitance,  $C_1$ , in a deep-depletion C-V characteristic.

The ACVS apparatus, shown schematically in Fig. 1, was used for automatic registration of the flatband voltage changes obtained at different BT stresses. The ACVS apparatus works as follows. Short triangular voltage pulses are applied to the MOS capacitor gate, giving rise to currents in the R resistor, which are proportional to momentary values of the MOS capacitor differential capacitance C. The duration of the voltage pulses is adjustable in the range from 10  $\mu\text{sec}$  to 1 msec. The time dependence of the voltage drop in the R resistor,  $V_R(t)$ , corresponds in this case with the deep-depletion type C-V characteristic of the MOS capacitor under test. Such characteristics are shown schematically in the insert of Fig. 1. The  $V_R(t)$  signal is amplified and compared with a preset reference voltage,  $V_1$ , which is so chosen as to correspond with a certain value,  $C_1$ , of the capacitance. A pulse sent from the comparator causes the  $V(t)$  voltage value which corresponds with  $C_1$  capacitance to be applied into a sample-and-hold circuit, and recorded continuously by a X-Y recorder. The horizontal input of the X-Y recorder is driven by a signal which sets the time scale or is proportional to the temperature applied. This way,  $\Delta V_{\text{FB}}(t)$  or  $\Delta V_{\text{FB}}(T)$  curves are automatically recorded. Triangular voltage pulses are superimposed at the output of the generator on a biasing voltage, which can be set in the range from  $-10$  to  $+10\text{V}$ . This voltage forces redistribution of charges in the dielectric. The triangular pulses are applied to the gate of the MOS capacitor in the from-accumulation-to-depletion direction. Measurements made with the pulses applied periodically, with periods ranging from 2 to 120 sec, pulse amplitudes in the range from 5 to 100V, and pulse duration in the range from 20  $\mu\text{sec}$  to 1 msec, have shown that these pulses do not affect the drift behavior (due to their short duration and low repetition rate). In cases of very short  $V_{\text{FB}}$  relaxation times ( $\tau < 10$  sec), measurements were made using the method of ionic polarization current integration (5).

### Results and Discussion

**Results of TVS measurements.**—All the MOS capacitors measured in the course of this work exhibited asymmetric TVS characteristics, which remains in agreement with previously published results for Al-SiO<sub>2</sub>-Si and Au-SiO<sub>2</sub>-Si structures (6), Cr-SiO<sub>2</sub>-Si structures (4, 7, 8), and Pt-SiO<sub>2</sub>-Si structures (2). The shape of the TVS current-voltage characteristic obtained for the from-positive-to-negative voltage sweep remains in agreement with the curve calculated using formulae derived in Ref. (3). The reduced TVS current peak obtained for the from-negative-to-positive voltage sweep is much wider, and not so well defined, as shown in Fig. 2. The areas under TVS current peaks

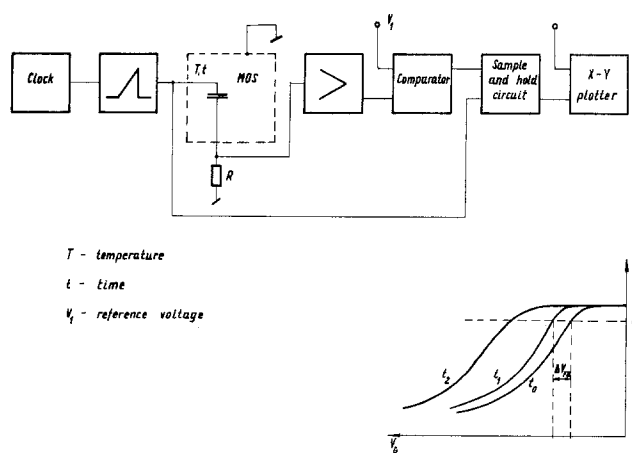


Fig. 1. Schematic diagram of the ACVS apparatus, and illustration of the drift of C-V deep-depletion characteristics (insert).



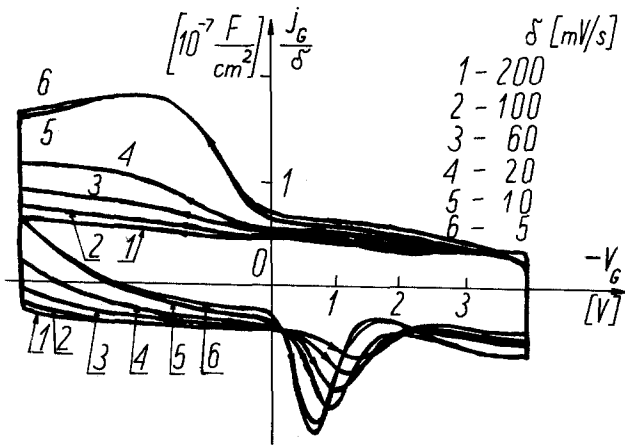


Fig. 2. The reduced TVS current vs. voltage curves of a Al-SiO<sub>2</sub>-Si structure for T = 250°C and various sweep rates.

for negative-to-positive and positive-to-negative voltage sweeps are close to each other, while the peak heights differ significantly. This property of TVS characteristics suggests that the same amount of mobile charge is transported in both directions through the dielectric layer, but the ions are trapped in deep traps at the metal-dielectric interface. Due to this fact, quasi-static condition is usually not fulfilled for the transport of ions from the metal to the silicon electrode, and the shape of the reduced TVS current peak for negative-to-positive voltage sweep is primarily determined by the properties of the metal-dielectric interface. For higher temperatures at which the electrodes are not ideally blocking any more, additional extrema ( $M_F$ ) appear in the TVS current-voltage characteristics, as shown in Fig. 3.

Results of our measurements of different MOS capacitors are summarized in Fig. 4. It can be seen in Fig. 4 that for all measured MOS capacitors, a "saturation" of  $Q_j$  and  $V_{Gmax}$  values is practically obtained for 250°C < T < 300°C, and  $\delta = 5$  mV/sec ( $V_{Gmax}$  is voltage corresponding with TVS current peak). This fact proves that quasi-equilibrium is maintained and that the electrodes are blocking in this temperature range, resulting in a constant value of  $Q_j$  as assumed in derivation of basic relations for the TVS method (2, 3).

Measurements of MOS capacitors built on p- and n-type silicon substrates of different resistivities have shown that the  $V_{Gmax}$  value changes with the resistivity of the substrate as predicted by the theory presented in Ref. (3). The agreement between theory and experiment is very good for Au-SiO<sub>2</sub>-Si capacitors, and slightly worse for Al-SiO<sub>2</sub>-Si capacitors, as shown in Fig. 5. The additional displacement of the TVS current peak along the voltage axis  $\Delta V_{Gmax} = 0.2-0.4V$  which is observed in the case of Al-SiO<sub>2</sub>-Si capacitors is probably due to the existence of a negative immobile charge in the SiO<sub>2</sub> layer.

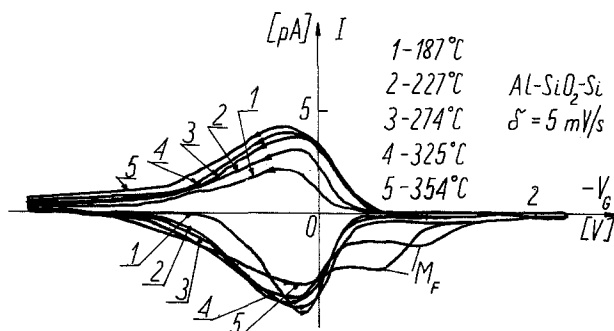


Fig. 3. TVS current-voltage characteristics with additional extrema ( $M_F$ ).

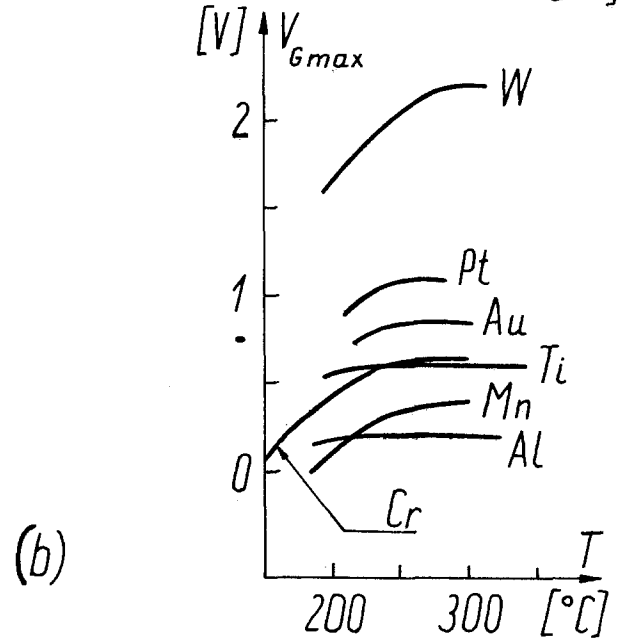
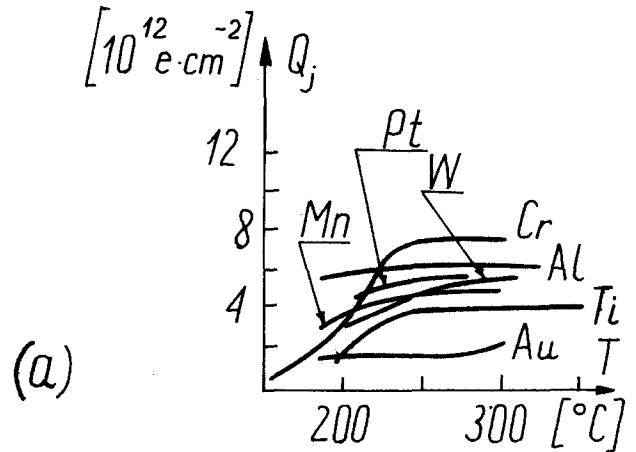


Fig. 4.  $Q_j$  vs. T (a) and  $V_{Gmax}$  vs. T (b) plots for MOS structures with different electrode materials.

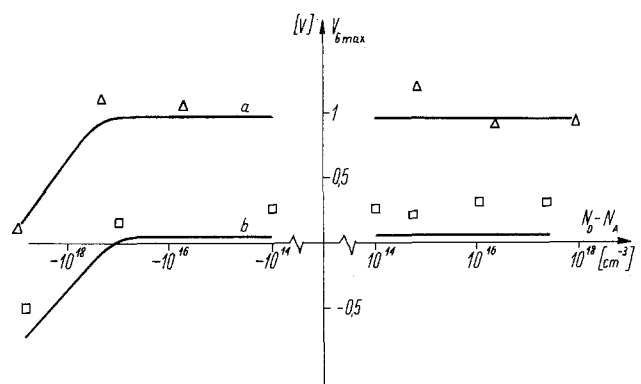


Fig. 5. A comparison of calculated and experimental dependencies of  $V_{Gmax}$  on the doping of silicon substrate  $N_D - N_A$ , for Au-SiO<sub>2</sub>-Si (curve a and triangles), and Al-SiO<sub>2</sub>-Si (curve b and squares) MOS structures.

Results of ACVS measurements.—Metal-SiO<sub>2</sub>-Si capacitors with Al, Au, Pt, and Ti metal electrodes were measured using the ACVS method described above. The range of temperatures used was from 70° to 200°C and the range of voltages applied to force the drift of mobile charges in the dielectric was from -6 to +6V. Changes of the flatband voltage  $\Delta V_{FB}$  and the biasing voltage  $V_B$  were of opposite signs (with the exceptions mentioned below). Time constants of drifts observed in the case of a positive voltage on the



metal electrode (positive BT stress) were one or two orders of magnitude higher than the time constants of drifts observed for opposite polarity (negative BT stresses). Typical drift  $\Delta V_{FB}(t)$  characteristics observed in the case of a positive BT stress are shown in Fig. 6. Drift characteristics of Al-SiO<sub>2</sub>-Si capacitors remain in good agreement with previously published data (11), i.e., for small values of  $t$ , are quite well described by a simple formula:  $\Delta V_{FB} = k\sqrt{t}$ , where  $k$  is a constant. For Pt-SiO<sub>2</sub>-Si capacitors a nearly linear dependence of  $\Delta V_{FB}$  on  $t$  was observed for small values of  $t$ . The Au-SiO<sub>2</sub>-Si capacitor  $\Delta V_{FB}(t)$  curves are often characterized by two values of time constants. The relaxation process is initially very fast, but becomes much slower later (see Fig. 6). The time constant of the initial (fast) relaxation process is comparable with the time constant of the drift observed for negative BT stresses. The  $\Delta V_{FB}(t)$  characteristic of a Ti-SiO<sub>2</sub>-Si capacitor differs significantly from analogous characteristics of MOS capacitors with electrodes made of other metals, and is included in Fig. 6 to demonstrate the possibilities offered by the ACVS method. The shape of this curve is due to the simultaneous action of ionic and trap instabilities, which tend to change the flatband voltage in opposite directions. Based on the temperature dependence of the above-mentioned time constants, activation energies of the relaxation processes were found for both positive and negative BT stresses. The activation energy,  $W_A$ , for positive BT stress conditions is  $1.05 \text{ eV} \leq W_A \leq 1.48 \text{ eV}$ , and for negative BT stresses is  $0.6 \text{ eV} \leq W_A \leq 0.8 \text{ eV}$ . Assuming that for positive BT stresses ions are emitted from Frenkel-Pool type trapping centers at the metal-SiO<sub>2</sub> interface, the trap potential well width may be found from the dependence of time constants on the value of biasing voltage (12). It was found that the trap potential well width,  $d$ , is  $20 \text{ \AA} \leq d \leq 100 \text{ \AA}$ .

The theory of redistribution of mobile ions in the dielectric of a MOS capacitor, which is caused by a voltage step, was developed in Ref. (11) and (12). In Ref. (11) a simplified model was considered in which redistribution of ions was diffusion limited. This diffusion was assumed to take place from a thin layer at the electrode-SiO<sub>2</sub> interface in which the ions were present in high concentration. This led to a classic formulation and solution of a diffusion problem. In Ref. (12) it was assumed that ions are trapped at the electrode-SiO<sub>2</sub> interface and ion emission from traps was considered the rate-limiting factor.

In this work two models were considered in detail (see Appendix). In the first case it was assumed that redistribution of ions is a bulk-limited process. Transport equation was solved numerically in this case, taking into account the existence of diffusion and drift components as well as built-in (Poisson-type) electric fields and various distributions of immobile charges in

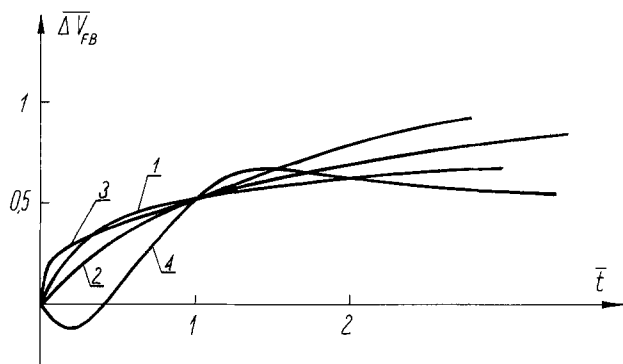


Fig. 6. Typical  $\Delta V_{FB}(t)$  drift characteristics for various MOS structures at positive BT stress. 1. Al-SiO<sub>2</sub>-Si structure, 2. Pt-SiO<sub>2</sub>-Si structure, 3. Au-SiO<sub>2</sub>-Si structure, 4. Ti-SiO<sub>2</sub>-Si structure.  $\Delta V_{FB} = \Delta V_{FB}/\Delta V_{FB}(\text{sat})$ ,  $\bar{t} = \text{normalized time}$ ,  $\bar{t} = 1$  for  $\Delta V_{FB} = 0.5$ .

the dielectric. In the second case, it was assumed that the only mechanism that determines the rate of the relaxation process is the emission of ions from traps located at the electrode-dielectric interface. Calculations of  $\Delta V_{FB}(t)$  characteristics were made, based on these two models, and the results of these calculations are compared in Fig. 7 with a typical experimental curve obtained for Al-SiO<sub>2</sub>-Si capacitors. The best agreement is obtained if ion trapping at the electrode-SiO<sub>2</sub> interface is assumed to be the rate-limiting factor. Higher values of activation energies obtained for redistribution processes occurring during positive BT stresses indicate the presence of deep ion traps at the metal-SiO<sub>2</sub> interface. The lower values of activation energies for relaxation processes occurring at negative BT stresses may be due either to the temperature dependence of ion mobility (bulk-limited process) or to the existence of shallow ion traps at the SiO<sub>2</sub>-Si interface (surface-limited process).

In the first case one would expect a nearly linear  $\Delta V_{FB}(t)$  dependence for small values of  $t$ , while in the second case a parabolic  $\Delta V_{FB}(t)$  curve would be expected (similarly as in the case of positive BT stress, illustrated in Fig. 7). Comparison of experimentally observed  $\Delta V_{FB}(t)$  characteristics, obtained at negative BT stresses with the curves calculated using both models described above, suggests that ion trapping at the Si-SiO<sub>2</sub> interface is more likely to be the rate-limiting factor.

Different values of activation energies obtained for drifts observed at positive and negative BT stresses may be due to different depths of potential wells created by the interaction of mobile ions with their image charges induced in the electrodes. Rough estimation of these potential wells (see Appendix), yields 0.94 eV for the metal-SiO<sub>2</sub> interface and 0.47 eV for the Si-SiO<sub>2</sub> interface. The lower limit of the activation energy found experimentally for drifts at negative BT stresses (0.6 eV) does not differ significantly from the depth of the image force potential well at the Si-SiO<sub>2</sub> interface (0.47 eV). This indicates the importance of image forces in the effect of ion trapping at the Si-SiO<sub>2</sub> interface.

The image force model alone is not sufficient, however, to explain the drift behavior of mobile ions at positive BT stresses. The experimental values of acti-

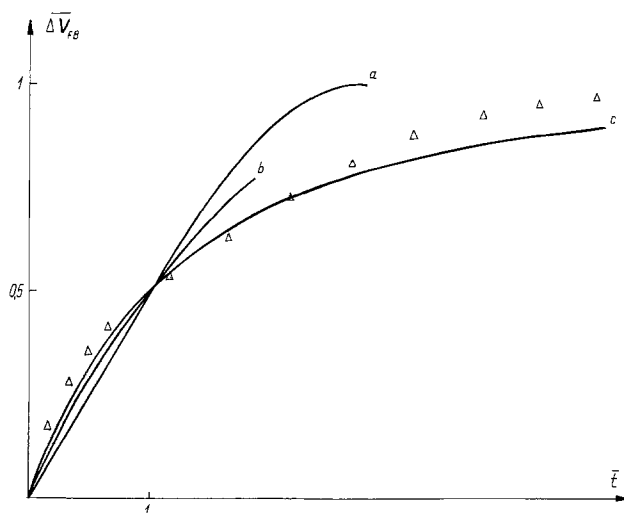


Fig. 7. Typical experimental  $\Delta V_{FB}(t)$  drift characteristic at positive BT stress for an Al-SiO<sub>2</sub>-Si structure (triangles) and curves calculated (solid lines) using three models: (a) the model in which diffusion and drift are taken into account, but the built-in field is assumed to be negligible, (b) the model in which drift, diffusion, and the built-in field are taken into account, (c) the model in which only emission of ions from traps at the electrode-SiO<sub>2</sub> interface is taken into account.

vation energies, the spread of these values, and a significant width of the potential well obtained indicate that besides the effect of image forces, another mechanism of ion trapping exists at the metal-SiO<sub>2</sub> interface. It is assumed in this work that this "additional" trapping mechanism is due to the presence of a thin layer of immobile negative charges in the dielectric, next to the metal-SiO<sub>2</sub> interface. Calculations have shown (see Appendix) that parabolic  $\Delta V_{FB}(t)$  curves, similar to the ones observed experimentally, are obtained if the presence of immobile negative charges at the metal-SiO<sub>2</sub> interface is assumed. Apart from the physical origin of the traps existing at the electrode-SiO<sub>2</sub> interfaces, excellent agreement between experimental and calculated  $\Delta V_{FB}(t)$  curves may be obtained for Al-SiO<sub>2</sub>-Si and Pt-SiO<sub>2</sub>-Si capacitors if adequate energy spectrum of traps is assumed. The "fast" and "slow" components of the drift observed in the case of Au-SiO<sub>2</sub>-Si structures may be due to the fact that only a part of the mobile ions is trapped at the interface. This may be caused by the presence of traps in a layer of SiO<sub>2</sub> (next to the metal-SiO<sub>2</sub> interface) which is thin in comparison with the width of the mobile ion distribution. Part of the mobile charge which is not trapped is responsible in this case for the "fast" component of the relaxation process, while ions emitted from traps are responsible for the "slow" component.

### Conclusions

Equilibrium and nonequilibrium properties of mobile charges in dielectric layers of MOS structures were studied experimentally. Basic models were proposed and discussed, allowing interpretation of measurement results. The main results of this work may be summarized as follows.

1. A wide variety of MOS structures was studied using the TVS method. It was shown that in most cases the TVS method yields meaningful results when applied in the temperature range of  $T = 250^\circ\text{--}300^\circ\text{C}$ , with the voltage ramp speed of  $\delta \leq 5$  mV/sec.

2. A new technique of quasi-continuous registration of the flatband voltage shift was developed (ACVS method) and proved to be useful in studies of nonequilibrium behavior of mobile ions.

3. Numerous MOS structures were measured using the ACVS method. The asymmetric properties of ion transport in MOS structures were always observed. It was also observed that the shape of the  $\Delta V_{FB}(t)$  curve depends on the material of the metal electrode.

4. Models were considered for nonequilibrium behavior of mobile ions, and calculations were made for the model in which  $V_{FB}$  relaxation processes are bulk limited and for the model in which electrode-SiO<sub>2</sub> interface properties determine the  $V_{FB}$  relaxation process.

5. By comparing the experimentally observed  $\Delta V_{FB}(t)$  curves with the curves calculated using the above-mentioned models, it was found that best agreement is obtained if trapping of mobile ions at the metal-SiO<sub>2</sub> interface is assumed. It is postulated that this trapping is primarily due to image forces and to the negative charges that may be present in the neighborhood of the metal-SiO<sub>2</sub> interface.

Manuscript submitted Dec. 3, 1975; revised manuscript received April 7, 1976. This was Paper 139 presented at the Dallas, Texas, Meeting of the Society, Oct. 5-9, 1975.

Any discussion of this paper will appear in a discussion Section to be published in the June 1977 JOURNAL. All discussions for the June 1977 Discussion Section should be submitted by Feb. 1, 1977.

### APPENDIX

Two models of the dynamic behavior of mobile ions in the dielectric of a MOS capacitor are considered.

*Model (a).*—It is assumed that uncompensated positive mobile ions are present in the dielectric as well

as negative immobile charges of various distributions. The redistribution of mobile ions is a bulk-limited phenomenon. With other assumptions being the same as in Ref. (10), this problem is represented for  $0 \leq x \leq l$ , and  $t \geq 0$  by the following set of equations

$$\frac{\partial P(x, t)}{\partial t} = D \frac{\partial^2 P(x, t)}{\partial x^2} - \mu \frac{\partial}{\partial x} [E(x, t) P(x, t)] \quad [\text{A-1}]$$

$$j(x, t) = q\mu P(x, t)E(x, t) - qD \frac{\partial P(x, t)}{\partial x} \quad [\text{A-2}]$$

$$\frac{\partial E(x, t)}{\partial x} = \frac{q}{\epsilon_1} [P(x, t) - N(x)] \quad [\text{A-3}]$$

where  $j$  is the current density,  $N(x)$  the concentration distribution of immobile negative charges,  $P(x, t)$  the concentration of positive mobile charges,  $D$  the diffusion coefficient,  $\mu$  the mobility,  $E$  the electric field,  $q$  the electron charge, and  $\epsilon_1$  is the permittivity of the dielectric.

Based on the solution obtained for steady-state distributions (10), the initial condition (initial distribution) is assumed to be

$$P(x) = P(0) \exp\left(-\frac{x}{\lambda_p}\right) \quad [\text{A-4}]$$

for  $t = 0$ , where  $P(0)$  is the value of  $P$  for  $x = 0$ , and  $\lambda_p$  is the parameter of the  $P(x)$  distribution for  $t = 0$ .

Boundary conditions are given by the assumption of blocking electrodes

$$\left. \frac{\partial P(x, t)}{\partial x} \right|_{x=0} = \frac{\mu}{D} E(x, t) P(x, t) \quad [\text{A-5}]$$

The biasing voltage is assumed to be

$$V_B(t) = \int_0^l E(x, t) dx \quad [\text{A-6}]$$

where the voltage drop in the semiconductor electrode was assumed to be negligible.

$$E(x, t) = E_B(t) - E(0, t) + \frac{q}{\epsilon_1} \int_0^x [P(x, t) - N(x)] dx \quad [\text{A-7}]$$

$$E(0, t) = \frac{Q_P}{\epsilon_1} [1 - X_{c1}^P(t)] - \frac{Q_N}{\epsilon_1} [1 - X_{c1}^N] \quad [\text{A-8}]$$

$$X_{c1}^P(t) = \frac{\int_0^l x P(x, t) dx}{\int_0^l P(x, t) dx} \quad [\text{A-9}]$$

$$X_{c1}^N = \frac{\int_0^l x N(x) dx}{\int_0^l N(x) dx} \quad [\text{A-10}]$$

where  $E_B(t) = V_B(t)/l$ , and  $Q_P$  and  $Q_N$  are the densities (per unit area) of positive mobile charges and negative immobile charges, respectively. The time dependence of the flatband voltage shift  $\Delta V_{FB}$  is given by

$$\Delta V_{FB}(t) = \frac{Q_P}{C_1} X_{c1}^P(t) \quad [\text{A-11}]$$

Equations [A-1]-[A-11] were solved numerically using the sparse matrix method and implicit discretization schemes, similarly as was done in the solution of the problem of carrier transport in p-n junctions (14, 15). Calculations were made for different concentrations of both mobile and immobile charges, and different biasing voltages. Examples of the results obtained are illustrated in Fig. 8 which shows the time dependence of mobile charge distributions for a MOS structure without immobile negative charge (a), and for a MOS structure with immobile negative charges residing in a thin layer adjacent to the metal-SiO<sub>2</sub> in-

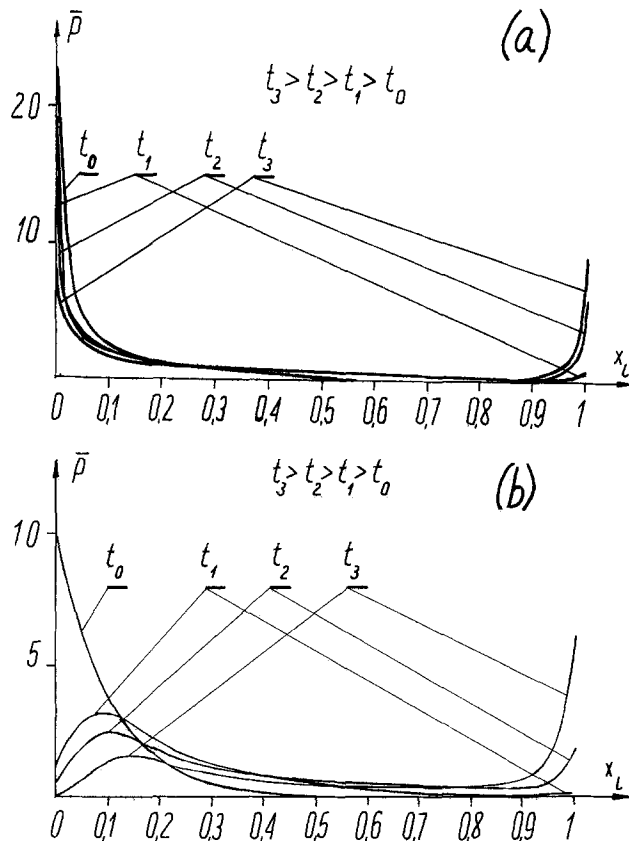


Fig. 8. Illustration of the time dependence of mobile charge distribution in  $\text{SiO}_2$  layer of a MOS structure without immobile negative charges (a), and with immobile negative charges residing in a thin layer adjacent to the metal- $\text{SiO}_2$  interface (b). MOS structure with following parameters was considered:  $Q_j = 10^{12} \text{ e/cm}^2$ ,  $\epsilon_{\text{ri}} = 3.9$ ,  $l = 10^{-5} \text{ cm}$ ,  $T = 538^\circ\text{K}$ ,  $V_B = 4.6\text{V}$ ; in case (b) the immobile negative charge  $Q_N = 10^{12} \text{ e/cm}^2$  is located at the metal- $\text{SiO}_2$  interface.  $\bar{p}$  is normalized mobile charge concentration,  $x$  is normalized distance.

interface (b). The shape of the  $\Delta V_{\text{FB}}(t)$  characteristic depends on the relation that exists between the externally applied field and the internal fields created by the space charge distributions. The  $\Delta V_{\text{FB}}(t)$  curve becomes nearly a straight line for very strong externally applied fields ( $E_B > Q_P/C_1 l$ ), and becomes nearly a parabolic curve  $\Delta V_{\text{FB}} = k t^{1/2}$  for relatively weaker externally applied fields ( $E_B < Q_P/C_1 l$ ).

*Model (b).*—It is assumed that the emission of ions from traps at the electrode- $\text{SiO}_2$  interfaces is the only mechanism that determines the  $V_{\text{FB}}(t)$  relaxation process. In this case, the time constant of the ion emission process,  $\tau_e$ , is higher than the transit time of the ions across the dielectric layer. For a discrete trap level one obtains (12)

$$\overline{\Delta V_{\text{FB}}(t)} = 1 - \exp(-t/\tau_e) \quad [\text{A-12}]$$

where  $\overline{\Delta V_{\text{FB}}(t)}$  is the normalized flatband voltage shift. For a gaussian distribution of traps and assuming that the emission of ions is governed by the Boltzmann statistic, one obtains (13)

$$\overline{\Delta V_{\text{FB}}(t)} = 1 - \frac{1}{\sigma\sqrt{2\pi}} \int_0^\infty \exp\left[-\frac{(W - W_0)^2}{2\sigma^2} - \frac{t}{\tau_e}\right] dW \quad [\text{A-13}]$$

where  $\sigma$  is standard deviation, and  $\tau_e$  is given by

$$\tau_e = \tau_e(W_0) \exp\left(\frac{W - W_0}{kT}\right) \quad [\text{A-14}]$$

One of the possible causes of ion trapping at the electrode interfaces is the existence of image forces (16). Assuming that the electrode- $\text{SiO}_2$  interface is a plane, and considering potential energy of an ion in the electrostatic field of its image charge, the following relation was obtained (16)

$$W(x) = \frac{q^2}{16\pi \epsilon_{\text{ri}} \epsilon_0 x} \left(\frac{\epsilon_{\text{ri}} - \epsilon_{\text{re}}}{\epsilon_{\text{ri}} + \epsilon_{\text{re}}}\right) \quad [\text{A-15}]$$

where  $\epsilon_{\text{ri}}$  and  $\epsilon_{\text{re}}$  are relative permittivities of the dielectric and the electrode material, respectively ( $\epsilon_{\text{ri}} = 3.9$  for  $\text{SiO}_2$ ,  $\epsilon_{\text{re}} = 11.8$  for Si electrode, and  $\epsilon_{\text{re}} \rightarrow \infty$  for metal electrode), and  $x$  is the distance of the ion from the interface plane. Equation [A-15] reflects the difference in the potential barriers at metal- $\text{SiO}_2$  and  $\text{SiO}_2$ -Si interfaces, which is one of the causes of the asymmetry of ion transport properties in MOS structures. For example, for  $x = 1\text{\AA}$ , which is considered to be the lowest distance of the ion from the interface plane for which Eq. [A-15] still holds (16), one obtains  $W = 0.94 \text{ eV}$  for the metal- $\text{SiO}_2$  interface and  $W = 0.47 \text{ eV}$  for the  $\text{SiO}_2$ -Si interface.

#### REFERENCES

1. B. E. Deal, *This Journal*, **121**, 198C (1974).
2. N. J. Chou, *ibid.*, **118**, 601 (1971).
3. H. M. Przewlocki and W. Marciniak, *Phys. Status Solidi, (a)*, **29**, 265 (1975).
4. M. Kuhn and D. J. Silversmith, *This Journal*, **118**, 966 (1971).
5. J. M. Eldridge and D. R. Kerr, *ibid.*, **118**, 986 (1971).
6. M. Yamin, *IEEE Trans. Electron Devices*, **ed12**, 88 (1965).
7. D. J. Silversmith, *This Journal*, **119**, 121 (1972).
8. R. J. Kriegler and R. Bartnikas, *IEEE Trans. Electron Devices*, **ed20**, 722 (1973).
9. W. Marciniak and H. M. Przewlocki, *Electron Technol. (Pol)* **3/4** (1975).
10. W. Marciniak and H. M. Przewlocki, *Phys. Status Solidi (a)*, **24**, 359 (1974).
11. E. H. Snow, A. S. Grove, B. E. Deal, and C. T. Sah, *J. Appl. Phys.*, **36**, 1664 (1965).
12. S. R. Hofstein, *IEEE Trans. Electron Devices*, **ed13**, 222 (1966).
13. S. R. Hofstein, *ibid.*, **14**, 749 (1967).
14. A. DeMari, *Solid-State Electron.*, **11**, 1021 (1968).
15. B. Funck, *Rev. Tech. Thomson-CSF*, **3**, 81 (1971).
16. R. Williams and M. H. Woods, *Appl. Phys. Letters*, **22**, 458 (1973).

# Galvanostatic Analysis of Polycrystalline Beta Alumina Resistivity

G. C. Farrington\*

General Electric Company, Research and Development Center, Schenectady, New York 12301

## ABSTRACT

Polycrystalline Na<sup>+</sup>-beta alumina resistivity has been examined with a fast response d-c technique using galvanostatic square waves of  $7 \times 10^{-9}$  sec risetime. Intragrain and intergrain resistance and capacitance components can be separately distinguished in many samples by resistivity analysis over the ca. 50 MHz-10 kHz effective frequency range of this technique. Polycrystalline beta alumina appears to be an aggregate of essentially single crystal grains separated by grain boundaries of markedly lower conductivity. Intrinsic intergrain and intragrain resistivities are typically  $10^7$  and 68 ohm-cm, respectively, at 23°C. Large intragrain capacitance effects which jeopardize the usefulness of multifrequency or galvanostatic analysis for separating intragrain and intergrain resistivity components in practical beta alumina ceramics have been observed. These effects, modeled as intragrain capacitance, are more likely initial observations of localized Na<sup>+</sup> ion exchange among the three nonequivalent sites available for mobile ion occupation in the beta alumina conduction plane.

Na<sup>+</sup>-beta alumina, a two-dimensional, solid ionic conductor into which a variety of monovalent cations including Ag<sup>+</sup>, Tl<sup>+</sup>, and K<sup>+</sup> (1) can be substituted, has a single crystal resistivity of 72 ohm-cm at 23°C (2), comparable to that of common nonaqueous organic electrolytes. For ease of fabrication, strength, and omnidirectional conductivity, it is generally used in practical devices as a dense, polycrystalline ceramic.

The bulk resistivity of polycrystalline beta alumina is typically 200-2000 ohm-cm at 23°C, more than that of single crystal material. It is divisible into intragrain and intergrain components. Intragrain resistivity is influenced by intrinsic grain composition and by the conduction path tortuosity, that is, the difference between the actual and apparent conduction path lengths between two points in a ceramic. The intergrain resistivity component varies widely and is highly dependent upon specific conditions of ceramic preparation and densification.

In optimizing ceramic processing, it is useful to separate total d-c resistivity of a specimen into its intragrain and intergrain components. Powers and Mitoff (3) have reported results of such an analysis of polycrystalline beta alumina resistivity obtained with a multifrequency, a-c technique. Their technique was useful in describing intergrain resistance and capacitance effects in a variety of beta alumina ceramics. But it was limited to a maximum frequency of 500 kHz which proved inadequate for characterizing many beta alumina specimens.

The present work was undertaken to examine the usefulness of a galvanostatic technique capable of examining the resistivity response of polycrystalline beta alumina over an effective frequency range of ca. 50 MHz-10 kHz. It was hoped with this simpler procedure to obtain intergrain resistance and capacitance data for a wider variety of beta alumina ceramics and describe intragrain ion transport at very short response times.

## Experimental Technique

Galvanostatic pulse analysis was used in this study for its simplicity in gathering resistivity data over a broad effective frequency range. Pulse and a-c measurements yield equivalent data from which real and imaginary impedance components can be derived as functions of frequency. However, Fourier analysis is

necessary to extract both of these components from pulse data. Fourier treatment has not been applied here.

Typical samples were tubes of fine-grained polycrystalline Na<sup>+</sup>-beta alumina, approximately 1.1 cm OD, 1.0 cm ID, and 9 cm in length. Tubes were prepared from Alcoa 'XB-2' beta alumina powder. Additional components were Y<sub>2</sub>O<sub>3</sub> (added as the oxalate), MgO (from the basic carbonate), and ZrO<sub>2</sub> (from grinding media wear). After mixing, the powder was calcined at 1400°C, suspended in amyl alcohol, and milled using zirconia grinding media. Tubes were formed by electrophoretic deposition and sintered in air at 1700°-1825°C.

The two specimens discussed in this paper, 6G3-2 and 6M2-2, differed only by 0.5% Y<sub>2</sub>O<sub>3</sub> incorporated in 6G3-2 as a sintering aid. Both specimens had random grain orientation and were single phase beta alumina.

Each sample was contacted at four points along its longer axis with ring electrodes of vapor-deposited Ag. Ag was chosen for electrodes because it can be applied readily and is electrochemically oxidized to an ion mobile within beta alumina. Since a pulse measurement repetitively passes unidirectional current, in contrast to a-c analysis, depletion of oxidizable material at the positive electrode occurs, gradually increasing sample resistance. Although these measurements neglect interfacial polarization, too large a sample resistance degrades pulse risetime and limits the time range of analysis. It is important, therefore, that the positive contact electrode be amply supplied with ions capable of injection into beta alumina. Ag serves this function well.

Alternate contact electrodes include tight Pt wire loops wetted with a solution of NaClO<sub>4</sub> in propylene carbonate. The advantage of Pt loops is their ease of attachment and removal. After analysis, a methanol wash quickly removes residual propylene carbonate solution and restores the sample to its original condition. However, the boiling point of propylene carbonate (241°C) and comparable liquids restricts the temperature range of analysis.

To measure resistivity, a constant current square wave is applied to the outer two electrodes and the differential voltage response between the inner electrodes recorded.

Figure 1 shows a sample tube mounted for study. Pt loops contact the Ag electrodes and suspend the sample in a small oven (Fig. 2). Binding lugs are provided on

\* Electrochemical Society Active Member.

Key words: beta alumina, solid electrolyte, polycrystalline, resistivity, square wave.

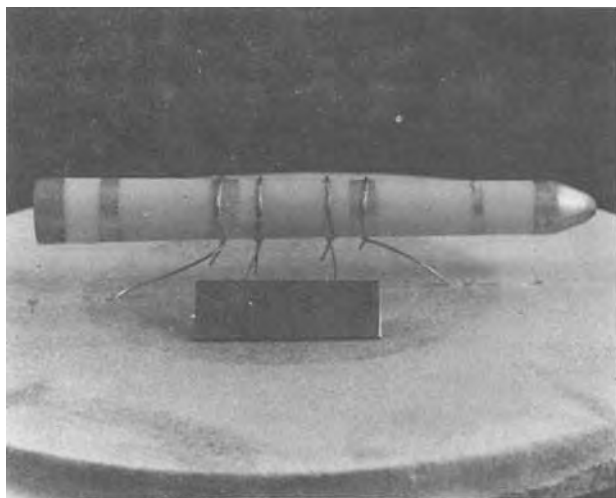


Fig. 1. Beta aluminum tube mounted for resistivity analysis



Fig. 2. Galvanostatic pulse generator and sample oven

the oven top for pulser and probe contact. The oven is warmed by heating tape and cooled by chilled dry  $N_2$  for multitemperature experiments.

Figure 3 is a circuit diagram of the constant current pulse generator used for all experiments reported here. Figure 2 shows the complete pulser which has an output range of  $40 \mu A$ -6.0 mA. The pulser was designed to minimize stray capacitance which would degrade output risetime. Output terminals protrude directly from the base of the pulser to minimize connecting lead lengths. Pulser output is off at a trigger input of  $\leq -2V$  and switches on for a trigger transition to  $\cong 0V$ .

The rising edge of a  $100 \mu A$  current pulse into a 500 ohm resistor is shown in Fig. 4. Its risetime ( $t_r$ ; 10-90%) of  $7 \times 10^{-9}$  sec is typical of the pulses used in this study. The rising edge shape follows an approximate RC response curve in which  $R$  is the total resistive

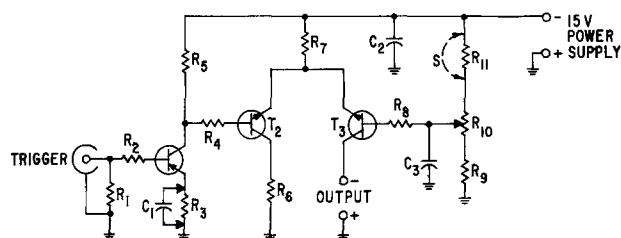


Fig. 3. Circuit diagram of galvanostatic pulse generator

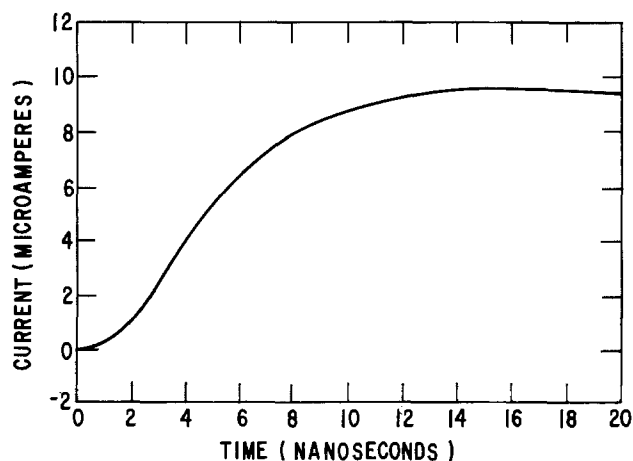


Fig. 4. Representative pulse rising edge;  $1000 \mu A$  into 500 ohm in series with sample.

load and  $C$  the capacitive load shunting the pulser output to ground.  $R$  is fixed by the sample under analysis.  $C$  has components within the pulser circuitry and distributed along the output load. Stray capacitance occurring within the pulser degrades the output before it encounters the sample and introduces no error into resistivity measurements. Capacitance distributed along the output load does cause error by creating disparity between the observed pulse shape monitored across the current-sensing resistor and the pulse shape actually perturbing the sample. Both sources of stray capacitance have negligible effects if the sample resistance is small ( $<1500$  ohm) and data are not measured at times  $<0.90 t_r$ .

For a resistivity measurement, one outer Ag electrode is connected through a 50 ohm high frequency current-monitoring resistor to pulser ground. The negative pulser terminal is connected to the opposite outer Ag band. For each elapsed time range, such as 10-40 nsec, the voltage rise as a function of time during a current pulse of appropriate duration is recorded with reference to pulser ground first across the high frequency current-sensing resistor and then at each of the two center sample electrodes. Each time range, thus, involves three separate current pulse measurements. The differential voltage rise as a function of time between the two center contacts is calculated and divided by the instantaneous current level monitored across the sensing resistor, yielding resistivity as a function of time. Analyses of six to ten time ranges are necessary to gather data from  $10^{-8}$  to  $10^{-3}$  sec.

Potential transients were captured with a Tektronix 7633 storage oscilloscope using a 6B53A time base and 6A11 vertical amplifier. Unit gain, 150 MHz bandwidth, and 1 megohm input impedance are three features of the 6A11 amplifier essential for these measurements. The probe-oscilloscope combination has a 60 MHz bandwidth, 5.9 nsec risetime, and vertical deflection accuracy of 3%. Stored traces were photographed for subsequent manual retrieval of potential/time information. The assembled apparatus was operated in a

single pulse mode by triggering the oscilloscope and pulser with a Datapulse Model 110B pulse generator.

**Results and Discussion**

*Model circuit.*—The resistivity/time behavior of a typical beta alumina tube (6G3-2) is shown in Fig. 5. Two impedance plateaus are apparent at 23°C, one between  $10^{-8}$ - $10^{-6}$  sec and a second in the region of  $10^{-4}$  sec. Each resistivity characteristic shifts toward longer elapsed times (lower frequencies) with decreasing temperature.

An equivalent circuit modeling this resistivity/time response is shown in Fig. 6.  $R_b$  and  $C_b$  are grain boundary resistance and capacitance, respectively;  $R_c$  and  $C_c$  are comparable grain parameters. Generally,  $R_b > R_c$  and  $C_b > C_c$ ; polycrystalline beta alumina, therefore, is considered an aggregate of essentially single crystal grains separated by grain boundaries of markedly lower conductivity. Maxwell and Wagner (4) first described the frequency dispersion of conductivity and dielectric constant expected for such a heterogeneous conductor. Koops (5) applied the circuit shown in Fig. 6 to model the a-c impedance of grain structured NiZn ferrite, and Mitoff (6) has suggested this circuit as a model for the resistivity of polycrystalline beta alumina.

Individual voltages arising from  $R_cC_c$  and  $R_bC_b$  are additive during perturbation by a constant current square wave

$$V_T = V_c + V_b \tag{1}$$

or

$$V_t = I_{in} \left[ \frac{1}{C_c \left( s + \frac{1}{R_c C_c} \right)} + \frac{1}{C_b \left( s + \frac{1}{R_b C_b} \right)} \right] \tag{2}$$

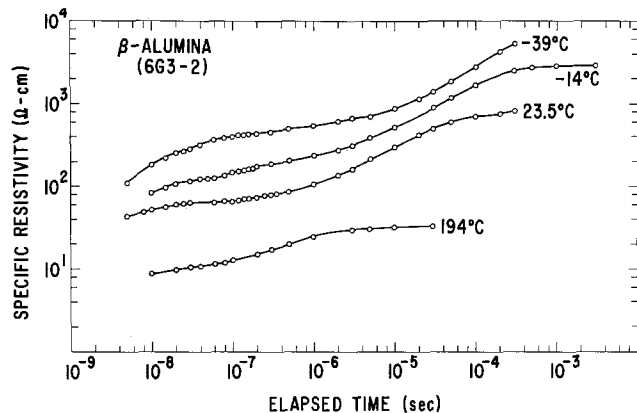


Fig. 5. Specific resistivity behavior of sample 6G3-2 as function of temperature.

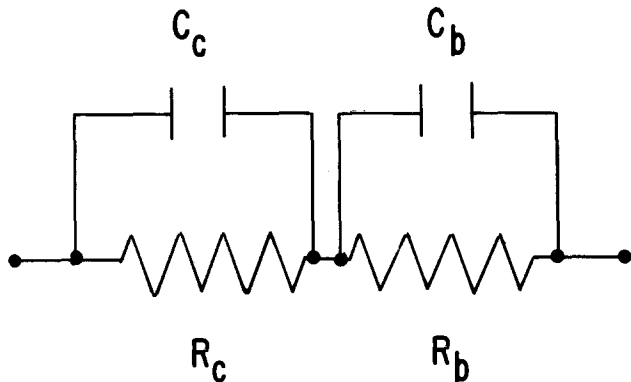


Fig. 6. Model circuit, ion transport in polycrystalline beta alumina.

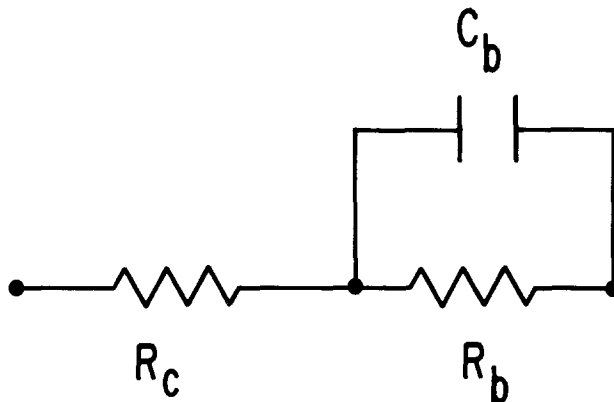


Fig. 7. Simplified model circuit, ion transport in polycrystalline beta alumina.

where  $s$  is the LaPlace operator and  $t$  is the elapsed time from the moment of current initiation, a point here defined as 10%  $t_r$ .

The response of this circuit to a constant current step

$$I_{in} = \frac{I_o}{s} \tag{3}$$

reduces to

$$\frac{V_T}{I_o} = R_t = R_c(1 - e^{-t/R_c C_c}) + R_b(1 - e^{-t/R_b C_b}) \tag{4}$$

If  $R_c C_c \ll R_b C_b$ , as is the case for 6G3-2, the effects of  $R_c C_c$  are essentially resolved before those from  $R_b C_b$  become significant. The equivalent circuit in Fig. 6 then can be simplified to that shown in Fig. 7 and Eq. [4] reduces to

$$R_t = R_c + R_b(1 - e^{-t/R_b C_b}) \tag{5}$$

Circuit resistance as a function of time is theoretically independent of pulse current magnitude. This is true for polycrystalline beta alumina over at least the 85-1650  $\mu A$  current range as the data for sample 6G3-2 in Table I demonstrate.

*Observed sample characteristics.*—Table II lists  $R_b$ ,  $R_c$ , and  $C_b$  observed as functions of temperature for sample 6G3-2 and 6M2-2. Certainly the most accurate figures are those for  $R_{dc}$ , which were obtained by extrapolating pulse data to direct current. Separating  $R_{dc}$  into  $R_b$  and  $R_c$  and calculating  $C_b$  is complicated by the failure of real ceramics to exhibit idealized resistivity behavior.

By comparing the observed resistivity response for 6G3-2 at 23°C with that predicted assuming  $R_b = 732$  ohm-cm,  $R_c = 68$  ohm-cm,  $C_b = 3.1 \times 10^{-8}$  F-cm<sup>-1</sup>, and  $C_c = 0$ , Fig. 8 illustrates that  $R_b C_b$  in a real ceramic is not a single time constant, but actually the mean of a time constant distribution. The observed response is more gradual than that predicted. Nonideal behavior arises because a single RC circuit can only approximate the three-dimensional RC network needed to accurately model conduction in polycrystalline beta alumina and because variations in intrinsic grain boundary

Table I. Observed resistivity of sample 6G3-2 at two current densities, 27°C

Elapsed time (nsec)	$R_t$ (ohm-cm) $i = 1650 \mu A$	$R_t$ (ohm-cm) $i = 85 \mu A$
40	44	48
60	51	53
80	56	55
100	59	59
200	66	68
300	72	73
500	76	79
1000	94	95
2000	120	123
3000	144	147

Table II. Variation of  $R_c$ ,  $R_b$ , and  $C_b$  with temperature

Sample 6G3-2				
Temperature (°C)	$R_{dc}$ (ohm-cm)	$R_c$ (ohm-cm)	$R_b$ (ohm-cm)	$C_b$ (F-cm <sup>-1</sup> )
-39	9004	424	8580	$3.1 \times 10^{-8}$
-14	2863	173	2690	$3.0 \times 10^{-8}$
23	800	68	632	$3.1 \times 10^{-8}$
194	32	10	22	$3.1 \times 10^{-8}$
Sample 6M2-2				
Temperature (°C)	$R_{dc}$ (ohm-cm)	$R_c$ (ohm-cm)	$R_b$ (ohm-cm)	$C_b$ (F-cm <sup>-1</sup> )
-12	3237	(173)*	3064	—
23	780	(68)	712	$8.5 \times 10^{-10}$
66	234	(28)	206	$8.8 \times 10^{-10}$
75	250	(24)	226	—
100	129	(16)	113	$6.1 \times 10^{-10}$
157	52	(8)	44	$1.1 \times 10^{-9}$

\* Values in parentheses are estimated assuming  $R_c$  (23°C) = 68 ohm-cm and  $E_c = 4.1$  kcal/mole.

characteristics occur within any particular ceramic specimen.

In sample 6G3-2,  $R_b C_b$  and  $R_c C_c$  are sufficiently different that its behavior at times  $> 10^{-8}$  sec can be modeled by the equivalent circuit shown in Fig. 7. With this simplification, it is possible to determine average values or  $R_c$ ,  $R_b$ , and  $C_b$  and 6G3-2 despite the distribution of  $R_b C_b$  time constants.

$R_b$  is equal to  $R_{dc} - R_c$ .  $R_c$  can be estimated from the second impedance plateau or determined more accurately by plotting  $\ln(R_{dc} - R_t)$  vs.  $t$  at points in the intergrain transition region.

For a model circuit such as Fig. 7 in which  $R_b C_b$  is a single time constant,  $\ln(R_{dc} - R_t)$  vs.  $t$  is a straight line of slope  $= -1/R_b C_b$  and intercept of  $\ln R_{t=0}$ , where  $R_{t=0} = R_b$ . The distribution of  $R_b C_b$  time constants introduces curvature into this relationship, but the plot is still sufficiently linear at times near the  $R_c$  plateau that  $R_c$  can be accurately determined.

$C_b$  is calculated at the inflection point of the intergrain transition where, for a symmetrical dispersion of grain boundary properties,  $R_t = (R_c R_b)^{1/2}$ . Were  $R_b C_b$  a single time constant, a constant value of  $C_b$  could be calculated at any point on the intergrain transition. However, calculation of  $C_b$  at multiple points on a distributed grain boundary transition (Fig. 8) yields a range of  $C_b$  values centering on that calculated at the inflection. Each value of  $C_b$  is that which brings a model  $R_b C_b$  transition into coincidence with the observed transition at its point of calculation.

The effects of  $R_c C_c$  and  $R_b C_b$ , separated in sample 6G3-2, merge in sample 6M2-2 (Fig. 9) and, when combined with a distributed  $R_b C_b$  response, make precise calculation of  $R_c$  extremely difficult. To obtain the values of  $R_b$ ,  $R_c$ , and  $C_b$  for 6M2-2 at various temperatures summarized in Table II, samples 6G3-2 and

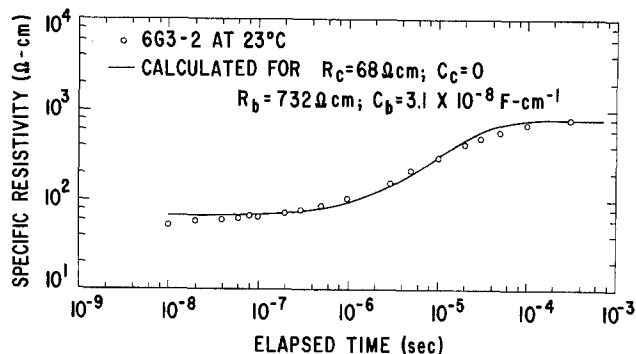


Fig. 8. Observed and calculated intergrain transition response, sample 6G3-2.

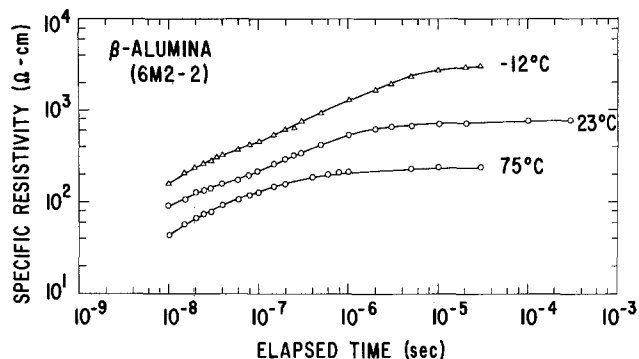


Fig. 9. Observed and calculated intergrain transition response, sample 6M2-2.

6M2-2 were considered identical in intragrain conduction behavior.  $R_c$  (6M2-2) at 23°C was taken to be 68 ohm-cm and its intragrain conduction activation energy,  $E_c$ , to be 4.1 kcal/mole. Implicit is the assumption that the presence (6G3-2) or absence (6M2-2) of  $Y_2O_3$ , because of the size of  $Y$ , has no effect on intragrain conduction.

*Nature of  $R_c$  and  $R_b$ .*— $R_c$  is not identical to but approximates the intrinsic resistivity of single crystal beta alumina. For sample 6G3-2,  $R_c$  at 23°C is 68 ohm-cm, close to that of 72 ohm-cm reported at 23°C by Whittingham and Huggins (2). Variation of  $R_c$  among different specimens and discrepancy between  $R_c$  and the intrinsic resistivity of single crystal beta alumina can arise from differences in composition and because the grains comprising polycrystalline samples are randomly oriented and separated by grain boundary regions.  $R_c$  is increased by a tortuous conducting path and decreased by capacitive shunting of grain boundaries.

$R_b$  is an aggregate grain boundary resistivity and should be contrasted with  $\rho_b$ , the intrinsic resistivity of an individual grain boundary. The difference between  $R_b$  and  $\rho_b$  lies in the geometric factor introduced in converting an observed sample d-c resistance (ohm) into resistivity (ohm-cm). That factor for these measurements is the annular tube area divided by the spacing between the center pair of electrodes. Grain boundaries, *per se*, occupy only a small portion of the ceramic between these two sensing electrodes; but the geometric factor measures the over-all area and distance between the sensing electrodes, not the actual grain boundary parameters.

Similarly,  $C_b$ , expressed in units of F-cm<sup>-1</sup>, is the aggregate capacitance of many individual grain boundaries, not an intrinsic grain boundary capacitance.

The aggregate grain boundary properties,  $R_b$  and  $C_b$ , vary with techniques of ceramic preparation, especially with grain size and distribution and the presence of sintering additives. One sintering additive that appears to concentrate at grain boundaries and greatly affects their electrical characteristics is  $Y_2O_3$ . Sample 6G3-2 was prepared with 0.5%  $Y_2O_3$  added as a sintering aid; sample 6M2-2 is free of  $Y_2O_3$ . The effects of  $Y_2O_3$  on grain boundary characteristics are evident in the relative values of  $C_b$  calculated for these two samples listed in Table II. In each case,  $C_b$  is independent of temperature within measurement accuracy but the average value of  $C_b$  is 41 times greater for 6G3-2 than 6M2-2.

A precise model of grain boundary behavior must consider that observed response results from many individual grain boundaries summed in a complex distributed series-parallel network. With great simplification, grain boundaries may be lumped to a single region of thickness,  $d$ , bounded by parallel plates of equal area,  $A$ . Thus

$$R_b C_b = \left( \rho_b \frac{d}{A} \right) \left( \epsilon_0 \epsilon_b \frac{A}{d} \right) \quad [6]$$

in which  $\rho_b$  and  $\epsilon_b$  are the specific intrinsic resistivity and dielectric constant of an individual grain boundary and  $\epsilon_0 = 8.85 \times 10^{-15} \text{ F-cm}^{-1}$ , the permittivity of free space.

At 23°C,  $R_b C_b$  and  $R_b$  are  $2.3 \times 10^{-5} \text{ sec}$  and  $632 \text{ ohm-cm}$ , respectively, for 6G3-2 and  $5.6 \times 10^{-7} \text{ sec}$  and  $712 \text{ ohm-cm}$ , respectively, for 6M2-2.

Considering

$$\frac{\left[ \left( \rho_b \frac{d}{A} \right) \left( \epsilon_b \epsilon_0 \frac{A}{d} \right) \right] (6G3-2)}{\left[ \left( \rho_b \frac{d}{A} \right) \left( \epsilon_b \epsilon_0 \frac{A}{d} \right) \right] (6M2-2)} = \frac{R_b C_b (6G3-2)}{R_b C_b (6M2-2)} \quad [7]$$

and

$$\frac{R_b (6G3-2)}{R_b (6M2-2)} = \frac{\rho_b \frac{d}{A} (6G3-2)}{\rho_b \frac{d}{A} (6M2-2)} \quad [8]$$

Then

$$\frac{\epsilon_b \frac{A}{d} (6G3-2)}{\epsilon_b \frac{A}{d} (6M2-2)} = 46 \quad [9]$$

Making the somewhat arbitrary assumptions that  $A/d$  (6G3-2) =  $A/d$  (6M2-2) and  $\epsilon_b$  (6M2-2) is a typical value such as 5, then  $\epsilon_b$  (6G3-2) = 230,  $\rho_b$  (6G3-2) =  $1 \times 10^7 \text{ ohm-cm}$ , and  $\rho_b$  (6M2-2) =  $1 \times 10^7 \text{ ohm-cm}$  at 23°C. Clearly, these are simplifications; nevertheless, the essential conclusion that the intrinsic resistivity of grain boundaries is approximately  $10^5$  times greater than that of grains is reasonable.

If  $\rho_b$  (6G3-2) =  $1 \times 10^7 \text{ ohm-cm}$  at 23°C, then the aggregate grain boundary thickness between the two larger faces of a  $1 \text{ cm}^2 \times 0.1 \text{ cm}$  section of the ceramic, assuming a model of alternating parallel grains separated by grain boundaries, is  $5 \times 10^{-4} \text{ cm}$ . A 1V potential drop across the ceramic in a direction normal to the larger faces produces a field of  $2 \times 10^3 \text{ V/cm}$  across the grain boundaries and  $8 \times 10^{-1} \text{ V/cm}$  across the grains at 23°C, and  $1.2 \times 10^3$  and  $3.7 \text{ V/cm}$ , respectively, at 350°C.

Localized grain boundary fields of greater intensity may arise from inhomogeneities in grain boundary resistivity and in grain size and distribution. For example, the total resistivity of a relatively large grain embedded in a matrix of smaller grains is lower than its neighboring region. Current flows preferentially through the grain, increasing the current density at its boundaries, producing greater localized fields than exist generally in the sample. These large grain boundary fields may be significant factors in the initiation and propagation of cracks that often appear in polycrystalline beta alumina upon extended electrochemical ionic transport.

*Variation of  $R_c$  and  $R_b$  with temperature.*—Arrhenius plots for intragrain and intergrain conductivity in sample 6G3-2 and intragrain conductivity in sample 6M2-2 are shown in Fig. 10 and 11, respectively.

The intragrain activation energy of  $4.1 \pm 0.1 \text{ kcal/mole}$  measured for sample 6G3-2 is slightly greater than that of  $3.8 \text{ kcal/mole}$  reported by Whittingham and Huggins (2) for beta alumina single crystals. Tortuosity of a polycrystalline sample should not influence the slope of its intragrain Arrhenius plot. The difference between these activation energies is significant, therefore; its cause may lie in small compositional differences between the samples of beta alumina analyzed.

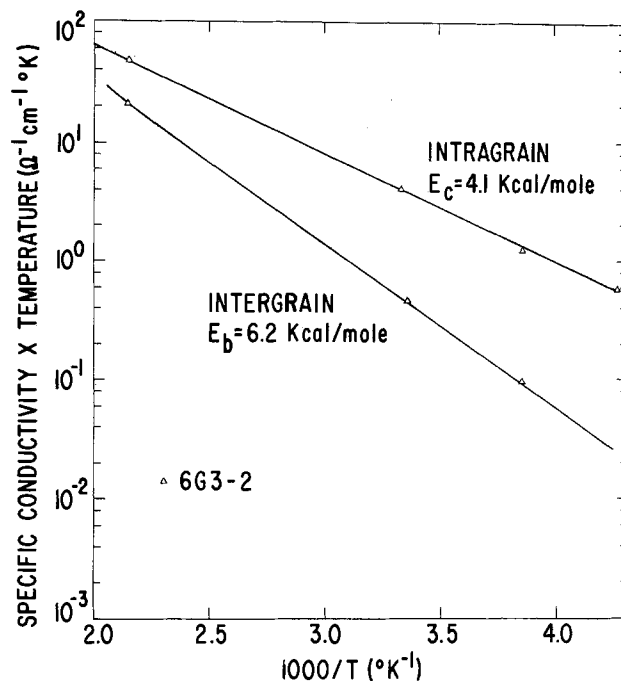


Fig. 10. Arrhenius plot, 6G3-2

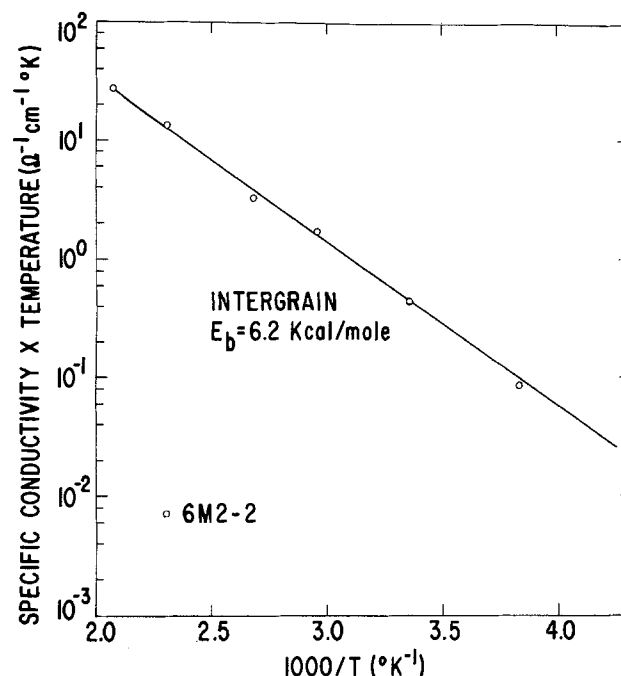


Fig. 11. Arrhenius plot, 6M2-2

Intergrain activation energies are the same, 6.2 kcal/mole, regardless of the presence (6G3-2; Fig. 10) or absence (6M2-2; Fig. 11) of  $\text{Y}_2\text{O}_3$ .

Nonlinear Arrhenius behavior might be observed for the temperature variation of polycrystalline beta alumina resistivity if the elapsed time, or its counterpart in frequency, at which resistivity is monitored falls on the intergrain or intragrain transition regions at some point in the temperature range of interest. For example, if the grain boundary conductance of sample 6G3-2 were monitored at 100 kHz from  $-58^\circ$  to  $300^\circ\text{C}$ , the resulting Arrhenius plot would be linear above ca.  $150^\circ\text{C}$ , in which range 100 kHz falls on the intergrain plateau, but would deviate from linearity at lower temperatures at which anomalously high conductivity would be observed. In deriving the Arrhenius plots presented here, the points at which resistivities were recorded for intergrain and intragrain transport were



adjusted with changing temperature to be clearly on the resistivity plateaus of interest.

**Nature of  $C_c$ .**—As Fig. 5 and 9 show, the resistivity of polycrystalline beta alumina decreases below  $R_c$  at short elapsed times. This effect, barely observable at 23°C but clear at -39°C, is modeled in the equivalent circuit (Fig. 6) by  $C_c$ , the intragrain capacitance.  $C_c$  expresses many polarization processes intrinsic to single crystal beta alumina, but is too large to result solely from electronic polarizations. Also, a simple geometric capacitance should not have so large a temperature variation.

Most materials have optical dielectric constants in the range 1-10. Were the intrinsic dielectric constant of beta alumina at 23°C a value such as 5,  $C_c$  (23°C) would be  $4.5 \times 10^{-14}$  F-cm<sup>-1</sup> and  $R_c C_c$ , considering  $R_c = 68$  ohm-cm, would be  $3.0 \times 10^{-12}$  sec. An RC response of this time constant should have a value of  $0.9 R_c$  or 62 ohm-cm at  $7 \times 10^{-12}$  sec. Actually,  $R(6G3-2)$  is 62 ohm-cm at  $1.14 \times 10^{-8}$  sec (23°C), making  $C_c = 8.9 \times 10^{-11}$  F-cm<sup>-1</sup> and  $R_c C_c = 6.1 \times 10^{-9}$  sec. From Eq. [6],  $R_c C_c = \rho_c \epsilon_c \epsilon_0$ , where  $\rho_c$  = single crystal beta alumina resistivity and  $\epsilon_c$  = single crystal dielectric constant. Then,  $\epsilon_c = 10^5$  to explain the observed behavior. Since  $10^5$  is an unreasonable optical dielectric constant,  $R_c C_c$  (see Fig. 6) must be a generalization of a more complex equivalent circuit needed to model intragrain, or single crystal, beta alumina impedance at shorter elapsed times than those encountered here. Possible origins for this complexity can be found in the structure and nature of ionic motion in the beta alumina conduction plane.

The structure of beta alumina was first determined by Bragg (7) and refined by Beevers and Ross (8) and Peters *et al.* (9). The work of Peters *et al.* addressed particularly sodium ion distribution within its conducting planes. Figure 12 maps the sodium and oxygen ion arrangement within the conducting plane. Two close-packed oxygen layers, the top removed and the bottom shown, symmetrically sandwich the conducting plane. Sodium ions are shown in d sites, one of three sites, d, b, and MO, available for mobile ion occupation.

A sodium ion in the center of each d site is hexagonally coordinated 2.88Å from each of three oxygens in the lower and three in the upper close-packed planes and equidistant at 3.25Å from three oxygens in the conducting plane. Sodium in the mid-oxygen (MO) is also hexagonally coordinated to six close-packed oxygens, three in each plane at a distance of 2.88Å, but its nearest neighbors are two oxygens in the conducting plane at a distance of 2.80Å. The b site, like the d site,

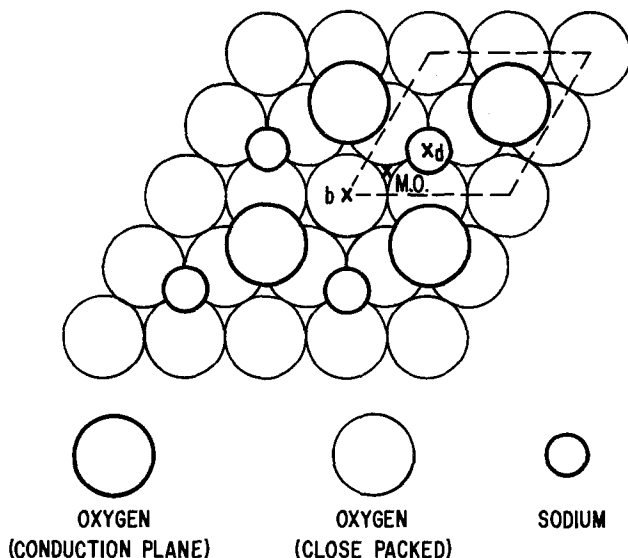


Fig. 12. Ionic arrangement in beta alumina conduction plane

has sodium trigonally coordinated 3.25Å away from three conduction-plane oxygens but placed between two close-packed oxygens only 2.38Å away.

If the Na<sup>+</sup> ion distribution presented by Peters *et al.* (11), which is averaged over many unit cells, actually represents ion distribution at the unit cell level, then Na<sup>+</sup> ion density at room temperature is concentrated in the d and MO sites. Density in the d site is shaped as a triangle with apical maxima 0.39Å from site center each pointing toward one of three neighboring MO sites; each d site has not one but three density maxima. Secondary density maxima occur at each MO site. Occupation of b sites is low in comparison. This density distribution becomes more uniform with increasing temperature. More sophisticated experimental techniques have essentially confirmed these observations (10).

The nonequivalency of Na<sup>+</sup> ion sites in beta alumina and of ion densities within those sites implies that a number of energetically different site-site ion transitions can occur. Therefore, measurement of intragrain (single crystal) beta alumina resistivity over an appropriate response range should reflect in its structure several different ion response times. The decline in resistivity at short elapsed times in Fig. 5 and 9 may be initial manifestations of these effects.

The resistivity data presented here only hint at what might be observed with more detailed measurements. For example, using NMR analysis, Story, Glowinkowski, and Roth (11) and Jerome and Boilot (12) report observing at least two distinct activation energies for Na<sup>+</sup> ion motion in beta alumina.

## Summary and Conclusions

Galvanostatic analysis is a useful approach for identifying and analyzing the several components of resistivity, both intergrain and intragrain, in polycrystalline beta alumina. Precise calculation of  $R_b$  and  $R_c$  is possible when  $R_b C_b \gg R_c C_c$  and  $R_b C_b$  is within the frequency range of measurement.

Grain boundaries dominate the resistivity of typical fine-grain beta alumina. Though their physical dimensions are small, they account for 92% of the d-c resistivity of sample 6G3-2 and 85% of the d-c resistivity of 6M2-2 at 23°C. Their properties are pivotal in determining the applications and temperatures for which polycrystalline beta alumina is a practical electrolyte.

A grain boundary can be modeled as an area of extremely low conductivity separating intragrain regions of much higher conductivities. Because of their large electrical fields, e.g.,  $10^3$  V/cm, grain boundaries may be focal points of electrochemically induced ceramic degradation.

Intragrain capacitance effects are observed in the elapsed time region of  $10^{-8}$ - $10^{-9}$  sec at 23°C and are considered the result of several different ion transitions possible among the three structurally nonequivalent sites available for mobile ion occupation in beta alumina. As a result, the intragrain transition region, beginnings of which are seen in these measurements, should not follow a single time constant but should exhibit complexity arising from multiple ion motions possible on a localized scale in the beta alumina conduction plane. An elucidation of the intragrain resistivity transition will require analysis at shorter elapsed times (higher frequencies) than those encountered here, but may illumine the intrinsic nature of ion transport in beta alumina.

Occurrence of intragrain capacitance effects at elapsed times as long as  $10^{-8}$  sec has one very practical consequence: it jeopardizes the usefulness of galvanostatic or multifrequency resistivity analysis in guiding beta alumina ceramic development. It was hoped that such techniques could be used to separate intragrain and intergrain resistivity components in polycrystalline beta alumina. Though satisfactory separation is ob-

served with yttria-containing ceramic such as 6G3-2, yttria is considered deleterious to ceramic life. Elimination of yttria yields samples such as 6M2-2 which appear to have approximately equivalent d-c resistivity to yttria-containing material but much smaller grain boundary capacitance. Consequently, the grain boundary ( $R_bC_b$ ) resistivity transition in 6M2-2 merges with its intragrain transition. Since the grain boundary response is not single valued and the nature of the intragrain transition unknown, resolution of  $R_c$  and  $R_b$  is not straightforward. Multifrequency analysis or its equivalent may be of little use in separating intragrain and intergrain resistivity components in such "improved" specimens of polycrystalline beta alumina.

Manuscript submitted March 10, 1975; revised manuscript received July 28, 1975.

Any discussion of this paper will appear in a Discussion Section to be published in the June 1977 JOURNAL. All discussions for the June 1977 Discussion Section should be submitted by Feb. 1, 1977.

Publication costs of this article were assisted by General Electric Company.

#### REFERENCES

1. Y. F. Y. Yao and J. T. Kummer, *J. Inorg. Nucl. Chem.*, **29**, 2453 (1967).
2. M. S. Whittingham and R. A. Huggins, *J. Chem. Phys.*, **54**, 414 (1971).
3. R. W. Powers and S. P. Mitoff, *This Journal*, **122**, 226 (1975).
4. K. W. Wagner, *Ann. Physik*, **40**, 817 (1913).
5. C. G. Koops, *Phys. Rev.*, **83**, 121 (1951).
6. S. P. Mitoff, in "Fast Ionic Transport in Solids," W. Van Gool, Editor, p. 415, American Elsevier, New York (1973).
7. W. L. Bragg, C. Gottfried, and J. West, *Z. Krist.*, **77**, 255 (1931).
8. C. A. Beevers and M. A. Ross, *ibid.*, **97**, 59 (1937).
9. C. R. Peters, M. Bettman, J. W. Moore, and M. O. Glick, *Acta Cryst.*, **B27**, 1826 (1971).
10. W. L. Roth, Personal communication.
11. H. S. Story, S. Glowinkowski, and W. L. Roth, Paper presented at American Physical Society, March 1975.
12. D. Jerome and J. P. Boilot, *J. Phys.-Lettres*, **35**, 1 (1974).

## Cathodoluminescence Saturation Phenomena in $Y_2O_3S:Eu$

D. J. Robbins

Royal Radar Establishment, Malvern, Worcestershire WR14 3PS, England

#### ABSTRACT

The importance of a thermal perturbation of  $Y_2O_3S:Eu$  (0.1%) under excitation by long (up to 30 msec) electron beam pulses is investigated using the measured differential thermal behavior of luminescence lines originating in the  $^5D_2$ ,  $^5D_1$ , and  $^5D_0$  states. An observed droop in light output, equivalent to a saturation of the phosphor brightness, is found to be inconsistent with a thermal perturbation of the system. Other experiments involving a-c electric field modulation of the luminescence from the  $^5D$  states suggest that the droop may be caused by electric field perturbation of the system. The saturation characteristics of the phosphor are changed reversibly during a 30 msec pulse, and irreversibly by mixing with a conducting matrix. It is suggested that space-charge fields are generated by trapping of charge in surface states of the phosphor grains, and a simple kinetic model for the saturation mechanism involving field-induced ionization of the charge transfer state and quenching of the  $^5D_2$  state is in qualitative agreement with the experimental data. The relevance of the model to saturation phenomena and to aging in CRT screens is discussed.

Most phosphors show some degree of saturation in their brightness vs. current density characteristic under electron beam excitation (1, 2). This saturation can clearly limit the brightness achievable from any CRT screen incorporating such a phosphor, and can prove troublesome in maintaining color balance in multicolor tubes (3-6). The phenomenon is therefore of great technological interest. Several workers have described techniques whereby the saturation characteristics of phosphors can be parameterized (3, 4, 7), but there have been rather few experimental investigations which can be used to provide insight into the fundamental mechanisms involved. This study was undertaken in order to test some of the generally accepted theories of current density saturation in phosphors.

Saturation of light output as pumping density increases is primarily a kinetic problem, and detailed kinetic models have been developed to explain the phenomenon in light-emitting semiconductor materials (8). In contrast the models applied to phosphor mate-

rials are much more general and qualitative in nature (9, 10), but the most probable causes of saturation may be summarized in the following way:

(i) A perturbation of the system kinetics at high current densities. It is usually assumed that this perturbation is thermal (3, 11) and that a temperature rise causes saturation by reducing the luminescent efficiency of the phosphor. However it should be remembered that excitation by a charged particle beam is involved in the CRT so that the perturbation might be electrical in nature.

(ii) True activator saturation, i.e., excitation of a large fraction of available activator sites causing significant depletion of the ground state population. Although this effect is often assumed in the analysis of phosphor kinetics (9) it is less likely to be significant in rare earth phosphors with several percent of activator ions in the lattice than in sulfide phosphors with activators at the ppm level. Such effects will also be sensitive to activator lifetimes.

(iii) The increasing importance at high excitation densities of higher order recombination pathways, or

Key words: phosphors, CRT, aging, space-charge electric field, surface states.

of self-absorption phenomena caused by the buildup in population of low energy excited states just above the ground state (12).

There is a lack of experimental data which can be used to decide the relative importance of the above mechanisms, but for rare earth phosphors and reasonable excitation densities mechanism (i) would appear most probable. Our first aim has therefore been to monitor the kinetics of a rare earth phosphor at increasing excitation current densities in order to determine whether effects related to saturation of light output were consistent with a thermal perturbation of the system. We thus sought a system with its own "internal thermometer," i.e., with spectral features sensitive to temperature in the range 300°-400°K. Such a system could be "calibrated" by measurement of its spectrum at various fixed temperatures, so that if a thermal perturbation were assumed to occur under electron beam excitation the effects could be predicted and the predictions checked against the experimental data. We shall show that for the rare earth phosphor material investigated here the kinetics are perturbed at higher current densities, but that the results cannot be explained by a rise in temperature of the system. However we shall present other evidence, including the electric field modulation of photoluminescence, which demonstrates that the effects are consistent with a perturbation of the kinetics caused by the buildup of an electric field in the phosphor particles during electron beam bombardment. This space-charge field may be created by trapping of charge in surface states of the phosphor.

The system chosen for study was  $\text{Y}_2\text{O}_3\text{S:Eu}$  (0.1%). The temperature dependence of the photoluminescence (PL) spectrum of this system has been extensively investigated by Struck and Fonger (13, 14), who have shown that between 300°-450°K emission from the  $^5\text{D}_2$  state is rapidly quenched, probably via the charge transfer (CT) state, whereas similar quenching of the lower lying  $^5\text{D}_1$  and  $^5\text{D}_0$  states does not begin until much higher temperatures. The relative intensities of the emission from  $^5\text{D}_2$ ,  $^5\text{D}_1$ , and  $^5\text{D}_0$  therefore constitute the internal thermometer which we have used to monitor the effective temperature of the luminescent ion as excitation current density is increased, and hence to determine the significance of any thermal perturbation. The energy level scheme and the wavelengths of the lines monitored are shown in Fig. 1.

Following the onset of electron beam excitation, energy transferred to the lattice phonons is rapidly relaxed; this relaxation is generally considered to be complete in a time  $\ll 10^{-10}$  sec, so that on the time scale of interest in our experiments the phonon subsystem can be considered to be instantaneously in local equilibrium with the electronic configuration of the activator ion. The relaxation between different electronic levels is much slower however, and can be strongly influenced by the strength of the electron-lattice coupling and by the mean phonon occupation numbers. The electronic relaxation times are obtained from the decay times of the states involved, and are of the order  $\tau \sim 1 - 5 \times 10^{-4}$  sec for the  $^5\text{D}_2$ ,  $^5\text{D}_1$ ,  $^5\text{D}_0$  states of  $\text{Eu}^{3+}$  at 300°K, and estimated to be  $\ll 10^{-8}$  sec for the charge transfer state (13). When an electron beam pulse is applied to the system the excitation rate is constant while the pulse is on, and the relative populations of the  $^5\text{D}_2$ ,  $^5\text{D}_1$ , and  $^5\text{D}_0$  electronic states will adjust to the new steady-state conditions in a time corresponding to  $\sim 5\tau$ , i.e.,  $\sim 0.5$ -2 msec. Since the kinetics are most easily interpreted in the steady-state condition rather than during the initial rapid rise of luminescence, relatively long electron beam pulses (up to 30 msec) have been applied to the system so that a steady-state condition should be reached. The temperature is expected to rise through the pulse, but as long as the rate of change is slow compared with the

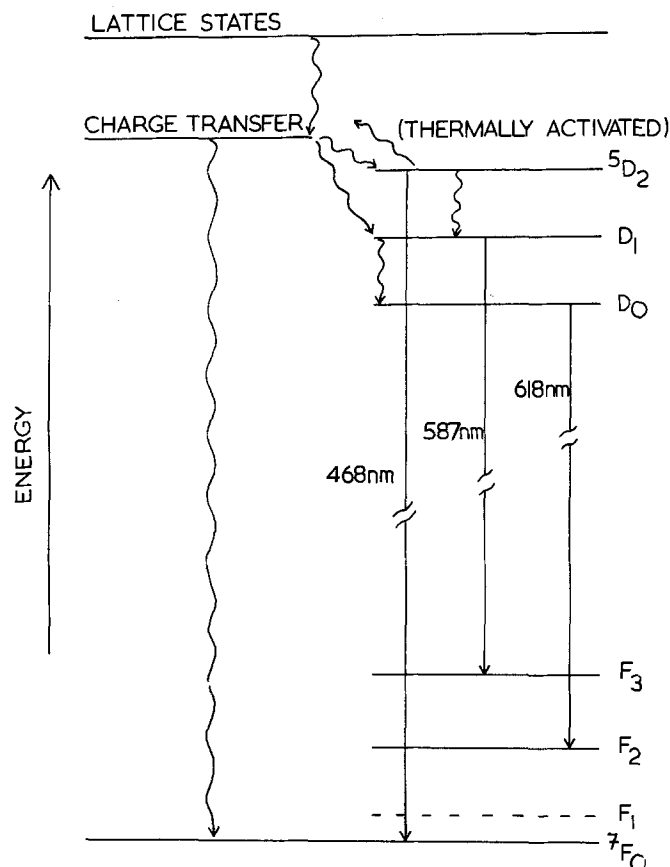


Fig. 1. Schematic energy level diagram for  $\text{Y}_2\text{O}_3\text{S:Eu}$ . The wavelengths of the emission lines used to monitor the kinetics of the excited states are shown.

electronic relaxation rates the relative populations of the excited states should reflect the effective temperature of the system throughout the pulse. Since the relative thermal behavior of the  $^5\text{D}_2$ ,  $^5\text{D}_1$ ,  $^5\text{D}_0$  states in  $\text{Y}_2\text{O}_3\text{S:Eu}$  (0.1%) is known (13), the relative populations of these states during electron beam excitation can be used to determine whether there is a significant thermal perturbation of the system as current density is increased.

It might seem more straightforward to calculate the expected temperature rise directly rather than use the experimental approach adopted here. However there are severe problems associated with such a calculation for a thin layer of phosphor powder settled on a substrate, not the least of these being the thermal conductivity to be used for small grains of material in point contact and associated with binder in the layer, and the volume and nature of the excitation caused by an electron beam penetrating a randomly oriented array of irregular particles. Archard and Einstein (15) have considered the problem of heating in phosphor screens under pulse electron beam excitation and have shown that the temperature rise can be treated as the sum of two parts: first, a rise in mean temperature, superimposed upon which is a pulse temperature rise occurring during the excitation period. If the electronic processes taking place at the excited activator ions are fast compared with the relaxation time of the thermal pulse, then the effective temperature experienced by the activator during the luminescence process will be higher than the mean screen temperature.

In view of these difficulties we have preferred to determine experimentally whether the light output of the phosphor system is significantly affected by thermal perturbation. Nevertheless it is useful to obtain a qualitative picture of the probable rate of change of temperature through the pulse using the method described by Carslaw and Jaeger (16), and used by

Archard and Einstein (15), since this will indicate whether our assumption that the rate of temperature change is slow compared with the electronic relaxation times is reasonable. If we assume the beam to penetrate a depth  $l$  into a semi-infinite solid with heat generated at a constant rate  $Q$  per unit time and area for time  $t > 0$ , and with no heat loss at the surface, then the temperature rise at depth  $l$  will be of the form (16)

$$T = \frac{KQt}{2kl} \left( 1 - 4i^2 \operatorname{erfc} \frac{l}{\sqrt{Kt}} \right) \quad [1]$$

where  $K = k/\rho c$ ,  $k$  is the thermal conductivity,  $\rho$  the density, and  $c$  the specific heat. The function  $i^2 \operatorname{erfc}(x)$  is tabulated in Ref. (16). Archard and Einstein (15) have measured a thermal conductivity for settled ZnS

$$k = 4 \times 10^{-4} \text{ cal cm}^{-1} \text{ } ^\circ\text{C}^{-1} \text{ sec}^{-1} \quad [2]$$

This is approximately the thermal conductivity of dry sandy soil (16), which is perhaps reasonable for a phosphor settled in silicate binder. Assuming this value for  $\text{Y}_2\text{O}_2\text{S}$ , and

$$\rho \approx 5 \text{ g cm}^{-3}$$

$$c \approx 0.1 \text{ cal g}^{-1} \text{ } ^\circ\text{C}^{-1} \quad [3]$$

then for a current density of  $0.5 \text{ mA cm}^{-2}$ , the maximum used in our experiment, the predicted temperature rise of the phosphor through a 30 msec electron beam pulse is shown in Fig. 2. With a repetition time of approximately 100 msec the background rise in temperature of the system calculated according to Archard and Einstein should be less than  $10^\circ\text{C}$ . The absolute magnitudes of these rises can only be crude estimates since we have neglected, among other things, heat losses to the metal substrate and to the surroundings, and the nonuniform intensity profile of the electron beam. However the calculation is sufficient to indicate that the rate of change of temperature through the pulse should be slow compared with the electronic relaxation times, and that therefore the relative intensities of emission from the  $^5\text{D}_2$ ,  $^5\text{D}_1$ , and  $^5\text{D}_0$  states of  $\text{Eu}^{3+}$  at any instant should reflect the temperature prevailing in the system.

With this background it is now possible to discuss the experimental results.

### Experimental

The  $\text{Y}_2\text{O}_2\text{S}:\text{Eu}$  (0.1%) was prepared at GEC Ltd. (Hirst Research Centre) by firing  $\text{Y}_2\text{O}_3$  with sulfur,  $\text{Eu}_2\text{O}_3$ , and  $\text{Na}_2\text{CO}_3$  at  $1200^\circ\text{C}$  for 2 hr in an open tube furnace and subsequently washing. The phase of the sample was checked by x-ray powder diffraction, and the activator content by x-ray fluorescence analysis. The cathodoluminescence (CL) measurements were

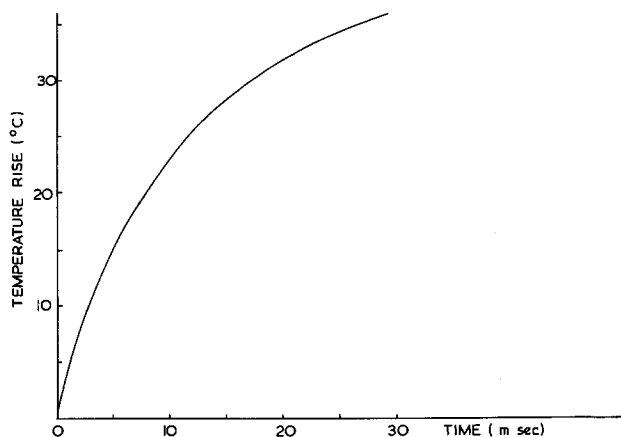


Fig. 2. Estimated temperature rise of  $\text{Y}_2\text{O}_2\text{S}:\text{Eu}$  powder layer through a long electron beam pulse, calculated from Eq. [1] for the highest current density used in our experiments.

made using an apparatus which has been described elsewhere (17). The electron beam was approximately  $800\mu$  in diameter and was variable from  $0.3\text{--}20 \mu\text{A}$  at the sample. The spot could be pulsed with variable dwell time and prf. The emitted light was focused onto the entrance slit of a  $0.25\text{m}$  grating monochromator and detected by a photomultiplier with a  $1 \text{ k}\Omega$  load. The signal/noise ratio was improved by averaging the output in a Hewlett-Packard 5480B multichannel signal analyzer with a time resolution of  $10 \mu\text{sec/channel}$ . The stored signal could then be displayed on a chart recorder. With this instrumentation it was possible to observe the light output profile throughout the electron beam pulse, and to measure decay times on switching off the pulse. All measurements were made at room temperature and with a  $20 \text{ kV}$  gun potential.

The phosphor was either gravity-settled through a dilute silicate binder using standard methods (18) onto small conducting glass or aluminum substrates, or dusted onto a thin layer of conducting silver-loaded epoxy adhesive (Johnson-Matthey Chemicals Ltd.) spread on an aluminum disk. The substrates were approximately  $1 \text{ cm}^2$  in area and the coverage approximately  $8 \text{ mg cm}^{-2}$ . The substrates bearing the phosphor samples were fixed to a rotating metal sample holder by conducting silver-DAG, so that each could be brought under the beam in turn. The samples were not aluminized, and were viewed from the electron-beam irradiated side.

Photoluminescence measurements were made in this laboratory by excitation at  $350\text{--}360 \text{ nm}$  with u.v. lines of an  $\text{Ar}^+$  laser used in conjunction with a u.v. band pass filter to remove interfering visible fluorescence lines, and by excitation at  $250 \text{ nm}$  with the monochromated output of a  $150\text{W}$  Xe arc source at GEC Ltd. Photoluminescence decay times were obtained using a  $\text{N}_2$  laser producing pulses with  $2 \text{ nsec}$  half-width at  $337 \text{ nm}$ . Variable temperature measurements were made using a commercial temperature controller in conjunction with an electrically heated sample mount.

### Results

Figure 3(a) shows the temperature dependence of the emission intensity from  $^5\text{D}_2$ ,  $^5\text{D}_1$ , and  $^5\text{D}_0$  states of  $\text{Eu}^{3+}$  for  $250 \text{ nm}$  excitation (19), and emphasizes the particular sensitivity of the  $^5\text{D}_2$  state in this temperature range. The system shows the same behavior under  $350\text{--}360 \text{ nm}$  excitation using the  $\text{Ar}^+$  laser, which excites into the CT band directly. The special role played by the CT state in feeding the  $^5\text{D}$  states has been discussed by Struck and Fonger (13, 14) and explains why excitation by electrons or photons at energies equal to or higher than the CT state energy produce the same relative emission intensities from the various  $^5\text{D}$  states of  $\text{Eu}^{3+}$  in  $\text{Y}_2\text{O}_2\text{S}$ .

Figure 3(b) shows the variation with temperature of the photoluminescence decay times. The data for  $^5\text{D}_2$  became uncertain at the higher temperatures because

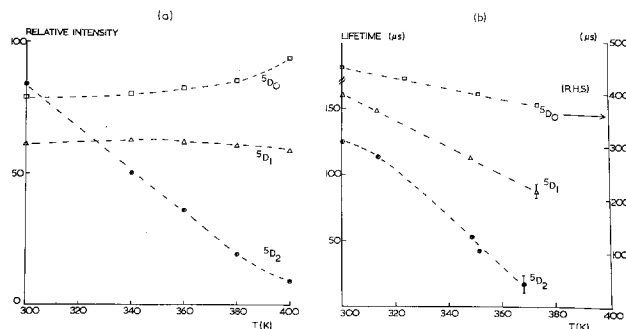


Fig. 3. Temperature dependence of PL of  $^5\text{D}_2$ ,  $^5\text{D}_1$ , and  $^5\text{D}_0$  states. (a) Relative intensity under  $250 \text{ nm}$  excitation. (b) Lifetime under  $337 \text{ nm}$  pulse excitation. ( $^5\text{D}_2$ ,  $^5\text{D}_1$ —L.H. scale,  $^5\text{D}_0$ —R.H. scale.) Quoted lifetimes are approximations to simple exponential behavior (see text).

the decay time approaches the resolution limit of the detection system used. With the time resolution available (10  $\mu\text{sec}/\text{channel}$ ) the rise time of the  ${}^5\text{D}_2$  state in response to the  $\text{N}_2$  laser pulse excitation was too fast to be measured, but the  ${}^5\text{D}_1$  and  ${}^5\text{D}_0$  emissions showed delayed buildup periods of approximately 50  $\mu\text{sec}$  and 200  $\mu\text{sec}$ , respectively, before the maxima in the emission intensity were reached. The reason for this difference in behavior is that the  ${}^5\text{D}_1$  and  ${}^5\text{D}_0$  states are fed partially or wholly via higher lying f-electron states with relatively slow relaxation rates, whereas the  ${}^5\text{D}_2$  state is fed principally from the CT state (13). The quoted decay times for the various states were measured over approximately one decade from the maxima in the response curves. The decays were reasonably approximated by exponential functions over this range, but since the decay characteristics of the  ${}^5\text{D}_1$  and  ${}^5\text{D}_0$  states are not simple first order decays from the end of the excitation pulse it is clear that the quoted decay times are not simply the characteristic decay times of the emitting states, but rather some combination of these.

Figure 4 shows typical measurements of the light output characteristics of the same  $\text{Y}_2\text{O}_3\text{S:Eu}$  (0.1%) phosphor material mounted in different ways and exposed to 30 msec electron beam pulses of increasing current density with a 300°K phosphor mount temperature. The behavior of lines originating from the  ${}^5\text{D}_2$  and  ${}^5\text{D}_1$  states only are shown for clarity, the  ${}^5\text{D}_0$  state having a characteristic very similar to that of  ${}^5\text{D}_1$ .

Consider first the results in Fig. 4(a) for phosphor settled through silicate binder onto a conducting glass substrate (similar results were obtained using aluminum substrates). Recalling the earlier discussion, the light output would be expected to rise, reaching a steady state in a time  $\sim 1$  msec, and, in the absence of other perturbation to stay constant though the pulse and finally decay rapidly at the end of the pulse. This is in fact the characteristic observed at the lowest beam currents, but as the current density is increased a "droop" appears in the output which would cause a sublinear increase in integrated light output with current density, i.e., a saturation effect. This droop is sensitive to the settling process, since the characteristic varied a little over the sample surface and a sample settled independently showed a more accentuated form of droop. For the samples reported in Fig. 4(a), the form of the droop was reasonably constant in time and the results were reproducible on increasing and subsequently decreasing the beam current within the quoted limits. There was a slow general decrease in over-all intensity of all the lines after prolonged exposure to the beam; this may have resulted from beam induced damage or contamination, or from the kind of energy storage phenomena described by Struck and

Fonger (20) leading to a depletion of the ground state activator concentration.

When the pulse length was shortened to 10 msec the light output obtained was the same as the curves for the first 10 msec period in Fig. 4(a), followed by rapid decay on switching off the pulse. The droop is also characteristic only of the excited state involved since the form of the curves was found to be independent of the final level when emissions from  ${}^5\text{D}_2$  to several components of the  ${}^7\text{F}$  ground state were measured. This shows that the droop is not the result of self-absorption phenomena caused by an increase in population of components of the  ${}^7\text{F}$  state just above the ground state (12).

At first sight it might appear that the droop is caused by a temperature rise through the pulse, and indeed previous reports of similar droop phenomena attributed them to thermal perturbation (11). However, consideration of the following points shows that this is unlikely to be the cause in our experiment:

1. The droop becomes significant for both  ${}^5\text{D}_2$  and  ${}^5\text{D}_1$  (and  ${}^5\text{D}_0$ ) states at approximately the same beam current, and although the droop of the  ${}^5\text{D}_2$  emission is greater than that of  ${}^5\text{D}_1$  the latter is quite substantial. The  ${}^5\text{D}_2$  state however is much more sensitive to temperature than  ${}^5\text{D}_1$  [see Fig. 3(a)], and indeed the intensity of emission from the latter is little changed over a temperature range which virtually quenches  ${}^5\text{D}_2$  emission. For a thermal perturbation one would therefore expect a large droop in the  ${}^5\text{D}_2$  characteristic before any significant effect on  ${}^5\text{D}_1$  occurred, and this conflicts with the experimental observation.

2. At higher currents the droop increases and the system tends to approach a limiting or equilibrium light output for long pulses which is not very sensitive to beam current. Again this is not expected for a thermal perturbation since the maximum temperature reached during the pulse should increase approximately linearly with beam current density (see Eq. [1]) and it would be necessary to argue that the increased pumping rates at higher current were exactly offset by increased thermal quenching. In fact this behavior is more characteristic of an electrical charging phenomenon, which would approach a steady state determined by the capacitance of the sample.

3. The droop observed is similar for phosphor settled on conducting glass and on aluminum substrates, i.e., is insensitive to the thermal conductivity of the substrate.

4. The power from the d-c  $\text{Ar}^+$  laser used in PL measurements corresponded to an excitation density of approximately  $1\text{W cm}^{-2}$ , which is only a factor of 2-3 smaller than the highest mean excitation density used in the electron beam experiments. The PL temperature dependence data taken with the  $\text{Ar}^+$  laser were the

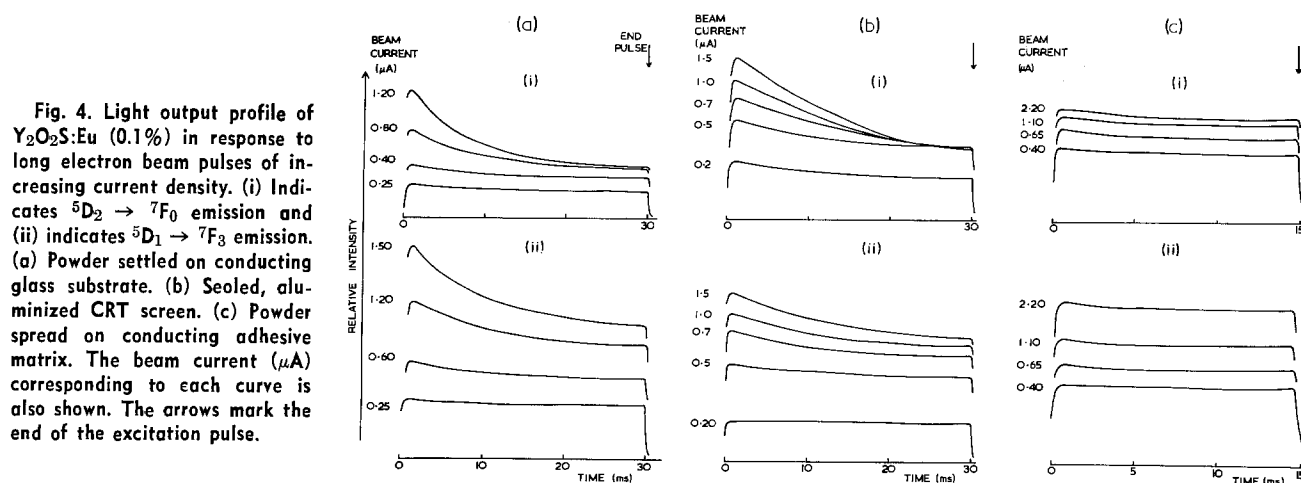


FIG. 4.

same as those taken at much lower power density with the monochromated Xe arc, showing that this level of excitation density does not produce significant perturbation of the luminescence process under photon excitation.

True activator saturation phenomena would not produce a droop characteristic, and it is unlikely that the droop can be caused by a depletion of the ground state activator concentration following CT dissociation and long-term energy storage (20), since this would affect all the  $^5D$  states equally and produce considerable changes in the light output characteristic as the number of pulses to which the sample was exposed increased. This was not observed in the measurements taken at 10 Hz prf. However since there is some evidence that the droop is associated with electrical charging effects, there exists the possibility that it is an artifact of the demountable system using nonaluminized samples. To eliminate this possibility sealed aluminized CRT screens were prepared by Ferranti Ltd. (Special Components Department) using the same phosphor material. The excitation conditions used in the demountable system were reproduced in the CRT, and the results are shown in Fig. 4(b) (21). These results are in excellent qualitative agreement with the demountable measurements, and show that the droop effect is not significantly altered by aluminizing the sample.

Two experiments were then carried out to test the sensitivity of the system to electrical perturbation. In the first the phosphor was lightly dusted onto a thin layer of conducting epoxy adhesive spread on an aluminum disk, and the excess shaken off. Any particles adhering were then in intimate contact with the conducting adhesive, so that the surface electrical properties of the particles were presumably quite different from those of the settled material. The light output observed on applying a long electron beam pulse is shown in Fig. 4(c), and it is clear that there is no significant droop. The mean brightness of these samples was also lower, probably as a result of the electric-field-induced quenching effects discussed later. However it is clear that changing the electrical properties of the phosphor layer markedly affects the droop characteristic.

In the second experiment a sandwich cell was constructed so that an electric field could be applied to the phosphor while it was being excited into the charge transfer state by the  $Ar^+$  laser (Fig. 5). The phosphor was settled in silicate binder onto a conducting glass plate which formed a transparent electrode transmitting the laser beam. The electrodes were nonblocking, and an a-c field was used to prevent polarization. With no field applied, the phosphor gave a steady d-c

light output level. However on applying 200V a.c. (rms) at 50 Hz, the light output was modulated at twice the field frequency as shown schematically in Fig. 5(b). At this field there was no interference from electroluminescence (EL), although a weak ACEL signal was observed at a field of 230V.

It should be noted that the light output is a maximum whenever the applied field is zero, and is partially quenched by any nonzero field. The form of the modulation was basically similar for all the  $^5D_j$  ( $j = 2,1,0$ ) states, the peak-peak modulation as a fraction of the unmodulated d-c light level being shown in Table I. Hence all three states are sensitive to the application of an electric field, the  $^5D_2$  being slightly more sensitive. This is in fact the same relative pattern of behavior as is observed in the drooping under electron beam excitation. Thus whereas the droop phenomenon cannot be explained by a thermal perturbation of the system kinetics the experimental data are entirely consistent with an electrical perturbation. The nature of this perturbation, and a possible model, are discussed in more detail below.

### Electric Field Effects on Cathodoluminescence

The quenching of both PL and CL of phosphor materials by electric fields is a well-known phenomenon and has been extensively reviewed by Ivey (22). Both bulk conductivity and surface effects may be important when considering the effects on the luminescence process. For example Dean and Male (23) have demonstrated a correlation between the bulk electrical conductivity of diamond, measured as conduction counting efficiency, and the electric field induced quenching of  $\beta$ -scintillations, the electric fields extracting secondary carriers and causing spatial separation of electrons and holes. Similarly Satchell (24) has shown that electric field modulation of the CL of ZnS:Mn crystals only occurred when the whole crystal volume between the electrodes was excited by the electron beam, i.e., when the bulk conductivity in the interelectrode region was increased by excitation.

The importance of surface effects has been shown in many ways. Kallman and his collaborators (25) have made extensive investigations of the changes in electrical conductivity which can occur when fields are applied to excited phosphors, and have shown that a state of "persistent internal polarization" can be created by separation of charges in the bulk material. Accumulation of charge at the natural barrier formed by the crystal surface may occur, and could be particularly important in powder material with a large surface/volume ratio. Charge storage near the surface of ZnS crystals has similarly been directly demonstrated (26), and in 1956 Lapovsky *et al.* (27) postulated that space charges were created in a phosphor screen during exposure to the electron beam, and that these space charges acted to control the secondary electron emission ratio of the screen. This postulate was necessary in order to explain the lack of a definite "sticking potential" for nonaluminized powder screens.

There have also been more direct demonstrations of the effect of surface charges on luminescence. For example Sedgwick (28) has shown that both quenching and enhancement of luminescence in ZnO can occur according to whether the surface is charged negative or positive by corona discharge, and the importance of space charge in the surface region of II-VI crystals in controlling both the Gudden-Pohl memory and luminescence quenching has been discussed by Peka and Proskura (29).

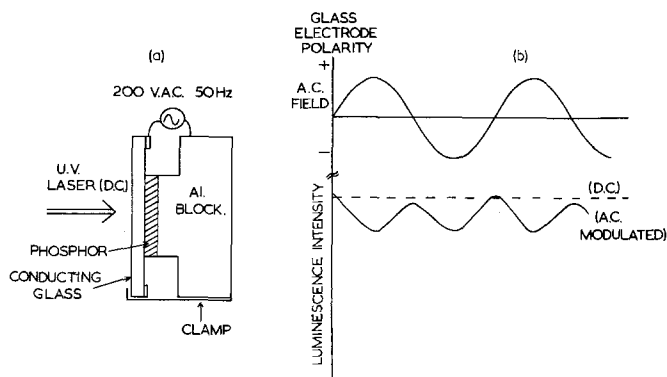


Fig. 5. (a) Sandwich cell structure used in a-c electric field modulation of PL under  $Ar^+$  laser excitation. (b) Upper curve shows phase of applied electric field. Lower curves show schematically the PL output in the absence of field (---) and when a field is applied (—). The form of the modulation is similar for all  $^5D$  states.

Table I. Approximate percentage modulation of PL intensity by application of an a-c electric field to  $Y_2O_3:Eu(0.1\%)$

$^5D_2$	16
$^5D_1$	11
$^5D_0$	10

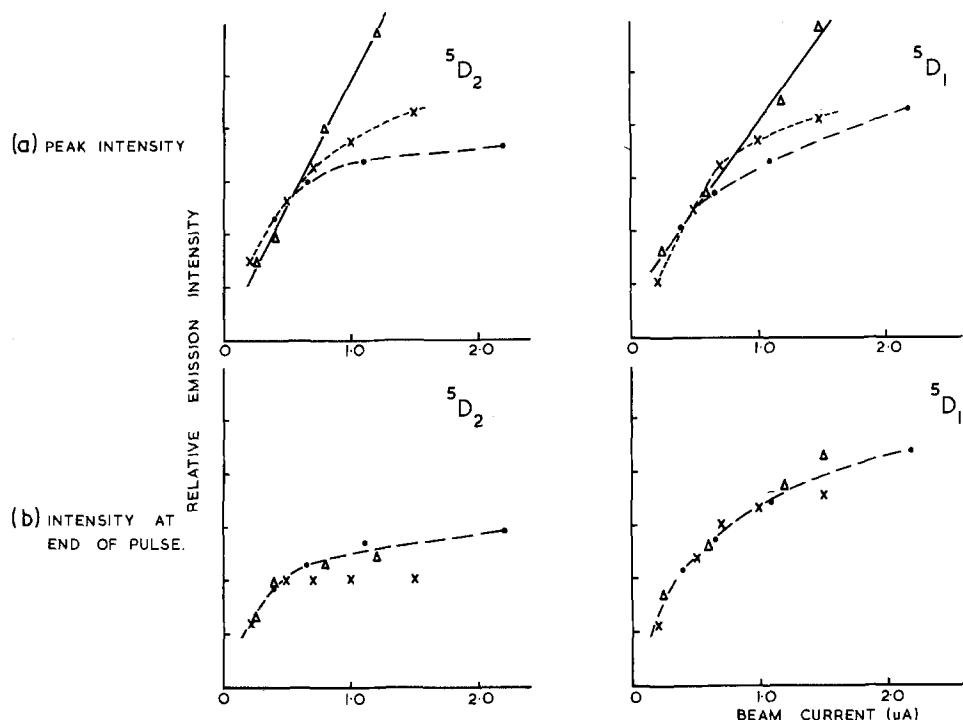
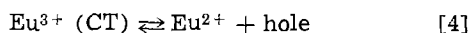


Fig. 6. Current saturation of  $Y_2O_2S:Eu(0.1\%)$  plotted from Fig. 4.  $\Delta$  = Powder settled on conducting glass substrate;  $\times$  = sealed, aluminized CRT screen;  $\bullet$  = powder spread on conducting adhesive matrix. (Curves normalized at  $0.5 \mu A$ .)

There is thus a considerable accumulation of evidence to support the idea that some electrical perturbation could quench the light output and therefore be responsible for the droop phenomenon in  $Y_2O_2S:Eu$ , and that this perturbation might be caused by the buildup of surface charge and associated space charge fields under electron beam bombardment. The effects on the saturation characteristics of the phosphor are shown in Fig. 6, where the peak light intensity and the intensity at long times after the onset of the electron beam pulse are plotted as a function of beam current for the materials whose output profiles are given in Fig. 4 (30). The significant points are: (i) The saturation of both  $^5D_2$  and  $^5D_1$  emission is generally more pronounced at long times, except for the epoxy-mounted material which shows the same behavior throughout the pulse. (ii) Emission from the  $^5D_2$  state shows greater saturation effects than that from  $^5D_1$  (or  $^5D_0$ ). (iii) At short times after the onset of the pulse the nonaluminized settled sample shows the least, and the epoxy-mounted material the greatest saturation, the aluminized screen being intermediate between these two. At long times all the samples reach an equilibrium output and show similar saturation behavior for any particular emitting state.

There are two particular experiments which provide useful guidelines for developing at least a qualitative explanation of these effects in  $Y_2O_2S:Eu$ . First, Struck and Fonger (20) have shown that the CT state can be thermally ionized leading to energy storage by charge separation and trapping; secondly, Dobrov and Buchanan (31) have shown that excitation into both the CT state and into the  $^5D_2$  state produces photoconductivity in  $La_2O_2S:Eu$  single crystals, and that there is a correlation between the temperature dependence of the photoconductive response for  $^5D_2$  excitation and thermal quenching of the  $^5D_2$  state. In contrast excitation of  $^5D_1$  and  $^5D_0$  does not lead to conductivity at  $300^\circ K$ . Both experiments suggest that the dissociation



produces mobile holes as majority carriers.

In order to explain the experimental results reported above we therefore propose the following model: that accumulation of charge in surface states of the  $Y_2O_2S:Eu$  phosphor generates electric fields within the powder grains which can accelerate dissociation of the CT

state, creating charge separation, and which can cause quenching of the  $^5D_2$  state directly. By analogy with the photoconductive response of  $La_2O_2S:Eu$ , there would be no significant direct emptying of the  $^5D_1$  and  $^5D_0$  states by these fields at  $300^\circ K$ . The precise form of the electric fields is not clear, but it is possible that accumulation of negative charge in surface states of the grains would cause drift of the mobile holes towards the surface region, and would markedly affect the nature of the surface states and surface potential which largely determine the nonradiative recombination probability for excess carriers reaching the particle surface. The data in Fig. 6 may then be interpreted to mean that there exist surface states of  $Y_2O_2S:Eu$  lying above the Fermi level which can be filled either by capture of low energy secondary electrons generated by the incident beam, as in the conventionally settled material, or by intimate contact with the silver-loaded epoxy adhesive which is assumed to have a Fermi level above the surface states. In the latter case the states are filled irreversibly before excitation so that the incident beam has little further effect on the surface potential, the equilibrium light output characteristic of the quenched state is reached instantaneously, and no droop is observed. When the phosphor is settled in the normal way, however, the surface states are largely empty and come to equilibrium relatively slowly following application of the electron beam as low energy secondary electrons are trapped. In this case the light output initially rises rapidly towards some steady-state level characteristic of the phosphor with empty surface states, but is then quenched towards the new equilibrium value as the surface states are filled. The traps fill and empty reversibly during the duty cycle, giving rise to the observed droop behavior. When the traps are filled by either mechanism the phosphor shows a common saturation behavior, as shown by Fig. 6(b), i.e., the states induced by a long pulse and by mixing with a conducting matrix are similar.

The qualitative effect of the space charge field associated with the filled surface traps on the relative populations of the  $^5D_j$  states may be illustrated in the following way. In the absence of electric field perturbation and activator ion saturation the steady-state populations of the CT state and the  $^5D_j$  states may be written as



$$C = \frac{G + \sum_j a_{jc} D_j}{\sum_j a_{cj}} \quad [5]$$

$$D_j = \frac{a_{cj} C + \sum_{j'} a_{j,j'} D_{j'}}{a_{jc} + a_j} \quad [6]$$

where  $G$  is the rate of CT excitation,  $a_{cj}$  is the cross-over rate from the CT state to  ${}^5D_j$  etc.,  $a_j$  is the sum of rates for all downward transitions from  ${}^5D_j$ ,  $a_{jc} \propto a_{cj} \exp[-E_j/kT]$ , and  $E_j$  is the energy gap between the CT state and  ${}^5D_j$ . The effects of an electric field can be introduced in a simplified fashion if we assume that the induced field is a function of both beam current and pulse length

$$E = E(I, t) \quad [7]$$

and that it approaches some steady value  $E^0$  for sufficiently long pulses. The steady-state equations [5] and [6] would then be modified to include field-dependent term

$$C^e = \frac{G + \sum_j a_{jc} D_j^e}{\sum_j a_{cj} + a_{ce} E^0} \quad [8]$$

$$D_j^e = \frac{a_{cj} C^e + \sum_{j'} a_{j,j'} D_{j'}^e}{a_{jc} + a_j + a_{je} E^0} \quad [9]$$

where  $a_{ce}$  and  $a_{je}$  represent rates of field-induced loss processes from the CT state and from  ${}^5D_j$ . In fact the photoconductivity data show that at 300°K  $a_{je}$  is only significant for  $j = 2$ , i.e., for the  ${}^5D_2$  state (31). Analysis of these equations shows that an electric field will lead to quenching of the steady-state populations of the CT state and of all  ${}^5D_j$  states ( $j = 2, 1, 0$ ). Because of the term in  $a_{2e}$ , however, the  ${}^5D_2$  state is quenched to a greater extent than  ${}^5D_1$ , and  ${}^5D_0$ , these latter states being expected to behave rather similarly. This is in qualitative agreement with the droop behavior of the lines (Fig. 4) and with the observed modulation of the line intensities by an applied a-c field (Table I).

### Discussion

We first consider the relevance of these observations to practical CRT screens (6). The dwell time of the beam at TV scan rates is of the order  $0.5-1.0 \times 10^{-7}$  sec, much shorter than the pulses used in our experiments, so that the results reported here are more directly relevant to slow writing speeds or cursive displays. However the rate of filling of surface traps will rise with beam current, and at moderate drive currents in CRT's ( $\sim 1-5$  A cm $^{-2}$ ) total charge dosage similar to that in our experiments could be delivered during a short dwell time. Charge loss by leakage would certainly be less during a short excitation period. Hence the light output from the CRT screen might be perturbed by these effects if sufficient charge were deposited during the dwell time to change significantly the surface potential, or if the surface states were relatively slow to relax so that a gradual accumulation occurred during screen operation. The existence of a state of persistent internal polarization in phosphor materials is evidence of the possibility of such long-lived space-charge fields. The concept of space-charge fields may also be relevant to the irreversible loss in light output often observed in CRT screens, i.e., to the problem of aging. Laponsky *et al.* (27) have shown that during the life of a nonaluminized tube the secondary electron emission ratio is changed, and it was suggested that this was caused by changes in the space-charge fields in the phosphor layer affecting the "sticking potential." It is therefore conceivable that as the total charge dosage received by the screen increases the nature of the phosphor surface states and the space-charge distribu-

tion are changed in such a way as to produce greater perturbation of the light output. For example any residual organic matter on the phosphor after aluminizing, the silicate binder, or the phosphor itself could be gradually decomposed by the beam, thereby changing the effective surface properties of the screen. Indeed the decomposition of willemite has recently been reported under electron beam bombardment (32).

In order to reduce these field-induced quenching effects one might conceive the preparation of phosphor particles essentially free of surface trapping states, or with bulk conductivities sufficiently large to screen the interior of the particle from the surface potential. It might also be possible to include in the screen a material with a Fermi level lying below the level of the phosphor surface states in such a way that it acts as a sink for emptying these states, rather than filling them as in the case of the silver-epoxy. In addition however it is probable that CRT screening methods can affect the surface properties and hence the saturation characteristics of the phosphor, since from Fig. 6 it can be seen that the degree of saturation of the sealed CRT at short times after application of the electron beam pulse is worse than that of the nonaluminized settled material. The implication is therefore that the screening process leads to partial filling of the existing surface traps in the material, or changes the nature or number of these traps so that they are more rapidly filled by the incident beam.

Finally we note that the proposed quenching mechanism, involving field-induced ionization of the CT state and subsequent spatial separation of electrons and holes, is formally similar to the Poole-Frenkel effect in semiconductor materials, in which the ionization energy of a donor is lowered by an applied electric field (33). It should be noted that the activator concentration in this investigation has been kept deliberately low so that emission from the  ${}^5D_2$  state could be observed. This situation is probably favorable to field-induced quenching since the diffusion length of separated electrons and holes will not then be limited by retrapping at activator sites, with subsequent light emission. The droop effect reported here may then be less significant at higher activator concentrations. Similarly the inclusion of co-dopants in the lattice could affect the electrical properties of the phosphor, and in this connection it is of interest to note the report by Yamamoto *et al.* (34) that small quantities of  $\text{Pr}^{3+}$  or  $\text{Tb}^{3+}$  in  $\text{Y}_2\text{O}_3\text{S:Eu}$  reduced the current saturation of the phosphor. These ions are often considered to act as hole trapping centers and may therefore limit the field-induced drift of holes towards nonradiative recombination centers in  $\text{Y}_2\text{O}_3\text{S:Eu}$ .

### Conclusions

It has been shown that the saturation characteristics of conventionally settled  $\text{Y}_2\text{O}_3\text{S:Eu}$  (0.1%) are different at short and long times after the onset of electron beam excitation, and that the transition between the two limits is associated with a droop in the CL light output during long electron beam pulses. This droop and the associated saturation cannot be caused by an increase in phosphor temperature as commonly suggested for other systems (11), since the data are not consistent with the known differential thermal behavior of the various excited  ${}^5D_j$  states. Neither can the droop be explained by depletion of the activator ground state population, nor by gross charging effects because the phenomenon is also observed in an aluminized screen.

Since none of the conventional models of current saturation can successfully account for these observations, a new model has been proposed. In this model saturation is the result of kinetic perturbations caused by space-charge electric fields which are themselves created by the filling of surface states in the phosphor



particles. These states may be filled either by application of sufficient charge to the phosphor, as during prolonged pulses of low current density, or by intimate mixing of the phosphor with a material having a relatively high Fermi level, e.g., the silver-loaded epoxy adhesive. Whatever the means of filling the traps, the data in Fig. 4 and 6 show that the result is to produce a quenched light output, and a common saturation curve. Predictions based on a simple kinetic model involving field-induced ionization of the CT state and quenching of the  $^5D_2$  state are in qualitative agreement with the observed droop characteristics. Such a model would be consistent with the general observation that CL saturation effects are greater at lower beam potentials (1), since the excitation is then produced nearer the surface and the system kinetics will be more sensitive to the surface potential. Improved control of the surface properties of a phosphor may therefore produce both better saturation characteristics and higher efficiency under low energy excitation.

At sufficiently high current densities of course an appreciable temperature rise may also occur at the screen. What we suggest here is that saturation phenomena may be caused by space-charge field effects at more moderate current densities, before significant heating takes place, if the particular activator/lattice combination involved is itself susceptible to electric field quenching of the luminescence.

#### Acknowledgments

The author is grateful to Dr. P. Greenough (GEC Ltd., Hirst Research Centre) for preparation of the phosphor material used in this study, and for measurement of the data in Fig. 3(a). He is also grateful to Mr. J. Leyland (Ferranti Ltd., Special Components Dept.) for the data in Fig. 4(b), and to Dr. P. J. Dean (RRE) for many helpful discussions.

Manuscript submitted Jan. 9, 1976; revised manuscript received April 12, 1976. This was Paper 429 RNP presented at the Toronto, Canada, Meeting of the Society, May 11-16, 1975.

Any discussion of this paper will appear in a Discussion Section to be published in the June 1977 JOURNAL. All discussions for the June 1977 Discussion Section should be submitted by Feb. 1, 1977.

#### REFERENCES

- H. W. Leverenz, "An Introduction to Luminescence of Solids," J. Wiley & Sons, Inc., New York (1950).
- G. F. J. Garlick, in "Luminescence of Inorganic Solids," P. Goldberg, Editor, Academic Press, New York (1966).
- V. D. Meyer and F. Palilla, *This Journal*, **116**, 535 (1969).
- E. F. Gibbons, R. G. DeLosh, T. Y. Tien, and H. L. Stadler, *ibid.*, **120**, 1730 (1973).
- S. Larach and A. E. Hardy, *Proc. IEEE*, **61**, 915 (1973).
- M. Stevens, L. Ozawa, G. Ban, and H. N. Hersh, *IEEE Trans. Consum. Electronics*, **21**, 1 (1975).
- O. J. Sovers, S. Yokono, and T. Yoshioka, Abstract 123, p 303, The Electrochemical Society Extended Abstracts, Spring Meeting, San Francisco, Calif., May 12-17, 1974.
- J. S. Jayson and R. Z. Bachrach, *Phys. Rev.*, **B4**, 477 (1971) and references therein.
- A. Bril, *Physica*, **15**, 361 (1949).
- M. Sayer, *Proc. Phys. Soc.*, **78**, 1017 (1961).
- P. A. Einstein, *Brit. J. Appl. Phys.*, **8**, 190 (1957).
- L. Ozawa and H. N. Hersh, *This Journal*, **122**, 1222 (1975).
- C. W. Struck and W. H. Fonger, *J. Luminescence*, **1**, 2, 456 (1970).
- W. H. Fonger and C. W. Struck, *J. Chem. Phys.*, **52**, 6364 (1970).
- G. D. Archard and P. A. Einstein, *Brit. J. Appl. Phys.*, **8**, 232 (1957).
- H. S. Carslaw and J. C. Jaeger, "Conduction of Heat in Solids," Oxford University Press, Oxford (1959).
- D. J. Robbins, B. Cockayne, B. Lent, and C. N. Duckworth, To be published.
- W. Espe, "Materials of High Vacuum Technology," Vol 3, Pergamon Press Ltd., Oxford (1968).
- P. Greenough, Private communication.
- C. W. Struck and W. H. Fonger, *Phys. Rev.*, **B4**, 22 (1971).
- J. D. Leyland, Private communication.
- H. F. Ivey, "Electroluminescence and Related Effects" in "Advances in Electronics and Electron Physics" Supplement 1, Academic Press, New York (1963).
- P. J. Dean and J. C. Male, *J. Phys. Chem. Solids*, **25**, 311, 1369 (1964).
- D. W. Satchell, *Brit. J. Appl. Phys.*, **13**, 589 (1962).
- J. R. Freeman, H. P. Kallman, and M. Silver, *Rev. Mod. Physics*, **33**, 553 (1961) and references therein.
- W. Ehrenberg and R. P. Shrivastava, *J. Phys.*, **D6**, 2079 (1973).
- A. B. Laponsky, M. J. Ozeroff, W. A. Thornton, and J. R. Young, *This Journal*, **103**, 498 (1956).
- T. O. Sedgwick, *ibid.*, **121**, 452 (1974).
- G. P. Peka and A. I. Proskura, *J. Luminescence*, **8**, 164 (1973).
- The author is grateful to the referee for pointing out the significance of plotting the data in this form.
- W. I. Dobrov and R. A. Buchanan, *Appl. Phys. Letters*, **21**, 201 (1972).
- J. M. Hurd Paper 88, p. 220, The Electrochemical Society Extended Abstracts, Spring Meeting, San Francisco, Calif., May 12-17, 1974.
- N. F. Mott and E. A. Davis "Electronic Processes in Non-Crystalline Materials", Clarendon Press, Oxford (1971).
- H. Yamamoto, T. Kano, Y. Otomo, and K. Urabe, Proc 9th Rare Earth Res Conference 503 (1971).

# Submicron GaAs Epitaxial Layer from Diethylgalliumchloride and Arsine

Yoshiro Nakayama, Shinji Ohkawa, Hisao Hashimoto, and Hajime Ishikawa\*

Fujitsu Laboratories Limited, Nakahara-ku, Kawasaki, Japan 211

## ABSTRACT

A submicron GaAs epitaxial layer has been grown using diethylgalliumchloride (DGC) and arsine on semi-insulating substrates. Layers with a mirror-smooth surface have been grown at a low temperature of 530°C. The growth rate can be controlled and 0.01  $\mu\text{m}/\text{min}$  is easily obtained by adjusting the temperature of the DGC source. The epitaxial layer without intentional doping is n-type and carrier concentration depends on the mole ratio of arsine to DGC in the gas introduced into the reactor. The mole ratio dependence of carrier concentration shows the opposite tendency to that in the growth using TMG or TEG. Carrier profile with steep decrease at the interface is obtained in the epitaxial layer.

The epitaxial growth of GaAs from an alkylgallium compound and arsine has the following advantages over growth in a Ga-AsCl<sub>3</sub>-H<sub>2</sub> system: (i) a simple apparatus having only one high temperature zone, (ii) a relatively low growth temperature which decreases the autodoping effect, and (iii) ease of heteroepitaxy (1, 5). In most studies concerned with this growth technique, trimethylgallium, (CH<sub>3</sub>)<sub>3</sub>Ga (TMG), or triethylgallium (C<sub>2</sub>H<sub>5</sub>)<sub>3</sub>Ga (TEG), was used as a gallium source (1-6). A very thin GaAs epitaxial layer is required for microwave electronic devices, e.g., a 0.2-0.3  $\mu\text{m}$  thick layer for field effect transistors. Diethylgalliumchloride, (C<sub>2</sub>H<sub>5</sub>)<sub>2</sub>GaCl (DGC), has lower vapor pressure and lower reactivity than TMG and TEG (7), properties of which are well suited to obtaining such a thin layer. This paper reports the growth characteristics and the electrical properties of the submicron GaAs epitaxial layer grown on (100) oriented semi-insulating GaAs substrate using DGC as the gallium source and arsine as the arsenic source.

## Experimental Conditions

**Growth apparatus.**—The growth apparatus is schematically shown in Fig. 1. The reactor is a horizontal quartz tube containing a SiC-coated carbon susceptor heated inductively. The diameter and the length of the tube are 63 mm and 80 cm, respectively. DGC was obtained commercially and used without further purification. Vapor of DGC was transported to the substrate by bubbling nitrogen gas through the liquid DGC. The concentration of the DGC vapor was controlled by heating the bubbler and/or by varying the flow rate of the bubbling gas. The temperature of the bubbler was in the range of room temperature to 60°C. The concentration of DGC was determined from amounts of CO and CO<sub>2</sub> formed by the reaction of DGC on oxygen. The mixture of nitrogen through the liquid DGC and oxygen at a flow rate of 100 ml/min was heated to 800°C. At this temperature, carbon atoms in the DGC molecule reacted on oxygen and became CO and CO<sub>2</sub>, amounts of which were determined by the gas phase chromatography. Arsine diluted to 1% in nitrogen gas was mixed with DGC vapor just before entering into the reactor. In addition, hydrogen gas at a flow rate of 1000 ml/min and nitrogen gas were used as carrier gases. The flow rate of the nitrogen gas was controlled to make the total gas flow rate constant, 2500 ml/min. In this system, oxygen and water were eliminated by passing through a purifier. Concentrations of oxygen and water in the carrier gas after purification were less than 2 and 5 ppm, respectively.

\* Electrochemical Society Active Member.

Key words: chemical vapor deposition, organic gallium source, gallium arsenide.

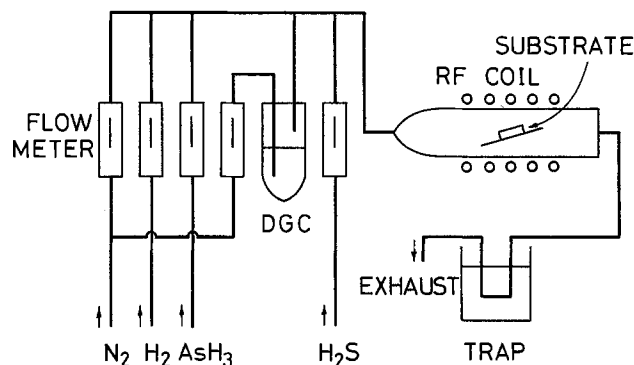


Fig. 1. Schematic of growth apparatus

Stainless steel tubing is widely used in the growth apparatus when TMG or TEG is employed as a gallium source. In this experiment, however, Teflon tubing was used because DGC potentially reacts on stainless steel.

**Procedure.**—The epitaxial growth was carried out on the boat-grown semi-insulating GaAs substrate doped with chromium. The orientation of the substrate was (100) or 2° off from (100) to (110). The substrate was obtained commercially with one face polished and was etched to remove 20-30  $\mu\text{m}$  from the depositing surface with H<sub>2</sub>SO<sub>4</sub>:H<sub>2</sub>O<sub>2</sub>:H<sub>2</sub>O (90:5:5) etchant just before the deposition. The substrate was placed on the susceptor and heated in the hydrogen-nitrogen mixture. When the temperature of the substrate was raised to 500°C, arsine was introduced into the reaction tube to prevent substrate decomposition. At a desired temperature, the substrate was maintained for additional 10 min before the introduction of DGC. Arsine flow was continued until the temperature dropped to 500°C after the growth had been completed. In this procedure, the temperature was monitored by an optical pyrometer. The error of the temperature measurement was less than 5° at 550°C.

**Thickness determination.**—The thickness of a grown layer was determined by the following methods.

(i) A substrate was partly covered with 2000Å thick SiO<sub>2</sub> film. After the growth, the SiO<sub>2</sub> film was etched off and the thickness of the epitaxial layer was determined by Talystep (Taylor Hobson). The layer was thicker near the edge of the covering SiO<sub>2</sub> film; therefore, thickness was measured at a distance of more than 500  $\mu\text{m}$  from the edge.

(ii) A cleaved plane was stained by HF:H<sub>2</sub>O<sub>2</sub>:H<sub>2</sub>O (1:1:10) staining solution. The thickness of the stained layer was measured by a microscope. For a submicron

layer, scanning electron microscope was employed to determine the thickness.

(iii) Schottky barriers were formed on the grown layer. The thickness of the layer was obtained from the carrier profile determined by  $C-V$  measurement. This method was used only for the sample in which the depletion region reached the interface between substrate and epitaxial layer within the breakdown voltage of the Schottky barrier.

### Growth Characteristics

**Surface feature.**—In the case of growth without hydrogen gas, the surface of a wafer appeared to be brownish. This was caused by a thin film covering the surface, which was not etched with an etchant for GaAs. By introduction of hydrogen gas into the reactor, deposition of this thin film was eliminated. These results show that the carbon from the ethyl radical in a DGC molecule is deposited on the wafer. This may be interpreted as follows: in the reaction system without hydrogen, partial pressure of nitrogen is high because nitrogen gas is used as the carrier and arsine is diluted with nitrogen. An ethyl radical in a DGC molecule may be thermally decomposed into carbon and hydrogen in this system. In order to prevent this decomposition, it is necessary to increase the partial pressure of hydrogen by introduction of hydrogen gas. Thus the ethyl radical forms a gaseous hydrocarbon such as ethane and is exhausted from the reactor.

Effects of the substrate off-orientation and the growth temperature on the surface feature were examined. A mirror-smooth layer was obtained on the substrate  $2^\circ$  off-oriented from (100) to (110) over the growth temperature of  $530^\circ$ – $600^\circ\text{C}$ , while many hillocks, as shown in Fig. 2(a), were observed in the layer deposited on the (100) oriented substrate over the same temperature range. For growth at a temperature higher than  $600^\circ\text{C}$  or lower than  $530^\circ\text{C}$ , a fine-ripple feature was observed even on  $2^\circ$  off-oriented substrate as shown in Fig. 2(b). The characterization of the epitaxial layer was carried out for the mirror-smooth layer in this experiment.

Electron diffraction patterns of the  $2\ \mu\text{m}$  thick layer were observed by the reflective method. A halo pattern was observed on the as-grown surface while Laue spots and Kikuchi lines were observed on a few hundred angstroms etched surface. This shows that the amorphous layer of a few hundred angstroms thick is formed on the as-grown layer. In the growth stage after stopping DGC flow, an anomalous growth may take place due to the imbalance between the concentrations of arsenic and gallium. This causes the thin amorphous layer at the surface.

**Growth rate.**—Growth was carried out under the following conditions: temperature of  $500^\circ$ – $700^\circ\text{C}$ , DGC flow rate of  $2 \times 10^{-6}$ – $1 \times 10^{-4}$  mole/min, and arsine flow rate of  $2 \times 10^{-5}$ – $3 \times 10^{-4}$  mole/min. The growth rate at the arsine flow rate of  $2 \times 10^{-4}$  mole/min is shown in Fig. 3 as a function of the growth temperature and the DGC flow rate. The growth rate is slightly changed with the growth temperature, but increases considerably with the DGC flow rate. The dependence of the growth rate on the DGC flow rate is linear. This shows that the growth rate is limited by the mass transport mechanism under the above conditions.

**Uniformity of thickness.**—The effect of a facing angle of the substrate to the gas flow on a thickness uniformity over the surface was examined. Curve 1 in Fig. 4 shows the thickness distribution of the epitaxial layer grown on the substrate which was placed parallel with the gas flow. The abscissa of Fig. 4 represents the distance from the upper edge of the substrate. The thicker layer is observed at the upper edge and the change in thickness is considerably large near the edge. Curve 2 shows the thickness distribution in the layer on the substrate placed perpendicular to the gas flow in the reactor. As can be seen, the uniformity of thickness was improved by placing the substrate per-

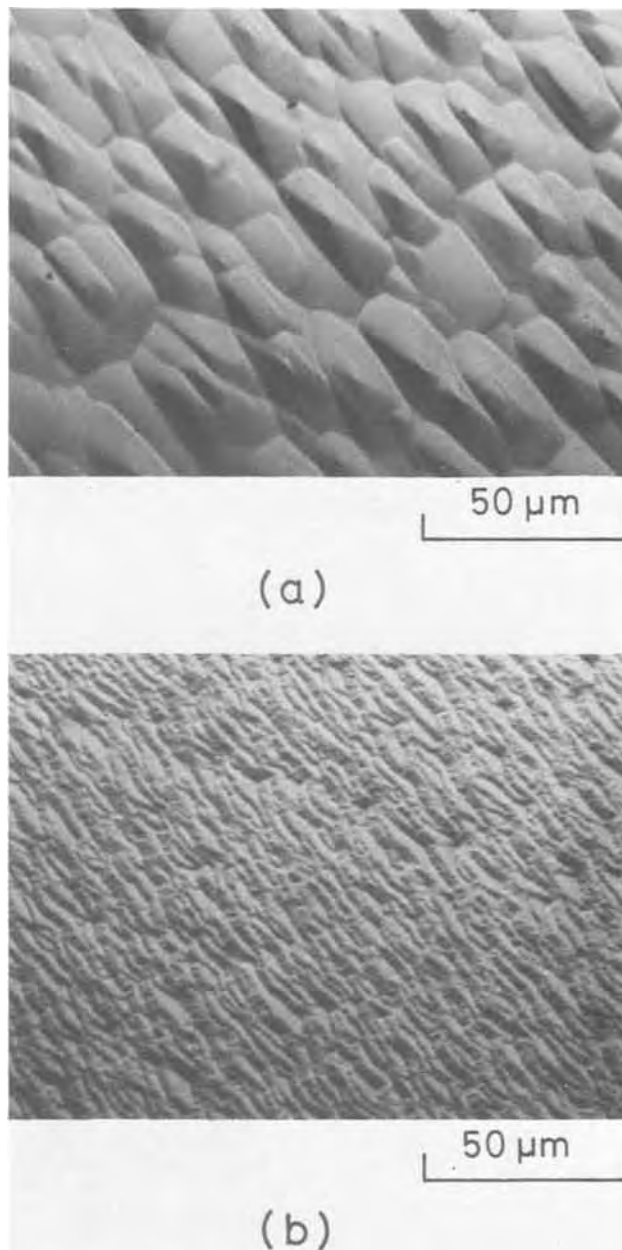


Fig. 2. Surface feature of epitaxial layer grown on (a) the (100) oriented substrate at  $550^\circ\text{C}$  and (b) the  $2^\circ$  off-oriented substrate at  $650^\circ\text{C}$ .

pendicular to the gas flow. The growth rate of GaAs depends mainly on the flow rate of DGC, namely the gallium concentration, in this experiment as shown in Fig. 3. Concentrations of gallium and arsenic in the reactor decrease downstream since gallium and arsenic atoms are used for GaAs deposition. Therefore, the growth rate also decreases downstream, that is, the thickness of the layer grown on the parallel-placed substrate decreases downstream. On the other hand, in the case of the growth on the substrate placed perpendicular, the thickness uniformity depends mainly on the distribution of the reacting species over the cross section of the reaction tube. When the area of the substrate is smaller than the cross-sectional area of the reaction tube, good uniformity of thickness could be obtained. The evaluation of the epitaxial layer was carried out for the layer grown on the perpendicular-placed substrate.

### Electrical Properties

Schottky diodes and a Hall bridge with a Schottky barrier which introduces a depletion region were fab-

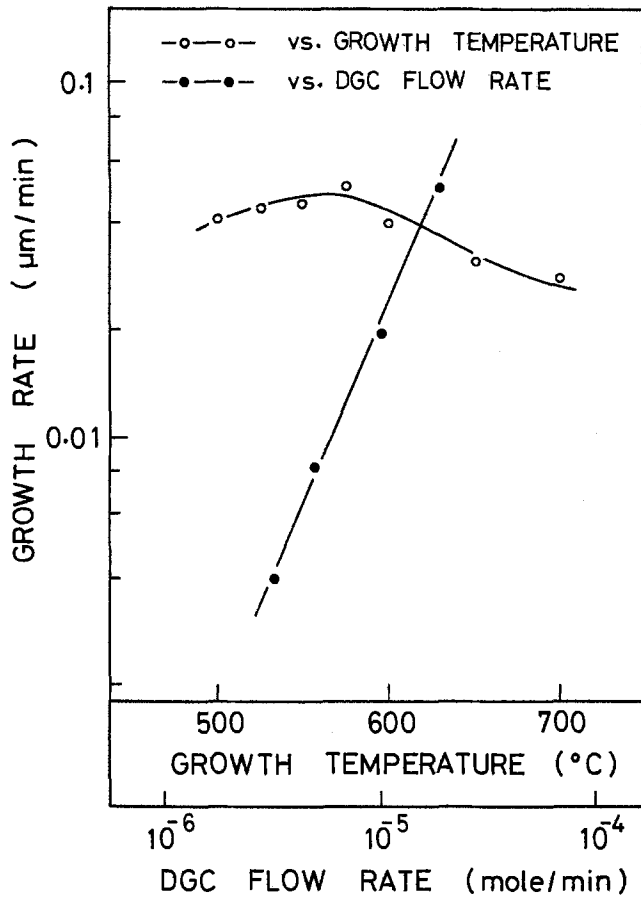


Fig. 3. Growth rate vs. growth temperature and DGC flow rate at arsine flow rate of  $2 \times 10^{-4}$  mole/min.

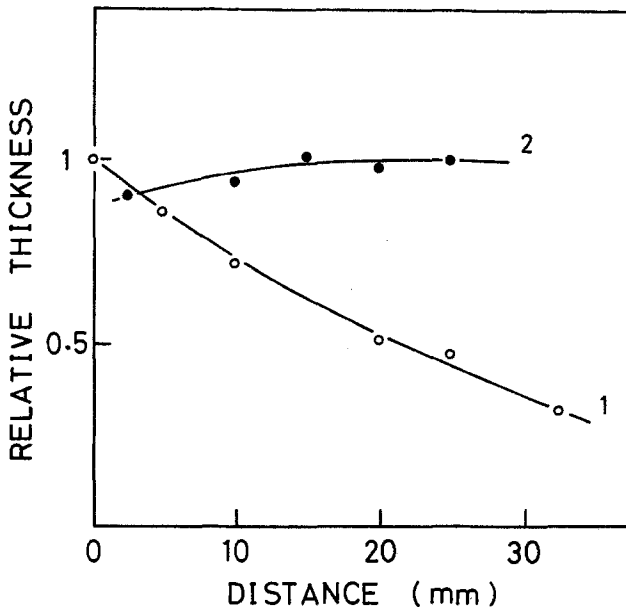


Fig. 4. Thickness distribution over the surface. Curves 1 and 2 represent thickness in the layer placed parallel and perpendicular to the gas flow, respectively.

ricated in the epitaxial layer for determination of electrical properties. The schematics of these devices are shown in Fig. 5. The width of the depletion region and hence the cross section of the conducting channel could be varied by biasing the Schottky barrier. The Schottky barrier was formed by evaporating Al and the ohmic contact was formed by alloying Au-Ge at 450°C.

**Carrier concentration.**—From the Hall measurement, all the epitaxial layers grown in this experiment were

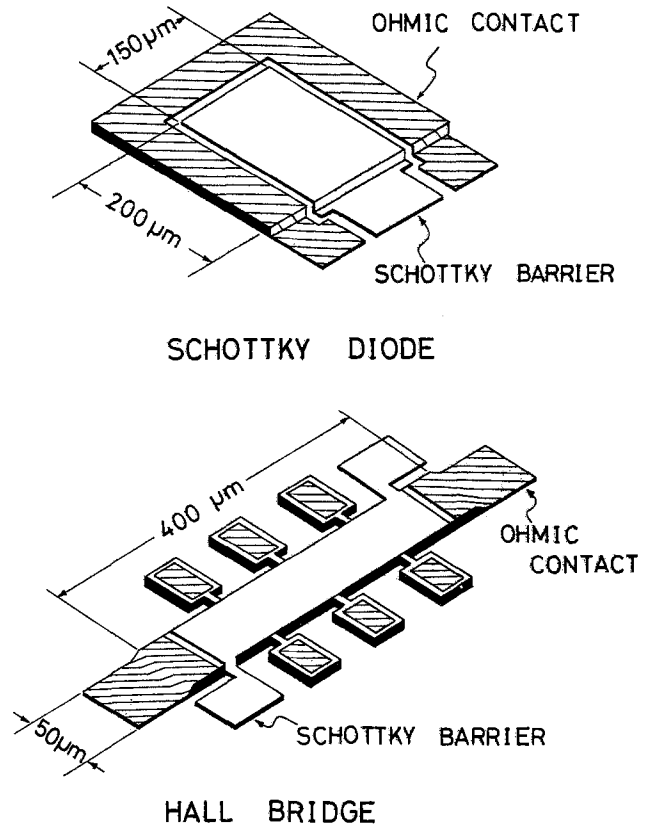


Fig. 5. Schottky diode and Hall bridge used for electrical property determination.

found to be n-type without intentional doping. Figure 6 shows the carrier concentration determined by C-V measurement as a function of the concentration ratio of arsenic to gallium, namely the mole ratio of arsine to DGC. The carrier concentration decreases with increasing the concentration ratio and very low carrier concentration was obtained for the large value of the ratio. It has been reported that conductivity of the epitaxial layer grown by using TMG or TEG depends on the mole ratio of arsine to the gallium source (5,

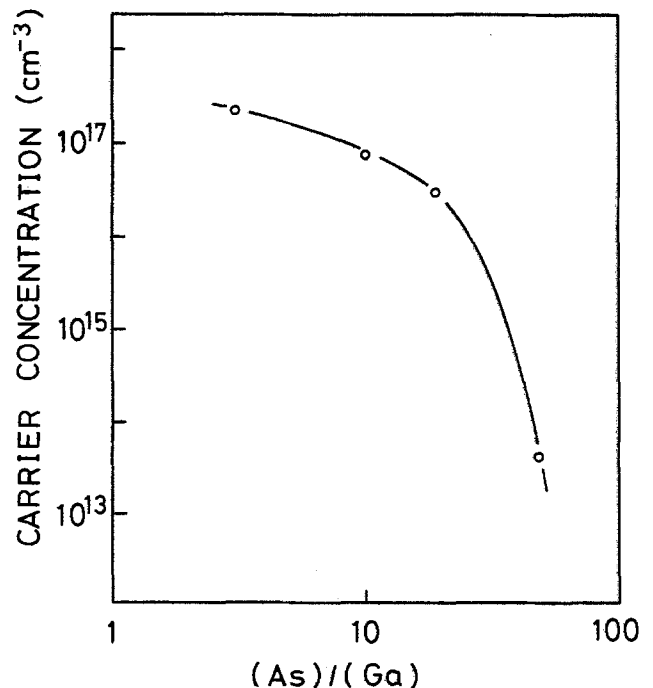


Fig. 6. Carrier concentration vs. concentration ratio of arsenic to gallium (As)/(Ga).

6). In those cases, carrier concentration of the n-type layer increases and that of the p-type layer decreases with increasing the mole ratio. This has been interpreted as follows: an atom of amphoteric impurity in a gallium site acts as a donor and that in an arsenic site acts as an acceptor. This amphoteric impurity is estimated to be an element of Group IV such as carbon or silicon contained in the gallium source. This interpretation, however, is not applicable to the result obtained here, in which the dependence of n-type carrier concentration on the mole ratio is opposite to that of the TMG or TEG source as described above. The mole ratio dependence in this experiment suggests that an atom of Group VI element in an arsenic site, rather than an atom of Group IV element in a gallium site, acts mainly as a donor.

**Hall mobility.**—Average Hall mobilities over the epitaxial layer determined by using the Hall bridge with a Schottky barrier were 5070 and 3500  $\text{cm}^2/\text{V sec}$  for the carrier concentration of  $5 \times 10^{16}$  and  $2 \times 10^{17} \text{ cm}^{-3}$ , respectively. These values are almost equal to the mobility of the epitaxial layer grown in the Ga-AsCl<sub>3</sub>-H<sub>2</sub> system. The average Hall mobility  $\bar{\mu}(z)$  and the sheet conductance  $\sigma_S(z)$  in the conducting channel were measured as a function of the distance from the interface,  $z$ , by biasing the Schottky barrier of the Hall bridge. The absolute Hall mobility  $\mu(z)$  was calculated using the following equation (8)

$$\mu(z) = \bar{\mu}(z) + \sigma_S(z) \partial \bar{\mu}(z) / \partial \sigma_S(z)$$

Figure 7 shows the profiles of the carrier concentration and the absolute mobility of the layer grown on the semi-insulating substrate. The carrier concentration changes very steeply near the interface between the grown layer and the substrate. Hall mobility decreases abruptly at the position of about 800 Å from the interface toward the surface. It is observed also in the epitaxial layer grown in the Ga-AsCl<sub>3</sub>-H<sub>2</sub> system that Hall mobility decreases at a point shallower than the interface determined from the profile of carrier concentration. This may be mainly caused by the increase of the space-charge scattering which is due to an anomalous growth such as deviation from the stoichiometry in the initial stage of growth (9).

Figure 8 shows the temperature dependence of Hall mobility at a distance of 0.26  $\mu\text{m}$  from the surface, together with the corresponding mobilities calculated

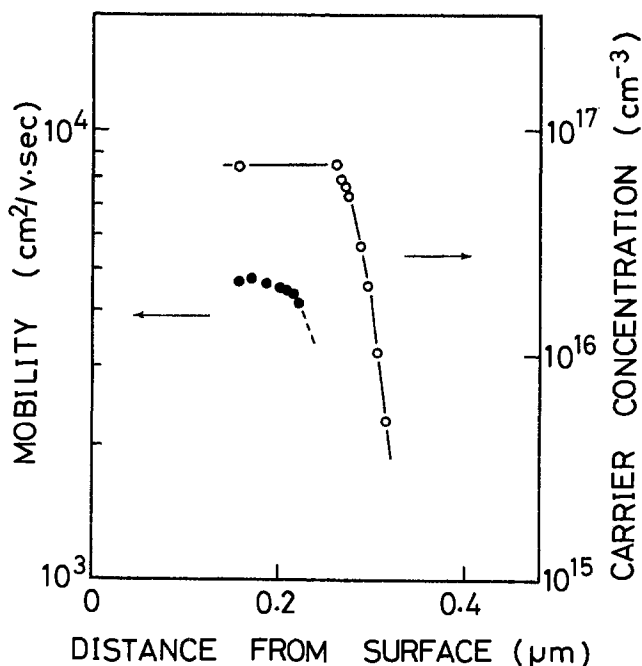


Fig. 7. Profiles of carrier concentration and Hall mobility

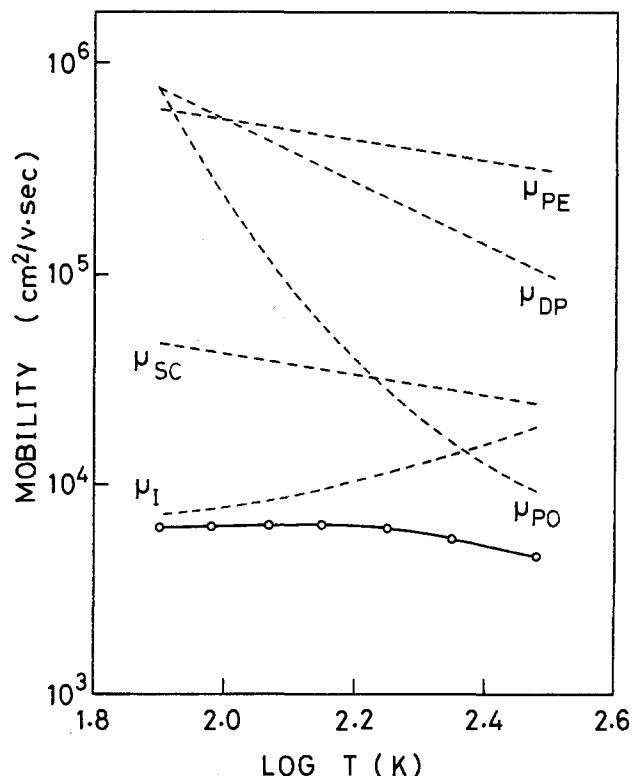


Fig. 8. Temperature dependence of Hall mobility.  $\mu_{SC}$ ,  $\mu_I$ ,  $\mu_{PO}$ ,  $\mu_{DP}$ , and  $\mu_{PE}$  represent the mobilities corresponding to space-charge, ionized impurity, polar optical phonon, deformation potential, and piezoelectric scattering, respectively.

for the various scattering mechanisms.  $\mu_{DP}$ , mobility due to deformation potential scattering (10), and  $\mu_{PE}$ , mobility due to piezoelectric scattering (11), are functions of absolute temperature, and  $\mu_{PO}$ , mobility due to polar optical phonon scattering (12), is a function of absolute temperature and carrier concentration which were determined by C-V measurement. Therefore,  $\mu_{DP}$ ,  $\mu_{PE}$ , and  $\mu_{PO}$  can be calculated.  $\mu_{SC}$ , mobility due to space-charge scattering (13), and  $\mu_I$ , mobility due to ionized impurity scattering (14), are functions of absolute temperature and  $N_s A$ , and absolute temperature and concentration of ionized impurity,  $N_A + N_D$ , respectively, where  $N_s A$  is the product of the density and scattering cross section of the space-charge regions. The reciprocal of absolute mobility is expressed as the sum of the reciprocals of these mobilities due to various scattering mechanisms. The open circles in Fig. 8 represent the measured values and the solid line is the theoretical curve with an optimum fit to the measured points.

The value of  $\mu_I$  is somewhat smaller, that is, the acceptor concentration is somewhat higher, but  $\mu_{SC}$  is considerably larger than that of the layer grown in the Ga-AsCl<sub>3</sub>-H<sub>2</sub> system. An amphoteric impurity, such as carbon generated from DGC, in an arsenic site may cause the higher acceptor concentration. The smaller space-charge scattering is estimated to be a result of lower growth temperature.

#### Doping Characteristics

The carrier concentration of the epitaxial layer depends on the mole ratio of arsine to DGC as mentioned above. In this experiment, a low concentration ratio of (As)/(Ga), that is, a high flow rate of DGC and/or a low arsine flow rate, was necessary to grow an epitaxial layer with higher carrier concentration. A high DGC flow rate results in a high growth rate which makes the growth of a very thin layer difficult and a low arsine flow rate may cause the unstable growth. In order to (i) obtain a carrier concentration higher than  $10^{18} \text{ cm}^{-3}$  without increasing the growth rate and

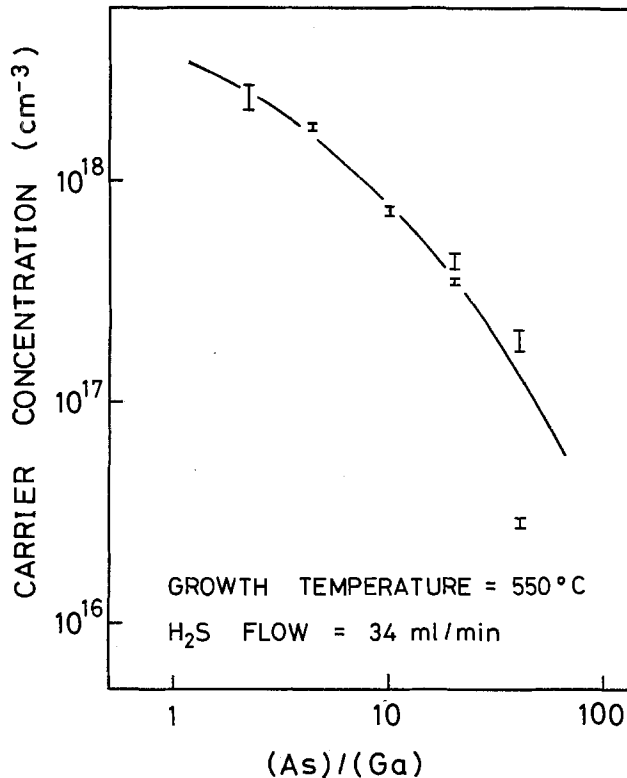


Fig. 9. Carrier concentration of sulfur-doped layer vs. (As)/(Ga)

(ii) control the carrier concentration with more accuracy, impurity doping was investigated.

Hydrogen sulfide diluted to 0.01% in nitrogen gas was used as a doping source. The doping gas was introduced into the reactor together with arsine when the substrate temperature was raised to 500°C. No considerable effect of the doping gas introduction was observed on the surface feature and the growth rate. Figures 9 and 10 show the carrier concentration as a function of the concentration ratio (As)/(Ga), which is equal to the mole ratio of arsine to DGC, and of the growth temperature, respectively. The mole ratio dependence of the carrier concentration has a similar tendency to that of the undoped epitaxial growth. This confirms the suggestion that the donor impurity in the undoped layer is an element of Group VI. By using this doping technique, a carrier concentration as high as  $2\text{--}3 \times 10^{18} \text{ cm}^{-3}$  was easily obtained. Electrical properties of the sulfur-doped layer were almost similar to those of the undoped layer having the same carrier concentration.

#### Conclusion

Very thin GaAs epitaxial layers have been grown from DGC and arsine. The growth rate depends mainly on the concentration of gallium in the gas introduced into the reactor and can be easily controlled to lower than  $0.01 \mu\text{m}/\text{min}$  by adjusting the temperature of the DGC source. Without intentional doping, n-type layers are obtained and the carrier concentration in the layer can be changed by varying the mole ratio of arsine to DGC in the gas flow, the increase of which results in the decrease of the carrier concentration. From the mole ratio dependence of the carrier concentration, the donor impurity is considered to be an element of Group VI in an arsenic site.

The carrier concentration of the epitaxial layer on a semi-insulating substrate decreases steeply at the interface between the epitaxial layer and the substrate. Hall mobilities of a  $0.3 \mu\text{m}$  thick layer are 5070 and  $3500 \text{ cm}^2/\text{V sec}$  at room temperature for the carrier concentrations of  $5 \times 10^{16}$  and  $2 \times 10^{17} \text{ cm}^{-3}$ , respectively.

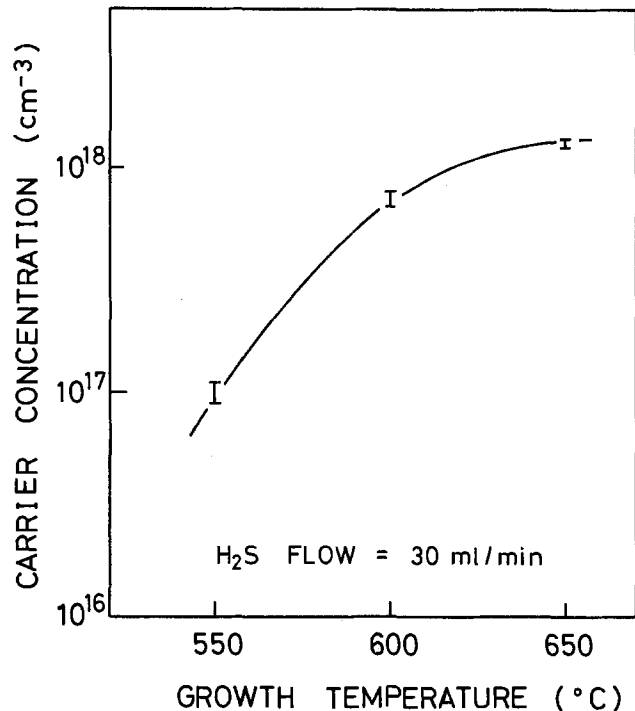


Fig. 10. Growth temperature dependence of carrier concentration of sulfur-doped layer.

#### Acknowledgments

The authors wish to thank Dr. M. Maeda for useful advice and encouragement during the course of this work. The electron diffraction study was performed by Mr. T. Furusawa and the measurement and analysis of Hall mobility were performed by Mr. N. Yokoyama. We also thank Mr. T. Matsumura for sample preparation.

Manuscript submitted Nov. 18, 1975; revised manuscript received March 22, 1976.

Any discussion of this paper will appear in a Discussion Section to be published in the June 1977 JOURNAL. All discussions for the June 1977 Discussion Section should be submitted by Feb. 1, 1977.

Publication costs of this article were assisted by Fujitsu Laboratories Limited.

#### REFERENCES

- H. M. Manasevit, *Appl. Phys. Letters*, **12**, 156 (1968).
- R. W. Thomas, *This Journal*, **116**, 1449 (1969).
- H. M. Manasevit and W. I. Simpson, *ibid.*, **116**, 1725 (1969).
- P. Rai-Choudhury, *ibid.*, **116**, 1745 (1969).
- S. Ito, T. Shinohara, and Y. Seki, *ibid.*, **120**, 1419 (1973).
- Y. Seki, E. Tanno, K. Iida, and E. Ichiki, *ibid.*, **122**, 1108 (1975).
- K. Lindeke, W. Sack, and J. J. Nickl, *ibid.*, **117**, 1316 (1970).
- M. Y. Darwish, *IEEE Trans. Electron Devices*, **ED-21**, 397 (1974).
- A. Shibatomi, N. Yokoyama, H. Ishikawa, K. Dazai, and O. Ryuzan, *J. Cryst. Growth*, **31**, 240 (1975).
- J. Bardeen and W. Shockley, *Phys. Rev.*, **80**, 72 (1950).
- A. R. Huston, *J. Appl. Phys.*, **32**, 2287 (1961).
- L. R. Weisberg, *ibid.*, **33**, 187 (1962).
- H. Brooks, in "Advances in Electronics and Electron Physics," Vol. 7, M. I. Marton, Editor, p. 85, Academic Press, New York (1955).
- D. J. Hawarth and E. H. Sondheimer, *Proc. Roy. Soc. (London)*, **A219**, 53 (1953).

# Incorporation of Si in Liquid Phase Epitaxial InP Layers

G. G. Baumann, K. W. Benz, and M. H. Pilkuhn

Physikalisches Institut und Kristalllabor, Universität Stuttgart, 7000 Stuttgart 80, West Germany

## ABSTRACT

It is demonstrated that Si is always incorporated in InP LPE layers as a shallow donor, i.e., it does not exhibit the amphoteric behavior known to LPE GaAs. Si-doped InP layers were grown with a concentration of  $N_D - N_A = 1 \cdot 10^{16} - 5 \cdot 10^{19} \text{ cm}^{-3}$  on (111), (110), and (100) oriented InP substrates. The growth temperature was varied from 715° to 550°C. The segregation coefficient for Si in InP LPE layers was estimated to be  $k_{\text{Si}} \approx 30$ . The layers were characterized by photoluminescence measurements at 1.8°K and Hall data. No emission line (energy range 1.42-1.35 eV) due to a shallow Si acceptor was observed. The difference in amphoteric behavior of Si in InP and GaAs is discussed on the basis of the atomic radii involved.

Si is one of the most frequently used and most important dopants in III-V compound semiconductors. In principle it behaves as an amphoteric dopant depending on whether it substitutes the Group III or Group V element. In AlSb (1), GaSb (2), and InSb (2), Si enters Sb sites and acts as an acceptor. In InAs (3, 4), however, Si enters on an In site and acts as a shallow donor. In GaAs (2, 5) and GaP (6) it can be incorporated on a Ga or As(P) site, acting as donor or acceptor.

By suitable control of the growth conditions during liquid phase epitaxy of GaAs, p-type and n-type material may be grown. High efficiency electroluminescent diodes have been fabricated by this technique with Si as the dopant in both the p- and n-type side of the junction (7). The p-type material can be grown below a certain conversion temperature,  $T_c$ .  $T_c$  is dependent on substrate orientation, which was experimentally shown for GaAs by Ahn *et al.* (8). For 0.1 atomic per cent (a/o) Si in the solution,  $T_c$  lies between 770° [(111)B substrates] and 918°C [(111)A substrates].

In previous studies, it was reported that InP:Si is always n-type (9, 10), even in the case of LPE layers, while the material was found to be rather inhomogeneous (10). The aim of this paper is to investigate what percentage of Si can be incorporated during LPE on P sites as a shallow acceptor. Detailed photoluminescence measurements at 1.8°K as well as Hall measurements were made at a series of LPE layers. The growth and incorporation of Si as a function of growth temperature and substrate orientation in search of a possible conversion temperature,  $T_c$ , was studied.

Low temperature photoluminescence measurement is a very sensitive tool in detecting a compensating acceptor level. The result of this study is that Si is not incorporated as a shallow acceptor even at high donor (Si) concentrations.

## Experimental Procedure

The layers were grown by LPE using a horizontal tipping system (11). The arrangement of the apparatus and the way in which the growth process was performed is discussed in more detail elsewhere (12).

Before the Si dopant was added to the In-P solution, high purity InP layers were grown in order to test the purity of the whole epitaxial system. The best values of net electron concentration and Hall mobility of these undoped layers were  $n = 2 \cdot 10^{14} \text{ cm}^{-3}$  (300°K) and  $\mu = 35,000 \text{ cm}^2 \text{ V}^{-1} \text{ sec}^{-1}$  (77°K). A very important point in our study of the doping behavior of Si was the elimination of additional donors and acceptors other than Si in the layer.

Key words: InP, liquid phase epitaxy, Si doping behavior, photoluminescence.

Special care was taken to determine the saturation temperature,  $T_s$ , before every growth series. Each growth series consisted of several growth runs. During each series the In-P solution remained unchanged. With the exact knowledge of  $T_s$  one can establish reproducible growth conditions at the beginning of each growth series.

On the basis of the amounts of In (Cominco, U.S.) and InP (MCP, England,  $n = 2 \cdot 10^{15} \text{ cm}^{-3}$ ),  $T_s$  was roughly calculated from the phase diagram (13). For an experimental and more exact determination of  $T_s$ , the baked In-P solution was heated up in a few minutes from room temperature to a temperature several degrees below  $T_s$ . After that, the solution was heated up in small temperature steps. At the various levels the temperature remained constant for 1 hr, and the solution was agitated gently by rotating the boat along its long axis. In approaching the saturation temperature,  $T_s$ , only some small InP crystallites were visible at the top of the solution. The crystallites disappeared within a temperature interval of 0.5°C, i.e.,  $T_s$  could be estimated with an accuracy of 0.5°C.

Prior to each run, the In-P solution was heated up 50°C above  $T_s$  in order to dissolve the InP quickly (Fig. 1). Then the solution was cooled down to the temperature  $T_{K1}$  which was 1°C below the previously measured saturation temperature,  $T_s$ . Before tipping the solution onto the substrate, the solution temperature was kept at  $T_{K1}$  for 5 min for homogenization. The small supersaturation of 1°C prevented an etchback of the substrate and initiated the growth of the epitaxial layer. After tipping, the solution was held at  $T_{K1}$  again for 5 min and was slowly agitated as described above.

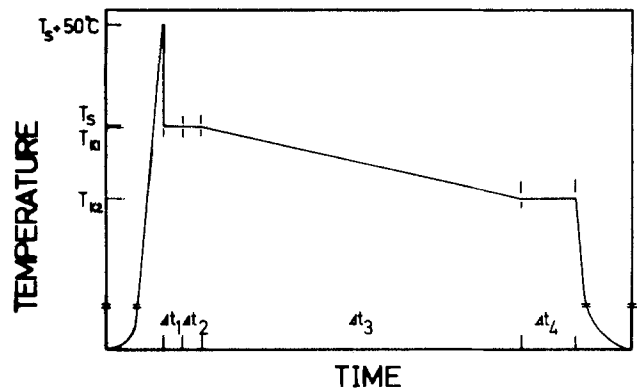


Fig. 1. Solution temperature vs. time during an epitaxial run.  $T_s$ : saturation temperature;  $T_{K1}$ ,  $T_{K2}$ : tipping temperatures;  $\Delta t_1 = \Delta t_2 = 5 \text{ min}$ ;  $\Delta t_3$ : cooling and growth period;  $\Delta t_4 = 15 \text{ min}$ .

Then the growth system was cooled down at a constant cooling rate. At the end of the cooling process, substrate and solution remained in contact for 15 min at the temperature  $T_{K2}$ . Finally, the substrate was withdrawn from the solution. During the whole process, no solid InP appeared at the top of the solution. Therefore,  $T_{K2}$  represented the tipping temperature,  $T_{K1}$ , for the next run.

Silicon has a rather low solubility in In (0.1 a/o at 700°C and 0.03 a/o at 610°C) (10). In order to get a low Si concentration in the layer, small Si ingots (30-90  $\mu\text{g}$ ) in 10g In solution were needed. Prior to use, the Si pieces ( $N_D + N_A < 10^{13} \text{ cm}^{-3}$ , Wacker-Chemitronic, Germany) were etched in high purity HF to remove  $\text{SiO}_2$  and taken into the graphite boat very quickly in order to prevent oxidation.

Under these conditions, we have grown single InP layers on (111), (110), and (100) undoped and Cr-doped InP substrates. The polished substrates which were available were cut  $\pm 2^\circ$  off orientation and were etched in a solution of 1% bromine in methanol and finally rinsed with 18 megohm water (Millipore System, England). In the different experimental runs,  $T_{K1}$  was varied between 715° and 590°C. The growth time was 1.5-4 hr and the cooling rate 4°-25°C/hr.

### Growth Results and Discussion

Table I shows growth results and conditions for different substrate orientations for some Si-doped layers with Si concentrations ranging from  $5 \cdot 10^{19}$  to  $1 \cdot 10^{16} \text{ cm}^{-3}$ . All grown layers were n-type, independent of growth temperature and orientation of the substrates.

We have estimated the segregation coefficient,  $k_{Si}$ , for Si in InP LPE layers as the ratio of net electron concentration in the layer to the amount of Si in the solution. This can be written as

$$k_{Si} = (N_D - N_A) \frac{AW_{Si} \cdot W_{Sol}}{N \cdot W_{Si} \cdot \delta_{In}}$$

where  $N_D - N_A$  = net electron concentration assumed equal to the concentration of Si atoms in the layer ( $\text{cm}^{-3}$ ),  $AW_{Si}$  = atomic weight of Si,  $W_{Sol}$  = weight of the In solution,  $W_{Si}$  = weight of the added Si,  $\delta_{In}$  = density of In = 7.30  $\text{g cm}^{-3}$ , and  $N$  = Avogadro's number. We obtained a value of  $k_{Si} \approx 30$ , which lies higher than that reported in the literature [ $k_{Si} \approx 4$  (10)]. It should be pointed out that after the first run there is a decrease in Si concentration from run to run mainly due to traces of water or oxygen which may enter the growth system and oxidize the Si to  $\text{SiO}_2$  (14). Exact knowledge of the amount of Si in the solution is not available for later runs. Therefore, we have estimated the segregation coefficient using only the first runs from several series.

In comparing the surface morphology of Si-doped layers with that of undoped layers, we find the following.

(i) The undoped layers grown on (100) and (111) surfaces show two types of surface structures: a shed

structure for layers grown at tipping temperatures  $T_{K1} \gtrsim 650^\circ\text{C}$  (12) and a terrace structure for layers grown at  $T_{K1} \lesssim 650^\circ\text{C}$ . These structures are due to misorientation of the substrates (15).

(ii) The surface structures of the Si-doped layers are dependent on the Si concentration and the misorientation of the InP substrates. Figure 2(a-c) shows the surfaces of layers with various Si concentrations for (100) substrate orientation. The layers with  $n > 5 \cdot 10^{18} \text{ cm}^{-3}$  (Fig. 2a) have a fairly flat mirrorlike surface. With decreasing Si concentration in the layer, the surface shows the typical terrace behavior of the undoped layers (Fig. 2c). An explanation of this effect may be the fact that higher Si concentration creates conditions that favor the formation of a large number of nucleating centers at the beginning of the growth (16). This will cause a reduction in step heights of the terrace structure and, as a result, the surface will be much smoother.

There is no difference in surface structure between (111)A, (111)B, and (100) surfaces. However, layers grown on (110) InP substrates always show, especially at high Si concentration, a new type of surface structure, depicted in Fig. 2d.

### Photoluminescence Results and Discussion

The Si-doped LPE layers were investigated by high resolution photoluminescence measurements at 1.8°K. The layers were excited with a He-Ne laser ( $P = 5 \text{ mW}$ ,  $\lambda = 632 \text{ nm}$ ) or a  $\text{Kr}^+$  laser ( $P = 11 \text{ mW}$ ,  $\lambda = 647 \text{ nm}$ ). The majority of the investigations were carried out on LPE layers grown on Cr-doped, semi-insulating InP substrates. These samples exhibit a broad emission near the bandgap as already reported by Astles *et al.* (10). The quantum efficiency of this emission is lower than in the case of doped layers on undoped substrates or high purity layers.

Figure 3 depicts the observed photoluminescence spectra at 1.8°K with various Si concentrations. In the energy range between 1.36-1.60 eV, two emission lines (A and B) can be resolved. With increasing Si concentration in the LPE layer, line A shifts from 1.42 eV ( $n = 1 \cdot 10^{16} \text{ cm}^{-3}$ ) to 1.60 eV ( $n = 5 \cdot 10^{19} \text{ cm}^{-3}$ ). At low Si concentrations line A is observed at approximately the energy gap [ $E_g = 1.4235 \text{ eV}$  (17)]. Line B remains nearly constant at 1.38 eV. Figure 4 shows the position of the emission maximum of line A as a function of the net electron concentration. The half-width of the high energy line A increases significantly with doping which is shown in Fig. 5. The half-width of the emission line B does not vary with electron concentration. The position and half-width of line A remains constant with increasing excitation intensity, whereas line B shifts from 1.3759 to 1.3772 eV by increasing the excitation intensity from 4 to 76  $\text{W cm}^{-2}$ .

It was found unambiguously that the major emission connected with the incorporation of Si is line A, whereas line B is associated with other residual impurities as discussed later. The major observed features of line A, its shift to higher energy and line broadening with increased doping, its dependence on excitation intensity, and its position, all indicate that it is due to band-to-band transition. The shift to higher energy can be explained by a Burstein-Moss shift, resulting from the incorporation of Si as a donor. The shift of Fermi level with carrier concentration  $n$  can be expressed in the following way

$$n = 4\pi (2m^*/h^2)^{3/2} \int_0^\infty \frac{E^{1/2}}{1 + \exp[(E - E_F)/kT]} dE$$

where electron effective mass  $m^* = 0.2 m_{e0}$  (18);  $E$  is the energy related to the conduction band minimum, and tail states are neglected. The position of the Fermi level,  $\xi = E_F - E_g$ , was calculated with the aid of a

Table I. Growth results and conditions for various InP:Si epitaxial layers

SAMPLE	$n(300\text{K})$ ( $\text{cm}^{-3}$ )	$\mu(300\text{K})$ ( $\text{cm}^2 \text{V}^{-1} \text{sec}^{-1}$ )	SUBSTRATE		$T_{K1}$ (°C)	$T_{K2}$ (°C)	$dT/dt$ (°C/hr)
			ORIENT.	DOPING			
F4	$4 \cdot 10^{19}$	940	100	Cr	690	673	8.5
F8	$2 \cdot 10^{19}$	760	110	Cr	590	550	20
F9	$4 \cdot 10^{18}$	1450	111B	Cr	686	670	8.5
J1	$2 \cdot 10^{19}$	1400	100	Cr	715	700	8.5
J3	$8 \cdot 10^{18}$	845	100	Cr	685	670	8.5
J7	$4 \cdot 10^{17}$	1790	100	Cr	622	600	8.5



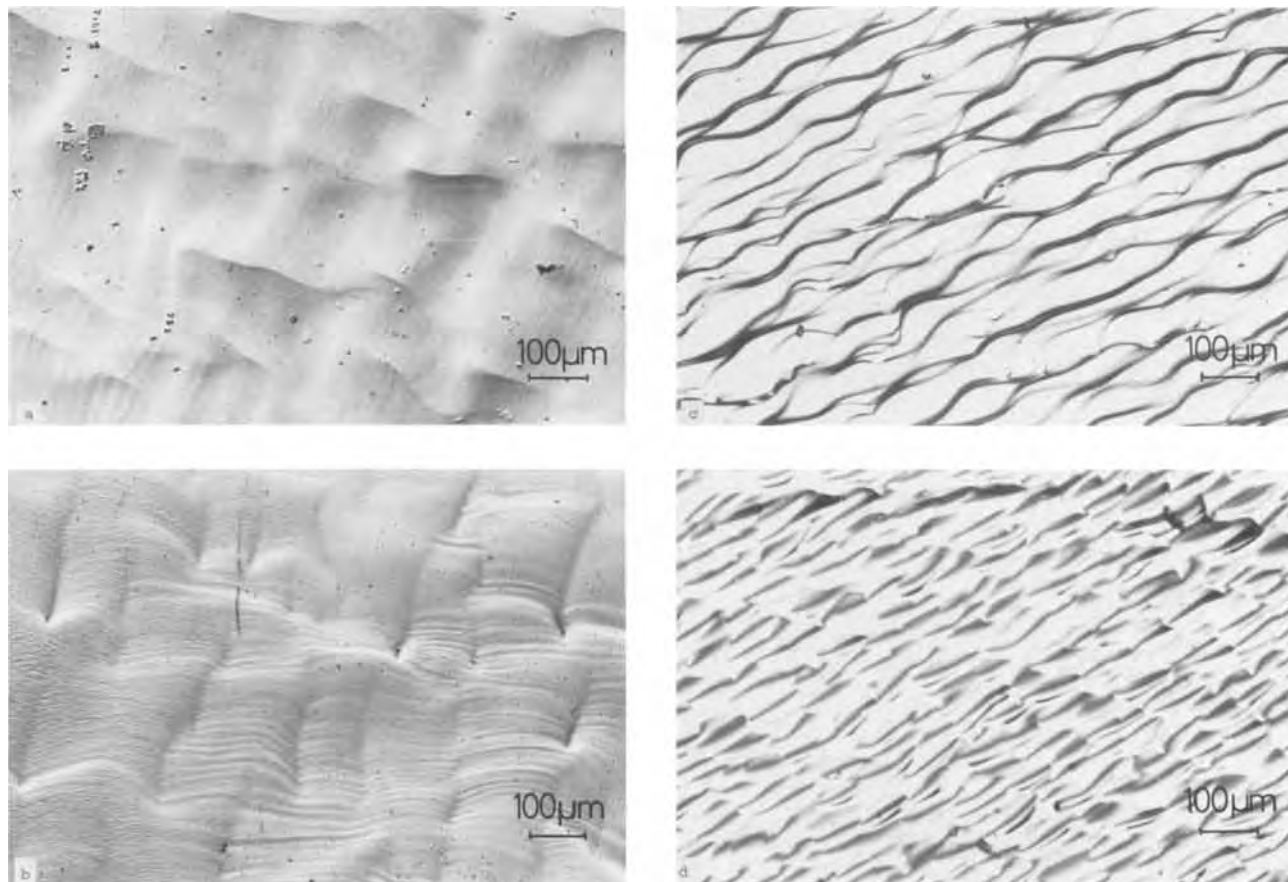


Fig. 2. Typical surfaces of InP:Si epitaxial layers grown on (100) oriented substrates (a-c) and (110) oriented substrate (d); net electron concentration of the layers:  $n = 2 \cdot 10^{19} \text{ cm}^{-3}$  (a),  $8 \cdot 10^{18} \text{ cm}^{-3}$  (b),  $4 \cdot 10^{17} \text{ cm}^{-3}$  (c), and  $2 \cdot 10^{19} \text{ cm}^{-3}$  (d).

nomogram published by Pankove and Annavegger (19). Experimentally,  $\xi$  was estimated from the high energy cutoff of line A and compared with the theoretical values for  $\xi$  (20). The experimentally deduced value for  $\xi$  and the theoretical one are plotted in Fig. 6 as a function of the net electron concentration.

The results in Fig. 6 can be taken as sufficient evidence for a Burstein-Moss shift; the deviation of the experimental data from the theoretical curve is the

typical one found for InP:Te (20). The deviation is due to tail states and/or the nonparabolicity of the conduction band. In agreement with the concept of band-to-band emission and with corresponding results in InP:Te (20), the linewidth increases with carrier concentration.

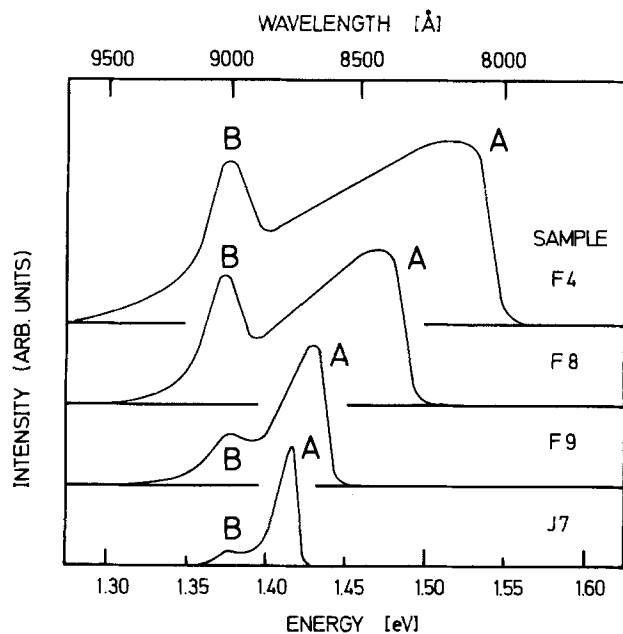


Fig. 3. Photoluminescence spectra at 1.8°K of four differently Si-doped InP LPE layers grown on Cr-doped substrates.

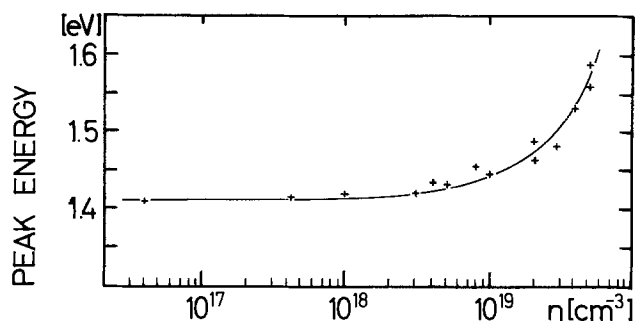


Fig. 4. Position of the emission maximum of line A as a function of the net electron concentration  $n$ .

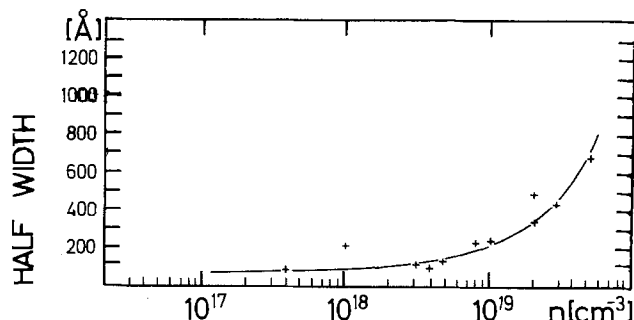


Fig. 5. Half-width of the emission line A at 1.8°K vs. net electron concentration  $n$ .

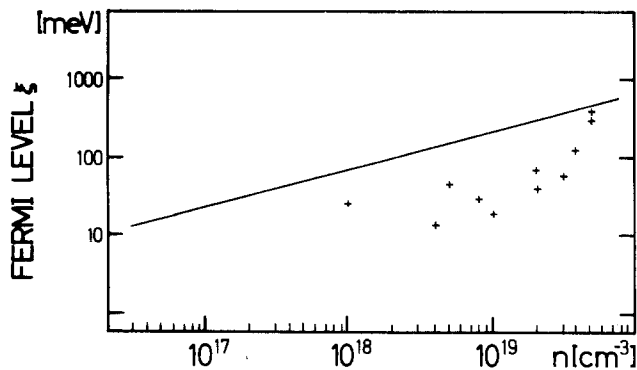


Fig. 6. Shift of Fermi level  $\xi$  with concentration  $n$ ; + experimental values; — theoretical curve.

From our results it can be concluded that the incorporation of Si can be described by a donor behavior leading to electron concentrations as high as  $5 \cdot 10^{19} \text{ cm}^{-3}$ . The question arises how much Si is incorporated as a compensating acceptor which may be expected in particular at high doping levels. Compensating acceptors would give rise to a band acceptor transition, i.e., an emission line which follows the A line in its energy shift with increasing doping at a distance of the acceptor binding energy. No such line is observed in high sensitivity photoluminescence, i.e., no evidence for any Si being incorporated as an acceptor was found.

Line B which is also observed in our samples is a well-known donor-acceptor pair transition due to the acceptor Zn (12). This Zn acceptor is incorporated as an undesired impurity in an uncontrolled manner in low-doped regions of the layer. Emission from regions with lower electron concentration is much more pronounced if undoped substrates are used. In the latter case, even the typical bound exciton emission lines ( $A^\circ, X$ ) and ( $D^\circ, X$ ) (12) may be observed in addition to the band-to-band luminescence induced by incorporation of Si.

### Conclusion

The main result of this investigation is that Si is incorporated in InP as a donor, i.e., on an In lattice site, whereas no incorporation on a P site as an acceptor was detected. This is different from the amphoteric behavior of Si in LPE GaAs. The incorporation of Si in InP on an In site can be explained qualitatively by the difference in covalent tetrahedral atomic radii of the elements In, P, and Si. Recent data of these radii (21) and those for Ga, Ge, Sn, As, and Sb are compiled in Table II. From early theoretical considerations by Welker (22), it is obvious that the doping element substitutes the lattice element with the greater tetrahedral radius in III-V semiconductors.

Let us first consider the incorporation of Si. In III-V compounds with nearly equal atomic radii of the components, Si shows the typical amphoteric behavior as observed in the case of GaAs and, though less pronounced, in GaP. Si in InP prefers the In site because there is a large difference between the atomic radii of In and P. Similar conclusions can be made for GaSb [Si predominate acceptor (23)] and InAs [Si predominate donor (4)].

The doping elements Ge and Sn in InP, having still larger atomic radii than Si, should also prefer to be incorporated on an In site as a donor, which is actually observed (10). Only C, with a very small atomic radius

( $r = 0.774 \text{ \AA}$ ) should be able to enter on a P site as an acceptor. In fact, the shallow " $A_1$ -acceptor" in InP with a binding energy of 41.1 meV (12) is presumably due to C on a P site.

### Acknowledgments

The cooperation of the Max-Planck-Institut für Festkörperforschung in Stuttgart, particularly stimulating discussion with Dr. E. Bauser and K. Hess, is gratefully acknowledged. We also thank Ms. K. Langer, Dr. J. U. Fischbach, P. Rossetto, and G. Mack for their assistance and interest.

Manuscript submitted Feb. 3, 1976; revised manuscript received April 7, 1976.

Any discussion of this paper will appear in a Discussion Section to be published in the June 1977 JOURNAL. All discussions for the June 1977 Discussion Section should be submitted by Feb. 1, 1977.

Publication costs of this article were assisted by Universität Stuttgart.

### LIST OF SYMBOLS

$k_{\text{Si}}$	segregation coefficient
$n$	$N_D - N_A$ net electron concentration
$AW_{\text{Si}}$	atomic weight of Si
$W_{\text{Sol}}$	weight of the In solution
$W_{\text{Si}}$	weight of the Si ingot
$N$	Avogadro's number
$\mu$	electron mobility
$T_s$	saturation temperature
$T_{K1}$	temperature of tipping the solution onto the substrate
$T_{K2}$	temperature of withdrawing the solution from the layer
$\lambda$	wavelength
$\xi$	$E_F - E_g$ Fermi level related to the conduction band minimum
$r$	covalent tetrahedral atomic radius

### REFERENCES

- D. Shaw, *Proc. Phys. Soc.*, **80**, 161 (1962).
- J. T. Edmond, *ibid.*, **73**, 622 (1959).
- E. Schillmann, *Z. Naturforsch.*, **11a**, 463 (1956).
- O. Mizuno, H. Watanabe, and D. Shinoda, *Japan. J. Appl. Phys.*, **14**, 184 (1975).
- C. J. Summer, R. Dingle, and D. E. Hill, *Phys. Rev.*, **B1**, 1603 (1970).
- M. R. Lorenz and M. H. Pilkuhn, *J. Appl. Phys.*, **38**, 61 (1967).
- H. Rupperecht, J. M. Woodall, K. Konnerth, and D. G. Pettit, *Appl. Phys. Letters*, **9**, 221 (1966).
- B. H. Alm, R. R. Schurtz, and C. W. Trussel, *J. Appl. Phys.*, **42**, 4512 (1971).
- E. W. Williams, W. Elder, M. G. Astles, M. Webb, J. B. Mullin, B. Straughan, and P. J. Tufton, *This Journal*, **120**, 1741 (1973).
- M. G. Astles, F. G. H. Smith, and E. W. Williams, *ibid.*, **120**, 1750 (1973).
- E. Grobe and H. Salow, *Z. Angew. Phys.*, **32**, 381 (1972).
- K. Hess, N. Stath, and K. W. Benz, *This Journal*, **121**, 1208 (1974).
- N. Sol, J. P. Clarion, N. T. Linh, and M. Moulin, *J. Cryst. Growth*, **27**, 325 (1974).
- O. G. Lorimor, S. E. Haszako, and P. D. Dapkus, *This Journal*, **122**, 1230 (1975).
- E. Bauser, M. Frik, K.-S. Löchner, and L. Schmidt, *J. Cryst. Growth*, **27**, 148 (1974).
- J. Crossley and M. B. Small, *ibid.*, **19**, 160 (1973).
- J. U. Fischbach, G. Benz, N. Stath, M. H. Pilkuhn, and K. W. Benz, *Solid State Commun.*, **11**, 721 (1972).
- R. Newman, *Phys. Rev.*, **111**, 1518 (1958).
- J. I. Pankove and E. K. Annavegger, *J. Appl. Phys.*, **36**, 3948 (1965).
- O. Roeder, U. Heim, and M. H. Pilkuhn, *J. Phys. Chem. Solids*, **31**, 2625 (1970).
- K. Hübner, *Kristall. Technik.*, **9**, 865 (1974).
- H. Welker, *Z. Naturforsch.*, **11**, 744 (1952).
- W. Jakowitz, To be published.

Table II. Covalent tetrahedral atomic radii  $r$  [ $\text{\AA}$ ] (21)

Al : 1.229	Si : 1.173	P : 1.127
Ga : 1.225	Ge : 1.225	As : 1.225
In : 1.405	Sn : 1.405	Sb : 1.405

# On the Maximum Position of Thermally Stimulated Depolarization Bands

A. Kessler

*Institute of Physics, University of Stuttgart, Stuttgart, Germany*

## ABSTRACT

It is shown by theoretical argument and by experiment that only in the case of a first order kinetics polarization do the TSD peaks occur invariably at a fixed temperature. Otherwise their position is shifting in a characteristic way with changing initial polarization. In the case of a space charge release, for example, the maximum temperature is increasing with polarization temperature and polarization time. Thus, peak position data for varying polarization conditions allow one to decide in particular whether a peak is due to a first order depolarization process, e.g., complex reorientation, or to the release of a space charge.

The thermally stimulated depolarization (TSD) of polar crystals by an increasing temperature usually shows several bands or peaks. This indicates that the depolarization is realized by several different processes. Two such processes are well known: the relaxation of aligned impurity-point defect complexes (1) and the relaxation of a space charge caused by mobile point defects accumulated at the electrodes (2, 3). But there are still other processes which cause TSD peaks which have not yet been identified (1, 4).

It is one of the fundamental problems of any investigation of TSD to relate the observed peaks to specific depolarization processes. From the experimental point of view, there are three quantities which characterize a given TSD peak, on which an analysis may be based: the maximum position, the magnitude of the peak, and the slope of the initial rise of the peak. The magnitude of the peak is eventually (1) a measure of the number of defects causing the polarization. The determination of the slope of the initial rise, which should yield the activation energy of the depolarization process, is in general a delicate task and if the peaks overlap too much, possibly no meaningful value can be obtained at all. However, it is comparatively easy to determine the approximate peak positions. We shall show how the peak position depends on the initial polarization of a sample, and that this can provide some information on the depolarization processes causing the peaks in question.

## Some General Considerations Concerning TSD

The TSD is usually investigated by measuring the "depolarization current"  $I_m(t, T)$  of a polarized sample of cross section  $A$  and thickness  $L$  which is connected to a galvanometer. The measured current density  $i_m(t, T) = I_m(t, T)/A$  is equal to the sum of the charge transport rate density  $e \cdot j(x, t)$  and the displacement current density  $\partial D(x, t)/\partial t$  at any arbitrary cross section of the investigated sample. Under ideal conditions, the measurement is carried out without any potential drop between the electrodes,  $\Delta V = \int_0^L E(x, t) \cdot dx = 0$ , and without any charge transfer to the electrodes, i.e.,  $j(0, t) = j(L, t) = 0$ . Under these conditions solely the displacement current density

$$i_m(t, T) = \left\{ \frac{\partial D(x, t)}{\partial t} \right\}_{x=0, L} \quad [1]$$

due to the redistribution of charges inside the sample is measured.

In general, there exist several different causes of polarization. However, we shall restrict ourselves here

**Key words:** thermally stimulated depolarization, current maxima, space charge relaxation, impurity-point defect complexes.

to two major cases: to the polarization due to an accumulation or/and depletion of mobile point defects (5) and to the polarization due to the reorientation of impurity defect complexes (1,5). Both the motion and the reorientation of these defects are thermally activated processes. For such processes, the rate of depolarization is expected to be proportional to some characteristic rate constant  $K(T) = K_0 \exp(-U/kT)$  with a pertinent activation energy  $U$  and to some "driving force"  $F(t)$ . It follows that the same is to be expected of  $i_m(t)$ , i.e.

$$i_m(t) = -K(T) \cdot F(t) \quad [2]$$

where the temperature  $T$  is a given function of time  $t$ ,  $T = f(t)$ . The derivative of  $i_m(t)$  with respect to  $t$  is thus

$$\frac{di_m(t)}{dt} = -K(T) \left\{ \frac{dT}{dt} \cdot \frac{U}{kT^2} \cdot F(t) + \frac{dF(t)}{dt} \right\} \quad [3]$$

$F(t)$  is decreasing with time and consequently  $dF/dt$  is negative. Hence there will exist a limiting rate of temperature increase,  $dT/dt$ , below which  $i_m(t)$  is monotonically decreasing and above which it is, for small values of  $t$  at least, increasing. Because  $i(t)$  becomes zero eventually, a current maximum must occur when  $\left\{ \frac{dT}{dt} \frac{U}{kT^2} + \frac{dF(t)/dt}{F(t)} \right\} = 0$ , with  $t = t_{mx}$ , and  $T = T_{mx} = f(t_{mx})$ . If the value of  $dT/dt = b = \text{const}$ , the maximum temperature  $T_{mx}$  will depend only on the properties of  $F(t)$  and on the value of the activation energy  $U$ .

Let us consider now the particular case of a polarization caused by impurity-vacancy complexes. Then  $F(t) = P(t)$ , the instantaneous polarization, and (5)

$$\frac{dP(t)}{dt} = -1/\tau \cdot P(t) \quad [4]$$

with  $\tau(T) = \tau_0 \cdot \exp(U/kT)$ , the relaxation time of reorientation. It follows from Eq. [4] that  $(dF/dt)/F(t) = -1/\tau(T)$ . Given  $b > 0$ , the maximum temperature will depend solely on the activation energy of reorientation  $U$  and on the relaxation time  $\tau(T_{mx})$  as found by Bucci and Fieschi (1);  $T_{mx} = \{(1/k) \cdot b \cdot U \cdot \tau(T_{mx})\}^{1/2}$ . It is to be noted, that Eq. [4] is a first order kinetics equation. It can, therefore, be concluded that, for any depolarization process with first order kinetics,  $T_{mx}$  will have a fixed value.

Let us now consider a depolarization with second order kinetics (6)

$$\frac{dP(t)}{dt} = -\gamma(T) \cdot P(t)^2; \quad \gamma(T) = \gamma_0 \cdot \exp\left(-\frac{U}{kT}\right) \quad [5]$$

For a constant value of  $b > 0$ , the solution of Eq. [5] for a given initial polarization  $P_0$  is

$$P(T) = \left[ \frac{1}{P_0} + \gamma_0/b \cdot \int_{T_0}^T \exp\left(-\frac{U}{kT'}\right) dT' \right]^{-1} \quad [5a]$$

and the condition for the occurrence of a maximum is  $\left\{ \frac{bU}{2kT^2} - P(T)^{-1} \right\} = 0$ . The maximum position thus depends on  $P(T)$  and, consequently (see Eq. [5a]), on the initial polarization  $P_0$ . It is easily shown that  $T_{mx}$  decreases as  $P_0$  is increased.  $P_0$  is determined by the conditions under which the sample was polarized. It may be said, therefore, that in the case of a depolarization process with second order kinetics,  $T_{mx}$  is a function of the polarization conditions.

A more intricate situation arises when the polarization is caused by an accumulation or/and depletion of mobile defects (5). In that case,  $K(T)$  stands for the mobility of the defects which cause the peak and  $F(t)$  is a function of the instantaneous defect concentration distribution  $n = n(x,t)$ . As shown in more detail in the Appendix

$$F(t) = \frac{e}{L} \int_0^L dx \int_0^x \frac{\partial}{\partial \xi} \left[ n(\xi,t) \cdot E(\xi,t) - \frac{kT}{e} \cdot \frac{\partial n(\xi,t)}{\partial \xi} \right] d\xi \quad [6]$$

where  $L$  is again the sample thickness, and  $E$  is the polarization field in the sample as it follows from the space charge distribution.

A general solution of the space charge formation and release, which would allow for a straightforward evaluation of  $[dF(t)/dt]/F(t)$ , is not known. But as demonstrated in Fig. 3,  $T_{mx}$  depends in principle on the initial TSD current density  $i_m(0)$  and on the integral

of  $i_m, Q_m = \int_0^\infty i_m(t) dt$ . Because of reasons which are given in the Appendix, it is to be expected that under favorable conditions the initial TSD current density  $i_m(0)$  increases with polarization temperature  $T_p$  or polarization time  $t_p$  less than the corresponding value of  $Q_m$ . In consequence,  $T_{mx}$  should increase with  $T_p$  or  $t_p$  and vice versa. If, on the other hand, a polarized sample is gradually depolarized,  $Q_m$  is decreased by each partial depolarization less quickly than  $i_m(0, T_0)$ . Therefore, repeated partial depolarization should result in a shift of  $T_{mx}$  to higher temperatures with each new heating cycle.

There is yet another property of the space charge relaxation which is of importance in connection with the TSD peak position. To achieve a complete relaxation of the polarization due to defect complexes, one-half of the complexes has to be activated. In the case of a space charge, any one of the accumulated defects has to be activated many times before the concentration gradient of the defects is leveled out. If one takes into account the fact that the activation probability of the defects associated into complexes and that of free defects is of about the same order of magnitude, it becomes evident that the space charge relaxation peaks ought to occur at higher temperatures than the peaks due to the relaxation complexes.

#### Experimental Data for the TSD Peak Position under Various Polarization Conditions

A number of TSD measurements on  $NH_4Cl$  and  $NH_4Cl:NiCl_2$  crystals polarized at different temperatures between  $-60^\circ$  and  $+25^\circ C$  and for two different polarization times have been carried out recently (7). These measurements always exhibited four peaks which were due to the polarization of the samples by an external field. The peak positions  $T_{mx}$  as a function of  $T_p$  and  $t_p$  are plotted in Fig. 1. The maximum posi-

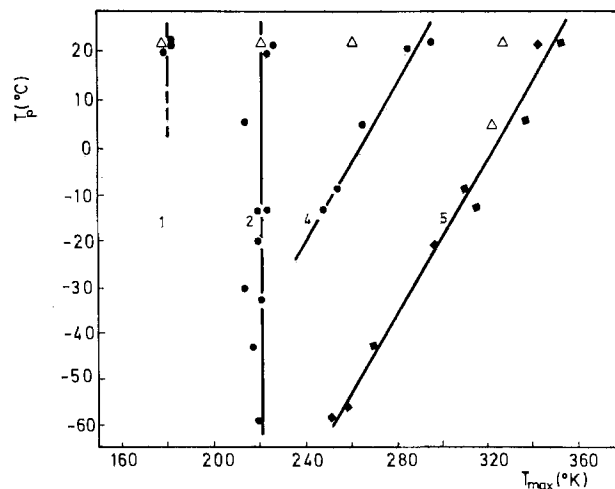


Fig. 1. Maximum position ( $T_{mx}$ ) of peaks 1, 2, 4, and 5 of  $NH_4Cl$  as a function of the polarization temperature  $T_p$  for a polarization time  $t_p$  of 30 min ( $\bullet$ ,  $\blacklozenge$ ) and 15 min ( $\triangle$ ), respectively.

tions of bands 1 and 2, which, occur at lower temperatures, are clearly independent of  $T_p$  and  $t_p$ . The maximum positions of bands 4 and 5, which occur at higher temperatures, however, increase with  $T_p$  and  $t_p$  and vice versa. One should thus expect the low temperature peaks to be caused by depolarization processes with first order kinetics; the high temperature peaks to be caused by space charge release.

It has been shown (7) that the magnitudes of peaks 1 and 4 increase with the  $NiCl_2$  concentration of the crystals. As, at the same time, the activation energy determined from the initial rise of peak 4 was found to be in good agreement with the activation energy of the motion of cation vacancies determined from conductivity data of  $NiCl_2$ -doped material (7), it seems highly probable that peak 1 is due to a relaxation of  $Ni^{2+}$ -cation vacancy complexes and that peak 4 is due to the relaxation of space charge formed partly by cation vacancies. The experimental results are thus found to agree with the theoretical predictions.

A further example of the dependence of  $T_{mx}$  on the polarization conditions is provided by Fig. 2, where the results of a "peak cleaning" i.e., a successive depolarization of the TSD of  $NH_4Cl$  crystals, are found. It can be seen that the maximum of peak 5 in Fig. 1 is shifted with the preceding depolarization toward higher temperatures, as predicted for the case of a gradual depolarization of a space charge. Peak 5 has been ascribed to the release of anion vacancies from the space charge in the undoped samples (7).

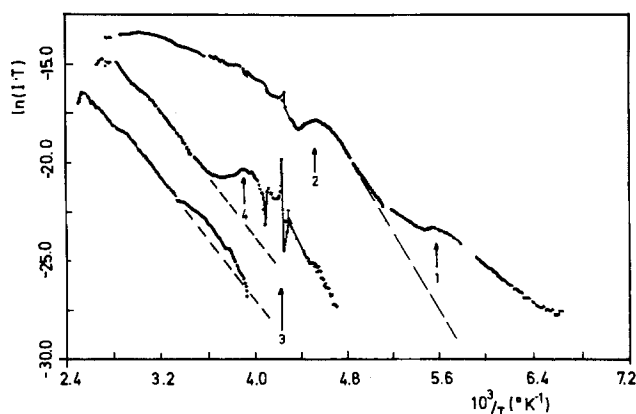


Fig. 2. Three consecutive runs of a partial TSD (peak cleaning) of undoped  $NH_4Cl$ . Peak 5  $10^3/T = 3.2-2.5$ .

Table I. Dependence of the TSD peak positions of CdF<sub>2</sub>:NaF on polarization temperature  $T_p$

Peak	$T_p$ (°K)	193	300
1	$T_{mx}$ (°K)	105-106	103-106
2		138	140
3		202-203	254

TSD measurements were also carried out on CdF<sub>2</sub>:NaF crystals polarized at different temperatures (8). Three peaks have been observed below room temperature, the maximum temperatures of which are found in Table I.

Peak 1 is due to defect-complex reorientation (2, 8), peak 3, according to Kessler and Caffyn (3), to a space charge caused by mobile point defects. It can be seen from Table I that  $T_{mx}$  is increasing with  $T_p$  for peak 3 and is independent of  $T_p$  for peak 1 as is to be expected.

Finally, it is worth mentioning that TSD measurements by other workers on CaF<sub>2</sub> crystals yielded a single peak which was assumed to be related to a second order kinetic depolarization process (6). This assumption was based, among others, on the fact that the experimental data fit Eq. [5] over three orders of magnitude of the depolarization. It was further found [see Fig. 3, Ref. (6)] that  $T_{mx}$  increases with decreasing initial polarization. The observed shift of  $T_{mx}$  is thus in agreement with theory.

### Summary

It has been shown theoretically that the TSD maximum positions are expected to depend in a characteristic way on the polarization conditions. Particularly in the case of a space charge polarization, the maximum temperature should increase with the polarization temperature and polarization time, whereas in the case of a first order kinetics depolarization, the maximum position should be invariable and occur at lower temperature than the space charge depolarization maxima. A comparison with experimental data on NH<sub>4</sub>Cl and on CdF<sub>2</sub> shows a good agreement between experiment and theory. This makes it possible, in particular, to find out whether a peak is due to first order kinetics or due to space charge release, if its maximum temperature as a function of polarization temperature or time is known.

Manuscript submitted Dec. 8, 1975; revised manuscript received April 12, 1976. This was Paper 104 presented at the Dallas, Texas, Meeting of the Society, Oct. 5-9, 1975.

Any discussion of this paper will appear in a Discussion Section to be published in the June 1977 JOURNAL.

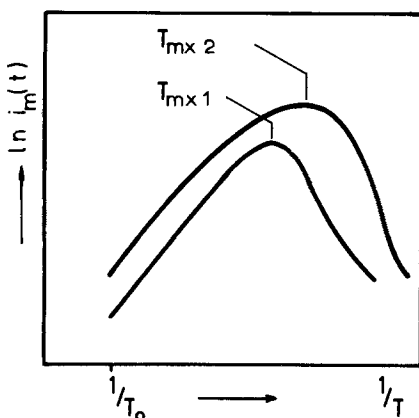


Fig. 3. Illustration of the maximum shift of a TSD peak due to a change of  $T_p$  or  $t_p$ .

All discussions for the June 1977 Discussion Section should be submitted by Feb. 1, 1977.

### APPENDIX

If a steady-state current is to pass through a polar crystal, all the ions arriving at the electrodes are to be "discharged." But at the moment the field is applied to the crystal, the rate of discharge will not necessarily be equal to the transport rate in the bulk. The effect that not all the defects arriving at an electrode are discharged is called blocking of the electrode. As a result of the blocking, defects are accumulated and/or depleted at the electrodes until the transport and the discharge rates become equal and a nonuniform concentration distribution of defects is established. If there is only one kind of mobile defect, the concentration of which is  $n_1 = n_1(x, t)$ , and the concentration of the complementary immobile defects,  $n_2$ , is constant, the displacement,  $D$ , caused by this defect distribution is

$$D(x, t) = e \int_0^L [n_1(x, t) - n_2] \cdot dx + D(0, t) \quad [A-1]$$

where  $D(x, t)$  has to satisfy the condition

$$\int_0^L E(x, t) \cdot dx = V_{apl} \quad [A-2]$$

This gives for a depolarization when  $V_{apl} = 0$

$$D(0, t) = \frac{en_2L}{2} - \frac{e}{L} \cdot \int_0^L dx \cdot \int_0^x n_1(\xi, t) \cdot d\xi \quad [A-3]$$

and thus the depolarization current is according to Eq. [1]

$$i_m(t) = -\frac{e}{L} \cdot \int_0^L dx \int_0^x \frac{\partial n_1(\xi, t)}{\partial t} \cdot d\xi \quad [A-4]$$

The derivative of  $n_1(x, t)$  may be expressed from the differential equation describing the defect distribution (5)

$$\frac{\partial n_1(x, t)}{\partial t} = \mu_1(T) \frac{\partial}{\partial x} \left[ n_1(x, t) \cdot E(x, t) - \frac{kT}{e} \frac{\partial n_1(x, t)}{\partial x} \right] \quad [A-5]$$

By identifying the mobility of the defects  $\mu_1(T)$  with the activation rate  $K(T)$  of Eq. [2], one obtains for  $F(t)$  the expression given in Eq. [6]. Using Eq. [A-4] and assuming that the sequence of integrations can be interchanged, one obtains for  $Q_m$

$$\begin{aligned} Q_m &= -\frac{e}{L} \int_0^\infty dt \left\{ \int_0^L dx \int_0^x \frac{\partial \mu_1(\xi, t)}{\partial t} d\xi \right\} \\ &= -\frac{e}{L} \int_0^L dx \int_0^x [n_1(\xi, \infty) - n_1(\xi, 0)] d\xi \end{aligned} \quad [A-6]$$

The first term in the brackets is a constant which is equal to the equilibrium defect concentration  $n_2$  for

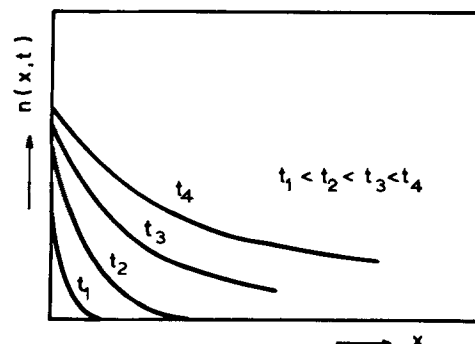


Fig. 4. Illustration of the buildup of a space charge with proceeding time of polarization  $t_p$ .  $x$  is the depth below the crystal surface.

crystals which are neutral. The second term is the initial defect concentration distribution.

Both  $i_m(0)$  and  $Q_m$  depend on the "shape" of the defect distribution and on the amount of accumulated defects. But while a steeper distribution of a fixed quantity of defects will decrease  $Q_m$ ,  $i_m(0)$  will be increased, at least in the case when the diffusion term in Eq. [6] is dominating. Consequently,  $T_{mx}$  would then be found at lower values (see Fig. 3).

A steeper distribution will occur if  $T_p$  is decreased because, as follows from the Nernst-Einstein relation, the diffusion is decreasing more rapidly with a decreasing temperature than the field drift (conductivity). Further, the distribution will become steeper if  $t_p$  is decreased. This follows directly from the way the space charge is built up with the proceeding polarization time (see Fig. 4).

## On Some Thermally Stimulated Depolarization Maxima in $\text{NH}_4\text{Cl}$ Due to Spontaneous Polarization

A. Kessler

*Institute of Physics, University of Stuttgart, Stuttgart, Germany*

### ABSTRACT

Two TSD peaks, which are observed in  $\text{NH}_4\text{Cl}$  crystals even if they are not polarized, were investigated. One, which occurs at the phase transition temperature at  $-30.6^\circ\text{C}$ , is due to a spontaneous polarization of the crystal in the course of the phase transition of crystals containing divalent impurities. The other, which occurs above  $0^\circ\text{C}$ , is due to a spontaneous current caused by an injection of defects formed under the influence of moisture on the sample surfaces.

The thermally stimulated depolarization (TSD) of  $\text{NH}_4\text{Cl}$  crystals exhibits several maxima as the temperature is increased (1, 2). But not all these maxima are due to the polarization caused by the field applied to polarize the investigated samples. Two of the maxima were observed during the heating even if the samples were not polarized previous to the heating. One peak occurs when the sample is undergoing the phase transition at  $-30.6^\circ\text{C}$ . Hence it will be called a phase transition maximum. The other peak is observed above room temperature and is due to a spontaneous current in the samples. This paper is a first report about these effects of which the former has already been observed by Uebele (3).

### The Phase Transition Peak

*Current peaks at phase transition.*—If a sample of a  $\text{NH}_4\text{Cl}$  crystal is placed between electrodes which are connected to a galvanometer, every time the temperature is decreased below or increased above the phase transition temperature,  $T_{ph} = -30.6^\circ\text{C}$ , a current peak is observed. The peak is detected even if the electrodes are insulated, and its maximum value  $I_{mx}$  was found to increase proportionally to the rate of temperature change  $dT/dt$ . The integral of the measured current  $\int_0^\infty I(t)dt$  has, for a given sample, a fixed value which changes the sign if the sample is heated instead of cooled and vice versa. To insulate the crystal samples, transformer oil was applied to the crystal electrode interfaces, because only in that way could both insulation and a good and reproducible thermal contact be achieved.

The above-mentioned facts show that a displacement current is measured, and that the spontaneous polariza-

tion,  $P$ , the change of which causes the measured current, is in the first approximation a function of the temperature  $T$  only

$$I(t) = \frac{dP}{dt} = \frac{dT}{dt} \cdot \frac{dP}{dT} \quad [1]$$

A graph of  $P$  vs.  $T$  is shown in Fig. 1.

*Correlation of the spontaneous polarization with the phase transition.*—To avoid any possible perturbation of the measurements, only the temperature of the electrodes was measured. If it is assumed that the "thermal resistance,"  $r$ , between the sample and the electrode has a fixed constant value, the lag  $\Delta T$  of the mean temperature of the sample behind  $T$  should be proportional to  $1/r$  and to  $dT/dt$ , because  $(mc) \cdot dT = 1/r \cdot \Delta T \cdot dt$ , where  $(mc)$  is the heat capacity of the sample. An extrapolation of  $T_{mx} = f(dT/dt)$  for  $dT/dt \rightarrow 0$  should thus yield the true temperature at which the current peak occurs. As shown in Fig. 2, this temperature, for both  $\text{NH}_4\text{Cl}$  and  $\text{ND}_4\text{Cl}$ , is in good agreement with the respective phase transition temperatures [see, for example, Ref. (4)]. This and the fact that the  $P(T)$  vs.  $T$  dependence is similar in principle to the dependence on  $T$  of both the order parameter of the  $\text{NH}_4^+$  ions (5) and the integral of the specific heat (6) shows that both polarization and depolarization are correlated with the phase transition.

*Dependence of the total polarization  $\Delta P$  on the impurity content of the crystals.*—The phase transition current peak  $I = f(t, T)$  of samples containing different impurity concentrations was measured and  $\Delta P = \int_{T_0}^{T_1} I(t)dt$  for  $T_0 \ll T_{ph} \ll T_1$  calculated. The results are given in Table I. It is obvious that  $\Delta P$  depends on the kind and quantity of the impurities built into the crystal. The highest polarization occurred in crystals

### REFERENCES

1. C. Bucci and R. Fieschi, *Phys. Rev. Letters*, **12**, 1 (1964); *Phys. Rev.*, **148**, 816 (1966).
2. I. Kunze and P. Müller, *Phys. Status Solidi (a)*, **13**, 197 (1972).
3. A. Kessler and J. E. Caffyn, *J. Phys. C: Solid State Phys.*, **5**, 1134 (1972).
4. C. Bucci and S. A. Riva, *J. Phys. Chem. Solids*, **26**, 363 (1965).
5. A. B. Lidiard, "Encyclopedia of Physics," Vol. XXII, Springer Verlag, Berlin (1957).
6. E. B. Podgorshak and R. P. Moran, *Phys. Rev. Letters*, **30**, 926 (1973).
7. P. Berteit, A. Kessler, and T. List, *Z. Physik*, **B24**, 15 (1976).
8. A. Kessler, *J. Phys. C: Solid State Phys.*, **6**, 1594 (1973).

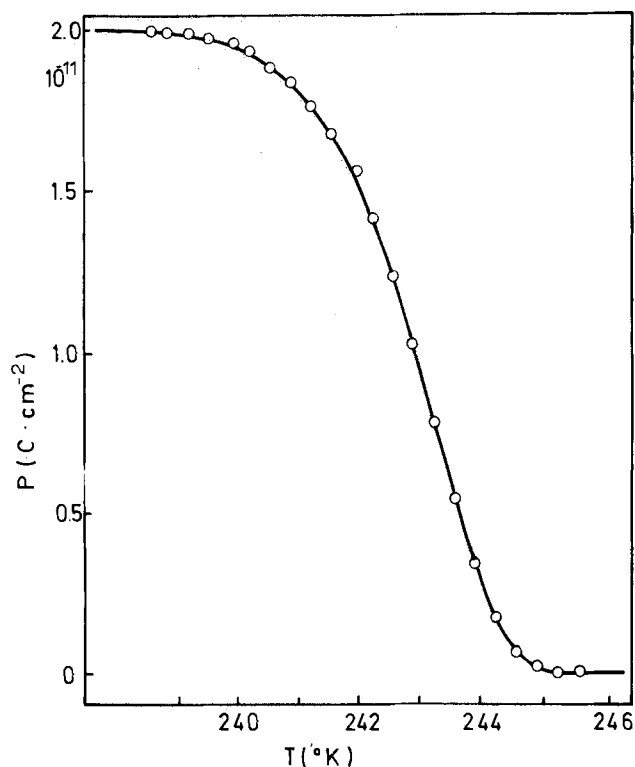


Fig. 1. The spontaneous polarization,  $P$ , of a  $\text{NH}_4\text{Cl}$  crystal sample at phase transition ( $242.5^\circ\text{K}$ ) as a function of temperature.

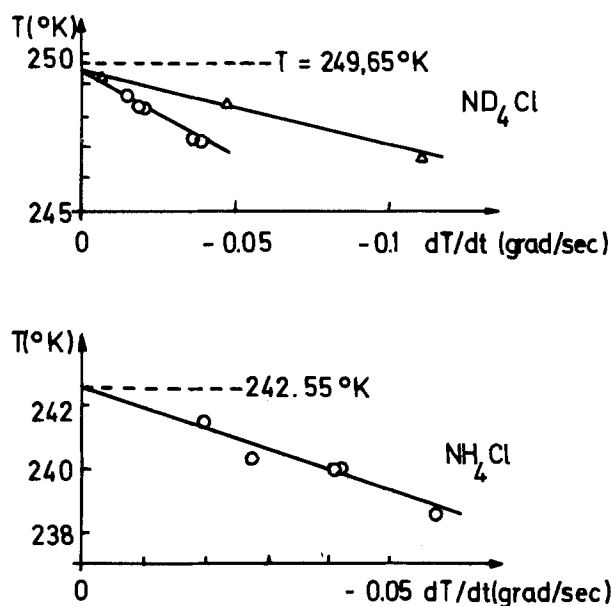


Fig. 2. Dependence of the observed peak position on the rate of temperature increase:  $\Delta$ , sample insulated with transformer oil;  $\circ$ , sample insulated with machine oil.

with built-in divalent impurities, which form impurity complexes with vacancies (2). In that case,  $\Delta P$  is clearly increasing with the concentration of the impurities. For crystals containing high concentrations of divalent copper in an interstitial position which forms neutral centers with  $\text{NH}_3$  [ $\text{Cu}^{2+}$ -center II (7)] or with  $\text{H}_2\text{O}$  [ $\text{Cu}^{2+}$ -center I (7)], the value of  $\Delta P$  is the same or smaller than for undoped crystals. Even if we take these results with some caution, we arrive at the conclusion that the polarization is not an inherent property of  $\text{NH}_4\text{Cl}$  but that it is caused by the built-in impurities. While for  $T > T_{\text{ph}}$  the complexes are no doubt randomly oriented, it seems possible that for  $T < T_{\text{ph}}$  there exists a preferential orientation. An alignment of

Table I. The total polarization,  $\Delta P$ , due to phase transition of crystals containing different kinds and concentrations of impurities

Crystal	Method of growth	Dopant	$P$ ( $\text{C}/\text{cm}^2$ )	$dT/dt$ (grad/sec)
$\text{ND}_4\text{Cl}$	Melt	—	$2.45\text{--}5.0 \times 10^{-11}$	$-0.07\text{--}0.11$
$\text{NH}_4\text{Cl}$	Melt	—	$2.1\text{--}3.2 \times 10^{-11}$	$-0.04\text{--}0.14$
$\text{NH}_4\text{Cl}$	Melt	10 ppm $\text{CuCl}_2$	$1.4\text{--}2.4 \times 10^{-10}$	$0.05\text{--}0.18$
$\text{NH}_4\text{Cl}$	Solution	5000 ppm $\text{Cu}^{2+}$ in center I	$1.0\text{--}2.0 \times 10^{-12}$	0.1
$\text{NH}_4\text{Cl}$	Solution	5000 ppm $\text{Cu}^{2+}$ in center II	$4.0\text{--}5.5 \times 10^{-11}$	0.1
$\text{NH}_4\text{Cl}$	Solution	100 ppm $\text{NiCl}_2$	$4.9\text{--}8.1 \times 10^{-10}$	$0.11\text{--}0.16$

the complexes would yield roughly a polarization like the measured one. Dipole moments caused by a geometric distortion of the lattice due to the built-in impurities, on the other hand, should be randomly oriented even for  $T < T_{\text{ph}}$  and would hardly yield a value which could account for the measured polarization. The centers I and II, which have normally no dipole moment and which are immobile, most probably do not contribute to  $P$ .

*Occurrence of more than one current peak at phase transition.*—Sometimes more than one peak is observed which, moreover, may vary in sign. It is believed that this effect is due to the existence of domains [see Ref. (8)] in the crystal. Because of the heat transmission to or from the crystal, there is necessarily a temperature gradient inside the crystal due to which the domains reach  $T_{\text{ph}}$  at different times. Furthermore, the existence of a hysteresis of the phase transition, which was observed between  $-72^\circ$  and  $-28^\circ\text{C}$  and is also attributed to the existence of domains (9), points to the above explanation of the multiple peaks. As far as the different signs of the peaks are concerned, they may be understood as a consequence of different orientations of the domains arranged so as to minimize the total polarization energy of the sample.

### Spontaneous Current Peak

The occurrence of a spontaneous current  $I_{\text{sp}}$  of some  $10^{-11}\text{--}10^{-8}\text{A}$  at room temperature is observed if a fresh, unpolarized sample of  $\text{NH}_4\text{Cl}$  crystal provided with graphite electrodes is connected to a galvanometer (2). The cross section of the samples was about  $1\text{ cm}^2$ . As the resistance of the samples is of the order of  $10^{11}$  ohm, voltages up to several thousands of volts would be needed to cause such currents to pass through the samples. As may be verified by using insulated electrodes, the current is caused "by the sample itself."

*Dependence of the spontaneous current on the quantity of adsorbed  $\text{H}_2\text{O}$ .*—One finds that  $I_{\text{sp}}$  is proportional to the water vapor pressure,  $p$ , acting on the contact surfaces of the samples (Fig. 3). This is achieved by sealing off the cylindrical surfaces of the samples and providing the contact surfaces, e.g., by a layer of colloidal graphite. The effect is strongest if only one contact surface is exposed to the water vapor (Fig. 3, curve 1). If the water vapor has access to both electrodes (Fig. 3, curve 3),  $I_{\text{sp}}$  is more than two orders of magnitude smaller. It is interesting to note that when vacuum-evaporated gold electrodes are used,  $I_{\text{sp}}$  is still increased if a high enough water vapor pressure is built up, but with a considerable delay after the build-up of  $p$ . Any decrease in  $p$  is followed by a decrease of  $I_{\text{sp}}$  after some delay. This delay shows that the  $\text{H}_2\text{O}$  molecules reach the crystal surface by diffusion through the metal layer.

Below  $p \sim 4$  Torr,  $I_{\text{sp}}$  is roughly independent of  $p$ . This is easily understood if it is assumed that there exists a certain minimum concentration of  $\text{H}_2\text{O}$  adsorbed on the crystal surface which depends mainly on the temperature and not on  $p$ . This notion is supported by the fact that, by heating the sample in a vacuum of  $5 \times 10^{-2}$  Torr to  $100^\circ\text{C}$ ,  $I_{\text{sp}}$  at first decreased to less

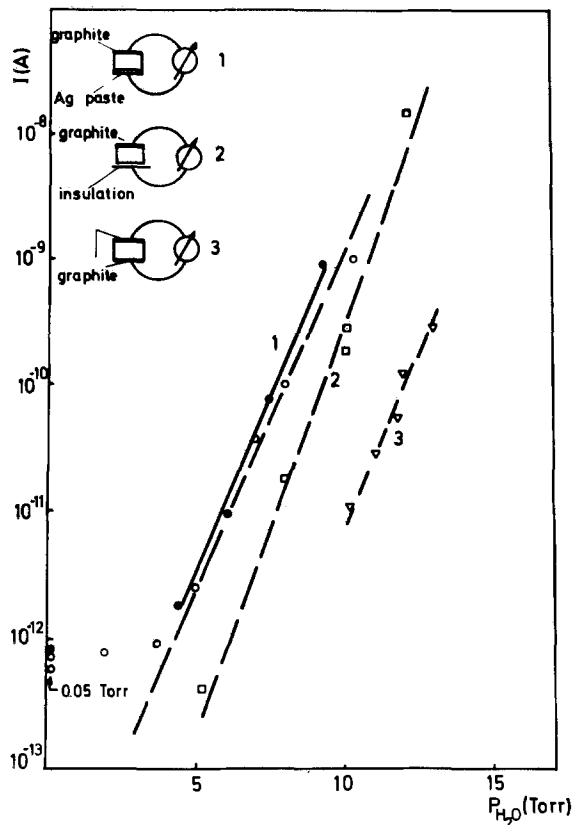


Fig. 3. Spontaneous current,  $I_{sp}$ , of a  $\text{NH}_4\text{Cl}$  crystal sample as a function of the water vapor pressure,  $p$ , in the measuring cell and of the electrode material.

than  $10^{-14}\text{A}$  at room temperature, but increased later to the original value of about  $8 \times 10^{-13}\text{A}$ . It is to be noted that above  $100^\circ\text{C}$  transitory decrease of the pressure in the measuring cell is observed, obviously due to an enhanced release of water.

**Dependence of the spontaneous current on temperature and time.**—If the temperature of the sample is decreased, one finds  $I_{sp}$  decreasing proportionally to  $\exp(-U/kT)$  with  $U \sim 1\text{ eV}$  (2) for undoped samples. If the temperature is increased above room temperature, a current maximum is observed (Fig. 4). The maximum position varies widely according to experimental conditions. All  $\text{NH}_4\text{Cl}$  crystals exhibit a spontaneous current, however, the magnitude is determined by the "history" of the sample. If  $I_{sp}$  is higher than  $10^{-12}\text{A}$ , it will decrease markedly with time, and the higher the initial value of  $I_{sp}$ , the higher the rate of decay.

**A first tentative interpretation of the findings.**—It is known that the abnormally high sublimation rate of  $\text{NH}_4\text{Cl}$  is caused by catalytic decomposure of  $\text{NH}_4\text{Cl}$  into  $\text{NH}_3$  and  $\text{HCl}$ . These neutral molecules are bound to the crystal with a lower energy than that of the  $\text{NH}_4^+$  and  $\text{Cl}^-$  ions. Consequently, they are easily "evaporated" (10). It seems that due to such a process vacancies should be created. It is to be expected that, due to an increasing amount of  $\text{H}_2\text{O}$  on the crystal surface, the decomposure will be enhanced. Because vacancies (and also  $\text{NH}_3$ ) are mobile in  $\text{NH}_4\text{Cl}$  crystals, they should penetrate into the bulk of the crystal (the cation vacancies at a higher rate) because they are more mobile (11). This should cause a net charge flow and if only one electrode is exposed to  $\text{H}_2\text{O}$  a current should be observed. In due time, an equilibrium will be reached, due to the buildup of a double layer.

It should be noted that the highest measured value of  $I_{sp}$  (see Fig. 3) would imply a rate of  $10^{11}$  vacancy/ $\text{cm}^2\text{ sec}$  entering the crystal. This is an extremely high, but still acceptable figure as compared with the ca.

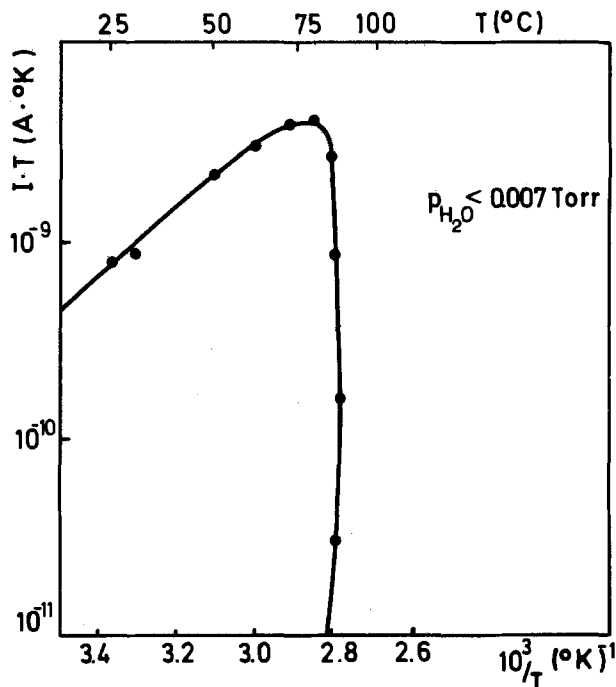


Fig. 4. Spontaneous current peak observed above room temperature on heating of an unpolarized sample.

$6 \times 10^{14}$  unit cells of the surface and taking into account the rapid decrease of  $I_{sp}$  after exposure.

If both electrodes are provided with permeable electrodes, theoretically, no current should be observed. But if no special provisions are made to safeguard identical conditions at both electrodes, a difference of about 1/100 of the current obtained with one single exposed electrode (see Fig. 3) seems a realistic value.

The decrease of  $I_{sp}$  with time should be a consequence of the buildup of a double layer, which to some extent can be compared with the double layer predicted by Lehovc (12). But a TSD peak as shown in Fig. 4 is most probably caused by the combined effect of the temperature dependence of the spontaneous current and by the evaporation of  $\text{H}_2\text{O}$  from the crystal surface. The peak occurs at a temperature at which the rate of loss of  $\text{H}_2\text{O}$  is higher than the increase in the mobility of the vacancies. Only in that way can the sudden drop in the current by orders of magnitude be understood.

Finally, it is to be emphasized that by the same mechanism, i.e. by the formation of mobile defects due to the catalytic effect of  $\text{H}_2\text{O}$  and the evaporation of the adsorbed  $\text{H}_2\text{O}$  at higher temperatures, some features of the conductivity of  $\text{NH}_4\text{Cl}$  have been explained (2).

Manuscript submitted Dec. 8, 1975; revised manuscript received April 12, 1976. This was Paper 105 presented at the Dallas, Texas, Meeting of the Society, Oct. 5-9, 1975.

Any discussion of this paper will appear in a Discussion Section to be published in the June 1977 JOURNAL. All discussions for the June 1977 Discussion Section should be submitted by Feb. 1, 1977.

#### REFERENCES

1. A. Kessler, *Solid State Commun.*, **12**, 697 (1973).
2. P. Berteit, A. Kessler, and T. List, *Z. Physik*, **B24**, 15 (1976).
3. P. Uebele, Thesis, University of Stuttgart (1973).
4. V. Hovi, Conference on Non-Metallic Crystals, p. 67, New Delhi (1969).
5. N. Kuroda and A. Kawamori, *J. Phys. Chem. Solids*, **32**, 1233 (1971).
6. F. Simon, *Ann. Phys.*, **68**, 4 (1922).



7. F. Boettcher and J. M. Spaeth, *Phys. Status Solidi (b)*, **61**, 465 (1974).
8. L. Vanotti, H. R. Zeller, K. Bachmann, and W. Känzig, *Phys. Kondens. Mater.*, **6**, 51 (1967).
9. P. Nissilä and J. Pöyhönen, *Phys. Letters*, **33A**, 345 (1970).
10. R. F. Chaiken, D. J. Sibbett, J. E. Sutherland, D. K. Van de Mark, and A. Wheeler, *J. Chem. Phys.*, **37**, 2311 (1962).
11. T. M. Harrington and L. A. K. Staveley, *J. Phys. Chem. Solids*, **25**, 921 (1964).
12. K. Lehovc, *J. Chem. Phys.*, **21**, 1123 (1953).

## Impurity and Substrate Diffusion in a Thin Contact Layer

R. P. Goel<sup>1</sup>

*Department of Mechanical Engineering, North Carolina Agricultural and Technical State University, Greensboro, North Carolina 27411*

and F. E. Bader

*Bell Laboratories, Columbus, Ohio 43213*

### ABSTRACT

Based on simplifying assumptions, diffusion phenomena of substrate and impurity through a thin contact layer have been compared. Results are presented in terms of nondimensionalized parameters  $k$  (a measure of diffusion rate, time, and contact thickness) and  $\bar{l}/l$  (film thickness/contact thickness). A single master curve is shown to represent each diffusion process. Numerical examples of practical interest are presented and the limitations of the theory are discussed.

Noble metals are typically used as contact layers because of their superior contact properties. In view of the high cost of these materials, it is desirable that a minimum thickness be used to attain a contact of desired quality. However, contact films resulting from mass diffusion of substrate material to the surface at elevated operating temperatures may set a lower limit on contact layer thickness. Impurities which are initially present in the contact layers may also diffuse to the surface and form films which degrade contact performance. In the case of electroplated gold, the most commonly used layer, small amounts of cobalt or nickel impurities are deliberately added to harden the gold.

The purpose of this study is to compare theoretically the relative rates of substrate and impurity diffusion. Although it is known that the presence of an impurity influences substrate diffusion and *vice versa*, it will be assumed that the processes are independent of each other. It will be shown that there may be regimes of time and temperature where one mechanism or the other will be clearly dominant.

The increasing use of elevated temperatures for various accelerated tests is another reason that diffusion rate studies are important. Contact resistance and/or film thicknesses are measured after elevated temperature exposures, and the data extrapolated to contact ambient temperatures. This can yield erroneous results if the dominant mechanism at elevated temperature is not the same as that at the operating temperature.

Equations governing the diffusion processes and their solutions along with the simplifying assumptions used to derive the solutions are presented below. Some examples of practical importance in the system of cobalt-hardened gold on a copper substrate are also discussed using diffusion rate data developed by Pinnel and Bennett (1) and Tompkins (2). Design guidelines are suggested, along with limitations of the present theory.

<sup>1</sup> Bell Laboratories Visiting Professor.  
Key words: cobalt, copper, gold, short-circuit diffusion mechanism.

### Theory

Diffusion in an electrical contact can be idealized by considering the following: (i) diffusion occurs only in the thickness direction of the medium (also called solvent) which is bounded by two planes, *e.g.*, the planes at  $x = 0$  and  $x = l$ ; (ii) no intermetallic compounds are formed; (iii) the substrate and impurity coefficients,  $D_s$ ,  $D_i$ , respectively, are independent of their respective concentrations; (iv) the two diffusion processes are independent of each other; (v) the contact layer is homogeneous throughout; (vi) the impurity and substrate arriving at the contact surface are oxidized instantaneously.

Diffusion through a homogeneous medium can be adequately described by Fick's second law. Thence, for substrate and impurity diffusion, respectively, we have

$$\frac{\partial C_s}{\partial t} = D_s \frac{\partial^2 C_s}{\partial x^2} \quad [1]$$

$$\frac{\partial C_i}{\partial t} = D_i \frac{\partial^2 C_i}{\partial x^2} \quad [2]$$

where  $C$  and  $t$  represent concentration and time and subscripts  $s$  and  $i$  denote substrate and impurity, respectively.

Let us assume that the initial concentration of the impurity,  $C_{i0}$ , is uniform throughout the medium and the medium is free from any substrate material at time  $t = 0$ . Therefore, we have

$$C_s(x, 0) = 0 \quad [3]$$

$$C_i(x, 0) = C_{i0} \quad [4]$$

Assumption (vi) implies sink effect at the contact surface,  $x = l$ . Such an assumption would be reasonable at lower temperatures at which diffusion rates are very low. However, if large oxide films are formed on the contact surface, this assumption will no longer hold. But by that time the contact material may already have

lost its effectiveness. In our applications, ambient temperature is relatively low and thus assumption (vi) is reasonably applicable. Hence we have

$$C_s(l, t) = 0 \tag{5}$$

$$C_i(l, t) = 0 \tag{6}$$

The impurity content present nearer to the contact surface will diffuse out at a faster rate than that present farther away from the surface because of high concentration gradient near the surface. And, therefore, this gradient at the interface of the substrate and the contact layer (farthest point from the contact surface) will virtually be zero. Consequently, we can simplify the solution of the boundary value problem by including its mirror image, which implies

$$C_i(-l) = 0 \tag{7}$$

(See Fig. 1.) One more condition is needed to solve Eq. [1]. That can be obtained by assuming that the Matano interface remains stationary, which implies that  $C_s$  remains constant at 50 atom per cent (a/o) at  $x = 0$ . Thus

$$C_s(0, t) = C_{s0} = 50 \text{ a/o} \tag{8}$$

It should be noted that concentration  $C$  can be given in a variety of units, but the flux is usually expressed in mass/area/time. Therefore,  $C$  must also be expressed in mass/volume units when using flux equations. The following conversion factors, CF, may be used to transform atom per cent or weight per cent (w/o) to mass/volume

$$\frac{C(\text{mass/vol})}{C(\text{a/o})} = \frac{\rho_1 \rho_2}{\rho_2 + \frac{M_2}{M_1} \rho_1} \frac{100 - C(\text{a/o})}{C(\text{a/o})} \equiv \text{CF}$$

$$\frac{C(\text{mass/vol})}{C(\text{w/o})} = \frac{\rho_1 \rho_2}{\rho_2 + \rho_1} \frac{100 - C(\text{w/o})}{C(\text{w/o})} \equiv \text{CF}$$

in which  $\rho_1, \rho_2, M_1,$  and  $M_2$  denote mass densities and atomic weights of the solute (substrate or impurity) and the solvent (contact layer), respectively.

Equations [1] and [2] along with the respective boundary and initial conditions are straightforward problems. Following Carslaw and Jaeger (3) and Crank (4), the solutions can be written as

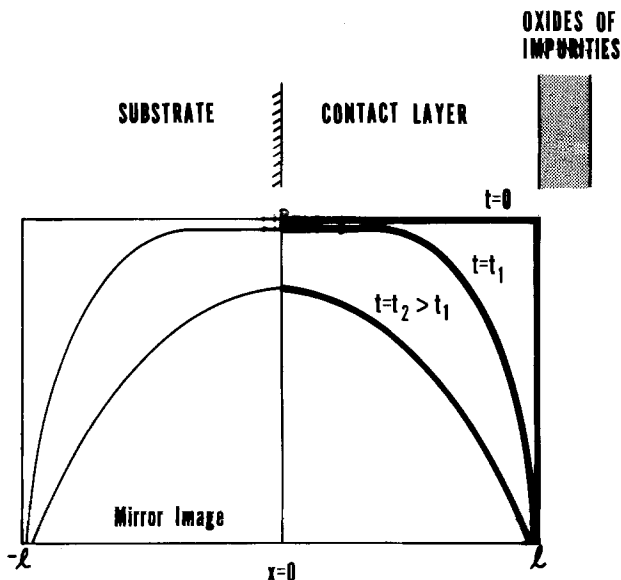


Fig. 1. Boundary conditions

$$C_s = C_{s0} \left[ 1 - \frac{x}{l} - \frac{2}{\pi} \sum_{n=1}^{\infty} \frac{1}{n} \sin(n\pi x/l) \exp(-n^2\pi^2 k_s) \right] \tag{9}$$

$$C_i = C_{i0} \sum_{n=0}^{\infty} \frac{(-1)^n}{\pi(2n+1)} \cos((2n+1)\pi x/2l) \exp[-(2n+1)^2\pi^2 k_i/4] \tag{10}$$

where  $k$  is a nondimensionalized parameter and is given by  $k = Dt/l^2$ .

If  $Q_s$  denotes the amount of substrate material appearing on the contact surface, then it can easily be given by

$$Q_s = \text{area} \times \left[ - \int_0^t D_s \frac{\partial C_s}{\partial x} \Big|_{x=l} dt \right] \tag{11}$$

Substituting Eq. [8] and [9] into [11] and after some algebraic manipulations, we get

$$Q_s = C_{s0} \times \text{area} \times l \left[ k_s + \frac{2}{\pi^2} \sum_{n=1}^{\infty} (-1)^{n+1} \frac{1}{n^2} \{ \exp(-n^2\pi^2 k_s) - 1 \} \right] \tag{12}$$

Similarly, following Tompkins (2), we can obtain the amount of impurity appearing on the surface, which is given by

$$Q_i = C_{i0} \times \text{area} \times l \left[ 2 - \frac{16}{\pi^2} \sum_{n=0}^{\infty} \frac{1}{(2n+1)^2} \exp\{-(2n+1)^2\pi^2 k_i/4\} \right] \tag{13}$$

Equation [13] can be approximated by the following simplified expression for times up to which 60% of the total impurity has diffused

$$Q_i = C_{i0} \times \text{area} \times l \left( \frac{4}{\pi} k_i \right)^{1/2} \tag{14}$$

In fact, the above approximation is an exact solution for a semi-infinite thick contact layer. It leads to quite an interesting result which we shall discuss later. Moreover, the underlying assumptions of the previous analysis are violated for times longer than that at which 60% or more of the total impurity has diffused out, and therefore, Eq. [14] would adequately describe the impurity diffusion process.

The aforesaid Eq. [12] and [14] yield the total amounts of substrate and impurity diffusants that have arrived at the contact surface at any given time. It may be more useful to know film thicknesses instead. This can be easily done by dividing both sides of Eq. [12] and [14] by  $\text{area} \times \rho_1$  resulting in the following equations (normalized by dividing by the layer thickness)

$$\frac{\bar{l}_s}{l} = \frac{C_{s0}}{\rho_1} \left[ k_s + \frac{2}{\pi^2} \sum_{n=1}^{\infty} (-1)^{n+1} \frac{1}{n^2} \{ \exp(-n^2\pi^2 k_s) - 1 \} \right] \tag{15}$$

$$\frac{\bar{l}_i}{l} = \frac{C_{i0}}{\rho_1} (4/\pi k_i)^{1/2} \tag{16}$$

where  $\bar{l}$  denotes the film thickness. As mentioned earlier, concentration  $C$  is usually expressed as atom per cent or weight per cent and thus conversion factors CF must be applied. Using appropriate CF's and assuming  $C_{s0} = 50 \text{ a/o}$ , Eq. [15] and [16] are solved for different values of  $k$ . Results are presented in Fig. 2 in which  $k$  and  $(1/2 \text{ MCF}) (\bar{l}/l)$  represent the ordinate and abscissa, respectively.  $\text{MCF} = \text{CF}/\rho_1$  is called the

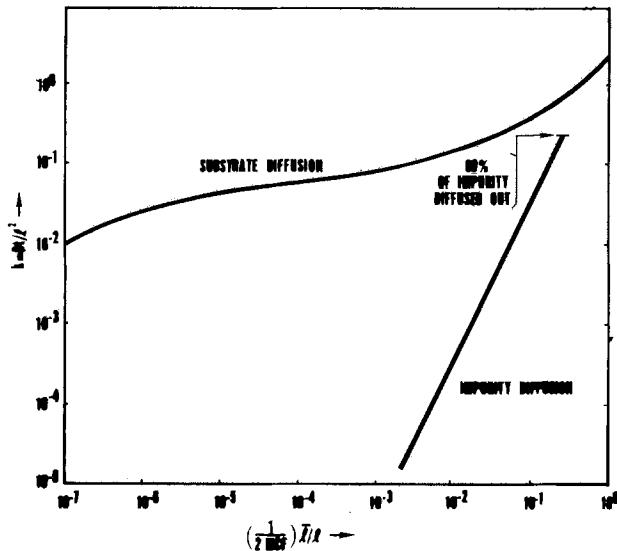


Fig. 2. Impurity and substrate diffusion

modified conversion factor. For any binary couple MCF can easily be calculated from the known values of atomic weights, mass densities, and concentration values.

Let us reexamine Eq. [16] and state the results observed by Tompkins (2) in his study of cobalt-hardened gold. Rewriting Eq. [16] and replacing  $k_1$  by  $D_1 t/l^2$  we get

$$\bar{l}_i = \frac{C_{i0}}{\rho_1} \left( \frac{4}{\pi} D_1 t \right)^{1/2} \quad [17]$$

which implies that the impurity film thickness,  $\bar{l}_i$ , is independent of contact thickness for times up to which less than 60% of the initial impurity content diffuses out of the contact layer. This occurs at  $k_1 \approx 2 \times 10^{-1}$ . Note, however,  $\bar{l}_i$  is directly proportional to initial concentration,  $C_{i0}$ .

Figure 2 represents two master curves, one for substrate diffusion and the other for impurity diffusion for all impurity concentration levels. For any binary planar couple which satisfies the assumptions stated earlier, one can estimate the film thicknesses at a given time and temperature. Next, we discuss some examples of practical interest to illustrate the use of these curves.

### Examples

The degradation of thin gold electroplates by mass diffusion of the base metal (copper) and interdiffusion of cobalt in cobalt-hardened gold are possible failure mechanisms in typical electrical connectors. Therefore, the results of the present theory will now be applied to cobalt-hardened gold on a copper substrate. Note that we have assumed the two processes to be independent of each other.

Diffusion rates for copper and cobalt through gold have been investigated, among others, by Pinnel and Bennett (1) and Tompkins (2), respectively. At test temperatures of 150°C, the rates were found roughly to be the same. Thence, we shall assume  $D_1 \approx D_s = D$  in our numerical examples.

Two examples of diffusion through 2.54  $\mu\text{m}$  (100  $\mu\text{in.}$ ) and 1.27  $\mu\text{m}$  (50  $\mu\text{in.}$ ) thick layers of gold at test temperature of 150°C are considered. The only impurity in gold is taken to be cobalt with an initial concentration of 0.25 w/o.

From Ref. (1, 2) we have

$$D_{\text{Cu}} \approx D_{\text{Co}} = D \approx 4 \times 10^{-16} \text{ cm}^2/\text{sec}$$

Modified conversion factors for Au-Cu ( $C_{s0} = 50 \text{ a/o}$ ) and Au-Co ( $C_{i0} = 0.25 \text{ w/o}$ ) are as follows

$$2 \text{ MCF}_{\text{Au-Cu}} = 0.8156$$

$$2 \text{ MCF}_{\text{Au-Co}} = 1.0875 \times 10^{-2}$$

If we assume the test time periods to be 1 day, 30 days, and 200 days then the corresponding values of  $k$  are given in Table I.

For each value of  $k$ , we can obtain  $(1/2 \text{ MCF}) (\bar{l}/l)$  from Fig. 2. Since we have assumed instantaneous oxidation of the solute (substrate and/or impurity) as it arrives at the contact surface, and if we further assume that Cu and Co are oxidized into  $\text{Cu}_2\text{O}$  and  $\text{CoO}$ , respectively, then the film thicknesses of Cu and Co, obtained from Fig. 2, can be converted into oxide film thicknesses by multiplying by 1.7278 and 1.9424, respectively. Results are presented in Table II which shows that in the early stages of diffusion very little copper has arrived at the surface while cobalt has appeared almost immediately. As the time progresses,  $\text{Cu}_2\text{O}$  film starts building up on the surface and soon exceeds the  $\text{CoO}$  film. It is quite possible that  $\text{CoO}$  film, almost instantaneously formed on the surface, may retard the formation of  $\text{Cu}_2\text{O}$  film or even the formation of  $\text{CoO}$  film may become slow for lack of free oxygen. But, nonetheless, the present analysis provides us with some degree of qualitative and quantitative relative measure of the two films.

### Discussion

Based on simplifying assumptions, diffusion phenomena of substrate and impurity through a thin contact layer have been compared. Results are presented in terms of nondimensionalized parameters  $k$  and  $(1/2 \text{ MCF}) (\bar{l}/l)$ . A single master curve is shown to represent each diffusion process.

On a log-log scale the substrate diffusion curve concaves down in the beginning but soon becomes concave up. It implies that substrate film thickness builds up slowly at first, then increases at a fast rate, and eventually becomes unbounded. However, as stated earlier, the later part of the curve is irrelevant because the underlying assumptions of the theory are violated.

Figure 2 suggests that there is a narrow range of  $k$  (between 0.01-0.1) over which most of the substrate diffusion, especially in applications of our interest, occurs. Therefore, the film thickness is very sensitive to the value of  $k = Dt/l^2$ . For a given material system, time, and temperature, the only parameter which a designer can effectively control is the contact thickness. Hence, once an upper limit on an acceptable substrate film thickness is determined, the designer can put a lower limit on the contact thickness assuming  $D$  is known. In the given example of gold on a copper substrate, recent data by Kulpa (5) and others have shown copper diffusion far in excess of that of Ref. (1). This is believed to be a "short circuit" mechanism, not predictable by analysis of the diffusion profile, and highly dependent on layer and substrate structure. This variability of the diffusion coefficient indicates the need for caution when using diffusion data

Table I. Value of  $k = Dt/l^2$ 

$l$ ( $\mu\text{m}$ )	$t$ (sec)	$8.64 \times 10^4$ (1 day)	$25.92 \times 10^5$ (30 days)	$17.28 \times 10^6$ (200 days)
1.27		$2.143 \times 10^{-8}$	$6.429 \times 10^{-2}$	$4.285 \times 10^{-1}$
2.54		$5.36 \times 10^{-4}$	$1.61 \times 10^{-2}$	$1.07 \times 10^{-1}$

Table II. Oxide film thicknesses ( $\text{\AA}$ )

$t$ (days)	2.54 $\mu\text{m}$		1.27 $\mu\text{m}$	
	$\text{Cu}_2\text{O}$	$\text{CoO}$	$\text{Cu}_2\text{O}$	$\text{CoO}$
1	0	7	0	7
30	<1	40	9	40
200	179	91	2678	91

and the desirability of further diffusion rate studies. For times up to which 60% of total impurity has diffused, the impurity film thickness depends upon the initial impurity content only, and this thickness does not depend upon the contact thickness.

As stated earlier, severe restrictions were imposed on the theory by making simplifying assumptions such as no interdependence of substrate and impurity diffusion processes, instant oxidation, etc. However, at low temperatures the diffusion rates are very small, the scatter in diffusion rate data is wide, and there exists very little quantitative information and relative comparison on diffusion of substrate and impurity processes, in spite of the relative importance of the subject. The present study, while being cognizant of its limitations, could provide an engineer with a useful design tool.

Manuscript submitted Nov. 19, 1975; revised manuscript received Feb. 19, 1976.

Any discussion of this paper will appear in a Discussion Section to be published in the June 1977 JOURNAL. All discussions for the June 1977 Discussion Section should be submitted by Feb. 1, 1977.

Publication costs of this article were assisted by Bell Laboratories.

#### REFERENCES

1. M. R. Pinnel and J. E. Bennett, *Met. Trans.*, **3**, 1989 (1972).
2. H. G. Tompkins, *This Journal*, **122**, 983 (1975).
3. H. S. Carslaw and J. C. Jaeger, "Conduction of Heat in Solids," Clarendon Press, New York (1959).
4. J. Crank, "The Mathematics of Diffusion," Oxford University Press, London (1970).
5. S. Kulpa, Private communications.

## Technical Notes



### On the Enhancement of Silicon Chemical Vapor Deposition Rates at Low Temperatures

Chin-An Chang<sup>1</sup>

*Materials and Molecular Research Division, Lawrence Berkeley Laboratory, Berkeley, California 94720*

Chemical vapor deposition (CVD) has been a widely used technique for thin film device fabrication. It is especially applicable to thin film silicon solar cells. A deposition rate of a few microns per minute can be easily obtained, and a p-n junction can be made by mixing silicon chemical vapors, such as silane and silicon tetrachloride, with dopant gases, like diborane and phosphine. In general, CVD of silicon is carried out at a substrate temperature *ca.* 1000°-1200°C, and a single crystal silicon wafer is used for an epitaxial growth of thin films. However, to make economic thin film solar cells for terrestrial photovoltaic applications, noncrystalline and often nonsilicon substrates are required. Furthermore, interaction between the substrate thus chosen and the silicon thin film deposited should be kept minimal. For example, at a substrate temperature *ca.* 1200°C, silicon thin films deposited on graphite show a significant diffusion of silicon and carbon and the formation of silicon carbide (1). Much less diffusion is noted, however, when the substrate temperature is below 800°C (2). Similar high temperature interaction between the silicon films deposited and other types of substrate has also been reported (3). Preferably, one should use the lowest possible substrate temperatures to minimize such interactions and diffusion.

At low substrate temperatures, however, other problems arise. First, silicon film thus deposited is polycrystalline with small grain size (4). Second, a much lower deposition rate than that at high substrate temperature is obtained using the CVD technique (5). Small grain size means a shortening of lifetime for the

charge carriers due to trapping at the grain boundaries (6); low deposition rate makes CVD a noneconomic technique for deposition. To solve the former problem, this author has developed a technique to increase the silicon crystallinity at low substrate temperatures. An enhancement of two to four orders of magnitude is obtained for the silicon films deposited on quartz and graphite at a 600°C substrate temperature (2, 7). The next goal is to increase the deposition rate of low temperature CVD. In doing so we make use of the observations that certain dopant gases enhance the silicon CVD rate and others hinder it (8). An understanding of these facts will obviously be useful to the enhancement of the silicon CVD rate at low temperatures. However, as pointed out later, these dopant gas effects cannot yet be consistently accounted for by the existing theories. Therefore, this paper presents a conceptual model which consistently explains the known dopant gas effects on the rate of silicon CVD. We believe that this work will not only lead to an enhancement of the low temperature silicon CVD rate needed for economic solar cells, but also be useful to guide experimentalists in carrying out the CVD process more effectively and to stimulating interest among theorists about the problems related to this topic. The proposed model is further tested for its predicted dopant gas effects on different CVD systems and other relevant work which needs to be done is also discussed.

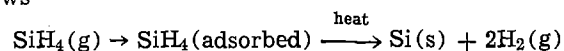
It is well known that the silicon deposition rate using silane and silicon tetrachloride is increased by diborane and boron tribromide, and decreased by phosphine and arsine (8). Existing theories considering either active site blocking (8b) or strong bonding between the chemical vapor molecules and both types of dopant gas molecules (8c) have not been advanced

<sup>1</sup> Present address: IBM Thomas J. Watson Research Center, Yorktown Heights, New York 10588.

Key words: silicon, CVD, enhanced rates, dopant effects, surface model.

enough to explain the known effects in a consistent way, nor can they be used to predict the dopant gas effect on other CVD systems. In this work we make use of the fact that diborane and boron tribromide, both p-type dopant gases for silicon, have an opposite effect on the deposition rate of silicon chemical vapor from that of phosphine and arsine which are n-type dopant gases. This implies a possible correlation between the electronic structure of the dopant atoms with the observed effects cited. The mechanism involved in the CVD process is, therefore, first analyzed, in order to see whether and how this property can be incorporated into the deposition process.

Chemical vapor deposition can be viewed as a two-step process: adsorption of the chemical vapor molecule on the substrate surface followed by its thermal decomposition. As an example, deposition of silane follows



The thermal decomposition involves a transfer of thermal energy from the substrate to the chemical vapor molecule needed for its decomposition. At a fixed substrate temperature, the maximal amount of thermal energy which can be acquired by the molecule is constant. The efficiency of this energy transfer, however, depends on the residence time of the molecule on the substrate surface. In other words, for an effective decomposition of the molecule to take place on the surface, a sufficient amount of thermal energy for such decomposition should be transferred to the molecule before it desorbs from the surface. Therefore, at a fixed substrate temperature, adsorption of the molecule determines its decomposition rate. This argument is in agreement with the work of Farrow who found that silane adsorption is the rate-limiting step for the decomposition of this molecule (8c). Accordingly, at a given substrate temperature, any factors which favor the adsorption of the molecule on the substrate surface should also enhance its decomposition and therefore its deposition rate. Our problem is thus simplified to that of the effect of dopant gas on the adsorption of silicon chemical vapor molecules.

Diborane, phosphine, and arsine all readily decompose on a hot surface into the dopant atoms and hydrogen. Boron tribromide also readily releases its boron upon reduction by hydrogen at high temperatures. Diborane and boron tribromide have quite different structures and polarities and such differences could have profound effect on their interactions with the silicon surface (9). The fact that both diborane and boron tribromide enhance the silicon CVD rate and that they both easily produce boron at high temperatures makes it reasonable to assume the dominant role of boron adatoms in determining the observed boron dopant gas effects. The same assumption is applied to the n-type dopant gases, *i.e.*, phosphine and arsine. The available data on diborane and arsine further show that, upon thermal decomposition, both boron and arsenic atoms strongly adsorb on the silicon surface (8c). In addition, complete coverage of the silicon surface with boron gives the highest silane deposition rate among all the experiments using various silane-diborane mixtures (8c). Some correlation with the boron adatom concentration is also noted. For a rigorous treatment of the dopant gas effects, the contribution from the adsorbed undecomposed dopant gas molecules, if any, should also be taken into account. However, this cannot yet be done due to the lack of knowledge on the surface lifetimes of these molecules on a hot silicon surface. Therefore, only the dopant adatom effect is considered here which is justified by the experimental facts cited above.

From a chemical point of view, silane has the partially ionic  $\text{Si}^+-\text{H}^-$  bonds (10). Being tetrahedral, such a molecule possesses no net dipole moment (11). How-

ever, the ionic character mentioned would make silane a molecule with four negatively charged hydrogen atoms surrounding a positively charged silicon atom in the center. A molecule of such polarity would be attracted by a surface with positive surface potential and be repelled from one with negative surface potential. In other words, making the surface potential more positive would enhance silane adsorption on the surface. The same argument applies to silicon tetrachloride which has  $\text{Si}^+-\text{Cl}^-$  ionic bonds, similar to those in silane.

First, we define a reference surface to be a silicon surface with only adsorbed silicon atoms. This is the case when pure silicon chemical vapor is used. A boron-adsorbed silicon surface can be seen to be different from the reference one. Boron, being a p-type dopant and electron deficient relative to silicon, should, relative to the reference surface, lower the local electron density on the surface silicon atoms around the adsorption site. This would increase the electron affinity of the local silicon surface around the adsorbed boron (12). According to Allen and Gobeli, an increase in surface electron affinity increases the positive surface potential (12). This has been observed on both Si and Ge (9, 12). A boron-adsorbed silicon surface would thus attract molecules like silane and silicon tetrachloride better than the reference surface. This should enhance the adsorption and, therefore, the deposition rate of these molecules. On the other hand, phosphorus and arsenic, which are n-type dopants and electron-excessive relative to silicon, would make the surface potential more negative than the reference one. Accordingly, the deposition rate of silane and silicon tetrachloride should be lowered when they are mixed with phosphine and arsine. The observed dopant gas effect on the deposition rates of silicon chemical vapor is thus satisfactorily and consistently explained. These results are summarized in Table I.

One further support to our model is the agreement between the predicted and observed deposition rate dependence on the dopant atom concentration. This can be better understood if we describe our model using the surface-state concept (13). Compared with a reference surface defined earlier, adsorbed boron atoms decrease the surface-state electron density, whereas phosphorus and arsenic atoms increase it. The induced local surface dipoles have their positive and negative ends, respectively, pointed toward the vacuum. Interaction with silane is, therefore, more attractive in the former case and more repulsive in the latter than in that of the reference surface. Both types of interaction increase with increasing coverage of the dopant adatoms on the surface. As the adatom concentration reaches *ca.*  $10^{12}$  atom/cm<sup>2</sup>, the induced surface dipoles emerge into a continuum (13). Furthermore, it is reasonable to assume the dominance of short-range interactions between the chemical vapor

Table I. Predicted and observed dopant gas effects on the deposition rates of silicon and carbon chemical vapors\*

	SiH <sub>4</sub>	SiCl <sub>4</sub>	CH <sub>4</sub>	CCl <sub>4</sub>
Bonding characters	Si <sup>+</sup> - H <sup>-</sup>	Si <sup>+</sup> - Cl <sup>-</sup>	C <sup>-</sup> - H <sup>+</sup>	C <sup>+</sup> - Cl <sup>-</sup>
B <sub>2</sub> H <sub>6</sub>	I	I	D	I
PH <sub>3</sub>	I <sup>a</sup> D	I <sup>a</sup> D	D <sup>b</sup> I	D
AsH <sub>3</sub>	D <sup>a</sup> D	D	I	D
	D <sup>a</sup>			

\* I and D indicate an increase and decrease, respectively, in deposition rate. The first row for each dopant gas is for the predicted effects, the second row for the observed effects.

<sup>a</sup> Ref. (8).  
<sup>b</sup> Ref. (17).

molecule and the surface (8c). One, therefore, expects appreciable dopant adatom effect beyond the concentration of  $10^{12}$  atom/cm<sup>2</sup> on the adsorption of silicon molecules. The observed onset of significant changes in the deposition rate of silane and silicon tetrachloride at the above dopant adatom concentration (8) is thus consistent with the theory.

A quantitative treatment of this problem involves calculation of the interaction between an adsorbed chemical vapor molecule and a differently dopant-atom adsorbed silicon surface. To date, such calculations are extremely difficult, if not impossible (14, 15). Therefore, only a qualitative test is given here. Some semi-quantitative work is in progress to estimate the dopant adatom effect on the local surface electron densities.

To test our model qualitatively, we chose a CV molecule of opposite polarity to that of SiH<sub>4</sub> and SiCl<sub>4</sub>. The dopant gas effect on the deposition rate of this chosen molecule should then be opposite to that for SiH<sub>4</sub> and SiCl<sub>4</sub>. One possible molecule is methane. Methane is also tetrahedral but has the C<sup>-</sup>-H<sup>+</sup> type of ionic bond. The polarity of methane is, therefore, opposite to that of silane. When carbon tetrachloride is used as a chemical vapor gas, its dopant gas effect should be similar to that of silane due to the C<sup>+</sup>-Cl<sup>-</sup> polarity of this molecule. The predicted dopant gas effects for methane and carbon tetrachloride are also listed in Table I. For a meaningful test of our model in carbon CVD, data on diamond deposition should be used. This is because the structure of diamond is similar to silicon, whereas the layer structure of graphite would complicate the deposition mechanism (16). The available literature data on the dopant gas effect on diamond deposition concern the methane-diborane system (17). The results clearly show that mixing methane with diborane lowers the diamond deposition rate from that observed using only methane. This is exactly the effect predicted by our model.

Although limited by the available information for a full qualitative test of our model, agreement with the existing data is encouraging. It is, therefore, worthwhile to point out some useful work that will be necessary to a better understanding of the CVD process. (i) Experiments for the lacking information listed in Table I should be carried out for a complete test of our model. Also, doping with other p- and n-elements, such as aluminum, should provide further testing of the model. (ii) As a test of the dopant adatom effect on the surface potential, a bias voltage of the proper polarity should be applied to the substrate and observation made of its effect on the deposition rate of pure chemical vapor molecules. A similar test should be made by the application of an electric field to the surface. (iii) Surface properties for silicon and diamond should be studied in the presence of adsorbed boron, arsenic, phosphorus, and other dopant atoms. Such properties include the surface states and work function, and surface lifetimes of adsorbed chemical vapor molecules. This study would allow a direct understanding of the adsorbed dopant atom effect on the surface properties and is essential to our final understanding of the problem discussed in this paper.

Once the suggested experiments are shown to support our model proposed above, it will then be possible to increase the deposition rate of silicon CVD at low temperatures. For example, by applying a suitable bias voltage which matches favorably with the polarity of the chemical vapor molecule, the substrate surface potential can be adjusted to increase the deposition rate beyond the current limit. It is also obvious that the right combination of molecule and dopant gas to allow the maximal increase in deposition rate must be chosen. Examples from Table I are SiH<sub>4</sub>-B<sub>2</sub>H<sub>6</sub>, CH<sub>4</sub>-PH<sub>3</sub>, CCl<sub>4</sub>-B<sub>2</sub>H<sub>6</sub>, etc. The remaining limiting factor will be the amount of thermal energy available at low substrate temperatures. One needs then to find a compromise be-

tween the maximal thermal energy available and the minimal interaction and diffusion allowed between the deposited thin film and the substrate chosen. All these principles should also be applicable to the CVD of other types of thin films, such as those for Si<sub>3</sub>N<sub>4</sub>, SiC, W, etc.

Finally, since our model is concerned mainly with the effect of one adsorbed species on the adsorption of another molecule, this work should also be useful to surface catalysis studies. In surface catalysis, molecular adsorption plays an essential role before decomposition or chemical reaction takes place. By varying the surface potential as described in this paper, one should observe changes of the chemical reaction rates between adsorbed molecules. This should allow a better understanding and control of the chemical reactions under study. In addition, varying the magnitude and sign of the surface potential should provide important information on the formation and strength of the chemisorptive bonds between the adsorbed molecule and the surface. Again, more experimental and theoretical work along this line is needed to further advance our idea to surface catalysis.

### Acknowledgment

This work was supported by the U.S. Energy Research and Development Administration.

Manuscript submitted Jan. 26, 1976; revised manuscript received April 7, 1976.

Any discussion of this paper will appear in a Discussion Section to be published in the June 1977 JOURNAL. All discussions for the June 1977 Discussion Section should be submitted by Feb. 1, 1977.

Publication costs of this article were assisted by the Lawrence Berkeley Laboratory.

### REFERENCES

1. C.-A. Chang and W. J. Siekhaus, *J. Appl. Phys.*, **46**, 3402 (1975).
2. C.-A. Chang and W. J. Siekhaus, *Appl. Phys. Lett.*, **29**, 208 (1976).
3. T. L. Chu, J. C. Lien, H. C. Mollenkopf, S. C. Chu, K. W. Heizer, F. W. Voltmer, and G. F. Wakefield, *Solar Energy*, **17**, 229 (1975).
4. (a) C.-A. Chang, Unpublished results. (b) A. Emmanuel and H. M.-Pollack, *This Journal*, **120**, 1586 (1973).
5. (a) H. C. Theuerer, *ibid.*, **108**, 649 (1961); F. C. Everstegn and G. H. Put, *ibid.*, **120**, 106 (1973); L. H. Hall and K. M. Koliwad, *ibid.*, **120**, 1438 (1973). (b) R. G. Frieser, *ibid.*, **115**, 401 (1968). (c) A. Emmanuel and H. M.-Pollack, *ibid.*, **120**, 1586 (1973).
6. T. I. Kamins, *J. Appl. Phys.*, **42**, 4357 (1971); Y. Matukura, *Japan. J. Appl. Phys.*, **2**, 91 (1963).
7. C.-A. Chang, W. J. Siekhaus, T. Kaminska, and D. T. Huo, *Appl. Phys. Letters*, **26**, 178 (1975).
8. (a) See Ref. (5a). (b) P. Rai-Choudhury and P. L. Hower, *ibid.*, **120**, 1761 (1973). (c) R. F. C. Farrow, *ibid.*, **121**, 899 (1974).
9. W. H. Brattain and J. Bardeen, *Bell System Tech. J.*, **32**, 1 (1953); H. C. Montgomery and W. L. Brown, *Phys. Rev.*, **103**, 865 (1956).
10. F. A. Cotton and G. Wilkinson, "Advanced Inorganic Chemistry," p. 466, John Wiley & Sons, New York (1966).
11. A. L. McCellan, "Tables of Experimental Dipole Moments," W. H. Freeman and Company, San Francisco (1963).
12. F. G. Allen and G. W. Gobeli, *Phys. Rev.*, **127**, 150 (1962).
13. J. Bardeen, *ibid.*, **71**, 717 (1947).
14. T. B. Grimley, *Proc. Phys. Soc.*, **90**, 751 (1967); see also R. Gomer, *Accounts Chem. Res.*, **8**, 420 (1975) and references therein.
15. J. R. Schrieffer, Private communication.
16. See, for example, S. Marinkovic, C. Suznjevic, and I. Dezarov, *Carbon*, **7**, 185 (1969); *ibid.*, **11**, 219 (1973).
17. D. J. Poferl, N. C. Gardner, and J. C. Angus, *J. Appl. Phys.*, **44**, 1428 (1973).

# Improvement of Lead-Free Flux Systems for the Growth of Bismuth-Substituted Iron Garnet Films by Liquid Phase Epitaxy

J. M. Robertson\*

Philips Research Laboratories, Eindhoven, The Netherlands

It has been shown that the Bi-substituted iron garnets are possible candidates for use in a magnetic bubble display (1) or in a beam-accessed thermomagnetic memory device (2). The first films grown for these purposes were from a PbO melt (3, 4), but they lacked the required optical properties. In particular the optical absorption coefficient,  $\alpha$ , was too large, and this was attributed to the simultaneous incorporation of Pb<sup>2+</sup> ions from the flux that occurs at the low growth temperatures required for high Bi substitutions (5).

Robertson *et al.* (6, 7) have shown that the use of a flux system based on Bi<sub>2</sub>O<sub>3</sub>:MeO<sub>2</sub> with Me = Si, Ge, Ti, or Ce leads to improved magneto-optic properties of the grown layers. A value for the figure of merit  $\theta/\alpha = 4.7^\circ/\text{dB}$  at 560 nm was obtained and this is very near to the 5°/dB required to make an efficient display device (1).

Several problems were encountered when using these new flux systems and this paper presents the work performed in improving the fluxes so that high quality Bi-substituted iron garnet films can be grown using the isothermal dipping technique of liquid phase epitaxy (8).

## Disadvantages of the Flux Systems

The incorporation of the Me<sup>4+</sup> ions of the flux into the garnet leads to higher optical absorption due to charge-compensating Fe<sup>2+</sup>. Thus it would be better if all four valent ions were eliminated from the fluxes. The second problem was the nature of the liquids themselves. When garnet growth is performed with the substrate in the horizontal plane, it is usual at the end of film growth, after the sample has been removed from the melt, to rotate it at high speed to throw off any remaining flux droplets. In the case of the present liquids this does not happen and instead the liquid gathers at the axis of rotation where it freezes and causes a degradation of the quality of the film by cracking or producing etch pits and mesas. This problem was solved to a large extent by dipping the substrate in the vertical plane and applying double harmonic motion in the manner as described by Brice *et al.* (9).

When we attempted to try to solve this second problem in another manner, *i.e.*, by lowering the surface tension of the liquids, we found that the first problem was also solved.

## Use of Alkali Metal Oxides in Flux Systems

A study was made of the effect that alkali-metal oxides would have on the surface tension of the flux system Bi<sub>2</sub>O<sub>3</sub>:MeO<sub>2</sub> discussed above. Table I gives a summary of some of the results obtained by Davies (10) when K<sub>2</sub>O was added to the system Bi<sub>2</sub>O<sub>3</sub>:CeO<sub>2</sub>. At the measurement temperature of 850°C it can be seen that the first 4 weight per cent (w/o) of K<sub>2</sub>O added has quite an effect on the value of the surface tension. Further additions do not have so much effect. With 6 w/o K<sub>2</sub>O the surface tension is very similar to that of PbO:Bi<sub>2</sub>O<sub>3</sub>, which was used to grow films of

good quality (3, 4). The numbers in parentheses indicate the values of other published data.

To verify these results, we used a melt containing 6 w/o K<sub>2</sub>O to grow garnet films by LPE. The melt composition was as follows: Bi<sub>2</sub>O<sub>3</sub>:CeO<sub>2</sub>:Y<sub>2</sub>O<sub>3</sub>:Fe<sub>2</sub>O<sub>3</sub>:Ga<sub>2</sub>O<sub>3</sub>:K<sub>2</sub>CO<sub>3</sub> = 349.5:1.30:2.10:11.2:1.5:30.8 (all values given in grams). The saturation temperature of the melt was ~ 870°C and the films grown had a lattice match within  $\pm 0.01\text{\AA}$  of the Gd<sub>3</sub>Ga<sub>5</sub>O<sub>12</sub> substrates. Films of good quality were grown and the viscoelastic nature of the liquids was no longer a deleterious factor.

The surface tension apparatus also allows an estimate of the melting points to be made. These data are also included in Table I, from which it can be seen that the addition of K<sub>2</sub>O lowers the melting points. If the viscosity remained low, it would be possible to eliminate the MeO<sub>2</sub> from the fluxes and thus reduce the tetravalent ion contamination in the garnet films.

Table II summarizes some data for the values of surface tension measured at 850°C and the melting points of the flux systems Bi<sub>2</sub>O<sub>3</sub> + 4 w/o R<sub>2</sub>O, where R = Li, Na, K, Rb, or Cs. It can be seen from the data that the lowest melting points are achieved with the system Bi<sub>2</sub>O<sub>3</sub>:Na<sub>2</sub>O and the lowest values for the surface tension with the system Bi<sub>2</sub>O<sub>3</sub>:K<sub>2</sub>O, although there is not much to choose between these two systems. For a trial growth of garnet films, the system Bi<sub>2</sub>O<sub>3</sub>:K<sub>2</sub>O was chosen and a melt of composition Bi<sub>2</sub>O<sub>3</sub>:Y<sub>2</sub>O<sub>3</sub>:Fe<sub>2</sub>O<sub>3</sub>:Ga<sub>2</sub>O<sub>3</sub>:K<sub>2</sub>CO<sub>3</sub> = 349.5:2.10:11.00:3.5:20.5 (all values given in grams) was premelted under oxygen into a crucible. This procedure was used to reduce the attack on the platinum crucibles [see Ref. (11) for more details]. The saturation temperature of the melt

Table I. Changes of surface tension when K<sub>2</sub>O is added to the flux Bi<sub>2</sub>O<sub>3</sub>:CeO<sub>2</sub> [see Ref. (10)]

Bi <sub>2</sub> O <sub>3</sub> (m/o)	CeO <sub>2</sub> (m/o)	Additive (w/o)	Surface tension at 850°C (dyne cm <sup>-1</sup> )	Melting point (°C)
100	0		213 (209)*	830 (825)
98	2		208	~800
98	2	K <sub>2</sub> O 1	175	
98	2	K <sub>2</sub> O 2	164	725
98	2	K <sub>2</sub> O 4	151	660-675
98	2	K <sub>2</sub> O 6	141	665-675
100	0	K <sub>2</sub> O 4	152	670-680
	PbO-Bi <sub>2</sub> O <sub>3</sub>		140	~720
	PbO-B <sub>2</sub> O <sub>3</sub>		131 (132)	800

\* Numbers in parentheses indicate other published data.

Table II. Data for the surface tension and melting points of the system Bi<sub>2</sub>O<sub>3</sub> + 4 w/o R<sub>2</sub>O with R = Li, Na, K, Rb, or Cs [see Ref. (10)]

R <sub>2</sub> O	Surface tension at 850°C (dyne cm <sup>-1</sup> )	Melting point (°C)
Li <sub>2</sub> O	171	620-640
Na <sub>2</sub> O	157	600-625
K <sub>2</sub> O	152	670-680
Rb <sub>2</sub> O	168	730-755
Cs <sub>2</sub> O	169	730-755

\* Electrochemical Society Active Member.

Key words: crystal growth, magneto-optics, surface tension, melting points, flux systems.

was about 827°C. With a  $Gd_3Ga_5O_{12}$  substrate vertically dipped (no rotation) into the melt at 804°C for 30 min, the resulting film had the following properties. The lattice parameter misfit was  $\Delta a = 0.011\text{\AA}$ , film thickness = 6.55  $\mu\text{m}$ , uniaxial anisotropy  $K_u = 13.8 \times 10^3$  erg  $\text{cm}^{-3}$ , saturation magnetization = 124G, and the magnetic bubbles had a mobility of 5000 cm/oe sec.

Particulars of other garnet film compositions grown from the system  $\text{Bi}_2\text{O}_3:\text{Na}_2\text{O}$  have been reported by Krumme *et al.* (12). Finally, although the evaporation rate has not been measured absolutely, it seems, from inspection of the tops of the furnaces, that the lead-free fluxes are less volatile than the  $\text{Bi}_2\text{O}_3:\text{PbO}$  mixtures.

### Conclusions

Improvements to flux systems that contain no lead have been investigated for the growth by LPE of bismuth-substituted iron garnet films and the best results were obtained with the system  $\text{Bi}_2\text{O}_3$  4 w/o  $\text{R}_2\text{O}$  where  $R = K$ , which has the lower value for the surface tension.

### Acknowledgments

The author would like to thank J. Davies for the use of his results on the surface tension and viscosity prior to publication and to M. Jansen for growing the films. F. de Leeuw and P. K. Larsen are thanked for their measurements on the layers. J. C. Brice and P. F. Bongers are thanked for their useful comments during the preparation of this manuscript.

Manuscript submitted Dec. 22, 1975; revised manuscript received March 29, 1976. This was Paper 224

presented at the Dallas, Texas, Meeting of the Society, Oct. 5-9, 1975

Any discussion of this paper will appear in a Discussion Section to be published in the June 1977 JOURNAL. All discussions for the June 1977 Discussion Section should be submitted by Feb. 1, 1977.

Publication costs of this article were assisted by Philips Research Laboratories.

### REFERENCES

1. J. E. Lacklison, G. B. Scott, R. F. Pearson, and J. L. Page, *IEEE Trans. Magnetics*, **MAG11**, 1118 (1975).
2. J. P. Krumme and H. J. Schmitt, *ibid.*, **MAG11**, 1097 (1975).
3. A. Akselrad, R. F. Novak, and D. L. Patterson, *AIP Conf. Proc.*, **18**, 949 (1974).
4. J. M. Robertson, J. C. Verplanke, S. Wittekoek, P. F. Bongers, M. Jansen, and A. Op den Buijs, *Appl. Phys.*, **6**, 353 (1975).
5. J. M. Robertson, S. Wittekoek, Th. J. A. Popma, and P. F. Bongers, *ibid.*, **2**, 219 (1973).
6. J. M. Robertson, P. K. Larsen, and P. F. Bongers, *IEEE Trans. Magnetics*, **MAG11**, 1112 (1975).
7. J. M. Robertson and J. C. Brice, *J. Cryst. Growth*, **31**, 371 (1975).
8. H. J. Levinstein, S. Licht, R. W. Landorf, and S. L. Blank, *Appl. Phys. Letters*, **19**, 485 (1971).
9. J. C. Brice, J. M. Robertson, and H. van der Heide, *J. Cryst. Growth*, **31**, 375 (1975).
10. J. E. Davies, To be published.
11. J. M. Robertson, J. P. Damen, H. D. Jonker, M. J. G. van Hout, W. Kamminga, and A. B. Voermans, *Platinum Metals Rev.*, **18**, 15 (1974).
12. J. P. Krumme, G. Bartels, P. Hansen, and J. M. Robertson, *Mater. Res. Bull.*, To be published

## Mechanical-Chemical Technique for Removal of Epitaxial Spikes

L. E. Katz\* and W. C. Erdman\*\*

Bell Laboratories, Allentown, Pennsylvania 18103

Epitaxial spikes have been a recurring problem over the years although defect levels have decreased with improved cleaning and handling techniques. The existence of these defects, which range in height from a fraction of a micrometer to several micrometers can result in mask damage when contact printing is used. It is the purpose of this paper to describe a simple, effective, and efficient technique for removing these defects without introducing any additional damage to the wafer. Proper utilization of the technique removes virtually all epi-spikes and results in a wafer which can be contacted to a mask without causing mask damage.

Prior attempts to remove or reduce the number and size of spikes have involved various mechanical methods which included scraping with a razor blade, crushing, or abrading. All of the simple mechanical removal techniques tend to be inadequate because of poor removal efficiency and an attendant high risk of surface contamination from particulates. A chemical etching technique was developed earlier (1) to selectively expose spikes to chemical etching. While the removal efficiency is high, the method suffers from an intermittent background of extraneous<sup>1</sup> etch pits that is in-

tolerable, especially as chip size is increased. An additional impetus for a new approach arises from the number of processing steps of the previous process which increases wafer cost.

### Experimental Procedure

The evaluation procedure involved counting and mapping the number of epi-defects on a particular group of wafers. Twenty-nine chips of the ~90 chips (~0.23 × 0.30 cm) present were mapped. The wafers were then subjected to the spike removal process and once again mapped; this time for spike removal pits. Counting repeatability was generally within ± 1 defect per 29 chips. The defects were examined optically to determine if the spike had been entirely eliminated. It is important that extraneous pits not be introduced since this can cause other processing problems later on. This new spike removal technique was also evaluated for mask damage. The procedure involved obtaining a defect count from a blank chrome mask, using a laser scanner (2). The wafer, after spike removal, was then contacted to the mask and once again a defect count obtained using the laser scanner. Since the number of defects was generally low, the damage was magnified either by multiple contacting of wafers to the same mask, or using wafers which had been grown with thick epi-layers in such a manner as to maximize the number of spikes. Such techniques provided a critical evaluation for the spike removal technique.

\* Electrochemical Society Active Member.

\*\* Deceased.

Key words: defects, mask damage, silicon.

<sup>1</sup> Extraneous etch pits are defined here as pits not related to epi-spikes but to the spike removal process. Spike removal pits are defined as those pits present, after spike removal, at the identical site of an epi-spike.



When a precision steel edge, typical of a commercial razor blade, is drawn across the surface of an epitaxial silicon wafer, any spikes present on the wafer have a high probability of being fractured. The remainder of a spike can be as damaging to a contact mask as the spike itself before the mechanical removal step. Earlier attempts to use mechanical methods as a sole treatment suffered from the effects of a fluctuating but significantly high number of partially removed spikes together with debris from the mechanical fracturing process. This "residual" spike effect can be almost totally eliminated by following the spike-fracturing step with a chemical etch, provided a protective oxide film is present.

The present method involves thermally oxidizing the epitaxial wafer to produce a film from 0.3 to 0.5  $\mu\text{m}$  thick. The wafer is then scraped with a commercial razor blade while the wafer is secured on a stable planar platform using a vacuum chuck. The blade is held on a machine assembly which draws the blade with a constant force, angle, and speed over the wafer surface. A few drops of dilute detergent (1000 parts deionized water to 1 part Triton X-100) placed on the wafer prior to fracturing the spikes is beneficial in removing the debris formed during the spike-fracturing process. The chuck is arranged to index to  $90^\circ$  of the original presentation to the blade and the blade is run again over the surface. The double mechanical treatment serves to increase the probability of at least some fracture to almost all spikes without causing appreciable extraneous surface damage. Hand manipulation of a blade is effective and can be used in lieu of a machine as long as the wafer is well secured on a vacuum chuck or equivalent.

After mechanical treatment, the wafer is placed in an etch bath of 5M aqueous KOH at  $85^\circ\text{C}$  for 15 min. The etch rate typical of the etchant, approximately 2  $\mu\text{m}/\text{min}$  on all silicon planes except the (111), is sufficient to destroy all damaged spikes within the 15 min interval. It should be noted that the spike need only be superficially fractured by the mechanical step to be removed if the protective oxide film is ruptured. The undamaged oxide film over the remainder of the epitaxial wafer is extremely efficient in protecting the surface. This is true because of the low inherent pin-hole density of thermal oxide films of this thickness and the relative slow etch rate of thermal  $\text{SiO}_2$  in KOH solution ( $\sim 50 \text{ \AA}/\text{min}$ ). The etch step in KOH is easily adapted to usual batch processing techniques. The etch bath can be easily thermostated ( $\pm 1^\circ\text{C}$  is sufficient) in a controlled external water bath.

### Experimental Results and Discussion

**Spike removal.**—Wafers from different lots were mapped with respect to spikes with the oxide present, and were mapped again after spike removal. Evaluation consisted of counting the total number of spikes on 29 chips on each wafer. Values obtained for various wafers ranged from 0 to 6. The number of spike removal pits for each wafer corresponded to the original number of spikes. The conclusion from this experiment is that the mechanical-chemical spike removal process is capable of removing spikes with little or no "background" of extraneous pits. This is not the case, as discussed previously, with the chemical etching technique.

Figure 1 shows a wafer surface including a spike at different stages of mechanical-chemical projection removal. The undamaged spike is shown in Fig. 1(a). Figure 1(b) shows the appearance of the spike after the mechanical damage step. Clearly only part of the spike is removed. It is obvious that mechanical removal alone is less than adequate for most purposes. The appearance of the spike site and surrounding wafer surface after KOH etching shows the total absence of debris and the complete removal of the spike as seen in Fig. 1(c).

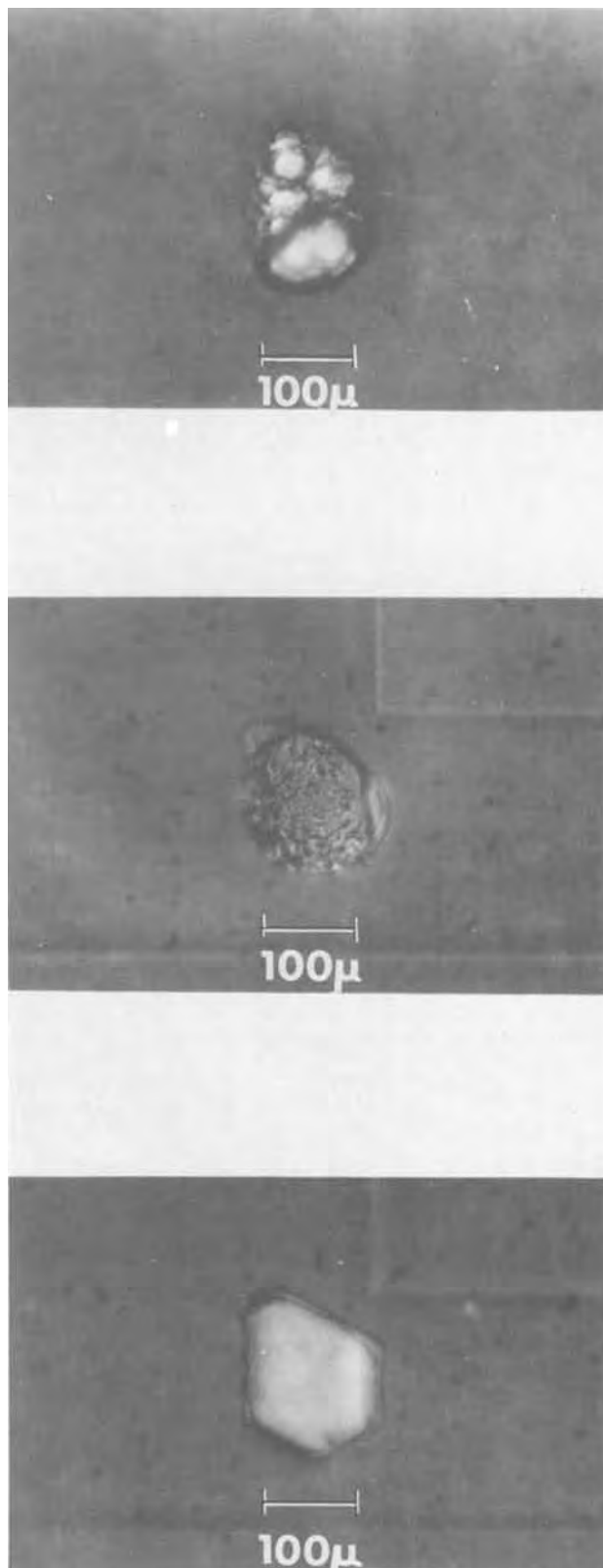


Fig. 1. Epitaxial silicon spike: (a, top) prior to spike removal; (b, center) after mechanical damage; (c, bottom) after mechanical-chemical spike removal.

**Mask damage.**—The procedure using blank chrome masks and laser inspection was described previously. The laser counting statistics involve an error bar equal to plus or minus the square root of the number of defects. The mask area examined was a 3.8 cm square. In all cases, two laser counts were taken on each mask prior to contacting and those masks showing a large number of the defects were discarded. The laser scan-

ner is capable of measuring defects  $\cong 1.8 \mu\text{m}$  in size. After contacting, two additional laser counts were taken.

Results showed that the mask defect density could be reduced from 10-60 (for wafers not subjected to spike removal) down to 1-2 (for wafers subjected to spike removal). These results were confirmed when several wafers which had been subjected to spike removal were contacted to the same mask.

As a severe test of the capability of the spike removal process, epi was grown on silicon substrates in such a manner as to obtain a high density of large spikes. Such wafers put through the spike removal process showed little or no mask damage within statistical limits. When high spike density wafers were contacted without the spike removal process, the mask defect counts were very high ( $>50$ ). The conclusion is that even high densities of large spikes can be successfully removed from the wafer with little or no subsequent mask damage.

### Conclusions

A new mechanical-chemical spike removal technique has been devised which effectively removes epi-spikes without introducing extraneous pits. No photoresist operations are involved. A mask damage evaluation technique has been described and used to evaluate masks contacted to wafers subjected to the new spike

removal technique. Results based on the mapping of defects and mask damage studies lead to the conclusions that the new spike removal technique efficiently removes epi-spikes and that wafers subjected to this process produce little mask damage when contacted to blank chrome masks.

Although epi-spike densities are generally low, this simple process guarantees that no damage will result from the few spikes which may have initially been present.

Manuscript submitted Feb. 19, 1976; revised manuscript received April 25, 1976.

Any discussion of this paper will appear in a Discussion Section to be published in the June 1977 JOURNAL. All discussions for the June 1977 Discussion Section should be submitted by Feb. 1, 1977.

Publication costs of this article were assisted by Bell Laboratories.

### REFERENCES

1. W. C. Erdman and P. Miller, Paper 195 RNP presented at The Electrochemical Society Meeting, Washington, D. C., May 9-13, 1971; U.S. Pat. 3,718,514.
2. D. F. Munro and J. D. Cuthbert, "Proceedings of the Technical Program, Electro-Optical Systems Design Conference," Industrial and Scientific Conference Management, Inc., Chicago, Illinois (1971).

## The Diffusion of Compensating Impurities in Single Crystal Cadmium Sulfide

J. L. Sullivan

University of Aston, Gosta Green, Birmingham, England

With a bandgap of about 2.5 eV, one would expect single crystal cadmium sulfide to exhibit high resistivity at room temperature. Due to a nonstoichiometric crystal structure, however, room temperature resistivities of 1 ohm-cm are typical in ultrahigh purity material. If a Group I impurity such as Cu, Ag, or Au diffuses into the crystals, the occupation of Cd lattice sites by the impurity atom results in the formation of deep electron traps. Thus a high resistance region is formed where the concentration of impurity atoms occupying Cd vacancies is great enough to remove most of the electron from the conduction band. This property is used in the production of many photoconductive devices.

It has been widely suggested that an interstitial-substitutional mechanism is dominant in compensating impurity diffusion. The CdS lattice is a tetrahedrally bonded wurtzite structure which is equally open in all directions. There are two major interstitial sites available for an impurity atom: a tetrahedral site of mean radius 0.10 nm and an octahedral site of mean radius 0.14 nm. Allowing for thermal relaxation, both sites are sufficiently large to accommodate an impurity. It is thus most likely that diffusion takes place via these sites and that an interstitial-substitutional mechanism is indeed responsible. If net compensation of crystal resistivity is to occur, however, the time spent by an impurity in an interstitial position must be very much less than that spent in a Cd vacancy. If this were not so, electrons donated to the conduction band by the interstitial impurity would compensate for those removed by impurities occupying vacancies and no net

change in resistivity would occur. Thus we must regard the energy required to remove an impurity from an interstitial site as very much less than that to remove the impurity from a substitutional site.

### The Migration Energy of Diffusion

Following an approach due to Glyde (1), an impurity atom residing at a Cd lattice site makes a jump to an adjacent interstitial site when its displacement from the equilibrium position is large enough and when the surrounding atoms move so that the impurity may pass. The probability of an atomic displacement  $u_\alpha$  along the  $\alpha$  axis (2) is

$$P(u_\alpha) = (2\pi \langle u_\alpha^2 \rangle)^{-1/2} \exp - \frac{1}{2} \left\{ \frac{u_\alpha^2}{\langle u_\alpha^2 \rangle} \right\} \quad [1]$$

If, for simplicity, we consider a cubic crystal [the difference between the wurtzite and zinc blende structures is small enough to make this assumption valid; for example, Bocchi and Ghezzi (3) have shown that the ratio of the mean square amplitudes parallel and perpendicular to the c axis in CdS is 1.09], it may then be shown (1, 4) that

$$P(u_\alpha) = \left\{ \frac{6\pi kT}{m\theta_D^2} \left( \frac{\hbar}{k} \right)^2 \right\}^{-1/2} \exp - \frac{1}{6} \left( \frac{k}{\hbar} \right)^2 \frac{\theta_D^2 u_\alpha^2 m}{kT} \quad [2]$$

where  $m$  is the mass of the diffusing atom,  $k$  is the Boltzmann constant,  $T$  is the absolute temperature, and  $\theta_D = \hbar\omega_D/k$ .

If the distance between a Cd vacancy,  $V_{Cd}$ , and an adjacent interstitial site,  $I$ , is  $b$ , then a jump occurs when  $u = b/2$ , and

$$P(b/2) = \left\{ \frac{6\pi kT}{m\theta_D^2} \left( \frac{\hbar}{k} \right)^2 \right\}^{-1/2} \exp - \frac{1}{24} \left( \frac{k}{\hbar} \right)^2 \frac{\theta_D^2 b^2 m}{kT}$$

Similar expressions may be derived (i) for the subsequent  $I \rightarrow V_{Cd}$  jump and (ii) for the movement of the surrounding atoms to allow the jumps to take place. The total probability of impurity movement from one vacancy to the next is the product of the individual probabilities. The effect of (i) is to modify the pre-exponential terms by a constant amount and to introduce a constant,  $g$ , into the exponential. The probabilities (ii) are not dependent on impurity mass and the effect of these is to change the preexponential term by a constant amount. Thus the total probability of impurity movement from one vacancy to the next is

$$P = \text{constant} \left\{ \frac{6\pi kT}{m\theta_D^2} \left( \frac{\hbar}{k} \right)^2 \right\}^{-1/2} \exp - \frac{g}{24} \left( \frac{k}{\hbar} \right)^2 \frac{\theta_D^2 b^2 m}{kT} \quad [3]$$

We may imagine the potential acting on an impurity atom in moving from vacancy A via an interstitial B to the next vacancy C to be as shown in Fig. 1 if the impurity compensates crystal resistivity  $E_{mv} \gg E_{mI}$  and the constant  $g$  is very close to unity.

Then from Eq. [3] we may write the diffusion jump rate as

$$\Omega = \Omega_0 \exp - \frac{E_m}{kT}$$

where  $E_m$  is the mean impurity migration energy, but  $\Omega \propto P$ . Hence

$$E_m = \frac{1}{24} \left( \frac{k\theta_D b}{\hbar} \right)^2 m \quad [4]$$

### The Activation Energy of Impurity Diffusion

The activation energy of the diffusion process may be written

$$Q = E_f + E_m \quad [5]$$

where  $E_f$  is the vacancy formation energy. If the impurity concentration is low, the vacancy formation energy is independent of the impurity atom. The activation energy for impurity diffusion therefore consists of a constant term,  $E_f$ , plus a term representing the migration energy of the diffusing species and dependent on the mass of that atom. Then

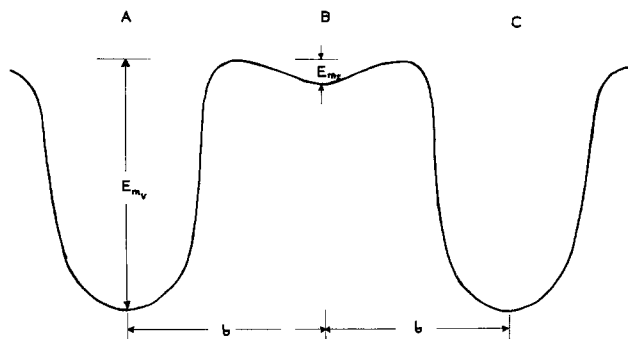


Fig. 1. Two-dimensional representatives of the potential acting on an atom in moving from vacancy A to vacancy C via an interstitial B.

$$Q = E_f + \frac{1}{24} \left( \frac{k\theta_D b}{\hbar} \right)^2 m \quad [6]$$

If all the impurity atoms follow the same net diffusion route,  $b$  is also constant and a plot of  $Q$  vs.  $m$  is linear of slope  $S$  and intercept on the  $Q$  axis equal to  $E_f$ . Inserting values of physical constants in Eq. [6] and rearranging in terms of  $b$  we have

$$b = 3.08 \times 10^{-13} S^{1/2} m \quad [7]$$

This value of  $b$  identifies the migration route of the diffusing atom and hence isolates the diffusion mechanism. The value of  $\theta_D$  used in Eq. [7] is that derived by Bocchi and Ghezzi (3) from mean square amplitudes.

### Discussion

Figure 2 shows the dependency of  $Q$  (taken from a series of recent measurements for atoms occupying Cd lattice position) on  $m$ . Considering the many different techniques employed in the measurements, the curve is reasonably linear. From the curve  $E_f = 0.6$  eV and  $b = 0.248$  nm, the expected error in  $b$  is  $\pm 12\%$ .

In his prediction of migration routes in spinels, Grimes (6) found that atoms behaved as though they were hard spheres. If we follow this approach there are two possible interstitial sites in CdS capable of accommodating the impurity ion: the tetrahedral interstitial site at a distance of 0.253 nm from a Cd lattice site and the octahedral site at distance 0.293 nm. The distance between the two interstitial sites is 0.245 nm. Due to close packing of the sulfur atoms, the only jump possible for an impurity atom occupying a Cd vacancy is to a tetrahedral interstitial site, a distance of 0.253 nm. Interstitial-interstitial migration is then possible, but since the time spent in interstitial positions must be small, the most likely movement of the impurity is to a Cd vacancy. Thus, the most probable diffusion route is  $V_{Cd} \rightarrow I_{tet} \rightarrow V_{Cd}$  with a mean jump size of 0.253 nm. Interstitial-interstitial migration is then possible, but since the time spent in interstitial positions must be small, the most likely movement of the impurity is to a Cd vacancy. Thus, the most probable diffusion route is  $V_{Cd} \rightarrow I_{tet} \rightarrow V_{Cd}$  with a mean jump size of 0.253 nm, although the route  $V_{Cd} \rightarrow I_{tet} \rightarrow I_{oct} \rightarrow I_{tet} \rightarrow V_{Cd}$  is possible. Here the mean jump size is 0.249 nm.

### Conclusion

Using a "hard-sphere" model, the expected mean jump size for an interstitial-substitutional diffusion mechanism lies between 0.249 and 0.253 nm and is probably much closer to the higher figure. From a relation-

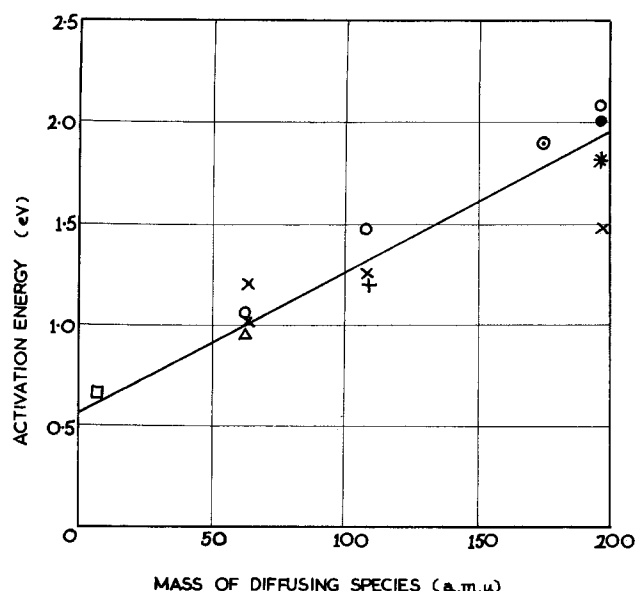


Fig. 2. Dependence of the activation energy for diffusion of compensating impurities in CdS on the mass of the diffusion atom.  $\circ$  Anderson and Chang (7),  $\bullet$  Dobrovinskya et al. (8),  $\bullet$  Malysheva (9),  $*$  Nebauer (10),  $\triangle$  G. A. Sullivan (11),  $\circ$  J. L. Sullivan (12),  $+$  Woodbury (13),  $\times$  Zmija and Damianiuk (14).

ship established between the migration energy and the mass of the diffusing element, the mean jump size calculated from recent experimental data is 0.248 nm  $\pm$  12%. Very acceptable agreement is thus found from the mean jump size derived from experimental data and that to be expected for an interstitial-substitutional mechanism. The agreement strongly suggests that this is the dominant mechanism for compensating impurity diffusion in single crystal CdS.

Manuscript submitted July 29, 1975; revised manuscript received April 5, 1976.

Any discussion of this paper will appear in a Discussion Section to be published in the June 1977 JOURNAL. All discussions for the June 1977 Discussion Section should be submitted by Feb. 1, 1977.

#### REFERENCES

1. H. R. Glyde, *J. Phys. Chem. Solids*, **28**, 2061 (1967).
2. A. A. Maradulin, E. W. Montroll, and G. H. Weiss,

- Solid State Phys. Suppl.*, **3**, 2 (1963).
3. C. Bocchi and C. Ghezzi, *J. Phys. Chem. Solids*, **36**, 421 (1975).
  4. H. R. Glyde, *Rev. Mod. Phys.*, **39**, 373 (1967).
  5. R. J. Finelstein, "Thermodynamics and Statistical Physics," Section 7.3, Freeman, Cooper & Company, San Francisco (1969).
  6. N. W. Grimes, *Phil. Mag.*, **25**, 67 (1972).
  7. W. W. Anderson and H. J. Chang, *This Journal*, **118**, 1451 (1971).
  8. E. P. Dobrovinskya *et al.*, *Ukr. Fiz. Zh.*, **13**, 861 (1968).
  9. G. K. Malsheva, *Soviet Phys. Semiconductors*, **5**, 420 (1971).
  10. E. Nebauer, *Phys. Status Solidi*, **29**, 269 (1968).
  11. G. A. Sullivan, *Phys. Rev.*, **184**, 796 (1969).
  12. J. L. Sullivan, *J. Phys. D*, **6**, 552 (1973).
  13. H. H. Woodbury, *J. Appl. Phys.*, **36**, 2287 (1965).
  14. J. Zmija and M. Damianiuk, *Acta. Phys. Polon.*, **A35**, 539 (1971).

## Brief Communications



### Vacuum Ultraviolet Excitation Spectra of Phosphors for Use in Gas Discharge Display Panels

A. W. de Jager-Veenis and A. Brill\*

Philips Research Laboratories, Eindhoven, The Netherlands

For use in gas discharge display panels, phosphors are required that have a high efficiency and a high light output (high absorption, *i.e.*, low reflection) for vacuum ultraviolet (v.u.v.) excitation, *e.g.*, from Xe, Kr, or Ar discharges. Well-known phosphors that could be used for this purpose are, for instance, willemite ( $Zn_2SiO_4$ -Mn) with low Mn concentration as a green-emitting phosphor,  $CaWO_4$ -(Pb) as a blue-emitting one, and the halophosphate Sb-Mn, which has a white emission (1-7). The relative excitation spectra of rare earth activated phosphors like  $Y_2O_3$ - $Eu^{3+}$  and  $YVO_4$ - $Eu^{3+}$  (red emitting),  $Y_2O_2S$ - $Tb^{3+}$  and  $SrGd_2S_4$ - $Eu^{2+}$  (green emitting), and  $Y_2SiO_5$ - $Ce^{3+}$  and  $Sr_3(PO_4)_2$ - $Eu^{2+}$  (blue emitting) have also been reported (2, 3, 6). In their experimental display panels, Ohishi *et al.* (6) used  $Y_2SiO_5$ -Ce in the blue,  $Zn_2SiO_4$ -Mn in the green, and  $Y_2O_3$ -Eu or  $YVO_4$ -Eu in the red region. Fukushima *et al.* (7) used  $M(P,V)O_4$ ,  $Zn_2SiO_4$ -Mn, and  $M(P,V)O_4$ - $Eu^{3+}$ , respectively (M = rare earth).

Searching for a guide to find an efficient "v.u.v. phosphor" we looked among the well-known efficient cathode ray (CR) phosphors and middle ultraviolet (m.u.v.) phosphors (*e.g.*, fluorescent lamp phosphors). With CR excitation, the excitation energy is absorbed in the host lattice, so that there should be transfer of absorbed energy to the luminescent centers. Many efficient m.u.v. phosphors are excited directly in the centers. These mechanisms might also hold for the respective types of phosphors when the excitation is

extended to the v.u.v. energy region. However, although the very efficient m.u.v. phosphor halophosphate-Sb-Mn, for example, is a good v.u.v. phosphor, too,  $YVO_4$ -Eu and  $Y_2O_2S$ -Eu are both efficient CR and m.u.v. phosphors with a poor light output in the v.u.v.

#### Experimental

Our excitation measurements extended from  $\lambda = 160$  up to 260 nm, at which latter wavelength the absolute quantum efficiency can be readily measured (8). If no light output could be obtained by excitation at  $\lambda = 260$  nm, the Cd spectral line at  $\lambda = 228.8$  nm was used as a radiation source for absolute measurements.

The excitation spectra were measured on a Seya-Namioka type McPherson 235 monochromator, the radiation source was a deuterium lamp with suprasil window, and the emitted (visible) radiation was detected with a spectrally calibrated EMI 9558Q photomultiplier (S20 cathode).

#### Results and Discussion

We measured among our own samples the excitation spectra and quantum efficiencies of some of the phosphors mentioned in Ref. (1-7) and found a reasonable agreement with those figures, as far as they are given absolutely. We did not measure the (low) diffuse reflections below  $\lambda = 220$  nm. The efficiency values below that wavelength were calculated on the assumption that the diffuse reflection and consequently the absorption did not change from  $\lambda = 220$  to 160 nm. None of the phosphors were optimized to obtain the highest efficiency for v.u.v. excitation. We found a rea-

\* Electrochemical Society Active Member.

Key words: excitation spectra, vacuum ultraviolet, luminescence, quantum efficiency.

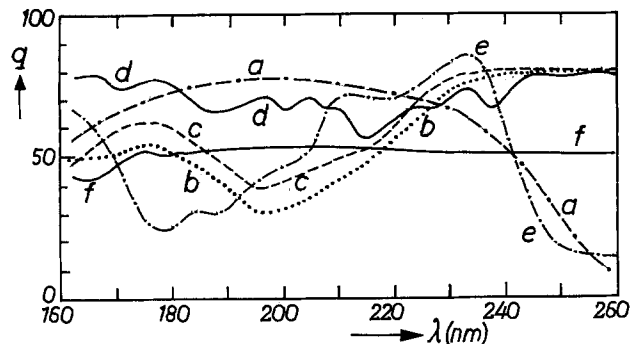


Fig. 1. The excitation spectra of (a)  $(\text{Ca,Mg})\text{SiO}_3\text{-Ti}$ ; (b)  $\text{Sr}_{5.5}\text{Mg}_6\text{Al}_{55}\text{O}_{94}\text{-Eu}^{2+}$ ; (c)  $\text{BaMg}_2\text{Al}_{16}\text{O}_{27}\text{-Eu}^{2+}$ ; (d)  $\text{CeMgAl}_{11}\text{O}_{19}\text{-Tb}^{3+}$ ; (e)  $\text{Sr}_3(\text{PO}_4)_2\text{-Tb}^{3+}$ ; (f)  $\text{CeF}_3\text{-Tb}^{3+}$ .

sonably good efficiency at  $\lambda_{\text{exc}} = 160$  nm for the phosphors made in our laboratories:  $(\text{Ca,Mg})\text{SiO}_3\text{-Ti}$  (blue emission) (9),  $(\text{Sr,Eu})_{5.5}\text{Mg}_6\text{Al}_{55}\text{O}_{94}$  (blue) (10),  $\text{BaMg}_2\text{Al}_{16}\text{O}_{27}\text{-Eu}^{2+}$  (blue) (10),  $\text{CeMgAl}_{11}\text{O}_{19}\text{-Tb}^{3+}$  (green) (10), which are known already to be good m.u.v. phosphors (applied in new generation "de luxe" fluorescent lamps),  $\text{Sr}_3(\text{PO}_4)_2\text{-Tb}^{3+}$  (green) (11), and  $\text{CeF}_3\text{-Tb}^{3+}$ . The latter has a green  $\text{Tb}^{3+}$  and u.v.  $\text{Ce}^{3+}$  emission; the ratio of green to u.v. emission shifts to green at higher  $\text{Tb}^{3+}$  concentrations (12). The v.u.v. radiation is absorbed in the  $\text{Ce}^{3+}$  ion and transferred partially to the  $\text{Tb}^{3+}$ ; in the excitation spectrum the  $\text{Ce}^{3+}$  absorption dominates the  $\text{Tb}^{3+}$  peaks [see Ref. (13)]. In particular, the phosphors  $\text{CeMgAl}_{11}\text{O}_{19}\text{-Tb}^{3+}$  and  $\text{CeF}_3\text{-Tb}^{3+}$  have a rather constant and high efficiency throughout the spectrum (see Fig. 1). We intend to describe separately the mechanism of energy absorption and transfer in the phosphors. Somewhat lower quantum efficiencies are found, for instance, for the phosphors:  $\text{CePO}_4\text{-Tb}^{3+}$  (green),  $2\text{CaO}\cdot\text{Al}_2\text{O}_3\cdot\text{SiO}_2\text{-Ce}^{3+}$  (gehlenite; blue),  $\text{YVO}_4\text{-Bi,Dy}^{3+}$  (yellow), and  $\text{CaWO}_4\text{-Tb}^{3+},\text{Nb}$  (blue green). The excitation curves are given in Fig. 2.

#### Acknowledgments

The authors are indebted to Miss R. B. Engelen for part of the measurements, to J. M. P. J. Verstegen of the Light Division for the preparation of the Eu- and Tb-activated aluminates, and to J. L. Sommerdijk for the preparation of the  $\text{CaNbWO}_4\text{-Tb}$  and  $\text{YVO}_4\text{-Bi,Dy}$ .

Manuscript received March 17, 1976.

Any discussion of this paper will appear in a Discussion Section to be published in the June 1977

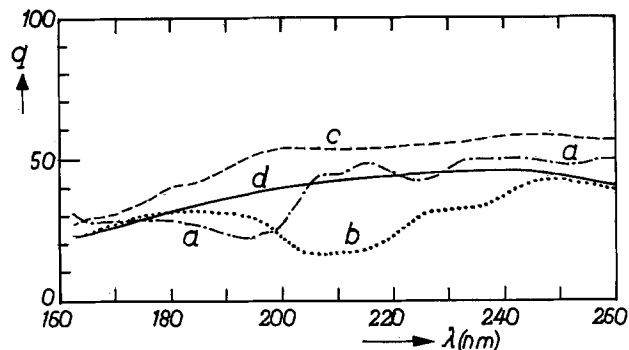


Fig. 2. The excitation spectra of (a)  $\text{CePO}_4\text{-Tb}^{3+}$ ; (b)  $2\text{CaO}\cdot\text{Al}_2\text{O}_3\cdot\text{SiO}_2\text{-Ce}^{3+}$ ; (c)  $\text{YVO}_4\text{-Bi}^{3+},\text{Dy}^{3+}$ ; (d)  $\text{CaWO}_4\text{-Tb}^{3+},\text{Nb}^{5+}$ .

JOURNAL. All discussions for the June 1977 Discussion Section should be submitted by Feb. 1, 1977.

Publication costs of this article were assisted by Philips Research Laboratories.

#### REFERENCES

1. P. D. Johnson, *J. Opt. Soc. Am.*, **51**, 1235 (1961).
2. R. L. Conklin, *ibid.*, **49**, 669 (1959).
3. D. H. Thurnau, *ibid.*, **46**, 346 (1956).
4. J. Janin, J. C. Bourcet, J. P. Jorus, and N. Bras, *Rev. Opt.*, **44**, 393 (1965).
5. J. D. Kingsley and G. W. Ludwig, *This Journal*, **117**, 353 (1970).
6. I. Ohishi, T. Kojima, H. Ikeda, R. Toyonaga, H. Murakami, J. Koike, and T. Tajima, *IEEE Trans. Electron Devices*, **ED22**, 650 (1975).
7. M. Fukushima, S. Murayama, T. Kaji, and S. Mikoshiba, *ibid.*, **22**, 657 (1975).
8. A. Bril and W. Hoekstra, *Philips Res. Rept.*, **16**, 356 (1961).
9. A. Bril and W. v. Meurs-Hoekstra, *ibid.*, **19**, 296 (1964).
10. J. M. P. J. Verstegen, *This Journal*, **121**, 1623 (1974); J. M. P. J. Verstegen, D. Radielovic, and L. E. Vrenken, *ibid.*, **121**, 1627 (1974).
11. A. Bril, W. L. Wanmaker, and J. W. ter Vrugt, *This Journal*, **115**, 776 (1968).
12. G. Blasse and A. Bril, *J. Chem. Phys.*, **51**, 3252 (1969); G. Blasse and A. Bril, *Philips Tech. Rev.*, **31**, 304 (1970), in particular pp. 328-330.
13. W. S. Heaps, L. R. Elias, and W. M. Yen, "Proceedings of the International Conference on Vacuum Ultraviolet Radiation Physics," E. E. Koch, R. Haensel, and C. Kunz, Editors, p. 407, Pergamon Vieweg, Brunswick (1974).

## Air Anneals of Unencapsulated InP/CdS Solar Cells

Sigurd Wagner and J. L. Shay

Bell Laboratories, Holmdel, New Jersey 07733

and K. J. Bachmann\* and E. Buehler

Bell Laboratories, Murray Hill, New Jersey 07974

The p-InP/n-CdS heterodiode solar cell (1-3) is a candidate for large scale terrestrial application. However, prior to its extensive development, a satisfactory operating lifetime and development of a polycrystalline thin film device are required. In this paper, we present results of annealing experiments in ambient air

\* Electrochemical Society Active Member.

Key words: InP/CdS, heterojunction, solar cells, life testing.

which provide convincing evidence for the stability and long life expectancy of this cell.

n-Type films of CdS were grown on p-type Cd-doped single crystals of InP essentially as previously reported (1, 2). However, for the present experiments, the Cd source temperature was raised from 350° to 375°C to increase the Cd to S flux ratio from 4.5 to 5.8. The InP substrates were kept at 240°C. Room temperature Hall

measurements on a typical CdS film with a thickness of 10  $\mu\text{m}$  gave the following results:  $\rho = 0.0063 \Omega\text{-cm}$ ,  $\mu = 140 \text{ cm}^2/\text{V}\text{-sec}$ ,  $n = 7.1 \times 10^{18} \text{ cm}^{-3}$ .

We have previously shown (2) that there is no appreciable interdiffusion of the components in the InP/CdS cell during 15 min anneals in air at temperatures up to at least 500°C. The capacitance-reverse voltage characteristic was unchanged by these anneals. However, for annealing temperatures above 400°C, the resistivity of the CdS with  $n \approx 2 \times 10^{18} \text{ cm}^{-3}$  increased enormously, as shown by the squares in Fig. 1. Such large CdS resistivities lead to large series resistances which dissipate power internally, thereby greatly reducing the solar cell efficiency. Nonetheless, it is intuitively obvious that rather long useful lifetimes will result under operating conditions ( $T \lesssim 50^\circ\text{C}$ ) since temperatures greater than 400°C are needed to deteriorate a cell's performance in 15 min.

It was with these observations in mind that we began a program of accelerated life tests for the InP/CdS cell. The objective of the program was to measure the time required for the CdS resistivity to increase to a value ( $\sim 1 \Omega\text{-cm}$ ) such that the fill factor and power delivered are appreciably ( $\sim 50\%$ ) reduced. If these "lifetimes" are plotted vs.  $T^{-1}$  and extrapolated to operating temperature ( $\sim 50^\circ\text{C}$ ), an upper limit to the useful lifetime can be estimated. (Of course, the extrapolation assumes identical degradation mechanisms at temperatures of test and of operation.)

Instead, we have found that the resistivity of CdS films with  $n \approx 1 \times 10^{19} \text{ cm}^{-3}$  is not appreciably altered by air anneals, and that it will not be the limiting factor determining the lifetime in ambient air. As shown by the circles in Fig. 1, the resistivity of these highly conducting films is essentially unchanged by 15 min anneals in air for temperatures up to 600°C. The error bars for 550°C indicate the spread in values obtained for three different samples. In Fig. 2, we show the variation of CdS resistivity for much longer anneals in air at 485°C. Whereas the resistivity of the earlier samples increases from 0.019 to 2  $\Omega\text{-cm}$  in 15 min, the resistivity of the new films only increases from 0.006 to 0.04  $\Omega\text{-cm}$  after 7 days at 485°C. A simple extrapolation of these data to  $\rho \sim 1 \Omega\text{-cm}$  indicates a lifetime of 1 month at 485°C. The open-circuit voltages indicated in Fig. 2 for  $\sim 1$ -3 day anneals are higher than both the maximum value of 0.72V previously reported (2) and

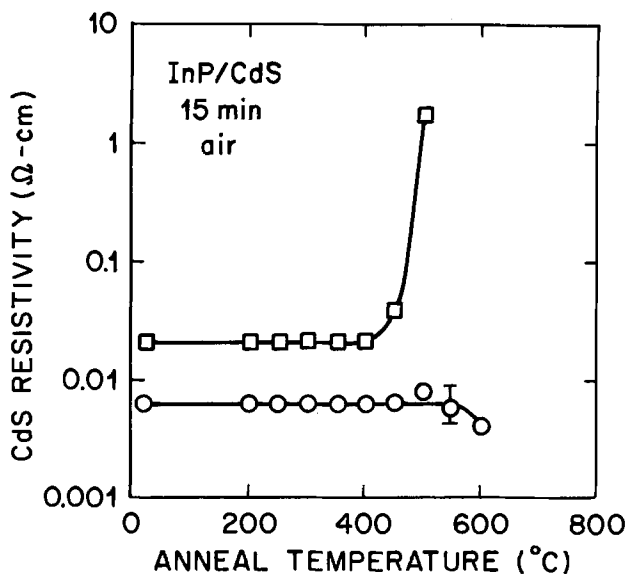


Fig. 1. Resistivity of CdS films (on p-InP substrates) subsequent to 15 min anneals in ambient air at various temperatures. The films with lower initial resistivity were prepared by having a larger Cd to S flux ratio.

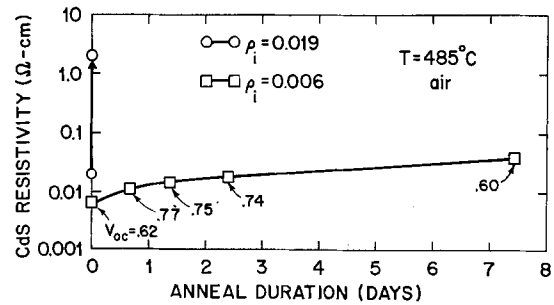


Fig. 2. Resistivity of CdS films (on p-InP substrates) for long duration air anneals at 485°C. Open-circuit voltages measured with a 3200°K tungsten-halogen lamp and a KG2 filter to simulate AM1 conditions (93 mW/cm<sup>2</sup>). No antireflection coatings were applied to the solar cells.

the band bending in the InP (0.65V) determined from capacitance measurements (4).

Since such a slight increase in resistivity is observed at 485°C, higher temperatures are required for accelerated life testing. We now show that higher temperature anneals change the morphology of the CdS film, and that these changes impair the effectiveness of the solar cell. The data shown in Fig. 1 are limited to temperatures  $\leq 600^\circ\text{C}$  since for anneals at 650°C in air or in forming gas (15% H<sub>2</sub> + 85% N<sub>2</sub>) the CdS becomes porous. The CdS layer detaches from the InP if an attempt is made to apply Ga-In or soldered In contacts. This behavior results from an attack of the CdS by ambient air (oxidation to CdO and SO<sub>3</sub>) or by forming gas (reduction to Cd and H<sub>2</sub>S). A very thin, whitish, resistive film, probably of CdO, developed on the CdS during the long duration anneals shown in Fig. 2. It was necessary to buff off this film using Linde B (0.05  $\mu\text{m}$ ) in order to perform the electrical measurements.

We have shown that this morphological change does not result from a chemical reaction between the InP and the CdS by annealing samples of InP/CdS in flowing argon, saturated with Cd and S vapor from an upstream source of CdS powder. During 15 min anneals at temperatures up to 750°C, the diodes are chemically

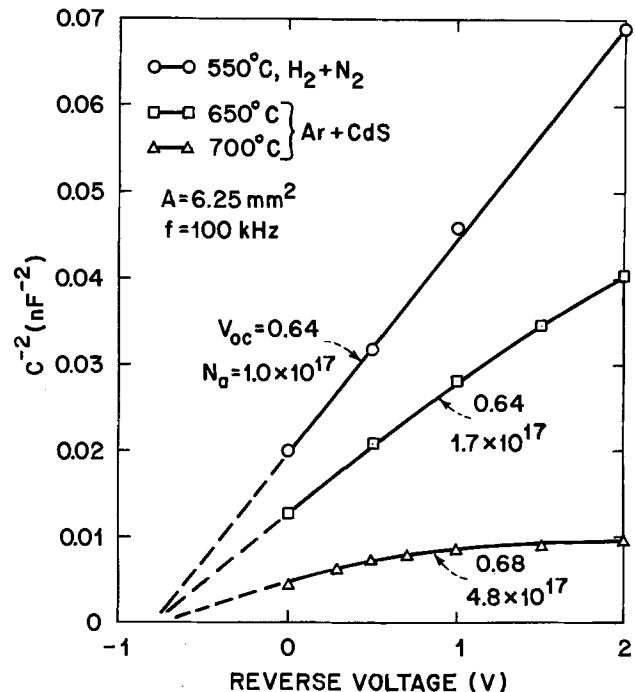


Fig. 3. Capacitance-reverse voltage characteristics for InP/CdS solar cells annealed for 15 min in argon plus CdS at 650° and 700°C, respectively. Capacitance measurements at 1 kHz and 10 kHz were typically a few percent larger.

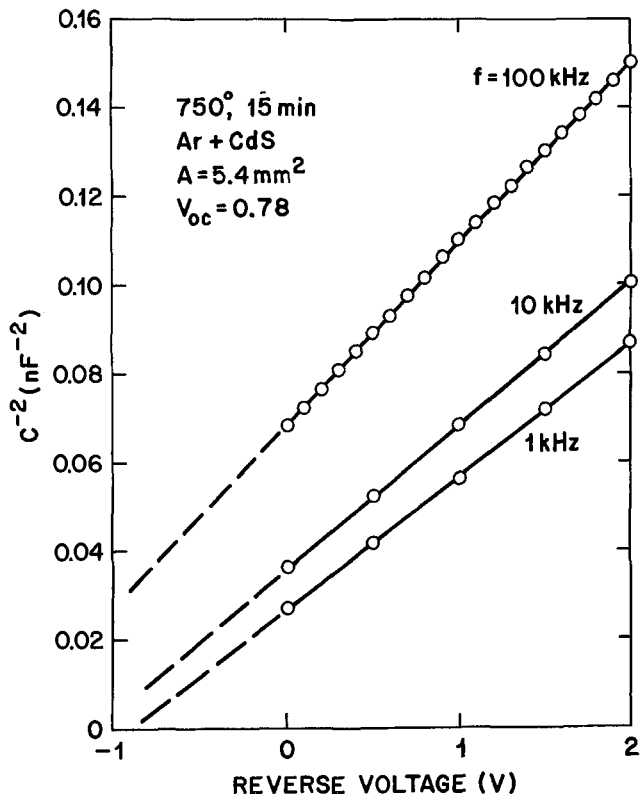


Fig. 4. Capacitance-reverse voltage characteristics for an InP/CdS solar cell annealed for 15 min in argon plus CdS at 750°C.

stable. At 800°C the CdS layer separates from the InP due to interfacial buildup of higher than atmospheric pressure of In<sub>2</sub>S, Cd, phosphorus, and sulfur. There is no significant interdiffusion of the components up to ~ 700°C, since the capacitance-voltage curves are well behaved (Fig. 3) and evidence only a gradual increase in the InP acceptor concentration from  $1.0 \times 10^{17} \text{ cm}^{-3}$

initially up to  $4.8 \times 10^{17} \text{ cm}^{-3}$  subsequent to the 700°C anneal. This increase in acceptor concentration may result from diffusion of excess Cd from the CdS into the InP. For an anneal at 750°C, the capacitance-voltage characteristic becomes frequency dependent as shown in Fig. 4.

From all of these results, we conclude that the useful lifetime of the InP/CdS solar cell in ambient air will be limited ultimately by a deterioration of the CdS morphology. Accelerated life testing under these conditions will be difficult since contacts must be applied initially which can withstand the high temperature anneals. Although our attempt to measure an accelerated lifetime for the InP/CdS cell has been frustrated by the electrical stability of the CdS films, it has certainly led to an encouraging result for terrestrial applications.

#### Acknowledgments

We are grateful to D. H. Olson and L. M. Schiavone for their technical assistance, and to Ms. Yolanda Martin for her technical assistance during the early stages of this work.

Manuscript submitted April 1, 1976; revised manuscript received May 5, 1976.

Any discussion of this paper will appear in a Discussion Section to be published in the June 1977 JOURNAL. All discussions for the June 1977 Discussion Section should be submitted by Feb. 1, 1977.

Publication costs of this article were assisted by Bell Laboratories.

#### REFERENCES

1. S. Wagner, J. L. Shay, K. J. Bachmann, and E. Buehler, *Appl. Phys. Letters*, **26**, 229 (1975).
2. J. L. Shay, S. Wagner, K. J. Bachmann, and E. Buehler, *J. Appl. Phys.*, **47**, 614 (1976).
3. K. Ito and T. Ohsawa, *Japan. J. Appl. Phys.*, **14**, 1259 (1975).
4. J. L. Shay, S. Wagner, and J. C. Phillips, *Appl. Phys. Letters*, **28**, 31 (1976).

## Etch Polishing of GaP Single Crystals by Aqueous Solutions of Chlorine and Iodine

A. Milch

Philips Laboratories, Briarcliff Manor, New York 10510

Investigations of the halogen etching of III-V semiconductors, GaP in particular, reported in the literature have employed two basic attack modes (1-4). They are a halogen dissolved in an organic liquid (1, 2, 3), or an aqueous solution of NaOCl and HCl (4). A third method is described in which the attack medium is an aqueous I<sub>2</sub>-KI-HCl solution, but was used only for the etching of gallium arsenide (5).

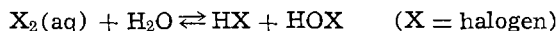
The present work originated with the need for a clean polishing etch for the controlled removal of material from very thin epitaxial layers of p-type GaP on n-type substrates. What was required was a chemically clean surface on a p-layer of about 3 μm thickness. The Cl<sub>2</sub>/methanol or Br<sub>2</sub>/methanol systems, cutting at values of approximately 10 μm/min (1), would necessitate uncontrollably short etch times. Moreover, the Cl<sub>2</sub>/organic solvent system is inconvenient and possibly dangerous.

The aqueous NaOCl-HCl etchant has the drawbacks of introducing nonvolatile alkali ions which have been known to degrade semiconductor performance (6, 7),

Key words: etch polishing, semiconductors.

and, insofar as the available literature reveals (4), requires electrolytic methods rather than the operationally simpler chemical etch techniques. An obvious expedient is to consider the halogen-water system since, in doing so, all of the above disadvantages are eliminated at once.

This communication recounts some observations on the etching and polishing of single crystal epitaxial GaP by aqueous solutions of chlorine and iodine. Disproportionation of both these halogens occurs (8) in aqueous solution according to the reaction



where both the dissolved halogen and the hypohalous acid may act as oxidizing agents. Note that with X = Cl, the system is somewhat equivalent to the NaOCl/HCl system mentioned above, but with the potentially deleterious effects of the Na<sup>+</sup> ion removed.

#### Experimental

*Chlorine.*—Experimentally, a sample of gallium phosphide of known surface area (neglecting surface

Table I. Etch rates of GaP by saturated chlorine water

Temperature (°C)	Cl <sub>2</sub> solubility (g/liter)	Etch rate (μm/min)	
		(111) B-face	(100)
6	11.3	0.45 ± 0.14	0.31 <sup>b</sup>
20	7.3	1.25 ± 0.25 <sup>a</sup>	—
20	7.3	0.32 ± 0.14	0.25 ± 0.06
45	4.2	1.9 <sup>a, b</sup>	—
45	4.2	1.0 <sup>b</sup>	—
67	2.8	0.014 ± 0.001	0.016 ± 0.002

<sup>a</sup> Sample held directly in bubble stream.

<sup>b</sup> One determination.

roughness) was waxed to a glass slide and suspended in the stirred etchant for a known period of time. The quantity of material removed was determined by weight loss using a Sartorius microbalance readable to ±0.001 mg on an optically projected vernier scale. Actual repeatability after successive weighings was generally better than ±0.01 mg while actual weight loss measurements were generally greater than 0.5 mg. Knowing the density of GaP (4.13 g/cm<sup>3</sup>), the thickness removed and etch rate are readily obtained.

The saturated chlorine solution was freshly prepared each day by bubbling the gas through distilled water for about 15 min prior to etching in order to achieve saturation. Following this, active bubbling was maintained throughout the etching experiments. Stirring was provided by the agitating action of the gas bubbles. Results of experiments conducted at four different temperatures on both B-face (111) and (100) surfaces are given in Table I. It is evident that etch values are sensitive to agitation as indicated by the high rates in the bubble stream. There appears to be a very weak peak in etch rate slightly above room temperature. This is presumably due to the strong and opposing effects of temperature on the solubility of Cl<sub>2</sub> in water on the one hand and on the reaction rate of the dissolved chlorine with the GaP on the other. The effects of agitation appear to be quite significant and may explain the spread of values in some of the grouped data. Nevertheless, the range of observed etch rates is very

satisfactory if it is desired to remove very thin layers of GaP.

Samples for etch experiments were chosen for heavy faceting in order to test the polishing action of the etchants. A typical result is displayed in Fig. 1. Visual comparisons indicate that (111) surfaces polish more readily than (100) surfaces and that the etch polishes about as effectively near room temperature as at 6°C. Etch rates at 67°C are so slow as to produce no visible changes over very protracted periods of time. It can be seen from the caption accompanying the photographs that considerable thickness of material had to be removed in these experiments in order to demonstrate polishing. This is an obvious result of the deliberate choice of heavily faceted material to begin with.

*Iodine as an etchant.*—Assuming no chemical reaction with water, the molar concentration of standard chlorine water at room temperature is about 0.1M. Accordingly, a 0.1M solution of iodine in about ½M HI was prepared and tested.<sup>1</sup> The etching action is practically zero: in two experiments, an etch rate of about 0.006 μm/min was observed during a 50 min etch period (equivalent to the removal of about 100 μg of GaP). In addition, considerable staining of GaP was observed. Hence iodine was quickly abandoned as a reasonable etchant for gallium phosphide.

### Conclusions

Water saturated with chlorine at room temperature is an excellent etch medium for GaP. It is convenient and clean, and the etch rate of about ½ μm/min is ideal for the metered removal of reasonable thickness of material with an acceptable degree of precision. It is a good polishing etch, with slightly better results being obtained with the (111) B-face of GaP. Aqueous HI<sub>3</sub> solutions are almost ineffective for etching GaP.

### Acknowledgments

I would like to thank Dr. E. H. Stupp for his encouragement and Mr. L. Dahlstedt for technical assistance during this work.

<sup>1</sup> Iodine is virtually insoluble in water. It dissolves in iodide solutions by virtue of the formation of the I<sub>3</sub><sup>-</sup> ion.

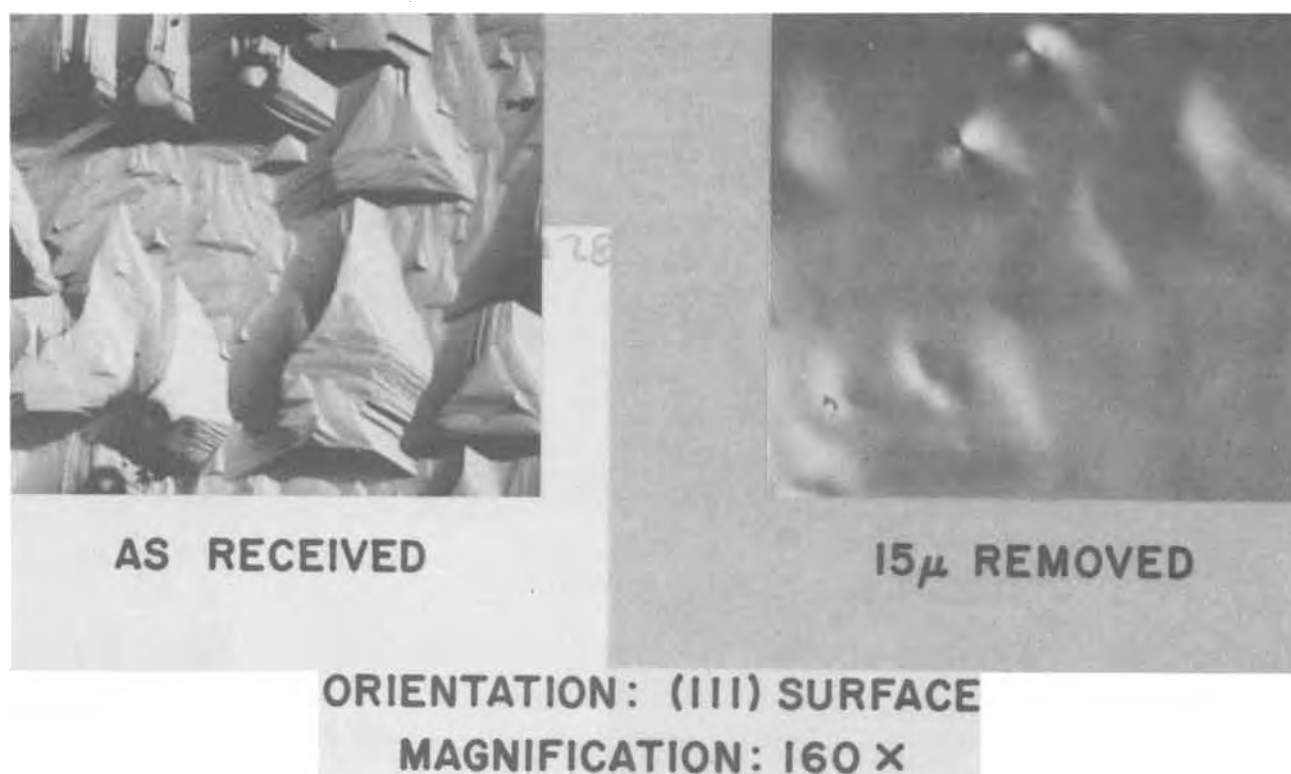


Fig. 1. Etch polishing of GaP by saturated chlorine water at room temperature



Manuscript submitted March 18, 1976; revised manuscript received April 19, 1976.

Any discussion of this paper will appear in a Discussion Section to be published in the June 1977 JOURNAL. All discussions for the June 1977 Discussion Section should be submitted by Feb. 1, 1977.

Publication costs of this article were assisted by Philips Laboratories.

#### REFERENCES

1. C. S. Fuller and H. W. Allison, *This Journal*, **109**, 880 (1962).
2. B. Schwartz, *ibid.*, **118**, 657 (1971).

3. A. V. Lishina and S. A. Medvedev, *Rost Kristallov, Akad. Nauk SSSR, Inst. Kristallogr.*, **6**, 239 (1965)
4. W. H. Hackett, Jr., T. E. McGahan, R. W. Dixon, and G. W. Kammlott, *This Journal*, **119**, 973 (1972).
5. G. M. Orlova and Kh. Binder, *Zh. Prikl. Khim.*, **39**, 1921 (1966).
6. A. S. Grove, "Physics and Technology of Semiconductor Devices," pp. 337-339, John Wiley & Sons, Inc., New York (1967).
7. R. Bhargava, Private communication.
8. N. V. Sidgewick, "The Chemical Elements and Their Compounds," pp. 1212-1217, Oxford University Press, London (1950).
9. F. W. Adams and R. G. Edmonds, *Ind. Eng. Chem.*, **29**, 447 (1937).

## Control of Palladium Adherence to Silicon Dioxide for Photolithographic Etching

M. S. Shivaraman and C. M. Svensson

Research Laboratory of Electronics, Chalmers University of Technology, Gothenburg, Sweden

The purpose of this note is to report a method for defining a pattern in a palladium film on silicon dioxide. The problem is the very low adherence of palladium to silicon dioxide (1) in which the Pd film may lift off the substrate immediately upon application of photoresist and also may lift off completely upon etching.

In our experiments, a silicon wafer was oxidized in dry oxygen to a thickness of 100 nm (at 1200°C). After that, 100 nm palladium was evaporated by e-gun evaporation. To be able to apply photoresist on the film the adherence to the substrate had to be increased. We then tried different annealing treatments. Annealing in argon at 500°C led to strong oxidation of the palladium probably due to trace amounts of water vapor or oxygen in the gas (the oxidized film could not be etched at all). Annealing in forming gas (10% H<sub>2</sub> in N<sub>2</sub>) for 5-15 min did not increase the adhesion. Instead, if it was done after an air anneal (see below), the adhesion decreased. Annealing in air at 150°C gave some increase in adhesion after a long annealing time (~ 16 hr). Annealing in air at 200° and 250°C did increase adhesion considerably; specifically, a treatment at 200°C in air for 30 min was found to give excellent results. After such a treatment the palladium film could be processed through photoresist application, drying, exposing, developing, and baking with no tendency to lift (using AZ 1350 positive resist). Annealing in air at 300°C again led to oxidation of the Pd film, making etching impossible.

In order to etch the film after photoresist patterning several etches were used. An etch consisting of sodium cyanide and ammonium sulfate described in the literature (2) did not work; instead, different forms of aqua regia were used. Standard aqua regia (3:1 HCl:HNO<sub>3</sub>) etched the palladium but before completion of the etching the whole film was lifted off the substrate. No damage of the photoresist was observed under the microscope. Modified aqua regia, with less HCl and more HNO<sub>3</sub>, gave, however, satisfactory results. By further moderating the etch with acetic acid, excellent results were obtained with smooth etching and no tendency for film lift-off. The etch used was 1:10:10 HCl:HNO<sub>3</sub>:CH<sub>3</sub>COOH with an etch rate of about 100 nm/min. After etching, the wafer was rinsed in distilled water and the resist was removed in acetone and rinsed in water again.

Key words: palladium, adhesion, etching.

The method can be summarized in the following way: (i) annealing in air at 200°C for 30 min; (ii) application of photoresist AZ 1350, spinning, drying, exposure, developing, and baking according to the standard procedure for this resist; (iii) etching with the etch described above (at 25°C); (iv) resist removal in acetone.

#### Discussion

The above observations suggest that hydrogen may play an important role in the adherence of palladium to silicon dioxide. It is well known that hydrogen diffuses rapidly through palladium at low temperatures (3). It is not expected that oxygen will diffuse through the film at temperatures of 500°C or less. The oxygen may, however, help extract hydrogen from the film (4).

The air annealing at 200°C is therefore assumed to extract hydrogen from the Pd-SiO<sub>2</sub> interface, and therefore increase the adhesion. The SiO<sub>2</sub> surface is probably covered with nonreactive silanol groups initially (5), and by extracting hydrogen from some of these groups the SiO<sub>2</sub> surface will become more reactive, thus increasing the adhesion. This hypothesis is also supported by the fact that a 500°C anneal in forming gas decreased the adhesion again.

During etching in standard aqua regia (HCl:HNO<sub>3</sub> 3:1) we may expect that H<sub>3</sub>O<sup>+</sup> may take part in the oxidation of palladium, forming hydrogen adsorbed in the film. This may lead to a decrease of the adhesion between Pd and SiO<sub>2</sub>. With an excess of the stronger oxidant NO<sub>3</sub><sup>-</sup>, this oxidant will dominate the process and no adsorbed hydrogen will be formed.

Manuscript received March 22, 1976.

Any discussion of this paper will appear in a Discussion Section to be published in the June 1977 JOURNAL. All discussions for the June 1977 Discussion Section should be submitted by Feb. 1, 1977.

Publication costs of this article were assisted by the Chalmers University of Technology.

#### REFERENCES

1. Cunningham, *Solid State Electron.*, **8**, 735 (1965).
2. E. M. Wise, "Palladium, Recovery, Properties and Uses," Academic Press, New York (1968).
3. F. A. Lewis, "The Palladium Hydrogen System," Academic Press, New York (1967).
4. Lundström, M. S. Shivaraman, and C. M. Svensson, *J. Appl. Phys.*, **46**, 3876 (1975).
5. M. L. Hair, *J. Non-Cryst. Solids*, **19**, 299 (1975).



## Reports on Electrochemical Society Summer Fellowship Awards

During the summer of 1975 the following graduate students received \$1000 each, representing the three Summer Fellowship Awards of The Electrochemical Society.

Miss Mary R. Suchanski, Northwestern University, Evanston, Illinois, was awarded the Edward Weston Fellowship.

Mr. James B. Flanagan, California Institute of Technology, Pasadena, California, was designated as the recipient of the Colin Garfield Fink Fellowship.

Mr. Thomas P. DeAngelis, University of Cincinnati, Cincinnati, Ohio, received the Joseph W. Richards Fellowship.

The Summer Fellowship Awards are made "without regard to sex, citizenship, race, or financial need, to a fellow or teaching assistant pursuing work between the degrees of B.S. and Ph.D. on a subject in a field of interest to The Electrochemical Society." They are intended to cover a period during which the recipient has no financial support for the continuance of his work.

### The Edward Weston Summer Fellowship Report

Miss Suchanski's report is given below.

#### Resonance Raman Spectroelectrochemistry of Tetracyanoquinodimethane Dianion and Tetrathiofulvalene Monocation

The planar aromatic molecules tetracyanoquinodimethane (TCNQ) and tetrathiofulvalene (TTF) are currently of great interest as the 1:1 complex TTF-TCNQ exhibits near-metallic behavior over a broad temperature range (1-3). Room temperature conductivities of TTF-TCNQ are on the order of 500 ( $\text{ohm}^{-1} \text{cm}^{-1}$ ) and increase by approximately one order of magnitude down to 58°K at which point a metal to insulator transition occurs (3). [Compare the room temperature conductivity of Cu which is  $6 \times 10^5$  ( $\text{ohm}^{-1} \text{cm}^{-1}$ ) (4).] The d-c conductivities of TTF-TCNQ are among the highest of all known organic conductors. Full characterization of the physical and chemical properties of highly conducting complexes such as TTF-TCNQ is necessary in developing criteria for designing organic metals with even better electrical behavior. This also involves study of the isolated components of such complexes.

The new technique of resonance Raman spectroelectrochemistry (RRSE) is valuable in studying species comprising organic charge transfer complexes. The highly resolved vibrational spectra obtained reflect the molecular geometry and the electronic distribution in the molecule. Other spectroelectrochemical techniques can yield this type of information. IR spectroelectrochemistry (5) provides molecularly specific vibrational data but is at least two orders of magnitude less sensitive in terms of sample concentration required. ESR spectroelectrochemistry compares more favorably with RRSE in terms of sensitivity and also yields structural data through the hyperfine coupling constant (6). While ESR is restricted to those molecules having net spin, resonance Raman spectroscopy requires only electronic absorption in the region of the excitation source.

As a spectroelectrochemical technique, RRSE also has the potential of other spectroelectrochemical meth-

ods for identifying the products of reaction sequences following electron transfer and monitoring the kinetics of such reactions. The feasibility of obtaining rate constants in the millisecond time range has recently been demonstrated (7).

The feature unique to RRSE is its ability to yield information about molecular excited states. While the observables in resonance Raman (RR) spectroscopy are those of molecular ground states, the actual process involves vibronic interactions between ground and excited states. Excited-state properties are related to the ground-state observables through the vibronic expansion of the Kramer-Heisenberg-Dirac dispersion relation for light-scattering processes (8). A recent study of the TCNQ radical anion in which the intensity of a ground-state vibrational mode is monitored as a function of excitation wavelength has yielded values of excited-state frequencies and excited-state vibronic level widths (9). Studies of this nature are valuable in the development of resonance Raman scattering theory.

A specific application of the utility of RRSE in studying ground-state properties of TTF and TCNQ is that of comparing frequency shifts which occur upon electron transfer with the corresponding computed bond order changes. This permits evaluation of those MO treatments which have calculated bond orders for the various TTF (10) and TCNQ (11, 12) moieties.

In addition, as vibrational frequencies are influenced by the electronic charge of a molecule, information about ground-state charge densities can be obtained via RRSE. The extent of charge transfer in TTF-TCNQ is a point of great contention, (13-19). Values have been estimated in the range of 0.5-1.0 electron transferred from TTF to TCNQ. From knowledge of radical ion and corresponding neutral vibrational frequencies, one can estimate the extent of electron transfer in solid conducting organic complexes. This comparison between solid-state and solution data is valid, as the frequency shifts in going from solution to a solid are small in comparison to those accompanying electron transfer. For example, see the work of Pecile *et al.* on TCNQ salts (20).

Reported here is an example of the use of RRSE in detecting and identifying decay products of electrochemically produced species. Positive identification of

the  $O_2$  decay product of  $TCNQ^{2-}$  has been made. Subsequent chemical routes led to isolation of  $TCNQ^{2-}$  in forms suitable for investigation via normal Raman (NR) spectroscopy. The NR spectra of two such  $TCNQ^{2-}$  moieties are reported. The vibrational frequencies obtained were used to compare computed CNDO bond order changes (12) with corresponding frequency changes accompanying electron transfer and electronic excitation in  $TCNQ^{\cdot-}$ .

Finally, the Raman spectroscopy of TTF is discussed. RRSE was employed to study TTF cation radical. The vibration data for TTF neutral were obtained via NR spectroscopy. A tentative assignment of the totally symmetric modes observed in the TTF<sup>+</sup> RR spectrum is made. Computed bond order changes are compared with the frequency changes accompanying the one electron oxidation process to form TTF<sup>+</sup>.

### Experimental

Several experimental configurations exist for obtaining Raman data via RRSE. The RRSE experiments reported here were all performed in the controlled potential electrolysis mode in which the species of interest are generated by exhaustive bulk electrolysis in a cell of conventional design with subsequent laser excitation of the species. The laser beam is scattered directly off the walls of the coulometry cell in oblique 180° scattering geometry. The details of the experimental configuration, cell construction, and solution preparation have been described earlier (21).

The  $TCNQ^{2-}$  was generated at  $-0.7V$  vs. SCE in thoroughly deoxygenated spectro grade acetonitrile solutions containing  $2.0 \times 10^{-4}$  to  $1.5 \times 10^{-3}M$   $TCNQ$  and  $0.1M$  tetrabutylammonium perchlorate (TBAP). The TTF cation radical was formed under similar conditions at  $+0.5V$  vs. SCE in solution containing  $1.0 \times 10^{-4}$  to  $3.0 \times 10^{-3}M$  TTF.

The reported resonance Raman scattering spectra and the normal Raman scattering spectra were obtained by excitation with a Spectra Physics Model 164 Ar<sup>+</sup> laser, a Coherent Radiation Model CR-8 Ar<sup>+</sup> laser, and a Coherent Radiation Model 490 jet stream dye laser pumped all-lines by the CR-8. Spectra were collected using either a 0.85m Spex Model 1401 double monochromator or a 0.75m Spex Model 1400-II double monochromator. Wavelengths reported are accurate to  $\pm 2$   $cm^{-1}$ . Further information regarding spectral calibration and data collection has been published (21).

Normal Raman scattering spectra of  $TCNQ^{2-}$  complexes and of neutral TTF were obtained by the rotating cell technique described by Shriver and Dunn (22). The powdered samples were sealed under vacuum in Pyrex ampuls to avoid air decomposition.

The  $TCNQ$  was purchased from Aldrich Chemical Company and was purified by a combination of high vacuum ( $10^{-5}$  Torr) sublimation at  $150^\circ C$  and recrystallization from acetonitrile. Neutral TTF was obtained from IBM Corporation and used without further purification.

The dianion of  $TCNQ$  was chemically prepared by two methods. The procedure of Basolo *et al.* (23) was followed for the reaction of  $TCNQ$  with the Schiff base complex  $N,N'$ -ethylenebis(acetylacetonimino) cobalt (II),  $[Co(acacen)]$  in the presence of pyridine to form  $[Co(acacen)(py)_2]_2TCNQ$ . Analysis calculated for  $C_{34}H_{32}CoN_8O_2$ : C, 62.10; H, 5.54; N, 15.52; found: C, 66.20; H, 5.89; N, 15.29.

Elemental analysis was performed by H. Beck of this department. The sample of dilithium tetracyanoquinodimethandiide tetrahydrofuranate ( $Li_2TCNQ \cdot THF$ ) was synthesized by Dr. Allen R. Siedle at NBS. Two equivalents of *n*-butyllithium are added to  $TCNQ$  in tetrahydrofuran at  $-78^\circ C$  to produce the white salt ( $Li_2TCNQ \cdot THF$ ) (24).

### Results and Discussion

The cyclic voltammogram of  $TCNQ$  and the optical spectroscopy of  $TCNQ$  dianion are shown in Fig. 1.

Peak A corresponds to formation of  $TCNQ^{\cdot-}$  ( $E_{pc} = +0.172V$  vs. SCE, scan rate  $V = 100$   $mV$   $sec^{-1}$ ). At peak B  $TCNQ^{\cdot-}$  is converted to  $TCNQ^{2-}$  ( $E_{pc} = -0.362V$  vs. SCE, scan rate  $V = 100$   $mV$   $sec^{-1}$ ). Measurement of the ratio of cathodic peak current to anodic peak current for peak B ( $i_{pc}/i_{pa} = 1.00 \pm 0.03$ ) indicates reversible formation of  $TCNQ^{2-}$  on the cyclic voltammetric time scale. In addition, at sweep rates lower than  $100$   $mV$   $sec^{-1}$  the anodic and cathodic peak separation  $\Delta E_p = 0.060V$ , indicating electrochemical reversibility.

The only previously reported optical spectrum of  $TCNQ^{2-}$  (11) had an absorption maximum at  $2.6$  eV ( $477$  nm). Attempts to repeat this work are shown by the solid line in Fig. 1. This electronic absorption spectrum of  $2.55 \times 10^{-4}M$   $TCNQ$  was recorded less than 5 min after bulk electrolytic generation under absence of  $O_2$ . In contrast to the results of Jonkman and Kommandeur (11), the absorption maxima occur at  $3.75$  eV ( $330$  nm),  $5.16$  eV ( $240$  nm), and  $5.9$  eV ( $210$  nm). Upon leakage of  $O_2$  into the bulk electrolysis cell, the

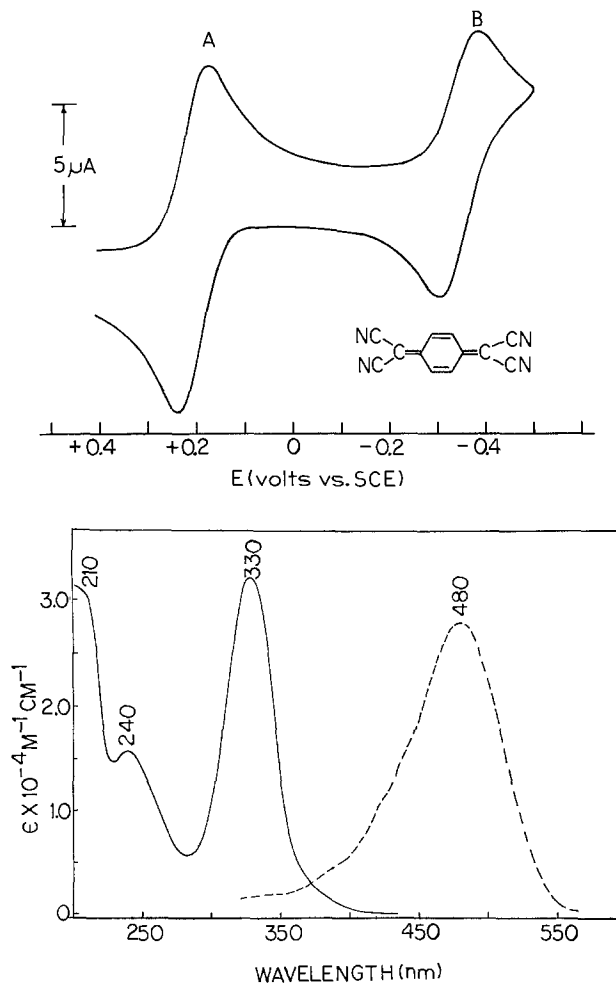


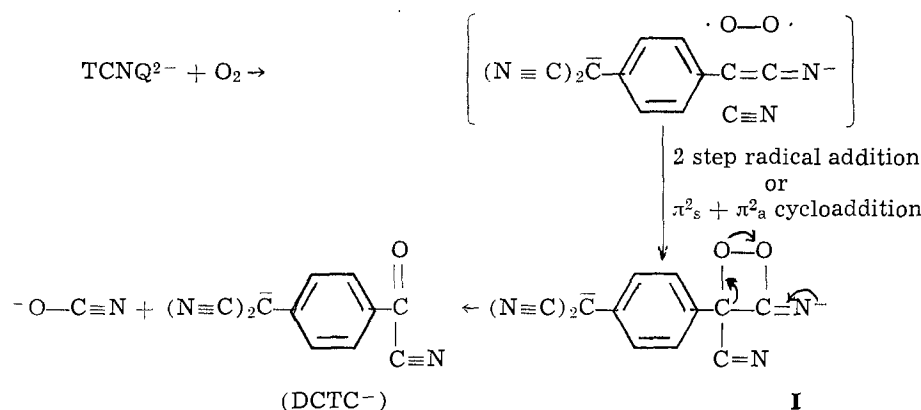
Fig. 1. Upper: First-scan cyclic voltammogram of  $0.66$   $mM$   $TCNQ$  in acetonitrile containing  $0.01M$  TBAP at a platinum disk microelectrode. The scan rate =  $0.100$   $V$   $sec^{-1}$ . Lower: Electronic absorption spectra of  $2.55 \times 10^{-4}M$   $TCNQ$  in  $0.1M$  TBAP-acetonitrile solution following exhaustive  $2e^-$  reduction at  $-0.70V$  vs. SCE. Solid line:  $TCNQ^{2-}$  absorption spectrum obtained by rigorous exclusion of  $O_2$  from the solution. Dotted line: absorption spectrum obtained by electrogenerating  $TCNQ^{2-}$  in the presence of  $O_2$  or by bubbling  $O_2$  through the solution originally giving the solid line spectrum. The extinction coefficient scale is quantitatively accurate for  $TCNQ^{2-}$  (solid line) spectrum only.

originally colorless solution of  $\text{TCNQ}^{2-}$  immediately turns orange. The ensuing visible absorption spectrum is indicated in Fig. 1 by the dotted line. The absorption maximum and extinction coefficient at the peak agree with that previously reported by Jonkman and Kommandeur (11) as being due to  $\text{TCNQ}^{2-}$ .

It was concluded that the orange product formed upon admitting  $\text{O}_2$  to a solution of  $\text{TCNQ}^{2-}$  was an oxygen decay product of  $\text{TCNQ}^{2-}$ . The identity of this species was established using resonance Raman as the spectroscopic monitor. The highly resolved vibrational Raman spectra are unique for each particular molecule or ion. Therefore, provided one has a good "guess" as to the identity of a product of an electrode reaction, comparison of a known sample to the unknown provides unambiguous identification.

Searching the cyanocarbon literature for oxygen containing compounds related to  $\text{TCNQ}$ , it was discovered that a carbanion [ $\alpha$ ,  $\alpha$ -dicyano-*p*-toluoyl cyanide ( $\text{DCTC}^-$ )] has an absorption maximum at 480 nm (26). The sodium salt of this carbanion can be prepared by the reaction of  $\text{TCNQ}$  neutral and  $\text{NaNO}_2$  (25). Figure 2 compares the RR spectrum of a solution of electrochemically generated  $\text{TCNQ}^{2-}$  exposed to air with that of a solution of  $\text{DCTC}^-$  formed from  $\text{TCNQ}$  neutral. The striking similarity of the two spectra confirms the identity of the  $\text{TCNQ}^{2-}/\text{O}_2$  decay product. The broad Raman signal at  $1638\text{ cm}^{-1}$  is probably a composite of  $\text{C}=\text{C}$  ring stretch and of carbonyl stretching. The  $2214\text{ cm}^{-1}$  band is ascribed to conjugated nitrile stretching. The corresponding bands in the infrared spectrum of  $\text{DCTC}^-$  are at  $1645$ ,  $2150$ , and  $2200\text{ cm}^{-1}$  (25).

A possible mechanism for formation of the carbanion is given by Scheme I. Triplet oxygen reacts via a two-step radical addition or by a  $\pi_s^2 + \pi_a^2$  cyclo-addition to form a dioxetane intermediate. Rearrangement of the intermediate results in  $\text{DCTC}^-$  formation with elimination of cyanate ion.



To obtain the RR spectrum of  $\text{TCNQ}^{2-}$  necessitates u.v. excitation. Not having u.v. excitation sources available at that time required developing routes to prepare  $\text{TCNQ}^{2-}$  in a form suitable for investigation via normal Raman (NR) spectroscopy, i.e., a solid. Two such solids were made chemically: (i) a brown, air-stable, diamagnetic cobalt Schiff base complex  $[\text{Co}(\text{III}) (\text{acacen})-(\text{py})_2]_2\text{TCNQ}$  discovered by Basolo (23) and (ii) a white, air-sensitive salt  $\text{Li}_2\text{TCNQ} \cdot \text{THF}$  prepared by A. Siedle (24). The NR spectra of these two compounds are shown in Fig. 3. The extra bands in the  $[\text{Co}(\text{III}) (\text{acacen})-(\text{py})_2]_2\text{TCNQ}$  spectra are ascribed to small amounts of resonance-enhanced

$\text{TCNQ}^{\cdot -}$  ( $339$ ,  $610$ ,  $677$ ,  $715$ ,  $1187$ ,  $1387$ ,  $1609$ ,  $1949$ , and  $2191\text{ cm}^{-1}$ ), to the acacen ligand ( $431$  and  $481\text{ cm}^{-1}$ ), and to Lewis-coordinated pyridine ( $647$ ,  $1024$ , and  $1048\text{ cm}^{-1}$ ). Assignment of the Raman signals at  $2106$ ,  $1304$ ,  $1194$ , and  $731\text{ cm}^{-1}$  to the totally symmetric modes  $\nu_2$ ,  $\nu_4$ ,  $\nu_5$ , and  $\nu_7$  of  $\text{TCNQ}^{2-}$  is made in analogy with the

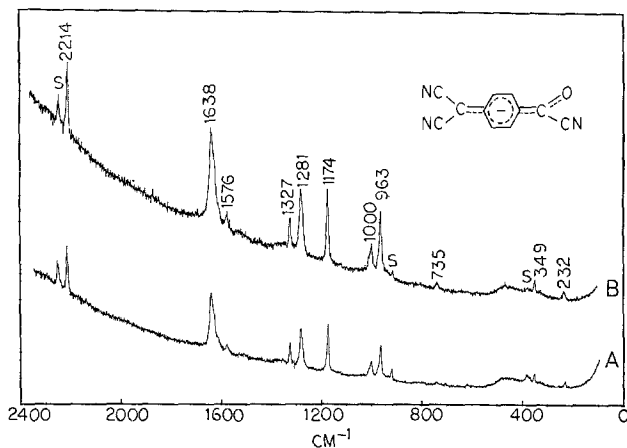


Fig. 2. Resonance Raman spectra of: (A) electrogenerated  $\text{TCNQ}^{2-}$  saturated with  $\text{O}_2$ ;  $[\text{TCNQ}^{2-}] = 1.42 \times 10^{-3}\text{ M}$ , laser power at  $4579\text{ \AA} = 80\text{ mW}$ , bandpass =  $2.3\text{ cm}^{-1}$ . (B) Authentic  $\text{DCTC}^-$  in  $\text{CH}_3\text{CN}:\text{H}_2\text{O}$  (10:1);  $[\text{DCTC}^-] = 1.43 \times 10^{-3}\text{ M}$ , laser power at  $4579\text{ \AA} = 30\text{ mW}$ , bandpass =  $2.3\text{ cm}^{-1}$ .  $\text{TCNQ}^{2-}$  was electrogenerated by controlled-potential coulometry at  $-0.70\text{ V}$  vs. SCE in  $0.1\text{ M}$  TBAP  $\text{CH}_3\text{CN}$ . All spectra were scanned at ca.  $50\text{ cm}^{-1}\text{ min}^{-1}$  using a  $1.00\text{ sec}$  counting interval. Plasma lines were removed with a  $4579\text{ \AA}$  interference filter.

vibrational designations of  $\text{TCNQ}^{\cdot -}$  (7) and by comparison with the lines in the  $\text{Li}_2\text{TCNQ} \cdot \text{THF}$  Raman spectrum. Although both nontotally symmetric and totally symmetric modes can be observed in NR spectroscopy, it is a general rule that the totally symmetric vibrations are more intense (26). Hence, all bands in the  $\text{Li}_2\text{TCNQ} \cdot \text{THF}$  spectrum are attributed to totally symmetric modes.

Table I summarizes the vibrational data for  $\text{TCNQ}^{\cdot -}$ .

in its ground state,  $\text{TCNQ}^{\cdot -}$  in its lowest  ${}^2\text{B}_{1u}$  state, and  $\text{TCNQ}^{2-}$  in its ground  ${}^1\text{A}_g$  state. The frequency changes occurring upon excitation of  $\text{TCNQ}^{\cdot -}$  to its lowest  ${}^2\text{B}_{1u}$  state and upon converting  $\text{TCNQ}^{\cdot -} ({}^2\text{B}_{3g})$  to  $\text{TCNQ}^{2-} ({}^1\text{A}_g)$  are also listed. A more extensive tabulation of vibrational frequencies for the  $\text{TCNQ}$  system will be published (24). An analysis of this type reveals the extent of electronic structure change corresponding to the various electron transfer and excitation processes. Modes  $\nu_2$  (terminal  $\text{C}\equiv\text{N}$  stretch) and  $\nu_4$  ( $\text{C}=\text{C}$  ring +  $\text{C}=\text{C}$  wing stretch) appear to be most sensitive to their electronic environment. For both processes (see Table I), the shift to lower frequencies reflects the promotion or addition of an electron to an antibonding orbital. One would expect the bond order changes accompanying these alterations to agree in relative order of magnitude with the corresponding

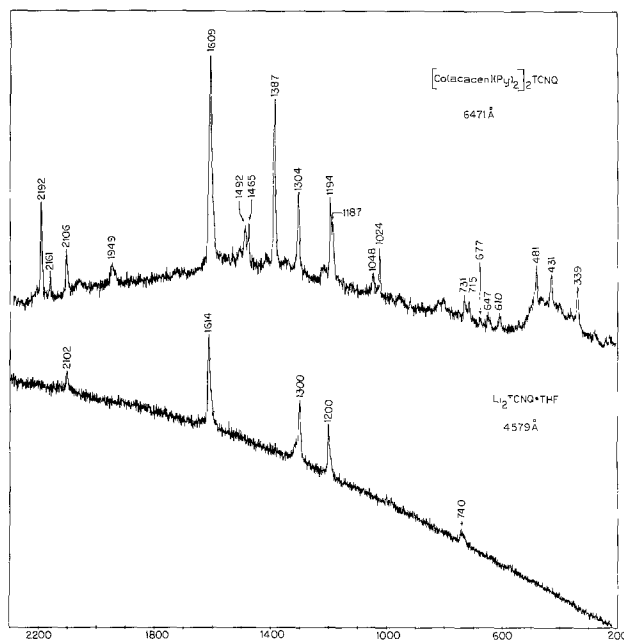


Fig. 3. Normal Raman scattering spectra of: (A)  $\text{Li}_2\text{TCNQ} \cdot \text{THF}$ , laser power at  $4579\text{Å} = 10\text{ mW}$ , bandpass  $= 2.0\text{ cm}^{-1}$ . (B)  $[\text{Co}(\text{acacen})(\text{py})_2]_2\text{TCNQ}$ , laser power at  $6471\text{Å} = 20\text{ mW}$ , bandpass  $= 4.0\text{ cm}^{-1}$ . Both samples were solid powders. Spectra were scanned at ca.  $50\text{ cm}^{-1}\text{ min}^{-1}$  using a  $1.0\text{ sec}$  counting gate. Plasma lines were removed at  $4579\text{Å}$  with an interference filter and at  $6471\text{Å}$  with a Claassen filter.

frequency changes. Such concurrence between bond order changes computed from CNDO/S MO theory for the TCNQ system (12) and the vibrational frequency changes does exist. This good agreement supports the frequency assignments of the totally symmetric modes in  $\text{TCNQ}^-$  ( ${}^2\text{B}_{1u}$  (1)). Further discussion of the excited state frequency assignments can be found elsewhere (27).

Turning to the other half of the conducting charge transfer complex TTF-TCNQ, the results for the tetrathiofulvalene neutral and monocation systems will be discussed. Figure 4 shows the cyclic voltammogram of TTF and the optical spectra of TTF neutral,  $\text{TTF}^+$  and  $\text{TTF}^{2+}$ . The two one-electron oxidations in the cyclic voltammogram correspond to generation of  $\text{TTF}^+$  (peak A,  $E_{\text{pa}} = +0.34\text{V vs. SCE}$  at a scan rate,

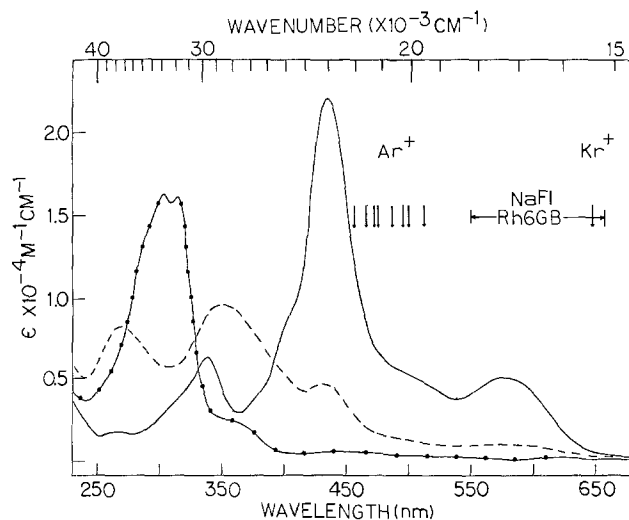
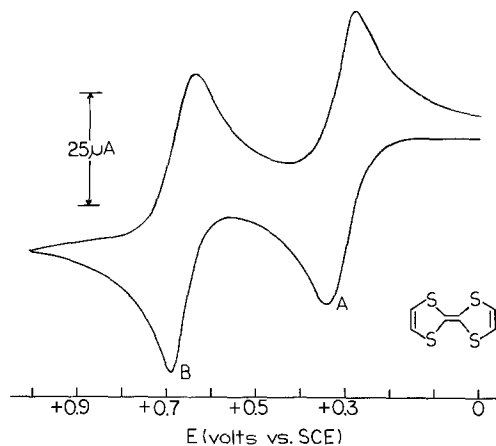


Fig. 4. Upper: First-scan cyclic voltammogram of  $6.0\text{ mM}$  TTF in acetonitrile containing  $0.10\text{M}$  TBAP at a platinum disk microelectrode. The scan rate  $= 0.10\text{ V sec}^{-1}$ . Lower: Electronic absorption spectra of TTF,  $\text{TTF}^+$ , and  $\text{TTF}^{2+}$ . (●-●-●-●-●-)  $4.38 \times 10^{-4}\text{M}$  TTF in acetonitrile. (————)  $\text{TTF}^+$  electrogenerated at  $+0.50\text{V vs. SCE}$  in acetonitrile containing  $0.1\text{M}$  TBAP.  $\text{TTF}^+ = 4.38 \times 10^{-4}\text{M}$ , cell pathlength  $= 0.10\text{ cm}$ . (-----)  $\text{TTF}^{2+}$  electrogenerated at  $+0.90\text{V vs. SCE}$  in acetonitrile containing  $0.1\text{M}$  TBAP.  $\text{TTF}^{2+} = 4.0 \times 10^{-4}\text{M}$ , cell pathlength  $= 0.10\text{ cm}$ . Residual  $\text{TTF}^+$  may be contributing to the  $\text{TTF}^{2+}$  absorption spectrum.

Table I. Raman vibrational data for totally symmetric fundamentals of TCNQ systems<sup>a</sup>

Assign.	$\text{TCNQ}^-$ ( ${}^2\text{B}_{3g}$ ) (6471Å) $\text{cm}^{-1b}$	$\text{TCNQ}^-$ ( ${}^2\text{B}_{1u}$ (1)) (5600- 6667Å) $\text{cm}^{-1}$	$\text{TCNQ}^{2-}$ ( ${}^1\text{A}_g$ ) <sup>c</sup> (4579Å) $\text{cm}^{-1}$	Process 1 $\Delta\nu_1^d$ $\text{cm}^{-1}$	Process 2 $\Delta\nu_1^e$ $\text{cm}^{-1}$
$\nu_1$	—	—	—	—	—
$\nu_2$	2192	2150	2102	+42	+90
$\nu_3$	1613	1613	1614	0	-1
$\nu_4$	1389	1335	1300	+54	+89
$\nu_5$	1195	1198	1200	-3	-5
$\nu_6$	976	—	—	—	—
$\nu_7$	724	—	740	—	-16
$\nu_8$	612	—	—	—	—
$\nu_9$	336	330	—	+6	—
$\nu_{10}$	—	—	—	—	—

<sup>a</sup> All Raman data pertain to TCNQ systems in  $\text{CH}_3\text{CN}$  solution and the frequencies are accurate to  $\pm 2\text{ cm}^{-1}$  unless otherwise indicated.

<sup>b</sup>  $\pm 5\text{ cm}^{-1}$ .

<sup>c</sup>  $\text{Li}_2\text{TCNQ} \cdot \text{THF}$  solid.

<sup>d</sup>  $\nu_1(\text{TCNQ}^- [{}^2\text{B}_{3g}]) - \nu_1(\text{TCNQ}^- [{}^2\text{B}_{1u}]) \pm 10\text{ cm}^{-1}$ .

<sup>e</sup>  $\nu_1(\text{TCNQ}^- [{}^2\text{B}_{3g}]) - \nu_1(\text{TCNQ}^{2-}) \pm 4\text{ cm}^{-1}$ .

$\text{V}$ , of  $100\text{ mV sec}^{-1}$ ) and to generation of  $\text{TTF}^{2+}$  (peak B,  $E_{\text{pa}} = +0.68\text{V vs. SCE}$  at a scan rate,  $\text{V}$ , of  $100\text{ mV sec}^{-1}$ ). Formation of TTF monocation is both chemically and electrochemically reversible, the former being demonstrated by the constancy of the quantity  $i_{\text{pa}}\text{V}^{-1/2}\text{C}^\circ$  as sweep rate  $\text{V}$  is varied.

In the lower half of Fig. 4 are the optical spectra of solid TTF neutral, of electrochemically generated  $\text{TTF}^+$ , and of electrochemically generated  $\text{TTF}^{2+}$ . The regions of  $\text{TTF}^+$  absorption are ideal from the standpoint of existing laser excitation sources. (See Fig. 4.)

Among the various MO treatments of  $\text{TTF}^+$ ; PPP (10), self-consistent statistical exchange multiple scattering (28), and Hückel (29), the PPP results with limited configuration interaction of Zahradnik *et al.* (10) are in best agreement with the transition energies and oscillator strengths of the  $\text{TTF}^+$  optical absorption spectrum. Hence, any further analysis of  $\text{TTF}^+$  electronic transitions are based on Zahradnik's results.

The RR spectrum of TTF cation radical was obtained upon excitation into the region of the  ${}^2B_{1u}$  to  ${}^2B_{2g}^{(2)}$  transition (4579Å excitation). (See Fig. 5.) Also reported in Fig. 5 is the NR spectrum of solid TTF neutral (excitation at 6000Å). Of the seven totally symmetric ( $A_g$ ) Raman active normal modes predicted for  $TTF^+$  (based on a  $d_{2h}$  point group), at least four have been ascribed to bands in the RR spectrum of  $TTF^+$ . These Raman lines are located at 265, 757, 1041, and 1427  $cm^{-1}$ . In comparing these vibrations with corresponding ones in the TTF spectrum, it is again assumed that all major bands are attributed to totally symmetric species. It is further assumed that site-symmetry effects and factor-group splitting are not manifested to any great extent in the neutral Raman spectrum. The TCNQ neutral Raman spectrum has been interpreted similarly (30).

The very intense fundamental at 1427  $cm^{-1}$  in the  $TTF^+$  RR spectrum is ascribed considerable central C=C character. This is in analogy with the C=C stretch in the RR spectrum of tetracyanoethylene anion radical (TCNE $^-$ ) at 1421  $cm^{-1}$  (21). The corresponding vibration in the TTF neutral spectrum occurs with equal intensity at 1513  $cm^{-1}$ . This shift upward of 86  $cm^{-1}$  is equated with strengthening of the central C=C bond when a bonding electron is added to  $TTF^+$ . Designation of the 1427  $cm^{-1}$  mode as  $\nu_2$  is made on the basis that  $\nu_1$  is due to the symmetric C—H stretch, even though it is not observed in the RR spectrum. The  $\nu_3$  fundamental at 1041  $cm^{-1}$  in the  $TTF^+$  spectrum (corresponding neutral band at 1089  $cm^{-1}$ ) is of unknown origin. Some C—S stretching may contribute to the Raman band of  $TTF^+$  at 757  $cm^{-1}$  (neutral frequency 796  $cm^{-1}$ ). Cyclic sulfides exhibit C—S stretching in the 550-700  $cm^{-1}$  region (31). Finally, the low frequency mode designated  $\nu_6$  at 265  $cm^{-1}$  is associated

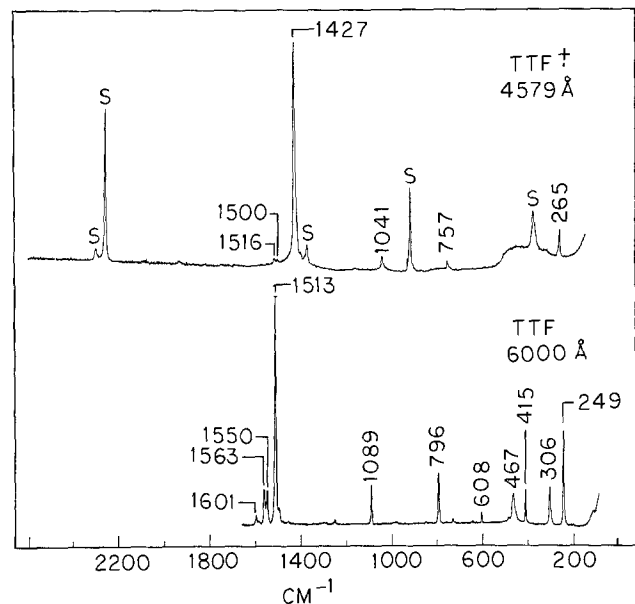


Fig. 5. Resonance Raman spectrum of electrogenerated  $TTF^+$  and normal Raman spectrum of TTF solid. Upper:  $TTF^+$  electro-generated by controlled-potential coulometry at +0.50V vs. SCE in 0.1M TBAP- $CH_3CN$  Excitation at 4579Å, 1.0 mM concentration, scanned at 0.333 Å/sec in second order, 1.00 sec counting interval, laser power = 70 mW, bandpass = 2.0  $cm^{-1}$  in second order. Plasma lines were removed with an interference filter. Lower: TTF powder at 6000Å excitation, scan rate = 0.25 Å/sec, 1.00 sec counting interval, laser power = 60 mW, bandpass = 1.2  $cm^{-1}$ .

Table II. Comparison of frequency changes and bond order changes for totally symmetric modes in the TTF system

$\nu_i$	Tentative assignment	TTF neutral 6000Å ( $cm^{-1}$ ) <sup>a</sup>	$TTF^+$ 4579Å ( $cm^{-1}$ )	$\Delta\nu_i$ (TTF- $TTF^+$ )	$\Delta P_i^c$ (TTF- $TTF^+$ )
$\nu_1$	C-H stretch	—	—	—	—
$\nu_2$	C=C stretch (central)	1513 vs <sup>b</sup>	1427 vs	+86	+0.185
$\nu_3$		1089 m	1041 w	+48	—
$\nu_4$		796 m	757 w	+39	—
$\nu_6$		249 m	265 m	-16	—
$\nu_7$		—	—	—	—

<sup>a</sup> All frequencies reported are accurate to  $\pm 2$   $cm^{-1}$ .

<sup>b</sup> w = weak, m = medium, vs = very strong.

<sup>c</sup> The bond order changes are based on the SCF calculations of R. Zahradnik et al. [Ref. (10)].

with the neutral band at 249  $cm^{-1}$ . It is possible that internal angle bending in the five-membered sulfur heteroatom ring contributes to this vibration. Low frequency modes in planar conjugated organic molecules have been attributed to bending motions (20, 30). Regarding  $\nu_2$  and  $\nu_7$ , no definitive assignment in either the  $TTF^+$  RR spectrum or TTF neutral Raman spectrum has been made. These results are summarized in Table II along with the PPP bond order changes.

Work is now underway to investigate the RR spectra  $TTF^+$  upon excitation with existing dye laser sources (5500-6500Å). It is hoped that complete characterization of the RR spectra of TTF moieties coupled with the related work on TCNQ species will ultimately lead to identification of the oxidation states of TTF and TCNQ in the highly conducting organic metal TTF-TCNQ.

#### Acknowledgments

The author would like to thank Dr. Allen R. Siedle for his synthesis of  $Li_2TCNQ \cdot THF$  and Dr. Jerry B. Torrance for supplying samples of TTF. The assistance of Dr. Richard P. Van Duyne throughout the course of this work as well as the support of this research by The Electrochemical Society is greatly appreciated.

#### REFERENCES

- J. Ferraris, D. O. Cowan, V. Walatka, and J. H. Perlstein, *J. Am. Chem. Soc.*, **95**, 948 (1973).
- M. J. Cohen, L. B. Coleman, A. F. Garito, and A. J. Heeger, *Phys. Rev.*, **B10**, 1298 (1974).
- S. Etemad, T. Penney, E. M. Engler, B. A. Scott, and P. E. Seiden, *Phys. Rev. Letters*, **34**, 741 (1975).
- CRC Handbook of Chemistry and Physics, p. 150, Chemical Rubber Publishing Company, Cleveland, Ohio (1973).
- W. R. Heineman, J. N. Burnett, and R. W. Murray, *Anal. Chem.*, **40**, 1974 (1968).
- R. S. Alger, "Electron Paramagnetic Resonance," pp. 267-272, Interscience, New York (1968).
- D. L. Jeanmaire and R. P. Van Duyne, *J. Electroanal. Chem.*, **66**, 235 (1975).
- J. Tang and A. C. Albrecht, in "Raman Spectroscopy—Theory and Practice," Vol. 2, H. A. Szymanski, Editor, Chap. 2, Plenum Press, New York (1967).
- D. L. Jeanmaire and R. P. Van Duyne, *J. Am. Chem. Soc.*, In press.
- R. Zahradnik, P. Carsky, S. Hunig, G. Kiesslich, and D. Scheutzw, *Int. J. Sulfur Chem.*, **C6**, 109 (1971).
- H. T. Jonkman and J. Kommandeur, *Chem. Phys. Letters*, **15**, 496 (1972).
- M. A. Ratner and K. Krogh-Jespersen, Private communication.
- J. B. Torrance, B. A. Scott, and F. B. Kaufman, Submitted to *Solid-State Commun.*
- W. D. Grobman, R. A. Pollack, D. E. Eastman, E. T. Maas, Jr., and B. A. Scott, *Phys. Rev. Letters*, **32**, 534 (1974).
- A. J. Epstein, N. O. Lipari, P. Nielsen, and D. J. Sandman, *ibid.*, **34**, 914 (1975).

16. W. T. Wozniak, G. DePasquali, M. V. Klein, R. L. Sweany, and T. L. Brown, *Chem. Phys. Letters*, **23**, 1 (1975).
17. P. Coppens, *Phys. Rev. Letters*, **35**, 98 (1975).
18. Y. Tomkiewicz, J. B. Torrance, B. A. Scott, and D. C. Green, *J. Chem. Phys.*, **60**, 5177 (1974).
19. V. E. Klymenko, V. Ya Krivnov, A. A. Ovchinnikov, I. I. Ukrainsky, and A. F. Shuets, Submitted to ITP, 75-6E (1975).
20. R. Bozio, A. Girlando, and C. Pecile, *Trans. Faraday Soc.*, **71**, 1237 (1975).
21. D. L. Jeanmaire, M. R. Suchanski, and R. P. Van Duyne, *J. Am. Chem. Soc.*, **97**, 1699 (1974).
22. D. F. Shriver and J. B. P. Dunn, *Appl. Spectry.*, **28**, 319 (1974).
23. S. G. Clarkson, B. C. Lane, and F. Basolo, *Inorg. Chem.*, **11**, 662 (1972).
24. M. R. Suchanski, A. R. Siedle, and R. P. Van Duyne, Submitted to *J. Am. Chem. Soc.*
25. W. R. Hertler, H. D. Hartzler, D. S. Acher, and R. E. Benson, *ibid.*, **84**, 3387 (1962).
26. D. M. Hanson and A. R. Gee, *J. Chem. Phys.*, **51**, 5052 (1969).
27. D. L. Jeanmaire and R. P. Van Duyne, *J. Am. Chem. Soc.*, To be published.
28. I. P. Batra, B. I. Bennet, and F. Herman, *Phys. Rev. B*, **11**, 4927 (1975).
29. A. J. Berlinsky, J. F. Carolan, and L. Weiler, *Can. J. Chem.*, **52**, 3373 (1974).
30. A. Girlando and C. Pecile, *Spectrochim. Acta*, **29A**, 1859 (1973).
31. S. K. Freeman, "Applications of Laser Raman Spectroscopy," Chap. 8, Wiley-Interscience, New York (1974).

## The Colin Garfield Fink Summer Fellowship Report

A summary of Mr. Flanagan's report is given below.

### Some Numerical Methods in Electrochemistry

The investigation into the use of fast, large potential step coulostatics to study electrode kinetics as described in the report previously published was pursued as far as using the technique to study the relatively slow  $Zn^{+2}$  reduction on mercury. The nonlinear regression-digital simulation proved to be quite successful in reproducing the values of the standard rate constant and transfer coefficient obtained by chronocoulometry. The maximum absolute rate observable by this technique seems to be about 0.3 cm/sec, a limit primarily imposed by the rate of injection of the charge. The injection must be very fast in order to measure the faster rates of electron transfer, and the existence of only a few ohms of uncompensated resistance is very effective in limiting the speed which can be obtained. New electrode designs are being studied which will facilitate the rapid injection of charge and thus make even faster electron transfer rates observable.

A new project was undertaken during the summer which was the study of differential pulse polarography as a tool in the observation of adsorption of electroactive species. An enhancement in the peak current is observed when adsorption of either product or reactant species is present. Equations were derived from approximate boundary conditions to try to quantify the effect. The use of differential pulse polarography in adsorption studies has several possible advantages: Adsorption can be studied easily in the region of the half-wave potential rather than by potential steps between the limiting-current regions as with chronocoulometry, thus making possible the study of potential dependence of adsorption in the region of the polarographic wave. Using differential pulse, the absolute amount of adsorption is not important, but rather the magnitude of the effect is related to the magnitude of the adsorption coefficient  $K$ , where  $\Gamma = KC_{SURFACE}$ . Thus the limits of detection of adsorption are in principle set only by the sensitivity of the instru-

ment at low concentrations. The lower limit on  $K$  seems to be about  $10^{-4}$  cm<sup>3</sup> for differential pulse sample times of greater than 5 msec. Evaluation of the raw data may be difficult for the worker without access to a computer, so if the technique proves to be generally useful, tabular or graphic working curves could be generated for distribution. The relevant equations, boundary conditions, and some experimental results for halide-induced adsorption of  $Cd^{+2}$  have recently been published in a preliminary note on the technique (1). Work is continuing on the study by using digital simulation to include the effects of uncompensated resistance and double-layer charging on the current response.

### REFERENCES

1. F. C. Anson, J. B. Flanagan, K. Takahashi, and A. Yamada, *J. Electroanal. Chem.*, **67**, 253 (1976).

## The Joseph W. Richards Summer Fellowship Report

Mr. DeAngelis' report is given below.

### Mercury Film Electrodes: Voltammetric and Optical Applicability

Since their inception thin film mercury electrodes (TFE) have found widespread applications in voltammetric analysis and have shown potential in spectroelectrochemical studies (1, 2). In both cases, desirable features are a working electrode with maximum hydrogen overvoltage and mercurylike characteristics. This necessitates that the substrate for the TFE interfere as little as possible with the thin mercury film, particularly with optically transparent electrodes (OTE), where, to retain transparency, one is restricted to a very thin mercury film.

Thin layer electrodes (TLE) have been used to good advantage in spectroelectrochemistry (3, 4) and in a variety of electrochemical measurements (5, 6) but have yet to be applied extensively in voltammetric analysis. The TLE does have the advantage of rapid electrolysis as a result of a short diffusional path and the capability of using small (<100  $\mu$ liter) solution volumes. Since the volume of solution available for analysis is sometimes small, particularly in biological samples, combining one of the most sensitive electroanalytical techniques, differential pulse anodic stripping voltammetry (DPASV), with the TLE would be advantageous. This should provide trace analysis capabilities on very small solution volumes. The TFE is ideally suited to the thin layer electrode configuration.

The objective of this study was (i) to develop a thin layer cell for DPASV on small solution volumes using a thin film mercury electrode and (ii) to evaluate substrates for TLE's. The substrates would be applicable to both mercury OTE's and TLE's using DPASV where no transparency is necessary.

### Experimental

*Apparatus.*—The thin layer cell was constructed of Lucite and Teflon. Details of the construction of the electrode will be published elsewhere (7).

A potentiostat of conventional operational amplifier design was used for electrochemical measurements. A Princeton Applied Research Model 174 polarographic analyzer was used for the differential pulse voltammograms. Signals were recorded on a Houston Instrument 2200-5-6 X-Y recorder.

*Electrodes.*—The following metal foils (Alfa Ventron) used were: tungsten, 0.127 mm thick; vanadium, 0.025 mm thick; iron, 0.0125 mm thick; chromium, 0.020 mm thick, epoxy backed.

*Reagents.*—The mercuric solution used for deposition on carbon and the metal foils was  $5.2 \times 10^{-3}M$



$\text{Hg}(\text{NO}_3)_2 \cdot \text{H}_2\text{O}$  (Baker, Analyzed), 1.0M  $\text{KNO}_3$  (Mal-linckrodt) at pH 6.4. Alternately, a  $5.9 \times 10^{-4}\text{M}$   $\text{Hg}(\text{NO}_3)_2 \cdot \text{H}_2\text{O}$  solution in 0.1N  $\text{HNO}_3$ , 0.5M  $\text{KNO}_3$  was also used to coat the metal foils. Methyl viologen dichloride (K and K Laboratories) was used without further purification. Lead solutions were prepared by dilution of 1000  $\mu\text{g}/\text{ml}$  atomic absorption standard (Fisher Scientific Company). Supporting electrolyte used for dilution of metal ion solutions was 1.0M potassium acetate (Baker, Analyzed) and 2M in acetic acid (E. I. du Pont) at pH 4.0. All solutions were diluted with distilled, deionized water.

**Procedure.**—The thin layer cell was assembled with a polished wax impregnated graphite electrode (WIGE) press-fitted into the Teflon plate. The  $5.2 \times 10^{-3}\text{M}$  mercuric solution was then added to the cell and mercury deposited at  $-0.3\text{V vs. SCE}$  until the current dropped and remained constant (usually 1-2 min). Mercuric solution was added and mercury deposited 14 more times. This gave a mercury film thickness of 300-400Å. Analyte solution was then added to the cell and the analysis performed.

The metal foils were prepared and coated with mercury in the following manner. A 1  $\text{cm}^2$  piece of foil was epoxied to a piece of Lucite leaving only one surface exposed. The electrode was dipped halfway into a small solution cup. Connection was made with a spring clip to the top half. A mercury film was formed on the foil by deposition of mercuric ions at  $-1.5\text{V vs. SCE}$  with moderate stirring. In between experiments the metal foils were wiped clean with a Kim Wipe. After coating with the appropriate mercuric solution, the sample to be analyzed was entered into the cell. All solutions were degassed with pure nitrogen for 20 min prior to use with the metal foil electrodes.

## Results and Discussion

Previously, the only OTE with mercurylike characteristics was the Hg-Pt OTE (8). Another approach to a mercury transparent electrode which was more easily adapted to the thin cell configuration was the mercury nickel minigrad electrode (9). In addition to its optical transparency, the Hg-Ni electrode showed potential for trace analysis of metal ions. However, the high residual current of the electrode at large negative potentials precluded its effective use in DPASV at levels below 300 ng/ml. An effort to lower this detection limit led to the present work, a search for better electrode substrates for use in voltammetric analysis in the TLE and mercury film OTE's. Metals which amalgamate very little with mercury were tried as substrates in an attempt to reduce the interference of the substrate metal with the mercury film.

**Thin layer cell.**—In many situations requiring analysis of samples, particularly biological samples, the amount of material the analyst has to work with is small. To analyze for heavy metals by DPASV one normally requires at least 2 ml total solution volume. This often requires dilution of the sample which introduces error into the analysis. In addition, DPASV normally requires solution degassing, reproducible stirring rates, and in the case of the HMDE, reproducible drop size, all of which tend to limit the effectiveness of the technique. The author has developed a cell which eliminates some of these sources of error.

The analyte lead solution was entered into the cell and deposited at a potential which reduced oxygen in the sample to water. The lead is exhaustively deposited into the thin film from the volume of solution above the carbon rod, very rapidly by diffusion, thus eliminating the necessity of stirring. Reproducible results were obtained when the cell was thoroughly rinsed with supporting electrolyte before each sample addition. Duplicate analyses on the same solution were

easily accomplished by depositing and stripping as many times as desired.

Three types of graphite were investigated for use in the thin layer cell: POCO FXI spectroscopic graphite, pyrolytic graphite (PG), and glassy carbon (GC). The POCO FXI WIGE was found to give the best results. A freshly cleaved pyrolytic graphite surface gives peak heights comparable to the WIGE; however, erratic results are obtained due to solution penetration of the edges of the PG. To try to overcome this problem in one case the outside of the PG rod was coated with epoxy and, in another, press-fitted into Teflon. This did not prevent solution from getting in between the graphite planes. This caused higher residual current and, at times, bubble formation at the edge of the electrode. GC was found difficult to coat evenly with mercury. The mercury film tended to form large mercury droplets visible on the surface of the GC. These were often lost when aspirating sample out of the cell. The very nature of GC makes it difficult to polish. Its small diameter (3 mm), compared to the POCO FXI WIGE, also makes edge concentration of analyte more pronounced.

Data collected with the WIGE gave peaks which are well defined with good resolution. The reproducibility of the data is well within acceptable limits for electrochemical trace metal analysis. Each analysis takes less than 5 min total time compared to approximately 30 min for DPASV in conventional electrochemical cells. Details of the use of this electrode and its applications will appear in the literature shortly (10).

**Metal foil electrodes.**—Vanadium, tungsten, chromium, and iron are very resistant to amalgamation with mercury (11). In addition, all except iron are quite corrosion resistant (12). First, the metals themselves were characterized as electrode materials and compared to presently available materials. Table I gives the cathodic potential limit as determined by the onset of hydrogen evolution for each metal at the given pH. Deposition of mercury to give various thicknesses did not increase the hydrogen overvoltage of the electrode. Cyclic voltammetry of  $\text{MV}^{2+}$  on the mercury-coated and uncoated electrodes showed multiple peaks and, in general, poor voltammetric behavior. There seems to be no advantage as yet to using these materials as optically transparent electrodes over currently available substrates such as platinum or nickel.

## Conclusion

A mercury, thin film, thin layer, electrochemical cell has been prepared and shown to be applicable to trace metal analysis on small volumes of solution. Of the various substrates for the mercury thin film which were tried, POCO FXI spectroscopic graphite, wax impregnated, gave the best results. The thin layer cell eliminates some of the sources of error, is as easy to use, and permits more rapid analysis on smaller sample volumes than conventional electrochemical cells.

Various metals were also evaluated for possible use as mercury film optically transparent electrode substrates. The metals used in this study as electrode sub-

Table I. Cathodic potential limits

Metal	$\text{H}_2$ evolution <sup>a</sup> (V vs. SCE)	$\text{H}_2$ evolution <sup>b</sup> (V vs. SCE)
Tungsten	-1.00	-0.57
Vanadium	-1.15	-0.43
Chromium	-1.00	-0.64
Iron <sup>c</sup>	—	—

<sup>a</sup> 1.0M  $\text{KNO}_3$  solution at pH 6.4.  $\text{H}_2$  evolution measured at  $I = 25 \mu\text{A}$ .

<sup>b</sup> 0.1N  $\text{HNO}_3$ , 0.5M  $\text{KNO}_3$  solution at pH 1.0.  $\text{H}_2$  evolution measured at  $I = 25 \mu\text{A}$ .

<sup>c</sup> Hydrogen evolution was not obtainable due to high ( $> 100 \mu\text{A}$ ) residual current.



strates do not amalgamate well with mercury; however, this fact apparently does not necessarily make the metal a good substrate for mercury film electrodes. Work is continuing in this area and will be reported in full at a later date.

#### Acknowledgments

The author wishes to thank Dr. W. R. Heineman for his valuable assistance and The Electrochemical Society for its financial support through the J. W. Richards Fellowship.

#### REFERENCES

1. G. E. Batley and T. M. Florence, *JEAC*, **55**, 23 (1974).
2. T. Kuwana, *BBG*, **77**, 858 (1973).
3. A. Yildiz *et al.*, *Anal. Chem.*, **40**, 1018 (1968).
4. D. Oglesby *et al.*, *ibid.*, **37**, 1317 (1965).
5. A. T. Hubbard and F. C. Anson, in "Electroanalytical Chemistry," Vol. 4, A. J. Bard, Editor, p. 129, Marcel Dekker, Inc., New York (1971).
6. A. T. Hubbard, *Crit. Rev. Anal. Chem.*, **19**, 201 (1973).
7. T. P. DeAngelis, To be published.
8. W. R. Heineman and T. Kuwana, *Anal. Chem.*, **43**, 1075 (1971).
9. W. R. Heineman, T. P. DeAngelis, and J. F. Goelz, *ibid.*, **47**, 1364 (1975).
10. T. P. DeAngelis, To be published.
11. A. F. Trotman-Dickenson, Editor, "Comprehensive Inorganic Chemistry," Vol. 3, pp. 283-285, Pergamon Press, London (1973).
12. F. A. Cotton and G. Wilkinson, "Advanced Inorganic Chemistry," 3rd ed., Interscience Publishers, New York (1972).



# Physical Properties of SnO<sub>2</sub> Materials

## I. Preparation and Defect Structure

Z. M. Jarzebski

Center for Interdisciplinary Studies in Chemical Physics, University of Western Ontario, London, Ontario, Canada

and J. P. Marton\*<sup>1</sup>

Welwyn Canada Limited, London, Ontario, Canada

### ABSTRACT

Stannic oxide in its pure form is an n-type wide-bandgap semiconductor. Its electrical conduction results from the existence of point defects (native and foreign atoms) which act as donors or acceptors. Some unique properties of SnO<sub>2</sub> make the material useful for many applications. Therefore, increasing attention is being paid to studies on this oxide, especially on the methods of preparation, and its electrical and optical properties. The purpose of this work is to provide a general up-to-date review of the investigations carried out and to help identify important areas for further studies. This part is concerned with the preparation and defect structure of single crystals, sintered polycrystalline samples, and thin films. Parts II and III<sup>2</sup> are reviews of the electrical and optical properties of SnO<sub>2</sub> materials.

SnO<sub>2</sub> crystallizes with tetragonal rutile structure with space group D<sub>4h</sub><sup>14</sup> [P4<sub>2</sub>/mnm (1)]. The unit cell contains six atoms, two tin and four oxygen as illustrated in Fig. 1. Each tin atom is at the center of six oxygen atoms placed approximately at the corners of a regular octahedron, and every oxygen atom is surrounded by three tin atoms approximately at the corners of an equilateral triangle. Thus, it is the structure of 6:3 coordination. The lattice parameters determined by Baur (2) are  $a = b = 4.737\text{\AA}$  and  $c = 3.185\text{\AA}$ . The  $c/a$  ratio is 0.673. The ionic radii for O<sup>2-</sup> and Sn<sup>4+</sup> are 1.40 and 0.71Å, respectively (3).

It is generally agreed that SnO<sub>2</sub> in its undoped form is an n-type, wide-bandgap semiconductor. Various specific and unique properties of this material make it very useful in many applications. Polycrystalline thin films and ceramics of SnO<sub>2</sub> have been extensively used for the production of resistors (4). Conducting SnO<sub>2</sub> films are well known as transparent electrodes, and when deposited on glass it is known as Nesa glass (5). SnO<sub>2</sub> films are also used as transparent heating elements (6), for the production of transistors (7, 8), for transparent antistatic coatings (9), and other parts in electric equipment where transparency is required. A polarized memory effect has also been observed in a Se-SnO<sub>2</sub> system (10).

Because of its practical importance, an increasing amount of work has been done on crystals and films in recent years. A great deal of experimental research has been carried out on the electrical and optical properties of single crystals, thin films, and sintered SnO<sub>2</sub> in the hope of gaining a detailed understanding of the semiconducting nature of this material. It is the purpose of this report to provide a general up-to-date re-

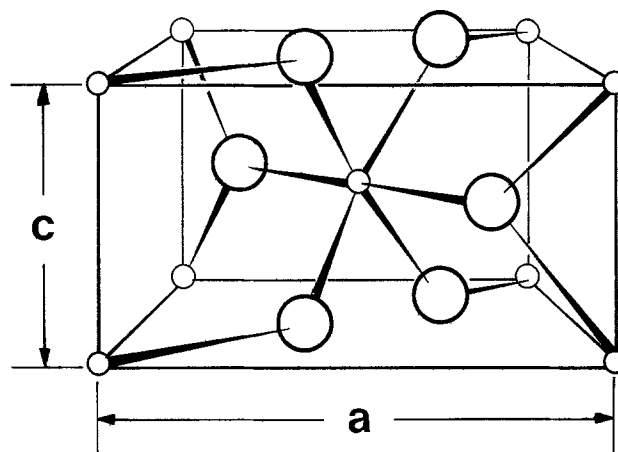


Fig. 1. Unit cell of the crystal structure of SnO<sub>2</sub>. Large circles indicate oxygen atoms and the small circles indicate tin atoms.

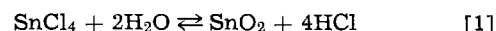
view of these investigations and to help identify important areas for further studies.

### Growth of SnO<sub>2</sub> Crystals

The growing of pure and intentionally doped single crystals of stannic oxide of good quality presents a difficult problem. However, since 1961 a rapid development in the techniques has taken place. The methods applied by various authors are compiled in Table I.

On the basis of past work, two techniques appear to be most promising, namely the growth of crystals by reaction of stannic chloride vapor with water vapor (13, 23) and growth using the reaction of stannic chloride vapor with hydrogen and oxygen (19, 24).

The first method described by Nagasawa *et al.* (13) is based on the following reaction



\* Electrochemical Society Active Member.

<sup>1</sup> Present address: Department of Engineering Physics, McMaster University, Hamilton, Ontario, Canada.

<sup>2</sup> To be published in THIS JOURNAL, September and October 1976, respectively.

Key words: single crystals, sintered material, thin films, native defects, doping, impurities.

Table I. Methods of growing SnO<sub>2</sub> single crystals

Year	Author	Reference	Method
1961	Marley and MacAvoy	(11)	Vapor phase growth from tin oxide powder based on reversible reaction $\text{SnO}(\text{g}) + \frac{1}{2} \text{O}_2 \rightleftharpoons \text{SnO}_2(\text{s})$ in a stream of mixture of helium and oxygen at 1920°K
1962	Reed, Roddy, and Mariano	(12)	Growth by a process involving the production of SnO(g) by the oxidation of tin followed by subsequent reoxidation and deposition of SnO <sub>2</sub> at 1620°K
1965	Nagasawa, Shionoya, and Makishima	(13)	Growth based on the reaction $\text{SnCl}_4 + 2\text{H}_2\text{O} \rightarrow \text{SnO}_2 + 4\text{HCl}$ at 1570°K
1965	Kunkle and Kohnke	(14)	Growth from a Cu <sub>2</sub> O flux at 1520°K
1965	Kusmina and Litvin	(15)	Hydrothermal growth using a solvent of LiOH solution at about 770°K and 2000 atm pressure
1966	Morgan and Wright	(16)	Growth by vapor reaction of tin vapor with oxygen at 1620°K
1968	Van Daal	(17)	Growth on top of sintered pellets of SnO <sub>2</sub> placed in a semiclosed alumina vessel and heated at 1920°K
1968	Gruner	(18)	Growth based on the reversible reaction $\text{SnO}(\text{g}) + \frac{1}{2} \text{O}_2 \rightleftharpoons \text{SnO}_2(\text{s})$ at 1570K
1969	Fonstad, Linz, and Rediker	(19)	Growth using the reaction $\text{SnCl}_4 + 2\text{H}_2 + \text{O}_2 \rightarrow \text{SnO}_2 + 4\text{HCl}$ at 1520°K and 10 Torr pressure
1969	Crabtree, Mehdi, and Wright	(20)	Growth based on reaction $\text{SnCl}_4 + 2\text{H}_2\text{O} \rightarrow \text{SnO}_2 + 4\text{HCl}$ as employed by Nagasawa <i>et al.</i> (13) with some modifications ( <i>e.g.</i> , including tin and using growth temperature of 1670°K)
1969	Caslavska and Roy	(21)	Epitaxial growth of SnO <sub>2</sub> on rutile single crystals using reaction $\text{SnI}_4 + 2\text{H}_2\text{O} \rightarrow \text{SnO}_2 + 4\text{HI}$ in the temperature range of 720°-920°K
1973	Takizawa and Sakurai	(22)	Growth similar to that used by Reed <i>et al.</i> (12) with some modifications; growth temperature was 1540°K
1974	Crabtree	(23)	Growth according to reaction $\text{SnCl}_4 + 2\text{H}_2\text{O} \rightarrow \text{SnO}_2 + 4\text{HCl}$ at 1520°K

A horizontal-type electric furnace with a constant temperature zone of 1570°K at the center was used together with an alumina-ceramic muffle tube as shown in Fig. 2. A fused quartz tube was fixed at the center of the furnace to provide a substrate on which to grow crystals. To introduce the vapors into the growing zone, two thin fused quartz tubes were used, one for water vapor, the other for SnCl<sub>4</sub> vapor. SnCl<sub>4</sub> and H<sub>2</sub>O were stocked separately in glass vessels immersed in thermostats to maintain the vapor pressures at constant values. Oxygen and nitrogen were used as carrier gases to transport H<sub>2</sub>O and SnCl<sub>4</sub> molecules, respectively, into the growing zone. The temperatures of the vapor sources were between 290° and 320°K. The flow rates of carrier gases were between 25 and 150 cm<sup>3</sup>/min. Single crystals with sizes up to 2 × 5 × 15 mm could be obtained in 24 hr.

Crabtree *et al.* (20) obtained SnO<sub>2</sub> single crystals applying the method which resembles that used by Nagasawa *et al.* (13). However, they have used an alumina liner tube instead of silica, employed a growth temperature of 1670°K, included a boat containing tin, and have also used argon as a carrier gas instead of nitrogen. The crystals produced had dimensions up to 2 × 2 × 12 mm.

In Fig. 3 a modification of the technique used by Crabtree *et al.* (20) is shown. The crystal growth occurs according to reaction [1]. SnCl<sub>4</sub> and H<sub>2</sub>O vapors are introduced to the furnace center by means of the tubes shown in Fig. 3. The temperature of the furnace center was 1520°K. The crystals of mm size have been grown within a few days (23).

The second method of growing SnO<sub>2</sub> single crystals mentioned above has been reported by Fonstad, Linz, and Rediker (19). The crystals obtained by their technique had higher Hall mobilities and higher purity

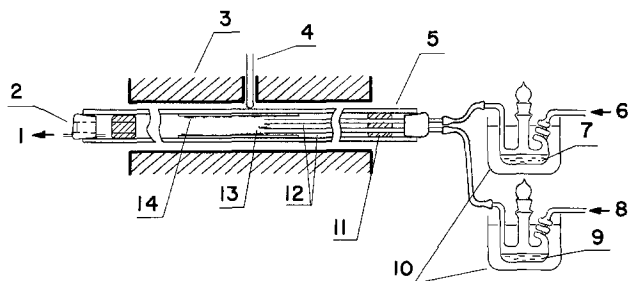
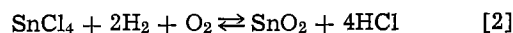


Fig. 2. Assembly for SnO<sub>2</sub> crystal growth by vapor reaction method using SnCl<sub>4</sub> and H<sub>2</sub>O vapors according to Nagasawa *et al.* (13). 1, gas blowoff; 2, viewing port; 3, electric furnace; 4, thermocouple; 5, muffle tube; 6, oxygen inlet; 7, water; 8, nitrogen inlet; 9, SnCl<sub>4</sub>; 10, thermostats; 11, alumina brick; 12, inlet tubes (fused quartz); 13, crystals; 14, growing tube (fused quartz).

than those grown by other methods. Furthermore, this method is compatible with introducing dopants during the growing process. The experimental arrangement for crystal growth is shown in Fig. 4, and is based on the reaction



The crystals grow in a quartz tube at 1520°K at 10 Torr pressure. Stannic chloride is produced by passing chlorine gas through a mesh of tin metal at 370°K

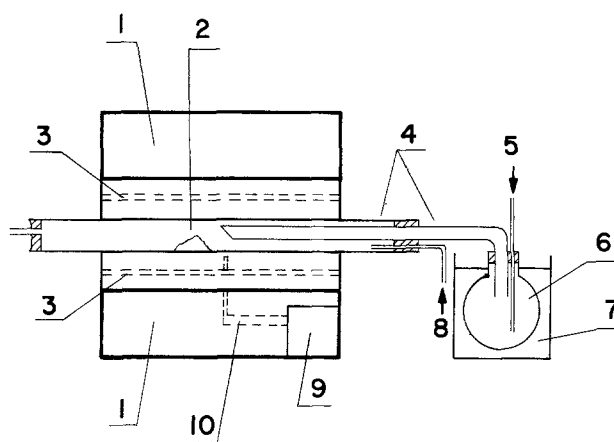


Fig. 3. Experimental arrangement for growth of SnO<sub>2</sub> crystals by reaction of SnCl<sub>4</sub> and H<sub>2</sub>O vapors according to Crabtree (23). 1, refractory brick insulation; 2, SnO<sub>2</sub> crystal; 3, SiC element; 4, quartz tube; 5, dry argon; 6, SnCl<sub>4</sub> at 373°K; 7, water bath; 8, steam argon; 9, ether temperature control; 10, thermocouple.

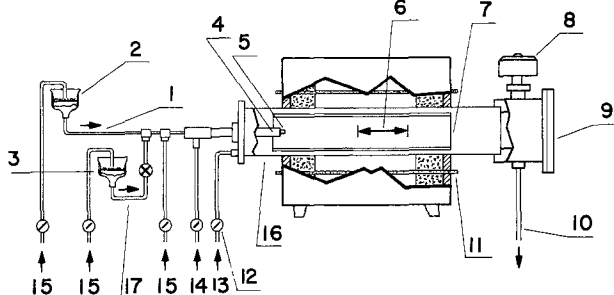


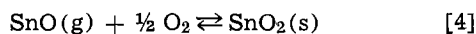
Fig. 4. Growing system of SnO<sub>2</sub> crystals based on reaction of stannic chloride, oxygen, and hydrogen (19, 24). 1, SnCl<sub>4</sub>; 2, pure reactor (Sn); 3, doping reactor (Sn + dopant); 4, quartz nozzle for hydrogen; 5, zirconia nozzle for SnCl<sub>4</sub>; 6, region of growth; 7, quartz tube; 8, pressure gauge; 9, viewing port; 10, to cold trap and vacuum; 11, global heater; 12, needle valves; 13, oxygen inlet; 14, hydrogen inlet; 15, chlorine inlet; 16, mullite tube; 17, SnCl<sub>4</sub> + doping chloride.

and at 10 Torr pressure according to the reaction



The reaction of tin with chlorine occurs in a Pyrex funnel kept at temperature about 370°K, sufficient at the pressure of 10 Torr to give a uniform and complete reaction. Dopants are introduced into the growing crystals by using reactors similar to those which generate SnCl<sub>4</sub> vapor in parallel with the SnCl<sub>4</sub> reactor, in which reactors the tin contains small amounts of the desired dopants, *e.g.*, antimony. The mullite furnace tube is horizontally mounted in a global furnace and is sealed with end caps. The O<sub>2</sub>, H<sub>2</sub>, Cl<sub>2</sub>, and SnCl<sub>4</sub> inlet tubes enter through the input end cap. The output end cap provides a mount for a pressure gauge, a quartz viewing window, and a connection to the cold traps and vacuum pump. A quartz tube fitting inside the main tube is used as the growing substrate. The crystals obtained by this technique were reported (24) to have carrier mobility of 8800 cm<sup>2</sup>/V sec at 77°K and of 13,500 cm<sup>2</sup>/Vsec at 45°K, which gives evidence of their high purity.

Other methods of single crystal growth include the one with the reaction



Historically, this was the first reported method used to grow SnO<sub>2</sub> crystals, and was described by Marley and MacAvoy (11). The crystals are grown in a horizontal two-zone platinum wound tube furnace. Both zones are independently controlled to allow a flexible temperature gradient. The temperature distribution is a constant high temperature zone maintained at 1920°K, followed by an area containing a decreasing temperature of approximately 20°K/in. Marley and MacAvoy used sintered alumina-ceramic muffle tubes throughout the furnace except where crystal deposition occurred. In this zone a removable mullite tube was substituted since at these temperatures the mullite provides a substrate to which crystals could firmly anchor. A gas entrainment apparatus was attached to the furnace and the furnace tube was charged with high purity SnO<sub>2</sub> powder which was placed in the high temperature zone. A stream of a mixture of helium and oxygen was passed over the SnO<sub>2</sub> powder to transport the resulting SnO vapor into the growing zone where supersaturation and crystal growth took place. In this way crystals up to 2 × 4 × 30 mm were obtained.

Van Daal (17) described the growth of SnO<sub>2</sub> crystals by a modification of this technique. Sintered pellets were placed in a semiclosed alumina vessel and then heated at 1920°K in air. Relatively large crystals were grown on top of these pellets. However, they contained appreciable amounts of various impurities, especially Al.

The growth of SnO<sub>2</sub> crystals by the reaction of tin vapor with oxygen was described first by Reed, Roddy, and Mariano (12). Zone-refined tin was placed in a quartz crucible having a neck for slow admission of air for oxidation of the tin. The crucible was kept at the temperature of 1620°K for several days. The SnO vapor produced by the oxidation of tin was reoxidized near the neck where the oxygen pressure was comparatively high, and SnO<sub>2</sub> crystals were deposited. They were up to 3 cm long and to 5 mm across. These crystals contained, however, a considerable amount of Si and other impurities.

In order to minimize the inclusion of Si, Takizawa and Sakurai (22) have recently grown SnO<sub>2</sub> crystals by this method at lower temperatures using a smaller crucible. They found that the most favorable growth occurred when 1g of zone-refined tin was put in a quartz crucible 10 cm long with a neck 20 cm in length, which was kept at the temperature of 1540°K for 7 days. The crystals obtained in this way have been

smaller than those prepared by Reed *et al.*, but had better qualities.

Applying a similar technique, Morgan and Wright (16) have grown SnO<sub>2</sub> crystals at 1720°K in about 10-15 days. They used a constant flow of a mixture of argon and oxygen upon an alumina boat, containing pure tin. The crystals grew on this boat, but they contained large amounts of various impurities. To obtain antimony-doped crystals, another alumina boat containing metallic Sb was introduced into the furnace.

Hydrothermal (15) and flux (14) methods may also be used to grow stannic oxide single crystals, but the possibility of contamination is much greater. Therefore, these methods are not popular for tin oxide crystal growth.

Other methods for the growth of single crystals of oxides in general may be found in a recent review on the subject (25) for further reference.

### Preparation of Sintered SnO<sub>2</sub> Materials

Conducting properties of pressed and sintered tin oxide have been investigated (26-32) as early as 1910. Recently, Van Daal (17) has described a method of preparing pure sintered tin oxide with a high density of about 95% of the bulk density by applying a gas transport reaction method (25). HBr was chosen as a transporting gas. The reaction between SnO<sub>2</sub> and HBr is exothermic, and the transport of SnO<sub>2</sub> in the apparatus is from the low temperature region of 1070°K to the high temperature region of 1170°K, producing a polycrystalline solid.

Loch (29) has obtained Sb-doped sintered SnO<sub>2</sub> by mixing reagent grade tin oxide with Sb<sub>2</sub>O<sub>3</sub> in an acetone slurry. The mixing was continued until the acetone evaporated and the dry powder was pressed at 8000 psi. Sintering followed at 1670°K in air.

Matthews and Kohnke (30) have prepared Zn-doped polycrystalline SnO<sub>2</sub> by adding an amount of ZnO to reagent grade tin oxide, treating the mixture with an acetone binder solution, pressing at 10,000 psi into pellets, and firing at 1730°K in air for 4 hr. In this way, sintered material of 95% theoretical density has been achieved.

Vincent and Weston (31) have described in detail a method of producing polycrystalline tin oxide by precipitation from solution. Sb-doped SnO<sub>2</sub> was prepared by coprecipitation with ammonium hydroxide of antimony and tin hydroxides from appropriate mixtures of antimony and tin chloride solutions in HCl, followed by a washing and heat-treatment. Samples obtained in this manner were subjected to heat-treatment at temperatures up to 1470°K.

### Deposition of SnO<sub>2</sub> Films

The current interest in applications of tin oxide films has led to more careful study of the techniques which can be employed to deposit these films and also to study the dependence of SnO<sub>2</sub> films on the mode of preparation. The methods applied by various authors are compiled in Table II. Earlier reviews were written by Bauer (33) and Fischer (34).

As can be seen from the table, many methods have been used to obtain SnO<sub>2</sub> thin films; however at present it seems that only two of them are promising for future development. These are gas-phase hydrolysis of volatile tin compounds, principally SnCl<sub>4</sub> using various carrier gases, and reactive sputtering.

*Hydrolysis.*—The method of hydrolysis is based on the reversible endothermic reaction [1] in the presence of HCl gas. Because this reaction proceeds very rapidly, the SnCl<sub>4</sub> is mixed with alcohol, some organic acid, or both (5). When spraying an atomized mixture of this solution onto a heated substrate, the reaction occurs in the forward direction resulting in the deposition of tin oxide in the form of a smooth, closely ad-

Table II. Deposition of SnO<sub>2</sub> films

Year	Author	Reference	Method
1953	Holland and Sidal	(9)	Reactive sputtering of Sn cathode
1954	Aitchison	(5)	Hydrolysis of SnCl <sub>4</sub> on heated glass substrate based on reaction $\text{SnCl}_4 + 2\text{H}_2\text{O} \rightleftharpoons \text{SnO}_2 + 4\text{HCl}$ at temperature range 770°-1070°K
1958	Ishiguro, Sasaki, Arai, and Imai	(35)	Solution of SnCl <sub>4</sub> ·5H <sub>2</sub> O crystal or SnCl <sub>4</sub> liquid in distilled water or in ethyl alcohol was sprayed on the glass, fused silica, or rock salt plates at temperatures 770°-870°K. The obtained SnO <sub>2</sub> films were comprised of crystallites.
1960	Arai	(36)	(i) Hydrolysis of SnCl <sub>4</sub> (ii) Heating with air the SnO films obtained by vacuum evaporation of SnO powder
1960	Kuznetsov	(37)	Hydrolysis of SnCl <sub>4</sub> without intentional doping
1963	Koch	(38)	Hydrolysis of SnCl <sub>4</sub>
1963	Sinclair and Peters	(39)	Reactive sputtering of Sn cathodes
1964	Maesen and Witmer	(40)	Hydrolysis of SnCl <sub>4</sub>
1964	Klasens and Koelmans	(7)	Vacuum evaporation process
1965	Sinclair, Peters, Stillinger, and Koonce	(41)	Reactive sputtering of Sn cathode
1965	Vainstein	(42)	Reactive sputtering of Sn cathode
1965	Tigane	(43)	Pyrolysis
1966	Sasaki, Nishimura, and Yamamoto	(44)	Hydrolysis of SnCl <sub>4</sub>
1966	Shiojiri Morikawa, and Suito	(45)	Vacuum evaporation of SnO <sub>2</sub>
1967	Spence	(46)	Vacuum evaporation of tin in oxygen atmosphere
1969	Bartholomew and Garfinkel	(47)	Producing SnO <sub>2</sub> films on silica glass substrate by oxidation of SnCl <sub>4</sub>
1969	Viscrian and Georgescu	(48)	SnO <sub>2</sub> films prepared using anhydrous tin chloride in alcohol
1969	Inagaki, Nishimura, and Sasaki	(49)	Droplet gas-phase reaction
1969	Caslavska and Roy	(21)	Epitaxial growth of SnO <sub>2</sub> films on rutile single crystal using reaction $\text{SnI}_4 + 2\text{H}_2\text{O} \rightleftharpoons \text{SnO}_2 + 4\text{HI}$
1969	Lieberman and Medrud	(50)	Reactive sputtering of Sn electrode
1969	Yamanaka and Ohashi	(51)	Reactive sputtering of SnO <sub>2</sub> itself
1970	Elliott, Zellmer, and Laitinen	(52)	Hydrolysis of solution of acidified SnCl <sub>4</sub> containing various percentages of SnCl <sub>4</sub> on a hot substrate (Pyrex, quartz, or polished platinum)
1970	Aoki and Sasakura	(8)	SnO <sub>2</sub> thin films were grown by transporting the vapor of (CH <sub>3</sub> ) <sub>2</sub> SnCl <sub>2</sub> onto the substrate with dried air and by decomposition and oxidizing
1970	Nishino and Hamakawa	(53)	Conductive SnO <sub>2</sub> films were obtained by two processes: (i) evaporation of tin on silicon and (ii) oxidation of these films at temperature range 570°-870°K for several minutes
1971	Vorob'eva and Polurotova	(54)	Hydrolysis of SnCl <sub>4</sub> without intentional doping
1972	Hecq and Portier	(55)	Reactive sputtering of Sn cathode
1972	Vossen and Poliniak	(56)	RF sputtering very thin films of SnO <sub>2</sub> :Sb and In <sub>2</sub> O <sub>3</sub> :Sn
1973	Kelly and Lam	(57)	Reactive sputtering of Sn cathode
1973	Aboaf and Marcotte	(58)	Hydrolysis of SnCl <sub>4</sub>
1974	Giani and Kelly	(59)	(i) Reactive sputtering of Sn cathode (ii) Anodizing of Sn in electrolyte of ammonium pentaborate in ethylene glycol with water
1974	Lepic and Marton	(60)	Hydrolysis of SnCl <sub>4</sub> on ceramic substrate. The films of SnO <sub>2</sub> :B:Sb were obtained by adding H <sub>3</sub> BO <sub>3</sub> or SbCl <sub>5</sub> to the solution

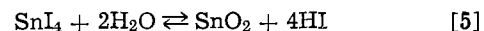
herent transparent film. The reaction proceeds slowly at 770°K, and is very rapid at temperatures higher than 1070°K. If the temperature of the substrate is higher than about 1270°K, metallic tin is formed. The optimum temperature range for SnO<sub>2</sub> film formation appears to be different in the experience of different workers. Aboaf and Marcotte (58) claim good results in the temperature range of 650°-870°K, while other authors (35, 5) prefer temperatures of 770°-870°K and 770°-1070°K.

An analysis of the SnO<sub>2</sub> films obtained in this way suggests contamination of chlorine and deviation from stoichiometry (36, 58). Cl contamination and oxygen deficiency are responsible for the rather high conductivity found in these films which are made without intentional doping (36, 37, 54). Usually, however, high conductivity tin oxide films are obtained by doping them with antimony (32, 36, 52, 60), boron (60), or other elements (58). To obtain SnO<sub>2</sub> films doped with antimony or boron, various percentages of SbCl<sub>3</sub> (or SbCl<sub>5</sub>) or H<sub>3</sub>BO<sub>3</sub> (60) are added to the acidified-atomized solution of SnCl<sub>4</sub>.

Because reaction [1] is reversible the structure and composition of SnO<sub>2</sub> films depend on the temperature, pressure, and rate of deposition. Recently, Aboaf and Marcotte (58) have described the deposition of SnO<sub>2</sub> films on heated silicon substrates by SnCl<sub>4</sub> hydrolysis at various temperatures between 650° and 870°K using ambients of N<sub>2</sub>, O<sub>2</sub>, and H<sub>2</sub>. Nitrogen gas was used to transport the high purity grade tin tetrachloride into the furnace tube by which either nitrogen, oxygen, or hydrogen was flowing. H<sub>2</sub>O vapor-saturated N<sub>2</sub> was fed into the furnace through a nozzle situated at some distance (about 5 cm) from the uniform hot zone for minimizing the reaction of SnCl<sub>4</sub> with H<sub>2</sub>O. The tin oxide films obtained in this manner were clear and virtually insoluble in acids and bases. The chlorine content was lowest when the films were deposited in a hydrogen atmosphere. SnO<sub>2</sub> films pre-

pared by the method of hydrolysis of SnCl<sub>4</sub> exhibit a small temperature coefficient of resistivity and are chemically stable at slightly elevated temperatures, but they are polycrystalline.

Caslavska and Roy (21) have obtained epitaxial oriented SnO<sub>2</sub> thin films on a rutile single crystal substrate by the reaction



in the temperature range of 720°-920°K. The experimental assembly consisted of a horizontal clam-shell furnace fitted with a silica-Pyrex reaction tube through which H<sub>2</sub>O vapor was flowing continuously. In the center of the reaction tube a rutile substrate was placed and was heated separately. The SnI<sub>4</sub> material was in a platinum crucible and was kept at a predetermined temperature at distances of 8, 11, and 20 cm from the substrate. The surface of the single crystal substrate was polished in a given orientation which was determined by x-ray diffraction.

*Reactive sputtering.*—Reactive sputtering is used by a number of investigators (25, 57, 59) to deposit SnO<sub>2</sub> films on various substrates. A simple system using two electrodes (55) has been used recently by Giani and Kelly (59). It consisted of an Sn cathode and substrates of chemically polished Al, Ta, and V, cleaved KCl, and air-annealed SnO<sub>2</sub> which were placed on the anode table 3 cm beneath the cathode. The d-c sputtering voltage ranged from 1000 to 3000V and the current was about 10 mA. As working gas, a 1:1 mixture of oxygen and argon was used at about 10<sup>-2</sup> Torr pressure. The sputtered SnO<sub>2</sub> films were amorphous as deposited on KCl or Ta substrates in the temperature range of 170°-470°K, and polycrystalline as deposited on SnO<sub>2</sub> at 470°K.

A more complicated apparatus is described by Lieberman and Medrud (50). It is constructed in such a way that it enables the simultaneous rotation and

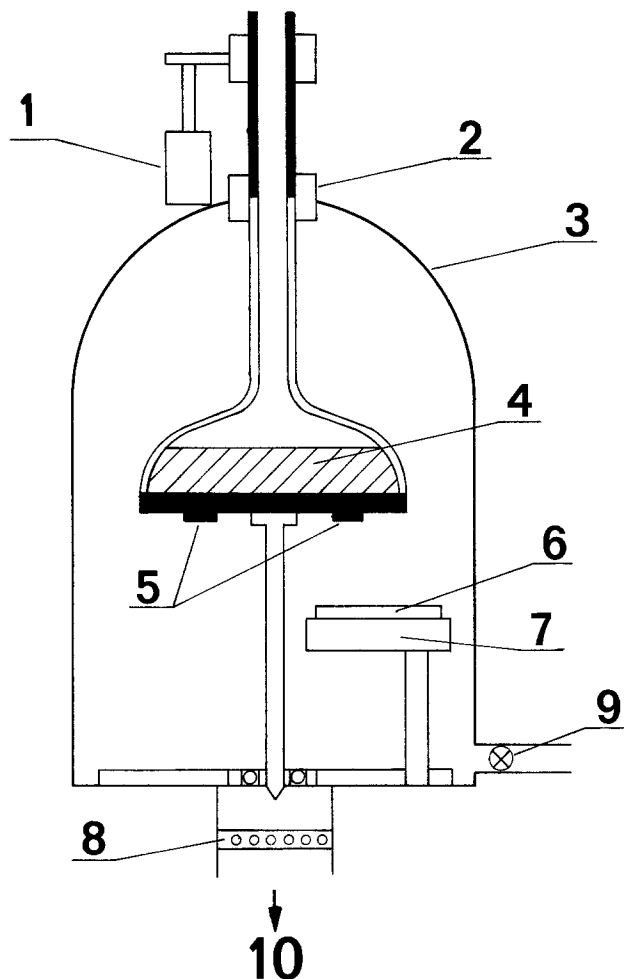


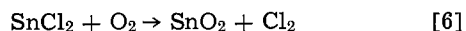
Fig. 5. Reactive sputtering apparatus which enables the simultaneous rotation and refrigeration of substrate during the sputtering process (50). 1, driving motor; 2, rotary seal; 3, bell jar; 4, refrigerant; 5, substrates; 6, tin cathode; 7, shield; 8, chevron baffle; 9, gas inlet; 10, vacuum pump.

refrigeration of substrates during the sputtering process. The outline of the apparatus is shown in Fig. 5. The rotation of the substrate helps to obtain films with uniform thickness, and also assists in the dissipation of heat from the substrate. The substrates are cooled by liquid nitrogen to increase the possibility of obtaining amorphous films. The liquid nitrogen-cooled vacuum flask is made of stainless steel, the base plate of this flask is a copper plate to which the glass substrates are attached, and the cathode is cooled by water flowing through the cathode supports.

Yamanaka and Oohashi (51) have prepared sputtered SnO<sub>2</sub> films using the cathode in the form of a tin oxide disk sintered from SnO<sub>2</sub> powder at 1770°K in air. The distance between the cathode and substrate was 6 cm and the sputtering voltage was 4500V.

The method of sputtering was used also by other authors for the etching of SnO<sub>2</sub> films (61). Descriptions of other reactive sputtering methods used to deposit oxide films may be found elsewhere (25, 57).

*Other methods.*—Bartholomew and Garfinkel (47) used anhydrous SnCl<sub>2</sub> as a starting material for preparing SnO<sub>2</sub> films. Stannous chloride with the melting point of 519°K was fused and subsequently oxidized to SnO<sub>2</sub> by the following reaction



The experiments were carried out either in an open or a closed system. The open system consisted of a Vycor glass crucible containing the SnO<sub>2</sub>. The crucible in turn was placed in a Vycor beaker and the whole as-

sembly was put in the furnace for fusing and oxidizing. In the closed system, a silica glass tube was used instead of the beaker. The tube was sealed at one end and had a silicone oil trap at the other end. The system was flushed with dry argon continuously while a film formed on the silica glass tube. Heat-treatment in air followed at temperatures between 670° and 800°K, with times ranging from 1 to 72 hr. In the case of a completely sealed system, no SnO<sub>2</sub> films was formed after 72 hr of heat-treatment.

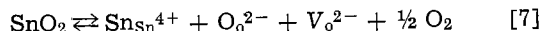
Aoki and Sasakura (8) have prepared SnO<sub>2</sub> films by transporting dimethyl tin dichloride (CH<sub>3</sub>)<sub>2</sub>SnCl<sub>2</sub> vapor onto a substrate surface by means of dried air, where the vapor was successively decomposed and oxidized. The assembly used by these workers is shown in Fig. 6. The thickness of the SnO<sub>2</sub> films was controlled by changing the flow rate of the air and the time of reaction, and their electrical conductivity was controlled by changing the temperature of the substrate.

Conductive tin oxide films have been grown by the evaporation of tin on a suitable substrate and the subsequent oxidation in an atmosphere containing oxygen (46, 53).

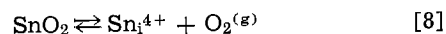
Giani and Kelly (59) have also prepared SnO<sub>2</sub> thin films by a high voltage anodizing method. The anode was an Sn sheet and the cathode was either an Al sheet or a Pt cylinder. The electrolyte used was an ammonium pentaborate in ethylene glycol which was varied by adding water. The anodizing voltage was 50V d.c. producing a current density of 10 mA/cm<sup>2</sup>.

#### Defect Structure

As it is well known, physical properties of oxides depend strongly on deviation from the stoichiometric composition (native disorder) and on nature and concentrations of foreign atoms incorporated into the crystal lattice (25). Because tin oxide is a semiconductor of n-type, therefore either oxygen vacancies, V<sub>o</sub>, or interstitial tin atoms, Sn<sub>i</sub>, are expected to be donors in pure SnO<sub>2</sub> (5, 11, 13). Thus, either defect reactions



or



may take place.

Recently, Samson and Fonstad (62) have concluded that in the partial oxygen pressure range from 10<sup>-2</sup> to 1 atm, and in the temperature range from 1370° to 1600°K, the doubly ionized oxygen vacancies predominate in SnO<sub>2</sub> according to the defect reaction [7] and following reaction



together with the neutrality condition

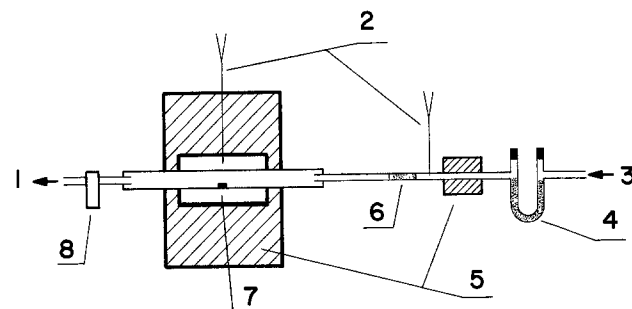
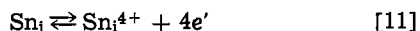


Fig. 6. An apparatus (8) for deposition of SnO<sub>2</sub> thin films from dimethyl tin dichloride (CH<sub>3</sub>)<sub>2</sub>SnCl<sub>2</sub>. 1, to aspirator; 2, thermocouple; 3, air inlet; 4, drying agent; 5, electric furnace; 6, (CH<sub>3</sub>)<sub>2</sub>SnCl<sub>2</sub>; 7, substrate; 8, flow meter.

This conclusion was based on the one-sixth dependence of electrical conductivity on the oxygen pressure  $\sigma \sim p_{O_2}^{-1/6}$ . It is well known, however, that from conductivity measurements similar results may be obtained also assuming the predominance of tin interstitials  $Sn_i^{4+}$ . If the mass action law is applied to defect reaction [8], and if the reaction



is used together with the neutrality condition

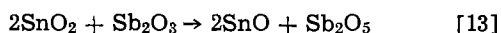
$$4[Sn_i^{4+}] = [e'] \quad [12]$$

we can obtain the dependence:  $\sigma \sim p_{O_2}^{-1/5}$ . Taking into account possible impurities incorporated into the crystals during the heat-treatment as well as the narrow oxygen pressure range investigated, it is difficult at present to decide which type of defect predominates in  $SnO_2$  materials. Thus, more detailed investigation is necessary to confirm the suggestion of Fonstad and Samson. Careful self-diffusion coefficient measurements as a function of oxygen pressure and temperature in thermodynamic equilibrium conditions may provide a more decisive answer.

It has been expected that  $SnO_2$  single crystals or thin films grown using the hydrolysis of  $SnCl_4$  may contain chlorine. This has been shown recently (58) for thin films. Aboaf and Marcotte (58) have found from x-ray measurements that chlorine is incorporated into  $SnO_2$  lattice either interstitially or substitutionally. Both interstitial and substitutional chlorine atoms give rise to donor levels and thus increase the charge carrier concentration in  $SnO_2$  films. This leads to increased conductivity.

The investigations of dislocations in  $SnO_2$  crystals grown by the vapor reaction method, described by Marley and MacAvoy (11), have been carried out by Koffyberg (63). However, his work is not discussed because the crystals obtained by this method are not of good quality.

Little is known about doped  $SnO_2$  materials in general. Recently, Vincent (32) reported a study on the thermodynamic stability of the oxides of tin and antimony. He concluded that the most probable configuration of tin-antimony oxide is a structure containing  $Sb_2O_3$  in  $SnO_2$ . This comes about because the reaction



is not probable, due to the relative instability of  $SnO$  with respect to  $SnO_2$ . However, it is not known whether the antimony atoms are substituted in Sn sublattice (37) or placed in the interstitial positions. It is expected that both cases may take place.

The nature of other impurities in the crystal lattice of  $SnO_2$  is not known. Depending on their relative positions to tin in the Periodic Table, they may act as either donors or acceptors.

### Conclusions

The best quality  $SnO_2$  single crystals are obtained by two techniques, namely the growth of crystals by the reaction of  $SnCl_4$  vapor with water vapor and growth using the reaction of  $SnCl_4$  vapor with hydrogen and oxygen. Pure sintered  $SnO_2$  material may be obtained by applying the gas-transport reaction method, e.g., by reaction between  $SnO_2$  and  $HBr$ .

The most promising methods for obtaining good  $SnO_2$  thin films are gas-phase hydrolysis of volatile tin compounds, especially  $SnCl_4$ , and reactive sputtering.

The nature of defect structure of pure  $SnO_2$  is not elucidated yet. Both doubly ionized oxygen vacancies and interstitial ions have been proposed, and either one is possible.

The detailed structure of doped  $SnO_2$  materials is not known at the present time.

### Acknowledgments

Z. M. Jarzebski has been a visiting fellow during the course of this work at the Centre for Interdisciplinary Studies in Chemical Physics and is grateful for the support from the Centre.

Manuscript submitted Aug. 19, 1975; revised manuscript received Feb. 4, 1976.

Any discussion of this paper will appear in a Discussion Section to be published in the June 1977 JOURNAL. All discussions for the June 1977 Discussion Section should be submitted by Feb. 1, 1977.

Publication costs of this article were partially assisted by the Centre for Interdisciplinary Studies in Chemical Physics.

### REFERENCES

1. R. W. G. Wyckoff, "Crystal Structures," Interscience, New York (1951).
2. W. H. Baur, *Acta Cryst.*, **9**, 515 (1956).
3. L. Pauling, "The Nature of the Chemical Bond," Cornell University Press, New York (1960).
4. R. H. W. Burkett, *J. Brit. I. R. E.*, **21**, 1 (1961).
5. R. E. Aitchison, *Australian J. Appl. Sci.*, **5**, 10 (1954).
6. J. W. Ward, *Appl. Ind.*, **16**, 408 (1955).
7. H. A. Klasens and H. Koelmans, *Solid-State Electron.*, **7**, 701 (1964).
8. A. Aoki and H. Sasakura, *Japan. J. Appl. Phys.*, **9**, 582 (1970).
9. L. Holland and G. Siddal, *Vacuum*, **3**, 375 (1953).
10. T. Matsushita, T. Yamagami, and M. Okuda, *Japan. J. Appl. Phys.*, **11**, 1657 (1972).
11. J. A. Marley and T. C. MacAvoy, *J. Appl. Phys.*, **32**, 2504 (1961).
12. T. B. Reed, J. T. Roddy, and A. N. Mariano, *ibid.*, **33**, 1014 (1962).
13. M. Nagasawa, S. Shionoya, and S. Makishima, *Japan. J. Appl. Phys.*, **4**, 195 (1965).
14. H. F. Kunkle and E. E. Kohnke, *J. Appl. Phys.*, **36**, 1489 (1965).
15. C. P. Kusmina and R. N. Litvin, *Sov. Phys. Cryst.*, **8**, 379 (1965).
16. D. F. Morgan and D. A. Wright, *Brit. J. Appl. Phys.*, **17**, 337 (1966).
17. H. J. Van Daal, *Solid State Commun.*, **6**, 5 (1968).
18. H. Gruner, *Naturwissenschaften*, **55**, 132 (1968).
19. C. G. Fonstad, A. Linz, and R. H. Rediker, *This Journal*, **116**, 1269 (1969).
20. D. F. Crabtree, R. N. S. M. Mehdi, and D. A. Wright, *J. Phys. D.*, **2**, 1503 (1969).
21. V. Caslavskaja and R. Roy, *J. Appl. Phys.*, **40**, 3414 (1969).
22. T. Takizawa and T. Sakurai, *Japan. J. Appl. Phys.*, **12**, 1323 (1973).
23. D. F. Crabtree, *J. Phys. D.*, **7**, L17 (1974).
24. C. G. Fonstad and R. H. Rediker, *J. Appl. Phys.*, **42**, 2911 (1971).
25. Z. M. Jarzebski, "Oxide Semiconductors," Pergamon Press, Oxford-New York (1973).
26. M. LeBlanc and H. Sachse, *Phys. Z.*, **32**, 887 (1931).
27. P. Guillery, *Ann. Phys.*, **14**, 216 (1932).
28. M. Foex, *Bull. Soc. Chim. France*, **11**, 6 (1944).
29. L. D. Loch, *This Journal*, **110**, 1081 (1963).
30. H. E. Matthews and E. E. Kohnke, *J. Phys. Chem. Solids*, **29**, 653 (1968).
31. C. A. Vincent and D. G. C. Weston, *This Journal*, **119**, 518 (1972).
32. C. A. Vincent, *ibid.*, **119**, 515 (1972).
33. G. Bauer, *Ann. Phys.*, **30**, 433 (1937).
34. A. Fischer, *Z. Naturforsch.*, **9**, 508 (1954).
35. K. Tshiguro, T. Sasaki, T. Arai, and I. Imai, *J. Phys. Soc. Japan*, **13**, 296, 755 (1958).
36. T. Arai, *ibid.*, **15**, 916 (1960).
37. A. Ya. Kuznetsov, *Sov. Phys.—Solid State*, **2**, 30 (1960).
38. H. Koch, *Phys. Status Solidi*, **3**, 1059, 1619 (1963).
39. W. R. Sinclair and F. G. Peters, *J. Am. Ceram. Soc.*, **46**, 20 (1963).
40. F. Maesen and C. H. M. Witmer, Proc. 7th Intern. Conf. on the Phys. of Semiconductors, p. 1211, Paris (1964).
41. W. R. Sinclair, F. G. Peters, D. W. Stillinger, and S. E. Koonce, *This Journal*, **112**, 1096 (1965).
42. V. M. Vainshtein, *Simp. Protsessy Sin. Rosta*

- Krist. Plenok Poluprov. Mater., Tezisy Dokl., p. 296, Novosibirsk (1965).
43. I. F. Tigane, *Sov. Phys.—Solid State*, **7**, 212 (1965).
  44. H. Sasaki, Y. Nishimura, and T. Yamamoto, Proceedings Elec. Comp. IEEE, p. 79 (1966).
  45. M. Shiojiri, H. Morikawa, and E. Suito, 6th Inter. Cong. for Electron Microscopy, p. 467, Kyoto (1966).
  46. W. Spence, *J. Appl. Phys.*, **38**, 3767 (1967).
  47. R. F. Bartholomew and H. M. Garfinkel, *This Journal*, **116**, 1205 (1969).
  48. I. Viscrion and V. Georgescu, *Thin Solid Films*, **3**, R17 (1969).
  49. T. Inagaki, Y. Nishimura, and H. Sasaki, *Japan. J. Appl. Phys.*, **8**, 625 (1969).
  50. M. L. Lieberman and R. C. Medrud, *This Journal*, **116**, 242 (1969).
  51. S. Yamanaka and T. Oohashi, *Japan. J. Appl. Phys.*, **8**, 1058 (1969).
  52. D. Elliott, D. L. Zellmer, and H. A. Laitinen, *This Journal*, **117**, 1343 (1970).
  53. T. Nishino and Y. Hamakawa, *Japan. J. Appl. Phys.*, **9**, 1085 (1970).
  54. O. V. Vorob'eva and T. F. Polurotova, *Izv. Akad. Nauk SSSR*, **7**, 206 (1971).
  55. M. Hecq and E. Portier, *Thin Solid Films*, **9**, 341 (1972).
  56. J. L. Vossen and E. S. Poliniak, *ibid.*, **13**, 281 (1972).
  57. R. Kelly and N. Q. Lam, *Radiation Effects*, **19**, 39 (1973).
  58. J. A. Aboaf and V. C. Marcotte, *This Journal*, **120**, 701 (1973).
  59. E. Giani and R. Kelly, *ibid.*, **121**, 394 (1974).
  60. D. A. Lopic, M.Eng. Thesis, McMaster University (1972).
  61. T. Hayashi and H. Tsukamoto, *Japan. J. Appl. Phys.*, **12**, 1457 (1973).
  62. S. Samson and C. G. Fonstad, *J. Appl. Phys.*, **44**, 4618 (1973).
  63. F. P. Koffyberg, *ibid.*, **36**, 844 (1965).





## A Sodium-Water Primary Cell with a Rotating Cathode

D. A. Fustier, W. F. Graydon,\* and F. R. Foulkes\*

Department of Chemical Engineering and Applied Chemistry,  
 University of Toronto, Toronto, Ontario, Canada M5S 1A4

### ABSTRACT

A primary cell utilizing the direct reaction of sodium metal with water is described. The cell was capable of delivering steady-state current densities in excess of 40 A/cm<sup>2</sup> at an output voltage of 0.3V. The cell mechanisms and the effects of several operating parameters such as sodium-feed rate and rotational speed of the steel disk cathode are discussed.

Recently, there has been much interest in electrochemical systems which utilize highly reactive substances such as sodium and lithium because of the high energy and power densities associated with these materials. One of the problems encountered in such systems is that conventional cathodes are not capable of sustaining the high discharge rates available at the anode, with the result that overvoltages prevailing at the cathode substantially limit cell capabilities. Furthermore, because of the relatively high operating temperatures and the corrosivity of the reagents involved, existing high power density systems such as sodium-sulfur, lithium-chlorine, and others require costly design and manufacturing techniques.

Recent work (1-4) has shown that alkali metals are able to develop a surface film in aqueous media when the composition of the medium is carefully controlled. The film acts somewhat like an ion-exchange membrane, permitting the anodic dissolution of the metal,  $M \rightarrow M^+ + e^-$ , while partially impeding the direct oxidation reaction with water. A substantial potential difference can be generated between metallic sodium and a solution if a convenient cathodic reaction is added to the system. If the cathodic process is simply the evolution of hydrogen from water, an inexpensive sodium-water-mild steel primary cell can be obtained.

A preliminary investigation was undertaken in order to ascertain the feasibility of such a system and its potential capabilities. It was decided to construct a cell of the "dynamic type" (1, 2), because of the high current densities reported for such a device.

### Experimental

Figure 1 shows the experimental apparatus. Metallic sodium was pressed mechanically onto a mild steel rotating disk moistened with water. In such a configuration the sodium becomes the anode, the steel the inert cathode, and the sodium hydroxide which is generated the electrolyte.

Prior to a run, the sodium was loaded into the brass container by means of an extrusion procedure using a manual hydraulic press. The inside surface of the brass container was previously polished and dried in an oven. (Runs were also preformed with sodium metal

which had been placed in the extruder in liquid form and allowed to solidify. No difference in results was obtained for this method of loading.) Sodium was

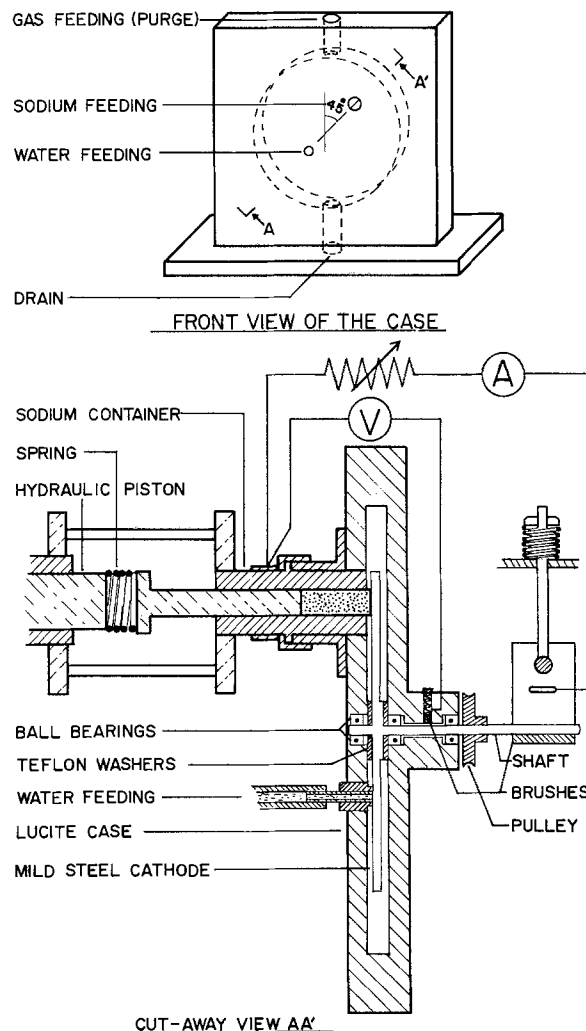


Fig. 1. Experimental apparatus

\* Electrochemical Society Active Member.  
 Key words: sodium primary cell, high energy electrochemical cell, alkali metal primary cell.

handled under a nitrogen atmosphere, and it was believed that the small amounts of sodium nitrides and sodium oxides eventually built up at its surface did not significantly affect the results.

During a run the sodium was extruded, by means of another hydraulic press fitted with a pressure gauge graduated from 0-2000 psi, through a rectangular aperture which measured  $\frac{3}{8} \times 0.060$  in. (0.145 cm<sup>2</sup>) and was situated about 1/32 in. from the rotating steel disk. The ratio of the sodium extrusion pressure over the hydraulic pressure was 9:1. Contact between the corrosion-sensitive brass and the electrolyte was prevented by covering the exposed brass with a Lucite frame. The sodium slab thus obtained was orientated so that its large dimension was directed toward the center of the rotating disk, the distance between the middle of the sodium aperture and the axis of the disk being 2 in.

The disk was driven by a 1/3 hp a-c electric motor fitted with a cone type Kopp variable drive for speed control. A belt and pulley coupling was employed to prevent electrical interaction between the motor and the cell.

The surface of the disk was mechanically polished with fine emery paper and buffing soap followed by a rinsing with distilled water and methanol. Only distilled water was used to rinse the cathode between consecutive runs.

The water was fed to the disk in a thin layer stream through a Tygon tube close to the surface of the disk, 1 in. from its axis and diametrically opposite the sodium. The entire cell, including the ball bearings used to stabilize the rotation of the disk shaft, was enclosed in a Lucite case.

The current on the cathode side was collected from the shaft through a spring-loaded brush made from Union Carbide Cophite 157 (93% copper, 7% carbon alloy). A second brush of the same type was added to monitor the cell potential without undergoing the IR-drop of the current collecting brush which had a resistance of 0.013Ω. The anode current was collected through a copper ring (2.5 in.<sup>2</sup> surface area) which was tightly fitted to the brass cylinder containing the sodium. The high pressure of sodium inside the container (~3000 psi) and its continuous motion were believed to provide good electrical contact between the sodium metal and its holder.

The voltage-current output of the cell was determined through the use of a variable resistive load placed in series in the external circuit. The current output was monitored through a Simpson 263 ammeter while the voltage output was recorded by means of a 610C-370 Keithley electrometer-recorder assembly. The quality of the d-c voltage output was continuously checked by means of an oscilloscope.

Throughout a run the cell was purged with either nitrogen or oxygen to prevent accumulation of explosive mixtures of hydrogen.

The cell was operated at room temperature with various water-feed rates. A water-feed rate of 0.35 cm<sup>3</sup>/min was found to optimize cell output characteristics under the conditions of sodium-feed rate discussed below. The cell output was quite insensitive to variations in water-feed rate. Unless otherwise stated, the rotational speed of the disk was maintained at 1000 rpm (corresponding to a velocity of 532 cm/sec 2 in. from the axis). Faradaic efficiencies were calculated by measuring sodium consumption and the number of coulombs passing through the external circuit. The over-all efficiency is defined as the product of the voltage efficiency and the Faradaic efficiency.

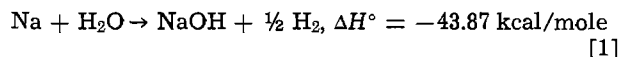
### Results and Discussion

As a consequence of the over-all reaction of sodium with water, a solution of sodium hydroxide is formed. The electrolyte, then, is self-generated and forms a thin layer adjacent to the disk. Although this layer of electrolyte is continuously removed by the action of

centrifugal force, it is also continuously regenerated by the reaction between fresh sodium and water, so that a steady-state sodium hydroxide concentration, probably in the order of 50-75% by weight (4), develops.

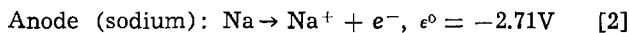
The operation of the cell can be explained by assuming that the sodium is converted to sodium hydroxide by two simultaneous processes:

I. Direct chemical combination at the sodium/electrolyte interface

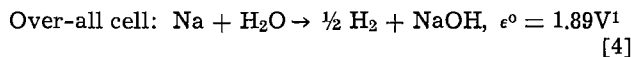
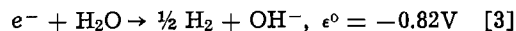


Conversion via reaction [1] results only in the production of heat.

II. Electrochemical conversion



Cathode (steel disk):



The over-all electrochemical reaction [4] produces the electrical energy collected in the external circuit ( $\Delta G^\circ = -43.49$  kcal/mole). The Faradaic efficiency gives the extent of the occurrence of process II relative to I.

It is also likely that reaction [3] occurs to some extent at the sodium, so that the anode potential is a mixed potential, and is somewhat more noble than -2.71V.

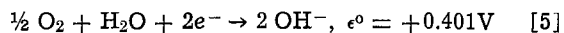
### Faradaic and Over-all Efficiencies

At constant sodium-feed rate the maximum obtainable current, i.e., 100% current efficiency, is fixed. Therefore the Faradaic efficiency is simply proportional to the current drawn, as shown in Fig. 2.

On the other hand, the over-all efficiency can be seen to pass through a maximum with increasing current density.

### Open-Circuit Voltages

When attempts were made to run the cell at low current densities under the high prevailing sodium-feed rates indicated in Fig. 2, cell operation became unstable. Under these conditions of extremely low efficiency the excessive heat production was observed to melt the sodium, not only giving rise to the erratic voltage-current behavior indicated in Fig. 2 at current densities below 10 A/cm<sup>2</sup>, but also making it impossible to obtain meaningful values of the open-circuit voltage. It was found that the open-circuit voltage could only be monitored at sodium-feed rates lower than about 0.4 g · cm<sup>-2</sup> · min<sup>-1</sup> (corresponding to a maximum theoretical current density of about 29 A/cm<sup>2</sup>). Under these conditions of low sodium-feed rate, when the cell was purged with nitrogen the open-circuit voltage was about 1.50V, whereas with an air or oxygen purge it was about 2.10V. This latter value, which is noticeably higher than the theoretical 1.89V, is believed to result from an increase in the potential of the steel cathode brought about in the presence of oxygen by the establishment of a mixed potential between reaction [3] and a reaction such as



### Cell Polarization Behavior

Figure 2 shows typical cell polarization behavior at three sodium-feed rates. Each curve was obtained by averaging the experimental results of three different runs. Reproducibility of the data was good (about ±5%) except, as mentioned earlier, for current densities less than 10 A/cm<sup>2</sup>. At the maximum feed rate shown (0.934 g · cm<sup>-2</sup> · min<sup>-1</sup>) current densities

<sup>1</sup>The reversible cell voltage will differ from 1.89V, because the reactants and products are not precisely at unit activity. Local overheating will not significantly affect the value.

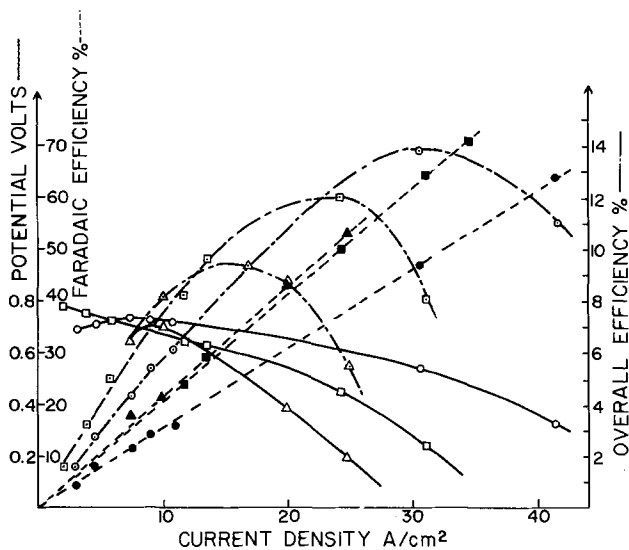


Fig. 2. Water-feed rate:  $0.35 \text{ cm}^3/\text{min}$ . Rotational speed of the cathode: 1000 rpm.  $\circ$ — $\circ$  Potential at an average sodium-feed rate, SFR =  $0.934 \text{ g} \cdot \text{cm}^{-2} \cdot \text{min}^{-1}$ ;  $\square$ — $\square$  potential at an average sodium-feed rate, SFR =  $0.692 \text{ g} \cdot \text{cm}^{-2} \cdot \text{min}^{-1}$ ;  $\triangle$ — $\triangle$  potential at an average sodium-feed rate, SFR =  $0.652 \text{ g} \cdot \text{cm}^{-2} \cdot \text{min}^{-1}$ ;  $\bullet$ — $\bullet$  Faradaic efficiency at SFR =  $0.934 \text{ g} \cdot \text{cm}^{-2} \cdot \text{min}^{-1}$ ;  $\blacksquare$ — $\blacksquare$  Faradaic efficiency at SFR =  $0.692 \text{ g} \cdot \text{cm}^{-2} \cdot \text{min}^{-1}$ ;  $\blacktriangle$ — $\blacktriangle$  Faradaic efficiency at SFR =  $0.652 \text{ g} \cdot \text{cm}^{-2} \cdot \text{min}^{-1}$ ;  $\odot$ — $\odot$  over-all efficiency at SFR =  $0.934 \text{ g} \cdot \text{cm}^{-2} \cdot \text{min}^{-1}$ ;  $\square$ — $\square$  over-all efficiency at SFR =  $0.692 \text{ g} \cdot \text{cm}^{-2} \cdot \text{min}^{-1}$ ;  $\triangle$ — $\triangle$  over-all efficiency at SFR =  $0.652 \text{ g} \cdot \text{cm}^{-2} \cdot \text{min}^{-1}$ .

greater than  $40 \text{ A/cm}^2$ , were obtained at about  $0.3 \text{ V}$  with Faradaic efficiencies in the order of 70%.

Table I summarizes some of the output characteristics of the cell at the maximum over-all efficiency for each sodium-feed rate. The irregular polarization behavior at current densities less than  $10 \text{ A/cm}^2$  is attributed to the initiation of the melting of the sodium which was referred to earlier.

The discharge of hydroxyl ions from water, reaction [3], is known to display Tafel behavior with a Tafel slope of  $-0.12 \text{ V/decade}$  up to current densities as high as  $100 \text{ A/cm}^2$  (6). In conventional cells, however, much of the overvoltage encountered with this reaction at very high current densities results from mass transport limitations, with the result that the over-all overvoltage is much greater than that from activation alone (6). For the present cell, as indicated previously, cell behavior was quite independent of water flow rate, indicating that mass transport limitations do not pose a serious problem. This effect is to be expected considering the dynamic nature of the cell. Furthermore, the extremely high  $IR$ -drops which have been found by other workers (5), and which have been attributed to increases in the resistance of the electrolyte resulting from the presence of hydrogen bubbles therein, are also not encountered in the dynamic cell because the hydrogen is removed before it can nucleate into macroscopic bubbles. Therefore activation po-

Table I. Output characteristics of the cell for 3 different sodium-feed rates and at a maximal over-all efficiency.  $\epsilon_t$  (over-all efficiency) and  $E_s$  (specific energy) are based on sodium utilization.

Sodium-feed rate ( $\text{g} \cdot \text{cm}^{-2} \cdot \text{min}^{-1}$ )	$i$ ( $\text{A/cm}^2$ )	$E$ (V)	$\epsilon_F$ (%)	$\epsilon_t$ (%)	$P$ ( $\text{W/cm}^2$ )	$E_s$ ( $\text{Whr/kg}$ )
0.910	30	0.56	48	14	17	313
0.707	24	0.45	50	12	11	254
0.652	15	0.55	33	9.5	8	210

Table II. Output characteristic of the cell for 3 different rotational speeds of the cathode at maximum current density obtainable (external resistance of  $0.077 \Omega$ ). Sodium feed rate  $0.886 \text{ g} \cdot \text{cm}^{-2} \cdot \text{min}^{-1}$ .

Rotation speed (rpm)	$i$ ( $\text{A/cm}^2$ )	$E$ (V)	$\epsilon_F$ (%)	$\epsilon_t$ (%)
600	32	0.25	53	6.9
1000	38.5	0.30	63	9.9
1400	31	0.24	50	6.3

larization accounts for most of the cathodic voltage losses.

A simple calculation using  $i_0 \approx 10^{-6} \text{ A/cm}^2$  as the exchange current density for reaction [3] on iron (6) and  $-0.12 \text{ V/decade}$  as the Tafel slope for this reaction indicates a cathodic activation polarization of about  $0.89 \text{ V}$  at  $25 \text{ A/cm}^2$ , which is consistent with observed values of cell voltage (Fig. 2). Halberstadt (2) observed comparable polarization behavior, but at much higher current densities, which were achieved through the use of thinner anode slabs ( $0.04 \text{ cm}$  wide) than were used in this work. Halberstadt's results could not be confirmed because the design of the present cell did not permit sufficiently high sodium-feed rates under comparable anode area to observe cell behavior at such high current densities.

#### Rotational Speed of Disk

Table II shows that increasing the speed of rotation of the disk from 600 to 1000 rpm results in a minor improvement in cell performance which can be attributed to improvements in the mass transport processes discussed in the previous section. However, when the speed is increased to 1400 rpm a decline in performance is observed which is probably due to mechanical difficulties such as vibration, frictional heat generation, and erosion of the film.

#### Conclusions

A primary electrochemical cell utilizing the reaction between sodium and water has been built and operated at current densities in excess of  $40 \text{ A/cm}^2$  at  $0.3 \text{ V}$ . The hydrogen evolved in the cell processes could be used as a further source of electrochemical energy.

The key to the useful harnessing of the reactions between alkali metals and oxidizing media lies in a clearer understanding of the nature of the anode film, and of the kinetics of the anodic dissolution taking place. These aspects are currently being investigated by the authors.

#### Acknowledgment

The authors gratefully acknowledge financial assistance from the National Research Council of Canada.

Manuscript submitted Nov. 10, 1975; revised manuscript received ca. April 28, 1976.

Any discussion of this paper will appear in a Discussion Section to be published in the June 1977 JOURNAL. All discussions for the June 1977 Discussion Section should be submitted by Feb. 1, 1977.

Publication costs of this article were assisted by the University of Toronto.

#### REFERENCES

- W. S. Geisler, U. S. Pat. 3,730,776 (1973).
- H. J. Halberstadt, in Proceedings of the 8th Inter-society Energy Conversion Engineering Conference, American Institute of Aeronautics and Astronautics, August 13-17, 1973.
- A. A. Lobanow, S. P. Poljakow, A. I. Sawitschkij, and E. A. Tkatschenko, German Pat. 2,316,979 (1973).
- L. S. Rowley, U.S. Pat. 3,791,871 (1974).
- F. Hine, M. Yasuda, R. Nakamura, and T. Noda, *This Journal*, 122, 9 (1975).
- K. J. Vetter, "Electrochemical Kinetics—Theoretical and Experimental Aspects," pp. 537-542, Academic Press, New York (1967).

# Experimental Optimization of Li/SOCl<sub>2</sub> Primary Cells with Respect to the Electrolyte and the Cathode Compositions

A. N. Dey\*

P. R. Mallory & Company Incorporated, Laboratory for Physical Science, Burlington, Massachusetts 01803

## ABSTRACT

The optimization of the Li/SOCl<sub>2</sub> C-size cells with respect to the parameters such as concentration of LiAlCl<sub>4</sub> source or purity of LiAlCl<sub>4</sub>, and the Teflon content of the carbon cathode showed that low Teflon content, low LiAlCl<sub>4</sub> concentration, and pure LiAlCl<sub>4</sub> improve the intrinsic capacity of the cells. The optimum cell performance at moderate to high rates was obtained with 1(M) salt concentration and 10% Teflon in the cathode.

The lithium-inorganic electrolyte system comprising Li anode, carbon cathode, thionyl chloride (SOCl<sub>2</sub>) depolarizer (and solvent), and LiAlCl<sub>4</sub> salt has been described in both the scientific (1, 2) and the patent (3, 4) literature. Earlier investigations in our laboratory (5) have shown the system to be capable of delivering high energy densities in unoptimized C-size (5) and D-size (6) cells. The object of this investigation is to optimize the system in regard to its fresh performance at ambient temperature. Based on the available data (1, 5) in regard to the material compatibility and the performance characteristics of experimental cells, the following specific materials were chosen for the optimization: Li anode, SOCl<sub>2</sub> solvent and depolarizer, LiAlCl<sub>4</sub> electrolyte salt, Teflon-bonded Shawinigan Black cathode on nickel exmet, and glass filter paper separator. The optimization was carried out with respect to the parameters such as concentration of LiAlCl<sub>4</sub> source or purity of LiAlCl<sub>4</sub>, and the Teflon content of the Shawinigan Black cathode according to a factorial matrix set up with several levels of each of the above parameters. The test vehicle chosen for the above factorial experiment was a C-size cell for which most of the hardware and the tooling were already available. At least four cells were made under each of the eighteen conditions and were tested at currents of 0.1, 0.3, 0.5, and 1.0A. The experimental details are furnished below.

## Experimental

A nickel-plated cold-rolled steel can (OD = 0.94 in., hgt = 2.00 in.) was used as a cell container. The Li anode (7.5 × 1.5 in.), the carbon cathode (8 × 1.5 in.), and the glass filter paper separator were wound into a tight roll and were packaged in the cell can. Other details of the cell construction are available elsewhere (5).

Two types of electrolytes were used for the optimization studies: (i) as prepared in our laboratory referred to as LPS electrolyte, described elsewhere (5); and (ii) as prepared from LiAlCl<sub>4</sub> received from Foote, referred to as Foote electrolyte. The latter type of electrolyte was prepared by dissolving known quantities of Foote LiAlCl<sub>4</sub> in distilled SOCl<sub>2</sub>. The color of this electrolyte was deep purple and it left an organic residue on the glass vessels after it was washed with water. The chemical composition of this residue has not been determined. However, it is soluble in CCl<sub>4</sub>. The LPS electrolyte, on the other hand, was colorless to light amber in appearance and did not leave any residue on the glass after washing with water.

The electrolytes were stored and dispensed from an all-glass (Pyrex) system. The weight of electrolyte added to each cell was recorded and was controlled to maintain 20 ± 2g.

\* Electrochemical Society Active Member.

Key words: thionyl chloride, lithium, inorganic electrolyte, high energy density, primary cells, C-size cell, carbon cathode, lithium aluminum chloride.

The carbon cathodes were made by pasting carbon and an appropriate amount of colloidal Teflon (du Pont) in water on the expanded nickel current collector. The electrodes were vacuum dried (1). Each cathode was weighed and the average weight of the carbon mix for all the cells was 1.62 ± 0.11g. The thickness of the cathodes was approximately 0.026 in. The porosity of the cathodes was approximately 70-80%.

The cells were tested at 25°C within 8 hr of cell filling at constant currents of 0.1, 0.3, 0.5, and 1.0A for each condition of cell construction. In addition, some cells were tested at -30°C at 0.3A. The cell potential was recorded as a function of time and the cell capacities were determined to a 2.0V cutoff.

## Results and Discussion

The cathode limiting nature of the C cells was established by constructing the cells in a cylindrical Teflon fixture (having the same internal diameter as the C-size cell described above) which had a Li reference electrode located above the electrode stack. The cells were discharged at currents of 0.1-3.0A and the potentials of both the carbon cathode and the Li anode were monitored against the Li reference electrode. The plots, shown in Fig. 1, indicate the cathode as the limiting electrode.

The variability of the performance of the C cells was determined by discharging four cells at 0.5A. The capacities to the 2.0V cutoff were 3.70, 3.60, 3.80, and 3.65 A-hr, respectively, indicating a standard deviation of ±0.085 A-hr or ±2.3%. This is exceptionally low. A

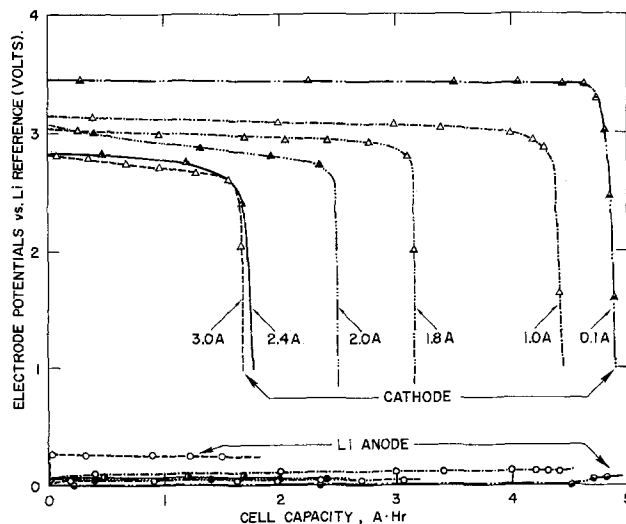


Fig. 1. Discharge curves of Li/SOCl<sub>2</sub> C-size cells with reference electrode. 1.0(M) LiAlCl<sub>4</sub> (LPS)-SOCl<sub>2</sub> electrolyte and 10% Teflon in the cathode, tested at 25°C at constant currents of 0.1, 1.0, 1.8, 2.0, 2.4, and 3.0A.

standard deviation of  $\pm 5\%$  is considered to be typical for these cells.

Typical discharge curves of a group of cells made with 1.0(M) LiAlCl<sub>4</sub> (LPS)-SOCl<sub>2</sub> electrolyte and 10% Teflon in the carbon cathode and tested at room temperature (25°C) at currents of 0.1, 0.3, 0.5, and 1.0A are shown in Fig. 2. Note that the cell voltage drops sharply at the end of the discharge and the cell capacities up to the 2.0V cutoff are very similar to the capacities up to the 3.0V cutoff.

The effect of Teflon content in the cathode on the performance of the C cells is shown in Fig. 3 which represents semilog plots of cell capacity vs. current for cells with 1.0(M) LiAlCl<sub>4</sub> (LPS)-SOCl<sub>2</sub> electrolyte and three levels (10, 20, and 30% by weight) of Teflon content in the cathode. The cell performance deteriorates with increasing Teflon content. This may be explained from the fact that Teflon acts as a binder of the carbon particles on which the SOCl<sub>2</sub> is discharged. Therefore, the quantity of the carbon is important in determining the cell capacity. Increasing the amount of Teflon automatically results in the decreasing of the total carbon content of the cathode, thus leading to a lower cell capacity. However, a minimum amount of Teflon is necessary in order to maintain the physical integrity of the carbon cathode. Experimentally, this minimum was found to be approximately 10% by weight.

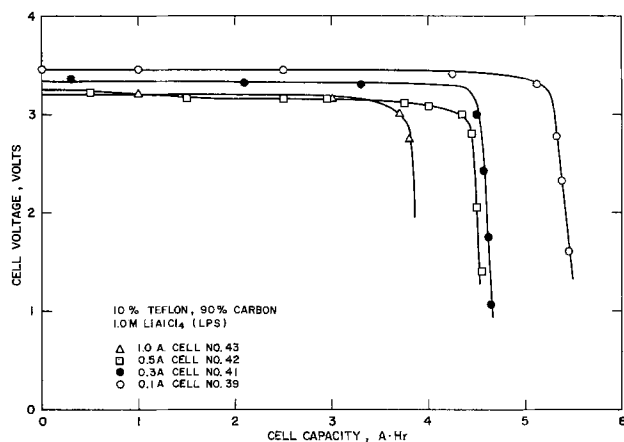


Fig. 2. Discharge curves of C-size cells made with 1.0(M) LiAlCl<sub>4</sub> (LPS)-SOCl<sub>2</sub> electrolyte and 10% Teflon in the cathode, tested at 25°C at constant currents of 0.1, 0.3, 0.5, and 1.0A.

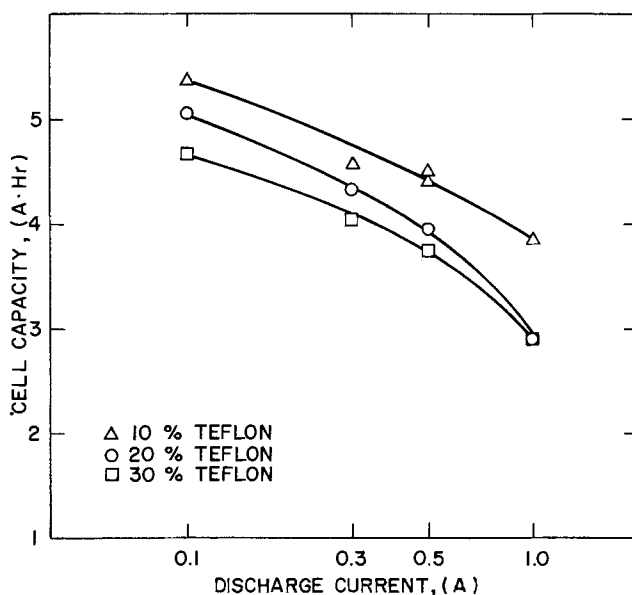
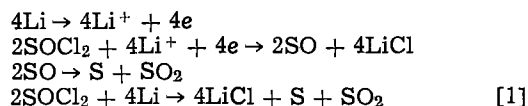


Fig. 3. Semilog plots of cell capacity vs. discharge current of C-size cells made with 1.0(M) LiAlCl<sub>4</sub> (LPS)-SOCl<sub>2</sub> electrolyte and 10, 20, and 30% by weight of Teflon in the carbon cathode.

The importance of the physical integrity of the cathode was further emphasized by the fact that while the capacity expressed in terms of ampere hours per weight of carbon mix (including Teflon) decreased with increasing Teflon content, the capacity expressed in terms of ampere hours per weight of carbon only increased with increasing Teflon content. The possible deactivation of the carbon particle due to the coating by the Teflon must be insignificant.

The effect of salt (LiAlCl<sub>4</sub>) concentration on the performance of the cells is demonstrated in Fig. 4 which shows semilog plots of cell capacity vs. discharge currents of cells made with 10% Teflon in the cathode and 0.5, 1.0, 1.5, and 2.0(M) LiAlCl<sub>4</sub> (LPS)-SOCl<sub>2</sub> electrolytes. At moderate to high currents (0.1-1.0A), the cells with 1.0(M) electrolyte performed significantly better than the other cells. We did not test the cells at lower currents. However, the graphical extrapolation of the data indicates that at low currents (0.03A) highest capacities may be obtained with 0.5(M) electrolyte. We found this to be true in the case of the D-size cells (7) The higher intrinsic capacity with low salt (LiAlCl<sub>4</sub>) concentration is explained as follows.

The cell reactions that conform to all the findings (5, 8) so far are



The formation of LiCl and S was found (8) to be quantitative. However, the SO<sub>2</sub> analysis was ambiguous because of its possible formation from the slow chemical decomposition of SOCl<sub>2</sub>. LiCl was found (8) to precipitate quantitatively in the cathode whereas S precipitates throughout the cell because of its solubility in SOCl<sub>2</sub>. Therefore, it is reasonable to assume that the limiting process involves the passivation of the carbon cathode by the precipitation of LiCl in its pores. In view of the fact that SOCl<sub>2</sub> is consumed during the discharge thereby causing the concentration of LiAlCl<sub>4</sub> to increase with the depth of discharge, the precipitation of LiAlCl<sub>4</sub> itself is expected to occur at a certain depth of discharge at which the concentration of LiAlCl<sub>4</sub> exceeds its solubility in SOCl<sub>2</sub>. The solubility of LiAlCl<sub>4</sub> in SOCl<sub>2</sub> was determined to be approximately 4.65(M) at room temperature (25°C). The change in concentration of LiAlCl<sub>4</sub> with the depth of discharge was calculated assuming cell reaction [1] and

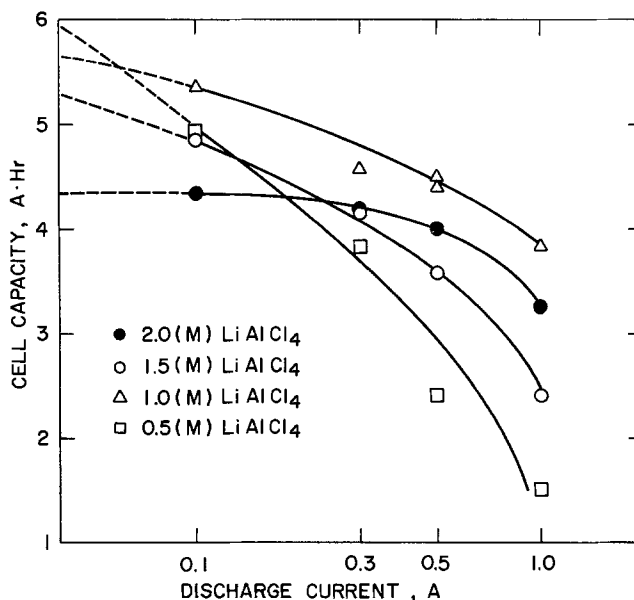


Fig. 4. Semilog plots of cell capacity vs. discharge current of C-size cells made with 10% Teflon in the cathode and 0.5, 1.0, 1.5, and 2.0(M) LiAlCl<sub>4</sub> (LPS)-SOCl<sub>2</sub> electrolytes.

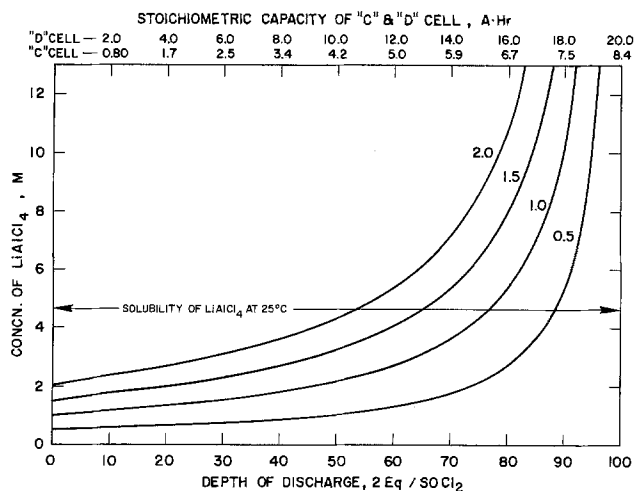


Fig. 5. Plots of  $\text{LiAlCl}_4$  concentrations as a function of the depth of discharge of C- and D-size cells calculated according to the cell reaction [1].

the plots for the various starting salt concentrations are shown in Fig. 5 for both the C- and D-size cells. The cell capacities for the various depths of discharge are also shown in the figure. It is clear that the depth of discharge at which  $\text{LiAlCl}_4$  begins to precipitate increases with the decrease in the starting salt concentration. This explains the higher intrinsic cell capacity with lower salt concentration.

The effect of the source or the purity of  $\text{LiAlCl}_4$  on the cell performance is demonstrated in Fig. 6 which shows semilog plots of capacity vs. current of cells made with 10% Teflon in the cathode, 1(M) salt, and two sources of  $\text{LiAlCl}_4$ . The LPS  $\text{LiAlCl}_4$  is clearly superior to the Foote  $\text{LiAlCl}_4$  which appeared to contain organic impurities. The organic impurities may enhance the passivation of the cathode.

### Conclusions

The following conclusions are drawn from the optimization studies.

1. The lowering of the Teflon content in the carbon cathode improves the performance of the  $\text{Li}/\text{SOCl}_2$  C cells.

2. The intrinsic capacity of the cells appears to increase with the decreasing salt ( $\text{LiAlCl}_4$ ) concentrations in the electrolyte. However, the best performance for moderate to high rate applications was obtained with 1(M)  $\text{LiAlCl}_4$ - $\text{SOCl}_2$  electrolyte.

3. The performance of the cells appears to depend on the purity of the  $\text{LiAlCl}_4$ ; better performance was obtained with laboratory-prepared  $\text{LiAlCl}_4$ .

### Acknowledgments

The author wishes to thank J. Miller for experimental assistance. The work was carried out under a

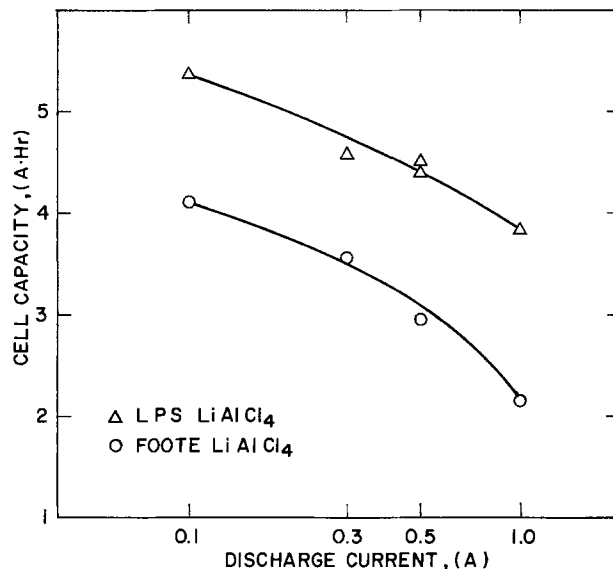


Fig. 6. Semilog plots of cell capacity vs. discharge current of C-size cells made with 10% Teflon in the cathode and 1(M) LPS and Foote  $\text{LiAlCl}_4$  salt.

contract from USA ECOM, Contract No. DAAB 07-74-C-0109.

Manuscript submitted March 29, 1976; revised manuscript received May 13, 1976. This was Paper 8 presented at the Washington, D. C., Meeting of the Society, May 2-7, 1976.

Any discussion of this paper will appear in a Discussion Section to be published in the June 1977 JOURNAL. All discussions for the June 1977 Discussion Section should be submitted by Feb. 1, 1977.

Publication costs of this article were assisted by P. R. Mallory & Company Incorporated.

### REFERENCES

- W. K. Behl, J. A. Christopoulos, M. Ramirez, and S. Gilman, *This Journal*, **120**, 1619 (1973).
- J. J. Auburn, K. W. French, S. I. Lieberman, V. K. Shah, and A. Heller, *ibid.*, **120**, 1613 (1973).
- D. L. Maricle and J. P. Mohns, U.S. Pat. 3,567,515 (1971).
- G. E. Blomgren and M. L. Kronenberg, German Pat. 2,262,256 (1973).
- A. N. Dey and C. R. Schlaikjer, Proceedings of the 26th Power Sources Symposium, Atlantic City, New Jersey, April 1974.
- A. N. Dey, *Electrochim. Acta*, In press.
- A. N. Dey and P. Bro, Proceedings of the International Power Sources Symposium, Brighton, England, 1976.
- J. R. Driscoll and G. L. Holleck, Abstract 34, p. 91, The Electrochemical Society Extended Abstracts, Fall Meeting, Dallas, Texas, Oct. 5-9, 1975.

# Casting and Properties of Grid Alloys for Maintenance-Free Batteries

T. W. Caldwell,<sup>1</sup> U. S. Sokolov,\* and L. M. Bocciarelli

NL Industries, Incorporated, Central Research Laboratory, Hightstown, New Jersey 08520

## ABSTRACT

Microstructure, hardness, castability, and hydrogen evolution rate of cast SLI battery grids were determined for a wide range of Pb-Ca and Pb-Ca-Sn alloy compositions. Calcium oxidation rate of the molten alloys was also studied. These properties were determined as a function of alloy composition, trace element content, and casting conditions. Grids were cast on a commercial calcium-lead grid casting machine under production conditions. Grids were cast from two base leads: a low bismuth primary lead and a refined secondary lead containing bismuth, antimony, copper, and silver. Calcium was found to affect hardness and initial aging rate, while tin influenced grain size, castability, and calcium oxidation rate. Hydrogen evolution rate was also found to be a function of alloy composition. Trace element additions influenced hardness and hydrogen evolution in Pb-Ca-Sn alloys, and calcium oxidation rate and castability in Pb-Ca alloys. Casting conditions influenced grain size and hardness at some alloy compositions.

A new type of lead-acid battery is under development for automotive applications. Called the maintenance-free battery, it is sealed and requires no periodic addition of water. Therefore, the rate of gassing during charging must be minimized to prevent excessive water loss. This restriction requires new low gassing grid alloys, as the conventional Pb-Sb alloys contribute heavily to hydrogen evolution (1). A low gassing Pb-Ca system has been employed for years in standby applications (2), and considerable attention is being given to the Pb-Ca and Pb-Ca-Sn systems for automotive application.

Recently, the effects of trace elements in typical commercial base leads on certain metallurgical and electrochemical properties of Pb-Ca and Pb-Ca-Sn alloys have been investigated (3,4). At the compositions studied, it was found that typical levels of bismuth, antimony, copper, and silver did not significantly affect the microstructure or hydrogen evolution rate under cathodically polarized conditions. As-cast and short term aged hardness increased at some alloy compositions in the presence of these trace elements. These investigations were performed on laboratory samples specially cast to duplicate actual grid solidification conditions.

In this study, the microstructure, hardness, castability, and hydrogen evolution rate of cast grids were determined for a wide range of Pb-Ca and Pb-Ca-Sn alloy compositions. The calcium oxidation rate of the molten alloys was also studied. These properties were determined as a function of alloy composition, trace element content, and casting conditions. "Alloy" refers to calcium and tin, and "trace elements" refers to bismuth, antimony, copper, and silver.

## Experimental

Grids were cast from both low bismuth primary and refined secondary base leads. Calcium and tin were added as a Pb-1Ca master alloy and Straits tin, respectively. Table I gives the compositions of the two base leads and the Pb-Ca master alloy, determined by emission spectroscopy. Elements are reported in ranges due to the use of more than one lot of each. Trace elements other than those indicated were each <0.001%. It is expected that antimony will be substantially removed by Ca<sub>3</sub>Sb<sub>2</sub> intermetallic formation when calcium

is added to the base lead. A composition range of 0.05-0.12Ca was studied with additions of 0, 0.5, 0.75, and 1.0Sn.

A Wirtz calcium-lead grid casting machine was employed for casting the grids. Nitrogen was used in place of natural gas as a melting pot cover gas, with a flow rate of 55 SCFH metered from two liquid N<sub>2</sub> tanks containing internal evaporators. Propane was employed to heat the metal transfer lines and as a pouring ladle cover gas. Modifications of ladle cam shape, tilt angle, and mold ejector pin settings were made from those normally prescribed for the machine to improve mold filling and grid ejection and to decrease dross buildup in the ladle. The standard pressure pad assembly in the trimming and planishing die was replaced with a specially designed water-cooled pressure pad to reduce thermal distortion of the trim die due to uneven cooling. The scrap return and ingot loading ports on the melting pot cover were sealed. Trim scrap was remelted only at the end of each run.

Figure 1 shows the cast grid configuration. The surface cut, 4M-type grid had a 9 × 23 wire pattern, 0.060 in. frame, and 0.055 in. wire thickness, and weighed 144g per twin. Over 100 casting runs were made, generally producing 1000-2000 grid twins/run. The duration of each run was sufficient to include mold coat deterioration; therefore the casting runs were representative of commercial production conditions. Longer runs of up to 4400 grid twins were made at some compositions. Casting conditions were held as constant as possible, producing 12 grid twins/min at a mold temperature of 400°-425°F, gate temperature of 475°F, and a pouring temperature of 900°-925°F.

Additional runs were made employing a second grid configuration, a staggered cut, 4H-type grid having an 8 × 26 wire pattern, weighing 148g per twin. Higher mold and metal temperatures were required to fill this mold because of the thinner and increased number of wires. Resulting grid properties were essentially the same as found with the 4M mold, except for a decrease in castability of about 11% at the compositions studied.

Table I. Base lead composition, ppm (wt)

	Bi	Sb	Cu	Ag
Low Bi primary	5	1	1	2-5
Refined secondary	110-180	5-20	5-10	20-30
Ca master	10	10	10	10

\* Electrochemical Society Active Member.

<sup>1</sup> Present address: NL Industries, Incorporated, Bearings Division, Toledo, Ohio 43614.

Key words: lead-acid battery, lead-calcium alloys, grid casting, hydrogen evolution, mechanical properties.

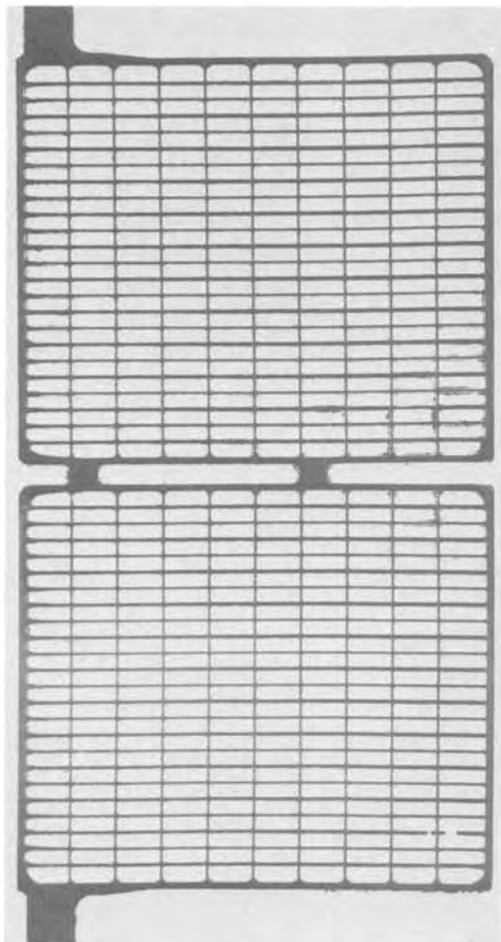


Fig. 1. Cast 4M grid configuration

Grid sections were mounted and examined metallographically. An acetic acid-hydrogen peroxide attack polish-etch was used, followed by an ammonium molybdate-citric acid etchant. The molybdate etch was effective only when all of the cold-worked surface produced during polishing was removed by the attack etching procedure. This was determined by the appearance of a bright surface after a number of polish-etch cycles.

A Barber-Coleman 936 Impressor was employed to measure grid hardness. This device was suitable for testing small cross-section specimens such as grids, and was sufficiently sensitive to measure the effects of composition, aging, and casting conditions. Hardness was measured at one day intervals from the time of casting to five days later. Fifteen hardness readings, five each from the top, side, and bottom borders of the grid twin, were averaged to obtain a single hardness reading for the grid at each time of measurement. Differences in hardness were observed among the top, side, and bottom borders of the grid, but the ranking of these three locations was not consistent. Generally, the bottom border gave the highest hardness readings. Analysis of hardness data was performed on a GE 635 time sharing computer using a nonlinear regression analysis to generate an age-hardening curve for each alloy. The best curve fits were obtained using a three parameter function

$$y = a + b/(x + c)$$

where  $y$  and  $x$  are 936 hardness and time, respectively, and  $a$ ,  $b$ , and  $c$  are constants determined by the regression program for each curve. The index of determination for each curve,  $R^2$  averaged 0.96, signifying excellent correlation between the computed curves and the actual data. (This index is the fraction of the over-

all variability in the data which is accounted for by the regression equation.) Molten metal and mold temperatures were held constant to eliminate effects of casting conditions on hardness.

The dependence of hardness on base lead composition was investigated with a statistical test for differences in hardness, performed at all combinations of calcium and tin composition where hardness data existed for both base lead systems. Because of the limited number of data points, the "T Statistic" method was employed with a 90% level of significance procedure. The test was performed at half-day intervals up to three days after casting, as differences between alloys of various trace element contents had been found previously to be significant only for a few days after casting (3).

The hydrogen evolution rate on cathodically polarized grids was measured as a function of potential, alloy composition, and trace element content. The grids were positioned symmetrically between two counter-electrodes in a glass and Teflon test cell. Grids were tested as-cast, with no surface preparation. The hydrogen evolution rate was expressed in terms of cathodic current density, measured at fixed potentials in 1.250 sp gr preelectrolyzed sulfuric acid at 70°F. Standard potentiostatic techniques were used with a saturated Hg/HgSO<sub>4</sub> reference electrode. Originally, the gas was collected and its volume measured. Once it was established that the coulombic input accounted for better than 97% of the gas evolved, gas collection was discontinued and only the current recorded. Since the property of interest is the current density, an electrostatic technique was developed to measure grid surface area. A test cell was constructed in which a grid was the middle plate of a three plate planar capacitor, positioned symmetrically between two solid lead sheets. The cell capacitance was measured using an impedance bridge and the grid surface area was determined by comparing the measured capacitance with a calibration curve. Calibration curves of capacitance vs. surface area were obtained by inserting lead sheets of known surface area in the cell in place of the grid and measuring the capacitance, using Nujol and toluene as dielectrics. Two dielectrics were used to determine if differences in dielectric surface tension would significantly affect wetted grid surface areas, and therefore capacitance. Surface area differences were <0.5%, illustrating the insensitivity of the technique to the choice of dielectric. In fact, surface area differences of <5% between grids of different casting lots could be reproducibly detected. The average grid surface area was 250 cm<sup>2</sup>.

One-hundred percent inspection of grids was performed employing representative criteria for antimonial lead grid production (5). Two types of rejects were classified: mold rejects which included porosity, flashing, and misfills, and mechanical rejects, which included grids damaged moving through the trim die and miscuts from the trimming operation.

The calcium content was measured at one-half hour intervals by atomic absorption spectrophotometry during each casting run. The tin content was measured only once during a run as it was found to be quite stable.

### Results and Discussion

*Microstructure.*—Figure 2 summarizes the major compositional influences on microstructure which were found. Grid side frame sections are shown. From left to right, the addition of calcium to the base lead refines the grain size (Fig. 2b) as is well known. The addition of tin (Fig. 2c and 2d) to Pb-Ca alloys results in an increase in grain size to approximately that of the base lead alone (3). Variations in tin level influence grain size, but not as significantly as when tin is first added to Pb-Ca. Grain size was not a function of base lead composition as shown by Fig. 3.

While not shown, it was found that as calcium was increased from 0.5 to 0.12 weight percent (w/o), grain



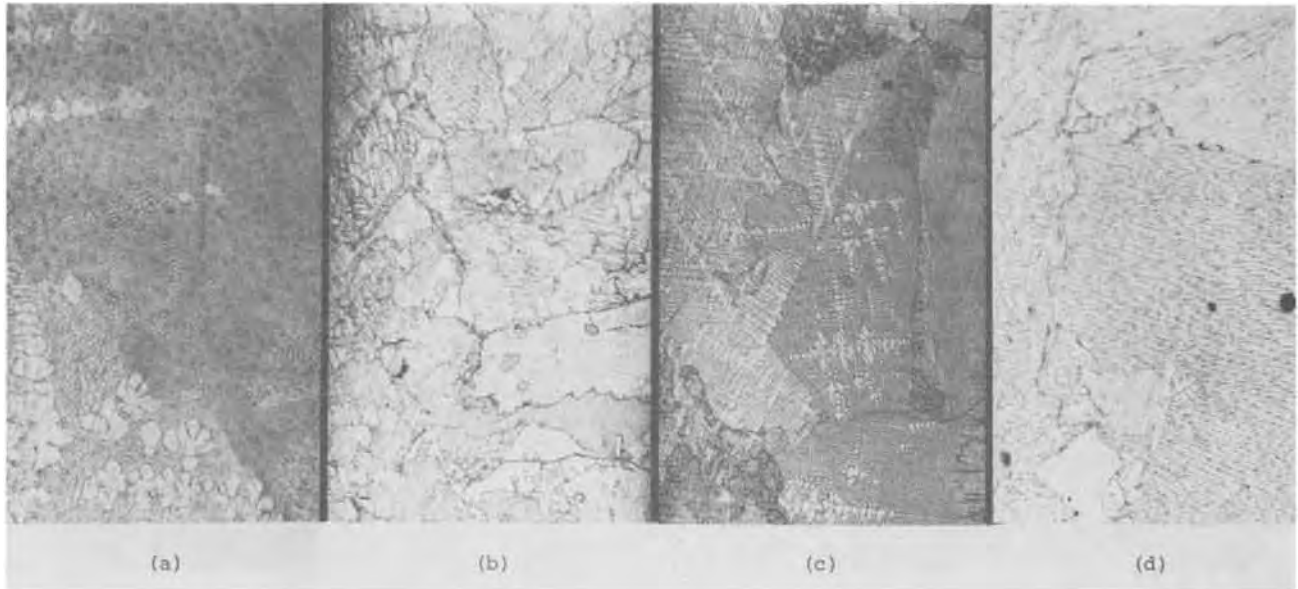


Fig. 2. Effects of alloy composition on microstructure, (a) base lead, (b) Pb-0.081Ca, (c) Pb-0.083Ca-0.45Sn, and (d) Pb-0.082Ca-1.0Sn, 52X.

size decreased in Pb-Ca alloys but the magnitude of grain refinement was found to be less than that reported in much of the literature (6-9). Part of this discrepancy may be due to the influence of solidification rate on grain size (7, 10), since specimens were produced under differing conditions in these studies. However, the molybdate etchant used herein is believed responsible for the particular grain sizes found and for the fibrous dendritic and branched dendritic structures within the grains which were always observed. The etching procedure used was more effective in removing the cold-worked surface layer formed during polishing than the standard acetic acid etchants. Many of the small, irregular grains and rows of grains in structures observed in the literature can be shown to violate Euler's law for the distribution of grain edges, corners, faces, and bodies in a space-fitting aggregate of polyhedral bodies (3, 11), and are therefore artifacts.

The fibrous dendritic morphology within grains as previously described (3, 8) was commonly observed. Breakdown of this structure into stubby-armed

branched dendrites was also found (Fig. 2-4). Fibrous dendritic or cellular structures have previously been observed in Pb-Ca alloys by other investigators (12-14). These structures have been extensively studied in dilute lead and tin-base alloys (15-20) and investigated in other alloy systems as well (21-23). While this structure has been described in Pb-Ca as an etching artifact (24), it is clearly real. Its significance is in its influence on the distribution of intragranular microstructural features which affect both hydrogen evolution (10) and corrosion (25). The presence of trace elements in the base lead had no observable effect on microstructural features.

Figure 4 indicates the variation of grain size with location in the grids. Grain size increased quickly away from the grid frame. There was some variation in grain size around the grid frame, but the variation along the frame was smaller than between frame and wire sections. Branched dendrites were observed in wire cross sections. A small but observable variation in grain size with casting conditions was also found, e.g., grain size

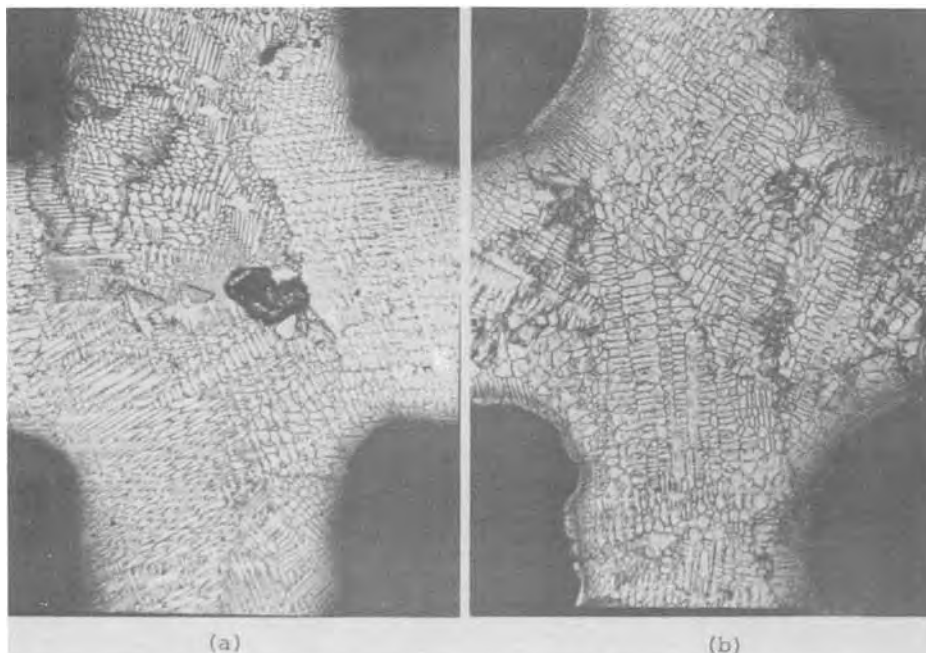


Fig. 3. Grid wire microstructure of Pb-0.08Ca-1.0Sn cast from (a) low Bi primary, and (b) refined secondary lead, 52X.

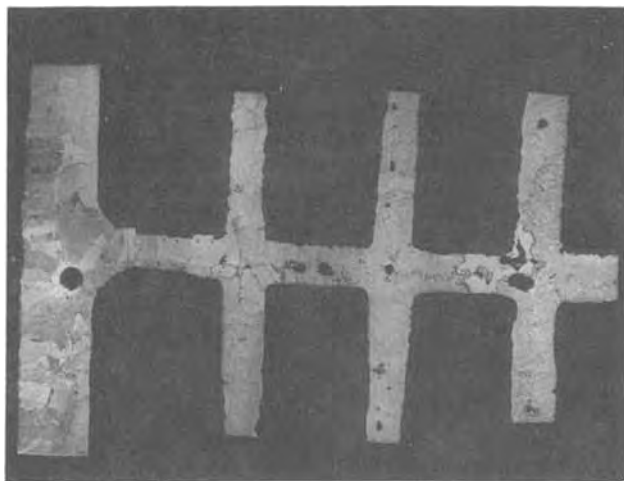


Fig. 4. Variation of grain size with location in grid, low Bi primary Pb-0.07Ca-0.75Sn, composite photograph, 52X.

increased as pouring temperature was raised from 900° to 1000°F at a constant 400°F mold temperature, in alloys containing 0.75Sn. Measurements were not made at other tin levels.

**Hardness.**—Hardness was measured as an indication of both tensile properties and grid handleability. While arbitrary hardness scales are generally nonlinear and values may be compared only on a qualitative basis, hardness measurement is an effective means of screening alloys and providing production quality control. Reasonably good correlation between hardness and tensile strength has been shown for Pb-Ca alloys (26). A cross plot of additional data in that study shows a reasonable correlation between hardness and yield strength, also.

Figure 5 illustrates the typical age-hardening behavior of Pb-Ca and Pb-Ca-Sn alloys. A similar plot was generated for alloys of other tin contents studied in both base lead systems. Hardness is observed to increase with both time and calcium content, as reported

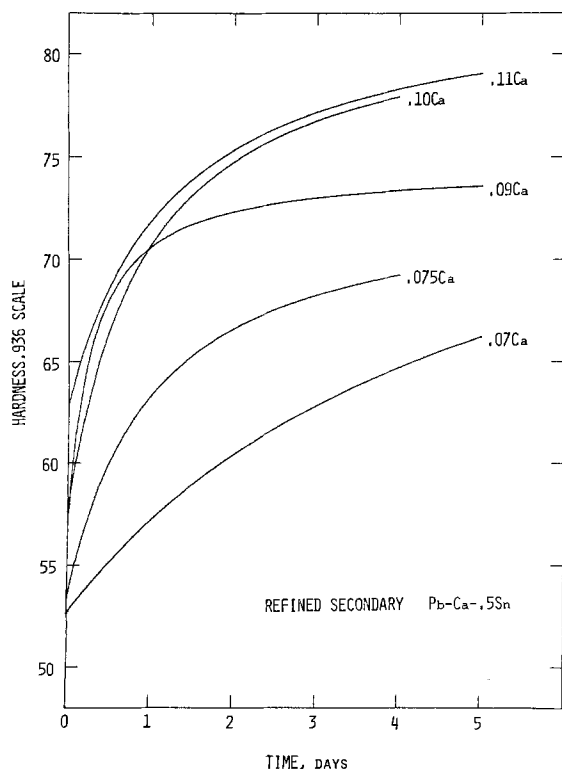


Fig. 5. Hardness vs. time after casting

previously for Pb-Ca alloys (hardness or tensile strength) by many investigators (9, 14, 27, 28). Initial aging rate was also observed to increase with increasing calcium content. The addition of tin to Pb-Ca alloys decreased hardness over the time interval studied, with hardness decreasing slightly as the tin content was increased from 0.5 to 1 w/o. However, tin additions did not influence initial aging rate within the accuracy of the measurement technique employed. Myers *et al.* (9) have shown that tin additions to Pb-Ca completely inhibit the onset of aging for at least 1 hr. The one day test interval used in this study was not designed to detect such short term effects. Tin is expected to have a positive influence on hardness at longer times (29, 30).

Mold and metal temperatures were held constant to eliminate effects of casting variables, as hardness was significantly influenced at some compositions by the particular ladle and mold temperatures employed, as shown in Fig. 6. On the left, the effect of three combinations of ladle and mold temperatures on the hardness of Pb-0.085Ca-0.75Sn is shown. Mold and ladle temperatures are in degrees Fahrenheit. The upper and lower mold temperatures were equal. Increases in both mold temperature (bottom and middle curves) and ladle temperature (bottom and top curves) increase hardness measurably. On the right, three curves are shown for Pb-0.075Ca-1Sn, but no strong dependence on ladle and mold temperature is evident, although some variation in initial hardness is indicated.

Figure 7 presents graphically the results of the statistical test for differences in hardness as a function of base lead composition. The data points indicate the calcium and tin compositions at which the significance test was performed. The solid circles identify compositions at which refined secondary lead alloys were statistically harder than low bismuth primary lead alloys. The solid squares identify compositions where the opposite was found. The open circles represent compositions where no statistical differences were indicated. No data is presented for Pb-Ca alloys as not enough hardness data were available for comparison between base leads.

It is observed that there are fairly well-defined compositional fields in which differences are observed between alloys of the two base leads. Below approximately 0.085Ca, refined secondary lead alloys exhibit higher hardness than low bismuth primary lead alloys. Above approximately 0.1Ca, a low bismuth primary lead alloy exhibited higher hardness. In the region between these compositions, there is no statistical difference. Within the limits of the available data, tin content did not influence the rankings, however, more data points would be required for clarification.

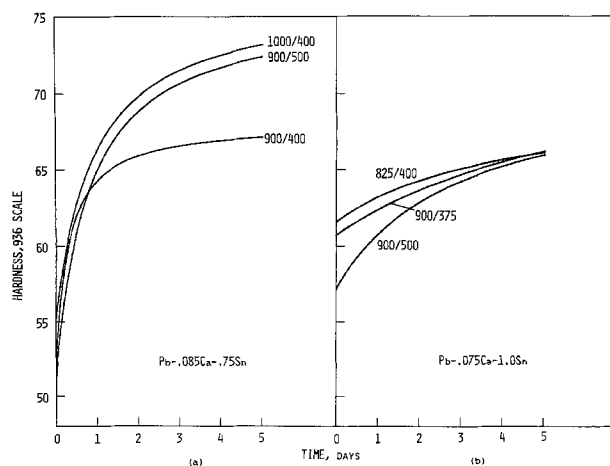


Fig. 6. Hardness vs. casting conditions in two alloy classes, (a) Pb-Ca-0.75Sn, and (b) Pb-Ca-1.0Sn, for different metal/mold temperature conditions.

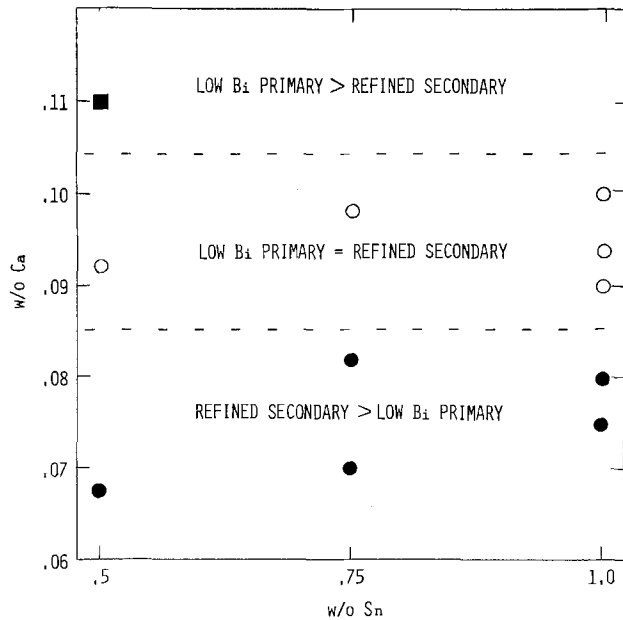


Fig. 7. Hardness vs. base lead composition at given calcium and tin levels.

The existence of fairly well-defined zones in which trace elements in the base lead have varying observed effects on hardness may be explained as follows: At low calcium levels where as-cast hardness is low, strengthening by trace elements is likely to be quite noticeable, as previously observed (3, 9). In Pb-Ca alloys, grain refinement has been suggested as the hardening mechanism (9). In Pb-Ca-Sn alloys, where no grain refinement is found [this study and others (3, 9)], some other mechanism such as solid solution strengthening must be operating. At higher calcium levels where as-cast hardness is higher, the effect of trace elements may not be observable (9). At very high calcium levels, i.e., higher than likely to be employed in a maintenance-free battery for reasons of corrosion resistance, the lattice straining effect of the trace elements in solid solution might contribute to overaging of the  $Pb_3Ca$  precipitates, causing low bismuth primary lead alloys to be harder. However, only one datum point exists where low bismuth primary Pb-Ca-Sn was harder than refined secondary Pb-Ca-Sn, and this effect must be investigated further.

At all calcium contents of interest, the results of this study indicate hardness is more easily controlled by adjustments in alloy composition and casting conditions than by adjusting base lead composition.

**Hydrogen evolution.**—The calibration technique developed for measuring grid surface area was found to be accurate and insensitive to the choice of dielectric. This was important since the accurate measurement of grid surface area was required to compare results on individual grids. The test cell is shown in Fig. 8. Table II lists results for Pb-Ca grids of different composition in both base leads. Unalloyed refined secondary base lead results are included for comparison. Unalloyed low bismuth primary base lead grids were too soft to handle and were not tested. The average rate of gassing is given for each potential. In all but one case, increasing calcium content increases gassing on both base leads. However, compared to the gassing on unalloyed refined secondary lead, it is not clear whether calcium increases or decreases gassing, or has any effect at all. It has previously been reported that calcium at similar compositions has no effect on gassing (31).

Table III presents results for Pb-Ca-Sn grids, for a number of different alloy compositions. Here, variations in gassing of 50% are observed as a function of alloy composition. At some compositions, e.g., Pb-0.085Ca-

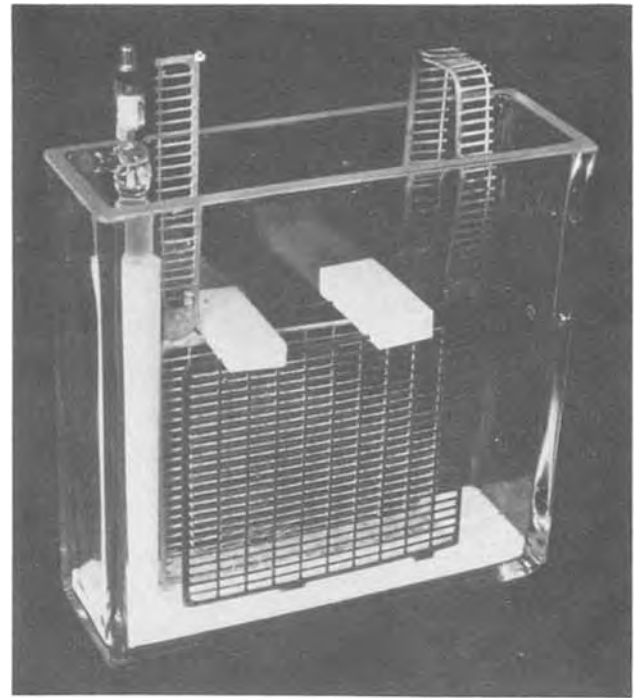


Fig. 8. Hydrogen evolution test cell

1.0Sn, refined secondary lead gasses less than low bismuth primary, while at others, e.g., Pb-0.07Ca-0.75Sn,

Table II. Gassing current density ( $\mu A/cm^2$ ) vs. base lead and Pb-Ca alloy composition

Potential (V)*	Base lead-low Bi primary			Unalloyed
	0.067 Ca	0.107 Ca	$\bar{X}$	
-1.1	17.55	20.19	18.87	
-1.2	18.25	23.72	21.00	
-1.3	22.88	25.51	24.19	
-1.4	32.42	40.48	36.45	

Potential (V)*	Base lead-refined secondary			Unalloyed
	0.08 Ca	0.11 Ca	$\bar{X}$	
-1.1	18.44	18.61	18.52	17.17
-1.2	19.06	20.49	19.77	20.68
-1.3	24.87	29.54	27.20	26.00
-1.4	40.39	36.91	38.65	43.95

\* Vs.  $Hg/Hg_2SO_4$  reference electrode.

Table III. Gassing current density ( $\mu A/cm^2$ ) vs. base lead and Pb-Ca-Sn alloy composition

Potential (V)*	Base lead-low Bi primary						$\bar{X}$
	0.084 Ca, 1.0 Sn	0.097 Ca, 1.0 Sn	0.071 Ca, 0.75 Sn	0.098 Ca, 0.75 Sn	0.081 Ca, 0.81 Sn		
-1.1	16.19	15.22	17.59	18.03	17.81	17.01	
-1.2	16.25	18.11	18.42	19.41	19.62	18.36	
-1.3	28.77	23.64	22.68	30.38	25.08	26.10	
-1.4	45.64	37.95	29.53	52.51	31.70	39.46	

Potential (V)*	Base lead-refined secondary					$\bar{X}$
	0.085 Ca, 1.0 Sn	0.108 Ca, 1.0 Sn	0.070 Ca, 0.73 Sn	0.073 Ca, 1.0 Sn	0.085 Ca, 0.7 Sn	
-1.1	15.23	17.73	19.19	18.19	17.40	17.55
-1.2	14.55	18.72	21.22	19.18	17.12	18.16
-1.3	19.31	28.91	27.35	25.36	20.48	24.30
-1.4	29.33	46.39	46.88	46.85	27.52	39.34

\* Vs.  $Hg/Hg_2SO_4$  reference electrode.

the opposite is true. It is not clear what is the general effect of calcium, tin, and trace element content on gassing, but it is observed that differences in gassing due to base lead composition are smaller than the effects due to variations in alloy content. Hence, gassing rate is more easily controlled by adjusting alloy content than by adjusting base lead composition. Recently, hydrogen evolution was measured in Pb-0.1Ca test cells in which trace elements were added to the electrolyte (32). This study indicated that antimony and arsenic at electrolyte concentrations > 1 ppm, and copper and bismuth at concentrations > 500 ppm increased gassing. However, it has yet to be demonstrated how electrolyte trace element concentration relates to grid alloy composition. Certainly, not all of a trace element in the grid alloy is available for solution into the electrolyte.

**Castability**

Industrial experience in the manufacture of Pb-Ca industrial batteries has indicated that the castability of Pb-Ca alloys would be inferior to that of antimonial lead in SLI grid configurations. Castability is defined here to be the combination of all factors influencing the net grid output of a casting machine per unit time. Figure 9 shows the reject percentage as a function of tin and base lead composition for all casting runs in the range 0.07-0.095Ca. The mold reject data points relate to the properties of the molten alloys and the skill of the machine operator. The difference between the total reject and the mold reject data points represents the percentage of mechanical rejects, which is related to grid strength and machine design.

A comparison of the two curves indicates that a mechanical reject percentage of 10-12% is quite constant at all compositions. This indicates that differences in hardness are not contributing to these rejects, rather, machine design must be modified if this 12% mechanical reject figure is to be reduced. The addition of 0.5Sn almost halves the total reject rate, but additions from 0.5 to 1.0Sn only have a small positive effect. Base lead composition has a significant effect only in Pb-Ca alloys. Differences between Pb-Ca-Sn alloys of different base leads are attributed to increased operator experience only, as the low bismuth primary lead alloys were cast first during the study. The effects of trace elements on hardness and castability reported herein conflict with those reported in a bench scale casting operation (33). In this study, repeated runs at a given composition often result in higher castability, indicating an operator learning factor, and that the results presented herein only indicate trends and general relationships.

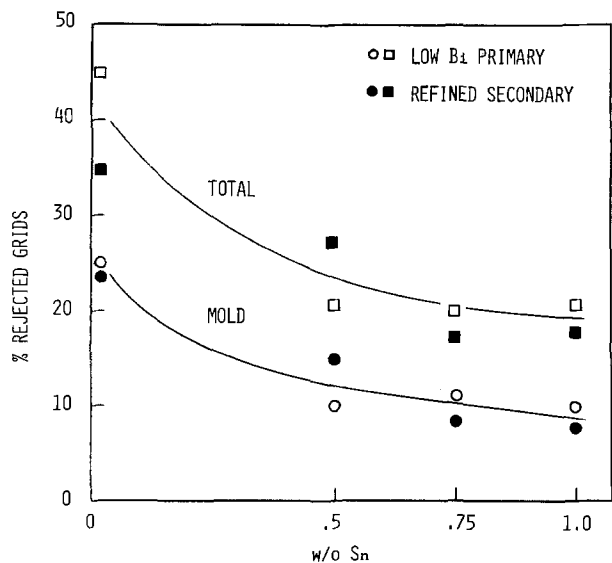


Fig. 9. Castability vs. tin and base lead composition showing mold and total reject percentages.

Furthermore, the absolute reject percentage is obviously a function of mold design and the inspection criteria employed.

**Calcium Oxidation Rate**

Unlike antimonial lead, molten calcium-lead alloys oxidize rapidly, even with the use of an enclosed melting pot and metal transport system. Figure 10 presents the rate of calcium loss as a function of tin content for the range 0.065-0.095Ca. Each data point represents the averaged loss rate for all casting runs in the given composition range. At all compositions, the calcium content decreased linearly with time, within the accuracy of the analytical technique.

While not shown, the calcium loss rate decreases somewhat with increasing calcium at each tin content. Oxidation rate in Pb-Ca is markedly lower for refined secondary base lead.

In Pb-Ca-Sn alloys, differences in loss rate with base lead composition are small. The frequency and thoroughness of drossing of the melting pot affect the absolute loss rates obtained, along with the effectiveness of the gas cover and scrap recycling procedures employed.

**Conclusions**

The most significant effects of calcium, tin, base lead compositions and casting conditions on the properties of Pb-Ca and Pb-Ca-Sn alloys studied herein are summarized as follows:

1. Hardness and initial aging rate increase with calcium content in the range 0.05-0.1Ca.
2. The addition of 0.5Sn to Pb-Ca alloys increases grain size and castability and decreases calcium oxidation rate. Further additions up to 1 w/o increase these properties slightly.
3. The addition of 110-180 ppm bismuth, 5-20 ppm antimony, 5-10 ppm copper, and 20-30 ppm silver increase hardness at <0.085Ca in alloys containing 0.5-1.0Sn.
4. The addition of the stated amounts of these elements also increases compositional stability and castability of Pb-Ca alloys but has no effect on Pb-Ca-Sn alloys for the compositions studied.
5. A capacitance method has been developed for accurately determining the surface area of cast grids, which for the grid design employed averaged 250 cm<sup>2</sup>.
6. The hydrogen evolution rate on cathodically polarized grids as a function of alloy composition varied in a seemingly random manner. Variations in calcium and tin composition affect gassing more than variations in trace element content.
7. At some compositions, casting conditions can exert as large an effect on hardness as changes in alloy composition.

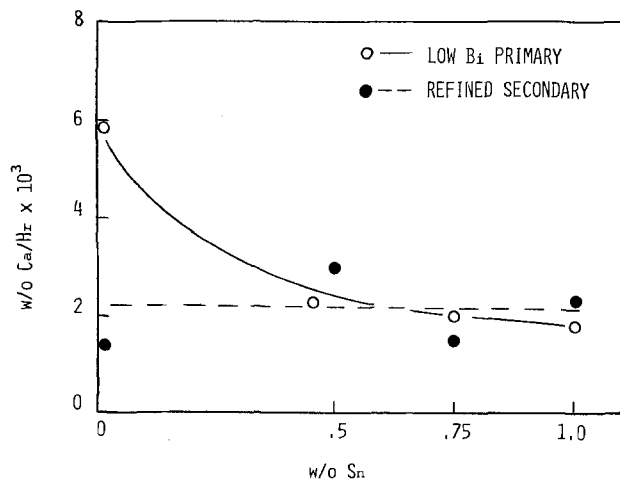


Fig. 10. Rate of calcium loss vs. tin and base lead composition

8. The doubling of tin content from 0.5 to 1.0 w/o has only a small effect on microstructure, hardness, castability, and calcium oxidation rate.

### Acknowledgments

The authors wish to thank Mrs. L. J. Crosby, R. A. Garini, D. Goodmacher, and K. Bibbo for assisting in the experimental portions of this work, S. Blinder for the statistical analyses, and members of the Analytical Services Department for the chemical analyses. The authors would also like to thank E. R. Hein and G. R. Kotler for helpful discussions and NL Industries for permission to publish this work.

Manuscript received April 23, 1976. This was Paper 36 presented at the Boston, Massachusetts, Meeting of the Society, Oct. 7-11, 1973.

Any discussion of this paper will appear in a Discussion Section to be published in the June 1977 JOURNAL. All discussions for the June 1977 Discussion Section should be submitted by Feb. 1, 1977.

Publication costs of this article were assisted by NL Industries, Incorporated.

### REFERENCES

- J. T. Crennel and A. G. Milligan, *Trans. Faraday Soc.*, **27**, 103 (1931).
- H. F. Haring and U. B. Thomas, *This Journal*, **68**, 293 (1935).
- T. W. Caldwell and U. S. Sokolov, *ibid.*, **123**, 972 (1976).
- U. S. Sokolov, T. W. Caldwell, and E. R. Hein, Paper 35, presented at The Electrochemical Society Meeting, Boston, Mass., Oct. 7-11, 1973.
- N. E. Hehner, "Storage Battery Manufacturing Manual," Independent Battery Manufacturers Association, Largo, Florida (1970).
- J. A. Young and J. B. Barclay, *Proc. 85th BCI*, p. 37 (1973).
- G. W. Mao, J. G. Larson, and P. Rao, *This Journal*, **120**, 11 (1973).
- J. Perkins and G. R. Edwards, *J. Mater. Sci.*, **10**, 136 (1975).
- M. Myers, H. R. Van Handle, and C. R. DiMartini, *This Journal*, **121**, 1526 (1974).
- T. W. Caldwell and U. S. Sokolov, "Power Sources 5," D. H. Collins, Editor, p. 73, Academic Press, New York (1975).
- C. S. Smith, *Met. Rev.*, **9**, 1 (1964).
- W. Hofmann, "Lead and Lead Alloys," English Trans. of 2nd German edition, p. 46, Springer-Verlag (1970).
- V. Goler, *Giesserei*, **25**, 242 (1938).
- J. N. Greenwood and C. W. Orr, *Proc. Aust. Inst. Min. and Met.*, **112**, 287 (1938).
- D. Walton, W. A. Tiller, J. W. Rutter, and W. C. Winegard, *Trans. AIME*, **203**, 1023 (1955).
- T. S. Plaskett and W. C. Winegard, *Can. J. Phys.*, **38**, 1077 (1960).
- G. S. Cole and W. C. Winegard, *J. Inst. Met.*, **92**, 322 (1963).
- G. A. Chadwick, "Fractional Solidification," M. Zief and W. R. Wilcox, Editors, p. 113, Marcel Dekker Inc., New York (1967).
- L. R. Morris and W. C. Winegard, *J. Crystal Growth*, **5**, 361 (1969).
- L. R. Morris and W. C. Winegard, *ibid.*, **6**, 61 (1969).
- H. Biloni, G. F. Bolling, and H. A. Domian, *Trans. AIME*, **233**, 1926 (1965).
- M. C. Flemings, D. R. Poirier, R. V. Barone, and H. D. Brody, *J. Iron Steel Inst.*, **208**, 371 (1970).
- R. M. Sharp and A. Hellawell, *J. Crystal Growth*, **6**, 334 (1970).
- "Metals Handbook," 7th ed., p. 300, American Society for Metals, Metals Park, Ohio (1972).
- S. Feliu, L. Galan, and J. A. Gonzalez, ILZRO Report LE-130 (1970).
- A. B. Townsend, USAEC Report Y-1307 (1960).
- E. E. Schumacher and G. M. Bouton, *Metals Alloys*, **1**, 405 (1930).
- E. E. Schumacher and G. S. Phipps, *This Journal*, **68**, 309 (1935).
- N. L. Parr, A. Muscott, and A. J. Crocker, *J. Inst. Met.*, **87**, 321 (1958/1959).
- E. R. Hein, Unpublished research.
- J. Burbank and C. P. Wales, NRL Report 5693 (1961).
- J. R. Pierson, C. E. Weinlein, and C. E. Wright, in "Power Sources 5," D. H. Collins, Editor, Academic Press, New York (1975).
- E. J. Ritchie, ILZRO Combined Reports LE-82 and LE-84 (1971).

## Some Observations on the Prediction of the State of Discharge of Batteries

F. Kornfeil\*

United States Army Electronics Command, Electronics Technology and Devices Laboratory,  
Fort Monmouth, New Jersey 07703

### ABSTRACT

A galvanostatic test method is described to determine the state of discharge of cells of the system Zn/KOH/HgO and the results compared with data obtained in loaded voltmeter tests. In a general treatment of battery testing equations are derived which show, *inter alia*, that for all electrochemical systems the sensitivity of galvanostatic tests is higher than the sensitivity of the loaded voltmeter method and which allow, *e.g.*, the calculation of the value of the external resistance yielding the maximal sensitivity attainable in a loaded voltmeter test.

Owing to the variety of electrochemical systems presently in use numerous test methods (1-3) to determine the state of discharge (SOD)<sup>1</sup> of galvanic cells have been employed, some modified with varying de-

grees of success to meet the demands of specific applications, chiefly to prevent the waste of still usable primary cells and, perhaps somewhat less importantly, to discern the need to replenish the charge of secondary batteries. One of the simplest and most widely used techniques is the loaded voltmeter test (4), so called because a voltmeter with a constant resistance (load) in parallel is attached to the cell terminals and the resulting voltage  $E$  used as an indication of the SOD of

\* Electrochemical Society Active Member.

Key words: battery testing, galvanostatic test method, loaded voltmeter test, electrode polarization, zinc-mercuric oxide cells.  
<sup>1</sup> In this paper the term "state of discharge" is used instead of the more prevalent "state of charge" because the latter conveys the concept of rechargeability, at least to this author's ears.

the cell. The loaded voltmeter test consists therefore, in effect, of the utilization, at constant external resistance  $R$ , of the overvoltage  $\eta$  of the cell as a function of the state of discharge and is known to produce results of acceptable accuracy with some, but by no means all, electrochemical systems.

It was the rather low sensitivity of the loaded voltmeter method when applied to cells of the system Zn/KOH/HgO (mercury cells) which prompted the investigation reported in this paper. Its aim was two-fold: to devise a rapid and nondestructive method of greater sensitivity for the prediction of the SOD of mercury cells; and to explore the consequences of a more generalized treatment of the polarization phenomena related to battery testing, thus perhaps eliminating at least part of the sometimes tedious empirical procedures.

### Experimental

**Test procedure.**—All experiments were performed at room temperature ( $21^\circ \pm 1^\circ\text{C}$ ) on mercury cells<sup>2</sup> of Type RM-4. These cells deliver from 30 to 33 hr of service when subjected to a continuous discharge through a  $12\Omega$  resistance to a cutoff voltage of 0.90V. Their open-circuit voltage  $E_o$  of 1.355V is remarkably uniform and stable and is very nearly constant over the entire discharge range, since no solid solutions between reactants and products are formed at either electrode and the electrolyte concentration remains virtually unchanged during discharge of the cells.  $E_o$  can, therefore, not be used as an indication of their SOD.

A series of preliminary experiments designed to explore the possible usefulness of the tangents drawn to  $E$ - $i$  curves at various currents as a function of the SOD proved unsuccessful, mainly because of the impossibility of attaining quasi-steady states at currents  $i > 200$  mA and at SOD's  $> 40\%$  of full capacity. These experiments lead, however, to the following galvanostatic test procedure.

The terminal voltage  $E$  of a fresh cell is measured 90 sec after the start of a constant discharge current, the current interrupted, and the cell, after recovery of the cell voltage to the original open-circuit value  $E_o$ , discharged through a  $12.0\Omega$  resistance for a recorded period of time. This procedure is repeated until the cell is almost completely discharged. Its remaining capacity is then determined by discharging it to an end voltage of 0.90V, this point representing the SOD of 100%.

Three curves obtained with this test method at different currents are shown in Fig. 1. Each curve represents the mean values of  $E$  of about thirty cells, plotted against the state of discharge  $C$  expressed in percent

<sup>2</sup> Mallory Battery Company, Tarrytown, New York.

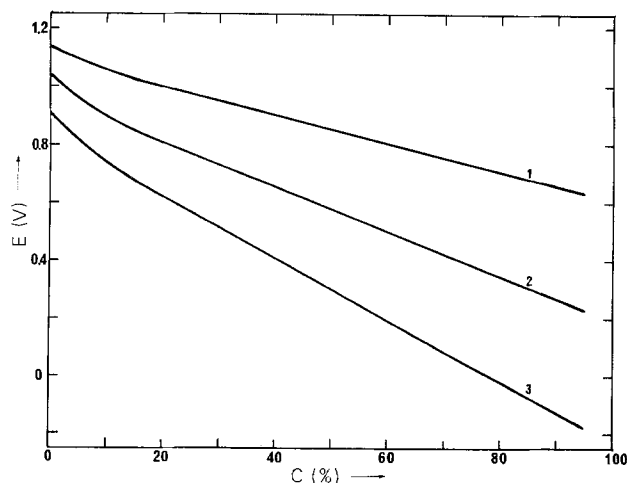


Fig. 1. Results of galvanostatic tests at different currents: curve 1, 200 mA; curve 2, 300 mA; curve 3, 400 mA.

of the total cell capacity  $C_o$ . At the test currents used the cell voltages exhibit a scatter of  $\pm 40$  mV. Except for the initial 10% of the abscissa  $E$  is seen to be a practically linear and rather sensitive function of the state of discharge. As an example, the slope of the linear portion of the curve obtained with a test current of 300 mA is 7.8 mV/%, contrasting quite favorably with loaded voltmeter tests performed under comparable conditions, as will be demonstrated below in greater detail. The interval of 90 sec before measuring  $E$  constitutes a compromise involving several factors. A period too short for a significant part of the mass transport to occur may result in the loss of a portion of the diffusion overpotential, thereby reducing the sensitivity of the test method.<sup>3</sup> Conversely, an unnecessary prolongation of the span may carry the system close to or into the limiting current condition and falsify the results, particularly when larger test currents are used. In addition, it is always desirable in any test to remove as minute a part of the cell capacity as possible. In the case of RM-4 cells one test of 90 sec duration at  $i = 300$  mA diminishes the capacity of a fresh cell by approximately 0.3%, a reasonably small fraction.

### Results and Discussion

**General considerations.**—At this point the question arises why, in fact, the overvoltage of a galvanic cell depends on its state of discharge. This is undoubtedly a problem of considerable complexity, however, for the purposes of the present discussion it is sufficient to consider only two factors. Firstly, as the cell is discharged the consumption of the electrode materials results in progressively smaller active electrode areas and consequently in correspondingly higher current densities and, therefore, higher overpotentials. Secondly, the accumulation of solid reaction products at the electrode surfaces changes the conditions of mass transport, giving rise to a gradual increase of the diffusion overpotential. These considerations will be valid for all systems in which a solid phase of the electrode participates directly in the electrode reaction but will not apply to redox systems (e.g., fuel cells) with inert electrodes whose sole function is to render the charge transfer step possible. It is fortunate that in these cases special methods to determine the state of discharge are not required since the reactants are stored outside of the galvanic cells and their quantities are easily measurable by other means.

**Relative sensitivity at  $i = \text{const}$  and  $R = \text{const}$ .**—The results depicted in Fig. 1 show that the test voltage  $E$  is a function of  $C$ , the state of discharge defined as  $100 C_r/C_o$ , where  $C_r$  denotes the capacity removed during a  $12\Omega$  continuous discharge and  $C_o$  is the total capacity available to an end point of 0.90V. A convenient way of treating the observed phenomena is to look at the decrease of  $E$  with increasing  $C$  as the result of a progressive increase of the total internal resistance  $R_i$  of the cell, i.e.,  $E = f(R_i)$ . Then  $R_i = d\eta/di$ ,  $\eta$  being the sum of the charge transfer, diffusion, reaction, crystallization and resistance overpotentials present at both electrodes (5).

From the equivalent circuit of the cell shown in Fig. 2, we observe that

$$E = E_o - iR_i \quad [1]$$

and

$$E = \frac{E_o R}{R + R_i} \quad [2]$$

expressing  $E = f(R_i)$  with either the current  $i$  or the external resistance  $R$  as the parameter. Capacitive effects are neglected because  $dE/dt \approx 0$  in all situations under discussion.

<sup>3</sup> It is for this reason that, *ceteris paribus*, tests using current pulses in polarization measurements are subject to a certain amount of scepticism. The use of pulse currents in the determination of, e.g., double layer capacities as a function of the SOD is, of course, another matter.

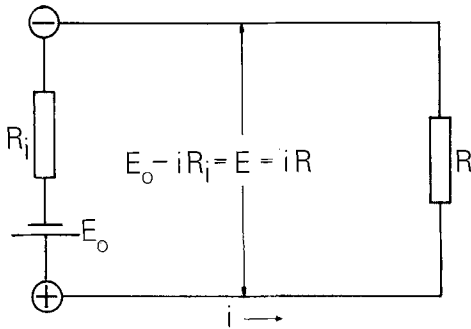


Fig. 2. Equivalent circuit and fundamental relations

Since  $R_i$  will, in general, be dependent on the current as well as the state of discharge it is convenient formally to separate  $R_i$  into two components,  $f(i)$  and  $F(C)$ , such that  $df(i)/dC = dF(C)/di = 0$

$$R_i = f(i) + F(C) \quad [3]$$

$f(i)$  and  $F(C)$  may be any single-valued function whatever of the current and the state of discharge, respectively, subject only to the following restrictions. Since  $d\eta/di > 0$  on thermodynamic grounds,  $f(i)$  must always be a positive quantity.  $F(C) = 0$  for  $C = 0$  and increases to a maximum at  $C = 100\%$  ( $C_r = C_o$ ), i.e.,  $dF(C)/dC = dR_i/dC > 0$  for all values of  $C$  which condition, obviously, is the *sine qua non* for the applicability of any test method based on electrode polarization.

Combining Eq. [1] and [3] we get

$$E = E_0 - i[f(i) + F(C)] \quad [4]$$

and

$$E = \frac{E_0 R}{R + f(i) + F(C)} \quad [5]$$

The sensitivities  $S_i$  of the galvanostatic method and  $S_R$  of the loaded voltmeter test are obtained by differentiation of Eq. [4] and [5] with respect to  $C$

$$S_i = -(\partial E / \partial C)_i = i \cdot dF(C) / dC = \frac{E}{R} dF(C) / dC \quad [6]$$

$$S_R = -(\partial E / \partial C)_R = \frac{E_0 R}{[R + f(i) + F(C)]^2} dF(C) / dC$$

$$= \frac{E}{R + f(i) + F(C)} dF(C) / dC \quad [7]$$

Division of Eq. [6] by Eq. [7] results in

$$S_i / S_R = 1 + \frac{f(i) + F(C)}{R} \quad [8]$$

Several interesting conclusions can immediately be drawn from the preceding equations. Since the second term on the right-hand side of Eq. [8] is always a positive quantity it follows that, for the same value of  $E$ ,  $S_i > S_R$  for every electrochemical system, no assumptions pertaining to its nature having been made in the derivation. Therefore, the galvanostatic method must invariably be more sensitive than a loaded voltmeter test performed at any load  $R$ , provided only that their respective  $E$ - $C$  curves have one point in common. Moreover, the ratio of the sensitivities will become greater as a cell of a given system approaches the state of full discharge [large  $F(C)$ ] and the more easily polarizable the system in question is [large  $f(i)$ ].

That this is indeed the case is illustrated in Fig. 3. In this diagram the solid line is the result of the galvanostatic tests performed at 300 mA and is a reproduction of curve 2 of Fig. 1. The dotted curves 1, 2, and 3 were obtained in loaded voltmeter tests in which  $E$  was also measured 90 sec after closing the circuit. The values of the external resistances were chosen such that

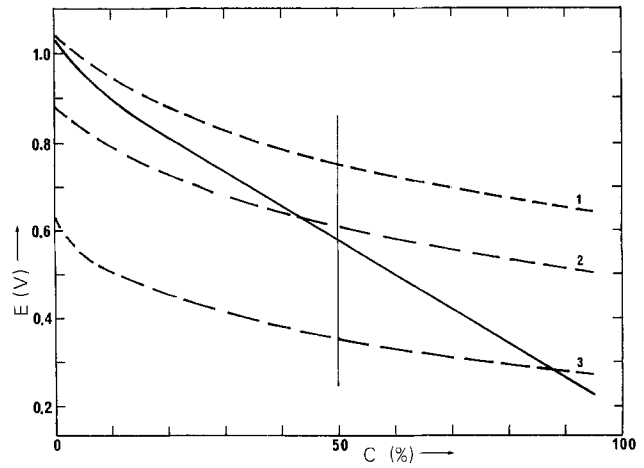


Fig. 3. Galvanostatic and loaded voltmeter test results. Solid line = galvanostatic test at 300 mA. Dotted lines = loaded voltmeter tests. Curve 1, 3.3Ω; curve 2, 2.2Ω; curve 3, 1.0Ω.

the curves would coincide with the galvanostatic line at states of discharge of approximately 0, 50, and 100%, respectively. As predicted, in all three series of loaded voltmeter tests the slopes are smaller than the slope of the galvanostatic curve. Obviously, the most appropriate comparison is made with curve 2 ( $R = 2.2\Omega$ ) because here the average current is roughly the same in the two tests, whereas in curve 1 ( $R = 3.3\Omega$ ) the loaded voltmeter test current is smaller and in curve 3 ( $R = 1.0\Omega$ ) larger than 300 mA for all states of discharge. The numerical values of the sensitivities, measured at  $C = 50\%$ , are  $S_i = 7.8$  mV/% and  $S_R = 3.0$  mV/%, i.e., at the midpoint the galvanostatic test is more sensitive by a factor of 2.6. This factor increases with increasing  $C$ , again in accordance with prediction, and reaches a value as high as 6.5 at  $C = 90\%$ .

The significance of the higher sensitivity of the galvanostatic test is brought out more clearly by considering the scatter of the test voltage due to the less than perfect uniformity achieved in the manufacture of the cells. Referring to Fig. 4, the maximal uncertainty  $\epsilon$  associated with a particular test method is related to its sensitivity  $S$  and the voltage scatter  $\sigma$  by the expression  $\epsilon = 2\sigma/S$ . As pointed out previously,  $\sigma$  is approximately 40 mV in the current range under consideration. Using this value the maximal uncertainty of the galvanostatic method is about 10% over the entire range at 300 mA, compared to about 27% for the loaded voltmeter test at  $C = 50\%$ . Taking an average slope of 2.1 mV/% between 50 and 90% discharge  $\epsilon = 38\%$  and it becomes clear that for mercury cells a loaded volt-

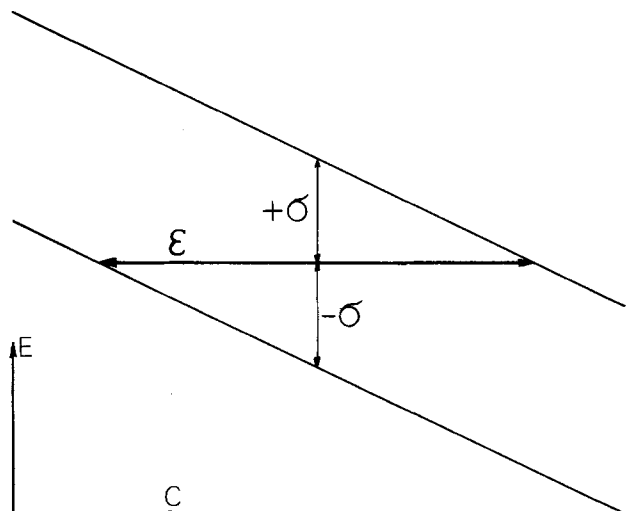


Fig. 4. Uncertainty due to scatter of test voltage



meter test with an average current of 300 mA is not accurate enough to distinguish a half-discharged from a nearly fully discharged cell with any degree of confidence.

**Absolute sensitivities.**—Referring to Eq. [4] it follows from the linearity (at least for mercury cells) of the galvanostatic  $E$ - $C$  curves that  $F(C)$  increases proportionally to  $C$  and that  $dF(C)/dC = \text{const}$ . According to Eq. [6] one should therefore expect  $S_i$  to increase linearly with the test current. Figure 5 shows this to be true, at least up to 400 mA, the highest value used to date (the quantity  $(\bar{S}_R)_{\text{max}}$  in the diagram will be discussed later). It should be noted that at this current cells of  $C > 85\%$  already exhibit a test voltage  $E < 0$ , requiring the use of an external d-c power source, a practice which was, at any rate, resorted to in all galvanostatic tests to facilitate the condition  $i = \text{const}$  during the 90 sec period. Accordingly, it appears that  $S_i$  can be raised to any desired value by increasing the test current, as long as the limiting current region is not reached, and provided that a possibly higher voltage scatter does not cancel the advantage so gained.

The relationship between the sensitivity  $S_R$  of the loaded voltmeter test and the external resistance  $R$  is rather more complicated than the simple linear dependence of  $S_i$  on the current. One aspect of this relationship becomes immediately apparent from an inspection of the slopes of the dotted lines shown in Fig. 3. Despite a more than threefold change of  $R$  the slopes at corresponding points on the abscissa differ by only about 30% and, at first perhaps surprisingly, actually increase with increasing  $R$ . The numerical values are, again at  $C = 50\%$ ,  $S_{R=1.0} = 2.3$ ,  $S_{R=2.2} = 3.0$ , and  $S_{R=3.3} = 3.4$  mV/%. This behavior can easily be understood by the following consideration. The external resistance chosen for a loaded voltmeter test can, obviously, have any value between  $0 \leq R < \infty$ . For both extremes the resulting  $S_R$  must be zero, independently of the state of discharge of the cell tested, since at  $R = 0$   $S_R = 0$  because the cell is short-circuited and  $E = 0$ , while at  $R = \infty$   $E = E_0$  and again  $S_R = 0$  unless  $E_0$  is itself a function of the state of discharge. Therefore, a maximal value  $(S_R)_{\text{max}}$  and a corresponding  $R_{\text{max}}$  must exist, and the question of whether the sensitivity increases or decreases with  $R$  depends entirely on the external resistance being smaller or larger than  $R_{\text{max}}$ .

It now remains to determine the position of  $(S_R)_{\text{max}}$  and, ideally, to calculate the absolute values of  $(S_R)_{\text{max}}$  and  $R_{\text{max}}$ .

**Values of  $(S_R)_{\text{max}}$ ,  $R_{\text{max}}$ ,  $(\bar{S}_R)_{\text{max}}$ ,  $\bar{R}_{\text{max}}$ .**—Equation [7] can be rewritten in the form

$$S_R = \frac{E_0 R}{(R + R_i)^2} dR_i/dC \quad [9]$$

and we see at once that the condition  $S_{R=0} = S_{R=\infty} = 0$

is satisfied because  $\lim_{R \rightarrow 0} R/(R + R_i)^2 = 0$  and also  $\lim_{R \rightarrow \infty} R/(R + R_i)^2 = 0$ . Equation [9] allows the calculation of the sensitivity of a loaded voltmeter test for any value of  $R$ , at any given state of discharge of the cell, once a single galvanostatic test curve has been established, since  $E_0$  is known and the numerical values of  $R_i$  and  $dR_i/dC = dF(C)/dC$  are readily accessible from Eq. [1] and [6], respectively. Although the knowledge of  $S_R$  for various values of  $R$  may be of interest in some particular instances, a determination of  $R_{\text{max}}$  will ordinarily be sufficient. Differentiation of Eq. [9] with respect to  $R$  and setting the result equal to zero yields

$$1/(R + R_i)^2 - 2R/(R + R_i)^3 = 0 \quad [10]$$

The value of  $R$  satisfying this equation is

$$R_{\text{max}} = R_i \quad [11]$$

Substitution into Eq. [9] leads to

$$(S_R)_{\text{max}} = \frac{E_0}{4} \frac{d}{dC} \ln R_i \quad [12]$$

Thus, at a given state of discharge, the maximal sensitivity of a loaded voltmeter test depends on the relative change of  $R_i$  and is realized when the external resistance used is equal to the internal resistance at this point. The calculated values of  $S_R$ , at  $C = 50\%$ , for the tests presented in Fig. 3, are  $S_{R=3.3} = 3.3$ ,  $S_{R=2.2} = 3.2$ , and  $S_{R=1.0} = 2.4$  mV/%, in good agreement with the experimental data.

In the derivation of Eq. [10]  $R_i$  was assumed to be independent of  $R$ , an obvious simplification since  $R_i$  contains the term  $f(i)$  and must consequently also be a function of  $R$ . However, the error due to this assumption is negligible, at least for mercury cells and probably also for other systems, as can be shown in the following way. A series of galvanostatic tests was carried out, at various currents, on fresh ( $C = 0$ ) cells for which  $F(C) = 0$ , by definition. Equation [4] then takes the form  $f(i) = (E_0 - E)/i$ , permitting the plotting, as a function of  $i$ , of  $f(i) = R_0$ , the value of  $R_i$  at  $C = 0$ . Figure 6 shows how after an initial decrease  $f(i)$  reaches a practically constant value of  $1.3\Omega$  between 200 and 400 mA, the range of currents used in the galvanostatic tests and, as will be demonstrated below, also in the loaded voltmeter tests conducted at maximal sensitivity. Remembering that  $f(i)_{C=0} = d\eta/di$ , the same curve can be obtained by drawing the tangents to the  $\eta - i$  curve of a fresh cell shown in Fig. 7. The rather long linear part of the curve is most likely caused by the gradual preponderance of the diffusion overpotential  $\eta_d$  (6), for which  $d^2\eta_d/di^2 > 0$ , over the charge transfer overpotential  $\eta_t$  (7), with  $d^2\eta_t/di^2 < 0$ . The question of whether this extended constancy of  $f(i)$  also occurs in other

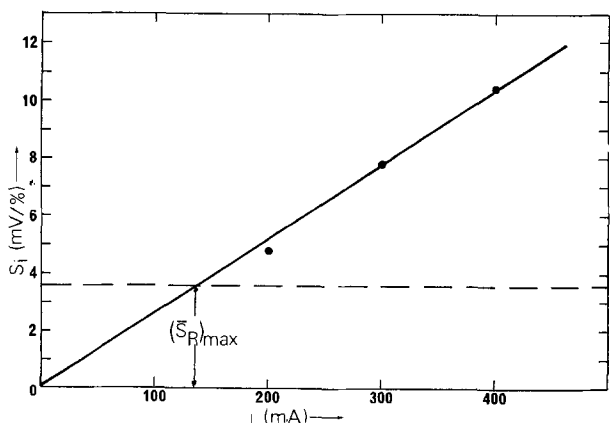


Fig. 5. Dependence of sensitivity of galvanostatic test on current

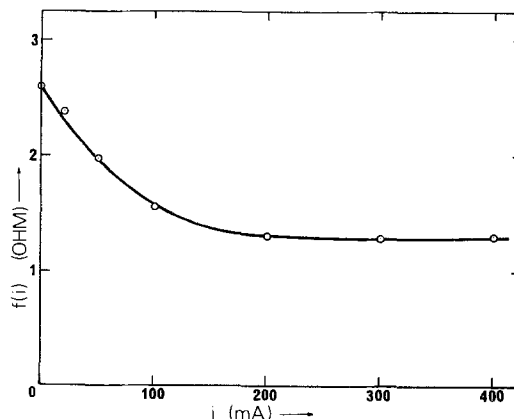


Fig. 6.  $f(i)$  as a function of current



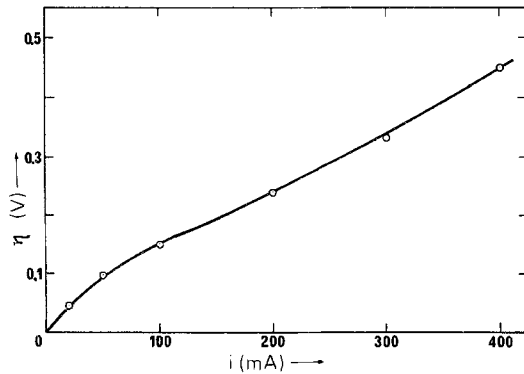


Fig. 7. Overvoltage of RM-4 cells as a function of current

systems is awaiting further experimentation and will be discussed in a subsequent publication.

It should perhaps be pointed out that it is not an uncommon mistake to assume  $(R_i)_{i \rightarrow 0}$  to be the ohmic component of the internal resistance because  $\eta$  approaches zero. Although  $\eta$  indeed vanishes  $(d\eta/di)_{i \rightarrow 0}$ , the polarization resistance (8), does not, and would be zero only if the exchange current densities, the diffusion coefficients of all species participating in the electrode reactions, and the rate constants of all chemical reactions preceding and following the charge transfer step were infinite.

Equations [11] and [12] refer to a specific point on the C-axis and hence to the individual value of  $R_i$  at that point and can, therefore, not directly be used to calculate  $(S_R)_{\max}$  and  $R_{\max}$  of a practical loaded voltmeter test for which, of course, a single value of  $R_{\max}$  is required. To this end it is necessary to maximize  $\bar{S}_R$ , the average sensitivity over all states of discharge. Consequently, we have

$$\begin{aligned} \bar{S}_R &= 1/100 \int_0^{100} S_R dC \\ &= \frac{E_0(R_{100} - R_0)}{100} \frac{R}{(R + R_0)(R + R_{100})} \quad [13] \end{aligned}$$

where use of Eq. [9] has been made and  $R_0$  and  $R_{100}$  denote the values of  $R_i$  at  $C = 0$  and  $C = 100$ , respectively. Setting the derivative  $dS_R/dR$  equal to zero we obtain the equation

$$\frac{1}{(R + R_0)(R + R_{100})} - \frac{R(2R + R_0 + R_{100})}{[(R + R_0)(R + R_{100})]^2} = 0 \quad [14]$$

the solution of which is

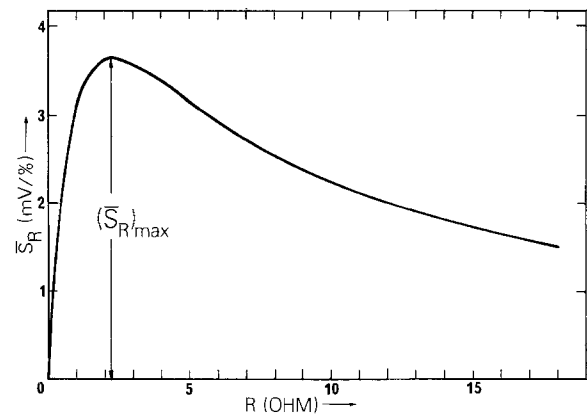
$$\bar{R}_{\max} = \sqrt{R_0 R_{100}} \quad [15]$$

i.e., in a loaded voltmeter test the external resistance yielding the maximal average sensitivity over the entire range of discharge of the cell is the geometric mean of the initial and final values of its internal resistance.

Substitution into Eq. [13] leads to

$$(\bar{S}_R)_{\max} = \frac{E_0(R_{100} - R_0)}{100} \frac{1}{2\sqrt{R_0 R_{100}} + R_0 + R_{100}} \quad [16]$$

Extrapolation of the linear part of a galvanostatic curve to  $C = 0$  and  $C = 100$  and use of the resulting values of  $E$  gives, in the case of the mercury cells tested,  $R_0 = 1.31$  and  $R_{100} = 3.90 \Omega$ . Substitution into Eq. [15] and [16] demonstrates that the average sensitivity of a loaded voltmeter test of RM-4 cells can never exceed 3.6 mV/% and is attained with an external resistance of 2.3  $\Omega$ . It is easily calculated that in this loaded voltmeter test the current varies between 220 and 380 mA and is within the range of virtual constancy of  $f(i)$ ,

Fig. 8.  $\bar{S}_R$  as a function of the external resistance, calculated with  $R_0 = 1.31 \Omega$ ,  $R_{100} = 3.90 \Omega$ .

again justifying the assumption  $dR_i/dR = 0$  implicit in Eq. [13], [15], and [16].

Figure 8 shows  $\bar{S}_R$  as a function of the external resistance, according to Eq. [13]. The sensitivity of the loaded voltmeter test increases rather slowly with decreasing  $R$ , reaches a maximum at  $R = 2.3 \Omega$  and then decreases sharply at still lower values of  $R$ . In order to facilitate the comparison of the galvanostatic and loaded voltmeter tests  $(S_R)_{\max} = 3.6$  mV/% has been inserted in the diagram of Fig. 5. It is apparent that a sensitivity of 3.6 mV/% can be achieved with a constant test current of only 140 mA, while the galvanostatic tests at 300 and 400 mA have sensitivities of 7.8 and 10.4 mV/%, respectively, clearly demonstrating the higher accuracy of the galvanostatic method.

One should, however, remember that the results reported here refer to cell capacities obtained at a single discharge rate (12  $\Omega$ ) at only one temperature (21°) and are likely to vary when these conditions are changed, a problem common to most, if not all, test methods. Experimental work is currently being conducted on mercury cells to permit the appropriate corrections to be made and also to test the application of the galvanostatic method, and its underlying theory, to different electrochemical systems.

Manuscript submitted Feb. 6, 1976; revised manuscript received May 10, 1976.

Any discussion of this paper will appear in a Discussion Section to be published in the June 1977 JOURNAL. All discussions for the June 1977 Discussion Section should be submitted by Feb. 1, 1977.

Publication costs of this article were assisted by the United States Army Electronics Command.

#### LIST OF SYMBOLS

$C$	state of discharge of cell, %
$E$	cell voltage, V
$E_0$	open-circuit voltage, V
$f(i)$	$i$ -dependent component of $R_i$ , $\Omega$
$F(C)$	$C$ -dependent component of $R_i$ , $\Omega$
$i$	test current, A
$R$	external resistance, $\Omega$
$R_i$	internal resistance of cell, $\Omega$
$R_0, R_{100}$	internal resistance at $C = 0$ and $C = 100$ , $\Omega$
$S_i$	test sensitivity at $i = \text{const}$ , mV/%
$\bar{S}_R$	sensitivity of loaded voltmeter test, mV/%
SOD	state of discharge
$\epsilon$	uncertainty of test method, %
$\eta$	overpotential, V
$\sigma$	scatter of test voltage, mV

#### REFERENCES

1. S. C. Levy and F. W. Reinhardt, SC-RR-70-332, Sandia Laboratories, Albuquerque, N.M. (June 1970).
2. R. G. Easterling and S. C. Levy, SC-RR-70-33, *ibid.* (June 1970).

3. J. J. Winter, J. T. Breslin, R. L. Ross, H. A. Leupold, and F. Rothwarf, *This Journal*, **122**, 1434 (1975).
4. E.g., F. John, Paper 23 presented at The Electrochemical Society Meeting, New York, N.Y., Sept. 29-Oct. 3, 1963.
5. K. J. Vetter, *Z. Elektrochem.*, **56**, 931 (1952).
6. J. N. Agar and F. P. Bowden, *Proc. R. Soc. London, Ser. A*, **169**, 206 (1939).
7. H. Gerischer, *Z. Elektrochem.*, **57**, 604 (1953).
8. K. J. Vetter, *Z. Phys. Chem.*, **194**, 284 (1950).

# ***In Situ* Studies of the Passivation and Anodic Oxidation of Cobalt by Emission Mössbauer Spectroscopy**

## **I. Theoretical Background, Experimental Methods, and Experimental Results for Borate Solution (pH 8.5)**

**G. W. Simmons,\* Elsie Kellerman, and Henry Leidheiser, Jr.\***

*Center for Surface and Coatings Research, Lehigh University, Bethlehem, Pennsylvania 18015*

### ABSTRACT

This paper is the first in a series of three that describe the application of emission Mössbauer spectroscopy to the *in situ* study of the cathodic and anodic behavior of cobalt. A brief review of the emission technique is given, along with a review of the chemical effects and Auger "after effects" that are associated with this experimental method. The surface sensitivity required to study thin anodic films was obtained by electrodepositing from 20 to 200Å thick Co<sup>57</sup> active layers on cobalt surfaces. Emission Mössbauer spectra from Fe<sup>57</sup> daughter ("probe") atoms were obtained during polarization (*vs.* SCE) of specimens in buffered borate, pH 8.5. The specimens were free of surface oxide during cathodic polarization at -1100 mV. The spectra of specimens polarized at low passivating potentials, -100 mV, indicated the presence of both +2 and +3 charges. The +3 oxidation state of the Fe<sup>57</sup> probe in the anodic film formed at this potential may arise from Auger after effects or chemical effects rather than from +3 states of the parent Co<sup>57</sup>. At higher passivating potentials +200 and +500 mV only the +3 oxidation state was observed. The existence of +2 oxidation state cannot be ruled out, however, because of the possibility for stabilization of defect charge states. Evidence for the +4 oxidation state in addition to +3 was found for specimens polarized at potentials in the transpassive range, +800 mV.

Since the first reported observation of passivity, a considerable amount of research on this subject has been published. Yet because of the complexity of the phenomenon and the limited experimental techniques available for *in situ* studies of surface films, there remains considerable uncertainty about many aspects of passivation. Passivity has been the subject of three international conferences co-sponsored by The Electrochemical Society and more recently it was the subject of a joint Japanese-American meeting in Hawaii in March 1975 (1). This latter conference resulted in three consensus summaries; and one of the principal objectives for future research was stated as follows: "It is hoped in the future to establish theoretical models to explain the cause of passivity and film-growth and dissolution kinetics in more detail and to develop critical experimental techniques which enable us to clarify the structure and composition of passive films." This paper describes an experimental technique which has led to the determination of the structure and composition of passive films on cobalt.

The electrochemical methods for studying passivity include galvanostatic and potentiostatic measurements which have been supplemented in some cases by potentiodynamic studies, a-c impedance investigations, and coulometry. These methods have been useful in characterizing the anodic behavior of metals, but the electrochemical techniques have not provided unambiguous information about the chemical composition and structure of anodically produced surface films. The nonelectrochemical approaches used thus far have also been of

limited value. Electron diffraction investigations require that the specimen be removed from its initial environment, and reasonable objections to the interpretation of results can be raised because of possible changes in composition of the specimen surface, such as dehydration, that may occur during the diffraction analysis. Although ellipsometry is a highly surface-sensitive technique and is applicable to *in situ* studies, the measured parameters for thin films, 10-50Å, lead only to information about the thickness. Mössbauer spectroscopy, on the other hand, offers the possibility of obtaining direct compositional and structural information about thin anodic films under *in situ* conditions. The major objective of our research has been to evaluate the emission Mössbauer spectroscopic technique for *in situ* determination of the chemical composition and structure of cobalt surfaces associated with the electrochemical behavior of this metal. Emission Mössbauer spectroscopic studies of the passivity of iron perhaps would have been more desirable than studies of cobalt because of the more extensive literature about the experimental and theoretical treatment of the passivation phenomena of iron. For reasons that are given later, the complications encountered in emission studies of iron surfaces are avoided in the cobalt system. Some aspects of this study, however, may also be helpful in understanding anodic behavior of the other ferrous metals iron and nickel. See Ref. (2) for studies of the passivation of iron by transmission Mössbauer spectroscopy.

The full report of our research has been divided into three parts. In the present paper, I, the experimental details are described, and theoretical considerations of

\* Electrochemical Society Active Member.

Key words: passivity, Mössbauer spectroscopy, cobalt, anodic oxidation, Co<sup>57</sup>, Fe<sup>57</sup>.

emission Mössbauer spectroscopy are presented along with details of experimental results in buffered borate solution, pH 8.5. Reference spectra of the cobalt compounds that may be constituents of anodic films on cobalt, are necessary for the interpretation of spectra obtained from cobalt during anodic polarization. There is only a limited amount of literature on emission Mössbauer spectroscopy of cobalt oxides, hydroxides, and oxyhydroxides, and therefore part II describes the spectra obtained from these compounds. Part III interprets the emission spectra obtained from anodic films formed on cobalt under different polarization conditions, and the results are discussed in terms of the electrochemical behavior of cobalt.

### Principles of Emission Mössbauer Spectroscopy Utilizing $\text{Co}^{57}$

The decay scheme of  $\text{Co}^{57}$  is shown in Fig. 1. The initial decay of  $\text{Co}^{57}$  by K-electron capture results in the formation of  $\text{Fe}^{57}$  with nuclear excited states which further decay to the ground state by  $\gamma$ -ray emission. The 14.4 keV  $\gamma$ -ray emitted from  $I = 3/2 \rightarrow I = 1/2$  transition is used in Mössbauer spectroscopy. The isomer shifts, quadrupole splittings, and magnetic hyperfine splittings of the  $I = 3/2$  and  $I = 1/2$  nuclear states of  $\text{Fe}^{57}$  are determined by the electron environment characteristic of the host matrix. The emission spectrum of the  $\text{Fe}^{57}$  nuclei is obtained by resonance absorption of the emitted radiation with an absorber that is designed to have only a single transition. The values obtained for the hyperfine parameters yield information about the chemical composition and structure of the emitter.

Many electrochemical reactions are slow in comparison to the average lifetime of the nuclear excited state of  $\text{Fe}^{57}$  ( $\sim 10^{-7}$  sec), and thus the application of emission Mössbauer spectroscopy is well suited to studies of cobalt. In other words, the time between the formation of the excited  $\text{Fe}^{57}$  nucleus and the emission of the  $\gamma$ -ray is so short that it is unlikely that the emission spectrum will contain any information about the chemical reactions of iron. The information derived from the spectra therefore depends principally on chemical changes in the parent  $\text{Co}^{57}$  atoms, although the  $\gamma$ -ray emission is actually from the  $\text{Fe}^{57}$  daughter atoms. Differences between the chemical potential of  $\text{Co}^{57}$  and substrates other than cobalt make the application of the  $\text{Co}^{57}$  doping technique impractical for studies of the oxidation behavior of other metals such as iron. For example, when the surface of iron is doped with  $\text{Co}^{57}$  and the specimen is oxidized at  $300^\circ\text{C}$  in air, the cobalt dopant remains in the elemental state as indicated by the Mössbauer emission spectrum. Presumably under these experimental conditions, the equilibrium

for the reaction,  $\text{Fe}_x\text{O}_y + \text{Co} \rightleftharpoons \text{Co}_m\text{O}_n + \text{Fe}$ , lies to the left.

The surface sensitivity required for studying passivation and anodic oxidation phenomena is obtained by controlling the amount of  $\text{Co}^{57}$  deposited on the specimen surface. The surface sensitivity of the emission method has been demonstrated in studies of surface lattice dynamics (3) and in investigations of the magnetic properties of thin films (4, 5) in which surface sensitivities approaching submonolayer dimensions were obtained. The composition and structure of thin anodic films can, therefore, be elucidated from the emission Mössbauer spectra of  $\text{Fe}^{57}$  probe atoms that have been incorporated into the anodic films as  $\text{Co}^{57}$ .

In the interpretation of emission Mössbauer spectra, two important chemical effects must be considered. One is the chemical influence of the host lattice environment on the  $\text{Fe}^{57}$  impurity atom, and the other, termed "after effects" is the variety of chemical consequences produced by the electron capture decay of  $\text{Co}^{57}$  to  $\text{Fe}^{57}$ . Details of chemical effects and after effects in emission spectroscopy can be found in published reviews on this subject (6, 7). Therefore, only a brief discussion of the origin of the chemical effects and after effects is presented.

The after effects are a result of the deexcitation of the vacant iron K level created after capture of a K electron by the  $\text{Co}^{57}$  nucleus. Deexcitation takes place by competitive x-ray fluorescence and Auger emission processes. When the deexcitation takes place only by x-ray emission the hole in the K level moves out to the valence levels, and in the absence of chemical interactions with the matrix, the daughter  $\text{Fe}^{57}$  has the same charge state as the parent  $\text{Co}^{57}$ . There is a probability for aliovalent species to be formed because of the likelihood for deexcitation by a radiationless process with the emission of electrons (Auger effect) and further ionization of the  $\text{Fe}^{57}$  atoms. The hole in the K shell may be filled by an electron from the L shell, and instead of  $\text{K}_\alpha$  x-ray emission, an electron may be ejected from the L shell. This process is termed a KLL Auger transition. The holes in the L levels are subsequently filled by electrons from the M levels with further emission of Auger electrons. This process is termed "Auger cascade" and can give rise to highly charged states on  $\text{Fe}^{57}$ . Pollak (8) has determined the probabilities for various charge states on  $\text{Fe}^{57}$  produced by the Auger cascade that follows electron capture decay of  $\text{Co}^{57}$ , and these results are given in Table I. After effects are not observed in metals because the time for charge equilibration of the high ionic states by the free conduction electrons is short compared to the lifetime of the  $\text{Fe}^{57}$  excited state ( $\sim 10^{-7}$  sec). In insulators, on the other hand, the highly ionized states (defect charge states) may have a sufficiently long lifetime to alter profoundly the immediate chemical environment of the  $\text{Fe}^{57}$  atoms, and these after effects are observed in the emission spectrum. The observable effects depend strongly on the nature of the host lattice, and it has

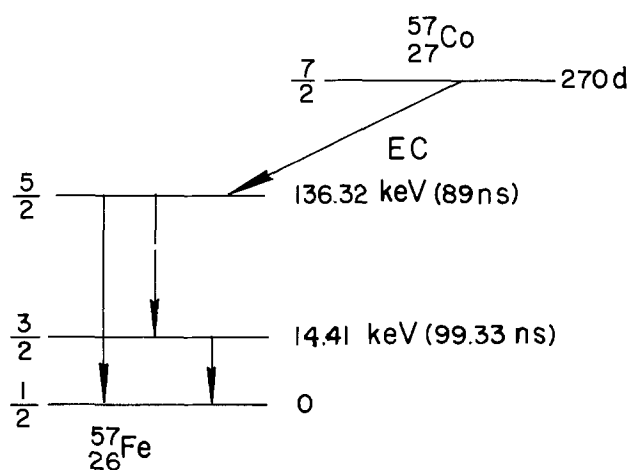


Fig. 1. Decay scheme of  $\text{Co}^{57}$  to  $\text{Fe}^{57}$ . Electron capture by the  $\text{Co}^{57}$  nucleus produces daughter  $\text{Fe}^{57}$  with nuclear excited states which decay to the ground state by  $\gamma$ -ray emission.

Table I. Probabilities for production of higher charge states of iron following electron capture decay of  $^{57}\text{Co}$

State of ionization	Probability (%) <sup>a</sup>	
	$\text{Co}^{2+}$	$\text{Co}^0$
0	—	1
1+	—	5
2+	5	21
3+	21.5	25
4+	25.3	29
5+	29.5	14
6+	14.2	4
7+	4.1	—
Total	99.6	99

<sup>a</sup> Two cases are considered: (a) cobalt initially in a 2+ charge state and (b) cobalt initially a neutral atom. Data taken from Ref. (8).

not been possible to predict *a priori* details of these effects. Furthermore, the mechanisms for producing the after effects in some cases are still poorly understood.

Radiolysis, size effects, and charge compensation have been proposed as mechanisms for the creation and/or stabilization of charge states in various types of compounds. An increasing tendency toward the stabilization of defect charge states with increasing degree of hydration in divalent cobalt salts has been attributed to the radiolysis of water molecules by the Auger electron ionization (9, 10). The oxidation of  $\text{Fe}^{+2}$  to  $\text{Fe}^{+3}$  in hydrated salts is suggested to be caused by the OH radicals produced during the radiolysis. The observation of  $\text{Fe}^{+3}$  lines in the transmission Mössbauer spectra of hydrated  $\text{Fe}^{+2}$  salts that have been subjected to ionizing radiation has been offered as supporting evidence for the radiolysis mechanism (11, 12).

Pollak (8) suggested that  $\text{Fe}^{+3}$  would be stabilized in divalent lattices whose metal ion is smaller than  $\text{Fe}^{+2}$ . Supporting evidence from data of  $\text{Co}^{57}$  doped metal fluorides with the rutile structure has been reported in which it was found that the smaller  $\text{Fe}^{+3}$  ion is preferentially stabilized in a lattice site smaller than that of  $\text{Fe}^{+3}$  in  $\text{FeF}_2$  (13). The differences in ionic sizes are not considered as completely sufficient for stabilization of the  $\text{Fe}^{+3}$  charge. It is assumed that charge compensating defects, such as trapped electrons or ionic vacancies, are also necessary. These defects are assumed to be produced by the Auger electron emission process and by the resulting highly charged states.

The  $\text{Fe}^{+3}/\text{Fe}^{+2}$  ratio in the emission spectra of CoO has been found to be a sensitive function of the method of specimen preparation (14-18). The presence of pre-existing charge compensating defects associated with the nonstoichiometry of the oxide is the generally accepted explanation for the stabilization of the  $\text{Fe}^{+3}$  charge state.

Cruset and Friedt (19) have proposed thermodynamic criteria for defect charge stabilization. The stabilization condition is given as

$$\Delta U \geq U_{ip} - E_{exc}$$

where  $U_{ip}$  is the ionization potential of  $\text{Fe}^{+2}$  in the solid state and  $E_{exc}$  is the energy of the electronically excited state produced by the electron capture decay.  $\Delta U$  is the electrostatic energy change associated with the substitution of  $\text{Fe}^{+2}$  by  $\text{Fe}^{+3}$  and is given by

$$\Delta U = [Z(\text{Fe}^{+3}) - Z(\text{Fe}^{+2})] \frac{e^2}{a} M$$

where  $M$  is the electrostatic potential at the Fe lattice site and  $a$  is the length of the unit cell. In general, therefore, the stability of the defect ionic species would be expected to increase with the macroscopic lattice energy of the host matrix. This correlation has been found in fact in a number of different chemical systems.

The charge state on the daughter iron atoms (ions) may be different from the parent cobalt for reasons that are completely independent of the Auger cascade. Specific charge states may be stabilized by chemical equilibration of the iron ions with the host matrix. Evidence for chemical or matrix effects is found for specimens in which 100% of the original  $\text{Co}^{+2}$  is observed in the emission spectrum as  $\text{Fe}^{+3}$ . Since there is a 5% probability for the empty K level to be filled by outer level electrons with emission of only x-rays (8), a few percent of  $\text{Fe}^{+2}$  should always be observed when only after effects mechanisms are operative. Complete valence change,  $\text{Co}^{+2}$  to  $\text{Fe}^{+3}$ , has been observed in emission spectra of  $\text{Co}^{57}$ -doped  $\text{Co}_3\text{O}_4$ ,  $\text{CoRh}_2\text{O}_4$ , and  $\text{CoFe}_2\text{O}_4$  (20). The fact that iron impurity in a trivalent charge state substitutes for divalent cobalt on the A sites in  $\text{CoRh}_2\text{O}_4$  has been suggested as further evidence that the change  $\text{Co}^{+2}$  to  $\text{Fe}^{+3}$  may be determined by a chemical preference rather than by after effects. These results do not rule out any possible after effects, but

do suggest that chemical stabilization must be considered when complete conversion of  $\text{Co}^{+2}$  to  $\text{Fe}^{+3}$  is observed in Mössbauer emission spectra. In addition to the charge compensating defects, ionic size, and crystalline energy considerations presented earlier, chemical stabilization mechanisms must also include crystal field effects and possible interactions such as red-ox reactions with surrounding cations.

From the narrowest point of view the after effects and chemical effects discussed above may be considered a limitation to the study of thin films by emission Mössbauer spectroscopic technique. As these phenomena become better understood, the complications with regard to interpretation of spectra become less serious, and in fact, the conditions for defect charge stabilization can be used for a more complete characterization of the chemical system under investigation. The studies of the passivation and anodic oxidation of cobalt were undertaken with a clear understanding of both the possible limitations and potential of the emission method for studying surfaces.

### Experimental

The cathodic and anodic behavior of cobalt polarized in deaerated borate solution, pH 8.5, was chosen for study. The polarization curve for cobalt was determined potentiostatically, and the current at each potential (*vs.* saturated calomel electrode, SCE) was recorded after the system reached steady state. Emission Mössbauer spectra were obtained at specific applied cathodic and anodic potentials in order to characterize the surface chemical species present during polarization. The growth rate and stability of the surface films that formed during polarization were determined from measurements of anodic current and of specimen radioactivity as a function of time.

Specimens used in the emission studies were prepared by casting  $10 \times 10 \times 0.5$  mm samples of 99.7% cobalt into the center surface of a 3 cm diam, 0.5 cm thick epoxy mount with the face of one side of the cobalt specimen parallel to the surface of the mount. Electrical contact was provided by means of a copper wire approximately 6 cm in length that was spot welded to the opposite face before the cobalt specimen was placed in the cast. The entire length of this wire was coated with epoxy to prevent its contact with the plating solution or with the solution used during the polarization studies. The specimen surfaces were first mechanically polished and then electrochemically etched in 50% phosphoric acid at a current density of 200 mA/cm<sup>2</sup>. The etching was done in the same cell in which depositions were made. Efforts were made to minimize the time the specimen was exposed to air during rinsing and solution changes. The deposition of  $\text{Co}^{57}$  onto the specimen surface was accomplished in a manner similar to that described by Dézsi and Molnár (21). To maximize the yield of  $\text{Co}^{57}$  deposition from the dilute solutions, the plating cell was designed to permit depositions from solution volumes of 5-10 ml. The solution used for the depositions was 2.5g/100 ml ammonium citrate with 2.5g/100 ml hydrazine hydrate adjusted to pH 10 with ammonium hydroxide. For current densities of 5-10 mA/cm<sup>2</sup> and plating times on the order of 1 hr, the plating efficiency has been reported to be on the order of 30% (21). The thickness of the  $\text{Co}^{57}$  active layer was controlled by adding specific amounts of natural cobalt ( $\text{CoCl}_2$ ) along with carrier-free  $\text{Co}^{57}$  (in HCl) to the plating solution. Relatively thin deposits (20-50Å) were required to obtain sufficient sensitivity to study changes in the cobalt surface at low passivating potentials. For anodic potentials in the range from the middle of the passive region to beyond the transpassive region, thicker deposits (50-200Å) were used. The actual thickness or uniformity of the active layer was not determined. An approximate range of deposit thickness was estimated from the plating efficiency and the cobalt content of the plating solution.

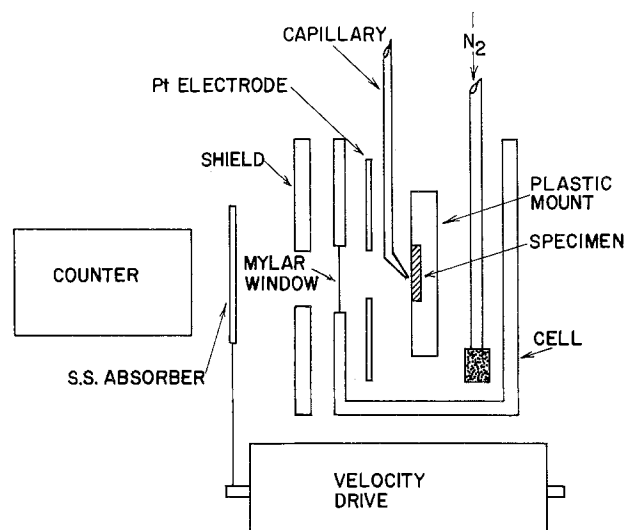


Fig. 2. Schematic of experimental arrangement used to obtain emission Mössbauer spectra of  $\text{Fe}^{57}$  cobalt during *in situ* polarization.

The experimental arrangement used for obtaining emission Mössbauer spectra of cobalt during polarization is shown schematically in Fig. 2. The cell was constructed from Plexiglas and was designed to minimize the amount of solution in the path of the emitted  $\gamma$ -rays. The distance between the specimen surface and a 0.04 mm thick Mylar window was approximately 3-4 mm. A SCE was separated from the polarization cell, and electrical continuity of the standard electrode with the cell was established via a capillary. Nitrogen gas was used to deaerate the solutions. A platinum counter-electrode was used; and an aluminum-brass-lead shield was mounted between the cell and the radiation detector in a manner that minimized the count rate from radiation originating from deposits of  $\text{Co}^{57}$  that formed on the platinum electrode during polarization of the specimen. Although  $\text{Co}^{57}$  ions that enter the solution during anodic polarization contribute to the background count rate, the  $\text{Fe}^{57}$  ions in solution produce no recoilless  $\gamma$ -rays and therefore do not contribute to the Mössbauer spectra. The specimen (emitter) was kept stationary, and the Mössbauer spectra were generated in the usual manner by measuring count rate as a function of velocity of a  $\text{Fe}^{57}$ -enriched stainless steel absorber. Positive velocities correspond to the absorber moving toward the specimen.

At all polarization potentials used in this study, with the exception of low passivating potentials, the corrosion rate was sufficiently slow that the surface active region was not lost during the time required to obtain the Mössbauer spectra. Additional experimental procedures were developed to make emission Mössbauer studies possible at low passivating potentials. A thin (20-50Å)  $\text{Co}^{57}$  active surface region was required to resolve the spectrum of the thin passive film formed at the low passivating potentials. Since the corrosion rate at these potentials was relatively high, the radioactive surface was stabilized by quenching the specimen and solution to liquid nitrogen temperature, and interrupting the applied potential after the passive film had formed. The specimen used in this case was prepared by epoxy coating a  $3.5 \times 9 \times 0.5$  mm sample of cobalt, except for a  $1 \text{ cm}^2$  area on which the  $\text{Co}^{57}$  layer (20-50Å) was deposited. One end of this specimen was attached to a brass block just outside of the electrolytic cell. This block was attached to a Dewar and could be readily maintained at liquid nitrogen temperature. The other end of the specimen was mounted in the cell in the manner already described (see Fig. 2). When the passive currents were reached and the count rate began to decrease, the Dewar was filled with liquid nitrogen. After the electrolyte had frozen, the applied potential

was removed. The spectrum was then obtained while the specimen was maintained near liquid nitrogen temperature. It was assumed that the quenching procedure and potential interruption did not produce significant changes in the passivated surface. A limitation of this procedure, not serious in our case, is the fact that  $\text{Co}^{57}$  ions that enter the solution and undergo hydrolysis during passivation may contribute to the emission spectrum since some fraction of the  $\gamma$ -rays emitted from the daughter  $\text{Fe}^{57}$  ions in the frozen solution are recoilless. The quenching procedure was only required for experiments conducted at low passivating potentials. Emission spectra were obtained at all other potentials at room temperature while the potential was maintained.

### Results and Discussion

Polarization of cobalt in the buffered borate solution produced a classical potential vs. current dependence as shown in Fig. 3. An active-to-passive transition occurs between -500 and -300 mV and cobalt remains passive at higher anodic potentials up to +500 mV. Above +500 mV, thick anodic film formation and oxygen evolution occurred commensurate with an increase in anodic current. Five specific polarization potentials were chosen for study which represented the different characteristic regions of the polarization curve shown in Fig. 3. These potentials were as follows: (a) cathodic potential of -1100 mV, (b) low passivating potential at -100 mV which is about 200 mV above the onset of passivity, (c) potential of +200 mV near the center of the passive region, (d) potential of +500 mV near the onset of transpassive behavior, and (e) potential of +800 mV which is in the transpassive region. Several experiments were conducted for each of these potentials. In some preparations of the surface active layer, it was found that a residual "oxide" layer could not be removed by cathodic reduction, and in other cases the surface sensitivity was not sufficient to detect the surface film that formed during anodic polarization. For the experiments in which cathodic polarization produced a "clean" surface and in which changes in the spectra were observed during anodic polarization, the results for each polarization potential were found to be reproducible. In the following sections typical results are presented for each of the polarization potentials.

*Cathodic polarization, -1100 mV.*—All of the specimens were polarized cathodically prior to the application of the anodic potentials. The emission Mössbauer

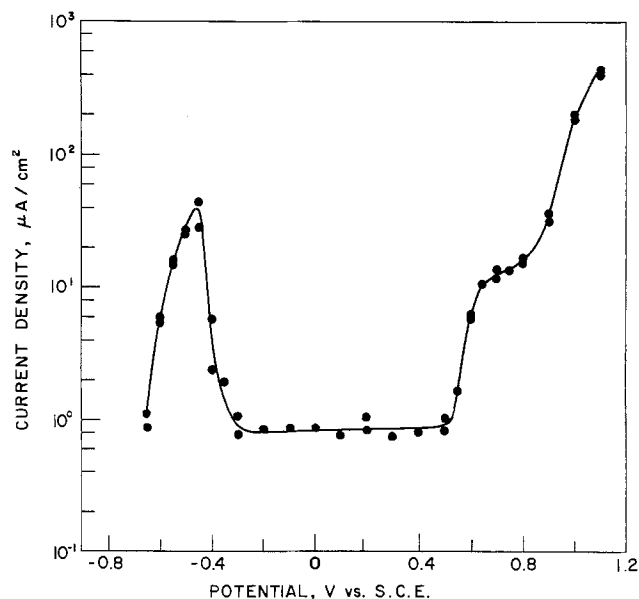


Fig. 3. Polarization curve of cobalt in buffered borate solution, pH 8.5. Potential is with reference to SCE.

spectra obtained during cathodic treatment were used to monitor the reduction of oxide or corrosion films that had formed subsequent to deposition of the  $\text{Co}^{57}$  layer or formed during previous anodic polarization of the specimen. Typical spectra obtained before and during cathodic polarization at  $-1100$  mV, current density  $20 \text{ mA/cm}^2$ , are shown in Fig. 4 and 5 for two specimens with different active layer thickness. The results obtained from these two specimens are discussed separately.

The relatively intense lines at the center of the spectrum shown in Fig. 4a for a 100-200Å specimen is indicative of a corrosion film that was present after preparation of the active  $\text{Co}^{57}$  layer. Cathodic polarization of the specimen gave rise to the spectrum presented in Fig. 4b which shows only the six lines expected from the magnetic hyperfine splitting of  $\text{Fe}^{57}$  in metallic cobalt. This result suggests that the corrosion film, which formed subsequent to the deposition of the active layer, was readily reduced by the cathodic treatment. Values of the hyperfine interactions measured for the 100-200Å film during cathodic polarization are summarized in Table II. Also summarized in Table II for comparison are results obtained for a bulk specimen which was annealed below the hexagonal to cubic transition temperature ( $400^\circ\text{--}500^\circ\text{C}$ ) and for a bulk specimen annealed above this temperature. The major differences in the hyperfine interactions of  $\text{Fe}^{57}$  nuclei in the bulk specimens which were annealed at  $400^\circ$  and  $800^\circ\text{C}$  is in the internal magnetic field. The difference of approximately 10 koe is attributed to the possibility that the  $400^\circ\text{C}$  specimen is hexagonal and that the  $800^\circ\text{C}$  specimen is mostly cubic. This result is consistent with studies in which the cubic phase was reported to be stable in fine grain specimens at room temperature (22, 23) after quenching from temperatures above  $500^\circ\text{C}$ . The hyperfine parameters in Table II indicate that the 100-200Å film is physically different from either of the bulk specimens. Impurities and de-

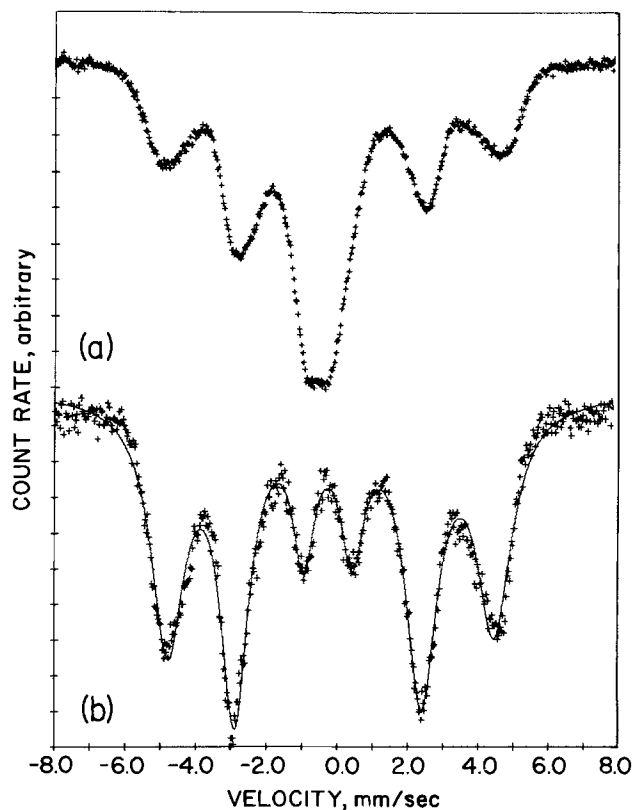


Fig. 4. (a) Emission spectrum of  $\text{Fe}^{57}$  in cobalt taken after deposition of 100-200Å  $\text{Co}^{57}$  layer. (b) Emission spectrum of same specimen taken during cathodic polarization at  $-1100$  mV. Spectra taken at room temperature.

Table II. Comparison of hyperfine parameters of  $\text{Fe}^{57}$  measured for thin film and bulk cobalt specimen doped with  $\text{Co}^{57}$

Specimen	IS (mm/sec) <sup>a</sup>	$H_{\text{eff}}$ (koe)	$\Delta_{56}\text{--}\Delta_{12}$ (mm/sec) <sup>b</sup>
Film 100-200Å	-0.20	296	0.19
Bulk (hcp) annealed $400^\circ\text{C}$	-0.15	331	0.21
Bulk (cubic) annealed $800^\circ\text{C}$	-0.13	322	0.20

<sup>a</sup> 310 SS reference.

<sup>b</sup>  $\Delta_{56}$  is difference between lines 5 and 6.  $\Delta_{12}$  is difference between lines 1 and 2.  $\Delta_{56}\text{--}\Delta_{12}$  is proportional to magnitude of quadrupole interaction.

fects in the film would contribute to lower values of the internal magnetic field and to the difference in isomer shift as compared with the bulk (24, 25). The measured parameters for the film may be a manifestation of the thickness of the specimen, of the fact that hydrogen may be present in the film during cathodic treatment, and of defects and impurities in the film. Further studies are required to ascertain the factors that determined the hyperfine interactions that were measured for the 100-200Å films during cathodic polarization.

As indicated in Fig. 4b, the relative intensities of the magnetic hyperfine lines of the thin cobalt surface layers were found to vary from the 3:2:1:1:2:3 expected from a bulk polycrystalline specimen. The relative intensities of the six line magnetic hyperfine spectra of  $\text{Fe}^{57}$  is a function of the angle,  $\theta$ , between the direction of  $\gamma$ -ray propagation and the principal axis of the magnetic field and are given by 3:x:1:1:x:3 where  $x = 4 \sin^2\theta / (1 + \cos^2\theta)$  (26). Ordinarily the angular dependency becomes important in studies of single crystals in which  $\theta$  is well defined. For thin polycrystalline ferromagnetic films, however, the magnetization vector and hence the axis of the internal magnetic field is parallel to the film surface. The angle  $\theta$  approaches  $90^\circ$  as the film thickness decreases, and the ratios of the peak intensities tend toward values of 3:4:1:1:4:3.

The spectrum shown in Fig. 5a was taken during anodic polarization of a 20-50Å cobalt film; and the relatively intense line(s) at the center of the spectrum originates from the anodic film. Subsequent cathodic polarization of this specimen effectively reduced the anodic film as evidenced by the reduction in the intensity of the center line(s) as shown in Fig. 5b. The spectra of the (20-50Å) cobalt surface films were considerably different from the spectra of the (100-200Å) cobalt surface films; compare spectrum of (20-50Å) film in Fig. 4b with spectrum of (100-200Å) film shown in Fig. 5b. The spectrum of the (20-50Å) specimen, Fig. 5b, indicates an apparent relaxation of the effective internal magnetic field of the  $\text{Fe}^{57}$  nuclei (26-28). The small peak at the center of the spectrum in Fig. 5b is probably the result of relaxation of the magnetic field, but it cannot be ruled out that this peak may originate from remnants of the corrosion film that was not reduced by the cathodic polarization. Relaxation of the hyperfine field in the thin surface film, in this case, is similar to that reported in Mössbauer spectroscopic studies of the magnetic properties of thin films (4, 5, 29). The relaxation spectra in the referenced studies may have been, in part, owing to superparamagnetism in ferromagnetic particles formed by growth of isolated "islands" of the metal on nonmagnetic substrates. Superparamagnetism is less likely to account for the apparent relaxation in the present studies, because magnetic isolation of the deposit probably did not occur on the magnetic cobalt substrate, even for a case of nonuniform deposition. The broadening of the lines shown in Fig. 5b may, therefore, be caused by a reduction of the magnetic moment on  $\text{Fe}^{57}$  nuclei in the surface of the film and/or by magnetic dilution of the  $\text{Fe}^{57}$  daughter atoms. Shinjo *et al.* (30) concluded in their

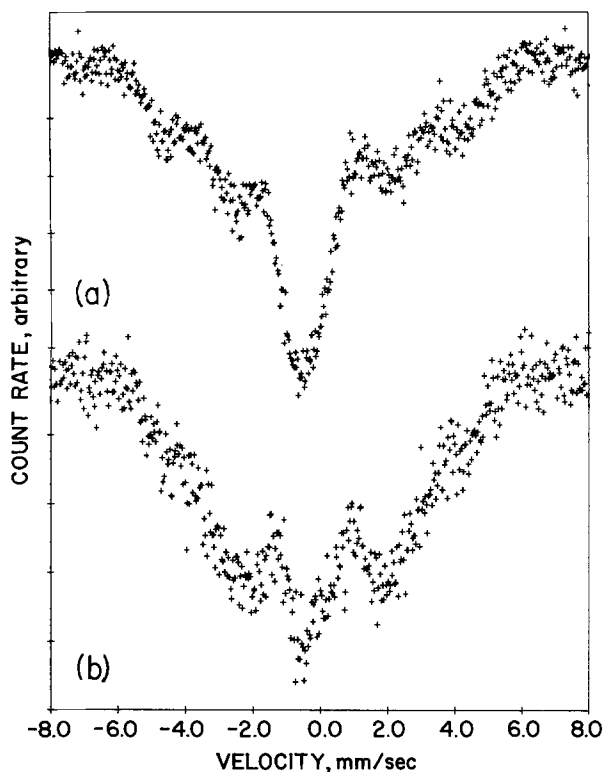


Fig. 5. (a) Emission spectrum of  $\text{Fe}^{57}$  in cobalt with anodic film present on surface. (b) Emission spectrum of same specimen taken during cathodic polarization at  $-1100$  mV. ( $\text{Co}^{57}$  active layer approximately  $20\text{-}50\text{\AA}$ .) Spectra taken at room temperature.

emission Mössbauer studies of monolayer  $\text{Co}^{57}$  deposits on cobalt substrates that the magnetic moment at the surface was not significantly different from the bulk value. They proposed that the line broadened spectra can be interpreted on the basis of a distribution of magnetic fields owing to the presence of vacancies and impurities such as stable  $\text{Fe}^{57}$ . Since specimens with thin surface active layers were deposited from very dilute solutions, the relative amounts of impurities that co-deposit with the cobalt is much higher than that encountered in the deposition of thicker films from more concentrated solutions. The concentration of defects and missing nearest neighbor atoms is also expected to be high in a thin film with high surface to volume ratio. It was not possible in the present study to determine whether relaxation effects or magnetic dilution effects are the predominate cause of the line broadening in the thin ( $30\text{-}50\text{\AA}$ ) specimens.

**Anodic polarization,  $-100$  mV.**—The potential of  $-100$  mV is just above the onset of passivity. The relatively high corrosion rate of cobalt at this potential did not permit *in situ* emission Mössbauer spectra to be obtained at room temperature. The specimen and solution were quenched to low temperature after the formation of the passive film as described in the experimental section. Since it was anticipated that the anodic film would be relatively thin at this potential, a specimen with  $\text{Co}^{57}$  surface layer on the order of  $30\text{-}50\text{\AA}$  thick was used. The specimen was cathodically reduced before application of the anodic potential. Figure 6 shows the changes in current and radioactivity of the specimen as a function of time after the  $-100$  mV potential was applied; and the times at which the system was quenched and the potential interrupted are also indicated. Anodic film formation and anodic dissolution account for the integrated current, which corresponds to the conversion of a surface region that is 2-3 times the estimated thickness of the  $\text{Co}^{57}$  active layer. Only approximately 30% of the radioactivity of the specimen, however, was lost during the anodic treatment.

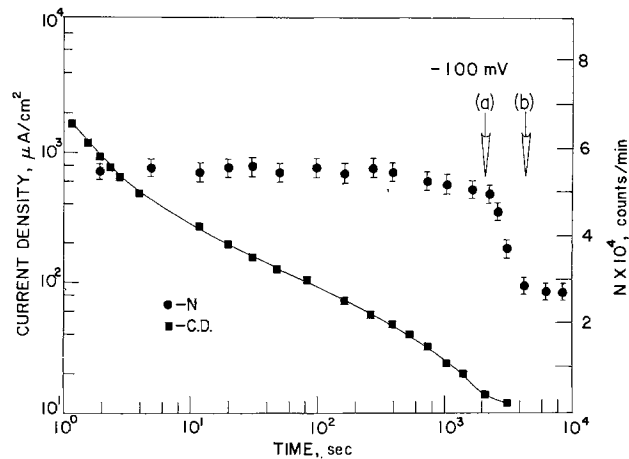


Fig. 6. Anodic current and count rate vs. time for specimen polarized at  $-100$  mV, (a) quenching initiated and (b) applied potential interrupted.

These facts suggest that the anodic film formation and dissolution did not take place uniformly over the specimen surface.

The emission Mössbauer spectrum of the specimen after polarization at  $-100$  mV is shown in Fig. 7. Resolution of the spectrum of the anodic film was enhanced by removing the background contribution of the unreacted metal. This was accomplished by subtracting an appropriately scaled spectrum of the same specimen taken during the cathodic polarization. The results of this subtraction are shown in Fig. 7b. The simplest combination of Lorentzian curves that gave a satisfactory computer fit to the spectrum is also shown in Fig. 7b. The spectrum apparently consists of two sets of quadrupole doublets, and the values for the isomer shift and quadrupole splitting of these resonant lines are

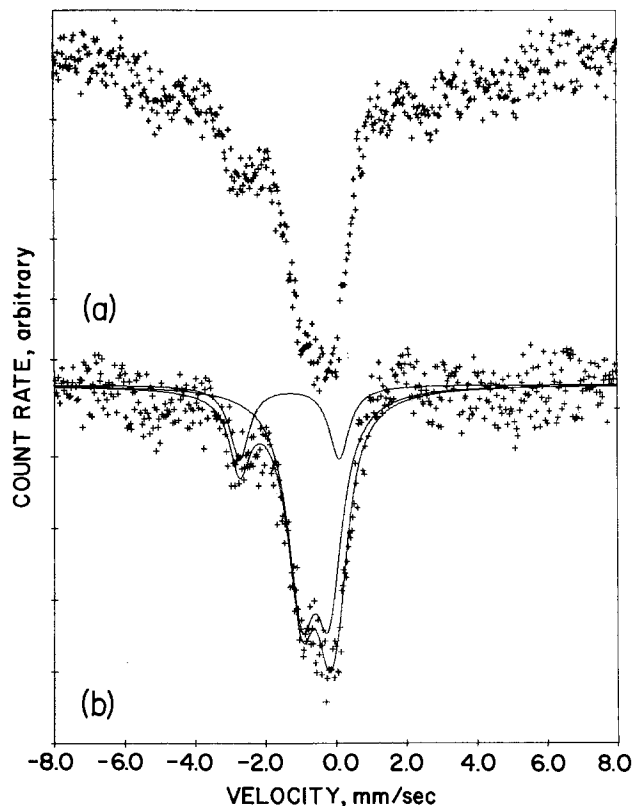


Fig. 7. Emission spectrum of  $\text{Fe}^{57}$  in cobalt anodically polarized at  $-100$  mV, (a) initial spectrum and (b) spectrum after subtraction of contribution from unreacted metal. Spectrum taken at liquid nitrogen temperature.

Table III. Hyperfine parameters for Fe<sup>57</sup> in anodically polarized cobalt surfaces doped with Co<sup>57</sup>

Anodic potential, mV (SCE)	Isomer shift <sup>a</sup> (mm/sec)	Quadrupole (mm/sec)
-100	-1.31 <sup>b</sup>	2.83 <sup>b</sup>
	-0.59 <sup>b</sup>	0.78 <sup>b</sup>
+200	-0.55	0.94
+500	-0.54	0.81
+800	-0.55 <sup>c</sup>	0.85 <sup>c</sup>
	0.14	

<sup>a</sup> Stainless steel reference.<sup>b</sup> Measured at liquid nitrogen temperature.<sup>c</sup> Values constrained during computer fitting.

given in Table III. The value of  $-1.31$  mm/sec for the isomer shift and the relatively large quadrupole splitting of  $2.83$  mm/sec for one set of lines correspond to Fe<sup>57</sup> (+2) in the anodic film. An isomer shift of  $-0.59$  mm/sec and a relatively small quadrupole splitting of  $0.78$  mm/sec for the other set of lines correspond to Fe<sup>57</sup> (+3). Because of the possibility of Auger after effects and chemical effects which were discussed earlier, the Fe<sup>57</sup> (+3) daughter atoms may not have originally existed as Co<sup>57</sup> (+3) parent atoms. It is possible therefore that the passive film formed at low passive potentials consists essentially of a divalent oxide or hydroxide.

**Anodic polarization, +200 and +500 mV.**—The experimental results obtained at +200 and +500 mV were found to be similar, and these results are, therefore, discussed together. Current and radioactivity measured as a function of time for specimens anodized at +200 and +500 mV are shown in Fig. 8 and 9, respectively. The thickness of the Co<sup>57</sup> layer on these specimens was on the order of 100–200 Å. The logarithmic time dependence of the initial changes in anodic current exhibited by cobalt at these potentials has been observed in other systems (31, 32). This current vs. time behavior has been attributed to the growth of the anodic film. Deviations from the logarithmic dependence at the longer times is caused by anodic dissolution. The rate of anodic dissolution was sufficiently slow at +200 and +500 mV, as indicated by the small changes in radioactivity, that emission Mössbauer spectra could be readily obtained *in situ* at room temperature without recourse to freezing. The corrosion rate after the surface was passivated was higher at the +200 mV potential than at the +500 mV potential as evidenced by the differences in the deviation of the current from logarithmic behavior and by the differences in the rate of decrease of radioactivity.

The emission Mössbauer spectra taken at +200 and +500 mV are shown in Fig. 10 and 11, respectively. The spectra taken at these two potentials are shown before

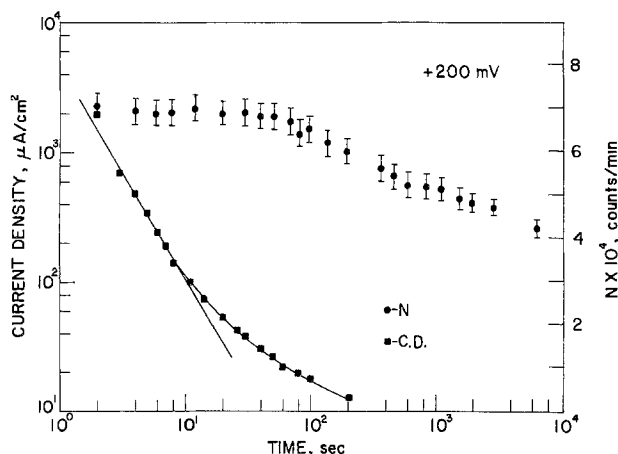


Fig. 8. Anodic current and count rate vs. time for specimen polarized at +200 mV.

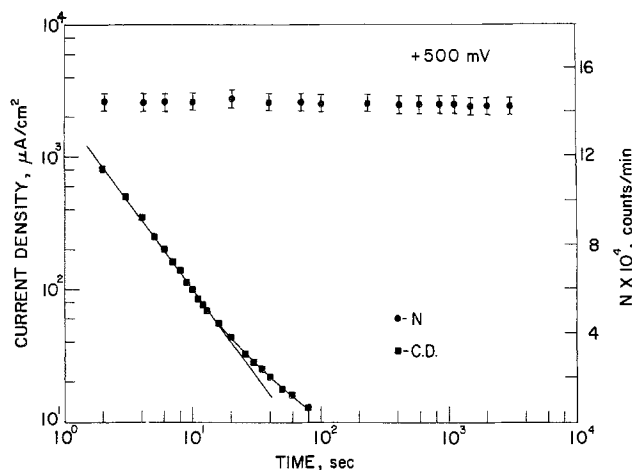
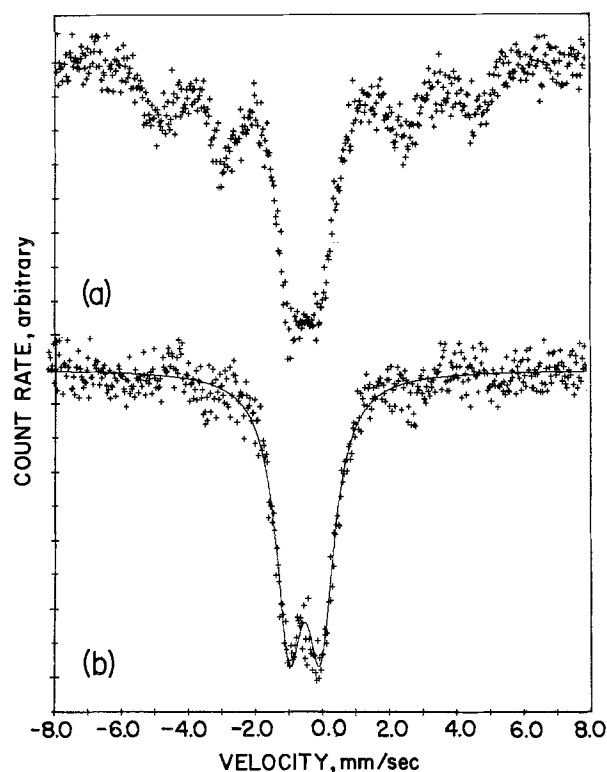


Fig. 9. Anodic current and count rate vs. time for specimen polarized at +500 mV.

Fig. 10. Emission spectrum of Fe<sup>57</sup> in cobalt anodically polarized at +200 mV, (a) initial spectrum and (b) spectrum after subtraction of contribution from unreacted metal. Spectrum taken at room temperature.

and after subtraction of the unreacted metal background. Two Lorentzian lines of equal intensity gave a satisfactory computer fit to the spectra obtained from both specimens. The isomer shift and quadrupole splitting associated with these lines for each specimen are listed in Table III and were essentially identical for each case. The values of  $-0.54$  and  $-0.55$  mm/sec for the isomer shifts and the small quadrupole splittings of  $0.81$  and  $0.94$  mm/sec are indicative of Fe<sup>57</sup> (+3). The composition of the passive films at +200 and +500 mV is apparently different from that of the film formed at  $-100$  mV, since no evidence of Fe<sup>57</sup> (+2) was found at these higher anodic potentials. The possible presence of Co<sup>+2</sup> in the anodic film formed at the higher potentials cannot be ruled out, however, since the daughter Fe<sup>57</sup> (+2) ions could have been converted to Fe<sup>57</sup> (+3) by Auger after effects or chemical effects.



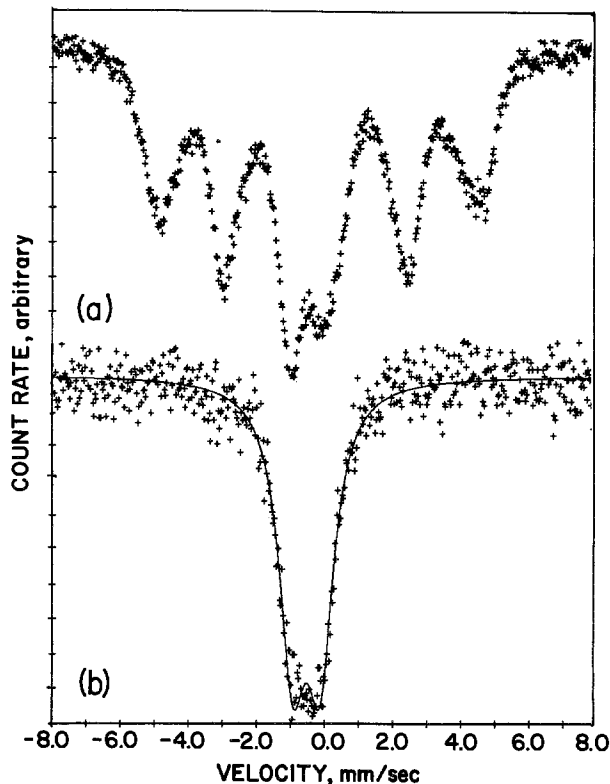


Fig. 11. Emission spectrum of  $\text{Fe}^{57}$  in cobalt anodically polarized at +500 mV, (a) initial spectrum and (b) spectrum after subtraction of contribution from unreacted metal. Spectrum taken at room temperature.

**Anodic polarization, +800 mV.**—The region of the polarization curve at which thick anodic films are formed and oxygen evolution occurs is referred to as transpassive. The potential of +800 mV is approximately 300 mV above the onset of this transpassive region. An emission Mössbauer spectrum obtained at this potential is shown in Fig. 12 before and after the subtraction of the unreacted metal contribution. The spectrum of the anodic film formed at +800 mV is similar to the spectra for the surface anodically treated at +200 and +500 mV. The asymmetry of the spectrum suggests, however, that anodic polarization at transpassive potentials produces a characteristic change in the anodic film. Apparently the major component of the film, in this case, is the same as that formed at the passive potentials, but part of the surface has been converted to a higher oxidation state. A satisfactory computer fit to the spectrum was obtained with a set of quadrupole split lines, similar to those found for the passive film, and an additional line with an isomer shift of 0.14 mm/sec. The hyperfine parameters based on the computer analysis are given in Table III. The isomer shift of 0.14 mm/sec for the resonance line that is characteristic of anodic polarization at +800 mV indicates the presence of  $\text{Fe}^{57}$  (+4) in the surface of the anodic film. In the computer fitting, the hyperfine parameters for the major component of the spectrum of the transpassive film were assumed to be identical with parameters obtained from the passive films formed at +200 and +500 mV.

### Summary and Conclusions

Emission Mössbauer spectroscopy technique was successfully demonstrated to be an effective method for *in situ* studies of changes in cobalt surfaces as a function of polarization. Despite the possible ambiguities introduced by effects associated with the emission technique, characteristic spectra were found for cobalt surfaces at specific applied potentials. These results are summarized as follows: (a) The cobalt was shown to be essentially free of a corrosion film during cathodic

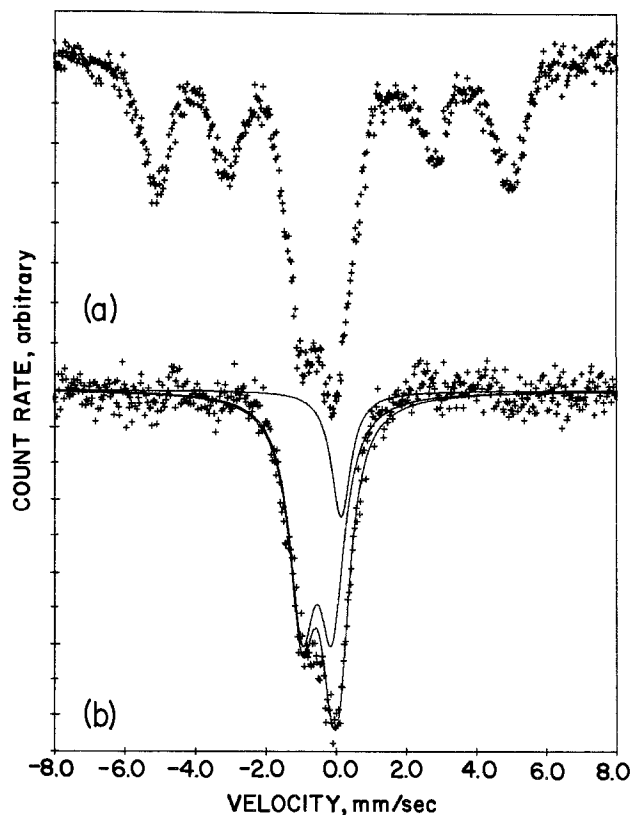


Fig. 12. Emission spectrum of  $\text{Fe}^{57}$  in cobalt anodically polarized at +800 mV, (a) initial spectrum and (b) spectrum after subtraction of contribution from unreacted metal. Spectrum taken at room temperature.

polarization (−1100 mV). (b) Resonance lines from both +2 and +3 oxidation states were found in the emission Mössbauer spectra of anodic films formed at low passivating potentials (−100 mV). (c) At potentials in the passive region of the polarization curve (+200 and +500 mV) the spectra indicated that the passive film contained primarily +3 oxidation state. (d) The anodic film formed at transpassive potentials (+800 mV) was found to consist of +3 and +4 oxidation states, and the +3 component of this film was shown to be likely the same as that formed at the passive potentials.

Auger after effects and chemical effects may give rise to a charge state on the  $\text{Fe}^{57}$  daughter (probe) that is different than the original charge on the parent  $\text{Co}^{57}$ . Further interpretation of the spectra obtained in this study, however, is possible with reference emission spectra for the oxides, hydroxides, and oxyhydroxides of cobalt. These reference spectra have been obtained and are described in paper II. Based on the interpretation of the spectra obtained during the anodic polarization of cobalt, the composition and structure of the anodic films are presented in paper III in conjunction with a description of the electrochemical behavior of cobalt.

### Acknowledgment

We acknowledge with appreciation support of this research by the Army Research Office-Durham. Our special thanks go to Dr. Henry Davis of this agency.

Manuscript submitted Feb. 9, 1976; revised manuscript received April 26, 1976.

Any discussion of this paper will appear in a Discussion Section to be published in the June 1977 JOURNAL. All discussions for the June 1977 Discussion Section should be submitted by Feb. 1, 1977.

Publication costs of this article were assisted by Lehigh University.

## REFERENCES

1. R. W. Staehle, Editor, "Passivity and Its Breakdown on Iron and Iron Base Alloys," Japan-U.S.A. Seminar, Honolulu, Hawaii (1975), National Association of Corrosion Engineers, In press.
2. W. E. O'Grady and J. O'M. Bockris, *Surface Sci.*, **38**, 249 (1973).
3. J. W. Burton and R. P. Godwin, *Phys. Rev.*, **158**, 218 (1967).
4. M. N. Varma and R. W. Hoffman, *J. Appl. Phys.*, **42**, 1727 (1971).
5. A. C. Zuppero and R. W. Hoffman, *J. Vac. Sci. Technol.*, **7**, 118 (1969).
6. N. N. Greenwood and T. C. Gibb, "Mössbauer Spectroscopy," pp. 373-379, Chapman and Hall Ltd., London (1971).
7. G. K. Wertheim, *Acc. Chem. Res.*, **4**, 373 (1971).
8. H. Pollak, *Phys. Status Solidi*, **2**, 720 (1962).
9. J. M. Friedt and J. P. Adloff, *C. R. Acad. Sci., Ser. C*, **264**, 1356 (1967); *Inorg. Nucl. Chem. Letters*, **5**, 163 (1969).
10. J. M. Friedt and J. P. Adloff, *C. R. Acad. Sci., Ser. C*, **268**, 1342 (1969).
11. P. Gütlich, S. Odar, B. W. Fitzsimmons, and N. E. Erickson, *Radiochim. Acta*, **10**, 147 (1968).
12. G. K. Wertheim and D. N. E. Buchanan, *Chem. Phys. Letters*, **3**, 87 (1969).
13. G. K. Wertheim, H. J. Guggenheim, and D. N. E. Buchanan, *J. Chem. Phys.*, **51**, 1931 (1969).
14. G. K. Wertheim, *Phys. Rev.*, **124**, 764 (1961).
15. A. J. Bearden, P. L. Mattern, and T. R. Hart, *Rev. Mod. Phys.*, **36**, 470 (1964).
16. C. J. Coston, R. Ingalls, and H. G. Drickamer, *Phys. Rev.*, **145**, 409 (1966).
17. V. G. Bhide and G. K. Shenoy, *ibid.*, **147**, 306 (1966).
18. J. G. Mullen and H. N. Ok, *Phys. Rev. Letters*, **17**, 287 (1966).
19. A. Cruset and J. M. Friedt, *Phys. Status Solidi*, **45**, 189 (1971).
20. C. D. Spencer and D. Schroerer, *Phys. Rev. (B)*, **9**, 3658 (1974).
21. I. Dézsi and B. Molnár, *Nucl. Instr. Methods*, **54**, 105 (1967).
22. O. S. Edwards and H. Lipson, *Proc. R. Soc. London, Ser. A*, **180**, 268 (1942).
23. A. R. Troiano and J. L. Tokich, *Met. Technol.*, **15**, 728 (1948).
24. J. Danon, in "Chemical Applications of Mössbauer Spectroscopy," V. I. Goldanskii and R. H. Herber, Editors, pp. 197-202, Academic Press, New York (1968).
25. N. N. Greenwood and T. C. Gibb, "Mössbauer Spectroscopy," pp. 303-324, Chapman and Hall, Ltd., London (1971).
26. H. Fraunfelder, D. E. Nagle, R. D. Taylor, D. R. F. Cochran, and W. M. Visscher, *Phys. Rev.*, **126**, 1065 (1962).
27. H. H. Wickman and G. K. Wertheim, in "Chemical Applications of Mössbauer Spectroscopy," V. I. Goldanskii and R. H. Herber, Editors, pp. 548-617, Academic Press, New York (1969).
28. F. Van Der Woude and A. J. Dekker, *Phys. Status Solidi*, **9**, 775 (1965).
29. W. Zinn, *Czech. J. Phys.* **B21**, 391 (1971).
30. T. Shinjo, T. Matsuzawa, T. Takada, S. Nasu, and Y. Murakami, *J. Phys. Soc. Japan*, **35**, 1032 (1973).
31. M. Nagayama and M. Cohen, *This Journal*, **109**, 781 (1962).
32. R. P. Frankenthal, *Electrochim. Acta*, **16**, 1845 (1971).

## Structure of Electroplated Hard Gold Observed by Transmission Electron Microscopy

Y. Okinaka\* and S. Nakahara\*\*

Bell Laboratories, Murray Hill, New Jersey 07974

### ABSTRACT

Transmission electron micrographs of gold films plated in baths containing cobalt or nickel as the hardening agent showed the presence of uniformly distributed nonmetallic objects with diameters ranging from 20 to 70Å. These objects are believed to represent single molecules, and their agglomerates, of the so-called "polymer" which has been isolated by several investigators in the form of a transparent film upon dissolution of gold deposits in aqua regia. Micrographs of gold films plated in room temperature baths containing no hardening agents revealed the presence of much larger nonmetallic objects (up to 150Å), which appeared to be gas bubbles, in addition to the features attributable to polymer molecules. Based on a comparison of the polymer content, estimated from the analysis of electron micrographs, with the total carbon content, it is suggested that the polymer is not the only source of carbon contamination in electroplated hard gold films. Possible effects of the co-deposition of polymer on grain size are also briefly discussed.

Hard gold deposits formed in acid cyanide baths containing a cobalt or nickel salt as the hardening-brightening agent are known to contain up to 1% carbon in addition to nitrogen, hydrogen, oxygen, potassium, and cobalt, or nickel (1-7). Munier (1) was the first to isolate transparent films, which were presumed to be an organic polymer, upon dissolution of gold deposits in aqua regia. On the basis of this result, it was suggested that the "polymer" is present in the deposits in the form of discrete layers.

\* Electrochemical Society Life Member.

\*\* Electrochemical Society Active Member.

Key words: polymer, carbon, phase contrast, through-focus imaging.

Holt and Stanyer (2) made a study using  $KC^{14}N$  of the dependence of  $\beta$ -emission count rate on deposit thickness, and concluded that the carbon is distributed uniformly across the thickness rather than in the form of layers. They speculated that the carbon-containing species are situated mainly at grain boundaries. On the other hand, Antler (6) made a scanning electron microscope study of fracture surfaces of hard gold deposits, and suggested that the polymer is occluded in discrete pockets ( $<1000\text{Å}$ ) in the deposits. As far as the chemical identity of the carbon-containing material is concerned, no agreement exists among investigators as to whether the carbon is de-

posited as a cyanide complex of codepositing metals (3, 7, 8), a cyanide of gold and/or potassium (7, 9), or an organic polymer (1, 6, 8).

The present study was prompted by the consideration that if the carbon-containing species is indeed present in the deposit in the form of an organic polymer, it may be directly observable by transmission electron microscopy (TEM) with the through-focus imaging technique, which is known to be a powerful method for observing nonmetallic inclusions in metal matrices (10-12).

### Experimental

**Plating.**—Cobalt-hardened gold films were plated from citrate-based proprietary as well as nonproprietary baths. The proprietary bath used was purchased from Sel-Rex Corporation (Autronex CI), whereas the nonproprietary bath contained 8.2g Au/liter as  $\text{KAu}(\text{CN})_2$ , 110 g/liter citric acid, 50 g/liter KOH, and 0.1g Co/liter as  $\text{CoSO}_4$ . Both baths were operated fresh at 10 mA/cm<sup>2</sup> at room temperature. The pH was adjusted to 4.0. Since the two baths yielded essentially the same electron microscopic information and more detailed analysis was made for the deposit from the proprietary bath, only the results obtained with the latter are presented. Nickel-hardened gold films were plated from Sel-Rex Corporation's Autronex N bath, which was also citrate-based and operated under the same experimental conditions as for the cobalt-containing baths. The cobalt- and nickel-containing baths will be called Co-bath and Ni-bath, respectively. Hard gold films from baths containing no metallic additives were prepared by J. J. Chick using the following two different baths: a citrate bath with pH 4.8 containing 40 g/liter  $\text{KAu}(\text{CN})_2$  and 100 g/liter dibasic ammonium citrate, and a phosphate bath with pH 4.5 containing 40 g/liter  $\text{KAu}(\text{CN})_2$  and 100 g/liter  $\text{KH}_2\text{PO}_4$ . These baths (hereafter called "additive-free baths") were operated at 15.5 mA/cm<sup>2</sup> and 25°C. All films were deposited on copper substrates prepared by cold-rolling OFHC material and annealing at 800°C for 2 hr in a hydrogen furnace. The substrate prepared in this manner consisted of very large grains and was suitable for observing epitaxy and grain refining phenomena involved in the process of deposit growth. The annealed copper substrate was etched in 1:2  $\text{HNO}_3$  before plating.

**Specimen preparation.**—Specimens were prepared from deposits ranging in thickness from 0.025 to 50  $\mu\text{m}$ . Thin deposits were stripped off the copper substrate in a mixture of  $\text{CrO}_3$  and  $\text{H}_2\text{SO}_4$  and collected on a microscope grid for direct observation. Thick deposits were electropolished using the conventional window or jet-polishing technique after stripping off the substrate. A cyanide-containing polishing solution described by Silcox and Hirsch (13) was used initially, but results were not satisfactory. Subsequently better results were obtained with a mixture of 25 ml ethyl alcohol, 25 ml glycerin, and 50 ml concentrated HCl (14).

**Transmission electron microscopy.**—TEM micrographs were taken with a JEM-200 electron microscope operated at 200 kV. The conventional imaging technique based on diffraction contrast is known to be unsuitable for observing organic or gaseous inclusions especially when they do not exert elastic strain and/or when their size is small (11). On the other hand, the technique known as through-focus imaging allows observation of such inclusions in metal matrices under defocused conditions. The images obtained by this technique are due to phase contrast arising from a difference in mean inner potential between the included material and metal matrix. Such inclusions are therefore generally called "phase objects" (10).

### Results and Discussion

**Deposits from Co- and Ni-baths.**—TEM examinations of gold deposits from the Co-bath were made with several samples of different thicknesses. The two micrographs in Fig. 1 were obtained with a nominally 500Å thick film in over-focused (a) and under-focused (b) conditions. The plating time used was only 10 sec, and no polishing was required. It is seen that numerous dark, circular features surrounded by white rings in Fig. 1(a) reverse their contrast when focusing conditions are reversed. This is characteristic of phase objects. Large, irregularly shaped white features with fringes (Fresnel fringes) in both micrographs are holes in the specimen. Large, black regions represent thick areas of the specimen through which electrons did not penetrate. Figure 2 is a stereo pair corresponding to a selected area of Fig. 1(a). It is seen that the phase objects are distributed uniformly throughout the thickness of the specimens. Several specimens prepared from thicker films (up to 25  $\mu\text{m}$ ) by electropolishing both sides showed images with essentially identical size and spatial distributions of phase objects. Deposits formed in the Ni-bath also yielded micrographs which are qualitatively similar to those in Fig. 1 and 2.

Figure 3 shows the size distribution of the phase objects in the above two deposits. A total of 100 measurements were made from each deposit. The data shown for the deposit from the Co-bath were obtained from Fig. 1a (thin deposit), while a specimen prepared from a 25  $\mu\text{m}$  thick deposit gave an essentially identical distribution curve. The deposit

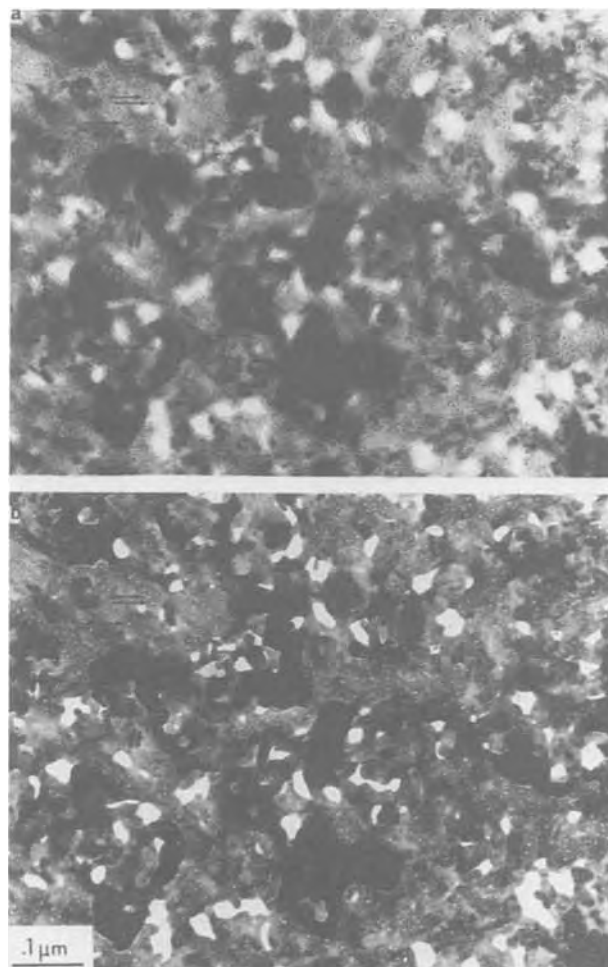
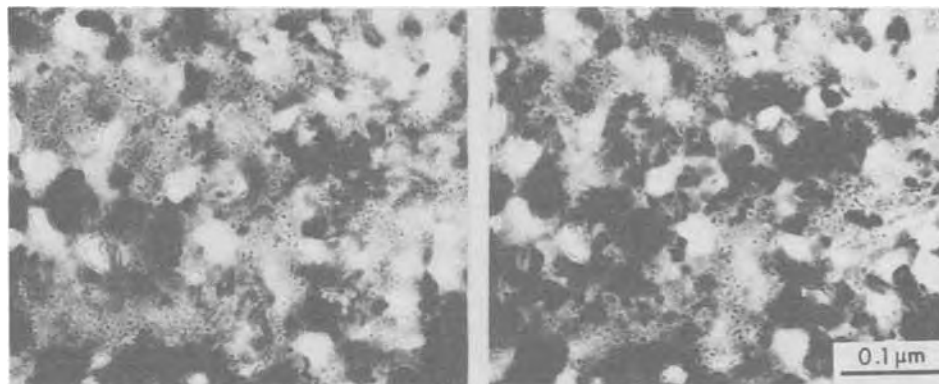


Fig. 1. TEM micrographs of 500Å thick cobalt-hardened gold deposit. (a) Over-focused,  $\Delta f = +3.9 \mu\text{m}$ ; (b) under-focused,  $\Delta f = -3.9 \mu\text{m}$ .

Fig. 2. Stereo pair showing spatial distribution of phase objects in deposit from Co-bath.



from the Ni-bath used to obtain the size distribution data was about 5000Å thick before polishing. It is noteworthy that the two distribution curves were practically identical; about 80% of the objects measured 25-35Å in diameter, and a small distinct peak was present at 50Å.<sup>1</sup> The fact that the majority of objects possess nearly the same size suggests that these objects may be the molecules of polymer that have been postulated to be present in hard gold deposits, rather than voids or gas bubbles. The objects giving the peak at 50Å may simply be agglomerates of the single polymer molecules. It is also possible that more than one kind of phase objects is involved, but this question cannot be resolved without carrying out more detailed studies. It is of interest to note in passing that deposits obtained with a proprietary high-speed hard gold plating bath yielded a distribution curve with only one sharp peak at 25Å. This bath was also citrate-based and contained a cobalt salt as the hardener and about 32g Au/liter in the form of  $\text{KAu}(\text{CN})_2$ . It was operated at 150 mA/cm<sup>2</sup> at 75°C with vigorous agitation.

Sanwald (15) described his finding of nonmetallic inclusions with diameters ranging from 20 to 200Å in electrodeposited gold. His study indicates that they were gas-filled voids, but no information is given in his paper concerning the plating bath and conditions

<sup>1</sup>The true size of phase objects is generally different from the image size. With overfocused conditions, this difference is relatively small; for example, when  $\Delta f = +3.9 \mu\text{m}$  (the amount of overfocus used for the size distribution measurement) and the image size <80Å, the image size is approximately equal to the true object size (12).

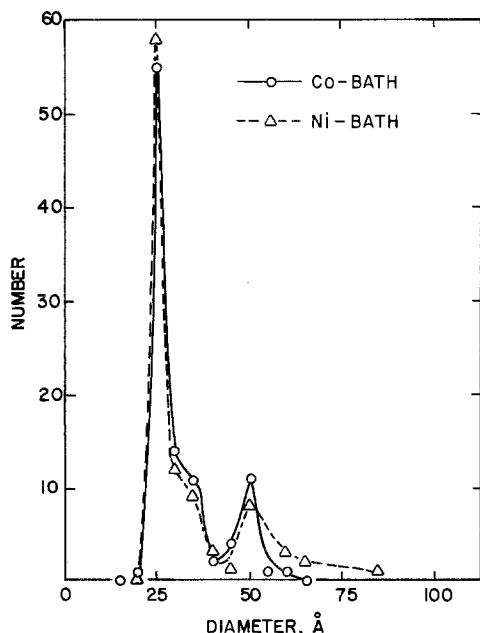


Fig. 3. Size distribution of phase objects in deposits from Co- and Ni-baths.

used. More recently, Willcox and Cady (16) reported that 0.4% nickel-hardened, electroplated gold contains gas-filled voids with a diameter of approximately 50Å. They gave a void density value of  $10^{17}/\text{cm}^3$  and a volume density of 0.6%, which are close to what we found for the polymer molecules in our deposits (see Table I). Based on the fact that the deposition of hard gold is a low current efficiency process and a significant quantity of hydrogen gas evolves during the deposition, they assumed that the "voids" are filled with hydrogen. Willcox (17) states that no evidence was found of the existence of carbon or carbon-containing material in the gold deposits that he studied. We also observed features which obviously looked like gas bubbles or gas-filled voids in some gold deposits, but the size and shape of these bubbles were clearly more random and nonuniform than those of the objects which we attribute to polymer molecules in this paper. The bubbles were found in the deposits from additive-free baths described in the next section as well as in some deposits formed in extensively used, citrate-based, cobalt-containing baths. We also reported recently on electron micrographs of electrodeless copper deposits containing numerous gas bubbles ranging from 20 to 300Å in diameter (18). These bubbles also had a shape and size distribution distinctly different from that of the polymer molecules.

In regard to the uniformity of spatial distribution of the polymer molecules, a question can be raised as to whether the molecules are situated at grain boundaries or within the grains, or both. Because of the small grain size (which is discussed in a subsequent section), the micrographs did not provide information concerning exact location of the molecules with respect to single grains.

*Deposits from additive-free baths.*—Munier (1) found that carbon-containing species codeposit even from baths containing no hardening agents, if they are operated at low current-efficiency conditions, i.e. at room temperature. Reinheimer (9) recently made a detailed investigation of carbon codeposition in such additive-free systems. Their results show that gold deposits formed in these baths contain less carbon

Table I. Comparison of polymer content, carbon content, and grain size of deposits from different paths

Bath	Population density (cm <sup>-3</sup> )	Volume density (%)	Calculated** maximum carbon content (%)	Grain size (Å)
Co-bath	$3 \times 10^{17}$	0.59	0.07	225-275
Ni-bath	$5 \times 10^{17}$	0.98	0.11	100-250
NH <sub>4</sub> -citrate (no additive)	$1 \times 10^{17}$ *	0.21	0.02	250-750
K-phosphate (no additive)	$1 \times 10^{17}$ *	0.25	0.03	250-750

\* Phase objects greater than 75Å were not included in the count.

\*\* See text for definition.

(up to  $\sim 0.1\%$ ) than cobalt- or nickel-hardened deposits. This was reconfirmed more recently by Raub, Knödler, and Lendvay (7).

The electron micrograph shown in Fig. 4 was obtained in an overfocused condition with a film plated in the additive-free citrate-buffered bath at  $25^\circ\text{C}$ . It is seen that this film contained phase objects with widely varying sizes. The size distribution is shown by the broken line in Fig. 5. The appearance of the large and small peaks at 25 and  $50\text{\AA}$  is strikingly similar to that found with the deposits from the Co- and Ni-baths (Fig. 3). This fact, with the broad distribution up to  $150\text{\AA}$ , is believed to indicate that this film contains both polymer molecules and gas bubbles. The gas bubbles perhaps consist of hydrogen. Deposits formed in the additive-free phosphate bath also appeared to contain both polymer molecules and bubbles. The size distribution of phase objects in these deposits is shown by the solid line in Fig. 5. Again, the peaks at 25 and  $50\text{\AA}$  are very distinct and essentially identical to those observed with other films. These results suggest that the polymer molecules formed in the additive-free baths are the same as those deposited from the Co- and Ni-baths.

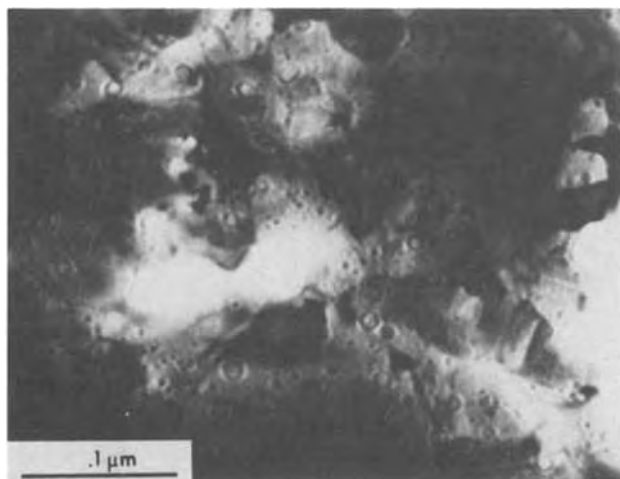


Fig. 4. TEM micrograph of deposit formed in additive-free citrate bath ( $\Delta f = + 3.9 \mu\text{m}$ ).

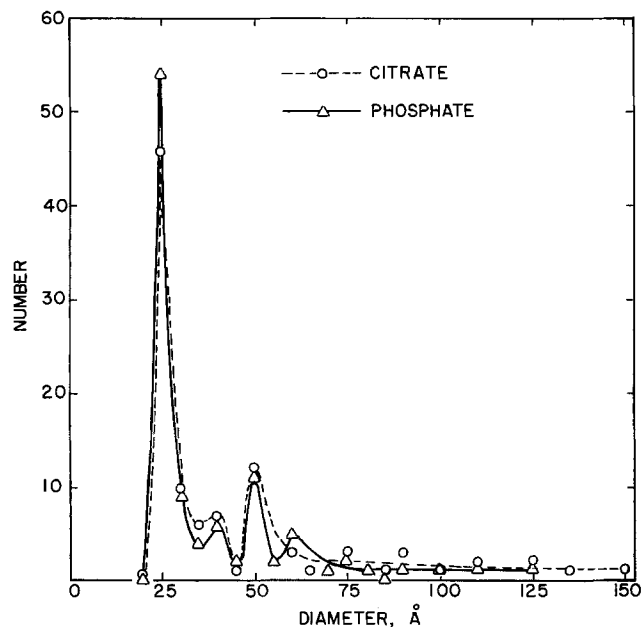


Fig. 5. Size distribution of phase objects in deposits from additive-free baths.

Concerning the form of incorporated carbon-containing species, Reinheimer (9) postulated that the carbon in gold deposits plated in additive-free baths is in the form of simple CN-containing species such as KCN, AuCN,  $\text{KAu}(\text{CN})_2$ , or HCN rather than in the form of a polymer. This suggestion was made on the basis of the finding that the carbon does not originate at the anode, where cyanide is known to form polymeric materials. As is discussed in the next section, the polymer apparently is not the only source of carbon contamination, but the codeposition of these simple CN-containing species may also be important.

*Polymer content, carbon content, and grain size.*—Table I lists the population density and volume density of the polymer molecules, the calculated maximum carbon content (see below), and the grain size of the deposits formed in the various baths. If a certain number is assumed for the specific gravity of the polymer, the weight percentage of this substance can readily be calculated from the volume density. If the specific gravity of graphite (2.25) is used, the weight percentage found may be regarded as a maximum possible carbon content attributable to the polymer. The values calculated in this manner are included in Table I as "Calculated maximum carbon content." The actual carbon content associated with the polymer should be appreciably less than this calculated carbon content, because most organic materials have specific gravity values much smaller than that of graphite. For the deposit formed in the Co-bath the calculated carbon content was  $0.07\%$ , which was significantly less than the total carbon content ( $\sim 0.25\%$ ) found by the combustion technique. Although no actual analytical data are available for the deposit from the Ni-bath, the recent study by Raub, Knödler, and Lendvay (7) indicates that the total carbon content of the nickel-hardened deposit from the type of bath employed in this study is not greatly different from that of the Co-bath. Thus, the calculated maximum carbon content of the deposit from the Ni-bath is also likely to be significantly lower than its total carbon content. A similar difference between calculated and total carbon contents was found for the deposit from the additive-free ammonium citrate bath. The total carbon content of this deposit was  $\sim 0.04\%$  as compared to the calculated maximum carbon content of  $0.02\%$ . Even if the uncertainty in the estimate of foil thickness is taken into consideration (a nominal value of  $500\text{\AA}$  was used), the differences described above are still considered quite significant. It is apparent from these comparisons that the polymer accounts for only a small fraction ( $\sim 10$  to  $25\%$ ) of the total carbon content. The rest of the carbon must be present in some other form(s) which is not visible by electron microscopy. Simple K-Au-CN species and/or Co-CN species are such possibilities (7, 9). It is of interest to note that both  $\text{Au}(\text{CN})_2^-$  (19) and  $\text{Co}(\text{CN})_4^{--}$  (20) are known to adsorb strongly on mercury.

A common feature of all hard gold deposits is the extremely small grain size. Since such small individual grains are difficult to resolve in micrographs taken in the bright-field, dark-field imaging was used to measure the grain size. A typical dark-field micrograph obtained with the deposit from the Co-bath is shown in Fig. 6. This specimen was prepared by electropolishing a  $25 \mu\text{m}$  thick film. The grain size of this film was quite uniform,  $250 \pm 25\text{\AA}$ . We also examined the early stages of deposit formation on large grains ( $> 10 \mu\text{m}$ ) of textured copper substrates. It was found that the deposit grows epitaxially only at the very early stages (up to only  $\sim 150\text{\AA}$ ), and subsequently becomes very fine-grained. On the other hand, deposits from high temperature, soft gold baths were found to grow epitaxially to a considerable thickness ( $> 1 \mu\text{m}$ ). Soft gold is known to contain very little

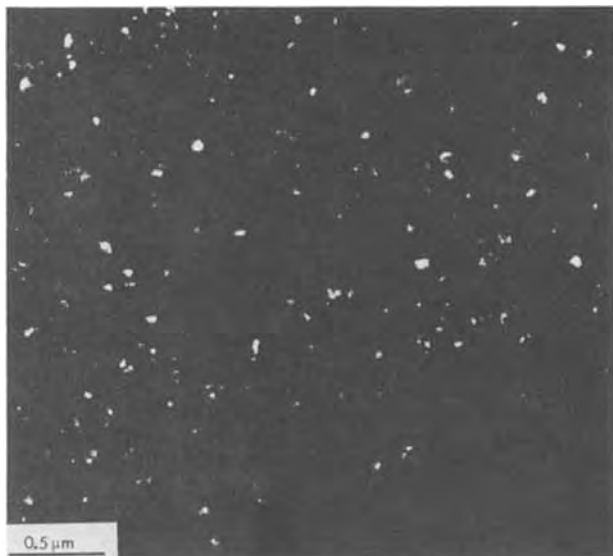


Fig. 6. Dark-field TEM micrographs of deposit from Co-bath ( $25\ \mu\text{m}$  deposit electropolished to about  $750\text{\AA}$ ).

carbon (1), and indeed no phase objects were found in such deposits. The deposit from the Ni-bath contained the largest quantity of polymer, and its grain size was smallest (Table I). On the other hand, as shown in Fig. 7(a) and (b), some large grains were

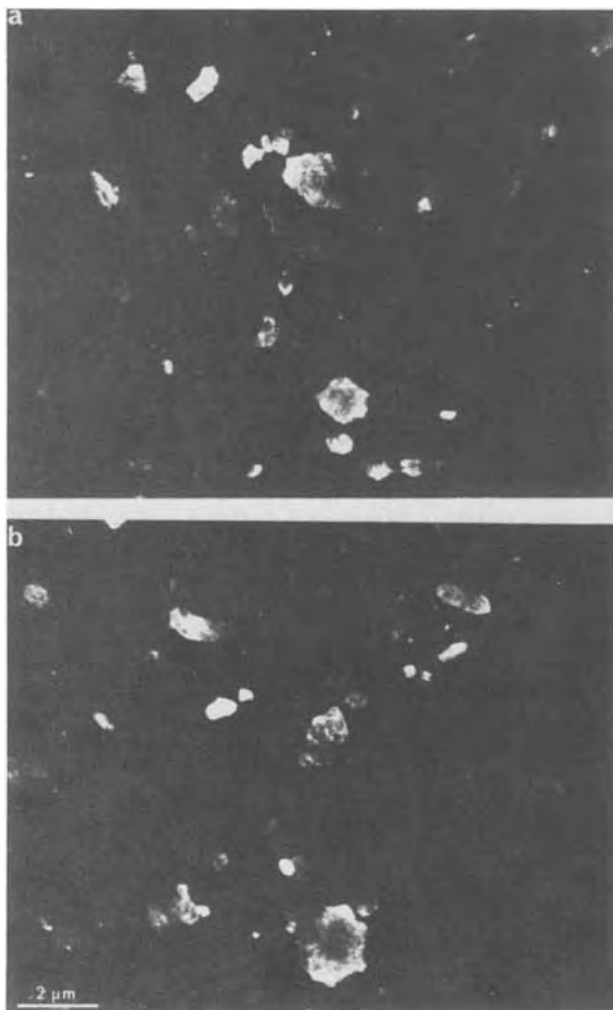


Fig. 7. Dark-field TEM micrographs of deposits from additive-free citrate (a) and phosphate (b) baths.

found in the deposits from the additive-free baths, which contained the least amount of polymer (Table I). From these results it would appear that the polymer content and grain size are interrelated. It is possible that the codeposited polymer molecules have a grain-refining effect which is due to the inhibition of crystal growth. Since the polymer is evidently not the only source of carbon, it is not clear whether the observed differences in grain size between the various deposits are entirely due to the differences in polymer content, or whether other carbon-containing species are also responsible. As already mentioned, the deposits from the additive-free baths appeared to contain gas bubbles. Unlike organic molecules or other adsorbed species, gas bubbles or voids are not likely to alter the grain size. With electroless copper deposits containing numerous gas bubbles, we observed no grain refining effect; epitaxial growth continued up to tens of micrometers (21).

It is generally recognized that the hardness of deposits is influenced by grain size. The Knoop hardness of the deposits from the four baths studied here ranged from 150 to 200 at 25g load. The relationship between grain size and hardness was not clear, and no effort was made to establish such a relationship in this investigation.

### Summary and Conclusion

1. Small phase objects (nonmetallic objects) ranging in diameter from 20 to  $70\text{\AA}$  found in hard gold deposits by the through-focus imaging technique of transmission electron microscopy are most likely to be single molecules and their agglomerates of the so-called polymer which has been isolated as a transparent film upon dissolution of gold in aqua regia. The polymer molecules appear to be distributed uniformly throughout the deposit.

2. The size distribution of the phase object is very tight and identical for deposits obtained from various different baths. Nearly 80% of the phase objects measure 25-35 $\text{\AA}$  in diameter. This is considered as evidence to support the conclusion that these objects are polymer molecules rather than voids or gas bubbles.

3. Features which appeared to be gas bubbles were found in deposits from the room temperature, additive-free baths as well as in deposits from an extensively used cobalt-containing bath. The shape and size distribution of these features are random and distinctly different from those of the polymer molecules.

4. A comparison of the polymer content estimated from the analysis of electron micrographs with the total carbon content indicates that the polymer accounts for only 10-25% of total carbon in gold deposits.

### Acknowledgment

The authors are indebted to J. J. Chick for supplying samples plated in the additive-free baths and for permitting us to use the experimental results in this communication.

Manuscript submitted Aug. 25, 1975; revised manuscript received April 19, 1976.

Any discussion of this paper will appear in a Discussion Section to be published in the June 1977 JOURNAL. All discussions for the June 1977 Discussion Section should be submitted by Feb. 1, 1977.

Publication costs of this article were assisted by Bell Laboratories.

### REFERENCES

1. G. B. Munier, *Plating*, **56**, 1151 (1969).
2. L. Holt and J. Stanyer, *Trans. Inst. Metal Finishing*, **50**, (1), 24 (1972).
3. L. Holt, R. J. Ellis, and J. Stanyer, *Plating*, **60**, 910 (1973).
4. L. Holt, R. J. Ellis, and J. Stanyer, *ibid.*, **60**, 918 (1973).

5. M. J. Vasile and D. L. Malm, *Anal. Chem.*, **44**, 650 (1972).
6. M. Antler, *Plating*, **60**, 468 (1973).
7. Ch. J. Raub, A. Knödler, and J. Lendvay, *ibid.*, **63**, 35 (1976).
8. F. H. Reid, American Electroplaters' Society Fifth Plating in the Electronics Industry Symposium, New York, March 24-25, 1975, p. 67.
9. H. A. Reinheimer, *This Journal*, **121**, 490 (1974).
10. L. Albert, R. Schneider, and H. Fischer, *Z. Naturforsch., Teil A*, **19**, 1120 (1964).
11. M. Rühle, Proceedings of International Conference on Radiation Induced Voids in Metals (1971).
12. S. Nakahara and Y. Okinaka, in "Properties of Electrodeposits—Their Measurement and Significance," R. Sard, H. Leidheiser, Jr., and F. Ogburn, Editors, chap. 3, The Electrochemical Society Softbound Symposium Series, Princeton, N. J. (1975).
13. J. Silcox and P. B. Hirsch, *Philos. Mag.*, **4**, 72 (1959).
14. P. Petroff, Private communication.
15. R. C. Sanwald, *Metallography*, **4**, 503 (1971).
16. P. S. Willcox and J. R. Cady, *Plating*, **61**, 1117 (1974).
17. P. S. Willcox Ph.D. Thesis, University of Southern California (1974).
18. Y. Okinaka and S. Nakahara, *This Journal*, **123**, 475 (1976).
19. Y. Okinaka, *ibid.*, **120**, 739 (1973).
20. H. S. Lim and F. C. Anson, *J. Electroanal. Chem.*, **31**, 297 (1971).
21. S. Nakahara and Y. Okinaka, To be published.

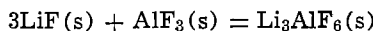
## Thermodynamics of the System LiF-AlF<sub>3</sub>

E. W. Dewing\*

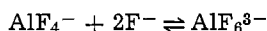
*Aluminum Company of Canada, Research Centre, Arvida, Quebec, Canada*

### ABSTRACT

It is demonstrated from the liquidus curve that solid Li<sub>3</sub>AlF<sub>6</sub> is stoichiometric. Solid-electrolyte concentration cells have been used to determine the free energy of



as  $\Delta G^\circ = -3668 - 7.051T$  cal (870°-1058°K) and  $\Delta G^\circ = -4138 - 6.510T$  cal (773°-870°K) with a standard deviation of  $\pm 11$  cal. At 1073°K liquid concentration cells with alumina diaphragms have given free energies of mixing for the system, the results being calculated with a transport number of Li<sup>+</sup> ions of  $0.957 \pm 0.008$  determined by coulometric titration of added AlF<sub>3</sub>. For liquid Li<sub>3</sub>AlF<sub>6</sub> the discrepancy between the results of the liquid cells and extrapolation of the results from solid cells is 100 cal. The free energies of mixing at 1073°K can be interpreted in terms of the equilibrium



with  $K = 14.9$  (in terms of anion fractions).

In earlier work, the free energy of the solid compounds Na<sub>3</sub>AlF<sub>6</sub> and Na<sub>5</sub>Al<sub>3</sub>F<sub>14</sub> was determined with solid-electrolyte concentration cells (1), and activities in liquid NaF-AlF<sub>3</sub> mixtures saturated with alumina were determined with concentration cells with alumina diaphragms (2). The object of the present work is to use similar methods on the LiF-AlF<sub>3</sub> system. At the same time a check is made to see whether solid Li<sub>3</sub>AlF<sub>6</sub> is nonstoichiometric in the same way that Na<sub>3</sub>AlF<sub>6</sub> seems to be (3).

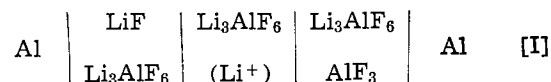
Romberger and Braunstein (4) measured the emf of concentration cells in the system LiF-BeF<sub>2</sub>. In that case the activities were already known, so that transport numbers could be calculated. In the present case neither activities nor transport numbers are available; it has thus been necessary to measure the transport number of Li<sup>+</sup> independently in a Hittorf-type experiment.

### Solid Li<sub>3</sub>AlF<sub>6</sub>

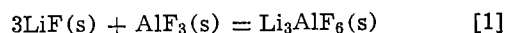
The check for nonstoichiometry is made by plotting the liquidus curve for Li<sub>3</sub>AlF<sub>6</sub> on the basis of  $\log(n_{\text{LiF}}^3 \cdot n_{\text{AlF}_3})$  against  $1/T$  (3). If the compound is stoichiometric the two branches of the liquidus will have at least a common tangent and may be superimposed. Figure 1, based on the results of Jensen (5), Rolin *et al.* (6, 7), and Matiasovsky and Malinovsky (8) shows that there is no effective separation of the lines except at the lowest temperature, and that consequently Li<sub>3</sub>AlF<sub>6</sub> may be treated as stoichiometric.

\* Electrochemical Society Active Member.  
Key words: lithium fluoride, aluminum fluoride, activities, transport number, concentration cell, lithium cryolite, dissociation.

The determination of the free energy of formation of solid Li<sub>3</sub>AlF<sub>6</sub> with a solid electrolyte cell is simple since the lithium analogue of chiolite, Na<sub>5</sub>Al<sub>3</sub>F<sub>14</sub>, does not exist. Hence, one cell



gives the desired result; if its emf is  $E$ , then for



$$\Delta G^\circ = -3EF/2 \quad [2]$$

[The theory of such cells has been given previously (1).]

The electrolyte was Li<sub>3</sub>AlF<sub>6</sub> doped with Mg<sup>2+</sup>. Crystals were recovered from a slowly cooled melt containing 8.4% MgF<sub>2</sub> and 7.5% excess AlF<sub>3</sub>. (This AlF<sub>3</sub> is equivalent to 3/2 MgF<sub>2</sub>.) The crystals were not analyzed. On each side of the doped material pure Li<sub>3</sub>AlF<sub>6</sub> was placed, and the powders were compacted into 5 mm ID alumina tubes, as in the earlier work. The liquid aluminum electrodes were kept in place by layers of graphite and silver.

EMF's were measured with a Guildline potentiometer and a Keithley 600 B electrometer as null-detector. The latter has an internal impedance of  $10^{14}\Omega$  and a recorder output, so that out of balance current could be recorded continuously with a sensitivity of 10 mV full scale. The emf's were in fact steady to a few tenths of a millivolt.



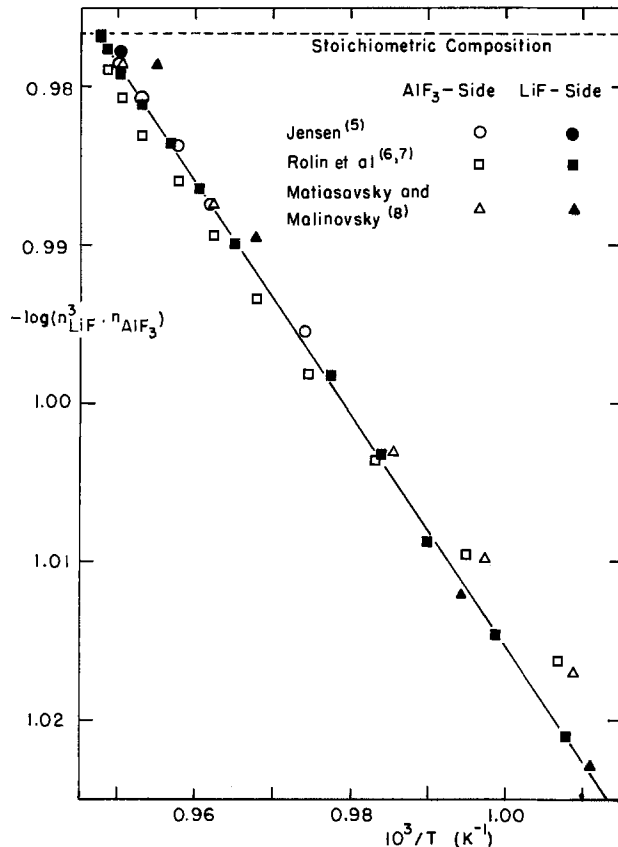


Fig. 1. Liquidus curve for  $\text{Li}_3\text{AlF}_6$ . (Some points omitted for clarity.)

The results are given in Table I in the order in which they were measured and are plotted in Fig. 2.

According to Jensen (5)  $\text{Li}_3\text{AlF}_6$  has transitions at 870° and 783°K. With the exception of the point at 745°K, which is well below the lower transition, the data were fitted by least squares to two straight lines intersecting at the upper transition point. The two equations are

$$\text{above } 870^\circ\text{K: } \Delta G^\circ = -3668 - 7.051T \quad [3]$$

$$\text{below } 870^\circ\text{K: } \Delta G^\circ = -4138 - 6.510T \quad [4]$$

The enthalpy of transition is 470 cal. The standard deviation of the points from the line is 11.5 cal, corresponding to 0.33 mV.

For comparison, Fig. 2 also shows the free energy given by the JANAF Tables (9). It differs by 0.9 kcal from this work.

#### Liquid LiF- $\text{AlF}_3$ Mixtures

The basis of the thermodynamic measurements is concentration cells with transport of the type

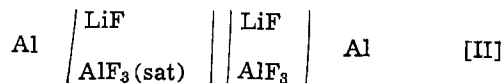


Table I. EMF of cells of type [I]

Cell	Temp (°K)	E (mV)	$-\Delta G^\circ$ (cal)
A	953.0	299.8	10,371
	866.8	282.3	9,765
	819.0	274.1	9,482
	818.0	293.4	10,149
	769.1	264.5	9,149
B	955.6	301.1	10,416
	745.6	261.7	9,053
	957.0	301.1	10,416
	896.1	288.9	9,993
	872.0	284.0	9,824
	818.6	273.6	9,464
	792.1	268.5	9,288

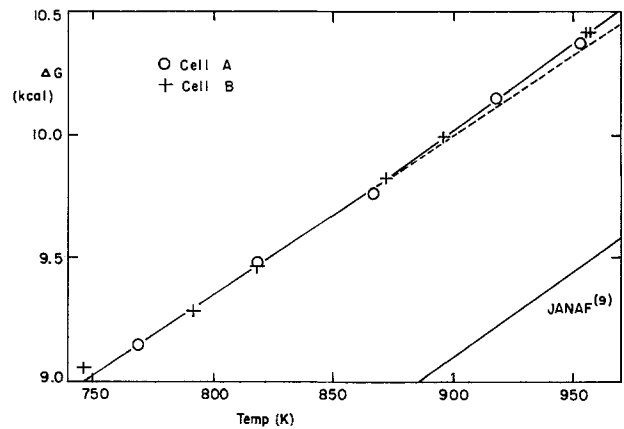


Fig. 2. Free energy of  $3\text{LiF}(\text{s}) + \text{AlF}_3(\text{s}) = \text{Li}_3\text{AlF}_6(\text{s})$

The left-hand side has a fixed composition since it is always saturated with  $\text{AlF}_3$ ; the right-hand side is variable. The mixtures were held in alumina tubes; since these are penetrated by cryolite melts the liquid junctions were formed within them. The electrodes were tungsten rods previously dipped in molten aluminum; effectively, for a period of minutes, they acted as reversible aluminum electrodes.

Mixtures were made up by weight from Reagent Grade LiF (Baker & Adamson-Allied Chemical) and  $\text{AlF}_3$  purified by sublimation. The latter contained 0.08 weight percent (w/o) NaF. They were put into 5 mm ID  $\times$  8 mm OD alumina tubes, enough to give 1-2 cm depth when melted. The tubes were immersed in a LiF- $\text{Li}_3\text{AlF}_6$  eutectic mixture (64.6 w/o LiF, 35.4 w/o  $\text{AlF}_3$ ) in a graphite crucible of 2 in. ID (Fig. 3). Seven tubes in all were immersed; five containing mixtures, one in the center containing a Pt-10% Rh thermocouple, and the other containing liquid aluminum. The latter served for coating and recoating the tungsten rods (1.5 mm diam) used as electrodes.

A few additional results were obtained in the course of the transport number work described below.

To make a measurement the two tungsten rods were taken out of the aluminum and placed in the reference mixture [ $\sim 60$  mol percent (m/o)  $\text{AlF}_3$  saturated with  $\text{AlF}_3$ ] and the one to be studied. An emf steady to within a millivolt or so was usually obtained within a few minutes. The electrodes were then removed,

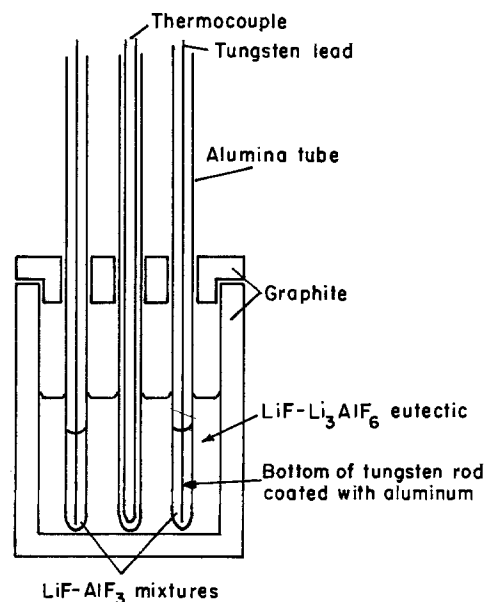


Fig. 3. Apparatus



cleaned of electrolyte with a file, and replaced in the aluminum.

Table II shows the results obtained at  $1073^\circ \pm 2^\circ\text{K}$  as a function of composition, and Table III shows the results as a function of temperature for a pair of electrodes in mixtures saturated with solid AlF<sub>3</sub> and solid LiF, respectively.

The theory of cells of this type has been given previously (2, 4, 10, 11). Activities are derived from emf by

$$d \ln a_{\text{LiF}} = - \frac{3F}{RT} \cdot \frac{dE}{r + 3t} \quad [5]$$

and

$$d \ln a_{\text{AlF}_3} = \frac{3F}{RT} \cdot \frac{r}{r + 3t} \cdot dE \quad [6]$$

where  $r$  is the molar ratio LiF/AlF<sub>3</sub> and  $t$  is the transport number of Li<sup>+</sup> ions. [It is assumed that the transport number of F<sup>-</sup> ions is  $(1 - t)$ , and hence that  $t_{\text{Al}^{3+}} = 0$ , which is reasonable if it is entirely complexed as AlF<sub>6</sub><sup>3-</sup> and AlF<sub>4</sub><sup>-</sup> (12).] Since these are differential equations they involve integrations and bring in unknown integration constants. These can be fixed if the integration can be started at a phase boundary where the activity is known.

From the phase diagram (5, 7) the LiF liquidus at  $1073^\circ\text{K}$  may be taken to lie at 8.1 m/o AlF<sub>3</sub>. The activity with respect to liquid LiF may be calculated from the JANAF (9) free energy of fusion as  $\Delta\bar{G}_{\text{LiF}} = -283$  cal, and  $a_{\text{LiF}} = 0.876$ . This provides the necessary integration constant for Eq. [5].

Figure 4 is a plot of the results. Examination shows that the line is not quite straight (there is no reason why it should be); and it has been represented by three straight-line segments

$$n_{\text{AlF}_3} < 0.25$$

$$E = 524 - 123.1 n_{\text{AlF}_3} \text{ mV}$$

$$0.25 < n_{\text{AlF}_3} < 0.30$$

$$E = 554 - 135.2 n_{\text{AlF}_3} \text{ mV}$$

$$n_{\text{AlF}_3} > 0.30$$

$$E = 494 - 115.3 n_{\text{AlF}_3} \text{ mV}$$

The last of these extrapolates to zero at 42.8 m/o

Table II. EMF of cells of type [II]

Mol % AlF <sub>3</sub>	Temp (°K)	EMF (mV)	Remarks
60.0	—	0	Taken as reference
4.9	1074	427	Saturated with LiF
15.1	1072	345	
25.0	1072	218	
35.5	1072	86	
10.3	1073	381	
19.9	1074	276	
30.1	1070	147	
38.1	1071	56	
4.9	1072	424	Saturated with LiF
10.0	1074	398	
40.0	1074	31	
39.8	1073	37	
25.0	1073	215	
25.0	1073	216	
26.8	1072	191	

Table III. EMF of melts saturated with solid LiF (reference: melt saturated with solid AlF<sub>3</sub>)

Temp (°K)	EMF (mV)
1074	427
1072	424
1023	359
1023	352
1025	355
1001	334
987	319
978	309
1047	394

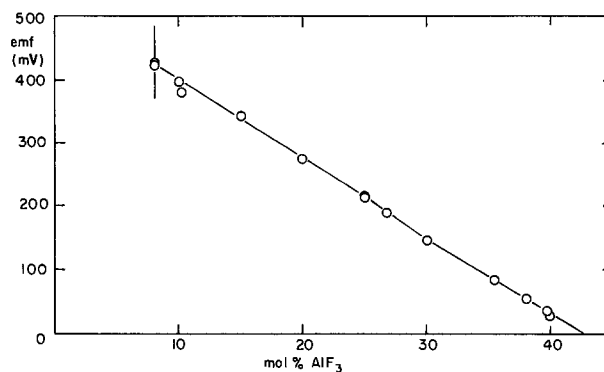
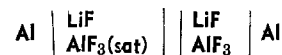


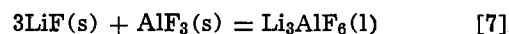
Fig. 4. EMF at  $1073^\circ\text{K}$  of the cell



AlF<sub>3</sub>, about 1.5 m/o higher than would be expected from the liquidus curve (5, 6) but hardly beyond experimental uncertainty.

The over-all standard deviation of the points from the lines is  $\pm 5.6$  mV.

Integration of Eq. [5] and [6] was first carried out numerically with the assumption that  $t = 1$ ; step size was 1 m/o. It was found that the  $\Delta G^\circ$  of formation of a 25 m/o AlF<sub>3</sub> mixture (i.e., for 0.75 LiF + 0.25 AlF<sub>3</sub>) was  $-3009$  cal (starting from liquid LiF and solid AlF<sub>3</sub>). This may be compared with the value derived from the free energy of formation of solid Li<sub>3</sub>AlF<sub>6</sub> (Eq. [3]). With the enthalpy of fusion of Li<sub>3</sub>AlF<sub>6</sub> of  $21,000 \pm 300$  cal at  $1058^\circ\text{K}$  given by Holm and Grønvdold (13) this gives for



$$\Delta G^\circ = 17,332 - 26.900T \quad [8]$$

and at  $1073^\circ\text{K}$ ,  $\Delta G^\circ = -11,532$ . To make comparison with the integral  $\Delta G$  of mixing this value must be divided by 4 (to put it on the basis of 1 mole total), and then  $-283 \times 0.75$  cal must be added to transfer to the liquid standard state for LiF. The final result is  $\Delta G = -3095$  cal. The discrepancy of 86 cal corresponds to 344 cal in the free energy of formation of Li<sub>3</sub>AlF<sub>6</sub>, and is an error of the order of 10 mV in the emf. One therefore questions whether the assumption of unit transport number for Li<sup>+</sup> ions is valid. If it be assumed that  $t$  is independent of composition, a value of 0.94 is needed to get rid of the discrepancy.

The transport number of Li<sup>+</sup> was determined by the direct coulometric titration of AlF<sub>3</sub>. The procedure was that a melt was made up by weight to have a molar ratio LiF/AlF<sub>3</sub> of 3. It was placed in an alumina tube which was in turn immersed in a LiF-Li<sub>3</sub>AlF<sub>6</sub> eutectic melt, as in the earlier work. The only difference was that the tube was 12 mm ID and the reference electrode was in a tube 8 mm ID. Dry argon was passed via a narrow alumina tube into the tube to exclude moisture; the top was plugged with glass wool. Aluminum-plated tungsten electrodes were used as before, except that the main one was not subsequently removed for replating. Aluminum was added to the crucible to act as anode.

At the start of a run, the emf between the two electrodes was found. A carefully weighed piece of coarsely crystalline AlF<sub>3</sub> was then dropped in, and the emf was redetermined. A current was then passed between the graphite crucible and the main electrode (cathodic) until the emf was above (or at least close to) the initial value. The duration of current was carefully timed and its value was measured with a calibrated resistor. (Since it had a small temperature

coefficient and since it heated when current was passed, its value was determined with a Kelvin bridge immediately after use. The current, from a Hewlett-Packard 6200B Power Supply, was kept flowing through the resistor at all times to ensure that it stayed at steady state.) Linear interpolation was made on the emf-time line to determine the number of coulombs passed when the potential was restored to its original value. More  $\text{AlF}_3$  was dropped in, and the process repeated. In this way a plot of coulombs vs. weight  $\text{AlF}_3$  added was obtained.

Figure 5 shows part of the emf-coulombs sequence, and Fig. 6 is the final plot of moles of  $\text{AlF}_3$  added vs. equivalents of charge passed. The slope of the least squares line is 1.5317 with a standard error of  $\pm 0.0025$  equiv./mole. The standard deviation is  $\pm 0.079$  mole equiv., or  $\pm 7.6\text{C}$ . This is based on 9 points, including the origin. If the origin is omitted the standard deviation increases, showing that it is a valid point. If, on the other hand, a tenth point is brought in the standard deviation again increases (by a factor of 1.6), implying that something is wrong with it. Possibly a fragment of the  $\text{AlF}_3$  failed to reach the bottom of the tube. It has been omitted from the final result.

If the slope of the line is  $n$  equiv./mole, the transport number is calculated as follows. Of 1 mole  $\text{AlF}_3$  added,  $n/3$  is destroyed by plating out Al onto the cathode. To restore the composition to the original molar ratio of 3,  $3(1 - n/3)$  moles LiF must be transported in. The transport number is thus

$$\begin{aligned} t &= 3(1 - n/3)/n \\ &= 3/n - 1 \\ &= 0.9586 \pm 0.0032 \end{aligned}$$

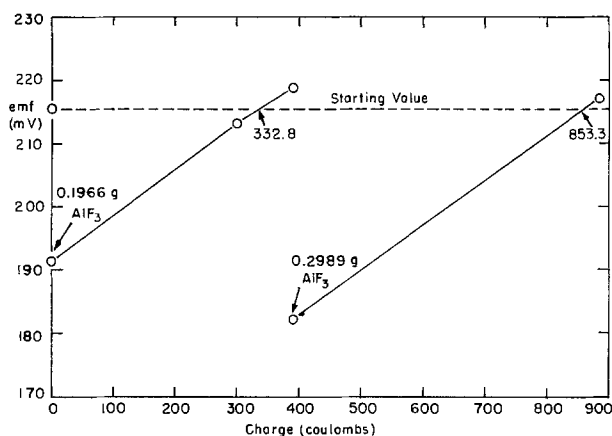


Fig. 5. Part of emf-coulombs sequence

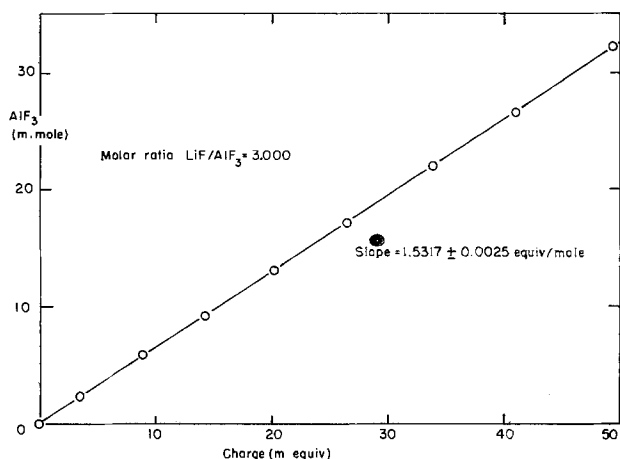


Fig. 6. Coulometric titration of  $\text{AlF}_3$

If it be assumed that the 0.082% NaF is the only impurity in the  $\text{AlF}_3$  (it is the most likely one), the value of  $t$  is reduced to 0.957.

The error quoted is a statistical standard error; systematic errors are much harder to estimate. The resistor was measured *in situ* with a precision of about  $\pm 0.2\%$ , timing the duration of the current is, say,  $\pm 1$  sec in 10 min or about 0.17%. The over-all precision on the coulombs is thus about  $\pm 0.26\%$ . This will make  $\pm 0.52\%$  in the value of  $t$ . If one takes this and two standard errors the over-all uncertainty is  $\sqrt{0.0064^2 + 0.0052^2} = \pm 0.0083$ . We may thus take  $t = 0.957 \pm 0.008$ .

Since  $t$  is very close to unity it is unlikely that a significant variation with composition could be determined experimentally, and it is assumed that it is constant. Integration of Eq. [5] and [6] is then straightforward, and the result is shown in Table IV. The  $\Delta G$  for (0.75 LiF, 0.25  $\text{AlF}_3$ ) is now  $-3070$  cal; the  $\pm 0.008$  uncertainty in the transport number makes  $\pm 11$  cal. The discrepancy with the calculated value of  $-3095$  cal is 25 cal, which is not really big enough to worry about. It would correspond to 3 mV in the emf.

### Discussion

That solid  $\text{Li}_3\text{AlF}_6$  is the only one of the alkali metal cryolites which does not show premelting effects (13) is probably associated with the fact demonstrated here that it is stoichiometric. The implication could be that the others are not.

It has been assumed in this work that alumina is essentially insoluble in lithium cryolite. Rolin and Muhlethaler (6) stated that the solubility was less than 1%; in fact their figures (14) indicate that it is about 0.2% at  $1073^\circ\text{K}$ . There was no obvious attack on the alumina tubes used in the concentration cells, and it is not believed that the solubility is high enough to have affected the thermodynamic values.

Although the values obtained are completely independent of any model of the melts it is interesting to see if they can be fitted to a reasonable model. One which has been adopted by numerous authors is the equilibrium



it being assumed that the various anionic species mix ideally. In the past it has been necessary to calculate for temperatures and compositions along the liquidus curve, but now isothermal data covering the whole composition range are available.

Since  $\text{Li}^+$  is the only (uncomplexed) cation present, and since we are assuming that the anionic species are mixing ideally, we may identify the activity of LiF as measured with the anion fraction of  $\text{F}^-$ . Having found that, and knowing the over-all composition,

Table IV. Thermodynamic functions for LiF- $\text{AlF}_3$  mixtures at  $1073^\circ\text{K}$  (transport number for  $\text{Li}^+ = 0.957$ )

$n_{\text{AlF}_3}$	$\Delta\bar{G}_{\text{AlF}_3}$ (cal)	$\Delta\bar{G}_{\text{LiF}}$ (cal)	$\Delta G$ (cal)	$a_{\text{AlF}_3}$	$a_{\text{LiF}}$
0.425	0	-5077	-2919	1.000	0.092
0.420	-129	-4983	-2944	0.941	0.097
0.400	-661	-4613	-3032	0.733	0.115
0.380	-1224	-4253	-3102	0.563	0.136
0.360	-1818	-3904	-3153	0.426	0.160
0.340	-2445	-3567	-3185	0.318	0.188
0.320	-3106	-3241	-3198	0.233	0.219
0.300	-3803	-2928	-3191	0.168	0.253
0.280	-4673	-2573	-3161	0.112	0.299
0.260	-5581	-2237	-3106	0.0730	0.350
0.250	-6052	-2076	-3070	0.0585	0.378
0.240	-6502	-1930	-3027	0.0474	0.405
0.220	-7419	-1656	-2924	0.0308	0.460
0.200	-8386	-1399	-2796	0.0196	0.519
0.180	-9404	-1161	-2644	0.0122	0.580
0.160	-10476	-941	-2467	0.00735	0.643
0.140	-11607	-741	-2263	0.00433	0.706
0.120	-12799	-563	-2032	0.00247	0.768
0.100	-14057	-408	-1773	0.00137	0.826
0.081	-15316	-283	-1501	0.00076	0.876

we can calculate the anion fractions of AlF<sub>4</sub><sup>-</sup> and F<sup>-</sup>, and then see if the model is working insofar as the equilibrium constant

$$K = a_{\text{Li}_3\text{AlF}_6} / (a_{\text{LiAlF}_4} \cdot a_{\text{LiF}}^2) \quad [10]$$

is constant.

If we start with an over-all composition  $n_{\text{LiF}}$  and  $n_{\text{AlF}_3}$  (the total = 1), and  $x_{\text{LiF}}$ ,  $x_{\text{LiAlF}_4}$ , and  $x_{\text{Li}_3\text{AlF}_6}$  denote numbers of moles of the individual species present, then

$$x_{\text{LiAlF}_4} + x_{\text{Li}_3\text{AlF}_6} = n_{\text{AlF}_3} \quad [11]$$

$$x_{\text{LiF}} + x_{\text{LiAlF}_4} + 3x_{\text{Li}_3\text{AlF}_6} = n_{\text{LiF}} \quad [12]$$

By substituting [11] in [12]

$$\begin{aligned} x_{\text{LiF}} &= n_{\text{LiF}} - n_{\text{AlF}_3} - 2x_{\text{Li}_3\text{AlF}_6} \\ &= 2n_{\text{LiF}} - 1 - 2x_{\text{Li}_3\text{AlF}_6} \end{aligned} \quad [13]$$

since  $n_{\text{AlF}_3} = 1 - n_{\text{LiF}}$ . The sum of the  $x$ 's is from [12]

$$x_{\text{LiF}} + x_{\text{LiAlF}_4} + x_{\text{Li}_3\text{AlF}_6} = n_{\text{LiF}} - 2x_{\text{Li}_3\text{AlF}_6} \quad [14]$$

Hence

$$a_{\text{LiF}} = \frac{x_{\text{LiF}}}{\text{Total}} = \frac{2n_{\text{LiF}} - 1 - 2x_{\text{Li}_3\text{AlF}_6}}{n_{\text{LiF}} - 2x_{\text{Li}_3\text{AlF}_6}} \quad [15]$$

and, rearranging

$$x_{\text{Li}_3\text{AlF}_6} = \frac{n_{\text{LiF}}(2 - a_{\text{LiF}}) - 1}{2(1 - a_{\text{LiF}})} \quad [16]$$

Once this is known, insertion into [11] gives  $x_{\text{LiAlF}_4}$ , and division by the sum of the  $x$ 's (Eq. [14]) gives the activities of Li<sub>3</sub>AlF<sub>6</sub> and LiAlF<sub>4</sub>.

If the model is working, and the equilibrium constant is constant, then a plot of  $a_{\text{LiF}}$  against  $\sqrt{a_{\text{Li}_3\text{AlF}_6}/a_{\text{LiAlF}_4}}$  should be straight. In Fig. 7 the results for  $n_{\text{AlF}_3} > 0.25$  are plotted. The line is remarkably straight. For  $n_{\text{AlF}_3} < 0.25$  problems arise because the quantity of AlF<sub>4</sub><sup>-</sup> present is so small that accuracy is lost, and another approach must be tried.

Fundamentally, the problem is: given the experimental emf's and assuming the model is applicable, what is the value of the equilibrium constant  $K$  which will minimize the scatter of the calculated and experimental emf's? The problem can be treated directly without doing any integrations since, for any composition, if  $K$  is specified the activities can be cal-

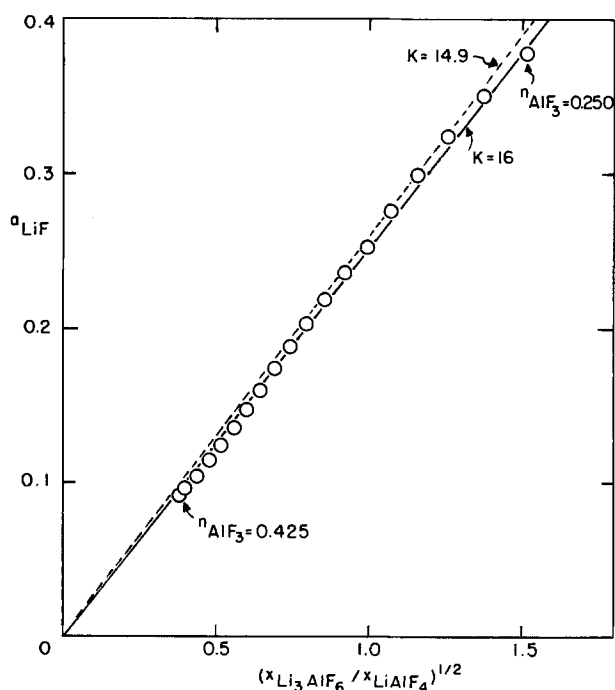


Fig. 7. Plot of  $a_{\text{LiF}}$  vs.  $(x_{\text{Li}_3\text{AlF}_6}/x_{\text{LiAlF}_4})^{1/2}$

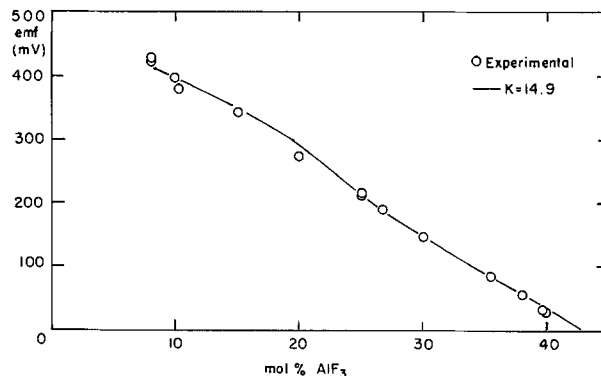


Fig. 8. Calculated emf-composition curve

culated uniquely and hence emf's with respect to some arbitrary standard composition. The only adjustment necessary is a constant to bring the arbitrary standard in line with the real one. In making the calculation it is of course necessary to insert the same transport number as used previously.

The best value of  $K$  is found to be 14.9. The resulting line is shown for comparison in Fig. 7 and the calculated emf composition curve is compared with the experimental points in Fig. 8. The standard deviation is  $\pm 8.5$  mV, which may be compared with the  $\pm 5.6$  mV standard deviation from the straight line segments. On the AlF<sub>3</sub>-side of Li<sub>3</sub>AlF<sub>6</sub> the fit is very good (as it is also in Fig. 7), but on the LiF-side there is a bend in the calculated curve which is not reproduced by the experimental values.

The simple dissociation model thus looks like a good first approximation, and is not inconsistent with Ratkje and Rytter's (15) finding that by Raman spectroscopy of LiF-Li<sub>3</sub>AlF<sub>6</sub> eutectic mixture (15 m/o AlF<sub>3</sub>) they could detect distorted AlF<sub>6</sub><sup>3-</sup> groups but no AlF<sub>4</sub><sup>-</sup>. With the value of the dissociation constant of 14.9 the composition is expected to be 74 m/o F<sup>-</sup>, 23 m/o AlF<sub>6</sub><sup>3-</sup>, and 2.8 m/o AlF<sub>4</sub><sup>-</sup>. It is thus perhaps not surprising that it was not detected. On the other hand, Gilbert, Mamantov, and Begun (16) did not see any AlF<sub>4</sub><sup>-</sup> in a Li<sub>3</sub>AlF<sub>6</sub>-Na<sub>3</sub>AlF<sub>6</sub> eutectic at 790°C. If  $K$  is around 15, then there should be 19 m/o AlF<sub>4</sub><sup>-</sup>. It is therefore quite possible that cation effects are not negligible, and that  $K$  varies with both the cation and the temperature. The assumption of ideal mixing of the anionic species may also be of limited application.

Now that thermodynamic functions are available it would be very interesting to have Raman spectra for the whole range of composition of LiF-AlF<sub>3</sub> mixtures at 1073°K. A direct comparison between activities and concentrations of various species would then be possible.

Manuscript submitted Oct. 20, 1975; revised manuscript received May 18, 1976. This was Paper 396 presented at the Washington, D. C., Meeting of the Society, May 2-7, 1976.

Any discussion of this paper will appear in a Discussion Section to be published in the June 1977 JOURNAL. All discussions for the June 1977 Discussion Section should be submitted by Feb. 1, 1977.

Publication costs of this article were assisted by the Aluminum Company of Canada.

#### REFERENCES

1. E. W. Dewing, *Metall. Trans.*, **1**, 2211 (1970).
2. K. Yoshida, and E. W. Dewing, *ibid.*, **3**, 682 (1972).
3. E. W. Dewing, *ibid.*, **3**, 2699 (1972).
4. K. A. Romberger and J. Braunstein, *Inorg. Chem.*, **9**, 1273 (1970).
5. B. Jensen, "Phase and Structure Relations for Some Alkali Aluminium Fluorides," Norges Tekniske Høgskole, Trondheim (October 1969).
6. M. Rolin and R. Muhlethaler, *Bull. Soc. Chem. Fr.*, **1964**, 2593.

7. M. Rolin, H. Latreille, and H. Pham, *ibid.*, **1969**, 2271.
8. K. Matiasovsky and M. Malinovsky, *Collect. Czech. Chem. Comm.*, **36**, 3746 (1971).
9. JANAF Thermochemical Tables, 2nd ed., U.S. National Standard Reference Data System, NSRDS-NBS 37, Washington, D. C. (1971).
10. C. Wagner, *Adv. Electrochem. Electrochem. Eng.*, **4**, 1 (1966).
11. K. B. Behl and J. J. Egan, *J. Phys. Chem.*, **71**, 1764 (1967).
12. I. S. Kachanovskaya, *Tr. Vses. Nauchno-Issled. Proekt. Inst. Alyumin., Magnievyi Elek. Prom.*, **1970**, 69.
13. B. J. Holm and F. Grønvald, *Acta Chem. Scand.*, **27**, 2043 (1973).
14. M. Rolin, Private communication.
15. S. K. Ratkje and E. Rytter, *J. Phys. Chem.*, **78**, 1499 (1974).
16. B. Gilbert, G. Mamantov, and G. M. Begun, *J. Chem. Phys.*, **62**, 950 (1975).

## Preparation and Applications of Graphite Substrate Lead Dioxide (GSLD) Anode

K. C. Narasimham and H. V. K. Udupa\*

*Central Electrochemical Research Institute, Karaikudi 623 006, India*

### ABSTRACT

The GSLD anodes have been developed for obtaining suitable size anodes for use in high amperage cells in the production of chlorates and perchlorates. The performance characteristics of the anodes in the preparation of chlorates and perchlorates are described. The use of the GSLD anode in other inorganic preparations like bromates iodates, and periodates is also included.

In recent years the quest for the development of indestructible anodes either as a substitute for costlier anodes or to increase the life of anodes in electrochemical processes has intensified. Increasing interest in the scientific development of inert and insoluble anodes provided a healthy atmosphere meriting considerable research effort both in the improvement of existing anodes and in the development of new anodes. The complex nature of the evaluation problem stems from the number of variables involved, such as electrode life, operating conditions of the cell, and replacement costs.

Graphite and platinum are widely well-known anodes in electrochemical processes and, less frequently, materials like magnetite, lead, and lead-silver or lead-antimony alloy are employed. But the recent researches on the indestructible or inert anodes are largely centered around the development of (i) platinum or its alloy coated over titanium and (ii) coating of oxide or mixed oxides of certain metals on suitable substrates.

The main requirements for an oxide anode are: (i) the possibility of forming ions of different valences to provide for high electrical conductivity, (ii) a high anodic potential at evolution of oxygen, (iii) absence of rectifying contacts at the boundary of oxide-metal current lead, and (iv) chemically inert.

The high cost of platinum has prompted several attempts to replace this metal by cheaper material. In the last two decades interest in the use of lead dioxide as anode in the place of platinum for the preparation of inorganic and organic electrochemicals (1) has been very much in evidence as seen by the considerable amount of work carried out to obtain lead dioxide deposits in a form suitable for anodes in the production of chlorates and perchlorates.

The successful development of a suitable GSLD anode for commercial scale operations in chlorates and perchlorates has been engaging the attention of the Central Electrochemical Research Institute. This paper reviews the developmental work on this project. Earlier attempts to prepare the lead dioxide electrodes as well

as the difficulties encountered by previous workers have been reviewed earlier by Narasimham and Udupa (2-4). Recently, Carr and Hampson (5) reviewed the studies on the electrodeposition of lead dioxide laying emphasis on the kinetics of electrodeposition.

### Preparation of GSLD Anode

A survey of the literature shows a continuous interest in the preparation of lead dioxide anodes beginning in 1934. Lead dioxide satisfies the major requirements given above for the oxide anode. Angel and Mellquist (6) reported the deposition of lead dioxide from lead tartrate bath. Though electrolysis of almost all soluble salts of lead (5, 7-10) gives lead dioxide deposit under suitable conditions on the anode, the lead nitrate bath is preferred since it may be readily controlled over long plating periods and also due to the high quality of deposit obtained from the bath over a wide range of operating conditions.  $\beta$ -PbO<sub>2</sub>, which has an oxygen overvoltage higher than  $\alpha$ -PbO<sub>2</sub>, is obtained from the nitrate bath. Japanese workers (11-16) used this nitrate bath extensively for depositing lead dioxide on nickel or mild steel substrate. When lead nitrate alone is used, a dendritic form of lead is also deposited on the cathode resulting in the shorting of the electrodes. Even though a diaphragm cell has been suggested (17) to prevent lead deposition on the cathode, the addition of copper salt to the extent of 2-3% to the bath for preventing the deposition of lead is by far the most important contribution (12) in the field of electrodeposition of lead dioxide. The copper, being more electropositive than lead in the electrochemical series, deposits preferentially on the cathode. Grigger *et al.* (18) and Schumacher *et al.* (19) reported the formation of lead dioxide from the nitrate bath on tantalum or platinum-clad tantalum.

Although much work had been done as described above, the preparation of lead dioxide electrodes involved certain disadvantages. In the process developed by the Japanese workers (11-16), massive lead dioxide electrodes were prepared by depositing lead dioxide up to 1 cm thick or more, then removing the same from the substrate, and finally cutting the deposit into suitable shapes with either an alundum or carborundum

\* Electrochemical Society Active Member.

Key words: electrodeposition, chlorates, perchlorates, insoluble anodes.

grinding stone. This operation needs special care as the deposit is brittle as well as very hard. The conventional clamp current-contact produces local heating and hence suitable modifications have to be done. On the other hand, costlier substrates were described for depositing lead dioxide in the methods described by Grigger *et al.* (18) and Schumacher *et al.* (19).

The successful electrodeposition of lead dioxide from lead nitrate-copper nitrate bath on graphite substrate carried out simultaneously by the authors (2, 20, 21) and by Gibson (22, 23) in the U.S. obviates the difficulties experienced by earlier workers. While Gibson (22) used a nonionic surface active agent in the bath, Narasimham and Udupa (2, 20, 21) employed rotation for the cylindrical rods and to-and-fro motion for the plates during deposition to inhibit gas bubbles from sticking to the surface, thereby avoiding pinholes and pitting in the coating. Although hydrodynamic factors, such as the decrease in the thickness of the diffusion layer and also the easy transport of ions to the interphase, do exist during the movement of the electrode, the important aspect in this case happens to be the dislodging of gas bubbles adhering to the surface of the electrode. Similarly, the use of surfactant lowers the interfacial tension, thereby enabling the easy release of gas bubbles from the anode surface. The electrodes thus developed have the following advantages: (i) a thin coating of lead dioxide on graphite is adequate; (ii) the graphite provides mechanical strength for the deposit and is completely protected against anodic attack; (iii) electrical contact to lead dioxide can conveniently be made on graphite; and (iv) preparation of such anodes for large scale operation does not present undue difficulty.

Cell assembly for oxide deposition differed with the size and shape of the anodes required to be coated. The electrolyte contained 325-350 g/liter lead nitrate and 25-30 g/liter copper nitrate, with an initial pH between 4 and 4.5. During electrolysis the pH became acidic due to the production of nitric acid and was maintained at 1-1.5 by adjusting the flow rate of the electrolyte. The acid produced was neutralized outside the cell by the addition of lead carbonate or lead monoxide and copper carbonate. Deposition was carried out at current densities of 3-5 A/dm<sup>2</sup> and at a temperature of 58°-65°C. It is most important to have precleaning operations for the graphite anode prior to deposition, which consist in electrolyzing a 10% (W/V) sodium hydroxide solution with the graphite as anode for 30 min, dipping the anode in 10% (V/V) nitric acid for 10 min, and finally washing it thoroughly with distilled water. Different rods and plates of GSLD prepared are given in Table I. These have been used in 200, 800, and 5000A cells for the production of chlorates and perchlorates. The thickness of the deposit depends on the process in which GSLD is used, e.g., 1.5-2.5 mm thick is sufficient for chlorate production while the thickness must be more than 3.5 mm for the production of perchlorate. Even if the lead dioxide peels off without any attack on the graphite surface, the lead dioxide can be deposited again on the same graphite. Some of the GSLD anodes given in Table I include such once or twice redeposited electrodes. Calculations for optimizing the size of the anode with respect to weight of graphite needed for different diameter graphite rods show that either 7.5 or 10 cm diameter GSLD rods are preferable (24).

Table I. GSLD rods and plates

Rods			Plates			
Length (cm)	Diameter (cm)	No. of specimens	Length (cm)	Width (cm)	Thickness (cm)	No. of specimens
30	5	60	30	15	1.25	148
30	7.5	65	30	15	2.5	86
60	7.5	100	90	18	3.0	48
75	20	8				

Figure 1 shows GSLD plates and rods of different sizes. The flow diagram of the process is given in Fig. 2.

The addition of different surface active agents to avoid pinholes has been described previously (13, 14, 25-27). In the course of the study on measurements of stress in electrodeposited lead dioxide (28), the authors found the addition of quaternary ammonium surfactants not only lowered the stress but also helped in obtaining a pore-free deposit on stationary graphite even at higher anode current densities (29).

### Application of GSLD Anodes

**Chlorates.—Sodium chlorate.**—A 200A cell with GSLD anode and stainless steel (30) or mild steel (31) cathode was operated continuously; the electrolyte being a solution containing 220-250 g/liter sodium chloride and 180-240 g/liter sodium chlorate with 1N HCl to maintain the pH between 6.4 and 6.8. Though this composition is not critical, but on cyclic use, the solution attained this composition after two or three runs. Table II gives the operating conditions of the cell. The anodes gave satisfactory service for 24 months with 50% of the anodes still in good condition. A current efficiency of 70-80% was obtained while depleting the chloride concentration of electrolyte from 250 to 100 g/liter. The energy consumption varied from 6.0 to 6.4 kWhr (d.c.)/kg of sodium chlorate (30). When the mild steel was used as container-cum-cathode the anode could be used for 12 months (31) at higher current density, thereby showing almost the same quantity of production per anode.

Based on the above results, scaling up of the cells to 800A was done for the production of sodium chlorate using GSLD (7.5 cm diam × 60 cm long) anodes (32). Two cells were operated continuously, one cell with a concrete container and stainless steel cathode and the



Fig. 1. Graphite substrate lead dioxide plates and rods of different sizes.

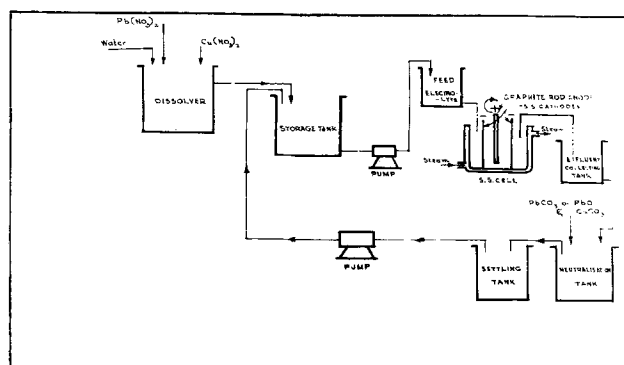


Fig. 2. Flow diagram for the production of GSLD anodes

Table II. Operating conditions of chlorate cells using GSLD anode

Characteristics	200A cell		800A cell	
	Cell with stain- less steel cathode	Cell with mild steel cathode	Cell with stain- less steel cathode	Cell with mild steel cathode
Cell voltage (V)	3.2	3.2-3.3	3.4-3.7	3.7-4.2
Anode current density (A/dm <sup>2</sup> )	3.4	5.2-5.7	4.9	10.5
Cathode current density (A/dm <sup>2</sup> )	—	2.5-3.0	1.4	1.13
Current concentration (A/liter)	6.5	15.4	3.2	2.9
Temperature (°C)	37	39	40-47	40-45
pH	6.6	6.4-6.8	6.2-6.8	6.2-6.8
Duration of working (months)	24	12	24	13
Current efficiency (%)	75-80	68-73	72-78	68-75
Energy consumption (kWhr/kg of NaClO <sub>3</sub> )	6.0-6.4	6.8-7.2	7.0-7.6	8.5-9.0

other with a mild steel container-cum-cathode. The performance of the cells employing the operating conditions given in Table II confirmed the results obtained with 200A cells. The chloride content could be brought down to less than 5 g/liter in the cell with the stainless steel cathode. No perchlorate formation was observed even at such low chloride concentration.

The recent trend in preparation of chlorates is in the use of 30% iridium-platinum coated titanium anodes. Considerable improvements in the efficiency of the electrolytic production of sodium chlorate are claimed for a process developed by Krebs (33,34). Major differences with usual practice lie in the anodes and in the use of higher current densities (30 A/dm<sup>2</sup>) and higher temperatures (>60°C) than current procedures. The consumption of activated alloy is reported to be 400-500 mg/ton of sodium chlorate. The advantage claimed with these anodes is the reduction in the power consumption, viz., 4800-5400 kWhr/ton of chlorate (34) as against 6000-6500 kWhr/ton in the existing processes. However, at present the preparation of this anode in India is dependent on the import of all the raw materials.

An electrolytic process for the preparation of sodium chlorate liquor of high concentration (630-660 g/liter NaClO<sub>3</sub> with 5-10 g/liter NaCl), suitable for the *in situ* production of chlorine dioxide for textile or paper industries, was developed by employing a GSLD anode and stainless steel cathode (35). The high concentration of sodium chlorate could be attained by saturating the cell liquor with solid sodium chloride during electrolysis with a current efficiency of 55-65% and an energy consumption of 8.8-11.5 kWhr (d.c.)/kg of NaClO<sub>3</sub>. However, the advantage of this method is that the cell effluent can be directly used for the production of chlorine dioxide without processing the liquor for getting solid sodium chlorate and this is possible only with the lead dioxide anode (and perhaps Pt-Ir coating the titanium anode), not with any other conventional anodes.

**Potassium chlorate.**—Potassium chlorate, which is mainly used in the manufacture of matches, was prepared by the electrolytic oxidation of potassium chloride in the 800A cell using GSLD anodes and stainless steel cathode (36). The cell was operated at an anode current density of 5 A/dm<sup>2</sup>, a temperature of 55°-60°C, and a pH of 6.0-7.0. A current efficiency of 82-85% was obtained with the energy consumption of 6.3-6.5 kWhr (d.c.)/kg of potassium chlorate. Efficiency in the production of potassium chlorate higher than sodium chlorate may be attributed to (i) the operation of the cell at higher temperature and consequent lowering of voltage by 0.1-0.2V and (ii) the conversion of less chloride to chlorate in view of solubility factors. A 5000A cell (37), which can be considered as a prototype commercial cell, was operated for about 150 days with a GSLD anode employing an anode current density of 15-17 A/dm<sup>2</sup> and a temperature of 50°-60°C. The cell voltage was 3.5-3.7V. The higher anode current density has the advantage of using a smaller cell with less initial investment on graphite. The cell effluent, being clear and free from suspended impurities, could be processed further without filtration and pure

potassium chlorate (>99%) was obtained by recrystallization.

Another process (38) using a GSLD anode for the production of potassium chlorate was developed on a 800A as well as on a 5000A scale (37) (Fig. 4) which consisted of the oxidation of sodium chloride to sodium chlorate using a mixed electrolyte consisting of sodium chloride, sodium chlorate, and potassium chlorate in the cell. Potassium chlorate was precipitated by adding solid potassium chloride. The chloride and chlorate concentrations in the electrolyte were maintained between 5 and 1 M/liter, respectively, in the feed electrolyte and *vice versa* in the effluent. The advantage of this method is that a higher concentration of sodium chlorate in liquor can be obtained in the cell which can be reacted with solid potassium chloride to precipitate the potassium chlorate, and the solution, after filtering off potassium chlorate, can be directly used as feed liquor. The novelty of this process is in the working out of the suitable range of compositions of feed and effluent liquor.

**Advantages of GSLD anodes in chlorate production.**—

It has been experimentally proved that GSLD anodes have the advantage of a life longer than the treated graphite anodes in the chlorate production (consumption of treated graphite is taken as 25-30 kg/ton of chlorate). Small dimensional change of the graphite anodes by the coating of PbO<sub>2</sub> does not call for much alteration in the design of the existing cells in industry. With GSLD anodes the cell effluent is clear and hence processing can be carried out without filtration. It is also possible to employ a higher current density which in turn helps in using a smaller cell with less initial investment on graphite.

**Perchlorates.**—**Oxidation of sodium chlorate to sodium perchlorate.**—Due to increasing demand for ammonium perchlorate in rocketry, attention was given to the replacement of costly platinum with GSLD anode in the production of perchlorate. At present, as metal oxide-coated titanium electrodes (like DSA) are not suitable, GSLD is the only alternative anode to platinum for the production of perchlorate. On the basis of results obtained on laboratory scale (39, 40), two cells of 75A and one of 400A were operated for the production of perchlorate using the GSLD anode (7.5 cm diam × 30 cm long with a deposit of 5 mm thick) (41). Six anodes were used in the 400A cell and only one anode in the 75A cell. A saturated solution of sodium chlorate containing NaF (2 g/liter), added to increase the oxygen overvoltage of the anode (13) and also to increase the current efficiency of the process, was electrolyzed using the anode current density of 15-25 A/dm<sup>2</sup>, temperature of 40°-45°C, and pH between 6 and 7. The current efficiency was 70-75% with an energy consumption of 3-3.3 kWhr (d.c.)/kg of sodium perchlorate. The presence of even small quantities of chromate in the electrolyte affected the current efficiency of the formation of perchlorate at lead dioxide (current efficiency of only 42%), thereby confirming the results of Sugino and Yamashita (42) and Schumacher *et al.* (19). It was pointed out that an insoluble film of lead chromate might be forming on the surface of lead dioxide and

thereby hindering the formation of perchlorate. It was found that the thickness of the deposit had a definite effect on the life of the anode and experiments showed that a thickness of 3.5-5 mm would be needed in the preparation of perchlorate (43).

**Direct oxidation of sodium chloride to sodium perchlorate.**—The methods so far in vogue for the electrolytic preparation of perchlorates involve two stages; the first stage being the oxidation of chloride to chlorate using graphite (44) or magnetite (45) or lead dioxide anodes (30-32), and the second stage being the oxidation of chlorate to perchlorate using platinum (46-49) or lead dioxide anodes (18, 19, 39, 40). In between these two stages, the electrolyte obtained in the first stage has to be processed to isolate the sodium chlorate and recover the unconverted sodium chloride.

Sugino (11) reported the direct oxidation of chloride to perchlorate using a lead dioxide anode having two discrete electrochemical stages wherein the temperatures of the electrolysis were different and the addition of sodium fluoride was made after all the chloride was converted to chlorate. Udupa *et al.* (50-52) found that GSLD could be used for preparing sodium perchlorate directly from sodium chloride in one cell without recourse to process in between to isolate chlorate. The operating conditions are given in Table III.

Large scale trials have been carried out (52) with two cells of 75A capacity and one 400A cell. The cells were run continuously at an anode current density of 20 A/dm<sup>2</sup> and a temperature of 45°-50°C. Six GSLD rods (7.5 cm diam × 30 cm long with 4-5 mm thick deposit) were used as anodes in the 400A cell and one rod was used in the 75A cells. The electrolyte was a saturated solution of sodium chloride containing NaF (2 g/liter). The loss due to evaporation was made up with further quantities of sodium chloride solution in such a way that the final cell liquor concentration would be 650-700 g/liter sodium perchlorate. Figure 3 is a graph showing the variation of the concentrations of chloride, chlorate, and perchlorate with duration of the electrolysis. The GSLD anode could be used for more than 450 days of continuous electrolysis in this process. A typical prototype commercial cell of 5000A (Fig. 4) was designed and operated continuously for 9 months at the optimum conditions (24). A current efficiency of 55-62% with energy consumption of 12.8-14.5 kWhr (d.c.)/kg of sodium perchlorate was obtained.

The novelty of this process is the oxidation of chloride to perchlorate in the same cell without alteration of operating conditions or recourse to intermediate processing. In contemplating the direct oxidation of sodium chloride to sodium perchlorate, none of the commonly used anodes, *viz.*, graphite, magnetite, or platinum, can be successfully employed as a single anode material and GSLD is the natural and economic choice at present. The addition of sodium fluoride can be made either at the beginning of the electrolysis or after the conversion of chloride (52).

Sodium perchlorate liquor obtained by both the above methods and having less than 10 g/liter sodium chlorate was used for double decomposition with either potassium chloride or ammonium chloride to give potassium perchlorate or ammonium perchlorate, respectively, and the products conformed to the required specifications (24).

Table III. Operating conditions for direct oxidation of sodium chloride to sodium perchlorate using GSLD anode

Anode current density (A/dm <sup>2</sup> )	15-20
Current concentration (A/liter)	18.5-25.0
Temperature (°C)	40-50
pH	6.2-6.8
Bath voltage (V)	4.0-4.6
Current efficiency (%)	53-60
Energy consumption (d.c.) (kWhr/kg of NaClO <sub>4</sub> )	11.5-12.3

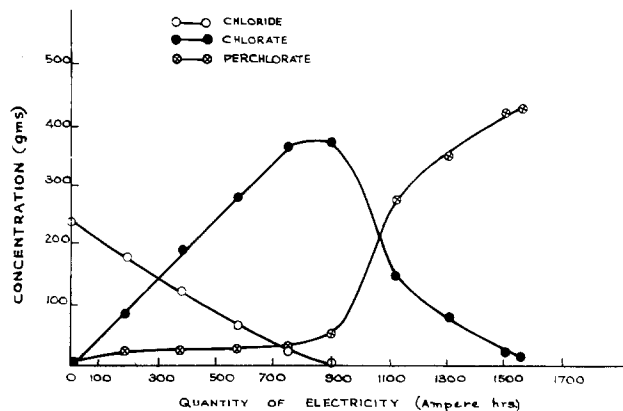


Fig. 3. Variation of the concentrations of chloride, chlorate, and perchlorate of sodium with quantity of electricity.

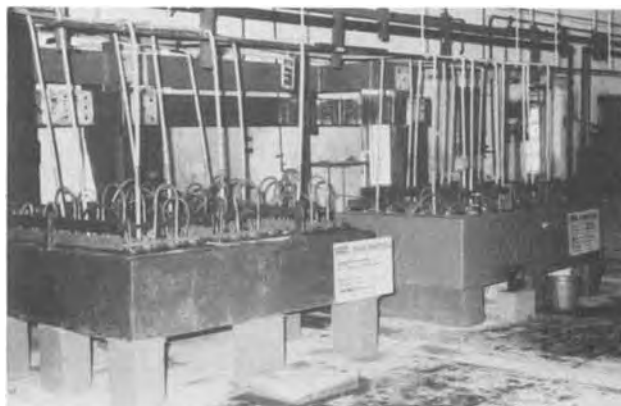


Fig. 4. Photograph of the 5000A chlorate and perchlorate cells

**Bromates, iodates, and periodates.**—Based on the resultant conditions of laboratory experiments (53), one 75A cell was run with a GSLD anode for the production of bromates employing an anode current density of 16-20 A/dm<sup>2</sup> and temperature of 55°-60°C. A current efficiency of 90-95% was obtained with an energy consumption of 4.0-4.5 kWhr (d.c.)/kg of sodium bromate. By treating highly soluble sodium bromate liquor with potassium bromide, potassium bromate could be obtained.

The electrochemical preparation of sodium iodate from iodine was studied using a GSLD anode and a nylon cloth-wrapped stainless steel cathode (54). Based on the laboratory scale experiments, one 250A cell was run and a current efficiency of 73-77% was obtained corresponding to an energy consumption of 3.0-3.4 kWhr (d.c.)/kg of sodium iodate.

In the oxidation of iodic acid to periodic acid (55), a GSLD anode with rough surface or prepolarized surface of lead dioxide gave better efficiency.

### Conclusion

Electrodeposited lead dioxide shows the promise of developing a high efficiency as an inert and insoluble anode in electrochemical processes and, at present, it is the only alternative anode to platinum for the production of perchlorates. Since the current-carrying capacity of GSLD is critical in view of the difference in the coefficients of graphite and lead dioxide, the proper choice of graphite plate or rod has to be made for depositing lead dioxide depending on its subsequent use. The deposition of lead dioxide on other substrates like titanium will have a better future.

### Acknowledgment

The authors thank all their colleagues connected with the project.



Manuscript submitted July 1, 1975; revised manuscript received April 7, 1976. This was Paper 169 presented at the Washington, D.C., Meeting of the Society, May 9-13, 1971.

Any discussion of this paper will appear in a Discussion Section to be published in the June 1977 JOURNAL. All discussions for the June 1977 Discussion Section should be submitted by Feb. 1, 1977.

## REFERENCES

- H. V. K. Udupa and K. C. Narasimham, *J. Indian Chem. Engr.*, **2**, 66 (1960).
- K. C. Narasimham and H. V. K. Udupa, Proceedings of the Symposium on Electrolytic Cells, Central Electrochemical Research Institute, p. 22, Karaikudi, India (1961).
- K. C. Narasimham, *Trans. SAEST*, **1**, 24 (1966).
- K. C. Narasimham and H. V. K. Udupa, *Chem. Ind. Dev.*, (*Chem. Process Eng., Bombay*), **6**, 26 (1972).
- J. P. Carr and N. A. Hampson, *Chem. Rev.*, **72**, 679 (1972).
- G. Angel and H. Mellquist, *Z. Elektrochem.*, **40**, 702 (1934).
- M. Fleischmann and M. Liler, *Trans. Faraday Soc.*, **54**, 1370 (1958).
- A. N. Kappanna and A. S. Dewagan, *J. Indian Chem. Soc.*, **34**, 439 (1957).
- U. B. Thomas, *Trans. Electrochem. Soc.*, **94**, 42 (1948).
- S. Kiyohara and Y. Shibazaki, Japan Pat. 13,370 (1969).
- K. Sugino, *Bull. Chem. Soc. Japan*, **23**, 115 (1950).
- K. Sugino and Y. Shibazaki, *J. Electrochem. Assoc. Japan*, **16**, 9 (1948).
- Y. Kato and K. Koizumi, *ibid.*, **2**, 309 (1934).
- Y. Kato, K. Sugino, K. Koizumi, and S. Kitahara, *Electrotech. J. Japan*, **5**, 45 (1941).
- S. Kitahara and T. Osuga, *J. Electrochem. Assoc. Japan*, **10**, 409 (1942).
- K. Sugino and Y. Shibazaki, Japan Pat. 176,954 (1948).
- Chemische Fabrik Griesheim-Electron, German Pat. 124,512 (1900) and 133,379 (1901).
- J. C. Grigger, H. C. Miller, and F. D. Loomis, *This Journal*, **105**, 100 (1958).
- J. C. Schumacher, D. R. Stern, and P. R. Graham, *ibid.*, **105**, 151 (1958).
- H. V. K. Udupa and K. C. Narasimham, Indian Pat. 66,195 (1958).
- K. C. Narasimham, S. Sundararajan, and H. V. K. Udupa, *J. Electrochem. Soc. Japan*, **29**, 137 (1961).
- F. D. Gibson, Jr., U.S. Pat. 2,945,791 (1960).
- F. D. Gibson, Jr., *Chem. Eng.*, **72**, 82 (1965).
- H. V. K. Udupa, K. C. Narasimham, M. Nagalingam, N. Thiagarajan, R. Palanisamy, S. Pushpavanam, M. Sadagopalan, V. Rangarajan, P. D. Jose, and P. U. John, To be published.
- Y. Shibazaki, *J. Chem. Soc. Japan*, **57**, 794 (1954).
- J. C. Grigger, U.S. Pat. 2,945,790 (1960).
- K. C. Narasimham and A. Narayanaswamy, Proceedings of the Symposium on Electrodeposition and Metal Finishing, Indian Section of The Electrochemical Society, p. 118 (1960).
- K. S. A. Gnanasekaran, K. C. Narasimham, and H. V. K. Udupa, *Electrochim Acta*, **15**, 1615 (1970).
- H. V. K. Udupa, K. C. Narasimham, and K. S. A. Gnanasekaran, Indian Pat. 124,215 (1969).
- H. V. K. Udupa, S. Sampath, K. C. Narasimham, S. Sundararajan, M. Nagalingam, N. Thiagarajan, P. Govinda Rao, C. J. Raju, T. J. V. Chandran, S. Kandasami, G. Subramanian, P. N. N. Namboodri, and S. Natarajan, *Indian J. Tech.*, **4**, 305 (1966).
- H. V. K. Udupa, S. Sampath, K. C. Narasimham, M. Nagalingam, N. Thiagarajan, T. J. V. Chandran, G. Subramanian, S. Kandasami, S. Natarajan, P. Subbiah, and R. Palanisamy, *Chem. Age India*, **22**, 21 (1971).
- H. V. K. Udupa, S. Sampath, K. C. Narasimham, M. Nagalingam, N. Thiagarajan, G. Subramanian, S. Natarajan, P. Subbiah, R. Palanisamy, S. J. Peter, S. Pushpavanam, and M. Sadagopalan, *Indian J. Tech.*, **9**, 257 (1971).
- Anon., Process in Europe, p. 11 (1971).
- Anon., *Platinum Metals Rev.*, **13**, 103 (1969).
- N. Thiagarajan, K. C. Narasimham, and H. V. K. Udupa, *Chem. Ing. Tech.*, **43**, 216 (1971).
- H. V. K. Udupa, S. Sampath, K. C. Narasimham, M. Nagalingam, N. Thiagarajan, G. Subramanian, P. Subbiah, R. Palanisamy, S. J. Peter, S. Pushpavanam, and M. Sadagopalan, *J. Appl. Chem. Biotech.*, **24**, 47 (1974).
- K. C. Narasimham, R. Palanisamy, M. Sadagopalan, P. D. Jose, P. U. John, V. Rangarajan, and H. V. K. Udupa, To be published.
- H. V. K. Udupa, S. Sampath, R. Viswanathan, N. Thiagarajan, K. C. Narasimham, M. Nagalingam, G. Subramanian, P. Subbiah, R. Palanisamy, S. J. Peter, and S. Pushpavanam, Indian Pat. 119,189 (1968).
- K. C. Narasimham, S. Sundararajan, and H. V. K. Udupa, *This Journal*, **108**, 798 (1961).
- K. C. Narasimham, S. Sundararajan, and H. V. K. Udupa, *Bull. Nat. Inst. Sci. India*, **29**, 279 (1961).
- K. C. Narasimham, H. V. K. Udupa, et al., Unpublished data.
- K. Sugino and M. Yamashita, *J. Electrochem. Soc. Japan*, **15**, 61 (1947).
- H. V. K. Udupa, S. Sampath, K. C. Narasimham, M. Nagalingam, N. Thiagarajan, G. Subramanian, R. Palanisamy, S. Pushpavanam, and M. Sadagopalan, Indian Pat. 123,290 (1969).
- P. H. Groggins, A. L. Pitman, J. McLaren, and F. H. Davis, *Chem. Met. Eng.*, **44**, 302 (1937).
- B.I.O.S. Final Report No. 1200.
- J. C. Schumacher, *Trans. Electrochem. Soc.*, **92**, 45 (1947).
- C. A. Hampel and P. W. Leppla, *ibid.*, **92**, 55 (1947).
- K. C. Narasimham, A. Narayanaswami, and B. B. Dey., *J. Sci. Ind. Res. (India)* **16A**, 512 (1957).
- H. V. K. Udupa, S. Sampath, K. C. Narasimham, M. Nagalingam, N. Thiagarajan, P. Govinda Rao, C. J. Raju, T. J. V. Chandran, S. Kandasami, G. Subramanian, S. Natarajan, P. Subbiah, and R. Palanisamy, *Indian Chem. Eng.*, **9**, 28 (1967).
- H. V. K. Udupa, S. Sampath, K. C. Narasimham, M. Nagalingam, C. J. Raju, and P. Govinda Rao, Indian Pat. 103,067 (1965); U.S. Pat. 3,493,478 (1970).
- M. Nagalingam, P. Govinda Rao, C. J. Raju, K. C. Narasimham, S. Sampath, and H. V. K. Udupa, *Chem. Ing. Tech.*, **41**, 1301 (1969).
- H. V. K. Udupa, K. C. Narasimham, M. Nagalingam, N. Thiagarajan, G. Subramanian, R. Palanisamy, S. Pushpavanam, M. Sadagopalan, and V. Gopalakrishnan, *J. Appl. Electrochem.*, **1**, 207 (1971).
- S. Sundararajan, K. C. Narasimham, and H. V. K. Udupa, *Chem. Process Eng.*, **43**, 438 (1962).
- M. S. Venkatachalapathy, S. Krishnan, M. Ramachandran, and H. V. K. Udupa, *Electrochem. Technol.*, **5**, 399 (1967).
- R. Ramaswamy, M. S. Venkatachalapathy, and H. V. K. Udupa, *Indian J. Tech.*, **1**, 115 (1963).



# Electrochemical Reduction of $\text{Al}_2\text{Cl}_7^-$ Ions in Chloroaluminate Melts

P. Rolland and G. Mamantov\*

Department of Chemistry, University of Tennessee, Knoxville, Tennessee 37916

## ABSTRACT

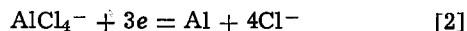
The electrodeposition of aluminum at glassy carbon, platinum, and tungsten electrodes in slightly acidic chloroaluminate melts has been studied using cyclic voltammetry, chronopotentiometry, chronoamperometry, and related techniques. The reduction of  $\text{Al}_2\text{Cl}_7^-$  ions involves a nucleation process at glassy carbon electrodes and to a lesser extent, at the platinum and tungsten electrodes. At platinum electrodes alloy formation is also involved. The discrepancies in the values of diffusion coefficients obtained by three different methods may be attributed to the nucleation effect.

The electrochemical behavior of aluminum in chloroaluminate melts ( $\text{AlCl}_3\text{-MCl}$  mixtures where  $\text{M}^+$  is an alkali cation) (1, 2) has been studied using primarily aluminum electrodes (3-7). In acidic ( $\text{AlCl}_3$ -rich) melts the oxidation of aluminum results in the formation of a poorly conducting (passivating)  $\text{Al}_2\text{Cl}_6$  layer at the electrode surface (5, 6). No evidence for the subvalent aluminum ions in these melts was obtained (7). Schulze and Hoff (4) from their galvanostatic double-pulse results calculated exchange current densities and transfer coefficients for the deposition and dissolution of aluminum in these melts.

It is well known (8-13) that the concentration of anions  $\text{AlCl}_4^-$  and  $\text{Al}_2\text{Cl}_7^-$  changes with the  $\text{AlCl}_3\text{-MCl}$  ratio. According to Tremillon and Letisse (3)  $\text{Al(III)}$  is reduced in two consecutive steps



and



$[\text{Al}_2\text{Cl}_7^-]$  changes from  $\sim 10^{-4}$  to  $\sim 1M$  in going from a  $\text{NaCl}$  saturated [ $\sim 49.8$  mole percent (m/o)  $\text{AlCl}_3$  at  $175^\circ\text{C}$ ] melt to a 52 m/o  $\text{AlCl}_3$  melt.

In this work we examined the electrochemical reduction of  $\text{Al}_2\text{Cl}_7^-$  ions at foreign substrates in melts of composition range 50.1-51 m/o  $\text{AlCl}_3$ , corresponding to  $[\text{Al}_2\text{Cl}_7^-]$  of  $6 \times 10^{-2}$  to  $4 \times 10^{-1}M$ . The purpose of this work was twofold: (i) To reach a better understanding of electrochemical reactions occurring at very cathodic potentials in these melts. This is necessary since some of the electrochemical reactions involving lower oxidation states of refractory metals, such as zirconium (14), hafnium (15), niobium (16), tantalum (17), and tungsten (18) occur at potentials near the deposition of aluminum. (ii) To learn whether the deposition of aluminum at solid electrodes other than aluminum itself involves nucleation phenomena of the type previously observed for the deposition of iron and the formation of insoluble  $\text{ZrCl}_3$  in these melts (14). Nucleation effects in the deposition of silver on platinum from molten alkali nitrates have been thoroughly studied by Hills, Schriffin, and Thompson (19, 20). These workers, however, pointed out that it is unlikely that similar nucleation effects would be observed in molten halides where predeposition reactions to form a monolayer frequently occur (21). Our results presented below show that nucleation phenomena are important in molten chloroaluminates.

## Experimental

Procedures for preparing acidic melts and most other experimental procedures have been described previ-

\* Electrochemical Society Active Member.  
Key words: aluminum electrochemistry, chloroaluminates, molten chloroaluminates, nucleation.

ously (14, 22). The background current density at the glassy carbon electrode was found to be about  $240 \mu\text{A}/\text{cm}^2$  at  $v = 0.1 \text{ V}/\text{sec}$  at  $+100 \text{ mV}$  with respect to the aluminum reference electrode in the same melt. Our value of the background current density at the glassy carbon electrode is  $\sim 50\%$  lower than the value reported by Boxall *et al.* (23) with the tungsten working electrode in molten  $\text{NaAlCl}_4$  at  $0.1\text{V}$  with respect to the aluminum reference electrode.

The procedure for making the glassy carbon electrode is similar to that of Gupta (24). This electrode was made of a 3.3 mm diameter glassy carbon rod (obtained from Beckwith Carbon Corporation, Van Nuys, California) sealed under vacuum in Pyrex tubing, then cut, polished with  $0.5\mu$  alumina and checked for leaks between the glass and carbon. The connection of the glassy carbon to a platinum wire was made with silver paint (Engelhard Industries) to give a good contact. Tungsten electrodes were cleaned by repeated oxidation and reduction using a saturated sodium hydroxide solution containing a small amount of sodium nitrite. Voltammograms and current-time curves were obtained with a PAR Model 174 pulse polarograph coupled to a PAR Model 175 universal programmer. The curves were recorded with either a Hewlett-Packard 7045A X-Y recorder or a Tektronix Model 549 oscilloscope.

$\text{Al}_2\text{Cl}_7^-$  concentrations were obtained from the known  $\text{AlCl}_3/\text{NaCl}$  mole ratios and the calculated mole fractions of Boxall *et al.* (10). Conversion to molar concentrations was made using the melt densities obtained by Fannin *et al.* (25). Molarities of  $\text{Al}_2\text{Cl}_7^-$  are given in Table I.

## Results and Discussion

**Voltammetric results.**—A typical cyclic voltammogram at a glassy carbon electrode in a slightly acidic melt is shown in Fig. 1. The voltammetric peak may be attributed to the  $\text{Al}_2\text{Cl}_7^-$  reduction. The peak current increases with the scan rate and with the  $\text{AlCl}_3/\text{NaCl}$  ratio (see below). This peak is followed by the  $\text{AlCl}_4^-$  reduction (3). Since  $\text{AlCl}_4^-$  is the main anionic constituent of the solvent, its concentration does not

Table I.  $\text{Al}_2\text{Cl}_7^-$  concentration as a function of  $\text{AlCl}_3\text{-NaCl}$  mole ratio at  $175^\circ\text{C}$

$\text{AlCl}_3$ (m/o)*	$[\text{Al}_2\text{Cl}_7^-]**$ (M)
50.15	0.06
50.20	0.09
50.30	0.12
50.80	0.28
51.00	0.38

\* Estimated precision  $\pm 0.02\%$ .  
\*\* Precision determined by the interpolation of the results from Ref. (10).

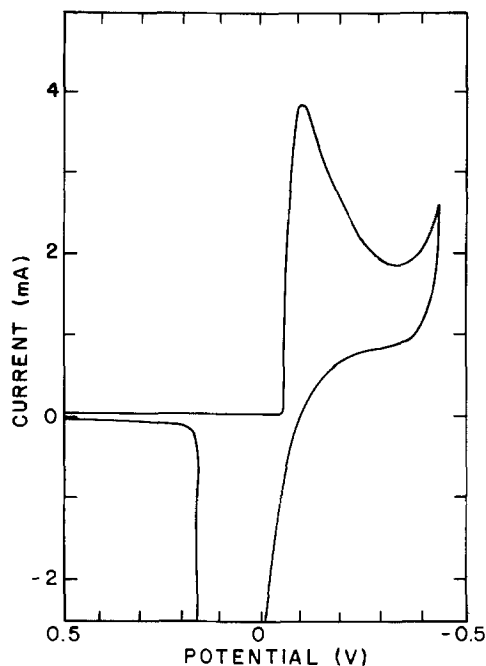


Fig. 1. Cyclic voltammogram at a glassy carbon electrode.  $v = 0.1$  V/sec;  $t = 175^\circ\text{C}$ ;  $[\text{Al}_2\text{Cl}_7^-] = 0.28\text{M}$ ; electrode area:  $0.085\text{ cm}^2$ . Potentials expressed with respect to the aluminum reference electrode in the same melt.

change significantly in the composition range studied (10). The reduction potential of  $\text{AlCl}_4^-$  remains constant in the melt composition range used for this study. When the acidity decreases the peak current decreases and shifts toward the reduction potential of  $\text{AlCl}_4^-$ , as expected for the case of an insoluble deposit (26). This peak disappears in basic melts; in this case only the  $\text{AlCl}_4^-$  limit is found. The equilibrium potential of an aluminum electrode is given by (3)

$$E = E^\circ + 4/3 RT/F \ln [\text{Al}_2\text{Cl}_7^-] \quad [3]$$

With the electrodes used, the activity of the aluminum metal is not fixed before the reduction and an underpotential deposition could occur (26). Such deposition at activity smaller than unity was observed at the platinum electrodes (Fig. 2). The reduction peak is

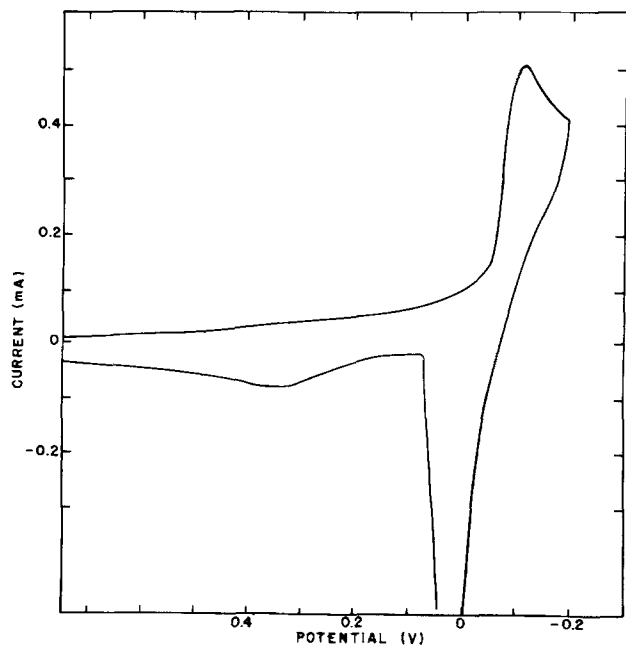


Fig. 2. Cyclic voltammogram at a platinum electrode.  $v = 0.02$  V/sec;  $t = 175^\circ\text{C}$ ;  $[\text{Al}_2\text{Cl}_7^-] = 0.09\text{M}$ ; area =  $0.100\text{ cm}^2$ .

preceded by an increasing current starting around  $+100\text{ mV}$  vs. the potential of the aluminum reference electrode. For the slow scan rates ( $<0.2\text{ V/sec}$ ) this increase is small but it becomes larger as the scan rate is increased; this is accompanied by the change in the shape of the wave from that corresponding to an insoluble deposit (26) to that of a soluble product. At the same time the reoxidation occurs in two steps; a second peak around  $+0.4\text{V}$  increases and shifts toward anodic potentials with the scan rate. If the aluminum reduction is avoided, the background does not show a reoxidation current peak at these potentials. This effect was observed only at platinum electrodes and may be attributed to alloy formation.

With the glassy carbon electrode (Fig. 1) an overpotential of  $\sim 50\text{ mV}$  was observed. A change in the slope of the reduction current at platinum (Fig. 2) occurs around the same overpotential value. At the tungsten electrode overpotential was much smaller.

For different melt compositions (Table I) the peak current increases with the square root of the scan rate (for slow scan rates) at the three electrodes. The results for the glassy carbon electrodes are shown in Fig. 3. Peak currents are proportional to the  $\text{Al}_2\text{Cl}_7^-$  concentration (Fig. 4).

At fast scan rates the peak current is no longer proportional to  $v^{1/2}$  (Fig. 5). A very large cathodic shift with increasing scan rate is also observed for the peak potential  $E_p$  (Fig. 6). Hills *et al.* (19) found a similar shift for the deposition of silver in nitrate melts, which was attributed to a nucleation process. In our case, however, the currents are much larger and ohmic drop effects are very difficult to separate from other causes of this shift. It should be noted that the shift is larger for the glassy carbon electrode and, therefore, in this case is not solely caused by an ohmic drop (the currents were comparable at the glassy carbon and tungsten). At platinum electrode the decrease of the param-

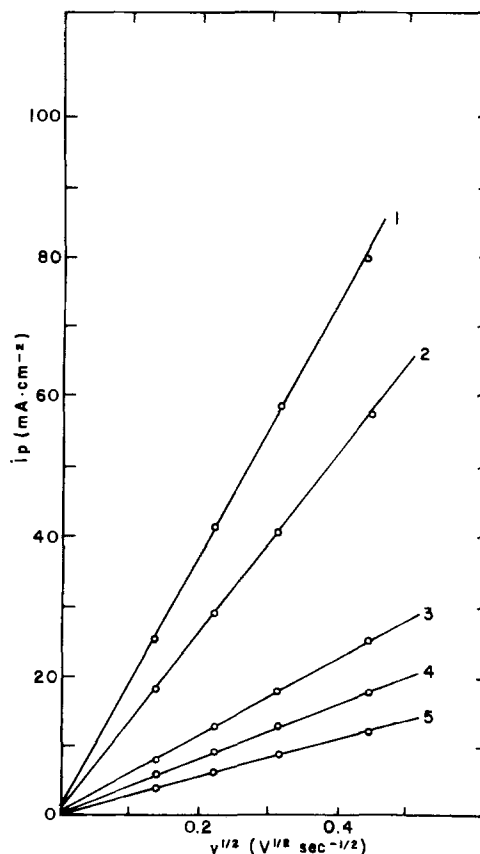


Fig. 3. Peak current density vs.  $v^{1/2}$  at a glassy carbon electrode.  $t = 175^\circ\text{C}$ .  $[\text{Al}_2\text{Cl}_7^-]$ : line 1,  $0.38\text{M}$ ; line 2,  $0.28\text{M}$ ; line 3,  $0.12\text{M}$ ; line 4,  $0.09\text{M}$ ; line 5,  $0.06\text{M}$ .

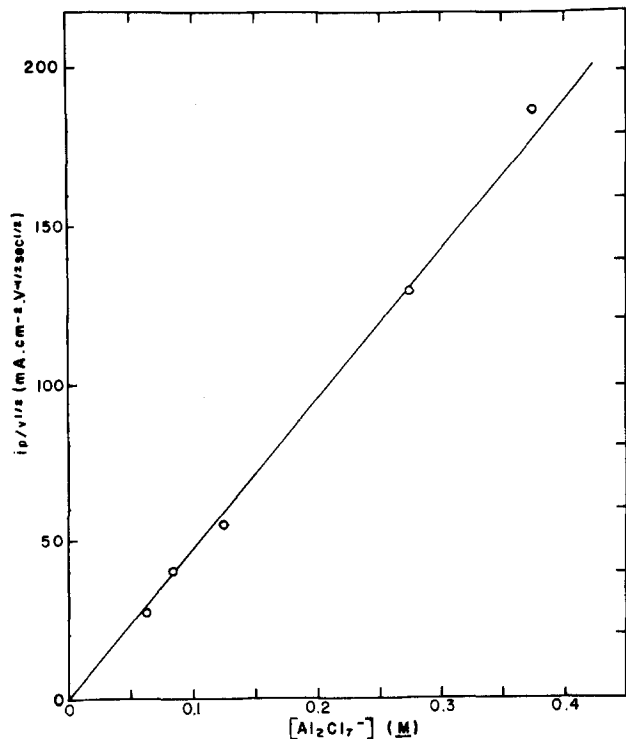


Fig. 4. Slope of straight lines in Fig. 3 vs.  $[\text{Al}_2\text{Cl}_7^-]$

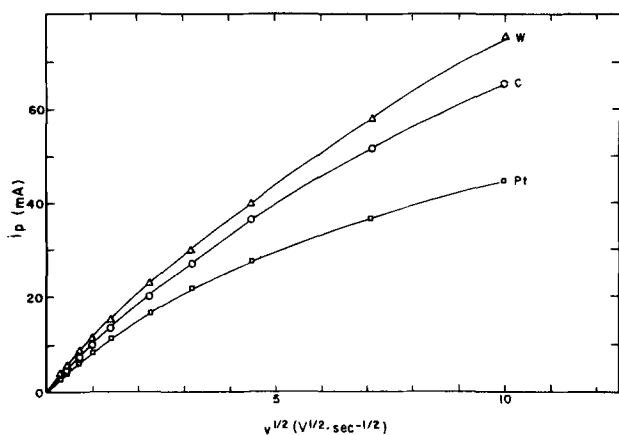


Fig. 5.  $i_p$  vs.  $v^{1/2}$  at tungsten, glassy carbon, and platinum electrodes.  $t = 175^\circ\text{C}$ ;  $[\text{Al}_2\text{Cl}_7^-] = 0.28\text{M}$ . Areas: C,  $0.085\text{ cm}^2$ ; Pt,  $0.100\text{ cm}^2$ ; W,  $0.12\text{ cm}^2$ .

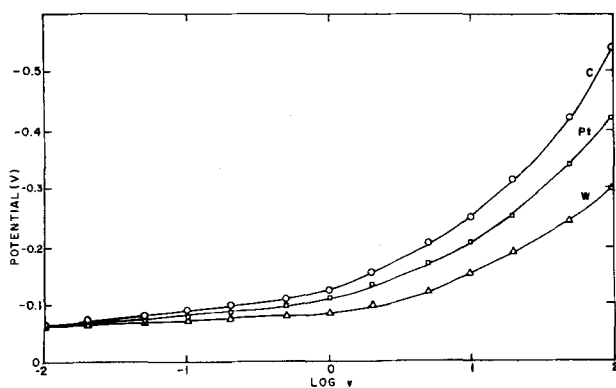


Fig. 6. Peak potentials vs.  $\log v$ . Experimental conditions same as in Fig. 5.

eter  $i_p/v^{1/2}$  with scan rate is probably caused by alloy formation which along with underpotential deposition becomes more important as the scan rate is increased.

**Chronoamperometric and chronopotentiometric results.**—Polarographic curves constructed from current-time curves (22, 27) at the tungsten electrode resulted in a linear relationship between  $E$  and  $\log(i_a - i)$  which shows that the reduction results in an insoluble product (26). The usual current decay with  $t^{-1/2}$  was observed. The slope for the  $\log(i_a - i)$  vs.  $E$  plot results in an  $n$  value of  $0.8 \pm 0.1$ , which is in reasonable agreement with the expected value of  $n = 0.75$  for reaction [1].

At glassy carbon electrodes the current-time curves show a different behavior. At small overpotentials there is no reduction current, which is in accord with the overpotential observed in linear sweep voltammetry for the same electrode. For overpotentials larger than  $-15\text{ mV}$ , after the capacitive current decay, the current increases slowly (Fig. 7a, b) then decreases after reaching a maximum (the decrease is not shown). The time to reach this maximum decreases as the applied cathodic potential is increased. It decreases from 1 min for an overpotential of  $-20\text{ mV}$  to very short times for potentials corresponding to the polarographic plateau. At the plateau potentials the parameter  $it^{1/2}$  for the current decay was constant indicating that the reduction is diffusion limited (this was true for the three electrodes used).

The increasing current has been attributed by Hills *et al.* (19) to the formation of growing nuclei at the electrode. This phenomenon has been previously observed in chloroaluminate melts for the reduction of Fe(II) and Zr(IV) (14). The current growth for the reduction of  $\text{Al}_2\text{Cl}_7^-$  was found to be linear with  $t^{1/2}$  with a slope that increases with the overpotential, similar to the results of Hills *et al.* (19). This has been attributed (19) to an instantaneous three dimensional nucleation followed by a growth controlled by hemispherical diffusion of ions to the nuclei. The reproducibility of the slope was affected by the history of the electrode. In order to get reproducible results in the nucleation studies, a stripping potential (1-2V) had to be applied for 10-20 min after the deposition of aluminum. The formation of chlorine at the electrode had to be avoided; if some chlorine was produced at the electrode the increasing current became very small and lasted for very long times even at high overpotentials

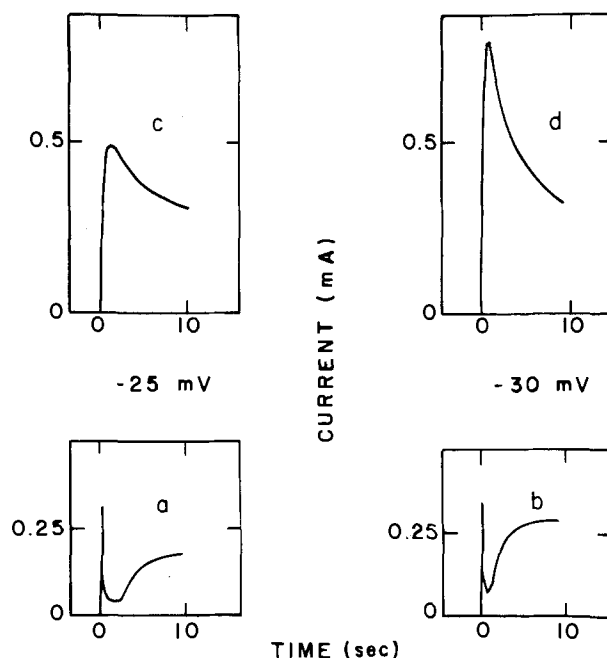


Fig. 7. Current-time curves at a glassy carbon electrode: (a) and (b) single step from the stripping potential (see text) to  $\eta$ ; (c) and (d) potential applied in two steps: stripping potential to  $+10\text{ mV}$ , then to  $\eta$ . (a) and (c):  $\eta = -25\text{ mV}$ ; (b) and (d):  $\eta = -30\text{ mV}$ .  $t = 175^\circ\text{C}$ ;  $[\text{Al}_2\text{Cl}_7^-] = 0.28\text{M}$ ; electrode area =  $0.085\text{ cm}^2$ .

indicating a completely different state of the surface of the electrode. For the stripping potentials used (1-2V) if the stripping time was less than 10 min, the nucleation current was found to increase after each cycle. In order to decrease the capacitive current observed when the step from the stripping potential to the reduction potential was applied, two potential steps were used. At first the potential was stepped to a positive potential (+10 mV) where no aluminum reduction occurs at the glassy carbon electrode. The residual current decays to a very small value in a few seconds. The reduction step was then applied and the current obtained (Fig. 7c, d) was much greater than in the case of a single step (Fig. 7a, b) from the stripping potential to the same reduction potential. The nucleation overlap (19) related to the time spent to reach the maximum, was reached in a shorter time and the beginning of the reduction was observed at a lower overpotential (-15 mV) than in the case of the direct step (-20 mV).

It should be stressed that the stripping parameters (time, potential) do not affect the current-time behavior observed at potentials corresponding to the  $i$ - $E$  plateau for the reduction of  $\text{Al}_2\text{Cl}_7^-$ . To show the effect of nucleation at small overpotentials a double pulse technique (20) was used. The potential was first stepped from the stripping potential to the potential  $\eta_G$  (Fig. 8). At this potential (0 to -20 mV with respect to the Al reference electrode) no reduction occurs if there are no nuclei sufficiently large to grow; only a small decreasing residual current is observed. The potential was then stepped for a short time  $t$  to a value  $\eta_P$ , where the nuclei are produced and grow. Upon stepping back to potential  $\eta_G$ , for nuclei of sufficient size, a current different from the residual current measured earlier was observed. Now the reduction occurs at  $\eta_G$  resulting in an increasing current. By changing the time spent at  $\eta_P$  a time lag can be found (19); for a time shorter than this time lag no growing current is observed; for a longer time the growth of nuclei is observed. The time lag vs.  $\eta_P$  at  $\eta_G = -10$  mV and -15 mV is shown in Fig. 8.

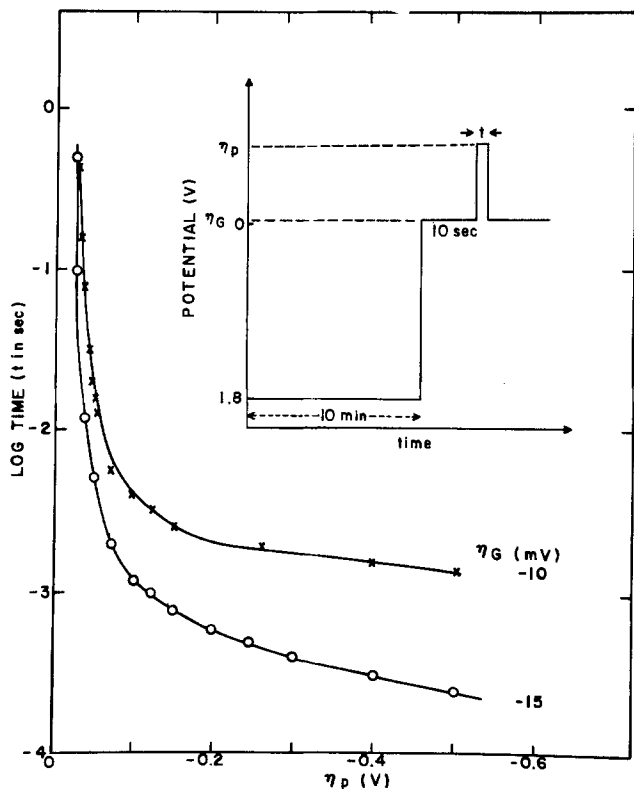


Fig. 8. Time lag vs.  $\eta_P$  at two  $\eta_G$ 's (see text). Glassy carbon electrode; same conditions as in Fig. 7. Potential-time sequence shown in the insert.

Table II. Diffusion coefficients ( $\text{cm}^2/\text{sec}$ ) of  $\text{Al}_2\text{Cl}_7^-$  ions determined using different electrodes and methods ( $t = 175^\circ$ ,  $[\text{Al}_2\text{Cl}_7^-] = 0.28\text{M}$ )

Method	Glassy carbon ( $A = 0.085$ $\pm 0.005 \text{ cm}^2$ )	Platinum ( $A = 0.100$ $\pm 0.005 \text{ cm}^2$ )	Tungsten ( $A = 0.12$ $\pm 0.01 \text{ cm}^2$ )
Chronopotentiometry	$5.0 \times 10^{-6}$	$9.6 \times 10^{-6}$	$3.7 \times 10^{-6}$
Chronoamperometry	$8.7 \times 10^{-6}$	$4.6 \times 10^{-6}$	$5.0 \times 10^{-6}$
Cyclic voltammetry	$5.5 \times 10^{-6}$	$3.2 \times 10^{-6}$	$4.1 \times 10^{-6}$

Support for the presence of a nucleation process was also found by chronopotentiometric results. The chronopotentiograms are distorted by an overshoot (14, 28, 29) due to a nucleation overpotential which can be as large as 100 mV at the glassy carbon electrode. The product  $i\tau^{1/2}$  is constant for glassy carbon and tungsten electrodes. For these electrodes the ratio of the reverse transition time  $\tau_R$  and the forward time  $t$  was found to be equal to one which indicates that the deposit is insoluble (30). For the platinum electrode, the shape of the chronopotentiogram changes with the current density. For small currents, a small overshoot is observed; the ratio  $\tau_R/t$  is close to one. When the current is increased the overshoot disappears, the curve becomes less well defined and the ratio  $\tau_R/t$  becomes 0.3 which shows that the reduction results in a soluble product (30).

**Diffusion coefficients.**—The diffusion coefficients were calculated using the straight portion of the linear sweep voltammetric  $i_p$  vs.  $v^{1/2}$  plot, the chronoamperometric  $i$  vs.  $1/t^{1/2}$  plots obtained at plateau potentials, and the chronopotentiometric  $i\tau^{1/2}$  results. The value of  $n = 0.75$  was used in the equations (see Eq. [1]; this was verified for the constructed polarograms at the tungsten electrode). The results are reported in Table II for the three methods and the three electrodes used. Hills *et al.* (19) found that the presence of the nucleation process introduces discrepancies in  $D$  values. This is also reflected in our results, particularly at the platinum electrode where nucleation and alloy formation occur at the same time.

### Acknowledgments

This work was supported by the National Science Foundation under Grant MPS 74-10357 A01. Preliminary work on this problem was performed by Dr. B. Gilbert, presently at the University of Liege, Belgium. The authors would like to acknowledge useful discussions with K. A. Bowman.

Manuscript submitted March 29, 1976; revised manuscript received May 18, 1976.

Any discussion of this paper will appear in a Discussion Section to be published in the June 1977 JOURNAL. All discussions for the June 1977 Discussion Section should be submitted by Feb. 1, 1977.

Publication costs of this article were assisted by the University of Tennessee.

### REFERENCES

1. For a review, see C. R. Boston, in "Advances in Molten Salt Chemistry," Vol. 1, J. Braunstein, G. Mamantov, and G. P. Smith, Editors, pp. 129-163, Plenum Press, New York (1971).
2. K. W. Fung and G. Mamantov, in "Advances in Molten Salt Chemistry," Vol. 2, J. Braunstein, G. Mamantov, and G. P. Smith, Editors, pp. 218-224, Plenum Press, New York (1973).
3. B. Tremillon and G. Letisse, *J. Electroanal. Chem.*, **17**, 387 (1968).
4. K. Schulze and H. Hoff, *Electrochim. Acta*, **17**, 119 (1972).
5. G. L. Holleck and J. Giner, *This Journal*, **119**, 1161 (1972).
6. B. Gilbert, D. L. Brotherton, and G. Mamantov, *ibid.*, **121**, 773 (1974).
7. R. J. Gale and R. A. Osteryoung, *ibid.*, **121**, 983 (1974).

8. G. Torsi and G. Mamantov, *Inorg. Chem.*, **10**, 1900 (1971).
9. G. Torsi and G. Mamantov, *ibid.*, **11**, 1439 (1972).
10. L. G. Boxall, H. L. Jones, and R. A. Osteryoung, *This Journal*, **120**, 223 (1973).
11. A. A. Fannin, L. A. King, and D. W. Seegmiller, *ibid.*, **119**, 801 (1972).
12. G. Torsi, G. Mamantov, and G. M. Begun, *Inorg. Nucl. Chem. Lett.*, **6**, 553 (1970).
13. G. M. Begun, C. R. Boston, G. Torsi, and G. Mamantov, *Inorg. Chem.*, **10**, 886 (1971).
14. B. Gilbert, G. Mamantov, and K. W. Fung, *ibid.*, **14**, 1802 (1975).
15. P. Rolland and G. Mamantov, Paper in preparation.
16. G. Ting, K. W. Fung, and G. Mamantov, *This Journal*, **123**, 624 (1976).
17. L. E. McCurry and G. Mamantov, Unpublished work.
18. D. L. Brotherton and G. Mamantov, Paper in preparation.
19. G. J. Hills, D. J. Schiffrin, and J. Thompson, *Electrochim. Acta*, **19**, 657 (1974).
20. G. J. Hills, D. J. Schiffrin, and J. Thompson, *ibid.*, **19**, 671 (1974).
21. G. J. Hills, D. J. Schiffrin, and J. Thompson, *This Journal*, **120**, 157 (1973).
22. G. Torsi, K. W. Fung, G. M. Begun, and G. Mamantov, *Inorg. Chem.*, **10**, 2285 (1971).
23. L. G. Boxall, H. L. Jones, and R. A. Osteryoung, *This Journal*, **121**, 212 (1974).
24. N. K. Gupta, *Rev. Sci. Instrum.*, **42**, 1368 (1971).
25. A. A. Fannin, F. C. Kibler, Jr., L. A. King, and D. W. Seegmiller, *J. Chem. Eng. Data*, **19**, 266 (1974).
26. T. Berzins and P. Delahay, *J. Am. Chem. Soc.*, **75**, 555 (1953).
27. G. Mamantov, P. Papoff, and P. Delahay, *ibid.*, **79**, 4034 (1957).
28. R. W. Stromatt, *This Journal*, **110**, 1277 (1963).
29. L. Martinot and G. Duyckaerts, *Inorg. Nucl. Chem. Lett.*, **5**, 909 (1969).
30. P. Delahay, "New Instrumental Methods in Electrochemistry," pp. 179-216, Interscience, New York (1954).

## Electrohydrodimerization Reactions

### VI. Rotating-Ring Disk Electrode and Macroscale Electrolysis Studies of the Second Reduction Wave of Diethyl Fumarate

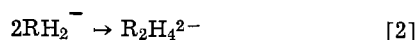
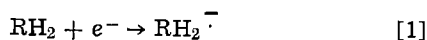
Jean-Maxime Nigretto<sup>1</sup> and Allen J. Bard\*

*Department of Chemistry, The University of Texas at Austin, Austin, Texas 78712*

#### ABSTRACT

The reactions occurring at potentials of the second reduction wave of diethyl fumarate (DEF) in dimethylformamide solutions, where a current dip is frequently observed in the voltammograms in the absence of added proton donors, was investigated. The over-all reaction order was determined by rotating disk electrode studies of the variation in the current at the dip with DEF concentration and theoretical results obtained by digital simulations. Analysis of products of macroscale electrolyses by NMR and mass spectroscopy was also undertaken. Several mechanisms are considered and one in which the electrogenerated dianion is protonated by the parent DEF to produce a carb-anion which can initiate formation of dimeric and trimeric species is proposed.

In recent years there have been numerous investigations dealing with the electrochemical reduction of deactivated olefins in aprotic media (1). For example, Baizer *et al.* (2) carried out polarographic, cyclic voltammetric, and macroscale electrolysis experiments and showed that the polarography of these compounds is characterized by two separate reduction waves. Numerous experimental studies of such systems (3-11), utilizing such electrochemical techniques as cyclic voltammetry, double potential step chronocoulometry, rotating-ring disk electrode (RRDE) voltammetry, and electron spin resonance (ESR) spectroscopy have shown that the predominant pathway of the electrohydrodimerization (EHD) reaction for reduction at the first wave consists of formation of the radical anion,  $\text{RH}_2^-$ , followed by dimerization and protonation



where  $\text{RH}_2$  represents the deactivated olefin. Very little work has been reported on the processes occurring at the second reduction step. The polarographic curves for many of the compounds studied show a second reduction wave, while others, like diethyl fumarate (DEF), (*trans*-  $\text{C}_2\text{H}_5\text{O}\cdot\text{CO}\cdot\text{CH}=\text{CH}\cdot\text{CO}\cdot\text{OC}_2\text{H}_5$ ) exhibit a current decrease or dip where a wave is expected (2). The presence of a dip where the dianion  $\text{DEF}^{2-}$  is supposed to be formed has been interpreted as oligo- or

polymerization initiated by the dianion. The mechanism of this reaction has not been established. By using cyclic voltammetric techniques and anhydrous working conditions with special steps taken to decrease the rate of the following homogeneous reaction(s) [through temperature reduction to  $-70^\circ\text{C}$  in DMF (9, 10) or the use of the low electrophilic solvent liquid ammonia at  $-43^\circ\text{C}$  (11)], the DEF dianion will exist for a sufficient time in the vicinity of the electrode surface to allow its observation. Its reactivity toward incoming parent molecules apparently can also be decreased by adding a proton source to the solution; the protonation of the doubly charged species then takes place, leading to the protonated species,  $\text{RH}_4$ . In this case, the dip at the second polarographic wave is suppressed and a definite wave is produced. Thus the final distribution of reaction products depends on the concentration of proton source present in the solution, including accidental sources, such as residual water. Cyclic voltammetric and ESR studies show that a third species, probably one formed after the first step, undergoes a reduction at a more negative potential (3, 9, 12). When stationary electrodes are used, the chemical reaction involving the dianion appears to produce some filming of the electrode surface, hindering complete usage of the experimental behavior following the first step for elucidation of the reaction path. However the forced radial convective flux near the electrode surface of the RRDE apparently sweeps away the products quickly enough to avoid these filming difficulties.

This work is aimed at extending the study of the reduction mechanism of DEF in *N,N*-dimethylformamide (DMF) at the second reduction step. The polarographic behavior exhibited by DEF has been sometimes encountered before with other redox systems and

\* Electrochemical Society Active Member.

<sup>1</sup> Present address: Department of Chemistry, Université Paris-Nord, 93206 Saint-Denis, France.

Key words: dianions, reductive coupling, rotating disk electrode, activated olefins, base-catalyzed reactions.

qualitatively interpreted. However, no quantitative treatment of this behavior at the RRDE has been reported. Because of the reactivity of the dianion toward any proton source, especially careful drying and purification procedures for the solvent and the electrolyte were employed. The second part of this paper deals with the identification of products obtained through bulk electrolysis and a proposed mechanism for the reaction.

### Experimental

The general experimental techniques were the same as those reported previously (3-5).

**Materials.**—The solvent, DMF, was purified as previously described. The supporting electrolyte, *tetra*-*n*-butylammonium iodide (TBAI), polarographic grade (Southwestern Analytical Chemicals, Austin, Texas) was dried under vacuum and stored under an inert atmosphere. Diethyl fumarate, puriss. (Aldrich Chemical Company, Incorporated, Milwaukee, Wisconsin), was used as received without further purification.

**Apparatus.**—Coulometric and preparative electrolysis experiments were carried out with a PAR Model 170 Electrochemistry System (Princeton Applied Research Corporation, Princeton, New Jersey). For the RRDE experiments, a Tacussel Electronique potentiostat Model BIPAD-2 was used. A Wavetek function generator provided the potential ramp for voltammetric studies recorded on a Mosley Model 2D-2 X-Y recorder. The RRDE, manufactured by the Pine Instrument Company (Grove City, Pennsylvania) was the same one as previously used (13); the platinum disk in it had a radius of 0.145 cm and was embedded in Teflon. It was driven with a Motomatic Model E 150 tachometer/generator motor (Electrocraft Corporation, Hopkins, Minnesota) using feedback control. The entire motor-electrode assembly was encased in a vacuum-tight mount, equipped with electrical feedthroughs to the motor and electrodes (13). The electrochemical cell used in the RRDE experiments had five glass joints leading to the working electrode assembly, the auxiliary electrode, and the reference compartment, with the remaining joints being devoted to solvent and solute transfers. The cell had a 50 ml capacity. A silver wire isolated in a compartment closed with a fine porosity sintered-glass disk was used as a reference electrode; its potential in the DMF-TBAI system was quite stable during each experiment. The auxiliary electrode was a platinum wire. The electrochemical cell used in preparative electrolysis and coulometric experiments comprised four compartments (auxiliary, intermediate-buffer to prevent catholyte contamination, reference, and working, the last having a 150 ml capacity). A mercury pool electrode was used as a working electrode; the auxiliary and reference electrodes were the same as those described above.

All the experiments were carried out in a glove box filled with a positive pressure of high purity helium (99.995% Matheson Gas Products, La Porte, Texas) and care was taken that neither purified solvent nor supporting electrolyte was ever in contact with the atmosphere following their purification. Furthermore, the following additional procedure was undertaken before each experiment to diminish the concentration of residual water or dissolved air in the solution. A weighed amount of supporting electrolyte was dissolved in the solvent under inert gas pressure and poured into a transfer vessel. After freezing and pumping of the solution, 5 ml of spectrograde benzene were added. Three freeze-pump-thaw cycles were performed and the water-benzene azeotrope was eliminated through vacuum distillation. The solution was then transferred under vacuum into the electrochemical cell, brought to atmospheric pressure with helium, and allowed to equilibrate. Before assembly the electrochemical cell was pumped down for about 1 hr and the platinum disk electrode polished with alumina. The same procedure

for purifying the solvent was used for the bulk electrolysis experiments. The catholyte solution had a volume of 120 ml and was saturated with supporting electrolyte (for TBAI, about 0.5M). Up to 0.2M depolarizer was added in several fractions and the electrolysis was conducted until each fraction had been converted before adding the next fraction. The basicity of the solution increased during electrolysis, and to avoid possible contamination a glass-embedded, rather than Teflon stirring bar, was used. After completion of the experiment, protonation of the remaining reactive species was achieved by pouring about 20 ml water into the solution. The mixture was then evaporated, the residue extracted with ether, washed with water, and the organic layer dried with anhydrous sodium sulfate. The solvent was removed by distillation and the analysis of the reaction products carried out.

### Results

A typical RRDE voltammogram of DEF is shown in Fig. 1. The disk curve exhibits a one-electron reduction wave, with  $E_{1/2} = -0.76V$  vs. the silver wire-reference electrode (Ag-RE), followed by a dip commencing at approximately  $-1.60V$  vs. Ag-RE. After the short plateau, characterized by the current  $i_{d,1}$ , the disk current,  $i_d$ , increases, due to the background limiting reduction of the DMF-TBAI system on platinum. For the same working conditions, the  $i_{d,1}$  value is reproducible within the experimental error and no appreciable filming of the electrode surface seems to occur, since two consecutive runs are essentially superimposable. On the same figure, curve b represents the ring current,  $i_r$ , as a function of disk potential,  $E_d$ , with the ring potential,  $E_r$ , held at 0.0V vs. Ag-RE. In absence of kinetic complication, the ratio  $i_r/i_d$  (the collection efficiency,  $N$ ) is only a function of the geometry of the electrode and can be calculated theoretically. In the case of RRDE curves of DEF, the experimental value of  $N$  for the first reduction wave equals its theoretical value (0.555 for this electrode), because the second-order rate constant,  $k_2$ , of the EHD reaction involving the  $DEF^-$  radical anion, [2], is so small that appreciable reaction of  $DEF^-$  does not occur during its transit from the disk to the ring [ $k_2 = 44$  liter/msec (3-6)]. At more negative  $E_d$  values, however, the concomitant decrease of  $i_d$  and especially  $i_r$ , which finally drops to zero, shows evidence of the high instability of the electrogenerated species.

The  $i_d$  value in that potential region is proportional to the concentration at the disk surface of species able to undergo reduction, DEF and  $DEF^-$ . Hence, the decrease of  $i_d$  in a region where the dianion,  $DEF^{2-}$ , is presumably formed (by comparison with the behavior

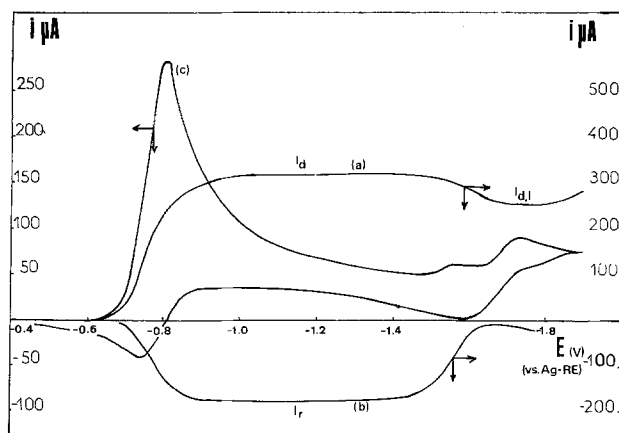


Fig. 1. Diethyl fumarate voltammograms in 0.1M TBAI-DMF solutions. RRDE voltammograms.  $\omega = 45 \text{ sec}^{-1}$ ;  $C = 9.4 \text{ mM}$ . (a)  $i_d$  vs.  $E_d$ , (b)  $i_r$  vs.  $E_d$  with  $E_r = 0.0V$  vs. Ag-RE. Cyclic voltammogram (c) 200 mV/sec,  $C = 12 \text{ mM}$ .

of olefins of similar structure) reveals the existence of a chemical stage involving the interception of incoming parent molecules by the dianion and/or by species formed after reactions of it. Thus the reaction kinetics are concentration dependent, so that for a sufficient concentration of DEF, the  $i_{d,1}$  value is lowered to a value smaller than that of the first diffusion plateau. A study of the variation of  $i_{d,1}$  with concentration of DEF,  $C$ , can then provide information about the nature and the kinetics of the reactions in this potential region. The "information content" of such an  $i_{d,1}$  vs.  $C$  plot is not sufficiently high that the elementary steps or their rate constants can be determined individually. What can be obtained is the over-all reaction order and rate constant. Our approach was to use digital simulations (14) of different reaction sequences involving the dianion assumed to be produced in the region of the dip. We assumed that no further reduction of the dianion at the electrode occurred at these potentials and that the predominant reaction of the dianion was that with DEF. Thus the rate of disappearance of the monomer DEF, by reaction with the dianion could be expressed as

$$-d[\text{DEF}]/dt = k_n[\text{DEF}^{2-}][\text{DEF}]^n \quad [4]$$

where  $n + 1$  represents the order of the equivalent over-all reaction and  $k_n$  is a composite rate constant, which is a function of the rate constants of the elementary bimolecular reactions involved in the reaction mechanism, as described later in this paper.

**Digital simulation procedure.**—A digital simulation of  $i_{d,1}$  for different values of  $k_n$  and  $n$  was undertaken. The general procedure involved the same theoretical treatment as that used previously for a variety of electrochemical and RRDE problems (3-5, 14-17). Its extension to the study of the DEF second reduction wave process of the RDE is fairly straightforward. The program written previously by Prater (15, 16) needed some modifications, with the diffusion and hydrodynamic parts remaining unaltered. The expression for the flux at the electrode surface, and accordingly the normalized current, was written to take care of the new boundary conditions involved in the two-step reduction. To do the simulation in terms of dimensionless parameters, it is convenient to define the current by the ratio of  $i_{d,1}$  over the value of twice the limiting current of the first reduction step. This ratio was called CONID. Another dimensionless variable used was  $XKTC^n$ , defined as

$$XKTC^n = (0.51)^{-2/3} \nu^{1/3} D^{-1/3} k_n \omega^{-1} C^n \quad [5]$$

which contains the rate constant  $k_n$  and the DEF concentration,  $C$ . We assumed the same diffusion coefficients for all of the species,  $D$ . The other parameters have their usual meaning. The digital program was tested by the simulation of an electrochemical process characterized by two separate reduction steps without kinetic complications. Simulated working curves were obtained for CONID as a function of  $\log(XKTC^n)$  for several values of  $n$ . One difficulty which often arises in the simulation of electrochemical systems with coupled chemical reactions with large rate constants is that the reaction layer thickness becomes much less than that of the diffusion layer so that only a few elements describe the concentration profile and the accuracy is diminished. In the present study this difficulty was overcome by determining the limiting CONID value for  $k_n \rightarrow \infty$  (practically  $10^7$ - $10^8$ ), i.e., by the simulation of a totally irreversible reaction of  $\text{DEF}^{2-}$  with  $n$  DEF molecules. Working curves spread across the whole range of normalized rate constants could be obtained by interpolating the accurate values at smaller rate constants toward the limiting one; typical working curves are shown in Fig. 2. From these results curves of CONID vs.  $\log(C)$  for each  $n$  and for several values of  $\log(XKT)$  (where  $XKT = XKTC^n/C^n$ ) were obtained and compared with the corresponding experimental points (Fig. 3). In the experiment  $i_{d,1}$  was taken

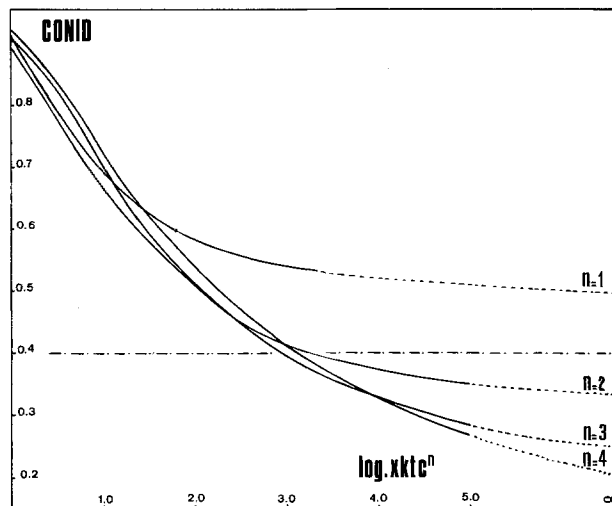


Fig. 2. Simulated CONID vs.  $\log(XKTC^n)$  curves for several values of  $n$ .

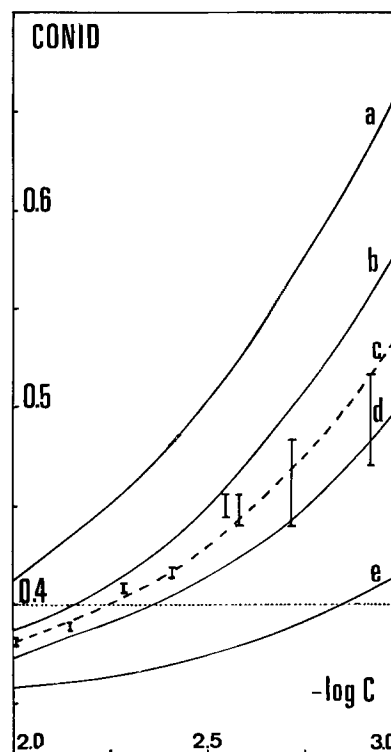


Fig. 3. Simulated CONID vs.  $\log C$  curves for  $n = 2$  and  $XKT$  values of: (a)  $7 \times 10^7$ , (b)  $3 \times 10^7$ , (d)  $10^8$ , (e)  $10^9$ . (c) (Dotted line) best fit to experimental results (yielding  $XKT = 5.6 \times 10^7$ ).

at  $E = -1.8\text{V}$  and the concentration was varied between  $10^{-2}$  to  $10^{-3}\text{M}$ . This concentration range proved to be the best for accurate measurements. At concentrations below  $10^{-3}\text{M}$  side reactions of the dianion with impurity proton donors may be a problem. Measurements were difficult at the relatively high currents observed for concentrations greater than  $10^{-2}\text{M}$ . The choice of the reaction order parameter was made as follows. The slopes of the simulated CONID vs.  $\log C$  plots, such as Fig. 3 at a given point (e.g.,  $\text{CONID} = 0.4$ ) differ for different values of  $n$ . A plot of the slope for different values of  $\log XKTC^n$  (Fig. 4) provides working curves which allow a more precise comparison of experimental and simulated data; this comparison leads, within the assumed mechanism, to an  $n$  of 2. Once  $n$  is known, the value of  $k_n$  can be estimated through the best fit between experimental and calculated CONID vs.  $(-\log C)$  curves. The average value for  $k_n$  was  $7 \times 10^8 \text{M}^{-1}\text{sec}^{-1}$ .

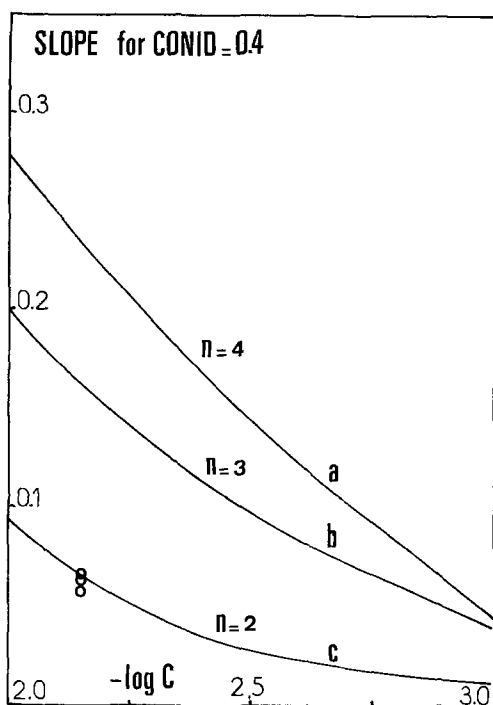


Fig. 4. Variation of the slope of CONID vs.  $\log(XKTC^n)$  simulated curves at  $\text{CONID} = 0.4$  vs.  $\log C$  for several values of  $n$ . Circles indicate experimental data.

**Macroscale electrolysis results.**—Bulk electrolysis experiments were performed to identify reaction products. The same working conditions as the RRDE experiments were used. The reduction was carried out at a continuously stirred mercury pool cathode at a controlled potential of  $-1.65\text{V}$  vs. Ag-RE in anhydrous DMF. For concentrations between  $5 \times 10^{-3}$  and  $0.2\text{M}$ , the apparent number of faradays per mole of DEF,  $n_{\text{app}}$ , was about the same as for the coulometric reductions performed after the first reduction wave. The vicinity of the third reduction peak and of the background reduction limit did not allow an accurate measurement of  $n_{\text{app}}$ , but most of the values fell in the range of 0.55–0.65. Thus  $n_{\text{app}}$  less than one is consistent with the existence of a reaction consuming parent molecules. During electrolysis, the working compartment solution showed a transient yellow color before turning gradually amber. The middle compartment remained colorless. Cyclic voltammograms taken during electrolysis showed a decrease of both reduction peaks with time. At all times during electrolysis no additional peaks were detected and the viscosity of the solution was apparently unchanged.

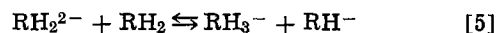
After completion of the electrolysis, no precipitate could be isolated, which might be formed by a polyaddition reaction initiated at the electrode and continuing in the bulk solution. Systematic attempts using gas chromatography to detect any ethanol (or ethanolate) that might be formed as a result of a subsequent reaction were unsuccessful. Such a possible pathway was first suggested by Nelson (18) to explain results based on ESR measurements. Recently, it was shown that a Dieckmann-type elimination of ethoxide stabilizes the dimeric cinnamate ester dianion (19, 20); however such a mechanism involves a different olefin under different working conditions. Our results demonstrate that  $\text{EtO}^-$  elimination from the DEF dianion does not occur. A proton NMR analysis was carried out on the isolated electrolysis products and the spectra compared with those of pure samples of hydrodimer, diethylsuccinate, and DEF. The results indicated that no dihydroproduct was formed. Moreover, no peak relative to protons carried by an  $\text{sp}^2$  carbon could be detected. The spectra exhibited two major groups at

$\delta = 4.15$  ppm( $\text{CH}_2$ ) and  $\delta = 1.30$  ppm( $\text{CH}_3$ ), arising from several nonequivalent ethyl groups. These major peaks were separated with numerous small groups in the CH and  $\text{CH}_2$  region. Integration of this region led to a value of 1.2 nonethyl protons/ethyl group. These results were qualitatively confirmed with C-13 NMR. We attempted to obtain additional information about the molecular weight of the reaction products by using mass spectroscopic techniques. The mass spectrum of pure hydrodimer ( $M = 346$ ) shows characteristic sequences of peak groups separated by loss of  $\text{C}_2\text{H}_5\text{O}$  units ( $m/e = 45$ ) and  $\text{C}_2\text{H}_5\text{COO}$  units ( $m/e = 73$ ) beginning with peaks at  $m/e = 301$ . The parent peak was absent. Qualitatively, the same type of spectra were obtained with the reaction products. The three first peak groups started, in the high range of  $m/e$  ratios, at 471, 472, 473–442, 443, 444 and 426, 427, 428. In the lower range, groups of peaks were positioned at  $m/e$  ratios arising from loss of units of 45 and 73. Since no peaks were detected at  $m/e$  values higher than the above limit, the mass spectra suggest formation of isomeric trimers as the predominant higher molecular weight species.

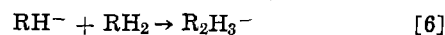
### Discussion

The experimental results indicate that formation of the dianion does not lead to polymer formation and both the RDE results (showing  $n = 2$ ) and the  $n_{\text{app}}$  results suggest predominant dimer and trimer formation. The absence of ethanol as a product demonstrates that a Dieckmann-type intramolecular cyclization does not occur. Three possible reaction schemes can be suggested, depending on the mode of reaction of the DEF dianion ( $\text{RH}_2^{2-}$ ) with parent molecule (structures are shown in Fig. 5).

1. **Proton transfer scheme.**—The DEF dianion is a strong base and could abstract a proton from incoming parent monomer



This type of reaction between electrogenerated dianion (as a base) and a second molecule has been discussed by Baizer and co-workers (21, 22) and Iverson and Lund (23). The carbanion  $\text{RH}^-$  could then react with an additional molecule of incoming parent



in a Michael reaction, with the dimeric species being protonated to yield  $\text{R}_2\text{H}_4$  or reacting with yet another molecule of  $\text{RH}_2$  to form the trimer,  $\text{R}_3\text{H}_6$ . If [5] is rapid and [6] is the rate-determining step, a kinetic expression of the form of [4] would result, with  $n = 2$ . The  $n_{\text{app}}$  found for this scheme would depend upon the fate of the  $\text{RH}_3^-$  species and whether protonation of any of the intermediates (e.g.,  $\text{RH}_3^-$  or  $\text{R}_2\text{H}_3^-$ ) generates  $\text{RH}^-$ .

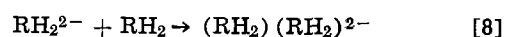
2. **Electron transfer scheme.**—The transfer of an electron between the dianion and parent is thermodynamically favored and would lead to two radical anions (reaction [7])



This route would lead to hydrodimer,  $\text{R}_2\text{H}_6$ , via reactions [2] and [3]. Since the radical anion coupling reaction is relatively slow, about  $44 \text{ M}^{-1}\text{-sec}^{-1}$  under

these conditions (3–6), a large fraction of the  $\text{RH}_2^{\cdot -}$  produced in the vicinity of the electrode will be reduced to dianion before coupling. The coupling intermediate  $\text{R}_2\text{H}_4^{2-}$  cannot be the major source of the current decrease in the vicinity of the second wave, since it is also produced at the first wave as well.

3. **Direct addition scheme.**—The direct addition of the dianion to parent would lead to a species formally the same as that resulting from the coupling of two radical anions





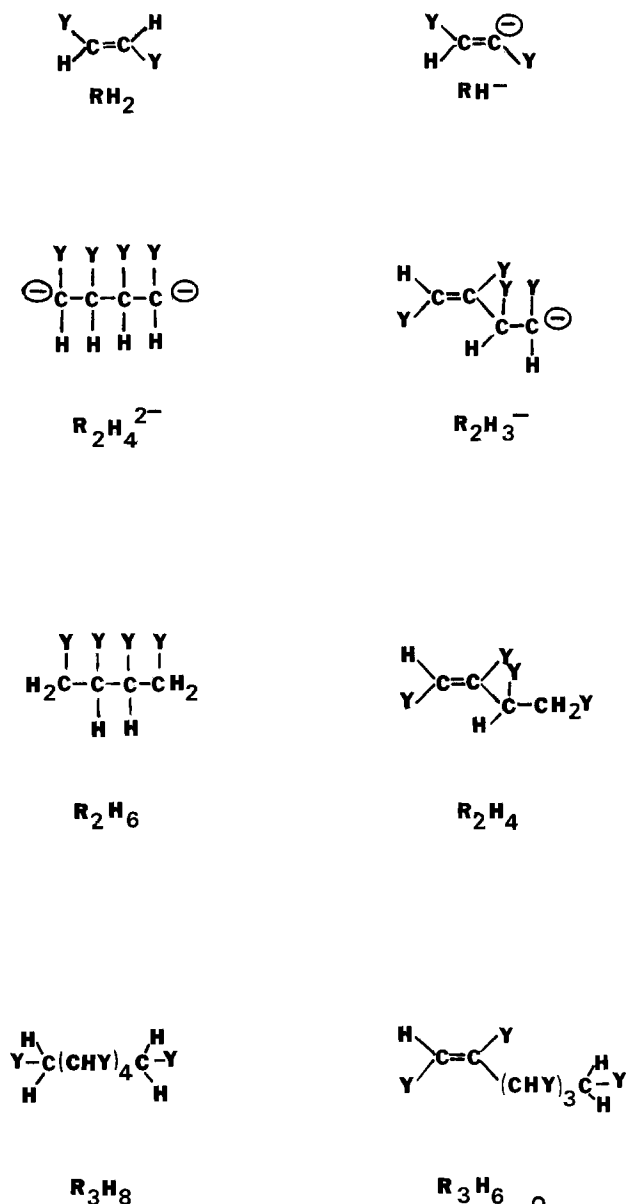
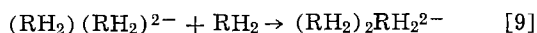


Fig. 5. Structures of various possible species. Y =  $-\text{C}-\text{OEt}$

If this species were identical to the  $\text{R}_2\text{H}_4^{2-}$  of reaction [2] appreciable reaction of it with parent, reaction [9], would not be expected. However if this species were different, at least for the time needed to undergo the



subsequent reaction, then production of the trimer,  $\text{R}_3\text{H}_8$ , would be possible at potentials of the second wave. The sequence of reactions [8] (rapid) and [9] (rate determining) would lead to an equation of the form of [4] with  $n = 2$ . The way in which the two dimeric dianionic species may differ might be analogous to the difference in behavior found in the cross-coupling and self-coupling rates of the radical anions of the *trans*- and *cis*-pair diethyl fumarate and diethyl maleate (17, 24). In that case the *trans*-radical anion couples rather slowly and does not react with acrylonitrile (AN), while the *cis*-radical anion, which isomerizes quite rapidly to the *trans*-form (25, 26), couples about two orders of magnitude more rapidly and reacts with AN. This rather speculative suggestion, that the dimeric dianion has some memory of its origin, at least for a time long enough for it to react further, will require more definitive experiments, probably in a less complicated system, before it can be considered established.

At this time scheme 1, the proton transfer scheme, appears most reasonable, although we did not detect an ethylenic double-bond in the products by NMR analysis, as would be expected in the unsaturated dimer or trimer  $\text{R}_2\text{H}_4$  or  $\text{R}_3\text{H}_6$ . These species might also be reducible at potentials of the second wave, since they contain the basic DEF grouping, and thus undergo further reduction and protonation in the macroscale electrolysis experiments. Addition of proton donor, even a relatively weak one such as water, causes an increase in the current at the second wave by competing with  $\text{RH}_2$  as a proton source. In the absence of  $\text{RH}^-$  interception of the incoming parent compound is avoided.

### Acknowledgment

The support of this research by the Robert A. Welch Foundation and the National Science Foundation (CHE 71-03344 A04) is gratefully acknowledged. We are indebted to Dr. M. Baizer for a sample of pure hydrodimer.

Manuscript submitted March 5, 1976; revised manuscript received April 25, 1976.

Any discussion of this paper will appear in a Discussion Section to be published in the June 1977 JOURNAL. All discussions for the June 1977 Discussion Section should be submitted by Feb. 1, 1977.

Publication costs of this article were assisted by The University of Texas at Austin.

### REFERENCES

- M. M. Baizer, in "Organic Electrochemistry," M. M. Baizer, Editor, Chap. XIX, Marcel Dekker, Inc., New York (1973).
- J. P. Petrovich, M. M. Baizer, and M. R. Ort, *This Journal*, **116**, 743 (1969).
- W. V. Childs, J. T. Maloy, C. P. Keszthelyi, and A. J. Bard, *ibid.*, **118**, 874 (1971).
- V. J. Puglisi and A. J. Bard, *ibid.*, **119**, 829 (1972).
- M. J. Hazelrigg and A. J. Bard, *ibid.*, **122**, 211 (1975).
- I. B. Goldberg, D. Boyd, R. Hirasawa, and A. J. Bard, *J. Phys. Chem.*, **78**, 295 (1974).
- E. Lamy, L. Nadjo, and J. M. Savéant, *J. Electroanal. Chem.*, **42**, 189 (1973).
- E. Lamy, L. Nadjo, and J. M. Savéant, *ibid.*, **50**, 141 (1974), and numerous references therein.
- R. D. Grypa and J. T. Maloy, *This Journal*, **122**, 377 (1975).
- R. D. Grypa and J. T. Maloy, *ibid.*, **122**, 509 (1975).
- I. Vartires, W. H. Smith, and A. J. Bard, *ibid.*, **122**, 894 (1975).
- I. B. Goldberg and A. J. Bard, in "Magnetic Resonance in Chemistry and Biology," J. N. Herak and K. J. Adamic, Editors, p. 297, M. Dekker, Inc., New York (1975).
- J. T. Maloy, K. B. Prater, and A. J. Bard, *J. Am. Chem. Soc.*, **93**, 5959 (1971).
- S. W. Feldberg, "Electroanalytical Chemistry," A. J. Bard, Editor, Vol. 3, Marcel Dekker, Inc., New York (1969).
- K. B. Prater, Ph.D. Dissertation, The University of Texas at Austin (1969).
- K. B. Prater and A. J. Bard, *This Journal*, **117**, 1517 (1970) and references therein.
- V. J. Puglisi and A. J. Bard, *ibid.*, **120**, 748 (1973).
- S. F. Nelson, *Tetrahedron Lett.*, **39**, 3795 (1967).
- L. H. Klemm and D. R. Olson, *J. Org. Chem.*, **38**, 3390 (1973).
- J. P. Petrovich, M. M. Baizer, and M. R. Ort, *This Journal*, **116**, 749 (1969).
- M. M. Baizer, J. L. Chroma, and D. A. White, *Tetrahedron Lett.*, **1973**, 5209.
- T. Troll and M. M. Baizer, *Electrochim. Acta*, **20**, 33 (1975).
- P. E. Iverson and H. Lund, *Tetrahedron Lett.*, **1969**, 3523.
- M. M. Baizer, *J. Org. Chem.*, **29**, 1670 (1964).
- A. J. Bard, V. J. Puglisi, J. V. Kenkel, and A. Lomax, *Faraday Discuss. Chem. Soc.*, **56**, 353 (1973).
- L. R. Yeh and A. J. Bard, Submitted to *This Journal*.

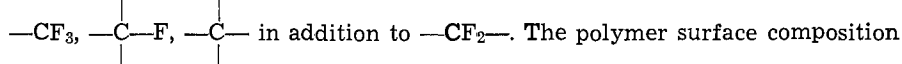
# Glow Discharge Polymerization of Tetrafluoroethylene, 1,1 Difluoroethylene, and Chlorotrifluoroethylene

D. W. Rice\* and D. F. O'Kane\*

IBM Corporation, General Products Division, Materials Science Laboratory, San Jose, California 95193

## ABSTRACT

Thin polymer films were prepared by electrodeless glow discharge polymerization of tetrafluoroethylene ( $\text{CF}_2=\text{CF}_2$ ), 1,1 difluoroethylene ( $\text{CF}_2=\text{CH}_2$ ), and chlorotrifluoroethylene ( $\text{CFCl}=\text{CF}_2$ ) monomers. The chemical composition of the films prepared both in and out of the glow discharge region was measured by x-ray photoelectron spectroscopy (XPS) and compared to bulk polymer standards. The glow discharge polymers exhibit a complex carbon 1s XPS spectrum as compared to the bulk standards. A minimum of four bonding states for carbon is clearly seen, with relatively high concentrations of



is clearly dependent on position with respect to the discharge region. The bond assignments are in close agreement with a simple electrostatic model. Polymer surface tensions were obtained using the concepts of critical surface tension and dispersion forces. They correlated well with the concentration of — $\text{CF}_3$ —, — $\text{CF}_2$ — on the surface as measured by XPS. The porosity of the films is shown to be significantly less than metal coatings of similar thickness.

Glow discharge polymerization offers an exciting alternative to classical methods of polymer synthesis. The types of polymers are potentially limitless because the combination of gases entering the discharge are equally as large. Thin, uniform, amorphous, pore-free films can be prepared with a variety of properties for optical, electronic, corrosion, wear, and surface applications. A large number of film types have been prepared by this process (1). The detailed deposition mechanisms are poorly understood. Electrons, metastables, ions, atoms, and free radicals are all present in the plasma and may be important in the polymerization process (2). Further complications are the presence of rf-generated photons and surface sputtering processes.

This study was designed to compare the deposition of thin polymer films prepared by the electrodeless glow discharge polymerization of tetrafluoroethylene ( $\text{CF}_2=\text{CF}_2$ ), chlorotrifluoroethylene ( $\text{ClCF}=\text{CF}_2$ ), and 1,1 difluoroethylene ( $\text{CF}_2=\text{CH}_2$ ) monomers. The former two monomers were chosen because of the excellent chemical stability and low permeability of bulk polymers prepared from them. The latter monomer,  $\text{CF}_2=\text{CH}_2$ , was chosen to test the relative stability of the two types of carbene free radicals;  $:\text{CF}_2$  and  $:\text{CH}_2$ . Particular emphasis was given to the polymer composition as a function of distance from the rf coils. A previous paper that discussed the process details for polymers prepared from  $\text{CF}_2=\text{CF}_2$  showed this to be very important (3). X-ray photoelectron spectroscopy, surface energy, and corrosion protection properties are the main topics of this paper. Fluoro-carbon-type films have been deposited by glow discharge polymerization in a capacitively coupled electrode-type system; the films that were deposited on alkali halide crystals were pinhole free, chemically resistant, and adherent (4).

## Experiment

Figure 1 shows the thin polymer film deposition system. A 500W, 13.56 MHz rf generator (LFE Corporation) was used to inductively couple to the respective monomers flowing through a fused silica tube. No carrier gas was used in these experiments.

\* Electrochemical Society Active Member.  
Key words: corrosion, deposition, film, monomers, polymerization.

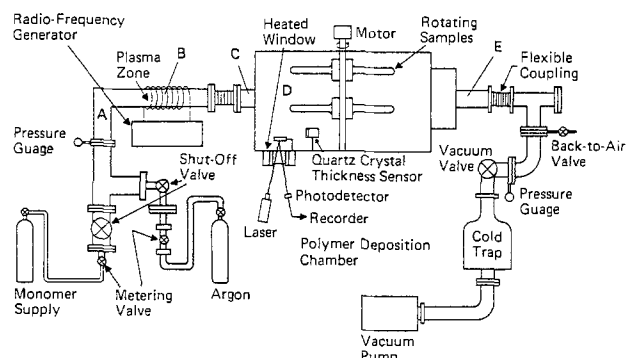


Fig. 1. Glow discharge thin polymer film deposition system

The unique feature of this system is the deposition chamber outside of the rf coil region. This minimizes substrate heating of materials that couple to the rf source. Deposition was carried out on NiFe (100 nM) coated glass microscope slides placed in regions A to E; however, for this report films prepared in the rf plasma region (region B) and in the deposition chamber (region D) will be the focus of our attention. A piezoelectric quartz thickness monitor in the deposition chamber was used to monitor film growth. Generally, the rate of deposition in the plasma region was  $10^3$  greater than in the deposition chamber. The substrates were ultrasonically cleaned in hexane, acetone, and isopropanol, followed by an *in situ* argon (60W) plasma cleaning just prior to polymerization. Table I shows the process conditions used for the three monomers in this report.

X-ray photoelectron spectra, commonly referred to as ESCA, were measured on a dispersion-compensated monochromatized spectrometer using  $\text{Al}(\text{K}\alpha)$  radia-

Table I. Glow discharge polymerization process conditions

Monomer	Inhibitor	Rf power (W)	Pressure ( $\mu$ )	Deposition rate in region D (nM/min)
$\text{CF}_2=\text{CF}_2$	1% $\alpha$ -terpinene	280	35	0.26
$\text{CF}_2=\text{CH}_2$	None	500	33	0.86
$\text{ClCF}=\text{CF}_2$	None	500	47	0.07

Table II. XPS binding energy results for bulk fluorocarbon polymers. The number in parenthesis following BE is full width half-maximum and that below is the BE reported by Clark (7)

Bonding Polymer	Carbon (1s)						F (1s)	Cl (2p <sub>3/2</sub> )
	CH <sub>2</sub>	CF	CF <sub>2</sub>	CF <sub>3</sub>	CFCI			
FEP Teflon	—	289.9 (1.2) (289.8)	291.8 (1.3) (291.8)	293.8 (1.0) (293.7)	—	—	689.1 (1.7) (690.2)	—
Polyvinylidene fluoride	286.4 (1.2) (286.3)	—	290.9 (1.0) (290.8)	—	—	—	687.9 (1.7) (689.6)	—
Polychlorotrifluoroethylene	—	—	291.1 (1.1) (291.9)	—	290.7 (1.1) (290.8)	—	688.2 (1.7) (690.8)	201.3 (201.1)

tion (Hewlett Packard ESCA 5950A). The resolution of this instrument is 0.8 eV for the carbon 1s binding energy (BE). The gold 4f<sub>7/2</sub>BE at 83.95 eV was used as the reference energy by evaporating a fraction of a monolayer of Au onto the polymer surface in the spectrometer. Argon ion etching was used to demonstrate the fragile nature of these type polymer materials to sputtering, a fact clearly demonstrated by Collins for bulk PTFE (5).

XPS is surface sensitive due to the short path length of the escaping photoelectrons. For example, 90% of the intensity comes from the top 3.5 (35Å), 2.3 (23Å), 3.7 (37Å) nM for the C(1s), F(1s), and Cl(2p) electrons, respectively, if one uses the escape depths published for homogeneous materials (6). There is considerable debate regarding the applicability of these escape depths to amorphous systems and the actual escape depth may be twice that given above. We assume the surface composition is the same as the bulk for this study. Evidence to support this assumption is that the bulk analysis of carbon and fluorine in a plasma polymer deposited from CF<sub>2</sub>=CF<sub>2</sub> agreed within 4% with the XPS quantitative results. Both peak position (BE) and integrated intensity (I) were measured. Manual curve fitting of the complex 1s spectrum was also used in making quantitative statements about the bonding of carbon. Sensitivity factors used in this study were based on our bulk standards work. These were 1.0, 0.20, and 0.48 for F(1s), C(1s), and Cl(2p), respectively.

XPS is well suited to fluoropolymer studies because of the highly electronegative fluorine atom that causes large C(1s) shifts and the long-lived final states that minimize relaxation effects observed in transition metals. The technique has been extensively applied to bulk fluorocarbon polymers (7, 8). We repeated bulk studies on FEP Teflon [(CF<sub>2</sub>-CF<sub>2</sub>)<sub>x</sub>(CF<sub>2</sub>-CF-CF<sub>3</sub>)<sub>y</sub>], polyvinylidene fluoride [(CF<sub>2</sub>-CH<sub>2</sub>)<sub>x</sub>], and polychlorotrifluoroethylene [(ClCF-CF<sub>2</sub>)<sub>x</sub>] for comparison to the plasma polymer analogs and as a check on our BE's. Table II shows the measured BE of the bulk polymers and compares them to the values obtained by Clark and Feast (7). The carbon (1s) levels are in good agreement; however, our F(1s) BE<sub>3</sub> are generally lower by 1-2 eV. It is not clear why these differ if one assumes both instruments were calibrated over the complete BE scale. Based on this assumption, the facts suggest our polymers had more ionic character in the C-F bond than those of Clark and Feast.

The surface energies of the deposited films were evaluated using both the concept of critical surface tension developed by Zisman (9) and dispersion force arguments popularized by Fowkes (10). The two methods agreed within experimental error, therefore, only an average solid surface tension (γ<sub>s</sub>) is reported. Contact angles were measured with a Rame Hart Model A-100 goniometer using hexane, heptane, tetradecane, hexadecane, 1 methylnaphthalene, ethylene glycol, and polyethylene glycols as reference fluids. Infrared spectra were taken on a Perkin Elmer 457 spectrometer. The complex nature of the deposited films coupled with the lack of precise group absorption assignment for macromolecules and broad CF

stretching bands makes the infrared work very qualitative.

The pore density of the coatings was measured optically after exposing the polymer-coated reactive NiFe metal/glass substrates to an accelerated gaseous test environment. The test conditions are given in Table III with time a variable. This environment "decorates" pores in the polymer film by corroding the metal film.

## Results and Discussion

Polymers were deposited from all three monomers. The deposition rate in the chamber (region D) differed by approximately a factor of 10; CF<sub>2</sub>=CH<sub>2</sub> going down most rapidly and ClCF=CF<sub>2</sub> least. The plasma polymers are quite different from bulk and exhibit a strong composition dependence on location with respect to the rf coils in most cases. The surface energy reflects these differences. Strong evidence for very high cross-linking is given. The polymers prepared in the plasma tend to be brittle and nonadherent. The films in this region take on a yellow to light brown color. The polymers deposited in the chamber (region D) are adherent and colorless. The failure of the reactive metal undercoat is via pores in the film not general film degradation. The pore density is significantly less than gold coatings of similar thickness. The polymers prepared from CF<sub>2</sub>=CF<sub>2</sub> and CF<sub>2</sub>=CH<sub>2</sub> are insoluble in Freon PCA while those prepared from ClCF=CF<sub>2</sub> are soluble.

Table IV gives the XPS and surface energy results for the three systems studied. Figure 2 graphically illustrates the carbon (1s) region of the XPS and clearly demonstrates the differences between plasma and bulk polymers. With these few introductory remarks, we will now discuss each system separately except for the pore density study.

CF<sub>2</sub>=CF<sub>2</sub>.—These glow discharge polymers show strong evidence of cross-linking and a relatively high concentration of -CF<sub>3</sub> functional groups in the XPS spectra. The assignment of particular C(1s) binding energies to a given functional group is based on a combination of the bulk standards and a simple electrostatic potential model for group electronegativities (11). Using the relative sensitivity and BE data in Table IV allows us then to calculate both total atomic composition and distribution of this composition between various functional groups. Table V summarizes these results.

The polymers prepared in the plasma show an atomic composition that is quite rich in carbon com-

Table III. Corrosion test environment to assess pore density

(Temperature, 25°C; gas velocity, 10 cm/sec;  
relative humidity, 70%)

Gas	Concentration (μg/M <sup>3</sup> )
SO <sub>2</sub>	810
NO <sub>2</sub>	940
O <sub>3</sub>	334
H <sub>2</sub> S	21
Cl <sub>2</sub>	8.6
Balance, purified air	

Table IV. XPS results

Starting monomer	Deposition position	BE (eV)	Carbon 1s					F(1s)	Cl(2p)	Binding energy (Au <sub>4f<sub>7/2</sub></sub> = 83.95) and measured relative peak areas (F(1s) = 100)		Critical surface tension (γ <sub>c</sub> = dyne/cm)
			1	2	3	4	5			I <sub>F(1s)</sub>	I <sub>C(1s)</sub>	
CF <sub>2</sub> =CF <sub>2</sub>	Plasma (region B) Chamber (region D)	BE	284.4	286.8	289.0	291.1	293.2	688.4	—	7.0 ± 0.5	22 ± 2	
		I	0.42	3.45	4.26	3.87	2.62	100	—	11.2 ± 0.3	12 ± 1	
		BE	—	287.0	289.2	291.7	293.8	688.9	—	10.3 ± 0.6	18.5 ± 1 (9)	
CF <sub>2</sub> =CH <sub>2</sub>	Plasma (region B) Chamber (region D)	BE	284.1	—	289.9	291.8	293.8	689.1	—	2.8 ± 0.2	31 ± 2	
		I	Trace	—	0.38	9.29	0.64	100	—	3.0 ± 0.4	26 ± 3	
		BE	—	285.8	287.7	290.4	292.9	687.6	—	5.4 ± 0.7	25 (9)	
CICF=CF <sub>2</sub>	Plasma (region B) Chamber (region D)	BE	285.0	285.4	—	290.9	—	687.9	—	5.1 ± 0.5	27.5 ± 2	
		I	2.6	9.91	—	8.96	—	100	—	6.7 ± 0.6	21 ± 2	
		BE	284.4	286.5	289.2	290.8	292.8	688.0	201.1	7.7 ± 0.6	30.8 (9)	
Polychlorotrifluoroethylene (bulk std.)	Plasma (region B) Chamber (region D)	BE	—	—	—	291.1	—	688.2	201.3	—	—	
		I	—	—	—	6.7	—	100	15.0	—	—	
		BE	—	—	—	6.3	—	—	—	—	—	

Table V. Group assignments and concentrations for polymers prepared from CF<sub>2</sub>=CF<sub>2</sub>

Deposition region	Atomic Composition	Group assignments and normalized percentage present			
		$\begin{array}{c} \text{C} \\   \\ \text{C}-\text{C}-\text{C} \\   \\ \text{C} \end{array}$ (286.8)	$\begin{array}{c} \text{F} \\   \\ \text{C}-\text{C}-\text{C} \\   \\ \text{C} \end{array}$ (289.5)	$\begin{array}{c} \text{F} \\   \\ \text{C}-\text{C}-\text{C} \\   \\ \text{F} \end{array}$ (291.5)	$\begin{array}{c} \text{F} \\   \\ \text{C}-\text{C}-\text{F} \\   \\ \text{F} \end{array}$ (293.5)
Region B (plasma)	CF <sub>1.4</sub> ± 0.1	24	30	27	18
Region D (chamber)	CF <sub>2.24</sub> ± 0.08	6	5	76	13
FEP Teflon bulk standard	CF <sub>2.06</sub> ± 0.12	—	4	90	6

pared to the starting monomer, while the chamber-deposited polymer shows enhanced levels of fluorine. Furthermore, as shown in Fig. 2, the polymers pre-

pared in the plasma have approximately equal quantities of the four major carbon functional groups ranging from carbon with four carbon nearest neighbors to —CF<sub>3</sub>. The network structure of this polymer is quite complex and suggests a high concentration of cross-links. The chamber-deposited polymer (region D) shows a preponderance of —CF<sub>2</sub>— with a relatively high concentration of —CF<sub>3</sub> (13%). The two lower BE peaks are small but significant. It is interesting to note that the FEP standard showed evidence

of —CF<sub>3</sub> and —C—F in addition to the main —CF<sub>2</sub>—

group. No evidence was seen for a carbon surrounded by four carbon nearest neighbors. When the chamber-deposited polymer is sputter etched for 60 sec with argon ions (1000V), the surface is dramatically converted to a spectra like that observed in the plasma

region, i.e., high carbon contents and large C—C—C concentrations. This merely suggests resputtering plays an important role in the plasma deposition process.

Millard and Pavlath have studied the plasma deposition of CF<sub>2</sub>=CF<sub>2</sub> on wool fabric and plastic surfaces. In their capacitively coupled system, they find a complex polymer much like that observed in our glow region. Our BE are in reasonable agreement; however, their functional group assignment is complicated by the presence of oxygen in the polymer and poor instrument resolution (12).

The infrared spectra of the polymers deposited in the two regions are quite different. The plasma-deposited films yield a very diffuse spectrum, while the deposition-chamber polymers have a spectrum much like PTFE. A small shoulder at 975 cm<sup>-1</sup> provides some evidence for C-F groups in agreement with XPS (3).

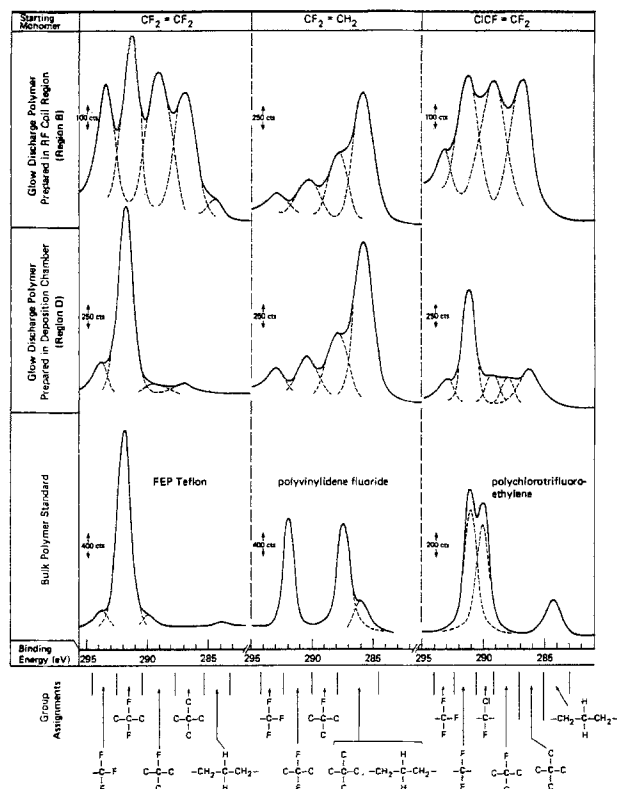


Fig. 2. Carbon (1s) x-ray photoelectron spectra of glow discharge polymers made from CF<sub>2</sub>=CF<sub>2</sub>, CF<sub>2</sub>=CH<sub>2</sub>, and CICF=CF<sub>2</sub> monomers.

The surface tension ( $\gamma_s$ ) of the glow discharge polymers is consistent with the XPS results. The chamber-deposited films have a very low surface tension, 12 dyne/cm, indicative of a high surface concentration of  $-\text{CF}_3$  (9). This is considerably lower than bulk FEP. The surface purity of the glow discharge polymers is significantly better than the bulk polymers. The XPS O(1s), N(1s), and C(1s) hydrocarbon intensities were used as a measure of purity. This may be an alternative explanation for the low surface tension in the chamber polymers. The polymers prepared in the plasma have higher surface tensions than the standard. The higher concentration of lower binding energy forms a carbon dominate in this latter case.

The lifetime of the reactive components, be they surface or gas phase, are quite different as indicated by the large differences in polymer composition with respect to the rf coils. One can speculate that in the deposition chamber adsorption of the monomer to free radical chain ends is the dominate propagation step. Resputtering is probably very minimal and, hence, the side groups would be formed in the gas phase. In the plasma zone resputtering processes are speculated to remove fluorine or  $-\text{CF}_2-$ ,  $-\text{CF}_3$  groups preferentially, yielding a far more complex propagation step.

$\text{CF}_2=\text{CH}_2$ .—The polymers prepared from  $\text{CF}_2=\text{CH}_2$  show marked similarity in both the plasma and deposition chamber compared to the significant differences observed for the  $\text{CF}_2=\text{CF}_2$  materials. They are quite complex and have a fluorine surface concentration significantly less than the bulk polymer. Table VI shows group assignments and distribution of carbon functional groups. It is important to note that XPS cannot detect hydrogen and, hence, interpretation of this system is more speculative. The low binding energy form of carbon can be a complex combination of carbon with four nearest carbon neighbors or  $\text{C}-\text{CH}_2-\text{C}$  (hydrocarbon). Infrared spectra confirm the presence of both CH stretching ( $2930\text{ cm}^{-1}$ ) and deformation ( $1450\text{ cm}^{-1}$ ).

The surface tensions for polymers prepared in both regions are greater than the bulk polymer. This supports the reduced levels of  $-\text{CF}_2-$  groups observed in the XPS study.

The deposition mechanism for this mixed hydro- and fluorocarbon system is not simply the deposition of a material originating from difluoro carbene in one region and dihydro carbene in another. The im-

portant reactive monomer may, however, be monofluoroacetylene originating from HF removal in the plasma. The carbon-to-fluorine ratio is consistent with this picture; however, the complex C(1s) XPS shows this not to be the whole story.

$\text{CICF}=\text{CF}_2$ .—Examination of the two deposition regions clearly demonstrates the complex nature of these plasma films compared to bulk polychlorotrifluoroethylene. Bond assignments are complicated in this system because of the various combinations of the constituents that yield similar binding energies, for example, the calculated BE of  $-\text{CCl}_2\text{F}$  is within 0.2 eV of  $-\text{CF}_2-$  (11). The atomic composition, as measured by XPS (Table VII), shows both fluorine and chlorine at lower levels in the plasma polymers. Just as in the  $\text{CF}_2=\text{CF}_2$  system, the polymers prepared in the plasma show a higher concentration of the lower binding energy forms of carbon.

The surface tension measurements show that the polymers prepared in both regions have lower values than the bulk. For the chamber-deposited films, where the  $\gamma_s$  is close to that of PTFE, the XPS peak at 291.0 must be predominately due to  $-\text{CF}_2-$  groups.

The relatively low concentration of chlorine in the chamber polymers supports preferential removal of  $-\text{Cl}$  from the monomer compared to fluorine.

### Barrier Properties

The pore density tests using a reactive transition metal (NiFe) substrate show convincingly that the polymers deposited in the deposition chamber provide superior atmospheric protection to metallic coatings of similar thickness. The pore sizes increased linearly as a function of test exposure time while the pore density reached a plateau. This is used as indirect evidence that these polymers are not severely degraded by the accelerated test conditions. Figure 3 shows the pore density of the chamber-deposited  $\text{CF}_2=\text{CF}_2$  films as a function of thickness and compares them to gold overcoats on nickel (13). The insert shows the time behavior of the pore size and pore density. The low pore density is speculated to result from the amorphous character of these materials coupled with the uniform *in situ* cleaning and deposition. These results support the work of Hollahan, Wydeven, and Johnson (4).

### Summary

Thin polymer films prepared by electrodeless glow discharge polymerization of  $\text{CF}_2=\text{CF}_2$ ,  $\text{CF}_2=\text{CH}_2$ , and

Table VI. Group assignments and concentrations for polymers prepared from  $\text{CF}_2=\text{CH}_2$

Deposition region	Atomic composition	Group assignments and normalized percentage present			
		$\begin{array}{c} \text{C} \\   \\ \text{C}-\text{C}-\text{CH}_2 \\   \\ \text{C} \end{array}$ (285.8)	$\begin{array}{c}   \\ -\text{C}-\text{F} \\   \end{array}$ (287.8)	$-\text{CF}_2-$ (290.5)	$-\text{CF}_3$ (292.9)
Region B (plasma)	$\text{CF}_{0.56}\text{H}_2$	54	23	15	8
Region D (chamber)	$\text{CF}_{0.60}\text{H}_2$	56	23	12	9
Polyvinylidene fluoride standard	$\text{CF}_{1.00}\text{H}_2$	53	0	47	0

Table VII. Group assignments and concentrations for polymers prepared from  $\text{CICF}=\text{CF}_2$

Deposition region	Atomic composition	Group assignments and normalized percentage present				
		$-\text{C}-$ (286.3)	$-\text{C}-\text{Cl}$ (287.8)	$-\text{CF}_2-$ , $-\text{CCl}_2-$ (289)	$-\text{CF}_2-$ (291.0) $-\text{CFCl}-$	$-\text{CF}_3$ (292.8)
Region B (plasma)	$\text{CF}_{1.16}\text{Cl}_{0.47}$	33	—	34	27	6
Region D (chamber)	$\text{CF}_{1.26}\text{Cl}_{0.22}$	24	8	12	47	9
Polychlorotrifluoroethylene standard	$\text{CF}_{1.54}\text{Cl}_{0.5}$	—	—	—	52	48
					( $-\text{CF}_2-$ ), ( $-\text{CClF}-$ )	

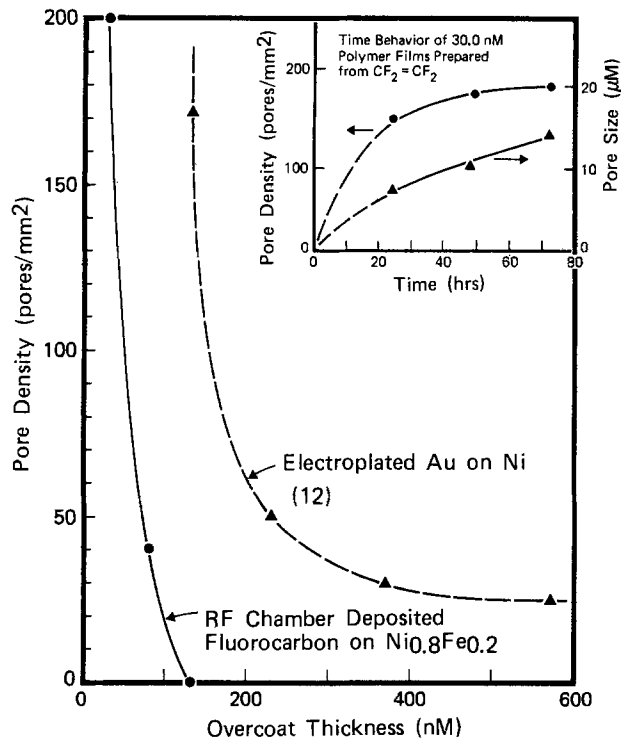


Fig. 3. Pore density as a function of film thickness for fluorocarbon-like plasma polymer on  $\text{Ni}_{0.8}\text{Fe}_{0.2}$  and Au on Ni. Insert shows time behavior of pore density and pore size for 30.0 nM polymer film.

$\text{CFCl}=\text{CF}_2$  monomers exhibit compositions and surface tensions significantly different than bulk polymers prepared from these monomers. The XPS data clearly demonstrate a deposition location dependent composition for the fully halogenated monomers. This method of deposition may provide valuable indirect evidence of reactive specie lifetime. A multitude of C(1s) binding energies are observed for all polymers deposited in the plasma (region B). The low binding energy form suggests cross-linking and complex network formation. The solid surface tensions can generally be rationalized by the relative amounts of  $\text{CF}_3$ ,  $-\text{CF}_2-$  surface concentrations. The barrier properties of these

films are much better than crystalline metallic coatings of similar thickness.

#### Acknowledgments

We would like to thank W. McChesney and R. Tremoureux for their technical assistance. Drs. H. R. Anderson, J. Coburn, R. Pollak, W. Hewett, R. Atkin, and J. Crowley provided technical discussion and valuable criticisms.

Manuscript submitted Feb. 9, 1976; revised manuscript received May 8, 1976.

Any discussion of this paper will appear in a Discussion Section to be published in the June 1977 JOURNAL. All discussions for the June 1977 Discussion Section should be submitted by Feb. 1, 1977.

Publication costs of this article were assisted by IBM Corporation.

#### REFERENCES

1. M. Millard, in "Techniques and Applications of Plasma Chemistry," J. H. Hollahan and A. T. Bell, Editors, pp. 177-214, John Wiley & Sons, Inc. New York (1974).
2. A. T. Bell, *ibid.*, pp. 1-56.
3. D. F. O'Kane and D. W. Rice, *J. Macromol. Sci., Chem.*, To be published; also *Polym. Prepr., Am. Chem. Soc., Div. Polym. Chem.*, **16**, (1), 92 (April 1975).
4. J. R. Hollahan, T. Wydeven, and C. C. Johnson, *Appl. Opt.*, **13**, 1844 (1974).
5. G. C. S. Collins, A. C. Lowe, and D. Nicholas, *Eur. Polym. J.*, **9**, 1173 (1973).
6. J. C. Tracy, in "Electron Emission Spectroscopy," W. Dekeyser, Editor, pp. 295-372, D. Reidel Publishing Co., Holland (1973).
7. D. T. Clark and W. S. Feast, *J. Macromol. Sci. Rev. Macromol. Chem.*, **12**, (2), 191 (1975).
8. C. R. Ginnard and W. M. Riggs, *Anal. Chem.*, **44**, 1310 (1972).
9. M. K. Bennett and W. A. Zisman, in "Adsorption at Interfaces," K. L. Mittal, Editor, pp. 199-211, American Chemical Society, Washington, D. C. (1975).
10. F. M. Fowkes, *Ind. Eng. Chem.*, **56**, (12), 40 (1964).
11. U. Gelius, P. F. Heden, J. Hedman, B. J. Lindberg, R. Manne, R. Nordberg, C. Nordling, and K. Siegbahn, *Physica Scripta*, **2**, 79 (1970).
12. M. M. Millard and A. E. Pavlath, *Polym. Prepr., Am. Chem. Soc., Div. Polym. Chem.*, **16**, (1), (April 1975).
13. S. J. Krumbein, *IEEE Trans. Parts, Mater., Packag., pmp-5*, **2** (1969).

# Electrochemical Investigations Concerning $\text{Ca}^{2+}$ Binding to Spectrin

E. Brauer,\* K.-D. Kupka, and V. Rudloff

*Institute of Physical Chemistry, University of Frankfurt/Main and*

*Max Planck Institute of Biophysics, Frankfurt/Main, Germany*

## ABSTRACT

Spectrin, a protein located at the inner surface of the red blood cell membrane, was isolated and investigated with respect to the binding of calcium. Aggregation phenomena were found to be due to the age of spectrin. The electrostatic interaction factor using the Linderstrøm-Lang method was found to be very weak,  $w < 0.01$ . Calcium binding occurred at 780 sites as indicated by Scatchard plots based on titration curves using a calcium-sensitive electrode. Titration curves showed in addition the occurrence of conformational changes. The presence of calcium caused the formation of filaments seen in the electron micrographs. The results of binding studies of calcium to spectrin may give information about the influence of calcium on the change of shape of red cell membranes in which spectrin is suggested to be involved.

In red cell membranes (RBC membrane) the presence of calcium controls the membrane transport and even determines the cell shape. Many investigations have been done for elucidating the mechanism of the calcium action with respect to cell shape (1-5). The interaction between calcium and the inner part of the cell membrane was found to be the reason for this phenomenon. Some investigators suggested a high molecular weight protein was responsible for the binding of calcium (6, 7). It was Marchesi (8) who first isolated a protein located at the inner surface of the membrane and called it spectrin.

Since the development of  $\text{Ca}^{2+}$ -sensitive electrodes by Ross (9), it is possible to examine directly the amount of  $\text{Ca}^{2+}$  ions bound by the protein and to estimate the interaction between this divalent cation and the protein, especially if it relates to the changes of cell shape.

## Preparation of the Material

Red blood cells were prepared according to the method of Dodge *et al.* (10). Spectrin was extracted by washing cells several times with Tris/HCl buffer, pH 7.6, and then haemolyzing them in the diluted buffer solution. The deciding step of separating the protein from its surroundings was bringing it into solution of low ion content. The composition of the material and the yield varied with pH, temperature, and the duration of incubation. It underwent an aging process which was dependent on such parameters as temperature, time between the isolation and the beginning of measurements, etc. (11).

Standard preparation was carried out in the following way: dialysis of the protein solution in low ionic strength solvent against distilled water adjusted with NaOH to pH 8 over night in the cold, thereafter separating the solubilized and unsolubilized membrane components in an ultracentrifuge at 50,000 rpm for 3.5 hr at pH 8. The material was controlled by SDS-gel electrophoresis, immediately after preparation as well as just before being used in the binding experiment. Neither EDTA nor mercaptanes were used during preparation. Electrophoretic analysis indicated that 80% of the solubilized material was spectrin and higher molecular aggregates of spectrin. Figure 1 shows a densitometer trace of spectrin prepared by the standard method.

\* Electrochemical Society Active Member through Deutsche Bunsen-Gesellschaft.  
Key words: calcium binding, bioelectrochemistry,  $\text{Ca}^{2+}$ -sensitive electrodes, spectrin.

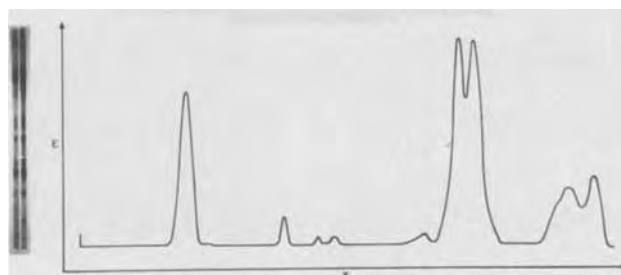


Fig. 1. Densitogram of an electrophoretic run of spectrin prepared at pH = 8.5.

## Electrometric Titration with Pure Spectrin

A possible way to identify ionizable amino acid side chains of a protein is afforded in principle by an electrometric titration. Spectrin prepared in the standard manner shows a maximum number of titratable groups in the alkaline region to be a function of time after preparation, Table I. It is obvious from these data that spectrin undergoes a process of aging finished 20 hr after preparation. This final state is found in presence of calcium ions (1 mmole/liter) immediately after preparation.

The complete titration curve allows the number of all groups titratable in spectrin to be estimated. There is protonation in an acid branch representing about 1000 groups and deprotonation in the alkaline branch representing about 500 groups. The total number of about 1500/molecule of spectrin is in rather good agreement with the recently published value of 1663 by Fuller (12).

*Multiple equilibria.*—The titration curve within a range of pH 2-11.5 was found to be reversible. Fuller (12) referring to a molecular weight of 460,000 reports 122 histidine imidazole groups. These groups have been reported by Tanford (13) to deprotonate from pH 7-9.5.

Table I. Titratable groups in the alkaline range as a function of the time after preparation

Time	No. of titratable groups
15 min	Not detectable
1 hr	136
2 hr	187
6 hr	235
20 hr	500

Since in this region no other groups dissociate or associate the application of the treatment developed by Linderstrøm-Lang (14) seems to be justified.

The model of Linderstrøm-Lang takes into account the electrostatic interaction of binding sites. One may obtain a measure of the interaction by evaluating the factor  $w$ , according to the equation

$$p_K - 0.868wz = \text{pH} + \log \left( \frac{\bar{\nu}}{n - \bar{\nu}} \right)$$

where  $p_K$  = internal  $p_K$  for imidazole groups, not identical with  $p_K$  for a single group,  $w$  = electrostatic interaction factor,  $z$  = number of elementary charges per molecule,  $\bar{\nu}$  = number of dissociated groups of a kind, and  $n$  = maximum number of  $\bar{\nu}$ .

Using the ionic strength of 0.01 we found  $w < 0.012$  with  $\text{pH} \sim 8$ . That means the electrostatic interaction is very weak. A comparison with the data of Tanford (Table II) shows a tendency of electrostatic interaction factor to decrease with increasing molecular weight.

### Ca<sup>2+</sup> Binding

**Electron micrographs.**—A growing tendency to form fibrils with increasing concentration of CaCl<sub>2</sub> could be detected by electron microscopic examination (Fig. 2). Alignment and formation of long chains were obviously a function of calcium ion content although this effect is overlapped by the drying process.

**Sedimentation constants.**—The conditions of aggregation in the original solution can be obtained using the analytical ultracentrifuge (Beckman/Spinco, Model E). The sedimentation constant of spectrin determined on solution (0.75 OD/ml), free of Ca<sup>2+</sup> in good agreement with Clarke (15), was found to be 5.3 sec. A solution containing 1 mmole/liter of CaCl<sub>2</sub> resulted in 10.4 sec, a twofold increase. It seems to be justified to assume that dimers of spectrin are built up in the presence of CaCl<sub>2</sub>.

**Titration with Ca<sup>2+</sup> sensitive electrode.**—Direct information concerning Ca<sup>2+</sup> binding was obtained by using the Ca<sup>2+</sup> ion selective electrode of Orion. It determines the concentration of free Ca<sup>2+</sup> in a solution. When the total Ca<sup>2+</sup> concentration of the sample is known, the amount of bound Ca<sup>2+</sup> can be calculated. A surprisingly high number of about 780 binding sites for Ca<sup>2+</sup> per molecule spectrin was found (Fig. 3).

Provided that the binding sites for Ca<sup>2+</sup> are equivalent and independent the representation of the results by a Scatchard plot (16) (Fig. 4) gives a straight line for each species of binding site. In the case of spectrin one can distinguish two kinds of sites. One branch indicates strong binding with a maximum number of  $n_1 = 180$  sites and  $k_{\text{assoc}}$  of  $22 \times 10^3$  liter/mole and a weaker binding with a maximum number  $n_2 = 600$  and  $k_{\text{assoc}} = 0.93 \times 10^3$  liter/mole.

The titration curve obtained on protein after one and three days does not fulfill the conditions for application of the Scatchard plot.

To give an idea of the mechanism of Ca<sup>2+</sup> binding the influence of pH can be used. Variation of pH showed clearly an increment of Ca<sup>2+</sup> binding with increasing pH. This may be interpreted as a competition effect of H<sup>+</sup> and Ca<sup>2+</sup> binding to the same amino acid side chains.

Table II. Calculated values for  $w$  at 25°C for different proteins according to Tanford (13)

Protein	Mol. wt	$w$ for ionic strength 0.01
α-Corticotropin	4,541	0.218
Ribonuclease	13,683	0.137
β-Lactoglobulin	35,500	0.088
Serum albumin	65,000	0.066
Spectrin	460,000	<0.012

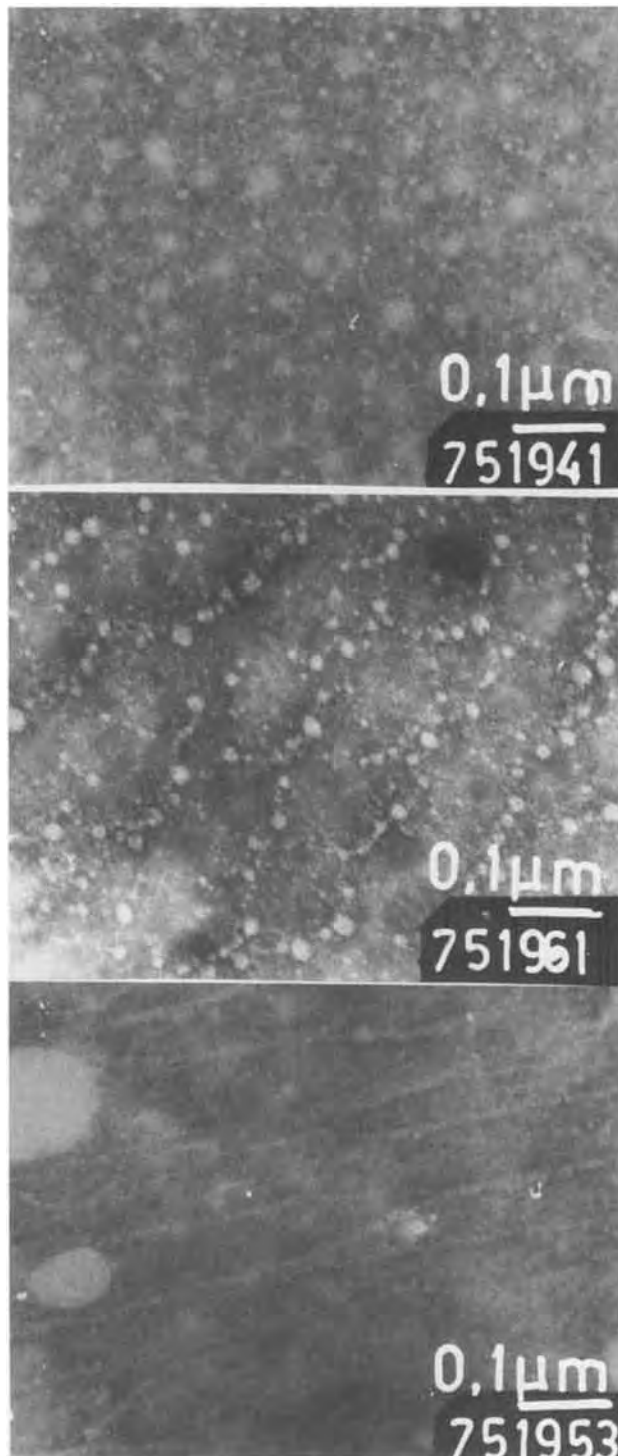


Fig. 2. Electron micrographs of (a, top) spectrin pure, (b, center) spectrin in 1 mmole/l CaCl<sub>2</sub>, and (c, bottom) spectrin in 2 mmole/l CaCl<sub>2</sub>, negative staining in 0.1 OD/ml spectrin, 1/100,000.

**Electrometric titration of spectrin solution containing Ca<sup>2+</sup>.**—In contrast to the acid-base titration of fresh pure spectrin we got a complete electrometric titration curve if Ca<sup>2+</sup> was present. Moreover this curve was not reversible in the range pH 7.5-10, which suggests conformational changes due to the presence of Ca<sup>2+</sup> (Fig. 5).

### Discussion

The Ca<sup>2+</sup> binding to spectrin depending on pH allows the estimation of the mechanism thereof. A competition between H<sup>+</sup> ions and Ca<sup>2+</sup> ions for the binding sites of the amino acid side groups seems to be possible.



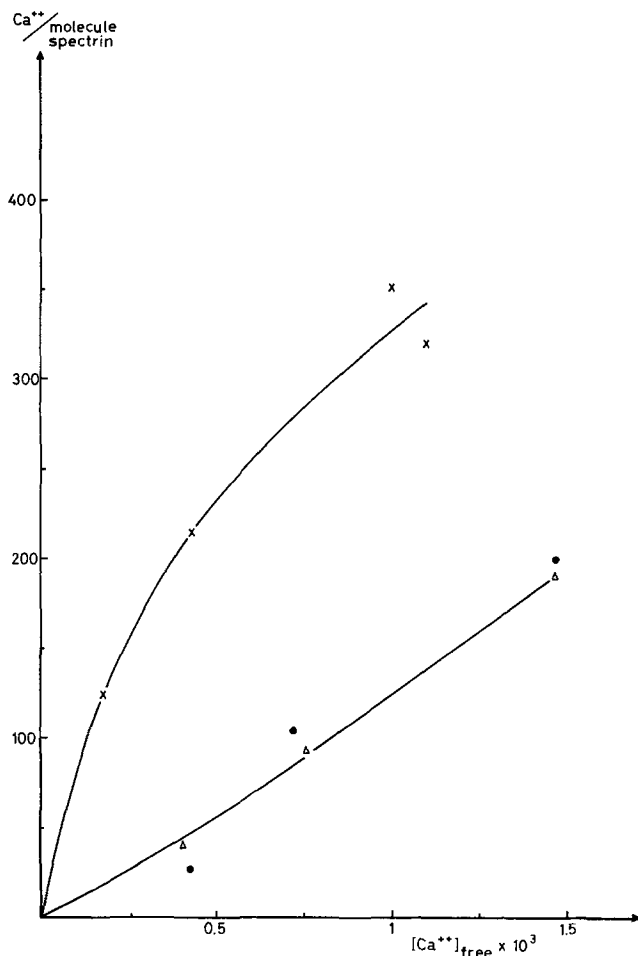


Fig. 3. Ca<sup>2+</sup> binding on spectrin prepared at pH = 8, measured at 22°C. × freshly prepared spectrin, Δ after 1 day, ● after 3 days.

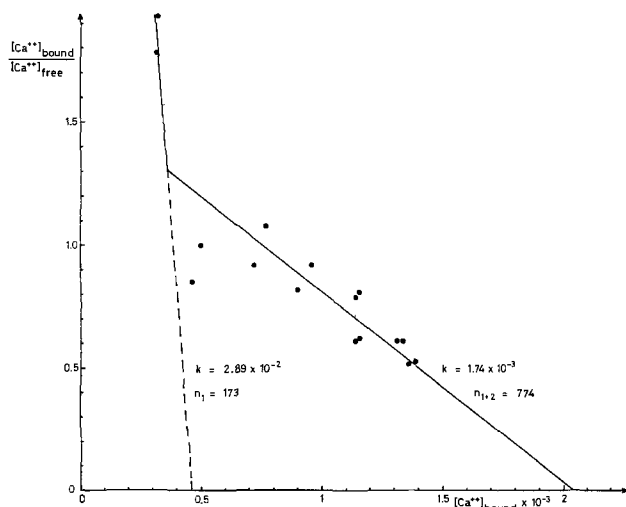


Fig. 4. Ca<sup>2+</sup> binding on spectrin. Scatchard plot of binding curve measured immediately after preparation at pH = 8 at 0°C (curve x in Fig. 3).

Forstner and Manery (17) state that carboxylic groups of glutamic acid and aspartic acid are responsible for high affinity calcium binding. Mikkelsen and Wallach (18) find high affinity calcium binding to the phenolic hydroxyl groups of tyrosine.

Another interpretation of the binding mechanism is offered for the low affinity binding sites. There are two reasons: (i) the high number of sites, and (ii) the observation of dimers and fibrils of spectrin in the

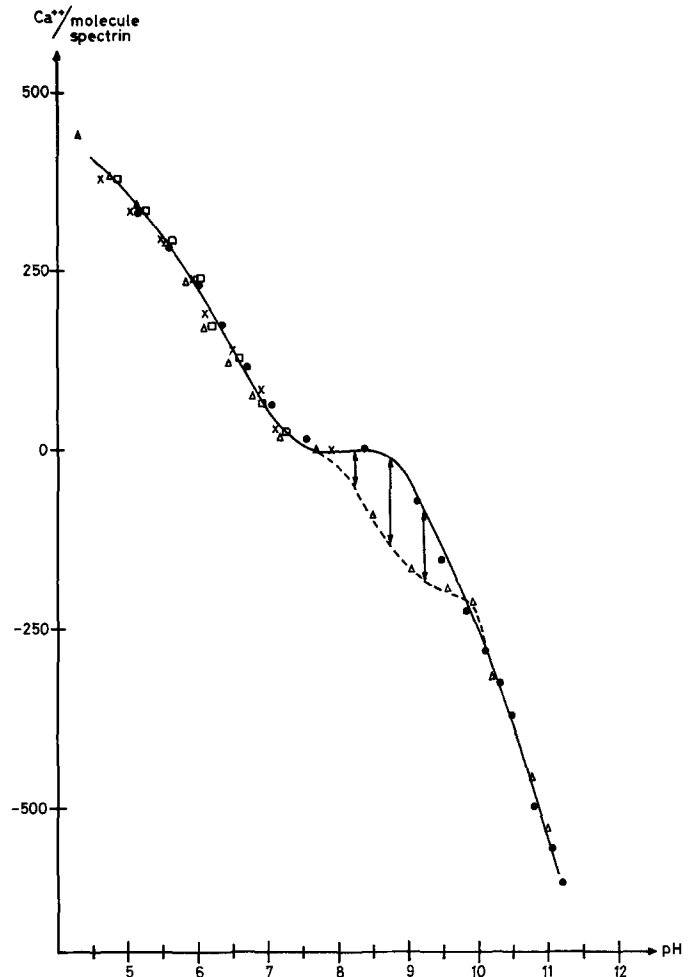


Fig. 5. Electrometric titration on spectrin freshly prepared with 1 mmole CaCl<sub>2</sub>. × neutral-acidic direction, ● acidic-basic direction, Δ basic-acidic direction, □ acidic-neutral direction.

presence of CaCl<sub>2</sub>. By analogy to the adsorption of Ca<sup>2+</sup> ions to the electrically charged surface of erythrocytes reported by Seaman *et al.* (19) the accumulation of Ca<sup>2+</sup> ions on spectrin molecules could be based on the electrostatic attraction of the negative charges, the number of which is determined by electrometric measurements being about 450 in the pH range 7-8.

The weak electrostatic interaction of the sites, found by the Linderström-Lang analysis, indicates the binding sites to be relatively strongly fixed in their surroundings. That means that a probable geometric arrangement of the Ca<sup>2+</sup> ions would be bridging two sites of neighboring molecules, respectively, thus causing the aggregation of spectrin molecules.

Long and Mouat (20) find the Ca<sup>2+</sup> binding to ghosts (haemolyzed erythrocytes) to be three times more effective than to intact erythrocytes. Duffy and Schwarz (7) suppose that 80% of the Ca<sup>2+</sup> binding to the RBC membrane is caused by the protein fraction. Therefore spectrin, as a prominent protein of the inner membrane surface [see Haggis (21); Nicolson, Marchesi, and Singer (8e)], is suggested to be responsible for the Ca<sup>2+</sup> binding.

This assumption is stressed by some observations that can be made under the influence of calcium on ghosts as well as on a solution containing 80% of pure spectrin in the protein fraction.

Rosenthal *et al.* (6) report on long chains 40-60Å in diameter that are built up by a fibrous protein of the RBC membrane in 2 mmoles CaCl<sub>2</sub> solution. Fibers of this protein extracted from the membrane under conditions of low ionic strength can be seen on the inner surface of ghost cells with the aid of electron micrographs (obtained by the same authors). This protein

could well be spectrin. Our own electron micrographs show exactly the same structures of spectrin.

Forstner and Manery (22) find a maximum of 300  $\mu$ moles  $\text{Ca}^{2+}$ /g protein bound to high affinity sites of ghosts. The high affinity  $\text{Ca}^{2+}$  binding to spectrin reported in this paper gives a value about one order of magnitude higher than that. The big difference can be due to several washings of the ghosts after  $\text{Ca}^{2+}$  incubation and/or to the specific  $\text{Ca}^{2+}$  binding conditions of spectrin. These authors also report an increase in  $\text{Ca}^{2+}$  binding to ghosts as a function of pH. We obtain the same results by measuring solutions of isolated spectrin.

Long and Mouat (20) detected three branches in the Scatchard plot of Ca binding to erythrocytes. One of them is due to sialic acid, the other two by proteins. That fits very well the observation of two branches in the Scatchard plot of  $\text{Ca}^{2+}$  binding to spectrin.

For all these reasons spectrin should be an important factor in  $\text{Ca}^{2+}$  binding to the RBC membrane and could easily be responsible for the shape changes of the RBC too.

#### Acknowledgment

The authors wish to acknowledge the financial support of this project by Deutsche Forschungsgemeinschaft and the grant for one of us (K.K.). Thanks are due to Professor Passow for helpful discussions, Miss D. Dahlem, MPI of Biophysics as well as Dr. Scherer, Hoechst AG.

Manuscript received June 30, 1975. This was Paper 364 presented at the Toronto, Canada, Meeting of the Society, May 11-16, 1975.

Any discussion of this paper will appear in a Discussion Section to be published in the June 1977 JOURNAL. All discussions for the June 1977 Discussion Section should be submitted by Feb. 1, 1977.

#### REFERENCES

1. R. I. Weed and B. Chailley, *Nouvelle Rev. Franc. Hématolog.*, **12**, 775 (1972).

2. M. A. Lichtmann and R. I. Weed, *ibid.*, **12**, 799 (1972).
3. P. L. La Celle, F. H. Kirkpatrick, M. P. Udkow, and B. Arkin, *ibid.*, **12**, 789 (1972).
4. J. Palek, W. A. Curby, and F. J. Lionetti, *Blood*, **40**, 261 (1972).
5. J. Palek, G. Stewart, and F. J. Lionetti, *ibid.*, **44**, 583 (1974).
6. A. S. Rosenthal, F. M. Kregenow, and H. L. Moses, *Biochem. Biophys. Acta*, **196**, 254 (1970).
7. M. J. Duffy and V. Schwarz, *ibid.*, **330**, 294 (1973).
8. (a) V. T. Marchesi and E. Steers, *Science*, **159**, 203 (1968).  
(b) V. T. Marchesi, E. Steers, T. W. Tillack, and S. L. Marchesi, in "Red Cell Membrane Structure and Function," G. A. Jamieson and T. J. Greenwalt, Editors, Lippincott Ltd. Philadelphia (1969).  
(c) E. Steers and V. T. Marchesi, *J. Gen. Physiol.*, **54**, 65s (1969).  
(d) T. W. Tillack, S. L. Marchesi, T. Marchesi, and E. Steers, *Biochem. Biophys. Acta*, **200**, 125 (1970).  
(e) G. L. Nicolson, V. T. Marchesi, and S. J. Singer, *J. Cell. Biol.*, **51**, 265 (1971).
9. J. W. Ross, *Science*, **156**, 1378 (1967).
10. J. T. Dodge, C. Mitchell, and D. J. Hanahan, *Arch. Biochem. Biophys.*, **100**, 119 (1963).
11. K.-D. Kupka and V. Rudloff, In preparation.
12. J. M. Fuller, J. M. Boughter, and M. Morazzani, *Biochemistry*, **13**, 3036 (1974).
13. Ch. Tanford, *Adv. Protein Chem.*, **17**, 69 (1962).
14. K. Linderström-Lang, *Compt. Rend. Trav. Lab. Carlsberg*, **15**, 7 (1924).
15. M. B. Clarke, Thesis, University of California, Berkeley (1971).
16. G. Scatchard, *Ann. N. Y. Acad. Sci.*, **51**, 660 (1949).
17. J. Forstner and J. F. Manery, *Biochem. J.*, **124**, 563 (1971).
18. R. B. Mikkelsen and D. F. H. Wallach, *Biochem. Biophys. Acta*, **336**, 211 (1974).
19. G. V. F. Seaman, P. S. Vassar, and M. J. Kendall, *Arch. Biochem. Biophys.*, **135**, 356 (1969).
20. C. Long and B. Mouat, *Biochem. J.*, **123**, 829 (1971).
21. G. H. Haggis, *Biochem. Biophys. Acta*, **193**, 237 (1969).
22. J. Forstner and J. F. Manery, *Biochem. J.*, **125**, 343 (1971).

# Tunable Voltage Clamp Method: Application to Photoelectric Effects in Pigmented Bilayer Lipid Membranes

Felix T. Hong and D. Mauzerall

The Rockefeller University, New York, New York 10021

## ABSTRACT

Pulsed dye laser excitation of magnesium porphyrins contained in bilayer lipid membranes produced a transient electrical response across the membrane caused by electron transfer from the pigment to the acceptor (ferrocyanide ion) in the adjacent aqueous phase, followed by their return. The photoreponse is measured by a tunable voltage clamp (TVC) method which is essentially a potentiostatic method with adjustable access impedance (time resolution 150 nsec). Comparison with the ideal potentiostatic and the ideal galvanostatic methods shows that the TVC method is superior in providing a complete characterization of the system in terms of an irreducible equivalent circuit. An intrinsic relaxation time constant identified with the reverse interfacial electron transfer is uniquely determined. This time constant can be decomposed into a resistive and a capacitive element. This novel chemical capacitance is required to account for the experimental observations. The model and the method are relevant to vision and photosynthesis research. The TVC method is also potentially applicable to photoelectrochemistry whenever an interfacial photoreaction is present.

Photoelectrochemistry is a particular area of electrochemistry where light-induced emf's instead of the usual current and voltage are used as perturbations of the system. The advent of lasers has made the method of pulsed light perturbation a powerful tool to investigate the fast kinetics of photoelectrochemical relaxations. The study of interfacial photoreactions is of particular interest to biologists because of their relevance to photobiological systems such as photosynthesis and vision. In these photobiological systems, the light-sensitive elements are bound to the membranes. In applying the conventional electrophysiological techniques to such membrane systems or their models, one encounters difficulty in achieving sufficient time resolution to study the fast kinetics of the photoevents. This is because of the presence of membrane capacitance which distorts the photoelectrical relaxation. We, therefore, propose a method of measurement and analysis which is specifically applicable to this type of problem. For reasons which will become apparent later, we call it the tunable voltage clamp (TVC) method. We shall illustrate this method with data obtained from a pigmented membrane system. Similar systems have been studied by means of conventional methods by a number of laboratories (1-5). The literature has been summarized by Tien (6).

### Description of the Measurement Method and Circuitry

The TVC method is a modified potentiostatic ("voltage clamp" as known to electrophysiologists) method with adjustable access impedance. The effect of this access impedance is included in a circuit analysis of the complete system: pigmented membrane system + electrodes + amplifier. The advantages of including a variable access impedance are discussed later.

The TVC method can be implemented in a number of ways. It suffices to describe a prototype: a two-electrode system as shown in Fig. 1, along with the equivalent circuit of the pigmented membrane system. Basically, a single 100 MHz operational amplifier is used in a negative feedback circuit. The same pair of electrodes are used for voltage sensing and for current injection. A d-c and pulsed command voltage source is connected in series with the membrane system. In a

Key words: interfacial photoelectrochemistry, lipid bilayer, chemical capacitance, pulsed laser.

measurement by means of the TVC method, the command voltage is maintained at a fixed d-c level and a short light pulse causes a perturbation to the pigmented membrane system. The negative feedback circuit is normally operated under the virtual ground condition. The circuit will operate as an ideal potentiostat if the access impedance of the electrodes plus the intervening electrolyte solutions is negligible as compared with the (source) impedance of the pigmented membrane system. This is indeed the case for relatively low frequency and d-c measurements. In the megahertz range, the source impedance may become as low as the access impedance because of the presence of membrane capacitance. The effect of the access impedance would then become quite significant. The system is potentiostated at the electrode inputs to the negative feedback circuit rather than at the two membrane-water interfaces. The error voltage at the interfaces is the voltage

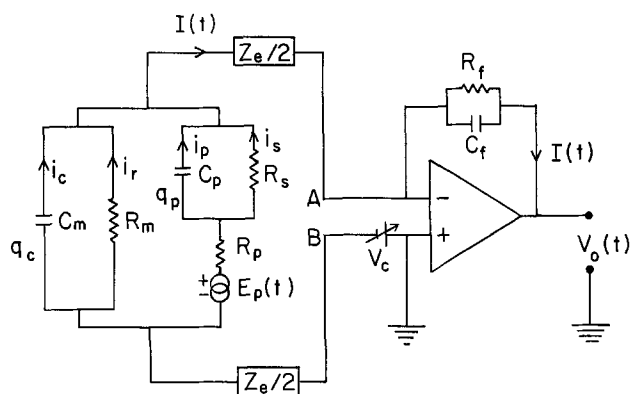


Fig. 1. Equivalent circuit of the pigmented BLM and its connection to the TVC circuit.  $E_p(t)$  is the photoemf, which has the same time course as that of the light pulse.  $R_m$  and  $C_m$  are the resistance and the capacitance of the membrane alone.  $R_p$ ,  $C_p$ , and  $R_s$  are caused by the pigment reactions.  $Z_e$  is the adjustable access impedance and can be replaced by an effective access resistance  $R_e$  over the time range of interest.  $R_f$  and  $C_f$  are the variable feedback resistance and capacitance, respectively.  $V_c$  is the externally applied command voltage source.  $I(t)$  is the current response and  $V_o(t)$  is the corresponding output voltage.

drop across the access impedance. As it is well known to electrochemists, it is difficult to completely eliminate the access impedance. The present method chooses to circumvent the difficulty by including the access impedance in the analysis. Variable precision resistances are added in series to the already existing access impedance of the electrodes and the electrolyte solutions. The total access impedance can be tuned to optimize the measurement (see section on Advantages of TVC Method). The negative feedback loop consists of a parallel RC network, which has the effect of a low pass filter on the output voltage ( $V_o(t)$  in Fig. 1) of the amplifier. There is a gain-bandwidth trade-off. The feedback resistance  $R_f$ , being proportional to the amplifier gain, must be kept high for maximum gain. On the other hand, the feedback RC time constant ( $\tau_f = R_f C_f$ ) must be kept small for good time resolution. Since it is difficult to reduce the feedback capacitance  $C_f$  to less than a few picofarads, further improvement of the instrumental time resolution can only be accomplished by reducing the feedback resistance  $R_f$  at the expense of the amplifier gain. We have found that a feedback capacitance of 15 picofarads (pf) (including stray capacitance) is sufficient to stabilize the amplifier. In order to achieve a time constant of 150 nsec, the feedback resistance  $R_f$  must then be 10 kohms. The over-all gain is still acceptable. This is because of the relationship of the photoemf  $E_p(t)$  and the RC's in the pigmented membrane as shown in Fig. 1. The reduction of the feedback resistance is compensated by the reduction of the source impedance at high frequency due to the presence of capacitances in the pigmented membrane system. The final consideration is then the signal-to-noise ( $S/N$ ) ratio. By reduction of extraneous noise sources and experimental artifacts (due to the laser flash discharge) and finally by signal averaging, good instrumental time resolution ( $\sim 150$  nsec) and an acceptable  $S/N$  ratio ( $> 100$  for the positive peak and  $> 10$  for the negative peak) can be achieved simultaneously.

The square wave command voltage pulse ( $V_c$ ) (rise-time  $< 5$  nsec) permits measurements of parameters required for a complete macroscopic characterization of the pigmented membrane system: the effective access resistance  $R_e$ , the membrane capacitance  $C_m$ , and the feedback time constant  $\tau_f$ .

The access impedance is measured by applying a square voltage pulse through the electrodes and the electrolyte solutions in the absence of a membrane. Although the electrode impedance has a complex frequency dependence because of the electrode capacitance, the access impedance was experimentally determined to vary less than 1.6% in the range of interest from 100 nsec to 500  $\mu$ sec. In terms of a simple circuit, this is because of the resistance in series with the electrode capacitance. It can therefore be replaced by an effective (pure) resistance for the circuit analysis in this frequency range. Henceforth,  $Z_e$  shall be regarded as a pure resistance and takes on the real value  $R_e$ . Application of a square pulse command voltage in the presence of a membrane permits the measurement of the charging time constant  $\tau_m \approx R_e C_m$ , which in turn leads to the determination of the membrane capacitance  $C_m$ , knowing the value of  $R_e$ . Application of a square wave command voltage with a precision resistor instead of the membrane and the electrodes at the input gives the instrumental time constant  $\tau_f$ .

The membrane resistance  $R_m$  can be determined by measuring the current response to a d-c command voltage change. The d-c pigment resistance is determined by means of the null current method described elsewhere (7).

The voltage output of the negative feedback amplifier passed through a second stage of amplification to avoid quantization error in the digitizer. The final output is then digitized by a transient recorder (Biomation Model 8100; time resolution 10 nsec; 8 bit resolution),

which is interfaced either to a Fabri-Tek Model 1060 signal averager or to a PDP 8/E minicomputer for signal averaging and data recording. The photocurrent response curve relaxes with two exponential components of opposite signs, with the time constant  $\tau_s$  and  $\tau_l$ , respectively ( $\tau_s < \tau_l$ ).

The light source is a flash-lamp-pumped dye laser (0.3  $\mu$ sec pulse duration; maximal output 120 mj with rhodamine 6G at 590 nm). The laser beam is focused to the thin bimolecular region of the membrane to exclude bulk liquid effects from the thick annular region (8).

### Materials and Methods of Forming Pigmented Bilayer Lipid Membranes

The phospholipid used here in the preparation of a bilayer lipid membrane (BLM) is egg lecithin (Sylvania, Millburn, New Jersey). The formula of the membrane-forming solution and the methodology of its formation are standard and have been described elsewhere (7, 8). The membrane-bound pigments are aliphatic esters of magnesium mesoporphyrin IX: diethyl and di-n-amyl. The preparation of these esters has been described (9). The pigment-containing BLM is formed on a Teflon plate (0.01 in.) around a hole of 2 or 3 mm<sup>2</sup>, and separates two aqueous KCl or NaCl solutions (1M) of 5 ml in volume. Potassium ferricyanide and ferrocyanide of specified concentrations are added to either or both aqueous solutions.

The chemistry of the pigmented BLM-aqueous redox system has been described in detail [Ref. (9) and Fig. 2 of Ref. (10)]. Photoexcitation of the pigmented membrane causes interfacial electron transfer from the excited pigment molecule in the membrane to the ferricyanide molecule in the aqueous phase. Subsequent reverse interfacial electron transfer from the ferrocyanide molecule in the aqueous phase to the pigment monocation in the membrane completes the cyclic reaction.

### Results

The current response of the pigmented BLM to a short pulse of light is biphasic: An initial positive peak is followed by a prolonged negative component which leads to restoration of the original dark level (Fig. 2). The polarity of the initial positive peak is in the direction expected for electron transfer from pigment in the membrane to the acceptor-rich aqueous phase. The physical meaning of the negative component is discussed later. The photocurrent relaxation can be fit with two exponential functions of opposite polarity; the ratio of their amplitudes closely equals the reciprocal of the ratio of their respective time constants. The dotted or noisy curves in Fig. 2 show the photocurrent response displayed on two different scales to clearly show the two components. It was measured by means of the TVC method at 0 mV with an effective access resistance  $R_e = 5.1$  kohms and an instrumental time constant of 1.5  $\mu$ sec. The apparent relaxation time constants of the two photocurrent components are 29 and 63  $\mu$ sec. The charging time constant  $\tau_m$  is determined to be  $42 \pm 0.5$   $\mu$ sec for this particular membrane. The laser pulse is delivered at  $t = 0$   $\mu$ sec. The data of Fig. 2 are analyzed in detail in the next section.

Figure 3 shows the rise of the photocurrent response to a single laser flash on a pigmented BLM, measured by the TVC method at 0 mV with an effective access resistance of 380 ohms and an instrumental time constant of 150 nsec. The laser pulse is also shown.

### Equivalent Circuit Analysis

The experimentally observed photocurrent relaxation can be accounted for quantitatively by the equivalent circuit shown in Fig. 1. This equivalent circuit includes a novel feature. A chemical capacitance ( $C_p$ ) in series with the photoemf is present in addition to the ordinary membrane capacitance ( $C_m$ ). In parallel with  $C_p$  is the transmembrane pigment resistance  $R_s$  which

represents the conductance pathway due to diffusion of pigmented molecules, both charged and uncharged. The photoevent is represented by an electrical channel in parallel with and independent of the ionic conductance channel represented by  $R_m$ . This independence has been established by a shunting experiment with nystatin which decreases the ionic resistance  $R_m$  (7). This proves the independence of the photoevent and the ionic event. A reason for introducing  $C_p$  is given later.

The equivalent circuit plus the access impedance can be explicitly analyzed by applying the two Kirchhoff rules (Appendix 1). The photocurrent at zero voltage (with a nonzero  $R_e$ ) is found to be

$$I(t) = \frac{1}{R_e C_m \left( \frac{1}{\tau_s} - \frac{1}{\tau_1} \right)} \left[ \left( \frac{1}{\tau_s} - \frac{1}{R_s C_p} \right) \int_0^t \frac{E_p(u)}{R_p} \exp\left(-\frac{u-t}{\tau_1}\right) du - \left( \frac{1}{\tau_s} - \frac{1}{R_s C_p} \right) \int_0^t \frac{E_p(u)}{R_p} \exp\left(-\frac{u-t}{\tau_1}\right) du \right] \quad [1]$$

where

$$\frac{1}{\tau_s} = \frac{1}{2} \left[ \left( \frac{1}{R_p C_m} + \frac{1}{\tau_p} + \frac{1}{\tau_m} \right) + \sqrt{\left( \frac{1}{R_p C_m} + \frac{1}{\tau_p} + \frac{1}{\tau_m} \right)^2 - 4 \left( \frac{1}{R_p C_m R_s C_p} + \frac{1}{\tau_p \tau_m} \right)} \right] \quad [2]$$

$$\frac{1}{\tau_1} = \frac{1}{2} \left[ \left( \frac{1}{R_p C_m} + \frac{1}{\tau_p} + \frac{1}{\tau_m} \right) - \sqrt{\left( \frac{1}{R_p C_m} + \frac{1}{\tau_p} + \frac{1}{\tau_m} \right)^2 - 4 \left( \frac{1}{R_p C_m R_s C_p} + \frac{1}{\tau_p \tau_m} \right)} \right] \quad [3]$$

$$\frac{1}{\tau_p} = \frac{1}{R_p C_p} + \frac{1}{R_s C_p} \quad [4]$$

$$\frac{1}{\tau_m} = \frac{1}{R_e C_m} + \frac{1}{R_m C_m} \quad [5]$$

In Eq. [2] and [3],  $\tau_s$  and  $\tau_1$  are expressed in terms of various RC parameters:  $R_p$ ,  $C_p$ , and  $R_s$  are unknown, the remaining parameters  $\tau_s$ ,  $\tau_1$ ,  $\tau_m$ ,  $R_m$ , and  $R_e$  are experimentally measurable. A third equation that is required to solve for the parameters  $R_p$ ,  $C_p$ , and  $R_s$  is given by

$$R_s + R_p = R_{sp} = \text{d-c pigment resistance} \quad [6]$$

The parameter  $1/R_{sp}$  is the difference between the conductance of pigmented BLM-redox system and that of a plain BLM, and can be readily measured by the null current method (7).

Although  $R_p$ ,  $C_p$ , and  $R_s$  can be solved for explicitly, it is hardly necessary to do so. Time-integration of the photocurrent shows the response goes to zero at long time. This indicates that  $R_s$  is relatively large. In fact,  $R_s \gg R_p$  and hence  $R_s \simeq R_{sp} = \text{d-c pigment resistance}$ . For TVC measurements with  $R_e \ll R_s$ , no significant error in computing  $R_p$  and  $C_p$  occurs by setting  $R_s$  to infinity (Appendix II). This leads to a simplified explicit solution for  $R_p$  and  $C_p$

$$\tau_p = \frac{\tau_s \tau_1}{\tau_m} \quad [7]$$

$$C_p = \frac{1}{R_e} (\tau_s + \tau_1 - \tau_m - \tau_p) \quad [8]$$

$$R_p = \frac{\tau_p}{C_p} \quad [9]$$

Therefore, there is a unique solution for  $R_p$  and  $C_p$ .

For the system shown in Fig. 2, we find that  $R_p = 34$  kohms,  $C_p = 1.3$  nF, and  $\tau_p = 44$   $\mu\text{sec}$ .

It remains to be demonstrated that the equivalent circuit predicts the correct time course of the photocurrent, given the above parameters. It is interesting to note that substitution of a delta function  $\delta(t)$  for the photoemf  $E_p(t)$  leads to the following expression

$$I(t) = \frac{1}{R_p R_e C_m \left( \frac{1}{\tau_s} - \frac{1}{\tau_1} \right)} \left[ \frac{1}{\tau_s} \exp\left(-\frac{t}{\tau_s}\right) - \frac{1}{\tau_1} \exp\left(-\frac{t}{\tau_1}\right) \right] \quad [10]$$

which states that the photocurrent is biphasic and consists of two exponential terms of opposite polarity with the amplitude ratio equal to the reciprocal of the ratio of their respective time constants. This is indeed consistent with experimental observations.

In carrying out the detailed computation of the photocurrent  $I(t)$ , the photoemf  $E_p(t)$  is assumed to follow the time course of the light pulse. This assumption is reasonable because of the following consideration: The singlet state of magnesium porphyrin lives about 1 nsec, and the triplet state less than 100 nsec under aerobic conditions. Thus the electron transfer from the excited state must be fast compared with the present instrumental time constant (150 nsec).

We also take into account the effect of the negative feedback loop as a low pass filter on the output photo-

current. The filtered current  $I_f(t)$  is given by

$$I_f(t) = \frac{1}{\tau_f} \int_0^t I(u) \exp\left(-\frac{u-t}{\tau_f}\right) du \quad [11]$$

where  $\tau_f = R_f C_f$  and  $I(u)$  is substituted with Eq. [1]. The computed time course is normalized with respect to its peaks and is shown in Fig. 2 as smooth curves. The theoretical positive and negative peak amplitude ratio of 6.6 compares favorably with the experimental peak amplitude ratio of 6.2.

A similar computation is also carried out for the rise phase of the photocurrent in Fig. 3 (smooth curve). The sigmoid-shaped rise of photocurrent is accountable by the low pass filter effect of the feedback RC constant of 150 nsec and the finite rise time of the laser pulse.

### Evidence That a Chemical Capacitance Does Exist

A pertinent question to raise is whether the equivalent circuit shown in Fig. 1 is a unique representation of the photoevent in the pigmented BLM. The circuit, being equivalent, is by no means unique because a more elaborate model can always be proposed which describes just as well or even better the photoevent. We shall demonstrate that to the best of our knowledge the equivalent circuit is unique in the sense that it is irreducible, being the simplest in the homologous series of circuits which are equivalent to the pigmented BLM system.

The distinct feature of the present equivalent circuit is the presence of a chemical capacitance  $C_p$ . Is there an alternative model without a  $C_p$  that describes the photoevent just as well? This alternative model without  $C_p$  can be ruled out by the following analysis. The photocurrent response of this model in the presence of a nonzero access resistance  $R_e$  is given by

$$I(t) = \frac{1}{R_e C_m} \int_0^t \frac{E_p(u)}{R_p + R_s} \exp\left(-\frac{u-t}{\tau}\right) du \quad [12]$$

where  $1/\tau = 1/R_e C_m + 1/R_m C_m + 1/(R_p + R_s) C_m \simeq 1/\tau_m$ , since  $R_s \gg R_e$ . In words, the photocurrent is the response of the photoemf  $E_p(t)$  to a low pass filter of time constant  $\tau_m$ . Without assuming a physically unrealistic time course of the photoemf and without as-

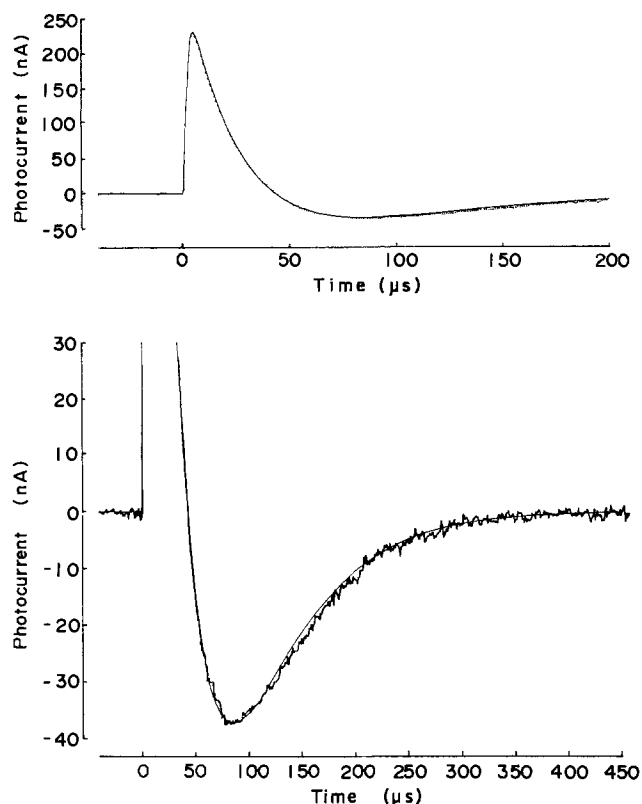


Fig. 2. Measured (dotted or noisy curve) and computed photoresponses to a dye laser pulse (0.3  $\mu$ sec) by means of the TVC method. The measured response is taken by means of the TVC method at 0 mV with  $R_e = 5.1$  kohms. The BLM is made from a membrane-forming solution which contains  $\sim 5$  mmolars magnesium mesoporphyrin IX di-n-omyl ester. The BLM separates two aqueous phases with 20 mmolars potassium ferricyanide and 0.5 mmolars potassium ferrocyanide on the acceptor-rich side and 20 mmolars potassium ferrocyanide on the donor-rich side. Both aqueous solutions also contain 1M NaCl and 10 mmolar phosphate buffer at pH 7.2. The temperature is maintained constant at 26°C. The exciting laser beam is focused to illuminate 19% of the thin bilayer of area 1.7 mm<sup>2</sup>. The instrumental time constant is 1.5  $\mu$ sec ( $R_f = 100$  kohms,  $C_f = 15$  pf). The average of 16 measurements from the same membrane is obtained with a signal averager. The same averaged record is displayed on two different scales. The computed response is based on the equivalent circuit of Fig. 1, assuming  $E_p(t)$  to have the time course of an equilateral triangular pulse with a half-width of 0.3  $\mu$ sec, the same as the exciting laser pulse. The input parameters for this computation are:  $R_e = 5.1$  kohms,  $R_m = 1.5 \times 10^9$  ohms,  $C_m = 8.2$  nf,  $R_p = 34$  kohms,  $C_p = 1.3$  nf,  $R_s = 10^9$  ohms. The computed curves are normalized with respect to the peaks. See text for details.

suming complex time dependence of the circuit parameters, the alternative model without  $C_p$  predicts a passive relaxation no faster than  $\tau_m$  (42  $\mu$ sec in Fig. 2). This prediction is contradicted by experiments in that a relaxation of 29  $\mu$ sec ( $\tau_s$  in Fig. 2) and indeed as fast as 5  $\mu$ sec can be observed (11).

To demonstrate that the fit does not depend on particular choices of the access impedance, the photocurrent responses measured from the same pigmented BLM under identical conditions except with two different values of  $R_e$  are compared (Fig. 4). Equivalent circuit analysis of the data in Fig. 4A and in Fig. 4B separately gives the following results:  $R_p = 40$  kohms,  $C_p = 1.1$  nf, and  $\tau_p = 43$   $\mu$ sec for Fig. 4A ( $R_e = 4.6$  kohms), and  $R_p = 37$  kohms,  $C_p = 1.2$  nf, and  $\tau_p = 44$   $\mu$ sec for Fig. 4B ( $R_e = 11$  kohms). The errors in this case are less than 5% except for the case of  $C_p$ , where the error is from 10 to 15%. The peak amplitudes of the

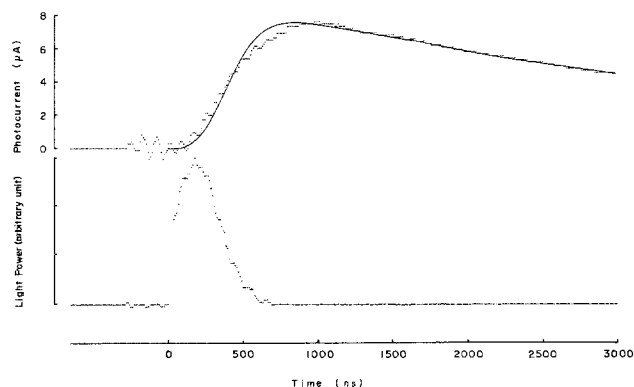


Fig. 3. The rise phase of the photocurrent and the time course of the laser pulse. The dotted curve is a single measurement from a BLM of area 2.5 mm<sup>2</sup> by means of the TVC method at 0 mV with  $R_e = 380$  ohm (25°C) and an instrumental time constant of 150 nsec. The quantization steps are present because of the 8 bit resolution of the digitizer. The pigmented BLM system has the same composition as that of Fig. 2, except that the pigment is the diethyl ester and that KCl replaces NaCl in the aqueous solutions. The solid smooth curve is the computed response including the 150 nsec instrumental time constant, as in Fig. 2. The laser pulse is measured by a photodiode (rise time 5 nsec). The spark gap discharge artifact is seen to precede the onset of the laser pulse. The jitter of the timing circuit and the breakdown delay of the spark gap in the dye laser is less than 40 nsec. The laser pulse is measured immediately following the photocurrent measurement. Fluctuations of the shape of the laser pulse produce an uncertainty of about 100 nsec in the peak of the pulse.

effective photoemf<sup>1</sup>  $E_p(t)$  are determined to be: 90 mV for Fig. 4A and 95 mV for Fig. 4B.

The mutual consistency of these two sets of data from the same membrane can be further visualized by using the data obtained at  $R_e = 4.6$  kohms to compute the photocurrent at  $R_e = 11$  kohms, and vice versa. These are shown as smooth curves in Fig. 4A and 4B.

Three sets of measurements referred to in this paper (Fig. 2, 4A, and 4B) are for the same experimental conditions and their agreement can be used to judge the precision of the analysis. These experiments demonstrate that the pigmented BLM does behave in accordance with the equivalent circuit of Fig. 1 at various access impedance. One is therefore free to "tune" the access impedance in order to optimize the measurement.

### Error Voltage

Because of the presence of the access impedance, the potentiostatic condition is not strictly fulfilled. The specified potential difference is maintained at the electrode inputs (points A and B in Fig. 1), but the two membrane-water interfaces are not at strictly constant potential difference. The error voltage is given by the voltage drop across the access impedance,  $I(t)R_e$ . In the example shown in Fig. 2 where the peak photocurrent is 230 nA and the effective access resistance 5.1 kohms, the maximal error voltage is 1.2 mV. For a nonlinear system such as the nerve membrane near its discharge threshold, an error voltage of a few millivolts would be significant. For a linear system such as the present photosystem, a voltage shift of  $\pm 100$  mV causes only a barely discernible change of the fast photocurrent responses. Thus, the effect of the error voltage is negligible.

### Advantages of the TVC Method

To appreciate the advantages of the TVC method, we must examine the ideal potentiostatic and the ideal galvanostatic methods. These are the two limiting

<sup>1</sup> The parameter  $E_p(t)$  is regarded as an effective photoemf because no attempt has been made to take into account the effect of focused illumination and the distinction of the forward charging and the reverse discharging interfacial resistance ( $R_p$ ) (10, 11).

cases with the access impedance equal to zero and to infinity, respectively. The circuit analyses are therefore similar to that of the TVC method with a finite and nonzero access impedance.

The photocurrent as measured by means of the ideal potentiostatic method at zero voltage is given by

$$I(t) = \frac{E_p(t)}{R_p} - \left( \frac{1}{\tau_p} - \frac{1}{R_s C_p} \right) \int_0^t \frac{E_p(u)}{R_p} \exp\left(\frac{u-t}{\tau_p}\right) du \quad [13]$$

where  $\tau_p$  is given in Eq. [4]. Using the measured and calculated parameters given in Fig. 2, the photocurrent response for an instrumental time constant of 1.5  $\mu\text{sec}$  is shown in Fig. 5. Notice that the filtered photocurrent retains the biphasic waveform. However, the data provide only one useful time constant  $\tau_p$ ; the other time constant is the instrumental time constant  $\tau_i$ . A decomposition of  $\tau_p$  in terms of  $R_p$  and  $C_p$  is not possible. The presence of a small access impedance in the TVC

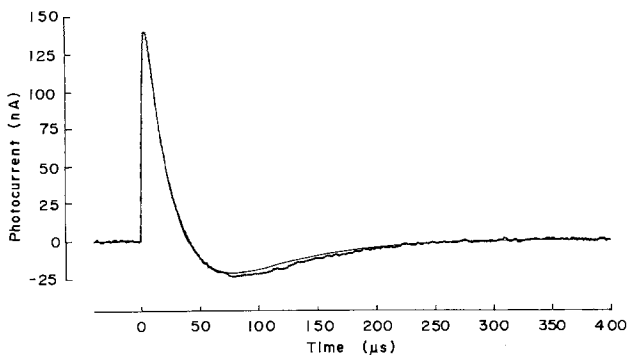
method causes interaction of the photochemical event with the membrane capacitance  $C_m$  to give rise to two useful time constants,  $\tau_s$  and  $\tau_i$ . This makes the decomposition of  $\tau_p$  possible. Thus more information can be obtained by means of the TVC method than by means of the ideal potentiostatic method.

The photovoltage as measured by means of the ideal galvanostatic method at zero current ("open-circuit" method) is given by

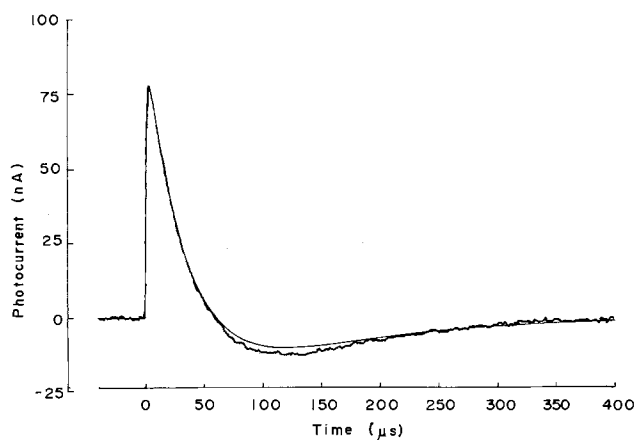
$$V(t) = \frac{\frac{1}{\tau_s'} - \frac{1}{R_s C_p}}{R_p C_m \left( \frac{1}{\tau_s'} - \frac{1}{\tau_i'} \right)} \int_0^t E_p(u) \exp\left(\frac{u-t}{\tau_s'}\right) du - \frac{\frac{1}{\tau_i'} - \frac{1}{R_s C_p}}{R_p C_m \left( \frac{1}{\tau_s'} - \frac{1}{\tau_i'} \right)} \int_0^t E_p(u) \exp\left(\frac{u-t}{\tau_i'}\right) du \quad [14]$$

where

$$\frac{1}{\tau_s'} = \frac{1}{2} \left[ \left( \frac{1}{R_p C_m} + \frac{1}{\tau_p} + \frac{1}{\tau_m'} \right) + \sqrt{\left( \frac{1}{R_p C_m} + \frac{1}{\tau_p} + \frac{1}{\tau_m'} \right)^2 - 4 \left( \frac{1}{R_p C_m R_s C_p} + \frac{1}{\tau_p \tau_m'} \right)} \right] \quad [15]$$



A



B

Fig. 4. Tuning the access impedance. The two measured photocurrent responses (noisy curve) are taken from a pigmented BLM (composition identical with that in Fig. 2) by means of the TVC method at 0 mV with  $R_e = 4.6$  kohms (A) and  $R_e = 11$  kohms (B). The instrumental time constant is 1.5  $\mu\text{sec}$ . The smooth curve in A is that computed with data obtained from the measured response in B but with  $R_e$  of 4.6 kohms, and vice versa for the smooth curve in B. The measurements were carried out on a single membrane. Even the absolute amplitudes agree to within 20%: measured amplitude 139 nA and predicted amplitude 172 nA for  $R_e = 4.6$  kohms; measured amplitude 77 nA and predicted amplitude 62 nA for  $R_e = 11$  kohms.

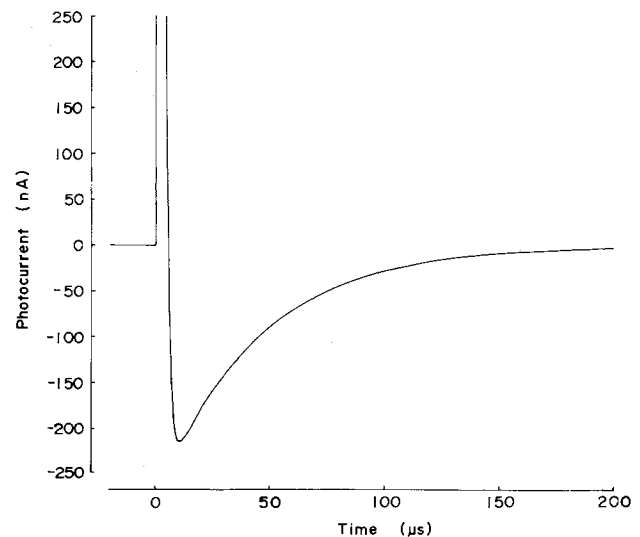
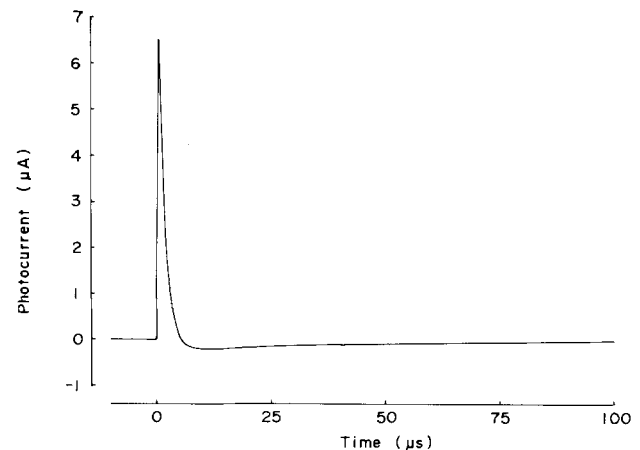


Fig. 5. The computed photocurrent response under ideal potentiostatic condition at zero voltage. The input data for the computation are from Fig. 2. The instrumental time constant of 1.5  $\mu\text{sec}$  is included. The response is displayed on two different scales.

$$\frac{1}{\tau_1'} = \frac{1}{2} \left[ \left( \frac{1}{R_p C_m} + \frac{1}{\tau_p} + \frac{1}{\tau_m'} \right) - \sqrt{\left( \frac{1}{R_p C_m} + \frac{1}{\tau_p} + \frac{1}{\tau_m'} \right)^2 - 4 \left( \frac{1}{R_p C_m R_s C_p} + \frac{1}{\tau_p \tau_m'} \right)} \right] \quad [16]$$

$$\frac{1}{\tau_m'} = \frac{1}{R_m C_m} \quad [17]$$

and  $\tau_p$  is again given by Eq. [4]. These expressions are similar to Eq. [1]-[5] except that  $\tau_m \approx R_e C_m$  is replaced by  $\tau_m' = R_m C_m$ . Using the same parameters as in Fig. 2, the computed photovoltage is shown in Fig. 6. Notice that two useful time constants  $\tau_s'$  and  $\tau_1'$  are available from such a measurement. In principle, a decomposition of the time constant  $\tau_p$  into a resistive element  $R_p$  and a capacitive element  $C_p$  is possible. In practice, this is hardly feasible. The computed photovoltage shows that the two components differ both in amplitudes and in time constants by over four orders of magnitude. The following analysis will clarify the situation.

From TVC data (e.g., Fig. 2),  $\tau_p \ll \tau_m'$ ,  $\tau_s' \ll \tau_1'$  and, to a crude approximation,  $C_p \approx C_m$ ,  $R_s \approx R_m$ . Therefore the following order-of-magnitude approximation is valid

$$\frac{1}{\tau_s'} \approx \frac{1}{\tau_s'} + \frac{1}{\tau_1'} = \frac{1}{R_p C_m} + \frac{1}{\tau_p} + \frac{1}{\tau_m'} \approx \frac{1}{R_p C_m} + \frac{1}{\tau_p} \approx \frac{2}{\tau_p} \quad [18]$$

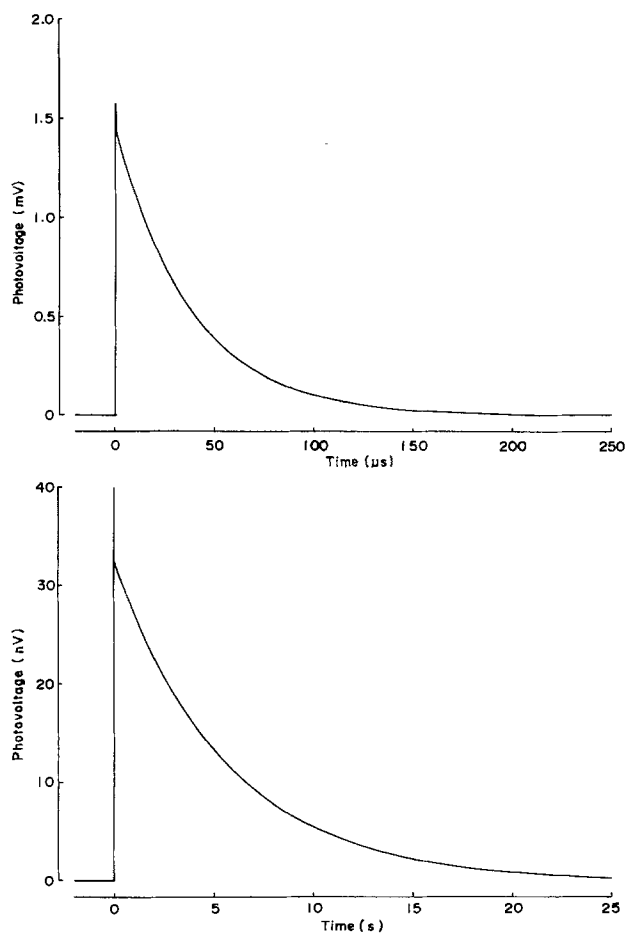


Fig. 6. The computed photovoltage response under the ideal galvanostatic condition at zero current. The input data for the computation are from Fig. 2. The instrumental time constant is taken to be zero since it does not appreciably affect this response. The response is displayed on two different scales. Notice that the units of both voltage and time in the two displays differ by over four orders of magnitude.

$$\frac{1}{\tau_s' \tau_1'} = \frac{1}{R_p C_m R_s C_p} + \frac{1}{\tau_p \tau_m'} \approx \frac{2}{\tau_p \tau_m'} \quad [19]$$

That is, to a crude approximation

$$\tau_p \approx 2\tau_s' \quad [20]$$

and

$$\tau_m' \approx \tau_1' \quad [21]$$

Except for a numerical factor of approximately 2, the representation of  $\tau_p$  by the negative component in the ideal potentiostatic condition is now replaced by its representation by the fast component in the ideal galvanostatic condition. The slow component in the latter case is almost purely membrane RC response. This is the case of excessive interaction between the photochemical event and the membrane capacitance. The calculation of  $R_p$  and  $C_p$  from the experimental data would involve subtraction of large numbers which are very close to each other, and is therefore not feasible. The present method of tuning the value of  $R_e$  enables us to optimize the measurement by bringing the two components into a range feasible for accurate measurements and calculation. The presence of the access impedance is therefore an asset rather than a nuisance. However, adequate S/N ratio is still necessary for the decomposition of  $\tau_p$  into  $R_p$  and  $C_p$ . Whereas the error in  $\tau_p$  is linear in  $\tau_1$ , this is not true for  $R_p$  and  $C_p$ . For example, a 5% variation of  $\tau_1$  in the data of Fig. 2 causes a change of  $\tau_p$  by 5% but a change of  $R_p$  by 10% and  $C_p$  by 15%.

### Conclusions

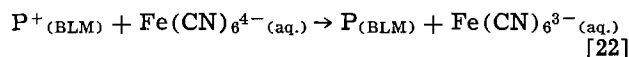
We have applied the TVC method to a model pigmented membrane system and have proposed an equivalent circuit to explain the observed photocurrent. The equivalent circuit has been interpreted in molecular terms (10). The presence of a chemical capacitance is the novel feature of the equivalent circuit and is required to account for the experimental results, in particular, the biphasic waveform of the photocurrent. This chemical capacitance has its physical origin in the photogenerated pigment monocation (10). These photogenerated pigment monocations can be regarded as fixed space charges which are localized at the acceptor-rich interface, on the microsecond time scale. Incomplete screening of these space charges by the electrical double layer near the acceptor-rich interface leads to polarization of the membrane dielectric. This interpretation has been substantiated by a theoretical calculation based on the Gouy-Chapman double layer theory (12). This later theoretical study indicates that the chemical capacitance is a characteristic of interfacial photoreaction involving membrane-bound pigment. The light-induced absorbance change in chloroplasts related to membrane potential (13) and the early receptor potential (ERP) in visual photoreceptors (14) have very fast rise times which are expected from our view of the chemical capacitance. The model and the method are therefore relevant to photobiology.

The TVC method applies specifically to a photoelectrochemical system in which a photogenerated interfacial emf is present. Viewed from outside the membrane system, the photoemf is connected in parallel with the membrane capacitance  $C_m$  but in series with the chemical capacitance  $C_p$ . It is this peculiar network relationship that makes the TVC method exquisitely sensitive and powerful in analyzing the fast interfacial kinetics. The photoemf injects current inside the double layer in contrast with perturbation due to an externally applied voltage.

In the TVC method, the effect of membrane capacitance is not eliminated but is reduced to such an ex-



tent (through proper choice of a small access impedance) that the perturbing effect can be accurately taken into account and that actually more information is made available than with the ideal potentiostatic method. The small value of  $R_p$  in the presence of a large  $R_s$  can still be measured accurately. This is not possible with the method of externally applied voltage perturbation when  $R_p$  and  $R_s$  are considered to be in series. The interfacial resistance  $R_p$  and the corresponding interfacial voltage drop have definite physical meanings (10). The TVC method thus provides a rapid and sensitive way of measuring interfacial photochemical kinetics. The calculated rate constant  $1/\tau_p$  is interpreted as the pseudo first-order rate constant of the reverse interfacial electron transfer reaction (where the aqueous ferrocyanide concentration on the acceptor-rich side is kept constant)



and is proportional to the constant concentration of the aqueous ferrocyanide solution. The calculated apparent second-order rate constant is  $(3.5 \pm 0.4) \times 10^7 M^{-1} \text{sec}^{-1}$  (10).

Although it might seem desirable to measure  $\tau_p$  explicitly by means of the ideal potentiostatic method, the latter method represents an unattainable ideal limit in experimental systems such as a pigmented membrane. Because of the presence of the chemical capacitance, the source impedance is reduced from its d-c value by several orders of magnitude in the megahertz range. A few hundred ohms of access impedance (e.g., due to electrodes and the electrolyte solutions) in the presence of a low source impedance cannot be considered negligible. On the other hand, this drastic reduction of source impedance enables one to achieve good instrumental time resolution and good  $S/N$  ratio simultaneously. With further reduction of noise and artifacts, it is not impossible to reach the ultimate time resolution set by the bandwidth of presently available operational amplifiers, namely 100 MHz.

With improved time resolution, it may be possible to study directly the relaxation of the electrical double layer using interfacial photoemf as a perturbation. The study of the photocurrent rise time in the present model system does not indicate any significant lag (<100 nsec) of the photocurrent following the stimulating light pulse.

The TVC method is potentially applicable to photoelectrochemistry where an interfacial photoreaction is involved, e.g., mercury electrode photoemission in electrolyte solutions (15). It is also potentially applicable in vision and in photosynthesis research.

### Acknowledgment

This work was supported by a National Institutes of Health Grant No. GM-20729.

Manuscript received June 30, 1975; This was Paper 365 presented at the Toronto, Canada, Meeting of the Society, May 11-16, 1975.

Any discussion of this paper will appear in a Discussion Section to be published in the June 1977 JOURNAL. All discussions for the June 1977 Discussion Section should be submitted by Feb. 1, 1977.

## APPENDIX I

### Equivalent Circuit Analysis

The equivalent circuit with access impedance  $Z_e$  is shown in Fig. 1. The following analysis gives the explicit expression for the photocurrent  $I(t)$  as measured by the TVC method at zero voltage and with an effective access resistance  $R_e$ . The TVC circuit keeps the summing point always at ground potential.

By definition

$$i_c = q_c \quad [A-I-1]$$

$$i_p = q_p \quad [A-I-2]$$

Application of Kirchhoff's two rules to the equivalent circuit results in the following relations

$$I = i_c + i_r + i_p + i_s \quad [A-I-3]$$

$$IR_e = -i_r R_m \quad [A-I-4]$$

$$i_s R_s = \frac{q_p}{C_p} \quad [A-I-5]$$

$$IR_e = E_p - \frac{q_p}{C_p} - (i_p + i_s) R_p \quad [A-I-6]$$

$$- \frac{q_c}{C_m} = E_p - \frac{q_p}{C_p} - (i_p + i_s) R_p \quad [A-I-7]$$

By differentiating Eq. [A-I-7], multiplying through by  $-C_m$ , and using Eq. [A-I-1], [A-I-2], and [A-I-5], we have

$$i_c = R_p C_m \left( q_p + \frac{\dot{q}_p}{R_p C_p} + \frac{\dot{q}_p}{R_s C_p} - \frac{\dot{E}_p}{R_p} \right) \quad [A-I-8]$$

By eliminating  $i_r$ ,  $I$ , and  $i_c$  from Eq. [A-I-3], [A-I-4], [A-I-6], and [A-I-8], using Eq. [A-I-2] and [A-I-5] and the definition for  $\tau_p$  and  $\tau_m$  (Eq. [4] and [5]), we have

$$q_p + \left( \frac{1}{R_p C_m} + \frac{1}{\tau_p} + \frac{1}{\tau_m} \right) \dot{q}_p + \left( \frac{1}{\tau_p \tau_m} + \frac{1}{R_p C_m R_s C_p} \right) q_p = \frac{\dot{E}_p}{R_p} + \frac{1}{\tau_m} \frac{E_p}{R_p} \quad [A-I-9]$$

The initial conditions for this second-order linear differential equation are

$$q_p(0) = 0 \quad [A-I-10]$$

and

$$i_p(0) = \dot{q}_p(0) = 0 \quad [A-I-11]$$

Standard techniques yield the following solution

$$q_p(t) = \frac{\frac{1}{\tau_s} - \frac{1}{\tau_m}}{\frac{1}{\tau_s} - \frac{1}{\tau_1}} \int_0^t \frac{E_p(u)}{R_p} \exp\left(\frac{u-t}{\tau_s}\right) du - \frac{\frac{1}{\tau_s} - \frac{1}{\tau_m}}{\frac{1}{\tau_s} - \frac{1}{\tau_1}} \int_0^t \frac{E_p(u)}{R_p} \exp\left(\frac{u-t}{\tau_1}\right) du \quad [A-I-12]$$

where  $\tau_s$  and  $\tau_1$  are defined by Eq. [2] and [3]. Knowing  $q_p(t)$ , it is then straightforward to obtain the explicit expression for  $I(t)$  as given by Eq. [1].

## APPENDIX II

### Existence and Uniqueness of Solution of Eq. [2] and [3] for $R_p$ and $C_p$

Solution of Eq. [2] and [3] for  $R_p$  and  $C_p$  when  $R_s$  is not small enough to be negligible is included here for completeness.

The following Eq. [A-II-1] and [A-II-2] are equivalent to Eq. [2] and [3]

$$\frac{1}{\tau_s} + \frac{1}{\tau_1} = \frac{1}{R_p C_m} + \frac{1}{\tau_m} + \frac{1}{\tau_p} \quad [A-II-1]$$

$$\frac{1}{\tau_s \tau_1} = \frac{1}{\tau_m \tau_p} + \frac{1}{R_p C_m R_s C_p} \quad [A-II-2]$$

We thus have

$$C_p = \frac{\frac{1}{R_p} + \frac{1}{R_s}}{\frac{1}{\tau_s} + \frac{1}{\tau_1} - \frac{1}{\tau_m} - \frac{1}{R_p C_m}} \quad [\text{A-II-3}]$$

The explicit solution for  $R_p$  and  $C_p$  follows

$$\frac{1}{R_p} = P \pm \sqrt{P^2 + Q} \quad [\text{A-II-4}]$$

$$C_p = T \pm \sqrt{T^2 - \frac{\tau_s \tau_1}{R_s^2}} \quad [\text{A-II-5}]$$

where

$$P = \frac{1}{2} \left[ SC_m + \frac{\frac{\tau_m}{\tau_s \tau_1} - \frac{1}{\tau_m}}{R_s \left( \frac{1}{\tau_m} + \frac{1}{R_s C_m} \right)} \right] \quad [\text{A-II-6}]$$

$$Q = \frac{SC_m}{R_s + \frac{\tau_m}{C_m}} \quad [\text{A-II-7}]$$

$$T = \frac{\tau_s \tau_1}{2} \left[ SC_m \left( \frac{1}{\tau_m} + \frac{1}{R_s C_m} \right) + \frac{1}{R_s} \left( \frac{\tau_m}{\tau_s \tau_1} + \frac{1}{\tau_m} \right) \right] \quad [\text{A-II-8}]$$

$$S = \frac{1}{\tau_s} + \frac{1}{\tau_1} - \frac{1}{\tau_m} - \frac{\tau_m}{\tau_s \tau_1} \quad [\text{A-II-9}]$$

It remains to be shown that one pair of solutions for  $R_p$  and  $C_p$  is physically meaningful and that the other pair is not. From Eq. [A-II-9], [A-II-1], and [A-II-2], it follows that

$$S = \frac{\tau_m}{R_p C_m} \left( \frac{1}{\tau_m} - \frac{1}{R_s C_p} \right) \approx \frac{\tau_m}{R_p C_m} \left( \frac{1}{R_e C_m} - \frac{1}{R_s C_p} \right) \quad [\text{A-II-10}]$$

For TVC measurement with the access resistance  $R_e < R_s$ , we have  $S > 0$ , since  $C_m$  and  $C_p$  are roughly of the same order of magnitude. Thus from Eq. [A-II-7] and [A-II-8] we have  $Q > 0$  and  $T > 0$ . As a consequence, we also have  $P + \sqrt{P^2 + Q} > 0$  and  $P - \sqrt{P^2 + Q} < 0$ . Therefore, there is one and only one physically meaningful solution for  $R_p$ , namely

$$\frac{1}{R_p} = P + \sqrt{P^2 + Q} \quad [\text{A-II-11}]$$

and one is forced to choose for  $C_p$

$$C_p = T + \sqrt{T^2 - \frac{\tau_s}{R_s^2}} \quad [\text{A-II-12}]$$

because of the choice of Eq. [A-II-11] for  $R_p$ .  $C_p$  must be real because of Eq. [A-II-3], and also positive because of Eq. [A-II-5] and  $T > 0$ .

This completes the proof of existence and uniqueness of  $R_p$  and  $C_p$  for the case with  $R_e$  smaller than  $R_s$ .

#### REFERENCES

1. J. S. Huebner and H. T. Tien, *Biochim. Biophys. Acta*, **256**, 300 (1972).
2. H.-W. Trissl and P. Läuger, *ibid.*, **282**, 40 (1972).
3. H.-M. Ullrich and H. Kuhn, *ibid.*, **266**, 584 (1972).
4. O. Froehlich and B. Diehn, *Nature*, **248**, 802 (1974).
5. M. Schadt, *Biochim. Biophys. Acta*, **323**, 351 (1973).
6. H. T. Tien, "Bilayer Lipid Membranes (BLM) Theory and Practice," pp. 245-321, Marcel Dekker, New York (1974).
7. F. T. Hong and D. Mauzerall, *Biochim. Biophys. Acta*, **275**, 479 (1972).
8. F. T. Hong and D. Mauzerall, *Nature New Biol.*, **240**, 154 (1972).
9. D. Mauzerall and F. T. Hong, in "Porphyrins and Metalloporphyrins," 2nd ed., K. Smith, Editor, pp. 701-725, Elsevier, Amsterdam (1975).
10. F. T. Hong and D. Mauzerall, *Proc. Nat. Acad. Sci. USA*, **71**, 1564 (1974).
11. F. T. Hong, Ph.D. Dissertation, The Rockefeller University, New York (1973).
12. F. T. Hong, *Federation Proc.*, **33**, 1268, Abstr. No. 249 (1974).
13. H. T. Witt, *Quart. Rev. Biophys.*, **4**, 365 (1971).
14. K. T. Brown, *Vision Res.*, **8**, 633 (1968).
15. R. P. Baldwin and S. P. Perone, *This Journal*, To be published.

# The Effects of Counterion Size on the Equilibrium Properties of Charged Interfaces

W. R. Fawcett\* and T. A. McCarrick

Department of Chemistry, University of Guelph, Guelph, Ontario, Canada

## ABSTRACT

The adsorption of iodide ion at mercury has been studied from two systems at constant ionic strength, namely,  $xM NaI + (0.25 - x)M NaF$  and  $xM KI + (0.25 - x)M KF$ . The surface excess of adsorbed iodide ions was calculated from differential capacity data using a modified version of the Hurwitz-Parsons analysis which takes into consideration variation in ionic activity coefficients with solution composition. The iodide surface excess was found to depend on the nature of the cation for a given bulk concentration and electrode charge density; comparison of the present data with those previously published shows a marked dependence of adsorbed surface excess on ionic strength. The effect of counterion nature on ionic adsorption is discussed within the framework of an electrostatic model for adsorption which takes the discrete nature of the charge at the interface into consideration. Counterion effects at charged monolayers, bilayer lipid membranes, and real membranes are compared with those observed at mercury.

Although numerous studies of the adsorption of ions at the mercury/solution interface have been carried out (1), the effect of the nature of the non-adsorbed counterion on the amount of adsorption and electrostatic properties of the interface has not been investigated. Thus, the adsorption of halide ions has been studied from aqueous solutions of KCl (2), KBr (3), and KI (4) at varying ionic strengths, and also from solutions of KCl + KF (5), KBr + KF (6),  $NH_4Br + NH_4F$  (7), and KI + KF (8) at constant ionic strength. In analyzing these data it has been customary to assume that neither the cation nor the fluoride anion in the mixed solutions is adsorbed on mercury. On the other hand, Grahame (9) showed that the double layer capacity in the absence of anion specific adsorption depends on the nature of the electrolyte cation when the latter is predominant in the double layer. These results can be interpreted as evidence that the thickness of the inner region of the double layer,  $x_d$ , increases with hydrated radius of the cation at the outer Helmholtz plane. Thus, the potential distribution in the inner layer and the electrostatic potential at the charge center of an adsorbed anion should depend on the nature of the nonadsorbed counterion. It then follows on the basis of the electrostatic model of ionic adsorption (10) that the amount of adsorption should depend on the nature of the counterion for constant charge on the electrode and constant bulk concentration of the adsorbing ion.

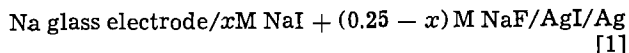
In order to test the above hypothesis, the adsorption of iodide ion has been studied from solutions of NaI + NaF and KI + KF at the same constant ionic strength (0.25M).  $Na^+$  and  $K^+$  were chosen as counterions because of their importance in biological systems where  $K^+$  is the predominant cation in the intracellular fluid and  $Na^+$ , predominant in the extracellular fluid.

## Experimental

Differential capacity against potential data for the mercury/aqueous solution interface were collected for 20 systems of composition  $xM NaI + (0.25 - x)M NaF$  and  $xM KI + (0.25 - x)M KF$  where  $x$  had the values 0, 0.0063, 0.01, 0.016, 0.025, 0.04, 0.063, 0.1, 0.16, and 0.25M. The capacity was measured at 1 kHz for 50 mV increments in potential except in potential regions where the capacity changed markedly with

potential; the potential increment was then reduced so that the capacity increment was  $< 5\mu F cm^{-2}$ . The data were obtained with an a-c bridge built according to the design of Hills and Payne (11), the potential of the mercury electrode being measured with respect to a saturated calomel electrode. The cell and associated electrodes have been described elsewhere (12). All experiments were carried out at  $25.0^\circ \pm 0.1^\circ C$ . Procedures for determining the area of the drop at balance and the potential of zero charge have been described previously (11, 12).

Variation in NaI activity with solution composition was determined by measuring the emf of the cell



The emf was determined by a null technique using a high input impedance electrometer ( $R > 10^{14}\Omega$ ). The sodium electrode was a Corning Model NAS 11-18 glass membrane electrode; the silver/silver iodide electrode was prepared by depositing silver iodide on silver using the procedure given by Ives and Janz (13).

The salts used were of AnalaR grade and were further purified by double recrystallization from pure water. The drying operation for the fluoride salts was carried out in platinum vessels. Conductivity grade water was obtained by doubly distilling deionized water.

## Analysis of the Thermodynamic Data

The original thermodynamic analysis for the mercury/mixed electrolyte solution interface at constant ionic strength by Dutkiewicz and Parsons (8) is limited to the case that the activity coefficients of the individual ions do not vary significantly with solution composition. More general analyses have been given by Hurwitz (14) and Lakshmanan and Rangarajan (15). The problem of activity coefficient variation is reconsidered here for simple 1-1 electrolyte mixtures for which Harned's rule is valid.

According to simple models for single ion activity coefficients (16), the activity coefficients for the ions in a MI-MF solution may be expressed as a function of the ionic strength  $\mu$  and the concentrations of oppositely charged ions. Thus, the activity coefficient for the cation M is given by

$$\ln \gamma_M = \frac{-A\mu^{1/2}}{1 + B\alpha_{M\mu}^{1/2}} + \beta_{MI}c_I + \beta_{MFCF} \quad [2]$$

\* Electrochemical Society Active Member.  
Key words: adsorption, double layer, iodide layer, counterion effects.

and for either anion by

$$\ln \gamma_J = \frac{-A\mu^{1/2}}{1 + B\mu^{1/2}} + \beta_{MJ}c_M \quad [3]$$

$A$  and  $B$  are the Debye-Hückel constants,  $a_i$ , the ionic size parameter for ion  $i$ ,  $c_i$ , its concentration, and  $\beta_{MJ}$ , the interaction coefficient between cation  $M$  and anion  $J$ . Since the ionic strength and concentration of the metal ion are held constant, only variation in  $\gamma_M$  with solution composition need be considered.

The Gibbs adsorption isotherm for the mixed electrolyte system may be written

$$-d\gamma = qdE_+ + \Gamma_I d\mu_{MI} + \Gamma_F d\mu_{MF} \quad [4]$$

where  $\gamma$  is the surface tension,  $q$ , the electrode charge density,  $E_+$ , the potential of mercury with respect to an electrode reversible to cation  $M^+$ ,  $\Gamma_I$ , the surface excess of anion  $J$ , and  $\mu_{MJ}$ , the chemical potential of salt  $MJ$ . Then, following Dutkiewicz and Parsons (8)

$$d\mu_{MI} = RT d \ln x + RT d \ln \gamma_M \quad [5a]$$

and

$$d\mu_{MF} = \frac{-x RT}{(1-x)} d \ln x + RT d \ln \gamma_M \quad [5b]$$

where  $x = c_I/(c_I + c_F)$ . For strong adsorption the position of the outer Helmholtz plane (OHP) is determined by the distance of closest approach of the cation and the Gibbs adsorption isotherm becomes

$$-d\gamma = qdE_+ + \Gamma_I^a RT d \ln x + (\Gamma_I + \Gamma_F) RT d \ln \gamma_{Na} \\ = qdE_+ + \Gamma_I^a RT d \ln x + (\Gamma_I + \Gamma_F) RT \beta x d \ln x \quad [6]$$

where  $\Gamma_I^a$  is the surface excess of iodide ion adsorbed in the inner layer and  $\beta = (\beta_{MI} - \beta_{MF})\mu$ .

When  $\beta$  is significant, the electrode potential measured with respect to a constant reference electrode  $E_r$  is related to the thermodynamic potential  $E_+$  by the equation

$$dE_r = dE_+ + \frac{RT}{F} d \ln \gamma_M = dE_+ + \frac{RT}{F} \beta dx \quad [7]$$

Thus, the electrode potential measured may be converted to a thermodynamic scale if  $\beta$  is known.

Introducing Parsons' function  $\xi_+ = \gamma + qE_+$  and converting surface excesses to the corresponding surface charge densities, Eq. [6] becomes

$$d\xi_+ = E_+ dq + q_a \frac{RT}{F} (1 + \beta x) d \ln x \\ + q_J^d \frac{RT}{F} \beta x d \ln x \quad [8]$$

where  $q_a$  is the adsorbed charge density due to iodide ions and  $q_J^d$  is the surface excess of anions in the diffuse layer.

The usual way of determining  $\xi_+$  is to integrate capacity against potential curves twice from a fixed negative potential  $E_+$  where adsorption of anions may be considered negligible and thus the charge on the electrode independent of solution composition. However, from Eq. [8], it is apparent that  $\gamma$  and  $\xi_+$  will not be independent of solution composition when  $q_I^a$  is zero. At constant charge density, the value of  $\xi_+$  at a fixed reference potential,  $\xi_+^r$  is given by

$$\xi_+^r = \xi_+^{r0} + q_J^d \cdot \frac{RT}{F} \beta x \quad [9]$$

where  $\xi_+^{r0}$  is the value of  $\xi_+^r$  when  $x = 0$ . Using this relationship the necessary integration constants may be calculated and  $\Delta\xi_+ = \xi_+ - \xi_+^0$  determined for any value of  $E_+$  or  $q$ .

Having determined  $\xi_+$  as a function of solution composition at constant  $q$ , one may determine  $q_I^a$  by differentiation. From Eq. [8]

$$\frac{F}{RT} \frac{1}{(1 + \beta x)} \left( \frac{\partial \xi_+}{\partial \ln x} \right)_q = q_a + q_J^d \frac{\beta x}{(1 + \beta x)} \quad [10]$$

When  $q + q_a$  is large,  $q_J^d$  approaches a constant value, given by  $(RT\epsilon\mu/2\pi)^{1/2}$  where  $\epsilon$  is the dielectric constant of the pure solvent. Thus, an approximate value of  $q_a$  may be calculated using the limiting value of  $q_J^d$ . The estimate is then improved using an iterative technique and the exact expression for  $q_J^d$  from Gouy-Chapman theory.

Examination of existing activity coefficient data reveals that the mean ionic activity coefficient for KI is approximately 1% higher than that for KF whereas that for NaI is 7% higher than that for NaF. Thus, any variation in  $\gamma$  for the KI-KF system would be difficult to determine experimentally and it is probably legitimate to assume  $\beta \approx 0$  for this system; however, as is shown below, variation in  $\gamma_{Na}$  in the NaI-NaF system can be detected experimentally. Thus, the exact analysis presented above was used for the latter system.

### Results

Experimental values of the emf of cell [1],  $\epsilon$  together with the corresponding values of  $\epsilon + (RT/F) \ln c_{NaCl}$  are recorded in Table 1 for varying values of  $x$  with  $\mu = 0.25M$ . From the Nernst equation for this cell

$$\epsilon + \frac{RT}{F} \ln c_{NaCl} = \epsilon_0 - \frac{RT}{F} \ln \gamma_{Na} \gamma_I \quad [11]$$

where  $\epsilon_0$  is the standard emf. The derivative  $d(\epsilon + (RT/F) \ln c_{NaCl})/dx$  is equal to 2 mV; thus, assuming  $\gamma_I$  is independent of solution composition,  $\beta = d \ln \gamma_{Na}/dx$  is equal to 0.078. From Eq. [10], it is apparent that neglect of variation of  $\gamma_{Na}$  would result in  $q_a$  being overestimated by approximately 8% when  $x = 1$ . The relative error decreases with decrease in  $x$ . It is also apparent that any variation in  $\gamma_K$  in the KI-KF could not be detected by using the equivalent cell to [1] for the  $K^+$  system when the precision of the emf measurements is  $\pm 1$  mV. Thus,  $\beta$  for the  $K^+$  system was assumed to be zero.

Typical capacity against potential curves for the KI-KF system are shown in Fig. 1. A small decrease in the slope of these curves followed by a steady increase is observed at potentials just positive of the point of zero charge. Similar but more pronounced effects are observed on capacity curves for  $Cl^-$  and  $Br^-$  systems (2, 3, 5-7) in water but are absent for the  $I^-$  systems in nonaqueous solvents (17). This effect is normally attributed to changes in the dielectric properties of the inner layer due to water molecule reorientation (1).

The capacity-potential curves were twice integrated from negative potentials ( $E_+ = -1.596V$  at  $q = -21 \mu C cm^{-2}$  for the KI-KF system and  $E_+ = -1.610V$  at  $q = -21 \mu C cm^2$  for the NaI-NaF system) where anion adsorption could be assumed negligible and  $\Delta\xi_+$  calculated for integral increments in  $q$  using well-established technique (3, 12) modified to take into account the variation in  $\gamma_{Na}$  in the NaI-NaF system as described above. The adsorbed charge density due to  $I^-$  was calculated according to Eq. [10], the derivative  $(\partial \Delta\xi_+ / \partial \ln x)_q$  being estimated by numerical differentiation using a least squares fit of a cubic equa-

Table 1. EMF of the cell Na glass electrode/ $xM$  NaI + (0.25 -  $x$ )M NaF/Ag I/Ag

$c_I, M$	$\epsilon, V$	$\epsilon + (RT/F) \ln c_{Na} + c_I, V$
0.001	-0.1965	-0.4096
0.01	-0.257	-0.4109
0.1	-0.3165	-0.4113
0.25	-0.341	-0.4122

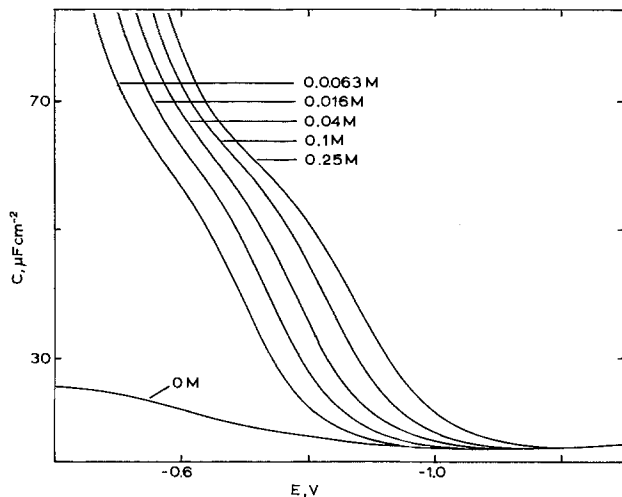


Fig. 1. Differential capacity of the mercury/solution interface,  $C$  against electrode potential,  $E$  (with respect to a saturated calomel electrode) for aqueous solutions of  $x\text{M KI} + (0.25 - x)\text{M KF}$  at  $25^\circ\text{C}$ . The concentration of KI is indicated on the figure.

tion to  $\Delta\xi^+$  against  $\ln x$  data over the total experimental range (18).

Adsorption isotherms for the KI-KF system at constant charge density are shown in Fig. 2. The curvature of these plots changed with  $q$  indicating that the isotherm is not congruent in this electrical variable. Similar results have been found for the adsorption of  $\text{Br}^-$  (6, 7) and  $\text{Cl}^-$  ions (5) whereas the adsorption isotherm for  $\text{I}^-$  ion from solutions of higher ionic strength (8) was found to be congruent in electrode charge density. The latter data were obtained only at more negative electrode charge densities ( $q < -6 \mu\text{C cm}^{-2}$ ) which may account for the difference in behavior with that observed here over a wider range of  $q$ . Comparison of the present data with those of Dutkiewicz and Parsons (8) also shows that the adsorbed charge density due to  $\text{I}^-$  ions,  $|q_a|$  is sig-

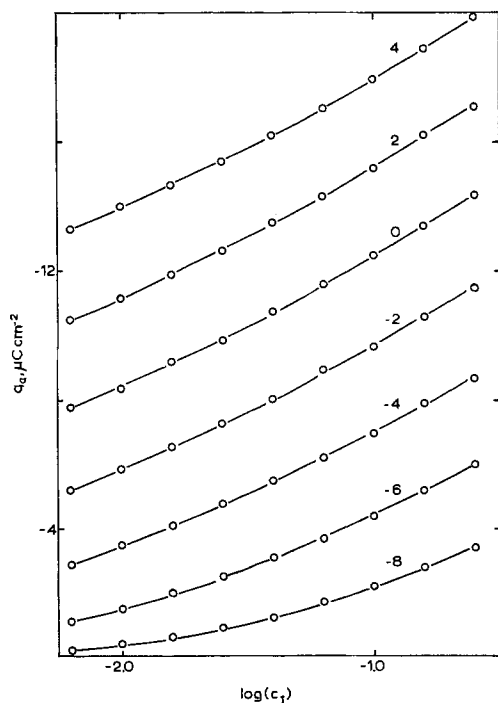


Fig. 2. Plots of the adsorbed charge density due to  $\text{I}^-$ ,  $q_a$  against the logarithm of  $\text{I}^-$  concentration in the bulk,  $\log(c_1)$  for various constant charge densities on the electrode (indicated by the integers adjacent to each curve) for adsorption from the KI-KF system.

nificantly less in the system of lower ionic strength. Although the amount of adsorption is less, similar adsorption isotherms are obtained for the NaI-NaF system. Results obtained at a bulk concentration of  $0.1\text{M I}^-$  in the present and previous studies are shown as a function of electrode charge density in Fig. 3. A large increase in  $|q_a|$  with ionic strength is readily apparent; a small but significant increase in  $q_a$  when the counterion is changed from  $\text{Na}^+$  to  $\text{K}^+$  at constant ionic strength is also observed.

Plots of the potential drop across the inner layer,  $\phi^{\text{md}}$ , against the adsorbed charge density,  $q_a$ , at constant electrode charge density are shown for the KI-KF system in Fig. 4. The plots were linear within experimental error but their slopes changed significantly with  $q$  indicating that the absorption could not be described by an isotherm congruent in electrode charge density. The plots for the NaI-NaF system were similar in appearance but had higher slopes. The reciprocals of the slopes of the above plots, that is,  $(\partial q_a / \partial \phi^{\text{md}})_q$  is plotted against electrode charge density in Fig. 5. In terms of the simple electrostatic model of the inner layer  $(\partial q_a / \partial \phi^{\text{md}})_q$  is equal to the integral capacity of the region between the adsorp-

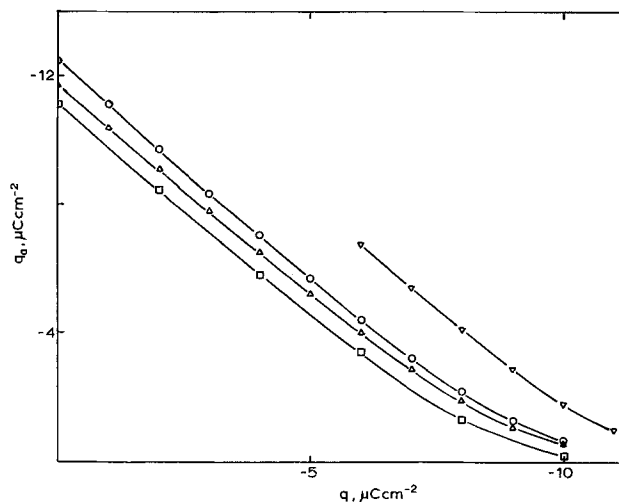


Fig. 3. Plots of the adsorbed charge density due to  $\text{I}^-$ ,  $q_a$  against the electrode charge density,  $q$  for constant bulk  $\text{I}^-$  concentration ( $0.1\text{M}$ ) but varying ionic strength and counterion:  $\square$ ,  $0.1\text{M KI}$  [Grahame (4)];  $\triangle$ ,  $0.1\text{M NaI} + 0.15\text{M NaF}$  (this work);  $\circ$ ,  $0.1\text{M KI} + 0.15\text{M KF}$  (this work);  $\nabla$ ,  $0.1\text{M KI} + 0.9\text{M KF}$  [Dutkiewicz and Parsons (8)].

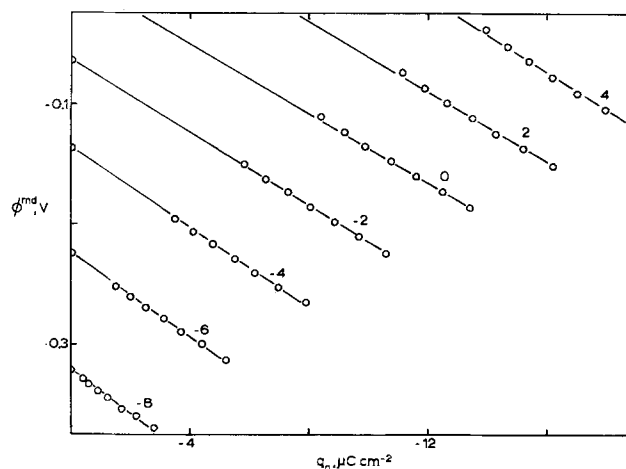


Fig. 4. Plots of the potential drop across the inner layer,  $\phi^{\text{md}}$  against the adsorbed charge density, due to  $\text{I}^-$ ,  $q_a$  at constant electrode charge density (indicated by the integer adjacent to each plot) for adsorption from the system  $x\text{M KI} + (0.25 - x)\text{M KF}$ .

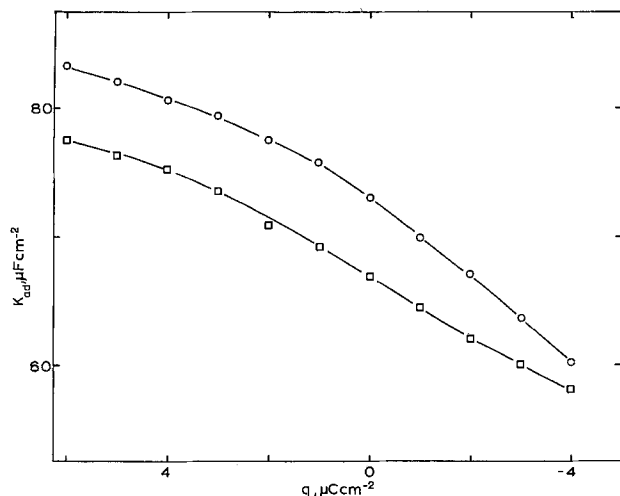


Fig. 5. Plots of the integral capacity of the region between the inner Helmholtz plane and the outer Helmholtz plane,  $K_{ad}$  against the electrode charge density,  $q$  for the NaI-NaF system (□) and KI-KF system (○).

tion or inner Helmholtz plane (IHP) and the OHP, that is,  $K_{ad}$ . The fact that  $K_{ad}$  is significantly lower for the NaI-NaF system suggests that the thickness of this region is greater in the  $\text{Na}^+$  system than in the  $\text{K}^+$  system.

The function  $\ln(-q_a/c_I) - f\phi^d$ , where  $\phi^d$  is the potential drop across the diffuse layer and  $f = F/RT$ , is plotted against  $q_a$  in Fig. 6. The linearity of these plots suggests that a virial isotherm with a term correcting for the diffuse layer (19) accounts for the data obtained. This type of adsorption isotherm is expected when the simple electrostatic model for ionic adsorption (10) is applicable and electrode coverage is small so that the entropic term in the isotherm,  $\ln(1 - \theta)$  may be approximated by the first two terms in its series expansion (19).

### Discussion

**Effects of activity coefficient variation.**—Two aspects of activity coefficient variation should be considered here: the variation in activity of iodide ion with nature of the cation for constant bulk concentration and ionic strength, and the variation in metal ion activity with solution composition for constant ionic strength and metal ion nature. From tabulated activity coefficient data, the mean ionic activity coefficients in 0.25M NaI and KI solutions are 0.741 and 0.718, respectively. Assuming  $a_{\text{Na}} = 4\text{A}$ ,  $a_{\text{K}} = 3\text{A}$  and  $a_{\text{I}} = 3\text{A}$  (20), and applying Eq. [2] and [3],  $\beta_{\text{NaI}}$  and  $\beta_{\text{KI}}$  are esti-

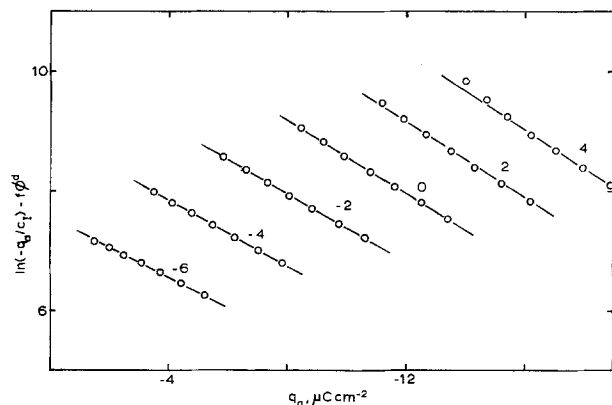


Fig. 6. Plots of the function  $\ln(-q_a/c_I) - f\phi^d$  against charge density due to adsorbed  $\text{I}^-$ ,  $q_a$  at constant electrode charge density (indicated by the integer adjacent to each plot) for the KI-KF system.

mated to be 0.019 and 0.016, respectively. Thus,  $\gamma_{\text{I}} = 0.727$  in 0.25M NaI and 0.718 in 0.25M KI. Other factors ignored, one would then expect more adsorption of  $\text{I}^-$  from the NaI system since its activity is higher at the same concentration. It then follows that one cannot attribute the decreased adsorption from the NaI system to a corresponding decrease in the bulk activity of the  $\text{I}^-$  ion.

The applicability of the above model may be tested by comparing the experimentally measured value of  $\beta$  for the NaI-NaF system with that estimated using Eq. [2] and [3]. Assuming  $a_{\text{F}} = 3.5\text{A}$  (20),  $\beta_{\text{NaF}} = -0.001$  and  $\beta = (\beta_{\text{NaI}} - \beta_{\text{NaF}})\mu = 0.079$ . This result agrees very well with that obtained experimentally and confirms that the estimates of single ion activities may be considered reliable.

It is worth mentioning that, although one might expect significant variation in single ion activities in some of the systems studied previously using the Hurwitz-Parsons method, only one attempt appears to have been made to consider this variation in the thermodynamic analysis (21). In that salt activities may be measured relatively easily using the emf technique with specific ion electrodes, this aspect of the Hurwitz-Parsons analysis of ionic adsorption should not be overlooked in future work. The data for systems with nonnegligible  $\beta$  previously published should also be reexamined.

**Adsorption of iodide ion at mercury.**—Although the data reported here are qualitatively similar to those presented earlier for halide ion adsorption (2-8), they can be used to elucidate several problems regarding ionic adsorption discussed in the recent literature (1). One point which has received a great amount of attention is the question of whether an isotherm congruent in either electrode charge density or electrode potential could be used to describe ionic adsorption. In more recent work it has been emphasized that a term to account for the contribution to the free energy of adsorption due to the potential drop across the diffuse layer must appear explicitly in the adsorption isotherm (7, 19). Since  $\phi^d$  is a function of both electrode charge density and bulk iodide ion concentration it follows that congruency in one or other of the electrical variables can be observed only when the diffuse layer term is negligibly small or fortuitously constant with change in bulk concentration of the adsorbing ion.

The present results provide direct evidence of the necessity of including the diffuse layer term in the isotherm. Thus, to a first approximation, the increase in  $|q_a|$  with increase in ionic strength at constant  $q$  may be attributed to a corresponding decrease in  $|f\phi^d|$ , that is, to a decrease in the repulsive field of the diffuse layer. More precisely, the electrostatic contribution to the free energy of adsorption of a monovalent anion may be written (10)

$$(\Delta G_a)_e = -F\phi^d - F(q + q_a)/K_{ad} + \xi_{sa} + \xi_{ds} \quad [12]$$

where the first two terms account for the difference between the average potential on the adsorption plane and that in the bulk of the solution,  $\xi_{sa}$  is the contribution due to the self-images formed by the adsorbing ion in the metal and diffuse layer (self-atmosphere potential) and  $\xi_{ds}$ , that due to the fact that the ion occupies finite area on the adsorption plane (disk potential). Other than the change in  $\phi^d$ , one may distinguish two other factors which contribute to a decrease in  $(\Delta G_a)_e$  with increase in ionic strength for constant  $q$  and  $q_a$ . It can be argued that the effective thickness of the inner layer decreases with increase in ionic strength; this change results mainly in an increase in  $K_{ad}$ , the effective capacity of the region between the adsorption plane and the outer Helmholtz plane (8) and thus in a decrease in  $(\Delta G_a)_e$ .

At the same time the self-atmosphere contribution  $\xi_{sa}$  becomes more negative due to the increased efficiency of image formation in the diffuse layer. The above effects are reduced somewhat by a decrease in the value of  $1/\xi_{ds}$ . The disk term is negative and given approximately by  $\xi_{ds} = Fg K_{md} q_a / K_{ma} K_{ad}$  where  $K_{md}$  is the integral capacity of the inner layer,  $K_{ma}$ , the capacity of the region between the metal and adsorption plane, and  $g$ , a dimensionless parameter approximately equal to unity (23). The increase in  $K_{ad}$  results in a smaller increase in  $K_{md}$  and thus a small decrease in  $1/\xi_{ds}$ . It is easily shown by calculations on the basis of models developed by Levine *et al.* (10, 22, 23) that the total effect of increase in  $K_{ad}$  with ionic strength is a corresponding decrease in  $(\Delta G_a)_e$ .

The variation in  $q_a$  with counterion nature at constant  $q$  and ionic strength can also be accounted for on the basis of the above electrostatic model. Although  $\phi^d$  is independent of counterion nature to a first approximation,  $K_{ad}$  increases when the counterion is changed from  $\text{Na}^+$  to  $\text{K}^+$  (Fig. 5). As argued above, this will result in a decrease in the second and third terms in Eq. [12], an increase in the fourth term, and an over-all decrease in  $(\Delta G_a)_e$ . Thus, one observes an increase in the difference in  $q_a$  for the  $\text{Na}^+$  and  $\text{K}^+$  systems as the difference between the corresponding values of  $K_{ad}$  increases. An alternative explanation of the cation effect on iodide ion adsorption is to attribute it to cation coadsorption, the amount of cation adsorption being larger in the  $\text{K}^+$  system. However, one would expect the amount of cation adsorption to increase as the charge on the electrode becomes more negative, and thus the difference between  $q_a$  in the  $\text{Na}^+$  and  $\text{K}^+$  systems to become more pronounced at negative charge densities. The present results show exactly the opposite trend and thus are evidence against this explanation of the cation effect. All results obtained are consistent with a model of the inner layer in which its thickness at negative charge densities is determined by the distance of closest approach of a solvated cation, the solvated radius of  $\text{Na}^+$  being larger than that of  $\text{K}^+$ . A similar explanation can be offered to account for all or part of the cation effect observed for the kinetics of electron transfer reactions occurring at negative charge densities on mercury (24, 25).

The Christie plots presented in Fig. 4 are normally interpreted in terms of a simple electrostatic model of the inner layer according to which

$$\phi^{md} = \frac{q}{K_{md}} + \frac{q_a}{K_{ad}} \quad [13]$$

If  $K_{md}$  and  $K_{ad}$  are independent of  $q_a$  for fixed  $q$ , then the slope of the Christie plot is equal to  $1/K_{ad}$ . In the more general case, the slope is given by

$$\frac{\partial \phi^{md}}{\partial q_a} = \frac{1}{K_{ad}} + q_a \left( \frac{\partial (1/K_{ad})}{\partial q_a} \right)_q + q \left( \frac{\partial (1/K_{md})}{\partial q_a} \right)_q \quad [14]$$

Since the Christie plots are linear, one may conclude that  $\partial(1/K_{ad})/\partial q_a \simeq 0$ . Considering the fact that the plots are not parallel, one would expect some contribution from the third term in Eq. [14]. However, its magnitude must be small or approximately independent of  $q_a$  for the range of values of  $q$  and  $q_a$  considered in Fig. 4. Since  $q$  is not large in this range and no curvature is apparent, one may conclude that the slope of the Christie plots is approximately equal to  $1/K_{ad}$  in the present case. Dutkiewicz and Parsons (8) found  $K_{ad}$  to be approximately constant ( $59 \mu\text{F}\cdot\text{cm}^{-2}$ ) in the 1M KI-KF system at negative charge densities ( $-12 < q < -6 \mu\text{coulombs}\cdot\text{cm}^{-2}$ ). The values obtained here are somewhat smaller ( $K_{ad} = 50 \mu\text{F}\cdot\text{cm}^{-2}$  at  $q = -8 \mu\text{coulombs}\cdot\text{cm}^{-2}$ ) and appear to decrease as the charge on the

electrode becomes more negative (Fig. 5). Several explanations could be offered for the disagreement. First, the numerical differentiation technique used to determine  $q_a$  becomes very inaccurate at large negative charge densities where the total change in  $\Delta\xi_+$  at constant  $q$  is small. On the other hand, Dutkiewicz and Parsons assumed that the isotherm is congruent and thereby avoided numerical differentiation, the values of  $q_a$  being obtained from  $\Delta E_+$ , the potential shift due to adsorption at constant electrode charge density (8). However, their procedure may be considered as a particular kind of data smoothing which necessarily results in approximately parallel Christie plots and a constant value of  $K_{ad}$  (1). The value of  $(\partial \phi^{md}/\partial q_a)$  obtained by Grahame (4) in pure KI solutions at the point of zero charge agrees well with that obtained here. At more negative or positive charge densities the agreement is poor. If  $K_{ad}$  changes with ionic strength, the disagreement can be attributed to increased contributions from the terms  $\partial(1/K_{ad})/\partial q_a$  and  $\partial(1/K_{md})/\partial q_a$  in Eq. [14].

Several attempts have been made (19, 26) to analyze adsorption data similar to that obtained here on the basis of the electrostatic model developed by Levine *et al.* (10, 23). In the case that the adsorbing ion is small, the adsorption isotherm may be written

$$\ln \theta - \ln(1 - \theta) = \ln \Gamma^a - (\Delta G_a)_c / RT - (\Delta G_a)_e / RT \quad [15]$$

where  $\theta = q_a/q_m$ ,  $q_m$  being the maximum adsorbed charge density, and  $(\Delta G_a)_c$  is the part of the free energy of adsorption which is independent of the electrical state of the interface. Since the coverage obtained in these experiments is small,  $q_m$  cannot be easily determined. Furthermore, the component capacities of the inner layer  $K_{ma}$  and  $K_{ad}$  can only be determined approximately from the Christie plots so that further analysis of the data presented in Fig. 6 does not seem worthwhile at present. However, it should be noted that the contribution to the free energy of adsorption due to the self-atmosphere potential (Eq. [12]) has been overlooked in previous analyses. Calculations have shown that this term is not negligible (22). Although it may not vary much with  $q_a$ , one would expect it to vary significantly with  $q$ .

#### Counterion effects at other charged interfaces.—

From a biological point of view studies of counterion effects at charged monolayers and bilayer lipid membranes (BLM) may be useful in elucidating the electrical behavior of membranes in living systems (26a). In this regard one may distinguish two cation effects at negatively charged monolayers and BLM. The first is the selectivity for cation transport which is often observed in these systems and which depends both on the chemical nature of the film and also on the presence of lipid soluble carriers such as valinomycin (27-29). The second effect and that with which this paper is concerned is the nature of the average and local potential profiles at the interfaces of the system and its influence on adsorption of other ions and dipolar molecules and on transport through the film.

Goddard and co-workers (30-33) have studied the effects of counterion nature on the surface pressure and potential at both positively and negatively charged monolayers. For negatively charged head groups, these properties depend both on the nature of the head group and on the nature of the cation in solution. The surface potential of an expanded arachidic acid monolayer ( $-\text{COO}^-$  head group) is negative in alkali metal hydroxide solution and decreases in magnitude in the sequence  $\text{K}^+ > \text{Na}^+ > \text{Li}^+$ . In the case of expanded docosyl sulfate monolayers, the sequence is reversed. Thus, Goddard (32) has argued that alkali metal cation interaction with ionized fatty acid monolayers increases as the crystallographic radius

of the cation decreases ( $\text{Li}^+ > \text{Na}^+ > \text{K}^+ > \text{Rb}^+ > \text{Co}^+$ ) whereas interaction with alkyl sulfate monolayers increases as the hydrated radius of the cation decreases ( $\text{Co}^+ \simeq \text{Rb}^+ > \text{K}^+ > \text{Na}^+ > \text{Li}^+$ ). In fact, the situation is undoubtedly much more complex. Examination of the literature on cation effects at negatively charged colloids reveals that cation interaction depends very much on the nature of the anionic group and that more than the above two interaction sequences for alkali metal cations are observed experimentally (34). Cation interaction with BLM does not appear to have been studied in any detail (28, 29) but electrical properties such as BLM capacitance have been found to depend on the nature and concentration of the electrolyte in the surrounding solution (28).

Erlander (34) has shown that cation interaction sequences at negatively charged colloids can be rationalized on the basis of the Frank and Wen model (35) of water structure surrounding the interacting ions with consideration of their effective dielectric constants. Accordingly, ions with high charge to radius ratios are surrounded by A-type water which is strongly bound to the ion by ion-dipole interactions. Most ions are also surrounded by B-type water in which the normal structure is broken and neither ion-dipole nor dipole-dipole interactions predominate. The normal water structure which is determined by dipole-dipole interactions and hydrogen bonding is designated C-type. Thus,  $\text{Li}^+$ ,  $\text{Mg}^{++}$ ,  $\text{Ca}^{++}$ ,  $\text{Sr}^{++}$ , and  $\text{Ba}^{++}$  ions are surrounded immediately by A water with a layer of B water beyond the tightly bound dipoles.  $\text{Cs}^+$ ,  $\text{Rb}^+$ ,  $\text{K}^+$ ,  $\text{Cl}^-$ ,  $\text{Br}^-$ , and  $\text{I}^-$  do not have any ordering effect and thus are surrounded by a B region only.  $\text{Na}^+$  and  $\text{F}^-$  are considered to have an A region but no B region. Erlander has estimated the effective dielectric constant of the B region surrounding the ions and has argued that ion-ion interaction increases when the effective dielectric constants are similar in magnitude (36). In order to apply these ideas to biological membranes one must know something about the effect of the charged groups at the surface on the structure of the surrounding water molecules. Erlander has argued that the phosphate group in phospholipids which is in close proximity to a base is surrounded by B water with a low effective dielectric constant. Thus, it interacts most strongly with  $\text{K}^+$  which has similar characteristics. The interaction sequence ( $\text{K}^+ > \text{Na}^+ > \text{Rb}^+ > \text{Li}^+ > \text{Cs}^+$ ) then depends on whether the cation has an A region and on the effective dielectric constant of the B region. Similar concepts can be applied to cation interaction with other common negative sites such as carboxylate (34).

In order to develop an electrostatic model for the potential distribution at the membrane/solution interface one must know the relative positions of the charged head group and counterions. At mercury the counterions are normally assumed to be  $\sim 5\text{\AA}$  from a homogeneous, geometrically smooth metal/solution interface; more precisely, the distance of closest approach of the counterion and thus the potential distribution at the interface depend on the nature of the interaction of both the charged metal surface and the counterion with surrounding water molecules. Considering the structure of phospholipid molecules it is quite possible that the counterions could penetrate beyond the plane through the charge centers of the phosphate groups. Since the membrane also contains protein and more than one type of phospholipid molecule (36a), often distributed in different ways on the inside and outside walls of the membrane (37), the local potential profile near the interface undoubtedly varies considerably over the surface of the membrane. Reeves and co-workers (38, 39) have developed an NMR technique for studying the orientation of

double layer ions at model membranes based on lyotropic liquid crystals. Application of this technique or another spectroscopic method to real membrane systems could be of considerable help in elucidating the spatial distribution of charged groups and ions at the membrane's surfaces. Levine *et al.* (40) have reviewed the electrostatic models developed to account for the surface potential and surface pressure observed at charged interfaces. They have emphasized the importance of considering the discrete nature of the charge as well as the distribution of counterions with respect to the charged head groups. Undoubtedly, the models developed for charged monolayers could be modified to deal with the potential distribution at each of the charged interfaces of the membrane. An understanding of the electrostatic situation could then be used to elucidate electrosorption, ionic surface excesses, and eventually the electrostatic factors which play a role in ion transport.

### Acknowledgments

The authors are indebted to Dr. J. B. M. Rattray for helpful discussions relating to the biological aspects of this paper. The financial support of the National Research Council of Canada is gratefully acknowledged.

Manuscript received June 30, 1975. This was Paper 358 presented at the Toronto, Canada, Meeting of the Society, May 11-16, 1975.

Any discussion of this paper will appear in a Discussion Section to be published in the June 1977 JOURNAL. All discussions for the June 1977 Discussion Section should be submitted by Feb. 1, 1977.

Publication costs of this article were assisted by the University of Guelph.

### REFERENCES

1. R. Payne, *J. Electroanal. Chem.*, **41**, 277 (1973).
2. D. C. Grahame and R. Parsons, *J. Am. Chem. Soc.*, **83**, 1291 (1961).
3. J. Lawrence, R. Parsons, and R. Payne, *J. Electroanal. Chem.*, **16**, 193 (1968).
4. D. C. Grahame, *J. Am. Chem. Soc.*, **80**, 4201 (1958).
5. R. Payne, *Trans. Faraday Soc.*, **64**, 1638 (1968).
6. A. R. Sears and P. A. Lyons, *J. Electroanal. Chem.*, **42**, 69 (1973).
7. G. J. Hills and R. M. Reeves, *ibid.*, **42**, 355 (1973).
8. E. Dutkiewicz and R. Parsons, *ibid.*, **11**, 100 (1966).
9. D. C. Grahame, *This Journal*, **98**, 343 (1951).
10. S. Levine, G. M. Bell, and D. Calvert, *Can. J. Chem.*, **40**, 518 (1962).
11. G. J. Hills and R. Payne, *Trans. Faraday Soc.*, **61**, 316 (1965).
12. W. R. Fawcett and M. D. Mackey, *J. Chem. Soc. Faraday Trans. I*, **69**, 634 (1973).
13. D. J. G. Ives and G. J. Janz, "Reference Electrodes," p. 198, Academic Press, New York (1961).
14. H. D. Hurwitz, *J. Electroanal. Chem.*, **10**, 35 (1965).
15. S. Lakshmanan and S. K. Rangarajan, *ibid.*, **27**, 127 (1970).
16. S. Lakshmanan and S. K. Rangarajan, *ibid.*, **27**, 170 (1970).
17. R. Payne, *Advan. Electrochem. Electrochem. Eng.*, **7**, 1 (1970).
18. W. R. Fawcett and J. E. Kent, *Can. J. Chem.*, **48**, 47 (1970).
19. C. V. d'Alkaine, E. R. Gonzalez, and R. Parsons, *J. Electroanal. Chem.*, **32**, 57 (1971).
20. J. Kielland, *J. Am. Chem. Soc.*, **59**, 1675 (1937).
21. L. M. Baugh and R. Parsons, *J. Electroanal. Chem.*, **58**, 229 (1975).
22. S. Levine, K. Robinson, and W. R. Fawcett, *ibid.*, **54**, 237 (1974).
23. S. Levine and K. Robinson, *ibid.*, **41**, 159 (1973).
24. W. R. Fawcett, *ibid.*, **22**, 19 (1969).
25. B. G. Chauhan, W. R. Fawcett, and T. A. McCarrick, *ibid.*, **58**, 275 (1975).
26. W. R. Fawcett and M. D. Mackey, *J. Chem. Soc. Faraday Trans. I*, **69**, 140 (1973).
- 26a. H. G. Bungenberg de Jong, in "Colloid Science," Vol. 2, H. R. Kruyt, Editor, Chap. 9, Elsevier, Amsterdam (1949).
27. G. Eisenman, G. Szabo, S. Ciani, S. McLaughlin,



- and S. Krasne, *Prog. Surface Membrane Sci.*, **6**, 140 (1973).
28. H. Ti Tien, "Bilayer Lipid Membranes, Theory and Practice," Marcel Dekker, New York (1974).
29. D. Papahadjopoulos, "Form and Function of Phospholipids," G. B. Ansell, J. N. Hawthorne, and R. M. C. Dawson, Editors, Chap. 7, Elsevier, Amsterdam (1973).
30. E. D. Goddard, O. Kao, and H. C. Kung, *J. Colloid. Interface Sci.*, **24**, 297 (1967).
31. E. D. Goddard, O. Kao, and H. C. Kung, *ibid.*, **27**, 616 (1968).
32. E. D. Goddard, *Croat. Chem. Acta*, **42**, 143 (1970).
33. E. D. Goddard and H. C. Kung, *J. Colloid. Interface Sci.*, **37**, 585 (1971).
34. S. R. Erlander, *J. Macromol. Sci., Part A*, **2**, 1073 (1968).
35. H. S. Frank and W. Y. Wen, *Discussions Faraday Soc.*, **24**, 133 (1957).
36. S. R. Erlander, *J. Macromol. Sci., Part A*, **2**, 833 (1968).
- 36a. S. J. Singer and G. L. Nicolson, *Science*, **175**, 720 (1972).
37. A. J. Verkleij, R. F. A. Zwaal, B. Roelofsen, P. Comfurius, D. Kastelijn, and L. L. M. Van Deenen, *Biochem. Biophys. Acta*, **323**, 178 (1973).
38. D. M. Chen, L. W. Reeves, A. S. Tracey, and M. M. Tracey, *J. Am. Chem. Soc.*, **96**, 5349 (1974).
39. D. M. Chen, K. Radley, and L. W. Reeves, *ibid.*, **96**, 5251 (1974).
40. S. Levin, J. Miggins, and G. M. Bell, *J. Electroanal. Chem.*, **13**, 280 (1967).

## Surface Charges on Nerve Membranes and Artificial Lipid Bilayers

B. Neumcke

*I. Physiologisches Institut der Universität des Saarlandes, 665 Homburg, Saar, Germany*

### ABSTRACT

The determination of membrane surface charges is described for membranes of unmyelinated and myelinated nerves and for artificial lipid bilayer membranes. In nerve membranes negative surface charges are found. Their density is larger at the external than at the internal interface. This result is discussed in terms of "flip-flop" transfer of charges between both surfaces across the membrane which is controlled by the electric field. Surface charge densities at lipid bilayer membranes formed from lipids with charged polar groups are higher than the corresponding densities at nerve membranes. The importance of discreteness of charge effects on the determination of membrane surface charges is estimated for nerve membranes and lipid bilayers and is illustrated by several examples.

Biological membranes are thin layers of proteins and lipids. Due to electrostatic and hydrophobic interactions the polar groups of these molecules are oriented toward the extra- and intracellular solutions whereas the lipophilic parts form the interior of the membrane. Charged polar groups thus are preferentially located at the membrane-solution interfaces. There is now growing evidence that these surface charges are essential for the structure and function of membranes. For example, the stability of membranes is critically affected by mutual repulsions of surface charges tending to disorder the orientation of polar head groups in the surface layers (1). The electrical conductivity of membranes depends on the membrane surface potential and can be controlled by specific surface charges near ion selective channels (2). Furthermore, surface charges may be sites for the adsorption of uncoupling agents (3) or even of macromolecular phages (4).

In this contribution surface charges are characterized for nerve membranes and compared with those at the surface of artificial lipid bilayers. For both types of membranes the exact shape of the surface and the location of charges are unknown. We, therefore, have to apply several idealizations: The membrane surface is considered as a plane interface separating two homogeneous phases with different dielectric constants. Dipole potentials and layers of adsorbed ions are neglected, and the surface charges are treated as uniformly distributed over the membrane surface. Some effects of discrete charge distributions are discussed in the last section of this contribution.

### Determination of Surface Charges

In principle there are two different approaches for determining membrane surface charges.

**Key words:** nerve membrane, lipid bilayer, membrane surface charge, discrete charge distributions

1. *Change of intramembrane field strength.*—The membrane surface potential depends on the ionic composition of the solutions in contact with the membrane. If a new solution is applied in which a different surface potential is generated, a corresponding change of the electric field strength in the membrane will occur though the externally applied voltage is kept constant. All field-dependent membrane parameters then are shifted along the voltage axis. The measured shift (corrected for the voltage drop at the membrane series resistances and for liquid junction potentials between the test solutions used) is equal to the change of the surface potential from which the density of surface charges can be calculated by applying the Gouy-Chapman theory of the diffuse double layer.

2. *Change of stationary ion flux.*—A change of the surface potential also affects the stationary ion flux. If the ion transport across the membrane is described as jump over a single symmetrical activation energy barrier, the stationary flux  $\Phi$  of univalent cations is proportional to (compare Eq. [A-9] of the Appendix)

$$\Phi \simeq \exp \left[ -\frac{F}{2RT} (\Psi' + \Psi'') \right] \left[ c' \exp \left( -\frac{FU}{2RT} \right) - c'' \exp \left( \frac{FU}{2RT} \right) \right] \quad [1]$$

where  $U$  is the externally applied voltage,  $c'$  and  $c''$  the bulk cation concentrations in the solutions,  $\Psi'$ ,  $\Psi''$  the surface potentials at the outer and inner membrane surface;  $F$  Faraday constant;  $R$  gas constant; and  $T$  absolute temperature. Thus  $\Phi$  is a function of the sum  $\Psi' + \Psi''$  of both surface potentials. For a symmetrical membrane and for identical ionic compositions of the solutions it is  $\Psi' = \Psi'' = \Psi$  and the expression [1] con-

tains the Boltzmann factor  $\exp(-F\Psi/RT)$ . The same result can be derived in the ohmic region  $U \rightarrow 0$  using the Nernst-Planck diffusion equation (5). The surface potential  $\Psi$  of a symmetrical membrane then can be determined in the following way: If the stationary ion flux through this membrane and the flux through a membrane without surface charges but otherwise identical composition are measured, the flux ratio is equal to the Boltzmann factor  $\exp(-F\Psi/RT)$  from which  $\Psi$  can be obtained.

### Surface Charges on Nerve Membranes

If the ionic strength of the internal perfusate of squid giant axons is lowered, the sodium inactivation curve is shifted along the voltage axis in the positive direction (6). This effect was attributed to the presence of negative fixed charges at the inside of the nerve membrane and the change of the internal field strength after altering the ionic strength. With the method 1 described above a density  $-1e_0/(27\text{\AA})^2$  ( $e_0$  is the elementary charge) was calculated for internal surface charges (6). At normal ionic strength of the intracellular solution this surface charge produces a surface potential of about  $-17$  mV. The surface charge density at the external membrane surface of squid giant axons was determined by varying the concentration of divalent cations in the extracellular solution. Higher amounts of these ions shift the potassium conductance-voltage curve in the positive direction from which a density  $-1e_0/(11\text{\AA})^2$  of negative outer surface charges and a surface potential of  $-46$  mV at physiological Ca concentrations were obtained (7). Shifts of almost identical size were found at squid giant axons for the curves relating the time constant of potassium activation and membrane potential at various extracellular Ca and Mg concentrations (8).

Surface charges at myelinated nerve fibers were determined for the nodal membrane of frog sciatic nerves. For this preparation the surface charge density can be calculated from the shifts of the ionic conductances in the positive direction which are induced by lowering the extracellular pH. This results in a density of  $-1e_0/(20\text{\AA})^2$  and an intrinsic  $pK_a = 4.3$  for unspecific external surface charges (2). [See also Ref. (8a, 8b).] The surface charge density at the internal surface of the nodal membrane cannot be determined directly. However, an estimate of  $-1e_0/(29\text{\AA})^2$  for this density can be derived by the hypothesis that the observed spontaneous shift of the steady-state sodium inactivation curve during long lasting voltage clamp experiments is caused by a decrease of negative interior surface charges (9). With the appropriate ionic compositions of intra- and extracellular solutions the surface potentials  $-19$  and  $-48$  mV are found for the internal and external surface potentials of myelinated nerves under physiological conditions.

It is evident that for squid giant axons and myelinated nerves the charge density at the external surface exceeds that at the internal one. This distribution would follow if the surface charges were not fixed at one interface but were able to diffuse across the hydrophobic interior of the nerve membrane toward the opposite membrane-solution interface. In this case the amount of surface charges at the external and the internal surface would be governed by the electric field strength in the membrane. This was recognized by McLaughlin and Harary (10) who calculated the equilibrium distribution of surface charges at giant axons at various membrane potentials. They concluded that at the resting state the charge density and surface potential at the outer surface would be substantially greater than the corresponding values at the inner surface. This prediction of the "flip-flop" diffusion of surface charges is in agreement with the charge densities found for the inner and outer surface of nerve membranes. If the redistribution of surface charges in nerve membranes were possible, more negative surface charges would be driven from the inner to the outer

membrane surface at holding potentials which are more negative than the resting potential. The surface potential  $\phi'$  at the outer membrane surface then would assume more negative values whereas the corresponding surface potential  $\phi''$  at the inner membrane surface would become less negative. This would modify the stationary ion flux  $\Phi$  at a given external voltage  $u$  according to the Eq. [A-6] derived in the Appendix. Increase or decrease of  $\Phi$  were determined by the asymmetry parameter  $\alpha$ . For  $\alpha = 1$  (energy barrier located at the inner membrane surface) the flux  $\Phi$  would decrease for flip-flop of negative surface charges from inside to outside (compare [A-8]). Instead an increase of the sodium and potassium currents was measured at more negative holding potentials than the resting potential (11). Therefore, the energy barrier must be located near the outer membrane surface if the observed increase of the ionic currents is caused by transverse motion of negative surface charges from inside to outside. In this case a change of the internal field strength should occur which should affect all field-dependent membrane parameters. However, no significant shift of the steady-state sodium inactivation was measured during fixed test pulses starting from different holding potentials (11, Fig. 2). Also, no evidence for a transmembrane motion of surface charges could be found during long depolarizations at squid axon membranes (12). Thus the existence of flip-flop of surface charges induced by a change of the holding potential is still questionable. However, a possible transverse diffusion of charged macromolecules in the interior of the nerve membrane can be inferred from the kinetics of the slow variations of the sodium current following changes of the holding potential or the extracellular pH. This analysis has been published elsewhere (13).

### Surface Charges on Lipid Bilayers

Artificial lipid bilayer membranes can be formed from various lipids with two hydrocarbon chains per lipid molecule. As in biological membranes the polar end groups of the molecules are preferentially located at the lipid-solution interfaces whereas the hydrocarbon chains are oriented toward the interior of the membrane. Bilayer membranes from lipids with charged polar groups thus bear surface charges. For lipids of known composition the approximate area per lipid molecule at the surface of lipid bilayers and thus the surface charge density can be estimated. As an example a value of about  $62\text{\AA}^2/\text{molecule}$  was reported for phosphatidylcholine (14). Similar surface densities are expected for other lipid molecules.

The surface potential of charged lipid bilayer membranes can be determined by comparing the stationary conductivity of membranes with and without surface charges (method 2, see above). In this way a high density of  $-1e_0/38\text{\AA}^2$  was obtained for negatively charged phosphatidylserine bilayer membranes from conductance measurements at these membranes and at neutral phosphatidylethanolamine bilayers (15). The binding of a pH sensitive fluorescence probe to a charged interface offers another possibility for determining its charge density. This probe will indicate the local pH at the interface thus showing a  $pK_a$  shift with respect to the bulk pH. Calculations on the basis of these shift measurements lead to charge densities at lipid-solution interfaces between  $1e_0/50\text{\AA}^2$  and  $1e_0/100\text{\AA}^2$  (16, 17). Thus the interpretation of the measured  $pK_a$  shifts in terms of membrane surface charges gives reasonable surface charge densities. Finally, the binding of the hydrophobic fluorescence probe ANS<sup>-</sup> (1-anilino-8-naphthalene sulfonate) to phospholipid membranes responds to the membrane surface potential and this probe, too, can be used to determine surface charge densities. An average distance of approximately  $8\text{\AA}$  between charged centers at the membrane surface was deduced from these binding experiments (18). In the

same investigation significant deviations from the ideal Gouy-Chapman behavior were found and interpreted in terms of discreteness of charge. These discrepancies between discrete and uniform charge distributions are discussed in the following section.

### Discrete Charge Distributions

Since the arrangement of surface charges on biological membranes and lipid bilayers is unknown, the values of surface charge densities given in the previous sections were calculated by ignoring the discreteness of charges, *i.e.*, by smearing the ions in the membrane-solution interface. Such an approximation can lead to serious errors. This complication was recognized very early in investigations of charge distributions near electrode surfaces and there have been many attempts to calculate surface potentials at electrode-solution interfaces when charge discreteness is not neglected [as an example compare with Ref. (19)].

In the physiological literature there have been only a few contributions dealing with discrete charge and dipole distributions (20-25). Cole (21) estimated that deviations between discrete and homogeneous charge distributions are negligible if the product  $\kappa b$  between the reciprocal of the Debye-Hückel length  $1/\kappa$  in the solution and the separation  $b$  of surface charges arranged in a hexagonal lattice is less than 1. For  $\kappa b > 1$  more discrete than uniformly distributed surface charges are required to obtain a given surface potential. We test this condition by inserting the values cited above for nerve membranes and lipid bilayers: For squid giant axons it is  $1/\kappa \approx 4\text{\AA}$  (ionic strength of the extra and intracellular solution approximately 500 mmoles). With a surface charge density of  $-1e_0/(27\text{\AA})^2$  at the inner (6) and  $-1e_0/(11\text{\AA})^2$  at the outer membrane surface (7) we have  $\kappa b \approx 7$  and 3 for these two interfaces indicating a significant difference between surface potentials generated by equal amounts of uniform and discrete charge distributions. Similar values of  $\kappa b$  are obtained for the membrane of myelinated nerve. Taking  $1/\kappa \approx 10\text{\AA}$  (ionic strength of the extra and intracellular solution approximately 100 mmoles) and the densities  $-1e_0/(29\text{\AA})^2$  and  $-1e_0/(20\text{\AA})^2$  for inner (9) and outer surface charges (2) we arrive at  $\kappa b \approx 3$  and 2, respectively. Thus all surface charge densities at nerve membranes cited above have to be considered as lower limits. The actual density of discrete charges may be significantly higher to be in accordance with the magnitude of measured surface potentials. For  $1/\kappa = 10\text{\AA}$  the concept of uniform charge distributions can be used for charge separations less than  $10\text{\AA}$ . Therefore, no corrections have to be applied to the charge densities reported for lipid bilayer membranes.

As an example for significant deviations between smeared and discrete charge distributions we discuss the determination of negative surface charges at the outer membrane surface of myelinated nerves. From our experiments the decrease of the surface potential at lowered extracellular pH values is obtained. By applying a smeared charge model these results can be fitted with a uniform surface charge density of  $-1e_0/(20\text{\AA})^2$  and an intrinsic  $pK_a = 4.3$  (2). If instead four discrete univalent negative charges are arranged around an ion selective channel of the nerve membrane, a charge distance of  $10\text{\AA}$  from the center of the channel and a  $pK_a = 4.3$  are needed to be in accordance with the experimental results. The calculation of the titration curve of these discrete surface charges was performed in close analogy to the work of Nelson and McQuarrie (25). Thus the  $pK_a$  value of the surface charges is the same for both charge distributions whereas significantly higher discrete than smeared charge densities are obtained.

### Acknowledgment

This work was supported by Deutsche Forschungsgemeinschaft, Sonderforschungsbereich 38 "Membran-

forschung." I thank Professor Dr. R. Stämpfli and Drs. H. Drouin, J. M. Fox, and W. Nonner for reading the manuscript.

Manuscript received June 30, 1975. This was Paper 371 presented at the Toronto, Canada, Meeting of the Society, May 11-16, 1975.

Any discussion of this paper will appear in a Discussion Section to be published in the June 1977 JOURNAL. All discussions for the June 1977 Discussion Section should be submitted by Feb. 1, 1977.

## APPENDIX

### Derivation of Eq. [1]

The stationary ion flux across a membrane will be calculated for the general case of different bulk ion concentrations in the solutions on both membrane sides, for unequal surface potentials at the outer and inner membrane surface, and for an asymmetrical potential barrier in the interior of the membrane (see Fig. 1).

We assume that the rate-limiting step for the ion transport is the passage through the interior of the membrane. This implies that diffusion polarization effects in the unstirred solution layers near the membrane can be neglected and that equilibrium for ion adsorption and desorption processes at the membrane-solution interfaces is maintained even in the stationary state. The aqueous concentrations  $c'_m$ ,  $c''_m$  of univalent cations at the membrane surfaces then are connected with the corresponding bulk concentrations  $c'$ ,  $c''$  by the Boltzmann distribution

$$\begin{aligned} c'_m &= c' \exp(-F\Psi'/RT) \\ c''_m &= c'' \exp(-F\Psi''/RT) \end{aligned} \quad [\text{A-1}]$$

( $\Psi'$  and  $\Psi'' < 0$  for negative surface charges.) For the ion transport of these univalent cations across the membrane interior we use Eyring's absolute rate theory (26) and assume one single activation energy barrier. The height  $H$  of this barrier is determined by the thickness and dielectric constant of the hydrophobic region of the membrane phase and by the radius of the permeant ion (27). Due to the externally applied voltage  $U$  (= potential in internal minus potential in external bulk solution) and due to surface potentials  $\Psi'$  and  $\Psi''$  at both membrane surfaces the activation energy  $B'$  of an ion jump from outside to inside is different from the energy  $B''$  for the reverse jump. Introducing the normalized quantities

$$\begin{aligned} h &= \frac{H}{RT}; \quad b' = \frac{B'}{RT}; \quad b'' = \frac{B''}{RT} \\ u &= \frac{FU}{RT}; \quad \phi' = \frac{F\Psi'}{RT}; \quad \phi'' = \frac{F\Psi''}{RT} \end{aligned} \quad [\text{A-2}]$$

we obtain from Fig. 1

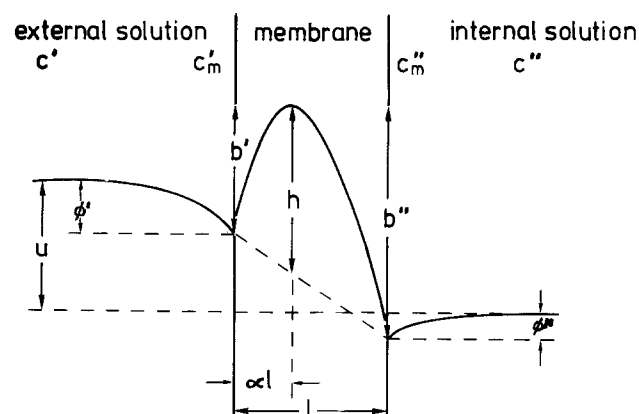


Fig. 1. Schematic plot of an asymmetrical energy barrier in the interior of the membrane and of the potential profile in the aqueous solutions for different surface charge densities on the outer and inner membrane surface.

$$b' = h + \alpha(u - \phi' + \phi'') \quad [\text{A-3}]$$

$$b'' = h - (1 - \alpha)(u - \phi' + \phi'') \quad [\text{A-4}]$$

The asymmetry parameter  $\alpha$  may assume values between 0 and 1. For  $\alpha = 0$  the energy barrier is located at the outer and for  $\alpha = 1$  at the inner membrane-solution interface. Following Eyring the stationary flux  $\phi$  of univalent cations from outside to inside is proportional to

$$\phi \simeq c'_m \exp(-b') - c''_m \exp(-b'') \quad [\text{A-5}]$$

The quantities contained in the proportionality factor (jump length, frequency factor) are assumed to be the same on both membrane sides and to be independent of the ion concentrations and membrane surface potentials. Inserting Eq. [A-1], [A-3], and [A-4] into [A-5] yields

$$\phi \simeq c' \exp[-(1 - \alpha)\phi' - \alpha(u + \phi'')] - c'' \exp[(1 - \alpha)(u - \phi') - \alpha\phi''] \quad [\text{A-6}]$$

This general expression can be simplified for the following special cases:

(a) energy barrier located at the outer interface ( $\alpha = 0$ )

$$\phi \simeq \exp(-\phi') [c' - c'' \exp(u)] \quad [\text{A-7}]$$

(b) energy barrier located at the inner interface ( $\alpha = 1$ )

$$\phi \simeq \exp(-\phi'') [c' \exp(-u) - c''] \quad [\text{A-8}]$$

(c) symmetrical energy barrier ( $\alpha = \frac{1}{2}$ )

$$\phi \simeq \exp\left(-\frac{\phi' + \phi''}{2}\right) \left[ c' \exp\left(-\frac{u}{2}\right) - c'' \exp\left(\frac{u}{2}\right) \right] \quad [\text{A-9}]$$

If the energy barrier is located at one interface, the stationary ion flux is determined solely by the surface potential of this membrane surface. For a symmetrical energy barrier the flux  $\phi$  depends on the sum  $\phi' + \phi''$  of both surface potentials (compare Eq. [A-9] which is identical to [1])

## REFERENCES

1. S. P. Verma, D. F. H. Wallach, and I. C. P. Smith, *Biochim. Biophys. Acta*, **345**, 129 (1974).
2. H. Drouin and B. Neumcke, *Pflügers Arch.*, **351**, 207 (1974).
3. S. McLaughlin, *J. Membrane Biol.*, **9**, 361 (1972).
4. W. S. Chelack, A. Petkau, and T. P. Copps, *Biochim. Biophys. Acta*, **274**, 28 (1972).
5. B. Neumcke, *Biophysik*, **6**, 231 (1970).
6. W. K. Chandler, A. L. Hodgkin, and H. Meves, *J. Physiol. (London)*, **180**, 821 (1965).
7. D. L. Gilbert and G. Ehrenstein, *Biophys. J.*, **9**, 447 (1969).
8. G. Ehrenstein and D. L. Gilbert, *ibid.*, **13**, 495 (1973).
- 8a. T. Brismar, *Acta Physiol. Scand.*, **87**, 474 (1973).
- 8b. B. Hille, A. M. Woodhull, and B. I. Shapiro, *Phil. Trans. R. Soc. London, Ser. B*, **270**, 301 (1975).
9. J. M. Fox, *Pflügers Arch.*, **355**, R69 (1975).
10. S. McLaughlin and H. Harary, *Biophys. J.*, **14**, 200 (1974).
11. J. M. Fox, *Biochim. Biophys. Acta*, **426**, 232 (1976).
12. G. Ehrenstein and D. L. Gilbert, *Biophys. J.*, **15**, 847 (1975).
13. B. Neumcke, J. M. Fox, H. Drouin, and W. Schwarz, *Biochim. Biophys. Acta*, **426**, 245 (1976).
14. R. Fettiplace, D. M. Andrews, and D. A. Haydon, *J. Membrane Biol.*, **5**, 277 (1971).
15. S. McLaughlin, G. Szabo, and G. Eisenman, *J. Gen. Physiol.*, **58**, 667 (1971).
16. M. Montal and C. Gitler, *Bioenergetics*, **4**, 363 (1973).
17. P. Fromherz and B. Masters, *Biochim. Biophys. Acta*, **356**, 270 (1974).
18. D. H. Haynes, *J. Membrane Biol.*, **17**, 341 (1974).
19. J. R. Macdonald and C. A. Barlow, Jr., *This Journal*, **113**, 978 (1966).
20. R. Friedenbergl, A. Blatt, V. Gallucci, J. F. Danielli, and I. Shames, *J. Theoret. Biol.*, **11**, 465 (1966).
21. K. S. Cole, *Biophys. J.*, **9**, 465 (1969).
22. J. R. Buysman and F. T. Koide, *J. Theoret. Biol.*, **32**, 1 (1971).
23. O. H. Griffith, P. J. Dehlinger, and S. P. Van, *J. Membrane Biol.*, **15**, 159 (1974).
24. R. H. Brown, *Prog. Biophys. Mol. Biol.*, **28**, 343 (1974).
25. A. P. Nelson and D. A. McQuarrie, *J. Theoret. Biol.*, **55**, 13 (1975).
26. B. Parlin and H. Eyring, in "Ion Transport Across Membranes," H. T. Clarke, Editor, Academic Press, New York (1954).
27. B. Neumcke and P. Läger, *Biophys. J.*, **9**, 1160 (1969).

## The Electrochemistry of Micelle-Solubilized Ferrocene

Peter Yeh\* and Theodore Kuwana†

Department of Chemistry, The Ohio State University, Columbus, Ohio 43210

### ABSTRACT

The electrochemistry of ferrocene solubilized by the use of nonionic detergent in aqueous phosphate solutions pH 7.0 was studied. The ferrocene molecules were incorporated as micelles which readily transferred electrons with a platinum electrode. Cyclic voltammetric and potentiometric data indicated that the electron transfer reaction was reversible. Micelle size calculated from electrochemical diffusion and light scattering data gave radii between 40-45 Å and molecular weights of ca. 130,000. The ferrocene-micelle served as an excellent mediator-titrant to couple electron transfer between an electrode and the heme proteins of cytochrome c, cytochrome c oxidase, and mixtures thereof.

Recently, ferricinium ion electrogenerated from ferrocene solubilized by the use of nonionic detergent has been employed for the redox titration of cytochrome c, cytochrome c oxidase, and mixtures thereof in aqueous pH 7.0 solutions (1). The detergent apparently formed micelles with the incorporation of ferrocene. The ferricinium/ferrocene couple is then

acting as a mediator to couple the electron transfer between the electrode and the heme proteins.

Ferrocene-micelles represent part of our effort to find water-soluble mediator-titrants (M-T's) with redox potentials suitable for use in the study of biological electron transport components. Requirements sought for these M-T's are: (a) both species of the redox couple of the M-T's need to be soluble in aqueous media buffered at or near pH 7; (b) the solubility of the M-T's should be 1 mM or more; (c)

\* Electrochemical Society Student Member.

† Electrochemical Society Active Member.

Key words: electrochemistry, ferrocene, micelle, mediator-titrants.

the rate of electron transfer with both electrode and heme proteins should be rapid; (d) the chemical stability should be adequate so that interferences with heme proteins be avoided; (e) the redox reaction mechanism should be uncomplicated, preferably involving one electron transfer ( $n = 1$ ); and (f) the optical absorbance of the M-T's should not interfere with those of the heme proteins. Very few M-T's fulfill all of the above requirements.

For working in the negative potential ranges, say  $-100$  to  $-500$  mV vs. NHE, the 4,4'-bipyridylum salts (commonly known as viologens or paraquats) have proved to be extremely useful (2). At potentials positive of ca.  $+300$  mV vs. NHE, the number of usable M-T's has been extremely limited. Ferricyanide/ferrocyanide has been commonly used, but has been found to produce deleterious effects or to complex with the hemes (2, 3). It is desirable to find M-T's with similar redox chemistry whose redox potentials could be altered through simple structural modifications.

From previous experience (4) with the electrochemistry of metallocenes in nonaqueous solvents, it was known that ferrocene, for example, underwent a fast one electron redox reaction at a positive potential. However, the low solubility of ferrocene (ca.  $10^{-5}$  M) in aqueous solutions prevented its use. Therefore, approaches to solubilization of these metallocenes were explored. Tween 20 was chosen for the present work because of our experience in the use of this surfactant in solubilizing heme proteins (2).

The number of electrochemical studies in which surfactant concentrations were deliberately increased above the critical micelle concentration for the solubilization of electroactive species has been limited. Hayano and co-workers (5, 6) have reported the use of several kinds of surfactants for the solubilization of dye molecules which exhibited reduction currents at dropping mercury electrode. Their results indicated that diffusion-limited currents could be attained and that the rate was limited by the diffusing micelle particles containing the dye. The effect of the surfactant-dye concentration ratio to the size-volume of the micelle was calculated from the experimentally obtained diffusion coefficient using the Stokes-Einstein relationship.

Westmoreland, Day, and Underwood (7) in 1972 reported the solubilization of azobenzene using surfactants such as sodium lauryl sulfate, cetylpyridinium chloride, and lauryltrimethylammonium bromide. Again, a diffusion-controlled wave attributable to micelle was found, and the reduction of azobenzene appeared to approach reversible behavior as the surfactant concentration decreased. In the above examples, reversibility and mechanism could be assessed only conditionally because of the fairly complex nature of the electron-transfer reaction, i.e.,  $n$  values greater than unity and possible involvement of protons.

In addition to our heme proteins studies (1), ferrocene (or dibutylferrocene) has been used as a mediator to couple electron transfer through lipid membranes as a model system for mitochondrial ion transport and respiratory control (8, 9). Ferrocene in these lipids (black lipid membranes and phospholipid vesicles) provided the coupling of electron transfer through the membrane with external redox reactants. The environment for ferrocene in the micelle is probably quite similar to that in the hydrophobic lipid membrane. Thus, a detailed study of the electrochemical and physical properties of ferrocene-micelle was of considerable interest and has stimulated the present work. The assessment of the formal redox potentials,  $E^{\circ}$ , of cytochrome *c* and cytochrome *c* oxidase using the ferrocene-micelle are discussed.

## Experimental

The electrochemical cell and instrumentation were similar to those previously described (9). A platinum optical transparent electrode (OTE) with surface resistance of ca.  $10 \Omega/\text{sq}$  was used for the electrochemistry. For optical measurements, another Pt OTE was placed in the reference beam of the spectrophotometer (Cary Model 15). The current-potential ( $i$ - $E$ ) curves were recorded using a Hewlett-Packard (Moseley Division) Model 7005B X-Y recorder. A silver-silver chloride (1M KCl) reference electrode was used for measurements of cell emf. The electrode potential of this reference half-cell was evaluated to be  $0.232$  V vs. NHE by measuring its potential vs. several reference saturated calomel electrodes. Temperature was maintained at  $20^{\circ} \pm 1^{\circ}\text{C}$ . The silver-silver chloride reference electrode was used because of the desire to duplicate the electrochemical cell used for heme protein studies (9).

Turbidity and refractive indices of the surfactant solutions were measured with the Brice-Phoenix light scattering photometer (Universal 1000 series) and a differential refractometer (Phoenix Precision Instrument). Viscosity measurements of solutions were made using a Ubbelohde viscometer (No. 1B-A356) which had been calibrated as described by Cannon (10). Filtration experiments were done with an ultra filtration cell (Model 202, Amicon Corporation) and Diaflo ultrafilters XM50 and XM100A under 15 psi of pressure.

An ultrasonic vibrator-cleaner (Heat Systems Ultrasonics, Incorporated) was used to assist in the solubilization of ferrocene and to pretreat glasswares for cleaning purposes.

Ferrocene (dicyclopentadienyliron) was obtained from Strem Chemical Company and was triply recrystallized from reagent grade ethanol. Tween 20 (Polysorbate 20, polyoxyethylene sorbitan monolaurate) with average molecular weight of 1650 was obtained from Sigma Chemical Company. It was purified by treatment through an alumina (aluminum oxide, basic, Alupharm Chemicals) column (18 in. long, 0.5 in. diameter). A very light straw-colored fraction was left on the column. Phosphate buffer, pH  $7.00 \pm 0.02$  (Buffer Titrosol, Merck and Company) was used for buffering all solutions. J. T. Baker and Company reagent grade potassium chloride and silver sulfate were used without further purification. Prepurified grade nitrogen gas (99.998%) was supplied by American Oxygen Service Corporation. Doubly distilled water was used to prepare all solutions.

The solubility of ferrocene is less than  $10^{-5}$  M in water at room temperature. It was solubilized by adding purified Tween 20 and a few milliliters of phosphate buffer directly to a weighed amount of ferrocene in a 100 ml volumetric flask. The amount of Tween 20 added was determined by the percentage of Tween desired in the final solution. The mixture was stirred and then agitated in an ultrasonic vibrator for about 30 min. The flask was filled to the mark and then stirred with a magnetic stirrer for another 12 hr. Attempts to solubilize ferrocene in water by dissolving ferrocene initially in alcohol or benzene and then adding water were unsuccessful since ferrocene precipitated as water was added.

## Results and Discussion

*Cyclic voltammetry of ferrocene-micelle.*—Since ferrocene was being investigated as a possible mediator-titrant, the working range of concentration selected for study was between 0.1 and 0.5 mM. At Tween concentrations below about 0.5% by volume of final solution, ferrocene was not totally solubilized as was evidenced by the nonreproducible electrochemical results. In the concentration range of 1.0-5.0% of Tween 20, ferrocene was completely solubilized and the cyclic voltammetric  $i$ - $E$  curves were reproducible. A typ-

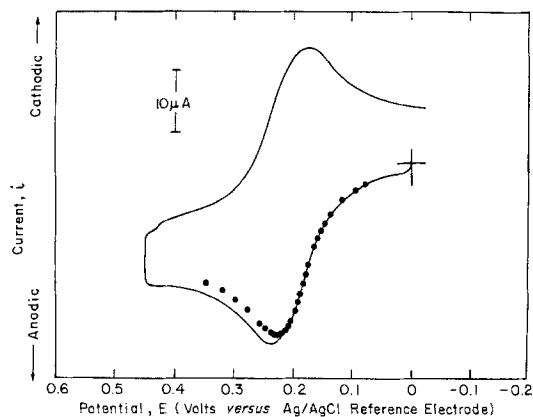


Fig. 1. Cyclic voltammetric  $i$ - $E$  curve of ferrocene (0.5 mM) and Tween 20 (3% v/v) in phosphate buffer (pH 7.00  $\pm$  0.02). Dotted curve is computer simulated according to Nicholson and Shain (11).

ical  $i$ - $E$  curve for micelle-solubilized ferrocene in phosphate buffer at pH 7.00 is shown in Fig. 1.

The experimental curve is well defined and is in close agreement with one which is computer-simulated for a reversible, one-electron transfer, electrode reaction using the relationship of Nicholson and Shain (11). The background  $i$ - $E$  which was added to the theoretical curve, was obtained for a Tween 20 solution in the absence of ferrocene. The value of the diffusion coefficient,  $D$ , chosen for the calculation was one which gave the closest match of the simulated  $i$ - $E$  curve to the experimental one. More will be said about the experimental  $D$  values shortly.

The dependence of Tween 20 concentration on the reversible electrode potential ( $E_{0.85}$  for cyclic voltammetry) and the separation of anodic and cathodic peak potentials ( $\Delta E_p$ ) is summarized in Table I. The ferrocene concentration was constant at 0.5 mM, the scan rate,  $\nu$ , was 96 mV/sec, and the Tween 20 concentration was varied between 1 and 3.5% by volume. The  $E_{0.85}$  and  $\Delta E_p$  values appear quite independent of Tween 20 concentration at this particular scan rate. The  $\Delta E_p$  of 60 mV indicates that the electrode reaction is essentially reversible under these particular experimental conditions.

The plots of the anodic peak current,  $i_p$ , vs. ferrocene concentration were linear for any given Tween 20 concentration at a constant scan rate. Also,  $i_p$  increased linearly proportional to the square root of scan rate as expected for a diffusion-limited electrode reaction for a constant Tween 20 and ferrocene concentration. However, the  $i_p$  was dependent on the Tween 20 concentration. In Table II, these  $i_p$  values (corrected for background current) are tabulated for Tween 20 concentration varying between 1 and 3.5% by volume. The ferrocene concentration was kept constant at 0.5 mM. The  $D$  values given in Table II were calculated from the slopes of the plots of  $i_p$  vs.  $\nu^{1/2}$  for each Tween 20 concentration. The calculation assumed the validity of the well-known Randle-Sevcik relationship

Table I. Dependence of  $E_{0.85}$  and  $\Delta E_p$  on Tween 20 concentration

Tween 20 concentration (% vol)	$E_{0.85}$ (mV vs. Ag/AgCl)*	$\Delta E_p$ (mV)
1.0	+180	60
1.5	190	63
2.0	195	65
2.5	190	63
3.0	190	60
3.5	208	60
	Avg 192 $\pm$ 6	62 $\pm$ 2

\* Each value is the average of 3 separate runs.

Table II.  $D$  and  $i_p$  values and dependence on Tween 20 concentration and scan rate

Scan rate (V/sec)	Peak currents* ( $\mu$ A) at various Tween 20 concentrations (% vol)				
	1%	2%	2.5%	3.0%	3.5%
0.023	8.75	12.0	12.1	14.3	12.3
0.047	13.5	16.5	17.1	19.0	16.0
0.071	15.8	21.2	20.7	22.5	20.7
0.096	20.8	23.5	24.3	24.8	22.8
0.120	24.5	26.9	26.3	29.0	26.0
Calculated slopes $\times 10^8$	79.8**	76.7	74.7	73.2	71.2
Intercepts	-4.03	0.11	0.70	2.93	1.07
Calculated $D \times 10^7$ ( $\text{cm}^2/\text{sec}$ )	4.87	4.50	4.27	4.10	3.88

\* Each value is average of 3 or 4 separate runs.  
\*\* Slopes and intercepts are least square values.

Table III. Viscosities of Tween 20 solutions

Concentration Tween 20 (% v/v)	Viscosity (cs)*
0	1.04
0.5	1.07
1.0	1.08
1.5	1.11
2.0	1.14
2.5	1.17
3.0	1.21
3.5	1.24
4.0	1.28

\* Viscosity,  $\eta$ , in centistokes was calculated using  $\eta = kt - b/t$ , where  $k$  is viscometer constant,  $b$  is calibration constant, and  $t$  is the time required for the test solution meniscus to pass between the two flow marks on the viscometer stem ( $k = 0.05193$  and  $b = 0.60$ ). All values are the average of 10 results.

$$i_p = kn^{3/2}AD^{1/2}C_0\nu^{1/2} \quad [1]$$

A value of  $2.64 \times 10^5$  was used for  $k$  in the computation of  $D$  (12). The  $D$  values decreased as the Tween 20 concentration increased.

The  $i_p$  and  $D$  value dependence on Tween 20 concentration was assumed to be due to the changing viscosity of the solutions. Thus, viscosities of Tween 20 solutions at concentrations between 0.5 and 4.0 volume percent (v/o) were determined using an Ubbelohde viscometer. The viscosity was found to vary linearly with concentration between 1.0 and 4.0 v/o Tween 20. The data are summarized in Table III.

In a simple diffusing system, the  $D$  value should be inversely proportional to the viscosity,  $\eta$ , assuming validity of the Stokes-Einstein relationship (13)

$$D = kT/6\pi\eta r \quad [2]$$

In Fig. 2,  $D$  value is plotted vs.  $1/\eta r$ . The linearity of the plot is excellent.

Calculation of micelle size.—The radius and molecular weight of the micelle can be computed from know-

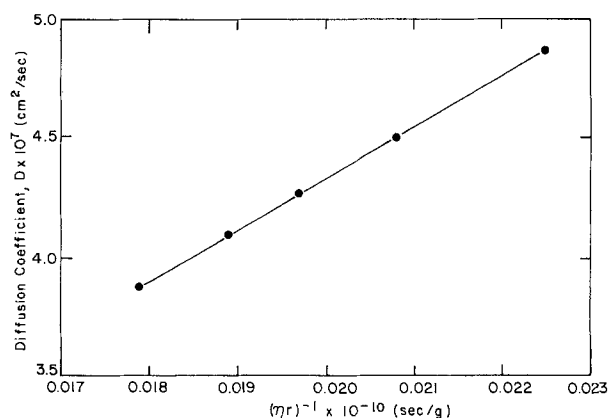


Fig. 2. Diffusion coefficient vs. reciprocal of  $\eta r$ .

ing the values of diffusion coefficients and viscosities. The shape of the micelle is assumed as spherical. The volume fraction,  $\phi$ , of the dispersed spherical micelles is determined by using the Guth and Simha equation (14, 15)

$$\eta/\eta_0 = 14.1\phi^2 + 2.5\phi + 1 \quad [3]$$

where  $\eta/\eta_0$  is the relative viscosity of the solution. The value of viscosity of the phosphate buffer solution in the absence of Tween 20 and ferrocene was used for  $\eta_0$ . The effective specific volume,  $\bar{V}$ , of one gram of surfactant, including any hydrated water, can be expressed as

$$\bar{V} = \phi/C' \quad [4]$$

where  $C'$  is the concentration of surfactant in the solution (grams/cubic centimeter).

The micelle weight,  $M$ , can be given in terms of the calculated  $\bar{V}$

$$M = \frac{(kt)^3 N}{162\pi^2 \eta^3 D^3 \bar{V}} \quad [5]$$

where  $N$  is Avogadro's number. The radius can be calculated from the value of  $\bar{V}$ , again assuming a spherical particle. Values of  $D$ ,  $\bar{V}$ ,  $\tau$ , and  $M$  as a function of Tween concentration are tabulated in Table IV. The average radius and molecular weight are 43 Å and 127,000 for the data listed in Table IV. From the data in this table, a slight increase in the radius and molecular weight of the micelles as the concentration of Tween increases can be seen. Whether or not this increase actually reflects size change due to increased amount of Tween 20 per micelle cannot be accurately ascertained. Similar increases of measured radius or molecular weight with increase of nonionic surfactant concentration have been previously reported (16). However, these increases may very well reflect changes in the micelle shape from spherical to ellipsoidal or in the number of hydrated water molecules associated with the micelle as a function of Tween 20 concentration.

The molecular weight of the micelle was also determined independently using the Debye method of light scattering (17). Measurements of turbidity of Tween 20 between 0 and 5% concentration in phosphate buffer were made with a Brice-Phoenix light scattering photometer at 0° and 90°. This photometer was calibrated with a dilute solution of Ludox (SM, du Pont) in water. The solute turbidity, or excess turbidity, upon which the molecular weight depends, is the apparent turbidity,  $\tau$ , of the solution with micelle minus the apparent turbidity,  $\tau_0$ , of the solvent, i.e., phosphate buffer without Tween 20 or ferrocene. The apparent difference in turbidity caused by the micelles and the refractive indices of the surfactant solutions can be related to molecular weight,  $M$ , through Eq. [6] and [7] as follows (17)

$$HC'/\tau = 1/M + 2BC' \quad [6]$$

and

$$H = \frac{32\pi^3 n_0^2 (n - n_0)^2}{3\lambda^4 N (C')^2} \quad [7]$$

$B$  is a constant depending on the solvent. All measurements were made with a blue filter ( $\lambda = 463$  nm).

Table IV. Micelle parameters as a function of Tween 20 concentration

Tween 20 (% v/v)	$C'$ (g/cm <sup>3</sup> )	$\bar{V}$ (cm <sup>3</sup> /g)	$\tau \times 10^8$ (cm)	$M$
1	0.010	1.48	41.2	119,000
2	0.020	1.68	42.2	113,000
2.5	0.025	1.57	43.4	132,000
3	0.030	1.67	43.7	127,000
3.5	0.036	1.60	45.1	144,000

Table V. Apparent turbidity and refractive index of Tween 20 solutions

Tween 20 (% v/v)	$\tau \times 10^8$ (cm <sup>-1</sup> )	$n_{463}^{25}$
0	0.09*	1.34127**
1	1.59	1.34231
2	2.35	1.34314
3	3.33	1.34421
4	2.49	1.34500
5	3.00	1.34600

\* Light scattering photometer calibration using dilute solution of Ludox (SM, du Pont).

\*\* Calibrated with KCl solution (0.09635 g/ml).

The apparent turbidities and the dependence of the refractive indices on Tween 20 concentration are tabulated in Table V. The refractive indices of the surfactant solution at temperature of 25°C was found empirically to follow the relationship

$$n = n_0 + 0.000944C' \quad [8]$$

where the value of  $n_0$  was determined to be 1.34127.

The molecular weight of micelle was determined by calculating  $HC'/\tau$  for the surfactant solutions and by plotting  $HC'/\tau$  vs.  $C'$  (Fig. 3). The extrapolated curve to zero concentration gave an intercept whose reciprocal value was equal to the molecular weight, which was 143,000. The over-all error was estimated to be  $\pm 10\%$ . The light scattering method assumes that the micelle size is independent of surfactant concentration and that the number of micelles is increasing with increased  $C'$ . There appears to be reasonable agreement between the molecular weight of the micelle as evaluated from both the electrochemical and the light scattering data.

Assuming the average molecular weight of Tween 20 to be 1650, the average aggregation number of micelle (data of Table IV) is in the order of  $77 \pm 5$  (molecules/micelle). An order of magnitude estimate of the ferrocene to micelle ratio is about 3:1 for a 2% by volume Tween 20 and 0.5 mM ferrocene concentration. For all of the experiments reported herein, the number of moles of ferrocene was greater than the number of moles of micelle present in the solution.

$E^{\circ}$  values.—An accurate assessment of the formal redox potential,  $E^{\circ}$ , is important for the use of the ferrocene-micelle as a M-T (2). The  $E^{\circ}$  value (assuming  $E^{\circ} \equiv E_{0.85}$ ) evaluated from cyclic voltammetry gave an average of  $424 \pm 6$  mV vs. NHE. As a further confirmation,  $E^{\circ}$  values were determined from potentiometric data for titration using  $Ag_2SO_4$  as oxidant and from A-E data obtained during the exhaustive coulometric oxidations. The concentration of ferricinium ion was monitored at wavelength of 615 nm

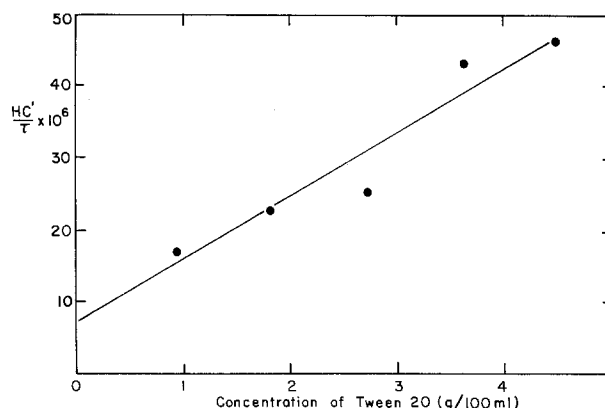


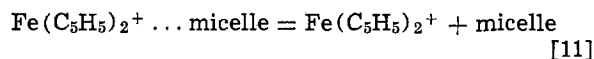
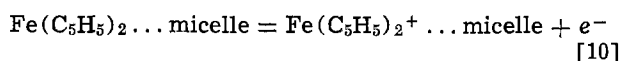
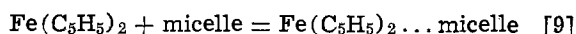
Fig. 3. Reciprocal specific turbidity of Tween 20 solutions



for the latter experiments. Nernstian slopes of  $58 \pm 2$  mV were obtained and the average value of  $E^{\circ}$  was  $425 \pm 10$  mV vs. NHE. The  $E^{\circ}$  values determined by these methods are in excellent agreement with that evaluated by cyclic voltammetry. Ferrocene had been proposed (18) as a redox standard from solvent to solvent because both ferrocene and ferricinium ion supposedly were minimally solvated. The formal potential for ferrocene has been reported to be 400 mV vs. NHE (18).

Hinkle (8) in his lipid work found the addition of small amounts of the anion tetraphenylboron to greatly enhance the effectiveness of ferrocene as a mediator. He suggested that the tetraphenylboron increased the solubility of ferricinium cation in the lipid phase of the membrane. Thus, the effect of tetraphenylboron to the cyclic voltammetry of ferrocene-micelle was examined. In a solution containing 2% Tween, 0.74 mM ferrocene, and 0.40 mM sodium tetraphenylboron, the cyclic  $i$ - $E$  curves were completely reversible with a  $\Delta E_p$  of  $60 \text{ mV} \pm 2 \text{ mV}$ . The  $E_{0.85}$  was 390 mV vs. NHE. The shift of potential to less positive value is consistent with stabilization of ferricinium ion by the anion, tetraphenylboron. Whether ferricinium ion interacted with tetraphenylboron inside of the micelle and thus shifted the equilibrium of reaction [11] could not be ascertained from the present data.

**Ferricinium ion.**—Ferricinium ion is known to be quite water soluble. Its partitioning between the micelles and solvent was qualitatively examined by filtering a ferricinium solution through a Diaflo filter (Amicon, XM50; M.W. separation 50,000) at 15 psi pressure in a stirred cell. The blue ferricinium ion was electrogenerated from ferrocene by controlled potential electrolysis in the Tween 20/phosphate buffer solution. The blue-colored filtrate indicated that ferricinium ion went through the filter and was not totally micelle bound. A similar experiment was performed with the ferrocene-Tween 20 solution. The filtrate in this case was clear and did not contain ferrocene, suggesting that ferrocene is indeed micelle bound. The reactions for the ferrocene/ferricinium system in the presence of micelle are suggested as



The  $K_{eq}$ 's are assumed to be greater than unity for both reactions [9] and [11].

The optical absorbance band at 615 nm was monitored during controlled potential coulometric oxidation of ferrocene to ferricinium ion in a stirred solution. The optical absorbance,  $A$ , at 615 nm changed linearly with the number of coulombs of charge.

The molar absorptivities,  $\epsilon$ , calculated for ferricinium ion and also ferrocene-micelle are tabulated in Table VI and compared to literature values (19). The large discrepancy of the molar absorptivity between our value and the literature value at wavelength of 250-235 nm is presently unexplored.

Ferricinium ion in aqueous media has been reported (19) to undergo decomposition. Thus, the stability of ferricinium ion was determined by following the decrease of the absorbance of the 615 nm band. A half-life of 14 hr was obtained for the ion in the pH 7.0 phosphate-buffered solution at temperature of 25°C. At pH 2.0, the half-life increased to 26 hr. This loss of ferricinium ion can affect results of long-term experiments or those where the ion concentration is high.

Table VI. Spectral properties of ferrocene-micelle and ferricinium ion

	Wavelength maxima (nm)	Molar absorptivity ( $\text{M}^{-1}\text{-cm}^{-1}$ )
Ferrocene-micelle	325 (325)* 440 (440)	96 (52)* 120 (91)
Ferricinium ion**	250 (235) 615 (617)	3,860 (12,000) 335 (340)

\* Literature values (19) in brackets; ferricinium ion data reportedly taken in solution alcohol-water containing tetraphenylborate anion.

\*\* Ferricinium ion generated by controlled potential coulometry.

**Ferrocene-micelle as mediator-titrant for heme proteins.**—As previously mentioned, methyl viologen was used as the M-T for the reduction of cytochrome c, cytochrome c oxidase, and mixtures thereof (2). In the respiratory chain,  $c(n = 1)$  is the component which transfers electrons to the enzyme bound cytochrome c oxidase ( $n = 4$ ). Oxidase is the enzyme which is responsible for the fast turnover of molecular oxygen to water and for coupling to oxidative phosphorylation.

The charge distribution between these heme components has been evaluated from the change in the optical absorbance,  $\Delta A$ , at 550 nm (cytochrome c) and 605 nm (cytochrome c oxidase) during indirect coulometric titration experiments (2). The plot of the oxidative  $\Delta A$ - $q$  ( $q = \text{electrochemical charge}$ ) was not a mirror image of the reductive one (20). The oxidant was  $\text{O}_2(n = 4)$  and the reductant was the viologen radical cation ( $n = 1$ ;  $E^{\circ} = -446\text{V vs. NHE}$ ) (9). Besides the obvious difference in the  $n$  values, a difference in the reactivity toward cytochrome c exists between the reductant and oxidant. The viologen radical reduces both the cytochrome c and cytochrome c oxidase rapidly (21). On the other hand,  $\text{O}_2$  oxidizes natured cytochrome c slowly. Thus, in a mixture of cytochrome c and cytochrome c oxidase, cytochrome c must be oxidized primarily by cytochrome c oxidase when  $\text{O}_2$  is used as the oxidant.

With use of electrogenerated ferricinium ion from the ferrocene-micelle, the  $\Delta A$ - $q$  curves were mirror images of the reductive ones (reductant:viologen radical) (1). These results suggest that the charge distribution between cytochrome c and the redox centers of cytochrome c oxidase are at equilibrium when the redox properties of the reductant and oxidant are similar.

Results to date indicate that the  $E^{\circ}$  values for cytochrome c oxidase are  $215 \pm 15$  and  $345 \pm 15$  mV vs. NHE. Each value of  $E^{\circ}$  involves two electrons and the metal centers of one iron and one copper. Since these  $E^{\circ}$  values are for cytochrome c oxidase isolated from the membrane (low lipid concentration) there is a question whether these values accurately reflect the cytochrome c oxidase potential in the mitochondrial system. It is also a question of why nature would have the  $E^{\circ}$  of cytochrome c ( $E^{\circ} = 257 \pm 17$  mV vs. NHE) (9) midway between the two potentials of cytochrome c oxidase.

Solubilization of M-T's by micelle formation provides (a) access to a wider variety of M-T's with opportunity for graded  $E^{\circ}$  values; (b) means of designing experiments to model biological electron transfer mechanisms a la Hinkle (8); and (c) an approach to kinetic studies to test whether electron-transfer rates to components in membranes can be accelerated by interactions with micelle bound M-T's.

There has been suggestion (22) that "... the detergent solution, which consists of lipoidal micellar regions dispersed throughout an essentially aqueous



phase, resembles the colloidal nature of biological environment."

### Acknowledgment

This investigation was supported by PHS-NIH Research Grant GM 19181 and NSF Grant No. MPS73-04882.

Manuscript received June 30, 1975. This was Paper 366 presented at the Toronto, Canada, Meeting of the Society, May 11-16, 1975.

Any discussion of this paper will appear in a Discussion Section to be published in the June 1977 JOURNAL. All discussions for the June 1977 Discussion Section should be submitted by Feb. 1, 1977.

Publication costs of this article were assisted by The Ohio State University.

### LIST OF SYMBOLS

$\nu$	scan rate
$I_p$	peak current
$\Delta E_p$	separation between anodic and cathodic peak potentials
$n$	number of electrons transferred per ferrocene molecule
$A$	area of electrode, cm <sup>2</sup>
$D$	diffusion coefficient, cm <sup>2</sup> /sec
$k$	Boltzmann constant
$T$	temperature, °K
$r$	radius, Å
$\eta$	viscosity
$\eta_0$	reference viscosity
$\phi$	volume fraction
$C'$	concentration (g/ml)
$M$	micelle molecular weight
$\bar{V}$	effective specific volume
$N$	Avogadro's number
$\tau$	apparent turbidity
$\tau_0$	apparent turbidity of solvent
$\lambda$	wavelength of light, nm
$n$	refractive index
$n_0$	refractive index of solvent

$\epsilon$	molar absorptivity
$A$	optical absorbance

### REFERENCES

1. Y. Fujihira, T. Kuwana, and C. R. Hartzell, *Biochem. Biophys. Res. Commun.*, **61**, 488 (1974).
2. T. Kuwana and W. R. Heineman, *Bioelectrochem. Bioenergetics*, **1**, 389 (1974).
3. L. N. Mackey, T. Kuwana, and C. R. Hartzell, Unpublished results.
4. T. Kuwana, D. E. Bublitz, and G. Hoh, *J. Am. Chem. Soc.*, **82**, 5811 (1960).
5. S. Hayano and N. Shinozuka, *Bull. Chem. Soc. Japan*, **42**, 1469 (1969); **43**, 2083 (1970); **44**, 1503 (1971).
6. H. Suzuki, N. Shinozuka, and S. Hayano, *ibid.*, **47**, 1093 (1974).
7. P. G. Westmoreland, R. A. Day, and A. L. Underwood, *Anal. Chem.*, **44**, 737 (1972).
8. P. Hinkle, *Biochem. Biophys. Res. Commun.*, **41**, 1375 (1970); *Federation Proc.*, **32**, 1988 (1973).
9. F. M. Hawkridge and T. Kuwana, *Anal. Chem.*, **45**, 1021 (1973).
10. M. R. Cannon, *Ind. Eng. Chem. Anal. Ed.*, **16**, 708 (1944).
11. R. S. Nicholson and I. Shain, *Anal. Chem.*, **36**, 706 (1964).
12. R. N. Adams, "Electrochemistry at Solid Electrodes," Marcel Dekker, New York (1969).
13. Robinson and Stokes, "Electrolyte Solutions," Academic Press, New York (1959).
14. T. Nakagawa and K. Shinoda, "Physicochemical Studies in Aqueous Solutions of Nonionic Surface Active Agents, in "Colloidal Surfactants," Shinoda, Nakagawa, Tamamushi, and Isemma, Editors, chap. 2, Academic Press, New York (1963).
15. E. Guth and R. Simha, *Kolloid Z.*, **74**, 266 (1936).
16. C. Tanford, *J. Phys. Chem.*, **78**, 2469 (1974).
17. P. Debye, *J. Phys. Colloid Chem.*, **51**, 18 (1947).
18. H. M. Koeppe, H. Wendt, and H. Strehlow, *Z. Electrochim.*, **64**, 483 (1960).
19. M. Rosenblum, "Chemistry of the Iron Group Metalloenes, Part 1" chap. 2, John Wiley & Sons, Inc., New York (1965).
20. Wm. R. Heineman and T. Kuwana, *Biochem. Biophys. Res. Commun.*, **50**, 892 (1973).
21. L. Mackey, Ph.D. Thesis, Ohio State University (1975).
22. M. B. Lowe and J. N. Phillips, *Nature*, **190**, 262 (1961).

## Investigation of Adsorbed Hydrogen on Platinum Electrode by Means of Dynamic Impedance Measurement

Tetsuya Ohsaka, Yoshimitsu Sawada, and Tadashi Yoshida\*

Department of Applied Chemistry, Waseda University, Tokyo 160, Japan

and Kohji Nihei

OKI Electric Industry Company, Limited, Fundamental Working Technology Laboratory, Tokyo 108, Japan

### ABSTRACT

Adsorbed hydrogen phenomena on a platinum electrode were investigated by an impedance method which draws potentiodynamically the in-phase and quadrature components of electrode admittance. The kinetic behavior of hydrogen adsorbed on platinum was examined in full with the complex capacitance representation. The kinetic experimental results were well explained on the basis of the proposed equivalent circuit which was composed of the pseudocapacitance, Warburg impedance, and ohmic component associated with the adsorption-desorption process of adsorbed hydrogen, together with the reaction resistance due to the Volmer reaction.

Impedance measurements at the electrode/solution interface have been developed recently (1) and used

extensively in solid electrode/solution systems (2-4). The impedance measurements can be classified into two groups: that using a-c bridges and that directly measuring the alternating current through a cell. The former enables us to determine the in-phase and quad-

\* Electrochemical Society Active Member.

Key words: dynamic impedance measurement, hydrogen adsorption phenomena.

ature components separately and to obtain accurate data. However, it has a disadvantage in that it requires too much time for measurement. Measurement using the latter technique has been developed as a well-known Breyer-type a-c polarography, and we can easily and rapidly get some data with this method. However, the results are scalar quantity, not divided into vector components. Therefore, the dynamic measurement of in-phase and quadrature components of alternating current has been recently attempted by some workers (4-6) for the purpose of removing the disadvantage mentioned above. The authors also constructed an instrument for dynamic impedance measurement as a function of electrode potential with the aid of a lock-in amplifier and by making use of the principle of the Breyer-type a-c polarograph. Since the heart of a lock-in amplifier is a phase sensitive detector, the impedance through the electrode/solution interface which is measured as the magnitude of cell admittance can be detected with the lock-in amplifier, dividing the alternating current into two components of in-phase and quadrature.

The hydrogen adsorption phenomena on a platinum electrode have been investigated by many workers (3, 7, 8). In particular, Frumkin (7) reviewed the kinetic behavior of adsorbed hydrogen on platinum from the results of impedance measurements. Recently, this subject has been discussed by some workers (9-13) from several points of view. In this paper, the kinetic behavior studied with the dynamic impedance circuit is discussed in reference to previous work.

### Instrumental

**Principle.**—The schematic arrangement of the dynamic impedance method is a small a-c level of frequency  $f$  imposed upon the d-c voltage controlled with a potentiostatic instrument. It is convenient to represent the equivalent circuit of a cell in a parallel combination of capacitance  $C_p$  and resistance  $R_p$ . The admittance of parallel circuit of  $C_p$  and  $R_p$  can be given as follows

$$Y = Z^{-1} = G + jS = R_p^{-1} + j\omega C_p \quad [1]$$

where  $\omega$  is the angular velocity ( $\omega = 2\pi f$ ),  $G$  the conductance, and  $S$  the susceptance. The alternating current through the electrode/solution interface can be divided into two components of  $I_i$  and  $I_q$  by a lock-in amplifier, and they correspond to  $EG$  and  $ES$ , respectively, because  $I = I_i + I_q = E \cdot Y = E(G + jS)$ . Therefore, we can measure directly and potentiodynamically  $R_p^{-1}$  as conductance and  $C_p$  as susceptance against the electrode potential with the scanning unit.

**The instrumental circuit.**—A block diagram of the present circuit is shown in Fig. 1. A small a-c voltage supplied by oscillator or function generator (OSC) is superimposed upon the scanning voltage, applied through potentiometer (P) and ramp generator (Ramp). The a-c voltage of the sinusoidal wave is adjusted with the attenuator to be less than 3 mV. Such a voltage is supplied to the working electrode by a fast-rise potentiostat (PS). The frequency range of the instrument is from 5 to 2000 Hz, which is checked with the dummy cell from the linearity of  $C_p$  or  $R_p^{-1}$ . The conductance and susceptance of the electrode/solution interface, which are directly proportional to the potential drop across the resistance  $r_s$ , are measured by the lock-in amplifier (L.I.A.) and calibrated with a standard resistance and capacitance as a dummy cell. After amplification with a lock-in amplifier, the voltage through the cell is supplied to a X-Y<sub>1</sub>-Y<sub>2</sub> recorder, directly drawing the conductance-potential and susceptance-potential relations, respectively.

### Experimental

A smooth platinum disk (0.07 cm<sup>2</sup>) was used as the working electrode. The counterelectrode was a platinum net having sufficiently large surface area. The po-

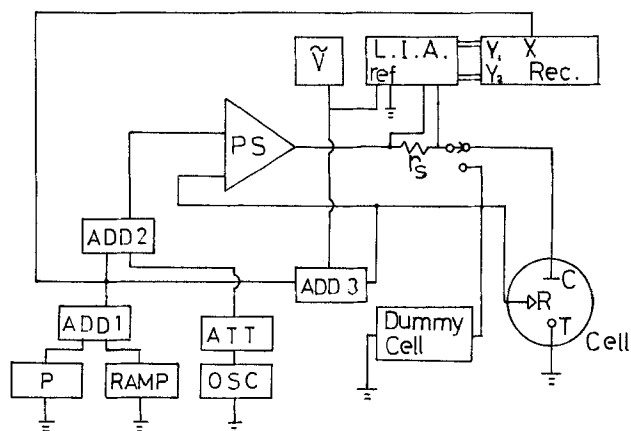
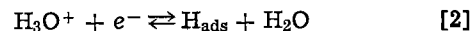


Fig. 1. Block diagram of dynamic impedance circuit. L.I.A. = lock-in amplifier (Princeton Applied Research, Model 129A), PS = potentiostat, P = potentiometer, RAMP = ramp generator, OSC = function generator (NF Circuit Design Block Company, Limited, Model FG-121B), ADD = adder, ATT = attenuator, X-Y<sub>1</sub>-Y<sub>2</sub> Rec. = 2-pen X-Y recorder (Yokogawa Electric Works Limited, Type 3078), V = electronic volt meter,  $r_s$  = standard resistance, T = test electrode, C = counterelectrode, R = reference electrode.

tential was determined in reference to the hydrogen electrode in the same solution (HE). The working electrode, cleaned with concentrated nitric acid, was pretreated by scanning the potential between 0.05 and 1.4 V<sub>HE</sub> at 10 V/sec for several decades of minutes. The reproducibility of the activated conditions of electrode was confirmed by the shape of  $i$ - $E$  (current-potential) curves in the above potential range. Solutions were prepared with reagent grade chemicals and triply distilled water. All the experiments were conducted in an atmosphere of purified nitrogen at 25°C in sulfuric acid.

### Results and Discussion

**Potential dependence of  $C_p$  and  $R_p^{-1}$ .**—The parallel capacitance  $C_p$  and conductance  $R_p^{-1}$  are potentiodynamically measured in the adsorbed hydrogen region on platinum with the scan rate of 2 mV/sec (shown in Fig. 2 and 3). During the anodic scan the adsorbed hydrogen is removed in acidic solutions according to the Volmer reaction in the so-called hydrogen region



Two pronounced peaks of capacitance or conductance appear in the  $C_p$ - $E$  or  $R_p^{-1}$ - $E$  curves similar to two current peaks in the anodic  $i$ - $E$  curves obtained by triangular scanning. There are some indications of the existence of a third peak in the adsorbed hydrogen region on platinum in the  $i$ - $E$  curves (10, 13, 14) and the small third current peak in acidic solution is observed. However, the third peak corresponding to the above is not revealed in the  $C_p$ - $E$  and  $R_p^{-1}$ - $E$  curves shown in Fig. 2 and 3. The potentials (i.e., 0.15 and 0.27 V<sub>HE</sub>) of the peaks in the  $C_p$ - $E$  and  $R_p^{-1}$ - $E$  curves are in agreement with those in the  $i$ - $E$  curves. These peak potentials in Breiter's results (3) shift to the cathodic side somewhat (i.e., 0.1 and 0.2V), while the data in Fig. 2 agree with those of Bagotzky *et al.* (25). The peaks in the  $C_p$ - $E$  curves in the low frequency region disappear gradually and become one peak with the increase in frequency, while the peaks in the  $R_p^{-1}$ - $E$  curves do not disappear in the frequency range observed. As shown in Fig. 2 and 3, the shapes of  $C_p$ - $E$  and  $R_p^{-1}$ - $E$  curves obtained with various frequencies in the adsorbed hydrogen region are approximately similar to those of Breiter (3) and Dolin *et al.* (15), obtained point by point. As for the frequency dispersion of  $C_p$ , the results in Fig. 2 differ from those of Bagotzky *et al.* (25) in which the parallel capacitance  $C_p$  depends on the

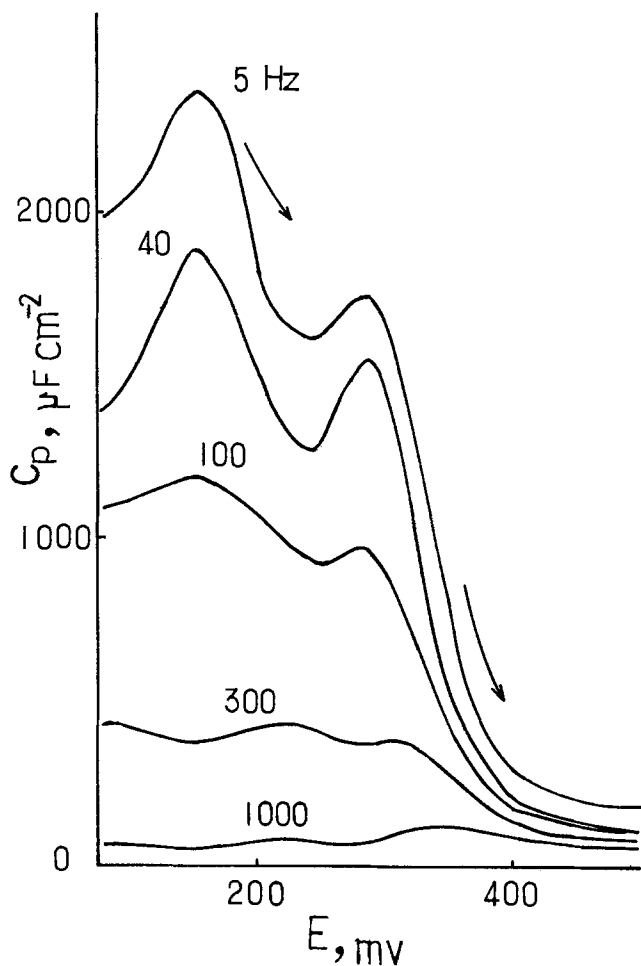


Fig. 2. Parallel capacitance vs. potential curves on Pt obtained potentiodynamically with various frequencies. 1N sulfuric acid, 25°C, 2 mV/sec, nitrogen gas atmosphere.

frequency in the range  $>1$  kHz and the frequency dispersion of  $C_p$  ceases at  $f < 1$  kHz. Breiter's data (3) show the frequency dispersion of  $C_p$  at below 1 kHz and the range  $< ca. 280$  Hz the dispersion ceases. In Fig. 2, the dispersion ceases in the frequency range  $< ca. 20$  Hz, however, there is good reproducibility. Therefore, the difference of the frequency at which the frequency dispersion of  $C_p$  ceases may not be attributed to an impurity or an unsuitable electronic system, but mainly to the reaction resistance  $r$  with a consideration of the behavior of frequency dispersion of  $C_p$ , as calculated by Eq. [3] or [7].<sup>1</sup> According to Dolin *et al.* (15), a simplified equivalent circuit to a platinum electrode in the adsorbed hydrogen region can be shown as that in Fig. 4(a), where  $C_D$  is the double layer capacitance,  $C_A$  the pseudocapacitance, and  $r$  the reaction resistance corresponding to reaction [2]. The following relationships for the conductance and the susceptance

<sup>1</sup>The frequency dependence of  $C_p$ , assuming the equivalent circuit (a) in Fig. 4 or 9, is affected partly by the difference of the solution resistance  $R_s$ , but largely by the reaction resistance  $r$ . When the reaction resistance becomes smaller, the frequency dispersion of  $C_p$  tends to shift to the higher frequency range. In the case of  $r = 0.02$ , the frequency dispersion ceases at  $f < 1$  kHz. The reaction resistance  $r$  obtained roughly from the results of Fig. 1 in the paper by Bagotzky *et al.* (25b) by means of the  $C_p R_p^{-1}$  relation is  $ca. 0.02$ . By using the value of  $r = 0.02$ , we can get the behavior of frequency dispersion similar to that of Bagotzky *et al.* According to the review by Frumkin (7),  $r^{-1}$  in 1N sulfuric acid is 3.4 ( $r = 0.29$ ), which approximately agrees with the present results (see Table I). However, there are higher values for  $r^{-1}$  in the table (*e.g.*,  $r^{-1} = 33.7$  in 8N sulfuric acid). Frumkin thought that higher values of  $r^{-1}$  are caused by greater activation of the electrode. Then, the data of Bagotzky *et al.* are considered to be obtained with a more activated electrode, which is also confirmed by the slight difference between bright and platinized platinum electrode in their work (25).

Moreover, the fact that our  $C_p$  values are twice those of Bagotzky *et al.* is attributed to the electrode area, *i.e.*, they show the data per true area while we use the projective one. Our data become approximately equal in magnitude to those of Bagotzky upon considering the roughness factor of  $1.7 \sim 2.5$  which is obtained with the same electrode.

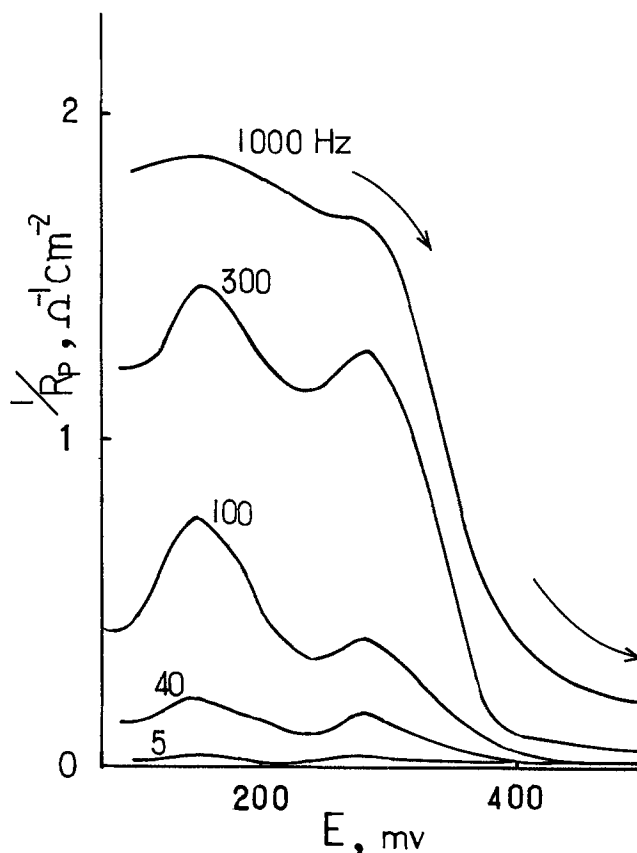


Fig. 3. Parallel conductance vs. potential curves on Pt obtained potentiodynamically with various frequencies. 1N sulfuric acid, 25°C, 2 mV/sec, nitrogen gas atmosphere.

can be derived from Eq. [3] with the assumption that the solution resistance equals zero

$$Y_1 = j\omega C_D + \{r + (j\omega C_A)^{-1}\}^{-1} \quad [3]$$

$$\left\{ \begin{aligned} G_p &= R_p^{-1} = \omega^2 r C_A^2 / (1 + \omega^2 r^2 C_A^2) & [4] \\ S_p &= \omega C_p = \omega \{C_D + C_A / (1 + \omega^2 r^2 C_A^2)\} & [5] \end{aligned} \right.$$

Then, we can get the relations of  $C_p \rightarrow (C_A + C_D)$  for  $\omega \rightarrow 0$ , and  $C_p \rightarrow C_D$ ,  $R_p \rightarrow r$  for  $\omega \rightarrow \infty$ . Moreover, we obtain the following equation by eliminating  $\omega$  from Eq. [4] and [5]

$$C_p = -C_A r R_p^{-1} + (C_A + C_D) \quad [6]$$

When the double layer capacitance  $C_D$  is determined in the potential range of the double layer,  $C_A$  and  $r$  can be computed by the gradient and intercept of the  $C_p R_p^{-1}$  relation, assuming the solution resistance to be negligible.

In practice, the conductance and the susceptance can be derived from the following equation, adding the solution resistance  $R_E$  in the equivalent circuit of (a) in Fig. 4

$$Y_2 = [R_E + \{j\omega C_D + \{r + (j\omega C_A)^{-1}\}^{-1}\}^{-1}]^{-1} \quad [7]$$

Since the solution resistance is very small, there is only a slight difference between  $Y_1$  and  $Y_2$ .

*Frequency dependence of  $C_p$  and  $R_p^{-1}$ .*—Figure 5 shows the frequency dependence of parallel capacitance  $C_p$  at the potentials of 0.15, 0.27, and 0.7  $V_{HE}$  in 1N sulfuric acid solution. At 0.7  $V_{HE}$  in the double layer region, the double layer capacitance  $C_D$  was determined as  $56 \mu F/cm^2$  by extrapolating  $C_p$  to a high frequency range, eliminating the faradaic components. The  $C_D$  in 4 and 8N sulfuric acid was also determined as 70 and  $77 \mu F/cm^2$ , respectively. Since the  $C_p$  in the adsorbed hydrogen region at low frequencies is much larger than  $C_D$ , the value of  $C_p$  might be approximately

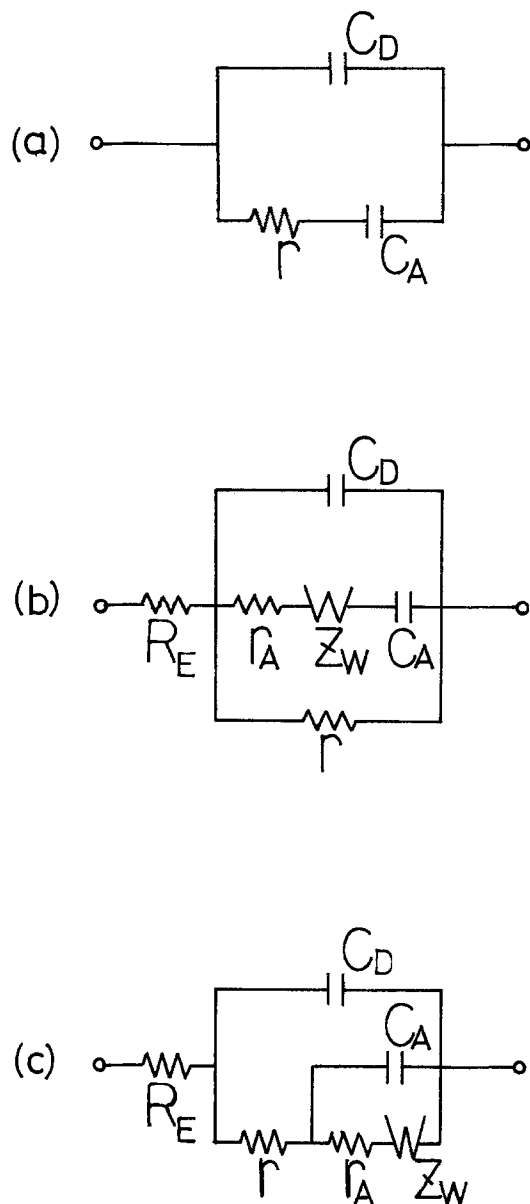


Fig. 4. Electrical equivalent circuits for adsorbed hydrogen on Pt electrode.

regarded as the pseudocapacitance due to adsorbed hydrogen. The frequency dependence of parallel conductance  $G_p$  in 1*N* sulfuric acid solution is shown in Fig. 6. The solution resistance  $R_E$  in 1*N* sulfuric acid was estimated from the data in Fig. 6 through Eq. [7]<sup>2</sup> for the conditions of  $\omega \rightarrow \infty$ . The more suitable value of 0.3  $\Omega\text{-cm}^2$  was chosen by an electronic computer in comparison with the experimental and theoretical data. The  $R_E$  in 4 and 8*N* sulfuric acid was also determined as 0.13  $\Omega\text{-cm}^2$ , respectively. Since the solution resistance results in very small value, the reaction resistance  $r$  and the pseudocapacitance  $C_A$  can be derived from Eq. [6] assuming  $R_E = 0$ . Figure 7 shows typical plots of  $C_p \cdot R_p^{-1}$ , which is expected to become linear with the gradient of  $-C_A r$  and the intercept of  $(C_A + C_D)$ . The results of the  $C_p \cdot R_p^{-1}$  plot become approximately linear and the approximate values of  $r$  and  $C_A$  can be determined from the linear part in Fig. 7. However, the linear relation deviates in the low frequency region. Such a deviation is more marked in the complex capacitance representation as shown in Fig. 8, that is,

<sup>2</sup>  $G_p$  can be derived from Eq. [7] as follows

$$G_p = R_p^{-1} = \frac{\omega^2(\omega^2 R_E L^2 + K^2 R_E + K C_A r - L)}{(1 - \omega^2 R_E L)^2 + \omega^2(C_A r + K R_E)^2} \quad [7a]$$

where  $K = C_D + C_A$  and  $L = C_D \cdot C_A r$ . When  $\omega \rightarrow \infty$ ,  $G_p \rightarrow R_E^{-1}$ .

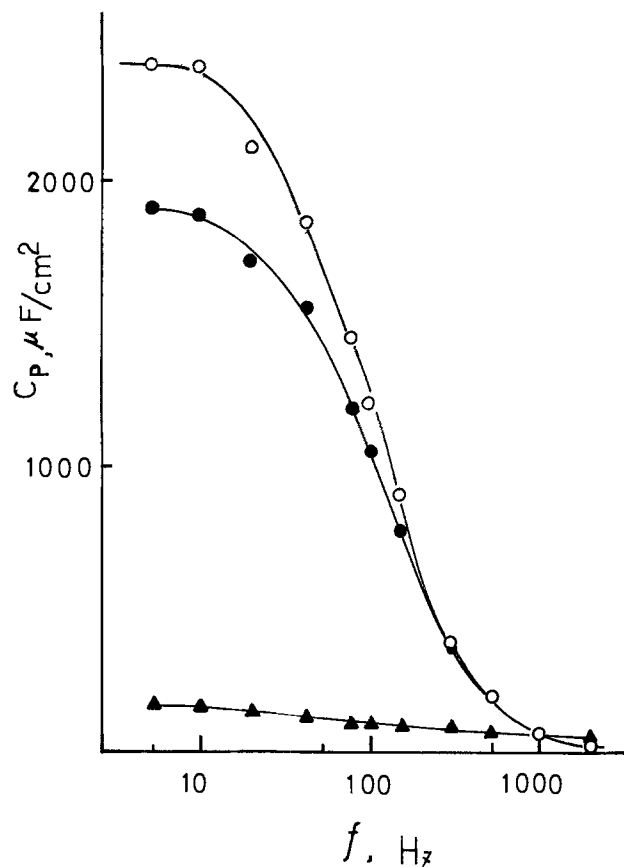


Fig. 5. Frequency dependence of parallel capacitance on Pt. 1*N* sulfuric acid, 25°C, 2 mV/sec, nitrogen gas atmosphere,  $\circ$  = measured at 0.15  $V_{HE}$ ,  $\bullet$  = at 0.27  $V_{HE}$ ,  $\blacktriangle$  = at 0.70  $V_{HE}$ .

the semicircular plots become linear in the region of low frequencies. Such results might indicate that the equivalent circuit shown in Fig. 4(a) is unsatisfactory and that the other electrical factors which affect the admittance through cell in the low frequency region must be considered.

*Complex capacitance representation.*—The data obtained from the impedance method are used for analysis with the representations of complex impedance (as  $Z$ ) and complex capacitance (as  $Y/\omega$ ), the latter being more convenient for the admittance measurement. Figure 8 shows the complex capacitance representations of the adsorbed hydrogen region in some acidic solutions. The plots in Fig. 8 are approximately semicircular, however, they become linear in the region of low frequencies. Such a deviation in the low frequency region seems to be more obvious with the increase in normality of sulfuric acid and is considered to be confirmed by the advantage that the results from the dynamic impedance measurement have especially good reproducibility in the low frequency region compared with those obtained point by point from the a-c bridge measurement for solid electrode/solution systems.

The analysis of a-c impedance in the presence of adsorption processes has already been discussed by various workers (16-26), and the most general case of adsorption with diffusion process has been investigated by a few workers (16-18). According to Lorenz *et al.* (17), the impedance  $Z_k$  due to the adsorption process corresponds to a series combination of capacitance  $\Delta C$ , adsorption resistance  $\tau/\Delta C$ , and Warburg impedance  $Z_w$  as follows

$$Z_k = (j\omega\Delta C)^{-1} + \tau/\Delta C + Z_w \quad [8]$$

where  $\Delta C = C_{LF} - C_{HF}$ ,  $C_{LF}$  and  $C_{HF}$  are low and high frequency limit capacitances,  $\tau$  the characteristic time constant for the adsorption step, and  $Z_w = (\xi/\omega\Delta C)(1 - j)$ ,  $\xi = (\partial\Gamma/\partial c)_E(\omega/2D)^{1/2}$ . The relationship be-

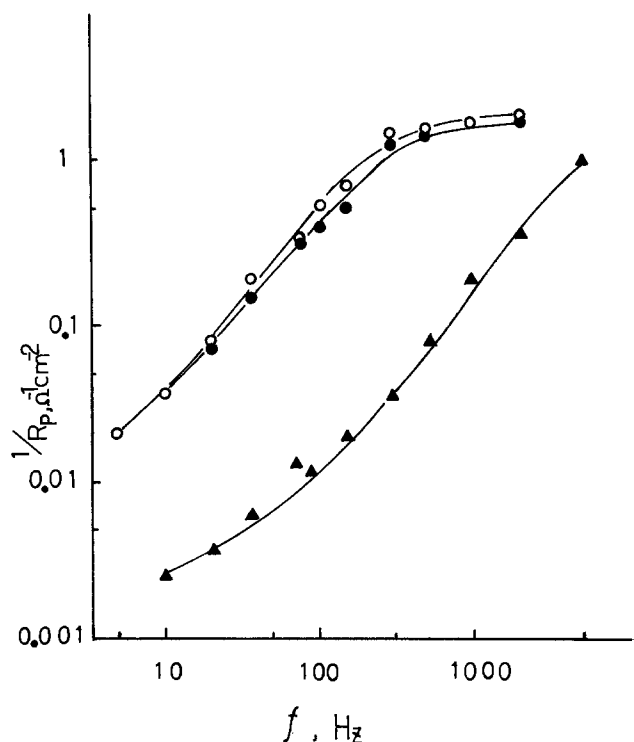


Fig. 6. Frequency dependence of parallel conductance on Pt. 1N sulfuric acid, 25°C, 2 mV/sec, nitrogen gas atmosphere, ○ = measured at 0.15  $V_{HE}$ , ● = at 0.27  $V_{HE}$ , ▲ = at 0.70  $V_{HE}$ .

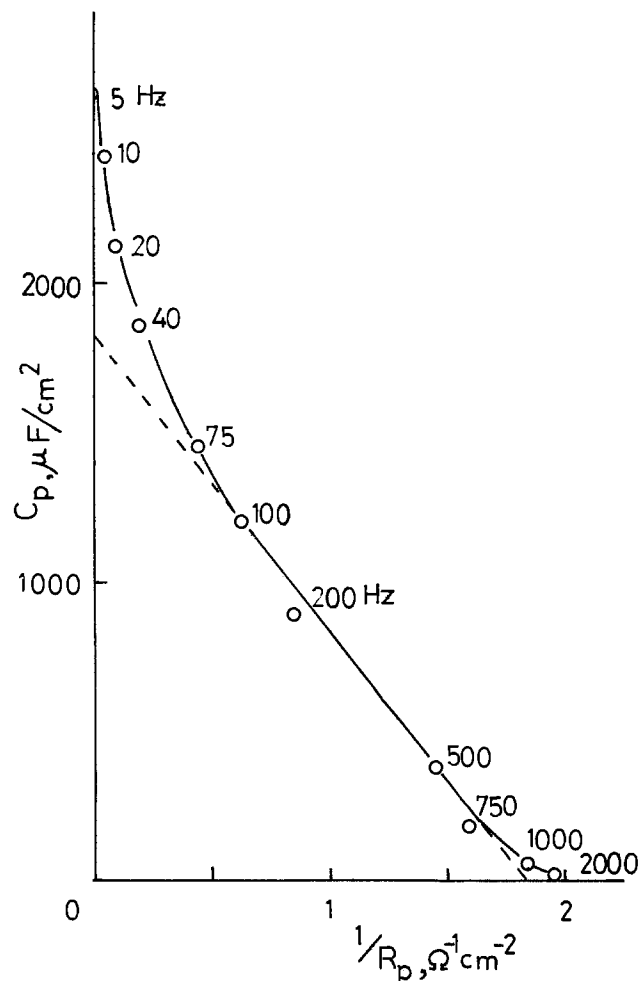


Fig. 7. Relation between parallel capacitance and parallel conductance in the adsorbed hydrogen region on Pt in 1N sulfuric acid, 25°C, nitrogen gas atmosphere, 0.15  $V_{HE}$ .

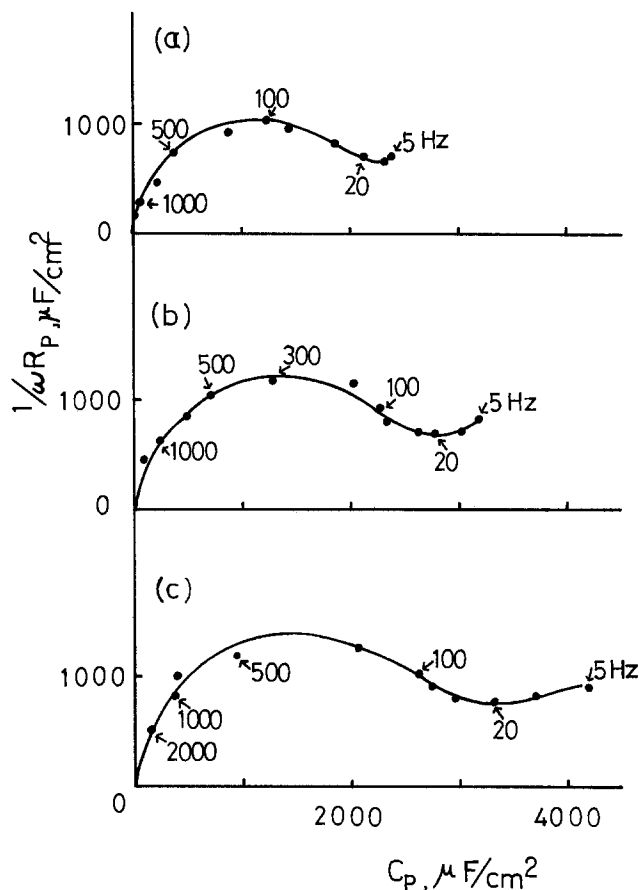


Fig. 8. Complex capacitance representation in the adsorbed hydrogen region on Pt. 25°C, nitrogen gas atmosphere, 0.15  $V_{HE}$ , (a) 1N sulfuric acid, (b) 4N sulfuric acid, (c) 8N sulfuric acid.

tween the equivalent circuit and the graphical representation corresponding to the above is given in Ref. (1) and (23). The apparently similar circuit to that of Lorenz *et al.* has been proposed by Bagotzky *et al.* (25) for the hydrogen adsorption on platinum, that is,  $Z_w$  is added in series to the impedance of  $Z_o = [(j\omega C_A)^{-1} + r]$  in Fig. 4(a). However, the theoretical representation of complex capacitance did not fit the experimental results shown in Fig. 8.<sup>3</sup> Therefore, the equivalent circuit for the hydrogen adsorption is naturally assumed to be (b) in Fig. 4 in which  $Z_k$  is connected with the impedance due to reaction resistance in parallel (26, 28). The equivalent circuit similar to (b) in Fig. 4 was also proposed by Randles *et al.* (19). Though the equivalent circuit in Fig. 4(c) is considered to be one of the most general case of specific adsorption of electroactive species, the theoretical representation of complex capacitance cannot elucidate the experimental results in Fig. 8. The concept of interaction between the faradaic and nonfaradaic components of electrode impedance was proposed by Llopis *et al.* (20) for the ferrous-ferrocyanide and halide-halogen reactions and its equivalent circuit was derived on the basis of Eq. [9] whose idea was also given by Delahay (24)

$$i_f = nFV + nF \frac{d\Gamma}{dt} \quad [9]$$

where  $i_f$  is the faradaic current,  $V$  the flux of reactant, and  $\Gamma$  the adsorbed amount stored at the interface. The equivalent circuit proposed by Llopis *et al.* (20) is shown in Fig. 4(c) in which the finite rate of adsorption and desorption appears as a resistance  $r_A$  in series with the Warburg impedance, and the pseudocapacitance  $C_A$  due to the storage of electroactive species is

<sup>3</sup>The representation of  $Y/\omega$  derived from the circuit of Bagotzky *et al.* (25) falls on a lemniscate-like curve [see Ref. (1) and (23)].

combined with the above impedance in parallel. The apparently same circuit was proposed by Levie *et al.* (5) for the biological membrane system. Sluyters *et al.* (28) examined this model for the  $Pb^{2+}/Pb(Hg)$  electrode system. Since the theoretical representation of the equivalent circuit of (c) in Fig. 4 accounts well for the experimental results in Fig. 8 (cf., Fig. 9), we adopt the equivalent circuit of (c) in Fig. 4 for the hydrogen adsorption on platinum and show the comparison of theoretical and experimental representations in Fig. 9. In the equivalent circuit of (c) in Fig. 4, the faradaic impedance due to reaction [2] is represented as a reaction resistance  $r$  in series with the impedance  $Z_k$  due to the adsorption or desorption process of adsorbed hydrogen, where  $Z_k$  is composed of  $C_A$  due to the storage of adsorbed hydrogen in parallel with the sum of  $r_A$  and  $Z_w$  caused by the adsorption rate and diffusion process of adsorbed hydrogen. The admittance for the circuit in Fig. 4(c) is represented as follows with the assumption of  $R_E = 0$

$$Y_3 = j\omega C_D + [r + [j\omega C_A + \{(\sigma r_A + \sigma\omega^{-1/2}) - j\sigma\omega^{-1/2}\}^{-1}]^{-1}]^{-1} \quad [10]$$

where  $Z_w = \sigma\omega^{-1/2} (1 - j)$  and  $\sigma$  the constant concerned with the Warburg impedance. Moreover, we can get the admittance with  $R_E \neq 0$ , though the apparent difference between  $Y_3$  and  $Y_4$  is almost negligible because of  $R_E \ll 1$  and  $C_D \ll C_A^4$

$$Y_4 = [R_E + [j\omega C_D + [r + [j\omega C_A + \{(\sigma r_A + \sigma\omega^{-1/2}) - j\sigma\omega^{-1/2}\}^{-1}]^{-1}]^{-1}]^{-1} \quad [11]$$

The values of each component of the equivalent circuit in Fig. 4(c) can be derived from the subtraction method after Levie (5b), *i.e.*,  $C_D$  is given by the graphical representation of  $Y/\omega$  with extrapolating to infinite frequency after subtraction of  $R_E$ ,  $r$  is given by extrapolating to high frequency in the graphical representation of  $Z$  after subtraction of  $C_D$  and  $R_E$ ,  $C_A$  is given by the graphical representation of  $Y/\omega$  after subtracting  $R_E$ ,  $C_D$ , and  $r$ , and  $r_A$  and  $\sigma$  are given by the remainder. The values of each component were estimated from the approximate linear relation in Fig. 7 and the above graphical method. The more precise values in Table I were determined by an electronic com-

<sup>4</sup> Though the frequency dispersion of  $C_D$  is somewhat dependent on the value of  $R_E$ , in the representation of  $Y/\omega$  the effect of the solution resistance is not so large in this system with the conditions of  $R_E \ll 1$  and  $C_D \ll C_A$ .

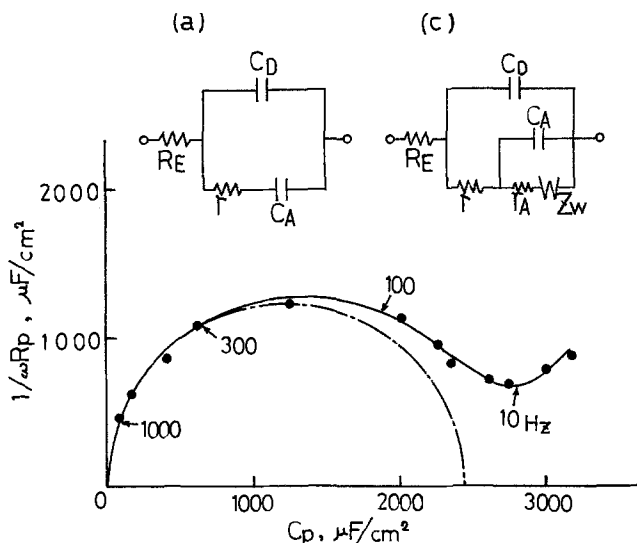


Fig. 9. Complex capacitance representation as  $Y/\omega$ . ● = experimental results in 4N sulfuric acid at 0.15  $V_{HE}$ ; --- = theoretical curve based on the circuit (a) with  $R_E$ ; — = theoretical curve based on the circuit (c), where  $R_E = 0.13 \Omega\text{-cm}^2$ ,  $C_D = 70 \mu\text{F/cm}^2$ ,  $C_A = 2400 \mu\text{F/cm}^2$ ,  $r = 0.22 \Omega\text{-cm}^2$ , and  $\sigma = 120 \Omega\text{-cm}^2/\text{sec}$ .

Table I. Values of components obtained experimentally from the assumption of the equivalent circuit (c) in Fig. 4

Sulfuric acid solution	1N	4N	8N
Potential ( $V_{HE}$ )	0.15	0.15	0.15
$C_D^*$ ( $\mu\text{F/cm}^2$ )	56	70	77
$R_E^{**}$ ( $\Omega\text{-cm}^2$ )	0.30	0.13	0.13
$C_A$ ( $\mu\text{F/cm}^2$ )	1800	2400	2700
$r$ ( $\Omega\text{-cm}^2$ )	0.58	0.22	0.20
$r_A$ ( $\Omega\text{-cm}^2$ )	0.4	0.4	0.4
$\sigma$ ( $\Omega\text{-cm}^2/\text{sec}$ )	150	120	110

\* The values of  $C_D$  were determined at 0.70  $V_{HE}$  by extrapolating  $\omega$  to  $\infty$ .  
 \*\* The values of  $R_E$  were determined at 0.70  $V_{HE}$ .

puter in comparison with the experimental and theoretical data.

In Table I, the values of  $C_D$ , which are determined in the double layer region on platinum, are considered to be appropriate, though they are somewhat higher than those obtained by other workers with impedance measurements (15, 27). The pseudocapacitance of adsorbed hydrogen,  $C_A$ , becomes somewhat large with the increase in normality of sulfuric acid solution, and such a trend might be caused by the increase of hydrogen ion concentration. Frumkin (7) listed the reaction resistance  $r$  obtained by various workers, and the results in Table I were approximately in agreement with some of them (*e.g.*, 0.294  $\Omega\text{-cm}^2$  in 1N  $H_2SO_4$  and 0.194  $\Omega\text{-cm}^2$  in 1N HCl), though he indicated the difference of apparent surface from true surface with freshly activated electrodes. As expected from the slow discharge theory (15), the results of  $r^{-1}$  are dependent on the hydrogen ion concentration in acidic solutions. Therefore, it follows from the results in Table I that the dynamic impedance measurement is satisfactorily applicable to solid electrode/solution systems.

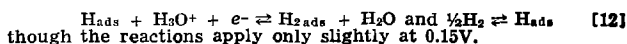
In Fig. 9, the theoretical representations of complex capacitance ( $Y/\omega$ ) calculated on the assumption of equivalent circuits are shown with a dotted line for (a) with adding  $R_E$  and a solid line for (c) of Fig. 4. The most simple circuit in Fig. 4(a) gives a semicircle with the intercept of  $C_D$  in the high frequency region, and the circuit including the solution resistance  $R_E$  reveals similar behavior (dotted line), though the intercept in the high frequency region becomes zero. The intercept in the low frequency region shows the sum of  $(C_A + C_D)$ . As seen in Fig. 9, the theoretical representation based on the circuit (a) of Fig. 4 is unsatisfactory to explain the experimental results shown with a black circle (●), while the theoretical solid line based on the circuit (c) of Fig. 4 coincides well with the results in the frequency range measured. Consequently, the equivalent circuit (c) of Fig. 4 is more available to elucidate the kinetic behavior of adsorbed hydrogen on a platinum electrode,<sup>5</sup> though the equivalent circuit (a) in Fig. 4 proposed by Dolin *et al.* is applicable to the approximate behavior in the relatively high frequency region.

Manuscript submitted Feb. 23, 1976; revised manuscript received May 18, 1976.

Any discussion of this paper will appear in a Discussion Section to be published in the June 1977 JOURNAL. All discussions for the June 1977 Discussion Section should be submitted by Feb. 1, 1977.

Publication costs of this article were assisted by OKI Electric Industry Company, Limited.

<sup>5</sup> It may be physically unclear as to why any Warburg component should be required for the present system. However, one might consider two possibilities, *i.e.*, the effects of the anions  $SO_4^{2-}$  and  $HSO_4^-$  on the adsorption states of hydrogen, which have been pointed out by some workers (13, 25) and the effects of the following reactions



## REFERENCES

1. D. E. Smith, in "Electroanalytical Chemistry," Vol. 1, A. J. Bard, Editor, p. 1, Marcel Dekker, Inc., New York (1966); M. Sluyter-Rehback and J. H. Sluyters, *ibid.*, Vol. 4, p. 1, Marcel Dekker, Inc., New York (1970); R. Parsons, in "Advances in Electrochemistry and Electrochemical Engineering," Vol. 7, P. Delahay, Editor, p. 177, Interscience, New York (1970).
2. For example, I. Epellboin and M. Keddum, *Electrochim. Acta*, **17**, 177 (1972); I. R. Burrows, J. A. Harrison, and J. Thompson, *J. Electroanal. Chem.*, **58**, 241 (1975); H. Kojima and A. J. Bard, *ibid.*, **63**, 117 (1975); R. D. Armstrong, K. Edmondson, and J. A. Lee, *ibid.*, **63**, 287 (1975).
3. M. W. Breiter, "Transactions of the Symposium on Electrode Processes, Philadelphia 1959," p. 307, John Wiley & Sons, New York (1961); *J. Phys. Chem.*, **68**, 2249 (1964).
4. H. G. Feller, H. J. Rätzer-Scheibe, and W. Wendt, *Electrochim. Acta*, **17**, 187 (1972); H. J. Rätzer-Scheibe and H. G. Feller, *ibid.*, **18**, 175 (1973).
5. (a) R. de Levie and A. A. Husovsky, *J. Electroanal. Chem.*, **20**, 181 (1969); *ibid.*, **49**, 153 (1974); *ibid.*, **58**, 123 (1975); *ibid.*, **62**, 111 (1975); (b) R. de Levie and D. Vukadin, *ibid.*, **62**, 95 (1975).
6. K. Matsuda, K. Takahashi, and R. Tamamushi, *Sci. Papers Inst. Phys. Chem. Res. (Tokyo)*, **64**, 62 (1970); *Bull. Chem. Soc. Jpn.*, **44**, 2880 (1971).
7. A. N. Frumkin, in "Advances in Electrochemistry and Electrochemical Engineering," Vol. 3, P. Delahay, Editor, p. 287, Interscience, New York (1963).
8. For example, K. J. Vetter, "Electrochemical Kinetics," p. 516, Academic Press, New York (1967); J. Horiuchi, in "Physical Chemistry," Vol. IXB, H. Eyring, D. Henderson, and W. Jost, Editors, p. 544, Academic Press, New York (1970); T. Erdey-Grúz, "Kinetics of Electrode Processes," p. 150, Adam Hilger, Ltd., London (1972).
9. V. S. Bagotzky, Yu. B. Vassiliev, and I. I. Pyshnograeva, *Electrochim. Acta*, **16**, 2141 (1971).
10. A. Capon and R. Parsons, *J. Electroanal. Chem.*, **39**, 275 (1972).
11. A. Bewick and A. M. Tuxford, *ibid.*, **47**, 255 (1973).
12. R. Woods, *ibid.*, **4**, 217 (1974).
13. N. Nakamura and H. Kita, *ibid.*, **68**, 49 (1976).
14. F. G. Will, *Electrochem. Technol.*, **112**, 451 (1965).
15. P. Dolin and B. Ershler, *Acta Physicochim. URSS.*, **13**, 747 (1940).
16. A. N. Frumkin and V. I. Melik Gaikazyan, *Dokl. Akad. Nauk SSSR*, **77**, 855 (1951).
17. W. Lorenz and F. Möckel, *Z. Elektrochem.*, **60**, 507 (1956); *ibid.*, **62**, 192 (1958).
18. K. Takahashi, *Electrochim. Acta*, **13**, 1609 (1968).
19. J. E. B. Randles and K. W. Somerton, *Trans. Faraday Soc.*, **48**, 937 (1952); H. A. Laitinen and J. E. B. Randles, *ibid.*, **51**, 54 (1955).
20. J. Llopis, J. Fernandez-Biarge, and M. Perez-Fernandez, "Transactions of the Symposium on Electrode Processes, Philadelphia 1959," p. 221, John Wiley & Sons, New York (1961); *Electrochim. Acta*, **1**, 130 (1959); *ibid.*, **6**, 167, 177 (1962).
21. B. E. Conway and E. Gileadi, *Trans. Faraday Soc.*, **58**, 2493 (1962); in "Modern Aspects of Electrochemistry," Vol. 3, J. O'M. Bockris and B. E. Conway, Editors, p. 347, Butterworths, London (1964).
22. J. Honz and L. Nemic, *Coll. Czech. Chem. Commun.*, **34**, 2030 (1969).
23. R. de Levie and L. Pospisil, *J. Electroanal. Chem.*, **22**, 277 (1969).
24. K. Holub, G. Tessari, and P. Delahay, *J. Phys. Chem.*, **71**, 2612 (1967); P. Delahay, *ibid.*, **70**, 2373 (1966).
25. (a) V. I. Luk'yanycheva, E. M. Strochkova, and V. S. Bagotsky, *Elektrokhimiya*, **6**, 701 (1970); (b) *ibid.*, **7**, 267 (1971).
26. J. O'M. Bockris and A. K. N. Reddy, "Modern Electrochemistry," Vol. 2, p. 1026, Plenum Press, New York (1970).
27. M. W. Breiter, H. Kammermaier, and Knorr, *Z. Elektrochem.*, **60**, 37 (1956); T. Brintseva and B. Kavanov, *Dokl. Akad. Nauk SSSR*, **132**, 686 (1960).
28. M. Sluyters-Rehbach, B. Timmer, and J. H. Sluyters, *J. Electroanal. Chem.*, **15**, 151 (1967); B. Timmer, M. Sluyters-Rehbach, and J. H. Sluyters, *ibid.*, **15**, 343 (1967); *ibid.*, **18**, 93 (1968).

# The Spectroelectrochemical Study of the Oxidation of 1,2-Diaminobenzene: Alone and in the Presence of Ni(II)

Alexander M. Yacynych\* and Harry B. Mark, Jr.\*

Department of Chemistry, University of Cincinnati, Cincinnati, Ohio 45221

## ABSTRACT

A rapid scanning spectrometer and classical electrochemical techniques have been combined in a spectroelectrochemical experiment using optically transparent electrodes to study electrode filming on the oxidation of 1,2-diaminobenzene; alone and in the presence of Ni(II). Spectroelectrochemical studies of short-lived redox intermediates and mechanisms of the oxidation at platinum electrodes are determined. Cyclic voltammetry showed the oxidation of 1,2-diaminobenzene to be irreversible, and on successive scans without cleaning the electrode the peak current dropped significantly with each scan until ultimately no current flowed. This situation is indicative of an insulating film completely coating the electrode. This behavior was observed both with and without Ni(II) being present in solution. However, there were significant differences in the rate and nature of the filming. Spectroelectrochemically, it was observed that the nature of the film on 1,2-diaminobenzene oxidation was independent of time and potential. A conducting film is initially formed, and on top of this a nonconducting film forms which eventually insulates the electrode. With Ni(II) present the oxidation mechanism is potential dependent. At lower potentials a product containing nickel is formed which does not coat the electrode. At higher potentials the product was found to be the same insulating film which coated the electrode in the oxidation of 1,2-diaminobenzene without the presence of Ni(II).

Often, electrochemical kinetic data are not sufficient to unambiguously determine the mechanism of an electrode reaction. This is especially true with reactions which are highly nonideal with respect to boundary conditions imposed by simple classical electrochemical models. An example of this nonideal electrochemical behavior is electrode filming, which often occurs with the oxidation of organic compounds. It is generally assumed but not proven that these electrode films are polymeric in nature (1, 2), however, the mechanisms and rates of their formation are unknown as the self-insulating nature of the films makes it very difficult to reduce the electrokinetic data to a mechanism. The elucidation of these types of mechanisms would benefit electrochemical organic oxidation studies in general and electrochemical polymerization mechanisms in particular.

In order to examine film formation, a separate but simultaneous optical monitoring of the electrode interface during the actual electrolysis (3-6) has been employed in this study. In this way, the information that can be obtained from the time-resolved spectra during electrolysis can be used for direct qualitative identification and the time dependency of products and/or intermediate(s) concentrations. By using spectroelectrochemical techniques, it is possible to obtain two independent sets of kinetic and mechanistic data. Thus, any mechanistic model which satisfies both the electrochemical and optical kinetic data simultaneously is more likely to be correct.

This particular example, the oxidation of 1,2-diaminobenzene, alone and in the presence of Ni(II), was chosen for study: first, because previous studies had shown that this system formed strongly adhering highly colored films at acidic pH values (1, 2, 7, 8); second, because it was felt that there was a possibility of forming a conductive organic film (polymeric cation radical system) which could have novel applications in the field of organic electrochemical synthesis and perhaps in the area of specific ion electrodes.

Previous studies on the electrochemical oxidation of 1,2-diaminobenzene have yielded only partial informa-

tion on the reaction mechanism (1, 2, 7-14). It was shown that the reaction products were pH dependent, with electrode filming occurring at lower and middle pH, but not at high pH (1, 2). Also, the half-wave potential changed with pH steadily decreasing with increasing pH (12).

## Experimental

In our spectroelectrochemical system, on-line experimental control, data acquisition, and reduction are accomplished by a Raytheon 704 computer, which assures that both the electrochemical and spectrophotometric experiments are on the same time base. A block diagram of the system is shown in Fig. 1. The computer sends a triangular waveform (maximum,  $\pm 10V$ ) from the digital-to-analog converter (DAC) to the digital trigger which simultaneously initiates the potentiostat and the rapid scanning spectrophotometer (RSS). The triangular waveform output by the computer is also used to control the RSS. The electrochemical data is then acquired on an oscilloscopy or X-Y recorder, and the spectral data is acquired by the computer through the analog-to-digital converter (ADC) and stored on magnetic tape.

The basic RSS is a commercially manufactured unit made by Harrick Scientific Corporation (15, 16). The spectrophotometer operates in the near ultraviolet and visible regions of the spectrum with a wavelength range of 280-600 nm. The electronic interface for the

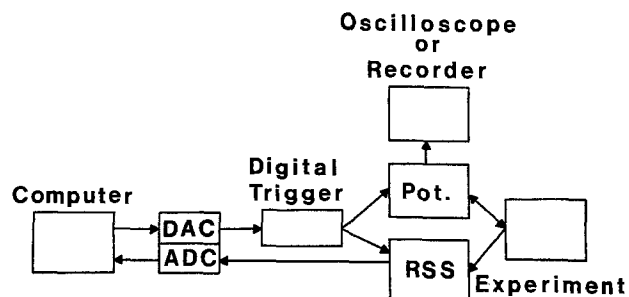


Fig. 1. A block diagram of the spectroelectrochemical system

\* Electrochemical Society Active Member.

Key words: optically transparent electrode, rapid scanning spectroscopy, electropolymerization, cyclic voltammetry.



RSS is composed of two circuits: a galvanometer drive circuit and a photomultiplier tube output signal conditioning circuit, which were described previously (17, 18). The galvanometer mirror (16) and, hence, wavelength scan, is driven electronically by a triangular waveform, computer generated, through the digital-to-analog (DAC) converter.

The RSS offers a high degree of experimental flexibility as the frequency of scan, the wavelength scan width, and wavelength region can all be varied by entering the proper commands on the teletype. RAPID is the main program of a package that was designed to drive and acquire data from the rapid scanning spectrometer. Details of the circuitry, operation, limitations of the system, and RAPID plus the subroutines associated with it have been described and listed previously (17-19).

The electrochemical cell was similar to the design used by Kuwana and Heineman (20). A platinum optically transparent electrode (OTE) was used as the working electrode, which was commercially manufactured by Harrick Scientific Corporation (15). These platinum OTE's generally have a metal film thickness of 50-250Å with a resistivity of 5-20  $\Omega$ -cm and an optical transmission in the visible region of the spectrum of about 10-20% (15). The light beam was perpendicular to the electrode surface (transmission mode). The working electrode was cleaned using a chromic acid cleaning solution, then rinsed with 3M nitric acid, and finally copiously rinsed with triply distilled water. This leaves the working electrode in an oxidized state, which is then electrochemically reduced at  $-0.2V$  vs. an Ag/AgCl reference electrode, then any adsorbed hydrogen is oxidized at  $+0.05V$ , and, finally, the working electrode is brought to starting potential, which in our case was  $0V$ . In the cleaning steps, the electrochemical reduction and oxidations were carried out until the current dropped almost to zero. This procedure, though tedious, assured a reproducible electrode surface at the start of every experiment (21). The counterelectrode, a coiled platinum wire, and the reference electrode, Ag/AgCl, were separated from the sample solution by Corning Vycor porous glass ("thirsty" glass) salt bridges. The supporting electrolyte was 0.1M phosphate buffer solution (pH = 7). The concentration of the samples used was 3 mM 1,2-diaminobenzene or 3 mM 1,2-diaminobenzene and 3 mM Ni(NO<sub>3</sub>)<sub>2</sub>. All electrolysis solutions were deaerated for 15 min with high purity grade nitrogen (Delta Products) prior to the initiation of the experiment and a nitrogen atmosphere was maintained over the solution during the course of the experiment.

The 1,2-diaminobenzene (practical grade) was purified by recrystallizing from dichloromethane three times using ordinary techniques, and was decolorized with activated carbon (2 g/liter) during the first recrystallization. The final product was pure white plate-like crystals with a melting point range of 100.3°-101.8°C. The literature value for the melting point range of pure 1,2-diaminobenzene is 102°-103°C (22). The Ni(NO<sub>3</sub>)<sub>2</sub> used was reagent grade and was not further purified.

X-ray fluorescence was used for the determination of nickel. An EDAX, energy dispersive x-ray analyzer, Nuclear Diodes (Model 707), was used for the analysis.

Infrared spectra were taken on a Beckman IR-12 spectrometer, with samples in the form of KBr pellets. The pellets were made using 2 mg of sample to 200 mg of reagent grade KBr, with a pressure of 1200 psi.

### Results and Discussion

A chronocoulometric study (23) gave anomalous results. Using a potential step from 0 to  $+0.6V$  which is well into an apparent diffusion-controlled region of the wave, a plot of charge vs. the square root of time data should yield an intercept on the charge axis for 1,2-diaminobenzene, both in the presence and absence of

Ni(II) representing charging and faradaic reactions of any adsorbed reactant (24). However, the plotted data (negative coulombs at  $t = 0$ ) had an intercept on the time axis, which is not consistent with an adsorbed reactant model. Examination of the potentiostat response showed that a relatively long time is required for the electrode to reach applied potential, 3 sec for a 600 mV potential step. The potentiostat response for the same potential step is only 30 msec in the supporting electrolyte solution. This degraded response time is probably responsible for the anomalous chronocoulometric results, and may be due to adsorption of 1,2-diaminobenzene and/or initial film formation in our system. This results in a huge pseudocapacitance and/or resistance effect and, hence, a large RC time constant for the electrode (24).

Figure 2 shows a typical cyclic voltammogram with a potential scan rate of 3 mV/sec for the oxidation of 1,2-diaminobenzene. The peak potential ( $E_p$ ) occurs at about  $+0.35V$  vs. a Ag/AgCl reference electrode. The oxidation wave is totally irreversible in nature, and on successive scans, without cleaning the electrode, the peak current dropped significantly with each scan until ultimately no current flowed, which is indicative of a nonconducting film completely coating the electrode.

Figure 3 shows a cyclic voltammogram for the oxidation of 3 mM 1,2-diaminobenzene in the presence of 3 mM Ni(II) under the same electrolysis conditions. In this case,  $E_p$  occurs at a slightly more negative potential of  $+0.33V$ . Other than this slight shift in half-wave potential, the two cyclic voltammograms are quite similar, with both oxidations being irreversible and film formation insulating the electrode on prolonged cycling.

As expected, the behavior on variation of sweep rates showed that the mechanism did not follow any of the model systems analyzed by Nicholson and Shain (25).

Obviously, by using only electrochemical techniques, little reliable mechanistic information could be obtained on this system. In fact, from this data alone, one

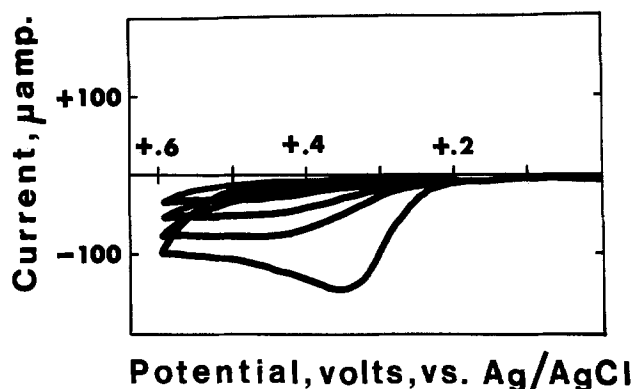


Fig. 2. Cyclic voltammogram of the oxidation of 1,2-diaminobenzene.

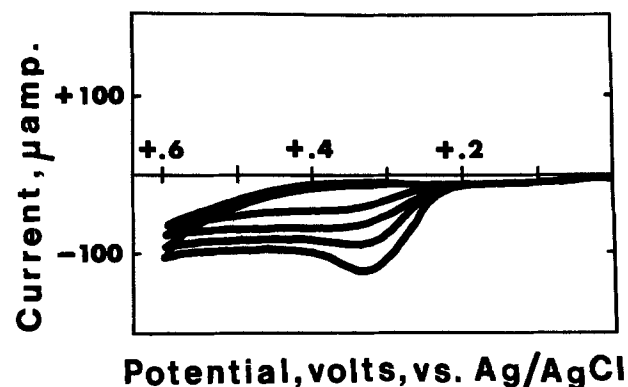


Fig. 3. Cyclic voltammogram of the oxidation of 1,2-diaminobenzene in the presence of Ni(II).

might be led to believe that the oxidation of 1,2-diaminobenzene alone and in the presence of Ni(II) is the same reaction or at least similar. Such is not the case, however, as can be seen from the spectroelectrochemical data given below.

### Spectroelectrochemical Results

All spectra were taken in the near-u.v. and visible regions of the spectrum (280-600 nm) at a scan rate of 20 spectra per second. A blank cell with an optically transparent electrode and sample solution was placed in the reference beam to subtract any absorbance not due to electrolysis products.

Two types of spectroelectrochemical experiments were performed. In one case, spectra of the electrode interface were taken during the oxidation while the potential was being scanned slowly (3 mV/sec). In the other case, spectra of the electrode interface were taken while the potential was stepped to various values along the oxidation wave up to solvent breakdown. In both types of experiments, the same absorbance peaks were observed which would seem to indicate that the reaction mechanisms are not time dependent with respect to the rate of applied potential change.

Typical voltammetric spectroelectrochemical results for 1,2-diaminobenzene are shown in Fig. 4. An absorbance peak at 460 nm appears at a potential of +0.25V, and a 360 nm absorbance peak appears at +0.30V. In this case it seems that we are observing two different species, an intermediate at 460 nm and the final product at 360 nm.

The voltammetric spectroelectrochemical results for 1,2-diaminobenzene in the presence of Ni(II) are shown in Fig. 5. An absorbance peak at 480 nm appears at +0.27V, and a 360 nm absorbance peak appears at

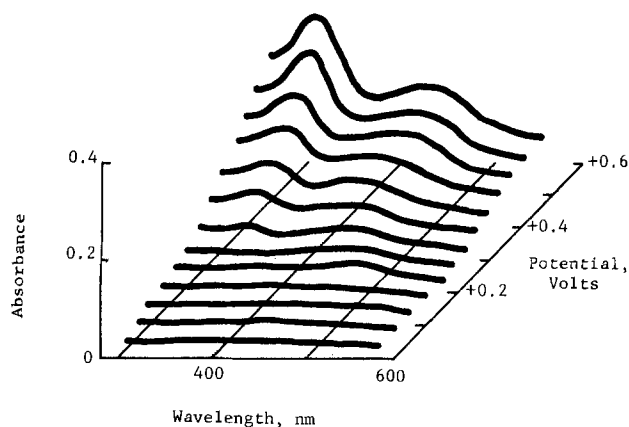


Fig. 4. Voltammetric spectroelectrochemical oxidation of 1,2-diaminobenzene.

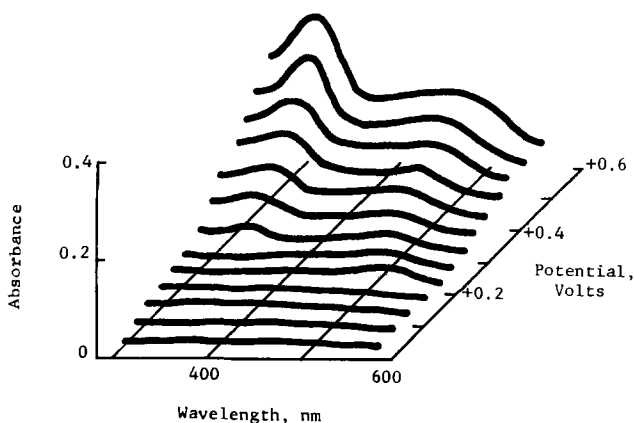


Fig. 5. Voltammetric spectroelectrochemical oxidation of 1,2-diaminobenzene in the presence of Ni(II).

+0.35V. Again, it appears that we are observing two different species.

In the potential step spectroelectrochemical experiments, the potential was stepped to the following points:  $E_{1/4}$  (+0.25V),  $E_{1/2}$  (+0.28V),  $E_{3/4}$  (+3.0V),  $E_p$  [+0.35V for 1,2-diaminobenzene alone and +0.33V for 1,2-diaminobenzene plus Ni(II)], +0.60V (plateau of the oxidation wave), +1.0V (almost to solvent breakdown). The electrochemical chronoamperometric behavior and the spectrophotometric behavior were monitored simultaneously. In these experiments it was found that there were significant differences in the rate and nature of the filming between 1,2-diaminobenzene alone and in the presence of Ni(II). With the oxidation of 1,2-diaminobenzene alone, filming occurred at all potential steps that were employed, but in the presence of Ni(II) no filming occurred at a potential less than +0.35V. The Cottrell behavior was plotted for all potential steps both with and without Ni(II) present and, as expected, diffusion-controlled Cottrell behavior was not observed (26).

Figure 6 shows the spectral behavior during the oxidation of 1,2-diaminobenzene with a potential step from 0V to  $E_p$  (+0.35V), which is also representative of the other potential steps. At all potential steps, an absorbance peak at 460 nm is initially formed, after which an absorbance peak at 360 nm grows until the electrode is completely insulated by the film.

The absorbance vs. time behavior for these two peaks for the  $E_p$  (+0.35V) step is shown in Fig. 7. The absorbance of the initial peak at 460 nm begins to level off after about 50 sec, while the absorbance at 360 nm is still growing after 100 sec. The electrode becomes insulated, and the absorbance peak at 360 nm stops growing after about 200 sec. No change was noticed in the spectrum on disconnecting the cell from the potentiostat or removing the solution from the cell and replacing it with distilled water.

The spectral behavior appears to indicate that the initial film formation (the 460 nm band) is a conducting organic film, and subsequent formation of a nonconducting film occurs on top of the conducting film, which eventually insulates the electrode. The absorbance peak at 360 nm corresponds to the nonconducting film product. An alternate, but less likely possibility is that the conducting film is transformed into the insulating film. This would necessitate a steady-state condition to explain the constant absorbance of the 460 nm peak after 50 sec. This steady-state condition seems unlikely with increasing insulation of the electrode.

Figures 8 and 9 show the spectral behavior during the oxidation of 1,2-diaminobenzene in the presence of Ni(II) with potential steps from 0V to  $E_p$  (+0.33V) and +1.0V, respectively. The  $E_p$  (+0.33V) potential step is representative of the  $E_{1/4}$  (+0.25V),  $E_{1/2}$

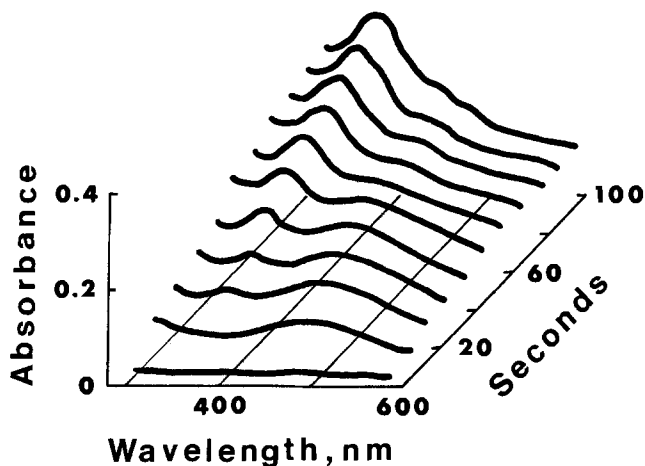


Fig. 6. Potential step ( $E_p$ ) spectroelectrochemical oxidation of 1,2-diaminobenzene.

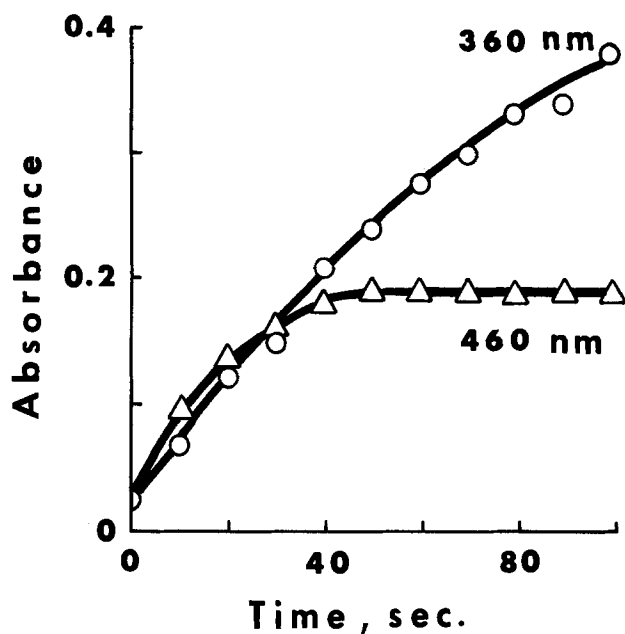


Fig. 7. Absorbance vs. time behavior for the  $E_p$  potential step spectroelectrochemical oxidation of 1,2-diaminobenzene.

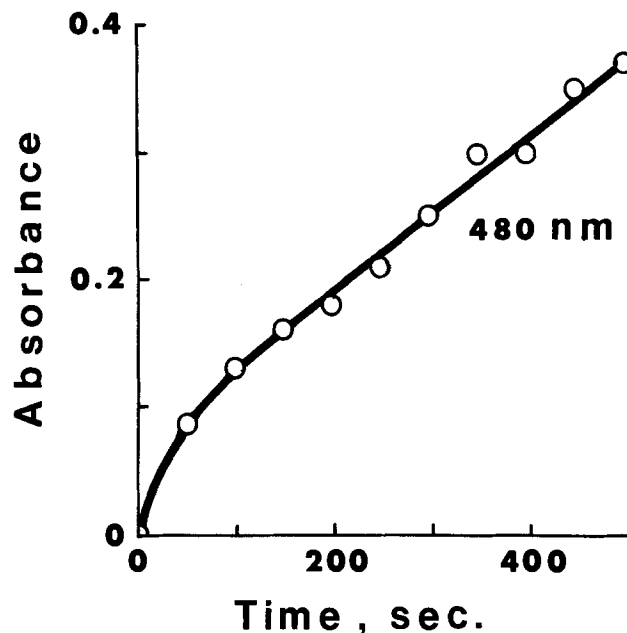


Fig. 10. Absorbance vs. time behavior for the  $E_p$  potential step spectroelectrochemical oxidation of 1,2-diaminobenzene in the presence of Ni(II).

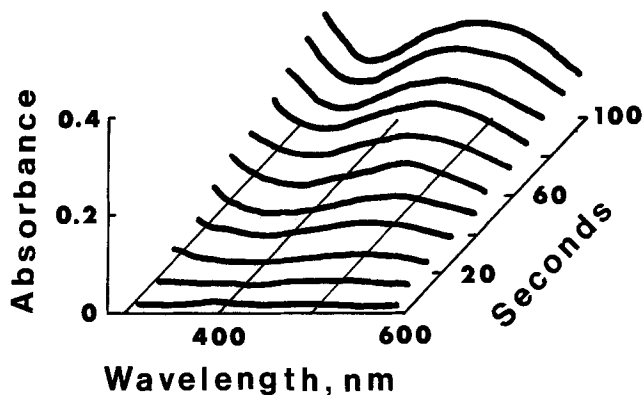


Fig. 8. Potential step ( $E_p$ ) spectroelectrochemical oxidation of 1,2-diaminobenzene in the presence of Ni(II).

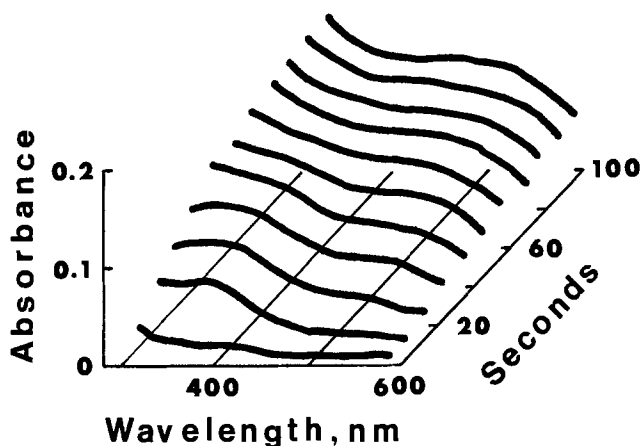


Fig. 9. Potential step (+1.0V) spectroelectrochemical oxidation of 1,2-diaminobenzene in the presence of Ni(II).

(+0.28V), and  $E_{3/4}$  (+0.30V) potential steps, and the +1.0V potential step is representative of the +0.6V potential step. At  $E_{1/4}$  (+0.25V),  $E_{1/2}$  (+0.28V),  $E_{3/4}$  (+0.30V), and  $E_p$  (+0.33V) potential steps, only one absorbance peak is evident, which occurs at 480 nm. The absorbance vs. time plot for this peak for the  $E_p$  (+0.33V) potential step is shown in Fig. 10. Note that the absorbance of this peak is still increasing after 500 sec with no signs of insulating filming occurring.

Similar behavior is observed at the lower potential steps, but when the magnitude of the potential step is increased a different reaction mechanism is observed. At +0.6 and +1.0V potential steps, only one absorbance peak is evident, but this peak occurs at 360 nm which is the same absorbance wavelength as the product formed in the oxidation of 1,2-diaminobenzene alone. The absorbance vs. time behavior for this peak for a +1.0V potential step is shown in Fig. 11. The behavior is similar for the +0.6V potential step. Note that this absorbance vs. time behavior is also similar to that obtained for the oxidation of 1,2-diaminobenzene, with the absorbance slowing significantly (but not leveling off) after about 200 sec and film formation eventually insulating the electrode.

Therefore, with Ni(II) present, it is evident that the mechanism and the products are potential dependent and, hence, may be governed by the potential-dependent rates of either the heterogeneous electron transfer or a surface chemical reaction. At lower potentials one obtains a product which does not film or insulate the electrode. At higher potentials one obtains a nonconducting film which insulates the electrode, and

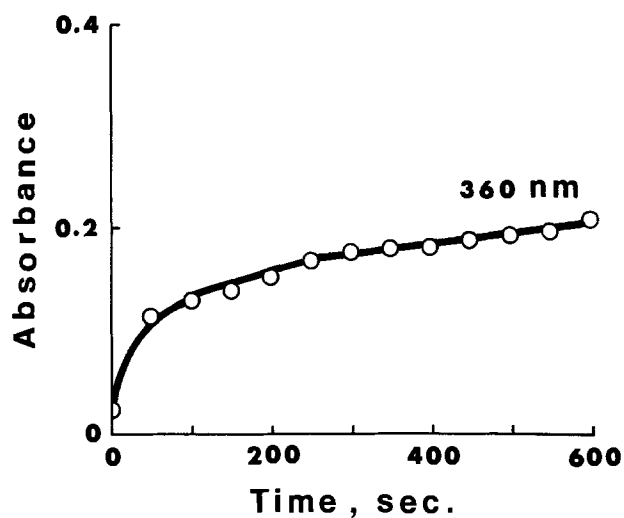


Fig. 11. Absorbance vs. time behavior for the +1.0V potential step spectroelectrochemical oxidation of 1,2-diaminobenzene in the presence of Ni(II).

is probably the same product that is formed without the presence of Ni(II), as the absorbance peak occurs at the same wavelength and the filming that occurs are identical.

The air oxidation product of 1,2-diaminobenzene alone and in the presence of Ni(II) has an absorbance peak at 415 nm. This absorbance peak is due to 3,5-dihydro-2-amino-3-imino-phenazine which is a tautomeric form of 2,3-diaminophenazine, which is the commonly accepted air oxidation product of 1,2-diaminobenzene (27, 28). This absorbance peak was not observed in any of the spectra due to the deaeration of the sample solution and maintenance of a nitrogen atmosphere over the solution during the experiment. Therefore, all the absorbance peaks observed in the spectra are due to electrochemical products or products formed in a direct follow-up chemical reaction to the electrolysis. Furthermore, this shows that the mechanisms and products of the electrochemical oxidations are totally different from those obtained by air oxidation.

Attempts were made to dissolve the films which insulated the electrode, and 22 different organic solvents were tried without success (18). Also, an attempt was made to determine the infrared spectra of the insulating films formed from the oxidation of 1,2-diaminobenzene alone and in the presence of Ni(II). The insulating films were formed on platinum optically transparent electrodes, using germanium as the substrate instead of quartz. No signal above the background was evident. This is probably due to the fact that extinction coefficients in the infrared region of the spectrum are generally less than those in the visible region of the spectrum. A literature survey on the spectra of the many oxidative polymerization products of 1,2-diaminobenzene did not reveal any which matched the u.v. spectrum of the insulating film (29-35).

It was noticed during the electrolysis of the 1,2-diaminobenzene in the presence of Ni(II) that a finely divided precipitate was formed near the electrode surface and fell to the bottom of the cell. This precipitate of soluble oxidation products appears to form via a polymerization reaction which takes place in the diffusion layer and not on the electrode surface. This is the final product of the nonfilming reaction which occurs at lower potentials. This product was filtered from the electrolysis solution, copiously washed with distilled water, and dried in a vacuum desiccator. It had a melting point of greater than 300°C, and was insoluble in the same 22 organic solvents that were tried on the insulating films (18).

An x-ray fluorescence analysis of the precipitation product showed the presence of two nickel peaks, a

principal emission line ( $K\alpha$ ) at 7.47 keV and a secondary line ( $K\beta_1$ ) at 8.26 keV, thereby, confirming the presence of nickel in the precipitation product.

A square planar Ni(II) (1,2-diaminobenzene)<sub>2</sub> complex is known where two 1,2-diaminobenzene molecules are complexed to Ni(II) as bidentate ligands (36, 37). However, this Ni(II) complex is not the same as the precipitation product that was obtained from electrolysis. The Ni(II) complex has absorbance peaks at 360 and 570 nm (36), and the infrared spectrum of the Ni(II) complex is different from the infrared spectrum of the electrolysis precipitation product (37).

A KBr pellet was made from the precipitation product and an infrared spectrum taken from 4000 to 200  $\text{cm}^{-1}$ , which is shown in Fig. 12. Not much structural information can be determined from the spectrum. The spectrum is made up of broad and diffuse bands with a large background. A band which is centered around 3200  $\text{cm}^{-1}$  is probably due to  $-\text{NH}_2$  stretching, a band at 1620  $\text{cm}^{-1}$  is due to N-H deformation of primary amines, a band at 1500  $\text{cm}^{-1}$  is due to aromatic C-C stretching, and a band at 755  $\text{cm}^{-1}$  is due to aromatic C-H bending. Thus, the product contains aromatic rings and amino groups, but no information concerning the nature of the polymeric linkages of the product can be determined. A C, H, N, and Ni elemental analysis of the precipitation product yielded the following results: C = 33.74%, H = 2.61%, N = 12.74%, and Ni = 21.87%. This elemental analysis does not match any of the simpler complexes of Ni(II) and 1,2-diaminobenzene, and it seems that the precipitation product is a more complex polymeric chelate. No polymeric chelates of Ni(II) and 1,2-diaminobenzene could be found in the literature with which to compare the above infrared spectrum and the elemental analysis.

### Conclusions

We were able to determine that the electrochemical oxidation mechanism of 1,2-diaminobenzene was neither time nor potential dependent in the context of the experiments employed. The reaction probably occurred with the initial formation of a nonconducting film which insulated the electrode. It would be attractive to speculate that the conductive organic film is formed by the polymerization of monocation radicals which are formed by the oxidation of the 1,2-diaminobenzene. Most organic electrochemical oxidations of this type form a monocation radical as the initial electrolysis product, and this product is then very often involved in a follow-up chemical reaction (38). The insulating film could then possibly be formed by the polymerization of the dication of the 1,2-diaminobenzene formed on disproportionation [this would require that the oxidation potentials for the cation radical and di-

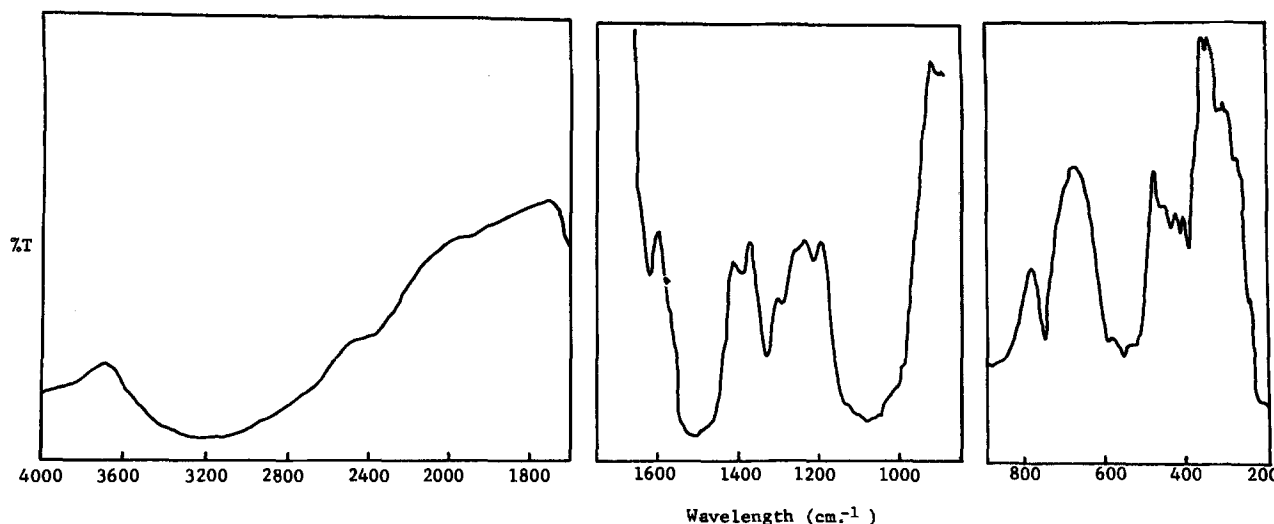


Fig. 12. Infrared spectrum (4000-200  $\text{cm}^{-1}$ ) of the nickel polymer precipitate. The sample was in the form of a KBr pellet

cation to be very close together (39)], or perhaps the monocation radical oxidizing at a conducting organic surface rather than the electrode surface yields a different product, the insulating film.

In the presence of Ni(II), the oxidation of 1,2-diaminobenzene was not time dependent with respect to rate of potential change, but was potential dependent. At lower potentials, the reaction produced a product which did not form a film but did eventually form a precipitate, and incorporated nickel in the structure. This product appears to have a relatively high molecular weight, because of the high melting point and its general insolubility in common organic solvents. At higher potentials, filming occurred, insulating the electrode. From the data available, it seems that this film is probably the same as the film formed without the presence of Ni(II). With the Ni(II) present, at lower potentials, the monocation radical formed by the oxidation of 1,2-diaminobenzene probably predominates, but at higher potentials the formation of the dication could predominate. At lower potentials the rate of the monocation polymerization on the electrode is slow compared to the rate of complexation with Ni(II) which forms a soluble intermediate product. This then polymerizes or aggregates and precipitates from solution. There was no evidence of the formation of a conducting organic film during the nickel polymer precipitation. At higher potentials the dication is probably preferentially formed, which then polymerizes on the electrode surface forming the insulating film over the electrode.

#### Acknowledgment

This research was supported in part by the National Science Foundation, Grant No. MPS 72-05014-A02. One of us (A.M.Y.) thanks the University of Cincinnati Research Council for travel funds to present this paper at the Toronto Electrochemical Society Meeting, May 1975.

Manuscript submitted Nov. 10, 1975; revised manuscript received May 15, 1976. This was Paper 393 presented at the Toronto, Canada, Meeting of the Society, May 11-16, 1975.

Any discussion of this paper will appear in a Discussion Section to be published in the June 1977 JOURNAL. All discussions for the June 1977 Discussion Section should be submitted by Feb. 1, 1977.

Publication costs of this article were assisted by the University of Cincinnati.

#### REFERENCES

- P. J. Elving and A. F. Krivis, *Anal. Chem.*, **30**, 1645 (1958).
- Ibid.*, 1648.
- A. Make and D. H. Geske, *J. Chem. Phys.*, **33**, 825 (1960).
- T. Kuwana, R. K. Darlington, and D. W. Leedy, *Anal. Chem.*, **36**, 2023 (1964).
- B. S. Pons and H. B. Mark, Jr., *ibid.*, **38**, 119 (1966).
- A. Prostack, H. B. Mark, Jr., and W. N. Hansen, *J. Phys. Chem.*, **72**, 2576 (1968).
- H. B. Mark, Jr. and F. C. Anson, *Anal. Chem.*, **35**, 722 (1963).
- K. B. Prater, *This Journal*, **120**, 356 (1973).
- S. S. Lord, Jr. and L. B. Rogers, *Anal. Chem.*, **26**, 284 (1954).
- R. E. Parker and R. N. Adams, *ibid.*, **28**, 828 (1956).
- R. Glicksman, *This Journal*, **108**, 1 (1961).
- V. D. Bezuglyi and Y. I. Beilis, *Zh. Obshch. Khim.*, **36**, 787 (1966).
- S. Wawzonek and T. W. McIntyre, *Electrochem. Technol.*, **114**, 1025 (1967).
- A. E. Lutskii, Y. I. Beilis, and V. I. Fedorchenko, *Zh. Obshch. Khim.*, **42**, 2535 (1972).
- Harrick Scientific Corporation, Ossining, New York.
- Data Sheet 5, Rapid Scanning Spectrophotometer, Harrick Scientific Corporation (1973).
- H. B. Mark, Jr., R. M. Wilson, T. L. Miller, T. V. Atkinson, A. M. Yacynych, and H. Woods, in "Information Chemistry; Computer Assisted Chemical Research Design," H. B. Mark, Jr. and S. Fujiwara, Editors, pp. 3-28, University of Tokyo Press, Tokyo (1975).
- A. M. Yacynych, Ph.D. Thesis, University of Cincinnati (1975).
- A. M. Yacynych and H. B. Mark, Jr., Submitted to *Chem. Instr.*
- W. R. Heineman and T. Kuwana, *Anal. Chem.*, **44**, 1972 (1972).
- R. N. Adams, "Electrochemistry at Solid Electrodes," pp. 206-208, Marcel Dekker, Inc., New York (1969).
- "Dictionary of Organic Compounds," Vol. 4, p. 2684, Oxford University Press, London (1965).
- J. H. Christie, G. Lauer, and R. A. Osteryoung, *J. Electroanal. Chem.*, **7**, 60 (1964).
- P. Delahay, "New Instrumental Methods in Electrochemistry," p. 132, Interscience Publishers, Inc., New York (1954).
- R. S. Nicholson and I. Shain, *Anal. Chem.*, **36**, 706 (1964).
- R. W. Murray and C. N. Reilley, "Electroanalytical Principles," pp. 2133-2137, Interscience Publishers, New York (1966).
- K. Wuthrich and S. Fallab, *Helv. Chim. Acta*, **47**, 1440 (1964).
- G. A. Swan and D. G. I. Felton, "The Chemistry of Heterocyclic Compounds, Phenazines," p. 11, Interscience Publishers, Inc., New York (1957).
- E. Tsuchida, *Asahi Garasu Kogyo Gijutsu Shoreikai Kenkyu Hokoku*, **15**, 537 (1969).
- J. K. Stille and E. L. Mainen, *Macromolecules*, **1**, 36 (1968).
- E. Tsuchida, M. Kaneko, and Y. Kurimura, *Makromol. Chem.*, **132**, 209 (1970).
- I. Bhatnagar and M. V. George, *J. Org. Chem.*, **33**, 2407 (1968).
- M. P. Terpugova, I. L. Kotlyarevskii, and E. K. Andrievskaya, *Izv. Akad. Nauk SSSR Ser. Khim.*, **4**, 713 (1966).
- V. G. Kostrovskii, E. D. Litman, A. I. Shjonko, V. G. Mazur, M. P. Terpugova, and I. L. Kothyarevskii, *Vysokomol. Soedin., Ser. A.*, **13**, 1721 (1971).
- Ya. M. Paushkin, O. Yu. Omarov, and V. I. Levashova, *Vysokomol. Soedin., Ser. B.*, **41**, 438 (1972).
- G. Maki, *J. Chem. Phys.*, **29**, 162 (1958).
- D. R. Marks, D. J. Phillips, and J. P. Fedfern, *J. Chem. Soc., A*, **64**, 2013 (1968).
- R. N. Adams, "Electrochemistry at Solid Electrodes," p. 305, Marcel Dekker, Inc., New York (1969).
- N. Winograd and T. Kuwana, *J. Am. Chem. Soc.*, **93**, 4343 (1971).

# The Anodic Oxidation of Platinum: Determining the Dependence of Current Density on Potential

J. L. Ord,\* D. J. DeSmet,<sup>\*1</sup> and M. A. Hopper<sup>\*2</sup>

Department of Physics, University of Waterloo, Waterloo, Ontario, Canada N2L 3G1

## ABSTRACT

The way in which current density depends on potential during the anodic oxidation of platinum in 0.1M H<sub>2</sub>SO<sub>4</sub> is studied using two different methods to determine values for the parameters in the relation  $i/i_0 = \exp((V - V^*)/V_0)$ . The first method determines values for the parameters from analysis of open-circuit transients, and correlates the  $V_0$  values with optical measurements of the thickness of the oxide film. The second method analyzes the dependence of potential on film thickness during galvanostatic oxidation to determine a second set of values for the parameters. This set differs significantly from the open-circuit set, and leads to a different model for the anodic oxidation process. The model based on open-circuit data appears to provide a more reasonable description of an anodic oxidation process controlled by the field in the oxide film. Reasons for the differences in the results are discussed, and the internal consistency of the methods is examined.

When platinum is oxidized anodically at constant current density, the three stages involved in the process show up clearly on a plot of potential *vs.* time. As the initial monolayer of oxide is formed,  $dV/dt$ , the rate of change of potential, decreases steadily from its initial double-layer charging value to the constant value it maintains during the second or layer-growth stage of oxidation. In the third stage,  $dV/dt$  again decreases as oxygen evolution competes with oxide formation and takes an increasing fraction of the current density. Our interest in this paper is in determining the dependence of current density on potential in the second stage where layer growth is the dominant process. In a previous paper (1) we argued that this stage of the anodic oxidation of platinum is limited by the electric field in the oxide film. Recent work from other laboratories (2-4) appears to support our conclusion that platinum undergoes field-limited oxidation in much the same way as does tantalum or niobium. Weaver surveyed the recent work in the field in his 1974 review of the electrochemical formation of thin oxide films on noble metals (5), and assessed the evidence for a model involving high field ion transport.

In this paper we direct our attention to the basic problem of inference involved in the determination of the dependence of current density on potential. The exponential dependence of current density,  $i$ , on potential,  $V$ , characteristic of an activation-controlled process can be written

$$i/i_0 = \exp((V - V^*)/V_0) \quad [1]$$

where  $V^*$  is the zero of overpotential,  $i_0$  is the exchange current density, and  $V_0$  is a Tafel slope expressed in terms of natural logarithms. Experiments usually are designed to determine values for the three parameters  $V^*$ ,  $i_0$ , and  $V_0$  under a variety of experimental conditions. For processes controlled by the overpotential,  $(V - V^*)$ , all three parameters are expected to have constant values, whereas processes controlled by the field in the film must have  $V_0$  proportional to the film thickness. Although all three parameters are required to specify completely the dependence of current density on potential, it is the behavior of the parameter  $V_0$  which distinguishes between field and overpotential control of the process. The parameter  $V^*$  identifies the potential at which oxidation commences.

\* Electrochemical Society Active Member.

<sup>1</sup> Present address: Department of Physics and Astronomy, The University of Alabama, University, Alabama 35486.

<sup>2</sup> Present address: Xerox Research Centre of Canada, Mississauga, Ontario, Canada L5L 1J9.

Key words: platinum, anodic oxidation, Tafel slope, ellipsometry.

Anodic oxidation is known to be a more complex process than the ideal activation-controlled process upon which Eq. [1] is based, and different approaches to the analysis of oxidation data may yield significant different values for the parameters  $V^*$ ,  $i_0$ , and  $V_0$  (6,7). Although the relative merits of the different approaches to data analysis can be debated at length, the ultimate choice between sets of parameter values is dictated by the answer to the question "which set leads to a more reasonable description of the behavior of the system?" Our aim in this paper is to show how one can go about attempting to answer this question for the anodic oxidation of platinum. We carry out an open-circuit transient analysis and a galvanostatic charging analysis on a common set of data. The two analyses give significantly different results, the results of the open-circuit analysis agreeing with our earlier work (1), and the results of the galvanostatic charging analysis agreeing with the work of Vetter and Schultze (2). After carrying out a detailed comparison of the results, we conclude that the parameter values from the open-circuit analysis provide the more reasonable description of the anodic behavior of platinum, and we offer an explanation of why this should be.

## Experimental

The optical measurements were made with a self-nulling ellipsometer which has been described in detail elsewhere (8). The instrument has a resolution of 0.01° in the settings of its polarizing prisms, and nulls both polarizer and analyzer approximately twice each second under the optical conditions encountered in this experiment. The standard deviation in the null readings is less than the resolution of the instrument, and some increase in resolution was obtained by averaging the data when the film thickness was not changing too rapidly. A helium-neon laser is used as the light source, and an angle of incidence of 60° is chosen to accommodate a cell made from a hollow equilateral glass prism. The cell is fitted with standard taper joints for mounting the electrode holder, platinum counter-electrode, mercurous sulfate reference electrode, and gas dispersion tube. The electrolyte, 0.1M H<sub>2</sub>SO<sub>4</sub>, was saturated with argon and measurements were made at room temperature, 23°C. Potentials are expressed relative to the normal hydrogen electrode.

The cylindrical single crystal sample of platinum used as the working electrode is clamped between Teflon washers in a glass electrode holder. A flat on one side of the cylinder is used for the optical measurements. A surface area of approximately 1.25 cm<sup>2</sup> is

exposed to the electrolyte in this configuration. The preparation of the surface of the sample is described in the next section.

The laboratory computer, a Hewlett-Packard 2114B, was programmed to carry out the experiments without operator intervention, recording the data on magnetic tape for recall by analysis programs written in BASIC. Both the electrochemical control circuitry and the circuitry which operates the ellipsometer are built into the multiplexed input-output interface of the computer. The computer reads the digital output from the ellipsometer directly, and uses digital-to-analog and analog-to-digital converters to control the current through the cell and read the electrode potential. A video display terminal and an X-Y point plotter are used extensively for graphical display during the performance of the experiment and the analysis of the data.

The experiments were performed under program control primarily to give the best optical data possible. It is difficult to obtain good optical data under conditions where the resolution of the instrument is 3% of the maximum range in the data, and variations in surface roughness or alignment can shift the data by an amount comparable to their range. Under program control, an entire series of experiments can be repeated precisely, and the reproducibility of the optical data can be given a very stringent test. Replication of the series of experiments also provides a stringent test of the estimates of the standard deviation in  $V_0$  values given by least squares analysis of open-circuit transients. Program control of both the performance of the experiment and the analysis of the data offers one further advantage which is qualitative rather than quantitative: it serves to emphasize the fact that there is nothing subjective about the differences between the results of the two approaches to data analysis.

Except for the open-circuit analysis program, the data reduction involves fitting straight lines only and requires no further comment. The basic equations governing open-circuit transients are obtained by writing the external current in the cell circuit,  $i_e$ , as the sum of  $i_c$ , the current charging the capacitance, and  $i$ , the Faradaic current through an element in parallel with the capacitance

$$i_c + i = i_e \quad [2]$$

With  $i_e = 0$ ,  $i_c$  written as  $C dV/dt$ , and  $i$  given by Eq. [1], Eq. [2] becomes

$$CdV/dt + i_0 \exp((V - V^*)/V_0) = 0 \quad [3]$$

This is the differential equation of an open-circuit transient. It can be integrated, assuming  $C$ ,  $i_0$ ,  $V_0$ , and  $V^*$  all constant, to give

$$V = V_1 - V_0 \ln(1 + t/\tau) \quad [4]$$

where the time constant  $\tau$  is defined by

$$\tau = CV_0/i_1 \quad [5]$$

and  $i_1$  and  $V_1$  are the values of  $i$  and  $V$  at  $t = 0$ . Analysis of open-circuit transients can be based on either Eq. [3] or [4]. In the analysis used here, the recorded values of  $V$  and  $t$  are fitted to Eq. [4] by varying  $\tau$  until a linear  $V$  vs.  $\ln(1 + t/\tau)$  least squares analysis gives the minimum deviation in  $V$ .

The open-circuit data are recorded in a form designed for this type of analysis. Although the potential is read at millisecond intervals, data are recorded only at specified potential increments. Hence the point density on the least squares line is uniform, the values of  $t$  are known exactly, and the standard deviation in  $V$  is approximately constant from point to point. Potentials are read using a 12-bit analog-to-digital converter with a one-half millivolt resolution. Eight successive conversions over a 200  $\mu$ sec interval are summed, then the least significant bit is dropped, leaving a 14-bit binary integer with a one-eighth millivolt resolution.

The standard deviation in  $V$  estimated from the open-circuit analysis is typically less than one-half millivolt, but it is systematic rather than random, indicating that second-order corrections to Eq. [1] are more significant than are random errors in  $V$ .

### Surface Preparation

Unless the surface of the platinum sample is prepared in a stable configuration, the polarizer and analyzer null settings for a nominally clean surface show a tendency to drift during a series of oxidation-reduction cycles. A typical set of optical data which exhibit this effect is shown in Fig. 1. Before the sample was inserted in the optical cell, its surface was roughened slightly by etching in aqua regia. The oxidation-reduction cycle consisted of oxidation at a current density of 20  $\mu$ A/cm<sup>2</sup> from 0.27 to 1.37V, followed by reduction at the same current density back to 0.27V. The optical data obtained on the bare surface at the beginning of the first cycle are plotted at A1 in the figure. As the oxidation proceeds, the data trace out the curve A1-B1. At point B1 the current is reversed, and the data proceed from B1 to a point slightly to the right of A1 in the figure. As the cycling continues, the data drift to the right in Fig. 1 along a zigzag path. The end points of cycles 4, 9, and 16 are shown in the figure along with the complete 27th oxidation cycle. Continued cycling beyond the 27th cycle produces a smaller and smaller drift in the optical data, indicating that an optically stable surface is being approached.

The change in the null settings represented by the displacements A1-B1 and A27-B27 in the figure can be attributed to the growth of an oxide film on the surface, whereas the displacement A1-A27 can be associated with a change in the roughness of the bare platinum surface. The film-growth displacements can be given a satisfactory (but not unique) analysis in terms of a change in the thickness of an oxide layer of constant refractive index, but there is no satisfactory technique for analyzing surface roughness. Experience shows that displacements to higher  $P$  values accompany decreases in surface roughness, and displacements to lower  $P$  values accompany roughening of the surface. Cycles of the type plotted in Fig. 1 can be used to reduce the roughness of a platinum surface provided care is taken to avoid gas evolution. If the cycling is continued, the surface eventually reaches a smooth, reasonably stable configuration, but the procedure is tedious even under program control.

There is a technique for preparing a smooth, stable platinum surface in one cycle. We discovered this technique by accident while studying the Kolbe reaction. Conway's extensive work on Kolbe synthesis [see for example Ref. (9) and (10)] led him to suggest (11) that we try using our self-nulling ellipsometer to detect the adsorption of organic molecules on both platinum and platinum oxide. The initial measurements appeared successful, for we found large optical changes associated with the Kolbe reaction, but further work showed that the optical changes were due to a re-

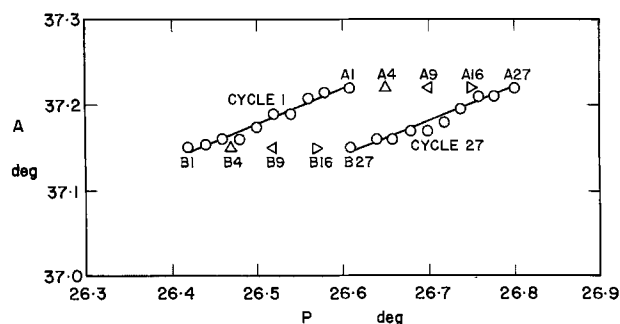


Fig. 1. Optical data obtained on cycling a roughened platinum electrode at 20  $\mu$ A/cm<sup>2</sup> between 0.27 and 1.37V in 0.1M H<sub>2</sub>SO<sub>4</sub>: A1-B1 first anodic cycle; A27-B27, twenty-seventh anodic cycle.

markable reduction in the roughness of the platinum surface during the Kolbe synthesis. When we concluded that the optical changes were not associated with the adsorption of organic molecules, we carried the work no further, but have continued to use this technique for preparing optical surfaces on platinum.

Optical data from a typical Kolbe cycle in 0.1M  $\text{H}_2\text{SO}_4 + 1.8\text{M CF}_3\text{COOH}$  are plotted in Fig. 2. In this instance, the surface of the platinum sample was roughened before the start of the experiment by evolving hydrogen on it rather than by etching it in aqua regia. The optical data trace out the curve A-B as an oxide film forms on the surface below the potential at which the Kolbe reaction begins. Once the Kolbe reaction begins, the optical data turn a sharp corner in the  $P$ - $A$  plot, and the polarizer readings start to increase. During Kolbe synthesis, the optical data trace out the curve B-C. As the experiment proceeded, the applied current density was increased from  $20 \mu\text{A}/\text{cm}^2$  at point B to  $1 \text{mA}/\text{cm}^2$  at point C. At C, the gas bubbles were shaken from the surface of the sample, and it was reduced at  $100 \mu\text{A}/\text{cm}^2$  until the oxide film was removed completely at point D. We interpret the net displacement of the optical data from A to C during the oxidation cycle as resulting from the superposition of a displacement from A to D due to reduction in surface roughness, and a displacement from D to C due to growth of an oxide film. We find that the sample can be rinsed and transferred to the optical cell with no deterioration in the condition of the surface provided that it is removed from the Kolbe cell with the oxide film on the surface, and the transfer is carried out reasonably quickly. The sample then remains smooth provided hydrogen is not evolved on its surface, and provided it is not exposed to the electrolyte for an extended period without an oxide film on the surface.

The surface roughness effects displayed graphically in Fig. 1 and 2 can equally well be expressed in terms of nominal values calculated for the refractive index of platinum at  $6328\text{\AA}$ . If point A in Fig. 2 is taken as characteristic of a clean platinum surface, a refractive index of 2.32-4.91i is obtained, whereas, if point D is taken, an index of 2.51-5.11i results. The latter value is undoubtedly better, because the calculation of the refractive index assumes that the metal surface is perfectly flat.

### Results

The data obtained during a typical oxidation-reduction cycle with no open-circuit transients are plotted in Fig. 3. The experiment begins with the potential of the working electrode set at 0.3V. At point A a constant oxidation current density, in this instance  $10 \mu\text{A}/\text{cm}^2$ , is applied to the working electrode, and its potential rises rapidly to B then more slowly to C as shown in the bottom portion of the figure. When the potential reaches 1.4V at point C, the applied current density is switched to  $-10 \mu\text{A}/\text{cm}^2$ , and the working electrode is reduced until the potential returns to 0.3V where it is held for 5 sec before the next cycle begins.

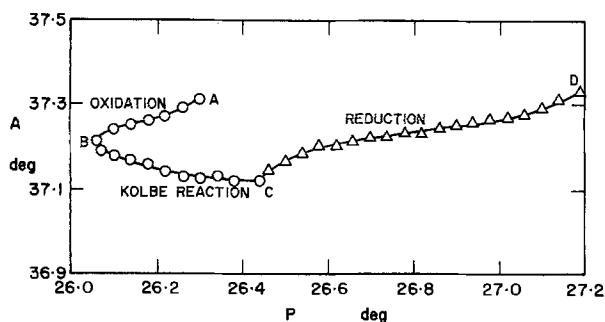


Fig. 2. Optical data obtained on a roughened platinum electrode during a Kolbe cycle in 0.1M  $\text{H}_2\text{SO}_4 + 1.8\text{M CF}_3\text{COOH}$ .

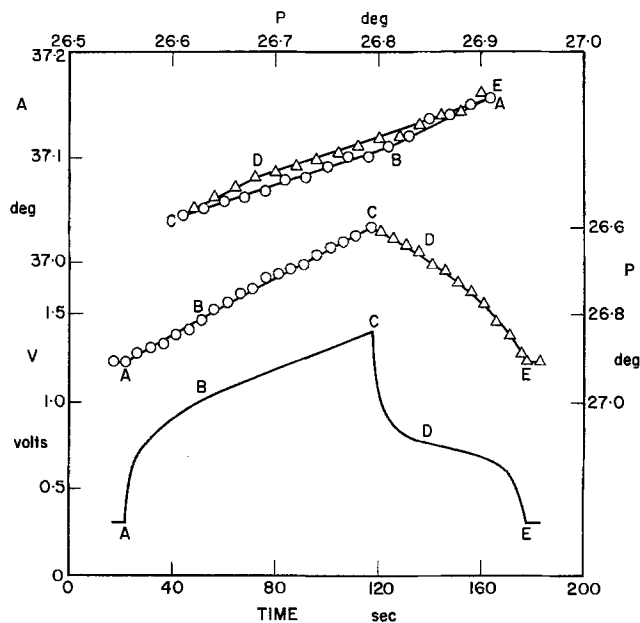


Fig. 3. Oxidation-reduction cycle at  $10 \mu\text{A}/\text{cm}^2$  for platinum in 0.1M  $\text{H}_2\text{SO}_4$ .

During the cycle, the null settings of the polarizer,  $P$ , and analyzer,  $A$ , are recorded at 1-sec intervals. These data are shown in plots of  $P$  vs. time in the center portion and  $P$  vs.  $A$  in the top portion of Fig. 3. Corresponding points labeled A, B, C, and D are identified on each of the three plots in the figure. Although the  $P$ - $A$  plot exhibits some fine structure, the dependence of  $P$  on  $A$  is essentially the linear relation expected for the growth of very thin films of constant refractive index. For such films there is also a linear relation between the film thickness and the  $P$  and  $A$  readings. Since  $P$  spans a greater range than  $A$ , we will use the change in  $P$  from its bare surface value as the optical measure of the average film thickness in our analysis of the data. Unique values for the thickness and refractive index of the oxide film cannot be determined from the analysis of our optical data, but the factor relating changes in film thickness to changes in  $P$  will be on the order of  $15 \text{\AA}/\text{degree}$  for reasonable values of the refractive index of the film.

The potential-time plot for an oxidation-reduction cycle with open-circuit transients is shown in Fig. 4. The experimental conditions are the same as for the data in Fig. 3, except that the computer is programmed to open the circuit at 100 mV intervals across the region from 0.9 to 1.4V. With a starting potential of 0.9V, as in Fig. 4, there will be six open-circuit transients during the cycle, and with a starting potential of 0.95V there will be five. Two sequences with 100 mV in-

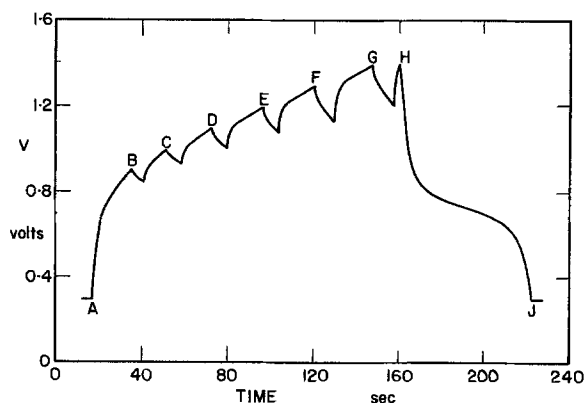


Fig. 4. Oxidation-reduction cycle at  $10 \mu\text{A}/\text{cm}^2$  with open-circuit transients for platinum in 0.1M  $\text{H}_2\text{SO}_4$ .



tervals are used rather than a single sequence with a 50 mV interval in order to allow the electrode more time to recover between transients. The detailed shape of the open-circuit transients cannot be shown accurately on the scale used in Fig. 4. The duration of a transient is equal to the time required for its slope to change by a factor of 16.

A series of cycles of the type plotted in Fig. 3 and 4 was carried out at oxidation current densities of 5, 10, 20, 40, and 80  $\mu\text{A}/\text{cm}^2$  both without open-circuit transients and with open-circuit transients at the two potential sequences. The complete series was then repeated under program control in order to test the reproducibility of the data. Throughout the experiment, the maximum offset noted in the optical data was 0.01 $\mu\text{A}/\text{cm}^2$ , and cycles with and without open-circuit transients were found to give indistinguishable optical data.

During an experiment of this kind, more data are recorded than can be handled conveniently. (Listing the data on the Teletype requires a full day.) We obtain a manageable set of 55 data points for use in further analysis if we select only the data recorded at the 11 open-circuit potentials for each of the 5 oxidation current densities. In order to free the laboratory computer for other experiments a Hewlett-Packard 9830 BASIC calculator was used to analyze the reduced data set. The values of  $P$ ,  $V_o$ , and  $1/C$  (calculated using Eq. [5]) were entered as 5 by 11 matrices with subscripts specifying current density and potential. The data were stored on the calculator tape cassette for least squares analysis and plotting programs. The remaining figures in the paper are tracings of graphs produced on the calculator plotter.

The analysis of open-circuit data involves a number of steps: first the transients are analyzed to determine the values of  $V_o$  and  $\tau$  (or  $1/C$ ), then the dependence of  $V_o$  on  $V_1$  at constant  $i_1$  is used to determine values for  $V^*$  and  $i_o$ , and finally the optical data are used to relate the  $V_o$  values to film thickness. In addition, the dependence of  $1/C$  upon film thickness can be investigated, but a simple relation is not expected in the case of platinum (1). In Fig. 5,  $V_o$  is plotted as a function of  $V_1$  for each of the 5 values of  $i_1$ , and in Fig. 6,  $V_o$  is plotted as a function of  $P$  for all values of  $i_1$  except 5  $\mu\text{A}/\text{cm}^2$ . One must be careful not to interpret Fig. 5 as expressing a dependence of  $V_o$  on  $V$  which can be substituted back into Eq. [1] to give a modified relation between  $i$  and  $V$ . As Fig. 6 clearly shows, the variations in  $V_o$  are due to the variations in film thickness which

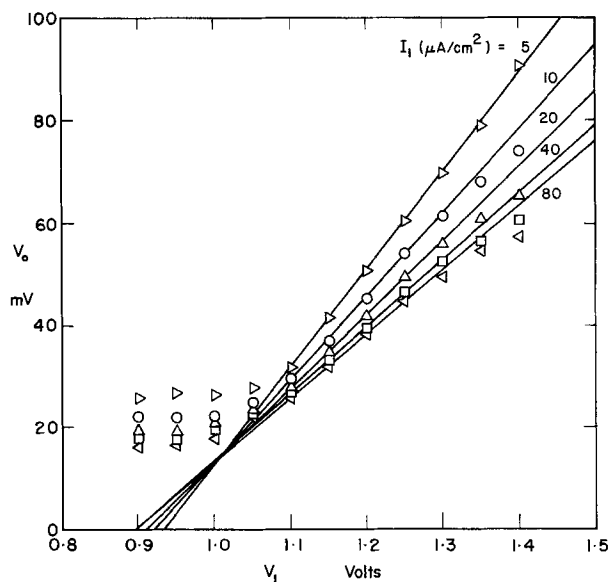


Fig. 5. Tafel slopes from open-circuit analysis vs. initial potential for oxidation current densities from 5 to 80  $\mu\text{A}/\text{cm}^2$ . The fitting region for the lines is from  $V_1$  equals 1.10-1.25V.

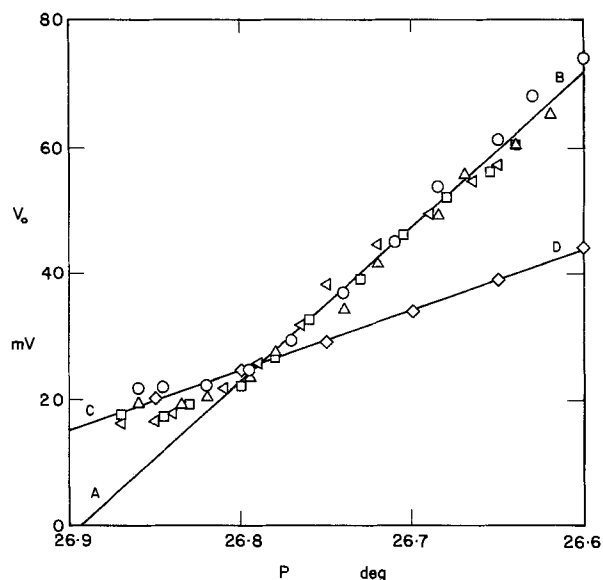


Fig. 6. Tafel slopes from open-circuit analysis vs. polarizer null setting for oxidation current densities from 10 to 80  $\mu\text{A}/\text{cm}^2$ . Oxidation current density is identified by plotting symbol as in Fig. 5. Line A-B is fitted to the data over the range from  $V_1$  equals 1.05-1.40V. Line C-D is fitted to the six data points plotted as diamonds which come from the galvanostatic charging analysis in Fig. 9.

accompany changes in  $V_1$  under our experimental conditions.

It is not possible to determine both  $V^*$  and  $i_o$  from the values of  $i_1$ ,  $V_1$ , and  $V_o$  for any one transient. If, however, a set of transients with a common value of  $i_1$  have  $V_o$  values which vary linearly with  $V_1$ , then we can find values for  $V^*$  and  $i_o$ , which are common to all transients in the set. If  $S$  is the slope  $dV_o/dV_1$ , then  $i_o$  is equal to  $i_1/\exp(1/S)$ , and  $V^*$  is given directly by the intercept of the line on the  $V_1$  axis. The lines in Fig. 5 are least squares fits to the  $V_o$  data at each  $i_1$  over the potential range from 1.1 to 1.25V. Below 1.1V the  $V_o$  data show the leveling expected for a field-limited process below monolayer coverage. Above 1.25V at the higher oxidation current densities, the data curve away from the linear relation predicted by elementary models of field-limited processes. The values of  $i_o$  and  $V^*$  determined from the least squares lines, in order of increasing  $i_1$ , are  $i_o$  equals 0.026, 0.022, 0.020, 0.019, and 0.028  $\mu\text{A}/\text{cm}^2$ , and  $V^*$  equals 0.934, 0.921, 0.911, 0.897, and 0.897V.

For  $i_1$  values from 10 to 80  $\mu\text{A}/\text{cm}^2$  all the  $V_o$  data fall on one line when plotted in Fig. 6 as a function of  $P$ . The expected deviation below monolayer coverage is still present, but there is no deviation corresponding to the curvature noted in Fig. 5 at higher  $V_1$ 's and  $i_1$ 's. A least squares line fitted to data with  $V_1 > 1.05$ V intersects the  $P$  axis at 26.89 degrees, and has a slope of 0.245V/degree. Average  $V^*$  and  $i_o$  values for the data falling on this line are  $V^* = 0.907$ V and  $i_o = 0.0225$   $\mu\text{A}/\text{cm}^2$ . The data for  $i_1 = 5$   $\mu\text{A}/\text{cm}^2$ , omitted from the figure for clarity, fall on a line of slightly (but significantly) steeper slope. This may be taken as indicating that all of the current density is not field-controlled for transients in which the current density ranges from 5  $\mu\text{A}/\text{cm}^2$  down to 5/16  $\mu\text{A}/\text{cm}^2$ . In order to make it easier to compare results, we have plotted the  $V_o$  values from galvanostatic charging analysis in Fig. 6 also.

The open-circuit analysis also provides values for the reciprocal capacitance, and these are plotted in Fig. 7 as a function of  $P$ . The reciprocal capacitance is not simply related to film thickness. It approximately doubles during monolayer coverage, then increases by

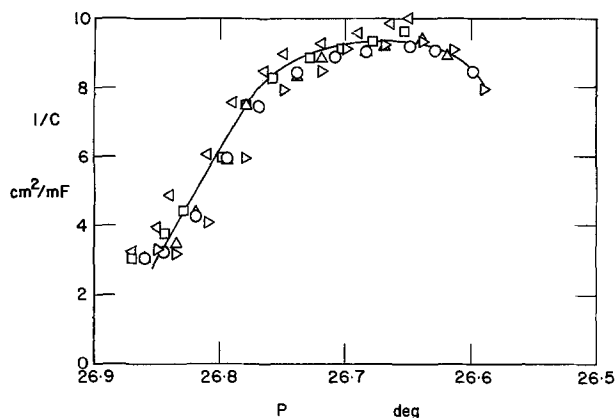


Fig. 7. Reciprocal capacitance from open-circuit analysis as a function of polarizer null setting. Oxidation current density is identified by plotting symbol as in Fig. 5.

only about a further 50% during film growth before leveling off and even dipping slightly.

This completes the reduction of the open-circuit transient data. We will now perform a second analysis of the data following an approach which does not use the open-circuit parameters  $V_0$  and  $\tau$ . This approach is usually based on analysis of the potential of the working electrode as a function of the charge accumulated at it for a set of constant oxidation current densities. In systems where the anodic oxidation process operates at nearly 100% efficiency, the charge accumulated on unit area of the working electrode is equated simply to the product of the oxidation current density and the time required to reach the potential in question. If there is reason to believe the reduction process to be more nearly 100% efficient, then the charge required to reduce the oxide is used instead. We prefer to use optical measurements of the thickness of the oxide film instead of charge measurements in our analysis, but we will refer to the analysis as galvanostatic charging analysis.

The data reduction begins with a plot of potential as a function of  $P$  at each of the 5 oxidation current densities. Our best such data, the set of 55 data points recorded at the initial potentials of the open-circuit transients, are plotted in Fig. 8. No following speed corrections need be applied to these data even at our

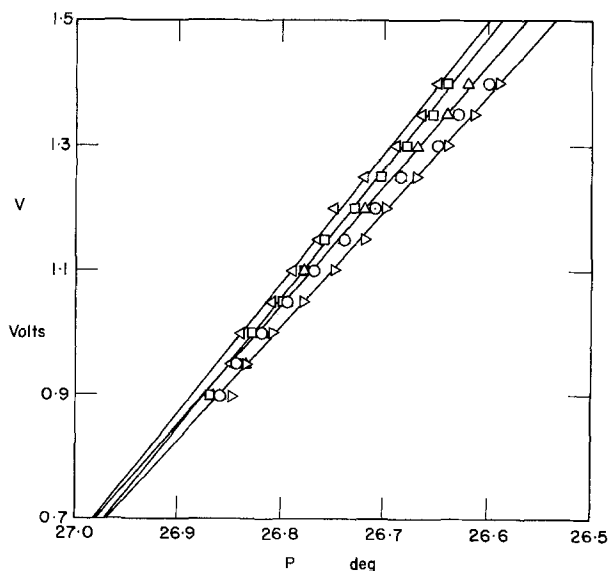


Fig. 8. Potential vs. polarizer null setting for galvanostatic charging at current densities from 5 to 80  $\mu\text{A}/\text{cm}^2$ . Current density is identified by plotting symbol as in Fig. 5. The lines are fitted over the potential range from 1.05 to 1.40V. The line fitted to the 10  $\mu\text{A}/\text{cm}^2$  data is not shown.

highest oxidation current density because the ellipsometer has time to reach a proper null while the circuit is open. For any particular value of  $i_1$ , the  $V_1$  data increase linearly with decreasing  $P$  at a slope which depends on the value of  $i_1$ . The  $V_1$ - $P$  slope gets steeper as the values of  $i_1$  get larger. The lines in the figure were fitted to the data over the 1.05-1.4V region using least squares. For clarity, the line for the  $i_1 = 10 \mu\text{A}/\text{cm}^2$  data is not shown in the figure because it obscures the trend illustrated by the other four lines.

Two techniques can be used for further reduction of the data in Fig. 8. Although they appear to be different, they are equivalent when applied to ideal data. In the first, plots of  $\log(i)$  vs.  $V$  are constructed for a set of different film thicknesses. Values of  $V^*$ ,  $i_0$ , and  $V_0$  as a function of film thickness can be determined directly from this plot. This technique, used widely in electrochemistry, is analogous to the technique used by Vetter and Schultze (2). In the second technique, used commonly in studies of the anodic oxidation of valve metals,  $\log(i)$  is plotted vs. the potential-film thickness slope. If the overpotential appears across the oxide film, this slope is equal to the field in the oxide film, and the plot directly shows the dependence of the current density on the electric field in the film.

In order to apply the first technique to the reduction of the data in Fig. 8, one draws lines perpendicular to the  $P$  axis at  $0.05^\circ$  increments between  $26.85^\circ$  and  $26.60^\circ$ . The intersections of these lines with the five least squares lines are then plotted vs.  $\log(i_1)$  to give current-potential characteristics at six different film thicknesses. This plot is shown in Fig. 9. The  $i$ - $V$  characteristics all show linear dependence of  $\log(i)$  upon  $V$  with the 10  $\mu\text{A}/\text{cm}^2$  points deviating significantly from the lines. If the characteristics have common values of  $i_0$  and  $V^*$ , lines fitted to the data in Fig. 9 should have a common intersection at the point where  $i$  equals  $i_0$  and  $V$  equals  $V^*$ . Least squares lines fitted to all but the 10  $\mu\text{A}/\text{cm}^2$  data do intersect at approximately the same point. Values of  $2.23 \times 10^{-8} \mu\text{A}/\text{cm}^2$  for  $i_0$ , and 0.539V for  $V^*$  are obtained by averaging the coordinates of the intersections of the 15 pairs of lines. The average  $i_0$  and  $V^*$  values from open-circuit analysis are shown in Fig. 9 for comparison purposes. The slopes of the lines in Fig. 9 give values for  $V_0$  as

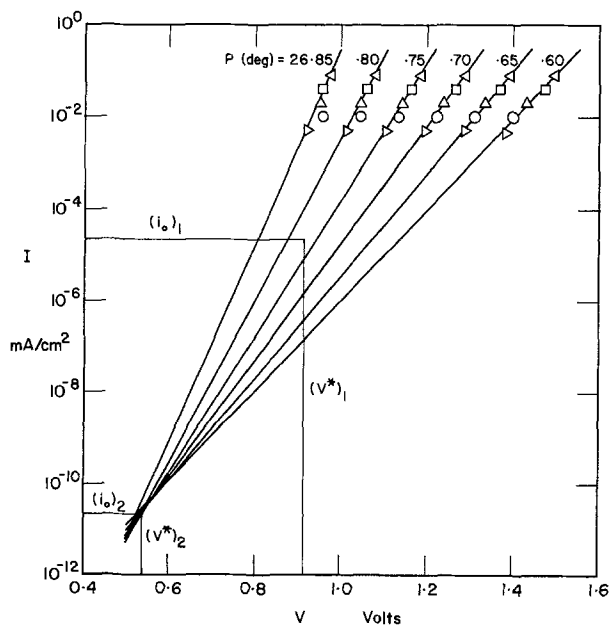


Fig. 9. Log current density vs. potential characteristics derived from the data in Fig. 8 for six polarizer null settings. The fitted lines exclude the 10  $\mu\text{A}/\text{cm}^2$  data. Values for the zero of overpotential,  $(V^*)_2$ , and the exchange current density,  $(i_0)_2$ , are given by the mean intersection of the fitted lines. The values from open-circuit analysis,  $(V^*)_1$  and  $(i_0)_1$ , are shown for comparison.

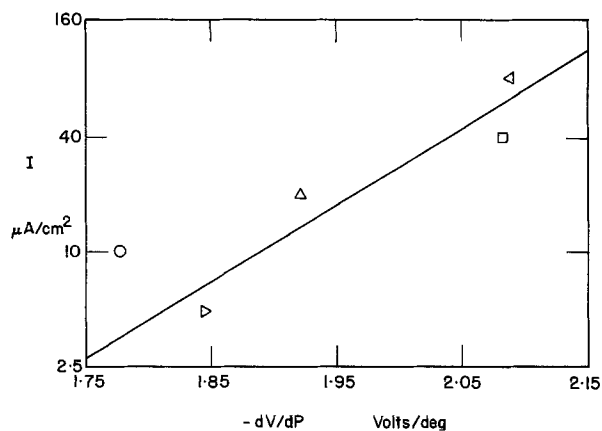


Fig. 10. Log current density vs. charging-curve slope from Fig. 8. The fitted line excludes the  $10 \mu\text{A}/\text{cm}^2$  data.

a function of  $P$ . These  $V_0$  values are plotted vs.  $P$  along with the open-circuit data in Fig. 6. A linear dependence of  $V_0$  and  $P$  is found with a  $P$  intercept at  $27.06^\circ$  and a slope of magnitude  $0.095 \text{ V}/\text{degree}$ .

The second technique for reducing the data in Fig. 8 is shown in Fig. 10. In this figure,  $\log(i)$  is plotted vs. the slope of the  $V$ - $P$  curve which is in turn proportional to the field in the film. The data show considerable scatter, but can be fitted reasonably well by a least squares line if the  $10 \mu\text{A}/\text{cm}^2$  data are ignored. If again  $i_0$  is assumed to have a common value for all of the points plotted, its value can be found by extrapolating the line back to the point where  $dV/dP$  equals zero. This extrapolation gives a value for  $i_0$  of  $2.6 \times 10^{-7} \mu\text{A}/\text{cm}^2$ . This is an order of magnitude greater than the value determined by the technique illustrated in Fig. 9, but it is still 5 orders of magnitude smaller than the open-circuit value for  $i_0$ .

### Discussion

The dependence of the values of  $i_0$ ,  $V_0$ , and  $V^*$  on the method of data analysis creates considerable confusion, and raises such questions as "how can this happen?" and "which method is correct?" The answers to these questions, although straightforward, require some discussion.

The basic reason for the differences between the parameter values may be stated simply: a three parameter equation such as Eq. [1] is inadequate to describe the process. In any method of data analysis, assumptions are made concerning what varies and what is constant under a particular set of experimental conditions. These assumptions, based on an idealized model of the process under study, are often unstated, and are tested only rarely in the experiment. The two different approaches we have taken to the data analysis, although both based on the same idealized field-limited model of the oxidation process, apply the assumptions of the model to different sets of experimental conditions. The analysis of open-circuit transients requires only that the parameters be well-behaved over individual open-circuit transients, whereas galvanostatic charging analysis requires that they be well-behaved over the entire set of charging experiments.

The question as to which method is correct has no answer. Both methods yield parameters which fit four out of the five sets of the data, so no distinction is possible on that basis. We prefer, for a number of reasons, to base analysis on the open-circuit transient data, but we do not wish to argue these reasons at this point. We propose to look instead at the models constructed from the results of the analyses to see which appears to be a more reasonable first-order description of the oxidation process.

Some aspects of this problem are not new. The case for applying open-circuit transient analysis to the anodic oxidation of tantalum has been argued in the

literature (7) with little apparent impact. In many respects, the anodic oxidation of tantalum and platinum are remarkably similar. In both systems higher values for  $i_0$  and  $V_0$  are obtained from open-circuit transients than from galvanostatic charging curves. The differences are significant, involving factors of  $10^6$  in  $i_0$  for platinum,  $10^8$  in  $i_0$  for tantalum, and 2.5 in the relation between  $V_0$  and film thickness for both. As a consequence, models of the oxidation process which are based on open-circuit transient data involve significantly lower values of the activation energy and valence-jump distance product than do models based on galvanostatic charging data. Since the present state of the theory of anodic oxidation does not make it very clear what values for these parameters should be considered reasonable, there is little to be gained from further discussion of these aspects of the problem.

Although tantalum tends to be easier to study than platinum due to the much wider range of oxide film thickness available experimentally, the platinum system is far superior for a study of the zero points on the thickness and potential scales. Looking first at the zero of overpotential, we see a very significant difference between the open-circuit transient result,  $V^* = 0.907\text{V}$ , and the galvanostatic charging result,  $V^* = 0.539\text{V}$ . Quite different models of the oxidation process result from the two  $V^*$  values. As can be seen in Fig. 3,  $V^* = 0.907\text{V}$  lies above the reduction plateau and below the linear oxidation region, whereas  $V^* = 0.539\text{V}$  lies below both the linear oxidation region and the reduction plateau. If one regards oxidation and reduction as reverse direction of the same reaction, then one would expect the zero of overpotential for oxidation to lie between the linear oxidation region and the reduction plateau. If, on the other hand, one regards oxidation and reduction as two different reactions with different zeroes of overpotential then  $V^*$  for oxidation could lie below the reduction plateau. In this case, the over-all reaction would have to be treated in much the same way as corrosion processes are treated.

We regard oxidation and reduction as reverse directions of essentially the same reaction, and hence we consider the  $V^*$  value of  $0.907\text{V}$  resulting from the open-circuit transient analysis to be reasonable, and the  $V^*$  value of  $0.539\text{V}$  resulting from galvanostatic charging analysis to be unreasonable. The subjective nature of this judgment is underscored by the fact that Vetter and Schultze (2) found a  $V^*$  value of  $0.530\text{V}$  in  $0.5\text{M H}_2\text{SO}_4$  from analysis of galvanostatic pulse measurements, and constructed what they apparently feel is a reasonable oxidation model using this value. We leave it to the reader to reach his own conclusion as to what is a reasonable value for  $V^*$ . We would like to emphasize that our galvanostatic charging analysis, although based on different measured quantities, gives parameter values which agree well with those of Vetter and Schultze. Our only point of difference concerns whether galvanostatic charging analysis gives results which lead to a reasonable model of the oxidation process.

Further information can be obtained by comparing the zero points on the thickness scale obtained from the two analyses. A high field model predicts proportionality between  $V_0$  and film thickness, hence the  $V_0$  data should reasonably be expected to extrapolate to zero at the point where the film thickness is zero. The extrapolation of the open-circuit  $V_0$  values in Fig. 6 intersects the axis  $0.02^\circ$  lower in  $P$  than the nominal bare surface point. The agreement with the model prediction is close, and there is some evidence that the  $0.02^\circ$  offset is associated with an optical change which precedes oxide film formation. The galvanostatic charging  $V_0$  values in Fig. 6 extrapolate to intersect the axis at a point which is  $0.15^\circ$  higher in  $P$  than the nominal bare surface point. We can find no way to reconcile an offset of this magnitude and in this direction with the proportionality between  $V_0$  and film thickness predicted by the model. Again we conclude that the open-

circuit analysis leads to a more reasonable model for the oxidation process than does the galvanostatic charging analysis.

At this point in the discussion, we doubt that many readers, even among those who find themselves agreeing with our view of what is reasonable, are particularly happy about basing oxidation models on parameters which can only be obtained from the analysis of open-circuit transients. Open-circuit transients are not widely used in oxidation studies, and it is not likely that they ever will be used as widely as galvanostatic charging measurements. The point we wish to make is not that there is anything wrong with galvanostatic charging measurements, but that unreasonable conclusions can result from charging analysis if the assumptions implicit in the usual treatment of the data are not valid.

We can illustrate this point by considering carefully the steps involved in determining  $V^*$  from the data in Fig. 8. In the standard analysis,  $V^*$  is the potential at which all of the  $V$ - $P$  lines should intersect. For the data in the figure, this point is rather poorly defined because the lines have slopes which differ little from each other. The intersection of one pair of lines appears in the figure at 0.914V, and the other five intersections occur off-scale to the lower left at 0.653, 0.651, 0.485, 0.267, and -7.119V. This last value, from the intersection of the 40 and 80  $\mu\text{A}/\text{cm}^2$  data lines, makes any attempt to average the data not very meaningful, but the median range, 0.485-0.651V does bracket the 0.539V value determined in Fig. 9. The techniques illustrated in Fig. 9 and 10 both use an additional stage of least squares fitting to smooth the data and improve the estimate of  $V^*$ . This is a reasonable procedure provided the problem is purely the statistical one of dealing with random errors. Unfortunately, the narrow range in the variation of the slopes of the lines in Fig. 8 makes it possible for second-order corrections to Eq. [1] to invalidate the standard approach to charging analysis. One example of such a correction would be a variation of  $i_0$  brought about by a change in the concentration of charge carriers at the activation barrier.

One way of determining the validity of charging analysis is to test its internal consistency. Comparison of the results of the analyses illustrated in Fig. 9 and 10 serves only as a test of the consistency of the statistical treatment of the second-order differences, not as a test of the basic assumptions of the analysis. We can test internal consistency by returning to the problem of determining  $V^*$  from the data in Fig. 8 and applying a method which does not involve second-order differences. For a field-controlled process,  $V^*$  is the potential coordinate at the point where the film thickness is zero on the lines in Fig. 8. If we take the film thickness to be zero at  $P = 26.91^\circ$ , we obtain values

for  $V^*$  of 0.807, 0.847, 0.833, 0.826, and 0.849V from the five sets of data in the figure. The average value obtained by this method, 0.833V, shows charging analysis to be internally inconsistent, and provides a further reason for our preference for open-circuit transients. If we take  $V^*$  to be 0.833V rather than 0.539V, we get closer agreement with the open-circuit value of 0.907V, but we are left with no obvious choice of a method to determine values for  $i_0$  and  $V_0$  from the charging data.

The discussion to this point has dealt mainly with determining the parameters  $i_0$ ,  $V_0$ , and  $V^*$  whereas our earlier work (1) dealt mainly with assessing the evidence for field control of the process. One may well ask whether the data presented in this paper strengthen or weaken our earlier conclusion that the field in the film controls the anodic oxidation process above monolayer thickness. We view the data presented in Fig. 6 as strengthening the case for field control. The  $V_0$  data show a proportionality to film thickness even in a region where the linear dependence of  $V_0$  on  $V_1$  no longer holds. From this we conclude that control of the process by the field in the film extends beyond the region of validity of elementary high field model in which  $i_0$  is considered constant.

### Acknowledgment

This work received support from the National Research Council of Canada under Grant No. A-1151.

Manuscript submitted Dec. 29, 1975; revised manuscript received May 10, 1976.

Any discussion of this paper will appear in a Discussion Section to be published in the June 1977 JOURNAL. All discussions for the June 1977 Discussion Section should be submitted by Feb. 1, 1977.

Publication costs of this article were assisted by the University of Waterloo.

### REFERENCES

1. J. L. Ord and F. C. Ho, *This Journal*, **118**, 46 (1971).
2. K. J. Vetter and J. W. Schultze, *J. Electroanal. Chem.*, **34** 141 (1972).
3. A. Damjanovic, A. T. Ward, B. Ulrick, and M. O'Jea, *This Journal*, **122**, 471 (1975).
4. L. B. Harris and A. Damjanovic, *ibid.*, **122**, 593 (1975).
5. M. J. Weaver, *J. Electroanal. Chem. Interfacial Electrochem.*, **51**, 231 (1974).
6. J. L. Ord, *This Journal*, **113**, 213 (1966).
7. J. L. Ord and D. J. DeSmet, *ibid.*, **116**, 762 (1969).
8. J. L. Ord, *Surf. Sci.*, **16**, 155 (1969).
9. A. K. Vijh and B. E. Conway, *Z. Anal. Chem.*, **224**, 160 (1967).
10. B. E. Conway and A. K. Vijh, *J. Phys. Chem.*, **71**, 3637 (1967).
11. B. E. Conway, Private communication.

# A New Capillary-Type Closed Viscometer for Molten Salt Research

N. van Os<sup>1</sup> and J. A. A. Ketelaar\*

Laboratory for Electrochemistry, University of Amsterdam, Amsterdam, The Netherlands

## ABSTRACT

A new capillary-type closed viscometer is described that can be used for many kinds of liquids. The viscometer is of simple design, incorporating a transparent measuring section and a suspended level enabling a flow of liquid under a constant mean hydrostatic head, the value of which is not affected by the total volume of liquid in the instrument. The viscometer is especially suitable for precise measurements with liquids having high vapor pressures, strongly corrosive properties, or showing chemical reactions with the atmosphere. As the viscometer has been used in molten salt research, a short description of the high temperature furnace, which involves an automatic optoelectronic device for recording the efflux time of the liquid, is also given. After a series of calibration experiments with molten  $\text{KNO}_3$ , the viscosity of molten  $\text{CdCl}_2$  was determined in the temperature range  $590^\circ\text{--}800^\circ\text{C}$ . Experimental results are given and compared with literature data.

## Construction and Working Principle of the Viscometer

In the literature, several closed capillary viscometers have been described which are useful for highly reactive and/or corrosive liquids or for liquids having appreciable vapor pressures, *e.g.*, for many molten salts. In some of these designs the capillary is enclosed in an outer vessel into which a submerged discharge from the capillary takes place (1-3).

A property which these instruments have in common is the application of an overflow adjustment device to ensure a constant working volume. As Greenwood (1) has already pointed out, surface tension effects may cause buildup in such an overflow, the result being that the bottom level of the hydrostatic head fluctuates and cannot be kept constant. Disadvantages of the viscometer described in (3) are its mechanical vulnerability and the fact that it is difficult to operate.

A second class of closed viscometers is patterned after Ostwald's design (4-7). Measurements over a wide range of temperatures are not so easy with some of these instruments (4-6), because they are charged with a fixed volume of liquid; furthermore, rather complicated techniques have to be applied for returning the liquid in order to make repeated measurement possible.

The Ostwald viscometer described by Timidei, Ledermann, and Janz (7) incorporates an overflow which ensures automatic adjustment of the working volume and at the same time reduces possible surface tension effects. Although this instrument has been used successfully in molten salt research, the design is more fragile and bulky.

Capillary viscometers applying suspended levels have been known since Ubbelohde (8), but so far most of these viscometers have been of the "open type," having a direct connection to the atmosphere or some pressurizing system. One exception is the viscometer described recently by Kang *et al.* (9), an instrument of the closed capillary type utilizing a suspended level. It has been used successfully in the measurement of the viscosity of a high vapor pressure organic electrolyte. Its design and construction seem rather delicate though, because of the side tube that is used for pressure equalization and because of the incorporation of an electrode system in the viscometer's tiny upper bulb.

The viscometer to be described in this article ensures automatic adjustment of the working volume by the

application of a suspended level type of outlet, thereby abandoning the overflow construction, while the containment of the viscometer within one cylindrical tube adds considerable mechanical strength to the design.

Figure 1 shows the new viscometer, fitted with the filling assembly which is used especially for salts and other liquefiable solids. For temperatures below  $500^\circ\text{C}$ , the construction material can be Pyrex; for higher temperatures quartz glass can be used.

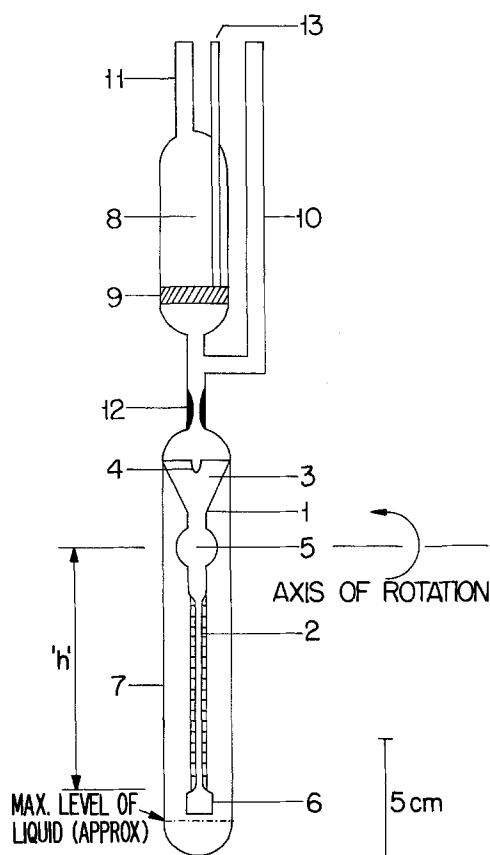


Fig. 1. Viscometer fitted with filling assembly. 1, Measuring tube; 2, capillary (diameter 0.45 mm, length 11 cm); 3, funnel sealed along the rim to 7; 4, slot or hole; 5, spherical reservoir; 6, suspended-level outlet; 7, cylindrical reservoir; 8, filtration chamber; 9, medium porosity fritted disk; 10, side tube; 11, salt fill tube; 12, constriction; 13, thermocouple protection tube.

\* Electrochemical Society Active Member.

<sup>1</sup> Present address: Koninklijke/Shell Laboratorium, Amsterdam, The Netherlands.

Key words: capillary, viscometer, molten salt, cadmium chloride.

The main feature of the viscometer is the outlet, which is of the suspended level type. Its function is to maintain at a constant value the bottom level of the hydrostatic head. The mean value of this head then also remains constant, this quantity is designated by 'h' in Fig. 1.

The viscometer is filled by introducing the salt sample into the filtration chamber through the fill tube. When the required quantity has been inserted, the fill tube and side tube are connected to a vacuum line, a thermocouple fitted for temperature measurement, and the apparatus lowered into an electrical furnace. The temperature of the furnace is raised slowly until all the solid has melted, the liquid salt being allowed to drip slowly through the frit into the viscometer. When the salt sample has passed into the viscometer, the apparatus is removed from the furnace; local heating is applied to the constriction enabling the filling assembly to be broken off and the viscometer to be sealed. The viscometer is now in its final form.

After sealing, the viscometer can be allowed to cool to room temperature or it can be transferred directly to a furnace suitable for the viscometry experiments.

In order to take measurements during the experiments, the salt must flow from the upper end of the viscometer into the spherical reservoir and down through the capillary tube to the outlet. When the viscometer reaches the required temperature in the test furnace it must be turned through 180° in the direction indicated in Fig. 1 to enable the upper part of the funnel with liquid salt through the slot or hole in the rim, 4 in Fig. 1, of the funnel sealed to the cylinder. When the salt has drained into this portion, the viscometer is quickly returned to its original position, whereupon the liquid will fill the funnel and reservoir and then flow through the capillary to accumulate in the bottom. Given a proper volume of liquid, little or none will spill through the slot in the funnel.

### Working Principle of the Furnace and Detection Equipment

The furnace that has been used in connection with the viscometer has two main features: first of all it provides a large hot zone at a uniform temperature; second, the furnace incorporates a means of recording the liquid flow time optically between two marked points.

One of the standard techniques in molten salt capillary viscometry is the use of platinum or platinum alloy wire electrodes, located at different levels in the reservoir of the viscometer, to measure the flow time. However, since this technique is restricted to conducting liquids, we have devised a new technique for molten salts for the present design, *i.e.*, an opto-electronic system.

The furnace, (shown in Fig. 2 with the viscometer in position), is an electric resistance furnace utilizing three Kanthal A resistors wound onto sillimanite tubes. It is, to a great extent, a descendant of that described by Motzfeldt (10).

Insulation is provided by firebricks and fiberfax, with stainless steel radiation shields in the upper end of the furnace and a plug of firebrick in the lower end. In addition, due to the fact that parts of the timing mechanism built into the furnace require cooling, a water-filled cooling system is provided. This cooling system fulfills a secondary function in that it enables heat to be "sunked" to a well-defined level, resulting in better furnace temperature regulation.

A silver tube is mounted within the working chamber in order to smooth minor temperature fluctuations, this tube also acting as a support for positioning the viscometer.

Viscometer temperature measurement is achieved using three Chromel-Alumel thermocouples, mounted in the positions indicated in Fig. 3, (this figure giving also details of the external equipment used in connec-

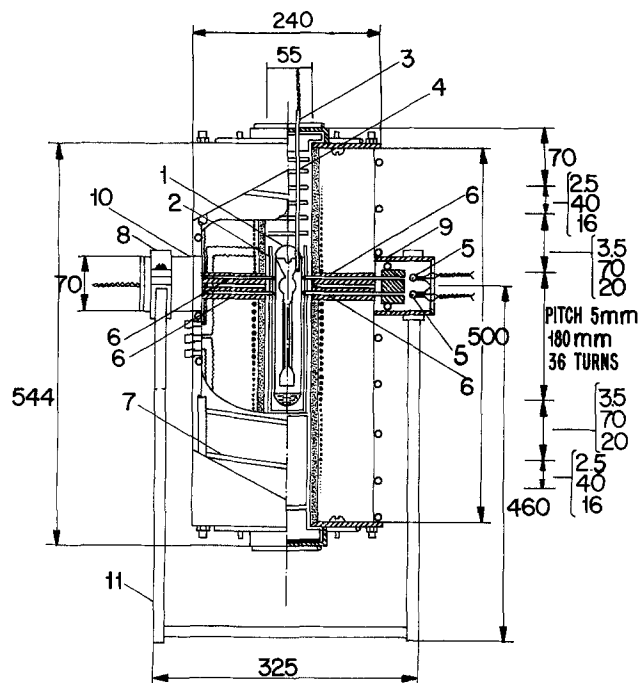


Fig. 2. Furnace for viscosity measurements (dimensions in mm). 1, Viscometer; 2, silver tube; 3, thermocouple; 4, radiation shielding; 5, timing lamps; 6, quartz rod light guides; 7, water-filled cooling system; 8, support bearing; 9, lamp housing; 10, housing for photodiodes and detector electronics; 11, furnace stand.

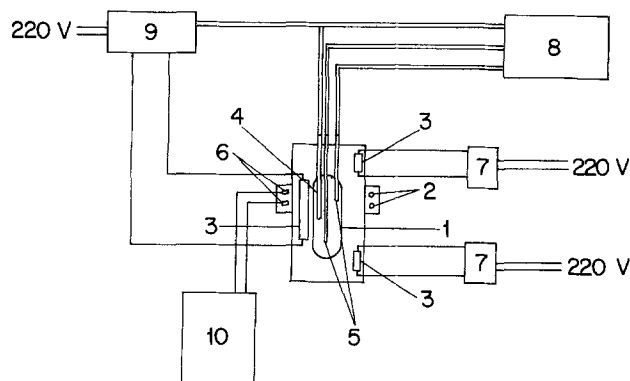


Fig. 3. Auxiliary equipment for the closed viscometer system. 1, Viscometer; 2, lamp; 3, Kanthal A resistor wound on sillimanite tube; 4, sensor thermocouple; 5, thermocouple; 6, photodiode detector; 7, Variac; 8, potentiometer; 9, Eurotherm temperature regulator; 10, millivolt recorder.

tion with the furnace and the viscometer). The middle thermocouple serves a dual purpose in that it also acts as a sensor for the "Eurotherm" temperature controller.

To provide for the necessary rotation of the viscometer, two brass tubes are mounted on opposite sides of the furnace coincident with the axis of rotation indicated in Fig. 1. The tubes are supported in bearings on a furnace stand, enabling the furnace to be rotated about a horizontal axis.

These brass tubes also serve as housings for the timing mechanism and are water-cooled. One of the brass tubes contains two lamps, each set equidistant above and below the axis of rotation (the center of the viscometer reservoir). The opposite tube is the housing for the detector electronics and two photodiodes, the diodes being in alignment with the lamps.

Two pairs of parallel quartz rods are set into the body of the furnace, one set between the photodiodes and the viscometer, the other between the viscometer and the lamps. These rods act as a light guide for each lamp and its opposing diode.

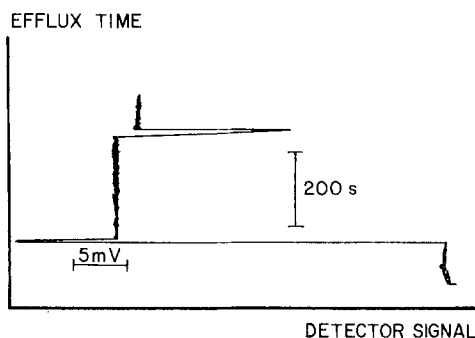


Fig. 4. Typical example of the level detector output. Potential peaks correspond to the signals emitted at the passage of liquid between the calibration levels.

Thus the viscometer is provided with an opto-electronic level detection system comprising: two lamps, two photodiodes, two sets of quartz rod light guides, and a timing system.

Because the furnace is itself a red light source and because of 50 Hz (stray) fields, the lamps are switched at 25 Hz and a synchronous detector is used. The detector is sensitive to the chopped light only and is not affected by radiation from the furnace or by the 50 Hz main supply. The signal from the detector is recorded on a millivolt recorder and shows two distinct peaks corresponding to the passage of liquid at the two levels, see Fig. 4. The efflux time can be easily measured with an accurate stopwatch, or alternatively the peak signal may be used to trigger an electronic counter.<sup>2</sup> Similar timing circuits triggered by photoelectric sensors have been described by Eicher and Zwolinski (11) and by Gramain and Libeyere (12).

#### Sources of Error

The viscosity equation that is normally used in capillary viscometry is written as

$$\frac{\eta}{\rho} = \nu = Ct - \frac{B}{t} \quad [1]$$

in which  $C$  and  $B$  are the viscometer's constants,  $\eta$  is dynamic viscosity,  $\rho$  is density,  $\nu$  is kinematic viscosity, and  $t$  is the efflux time. The quantity  $B/t$  of Eq. [1] is called the kinetic energy correction and has been discussed in detail by Wellman *et al.* (13). These authors, as well as many others (1, 7, 8, 14-16), have noted and critically reviewed other sources of error in capillary viscometry and it is considered sufficient to discuss one remaining source of error especially important with regard to high temperature viscometry, *i.e.*, temperature inhomogeneity.

Temperature profiles recorded with sliding thermocouples indicated that temperature inhomogeneities within the working chamber of the high temperature furnace could well be kept within  $\pm 1^\circ\text{K}$ . Since for the molten salts investigated the temperature coefficient of the dynamic viscosity is  $\frac{1}{2}\%$ /degree or less, we can conclude that the viscosities of these salts can be measured with an accuracy better than 1% as far as the

<sup>2</sup> Details of the electronic circuitry may be obtained through the first author.

Table I. Efflux times for molten  $\text{KNO}_3$

$T_1 = 368^\circ\text{C}$		$T_2 = 469^\circ\text{C}$	
Test No.	Efflux time (sec)	Test No.	Efflux time (sec)
1	528.6	1	349.1
2	529.1	2	349.9
3	529.7	3	350.6
4	531.0	4	351.1
5	529.0	5	352.1
6	529.1	6	349.9
Mean value $t_1 = 529.3$ sec $\nu_1 = 1.34$ cst		Mean value $t_2 = 350.5$ sec $\nu_2 = 0.87$ cst	

temperature inhomogeneity is concerned. The reproducibility of the viscosity measurements has turned out to be of the order of 1%.

#### Calibration Experiments

The viscometer constants of Eq. [1] have been determined with molten  $\text{KNO}_3$  as the calibration liquid. A simple technique has been used to purify this salt (14) which is not strongly hydrated, similar techniques have been described elsewhere (7, 17, 18). Absolute values for the dynamic viscosity of molten  $\text{KNO}_3$  have been known since Dantuma (19), whose measurements are considered to be as good as any latterly published results.

Efflux times for molten  $\text{KNO}_3$  were determined in our viscometer in the range  $350^\circ\text{C}$ - $450^\circ\text{C}$ . The constants  $C$  and  $B$  in Eq. [1] were calculated using  $\nu_1$  and  $\nu_2$ , the kinematic viscosities of molten  $\text{KNO}_3$  at temperatures  $T_1$  and  $T_2$ , respectively, and the equations

$$C = \frac{\nu_2 t_2 - \nu_1 t_1}{t_2^2 - t_1^2} \quad [2]$$

$$B = \frac{t_1 t_2}{t_2^2 - t_1^2} (\nu_2 t_1 - \nu_1 t_2)$$

Table I shows the efflux times at two typical temperatures for molten  $\text{KNO}_3$ . The values of  $\nu_1$  and  $\nu_2$  were obtained from the literature (17). According to Eq. [2] the value of  $C$  is  $2.57 \cdot 10^{-3}$  cst/sec and  $B$  is 10 cst  $\cdot$  sec.

#### Viscosity of Molten $\text{CdCl}_2$

Literature concerning the viscosity of liquid  $\text{CdCl}_2$  is available. Karpachev's results were the first to be reported (20), while those of Bloom *et al.* are more recent (21).

Liquid  $\text{CdCl}_2$  is an interesting compound to work with in a closed viscometer because of its high vapor pressure. It also requires attention during the initial stages of the experiment, especially in drying and handling, since hydrolysis may occur. The procedure that we followed for the purification of  $\text{CdCl}_2$  was derived from that described by Hill *et al.* (22) and has been described elsewhere in detail (14).

In Table II the experimental efflux times of liquid  $\text{CdCl}_2$  are given as a function of temperature. With the aid of the constants  $C$  and  $B$  determined previously, the viscosity of liquid  $\text{CdCl}_2$  was calculated. Density values for molten  $\text{CdCl}_2$  to convert from kinematic viscosity to dynamic viscosity were obtained from our own measurements (14), summarized by the equation

Table II. Viscosity of molten  $\text{CdCl}_2$  as a function of temperature

Temperature, $T$ ( $^\circ\text{C}$ )	Efflux time, $t$ (sec)*	Kinematic viscosity, $\nu$ (cst)	Dynamic viscosity, $\eta$ (cp)	Dynamic viscosity (21), $\eta$ (cp)	Dynamic viscosity (20), $\eta$ (cp)
$594 \pm 1.5$	$273.4 \pm 0.6$	$0.67 \pm 0.01$	$2.26 \pm 0.03$	$2.30 \pm 0.03$	—
$645 \pm 1$	$242.3 \pm 0.9$	$0.58 \pm 0.01$	$1.93 \pm 0.03$	$2.00 \pm 0.03$	2.14
$694 \pm 1.5$	$217.8 \pm 0.2$	$0.51 \pm 0.01$	$1.69 \pm 0.03$	$1.80 \pm 0.03$	1.90
$743 \pm 1.5$	$198.8 \pm 0.3$	$0.46 \pm 0.01$	$1.49 \pm 0.03$	—	1.72
$797 \pm 1.5$	$180.0 \pm 0.5$	$0.41 \pm 0.01$	$1.32 \pm 0.02$	—	—

\* Efflux times are mean values determined from at least five separate measurements.

$$\rho = 4.235 - 9.45 \times 10^{-4} T \quad [3]$$

with  $\rho$  the density in  $\text{g/cm}^3$  and  $T$  the temperature in  $^\circ\text{K}$ . Our values of the dynamic viscosity of liquid  $\text{CdCl}_2$  are also given in Table II together with literature data. Figure 5 is a graph showing the dynamic viscosity of molten  $\text{CdCl}_2$  against temperature, Fig. 6 shows a graph of  $\ln \eta$  against  $1/T$ . The temperature dependence can be expressed as the following exponential function  $1/T$

$$\eta = 0.133 \times \exp(4880/RT) \quad [4]$$

( $\eta$  in cp,  $R = 1.987 \text{ cal K}^{-1} \text{ mol}^{-1}$ ) with a correlation coefficient of 0.999.

The post exponential factor found by Bloom *et al.* (21) was equal to 4.0 kcal/mole, while that found by Karpachev was equal to 4.1 kcal/mole.

### Discussion

With the closed capillary viscometer described in this article, it is possible to measure accurately the viscosity of many liquids but especially those having properties which make them less suitable for other types of viscometer. The advantages of this instrument can be summarized as follows:

1. The hydrostatic head adjusts itself automatically by virtue of the suspended level and is independent of the total amount of liquid.

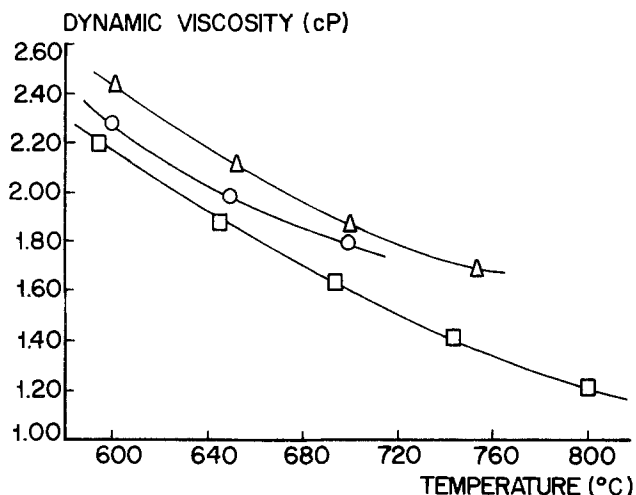


Fig. 5. Dynamic viscosity-temperature curves for liquid  $\text{CdCl}_2$ , according to: ( $\Delta$ ) Karpachev and Stromberg (20); ( $\circ$ ) Bloom, Harrap, and Heymann (21); ( $\square$ ) the authors.

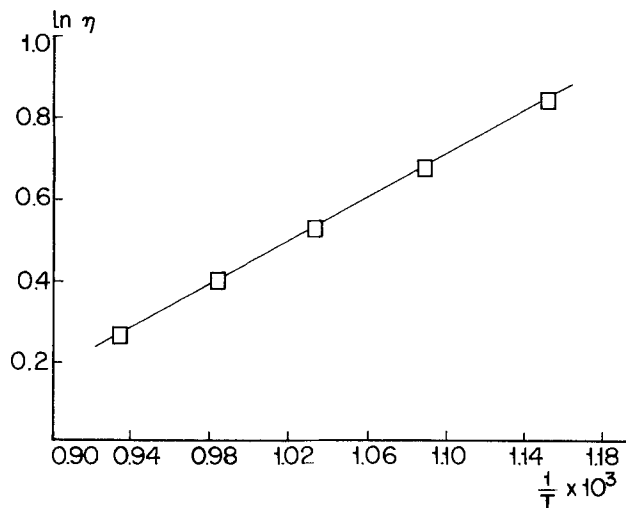


Fig. 6. Graph of  $\ln \eta$  (ln of dynamic viscosity) of liquid  $\text{CdCl}_2$  against the reciprocal of  $[T$  (temperature)  $\times 10^{-3}]$ , where  $T$  is in  $^\circ\text{K}$ .

2. Because surface tension in the measuring bulb and the suspended level are of an opposing nature they will cancel each other to a great extent.

3. The change of liquid volume with temperature has no influence.

4. Repeated measurements are readily obtained.

5. When the viscometer is slowly rotated during cooling no fracturing occurs on freezing.

6. The simple and robust construction is very attractive for high temperature work.

7. The viscometer has a very good reproducibility, as can be seen from the results in Table I.

As to the present values of the dynamic viscosity of molten  $\text{CdCl}_2$ , it is the authors' view that the viscometry of low viscosity liquids (1-10 cp) at high temperatures is a very difficult experimental undertaking and it is not uncommon to find that single salt viscosities differ by more than 50% (13), especially with regard to data obtained by earlier authors.

In an attempt to obtain more reliable viscosity data, Øye and co-workers (13, 23) have recently redetermined the viscosities of the molten alkali chlorides, using the torsional pendulum method. They predicted the use of the capillary tube method on the grounds that etching of the capillary material could result in a slight alteration to the capillary diameter and that difficulties could be expected in the maintenance of a large zone of uniform temperature in the furnace and in liquid flow measurement.

However, it is our opinion that etching of the capillary material takes place at high temperatures only in the presence of water, since no visible etching was observed in these experiments using carefully dehydrated salts. Moreover, a redetermination of the constants  $C$  and  $B$  of Eq. [1] after the  $\text{CdCl}_2$  experiment showed them to be equal to the formerly determined values, with an uncertainty of 1.5%. In addition, the other two objections against high temperature capillary viscometry have also been successfully dealt with in the foregoing paragraphs.

Apart from these experimental considerations, the present authors are also of the opinion that, from a methodological point of view, the capillary tube method should not be precluded. In the torsional pendulum method, *i.e.*, an absolute method, the extreme attention that must be paid to the accurate determination of the radius of the oscillating sphere and to first-class machining of the assembly has been stressed (23). However, in a relative method such as the capillary tube method, we have the advantage that, after an accurate calibration, all measurements can be done in a relatively short time without the need to redetermine the critical dimensions of the apparatus.

Finally, our choice of the capillary tube method has been justified by our measurements of the dynamic viscosity of molten  $\text{KCl}$  and molten  $\text{CsCl}$ . The agreement of our data (14) with those obtained recently by Brockner *et al.* [(13) including our data] and by Zuca and Borcan (24) is considered to be good although these data are different from those reported earlier by Murgulescu and Zuca (25) which were also obtained by the oscillating sphere method.

With regard to the present data on molten  $\text{CdCl}_2$ , it is interesting to note that the values of Bloom *et al.* (21) have also been obtained with a capillary viscometer. According to these authors, no kinetic energy correction  $B/t$  (see Eq. [1]) is necessary as capillaries with trumpet-shaped ends have been used. However, regardless of the shape of the end sections of the capillary, the kinetic energy correction should be applied, as has been demonstrated by Wellman *et al.* (18), and thus the values of Bloom *et al.* (21) should be somewhat lower and hence come closer to our values (see Fig. 5). It is also clear from Fig. 5 that the difference between the two sets of data increases with increasing temperature. This is to be expected if the  $B/t$  term is neglected, since with increasing temperature the efflux



times decreases and the correction  $B/t$  will increase. It is difficult to say whether these discrepancies can be attributed to the kinetic energy correction only but certainly the trend is explained.

The values of Karpachev and Stromberg (20) have been obtained with an oscillating sphere viscometer and while most earlier viscosity data are considerably higher than corresponding data reported recently, a tentative explanation of this phenomenon has been forwarded by Øye and co-workers (13). The latter remark that most sources of error, for instance melt impurities, will result in higher viscosity values. In addition, for oscillation methods, lateral movement of the pendulum will also give rise to a viscosity higher than the true value. A combination of these effects may have caused the high viscosity values reported by Karpachev and Stromberg (20).

#### Acknowledgment

The present investigations have been carried out under the auspices of the Netherlands Foundation for Chemical Research (S.O.N.) and with financial aid from the Netherlands Organization for the Advancement of Pure Science (Z.W.O.). The authors gratefully acknowledge the assistance by Messrs. Voogt, Baker, and Keuning in the design and construction of various pieces of the equipment.

Manuscript submitted March 10, 1976; revised manuscript received May 10, 1976.

Any discussion of this paper will appear in a Discussion Section to be published in the June 1977 JOURNAL. All discussions for the June 1977 Discussion Section should be submitted by Feb. 1, 1977.

Publication costs of this article were assisted by the University of Amsterdam.

#### REFERENCES

1. N. N. Greenwood and K. Wade, *J. Sci. Instr.*, **34**, 288 (1957).
2. A. A. Banks, A. Davies, and A. J. Rudge, *J. Chem. Soc.*, **1**, 732 (1953).
3. C. J. Planck and H. Hunt, *J. Am. Chem. Soc.*, **61**, 3590 (1939).
4. E. N. Da Andrade and K. E. Spells, *J. Sci. Instr.*, **9**, 316 (1932).
5. J. R. Lewis, *J. Am. Chem. Soc.*, **47**, 626 (1925).
6. C. T. Ewing, J. A. Grand, and R. R. Miller, *ibid.*, **73**, 1168 (1951).
7. A. Timidei, G. Ledermann, and G. J. Janz, *Chem. Instr.*, **2**, 309 (1970).
8. L. Ubbelohde, "Zur Viskosimetrie," S. Hirzel Verlag, Stuttgart (1965).
9. H. Y. Kang, and P. Bro, *This Journal*, **122**, 1155 (1975).
10. K. Motzfeldt, in "Physico-Chemical Measurements at High Temperatures," J. O'M Bockris, J. L. White, and J. D. Mackenzie, Editors, chap. 3, Butterworths, London and Washington (1959).
11. L. D. Eicher and B. J. Zwolinski, *J. Phys. Chem.*, **75**, 2016 (1971).
12. P. Gramain and R. Libeyere, *J. Appl. Polym. Sci.*, **14**, 383 (1970).
13. W. Brockner, K. Grjotheim, T. Ohta, and H. A. Øye, *Ber Bunsenges. Phys. Chem.*, **79**, 344 (1975).
14. N. van Os, Thesis, University of Amsterdam (1975).
15. R. C. Hardy, *Nat. Bur. Std. (U.S.) Monograph* 55 (1962).
16. K. Schwabe, "Physikalisch Chemische Messverfahren," Part 1, Leipzig (1973).
17. G. J. Janz, "Molten Salts Handbook," Academic Press, New York (1967).
18. R. E. Wellman, R. De Witt, and R. B. Ellis, *J. Chem. Phys.*, **44**, 3070 (1965).
19. R. S. Dantuma, *Z. Anorg. Allg. Chem.*, **175**, 1 (1928).
20. S. Karpachev and A. Stromberg, *Zh. Fiz. Khim.*, **11**, 852 (1938).
21. H. Bloom, B. Harrap, and E. Heymann, *Proc. R. Soc. London, Ser. A*, **194**, 237 (1948).
22. D. Hill, *This Journal*, **107**, 699 (1960).
23. T. Ohta, O. Borgen, W. Brockner, D. Fremstad, K. Grjotheim, K. Tørklep, and H. A. Øye, *Ber. Bunsenges. Phys. Chem.*, **79**, 335 (1975).
24. S. Zuca and R. Borcan, *Rev. Roum. Chim.*, **19**, 553 (1974).
25. I. G. Murgulescu and S. Zuca, *Z. Phys. Chem. (Leipzig)*, **222**, 300 (1963).

# Analysis of Porous Electrodes with Sparingly Soluble Reactants

## III. Short Time Transients

Hiram Gu\* and Douglas N. Bennion\*\*

*Energy and Kinetics Department, School of Engineering and Applied Science,  
University of California, Los Angeles, California 90024*

and John Newman\*\*

*Materials and Molecular Research Division, Lawrence Berkeley Laboratory and  
Department of Chemical Engineering, University of California, Berkeley, California 94720*

### ABSTRACT

A mathematical model which describes the operation of porous battery electrodes has been developed. It includes short time transient behavior of electrolyte concentration, porosity, current distribution, reaction rate, and detailed solution diffusion descriptions of a sparingly soluble reactant. Calculations were made for constant current (50 and 25 mA/cm<sup>2</sup>) charging and discharging of Ag/AgCl electrodes. Results of calculations indicate that the concentration of the electrolyte, KCl, inside the porous electrode plays an important role in the performance of the electrode. During charging, the electrolyte concentration falls in the depth of the electrode, thereby decreasing the solution electrical conductivity. Reaction penetration depth on charging is very shallow, less than 0.3 mm, for the current densities investigated. On discharging, the electrolyte concentration in the depth of the electrode increases. Consequently, the electrical conductivity of the solution as well as the solubility of AgCl increases. A high reaction rate in the depth of the electrode is possible even at high current discharge. Charge utilization over 90% is predicted if the charge is stored uniformly by employing a slow charging rate.

Porous electrodes have larger reactive surface to volume ratios than do plane electrodes. Consequently their use is common in primary and secondary batteries as well as continuous flow galvanic cells. Many mathematical models have been proposed to explain the operation of porous electrodes. Progress in the mathematical modeling of flooded porous electrodes prior to 1974 has been reviewed by de Levie (1) and by Newman and Tiedemann (2). A recent mathematical model for the negative plate of the lead-acid battery was reported by Micka and Rousar (3). Like their previous model for the lead dioxide plate (4), reversible electrode kinetics was assumed.

The mathematical model proposed here describes transient behavior of flooded porous electrodes with sparingly soluble reactants. The present model is an extension and refinement of a previously proposed model (5).

In the previous model, a pseudo steady-state approximation was used to calculate time-dependent results. The time-dependent concentration term  $\partial c_e/\partial t$  in the conservation equation was eliminated. The solution from the steady-state ordinary differential equations was used to predict the electrode conditions for one time increment later. A new steady-state solution was then found for the new time step and so on.

In the present model, the partial differential equations were solved including all  $\partial/\partial t$  terms. An accurate account of the electrolyte concentration variation with time is important since the electrolyte concentration inside the electrode greatly affects the behavior of a porous electrode. Frequently,  $\partial c_e/\partial t$  type terms are important in predicting concentration distributions under conditions similar to practical operating situations. Simonsson (6) solved his mathematical model for the porous lead dioxide electrode including the  $\partial c_e/\partial t$  term. The results of his model calculations showed that the discharge capacity of the electrode is caused by acid depletion.

A macroscopic treatment is used in the present model, replacing the previous single pore geometry (5).

\* Electrochemical Society Student Member.

\*\* Electrochemical Society Active Member.

Key words: current distribution, concentration distribution, battery, mathematical model.

This means that averaging is performed over a volume element in the porous electrode. The electrode is treated as a superposition of two continua, one of the electrode matrix phase and one of the solution phase. Although this change is rather minor mathematically, it allows a more realistic description of the tortuosity effect.

Application of the present model is restricted to the class of porous electrodes whose transport of reactants involves a solution phase diffusion step. Specifically, the present model can be applied to Ag/AgCl porous electrodes such as those used in seawater batteries. The AgCl is the sparingly soluble reactant. Previous studies indicate that the transfer between Ag and AgCl involves solution diffusion of  $\text{AgCl}_{n+1}^{-n}$ , where  $n = 0, 1, 2, 3$  (7 and 8). A mass transfer coefficient,  $k_m^*$ , can be used to describe the diffusion of  $\text{AgCl}_{n+1}^{-n}$ . As an improvement to the previous model, the mass transfer coefficient used in the present model is in a physically more realistic and mathematically simpler form. In addition, the present model includes the rate of nucleation of AgCl during charging of the electrode.

The formulation of the coverage of the metal surface by salt crystallites in the present model is specifically for the Ag/AgCl system. Based on experimental observations (8, 9), two modes of AgCl growth are postulated. The first mode involves the forming of AgCl nuclei and the growing together of AgCl mounds. The second mode involves the thickening of a "porous" AgCl film.

For a given set of initial conditions such as electrolyte concentration, porosity, and the state of charge, the mathematical model calculations will predict the current density  $i_2$ , the potential  $\phi_2$ , the electrolyte concentration  $c_e$ , the concentration of sparingly soluble reactant  $c_R$ , the porosity  $\epsilon$ , the local reaction rate  $j$ , and the bulk solution velocity  $v$  as functions of time and position with respect to the front face of the electrode.

### Description of the Model

A one dimensional approach is used in which variation of properties occur only along the axis perpendicular to the face of the electrode. Geometric features of the model are shown in Fig. 1. The front face of the

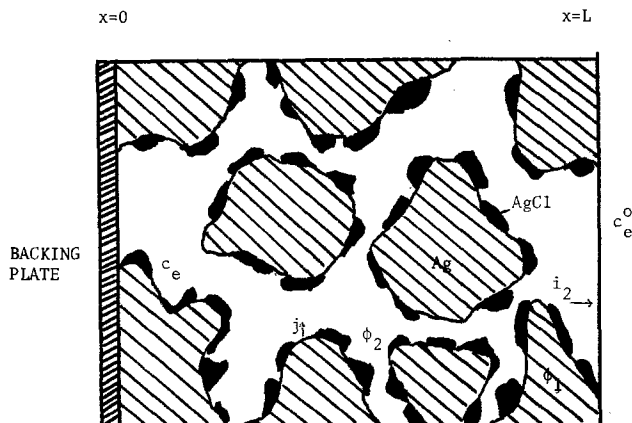


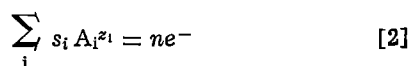
Fig. 1. Macroscopic model of porous electrodes

electrode is at  $x = L$ . The current collecting plate is at  $x = 0$ . The current density  $i_2$  is a superficial current density in the solution phase. At  $x = L$ ,  $i_2$  is equal to the total applied current density  $I$ . Inside the porous electrode, the following relationship applies

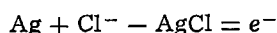
$$i_1 + i_2 = I \quad [1]$$

where  $i_1$  is the superficial current density in the solid phase. At the backing plate,  $i_2$  is zero. A positive sign is used for anodic currents and a negative sign for cathodic currents. The potential in the metal phase is assumed to be at ground potential (that is,  $\phi_1 = 0$ ) which implies that we have neglected the metal phase ohmic resistance relative to the solution phase ohmic resistance. The potential in the solution phase,  $\phi_2$ , is the potential that one would measure with respect to the working electrode if a reference electrode of the same kind as the porous electrode is placed in the solution phase within the pores of the porous electrode.

The stoichiometric reaction representing the chemical process within the porous electrode is



where  $s_i$  are stoichiometric coefficients and  $z_i$  are the charges on species  $A_i$ . The number of electrons transferred for the reaction as written is  $n$ . For the Ag/AgCl electrode, the reaction is written as



A modified Ohm's law applied to the solution phase in the porous electrode is

$$i_2 = -\kappa \epsilon^{(1+t)} \frac{d\phi_2}{dx} - \frac{\kappa \epsilon^{(1+t)} \nu RT}{F c_o \bar{V}_o} \left[ 1 + \frac{d \ln \gamma_{\pm}}{d \ln m_e} \right] \left[ \frac{s_+}{n\nu_+} + \frac{t_+^o}{z_+\nu_+} - \frac{s_o c_e}{n c_o} \right] \frac{1}{c_e} \frac{dc_e}{dx} \quad [3]$$

Here  $\phi_2$  is the potential in the solution phase;  $\kappa$  is the electrolyte conductivity;  $t$  is the tortuosity factor;  $\epsilon$  is the porosity;  $c_o$  is the solvent concentration;  $\bar{V}_o$  is the solvent partial molar volume;  $\nu$  is the number of ions per electrolyte molecule;  $\nu_+$  is the number of cations;  $\gamma_{\pm}$  is the mean molal activity coefficient;  $m_e$  is the molality of the electrolyte;  $t_+^o$  is the transference number of the cation referred to solvent velocity; and  $s_+$  and  $s_o$  are stoichiometric coefficients of the cation and solvent, respectively, according to reaction [2]. The boundary conditions for the superficial current density in the solution phase,  $i_2$ , and the concentration of the electrolyte,  $c_e$  are as follows

$$\text{at } x = 0, \quad i_2 = 0, \quad \frac{dc_e}{dx} = 0 \quad [4]$$

$$\text{at } x = L, \quad i_2 = I \quad \text{and} \quad c_e = c_e^o \quad [5]$$

where the superscript  $o$  refers to conditions outside the electrode.

The redox kinetic expression that relates the local transfer current density,  $j$ , to the surface overpotential between the solid matrix and the solution,  $(\phi_1 - \phi_2)$ , can be written as

$$j = \theta i_o [\exp(-\alpha_a F \phi_2 / RT) - \exp(\alpha_c F \phi_2 / RT)] \quad [6]$$

where  $\phi_1$  is taken to be zero as previously stated. The exchange current density depends on the concentration of the sparingly soluble reactant and the electrolyte concentration in the following way

$$i_o = i_o^o \left( \frac{c_R}{c_R^*} \right)^\gamma \left( \frac{c_e}{c_e^o} \right)^\zeta \quad [7]$$

where  $i_o^o$  is concentration independent. Here  $c_R$  is the concentration of complexed ions at the metal surface and  $c_R^*$  is the equilibrium concentration of complexed ions at electrolyte concentration  $c_e^o$ . The order of dependence of  $i_o$  on  $c_R$  and  $c_e$  are  $\gamma$  and  $\zeta$ , respectively.

The conservation of charge requires that

$$aj = \frac{di_2}{dx} \quad [8]$$

where  $a$  is the electrode surface area per unit volume of the electrode. Equation [8] relates local transfer current density to superficial current density in the solution phase.

Due to the differences in partial molar volumes of the salt and the metal, the porosity of the electrode will change with time according to the local reaction rate

$$\frac{\partial \epsilon}{\partial t} = \left( \frac{1}{nF} \sum_{\text{species}} \bar{V}_i \bar{V}_i s_i \right) \frac{\partial i_2}{\partial x} \quad [9]$$

As the relative volume of liquid to solid in the pores changes, a convective flow of liquid into or out of the electrode results. This bulk flow motion can be described by an over-all continuity equation

$$\frac{\partial \epsilon}{\partial t} + \frac{\partial v \square}{\partial x} = -\frac{1}{F} \left( \frac{\bar{V}_e t^- o}{z_- \nu_-} + \frac{\bar{V}_e s_-}{n \nu} + \frac{\bar{V}_o s_o}{n} \right) \frac{\partial i_2}{\partial x} \quad [10]$$

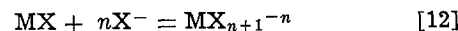
Here  $v \square$  is the superficial volume average velocity.

The concentration variation of the electrolyte in the pores is expressed by the electrolyte continuity equation

$$\epsilon \frac{\partial c_e}{\partial t} + v \square \frac{\partial c_e}{\partial x} = \frac{\partial}{\partial x} \left[ D \epsilon^{(1+t)} \frac{\partial c_e}{\partial x} \right] - \left[ \frac{c_o \bar{V}_o t_+^o}{z_+ \nu_+} + \frac{c_o \bar{V}_o s_+}{n \nu_+} - \frac{s_o c_e \bar{V}_o}{n} \right] \frac{1}{F} \frac{\partial i_2}{\partial x} \quad [11]$$

where  $D$  is the diffusion coefficient of the electrolyte.

Finally, the reaction rate is determined by the diffusion of complexed ions formed through the reaction



By defining an over-all mass transfer coefficient  $k_m^*$ , the reaction rate can be written as

$$j = \frac{-nF}{s_R} k_m^* c_R^{\text{eq}} (C_1 - 1) \quad [13]$$

where  $C_1 = c_R / c_R^{\text{eq}}$  and where the equilibrium concentration of the complexed ion,  $c_R^{\text{eq}}$  is related to the electrolyte concentration,  $c_e$ , through the equilibrium constant  $K$  associated with reaction [12] hereafter referred to as a dissolution constant.

The over-all mass transfer coefficient,  $k_m^*$  is dependent on the amount of metal surface area available for the reaction to occur. It is related to  $\theta$  by

$$k_m^* = k_m^o (\theta)^{1/2} (1 - \theta)^{1/2} + k_{\text{nuclei}} \theta \quad [14]$$

Here,  $k_m^0$  is a function of the diffusion coefficient and the effective diffusion path of  $\text{MX}_{n+1}^{-n}$ . The mass transfer coefficient for nucleation,  $k_{\text{nuclei}}$  represents the formation of salt nuclei in addition to the diffusion of  $\text{MX}_{n+1}^{-n}$  from metal surface to the salt surface during charging. It is related to the level of supersaturation of the sparingly soluble salt as well as the surface condition of the metal. During discharge  $k_{\text{nuclei}}$  is zero.

The surface coverage of metal by the salt depends on the state of charge. For the Ag/AgCl electrode (or possibly other similar electrodes), the charge dependence of the surface coverage can be divided into two regions during anodic operation, charging for this case. The first region involves the nucleation of AgCl at various sites and the spreading of adsorbed AgCl from the nuclei. This region of AgCl growth is represented by

$$\theta_s = (1 - Q/Q^*)^S \quad [15]$$

where  $Q$  is the charge stored and  $Q^*$  is a charge parameter. The value of the shape factor,  $S$ , will depend on the morphology of the sparingly soluble salt crystallites. A large  $S$  indicates flat plate-type crystals while a small  $S$  indicates needle-type crystals. In the second region, patches of adsorbed AgCl molecules (crystals) have grown together to form a porous film. As the film thickens, micropores incorporated in the AgCl film gradually diminish. The function used to describe the fraction of the metal exposed for the second region is

$$\theta_p = (P)^{Q/Q^*} \quad [16]$$

The value of the porosity factor,  $P$ , depends on the density (porosity) of the salt film. A small  $P$  indicates a dense salt film. It is expected that the value of  $P$  will fall between 0 and 0.3. The charge parameter,  $Q^*$ , represents the state of charge when all salt patches have united to form a porous film. The charge  $Q^*$  has a fractional value of the maximum charge that can be stored in the pores

$$Q^* = \lambda Q_{\text{max}} \quad [17]$$

A value of 0.5 for  $\lambda$  is used in the present model. The maximum amount of charge that can be stored is limited by complete filling of pores by the salt. It can be expressed as

$$Q_{\text{max}} = Q_0 - nF \frac{\epsilon_0}{\sum_i s_i \bar{V}_i} \quad [18]$$

solid  
species

Here  $Q_0$  and  $\epsilon_0$  are initial charge and initial porosity, respectively. It is also possible, but not likely for practical electrodes, that the amount of metal available for conversion to salt is limiting. In this case

$$Q_{\text{max}} = Q_0 + \frac{nF}{\bar{V}_M S_M} \left( 1.0 - \epsilon_0 + \frac{Q_0 \bar{V}_{\text{MX} S_{\text{MX}}}}{nF} \right) \quad [19]$$

Solutions to the mathematical model were obtained numerically. The equations described were combined and reduced to one second-order and two first-order partial differential equations. For the Ag/AgCl electrode, the three equations are

$$i_2 = -\kappa \epsilon^{(1+t)} \frac{d\phi_2}{dx} - \frac{2\kappa \epsilon^{(1+t)} RT}{F c_0 \bar{V}_0} \left[ 1 + \frac{d \ln \gamma_{\pm}}{d \ln m_e} \right] \left[ \frac{t_+^0}{c_e} \right] \frac{dc_e}{dx} \quad [20]$$

$$\frac{di_2}{dx} = a \theta_i i_0^0 \left[ \frac{c_e}{c_0} \right]^{\gamma+\zeta} \left[ 1 - \frac{\frac{di_2}{dx}}{a F k_m^* K c_e} \right]^{\gamma} \left[ \exp \left( \frac{-\alpha_a F \phi_2}{RT} \right) - \left( \exp \frac{\alpha_c F \phi_2}{RT} \right) \right] \quad [21]$$

and

$$\epsilon \frac{\partial c_e}{\partial t} + \left[ \frac{-\bar{V}_e t_0^+ - \bar{V}_M + \bar{V}_{\text{MX}}}{F} \right] i_2 \frac{\partial c_e}{\partial x} = \frac{\partial}{\partial x} \left[ D \epsilon^{(1+t)} \frac{\partial c_e}{\partial x} \right] + t_0^+ \left[ \frac{1 - c_e \bar{V}_e}{F} \right] \frac{\partial i_2}{\partial x} \quad [22]$$

The three equations in their linearized form were then solved using the numerical technique of Newman [10].

### Results of Calculations

Results of several calculations applied to porous Ag/AgCl electrodes are presented here. The electrode was assumed to be 1 mm thick (that is, from  $x = 0$  to  $x = L$ ). The electrolyte was 1N KCl. The exchange current density,  $i_0^0$ , was assumed to be  $10^{-4}$  A/cm<sup>2</sup>. A value of  $1.735 \times 10^{-5}$  as reported by Giles [7] was used for the dissolution constant  $K$ . The values of  $k_m^0$  and  $k_{\text{nuclei}}$  were chosen to be 0.3 and 0.1 cm/sec, respectively, based on experimental data of Katan *et al.* (8, 9). Kinetic parameters  $\alpha_a$  and  $\alpha_c$  were given the same value of 0.5. A value of 2/3 was used for the shape factor,  $S$ , based on observed surface morphology (9). The value of  $P$  was chosen to be 0.184 so that the change of AgCl growth mode would occur at  $Q/Q^* = 0.9$ . Other concentration dependent physical properties were calculated based on previously published values (11, 12).

**Charging behavior.**—Calculations were made for the charging of a porous electrode initially composed of pure silver only. The initial porosity was assumed to be 0.571 and the specific surface area was assumed to be 4700 cm<sup>2</sup>/cm<sup>3</sup>. Electrode behavior under constant charging current densities of 50 and 25 mA/cm<sup>2</sup> were examined. The electrode overpotentials as functions of the total amount of charge passed are shown in Fig. 2. By picking a cutoff potential of  $-0.19$  V, one can see that the 25 mA/cm<sup>2</sup> charging allows the electrode to store approximately 71% more charge.

Local transfer current density distributions inside the porous electrode are shown in Fig. 3. At the beginning stage of charging (3 C/cm<sup>2</sup>), the reaction distributions are mainly controlled by the ohmic resistance of the electrolyte in the pores with a higher reaction rate at the front of the electrode. At a later stage of charging, the electrolyte concentration becomes lower in the back (see Fig. 4), causing even higher reaction rate at the front of the electrode (see curve for 50 mA/cm<sup>2</sup> charged to 24 C/cm<sup>2</sup> in Fig. 3). The front of the electrode may reach a condition where most of its reacting surfaces are covered by AgCl. As a result, a maximum in the local transfer current density distribution may occur inside the electrode as demonstrated by the 25 mA/cm<sup>2</sup> charging at the stage of 54 C/cm<sup>2</sup> (see Fig. 3). At the end of charging, a porous AgCl film covers the surfaces of the front portion of the electrode and the electrolyte concentration is very low in 3/4 of the elec-

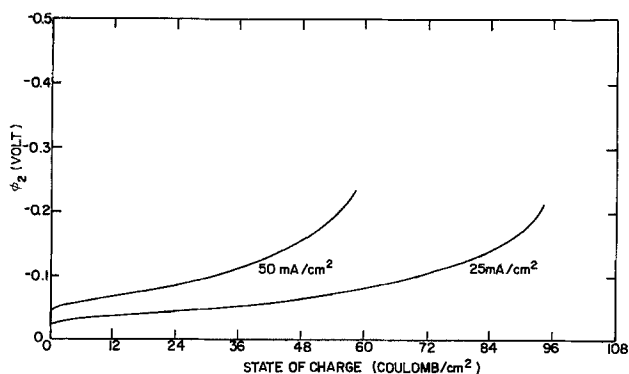


Fig. 2. Anodic electrode overpotential ( $\phi_2$  at  $x = L$ ) vs. state of charge.

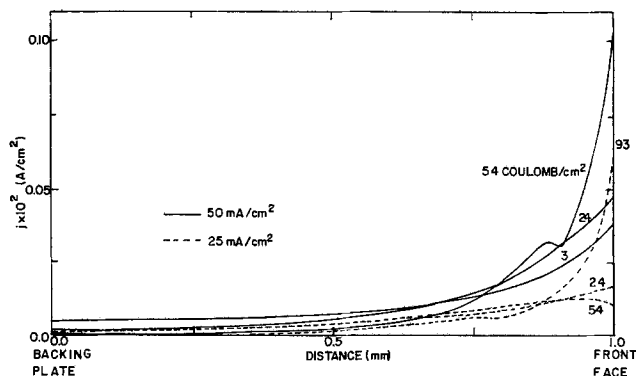


Fig. 3. Local transfer current density distributions at various stages of charge. Charging currents: —, 50 mA/cm<sup>2</sup>; ---, 25 mA/cm<sup>2</sup>.

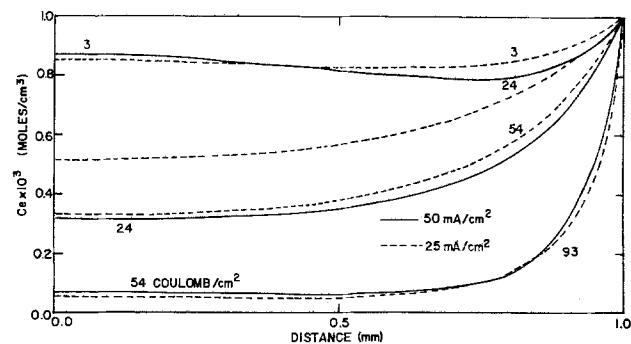


Fig. 4. Electrolyte concentration distributions at various stages of charge. Charging currents: —, 50 mA/cm<sup>2</sup>; ---, 25 mA/cm<sup>2</sup>.

trode (see Fig. 4). These conditions force the reaction to concentrate at the very front of the electrode as shown by 50 mA/cm<sup>2</sup> charging at 54 C/cm<sup>2</sup> and 25 mA/cm<sup>2</sup> charging at 93 C/cm<sup>2</sup> (see Fig. 3).

A cross-examination of Fig. 2 and 4 shows that the concentration distributions are about the same when the electrode overpotentials are the same for the high current and low current charging. This indicates that the electrolyte concentration inside the electrode may be the controlling factor in the behavior of Ag/AgCl porous electrodes.

The charge distributions are shown in Fig. 5. For the high current charging, about 73.5% of the charge, stored as AgCl, is located in the front quarter (0.25 mm) of the electrode at a potential,  $\phi_2$ , of -0.19V. Even with the 25 mA/cm<sup>2</sup> charging, about 57% of

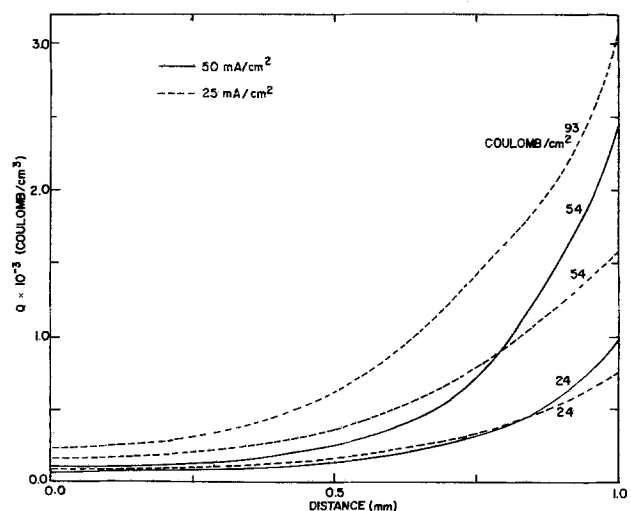


Fig. 5. Charge distributions at various stages of charge. Charging currents: —, 50 mA/cm<sup>2</sup>; ---, 25 mA/cm<sup>2</sup>.

the charge is stored in the front quarter at the same shut-off potential. At 54 C/cm<sup>2</sup>, the electrode charged at 50 mA/cm<sup>2</sup> stores 18.5% more charge in the front 0.25 mm of the electrode when compared to the electrode charged at lower current density.

One conclusion which can be drawn from these results is that more than half of the 1 mm electrode is ineffective in terms of charge storage in the range of current densities investigated.

**Discharging behavior.**—The discharging behavior of a porous Ag/AgCl electrode with uniformly distributed charge (540 C/cm<sup>3</sup>) was investigated. Calculations were made for discharge current densities of 50 and 25 mA/cm<sup>2</sup>. The initial porosity was assumed to be 0.484 and the specific surface area of the electrode was assumed to be 4700 cm<sup>2</sup>/cm<sup>3</sup>. The variations in total overpotentials are shown by the solid curves in Fig. 6. The overpotential decreases in the beginning due to the rise in electrolyte concentration and the increase in electrolyte conductivity (see Fig. 7). As the active material (AgCl) is being depleted, the overpotential rises and the electrode finally shuts off when limiting current densities are reached. According to Fig. 6, the discharge efficiency is 92% at 50 mA/cm<sup>2</sup> discharge and 97% at 25 mA/cm<sup>2</sup> discharge. Evidently, due to the high level of concentration that can be reached inside the electrode, the discharge efficiency is less dependent on current densities as compared to the charge storage capacity in charging. The concentration in the back of the electrode during discharge can actually reach 2.5 moles/liter as shown in Fig. 7.

The local transfer current densities for the discharge case is more uniformly distributed relative to the

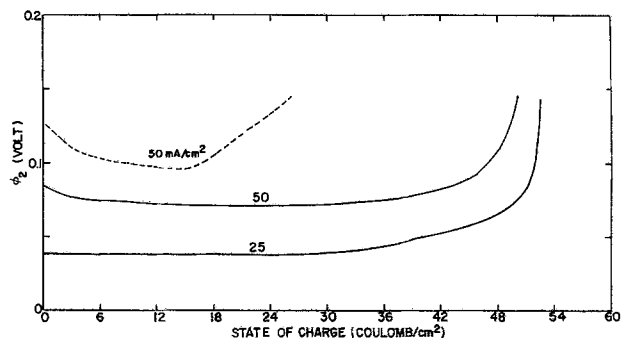


Fig. 6. Cathodic electrode overpotential ( $\phi_2$  at  $x = L$ ) vs. state of charge. —, Initial charge uniformly distributed (540 C/cm<sup>3</sup>); ---, charged initially by 50 mA/cm<sup>2</sup> for 18 min. (Total charge is the same for each case.)

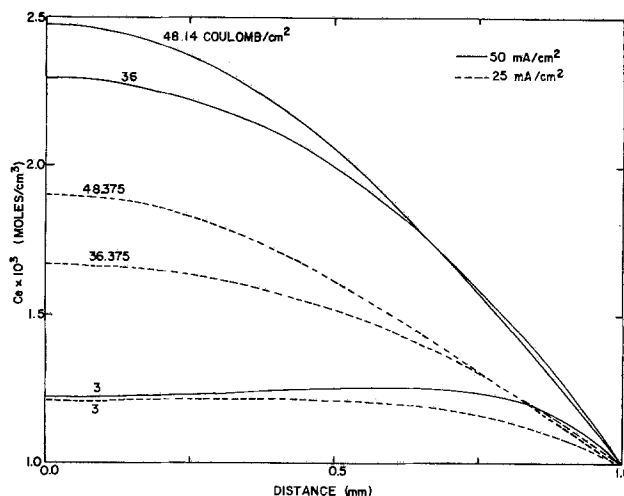


Fig. 7. Electrolyte concentration distributions at various stages of discharge. Discharging currents: —, 50 mA/cm<sup>2</sup>; ---, 25 mA/cm<sup>2</sup>. Uniform charge initially.

charging case. The maximum of the reaction rate moves toward the rear as the electrode is being discharged (Fig. 8). At the end of the discharge, the local transfer current density is actually the highest in the back of the electrode. For the high current discharge, the reaction rate distribution is such that the active material a little way inside the electrode is actually depleted first before the charge at the very front is used up as shown in Fig. 9. The low current discharge, however, consumes the charge at the front of the electrode first.

**Cycling behavior.**—To examine the cycling behavior of Ag/AgCl porous electrodes, calculations were made for the discharge of an electrode previously charged to 54 C/cm<sup>2</sup> at 50 mA/cm<sup>2</sup>. The initial charge distribution is shown in Fig. 5. The total overpotential with respect to degree of discharge is shown in Fig. 6. As shown by the dashed line, only about 48% of the charge stored is retrievable before the limiting current is reached. The electrolyte concentration inside the electrode can again reach a very high level as shown in Fig. 10. As a result, the reaction rate can be quite high in the back of the electrode as can be seen from Fig. 11. As the discharge continues, the little active material available in the rear of the electrode is soon depleted (see Fig. 12). The reaction rate at the front of the electrode, therefore, becomes higher. However, since the front of the electrode contains most of the stored charge, it has most of its surface covered by AgCl. The high local transfer current densities and the lack of reaction surfaces soon cause the limiting current den-

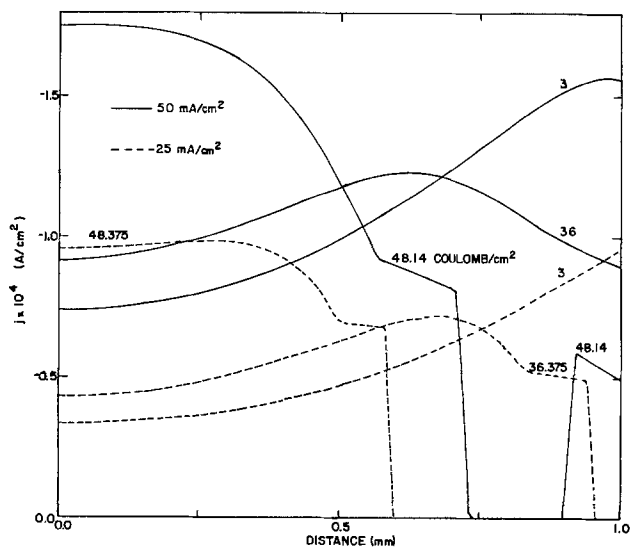


Fig. 8. Local transfer current density distributions at various stages of discharge. Discharging currents: —, 50 mA/cm<sup>2</sup>; ---, 25 mA/cm<sup>2</sup>. Uniform charge initially.

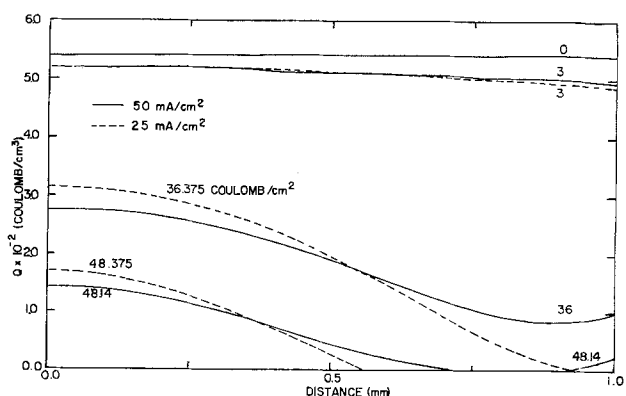


Fig. 9. Charge distributions at various stages of discharge. Discharging currents: —, 50 mA/cm<sup>2</sup>; ---, 25 mA/cm<sup>2</sup>. Uniform charge initially.

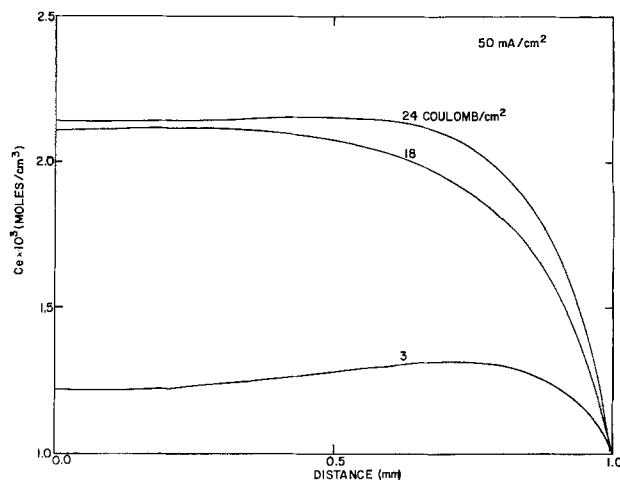


Fig. 10. Electrolyte concentration distributions during the discharge half-cycle. Current density 50 mA/cm<sup>2</sup>.

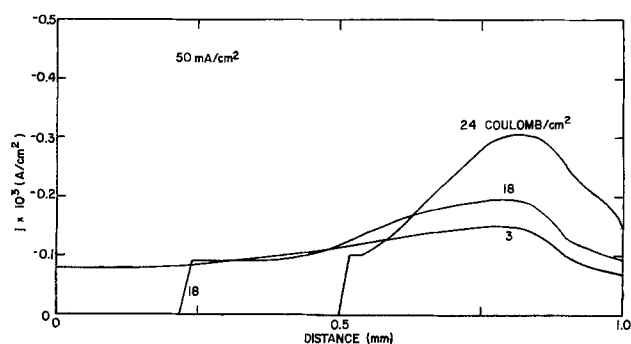


Fig. 11. Local transfer current density distributions during the discharge half-cycle. Current density, 50 mA/cm<sup>2</sup>.

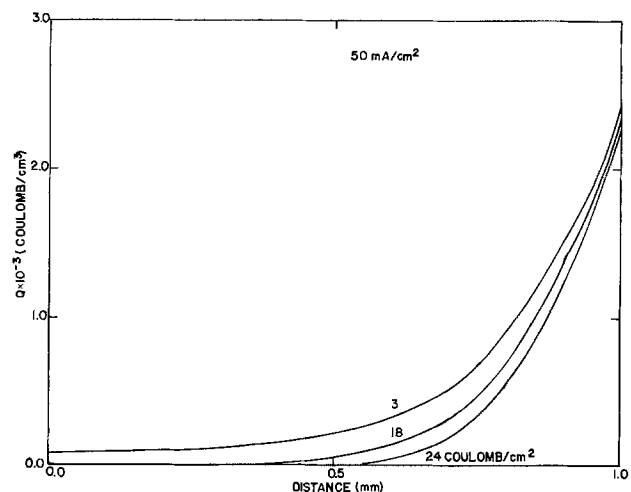


Fig. 12. Charge distributions during the discharge half-cycle. Current density, 50 mA/cm<sup>2</sup>.

ties to be reached before the charge stored as AgCl can be used efficiently.

### Discussion and Conclusions

The mathematical model can provide information for the design and improvement of electrode plates. For example, the charging behavior predicted for the Ag/AgCl electrode indicates that a large portion of the 1 mm electrode thickness from the electrode face to the center of the electrode plate was not used effectively for the current densities considered. Therefore, the optimum thickness of a real Ag/AgCl electrode plate should probably be less than 2 mm if operation above 25 mA/cm<sup>2</sup> is necessary for a large fraction of the charging cycle. The cycling calculations suggest

that the electrode should be charged at a low current density. In the charged state the AgCl should be uniformly distributed so that most of the stored charge can be used when the electrode is being discharged. No parts inside the porous electrode should exceed limiting current densities (and thus induce gasing) before the charge is fully utilized. The calculated results indicate that the concentration of the electrolyte inside the porous electrode plays an important role in the electrode performance for both charging and discharging.

There are still shortcomings in the proposed mathematical model. The specific surface area used in the model was assumed to be constant. This is not quite true since the morphology of the electrode surfaces changes during charging or discharging. The inclusion of the variation of surface area with time should be based on future experimental observations.

The functional dependence of  $\theta$  on the state of charge used in the present model is still not ideal. The amount of surface coverage with respect to the state of charge is not known accurately. An improvement in the description of  $\theta$  variations based on actual experimental observations is needed.

The value of  $k_m^0$  depends on the effective diffusion path of complex ions. The effective diffusion path of  $\text{AgCl}_{n+1}^{-n}$  conceivably changes during charging or discharging. The value of  $k_m^0$ , therefore, will actually vary with the state of charge. The nucleation mass transfer coefficient,  $k_{\text{nuclei}}$ , is dependent on the supersaturation level, local transfer current density, and surface condition. In the present model, both  $k_m^0$  and  $k_{\text{nuclei}}$  are assumed constant. The present treatment also does not include the effect of temperature differences resulting from nonuniform current distributions.

The plateau regions in the local transfer current density distributions shown in Fig. 8 and 11 are results of letting  $k_m^*$  be constant when  $\theta$  has reached 0.99. This limitation was applied to minimize the cost of computer calculations. During discharge calculations, as  $k_m^*$  was approaching zero, the local transfer current densities were very close to limiting current densities. If  $k_m^*$  was not limited, very short time steps were required to avoid exceeding limiting current densities by the calculated current densities before the true solution was reached.

### Acknowledgment

Financial support for this work was provided by the Office of Naval Research under contract No. N0014-75-C-0794 and the University of California.

Manuscript received Feb. 17, 1976. This was Paper 54 presented at the Dallas, Texas, Meeting of the Society, Oct. 5-9, 1975.

Any discussion of this paper will appear in a Discussion Section to be published in the June 1977 JOURNAL. All discussions for the June 1977 Discussion Section should be submitted by Feb. 1, 1977.

Publication costs of this article were assisted by the University of California with funds provided by the Office of Naval Research.

### LIST OF SYMBOLS

$A_i$	chemical symbol for species $i$
$a$	specific surface area per unit volume of the electrode, $\text{cm}^2/\text{cm}^3$
$C_1$	ratio of surface concentration to bulk saturation concentration of complexed ions, $c_R/c_R^{\text{eq}}$
$c_0$	solvent concentration, moles/ $\text{cm}^3$
$c_e$	electrolyte concentration, moles/ $\text{cm}^3$
$c_e^0$	electrolyte concentration outside the pores of the electrode, a constant, moles/ $\text{cm}^3$
$c_i$	concentration of species $i$ , moles/ $\text{cm}^3$
$c_R$	concentration of complexed ions at metal surface, moles/ $\text{cm}^3$
$C_R^{\text{eq}}$	equilibrium concentration of complexed ions with respect to electrolyte concentration $c_e$ , moles/ $\text{cm}^3$
$c_R^*$	equilibrium concentration of complexed ions with respect to the reference concentration $c_e^0$ , moles/ $\text{cm}^3$

$D$	diffusion coefficient of the electrolyte, $\text{cm}^2/\text{sec}$
$e^-$	symbol for the electron
$F$	Faraday's constant, 96,487 C/equiv.
$I$	superficial applied current density, A/ $\text{cm}^2$
$i_1$	superficial current density in metal phase, A/ $\text{cm}^2$
$i_2$	superficial current density in solution phase, A/ $\text{cm}^2$
$i_0$	exchange current density, A/ $\text{cm}^2$
$i_0^0$	concentration independent exchange current density, A/ $\text{cm}^2$
$j$	local transfer current density (anodic current positive), A/ $\text{cm}^2$
$K$	dissolution constant for complexation reaction
$k_m^*$	over-all mass transfer coefficient, $\text{cm}/\text{sec}$
$k_m^0$	mass transfer coefficient, $\text{cm}/\text{sec}$
$k_{\text{nuclei}}$	nucleation rate coefficient, $\text{cm}/\text{sec}$
$L$	electrode thickness, $\text{cm}$
$MX_n$	chemical symbol for a metal salt
$m_e$	molality of the electrolyte, moles/kg
$n$	numbers of electrons transferred in the electrode reaction
$P$	porosity factor for porous salt film
$Q$	amount of charge stored at a point within the electrode, C/ $\text{cm}^3$
$Q_{\text{max}}$	the maximum amount of active material storable in the pores, C/ $\text{cm}^3$
$Q^*$	a charge parameter indicating the transition of AgCl growth regions, C/ $\text{cm}^3$
$RT$	gas constant multiplied by the absolute temperature, joules/mole
$S$	shape factor for salt crystallites
$s_i$	stoichiometric number for species $i$ , subscripts 0 for solvent, + for cation, - for anion, M for metal, and R for reactant
$t$	time, sec; tortuosity factor (when in exponents)
$t_{+0}$	transference number of cation referred to solvent velocity
$v_{\square}$	superficial volume average velocity, $\sum_i c_i \bar{v}_i v_i$ , $\text{cm}/\text{sec}$
$v_i$	velocity of species $i$ in solution, $\text{cm}/\text{sec}$
$\bar{V}_i$	partial molar volume of species $i$ ; subscripts 0 for solvent, e for electrolyte, M for metal, and MX for salt; $\text{cm}^3/\text{mole}$
$x$	distance from backing plate, $\text{cm}$
$X^-$	symbol for an anion
$z_i$	charge number of species $i$

### Greek Symbols

$\alpha_a, \alpha_c$	kinetic parameters
$\gamma$	exponent in composition dependence of the exchange current density
$\gamma_{\pm}$	mean molal activity coefficient of the electrolyte
$\epsilon$	volume of pores to total volume of electrode
$\theta$	fraction of the metal area exposed, subscript $s$ represents the AgCl patch growth region and subscript $p$ represents the film thickening region
$\kappa$	conductivity, mho/cm
$\nu$	number of moles of ions into which a mole of electrolyte dissociates
$\nu_+, \nu_-$	number of cations (anions) into which a molecule of electrolyte dissociates
$\phi_1$	potential in metal phase, V
$\phi_2$	potential in solution phase, V
$\zeta$	exponent in composition dependence of the exchange current density

### REFERENCES

1. R. de Levie, *Adv. Electrochem. Electrochem. Eng.*, **6**, 329 (1967).
2. John Newman and W. H. Tiedemann, *Am. Inst. Chem. Engrs. J.*, **21**, 25 (1975).
3. K. Micka and I. Roušar, *Electrochim. Acta*, **19**, 499 (1974).
4. K. Micka and I. Roušar, *ibid.*, **18**, 629 (1973).
5. J. S. Dunning, D. N. Bennion, and John Newman, *This Journal*, **120**, 906 (1973).
6. D. Simonsson, *J. Appl. Electrochem.*, **3**, 261 (1973).
7. R. D. Giles, *J. Electroanal. Chem. Interfacial Electrochem.*, **27**, 11 (1970).
8. T. Katan, S. Szpak, and D. N. Bennion, *This Journal*, **120**, 883 (1973).
9. T. Katan, S. Szpak, and D. N. Bennion, *ibid.*, **121**,

- 757 (1974).  
 10. John Newman, *Ind. Eng. Chem., Fundam.*, **7**, 514 (1968).  
 11. Thomas W. Chapman, Ph.D. Dissertation, Chem.

- Eng., University of California, Berkeley (1967).  
 12. T. W. Chapman and John Newman, University of California Lawrence Radiation Lab. Report UCRL-17767 (May 1968).

# Analysis of Porous Electrodes with Sparingly Soluble Reactants

## IV. Application to Particulate Bed Electrode: Ag/AgCl System

Theodore Katan\*

Lockheed Palo Alto Research Laboratory, Materials Sciences, Palo Alto, California 94304

and Hiram Gu\*\* and Douglas N. Bennion\*

Energy and Kinetics Department,  
 School of Engineering and Applied Science, University of California, Los Angeles, California 90024

### ABSTRACT

Experiments were conducted to characterize critical processes which determine performance of totally immersed, porous, secondary electrodes having sparingly soluble reactants. Particulate beds comprised of silver spheres,  $37.7 \pm 4.2 \mu\text{m}$  in diameter, were used as Ag/AgCl electrodes in 1N KCl. Silver chloride product distribution and facial potential as functions of time during galvanostatic charging are compared to predictions of a recently developed mathematical model. Good accord is shown over the tested time range, 1-19 min, and exterior current density  $50 \text{ mA cm}^{-2}$ . Time for onset of pore blockage with failure to accumulate charge, about 18 min, and the reaction penetration, mostly less than 0.03 cm, are predicted with reasonable accuracy. A characteristic minimum in polarization occurs during galvanostatic discharge due to reduction in pore blockage at the beginning of discharge, increase in KCl concentration in the depth of the electrode, and increase in effective matrix electronic conductivity with silver deposition. A final rise in polarization occurs when silver chloride is depleted. Theory is used to show how governing rate processes are shifted by the occurrence of blockages of the first and second kinds.

In principle, the analyses of experimental studies of current distributions and morphological changes can be used to improve the design of battery electrodes. Rational design is possible only if it is known how electrode structure affects changes in distributions and morphology. Such experimental studies, however, are carried out with difficulty. Currents and structural changes occur within poorly accessible regions of thin electrodes often having pores less than  $10 \mu\text{m}$  in diameter (1). External devices used for experimental observations can disturb the conditions of normal operation.

Nevertheless, such experiments have now progressed along two paths: those dealing directly with idealized single pores (2-4) and those treating aggregates of pores in model porous electrodes more or less representing a real battery electrode (5-10).

In single pore studies the pore is considered to represent a real electrode constituted of multiple aggregates of this pore. Notably, Brodd (2) and Szpak *et al.* (3) attempted to provide an experimental basis for theoretical treatments of current distribution in segmented single pores larger than  $800 \mu\text{m}$  in diameter. Szpak and Katan (4) reduced the pore spacing to  $60 \mu\text{m}$  using microelectronic techniques and were able to observe the evolution of reaction profile. Serious application of these single pore studies has been somewhat delayed, mainly because practical porous electrodes often have smaller pores which are in fact interconnected and tortuous, and, also, theory needed to translate the findings is still under development.

Model electrodes having some resemblance to real electrodes have been studied with varying degrees of success in understanding the prevailing reaction modes and distributions, *i.e.*, by Alkire *et al.* for the Cu/CuSO<sub>4</sub> system (5, 6), by Bro and Kang for Cd/Cd(OH)<sub>2</sub> (7), by Nagy and Bockris for Zn/Zn(OH)<sub>2</sub> (8), by Szpak *et al.* for Ag/AgCl (9), and by Simonsson for PbSO<sub>4</sub>/PbO<sub>2</sub> (10). In some of these studies electrodes were cut into sections after charging or discharging, and the current distribution was inferred from the amount of chemical change that occurred in each section. This approach is used in the work presented here.

The merit of model or real electrodes over single pore electrodes lies in the more direct conformity of results. Mathematical representation can be given for the observed distribution curves with more assured application, and effects of the phenomena of blockage of the first and second kinds can often be distinguished and interpreted. Either the experimental studies or the developed mathematical representation can be used individually, but together they provide the most valuable means for insight into the principles involved in electrode operation.

It is the aim of this work to test the applicability of theory developed by Bennion and co-workers (11) for describing performance of totally immersed, porous, secondary electrodes having a sparingly soluble reactant. The theory has a fundamental basis on principles of transport and electrochemistry. Comparisons with experiment are made for AgCl product distribution in an Ag/AgCl electrode and for facial potential as a function of time during galvanostatic charging. Facial potential is also compared for the discharge cycle. After a series of preselected galvanostatic anodic treatments, the electrode is sectioned and each section is analyzed

\* Electrochemical Society Active Member.

\*\* Electrochemical Society Student Member.

Key words: porous electrodes, electrode design, batteries, silver/silver chloride electrode.



for AgCl content for the comparisons. Microscopic examinations are made of fully charged and discharged electrodes to assist in the interpretations.

The Ag/AgCl system was selected as representative of cathodes having sparingly soluble reactant because much is known of its electrochemical behavior. The system has been the subject of many detailed kinetic investigations, and the elementary processes controlling charge and discharge have been established for Ag surfaces partially covered with AgCl [e.g., see (12) and (13)]. Particulate beds consisting of loosely stacked uniform silver spheres, about 40  $\mu\text{m}$  in diameter, were used. The beds are conveniently prepared and easily sectioned without disturbing unsectioned portions. With uniform sphere beds, the initial porosity is essentially unchanged while specific surface is varied by changing sphere size. Transfer current is strongly dependent on depth rather than location at a given depth because of the uniformity in particle size. The structure is simple, easily reproduced, and has good matrix conductance for the 40  $\mu\text{m}$  silver spheres, about  $1.0 \Omega^{-1}\text{-cm}^{-1}$ .

### Experimental

**Apparatus.**—The apparatus consisted of a cell which housed the particulate bed electrode, a porous Ag/AgCl counterelectrode, and an Ag/AgCl reference electrode, together with associated instrumentation: a galvanostat, ammeter, and recording potentiometer. In Fig. 1 the general arrangement of the cell is shown. Details of the components have been previously described (13), with the exception of the reference electrode which is now differently placed. From its separate container, the Ag/AgCl reference (14) now communicates with the

front face of the particulate bed via a ca. 1/64 in. slit which surrounds the frontal face of the bed and which forms the junction of the upper removable part of the cell with the lower part having the spheres in a cuplike enclosure. A Saran film bag containing the reference electrode is sealed to the tubular Pyrex cell by Teflon pipe thread sealant tape. The particulate bed working electrode was always made 2.00 mm thick in the 1.41 cm diameter cup having a movable silver disk bottom for electrical contact, positioning, and sectioning. Electrolyte was 1N KCl.

**Experimental procedure.**—Silver spheres,  $37.2 \pm 4.2 \mu\text{m}$  in diameter, were washed and dried as previously described (13) and placed from a slurry with 1N KCl into the cup with the silver disk bottom. The disk was raised and silver particles were swept from the frontal plane with the straight edge of a spatula using the cup's rim as a guide to form a planar electrode face. The particles were swept onto a surrounding Teflon collar temporarily attached to the cup. This process was repeated, using a micrometer screw setting below the disk until the bed thickness was  $2.00 \pm 0.01 \text{ mm}$ . The Teflon collar was then removed and the cell was assembled.

During charging and discharging, the porous Ag/AgCl counterelectrode about 7 cm above the bed electrode collected the galvanostatic current, and the Ag/AgCl reference electrode with its exit slit placed at the facial edge of the bed was used to monitor potential. All charging and discharging in this work was at constant exterior current density, 50  $\text{mA cm}^{-2}$ . Some of the electrodes were cycled: charging until after the onset of a sharp increase in the rate of polarization increase, for about 25 min, and then discharging for the same time or coulombs, repeating for 5 cycles. Other electrodes were charged without cycling for time intervals from 1 to 8 min, differing by 1 min increments, and from 10 to 22 min, with 2 min increments. These charged electrodes were subsequently sectioned for analyses for AgCl. Prior to an experiment, the Ag/AgCl counterelectrode was anodically charged in a separate container with an amount of silver chloride in excess of that consumed during charging of the working electrode.

After a particulate bed was charged for a preselected time, the cell was disassembled and the electrode was sliced into ten sections, each section approximately 0.02 cm thick. Sectioning was conducted with a stainless steel blade with a fine saw-tooth edge after the electrode was raised above the rim of the holding cup with the micrometer screw, Fig. 1. The cut section was then removed to a Teflon collar and then to a beaker and the sectioning repeated. Each sliced section was treated with 20  $\text{cm}^3$  of deaerated 1.0M sodium thiosulfate solution to dissolve the accumulated AgCl, and the solution was then analyzed for Ag by the atomic absorption method. The metallic Ag from each section was weighed afterward so that the layer thicknesses could be calculated accurately.

In general, the equivalent number of coulombs of AgCl found experimentally exceeded the coulombs passed through the electrode during charging. Air was not excluded from the sample bottles containing the sectioned specimens, and the dissolution of oxides of silver in the 1M  $\text{Na}_2\text{S}_2\text{O}_3$  could account for the observed higher values determined by atomic absorption analyses. The discrepancy in coulombs was found to increase with passage of time, which was never over 4 days before analyses, indicating a continuing dissolution process of the silver specimen. For a given time after sampling the charge discrepancy was constant, never exceeding 20% of the total coulombs passed. An averaged constant discrepancy was subtracted from each section to make the value of the sum of the charge from each section equal to the galvanostatically passed coulombs. The data reported here are so corrected.

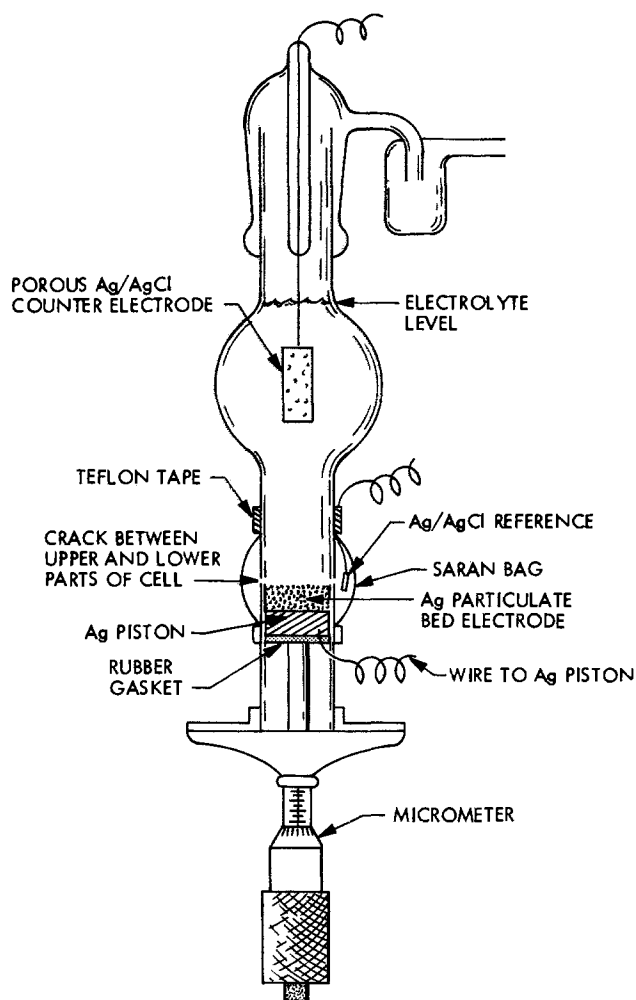


Fig. 1. Arrangement of particulate bed and counterelectrode in the sectioning cell. Cell is disassembled and micrometer screw is actuated for sectioning the bed.

The data collected from the AgCl analyses were plotted with charge,  $C\text{ cm}^{-3}$ , as a function of position for the various time intervals studied up to the onset of severe polarization, about 18 min at the  $50\text{ mA cm}^{-2}$  current density. The determined polarization as a function of time was also plotted for both the charging mode and the discharge mode during cycling.

**Microscopy.**—Optical and scanning electron microscopy were used to ascertain morphological changes leading to the onset of severe polarization which prevented further accumulation of AgCl charge and to compare the penetration depth with that determined by the slicing of the electrode into ten parts. Optical microscopy was conducted after the fully charged, unsliced electrode was dried, vacuum-impregnated with epoxy, sectioned, and polished metallographically. Electron microscopy was conducted with unsliced, fully discharged, previously cycled electrodes which were dried and then broken in half to reveal the internal structure. The charged and the cycled electrodes were found to have some structural strength; the particulate bed was bonded together by the electrochemical treatment, either by deposited silver chloride or silver (13).

For one fully charged electrode, an elemental electron microprobe analysis was conducted with an ARL electron microprobe Model EMX with  $67\text{ }\mu\text{m}$  intervals every 40 sec. Line width of the field was  $0.005\text{ mm}$  with a  $0.7\text{ mm}$  line length, the probe movement perpendicular to the line. In this way, by encompassing several sphere diameters at one depth into the electrode, statistical scatter was minimized. Calibration was with reagent grade AgCl, and the passed coulombs matched the sum of the sections to within 1%.

### Results and Interpretation

**Microscopic examinations.**—A metallographic section of the epoxy impregnated, fully charged electrode is shown in Fig. 2. This electrode was charged for 26 min at  $50\text{ mA cm}^{-2}$  when it could no longer accept further galvanostatic charging but suffered an onset of severe polarization and subsequent gas evolution. A layer of AgCl covers the electrode's frontal surface and blocks all passages to the internal parts of the particulate bed. Within the structure, for a distance of about  $0.02\text{ cm}$ , we also see Ag particles enveloped in AgCl. It appears that the final inability of the electrode to ac-

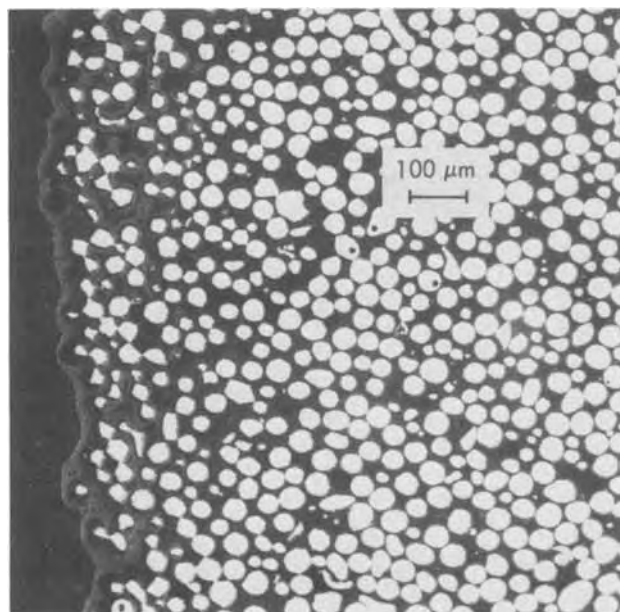


Fig. 2. Cross section of charged particulate Ag bed electrode with AgCl charge on frontal surface and inside the bed. Section taken after electrode held anodically at  $50\text{ mA cm}^{-2}$  for 26 min in  $1\text{N KCl}$ ,  $23^\circ\text{C}$ .

cept charge is caused both by this extensive blockage of the pores, blockage of the first kind, and of the pore walls, blockage of the second kind. The increased ohmic resistance for these two reaction paths could cause the observed severe polarization.

The electron microprobe analysis shown in Fig. 3, also indicates the sharp increase in AgCl charge near the frontal surface, at depths of  $0.01\text{ cm}$  or less, until the electrode is about 92% AgCl. This observation confirms the optical microscopy of Fig. 2 in that a nearly pure layer of AgCl coats the frontal portion of the electrode.

After a final discharging of the electrodes (five complete cycles), metallographic sections reveal the onset of a new silver morphology in the reaction zone, consisting mostly of very fine particles less than  $2\text{ }\mu\text{m}$  in diameter, with estimated porosity and specific surface area of 50% and  $15,000\text{ cm}^2\text{ cm}^{-3}$  (15, 16). The change in morphology extends ca.  $0.01\text{ cm}$  from the frontal plane, and remnants of the original  $37.2\text{ }\mu\text{m}$  diameter spheres are present, Fig. 4. The shape of the spheres originally present is changed, and the spheres' surfaces have become roughened. Erosion of the original spherical shape occurs within the reaction region with the reformation of a typical, small-particle morphology.

More details of the change in morphology can be seen in SEM photos as shown in Fig. 5. In the frontal region, about  $50\text{ }\mu\text{m}$  from the front face, small Ag crystallites, about  $0.5\text{ }\mu\text{m}$  in size, are clustered and mingled with larger Ag crystallites, about  $3\text{ }\mu\text{m}$  in size, Fig. 5b. A solid electrical path always exists through the clumps of crystallites which have grown together. Deeper into the electrode, about  $100\text{ }\mu\text{m}$  from the frontal plane, most Ag crystallites are larger, about  $2\text{--}3\text{ }\mu\text{m}$  in size, Fig. 5c. This effect of increase in crystal size with depth into the electrode is also evident in Fig. 4. The increase in specific surface area which results with the cycling is more effective at the lesser depths. This action occurs if the reaction penetration depth decreases with in-

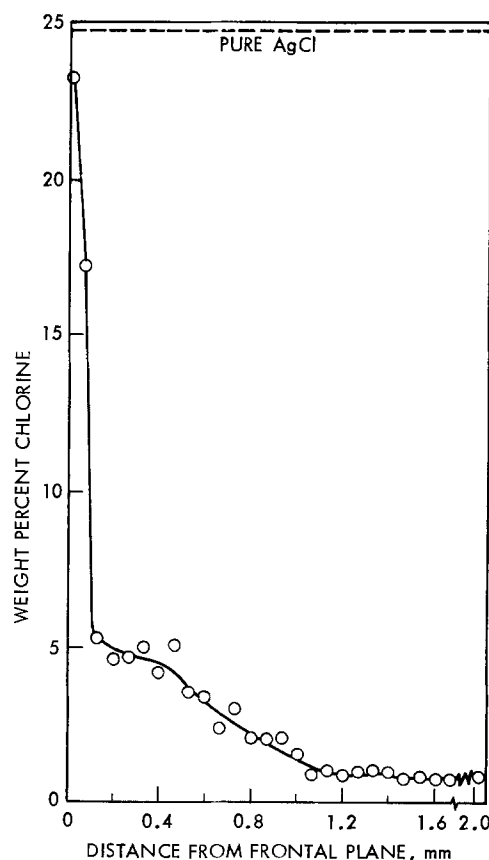


Fig. 3. Electron microprobe elemental analysis of charged Ag particulate bed electrode shown in Fig. 2. Probe moved perpendicular to field length,  $0.7\text{ mm}$ , and was taken at  $67\text{ }\mu\text{m}$  intervals.

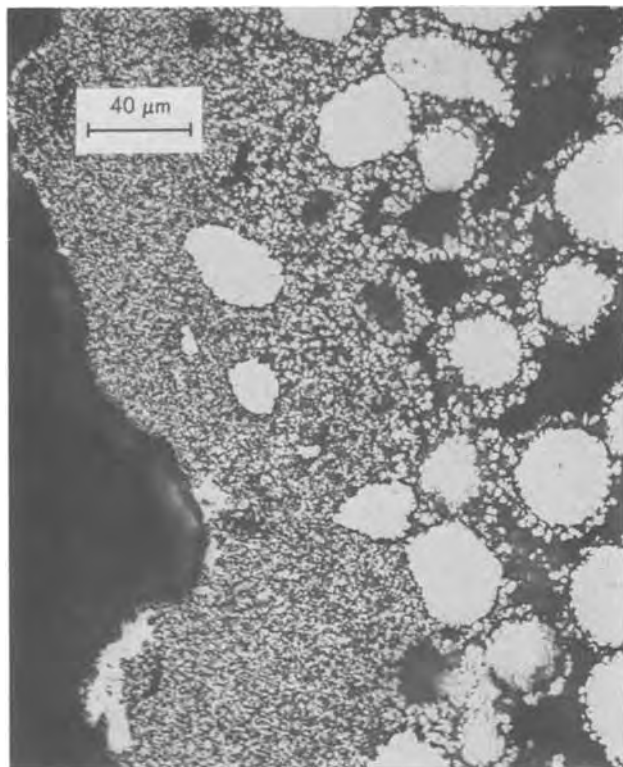


Fig. 4. Change in morphology of spherical silver structure in frontal region of particulate bed electrode, after five cycles of complete charge and discharge. Each cycle was for 50 min at  $50 \text{ mA cm}^{-2}$ .

creased specific surface area (17). Each cycle results in shallower penetration, and the frontal regions become most affected.

At about  $450 \mu\text{m}$  from the frontal plane, the texture of the original sphere surface becomes apparent as a heavily pitted and etched body, Fig. 5d. Metal has been removed from imperfection sites and grain boundaries (13).

*Potential/time relation for charging.*—Polarization during galvanostatic charging abruptly assumes a value of  $0.1\text{V}$  and then gradually increases to about  $0.3\text{V}$  after ca. 18 min, region I in Fig. 6. Thereafter, a sharp increase in polarization commences with eventual evolution of bubbles of gas, smelling of chlorine, and a consequent erratic response of polarization, region II. Polarization beyond  $1.2\text{V}$  brings the electrode into the potential region favorable for oxygen and chlorine evolution (18).

The more severe increase in polarization, region II of Fig. 6, is attributed to onset of nearly complete blockage both of the pore volume and pore surface by AgCl as indicated by the optical microscopy in Fig. 2 and by our previous communications (12, 13). It was shown that AgCl deposits at an approximately uniform thickness of about  $3500\text{\AA}$  at various locations on the pore walls and that these deposits first grow laterally until surface coverage is nearly completed. Thereupon, the film starts to thicken as polarization is increased (13, 19, 20). Within the particulate bed, the loss of Ag surface by AgCl film formation, blockage of the second kind, at the frontal regions of the electrode is followed by film thickening, resulting in blockage of the first kind, i.e., pore blockage by the accumulating AgCl. Eventually the front part of the electrode is covered by a thick AgCl layer blocking all of the pores

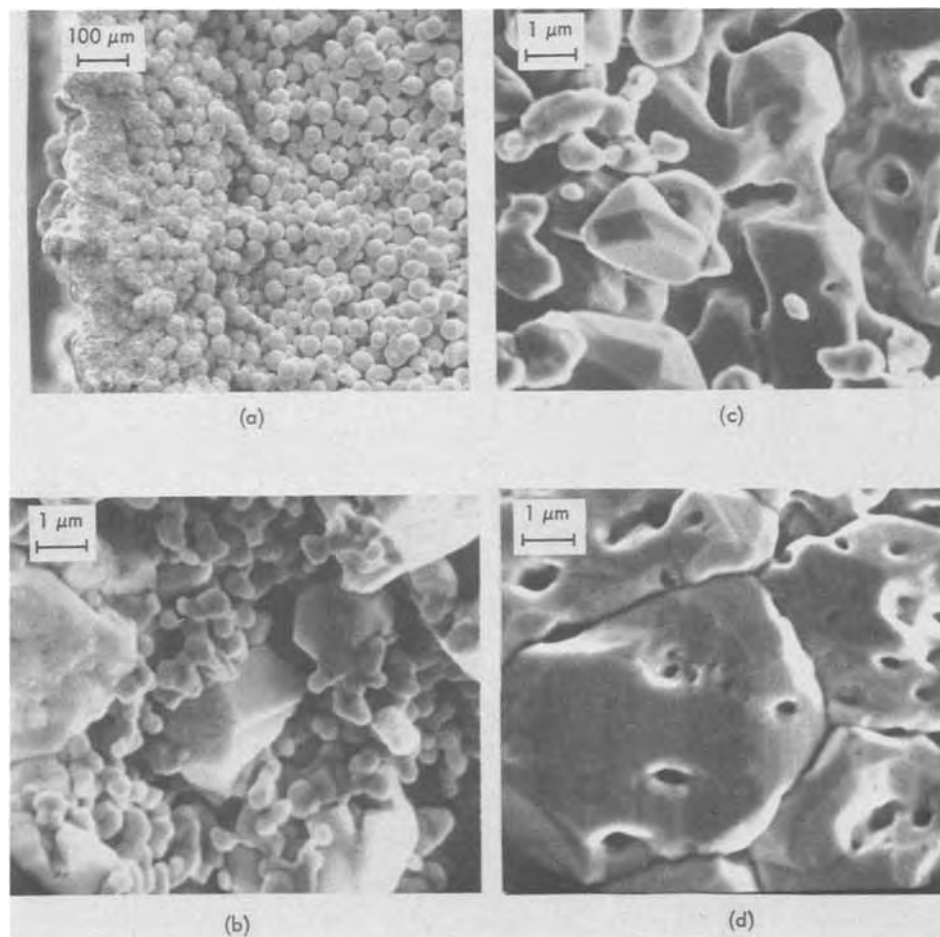


Fig. 5. SEM photographs showing cross section of cycled electrode. Five complete galvanostatic cycles were run, each 25 min of charge (anodic) and 25 min of discharge (cathodic) with a final reduction,  $50 \text{ mA cm}^{-2}$  in  $1\text{N KCl}$ ,  $23^\circ\text{C}$ . The Ag spheres in the bed originally appeared smooth and were about  $37.7 \mu\text{m}$  in diameter. (a) Morphological changes are shown as a function of depth into the electrode with the frontal plane shown on the left mostly affected; (b) Ag morphology at a  $50 \mu\text{m}$  depth is constituted of small Ag crystallites reformed from the spheres; (c) at a  $125 \mu\text{m}$  depth the reformed Ag crystallites can also be seen but are somewhat larger than at the frontal region; and (d) at a  $450 \mu\text{m}$  depth no crystallites are found but the crystal grain boundaries on the original spheres are deeply etched and isolated pits are formed (13).

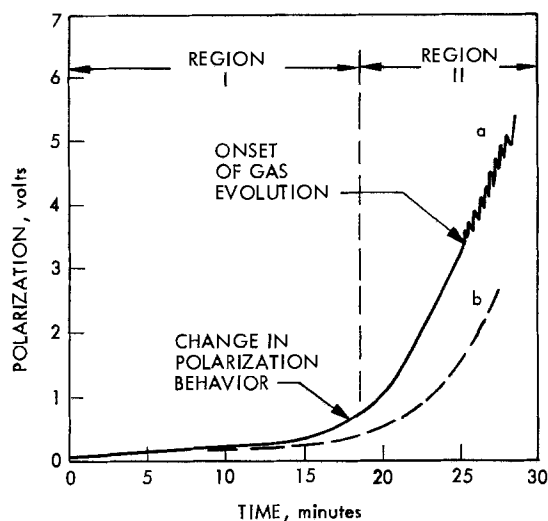


Fig. 6. Polarization increase during application of  $50 \text{ mA cm}^{-2}$  anodic current density to particulate bed electrode in  $1N \text{ KCl}$ ,  $23^\circ\text{C}$ . (a) Increase in polarization with a freshly prepared electrode; and (b) increase in polarization after the electrode has been charged for 25 min at  $50 \text{ mA cm}^{-2}$  and then fully discharged.

as shown in Fig. 2. Blockage of the first kind by KCl depletion and AgCl accumulation, with resultant increase in resistive path through the electrolyte, prevents the complete coverage of Ag surface by AgCl at depths greater than ca.  $0.01 \text{ cm}$ , Fig. 2 and 3.

Comparisons could be made of the experimentally determined polarization/time dependence with the results of theoretical treatment detailed by Gu *et al.* in the preceding study (11), i.e., for region I and the first part of region II in Fig. 5. Using parameters of the system given in Table I, we apply the theory as previously described to obtain the relation shown in Fig. 7 [cf. Fig. 2 in Ref. (11)]. Here, theory indicates the onset of severe polarization after 18 min in accord with experimental findings. Agreement for the polarization/time curve is seen to be good throughout the theoretically treated region to 19 min. These results are considered as evidence for validation of the theoretical method employed in this analysis of electrode behavior.

In application of the theory, a different expression was used for the fraction of exposed Ag area,  $\theta$ , for the condition when AgCl grows as a film parallel to the surface than that used for the condition when the AgCl film is thickening after the nearly complete coverage. Before film thickening occurs we use  $(1 - Q/Q^*)^s$ , an expression similar to that of Simonsson (21) having geometrical significance, while afterwards we use  $p^{(Q/Q^*)}$ , an expression whose functional de-

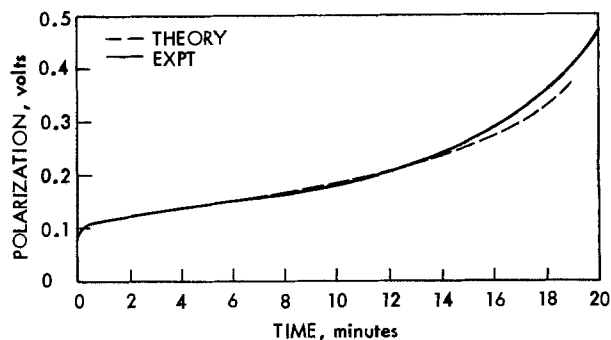


Fig. 7. Comparison of experimental results with computed curve. Theory of Gu *et al.* (11) applied with parameters of Table I, showing region I of Fig. 6 in more detail.

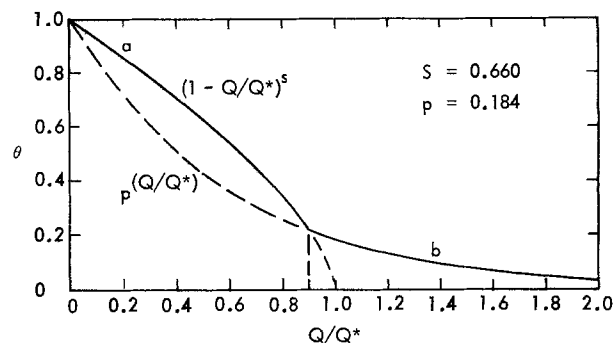


Fig. 8. Functional dependences of fractional coverage by AgCl,  $\theta$ , on the accumulated charge fraction,  $Q/Q^*$ . (a) For lateral film growth mode; and (b) for film thickening mode.

pendence appears reasonable for the situation of film thickening. Here,  $s$  and  $p$  are constants,  $Q$  is the charge, and  $Q^*$  is the charge required for nearly complete surface coverage, i.e., when the film thickening mechanism becomes active. In Fig. 8 we plot the two expressions for  $\theta$ . The term  $p^{(Q/Q^*)}$  is used after the intersection of the two curves when the process of film thickening is assumed to predominate for fractional surface coverage greater than 0.9.

If the electrode is cathodically reduced after charging and then charged again, polarization during the second charging is less throughout both regions of charging, Fig. 6, and the sharp increase in polarization then starts later, after ca. 21 min. The increased specific surface area after electrode reduction, from 1000 to an estimated  $15,000 \text{ cm}^2 \text{ cm}^{-3}$ , results in improved electrode performance, and a greater utilization is possible of the solid Ag present. With the cycled electrodes, the

Table I. Parameters of the Ag/AgCl particulate bed electrode used with theory of Gu *et al.* (11) to describe electrode's behavior, Fig. 7-10

Parameter	Value	Basis of parameter selection
Exterior current density, $\text{mA cm}^{-2}$	50	Measured
Temperature, $^\circ\text{C}$	25	Approximate measured value
Electrode thickness, mm	2.0	Measured
KCl concentration, $N$	1.0	Measured
Porosity at frontal plane	0.53	Estimated from photomicrographs
Porosity at depths greater than $0.45 \text{ mm}^*$	0.40	Approximate, measured value, Ref. (13)
Specific surface area at frontal plane, $\text{cm}^2 \text{ cm}^{-3}$	758	Calculated from porosity and sphere diameter, Ref. (15)
Specific surface area at depths greater than $0.45 \text{ mm}$ , $\text{cm}^2 \text{ cm}^{-3}$	970	Calculated from porosity and sphere diameter, Ref. (15)
Mass transfer coefficient, $k_m$ , $\text{cm sec}^{-1}$	0.3	Calculated from estimated diffusion coefficient, Ref. (12), and diffusion path, Ref. (13)
Concentration independent exchange current density, Ref. (11), $A \text{ cm}^{-2}$	$0.6 \times 10^{-4}$	Best value fitting data
Charge parameter, $Q^*$ , $C \text{ cm}^{-3}$	1.3A	From Ref. (12) where $A$ is specific surface area in $\text{cm}^{-1}$ and from assumption of 0.9 coverage factor, Fig. 8
Porosity factor, $P$	0.184	Assumed functional dependence and mode change at 0.9, Fig. 8
Shape factor, $S$	0.66	Geometrical reasoning, e.g., Ref. (21)

\* A parabolic decrease with distance is assumed for the porosity change at depths from 0 to  $0.45 \text{ mm}$  as an approximation based on photomicrographs.

\*\* Surface is calculated according to Ref. (15) from the porosity and sphere radius for depths from 0 to  $0.45 \text{ mm}$ .

smaller sized particles enable the accumulation of a greater charge, as observed in curve b, Fig. 6. Porosity of the original particulate bed and the reaction zone after 5 cycles changed less drastically, from 39 to an estimated 50%.

**Potential/time relation for discharging.**—The polarization/time relation for discharge was determined for a bed electrode previously charged *in situ* at 50 mA cm<sup>-2</sup> for 26 min, Fig. 9. Polarization was initially high during galvanostatic discharge because of the previous loss of electrically conductive paths caused by AgCl blockage at full charge, Fig. 2. Polarization sharply decreased, however, as electrically conductive paths were formed (20, 22), and then decreased more slowly as a balance was established between the processes of AgCl dissolution, diffusion, and electroreduction (12, 13) within the opened pores, Fig. 9. Pores are opened as the more bulky AgCl is reduced to Ag, *i.e.*, with the ratio of molar volumes of 2.51 to 1, respectively. Also, electrolyte conductivity is increased with AgCl reduction by the release of Cl<sup>-</sup>, and AgCl solubility increases. Finally, as AgCl area becomes very small, the over-all process becomes dissolution limited, and polarization increases sharply.

An accurate polarization/time dependence was not calculated (11) because the cost of running the computer code became prohibitive for times greater than 19 min on charging. Thus, the needed theoretical charge distributions for the full 26 min of charging could not be calculated. Also, the increase in silver surface area during discharging is not included in the present mathematical model. However, an approximate comparison of theory and experiment could be made by assuming constant initial AgCl charge density throughout the electrode. Applying the theory as previously described (11), we make this comparison in Fig. 9 [cf. Fig. 6 in Ref. (11)]. Here, fair agreement is obtained for the shape and magnitude of the curves. For a theoretically uniformly AgCl-charged electrode, the sharp initial decrease in polarization was not predicted, compare curves a and b, Fig. 9. Nevertheless, the gradual decrease in polarization could be shown as a result of electrolyte conductivity increase, curve b, Fig. 9, and the final increase matches fairly well with the experimental curve.

**AgCl charge distribution.**—Typical charge distributions are shown in Fig. 10. Here, results of experimental analyses of sections taken from galvanostatically charged electrodes are compared with results of theoretical treatment using parameters of Table I (cf. Fig. 5 in Ref. (11)). Agreement is generally good for the time span studied, 1-18 min. The accumulated AgCl charge density undergoes a characteristic rapid decrease with increased penetration into the electrode, and both theory and experiment show that the reaction's penetration depth does not change substantially

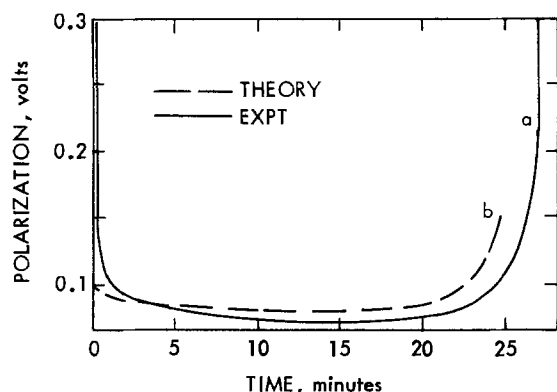


Fig. 9. Typical polarization behavior during a cathodic galvanostatic discharge, 50 mA cm<sup>-2</sup>, of previously AgCl charged electrode, 1N KCl, 23°C. The initial polarization drop is explained in terms of a removal of blockages whereas the final increase is explained by the removal of AgCl.

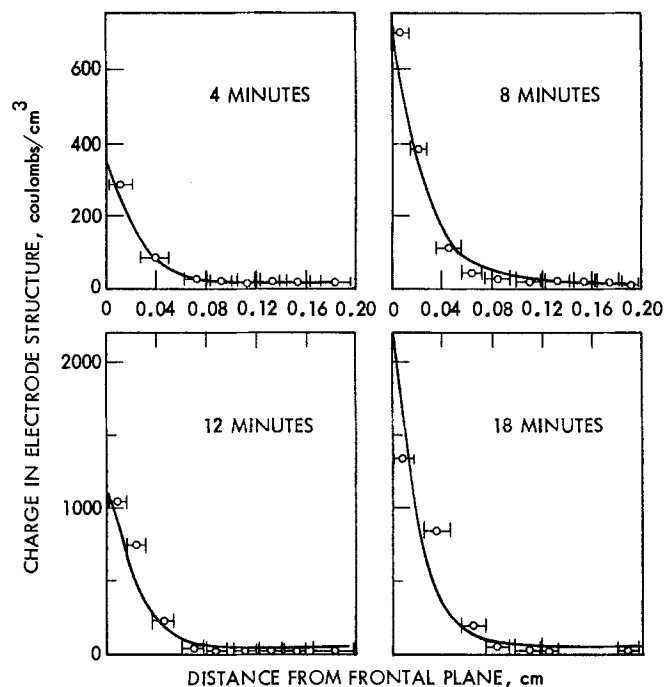


Fig. 10. Typical AgCl distribution within the particulate bed electrode. Experimentally determined distributions are shown by circles and theoretically computed curves are shown as a solid line. Charging times at 50 mA cm<sup>-2</sup> are indicated in each figure, 1N KCl, 23°C.

from a value less than *ca.* 0.03 cm over the full range of charging. Most of the reaction always takes place within a 0.03 cm depth at 50 mA cm<sup>-2</sup> even though the total accumulated charge undergoes an 18-fold change.

Charge penetration to within a small frontal region of the electrode is also shown by the SEM photos, Fig. 5a, and the cross section, Fig. 4, taken after 50 min of charging and discharging in 5 cycles. Here the penetration depth, judged from marked morphological change, can be seen to be about  $0.01 \pm 0.002$  cm. At greater depths the lesser extent of reaction is limited to the Ag sphere's surface, while at shallower depths reaction is so extensive that the original spherical shapes are no longer present. Repeated cycling tends to accent this effect because the Ag surface area is increased in the reaction zone, acting to bring the reaction even closer to the frontal plane (17).

## Discussion

Results have shown that theory developed by Gu, Bennion, and Newman (11) agrees consistently with the experimental findings with the selection of reasonable physical parameters for the system. The theory is shown to yield a good description of the actual increase in polarization with time, Fig. 7, and dependence of charge profile on time, Fig. 10.

Aside from this descriptive nature, the treatment can also yield an understanding of the governing processes which are undergoing dynamic changes during charge and discharge and which caused blockage of the first or second kinds. For example, during the charging process it can be determined from the programmed theory that the causes of the steep rise in polarization after 18 min are the onset of electrolyte depletion with decreased conductivity together with the loss of active Ag surface by coverage with AgCl. It can be seen that the depletion of Cl<sup>-</sup> by AgCl formation causes the current profile to be thrown toward the frontal region of the electrode, by the decrease of conductance in the modified Ohm's law expression of the theory (11), while the more gradual decrease in active surface,  $\theta$ , renders the reaction more difficult there, affecting the utilized redox kinetic expression (11). Thusly, the in-

terplay of blockage of the first and second kinds caused by changing rate processes may be realized. Ultimately, after 26 min, it could be shown from the Ohm's law expression that fractional void volume becomes so small that pore blockage by AgCl is essentially complete, as observed, Fig. 2.

The expressions of the theory may also be examined to find the extent of film thickening which occurs, here preferentially at the frontal surfaces, from the state of charge,  $Q/Q^*$  in Fig. 2. The constants  $p$  and  $s$  determine how effective the blockage is as the film starts to thicken rather than grow in a surface-spreading mode.

During discharge, the theory accounts for an initial decrease in polarization, Fig. 9, by the opening of blocked pores and by the increased conductivity of electrolyte from the released  $\text{Cl}^-$ . Finally, as AgCl is depleted the polarization rises, as observed. The alleviation of polarization during initial discharge by the growth of Ag filaments (22), which may be called the removal of blockage of the third kind, was not programmed into the theory.

### Conclusions

Theory developed by Gu, Bennion, and Newman (11) was found to give a good description of performance of a particulate bed electrode comprised of Ag spheres,  $37.7 \pm 4.2 \mu\text{m}$  in diameter, in 1N KCl. With reasonably selected physical parameters the theory could predict the onset of failure to accumulate charge, after 18 min at  $50 \text{ mA cm}^{-2}$ , the location of reaction profile mostly within a depth of 0.03 cm, and the shifts in governing rate processes which cause blockages during charge and discharge. The conformity of experiment and theory is submitted as evidence for the applicability of the given treatment as well as the usefulness of the theory in interpretation of morphological changes and electrode behavior.

### Acknowledgment

This work was supported by the Office of Naval Research.

Manuscript submitted Jan. 9, 1976; revised manuscript received April 6, 1976. This was Paper 55 presented at the Dallas, Texas, Meeting of the Society, Oct. 5-9, 1975.

Any discussion of this paper will appear in a Discussion Section to be published in the June 1977 JOURNAL. All discussions for the June 1977 Discussion Section should be submitted by Feb. 1, 1977.

Publication costs of this article were assisted by Lockheed Palo Alto Research Laboratory.

### REFERENCES

1. S. U. Falk and A. J. Salkind, "Alkaline Storage Batteries," John Wiley & Sons, Inc., New York (1969); G. W. Vinal, "Storage Batteries," 4th ed., John Wiley & Sons, Inc., New York (1924).
2. R. J. Brodd, *Electrochim. Acta*, **11**, 1107 (1966).
3. S. Szpak, J. D. Elwin, and T. Katan, *ibid.*, **11**, 934 (1966).
4. S. Szpak and T. Katan, *This Journal*, **122**, 1063 (1975).
5. R. C. Alkire, Ph.D. Thesis, University of California, Berkeley (1968).
6. R. C. Alkire, E. A. Grens, and C. W. Tobias, *This Journal*, **116**, 1328 (1969).
7. P. Bro and H. Y. Kang, *ibid.*, **118**, 519 (1971).
8. Z. Nagy and J. O'M. Bockris, *ibid.*, **119**, 1129 (1972).
9. S. Szpak, A. Nedoluha, and T. Katan, *ibid.*, **122**, 1054 (1975).
10. D. Simonsson, *ibid.*, **120**, 151 (1973).
11. H. Gu, D. N. Bennion, and J. Newman, *ibid.*, **123**, 1364 (1976).
12. T. Katan, S. Szpak, and D. N. Bennion, *ibid.*, **120**, 883 (1973).
13. T. Katan, S. Szpak, and D. N. Bennion, *ibid.*, **121**, 757 (1974).
14. A. S. Brown, *J. Am. Chem. Soc.*, **56**, 646 (1934).
15. T. Katan and H. F. Bauman, *This Journal*, **122**, 77 (1975).
16. H. W. Chalkley, J. Cornfield, and H. Park, *Science*, **110**, 295 (1949).
17. L. Nanis, *Plating*, **58**, 805 (1971).
18. W. M. Latimer, "Oxidation Potentials," 2nd ed., Prentice Hall, Inc., Englewood Cliffs, New Jersey (1952).
19. L. Y. Kurtz, *C. R. Acad. Sci., USSR*, **2**, 383 (1935).
20. W. Jaenicke, R. P. Tischer, and H. Gerischer, *Z. Elektrochem.*, **59**, 448 (1955).
21. D. Simonsson, *J. Appl. Electrochem.*, **3**, 261 (1973).
22. V. B. Aleskovskii, E. V. Bairachnyi, E. G. Ivanov, and V. A. Nikolskii, "Sbornik Rabot po Khimicheskim Istochnikam Toka," No. 4, p. 241, Energiia Press, Leningrad (1969).

## Technical Notes



### Long-Lived Sn(IV) Sensitizer Baths for Photoselective Metal Deposition

B. K. W. Baylis, A. Busuttill, N. E. Hedgecock, and M. Schlesinger\*

Department of Physics, University of Windsor, Windsor, Ontario, Canada N9B 3P4

In a previous publication (1) we reported that Sn(IV) can be used as a sensitizer for Cu plating and for Ni-P plating from an acidic bath. Irradiation of the catalyzed surface with ultraviolet light after the Pd(II) activation step was shown to be a necessary condition for copper plating, but was found to prevent Ni-P plating. Ni-P plating occurs on the catalytic surface not exposed to u.v. light; hence the images resulting from irradiation through a mask and subsequent Ni-P plat-

ing replicate the mask, i.e., are positive images. It should be emphasized that copper plating occurs only on the irradiated catalyst, resulting in a clean negative image of the mask. This "stimulated" negative, where irradiation is necessary for plating, since no plating occurs on nonirradiated areas, is of course strikingly different from the negatives we reported earlier (2), obtained with Sn(II) as the sensitizer and u.v. irradiation following the postactivation rinse. In this latter case, the nonirradiated area plates as usual, but the irradiated area plates faster. This gives an image of

\* Electrochemical Society Active Member.

Key words: electroless, sensitizer, photoselective, thin films.



low contrast. For practical applications, particularly in the fabrication of printed circuitry, the "stimulated" negative image, having much higher contrast, is more useful.

It was further reported in Ref. (1) that the Sn(IV) sensitizer is only effective for imaging if it is between ~20 and ~45 hr old. We have now been able to extend the useful lifetime of Sn(IV) sensitizer baths for up to three months. The technique is to let hydrolysis of the Sn(IV) chloride proceed until the bath is cloudy and to add hydrochloric acid to slow further hydrolysis and to prevent formation of long colloidal particles. Because these baths are left in beakers covered only by watch glasses, the evaporation occurring over such a long time is quite significant. Nonetheless they can be used for making sharp images even after their volume has halved and the colloid has redissolved, leaving a clear solution. [See Ref. (1).]

These baths were made by diluting 2.5 ml of a stock solution, which contains 10g SnCl<sub>4</sub> · 5H<sub>2</sub>O in 12.5 ml concentrated HCl, to 200 ml with distilled water. After

anywhere from 26 to 55 hr (i.e., after the solution became cloudy), 1 ml concentrated HCl was added. After a week or more, another 1 ml concentrated HCl was added. This second addition has been made after from 6 to 13 days, resulting in solutions which remained highly effective for up to three months.

#### Acknowledgment

This research has been supported by the National Research Council of Canada.

Manuscript received April 26, 1976.

Any discussion of this paper will appear in a Discussion Section to be published in the June 1977 JOURNAL. All discussions for the June 1977 Discussion Section should be submitted by Feb. 1, 1977.

Publication costs of this article were assisted by the University of Windsor.

#### REFERENCES

1. B. K. W. Baylis, A. Busuttill, N. E. Hedgecock, and M. Schlesinger, *This Journal*, **123**, 348 (1976).
2. M. Schlesinger, *ibid.*, **121**, 667 (1974).

## Application of Wagner's Theory to the Electropolishing of Aluminum

M. Zamin,\* P. Mayer,\*\* and M. K. Murthy

Ontario Research Foundation, Mississauga, Ontario, Canada L5K 1B3

It is known (1) that during the electropolishing of metals, a horizontal plateau is obtained when the anode current density ( $i$ ) is plotted against the cell voltage ( $V$ ). Edwards (2, 3) has suggested that this plateau is due to the diffusion of an "acceptor" to the anode for metal ions. Thus, the plateau corresponds to a maximum concentration gradient when practically all the acceptor approaching the anode readily reacts with the metal ions resulting in a much lower acceptor concentration at the anode as compared to its bulk concentration. Wagner (4) suggests that this interpretation of the  $i$ - $V$  curve implies "that either the standard free energy of non-hydrated cations is much higher than that of hydrated cations, or the activation energy for the formation of non-hydrated cations is considerably greater than the activation energy for the formation of hydrated cations." Such a process has been termed "an ideal electropolishing process" by Wagner (4) who published the first quantitative mathematical description of the electropolishing process.

A detailed outline of Wagner's theory can be found in the original paper (4). However, in order to help clarify the use of the theoretical equations, a brief account of the essential features is summarized below.

Consider a surface whose roughness can be described by a sine-wave profile with a wavelength,  $a$ , and an amplitude,  $b$ . If an "ideal electropolishing process" is considered then the metal ions are consumed immediately upon arrival to the outside of the hydrodynamic polishing layer of thickness,  $\delta$ . For such a process the displacement  $u$  for a decrease of the amplitude from  $b_0$  to  $b$  is given by

$$u = \frac{a}{2\pi} \ln \frac{b_0}{b} \quad \text{if } b \ll a, a \ll \delta \quad [1]$$

where  $b_0$  and  $b$  are the amplitudes of the sine-wave surface profile at times  $t = 0$  and  $t = t$ , respectively.

\* Electrochemical Society Student Member.

\*\* Electrochemical Society Active Member.

Key words: aluminum, electropolishing, Wagner's theory, metal removal rate.

The corresponding loss of metal per unit area,  $\Delta m/A$ , is

$$\frac{\Delta m}{A} = u\rho = \frac{a\rho}{2\pi} \ln \frac{b_0}{b} \quad [2]$$

The charge consumed in the electropolishing process is given by

$$Q = it = \frac{96,500}{EqW} \frac{a\rho}{2\pi} \ln \frac{b_0}{b} \quad [3]$$

where  $EqW$  is the equivalent weight of the metal, 96,500 is the Faraday constant in coulombs per equivalent,  $i$  is the polishing current density, and  $t$  is the time.

#### Experimental

Specimens were made from commercial purity aluminum<sup>1</sup> which was in the form of rods, 1.2 cm in diameter and 16 cm long. One end of the rod was machined on a lathe and threads were cut over a length of 5 cm by a flat-wedged tool bit. The resultant profile of the surface was determined by the Talysurf 4.<sup>2</sup>

The electropolishing solution was a commercially available product called Electro Glo 100.<sup>3</sup> For use, 1 part by volume of this product is mixed with 3 parts by volume of orthophosphoric acid (85%). The temperature of the solution was maintained in the range 70° ± 2°C by a hot plate. The polishing cell consisted of a beaker 12 cm in diameter and 15 cm deep with a cylindrical lead cathode. The solution was stirred mechanically by a Teflon stirrer. A conventional series circuit was used. The power was supplied by a Hewlett-Packard d-c power supply<sup>4</sup> and the anodic current was measured by an ammeter. The surface profile of the specimen was determined by the Talysurf. The results reported are for the same specimen polished for various periods of time. The experimental procedure was

<sup>1</sup> Analysis in weight percent: Cu 0.15-0.4; Si 0.40-0.8; Fe 0.70; Mn 0.15; Mg 0.8-1.2; Zn 0.25; Cr 0.04-0.35; Ti 0.15.

<sup>2</sup> Manufactured by Rank Precision Industries Limited, Leicester, England.

<sup>3</sup> Trademark of the Electro-Glo Company, Chicago, Illinois.

<sup>4</sup> Model 6269B, 0-60V, 0-50A.

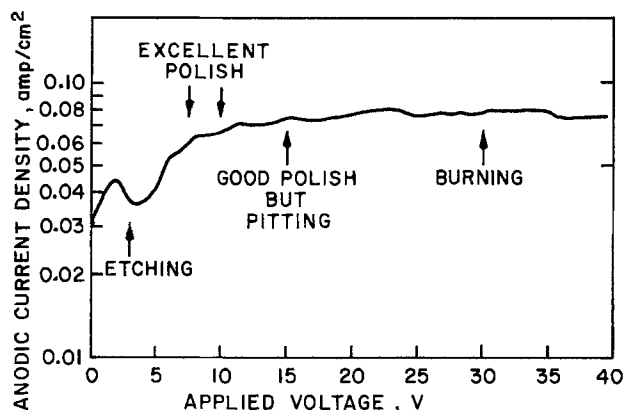


Fig. 1. The anodic current density-applied voltage curve for the electropolishing of aluminum.

as follows: The surface profile of the initial surface was noted by the Talysurf. The specimen was cleaned by dipping in an ultrasonic bath containing petroleum ether for 5 min, air dried, and then polished for various periods of time. After each polish, the specimen was washed in tap water, dipped in the petroleum ether solution, air dried, and then its surface profile determined.

### Results and Discussion

The anodic current density-applied voltage curve for the electropolishing of aluminum in Electro Glo 100 is shown in Fig. 1. It is to be noted that although a typical plateau, similar to the one noted by Jacquet (1) and Elmore (5) is obtained over an extremely large potential range, not all regions of the curve are suitable for electropolishing. In fact, there is only a small range (7-10V) in which the polishing is excellent. Lower voltages lead to etching of the surface whereas higher voltages cause burning. The results shown in Fig. 1 are very similar to those of Powers (6) for the electropolishing of copper in phosphoric acid solutions containing 10-15 g/liter of cupric ions. Powers (6) observed a current density plateau over a large anodic overvoltage region, but found that only part of the curve was suitable for electropolishing.

The values of  $a$  and  $b$ , the wavelength and amplitude, as determined from the surface profile are given in Table I. It is to be noted that with time of electropolishing, the amplitude ( $b$ ) decreases signifying smoothening, although the wavelength ( $a$ ) does not change.

Since the equivalent weight of aluminum is 8.99g, Eq. [3] simplifies to

$$Q = 80.76 \ln \frac{b_0}{b}, \quad \text{C/cm}^2 \quad [4]$$

The value of the charge consumed during the process of electropolishing ( $Q$ ) can be determined in two ways. First, the anodic current density (in amperes per square centimeter) can be multiplied by the time of polishing (in seconds) and the charge ( $Q_{\text{obs}}$ ) obtained (in coulombs per square centimeter). In the present case,  $Q_{\text{obs}}$  is the total charge passed up to that instant of polishing. Secondly, the charge can be calculated ( $Q_{\text{cal}}$ ) from Eq. [4] knowing the decrease in amplitude.

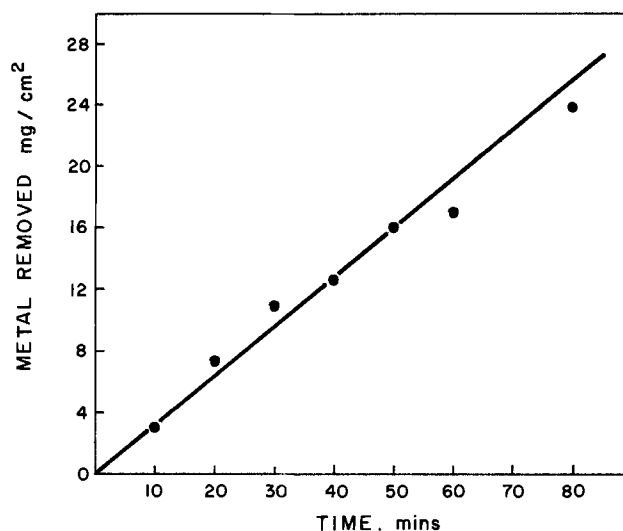


Fig. 2. Metal removed as a function of time for the electropolishing of aluminum.

These charges can be compared and taken as a test for the Wagner theory. These calculations are presented in Table I. It can be seen that although the calculated charge is generally less than the observed charge, the values are within 15% of one another. It is, therefore, evident that the electropolishing of aluminum provides a fair test for the validity of Wagner's theory (4).

Two possible causes for the discrepancy in the calculated and observed charges can be considered. First, the experimental error and, secondly, a lower current efficiency for metal dissolution. The experimental error can account for a discrepancy up to about 8%. More important perhaps is the fact that Eq. [3] has been derived under the assumption that all the charge is involved in the polishing process with no side or extraneous reactions occurring. In other words, a 100% current efficiency has been assumed. However, if the anodic current density is also involved in any side reactions, for example oxygen evolution, then the current efficiency will be less than 100%. Since gas evolution was observed at the anode during the electropolishing process, an error in the observed and calculated values of the charge is then due most likely to a lower current efficiency for the electropolishing process rather than any discrepancy in the theory. Lower current efficiencies for metal dissolution are known to be present in the electropolishing of metals (7).

The amount of metal removed per unit area as calculated from Eq. [2] is shown in Fig. 2 as a function of the polishing time. The rate of metal removed as determined from the slope of the curve is 0.32 mg/cm<sup>2</sup>/min which is equivalent to a rate of 1.2  $\mu\text{m}/\text{min}$ . This rate is lower than that reported in literature (3  $\mu\text{m}/\text{min}$ ) for the electropolishing of aluminum in perchloric acid-acetic anhydride solution (8). A possible reason for the discrepancy is that perchloric acid base solutions are inherently more "aggressive" than phosphoric acid based ones. For example, the electrolytic polishing of 18/8 stainless steel in the two solutions gives the following metal removal rates (8): perchloric acid-acetic

Table I. The wavelength and amplitude variation during the electropolishing of aluminum

Time (min)	$a$ (cm)	$b$ (cm)	$\ln \frac{b_0}{b}$	$i$ (A/cm <sup>2</sup> )	$Q_{\text{obs}}$ (C/cm <sup>2</sup> )	$Q_{\text{cal}}$ (C/cm <sup>2</sup> )	$\frac{Q_{\text{cal}}}{Q_{\text{obs}}}$
0	0.0175	0.00153	—	—	—	—	—
10	0.0175	0.00100	0.486	0.066	39.6	32.8	0.83
20	0.0175	0.000572	0.981	0.066	79.2	79.2	1.00
30	0.0175	0.000351	1.47	0.072	122.4	118.7	0.97
40	0.0175	0.000237	1.67	0.062	159.6	134.9	0.85
50	0.0175	0.000178	2.15	0.055	192.6	173.6	0.90
60	0.0175	0.000160	2.26	0.062	229.8	181.7	0.79
80	0.0175	0.000064	3.18	0.062	304.2	256.8	0.85



anhydride = 0.60  $\mu\text{m}/\text{min}$ ; orthophosphoric acid-glycerine = 0.15  $\mu\text{m}/\text{min}$ .

Lower metal removal rates have the distinct advantage in that they offer better control of the polishing process. Apart from the fact that orthophosphoric acid electrolytes yield surface finishes which are superior to perchloric acid electrolytes, they are much safer to use as well (8).

The diffusion of an "acceptor" to the anode is the controlling mechanism in the Wagner theory (4). However, recently Kojima and Tobias (9) showed that for the electropolishing of copper in phosphoric acid solutions, the outward diffusion of the anodic reaction product (copper phosphate) is the rate-limiting step. It is difficult to distinguish between the two mechanisms on the basis of the results reported here. Interestingly enough, however, Nicholas and Tegart (10) pointed out that results similar to those predicted by Wagner's theory can be obtained without making any assumptions about the mechanism of the polishing process.

#### Acknowledgments

This work was carried out under a grant from the Ontario Government, Ministry of Industry and Tourism, to the Ontario Research Foundation.

Manuscript submitted March 19, 1976; revised manuscript received May 14, 1976.

Any discussion of this paper will appear in a Discussion Section to be published in the June 1977 JOURNAL. All discussions for the June 1977 Discussion Section should be submitted by Feb. 1, 1977.

Publication costs of this article were assisted by the Ontario Research Foundation.

#### REFERENCES

1. P. A. Jacquet, *Nature*, **135**, 1076 (1935); *Trans. Electrochem. Soc.*, **69**, 629 (1936).
2. J. Edwards, *J. Electrodepositors Tech. Soc.*, **28**, 137 (1952).
3. J. Edwards, *This Journal*, **100**, 189C, 223C (1953).
4. C. Wagner, *ibid.*, **101**, 225 (1954).
5. W. C. Elmore, *J. Appl. Phys.*, **10**, 724 (1939); **11**, 797 (1940).
6. R. W. Powers, *Electrochem. Tech.*, **2**, 274 (1964).
7. M. Datta and D. Landolt, *This Journal*, **122**, 1466 (1975).
8. W. Tegart, "The Electrolytic and Chemical Polishing of Metals," p. 111, Pergamon Press (1959).
9. K. Kojima and C. W. Tobias, *This Journal*, **120**, 1026 (1973).
10. J. F. Nicholas and W. Tegart, *ibid.*, **102**, 93C (1955).



## Silicon Oxidation Studies: Analysis of SiO<sub>2</sub> Film Growth Data

E. A. Irene\* and Y. J. van der Meulen\*

IBM Thomas J. Watson Research Center, Yorktown Heights, New York 10598

### ABSTRACT

This study is aimed toward identifying the reasons why large discrepancies exist in the literature relative to the kinetic constants which are supposed to describe the thermal oxidation of single crystal silicon (Si) in pure oxygen (O<sub>2</sub>). In order to obtain sufficient quality and quantity of silicon dioxide (SiO<sub>2</sub>) film growth thickness-time data, an automated ellipsometer was used to measure the SiO<sub>2</sub> thickness *in situ*. The resulting data was fitted to the generally accepted linear-parabolic model by several commonly used methods and the results compared. Careful attention was given to eliminating trace amounts of H<sub>2</sub>O and Na so that the data are representative of oxidation in pure O<sub>2</sub>; the oxidation data was compiled in the temperature range of 780°-980°C. Calculated standard deviation values were used to evaluate the quality of the fit of the data to the model. From this analysis an initial regime of rapid oxidation was identified which does not conform to linear-parabolic kinetics. This regime extends up to about 350Å. A best fit of the data to the model was achieved using data above 350Å. By using either data below 350Å or only data greater than about 1100Å, large curve-fitting errors (~50% in terms of rate constants) were obtained. It was concluded that this source of error in combination with impurity effects, insufficient data, and the specific form of the curve-fitting equation could yield the large reported discrepancies. The activation energy calculated from the linear rate constants of this study (1.5 eV) indicates that O-O bond breaking is important for linear kinetics and the activation energy for the parabolic rate constants (2.3 eV) is too large to be correlated with a reported value (1.2 eV) for the diffusion of O<sub>2</sub> through SiO<sub>2</sub>.

As evidenced by the large number of publications on the subject, the thermal oxidation process by which thin films of silicon dioxide (SiO<sub>2</sub>) are formed on silicon (Si) is of great technological importance. Surprisingly, however, there is considerable variance among the reported rate constants which are supposed to describe the oxidation process. As shown in Table I, there is a spread of about 300 and 50% in the linear and parabolic rate constants, respectively. Yet there is almost general agreement that the thermal oxidation of Si follows mixed linear-parabolic kinetics [see, for example, Ref. (1)-(5)]. The present study is aimed at finding the reasons for the larger discrepancies in the reported rate constants and thereby provide accurate rate constants for further interpretation. With this purpose in mind it is useful for comparison to consider the two commonly used forms for the linear-parabolic equation utilized to describe the SiO<sub>2</sub> film growth data.

The first equation has received attention due to Deal and Grove (1) who applied the mixed linear-parabolic oxidation rate law derived by Evans (6) to the thermal oxidation of Si. The resulting integrated rate equation has the form

$$t - t_0 = A(d - d_0) + B(d^2 - d_0^2) \quad [1]$$

where  $d$  is the film thickness for an oxidation time  $t$ ; and  $A$  and  $B$  are the reciprocals of the linear ( $k_{LIN}$ ) and parabolic ( $k_{PAR}$ ) rate constants, respectively. The

terms  $d_0$  and  $t_0$  can represent either an initial oxide thickness which is present prior to an oxidation experiment (at  $t_0 = 0$ ) or a regime of initial oxidation defined by ( $d_0, t_0$ ) which precedes the linear-parabolic regime. Several publications [see, for example, Ref. (1)-(5)] assert that the linear-parabolic mode is preceded by a more rapid oxidation regime. Essentially, Eq. [1] is derived from a consideration of three fluxes in a steady state: the flux of oxidant from an ambient gas to the gas-SiO<sub>2</sub> interface; the flux of oxidant through the SiO<sub>2</sub> film; and the flux which represents the extent of reaction of oxidant with Si at the SiO<sub>2</sub>-Si interface.

The second equation [see, for example, Ref. (2)] has the form of a truncated Taylor series

$$t - t_0 = A'(d - d_0) + B'(d - d_0)^2 \quad [2]$$

Table I. Sample rate constants for the oxidation of silicon (<111> Si, dry O<sub>2</sub>, 1 atm, 900°C)

$k_{LIN}$ (Å/min)	$k_{PAR}$ (Å <sup>2</sup> /min)	Reference
2.8	6800	(1)
9.7	6220	(2)
5	—	(4)
(2 for <100> Si)	—	(4)
7	4800	(5)
(4 for <100> Si)	(2300 for <100> Si)	(5)

\* Electrochemical Society Active Member.

Key words: insulating films, oxidation kinetics, rate constants.

The terms in this equation are defined the same as those for Eq. [1]. Equation [2] is not mathematically derived from a physical description of the oxidation system, but rather is simply the sum of a linear term which represents first order kinetics for the reaction of Si and oxidant and a parabolic term which represents a diffusional limitation of oxidant through the SiO<sub>2</sub> film. Since for Eq. [2] there is no specific physical model, the rate constants obtained by Eq. [2] cannot be directly correlated with physical parameters of the oxidation system.

Equations [1] and [2] have the same mathematical form and therefore, when experimental data is fitted to either equation using identical procedures, equivalent curve-fitting errors will be obtained but different numerical values for the rate constants will result. The rate constants for Eq. [1] and [2] are related as shown later (Eq. [3]). However, the spread in the reported experimental rate constants shown in Table I, which were obtained using the above equations, is outside the range anticipated based on the mathematical differences between Eq. [1] and [2]. Therefore it is of interest to examine other causes for the large discrepancies such as previously reported impurity effects (2, 5), the sufficiency and accuracy of the experimental data, and the particular method of data analysis.

The purpose of the present study was to obtain SiO<sub>2</sub> film growth time-thickness data of sufficient quality and quantity to provide accurate rate constants for a thorough analysis of the above-mentioned possible sources of error. In this context, particular attention was given to the exclusion of Na (2) and H<sub>2</sub>O (5) effects and we believe that the data are representative of the oxidation of Si in pure oxygen. An automated ellipsometer (7) capable of measuring the SiO<sub>2</sub> film thickness *in situ* during an actual oxidation experiment was used to obtain the data for this study.

### Experimental Procedures

**Sample preparation.**—All substrates were <100> oriented chem-mechanically polished silicon wafers measuring 3.2 cm in diameter and 0.025 cm in thickness. All the wafers were p-type with a nominal resistivity of 2 ohm-cm. It was reported previously (5) that the resistivity type or value in the range 0.5-10 ohm-cm had no influence on the oxidation process. The wafers were cleaned as reported elsewhere (5) and an initial oxide thickness of from 3 to 6 Å SiO<sub>2</sub> was measured at room temperature. Previously (4, 5), a thickness of 10-12 Å was reported for the initial oxide film. With the automated ellipsometer (to be described later) the cleaned Si wafers could be immediately placed in a dry N<sub>2</sub> ambient, whereas in previous studies the wafers were exposed to room air for about 10 min during the ellipsometric measurements. After the initial SiO<sub>2</sub> film measurement, the samples were heated in dry N<sub>2</sub> (10-15 min) to the experimental oxidation temperature and the SiO<sub>2</sub> film thickness was remeasured. The SiO<sub>2</sub> film now measured 7-8 Å. After continuous heating for 5 hr at 900°C in dry N<sub>2</sub>, the total film thickness never exceeded 11 Å. Apparently there is some small amount of oxidant either present in the N<sub>2</sub> or desorbing from the walls of the reaction vessel, but the relative amount of SiO<sub>2</sub> growth is negligible for this study.

**Gas purity.**—Both N<sub>2</sub> and O<sub>2</sub> were supplied by boil-off from liquid sources. Dew points of the gases were measured by means of a hygrometer (5). As previously reported (5), the O<sub>2</sub> was shown to contain trace amounts of methane (~17 ppm) which at the experimental oxidation temperature combusts to form H<sub>2</sub>O. This trace H<sub>2</sub>O substantially increases the rate of oxidation (5). To preclude this H<sub>2</sub>O effect, the methane in the O<sub>2</sub> was removed by the procedure outlined previously (5). The H<sub>2</sub>O content of the N<sub>2</sub> and O<sub>2</sub> (after purification) was found to be less than 1 ppm as measured after the oxidation furnace.

**Automated ellipsometer.**—The instrument used for this study has been described in detail elsewhere (7). Basically, the ellipsometer uses a laser light source, polarizer, compensator, and a rotating analyzer-encoder. The light intensity measurement after the analyzer is automated. The ellipsometry measurements are made with the sample in a fused silica rf-heated reaction tube. Therefore it is possible to collect and analyze ellipsometer data as the SiO<sub>2</sub> film grows without interrupting the oxidation run. The optical constants characteristic of the Si surface as a function of temperature were previously measured (7).

**SiO<sub>2</sub> quality.**—In order to check on the charge levels in the SiO<sub>2</sub> films grown, capacitance-voltage (C-V) measurements were made on some oxides. Evaporated aluminum counterelectrodes were used as electrical contacts. The C-V measurements (at 1MHz) revealed an average fixed positive charge level of  $\sim 5 \times 10^{10}$  charges/cm<sup>2</sup>. Bias-temperature stressing ( $\pm 10^6$  V/cm at 200°C for 15 min and subsequent cooling under bias) revealed an average mobile positive charge level of  $\sim 7 \times 10^{10}$  charges/cm<sup>2</sup>. These values are characteristic of MOS quality oxide.

### Data Analysis

The experimental SiO<sub>2</sub> film thickness *vs.* time of oxidation data obtained with the automated ellipsometer is displayed in Fig. 1.

In order to compare the rate constants obtained in this study with previously reported values (1, 2, 5), the data was analyzed by three methods. Both Eq. [1] and [2] were used and the two previously mentioned ways to choose ( $d_0, t_0$ ) were compared. Table II outlines the essential differences among the three methods of data analysis. Each method utilizes linear least squares (LLS) analysis of the data in accordance with the equation tested (Eq. [1] or [2]) and the way in which ( $d_0, t_0$ ) is chosen. For each LLS iteration in a given method, the smallest remaining ( $d, t$ ) value is dropped from the analysis; and for each iteration numerical values are calculated for the slope, intercept, and standard deviation values for the over-all fit,  $\sigma_F$ , the slope,  $\sigma_S$ , and the intercept,  $\sigma_I$ . The reciprocals of the slope and intercept are the parabolic ( $k_{PAR}$ ) and linear ( $k_{LIN}$ ) rate constants, respectively. The equations which define the calculated standard deviation values were obtained from Ref. (8).

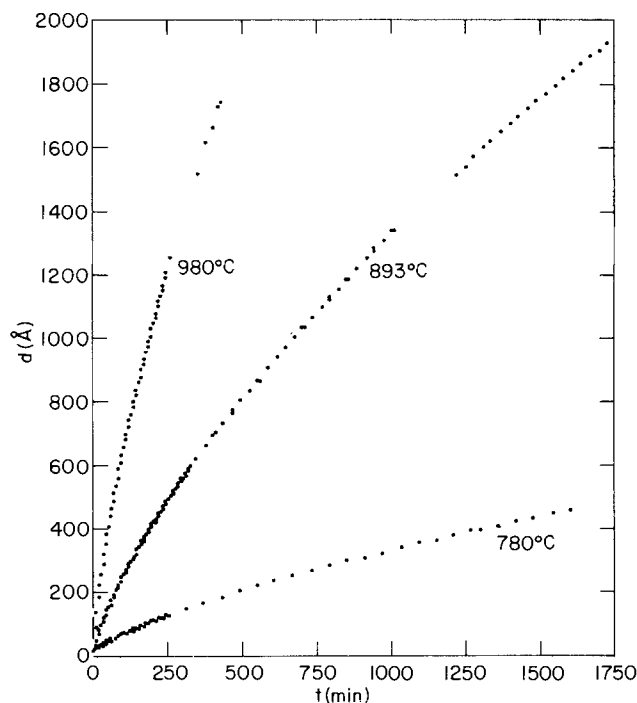


Fig. 1. SiO<sub>2</sub> film thickness  $d$  (Å) is plotted vs. time for oxidation  $t$  (min) for 780°, 893°, and 980°C oxidations of (100) Si in O<sub>2</sub>.

Table II. Outline of the three methods of data analysis

Method	LLS relationship	Values for $d_0$ and $t_0$	Description
I	Eq. [2] $(t - t_0)/(d - d_0)$ vs. $(d - d_0)$	$d_0 = 10\text{\AA}$ $t_0 = 0$	Iterative LLS; each iteration sequentially drops the smallest $(d,t)$ value from the analysis
II	Eq. [2] $(t - t_0)/(d - d_0)$ vs. $(d - d_0)$	$(d_0, t_0)$ is taken as the $(d,t)$ value dropped from the iteration	Same as I
III	Eq. [1] $(t - t_0)/(d - d_0)$ vs. $(d + d_0)$	Same as II	Same as I

This LLS technique scans a different subset of the data for each iteration and the standard deviation values enable a judgment as to which  $(d,t)$  subset yields the best fit to linear-parabolic kinetics.

A representative plot of the standard deviation,  $\sigma_F$ , for the fit of the data to Eq. [2] vs. the number of data (# DATA) included in the LLS iteration using method III and the 893°C data is shown in Fig. 2. Each point on Fig. 2 is obtained from a different subset of a data set; each subset is formed by dropping the smallest thickness-time value from the previous subset. The subsets are identified by the number of thickness-time data points in the subset. The shape of this plot was the same for the other two methods, as well as for the standard deviation values for the slope and intercept, and for the other two experimental temperatures. The characteristic features for all the error plots as represented by Fig. 2 are as follows.

**Region 1.**—With the small thickness-time data included in the analysis (i.e., # DATA is relatively greater), larger curve-fitting errors are obtained. This confirms the existence of an initial oxidation regime which does not conform to the linear-parabolic model (1, 5). Additionally, the analysis provides an estimation of the influence of this regime which for the 893°C data extends up to about 340Å.

**Region 2.**—A level region of relative best fit is obtained in the range of 85-40 data points. From the 893°C oxidation data, this region is found to correspond to thicknesses in the range of 340-1100Å. In order that a time-thickness data set yield minimum curve-fitting errors, hence more accurate rate constants, data in the best fit range must be adequately represented.

**Region 3.**—As the analyzed data subset includes only thickness data greater than about 1100Å, the curve-fitting errors again rise. This is a consequence of including thickness-time data which predominantly represent the diffusional aspect of the kinetic model and is therefore anticipated to occur for the greater film

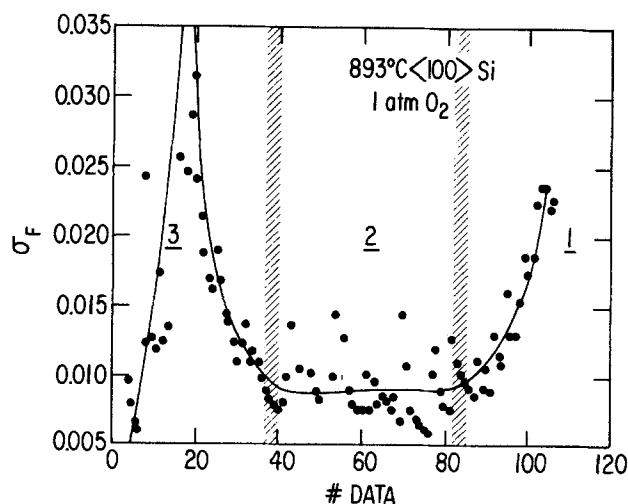


Fig. 2. The error values for the fit,  $\sigma_F$ , vs. the number of data points for the LLS analysis according to method III for the 893°C oxidation data. (The  $\sigma_F$  values near # DATA = 20 rises to a maximum of about 0.060 but were omitted for scaling purposes.)

thickness. If the analysis is continued further to include an even smaller number of data (<10), the errors again decrease to zero for two data points as expected.

From the standard deviation plots and the experimental data, the  $(d_0, t_0)$  values are obtained at the position on the standard deviation plots where the errors begin to level. Therefore, the  $(d_0, t_0)$  values represent the upper thickness limit for the predominant influence of the initial rapid oxidation regime. The slopes and intercepts which correspond to the  $(d_0, t_0)$  values are used to calculate the rate constants. Table III contains the  $k_{LIN}$ ,  $k_{PAR}$ , and  $d_0$  values obtained from methods I, II, and III. These constants describe the data with an average precision of about 2% for thickness values greater than the  $d_0$  value reported in Table III.

All the error plots show the existence of an initial oxidation regime extending to nearly 400Å which does not conform to linear-parabolic kinetics. Hence method I which pins  $d_0 = 10\text{\AA}$ ,  $t_0 = 0$  is deemed unacceptable. However, this way of choosing  $d_0$  has been utilized to calculate rate constants (2) and, therefore, is considered in this study for comparison. Methods II and III differ only in the equation fitted (Eq. [1] or [2]). Since both equations are of the same form, identical curve-fitting errors were obtained. By comparing Eq. [1] and [2] it is easily shown that the slopes (hence  $k_{PAR}$ ) should be identical and indeed the measured  $k_{PAR}$  values are very close in value. The  $k_{LIN}$  values for methods II and III are related by the equation

$$\frac{1}{k_{LIN}(III)} = \frac{1}{k_{LIN}(II)} - \frac{2d_0}{k_{PAR}(II)} \quad [3]$$

Therefore, as shown in Table III, the differences in reported rate constants as large as 300% for a given Si orientation cannot be explained on the basis of the different methods of analysis. Nor can the effect (~25%) of trace amounts of H<sub>2</sub>O be responsible for the large reported differences.

To clarify this situation, representative plots of the calculated values for the slopes and intercepts are shown in Fig. 3. It is seen that three rather distinct regions are found analogous to the error plot (Fig. 2). First, as small thickness values are eliminated, the slope and intercept values change rapidly. Then, there is a region in which there is smaller variation in the slope and intercept which corresponds to the best fit region of Fig. 2. Finally, when only data of 1100Å and thicker are considered, a more rapid variation is again

Table III. Rate constants obtained from methods I, II, and III

T (°C)	$k_{LIN}$ (Å/min)	Std dev $k_{LIN}$	$k_{PAR}$ (Å <sup>2</sup> /min)	Std dev $k_{PAR}$	$d_0^*$ (Å)	Method
780	0.66	0.007	220	3	75	I
	0.46	0.003	260	5	50	II
	0.56	0.006	265	5	50	III
893	2.6	0.02	3500	31	375	I
	1.7	0.003	4340	27	340	II
	2.2	0.005	4350	28	340	III
980	9.9	0.14	11600	188	450	I
	5.3	0.03	14000	127	380	II
	7.7	0.06	14000	127	380	III

\* The  $d_0$  value reported here represents the extent of the initial stage of oxidation which does not fit a purely linear-parabolic regime.

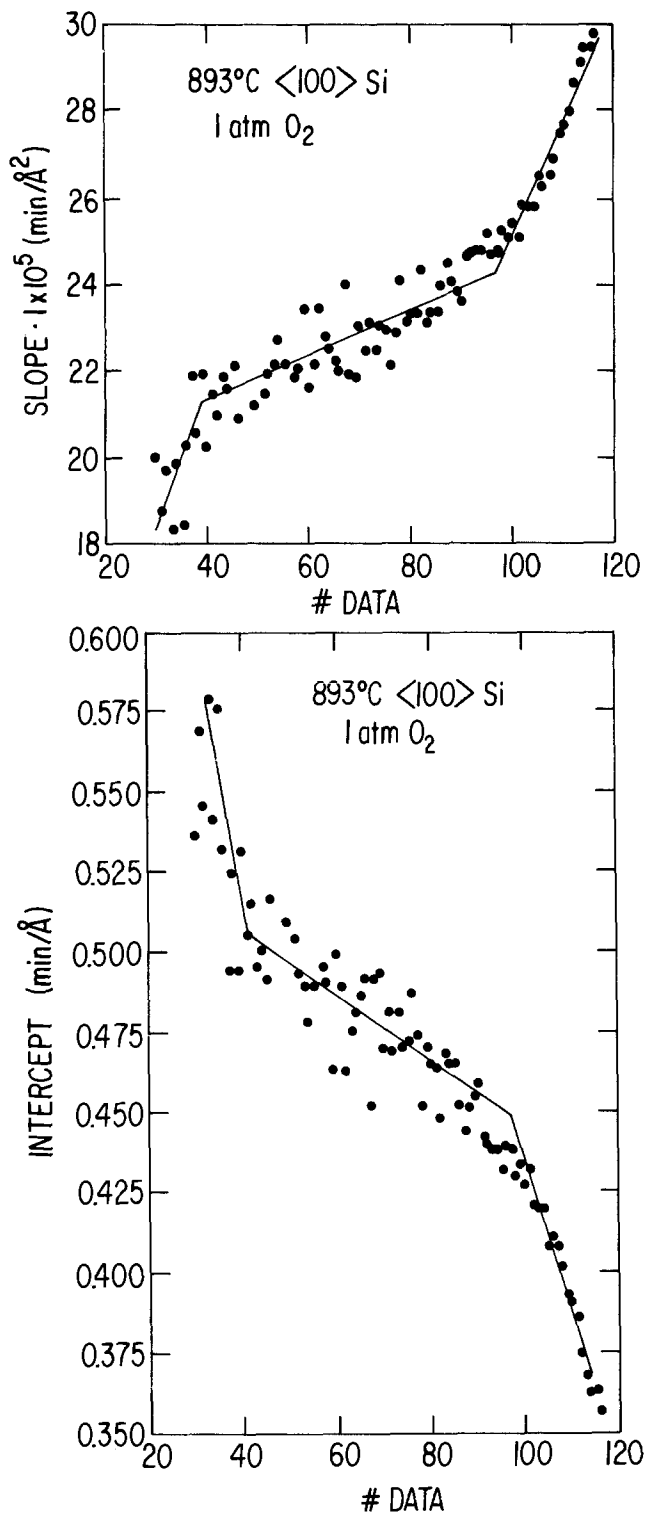


Fig. 3. Values for the slope (top) and intercept (bottom) vs. the number of data points for the LLS analysis according to method III for the 893°C oxidation data.

evidenced. A total variation of up to 50% could be obtained for rate constants calculated using data outside the region of best fit. Within the best fit region about 10% variation could be obtained and this variation could possibly be accounted for by modifying the Deal and Grove (1) derivation to include such effects as the moving Si-SiO<sub>2</sub> boundary, possible ionic oxidant species, SiO<sub>2</sub> film porosity, and chemisorption. Further theoretical and experimental studies are required to test these modifications.

Therefore, rather than a single source of error being responsible for the large variation of the reported rate constants, it is concluded that a combination of errors such as those resulting from trace H<sub>2</sub>O (~25%), from

the form of the linear-parabolic equation (~25%), from data not adequately representing the best fit regime (~50%), and from insufficient data [previous studies (1-5) utilized about ten data points for curve fitting] could account for the large variations in the literature.

Considering that the above-mentioned sources of error are minimized in the present study and permitting 10% error in the rate constants due to the variation of the rate constants in the best fit regime, it would be useful to examine the additional kinetic information obtainable from this analysis.

Activation energies,  $E_a$ , and preexponential factors,  $k_0$ , calculated according to an Arrhenius equation of the form

$$k = k_0 e^{-E_a/RT} \quad [4]$$

are shown in Table IV. (There is an estimated 10% uncertainty in both these values.) The values are not very different for the three methods and this suggests that the trends in the kinetic data can be represented by any of the methods. Previously reported data (5) showing the effects of trace amounts of H<sub>2</sub>O in oxidation were recalculated according to method III [originally method I was used (5)]. A sample of the results is shown in Table V. The agreement with the present analysis is reasonable in view of the sources of potentially large errors discussed above, especially that only ten data points were used in the previous study (5). Moreover, all the trends previously reported (5) were confirmed.

From Table IV the activation energy of 1.5 eV for the linear rate constant,  $E_{a,LIN}$ , corresponds to the reaction at the Si-SiO<sub>2</sub> interface. This value correlates more closely with the 0-0 bond energy of 1.44 eV (9) than, as previously reported (1, 5), with the Si-Si bond energy of 1.8 eV (9). The  $E_{a,PAR}$  value of 2.3 eV is larger than either reported values of 1.4 eV for <111> Si (1) and 2.0 eV and 1.7 eV for <100> and <111> Si (5), respectively. This larger value for  $E_{a,PAR}$  does not correlate well with the 1.2 eV reported for the activation energy for the diffusion of oxygen through fused silica (10). Based on the diffusivity of oxygen in SiO<sub>2</sub> (10) and the kinetic data in this study, the concentration of oxygen in the SiO<sub>2</sub> films at 1000°C was calculated to be about 20% less than the values previously reported (1).

The above findings do not negate the utility of the simple model proposed by Deal and Grove (1). For oxidation resulting in film thickness of 300Å and thicker, the rate constants will predict the final film thickness with 10% accuracy. However, the model does not include other mechanisms (previously listed) which when considered could further increase the accuracy of the formulation. Therefore, the linear-parabolic model should be treated as a reasonably good approximation for the oxidation of Si from about 300Å SiO<sub>2</sub> upwards. Further studies are in progress to cor-

Table IV. Arrhenius activation energies ( $E_a$ ) and preexponential factors ( $k_0$ ) for the linear and parabolic rate constants

Method	$E_{a,LIN}$ (eV)	$k_{0,LIN}$ (cm/sec) · 10 <sup>3</sup>	$E_{a,PAR}$ (eV)	$k_{0,PAR}$ (cm <sup>2</sup> /sec) · 10 <sup>5</sup>
I	1.5	1.8	2.3	3.2
II	1.4	0.3	2.3	4.8
III	1.5	1.0	2.3	4.4

Table V. Kinetic values from literature data (5) according to method III

T (°C)	$k_{LIN}$ (Å/ min)	$k_{PAR}$ (Å <sup>2</sup> / min)	$E_{a,LIN}$ (eV)	$k_{0,LIN}$ (cm/ sec) · 10 <sup>3</sup>	$E_{a,PAR}$ (eV)	$k_{0,PAR}$ (cm <sup>2</sup> / sec) · 10 <sup>5</sup>
800	0.6	400				
927	5	2900	1.7	4.0	2.0	2.4
996	9	12400				

rect the model, to investigate the thickness regime below 300Å, and to more accurately define the effects of trace impurities in the oxidant.

### Conclusions

The data and analysis of this study confirm that mixed linear-parabolic kinetics enable a reasonably accurate representation of the oxidation data provided that there is sufficient data in the proper thickness range. The initially rapid regime of oxidation is identified.

While the three methods of data analysis yield approximately equal representations of the experimental data, one of these methods, method III, is directly related to a physical model and therefore recommended. The large variation of published rate data cannot be attributed to a single cause but rather, is due to a lack of sufficient data for accurate curve fitting, data in inappropriate thickness ranges, and trace impurity effects.

The sensitivity of the iterative LLS analysis with the abundance of reliable oxidation data from the automated ellipsometer has shown that the simple rate law proposed by Deal and Grove (1) requires modification in order to provide rate constants with better than 10% accuracy.

### Acknowledgment

The authors gratefully acknowledge Dr. R. Ghez for many helpful discussions and several computer programs and are grateful to Drs. R. Ghez and T. B. Light for critically reviewing this manuscript.

Manuscript submitted Dec. 22, 1975; revised manuscript received ca. May 13, 1976. This was Paper 101 presented at the Dallas, Texas, Meeting of the Society, Oct. 5-9, 1975.

Any discussion of this paper will appear in a Discussion Section to be published in the June 1977 JOURNAL. All discussions for the June 1977 Discussion Section should be submitted by Feb. 1, 1977.

Publication costs of this article were assisted by IBM Corporation.

### REFERENCES

1. B. E. Deal and A. S. Grove, *J. Appl. Phys.*, **36**, 3770 (1965).
2. A. G. Revesz and R. J. Evans, *J. Phys. Chem. Solids*, **30**, 551 (1969).
3. T. Nakayama and F. C. Collins, *This Journal*, **113**, 706 (1965).
4. Y. J. van der Meulen, *ibid.*, **119**, 530 (1972).
5. E. A. Irene, *ibid.*, **121**, 1613 (1974).
6. U. R. Evans, "The Corrosion and Oxidation of Metals," Chap. XX, p. 826, Edward Arnold Ltd., London (1960).
7. Y. J. van der Meulen and N. C. Hien, *J. Opt. Soc. Am.*, **64**, 804 (1974).
8. H. D. Young, "Statistical Treatment of Experimental Data," Chap. IV, McGraw-Hill Co., Inc., New York (1962).
9. L. Pauling, "The Nature of the Chemical Bond," 3rd ed., p. 85, Cornell University Press, Ithaca, New York (1960).
10. F. J. Norton, *Nature*, **171**, 701 (1961).

## Ce<sup>3+</sup>-Activated Photoluminescence in the BaO-SrO-SiO<sub>2</sub> System

### I. Crystalline Phases

P. Victor Kelsey, Jr. and Jesse J. Brown, Jr.

Division of Minerals Engineering, Virginia Polytechnic Institute and State University, Blacksburg, Virginia 24061

### ABSTRACT

All single phase regions (compounds and solid solutions) in the BaO-SrO-SiO<sub>2</sub> system were activated with 0.01 mole percent (m/o) Ce<sup>3+</sup> (with equimolar amounts of Li<sup>+</sup>, Na<sup>+</sup>, or K<sup>+</sup> added to compensate charges) and the resulting ultraviolet excitation and emission spectra were characterized. Brightest phosphors were obtained from the solid solution phases in the BaSiO<sub>3</sub>-SrSiO<sub>3</sub> and Ba<sub>2</sub>SiO<sub>4</sub>-Sr<sub>2</sub>SiO<sub>4</sub> systems at the approximate compositions of (Ba<sub>0.8</sub>, Sr<sub>0.6</sub>) SiO<sub>3</sub>:Ce<sup>3+</sup>, K<sup>+</sup> and (Ba<sub>0.2</sub>, Sr<sub>0.8</sub>)<sub>2</sub>SiO<sub>4</sub>:Ce<sup>3+</sup>, Li<sup>+</sup>, respectively. All phosphors exhibit a peak emission wavelength at approximately 390 nm with slight variations resulting from compositional changes.

It is well established that most Ce<sup>3+</sup> activated phosphors emit in the 300-500 nm spectral range (ultraviolet to blue green) and that their luminescent decays are fast. These two characteristics make this class of phosphors especially attractive as materials for applications in fast response optical conversion systems such as flying-spot-scanners. In addition, Ce<sup>3+</sup> is a relatively large activator (1.03Å ionic radius) and substitutes easily in solids for other large ions such as Ba<sup>2+</sup>, Sr<sup>2+</sup>, and rare earth ions. The resulting phosphors with their large mass absorption coefficients and fast decay times must be considered potential x-ray excited phosphors for use in real-time radiographic systems.

In the present investigations, crystalline phases in the SrO-BaO-SiO<sub>2</sub> ternary system are activated by Ce<sup>3+</sup> and the resulting u.v. luminescence examined. In a subsequent study, the x-ray excited emission characteristics will be described.

\* Electrochemical Society Active Member.

Key words: Ce<sup>3+</sup> photoluminescence, phosphors, barium silicates, strontium silicates.

### Related Literature

The Ce<sup>3+</sup> ion has only one electron in the 4f orbital which is raised to a 5d level when the ion is excited. The resulting 5d-4f emission is often located in the near u.v. region of the spectrum and is in the form of two broad bands which arise from the doublet ground states (<sup>2</sup>F<sub>5/2</sub> and <sup>2</sup>F<sub>7/2</sub>) (1, 2). The unshielded 5d excited state is strongly influenced by the crystal field (3), the strength of which causes variations in the peak emission wavelengths (1), and the symmetry of the crystal field causes d-orbital splittings (4).

Blasse and Brill (1) have examined the excitation and emission spectra of a number of Ce<sup>3+</sup> activated compounds including Y<sub>3</sub>Al<sub>5</sub>O<sub>12</sub>, ScBO<sub>3</sub>, YAl<sub>3</sub>B<sub>4</sub>O<sub>12</sub>, YPO<sub>4</sub>, and others. Frequently, they are able to deduce the site symmetry of the Ce<sup>3+</sup> ion from the splittings evident in the excitation spectra. On the other hand, the emission spectra generally contain two broad bands (resulting from the two ground states) whose wavelengths are strongly dependent upon the strength of the crystal field. Similar emission spectra have been

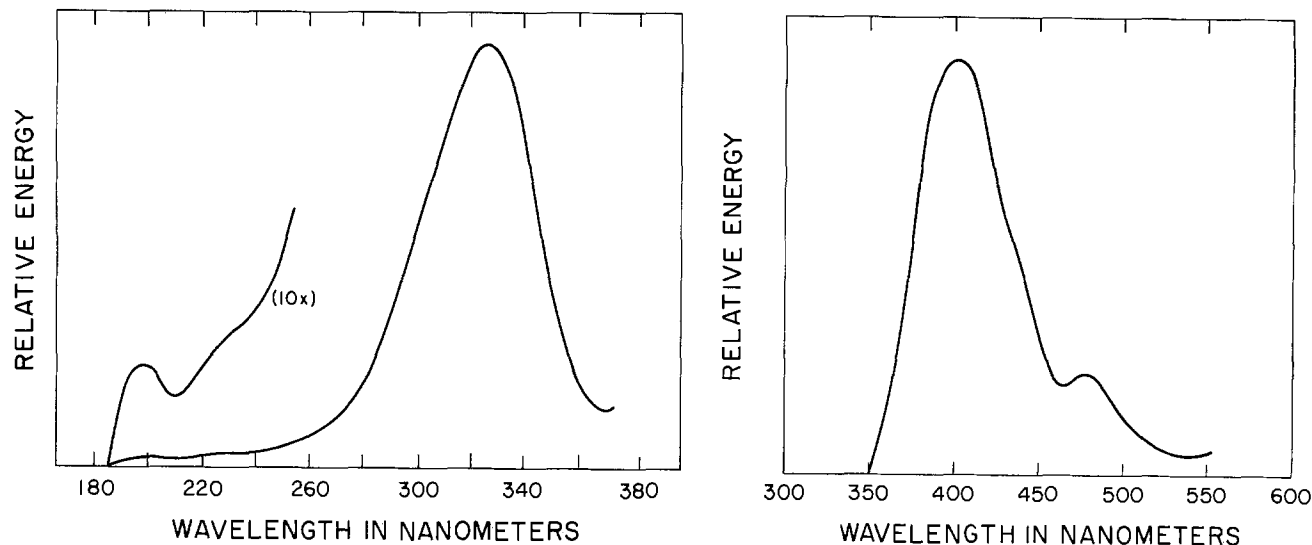


Fig. 1. The excitation (left) and emission (right) spectra of BaSiO<sub>3</sub>:Ce<sup>3+</sup> (no charge compensation)

observed for Ce<sup>3+</sup> in Ca<sub>3</sub>(PO<sub>4</sub>)<sub>2</sub> (5), alkaline earth sulfides (6-8), and alkaline earth fluorides (9).

Although no data are given with regard to Ce<sup>3+</sup> luminescence in Ba or Sr silicates, the phase equilibrium relationships in the BaO-SrO-SiO<sub>2</sub> system were recently determined by Fields *et al.* (10). Complete solid solubility exists between Ba<sub>2</sub>SiO<sub>4</sub> and Sr<sub>2</sub>SiO<sub>4</sub> and limited solubility between BaSiO<sub>3</sub> and SrSiO<sub>3</sub>. In addition, a ternary compound, BaO·SrO·3SiO<sub>2</sub>, exists.

#### Experimental Procedure

All ingredients were weighed to 0.1 mg and were formulated with reagent grade BaCO<sub>3</sub>, SrCO<sub>3</sub>, silicic acid, and cerium oxalate. Crystalline samples were fired in air at 1100°C for 2 hr, reground, and then refired at 1100°C for two additional hours. After regrounding, the material was fired under an atmosphere of argon and hydrogen at 1100°C for 4 hr.

The emission spectra were determined using a 200W high pressure mercury lamp and a Heath EU-700 monochromator. The entrance and exit slits of the analyzer spectrometer were set at 200 μm, which gave a spectra resolution of  $\lesssim 2\text{Å}$  over the wavelength range used. The spectrometers were calibrated for wavelength reproducibility and accuracy using a mercury pen-lamp and correlating the observed spectra with published data for Hg lines.

The excitation spectra were obtained by exciting the sample with a Heath EU-701-50 deuterium light source and focusing the resultant light output into the Heath spectrometer. Because of the need for increased inten-

sity for the second analyzing spectrometer, the slits of the Heath spectrometer were opened to the maximum setting of 2 mm.

All spectra were corrected for photomultiplier response and monochromator sensitivity where appropriate.

Identification of the crystalline phases present in the reacted samples was made with a Philips x-ray powder diffractometer operating at 40 kV and 15 mA using CuK $\alpha$  nickel filtered radiation. Diffractometer scans used for phase identification were obtained using a scanning rate of 1°-2 $\theta$  per minute.

The relative brightness measurements were taken by comparison of relative peak heights of the most intense band of the emission spectra to that of Sylvania Type 212 (SrMgP<sub>2</sub>O<sub>7</sub>:Eu<sup>2+</sup>).

#### Results and Discussion

The phosphor compositions examined in this investigation are summarized in Table I. Also tabulated are the phase(s) present in the reacted sample, the percent relative emission peak height, and the excitation and emission peak wavelengths. All phosphors were activated by 0.01 moles of Ce<sup>3+</sup> substituted for Ba<sup>2+</sup> and/or Sr<sup>2+</sup> and, where indicated, Li<sup>+</sup>, Na<sup>+</sup>, and K<sup>+</sup> were used to compensate for the imbalance of charges resulting from the substitution of a trivalent ion for a divalent ion.

*BaSiO<sub>3</sub> phosphors.*—The excitation and emission spectra of cerium-activated BaSiO<sub>3</sub> (not charge compensated) are shown in Fig. 1. The low solubility of

Table I. Compositions, phase analyses, and Ce<sup>3+</sup> activated luminescence characteristics of phosphors studied

Composition	Phase(s)	% Relative emission peak height*	Excitation bands	Emission bands (nm)
BaSiO <sub>3</sub> :Ce	BaSiO <sub>3</sub>	16	190, ~230, 330	392, 475
(Ba <sub>0.8</sub> Sr <sub>0.2</sub> )SiO <sub>3</sub> :Ce	BaSiO <sub>3</sub> <sub>ss</sub>	17	—	400, 475
BaSiO <sub>3</sub> :Ce:Li	BaSiO <sub>3</sub>	33	230, 250; 290, 330	387
(Ba <sub>0.8</sub> Sr <sub>0.2</sub> )SiO <sub>3</sub> :Ce:Li	BaSiO <sub>3</sub> <sub>ss</sub>	42	230, 245; 295, 337, 343	395, 480
(Ba <sub>0.6</sub> Sr <sub>0.4</sub> )SiO <sub>3</sub> :Ce:Li	BaSiO <sub>3</sub> <sub>ss</sub>	25	230, 250; 295, 340, 345	402.5, 480
(Ba <sub>0.2</sub> Sr <sub>0.8</sub> )SiO <sub>3</sub> :Ce:Li	SrSiO <sub>3</sub> <sub>ss</sub>	15	230, 250; 300, 318, 350	361.5
SrSiO <sub>3</sub> :Ce:Li	SrSiO <sub>3</sub>	27	230, 250; 300, 320, 353	362.5
BaSiO <sub>3</sub> :Ce:Na	BaSiO <sub>3</sub>	41	235, 250; 330, 300	389
(Ba <sub>0.8</sub> Sr <sub>0.2</sub> )SiO <sub>3</sub> :Ce:Na	BaSiO <sub>3</sub> <sub>ss</sub>	56	235, 250; 290, 340	393, 480
(Ba <sub>0.6</sub> Sr <sub>0.4</sub> )SiO <sub>3</sub> :Ce:Na	BaSiO <sub>3</sub> <sub>ss</sub>	51	235, 250; 290, 345	395, 480
(Ba <sub>0.2</sub> Sr <sub>0.8</sub> )SiO <sub>3</sub> :Ce:Na	SrSiO <sub>3</sub> <sub>ss</sub>	26	230, 250; 283, 350	397, 435, 474
SrSiO <sub>3</sub> :Ce:Na	SrSiO <sub>3</sub>	16	230, 250; 283, 350	405, 366, 475
BaSiO <sub>3</sub> :Ce:K	BaSiO <sub>3</sub>	57	230, 245; 300, 335	390
(Ba <sub>0.8</sub> Sr <sub>0.2</sub> )SiO <sub>3</sub> :Ce:K	BaSiO <sub>3</sub> <sub>ss</sub>	71	230, 245; 290, 337	390, 480
(Ba <sub>0.6</sub> Sr <sub>0.4</sub> )SiO <sub>3</sub> :Ce:K	BaSiO <sub>3</sub> <sub>ss</sub>	61	235, 245; 290, 341	395, 480
(Ba <sub>0.2</sub> Sr <sub>0.8</sub> )SiO <sub>3</sub> :Ce:K	SrSiO <sub>3</sub> <sub>ss</sub>	29	230, 250; 280, 347	401, 475
SrSiO <sub>3</sub> :Ce:K	SrSiO <sub>3</sub>	23	230, 250; 280, 250	404, 475
Ba <sub>2</sub> SiO <sub>4</sub> :Ce:Li	Ba <sub>2</sub> SiO <sub>4</sub>	31	230, 250; 300, 335	369.5, 480
(Ba <sub>0.4</sub> Sr <sub>0.6</sub> )SiO <sub>4</sub> :Ce:Li	Ba <sub>2</sub> SiO <sub>4</sub> <sub>ss</sub>	78	230, 245; 295, 340	388
(Ba <sub>0.2</sub> Sr <sub>0.8</sub> )SiO <sub>4</sub> :Ce:Li	Ba <sub>2</sub> SiO <sub>4</sub> <sub>ss</sub>	100	230, 250; 290, 345	388
Sr <sub>2</sub> SiO <sub>4</sub> :Ce:Li	Sr <sub>2</sub> SiO <sub>4</sub>	91	230, 250; 285, 345	384

\* 100% corresponds to 15% of Sylvania Type 212.

$Ce^{3+}$  in  $BaSiO_3$  is reflected in the gray body color and low brightness of the phosphor. The excitation spectrum shows three bands at 190,  $\sim 230$ , and 330 nm. The emission spectrum contains the normal  $Ce^{3+}$  emission bands which peak at 392 and 475 nm with the latter showing a high wavelength tail up to nearly 550 nm.

The excitation spectra of  $BaSiO_3:Ce^{3+}$  phosphors charge compensated by  $K^+$  and  $Li^+$  are shown by curves (a) in Fig. 2 and 3, respectively. These indicate little change in the environment of  $Ce^{3+}$  ion as the size of the compensating ion increases. The corresponding emission spectra are shown by curves (a) in Fig. 4 and 5. Most significant is the improvement in brightness that accompanies the increase in size of the compensating ion as shown by Fig. 6. For example, the relative brightness of  $BaSiO_3:Ce^{3+}$  is 16% which increases to 33, 41, and 57%, when an equimolar amount of  $Li^+$ ,  $Na^+$ , and  $K^+$ , respectively, is added to the phosphor.

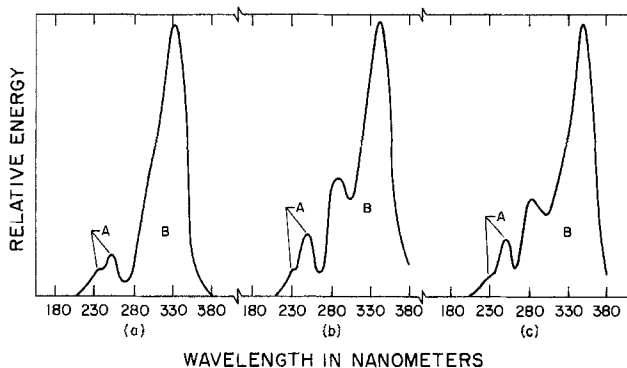


Fig. 2. The excitation spectra of (a)  $BaSiO_3:Ce^{3+},K^+$ ; (b)  $(Ba_{0.6},Sr_{0.4})SiO_3:Ce^{3+},K^+$ ; and (c)  $SrSiO_3:Ce^{3+},K^+$ .

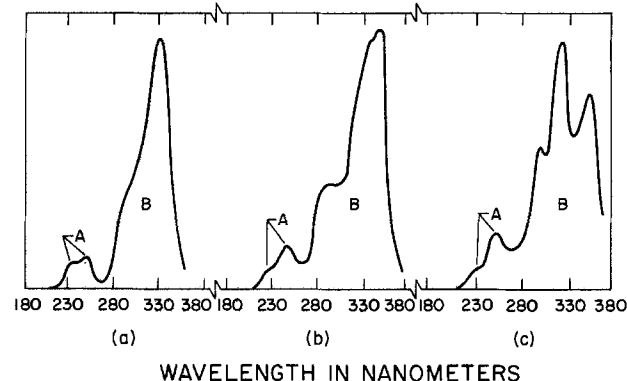


Fig. 3. The excitation spectra of (a)  $BaSiO_3:Ce^{3+},Li^+$ ; (b)  $(Ba_{0.6},Sr_{0.4})SiO_3:Ce^{3+},Li^+$ ; and (c)  $SrSiO_3:Ce^{3+},Li^+$ .

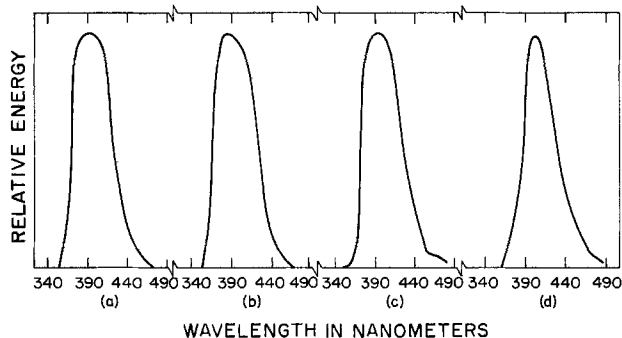


Fig. 4. The emission spectra of  $K^+$  compensated  $Ce^{3+}$  activated (a)  $BaSiO_3$ ; (b)  $(Ba_{0.6},Sr_{0.2})SiO_3$ ; (c)  $(Ba_{0.6},Sr_{0.4})SiO_3$ ; and (d)  $SrSiO_3$ .

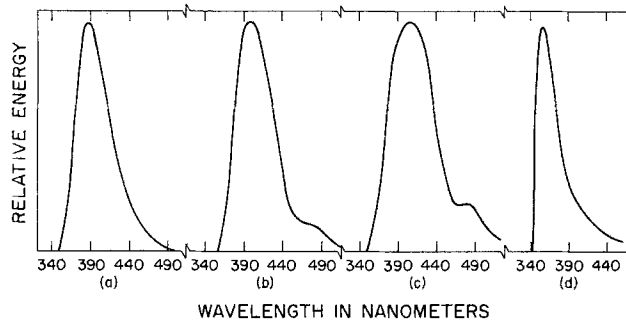


Fig. 5. The emission spectra of  $Li^+$  compensated  $Ce^{3+}$  activated (a)  $BaSiO_3$ ; (b)  $(Ba_{0.8},Sr_{0.2})SiO_3$ ; (c)  $(Ba_{0.6},Sr_{0.4})SiO_3$ ; and (d)  $SrSiO_3$ .

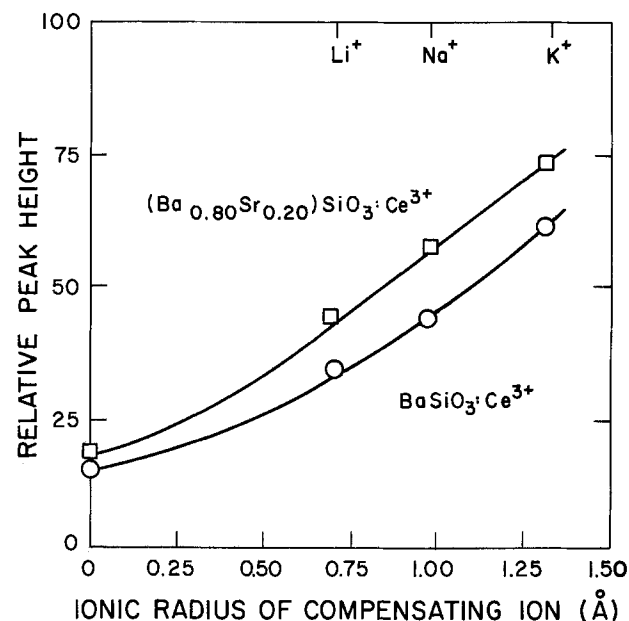


Fig. 6. Variation of phosphor brightness of  $BaSiO_3$  and  $(Ba_{0.8},Sr_{0.2})SiO_3$  as a function of ionic size of compensating ion.

The visual body color of the charge-compensated phosphors are uniformly white, not discolored like the uncompensated phosphors, and there is an increase in the sharpness of the emission spectra as well as an accompanying increase in peak height. The compensating effect appears to increase as the compensating ion increases in size from  $Li^+$  (0.78 Å) to  $Na^+$  (0.98 Å) to  $K^+$  (1.33 Å). This is not surprising because the  $K^+$  ion is closer in size to  $Ba^{2+}$  (1.43 Å) than the other two. Because of the improved qualities of the charge-compensated phosphors, all subsequent phosphors prepared in this study were charge compensated.

**$BaSiO_3$ - $SrSiO_3$  phosphors.**—The  $BaSiO_3$ - $SrSiO_3$  system contains two regions of limited solid solubility at both extremities of the system (10). Phosphors were prepared at 10 m/o intervals across both these solid solution regions.

The excitation spectra of the  $K^+$  and  $Li^+$  charge-compensated phosphors are shown in Fig. 2 and 3. Characteristically, these phosphors show a high energy excitation band (A) at  $\sim 235$ -250 nm and a low energy excitation band (B) at  $\sim 290$ -345 nm. The first doublet (A) appears to be composition independent whereas the second doublet (B) was found to vary in position in accordance with the host composition and the compensating ion.

The excitation spectrum for  $Li^+$  compensated  $SrSiO_3$  solid solution phosphors appears to be somewhat



unique. Excitation band (B) very distinctly splits into three components. While the components of the high energy band (A) are stationary at 235 and 250 nm across the solid solution region, the low energy band is split into three distinct components at 300, 318, and 350 nm for (Ba<sub>0.2</sub>, Sr<sub>0.8</sub>)SiO<sub>3</sub>. The two low energy components of this triplet are shifted to higher wavelengths as SrSiO<sub>3</sub> is added into solid solution, with the SrSiO<sub>3</sub> end member having three distinct excitation bands at 300, 320, and 353 nm.

With the exception of the (Sr<sub>1-x</sub>, Ba<sub>x</sub>)SiO<sub>3</sub>:Ce<sup>3+</sup>, Li<sup>+</sup> (0 ≤ x ≤ 0.2) phosphors, the most intense excitation peak for all compositions is the lowest energy level (or highest wavelength peak). The most intense excitation band for this series of phosphors is the second highest energy band, as indicated by curve (c) in Fig. 3.

The emission spectra of the Na<sup>+</sup> and K<sup>+</sup> compensated phosphors are very similar. Typical emission spectra, as shown in Fig. 4 for BaSiO<sub>3</sub>:Ce<sup>3+</sup>, K<sup>+</sup>, consist of strong bands at about 390 nm. Additions of SrSiO<sub>3</sub> into solid solution generally produce shifts of this emission band to higher wavelengths. The doublet ground state of the Ce<sup>3+</sup> ion is evidenced in the emission spectra by the appearance of a second, rather weak band at about 480 nm. Generally, the emission peak wavelengths for Na<sup>+</sup> compensated phosphors are slightly lower (3-5 nm) than for phosphors compensated with K<sup>+</sup>. Weak unidentified emission bands for the (Sr<sub>0.8</sub>, Ba<sub>0.2</sub>)SiO<sub>3</sub>:Ce<sup>3+</sup>, Na<sup>+</sup> and SrSiO<sub>3</sub>:Ce<sup>3+</sup>, Na<sup>+</sup> phosphors are observed at 435 and 366 nm, respectively.

The variation of peak emission wavelength with composition for Ce<sup>3+</sup> activated BaSiO<sub>3</sub>-SrSiO<sub>3</sub> phosphors is shown in Fig. 7. Generally, there is a small increase in peak emission wavelength as the strontium content increases. Again, the Li<sup>+</sup> compensated SrSiO<sub>3</sub>:Ce<sup>3+</sup> phosphors are unusual in that their peak emission wavelengths are unusually low.

In interpreting the excitation spectra of the Ce<sup>3+</sup> activated phosphors, it is reasonable to assume that the character of the spectra is a result of electronic transitions from the ground state of the Ce<sup>3+</sup> ion to excited states. The presence of multiple excitation bands which change with compensating ion is indicative of electronic transition within the activator ion.

The site symmetry of the Ce<sup>3+</sup> ion, as indicated by the excitation spectra for all phosphors on the BaSiO<sub>3</sub>-SrSiO<sub>3</sub> binary regardless of the charge compensator, appears to be low. The degeneracy appears to be nearly removed for K<sup>+</sup> and Na<sup>+</sup> compensated phosphors as indicated by four excitation bands, and is totally removed for Li<sup>+</sup> compensated phosphors as indicated by the existence of five distinct bands.

The higher energy emission peaks of the (Sr<sub>1-x</sub>, Ba<sub>x</sub>)SiO<sub>3</sub>:Ce<sup>3+</sup>, Li<sup>+</sup> phosphors indicate a photoemission process that proceeds from the second lowest excitation level (Fig. 4d) to the ground state.

**Ba<sub>2</sub>SiO<sub>4</sub>-Sr<sub>2</sub>SiO<sub>4</sub> phosphors.**—Phosphors within the Ba<sub>2</sub>SiO<sub>4</sub>-Sr<sub>2</sub>SiO<sub>4</sub> binary, which exhibits complete solubility across the entire join at high temperatures (10), were prepared at 20 m/o intervals.

The body color of the Na<sup>+</sup> and K<sup>+</sup> compensated phosphors is off-white on the strontium-rich side of (Ba<sub>0.8</sub>, Sr<sub>0.2</sub>)<sub>2</sub>SiO<sub>4</sub>. These compounds were nearly inert under u.v. excitation because of the reabsorption of emitted light.

The excitation spectra of (Ba<sub>1-x</sub>, Sr<sub>x</sub>)<sub>2</sub>SiO<sub>4</sub>:Ce<sup>3+</sup>, Li<sup>+</sup> and (Ba<sub>1-x</sub>, Sr<sub>x</sub>)SiO<sub>3</sub>:Ce<sup>3+</sup> phosphors are very similar to those previously discussed. An upper energy doublet at 230 and 250 nm remains stationary for compositions across the entire system. A lower energy doublet, also present in all (Ba<sub>1-x</sub>, Sr<sub>x</sub>)<sub>2</sub>SiO<sub>4</sub>:Ce<sup>3+</sup>, Li<sup>+</sup> phosphors, broadens as SrSiO<sub>4</sub> is added to Ba<sub>2</sub>SiO<sub>4</sub> via solid solution. The lowest energy excitation band shifts from 335 nm for Ba<sub>2</sub>SiO<sub>4</sub> to 345 nm for Sr<sub>2</sub>SiO<sub>4</sub>, and the higher energy band of this doublet moves to lower wavelengths with increased Sr<sub>2</sub>SiO<sub>4</sub> additions as indi-

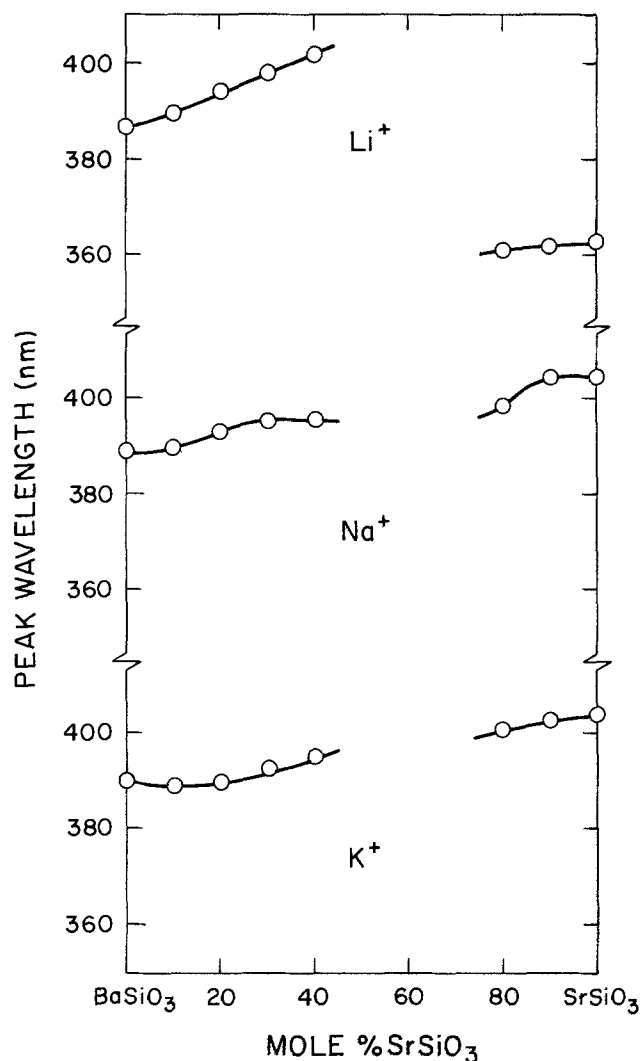


Fig. 7. Variation of peak emission wavelength with composition for Li<sup>+</sup>, Na<sup>+</sup> and K<sup>+</sup> charge-compensated (Ba<sub>1-x</sub>, Sr<sub>x</sub>)<sub>2</sub>SiO<sub>4</sub>:Ce<sup>3+</sup> phosphors.

cated by the peak wavelength shift from 300 nm (Ba<sub>2</sub>SiO<sub>4</sub>) to 285 nm (Sr<sub>2</sub>SiO<sub>4</sub>).

The emission spectra of the Li<sup>+</sup> charge-compensated solid solutions indicate a continuous shift of the principal emission peak wavelength from 384 nm for Ba<sub>2</sub>SiO<sub>4</sub> to 399.5 nm for Sr<sub>2</sub>SiO<sub>4</sub>. A less intense secondary emission band appears at 480 nm for the composition (Ba<sub>0.6</sub>, Sr<sub>0.4</sub>)<sub>2</sub>SiO<sub>4</sub> and remains for all compositions up to and including Sr<sub>2</sub>SiO<sub>4</sub>.

The (Ba<sub>1-x</sub>, Sr<sub>x</sub>)<sub>2</sub>SiO<sub>4</sub>:Ce<sup>3+</sup>, Li<sup>+</sup> series of phosphors is relatively bright, as indicated in Table I. A considerable improvement in brightness is obtained by solid solution of Sr<sub>2</sub>SiO<sub>4</sub> in Ba<sub>2</sub>SiO<sub>4</sub> with the relative brightness increasing from 49% for the Ba<sub>2</sub>SiO<sub>4</sub> phosphor to 100% for the composition (Sr<sub>0.8</sub>, Ba<sub>0.2</sub>)<sub>2</sub>SiO<sub>4</sub>. The Sr<sub>2</sub>SiO<sub>4</sub> phosphor has a brightness of 91%.

The change of configuration of the low energy doublet observed in the spectra with the addition of Sr<sub>2</sub>SiO<sub>4</sub> to Ba<sub>2</sub>SiO<sub>4</sub> via solid solution is a result of a similar lattice constriction described for the (Ba<sub>1-x</sub>, Sr<sub>x</sub>)SiO<sub>3</sub> phosphors. The constriction forces the lowest energy excitation band to shorter wavelengths which is directly reflected in the emission spectra.

Manuscript submitted Nov. 3, 1975; revised manuscript received May 12, 1976. This was Paper 199 presented at the Toronto, Canada, Meeting of the Society, May 11-16, 1975.

Any discussion of this paper will appear in a Discussion Section to be published in the June 1977 JOURNAL. All discussions for the June 1977 Discussion Section should be submitted by Feb. 1, 1977.

Publication costs of this article were assisted by the Virginia Polytechnic Institute and State University.

## REFERENCES

- G. Blasse and A. Bril, *J. Chem. Phys.*, **47**, 5139 (1967).
- G. Blasse and A. Bril, *Appl. Phys. Letters*, **11**, 53 (1967).
- G. Blasse, "Analysis and Application of Rare Earth Materials," NATA Advanced Study Institute, Universitetsforlaget, Oslo, Norway (1973).
- M. G. Day and J. Selbin, "Theoretical Inorganic Chemistry," p. 292, Reinhold Publishing Corp., New York (1962).
- T. P. J. Botden, *Philips Res. Rept.*, **7**, 197 (1952).
- W. Lehmann and F. M. Ryan, *This Journal*, **118**, 477 (1971).
- J. W. Gilliland, *J. Appl. Phys.*, **38**, 2427 (1967).
- E. Banks and R. Ward, *Trans. Electrochem. Soc.*, **96**, 297 (1949).
- E. Loh, *Phys. Rev.*, **154**, 270 (1957).
- J. M. Fields, P. S. Dear, and J. J. Brown, *J. Am. Ceram. Soc.*, **55**, 585 (1972).
- L. Pauling, "Nature of the Chemical Bond," 3rd ed., Cornell University Press, Ithaca, New York (1960).

## Boron Impurity Profile Tailoring in Silicon by Ion Implantation and Measurement by Glow Discharge Optical Spectroscopy

G. T. Marcyk and B. G. Streetman

Coordinated Science Laboratory and Department of Electrical Engineering,  
University of Illinois at Urbana-Champaign, Urbana, Illinois 61801

## ABSTRACT

Glow discharge optical spectroscopy (GDOS) is used to measure distributions of implanted B in Si before and after annealing. Methods for GDOS measurement are discussed, and data are presented indicating the resolution and sensitivity of this technique. Impurity profiles are synthesized by multiple B implantations, and examples of uniform and  $x^{-3/2}$  hyperabrupt distributions are presented. Measurements of these profiles with GDOS exhibit excellent agreement with theoretical predictions. Distortion of the B distribution due to diffusion during annealing is less pronounced in the multiple implant profiles than is the case for a single gaussian.

Because of the widespread use of ion implantation in semiconductor device fabrication, there is a strong need for simple and reliable methods for measuring implanted impurity distributions. This is particularly true in applications requiring tailored profiles by multiple implantations (1-3), in which the impurity distribution after annealing is critical to the performance of the device. Various methods for measuring the electrically active impurity profile have been developed, including differential capacitance (4, 5) and successive electrical measurements combined with stripping procedures (6). These measurements suffer from problems of accuracy, particularly when sharp impurity gradients are encountered (7). Techniques for measuring the total impurity profile usually involve sputtering through the implanted layer, while monitoring some property of the impurity of interest. The most widespread methods of this type are the secondary ion mass spectroscopy (SIMS) (8) and the Auger electron spectroscopy (AES) (9) techniques. Each of these methods has been successful in monitoring certain impurities (10), although the SIMS and AES systems require rather elaborate equipment (11). In 1974 Greene *et al.* (12) reported the application of glow discharge optical spectroscopy (GDOS) to this problem. This approach is particularly attractive because of its simplicity, accuracy, and versatility. A number of improvements have been made in the application of the GDOS technique to semiconductor impurity profiling, as demonstrated by the measured profiles of implanted boron in silicon discussed here.

### The GDOS System

Greene and Whelan (13) first proposed GDOS as a method for analyzing thin films. This technique has since then been used to measure the composition of bulk samples (14) and to profile diffused and implanted

impurities in Si (12, 15). In GDOS, a sample is placed on the cathode of a low pressure d-c gas (e.g., Ar) discharge. The sample is slowly eroded by cathode sputtering, the sputtered material leaving primarily as neutral atoms (16). These sputtered neutrals are collisionally excited in the cathode glow region of the discharge and emit light with wavelengths characteristic of the atom. The resulting light intensity at a given wavelength has been shown to be proportional to the concentration of impurities in the sample (15). An impurity profile is obtained by monitoring the intensity of a single emission line as a function of time. The depth scale is determined by an independent measurement of the sputtering rate, which is held constant during the experiment. An absolute impurity concentration calibration can be obtained by measuring the intensity from standard samples during sputtering under identical conditions. The resolution of the GDOS system is determined by the sputtering rate, which can be conveniently held to  $\sim 500$  Å/min for typical semiconductor targets.

### Experimental Procedure

A schematic diagram of the GDOS system used in this experiment is shown in Fig. 1. The discharge chamber is a 4½ in. diam glass cylinder with a fused quartz window mounted perpendicular to the sample and positioned to receive light from the cathode glow region of the discharge. The copper electrodes are water cooled, and their separation is adjustable by a bellows on the anode. The edge region of the cathode is protected by a Pyrex glass shield (Fig. 2). The 1 cm<sup>2</sup> sample is mounted with silver conducting paint onto a larger (1.5 in. diam) backing plate which covers that portion of the cathode not shielded by the glass. For these experiments the backing plate is n-type Si with a negligible B concentration. The use of such a backing plate prevents sputtering of the cathode material, which may contain trace contaminants of the

Key words: boron implantation, ion implantation, silicon doping, impurity profiling.

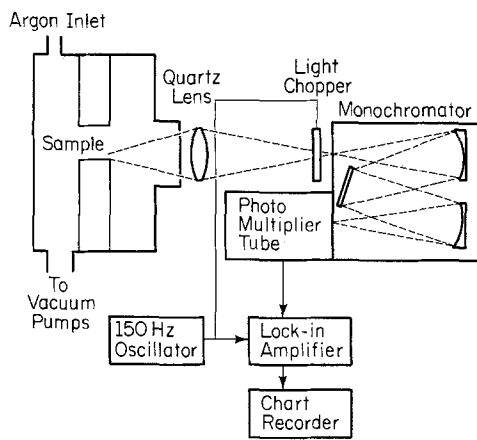


Fig. 1. Schematic diagram of the GDOS system

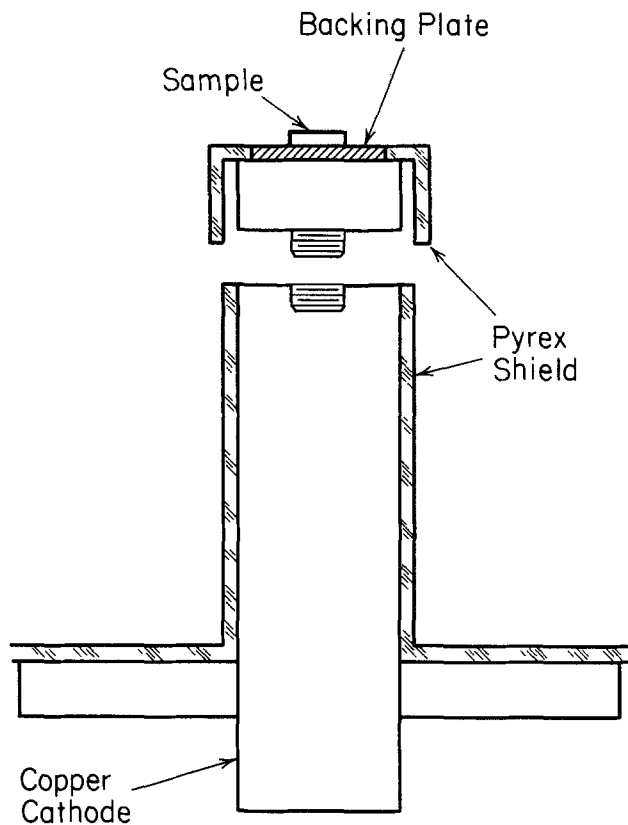


Fig. 2. Cathode assembly with detachable sample holder and backing plate.

impurity being studied. The area of the backing plate should be several times that of the sample centered upon it, to avoid nonuniform sputtering near the edge of the cathode by placing the sample in a more uniform field region of the discharge.

Before each measurement the system is evacuated to below  $10^{-5}$  Torr and is then backfilled with high purity Ar to the desired pressure. Argon is constantly flowed through the system during sputtering, and once stabilized the pressure can be held constant over long periods. In these experiments, pressures are chosen in the range  $10\text{--}25\mu$  and held constant to within  $1\mu$ , as measured by a thermocouple gauge. With such Ar pressures and an applied voltage of 3 kV, the sputtering rate is  $\sim 500$  Å/min.

Light from the cathode region passes through the window and is collected by a quartz lens. A  $\frac{3}{4}$ m monochromator containing a  $102 \times 102$  mm grating with 1200 lines/mm blazed at  $3000\text{Å}$  is used to resolve the emission. In measuring B profiles we monitor the strong

2497.7Å line of the boron spectrum (17). Typical slit widths used in this experiment range from  $50\text{--}100\mu$ . The intensity of the monitored line is detected by a u.v.-sensitive photomultiplier tube, and the output is analyzed by either a lock-in amplifier or a photon counting system, depending on the sensitivity required. The resulting plot of intensity vs. time is converted to impurity concentration vs. distance by appropriate calibration. The intensity scale is calibrated using Si samples of known uniform B concentration, and the sputtering rate is calibrated by measuring step heights on samples with regions masked by  $\text{SiO}_2$  and sputtered for various times at a given voltage and pressure.

The sputtering rate can be held constant to within 5% throughout the experiment, as determined by monitoring emission from the host Si atoms. The uniformity of sputtering over the sample surface can be ascertained from the abrupt disappearance during sputtering of a thin deposited film. For example, a  $1000\text{Å}$  Ni film deposited on the Si surface has been sputtered at  $100$  Å/min while monitoring a dominant Ni line. The Ni emission goes from full intensity to the zero level in less than 1 min at the Ni-Si interface. This corresponds to an interface uncertainty of less than  $100\text{Å}$ . The appearance of Si emission occurs over the same time period, as the metal-semiconductor interface is sputtered. This experiment indicates very little nonuniform sputtering, which would result in a much more diffuse transition across the interface.

One problem encountered in GDOS (15) is exact determination of the surface location, in view of the fact that initiation of the discharge results in uncalibrated sputtering until steady state is reached (about 1 min) (18). This problem can be overcome by depositing a metal film of known thickness over the surface and sputtering through the film and into the semiconductor at calibrated rates. Using this method, the discharge has reached a steady-state condition before the Si surface is encountered.

### Measurement of Implanted B Profiles in Si

The sensitivity and resolution of the GDOS measurement system for B in Si are illustrated by the experimental results shown in Fig. 3. In this experiment a  $4\ \Omega\text{-cm}$   $\langle 111 \rangle$  n-type Si wafer was implanted with  $^{11}\text{B}^+$  ions at  $120$  keV to a fluence of  $10^{15}\text{ cm}^{-2}$ . The wafer was tilted  $7^\circ$  from the beam normal to minimize

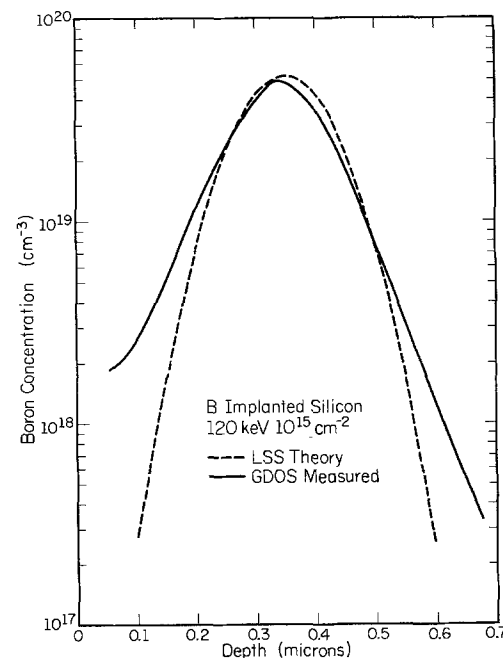


Fig. 3. Implanted boron impurity profile as measured by GDOS, compared to LSS predicted distribution.

channeling. The projected range and straggle of the unannealed B profile as measured by GDOS (Fig. 3) are within  $\sim 10\%$  of the values predicted by the LSS theory using corrected cross sections (19). This allows us to use a gaussian approximation for the boron distributions in the subsequent profile tailoring. Some deviation from the actual distribution may be due in part to a slightly slower sputtering rate within the unannealed implanted region. In addition, departures from the gaussian approximation are expected, based on other experiments (10). By monitoring the Si line during sputtering of similarly damaged layers, we estimate that the sputtering rate is constant to within 10% throughout the unannealed implanted region. Figure 3 demonstrates the lower limit of detection for B using the present experimental setup and photon counting. Boron concentrations as low as  $3 \times 10^{17} \text{ cm}^{-3}$  can be reliably measured.

Three identical samples were implanted at 240 keV to a fluence of  $10^{15} \text{ cm}^{-2}$  to study the effects of annealing on the B profile. One sample was measured unannealed, and the remaining two were annealed for 30 min in an Ar atmosphere, one at 600°C and the other at 900°C. The measured profiles (Fig. 4) illustrate diffusion during the higher temperature anneal. The unannealed and 600°C annealed samples exhibit essentially identical profiles. However, the straggle of the distribution after 900°C annealing has increased by about 30%. This degree of diffusion is typical for single gaussians annealed at this temperature (20).

Of particular interest in many semiconductor device applications is the use of implantation to achieve tailored profiles. Using a computer program incorporating an optimization routine which assumes gaussian profiles to determine parameters for multiple implants (21), we have synthesized two particularly useful profiles, namely, the uniform and the  $x^{-3/2}$  hyperabrupt distributions. Figure 5 illustrates an essentially uniform profile constructed by the summation of four implants. The desired distribution was a constant  $10^{19} \text{ cm}^{-3}$  concentration from 0.2 to 0.8  $\mu$ . Of course, a better approximation could be obtained by using more implants. The unannealed profile measured by GDOS (Fig. 5) is extremely close to the computed distribution (dashed curve). The peak of the lowest energy implant is quite low compared with the predicted value, and we believe this is due to an error in fluence rather than the GDOS measurement. The GDOS experimental curves are presented here as obtained from the measurement with previously described calibrations; no curve fitting with the calculated profiles was employed. In view of this, the details of peak positions and separa-

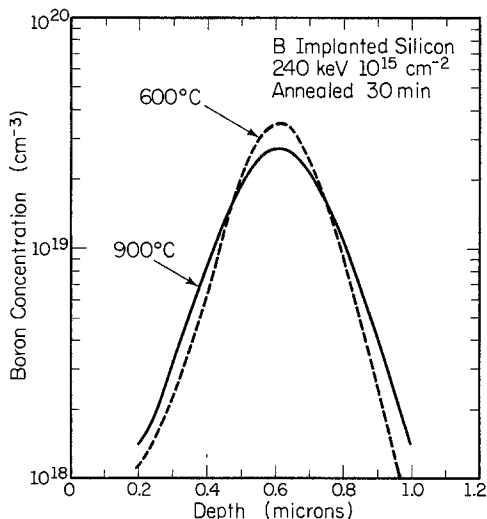


Fig. 4. Measured distribution of implanted boron after annealing at 600°C and 900°C. The measured profile before annealing is essentially identical to the 600°C curve.

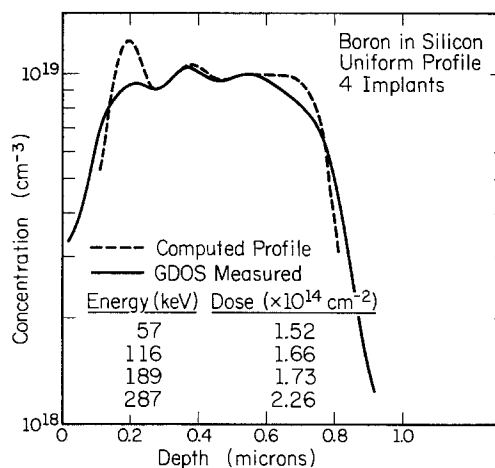


Fig. 5. Comparison of predicted and measured boron profiles for a uniform  $10^{19} \text{ cm}^{-3}$  distribution synthesized by four implants.

tion displayed in Fig. 5 demonstrate the precision of the GDOS measurement.

An impurity distribution of particular interest for varactor fabrication is the hyperabrupt profile with  $x^{-3/2}$  dependence (22, 23). If such a distribution is used in the more lightly doped side of a junction, the reverse bias capacitance varies as  $V^{-2}$  (24). When this device is placed in an L-C resonant circuit, the resonant frequency varies linearly with the voltage applied across the diode. Although such a varactor has interesting applications, the close profile control is difficult to achieve. As illustrated in Fig. 6, the  $x^{-3/2}$  dependence can be synthesized over a limited range by successive implantations. The computer simulation using four implants places the highest concentration 0.1  $\mu$ m below the surface. In varactor fabrication this initial layer could be doped  $n^+$  to form the hyperabrupt junction. Alternatively, the 0.1  $\mu$ m surface layer could be removed by etching (or the implants could be per-

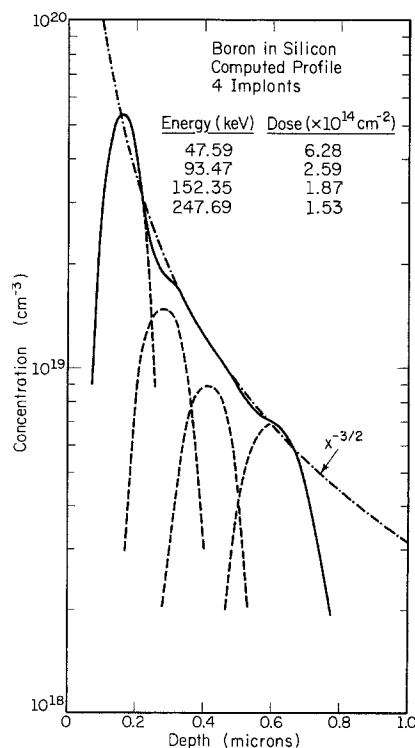


Fig. 6. Sum of four gaussian profiles computed to simulate an  $x^{-3/2}$  distribution. Implantation energies produced by the optimization program are rounded off to the nearest keV during the actual implant.

formed through SiO<sub>2</sub> of appropriate thickness) for Schottky barrier varactor fabrication.

The four implants prescribed by the computer simulation were performed in a 4  $\Omega$ -cm p-type Si wafer. The resulting profiles as measured by GDOS are shown in Fig. 7. The unannealed sample exhibits a B profile which follows the  $x^{-3/2}$  distribution over a considerable range. Of further interest, a 30 min anneal at 900°C does not distort the profile as much as might be expected. Apparently, the reduced gradient of the  $x^{-3/2}$  distribution compared with a simple gaussian results in very limited diffusion during the anneal.

### Conclusions

In this work we have demonstrated that complex and otherwise unattainable impurity distributions can be obtained by performing appropriate multiple implants. The measured profiles agree well with the computed distributions, even after annealing. The GDOS measurement system is a simple yet accurate method for determining actual profiles of implanted boron in Si. In addition to the results reported here, we have successfully measured implanted As profiles in Si, and Be in GaAs using GDOS. Not all impurities are amenable to the GDOS approach, however. For example, attempts to measure implanted profiles of N in GaP have been unsuccessful, due to a buildup of N concentration in the chamber during the measurement. Application of the GDOS method to specific impurities depends on the tendency for the atom to stick to the vessel walls rather than remaining in the low pressure gas. In addition, the strength of emission lines varies considerably among impurities. For example, an impurity which emits in many lines of comparable strength may provide too little intensity in any one for reasonable detection. Such information must be obtained by experiment (14), since the strength of

emission for atoms in the discharge is difficult to predict.

### Acknowledgment

This work was supported by the National Science Foundation under Grants GH40450 and DMR73-02359 A01, and the Joint Services Electronics Program (U. S. Army, U. S. Navy, and U. S. Air Force) under Contract DAAB-07-72-C-0259.

Manuscript submitted Feb. 17, 1976; revised manuscript received May 3, 1976. This was Paper 253 RNP presented at the Dallas, Texas, Meeting of the Society, Oct. 5-9, 1975.

Any discussion of this paper will appear in a Discussion Section to be published in the June 1977 JOURNAL. All discussions for the June 1977 Discussion Section should be submitted by Feb. 1, 1977.

Publication costs of this article were assisted by the University of Illinois at Urbana-Champaign.

### REFERENCES

1. T. E. Seidel, R. E. Davis, and D. E. Iglesias, *Proc. IEEE*, **59**, 1222 (1971).
2. D. H. Lee and R. S. Ying, in "Ion Implantation in Semiconductors," S. Namba, Editor, Plenum Press, New York (1975).
3. R. M. Allen, *Electron. Letters*, **5**, 111 (1969).
4. See for example, J. Hilibrand and R. D. Gold, *RCA Rev.*, **21**, 245 (1960).
5. T. E. Seidel, in "Ion Implantation in Semiconductors," I. Ruge and J. Graul, Editors, Springer-Verlag (1971).
6. See for example, B. L. Crowder, *This Journal*, **118**, 943 (1971).
7. C. P. Wu, E. C. Douglas, and C. W. Mueller, *IEEE Trans. Electron Devices*, **ED-22**, 319 (1975).
8. Recently reviewed by H. Liebl, *J. Phys. E: Sci. Instrum.*, **8**, 797 (1975).
9. Recently reviewed by J. M. Morabito, *Thin Solid Films*, **19**, 21 (1973).
10. An excellent review of boron implanted profiles is given by W. K. Hofker, *Philips Res. Rept., Suppl.* **8** (1975).
11. For a comparison of AES and SIMS, see for example, C. A. Evans, Jr., *J. Vacuum Sci. Technol.*, **12:1**, 144 (1975).
12. J. E. Greene, F. Sequeda-Osorio, B. G. Streetman, J. R. Noonan, and C. G. Kirkpatrick, *Appl. Phys. Letters*, **25**, 435 (1974).
13. J. E. Greene and J. M. Whelan, *J. Appl. Phys.*, **44**, 2509 (1973).
14. J. E. Greene, F. Sequeda-Osorio, and B. R. Natarajan, *ibid.*, **46**, 2701 (1975).
15. J. E. Greene, F. Sequeda-Osorio, and B. R. Natarajan, *J. Vacuum Sci. Technol.*, **12**, 366 (1975).
16. J. Comas and C. G. Burleigh, *J. Appl. Phys.*, **38**, 2956 (1967).
17. Massachusetts Institute of Technology, "Wave Length Table," M.I.T. Press (1969).
18. J. E. Houston and R. D. Bland, *J. Appl. Phys.*, **44**, 2504 (1973).
19. J. F. Gibbons, W. S. Johnson, and S. W. Mylroie, "Projected Range Statistics," 2nd edition, Halsted Press, Somerset, New Jersey (1975).
20. W. R. Hofker, H. W. Werner, D. P. Oosthoek, and H.A.M. de Grefte, in "Ion Implantation in Semiconductors and Other Materials," B. L. Crowder, Editor, Plenum Press, New York (1973).
21. A. J. Zaremba, G. T. Marcyk, and B. G. Streetman, Unpublished.
22. P. Brook and C. S. Whitehead, *Electron. Letters*, **4**, 335 (1968).
23. R. A. Moline and G. F. Foxhall, *IEEE Trans. Electron Devices*, **ED-19**, 267 (1972).
24. M. Norwood and E. Schatz, *Proc. IEEE*, **56**, 788 (1968).

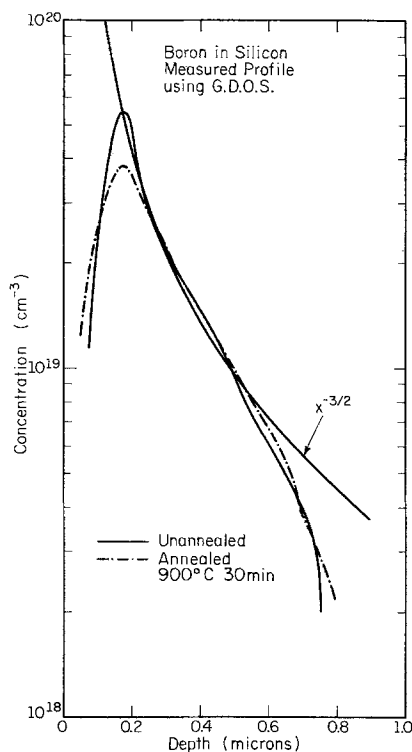


Fig. 7. Measured boron profiles of the  $x^{-3/2}$  structure, before and after annealing.

# Relationships of the Chemical and Electrical Interfacial Properties of Germanium-SiO<sub>2</sub> Systems

K. L. Wang and P. V. Gray

General Electric Company, Research and Development Center, Schenectady, New York 12301

## ABSTRACT

Germanium-silicon dioxide structures were prepared by depositing SiO<sub>2</sub> on cleaned germanium wafers using chemical vapor deposition (CVD) from the silane-oxygen reaction at 450°C. The structures were then annealed in various gas environments, Ar, O<sub>2</sub>, and a 10% H<sub>2</sub> and 90% N<sub>2</sub> forming gas, at 600°C for 2 hr. For samples annealed in forming gas, the interface state density measured by C-V techniques shows a high density near the band edges (10<sup>14</sup>/cm<sup>2</sup>-eV). For samples annealed in oxygen, it decreases to 10<sup>11</sup>/cm<sup>2</sup>-eV. High surface recombination velocity was observed in the samples annealed in forming gas. The measured results of charge generation and injection indicated charge losses to the interface states but not to oxide traps, whose time constant for trapping is longer than the normal injection time (1 ~ 10<sup>-8</sup> sec). In order to understand the effects of annealing with different gas environments, profile analyses of the structures were carried out using secondary ion mass spectrometry (SIMS) and Auger electron spectroscopy (AES). For the samples annealed in oxygen, the presence of germanium oxide was identified by observing the low energy Auger spectrum at the interface in comparison with the spectrum obtained for a standard GeO<sub>2</sub> sample. The profile of the germanium spectrum obtained using SIMS can be used to identify the presence of the oxide because of the enhanced secondary ion yield of the oxide. In the case of the forming gas anneal, the hydrogen appears to diffuse into the interface resulting in a high interface state density. The profile of hydrogen concentration for the structures was also obtained. It is concluded that the increase of the interface state density of a germanium-SiO<sub>2</sub> system due to the forming gas anneal appears to result from dissolved hydrogen diffusing through the SiO<sub>2</sub>. The reduction of interface state density of the structure annealed in oxygen is probably due to the oxidation of germanium and dissolved hydrogen, which reduces the defects originally present in the interface region following the SiO<sub>2</sub> deposition.

The interface properties of the germanium-insulator system have been a subject of interest for some time. Sedgewick (1) has investigated the C-V behavior of a Ge-SiO<sub>2</sub> system. There the SiO<sub>2</sub> film was deposited by decomposition of tetraethylorthosilicate. The characterization of interface properties of a Ge-silox SiO<sub>2</sub> system has also been reported earlier (2). Recently the passivation of germanium was carried out using several different insulators (3). The interface of a Ge-SiO<sub>2</sub> system appears to have low interface state density. However no systematic study of the interface characterization has been reported. Furthermore, no chemical study of the interface has been done. As is demonstrated later, such a study of its chemical constitution is useful in the understanding of the annealing processes.

It is the purpose of this article to describe the measurement of interface state density for samples annealed in different ambients. Further the investigation of electronic properties of resulting MIS structures such as surface minority carrier generation and field effect mobility are also reported. The relationship between interface chemical composition, as studied by Auger electron spectroscopy (AES) and secondary ion mass spectrometry (SIMS), and the measured interface state density are correlated.

## Experimental

*Sample preparation.*—Germanium/SiO<sub>2</sub> structures were prepared similarly to the procedures described elsewhere (2). The thickness of the SiO<sub>2</sub> films was varied from 30 to 1500Å. The structures having a thin SiO<sub>2</sub> film were used for chemical analyses in order to obtain a high depth resolution, and other structures with a thicker SiO<sub>2</sub> film (500 ~ 1500Å) were used for the measurement of interface state density and for other investigations of interfacial properties.

Key words: MOS, MIS, surface state(s), secondary mass spectrometry, dark current, Auger electron spectroscopy, Zerbst plot.

Ge-SiO<sub>2</sub> structures were annealed in various gas ambients (argon, oxygen, a forming gas consisting of 10% H<sub>2</sub> and 90% N<sub>2</sub>) at 600°C for 2 hr. After this annealing, an Al, Au, or Mo dot matrix of 2 mm diam dots was evaporated over the SiO<sub>2</sub> surface. The constituents of the interfaces of the structures were then analyzed with Auger electron spectroscopy (AES) and secondary ion mass spectrometry (SIMS). The interface state density was measured using C-V techniques, and minority carrier generation and field effect mobility were investigated as is described later.

*Chemical study using AES.*—AES simultaneous with ion sputter-etch was used to analyze the samples. The analysis system used is from Physical Electronics Industries, Inc. The Auger peak energies correspond to the points of maximum negative slope of the energy distribution which is calibrated to the elastic peak. The characterization of the Auger spectrum was carried out, particularly in the low energy spectrum, to investigate the chemical state of the constituents in the interface. The spectrum obtained from a standard, thermally oxidized germanium oxide film (grown at 500°C in oxygen) was compared with another standard spectrum for germanium and the corresponding energies are listed in Table I. For example, a valence state of germanium corresponding to Auger transition of M<sub>45</sub>N<sub>23+2</sub>N<sub>23+2</sub> (2) appears to have shifted from 22.5 to 18 eV when oxidized. In the case of germanium oxide, a new peak at 63 eV appears while the transition at 76 eV corresponding to L<sub>1</sub>L<sub>2</sub>L<sub>45</sub> in the germanium spectrum disappears.

Samples which had undergone various annealings were investigated using AES. Some samples were annealed in oxygen at 600°C for 2 hr after a 30Å SiO<sub>2</sub> film was deposited on a Ge substrate. In these the presence of germanium oxide between the deposited SiO<sub>2</sub> film and the Ge substrate was identified by comparing the

Table I. Germanium strong Auger transitions and chemical shifts of its oxide

Apparent transitions	Calculated energy	M <sup>a</sup>	Measured energy	Oxide energy	Energy shifts
M <sub>1</sub> M <sub>3</sub> M <sub>45</sub>	14.5	(20)	14	10	-4
M <sub>45</sub> N <sub>23-2</sub> N <sub>23-2</sub>	23.0	(40)	22.5	18	-4.5
M <sub>1</sub> M <sub>3</sub> N <sub>23-2</sub>	46.5	(8)	46.5	46.5	—
M <sub>3</sub> M <sub>45</sub> M <sub>15</sub>	52.0	(10)	50.5	50	-0.5
L <sub>1</sub> L <sub>2</sub> M <sub>45</sub>	74	(10)	76	63	-13
M <sub>3</sub> M <sub>45</sub> N <sub>23-2</sub>	84	(40)	87	84	-3
M <sub>3</sub> M <sub>45</sub> N <sub>32-2</sub>	91	(20)	—	—	—
L <sub>1</sub> L <sub>3</sub> M <sub>45</sub>	108.0	(20)	106	101.5	4.5

<sup>a</sup>Multiplicity: The products of number of electrons in the three levels involved in the transitions, normalized to a maximum of 100 for a largest such product for given element.

AES spectrum with the spectrum of the standard obtained previously. The thickness of the germanium oxide film depends on the annealing ambient, temperature, and time. This can best be demonstrated in the SIMS analyses discussed in the following section.

As is discussed later, the forming gas annealed samples give a much higher interface state density than the samples annealed in argon. On the other hand, SIMS (and also AES) shows a very small difference in the thickness of germanium oxide; it suggests that hydrogen may play an important role at the interface. However since AES does not provide an easily accessible means to identify hydrogen, SIMS, which has high sensitivity and depth resolution, appears as an alternative technique.

*Profiling of SiO<sub>2</sub>-Ge structures using SIMS.*—The instrument used for analyzing the samples is an ion microprobe mass analyzer manufactured by Applied Research Laboratories. Primary ion beams of <sup>40</sup>Ar<sup>+</sup> or <sup>32</sup>O<sub>2</sub><sup>+</sup> were raster-scanned over a small area (10<sup>4</sup> μm<sup>2</sup>) to sputter-etch a rather uniform crater. Furthermore, the secondary ion signal was electronically gated in such a fashion that only those secondary ions from the central region of a sputtered crater were detected. This technique of using an electronic aperture greatly enhanced the depth resolution.

The secondary ion yield of a solid substrate depends strongly on the constituent matrix of the substrate and the type of primary ion used (4). In general the positive secondary ion yield increases as the electron availability of a substrate decreases. Thus, in using <sup>40</sup>Ar<sup>+</sup> as primary ions, the positive ion yield is enhanced and controlled by the presence of neighboring electronegative species such as oxygen in a sample. Si and Ge in the form of oxide will have a higher secondary ion yield than in the elemental state. Therefore when a <sup>40</sup>Ar<sup>+</sup> primary ion beam was used, the presence of oxide in the interface showed as a prominent peak. The analyzed results are described in the following.

The profiles of <sup>92</sup>GeO<sup>+</sup>, <sup>74</sup>Ge<sup>+</sup>, and <sup>30</sup>Si<sup>+</sup> for the identical sample analyzed by AES (annealed in oxygen with a 30Å-SiO<sub>2</sub> film, 100N-3) are shown in Fig. 1. As shown in the figure, the β-current is the current collected in the electrostatic sector analyzer aperture, which is approximately proportional to the total secondary ion current.

The sputter rates of SiO<sub>2</sub> and GeO<sub>2</sub> were calibrated using the known thickness of two standards as determined by ellipsometry and interferometry. The depth of the analyzed sample was then calculated using the simple relation

$$S_c = C_1 S_1 + C_2 S_2 \quad [1]$$

where  $S_c$  = effective sputter rate of the sample;  $S_1$  = sputter rate of SiO<sub>2</sub>;  $S_2$  = sputter rate of GeO<sub>2</sub>;  $C_1$  and  $C_2$  are fractional molecular concentrations of SiO<sub>2</sub> and GeO<sub>2</sub>, respectively.

From Fig. 1, both <sup>92</sup>GeO<sup>+</sup> and <sup>74</sup>Ge<sup>+</sup> profiles indicate a similar distribution of a GeO<sub>2</sub> layer, about 300Å thick. This layer of GeO<sub>2</sub> was grown during the oxygen

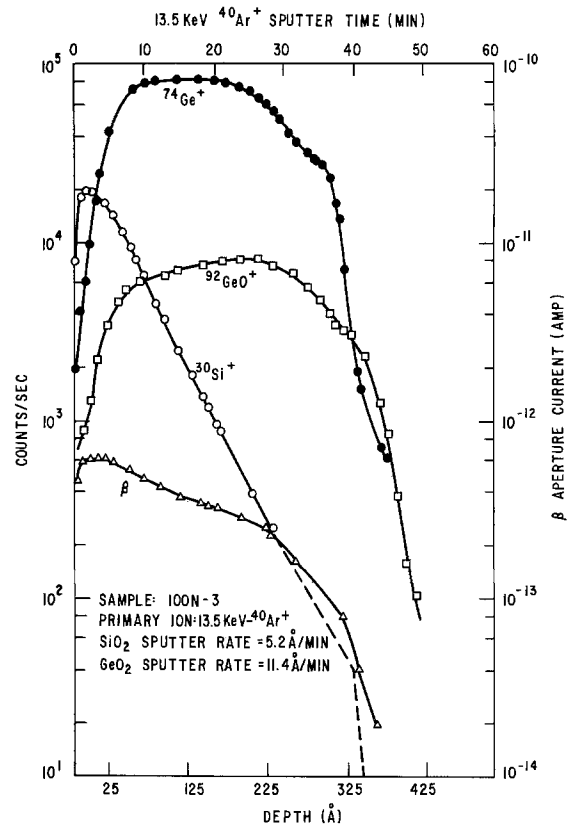


Fig. 1. Profile of <sup>30</sup>Si<sup>+</sup>, <sup>74</sup>Ge<sup>+</sup>, and <sup>92</sup>GeO<sup>+</sup> for sample 100N-3 annealed in oxygen ambient at 600°C for 2 hr. The depth shown is calculated using the sputter rate obtained from Eq [1]. The β aperture current, also shown is the secondary ion current intercepted at the exit of the electrostatic sectors.

anneal at 600°C. A similar GeO<sub>2</sub> layer was observed for a sample, having a 410Å SiO<sub>2</sub> film following an oxygen anneal.

For samples treated in argon at 600°C for 2 hr, a very small amount of GeO<sub>2</sub> was observed. This is illustrated in the profiles of <sup>74</sup>Ge<sup>+</sup> in Fig. 2. The other profiles of <sup>28</sup>Si<sup>+</sup> and β-current are also illustrated. The thickness of germanium oxide is about 30Å, which is consistent with AES data.

For samples treated in a forming gas ambient (90% N<sub>2</sub>; 10% H<sub>2</sub>), a C-V study indicates a high interface density. Samples under identical heat-treatment, with a thin SiO<sub>2</sub> film, were analyzed. The profiles of major constituents are illustrated in Fig. 3. The general feature of <sup>28</sup>Si<sup>+</sup>, <sup>74</sup>Ge<sup>+</sup>, and <sup>90</sup>GeO<sup>+</sup> signals are similar to those for sample 100N-4, previously described. The thickness of GeO<sub>2</sub> appears to be somewhat thinner: about 24Å.

*Hydrogen concentration.*—Since hydrogen anneal of germanium MIS structures produces a very high interface state density, its concentration profiles were investigated. Due to the presence of a high background H<sup>+</sup> signal, a cold plate near the sample had to be chilled to liquid nitrogen temperature during the profilings. The profile of hydrogen concentration illustrated was normalized to a primary ion current of 5 × 10<sup>-9</sup>A. A sample annealed in the oxygen and argon cycle (111N-7) was compared with a sample annealed in forming gas (sample 100N-8). Near the GeO<sub>2</sub>/SiO<sub>2</sub>-Ge interface the hydrogen concentration of the sample annealed in forming gas is about seven times higher than that of the sample annealed in oxygen and argon. Furthermore, in the latter sample, some of the hydrogen signal may be attributed to the background.

To assure that the profile observed was actually due to hydrogen and not to composition matrix effects due to the presence of electronegative ions, a primary ion beam using oxygen was also employed. Figure 4 shows the high hydrogen concentration of sample 100N-8,

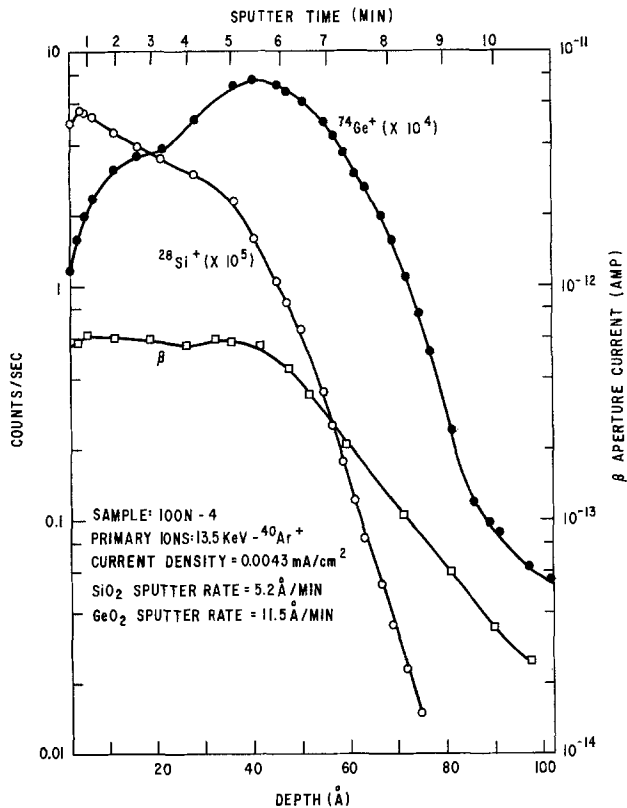


Fig. 2. Profiles of  $^{28}\text{Si}^+$ ,  $^{74}\text{Ge}^+$ , and the total secondary ion current ( $\beta$ ) for sample 100N-4 annealed in an argon ambient at 600°C for 2 hr. The depth profile shown is also calculated using the sputtering rates obtained from Fig. 1.

annealed in forming gas at 600°C for an hour. The hydrogen concentration remains high near the  $\text{SiO}_2$ -Ge interface

**Interface state measurements.**—The samples used here were processed identically to those used for the chemical analyses described previously. The thickness of an  $\text{SiO}_2$  film used here is about 500-1500Å for convenience in C-V and other electrical measurements.

In the C-V measurements, all the high frequency MOS differential a-c capacitance measurements were carried out at 1 MHz using a Boonton Electronics 72A capacitance meter. For ohmic contact, Ga-In liquid metal was used on the back of the wafers. Typical C-V curves taken at 300° and 77°K are shown in Fig. 5 for samples annealed in oxygen and forming gas, respectively. A significant flatband voltage shift from 300° to 77°K for the forming gas treatment indicates a much higher interface state density. Furthermore at 77°K, the depletion capacitance departs from the theoretically calculated curve, as shown in flat region. This is due to the contributions of interface state capacitance. The interface state density was measured similarly to that described by Gray and Brown (5). The method of measurement is to record the flatband voltage shift while varying the sample temperature from 300° to 78°K. The flatband condition is maintained by holding the flatband capacitance with a feedback amplifier. The shift in flatband bias is a measure of the number of interface states located at the energy between the Fermi levels of incremental temperatures. This is a direct measurement of a majority of interface states located at the upper half of the bandgap for n-type samples; and similarly at the lower half of the bandgap for p-type samples, that is

$$n_{\text{FS}} = \frac{dN_{\text{FS}}}{dE} = \frac{C_0}{qA} \frac{dV_{\text{FB}}}{dT} \bigg/ \frac{dE_{\text{F}}}{dT} \quad [2]$$

Since there are electron traps as revealed by hysteresis in the C-V curves, it is difficult to estimate exactly

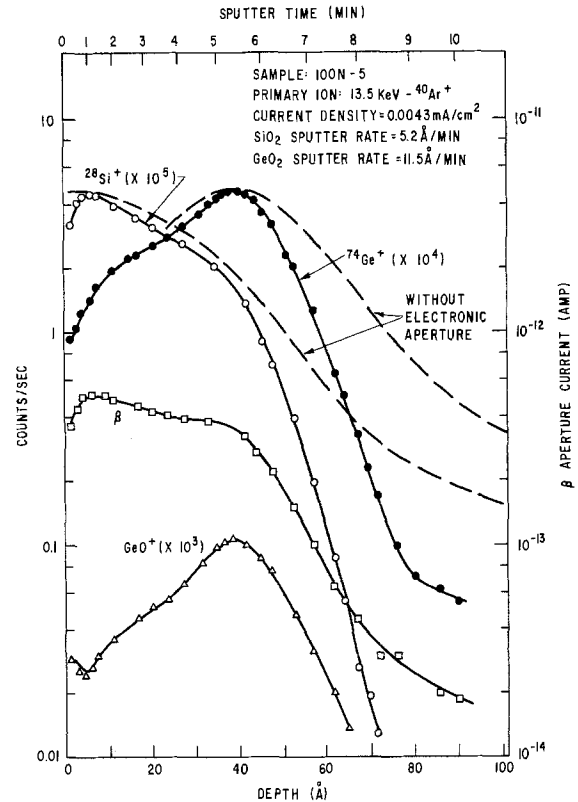


Fig. 3. Profiles of  $^{28}\text{Si}^+$ ,  $^{74}\text{Ge}^+$ ,  $^{90}\text{GeO}^+$ , and the secondary ion current ( $\beta$ ) for sample 100N-5, annealed in forming gas. The profiles of  $^{28}\text{Si}^+$  and  $^{74}\text{Ge}^+$  without the use of the electronic aperture is also plotted to illustrate the improvement of resolution by its use.

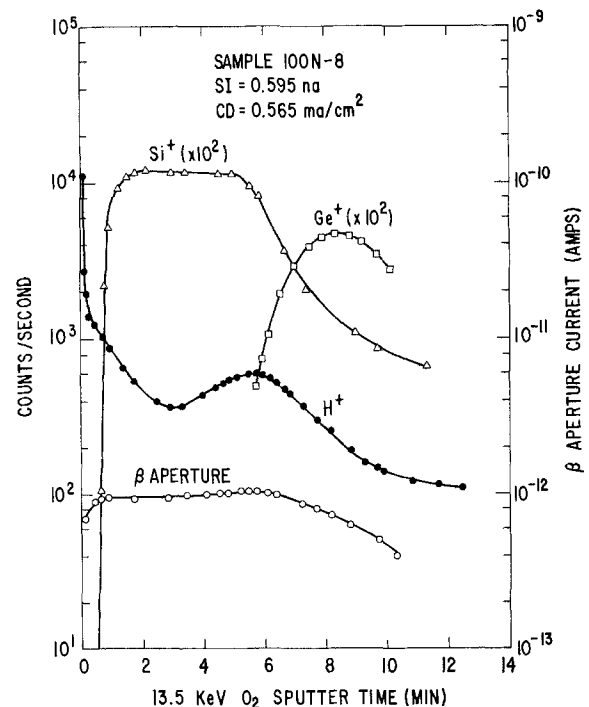


Fig. 4. The profile of  $\text{H}^+$  for sample 100N-8 using a 13.5 keV  $^{32}\text{O}_2^+$  beam. The sample has a 340Å  $\text{SiO}_2$  film and was annealed in forming gas at 600°C for 2 hr. A peak of hydrogen concentration near the interface is shown. The sputter rate is about 51 Å/min.  $\text{Si}^+$ ,  $\text{Ge}^+$ , and the  $\beta$  aperture current are also plotted.

the shift of the flatband potential due to the fast states. This is also true for the use of other C-V techniques. Therefore, there is a certain amount of uncertainty in measuring the fast state density. Further, the interface



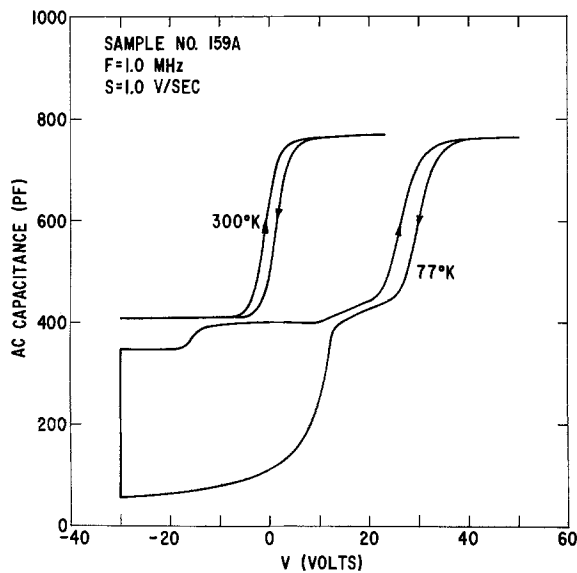
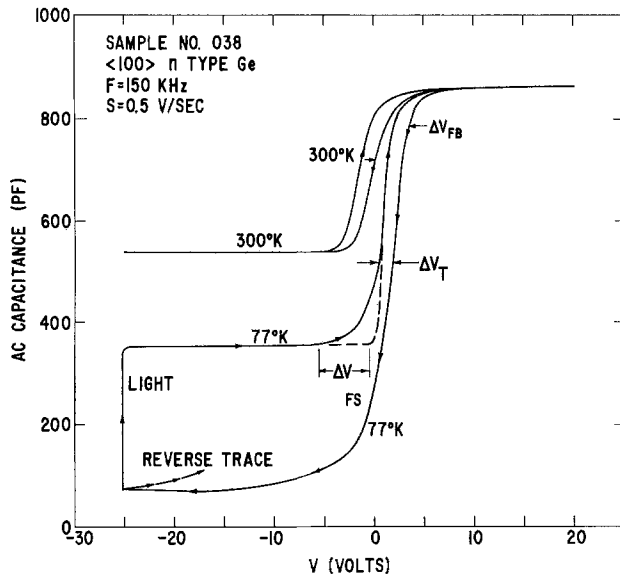


Fig. 5. Typical C-V curves (a, top) at 300° and 77°K; for samples annealed in oxygen; (b, bottom) for samples annealed in forming gas.

state density induced by the forming gas anneal is so high that it always contributes to the capacitance values, particularly near room temperature. Thus the precise density of states cannot be determined in this case.

The interface state densities for several samples under different annealing conditions, shown in Fig. 6 were obtained using Eq. [2] by numerically differentiating the  $\Delta V_{FB}-T$  curves. Samples annealed both in oxygen and forming gas environments show a similar distribution increasing toward the band edge. The forming gas annealed samples have much higher interface state densities ( $10^{14}/\text{cm}^2$ ) than those annealed in oxygen. The reduction of the states, when annealed in oxygen, can be attributed to the growth of  $\text{GeO}_2$  between the  $\text{SiO}_2$ -Ge interface as discussed previously.

Some 77°K curves show a well-defined region ("ledge") of nearly constant capacitance above the inversion capacitance of the reverse trace ( $\Delta V_{FS}$ ). The length of this region is also a measure of the interface state density (6). Therefore, the total interface state density can be estimated from either

$$N_{FS} \cong \Delta V_{FS} C_o/e$$

or

$$N_{FS} \cong 2\Delta V_{FB} C_o/e$$

[3]

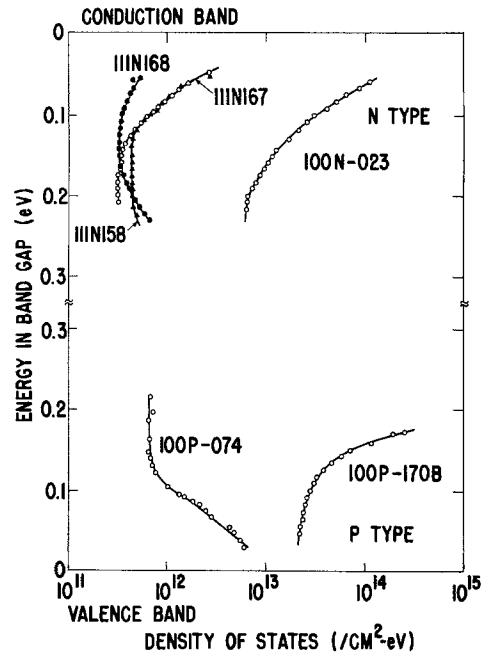


Fig. 6. Interface state densities for samples annealed in oxygen ambient (samples 74, 167, 168, and 158) in forming gas (sample 23), and with Ni contamination (sample 170B).

The results are in agreement with the previous measurements of the shift of flatband voltage with temperature.

*Measurement of minority carrier generation using the capacitance vs. time technique.*—When a MIS structure is biased to deep depletion, minority carriers will gradually accumulate at the  $\text{SiO}_2$ -Ge interface to invert the surface as a result of electron-hole pair generation. The time required for a MIS device to invert from depletion without external excitation is defined here as the recovery time or the storage time. For an n-type substrate, the generation rate of holes per unit area may be written (7-11)

$$\frac{dP_s}{dt} = G_d + G_s + G_b + G_e \quad [4]$$

where  $G_d$  is the generation rate in the space charge region (or the depletion region),  $G_s$  is the surface generation,  $G_b$  is the bulk generation outside the space charge region, and  $G_e$  is external excitation, such as optical generation.

Assuming the capture cross sections for electrons and holes are comparable, the minority carrier generation in the depletion region ( $n_p \ll n_i$ ) may be expressed simply as (7)

$$G_d = \frac{n_i}{\tau_b} (w - w_f) \quad [5]$$

where  $w$  and  $w_f$  are the depletion and inversion widths, respectively;  $n_i$  is the intrinsic carrier concentration, and  $\tau_b$  is the bulk lifetime. Similarly, the generation due to interface states can be written as (7, 10)

$$G_s = n_i S \quad [6]$$

where  $S$  is the surface recombination velocity. Minority carriers originating from electron-hole pairs generated outside the space charge region may diffuse into the depletion region and be swept by the field toward the interface. This generation rate may be obtained (12) by using the diffusion equation and bulk generation rate to give

$$G_b = \frac{n_i^2}{N_b} \left( \frac{D_p}{\tau_b} \right)^{1/2} \quad [7]$$

By substituting each generation component into Eq. [4] and expressing it in terms of capacitance, one obtains

$$-\frac{N_D \epsilon_s}{2C_{ox}} \left[ \frac{d}{dt} \frac{C_{ox}}{C} \right]^2 = \frac{n_i}{\tau_b} \epsilon_s \left( \frac{1}{C} - \frac{1}{C_f} \right) + S n_i + \frac{n_i}{N_D} \left( \frac{D_p}{\tau_b} \right)^{1/2} \quad [8]$$

To investigate the physical parameters controlling the generation and recombination in a MIS structure, a pulsed C-V technique is used. Square-wave pulses were applied to MIS devices and capacitance vs. time (C-t) curves were observed on an oscilloscope. The sample temperature was varied in a cryostat. The C-t curves for various interface state densities ( $10^{11}/\text{cm}^2\text{-eV}$  and  $10^{14}/\text{cm}^2\text{-eV}$ ) were taken, and then the recovery time from deep depletion to inversion was plotted vs.  $1/T$  as shown in Fig. 7.

The storage time vs.  $1/T$  plot shows a slope of 0.668 eV at 250°K for sample 100N-037 which has a low interface state density similar to samples 167 and 168 shown in Fig. 6. (These samples had been heat-treated in wet oxygen at 600°C for 2 hr and subsequently in dry air at 350°C for 18 hr.) This slope is close to the bandgap  $E_g = 0.684$  eV at this temperature, indicating that the generation and recombination are dominated by a bulk phenomenon. Most of the minority carriers reaching the interface come from outside the space charge region through the carrier diffusion process. If one assumes that bulk generation dominates Eq. [4], then Eq. [5] reduces to

$$\frac{d}{dt} \left( \frac{C}{C_{ox}} \right) = \left( \frac{C}{C_{ox}} \right)^3 \left( \frac{n_i}{n_D} \right)^2 \frac{\epsilon_{ox}}{\epsilon_x} \frac{1}{t_{ox}} \left( \frac{D_p}{\tau_b} \right)^{1/2} \quad [9]$$

The plot of

$$\frac{d}{dt} \left( \frac{C}{C_{ox}} \right) \text{ vs. } \left( \frac{C}{C_{ox}} \right)^3$$

as shown in Fig. 8, is linear. The linearity is a further evidence of bulk generation and also gives  $D_p/\tau_b$  from the slope of the straight line. Sample 111N-197 was annealed in forming gas at 600°C for 2 hr, and has a high interface state density. The same plot shows a slope of 0.309 eV, which is close to one-half the energy band-

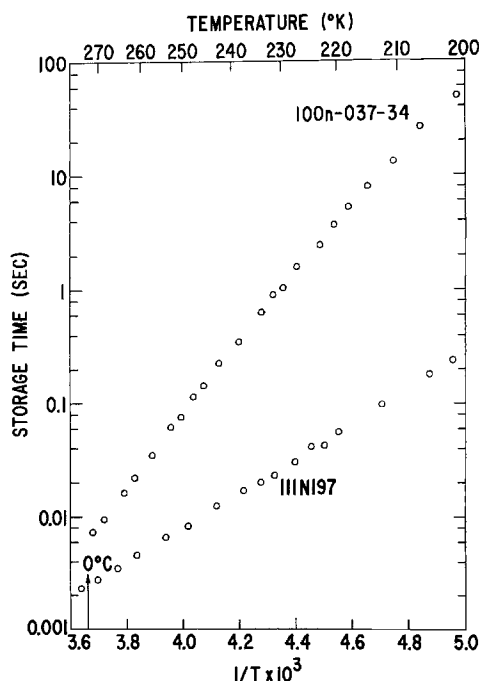


Fig. 7. Recovery time from depletion to inversion for sample annealed in oxygen (sample 37) and for sample annealed in forming gas (sample 197).

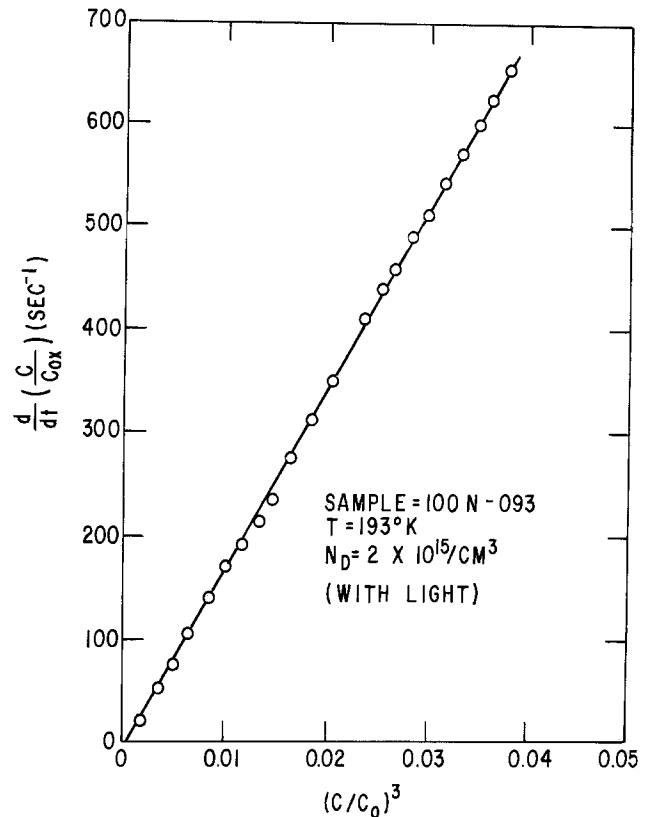


Fig. 8.  $d/dt (C/C_{ox})$  vs.  $(C/C_{ox})^3$  plot for sample annealed in oxygen. The linearity indicates that bulk generation is dominant when the sample is in the dark.

gap. It is clear from Eq. [6] that the surface generation due to the interface states would have this dependence.

It should also be noted that as temperature varies, the shapes of the C-t curves in the dark for the same sample change. This change results from the transition of the dominant generation components from a diffusion process to generation in the space charge region and other field-induced processes in the germanium substrate as temperature decreases. At temperatures above 235°K, the linear relationship of

$$\frac{dC/C_o}{dt} \text{ vs. } \left( \frac{C}{C_o} \right)^3$$

plots suggest a diffusion process. This implication is demonstrated from the relationship of the storage time and  $1/T$ , shown in Fig. 7 which is linear above 235°K. The change in slope at about 235°K can be related to the temperature dependence of the reverse current in a p-n junction (12). For the temperature region between 300° and 230°K, the minority carriers are generated in the bulk and arrive at the surface via the diffusion process. Particularly for the samples annealed in oxygen, the generation due to the low interface state density near the midgap does not constitute a significant contribution (13). This is demonstrated in the previous section in the dependence of the recovery time on temperature as  $\exp(-E_g/kT)$  and the linear relationship of  $dC/dt$  and  $C^3$ .

**Channel mobility measurements.**—Germanium IGFET's were fabricated using a process similar to that of silicon RMOS as described elsewhere (2). The channel mobility of samples annealed in forming gas (IGFET 111N577) is much lower than the sample annealed in oxygen (IGFET 111N-563) as illustrated in Fig. 9: The channel mobility of IGFET 563 increased from 280  $\text{cm}^2/\text{V-sec}$  to 550  $\text{cm}^2/\text{V-sec}$  as the temperature decreased from 300°K to 78°K. This increase in channel mobility reflects the decrease of lattice scattering at lower temperature. On the other hand, the

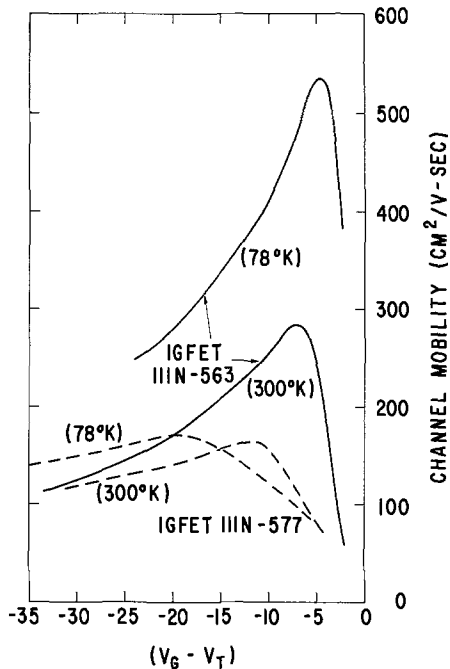


Fig. 9. Channel mobilities for FET's which were processed with oxygen annealing (sample 563) and processed with forming gas annealing (sample 577).

channel mobility of IGFET 577, annealed in forming gas, does not show a significant increase as temperature decreases indicating surface charge scattering. In fact when the surface field is low (near the turn-on voltage) in a weak inversion condition, the channel mobility at 78°K is somewhat lower than that at 300°K. This is due to the increasing occupation of the acceptor states (negatively charged when occupied) induced by the forming gas anneal as Fermi level moves close to the conduction band when the temperature decreases. Thus the coulomb scattering due to these surface charges increases and the mobility thereby is reduced.

### Discussion

The electrical measurements of interface state properties by C-V and capacitance recovery time are consistent with the measured density of states. The results indicate that interface states are induced by hydrogen. Dissolved hydrogen in germanium has no known electrical activity. Recently in work on high purity germanium detectors, Armantrout *et al.* (14) observed degradation of the detector, *i.e.*, increase in reverse leakage current from microamperes to milliamperes, for germanium grown in hydrogen and for devices packaged in a hydrogen ambient. The degradation has been shown to be due to the formation of surface states as hydrogen slowly diffuses to the surface. The formation of a p-type inversion layer has also been reported for surfaces with adsorbed hydrogen (15, 16).

From the measured result of interface state properties in the case of the forming gas anneal, it is suggested that the hydrogen-induced states are very localized at the surface. The actual surface bonding has been suggested to be different from covalent for the absorbed hydrogen. Appelbaum and Hamann (17) reported the calculated results of the potential, charge density, and electron energy level structures for a Ge surface using the Hartree Fock self-consistent technique. The electron energy level structure of the germanium <111> surface is similar to that of the silicon surface, having two deep bands of surface states. They suggested that unlike silicon the second surface layer of germanium can participate in a chemisorbed bond to form additional surface states, giving a fivefold coordination. A similar coordination may exist at the interface between SiO<sub>2</sub> and Ge. Such a coordination may be responsible for the observed interface states here.

The presence of germanium oxide when annealed in O<sub>2</sub> ambient is established in the AES and SIMS studies. Infrared absorption spectroscopy has also been used to demonstrate the presence of GeO<sub>2</sub> (18). A factor of 4 in reduction of interface state density has been achieved. As a result, an infrared imager of charge injection type (CID) has been fabricated. Schroder (19) has also fabricated charge-coupled devices (CCD). There, the efficiency should improve through the use of O<sub>2</sub> anneal and buried channel approach via ion implant. In this case of germanium MOS systems, the high residual interface state density tends to suggest that the CID approach in imaging has an intrinsic advantage of high efficiency.

### Conclusion

The interface properties of germanium-SiO<sub>2</sub> MIS structures following different annealings were investigated. The chemical composition of the interface was analyzed by the use of AES and SIMS. The correlation of these studies, namely the profiles of GeO<sub>2</sub> and H with interface state distribution, suggests that the interface state density can be reduced by annealing the samples in an oxygen ambient to grow GeO<sub>2</sub> and thus eliminate some defects originally present following the CVD deposition of the SiO<sub>2</sub> film. An annealing in forming gas gives rise to a much higher interface state density. The interface states indeed are shown to be responsible for a high surface minority carrier generation in a MIS structure which is depleted initially. This also increases surface charge scattering in the carrier transport process as measured using IGFET's. The hydrogen-induced states are believed to be very localized, for hydrogen has no electrical activity in the bulk germanium. It should also be pointed out that due to the high state density a precise determination of surface potential and therefore the distribution of interface state density is difficult. The use of ion implantation to introduce a controlled amount of hydrogen is being carried out. The results will be reported at a later date.

### Acknowledgment

This research was supported in part by the Advanced Research Projects Agency of the Department of Defense and was monitored by USAERDL under contract DAAK02-73-C-0060.

Manuscript submitted Feb. 6, 1976; revised manuscript received April 30, 1976.

Any discussion of this paper will appear in a Discussion Section to be published in the June 1977 JOURNAL. All discussions for the June 1977 Discussion Section should be submitted by Feb. 1, 1977.

Publication costs of this article were assisted by General Electric Company.

### REFERENCES

1. T. O. Sedgewick, *J. Appl. Phys.*, **39**, 5066 (1968); also T. Yashino, *Japan J. Appl. Phys.*, **9**, 740 (1970).
2. K. L. Wang and P. V. Gray *IEEE Trans. Electron Devices*, **ED-22**, 357 (1975); K. L. Wang and A. Josni, *J. vac. Sci. Technol.*, **12**, 927 (1975).
3. H. Nagai, *Rev. Elec. Commun. Lab. (Tokyo)*, **22**, 1043 (1974); T. Tashio, for example, see H. Nagai and K. Yano, *ibid.*, **22**, 1057 (1974); S. Iwauchi and T. Tanaka, *Jpn. J. Appl. Phys.*, **10**, 1260 (1971).
4. C. A. Anderson, *Int. J. Mass Spectrom. Ion Phys.*, **2**, 61 (1969); *ibid.*, **3**, 413 (1970).
5. P. V. Gray and D. M. Brown, *Appl. Phys. Lett.*, **8**, 31 (1966).
6. P. V. Gray, *IEEE Proc.*, **57**, 1543 (1969).
7. D. K. Schroder, *IEEE Trans. Electron Devices*, **ED-19**, 1018 (1972).
8. D. K. Schroder and H. C. Nathanson, *Solid-State Electron.*, **13**, 577 (1970).
9. D. K. Schroder and J. Guldborg, *ibid.*, **14**, 1285 (1971).
10. M. Zerbst, *Z. Angew. Phys.*, **22**, 30 (1966).
11. C. St. L. Rhodes and C. A. T. Salama, *J. Phys. D*,

- 6, 1798 (1973).
12. A. S. Grove, "Physics and Technology of Semiconductor Devices," p. 179, John Wiley & Sons, Inc., New York (1967).
  13. D. J. Fitzgerald and A. S. Grove, *Surf. Sci.*, **9**, 347 (1968).
  14. G. A. Armantrout, R. Wichner, and S. P. Swierkowski, *IEEE Trans. Nucl. Sci.*, **ns-21**, 344 (1974).
  15. K. H. Maxwell and M. Green, *J. Phys. Chem. Solids*, **14**, 94 (1960).
  16. R. C. Franck and J. E. Thomas, *ibid.*, **16**, 144 (1960).
  17. J. A. Appelbaum and D. R. Hamann, *Phys. Rev. Lett.*, **32**, 225 (1974); Private communication.
  18. M. Kuisl, *Solid State Electron.*, **15**, 595 (1972).
  19. D. K. Schroder, *Appl. Phys. Lett.*, **25**, 747 (1974).

## Effect of Evaporated Dielectric Materials on the Surface of High Purity Germanium

R. J. Dinger

Atomic Energy of Canada Limited, Chalk River Nuclear Laboratories, Chalk River, Ontario, Canada K0J 1J0

### ABSTRACT

The effect of evaporated dielectrics on real Ge surfaces has been investigated at 80°K. Using high purity Ge ( $|N_D - N_A| < 10^{11} \text{ cm}^{-3}$ ), insulated gate field transistors (MISFET) were made and coated with an evaporated dielectric layer. The number of surface states and the density of states per unit energy have been deduced from the forward transconductance. It has been found that some dielectrics introduce a large number of surface states near the center of the bandgap.

The protection of the surface of the active volume of germanium detectors for infrared light,  $\gamma$ -radiation, or particles is a problem which differs in many respects from the surface passivation problem in the silicon transistor or integrated circuit technology. The solutions developed for the latter cannot be applied to these Ge devices for a variety of reasons. The main one is that the crystal material must at no stage of the fabrication of the device be heated to more than 300°-350°C (1).

The large size of the Ge detectors (active volume 0.5-100 cm<sup>3</sup>) compared to transistors suggests that any electronically disturbed surface layers are such a small fraction of the total volume that their influence on the detection properties is negligible; experiments show that this is not so. Figure 1 shows the response of a small (0.5 cm<sup>3</sup>) Ge  $\gamma$ -ray detector to the 662 keV  $\gamma$ -rays from a <sup>137</sup>Cs source (2). The top spectrum was taken just after the manufacture of the device, the middle spectrum after it had been exposed to oxygen (about 100 Pa · sec), and the lower spectrum after a "bake-out" at room temperature for 30 min (the device is operated at ~80°K). All spectra were taken for the same duration. It is obvious that the effect of the exposure to oxygen was to reduce the area underneath the peak (full energy peak efficiency), which is proportional to the sensitive volume, to about one-third of its original value. The moderate bake-out partly recovered the original performance.

Recent investigations (2, 3) have shown that this degradation is due to the formation of "surface channels." Surface channels were first discovered by Brown (4) and found to be the cause for poor Ge transistor characteristics. The thickness of the surface channels is related to the effective Debye length,  $L_D$  (5), which can become as large as 0.3 mm in the very pure material used for Ge detectors.

To protect the surfaces of Ge detectors against the effect of adverse ambient atmospheres, encapsulation techniques have been used with varying success (6, 7). Another method of surface protection consists of stabilizing the position of the Fermi level at the surface by an electronic interaction of the Ge with a suitable

Key words: Ge detectors, surface protection, surface state density.

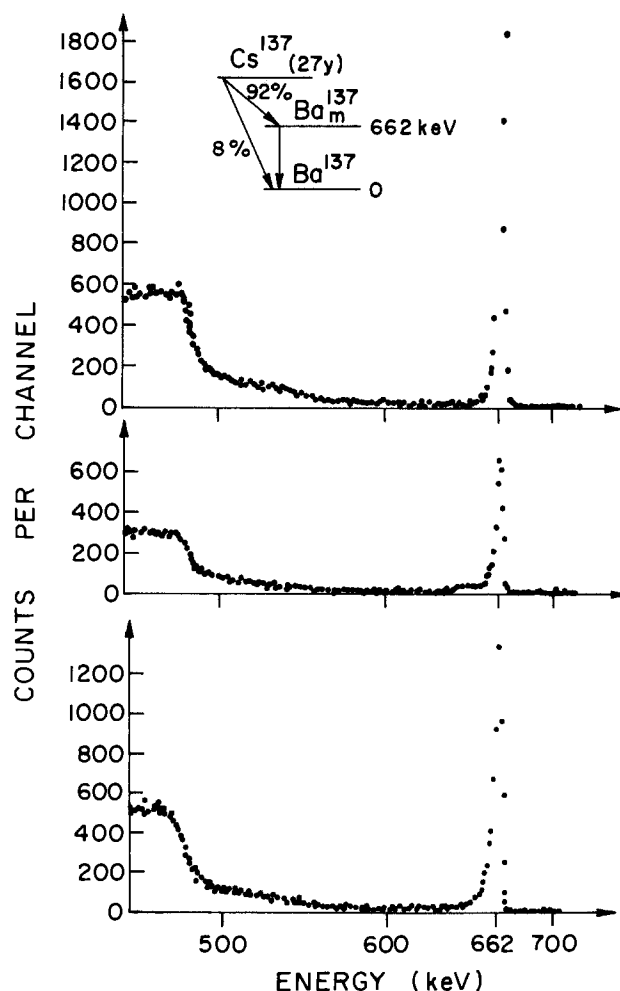


Fig. 1.  $\gamma$ -Ray spectrum of <sup>137</sup>Cs taken with a 0.5 cm<sup>3</sup> Ge  $\gamma$ -ray detector. Top = after the manufacture of the device; middle = after exposure to 100 Pa · sec of oxygen; bottom = after bake-out at 300°K in good vacuum [after Ref. (2)].

coating material. This paper deals with the effect of evaporated coatings on real Ge surfaces. Although it is quite clear that an evaporated layer will hardly be comparable to a thermally grown oxide such as SiO<sub>2</sub> with respect to pinholes, included impurities, etc., it has been found that certain dielectrics show an electronic interaction with the underlying Ge which stabilizes the Ge surface by effectively anchoring the Fermi level at a favorable position. The protection mechanism involved is therefore such that a great number of deliberately introduced surface states at an energetically favorable position overcomes the effect of additional states produced by the ambient.

The electronic properties of the Ge surface before and after the evaporation of the coating were investigated using a metal-insulator-semiconductor transistor (MIS transistor) arrangement. Because the devices to be protected with these coatings are normally cooled with liquid nitrogen and operated at ~80°K, all measurements were taken at that temperature.

**Theory**

The energy band diagram for a p-type semiconductor with an n-type inversion layer is shown in Fig. 2. The occupancy of the surface states at the boundary of the crystal and within the evaporated dielectric is given by the Fermi level. The net surface charge due to the surface states must be compensated for by an equal amount of charge of opposite sign within the bulk of the semiconductor. In Fig. 2 it is assumed that the surface charge due to the surface states is positive which requires the energy bands to be bent downwards. The semiconductor shows an n-type conducting surface channel (inversion layer) of thickness of the order of magnitude of the effective Debye length, *L<sub>D</sub>*, where

$$L_D = \sqrt{\frac{\epsilon_0 \cdot \epsilon_r \cdot kT}{q^2(n_b + p_b)}} \quad [1]$$

and  $\epsilon_0$  = permittivity of the vacuum,  $\epsilon_r$  = relative dielectric constant,  $k$  = Boltzmann's constant,  $T$  = absolute temperature,  $q$  = electronic charge,  $n_b$  = concentration of free electrons, and  $p_b$  = concentration of free holes in the bulk of the semiconductor.

Under the present experimental conditions, the sum of the concentrations of the free carriers in the bulk may be approximated by the net ionized concentration of dopants  $N$

$$n_b + p_b \approx |N_D - N_A| \equiv N \quad [2]$$

$N_D$  being the concentration of ionized donors and  $N_A$  the concentration of ionized acceptors.

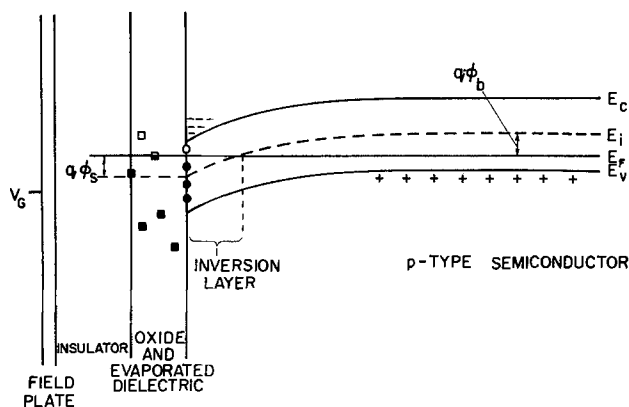


Fig. 2. Energy band diagram of the field effect experiment.  $E_c$ ,  $E_i$ ,  $E_F$ , and  $E_v$  are the conduction band edge, the intrinsic Fermi level, the Fermi level, and the edge of the valence band.  $\phi_b$  and  $\phi_s$  are the bulk potential and the surface potential.  $\blacksquare$  and  $\square$  are slow,  $\bullet$  and  $\circ$  fast surface states. The energy levels are shown for zero voltage at the field plate.

If any voltage is applied to the field plate, which is parallel to the surface as shown in Fig. 2, charge neutrality requires that

$$C_G \cdot V_G = q(N_t(\phi_s) - \Delta N) + Q(\phi_s) \quad [3]$$

where  $C_G$  is the capacitance between the field plate and the semiconductor,  $N_t$  is the number of surface states, and  $\Delta N$  the number of free excess electrons created by the bending of the bands in the inversion layer (all per unit surface area).  $V_G$  is the voltage at the field plate with respect to the semiconductor,  $\phi_s$  is the surface potential (see Fig. 2), and  $Q(\phi_s)$  is the charge per unit area due to the depletion of the majority carriers in the surface space charge layer. The sign of  $q$  is the same as the sign of the minority carriers in the inversion layer. Using Eq. [1],  $Q(\phi_s)$  is of the order of

$$Q(\phi_s) \approx N \cdot L_D \quad [4]$$

In strong inversion layers the number  $\Delta N$  of excess minority carriers per unit area in the surface space charge region is much larger than  $N \cdot L_D$  and Eq. [3] reduces to

$$C_G \cdot V_G = q(N_t(\phi_s) - \Delta N) \quad [5]$$

Since the surface potential  $\phi_s$  is a definite function of  $\Delta N$ , the knowledge of  $\Delta N$  and the parameters  $C_G$  and  $V_G$  allows the number  $N_t$  of surface states per unit area as a function of  $\phi_s$  to be determined. The measurement of  $\Delta N$  is done by applying an electric field parallel to the surface and observing the conductivity  $\sigma$  of the minority carriers in the inversion layer. In the concentric contact geometry used the conductivity  $\sigma(\Omega^{-1})$  is given by

$$\sigma = \frac{2\pi}{\ln r_1/r_2} \cdot \Delta N \cdot \mu_s \cdot q \quad [6]$$

where  $r_1$  and  $r_2$  are the outside and inside radii, respectively, of the active surface (inversion layer in Fig. 3) and  $\mu_s$  is the mobility in the inversion layer. The latter was measured in the same arrangement by applying to the field plate a voltage pulse  $\delta V_G$  which is short compared to the relaxation time of the fast surface states. This means that the surface state density remains constant during the voltage pulse and the mobility can be determined using Eq. [5] which further simplifies to

$$C_G \cdot \delta V_G = q \cdot \delta(\Delta N) = \frac{\delta\sigma}{\mu_s} \cdot \frac{\ln r_1/r_2}{2\pi} \quad [7]$$

In this work the number of surface states in equilibrium ( $V_G = 0$ ) is of main importance. This equation may be obtained by combining Eq. [5] and [6]

$$[N_t]_{V_G=0} = \frac{\sigma \cdot \ln r_1/r_2}{2\pi \cdot \mu_s \cdot q} \quad [8]$$

The above formulas show that a d-c field effect experiment and a pulsed field effect experiment (for the measurement of the mobility) are sufficient to determine the number of surface states per unit area present.

In order to obtain the density of surface states per unit energy, it is necessary to know the relation between the number of minority carriers  $\Delta N$  per unit area in the inversion layer and the surface potential  $\phi_s$ . Numerical computations of this relation were carried out by Many *et al.* (5). Their results show that when the average concentration of minority carriers in the surface inversion layer  $\Delta N/L_D$  exceeds the net concentration of dopants  $N$

$$|v_s| - |u_b| \approx 2 \cdot \ln \frac{\Delta N}{L_D \cdot N} \quad [9]$$

where  $v_s$  and  $u_b$  are defined as

$$v_s = \frac{q}{kT} \phi_s \text{ and } u_b = \frac{q}{kT} \phi_b \quad [10]$$

where  $\phi_b$  is the bulk potential. The change in surface potential, associated with an increase or decrease of the channel conductivity  $d\sigma$  (due to a change in the voltage at the field plate  $dV_G$ ), becomes

$$dv_s = 2 \frac{d(\Delta N)}{\Delta N} = 2 \frac{d\sigma}{\sigma} \quad [11]$$

Usually the density of surface states is high enough such that an increase in the voltage at the field plate  $dV_G$  produces many more surface states than free carriers in the inversion layer (cf. Eq. [4]  $dN_t \gg d(\Delta N)$ ). The contribution of the change in the number of free carriers  $d(\Delta N)$  to the charge may therefore be neglected and  $dN_t$  is given by

$$dN_t = \frac{C_G}{q} \cdot dV_G \quad [12]$$

Substituting  $dE/kT$  for  $dv_s$  in Eq [11],  $E$  being energy in electron volts, the density of surface states per unit energy becomes

$$\frac{dN_t}{dE} = \frac{C_G}{2 \cdot q \cdot kT} \cdot \frac{dV_G}{d\sigma/\sigma} \quad [13]$$

It should be noted that neither the carrier mobility nor the device geometry is necessary to determine the density of surface states per unit energy. Equation [13] is valid as long as the average concentration of minority carriers in the surface channel  $\Delta N/L_D$  equals or exceeds the bulk dopant concentration  $N$  and, in the present experimental arrangement at 80°K, if the surface state density is larger than  $10^{13} \text{ cm}^{-2} \cdot \text{eV}^{-1}$ .

### Experimental Arrangement

Figure 3 shows the experimental arrangement. The device consists of a circular disk of  $\sim 3$  cm diameter of p-type Ge of high purity ( $N < 10^{11} \text{ cm}^{-3}$ ) with two concentric n-contacts. (Devices from n-type Ge with p-contacts were made as well.)<sup>1</sup> The concentric contact configuration eliminates any undesirable edge effects. After the chemical surface treatment (lap, polish, etch in 3:1 by volume of 70%  $\text{HNO}_3$  and 40%  $\text{HF}$  with quench and rinse in doubly distilled water), a 0.01 mm thick polyester insulating disk and the field plate were placed on top as shown in the figure. This device is essentially an n-channel metal-insulator-semiconductor (MIS) field effect transistor with an active surface area of about  $2 \text{ cm}^2$ .

To measure the conductivity between the center contact and the outside ("drain" and "source"), a 60 Hz a-c voltage of 0.1-0.5V produced by a shielded transformer was applied and the current was measured with a RMS ammeter. A voltage of up to  $\pm 300\text{V}$  could be applied to the field plate ("gate") corresponding to an induced charge of up to  $10^{12}$  electrons per  $\text{cm}^2$ . For the measurement of the mobility, a 0.5V d-c voltage was

<sup>1</sup>To avoid the risk of contamination of the material, low temperature processes were used to make the contacts. The n-contacts were made by diffusion of Li at 300°C, the p-contacts by alloying with In at 300°C or by the evaporation of a metal surface barrier.

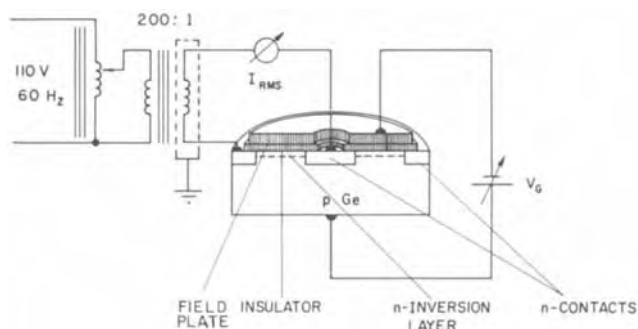


Fig. 3. Experimental arrangement.

applied across the channel and a voltage pulse of 15V to the gate. The increase in conductivity  $\delta\sigma$  was observed with an oscilloscope (terminated with  $50\Omega$ ).

### Results

**Mobility.**—Results of the measurement of the mobility are shown in Fig. 4. Plotted is the ratio of the mobility  $\mu_s$  is the surface inversion layer to the bulk mobility  $\mu_b$ . The bulk mobilities were taken as  $3.6 \times 10^4 \text{ cm}^2 \cdot \text{V}^{-1} \cdot \text{sec}^{-1}$  for electrons and  $4.2 \times 10^4 \text{ cm}^2 \cdot \text{V}^{-1} \cdot \text{sec}^{-1}$  for holes (8). The horizontal axis shows the "strength" of the surface channel given both as the number of minority carriers per unit area divided by the Debye length and the normalized excess surface potential  $|v_s| - |u_b|$ . This is the barrier height in units of  $kT$  except for an additive constant. The measurements were made with Ge of  $N \approx 5 \times 10^{10} \text{ cm}^{-3}$ . The figure shows that the stronger the surface channel gets the more the mobility is reduced. Schrieffer (9), and, later, other workers (10-13) have predicted such an effect. They calculated the reduction in mobility due to the fact that the carriers in the surface channel have to move in a potential valley of width  $L_D$ , which in more highly doped samples is narrower than the thermal mean free path. It should be mentioned that Schrieffer's calculations assume completely diffuse scattering of the carriers at the surface and that measurements (14,15) at higher temperatures and with much more highly doped material showed that the theory predicts too great a reduction in mobility (which means that the surface reflects the carriers in a partly specular manner). However, the measurements with this high purity material (where the thermal mean free path is only about  $1 \mu\text{m}$  and the Debye length about  $10 \mu\text{m}$ ) show that the mobility is even more reduced than Schrieffer's theory predicts. According to the theory, the three curves in Fig. 4 should coincide. The measurements with material of this purity show that the mobility in the surface channel obviously depends strongly on the surface treatment. In addition to Schrieffer's theory, another mechanism must therefore be responsible for the observed strong reduction in

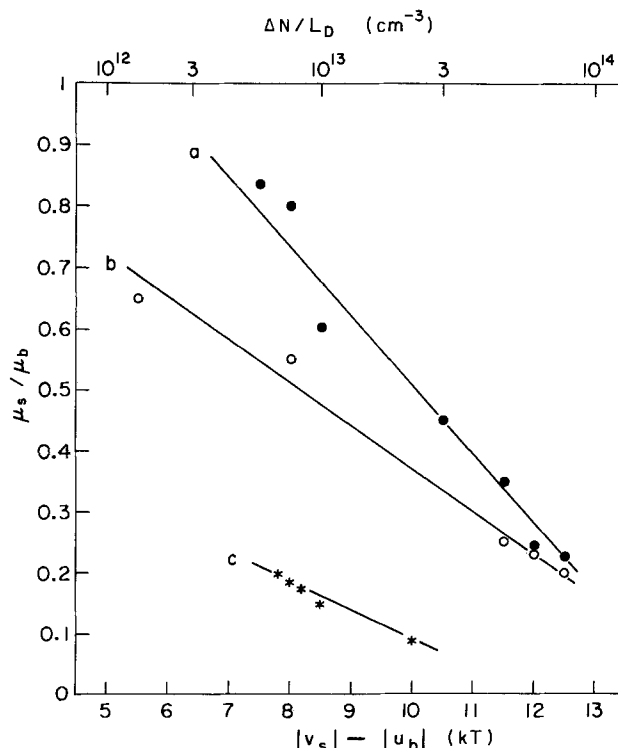


Fig. 4. Ratio of the mobility in the surface inversion layer,  $\mu_s$ , to the bulk mobility,  $\mu_b$ , as a function of the barrier height: a = n-channel MIS transistor; b = the same sample as a but after the chemical surface treatment has been repeated; c = p-channel MIS transistor.

mobility. A possible explanation would be that because of their small thermal mean free path the carriers are "trapped" in the potential wells created by local fluctuations in the surface potential and move along the surface, "hopping" from one of these wells to the next. Since the mobility is strongly nonlinear with the electric field, any such effect will reduce it. In addition, such a model could explain the dependence on the etch treatment observed here and by other workers (15). A "hopping" model, similar to that described, has been proposed by Mott (16) and found to be adequate to describe low temperature mobilities in inversion layers of silicon MIS transistors (17, 18) and thin amorphous germanium films (19).

**Surface state density after the surface treatment.**—Figure 5 shows the result of the field effect experiment on an n-channel Ge sample of  $5 \times 10^{10} \text{ cm}^{-3}$  dopant concentration, which was carried out as soon as possible after the chemical surface treatment. As expected from Eq. [3], increasing gate voltage also increases the conductivity  $\sigma$ . However, as shown in Fig. 4, the stronger the inversion layer gets, the more the mobility is reduced. Hence the conductivity seems to approach a limiting value. The number of electrons in the inversion layer, calculated according to Eq. [6] from the conductivity and the mobility (which were measured simultaneously, for this sample), shows a linear dependence upon the gate voltage. This linear dependence suggests that the surface state density is very small in this sample and calculation using Eq. [5] shows that in fact the charge induced by the gate voltage equals the number of electrons in the inversion layer within the experimental limits. The upper limit for the surface state density is therefore  $\sim 10^{12} \text{ cm}^{-2} \cdot \text{eV}^{-1}$ . At zero gate voltage there are nevertheless  $5 \times 10^9 \text{ cm}^{-2}$  surface states present which produce an n-type surface.

It should be mentioned that this particular sample showed the lowest observed density of surface states per unit energy. The surface condition just after the surface treatment depends upon the chemical surface

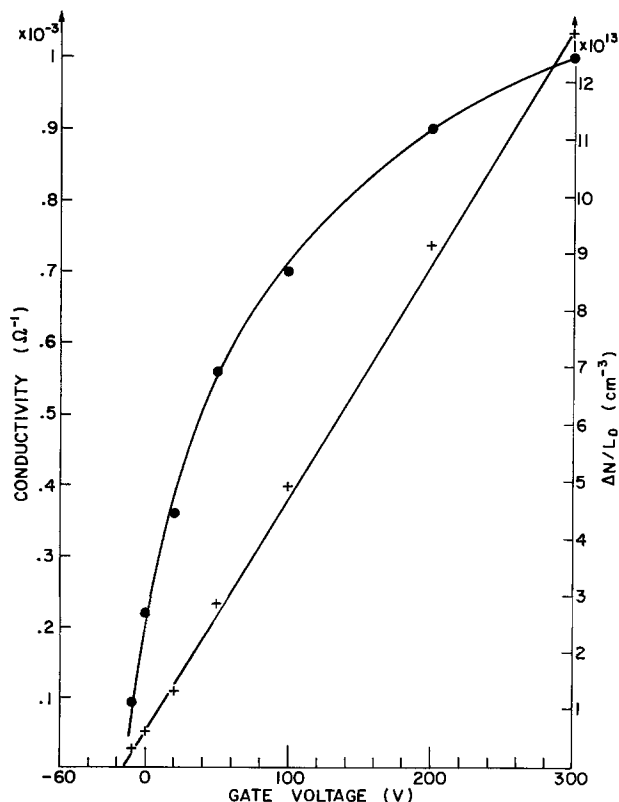


Fig. 5. Characteristics of an n-channel MIS transistor: ● = conductivity  $\sigma$  and + = excess surface carrier concentration  $\Delta N/L_D$  as a function of gate voltage.

treatment itself and the crystal material used. A surface state density of  $10^{13} \text{ cm}^{-2} \cdot \text{eV}^{-1}$  is often observed but the position of the Fermi level varies from sample to sample.

**Effect of the dielectrics on the surface of Ge.**—The effect of dielectrics on the surface of Ge has been investigated by comparing the surface state density just after the chemical surface treatment with the figures obtained after subsequent coating with an evaporated layer of 100-1000 nm thickness. To test the coatings for their ability to protect the Ge from adverse ambients, the coated devices were exposed to atmospheres of  $\text{H}_2$ , wet  $\text{N}_2$ ,  $\text{O}_2$ , dry  $\text{N}_2$ , etc., for up to 100 hr. For these tests the devices were at room temperature and were cooled to 80°K only for the measurements.

The following dielectrics have been tested:  $\text{SiO}_2$ ,  $\text{SiO}$ ,  $\text{TiO}_2$ , polytetrafluoroethylene (PTFE),  $\text{MgF}_2$ ,  $\text{Al}_2\text{O}_3$ , and the glasses Corning 7740 and Schott 8329. Except for  $\text{SiO}$  which was evaporated from a sublimation source, all of the insulators were evaporated using an electron gun evaporator. The vacuum was usually  $\sim 10^{-4} \text{ Pa}$  except for the evaporation of PTFE which produces large amounts of gaseous cracking products when "evaporated."<sup>2</sup>

Considerable differences between the various dielectrics have been observed with respect to their effect on the electronic properties of the Ge surface. Some dielectrics react very strongly with the Ge surface (e.g.,  $\text{SiO}$  and  $\text{TiO}_2$ ) while for others no interaction could be detected (e.g.,  $\text{SiO}_2$ ,  $\text{Al}_2\text{O}_3$ , etc.). An example of a strong interaction is shown in Fig. 6. The figure shows the characteristics of a p-channel MIS transistor. The zero intercept of the curves is proportional to the num-

<sup>2</sup> The "evaporation" of PTFE with an electron gun, according to de Wilde (20), is mainly a cracking process of the bulk material and the gaseous fractions recombine under the bombardment of stray electrons from the electron gun.

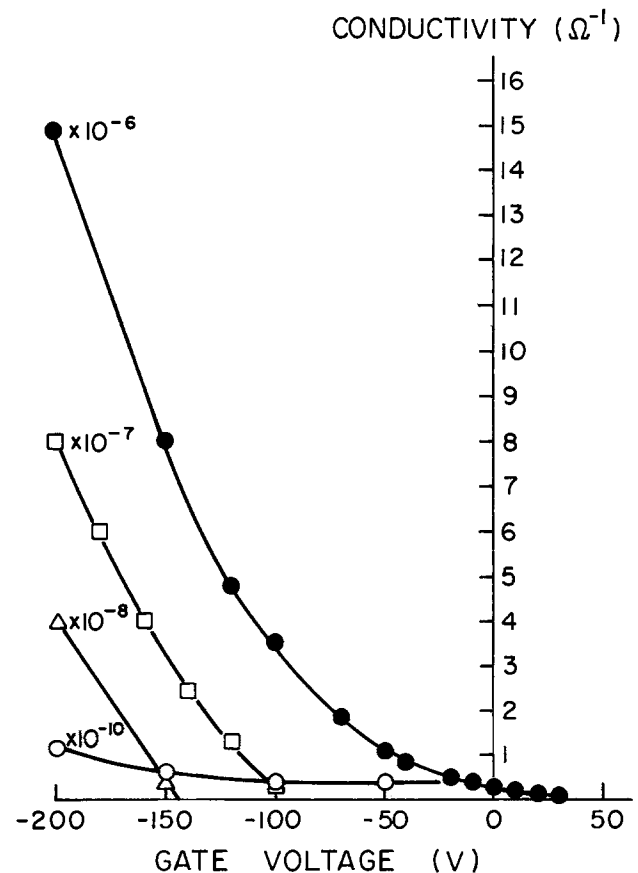


Fig. 6. Characteristics of a p-channel MIS transistor: ● = after the manufacture; ○ = after evaporation of 100 nm of  $\text{SiO}_2$ ; Δ = after  $\text{H}_2$  for 3 days; □ = after wet  $\text{N}_2$  for another day. The notations at each curve give the order of magnitude of the conductivity ( $\sigma$ ).

ber of surface states present at a particular surface condition (cf. Eq. [8]) and the density of surface states per unit energy is inversely proportional to the relative slope  $(d\sigma/\sigma)/dV_G$  of the curves (cf. Eq. [13]). Just after the chemical surface treatment ( $\bullet$ ), the device shows a weak inversion layer with a low density of surface states per unit energy. After coating with an evaporated layer of 100 nm of SiO ( $\circ$ ), the channel conductivity remains at the noise level up to a gate voltage of  $-150V$ . The slight rise in the conductivity  $\sigma$  for gate voltages larger than  $-150V$  indicates that the surface state density has become very high. However the very small channel conductivity ( $\sim 10^{-10} \Omega^{-1}$ ) shows that the number of holes in the inversion layer divided by the Debye length  $\Delta N/L_D$  is much smaller than the bulk dopant concentration  $N$  (which was  $5 \times 10^{10} \text{ cm}^{-3}$  for this sample). This means that Eq. [13] is no longer valid and the results plotted in Fig. 6 can only be interpreted qualitatively. It may be seen that exposure to a  $H_2$  atmosphere for 3 days ( $\Delta$ ) and wet  $N_2$  atmosphere for another day ( $\square$ ) worsens the device but the conductivity is still very low and is below the noise level at  $V_G = 0$ . The situation has been found to be even more favorable with n-channel devices. Usually after the evaporation of a coating of SiO, no conductivity can be detected and different ambients do not change this characteristic. The experiment shows that the SiO layer introduces a great number of surface states at an energy level which is close enough to the intrinsic position of the Fermi level to deplete the surface.

By either the chemical surface treatment or the influence of the ambient atmosphere before the evaporation of the dielectric layer, it is, however, possible to produce surface channels which show a large enough surface state density that the number of surface states introduced by the coating dielectric cannot shift the Fermi level sufficiently to deplete the surface. Two examples of this are shown in Fig. 7. Characteristics of p-channel devices are shown just after manufacturing ( $\bullet$  and  $\blacksquare$ ) and after having been coated with 100 nm

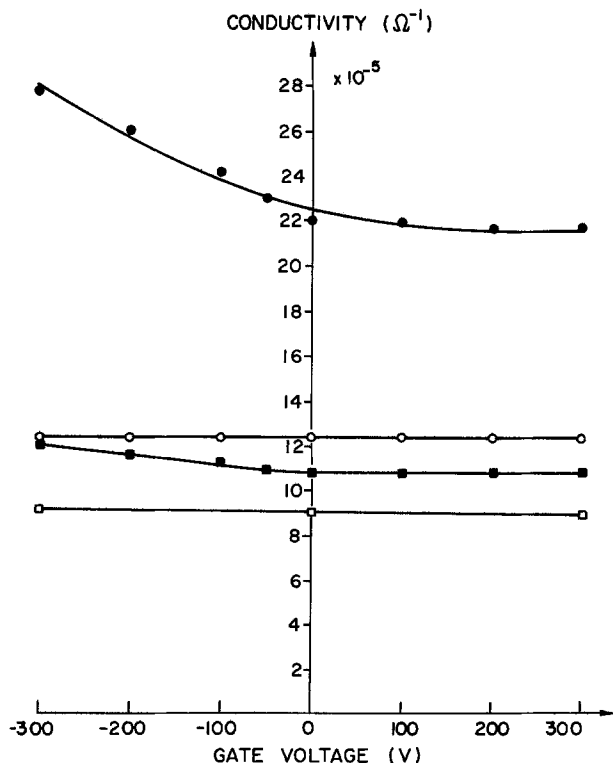


Fig. 7. Characteristics of two p-channel MIS transistors:  $\bullet$  = after the manufacture and  $\circ$  = after coating with 100 nm of SiO, and  $\blacksquare$  = after the manufacture and  $\square$  = after coating with 100 nm of TiO<sub>2</sub>.

of SiO ( $\circ$ ) or TiO<sub>2</sub> ( $\square$ ). It may be seen that neither of the two dielectrics used is able to cause the strong surface channels to disappear.

The surface protection qualities of the dielectrics may be attributed to the total number of surface states per unit area produced and their energetic position. This information may be obtained from the experiments described in Fig. 7. Table I gives the result of these experiments for all the dielectrics tried in the course of this work.

The table shows that four dielectrics show interactions with the Ge surface that are smaller than the detection limit of the method outlined above. Although the field effect experiment is capable of detecting very small changes in the electronic properties of the Ge surface, it should be mentioned that the manipulations necessary to perform the experiment described in Fig. 7 introduce changes in the surface due to the effect of the ambient atmosphere the sample is exposed to. (To determine the figures given in Table I, the sample has to be put in the measuring cryostat, evacuated and cooled, measured, warmed up and transferred in air into the evaporator, evacuated and coated with the dielectric, transferred back into the cryostat, evacuated, cooled, and measured again.) The ambient atmosphere has been found to introduce typically about  $10^{11} \text{ cm}^{-2}$  surface states which is therefore the lower limit of detection for the effect of the evaporated dielectric on the surface of Ge.

Four of the dielectrics tried show a pronounced interaction with the Ge surface. The two dielectrics SiO and TiO<sub>2</sub> introduce their surface states close enough to the intrinsic position of the Fermi level to deplete the surface. (Due to the very low intrinsic carrier concentration at 80°K the Fermi level may deviate by as much as 36 kT (= 0.24 eV) from its intrinsic position without producing an excess carrier concentration at the surface  $\Delta N/L_D$  exceeding  $10^{10} \text{ cm}^{-3}$ ).

For the two glasses tried it was found that they introduce surface states close to or within the position of the valence band at the surface. This means that regardless of the surface condition created by previous surface treatments the evaporation of one of these glasses leads to a more p-type surface.

*Mechanism of interaction.*—Theoretical calculations (21, 22) show that real Ge surfaces such as the ones produced by the chemical surface treatment used in the present work should not show any nonlocalized surface states. This means that the dangling bonds of the Ge surface atoms are saturated with the bonds originating at the oxygen atoms of the native surface oxide layer. Ideally, such a well-oxidized surface has no surface states. The Fermi level at the surface has the same position as in the bulk material and the energy bands go horizontally right to the surface of the crystal ("flat-band condition"). If this oxide layer is thick enough, it is an ideal surface protection in the sense that additional covering of the surface with any material cannot produce surface states because the additional layer has no access to the bare Ge surface and the oxide is thick enough to inhibit carrier exchange by tunneling, etc. The usual method of protecting a real surface is, therefore, to grow a thick and good oxide. The surface

Table I. Energetic position and number of surface states per unit area produced by the dielectric layers on real Ge surfaces

Dielectric material	Number of surface states produced per unit area ( $\text{cm}^{-2}$ )	Energetic position of the surface states
SiO	$10^{14}$	within $\pm 0.25$ eV of the intrinsic position of the Fermi level
TiO <sub>2</sub>	$10^{13}$	
Glass 7740	$10^{12}$ - $10^{13}$	within the valence band
Glass 8329	$10^{12}$ - $10^{13}$	
MgF <sub>2</sub>	$\leq 10^{11}$	
PTFE	$\leq 10^{11}$	
Al <sub>2</sub> O <sub>3</sub>	$\leq 10^{11}$	
SiO <sub>2</sub>	$\leq 10^{11}$	



states observed after the chemical surface treatment used in this work are localized states. They originate at local imperfections (e.g., pinholes) in the oxide layer. The well-known sensitivity of these Ge surfaces to changes in the ambient atmosphere may be due to additional states created at the pinholes in the oxide.

Two possible mechanisms of interaction can explain the effect of the evaporated dielectric materials. The relatively large number of surface states may either be produced by an electronic interaction of the coating material through the oxide or else the surface states are produced at the pinholes of the oxide. To get some information which might allow a distinction between these two possible mechanisms, measurements were made of the total number of surface states produced as a function of the thickness of the native Ge oxide layer.

According to ellipsometric measurements done by Baertsch (23), the chemical surface treatment mainly used in this work produces a Ge oxide layer of about 1.5 nm thickness. The same author has made measurements on the subsequent growth of the oxide layer when the samples are exposed to laboratory air for periods between 1 hr and 50 days. MIS transistors with various native oxide thicknesses were made by oxidizing the samples in air before a coating layer of 100 nm of SiO was applied. Figure 8 shows the total number of surface states produced by the SiO layer as a function of the thickness of the native Ge oxide using the results of Baertsch (23).

Although the further growth of the native oxide layer in air is relatively slow (it takes about three weeks to double the thickness of the oxide produced by the chemical surface treatment), the figure shows that the total number of states produced by the SiO layer decreases very rapidly with increasing oxide thickness. It may be seen that doubling the native oxide layer thickness reduces the total number of surface states produced by the coating dielectric by about two orders of magnitude. It is unlikely that this thickness dependence is caused by an interaction through the oxide because (i) extrapolation to zero oxide thickness would lead to  $10^{16}$ - $10^{17}$  cm<sup>-2</sup> surface states which is ten to

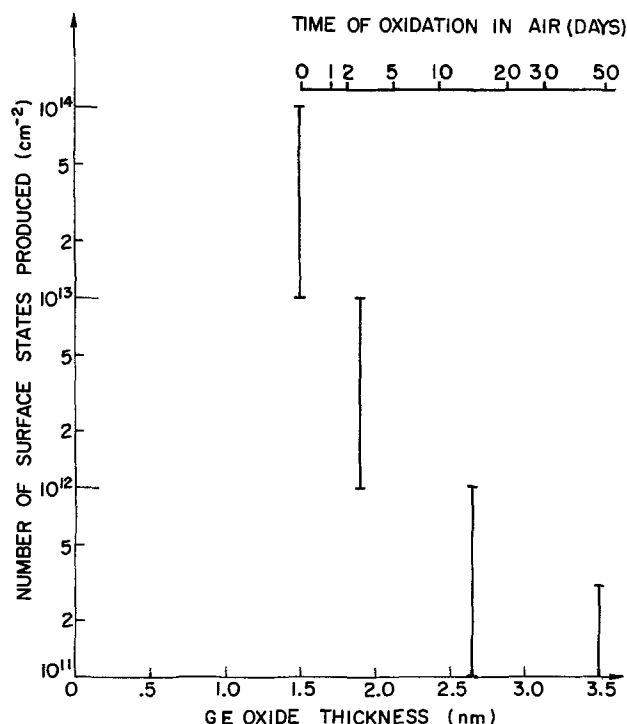


Fig. 8. Total number of surface states produced by an evaporated layer of 100 nm of SiO as a function of the thickness of the native germanium oxide. The Ge oxide thickness was increased prior to the evaporation of the SiO layer by oxidizing the sample in air (300°K) for the times indicated.

one hundred times higher than the number of Ge atoms per unit surface area ( $10^{15}$  cm<sup>-2</sup>); (ii) other chemical surface treatments which result in thicker oxide layers still lead to  $10^{13}$ - $10^{14}$  cm<sup>-2</sup> surface states if coated with one of the effective dielectrics shortly after the surface treatment; and (iii) since a direct overlap of the electron orbitals from the coating molecule with the orbitals from the Ge atoms is unlikely because of the relatively thick oxide layer and because of the theoretical considerations mentioned above, an interaction through the native oxide would have to be an exchange of electrons through the oxide. In such a mechanism the native oxide acts as a conductor between a layer containing the surface states and the Ge. A thicker oxide layer thus leads to a longer time constant to reach the equilibrium position of the Fermi level at the surface, but does not affect the total number of surface states produced by an additional surface layer.

It is, therefore, concluded that the interaction of the Ge and the evaporated dielectrics occurs at the pinholes in the oxide produced during the surface treatment. The reason for the decreasing number of surface states produced if the sample is further oxidized is the decreasing number of pinholes in the oxide. This agrees well with the observation that an "old" (uncoated) surface is much less sensitive to the influence of adverse ambients than a freshly etched one.

### Discussion and Conclusions

The real surfaces investigated in the present work are covered with an oxide layer of 1-2 nm thickness. Nevertheless, it was found that evaporated layers of certain dielectric materials produce up to  $10^{14}$  cm<sup>-2</sup> surface states. These surface states are created at pinholes in the oxide film. For some of the dielectrics tried, the energetic position of the surface states is within  $\pm 0.2$  eV of the intrinsic position of the Fermi level. This means that, except for surfaces which are strongly p- or n-type after the surface treatment, the evaporation of one of the effective dielectrics leads to a surface potential which is lower than the bulk potential of the crystal. Hence for devices which must be depleted for successful operation (e.g., radiation detectors), there are no surface layers which cannot be depleted and, thus, window effects (2, 3) are greatly reduced. [The charge collection properties at the surface of these devices are degraded as long as there is a bending of the energy bands in either direction, but the effect on the performance of the detectors is much worse when the surface layers cannot be depleted (24).] In addition, it has been found that Ge surfaces coated with one of the effective dielectrics are much less sensitive to deterioration due to the influence of the ambient atmosphere.

It might be interesting to mention that similarly prepared surfaces of material of comparable impurity concentration have also been found (25) to show about  $10^{14}$  cm<sup>-2</sup> surface states after the evaporation of different metals. In that work the number of surface states was determined from the properties of Schottky barriers formed by the metals on the Ge surface.

In conclusion, this paper has shown that the evaporation of certain dielectric materials provides a means of surface protection for those Ge devices which require a surface potential as low as possible,<sup>3</sup> but not for devices which require a low density of surface states, e.g., field effect transistors. It is however clear that none of the dielectrics tried provides a perfect surface protection in the sense that it will cause a surface channel of any strength to disappear and completely eliminate the effect of the ambient atmosphere.

### Acknowledgments

I would like to thank I. L. Fowler and H. L. Malm for many helpful and encouraging discussions and the revision of the manuscript.

<sup>3</sup> Patent pending on the use of evaporated dielectrics for passivation of semiconductor nuclear radiation detectors by NRD Division, Aptic Engineering Limited, Downsview, Ontario, Canada.

The author is currently in receipt of a Fellowship from the National Research Council of Canada.

Manuscript submitted Dec. 29, 1975; revised manuscript received May 10, 1976. This was Paper 131 presented at the Toronto, Canada, Meeting of the Society, May 11-15, 1975.

Any discussion of this paper will appear in a Discussion Section to be published in the June 1977 JOURNAL. All discussions for the June 1977 Discussion Section should be submitted by Feb. 1, 1977.

Publication costs of this article were assisted by Atomic Energy of Canada, Limited.

#### REFERENCES

1. R. N. Hall, *J. Appl. Phys.*, **35**, 379 (1964); see also Int. Conf. on Lattice Defects in Semiconductors, Freiburg, July 1974.
2. R. Dinger, *Helv. Phys. Acta*, **47**, 220 (1974).
3. R. Dinger, *IEEE Trans. Nucl. Sci.*, **22**, 135 (1975).
4. W. L. Brown, *Phys. Rev.*, **91**, 518 (1953).
5. A. Many, Y. Goldstein, and N. B. Grover, "Semiconductor Surfaces," p. 136 ff, North-Holland Publishing Company, Amsterdam (1965).
6. P. P. Webb *et al.*, *IEEE Trans. Nucl. Sci.*, **13**, 351 (1966).
7. G. Armantrout *et al.*, *ibid.*, **21** (1974) 344
8. G. Bertolini and A. Coche, Editors, "Semiconductor Detectors," p. 14, North-Holland Publishing Company, Amsterdam (1968).
9. J. R. Schrieffer, *Phys. Rev.*, **97**, 641 (1955).
10. R. F. Greene, D. R. Frankl, and J. Zemel, *ibid.*, **118**, 967 (1960).
11. R. F. Greene, *J. Phys. Chem. Solids*, **14**, 291 (1960).
12. N. B. Grover, Y. Goldstein, and A. Many, *J. Appl. Phys.*, **32**, 2538 (1961).
13. Y. Goldstein, N. B. Grover, A. Many, and R. F. Greene, *ibid.*, **32**, 2540 (1961).
14. A. Many, N. B. Grover, Y. Goldstein, and E. Harnik, *Phys. Chem. Solids*, **14** 186 (1960).
15. N. B. Grover and R. Oren, *ibid.*, **24**, 693 (1963).
16. N. F. Mott, *Adv. Phys.*, **16**, 49 (1968).
17. M. Pepper, S. Pollitt, C. J. Adkins, and R. E. Oakley, *Phys. Lett. A*, **47**, 71 (1974).
18. D. C. Tsui and S. J. Allen, Jr., *Phys. Rev. Lett.*, **32**, 1200 (1974).
19. M. L. Knotek, M. Pollak, T. M. Donovan, and H. Kurtzmann, *ibid.*, **30**, 853, 856 (1973).
20. W. de Wilde, *Thin Solid Films*, **24**, 101 (1974).
21. R. O. Jones, *Phys. Rev. Lett.*, **20**, 992 (1968).
22. M. Henzler, *Festkörperprobleme*, **11**, 187 (1971).
23. R. D. Baertsch, *IEEE Trans. Nucl. Sci.*, **21**, 347 (1974).
24. H. L. Malm and R. Dinger, *ibid.*, **23**, 76 (1976).
25. H. L. Malm, *ibid.*, **22**, 140 (1975).

## Technical Notes



### Repeated Removal of Thin Layers of Silicon by Anodic Oxidation

H. D. Barber\*

Linear Technology Incorporated, Burlington, Ontario, Canada

H. B. Lo

Department of Engineering Physics, McMaster University, Hamilton, Ontario, Canada

and J. E. Jones

Bowmar Canada Limited, Ottawa, Ontario, Canada

The electrical characteristics of semiconductor devices are primarily determined by the impurities incorporated into the body of the semiconductor and by their spatial distribution. Three basic methods are available to determine impurity profiles in semiconductors. The first is spreading resistance (1-3) which will give a complete profile on a small area, rapidly and to any depth. However, the equipment is expensive, calibration is difficult and variable, computer analysis for interpretation is usually necessary, and step sizes are normally larger than 500Å. The second method determines the profile from C-V measurements (4-6). A complete profile cannot usually be determined by this method since the distance over which the profile can be determined is limited by the avalanche breakdown of the semiconductor. The third method involves successive measurements following the removal of controlled amounts of the semiconductor. C-V measurements, radio-tracer counting (7, 8) or dif-

ferential sheet resistivity measurements (7, 9) using either a four-point probe (7, 10-12) or the Hall effect (13, 14) can be performed in conjunction with the sectioning to determine the impurity profile.

Three basic techniques for sectioning exist: mechanical grinding (15), chemical etching (16, 17), and oxidation followed by etching of the oxide. Removal by anodic oxidation is strain free, planar, reproducible, practically independent of dopant, independent of crystal orientation, and causes insignificant impurity redistribution. Anodic oxidation can be carried out in a simple, inexpensive cell without the necessity of any expensive facilities. It does, however, suffer the disadvantage that many anodizations must be carried out to obtain the profiles of thick layers. In comparison to other methods, the determination of impurity profiles by anodization, etching, and four-point probe resistivity measurements is often very attractive.

This paper describes an investigation of the variables affecting anodic oxidation and a simple, highly accurate anodization procedure is outlined.

\* Electrochemical Society Active Member.

Key words: silicon, anodization, impurity profiling, sectioning.

### Electrolyte

Nonaqueous solutions were selected for the anodization of silicon because they allow higher forming voltages, cause less contamination, and give denser oxides than the acid or borate solutions (7). Pure water (18) with a resistivity in excess of 0.5 megohm-cm may be used but the rate of oxide formation is much lower than that for nonaqueous electrolytes.

Several nonaqueous solutions such as N-Methylacetamide (NMA) (19, 20), tetrahydrofurfuryl alcohol (21, 22), and ethylene glycol (23-26) were evaluated. Ethylene glycol containing 0.04N  $\text{KNO}_3$  and small amounts of water was selected because it produced uniform and compositionally reproducible oxides. In addition, it has the advantages of low cost, high purity, good electrolyte solubility, and good stability towards heat and electrolysis.

For good anodizations this electrolytic solution must contain water. Duffek (23) suggests that 0.5-5% water by volume is optimum since for higher concentrations the Si:O<sub>2</sub> ratio becomes a function of water concentration and thus the silicon removed is not simply related to the measurements of oxide thickness. Others (24, 26) have used up to 10% water and the interpretation of their work where oxide measurements are used to determine silicon removed suffers from this difficulty. In this work 2.5% water was used. Because ethylene glycol is hygroscopic it is necessary, if the water concentration is to be kept constant, to keep the solution in tightly stoppered containers and to have samples dry before inserting them into the cell.

During multiple runs in the same electrolytic solution, the current efficiency increased while the voltage at which oxide stripping began decreased. Manara *et al.* (26) show that fluoride ions increase the current efficiency while Croset and Dieumegard (27) identified fluoride ions as the cause of the stripping. Croset and Dieumegard (27) suggest the addition of 1-2g of  $\text{Al}(\text{NO}_3)_3 \cdot 9\text{H}_2\text{O}$  per liter to inhibit the effects of the fluoride ion. The effects of the addition of  $\text{Al}(\text{NO}_3)_3 \cdot 9\text{H}_2\text{O}$  were investigated. Electrolyte A did not contain  $\text{Al}(\text{NO}_3)_3 \cdot 9\text{H}_2\text{O}$  while electrolyte B did.

Two methods of anodization are possible. In the first method a constant voltage is applied across the electrode and the current is allowed to fall until a predetermined value is reached. In the second method a constant current is forced to flow between the electrodes and the voltage is allowed to rise until a preset value is reached. The constant current method was used in this work. In constant current anodization the thickness of the oxide is directly proportional to the net forming voltage provided no oxide stripping occurs during the anodization. The net forming voltage or net voltage is defined as the final cell voltage minus the initial cell voltage for a clean sample at the start of anodization.

### Apparatus

A HP 6186B d-c current source capable of delivering up to 100 mA at voltages up to 300V was used to power the cell. An enclosure was placed over the cell to eliminate ambient light, and a projection lamp was used to provide uniform, controlled intensity of illumination on the sample. A circular groove in the cell lid provided simple and accurate positioning of the electrodes with a 2.5 cm spacing in a standard 400 ml beaker. This beaker was placed in a water bath which was used to control the operating temperature and to act as a heat sink to minimize the effects of the self-heating during anodization. A magnetic stirrer provided the constant agitation and mixing necessary for reproducible and uniform anodization. The insert cathode was composed of platinum mesh stretched over 1/16 in. stainless steel frame for rigidity. The cathode had an area of 14.5 cm<sup>2</sup>. With this mesh cathode, the anode sample surface was easily illuminated through the cathode and the continual mixing of the solution was not impeded.

The sample holder of chemically inert Teflon is shown in detail in Fig. 1. The wafer was waxed to a

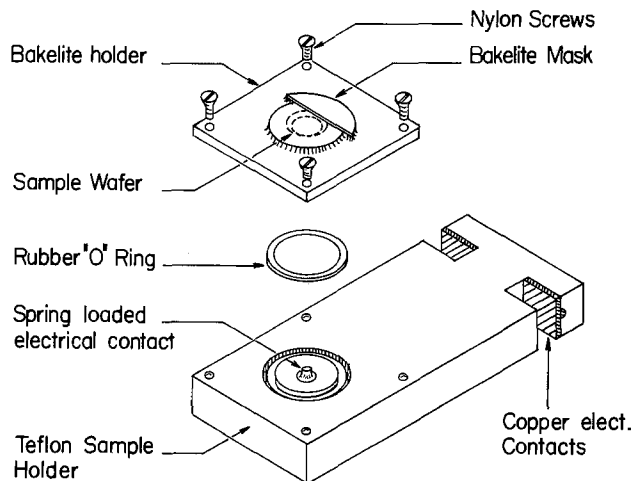


Fig. 1. Anodization sample holder and sample mount

thin Bakelite square, which was mounted and sealed on the anode structure by means of nylon screws and an O ring as shown in Fig. 1. A small Bakelite sheet was waxed to an area on the wafer surface to mask it from the anodization and provide a reference surface.

### Sample Preparation

The silicon samples were degreased and rinsed in running deionized water. They were then etched in 8% HF until wetting ceased, rinsed in running deionized water, and blown dry. A 2000Å thick aluminum layer was evaporated onto the back of the wafer to ensure good uniform electrical contact.

The wafer was mounted by placing wax on the Bakelite support and heating it in an oven at about 200°C until the molten wax formed a smooth layer about 1/16 in. thick. The sample was then pushed down into the molten wax until a uniform bead of wax formed around the entire edge of the sample.

### Anodization Technique

Anodization was carried out in the 400 ml cell using 325 ml of solution. The power supply was set to the current required to provide the desired current density and anodization proceeded until the predetermined net forming voltage was reached. The sample holder was removed from the cell and rinsed in running deionized water. The wafer surface was scrubbed lightly during the rinse to ensure complete removal of the ethylene glycol. Any ethylene glycol residues prevent uniform removal of the oxide. After the oxide removal in 8% HF, the sample was rinsed in deionized water and blown dry. Care was taken to insure that the holder was dry before reinsertion.

### Measurements of Silicon Removed

Three methods were employed to accurately measure the thickness of silicon removed during anodization.

An interference angstrometer employing a sodium monochromatic light source was used throughout the experiments to measure both the thickness of silicon removed and the anodic oxide thickness. The method was as follows. An area of the sample surface was masked against the anodization as shown in Fig. 1. After a number of anodizations, the sample was removed from the Bakelite holder and cleaned. Part of the area covered with anodic oxide was masked by Apiezon wax and the rest was removed. The sample was then cleaned and 500Å of aluminum was evaporated onto the surface to improve the reflectivity. The interference pattern from the surface was photographed and a travelling microscope was used to measure the step heights from the interference patterns. Measurements of these steps gave thickness values for both silicon removed and anodic oxide formed.

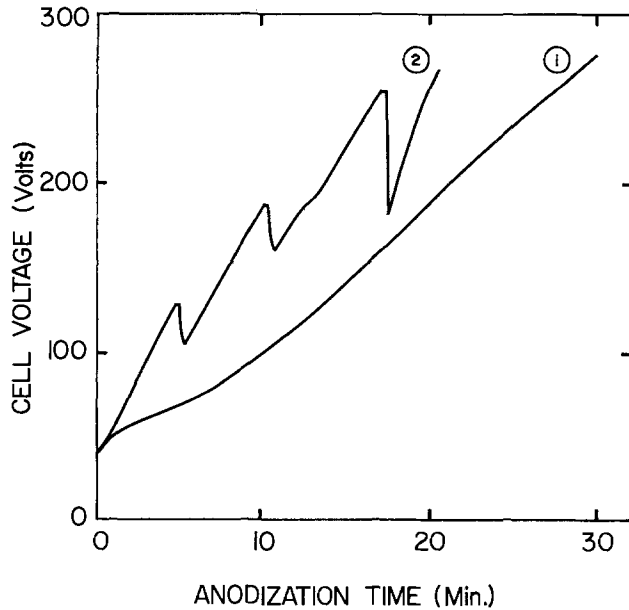


Fig. 2. Typical anodization cell voltage curves for (1) electrolyte B and the first two runs of electrolyte A and for (2) subsequent runs of electrolyte A showing oxide stripping above 125V.

Single readings by this technique were accurate to  $\pm 50\text{\AA}$ .

The anodic oxide thickness was also measured by ellipsometry (30). Because it was not necessary to remove the sample from the Bakelite mount for this measurement, it was used extensively to monitor the reproducibility of anodization from run to run. Oxide thickness measurements from the angstrometer agreed with those from the ellipsometer to within  $\pm 5\%$  based on a value of 1.46 assumed for the refractive index of the anodized oxide films. Because the refractive index of anodic oxides does depend on the electrolyte, this value may not apply for other electrolytes. Ellipsometry measurements of the oxide thickness from run to run agreed to within  $\pm 3\%$  which was the probable deviation of the oxide thickness formed during multiple anodizations.

The silicon removed was determined from the change in weight after a predetermined number of anodizations. In order to obtain an accuracy of  $\pm 5\%$ , a large number of anodizations was necessary so this method was only employed during profiling. The results obtained agreed within 5% with those obtained from the interference measurements.

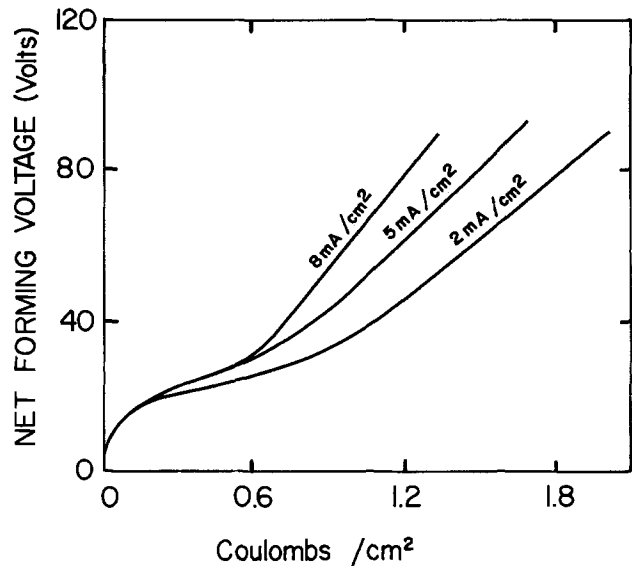


Fig. 3. Net forming voltage vs. total charge passed through the cell per unit sample area for various current densities.

### Experimental Results

The cell voltage as a function of the duration of the anodization is shown in Fig. 2 for a number of runs of both electrolyte A and electrolyte B which contained  $\text{Al}(\text{NO}_3)_3 \cdot 9\text{H}_2\text{O}$ . The first two runs for electrolyte A and all runs for B continue without interruption to the maximum voltage as shown in curve 1. All of the other runs for electrolyte A have discontinuities arising from a stripping of the oxide as shown in curve 2. The first discontinuity occurred repeatedly at about 125V corresponding to a net forming voltage,  $V_N$ , of 100V. Where anodizations using electrolyte A were terminated at a net forming voltage of 90V, stripping of the oxide was avoided. Stripping is undesirable because it causes surface roughness and errors in the silicon removed.

The amount of silicon removed by anodization and etching was found to be independent of the current density in the range 2-8  $\text{mA}/\text{cm}^2$  and directly dependent on the net forming voltage (see Table I). Figure 3 shows the net forming voltage vs. the total charge per unit area for electrolyte A anodizations. The increase in current efficiency with increasing current density previously reported by Schmidt (19) is clearly evident. Because of the higher current efficiency and the

Table I. Anodization results showing the effects of current density, net forming voltage, temperature and type and resistivity of silicon and the averages for optical and ellipsometric measurements and for weight measurements

Sample type*	Electrolyte type	Temp. ( $^{\circ}\text{C}$ )	Current density ( $\text{mA}/\text{cm}^2$ )	Net voltage (V)	Number of anodizations	Silicon removed (A/V)
3	A	24	2	90	16	2.19
3	A	24	5	90	16	2.13
3	A	24	8	90	32	2.24
4	A	24	8	90	8	2.23
4	A	24	8	135	2	2.30
4	A	24	8	180	1	2.42
4	A	24	8	225	1	2.32
3	B	3	8	260	16	2.35
4	A	24	8	270	1	2.41
3	B	3	8	280	8	2.36
1-4	A, B	3	8	90-280	60	2.23
1-4	A	24	8	90	60	2.22
1-4	A	50	8	90	39	2.09
1 (1 $\Omega\text{-cm}$ n)	A	3-50	8	90	29	2.08
2 (10 $\Omega\text{-cm}$ p)	A	3-50	8	90	30	2.22
3 (p <sup>+</sup> diffusion)	A	3-50	2-8	90	84	2.18
4 (n <sup>+</sup> diffusion)	A	3-50	8	90	24	2.14
3 (p <sup>+</sup> diffusion)	B	3	8	260-280	24	2.35
Total optical and ellipsometric measurements						
1-4	A, B	3-50	2-8	90-280	197	2.19
Total weight measurements						
3, 4	A	3	8	90	368	2.21

\* Samples: 1 = 1  $\Omega\text{-cm}$  n-type; 2 = 10  $\Omega\text{-cm}$  p-type; 3 = 1  $\Omega\text{-cm}$  n-type wafer with 170  $\Omega/\square$ ,  $3\mu$  deep p<sup>+</sup> diffusion; 4 = 10  $\Omega\text{-cm}$  p-type wafer with 3.6  $\Omega/\square$ ,  $3\mu$  deep n<sup>+</sup> diffusion.

shorter anodization time, the 8 mA/cm<sup>2</sup> current density was used in subsequent anodizations.

From Fig. 2 it is clear that the cell voltage at the start of an anodization is not zero. The initial voltage,  $V_i$ , arises primarily from the resistivity of the electrolyte solution. Thus

$$V_i = IR = \frac{JA\rho_e d}{A'} \quad [1]$$

Measurements confirmed that the initial voltage was a linear function of the current density,  $J$ ; the separation between the anode and the cathode,  $d$ ; and the resistivity of the solution,  $\rho_e$ . However, they indicated that it was a weaker function of the sample area,  $A$ . This weaker dependence on  $A$  is due to the fact that  $A'$ , the effective cross-sectional area for the electrolyte solution, is also a function of the silicon anode area,  $A$ . No change in  $V_i$  was detected when changing from electrolyte A to B.

The temperature at which the anodization takes place affects a number of variables. The viscosity of the solution and thus its resistivity increase as the temperature decreases. This results in higher values of the initial voltage,  $V_i$ , and in less efficient mixing of the solution. However, as the temperature of the solution is increased, the adhesion of the wax is reduced and creep of the electrolyte along the wafer-wax interface results in partial anodization of the wafer back. For these reasons, a temperature between 15 and 20°C is considered desirable and can be easily realized by means of a flowing water bath to carry the excess heat from the anodization cell. As shown in Table I, the amount of silicon removed per volt of net anodization voltage was essentially independent of temperature in the range 3°-50°C.

Figure 3 shows a decrease in the time necessary to reach a fixed net forming voltage with increasing number of runs for electrolyte A. Electrolyte B containing  $\text{Al}(\text{NO}_3)_3 \cdot 9\text{H}_2\text{O}$  did not exhibit this increasing current efficiency with the number of anodizations. Furthermore, for electrolyte B, the stripping and consequent surface roughness observed after the occurrence of stripping in electrolyte A did not occur up to the 320V limit of the power supply. These results support the work of Croset and Dieumegard (27) who identified the presence of fluorine in the electrolyte as the cause of oxide stripping.

Table I also gives results indicating that the amount of silicon removed per volt of net anodization voltage is essentially independent of both the type and resistivity of silicon for  $n \leq 10^{20} \text{ cm}^{-3}$  and  $p \leq 3 \times 10^{18} \text{ cm}^{-3}$ . This agrees with the work of Manara *et al.* (26) who reported no dependence for p-type material and about a 10% decrease in silicon removal for 0.0001  $\Omega\text{-cm}$  ( $n \geq 10^{21} \text{ cm}^{-3}$ ) n-type silicon anodized to a net voltage of 100V. For high resistivity silicon, metallization of the wafer backs is essential for uniform anodization.

Two rate-limiting processes for n-type material are shown in Fig. 4. The initial rapid growth for the n-type material in the dark was also observed by Schmidt and Michel (19). This effect is due to a field in the silicon surface arising because of the depletion of electrons and the lack of holes. This field reduces the energy required to remove a silicon atom from the surface and therefore increases the anodic current efficiency. Illumination increases the hole concentration and reduces the field. Regardless of the rate of reaction, the same amount of silicon is removed for the same value of net forming voltage. Above the dashed line in Fig. 4 the effect of illumination disappears and the slopes of the curves, which are the rates of reaction, are approximately the same. In this region a different rate-limiting process controls the reaction. The thickness of the oxide at which this rate limitation begins is 250Å, differing from the 400Å found by Schmidt and Michel (19). To avoid variations in initial conditions, sufficient illumination should be provided to ensure that the starting voltage is minimum.

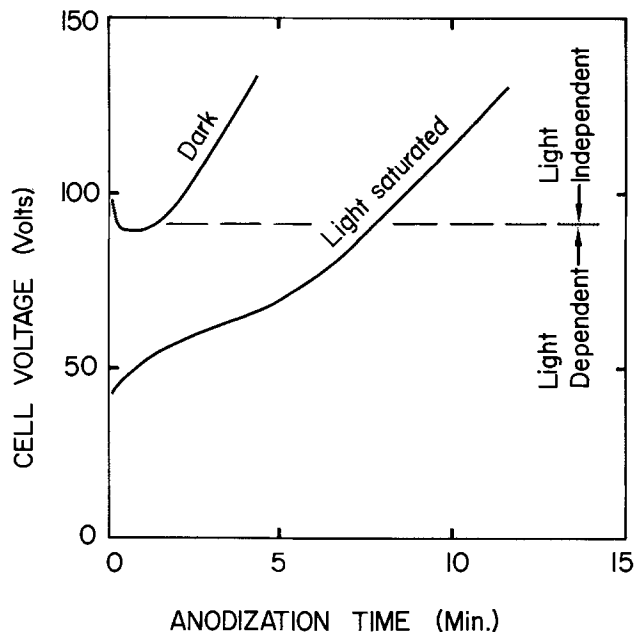


Fig. 4. Anodization voltage behavior for 1  $\Omega\text{-cm}$  n-type silicon with and without illumination.

Five samples were profiled by anodization and etching and the average thickness of silicon removed was determined by weight difference to be 2.21 Å/V with  $\sigma = 0.06$  Å/V in excellent agreement with 2.19 Å/V with  $\sigma = 0.13$  Å/V determined by the angstrometer. The much smaller deviation in the weight difference is due to the fact that each measurement is an average of a large number of anodizations.

### Profiling

As an example of the use of this method of sectioning, the impurity profiles for  $n^+$  and  $p^+$  diffused layers were determined by differential sheet resistivity measurements employing a four-point probe.

The NBS "Tentative Method of Test for Resistivity of Silicon Slices by Four-Point Probes" (10) was used except that the wafer was left on the sample holder rather than being placed on a heat sink. Plots of sheet resistivity,  $\rho_s(x)$ , per anodization are presented in Fig. 5 and 6.

Converting this data into an impurity profile is a two-stage process. First, the differential sheet resistivity,  $\rho_d(x)$  must be calculated. Tannenbaum (7) proposes

$$\rho_d(x) = [d(1/\rho_s(x))/dx]^{-1} \quad [2]$$

while Evans and Donovan (9) modified it to

$$\rho_d(x) = 0.4343 \rho_s(x) / d \log [\rho_s(x)] dx \quad [3]$$

When an analytic expression is calculated to fit  $\rho_s(x)$ , the results are the same for either method. In this case a polynomial

$$\log [\rho_s(s)] = a_0 + a_1s + a_2s^2 + a_3s^3 \quad [4]$$

was fitted to the sheet resistivity data where  $s$  was the number of anodizations. The sublayer resistivity was related to the impurity concentration by Irwin's curves (21) and the resulting impurity profiles are also shown in Fig. 5 and 6.

The shapes of these profiles agree with the results reported by others (32-34). In particular, the redistribution of the boron due to out-diffusion during the drive diffusion is in excellent agreement with the work of Kato and Nishi (33).

This method of sectioning has also been used successfully with the Hall effect as the measurement in the profiling of thin epitaxial multilayer structures (35).

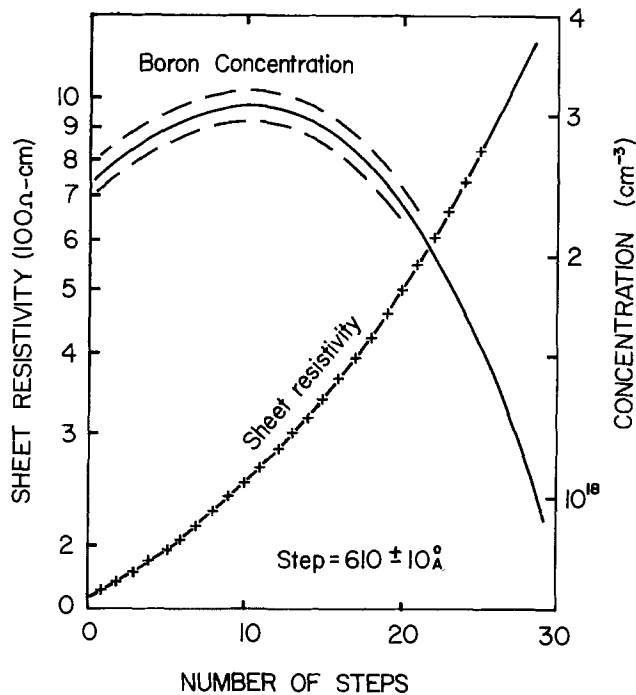


Fig. 5. Impurity profile of a boron diffusion. The dotted curves are limits resulting from the  $\pm 10 \text{ \AA}$  step size uncertainty.

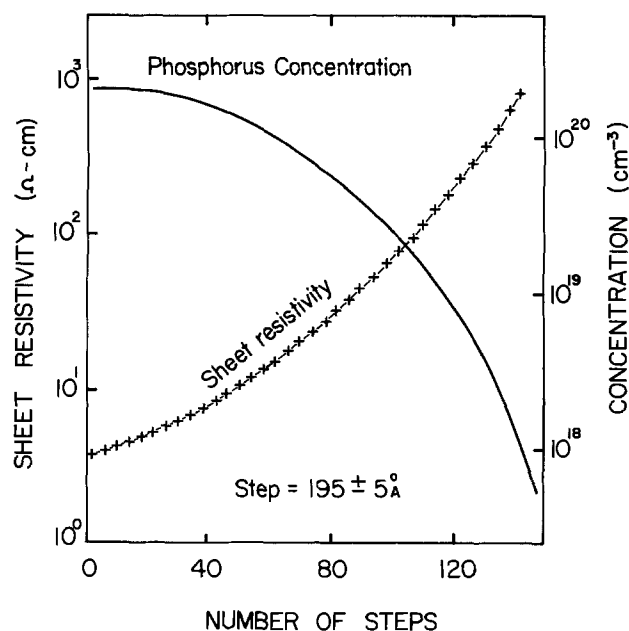


Fig. 6. Impurity profile of a phosphorus diffusion

### Conclusions

Anodic oxidation followed by etching of the oxide is a successful means of sectioning silicon. Constant current anodization was used with an electrolyte solution of ethylene glycol with 0.04N  $\text{KNO}_3$ , 2.5% water, and 1-2 g/liter of  $\text{Al}(\text{NO}_3)_3 \cdot 9\text{H}_2\text{O}$ . To insure reproducible results, the back of the wafer must be metallized for high resistivity samples, the electrolytic solution must be agitated, and the wafer surface must be illuminated. The amount of silicon removed was independent of the current density between 2 and 8  $\text{mA}/\text{cm}^2$ , the temperature between 3° and 50°C and the type and resistivity of the silicon up to concentrations of  $10^{20} \text{ cm}^{-3}$ . The oxide formed was uniform and reproducible with an average Si:  $\text{SiO}_2$  thickness ratio of  $0.44 \pm 0.04$  in excellent agreement with the accepted value of 0.44 for thermal oxides. The thickness of silicon removed was found to be a linear function of the net forming voltage with a proportionality constant of 2.20  $\text{\AA}/\text{V}$  having

a standard deviation of 0.13  $\text{\AA}/\text{V}$ . Any voltage dependence of silicon removal for net voltages up to 280V was not significant and was less than previously reported (26).

Both the increasing current efficiency and the oxide stripping with the number of runs were due to the fluoride ion and were eliminated by the addition of  $\text{Al}(\text{NO}_3)_3 \cdot 9\text{H}_2\text{O}$ . After studying the temperature dependence of the different parameters, particularly electrolyte creep along the wafer-wax interface, it was determined that a temperature between 15° and 20°C (which can be easily realized by means of a flowing water bath) is optimal.

This sectioning technique combined with differential sheet resistivity measurements forms an excellent, inexpensive, uncomplicated means of profiling silicon.

### Acknowledgments

This work was carried out with support from the National Research Council of Canada.

Manuscript submitted April 10, 1975; revised manuscript received May 29, 1976.

Any discussion of this paper will appear in a Discussion Section to be published in the June 1977 JOURNAL. All discussions for the June 1977 Discussion Section should be submitted by Feb. 1, 1977.

Publication costs of this article were assisted by Linear Technology Incorporated.

### REFERENCES

1. R. G. Mazur and D. H. Dicky, *This Journal*, **113**, 255 (1966).
2. J. M. Adley, M. R. Poponiak, C. P. Schneider, P. A. Schamann, Jr., and A. H. Tong, in "Semiconductor Silicon," R. R. Haberecht and E. L. Kern, Editors, p. 721, The Electrochemical Society Soft-sound Symposium Series, New York (1969).
3. P. J. Severin, *Philips Res. Rept.*, **26**, 359 (1971).
4. C. van Opdorp, *Solid-State Electron.*, **11**, 397 (1968).
5. J. A. Copeland, *IEEE Trans. Electron Devices*, **ed-16**, 445 (1969).
6. P. J. Severin and G. J. Poedt, *This Journal*, **119**, 1384 (1972).
7. E. Tannenbaum, *Solid-State Electron.*, **2**, 123 (1961).
8. G. B. Larrabee and J. A. Keenan, *This Journal*, **118**, 1351 (1971).
9. R. A. Evans and R. P. Donovan, *Solid-State Electron.*, **10**, 155 (1968).
10. F. M. Smits, *Bell Syst. Tech. J.*, **37**, 711 (1958).
11. "Tentative Method of Test of Resistivity of Silicon Slices Using Four-Point Probes," NBS F 84-67T, Rev. 1, Washington, D.C. (Dec. 1967).
12. P. J. Severin, *Philips Res. Rept.*, **26**, 279 (1971).
13. L. V. van der Pauw, *ibid.*, **13**, 1 (1958).
14. N. G. E. Johansson and J. W. Mayer, *Solid-State Electron.*, **13**, 317 (1970).
15. M. F. Lamorte, *ibid.*, **1**, 164 (1960).
16. P. A. Iles and B. Leibenhaut, *ibid.*, **5**, 331 (1962).
17. H. C. Gatos and C. Garret, *Prog. Semicond.*, **9**, 1 (1965).
18. L. A. Dubroski, V. G. Mel'nik, and L. L. Odyets, *Russ. J. Phys. Chem.*, **36**, 1188 (1962).
19. P. F. Schmidt and W. Michel, *This Journal*, **104**, 233 (1957).
20. E. F. Duffek, C. Mylroie, and E. A. Benjamini, *ibid.*, **111**, 1042 (1964).
21. P. F. Schmidt and A. E. Owen, *ibid.*, **111**, 682 (1964).
22. J. C. C. Tsai, *Proc. IEEE*, **57**, 1499 (1969).
23. E. F. Duffek, E. A. Benjamini, and C. Mylroie, *Electrochem. Technol.*, **3**, 75 (1965).
24. K. M. Busen and R. Linzey, *Trans. Metall. Soc. AIME*, **236**, 306 (1966).
25. R. Dreiner, *This Journal*, **113**, 1210 (1966).
26. A. Manara, A. Ostidich, G. Pedroli, and G. Restelli, *Thin Solid Films*, **8**, 359 (1971).
27. M. Croset and D. Dieumegard, Paper 87 presented at The Electrochemical Society Meeting, Cleveland, Ohio, Oct. 3-7, 1971; *This Journal*, **120**, 526 (1973).
28. V. B. Flynn, *ibid.*, **105**, 715 (1958).
29. E. A. Benjamini, E. F. Duffek, and F. Schulenburg, RNP presented at The Electrochemical Society

Meeting, New York, N.Y., Sept. 29-Oct. 3, 1963.

30. R. J. Archer, "Ellipsometry in the Measurements of Surface and Thin Films," p. 261, National Bureau of Standards, Washington, D.C. (1964).
31. J. C. Irvin, *Bell Syst. Tech. J.*, **41**, 387 (1962).
32. M. M. Atalla and E. Tannenbaum, *ibid.*, **39**, 933 (1960).
33. T. Kato and Y. Nishi, *Jpn. J. Appl. Phys.*, **3**, 377 (1964).
34. S. Horinchi and J. Yamaguchi, *ibid.*, **1**, 314 (1962).
35. D. King and J. Shewchun, To be published.

## New Flash Evaporation Method Improves Film Preparation

N. S. Platakis

IBM Corporation, San Jose, California 95193

and H. C. Gatos\*

Department of Materials Science and Engineering,  
Massachusetts Institute of Technology, Cambridge, Massachusetts 02193

A new flash evaporation method has been developed which eliminates the major disadvantages of conventional flash evaporation and permits the preparation of films which are significantly improved in structural and chemical homogeneity. This new method is restricted to congruently melting materials with melting points below the quartz softening temperature when the apparatus is made of quartz.

Melting in an open boat, chemical vapor deposition, sputtering, and flash evaporation are most commonly used in the preparation of films. Each of them has its advantages and disadvantages (1); the choice lies heavily on the characteristics of the material to be evaporated. Flash evaporation is particularly suitable for relatively low melting materials whose constituents exhibit large differences in their vapor pressure. In the normal method of flash evaporation (2), powder of the material to be evaporated is fed into a furnace which is preheated to a temperature several hundred degrees above the melting point of the material; the powder melts, vaporizes instantaneously, and is deposited onto the desired substrate. The main problems with this method are (i) the feeding rate of the powder and thus the evaporation rate (an important parameter in achieving chemical and structural homogeneity) is intermittent and in some cases also inconsistent and (ii) a molten phase is occasionally accumulated in the furnace due to surcharges of powder which leads to fractional vaporization and thus to phase separation in the film.

The flash evaporation method reported here essentially eliminates the above problems. The method is schematically illustrated in Fig. 1. The material to be vaporized is sealed off under vacuum in a quartz ampul one end of which is drawn to a capillary tube; the tip of the capillary tube is then broken and the ampul containing the material is positioned as shown in Fig. 1. Current is passed through coil A to attain the desired high temperature (see Table I) and when it is stabilized, power is applied to coil B to melt the material. Due to the vapor pressure in the ampul, the molten material flows through the capillary into the space heated by coil A where it vaporizes instantaneously. The vapor emerges from the other end of the quartz U tube to be deposited on the substrate. The flow of the molten material is controlled by the vapor pressure above the melt which in turn is controlled by the temperature of the ampul; this temperature is monitored by a thermocouple placed near the ampul. In this way,

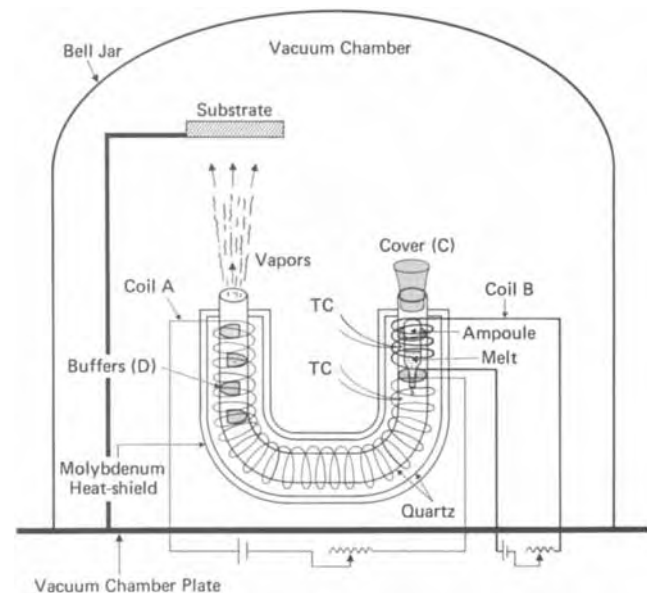


Fig. 1. The new flash evaporation method

continuous injection or drop-by-drop feeding can be attained. Thus, vaporization can take place either only at the tip of the capillary (which is continuously fed) or after the drop leaves the capillary but before it reaches the walls of the heated quartz tube. A small opening in the molybdenum heat shield permits observation of the material flow at the tip of the capillary. Cover C prevents the escape of vapors from that end and the quartz tube itself prevents contamination from the molybdenum heating coils. A set of buffers (D) prevents drops of molten material, formed ac-

Table I

	Material	Melting point (°C)	T <sub>1</sub> * (°C)	T <sub>2</sub> ** (°C)
x = 0	As <sub>2</sub> Se <sub>3</sub>	370 ± 2	400	620
x = 0.2	0.8 As <sub>2</sub> Se <sub>3</sub> · 0.2 Sb <sub>2</sub> Se <sub>3</sub>	391 ± 5	530	661
x = 0.4	0.6 As <sub>2</sub> Se <sub>3</sub> · 0.4 Sb <sub>2</sub> Se <sub>3</sub>	461 ± 5	506	736
x = 0.6	0.4 As <sub>2</sub> Se <sub>3</sub> · 0.6 Sb <sub>2</sub> Se <sub>3</sub>	526 ± 5	576	806
x = 0.8	0.2 As <sub>2</sub> Se <sub>3</sub> · 0.8 Sb <sub>2</sub> Se <sub>3</sub>	574 ± 5	628	858
x = 1	Sb <sub>2</sub> Se <sub>3</sub>	612 ± 2	670	900

\* Electrochemical Society Active Member.

Key words: vacuum deposition, film composition, homogeneity, alloys.

\* Temperature of the melt in the ampul (coil B).

\*\* Temperature of chamber where the melt evaporates (coil A).

identally, from escaping through the high temperature region.

Thus, the basic features that distinguish the new method from the conventional one are (i) the material is stored and homogenized in the molten state (in the ampul) without being subjected to vaporization except through a capillary tip, and (ii) the molten material is injected for vaporization by its own vapor pressure which is constant at a given precisely controlled temperature.

The present method (using a U quartz tube 1 cm in diameter and 9 cm in height) was successfully applied to the preparation of films of a number of materials including the system  $(1-x)\text{As}_2\text{Se}_3 \cdot x\text{Sb}_2\text{Se}_3$ . Prior to evaporation, the pressure in the bell jar was brought down to  $10^{-7}$  Torr. However, during evaporation the vacuum in the chamber dropped to the  $10^{-5}$  Torr range. The ampul and evaporation chamber temperatures in actual work with alloys  $(1-x)\text{As}_2\text{Se}_3 \cdot x\text{Sb}_2\text{Se}_3$ , which were deposited on quartz wafers, are given in Table I. X-ray analysis of such films by scanning electron microscope, whose beam diameter and sensitivity were  $\sim 300\text{\AA}$  and a few hundred parts per million, respectively, showed no difference in chemical composition between the feed material and the prepared films. Furthermore, no variation in composition was detected within the  $20\ \mu\text{m}$  thick films. The physical characteristics of these films, including electrical conductivity, were also highly reproducible.

In contrast, films prepared by the conventional flash evaporation methods and under the same temperature and vaporization rate conditions were at least 5% richer in  $\text{As}_2\text{Se}_3$  than the feed material. This analysis was performed on a flat edge of the film which was obtained by cleaving a thin Si wafer on which the  $20\ \mu\text{m}$  thick film had been deposited. The electron beam was focused on a number of points along the thickness of the film and the intensity of x-rays was recorded using an energy-dispersive x-ray detector. The  $\text{AsK}\alpha$  and  $\text{SbL}\alpha$  intensities from each of these points were compared to those obtained from a series of homogeneous standard (specimens of known compositions) which included a specimen with the composition of the bulk materials used to prepare the film.

Manuscript submitted March 22, 1976; revised manuscript received April 30, 1976.

Any discussion of this paper will appear in a Discussion Section to be published in the June 1977 JOURNAL. All discussions for the June 1977 Discussion Section should be submitted by Feb. 1, 1977.

Publication costs of this article were assisted by IBM Corporation.

#### REFERENCES

1. "Handbook of Thin Film Technology," L. I. Maissel and R. Glang, Editors, Chap. 1, pp. 65-97; Chap. 4, p. 2; Chap. 5, pp. 22-24; McGraw-Hill Book Co., New York (1970).
2. *Ibid.*, Chap. 1, pp. 92-95.

## Determination of Reactant Gas Concentration by Quadrupole Mass Analyzer during PSG Film Formation Using Organic Compounds

Takeo Yoshimi, Hideo Sakai, and Katsuro Sugawara\*

Hitachi, Limited, Semiconductor and Integrated Circuits Division, Kodaira, Tokyo, Japan

Gas analysis in CVD (chemical vapor deposition) reactions is essential, both to investigate the reaction mechanism and to control the film thickness and the composition precisely. In general, reactant gases have been analyzed by infrared absorption in  $\text{SiH}_4\text{-O}_2$ ,  $\text{SiH}_4\text{-N}_2\text{O}$ , and  $\text{SiH}_4\text{-CO}_2\text{-H}_2$  reactions (1) and in  $\text{SiH}_4\text{-PH}_3\text{-O}_2$  reaction (2, 3), quadrupole mass analysis for gas present under vacuum (4) and in molecular beam epitaxy of GaAlAs superlattice (5), time-of-flight mass analysis in  $\text{GaAs}_x\text{P}_{1-x}$  (6), GaN (7),  $\text{In}_{1-x}\text{Ga}_x\text{As}$  (8, 9) and  $\text{SiH}_2\text{Cl}_2\text{-H}_2$ ,  $\text{SiHCl}_3\text{-H}_2$ ,  $\text{SiCl}_4\text{-H}_2$  (10, 11) CVD reactions, and Raman scattering in  $\text{SiH}_4$  decomposition and  $\text{SiH}_4\text{-NH}_3$  reactions (12).

In a previous paper (13), phosphosilicate glass (PSG) films using organic compounds,  $\text{Si}(\text{OC}_2\text{H}_5)_4$  and  $\text{PO}(\text{OCH}_3)_3$ , were formed under reduced pressure, to improve film thickness uniformity and step coverage over a silicon substrate. In this evacuated system, quantitative determination of the organic sources was difficult, due to the small amount of source evaporation and to measurement under vacuum. In the present study, determination was attempted by the infrared absorption and the quadrupole mass analyses. The gas concentration could not be measured by the former method, because of its poor sensitivity to the small amount of organic compounds. Therefore the quadrupole mass analyzer which had a high sensitivity and

was well suited to the evacuated system was used. This note describes reactant gas analysis using the mass analyzer, with regard to the quantitative determination of the reactant gases and the correlation between the phosphorus concentration in the gas phase and that in the solid film.

The PSG film was formed in a resistance-heated furnace at reduced pressure, as shown in Fig. 1. The quartz reaction tube was 9 cm ID, 180 cm long, and its hot zone was 80 cm long. In principle, this reaction

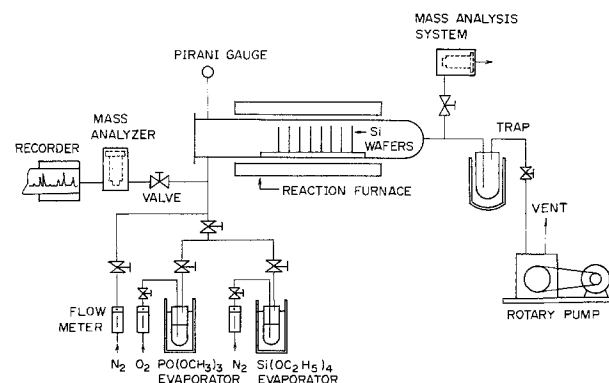


Fig. 1. Schematic diagram of the PSG film deposition reactor. A quadrupole mass analyzer was attached to it to determine the concentration of the reactant gases at reduced pressure.

\* Electrochemical Society Active Member.

Key words:  $\text{Si}(\text{OC}_2\text{H}_5)_4\text{-PO}(\text{OCH}_3)_3$  reaction, correlation of gas- and solid-phosphorus concentration, quantitative determination of phosphorus concentration.



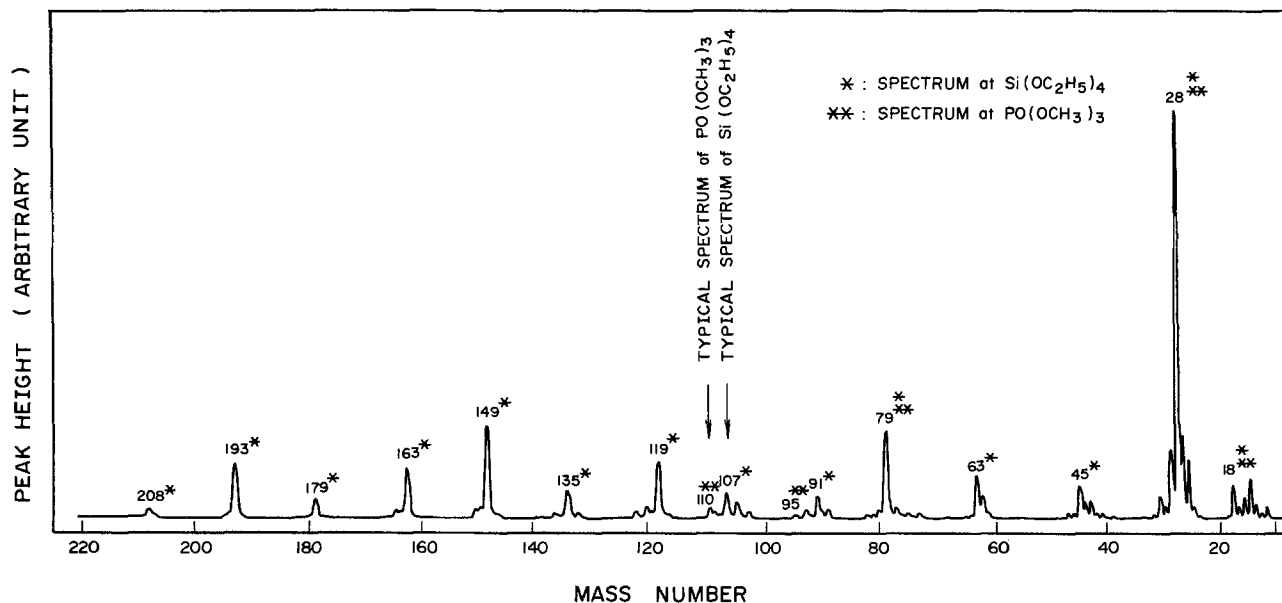


Fig. 2. Mass spectrum patterns of  $\text{Si}(\text{OC}_2\text{H}_5)_4 + \text{PO}(\text{OCH}_3)_3$  reactant gases

system was based on the same method that had been used in LTP (low temperature passivation) (14, 15) in which only one component of  $\text{Si}(\text{OC}_2\text{H}_5)_4$  was for LTP  $\text{SiO}_2$  film formation. However, two components (16),  $\text{Si}(\text{OC}_2\text{H}_5)_4$  and  $\text{PO}(\text{OCH}_3)_3$ , were used for the PSG film deposition in this experiment; the purity of both materials was 99.999%. The typical deposition temperature and pressure were  $740^\circ\text{C}$  and 3 Torr, respectively. The phosphorus doping concentration and the deposition rate were investigated. The concentration of the silicon and phosphorus compounds in the reaction gas was monitored during the deposition by the quadrupole mass analyzer, UTI 100C. The phosphorus concentration in the solid film was determined by the x-ray fluorescence method. The PSG film on the silicon substrate was partially removed by etching and the film thickness was measured with a Talystep.

Figure 2 shows the mass spectrum patterns of  $\text{Si}(\text{OC}_2\text{H}_5)_4 + \text{PO}(\text{OCH}_3)_3$ . Typical spectra,  $m/e = 107$  for  $\text{Si}(\text{OC}_2\text{H}_5)_4$  and  $m/e = 110$  for  $\text{PO}(\text{OCH}_3)_3$ , were selected for the determination of each concentration; these two spectra were adjacent to, but did not interfere with each other. Ionized decomposition species of the  $\text{Si}(\text{OC}_2\text{H}_5)_4$  and  $\text{PO}(\text{OCH}_3)_3$  compounds,  $\text{SiO}_3\text{OCH}_3^+$  for  $m/e = 107$  and  $\text{PO}(\text{OCH}_3)\text{O}_2^+$  for  $m/e = 110$ , are supposed identifications of the mass numbers. The concentration of the reactant gases was quantitatively acquired by correlation between the peak height and flow rate of the organic sources. Figure 3 shows the relationship between the spectrum peak height ratio of  $\text{Si}(\text{OC}_2\text{H}_5)_4$  and  $\text{PO}(\text{OCH}_3)_3$  in the reactant gases and the phosphorus concentration in the PSG films. This indicates that the measurement of the spectrum peak height by the quadrupole mass analyzer can be used to monitor the phosphorus concentration, even in a system with small amounts of the organic compounds, during the deposition reaction.

The concentration of the reactant gases was analyzed at various reaction temperatures. The abrupt decrease of both peak heights above  $700^\circ\text{C}$  in Fig. 4 demonstrates the promotion of the reaction in this temperature range. In the low temperature range between  $400^\circ$  and  $600^\circ\text{C}$ , no deposition of the PSG film on the silicon substrate was observed and inlet and outlet gas concentrations showed the same value. Therefore, taking  $740^\circ\text{C}$  for instance, the concentration of the  $\text{Si}(\text{OC}_2\text{H}_5)_4$  compound and that of the  $\text{PO}(\text{OCH}_3)_3$  at the outlet decreased to  $\sim 1/100$  and  $\sim 1/2$  of the initial inlet concentration, respectively, as shown in this figure. Then, the deposition rate and phosphorus concentration were

measured at temperatures between  $650^\circ$  and  $850^\circ\text{C}$ . The former showed a tendency of increase-maximum-decrease with an increase in reaction temperature as in Fig. 5. From  $650^\circ$  to  $780^\circ\text{C}$ , the behavior was surface-reaction limited ( $E_{\text{act}} = 36$  kcal/mole); above  $780^\circ\text{C}$  diffusion limited. Above  $800^\circ\text{C}$  the behavior was consistent with that expected due to homogeneous nucleation region (17). With high supersaturation and excessive heating of the reactant gases, precipitation of the reaction products can occur, causing a reduction of the deposition rate on the substrate. The deposition rate

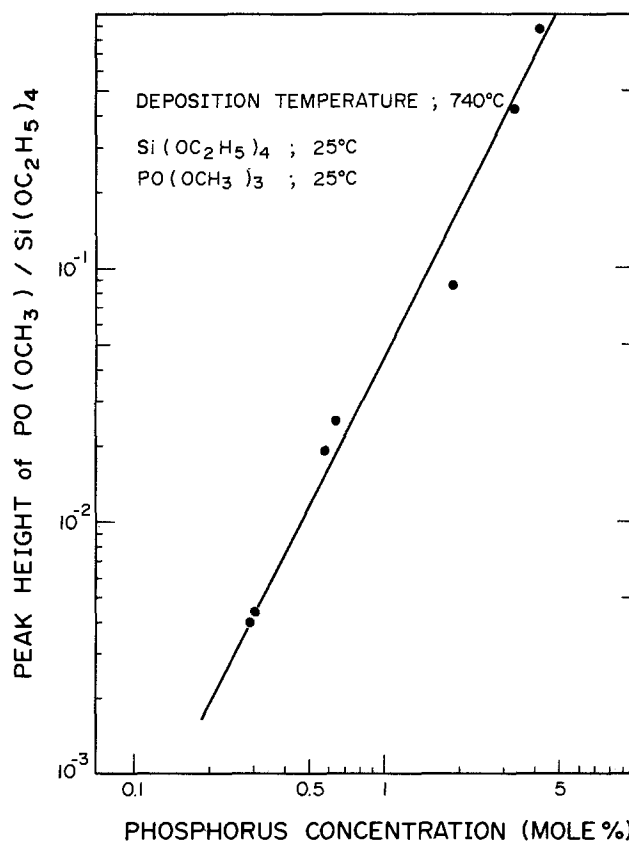


Fig. 3. Correlation between the spectrum peak height ratio of  $\text{Si}(\text{OC}_2\text{H}_5)_4$  and  $\text{PO}(\text{OCH}_3)_3$  reactants and the phosphorus concentration in the PSG film.

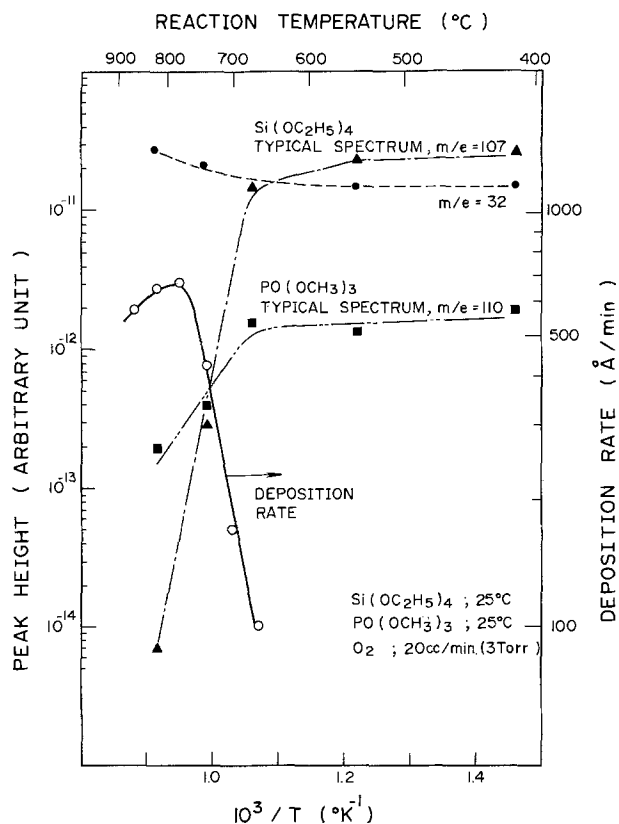


Fig. 4. Dependence of the spectrum peak heights measured by the quadrupole mass analyzer on the reaction temperature.

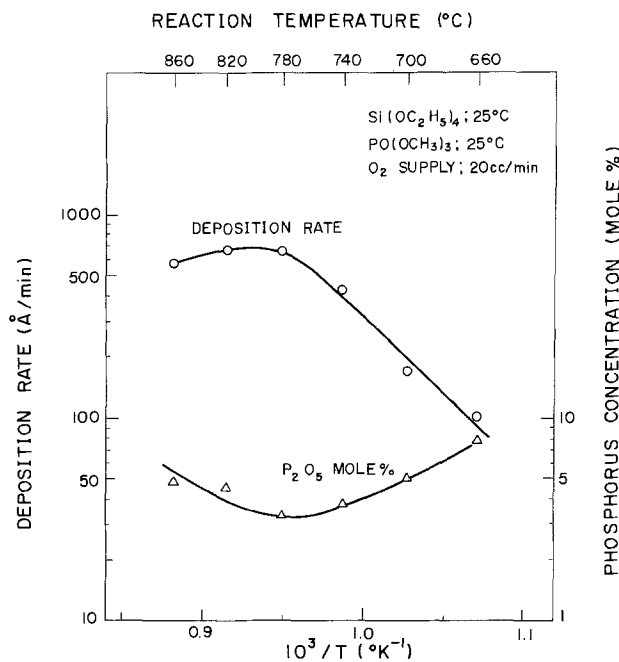


Fig. 5. Dependence of the deposition rate and phosphorus concentration on deposition temperature.

had a tendency similar to the reactivity of the silicon compound except for the homogeneous nucleation above 800°C, shown in Fig. 5. The temperature dependence of the phosphorus concentration in Fig. 5, decrease-minimum-increase, may be explained by the

ratio of these two peak heights, dependence of the P compound was smaller than that of the Si compound as shown in Fig. 4, and by the consideration of the homogeneous nucleation.

Using  $\text{Si}(\text{OC}_2\text{H}_5)_4$  and  $\text{PO}(\text{OCH}_3)_3$  organic compounds, PSG film was deposited at 740°C and 3 Torr. In this reaction system, the concentration of the reactant gases was determined by the quadrupole mass analyzer, and the correlation between the phosphorus concentration in the gas phase and that in the solid film was quantitatively clarified. By using the analyzer, correlation was investigated between the temperature dependence of reactivity in the gaseous concentration and that of the film deposition rate and film phosphorus concentration.

### Acknowledgments

The authors wish to express their deep appreciation to Mr. S. Nishida and Mr. M. Ohno for their valuable discussions and encouragement throughout this experiment, to Mr. H. Ono of Kokusai Electric Company for the various suggestions in the mass analysis, to Mr. T. Nohara and Mr. S. Hosoda for their helpful discussions, and to Mr. K. Akiba for assistance in fabrication of the experimental reactor.

Manuscript submitted June 26, 1975; revised manuscript received March 8, 1976.

Any discussion of this paper will appear in a Discussion Section to be published in the June 1977 JOURNAL. All discussions for the June 1977 Discussion Section should be submitted by Feb. 1, 1977.

Publication costs of this article were assisted by Hitachi, Limited.

### REFERENCES

1. K. Strater, *RCA Rev.*, **29**, 618 (1968).
2. M. Shibata and K. Sugawara, *This Journal*, **122**, 155 (1975).
3. M. Shibata, T. Yoshimi, and K. Sugawara, *ibid.*, **122**, 157 (1975).
4. G. B. Bunyard, *Solid State Technol.*, **78** (March 1970).
5. L. L. Chang, L. Esaki, W. E. Howard, and R. Ludeke, *J. Vac. Sci. Technol.*, **10**, 11 (1973).
6. V. S. Ban, *This Journal*, **118**, 1473 (1971).
7. V. S. Ban, *ibid.*, **119**, 761 (1972).
8. V. S. Ban, *J. Cryst. Growth*, **17**, 19 (1972).
9. V. S. Ban and M. Ettenberg, in "Chemical Vapor Deposition," G. F. Wakefield and J. M. Blocher, Jr., Editors, p. 30, The Electrochemical Society Softbound Symposium Series, Princeton, New Jersey (1973).
10. V. S. Ban and S. L. Gilbert, *This Journal*, **122**, 1382 (1975).
11. V. S. Ban, *ibid.*, **122**, 1389 (1975).
12. T. O. Sedgwick and J. E. Smith, Jr., Paper 212 presented at The Electrochemical Society Meeting, New York, N.Y., Oct. 13-17, 1974.
13. K. Sugawara, T. Yoshimi, and H. Sakai, in "Chemical Vapor Deposition, Fifth International Conference," J. M. Blocher, Jr., H. E. Hintermann, and L. H. Hall, Editors, p. 407, The Electrochemical Society Softbound Symposium Series, Princeton, New Jersey (1975).
14. T. Tokuyama, *Proc. IEEE*, **52**, 723 (1964).
15. M. Yamamoto, K. Sato, Y. Watanabe, Y. Koga, E. Yamada, and Y. Wakashima, *Hitachi Rev.*, **18**, 364 (1969).
16. E. Tanikawa, O. Takayama, and K. Maeda, in "Chemical Vapor Deposition," G. F. Wakefield and J. M. Blocher, Jr., Editors, p. 261, The Electrochemical Society Softbound Symposium Series, Princeton, New Jersey (1973).
17. J. M. Blocher, Jr., in "Vapor Deposition," C. F. Powell, J. H. Oxley, and J. M. Blocher, Jr., Editors, p. 11, John Wiley & Sons, Inc., New York (1966).

# Annealing of Ion-Implanted GaAs in a Controlled Atmosphere

R. M. Malbon,\* D. H. Lee,\* and J. M. Whelan\*.<sup>1</sup>

Hughes Aircraft Company, Torrance Research Center, Torrance, California 90509

Implantation is considered to be an attractive alternative to diffusion for the creation of thin heavily doped n-type regions in GaAs (1-15). We have utilized ion implantation to fabricate high-low READ GaAs IMPATT diodes (6) and state-of-the-art Ka-band GaAs Gunn effect diodes (7). However, the results reported to date indicate that, in general, the doping efficiencies of the n-type implanted species are low unless long annealing periods are used. Lengthy annealing times are unattractive because diffusion tends to excessively broaden the impurity doping gradients and thus impair device performance. Even for short anneal times within the range of commonly used annealing temperatures, 700°-900°C, it is necessary to take special precautions to minimize erosion of the GaAs surfaces. A variety of approaches have been used. These include sealing the GaAs both with and without a dielectric encapsulant in evacuated quartz ampuls prior to annealing (4, 8). The encapsulants have included SiO<sub>2</sub> (3, 4, 6, 9), Si<sub>3</sub>N<sub>4</sub> (8, 9), Al<sub>2</sub>O<sub>3</sub> (11, 12), and Ga-doped SiO<sub>2</sub> (13, 14). However various problems associated with uncontrolled contamination and interdiffusion at the encapsulant-GaAs interface have been noted (15).

This paper describes the results of substituting a controlled atmosphere for the dielectric encapsulant to protect the GaAs surface during high temperature anneals. Epitaxial materials technology has demonstrated that polished substrates can be maintained at elevated temperature with minimal surface degradation in a flowing high purity hydrogen atmosphere. Taking advantage of this experience, an anneal system was designed which utilizes a controlled atmosphere of high purity hydrogen (H<sub>2</sub>) in conjunction with an arsenic (As) source to protect the GaAs surface during annealing. The system was used to anneal epitaxial GaAs films implanted with either silicon ions or sulfur ions to create thin, highly doped n-type layers. The epitaxial surfaces exhibited no degradation after anneals at 800°C for 20 min. The electrical results indicate that the apparent electrical conversion efficiencies achieved for the implanted layers were as high as 85% for the 800°C, 20 min anneal.

## Experimental

The GaAs epitaxial material used in this investigation was grown by the H<sub>2</sub>-Ga-AsCl<sub>3</sub> vapor phase technique on heavily Te-doped n<sup>+</sup>-substrates oriented 3° off the <100> toward the <111>. The epitaxial layers were doped with sulfur and were electrically uniform in depth with net donor concentrations within the range 2-8 × 10<sup>15</sup> cm<sup>-3</sup>. The epitaxial layers were implanted at room temperature with either 120 keV silicon ions or 140 keV sulfur ions. In the case of the silicon implants it was concluded after careful analysis of the separated ion spectrum that the implanted species was <sup>28</sup>Si<sup>+</sup> with less than 1% of other possible molecular components (e.g., N<sub>2</sub><sup>+</sup>). To minimize channeling effects, the GaAs lattice was oriented to appear random to the incident ion beam. Under this condition, a first order approximation to the implanted ion distribution is Gaussian with a mean projected range R<sub>p</sub> and standard deviation ΔR<sub>p</sub>. For the 120 keV silicon implants, the ion dose, N<sub>D</sub> (number of ions/cm<sup>2</sup>), was varied between 5.6 × 10<sup>12</sup> and 2.3 × 10<sup>13</sup>. Based on the range theory of Lindhard, Scharff, and Schiøtt (15),

R<sub>p</sub> = 0.103 μm and ΔR<sub>p</sub> = 0.051 μm. For the 140 keV sulfur, the ion dose was 2.53 × 10<sup>13</sup> ions/cm<sup>2</sup>. In this case the theory of Lindhard et al. predicts R<sub>p</sub> = 0.104 μm and ΔR<sub>p</sub> = 0.051 μm. After ion implantation, the GaAs epitaxial layers were annealed under a H<sub>2</sub> atmosphere using a quartz envelope furnace assembly shown schematically in Fig. 1. Inlet H<sub>2</sub> from a liquid source was preheated by passage through one leg of the horizontal U tube and was subsequently passed over a quartz boat containing a liquid Ga/GaAs solution saturated with As. This source supplied As to the atmosphere at a pressure near that required for equilibrium with the GaAs-implanted surface. The Ga/GaAs also served as a reaction site for the trace amounts of H<sub>2</sub>O in the hydrogen stream and thus minimized erosion of the implanted surface by this atmospheric impurity. Samples to be annealed were placed on a quartz support assembly and loaded into the main tube. After loading, the chamber was flushed for a minimum of 1 hr so that the (air + H<sub>2</sub>O) concentrations were under 3 ppm. Based on prior experience, the H<sub>2</sub>O concentration rises to 10 ppm or less due to outgassing of the quartz at the annealing temperature (17). No surface degradation was observed with an optical microscope at 700X with interference contrast after the 800°C, 20 min anneal cycles reported here.

The ion-implanted donor profiles were determined from capacitance-voltage (C-V) measurements on reverse-biased Schottky barrier diodes. The Al or Au Schottky barriers were vacuum deposited on the implanted layers after a Au-Ge ohmic contact was alloyed on the n<sup>+</sup>-substrate. An automatic impurity profile plotter<sup>2</sup> was used in conjunction with some forward-biased C-V measurements to obtain as large a portion of the free carrier profile as possible. Etch step techniques were combined with the Schottky barrier measurements to obtain the complete net donor tail distribution. Steps of approximately 1000Å each were etched into the ion-implanted epitaxial layer using a volume ratio 5:1:1 (H<sub>2</sub>SO<sub>4</sub>, H<sub>2</sub>O<sub>2</sub>, H<sub>2</sub>O) as the etchant. The step heights were measured with a commercial step height analyzer to complete the profile data. Although the C-V technique exhibits certain limitations in its ability to accurately reproduce rapidly varying profiles (18), it was concluded by comparison of the results from the various etch steps that no significant deviation was occurring.

## Results and Discussion

The profile evaluations for the silicon implants into the GaAs epitaxial layers are illustrated in Fig. 2 and

<sup>2</sup> The differential C-V measurements were obtained by the application of a 15 mV signal at a frequency of 1 MHz.

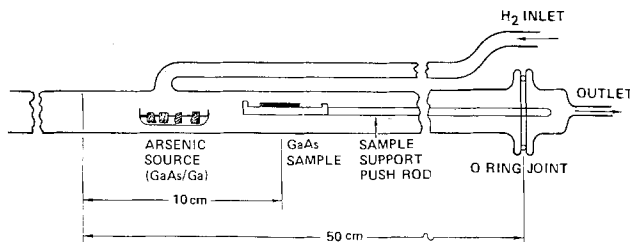


Fig. 1. Quartz annealing assembly for ion-implanted GaAs samples. A 50 cm long resistance furnace on tracks may be centered on the sample or rolled to the left for rapid sample cooling.

\* Electrochemical Society Active Member.

<sup>1</sup> Present address: Materials Science Department, University of Southern California, Los Angeles, California 90007.

Key words: compound semiconductors, implanted silicon, implanted sulfur.

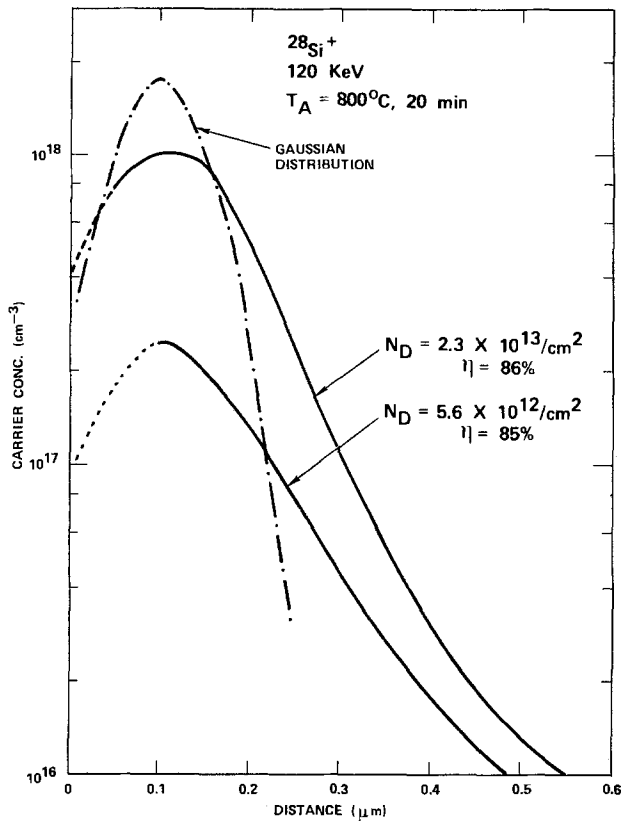


Fig. 2. Measured carrier concentration vs. the distance from the sample surface for ion-implanted silicon in GaAs. The samples were annealed at 800°C for 20 min.

3. Figure 2 shows the resultant donor profiles for 120 keV Si implants annealed at 800°C for 20 min. The measured profiles for the two different doses ( $2.3 \times 10^{13}$  and  $5.6 \times 10^{12}$  ions/cm<sup>2</sup>) are indicated by the solid curves. The first order theoretical distribution based on the theory of Lindhard *et al.* is the dot-dashed line which indicates the projected range of the implants for the energy used. The apparent electrical activities were estimated by integrating under the solid measured profile curves and their projected sections shown as dotted lines in the figure. (The C-V profile technique is limited by the depletion depth of the Schottky barrier diode.)

The apparent electrical conversion efficiency,  $\eta$ , is the ratio of the integrated net donors to the dose. For the 800°C, 20 min anneal,  $\eta$  was calculated to be approximately 85% for both doses. The measured donor profiles agreed within 20% of the projected range and tended to be slightly deeper in both cases. Figure 3 compares the resultant donor profiles for 120 keV Si implants annealed at 700°C for 20 min. The solid curves are the measured profiles for the two different doses utilized ( $2.3 \times 10^{13}$  and  $5.6 \times 10^{12}$  ions/cm<sup>2</sup>). The dotted lines indicate the projected distribution utilized to calculate the apparent electrical conversion efficiency. In this case,  $\eta$  was higher for the higher dose implant; 62% for the  $2.3 \times 10^{13}$ /cm<sup>2</sup> dose and 56% for the  $5.6 \times 10^{12}$ /cm<sup>2</sup> dose. In both cases, however,  $\eta$  was significantly lower than that obtained for the 800°C, 20 min anneal. The measured profile distribution peaks agreed quite well with the projected range and tended to be slightly deeper.

The profile evaluation for the sulfur implant is illustrated by the solid curve in Fig. 4. The measured profile indicates the resultant donor profile for the 140 keV S implant after the 800°C, 20 min anneal. The dose in this case was  $2.5 \times 10^{13}$  ions/cm<sup>2</sup>. The first order theoretical distribution based on the theory of Lindhard *et al.* is the dot-dashed line which indicates the projected range of the implants for the energy used. As

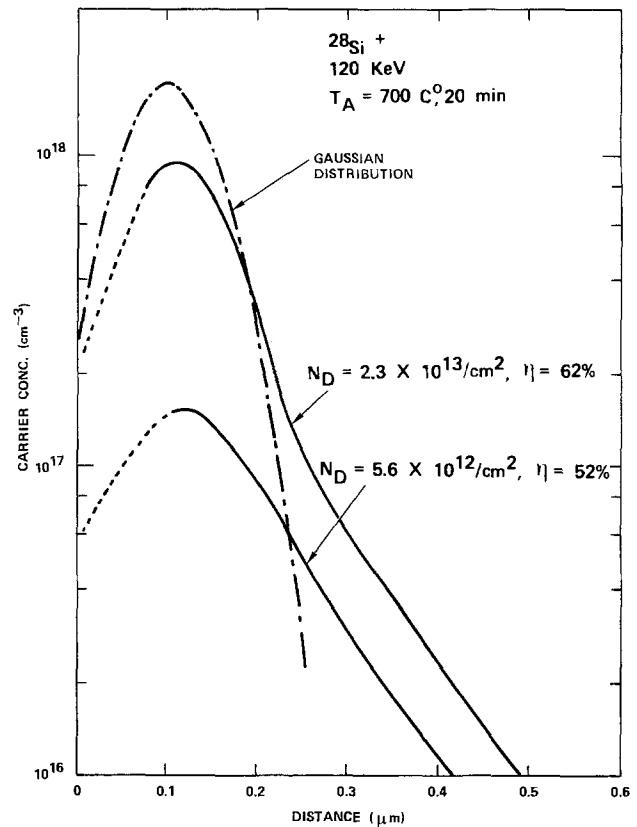


Fig. 3. Measured carrier concentration vs. the distance from the sample surface for ion-implanted silicon in GaAs. The samples were annealed at 700°C for 20 min.

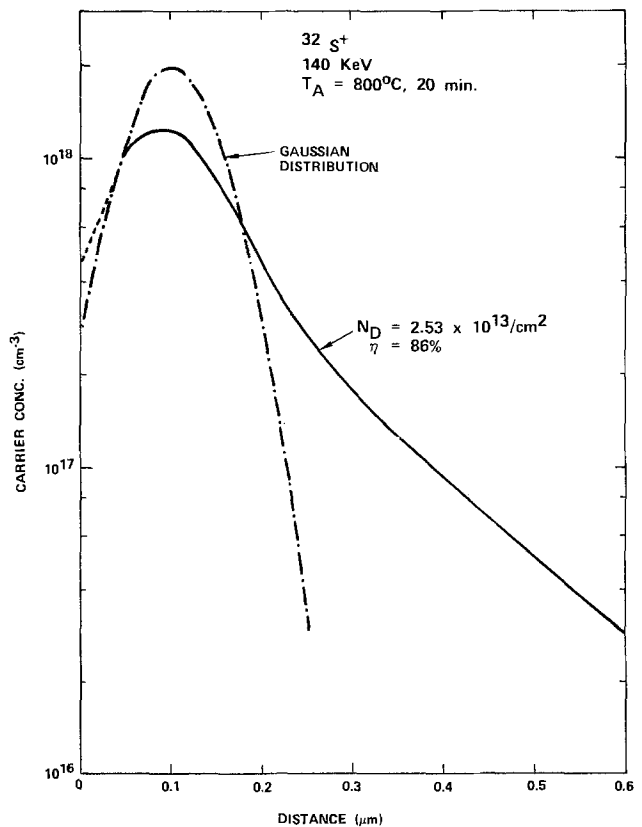


Fig. 4. Measured carrier concentration vs. the distance from the sample surface for ion-implanted sulfur in GaAs. The samples were annealed at 800°C for 20 min.

above,  $\eta$  was estimated using the same technique described for the silicon implants. For the 800°C 20 min anneal with the controlled atmosphere technique,  $\eta$

was calculated to be 82%. The measured donor profile for the S-implanted profile agrees within 20% of the projected range but exhibits a significantly deeper tail than that encountered with the annealed Si profiles.

To ensure that the anneal process was not influencing the ion-implanted results reported above, unimplanted epitaxial layers of known impurity concentration were annealed in the system at 800°C for 30 min and reevaluated. In all cases, the background impurity concentration distributions in the epitaxial layers remained unchanged from their value prior to the anneal. This indicates that no unusual redistribution of the background impurities was occurring during the high temperature anneal. If the anneal times were extended to 60 min at 800°C, a slight surface degradation was noted at  $700\times$  indicating that some dissociation or H<sub>2</sub>O vapor etching of the GaAs was occurring.

Comparison of Fig. 2 and 3 for the silicon implants indicates that diffusion broadening of the profile is taking place during the 800°C, 20 min anneal. It is also apparent that higher peak concentrations are obtained with the 800°C anneal. For the low dose, the peak concentration increased by 60% using an 800°C anneal as compared to a 700°C anneal. However, for the higher dose case, only a 6% improvement was noted. This suggests the possibility that the electrical activity is dose dependent at lower anneal temperatures. Comparison of the profile data for the silicon (Fig. 2) to those for the sulfur (Fig. 4) annealed under the same conditions, suggests that diffusion broadening of the sulfur profile is more significant. However, these results may be influenced to some extent by the inability of the C-V technique to accurately reproduce rapidly varying tail distributions (18).

It is of interest that upon annealing at 700°-800°C, ion-implanted Si acts as a relatively high efficiency donor. This is in accord with the results of other authors (4, 8, 14), but opposite to the observations that lightly Si-doped GaAs epitaxial films grown from Si-doped Ga solutions at approximately 815° and 730°C are p-type (19). The Ga and As fugacities used to prepare these liquid phase epitaxy samples were similar to those used in our anneals. It is possible that their results are more nearly representative of thermal equilibrium and that their dominant acceptor is not simply a Si atom on an As lattice site. This view is consistent with the results of Spitzer and Pannish (20) who found the concentration of Si on Ga sites to be larger than that on As sites in heavily Si-doped GaAs grown from Ga solutions. Their results suggested a complex acceptor defect was responsible for the p-type character. Due to the high donor doping efficiencies we find, it is presumed that the acceptor complex is not present at large concentrations in our Si-implanted GaAs. Hicks and Green (19) did not find that the acceptor doping efficiency of Si increased as the growth temperature decreased from 815° to 730°C. This may be one reason why we find a lower donor doping efficiency upon annealing at 700°C as compared to 800°C.

The relatively high and reproducible electrical activities described above are in a large part directly attributable to the anneal technique. As reported by a number of authors, an anneal temperature of at least 600°C is required to eliminate the lattice disorder associated with the implant. In addition, most authors have reported very low electrical activity for anneal temperatures below 700°C. However, dissociation of the GaAs surface can begin as low as 600°C unless special precautions are taken to either control the atmosphere or encapsulate the surface. Our initial attempts using dielectric encapsulation resulted in some attractive profiles and excellent device results (6, 7). However, controlled profiles were difficult to reproduce regularly due to the poor quality of the dielectric encapsulants. Although the dielectric encapsulants maintained surface integrity, problems associated with impurities diffusing out of the encapsulant into the GaAs

as well as Ga diffusing into the encapsulating layer (15) have influenced the reproducibility greatly. Use of the controlled atmosphere anneal has significantly reduced these problems. It is not known at present to what extent this technique can be extended to longer and/or higher temperature anneals through better hydrogen purification procedures and more direct control of the As vapor pressure.

### Conclusions

In this paper we have described a simple reproducible technique for annealing ion-implanted layers in GaAs. A controlled atmosphere is utilized instead of a dielectric encapsulant to prevent dissociation of the GaAs surface during the anneal. A controlled atmosphere is preferable as it minimizes the possibility of unwanted impurities diffusing out of the encapsulant into the ion-implanted region, thus disturbing the net impurity concentration. The ion-implanted results reported indicate that exceptionally high apparent conversion efficiencies (85%) can be obtained with this technique for n-type dopants in GaAs.

### Acknowledgments

The authors are grateful to D. Jamba for assistance with the implantation, W. B. Henderson for the epitaxial material, and C. A. Reamer for sample preparation. We also wish to thank Dr. J. K. Kung for many useful discussions.

Manuscript submitted April 9, 1976; revised manuscript received May 6, 1976.

Any discussion of this paper will appear in a Discussion Section to be published in the June 1977 JOURNAL. All discussions for the June 1977 Discussion Section should be submitted by Feb. 1, 1977.

Publication costs of this article were assisted by Hughes Aircraft Company.

### REFERENCES

1. R. G. Hunsperger and O. J. Marsh, *Radiation Effects*, **6**, 236 (1970).
2. R. G. Hunsperger and O. J. Marsh, *This Journal*, **116**, 488 (1969).
3. A. G. Foyt, J. P. Donnelly, and W. T. Lindley, *Appl. Phys. Letters*, **14**, 372 (1969).
4. J. D. Sansberry and J. F. Gibbons, *Radiation Effects*, **6**, 269 (1970).
5. F. Eisen, Proceedings of the Fourth International Conference on Ion Implantation, Osaka, Japan, 1974.
6. J. J. Berenz, R. S. Ying, and D. H. Lee, *Electron. Letters*, **10**, 157 (1974).
7. D. H. Lee, J. J. Berenz, and R. L. Bernick, *ibid.*, **11**, 189 (1975).
8. J. M. Woodcock, J. M. Shannon, and D. J. Clar, *Solid-State Electron.*, **18**, 267 (1975).
9. E. C. Bell, A. E. Glaccum, P. L. F. H. Hemet, and B. J. Sealy, *Radiation Effects*, **22**, 253 (1974).
10. T. Miyazaki and M. Tamura, Proceedings of the Fourth International Conference on Ion Implantation, Osaka, Japan, 1974.
11. B. J. Sealy and A. D. E. D'Cruz, *Electron. Letters*, **11**, 323 (1975).
12. P. L. F. Hemment, B. J. Sealy, and K. G. Stevens, Proceedings of the Fourth International Conference on Ion Implantation, Osaka, Japan, 1974.
13. D. E. Davies, S. Roosild, and L. Lowe, *Solid-State Electron.*, **18**, 733 (1975).
14. D. E. Davies, J. K. Kennedy, and C. E. Ludington, *This Journal*, **122**, 1374 (1975).
15. J. Gyulai, J. W. Mayer, and I. V. Mitchell, *Appl. Phys. Letters*, **17**, 332 (1970).
16. J. Lindhard, M. Scharff, and H. Schiøtt, *Mat. Fys. Medd. Dan. Fys. Selsk.*, **33**, 1 (1963).
17. P. S. Vijayakamur, Private communication, representative data to be published.
18. C. P. Wu *et al.*, *IEEE Trans. Electron Devices*, **ED-22**, 319 (1975).
19. H. G. B. Hicks and P. D. Green, Proceedings of the 3rd International Symposium on Gallium Arsenide, Institute of Physics and the Physics Society, p. 92 (1970).
20. W. G. Spitzer and M. B. Pannish, *J. Appl. Phys.*, **40**, 4200 (1969).

# Restrained Diffusion of Boron and Phosphorus in Silicon under HCl-Added Oxygen Atmosphere

Yasumasa Nabeta, Tadashi Uno, Shuji Kubo,\* and Hirokazu Tsukamoto

Matsushita Research Institute Tokyo, Incorporated, Ikuta, Tamaku, Kawasaki, Japan

The enhanced diffusion of boron and phosphorus in silicon in oxidizing atmosphere has been reported by several workers (1-3). This paper describes experimental results of diffusion behavior of these impurities in HCl-added oxygen gas. It was found that the impurities are restrained in a presence of HCl gas in the oxidizing diffusion atmosphere.

Samples used in this experiment were n-type silicon crystals of 70  $\Omega$ -cm and p-type silicon crystals of 25  $\Omega$ -cm with (100) plane. P-type silicon crystals of 45  $\Omega$ -cm with (111) plane were also used. The experimental procedure was as follows: (i) CVD film (borosilicate or phosphosilicate glass) is deposited on silicon surface at a temperature of 450°C; (ii) boron or phosphorus in the CVD film is pre-diffused in the surface layer of the sample at a temperature of 1000°C for 10 min in the nitrogen atmosphere; (iii) CVD film is then removed; (iv) diffusion is carried out in three different atmospheres, i.e., 30°C wet oxygen (wet O<sub>2</sub>), HCl-added oxygen (HCl-O<sub>2</sub>), and nitrogen (N<sub>2</sub>). An oxidation rate of 6% HCl-O<sub>2</sub> is equal to that of 30°C (wet O<sub>2</sub>) at a temperature of 1100°C.

The junction depth,  $X_j$  was measured by angle lapping and staining. The surface concentration,  $C_s$  was obtained from  $X_j$  and sheet resistivity,  $\rho_s$ , using the data of Irvin (4) under the assumption of the gaussian distribution. The diffusion coefficient,  $D$ , was calculated from the values of  $X_j$  and  $\rho_s$  by using the gaussian diffusion function.

The experimental results for boron impurities after drive-in at the temperature 1100°C with different times are summarized in Table I. The diffusion coefficient was also calculated by incorporating the measured values of  $X_j$  into the theoretical formula of the Kato and Nishi model (5). It is clear from Table I that the diffusion coefficient values obtained by these two methods show relatively good agreement. Similar results for phosphorus impurities are shown in Table II. From these tables it is found that the values of junction depth for the HCl-O<sub>2</sub> diffusion are close to that for the N<sub>2</sub> diffusion for the same diffusion time, but are much smaller than that for the wet-O<sub>2</sub> diffusion. The

\* Electrochemical Society Active Member.

Key words: diffusion, silicon, boron, phosphorus, HCl-added oxygen.

Table I. Summary of results on boron diffusion in Si at 1100°C

Drive-in time (min)	Drive-in ambient	Junction depth $X_j$ ( $\mu$ m)	Sheet resistivity $\rho_s$ ( $\text{ohm}/\square$ )	Cs (Gaussian) (atoms/cm <sup>2</sup> )	$\sqrt{D}$ ( $\mu\text{m}/\sqrt{\text{hr}}$ )	
					(Gaussian)	(Kato and Nishi) <sup>†</sup>
14	dry-N <sub>2</sub>	0.72	96.1	$6.3 \times 10^{19}$	0.204	0.180
	6% HCl+dry O <sub>2</sub>	0.90	154	$3.0 \times 10^{19}$	0.262	0.255
	wet O <sub>2</sub>	1.25	154	$2.0 \times 10^{19}$	0.369	0.370
64	dry-N <sub>2</sub>	1.31	87.6	$3.8 \times 10^{19}$	0.178	0.177
	6% HCl+dry O <sub>2</sub>	1.37	172	$1.6 \times 10^{19}$	0.190	0.203
	wet O <sub>2</sub>	2.19	175	$8.5 \times 10^{18}$	0.313	0.329
124	dry-N <sub>2</sub>	1.73	81.8	$2.9 \times 10^{19}$	0.168	0.173
	6% HCl+dry O <sub>2</sub>	1.83	193	$1.0 \times 10^{19}$	0.185	0.202
	wet O <sub>2</sub>	2.98	175	$5.8 \times 10^{18}$	0.309	0.329

After the pre-diffusion, junction depth and surface concentration, assuming the complementary error function, were 0.41  $\mu$ m and  $1.6 \times 10^{20}$  atoms/cm<sup>2</sup>, respectively.

<sup>†</sup> Calculated using the segregation coefficient  $k = 10$  and oxidation constant  $K = 1.20 \times 10^{-13}$  cm<sup>2</sup>/sec for HCl-O<sub>2</sub> and  $K = 1.23 \times 10^{-13}$  cm<sup>2</sup>/sec for wet-O<sub>2</sub>.

Table II. Summary of results on phosphorus diffusion in Si at 1100°C

Drive-in time (min)	Drive-in ambient	Junction depth $X_j$ ( $\mu$ m)	Sheet resistivity $\rho_s$ ( $\text{ohm}/\square$ )	Cs (Gaussian) (atoms/cm <sup>2</sup> )	$\sqrt{D}$ ( $\mu\text{m}/\sqrt{\text{hr}}$ )	
					(Gaussian)	(Kato and Nishi) <sup>†</sup>
14	dry-N <sub>2</sub>	0.82	52.4	$6.6 \times 10^{19}$	0.249	0.220
	6% HCl+dry O <sub>2</sub>	0.90	52.6	$5.4 \times 10^{19}$	0.275	0.262
	wet O <sub>2</sub>	1.20	47.3	$4.8 \times 10^{19}$	0.369	0.365
64	dry-N <sub>2</sub>	1.45	48.9	$3.4 \times 10^{19}$	0.211	0.208
	6% HCl+dry O <sub>2</sub>	1.54	51.9	$3.1 \times 10^{19}$	0.225	0.235
	wet O <sub>2</sub>	2.21	45.3	$2.3 \times 10^{19}$	0.327	0.338
124	dry-N <sub>2</sub>	1.92	48.6	$2.6 \times 10^{19}$	0.202	0.201
	6% HCl+dry O <sub>2</sub>	1.87	52.1	$2.5 \times 10^{19}$	0.197	0.207
	wet O <sub>2</sub>	2.88	43.4	$1.8 \times 10^{19}$	0.309	0.324

After the pre-diffusion, junction depth and surface concentration, assuming the complementary error function, were 0.44  $\mu$ m and  $2.7 \times 10^{20}$  atoms/cm<sup>2</sup>, respectively.

<sup>†</sup> Calculated using the segregation coefficient  $k = 0.1$  and oxidation constant  $K = 1.20 \times 10^{-13}$  cm<sup>2</sup>/sec for HCl-O<sub>2</sub> and  $K = 1.23 \times 10^{-13}$  cm<sup>2</sup>/sec for wet O<sub>2</sub>.

surface concentrations for HCl-O<sub>2</sub> and N<sub>2</sub> are larger than for wet O<sub>2</sub>.

Relations between surface concentration and diffusion coefficient for boron and phosphorus impurities are shown in Fig. 1 and 2, respectively. In these fig-

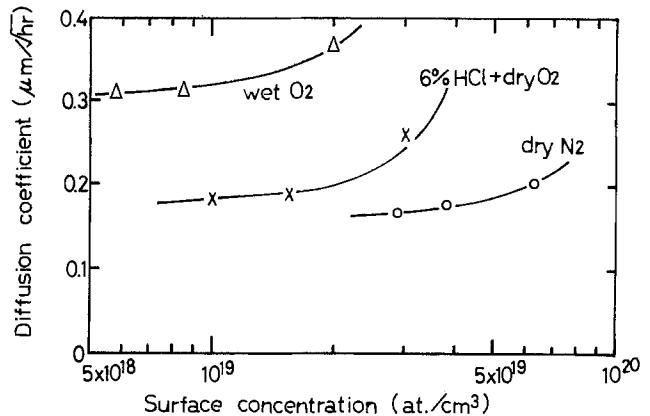


Fig. 1. Diffusion coefficient vs. surface concentration for boron diffusion at 1100°C.

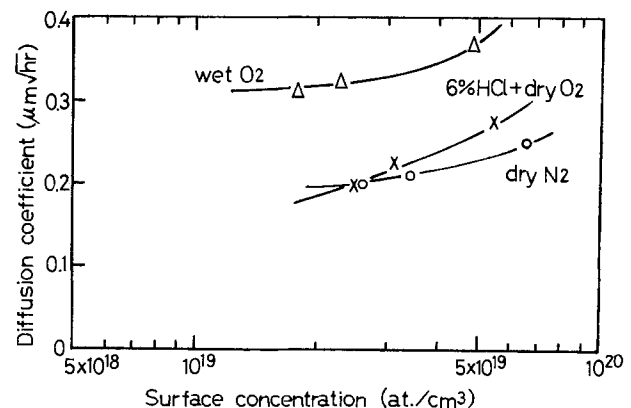


Fig. 2. Diffusion coefficient vs. surface concentration for phosphorus diffusion at 1100°C.

ures, it is interesting to note that the diffusion coefficients of boron and phosphorus in silicon in wet O<sub>2</sub> are larger than those in N<sub>2</sub> and HCl-O<sub>2</sub>. This result indicates that the diffusion of boron and phosphorus in silicon in wet O<sub>2</sub> is enhanced as has been reported, but not for HCl-O<sub>2</sub>, particularly in a lower range of surface concentration.

This effect of restrained diffusion is varied with the process condition. Figures 3 and 4 show these experimental results of diffusion coefficients for boron and

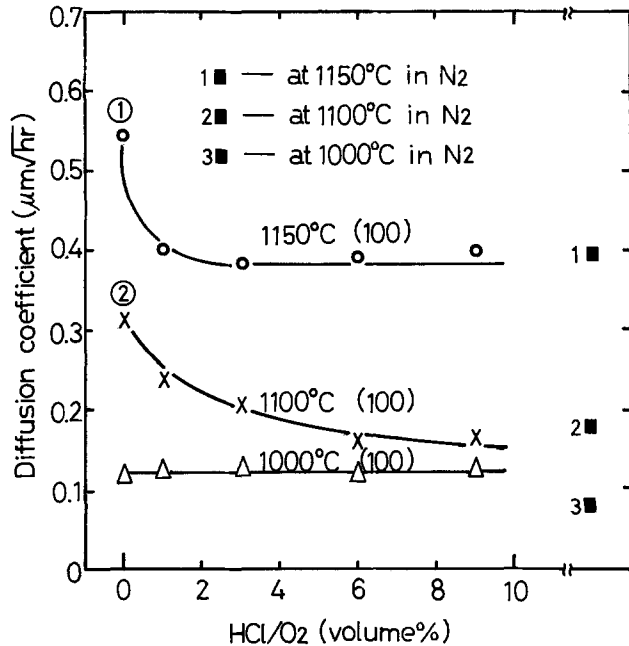


Fig. 3. Diffusion coefficient of boron in silicon at different temperatures and HCl volume ratios.

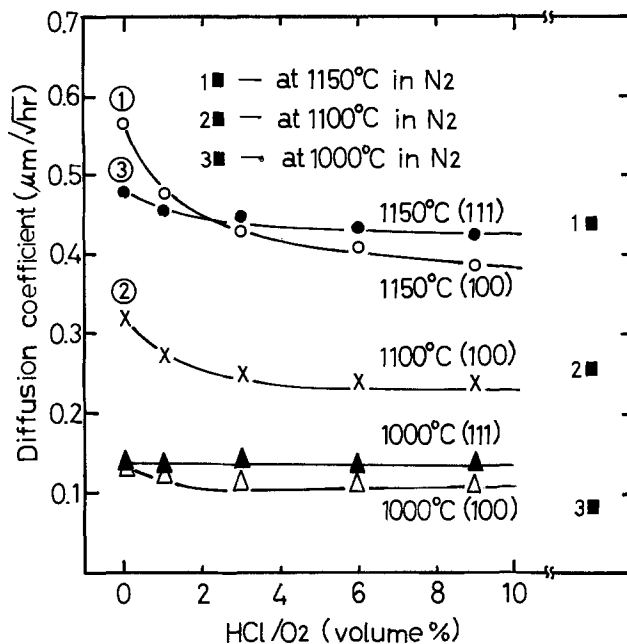


Fig. 4. Diffusion coefficient of phosphorus in silicon at different temperatures and HCl volume ratios.

phosphorus for the diffusions at temperatures of 1000°, 1100°, and 1150°C, varying volume ratios of HCl gas to dry oxygen. From these figures, the following behavior of impurity diffusion can be observed.

(i) The diffusion coefficient of boron and phosphorus for (100) crystal treated in HCl-O<sub>2</sub> at temperatures above 1100°C gradually decreases with increasing volume ratio of HCl gas up to 9% and reaches the diffusion coefficient of that in N<sub>2</sub>, which has been evaluated by several workers (6, 7). The rate of decrease of the diffusion coefficient with increasing HCl gas content is more prominent for (100) crystal at 1150°C, as seen from curves ① and ② in Fig. 3 and 4. This behavior of the diffusion coefficient as a function of HCl gas content and temperature seems to correlate to the results of Shiraki's work (8) on decreasing stacking faults as a function of HCl gas content and temperature.

(ii) The diffusion coefficient of phosphorus for (111) silicon crystal is less dependent on the HCl gas content than that for (100) crystal, as seen from curves ① and ③ in Fig. 4. This can be interpreted from Shiraki's result that during dry-O<sub>2</sub> oxidation stacking faults tend to generate for the (100) plane rather than for the (111) plane.

(iii) The restrained diffusion effect is not prominently shown at any HCl gas content at temperatures lower than 1000°C. This corresponds to the report by Kobayashi *et al.* (9) indicating that the HCl-O<sub>2</sub> process below 1060°C does not give any improved effect of Si-SiO<sub>2</sub> interface.

In summary, experimental study for boron and phosphorus diffusion in silicon in various atmospheres was carried out. It was found that the diffusion of these impurities is restrained in the presence of HCl gas in the oxidizing diffusion atmosphere at certain conditions of temperature and HCl gas content. These conditions show strong similarity to the behavior of stacking fault generation in HCl-added oxygen atmosphere. The restrained diffusion of impurities, therefore, seems to result from the elimination of stacking faults at the Si-SiO<sub>2</sub> interface, which varied with the HCl-added atmosphere.

#### Acknowledgments

The authors express deep thanks to Dr. M. Onuki for his valuable discussions.

Manuscript submitted Dec. 16, 1975; revised manuscript received May 19, 1976.

Any discussion of this paper will appear in a Discussion Section to be published in the June 1977 JOURNAL. All discussions for the June 1977 Discussion Section should be submitted by Feb. 1, 1977.

Publication costs of this article were assisted by the Matsushita Research Institute Tokyo, Incorporated.

#### REFERENCES

1. G. Masetti, S. Solmi, and G. Soncini, *Solid-State Electron.*, **16**, 1419 (1973).
2. W. G. Allen and K. V. Amand, *ibid.*, **14**, 397 (1971).
3. M. Okamura, *Jpn. J. Appl. Phys.*, **9**, 849 (1974).
4. J. C. Irvin, *Bell Syst. Tech. J.*, **41**, 387 (1962).
5. T. Kato and Y. Nishi, *Jpn. J. Appl. Phys.*, **3**, 377 (1964).
6. G. L. Masetti, *Solid-State Electron.*, **16**, 1419 (1973).
7. M. L. Barry and P. Olofsen, *This Journal*, **116**, 854 (1969).
8. H. Shiraki, *Jpn. J. Appl. Phys.*, **15**, 83 (1976).
9. K. Kobayashi *et al.*, *Denki Kagaku*, **42**, 294 (1974).



## Depth Analysis of Passive Films on Iron in Neutral Borate Solution

Norio Sato,\* Kiyokatsu Kudo, and Rokuro Nishimura

*Corrosion Research Group, Faculty of Engineering, Hokkaido University, Sapporo 060, Japan*

### ABSTRACT

Composition depth profiles of passive films on iron in a borate solution at pH 8.42 have been obtained by means of cathodic reduction combined with ellipsometry and chemical analysis. Results revealed that the compositional profile varied depending primarily on the potential and to some degree on the time of film growth. The barrier layer in contact with the metal changed in composition from an iron(II-III) mixed oxide at potentials below the Flade potential to an iron(III) oxide at more noble potentials. The deposit layer next to the solution was a hydrated iron(III) oxide and adsorbed iron(II) ions at less noble potentials. There was found a peak or a decrease in iron concentration at the barrier/deposit boundary. The iron-rich boundary was gradually replaced by the iron-depleted as the potential was shifted to more noble direction. It was the barrier layer alone that increased in thickness during the film growth at potentials above the Flade potential. In the transpassive potential region the barrier layer ceased growing with potential and tended to contain a small concentration of iron(II) ions. It is suggested that the ion transport in the layers plays a role in determining the passive film composition.

In previous papers (1-6) it has been shown that the passive film formed on iron in a borate solution at pH 8.42 is a bilayered film consisting of a barrier layer of  $\gamma\text{-Fe}_2\text{O}_3$  next to the metal phase and a deposit layer of hydrated iron(III) oxide next to the solution phase. The barrier layer was potential dependent and its thickness at steady state was proportional to the overpotential of the layer formation. The deposit layer, which was stable only in the neutral and basic pH range, appeared to differ in thickness with different passivation processes and also with different solution environments such as pH and anion.

The picture is, however, not altogether clear in an extended range of potential at which the film is formed. This work has therefore been undertaken to throw light into the composition profile of the passive film formed at different potentials in a borate solution of pH 8.42.

### Experimental

The materials, instruments, and methods employed are essentially the same as those described in previous papers (5, 6). The specimen was polycrystalline iron of 99.9% purity in the form of sheet. The solution in which the specimen was passivated was a nitrogen-saturated oxygen-free 0.15M boric acid-sodium borate solution of pH 8.42.

For depth analysis of the passive film, a galvanostatic-cathodic reduction technique combined with ellipsometry and chemical analysis (6, 7) was employed by using an oxygen-free 0.15M boric acid-sodium borate solution at pH 6.48 in which the passive film on iron was proved to cathodically dissolve layer by layer

without any appreciable change in its original composition profile (7).

The specimen surface free from oxide films was prepared by cathodic reduction at pH 8.42 and, immediately after renewing the solution, was anodically oxidized at a constant potential for 1 hr to form the passive film on it. The response time of the potential shift from the cathodic region to the passive potential region was less than 2 sec. After exchanging the solution from pH 8.42 to pH 6.48, the passive film was cathodically reduced at a constant current of  $6.0 \mu\text{A}/\text{cm}^2$  and the solution was analyzed for iron by absorption spectroscopy as a function of time of cathodic reduction.

Furthermore, optical measurements of light-intensity-following ellipsometry (8, 9) were carried out during galvanostatic cathodic reduction of the passive film at an angle of incidence of  $74.485^\circ$  and at a wavelength of light 546.1 nm with an ellipsometer (Rudolph 43702-200E).

All measurements were carried out at  $20^\circ \pm 1^\circ\text{C}$ . The electrode potential was measured in reference to a saturated calomel electrode and was converted into the standard hydrogen electrode scale.

### Results and Discussions

*Film thickness.*—A number of film thickness measurements by ellipsometry have been carried out in the authors' laboratory (1-4). Figure 1 shows the film thickness and anodic current as a function of potential at which the passive film has been formed by anodic 1 hr oxidation. The Flade potential (10),  $E_f = +0.58\text{-}0.059 \text{ pH}$ , may divide the passive potential region into two regions, I and II. Transpassivation began to occur at  $+1.55\text{V}$  almost independent of pH (11).

\* Electrochemical Society Active Member.  
Key words: iron passivity, anodic oxide film, ellipsometry, cathodic reduction, composition depth profiling, film growth.



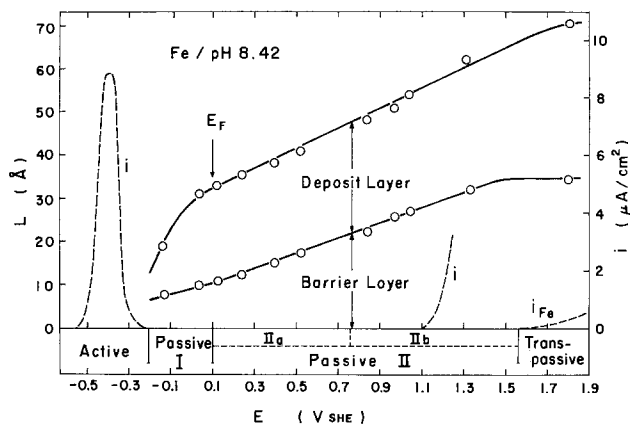
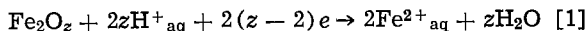


Fig. 1. Anodic current-potential curve of iron and thickness-potential curve for the passive film on iron anode in borate solution of pH 8.42. The films were formed potentiostatically each on the oxide-free surface for 1 hr.  $i_{Fe}$  = transpassive dissolution current,  $E_F$  = Flade potential.

Evidently, the barrier layer is potential dependent except for the potential region of transpassivation where the layer thickness remained nearly constant. The barrier layer thickness for unit voltage was 1.54 nm/V ( $6.5 \times 10^6$  V/cm) in region I and 1.75 nm/V ( $5.7 \times 10^6$  V/cm) in region II. It was also observed that the deposit layer thickness increased with potential in region I and remained almost unchanged in region II. As reported previously, the amount of iron(II) ion dissolved in an early stage of passivation has a direct effect on the deposit layer thickness (5).

**Depth profiling by cathodic reduction.**—The cathodic reduction of the film produces iron(II) ions in the solution



where  $z$  represents the oxidized state of iron in the film. Previous studies (6, 7) have shown that, in the solution at pH 6.48, the reaction for ferric oxide films proceeds with equivalent coulomb (current efficiency = 1) at a constant cathodic current of  $6.0 \mu A/cm^2$ . Figures 2, 3, and 4 show the amount of iron(II) ions dissolved,  $W_{Fe^{2+}}$ , along with the film thickness,  $L$ , as a function of cathodic charge passed. Reference lines in the figures correspond to stoichiometric iron oxides,  $z_{Fe} = +2.67$  ( $Fe_3O_4$ ) and  $z_{Fe} = +3.00$  ( $\gamma-Fe_2O_3$ ), and their slopes can be used as a reference for the oxidized state of the film. There are two regions where  $W_{Fe^{2+}}$  increases linearly with  $Q_c$  in the curve, corresponding to the deposit

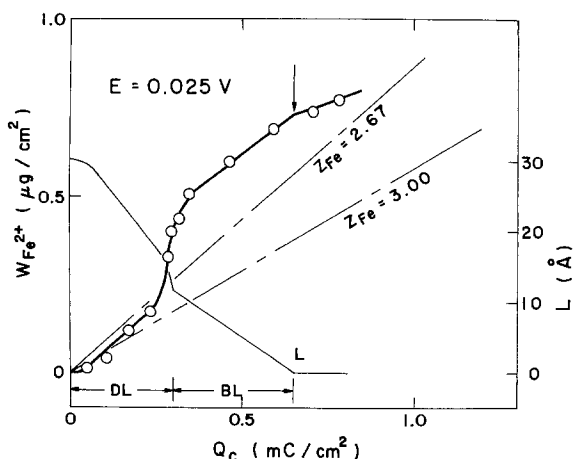


Fig. 2. Cathodic dissolution and thickness reduction curves of the passive film formed at +0.025V in potential region I in borate solution of pH 8.42.  $Q_c$  = cathodic charge passed during galvanostatic film reduction at pH 6.35.

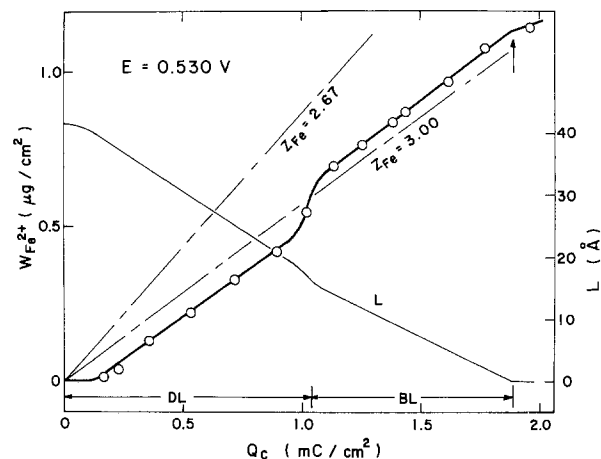


Fig. 3. Cathodic dissolution and thickness reduction curves of the passive film formed at +0.53V in potential region IIa.

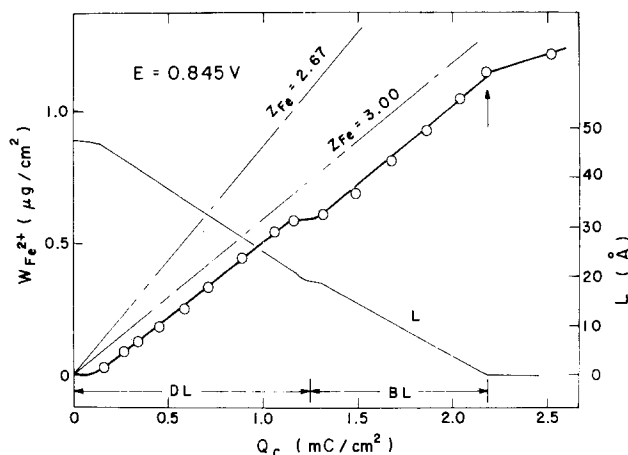


Fig. 4. Cathodic dissolution and thickness reduction curves of the passive film formed at +0.845V in potential region IIb.

layer and the barrier layer. From the slope of the curve, the oxidized state of iron in both layers can be estimated: the results are shown later (Fig. 6).

It is noticeable that the film dissolution curve is inflected with a distinct shift at the boundary between the deposit layer and the barrier layer. This shift, which varied depending on the potential of film formation, indicates that either excess iron ions or iron ion vacancies are concentrated at the barrier/deposit boundary. A discontinuous change at the boundary was also observed by light-intensity-following ellipsometry, as shown in Fig. 5, which illustrates the locus of two ellipsometric parameter  $\Delta$  and  $\Psi$  during the cathodic reduction of the film formed at different potentials.

The  $\Delta$ - $\Psi$  locus is in theory related to the optical constant and thickness of the film, and therefore can be used to determine the optical constant and thickness of the film. Computer calculations (12) were carried out, in which coulometric estimates of the film thickness were taken into account and the optical constant,  $n - ik$ , was limited to a range of  $n = 1.7 \sim 3.2$  and  $k = 0.0 \sim 1.0$ , within which all the optical constants of known iron oxides or hydroxides are found. It was thus estimated that the complex refractive index of the barrier layer was 2.50-0.14i in region I, 2.50-0.30i in region II, and 2.50-0.22i in the transpassive potential region. The index of the deposit layer could be estimated only roughly as 2.20-0.10i. The error involved in the layer thickness estimation was less than 10% for the barrier layer and about 20% for the deposit layer.

From the slope of  $W_{Fe^{2+}}-Q_c$  curves the mean ionic valency of iron,  $z_{Fe}$ , can be estimated for the barrier and deposit layers. Furthermore, the iron density,  $dW_{Fe}/dL$ ,

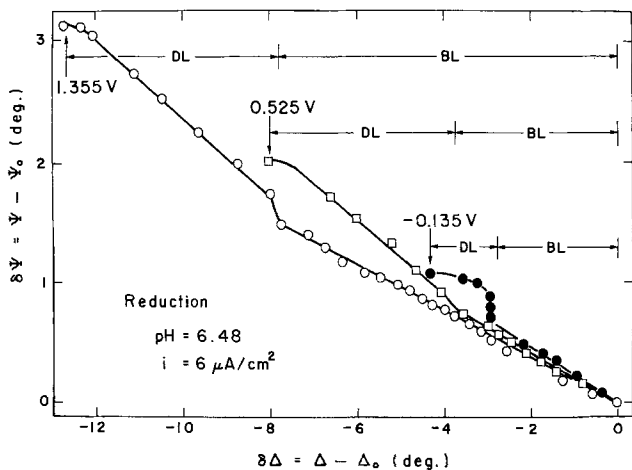
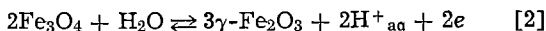


Fig. 5. Change in ellipsometric parameters  $\Delta$  and  $\Psi$  during cathodic dissolution at pH 6.48 of the passive films formed at  $-0.135$ ,  $+0.525$ , and  $+1.355$  V in borate solution at pH 8.42. The optical constant was  $3.01 - 3.47i$  for the cathodically reduced iron surface ( $\Delta_0, \Psi_0$ ) and  $1.336$  for the solution of pH 6.48.

in the layers can be obtained from the  $L-Q_c$  and  $W_{Fe}-Q_c$  curves during cathodic reduction:  $dW_{Fe}/dL = (dW_{Fe}/dQ_c)/(dL/dQ_c)$ . Figure 6 shows  $z_{Fe}$  and  $dW_{Fe}/dL$  in the two layers as a function of potential.

In the passive region II, the barrier layer was in the oxidized state of iron(III) and had an iron density equal to that of  $\gamma\text{-Fe}_2\text{O}_3$ . In the passive region I, however, it contained some amount of iron(II) in addition to iron(III). This may be attributed to the electrochemical thermodynamic stability of  $\gamma$ -iron(III) oxide and magnetite. The Flade potential, which separates region I from region II, has been explained as the equilibrium potential of the reaction (10, 13)



Magnetite is thermodynamically stable in region I and  $\gamma$ -iron(III) oxide in region II. Wagner (13) described  $\gamma$ -iron(III) oxide as an iron-deficient magnetite ( $\text{Fe}_{3-\Delta}\text{O}_4$ ) saturated with iron vacancies ( $\Delta = 1/3$ ) and explained the Flade potential as corresponding to a halfway ( $\Delta = 1/6$ ) between stoichiometric magnetite and iron-vacancy-saturated magnetite.

In the transpassive potential region where anodic iron dissolution was detectable, the barrier layer was again found to contain a little amount of iron(II) and, correspondingly, its iron density increased to a value close to that of magnetite. This is a fact which may agree with an electron diffraction analysis result obtained by Foley, Kruger, and Bechtoldt (14), who found a detectable amount of magnetite in the passive film

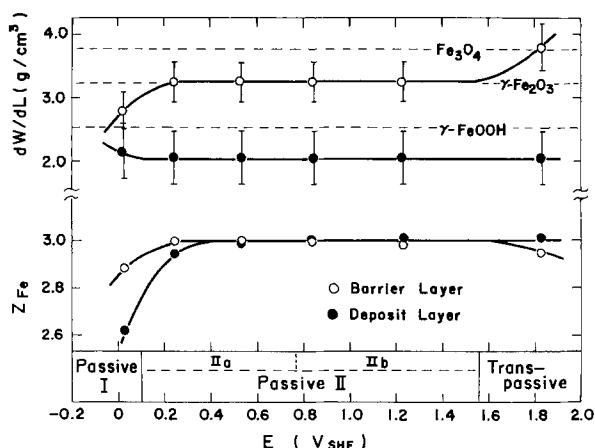


Fig. 6. Iron ion valency  $z_{Fe}$  and iron density  $dW_{Fe}/dL$  in the barrier and deposit layers as a function of potential.

formed in the potential region of oxygen evolution. This fact appears to contradict the thermodynamic stability of iron oxides that the oxidized state becomes higher as the potential is more noble. It should be mentioned, however, that the film is not in thermodynamic equilibrium, because of an appreciable dissolution current requiring a nonequilibrium iron transport through the transpassive surface film. A possible explanation is based on the transport ratio of iron ions and oxygen ions, which is likely to determine the nonequilibrium composition of the barrier layer. Further discussion will be reported elsewhere.

The deposit layer of hydrated iron(III) oxide exhibits no significant composition change in the whole range of potential, except for an absorption of iron(II) ions in region I. This may suggest that the deposit layer is formed by anodic oxidation of iron(II) ions dissolved in solution in an early stage of passivation



The anodic deposition film of this kind has recently been identified by Hashimoto and Cohen (15) as  $\gamma\text{-FeOOH}$ .

**Barrier/deposit boundary.**—As mentioned above, there was a shift in the cathodic dissolution curve of the film at the barrier/deposit boundary. There was also an induction period of film dissolution in an early stage of the cathodic reduction. No direct relationship, however, was found between the shift and the induction. The induction period requires a cathodic charge for polarizing the passive film to the potential where the film dissolution occurs, and therefore may represent the apparent electrical capacity of the film, whatever the mechanism may be. The shift, on the other hand, can be considered as an indication of excess iron ions or iron ion vacancies that concentrate at the barrier/deposit boundary. This shift was therefore determined quantitatively in terms of the amount of iron, and is plotted as a function of potential in Fig. 7. It is thus seen that the boundary composition changed from iron ion excess to iron ion deficiency as the potential was more noble. Schematic depth profiles of iron in the passive film formed in four different potential regions are also shown in Fig. 7. The passive region II may be divided into two regions, region IIa with excess iron ions and region IIb with iron ion vacancies at the barrier/deposit boundary.

It is worth showing that the barrier/deposit boundary composition is not a reversible function of potential but differs with different processes of film formation. Figure 8 illustrates in thickness and schematic composition depth profile the difference that arose between the film formed at  $+0.245$  V for 1 hr and the film first formed at  $+0.845$  V for 1 hr and then polarized to  $+0.245$  V for another hour. The film formed at  $+0.845$  V

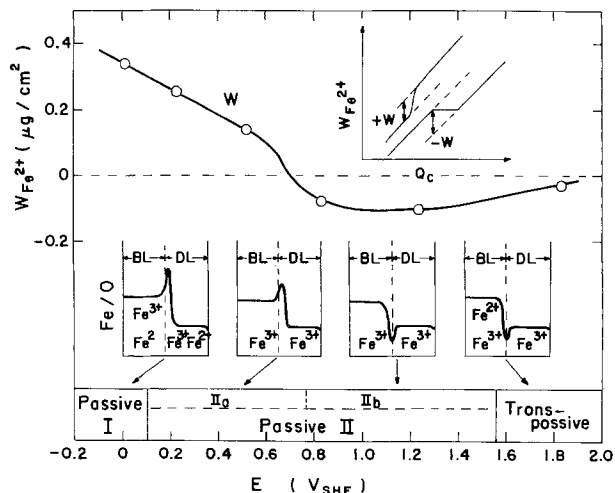


Fig. 7. Iron excess or deficiency at the barrier/deposit boundary as a function of potential.

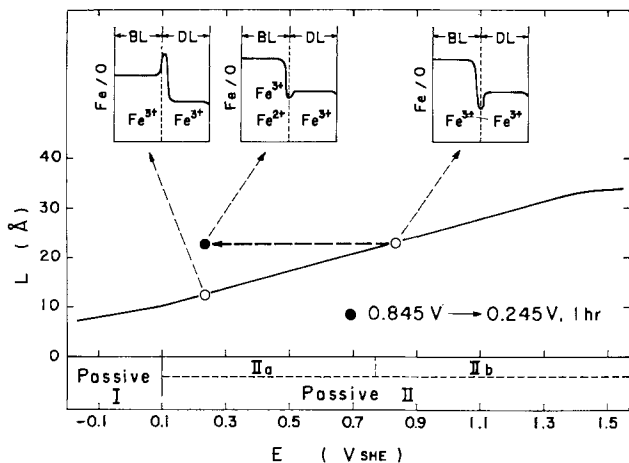
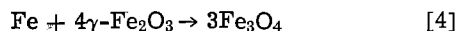


Fig. 8. Barrier layer thickness and schematic depth profile of the passive film formed at +0.245V 1 hr, the film formed at +0.845V 1 hr, and the film first formed at +0.845V 1 hr followed by 1 hr aging at +0.245V.

and aged at +0.245V had iron ion vacancies at the barrier/deposit boundary, as contrasted with excess iron ions concentrated at the boundary in the film fresh formed at +0.245V.

It should also be noted that the aging at +0.245V of the film formed at +0.845V caused the barrier layer, which was iron(III) oxide before aging, to contain a small amount of iron(II) ions. This aging effect can probably be explained as resulting from a diffusion of iron through the barrier layer, i.e., an oxide conversion proposed by Sato and Cohen (16)



**Potentiostatic film growth.**—The passive film was grown at constant potential for different periods of time in the solution of pH 8.42, and then the depth analysis of the film was carried out by galvanostatic-cathodic reduction at pH 6.35. Figure 9 shows the thickness and the iron ion valency of the barrier and deposit layers as a function of time during the film growth at a constant potential in region II. Evidently, it is the barrier layer that grew in thickness and the deposit layer remained practically unchanged. This is a fact which one should bear in mind when studying the film growth kinetics in the passive potential region. Notice also that the barrier layer changed from  $z_{\text{Fe}} < +3$  in an early stage to  $z_{\text{Fe}} = +3$  in the later stage of film growth.

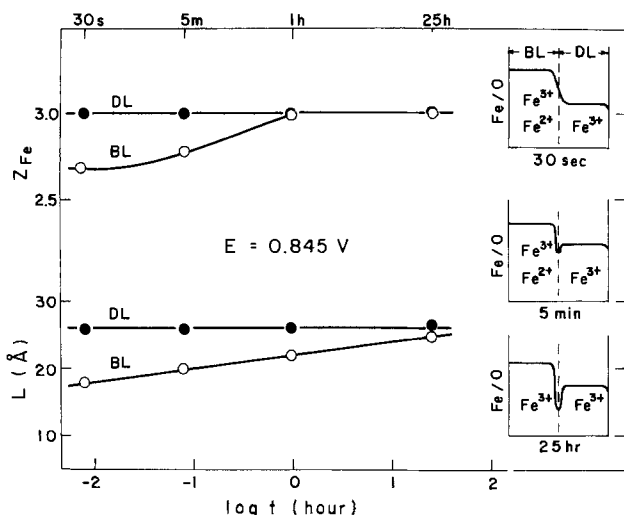
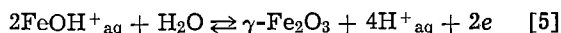


Fig. 9. Thickness, iron ion valency, and schematic depth profile of the passive film as a function of time of potentiostatic film growth in potential region II.

The composition change that occurred at the barrier/deposit boundary is also schematically illustrated in Fig. 9. Excess iron ions initially accumulated at the barrier/deposit boundary are gradually replaced by iron ion vacancies in the later stage. This may probably be attributed to the electrified double layer structure that forms at the barrier/deposit boundary, but the mechanism remains unclear in detail.

The film growth is somewhat different in the passive I region from that in the passive II region. Figure 10 shows the film growth process that occurred in region I. Notice that the iron ion valency changed in both the barrier layer and the deposit layer. The barrier layer, which was iron(III) oxide in an early growth stage, gradually changed in composition to iron(II-III) mixed oxide with more iron(II) than in magnetite after an extended period of time. In this potential region, magnetite is thermodynamically more stable than  $\gamma$ -iron(III) oxide according to reaction [2], while  $\gamma$ -iron(III) oxide is also stable when the iron(II) ion concentration in the solution exceeds the equilibrium concentration with the following reaction



It is therefore suggested from the results that in the passive region I, the barrier layer is formed initially by reaction [5] in the presence of iron(II) ions and then undergoes a transformation from  $\gamma$ -iron(III) oxide to magnetite by reaction [2] or [4]. During the oxide conversion a gradual increase in thickness of the barrier layer was observed.

The deposit layer was also observed to grow in thickness while undergoing a compositional change from iron(II-III) mixed hydroxide toward iron(III) hydroxide. This may be explained by the following reactions simultaneously taking place in region I:  $\text{FeOH}^+_{\text{aq}} + \text{H}_2\text{O} \rightarrow \text{Fe}(\text{OH})_2 + \text{H}^+_{\text{aq}}$ ,  $\text{Fe}(\text{OH})_2 \rightarrow \text{FeOOH} + \text{H}^+_{\text{aq}} + e$ , and  $\text{FeOH}^+_{\text{aq}} + \text{H}_2\text{O} \rightarrow \text{FeOOH} + 2\text{H}^+_{\text{aq}} + e$ .

## Conclusions

The galvanostatic cathodic reduction technique employing appropriate solution and current density provides a depth profiling analysis of the passive film on iron.

The potential region of iron passivity in borate solution at pH 8.42 may be divided by the Flade potential into two regions, I and II, with which the passive barrier layer changes in composition and refractive index.

In region I, the barrier layer was an iron(II-III) mixed oxide and its thickness for unit voltage at steady state was 1.54 nm/V ( $6.5 \times 10^6$  V/cm). In region II, it was an iron(III) oxide [probably  $\gamma$ -iron(III) oxide] with thickness 1.75 nm/V ( $5.7 \times 10^6$  V/cm).

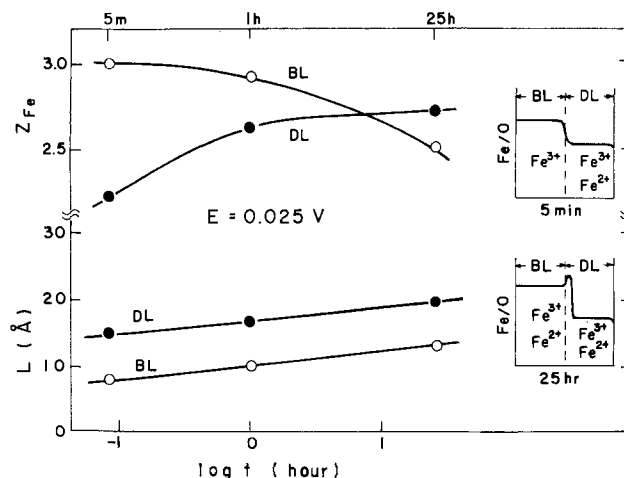


Fig. 10. Thickness, iron ion valency, and schematic depth profile of the film as a function of time of potentiostatic film growth in potential region I.

Transpassivation caused the barrier layer to cease growing with rise of potential and to reduce its oxidized state to less than  $\alpha_{Fe} = +3$ .

The deposit layer, which was always formed on the barrier layer, was a hydrated iron(III) oxide (probably  $\gamma$ -FeOOH) and exhibited no significant composition change with potential, except for an absorption of iron(II) ions in region I.

There was a peak or a decrease in iron ion concentration at the barrier/deposit boundary in the depth profile of the film. At relatively less noble potentials the boundary adsorbed excess iron ions, which were gradually replaced by iron ion vacancies as the potential was more noble.

It is the barrier layer alone that increased in thickness during the growth of the passive film in the potential region II.

### Acknowledgments

The authors wish to thank the Ministry of Education of Japan who provided finance with the ellipsometer and awarded Science Research Grants in 1972-1973.

Manuscript submitted March 19, 1976; revised manuscript received ca. June 8, 1976.

Any discussion of this paper will appear in a Discussion Section to be published in the June 1977 JOURNAL. All discussions for the June 1977 Discussion Section should be submitted by Feb. 1, 1977.

Publication costs of this article were assisted by Hokkaido University.

### REFERENCES

1. N. Sato, K. Kudo, and T. Noda, *Z. Phys. Chem. N.F.*, **98**, 271 (1975).
2. N. Sato, *Corros. Eng. (Tokyo) (Boshoku Gijutsu)*, **23**, 535 (1974).
3. N. Sato, T. Noda, and K. Kudo, *Electrochim. Acta*, **19**, 471 (1974); Proc. 5th International Congress on Metallic Corrosion, Tokyo, 1972, 218 NACE (1975).
4. T. Noda, K. Kudo, and N. Sato, *J. Jpn. Inst. Met.*, **37**, 951 (1973).
5. N. Sato and K. Kudo, *Electrochim. Acta*, **16**, 447 (1971).
6. N. Sato, K. Kudo, and T. Noda, *ibid.*, **16**, 1909 (1971).
7. R. Nishimura, K. Kudo, and N. Sato, *J. Electrochem. Soc. Jpn. (Denki Kagaku)*, **44**, 198 (1976); *ibid.*, **44**, No. 10, in press (1976).
8. R. Nishimura, K. Kudo, and N. Sato, *Corros. Eng. (Tokyo) (Boshoku Gijutsu)*, **25**, 83 (1976).
9. R. Nishimura, K. Kudo, and N. Sato, *J. Jpn. Inst. Met.*, **40**, 118 (1976).
10. H. Göhr and E. Lange, *Z. Elektrochem.*, **61**, 1929 (1952).
11. T. Noda, Dissertation, Hokkaido University (1972).
12. K. Kudo and N. Sato, *Bull. Faculty of Eng., Hokkaido Univ.*, No. 61, p. 45 (1971).
13. C. Wagner, *Ber. Bunsenges. Phys. Chem.*, **77**, 1090 (1973).
14. C. L. Foley, J. Kruger, and C. J. Bechtoldt, *This Journal*, **114**, 994 (1976).
15. K. Hashimoto and M. Cohen, *ibid.*, **121**, 37 (1974).
16. N. Sato and M. Cohen, *ibid.*, **111**, 624 (1964).

## Current and Potential Distributions in Plating Corrosion Systems

William H. Smyrl\*

Sandia Laboratories, Albuquerque, New Mexico 87115

and John Newman\*

Materials and Molecular Research Division, Lawrence Berkeley Laboratory, and  
Department of Chemical Engineering, University of California, Berkeley, California 94720

### ABSTRACT

The numerical determination of current and potential distributions has been performed for plating corrosion systems, where failure to coat a small area leads to corrosion at the pinhole. The distributions depend on characteristic parameters for the disk anode and surrounding plane cathode and reveal that each of the electrodes influences the other due to their proximity. The results were applied to an array of disks, and it was found that the corrosion potential of the system is a linear function of the area ratio of anode to cathode when ohmic effects are important. This may be contrasted to the logarithmic dependence found when ohmic effects are neglected. Other applications are discussed.

The protection of active metals by electroplated noble metals has been an established practice for many years. In the electronics industry, for example, copper is protected by plating gold over the substrate. In order to minimize costs, the thickness of the gold coating is reduced as much as possible, and this introduces pores in the overplate. These pores will permit corrosion of the underlying copper substrate, and if there is a cathodic reaction on the gold, the corrosion of copper will actually be enhanced because of galvanic effects. Therefore, one seeks the minimum thickness of the gold electroplate which will adequately eliminate corrosion.

Several techniques have been introduced to determine the porosity of the electroplate for various plat-

ing thicknesses. Chemical etch techniques for the copper-gold system (1, 2) decorate the pores and permit them to be counted by microscopic techniques. The measurement of anodic current in a system where the gold is completely inert and only copper is active has been very successful (2, 3) in determining the total surface area of copper exposed in pores, but it does not reveal the distribution of pores nor their size on electroplated pieces. A similar technique (4-7) is the determination of resistance when an electroplated specimen is polarized under potentiostatic control. Finally, measurement of the corrosion potential for the galvanic couple, substrate/coat, has been proposed (8-11) as a technique to measure the ratio of areas of the two metals. We have chosen this final technique for further discussion and study here.

Galvanic corrosion, in this case the corrosion of an active metal in a pore driven by a cathodic reaction

\* Electrochemical Society Active Member.  
Key words: corrosion, porous coatings, current distribution, potential distribution, corrosion potential, electrode interaction.

on the surrounding noble electroplate, is a complex phenomenon which may involve electrode-kinetic effects on both the anode and cathode, mass-transfer effects, and ohmic effects. In addition, the proximity of the two "electrodes" in plating corrosion can lead to interaction effects not normally seen on separated electrodes.

Stern (9) first derived the relationship between the area ratio of a galvanic couple and its corrosion potential. The development was based on the assumptions that the electrochemical reaction kinetics on each electrode were of the Tafel form and that the respective reactions were uniform on the anode and cathode of the couple. This development does not take into account ohmic effects in the solution. The relationship derived is (9)

$$\eta_{\text{corr}} = -\frac{E_a \beta_c}{\beta_c + \beta_a} - \frac{\beta_c \beta_a}{\beta_c + \beta_a} \ln(A_a i_{ac}) + \frac{\beta_c \beta_a}{\beta_c + \beta_a} \ln(A_c i_{oc}) \quad [1]$$

where  $\beta$  = Tafel slope of the respective reaction,  $i_o$  = exchange current density of the respective reaction,  $A_a$  = area fraction of anode,  $A_c$  = area fraction of cathode,  $\eta_{\text{corr}}$  = corrosion potential of the couple relative to the reversible potential of the cathode, and  $E_a$  = standard reversible potential of the anode with respect to the reversible potential of the cathode. Thus it may be seen that the corrosion potential has a logarithmic dependence on the area ratio  $A_a/A_c$ , with a slope of  $-\beta_c \beta_a / (\beta_c + \beta_a)$ . Stern (9) notes that this equation is not valid in the limit that  $A_a$  or  $A_c$  approaches 1.

Oldham and Mansfeld (11) recently extended this treatment to include both an oxidation reaction and reduction reaction on the cathode of the couple. Their development again does not take ohmic effects into account, but they do treat the case of diffusion control on the cathode.

Mansfeld has also treated other special cases (12) including that for diffusion control on both anode and cathode. For this case, the "catchment principle" is derived, i.e., the corrosion potential is found to be linearly related to the area ratio for the galvanic couple.

Levich and Frumkin (13) treated a system of a cathodic disk in a surrounding anodic plane, which is the reverse of the system to be treated here. The current density on the small disk was uniform, and the potential of the surrounding plane was uniform (i.e., completely reversible kinetics on the plane). This treatment specifically includes ohmic effects in solution. More recently, McCafferty (14) has presented an analysis of current and potential distribution for an anodic disk in a surrounding cathodic plane, using an assumed linear form for the electrode kinetics on the disk and plane. This treatment also includes the effect of ohmic resistance in solution.

The present contribution describes the general analysis of current and potential distribution for an anodic disk in a cathodic plane. General mathematical expressions for the electrode kinetics are employed, which reduce to the special treatments listed above as limiting cases. This analysis also provides a systematic treatment of the effect of the proximity of the electrodes on the current and potential distribution of each electrode. The broader understanding of galvanic corrosion in this simple system then allows one to predict the behavior of arrays of disks, and therefore the influence of porosity of the electroplate on the corrosion potential of the couples.

### Mathematical Treatment

The system to be studied here is illustrated in Fig. 1. The anodic disks are distributed randomly on the surface, are coplanar with the surrounding plane, and are all of the same radius,  $r_d$ . They are also assumed to be far apart. The effect of recessing the pores is dis-

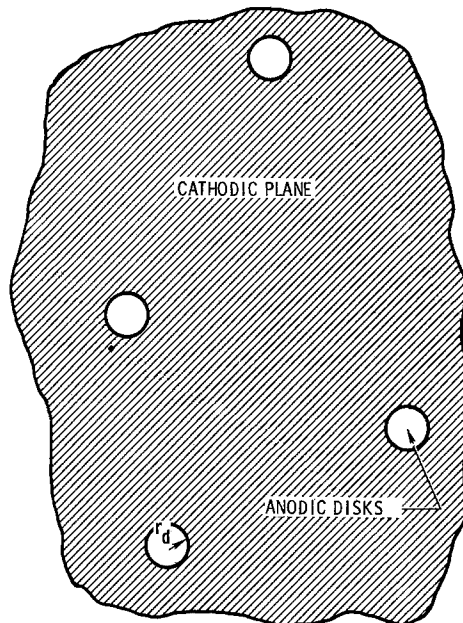


Fig. 1. Corroding disks in a cathodic surrounding plane

cussed briefly, but a detailed study will be treated in a later paper.

The current and potential distributions in an electrochemical system may be determined mathematically by solving Laplace's equation

$$\nabla^2 \phi = 0 \quad [2]$$

subject to boundary conditions on the electrodes imposed by the kinetics of the reactions occurring there. Electrodes with highly reversible reactions have a constant-potential boundary condition everywhere on the surface since polarization causes an ohmic potential drop in solution without changing the surface potential of the electrode. The current and potential distributions on an electrode with this boundary condition depend on geometric ratios for the system, but do not depend on the absolute size. Boundary conditions suitable for slower reactions cause the current and potential distribution to depend on an absolute length of the electrode, as well as the geometric ratios characteristic of a purely ohmically determined distribution. Also, it is shown below that the distribution on one electrode depends on the distribution on the counterelectrode as well when the electrodes are near one another.

For the analysis which follows, attention is focused on one disk first, and the array of disks is treated later. The origin of the coordinate system is chosen as the center of the disk. Radial distance,  $r$ , is measured from the axis of the disk, parallel to the surface. The distance,  $z$ , is measured normal to the surface. We choose the rotational elliptic coordinate system, which has been shown (15, 16) to be especially suitable for disk geometries and is related to the coordinates  $r$ ,  $z$ , by

$$z = r_d \eta \xi \quad [3]$$

$$r/r_d = [(1 + \xi^2)(1 - \eta^2)]^{1/2} \quad [4]$$

where  $r_d$  is the disk radius. The disk in a surrounding plane is now described geometrically in rotational elliptic coordinates as shown in Fig. 2. The disk electrode is at  $\xi = 0$ , and its axis is  $\eta = 1$ . The surrounding plane is located at  $\eta = 0$ . The plane  $\xi = \xi_{\text{max}}$  is far from the disk and in cylindrical coordinates is approximately a hemisphere in the solution which intersects the surrounding plane at a radial distance  $r_{\text{max}}$ .

Laplace's equation in this coordinate system is (16)

$$(1 - \eta^2) \frac{\partial^2 \phi}{\partial \eta^2} + (1 + \xi^2) \frac{\partial^2 \phi}{\partial \xi^2} + 2\xi \frac{\partial \phi}{\partial \xi} - 2\eta \frac{\partial \phi}{\partial \eta} = 0 \quad [5]$$

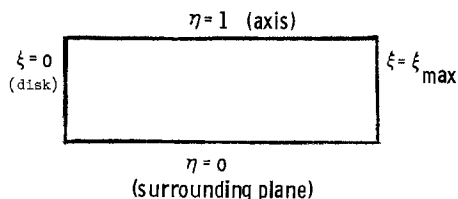


Fig. 2. The disk-plane system in rotational elliptic coordinates

and is to be solved subject to the boundary conditions (where  $\kappa$  is the conductivity of the electrolytic solution)

(a) on the disk,  $\xi = 0$

$$i_d = -\frac{\kappa}{r_d \eta} \frac{\partial \phi}{\partial \xi} \Big|_{\xi=0} \quad [6]$$

$$= i_{od} \left[ \exp \left\{ \frac{\alpha_{ad} \mathbf{F}}{RT} (V_d - \phi^{\circ}_d - E^{\circ}_d) \right\} - \exp \left\{ \frac{-\alpha_{cd} \mathbf{F}}{RT} (V_d - \phi^{\circ}_d - E^{\circ}_d) \right\} \right] \quad [7]$$

(b) on the surrounding plane,  $\eta = 0$

$$i_p = -\frac{\kappa}{r_d \xi} \frac{\partial \phi}{\partial \eta} \Big|_{\eta=0} \quad [8]$$

$$= i_{op} \left[ \exp \left\{ \frac{\alpha_{ap} \mathbf{F}}{RT} (V_p - \phi^{\circ}_p - E^{\circ}_p) \right\} - \exp \left\{ \frac{-\alpha_{cp} \mathbf{F}}{RT} (V_p - \phi^{\circ}_p - E^{\circ}_p) \right\} \right] \quad [9]$$

(c)  $\phi$  well-behaved at  $\eta = 1$

(d) at  $\xi = \xi_{\max}$  two different boundary conditions were employed, i.e.

$$* \frac{\partial \phi}{\partial \xi} = 0 \quad \text{at} \quad \xi = \xi_{\max} \quad [10]$$

$$* \frac{\partial \phi}{\partial \xi} = -\frac{2\phi}{\xi_{\max}} \left\{ \frac{P_1(\eta) + \frac{3P_2(\eta)}{\xi_{\max} P_2(0)} J_p}{P_1(\eta) + \frac{2P_2(\eta)}{\xi_{\max} P_2(0)} J_p} \right\} \quad [11]$$

Equation [10] would be appropriate for an insulating surface at  $\xi_{\max}$ , and Eq. [11] is an approximation to the derivative at  $\xi_{\max}$  when the solution actually extends to infinity. In the latter case, the potential  $\phi$  is measured relative to the reversible or open-circuit potential for the surrounding plane. The quantity  $(V - \phi^{\circ} - E^{\circ})$  in Eq. [7] and [9] is the surface overpotential for the respective reaction (16), and  $\phi^{\circ}$  is the potential in solution at the electrode surface. The derivation of Eq. [11] is given in Appendix A.

The Butler-Volmer relationship for kinetics on an electrode is given by Eq. [7] or [9]. For corrosion systems where simultaneous reactions occur on a homogeneous surface, such a relationship would be appropriate for each reaction. Polarization of a reaction far from its reversible potential  $E^{\circ}$  will cause one term of the relationship to dominate, and the polarization is said to be in the Tafel region. For two different reactions occurring simultaneously, one anodic and one cathodic on the same surface, one has for Tafel polarization

$$i_{\text{anodic}} = i_{oa} \exp \left[ \frac{\alpha_a \mathbf{F}}{RT} (V - \phi^{\circ}_a - E^{\circ}_a) \right]$$

and

$$i_{\text{cathodic}} = -i_{oc} \exp \left[ \frac{-\alpha_c \mathbf{F}}{RT} (V - \phi^{\circ}_c - E^{\circ}_c) \right]$$

Following Wagner and Traud (17), the local (net) current density at a point on the surface is the sum of the current density for each reaction, i.e.

$$i_{\text{net}} = i_{\text{anodic}} + i_{\text{cathodic}} \\ = i_{oa} \exp \left[ \frac{\alpha_a \mathbf{F}}{RT} (V - \phi^{\circ} - E^{\circ}_a) \right] - i_{oc} \exp \left[ \frac{-\alpha_c \mathbf{F}}{RT} (V - \phi^{\circ} - E^{\circ}_c) \right]$$

For zero net current

$$i_{\text{anodic}} = -i_{\text{cathodic}}$$

or

$$i_{oa} \exp \left[ \frac{\alpha_a \mathbf{F}}{RT} (V - \phi^{\circ} - E^{\circ}_a) \right] = i_{oc} \exp \left[ -\frac{\alpha_c \mathbf{F}}{RT} (V - \phi^{\circ} - E^{\circ}_c) \right] \\ = i_{\text{corr}}$$

where  $i_{\text{corr}}$  is the corrosion current density at the mixed or corrosion potential.  $U_{\text{corr}}$  is the corrosion potential identified as

$$U_{\text{corr}} \left[ \frac{\alpha_a \mathbf{F}}{RT} + \frac{\alpha_c \mathbf{F}}{RT} \right] = -\ln \frac{i_{oa}}{i_{oc}} - \frac{\alpha_a \mathbf{F}}{RT} E^{\circ}_a - \frac{-\alpha_c \mathbf{F}}{RT} E^{\circ}_c$$

which is identical to Eq. [1] when  $E^{\circ}_c$  is zero. The expression for the net current may now be written

$$i_{\text{net}} = i_{\text{corr}} \left\{ \exp \left[ \frac{\alpha_a \mathbf{F}}{RT} (V - \phi^{\circ} - U_{\text{corr}}) \right] - \exp \left[ \frac{-\alpha_c \mathbf{F}}{RT} (V - \phi^{\circ} - U_{\text{corr}}) \right] \right\}$$

This expression for the net current is similar to Eq. [7] or [9] where  $i_o$  is replaced by  $i_{\text{corr}}$  and  $E^{\circ}$  is replaced by  $U_{\text{corr}}$ . Therefore, Eq. [7] may be written for a corroding disk as

$$i_d = i_{\text{corr},d} \left\{ \exp \left[ \frac{\alpha_{ad} \mathbf{F}}{RT} (V_d - \phi^{\circ}_d - U_{\text{corr},d}) \right] - \exp \left[ \frac{-\alpha_{cd} \mathbf{F}}{RT} (V_d - \phi^{\circ}_d - U_{\text{corr},d}) \right] \right\} \quad [12]$$

For a corroding plane

$$i_p = i_{\text{corr},p} \left\{ \exp \left[ \frac{\alpha_{ap} \mathbf{F}}{RT} (V_p - \phi^{\circ}_p - U_{\text{corr},p}) \right] - \exp \left[ \frac{-\alpha_{cp} \mathbf{F}}{RT} (V_p - \phi^{\circ}_p - U_{\text{corr},p}) \right] \right\} \quad [13]$$

The boundary conditions [12] and [13] along with the expressions for the current in solution at the electrode surfaces yield the characteristic "polarization parameters" for the problem (18). First we have the ratios of the transfer coefficients  $\alpha_{ad}/\alpha_{cd}$  and  $\alpha_{ap}/\alpha_{cp}$ . For all the calculations reported here, it has been assumed that these ratios are both unity, that is, that the cathodic Tafel slope equals the anodic Tafel slope for either the disk or the plane. Following Newman (18), we identify the additional polarization parameters as

$$J_d = \frac{i_{\text{corr},d} (\alpha_{ad} + \alpha_{cd}) \mathbf{F} r_d}{\kappa RT} \quad [14]$$

and

$$\delta_d = \frac{|i_{\text{avg},d}| \alpha_{ad} \mathbf{F} r_d}{\kappa RT} \quad [15]$$

for the disk and

$$J_p = \frac{i_{\text{corr,p}}(\alpha_{\text{ap}} + \alpha_{\text{cp}})F r_d}{\kappa RT} \quad [16]$$

for the plane. These three quantities all represent ratios of the ohmic potential drop (of order  $i_{\text{avg}} r_d / \kappa$ ) to the surface overpotential. The quantities  $J_d$  and  $J_p$  contain  $i_{\text{corr}}$  and are especially relevant in a potential range where the corresponding Eq. [12] or [13] can be linearized. The quantity  $\delta_d$  is especially relevant when the Eq. [12] can be approximated by a Tafel expression. With retention of the full forms of Eq. [12] and [13], all these dimensionless parameters can have some influence on the current and potential distributions. The parameter  $J_p$  for the plane involves  $r_d$  since this is the only characteristic dimension. Since the total current on the anode must be equal in magnitude to the total cathodic current, there is no additional parameter, like  $\delta_d$ , for the plane. If a net current were being imposed on the disk-plane system by a third electrode, then there would be a total of six parameters for the disk and the plane.

For large values of  $J_d$  and  $\delta_d$ , the current distribution on the disk becomes highly nonuniform and approaches the ohmically determined distribution (uniform potential on the electrode). For small values of these parameters, the current distribution is controlled by the kinetics and becomes uniform.

By the method of separation of variables, one can write the general solution of Eq. [5] as

$$\phi = \sum_{n=1}^{\infty} B_n P_n(\eta) M_n(\xi) \quad [17]$$

where  $P_n$  is the Legendre polynomial and  $M_n$  is the Legendre function of imaginary argument (15). The solution for the present problem involves both odd and even orders in both  $P_n$  and  $M_n$ , and this prevents one from obtaining an orthogonality relationship to calculate the  $B$  coefficients in the infinite series. Equation [17] is not very useful for this reason, and it is necessary to seek another means to solve Eq. [5] for the present study. It has been found that the numerical solution of Eq. [5] by finite difference techniques provides very satisfactory results. The remainder of this paper is devoted to the discussion of this technique and the results obtained.

As an aside, it is noted that Levich and Frumkin (13) found that only the first term of Eq. [17] was needed to solve the problem they treated. From the form of the first few terms in Eq. [17], it is expected that the dominant term for large values of  $\xi$  (far from the disk) is the first term. This leads one to expect that the present results should show parallel behavior to the results of Levich and Frumkin (13) at large values of  $\xi$ . These authors found

$$B_1 = \frac{2i_d r_d}{\pi \kappa}$$

and thus

$$\phi = \frac{2i_d r_d}{\pi \kappa} \eta (\xi \cot^{-1} \xi - 1) \quad [18]$$

where  $i_d$  is the (uniform) current density on the disk. This result provides a convenient basis for comparison for our results and a means of calculating the contribution of an individual pore to the potential detected by a distant reference electrode (the measured corrosion potential). See also Appendix A which discusses the asymptotic behavior of the potential distribution when electrode-kinetics on the surrounding plane is not ignored.

### Numerical Analysis

Following Klingent, Lynn, and Tobias (19) and Fleck (20), we use the five-point, central difference approximation to obtain Laplace's equation in finite difference form

$$\begin{aligned} \phi_o &= \left[ \frac{2(1 - \eta_o^2)}{h_\eta^2} + \frac{2(1 + \xi_o^2)}{h_\xi^2} \right] \\ &= \phi_1 \left[ \frac{1 + \xi_o^2}{h_\xi^2} + \frac{\xi_o}{h_\xi} \right] + \phi_2 \left[ \frac{1 - \eta_o^2}{h_\eta^2} - \frac{\xi_o}{h_\xi} \right] \\ &+ \phi_3 \left[ \frac{1 + \xi_o^2}{h_\xi^2} - \frac{\xi_o}{h_\xi} \right] + \phi_4 \left[ \frac{1 - \eta_o^2}{h_\eta^2} + \frac{\eta_o}{h_\eta} \right] \quad [19] \end{aligned}$$

where  $h_\xi$  and  $h_\eta$  are mesh spacings as defined in Fig. 3. This equation is solved for  $\phi_o$  and is identified as  $\phi_{o,\text{try}}$ . A new value of  $\phi_o$  is calculated by

$$\phi_{o,\text{new}} = \phi_{o,\text{old}} + \Omega(\phi_{o,\text{try}} - \phi_{o,\text{old}})$$

where  $\Omega$  is the overrelaxation factor. This value of  $\phi_{o,\text{new}}$  is used in the calculation of  $\phi$  for adjacent points. All the interior points in the space are treated this way for one iteration, and the iteration procedure is repeated until  $\phi$  converges to within some error limit at each point. The procedure outlined above is the Liebmann (Gauss-Siedel) iteration procedure with successive overrelaxation.

At boundary points on the electrodes, use of the five-point central difference technique produces "image" points outside the physical space. These image points are eliminated by using the boundary conditions [6] and [8] along with [12] and [13] (or [7] and [9]), expressed in finite difference form. This yields on the plane electrode

$$\begin{aligned} \phi_o &= \left[ \frac{2(1 - \eta_o^2)}{h_\eta^2} + \frac{2(1 + \xi_o^2)}{h_\xi^2} \right] \\ &= 2\phi_2 \left( \frac{1 - \eta_o^2}{h_\eta^2} \right) + \phi_1 \left[ \frac{1 + \xi_o^2}{h_\xi^2} + \frac{\xi_o}{h_\xi} \right] \\ &+ \phi_3 \left[ \frac{1 + \xi_o^2}{h_\xi^2} - \frac{\xi_o}{h_\xi} \right] + 2\xi_o h_\eta F_p \left[ \frac{1 - \eta_o^2}{h_\eta^2} + \frac{\eta_o}{h_\eta} \right] \quad [20] \end{aligned}$$

where

$$F_p = \frac{r_d}{\kappa} i_{\text{corr,p}} \left\{ \exp \left[ \frac{\alpha_{\text{ap}} F}{RT} (V_p - \phi_p - U_{\text{corr,p}}) \right] - \exp \left[ \frac{-\alpha_{\text{cp}} F}{RT} (V_p - \phi_p - U_{\text{corr,p}}) \right] \right\}$$

A similar relationship is obtained for boundary points

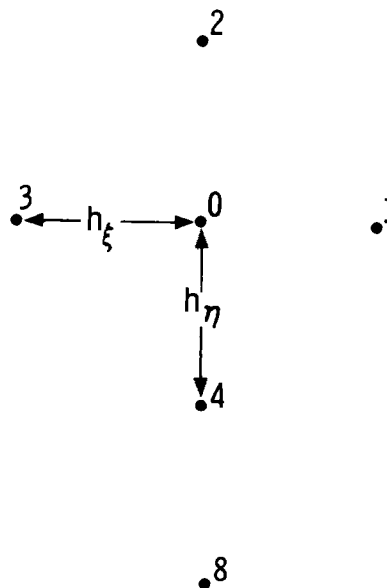


Fig. 3. Relationship of the mesh points and mesh distances  $h_\xi$  and  $h_\eta$ .

on the disk. Equation [20] is a nonlinear equation in  $\phi_p$ . The treatment of these nonlinear boundary conditions is discussed in more detail in Appendix B. For convenience,  $U_{\text{corr},p}$  was taken to be zero for the calculations.

The boundary at  $\eta = 1$  was treated by dropping the term

$$(1 - \eta^2) \frac{\partial^2 \phi}{\partial \eta^2}$$

from Eq. [5] and using backward difference relations in  $\eta$ , central differences in  $\xi$ , to obtain

$$\begin{aligned} \phi_0 \left[ \frac{2(1 + \xi_0^2)}{h_\xi^2} + \frac{3}{h_\eta} \right] &= \phi_1 \left[ \frac{1 + \xi_0^2}{h_\xi^2} + \frac{\xi_0}{h_\xi} \right] \\ &+ \phi_3 \left[ \frac{1 + \xi_0^2}{h_\xi^2} - \frac{\xi_0}{h_\xi} \right] + \phi_4 \left[ \frac{4}{h_\eta} \right] - \phi_8 \left[ \frac{1}{h_\eta} \right] \end{aligned} \quad [21]$$

where the points are identified on Fig. 3. The iteration procedure and successive overrelaxation used for these boundary points were similar to that employed for the interior points.

The boundary at  $\xi = \xi_{\text{max}}$  was treated with two different boundary conditions. The boundary condition expressed by Eq. [10] was used to simulate the situation which would be encountered for a single disk in a plane with an insulating surface at  $\xi_{\text{max}}$ . The boundary points were treated in the same way as interior points, and the image points were eliminated by using Eq. [10] in finite difference form. The iteration procedure and successive overrelaxation for these points were the same as for interior points. The boundary condition expressed by Eq. [11] was used to obtain results which could be used with multiple disks in the plane. The relationship [11] was expressed in finite-difference form to eliminate image points, and the iteration procedure and successive overrelaxation were used as before. For large values of  $\xi_{\text{max}}$ , both boundary conditions give essentially identical results for the potential and current distribution on and near the disk. The results differ in the region near  $\xi_{\text{max}}$  where boundary condition [10] causes the current density on the plane to be higher near  $\xi_{\text{max}}$  than does [11], for the same total current to the disk. This is discussed in more detail below.

### Results and Discussion

The results which have been obtained are rather complex. In order to discuss them clearly and concisely, the presentation of the results is divided into four parts. In the first part, the general behavior is discussed with particular emphasis on accuracy and the influence of boundary conditions. Following this is the description of the calculated current and potential distributions as influenced by system parameters. The third part discusses the implications of these results for disk arrays, and the final part presents other applications.

*General.*—The finite-difference technique used here was found to be efficient, fast, and accurate for determining the current and potential distribution on the disk and plane. The use of overrelaxation and successive iteration procedures discussed earlier reduces the computational time required for convergence as compared to other iteration procedures without overrelaxation [see Fleck (20)]. Iteration was concluded when all points in the domain changed less than a given error limit for two successive iterations. Accuracy was assumed adequate when (i) reducing the error limit caused a change of less than 0.1%, and (ii) doubling the number of mesh points in each direction caused a change of less than 0.1%. Finally, calculations were made for the disk-insulating plane system discussed by Newman (15), and the uniform disk-reversible plane system discussed by Levich and Frumkin (13). It was possible to achieve agreement with both cases

to within 0.1%. Therefore, it is believed that the results presented here are accurate to 0.1%, unless otherwise noted.

In general, the current density on the disk and plane is larger in absolute magnitude near the edge of the disk than elsewhere. The effect of slow kinetics, small size, and high conductivity is to reduce this nonuniformity. In the limit of uniform current density on both the disk and surrounding plane, the system behavior should approach that described by Stern (9) and Oldham and Mansfield (11).

The use of the insulator boundary condition, Eq. [10], forces the total current on the plane to be equal in magnitude to the total current on the disk. These results would be useful for studies of galvanic corrosion of a single disk in a surrounding plane, with an insulator surface at  $\xi_{\text{max}}$ . Since the primary interest here is for disk arrays, and the insulator boundary condition results are not relevant to arrays, they are not discussed further. It is sufficient to state that the current distribution on the disk is unaffected by the boundary condition at  $\xi_{\text{max}}$  for the range of parameters discussed below. The current distribution on the plane is affected only near  $\xi_{\text{max}}$ , where current is forced to go due to the insulator boundary condition. Therefore, the general behavior of the system is identical for either boundary condition, except as noted, and the behavior is described only for Eq. [11].

Condition [11] relates the potential  $\phi$  and the gradient  $\partial\phi/\partial\xi$  at  $\xi_{\text{max}}$ , and current may pass through this surface. The amount of current that "leaks" through this surface at  $\xi_{\text{max}}$  will depend on the location of  $\xi_{\text{max}}$  as well as the nonuniformity of current density on the plane. For a given value of  $J_p$  for the plane, the fraction of current that leaks past  $\xi_{\text{max}}$  decreases as  $\xi_{\text{max}}$  increases.

The current distribution on the disk is determined by the parameter  $J_d$  for  $i \ll i_{\text{corr}}$ , and is independent of the current level and therefore the potential difference between the disk and plane. For currents much larger than  $i_{\text{corr}}$ , the current distribution is determined by the current level as measured by  $\delta_d$ . For intermediate currents, values of  $\alpha_{\text{ad}}/\alpha_{\text{cd}}$  and  $\delta_d$  characterize the current distribution. In addition, the polarization characteristics of the plane influence the current distribution on the disk as will be shown.

*Current and potential distribution on the disk and plane.*—The potential distribution in the solution on the disk and plane for an insulating plane is shown in Fig. 4. The potential at the surface is highest near the center of the disk and decreases to zero far from the disk. This is compared to the potential distribution calculated for a conducting plane with reversible kinetics ( $J_p \rightarrow \infty$ ) shown in the lowest curve on this figure. The influence of the conducting plane is to lower the potential near the center of the disk, and the po-

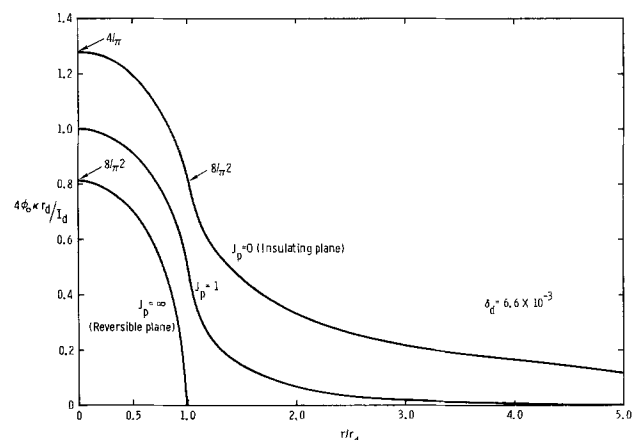


Fig. 4. Potential distribution at the surface of the disk and surrounding plane.



tential becomes zero at the edge where the two electrodes join. The gradient of the potential is larger near the edge of the disk for a conducting plane.

To make the influence of the plane polarization more quantitative, the potential difference across the disk is shown in Fig. 5 as a function of  $J_p$  for different values of  $\delta_d$ .  $\Delta\phi$  is made dimensionless by multiplying by  $4\tau_d\kappa/I$  where  $I$  is the total (disk) current. The influence of increasing  $\delta_d$  is to decrease the importance of electrode kinetics relative to the ohmic potential drop, and thus to decrease the potential difference between the center and edge of the disk. The intercept as  $J_p \rightarrow 0$  for each curve was calculated for an insulating plane, and the general curve is shown in Fig. 6, where the intercept is from Newman (15). In the other extreme, as  $J_p \rightarrow \infty$ , the potential difference across the disk is shown in Fig. 7 as a function of  $\delta_d$ . The intercept for  $\delta_d \rightarrow 0$ ,  $J_p \rightarrow \infty$ , is that for the Levich-Frumkin calculation, i.e.,  $8/\pi^2$ . The results shown on Fig. 7 are less accurate than other results reported herein because of the large gradients in the corner where the disk and plane join. Problems with accuracy were also encountered for the calculations of Fig. 5 for values of  $J_p$  greater than 20. The results for large values of  $J_p$  and  $\delta_d$  will be reported at a later date.

The current distribution on the disk is shown in Fig. 8 where the curve for  $J_p = 0$  is for an insulating plane and agrees with the results of Newman (15). The other curves were calculated for a conducting plane with different values of the plane polarization parameter. As noted already, increasing  $J_p$  distorts the current distribution on the disk, causing a larger current density at the edge of the disk. This results from decreasing the influence of electrode kinetics on the plane as compared

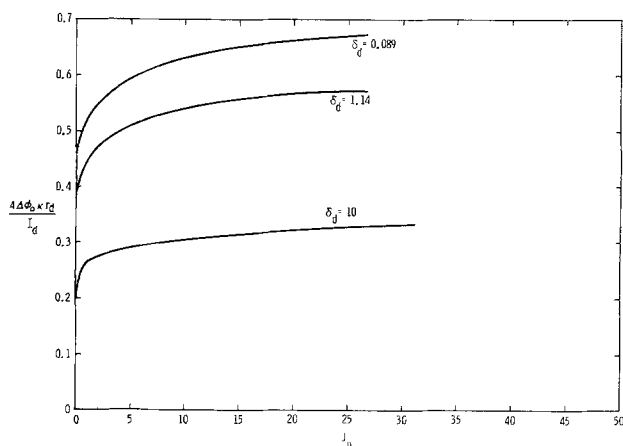


Fig. 5. Potential difference between the center and edge of the disk as a function of plane polarization parameter  $J_p$ .

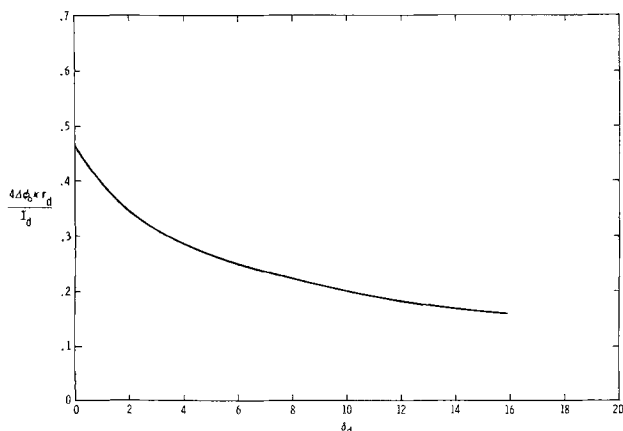


Fig. 6. Potential difference between the center and edge of the disk in an insulating plane as a function of  $\delta_d$ .

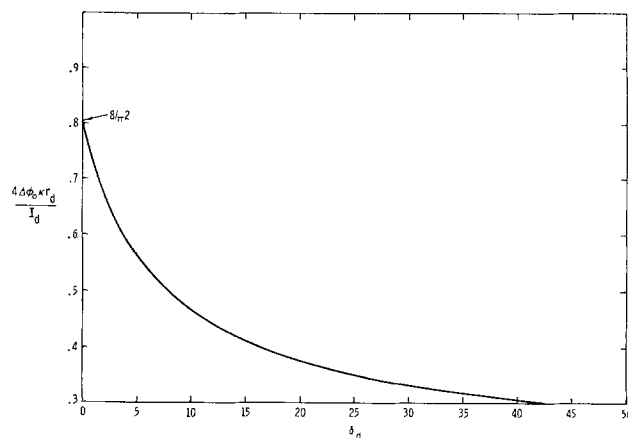


Fig. 7. Potential difference between the center and edge of a disk in a conducting (reversible) plane as a function of  $\delta_d$ .

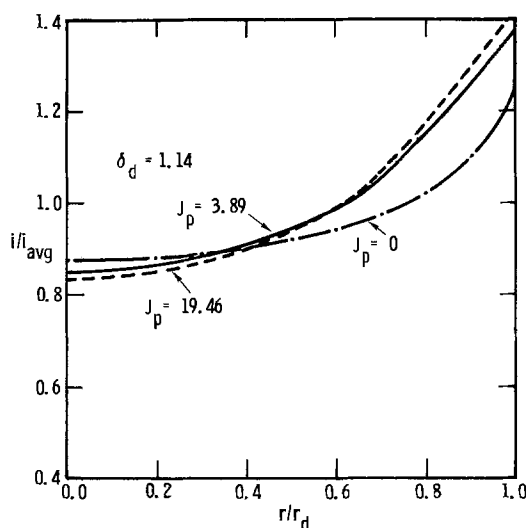


Fig. 8. Current distribution on a disk in a conducting plane for different values of the plane polarization parameter,  $J_p$ .

to the ohmic influence. All curves were calculated for Tafel polarization on the disk, with identical values of  $\delta_d$ . The influence of a conducting plane on a disk with linear kinetics is qualitatively the same.

The current density on the cathodic plane is shown in Fig. 9 as a function of distance from the disk. The polarization behavior of the disk influences the current distribution on the plane only very near the disk for large values of  $J_p$ . The potential and current distribution far from the disk are then rather insensitive to the disk polarization parameters. Also shown in this figure is the calculation for a uniform current disk and reversible plane, labeled "Levich." The parallel behavior of the two curves indicates that for large values of  $\xi$ , the current and potential distribution for both cases have the same dependence on  $\xi$ . Thus one expects that only the first term of the expansion for the potential, Eq. [17], is important for the present case for  $J_p$  greater than about 1. The two curves were calculated for identical values of the total disk current.

These observations lead us to propose that the value of  $B_1$  for Eq. [17] may be calculated by comparison with the Levich-Frumkin result, even though it may not be calculated directly as discussed earlier. The ratio  $B_1/B_{1L}$  ( $B_{1L}$  is the value obtained by Levich and Frumkin, see Eq. [18]) is equivalent to the ratio of the current density from Fig. 9 to the Levich-Frumkin current density at a particular value of  $\xi$ . Knowledge of the value of  $B_{1L}$  for the uniform current disk, reversible plane permits calculation of  $B_1$ . The ratio  $B_1/B_{1L}$  is influenced by the value of  $J_p$  as shown in Fig. 10, but

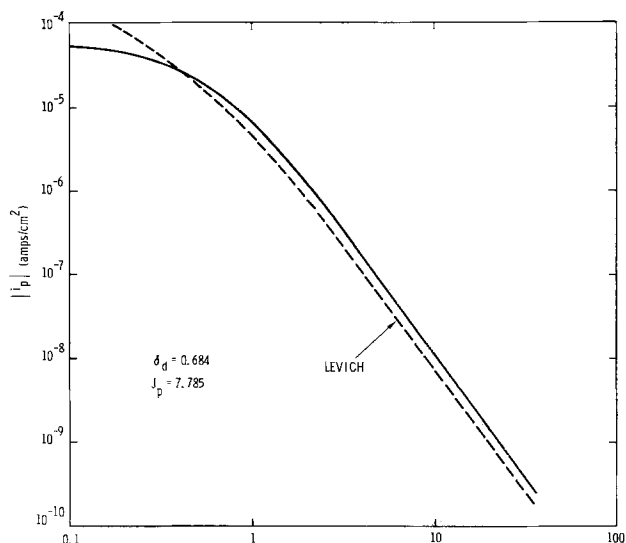


Fig. 9. The cathodic current density of the surrounding plane as a function of the distance  $\xi$  from the edge of the disk, compared to the Levich-Frumkin behavior for a reversible plane.

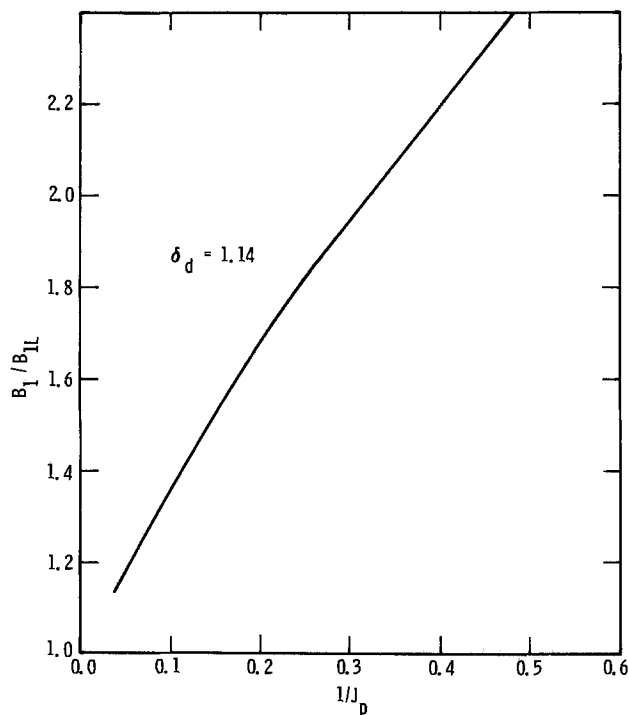


Fig. 10. The departure of the behavior of the cathodic plane from Levich-Frumkin behavior, measured by the ratio  $B_1/B_{1L}$ , as a function of the reciprocal of the plane polarization parameter,  $1/J_p$ .

nearly independent of the disk behavior as shown in Fig. 11. It should be mentioned that the parallel behavior of the two curves in Fig. 9 for large values of  $\xi$  is also observed for the boundary condition [8] except near  $\xi_{max}$ .

The influence of the disk on the behavior of the plane is concentrated to a region near  $\xi = 0$ . This influence is depicted on Fig. 12 where the value of  $|i_p|/i_{corr,p}$  at  $\xi = 0$  is given as a function  $\delta_d$  for different values of  $J_p$ . This reveals that  $|i_p|/i_{corr,p}$  at  $\xi = 0$  is large, even for small values of  $J_p$ . For all values of  $J_p$  shown here, the value of  $|i_p|/i_{corr,p}$  is smaller by at least five orders of magnitude at  $\xi = 200$ . The decrease is sharper for larger values of  $J_p$ .

The wide range of current density on the plane in Fig. 9 indicates how essential it is that the general ex-

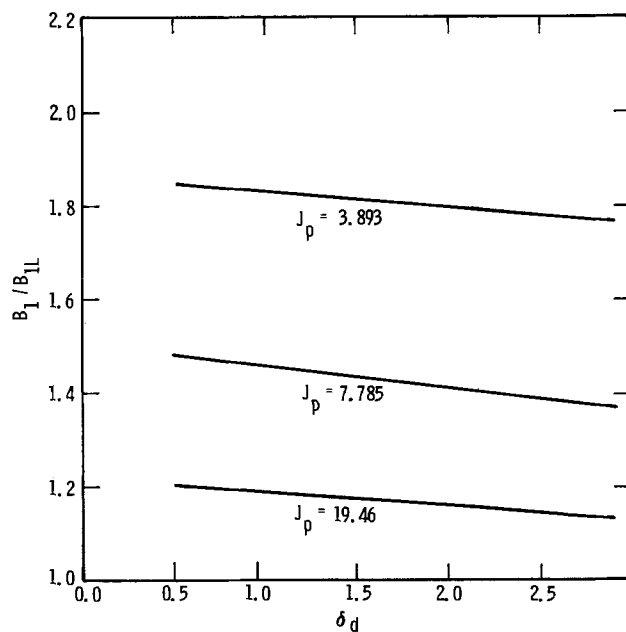


Fig. 11. The departure of the behavior of the cathodic plane from Levich-Frumkin behavior, featured by the ratio  $B_1/B_{1L}$ , as a function of the disk polarization parameter,  $\delta_d$ , at three values of  $J_p$ .

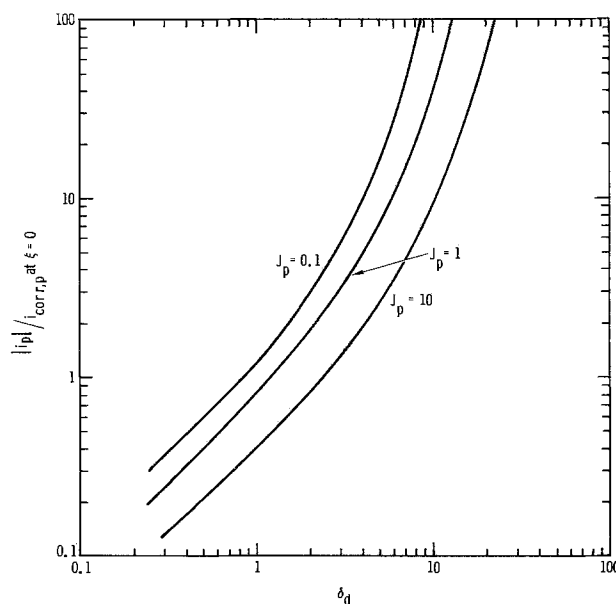


Fig. 12. The current density to the plane at  $\xi = 0$ , as compared to the corrosion current density for the plane, as a function of  $\delta_d$  and for three values of  $J_p$ .

pression for the kinetics, Eq. [13], be used. For large values of  $J_p$ , the ratio  $|i_p|/i_{corr,p}$  approaches a large value at  $\xi = 0$ . For small  $J_p$ , the value of  $|i_p|/i_{corr,p}$  at  $\xi = 0$  is still large, and in either case  $|i_p|/i_{corr,p} \rightarrow 0$  as  $\xi_{max} \rightarrow \infty$ . Both the large value of  $|i_p|/i_{corr,p}$  and its large variation from  $\xi = 0$  to  $\xi \rightarrow \infty$ , preclude the use of linear kinetics on the plane, except for extremely large values of  $J_p$  and small values of  $\delta_d$ . The Tafel approximation for plane kinetics would not be appropriate either because of the value of  $|i_p|/i_{corr,p}$  at  $\xi \rightarrow \infty$ . Therefore, the present technique provides results which could probably never be obtained theoretically, because boundary condition [13] or [7] describes the kinetic behavior everywhere on the plane, including the extremes at small and large  $\xi$ .

*Array of disks.*—The results discussed in the previous section provide a background for the analysis of the behavior of an array of disks. The random array of disks which are all of the same radius and are far apart are treated here. Following Levich (13b), the average

potential in solution at some large distance from the surface is

$$\bar{\phi}_{(\text{large } z)} = \bar{n} \int_0^{\infty} \phi(r) 2\pi r dr \quad [22]$$

where  $\bar{n}$  is the number of disks per square centimeter of surface. In the previous section it was found that the potential far from the surface can be approximated by the first term of Eq. [17], i.e.

$$\begin{aligned} \phi &= B_1 P_1(\eta) M_1(\xi) \text{ at large } \xi \\ &= \left( \frac{B_1}{B_{1L}} \right) B_{1L} \eta [\xi \cot^{-1} \xi - 1] \end{aligned} \quad [23]$$

For large  $z$ ,  $\xi$  is also large and

$$\phi = - \frac{B_1}{B_{1L}} (B_{1L}) \eta \left[ \frac{1}{3\xi^2} \right] \text{ as } \xi \rightarrow \text{large} \quad [24]$$

where  $B_{1L} = -2I_d/\pi^2 r_d \kappa$ . The equation for  $\bar{\phi}_z$  now becomes

$$\bar{\phi}_z = - \frac{2\pi B_1 \bar{n}}{3B_{1L}} (B_{1L}) \int_0^{\infty} \frac{\eta}{\xi^2} r dr \quad [25]$$

Using the relationships in Eq. [3] and [4], for large  $\xi$ , it may be shown that

$$\bar{\phi}_z = - 2\pi \left( \frac{B_1}{B_{1L}} \right) B_{1L} \bar{n} (r_d^2) \quad [26]$$

The ratio of anode area to cathode area,  $A_a/A_c$ , is

$$A_a/A_c = \bar{n} \pi r_d^2$$

and

$$\bar{\phi}_z = \frac{4I_d}{3\pi^2 r_d \kappa} \left( \frac{B_1}{B_{1L}} \right) (A_a/A_c) \quad [27]$$

Thus, the corrosion potential of an array of disks will be proportional to the area ratio when ohmic effects are important. This is contrasted to the behavior expected when only kinetic effects are important, e.g., Eq. [1]. It should be noted that the corrosion potential,  $\bar{\phi}$ , is independent of the value of  $z$ , and may be measured with an appropriate reference electrode in any arbitrary location far from the disk-plane surface.

Equation [27] was derived with the assumption that the pores are far enough apart that they interact to a negligible extent through the small ohmic drop far from a disk. This should be a good approximation when the distance separating the disks is large enough that only a small current density flows to the midpoint of the separation distance. This suggests that the minimum distance of separation for negligible interaction is dependent on the magnitude of  $J_p$ . The larger the value of  $J_p$ , the smaller may be the separation distance for the disks for independent behavior. The polarization parameters on the disk have a small influence on the plane behavior, as noted previously, so the most important parameter influencing interaction will be  $J_p$ . Preliminary calculations indicate that 99% of the plane current would go to a distance less than  $\xi_{\max}$  when the product

$$J_p \xi_{\max} \cong 195 \quad [28]$$

For large values of  $\xi_{\max}$

$$\begin{aligned} \xi_{\max}^2 &\cong \frac{\text{area of cathode (plane)}}{\text{area of anode (disk)}} \\ &= \frac{r_{\max}^2 - r_d^2}{r_d^2} \end{aligned}$$

and from Eq. [28] one may obtain a value of the minimum separation distance or area ratio for this level of interaction for given  $J_p$  (and  $r_d$ ). For example, if

$$J_p = 0.7$$

the area ratio of cathode to anode is  $10^6$ . This would

then be the minimum area ratio for which the corrosion potential would be expected to obey Eq. [27]. More detailed results will be reported at a later date.

*Applications.*—The importance of ohmic effects in galvanic corrosion in plating systems may be estimated by calculation of the polarization parameters of the disk and plane. These calculations require the values of the corrosion current density for both surfaces, the value of a characteristic dimension for the disk,  $r_d$ , the average current density on the disk, and the conductivity of the electrolyte. Small values of the polarization parameters for the disk and plane would indicate that the kinetic effects are more important than ohmic considerations, and that the current distribution on each will tend to be uniform. As the polarization parameters approach zero, the behavior of a disk array will tend toward that predicted by Stern (9) and Oldham and Mansfeld (11). These polarization parameters are very important and very useful diagnostic criteria.

The exposed substrate disk in a plating system would be expected to be small, and this small characteristic dimension would be expected to force both  $J_d$  and  $\delta_d$  to be small. Therefore, the current distribution on such a disk would be rather uniform.

The cathodic plane would tend to have a nonuniform distribution of current because of its size unless both the corrosion current density is low and the conductivity is high. For values of the parameters of  $\kappa = 0.001 \Omega^{-1}\text{-cm}^{-1}$ ,  $F = 96,500 \text{ C-equiv.}^{-1}$ ,  $T = 298.15^\circ\text{K}$ ,  $R = 8.315 \text{ joules } (^\circ\text{K})^{-1} \text{ mole}^{-1}$ ,  $r_d = 10^{-3} \text{ cm}$ ,  $i_{\text{corr,p}} = 10^{-2} \text{ A-cm}^{-2}$ , and  $(\alpha_{\text{ap}} + \alpha_{\text{cp}}) = 1$ , then  $J_p = 0.3893$ . For a value of  $\delta_d = 10^{-3}$  (virtually uniform disk current), and the above value of  $J_p$ , the current density to the plane is found to be nonuniform. The plane current density at a distance of three disk radii is decreased by an order of magnitude from the value at  $\xi = 0$ . It is reduced by five orders of magnitude at about 98 disk radii. This nonuniform current distribution on the plane would cause the corrosion potential to follow Eq. [27].

More specifically, the transition in behavior from that described in Eq. [27] to that given by Eq. [1] occurs at a specific area ratio for a given system. The quantity

$$J_p \xi_{\max} \cong 195$$

may be used to estimate the area ratio at which this transition occurs. For

$$J_p = 10$$

the value of  $\xi_{\max}$  is 19.5 and this corresponds to a ratio of anode area to cathode area of

$$\frac{A_a}{A_c} \cong 2.6 \times 10^{-3}$$

For smaller area ratios the system would follow Eq. [27]. For larger area ratios the system would behave as described in Eq. [1]. The transition between the two regions would be smooth, and the behavior would not follow either relationship exactly. The size of the transition region has not been determined here, but is the subject of a continuing study.

For a single pore in a finite plane, the behavior will be similar to that described above in general. That is, at area ratios ( $A_a/A_c$ ) smaller than that given by

$$J_p \xi_{\max} \cong 195$$

the ohmic effects will be important. At larger area ratios the transition to the behavior given by Eq. [1] will occur. The exact description of the behavior of this finite system with ohmic effects is being determined and will be reported later, along with the behavior of interacting arrays of pores, which is another finite system of considerable importance.

For systems where  $\delta_d$  is unknown because  $i_{\text{avg,d}}$  is unknown, one may estimate  $\delta_d$  from Fig. 13. Here, the value of  $U$ , the corrosion potential difference of the separated metals,  $J_p$ , and  $J_d$  can be used to predict  $\delta_d$ .

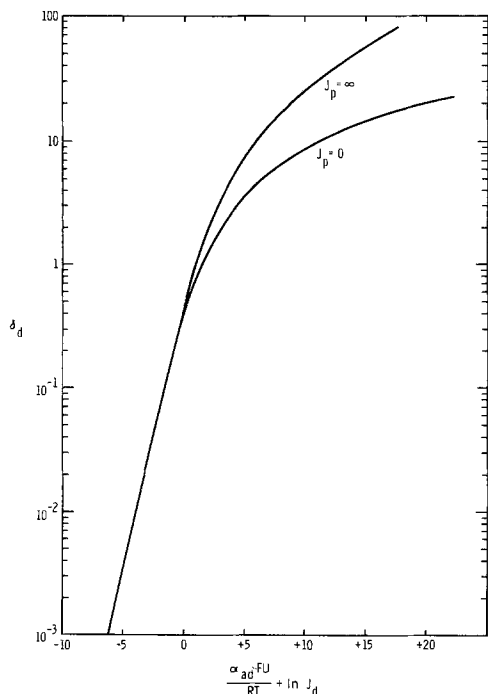


Fig. 13.  $\delta_d$  as a function of  $(\alpha_a F U / RT) + \ln J_d$  for a reversible plane and an insulating plane.

For small values of  $[(\alpha_a F U / RT) + \ln J_d]$ , the polarization parameter of the plane does not influence  $\delta_d$  because kinetic effects predominate. For larger values of  $[(\alpha_a F U / RT) + \ln J_d]$ , Fig. 13 may be used and the value of  $J_p$  is important for predicting  $\delta_d$ . The total spread of values between  $J_p = 0$  and  $J_p = \infty$  is not large until  $[(\alpha_a F U / RT) + \ln J_d]$  becomes greater than 10, a value seldom encountered in practice. Knowledge of  $\delta_d$  with the other parameters can then be used to predict current distribution on the disk and plane from Fig. 8 and 9. The potential distribution across the disk can be estimated from Fig. 5. For an insulating plane, the value of  $\ln \delta_d$  becomes proportional to  $[(\alpha_a F U / RT) + \ln J_d]$  at small values of  $\delta_d$ . At large  $\delta_d$ , a linear relationship between  $\delta_d$  and  $[(\alpha_a F U / RT) + \ln J_d]$  is observed with a slope of  $4/\pi$ . A disk with a reversible plane has the same behavior at small  $\delta_d$ , as shown. For large  $\delta_d$ , a linear relationship between  $\delta_d$  and  $[(\alpha_a F U / RT) + \ln J_d]$  is again observed, but with a slope of  $16/\pi$ . These results will be discussed in a forthcoming publication (21). It should be noted that these curves have been determined for a surrounding plane of infinite extent.

Knowledge of these parameters allows one to estimate  $B_1/B_{1L}$  from Fig. 10 and 11. This can be used to predict the slope of the corrosion potential-area ratio curve for a collection of pores in a plating system, and this can be verified by experiment.

These results would also be applicable to the situation of a cathodic inclusion on an anodic plane. The physical consequences predicted by this treatment are nonuniform anodic dissolution on the plane, with the largest dissolution near the inclusion. This could lead to undermining the inclusion with eventual pit formation if the inclusion is dislodged.

### Summary

Numerical analysis of a conducting disk in a conducting plane has been performed by finite difference techniques. The current and potential distribution on both the disk and the plane have been determined for a wide range of parameters. The distributions have been shown to depend not only on the individual parameters of the disk and plane, but the disk and plane influence each other as well because of their proximity. The results have been used to determine the behavior of an array of disks, and the application and use of the results for other situations have been discussed.

### Acknowledgment

This work was supported by the U. S. Energy Research & Development Administration. Portions of this paper were presented at the Washington, D.C., Meeting of the American Institute of Chemical Engineers, December 1974.

Manuscript submitted March 8, 1976; revised manuscript received May 28, 1976.

Any discussion of this paper will appear in a Discussion Section to be published in the June 1977 JOURNAL. All discussions for the June 1977 Discussion Section should be submitted by Feb. 1, 1977.

Publication costs of this article were assisted by Sandia Laboratories.

### APPENDIX A

#### Boundary Condition Far from the Disk

The surface  $\xi = \xi_{\max}$  defines a hemisphere in  $r, z$  coordinates. If the hemisphere is an insulator, no current may pass through it, and one uses the boundary condition specified in Eq. [8]. We have also used a second boundary condition in which current is allowed to pass through this hemispherical boundary, and we approximate the potential gradient in solution nearby by a relationship which is similar to the Levich-Frumkin distribution. We have found that both boundary conditions give the same results for current and potential distribution everywhere except near the boundary  $\xi = \xi_{\max}$ . The insulator boundary condition forces more current to flow to the plane in the corner near  $\xi = \xi_{\max}$ .

Levich and Frumkin found, for a reversible plane and uniform current on the disk, that the potential far from the disk is

$$\phi = \frac{2i_d r_d}{\pi \kappa} \eta [\xi \cot^{-1} \xi - 1] \quad [18]$$

where  $i_d$  is the (uniform) current density on the disk.

For the present problem we use the expansion

$$\phi = \sum_{n=1}^{\infty} B_n P_n(\eta) M_n(\xi) \quad [17]$$

and retain only the first two terms of the expansion in anticipation that higher terms are negligible for large values of  $\xi$ . The first term is identical to the Levich-Frumkin result except for the value of  $B_n$ , i.e.

$$P_1(\eta) = \eta \quad [A-1]$$

$$M_1(\xi) = -[\xi \cot^{-1} \xi - 1] \quad [A-2]$$

and the second term is

$$P_2(\eta) = \frac{1}{2} (3\eta^2 - 1) \quad [A-3]$$

$$M_2(\xi) = -\frac{2}{\pi} [(3\xi^2 + 1) \cot^{-1} \xi - 3\xi] \quad [A-4]$$

For large values of  $\xi$  [see Ref. (22)]

$$M_1(\xi) \rightarrow \frac{1}{2\xi^2} \text{ as } \xi \rightarrow \infty \quad [A-5]$$

and

$$M_2(\xi) \rightarrow -\frac{1}{15\pi\xi^3} \text{ as } \xi \rightarrow \infty \quad [A-6]$$

Near the plane, the potential must also satisfy the boundary condition for passage of current to the plane, and this provides a relationship between  $B_1$  and  $B_2$ . On the plane, it is assumed that we are far enough from the disk that the kinetics may be approximated by the linear relationship, i.e.

$$\left. \frac{-\kappa}{r_d \xi} \frac{\partial \phi}{\partial \eta} \right|_{\eta=0} = i_p = \frac{(\alpha_{ap} + \alpha_{cp}) F}{RT} (U_{\text{corr},p} - \phi_{op}) i_{\text{corr},p} \quad [A-7]$$

We arbitrarily set  $U_{\text{corr},p} = 0$ , and find

$$-\frac{1}{\xi} \left[ \frac{B_1}{2\xi^2} \right] = J_p \left[ \frac{8}{15\pi\xi^3} B_2 P_2(0) \right] \quad [\text{A-8}]$$

where terms of order  $(1/\xi^4)$  have been neglected, and

$$J_p = \frac{(\alpha_{ap} + \alpha_{cp}) r_d F}{\kappa RT} i_{\text{corr},p} \quad [\text{A-9}]$$

This leads to

$$B_1 = -\frac{16}{15\pi} J_2 P_2(0) B_2 \quad [\text{A-10}]$$

and with this relationship we may now derive an expression for the potential gradient near  $\xi_{\text{max}}$  valid for large values of  $\xi_{\text{max}}$ . Now

$$\begin{aligned} \phi &= \frac{B_1}{2\xi^2} P_1(\eta) - \frac{16B_2}{15\pi\xi^3} P_2(\eta) \\ &= \frac{8B_2}{15\pi} \left\{ \frac{P_2(0) P_1(\eta) J_p}{\xi^2} + \frac{2P_2(\eta)}{\xi^3} \right\} \quad [\text{A-11}] \end{aligned}$$

and

$$\begin{aligned} \left. \frac{\partial \phi}{\partial \xi} \right|_{\xi=\text{max}} &= \frac{8B_2}{15\pi} \left\{ \frac{2P_2(0) P_1(\eta) J_p}{\xi^3} + \frac{6P_2(\eta)}{\xi^4} \right\} \\ &= -\frac{2\phi}{\xi_{\text{max}}} \left\{ \frac{P_1(\eta) + \frac{3P_2(\eta)}{\xi_{\text{max}} P_2(0) J_p}}{P_1(\eta) + \frac{2P_2(\eta)}{\xi_{\text{max}} P_2(0) J_p}} \right\} \quad [\text{A-12}] \end{aligned}$$

and this reduces to the Levich-Frumkin functional relationship as  $\xi_{\text{max}} \rightarrow \infty$ .

## APPENDIX B

### Finite Difference Approximations for Nonlinear Boundary Conditions

Equation [20] is a finite difference relationship for the surrounding plane involving a function  $F_p$  which is exponential in  $\phi_p$ . This nonlinear relationship for  $\phi_p$  is rather unstable, and diverges rapidly unless the initial potential approximation is near the final, converged value. We have adopted the following treatment which eliminates these divergence problems.

We approximate the value of  $F_p$  by

$$\begin{aligned} F_p &= F_p(V_p - \phi_p - U_{\text{corr},p}) \\ &+ (\phi_p(r) - \phi_{p,\text{old}}) F_p' \quad [\text{B-1}] \end{aligned}$$

where  $\phi_{p,\text{old}}$  is the previous value of  $\phi_p$  at the central point,  $\phi_p(r)$  is the value of  $\phi_p$  at the central point to be calculated, and  $F_p'$  is the derivative of  $F_p$  with respect to the overpotential  $(V_p - \phi_p - U_{\text{corr},p})$ .

Equation [19] becomes now

$$\begin{aligned} \phi_o \left[ \frac{2(1-\eta_o^2)}{h_\eta^2} + \frac{2(1+\xi_o^2)}{h_\xi^2} \right. \\ \left. + 2F_p' \xi_o h_\eta \left( \frac{1-\eta_o^2}{h_\eta^2} + \frac{\eta_o}{h_\eta} \right) \right] \\ = 2\phi_2 \left( \frac{1-\eta_o^2}{h_\eta^2} \right) + \phi_1 \left[ \frac{1+\xi_o^2}{h_\xi^2} + \frac{\xi_o}{h_\xi} \right] \\ + \phi_3 \left[ \frac{1+\xi_o^2}{h_\xi^2} - \frac{\xi_o}{h_\xi} \right] + 2\xi_o h_\eta (F_p + \phi_{o,\text{old}} F_p') X \\ \left[ \frac{1-\eta_o^2}{h_\eta^2} + \frac{\eta_o}{h_\eta} \right] \quad [\text{B-2}] \end{aligned}$$

or

$$\begin{aligned} \phi_o \left[ \frac{2}{h_\eta^2} + \frac{2(1+\xi_o^2)}{h_\xi^2} + 2F_p' \xi_o \left( \frac{1}{h_\eta} \right) \right] \\ = \frac{2\phi_2}{h_\eta^2} + \phi_1 \left[ \frac{1+\xi_o^2}{h_\xi^2} + \frac{\xi_o}{h_\xi} \right] \\ + \phi_3 \left[ \frac{1+\xi_o^2}{h_\xi^2} - \frac{\xi_o}{h_\xi} \right] + \frac{2\xi_o}{h_\eta} (F_p + \phi_{o,\text{old}} F_p') \quad [\text{B-3}] \end{aligned}$$

where we have introduced  $\eta_o = 0$  on the plane.

This equation is solved for  $\phi_o$ , called  $\phi_{o,\text{try}}$ , and a new value of  $\phi_o$  is calculated by

$$\phi_{o,\text{new}} = \phi_{o,\text{old}} + \Omega(\phi_{o,\text{try}} - \phi_{o,\text{old}})$$

The same value of the overrelaxation parameter is used for the boundary as for interior points.

An analogous treatment of the generally nonlinear boundary condition on the disk was adopted.

Successive iterations with this approximation technique lead to convergence and a rigorous result, since the second term of [B-1] approaches zero as the potential approaches the converged value.

## REFERENCES

1. F. I. Nobel, B. D. Ostrow, and D. W. Thomson, *Plating*, **52**, 1001 (1965).
2. A. A. Khan, *ibid.*, **56**, 1374 (1969).
3. R. A. Ehrhardt, *Proc. Am. Electroplaters Soc.*, **47**, 78 (1960).
4. M. Clarke and J. M. Leeds, *Trans. Inst. Met. Finishing*, **43**, 50 (1965).
5. M. Clarke and A. M. Chakrabarty, *ibid.*, **48**, 99 (1970).
6. M. Clarke, *ibid.*, **51**, 150 (1973).
7. M. Clarke, *ibid.*, **52**, (Part 2), 48 (1974).
8. T. P. Hoar, *J. Electrodepositors' Tech. Soc.*, **14**, 42 (1938).
9. M. Stern, *Corrosion*, **14**, 329t (1958).
10. R. J. Morrissey, *This Journal*, **117**, 742 (1970).
11. K. B. Oldham and F. Mansfeld, *J. Appl. Electrochem.*, **2**, 183 (1972).
12. F. Mansfeld, *Corrosion*, **27**, 436 (1971).
13. (a) B. Levich and A. Frumkin, *Acta Physicochim. URSS*, **18**, 1 (1943); (b) B. Levich, "Physicochemical Hydrodynamics," Prentice-Hall, Englewood Cliffs, N.J. (1962).
14. E. McCafferty, Naval Res. Lab. Rept., NRL 7835 (Jan. 31, 1975).
15. J. Newman, *This Journal*, **113**, 1235 (1966).
16. J. Newman, in "Electroanalytical Chemistry," Vol. 6, A. J. Bard, Editor, chap. 3, Marcel Dekker, New York (1973).
17. C. Wagner and W. Traud, *Z. Elektrochem.*, **44**, 391 (1938).
18. J. Newman, "Electrochemical Systems," Prentice-Hall, Englewood Cliffs, N.J. (1973).
19. J. A. Klingert, S. Lynn, and C. W. Tobias, *Electrochim. Acta*, **9**, 297 (1964).
20. R. N. Fleck, UCRL-11612 (September 1964).
21. W. H. Smyrl and J. Newman, Abstract 256, p. 638, The Electrochemical Society Extended Abstracts, Spring Meeting, Washington, D.C., May 2-7, 1976.
22. J. J. Miksis, Jr., LBL-4537 (November 1975).

# The Comparative Crevice Corrosion Resistance of Co-Cr Base Surgical Implant Alloys

T. M. Devine<sup>\*,1</sup> and J. Wulff

Department of Metallurgy and Materials Science, Massachusetts Institute of Technology, Cambridge, Massachusetts 02139

## ABSTRACT

Different electrochemical and direct immersion tests were used to compare the relative crevice corrosion resistance of currently used or recommended nontitanium surgical implant alloys. Measurement of the anodic corrosion current vs. time of creviced specimens in deaerated isotonic salt solution at 37°C and in a 10% HCl + 1% FeCl<sub>3</sub> solution at a series of constant applied potentials lying in the passive range of the alloys provided the same comparative rating of the different alloys as potential-time measurements as well as direct immersion tests. According to the tests, recently developed stronger wrought versions of the Co-Cr-Mo-C alloy H.S. 21 (modified Vitallium) and a wrought Co-20Cr-10Mo alloy were found to possess greater crevice corrosion resistance in both solutions than as-cast H.S. 21 and wrought alloys such as H.S. 25, M.P. 35N., Elgilloy, and 316L stainless steel.

The three most widely used surgical implant alloy systems are molybdenum containing wrought austenitic stainless steel, precision cast cobalt-chromium-molybdenum-carbon alloys such as H.S. 21 and Vitallium, and wrought commercial titanium and some of its alloys. Unfortunately, none of these alloys can be regarded as ideally suitable surgical implant material. Stainless steel possesses inadequate corrosion resistance in body fluids (1-6). While precision cast cobalt-chromium-molybdenum alloys exhibit superior corrosion resistance, they possess insufficient mechanical properties for safe use in some weight-bearing implants (7-10). Ordinary commercial titanium and some of its alloys exhibit superior long-time corrosion resistance in body fluids relative to the other two alloy systems (11). Unfortunately, however, titanium and some of its alloys undergo a high initial rate of corrosion in body fluids (12, 13) and possess little wear resistance when in rubbing contact with themselves or other metallic implant materials (14).

Because of the low mechanical properties of cast H.S. 21-type alloys implant fabricators have substituted the wrought, high strength cobalt-chromium-tungsten-nickel alloy, H.S. 25, for the cast H.S. 21 alloy in certain weight-bearing implant parts. However, such H.S. 25 parts are susceptible to crevice corrosion, albeit after long residence in patients (15, 16). More recently one fabricator has begun substituting M.P. 35N. for cast H.S. 21 parts (17). Preliminary experiments conducted in our laboratory have indicated that the recently developed wrought versions of H.S. 21 and the No. 7 alloy (Co-20Cr-10Mo) may be ideally suitable for substitution for cast H.S. 21 parts since they can be thermomechanically processed to remarkably high strength levels without impairment in corrosion resistance (18-20).

The purpose of the investigation reported in this paper was to compare the crevice corrosion resistance of the wrought H.S. 21 and No. 7 alloys with currently used or recommended (nontitanium) implant alloys. Investigation of crevice corrosion resistance was undertaken, since examination of excised implants of all kinds has shown that crevice corrosion is responsible for the major corrosion damage of implants (21). It occurs not only at metal/metal contacts in multipiece implants but also at metal/bone contacts. Like pitting,

crevice corrosion in saline media is due to localized chloride ion attack. It can occur in narrow crevices even in weak saline solution like body fluid where the chloride as well as the hydrogen ion content can build up to extremely high levels in the crevice solution (22-24). This occurs without significant change in the solution external to the crevice where convection prevents such localized concentrations.

In their comparison of corrosion resistance of a long list of iron-, nickel-, cobalt-, and titanium-base alloys in isotonic salt and physiological solutions, Hoar and Mears (7) have found that measurements of anodic current vs. time (up to 400 hr) of potentiostatically polarized noncreviced specimens at a constant potential provide a more quantitative assessment of general and localized corrosion resistance than rest potential-time measurements of noncreviced specimens. Jones and Greene (25) and Rosenfeld and Marshakov (26) have shown that potential-time measurements of specimens immersed in aqueous solutions can also be used to assess the localized corrosion resistance of alloys. Direct immersion crevice corrosion test of alloy samples in aggressive corrodents such as 10% HCl + 1% FeCl<sub>3</sub> have long been used in alloy development studies for screening purposes (27). We have used all three types of tests in this investigation to compare the crevice corrosion resistance of recently developed stronger versions of cast Vitallium or H.S. 21-type alloys with currently used or recommended nontitanium surgical implant alloys such as 316L stainless steel, Elgilloy, M.P. 35N., H.S. 25, and as-cast H.S. 21.

## Experimental

*Materials.*—The nominal chemical compositions of the alloys tested are listed in Table I. The wrought 316L, Elgilloy, M.P. 35N., and H.S. 25 were all obtained as cylindrical rods in the mill-annealed state. H.S. 21 was supplied as 0.5 in. diameter investment castings. One

Table I. Nominal compositions of some commercially available surgical implant alloys and experimental alloy No. 7

Alloy	Cr	Mo	W	Ni	C	Fe	Co
316L	17-20	2-4	—	10-14	0.03	Bal	—
Elgilloy	20	7	—	15	0.15	Bal	40
M.P. 35N.	20	10	—	35	—	—	35
H.S. 25	19-21	—	14-16	9-11	0.15	3	Bal
H.S. 21	27.5	5.5	—	2.5	0.35	2.0	Bal
No. 7	20	10	—	—	—	—	Bal

\* Electrochemical Society Active Member.

<sup>1</sup> Present address: General Electric Company, Research and Development Center, Schenectady, New York 12301.

Key words: crevice corrosion, surgical implants, cobalt alloys.

set of the wrought experimental alloys No. 7 and H.S. 21 were hot extruded in a single pass (80% reduction in area) from 1 in. diameter vacuum-cast ingots. Another set was hot press forged (1200°C) from 30 lb ingots with frequent intermediate anneals and then hot rolled at ~1200°C to a 0.38 in. thick strip.

Test specimens having a length of 1.000 in. and a diameter of 0.250 in. were cut, machined, and polished to 4 × 0 grit paper. One end of each specimen was rounded and for the electrochemical tests the other end was drilled and tapped to fit into a Stern-Makrides (28) electrode holder.

Teflon rings were all machined from the same cylindrical rod stock of Teflon, finished with 4 × 0 grit paper to have a width of 0.125 in. and an internal diameter of 0.235 in. Sharp edges were rounded.

After ultrasonic degreasing in trichlorethylene all metal specimens were washed and rinsed in distilled water and absolute alcohol, dried, and stored in vacuum dessicators. The Teflon rings were also degreased, washed, rinsed, and dried before they were force-fitted to the middle of the cylindrical alloy specimens with the aid of a mechanical jig. The latter was used to avoid damaging the surface finish with hand tools. After force fitting, the metal external to the Teflon ring was lightly abraded with 4 × 0 grit paper to remove adherent Teflon and carefully cleaned with absolute alcohol.

Two test solutions were employed, isotonic salt solution, 0.9% NaCl, and a highly aggressive solution of 10% HCl + 1% FeCl<sub>3</sub>. The two corrodents used in the corrosion tests were made from reagent grade chemicals and doubly distilled water. Purified nitrogen was used for deaeration and tank oxygen for aeration of the corrodents used in the electrochemical cells. The quiescent solutions used in the beaker tests were renewed for test runs of over 10 days at regular intervals.

**Corrosion tests.**—The electrochemical cells, auxiliary electrical apparatus, and techniques of measurement duplicated that recommended by Greene (29) and used by Revie and Greene (12, 13). A nonpolarizable Ag-AgCl electrode ( $E^\circ = 0.216V$  at 37°C) was used for reference. Measurements of open-circuit potential *vs.* time in oxygenated solution at 37°C and anodic polarization curves in deaerated electrolytes at 37°C were first made to determine rest and breakdown potentials. These were followed by similar measurements of the open-circuit potential variation with time of creviced alloy specimens and anodic current *vs.* time of creviced alloy specimens at a series of fixed potentials lying in the passive region of the noncreviced alloy specimens. The electrochemical cells were housed in an incubator which was maintained at 37° ± 0.5°C. After the termination of each test run, the Teflon ring was carefully cut away and the electrode scrubbed with a bristle brush in running water. The specimen was then rinsed with alcohol, dried, and examined at high magnification using intense oblique illumination for evidence of etching and pitting.

Two types of direct immersion tests in the aggressive corrodent were employed. In both, a minimum of six specimens were used for each test and only one specimen was immersed in each beaker. These were housed in incubators maintained at 37° ± 0.5°C. In the first set of tests in the 10% HCl + 1% FeCl<sub>3</sub> solution, test runs were terminated at 4 hr intervals after immersion for times up to 4 days. In another series using creviced as well as noncreviced alloy specimens the test runs were terminated after 10 day intervals. After the termination of each test and removal of the Teflon rings and cleaning of the specimens, all specimens were examined for evidence of isolated pitting and crevice corrosion as well as etching. In the case of the 10 day tests in the 10% HCl + 1% FeCl<sub>3</sub> solution loss in weight measurements were also made. Similar tests in

the isotonic salt solution were terminated at 10 day intervals for periods up to 60 days.

## Results

The results of the beaker tests employing a quiescent 10% HCl + 1% FeCl<sub>3</sub> solution at 37°C are summarized in Table II. Column A lists the times to onset of the first two to four crevice corrosion pits in all 6 samples of each alloy on test runs up to 4 days. The loss in weight after 10 day immersion tests of the creviced alloys is listed in column B of Table II and the loss in weight of noncreviced specimens of the same alloys is shown in column C. In all three sets of observations it is apparent that the crevice corrosion resistance as well as general corrosion resistance of cast and solutionized H.S. 21, wrought H.S. 21, and the wrought No. 7 alloy are greater in this solution than Elgilloy, M.P. 35N., H.S. 25, and as-cast H.S. 21.

Table III lists the results of the direct immersion corrosion tests conducted in 0.9% NaCl. Obtaining weight loss measurements of highly corrosion resistant alloys in such a relatively weak corrodent requires extremely long immersion times. Consequently, the alloys' resistances to crevice corrosion in 0.9% NaCl were determined in a highly qualitative fashion by sacrificing 4 specimens of each alloy at 10 day intervals and determining the time at which crevice corrosion pits could be observed at 200× in two of the four specimens. The alloys are rated in the same manner as the direct immersion corrosion tests in 10% HCl + 1% FeCl<sub>3</sub>. For comparison purposes the data obtained from examination of excised implants are listed in column B of Table III.

Figures 1 and 2 list the anodic polarization characteristics of the alloys examined in deaerated solutions of 10% HCl + 1% FeCl<sub>3</sub> and 0.9% NaCl, respectively. The samples were immersed for 1 hr in the test solution prior to polarization which was accomplished by sweeping the potential at a rate of 10 mV/min. The anodic polarization behavior of 316L stainless steel was not determined in 10% HCl + 1% FeCl<sub>3</sub> since the alloy was visibly pitted within minutes following immersion.

Table II. Results of beaker tests in 10% HCl + 1% FeCl<sub>3</sub> at 37°C

Alloy	A*	B†	C‡
Elgilloy	4 hr	0.0864	0.0640
M.P. 35N.	8 hr	0.0454	0.0350
H.S. 25	8 hr	0.0352	0.0128
As-cast H.S. 21	72 hr	0.0053	0.0015
As-cast and solutionized H.S. 21	No pitting in 28 days	0.0005	0.0002
Wrought H.S. 21	No pitting in 28 days	0.0001	0.0001
Wrought No. 7	No pitting in 28 days	0.0000	0.0000

\* A. Time to onset of first observable crevice corrosion pits.

† B. Average loss in weight in grams during 10 day test of creviced specimens.

‡ C. Average loss in weight in grams of bare (noncreviced) specimens in 10 day test.

Table III. Results of direct immersion corrosion tests in 0.9% NaCl

Alloy	A*	B†
316L stainless steel	10 days	<2 months
Elgilloy	30-40 days	<6 months
M.P. 35N.	40-60 days	Not reported
H.S. 25	50-60 days	<4 years
As-cast H.S. 21	None in 60 days	Not reported
As-cast and solutionized H.S. 21	None in 60 days	—
Wrought H.S. 21	None in 60 days	—
Wrought No. 7	None in 60 days	—

\* A. Time to onset of first observable crevice corrosion pits in creviced specimens of alloys immersed in isotonic salt solution at 37°C.

† B. Shortest time reported for excision of implants in which crevice corrosion pitting was observed.

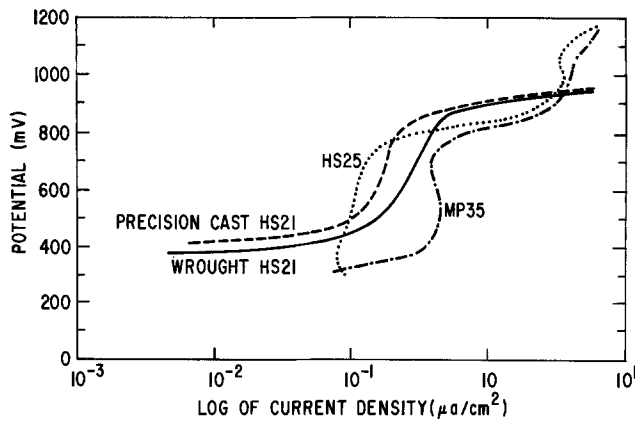


Fig. 1. Anodic polarization characteristics of the alloys in deaerated 10% HCl + 1% FeCl<sub>3</sub> at 37°C.

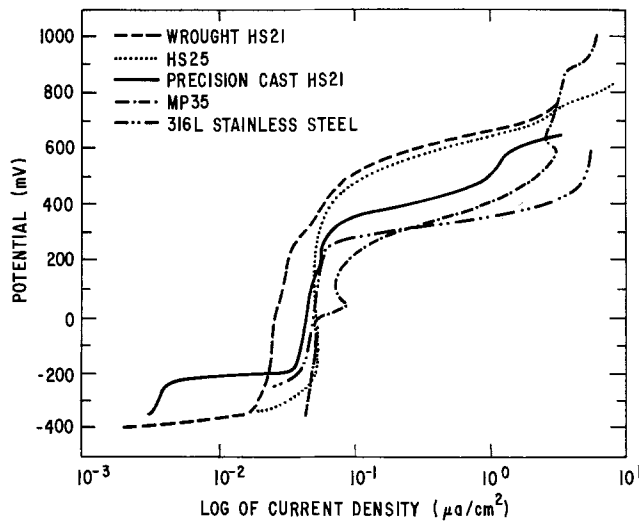


Fig. 2. Anodic polarization characteristics of the alloys in deaerated 0.9% NaCl at 37°C.

Figure 3 depicts the variation of open-circuit potential with time of Teflon creviced specimens of all the alloys except 316L stainless steel in the oxygenated 10% HCl + 1% FeCl<sub>3</sub> solution at 37°C. Stainless steel is active in this solution and the metal external to the Teflon ring extensively corrodes immediately after immersion. The smooth, monotonic increase of potential with time of creviced samples of wrought H.S. 21, wrought No. 7, and as-cast and solutionized H.S. 21 indicates no localized corrosion occurred in these alloys (25, 26). The potential of as-cast H.S. 21, however, is seen to continuously decrease approximately 15 hr after immersion. Upon completion of the test the as-cast H.S. 21 specimen showed mild crevice attack in the form of two parallel discontinuous rings of pits at the

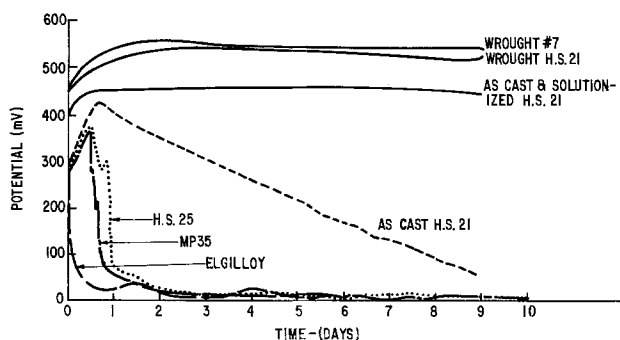


Fig. 3. Potential variation with time of creviced samples in oxygenated 10% HCl + 1% FeCl<sub>3</sub> at 37°C.

two former Teflon-metal-solution interfaces. The potentials of creviced samples of H.S. 25 and M.P. 35 dropped to active values in approximately 10 hr. Severe crevice corrosion was observed under their Teflon rings when the tests were terminated 8 days after immersion. The potential of a creviced sample of Elgilloy dropped to an active value in less than 1 hr after immersion. The sample exhibited extensive crevice corrosion.

The results of the rest potential measurements conducted on creviced samples in 0.9% NaCl are depicted in Fig. 4. Serrations indicative of localized attack were only observed in 316L stainless steel and, to a much lesser extent, in Elgilloy. The stainless steel specimen exhibited a few tiny crevice corrosion pits underneath the Teflon ring. No crevice corrosion occurred in any of the other alloys during this 10 day test.

In the measurement of the anodic corrosion current of creviced alloy electrodes for times up to a thousand minutes or more at fixed potentials in a deaerated solution it was possible to observe a potential at which the current abruptly increased. Only in the case of solutionized H.S. 21, wrought H.S. 21, and the No. 7 alloy was that potential found to be equivalent to the breakdown potential of noncreviced specimens of the same alloy. The anodic corrosion current measured divided by the area of metal outside the Teflon ring is plotted as log<sub>10</sub> of corrosion current density vs. log<sub>10</sub> time as shown in Fig. 5 for 316L stainless steel in 0.9% NaCl. Initially, at all applied potentials, the corrosion rate decreases monotonically with time and the alloy exhibits typical passive behavior. However, at potentials

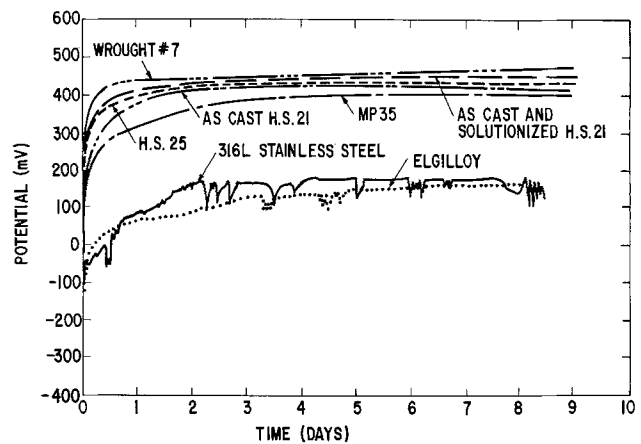


Fig. 4. Potential variation with time of creviced samples in oxygenated 0.9% NaCl at 37°C.

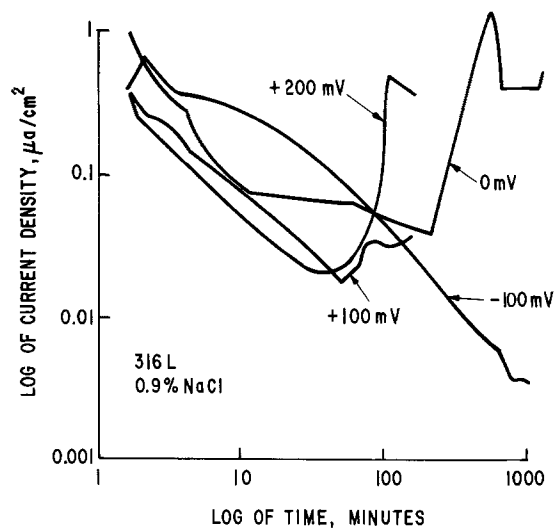


Fig. 5. Corrosion current density variation with time of creviced samples of 316L stainless steel in deaerated 0.9% NaCl at 37°C as a function of applied potential.



of 0 mV and higher the corrosion rate abruptly increases after a certain incubation period and crevice corrosion could be seen under the Teflon rings after termination of the test. Tables IV and V list the lowest applied potential at which crevice corrosion occurred in each of the alloys in 10% HCl + 1% FeCl<sub>3</sub> and 0.9% NaCl, respectively. No crevice corrosion was observed in samples of wrought H.S. 21 or alloy No. 7 in either test solution. Despite the applied potential, the Teflon ring affixed samples of these two alloys continued to exhibit passive behavior and no localized corrosion.

### Discussion and Conclusions

All of the corrosion test results clearly indicate the superiority of cast and solutionized H.S. 21, wrought H.S. 21, and the wrought No. 7 alloy whose compositions are listed in Table I. All three appear to be immune to localized corrosion; even when their passive films break down during anodic polarization above the breakdown potentials in the two corrodents used, they corrode generally rather than locally. The superior crevice corrosion resistance of the wrought H.S. 21 relative to the cast H.S. 21 can in large measure be attributed to the greater chemical as well as structural homogeneity of the wrought material (19, 20, 30). Evidently a 1 hr solutionizing heat-treatment at 1230°C removes a sufficient amount of coring and microsegregation to realize the improvements reported in corrosion resistance relative to the as-cast material. However, metallography and x-ray diffraction studies indicate that such a solutionizing treatment does not completely remove all of the secondary phases such as carbides and sigma phase that are present in the as cast condition (30). Nevertheless, this heat-treatment also improves the ductility and tensile strength of the cast alloys (31).

The present finding that H.S. 25 is inferior to cast H.S. 21 is confirmed by the *in vivo* results of Cohen and Wulff (15) and Rose *et al.* (16) who reported incidents of crevice corrosion in H.S. 25 implant parts coupled to cast H.S. 21 parts which were free of corrosion. All of the corrosion tests conducted indicate the high strength, wrought M.P. 35N alloy possesses the same general and crevice corrosion resistance as H.S. 25, and though M.P. 35N is currently used by at least one fabricator (17) for the weight bearing members of implant parts formerly made of cast H.S. 21, the present results indicate that M.P. 35N will eventually be found lacking in crevice corrosion resistance as is the case for H.S. 25.

Table IV. Lowest applied potential at which crevice corrosion initiates in deaerated 10% HCl + 1% FeCl<sub>3</sub>

Alloy	Potential (mV)	Time (min)
Elgilloy	400	7
M.P. 35N	400	350
H.S. 25	400	600
H.S. 21 as-cast	800	850
H.S. 21 cast and solutionized	No crevice corrosion at any applied potential	
H.S. 21 wrought	No crevice corrosion at any applied potential	
No. 7	No crevice corrosion at any applied potential	

Table V. Lowest applied potential at which crevice corrosion initiates in deaerated 0.9% NaCl at 37°C

Alloy	Potential (mV)	Time (min)
316L	100	200
Elgilloy	100	200
M.P. 35N	300	85
H.S. 25	300	100
H.S. 21 as-cast	300	1000
H.S. 21 as-cast and solutionized	No crevice corrosion at any applied potential	
H.S. 21 wrought	No crevice corrosion at any applied potential	
No. 7 wrought	No crevice corrosion at any applied potential	

Although Elgilloy possesses admirable mechanical properties, its crevice corrosion resistance is far inferior to the above cobalt-base alloys. The remarkably high tensile and fatigue strengths of wrought H.S. 21 and No. 7 combined with their superior general and crevice corrosion resistances should make them an attractive substitute for Elgilloy (20, 30). 316L stainless steel, the most widely used surgical implant alloy, exhibited the least resistance to crevice corrosion. This is substantiated by numerous *in vivo* results indicating the high susceptibility of 316L stainless steel implant parts to crevice corrosion (4-6, 21). The occurrence of crevice corrosion in 316L specimens affixed with Teflon rings within 10 days of immersion in 0.9% NaCl questions the suitability of this material for use even in short term implant parts. It is hoped that the simple solutionizing anneal treatment for cast H.S. 21 would be adopted by all implant fabricators to assist them in producing consistently stronger and more corrosion resistant parts. Adoption of the high strength wrought version of H.S. 21 or the No. 7 alloy by implant fabricators will no doubt take time for shaping implant parts out of either alloy from wrought bar, plate, or sheet stock requires for all but the simplest implant parts hot closed-die forging, since machining these alloys is difficult although not impossible, according to presently known techniques. In this regard the Co-20Cr-10Mo alloy is probably more workable because of its low carbon content. That this alloy also appears somewhat more corrosion resistant than wrought H.S. 21, can probably be attributed to its higher Mo/Cr ratio than H.S. 21 or Vitallium. We are led to this viewpoint by earlier studies of Tomashov and Chernova (32) regarding additions of molybdenum to austenitic-type stainless steels. As Rhodin (33) pointed out, molybdenum has a tendency to stabilize the passive film and make it more resistant to chloride-ion penetration.

Hoar and Mears (7) have suggested that measurements of corrosion current as a function of time of bare (noncreviced) specimens at fixed applied potentials which lie in their passive region provide a more quantitative assessment of localized corrosion susceptibility than potential-time measurements. We believe however that the use of creviced samples in such measurements is not only less time consuming but more meaningful, for crevice corrosion is the major origin of corrosion damage in surgical implants.

The direct immersion tests of the onset of crevice corrosion in the 10% HCl + 1% FeCl<sub>3</sub> solution, it is necessary to emphasize, provide as reasonable an assessment of crevice corrosion resistance as the potential-time measurements in the same solution or for that matter as the passive current-time measurements in the same solution. For initial screening purposes in alloy development studies such tests are simple and less time-consuming but like all crevice corrosion tests, their reproducibility depends to a large measure on the care exercised in reproducing crevice geometry.

Although the pitting potential of titanium alloys in isotonic salt solution are higher than those of wrought H.S. 21, their initial rate of corrosion in the first 1000 or more minutes after immersion in an isotonic salt solution is no different (12, 14). Kummer (14) has shown that in a 10-20% HCl solution at 37°C their long time corrosion rates are no better than wrought H.S. 21. For patients who exhibit sensitivity to nickel or cobalt corrosion products the use of titanium alloy implants is of course mandatory, but for other patients it is important to realize that the tensile and fatigue strengths of the wrought H.S. 21 are equivalent to those of fully hardened Ti-6Al-4V. However, in that state Ti-6Al-4V appears to have greater notch sensitivity than wrought H.S. 21. In any case, the superior wear resistance of wrought or cast H.S. 21 requires its use at least for the present in the rubbing members of certain total joint replacement prostheses since titanium alloys have inadequate wear characteristics (14).

Finally, it should be noted that hot isostatic pressing of investment cast implants is a third technique, in addition to the solutionizing heat-treatment and hot working, for improving the strength and corrosion resistance of Co-Cr-Mo-C alloys. That this technique can increase the tensile properties of cast H.S. 21 has been demonstrated in a separate investigation (31). Since such processing heals microvoids, reduces coring, and dissolves carbides and other secondary phases, the corrosion resistance of hot isostatically pressed cast implants should be favorably affected. Experiments are currently underway to determine if such is the case.

#### Acknowledgments

For the financial support of the investigation of which the present study was a part we are grateful to the National Science Foundation. For cooperation in the development of wrought H.S. 21 and No. 7 alloy we are indebted to Dr. S. Wlodek of the Haynes Stellite Division of the Cabot Corporation. The technical assistance of Dr. F. J. Kummer and Mr. G. Arndt of M.I.T. is also thankfully acknowledged.

Manuscript received June 30, 1975. This was Paper 369 presented at the Toronto, Canada, Meeting of the Society, May 11-16, 1975.

Any discussion of this paper will appear in a Discussion Section to be published in the June 1977 JOURNAL. All discussions for the June 1977 Discussion Section should be submitted by Feb. 1, 1977.

*Publication costs of this article were assisted by General Electric Company.*

#### REFERENCES

1. J. T. Scales, G. D. Winter, and H. T. Shirley, *J. Bone Joint Surg.*, **41B**, 810 (1959).
2. J. H. Hicks and W. H. Cater, *ibid.*, **44B**, 122 (1962).
3. J. Brettle and A. N. Hughes, United Kingdom Atomic Energy Authority Report No. GRO/44/83/12 (Ex).
4. F. W. Bultitude and J. R. Morris, United Kingdom Atomic Energy Authority Report No. GRO/44/83/22 (Ex).
5. V. J. Colangelo and N. D. Greene, Report to National Institute of Health GM-12661-01 (1968).
6. J. T. Scales, B. M. Roantree, R. Perry, and R. Eborall, *Eng. Medicine*, **2**, 51 (1973).
7. T. P. Hoar and D. C. Mears, *Proc. R. Soc. London, Ser. A*, **294**, 486 (1966).
8. K. Asgar and F. A. Peyton, *J. Dental Res.*, **40**, 73 (1961).
9. J. Charnley, *J. Bone Joint Surg.*, **53B**, 342 (1971).
10. J. Brettle, United Kingdom Atomic Energy Authority Report No. GRO/44/83/13 (Ex).
11. P. G. Laing, A. B. Ferguson, and E. S. Hodge, *J. Biomed. Mater. Res.*, **1**, 135 (1967).
12. R. W. Revie and N. D. Greene, *ibid.*, **3**, 465 (1969).
13. R. W. Revie and N. D. Greene, *Corros. Sci.*, **9**, 755 (1969).
14. F. J. Kummer, M.I.T. Ph.D. Thesis, (June 1973).
15. J. Cohen and J. Wulff, *J. Bone Joint Surg.*, **54A**, 617 (1972).
16. R. M. Rose, A. Schiller, and E. Radin, *ibid.*, **54A**, 854 (1972).
17. Sulzer Catalogue of Surgical Implant Prostheses.
18. T. M. Devine, M.I.T. SB-SM Thesis (May 1971).
19. T. M. Devine, F. J. Kummer, and J. Wulff, *J. Mater. Sci.*, **7**, 126 (1972).
20. T. M. Devine and J. Wulff, *J. Biomed. Mater. Res.*, To be published.
21. J. T. Scales, *J. Bone Joint Surg.* **53B**, 344 (1971).
22. M. G. Fontana and N. D. Greene, "Corrosion Engineering," p. 322, McGraw-Hill Book Co., New York (1967).
23. N. D. Greene and G. Judd, *Corrosion*, **21**, 15 (1965).
24. I. L. Rosenfeld and I. K. Marshakov, *ibid.*, **20**, 115t (1964).
25. D. A. Jones and N. D. Greene, *ibid.*, **25**, 367 (1967).
26. I. L. Rosenfeld and I. S. Danilov, *Corros. Sci.*, **7**, 129 (1967).
27. G. D. Smith, U. S. Pat. 3,356,542 (1967).
28. M. Stern and A. C. Makrides, *This Journal*, **107**, 782 (1960).
29. N. D. Greene, "Experimental Electrode Kinetics," R.P.I. Press, Troy, N.Y. (1965).
30. T. M. Devine, M.I.T. PhD Thesis, (February 1974).
31. R. Hollander and J. Wulff, *Metals Eng. Q.*, **14**, 37 (1974).
32. G. P. Chernova, N. D. Tomashov, and O. N. Marcova, *Corrosion*, **20**, 166T (1964).
33. T. N. Rhodin, *ibid.*, **12**, 465 (1956).

# Streaming Potential Measurements of Biosurfaces

R. A. Van Wagenen and J. D. Andrade

Department of Material Science and Engineering, University of Utah, Salt Lake City, Utah 84112

and J. B. Hibbs, Jr.

Veterans Administration Hospital and Department of Medicine, University of Utah Medical Center, Salt Lake City, Utah 84132

## ABSTRACT

A technique based on the measurement of streaming potentials has been developed to evaluate the electrokinetic region of the cell periphery. This approach is feasible for cell lines propagated in *in vitro* cell culture in monolayer form. The advantage of this system is that cells may be evaluated in the living state attached to a substrate. Thus it is not necessary to subject the cells to enzymatic, chemical, or mechanical trauma required to obtain monodisperse suspensions which are then normally evaluated by microelectrophoresis. In this manner it should be possible to study the influence of substrate and environmental factors on the charge density and potential at the cell periphery. The apparatus and procedure are described as well as some results concerning the electrokinetic ( $\zeta$ ) potential of borosilicate capillaries as a function of ionic strength, pH, and temperature. The effect that turbulence and entrance flow conditions have on accurate streaming potential measurements is discussed. The  $\zeta$ -potential of BALB/c 3T12 fibroblasts has been quantitated as a function of pH, ionic strength, glutaraldehyde fixation, and Giemsa staining.

The electrokinetic properties of monodisperse suspensions of blood cells have been comprehensively investigated. Electrokinetic studies have been carried out on erythrocytes as a function of pH, ionic strength, and anion binding (1), various chemical treatments (2, 3), and proteolytic enzyme exposure (4). Similar studies have been conducted on lymphocytes (5), leukocytes (6, 7), and platelets (8). Seaman and Heard (9) have modified a microelectrophoresis apparatus originally designed by Bangham *et al.* (10) for analysis of biological materials in monodisperse form.

However, the great majority of cell types are not free and monodispersed in their natural state but, rather, are intimately associated in tissues. Investigators have attempted to characterize cells from *in vivo* sources (11) and cells from *in vitro* tissue cultures (12) using the microelectrophoresis technique. This usually necessitates a dissolution of the tissue or cell monolayer by mechanical, chemical, or enzymatic means to yield a monodispersed suspension. The assumption that such treatments do not significantly alter the peripheral region of the cells and thus their electrokinetic behavior is unsound. Ponder (13) and Seaman and Heard (14) have shown that trypsinization significantly reduces the electrophoretic mobility of human erythrocytes. Seaman and Uhlenbruck (4) extended this analysis to a number of proteolytic enzymes and erythrocytes derived from a variety of species. In most instances there was a significant alteration in measured electrophoretic mobility. Also, it is possible that the association of cells in tissues or monolayers in *in vitro* culture results in profound alterations in their electrokinetic properties compared to those commonly observed in suspension microelectrophoresis.

The initial objective of this research was to develop an apparatus and experimental technique which could directly measure the electrokinetic properties of cells grown in *in vitro* tissue culture. The approach chosen was based on the streaming potential phenomena originally quantitated by Helmholtz and Smoluchowski (15) and explained in some detail by Davies and Rideal (16).

The relationship between the measured streaming potential and the potential at the hydrodynamic shear

**Key words:**  $\zeta$ -potential, cell periphery, borosilicate, entrance effects.

plane, the zeta ( $\zeta$ )-potential is given as

$$\zeta = \frac{4\pi\eta}{\epsilon} \frac{Estr}{P} \left[ K_B + \frac{2K_s}{a} \right] \quad [1]$$

where  $\eta$  and  $\epsilon$  are viscosity and dielectric constant, respectively, in the diffuse double layer,  $Estr$  is the streaming potential measured across the streaming capillary,  $P$  is the pressure difference across the capillary responsible for the flow of electrolyte,  $a$  is the radius of the capillary, and  $K_B$  and  $K_s$  are the specific bulk and surface conductance. The  $\zeta$ -potential can be calculated from measurements of streaming potential and driving pressure if surface conductance is accounted for. This is accomplished by utilizing Eq. [2]

$$\zeta = \frac{4\pi\eta}{\epsilon} \frac{Estr C}{P R} \quad [2]$$

Here  $C$  is a predetermined system constant and  $R$  is the measured a-c resistance of the capillary-electrolyte system.

Normally Eq. [2] is utilized when ionic strength is so low that surface conductance comprises a significant proportion of the total conductance. At high ionic strengths, *i.e.*, physiological electrolyte concentrations, surface conductance is negligible compared to the total conductance, and Eq. [1] simplifies to Eq. [3]

$$\zeta = \frac{4\pi\eta K_B}{\epsilon} \frac{Estr}{P} \quad [3]$$

$K_B$  can then be determined in a standard conductivity cell utilizing platinized gray platinum electrodes. Viscosity and dielectric constant in the diffuse layer are assumed to be equal to bulk values; however, this is probably incorrect according to Hayden (17).

Ball and Fuerstenau (18) have reviewed the streaming potential literature in regard to  $Estr/P$  data. They have concluded that, due to as yet unexplained flow and asymmetry potentials common to a wide variety of electrode types, the slope of the loci of  $Estr$  data at a number of driving pressures in opposite flow directions ( $\Delta E_{str}/\Delta P$ ) should be utilized in Eq. [1], [2], and [3]. This has been the case in this research where the loci of streaming potential data as a function of driving pressure in both flow directions have been fitted to a

linear regression best fit straight line using a Hewlett Packard (Model 9820A) programmable calculator.

### Apparatus

The streaming potential apparatus is illustrated in Fig. 1. It is composed entirely of borosilicate (Corning 7740) glass with the exception of two sections of Silastic (Dow Corning polydimethyl siloxane medical grade) tubing (F) used to connect the streaming capillary (E) to the electrode chambers (C). The electrodes are of the silver, silver chloride type and are prepared by the anodic electrolytic deposition of an AgCl coating on a silver wire (A. D. Mackay, New York). The wire electrodes are in the form of a spiral and are epoxied into 7/15  $\frac{1}{8}$  glass joints which mate with the electrode chambers. Two 200 ml reservoirs (A) serve as containers for the streaming fluid and are connected to the electrode chambers (C) and an N<sub>2</sub> pressure source via section B. Section D is a dip tube extending to the bottom of each reservoir. Sections A, B, C, and D are connected together via 7/15 and 19/22  $\frac{1}{8}$  glass joints and were made small enough to be rf glow discharged prior to each streaming experiment.

The reservoirs are positioned in a constant temperature bath and stirring can be accomplished with a magnetic stirrer. The system pH (Corning Model 12 pH meter and glass electrode combination) and temperature (0-100°C, accurate to 0.1°C) can be monitored continuously. Purified N<sub>2</sub> gas (99.999% pure) serves as a pressure source utilized to drive the streaming fluid through the capillary. The four-way ball valve (V) (Whitey Model B-43YF2) simultaneously exposes one reservoir to N<sub>2</sub> driving pressure and the other to atmospheric pressure. A 90° rotation of the valve applies pressure to the opposite reservoir and reverses the electrolyte flow. Pressure is adjusted with a two-stage oxygen regulator (Matheson Gas Products Model 3104) with an adaptor for N<sub>2</sub> and a Tycos pressure gauge (T) (0-300 mm Hg, accurate to 1 mm Hg). The components of the pressure drive system are connected to the streaming apparatus via Silastic tubing. The streaming potential is measured with a high input impedance digital electrometer (Keithley Model 616), and the resistance or conductance of the streaming fluid is measured with an a-c bridge at a frequency of 1 kHz (General Radio Model 1650B). The streaming apparatus is electrically isolated from extraneous electrical signals by a Faraday cage (copper screen 50 mesh/in.) (FC).

### Procedure

Streaming potential data were obtained by measuring streaming potentials at a driving pressure of 2 cm Hg, then reversing the flow direction and repeating the measurement. The driving pressure was increased by 2 cm Hg and streaming potentials were again measured

in both flow directions. This process was repeated until the driving pressure reached 12-14 cm Hg. The slope,  $\Delta E_{str}/\Delta P$ , of the best fit straight line was utilized in Eq. [3]. Solution specific conductance was determined in a precalibrated cell with platinized platinum electrodes. The cell constant, *C*, of the streaming capillary and the conductivity cell were predetermined using a 0.1N KCl solution of known specific conductance (19). Following streaming measurements, the resistance of the capillary electrode system was measured with the a-c bridge. In most instances where ionic strength was high, solution conductance masked surface conductance and *K<sub>B</sub>* was determined in a conventional conductivity cell. Equation [3] was then utilized. This was the case for all data reported here.

Radio frequency glow discharge (RFGD) of the streaming cell components was carried out to eliminate problems with surface contamination which occasionally developed. RFGD (Commercial Plasmod System, Tegal Corporation, Richmond, California) in argon gas at 100  $\mu$ m Hg and an rf power density of 50W for 5 min was highly effective in removing surface contamination.

All chemicals utilized were analytical reagent grade (Fisher Scientific Company, Fairlawn, New Jersey). Water used in this study was twice distilled over Pyrex glass (Corning Still Model AG-11) and had a conductivity of  $1 \pm 0.1 \mu$ mho/cm. Phosphate buffered saline (PBS) was made up as 0.145M NaCl,  $2 \times 10^{-4}$ M KH<sub>2</sub>PO<sub>4</sub>, and  $8 \times 10^{-4}$ M Na<sub>2</sub>HPO<sub>4</sub> using twice distilled water. Glutaraldehyde was employed as a fixative in a 2% (v/v) solution in PBS (obtained in purified form as an 8% (v/v) unbuffered aqueous solution sealed under pure N<sub>2</sub> from Polysciences, Incorporated, Warrington, Massachusetts). Giemsa biological stain (Fisher Scientific Company, Fairlawn, New Jersey) was utilized at 10% (v/v) in twice distilled water. Nigrosin (Eastman Organic Chemicals, Rochester, New York) dye exclusion was used as a test of membrane viability at a concentration of 1% (wt/v) in PBS. Dulbeccos modified Eagle Medium (Grand Island Biological Labs) supplemented with penicillin (100 units/ml), streptomycin (100 mg/ml), and 20 mM HEPES (N-2-hydroxyethyl piperazine-N-2-ethane sulfonic acid, ICN Pharmaceuticals, Cleveland, Ohio) buffer was utilized as the cell culture medium and will be referred to as DMM. Fetal bovine serum (fbs) was added as specified.

An established line of BALB/c 3T12 mouse fibroblasts (noncontact-inhibited, tumorigenic cells) were cultured to confluency in borosilicate capillaries  $600 \pm 20 \mu$ m ID. The cells were harvested from milk dilution bottles by trypsinization [6 ml of 0.25% (v/v) trypsin], resuspended in DMM supplemented with 10% (v/v) fbs, and centrifuged at 200g for 5 min. The cells were then resuspended in DMM, counted in a hemocytometer, washed in DMM twice, and resuspended at a seeding concentration of  $1 \times 10^6$  cell/ml in DMM. The cells were seeded by drawing the cell suspension into the capillary using a 1 cm<sup>3</sup> syringe. Both ends of the capillary were capped with Silastic tubing and clamps; the capillary was placed in an incubator at 37°C, 90% humidity, and 95% air/5% CO<sub>2</sub> for 20-30 min. This was sufficient time to allow the cells to contact and form an adhesive bond with the glass surface. Fresh DMM supplemented with 10% (v/v) fbs was then drawn into the capillary. After approximately 5-10 hr the capillary was removed from the incubator and reseeded in another position on the internal circumference in the same manner. Four to five cell seedings over a 24-36 hr period were sufficient to get a uniform distribution of cells on the interior of the capillary. Glass syringes of 30 ml capacity were attached to each end of the capillary via Silastic rubber tubing. Supplemented medium (DMM, 10% fbs) was continuously perfused through the capillary at a flow rate of 0.5 ml/hr using a Sage syringe pump (Sage Instruments Model 341). This was sufficient to keep the cells metabolically and mitotically

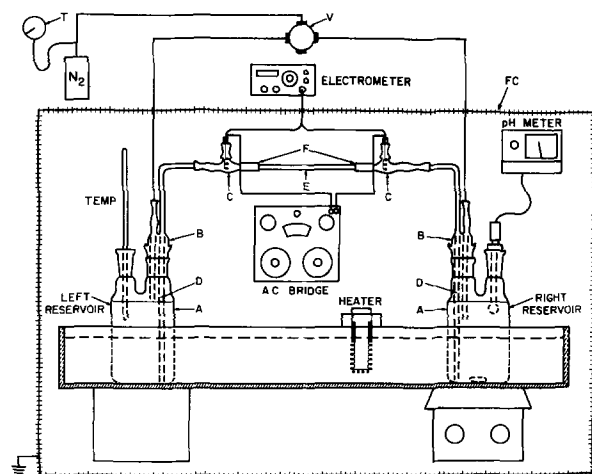


Fig. 1. A schematic diagram of the streaming potential apparatus

Table I. Composition of aqueous electrolyte utilized in electrokinetic evaluation of living cells

Component	Millimoles/L of component
NaCl	133.00
CaCl <sub>2</sub>	1.80
KCl	5.36
MgSO <sub>4</sub> · 7H <sub>2</sub> O	0.81
KH <sub>2</sub> PO <sub>4</sub>	0.20
Na <sub>2</sub> HPO <sub>4</sub>	0.80
D-glucose (anhydrous)	5.55

active, and after 24-36 hr the cells had proliferated to monolayer density.

The capillary was removed from the perfusion apparatus and rinsed in 5 ml of cell streaming solution (Table I) at 5 ml/min. It was then inserted into the streaming apparatus and evaluated within 10-15 min. Following this, the cells in the capillary were fixed in a 2% (v/v) glutaraldehyde PBS solution for 30 min at 37°C. After fixation the electrokinetic properties of the cells were evaluated as a function of pH and ionic strength. When the electrokinetic evaluations were completed, the cells were stained in a 10% Giemsa solution in distilled water, reevaluated electrokinetically, and photographed in both transmitted light and the scanning electron microscope. The cells on glass substrates were post fixed in 1% osmium tetroxide PBS solution at 37°C for 15 min, dehydrated in a graded series of ethanol water solutions, critical point dried in liquid CO<sub>2</sub>, mounted, coated with carbon and gold, and observed in a Cambridge stereoscan scanning electron microscope.

For streaming studies on glass and cell monolayers as a function of pH, pH was adjusted with solutions of NaOH or KOH and HCl having the same ionic strength as the streaming solution. In all studies where pH was maintained constant, phosphate buffer (2 × 10<sup>-5</sup>M KH<sub>2</sub>PO<sub>4</sub>, 8 × 10<sup>-5</sup>M Na<sub>2</sub>HPO<sub>4</sub>) was added to the streaming electrolyte. The temperature was maintained constant at 24°C in all studies.

### Results and Discussion

Preliminary investigations concerning the effect of capillary geometry on measured streaming potential indicated a linear decrease in  $\Delta E_{Str}/\Delta P$  as the length of the capillary decreased. This was at odds with the conclusion inherent in the derivation of the streaming potential equation in that capillary geometry should not affect the streaming potential. An analysis of flow turbulence and entrance effects on streaming potential was carried out to determine the cause of the discrepancy.

Figure 2 is an  $E_{Str}$  vs.  $P$  plot for two streaming tubes. Tube A is 600  $\mu$ m ID and 30 cm in length, while tube

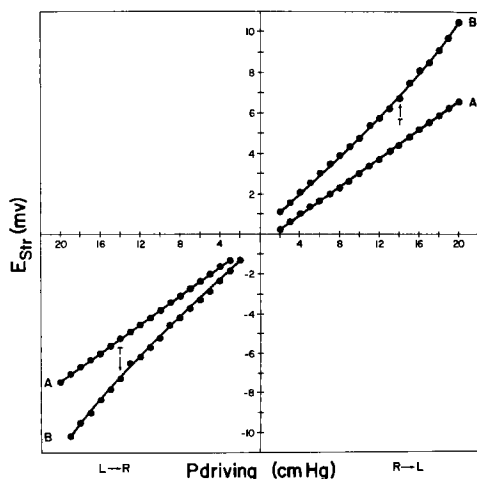


Fig. 2.  $E_{Str}$  vs.  $P_{driving}$  for two borosilicate capillaries A and B. The streaming solution was 0.01M KCl buffered to a pH of 7.

B is 1250  $\mu$ m ID and 30 cm long. In the case of tube A the data is linear and the slope ( $\Delta E_{Str}$  vs.  $\Delta P$ ) is equal in both flow directions. Measured flow rates and subsequently calculated Reynolds numbers indicated laminar flow throughout the measured pressure range for tube A. In the case of the larger tube (B), the data at low driving pressures is linear and the slopes are equal in both flow directions; however, at a pressure of 14 cm Hg the flow becomes turbulent ( $R > 2000$ ) and the data becomes nonlinear at higher driving pressures. This seems to indicate a marked deviation in the  $\Delta E_{Str}/\Delta P$  data obtained if the flow changes from laminar to turbulent. This is at odds with data published by others (19) for turbulent flow in aqueous systems. One can also see a difference in  $\Delta E_{Str}/\Delta P$  for tubes A and B which would seem to indicate that turbulent flow is not the only cause of deviations in the calculated  $\zeta$ -potential for tubes of various sizes.

The results of streaming potential studies on borosilicate capillaries as a function of length and internal diameter are shown in Fig. 3. Each tube was evaluated at its greatest length and then successive portions were removed and it was reevaluated. This was continued until no tube remained. The only variable was length since  $\eta$  and  $\epsilon$  are assumed constant and  $K_B$  greatly predominated over  $K_S$  at this high ionic strength (0.01 g ions/L). Capillaries B (1284  $\pm$  34  $\mu$ m ID) and C (595  $\pm$  15  $\mu$ m ID) were commercial borosilicate; there was no significant variation in ID along the length. Both capillaries exhibited a constant  $\Delta E_{Str}/\Delta P$  value until a critical length was reached whereupon there was a marked drop in  $\Delta E_{Str}/\Delta P$ . The critical length ( $L_c$ ) at which this occurred was 58 cm for tube B and 20 cm for tube C. Capillary A was hand drawn from a larger tube. There were significant variations in ID along its length. Points 1 and 2 shown in Fig. 3 were obtained when the capillary was 190  $\pm$  12  $\mu$ m ID, while equivalent lengths taken from the center of the tube gave lower  $\Delta E_{Str}/\Delta P$  values and had an ID of 160  $\pm$  5  $\mu$ m. This would seem to indicate that at lengths less than some critical length the diameter and length of the streaming capillary markedly affect the measured streaming potential, while at lengths greater than  $L_c$  minor variations in diameter and length have no measurable effect.

The onset of turbulent flow does not seem to cause this behavior since flow was laminar in all cases for tubes A and C and there seemed to be no significant effect due to turbulent flow for tube B. If one compares the measured flow rates,  $Q_m$ , in the three tubes with the theoretical flow rates,  $Q_t$ , calculated using Poiseuille's law as expressed in Eq. [4]

$$Q_t = \frac{\pi r^4}{8 \eta} \frac{dP}{dX} \quad [4]$$

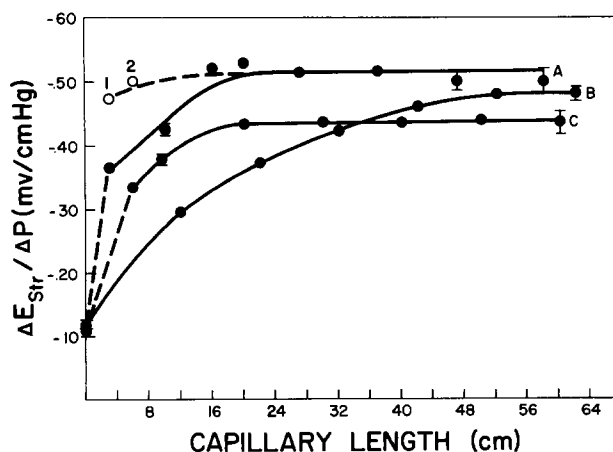


Fig. 3.  $\Delta E_{Str}/\Delta P$  vs. streaming tube length for three borosilicate tubes A, B, and C. The streaming solution was 0.01M KCl buffered to a pH of 7. Error ranges correspond to one standard deviation.

where  $r$  is the tube radius,  $\eta$  is the fluid viscosity, and  $dP$  is the pressure drop across a flow length  $dX$ , it is found that  $Q_t$  and  $Q_m$  are equal until the critical length,  $L_c$ , is reached, i.e., 20 cm for tube C and 58 cm for tube B. It can be concluded from this that the streaming data and calculated  $\zeta$ -potential are independent of capillary geometry (the variations in plateau values of  $\Delta E_{str}/\Delta P$  are expected since the tubes were from different sources and most probably had different surface histories) as long as Poiseuille flow exists. This is what Helmholtz predicted as Bocquet has pointed out (20). Poiseuille flow actually requires that four basic conditions exist, i.e., the flow is steady, incompressible, laminar, and established.

Many investigators have simply ignored the established flow criteria. It takes a certain length,  $L_e$ , past the entrance of a cylindrical flow system, to establish a parabolic velocity profile during steady laminar flow of an incompressible fluid. The value of  $L_e$  has been found both experimentally (21) and theoretically (22) to be given by Eq. [5]

$$L_e \approx 0.06RD \quad [5]$$

Here  $R$  is the Reynolds number and  $D$  is the diameter. On the basis of this analysis, it seems that if  $L_e$  is greater than  $10 \pm 1\%$  of the total streaming tube length, the  $\Delta E_{str}/\Delta P$  ratio and subsequently calculated  $\zeta$ -potential will be anomalously low.

Electrode asymmetry at high ionic strength can develop, particularly if the electrodes have aged appreciably over the course of several months' use, and if they have been exposed to protein or other adsorbable solutes. This is illustrated in Fig. 4. Curves 8B through 12B were obtained utilizing silver, silver chloride electrodes which had previously been exposed to a streaming capillary with a surface of adsorbed fetal bovine serum. The asymmetry developed at that time. It was absent in earlier experiments at high ionic strength (0.1 g ions/L) where protein was not present (not shown). The asymmetry diminished with continuous streaming of electrolyte in approximately 30 min (8B-10B). As long as streaming continued, the slope  $\Delta E_{str}/\Delta P$  (10B-12B) remained constant.

If flow ceased for any length of time, asymmetry reappeared and it required another 30-40 min of streaming to obtain good linearity and reproducibility. At lower ionic strength (0.01 g ions/L) the asymmetry was not evident (1B and 4B, Fig. 4). When fresh electrodes were prepared and protein contamination was absent, there was no deviation from linearity at low ionic strength (0.01 g ions/L) or high ionic strength (0.1 g ions/L) as shown in Fig. 5.

The asymmetry exhibited by aged silver, silver chloride electrodes at high ionic strength may be due

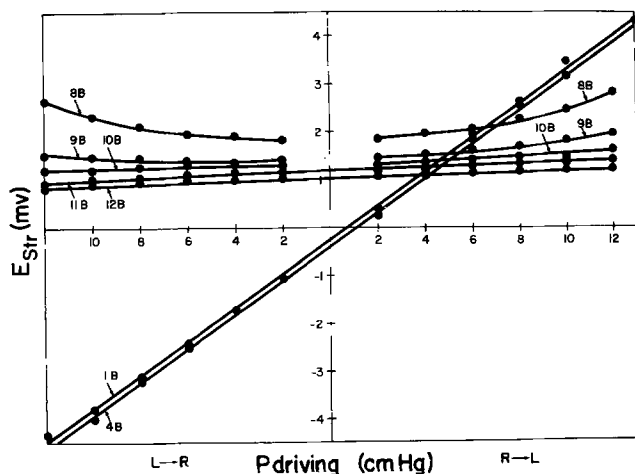


Fig. 4.  $E_{str}$  vs.  $P_{driving}$  for a borosilicate capillary. The streaming solution was 0.1M KCl (unbuffered) for curves 8B-12B and 0.01M KCl (unbuffered) for curves 1B and 4B.

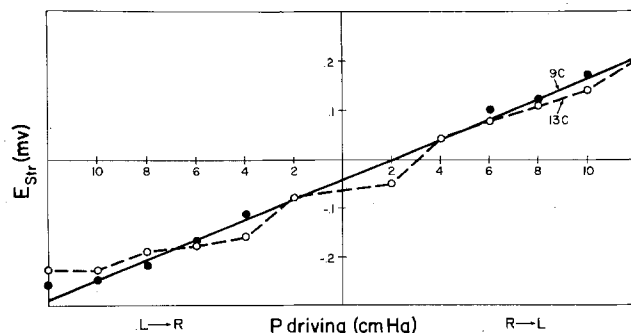


Fig. 5.  $E_{str}$  vs.  $P_{driving}$  for a borosilicate capillary. The streaming solution was 0.1M KCl. 13C was immediately after chloridization while 9C was after equilibration and short-circuiting in streaming solution for 30 min.

to protein adsorption in the pores of the AgCl coating. Janz and Ives (23) maintain that silver may form stable complexes with amino and sulfhydryl groups of organic molecules which can compete with the insolubility of the AgCl thus negating the proper functioning of the electrodes. It has also been suggested (23) that 10-25% of the silver should be chloridized to AgCl to produce electrodes having good reproducibility and stability. The electrodes exhibiting asymmetry problems had only 1% conversion (assuming 100% current efficiency) of Ag to AgCl. Srinivasan (24) has recommended that silver, silver chloride electrodes be prepared in a slowly alternating a-c fashion utilizing anodic deposition of AgCl and cathodic current to increase surface area by enhanced pore formation. The above recommendations were followed. Silver, silver chloride electrodes were prepared electrolytically with a slowly alternating current (5 min anodic, 2 min cathodic, etc.); the gross surface area per electrode was 1 cm<sup>2</sup> and the net anodic current density time product was 6.9 A-sec/cm<sup>2</sup>. There was a theoretical conversion of silver to silver chloride of 16%. Electrodes freshly prepared in this fashion are stable and have never shown prolonged asymmetry at high ionic strength even upon protein adsorption.

Figure 6 comprises 4 SEM micrographs of silver, silver chloride electrode surfaces. The general shape of the electrodes used in this study are shown in Fig. 6a. They consist of silver wire coils 6 mm long and 3.8 mm OD. The gross surface area is 1 cm<sup>2</sup>. Figure 6b illustrates the AgCl surface of a freshly prepared electrode (anodic 5 mA/cm<sup>2</sup> for 4 min, 1% conversion of Ag to AgCl). A number of pores can be seen as well as some microgranularity on a cobblestone surface. Figure 6c is the same electrode after approximately 3 months use. This was the same electrode which developed asymmetry at high ionic strength and protein exposure. The cobblestone appearance is still partially evident; however, much of the pore structure and all of the microtexture are lost. The pores between the cobblestones are now replaced by smaller pores in an incomplete cobblestone structure. Figure 6d is the surface of a freshly prepared electrode employing the alternating anodic and cathodic deposition of AgCl previously described. The highly porous structure obviously increases the surface area available for current transport. Electrodes prepared in this manner have not exhibited asymmetry at high ionic strength and exposure to protein solutions as long as they are equilibrated several hours prior to use.

The calculated  $\zeta$ -potential of borosilicate glass as a function of temperature is shown in Fig. 7. The standard deviations at both ionic strengths are rather large, particularly for 0.1M NaCl. This is due primarily to the variation in  $\Delta E_{str}/\Delta P$  slopes obtained at various temperatures and not so much to the inability to get accurate slopes at constant equilibrium temperatures. Due to the wide standard deviations it can only be con-

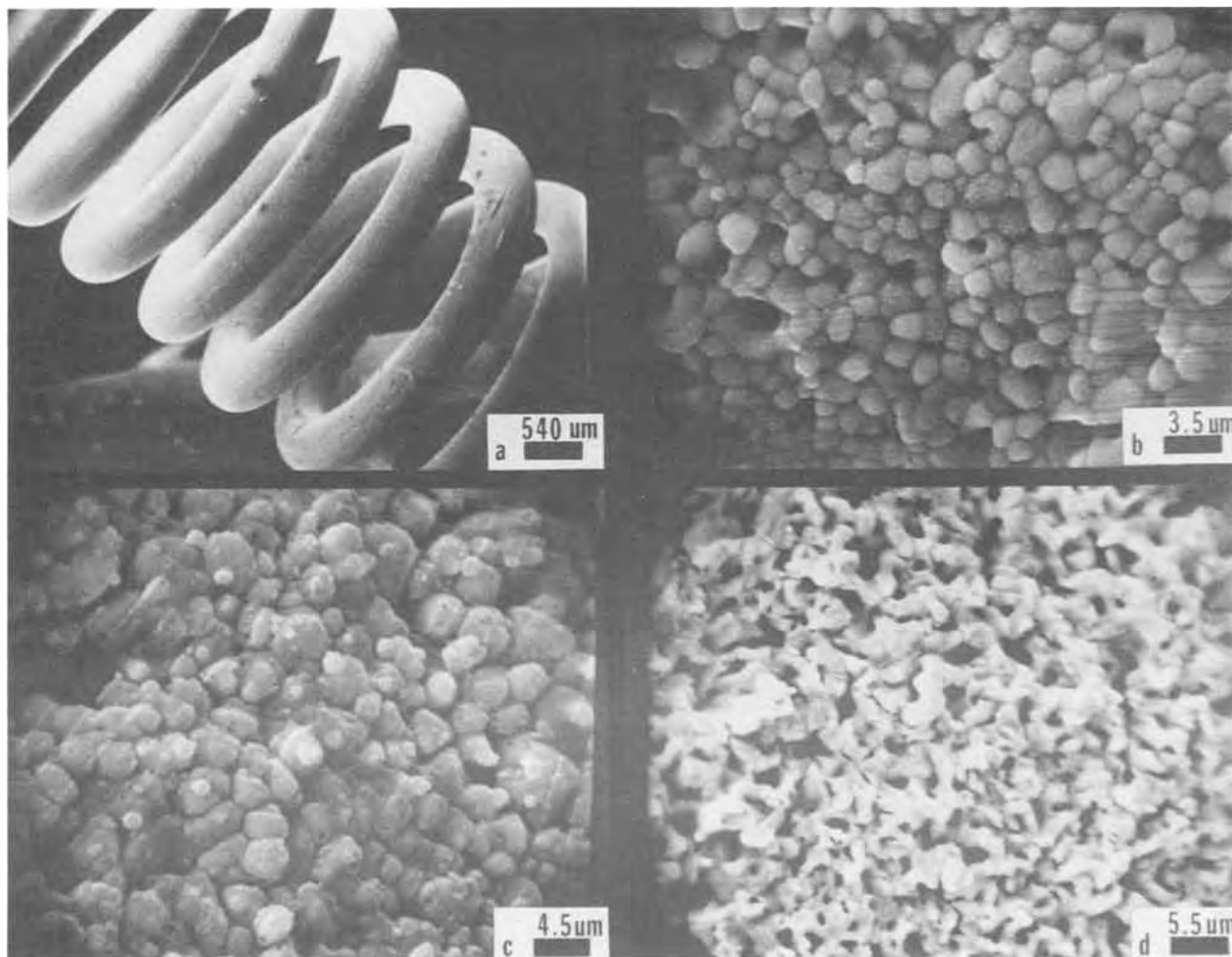


Fig. 6. SEM micrographs of silver, silver chloride electrode surfaces

cluded that there is no statistically significant variation in  $\zeta$  as a function of temperature.

The variation in  $\zeta$ -potential with pH for borosilicate glass is shown in Fig. 8. The data indicates that borosilicate has a  $pK_a$  of  $\sim 5.7$  assuming that all the surface charge is due to the ionization of ionogenic  $\equiv Si-OH$  (silanol) groups in the hydrated region of the glass. This is at variance with the data of Hair and Hertl (25) and Marshall *et al.* (26) which suggests a  $pK_a$  for surface silanol groups of 7.1-7.2. However, it is quite prob-

able that high concentrations of hydronium ions exist in the hydrated surface region of the glass due to cation exchange. If this were the case, the  $\zeta$ -potential at acidic pH could be considerably less than that occurring as a result of charge generation purely by ionogenic silanol groups. The result would be an apparent shift in  $pK_a$ . A second cause of the discrepancy may be due to the presence of boranol groups ( $\equiv B-OH$ ) in significant numbers at the hydrated surface of borosilicate glass. The proportion of boron to silicon in the porous surface may be as high as 1:3 rather than 1:18

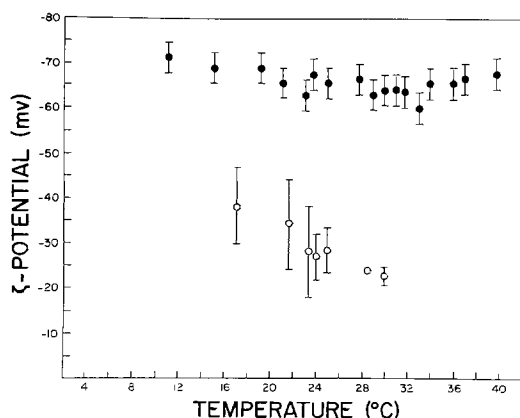


Fig. 7. Calculated  $\zeta$ -potential of borosilicate glass as a function of temperature. Streaming solution was 0.01M KCl ( $\bullet$ ) and 0.1M NaCl ( $\circ$ ); both solutions were buffered to a pH of 7.0. Error ranges correspond to one standard deviation.

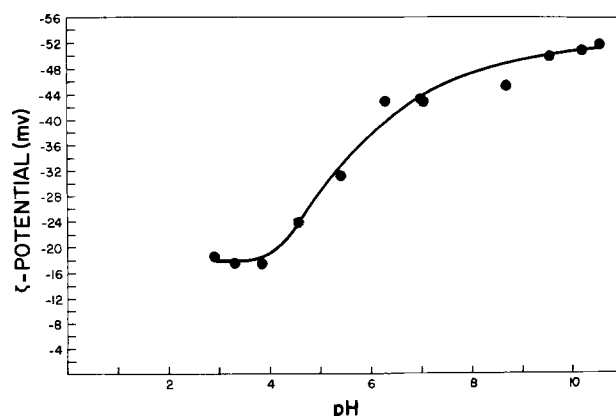


Fig. 8. Calculated  $\zeta$ -potential of borosilicate glass as a function of pH. Streaming solution is 0.01 M KCl. The pH was altered with KOH and HCl solutions of the same ionic strength.



as expected in the bulk (27). The  $pK_a$  of boranol groups is 5.1 and this would also tend to shift the resultant surface  $pK_a$  to a more acidic region.

Figure 9 illustrates the increase in  $\zeta$ -potential with decreasing ionic strength (KCl) at constant pH (7.1) and temperature ( $24^\circ\text{C}$ ). The linear portion of the curve corresponds to the expansion of the electrical double layer as ionic strength decreases. At an ionic strength of less than  $3 \times 10^{-4}$  g ions/L there is a deviation from linearity due to the onset of surface conductance which was not accounted for in the calculation of  $\zeta$ . This is in agreement with the detailed analysis of surface conductance made by Rutgers and DeSmet (28) and Li and DeBruyn (29).

Streaming potential studies on living 3T12 cells were carried out using cell streaming solution as described in Table I. It was necessary to incorporate divalent cations and glucose in the electrolyte to maintain good cell substrate adhesion during streaming since the high flow rates (typically  $10 \text{ cm}^3/\text{min}$ ) are sufficient to shear off cells with altered adhesive properties. Even in the solution used, the cells begin to lose adhesiveness after approximately 20 min. For this reason streaming evaluations on living cells were limited to 10-12 min. Nigrosin staining (30) of 3T12 cells indicated that their membranes retained semipermeability for more than 60 min in streaming solution, even though most cells had retracted off the surface in monolayer sheets. Apparently, the cells sacrifice cell-substrate bonds rather than cell-cell bonds and retain membrane function and viability even after 60 min of exposure to streaming solution at room temperature. The  $\zeta$ -potential of living cells was  $-28.8 \pm 2.5 \text{ mV}$  (streaming solution Table I, ionic strength 0.145, pH 7.3, temperature  $24^\circ\text{C}$ ). Following 2% glutaraldehyde fixation, the  $\zeta$ -potential dropped to  $-17.6 \pm 2.6 \text{ mV}$  under the same conditions. The decrease in electrokinetic potential following glutaraldehyde fixation may be due to a loss of free draining volume in the cell periphery, that is, the region of hydrodynamic slip containing a portion of the peripheral charge is eliminated due to glutaraldehyde cross-linking of membrane protein, thus preventing the detection of this charge by electrokinetic techniques. Following fixation the cells were evaluated as a function of ionic strength and pH.

The effect of pH on fixed 3T12 cells is shown in Fig. 10. Ionic strength was constant at 0.01 g ions/L (NaCl). In a qualitative sense the data is similar to that of Vassar *et al.* (3) for fixed human erythrocytes. In the plateau region from pH 7 to 10 there is no variation in  $\zeta$ -potential; however, there is a precipitous and quite linear decrease in  $\zeta$ -potential below pH 6 indicating the presence of an ionogenic molecular type(s) with an acidic  $pK_a$  of 4.5 or less. There is no indication of an

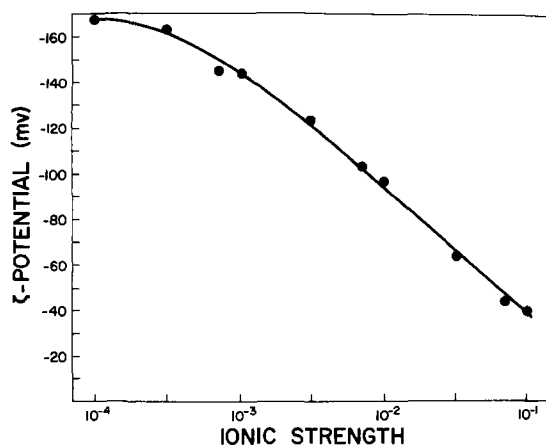


Fig. 9. Calculated  $\zeta$ -potential of borosilicate glass as a function of ionic strength. The streaming solution is KCl buffered to a pH of 7.1.

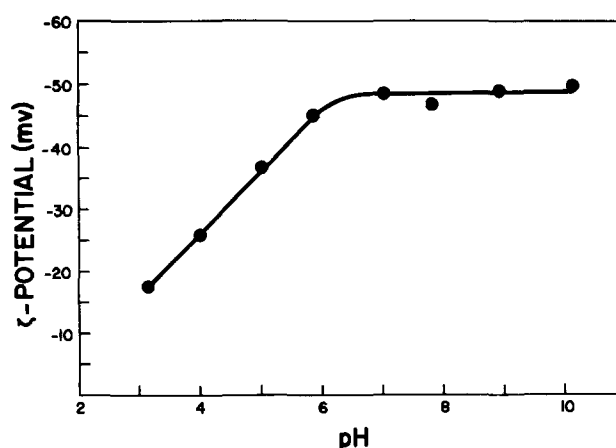


Fig. 10. Calculated  $\zeta$ -potential of 3T12 cells cultured in borosilicate capillaries following fixation in glutaraldehyde. The streaming solution was 0.01M NaCl. The pH was altered with NaOH and HCl solutions of equal ionic strength.

ionogenic species of  $pK_a \sim 6.5$  due to glutaraldehyde fixation as reported by Vassar *et al.* (3). This discrepancy is further accentuated when it is realized that glutaraldehyde fixation caused a 38% decrease in the  $\zeta$ -potential of 3T12 fibroblasts, while it resulted in about a 10% increase in electrophoretic mobility of human erythrocytes. However, when making comparisons of this sort and attempting to see relationships, it should be kept in mind that at least two variables could and probably do invalidate any present attempt at comparison. (i) Different electrolyte components, ionic strengths, and buffers were utilized. (ii) Cell types evaluated were different.

The  $\zeta$ -potential as a function of ionic strength (NaCl) relationship for fixed 3T12 cells is shown in Fig. 11. The expansion of the double layer at lower ionic strength results in a higher  $\zeta$ -potential. The increase is quite linear, and there is no indication of the predominance of surface conductance at low ionic strengths ( $1 \times 10^{-3}$  g ions/L). This data is similar to that of Heard and Seaman (1) for unfixed human erythrocytes; however, in the case of 3T12 cells, the slope over the ionic strength range 0.1-0.01 g ions/L is not as steep as is the case for the erythrocytes. Here again the differences between cell type, fixation, and the presence of sorbital during microelectrophoresis prevents direct comparison.

Following the evaluation of the 3T12 electrokinetic surface, *i.e.*, that region of the cell periphery within  $\sim 10\text{\AA}$  of the hydrodynamic shear region, several

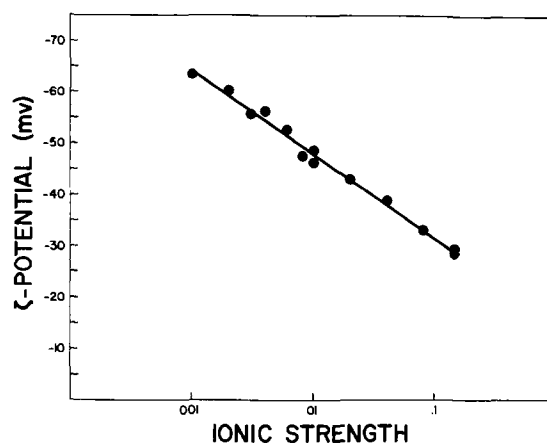


Fig. 11. Calculated  $\zeta$ -potential of 3T12 cells following fixation in glutaraldehyde as a function of ionic strength. Streaming solution was NaCl buffered to a pH of 7.3.



streaming experiments were repeated under identical conditions of ionic strength and pH. There was no significant deviation from original data after 5 days storage in PBS. This would seem to substantiate the assumption that glutaraldehyde fixation produces a stable cell membrane in the electrokinetic sense. The cells were stained in Giemsa to enhance microscopic evaluation of the uniformity of the 3T12 cell layer. Giemsa staining at 25°C for 8 min resulted in a 20% reduction in calculated  $\zeta$ -potential, i.e.,  $-46.2 \pm 1.3$  mV to  $-36.7 \pm 0.8$  mV (0.01M NaCl, phosphate buffer, 25°C, pH 7.2).

Comparative scanning electron micrographs of stained and unstained 3T12 monolayers indicated that Giemsa-stained cells were altered morphologically. Nonstained cells were well spread and in contact with the substrate, while stained cells had a more rounded appearance and had lost some contact with the glass. The decrease in  $\zeta$ -potential may have been due to the effect of Giemsa stain on the cell periphery or the altered morphology of the cells. Giemsa is composed of Azure II, Eosin, glycerin, and methanol and any of these may have been the cause of the decrease in  $\zeta$ .

Recently, a technique of evaluating cells cultured in capillary tubes utilizing electroosmosis has been reported by Fike and Van Oss (31). The advantage of this approach is that the cells may be evaluated for long times in the living state; however, the disadvantage is that the ionic strength must be an order of magnitude lower than physiological to obtain accurate measurements.

In conclusion, a streaming potential apparatus and technique have been developed which make it possible to evaluate the electrokinetic properties of cells grown in *in vitro* cell culture. The results for borosilicate glass substrate and 3T12 mouse fibroblasts cultured to confluency on this substrate attest to the feasibility of the approach. The usefulness of various electrokinetic techniques applied to investigations of cell membranes has been established. Microelectrophoresis, streaming potential, and electroosmosis have all been utilized on various cell types, but no single technique seems feasible for a detailed study of a wide variety of cells under all conditions. Rather, the three mentioned techniques must be utilized in conjunction to gain a more complete understanding of the similarities and differences in cell membranes over a wider range of cell types.

#### Acknowledgments

Portions of this work were supported by NASA Contract NAS 8-30253, NSF Grant No. GH38996X, NIH Grant CA15811, the Veterans Administration Hospital, and the University of Utah Faculty Research Committee. We thank Dr. S. Srinivasan for encouragement and consultation; C. C. Moore, D. Coleman, and R. R. Taintor for technical assistance; and R. Kocour and M. Knowlton for preparation.

Manuscript received Aug. 29, 1975. This was Paper 382 presented at the Toronto, Canada, Meeting of the Society, May 11-16, 1975.

Any discussion of this paper will appear in a Discussion Section to be published in the June 1977 JOURNAL. All discussions for the June 1977 Discussion Section should be submitted by Feb. 1, 1977.

Publication costs of this article were assisted by the University of Utah.

#### LIST OF SYMBOLS

$\zeta$	zeta potential (mV)
$\eta$	viscosity in double layer (poise)
$\epsilon$	dielectric in double layer
$E_{str}$	measured streaming potential (mV)
$P$	pressure difference driving electrolyte through capillary (cm Hg)
$a$	capillary radius (cm)
$K_B$	specific bulk conductance (mho/cm)
$K_s$	surface conductance (mho)
$R$	resistance ( $\Omega$ )

#### REFERENCES

1. D. H. Heard and G. V. F. Seaman, *J. Gen. Physiol.*, **43**, 635 (1960).
2. D. A. Haydon and G. V. F. Seaman, *Arch. Biochem. Biophys.*, **122**, 126 (1967).
3. P. S. Vassar, J. M. Hards, D. E. Brooks, B. Hagenberger, and G. V. F. Seaman, *J. Cell Biol.*, **53**, 809 (1972).
4. G. V. F. Seaman and G. Uhlenbruck, *Arch. Biochem. Biophys.*, **100**, 493 (1963).
5. P. S. Vassar, J. M. Hards, and G. V. F. Seaman, *Biochim. Biophys. Acta*, **291**, 107 (1973).
6. P. S. Vassar, M. J. Kendall, and G. V. F. Seaman, *Arch. Biochem. Biophys.*, **135**, 350 (1969).
7. G. V. F. Seaman, P. S. Vassar, and M. J. Kendall, *ibid.*, **135**, 356 (1969).
8. G. V. F. Seaman and P. S. Vassar, *ibid.*, **117**, 10 (1966).
9. G. V. F. Seaman and D. H. Heard, *Blood*, **18**, 599 (1961).
10. A. D. Bangham, D. H. Heard, R. Flemans, and G. V. F. Seaman, *Nature (London)*, **182**, 642 (1958).
11. I. Simon-Reuss, G. M. W. Gook, G. V. F. Seaman, and D. H. Heard, *Cancer Res.*, **24**, 2038 (1964).
12. T. Yamada, T. Takaoka, H. Katsuta, M. Namba, and J. Sato, *Jpn. J. Exp. Med.*, **42**, 377 (1972).
13. E. Ponder, *Blood*, **6**, 350 (1957).
14. G. V. F. Seaman and D. H. J. Heard, *J. Gen. Physiol.*, **44**, 251 (1960).
15. M. Helmholtz, *Wied. Ann.*, **7**, 337 (1879); M. Smoluchowski, "Handbuch der Elektrizität und des Magnetismus," Vol. 11, Graetz, Editor, p. 366, Barth, Leipzig (1921).
16. J. T. Davies and E. K. Rideal, "Interfacial Phenomena," 2nd ed., p. 108, Academic Press, New York (1963).
17. D. A. Haydon, *Recent Prog. Surf. Sci.*, **1**, 94 (1964).
18. B. Ball and D. W. Fuerstenau, *Miner. Sci. Eng.*, **5**, 267 (1973).
19. G. Jones and B. C. Bradshaw, *J. Am. Chem. Soc.*, **55**, 1780 (1933).
20. P. E. Bocquet, Ph.D. Thesis, University of Michigan (1952).
21. L. Prandtl and O. G. Tietjens, "Applied Hydro- and Aeromechanics," p. 22, McGraw-Hill Book Co., New York (1934).
22. H. L. Langhaar, *Trans. Am. Soc. Mech. Eng.*, **64**, A55 (1942).
23. G. T. Janz and D. J. C. Ives, *Ann. N. Y. Acad. Sci.*, **148**, 210 (1968).
24. S. Srinivasan, Personal communication.
25. M. L. Hair and W. J. Hertl, *J. Phys. Chem.*, **74**, 91 (1970).
26. K. Marshall, G. L. Ridgewell, C. H. Rochester, and J. Simpson, *Chem. Ind. (London)*, **19**, 775 (1974).
27. F. M. Ernsberger, *Annu. Rev. Mater. Sci.*, **2**, 529 (1972).
28. A. J. Rutgers and M. DeSmet, *Trans. Faraday Soc.*, **43**, 102 (1947).
29. H. C. Li and P. L. DeBruyn, *Surf. Sci.*, **5**, 203 (1966).
30. J. P. Kaltenbach, M. H. Kaltenbach, and W. B. Lyons, *Exp. Cell Res.*, **15**, 112 (1958).
31. R. M. Fike and C. J. Van Oss, Personal communication.

# Donor Recipient Lymphocyte Recognition in Kidney Transplantation

## Electrochemical Techniques for Evaluating Donor Recipient Tissue Compatibility

P. N. Sawyer, B. Stanczewski, N. Ramasamy,\* D. V. Raman, W. Wrezlewicz, I. Parsa, J. Pindyck, S. L. Kountz, and K. Butt

*Electrochemical and Biophysical Laboratories, Transplantation Service, and Vascular Surgical Services, Departments of Surgery and Surgical Research, State University of New York, Downstate Medical Center, Brooklyn, New York 11103*

### ABSTRACT

Classical methods based on cell recognition *in vitro* do not yield full information on tissue-host compatibility. Acute rejection episodes are thus common in patients with transplanted kidneys. Determination of surface charge of lymphocytes has been employed to provide information on cell recognition. The results from 40 sets of matched kidney donors and recipients indicate that cell electrophoresis could be used to determine tissue-host compatibility. Acute rejection occurs in cases where the electrophoretic mobility of mixed lymphocyte ( $EM_{mix}$ ) is much higher or lower than that of the recipient ( $EM_R$ ). If  $EM_{mix}$  is only marginally lower than  $EM_R$  ( $\pm 5\%$ ) the transplanted organ rejection rate is markedly reduced.

This group has studied "surface recognition phenomena" in biological systems intermittently since 1950. One aspect of this interest has been the study of intravascular thrombosis which entails special surface chemical recognition characteristics (1-5). Another aspect of this interest has been investigative evaluation of the immune response, as a surface recognition or surface chemical event. This area was first investigated by us when we studied slow rejection and thrombosis in fresh and freeze-dried homo transplanted arterial grafts in dog and man in 1950 through 1953 (2, 4, 5). Freeze-dried homo grafts displayed less immunogenicity and thrombosed less than did fresh grafts implanted into the recipient artery (Fig. 1).

**Surface recognition.**—One of the initial steps in the immune response is the recognition of the foreign tissue by the immunocompetent cells as nonself.

If rejection involves "recognition," both should be modified by "electrical masking," (4, 6, 7) that is by modification or rearrangement of the surface charges in the donor tissues, thus preventing antigen-antibody recognition and/or recipient recognition cells principally lymphocytes from attaching to the surface prosthetic groups of the organ transplant (8-12).

In the first experiment, an attempt was made to modify the recognition faculty of the immunocompetent cells of the recipient by inserting a charged metallic pipe prosthesis between donor and recipient arteries at the inflow site. Whether the "electrode pipe" was charged or uncharged the survival of transplanted kidneys was not enhanced (Fig. 2a and b).

An attempt to influence rejection rates in an acute immune response model using an *ex vivo* heterologous rabbit liver perfused by dog was next carried out, and was found to reveal several interesting effects of electrical phenomena. Applied electrodes and developed fields were found to delay the rejection in specific areas of the heterologous liver depending on the configuration of the field (13) (Fig. 3a b, and c). The observations were substantiated by time lapse photography, histologic and biochemical studies of the blood flowing through the *ex vivo* liver, and by mapping the shape and density of the applied electric field. These were compared with the visible rate and type of rejection seen on the surfaces of the exposed livers which were

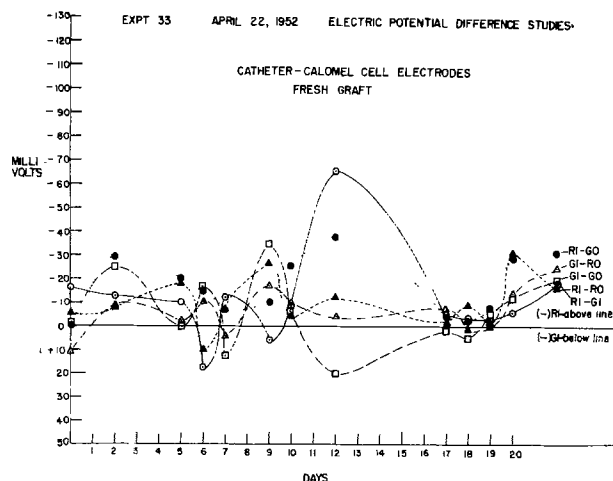


Fig. 1. The six daily readings of a fresh graft and recipient aorta plotted against time, showing initial potential difference in the graft (GI-GO), the early peak at 2 days, the positive peak at 9-13 days, and final negative deflection at 18 days. The graft displayed considerable grade 3+ thrombus formation at autopsy with cicatrization and connective tissue reaction around it. RI-RO shows repeated peaks of potential, positive at 5 days, negative at 10-14 and 18-20 days. These peaks are thought to occur at the point of maximum antigenic response of the host to the fresh homograft. Some superficial infection occurred in this dog. It should be noted that even in 1950-1951, we recognized that changes in the inter-face potential of a fresh or freeze-dried homograft might change with rejection.

photographed. The results indicated that recognition involved an "electron to electron look" which obviously can be masked at least in part by the applied field (10-14). However, the experiment was impossibly expensive and time consuming. A less expensive model was sought.

### The Modern Scene

In 1952, the first successful renal transplantation was carried out using identical sibling kidneys between donor and recipient (15). As time progressed, renal transplantation has become an accepted modality of treatment for end stage renal failure in patients and is being applied on an ever wider scale (16). However, the results of renal transplantation have reached a

\* Electrochemical Society Active Member.  
Key words: electrophoresis, compatibility, recognition, transplantation.

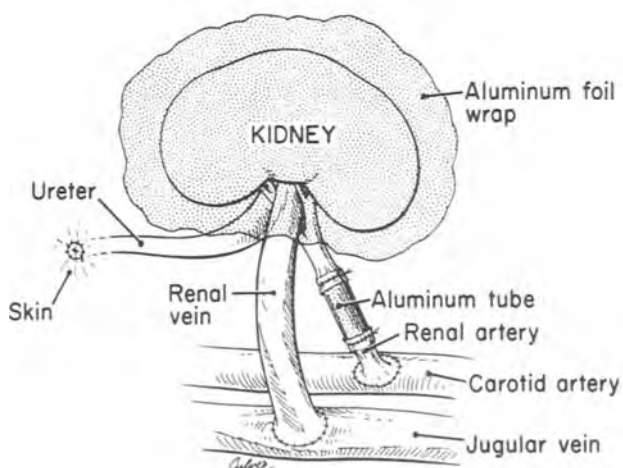
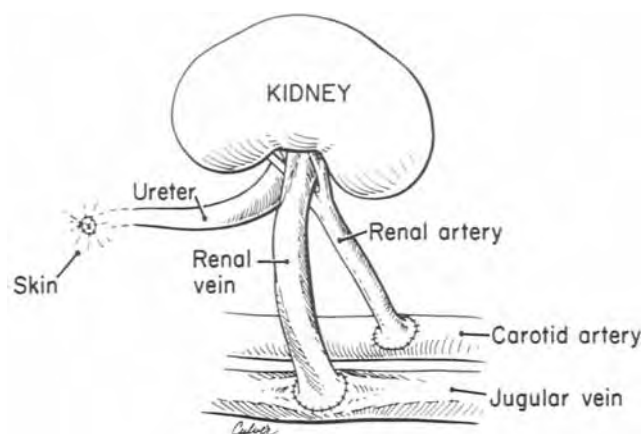


Fig. 2. (a, top) Schematic diagrams of kidneys transplanted from one dog to another dog. The ureter is run through the skin to make a cutaneous fistula. The renal artery is attached to the carotid artery. The renal vein is anastomosed to jugular vein. (b, bottom) Attempts to modify kidney rejection were carried out in one of three ways: (i) either by the implantation of a metal tube between the carotid and the renal artery, (ii) making the tube electrically positive or negative, or (iii) wrapping the kidney with aluminum foil. Size and electric polarity of charge, aluminum foil wrap, or isolation of the kidney, did not modify rejection rate.

plateau and have not shown improvement in the last five years (16). In an effort to try to improve the immediate and long term results of kidney grafting, three broad approaches have been investigated: (i) improved immunosuppression of the host (17, 18), (ii) alteration of the antigenicity of the graft (19), and (iii) improved donor and recipient pair selection (20, 21). While the first two categories of studies have shown significant gains at the present time, they are in general only applicable to the human situation in a limited way. Logistically, improved selection of donor kidneys, particularly those from cadavers, has become increasingly important.

### Synthesis

The solution to making further progress in the evaluation of interfacial phenomena and immune rejection was the clear indication that lymphocytes, probably in this instance T lymphocytes with B lymphocytes as complement, under specified conditions are a major source of immunocompetence (8-12, 14). Modern dogma has it that modification or neutralization of T and B lymphocytes should decrease transplant organ rejection. This has in general only partly been borne out

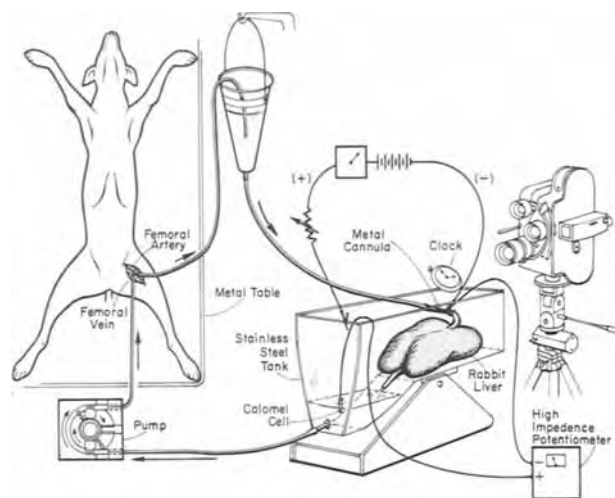


Fig. 3a. Canine blood from the femoral artery perfuses the portal vein of an *ex vivo* liver placed in perfusion tank. The blood flows into the liver through the portal vein and out the inferior vena cava into a well in the tank. It is then pumped back into a dog femoral vein via a blood pump. Changes in the liver are photographed as illustrated including the time lapse clock in the right upper corner of the picture. The perfusion tanks were made either of stainless steel or Plexiglas. The metal catheters are made of a number of different materials in an attempt to influence rejection.

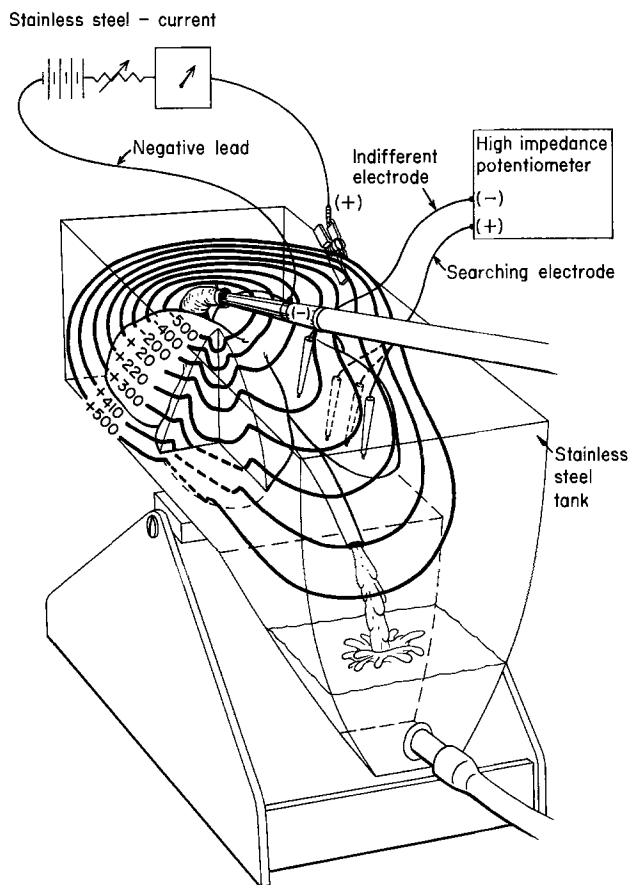


Fig. 3b. The addition of a battery, ammeter, and variable resistance was used to modify the electric potential on the surface of the liver cells in the attempt to modify rejection as shown in this figure. The negative pole of the battery is attached to the metal perfusion cannula. The positive pole here is attached to the wall of the tank.

(22). This belief has led to a series of tests to evaluate compatibility between donor and recipient lymphocytes. The tests most commonly applied include HLA

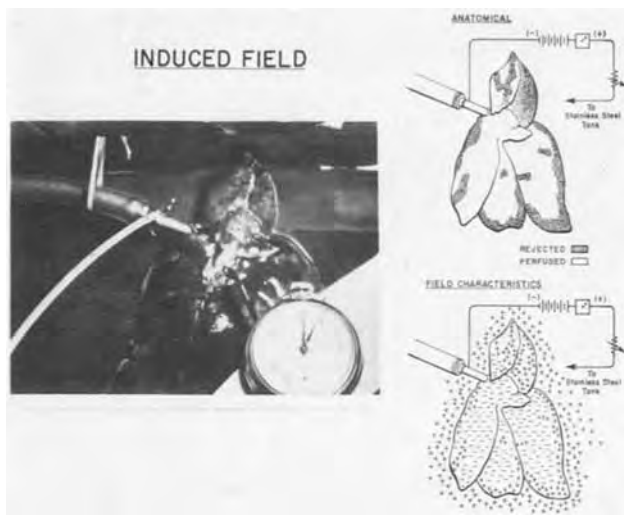


Fig. 3c. With the metal cannula charge negative and the wall of the tank charged positive the lobe of the liver nearest the wall of tank rejects most rapidly. Rejection is somewhat slower than under control conditions. The periphery rejects rather rapidly and stabilizes this way because the field developed by the negatively charged cannula implanted into it is placed near the center of the mass of the *ex vivo* liver. In general, where there is a high concentration of electrons negatively charged ions in this system, there is slower rejection.

and mixed leukocyte culture (MLC) tests (21, 23). Attempts to decrease the immunocompetence of both donor and recipient lymphocytes which carry immune recognition capability has been carried out through infusion of antilymphocyte and antithymocyte serum. Both tend to "mask" lymphocyte surface antibodies.

### Progress

In spite of our recognition of the classical problems of immune rejection, improvement in donor-recipient selection techniques with improved survival and function have really been improving at a great rate only in living related transplants. For example it has clearly been shown that homografts between identical twins or HLA identical siblings have a better than 95% long term chance of survival (16, 20). However, the same serological techniques for determining HL antigens have not been overly successful in selecting satisfactory cadaveric transplants or those from unrelated donors (24). Human lymphocyte antigen tests theoretically are capable of indicating differences in the antigen structure of lymphocytes, red cells, and other cells from nonidentical humans. However, the HLA technique has been found inapplicable in large degree to unrelated donor-recipient pairs suggesting that some subtle antigens which require testing have not been recognized.

The MLC tests require that lymphocytes be extracted from lymph nodes of both donor and recipient and that they be cultured together to determine if during long term culture in a nutrient medium they have a tendency to form "blast cell" forms or not (25). Three days to a week are required to obtain sufficiently good cultures to determine compatibility. This is not useful in cadaveric transplants which require implantation with a maximum delay of 24 hr.

It seemed obvious therefore that if we could look at the changing electrophoretic characteristics of lymphocytes under conditions where donor and recipient lymphocytes were mixed together, and their surfaces allowed to interact, the results might be indicative of "compatibility."

Moreover, an appropriate electrochemical evaluation of donor-recipient lymphocyte compatibility might be used simultaneously as a new model of immunocompetence and/or rejection, as well as a technique for measuring organ acceptance in the new host.

In order to prove utility, it was first necessary to show that, (i) Lymphocytes display electrophoretic mobility. This has previously been shown by many people (26, 27) and been shown modifiable by various surface chemical reactants (10). (ii) Electrophoretic mobilities are reproducible (10-12, 26, 27). (iii) Electrophoretic mobilities for "different lymphocytes" T and B, and from different people vary (14, 28) and why (10-12). (iv) Donor-recipient lymphocyte compatibility is measured by variation in electrophoretic mobility following incubation together. (v) One could determine from the electrophoresis of two lymphocyte groups incubated together whether or not organ transplant could be successful. (vi) Various modifications of the basic tests permit a scientific determination of the lymphocyte surface characteristics which are being evaluated.

### The New Model

The new "model" which is capable of sequential manipulation involves the removal of lymphocytes from donor and recipient lymph nodes or peripheral blood and the mixing of these lymphocytes together to determine whether they inter-react and effect each other in terms of their movement in an electric field, *i.e.*, electrophoresis (Fig. 4). The surfaces of the lymphocytes removed from either blood or lymph nodes can be evaluated electrophoretically, using a microelectrophoresis apparatus (29).

These cells can then be compared with lymphocytes from another person in whom one is contemplating transplanting an organ.

Results of lymphocyte cultures from unrelated donors and cadavers can be compared with those from related donors and from family related donor-recipient pairs. In addition, lymphocytes from the donor can be compared with the serum of recipient and vice versa. The effect of temperature can be measured to deter-

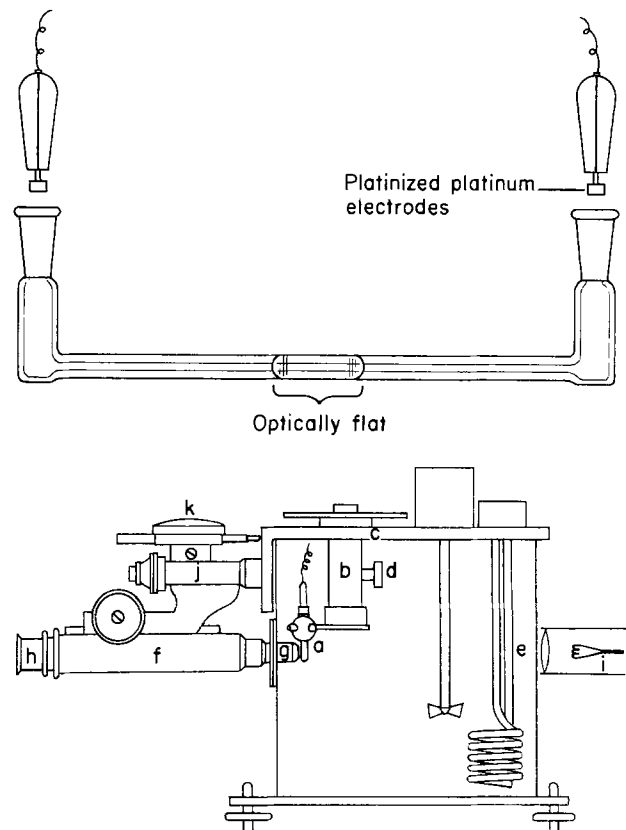


Fig. 4. Diagram of a Seamen's microelectrophoresis apparatus. The most interesting aspect of this modification of the electrophoresis apparatus is Seamen's placing the microscope on horizontal axis to look at a vertical electrophoresis chamber, a novel and very useful development.

mine whether the donor-recipient changes in electrophoresis are complement related. Collateral studies of donor-recipient lymphocytes and/or their serum include: (a) effect of ABO, MN compatibility on electrophoresis; (b) effect of temperature to determine if "complement" is involved; (c) effect of steroids; (d) effect of immuran; (e) comparison of motility of lymph node lymphocytes in comparison with peripheral circulating lymphocytes from the same patient under the same conditions; (f) the effect of washing lymphocytes with either Ringer's solution or distilled water to produce ghosts and the comparison of these suspended treated cells with their precursors or following poisoning; (g) the obvious determination of the effects of storage and incubation time and temperature; (h) effect of aging lymphocytes while stored within and out of lymph nodes in various bathing solutions, etc.; (i) correlatedly the effect of freezing and storage; and (j) effect of anti lymphocyte globulin (ALG) or anti thymocyte globulin (ATG) and other surface active inhibitors on the surface charges to decrease or increase electrophoretic mobility and the ionic structure of the cell interface.

The results of many of these studies will be presented in subsequent presentations. The most important aspect of this determination, that transplant rejection can often be predicted by recipient lymphocyte incubation and electrophoresis, was established.

### Materials and Methods

Electrophoresis was carried out using a Seaman, Cambridge micro electrophoresis apparatus (29) (Fig. 4 and 5).

I. Source of lymph nodes: Lymph nodes were taken from the renal hilum and peri-aortic areas of donor and peri-iliac areas of the recipient.

II. Lymphocytes removed from lymph nodes were prepared by mincing lymph nodes at room temperature and extracting the lymphocytes into Ringer's solution. These were then diluted to approximately 300,000 lymphocytes/cm<sup>3</sup> of Ringer's as measured in a hemocytometer.

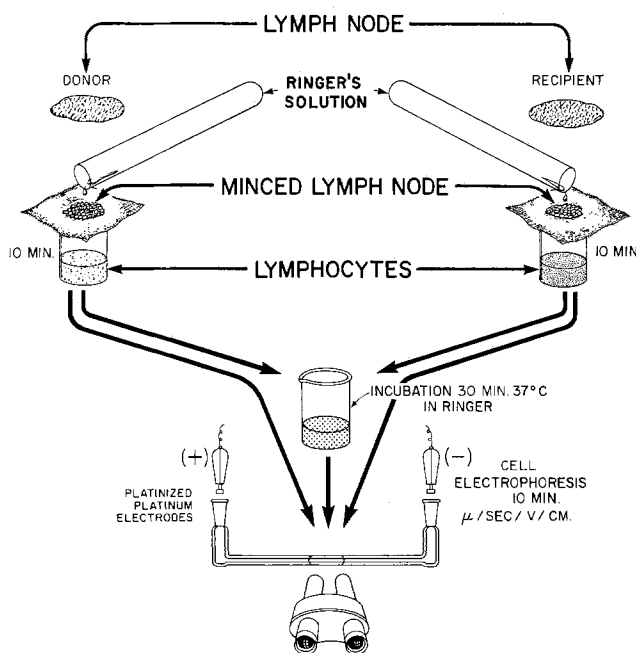


Fig. 5. Lymph nodes removed from both donor and recipient are minced, lymphocytes extracted and suspended in Ringer's solution. The lymphocytes at a concentration of 300,000/cm<sup>3</sup> are then put in a microelectrophoresis apparatus and electrophoresis determined for first donor and then recipient lymphocytes. Finally equal numbers of donor and recipient lymphocytes are mixed together, incubated at 37°C for 30 min and electrophoresis repeated. The results are compared.

III. The cells were suspended in Ringer's solution or isologous serum unless otherwise specified. The electrophoretic mobility of each set of lymphocytes was determined. Following this, equal numbers of donor and recipient lymphocytes were mixed together and incubated at room temperature or at 37°C for one-half hour. Measurements of the electrophoretic mobility of the incubated cells were then repeated, then placed in the electrophoresis apparatus for comparison with the individual electrophoretic mobilities of donor and recipient lymphocytes.

IV. In several experiments lymphocytes from both donor and recipient were each mixed with serum from the opposite to determine the significance of circulating antibodies, complement, and the effect of increasing temperature on each of these.

V. Lymphocytes were washed in some experiments to determine the effect of removal of surface water soluble antigens or antibodies from the lymphocytes. Washing was commonly done with Ringer's solution at room temperature or in some instances distilled water to make lymphocyte ghosts.

VI. Separation of peripheral lymphocytes from peripheral blood was accomplished by removing the supernatant from heparinized blood and treating the supernatant with equal amounts of Ficoll-hypaque solution.

### Results

I. It was found many years ago that lymphocytes were electrophoretically mobile (26) (Fig. 6).

II. It has recently been shown that electrophoretic mobility of the lymphocyte is modified by systemic illness of many sorts (27).

III. In our experiment it was found that lymphocytes removed from lymph nodes in unrelated donors displayed significant differences in electrophoretic mobility initially and following mixing suggesting that unrelated donor incompatibility is reflected in the electrophoretic mobility of lymphocytes from the donor and recipient when mixed together and incubated for 30 min. Surprisingly, the changes most frequently observed are an increase rather than a decrease in electrophoretic mobility (Fig. 7).

#### The Cataphoresis of Platelets in Plasma.

The speed of polymorphonuclear leucocytes is given in the last column. Although red cells and small lymphocytes have different velocities, note that platelets and polymorphonuclear leucocytes have the same velocity (six horses).

Plasma	Age	Platelets		Polymorphonuclear leucocytes
		$V_0$	$V$	
	hrs.	$\mu$ per sec. per volt per cm.	$\mu$ per sec. per volt per cm.	$\mu$ per sec. per volt per cm.
1	30	.71	.41	.46
	6	.82	.59	.57
2	30	.76	.55	.60
	6	.65	.46	.52
3	6	.65	.46	.52
	6	.57	.40	.43
4	6	.57	.40	.43
	6	.67	.51	.53
5	6	.67	.51	.53
	6	.68	.46	.54
Mean excluding No. 2			.45	.49
$\zeta$ potential (millivolts)			12	13
(26.5 $\times \mu$ per sec. per volt per cm.)				

Fig. 6. A table from Abramson's classical monograph indicating the electrophoretic mobility of polymorphonuclear leucocytes, platelets, and ultimately lymphocytes. His early classical work measured the standard electrophoretic mobility of a number of cells which displayed sufficient variability in each animal to suggest that the surface characteristics of the lymphocytes were not a fixed unvarying phenomenon. Note that the cells being negatively charged always moved toward the positive electrode in the electrophoresis apparatus.

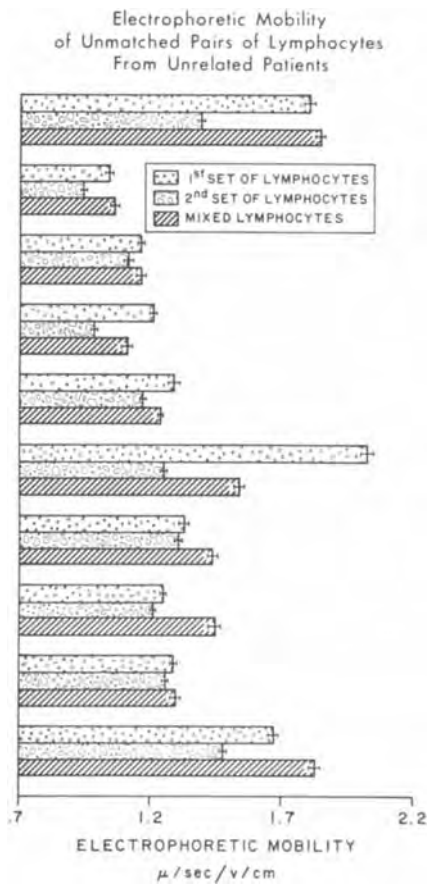


Fig. 7. This table is a determination of electrophoretic mobility of lymphocytes removed from lymph nodes of unmatched pairs of patients at surgery. The figure is extremely interesting in that it shows electrophoretic mobility of lymphocytes from different people is inherently different. The lymphocytic mobility does not follow a fixed pattern. Incubation of the donor-recipient lymphocytes at 37°C or 30 min in this group of patients produces very significant differences in the net electrophoretic pattern.

IV. In a second series of experiments, lymph nodes taken from related donor-recipient pairs provided information that electrophoretic mobility was both more closely matched initially and following incubation in related populations (Fig. 8).

V. Retrospective evaluation reveals that lymphocytes from lymph nodes removed from cadavers preparatory to transplantation when mixed with lymph node lymphocytes from the recipient suggests a very definite improvement in long term viability and function of the transplanted kidney when mixed lymphocyte electrophoresis did not change more than 20% following 30 min incubation at 37°C in Ringer's solution (Table I).

Table I. Electrophoretic mobility and long term survival of the transplanted kidney

Δ EM* (zeta-potential in mV)	No. of months of function before rejection	No. of months of good function	Rejection	Good function
Increase	2, 2, 1, 2, 2, 7d, 1d, 3, 10d	12, 6, 5, 1½, 1½, 1½	9	6
Decrease 0-2	1, 2	14, 14, 14, 15, 15, 15, 6, 6, 6, 5, 1½, 1	2	12
Decrease 2-4	3, 7d	11	2	1
Decrease 4-7	7d, 1½	9, 12	2	2
Decrease >7	2, 2	—	2	—

\* Δ EM = EM<sub>Recipient</sub> - EM<sub>mix.</sub>

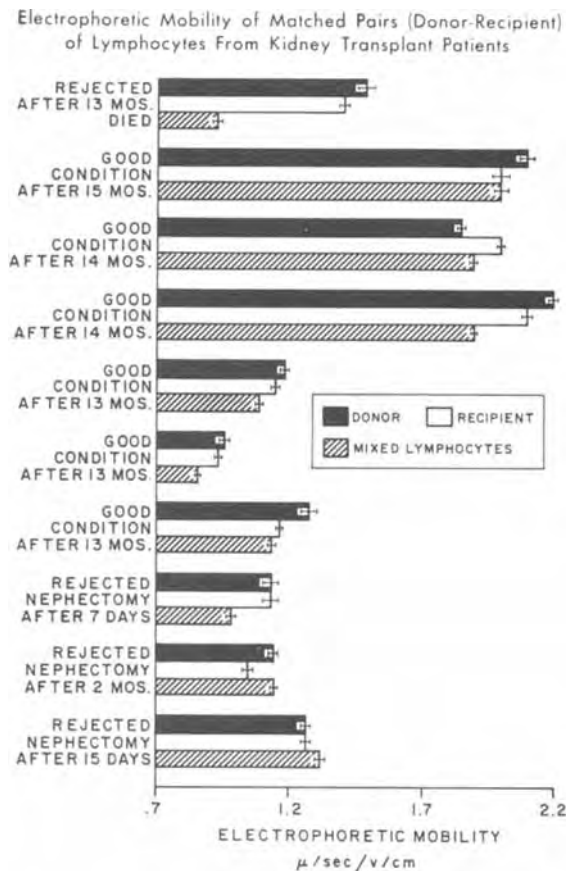


Fig. 8. Kidney transplantation in the large transplant service at the Downstate Medical Center provides an excellent opportunity for evaluation of transplant survival times in a large number of patients. Here we show the electrophoretic mobility of matched pairs of donor-recipient lymphocytes from transplanted kidney patients on the transplant service. Here even more strongly than in unrelated pairs, if gross differences in the electrophoretic mobility of the mixed lymphocytes were observed, rejection almost certainly occurred. In instances where electrophoretic mobility of the mixed lymphocytes was no more than 20% different than the electrophoretic mobility of either donor or recipient lymphocytes, chances of rejection were markedly reduced and chances of long term function were improved.

However, in most instances, recipient lymph nodes were taken from patients already subjected to immunosuppression at the time the lymph nodes were removed so that this factor enters into the problem. This problem illustrates the need to obtain lymphocytes prior to the application of immuno therapy.

Therefore, a prospective study is now going on comparing peripheral and lymph node lymphocytes prior to immunosuppression in contact with donor and recipient serum as well as with donor-recipient lymphocytes incubated for 30 min at 37°C (Fig. 9). This is being done in order to determine the predictive utility of this determination in organ transplantation.

Most important, the predictive results of the mixed donor-recipient lymphocytes in terms of indicating long term acceptability of the transplanted kidney has been compared with both HLA and MLC determinations of the identical donor-recipient pairs.

Discussion

I. It is now probable that electrophoretic techniques may be used to determine in at least a relative sense donor-recipient transplant organ compatibility.

II. The more closely related the donor-recipient pair the more nearly the lymphocyte electrophoretic mobilities are alike following mixing and incubation.

III. Though lymphocytes from related donors when mixed display similar electrophoretic mobilities, washing, grossly denaturing in distilled water, and heating

Electrophoretic Mobility of Lymphocytes From Kidney Transplant Patients  
(Matched Against Serum and Lymphocytes of Donors and Recipients)

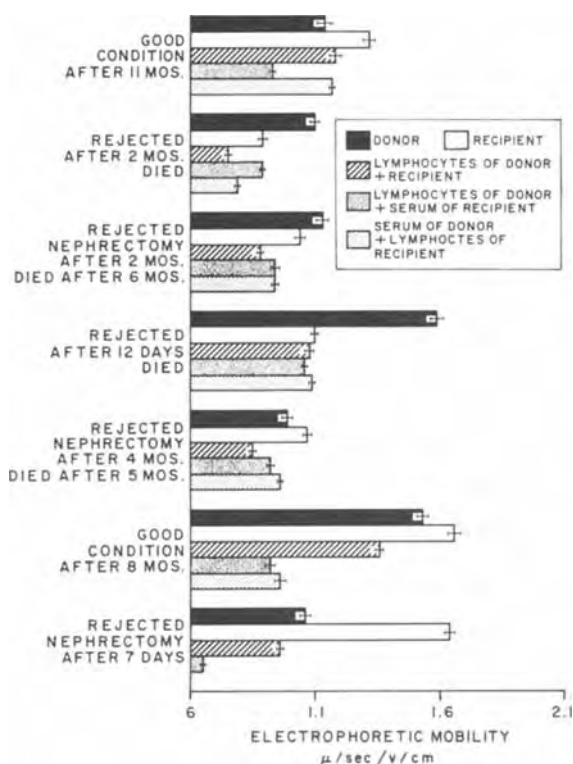


Fig. 9. The electrophoretic mobility of lymphocytes is determined individually and following incubation for 30 min at 37°C. In addition, the lymphocytes are mixed with serum of the opposite member of the transplant group so that donor-recipient comparisons can be made. Here again, significant differences in electrophoretic mobility of the mixed lymphocytes indicated a very short life span for the transplanted kidney. The absolute significance of the lymphocyte serum mixtures and how these relate to the electrophoresis of cell in man is not known. The electrophoretic mobility of donor-recipient pairs in a large human transplant population suggests that this technique might be quite useful as a model of immune rejection as well as a useful predictive test for the suitability of a projected donor-recipient transplant.

all tend to change the electrophoretic mobility of the lymphocytes. The response of the mixing and incubation of lymphocytes from donor-recipient serum and vice versa suggests that much of the immune response measured in the model exists in circulating antibodies. The return of electrophoretic mobility to control rates with heating indicates participation of some form of complement. The reaction, therefore, must be complex. One of the most significant aspects of the finding if not the most important has been the observation of increasing electrophoretic mobility with decreasing transplant tolerances. This indicates uncovering of underlying negative charged groups such as sialic acid, etc. when the antigen antibody reaction occurs on the surfaces of the lymphocytes.

IV. The technique of lymphocyte electrophoresis is rapid. It is easily susceptible to being mechanically taught to large numbers of people and applied in the same way as the classical Landsteiner (30) techniques were easily applied to human blood cross-matching for transfusion. The finding that electrophoretic measurements possibly are informative in terms of kidney transplant survival and function should prove quite useful if confirmed.

V. The study which we have described can provide answers concerning donor-recipient compatibility within at most 1-2 hr following removal of the lymph nodes from donor and recipient. In addition, the studies give additional insight into the basic recognition and charge

characteristics on the surfaces of donor and recipient lymphocytes which relate to rejection. With increasing information, more successful manipulation should be possible, ultimately with more effective utilization of the transplant compatibility determinations (10, 11, 23).

VI. Possibly a more important application of the technique is its use as a model of immunocompetence among various members of a species. The test is inexpensive, easy to use, and is with further definition easily susceptible to measurement and evaluation of the modification of the surface proteins deposited on the lymphocyte, etc. More subtle manipulations may provide very real information concerning specific special immunochemistry of donor-recipient lymphocyte recognition and possibly help in describing their stereochemistry.

Thus, there is promise that the technique will provide dual utility in the immunologic field, one immediately practical and the other ultimately useful. The gross differences in lymphocyte electrophoretic mobilities have not been explained by the study. However, the studies of Mehrishi, Katz, and Zeiller, Seaman, Weiss and the clinical results of transplantation as shown by Kountz, Belzer, and associates and many other investigators give information which may be useful in explaining the observed variations, and give thought for the future.

Manuscript received June 30, 1975. This was Paper 359 presented at the Toronto, Canada, Meeting of the Society, May 11-16, 1975.

Any discussion of this paper will appear in a Discussion Section to be published in the June 1977 JOURNAL. All discussions for the June 1977 Discussion Section should be submitted by Feb. 1, 1977.

#### REFERENCES

1. J. W. Pate, P. N. Sawyer, R. A. Deterling, W. Blunt, and M. S. Parsley, *Surg. Forum, Am. Col. Surg. W. B. Saunders Co.*, **3**, 147 (1952).
2. P. N. Sawyer and J. W. Pate, Research Report Project NM 007 081.10.06, Naval Medical Research Institute, National Naval Medical Center, Bethesda, Md., **11**, 69 (1953).
3. P. N. Sawyer, J. W. Pate and C. S. Weldon, Research Report, Project NM 007, 081 10.08, Naval Medical Research Institute, National Naval Medical Center, Bethesda, Md., **11**, 155 (1953).
4. P. N. Sawyer and S. Srinivasan, *Bull. N.Y. Acad. Med.*, **48**, 235 (1972).
5. J. R. Barberio, J. W. Pate, P. N. Sawyer, and C. W. Hufnagel, *Surg.*, **33**, 827 (1953).
6. J. W. Bothwell, G. B. Lord, N. Rosenberg, C. B. Burrows, S. A. Wesolowski, and P. N. Sawyer, in "Biophysical Mechanisms in Vascular Homeostasis and Intravascular Thrombosis", P. N. Sawyer, Editor, p. 306, Appleton-Century-Crofts, New York (1965).
7. P. N. Sawyer and J. W. Pate, *Surg.*, **34**, 491 (1953).
8. D. H. Katz, T. Hamaoka, M. E. Dorf, and B. Benacerraf, *Proc. Nat. Acad. Sci.*, **70**, 2624 (1973).
9. D. H. Katz, T. Hamaoka, and B. Benacerraf, *ibid.*, **70**, 2776 (1973).
10. J. N. Mehrishi, *Int. Arch. Allergy*, **42**, 69 (1972).
11. J. N. Mehrishi, *Prog. Biophys. Mol. Biol.*, **25**, 1 (1972).
12. J. N. Mehrishi and K. Zeiller, *Eur. J. Immunol.*, **4**, 474 (1974).
13. P. N. Sawyer, R. Rubin, B. Stanczewski, A. Parmeggiani, M. Costello, T. Lucas, and S. Srinivasan, *Eur. Surg. Res.*, **5**, 90 (1973).
14. K. Zeiller and L. Dolan, *Eur. J. Immunol.*, **2**, 439 (1972).
15. D. M. Hume, J. Merrill, and B. Miller, *J. Clin. Invest.*, **31**, 640 (1952).
16. S. L. Kountz and F. O. Belzer, *Ann. Surg.*, **176**, 509 (1972).
17. D. M. Hume, H. M. Lee, G. M. Williams, H. J. O. White, J. Ferre, J. S. Wolfe, G. R. Prout, M. Slapak, J. O'Brien, S. J. Kilpatrick, H. M. Kauffman, and R. J. Cleveland, *ibid.*, **164**, 352 (1966).
18. R. E. Wolf, A. R. Remmers, H. E. Sarles, J. C. Fish, J. D. Lindley, J. A. E. Murillo, and S. E. Ritz-



- mann, *Res. J. Reticuloendothelial Soc.*, **10**, 283 (1971).
19. S. L. Kountz and B. Cohn, *Lancet*, **1**, 338 (1969).
20. M. R. Margules, P. M. Thibault, F. O. Belzer, and S. L. Kountz, *Transplantation Proc.*, **4**, 735 (1972).
21. B. G. Hattler and J. Miller, *ibid.*, **4**, 655 (1972).
22. J. S. Najarian, R. L. Simmons, H. Gewurz, A. Moberg, F. Merkel, and G. E. Moore, *Ann. Surg.*, **170**, 617 (1969).
23. V. P. Eijsvoogel, L. Koning, L. deGroot-Kooy, L. Huisman, J. J. van Rood, A. van Leeuwen, and E. D. du Toit, *Transplantation Proc.*, **4**, 199 (1972).
24. A. Ting and P. J. Terasaki, *ibid.*, **8**, 371 (1974).
25. H. Boehmer, *J. Immunol.*, **112**, 70 (1974).
26. H. A. Abramson, in "Biophysical Mechanism in Vascular Homeostasis and Intravascular Thrombosis," P. N. Sawyer, Editor, p. 3, Appleton-Century-Crofts, New York (1965).
27. G. Ruhenstroth-Bauer, *ibid.*, p. 42.
28. K. Zeiller, E. Holzberg, G. Pascher, and K. Hanning, *Hoppe-Seyler's Z. Physiol. Chem.*, **353**, 105 (1972).
29. G. V. F. Seaman, in "Cell Electrophoresis," E. J. Ambrose, Editor, p. 4, Little, Brown and Company, Boston (1965).

## Effect of Moisture on the Electrical Properties of Bone

G. B. Reinish<sup>1</sup> and A. S. Nowick\*

*School of Engineering and Applied Science, Columbia University, New York, New York 10027*

### ABSTRACT

Both a-c (1000 Hz) and d-c electrical conductivity of human cortical bone are studied after equilibration at various relative humidities. At the same time weight change measurements are carried out as a function of humidity, so as to determine the moisture content of the bone. Both the electrical properties and weight changes show striking hysteresis when plotted vs. relative humidity. However, when electrical properties are plotted as functions of moisture content the hysteresis is eliminated. The hysteresis effects are attributed to capillary condensation in pores. Measurements were made on samples soaked in Ringer's solution as well as samples washed in distilled water, and also with electric field both parallel and perpendicular to the bone axis. The results of these measurements strongly suggest that the large effect of moisture on conductivity is from ionic salt solutions located in pores and channels.

Since the discovery that dry bone and dry collagen were piezoelectric (1, 2), there has been much interest in the possibility that the mechanism controlling osteogenesis, that is, production of new bone cells, is electrical. Recent work on electrical stimulation of bone growth (3, 4) has emphasized the need to study both electrical and piezoelectric properties of bone under varying degrees of moisture content so as to bridge the gap between the well-characterized behavior of dry bone and the very elusive behavior of living bone.

This paper describes the hysteresis, or history dependence, of the moisture content of cortical bone as a function of relative humidity, and the effect of this behavior on electrical properties. Specifically, the conductivity at 1000 Hz and the d-c conductivity, are studied as functions of relative humidity and moisture content, as well as of the orientation of the electric field and the salt content of the bone.

### Experimental Methods

**Sample preparation.**—Fresh cortical bone from the human femur was cut into 4 mm cube-shaped specimens with one pair of faces parallel to the periosteal and endosteal surfaces and another pair perpendicular to the bone axis. Some specimens were stored in Ringer's solution, hereafter referred to as "Ringer's specimens." Other specimens were washed for three weeks in distilled water, with the water changed daily for the first week, and every other day for the next two weeks. These will be referred to as "washed specimens."

Electrodes consisted of silver conductive epoxy cement which was fixed to room-dried specimens; platinum wires were fixed to these electrodes. Some

specimens were prepared with electrodes attached to the endosteal and periosteal surfaces, so as to produce an electric field perpendicular to the bone axis. Others had electrodes attached to the surfaces perpendicular to the bone axis, so that the electric field would be parallel to the bone axis.

**Apparatus.**—A long, water-jacketed, glass cylinder (Fig. 1) was constructed and connected through a Teflon collar to a water-jacketed vessel in which salt solutions were used to maintain the desired relative humidities (5). The apparatus was designed to allow simultaneous measurement of moisture content (i.e., of mass) and electrical properties on identical specimens. The Teflon collar permits equilibration of the air in the lower vessel with that in the long cylinder, but provides an air-tight seal to the outside, by means of rubber O-rings and a clamp. Water was pumped from a thermostatically controlled temperature bath, maintained at 30°C, through the water jackets. To prevent an appreciable temperature gradient in the unjacketed region of the Teflon collar, Tygon tubing with water at 30°C flowing through it was wrapped around this portion of the apparatus, and asbestos insulation was then wrapped around the tubing. In this way the temperature gradient was reduced to less than  $\pm 0.5^\circ\text{C}$ .

A sensitive calibrated quartz spring was suspended in the long cylindrical chamber with a bone specimen hanging from its end. The position of a reference point on the quartz spring was measured by sighting through the glass column, using a micrometer-controlled cathetometer. The change in spring length could be read to 0.01 mm, corresponding to a mass change of 0.01 mg, or to 0.008% of the mass of the bone specimen.

Platinum wires were brought out, through the Teflon collar, from two bone specimens mounted within the chamber (see section A-A of Fig. 1). An impedance bridge was used with an external oscillator

\* Electrochemical Society Active Member.

<sup>1</sup> Permanent address: Department of Electrical Engineering, Fairleigh Dickinson University, Teaneck, New Jersey 07666.

Key words: electrical conductivity, bone (cortical), capillary condensation.



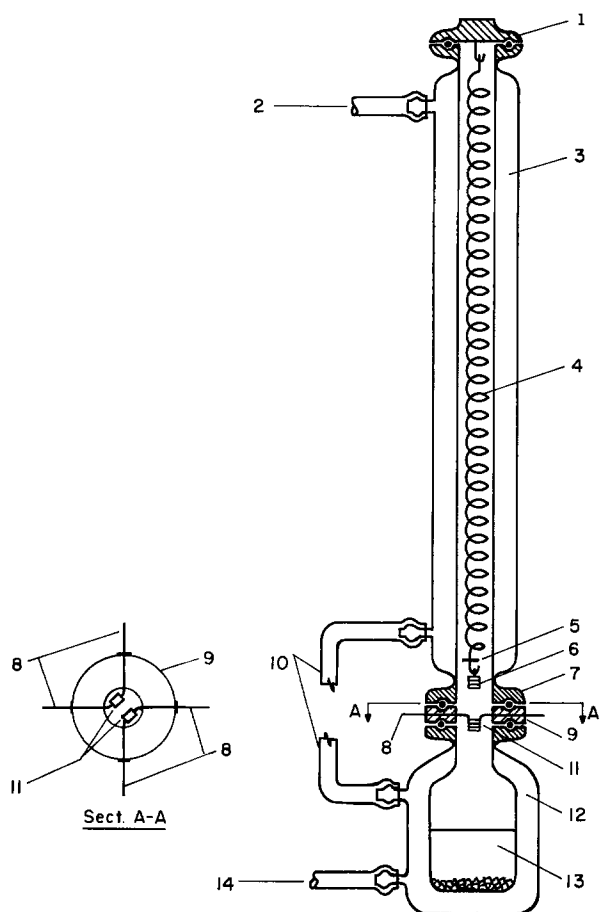


Fig. 1. Apparatus for combined mass and electrical measurements: 1 and 7, clamped flanged joints with O-ring seal; 2 and 14, Tygon tubing to constant temperature bath; 3 and 12, water jackets; 4, quartz spring; 5, spring reference mark; 6 and 11, bone specimens; 8, platinum wires; 9, Teflon collar; 10, Tygon tubing coiled around unjacketed region; 13, saturated salt solution.

and an external detector, so that conductance and capacitance of the bone specimens could be measured over a frequency range of 50-20,000 Hz. Low capacity cables were used, and correction was made for leakage conductance and capacitance by making measurements between leads going to adjacent specimens. An electrometer and d-c power supply were used to measure d-c conductance.

**Procedure.**—Eight different saturated salt solutions were used to provide controlled relative humidities covering the range between zero and 100%. It was found necessary to allow at least one week for equilibration at each humidity. Figure 2 illustrates the

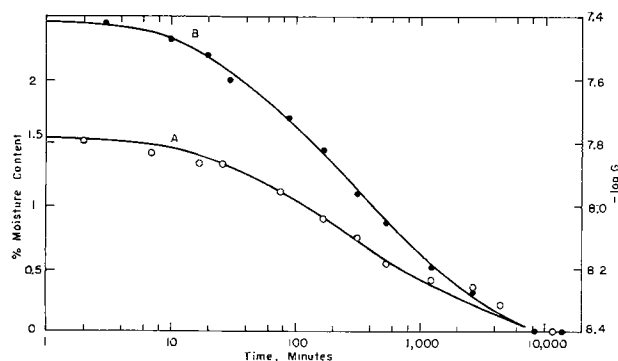


Fig. 2. Kinetic curves of moisture content (open circles, curve A) and conductance (solid circles, curve B) of Ringer's specimens following an abrupt change of humidity from 75 to 30%.

kinetics of equilibration, by showing the variation, with time, of moisture content and conductivity of two bone specimens, simultaneously measured in the same chamber, when the relative humidity was abruptly changed from 75 to 30%. A logarithmic scale was chosen for the abscissa in order to cover conveniently the full period of one week ( $10^4$  min) required to attain equilibrium.

After equilibrium is reached at each humidity, the change in weight of the bone specimen on the spring was measured. The percent moisture content of the bone was then obtained by dividing the change in spring length by the spring calibration and the dry weight of the sample.

At each equilibrium condition, electrical measurements (both a-c and d-c) were made on the two bone specimens mounted on the Teflon collar. In this paper, for the a-c measurements we report primarily the conductance at 1000 Hz. The d-c conductivity, on the other hand, is obtained in two ways: first by a direct electrometer measurement, and second, by extrapolation of a-c data, based on a heterogeneous dielectric model of bone which will be described in a forthcoming paper (6). Measurements were made on Ringer's specimens with electric field perpendicular to the bone axis, and on washed specimens with field both perpendicular and parallel to the bone axis.

The results reported herein are typical of those obtained using ten different specimens in three chambers of the type described above.

## Results

It was found that the moisture content of a sample of bone, as obtained from the weight measurements, is not a unique function of the relative humidity of the atmosphere with which the sample has equilibrated. Specifically, the moisture content is always higher during drying (desorption) than it is during wetting (adsorption). Such results are illustrated in Fig. 3 for both a Ringer's and a washed specimen. The striking aspects of the figure, aside from the existence of pronounced hysteresis, are that the washed and Ringer's samples both follow the same curves, and

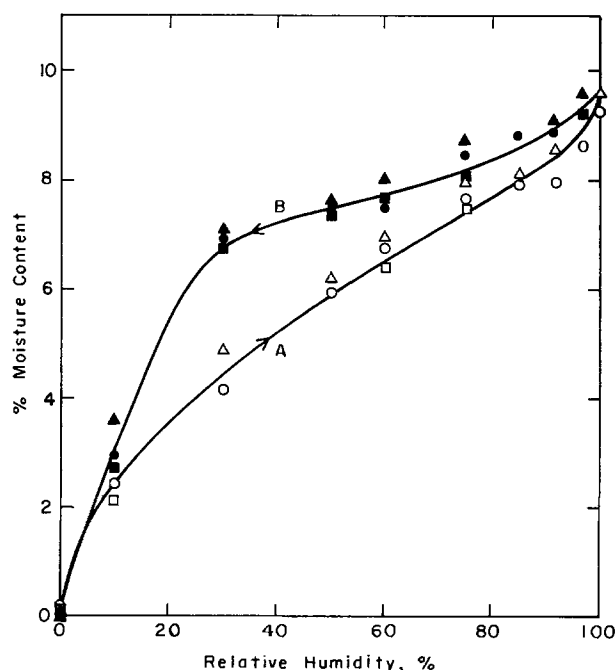


Fig. 3. Equilibrium moisture content of bone as a function of relative humidity: Ringer's specimen, first cycle:  $\circ$  adsorption,  $\bullet$  desorption, second cycle:  $\square$  adsorption,  $\blacksquare$  desorption; washed specimen:  $\triangle$  adsorption,  $\blacktriangle$  desorption.

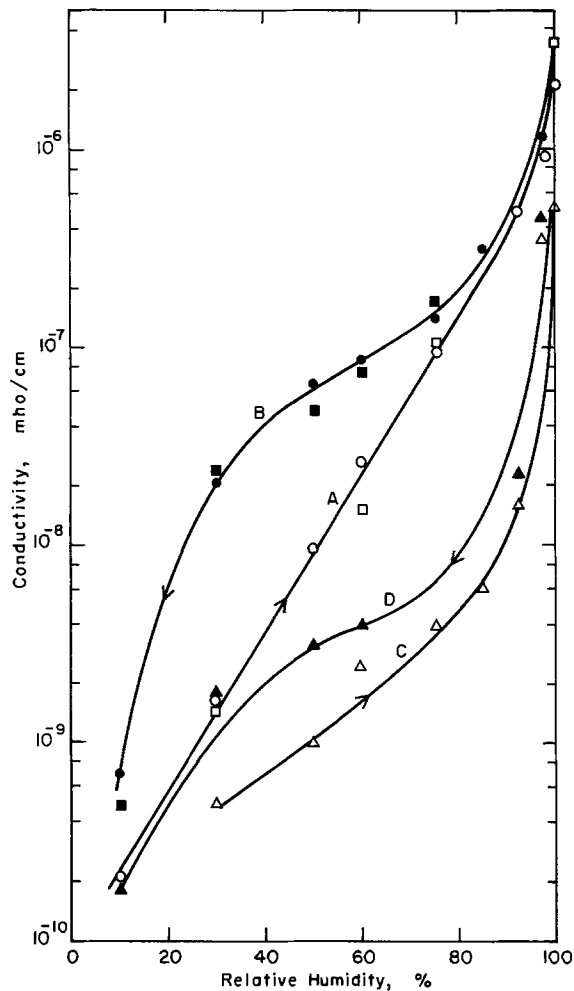


Fig. 4. Conductivity of bone samples at 1000 Hz, with electric field perpendicular to bone axis, as function of relative humidity. Symbols same as in Fig. 3.

also that the curves are very reproducible under repeated cycling.

In Fig. 4, a-c conductivity at 1000 Hz of a Ringer's specimen and a washed specimen are shown as functions of relative humidity under the same conditions of cycling used in the weight measurements. Hysteresis is present for both samples, though it is greater in the case of the Ringer's specimen. Again, the curves are reproducible upon successive cycling.

Because the weight changes were measured concurrently with the conductivity, it becomes possible, using the results of Fig. 3, to convert the data of Fig. 4 into plots of conductivity vs. moisture content. Such plots, given in Fig. 5, show clearly that the hysteresis is completely eliminated, meaning that the conductivity,  $\sigma$ , is a single valued function of moisture content. It follows that the hysteresis observed in plots of  $\sigma$  vs. humidity can be ascribed entirely to the hysteresis in moisture content as a function of humidity (Fig. 3).

Further examination of Fig. 5 brings out additional points of interest. First, dry bone is a very good insulator, with  $\sigma \approx 10^{-11}$  mho/cm. Second, the introduction of moisture increases the conductivity of bone by as much as a factor of  $10^6$ . In fact, an exponential dependence of  $\sigma$  on moisture content is obeyed up to about 8% moisture content. Such an exponential dependence has also been found for collagen (7). Third, the effect of washing salts out of the bone produces a reduction of  $\sigma$  by about one decade over most of the range studied, although the extrapolated value at zero moisture content appears to be the same as for the Ringer's sample. (The absence of data for  $\sigma$

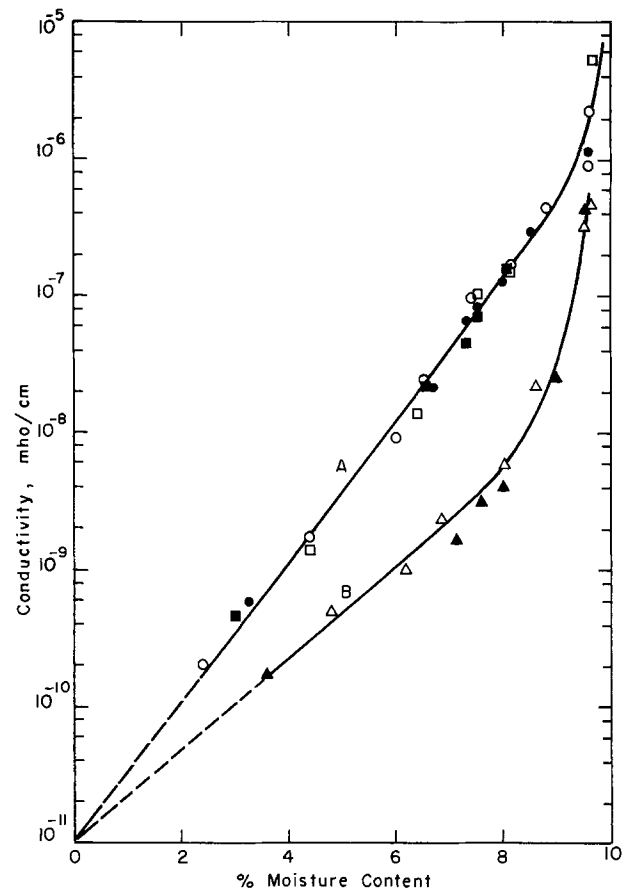


Fig. 5. Conductivity of bone samples at 1000 Hz, with electric field perpendicular to bone axis, as a function of moisture content. Curve A: Ringer's specimen; curve B: washed specimen. Symbols same as Fig. 3.

$< 10^{-10}$  ( $\Omega\text{-cm}$ ) $^{-1}$  is due to limitations imposed by the instruments and by leakage conductance.)

We have also observed hysteresis behavior analogous to that of Fig. 4 both for the real part of the dielectric constant ( $\epsilon'$ ) and for the principal piezoelectric coefficient ( $d_{14}$ ), when these properties are measured cyclically vs. relative humidity (6, 8). In both cases, the hysteresis was eliminated when the data were replotted vs. moisture content.

There is, however, one striking exception to the single valued electrical properties vs. moisture content, in the case of the d-c conductivity of a specimen having the electric field perpendicular to the bone axis. Figure 6 shows the d-c conductivity vs. humidity for such a washed specimen. (This figure includes points obtained both by direct d-c measurements and as calculated from extrapolation of a-c data, as mentioned in the Experimental Methods section. The "calculated" values are believed to be the more reliable because the direct measurements may be influenced by contributions from electrode impedance.) In any case, it is clear from Fig. 6 that there is very little, if any, hysteresis. Similar results are obtained for a Ringer's specimen with the same field orientation, except that the conductivity levels are somewhat higher than for the washed specimen.

A reasonable interpretation for the lack of hysteresis in this particular case is that the d-c conductivity of these samples is a measure of surface conductivity; the amount of moisture on the surface should be determined uniquely by the humidity of the ambient. By contrast to the above case in which the electric field is perpendicular to the bone axis, the d-c conductivity of similar specimens does show pronounced hysteresis vs. the humidity when the electric field is parallel to the bone axis. In this case we

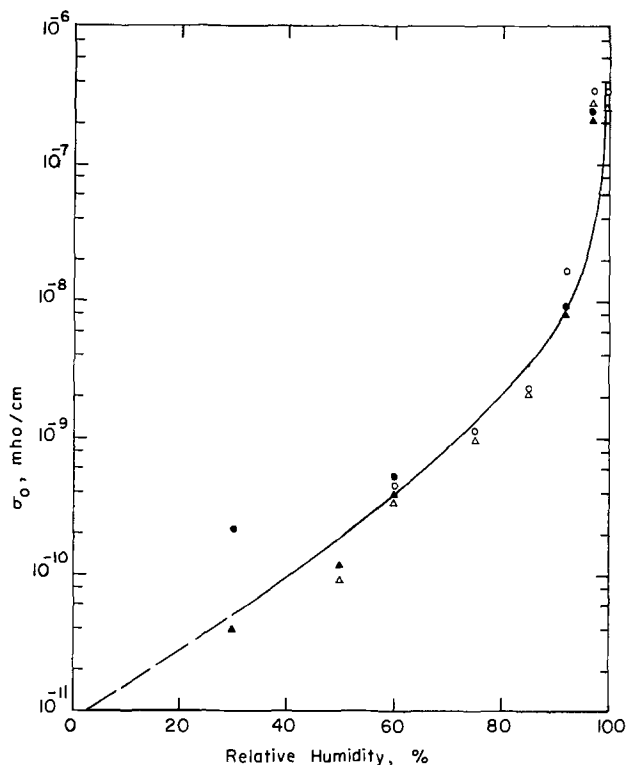


Fig. 6. D-C conductivity,  $\sigma_0$ , of a washed specimen (electric field perpendicular to bone axis) as a function of relative humidity. "Calculated"  $\sigma_0$ :  $\circ$  adsorption,  $\bullet$  desorption. Measured  $\sigma_0$ :  $\Delta$  adsorption,  $\blacktriangle$  desorption.

must have contributions from the bulk as well as surface conductivity. Accordingly, it is anticipated that the bulk contribution alone can be obtained by subtracting the d-c conductivity of a perpendicular-field specimen from that of the corresponding parallel-field specimen. This difference is shown in Fig. 7 as a function of relative humidity for the case of two washed specimens, and again in Fig. 8 as a function of moisture content. The pronounced hysteresis shown in Fig. 7 is completely eliminated in the plot vs. moisture content of Fig. 8.

### Discussion

This work has demonstrated striking hysteresis effects in various electrical properties of bone as functions of humidity when measurements are made over a complete adsorption-desorption cycle. This behavior has been related to the hysteresis in the moisture content as a function of humidity, which may be obtained reproducibly during repeated cycling, and which is the same for both Ringer's and washed samples (as seen from Fig. 3). Such hysteresis behavior has been observed before on a wide variety of porous materials (9, 10). It is attributed to the condensation of water in capillaries or pores, and to the fact that surface tension acts to prevent the removal of previously condensed moisture in the desorption part of the cycle. The presence of "ink bottle" shaped pores, which are wider in the interior than at the exit, accentuates the effect, since water is trapped in a relatively large cavity which cannot empty until the vapor pressure drops below that at the access channel.

The theory of Brunauer, Emmett, and Teller (11, 10) (widely known as the BET theory), which is based on the concept of multilayer physical adsorption of gas molecules, predicts a straight line relationship between  $x/M(1-x)$  and  $x$ , where  $M$  is the moisture content and  $x$  is the relative vapor pressure (here, the relative humidity). Such "BET plots" have been very successful in fitting empirical

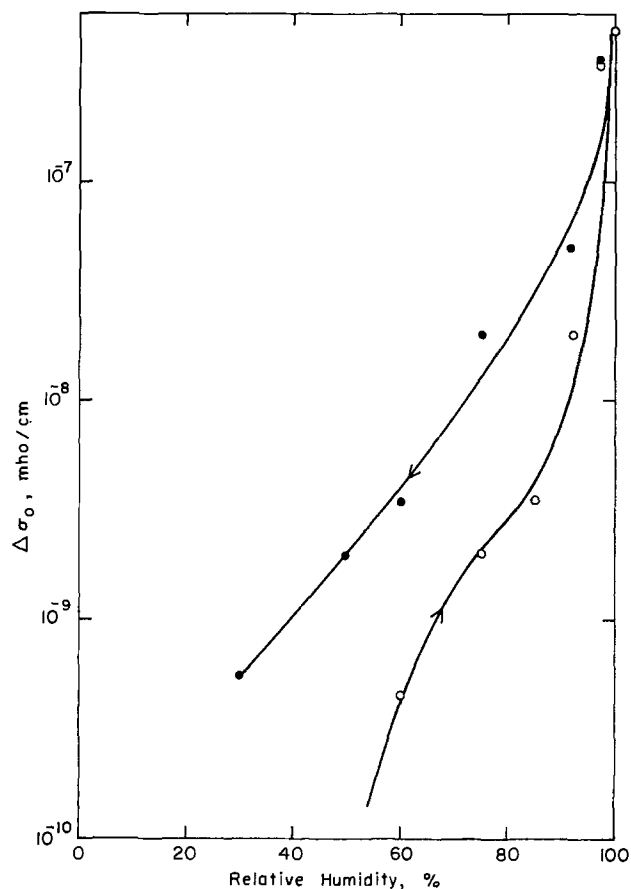


Fig. 7. Difference,  $\Delta\sigma_0$ , between  $\sigma_0$  with parallel field and perpendicular field as a function of relative humidity for washed specimens.  $\circ$  Adsorption,  $\bullet$  desorption.

isotherms, although the theoretical basis has been severely questioned. A BET plot is shown in Fig. 9 both for the adsorption and desorption data of Fig. 3. Departure from linearity occurs at about 32% humidity for the adsorption and 25% humidity for the desorption curve. Such departures can be attributed to the presence of the pores, which not only limit the number of possible layers of adsorption, but introduce the complexity of capillary condensation which is not considered in the BET theory.

From the results of the present work, we may conclude that a major part of the effect of moisture on conductivity involves conduction through ionic salt solutions located in pores and channels. The main evidence for this conclusion is: (a) the existence of large hysteresis effects and the interpretation of such effects, (b) the decrease by one order of magnitude in the conductivity of moist bone which has been "washed" as against the Ringer's sample, and (c) the very high conductivity values attained by moist bone. With regard to the last item, it is interesting to compare the conductivity of wet bone (Fig. 4) with that of pure Ringer's solution (0.014 mho/cm) and that of pure collagen at 12% moisture content<sup>2</sup> ( $\approx 10^{-11}$ - $10^{-12}$  mho/cm) (7). Such a comparison clearly indicates that wet collagen has a conductivity several orders of magnitude lower than wet bone, a difference which is most readily interpreted as a salt-solution effect in the bone. Finally, the fact that the d-c conductivity measured parallel to the bone axis showed a hysteretic component, while that measured perpendicular to the bone axis showed no such contribution, is also consistent with the above conclusion. Such a d-c contribution is interpreted as resulting from interconnected channels containing salt solutions. The re-

<sup>2</sup> This value is believed to be the moisture content of the collagen in bone at 100% humidity (8).

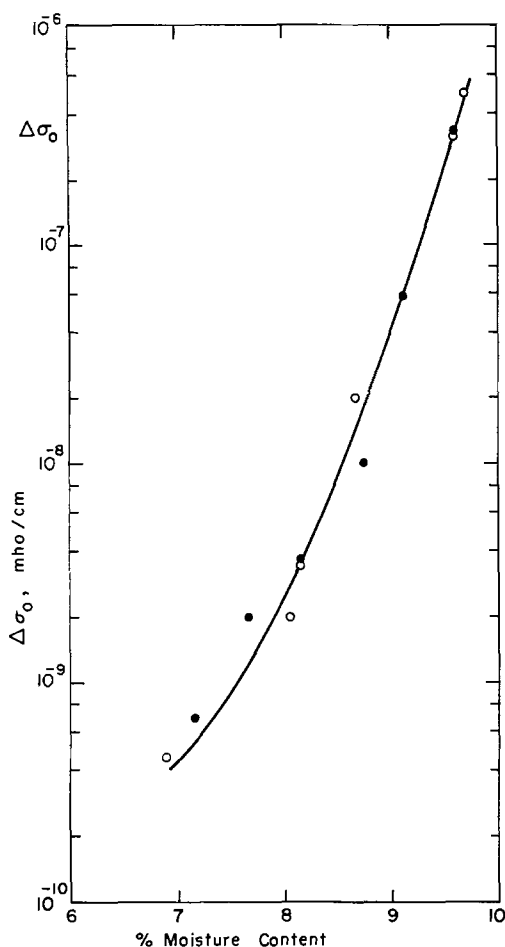


Fig. 8. Data for  $\Delta\sigma_0$  of Fig. 7, replotted vs. moisture content

sults are then in accord with the fact that the open channels in bone run primarily parallel to the bone axis (12).

In contrast to the d-c values, the a-c conductivity also includes contributions from solutions in pores of various sizes which are not interconnected. The presence of such solution-filled pores means that bone is, in fact, a heterogeneous dielectric. In fact, data on the frequency dependence of both the real and imaginary parts of the dielectric constant are consistent with such a picture (6).

There has been much discussion of the concept of "free" water as against "bound" water in proteins and biological systems (13). From the above considerations, it seems clear that in the major range of moisture content covered by these experiments we are dealing primarily with free water. This conclusion is in striking contradiction to the viewpoints expressed by other authors (14). It is possible, however, that at the low humidity end, particularly below the point where the adsorption and desorption curves come together in Fig. 3 (e.g., at  $\leq 5\%$  relative humidity), water that is chemically bound to either the collagen or the mineral constituent of bone may determine the electrical properties. For this reason, a further detailed study of the low humidity region would be of interest.

#### Acknowledgment

One of us (G.B.R.) received partial support from an N.I.H. training grant to the Orthopaedic Research Laboratories at Columbia University. We thank Dr. C. A. L. Bassett for the specimens and for helpful discussions.

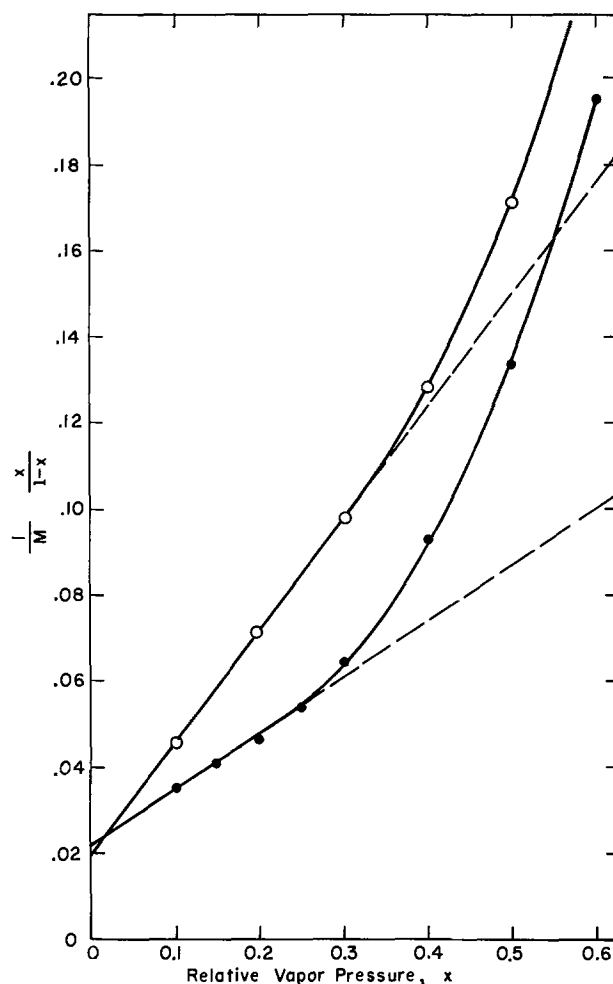


Fig. 9. BET plots for adsorption and desorption of water by bone, from the data of Fig. 3.  $M$  is the fractional moisture content and  $x$  is the relative water vapor pressure.  $\circ$  Absorption,  $\bullet$  desorption.

Manuscript received June 30, 1975. This was Paper 356 presented at the Toronto, Canada, Meeting of the Society, May 11-16, 1975.

Any discussion of this paper will appear in a Discussion Section to be published in the June 1977 JOURNAL. All discussions for the June 1977 Discussion Section should be submitted by Feb. 1, 1977.

#### REFERENCES

1. E. Fukada and I. Yasuda, *J. Phys. Soc. Jpn.*, **12**, 1158 (1957).
2. E. Fukada and I. Yasuda, *J. Appl. Phys.*, **3**, 117 (1964).
3. C. A. L. Bassett, R. J. Pawluk, and A. A. Pilla, *Science*, **184**, 575 (1974).
4. See several papers in the Symposium: "Electrically Mediated Growth Mechanisms in Living Systems," in *Ann. N.Y. Acad. Sci.*, **238** (1974).
5. F. E. O'Brien, *J. Sci. Instrum.*, **25**, 73 (1948).
6. G. B. Reinish and A. S. Nowick, To be published.
7. V. P. Tomaselli and M. H. Shamos, *Biopolymers*, **13**, 2423 (1974).
8. G. B. Reinish and A. S. Nowick, *Nature*, **253**, 626 (1975).
9. C. O. Seborg, *Ind. Eng. Chem.*, **29**, 169 (1937).
10. A. Adamson, in "Physical Chemistry of Surfaces," chap. XIII, John Wiley & Sons, Inc., New York (1967).
11. S. Brunauer, P. H. Emmett, and E. Teller, *J. Am. Chem. Soc.*, **60**, 309 (1938).
12. J. M. Vaughan, "The Physiology of Bone," Clarendon Press, Oxford (1970).
13. I. D. Kuntz, Jr. and W. Kauzmann, *Adv. Protein Chem.*, **28**, 239 (1974).
14. A. A. Marino, R. O. Becker, and C. H. Bachman, *Phys. Med. Biol.*, **12**, 367 (1967).

# The Topography of Cell Surface Ionogenic Groups

J. R. Subjeck and L. Weiss

Department of Experimental Pathology, Roswell Park Memorial Institute, Buffalo, New York 14263

## ABSTRACT

The interaction of cells with their environment appears to be partially regulated by the electrical properties of their surfaces. The adsorption of positively charged, electron dense, colloidal particles visible by electron microscopy, have been used to study the negative charges at the surfaces of normal, transformed, and revertant cell lines and various classes of lymphoid cells.

The surfaces of all mammalian cells so far examined carry a net negative charge (1). Among the surface anionic moieties of interest in this respect are sialic acids (2) and ribonuclease-susceptible groups (3). It seems likely that, in a complex manner, the densities and distributions of ionogenic sites at their peripheries partially regulate some cell interaction phenomena (4).

In this paper we review work which has utilized electron microscopy to map the binding of positively charged particles to negatively charged cell surface sites. Some of the cells were incubated with neuraminidase and/or ribonuclease prior to fixation with subsequent reaction with positively charged particles. The first section of this paper examines the topography of binding sites for the particles on Ehrlich ascites tumor (EAT) cells; the second section considers the use of this technique in examining other cell types.

The principal cationic stain utilized in our investigations is colloidal iron hydroxide (CIH) as developed by Hale (5) and Mowry (6), and later applied in electron microscopy by Gasic *et al.* (7). This colloidal reagent is prepared and used at a pH of 1.9. The CIH particles have been measured and found to have a mean diameter of 8-10 nm (8).

The application of such an acidic stain to the investigation of biological material requires prior fixation in glutaraldehyde. The aldehyde fixative would be expected to react and cross-link positively charged amino, imino, and guanidino surface groups (9). Such groups have been found to account for 5% of the  $\zeta$ -potential of Ehrlich ascites tumor cells (10), which have been used in much of the work reported here. The effects of aldehyde fixation on the topographic arrangement and susceptibility to staining of the negatively charged groups discussed in this paper are uncertain, and this artifact must be constantly borne in mind.

### Variations in Electrical Properties from One Region to Another of the Surface of the Same Cell

The description of the periphery of cells using electrophoresis, microelectrode, or chemical analysis yields an estimate of the spacial average of the measured property over the cell surface. With respect to contact and adsorption of charged drugs, antibodies, viruses, cellular probes (diameter  $\sim$  100 nm), and other entities to cell surfaces, spacial heterogeneities in the distribution of peripheral cellular constituents would be expected to be of significance.

The data reported here are obtained from examination of Ehrlich ascites tumor (EAT) cells, which are maintained by us in single cell suspension culture. The CIH binding has been investigated on EAT cells which have been seeded onto substrates of embedding

plastic or taken directly from suspension. For the adherent cells the topography of CIH binding was examined at cell surfaces that are far distant from other cells, or alternatively are apparently ready to contact or have contacted other cells.

Cells often appear to contact one another via low radius or curvature probes, for which the generic name microvilli is used here. Calculations of the energies of repulsion between two negatively charged surfaces (4) indicate that contact between the surfaces would be facilitated if one or both surfaces were capable of extending such low radius of curvature projections. The density of CIH particles on the cylindrical microvilli probes of EAT cells was determined and then compared with the density found on the regions of the cell surface intermediate between microvilli (the intermicrovillus or IMV surface). The results obtained were found to be independent of whether the cells were reacted with CIH immediately after removal from suspension culture or reacted after a period of 7 hr during which the cells were allowed to spread and adhere to the substrate. For the monolayer prepared material electron micrographs were taken from surfaces of cells which were not in the apparent vicinity of neighboring cells. The data for adherent, isolated cells are summarized in Table I. From this table it is seen that the density of particles adsorbed to the microvilli is approximately twice that found on the IMV surface (9). Prior incubation of cells with ribonuclease reduces the density of particles bound to both the IMV and microvilli surfaces but a twofold difference is maintained. However, prior incubation with neuraminidase shows that while the density of particles on both the microvilli and IMV surfaces is reduced to a very low value, the twofold difference between the surfaces is removed, indicating that the original higher density of particles bound to the microvilli was due to an increased density of sialic acid binding sites on these surfaces.

In this work the stability of the CIH colloid predetermined that cells be reacted at a pH value of 2 under nonphysiological conditions of ionic strength and composition. At this pH value surface groups of higher pK values would be partially or totally protonated,

Table I. Densities of CIH particles bound to microvilli of EAT cells and to their intermicrovillus spaces\*

	Particles/4000 nm <sup>2</sup> $\pm$ SE (No. observations)		
	Treatment		
	Control	RNase	NANase
IMV spaces	2.10 $\pm$ 0.19 (21)	1.69 $\pm$ 0.13 (19)	0.16 $\pm$ 0.05 (19)
Microvilli	4.26 $\pm$ 0.29 (25)	3.51 $\pm$ 0.30 (21)	0.16 $\pm$ 0.03 (25)
Ratio	1:2	1:2	1:1

\* After enzyme treatment indicated.

Key words: colloid, particles, lymphocyte, microvilli.

Table II. Densities of cationized ferritin particles bound to microvilli of EAT cells and to their intermicrovillus spaces\*

	Particles/3000 nm <sup>2</sup> ± SE (No. observations) Treatment	
	Control	NANase
IMV spaces	3.85 ± 0.15 (23)	2.99 ± 0.15 (23)
Microvilli	6.41 ± 0.33 (24)	5.12 ± 0.22 (22)
Ratio	1.0:1.7	1.0:1.7

\* After treatment indicated.

and therefore would be nonreactive with the CIH stain. To determine if the reported differences in the density of neuraminidase- and ribonuclease-susceptible sites extended to other anionic sites having higher pK values, we have used another stain under conditions of physiological pH and ionic strength. The reagent used was cationized ferritin, prepared according to the method of Dannon *et al.* (11) and reacted at pH 7.4 in physiologic phosphate buffered saline. The results of the use of this reagent following fixation, to the surfaces of EAT cells is presented in Table II (12). The microvilli are again found to exhibit a higher density of anionic binding sites. However in this case the increase over the microvilli is not removed by neuraminidase; suggesting the existence of additional anionic sites over the microvilli, which were not revealed at the low pH value.

The tonicity and pH of this stain make it suitable for application to living material. However we have found that due to the essentially dynamic nature of the cell periphery, the cationized ferritin particles become clustered at the cell surface and in some cases appear to be endocytosed (12). Therefore the interaction of this investigative probe with the cell periphery precludes its use in the study of living material.

### Charge Topography and Contact

In our analysis of the surfaces of EAT cells adjacent to neighboring cells, we have attempted to locate sites of impending contact between cells by projecting the axes of microvilli of one cell onto the surface of an opposing cell (Fig. 1). When comparing the binding of CIH particles in the regions at which the microvilli appear to be "aimed," it was found that the mean density was less than half the density for nonaligned regions and that this difference was significant at the 0.1% level (13). The results of this analysis are presented in Table III where the zero point is defined

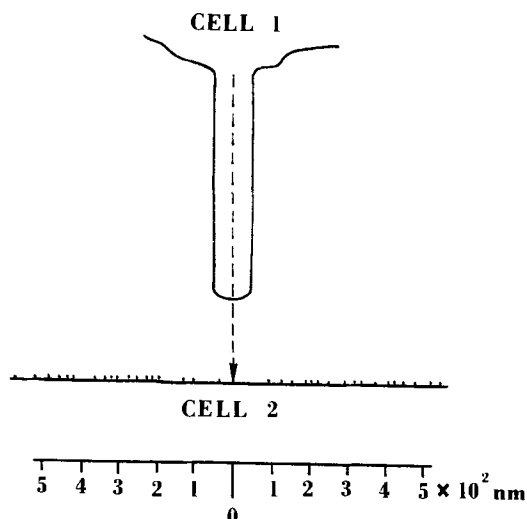


Fig. 1. Schematic drawing of an electron micrograph of the microvillus of one cell opposed to a low density region of colloidal iron hydroxide particles on the IMV surface of a second cell.

Table III.

Distance from center of projected microvillus contact area (nm)	Particle density per 100 nm of surface ± SE (No. observations)
0-100	1.72 ± 0.31 (57)
50-150	2.61 ± 0.52 (57)
150-250	3.91 ± 0.55 (57)
250-350	4.75 ± 0.58 (56)
350-450	3.84 ± 0.46 (50)
450-550	4.39 ± 0.63 (46)
550-650	4.13 ± 0.58 (38)

as the intersection of the projection of the axis of the microvillus with the opposing IMV surface.

Due to the essentially static nature of electron micrographs it may not be determined whether an individual microvillus which is aligned with a low density region of another cell would actually have made contact with it in the undisturbed situation. Therefore, it cannot be stated for an individual situation whether a microvillus was actually moving in the direction of the opposing surface rather than away from it.

Despite these difficulties the data show a noncoincidental alignment of a microvillus from one cell with a low density CIH region on a neighboring cell. This result insists on some kind of interaction occurring between the microvillus and opposing IMV surface. Whether this interaction occurs prior to or following contact, or in the absence of contact, cannot be unequivocally answered. Since alignment is observed to occur in 91% of the samples observed, it is highly possible that in many cases the alignment occurs prior to contact (or even in its absence). In this instance it is of interest to examine mechanisms via which alignment may take place. A mechanism to induce alignment will be dependent on the distance of separation between the microvillus tip and the adjacent IMV surface. As data are obtained from thin sections, it is therefore possible that an observed microvillus may leave the section and produce an apparent separation distance different from the true distance. For this reason the real distance of separation cannot be accurately determined; however, it appears possible that interactions occurred between opposed cell surfaces separated by distances as great as 200 nm, which was the greatest distance selected for these results. A detailed theoretical analysis of possible interaction mechanisms as a function of distances of this order is discussed elsewhere (14). One proposed mechanism for alignment is that net negatively charged macromolecules diffusing out of cells in the region of their microvilli, electrostatically repel CIH-binding anionic sites in the fluid periphery of the opposed cell, causing gaps in their distribution.

It must be emphasized that despite the fact that the true separation distance between the microvillus and opposing IMV surface is uncertain; contact out of the section as an explanation for the observed redistribution is excluded, because examination of particle densities of microvilli in contact with two cells (in the same section) indicates that corresponding low density regions bear no constant distribution relative to the contact point (13).

### Variations in Electrical Properties Between Different Cell Types

**3T3 cells.**—Cultures of fibroblasts from normal tissue are found to contain few dividing cells after confluency of the culture is achieved. In contrast, fibroblasts that have been transformed by an oncogenic virus such as Simian virus 40 (SV40) lack this contact inhibition of growth. A cloned transformed cell line, however, has been found to be composed of a heterogeneous population of cells, a small number of which are contact-inhibited. By employing the differential agglutinability exhibited by plant lectins such as Concanavalin A toward normal and transformed cultures, it is possible

to select out and clone those contact inhibited variants of the transformed line. These new "revertant" cultures exhibit general morphology and growth densities characteristic of the normal state.

We have investigated normal and SV40 transformed Balb/3T3 (15) cultures together with two revertant lines. Inoculations of these various cell lines into susceptible mice show the normal and revertant cultures to be essentially nonmalignant, while the SV40 transformed Balb/3T3 cells form cancers.

The CIH stain has been applied to the 3T3 system with the results presented in Table IV. It is clear that the surfaces of both the normal and revertant 3T3 cells bind approximately the same density of CIH particles on their IMV surface and that the SV40 transformed line yields a CIH density which is significantly reduced. Therefore in this cellular system, there appears to be a correlation between the electrical properties of the cell surfaces measured with the CIH probe, and malignant transformation and reversion.

**Lymphoid cells.**—It is generally accepted that two distinct classes of lymphocytes are present in different mammalian species including man (16). These are B or bone-marrow derived and T or thymus-derived lymphocytes. Although generally similar in appearance, these two cell types are found to have widely differing functions. T lymphocytes may be cytotoxic to cells carrying foreign surface antigens. This class of lymphoid cells is also known to cooperate in an as yet undefined manner with B lymphocytes in initiating the proliferation of the B cells into specific antibody-producing clones. These two groups have distinguishable surface characteristics as has been revealed electrophoretically (17), serologically (18), and with respect to their differential sensitivity to lectins (19). In addition to these two classes, at least one serologically distinguishable subgroup of T lymphocytes is also recognized; the thymus-located lymphocytes, or thymocytes, which appear to represent differentiating precursor T lymphocytes (20).

The affinity of mouse-derived thymocytes, B and T lymphocytes for CIH is shown in Table V. These results indicate that thymocytes and T lymphocytes constitute a class distinguishable (at the 0.1% level) from the B lymphocyte group. The role of the cell periphery

in the differential functions of these lymphocyte classes is as yet unknown. However it is apparent that the specific electrical property revealed by the binding of the CIH colloid is of value in distinguishing the B from the T or thymus cell classes.

### Conclusions

Heterogeneities between different regions of the surface of the same cell may be of influence in some interaction phenomena occurring between cells. The average electrical property studied here is significantly different in at least some cells with differential function.

### Acknowledgments

We wish to thank Dr. George Poste and Dr. Dorothy Graves for providing us with the various 3T3 and lymphoid cells used in some of our studies. This work was partially supported by Grant No. BC-87G from the American Cancer Society Inc.

Manuscript received Aug. 2, 1975. This was Paper 354 presented at the Toronto, Canada, Meeting of the Society, May 11-16, 1975.

Any discussion of this paper will appear in a Discussion Section to be published in the June 1977 JOURNAL. All discussions for the June 1977 Discussion Section should be submitted by Feb. 1, 1977.

Publication costs of this article were assisted by Roswell Park Memorial Institute.

### REFERENCES

1. L. Weiss, in "The Chemistry of Biosurfaces," M. L. Hair, Editor, p. 337, M. Dekker Inc., New York (1972).
2. L. Weiss, *Behring Inst. Mitt.*, **55**, 185 (1974).
3. L. Weiss and E. Mayhew, *Int. J. Cancer*, **4**, 626 (1969).
4. L. Weiss and J. P. Harlos, *Prog. Surface Sci.*, **1**, 355 (1971).
5. C. W. Hale, *Nature*, **58**, 202 (1946).
6. R. W. Mowry, *Ann. N.Y. Acad. Sci.*, **106**, 402 (1963).
7. G. J. Gasic, L. Berwick, and M. Sorrentino, *Lab. Invest.*, **18**, 63 (1968).
8. L. Weiss and R. Zeigel, *J. Cell Physiol.*, **77**, 179 (1971).
9. L. Weiss and J. R. Subjeck, *J. Cell Sci.*, **14**, 215 (1974).
10. L. Weiss, *Exp. Cell Res.*, **83**, 311 (1974).
11. D. Dannon, L. Goldstein, Y. Marikovsky, and E. Skutelsky, *J. Ultrastruct. Res.*, **38**, 500 (1972).
12. J. R. Subjeck and L. Weiss, *J. Cell Physiol.*, **85**, 511 (1975).
13. L. Weiss and J. R. Subjeck, *Int. J. Cancer*, **13**, 143 (1974).
14. L. Weiss, S. Nir, J. P. Harlos, and J. R. Subjeck, *J. Theor. Biol.*, In press (1975).
15. S. A. Aaronson and G. J. Todaro, *J. Cell. Physiol.*, **72**, 141 (1968).
16. M. C. Raff, *Transplant. Rev.*, **6**, 52 (1971).
17. S. Nordling, L. C. Andersson, and P. Hayry, *Eur. J. Immunol.*, **2**, 405 (1972).
18. T. Takahashi, L. J. Old, R. K. McIntire, and E. A. Boyse, *J. Exp. Med.*, **134**, 815 (1971).
19. J. Andersson, O. Sjöberg, and G. Moller, *Transplant. Rev.*, **11**, 181 (1972).
20. M. C. Raff and H. Cantor, in "Progress in Immunology," B. Amos, Editor, pp. 83-93, Academic Press, New York (1971).

Table IV. Densities of CIH particles on the IMV surface of normal, SV40 transformed, and two revertant (Rev 3 and Rev 5) BALB/3T3 cell lines

Normal	Particles/4000 nm <sup>2</sup> ± SE (No. observations)			Rev 5
	SV40	Rev 3	Rev 5	
4.21 ± 0.27 (22)	2.17 ± 0.12 (27)	3.96 ± 0.19 (18)	4.05 ± 0.20 (24)	

Table V. Densities of CIH particles on different lymphoid cell classes

B	Particles/4000 nm <sup>2</sup> ± SE (No. observations)		Thymocytes
	T	Thymocytes	
3.88 ± 0.13 (83)	2.35 ± 0.11 (71)	2.29 ± 0.11 (88)	

# Periodic Variations of Overvoltages for Water Electrolysis in Acid Solutions from Cyclic Voltammetric Studies

M. H. Miles\* and M. A. Thomason

Department of Chemistry and Physics, Middle Tennessee State University, Murfreesboro, Tennessee 37132

## ABSTRACT

Cyclic voltammetry was used to determine the electrocatalytic activities of 31 metals for the hydrogen and oxygen evolution reaction in 0.1M H<sub>2</sub>SO<sub>4</sub> at 80°C. For the hydrogen evolution reaction, properties of the metals such as electronic structures, work functions, and metal-hydrogen bond strengths tend to correlate with the observed electrocatalytic activities. The best electrocatalysts for the hydrogen evolution reaction in the order of decreasing catalytic activity are Pd > Pt ≈ Rh > Ir > Re > Os ≈ Ru > Ni. For the oxygen evolution reaction, the order of catalytic activity is Ir ≈ Ru > Pd > Rh > Pt > Au > Nb. Most other metals undergo anodic corrosion and cannot be used for the evolution of oxygen in acid solutions. The potentials at which corrosion is observed are presented for these metals.

Most commercial water electrolyzers operate at 70°-90°C in 25-35 weight percent (w/o) potassium hydroxide solutions using nickel anodes (1, 2). A possible improvement in water electrolysis as a route for hydrogen production is the use of solid polymer electrolytes such as General Electric's perfluorinated sulfonic acid polymer. During electrolysis, the hydrogen ions produced by the oxidation of water move across the solid polymer electrolyte and are reduced to form hydrogen at the cathode. One disadvantage of such a system is the acid environment which develops at the anode causing corrosion of metals such as nickel. In this study, various metals are investigated for possible use as electrocatalysts for water electrolysis in an acid medium at 80°C. A previous study in alkaline solutions has shown that cyclic voltammetry is a convenient method for evaluating electrocatalysts for water electrolysis (3).

## Experimental

The cyclic voltammetric measurements were made with a PAR Model 170 instrument using a potential sweep rate of 50 mV/sec. Most electrodes consisted of high purity wires which were spot-welded to nickel or copper leads and sealed into glass tubing with clear epoxy. These electrodes were mechanically polished with emery paper prior to use. The ruthenium and osmium electrodes were formed by electroplating the metal onto a platinum wire electrode. A ruthenium oxide electrode formed on titanium (RuO<sub>2</sub>/TiO<sub>2</sub>) similar to those used in the chlor-alkali industry (4) was also tested. The hydrogen evolution reaction was investigated first in order to minimize surface changes due to electrode oxidation or oxide film formations.

Reagent sulfuric acid (Baker) and distilled water were used to prepare the 0.1M H<sub>2</sub>SO<sub>4</sub> solution. Measurements were made in a beaker-type glass cell equipped with a cap, a cylindrical platinum screen counterelectrode, a saturated calomel reference electrode (SCE) with a ceramic junction which gives a negligible leak rate, and the test electrode. The temperature was controlled at 80° ± 2°C in all experiments.

## Results

The cyclic voltammetric traces for the iridium electrode in 0.1M H<sub>2</sub>SO<sub>4</sub> at 80°C are shown in Fig. 1. The short potential cycles at each end show the results for studies of the hydrogen and oxygen evolution reactions, while the dashed lines show the behavior for the full potential sweep. The horizontal line segments

show where the current attains a value of 2 mA/cm<sup>2</sup> based on the geometrical area of the electrode. At this current density, gas evolution is clearly visible and the current changes rapidly with small changes in potential. Therefore, experimental overvoltages for water electrolysis obtained by this method are rather insensitive to differences in surface roughness factors. From the Tafel equation

$$\eta = a + b \log i \quad [1]$$

the experimental overvoltages for hydrogen or oxygen evolution at 2 mA/cm<sup>2</sup> for the various metals should reflect changes in the Tafel parameter, *a*, and hence changes in the exchange current density, *i*<sub>0</sub> = 10<sup>-*a*/*b*</sup>, as long as the Tafel slope, *b*, remains constant for a given reaction on various metals.

Figure 2 presents the summary of all cyclic voltammetric results on various metals in 0.1M H<sub>2</sub>SO<sub>4</sub> at 80°C. The potentials where the current density attains 2 mA/cm<sup>2</sup> using a potential sweep rate of 50 mV/sec are shown as a function of the atomic numbers of the elements. The horizontal dashed lines represent the estimated reversible potentials for the hydrogen and oxygen electrode reactions at the experimental conditions used. The solid circles at the negative potentials locate hydrogen evolution at 2 mA/cm<sup>2</sup>; the solid circles at the positive potentials locate oxygen evolution at this current density. The open circles show the potentials at which the current density exceeds 2 mA/cm<sup>2</sup> due to some other anodic proc-

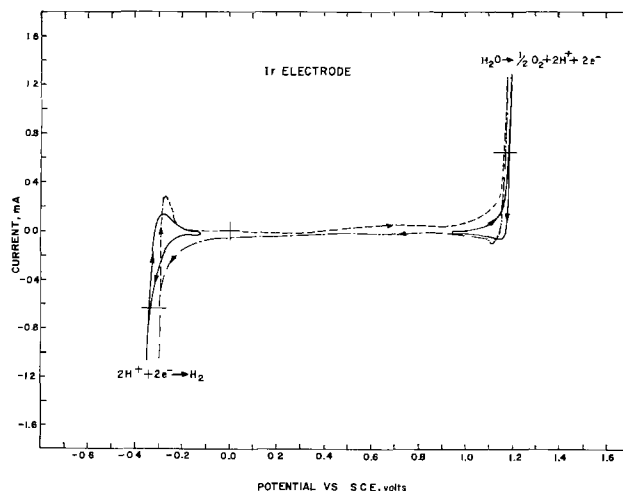


Fig. 1. Cyclic voltammograms for an iridium electrode of 0.32 cm<sup>2</sup> geometrical area in 0.1M H<sub>2</sub>SO<sub>4</sub> at 80°C.

\* Electrochemical Society Active Member.

Key words: adsorption, corrosion, electrocatalyst, hydrogen, oxygen, work function.



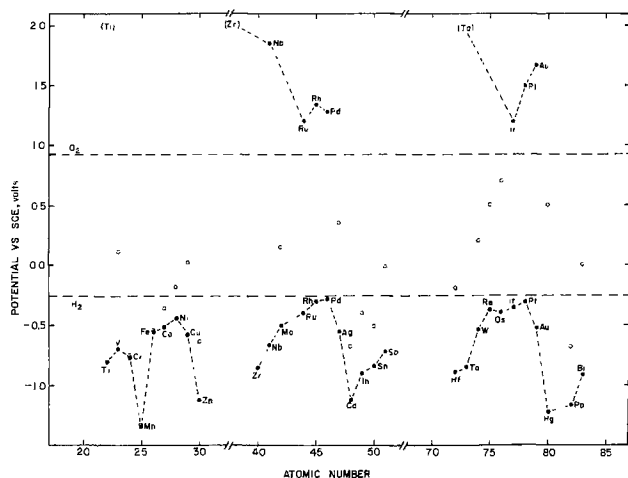


Fig. 2. Summary of cyclic voltammetric results for various metallic elements in 0.1M  $H_2SO_4$  at  $80^\circ C$ . The potential vs. SCE is shown where the current density attains  $2 \text{ mA/cm}^2$  using a potential sweep rate of  $50 \text{ mV/sec}$ .

ess such as corrosion of the metal. For Cr, Mn, and Fe, hydrogen evolution and anodic oxidation are observed at about the same potential, hence their location could be influenced by a mixed potential (5). The potentials at  $2 \text{ mA/cm}^2$  for Ti, Zr, Hf, Ta, and Pd were not as reproducible as those for other metals. This is likely due to hydride formation which changes the surface properties. The electrochemical formation of palladium hydride can even be observed at potentials somewhat positive to the reversible hydrogen potential (6). During hydrogen ion reduction, the experimental potential at  $2 \text{ mA/cm}^2$  at palladium changed from about  $-0.1V$  to about  $-0.3V$  vs. SCE. For hafnium, the anodic limit observed at about  $-0.2V$  probably results from oxidation of the metallic hydride. No reproducible anodic limits were observed for Ti, Zr, and Ta. Although oxygen evolution was initially observed on these metals, their surfaces soon passivate due to formation of insulating oxide films. The resistance of these metals to corrosion would make them useful as structural metals in water electrolysis cells operating in acid environments at high temperatures.

### Discussion

Periodic variations of hydrogen overvoltages with atomic numbers of the electrode metals are evident from Fig. 2. The overvoltages show minima for Ni, Pd, and Pt which have  $d^8s^2$ ,  $d^{10}s^0$ , and  $d^9s^1$  electronic configurations, respectively. Large hydrogen overvoltages are observed for Zn, Cd, and Hg which are all of the  $d^{10}s^2$  electronic configurations. As observed for a similar study in alkaline solutions (3), Cr and Mn show a decrease in catalytic activity with increasing atomic number. It is possible that mixed potentials established at these metals in acid solutions could contribute to the larger experimental overvoltages, nevertheless  $i_0$  values in acid solutions show a similar decrease with an unusually low  $i_0$  value for Mn (7, 8). Other studies of the hydrogen evolution reaction have also established general periodic trends for exchange current densities (9) and for overvoltages (10, 11), however, these studies often use data gathered from differing sources, thus the data are not necessarily homogeneous. The differing  $i_0$  values selected contribute to the conflicting conclusions regarding correlations with other properties (8, 12). Furthermore, electrochemical studies at temperatures and conditions used in water electrolysis are sparse.

The periodic trends observed for hydrogen overvoltages show a high correlation with the work functions of the transition metals. Using the same work

function values adopted by Trasatti (8), the location of the experimental potential,  $E$  vs. SCE, at  $2 \text{ mA/cm}^2$  for the transition metals is given by

$$E = 0.64\phi - 3.5 \quad [2]$$

where  $\phi$  is work function in electron volts. Figure 3 shows the  $E$  vs.  $\phi$  plots for both transition metals and sp metals. The correlation coefficient for the least squares fit for the transition metals is 0.88 suggesting a high correlation between the observed hydrogen overvoltage and the work function. For the nontransition metals tested, the correlation between the observed hydrogen overvoltage and the work function is much less precise and the calculated correlation coefficient is only 0.29. The overvoltages on Zn, Cd, Hg, and Pb actually seem to be nearly independent of the work function.

The heat of adsorption of hydrogen on metals is theoretically related to the rate of electrolytic hydrogen evolution (13-15) and experimental correlations have been observed (8, 12). Figure 4 shows the least squares plot of the potential observed at  $2 \text{ mA/cm}^2$  against the M-H bond strength of the metal as derived by Krishtalik (15) from experimental data for hydrogen evolution. The predicted volcano-shaped curve is obtained and looks similar to results based on  $i_0$  values (8). Assuming that differences in experimental overvoltages and exchange current densities on various metals reflect mainly changes in the Tafel parameter,  $\alpha$ , then the slopes of such plots should be related by

$$\text{slope} = \frac{\Delta\eta}{\Delta M-H} = \frac{b \Delta \log i_0}{\Delta M-H} \quad [3]$$

Using  $b = 0.14V$  in Eq. [3], the slopes of the curves in Fig. 3 are similar to the slopes reported by Trasatti (8) using  $i_0$  values obtained at room temperature. Figure 3 suggests the presence of a horizontal region where the overvoltage remains small for M-H bond strengths between 52-60 kcal/mole. Such horizontal regions are predicted when the adsorption equilibrium follows a Temkin isotherm (13).

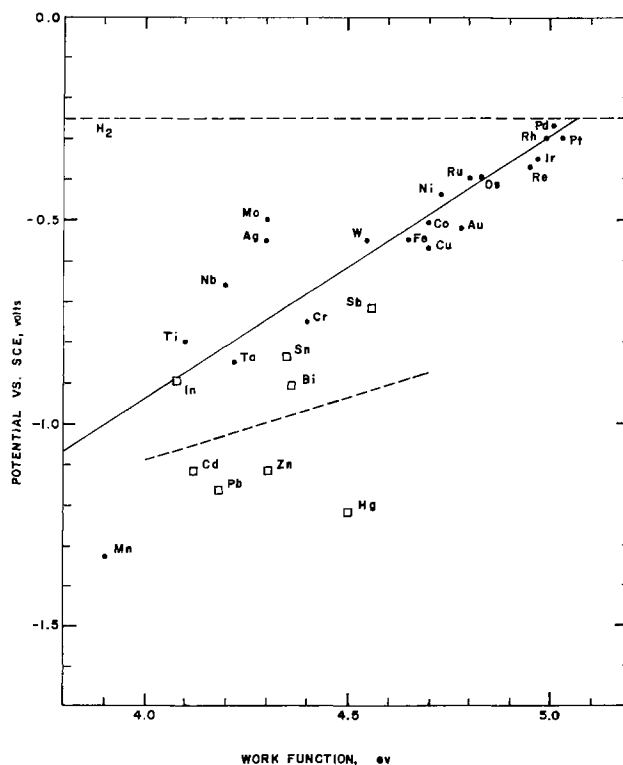


Fig. 3. The potential vs. SCE at  $2 \text{ mA/cm}^2$  vs. the values of the work function of the metal given by Trasatti (8). Symbols used are: ● transition metals; □ sp metals.

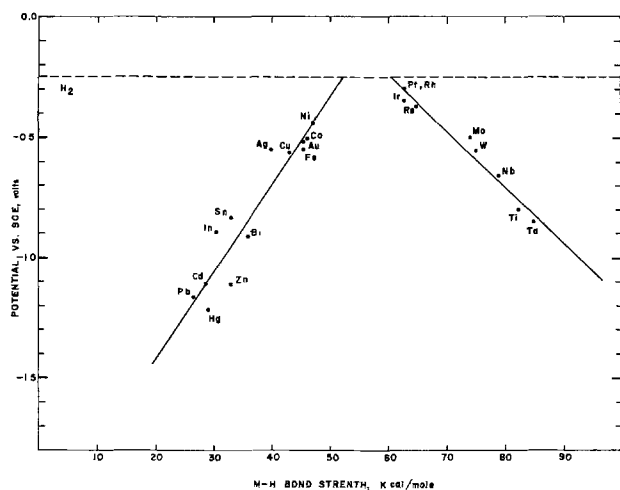


Fig. 4. The potential vs. SCE at 2 mA/cm<sup>2</sup> vs. the M-H bond strength as derived by Krishtalik (15).

The best electrocatalysts for the hydrogen evolution reaction in 0.1M H<sub>2</sub>SO<sub>4</sub> at 80°C in order of decreasing catalytic activity are Pd > Pt ≈ Rh > Ir > Re > Os ≈ Ru > Ni. For the electroplated ruthenium and osmium electrodes, a roughness factor of about 20 relative to the other metals was assumed. Judging from Fig. 2-4, an ideal electrocatalyst lacks two electrons in filling its outermost d and s sublevels, has a work function of about 5 eV, and forms M-H bonds with energies of about 50-60 kcal/mole.

For the oxygen evolution reaction, the catalytic activity in acid solution is found to be in the order Ir ≈ Ru > Pd > Rh > Pt > Au > Nb. Nearly all other metals either undergo anodic corrosion or form passivating oxide films in 0.1M H<sub>2</sub>SO<sub>4</sub> at 80°C. Based on these cyclic voltammetric results, iridium and ruthenium appear to be considerably better than platinum as electrocatalysts for oxygen evolution in acid solutions. The high electronic conductivities of IrO<sub>2</sub> and RuO<sub>2</sub> (16-18) apparently promote the slow electron transfer through the oxide layer (19). Results for ruthenium plated onto platinum and for the RuO<sub>2</sub>/TiO<sub>2</sub> electrode were similar, except that the ruthenium-plated electrode gradually disintegrated during oxygen evolution. Potentiostatic steady-state measurements in acid solutions at 80°C also indicate that Ir is considerably better than Pt as an electrocatalyst for the oxygen evolution reaction. In fact the separation of the Tafel lines (300 mV) at various current densities is practically identical to the observed difference in cyclic voltammetric measurements presented in Fig. 2.

### Conclusions

1. Properties of metals which influence their electrocatalytic activities when used as cathodes for water electrolysis under acid conditions include electronic structures, work functions, and M-H bond strengths.

2. For metals used as anodes in water electrolysis under acid conditions, the properties of the metal

oxide seem to be the dominant factor in affecting electrocatalytic activities.

3. The cyclic voltammetric method used in this study provides a rapid method for comparing properties of electrocatalysts. The observed trends are in good agreement with results based on the more tedious determinations of exchange current densities.

### Acknowledgments

The authors wish to thank Dr. S. Srinivasan, Mr. F. J. Salzano, and Dr. R. H. Wiswall for helpful discussions and encouragement regarding this work. A summer appointment as a visiting scientist for M. H. Miles in 1975 by Brookhaven National Laboratory is gratefully acknowledged. We wish to acknowledge financial support provided by Brookhaven National Laboratory under Contract No. 347505S and by the Faculty Research Committee at Middle Tennessee State University.

Manuscript submitted Dec. 5, 1975; revised manuscript received May 24, 1976.

Any discussion of this paper will appear in a Discussion Section to be published in the June 1977 JOURNAL. All discussions for the June 1977 Discussion Section should be submitted by Feb. 1, 1977.

Publication costs of this article were assisted by Middle Tennessee State University.

### REFERENCES

1. E. A. Chapman, *Chem. Process Eng.*, **46**, 387 (1965).
2. D. H. Smith, in "Industrial Electrochemical Processes," A. T. Kuhn, Editor, pp. 127-157, Elsevier Publishing Co., New York (1971).
3. M. H. Miles, *J. Electroanal. Chem.*, **60**, 89 (1975).
4. A. T. Kuhn and C. J. Mortimer, *This Journal*, **120**, 231 (1973).
5. K. J. Vetter, "Electrochemical Kinetics," pp. 732-734, Academic Press, New York (1967).
6. G. C. Libowitz, "The Solid-State Chemistry of Binary Metal Hydrides," pp. 92-93, W. A. Benjamin, New York (1965).
7. A. Bélanger and A. K. Vijh, *This Journal*, **121**, 225 (1974).
8. S. Trasatti, *J. Electroanal. Chem.*, **39**, 163 (1972).
9. H. Kita, *This Journal*, **113**, 1095 (1966).
10. J. O'M. Bockris, *Trans. Faraday Soc.*, **43**, 417 (1947).
11. N. E. Khomutov, *Zh. Fiz. Khim.*, **39**, 532 (1965).
12. A. T. Kuhn, C. J. Mortimer, G. C. Bond, and J. Lindley, *J. Electroanal. Chem.*, **34**, 1 (1972).
13. R. Parson, *Trans. Faraday Soc.*, **54**, 1053 (1958).
14. P. Delahay, "Double Layer and Electrode Kinetics," pp. 260-268, John Wiley & Sons, Inc., New York (1965).
15. L. J. Krishtalik, in "Advances in Electrochemistry and Electrochemical Engineering," Vol. 7, P. and C. W. Tobias, Editors, John Wiley & Sons, Inc., New York (1970).
16. W. D. Ryden, A. W. Lawson, and C. C. Sartain, *Phys. Lett.*, **26A**, 209 (1968).
17. D. B. Rogers, R. D. Shannon, A. W. Sleight, and J. L. Gillson, *Inorg. Chem.*, **8**, 841 (1969).
18. J. M. Honig, in "Fast Ion Transport in Solids," W. van Gool, Editor, North Holland Publishing Co., Amsterdam (1973).
19. J. W. Schultze and K. J. Vetter, *Electrochim. Acta*, **18**, 889 (1973).

# Mathematical Model of a Lithium-Water Electrochemical Power Cell

Douglas N. Bennion\*

Energy and Kinetics Department, School of Engineering and Applied Science,  
University of California, Los Angeles, California 90024

and E. L. Littauer\*

Lockheed Missiles & Space Company, Incorporated, Lockheed Palo Alto Research Laboratories,  
Palo Alto, California 94304

## ABSTRACT

A mathematical model has been developed which describes the operation of a lithium-water, electrochemical power cell. The current density, current efficiency, powder density, and specific energy are calculated as functions of cell potential, lithium hydroxide concentration, temperature, electrolytic solution flow velocity, position along the flow channel, spacing between electrodes, and flow channel width. Anode to cathode contact pressure is not included in this initial model. A large dependence of power density on LiOH concentration is predicted. For example, at an LiOH concentration of 2M, a power maximum of 394 mW/cm<sup>2</sup> is calculated, and in 5M LiOH the power maximum is calculated to be 25 mW/cm<sup>2</sup>. Temperature and flow velocity show similar but smaller effects.

Design and performance characteristics of lithium-water electrochemical power cells have been described in the literature (1-4). The object of this paper is to present a general, theoretical description of the operation of such a system which illustrates and describes some principal, controlling processes and design variables. An idealized design is used to achieve this purpose. The effects of pressing the cathode grid against the anode surface, insulated by the LiOH film, are not included in this model. Recent results have shown that the effect of this cathode to anode pressure is a dominant variable allowing greatly improved performance and cell control.

The anode, in the simple geometry used here, is a plane sheet of lithium covered with a film of hydrated lithium oxide. The cathode is a plane sheet of nickel or other inert metal. Spacers provide flow channels between the anode and cathode through which a lithium hydroxide-water solution is circulated. Hydrogen is evolved from both the anode and cathode during cell operation. Hydrogen evolved at the cathode is part of the energy producing cell reaction. Hydrogen evolved at the anode is simply a corrosion reaction which represents a loss in current efficiency.

The object of this study has been to describe the local current density, current efficiency, power density, and specific energy as quantitative functions of the cell potential, lithium hydroxide concentration, temperature, electrolytic solution flow velocity, position along the flow channel, spacing between electrodes, and flow channel width. The last two independent variables are listed as separate entries since in more advanced designs the electric current path in the electrolytic solution is not the same as the flow channel width. The physical and chemical processes believed to control the system are described by mathematical equations. The equations have been solved numerically using high speed digital computing machinery.

## Theoretical

*Physical processes.*—The basic geometry of the model is shown in Fig. 1. A film of hydrated lithium oxide is assumed to form on the surface of the lithium. The

rate of parasitic hydrogen evolution on the surface of the lithium is limited by the rate of transport of water through the hydrated lithium oxide film. The water transport may be by diffusion through the solid film, liquid phase convection and diffusion through micropores in the film, or a combination of both. This elementary model does not distinguish the mode of transport, and the diffusion parameter defined later is an effective or over-all parameter characteristic of the over-all, steady-state water transport rate across the film. The solution surface of the film is in equilibrium with a saturated solution of lithium hydroxide in water. The lithium oxide film is continually dissolving in an operating power cell. The lithium hydroxide diffuses through a hydrodynamic diffusion boundary layer into the bulk solution where it is circulated out of the cell. The thickness of the hydrodynamic diffusion boundary layer,  $\delta_0$ , is governed by the forced convection flow of electrolytic solution and the stirring action of the parasitic hydrogen evolution reaction.

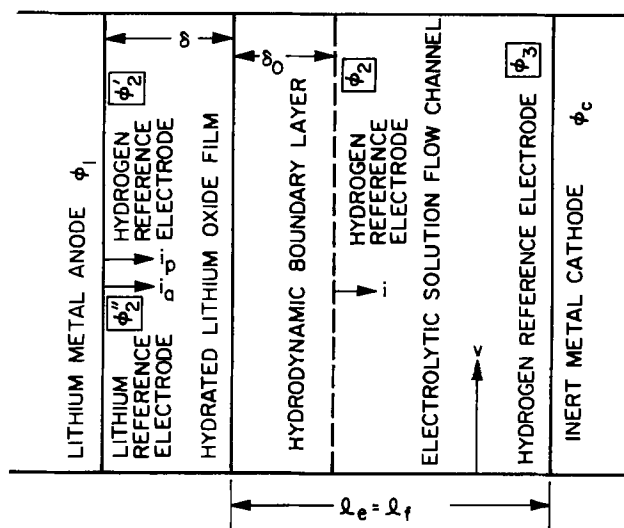


Fig. 1. Lithium water primary power cell. Idealized, geometric representation of the theoretical model.

\* Electrochemical Society Active Member.

Key words: lithium hydroxide, battery, mechanically rechargeable fuel cell, corrosion.

The hydrated lithium oxide film is assumed to be in a dynamic steady state. Lithium ions are continually being formed at the interface between the metallic lithium and the lithium oxide film and then transported to the film-electrolytic solution interface. Water is continually being transferred through the film in the opposite direction from the film-electrolytic solution interface to the surface of the metallic lithium. A steady-state film thickness is established when the rate of production of lithium ions at the lithium metal surface equals the rate of dissolution of lithium hydroxide at the film-solution interface.

The total cell current,  $i$ , is equal to minus the hydrogen evolution reaction rate at the cathode,  $i_c$ . The total cell current,  $i$ , is also equal to the sum of the rate of lithium oxidation,  $i_a$ , and the parasitic hydrogen evolution rate  $i_p$ , occurring at the anode

$$i = -i_c = i_a + i_p$$

All cathodic current densities are negative numbers. Thus,  $i_p$  will be a negative number, and  $i$  will be less than  $i_a$ .

Each of the electrode reactions, represented by  $i_a$ ,  $i_p$ , and  $i_c$ , can be described as functions of a local surface overpotential using well-known oxidation-reduction, exponential kinetic rate expressions. The exchange current density for the parasitic hydrogen evolution reaction,  $i_p$ , is assumed to be proportional to the 0.5 power of the water activity in the lithium oxide film at the surface of the lithium metal. This is equivalent to assuming  $\alpha$  is 0.5. The basis for developing the rate expression has been given by Delahay (5). Surface overpotentials which drive the electrode reactions at the metallic surfaces are defined as the electrical potential of the metallic electrode minus the potential of a reference electrode placed just outside the double layer at the surface of the working electrode, see Fig. 1. The potential of the lithium metal,  $\phi_1$ , is assumed to be zero; all other potentials are referred to this potential. A hypothetically reversible lithium reference electrode of potential  $\phi_2''$  is imagined to be imbedded in the lithium oxide film next to the metallic lithium electrode. A hypothetically reversible hydrogen reference electrode of potential  $\phi_2'$  is similarly imagined to be imbedded in the lithium oxide film next to the metallic lithium electrode. For simplicity in writing rate expressions, hydrogen gas is assumed to be dissolved in all phases and at unit activity throughout the cell. A hypothetically reversible hydrogen reference electrode of potential  $\phi_2$  is also imagined to be placed in the bulk electrolytic solution just outside the hydrodynamic diffusion boundary layer at the surface of the lithium oxide film. A third hydrogen reference electrode of potential  $\phi_3$  is imagined in the bulk electrolytic solution adjacent to the cathode. The potential of the working, inert cathode,  $\phi_c$ , is also the cell potential since the potential of the anode,  $\phi_1$ , is taken as the zero of potential.

The hydrated lithium oxide film is to be described by three averaged parameters: the effective film thickness  $\delta$ , the effective ionic electrical conductivity of the film  $\kappa_f$ , and the effective diffusivity of water in the film  $D^*$ . The transport of lithium ions across the film is not considered explicitly other than in the contribution of lithium ion movement to  $\kappa_f$ . The use of only three parameters to describe the rather complex transport processes occurring in the hydrated lithium oxide film does represent a considerable simplification of the actual processes that are occurring. The treatment could be improved by a more complete description of the film transport mechanisms. However, the three-parameter approach does appear to incorporate the most important rate processes at a reasonable computational cost. It appears obvious that the hydrated lithium oxide film is not homogeneous. Water content

varies. The film may or may not contain pores or fissures through which hydrogen escapes, and water is transported toward the lithium metal. The three parameters  $\delta$ ,  $\kappa_f$ , and  $D^*$  are to be viewed as effective or averaged values describing the film as a whole. A more complete model would allow for property and transport process changes with position in the film.

*Mathematical equations.*—It proves convenient mathematically and for notation purposes to choose all electrode kinetic transfer coefficients,  $\alpha$ , to equal 0.5. In reviewing experimental results for the lithium and hydrogen electrochemical reactions, this assumption appears reasonable. It is also convenient to let the group  $RT/\alpha F$  equal  $\psi$ . Symbols are all defined at the end of the paper or in Eq. [13]–[23].

Recalling the definitions of  $\phi_1$ ,  $\phi_2''$ ,  $\phi_2'$ ,  $\phi_3$ , and  $\phi_c$  from the previous section and assuming that the exchange current density for the hydrogen evolution reaction depends on the 0.5 power of water activity, we write the following equations relating surface reaction rates to electrical potentials

$$i_a = i_{o,a}^0 [\exp(-\phi_2''/\psi) - \exp(\phi_2''/\psi)] \quad [1]$$

$$i_p = i_{o,p}^0 a_{o,s}^{0.5} [\exp(-\phi_2'/\psi) - \exp(\phi_2'/\psi)] \quad [2]$$

$$i_c = -i = -i_a - i_p = i_{o,c}^0 [\exp((\phi_c - \phi_3)/\psi) - \exp((\phi_3 - \phi_c)/\psi)] \quad [3]$$

The surface reaction rates for the lithium oxidation,  $i_a$ , parasitic hydrogen evolution,  $i_p$ , and hydrogen evolution at the cathode,  $i_c$ , are all expressed as equivalent current densities and have been discussed in the previous section.

The electrical potential variation in the electrolytic solution is assumed to follow Ohm's law

$$\phi_2 - \phi_3 = (i_a + i_p) l_e/\kappa \quad [4]$$

The rate of parasitic hydrogen evolution is assumed proportional to the rate of water transport through the lithium oxide film to the metallic lithium surface

$$i_p = -(D^*/\delta) F c_o^{\text{sat}} (a_o^{\text{sat}} - a_{o,s}) \quad [5]$$

The water activity,  $a_o$ , is defined as a dimensionless quantity referred to the activity of pure water as one. It is related to the molality of the LiOH through an empirical fit to experimental data (6).

The potential difference between the lithium and hydrogen reference electrodes in the lithium oxide film adjacent to the metallic lithium is the sum of two standard electrode potentials,  $U$ , plus a term for the activity of water at the film-metal interface. The correction terms for deviations of LiOH and H<sub>2</sub> from their standard states are assumed to be negligible for these calculations and are not shown in Eq. [6]

$$\phi_2' - \phi_2'' = U + (RT/F) \ln a_{o,s} \quad [6]$$

The electrical potential drop across the hydrated lithium oxide film is assumed to be an Ohm's law term plus terms for changes in lithium ion activity and water activity. Activity corrections across the liquid phase diffusion boundary layer are included in Eq. [7] rather than in Eq. [4]. This choice is arbitrary. To help avoid further complexity, the activity of lithium ions at the surface of the metallic lithium are assumed equal to the activity of lithium hydroxide in a saturated aqueous solution,  $a_e^{\text{sat}}$ . The loss in descriptive accuracy by using this assumption seems negligible compared to other assumptions, and it obviates the need to write another equation for the transport of lithium ions across the hydrated lithium oxide film. A result is that the second term on the right-hand side

of Eq. [7] is effectively a constant which depends weakly on temperature

$$\phi_2' - \phi_2 = (i_a + i_p) \delta / \kappa_f + (2RT/F) t_{+0} \ln(a_{e^b} / a_{e^{\text{sat}}}) + (RT/F) \ln(a_{o,s} / a_{o,b}) \quad [7]$$

The lithium hydroxide activity coefficients are reasonably constant in the concentration range of interest here. For the bulk solution, the activity coefficient was assumed constant at 0.5. For the saturated solution, the activity coefficient was assumed constant at 0.45. The activities are dimensionless, referred to a hypothetically ideal solution of unit molality.

Equation [8] equates the lithium oxidation rate,  $i_a$ , to the dissolution rate of the lithium hydroxide at the liquid interface of the solid film. The assumptions involved in this equation imply a steady-state film transport condition and a film thickness  $\delta$  which is independent of time

$$i_a = F k_m (c_e^{\text{sat}} - c_e^b) \quad [8]$$

The mass transfer coefficient,  $k_m$ , is assumed to be the sum of a convective mass transfer coefficient,  $k_c$ , and a mass transfer coefficient,  $k_b$ , associated with the formation and breaking away of hydrogen bubbles. This interpretation of  $k_m$  roughly parallels Rohsenow's development of nucleate boiling heat transfer coefficients with forced convection as discussed by Kreith [7]

$$k_m = k_c + k_b \quad [9]$$

The forced convection Reynold's number for the flow channel being considered is typically below 1000, thus the following expression for entrance region flow is selected (8)

$$k_c = (D/2l_f) a_c (\text{Re Sc } 2l_f/x)^\gamma \quad [10]$$

Here  $a_c$  equals 1.2325 for  $x$ , the distance along the flow channel. For average values where  $x$  equals total channel length,  $a_c$  is 1.8488. A value of 1/3 for  $\gamma$  is recommended for laminar flow in an entrance region and is also taken as 1/3 in Eq. [11].

The bubble mass transfer coefficient is correlated as follows

$$k_b = (D/l_b) a_b \text{Re}_b^\beta \text{Sc}^\gamma \quad [11]$$

The bubble Reynolds number  $\text{Re}_b$  is calculated as a function of the parasitic hydrogen evolution rate,  $i_p$ , as follows

$$\text{Re}_b = l_b v_b / \nu = - l_b i_p RT / (\nu F P (0.20265)) \quad [12]$$

The numerical constant converts  $P$  from atmospheres to joules per cubic centimeter and includes a 2 since two equivalents are needed to produce a mole of hydrogen. The velocity of bubble growth into the solution,  $v_b$ , is assumed equal to the hydrogen evolution rate at the anode.

The parameters  $a_b$ ,  $\beta$ ,  $D^*$ , and  $i_{o,c}$  were adjusted within physically meaningful limits to fit experimental data. Since  $\beta$  was used as a fitting parameter, the bubble diameter  $l_b$  is arbitrary, and a value of 0.02 cm was selected.

Temperature dependence is included by inserting the expected temperature dependence of the physical parameters

$$\rho = \rho_0 + A_\rho (T - T_0) \quad [13]$$

$$\rho_0 = 0.997 + 29.96 c_e^b - 0.003003 (c_e^b \cdot 1000)^{1.5} \quad [13a]$$

$$\mu = \mu_0 (T_0/T) \exp [-E^\dagger_\mu (T - T_0)/RTT_0] \quad [14]$$

$$\mu_0 = 0.008937 [1 + 0.04 (c_e^b \cdot 1000)^{0.5} + 0.000259 c_e^b] \quad [14a]$$

$$D = D_0 (T/T_0) \exp [E^\dagger_D (T - T_0)/RTT_0] \quad [15]$$

$$D_0 = (1.728 \times 10^{-5}) (0.008937) / \mu_0 \quad [15a]$$

$$D^* = D^*_0 (T/T_0) \exp [E^\dagger_*(T - T_0)/RTT_0] \quad [16]$$

$$\kappa = \kappa_0 (T/T_0) \exp [E^\dagger_\kappa (T - T_0)/RTT_0] \quad [17]$$

$$\kappa_0 = (175 - 19,000 c_e^b) c_e^b \quad [17a]$$

$$\kappa_f = \kappa_f^0 (T/T_0) \exp [E^\dagger_f (T - T_0)/RTT_0] \quad [18]$$

$$U = U_0 (T/T_0) + \Delta H^0_U (T - T_0)/FT_0 \quad [19]$$

$$i_{o,a} = i_{o,a}^0 (T/T_0) \exp [E^\dagger_a (T - T_0)/RTT_0] \quad [20]$$

$$i_{o,p} = i_{o,p}^0 (T/T_0) \exp [E^\dagger_p (T - T_0)/RTT_0] \quad [21]$$

$$i_{o,c} = i_{o,c}^0 (T/T_0) \exp [E^\dagger_c (T - T_0)/RTT_0] \quad [22]$$

$$c_e^{\text{sat}} / c_e^{\text{sat } 0} = 1 + (5.9828 \times 10^{-4}) (T - T_0) + (1.6644 \times 10^{-5}) (T - T_0)^2 + (6.7019 \times 10^{-7}) (T - T_0)^3 \quad [23]$$

$$c_0^{\text{sat}} = (\rho_{\text{sat}} - c_e^{\text{sat}} (23.95)) / 18.016 \quad [23a]$$

Equation [23] is an empirical fit of data given by Adams and Anderson (4). Symbols are defined at the end of the paper.

Equations [1] through [8] represent a total of eight independent, algebraic equations, and they contain eight unknowns or dependent variables:  $i_p$ ,  $\phi_2$ ,  $\phi_3$ ,  $\delta$ ,  $a_{o,s}$ ,  $\phi_2'$ ,  $\phi_2''$ , and  $i_a$ . Equations [9] through [23a] relate various parameters to the dependent or independent variables. The independent variables, which can be viewed as the controllable design or operating conditions, are: cell potential  $\phi_c$ , bulk lithium hydroxide concentration  $c_e$ , temperature  $T$ , bulk electrolytic solution velocity  $v$ , position along the flow channel  $x$ , effective electrical current path length in the electrolytic solution  $l_e$ , and the flow channel width  $l_f$ .

The problem of predicting the dependent variables as functions of the independent variables and physical parameters is now specified, and solutions are a matter of mathematical manipulation.

It is to be noted that there is considerable correspondence between the geometric aspects of this model and one for transient zinc electrode polarization presented by Farmer and Webb (9). However, the mathematical representation of the controlling processes, the purpose of the models, and the systems treated are quite different. Farmer and Webb concentrate on film growth rate as controlled by unsteady-state zinc ion transport through an oxide film and dissolution of the film. The lithium electrode model is for steady-state conditions, it includes surface overpotentials and cell potential, and it includes both water and lithium ion transport using simplified, steady-state transport equations.

*Numerical calculations.*—The equations were linearized and the resulting matrix inverted and iterated upon using a numerical approach described by Newman (10). The technique guarantees rapid convergence if the initial estimates are reasonably close to the correct answer. If estimates are too far from the correct answer, the procedure does not converge. In a series of calculations, the code uses previous solutions as the estimate for the next problem it reads. Once a converged answer is found, the dependent variables for the next problem must be changed by an amount small enough to insure convergence. As a rule of thumb, the following changes per problem in the independent variables were found to be satisfactory:  $\phi_c = 0.1-0.2V$ ,  $c_e = 10^{-3}$  mol/cm<sup>3</sup>,  $T = 10^\circ K$ ,  $v = 10$  cm/sec,  $x = 10$  cm,  $l_e = 0.01$  cm, and  $l_f = 0.5$  cm. A list of parameter inputs is shown in Table I.

In examining system behavior and attempting to "fit" results to experimental results, it is important to recognize the number and definitions of independent parameters. A dimensional analysis of the equations yielded the following as independent input parameters

Table I. Input parameters

Symbol	Description	Magnitude	Reference
$A_p$	Constant in $T$ dependence of density	$-5.922 \times 10^{-4}$	(13)
$a_b$	Coefficient in expression for $k_b$	2.8	Fitted
$a_c$	Coefficient in expression for $k_c$	1.2325	(9)
$c_e^{sat}$	Concentration of LiOH at saturation at 25°C	$5.34 \times 10^{-3}$ mol/cm <sup>3</sup>	(15)
$D^*$	Effective diffusivity of H <sub>2</sub> O in Li <sub>2</sub> O film	$6 \times 10^{-7}$ cm <sup>2</sup> /sec	Fitted
$E_a^\dagger$	Activation energy for $i_{o,a}$	$8.372 \times 10^4$ J/mol	Estimated
$E_c^\dagger$	Activation energy for $i_{o,c}$	$8.372 \times 10^4$ J/mol	Estimated
$E_D^\dagger$	Activation energy for liquid diffusion	$1.2558 \times 10^4$ J/mol	Estimated
$E_f^\dagger$	Activation energy for Li <sub>2</sub> O film conductivity	$4.186 \times 10^4$ J/mol	(4)
$E_p^\dagger$	Activation energy for $i_{o,p}$	$8.372 \times 10^4$ J/mol	Estimated
$E_k^\dagger$	Activation energy for liquid conductivity	$1.2558 \times 10^4$ J/mol	Estimated
$E_\mu^\dagger$	Activation energy for viscosity	$1.2558 \times 10^4$ J/mol	Estimated
$E_*^\dagger$	Activation energy for Li <sub>2</sub> O film diffusion	$4.186 \times 10^4$ J/mol	(4)
$\Delta H^{\circ U}$	Enthalpy of reaction $Li + H_2O \rightarrow LiOH + \frac{1}{2}H_2$	$-5.0234 \times 10^6$ J/mol	(14)
$i_{o,n}^0$	Lithium exchange current at 25°C	$7.8 \times 10^{-2}$ A/cm <sup>2</sup>	(4)
$i_{o,c}^0$	Cathode hydrogen exchange current at 25°C	$1 \times 10^{-7}$ A/cm <sup>2</sup>	(11) fitted
$i_{o,p}^0$	Parasitic hydrogen exchange current at 25°C	$1 \times 10^{-10}$ A/cm <sup>2</sup>	(11)
$l_b$	H <sub>2</sub> gas bubble diameter	0.02 cm	Estimated
$P$	Pressure in flow channel	2 atm	Estimated
$t_+^0$	Transference number of Li <sup>+</sup> in solution	0.15	(12)
$U_0$	Standard cell potential for $Li = Li^+ + e^-$ at 25°C	2.217V	(14)
$\alpha$	Transfer coefficient	0.5	(11)
$\beta$	Exponent of bubble Reynold's number in $k_b$	0.8	Fitted
$\gamma$	Exponent of Schmidt number in $k_c$ and $k_b$	0.33333	(9)
$\kappa_f^0$	Li <sub>2</sub> O film electrical conductivity at 25°C	$1.608 \times 10^{-2}$ mho/cm	(4)

in addition to the independent variables:  $D^*F c_e^{sat}/\kappa_f$ ,  $i_{o,p}/i_{o,c}$ ,  $i_{o,a}/i_{o,c}$ ,  $l_b i_{o,c}/\kappa_f \psi$ ,  $Re$ ,  $Re_b$ ,  $a_c$ ,  $a_b$ ,  $\beta$ , and  $\gamma$ . Parameters which depend only on temperature are:  $\psi$ ,  $U$ , and  $t_+^0$ . There are alternative ways of grouping the parameters; however, mathematically, the number of independent parameters remains constant.

The results were found to depend only weakly on  $l_b i_{o,c}/\kappa_f \psi$ . Thus  $D^*$  and  $\kappa_f$  enter only as a ratio in  $D^*F c_e^{sat}/\kappa_f$ . In the numerical parameter fitting,  $\kappa_f$  was fixed at  $1.6081 \times 10^{-2}$  mho/cm at 25°C, and  $D^*$  was used as a fitting parameter. A value for the hydrated lithium oxide film thickness could be predicted only if a unique, correct value of  $\kappa_f$  is known. Such information is not available under the actual operating conditions being studied. However, Adams and Anderson (4) do provide some information based on static conditions. They report film resistances between 0.33 and 4.55  $\Omega$ -cm<sup>2</sup> with 1.21  $\Omega$ -cm<sup>2</sup> as a best estimate for  $\delta/\kappa_f$ . The value of  $1.6081 \times 10^{-2}$  mho/cm for  $\kappa_f^0$  was selected to yield values of  $\delta/\kappa_f$  which compared well with Adams and Anderson's results. The predicted values of  $\delta$  depend on the value of  $\kappa_f$  selected and can only be as accurate as that selection. Accurate measurements of film thickness,  $\delta$ , under dynamic, operating conditions could provide further, more definitive tests of the accuracy of the model.

## Results

**Comparison of theory and experiments.**—Figure 2, 3, and 4 have been prepared from the results of the computer code, and superimposed are data extracted from Ref. (2).

The values of  $D^*i_{o,c}$ ,  $\beta$ , and  $a_b$  were fitted as discussed in the previous section so as to achieve the degree of agreement exhibited between the experimental and calculated results. Values used are shown in Table I. The fitting parameter values appear to be within expected physical limits. Direct measurements of  $D^*$  are unknown. The value of  $i_{o,c}$

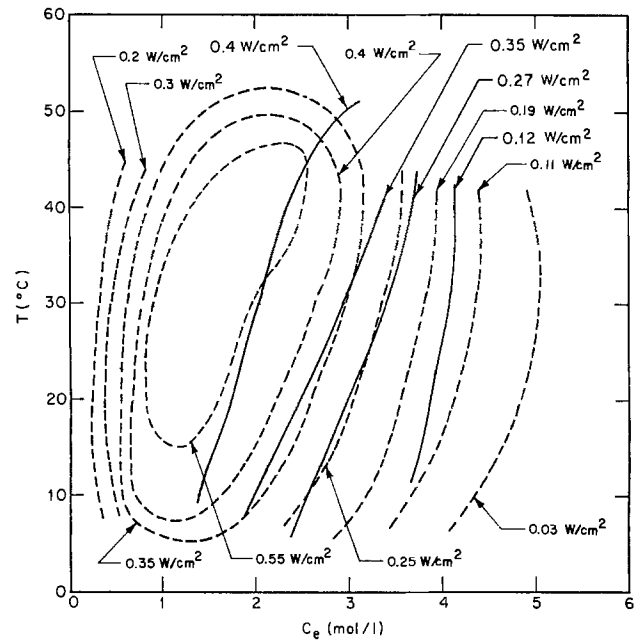


Fig. 2. Power contours at 1.0V cell potential. Dashed lines are constant power contours through array of computer calculations. Solid lines are experimental data from Ref. (2). Extension of dashed contours above 35°C and below 15°C are extrapolations of calculations and are for illustration only.  $\phi_c = 1.0V$ ,  $\nu = 12.2$  cm/sec,  $L = 6.35$  cm,  $l_e = 0.05$  cm,  $l_f = 0.1524$  cm. Values are averages for a complete Li-H<sub>2</sub>O cell.

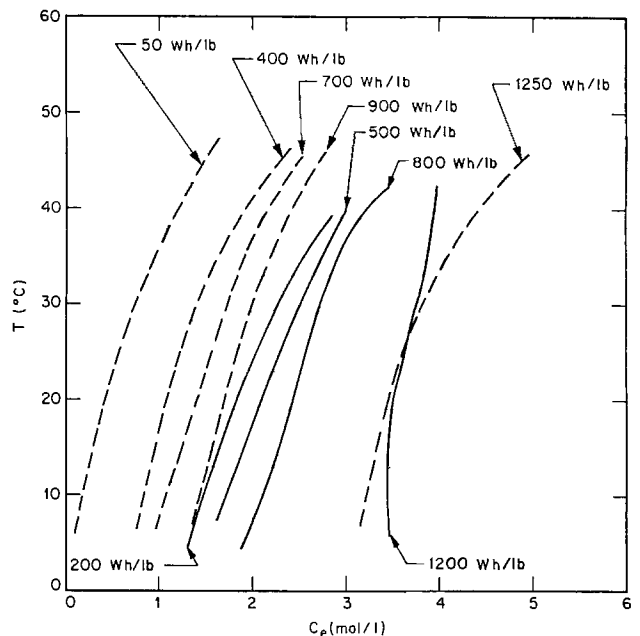


Fig. 3. Specific energy contours at 1.0V cell potential based on mass of lithium consumed. Dashed lines are constant specific energy contours through array of computer calculations. Solid lines are experimental data from Ref. (2).  $\phi_c = 1.0V$ ,  $\nu = 12.2$  cm/sec,  $L = 6.35$  cm,  $l_e = 0.05$  cm,  $l_f = 0.1524$  cm. Values are averages for a complete Li-H<sub>2</sub>O cell. Theoretical specific energy based on 2.196V cell potential is 3847 W-hr/lb.

is within limits reported by Kita (11). Ibl and Venzel (16) derived  $\beta$  equal 0.5 and  $a_b$  equal 1.95 using a surface renewal theory. Janssen and Hoogland (17) found  $\beta$  experimental values to vary between 0.36 and 0.87 for gas evolution on a flat plate. Considering the difference in experimental conditions, the agreement is considered good. The agreement between calculated and experimental performance is within experimental accuracy especially when it is realized that the experimental data were obtained using seawater in place of fresh water. Subsequent laboratory tests have

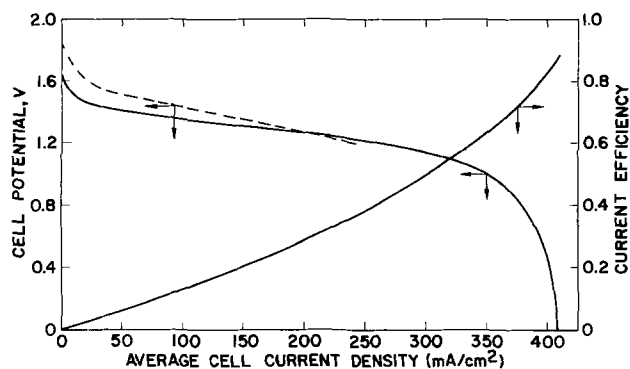


Fig. 4. Current-voltage curve and current efficiency curve. Solid lines are based on computer calculations. Dashed line is experimental results from Ref. (2).  $c_e^b = 3.0M$ ,  $v = 85$  cm/sec,  $L = 26.67$  cm,  $T = 25^\circ C$ ,  $l_e = 0.05$  cm,  $l_f = 0.1524$  cm. Values are averages for a complete Li-H<sub>2</sub>O cell.

shown that calcium, magnesium, and carbonate ions in seawater influence the nature of the anodic film and the polarization behavior in an unpredictable way.

The theoretically determined (dashed) curves of Fig. 2 at the lowest and highest power levels are somewhat different from those obtained experimentally. However, at intermediate power, the experimental data actually have good concordance with the theoretically calculated numerical values. It should be mentioned here that the closing of the dashed curves at the upper and lower regions are for illustration only, since actual calculations were not made for those areas. However, the shape appears to be logical.

Figure 3 shows current efficiency as a function of temperature and concentration at 1.0V cell potential. The theoretical lines of constant specific energy are more spread out than the experimental lines, but they have similar slope. As mentioned above, the discrepancy can be partly ascribed to the fact that the experimental tests were performed with seawater rather than fresh water-based electrolytes.

The theoretical and actual polarization curves of Fig. 4 show good agreement. The similar curve configuration as the current is reduced to zero should be noted.

**Effects of independent variables on operating conditions.**—The independent variables are  $\phi_c$ ,  $c_e^b$ ,  $T$ ,  $v$ ,  $x$ ,  $l_e$ , and  $l_f$ . Performance is described in terms of local current density  $i$ , local current efficiency  $\eta$ , local power density  $p$ , and local specific energy  $w$ . Power density and specific energy are of greatest importance to practical operation of the system.

Figure 5 illustrates the effect of flow velocity and position along the flow channel on the local current

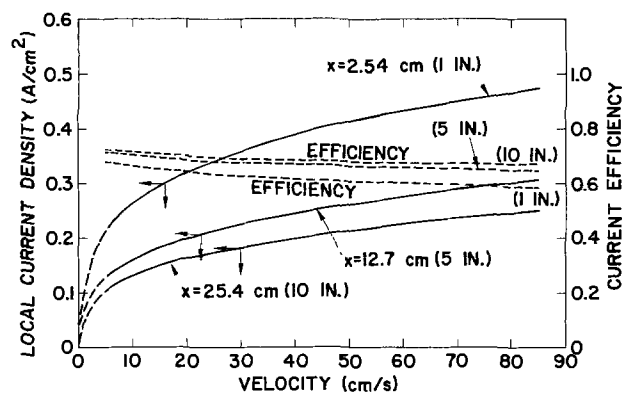


Fig. 5. Current density and current efficiency at 1.0V cell potential as function of electrolytic solution flow velocity and position along flow channel.  $\phi_c = 1.0V$ ,  $c_e^b = 3.0M$ ,  $T = 25^\circ C$ ,  $l_e = 0.05$  cm,  $l_f = 0.1524$  cm.

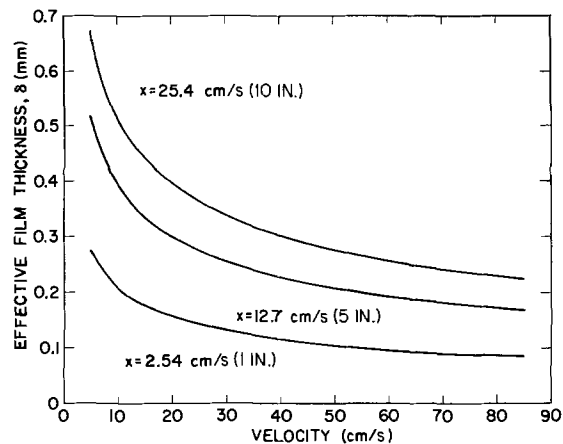


Fig. 6. Effective thickness of lithium oxide (hydroxide) film as a function of electrolytic solution flow velocity and position along flow channel.  $\phi_c = 1.0V$ ,  $c_e^b = 3.0M$ ,  $T = 25^\circ C$ ,  $l_e = 0.05$  cm,  $l_f = 0.1524$  cm.

density and current efficiency. Figure 6 shows how the effective thickness of the hydrated lithium oxide film varies with flow velocity and position.

Figures 7 and 8 further illustrate the dependence of cell performance on channel flow velocity. Figure 7 is a collection of theoretical current voltage curves and current efficiency curves for varying flow channel velocities. Higher currents can be achieved at higher flow rates, but at the expense of increased parasitic pumping energy. Such design trade-offs have not been attempted here, but the results can be used to develop such optimization information. Figure 8 shows how power density in milliwatts per square centi-

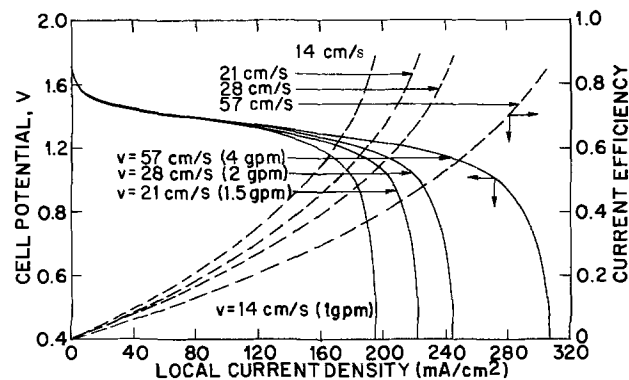


Fig. 7. Current-potential curves and current efficiency for various electrolytic solution flow velocities.  $c_e^b = 3.0M$ ,  $T = 25^\circ C$ ,  $x = 12.7$  cm,  $l_e = 0.05$  cm,  $l_f = 0.1524$  cm.

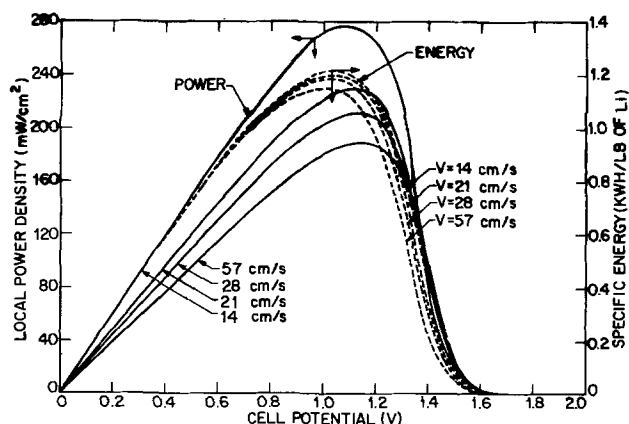


Fig. 8. Power and specific energy as functions of cell potential,  $\phi_c$ , and electrolytic solution flow velocities,  $v$ .  $c_e^b = 3.0M$ ,  $T = 25^\circ C$ ,  $x = 12.7$  cm,  $l_e = 0.05$  cm,  $l_f = 0.1524$  cm.

meter and specific energy in kilowatt-hours per pound of lithium vary with cell potential and flow velocity.

Figures 9 and 10 show the effects of temperature on cell performance in terms of variations in current voltage curves, current efficiency, power density, and specific energy. Figures 11 and 12 show the same cell performance characteristics with electrolytic solution concentration as a variable.

Comparison of velocity, temperature, and concentration with regard to their effects on cell performance shows that the lithium hydroxide concentration in the circulating solution has the most important influence on cell performance. Figure 13 is an illustration of how control of lithium hydroxide concentration can be used to optimize cell operation. For example, if a power setting of 160 mW/cm<sup>2</sup> is desired, a

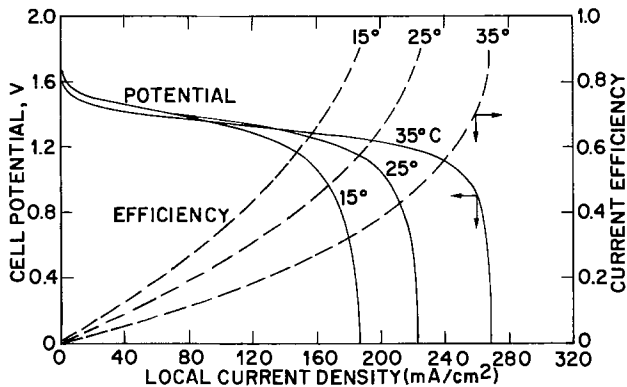


Fig. 9. Current-potential curves and current efficiency for various operating temperatures.  $v = 21.3$  cm/sec,  $c_e^b = 3.0M$ ,  $x = 12.7$  cm,  $l_e = 0.05$  cm,  $l_f = 0.1524$  cm.

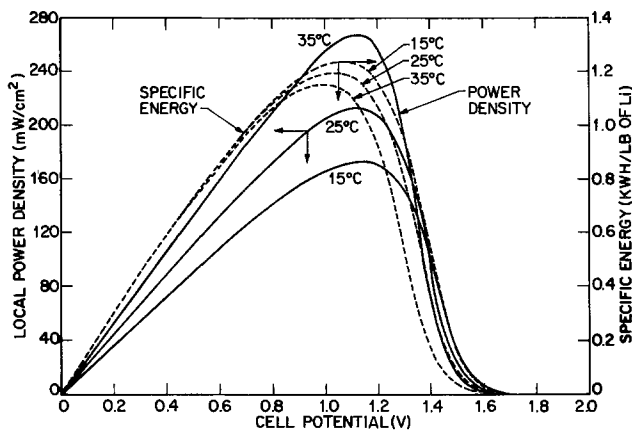


Fig. 10. Power and specific energy as functions of cell potential,  $\phi_c$ , and cell operating temperature.  $v = 21.3$  cm/sec,  $c_e^b = 3.0M$ ,  $x = 12.7$  cm,  $l_e = 0.05$  cm,  $l_f = 0.1524$  cm.

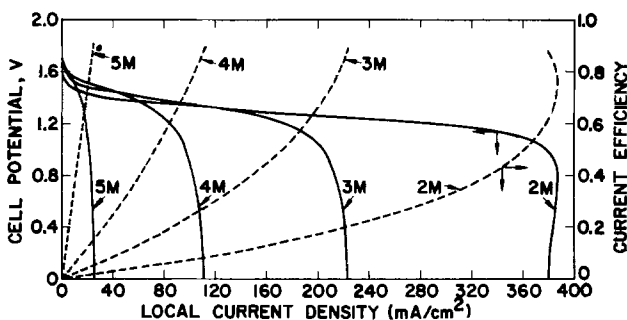


Fig. 11. Current potential curves and current efficiency for various electric solution concentrations.  $v = 21.3$  cm/sec,  $T = 25^\circ C$ ,  $x = 12.7$  cm,  $l_e = 0.05$  cm,  $l_f = 0.1524$  cm.

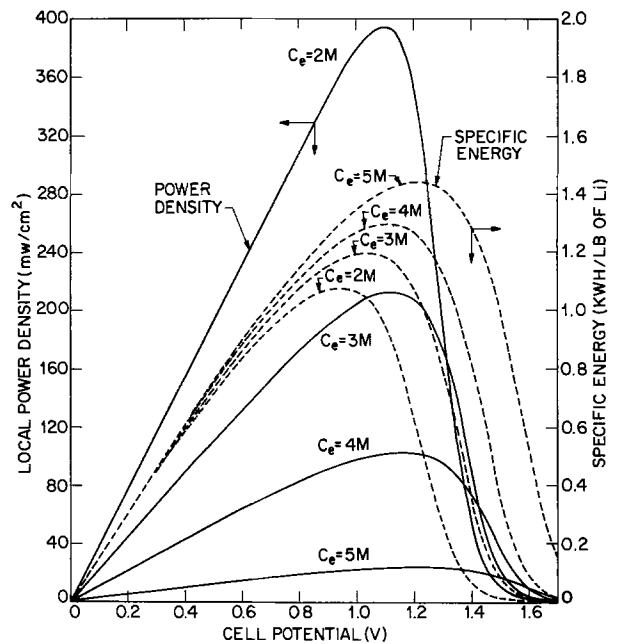


Fig. 12. Power and specific energy as functions of electrolytic solution concentration.  $v = 21.3$  cm/sec,  $T = 25^\circ C$ ,  $x = 12.7$  cm,  $l_e = 0.05$  cm,  $l_f = 0.1524$  cm.

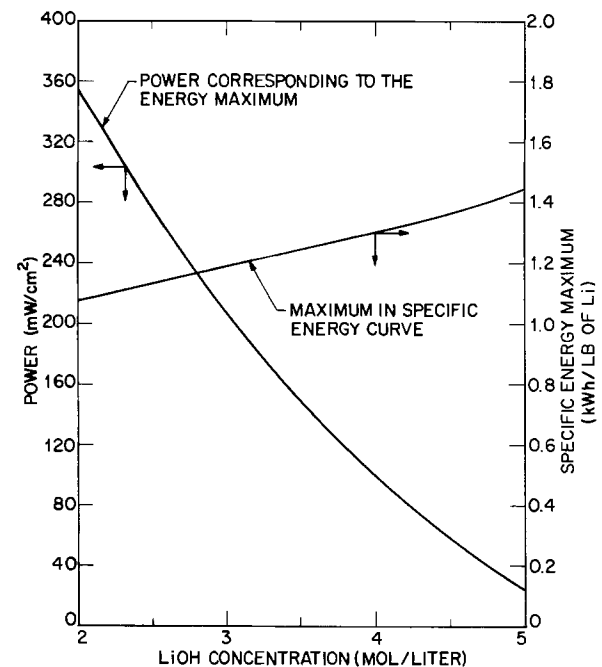


Fig. 13. Power corresponding to specific energy maximums.  $v = 21.3$  cm/sec,  $T = 25^\circ C$ ,  $x = 12.7$  cm,  $l_e = 0.05$  cm,  $l_f = 0.1524$  cm.

maximum in specific energy of 1.23 kW-hr/lb of lithium will be achieved at a solution concentration of 3.40M. Inspection of Fig. 12 shows that this optimum setting occurs at 1.11V cell potential implying a current of 144 mA/cm<sup>2</sup>. These optimum settings are on rather narrow maximums, and settings far from the maximum will yield poor efficiency. As an example, for 160 mW/cm<sup>2</sup> at a concentration of 3.0M and assuming operation along the high voltage branch at 1.3V, Fig. 12 indicates a specific energy of only 0.69 kW-hr/lb of lithium. If the lower voltage branch is used, the cell potential would be 0.734V with a lithium utilization of 1.02 kW-hr/lb. Both settings are well below the optimum (for the cell configuration used in this study) of 1.25 kW-hr/lb, but the lower voltage off optimum setting is less serious a loss than the



high voltage setting. This example illustrates that ideal settings are single valued as shown in Fig. 13, but off optimum settings are double valued. When off the ideal, the lower voltage selection yields a higher efficiency for lithium utilization than the higher setting. Figure 13, when used with Fig. 11 and 12, allows selection of best settings for fixed temperature and flow rate. Figures 5 through 10 illustrate, generally, the effects of varying temperature and flow rate.

### Discussion

The bell-shaped power maximum curves shown in Fig. 8, 10, and 12 are not unique to the lithium-water system. Any battery or fuel cell power-potential curves have the same general shape. For most electrochemical power sources, the high voltage branch will yield the most efficient materials utilization. However, the lithium-water system involves a parasitic hydrogen evolution reaction or corrosion reaction which becomes relatively less important along the lower voltage branch of the curve. Thus, in the cases studied, the increase in current efficiency more than offsets the loss in cell potential. Based on the limited cases examined in this work, it appears to be a reasonable guideline to operate as close to the power maximum as possible and to insure that deviations tend to the low voltage side of the maximum. Power and energy maximums occur very close together so that, practically, it is not important to distinguish between the two.

Changes in cell output appear only mildly affected by electrolytic solution flow velocity as compared to the effects of changing the bulk lithium hydroxide concentration or the operating temperature. This appears to be due in part to the stirring effect of the hydrogen evolution, particularly from the parasitic reaction. The parameters associated with the effect of the parasitic hydrogen evolution rate on the mass transfer of ions into the bulk solution made important changes in the numerical results.

In summary, the mathematical model has correlated early experimental results sufficiently well that reasonable confidence can be placed in the description of the principal factors controlling the lithium anode. However, experimental work performed subsequently has shown the importance of anode to cathode contact pressure for optimization of cell performance. Thus, faradaic efficiencies approaching 100% and cell potentials of 1.3V are obtained when the electrodes are pressed together at 10 psi. This operational feature then results in gravimetric energy densities of 2 kW-hr/lb lithium. The importance of this effect needs to be factored into the model since examination of Fig. 8, 10, and 12 shows that the predicted maximum energy density is only between 1 and 1.5 kW-hr/lb lithium. This result implies 26-38% thermodynamic efficiency, a value which compares well with other devices for converting chemical energy to mechanical or electrical energy. The lithium oxidation involves the formation of a hydrated lithium oxide film on the surface of the lithium. The lithium hydroxide continually dissolves into the bulk electrolytic solution through a hydrodynamic diffusion boundary layer. The rates of lithium oxidation and the parasitic or corrosion hydrogen evolution are controlled by the mass transport of water, hydroxyl ions, and lithium ions through the hydrated lithium oxide film. The thickness of the film is established by a steady-state balance between the various rate processes.

### Acknowledgments

The authors acknowledge the helpful assistance of G. B. Adams and J. J. Redlien of Lockheed. They provided the cell characterization data and participated in the technical discussion. Financial support for this work has been provided by Lockheed Missiles & Space Company, Incorporated. The development of

the mathematical modeling techniques has been supported financially by the U.S. Naval Air Systems Command and the U.S. Office of Naval Research. The basic conception for the model presented here came from the Palladium Medal Address given by T. P. Hoar (18).

Manuscript submitted Jan. 30, 1976; revised manuscript received May 28, 1976.

Any discussion of this paper will appear in a Discussion Section to be published in the June 1977 JOURNAL. All discussions for the June 1977 Discussion Section should be submitted by Feb. 1, 1977.

Publication costs of this article were assisted by Lockheed Missiles & Space Company, Incorporated.

### LIST OF SYMBOLS

$a_e^b$	activity of LiOH in bulk solution, dimensionless
$a_e^{sat}$	activity of LiOH at saturation, dimensionless
$a_{o,b}$	activity of water in bulk electrolytic solution compared to pure water, dimensionless
$a_{o,s}$	activity of water at lithium surface compared to pure water, dimensionless
$a_o^{sat}$	activity of water in solution saturated with LiOH compared to pure water, dimensionless
$c_e^b$	concentration of LiOH in bulk electrolytic solution, mol/cm <sup>3</sup>
$c_e^{sat}$	concentration of LiOH in solution saturated with LiOH, mol/cm <sup>3</sup>
$c_o^{sat}$	concentration of water in solution saturated with LiOH, mol/cm <sup>3</sup>
$D$	diffusion coefficient of LiOH in electrolytic solution, cm <sup>2</sup> /sec
$F$	Faraday constant, 96,487 C/equiv.
$i$	net or observed cell current density, A/cm <sup>2</sup>
$i_a$	total anodic rate of lithium oxidation, A/cm <sup>2</sup>
$i_c$	rate of hydrogen evolution at cathode, A/cm <sup>2</sup>
$i_p$	rate of parasitic hydrogen evolution at anode, A/cm <sup>2</sup>
$k_m$	mass transfer coefficient for LiOH dissolution, cm/sec
$k_c$	convective mass transfer coefficient, cm/sec
$k_b$	bubble mass transfer coefficient, cm/sec
$l_e$	electric current path length, cm
$l_f$	flow channel width, cm
$R$	universal gas constant, 8.3143 J/mol·°K
$Re$	Reynolds number
$Sc$	Schmidt number
$T$	temperature, °K
$T_o$	reference temperature, 298.15°K
$U$	standard cell potential, u
$v$	electrolytic solution flow velocity, cm/sec
$x$	position along flow channel, cm
$\delta$	hydrated lithium oxide effective film thickness, cm
$\delta_o$	diffusion boundary layer thickness, cm
$\kappa$	solution electrical conductivity, mho/cm
$\kappa_f$	film electrical conductivity, mho/cm
$\mu$	viscosity, poise
$\nu$	kinematic viscosity, cm <sup>2</sup> /sec
$\rho$	density of electrolytic solution, g/cm <sup>3</sup>
$\phi_1$	potential of lithium electrode, V
$\phi_2''$	potential of lithium reference electrode, V
$\phi_2'$	potential of hydrogen reference electrode at anode, V
$\phi_2$	potential of hydrogen reference electrode in solution near anode, V
$\phi_3$	potential of hydrogen reference electrode in solution near cathode, V
$\phi_c$	potential of cathode, V
$\psi$	$RT/aF$

### REFERENCES

1. E. L. Littauer and K. C. Tsai, Proceedings 26th Power Sources Symposium, Atlantic City, May 1974, p. 57.
2. Lockheed Missiles & Space Co., Report to U.S. Navy on Contract N00017-72-C-4449, Report LMSC D 311256 (Nov. 1972).
3. E. L. Littauer and J. J. Redlien, Proceedings 9th Intersociety Energy Conversion Engineering Conference, San Francisco, 1974, p. 615.
4. G. B. Adams and L. B. Anderson, Lockheed Missiles & Space Co., Inc., Internal Report No. LMSC-D313433 (January 1973).

5. P. Delahay, "Double Layer and Electrode Kinetics," pp. 158 and 164, Interscience Publishers, New York (1965).
6. R. A. Robinson and R. H. Stokes, "Electrolytic Solutions," pp. 483 and 491, Butterworths, London (1959).
7. F. Kreith, "Principles of Heat Transfer," pp. 441-453, International Textbook Co., Scranton, Pa. (1965).
8. J. Newman, "Electrochemical Systems," p. 318, Prentice Hall, Englewood Cliffs, N.J. (1973).
9. E. D. Farmer and A. H. Webb, *J. Appl. Electrochem.*, **2**, 123 (1972).
10. J. Newman, "Electrochemical Systems," pp. 414-425, Prentice Hall, Englewood Cliffs, N.J. (1973).
11. H. Kita, *This Journal* **113**, 1095 (1966).
12. J. Newman, "Electrochemical Systems," p. 230, Prentice Hall, Englewood Cliffs, N.J. (1973).
13. L. S. Darken and H. J. Meier, *J. Am. Chem. Soc.*, **64**, 621 (1942).
14. N. A. Lange, Editor, "Handbook of Chemistry," 8th ed., p. 1639, Handbook Publishing, Inc., Sandusky, Ohio (1952).
15. "Handbook of Chemistry and Physics," 53rd ed., p. B104, Chemical Rubber Co., Cleveland, Ohio (1972).
16. N. Ibl and J. Venzel, *Metalloberfläche*, **24**, 365 (1970).
17. L. J. J. Janssen and J. G. Hoogland, *Electrochim. Acta*, **18**, 543 (1973).
18. T. P. Hoar, *This Journal*, **117**, 17C (1970).

## Ionic Conductivity of Some Lithium Silicates and Aluminosilicates

I. D. Raistrick, Chun Ho,\* and R. A. Huggins†

*Center for Materials Research, Stanford University, Stanford, California 94305*

### ABSTRACT

Lithium silicates and aluminosilicates exhibiting a variety of typical silicate structures have been synthesized, and their ionic conductivities measured over a wide range of temperature and frequency, using a-c methods and blocking electrodes. The frequency dispersion of the conductance and capacitance has been analyzed, and an equivalent circuit containing temperature and frequency dependent components is proposed. Frequency independent bulk conductances and activation enthalpies have been extracted and these are discussed in terms of the structural properties of these materials. The importance of a careful analysis of the frequency dispersion is demonstrated.

At the present time there is considerable interest in finding a lithium ion conducting solid electrolyte with properties appropriate for utilization in high energy density battery systems. The conductivities of a number of lithium containing electrolytes have recently been reviewed by Pizzini (1, 2).

As part of a general screening program for good lithium solid electrolytes, it was decided to investigate the electrical properties of some silicates and aluminosilicates. A number of materials (Li<sub>2</sub>Si<sub>2</sub>O<sub>5</sub>, Li<sub>2</sub>SiO<sub>3</sub>, LiAlSiO<sub>4</sub>, and LiAlSi<sub>2</sub>O<sub>6</sub>) were chosen with structures representative of the main silicate types with the objective of adding to the understanding of the relationship between structure and ionic mobility.

Several lithium silicates have been investigated previously. Li<sub>4</sub>SiO<sub>4</sub> (lithium orthosilicate) has been studied by Gratzner *et al.* (3) and West (4, 5). It is one of the best lithium conductors. The conductivity of β-spodumene, LiAlSi<sub>2</sub>O<sub>6</sub>, was measured by Pizzini (1) who also showed by emf measurements that lithium was the mobile species, and recently some data have been presented by Johnson *et al.* (6, 7) for glassy and "glassy-ceramic" LiAlSiO<sub>4</sub> (β-eucryptite).

The major difficulty encountered in the measurement of ionic conductivities of solids is polarization at the electrode/electrolyte interface, and at the grain boundaries in a polycrystalline solid. While the electrode polarization can in principle be eliminated by using ideally reversible electrodes, an alternative procedure, that of studying the frequency dispersion of the a-c response using blocking electrodes, was adopted here, in the hope of obtaining additional information about grain boundary effects, minority carrier conduction, and interfacial and bulk capacitances.

The problem of analysis of frequency dispersion in ionic conductors has received some attention in recent years. For example, Macdonald (8-10) has presented exact solutions of the diffusion equations for a variety of theoretical conditions, and some experimental work has been carried out by Armstrong and co-workers (11-13), on the effect of grain boundaries etc. on the nature of the dispersion. In addition, a large amount of information is contained in the dielectric loss literature. Some of these latter data have been recently brought together by Jonscher (14). Dielectric loss has been used directly to determine the conductivities of solid electrolytes in a number of instances (15, 16).

The method of data analysis presented in this paper is primarily empirical. The complex plane method originally due to Cole and Cole (17) is employed. Equivalent circuits and admittance equations are introduced which reproduce the data well over wide ranges of experimental parameters. Recent examples of this approach can be found in the publications of Macdonald (10), Armstrong (11, 13), Mitoff and Charles (18), Franklin (19), Bert *et al.* (20), and Bauerle (21). The importance of this kind of analysis is demonstrated by showing that erroneous values for both conductivities and activation enthalpies can result from a disregard of frequency dispersion effects.

### Materials Investigated

This section briefly describes the main structural features of the four lithium-containing compounds, LiAlSi<sub>2</sub>O<sub>6</sub>, LiAlSiO<sub>4</sub>, Li<sub>2</sub>Si<sub>2</sub>O<sub>5</sub>, and Li<sub>2</sub>SiO<sub>3</sub>.

*LiAlSi<sub>2</sub>O<sub>6</sub>, β-spodumene.*—LiAlSi<sub>2</sub>O<sub>6</sub> exists in three modifications. The low temperature form has a diopside chain structure, a high temperature form is a "stuffed" 2/1 keatite structure, and a high temperature-high pressure form has a stuffed β-quartz structure (23). In nature, only the first is found, while the usual lab-

\* Electrochemical Society Student Member.

† Electrochemical Society Active Member.

Key words: solid electrolytes, complex plane analysis, frequency dependence, lithium ionic conductors.

oratory preparation at atmospheric pressure results in the second: known as  $\beta$ -spodumene, stable above 500°C but metastable at room temperature. A wide range of  $\beta$ -spodumene solid solution is known to exist (24), lying approximately between 60 and 80 mole percent (m/o)  $\text{SiO}_2$ . Close to the ideal composition, the tetragonal unit cell has the parameters  $a_0 = 7.53$ ,  $c_0 = 9.14\text{\AA}$ .

Keatite is a high temperature-high pressure modification of  $\text{SiO}_2$  (25), ( $a_0 = 7.456$ ,  $c_0 = 8.604\text{\AA}$ ). It is constructed of corner-sharing  $\text{SiO}_4$  tetrahedra arranged in spirals around the lines  $x = 0$ ,  $y = \frac{1}{2}$ , and  $x = \frac{1}{2}$ ,  $y = 0$ . The spirals are linked by Si atoms in such a way that each Si is linked to the oxygen of four different spirals, resulting in five-membered rings, the cavities of which extend throughout the structure. In  $\beta$ -spodumene 1/3 of the Si atoms are replaced by aluminum atoms randomly, and the lithium ions occupy either of two equivalent positions within the rings. There are twice as many sites as lithium ions. The large channels presumably account for the ion exchange properties of this compound (26). This fact led to the present interest in this material as a possible solid electrolyte.

*LiAlSiO<sub>4</sub>,  $\beta$ -eucryptite.*—This material is another example of a "stuffed" structure, (27), but this time it is a superstructure of the  $\beta$ -quartz modification of  $\text{SiO}_2$ , rather than keatite. Quartz is the closest packed of the three common silica modifications. It is composed of interlinked helical chains of corner-shared  $\text{SiO}_4$  tetrahedra. The interstices, which are occupied by  $\text{Li}^+$  ions in  $\beta$ -eucryptite, are much smaller than the interstices in keatite, cristobalite, or tridymite.

*Li<sub>2</sub>Si<sub>2</sub>O<sub>5</sub> and Li<sub>2</sub>SiO<sub>3</sub>.*—By contrast with the previous two structures, the  $\text{Li}^+$  ions in  $\text{Li}_2\text{Si}_2\text{O}_5$  and  $\text{Li}_2\text{SiO}_3$  are not "interstitial" in nature but are essential to the cohesion of the framework. In  $\text{Li}_2\text{Si}_2\text{O}_5$  (as in  $\text{LiAlSi}_4\text{O}_{10}$ , petalite) the silicate tetrahedra form six-membered rings, which share vertices leading to infinite sheets. Two sheets are held together by ionic bonding through  $\text{Li}^+$ , positioned between the layers (28).

In  $\text{Li}_2\text{SiO}_3$ , rather than forming sheets, the  $\text{SiO}_4$  tetrahedra form zigzag chains, which are again held together by lithium ions lying between them (29).

### Preparation and Characterization of Materials

Standard solid-state preparative methods were used to synthesize  $\text{LiAlSi}_2\text{O}_6$ ,  $\text{LiAlSiO}_4$ , and  $\text{Li}_2\text{SiO}_3$ . The starting materials were  $\text{Al}_2\text{O}_3$ ,  $\text{SiO}_2$ , and  $\text{Li}_2\text{CO}_3$ . Mixtures of appropriate composition were heated in alumina crucibles between 1050° and 1200°C.  $\text{Li}_2\text{Si}_2\text{O}_5$  was prepared by melting a mixture of  $\text{Li}_2\text{CO}_3$  and  $\text{SiO}_2$  at 1200°C and quenching to room temperatures, followed by solid-state annealing at 900°C. All x-ray diffraction patterns were in excellent agreement with previously published results.

### Experimental Aspects of the Electrical Measurements

*Preparation of samples for measurements.*—A small quantity of the ground material was hot pressed at temperatures between 800° and 1000°C and at a pressure of 6000 psi, in graphite dies. Carbon was then burned off the resulting disks at 800° in air.

The surfaces of the disks were polished using 400 mesh silicon carbide paper and both surfaces of the pellets x-rayed to ensure that the surface was still composed of the correct material. 1000Å of platinum was then sputtered onto both surfaces and electrical contact was made by spring-loaded platinum foil disks.

*A-C measurements.*—The a-c measurements were made using one or more of three different bridges; General Radio 1608, 1615, and Hewlett-Packard 4270 A, the 1615 bridge being used at conductivity values below 100  $\mu\text{mhos}$ . The frequency range used was between 20 Hz and 1 MHz, although the exact range available depended on the conductance of the sample. Materials with a high conductivity generally exhibited too great a loss at low frequencies (< 100 Hz) to allow accurate

measurement with available equipment. The signal amplitude was maintained below a few millivolts.

### Introduction to Analysis of the Frequency Dependence

At any given temperature the frequency dispersion can be represented as a line in a complex admittance, impedance or dielectric constant plane. As the temperature is varied the various time constants change and hence the observable portion of the total frequency-dependent response shifts. Thus, by making measurements over a sufficiently wide range of temperatures, it is possible to construct a composite picture of the total behavior. Such a composite diagram for the silicates is given schematically in Fig. 1. The frequency- and temperature-dependent response of all four materials was found to be sufficiently similar to enable them to be discussed together.

As may be seen from Fig. 1, two main regions of response are discernible. At the low frequency end, the admittance ( $B$ - $G$ ) plot is a closed circular arc, whereas data in the high frequency region lead to an open figure. The converse is true for the impedance ( $X$ - $R$ ) plot. The two regions are separated at a real resistance  $R_B$  in both cases. The shapes of the experimental curves indicate that at low frequencies a series  $R$ - $C$  circuit is dominant, with an associated capacitance of the order of microfarads, whereas at high frequencies a parallel  $R$ - $C$  circuit with an associated capacitance of the order of picofarads more closely models the characteristic response. The temperature-dependent resistance  $R_B$  is common to both networks and has been taken as the bulk resistivity of the electrolyte. Note that the lowering of the centers of the circular portions of the plots below the real axes, characterized by the angles  $\theta_Y$  and  $\theta_Z$ , corresponds to a deviation of the open-ended portions of the complementary figure from the vertical.

Such data cannot be modeled by any equivalent circuit composed entirely of frequency-independent com-

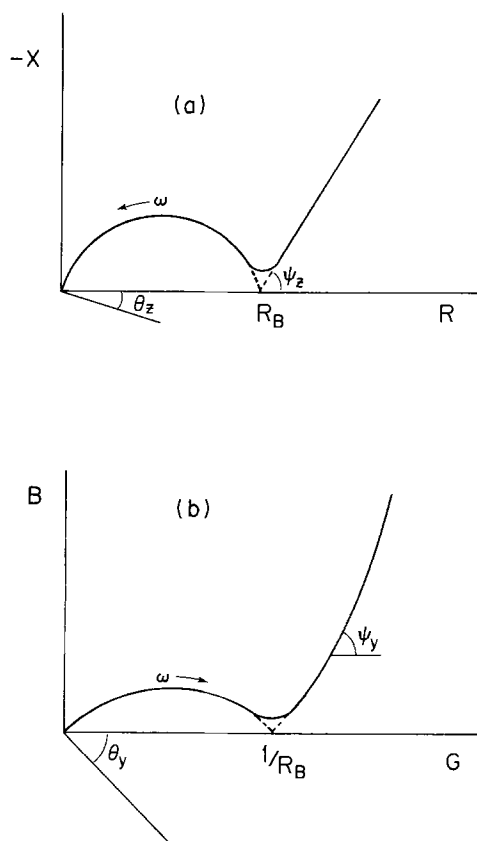


Fig. 1. Schematic representation of the complex impedance (a) and complex admittance (b) of the solid electrolyte/blocking electrode system.

ponents; nonfinite or frequency-dependent components must be included in order to explain circular arcs whose centers lie below the real axis.

**Results of the Analysis of the Low Temperature-High Frequency Response**

All four materials showed similar low temperature frequency dispersion and will be considered together here. The *B-G* plots are curves inclined at an angle  $\psi_Y (\pi/4 < \psi_Y < \pi/2)$  to the real (*G*) axis. The higher the frequency the closer  $\psi_Y$  approaches  $\pi/2$ . A low frequency "tail" is evident which, as the temperature is raised, eventually goes through a minimum leading into the low frequency (high temperature) region, discussed in the next section. Typical *B-G* plots are shown in Fig. 2 and 3

The corresponding *X-R* plots (Fig. 4) are approximately semicircular arcs with the high frequency intercept at the origin. A low frequency tail is again evident. The center of the circle is a few degrees below the real (*R*) axis.

If the effective parallel capacitance,  $C_p$ , is plotted against  $\log \omega$  (Fig. 5), it can be seen that at very high frequencies  $C_p$  extrapolates to a constant value ( $C_\infty$ ) which is almost temperature independent, and of the order of a few picofarads. Similar values were obtained for all the materials. The occurrence of a limiting high frequency capacitance is not unexpected: the physical arrangement of a material of finite dielectric constant sandwiched between two parallel metal electrodes has a geometrical, or bulk, capacitance which is expected to be of the order of a few picofarads for the sample and electrode geometry used here. The most obvious effect of temperature is to drastically increase  $C_p$  at low frequencies.

The shape of the  $C_p$  vs.  $\log \omega$  curve (Fig. 5) suggested a dependence of  $\log (C_p - C_\infty)$  upon  $\log \omega$ . This was confirmed by plotting these two quantities against one another, producing straight lines at several temperatures (Fig. 6).

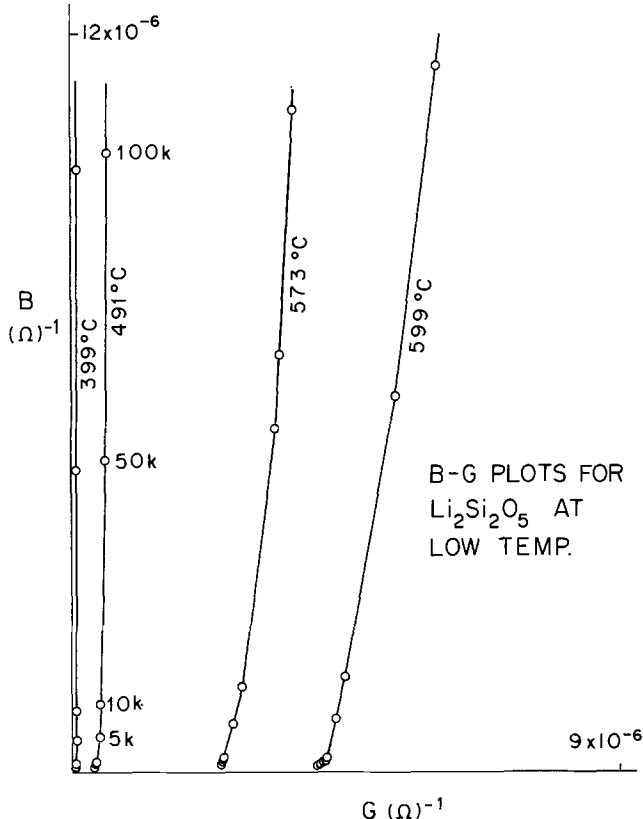


Fig. 2. Complex admittance plot for  $\text{Li}_2\text{Si}_2\text{O}_5$  at low temperatures

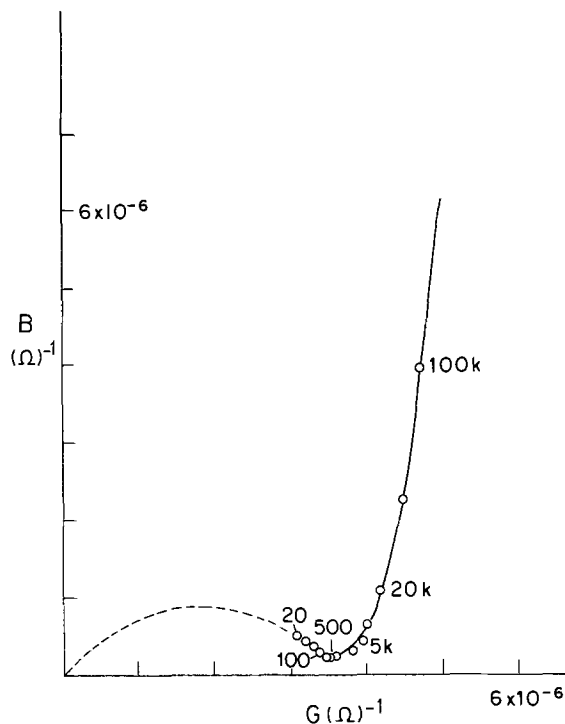


Fig. 3. Complex admittance plot for  $\text{LiAlSiO}_4$  at an intermediate temperature ( $421^\circ\text{C}$ ).

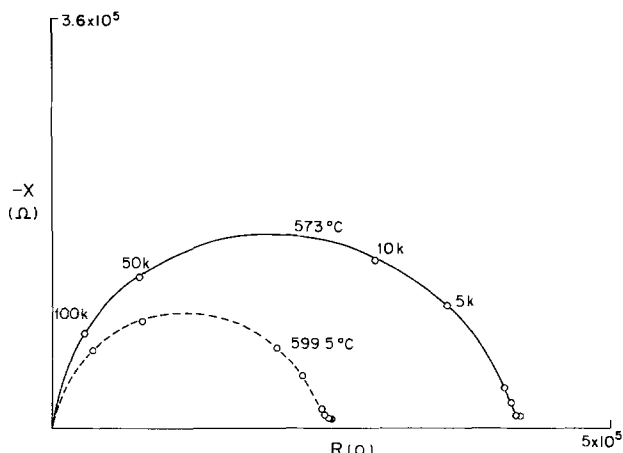


Fig. 4. Complex impedance plot for  $\text{Li}_2\text{Si}_2\text{O}_5$  at low temperatures

Thus, we can write

$$\log (C_p - C_\infty) = \log B_B + \delta \log \omega$$

where  $\delta$  is the slope and  $\log B_B$  is the  $\log \omega = 0$  intercept. Hence

$$C_p = C_\infty + B_B \omega^\delta$$

In the same way, a plot of  $\log (G_p - 1/R_B)$  vs.  $\log \omega$  gave straight lines of slope  $+\beta$  and intercept  $\log A_B$ . Therefore

$$G_p = \frac{1}{R_B} + A_B \omega^{+\beta}$$

Approximate values of  $C_\infty$  and  $R_B$  were obtained from Cole-Cole and complex impedance plots and were then varied using a digital computer so as to minimize the squared error in the straight line fit. Values for  $A_B$ ,  $B_B$ ,  $\beta$ , and  $\delta$  are given for  $\text{Li}_2\text{SiO}_3$  in Tables I and II at various temperatures.

The complete admittance equation for the high frequency (low temperature) response is therefore

$$Y^* = G_p + j\omega C_p = \frac{1}{R_B} + A_B \omega^{+\beta} + j(\omega C_\infty + B_B \omega^{1+\delta})$$

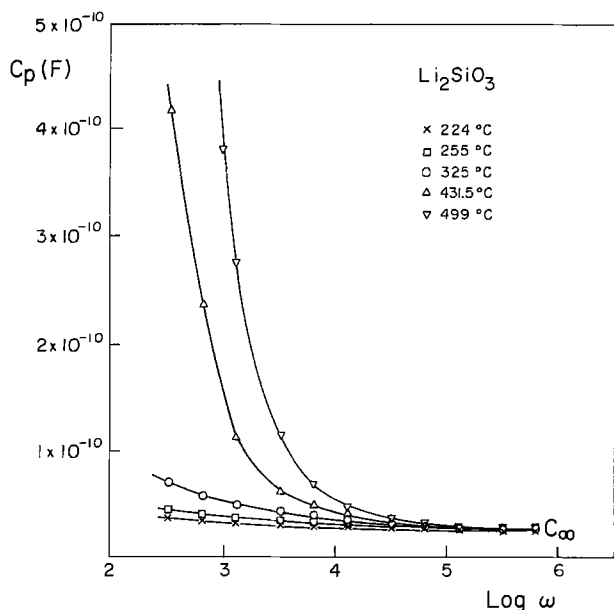


Fig. 5. Plot of measured parallel capacitance ( $C_p$ ) vs. logarithm of angular frequency for  $\text{Li}_2\text{SiO}_3$  at various temperatures.

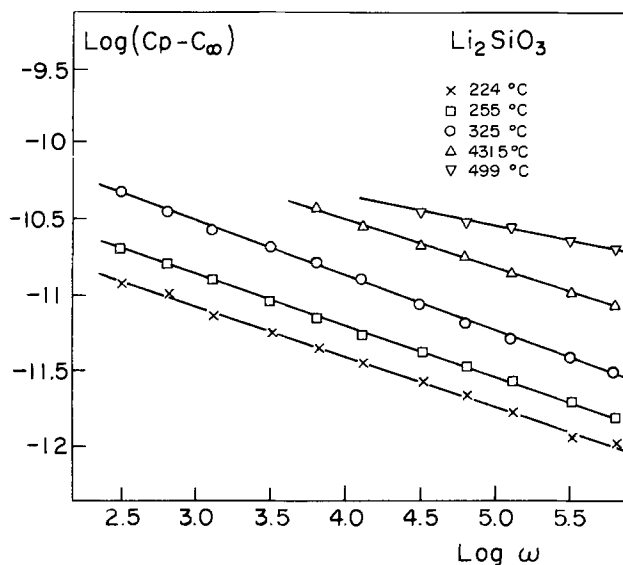


Fig. 6. Plot of logarithm of parallel capacitance after subtraction of high frequency limiting capacitance vs. logarithm of angular frequency for  $\text{Li}_2\text{SiO}_3$  at various temperatures.

and the appropriate equivalent circuit for this region is shown in Fig. 7a, where  $Y_B^*$  is a frequency-dependent circuit element having an admittance of the form

$$Y_B^* = A_B \omega^{+\beta} + jB_B \omega^{1+\delta}$$

Table I. Bulk complex admittance parameters for  $\text{Li}_2\text{SiO}_3$  (imaginary part)

T (°C)	Slope ( $\delta$ )	Intercept ( $\log B_B$ ) ( $B_B$ in $\Omega^{-1}$ )	$B_B$ ( $\Omega\text{-cm}^{-1}$ )	$C_\infty$ ( $\text{F}\text{-cm}^{-1}$ )
224*	-0.334	-10.09	$2.25 \times 10^{-11}$	$6.59 \times 10^{-13}$
255*	-0.342	-9.845	$3.94 \times 10^{-11}$	$6.45 \times 10^{-13}$
325*	-0.362	-9.442	$9.98 \times 10^{-11}$	$6.34 \times 10^{-13}$
431.5†	-0.318	-9.237	$1.60 \times 10^{-10}$	$3.29 \times 10^{-13}$
499†	-0.191	-9.596	$6.97 \times 10^{-11}$	$3.78 \times 10^{-13}$

\*, † Results marked \* and † were taken in different cells. This may be of relevance since cell geometry, size of electrode plates, etc., might make a contribution to  $C_\infty$ .

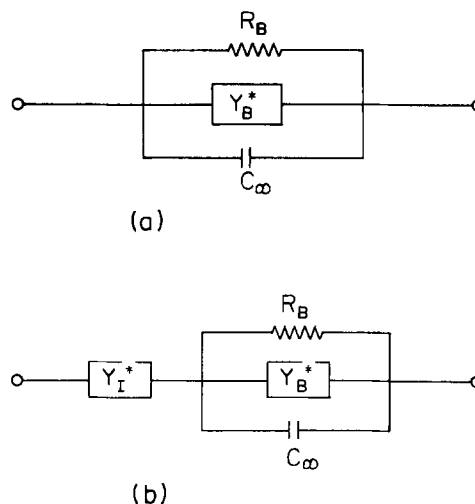


Fig. 7. Equivalent circuit models for the total electrolyte/electrode response: (a) low temperature, high frequency regime; (b) full experimental range.

From Tables I and II it can be seen that  $A_B$  and  $B_B$  are of the same order of magnitude, as are  $\beta$  and  $(1 + \delta)$ . When  $\omega(C_p - C_\infty)$  and  $(G - 1/R_B)$  are plotted against each other a straight line of slope  $\sigma$  results (Fig. 8). Thus

$$\frac{dB}{dG} = \frac{B_B(1 + \delta)\omega^\delta}{A_B\beta\omega^{(\beta+1)}} = \sigma, \text{ a constant}$$

Since  $\sigma$  is independent of frequency (Fig. 8)

$$\delta = \beta - 1$$

Thus

$$\sigma = B_B/A_B$$

Thus the frequency exponents in the two terms in the admittance equation are the same, in accordance with the Kramers-Krönig relations, but  $A_B$  and  $B_B$  may be different, the ratio of these latter quantities,  $\sigma$ , determines both the slope of the  $B$ - $G$  plot and the extent of the lowering of the center of the semicircle below the real axis in the  $X$ - $R$  plots. The final form of this bulk admittance is therefore

$$Y^*_{\text{bulk}} = A_B \omega^{+\beta} + jB_B \omega^{+\beta}$$

or, transforming this to an impedance equation

$$Z^*_{\text{bulk}} = \left( \frac{A_B}{A_B^2 + B_B^2} \right) \omega^{-\beta} - j \left( \frac{B_B}{A_B^2 + B_B^2} \right) \omega^{-\beta}$$

The physical origin of an admittance of this form is at the present time uncertain. The most likely hypothesis is that it is connected with diffusional grain boundary charge storage and dissipation. It is possible to write a number of infinite circuits, all of which show an admittance of the form described above. Scheider (30) has discussed some of these in a slightly different context. Until more specific experiments are carried out to determine the effect of grain boundaries on the electrical response of such an electrolyte-electrode system, the explanation offered here should be regarded as speculative.

Table II. Bulk complex admittance parameters for  $\text{Li}_2\text{SiO}_3$  (real part)

T (°C)	Slope ( $\beta$ )	Intercept ( $\log A_B$ ) ( $A_B$ in $\Omega^{-1}$ )	$A_B$ ( $\Omega\text{-cm}^{-1}$ )	$1/R_B$ ( $\Omega\text{-cm}^{-1}$ )
244	0.738	-10.61	$6.31 \times 10^{-12}$	$1.51 \times 10^{-9}$
255	0.670	-10.12	$1.93 \times 10^{-11}$	$5.33 \times 10^{-9}$
325	0.650	-9.69	$5.28 \times 10^{-11}$	$6.36 \times 10^{-9}$
431.5	0.707	-9.66	$5.67 \times 10^{-11}$	$8.85 \times 10^{-9}$
499	0.705	-9.50	$8.19 \times 10^{-11}$	$2.73 \times 10^{-9}$

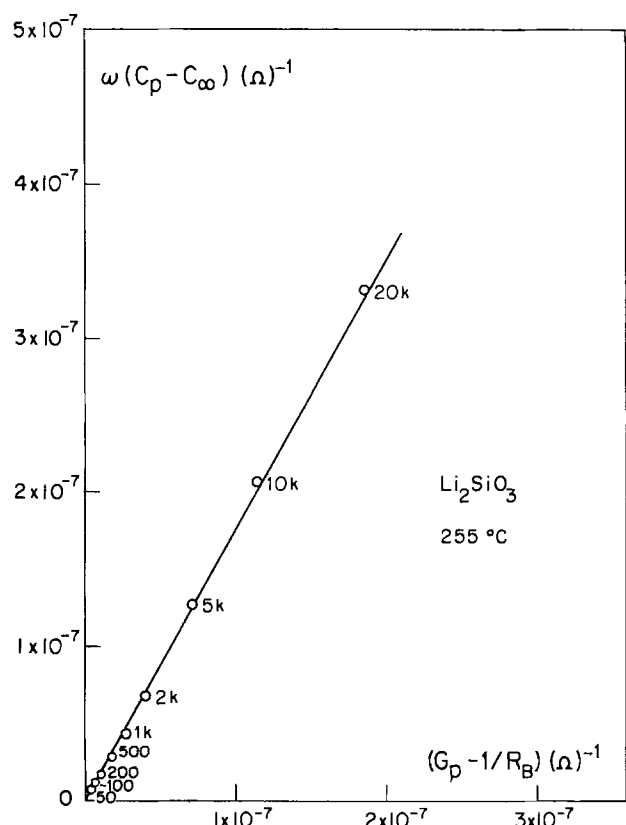


Fig. 8. Complex admittance plot after subtraction of  $\omega C_\infty$  from the susceptance and  $1/R_B$  from the conductance.

**Analysis of the High Temperature-Low Frequency Region of Electrical Response**

The two materials with the highest conductivities,  $\text{LiAlSiO}_4$  ( $\beta$ -eucryptite) and  $\text{LiAlSi}_2\text{O}_6$  ( $\beta$ -spodumene) exhibit very similar high temperature (low frequency) a-c response. Measurements on  $\text{Li}_2\text{SiO}_3$  and  $\text{Li}_2\text{Si}_2\text{O}_5$  were not carried out at sufficiently high temperatures to observe analogous response, the lower conductivities of these materials implying that the typical high temperature (low frequency) response is not seen in the experimentally available frequency spectrum until higher temperatures.

The general form of the high temperature response is shown in Fig. 9 and 10 in terms of  $B$ - $G$  and  $X$ - $R$  plots.

The  $B$ - $G$  plots are portions of circles, with their centers much below the real axis at low temperatures. The angle  $\theta_X$ , defined at the origin by the position of the center of the circle, is given in Table III for  $\text{LiAlSi}_2\text{O}_6$

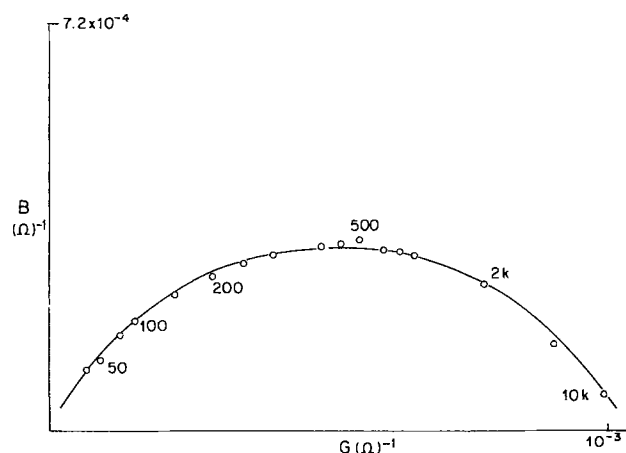


Fig. 9. High temperature complex admittance plot for  $\text{LiAlSi}_2\text{O}_6$  at  $644^\circ\text{C}$ .

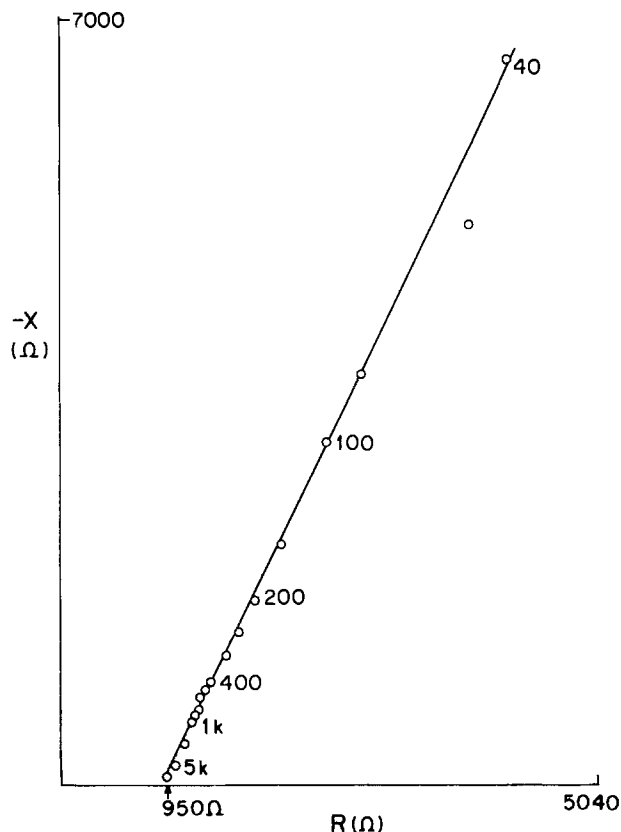


Fig. 10. High temperature complex impedance plot for  $\text{LiAlSi}_2\text{O}_6$  at  $692^\circ\text{C}$ .

at several temperatures. The high frequency end of the semicircle has a tail at low temperatures which leads into the bulk response region discussed in the previous section.

As the temperature is increased, the circular portions of the  $B$ - $G$  plots rise until at the highest temperatures studied ( $>900^\circ\text{C}$ ) the semicircle has its center on the real axis. The  $X$ - $R$  plots are straight lines inclined at an angle  $\psi_z$  to the real axis ( $\pi/2 > \psi_z > \pi/4$ ). As the temperature is increased the  $X$ - $R$  plot approaches a vertical straight line.

The occurrence of a circular arc in a  $B$ - $G$  plot is equivalent to a straight line in the  $X$ - $R$  plot. From the latter, we can write

$$-X = \psi_z(R - R_B)$$

where  $\psi_z$  is the slope of the line and  $R_B$  is the extrapolated intercept on the real ( $R$ ) axis corresponding to the bulk electrolyte resistance.

Thus,  $dX/dR = -\psi_z$ , which is a constant and independent of frequency even though both  $X$  and  $R$  are functions of frequency.

Plots of  $\log(-X)$  and  $\log(R - R_B)$  vs.  $\log \omega$  were both found to be straight lines having the same slope,  $-\alpha$ . Thus

$$R - R_B = A_I \omega^{-\alpha}$$

and

$$-X = B_I \omega^{-\alpha}$$

Therefore

$$\psi_z = B_I/A_I$$

and is independent of  $\omega$ .

Table III. Angle subtended at origin of  $B$ - $G$  plot by the center of low frequency semicircle for  $\text{LiAlSi}_2\text{O}_6$  ( $\beta$ -spodumene)

$T$ ( $^\circ\text{C}$ )	$\theta_X$ (degrees)	$T$ ( $^\circ\text{C}$ )	$\theta_X$ (degrees)
421	$\sim 37$	711	28
609	33	775	19
667	31.5	938	$\sim 0$

We may, therefore, represent the electrical response of the sample-electrode system in the low frequency-high temperature regime by the impedance

$$Z^*_I = A_I \omega^{-\alpha} - jB_I \omega^{-\alpha}$$

in series with the bulk resistance  $R_B$ .

The corresponding admittance in this regime (excluding the bulk resistance) is

$$Y^*_I = \frac{A_I}{A_I^2 + B_I^2} \omega^\alpha + j \frac{B_I}{A_I^2 + B_I^2} \omega^\alpha$$

In Table IV, values of  $A_I$ ,  $B_I$ , and  $\alpha$  are given at three different temperatures for  $\beta$ -spodumene and  $\beta$ -eucryptite.

The form of this low frequency (high temperature) impedance is significantly different from the normal description of a blocking electrode double layer. It has usually been assumed that the electrical double layer could be described as a frequency-independent capacitance in series with the bulk resistance. The present description allows resistive as well as capacitive components to act at the interface, and these are related in such a way that the dissipation factor, the ratio of energy dissipated to energy stored, is fixed and independent of frequency. The coefficients  $A_I$  and  $B_I$ , however, may change with temperature. Unfortunately, the instability of the interface morphology at these high temperatures prevented further meaningful numerical analysis, which would give the dependence  $A_I$ ,  $B_I$ , and  $\alpha$  on temperature. At the present time, low temperature measurements on better ionic conductors are in progress in the hope of defining the interface parameters and their properties more exactly (31).

#### Effect of Frequency Dependence on Measured Activation Enthalpies of Lithium Silicates and Aluminosilicates

As discussed in the previous two sections, the frequency response of the silicates using sputtered platinum electrodes is well modeled by the equivalent circuit shown in Fig. 7b, where

$$Y^*_B = A_B \omega^\beta + jB_B \omega^\beta$$

and

$$Y^*_I = \frac{A_I}{\rho} \omega^\alpha + j \frac{B_I}{\rho} \omega^\alpha$$

$$\rho = A_I^2 + B_I^2$$

Although the magnitudes of both the constants and the frequency exponents of  $Y^*_I$  and  $Y^*_B$  are quite different, the same value of the frequency-independent resistance ( $R_B$ ) can be extracted from the data in both frequency/temperature regimes. It will be seen shortly that the conductivity-temperature product related to this resistance varies exponentially with temperature in accordance with the Arrhenius relation. The high frequency limiting capacitance  $C_\infty$  is associated with the high frequency dielectric constant of the silicates. It may also include a contribution from the leads and measuring equipment, although this factor was eliminated experimentally so far as possible.

It should be noted that  $C_\infty$  may be placed over the entire circuit, rather than just across  $Y^*_B$ , but this would involve essentially no changes in either the form

Table IV. Interface complex impedance parameters for  $\text{LiAlSi}_2\text{O}_6$  and  $\text{LiAlSiO}_4$

Compound	T (°C)	$A_I$ ( $\Omega\text{-cm}^2$ )	$B_I$ ( $\Omega\text{-cm}^2$ )	$\alpha$
$\text{LiAlSi}_2\text{O}_6$	692	$2.97 \times 10^5$	$5.43 \times 10^5$	0.85
$\text{LiAlSi}_2\text{O}_6$	786	$1.78 \times 10^6$	$2.01 \times 10^6$	0.73
$\text{LiAlSi}_2\text{O}_6$	931.5	$3.72 \times 10^5$	$5.95 \times 10^6$	0.80
$\text{LiAlSiO}_4$	667	$1.19 \times 10^6$	$1.99 \times 10^5$	0.79
$\text{LiAlSiO}_4$	775	$9.44 \times 10^4$	$1.63 \times 10^6$	0.76
$\text{LiAlSiO}_4$	923	$1.10 \times 10^6$	$9.89 \times 10^4$	0.70

of the magnitudes of the results. Also a d-c electronic resistance might be included in parallel to the whole circuit. However, the low frequency data extrapolate to very low d-c conductances indicating a very low electronic transference number. This was confirmed by independent d-c measurements.

The circuit element  $Y^*_I$  is obviously associated with the electrolyte-electrode interface, and  $Y^*_B$  with the bulk response. Because of the large difference in their time constants, in principle, the two response regimes are clearly separated at  $R_B$  when represented in either the admittance or impedance complex plane.

However, the range of frequencies readily accessible to experimental measurements often does not span the full range of behavior theoretically expected. At low temperatures the bulk-dominated response region generally lies within the accessible frequency range; and at high temperatures the interface-dominated response is observed. The effect of this shift in the "frequency window" with temperature is that numerical extrapolations to obtain  $R_B$  must typically be made to low frequencies at lower temperatures, and to high frequencies at higher temperatures. This is contrary to the traditional practice of extrapolating all measurements to infinite frequency and assuming that all polarization effects have been eliminated. In Fig. 11 and 12 both monofrequency data taken at 10 kHz and the results obtained from data obtained over a wide frequency range and corrected for frequency dependence by appropriate extrapolation are plotted as  $\log \sigma T$  vs.  $1/T$  for  $\text{Li}_2\text{Si}_2\text{O}_5$  and  $\text{Li}_2\text{SiO}_3$ .

The following observations may be made:

1. The general tendency is for monofrequency data at low temperatures to imply greater conductivities and lower activation enthalpies than are actually present. In Table V, numerical values of the 10 kHz and corrected data are compared.
2. Apparent discontinuities in the conductivity vs. temperature plots obtained in monofrequency experiments are either eliminated or removed to much lower

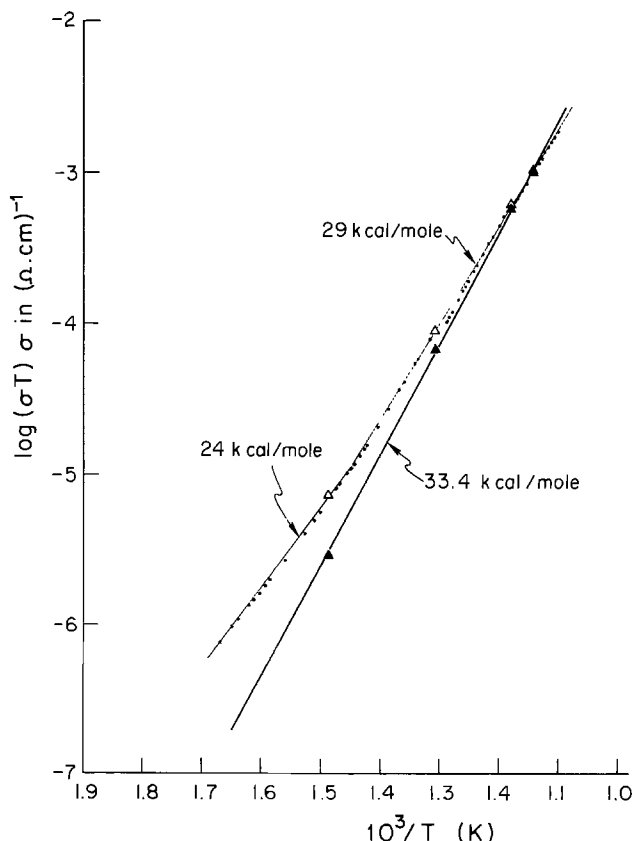


Fig. 11. Monofrequency data ( $\Delta$ , 10 kHz) and frequency-independent conductivity data ( $\blacktriangle$ , corrected for frequency dependence) for  $\text{Li}_2\text{Si}_2\text{O}_5$ .

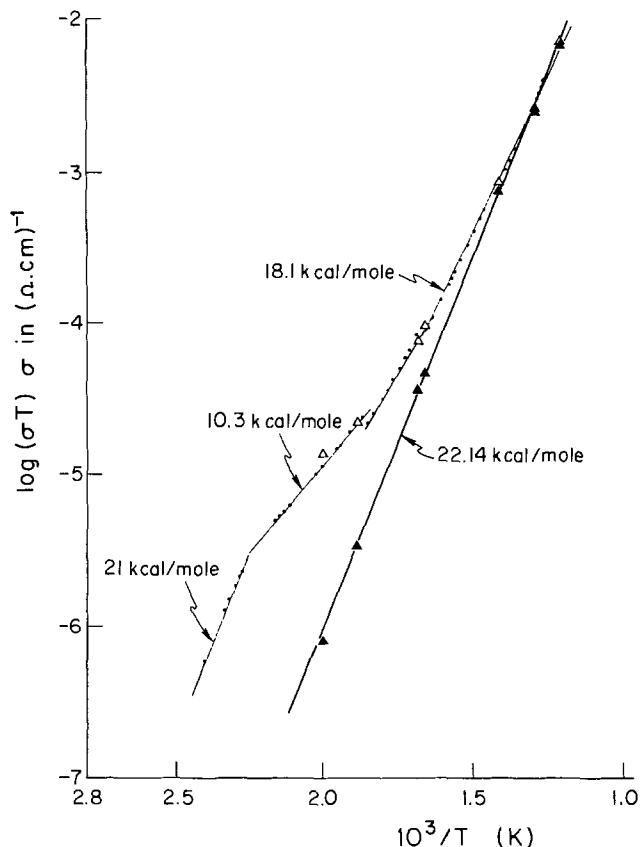


Fig. 12. Monofrequency data ( $\Delta$ , 10 kHz) and frequency-independent conductivity data ( $\blacktriangle$ , corrected for frequency dependence) for  $\text{Li}_2\text{SiO}_3$ .

temperatures by proper analysis. The behavior of  $\text{Li}_2\text{SiO}_3$  may be taken as an example. The 10 kHz data might be interpreted by several approximately linear regions, whereas the corrected data show a straight line with a single value of activation enthalpy. Such apparent changes in slope are often interpreted in terms of transitions between intrinsic and extrinsic behavior. This is not to say that an extrinsic-intrinsic transition is never found, but merely that the quantitative analysis of such behavior should be treated with circumspection if the frequency dispersion of the sample-electrode system has not been examined.

3. At very high temperatures monofrequency conductivity values observed may be less than the true values, leading to apparent curvature of the conductivity vs. temperature plot.

4. It has not proved possible in the present case to separate inter- and intragranular resistances. Only one resistance was necessary to model the data. It is possible, therefore, that the conductivity values given here may include a contribution from the grain boundaries. Further work is needed on this important consideration.

#### Relationship Between Structure and Ionic Conductivity in the Lithium Silicates and Aluminosilicates

In Fig. 13 frequency-independent conductivities are plotted as a function of temperature for the silicates

Table V. Comparison of real and apparent activation energies for  $\text{Li}_2\text{SiO}_3$  and  $\text{Li}_2\text{Si}_2\text{O}_5$

Sample	Temperature range ( $^{\circ}\text{C}$ )	Apparent activation enthalpy (kcal/mole)	Real activation enthalpy (kcal/mole)
$\text{Li}_2\text{SiO}_3$	140-171	21	22
$\text{Li}_2\text{SiO}_3$	171-268	10.34	—
$\text{Li}_2\text{SiO}_3$	268-527	18.75	—
$\text{Li}_2\text{Si}_2\text{O}_5$	337-415	24	33
$\text{Li}_2\text{Si}_2\text{O}_5$	415-650	29.4	—

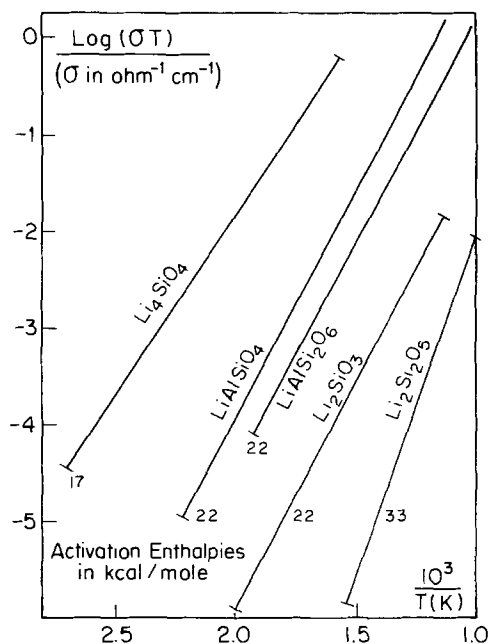


Fig. 13. Collected frequency-independent conductivity results for the silicates and aluminosilicates.

and aluminosilicates described above. Also included in this diagram are corrected conductivity values for  $\text{Li}_4\text{SiO}_4$ , lithium orthosilicate. Conductivity measurements on this material have been made in this laboratory over a wide range of frequency, as well (32). Details of this work and a comparison with the corresponding germanate (33) will be published separately.

In Table VI conductivities at  $400^{\circ}\text{C}$  and corresponding activation enthalpies are given. As may be seen, the lowest conductivities and highest activation enthalpies are exhibited by the chain and sheet silicates. Intermediate conductivities are shown by the "stuffed" quartz structures, and lithium orthosilicate has by far the highest conductivity. Indeed, it is one of the best lithium solid electrolytes known.

The general trend of these results is not unexpected, and can be qualitatively rationalized on the basis of the crystal structures of these materials.

In the layer and sheet silicates, the lithium ions are essential for the cohesion of the structure as a whole. They occupy tetrahedral sites, linking together the  $\text{SiO}_4$  tetrahedra through short, strong bonds.  $\text{Li}_2\text{Si}_2\text{O}_5$  has the shortest Li-O bond length (1.94Å) (28) suggesting the strongest bond, and correspondingly this compound has the lowest ionic conductivity and the highest activation enthalpy among the materials examined here. The stuffed structures have rather weaker lithium-oxygen bonds, e.g.,  $\text{LiAlSi}_2\text{O}_6$  has a Li-O bond length of 2.08Å. The lithiums are not an essential part of the structure, as evidenced by the existence of these crystallographic forms in pure silica.

The best ionic conductor is  $\text{Li}_4\text{SiO}_4$ . Its structure consists of isolated  $\text{SiO}_4$  tetrahedra linked through 4 coordinated Li ions. In addition, however, there are extra 5 and 6 coordinated lithium sites which are also partially occupied. The mean bond lengths for the 5 and 6 coordinated ions are 2.099 and 2.247Å, respectively. These figures may be compared with an average 4 co-

Table VI. Conductivities at  $400^{\circ}\text{C}$  and activation enthalpies

Compound	$\sigma_{400^{\circ}\text{C}}$ ( $\Omega\text{-cm}$ ) $^{-1}$	$\Delta H$ (kcal/mole)
$\text{Li}_2\text{Si}_2\text{O}_5$	$4.5 \times 10^{-9}$	33
$\text{Li}_2\text{SiO}_3$	$5.6 \times 10^{-7}$	22
$\text{Li}_2\text{Si}_2\text{O}_6$	$1.4 \times 10^{-6}$	22
$\text{LiAlSiO}_4$	$4.7 \times 10^{-6}$	22
$\text{Li}_4\text{SiO}_4$	$2.2 \times 10^{-4}$	17



ordinated lithium-oxygen bond length of 1.98Å. It is probably not unreasonable to suppose that the weakly bound ions in the 5 and 6 positions are primarily responsible for the high conductivity of this compound.

Good ionic conductivity in the silicates is therefore expected to be associated with one or more of the following structural features: a framework-type structure, with long alkali metal-oxygen bond distances (ions in sites of high coordination number), and fractional occupancy of alkali ion sites.

#### Acknowledgment

This research was supported by the Defense Advanced Research Projects Agency, and was monitored by the Office of Naval Research under Contract No. N00014-67-A-0075 and N00014-75-C-1056.

Manuscript submitted Dec. 9, 1975; revised manuscript received June 1, 1976.

Any discussion of this paper will appear in a Discussion Section to be published in the June 1977 JOURNAL. All discussions for the June 1977 Discussion Section should be submitted by Feb. 1, 1977.

Publication costs of this article were assisted by Stanford University.

#### REFERENCES

1. S. Pizzini, *J. Appl. Electrochem.*, **1**, 153 (1971).
2. S. Pizzini, G. Monari, and R. Morlotti, *This Journal*, **118**, 796 (1971).
3. W. Gratzel, H. Bittner, H. Novotny, and K. Seifert, *Z. Kristallogr.*, **133**, 260 (1971).
4. A. R. West, *J. Appl. Electrochem.*, **3**, 327 (1973).
5. A. R. West and E. P. Glasser, *J. Mater. Sci.*, **5**, 676 (1970).
6. R. T. Johnson, R. M. Biefeld, M. L. Knotek, and B. Morosin, *This Journal*, **123**, 680 (1976).
7. R. T. Johnson, B. Morosin, M. L. Knotek, and R. M. Biefeld, *Bull. Am. Phys. Soc.*, **20**, 330 (1975).
8. J. R. Macdonald, *J. Chem. Phys.*, **58**, 4982 (1973).
9. J. R. Macdonald, *J. Appl. Phys.*, **44**, 3455 (1973).
10. J. R. Macdonald, *J. Electroanal. Chem.*, **53**, 1 (1974).
11. R. D. Armstrong, *ibid.*, **52**, 413 (1974).
12. R. D. Armstrong, T. Dickinson, and P. M. Willis, *ibid.*, **48**, 47 (1973).
13. R. D. Armstrong, T. Dickinson, and P. M. Willis, *ibid.*, **53**, 389 (1974).
14. A. Jonscher, *Nature*, **253**, 717 (1975).
15. R. H. Radzilowski, Y. F. Yao, and J. T. Kummer, *J. Appl. Phys.*, **40**, 4716 (1969).
16. J. Singer, H. F. Kautz, W. L. Fielder, and J. S. Fordyce, in "Fast Ion Transport in Solids," W. van Gool, Editor, p. 653 North-Holland, Amsterdam (1973).
17. K. S. Cole and R. H. Cole, *J. Chem. Phys.*, **9**, 341 (1941).
18. S. P. Mitoff and R. J. Charles, *J. Appl. Phys.*, **43**, 927 (1972).
19. A. D. Franklin, *J. Am. Ceram. Soc.*, **58**, 465 (1975).
20. J. Bert, J. L. Picot, and J. Dupuy, *Phys. Status Solidi A*, **19**, 119 (1973).
21. J. E. Bauerle, *J. Phys. Chem. Solids*, **30**, 2657 (1969).
22. M. J. Buerger, *Am. Mineral.*, **39**, 600 (1954).
23. C. T. Li and D. R. Peacor, *Z. Kristallogr.*, **126**, 46 (1968).
24. R. Roy, D. M. Roy, and E. F. Osborn, *J. Am. Ceram. Soc.*, **33**, 152 (1950).
25. J. Shropshire, P. P. Keat, and P. A. Vaughn, *Z. Kristallogr.*, **112**, 409 (1959).
26. G. D. White and T. N. McVay, U. S. Energy Comm. ORNL-2450 (1958).
27. H. G. F. Winkler, *Acta Crystallogr.*, **1**, 27 (1947).
28. F. Liebau, *ibid.*, **14**, 389 (1961).
29. H. J. Seeman, *ibid.*, **9**, 251 (1956).
30. W. Scheider, *J. Phys. Chem.*, **79**, 127 (1975).
31. I. D. Raistrick, C. Ho, Y-W. Hu, and R. A. Huggins, To be published in *J. Electroanal. Chem. Interfacial Electrochem.*
32. Y-W. Hu, Unpublished work.
33. B. E. Liebert, *Mater. Res. Bull.*, To be published.

## Technical Note



# The Electrochemical Reactions of Carbon Monoxide, Nitric Oxide, and Nitrogen Dioxide at Gold Electrodes

J. M. Sedlak\* and K. F. Blurton\*

Energetics Science, Incorporated, Elmsford, New York 10523

Previously, an instrument for the measurement of carbon monoxide in ambient air was described (1, 2). The operating principle of that analyzer was based on the electrochemical oxidation of carbon monoxide (3) at a platinum-catalyzed Teflon-bonded diffusion electrode (4); the potential of this sensing electrode being maintained constant at a value where neither oxygen reduction nor electrolyte decomposition interfered with the measurement of the pollutant.

Utilization of this technique for the measurement of nitric oxide (NO) and nitrogen dioxide (NO<sub>2</sub>) required selective analysis of both gases in the presence of each other and in the presence of relatively large carbon monoxide concentrations. For example, typical ambient air concentrations of CO, NO, and NO<sub>2</sub>

are 10, 0.03, and 0.03 ppm (parts per million on a volumetric basis), respectively (5), while in industrial environments the pollutant levels can be substantially higher.

In general, instrument specificity can be achieved either by using selective gas filters or by optimizing the electrode catalyst and potential. Since it is impossible to filter CO selectively from air streams containing NO and NO<sub>2</sub>, specificity was achieved by the second approach. Therefore, the electrochemical reactions of NO, NO<sub>2</sub>, and CO on gold were investigated and are reported here.

#### Experimental

The electrochemical cell used was similar to that described previously (1) except for the sensing electrode catalyst. For this experimental study the cell contained three electrodes with 4.0M H<sub>2</sub>SO<sub>4</sub> solution as

\* Electrochemical Society Active Member.  
Key words: carbon monoxide, nitric oxide, nitrogen dioxide, gold electrode, gas sensor, diffusion electrode.

the electrolyte. Both sensing and counterelectrodes were gold-catalyzed Teflon-bonded diffusion electrodes (geometric area 5 cm<sup>2</sup> and catalyst loading 7-13 mg/cm<sup>3</sup>), and the reference electrode was a mercury/mercury sulfate electrode. The electrodes were prepared by the usual method (6).

When measurements were taken, the gas was passed over the back of the potentiostated gold diffusion electrode, and the current generated by the electrochemical reaction was measured by determining the potential drop across a standard resistor with a recorder (Hewlett-Packard Company, Model 680). The potentiostat was designed and constructed in-house. All potentials refer to the reversible hydrogen electrode potential in 4.0M H<sub>2</sub>SO<sub>4</sub> solution.

Analyzed cylinders of 6.8, 39, and 349 ppm NO in nitrogen and of zero grade air were obtained from Airco Incorporated (nitrogen was used as the diluent for NO to preclude reaction with oxygen). Samples containing up to 5 ppm NO<sub>2</sub> in air were prepared using zero grade air and thermostated permeation tubes (Metronics Associates). Unanalyzed CO in air mixtures containing approximately 50, 90, and 735 ppm were obtained from Matheson Gas Products Company.

### Discussion of Results

Current/potential curves for NO, NO<sub>2</sub>, and CO were obtained by initially potentiostating the gold electrode at 0.6V for 24 hr. The current was then measured for zero air and subsequently for each of the test gas mixtures at a flow rate of 0.7 liter/min. The electrode potential was then increased stepwise to 1.6V and the currents at each potential were determined after potentiostating for 24 hr. At each potential there was a small current (<10 μA) when zero air was passed into the sensor which was cathodic below about 1.05V. This current was subtracted from the current measured with the test gases. The potential range was restricted to 0.6-1.6V to minimize currents due to O<sub>2</sub> reduction and evolution. The current potential plots in Fig. 1 and 2 were obtained with one sensor but qualitatively similar behavior was noted with six additional cells.

Nitric oxide was electro-oxidized on Au only at potentials >0.9V, and this is similar to previously reported data with Pt electrodes (7, 8). Nitrogen dioxide was electro-oxidized at potentials >1.0V and electro-reduced at the more cathodic potentials. A plateau in the NO oxidation curve was obtained at potentials >1.2V and the value of this current was 7.8 μA/ppm. Similarly the maximum current for NO<sub>2</sub> oxidation was 3.8 μA/ppm and for NO<sub>2</sub> reduction was 8.2 μA/ppm. The value of this maximum current varied with each sensor and increased to approximately 13 μA/ppm for NO oxidation and NO<sub>2</sub> reduction with the higher catalyst loadings investigated.

The current for CO oxidation on Au electrodes (Fig. 2) was in marked contrast to that obtained with platinum electrodes (3). At potentials <1.0V, this current was very small. As the electrode potential approached that for gold oxide formation (9), the oxidation current increased to a maximum of 0.04 μA/ppm and subsequently decreased at potentials >1.4V.

From the current/potential behavior of CO, NO, and NO<sub>2</sub> with the gold catalyzed electrodes, an instrument for the separate and direct determination of NO and NO<sub>2</sub> was developed (10). The NO<sub>2</sub> sensor was biased at 0.8V since both NO and CO are unreactive at this potential. The NO sensor was operated at 1.5V where CO is again quite unresponsive and since NO<sub>2</sub> can easily be selectively filtered from NO/NO<sub>2</sub> mixtures (11).

Nitrogen oxides can undergo a variety of charge transfer processes at electrode surfaces. We have used the above-described cell to determine the over-all reactions for NO<sub>2</sub> reduction at 0.8V and for NO oxidation at 1.5V.

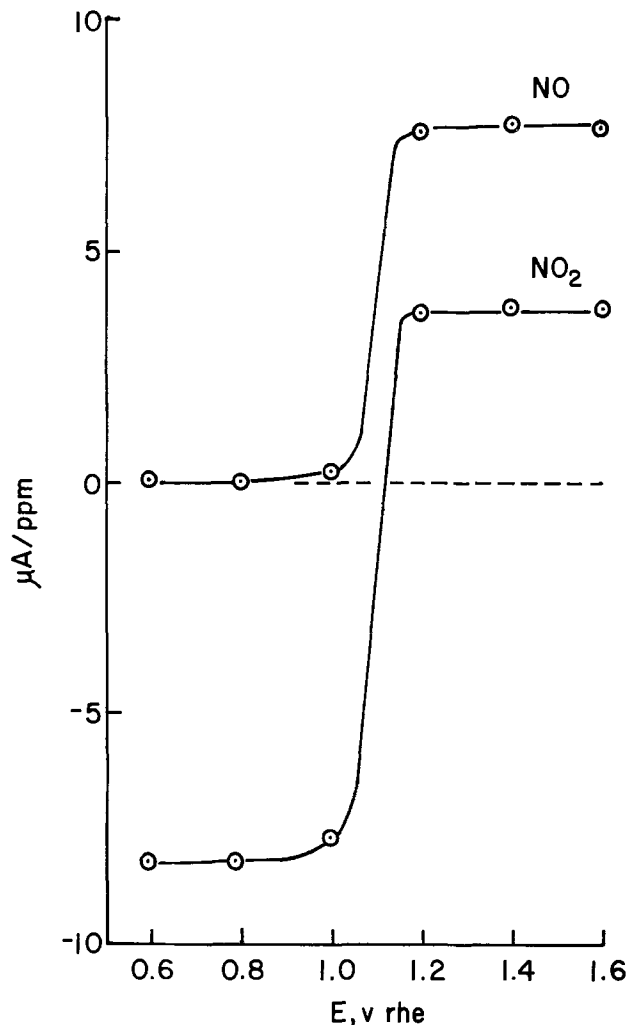


Fig. 1. NO oxidation currents and NO<sub>2</sub> oxidation and reduction currents on gold between 0.6 and 1.6V. Gas flow rate of 0.7 liter/min.

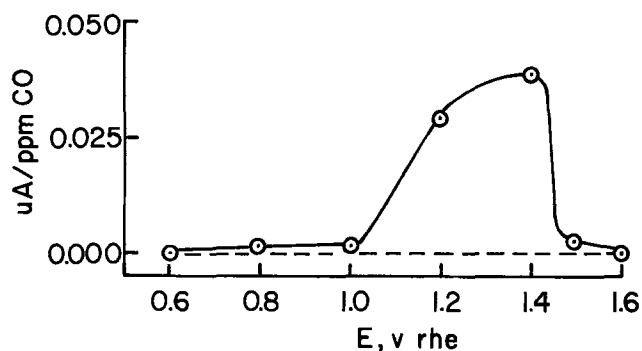


Fig. 2. CO oxidation currents on gold between 0.6 and 1.6V. Gas flow rate of 0.7 liter/min.

The theory of this diffusion electrode sensor relates the steady-state current,  $i_1$  (μA), to the electroactive gas concentration,  $n_o$  (ppm), molar volume,  $V$  (cm<sup>3</sup>/mole), and sample gas flow rate through the sensor,  $G$  (cm<sup>3</sup>/sec), by (2)

$$i_1 = \frac{zFn_oG}{V} [1 - \exp(-\{\lambda - k\}whL/G)] \quad [1]$$

where  $z$  is the number of electrons transferred per gas molecule reacted,  $\lambda$  (sec<sup>-1</sup>) the system response time constant,  $k$  (sec<sup>-1</sup>) the over-all rate constant for the electrode process, and  $w$ ,  $h$ , and  $L$  (cm), respectively, are the width, height, and length of the gas pathway on the back side of the diffusion electrode.

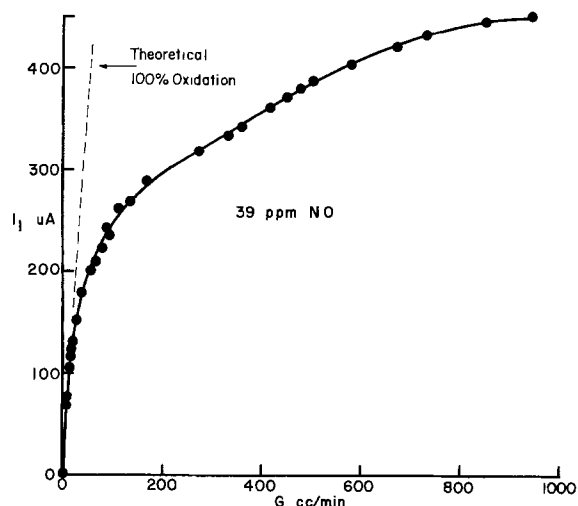


Fig. 3. Oxidation currents for 39 ppm NO at 1.5V as a function of gas flow rate.

At 0.7 liter/min about 8% of the NO<sub>2</sub> (0.8V) or NO (1.5V) entering the sensor actually reacts. The remainder leaves the sensor in the exit gas stream. For example, Fig. 3 shows the measured current-flow rate behavior for 39 ppm NO as compared to the theoretical *i*-*G* line (dotted) for 100% oxidation at all flow rates. It follows from Eq. [1] that

$$\lim_{G \rightarrow 0} (i_1/G) = zFn_0/V \quad [2]$$

As the flow rate is decreased, a point is reached at which all of the NO entering the sensor reacts. Thus, current measurements at very low flow rates permit calculation of *z* or *n*<sub>0</sub>.

To demonstrate the application of this method, it was used to analyze two CO-air mixtures for which *z* can only be 2 (12). Unanalyzed CO-air mixtures prepared to 50 ppm ( $\pm 10\%$ ) and 90 ppm ( $\pm 10\%$ ) were passed into a sensor with a Pt-catalyzed anode (3) at 5 cm<sup>3</sup>/min. The resulting oxidation currents were used to calculate gas concentrations of  $53.2 \pm 2.0$  and  $96.8 \pm 3.6$  ppm CO, respectively, by means of Eq. [2].

Similar experiments were carried out with gold-catalyzed NO<sub>2</sub> and NO sensors potentiostated at 0.8 and 1.5V, respectively, using gases of known concentrations. The apparent value of *z* calculated from Eq. [2] was plotted vs. the gas flow rate (Fig. 4). The limiting values *z* (i.e., for 100% gas reaction) were 3 for NO electro-oxidation and 2 for NO<sub>2</sub> electro-reduction. The precision of *z* as determined by this method is well within the usual limits of uncertainty inherent in other electrochemical methods (13).

From these data it is proposed that the over-all electrochemical process for NO at 1.5V is



Support for this proposed reaction is provided by pre-

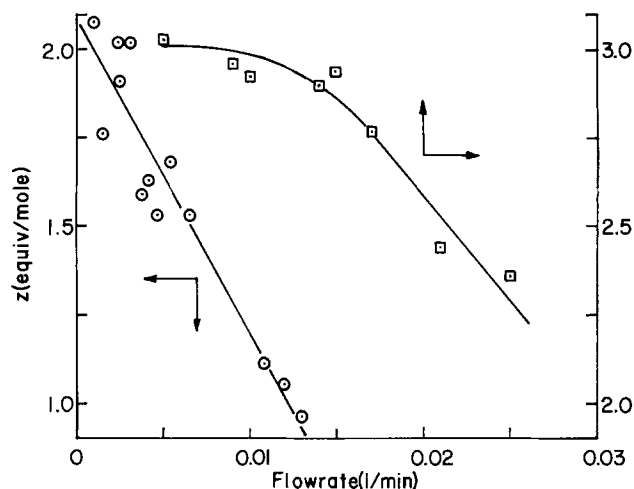


Fig. 4. Apparent values of *z* for NO oxidation at 1.5V and for NO<sub>2</sub> reduction at 0.8V as a function of gas flow rate.

vious work (8) and by the observation that NO<sub>2</sub> is also electro-oxidized at this potential (Fig. 1).

The over-all process for NO<sub>2</sub> reduction at 0.8V is



as evidenced by the nonreactivity of NO and by the rapid reduction of the trivalent NO<sub>2</sub><sup>-</sup> at this potential.

Manuscript submitted April 14, 1976; revised manuscript received June 10, 1976. This was Paper 410 presented at the Toronto, Canada, Meeting of the Society, May 11-16, 1975.

Any discussion of this paper will appear in a Discussion Section to be published in the June 1977 JOURNAL. All discussions for the June 1977 Discussion Section should be submitted by Feb. 1, 1977.

Publication costs of this article were assisted by Energetics Science, Incorporated.

#### REFERENCES

1. K. F. Blurton and H. W. Bay, *Am. Lab.*, **6**, 50 (1974).
2. H. W. Bay, K. F. Blurton, J. M. Sedlak, and A. M. Valentine, *Anal. Chem.*, **46**, 1837 (1974).
3. J. M. Sedlak and K. F. Blurton, *This Journal*, **121**, 1315 (1974).
4. J. P. Hoare, "Electrochemistry of Oxygen," Interscience, New York (1968).
5. "Cleaning Our Environment," American Chemical Society, Washington, D.C. (1969).
6. W. M. Vogel and J. T. Lundquist, *This Journal*, **117**, 1512 (1970).
7. R. R. Gaddi and S. Bruckenstein, *J. Electroanal. Chem. Interfacial Electrochem.*, **50**, 163 (1974).
8. D. Dutta and D. Landolt, *This Journal*, **119**, 1320 (1972).
9. S. B. Brummer and A. C. Makrides, *ibid.*, **111**, 1122 (1964).
10. J. M. Sedlak and K. F. Blurton, *Talanta*, In press.
11. D. A. Levaggi, W. Siu, M. Feldstein, and E. L. Kothny, *Environ. Sci. Technol.*, **6**, 250 (1972).
12. E. Gileadi, in "Modern Aspects of Electrochemistry," Vol. IV, J. O'M. Brockris, Editor, pp. 100-102, Butterworths, London (1966).
13. R. G. Barradas, M. C. Giordano, and W. H. Sheffield, *Electrochim. Acta*, **16**, 1235 (1971).



## The Dielectric Breakdown of Anodic Aluminum Oxide

H. J. de Wit, Ch. Wijenberg, and C. Crevecoeur

*Philips Research Laboratories, Eindhoven, The Netherlands*

### ABSTRACT

Nonshorting breakdowns of anodic alumina films, 200-2500Å thick, have been measured. These measurements reveal the existence of a thickness-independent breakdown field which is close to the anodizing field. The existing theories, which make use of electron avalanching, cannot explain these facts and it is suggested that the breakdown is initiated by ionic movement and that it is related to the anodizing process.

The dielectric breakdown of thin anodic  $\text{Al}_2\text{O}_3$  layers has been measured by, among others, Nicol (1), Lomer (2), Merrill and West (3), and Odynets *et al.* (4). Their results, differing in breakdown level, have in common a decrease of the breakdown field with increasing layer thickness. This is ascribed to electron avalanching, and several theoretical dependences given by Forlani and Minnaja (5, 6) and by O'Dwyer (7, 8) have been fitted to the various experiments. Carnes and Duffy (9), however, showed that the breakdown field of aluminum oxide films deposited on silicon substrates by the pyrolysis of aluminum isopropoxide and measured with the nonshorting breakdown technique (10) is essentially independent of thickness in the range from 200 to 6000Å and is equal to  $7.5 \times 10^6$  V/cm (Si positive on p-type substrate). Korzo (11) has measured dielectric breakdown of  $\text{Al}_2\text{O}_3$  grown by decomposition of aluminum acetylacetonate in an hf discharge plasma using u.v. radiation for activation. He found a decrease of the breakdown field from  $1.2 \times 10^7$  V/cm at  $d = 600\text{Å}$  to  $3 \times 10^6$  V/cm at  $d = 4 \mu\text{m}$  (substrate positive).

In view of these widely divergent results, we decided to reinvestigate anodic oxide layers on aluminum, with the nonshorting breakdown technique, using a thin counterelectrode. Evaporated gold contacts were mainly used because the poor adhesion to the oxide layer favors the occurrence of nonshorting breakdown. When a breakdown occurs, the oxide layer melts in places (Fig. 1b) and over a relatively large surface the gold contact evaporates, thus leaving the breakdown isolated (Fig. 1a). A preliminary account of this work was given in Ref. (12). The present paper first describes how the specimens are prepared and how values for the breakdown voltage are obtained. These are analyzed statistically to give a definite value for the breakdown voltage or field. The results are first compared with those obtained by other workers (1-4) and then with theories on the avalanche breakdown of  $\text{Al}_2\text{O}_3$  (4-8). Considerable attention has recently been paid to dielectric breakdown of  $\text{SiO}_2$  layers and our results on  $\text{Al}_2\text{O}_3$  will also be confronted with the explanations proposed for  $\text{SiO}_2$ .

### Experiment

Aluminum of 99.95% purity (Merck) was cleaned, electropolished, annealed at 600°C, electropolished once

Key words: dielectric strength, statistical analysis, electron avalanche, ionic movement.

more, and etched in a  $\text{HF-H}_2\text{SO}_4$  solution in water, all as described in Ref. (13). The anodizing solution consisted of 17g of ammonium pentaborate in 100 ml of glycol at room temperature; a constant current density of 0.35 mA/cm<sup>2</sup> was used. The anodizing field is then  $8.7 \times 10^6$  V/cm (14). With this value the oxide thickness was calculated from the forming voltage. Before anodization of the main part of the specimen, a small part had previously been anodized up to 180V to provide thick oxide. Contact to the counterelectrode, which covered the thick oxide as well as the oxide to be investigated, was made with a platinum wire above the thick oxide and some silver paint (leitsilber) (see Fig. 2). In this way breakdowns underneath the platinum wire, which easily lead to a short circuit, could be avoided.

For metallic counterelectrodes evaporated gold ( $\approx 500\text{Å}$  thick) and aluminum ( $\approx 200\text{Å}$ ) were used, with contact area 5-100 mm<sup>2</sup>. We also performed measurements with counterelectrodes made of  $\text{MnO}_2$ , a material which is interesting because of its widespread use as a counterelectrode for solid electrolytic capacitors. It was obtained in two ways, by pyrolysis and by sputtering. Pyrolysis resulted from spraying a solution of manganese nitrate onto an anodized aluminum specimen heated to 300°-350°C as described by Rosztochy and Read (15).

Sputtered  $\text{MnO}_2$  was prepared by reactive d-c sputtering of metallic Mn with oxygen at a pressure of 60-80 mTorr and at a voltage of 1100-1400V. The sputtering apparatus was completely similar to that used by Valletta and Pliskin (16). The specimens were clamped against a water-cooled plate. In this way and by using a very low sputtering rate ( $\approx 4-5$  Å/min), the temperature of the specimens could be held below 100°C as was measured with a thermocouple and with an IRCON infrared radiation thermometer.

Table I gives data for the  $\text{MnO}_2$  thus prepared. On top of the  $\text{MnO}_2$ , which covered most of the specimen surface, a gold contact was evaporated, since the sheet resistance of the  $\text{MnO}_2$  itself was too high to cause nonshorting breakdowns.

### Measurements

Breakdowns were measured in ramp tests. A diagram of the apparatus is drawn in Fig. 3. At the beginning of a measurement the  $dV/dt$  generator is started. A fraction of the voltage across the specimen

1555

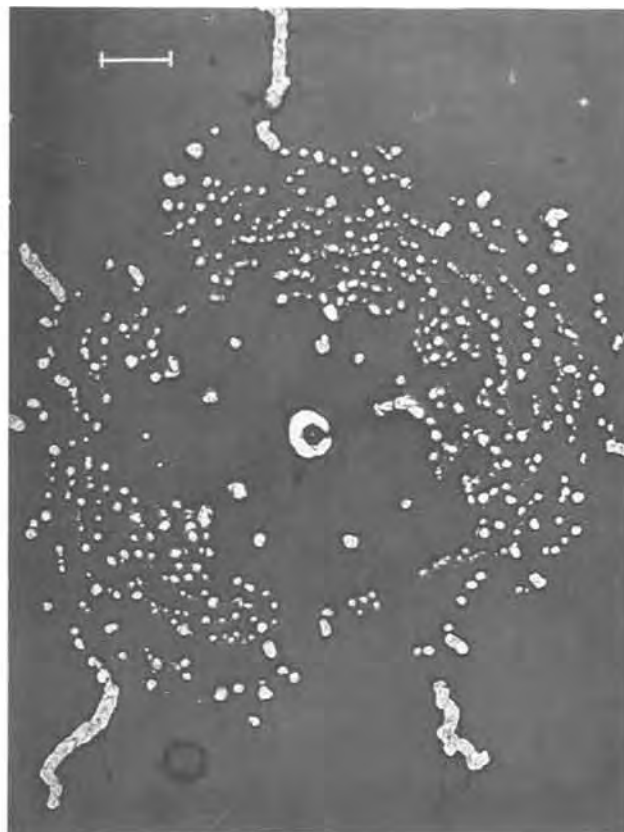
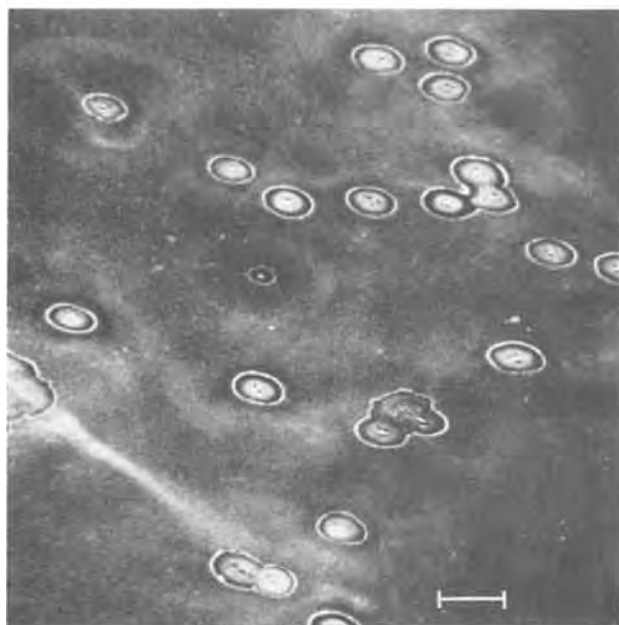


Fig. 1. (a, left): Scanning electron micrograph of an anodized aluminum specimen with gold contact after a number of severe breakdowns have occurred. (The bar represents  $100\ \mu\text{m}$ , tilt  $70^\circ$ ). (b, right): Transmission electron micrograph of an  $\text{Al}_2\text{O}_3$  layer detached from the aluminum after a breakdown experiment. The bar represents  $10\ \mu\text{m}$ .

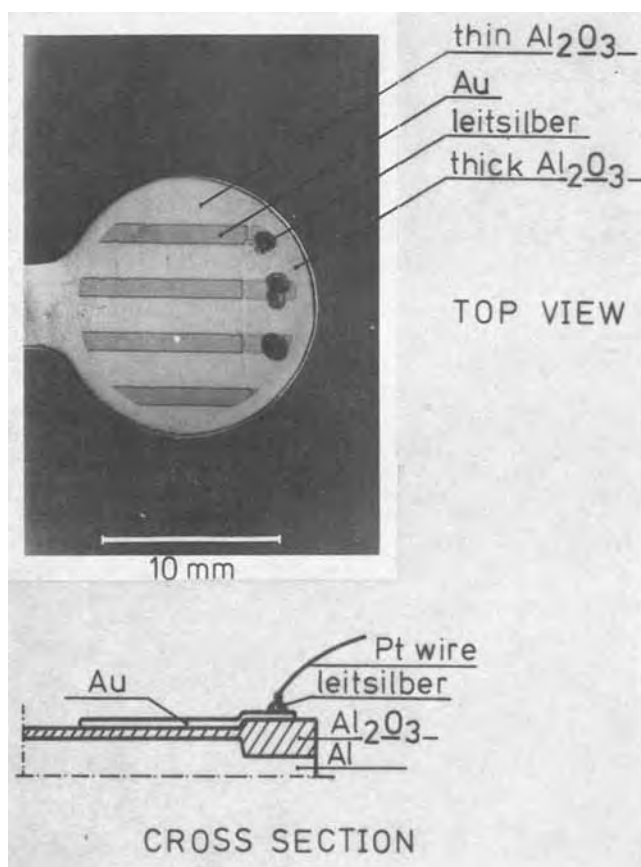


Fig. 2. Anodized aluminum specimen with gold counterelectrodes. Contact with the counterelectrode is made above the thick oxide with a platinum wire and silver paint (leitsilber).

is compared with and made equal by feedback to the voltage of the generator. The comparator has frequency characteristics such that the internal resistance of the voltage source as a whole is low for slow variations and high for rapid variations of the load, the dividing time being  $\sim 1$  msec.

When a breakdown occurs, a rapid voltage drop across the specimen is detected by the trigger and the analog switch short-circuits the input of the voltage amplifier and halts the  $dV/dt$  generator, the voltage of which is then measured and punched on paper tape. Once this is done, the  $dV/dt$  generator returns to zero and the process starts again. For series of hundreds of breakdown measurements, we found a one-to-one correspondence between the occurrence of a spark and the detection of a breakdown by the apparatus.

Figure 4 gives the results of 200 successively measured breakdowns of positive polarity on a specimen with a gold contact (which is then negative). We see

Table I  
Manganese Dioxide

	pyrolyzed	sputtered
composition	$\text{MnO}_{1.9}$	$\text{MnO}_{1.88}$
sheet resistance	100–200 k $\Omega$	$\approx 300\text{ k}\Omega$
thickness	1–10 $\mu\text{m}$	.1–.2 $\mu\text{m}$
specific resistivity	10–100 $\Omega\text{ cm}$	$\approx 5\ \Omega\text{ cm}$
deposition temperature	350 $^\circ\text{C}$	$< 100\ ^\circ\text{C}$

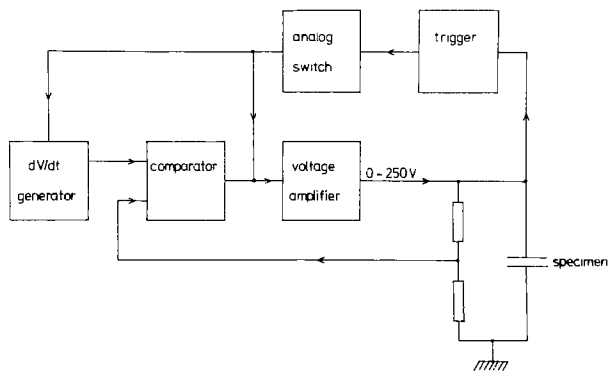


Fig. 3. Block diagram of the apparatus for determining breakdown voltages.

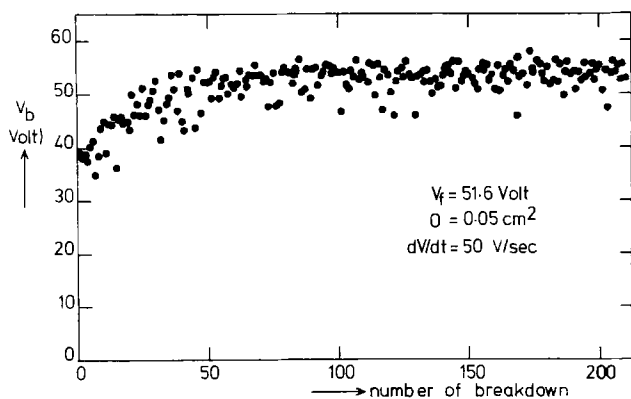


Fig. 4. Breakdown voltages successively measured on a specimen with gold contact and with positive polarity (Al +).

that the breakdown level increases at first when weak spots are being removed. Then the breakdown voltages are distributed with a fairly large spread round a constant level which is quite close to the forming voltage of the specimen.

We would like to draw attention to the fact that breakdowns do not occur at progressively higher voltages, as would be expected if the mechanism implied a removal of progressively less weak spots. Instead, higher and lower breakdown voltages alternate. As has been pointed out by Albert *et al.* (17), this is due to the statistical nature of the breakdown phenomenon; at a given voltage and contact area there is a definite probability per unit of time that a breakdown will occur. For the analysis of our breakdown voltage distribution, we assume on the basis of Albert *et al.* that in a test at constant voltage, not in a ramp test, (i) the breakdowns occur randomly in surface and time and (ii) the average number of breakdowns per second,  $n$ , increases exponentially with the applied voltage,  $V$ , as  $n = n_0 O \exp(BV)$ , where  $n_0$  and  $B$  are constants, and  $O$  is the contact area. ( $BV \approx 30$  in our experiments).

The breakdown voltage distribution has then to be calculated for the case that the applied voltage increases linearly. This has already been done for fairly general conditions by Lewis and Ward (18) and Briggell (19). In our case the derivation runs as follows: The voltage is increased at a constant rate,  $V/t = r$ . We now wish to know the probability that a breakdown has not yet occurred at time  $t$ , and voltage  $V = rt$ . We divide  $t$  into  $N$  small equal intervals.

The probability that no breakdown has occurred in the  $i^{\text{th}}$  interval is equal to  $(1 - n(V_i)t/N)$  in which

$V_i = irt/N$  is the voltage across the specimen in the  $i^{\text{th}}$  interval. Thus

$$(1 - n(V_i)t/N) = 1 - n_0 O \exp(Birt) t/N$$

The probability that no breakdown has occurred in any of the  $N$  intervals up to  $t$  is then equal to

$$F_0(t) = \prod_{i=1}^N (1 - n_0 O \exp(Brit/N) \cdot t/N)$$

$$\ln F(t) = \sum_{i=1}^N \ln \{1 - n_0 O \exp(Brit/N) \cdot t/N\}$$

$$\cong - \sum_{i=1}^N \{n_0 O \exp(Brit/N) \cdot t/N\}$$

If the summation is replaced by an integration, we obtain

$$\ln \{F_0(t)\} = - (n_0 O / Br) \cdot (\exp(Brt) - 1)$$

and the probability that no breakdown has occurred before voltage  $V$  is given by

$$F_0(V) = \exp \{- (n_0 O / Br) (\exp(BV) - 1)\} \quad [1]$$

It will be readily seen that  $\exp BV \gg 1$  and we will consequently ignore the term  $-1$  henceforth.

The breakdown voltage distribution is obtained by differentiating Eq. [1]

$$f(V)dV = n_0 O / r \{ \exp(BV - (n_0 O / rB) \exp BV) \} dV \quad [2]$$

$f(V)dV$  is the probability density that a breakdown occurs between  $V$  and  $V + dV$ . This distribution has been fitted to the experimental histograms in the standard manner [see, for example, Cramer (20)] by minimizing the quantity  $\chi^2$  with, in this case,  $B$  and  $\ln(n_0 O / rB)$  as free parameters. The values thus obtained for  $\chi^2$  bear out very well the hypothesis that Eq. [2] describes the measured histograms.

Figure 5 provides an example. For the purpose of fitting, all measured breakdown voltages exceeding 28.25V were grouped together in one class and those below 25.75V in another. The resulting  $\chi^2$  value was 2.4 which is reasonable for the four remaining degrees of freedom in this case ( $P\chi^2 > \chi_p^2 = 65\%$ ). See also Solomon, Klein, and Albert (21) for an example.

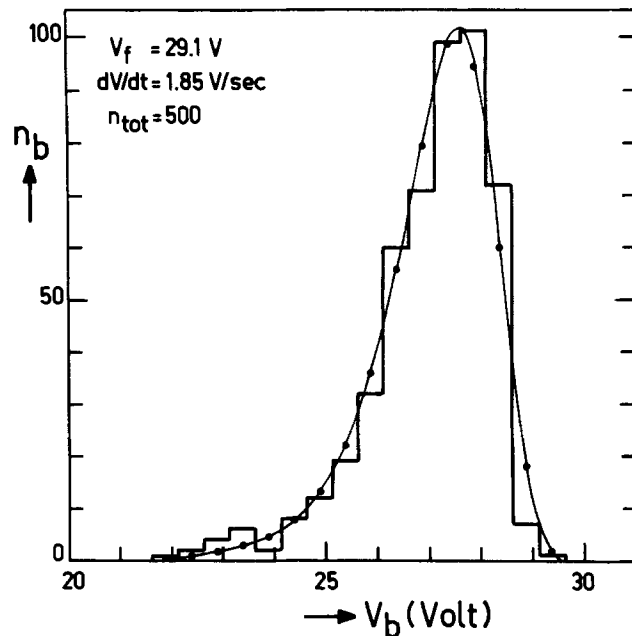


Fig. 5. Measured and calculated breakdown voltage distributions (Eq. [2]).

A value for the breakdown voltage is defined by taking, for instance, the maximum of the fitted distribution (28.6V in Fig. 5). An alternative way is to take the values of successive breakdowns together in groups of ten and to determine the average value of the maxima of these groups. The latter quantity which lies  $\approx 3\%$  higher than the former is very easily calculated directly from the measurement and this method has the advantage that very low breakdown values which occasionally occur with aluminum and manganese oxide counterelectrodes because of imperfect healing are discarded automatically. The value of the breakdown voltage depends to some extent on the particular choice. The maximum  $f(V)$  lies at

$$V_{\max} = (1/B) \cdot \ln(\tau B/n_0 O) \quad [3]$$

In Fig. 6 the breakdown voltages (relative to the forming voltages) of layers with the same thickness are plotted as a function of log (capacitance) at constant  $dV/dt$  and as a function of log (ramp rate) at constant capacitance. The capacitance is proportional to the contact area. Linear relations in agreement with Eq. [3] are found. Lines with the same absolute slope ( $B = 0.55V^{-1}$ ) but opposite sign have been drawn through these points. This shows incidentally that  $BV \approx 27.5$  in this case, so that  $\exp(BV) \gg 1$  as was used for the derivation of Eq [2].

In Fig. 7 the quantity  $B$ , as found from curve fitting for specimens formed to different voltages, is plotted as

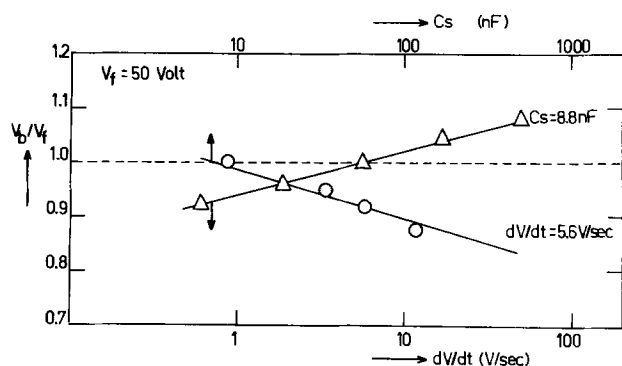


Fig. 6. Dependence of the breakdown voltage (relative to the forming voltage) on contact area (proportional to capacitance) and on  $dV/dt$ . All specimens formed to the same voltage.

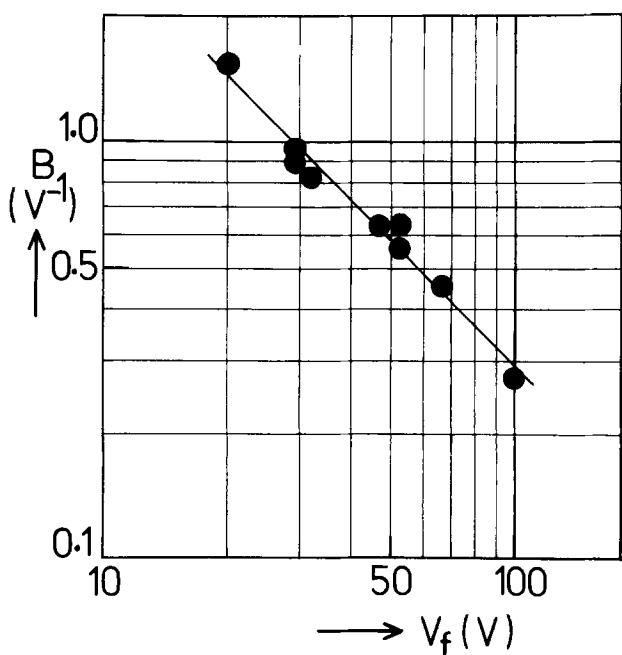


Fig. 7. Thickness dependence of  $B$

a function of  $V_f$ . It is obvious that  $B$  is inversely proportional to  $V_f$  and therefore to specimen thickness  $d$ . We substitute  $\beta/d = B$  accordingly and obtain for the field at the maximum of the distribution

$$F_{\max} = (1/\beta) \cdot \ln(\tau\beta/n_0 O d) \quad [4]$$

Curve-fitting also yields the quantity  $\ln(n_0 O/rB)$  from which  $n_0$  can be calculated. However, since the relative scatter in  $B$  and in  $\ln(n_0 O/rB)$  is of the same magnitude, the precision with which  $n_0$  itself is determined is very low. For the measurements shown in Fig 7, the values for  $n_0$  lie between  $5 \times 10^{-10}$  and  $7 \times 10^{-12}/\text{sec cm}^2$ . This makes it impossible to decide whether or not  $n_0$  is dependent on thickness.

In the following we will assume that  $n_0$  is constant. If we average  $\ln(n_0)$ , we obtain  $n_0 = 3.4 \times 10^{-11}/\text{cm}^2 \text{ sec}$  and  $\beta = 3.35 \times 10^{-6} \text{ cm/V}$  if we take  $8.7 \times 10^6 \text{ V/cm}$  for the forming field.

If  $n_0$  and  $\beta$  are independent of  $d$ , Eq. [4] predicts for a constant  $dV/dt = r$  a breakdown field which decreases logarithmically with thickness. If we perform the measurements at constant  $dF/dt$ , i.e. if we take  $r$  proportional to  $d$ , we expect a constant breakdown field. Figure 8 gives our experimental results (black spots) obtained with gold as the counterelectrode, at room temperature, corrected for the  $dV/dt$  dependence so that they represent measurements at constant  $dF/dt$ , with positive polarity. We obviously obtain a breakdown field which is completely independent of the specimen thickness to within a few percent in the thickness range 230-1700Å. This shows that our results can be consistently described with the assumptions that at constant field breakdowns occur randomly in surface and time and that the number of breakdowns per unit of time is exponentially dependent on the applied field as  $n = n_0 O \exp(\beta F)$  with certainly  $\beta$  and possibly  $n_0$  independent of specimen thickness. The results of other workers are also indicated in the figure. The agreement is nonexistent. We shall come back to this point in the Discussion.

In Fig. 9 the same results are plotted once more, together with results obtained with aluminum and sputtered manganese dioxide counterelectrodes, for both polarities. They have been taken at constant  $dV/dt$  and not at constant  $dF/dt$ . This accounts for the slow decrease of the breakdown field at greater thicknesses. Nonshorting breakdowns are more difficult to obtain with Al and  $\text{MnO}_2$  contacts than with gold contacts. Very low breakdown voltages are sometimes found and short circuits also often occur, so that the total number of breakdowns in one measurement with these contacts is limited. The measurements with these contacts are therefore by no means as accurate as in the case of gold, and in particular the statistical analysis of these

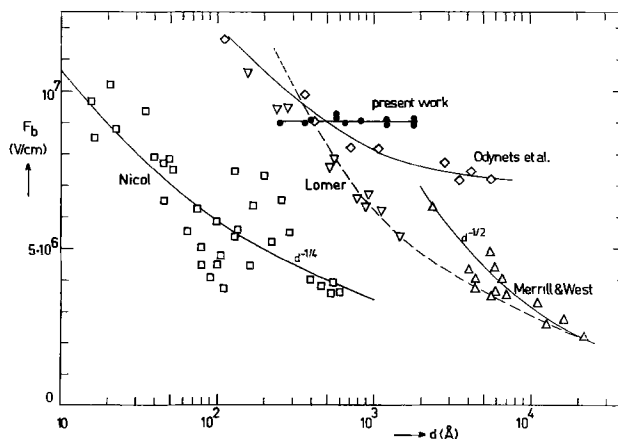


Fig. 8. Comparison of our measured breakdown field (black spots), obtained at a constant  $dF/dt$  of  $8.7 \times 10^6 \text{ V/cm sec}$  and with contact area  $6.5 \text{ mm}^2$ , with results of other workers.

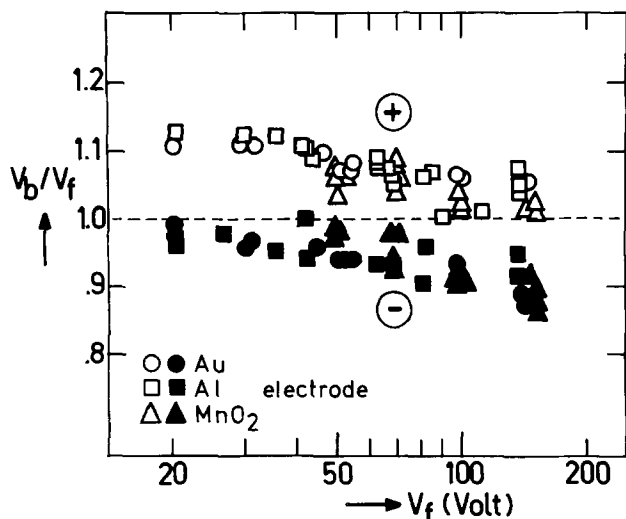


Fig. 9. Breakdown voltage (relative to forming voltage) obtained at a constant  $dV/dt$  of 50 V/sec, as a function of forming voltage for specimens with gold, aluminum, and sputtered manganese dioxide counterelectrodes, for both directions of the applied field. Contact area  $\approx 6 \text{ mm}^2$ .

results presented above has been validated for gold contacts only. Nevertheless, it is quite clear that the results obtained with Al and sputtered  $\text{MnO}_2$  do not differ significantly from those with gold. For all three contacts it is noteworthy that the breakdown field in the reversed direction is about 10% lower. A much steeper field dependence of the breakdown was measured on pyrolyzed  $\text{MnO}_2$ . However, since this was also found with reverse voltage, it is not thought to be due to a qualitatively different behavior of the contact, but to damage caused to the oxide layers by the pyrolyzation process. Some measurements were effected at liquid nitrogen temperature. The breakdown field for gold contacts with positive polarity then was about 20% higher, which agrees with the temperature dependence found, for example, by Odynets *et al.* (4).

### Discussion

**Contrast with other experiments.**—Breakdown experiments on anodized aluminum oxide have also been performed by Nicol (1), Lomer (2), Merrill and West (3), and Odynets *et al.* (4). Their measurements have been included in Fig. 8. The reason for the discrepancies is still undecided. Although all these experiments were performed on anodic oxide, the preparation methods were widely different. Nicol prepared his layers in a plasma and obtained  $\gamma\text{-Al}_2\text{O}_3$ , Lomer anodized in an aqueous solution of ammonium phosphate, Merrill and West used oxalic and/or boric acid, and Odynets *et al.* used an aqueous solution of boric acid. The methods of measuring the breakdown voltage were also different. It is not clear what method Nicol used ("Breakdown voltages were measured on a Tektronix 575 Curve Tracer").

Odynets *et al.* and Lomer obtained their results with a steel ball as the counterelectrode. As shown above, the contact area influences the breakdown field and it is not clear how large this area is when a steel ball is used. These measurements may consequently not be directly comparable with ours. Merrill and West used the same method as we did, *viz.*, nonshorting breakdowns. They do not specify the counterelectrode material. To obtain such thick layers, they had to use porous oxide formation in oxalic acid followed by dense formation in boric acid and it is not clear whether the breakdown is influenced by inhomogeneous composition of the layer. A major difference appears to be the use of aqueous electrolytes, instead of the glycol borate used by us. A drawback of the latter electrolyte is, of course, that the thickness range it allows is small.

This is, however, more than compensated by the fact that the anodization properties of this solution are very well known, thanks to the work of Bernard and Cook (14), who established, in particular, that the current efficiency is unity, *i.e.*, that all the charge passed is used for oxide formation. Moreover, it is known from electron microscopy (13) that very homogeneous dense layers are formed. This makes it possible to use the forming voltage as an accurate measure for the thickness of the layer.

Compared with this relatively simple situation, anodization in aqueous electrolyte is an intricate affair. This is evident from the work of Odynets *et al.* in which it is found that measurements on these layers in air give a large spread in results due to the humidity of the air, to which our layers are not susceptible. In general, the efficiency of the anodization process is lower than unity, while the border line between barrier oxide formation and porous oxide formation is often ill defined. Randall and Bernard (22), reporting recently on aqueous phosphate solutions (the same electrolyte used by Lomer), stated that depending on current density and whether the solution is stirred or not, porous or dense oxide is formed. Whether this difference in the electrolyte is indeed the main cause of the difference in results is at present under investigation.

**Comparison with theory.**—A number of approaches has been used to describe the dielectric breakdown of  $\text{Al}_2\text{O}_3$  and  $\text{SiO}_2$ . In this section the following points are discussed: (i) the avalanche model of Forlani and Minnaja; (ii) the model of O'Dwyer in which the positive space charge left after avalanching plays a crucial role; (iii) The approach of Ridley, who assumes that joule heating, caused by currents injected at irregularities of the cathode, is responsible for breakdown; and (iv) the possibility that ionic movement causes breakdown.

**Avalanching following Forlani and Minnaja.**—These authors (5), as well as O'Dwyer and Ridley, assume that electrons are injected at the cathode following the Fowler-Nordheim mechanism

$$j_i = j_0 \exp(-F_{FN}/F) \quad [5]$$

where  $j_0$  and  $F_{FN}$  are constants (we have neglected the pre-exponential field dependence on  $F$  here). Then they calculate the probability  $P(F)$  that an electron is accelerated by the field into such a state that it gains more energy from it than it loses to optical phonons. In this state ionization occurs every time an ionization energy  $V_0$  is reached. The current then is given roughly by

$$j = j_i P(F) \exp(eFd/V_0)$$

They postulate that breakdown occurs if  $j$  exceeds a certain value. Two situations can occur depending on whether  $F_{FN}$  is large or small. In the first case  $P(F) \approx 1$  which leads to a thickness dependence  $F_B \sim d^{-1/2}$ . In the second case  $P(F) \ll 1$  and  $F_B \sim d^{-1/4}$  is found. The line through the results of Merrill and West in Fig. 8 was drawn according to this  $d^{-1/2}$  dependence by Forlani and Minnaja whereas the line through Nicol's points was drawn according to  $d^{-1/4}$  by himself.

If we compare these theoretical dependencies with our measurements, it is clear that they cannot explain them, even the weaker thickness dependence  $d^{-1/4}$  predicts a change of about 60% over the thickness range covered by us, whereas our breakdown field remains constant to within a few percent. Furthermore, it is very doubtful whether  $d^{-1/4}$  can be used in the range of very small thicknesses as was done by Nicol. It is valid if  $P \ll 1$ . To make the current  $j$  larger than the injected current  $j_i$ ,  $eFd/V_0$  must be much larger than 1. For a breakdown field of  $10^7 \text{ V/cm}$  and  $d = 100 \text{ \AA}$ , however,  $eFd/V_0 = 1$  for  $V_0 = 10 \text{ eV}$ . Also the  $d^{-1/2}$  as applied to the results of Merrill and West is



open to objections. The breakdown field changes by a factor of three.  $P$  is by no means  $\approx 1$  over this whole field range as was assumed for the derivation of the  $d^{-1/2}$  relation [see Fig. 4 of Forlani and Minnaja (5)].

**O'Dwyer's theory.**—O'Dwyer (7, 8) has drawn attention to the influence of the positive charges that are left behind by the knocked-off electrons. In his approach it is assumed that the mobility of the holes is very much smaller than that of the electrons. Therefore a net positive charge remains by which the field at the cathode is increased leading to injection of more electrons and so on. The degree to which the breakdown field depends on thickness in this theory depends on the numerical values of the various quantities. To show this, we give a very simple derivation of the breakdown field which is somewhat similar to an approach recently put forward by Solomon and Klein (23) and in which it is additionally assumed that the field distortions are small compared with the applied field  $F$ .

O'Dwyer assumes that the collision ionization rate per unit length,  $\alpha$ , is given by

$$\alpha = \alpha_0 \exp(-F_\alpha/F) \quad [6]$$

with  $\alpha_0$  and  $F_\alpha$  constants. If Eq. [5] and [6] are combined, the total number of holes created per second is

$$j_i/e \cdot (\exp(\alpha d) - 1) \\ = j_i/e \cdot (\exp(\alpha_0 d \exp(-F_\alpha/F)) - 1)$$

In equilibrium the number of holes created must be equal to the number that disappears. We assume that this happens by drift to the cathode with a mobility  $\mu_p$ , that the positive charge density is uniform over the specimen thickness, and that the drift is caused by the average applied field  $V/d$ . (In this we differ from DiStefano and Shatzkes (24) who assume for the case of  $\text{SiO}_2$  that the holes are removed by recombination). We find  $p\mu_p F = j_i/e (\exp(\alpha d) - 1)$  with  $p$  the hole density.

Here we already see the origin of the current runaway, at low fields all the holes created are swept away by the field. If the field becomes higher, the number of holes created increases rapidly because of the term  $\exp(-F_\alpha/F)$  and also because the field at the cathode increases so that more electrons are injected. Eventually holes cannot be removed quickly enough and the current shoots to a very high value. In the case of a uniform concentration of holes  $p$  the field at the cathode is given by  $F_{\text{cath}} = V/d + \Delta F = V/d + epd/2\epsilon$  with  $\epsilon$  the dielectric constant. If we put these expressions together we obtain the following equation for the current injected at the cathode

$$j_i/e = j_0/e \cdot \exp(-F_{\text{FN}}/(F + \Delta F)) \\ = j_0/e \cdot \exp(-F_{\text{FN}}/(F + (dj_i/2\epsilon\mu_p F))) \\ \{\exp(\alpha_0 d \exp(-F_\alpha/F)) - 1\} \quad [7]$$

This equation can be solved easily by iteration and be used to obtain numerical results. However, a simple estimate of the breakdown field can be obtained if we use a further simplification for the case of very thin layers, assuming that multiplication occurs rarely so that  $\alpha d < 1$ . The current increase due to the field distortion becomes important if  $F_{\text{FN}}/F = F_{\text{FN}}/(F + \Delta F) \approx 1$ .

As  $F_{\text{FN}}/F \gg 1$ , this can be written as

$$F_B^2 \approx F_{\text{FN}} \Delta F = F_{\text{FN}} (d^2 \alpha_0 j_i / 2\epsilon \mu_p F_B) \exp(-F_\alpha/F_B)$$

As an estimate for  $j_i$  we use the undistorted value

$$j_i/e = j_0/e \cdot \exp(-F_{\text{FN}}d/V)$$

and thus obtain

$$F_B = \frac{F_{\text{FN}} + F_\alpha}{\ln(F_{\text{FN}} d^2 \alpha_0 j_0 / 2\epsilon \mu_p F_B^3)}$$

This simple equation shows the following features: (i)  $F_B$  is directly proportional to  $F_{\text{FN}} + F_\alpha$ , therefore a

difference in contact potential shows up directly in  $F_B$ ; (ii)  $F_B$  is thickness dependent. Viewed qualitatively this theory will not be able to explain our results, *viz.*, a breakdown field which is independent on thickness and independent on contact material.

For a more quantitative approach the different quantities in Eq. [7] must be estimated. This is carried out in the Appendix. The result for the case of a gold counterelectrode is shown in Fig. 10, together with our experimental facts. If we use aluminum instead of gold as a contact, we obtain from Eq. [7] a breakdown field at  $d = 10^{-5}$  cm, equal to  $6.6 \times 10^6$  V/cm.

In view of the dependence on the barrier height and, even in this case, the considerable  $d$  dependence, we conclude that the avalanche theory cannot explain our results. Only if  $F_\alpha$  is much higher than the value inserted here can the  $d$  dependence found be reproduced.

**Joule heating.**—A different theory of breakdown has been put forward by Ridley (25). In essence, this is a theory of thermal breakdown, due to joule heating by Fowler-Nordheim currents injected at the cathode. It is easy to show that homogeneous heating cannot occur. Ridley therefore assumes that such high current densities are due to field enhancement at cathodic protuberances which he estimates to be of the order of 10% of the specimen thickness. He remarks that "protuberances of this size are scarcely observable with existing techniques so our assumption that they exist is at present unverified, but presumably not unverifiable." However, Fig 11, which shows a transverse section of an  $\text{Al}_2\text{O}_3$  layer, indicates that protuberances on the

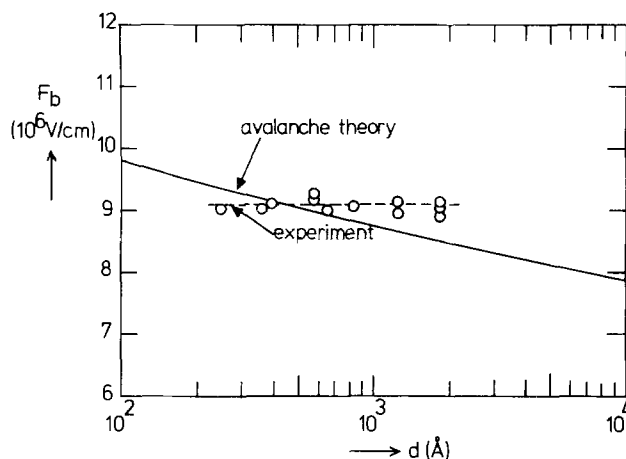


Fig. 10. Comparison of the measured breakdown field (same results as in Fig. 8) with values calculated from O'Dwyer's space charge avalanche theory.



Fig. 11. Transmission electron micrograph of a 500Å thick cross-section of an anodized Al sample. The lower part is the metal. The oxide layer is about 2600Å thick.

scale assumed by Ridley (for  $\text{SiO}_2$ ) do not occur in anodic  $\text{Al}_2\text{O}_3$ . Moreover, this theory predicts again a dependence on thickness and on the electrode material.

**Ionic movement.**—What then is the mechanism of dielectric breakdown in  $\text{Al}_2\text{O}_3$ ? A significant fact is that the breakdown field is close to the anodizing field of the material. In this respect,  $\text{Al}_2\text{O}_3$  differs markedly from  $\text{SiO}_2$  in which the breakdown field  $\approx 10^7$  V/cm is about half the anodizing field, which according to Fritzsche (26) is  $1.9 \times 10^7$  V/cm.

At the anodizing field considerable ionic currents set in. Therefore it forms an upper limit for the field that the material can stand ultimately. It seems more reasonable, therefore to assume that ionic movement starts the dielectric breakdown, a suggestion made recently by Shousha (27) also. There are a number of interesting facts in connection with such an assumption.

1. The steady-state ionic current density during anodization at a field of  $8.7 \times 10^6$  V/cm is equal to 0.35 mA/cm<sup>2</sup>, when  $\approx 10^{15}$ /cm<sup>2</sup> sec charge carriers cross the surface. At that field the number of breakdowns is 160/cm<sup>2</sup> sec. If it is assumed that during a breakdown test the steady state is reached and also that every single moving ion has a certain probability to start a breakdown, then this probability is remarkably low.

2. The field dependence of  $n$ , described by the quantity  $\beta = 3.35 \times 10^{-6}$  cm/V, is definitely lower than that of the forming current density for which Bernard and Cook found the value  $4.83 \times 10^{-6}$  cm/V if it is written as  $j = j_0 \exp(B_F \cdot F)$ . It is, however, interesting to note that the field dependence of the forming current density at high frequency is lower than for low frequency, [see Winkel, Pistorius, and van Geel (28)]. For instance, we found (29) at a current density of 0.14 mA/cm<sup>2</sup> that  $B_F$  changes from the d-c value  $4.8 \times 10^{-6}$  cm/V to  $1.57 \times 10^{-6}$  cm/V if the frequency increases from below 0.1 Hz to above 8 Hz. The difference of the two dependences is  $3.2 \times 10^{-6}$  cm/V and it is striking that this quantity is so close to the field dependence of the breakdown rate. This frequency dependence of  $B_F$  is directly connected with the occurrence of current transients when the applied field is suddenly increased. It has been shown by Young (30) on Ta and by Dignam and Ryan (31) on Al that the build up of the current in a transient is an autocatalytic process, the nature of which has not yet been fully clarified. The fact that the value of that part of the field dependence of  $B_F$  which is determined by this autocatalytic process is close to  $\beta$  suggests that this process plays a role during breakdown.

3. The breakdown field is independent of thickness and follows very well the relation  $F_{\max} = 1/\beta \ln(\tau_F \beta / n_0 O)$  in which we have substituted  $r_F = dF/dt = r/d$ , the rate of change of the applied electric field. This equation was derived on the assumption that  $n_0$  is a probability per unit surface area and not per unit volume of the oxide. If the latter is assumed, the factor  $O$  has to be replaced by  $Od$ . Therefore, the fact that the breakdown field is independent of thickness implies that breakdown, although independent of the contact material, is still a surface phenomenon and not a volume phenomenon. It has been argued by Dignam and co-workers [see, for example, Ref. (32)] that the anodization process itself is controlled at one of the interfaces.

If these facts are combined, the following picture emerges. Breakdown is completely determined by the introduction of an ion from the surface into the volume of the oxide. Once this has occurred ionic conduction at that spot starts up, which may lead to a breakdown either by heating, as described by Ridley, or by the buildup of space charge followed by electron injection, as suggested also by Shousha. If breakdown occurs not here but somewhere else, the remaining charge carriers are swept away during the next run. This would consequently explain why the breakdown field does not decrease during subsequent measurements, as would

happen if space charges had remained in the specimen. The difference between the forward and backward directions could be due to a variation of the composition of the anodic layer or to a built-in electric field created by space charge. This description is essentially connected with the mechanism of anodization and it has possibly the advantage that the phenomenon of sparking during anodization can be considered from the same point of view. Its drawback, however, is that since there is no generally accepted microscopic theory of anodization, a quantitative elaboration of this very speculative picture cannot be given at present.

### Acknowledgments

We are grateful to H. J. van de Berg for the preparation and photomicrography of slices of anodic oxide, to H. B. Haanstra for the photomicrographs of the breakdowns, to L. P. van Kemenade for technical assistance, to H. J. Prins for the statistical analysis of the results, to L. Willemsse for the construction of the apparatus, and to Professor N. Klein for a discussion on the subject.

Manuscript submitted April 26, 1976; revised manuscript received June 21, 1976. This was Paper 83 presented at the Toronto, Canada, Meeting of the Society, May 11-16, 1975.

Any discussion of this paper will appear in a Discussion Section to be published in the June 1977 JOURNAL. All discussions for the June 1977 Discussion Section should be submitted by Feb. 1, 1977.

Publication costs of this article were assisted by Philips Research Laboratories.

### APPENDIX

For a calculation of the breakdown field from Eq. [7], the quantities  $j_0$  and  $F_{FN}$  in Eq. [5],  $\alpha_0$  and  $F_\alpha$  in Eq. [6], and  $\mu_p$  must be estimated.

$j_0$  and  $F_{FN}$ .—Fowler-Nordheim tunneling is described numerically by

$$j = 1.54 \times 10^6 \frac{F^2}{Q} \exp\left(-68.3 \frac{Q^{3/2}}{F}\right)$$

where  $Q$  is the barrier height in eV and  $F$  the field in MV/cm. [Ref. (8) p. 77]. Field emission (33) experiments have yielded  $Q = 1.5$ - $1.85$  eV for Al/ $\text{Al}_2\text{O}_3$  and 2.5 eV for Au/ $\text{Al}_2\text{O}_3$ . This gives  $j_0 = 6 \times 10^7$  A/cm<sup>2</sup> and  $F_{FN} = 2.7 \times 10^8$  V/cm for Au and  $j_0 = 1.03 \times 10^8$  A/cm<sup>2</sup> and  $F_{FN} = 1.25 \times 10^8$  V/cm for Al.

$\alpha_0$  and  $F_\alpha$ .—O'Dwyer obtained  $\alpha_0$  and  $F_\alpha$  from fitting his theory to the measurements of Lomer and of Merrill and West. The relation obtained is also shown in Fig. 7. It gives  $F_\alpha = 20 \times 10^6$  V/cm and  $\alpha_0 = 7.5 \times 10^6$ /cm. These fairly low values are necessary to reproduce the steep measured field dependence. The only other experimental evidence concerning electron multiplication seems to be the laser breakdown measurements on sapphire by Fradin and Bass (34), who showed that breakdown with  $t_p = 4.7$  nsec pulses at a wavelength of 1.06  $\mu\text{m}$  occurs at  $(6.3 \pm 1.6) \times 10^6$  V/cm. If this is interpreted in accordance with Bloembergen (35) as the time needed to build up an avalanche of  $2^{40}$  electrons we obtain  $\eta(F)t_p \approx 18$ , where  $\eta$  is the ionization rate per second. This can be converted in an ionization rate per centimeter if the velocity of the electrons at a field of  $10^7$  V/cm is known. This has been calculated by Thornber and Feynman (36), who obtain a value of  $\approx 2 \times 10^7$  cm/sec.

Taking all these figures into account and also assuming that anodic  $\text{Al}_2\text{O}_3$  and sapphire behave the same in this respect, we obtain  $\alpha(6.3 \times 10^6 \text{ V/cm}) = 180/\text{cm}$ . This is low compared with the value obtained with O'Dwyer's constants ( $\alpha = 3.1 \times 10^5/\text{cm}$ ), but it is quite close to the values obtained for  $\text{SiO}_2$  by Solomon and Klein (23). For lack of something better, we will take the field dependence of  $\text{SiO}_2$   $F_\alpha = 1.8 \times 10^8$  V/cm, as applying to  $\text{Al}_2\text{O}_3$ , which gives  $\alpha_0 = 4.6 \times 10^{14}/\text{cm}$ .

$\mu_p$ .—The only constant then missing is the hole mobility. If the breakdown field at 500Å calculated with

Eq. [7] is fitted to our experimental results, we obtain  $\mu_p = 10^{-8}$  cm<sup>2</sup>/Vsec which seems not unreasonably high in view of the results obtained again on SiO<sub>2</sub> by Hughes (37), who found  $4 \times 10^{-9}$  cm<sup>2</sup>/Vsec at room temperature. Figure 10 gives our experimental facts compared with the theoretical dependence calculated with Eq. [7]. It is instructive to consider the various quantities that follow from the calculation. At 1000Å we find

breakdown field	$F_B = 8.81 \times 10^6$ V/cm
Fowler-Nordheim current calculated with $F = V/d$	$J_{FN} = 2.97 \times 10^{-6}$ A/cm <sup>2</sup>
actual injected current	$J_{cath} = 1.38 \times 10^{-5}$ A/cm <sup>2</sup>
total current = injected electrons + ionized electrons + holes	$J_{total} = 6.7 \times 10^{-3}$ A/cm <sup>2</sup>
hole density	$p = 2.37 \times 10^{17}$ /cm <sup>3</sup>
total number of holes	$pd = 2.37 \times 10^{12}$ /cm <sup>2</sup>
change of the field at the cathode	$\Delta F = 2.5 \times 10^5$ V/cm

The change of the field is very small. Furthermore, we can compare drift with recombination. The number of holes removed per second by drift is equal to  $\mu_p p F$ . The number of holes removed per second by recombination is smaller than  $n_e p d \langle \sigma \rangle$ , with  $\langle \sigma \rangle$  a cross section of recombination and  $n_e$  the total electron current density.

Inserting the numbers given above and  $\langle \sigma \rangle = 10^{-18}$  cm<sup>2</sup>, the value used by DiStefano and Shatzkes (24), we obtain  $\frac{(dp/dt)_{\text{recombination}}}{(dp/dt)_{\text{drift}}} = 2 \times 10^{-6}$ . The approach chosen here is at least self-consistent.

If we use aluminum instead of gold as a contact, with the numbers  $j_o = 1.03 \times 10^8$  and  $F_{FN} = 1.25 \times 10^8$  (Q = 1.5 eV), we obtain from Eq. [7] a breakdown field at  $d = 10^{-5}$  cm equal to  $6.6 \times 10^6$  V/cm.

#### REFERENCES

- W. S. Nicol, *Proc. IEEE*, **56**, 109 (1968).
- P. D. Lomer, *Proc. Phys. Soc. London, Sect. B*, **63**, 818 (1950).
- R. C. Merrill and R. A. West, Abstract 1, p. 1, The Electrochemical Society Extended Abstracts, Spring Meeting, Pittsburgh, Pa., April 15-18, 1963.
- L. L. Odynets, F. S. Platonov, and E. M. Prokopchuk, *Radiotekh. Elektron.*, **16**, 1739 (1971); *Radio Eng. Electron. Phys. (Engl. Transl.)*, **16**, 1576 (1971).
- F. Forlani and N. Minnaja, *Phys. Status Solidi*, **4**, 311 (1964).
- F. Forlani and N. Minnaja, *J. Vac. Sci. Technol.*, **6**, 518 (1969).
- J. J. O'Dwyer, *J. Phys. Chem. Solids*, **28**, 1137 (1967).
- J. J. O'Dwyer, "The Theory of Electrical Conduction and Breakdown in Solid Dielectrics," Clarendon Press, Oxford (1973).
- J. E. Carnes and H. T. Duffy, *J. Appl. Phys.*, **42**, 4350 (1971).
- N. Klein, *IEEE Trans. Electron Devices*, **ed-13**, 788 (1966).
- V. F. Korzo, *Fiz. Tverd. Tela*, **11**, 3038 (1969); *Sov. Phys. Solid State, (Engl. Transl.)*, **11**, 2469 (1970).
- H. J. de Wit and C. Crevecoeur, *Phys. Lett. A*, **50**, 365 (1974).
- C. Crevecoeur and H. J. de Wit, *This Journal*, **121**, 1465 (1974).
- W. J. Bernard and J. W. Cook, *ibid.*, **106**, 643 (1959).
- F. E. Rosztoczy and M. H. Read, *ibid.*, **116**, 1752 (1969).
- R. M. Valletta and W. A. Pliskin, *ibid.*, **114**, 944 (1967).
- M. Albert, N. Klein, and P. Solomon, *Thin Solid Films*, **13**, 221 (1972).
- T. J. Lewis and B. W. Ward, *Proc. R. Soc. London, Ser. A*, **269**, 223 (1962).
- J. E. Brignell, *Proc. IEE*, **113**, 1683 (1966).
- H. Cramer, "Mathematical Methods of Statistics," Princeton University Press, Princeton, New Jersey (1964).
- P. Solomon, N. Klein, and M. Albert, *Thin Solid Films*, **35**, 321 (1976).
- J. J. Randall, Jr. and W. J. Bernard, *Electrochim. Acta*, **20**, 653 (1975).
- P. Solomon and N. Klein, *Solid State Commun.*, **17**, 1397 (1975).
- T. H. DiStefano and M. Shatzkes, *Appl. Phys. Lett.*, **25**, 685 (1974).
- B. K. Ridley, *J. Appl. Phys.*, **46**, 998 (1975).
- C. R. Fritzsche, *J. Phys. Chem. Solids*, **30**, 1885 (1969).
- A. H. M. Shousha, *J. Non-Cryst. Solids*, **17**, 108 (1975).
- P. Winkel, C. A. Pistorius, and W. Ch. van Geel, *Philips Res. Rep.*, **13**, 277 (1958).
- H. J. de Wit and C. Crevecoeur, To be published.
- L. Young, *Proc. R. Soc. London, Ser. A*, **263**, 395 (1961).
- M. J. Dignam and P. J. Ryan, *Can. J. Chem.*, **46**, 549 (1968).
- D. F. Taylor and M. J. Dignam, *This Journal*, **120**, 1299 (1973).
- A. Braunstein, M. Braunstein, G. S. Picus, and C. A. Mead, *Phys. Rev. Lett.*, **14**, 219 (1965).
- D. W. Fradin and M. Bass, *Appl. Phys. Lett.*, **22**, 157 (1973).
- N. Bloembergen, *IEEE J. Quantum Electron.*, **qe-10**, 375 (1974).
- K. K. Thornber and R. P. Feynman, *Phys. Rev. B*, **1**, 4099 (1970).
- R. C. Hughes, *Appl. Phys. Lett.*, **26**, 436 (1975).

# Initial Stages of Oxide Growth and Pore Initiation in the Porous Anodization of Aluminum

C. J. Dell'Oca<sup>\*,1</sup> and P. J. Fleming<sup>\*,1</sup>

Fairchild Semiconductor, Mountain View, California 94040

## ABSTRACT

Ellipsometry studies of evaporated aluminum films anodized in 0.6M H<sub>3</sub>PO<sub>4</sub> at constant current indicate that the anodic oxide produced is at first homogeneous with a refractive index of 1.62, as found for barrier anodic oxide of thin film and bulk Al. As the thickness increases, the optical properties change signifying the onset of pore formation. This occurs at increasing thicknesses with increasing current density, however, pore formation always occurs well before the peak in voltage is reached at constant current. Ellipsometry indicates that the mode of development of the oxide prior to pore initiation is similar to that of barrier anodic oxides. However, the efficiency of oxide growth and the electric field required to pass a given ionic current,  $J$ , are generally lower and approach values for barrier oxides (of thin film and bulk Al) only at high current densities. The curvature of the  $\log J$  vs.  $E$  curve is in the opposite sense to that normally observed for anodic oxides and it is interpreted in terms of cation and anion motion. After pore formation the efficiency of oxide growth increases and becomes near unity when steady-state formation conditions are reached. These results appear consistent with the model that dissolution at the pore bases is an electric field-aided process.

Anodization of evaporated aluminum films is becoming increasingly important in the fabrication of monolithic, large-scale integrated circuits utilizing aluminum metal electrical interconnections where anodization provides both improved processing and reliability (1). In order to arrive at optimum processing, it is necessary to understand the anodization properties of aluminum films. In a previous paper, the barrier anodization properties were studied and found to be essentially the same as those of bulk aluminum (2). The present study is concerned with porous anodization. In particular, the initial stages of oxide growth and the onset of pore formation are quantitatively characterized using ellipsometry. This has not been done previously for porous anodization of aluminum and the results should be valuable in arriving at the mechanism of pore formation.

Of the vast literature on porous anodization of aluminum, very little deals with initial stages of film formation. That which does is mostly qualitative because of the difficulties involved with measuring very thin films. The evidence that is presented indicates that a barrierlike film initially forms, followed by pore initiation and porous oxide growth. For example, the anodization characteristics, such as the time development of current at constant voltage (3) or of voltage at constant current, are at first similar to those observed in barrier anodizations. Also, direct observations of the surface with electron microscopy indicate that surface roughness occurs after some growth has taken place (3, 4). Thus, the oxide formed in the initial stages of porous oxide growth and that which remains interposed between the pore-containing layer and the metal is often referred to as a barrier layer. In this paper, these layers will be respectively referred to as the initial film (or oxide) and the pore-free layer. To avoid ambiguity, the term "barrier" will be reserved to describe oxides formed in a barrier anodization.

The basic difficulty involved with the study of the initial film is the measurement of thickness. Previous methods include reanodization in barrier film forming electrolyte (5) and direct observation of thickness

using cross sections and electron microscopy (4). The first method assumes that the ionic conductivity of the initial film is the same as that of barrier oxides. These methods have limited resolution and accuracy and, in addition, are destructive and therefore cumbersome. In the present study these drawbacks are overcome using ellipsometry. This is a nondestructive optical technique that is very sensitive to the presence of and changes in thin surface layers. Thus, it has been widely used to characterize properties of thin films (6) including those of barrier oxides formed on bulk (7, 8) and thin film aluminum (2).

If the initial film growth characteristics are as have been presented, then it should be possible with ellipsometry not only to determine the growth properties but also to determine the onset of pore formation. That is, the optical properties of the initial film should at first be similar to those of barrier oxides which have been found to be optically homogeneous (2, 7). The advent of pore formation causes a change of optical properties which should be detectable by ellipsometry. This turns out to be the case.

## Experimental

The investigation was carried out with 2  $\mu$ m thick aluminum films deposited on thermally oxidized polished silicon wafers by the electron beam evaporation of 99.999% pure aluminum under high vacuum. Films deposited under these conditions have barrier anodization properties which are not detectably different than those of bulk aluminum (2). The thin film is more convenient to use than bulk aluminum because a smooth surface suitable for anodization is obtained directly without polishing and because photolithography and etching can be used to precisely define the anodization area.

Two types of specimens were used and these are shown schematically in Fig. 1. One type had a 3.22 cm<sup>2</sup> anodization area defined using photolithography and etching of a previously formed, 2700Å thick, barrier anodic oxide on the aluminum film. The other type had a circular 10 cm<sup>2</sup> aluminum area defined by photolithography and etching of the deposited aluminum film. An aluminum strip 1 mil wide was left to connect the aluminum in the contact area to the anodization area. The strip is of negligible area but

\* Electrochemical Society Active Member.

<sup>1</sup> Present address: Hewlett-Packard Company, Palo Alto, California 94304.

Key words: anodization, aluminum oxide, ellipsometry.

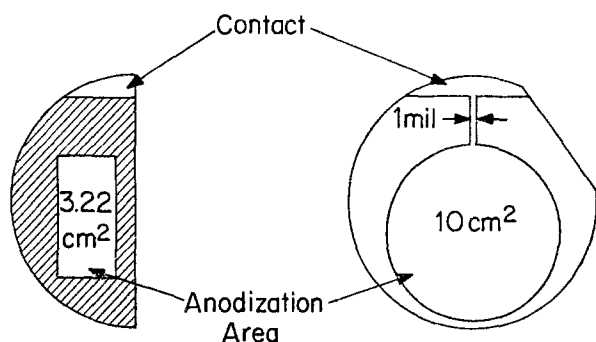


Fig. 1. Schematic representation of the two types of thin film aluminum specimens used in this study.

it is sufficiently long to keep the contact area above the electrolyte during anodization. The first type of specimen was used mostly for kinetic studies while the second type was used for density measurement. No noticeable difference in oxide growth was noted between these two surface preparation methods.

The anodizations were carried out at constant current (regulated to 0.3%) in a stirred 0.6M  $H_3PO_4$  electrolyte held at  $25^\circ \pm 0.2^\circ C$ . This electrolyte was chosen because the pore-free portion of the porous oxide can, depending on current density, be varied over a substantial thickness range, leading to a more precise determination of film properties. The anodizations were carried out in a stepwise fashion with ellipsometry measurements made on the surface prior to anodization and after each anodization step. All ellipsometry measurements were made at  $70^\circ$  angle of incidence using a He-Ne laser unpolarized light source of  $6328\text{\AA}$  wavelength. Other experimental details are as described in a previous paper (2).

### Results

**Optical properties.**—Since the analysis of ellipsometry results from the initial film relies heavily on the ellipsometry characteristics of barrier anodic oxide formed on evaporated aluminum films, the latter results are quoted in Fig. 2 (2). This figure presents the conventional  $\Delta$  vs.  $\psi$  plot used in ellipsometry, where  $\Delta$  and  $\psi$  are the quantities determined in ellipsometry and are related to the properties of the film and underlying substrate. The experimental results begin at the point marked "bare" substrate which represents the surface of the aluminum film prior to barrier anodization in a tartrate solution. As the surface is anodized and remeasured at intervals, the experimental points obtained (denoted by crosses) trace out, in a counterclockwise direction, an elliptically shaped curve which eventually recycles on itself as indicated by the circular points. The curve in the figure represents the best fit to the experimental points indicating a uniform oxide with an index of refraction ( $N = n - jk$ ) of 1.62 on aluminum having a refractive index of 1.3-6.5.

As expected, the ellipsometry results characteristic of initial film growth in 0.6M  $H_3PO_4$  are at first similar to those of barrier oxides. Figure 3 shows a superposition of results from various anodization current densities. The dashed curve in this figure is the ellipsometry curve for barrier anodization taken from Fig. 2 and it serves as a reference. The ellipsometry measurements taken at intervals during porous anodization at first are coincident with the reference curve indicating that the initial film has the optical properties of barrier films. For sake of clarity, the experimental points are not shown. Eventually, the experimental curve deviates from the reference curve signifying a change in optical properties, i.e., the presence of pores. The reproducibility of these results is good in the region before deviation and for some time

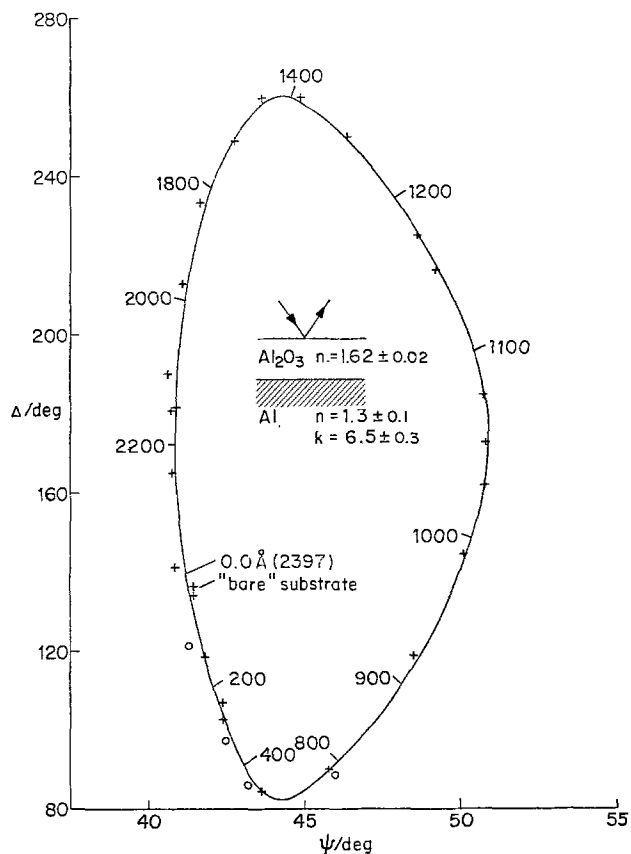


Fig. 2. Ellipsometry results and fitted curve for anodization of aluminum films in 3% tartaric acid (pH of 5.5) at  $25^\circ C$  (2). Numbers along curve indicate film thickness.

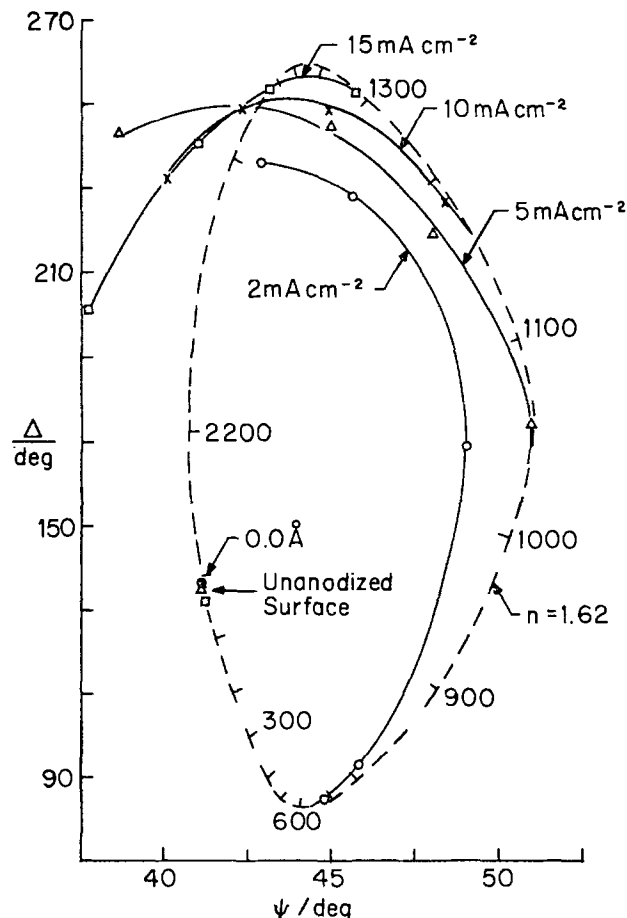


Fig. 3. Departure from dashed curve representing the homogeneous film in Fig. 2 of ellipsometry results from oxides formed at various current densities on Al in 0.6M  $H_3PO_4$ .

after deviation from the reference curve. The reproducibility becomes less good at large deviations, i.e., near the ends of the experimental curves.

A quantitative analysis of these results is not feasible because of the complex mode of film growth after pore initiation. That is, the growth rates of the initial and pore containing layers are expected to, respectively, decrease and increase in a complex way. In addition, the size and number of pores is expected to change with voltage until the steady-state voltage is reached in the constant current anodization (4). A further complication to this picture is that in addition to pore formation at the upper surface of the growing film, after a while, roughening of the aluminum also occurs, effectively changing its optical properties.

A qualitative analysis of the experimental results is instructive and can be made using a simplified model of growth. In this model it is assumed that, once the pores begin to form, these pores have a fixed size and they penetrate the growing layer at some fixed rate. Indicative calculated ellipsometry curves are given in Fig. 4 and 5. The respective thicknesses at which pore formation begins are chosen as 500Å (Fig. 4) and 1000Å (Fig. 5) to, respectively, correspond to the 2 and 5 mA/cm<sup>2</sup> formation currents.

The simplest case is one where the pores grow at a rate equal to film growth. In other words, the initial layer remains fixed at the pore-initiation thickness. Optically, this corresponds to a porous layer growing over a pore-free layer of fixed thickness and refrac-

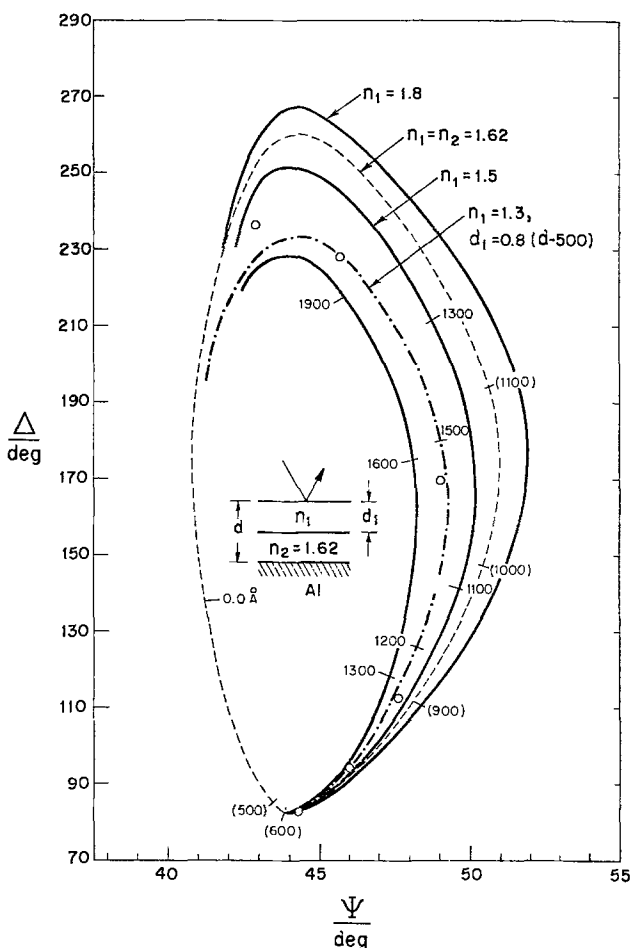


Fig. 4. Calculated ellipsometry curves using a two-layer approximation of film growth after pore initiation occurs at 500Å. — Layer 2 fixed at 500Å; - - - layer 2 contributes 20% of the total film growth; — — — reference curve from Fig. 1; ○ ○ ○ = 2 mA/cm<sup>2</sup> experimental points from Fig. 3; numbers indicate total film thickness, *d*, and bracketed numbers apply to reference curve.

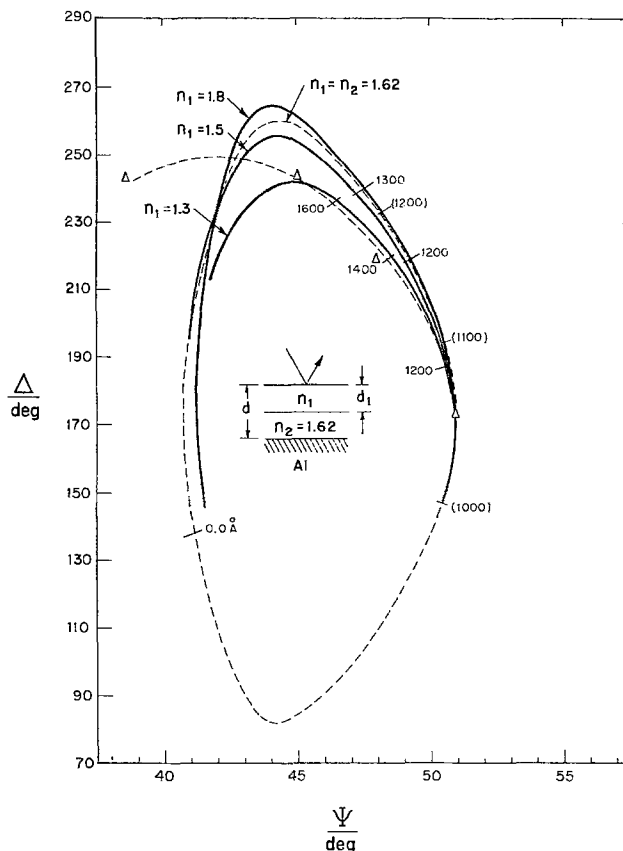


Fig. 5. Same as in Fig. 4 but for the case of pore initiation at 1000Å and layer 2 fixed at 1000Å (—△—△ = 5 mA/cm<sup>2</sup> experimental points from Fig 3).

tive index of 1.62. This simple model predicts that the refractive index of the porous layer must be lower than that of the barrier films in order to obtain ellipsometry curves that deviate on the correct side of reference curve (Fig. 4 and 5). This behavior is expected since the presence of pores decreases the density of the oxide.

A pore growth rate less than that of film growth, i.e., an initial layer that continues to grow at some rate after pore initiation, has the effect of moving the calculated curves in Fig. 4 and 5 closer to the reference curve. In the extreme case where only the initial layer grows (i.e., no pore formation), the reference curve is regained. A calculated curve which comes close to the 2 mA/cm<sup>2</sup> results is shown in Fig. 4. In this case, after pore initiation at 500Å, a porous layer of refractive index 1.3 contributes 80% of the total increase in film thickness.

One characteristic difference between the calculated and experimental curves is that with increasing thickness the former turn and proceed to pass near the point marked 0.0Å, which represents the original surface. The experimental results do not have this tendency because as the pores grow, a scallop is developed in the aluminum surface under each pore cell (4). The result is a fine grain surface roughness which effectively changes the refractive index of the aluminum and shifts the ellipsometry results.

*Pore initiation.*—As a first approximation, the onset of pore formation is determined from the point where the ellipsometry curve begins to deviate from the reference curve (Fig. 3). This point occurs approximately at 600, 1050, 1150, and 1275Å, respectively, for formation currents of 2, 5, 10, and 15 mA/cm<sup>2</sup>. The accuracy within which these points can be determined depends on where the deviation occurs on the reference curve. The sensitivity is higher in the 900-1200Å region than at the apex of the reference curve.

The voltage of pore initiation is determined from the above thickness using a graph of voltage vs. thickness for the various anodization current densities. (This figure is presented later in the section on growth properties.) The important result here is that pore initiation occurs well before the peak in voltage is reached in the constant current anodizations. Figure 6 shows the voltage-time curves which are characteristic of porous aluminum anodization and typical for the present experiments. The onset of pore formation occurs at about 70% of the steady-state voltage. O'Sullivan and Wood using electron microscopy have reported for anodizations at 5 mA/cm<sup>2</sup> in 0.4M H<sub>3</sub>PO<sub>4</sub> at 25°C that very minor film roughening is noted after 40 sec of growth (4). This is in agreement with the present results at the same current density in a somewhat more concentrated electrolyte.

The thickness at which the onset of pore formation occurs has probably been overestimated to some degree. This is because the deviation from the reference curve occurs slowly with changing film thickness. Some indications of how slowly can be obtained from the calculated curves of Fig. 4 and 5. If a similar estimation of pore initiation is made for these curves, then the onset of pore formation would be thought to occur at about 600Å (Fig. 4) and 1050Å (Fig. 5) when, in actuality, it began at 500 and 1000Å, respectively.

However, it is highly unlikely that pores are present and grow from the outset of the anodization. This would require the pore-containing portion of the film to remain relatively insignificant until near the point of deviation and then almost abruptly become significant. To be insignificant, the pore-containing layer should change the refractive index of the over-all film by less than 1% for the formations above 2 mA/cm<sup>2</sup>. In addition to this argument, the thickness determined by ellipsometry was checked at various points along the 10 mA/cm<sup>2</sup> anodization by an independent method utilizing the Tolansky interference measurement of the height of a silvered step formed in the anodic oxide. These measurements were found to be in agreement.

**Characteristics of initial film growth.**—The characteristics of initial film growth at constant current in 0.6M H<sub>3</sub>PO<sub>4</sub> at 25°C were found to be similar to those of barrier oxide growth. That is, the thickness increases linearly with time and the voltage increases linearly with thickness. Typical results are given in Fig. 7 and 8. The thickness was determined using ellipsometry and the optical properties of barrier film (reference curve of Fig. 3). In some cases the thickness was checked by the independent method

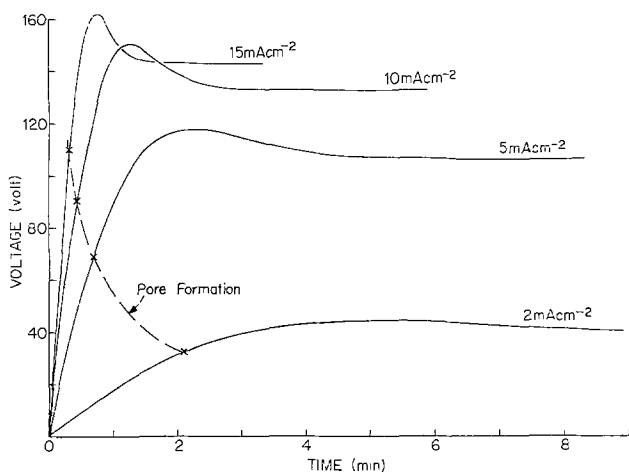


Fig. 6. Time development of voltage for porous anodization at various current densities showing the onset of pore formation.

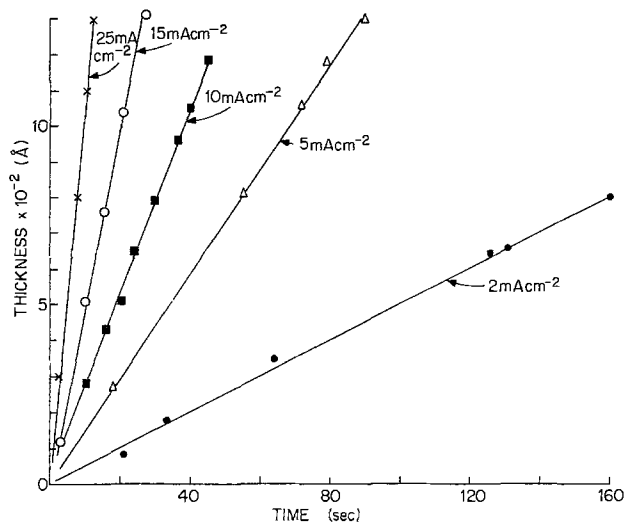


Fig. 7. Typical initial film thickness development with time for various anodization current densities.

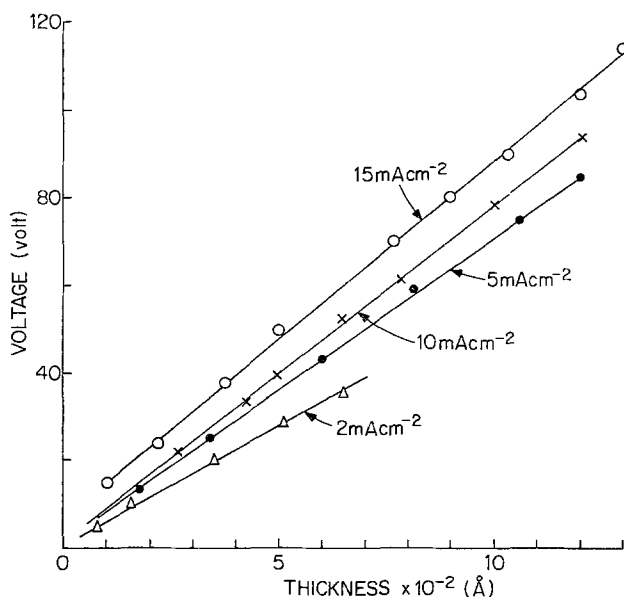


Fig. 8. Typical cell voltage development with initial film thickness for various anodization current densities.

already mentioned. These results were generally quite reproducible.

The efficiency of oxide growth, *i.e.*, oxygen uptake, and the efficiency of aluminum consumed during the anodization were determined and found to be different. The efficiency of oxide growth is low and increases with current density of formation (Table I). The efficiency is calculated using Faraday's law for an oxide of formula Al<sub>2</sub>O<sub>3</sub>, and the rate of film growth determined from the experimental thickness vs. time curves. An oxide density of 3 g/cm<sup>3</sup> was used in these calculations. This is within the range of values (2.90-3.2 g/cm<sup>3</sup>) obtained from our measurements of density and is a value that has been used by others (9). By comparison, barrier films formed in a tartrate

Table I. Efficiency of initial oxide growth in 0.6M H<sub>3</sub>PO<sub>4</sub> at 25°C

Applied current (mA/cm <sup>2</sup> )	Electric field (10 <sup>6</sup> V/cm)	Growth rate (Å/sec)	Growth efficiency (%)
2	5.5	5	43
5	6.74	14	47
10	7.66	30	51
15	8.2	51	58
25	8.6	109	74

solution at the same temperature, have efficiencies close to 70 and 80%, respectively, at 2 and 10 mA/cm<sup>2</sup> formation (2). While the efficiency of oxide formation is low, the efficiency of aluminum used in the anodization approaches unity. This was determined from calculations based on the difference in weight from prior to anodization to after anodization and removal of the anodic oxide. That is, the amount of aluminum used in the anodization corresponds to that predicted from Faraday's law for the charge passed. This indicates that, within experimental error, electronic currents are not contributing to current transport through the oxide. Hence, the low efficiencies observed for oxide growth occur from the loss of aluminum to the electrolyte by oxide dissolution.

The open-circuit oxide dissolution rate in the electrolyte was measured and found to be less than 0.2A/sec which is insignificant when compared to the rates of oxide growth. The effect was further minimized by minimizing the open-circuit exposure of oxide to the electrolyte. Thus, oxide dissolution must be a function of electric field in the oxide in order to cause the observed loss in oxide growth efficiency. This is discussed later.

The growth kinetics of the initial oxide, i.e., the log of ionic current density *vs.* electric field, are given in Fig. 9. The electric field is obtained from the slope of the voltage *vs.* thickness curves. The ionic current density (dashed curve, Fig. 9) is the applied current density (left curve, Fig. 9) corrected for efficiency of growth. The curve on the right in Fig. 9 represents the growth kinetics for barrier oxide formed in a tartrate solution. It is seen that at high current densities the growth kinetics of the initial oxide approach that of barrier oxides. At lower currents, the ionic conductivity of the initial film is significantly higher than that of barrier oxides. Also, note that the electric fields are lower than the 10<sup>7</sup> V/cm which have been reported to occur across the dense oxide after steady-

state porous oxide growth is reached in the same electrolyte (4).

The higher ionic conductivity of the initial film does not appear to be an artifact of the thickness measurements. Systematic measurement errors in thickness do not enter because rates of change rather than absolute values are used to determine growth efficiency and electric field. In order to observe a lower field, the initial film thickness must be overestimated by a factor that increases with thickness. This is highly unlikely even if it is assumed that pore formation occurs far earlier than estimated. If pore formation occurred much earlier than has been estimated, then it might be expected that the effective film thickness for ionic conduction would be less, hence reducing the required voltage and leading to a lower estimate of electric field. Contrary to this is the fact that the presence of pores effectively decreases the anodization area and hence increases the effective current density and, in turn, the electric field. Thus, the measured electric field across the pore-free layer is far greater than that of the barrier films, being on the order 10<sup>7</sup> V/cm (4). In addition, if pores are present, the qualitative indications (Fig. 4 and 5) are that using the reference curve, ellipsometry would underestimate the thickness of the film and hence the efficiency of oxide growth would also be underestimated. This would have the effect of bringing the ionic current (Fig. 9) closer to the applied current and hence lowering the electric field. Thus, it is not clear that early pore formation would lead to an underestimation of the electric field. In any event, the present evidence and that from direct observation (4) almost exclude early pore formation.

*Steady-state porous oxide growth.*—Although it is not the intention of this paper to characterize porous film growth, it was found that the growth rate is significantly higher during steady-state porous anodization. That is, after the voltage reaches a more or less constant value under constant applied current. A typical result for the 10 mA/cm<sup>2</sup> anodization is shown in Fig. 10. The thickness of the initial film was determined by ellipsometry and by Tolansky interference measurement of step height. The thickness of the porous film was determined solely by the latter method and also by a mechanical surface profilometer. The results extend out to film thicknesses beyond 3 μm.

## Discussion

*Kinetics of oxide growth.*—The optical properties of the initial oxide formed in a porous anodization of aluminum are similar to those of the barrier anodic oxides. The log *J vs. E* characteristics do appear to be different, but this does not necessarily imply a different mechanism of ionic conduction. In fact, it may be argued that these results are consistent with the high field Frenkel defect theory of ionic conduction in anodic oxides and the mobility of both oxygen (anions) and metal (cations) ions during oxide growth. There is a body of evidence indicating that both ions are mobile and contribute to oxide growth at the oxide-electrolyte and metal-oxide interface, respectively. [For a review of anodic oxides see Ref. (11) and (12).] According to the Frenkel defect theory (10), ionic conduction occurs by a thermally activated electric field-aided process in which ions of charge *q* overcome energy barriers of height *W* and have a half-jump (activation) distance of *a*. The ionic current density then is  $J = Ae^{-(W-qaE)/kT}$ , with *A*, *W*, and *qa* characteristic of the particular ion species. In a log *J vs. E* plot, each ion current will be represented by a straight line of slope proportional to the product *qa*. The two lines will intersect at some point. The total current (sum of the ion currents) will be dominated by the ion with the lower *qa* below this point and by the ion with the higher *qa* above this point. Thus, the

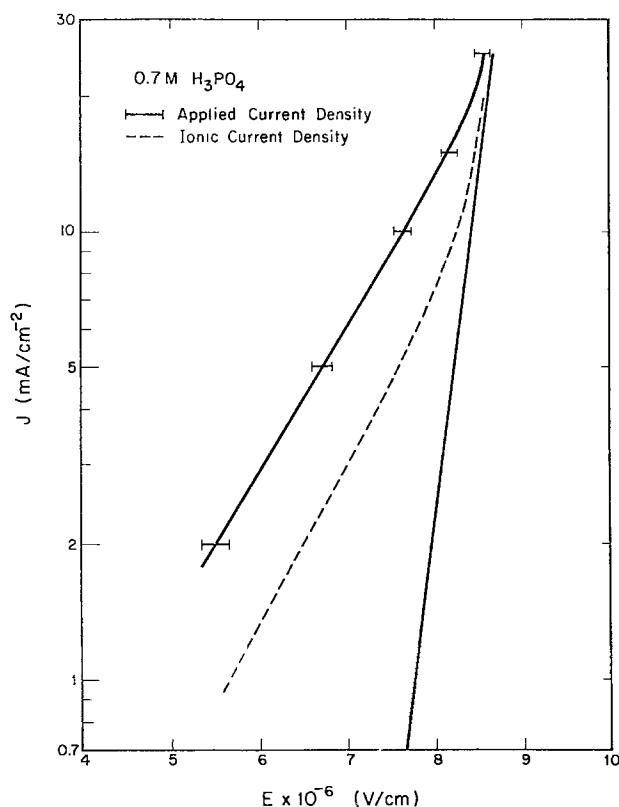


Fig. 9. Constant current kinetics of initial film growth in 0.6M H<sub>3</sub>PO<sub>4</sub> at 25°C. Curve to the left represents applied current density. Dashed curve is the ionic current density. The curve on the right gives the kinetics obtained in the barrier anodization of Al films (2).



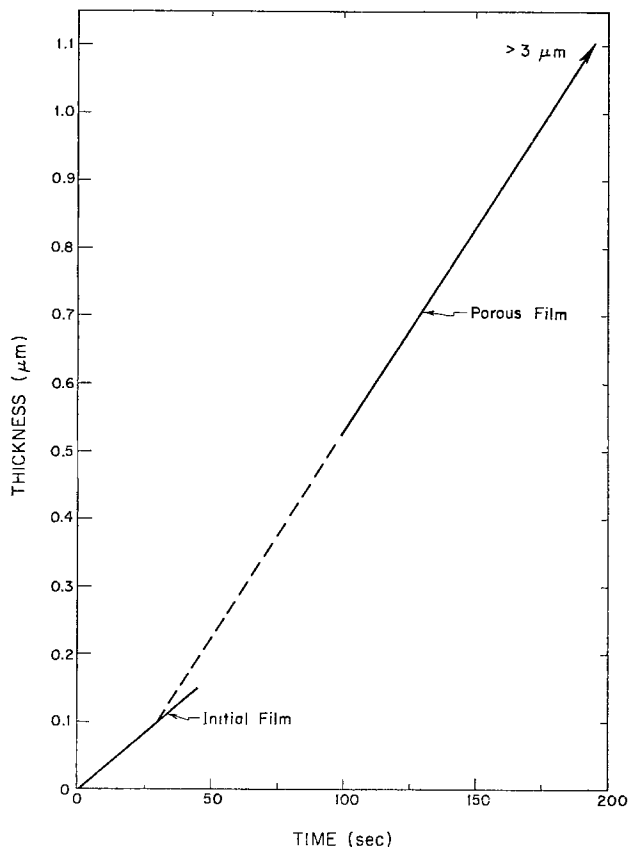


Fig. 10. Development of film thickness with time for a 10 mA/cm<sup>2</sup> porous anodization in 0.6M H<sub>3</sub>PO<sub>4</sub> at 25°C.

total current will have a curve whose slope increases with electric field as is observed in this study.

The foregoing argument was first presented (11) to show the inconsistency of the Frenkel defect theory and the curvature observed for anodic oxides of Ta, Al, and Nb. The curvature for these oxides is in the opposite sense, *i.e.*, the  $\log J$  vs.  $E$  curve slowly decreases in slope with increasing electric field, giving a  $\log J \propto \alpha E - \beta E^2$ . While numerous models have been proposed [see Ref. (11) and (12)], it is not known whether the effect is intrinsic to ionic conduction or whether, as has been proposed (13), caused by incorporation of electrolyte impurities into the oxide. It has been found that the curvature is enhanced for Ta anodized in dilute H<sub>3</sub>PO<sub>4</sub> or more concentrated H<sub>2</sub>SO<sub>4</sub>, where impurity incorporation is more pronounced (12).

If impurities cause curvature, why is the curvature not noted for the present anodization in H<sub>3</sub>PO<sub>4</sub>? Perhaps impurity incorporation is much smaller in Al<sub>2</sub>O<sub>3</sub>. Or, the effect may simply be overwhelmed by the change from oxygen to metal ion current domination. However, it is certain that the low efficiencies, particularly at low currents, serve to minimize the fraction of oxide-containing impurities. If the incorporated impurities are, as has been indicated (14), immobile with respect to the rate of oxide growth, then incorporation of the impurities into the oxide will only occur if the metal ion transport number,  $t_m$ ,<sup>2</sup> is greater than the difference between the efficiency of oxide growth and unity. The  $t_m$  for Al anodization in H<sub>3</sub>PO<sub>4</sub> is not known. However, it is expected to increase with current density of formation. For example, for the anodization of Al in another aqueous electrolyte (ammonium citrate),  $t_m$  varied from 0.56 at 1 mA/cm<sup>2</sup> to 0.72 at 10 mA/cm<sup>2</sup> (15). Since both the efficiency and  $t_m$  increase with current density, the effect of

<sup>2</sup>  $t_m$  is the fraction of oxide which grows at the oxide-electrolyte interface from metal ion transport. The remaining oxide grows at the metal-oxide interface from oxygen in transport.

incorporation will become more noticeable at higher currents. In fact, if impurity incorporation occurs with Al<sub>2</sub>O<sub>3</sub>, it should be expected that at higher currents than those used in this study the  $\log J$  vs.  $E$  curve for the initial oxide would tend to curve back in the direction found for oxides of Ta, Al, and Nb.

Thus it appears that the kinetics of initial film growth can be analyzed in terms of anion and cation currents. Then, in the linear region, *i.e.*, at low currents, the activation or half-jump distance should be calculated for an anion with a valence charge of  $q = -2e$  for O<sup>2-</sup> or  $q = -e$  for OH<sup>-</sup> as proposed by Hoar and Mott (16). The activation distance found is 1.1 and 2.2Å, respectively, which are not unrealistic values. An activation distance for cation motion cannot be obtained because the present data do not reach high enough currents where presumably the linear region for cation-dominated conduction is found. However, there seems to be a tendency toward a line similar to that of the barrier oxide kinetics. Based on a metal ion with  $q$  of 3 $e$ , an activation distance close to 3Å is obtained both for barrier oxides formed on thin film (2) and bulk aluminum (9).

**Pore formation.**—The two observations important to pore formation and growth are the efficiency of initial film formation and its increase during porous film growth. Both of these observations are in direct support of the model that etching at the pore bases is an electric field-aided process (16). First, although the efficiency of initial film growth increases with current density (and hence electric field), the net dissolution rate (inefficiency) also increases with current density or electric field. In fact, the rate of dissolution increases exponentially with electric field, except at the higher current density where the rate of increase is slower. Secondly, as the porous film grows, the electric field across the porous oxide becomes much less than across the pore-free layer; therefore, the efficiency of growth should become near unity since the surface dissolution is decreasing.

In addition to field-assisted dissolution, it is also claimed that some anion motion is necessary to sustain porous film growth (16). Dissolution requires high fields. Fields corresponding to 10<sup>7</sup> V/cm have been observed across the pore-free layer for anodization in dilute H<sub>3</sub>PO<sub>4</sub> (4). However, from the observation of initial film growth, anion-current dominance occurs at lower fields. There are several explanations for this apparent inconsistency. One is that oxide curvature tends to increase the electric field at the surface of the pore base while the bulk of the pore-free oxide experiences lower fields. However, in order to explain this in terms of anion and cation electric field dependent currents, it is necessary to postulate the buildup of space charge in the oxide. A more likely explanation appears to be that of fringing electric fields. That is, ionic conduction takes place not only as postulated through the oxide surrounding the pore base (4) but also for some distance up the pore wall. The idea is not unreasonable, when it is considered that ionic conduction through the initial film is observed to occur at fields that are considerably lower than that effectively across the pore base oxide. Thus, ionic conduction can occur to (or from) points on the pore wall surface which are separated from the metal by distances considerably larger than the thickness of the oxide under the pore base. Proceeding from the pore base up the pore wall, the electric field will decrease in some fashion. The decreasing field is accompanied by decreasing ionic current which, in turn, has an increasing oxygen ion component. Since this current flow is toward the metal under the pore wall, this is exactly what is necessary to build up the pore wall. In addition, since the fringing fields also support dissolution, a variety of pore shapes near the pore base are possible depending on whether the

fringing field causes net growth or dissolution at a point.

Turning to the mechanism of pore initiation, it is difficult to reconcile the present ideas of field-aided ionic conduction and oxide dissolution with an oxide thickness instability resulting in a pore. What is even more perplexing is that at a given current density pore initiation occurs after a certain oxide thickness is reached. Perhaps, at a given current density, a certain thickness must be reached before the allowed local variation in oxide thickness reaches a value where the probability of pore initiation is high. Pore initiation might occur at the edge of such a region where the gradient in electric field gives rise to a varying interplay of dissolution, oxide growth, and perhaps metal and oxygen ion motion.

### Conclusions

Ellipsometry has been shown to be a useful technique for studying initial film growth in porous aluminum anodization. It can be used to determine both the growth properties and the onset of pore formation.

The initial films formed in the course of porous anodization resemble ordinary barrier films both optically and in their mode of development. However, the electric field required to grow these films is significantly lower and approaches values for ordinary barrier films only at high current densities.

The observations that film dissolution increases with field, that the efficiency of oxide growth increases after pore initiation, and that the fields causing growth are significantly smaller prior to pore formation appear to be in direct support of the model presented by Hoar and Mott (16), that the dissolution at the pore base is a field-aided process.

Manuscript submitted Jan. 13, 1976; revised manuscript received June 18, 1976.

Any discussion of this paper will appear in a Discussion Section to be published in the June 1977 JOURNAL. All discussions for the June 1977 Discussion Section should be submitted by Feb. 1, 1977.

### REFERENCES

1. See Ref. 1-5 of C. J. Dell'Oca, *Thin Solid Films*, **26**, 371 (1975).
2. C. J. Dell'Oca, *ibid.*
3. T. P. Hoar and J. Yahalom, *This Journal*, **110**, 614 (1963).
4. J. P. O'Sullivan and G. C. Wood, *Proc. R. Soc. London, Sec. A*, **317**, 511 (1970).
5. M. S. Hunter and P. Fowle, *This Journal*, **101**, 481 (1954).
6. See, for example, E. Passaglia, R. R. Stromberg, and J. Kruger, Editors, "Ellipsometry in the Measurement of Surfaces and Thin Films," NBS Misc. Pub. 256, Washington, D.C. (1963).
7. R. M. Goldstein, R. J. Lederich, and F. W. Leonard, *This Journal*, **117**, 503 (1970).
8. M. A. Barret and A. B. Winterbottom, in "First International Congress on Metallic Corrosion," p. 657, Butterworths, London (1961).
9. A. C. Harkness and L. Young, *Can. J. Chem.*, **44**, 2409 (1966).
10. L. Young, "Anodic Oxide Films," Academic Press, New York (1961).
11. W. S. Goruk, L. Young, and F. G. R. Zobel, in "Modern Aspects of Electrochemistry," Vol. 4, p. 176, Plenum Press, New York (1966).
12. C. J. Dell'Oca, D. L. Pulfrey, and L. Young, in "Physics of Thin Films," Vol. 6, p. 1, Academic Press, New York (1971).
13. C. J. Dell'Oca and L. Young, *This Journal*, **117**, 1548 (1970).
14. J. J. Randall, W. J. Bernard, and R. R. Wilkinson, *Electrochim. Acta*, **10**, 183 (1965).
15. J. A. Davies, B. Domeij, J. P. S. Pringle, and F. Brown *This Journal*, **112**, 675 (1965).
16. T. P. Hoar and N. F. Mott, *J. Phys. Chem. Solids*, **9**, 97 (1959).

## Line Emission Penetration Phosphors: Preparation and Cathodoluminescent Properties

S. Ignasiak\*<sup>1</sup> and H. Veron<sup>2</sup>

Sperry Research Center, Sudbury, Massachusetts 01776

### ABSTRACT

The preparation of three rare earth phosphors with onionskin barrier layers is described. The new materials are lanthanum oxysulfides and oxysulfates activated with terbium and in some cases coactivated with europium. When these phosphors with high dead voltage, and green emission are mixed with a commercial phosphor, such as  $YVO_4:Eu$ , a penetration phosphor results which has four distinct colors as a function of voltage in CRT displays. The emission from this phosphor system is at all times narrow band.

Several methods have been developed which allow the generation of multicolor displays on cathode-ray tubes (CRT). When the color is determined by the accelerating potential on the electrons from a single electron gun, these devices often use several phosphor layers either as discrete layers on the face of the CRT (1-3) or as layered "onionskin" particles (4). Among the latter group a practical phosphor mixture has been developed using a sulfide phosphor with green emission and an inert onionskin coating or containing

a phosphor poison (5, 6). This coated phosphor is mixed with a commercial red-emitting phosphor. When the mixture is excited by an electron beam, the red emission is visible at low energies, but as the energy of the electrons is increased, the barrier of the coated phosphor is penetrated and green light is emitted. The gradual increase in green emission with increasing beam voltage creates orange, yellow, and finally green light. This particular system has a broad wavelength emission in the green portion of the visible spectrum as opposed to the line emission typical of rare earth ions.

Three new onionskin phosphors have been developed. They have a barrier layer and they emit intense narrow wavelength green light only at sufficiently high accelerating voltages. These rare earth barrier phosphors

\* Electrochemical Society Active Member.

<sup>1</sup> Present address: Coulter Information Systems, Incorporated, Bedford, Massachusetts 01730.

<sup>2</sup> Present address: Mitre Corporation, Bedford, Massachusetts 01730.

Key words: lanthanum oxysulfide, lanthanum oxysulfate, barrier layer phosphors, europium, terbium.

operate in the same manner as the sulfide phosphor when mixed with commercial red-emitting phosphors. The purpose of this paper is to describe the synthesis and cathodoluminescent characteristics of these rare earth barrier phosphors and their behavior in penetration phosphor mixtures.

### Composition and Mechanism

A method was desired for creating a poisoned surface on rare earth phosphors analogous to the use of cobalt diffusion in zinc sulfide phosphors (6). Possible mechanisms for achieving this effect were examined. Since intense green emission is obtained from terbium ions in a number of host lattices, the immediate problem was to quench the terbium emission in the outer surface of a terbium-activated phosphor. This could be accomplished by concentration quenching (7), energy transfer (8-10), or a change in host lattice in the barrier region (4). All three effects or combinations of them were found to yield barrier layers permitting the adjustment of the threshold voltage to a higher value. Typical values of threshold voltages for rare earth phosphors are approximately 1-2 kV. The dead voltage (defined as the extrapolation to zero intensity of the linear portion of a brightness vs. voltage curve) for a typical barrier phosphor is approximately 8-10 kV.

The composition of the three materials is summarized in Table I. Shown in Table I is the composition of the inner core and that of the onionskin portion with respect to host lattice and activators. Mechanisms by which the terbium emission is quenched in the barrier layer are discussed in the following paragraphs, numbered to correspond with the phosphor types listed in Table I.

I. In this case the entire particle has a host lattice of  $\text{La}_2\text{O}_2\text{S}$  (hexagonal crystal structure) which is activated by terbium ions homogeneously dispersed throughout. The barrier region is coactivated with europium ions which quench the emission of the terbium ions in their neighborhood. The decrease in terbium emission is attributed to two effects. The first effect is concentration quenching. The additional europium ions increase the total concentration of activator ions so that the optimum brightness is no longer obtained. The brightness of a terbium-doped phosphor is sensitive to the activator concentration (7). Moreover, the effect of coactivation of rare earth lattices has been found to reduce the brightness of a phosphor relative to a phosphor containing only one activator (7). The concentration quenching effect can be obtained by the addition of any of several of the rare earth ions including terbium itself. Europium is chosen for coactivation because the emission from europium ions is red and is generally more intense than that of other red-emitting rare earth ions, also there is energy transfer from Tb to Eu. The second effect, energy transfer, has been demonstrated in several hosts for terbium-europium coactivated materials (8-10).

II. In this case the core material is the same as in case I. The coating material is lanthanum oxysulfate (orthorhombic crystal structure) (11). The terbium activator ions are homogeneously dispersed throughout the phosphor particle but since the coating material is a poor host lattice the emission is weak in the barrier region. This quenching effect is caused by the change in the crystal structure.

III. In the third material the core is again the same. The quenching effect on the terbium ions in the coating

is achieved by a combination of the effects described in cases I and II.

In all three materials the core provides intense green emission when excited by high energy electrons, whereas low energy electrons do not penetrate to the core. Any of the above barrier phosphors can be mixed with a red-emitting phosphor. The resulting phosphor mixture emits red at low voltages, then orange, yellow, and green with increasing voltages. In penetration phosphor mixtures using barrier phosphors type I and III it is fortuitous that some additional red emission can be obtained at low voltages from the europium in the barrier coating.

### Synthesis

The problem in the synthesis of the barrier phosphors, types I and III, is to diffuse europium ions to a specified depth with a reasonable degree of precision. (The thickness of the barrier region is discussed in the Appendix.) For barrier phosphors, types II and III, it is necessary to oxidize the lanthanum oxysulfide to lanthanum oxysulfate to a specified depth on each particle. Both of these problems are related by the fact that europium diffusion in lanthanum oxysulfide is negligible, whereas in lanthanum oxysulfate it is appreciable. In order to diffuse europium into the barrier region it is necessary first to form the oxysulfate structure. This is the main reason that lanthanum was chosen as the host lattice ion, its chemistry differs from that of other rare earths in that the oxysulfate is stable (12).

To demonstrate the diffusion of europium in lanthanum oxysulfate a series of materials was produced starting from  $\text{La}_2\text{O}_2\text{S:Tb}$  (a commercial phosphor, JEDEC No. P-44). This commercial phosphor has a dead voltage of approximately 2 kV as shown in Fig. 1. The phosphor was mixed with a chelate of europium and annealed under conditions which excluded excess oxygen at a temperature above  $700^\circ\text{C}$ . The decomposition of the chelate released the oxygen which it contained.

Since the amount of oxygen was limited, the phosphor particles were only partially converted to the oxysulfate and europium diffused only in the outer oxysulfate portion of each particle. In this manner a new material (A) was formed with a dead voltage of 5 kV (refer to curve A in Fig. 1). After several cycles of mixing with an oxygen-containing chelate of euro-

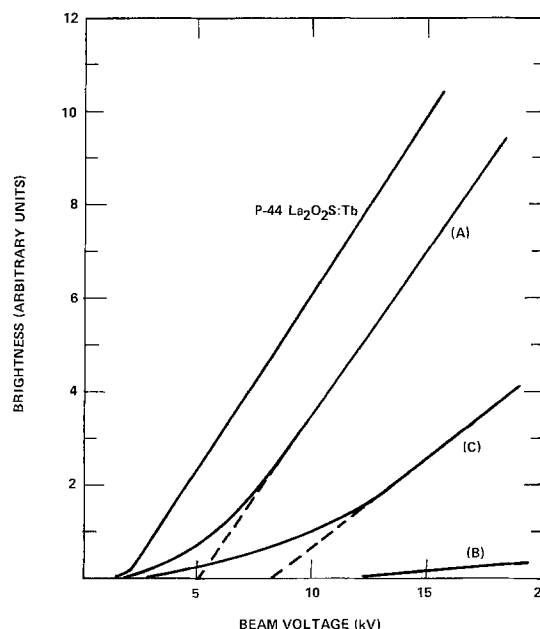


Fig. 1. Brightness vs. beam voltage for commercial P-44  $\text{La}_2\text{O}_2\text{S:Tb}$  and a type I barrier phosphor with a dead voltage of 5 kV (A), a lanthanum oxysulfate phosphor (B), and a type I barrier phosphor with a dead voltage of 8 kV (C).

Table I. Barrier layer phosphors

Type	Core		Onionskin	
	Host lattice	Activator	Host lattice	Activator
I	$\text{La}_2\text{O}_2\text{S}$	Tb	$\text{La}_2\text{O}_2\text{S}$	Tb, Eu
II	$\text{La}_2\text{O}_2\text{S}$	Tb	$\text{La}_2\text{O}_2\text{SO}_4$	Tb
III	$\text{La}_2\text{O}_2\text{S}$	Tb	$\text{La}_2\text{O}_2\text{SO}_4$	Tb, Eu

europium and annealing no increase in dead voltage is obtained. This process will not produce a barrier phosphor with a dead voltage above 5 kV because the oxygen released by the chelate cannot penetrate any further during the short time it is available. The anneal which decomposed the chelate was performed under an atmosphere of argon containing hydrogen sulfide and water vapor (13). Under these conditions the crystal structure was converted to the original oxysulfide form after the chelate was destroyed. Material A is a type I barrier phosphor having a core of  $\text{La}_2\text{O}_2\text{S:Tb}$  with an outer surface of  $\text{La}_2\text{O}_2\text{S:Tb,Eu}$ .

A sample of the europium-coated  $\text{La}_2\text{O}_2\text{S:Tb}$  (material A) was next oxygen annealed to produce phosphor particles which were mainly lanthanum oxysulfate (material B). As expected this material is a poor host because of the change in crystal structure and emission is very weak as is shown by curve B in Fig. 1. Finally, a sample of material B was reconverted to the oxysulfide form (material C). The brightness increased compared to the oxysulfate form (B) and the extrapolated threshold voltage increased (refer to curve C in Fig. 1). The increase in dead voltage indicates that europium diffusion took place in the lanthanum oxysulfate phase during the oxygen anneal.

By controlling the amount of oxygen available or the temperature and time of the oxygen anneal the formation of lanthanum oxysulfate can be limited. When a thin (submicron) onionskin layer of lanthanum oxysulfate is formed on lanthanum oxysulfide, it provides a barrier phosphor of type II. If europium is diffused into the oxysulfate a barrier phosphor of type III is obtained. When a type III phosphor is annealed under an atmosphere containing hydrogen sulfide and water vapor a type I barrier phosphor is obtained.

An important consideration in the synthesis of barrier phosphors is the maintenance of temperature equilibrium over the entire sample during the oxygen anneal. If temperature equilibrium is not maintained, the rate of formation of lanthanum oxysulfate will vary and result in uneven coating thickness. This in turn will increase the nonlinearity of the brightness vs. voltage curve for the sample. Also, the slope of the brightness vs. voltage curve will be reduced, that is, it will not be parallel to the curve for an untreated phosphor. In order to obtain a wide spread in color coordinates with changing voltage in the final mixture the slope of the brightness vs. voltage curve for the barrier phosphor must be steep. In other words, the brightness vs. voltage curve should be parallel to the curve for a phosphor without a barrier layer but should have a higher threshold.

The oxygen anneal is most easily carried out in a rotating quartz chamber. This is especially necessary when the bulk of a large sample becomes so great that it is not uniformly in contact with oxygen. Indentations in the chamber insure that the powder is tumbled during the anneal. The dimensions of the chamber should be kept within the constant temperature zone of the oven. Samples were prepared using a quartz reaction chamber attached to a thick-walled quartz tube which extended beyond the horizontal furnace. A controlled atmosphere was obtained by passing gases through the tube. A ball and socket joint allowed the rotation of the reaction chamber in the oven during the anneal (Fig. 2).

In the following syntheses europium-tris-2, 2, 6, 6-tetramethylheptanedionate is used to coat the surface of the phosphor with europium. Many other europium-containing compounds will produce adequate results. However, with some materials there are side reactions as with europium trichloride which yields lanthanum oxychloride. Therefore, satisfactory results are most easily obtained with organic chelates containing only carbon, hydrogen, and oxygen in addition to the rare earth ion. Another suitable chelate can be made with pentanedione (acetyl acetone) and europium (14).

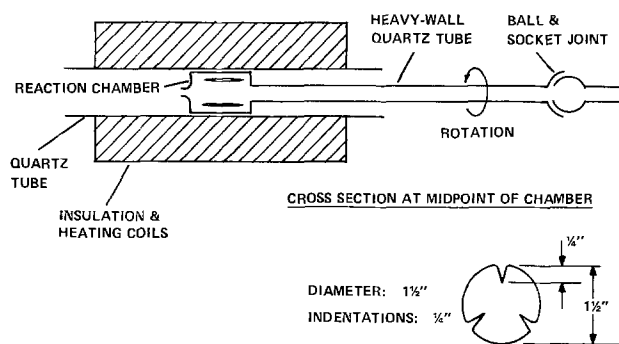


Fig. 2. Rotating quartz reaction chamber

**Synthesis of  $\text{La}_2\text{O}_2\text{S:Tb-La}_2\text{O}_2\text{S:Tb,Eu}$  (type I).**—In a polyethylene bottle 20.0g  $\text{La}_2\text{O}_2\text{S:Tb}$  (General Electric phosphor No. 118-2-35) ( $5.85 \times 10^{-2}$  mole) was added to 405 mg Eu(III)-tris-2, 2, 6, 6-tetramethylheptanedionate ( $5.7 \times 10^{-4}$  mole). The chelate was presieved through a  $53\mu$  mesh. After tumbling the mixture it was fired in a quartz reaction chamber in a horizontal tube furnace. The chamber contents were kept under argon until a temperature of  $750^\circ\text{C}$  was reached. At this point oxygen replaced the argon flow and the chamber was rotated for 20 min. The material was air quenched and a sample was removed for analysis. The remaining material was replaced in the furnace under a flow of argon bubbled through water at  $25^\circ\text{C}$  and approximately 30% hydrogen sulfide. After 6 hr at a maximum temperature of  $1000^\circ\text{C}$  the product was cooled under argon.

X-ray analyses showed the sample that was removed after the oxygen anneal to be approximately 15 mole percent (m/o) lanthanum oxysulfate and the final product was 100% lanthanum oxysulfide. When brightness under cathode-ray excitation was plotted as a function of beam voltage the extrapolated dead voltage was 8.5 kV. The reflected color was white.

**Synthesis of  $\text{La}_2\text{O}_2\text{S:Tb-La}_2\text{O}_2\text{SO}_4\text{:Tb}$  (type II).**—A 10g sample of  $\text{La}_2\text{O}_2\text{S:Tb}$  (General Electric No. 118-2-35) was oxygen annealed in a rotating quartz chamber for 25 min at  $750^\circ\text{C}$ . The material was kept under argon flow until the anneal temperature was reached and at the end of the anneal it was air quenched. X-ray analysis indicated approximately 9 m/o lanthanum oxysulfate. The reflected color was white and the dead voltage was 6.2 kV.

**Synthesis of  $\text{La}_2\text{O}_2\text{S:Tb-La}_2\text{O}_2\text{SO}_4\text{:Tb,Eu}$  (type III).**—In a polyethylene bottle 10.0g  $\text{La}_2\text{O}_2\text{S:Tb}$  (General Electric No. 118-2-35) ( $2.9 \times 10^{-2}$  mole) was combined with 400 mg Eu-tetramethylheptanedionate ( $5.7 \times 10^{-4}$  mole). After mixing, the material was oxygen annealed for 30 min at  $725^\circ\text{C}$  and air quenched. X-ray analysis indicated 12 m/o lanthanum oxysulfate.

Several more samples of barrier layer phosphors prepared by one of the procedures described above are described in Table II. The anneal time under oxygen atmosphere and anneal temperature are listed. The samples were kept under argon until the anneal temperature was reached and while cooling to room temperature. Different furnaces and controllers were used, so the accuracy of the temperature reading varies. The mole percent lanthanum oxysulfate was determined from x-ray diffraction intensities. The relationship between the amount of oxysulfate formed and the dead voltage is discussed in the Appendix.

### Measurements

**Apparatus.**—In order to measure the cathodoluminescent properties of phosphor samples, a demountable CRT was assembled. The unit was constructed by adapting a standard oil diffusion vacuum coating apparatus. The pumping system provided pressures on the order of  $10^{-7}$  Torr.

Table II. Oxygen anneal conditions for barrier layer formation

Anneal time in oxygen (min)	Anneal temperature (°C)	M/O La <sub>2</sub> O <sub>3</sub> :SO <sub>4</sub> *	Dead voltage (kV)
30	~750	22	10.5
60	~780	20	9
30	~770	20	9
30	~750	20	8.5
25	740-60	19	7.5
30	747 ± 5	17.5	9.5
80	~778	17	8
30	750-65	15	9
180	705 ± 5	14	—
60	~725	13	8.5
42	~750	13	7
30	725-45	13	6.2
30	725 ± 5	12	—
30	725-35	11	7.5
40	725 ± 5	10	—
25	~750	9	6.2
30	~750	8	5.5
30	~725	7	3.5

\* Refer to Appendix.

The demountable CRT was assembled using a Pyrex Tee with a 6-in. diameter which served as the test volume. The bottom portion of the Tee was connected to the vacuum pump. The 18 in. horizontal portion of the Tee contained a standard black and white electron gun and yoke on one end and the phosphor target holder on the opposite end. For ease of replacement, the electron gun was inserted into a quick-disconnect mounted on a stainless steel flange. A sample holder was fabricated so that 16 samples could be tested at one time. The phosphors were gravity settled using standard techniques on Nesatron glass and remained unaluminized for the results reported in this paper.

For simplicity of measurement, a pulsed electron beam was used rather than a raster scan. The measurements were made in the unsaturated mode of the cathodoluminescent behavior of the phosphors. The cathodoluminescent spectra and brightness were measured via transmission through the sample. The brightness from the electron beam spot on the phosphor target was measured with a Spectra® Brightness Spot Meter (Model UB½, Photo Research Corporation). Brightness was measured at constant beam current. The spot diameter was focused to 0.20 in. on a removable overlay grid with 0.050 in. divisions for each level of accelerating voltage. The emission spectrum was obtained using a Jarrel-Ash ½ meter Ebert scanning monochromator. The color coordinates were determined from the corrected spectra and the 1931 C.I.E. standard tables. It should be pointed out that the brightness measurements were always compared to a commercial P-44 phosphor sample whose thickness was optimized so as to obtain maximum brightness. All other samples were deposited with the same thickness as the P-44 La<sub>2</sub>O<sub>2</sub>S:Tb phosphor.

**Results.**—Samples of penetration phosphor were prepared by mixing green phosphor which had a barrier layer with a commercial red-emitting phosphor. In the two examples given below the commercial phosphor was YVO<sub>4</sub>:Eu, approximately 15 weight percent of the total mixture. Barrier phosphors of types II and III were used. Table III gives the color coordinates of these mixtures at various beam voltages. The efficiency in lumens per watt is listed.

### Summary

Controlled oxidation of lanthanum oxysulfide yields particles coated with lanthanum oxysulfate. While europium diffuses readily in La<sub>2</sub>O<sub>2</sub>SO<sub>4</sub> at several hundred degrees centigrade, it does not diffuse in La<sub>2</sub>O<sub>2</sub>S to any appreciable extent under the same conditions.

A barrier layer containing Eu<sup>+3</sup> ions will quench the emission from La<sub>2</sub>O<sub>2</sub>S:Tb phosphor particles. An onion-

Table III. Color co-ordinates of penetration phosphors

Beam voltage (kV)	X	Y	Lumens/Watt
Sample 1			
Type II La <sub>2</sub> O <sub>2</sub> S: Tb—La <sub>2</sub> O <sub>2</sub> SO <sub>4</sub> : Tb with YVO <sub>4</sub> : Eu			
5	0.587	0.395	2.0
7	0.574	0.405	2.1
10	0.538	0.435	3.4
14	0.489	0.479	5.4
18	0.461	0.501	7.6
Sample 2			
Type III La <sub>2</sub> O <sub>2</sub> S: Tb—La <sub>2</sub> O <sub>2</sub> SO <sub>4</sub> : Tb, Eu with YVO <sub>4</sub> : Eu			
5	0.568	0.413	4.3
12.5	0.514	0.460	7.0
18	0.470	0.494	9.6

skin barrier layer of lanthanum oxysulfate will also produce this effect.

Green-emitting phosphors with high dead voltages (8-10 kV) can be obtained using either or both of the quenching effects described above.

Barrier phosphors made from La<sub>2</sub>O<sub>2</sub>S:Tb can be mixed with commercial red phosphors such as YVO<sub>4</sub>:Eu. to produce penetration phosphors with line emission whose color is a function of voltage.

### Acknowledgment

The authors wish to acknowledge the able assistance of Dario Dorigo in several phases of sample preparation and measurement.

Manuscript submitted March 19, 1976; revised manuscript received May 27, 1976.

Any discussion of this paper will appear in a Discussion Section to be published in the June 1977 JOURNAL. All discussions for the June 1977 Discussion Section should be submitted by Feb. 1, 1977.

Publication costs of this article were assisted by Sperry Research Center.

### APPENDIX

#### Analysis of Barrier Thickness

The barrier layer on the lanthanum phosphors is not a "coating" in the sense that additional material is added to each particle. However, since the density of lanthanum oxysulfate (5.52 g/cm<sup>3</sup>) is less than that for lanthanum oxysulfide (5.73 g/cm<sup>3</sup>) there is probably a slight but insignificant increase in particle diameter in materials of types II and III (see Table I). The typical median particle diameter for P-44 La<sub>2</sub>O<sub>2</sub>S:Tb is 10.0μ as determined by Coulter Counter.<sup>3</sup> Scanning electron micrographs indicate the particles to be irregular polyhedra, only roughly spherical. No significant detectable change in particle size or shape after formation of a barrier layer was seen in scanning electron micrographs.

In order to obtain an estimate of the thickness of the barrier layer in the materials described above the following modified model of dead voltage as a function of barrier thickness was used.

A general equation describing electron penetration of solids is

$$d = CV^n \quad [1]$$

where  $d$  is the depth of penetration,  $V$  is the energy of the electrons and  $C$  and  $n$  are constants characteristic of the material. Kingsley and Prener (5, 6) have determined experimentally values for  $C$  and  $n$  in Eq. [1] for zinc sulfide phosphors where  $C = 7.3 \times 10^{-7}$  and  $n = 1.77$  when  $V$  is in kilovolts and  $d$  is in centimeters. The coefficient,  $C$  was modified by correcting for differences in atomic number, molecular weight, and density between zinc sulfide and lanthanum oxysulfide to obtain

$$d = 5.7 \times 10^{-7} V^{1.77} \quad [2]$$

where  $d$  is in centimeters and  $V$  is the accelerating potential on the electrons in kilovolts. The correction fac-

<sup>3</sup> General Electric Product Data Sheet for P-44 La<sub>2</sub>O<sub>2</sub>S:Tb (No. 118-2-35).

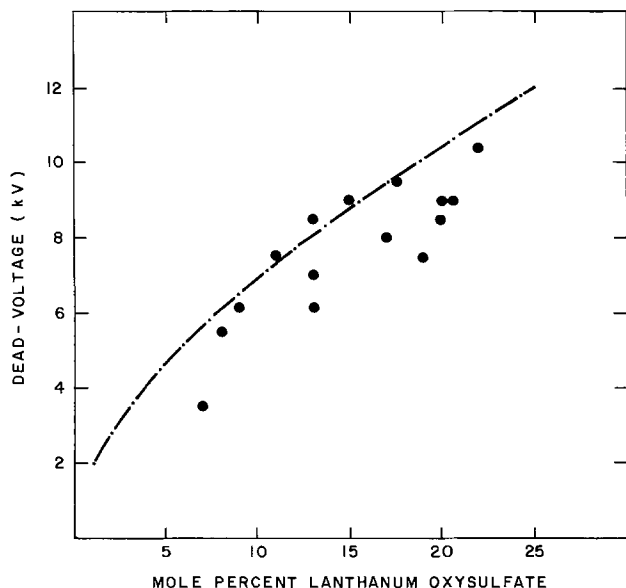


Fig. 3. Dead voltage vs. mole per cent lanthanum oxysulfate. The solid line is the expected relationship for  $10\mu$  diameter particles using Eq. [2].

tor for the coefficient, 0.776, was obtained by multiplying the ratio of molecular weights by the inverse of the ratios of the densities and number of electrons for  $\text{La}_2\text{O}_3\text{S}/\text{ZnS}$ . The depth of penetration is proportional to molecular weight and inversely proportional to density and number of electrons (5, 15). The thickness of a barrier layer is represented by  $d$  when  $V$  is the dead voltage in kilovolts.

For a desired dead voltage the modified equation predicts a barrier thickness. The predicted value for barrier thickness can be used to calculate the amount of lanthanum oxysulfate it will be necessary to form in a  $10\mu$  diameter particle. The volume occupied by the onionskin is calculated assuming spherical particles. The percent active phosphor material remaining in the core determines the maximum possible brightness which can be obtained from the resulting barrier phosphor. Using the modified Eq. [2] and assuming that the median particle diameter of the phosphor is  $10\mu$  it is calculated that 13-19% of each oxysulfide particle must be converted to oxysulfate in order to obtain a barrier phosphor with a dead voltage of 8-10 kV.

To check these predictions two methods were used for measuring the amount of material in the barrier region. The first method depended on the atomic absorption analysis of the europium and terbium content of dissolved samples of barrier phosphor. When the europium/terbium ratio of a completely dissolved sample was compared to that for a partially dissolved sam-

ple it indicated that the europium was contained in a surface layer less than  $1\mu$  thick. Because this analysis is destructive and sample preparation is difficult, this method was abandoned in favor of the second.

The second method was based on quantitative x-ray diffraction. Standards of known ratios of lanthanum oxysulfide and lanthanum oxysulfate were prepared. By comparison with the standards the amount of oxysulfate coating in the samples of barrier phosphor was estimated. The results are summarized in Table II. The mole percent lanthanum oxysulfate as determined by comparison of x-ray diffraction patterns has an estimated error of  $\pm 2$  m/o. The dead voltage is determined from a brightness vs. voltage curve for each sample. A graph of dead voltage vs. mole percent oxysulfate for several samples annealed under oxygen indicates that the expected trend is followed (Fig. 3). The data points are scattered around the prediction (solid line in Fig. 3) based on the modified equation and  $10\mu$  diameter particles. The empirical relationship derived for zinc sulfide was sufficiently accurate when modified to be useful in preparing barrier layers of desired thickness on lanthanum oxysulfide phosphors.

#### REFERENCES

1. A. F. Martin and J. P. Galves, "New Trends in Professional Colour Multilayer CRT's," Thomson-CSF, St Egreve, France.
2. R. V. Alves, R. A. Buchanan, and T. G. Maple, *Appl. Phys. Lett.*, **21**, 530 (1972).
3. J. P. Dismukes, J. Kane, B. Binggeli, and H. P. Schweizer, in "Chemical Vapor Deposition, Fourth International Conference," G. F. Wakefield and J. M. Blocher, Jr., Editors, pp. 275-286, The Electrochemical Society Softbound Symposium Series, Princeton, N.J. (1973).
4. M. Tecotzky and J. J. Mattis, Paper 159 presented at the Electrochemical Society Meeting, Cleveland, Ohio, Oct. 3-7, 1971.
5. J. D. Kingsley and J. S. Prener, *J. Appl. Phys.*, **43**, 3073 (1972).
6. J. S. Prener and J. D. Kingsley, *This Journal*, **119**, 1254 (1972).
7. R. C. Ropp, "Optimum Activator Concentrations in Rare Earth Oxide Phosphors," Fifth Rare Earth Research Conference, Book One, pp. 53-63, August 30-September 1, 1965.
8. W. W. Holloway, M. Kestigian, and R. Newman, *Phys. Rev. Lett.*, **11**, 458 (1963).
9. L. G. Van Uitert, E. F. Dearborn, and H. M. Marcos, *Appl. Phys. Lett.*, **9**, 255 (1966).
10. L. G. Van Uitert and R. R. Soden, *J. Chem. Phys.*, **36**, 1289 (1962).
11. R. Ballestracci and J. Mareschal, *Mat. Res. Bull.*, **2**, 993 (1967).
12. J. W. Haynes and J. J. Brown, *This Journal*, **115**, 1060 (1968).
13. D. W. Ormand and E. Banks, *ibid.*, **122**, 152 (1975).
14. K. J. Eisentraut and R. E. Sievers, *J. Am. Chem. Soc.*, **87**, 5254 (1965).
15. C. Feldman, *Phys. Rev.*, **117**, 455 (1960).

# Control of Sulfur Doping for Gallium Arsenide Epitaxial Layers

M. A. Savva

British Post Office, Research Department, London NW2 7DT

## ABSTRACT

In growing gallium arsenide epitaxial layers for device manufacture it is necessary to control the dopant (usually n-type) concentration in the gas stream. A novel method is presented for introducing known and controlled concentrations of sulfur compounds based on "the modified entrainment method." The dopant is confined to a small bottle with a capillary, which acts as a resistance, and the rate at which the dopant is transported out of the bottle depends on the vapor pressure, the capillary dimensions, and the diffusion coefficient. Using this method, the rates of weight loss of sulfur, thionyl chloride, and sulfur dichloride were measured in nitrogen over a range of temperatures. From these measurements the diffusion coefficient of the compounds is calculated and it is concluded that the method can be used to give controlled dopant concentrations in the gas stream of an epitaxial reactor. Using these data the dopant concentrations in a typical reactor are calculated as a function of temperature for different size capillaries. The distribution coefficient of sulfur between the epitaxial layer and the gas phase is found to be about 60 for carrier concentrations in the region of high  $10^{16}$  carriers  $\text{cm}^{-3}$ .

The growth of gallium arsenide epitaxial layers by the Ga/AsCl<sub>3</sub>/H<sub>2</sub> process (1), for the manufacture of devices such as IMPATT diodes, requires the material to be doped n-type at various controlled levels. Generally, the epitaxial layers are sulfur doped and the mole fractions of hydrogen sulfide required in the gas stream are less than  $10^{-6}$ . In order to grow doped epitaxial layers reproducibly, and indeed to understand the mechanisms of dopant incorporation, it is necessary to control and know the concentration of dopant injected into the gas stream.

Bachem and Bruch (2) have pointed out some of the obvious weaknesses of introducing the dopant, either directly as hydrogen sulfide from a gas cylinder, or indirectly by heating sulfur vapor, from a solid source, in the hydrogen gas stream and converting it to hydrogen sulfide. They have attempted to obtain better control over the direct method by restricting the flow from the reducing valve of the gas cylinder, using a small capillary. Also, they have doped the transporting agent, arsenic trichloride, with sulfur monochloride and deduced the concentration of dopant in the gas stream by assuming that the solution is ideal. Both of their methods seem to be consistent each yielding epitaxial layers at the same carrier concentration for a given concentration in the gas stream. However, the ratio of the carrier concentration to the dopant concentration in the gas stream is much lower than that reported by other workers (3-5) and is lower than we observed in our work. In this paper we present a novel method for introducing known and controlled concentrations of sulfur compounds into the gas stream of an epitaxial reactor. The method is easy to set up and operate and can cope with a wide range of dopant concentrations.

This method is adapted from the modified entrainment method, which has been developed from the early work of Stefan [see Ref. (6)], and used for measuring vapor pressures (7), diffusion coefficients (8), and heterogeneous equilibrium constants (9, 10). The theory is described in detail elsewhere (7) and here we only outline the principles of the modified entrainment method in its application to dopant control. The dopant is placed in a small bottle and is allowed to diffuse along a capillary of known dimen-

sions and at the end of the capillary it is swept away by the gas stream. The capillary acts as a resistance, thus permitting the dopant to reach its equilibrium vapor pressure inside the bottle. Hence, at a given temperature, the rate of transport of the dopant out of the bottle is well defined, and its concentration in the gas stream can be calculated, if the flow rate over the bottle is known.

So as to validate the method for its application for introducing a sulfur compound into an epitaxial reactor, we have measured the rates of loss of liquid sulfur, thionyl chloride, and sulfur dichloride from such a bottle over a range of temperatures. From these measurements we can be sure that the equilibrium vapor pressures are attained in the bottle, and by using available data for vapor pressures we can determine the diffusion coefficients for the above species. From these data we can then calculate the concentration of the dopant that is injected into the gas stream of an epitaxial reactor.

## Theory

For a single species, A, evaporating into a stream of an inert gas the vapor pressure ( $p^{\circ}_A$ ) of that species is given by

$$p^{\circ}_A = p[1 - e^{-\xi}] \quad [1]$$

where  $p$  is the total pressure and  $\xi$ , the transport function, is

$$\xi = \frac{\dot{W}RTl}{DpM_A\pi r^2} \quad [2]$$

where  $\dot{W}$  is the rate of weight loss of species A through a capillary of length  $l$  and radius  $r$ , at a temperature  $T$ .  $M_A$  is the molecular weight of A and  $D$  is the diffusion coefficient of A in the inert gas. The temperature dependence of the diffusion coefficient can be expressed as

$$D = \frac{D_0 p_0}{p} \left( \frac{T}{T_0} \right)^{1+s} \quad [3]$$

where  $D_0$  is the diffusion coefficient at a reference temperature  $T_0$  and a reference pressure  $p_0$ , and  $s$  has a value between 0.5 and 1, which is usually close to 0.8 (11). The reference pressure is taken as 1 atm

Key words: gallium arsenide, vapor phase epitaxy, sulfur doping, diffusion coefficient.

which is also the pressure at which the measurements are made.

From Eq. [1]-[3], the vapor pressure of a species can be calculated by estimating a value for  $D_0$  and  $s$ . Therefore, by measuring the rate of weight loss as a function of temperature, the enthalpy ( $\Delta H_v$ ) and the entropy ( $\Delta S_v$ ) of evaporation can be calculated since

$$R \ln p^{\circ}_A = -\Delta H_v/T + \Delta S_v \quad [4]$$

If the boiling point is known then a value of  $D_0$  can be chosen so that, for the calculated values of  $\Delta H_v$  and  $\Delta S_v$ , the vapor pressure is unity at the boiling point. When the vapor pressure of a species is known, then, from Eq. [1] and [2], the diffusion coefficient can be calculated. The values for  $D_0$  and  $s$  can be obtained using Eq. [3] by plotting  $\log D$  vs.  $\log T$ .

In some instances, the vapor may contain polymeric species, for example sulfur exists mainly as  $S_8$ ,  $S_6$ ,  $S_4$ , and  $S_2$  up to the boiling point with  $S_8$  predominating. In such cases the total rate of weight loss can be related to the individual partial pressures from a series of Eq. [1] and [2]

$$\dot{W} = \frac{p_{A_n} \pi r^2}{RTl} \sum n D_{A_n} \ln \left( 1 - \frac{p^{\circ}_{A_n}}{p} \right) \quad [5]$$

where  $p^{\circ}_{A_n}$  is the partial pressure of species  $A_n$  with a diffusion coefficient of  $D_{A_n}$  in the inert gas.  $M_A$  is the molecular weight of the monomer. The diffusion coefficients of each species can be related to the diffusion coefficient of the dominant species by Graham's law

$$\frac{D_{A_n}}{D_{A_m}} = \sqrt{\frac{M_{A_m}}{M_{A_n}}} = \sqrt{\frac{m}{n}} \quad [6]$$

Thus, from measurements of rate of weight loss at different temperatures, values for  $D_0$  and  $s$  can be calculated for the dominant species, as described earlier, if the partial pressure of each species is known as a function of temperature.

### Experimental

The apparatus is illustrated in Fig. 1 and is similar to that described by Battat *et al.* (7). The effusion bottle was suspended on a silica fiber from a CI Electronics 2CT5 microforce balance. The bottle was hung either inside a tube which was heated with a small furnace up to 400°C to give a flat temperature profile, or else inside a glass condenser which was temperature controlled in the range -5° to 55°C. The temperature was measured either with a Chromel-Alumel thermocouple or with a mercury-in-glass thermometer just beneath the bottle. The gas inlet through the balance was controlled using a mass flow controller.

### Results

**Evaporation of sulfur in nitrogen.**—The sample of crystalline sulfur was 99.999% pure (Koch-Light Limited, England). The experimental rates of weight loss in nitrogen and at various temperatures, using a capillary 1.991 cm in length and 0.201 cm in diameter, are given in Fig. 2. From these results the diffusion coefficient of  $S_8$  in nitrogen was calculated using Eq. [5] and [6], so as to take into account all species of sulfur, and the vapor pressure data of Braune *et al.* (12), which are recommended by Nesmeyanov (13). The calculated values of the diffusion coefficient are plotted out as a function of temperature in Fig. 3 from which we obtain a value of  $0.068 \text{ cm}^2 \text{ sec}^{-1}$  for the diffusion coefficient at 20°C and a temperature dependence of  $T^{1.86}$  (i.e.,  $s = 0.86$ ).

**Evaporation of thionyl chloride in nitrogen.**—The experimental rates of weight loss for thionyl chloride (Hopkin and Williams Limited, England) in nitrogen and at various temperatures, using a capillary 2.000

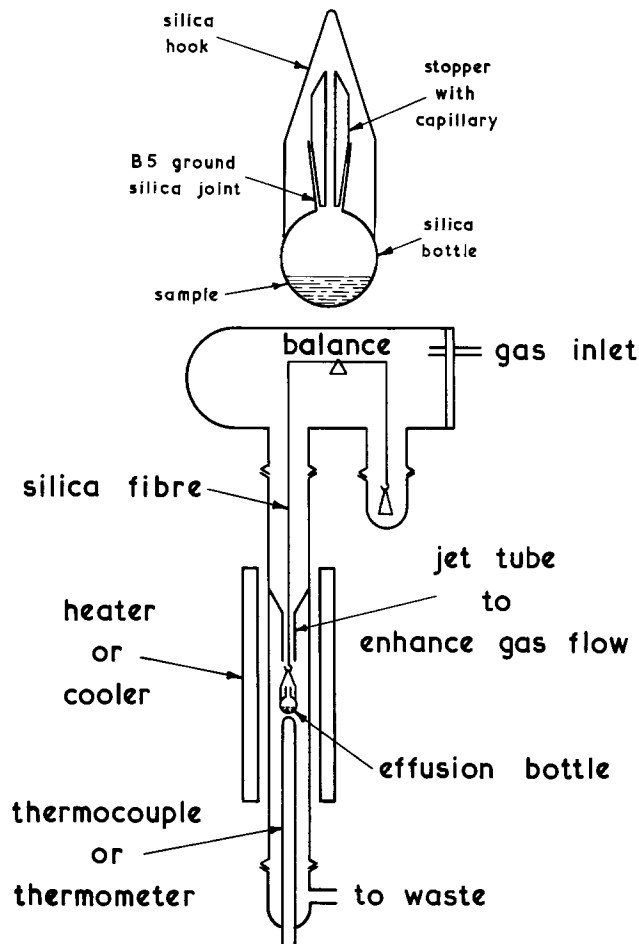


Fig. 1. Effusion bottle (top) and experimental system (bottom)

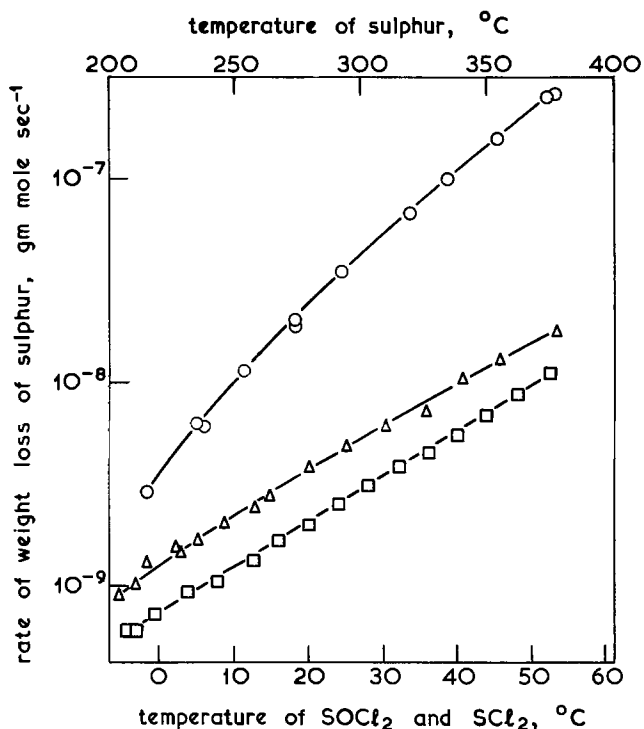


Fig. 2. Rate of weight loss as a function of temperature: ○ = sulfur, □ = thionyl chloride, △ = sulfur dichloride.

cm in length and 0.097 cm in diameter, are given in Fig. 2. From these results the diffusion coefficient of thionyl chloride in nitrogen was calculated using Eq. [1] and [2], and the vapor pressure data given



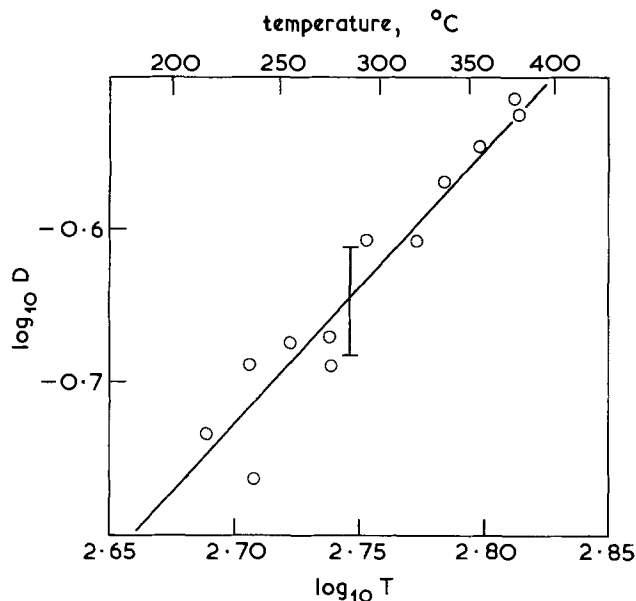


Fig. 3. Diffusion coefficient for  $S_8-N_2$  as a function of temperature: bar  $\equiv$  5% deviation;  $D = 0.0688 \left( \frac{T}{293.2} \right)^{1.86} \text{ cm}^2 \text{ sec}^{-1}$ .

in the literature (14). The calculated values of the diffusion coefficient are plotted out as a function of temperature in Fig. 4 from which we obtain a value of  $0.101 \text{ cm}^2 \text{ sec}^{-1}$  for the diffusion coefficient at  $20^\circ\text{C}$  and a temperature dependence of  $T^{1.86}$  (i.e.,  $s = 0.86$ ).

*Evaporation of sulfur dichloride in nitrogen.*—The experimental rates of weight loss of sulfur dichloride (Hopkin and Williams Limited, England) in nitrogen and at various temperatures, using a capillary 2.189 cm in length and 0.103 cm in diameter, are given in Fig. 2. As we do not consider the literature values for the vapor pressure of sulfur dichloride (14) to be reliable (see below), we have chosen  $D_0$  at  $20^\circ\text{C}$  to be  $0.082 \text{ cm}^2 \text{ sec}^{-1}$  with  $s = 0.8$  and using Eq. [1]–[3] we have calculated the vapor pressure of sulfur dichloride. From the plot of the vapor pressure vs. temperature in Fig. 5 we calculate second law values for  $\Delta H_v$  and  $\Delta S_v$  as  $28.0 \text{ kJ mole}^{-1}$  and  $84.1 \text{ J mole}^{-1}$

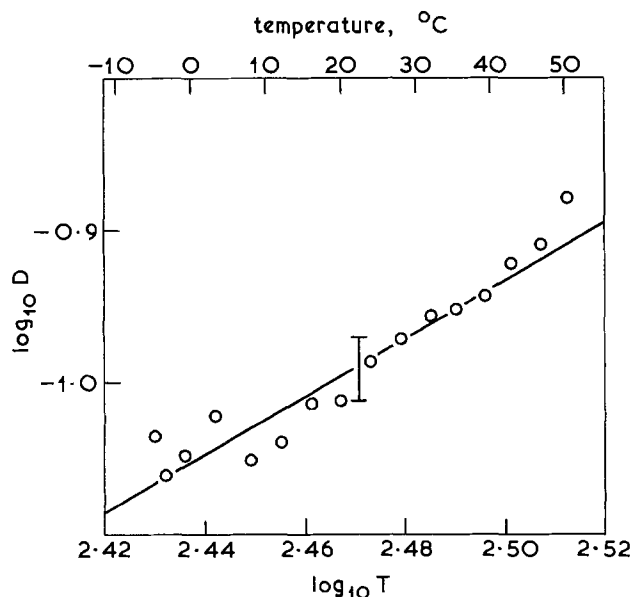


Fig. 4. Diffusion coefficient for  $SOCl_2-N_2$  as a function of temperature: bar  $\equiv$  5% deviation;  $D = 0.101 \left( \frac{T}{293.2} \right)^{1.86} \text{ cm}^2 \text{ sec}^{-1}$ .

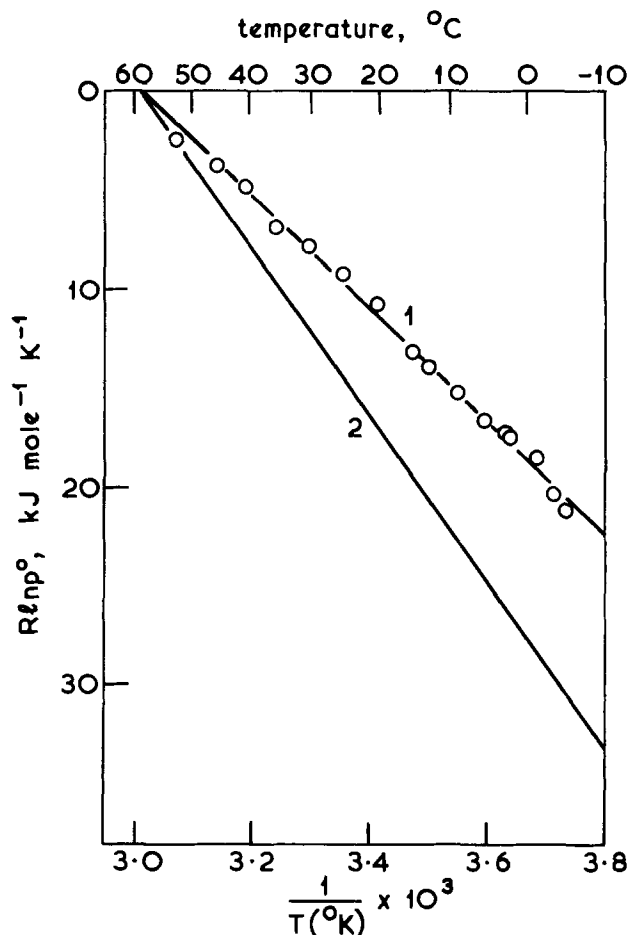


Fig. 5. Vapor pressure of  $SCl_2$  as a function of temperature: 1 = this work  $R \ln p^\circ = - \frac{28.0 \times 10^3}{T} + 84.1 \text{ kJ mole}^{-1} \text{ K}^{-1}$ ; 2 = from Ref. (14).

$\text{K}^{-1}$ , respectively, at our mean temperature of  $25^\circ\text{C}$ . The value of  $D_0$  was chosen so that the plot in Fig. 5 went through the boiling point of sulfur dichloride ( $59^\circ\text{C}$ ) at a vapor pressure of 1 atm.

### Discussion

The diffusion coefficients at  $20^\circ\text{C}$  that we have calculated from our experimental results are compared with the listed values of other species in nitrogen (11, 15) in a plot of  $1/D$  against  $\sqrt{M}$  as shown in Fig. 6. From the plot it is apparent that the relationship is linear for the rare gases, and all other species have a relatively lower diffusion coefficient. Our calculated diffusion coefficients and values for the temperature dependence are consistent with the general trend.

In analyzing the results of sulfur dichloride, we considered the literature values for the vapor pressure dependence on temperature to be unreliable since  $\Delta S_v$  has a reported value of about  $125 \text{ J mole}^{-1} \text{ K}^{-1}$ , whereas from Trouton's rule it should be nearer  $92 \text{ J mole}^{-1} \text{ K}^{-1}$  (we calculated  $84.1 \text{ J mole}^{-1} \text{ K}^{-1}$ ). Consequently, the literature value of  $\Delta H_v$  is over  $12 \text{ kJ mole}^{-1}$  higher than our value of  $28 \text{ kJ mole}^{-1}$ . The issue is complicated further as it is commonly reported (16) that sulfur dichloride is nearly completely dissociated into sulfur monochloride and chlorine at the boiling point. However, Stevenson (17) has looked at the dissociation of sulfur dichloride and sulfur monochloride into sulfur and chlorine at high temperatures, and it is apparent from his data that only about 10% of the dichloride will dissociate into the monochloride and chlorine at  $500^\circ\text{C}$ . Therefore, in our analysis we have assumed no dissociation

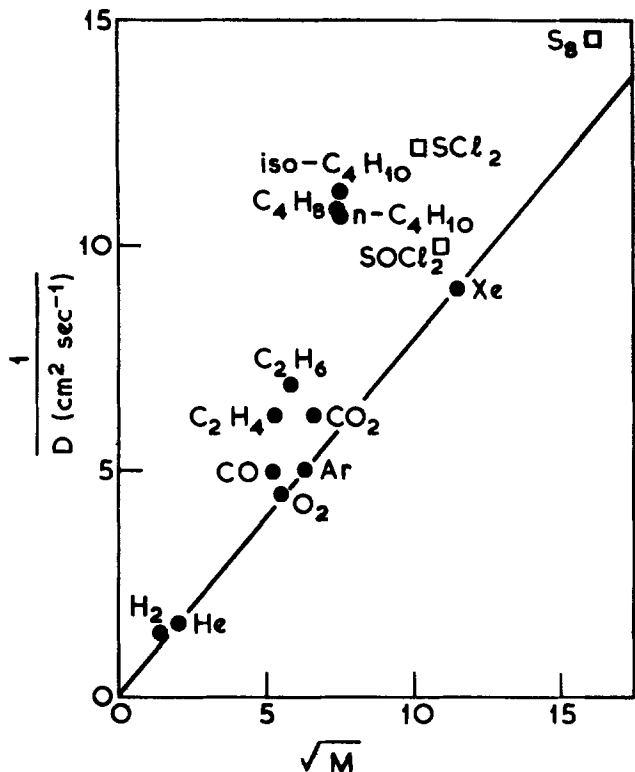


Fig. 6. Diffusion coefficients of various gases in nitrogen at 20°C as a function of molecular weight: ● = values from Ref. (11) and (15), □ = values derived in this work.

and we calculated values for the entropy of evaporation and for the diffusion coefficient in nitrogen.

The modified entrainment method is designed so that equilibrium is attained in the effusion bottle. If equilibrium is not attained, then the rates of weight loss would be low and have a higher dependence on temperature than expected. Consequently, in the case of sulfur and thionyl chloride, the calculated temperature dependence of the diffusion coefficient would be extraordinarily high. In the case of sulfur dichloride,  $\Delta S_v$  would be high. Our results do not bear this out in the temperature range of our measurements and we are confident that the equilibrium vapor pressures are approached closely in the effusion bottle. Therefore, the modified entrainment method can be used for introducing known and controlled concentrations of dopant into a gas stream.

Rates of weight loss for sulfur below 200°C were made over several hours and during that time the ambient temperature changed, giving fluctuations in the balance output that were comparable with the rates of weight loss ( $\sim 5 \times 10^{-8}$  g sec<sup>-1</sup>). Therefore, the low temperature results were disregarded. In order to make reliable measurements down to the melting point, and indeed for crystalline sulfur, we would need to compensate in some way for changes in ambient temperature. It is desirable to go down to lower temperatures so that we can determine the point at which the vapor pressure in the bottle is dictated by surface kinetic limitations rather than equilibrium conditions. Similarly, it would be useful to investigate the sulfur chlorides at lower temperatures but the balance used cannot measure low rates of evaporation. Furthermore, by using high temperatures there is no need to use solid sulfur. This avoids any irreproducibility of vapor pressures due to the slow transformation from monoclinic to rhombic sulfur, as reported by Kniepkamp *et al.* (18).

#### Doping in an Epitaxial Reactor

The work described above demonstrates that over the specified temperature ranges it is possible to ob-

Table I. Ratio of diffusion coefficients in H<sub>2</sub> and N<sub>2</sub>

Gas	Diffusion coefficient in hydrogen (cm <sup>2</sup> sec <sup>-1</sup> ) at 20°C (15)	Diffusion coefficient in nitrogen (cm <sup>2</sup> sec <sup>-1</sup> ) at 20°C (15)	Ratio
Ar	0.77	0.20	3.85
O <sub>2</sub>	0.697	0.181	3.85
CO	0.651	0.192	3.39
CO <sub>2</sub>	0.550	0.144	3.82
C <sub>2</sub> H <sub>4</sub>	0.602	0.163	3.69
C <sub>2</sub> H <sub>6</sub>	0.537	0.148	3.63
cis-butene-2	0.378	0.095	3.98

Average  $3.74 \pm 0.15$

tain known dopant concentrations in a gas stream by controlling the temperature of a dopant which is confined to a small bottle with a capillary. The method is simple to set up and use.

In applying this method of dopant control to a gallium arsenide epitaxial reactor we need to know the diffusion coefficient in hydrogen rather than in nitrogen. From Graham's law, the diffusion coefficient should be 3.74 times higher (*i.e.*,  $\sqrt{28/2}$ ). In Table I we list the reported diffusion coefficients, at 20°C, of various species in hydrogen and nitrogen (11, 15) and calculate the ratios. The average of these ratios is  $3.74 \pm 0.15$  and it is reasonable, therefore, to use Graham's law in our application.

Now the concentration of dopant used during the growth of gallium arsenide is small and therefore the resistance of the capillary would have to be higher than that used during our measurements. As a guide, we have calculated the concentration of dopant in an epitaxial reactor, which has 200 ml min<sup>-1</sup> (measured at room temperature) of hydrogen flowing through it, as a function of dopant temperature for capillaries 1 cm in length but with different diameters. Figure 7 shows the concentration of sulfur in the temperature range from the melting point to boiling

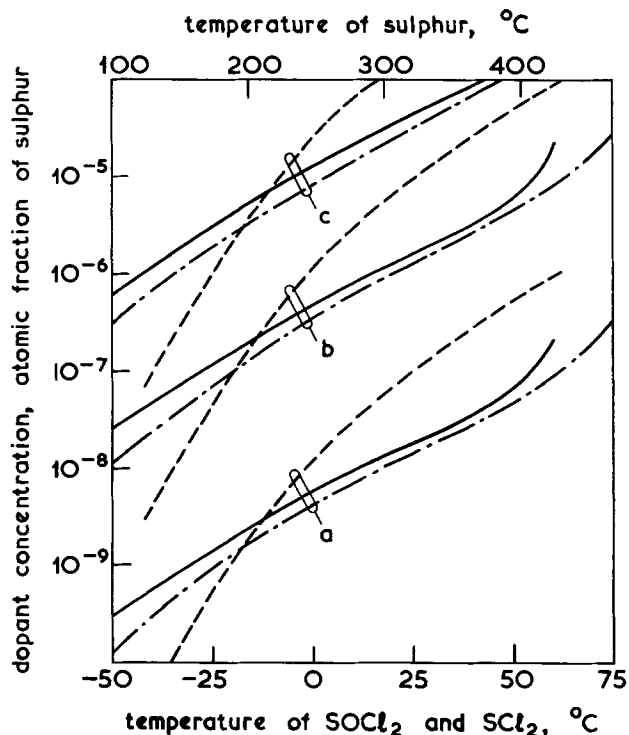


Fig. 7. Dopant concentration in the gas stream as a function of effusion bottle temperature for a hydrogen flow rate of 200 ml min<sup>-1</sup> and a capillary 1 cm long with a diameter of (a) 0.001 cm, (b) 0.01 cm, (c) 0.05 cm. - - - Sulfur; - · - · thionyl chloride, — sulfur dichloride.

point and the concentration of thionyl chloride and sulfur dichloride from  $-50^{\circ}\text{C}$  to the boiling point. In these calculations the temperature range has been extended to lower temperatures than those used during our measurements. This is not too unreasonable since for higher resistance capillaries the temperature at which surface kinetics begin to influence the vapor pressure in the bottle will be lower. However, it is better to use high temperatures and high resistance capillaries so as to ensure that equilibrium vapor pressures are attained and thereby yielding reproducible results.

Our epitaxial reactor is based on the Ga/AsCl<sub>3</sub>/H<sub>2</sub> system and we find that a hydrogen sulfide concentration of  $5 \times 10^{-8}$ , obtained from sulfur by the method described in this paper, in the gas stream yields layers grown on (100) surfaces in the region of high  $10^{16}$  carriers  $\text{cm}^{-3}$ . If we assume that the concentration of carriers is equivalent to the concentration of sulfur in the layer, then we obtain a distribution coefficient ( $k$ ) of  $\sim 60$  with

$$k = \frac{\text{atomic fraction of sulfur in the epitaxial layer}}{\text{atomic fraction of sulfur in the gas stream}}$$

We hesitate to be more precise in our value of  $k$  since we have found, in common with others (4), that the growth rate can have a dramatic influence on dopant incorporation. This work will be reported in a future communication (19).

Our value of  $k$  differs markedly from that of some workers (2, 3) but is consistent with that of other workers (4, 5). Bachem and Bruch (2) obtained a value of  $\sim 1$  for  $k$  while from the work of DiLorenzo and Moore (3) we extract a value of  $\sim 1000$ . The work of Hollan and Mircea (5) suggests that  $k$  has a value of at least  $\sim 40$  while Luther and DiLorenzo (4) have extracted from their results a value of  $\sim 20$  and found that the value depended on the growth rate.

### Conclusions

We have presented a method for introducing known and controlled concentrations of sulfur compounds into an epitaxial reactor based on the modified entrainment method. We have shown that over the temperature range studied the method is reproducible as equilibrium vapor pressures are attained in the effusion bottle. The diffusion coefficients of sulfur, thionyl chloride, and sulfur dichloride, which are needed to calculate the dopant concentration introduced into the epitaxial reactor, have been determined.

### Acknowledgments

Acknowledgment is made to J. Singh for his experimental assistance and to the Director of Research of the British Post Office for permission to publish this paper.

Manuscript submitted Dec. 16, 1975; revised manuscript received May 3, 1976.

Any discussion of this paper will appear in a Discussion Section to be published in the June 1977 JOURNAL. All discussions for the June 1977 Discussion Section should be submitted by Feb. 1, 1977.

Publication costs of this article were assisted by the British Post Office.

### LIST OF SYMBOLS

$A_n$	polymeric species consisting of $n$ monomers
$D_i$	diffusion coefficient of species $i$ , $\text{cm}^2 \text{sec}^{-1}$
$D_0$	diffusion coefficient at a reference temperature $T_0$ and a reference pressure $p_0$ , $\text{cm}^2 \text{sec}^{-1}$
$\Delta H_v$	enthalpy of evaporation, $\text{kJ mole}^{-1}$
$k$	distribution coefficient
$l$	length of capillary, $\text{cm}$
$M$	molecular weight
$p^{\circ}_A$	vapor pressure of species $A$ , $\text{atm}$
$p$	total pressure, $\text{atm}$
$p_0$	a reference pressure, $\text{atm}$
$r$	radius of capillary, $\text{cm}$
$R$	gas constant, $\text{kJ mole}^{-1} \text{K}^{-1}$ in Eq. [4]; $\text{cm}^3 \text{atm mole}^{-1} \text{K}^{-1}$ in Eq. [2] and [5]
$s$	$1 + s$ is the temperature dependence of the diffusion coefficient
$\Delta S_v$	entropy of evaporation, $\text{J mole}^{-1} \text{K}^{-1}$
$T$	temperature, $^{\circ}\text{K}$
$T_0$	a reference temperature, $^{\circ}\text{K}$
$\dot{W}$	rate of weight loss, $\text{g sec}^{-1}$
$\xi$	transport function.

### REFERENCES

1. D. Effer, *This Journal* **112**, 1020 (1965).
2. K. H. Bachem and H. Bruch, *ibid.*, **122**, 1000 (1975).
3. J. V. DiLorenzo and G. E. Moore, *ibid.*, **118**, 1823 (1971).
4. L. C. Luther and J. V. DiLorenzo, *ibid.*, **122**, 760 (1975).
5. L. Hollan and A. Mircea, GaAs and Related Compounds, 1972 Symposium Proceedings, The Institute of Physics, p. 217, London (1973).
6. D. A. Frank-Kamenetskii, "Diffusion and Heat Transfer in Chemical Kinetics," Wiley, New York (1967).
7. D. Battat, M. M. Faktor, I. Garrett, and R. H. Moss, *J. Chem. Soc. Faraday Trans. 1*, **70**, 2267 (1974).
8. D. Battat, M. M. Faktor, I. Garrett, and R. H. Moss, *ibid.*, **70**, 2280 (1974).
9. D. Battat, M. M. Faktor, I. Garrett, and R. H. Moss, *ibid.*, **70**, 2293 (1974).
10. D. Battat, M. M. Faktor, I. Garrett, and R. H. Moss, *ibid.*, **70**, 2302 (1974).
11. S. Chapman and T. H. Cowling, "The Mathematical Theory of Non-Uniform Gases," Cambridge University Press, Cambridge (1960).
12. H. Braune, S. Peter, and U. Neveling, *Z. Naturforsch. Teil A*, **6**, 32 (1951).
13. A. N. Nesmeyanov, "Vapour Pressure of the Elements," Infosearch (1963).
14. "Selected Values of Properties of Chemical Compounds," Manufacturing Chemists Association Research Project (1974).
15. J. O. Hirschfelder, C. F. Curtiss, and R. B. Bird, "Molecular Theory of Gases and Liquids," Wiley, London (1964).
16. D. M. Yost and H. Russell, Jr., "Systematic Inorganic Chemistry of the Fifth- and Sixth-Group Non-metallic Elements," Prentice-Hall, Englewood Cliffs, New Jersey (1944).
17. D. P. Stevenson, Unpublished calculations. See also *op. cit.*, p. 300.
18. H. Kniepkamp, S. Gisdakis, W. Kellner, and D. Ristow, *Siemens Res. Dev. Rep.*, **4**, 274 (1975).
19. A. K. Chatterjee, I. Garrett, and M. A. Savva, Unpublished work.

# Thin Film Epitaxial Growth of $\text{In}_x\text{Ga}_{1-x}\text{As}$ on GaAs

S. B. Hyder

Varian Associates, Corporate Research Laboratories, Palo Alto, California 94303

## ABSTRACT

Thin film, n-type single crystal epitaxial  $\text{In}_x\text{Ga}_{1-x}\text{As}$  was grown on semi-insulating GaAs substrates using an open-tube Ga-In-AsCl<sub>3</sub>/H<sub>2</sub> CVD system. Electron concentrations of about  $10^{17} \text{ cm}^{-3}$  were obtained using H<sub>2</sub>S doping. Semi-insulating layers were produced using CrO<sub>2</sub>Cl<sub>2</sub> as a dopant. InAs concentration of up to 23 mole percent (m/o) was obtained by compositional grading for lattice matching. The active layers were less than a micron thick and growth rates as low as 0.01  $\mu\text{/min}$  were achieved. The epitaxial layers were evaluated for surface quality, InAs concentration, electron concentration, and electron mobility for use in fabrication of microwave Schottky barrier gate field effect transistors. Good surfaces were obtained with all concentrations of InAs. Electron mobilities generally higher than those so far reported in the literature were obtained when care was taken to optimize the grading layer.

The  $\text{In}_x\text{Ga}_{1-x}\text{As}$  alloy system has attracted considerable attention recently because of its device application potential. Stillman *et al.* (1) and Nahory, Pollock, and DeWinter (2) have successfully fabricated detectors; and Nuese *et al.* (3) have constructed lasers for the 1.06 $\mu$  region. Application for use in near-infrared photocathodes has also been shown (4, 5). A preliminary report (6) has been made of the performance of this material in a microwave Schottky barrier field effect transistor application. This paper describes the work undertaken to produce the material for the microwave FET fabrication.

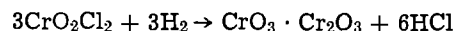
$\text{In}_x\text{Ga}_{1-x}\text{As}$  can be grown by liquid phase epitaxy (7-9), but homogeneous FET quality material is difficult to obtain, and uniform compositional grading is also difficult by this method. Growth by chemical vapor deposition (10-12), on the other hand, lends itself easily to preparation of homogeneous material of any desired composition and donor concentration by facilitating lattice matching through compositional grading. Mass spectroscopic studies have been reported recently by Ban and Ettenberg (13) who applied equilibrium thermodynamics to  $\text{In}_x\text{Ga}_{1-x}\text{As}$  CVD system and found reasonable agreement with experimental data. Mixed sources of In and Ga as well as separate In, Ga, and As sources have been used (10-12) with AsH<sub>4</sub>, HCl, and AsCl<sub>3</sub> systems.

In the present work, separate sources of In and Ga were used to ensure that no change of composition occurs during growth due to depletion of one source. Transport by AsCl<sub>3</sub>/H<sub>2</sub> was used to achieve the highest attainable purity. The advantage of this method is the use of only two sources with AsCl<sub>3</sub> supplying the As as well as HCl that is necessary for transport of In and Ga.

## Experimental Procedure

The  $\text{In}_x\text{Ga}_{1-x}\text{As}$  growth system and reactor are shown schematically in Fig. 1. Tylan Corporation's electronic mass flow controllers control the flow of purified H<sub>2</sub>. The AsCl<sub>3</sub> bubbler is kept at any desired temperature by a thermal bath and is connected to the In and Ga chambers; the AsCl<sub>3</sub>/H<sub>2</sub> flow over each element being separately controlled. The flow line to In is also connected through valved bypasses to an etch line entering the reactor chamber, and the flow can be diverted to this line if desired. The H<sub>2</sub>S

tank gas (310 ppm in H<sub>2</sub>) is further diluted with H<sub>2</sub> in a mixing chamber and the diluted gas is fed into the reactor ahead of the substrate position for S doping. Chromium doping is achieved using a CrO<sub>2</sub>Cl<sub>2</sub> bubbler and a cracking furnace kept at 500°C. The CrO<sub>3</sub>/H<sub>2</sub> mixture enters the reactor between the sources and the substrate, according to the reaction



The monochloride vapors of Ga and In are mixed in the reactor by means of a baffle placed at the exit of the In/Ga chambers to ensure homogeneous mixing. A 0.4 mm thick substrate of area about 5 cm<sup>2</sup> is placed horizontally in a holder, and a thermocouple inserted into a well incorporated in the holder records

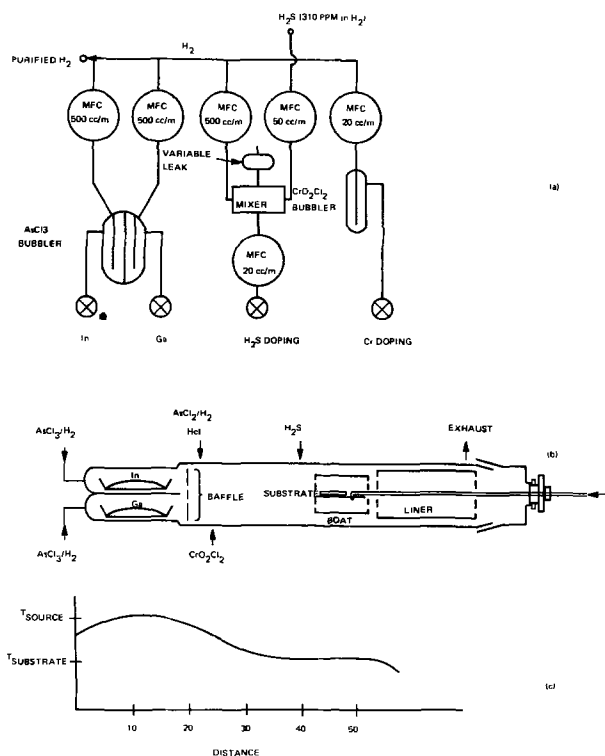


Fig. 1. Deposition reactor and system

\* Electrochemical Society Active Member.  
Key words: AsCl<sub>3</sub> CVD, compositional grading, Schottky barrier gate FET, CrO<sub>2</sub>Cl<sub>2</sub> doping.

the temperature. A quartz liner protects the reactor from monochlorides depositing in the cold region. All the glassware in the high temperature region is made from Spectrosil grade quartz. The reactor tube of cross-sectional area 9 cm<sup>2</sup> is held in a horizontal position and the furnace is rolled onto it to start the deposition process. An approximate temperature profile of the furnace when placed over the reactor is shown in Fig. 1(c). The source temperature was about 780°C, and the substrate temperature was usually about 720°C. Temperature variation over the length of the substrate was less than a degree per centimeter and about 5°C over the length of the source boats, which were 8 cm long with the source surface area of about 12 cm<sup>2</sup>.

### Vapor Phase Deposition

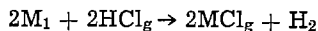
**Source preparation and saturation.**—50g of elemental In and Ga of minimum purity 99.9999% are used. Gallium is poured into the source boat as received, but indium is baked in H<sub>2</sub> stream at about 900°C for 72 hr before transferring it to the source boat in the reactor. Use of AsCl<sub>3</sub> and elemental sources requires that the sources are saturated with As until a crust of InAs and GaAs is formed on the respective sources. Transport and epitaxial growth occurs only after the sources are saturated.

The source temperature during saturation was kept at about 770°C. The AsCl<sub>3</sub> vapor pressure was 9.15 × 10<sup>-3</sup> atm at 20°C bubbler temperature. Using a H<sub>2</sub> flow rate of 300 cm<sup>3</sup>/min, the saturation time of 5.6 hr was calculated using the relation given by Shaw (14) for Ga

$$t_{\text{sat}} = \frac{RT_1}{p_{\text{AsCl}_3} F_1} \cdot \left[ \frac{X_{\text{As}}}{1 - X_{\text{As}}} \right] \frac{W}{mw}$$

where  $t_{\text{sat}}$  = saturation time in minutes,  $p_{\text{AsCl}_3}$  = AsCl<sub>3</sub> vapor pressure (atm),  $T_1$  = source temperature,  $F_1$  = flow rate in liters per minute,  $X_{\text{As}}$  = mole fraction As in saturated source,  $W$  = weight of the source,  $mw$  = molecular weight of the element, and  $R$  = gas constant 0.0821 atm/deg-mole. Arsenic solubility was taken from Hall's (15) data shown in Fig. 2 for Ga and In.

Ban and Ettenberg (13) have calculated that at a deposition temperature of 1000°K, about 10% of InCl is converted into solid from the gas phase as compared to about 60% for GaCl. This also indicates that the In source is depleting faster than the Ga source in the same ratio since depletion of the elemental source occurs according to the relation



For a source temperature of 780°C it was observed that after a series of test depositions the Ga source depleted about 20% whereas the In source depleted as much as 80%. Considering this faster depletion of In source, the saturation time for the In source was estimated by dividing Shaw's (14) expression by four. Indium saturation time was then calculated to be about 11 hr in reasonable agreement with the experimentally observed time of about 10 hr for In saturation with As.

After temperature equilibration, during which some desaturation occurs, the sources were resaturated initially with 300 cm<sup>3</sup>/min of AsCl<sub>3</sub>/H<sub>2</sub> flow over the In source and 100 cm<sup>3</sup>/min over the Ga source. After a series of depositions, the In source was found to deplete from the high temperature side of the source boat. This situation does not interfere with normal growth in any way until the source size is depleted about 80% or so after a considerable number of hours of saturations and depositions. The effect on the growth surface is then observed as formation of hillocks running along the (110) direction as shown in Fig. 3.

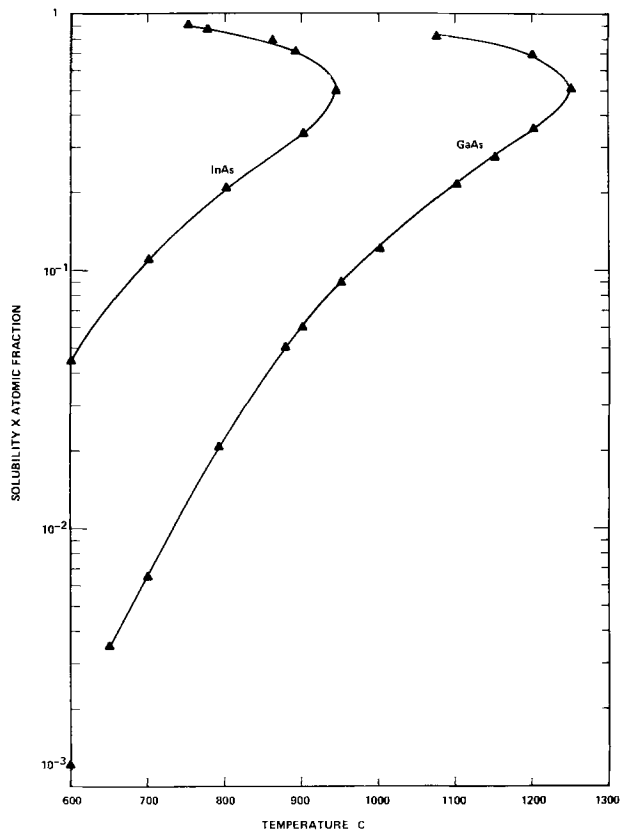


Fig. 2. Solubility curves for As dissolution in In and Ga (after Hall).

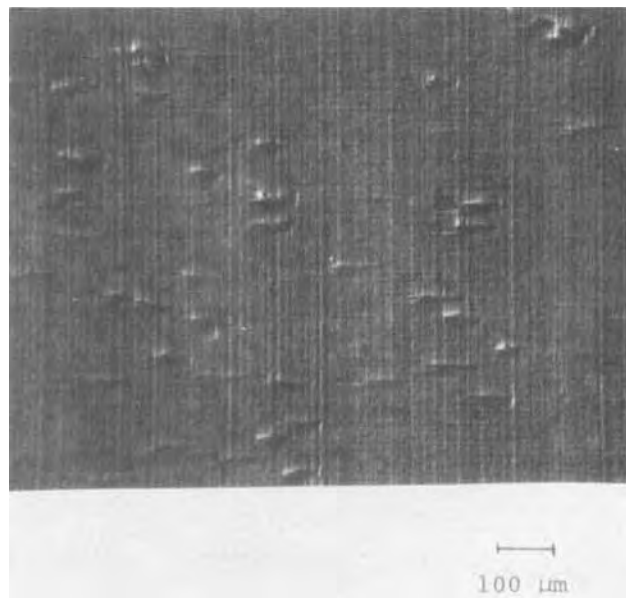


Fig. 3. Hillock formation with high flow rates and small source volume.

Reduction of AsCl<sub>3</sub>/H<sub>2</sub> flow at this point in the life of the source seems to eliminate hillock formation.

**Compositional grading and epitaxial growth.**—During grading for lattice matching and epitaxial growth, the substrate was kept at a temperature between 713° and 725°C and the sources were kept at 780°C. The composition of the deposited In<sub>x</sub>Ga<sub>1-x</sub>As layers was varied by varying the AsCl<sub>3</sub>/H<sub>2</sub> flow over the In and Ga sources. Experiments were conducted to determine the composition of epitaxial In<sub>x</sub>Ga<sub>1-x</sub>As as a function of fractional AsCl<sub>3</sub>/H<sub>2</sub> flow ratio over the Ga source. The results are shown in Fig. 4 and com-

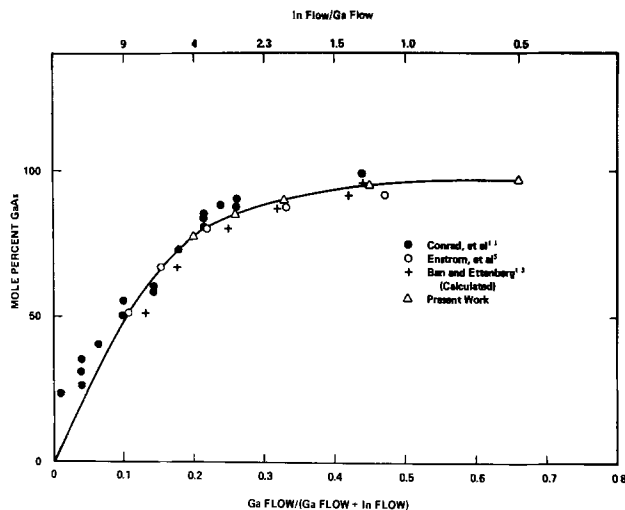


Fig. 4. Variation of epitaxial  $\text{In}_x\text{Ga}_{1-x}\text{As}$  composition with  $\text{AsCl}_3/\text{H}_2$  flow over Ga and In.

pared with previous experimental data (5, 11) and calculated values of Ban and Ettenberg (13). Compositional grading to the desired composition was accomplished by continuously controlling the input flow ratios to Ga and In (according to the data shown in Fig. 4) by means of a dual-channel electrostatic-curve-following programmer. Both the In and Ga flows were varied to keep the total flow constant. Since the composition of the deposited  $\text{In}_x\text{Ga}_{1-x}\text{As}$  is governed by equilibrium thermodynamics, letting the flow rate change during compositional grading by keeping flow through one source constant changes the growth rate during grading and results in degradation of surface quality and of electrical properties. Figure 5 shows the surface of epitaxially grown  $\text{In}_x\text{Ga}_{1-x}\text{As}$  with 14 m/o InAs, with (a) ungraded growth, (b) with 1  $\mu\text{m}$  of graded layer, and (c) with 3.9  $\mu\text{m}$  of graded layer. The better quality of the 3.9  $\mu\text{m}$  layer grown with constant flow rate is immediately obvious. Figure 6 shows the electron mobility at 300°K of some of the films grown with different thickness of graded layers and ungraded growth. The material was doped to about  $10^{17}/\text{cm}^3$  electron density with  $\text{H}_2\text{S}$ . The graded layer was made semi-insulating with Cr doping using  $\text{CrO}_2\text{Cl}_2$  as indicated in Fig. 1. The best results were obtained for graded layers of  $> 3 \mu\text{m}$  thickness using constant total flow rates, with mobilities of 6920 and 6840  $\text{cm}^2/\text{Vsec}$ , indicated by 4.9 and 4.8, respectively, in Fig. 6. Samples 4.11 and 4.10 were also grown with constant flow rates, but the graded layers were only 2.5  $\mu\text{m}$  and 2.8  $\mu\text{m}$  thick, respectively. Specimen 4.1 has a 2.5  $\mu\text{m}$  graded layer, but the flow rate was not constant throughout the grading. Effect of both variable flow rate and smaller graded thickness is depicted by specimen 4.4 with a room temperature mobility of only 2770  $\text{cm}^2/\text{Vsec}$ . The higher InAs concentration in this specimen with improper grading and gas flow rate also contributes to lower mobility. These can be compared with specimen 6.5, with a mobility of 6360  $\text{cm}^2/\text{Vsec}$  which had a 2.9  $\mu\text{m}$  graded layer and was grown at a constant gas flow rate.  $\text{In}_x\text{Ga}_{1-x}\text{As}$  grown directly on the GaAs substrate is exemplified by specimen 3.15. The mobility is 4190  $\text{cm}^2/\text{Vsec}$  as compared with about 5200  $\text{cm}^2/\text{Vsec}$  obtained by Glicksman *et al.* (12), but is better than specimens 4.4 and 4.1 only because the InAs mole percent is much smaller, and lattice mismatch is not too large (0.3% as compared to about 1.4%).

$\text{CrO}_2\text{Cl}_2$  flow of about  $3.4 \times 10^{-7}$  mole/min was used for doping graded layers which yielded epilayer resistivity of the order of  $2 \times 10^8 \Omega\text{-cm}$  with a total

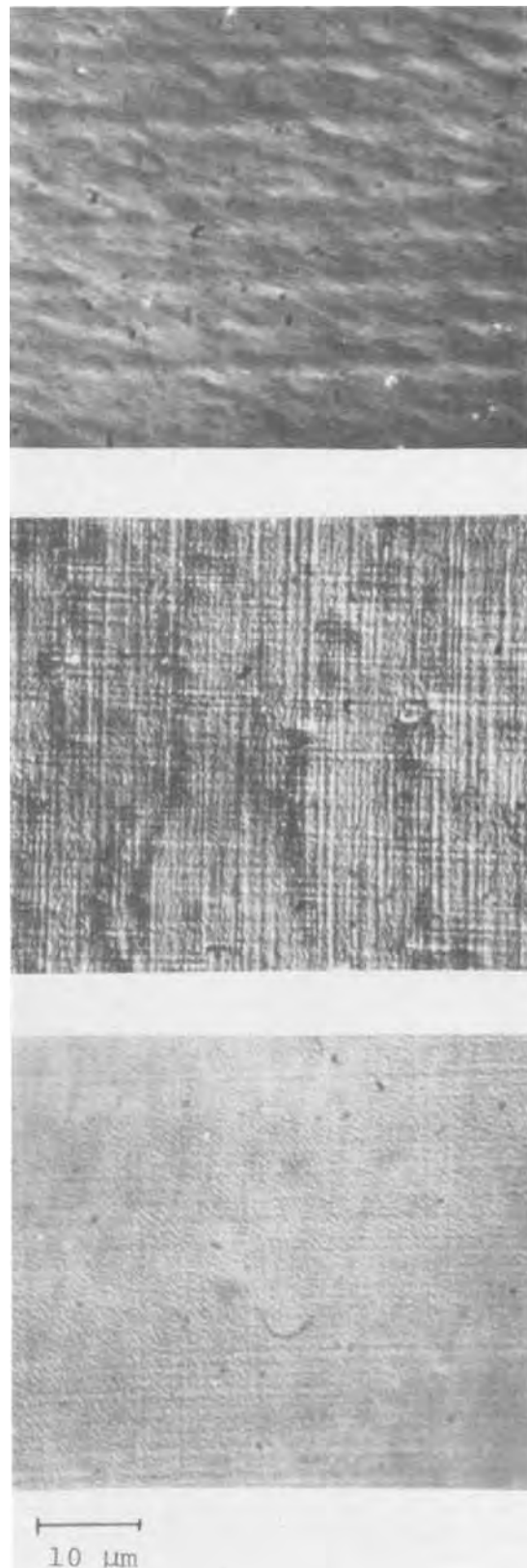


Fig. 5. Surface of epitaxially grown  $\text{In}_{0.14}\text{Ga}_{0.86}\text{As}$  grown on ungraded and lattice-matched graded layers: a = ungraded, b = 1  $\mu\text{m}$  graded layer, c = 3.9  $\mu\text{m}$  graded layer.

$\text{AsCl}_3/\text{H}_2$  flow of 460  $\text{cm}^3/\text{min}$ . When lower total  $\text{AsCl}_3$  flows were used, surface imperfections, shown in Fig. 7, were observed running along the (110) direction. These are possibly due to excessive Cr. Similar imperfections have been observed by Mizuno, Kikuchi, and Seki (16) and were attributed to  $\text{Ga}_2\text{O}_3$  formation when water vapor produced in the reaction

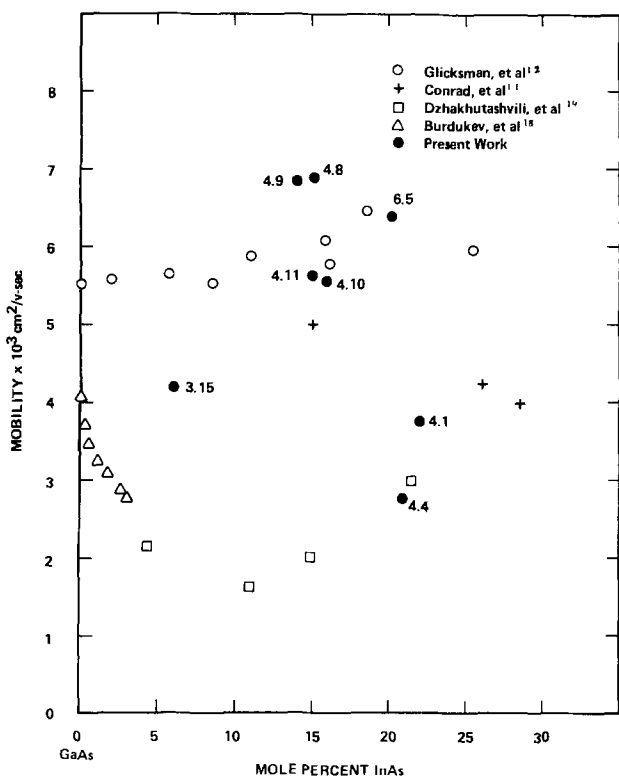


Fig. 6. Hall mobility as a function of mole percent InAs

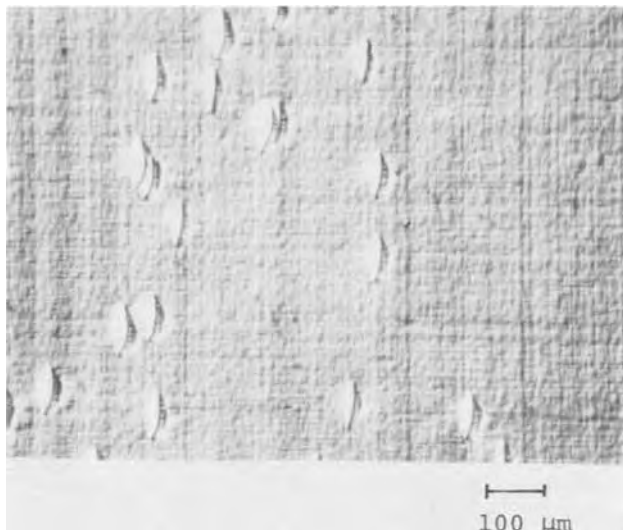


Fig. 7. Surface defects formed at high  $\text{CrO}_2\text{Cl}_2$  flow

reacted with the Ga source. Since the  $\text{CrO}_2\text{Cl}_2$  does not pass over the Ga source in our arrangement, the defects observed are tentatively attributed to the formation of stoichiometric CrAs which is found to give needle-shaped precipitates in Czochralski grown GaAs (17). No attempt at compositional analysis, however, was made to confirm this speculation.

To establish desirable equilibrium growth conditions with the InGaAs system described in Fig. 1, the input  $\text{AsCl}_3$  vapor pressure was adjusted by varying the  $\text{AsCl}_3$  vaporizer temperature. Complete conversion of HCl to the monochloride of In and Ga was determined by placing a GaAs substrate partially covered with  $\text{SiO}_2$  in the high temperature zone and measuring the amount of material etched. Increasing  $\text{AsCl}_3$  vapor pressure was found to increase etching due to increased HCl production, while at lower  $\text{AsCl}_3$  vapor pressures growth occurred at the sub-

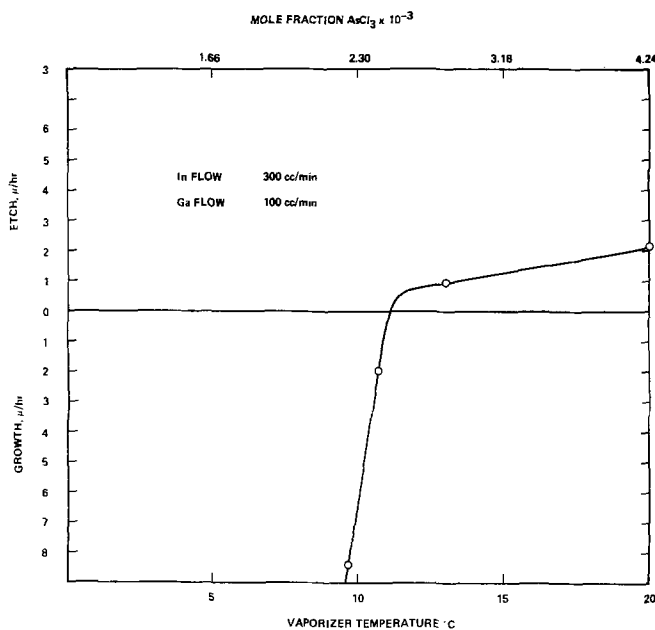


Fig. 8. Etch and growth rate at high temperature as a function of mole fraction  $\text{AsCl}_3$ .

strate. Figure 8 shows the etch rate as a function of  $\text{AsCl}_3$  vaporizer temperature. Complete conversion seems to occur at a vaporizer temperature of about  $11^\circ\text{C}$ , below which growth occurs in the high temperature region. Since in this series of experiments  $\text{CrO}_2\text{Cl}_2$  is also used to provide Cr doping, extra HCl enters the reactor through the reaction of  $\text{CrO}_2\text{Cl}_2$  and  $\text{H}_2$ . Use of an  $\text{AsCl}_3$  vaporizer temperature of  $11^\circ\text{C}$  can therefore cause severe etching of the substrate. Figure 9 shows the growth surface with  $\text{AsCl}_3$  vaporizer temperature of  $11^\circ\text{C}$  and  $\text{CrO}_2\text{Cl}_2$  addition. An  $\text{AsCl}_3$  vaporizer temperature of  $7^\circ\text{C}$  was therefore selected for the growth of material reported here, as a compromise among smooth etching, complete conversion, and low growth rates.

Typically, S-doped  $\text{In}_x\text{Ga}_{1-x}\text{As}$  epitaxial layers with electron densities of the order of  $10^{17}\text{ cm}^{-3}$  were grown on semi-insulating GaAs (100) wafers orientated about  $2^\circ$  off axis toward the (110) plane. Graded layers for lattice matching were made semi-insulating with Cr doping. The GaAs substrate was placed in a horizontal position on the substrate holder and

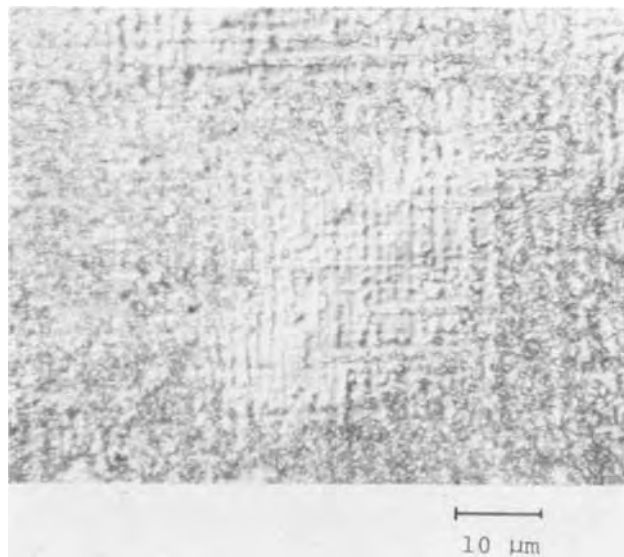


Fig. 9. Growth surface with the  $\text{AsCl}_3$  bubbler at  $11^\circ\text{C}$  in the presence of  $\text{CrO}_2\text{Cl}_2$ .

pushed into the hot zone during temperature equilibration and resaturation of the sources. After HCl etch cleaning, the substrate was pulled back just beyond the S-doping line (Fig. 1), and a graded layer grown on it to the desired InAs composition, as determined from the curve of Fig. 4. After a graded layer of about 3  $\mu\text{m}$  or more was grown, the substrate was pulled further down in the deposition region where S-doped  $\text{In}_x\text{Ga}_{1-x}\text{As}$  was grown. This growth rate was found to depend on the total flow rate. For a typical flow rate of about 460  $\text{cm}^3/\text{min}$   $\text{AsCl}_3/\text{H}_2$ , the growth rate was found to be about 0.03  $\mu\text{m}/\text{min}$ . A growth rate of 0.01  $\mu\text{m}/\text{min}$  was obtained when the total flow rate was reduced to 260  $\text{cm}^3/\text{min}$ . The growth rate during grading was typically 0.07  $\mu\text{m}/\text{min}$ . The effect of flow rate and substrate temperature on composition and growth rates is being investigated and will be the subject of another report.

After the desired epitaxial growth thickness had been obtained, the doping line and  $\text{AsCl}_3$  flow was shut off and the furnace rolled off from the reactor tube. The substrate was cleaned and stained to delineate the growth layers and the growth thickness was determined optically. Surface structure was observed optically under a Zeiss microscope. The electron density was determined using an impurity profile plotter. The InAs molar concentration was determined by measuring the bandgap (8) by photoluminescence and by x-ray diffraction determination of lattice constants. Hall mobilities were measured by the Van der Pauw method on square samples with alloyed In contacts on the corners. No correction for submicron layer thicknesses was made.

### Results and Discussion

Earlier measurements of electron mobility in melt-grown  $\text{In}_x\text{Ga}_{1-x}\text{As}$  with impurity concentrations of the order of  $10^{17} \text{ cm}^{-3}$  showed a drastic decrease in mobility with increasing concentration of InAs (18, 19). This decrease in electron mobility was attributed to alloy scattering. A similar effect was observed by Ku (20) in  $\text{GaAs}_{1-x}\text{P}_x$  with a carrier concentration of  $1.5 \times 10^{17} \text{ cm}^{-3}$ . As opposed to  $\text{GaAs}_{1-x}\text{P}_x$  [where a direct-to-indirect bandgap crossover occurs at  $x = 0.44$  (21)],  $\text{In}_x\text{Ga}_{1-x}\text{As}$  has direct bandgap through all compositions from GaAs to InAs. The expression for the variation of bandgap with InAs concentration is given by Nahory, Pollack, and DeWinter (2). The energy of the  $\Gamma$  conduction band minimum in  $\text{In}_x\text{Ga}_{1-x}\text{As}$  decreases rapidly with increasing  $x$  whereas the energy of the  $x$  minimum increases slowly. The electrons are thus characterized by decreasing effective mass. Experimentally determined conduction band effective masses have been found by Fetterman, Waldman, and Wolfe (22) to decrease linearly with increasing InAs concentration. The decrease in electron mobility observed in melt-grown alloys is too large to be explained on the basis of alloy scattering and is probably due to material being inhomogeneous. Purer and more homogeneous material grown from vapor has been shown to have a less marked decrease in mobility [Conrad, Hoyt, and Martin (11) and

Fetterman, Waldman, and Wolfe (22)]. Glicksman *et al.* (12), on the other hand, found practically no effect of composition up to a composition of  $x = 0.25$  InAs. In Fig. 6, the data points labeled with sample numbers show the mobilities obtained in some good and bad samples of thin film  $\text{In}_x\text{Ga}_{1-x}\text{As}$ , all grown from vapor with a donor concentration of the order of  $10^{17} \text{ cm}^{-3}$ . Results of other work reported in literature are also shown for comparison. All the alloy layers grown in the present study were of the order of a micron or less in thickness as shown in Table I, and the graded layers for compositional lattice matching were made semi-insulating as indicated earlier. The difference between the  $N_D - N_A$  value obtained from d-c Hall data and the charged carrier concentration obtained by differential capacitance measurement is due to the nature of the latter measurement which is carried out at 100 kHz frequency and is less sensitive to carrier trapping at room temperature.

Our data do not confirm the downward trend in mobility with increase of InAs content noted in earlier literature. In this respect, our results agree with those of Glicksman *et al.* (12). On the other hand, quality of the surface and quality and thickness of graded layers seem to affect the electrical properties. For slow growth rates that were used, a thickness of the graded layer of about 3-5  $\mu\text{m}$  seems to be sufficient. Using constant flow rates, as mentioned earlier, also seems to improve the quality of the film. Sample 3.15 was ungraded and seems to have a moderately highly compensating acceptor impurity. Sample 4.1 was grown on an undoped graded layer. It is seen from these results that for a properly grown  $\text{In}_x\text{Ga}_{1-x}\text{As}$  layer such as 4.8 and 4.9, for example, the room temperature mobility is higher than previously reported for any alloy of comparable composition and carrier density. The degradation in mobility seems to be due only to inhomogeneity and other structural disorders in the epitaxially grown alloys. Effort is under way to increase the InAs concentration up to about 50% and study the effect on mobility of higher InAs concentration in moderately heavily n-doped  $\text{In}_x\text{Ga}_{1-x}\text{As}$ .

### Conclusions

Submicron epitaxial layers of  $\text{In}_x\text{Ga}_{1-x}\text{As}$  were grown successfully on high resistivity graded epilayers to lattice match with GaAs substrates. N-type active layers doped to a carrier concentration of  $10^{17} \text{ cm}^{-3}$  showed high electron mobilities. It is concluded that alloy scattering as assumed in earlier work does not play any important role in homogeneous  $\text{In}_x\text{Ga}_{1-x}\text{As}$  alloys grown by chemical vapor deposition. Structural defects, on the other hand, can degrade mobility. The effect of impurity concentration is to reduce mobility in general according to accepted laws, but composition variation alone has minimal or no effect on the electrical properties of the material.

### Acknowledgments

Thanks are due to R. Fairman and D. Tringali for designing and setting up the  $\text{In}_x\text{Ga}_{1-x}\text{As}$  reactor

Table I

Sample No.	Thickness		InAs conc $x$ (%)	Resistivity ( $\Omega\text{-cm}$ )	Hall mobility 300°C ( $\text{cm}^2/\text{Vsec}$ )	$N_D - N_A$ (Hall) ( $\text{cm}^{-3}$ )	Carrier conc (differential capacitance) ( $\text{cm}^{-3}$ )
	Grading ( $\mu\text{m}$ )	Epitaxial ( $\mu\text{m}$ )					
4.1	3.5	0.7	23	0.002	3750	$7.62 \times 10^{17}$	$7.8 \times 10^{17}$
4.4	1	0.3	22	0.023	2770	$3.51 \times 10^{19}$	$1.5 \times 10^{17}$
4.8	3.4	0.53	15	0.015	6920	$5.9 \times 10^{19}$	$1.1 \times 10^{17}$
4.9	3.9	1.0	14	0.016	6840	$5.62 \times 10^{19}$	$1.2 \times 10^{17}$
4.10	2.8	0.4	16	0.01	5560	$1.15 \times 10^{17}$	$1.3 \times 10^{17}$
4.11	2.5	0.35	15	0.037	5630	$3 \times 10^{19}$	$1 \times 10^{17}$
6.5	2.9	0.7	20	0.015	6360	$6.4 \times 10^{19}$	$1.2 \times 10^{17}$
3.15	—	0.5	6	0.33	4190	$4.46 \times 10^{15}$	$1.5 \times 10^{17}$



system and also for initial preparation of samples. Thanks are also due to S. von Szeremy for obtaining the mobility data and L. Garbini for x-ray analysis. I am also grateful to R. Moon, R. Sankaran, and R. Fairman for numerous discussions and to M. Omori for analysis of the electrical data. Analysis of the microwave data by S. Bandy, which will be reported elsewhere, is also highly appreciated.

This work was supported in part by the Office of Naval Research, Arlington, Virginia, under Contract N00014-75-C-0125, and in part by Varian Associates.

Manuscript submitted March 11, 1976; revised manuscript received June 15, 1976.

Any discussion of this paper will appear in a Discussion Section to be published in the June 1977 JOURNAL. All discussions for the June 1977 Discussion Section should be submitted by Feb. 1, 1977.

Publication costs of this article were assisted by Varian Associates.

#### REFERENCES

1. G. E. Stillman, C. M. Wolfe, A. G. Foyt, and W. T. Lindley, *Appl. Phys. Lett.*, **24**, 8 (1974).
2. R. E. Nahory, M. A. Pollack, and J. C. DeWinter, *ibid.*, **25**, 146 (1974).
3. C. J. Nuese, M. Ettenberg, R. E. Enstrom, and H. Kressel, *ibid.*, **24**, 224 (1974).
4. J. J. Uebbing and R. L. Bell, *Proc. IEEE*, **56**, 1624 (1968).
5. R. E. Enstrom, D. Richman, M. S. Abrahams, J. R. Apert, D. G. Fisher, A. H. Sommer, and B. F. Williams, "Proceedings of the Third International Symposium on Gallium Arsenide and Related Compounds," Institute of Physics and the Physics Society, London (1970).
6. D. R. Decker, R. D. Fairman, and C. K. Nishimoto, "Proceedings of the Fifth Biennial Cornell Electrical Conference," Vol. 5, p. 305, Ithaca, New York (1975).
7. G. A. Antypas, *This Journal*, **117**, 1393 (1970).
8. R. E. Nahory, M. A. Pollack, and J. C. DeWinter, *J. Appl. Phys.*, **46**, 775 (1975).
9. R. Sankaran, R. L. Moon, and G. A. Antypas, *J. Cryst. Growth*, **33**, 000 (1976).
10. H. T. Minden, *This Journal*, **112**, 300 (1965).
11. R. W. Conrad, P. L. Hoyt, and D. D. Martin, *ibid.*, **114**, 164 (1967).
12. M. Glicksman, R. E. Enstrom, S. A. Mittleman, and J. R. Apert, *Phys. Rev. B*, **9**, 1621 (1974).
13. V. S. Ban and M. Ettenberg, in "Chemical Vapor Deposition, Fourth International Conference," G. F. Wakefield and J. M. Blocher, Jr., Editors, p. 31, The Electrochemical Society Softbound Symposium Series, Princeton, New Jersey (1973).
14. D. W. Shaw, *J. Cryst. Growth*, **8**, 117 (1971).
15. R. N. Hall, *This Journal*, **110**, 385 (1963).
16. O. Mizuno, S. Kikuchi, and Y. Seki, *Jpn. J. Appl. Phys.*, **10**, 208 (1971).
17. F. A. Gimelfarb, B. G. Girich, M. G. Milvidskii, O. V. Pelevin, and V. I. Fistul, *Sov. Phys.-Solid State*, **11**, 1612 (1970).
18. Yu. M. Burdukov, O. V. Emelyanenko, D. N. Nasledov, and Kh. A. Khalikov, *Sov. Phys. Semicond.*, **4**, 1697 (1971).
19. T. V. Dzhakhutashvili, A. A. Mirtskhulava, L. G. Sakvarelidze, A. L. Shkolnik, and M. S. Matinoun, *ibid.*, **5**, 190 (1972).
20. S. Ku, *This Journal*, **110**, 991 (1963).
21. J. J. Tietjen and L. R. Weisberg, *Appl. Phys. Lett.*, **7**, 261 (1965).
22. H. Fetterman, J. Waldman, and C. M. Wolfe, *Solid State Commun.*, **11**, 375 (1972).

# Preparation of p-Type InP Films on Insulating and Conducting Substrates via Chemical Vapor Deposition

K. J. Bachmann\* and E. Buehler

Bell Laboratories, Murray Hill, New Jersey 07974

and J. L. Shay, S. Wagner, and M. Bettini

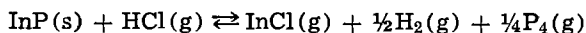
Bell Laboratories, Holmdel, New Jersey 07733

## ABSTRACT

Polycrystalline p-type InP films were grown on various insulating and conducting substrates, e.g., glass or carbon, via chemical vapor deposition in an open-tube In/H<sub>2</sub>/PCl<sub>3</sub> flow system. Zn and Cd were used as dopants. Noticeable differences in growth characteristics are observed as compared to epitaxial layer growth on InP single crystal substrates. Preliminary polycrystalline CdS/InP solar cells have a power conversion efficiency of 2.8%.

Heterodiodes n-CdS/p-InP have potential for solar cell applications since the bandgaps and the excellent lattice match of these materials result in a high solar power conversion efficiency and the stability of the two compounds assures good resistance against degradation. Present state-of-the-art single crystal CdS/InP solar cells have a power conversion efficiency of 14% at air mass 2 (1) and recent accelerated lifetime tests showed that such cells can be heated in air at 485°C for 1 week without significant decay in the device performance (2). InP has a direct bandgap and correspondingly low ( $\lesssim 1 \mu\text{m}$ ) absorption lengths for solar light with  $0.50 \mu\text{m} \lesssim \lambda \lesssim 0.96 \mu\text{m}$ . Over this entire "window" of the InP/CdS cell, InP grain sizes of a few micrometers should thus suffice for efficient collection of photogenerated minority carrier electrons. The cell is therefore an attractive candidate for production in thin film form. At the present stage of development, the preparation of polycrystalline CdS/InP solar cell hinges on the fabrication of p-type films of InP on a suitable substrate material.

In this paper we report on the growth of polycrystalline films of p-type InP on transparent insulators, and on conducting substrates that provide a large area contact to the InP, utilizing the In/H<sub>2</sub>/PCl<sub>3</sub> growth method (3). In this system, the temperature dependence of the equilibrium constant of the reaction



regulates transport of InP from an InP crust on an In

\* Electrochemical Society Active Member.

Key words: thin film solar cells, polycrystalline InP.

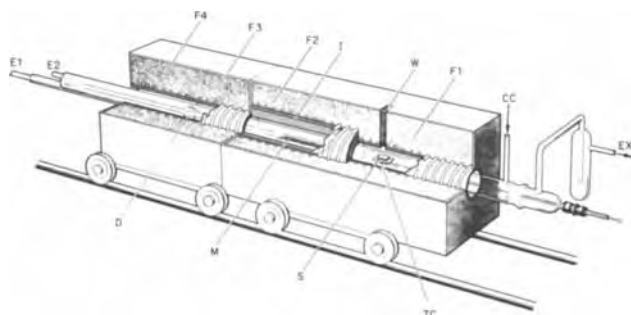


Fig. 1. Open-tube H<sub>2</sub> flow system for chemical vapor deposition of InP. E1 = entrance for the PCl<sub>3</sub>/H<sub>2</sub> mixture, E2 = entrance for pure H<sub>2</sub>, D = dopant source, M = InP saturated In source, F1-F4 = furnaces, I = isothermal furnace linear, W = window, CC = counter current of pure H<sub>2</sub>, S = substrate, TC = thermocouple, EX = exhaust.

metal source formed by reaction with PCl<sub>3</sub> to a distant substrate in an open-tube hydrogen flow system. The thermodynamic foundation of the HCl transport of InP has been investigated by Seki and Minagawa (4) and by Shaw (5). Also, there exist several experimental studies of the chemical vapor deposition (CVD) of epitaxial InP layers on single crystal InP substrates (6-11) which were mostly directed towards the fabrication of microwave oscillators.

## Experimental

A drawing of the experimental arrangement is shown in Fig. 1. A stream of Pd-diffused H<sub>2</sub> is passed through a bubbler filled with PCl<sub>3</sub> which is kept at +2.2°C corresponding to a saturation pressure of 40 Torr. The PCl<sub>3</sub>-saturated H<sub>2</sub> is diluted by pure H<sub>2</sub> to attain proper molar fractions  $x_{\text{PCl}_3}$  of PCl<sub>3</sub>, typically 2%, and is injected into entrance E2 to the deposition tube. Also, part of the pure H<sub>2</sub> is channeled through a separate entrance on the downstream end of the deposition tube establishing a counter current flow, CC, on the outer side of a quartz liner that surrounds the seed

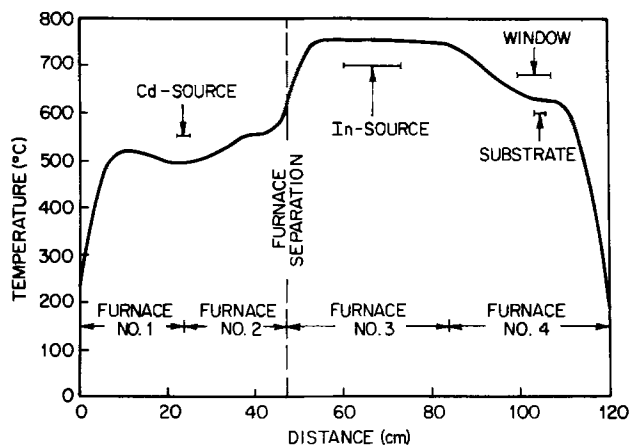


Fig. 2. Temperature profile of F1-F4

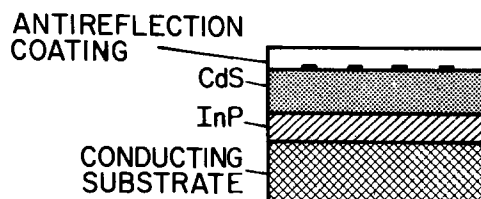


Fig. 3. Schematic cross section of a CdS/InP solar cell

holder so that all reaction products are deposited inside this liner and are removed with the substrate, S, after the experiment is terminated. S can be positioned by means of a quartz push rod for *in situ* visual inspection through window, W, in furnace F1 that controls the deposition temperature. The push rod contains a thermocouple, TC, for monitoring the substrate temperature. The boat, M, contains In-metal that is saturated with InP prior to the CVD experiment as described by Clarke, Joyce, and Wilgoss (8) and is kept by means of furnace F2 at a constant temperature which is typically 750°C. An isothermal furnace liner, I, is inserted into F2 to provide an ~ 20 cm long isothermal section in F2 that warrants equal temperature for all parts of M. The p-type dopant, D, is contained in a separate quartz tube which ends shortly before M and is swept by pure H<sub>2</sub> injected into entrance E1. Furnaces F3 and F4 are used to establish a temperature profile that keeps D inside the spherical section shown in Fig. 1. A typical temperature profile for the entire furnace assembly is shown in Fig. 2.

Both pure Cd and Zn have been used as dopant materials yielding net acceptor concentrations of  $N_A - N_D \leq 2 \times 10^{18} \text{ cm}^{-3}$ . The dopant concentration in the vapor phase is typically  $10^{-3}$ - $10^{-2}$ , e.g., a molar frac-

tion of Zn of  $1.8 \times 10^{-3}$  in the vapor phase results in epitaxial InP layers that have a resistivity  $\rho = 0.07 \text{ } \Omega\text{-cm}$ ,  $N_A - N_D = 9 \times 10^{17} \text{ cm}^{-3}$ , and  $\mu_h = 97 \text{ cm}^2/\text{Vsec}$  on Fe-doped semi-insulating (100) InP single crystal substrates. Alternatively, anhydrous CdCl<sub>2</sub> or ZnCl<sub>2</sub> may be used as dopant materials which eliminates the need for separating D from the HCl-containing vapor atmosphere.

Figure 3 shows a schematic drawing of a cross section through a polycrystalline CdS/InP solar cell consisting of a large area contact to the InP layer, the p-n junction, and a contact grid on top of the CdS which is covered by an antireflection coating. If a suitable conducting substrate is used, the formation of the large area contact to the InP film is included in the CVD step. If an insulating substrate, e.g., glass, is used then the contact to the InP would have to be provided by a contact grid previously deposited on the glass or subsequently attached to a part of the InP layer that is masked from the following CdS deposition.

Figure 4 shows InP coatings produced via CVD on various substrate materials that match the thermal expansion of InP: (A) Corning 7059 glass. (B) molybdenum, (C) carbon, and (D) Fe 30% Ni steel. Note that severe peeling of the InP occurs on the Fe/Ni

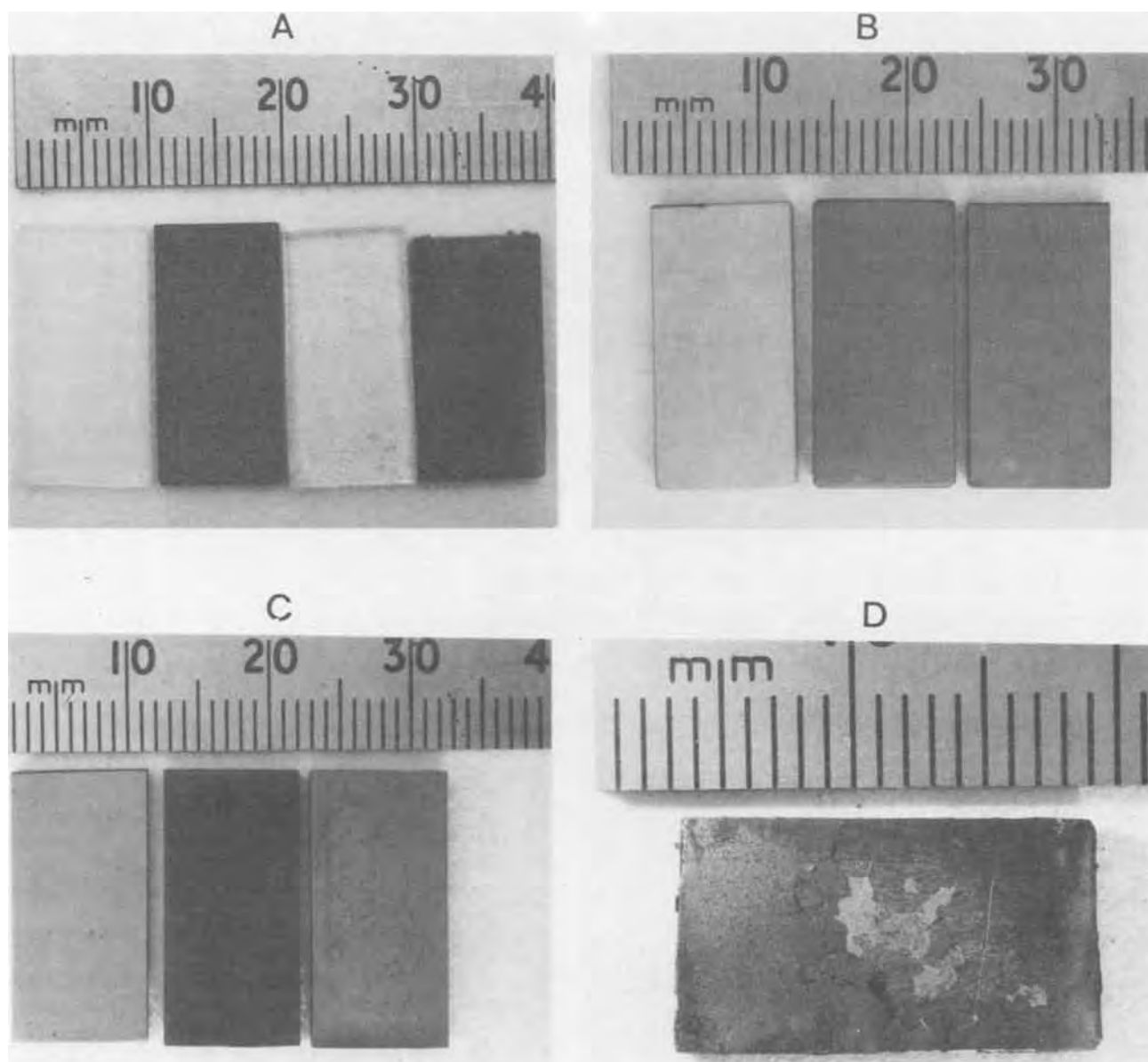


Fig. 4. InP coatings on various substrates: A = glass substrates (left etched, right not etched); B = etched Mo substrate, InP-covered Mo substrates; C = AEC carbon covered with InP, uncovered AEC carbon, InP covered POCO graphite; D = InP on a Fe 30% Ni substrate.

substrate and the reason for this behavior is revealed by Fig. 5 that shows a scanning electron micrograph of a cross section through such a layer, the substrate being on the right-hand side. The top part of Fig. 5 shows x-ray emission analysis traces obtained at various locations marked by arrows on the cross section. The second trace from bottom (No. 4) is an x-ray emission analysis of the original Fe 30% Ni alloy. Clearly In is diffusing into the base alloy (top trace) while Fe and to a lesser extent Ni are reacting with the InP films to form  $\text{Fe}_3\text{P}$  and  $\text{Ni}_3\text{P}$  that do not match the lattice of InP and do not have a similar expansion coefficient as the base alloy. Because of this, the film cracks off at the  $\text{Fe}_3\text{P}$ /alloy interface and Fe/Ni is, therefore, not a suitable substrate material. A similar behavior is observed for Kovar which has both a better match to the expansion characteristics of InP and a somewhat better chemical stability. Therefore, a diffusion barrier layer would have to be used with all Fe-base alloys as substrate materials.

Glass, molybdenum, and carbon are all well suited for coating with InP via HCl transport and no cracking and excellent adhesion of the InP to the substrate is obtained for these substrates. For glass (Corning 7052, Nonex, etc.), more uniform nucleation is obtained on matted surfaces prepared by either mechanical abrasion or by a slight etch in HF. The Mo substrates were etched in a mixture of  $\text{HNO}_3:\text{HF} = 30:1$  and the carbon substrates (AEC carbon, POCO graphite) were cleaned by heating to  $\sim 1000^\circ\text{C}$  in vacuum.

Figure 6 shows scanning electron micrographs of p-type InP coatings on molybdenum (A and C) and carbon (B and D) substrates. The grain size is comparable or larger than the absorption length for InP, i.e.,  $\sim 1 \mu\text{m}$ , and one can, therefore, expect that grain boundaries will not substantially reduce the quantum efficiency of CdS/InP solar cells prepared from such InP films. The morphology of the InP grains on carbon is favorable to that obtained on Mo, and because of its chemical inertness, mechanical stability, abundance, and low cost, we consider graphitized carbon as a possible substrate choice for the preparation of large area solar cells.

The growth rate of the InP films on substrates like carbon or glass is strongly influenced by kinetic factors and, in general, does not follow thermodynamic predictions. Thermodynamic calculations result, at constant input partial pressure  $p_{\text{PCl}_3}$  of  $\text{PCl}_3$  and constant source temperature  $T_1$ , in an equilibrium transport rate from the source to the substrate that increases approximately exponentially with decreasing substrate temperature  $T_2$  (5). The actual growth rate vs.  $\Delta T = T_1 - T_2$  relation on a carbon substrate is shown in Fig. 7 for  $x_{\text{PCl}_3} = 2.3 \times 10^{-2}$  and  $T_1 = 740^\circ\text{C}$ . Due to hindrances in the formation of three-dimensional nuclei of InP on the carbon, the growth rate remains zero<sup>1</sup> up to a critical temperature difference  $\Delta T_c$ . At  $\Delta T > \Delta T_c$  the growth rate increases steeply within a narrow range of  $\Delta T$  and changes relatively little for further increases in  $\Delta T$ .

In contrast to the conditions for CVD of InP on single crystal InP substrates, a foreign substrate does not provide a preferred nucleation site for the InP as compared to fused silica. Therefore,  $\Delta T_c$  is strongly affected by competitive nucleation and growth of InP on the quartzware in the vicinity of the substrate. That is, due to such competitive deposition, the actual supersaturation at the location of the substrate may be reduced below the value indicated by  $\Delta T'$  and geometric factors. The temperature distribution in the vicinity of the substrate and the flow rate may, therefore, affect the experimentally obtained  $\Delta T_c$ . Large flow rates tend to reduce these effects. Usually we worked at a linear flow velocity  $v_1 = 30 \text{ cm/min}$  and  $x_{\text{PCl}_3} \gtrsim 1.5\%$ .

<sup>1</sup>Zero growth rate means that within an incubation time of 3 hr no critical InP nuclei have formed on the carbon.

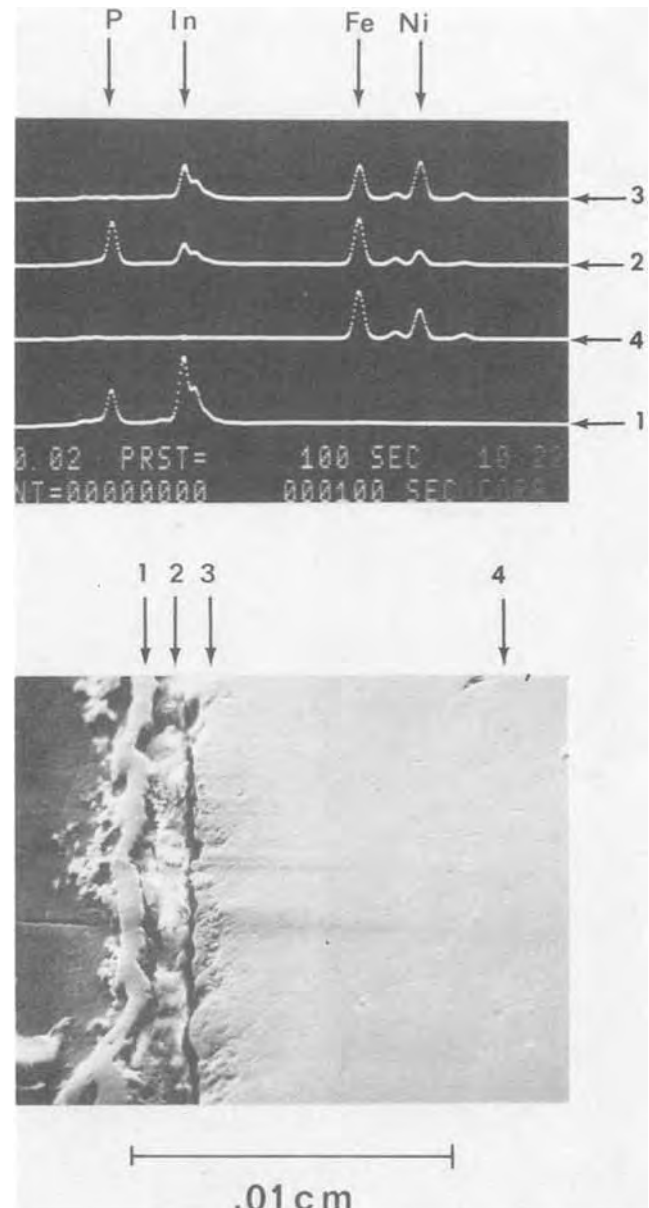


Fig. 5. Scanning electron micrograph of a cross section through InP/Fe 30% Ni (bottom), x-ray emission analysis traces (top).

The kinetics of InP transport in a  $\text{PCl}_3/\text{H}_2$  flow system to isolated (110), (111), and (100) faces of InP single crystal substrates has been examined recently by Mizuno (12). For deposition on InP single crystals and small  $\Delta T$ , the growth rate followed qualitatively the  $\Delta T$  characteristics predicted by thermodynamic calculations. However, depending somewhat on the crystallographic orientation and on the  $\text{PCl}_3$  flow rate, the growth rate becomes kinetically limited at  $\Delta T \gtrsim 100^\circ\text{C}$ . Because of the existence of a nucleation barrier that has to be overcome in polycrystalline film growth on foreign substrates, one is forced to work in the kinetically limited range, at least during the nucleation stage of film growth. Also, in the preparation of p-type InP layers, it is necessary to work at relatively high  $\text{PCl}_3$  concentrations, which are usually one order of magnitude larger than those used in Ref. (12), thereby shifting the onset of kinetically limited growth towards lower  $\Delta T_c$ , to suppress a high background donor concentration that arises when working with  $x_{\text{PCl}_3} < 1\%$  (10).

X-ray pole figure studies of polycrystalline InP films grown on C, Mo, or glass reveal that the crystallographic orientation of the InP crystallites in such films

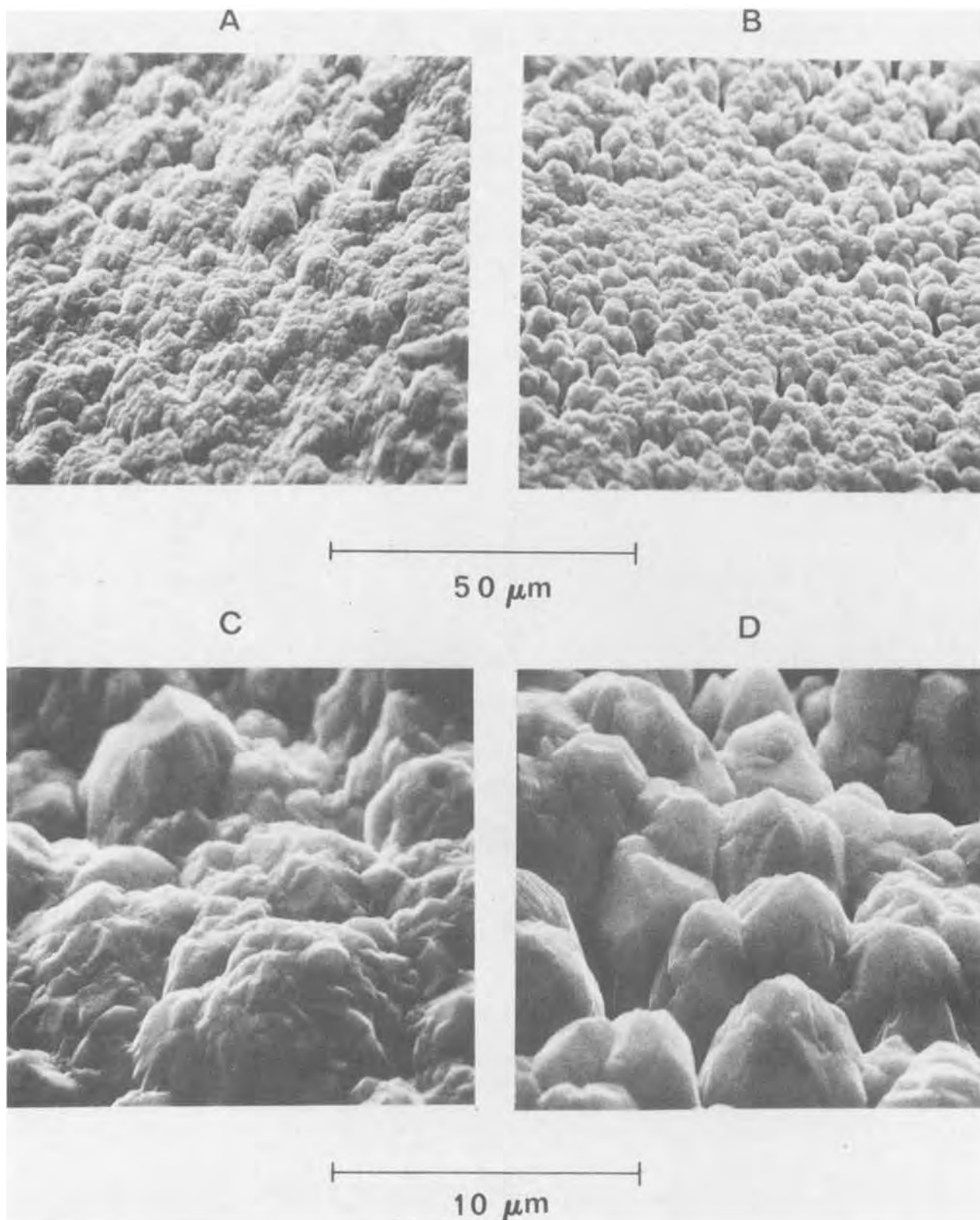


Fig. 6. Scanning electron micrographs of p-type InP layers on molybdenum and carbon substrates

is random. Therefore, effects of the anisotropy in growth rate usually average out in polycrystalline film growth and the grains are more or less equiaxed (compare Fig. 6). However, drastic anisotropies in growth rate and dramatic increases in its magnitude may be induced by the presence of impurities which, in extreme cases, lead to whisker growth that is detrimental to the preparation of solar cells. A study of the conditions and of the morphological characteristics of InP

whisker growth will be presented in a separate publication (13).

#### Preliminary Polycrystalline CdS/InP Solar Cells

Polycrystalline n-CdS/p-InP solar cells were prepared by depositing  $\sim 10 \mu\text{m}$  thick layers of CdS onto the above-described InP films utilizing a vacuum deposition technique described previously (14). A comparison between the properties of a representative poly-

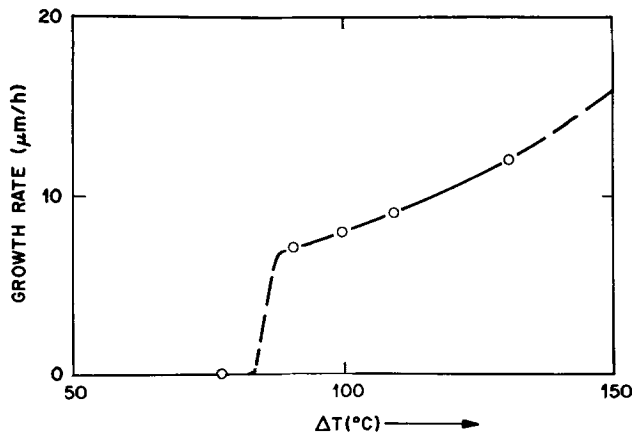


Fig. 7. Growth rate vs. temperature difference between source and substrate, carbon substrate,  $v_1 = 30$  cm/min,  $x_{PCl_3} = 2.3\%$ .

crystalline thin film CdS/InP solar cell grown on a carbon substrate and of a typical single crystal CdS/InP solar cell is made in Table I. The short-circuit current density,  $I_{sc}$ , is virtually identical for both types of CdS/InP solar cells. However, the open-circuit voltage,  $V_{oc}$ , and the fill factor,  $F$ , of the polycrystalline solar cell are considerably smaller than for single crystal devices. Therefore the solar power conversion efficiency,  $P$ , of the preliminary polycrystalline cells described above is presently limited to 2.8% as compared to 14% for annealed single crystal devices. For more detailed information on the properties of our present thin film CdS/InP solar cells we refer the reader to a forthcoming publication (15).

#### Acknowledgments

We would like to thank G. K. Kammlott for providing the scanning electron micrographs of the InP films.

Manuscript submitted April 22, 1976; revised manuscript received June 2, 1976. This was Paper 241 presented at the Washington, D.C., Meeting of the Society, May 2-7, 1976.

Any discussion of this paper will appear in a Discussion Section to be published in the June 1977

Table I. Comparison of the properties of present polycrystalline and single crystalline CdS/InP solar cells (SiO antireflection coating, AM1, 93 mW/cm<sup>2</sup>)

Property	$I_{sc}$ ( $\frac{mA}{cm^2}$ )	$V_{oc}$ (V)	$F$	$P$ (%)
Polycrystalline cell	21	0.40	0.31	2.8
Single crystal cell	25	0.72	0.72	14

JOURNAL. All discussions for the June 1977 Discussion Section should be submitted by Feb. 1, 1977.

Publication costs of this article were assisted by Bell Laboratories.

#### REFERENCES

- J. L. Shay, S. Wagner, K. J. Bachmann, and E. Buehler, *J. Appl. Phys.*, **47**, 614 (1976).
- S. Wagner, J. L. Shay, K. J. Bachmann, and E. Buehler, *This Journal*, **123**, 1254 (1976).
- B. D. Joyce and E. W. Williams, Proceedings of the Third International Symposium on GaAs and Related Compounds, Institute of Physics, p. 57, London (1971).
- H. Seki and S. Minagawa, *Jpn. J. Appl. Phys.*, **7**, 1142 (1968).
- D. W. Shaw, *J. Phys. Chem. Solids*, **36**, 111 (1975).
- H. Seki and M. Kinoshita, *Jpn. J. Appl. Phys.*, **7**, 1142 (1968).
- S. Narita, B. Choe, and H. Harada, *ibid.*, **8**, 500 (1969).
- R. C. Clarke, B. D. Joyce, and W. H. E. Wilgoss, *Solid-State Commun.*, **8**, 1125 (1970).
- M. C. Hales, J. R. Knight, and C. W. Wilkins, Proceedings of the Third International Symposium on GaAs and Related Compounds, Institute of Physics, p. 50, London (1971).
- R. C. Clarke, *J. Cryst. Growth*, **23**, 166 (1974).
- R. C. Clarke and L. L. Taylor, *ibid.*, **31**, 190 (1975).
- O. Mizuno, *Jpn. J. Appl. Phys.*, **14**, 451 (1975).
- K. J. Bachmann, S. Mahajan, and G. K. Kammlott, *J. Cryst. Growth*, To be published.
- S. Wagner, J. L. Shay, K. J. Bachmann, and E. Buehler, *Appl. Phys. Lett.*, **26**, 229 (1975).
- K. J. Bachmann, J. L. Shay, S. Wagner, and E. Buehler, *ibid.*, **29**, 121 (1976).

# Film-Substrate Interaction in Si/Ta and Si/Ta<sub>2</sub>O<sub>5</sub> Structures

A. G. Revesz and T. D. Kirkendall

COMSAT Laboratories, Clarksburg, Maryland 20734

## ABSTRACT

Gravimetric and SIMS analyses of vacuum-deposited Ta films on Si substrates as well as Ta<sub>2</sub>O<sub>5</sub> films obtained by their thermal oxidation demonstrate a significant interaction in Si/Ta (Ta<sub>2</sub>O<sub>5</sub>) structures well below the usual temperatures required to form TaSi<sub>2</sub> or SiO<sub>2</sub> on silicon. The interaction begins during the deposition of the Ta film, leading to the incorporation of silicon in the film. It is suggested that oxygen gettering by tantalum facilitates this process. During oxidation of the Ta film, the silicon in the film is co-oxidized and oxygen diffusing through the already formed oxide enhances the further entry of silicon into the film. Oxygen diffusing through the completely oxidized Ta film further reacts with the silicon substrate during postoxidation heat-treatment in oxygen. There is no evidence that the interaction during any of these three steps is caused by intermixing elemental tantalum and silicon. The results of gravimetric and SIMS analyses are qualitatively consistent with the measured dielectric parameters of the film and the observed electronic properties of the Si/Ta<sub>2</sub>O<sub>5</sub> interface.

Tantalum and niobium oxides have recently been developed as antireflection films in silicon solar cells with increased conversion efficiency (1, 2). These oxide films, obtained by thermal oxidation of vacuum-deposited Ta or Nb film, are noncrystalline with a high degree of short-range order. During the development work, it has been observed that an unexpected interaction between the film and silicon substrate occurs significantly below the temperatures at which silicon is oxidized or Ta silicide is formed. This interaction results in a graded refractive index of the Ta oxide film (3).

Detailed investigations of the optical properties (4) and Rutherford backscattering (RBS) analysis (5) of Ta oxide films on silicon have revealed that these films are, to a first approximation, stoichiometric Ta<sub>2</sub>O<sub>5</sub>. However, their refractive indexes vary from ~1.9 to ~2.4, the particular value depending on the thickness of the Ta film, oxidation conditions, and postoxidation treatments. This effect has been attributed to the incorporation of varying amounts of silicon into the noncrystalline Ta<sub>2</sub>O<sub>5</sub>. However, the amount of silicon estimated by RBS analysis appears to be insufficient to explain the observed large variation, indicating that Si-O bonds present in Ta<sub>2</sub>O<sub>5</sub> have a profound effect on the polarizability of the Ta-O bonds, and hence on the refractive indexes (4).

The work reported herein is intended to study the film-substrate interaction in Si/Ta (Ta<sub>2</sub>O<sub>5</sub>) structures by secondary ion mass spectroscopy (SIMS) and gravimetry. It is shown that silicon is already present in the vacuum-deposited Ta film, and that its amount further increases during oxidation. However, the quantitative aspects of the silicon incorporation are not yet fully resolved. This interaction is compared with those observed in other silicon/thin film structures as well as with those occurring during heat-treatment of anodically prepared Ta<sub>2</sub>O<sub>5</sub> films on tantalum.

## Experimental

Polycrystalline ( $\beta$ -tetragonal) tantalum films about 28 nm thick were deposited on silicon substrates in a vacuum of better than 10<sup>-6</sup> Torr obtained with a diffusion pump using a liquid N<sub>2</sub> trap. The high purity source was heated with electron beams and a shutter was used. The average area of the substrates was 4.05 cm<sup>2</sup>. The substrate temperature during Ta deposition

was estimated to be less than ~50°C.<sup>1</sup> In a few cases the films were deposited on previously oxidized (~250 nm thick SiO<sub>2</sub>) Si substrates. Oxidation was carried out in oxygen atmosphere at 530°C for 15 min. Under these conditions the tantalum was fully converted into a ~60 nm thick Ta<sub>2</sub>O<sub>5</sub> film. More details on preparation conditions are given in Ref. (2), (4), and (5).

Both the Ta and Ta<sub>2</sub>O<sub>5</sub> films were analyzed gravimetrically and with SIMS. For the gravimetric analysis, the weights of four samples were determined from five measurements performed with a Cahn microbalance (Model RH 2501 UHV, sensitivity = 2  $\mu$ g) at each of the following stages: before processing, after metal deposition, after oxidation, and following dissolution of the oxide film in HF. The results were evaluated by statistical methods.

The SIMS analysis was performed with a CAMECA instrument using mainly O<sub>2</sub><sup>+</sup> as the primary beam, although some samples were also analyzed with an Ar<sup>+</sup> beam. (Qualitatively, the results were similar.) In both cases, the profiles of two species were determined simultaneously. The primary ion beam was raster scanned over a large area (~300  $\mu$ m diameter) while the secondary ion collection was limited to a small central region (~70  $\mu$ m diameter) in the bottom of the crater to avoid edge effects. Since no standards were used, the results of this analysis were essentially qualitative. At the completion of the crater formation, a spectral analysis over the mass range of 190-270 amu was taken at the crater edge where all species in the exposed film could be measured simultaneously.

The thickness of the oxide films was determined with ellipsometry.

## Results

**Gravimetric analysis.**—The results of the gravimetric analysis are shown in Table I. Several points should be mentioned in connection with this table. The density of the Ta films, as calculated from the average weight and thickness is about 13 gcm<sup>-3</sup>. This value is less than the bulk density (16.6 gcm<sup>-3</sup>), indicating that the Ta films are porous. The thickness of the oxide

<sup>1</sup> This temperature was estimated by considering that the power radiated from tantalum at 3500°K is absorbed in the silicon sample held at 50 cm distance from the Ta source. The absorbed power is then reradiated so that the Si sample is in thermal equilibrium. The following approximate values were used in the calculation: emissivity of Ta = 0.1, absorptivity and emissivity of silicon = 0.8.



Table I. Gravimetric analysis of four samples of thermally oxidized Ta<sub>2</sub>O<sub>5</sub> films on silicon (all weights are in  $\mu\text{g}$ )

	Weights and probable error of individual samples (5 determinations each)				Avg	Std dev	Avg prob error*
	1	2	3	4			
Deposited Ta	142 $\pm$ 2.3	151 $\pm$ 2.3	162 $\pm$ 1.5	155 $\pm$ 1.7	152	7.2	2.0
Oxygen uptake	34 $\pm$ 1.9	43 $\pm$ 1.7	41 $\pm$ 1.4	33 $\pm$ 1.6	38	4.3	1.6
Excess oxygen	2.6 $\pm$ 2.0	9.6 $\pm$ 1.8	5.2 $\pm$ 1.4	-1.2 $\pm$ 1.7	4.0	4.0	1.7
Wt of Ta + O	2.6 $\pm$ 2.0	9.6 $\pm$ 1.8	5.2 $\pm$ 1.4	—	5.8**	2.9	1.7
Wt of oxide as determined by HF dissolution	176 $\pm$ 2.2	194 $\pm$ 2.0	203 $\pm$ 1.2	188 $\pm$ 1.2	190	9.8	1.7
Loss of Si after dissolution	208 $\pm$ 1.8	216 $\pm$ 1.7	214 $\pm$ 1.2	203 $\pm$ 2.0	210	5.1	1.7
	32 $\pm$ 2.3	22 $\pm$ 2.3	11 $\pm$ 1.3	15 $\pm$ 2.1	20	8.0	2.0

\* At the usual 50% confidence level.

\*\* This average weight is based on 3 samples, the fourth being excluded because the error exceeds the value itself.

film calculated from the amount of tantalum is 57 nm, assuming that the oxide is Ta<sub>2</sub>O<sub>5</sub> with a density of 8.0 gcm<sup>-3</sup> (the value for noncrystalline anodic Ta<sub>2</sub>O<sub>5</sub>). However, the experimentally determined thickness is  $\sim$ 60 nm, indicating that the density is less than 8.0 gcm<sup>-3</sup> and/or the oxide is not pure Ta<sub>2</sub>O<sub>5</sub>. For each sample the amount of oxygen needed to convert the particular amount of tantalum into Ta<sub>2</sub>O<sub>5</sub> (corresponding to the highest oxidation state of tantalum) has been subtracted from the oxygen uptake associated with the oxidation. Since, except for one sample, the difference is positive, this difference is labeled excess oxygen.

Table I shows that the sum of deposited tantalum and oxygen uptake is significantly less than the weight of the oxide film determined by dissolution. The reason for this is that some amount of silicon was lost when the oxide film was dissolved, as shown in the last row. The average value of the silicon loss reported here is less than the result of the preliminary investigation (40  $\mu\text{g}$ ) (3), but, statistically, it is still highly significant, as indicated by both the standard deviation and average probable error values. The previous result was obtained without statistical analysis. Even if the unusually strict 95% (rather than the usual 50%) confidence limit is considered, the individual error terms vary from 25 to 52%. Hence, the loss must be due to a real effect. Indeed, no significant change has been observed in the weight of similarly treated silicon control samples without Ta film. Thus, it is concluded that the Ta oxide film on silicon contains a significant amount of silicon. This is the reason why the oxide film is thicker than expected.

The question of how this silicon is incorporated in the oxide cannot be easily answered. If it is assumed that the Si is incorporated in the oxidized Ta film as SiO<sub>2</sub>, the amount of excess oxygen taken up (average 5.8  $\mu\text{g}$ ) corresponds to 5.1  $\mu\text{g}$  Si, much less than the Si loss (average 20  $\mu\text{g}$ ) determined by HF dissolution of the film. On the basis of ellipsometric measurements, the possibility that there is a discrete layer of SiO<sub>2</sub> between the Si substrate and the Ta<sub>2</sub>O<sub>5</sub> film has been eliminated (3). This suggests that the silicon atoms in the noncrystalline Ta-O network form bonds with oxygen atoms which are associated with one or more tantalum atoms. Consequently, the O to Si ratio corresponds to 0.5 rather than 2, as it would for SiO<sub>2</sub> (if a uniform distribution of Si atoms in the oxide were assumed).

Another approach to the problem is to consider the density of the oxide film. From the weight of tantalum and the oxygen uptake, the average density is 7.5 gcm<sup>-3</sup>, whereas its value determined from the weight loss in HF is 8.3. These values can be compared with the reported density of noncrystalline anodic Ta<sub>2</sub>O<sub>5</sub> (8.0 gcm<sup>-3</sup>) and noncrystalline SiO<sub>2</sub> (2.20 gcm<sup>-3</sup>). A further comparison can be made with the "apparent" density of similarly prepared Ta<sub>2</sub>O<sub>5</sub> films on silicon determined by RBS analysis [6.3-6.6 gcm<sup>-3</sup> for about 60 nm thick oxide films (5)]. These values have been obtained from the areal density of Ta atoms using the

ellipsometric thickness value of the oxide, which is assumed to be Ta<sub>2</sub>O<sub>5</sub>. The unrealistically low apparent density values indicate that a significant amount of foreign constituent in the oxide has not been detected with the RBS technique.

The amount of silicon determined gravimetrically corresponds to 0.85 Si atom/Ta atom in the oxide film. This value is much higher than even the most conservative limit of detection of the RBS technique: 0.16 Si atom/Ta atom (5). This discrepancy is not yet resolved, but does suggest that the majority of the Si atoms incorporated in the film are concentrated near the interface rather than distributed more uniformly in the film. The SIMS results, discussed below, corroborate this hypothesis. On the other hand, the behavior of the refractive index of Ta<sub>2</sub>O<sub>5</sub> films on silicon indicates that, in qualitative agreement with gravimetric analysis, a significant amount of Si-O bonds must be present throughout the oxide film. These considerations are based on the assumption that the polarizability of the Si-O and Ta-O bonds in these films is the same as in vitreous silica and anodic Ta<sub>2</sub>O<sub>5</sub>, respectively, and that the bond polarizability is additive (4).

In conclusion, the results of the gravimetric analysis demonstrate that thermally grown Ta<sub>2</sub>O<sub>5</sub> films on silicon contain a significant amount of silicon. This may qualitatively explain the large variation in the refractive index and its gradient within the oxide (decreasing toward the Ta<sub>2</sub>O<sub>5</sub>/Si interface), but there is an unresolved discrepancy between these results and those obtained with the RBS technique.

**SIMS analysis.**—The results obtained for an as-deposited Ta film on silicon are shown in Fig. 1, which indicates that all four species, <sup>28</sup>Si<sup>+</sup>, <sup>56</sup>Si<sub>2</sub><sup>+</sup>, <sup>32</sup>O<sub>2</sub><sup>+</sup>, and <sup>60</sup>SiO<sub>2</sub><sup>+</sup>, exhibit an apparent gradient at the outer surface. Since this gradient occurs within an estimated thickness less than  $\sim$ 10 nm, it may be due to spurious surface effects; therefore, it is designated as apparent. However, no gradient, not even an apparent one, would have been observed unless these species were present in the Ta film.

In addition, the distribution profiles of both silicon species exhibit a kink on the Ta side of the Ta/Si interface, i.e., the number of counts there is higher than expected from a sharp Ta/Si interface. This also indicates that some silicon is present in the Ta film. Significant impurity effects in Ta films on silicon have also been observed with the RBS technique; they have been attributed mainly to gettering of oxygen, but it is also possible that silicon is present in the Ta film (5).

Although the Ta films are porous, they are not discontinuous in the sense that x-ray surface diffraction analysis showed only the structure of tantalum but not of silicon. Also, very thin ( $\sim$ 20 nm) Ta<sub>2</sub>O<sub>5</sub> films are very uniform morphologically and optically (4), indicating that even Ta films which are much thinner than  $\sim$ 28 nm are continuous.

Figure 2 shows the results obtained with Ta<sub>2</sub>O<sub>5</sub> films on silicon using an Ar<sup>+</sup> ion beam. Qualitatively, the



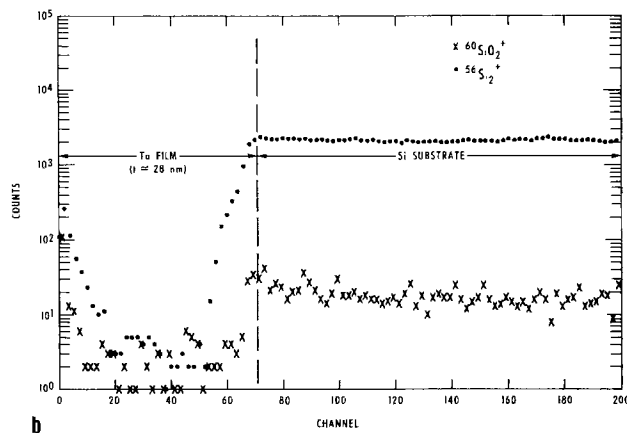
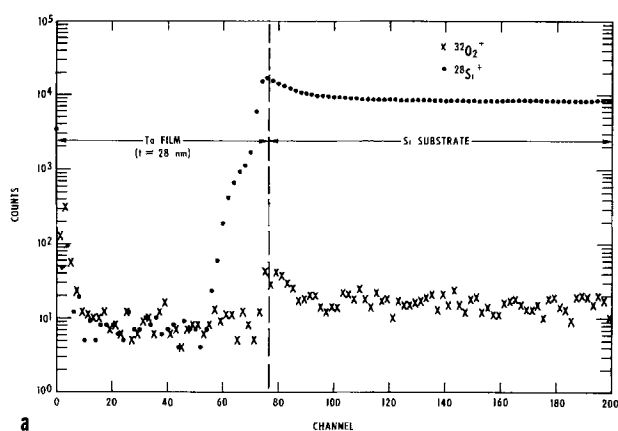


Fig. 1. SIMS analysis of Ta film on silicon. The beam is  $O_2^+$ . a and b represent two separate scans on the same sample which has been prepared by electron beam deposition of Ta on Si. The apparent rise in the  $^{28}Si^+$  curve at the Ta/Si interface relative to the bulk silicon is probably a chemical enhancement effect.

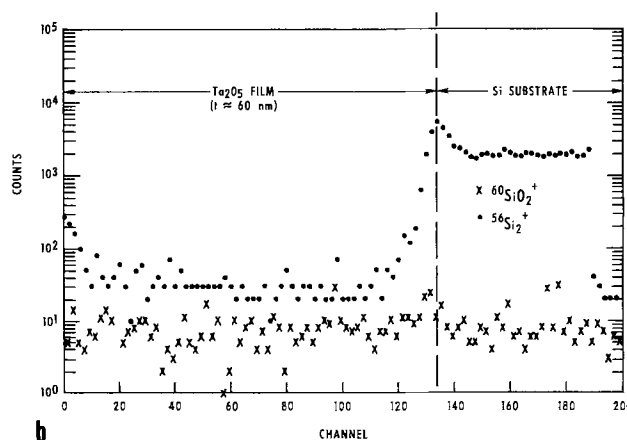
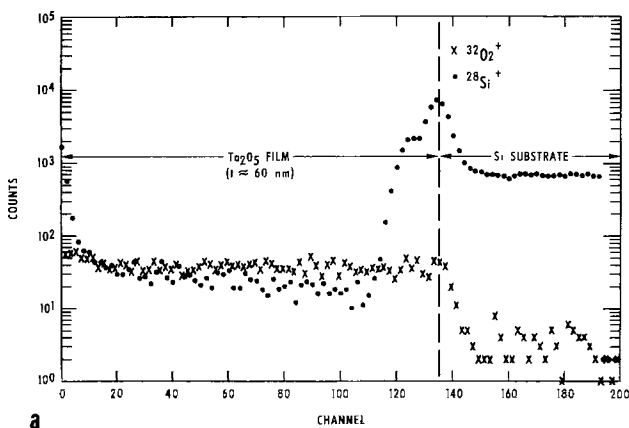


Fig. 2. SIMS analysis of  $Ta_2O_5$  film on silicon. The beam is  $Ar^+$ . a and b represent two separate scans on the same sample which has been prepared by thermal oxidation at  $530^\circ C$  of EB-deposited Ta on Si. The location of the  $Ta_2O_5/Si$  interface has been estimated from the negligible solubility of oxygen in silicon.

essential features are the same as in Fig. 1; however, the  $^{60}SiO_2^+$  level is now uniform across the whole sample and both silicon species exhibit an enhancement effect on the silicon side of the  $Ta_2O_5/Si$  interface. Comparison with the  $^{56}Si_2^+$  and  $^{60}SiO_2^+$  profiles obtained with an  $O_2^+$  beam (see Fig. 3) indicates that the enhancement of  $^{56}Si_2^+$  on the silicon side of the  $Ta_2O_5/Si$  interface is probably due to the presence of an oxide film [a similar effect has been observed at the  $SiO_2/Si$  interface (6)], but the enhancement of  $^{60}SiO_2^+$  at the  $Si/Ta_2O_5$  interface in Fig. 3 is probably an artifact caused by the  $O_2^+$  beam. Obviously there is no  $SiO_2$  in the Si substrate. On the basis of arguments similar to those used above for the Ta films on silicon, and from the qualitative feature of the  $^{28}Si^+$  and  $^{56}Si_2^+$  profiles, it is concluded that silicon is present in the oxide film.

The mass spectrum taken at the completion of the crater formation (Fig. 4) demonstrates that a large variety of Ta-Si-O complexes were present among the ions detected. It is possible that, due to some reactions with the ion beam, not all the species shown in the spectrum were present as such in the film and/or not in that relative concentration. Nevertheless, it is very unlikely that all the complexes resulted from spurious effects.

Similarly, it was observed that several constituents of a glassy substrate, especially silicon, became incorporated in  $Ta_2O_5$  films obtained by thermal oxidation of sputtered Ta films (7). In this case, the concentration of silicon was estimated as  $\sim 0.5$  atomic percent (a/o), most of which was in oxidized form. Apparently, some interaction took place between the glass and Ta and/or  $Ta_2O_5$  film. Since silicon is more

reactive than glass, it is plausible that the concentration of silicon in the  $Ta_2O_5$  film on silicon would be higher than in the case of a glass substrate.

The possibility of an interaction with a silica substrate has not been investigated in great detail. Nevertheless, it is instructive to compare the profiles shown in Fig. 2 and 3 with those characteristic of a  $Ta_2O_5$  film on an oxidized silicon substrate (see Fig. 5). In this figure, the counts for both  $^{60}SiO_2^+$  and  $^{56}Si_2^+$  on the  $Ta_2O_5$  side of the  $Ta_2O_5/SiO_2$  interface fall into the noise level, whereas in Fig. 2b and 3 the  $^{56}Si_2^+$  counts are higher than the  $^{60}SiO_2^+$  counts and their noise

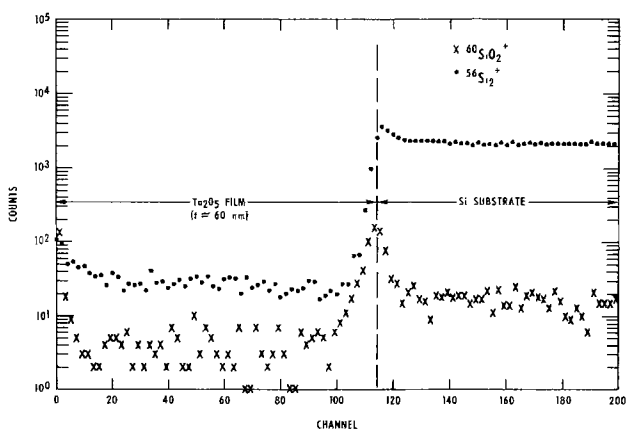


Fig. 3. SIMS analysis of  $Ta_2O_5$  films on silicon. The beam is  $O_2^+$ . The inflection of the  $^{60}SiO_2^+$  signal at the  $Ta_2O_5/Si$  interface is more pronounced than in the case of  $Ar^+$  (Fig. 2b).

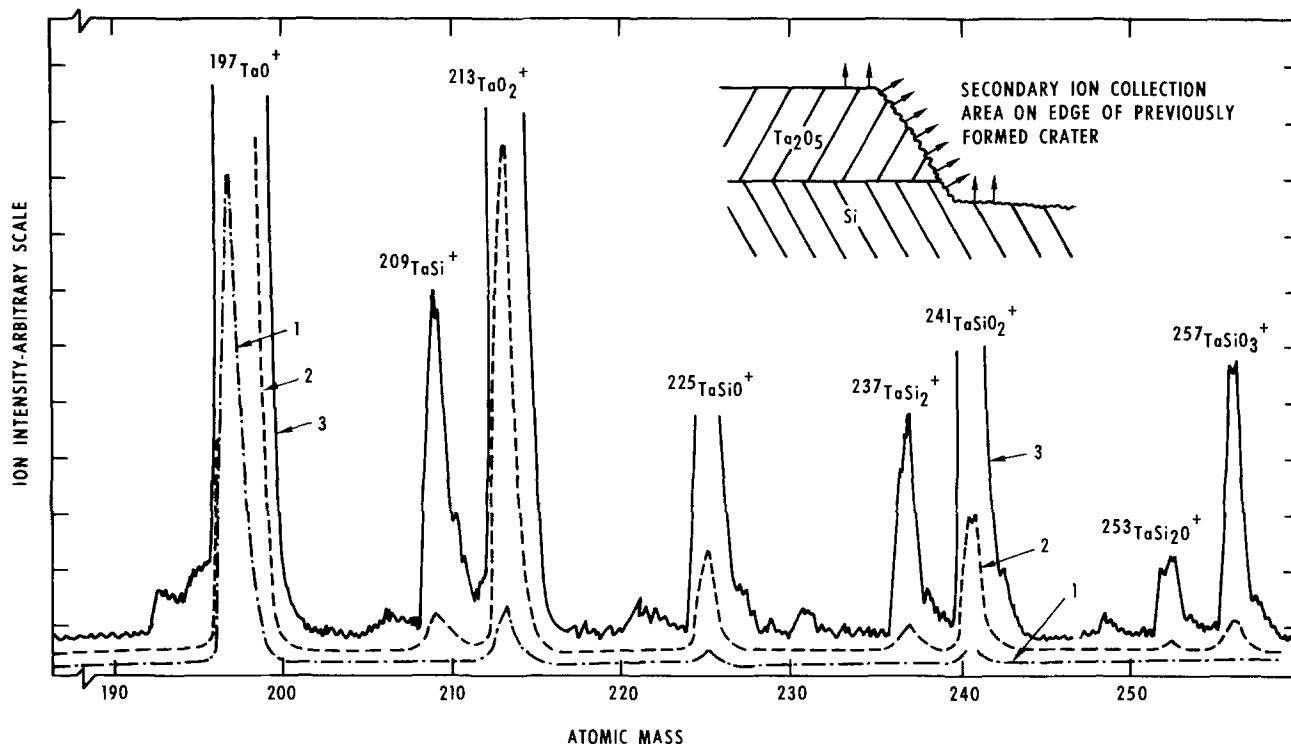


Fig. 4. Mass spectrum taken at the completion of the crater. The beam is  $O_2^+$ . The ions shown in the spectrum originate mostly from the edge of the crater to include species in the film and interface region. Each trace has 10 times greater sensitivity than the preceding. The insert is not to scale.

level is much less than that of the  $^{60}SiO_2^+$  profile. This may indicate that the extent of the film-substrate interaction is less, if any, for a  $SiO_2$  than for a Si substrate.

Because of the interest in applying  $Nb_2O_5$  as an antireflection film in silicon solar cells (1, 2), thermally grown  $Nb_2O_5$  films on silicon were also analyzed to a limited extent. The SIMS results were essentially the same as those obtained for  $Ta_2O_5$  films. Preliminary Auger analysis indicated that silicon is present at the outer surface of both  $Ta_2O_5$  and  $Nb_2O_5$  films.

The results of the SIMS analysis demonstrate qualitatively that silicon is present in both vacuum-deposited Ta and thermally grown  $Ta_2O_5$  films on silicon substrates. Together with the results of the gravimetric analysis, they indicate a film-substrate interaction in the Si/Ta ( $Ta_2O_5$ ) structure.

### Discussion

The results presented above show that an interaction with the silicon substrate occurs during the vacuum

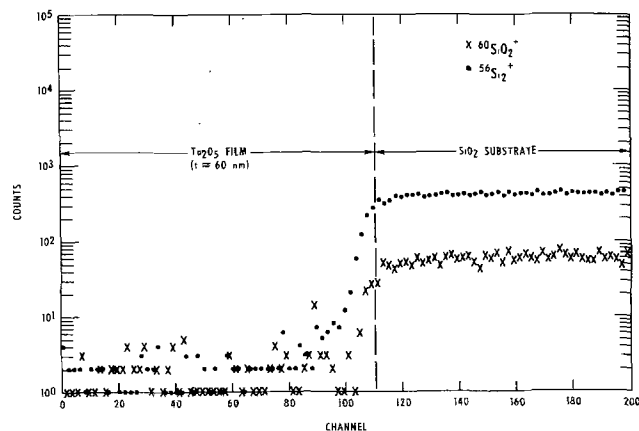


Fig. 5. SIMS analysis of  $Ta_2O_5$  film on  $SiO_2$ . The beam is  $O_2^+$ . The substrate is  $\approx 250$  nm of  $SiO_2$  prepared by thermal oxidation of Si. The  $Ta_2O_5$  film has been prepared by EB deposition of Ta with subsequent oxidation at  $530^\circ C$  for 15 min in oxygen.

deposition of the tantalum film, leading to the entry of Si atoms into the metal film. The compositionally rather ill-defined thin ( $\sim 2$  nm) oxide film that covers the silicon surface at room ambient is probably destroyed during this process. This interaction must be quite different from that resulting in silicide formation, since the temperature of the substrate (not purposely heated) is far below  $650^\circ C$ , the temperature at which  $TaSi_2$  has been reported to form in silicon-Ta film structures (8).<sup>2</sup> However, the observed interaction resembles the diffusion of silicon into a Pt film, which has been reported to proceed to the extent of 20-40 nm during the deposition process, and to be independent of the deposition method. The silicon content of an as-deposited Pt film on Si has been given as 3 a/o (9).

Based on the assumption that oxygen is the only contaminant, it has been inferred from RBS analysis (5) that oxygen is also present in vacuum-deposited Ta films (corresponding to 0.15-0.60 O atom/Ta atom). Hence, the incorporation of silicon, e.g., by grain boundary diffusion, into the Ta film may have been facilitated by oxygen due to the formation of strong Si-O bonds. Consequently, silicon incorporation occurs at a much lower temperature than that needed to form  $TaSi_2$ .

Following the deposition, the oxygen content of the film rapidly increases during thermal oxidation, resulting in a  $Ta_2O_5$  film. During this process, silicon already present in the film is co-oxidized with tantalum and further interaction with the Si substrate takes place. This process occurs at a temperature at which only an extremely thin  $SiO_2$  film can be obtained when silicon alone is oxidized. To wit, oxidation of bare silicon at  $600^\circ C$  (as opposed to  $530^\circ C$  in these experiments) for 30 min results in only a 2 nm thick  $SiO_2$  film (10). As mentioned above, no oxidation of silicon has been observed at  $530^\circ C$  in addition to the room ambient oxide film.

The interaction in the Si/Ta ( $Ta_2O_5$ ) structure resembles to some extent the formation of an  $SiO_2$  layer

<sup>2</sup> In accordance with Ref. (8), low angle x-ray diffraction investigation of Ta/Si structure heat-treated at  $500^\circ C$  in neutral ambient did not show the presence of  $TaSi_2$ .

on the top of vacuum-deposited gold films on silicon substrates (11). That process occurs at 150°-250°C, which is also well below the oxidation temperature of silicon. The significant difference is that gold cannot be oxidized so that a separate SiO<sub>2</sub> film forms, whereas the tantalum is oxidized to Ta<sub>2</sub>O<sub>5</sub> film, which contains silicon associated with oxygen (Si-O bonds). However, there is also a strong similarity: in both cases the entry of silicon into the metal film, its migration there, and its oxidation are closely related processes. In the case of gold on silicon, this relationship is manifested in the fact that no intermixing of silicon and gold (as shown by the disappearance of a sharp Si-Au interface in terms of both Si and Au distributions) below the eutectic point (375°C) has been observed when the sample is heated in a nonoxidizing ambient, thus precluding the formation of an SiO<sub>2</sub> film on the gold surface (11). Apparently, a significant intermixing of gold and silicon at low temperatures is possible only when the Si atoms can be tied to oxygen atoms.<sup>3</sup> That is, the Au/SiO<sub>2</sub> interface acts as a sink for the Si atoms migrating from the Si-Au mixed phase through the Au layer to the Au/SiO<sub>2</sub> interface.

According to the model proposed in Ref. (11), the intermixed Si-Au layer plays a key role in the formation of a SiO<sub>2</sub> film on the gold surface. The RBS results have shown that, in terms of tantalum distribution, both the Si/Ta and Si/Ta<sub>2</sub>O<sub>5</sub> interfaces are very sharp, indicating that Ta is not present in the Si substrate. Accordingly, the film-substrate interaction in Si/Ta (Ta<sub>2</sub>O<sub>5</sub>) structures must involve some phenomenon other than the formation of an intermixed layer.

It is interesting to note that the SIMS results indicate the possibility of silicon enhancement at the outer surface of Ta films (see Fig. 1). The reason for this effect may be a similar "sink effect" due to oxygen, since oxygen is also accumulated at the outer surface of Ta films.

It is important to realize that during the thermal oxidation of a Ta film on silicon there is no sharp boundary in the oxygen concentration between Ta<sub>2</sub>O<sub>5</sub> on the surface and "unoxidized" tantalum beneath it (5). Therefore, concomitant with the formation of Ta<sub>2</sub>O<sub>5</sub> and co-oxidation of silicon already present in the Ta film, the oxygen concentration further increases in that region of the Ta film which has not yet been converted into Ta<sub>2</sub>O<sub>5</sub>. Thus, the entry of silicon into the Ta film is further enhanced. This model is consistent with the observed decrease in silicon enhancement at the outer surface after the Ta film has been fully oxidized (compare Fig. 1a and 3). It also explains the decrease in the refractive index from the outer surface of the Ta<sub>2</sub>O<sub>5</sub> film toward the Si/Ta<sub>2</sub>O<sub>5</sub> interface (3, 4); this decrease results from the increased concentration of Si-O bonds toward the Si/Ta<sub>2</sub>O<sub>5</sub> interface. This increase may be the reason for the presence of a kink in the silicon distribution profile at the Si/Ta and Si/Ta<sub>2</sub>O<sub>5</sub> interfaces.

The film-substrate interaction in Si/Ta (Ta<sub>2</sub>O<sub>5</sub>) structures does not stop when the Ta film is fully oxidized. It has been observed that the determination of the end point of the oxidation process is somewhat complicated by a continuous increase in the oxide thickness and decrease in the oxide refractive index (3). Similar effects have been observed during post oxidation heat-treatment in an oxidizing ambient (4). These observations demonstrate that the oxidation of silicon and its incorporation into the oxide film proceed even when no more metallic tantalum is present. Furthermore, this process also occurs at temperatures at which bare silicon cannot practicably be oxidized. This observation further emphasizes the role of oxygen in the film-substrate interactions, especially its diffusion through the Ta<sub>2</sub>O<sub>5</sub> film and its reaction with

silicon. It is important to realize that there are no grain boundaries present in the morphologically and optically very homogeneous noncrystalline Ta<sub>2</sub>O<sub>5</sub> film. Hence, the migration of silicon there cannot proceed via grain boundary diffusion.

The Ta<sub>2</sub>O<sub>5</sub> films on silicon discussed in this paper are noncrystalline. The properties of noncrystalline Ta<sub>2</sub>O<sub>5</sub> films obtained by thermal oxidation of bulk tantalum are not well known, but noncrystalline Ta<sub>2</sub>O<sub>5</sub> films prepared by anodic oxidation of tantalum have been studied extensively. For instance, it has been reported that oxygen can easily diffuse through anodic Ta<sub>2</sub>O<sub>5</sub> films in the temperature range of 400°-600°C and then gets absorbed in the underlying tantalum (12). Very significantly, the diffusion of oxygen through the anodic Ta<sub>2</sub>O<sub>5</sub> film has not resulted in additional oxide growth when the anodic oxidation is reasonably thick (e.g., a 50 nm oxide has remained unchanged for 24 hr at 500°C). Thus, the bulk tantalum acts simply as an oxygen sink. Similarly, in the case of Si/Ta (Ta<sub>2</sub>O<sub>5</sub>) structures, the silicon substrate may act as an oxygen sink after complete oxidation of the Ta film. It can be estimated from the data in Ref. (12) that the diffusion of oxygen at 530°C through a 60 nm thick Ta<sub>2</sub>O<sub>5</sub> film can oxidize about 20 μg of silicon on a 4.05 cm<sup>2</sup> wafer within 20 min. The agreement between this value and the measured silicon loss (Table I) is probably fortuitous, but the important point is that oxygen can be supplied for further oxidation through the already formed Ta<sub>2</sub>O<sub>5</sub> film.

It is more difficult to explain why the oxidation of silicon proceeds at a lower temperature at the Si/Ta<sub>2</sub>O<sub>5</sub> interface than at the Si/SiO<sub>2</sub> interface (as is the case during the usual thermal oxidation). It may be argued that, before the oxidation of the Ta film is complete, oxidation of silicon already present in the Ta film may occur at a lower temperature than oxidation of bulk silicon because in the former the Si atoms are not bound to other Si atoms. Thus, the situation is somewhat similar to the Si/Au structure, where Si atoms arriving on the gold surface also combine with oxygen at even lower temperatures because they are not part of the silicon crystal. However, this is no longer the case after the Ta film has been fully oxidized. Thus, it is apparently easier to transfer a silicon atom from the silicon crystal into Ta<sub>2</sub>O<sub>5</sub> than into SiO<sub>2</sub>.

As a result of the incorporation of Si atoms into the Ta<sub>2</sub>O<sub>5</sub> film, the Si/Ta<sub>2</sub>O<sub>5</sub> interface does not coincide with the original Si surface or Si/Ta interface. In this respect, this process resembles the oxidation of silicon, which, under proper conditions, results in a nearly perfect semiconductor-insulator interface. The perfection of the Si/SiO<sub>2</sub> interface results from two basic features: (i) a growth process (i.e., transfer of Si atoms from the silicon crystal into the SiO<sub>2</sub> film) by which the silicon surface is displaced from its original position into a new one which was formerly in the bulk, and (ii) the structural flexibility of noncrystalline SiO<sub>2</sub>, which is essential for the accommodation of the two solids at the interface with minimum disorder (13). The Si/Ta<sub>2</sub>O<sub>5</sub> structures exhibit similar characteristics. Indeed, there are indications that the Si/Ta<sub>2</sub>O<sub>5</sub> interface has a perfection that is unexpected for an extrinsic (i.e., non-SiO<sub>2</sub>) oxide film on silicon (2, 14).

The nature of the Si/Ta<sub>2</sub>O<sub>5</sub> interface is, of course, intimately related to the existence of the Si-O, Si-O-Ta, and the somewhat improbable Si-Ta bonds in the oxide. The mass spectrum in Fig. 4 indicates a large variety of possible combinations of Si, Ta, and O atoms. However, some of these combinations may not occur in the oxide but may be artifacts produced in the course of the analysis. Polarizability considerations have indicated that this oxide somehow lies intermediate between Ta<sub>2</sub>O<sub>5</sub> and SiO<sub>2</sub>, where the role of Si-O bonds appears to be disproportionately large and may even affect the Ta-O bonds (4). Unfortunately, very little

<sup>3</sup> It should be noted that the model proposed in Ref. (11) does not provide an explanation for the observation that no Si-Au intermixed layer formed below the eutectic point in a nonoxidizing ambient.

is known about the structure of noncrystalline Ta<sub>2</sub>O<sub>5</sub> and the relationship with its properties. However, from the above discussion it is clear that a significant interaction occurring in Si/Ta and Si/Ta<sub>2</sub>O<sub>5</sub> structures plays a predominant role in obtaining an oxide film with remarkable properties. Some of these properties can be varied in a controlled manner within a very wide range.

### Conclusions

According to gravimetric analysis, Ta<sub>2</sub>O<sub>5</sub> films on silicon substrates obtained by thermal oxidation of vacuum-deposited tantalum contain a significant amount of silicon. Corroborative secondary ion mass spectroscopy further indicates that silicon is already present in the as-deposited Ta film. These results agree qualitatively with the behavior of the refractive index and dielectric constant of these oxide films described previously, although comparison with former RBS data shows an inconsistency. A model is suggested in which an interaction between silicon and oxygen is responsible for the incorporation of silicon into the Ta and Ta<sub>2</sub>O<sub>5</sub> film at temperatures well below the usual temperature for oxidation of silicon.

### Acknowledgments

The authors are indebted to J. Allison, who prepared the samples, and B. Phillips (formerly with Battelle Memorial Institute), who collaborated on the SIMS analysis. This paper is based upon work performed in COMSAT Laboratories under the sponsorship of the Communications Satellite Corporation.

Manuscript submitted Feb. 4, 1976; revised manuscript received May 5, 1976.

Any discussion of this paper will appear in a Discussion Section to be published in the June 1977 JOURNAL. All discussions for the June 1977 Discussion Section should be submitted by Feb. 1, 1977.

Publication costs of this article were assisted by COMSAT Laboratories.

### REFERENCES

1. A. G. Revesz, *COMSAT Tech. Rev.*, **3**, 449 (1973); also, Conference Record of the 10th IEEE Photovoltaic Specialists Conference, p. 180, Palo Alto, California, Nov. 1973.
2. A. G. Revesz, J. Allison, and J. Reynolds, *COMSAT Tech. Rev.*, **6**, 57 (1976).
3. A. G. Revesz, J. Allison, T. Kirkendall, and J. Reynolds, *Thin Solid Films*, **23**, S63 (1974).
4. A. G. Revesz, J. Reynolds, and J. Allison, *This Journal*, **123**, 889 (1976).
5. J. Hirvonen, A. G. Revesz, and T. Kirkendall, *Thin Solid Films*, **33**, 315 (1976).
6. H. L. Hughes, R. D. Baxter, and B. Phillips, *IEEE Trans. Nucl. Sci.*, **19**, 256 (1972).
7. J. M. Morabito and R. K. Lewis, *Anal. Chem.*, **45**, 869 (1973).
8. H. M. Day and A. Christou, AIME Electronic Materials Conference, Princeton, New Jersey Aug. 1975.
9. M. J. Rand and J. F. Roberts, *Appl. Phys. Lett.*, **24**, 49 (1974).
10. A. M. Goodman and J. M. Breece, *This Journal*, **117**, 982 (1970).
11. A. Kiraki, E. Lugujo, and J. W. Mayer, *J. Appl. Phys.*, **43**, 3643 (1972).
12. R. E. Pawel and J. J. Campbell, *This Journal*, **113**, 1204 (1966).
13. A. G. Revesz, *J. Non-Cryst. Solids*, **11**, 309 (1973).
14. A. G. Revesz and J. Allison, *IEEE Trans. Electron Devices*, **ed-23**, 527 (1976).

## Gel Formation in Negative Electron Resists

Nobufumi Atoda and Hisazo Kawakatsu

*Electrotechnical Laboratory, Tanashi, Tokyo, 188 Japan*

### ABSTRACT

Exposure characteristics of negative electron resists are described on the basis of Charlesby's theory on gel formation by a chain reaction. By use of the theory, the important resist parameters, contrast and sensitivity, can be related to the chemical properties of the resist materials. Applicability of the theory to exposure curves of Kodak thin film resist (KTFR), polymethylvinylsiloxane (PMVS), and epoxidized polybutadiene (EPB) is experimentally verified. The radiation yield for the reaction initiated directly by the electron irradiation and that for the over-all reaction propagated via radicals is separately estimated. It is found that the sensitivity of styrene-butadiene copolymers (SB) is increased by an introduction of  $\alpha$ -phenylmaleimide. This increase in sensitivity is also explained by the theory. The observed lowering in contrast associating the improvement in sensitivity by  $\alpha$ -phenylmaleimide in SB, by epoxidation in polybutadiene, and by introduction of vinyl groups in polysiloxanes is in good agreement with the theoretical results. It is concluded that if a resist with higher contrast than 1.0 is required, the chain reaction must be inhibited so that the inhibition factor is larger than about 0.5.

Electron beam lithography has become important in order to fabricate master masks or direct devices having high resolution structures. If the electron beam parameters and resist properties are properly combined, a minimum linewidth down to 1000Å can be obtained with an electron optical system of the scanning electron microscope type (1). However, for practical processes, further development concerning the pattern-fabricating speed is required. The amount of time for writing a desired pattern is restricted by

Key words: electron lithography, chain reaction, radiation yield, contrast, sensitivity.

the electron beam current and the sensitivity of the resist. Since the electron current is limited by the brightness of the electron source and decreases rapidly with the spot diameter (2), resists with high sensitivity are needed for writing the desired pattern with satisfactory resolution in a reasonable amount of time.

Resist materials are classified into two categories: negative resists, which are cross-linked and converted to insoluble gels by electron irradiation, and positive resists, which are degraded and dissolved in the irradiated area. Negative resists are, in general, more sensitive than positive resists, although positive re-

sists are preferable for high resolution applications (3). The comparatively low resolution of negative resists is mainly due to the fact that electrons back scattered from the substrate cause a gradual slope at the edge of the developed pattern (4). The extent of this effect strongly depends on the contrast,  $\Gamma$ , of the resist, which is defined as the slope of the exposure characteristic curve. It is noted that if negative resists with high contrast ( $\Gamma > 1.0$ ) are properly processed, resolutions close to the diameter of the electron beam can be obtained (5). However, negative resists with high sensitivity tend to exhibit comparatively low contrast, especially when the sensitivity is improved by the introduction of a reactive chemical group, such as epoxy or vinyl. Then the contrast is lowered in comparison with that of the original material (6, 7).

In the present work, gel formation in negative resists is studied on the basis of radiation chemistry, with the intention of understanding the dependence of contrast and sensitivity on the chemical properties of resist materials. The study on gel formation by electron irradiation can be reduced into two steps. The first is formation of cross-links by electron irradiation, which is conveniently discussed in terms of radiation yield, independent of any detailed mechanism. In the second, gel fraction is related to the extent of cross-linking. This problem has been theoretically treated in detail by Charlesby (8). A radiation chemical approach to the insolubilization of electron resists has been first reported by Ku and Scala (9). Although their result provides valuable information as to dependence of the critical dose on chemical properties of resists, such as average molecular weight and radiation yield, it cannot offer any information as to the important resist parameter, contrast. Moreover, it is not always applicable to every resist system. In resist materials which contain epoxy or vinyl groups, it is supposed that the insoluble gel is formed through chain reactions of cross-linking. For such a case, a Charlesby theory on random cross-linking (10), which is implicitly postulated in the treatment by Ku and Scala, is no longer valid.

The chain reaction has been used to explain experimental results. Broyde has estimated the radiation yield of Kodak thin film resist (KTFR) assuming the chain reaction (11). Paal *et al.* (12) and Roberts (6) have attributed the high sensitivity of newly developed resists to the chain reaction. However, the applicability of chain process to the resist systems has not been fully verified. The work reported by Nonogaki *et al.* is taken as experimental evidence, in which the dependence of the sensitivity of epoxidized polybutadiene (EPB) (13) on the epoxy content is empirically formulated by assuming chain process (14), while Feit *et al.* have observed little dependence in the same experiments (7). Moreover, theoretical treatments and quantitative descriptions of contrast have not been reported.

The theory on gel formation by the chain mechanism has been given by Charlesby (15). By use of the theory, contrast as well as sensitivity can be related quantitatively to the extent of chain propagation. In the present work, the applicability of the theory to exposure curves of KTFR, EPB, and PMVS (poly-methylvinylsiloxane) (16) is examined. Further, the observed tendency that improvement in sensitivity by the introduction of vinyl, epoxy, or  $\alpha$ -phenylmaleimide ( $\alpha$ -PMI) is accompanied by a lowering in contrast is studied according to the theory.

### Theoretical Basis

*Gel formation through a chain reaction.*—A mathematical analysis applicable to gel formation through a chain reaction has been given by Charlesby (15). It is assumed in the analysis that a double bond on a

polyester molecule is converted to two radicals by irradiation, and that the radical reacts with a double bond on a neighboring molecule, forming a cross-link and at the same time producing a radical on the molecule. Another assumption is the inhibition of the reaction, which determines the length of the chain propagation. Thus the important material parameters are  $\nu$ , the average number of reacting sites per molecule of number average molecular weight, and  $i$ , the inhibitor activity defined as the probability that a growing chain is terminated at any one step by cyclization, resonance stabilization, mutual termination of two radicals, or termination by an additive.

Charlesby's result is presented in a form of somewhat complicated simultaneous equations including a parameter which should be eliminated by numerical calculations. On the basis that  $\nu$  is in general large compared with one in actual resist materials, we can obtain rather simplified formulas approximated from the original equations. The result depends on the initial molecular weight distribution of the polymer. If all molecules are initially of the same size (uniform distribution)

$$g = 1 - \exp\{-\delta g f(g, i)\} \quad [1]$$

and for a random distribution

$$g = 1 - \frac{1}{\{1 + \delta g f(g, i)/2\}^2} \quad [2]$$

where  $g$  is the gel fraction and  $\delta$  the cross-linking coefficient defined as the average number of cross-linked sites per molecule of weight average molecular weight.  $f(g, i)$  is a function of  $g$  and  $i$ , which implies the effect of the chain reaction

$$f(g, i) = \frac{g + \frac{2i}{1-i}}{\left(g + \frac{i}{1-i}\right)^2} \quad [3]$$

If  $f(g, i)$  is equated to 1, Eq. [1] and [2] become the formulas for the case where cross-linking takes place at random without any chain reaction (10).

In Fig. 1, calculated curves of Eq. [1] (solid line) and Eq. [2] (broken line) for  $i = 0.04$  and  $0.25$  are shown. Curves for nonchain process are also shown for comparison, where the relationship between  $g$  and  $\delta$  is independent of material, and the gel point where gel formation first starts is  $\delta_m = 1$ . In the case of the chain reaction, the same value of  $g$  as in the non-chain process is obtained at a value of  $\delta$  lowered by a factor  $1/f(g, i)$ . Since  $f(g, i)$  is nearly equal to  $2(1-i)/i$  for small  $g$ , the gel point is

$$\delta_m = \frac{i}{2(1-i)} \quad [4]$$

Therefore, as shown in Fig. 1, the smaller the value of  $i$ , the smaller the gel point and the slope of the curve. The effect of the molecular weight distribution on the slope of the curve is also seen from the figure, that is, the slope for a random distribution (polydispersity  $\overline{M}_w/\overline{M}_n = 2$ , where  $\overline{M}_w$  is the weight average molecular weight and  $\overline{M}_n$  is the number average molecular weight) is more gradual than that for a uniform distribution ( $\overline{M}_w/\overline{M}_n = 1$ ).

In comparison with experimental results, the gel fraction  $g$  is equivalent to the normalized film thickness  $d/d_0$ , where  $d$  is the film thickness after development and  $d_0$  is the initial film thickness. On the other hand, in order to relate the cross-linking coefficient  $\delta$  with the exposure dose  $q$ , the absorption of irradiated energy and subsequent chemical events must be known. These processes are described con-

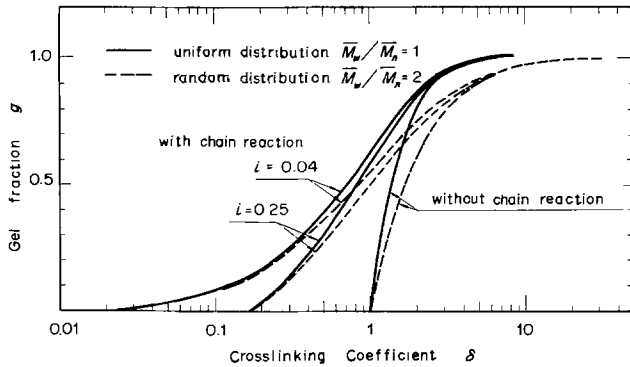


Fig. 1. Theoretical relationships between gel fraction  $g$  and crosslinking coefficient  $\delta$  for the cases without chain reaction and with chain reaction corresponding to an inhibitor activity  $i = 0.04$  and  $0.25$ .

veniently by use of the empirical depth-dose function (17) and the radiation yield  $G$  defined as the number of cross-links effected per 100 eV of the energy absorbed. For a nonchain process, a relationship between  $\delta$  and  $q$  has been given (18), assuming no chain scission

$$\delta = \delta_0 \{1 - \exp(-Kq/\delta_0)\} \quad [5]$$

with

$$K = \frac{GM_w \Delta E}{50e\rho N_A}$$

where  $\delta_0$  is the total number of cross-linkable sites per molecule,  $\Delta E$  the energy absorbed per unit length,  $\rho$  the density,  $e$  the electronic charge, and  $N_A$  Avogadro's number. In electron resists,  $\delta_0$  is in general much larger than 100, whereas gel fraction almost saturates when  $\delta$  is larger than 10. Therefore, Eq. [5] can be reduced to a linear relationship between  $\delta$  and  $q$ .

In the case of a chain reaction,  $\delta$  appearing in Eq. [1] and [2] is the over-all cross-linking coefficient, including the effect of chain propagation. Since each radical produced directly by electron irradiation gives rise to a chain reaction linking together  $1/i$  molecules on the average (in this sense,  $\alpha \equiv 1/i$  may be called the chain reaction coefficient), a linear relationship between  $\delta$  and  $q$  is obtained

$$\delta = Kq/i \quad [6]$$

The factor  $K$  determines the sensitivity and therefore is called the sensitivity factor in this work.

Assuming the critical dose  $q_m$ , defined as the minimum dose required for insolubilization, corresponds to the gel point predicted theoretically, Eq. [6] yields

$$G_a = \frac{G_i}{i} = \frac{50e\rho N_A \delta_m}{M_w \Delta E q_m} \quad [7]$$

Here,  $G_i$  is the radiation yield for the reaction initiated directly by the electron irradiation and  $G_a$  is the radiation yield for the over-all reaction propagated via radicals. If  $i = 1$  and  $\delta_m = 1$ , Eq. [7] gives the formula derived by Ku and Scala (9).

**Contrast and sensitivity.**—Contrast is a measure of the gradient of the exposure curve of the resist and is one of the main factors determining the edge acuity of the exposed and developed pattern. A gradual slope at the pattern edge is a reflection, through the shape of the exposure curve of the resist, of the spatial distribution of the exposing beam and the subsequently scattered electrons (19, 20).

The definition of contrast as the slope of the linear portion of the exposure curve does not include the tailing at low dosages as in the EPB results shown later, which effectively affects the cutoff of the edge

(21). Moreover, exposure with low dosage is preferable for high resolution work since the effect of scattered electrons becomes significant in the high dosage region. Thus, the slope between the critical dose  $q_m$  and the dose required for  $d/d_0 = 0.5$ ,  $q_{0.5}$ , is employed as the definition of contrast and denoted  $\Gamma_{0.5}$

$$\Gamma_{0.5} \equiv \frac{0.5}{\log(q_{0.5}/q_m)} \quad [8]$$

In many cases, this definition gives a good linear approximation to the lower portion of the exposure curve.

A theoretical value of  $\Gamma_{0.5}$  for a uniform distribution is given from the definition and Eq. [1]

$$\Gamma_{0.5} = \frac{0.5}{\log(\delta_{0.5}/\delta_m)} \approx \frac{0.5}{\log\{1.39(1+i)^2/i(1+3i)\}} \quad [9]$$

where  $\delta_{0.5}$  is the cross-linking coefficient for  $g = 0.5$ .  $q_{0.5}$  is employed as a measure of sensitivity. Using Eq. [6]

$$q_{0.5} = \frac{i\delta_{0.5}}{K} \approx \frac{0.693i(1+i)^2}{K(1+3i)(1-i)} \quad [10]$$

For a random distribution, similar equations can be derived which differ only in factors, that is, 1.39 in Eq. [9] is replaced by 1.66 and 0.693 and in Eq. [10] by 0.828.

Calculated results of  $\Gamma_{0.5}$  and  $q_{0.5}$  are shown in Fig. 2, where the curves with solid lines are for a uniform distribution, and those with broken lines are for a random one.  $q_{0.5}$  is a function of both  $K$  and  $i$ , while  $\Gamma_{0.5}$  is determined only by  $i$ . The axes of  $i$  for uniform and random distributions are shown on the right side. It is shown in the figure that when the inhibition of chain reaction  $i$  decreases, the sensitivity increases, while the contrast decreases. It is also shown that with an increase in  $i$ , the contrast approaches saturation values, 3.5 in a uniform distribution and 2.3 in a random distribution, which are the contrast values in the nonchain process. On the other hand, with the increase in the sensitivity factor  $K$  as shown in the figure for  $K = 10^4, 10^5, 10^6$ , and  $10^7$  ( $\text{cm}^2/\text{C}$ ), these curves are shifted laterally toward high sensitivity without changing contrast.

## Experimental

**Experimental procedures.**—Resist materials studied were KTRF (Eastman Kodak Company), PMVS (Toray Silicone Company, SH 410), EPB (Tokyo Ohka Kogyo Company), and a styrene-butadiene copolymer with  $\alpha$ -PMI (Somar Manufacturing Company). These materials contain a double bond, epoxy,

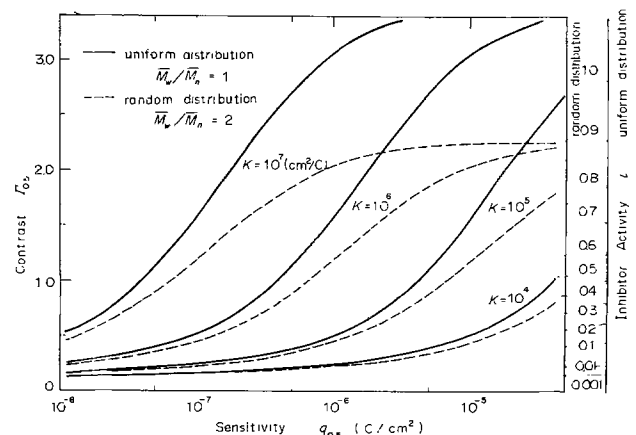


Fig. 2. Theoretical relationships between contrast  $\Gamma_{0.5}$  and sensitivity  $q_{0.5}$  ( $\text{C}/\text{cm}^2$ ) for the sensitivity factor  $K = 10^4, 10^5, 10^6$ , and  $10^7$  ( $\text{cm}^2/\text{C}$ ).

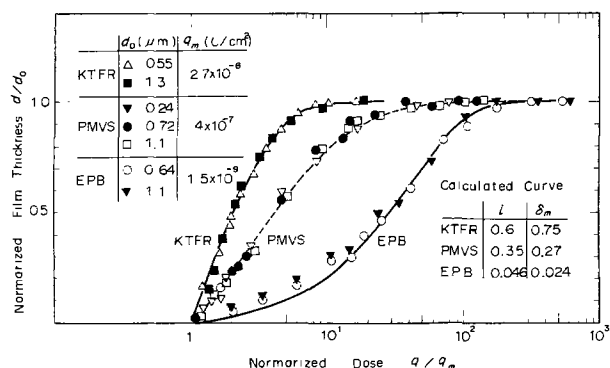


Fig. 3. Comparison of exposure characteristics of KTFR, PMVS, and EPB with the theoretical curves. The curves with solid lines for KTFR and EPB are calculated from the equation for uniform molecular weight distribution, and the curve with the broken line for PMVS is for a random distribution

or  $\alpha$ -PMI which can initiate chain reactions, and the critical doses ranged from  $1.5 \times 10^{-9}$  to  $2.7 \times 10^{-6}$  C/cm<sup>2</sup>.

Resist films were prepared by the conventional spin-coating method on aluminum films of about 150Å thickness evaporated on glass plates. In order to prevent spontaneous cross-linking (22) affecting reproducibility, the resist films were coated just before the electron exposure. After exposure to a uniformly diverging electron beam, the resist film was developed with the proper solvent. Then the thickness of the insoluble film left on the substrate  $d$  was measured with a Tolansky-type interferometer.

**Results and discussions.—Gel-dose relation.**—Measured relationships between normalized film thickness after development  $d/d_0$  and normalized exposure charge density  $q/q_m$  for EPB and PMVS at the incident electron energy  $E_0 = 20$  keV, and for KTFR at  $E_0 = 40$  keV are shown in Fig. 3. The thickness of the saturation  $d_0$  is found to closely coincide with the initial thickness in PMVS and KTFR. In EPB, deformation of the film during development is significant in the saturating region. Consequently, measurement of the saturation thickness is often affected, and the accuracy of the characteristics for EPB is not as precise as for PMVS and KTFR. The obtained curve, however, is qualitatively similar in shape to that given by Feit *et al.* (7).

By equating the experimental value of  $q_{0.5}/q_m$  to the theoretical expression of  $\delta_{0.5}/\delta_m$  by Eq. [1] or [2], values of  $i$  and consequently of  $\delta_m$  by Eq. [4] are obtained. The curves in Fig. 3 are the calculated results. It is seen that the experimental points fit fairly well to the calculated curves of Eq. [2] for  $i = 0.35$  in PMVS, and of Eq. [1] for  $i = 0.6$  and  $0.046$  in KTFR and EPB, respectively.

In order to estimate the radiation yield,  $\Delta E$  is calculated using the depth-dose function given by Hoff and Everhart (17), and  $\bar{M}_w$  is measured with a gel permeation chromatograph (Hitachi GPC-635). In each resist, average values of  $\Delta E$  and  $q_m$  are used for different  $d_0$ . In Table I the values obtained for  $i$ ,  $\delta_m$ ,  $G_i$ ,

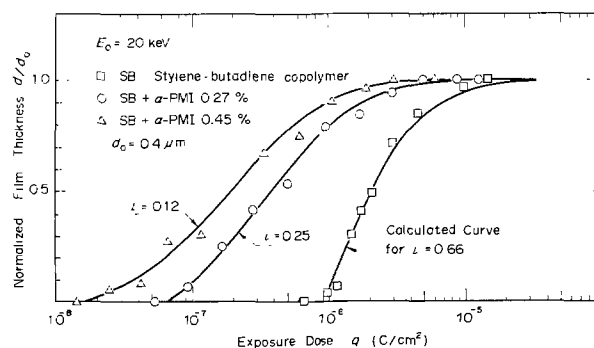


Fig. 4. Variation of the exposure characteristic in SB due to the introduction rate of  $\alpha$ -PMI. The curves are calculated from the equation for random molecular weight distribution with the inhibitor activity  $i = 0.66$  for the original SB, and  $i = 0.25$  and  $0.12$  for SB with 0.27 and 0.45 m/o  $\alpha$ -phenylmaleimided styrenes, respectively.

and  $G_a$  are shown, together with the material and the experimental parameters.  $G_a = 1.14$  in KTFR is comparable to the value 1.20 which has been obtained by assuming that  $G_1$  is equal to the  $G$  value of KPR (Kodak photo resist) (11). The high sensitivity (small value of  $q_m$ ) in EPB, in spite of the small value of  $G_i$ , is due to the fact that  $\delta_m$  is much less than one and the multiplication of the reaction by chain propagation amounts to over 20 times.

Radiation-induced scission was proposed as a partial explanation for the slow rate of gel formation in EPB by Feit *et al.* (7). According to the theory of simultaneous cross-linking and main chain scission for a nonchain process (23), the maximum gel fraction attainable,  $g_0$ , decreases and the gel point increases with an increase in the ratio of degradation to cross-linking,  $p_0/q_0$ . However, it is found that when the calculated relationships between gel fraction and cross-linking coefficient are reduced to a normalized form,  $g/g_0$  vs.  $\delta/\delta_m$ , the shapes of the curves are almost independent of the value of  $p_0/q_0$ . Another possibility is the scission of cross-links (7). In this case, a term of  $-q^2$  will be added to the linear relationship between  $\delta$  and  $q$ , since the increment of scission is proportional to the number of cross-links already formed. Then the gel-dose curve will become more gradual than those shown in Fig. 3 especially in the high dose region.

**Contrast and sensitivity.**—It was found that the sensitivity of SB (styrene-butadiene copolymer) can be increased by introduction of  $\alpha$ -PMI ( $\alpha$ -phenylmaleimide) to phenyl groups on the styrene molecules. In Fig. 4, the exposure characteristics of SB's with 0.27 and 0.45 mole percent (m/o) of  $\alpha$ -phenylmaleimided styrenes are shown in comparison with that of the original SB which is a copolymer of 40 m/o styrene and 60 m/o butadiene. It can be seen that a lowering of the critical dose by over one order of magnitude is achieved by a small introduction of  $\alpha$ -PMI. This suggests that a chain process must be included in the reaction. Comparison with the theoretical formula of the chain reaction for a random dis-

Table I. Experimental parameters and radiation yields

Resist	Molecular weight, $\bar{M}_w$	Electron energy, $E_0$ (keV)	Critical dose, $q_m$ ( $\text{C}/\text{cm}^2$ )	Inhibitor activity, $i$	Gel point, $\delta_m$	Radiation yield for	
						Initiation, $G_i$	Over-all reaction, $G_a$
KTFR	$1.0 \times 10^{5*}$	40	$2.7 \times 10^{-6}$	0.6	0.75	0.68	1.14
PMVS	$2.3 \times 10^5$	20	$4.0 \times 10^{-8}$	0.35	0.27	2.1	6.0
EPB	$3.8 \times 10^5$	20	$1.5 \times 10^{-9}$	0.046	0.024	0.36	7.8

\* Ref. (11).

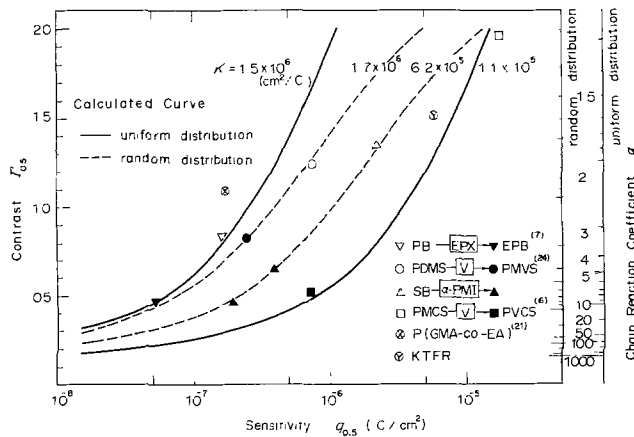


Fig. 5. Comparison of experimental data on contrast  $\Gamma_{0.5}$  and sensitivity  $q_{0.5}$  with the calculated curves. Abbreviations used in the figure are as follows: EPX = epoxidation, V = introduction of vinyl groups,  $\alpha$ -PMI =  $\alpha$ -phenylmaleimidation.

tribution, Eq. [2], shows that the best fits are obtained when  $i = 0.66$  for the original SB,  $i = 0.25$  for SB with 0.27%  $\alpha$ -PMI, and  $i = 0.12$  for SB with 0.45%  $\alpha$ -PMI. In the original SB where  $i = 0.66$ , the gel point is close to 1 and the chain reaction coefficient  $\alpha$  is about 1.5. This means that the chain process is not dominant in the original SB. The curves in Fig. 4 are the calculated results, showing good agreement with the experimental data.

The observed variation of contrast  $\Gamma_{0.5}$  and sensitivity  $q_{0.5}$  of SB with the introduction rate of  $\alpha$ -PMI is shown in comparison with the calculated curve for  $K = 6.2 \times 10^5$  ( $\text{cm}^2/\text{C}$ ) in Fig. 5, where the axis of the chain reaction coefficient  $\alpha \equiv 1/i$  corresponding to contrast  $\Gamma_{0.5}$  is at the right side. Similar variations can be seen in experimental data previously reported, which are also shown in Fig. 5. EPB is reported to present higher sensitivity and lower contrast than the original PB (1,4-polybutadiene, CB221) (7). The data are compared with the calculated curve for  $K = 1.5 \times 10^6$  ( $\text{cm}^2/\text{C}$ ). It can be seen that, as suggested by Feit *et al.* (7), gel formation in CB221 includes chain processes, and the shift towards high sensitivity and low contrast in EPB coincides with the calculated variation, corresponding to the increase in the chain reaction coefficient  $\alpha$  from 3 to 10.

PMVS has a molecular structure in which methyl groups of polydimethylsiloxane (PDMS) are replaced by vinyl groups to more than 1 m/o (16). Experimental data of PMVS and PDMS (24) are shown in Fig. 5, compared with the calculated curve for  $K = 1.7 \times 10^6$  ( $\text{cm}^2/\text{C}$ ). Experimental points of polymethylcyclosiloxane (PMCS) and polyvinylcyclosiloxane (PVCS) obtained from exposure curves by Roberts (6) are also shown in comparison with the calculated curve for  $K = 1.1 \times 10^5$  ( $\text{cm}^2/\text{C}$ ). Although precise measurements on molecular parameters and detailed investigation into the gel formation mechanism

in individual resist materials are not carried out, fairly good agreement between the experimental data and the calculated curves supports the applicability of the theory to those materials.

Experimental values of  $\Gamma_{0.5}$  and  $q_{0.5}$ , and estimated values of  $i$ ,  $\delta_m$ ,  $\alpha$ , and  $K$  for each resist are listed in Table II. The value of  $i$  is obtained by equating  $\Gamma_{0.5}$  to the theoretical formula Eq. [9], then  $\delta_m$  is given by Eq. [4] and  $K$  is calculated from Eq. [6] using  $i$ ,  $\delta_m$ , and  $q_m$ . The estimated values of  $K$  in each group of the resist material are not greatly changed by the improvement in sensitivity. This suggests that the change in  $G$  is not so significant as to result in an increase in sensitivity by one order or more, since  $\overline{M}_w$ , the other changeable parameter in  $K$ , is probably not changed significantly by the introduction of epoxy, vinyl, or  $\alpha$ -PMI. In fact,  $G_i = 2.1$  obtained for PMVS is comparable to  $G = 2.2$ -2.5 in PDMS obtained by irradiation of 800 kV electrons (25, 26). Thus the improvement in sensitivity by the introduction of epoxy, vinyl, or  $\alpha$ -PMI is mainly due to the increase in the subsequent multiplication of the reaction by chain propagation, indicated by  $\alpha$ , and the decrease in the gel point  $\delta_m$ .

As a result, it may be concluded that in order to obtain resists with high contrast and high sensitivity, large  $K$  and small  $\alpha$  are preferable. If a high contrast larger than 1.0 is required, the chain reaction should be restricted so that  $\alpha$  is less than about 2, when the chain process becomes no longer dominant, as in P(GMA-co-EA) (21), PDMS (16, 24), SB, and PMCS (6).

## Conclusions

Exposure characteristics of negative electron resists are studied on the basis of Charlesby's theory on gel formation through chain reactions. By use of the theory, the important resist parameters, sensitivity and contrast, can be related quantitatively to the chemical properties of the material. Some important aspects are summarized as follows.

1. It is experimentally verified that Charlesby's theory on gel formation by chain reactions is applicable to exposure curves of KTFR, PMVS, and EPB.
2. By use of the theory, the radiation yield for the reaction initiated directly by the electron irradiation  $G_i$  and that for the over-all reaction including the effect of chain propagation  $G_a$  is separately estimated.  $G_i$  is small even in EPB, the resist of the highest sensitivity previously reported. The high sensitivity is mainly due to the decrease in the gel point and to the increase in the chain reaction coefficient.
3. It is found that the sensitivity of styrene-butadiene copolymers is increased by the introduction of  $\alpha$ -PMI. This increase in sensitivity is also explained by the theory.
4. Theoretical formulas of contrast and sensitivity are given as functions of the inhibitor activity of the chain reaction  $i$  and the sensitivity factor  $K$ . Improvement in sensitivity and associated lowering in contrast by epoxidation in polybutadiene, by  $\alpha$ -phenyl-

Table II. Parameters related to contrast and sensitivity

Resist material	Contrast, $\Gamma_{0.5}$	Sensitivity, $q_{0.5}$ ( $\text{C}/\text{cm}^2$ )	Inhibitor activity, $i$	Chain reaction coefficient, $\alpha$	Gel point, $\delta_m$	Sensitivity factor, $K$ ( $\text{cm}^2/\text{C}$ )
Polybutadiene						
Original (CB221) (7)	0.83	$1.6 \times 10^{-7}$	0.31	3.2	0.22	$1.8 \times 10^6$
Epoxidized (EPB-9) (7)	0.45	$5.2 \times 10^{-7}$	0.099	10.1	0.055	$1.4 \times 10^6$
Polysiloxane						
Original (PDMS) (24)	1.24	$7.4 \times 10^{-7}$	0.60	1.7	0.75	$1.6 \times 10^6$
Vinyl-introduced (PMVS) (24)	0.83	$2.4 \times 10^{-7}$	0.37	2.7	0.29	$1.8 \times 10^6$
Styrene-butadiene copolymer						
Original	1.36	$2.1 \times 10^{-6}$	0.66	1.5	0.97	$7.0 \times 10^5$
$\alpha$ -PMI 0.27%	0.65	$3.8 \times 10^{-7}$	0.25	4.0	0.17	$6.5 \times 10^5$
$\alpha$ -PMI 0.45%	0.45	$1.9 \times 10^{-7}$	0.12	8.3	0.067	$5.4 \times 10^5$
Polycyclosiloxane						
Original (PMCS) (6)	1.96	$1.8 \times 10^{-5}$	0.72	1.4	1.3	$9.3 \times 10^4$
Vinyl-introduced (PVCS) (6)	0.52	$7.0 \times 10^{-7}$	0.14	7.1	0.081	$1.5 \times 10^5$



maleimidation in SB, and by introduction of vinyl groups in polysiloxanes are in good agreement with the theoretical results.

5. In order to obtain resists with high sensitivity, large  $K$  and small  $i$  are preferable. On the other hand, for high contrast,  $i$  must be large. If a contrast higher than 1.0 is required, the chain reaction should be inhibited, so that  $i$  is larger than about 0.5.

#### Acknowledgments

The authors wish to thank Prof. K. Kanaya of the University of Kogakuin for helpful advice. They would like to thank Profs. Y. Shibata and S. Ono of Tohoku University for their valuable discussions. Thanks are also due to Dr. K. Nagasawa, H. Ochi, and F. Tanaka of the Research Department of Somar Manufacturing Company, Limited for preparation of the SB samples and for valuable discussions.

Manuscript submitted Nov. 3, 1975; revised manuscript received June 11, 1976.

Any discussion of this paper will appear in a Discussion Section to be published in the June 1977 JOURNAL. All discussions for the June 1977 Discussion Section should be submitted by Feb. 1, 1977.

Publication costs of this article were assisted by the Electrotechnical Laboratory.

#### REFERENCES

1. A. N. Broers and M. Hatzakis, "Proceedings of the 7th International Congress on Electron Microscopy," p. 249, Grenoble (1970).
2. T. H. P. Chang and B. A. Wallman, "Record of 11th Symposium on Electron, Ion, and Laser Beam Technology," p. 471, San Francisco Press, San Francisco (1971).
3. M. Hatzakis, *J. Vac. Sci. Technol.*, **11**, 95 (1974).
4. M. Hatzakis, *This Journal*, **116**, 1033 (1969).
5. L. F. Thompson, *Solid State Technol.*, **17**, 27 (July 1974).
6. E. D. Roberts, *This Journal*, **120**, 1716 (1973).
7. E. D. Feit, R. D. Heidenreich, and L. F. Thompson, *Appl. Polym. Symp.*, **23**, 125 (1974).
8. A. Charlesby, "Atomic Radiation and Polymers," Pergamon Press, New York (1960).
9. H. Y. Ku and L. C. Scala, *This Journal*, **116**, 980 (1969).
10. A. Charlesby, *Proc. R. Soc. London, Ser. A*, **222**, 542 (1954).
11. B. Broyde, *This Journal*, **116**, 1241 (1969).
12. G. Paal, U. D. Strähle, and G. Kielhorn, *ibid.*, **120**, 1714 (1973).
13. T. Hirai, Y. Hatano, and S. Nonogaki, *ibid.*, **118**, 669 (1971).
14. S. Nonogaki, H. Morishita, and N. Saitou, *Appl. Polym. Symp.*, **23**, 117 (1974).
15. A. Charlesby, *Proc. R. Soc. London, Ser. A*, **241**, 495 (1957).
16. Y. Yatsui, T. Tanaka, and K. Umehara, *This Journal*, **116**, 94 (1969).
17. P. H. Hoff and T. E. Everhart, "Record of 10th Symposium on Electron, Ion, and Laser Beam Technology," p. 454, San Francisco Press, San Francisco (1969).
18. R. D. Heidenreich, L. F. Thompson, E. D. Feit, and C. M. Melliar-Smith, *J. Appl. Phys.*, **44**, 4039 (1973).
19. S. Arakawa, N. Atoda, H. Kawakatsu, and K. Kanaya, *Rep. Kohgakuin Univ.*, **38**, 149 (1975).
20. R. D. Heidenreich, J. P. Ballantyne, and L. F. Thompson, *J. Vac. Sci. Technol.*, **12**, 1284 (1975).
21. L. F. Thompson, *Solid State Technol.*, **17**, 41 (August 1974).
22. L. F. Thompson, E. D. Feit, C. M. Melliar-Smith, and R. D. Heidenreich, *J. Appl. Phys.*, **44**, 4048 (1973).
23. A. Charlesby and S. H. Pinner, *Proc. R. Soc. London, Ser. A*, **249**, 367 (1959).
24. N. Atoda and K. Kanaya, *Bull. Electrotech. Lab., Tokyo*, **33**, 1297 (1969).
25. L. E. St. Pierre, H. A. Dewhurst, and A. M. Bueche, *J. Polym. Sci.*, **36**, 105 (1959).
26. W. Barnes, H. A. Dewhurst, R. W. Kilb, and L. E. St. Pierre, *ibid.*, **36**, 525 (1959).

## VPE Growth of n-AlAs on GaAs for Heterojunction Devices

W. D. Johnston, Jr. and W. M. Callahan

Bell Laboratories, Holmdel, New Jersey 07733

#### ABSTRACT

Vapor phase epitaxial growth of AlAs on Zn-doped GaAs substrates by chloride transport in an all-alumina reactor yields useful n-AlAs/p-GaAs heterojunction material. Smooth, planar interfaces and gently hummocked top surfaces have been obtained. The heterojunctions are found to be abrupt, both metallurgically and electrically, and have been used to demonstrate large area, high efficiency solar cells. The utility of Mn and Be as p-type dopants for vapor phase AlAs growth has been explored, without success.

In contrast to the extensive (and highly successful) efforts which have been devoted to the preparation by liquid phase epitaxy (LPE) of heterostructure materials and devices based on the  $\text{Al}_x\text{Ga}_{1-x}\text{As}$ -GaAs system, little interest has been shown in the growth of such material by vapor phase epitaxy (VPE). It is much more difficult to prepare  $\text{Al}_x\text{Ga}_{1-x}\text{As}$  of high quality by VPE for  $x$  appreciably different from 0 or 1. Alloys with  $x \sim 1$  are unstable in moist air and are more difficult to contact and process than those with significant Ga content. To date, VPE AlAs has only been obtained as n-type material and no satisfactory way to grow p-type layers of AlAs has been re-

ported. In earlier work by Sigai *et al.* (1), a type-converted interfacial layer was reported at the interface between substrate GaAs and VPE AlAs. Taken together, the device potential of VPE AlAs material appeared discouraging, particularly in contrast to the successes achieved with LPE heterostructure growth (2).

We have recently reported progress in overcoming some of these difficulties, showing that suitable anodization (3) of AlAs provides adequate protection for standard device processing, and that n-AlAs can be grown by VPE on p-GaAs substrates to provide multi-square-centimeter junctions comparable in quality to LPE material of similar area, and having

Key words: solar cells, vapor phase epitaxy, III-V compounds.

similar potential for high performance solar cells (4). This successful initial demonstration of useful AIAs device material makes further study of VPE AIAs worthwhile, and in this paper we describe our growth apparatus and technique, our observations of the relation of surface morphology to growth variables, the bulk layer electrical properties and results of our efforts to grow p-type material, and the interface properties of our n-AIAs/p-GaAs heterojunctions.

### Growth Apparatus and Technique

Our growth reactor, shown schematically in Fig. 1, is similar in general design to that described by Ettenberg *et al.* (5). In an effort to minimize problems (1, 5) arising from the reactivity of  $\text{SiO}_2$  with Al compounds, we have completely excluded fused quartz components. All components in the heated zone, save for a small quantity of tungsten sheet ( $0.2 \text{ mm} \times 1.5 \text{ cm}^2$ ) and wire ( $0.1 \text{ mm} \times 10 \text{ cm}$ ) used for securing the substrate, are made from 99.8%  $\text{Al}_2\text{O}_3$  ceramic (6). This material is vacuum tight to at least  $1300^\circ\text{C}$  and tubing to 2.5 cm diameter by 1m long has adequate mechanical strength for self-supported design. Our main reactor tubes ( $2\text{m} \times 7 \text{ cm}$  diameter, 0.4 cm wall) required over-all support to prevent cracking from their own weight under high temperature and high temperature gradient conditions. Provisions also had to be made for the tube to expand freely and move to relieve stress from thermal expansion. These ends were accomplished by mounting the  $\text{Al}_2\text{O}_3$  tube within a larger mullite tube, leaving an annular space of  $\sim 0.5 \text{ cm}$  filled loosely with expanded alumina insulating beads. Connections to gas inlet lines were made through flexible stainless steel hose at one end, and via a lightweight neoprene bellows to a gate valve at the substrate insertion (exhaust) end.

Since the growth of AIAs in the  $1000^\circ\text{--}1100^\circ\text{C}$  range is rather far from equilibrium, *i.e.*, AIAs is formed directly in the mixing region, provision must be made to extend that region to accommodate substrate placement. In the work described in Ref. (1) and (5), restriction of the  $\text{AlCl}_3\text{--H}_2$  flow by a perforated plug was used to increase the stream velocity. We use a closed-end, 2.5 cm diameter  $\text{Al}_2\text{O}_3$  tube to hold the aluminum source (5N metal), with several 1 mm holes drilled into the closed end (see Fig. 1b). Since we have noticed no important differences whether one hole or twenty-four are used in deposition geometry with the same total flow conditions, we feel that the stream velocities in our apparatus are all sufficiently low as to be unimportant compared to diffusive gas mixing. Nevertheless, the restrictions tend to prevent growth of AIAs within the Al source tube, and we normally use 20-24 evenly patterned perforations. We have grown layers with less than 10% thickness variation over  $4 \times 4 \text{ cm}$  substrates positioned 2.5 cm from the tube end.

The alumina substrate support tube is closed at the substrate end and contains a Pt-Pt/Rh thermocouple to monitor temperature at the substrate position. The motion required for substrate insertion and withdrawal is accommodated with a 1.2m long flexible "bellows" seal made from thin wall, large diameter rubber tubing. The assembly is leak-free under vac-

uum or  $\text{H}_2$  overpressure to  $1400^\circ\text{C}$ . A three-zone furnace with independent temperature controllers provides  $\pm 1^\circ\text{C}$  stability in the source and growth regions.

Additional  $\text{Al}_2\text{O}_3$  ceramic tubes permit other metal species to be introduced into the growth region. Ga, Be, or Mn can be transported as chlorides by introducing gaseous  $\text{HCl}$  into the  $\text{H}_2$  flow through the appropriate tube. In the initial stages of this work, an  $\text{AlCl}_3$  sublimation source external to the main reactor was used. We were unable to obtain good epilayer growth, which we attribute to the presence of excess  $\text{HCl}$  [ $\text{AlCl}$  is the stable species at our growth temperatures (5)]. At the inlet end of the growth apparatus the ceramic tubes are sealed with Viton O-rings and Monel fittings. The  $\text{Al}_2\text{O}_3$  ceramic is neither particularly round nor smooth compared to fused silica tubing, but vacuum- and pressure-tight demountable static seals can be achieved with care. The inlet gas plumbing utilized standard commercial stainless steel and Monel components and included manual differential pressure-type flow controllers.

The apparently trivial task of devising a substrate holder proved difficult owing to the corrosive  $\text{HCl}/\text{AlCl}$  atmosphere, the large temperature excursion, etc. Commercial "high alumina" ceramic cements disintegrate due to chloride attack on proprietary binder materials, apparently sulfates and silicates or silica. A satisfactory solution was obtained with a small quantity of tungsten wire and sheet and small diameter alumina rod as shown in Fig. 1b. The tungsten suffers typical hydrogen embrittlement and eventual fracture after several dozen growth runs, but is available for inspection and replacement after each run as needed and does not appear to be attacked by the chloride vapors.

In normal operation the furnace is brought to temperature at about  $100^\circ\text{K}$  per hour and maintained at growth temperature for many runs. Cooling is accomplished at a similar rate to avoid thermomechanical stresses on the alumina components. Except for modifications, metals reloading, or cleaning, a flow of high purity hydrogen is maintained through the reactor tubing assembly.

The growth sequence is straightforward: commercially obtained GaAs substrates, typically (100) oriented with a Syton-NaOCl polish, were etched for 20 min in 4:1:1  $\text{H}_2\text{SO}_4/\text{H}_2\text{O}/\text{H}_2\text{O}_2$ , rinsed in deionized water, 2% Br-methanol, and high purity methanol, and mounted on the substrate holder rod. The air lock chamber is closed, evacuated, and flushed with  $\text{H}_2$ , the gate valve to the growth reactor opened, the  $\text{AsH}_3$  flow initiated, and the substrate inserted, allowing a few minutes to equilibrate at about  $500^\circ$  and  $800^\circ\text{C}$ , before insertion to the final position in the  $1000^\circ\text{--}1100^\circ\text{C}$  range. The quality of the GaAs/AIAs interface depends on the timing of initiation of  $\text{HCl}$  flow over the Al during this insertion, since thermal etching of the GaAs is rapid at  $1000^\circ\text{C}$  and growth must start promptly. The  $\text{HCl}$  flow must not be initiated too soon, on the other hand, as the downstream  $\text{HCl}$  leads to chemical vapor etching at temperatures as low as  $600^\circ\text{C}$ . Both the high temperature thermal etching and the  $\text{HCl}$  vapor etching are selective and preferentially

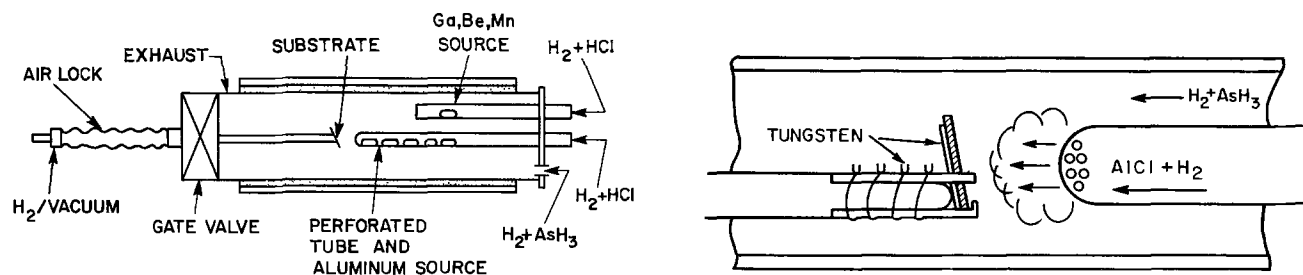


Fig. 1. (a, left) Schematic drawing of growth reactor. (b, right) Detail of substrate holder and aluminum source tube

attack residual work damage, points of dislocation emergence, etc.

The typical flow rates for our reactor are 4 cm<sup>3</sup>/min for HCl and AsH<sub>3</sub> and a total of 2 liters/min of H<sub>2</sub>. (The HCl and AsH<sub>3</sub> are both obtained as 2% dilutions in H<sub>2</sub>, and further diluted in the reactor.) Reactant flow is continued for the desired time (growth may be varied from ~10 to ~60 μm per hour), after which the substrate is withdrawn and reactant flows returned to pure H<sub>2</sub>. Growth of alternating layers of GaAs and AlAs is accomplished by partially withdrawing the substrate to an appropriate position in the 600°-800°C range and switching the HCl flow from the Al source to the Ga source, then reversing the procedure to grow another AlAs layer, etc. In this way we have grown alternating layers with good planarity as thin as 0.5 μm.

The primary attractive feature of VPE as compared to LPE or molecular beam epitaxy (7) (MBE) is the potential ease of transfer from research scale to economical production scale growth. The alumina ceramic components of our furnace are presently available commercially (6) in larger sizes which would permit a tenfold increase in production rate, from ~50 cm<sup>2</sup>/hr which we have achieved with the apparatus of Fig. 1 (for 20 μm thick epitaxial layers) to at least 600 cm<sup>2</sup>/hr. Such a capability is of paramount importance if significant penetration of the space solar cell market [presently 500 m<sup>2</sup> per year (8) for silicon arrays] is seriously contemplated, and absolutely essential for significant terrestrial electric power impact (9), for which a production capacity several orders of magnitude larger must be considered.

#### Surface Morphology and Reactivity of AlAs Epilayers

The nature of the surface of our VPE AlAs epilayers depends on growth temperature, flow ratio of

HCl (over Al) to AsH<sub>3</sub>, absolute concentration of HCl and AsH<sub>3</sub>, total gas flow rate, substrate orientation and surface treatment, position of substrate relative to the perforated end of the Al source tube, the detailed sequence and timing of substrate insertion and reactant flow initiation, and the long term history of the growth reactor. The last three factors arise from the necessity of growing at a temperature substantially lower than would be desirable from thermodynamic considerations of the As-AlCl reaction kinetics (5). In the 1000°-1100°C range this reaction goes strongly to form AlAs and the deposition range is limited to a few centimeters from the point of AlCl injection into the As atmosphere. Growth occurs in the vicinity of the substrate on the reactor walls, on the perforated tube end, and on the substrate holder as well as on the substrate, and eventually the reactor must be cooled down and cleaned of this deposit. As an alternative, the temperature at the growth region may be raised temporarily above ~1300°C to move the deposit downstream from the substrate position. This permits extension of the time between cleanings, which otherwise are necessary after 30-40 hr of growth operation.

The epitaxial surfaces may be grossly characterized as specular, as having hillocks or hummocks, or as terraced. Misfit dislocation arrays are apparent as (110) directed rectilinear grids, most simply seen in Nomarski interference contrast micrographs, and are a typical feature. The misfit dislocation arrays were observed on all surfaces except those with grossly disturbed topography. Examples of surface appearance are shown in Fig. 2.

Several distinctions may be made with the more familiar VPE growth of GaAs layers. First, terracing is not a typical feature of the AlAs layers, and appears to occur only in conjunction with a characteristic "rectangular etch pit" attack of the substrate prior to

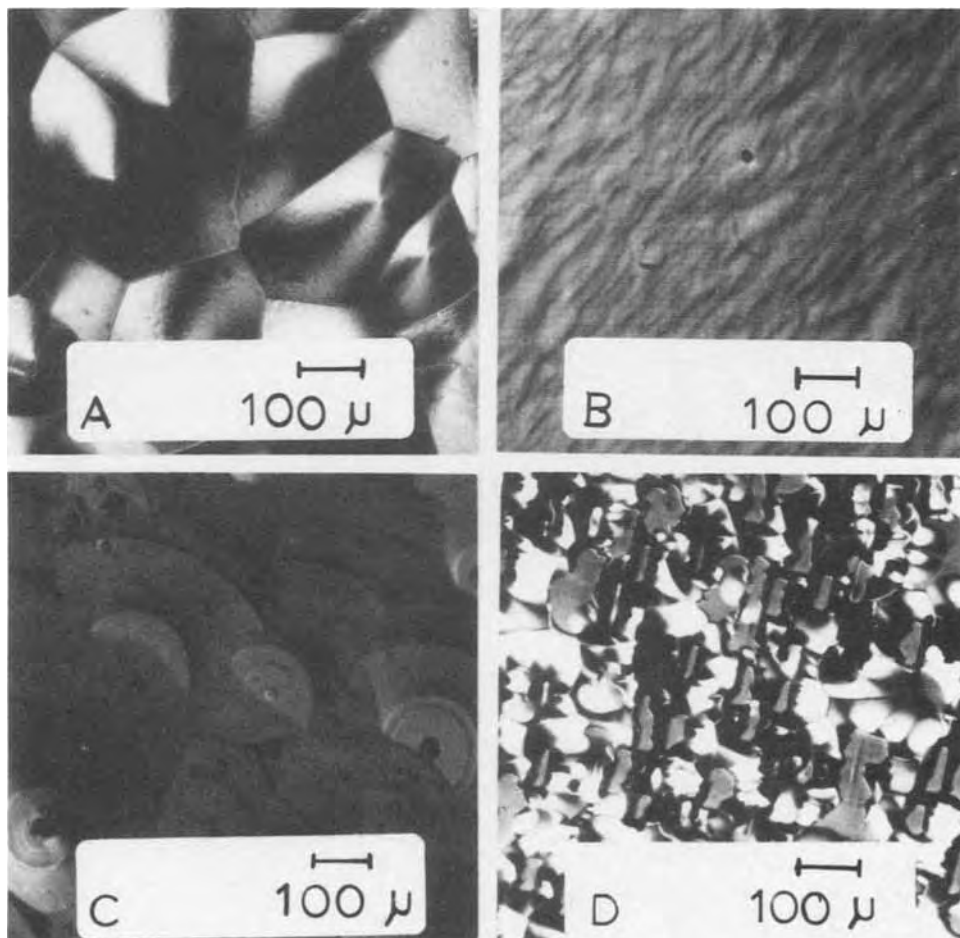


Fig. 2. Differential interference contrast micrographs of surfaces of AlAs VPE layers: A = hillocks, growth at 32 μm/hr; B = "smooth," growth at 12 μm/hr; C = terracing, low As partial pressure; D = rough, disordered surface indicative of severe selective thermal etching of GaAs substrate as in Fig. 5A. Surfaces A and B are more stable and surface D much less stable than surface C in humid air.

growth. This is an effect which may be prevented by ensuring that As vapor is present at the concentration to be used during growth before the substrate is introduced into the high temperature region of the reactor and by proper sequencing of the HCl flow initiation. Terrace planes were observed in the transition region between correct Al/As stoichiometry and the As-rich, Al-poor periphery where spotty, imperfect growth took place, using a single hole Al source tube and low AlCl/AsH<sub>3</sub> flow ratios. GaAs layers grown in this apparatus often showed stacking faults, particularly for growth above 800°C, but this behavior was not seen for any AlAs layers grown up to the 1130°C maximum temperature investigated. Substrate orientation is a matter of some importance in obtaining smooth layers for GaAs, but we were unable to observe consistent behavior for AlAs epitaxy, i.e., whether orientation was nominally on <100> or 2°-4° off <100> [toward (110)] did not make much difference. The growth rate and topography were determined by local reactant stoichiometry (mostly reflecting Al source/substrate geometry). In several instances highly specular, featureless layers were grown at about half the usual growth rate on substrates that appeared to be oriented almost exactly to the (100) plane, i.e., much more closely than the nominal ±10' typical orientation accuracy.

These differences may all be understood qualitatively as reflecting the very substantial departure from equilibrium growth. For near-equilibrium growth relations among growth rate, stacking fault occurrence, terrace formation, and surface energy are beginning to be understood (10), but the relevant approximations do not apply for AlAs growth under our conditions. The typical hummock pattern is also seen for VPE growth of InP, AlP, GaAs, and Si when the substrate temperature is low and reactant supply high. At the highest growth temperatures we investigated, specular surfaces were more often obtained and hummock density was much reduced, but difficulties with evaporation of the GaAs substrate and deterioration of the bulk electrical properties of the AlAs layer became substantial.

The stability of the AlAs layers in air depends on surface quality, relative humidity, and surface post-growth history. Below about 25% relative humidity, surfaces with low hummock density form a protective oxide layer and are stable against further change for several days. The layers may be stored without oxide formation in a low humidity environment (N<sub>2</sub>, dry air, or O<sub>2</sub>) or under hexane, trichloroethylene, etc. A controlled, stable oxide layer is most easily formed by anodization (3) in highly pure water (resistivity greater than 18 megohm-cm) to which H<sub>3</sub>PO<sub>4</sub> has been added to modify the pH to the 1.9-2.0 range. This oxide is uniformly formed regardless of surface topography on electrically uniform layers, in contrast to that produced by radio frequency plasma oxidation (11) in oxygen, which produces a uniform oxide only on the smooth surfaces. The rf plasma oxide is also substantially less stable than the anodic oxide in moist air. Both oxides are preferentially attacked at mechanical defects such as scratches, cleaved edges, and at the apexes of topographical features such as hummock peaks where the local surface curvature is a maximum.

Similar surface effects were noted for interaction with evaporated oxides. SiO<sub>x</sub> layers were found to react with as-grown AlAs preferentially at regions of high local curvature, followed by rapid deterioration in moist air. SnO<sub>2</sub>-evaporated films react with AlAs at 400°C in dry air. Indium-tin-oxide (ITO, 91% In) films (12) did not react on smooth AlAs layers but were reduced on the hillock-covered AlAs surfaces under the same conditions. (A 400°C air bake is used to convert the SnO<sub>2</sub> and ITO films to a high conductivity,

high transparency state from the as-evaporated state which is excessively deficient in oxygen.)

The solution to these difficulties is obviously growth at higher temperature. However, as discussed below, this expedient may be undesirable for other reasons, if the ultimate goal is production of heterojunctions to GaAs. With careful control of substrate-Al source geometry, reasonably smooth layers exceeding 15 cm<sup>2</sup> in area may be reproducibly grown as low as 990°C. Such layers are entirely adequate for single heterostructure device applications, but the remaining surface nonplanarity gives rise to problems with multi-heterostructure material as would be required, for instance, for continuous wave laser diodes.

### Electrical Properties of AlAs Layers

The layers grown in this study were all found to be n-type, with conductivities ranging from 0.02 to 1.0 Ω-cm. Four types of growth were attempted: undoped "high purity" layers (i.e., lowest attainable carrier concentration with highest Hall mobility), undoped layers with reproducible and controlled carrier concentration in the 10<sup>17</sup>-10<sup>18</sup> cm<sup>-3</sup> range, and layers doped with Be or Mn, intended to be p-type. Electrical characterization was made by the Van der Pauw (13) method using spark-formed contacts with 80 μm Au-2% Sn wire. Conductivity type was verified with a thermal probe. The results are summarized in Fig. 3.

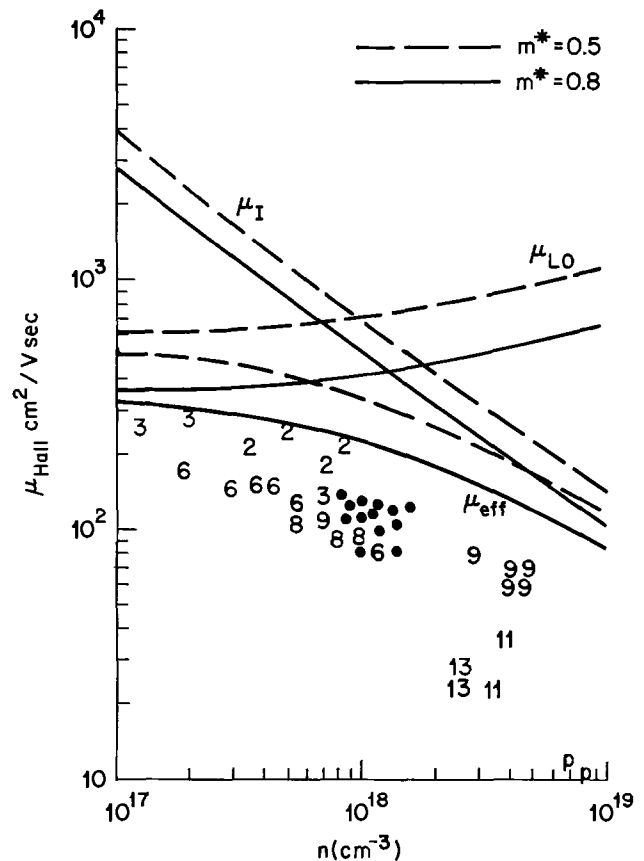


Fig. 3. Mobility and carrier concentration from Hall measurements. The numeric symbols relate to growth temperature as (10 × symbol) + 1000 in °C, and represent runs for which flow rates and geometry were adjusted for maximum mobility. The solid points represent runs at 1000°-1030°C for which growth rates of ~20 μm/hr, good large area uniformity, and fairly smooth surfaces were obtained together with a desired carrier concentration in the 0.7-2.0 × 10<sup>18</sup> cm<sup>-3</sup> range. The points marked p represent Be-doped material for which N<sub>Be</sub> ~ 4 × 10<sup>18</sup>, N<sub>Si</sub> > 10<sup>19</sup>, N<sub>Mg</sub> ~ 5 × 10<sup>17</sup> cm<sup>-3</sup> levels were inferred, and except for addition of BeCl<sub>2</sub> were grown identically to the runs shown as points. Theoretical curves represent limiting mobilities predicted: μ<sub>I</sub>, from ionized impurity scattering assuming no compensation; μ<sub>LO</sub>, from optic phonon scattering; and μ<sub>EFF</sub> (μ<sub>EFF</sub><sup>-1</sup> = μ<sub>LO</sub><sup>-1</sup> + μ<sub>I</sub><sup>-1</sup>).

After a series of growth runs at constant temperature and flow conditions, samples of bulk AlAs ( $\sim 1$ g) deposited in the vicinity of the substrate were analyzed qualitatively by emission spectroscopy and quantitatively by atomic absorption spectroscopy. For the undoped runs, particular attention was paid to Mg, Cu, Fe, and Si on the basis of analysis of the  $\text{Al}_2\text{O}_3$  ceramic material. Of these elements, only Si was detected as a "faint trace," substantially below the quantitative limit of 2 ppm. We can thus state that less than 2 ppm Si was present, with a best estimate of  $\sim 0.2$  ppm. If fully electrically active, this would provide an estimated donor concentration of  $\sim 1.6 \times 10^{16} \text{ cm}^{-3}$ , nearly two orders of magnitude below that actually observed. Thus we conclude that while Si contamination has not been eliminated in our apparatus, a native defect donor is the more likely cause of the observed n-type conductivity.

The level of conductivity may be reproducibly controlled by fine (i.e. millimeter increments) adjustment of the Al source/substrate distance, by modification of the growth rate through the absolute HCl and  $\text{AsH}_3$  inlet flows, and to a lesser degree by adjustment of the HCl/ $\text{AsH}_3$  inlet ratio or substrate temperature. With increasing growth temperature, the net donor concentration increased, passed through a maximum at about  $1090^\circ\text{C}$ , and then decreased again at higher temperatures. Over this range the mobility decreased monotonically. The highest mobility is obtained at low temperatures ( $\sim 1000^\circ\text{C}$ ) and low growth rates ( $\sim 10 \mu\text{m/hr}$ ), conditions which produce a combination of hillocks and terraces on the surface and a moderately roughened layer-substrate interface. For fixed-growth conditions, the net carrier concentration is one of the most reproducible features of our material, varying less than 20% among repeated runs. This corresponds to the variation from corner to corner over a given substrate and is about the same as the accuracy of our electrical characterization technique.

It would be desirable to be able to prepare p-type AlAs layers without resorting to postgrowth diffusion. Sigai *et al.* (1) have reported a lack of success in growing AlAs with Zn incorporation during growth. We have tried incorporation of Be or Mn, both of which may be readily transported as chlorides at the temperatures in our reactor. With Be, we were able to obtain levels of about  $10^{18} \text{ cm}^{-3}$  as determined by atomic absorption spectroscopy. At the same time, however, about  $2 \times 10^{17} \text{ Mg atoms/cm}^3$  and  $8 \times 10^{18} \text{ Si atoms/cm}^3$  were incorporated. The result was compensated n-type conductivity with net donor concentrations in the  $7\text{--}8 \times 10^{18}$  range and Hall mobilities of 8–10. This more-than-three order of magnitude increase of Si appears to be due to attack on the  $\text{Al}_2\text{O}_3$  ceramic by  $\text{BeCl}_2$  vapor, in which BeO and AlCl are formed. White needles were observed growing from the Al source tube in the vicinity of the substrate as well as on the walls of the Be source. Si is apparently liberated from the 0.1%  $\text{SiO}_2$  impurity content of the alumina ceramic as volatile chlorides or oxychlorides and incorporated in the growing AlAs. The greater fraction ( $\sim 0.8$ ) of the  $\text{BeCl}_2$  formed must have reacted with the  $\text{Al}_2\text{O}_3$  ceramic in this way to account for the quantity of Si observed. The Be used contained less than 15 ppm Si and remains in solid form throughout the growth procedure so direct transport of the observed quantity of Si from the Be metal seems unlikely.

The observed Hall mobility and concentrations of Si, Be, and net carriers are consistent with the assumption that all the Be is present as an electrically active acceptor, so it would appear that p-type AlAs could be grown in an apparatus resistant to  $\text{BeCl}_2$  attack. BeO ceramic tubing is an obvious choice but was not available to us in the required sizes during this work.

In contrast, the results with Mn are less encouraging. We were unable to obtain Mn incorporation into the growing epilayer, due to the formation of  $\text{Mn}_2\text{As}$  at the

point of injection into the As atmosphere. (A black crystalline mass,  $\text{Mn}_{2.1}\text{As}$  by analysis, was recovered from the region between the Mn source and the substrate.) The conversion of Mn to  $\text{MnCl}_2$  and transport thereof was quantitative. An arrangement where the Mn and Al chlorides are mixed and injected together into the As ambient at the vicinity of the substrate would be more suitable.

Also shown in Fig. 3 are theoretical curves of limiting mobility due to scattering by polar optical phonons ( $\mu_{\text{LO}}$ ) and scattering by ionized impurities ( $\mu_{\text{I}}$ ). The following equations were used

$$\mu_{\text{I}} \approx \frac{3.2 \times 10^{15} (m_0/m^*)^{1/2} e^2 T^{3/2} / (N_{\text{D}} + N_{\text{A}})}{\ln[1.3 \times 10^{14} T^2 \epsilon (m^*/m_0) / N_{\text{D}} - N_{\text{A}}]} \quad [1]$$

$$\mu_{\text{LO}} = 0.199 (T/300)^{1/2} (e/e^*)^2 (m/m^*)^{3/2} (10^{22} M) \times (10^{23} v_{\text{a}}) (10^{-13} \hbar\omega) (e^z - 1) (e^{-\xi G^{(1)}}) \quad [2]$$

In Eq. [1] [see Ref. (14)]  $N_{\text{D}}$  and  $N_{\text{A}}$  are the densities of donor and acceptor impurities,  $\epsilon$  is the (static) dielectric constant ( $= 10.9$  for AlAs) and  $m^*$  the electron effective mass. In Eq. [2] [see Ref. (15)]  $M$  and  $v_{\text{a}}$  are the reduced mass and volume of an Al and As atom pair,  $\hbar\omega$  is the LO phonon energy (49 meV),  $e^*$  is the screened charge given (15) by  $0.0345 (10^{22} M) (10^{-13} \hbar\omega)^2 \times (10^{23} v_{\text{a}}) (\epsilon_{\infty}^{-1} - \epsilon^{-1})$  with  $\epsilon_{\infty}$  the dynamic dielectric constant ( $= 8.5$ ). Numerical values for AlAs were taken from Ref. (16). The remaining factors are  $z = \hbar\omega/kT$  and  $e^{-\xi G^{(1)}}$ , a function plotted in Ref. (15) which varies from 0.65 to 0.75 for AlAs,  $300^\circ\text{K}$ ,  $n \leq 10^{19}$ .

Equation [2] assumes the validity of Boltzmann statistics and a simple parabolic band. The conduction band minima in AlAs may reasonably be assumed to lie at the X point, giving three equivalent (100) valleys, each presumably ellipsoidal by analogy with GaAs. From symmetry considerations, the ground state of a donor impurity must have a degeneracy factor  $g = 2$  or  $4$  (including spin). Whitaker (17) has measured  $m^{*3/2}/g$  and determined  $m^* = 0.5$  or  $0.8$ , respectively. The relation for an effective mobility  $\mu_{\text{eff}}^{-1} = \mu_{\text{LO}}^{-1} + \mu_{\text{I}}^{-1}$  is not strictly valid theoretically (18) but is useful within the experimental limits and the theoretical approximation (single effective mass, parabolic band) here.

From Fig. 3 it can be seen that polar optic mode scattering should dominate at room temperature for carrier concentrations below about  $10^{18} \text{ cm}^{-3}$ . For carrier or ion concentrations above about  $2 \times 10^{18}$ , the scattering should predominantly arise from the impurity ions. Qualitatively at least, the data points are consistent with this picture. If the value of 0.8 is correct for  $m^*$ , our highest mobility samples would appear to be relatively uncompensated. The value of  $m^*$  for the  $x_{\text{ic}}$  conduction band minimum in GaAs is known (19) to be 0.85, which lends some plausibility to this argument.

### AlAs-GaAs Interface and Junction Properties

The difficulties encountered in growing p-type AlAs by VPE ruled out the study of p-AlAs/n-GaAs heterojunctions at this time. We have, however, investigated VPE grown n-p and n-n heterostructures. The planarity of the AlAs-GaAs transition is a function of the substrate pregrowth treatment and the timing of the thermal etch-growth initiation sequence. In Fig. 4 are shown typical optical micrographs of cleaved sections for layers grown with the empirically determined optimum sequence and with either early or late initiation of AlCl flow. The distribution of interface roughness is easily seen on samples from which the AlAs layer has been stripped with 2% HCl. The examples in Fig. 5 illustrate the selective nature of the thermal etch, since the substrates are introduced into the reactor in an essentially featureless condition. A rough interface is undesirable since it gives rise to a rougher-than-normal top surface and because rough interfaces are as-

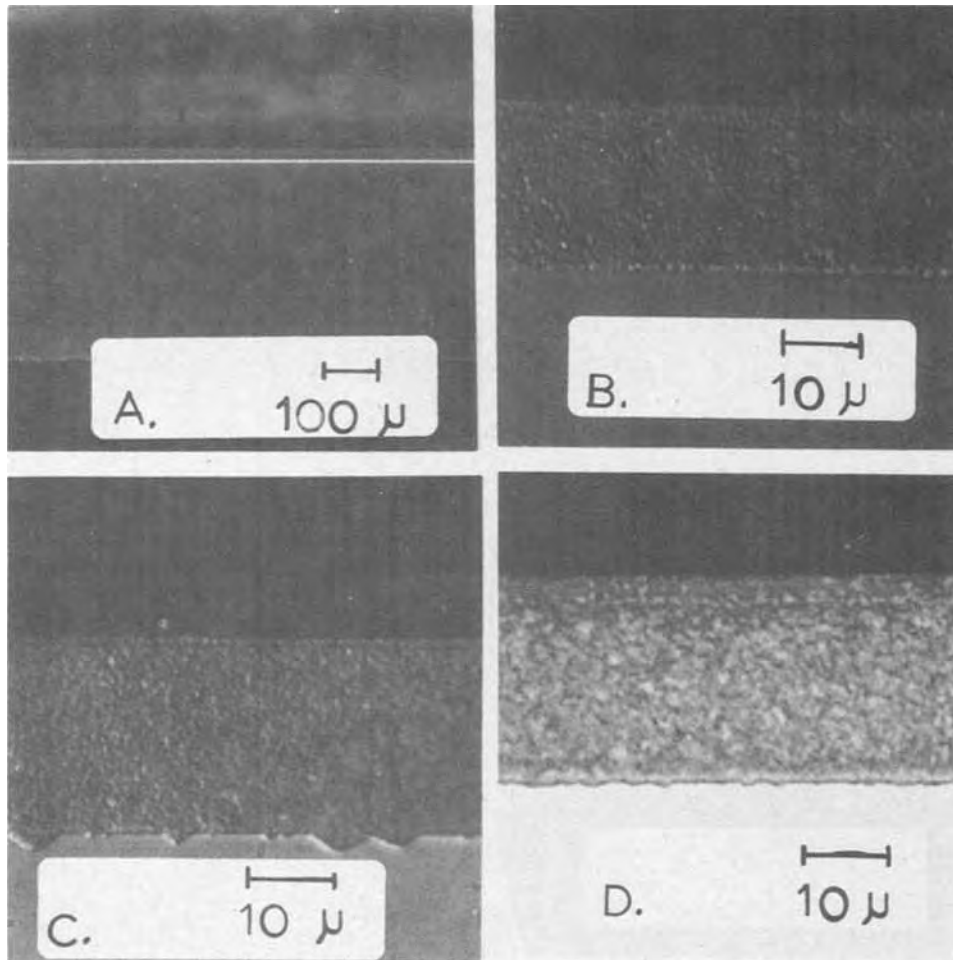


Fig. 4. Optical micrographs of cleaved sections showing AlAs-GaAs interface for optimum sequence of substrate insertion and AICI flow initiation (A and B) and roughened interfaces for late (C) and early (D) AICI flow initiation.

sociated with poor heterojunction  $I$ - $V$  characteristics. Optical micrographs such as those in Fig. 4 or similar ones taken after use of selective chemical stains (20) show no sign of an interfacial layer nor an extended transition region. This conclusion remains the same under scanning electron microscope examination. We believe that the Al-Ga transition is in fact atomically abrupt, but the precision of our measurements dictates an upper limit of 200Å for metallurgical grading.

The p-n junction for growth on Zn-doped GaAs substrates is located coincidentally with the Al-Ga transition. Figure 6 shows an electron beam-induced current trace indicative of this. Additional evidence is that In-Ga slush contacts melted to the substrate surface after removal (with 2% HCl) of the AlAs give a p-type thermal probe result, and the photoresponse (4) extends to 900 nm, completely ruling out the possibility that the junction lies in the AlAs. Results of capacitance-voltage characterization of the junctions (21) are well fit by the abrupt junction Anderson (22) model. The slope of  $C^{-2}$  vs. voltage plots, and extrapolated voltage intercepts, are in excellent agreement with those calculated from the substrate and epilayer carrier concentrations deduced from Hall data. Apparently Zn diffusion from the substrate during layer growth is not significant, at least over distances on the scale of the 250Å depletion layer width calculated for the  $\sim 10^{18}$  cm $^{-3}$  doping in these diodes.

The current-voltage plots for these diodes follow a  $J \sim J_s \exp(eV/\eta kT)$  dependence, with  $\eta$  typically 1.95. Values of saturation current density  $J_s$  vary over several orders of magnitude. When growth variables were held constant,  $J_s$  was found to be determined primarily by choice of substrate, with diodes grown on substrates cut from particular ingots grouping together. The open-circuit voltage measured for solar cells at an illumination intensity yielding  $J_{ph}$  short-circuit current density is given by

$$V_{oc} \sim (\eta kT/q) \ln(J_{ph}/J_s + 1)$$

This equation is valid for currents where series resistance may be ignored and where  $\eta$  has a well-defined value. Except for diodes with poor contacts or pathological growth problems, this was found to be the case over several decades of junction current with  $\eta$  for various diodes in the range  $2 \pm 0.1$ . This suggests strongly that generation-recombination components dominate the reverse saturation current density, which may then be written (23) as

$$J_s = kT(A + B)/[V_D(V_D - V)]^{1/2}$$

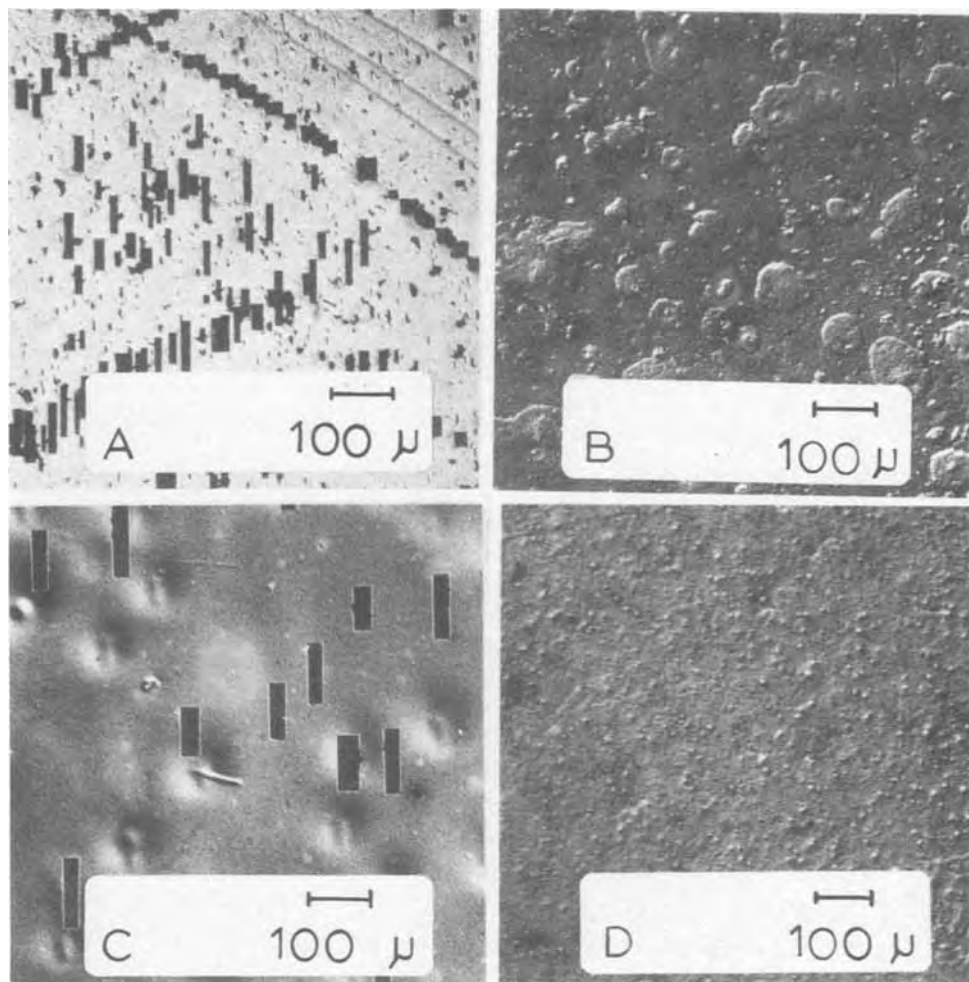
Here,  $V_D$  is the "built-in" voltage of the diodes as given by the capacitance-voltage plots and is 1.9-2.0V.  $A$  and  $B$  are constants depending on the material parameters of the AlAs and GaAs, respectively, and are given, for equal doping, by  $A \approx n_i \cdot l/\tau$  with  $n_i$  the intrinsic carrier density,  $l$  the zero-bias depletion layer width, and  $\tau$  the minority carrier lifetime in the depletion region of the AlAs. A similar expression for  $B$  applies to the GaAs. Thus, at the illumination level producing a particular short-circuit photocurrent density (25 mA/cm $^2$  is a convenient number corresponding roughly to unfocused terrestrial solar illumination), the open-circuit voltage for a given cell will vary as

$$V_{oc} \sim 0.05 \ln \tau_p + \text{const.}$$

since  $n_{iAlAs} \ll n_{iGaAs}$ . We thus can conclude on the basis of this model that the saturation currents and hence open-circuit voltages for our diodes should be determined dominantly by the electron lifetime in the p-GaAs. This has been verified by photoluminescence studies (21) on cells made on substrates cut from different ingots of p-GaAs which were similar in electrical properties but differed widely in photoluminescent efficiency.



Fig. 5. Differential interference contrast micrographs of top surface of GaAs after growth and removal of AlAs epilayer: A =  $\langle 110 \rangle$  defined rectangular etch pits, late initiation of AlCl flow; B = early AlCl flow (thermochemical etching in As and HCl atmosphere); C = thermal etching in As deficient atmosphere; D = interfacial surface for near optimum growth initiation. The best interfacial surfaces appear similar to the featureless regions in C.



### Conclusions and Discussion

The finding of principal importance in this work is that it is possible, by the use of commercially available high purity  $\text{Al}_2\text{O}_3$  ceramic furnace components, to grow AlAs by VPE on GaAs substrates without formation of a disturbed interfacial layer. This permits the fabrication of usefully efficient heterojunction solar cells which at present are performance limited by the quality of the substrate material. In several respects, however, the alumina ceramic is less than ideal. Residual Si contamination is still present, although we believe native donor defects to be the more likely cause of the minimum carrier concentration of  $\sim 10^{17} \text{ cm}^{-3}$  in our highest mobility epitaxial AlAs layers. Our results with Be doping indicate that useful, p-type VPE AlAs should be obtainable if the alumina ceramic were replaced by a material not attacked by  $\text{BeCl}_2$  (or AlCl) vapor in the  $1100^\circ\text{C}$ ,  $\text{H}_2$  ambient.

The interface between the AlAs layer and the GaAs can be reproducibly smooth and planar over the entirety of large area substrates up to  $15 \text{ cm}^2$  at least. This requires growth at the lower end of the temperature range for AlAs VPE and careful control of the thermal etch-VPE growth transition. At these temperatures ( $1000^\circ\text{--}1050^\circ\text{C}$ ), the AlAs surface morphology consists of hillocks, the density of which depends primarily on substrate-AlCl source spacing. The surface quality is not strongly dependent on the crystallographic orientation of the substrate, growth temperature gradient, or exact Al/As flow ratio, but is moderately dependent on absolute Al and As supply rates.

The heterojunction formed between the n-AlAs and Zn-doped GaAs is well described by an abrupt model. The reverse saturation current of these junctions is determined by the bulk minority carrier lifetime in the GaAs. For many heterojunction device applications,

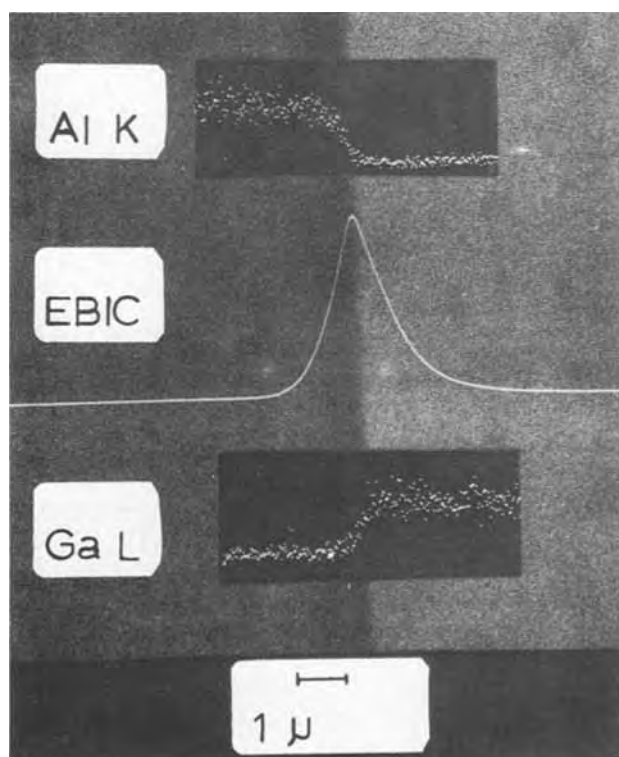


Fig. 6. Scanning electron (secondary emission) micrograph of n-AlAs-p-GaAs interface with superimposed Al K and Ga  $L_{\alpha}$  x-ray emission scans and electron-beam-induced junction current (EBIC) scan.

the low bandgap member is the important one with regard to minority carrier life, and the quality requirements on the wide gap member are relatively much less stringent. Thus, in spite of the fact that all our layers show misfit dislocation arrays of  $10^5$ - $10^6$  cm<sup>-2</sup> density, we have no evidence for deleterious effects arising from the interface. We have measured external short-circuit-current quantum efficiencies exceeding 95%, with antireflection coating, and these appear to be limited solely by the electron diffusion length in the p-GaAs bulk.

In spite of eliminating the interfacial layer found by others (1, 5), we have obtained no improvement in mobility or reduction in donor concentration. A calculation of the theoretically expected mobility should properly include (at least) the effects of polar optic mode scattering and ionized impurity scattering which interact in a complex way (18). Approximate calculations indicate that polar phonon scattering limits the mobility in AlAs at 300°K for electron concentrations below  $10^{18}$  in the absence of significant compensation. For total donor and acceptor concentrations above about  $2 \times 10^{18}$  cm<sup>-3</sup>, ionized impurity or native defect scattering should dominate. Our results are consistent with these expectations.

Manuscript submitted April 22, 1976; revised manuscript received June 14, 1976.

Any discussion of this paper will appear in a Discussion Section to be published in the June 1977 JOURNAL. All discussions for the June 1977 Discussion Section should be submitted by Feb. 1, 1977.

Publication costs of this article were assisted by Bell Laboratories.

#### REFERENCES

1. A. G. Sigai, M. S. Abrahams, and J. Blanc, *This Journal*, **119**, 952 (1972).
2. For example continuous wave diode lasers at room temperature [I. Hayashi and M. B. Panish, *J. Appl. Phys.*, **41**, 150 (1970)] and high efficiency solar cells [H. J. Hovel and J. M. Woodall, *This Journal*, **120**, 1246 (1973)].
3. W. D. Johnston, Jr., *ibid.*, **123**, 442 (1976).
4. W. D. Johnston, Jr. and W. M. Callahan, *Appl. Phys. Lett.*, **28**, 150 (1976).
5. M. Ettenberg, A. G. Sigai, A. Dreeben, and S. L. Gilbert, *This Journal*, **118**, 1355 (1971).
6. Coors Porcelain Company, Golden, Colorado and McDanel Refractory Products, Beaver Falls, Pennsylvania.
7. A. Y. Cho, *J. Vac. Sci. Technol.*, **8**, S31 (1971).
8. M. Wolf, *ibid.*, **12**, 984 (1975).
9. For example, an eventual production rate of the order of  $10^6$  m<sup>2</sup> per year is required, even with solar concentration of 500 times, to satisfy the goals of the United States National Solar Energy Research, Development and Demonstration Program. "Definition Report ERDA-49," Energy Research and Development Administration, Division of Solar Energy, Washington, D.C. (June 1975).
10. cf. D. L. Rode, *Phys. Status Solidi A*, **32**, 425 (1975).
11. R. P. H. Chang and A. K. Sinha, *Appl. Phys. Lett.*, **29**, 56 (1976).
12. D. B. Fraser and H. D. Cook, *This Journal*, **119**, 1368 (1972).
13. L. J. Van der Pauw, *Philips Res. Rep.* **13**, 1 (1958).
14. A. G. Milnes, "Deep Impurities in Semiconductors," p. 68, John Wiley & Sons, New York (1973).
15. H. Ehrenreich, *J. Phys. Chem. Solids*, **8**, 130 (1959).
16. M. Neuberger, "III-V Semiconducting Compounds," IFI/Plenum, New York (1971).
17. J. Whitaker, *Solid-State Electron.*, **8**, 649 (1965).
18. H. Ehrenreich, *Phys. Rev.*, **120**, 1951 (1960).
19. G. D. Pitt and J. Lees, *Solid State Commun.*, **8**, 419 (1970).
20. G. H. Olsen and M. Ettenberg, *J. Appl. Phys.*, **45**, 5112 (1974).
21. W. D. Johnston, Jr., Unpublished.
22. R. L. Anderson, *Solid-State Electron.*, **5**, 341 (1962).
23. A. G. Milnes and D. L. Feucht, "Heterojunctions and Metal-Semiconductor Junctions," Academic Press, New York (1972).

## Studies of the Push-Out Effect in Silicon

### II. The Effect of Phosphorus Emitter Diffusion on Gallium-Base Profiles, Determined by Radiotracer Techniques

Christopher L. Jones and Arthur F. W. Willoughby

*Engineering Materials Laboratories, The University, Southampton, Hants SO9 5NH, England*

#### ABSTRACT

The push-out of gallium-diffused base layers underneath subsequently diffused phosphorus emitters, has been studied using <sup>67</sup>Ga to obtain the complete tracer profiles of the base both within and beyond the emitter. The profiles show two major features which can be treated separately. Firstly, the depression of the base-collector junction in push-out is found to be due entirely to movement of Ga atoms, representing a very large enhancement of diffusion beyond the emitter. For the emitter diffusions used in this work, the magnitude of this enhancement varies from ~8 for a 1050°C emitter diffusion to ~100 for a 900°C emitter diffusion. The mechanism of diffusion enhancement in push-out is discussed in the light of the new data, and is considered to be due to production of an excess of a mobile point defect by high concentration phosphorus diffusion. The nature of the point defect, and the generation mechanism are, however, still to be resolved. Secondly, the tracer profiles also show a pronounced dip in the gallium concentration within the emitter. It is shown that the electric field created during the emitter diffusion could be the cause of such a dip, and the dip position, predicted on such a model, is close to that found experimentally. Similar effects produced by the diffusion of arsenic emitters are compared with these new observations on the effects of phosphorus emitter diffusions.

The push-out or emitter-dip effect is one of the most important anomalous diffusion effects that occur in the

Key words: diffusion, enhancement, emitter push, radiotracer, electric field.

manufacture of silicon bipolar transistors (1, 2). The effect can be described as the depression of a base/collector junction beneath a localized emitter diffusion. Figure 1 is a section through a pushed-out structure



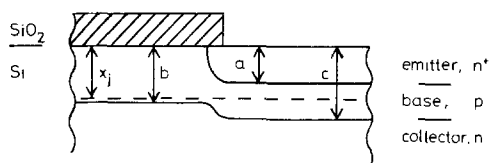


Fig. 1. Section through a transistor structure showing the depths measured:  $x_j$ , the initial base depth, is measured before emitter diffusion;  $a$ ,  $b$ , and  $c$  after the emitter diffusion.

showing the deeper penetration,  $c$ , of the base under the emitter compared with the base depth,  $b$ , away from the emitter. The difference between the base depths,  $(c - b)$ , will be referred to as the amount of push-out.

As discussed in Part I (3) of this work push-out creates particular problems in the fabrication of micro-wave n-p-n transistors using phosphorus-doped emitters, yet the cause of push-out is still not certain. Although there is a growing body of information concerning the influence of various process parameters on the amount of push-out, as measured by junction depths (3-8), there is still virtually no information about the shape of the pushed-out base doping profile. A certain amount of electrical profiling in the pushed-out base has been carried out (3, 4, 9, 10) but as pointed out in Part I (3) electrical profiling is of very limited value for studying diffusion processes because so little of the base profile can be measured. The purpose of this work was to gain a greater understanding of sequential diffusions involving push-out by the radiotracer profiling of the complete base profile both within and beyond the emitter.

The conventional boron base cannot be profiled by tracer techniques because boron does not have an isotope of sufficiently long half-life ( $^{10}\text{B}$  and  $^{12}\text{B}$  half-lives are  $< 1$  sec) so in this work gallium-base layers have been employed. In Part I (3) the push-out of gallium was compared with boron by junction depth measurements and found to be very similar. It is therefore felt that the results to be described below must be closely related to the usual boron-base, phosphorus-emitter structure.

A preliminary report of the gallium tracer work has already been published (11). In the present paper the experiments are described in detail and the results are analyzed by considering the electric field effect and a general diffusion enhancement caused by the emitter diffusion. The possible reasons for this diffusion enhancement, which produces push-out, are discussed in the light of the new information, and the possibility of predicting the complete base profile shape is also considered.

### Experimental Techniques

**Material.**—The silicon used was n-type, 5-10  $\Omega$ -cm, in (111) oriented wafer form, chemically polished on one side. Before diffusion the wafers were thoroughly cleaned as described in Part I (3).

**Gallium-base diffusions.**—The open-tube system described in Part I was used to form the Ga-base layers. The source was  $\text{Ga}_2\text{O}_3$  powder containing the radioisotope  $^{67}\text{Ga}$ . The use of  $^{67}\text{Ga}$  was preferred to the more usual  $^{72}\text{Ga}$  because of the former's longer half-life.  $^{67}\text{Ga}$  has a half-life of 78 hr and is a  $\gamma$ -emitter, the main  $\gamma$ -energy being 0.092 MeV. The sources were specially prepared from  $^{67}\text{GaCl}_3$  solution at the Radiochemical Centre, Amersham, and the source mass was made as small as could conveniently be handled ( $\sim 40$  mg) so as to maximize specific activity within the limited total activity allowed for safety reasons (0.5 mCi). During a diffusion the source was at  $1050^\circ\text{C}$  and the silicon samples at  $1100^\circ \pm 2^\circ\text{C}$  while a mixture of  $\text{H}_2$  and  $\text{N}_2$  gases transferred dopant from the source to the silicon (12).

**Phosphorus-emitter diffusions.**—These were carried out as described in Part I using a  $\text{POCl}_3$  liquid source at  $0^\circ\text{C}$  and an  $\text{O}_2/\text{N}_2$  carrier gas mixture. Two experiments used an emitter diffusion temperature of  $1050^\circ \pm 1^\circ\text{C}$  and one experiment used a temperature of  $900^\circ \pm 1^\circ\text{C}$ . A light weight furnace boat was used to keep wafer warm-up time to a minimum and all samples were cooled rapidly following the diffusion.

**Junction depth measurement.**—Junction depths  $a$ ,  $b$ ,  $c$ , and  $x_j$  of Fig. 1 were measured on stained grooves by sodium light interferometry, see Part I. The measurements were made on test pieces processed at the same time as the samples used for profiling.

**Profiling.**—Analysis of the diffused layers was made by layer removal combined with sheet resistance and radioactivity measurements. The layers were removed by anodizing the silicon and then etching off the anodic oxide in HF solution. The thickness of each layer was determined from the anodic oxide color which had been previously calibrated. The  $^{67}\text{Ga}$  activity in each layer of silicon removed was measured using a  $\gamma$ -counting system consisting of a sodium-iodide well-crystal scintillator, photomultiplier, amplifier, pulse height analyzer, ratemeter, and scaler/timer. Profiling was carried out both by counting the activity of the oxide etch only and by counting oxide etch and anodizing electrolyte together and, although some gallium was found in the electrolyte, profiles obtained by the two methods were of closely similar shape. To obtain the "electrical" impurity profile on the same sample as the tracer gallium profile, sheet resistance measurements were made after each HF etch step using a four-point probe. The sheet resistance vs. depth data were converted to concentration vs. depth profiles by the method of Evans and Donovan (13) and using Irvin's (14) curves to convert resistivity to concentration. The conversion of radioactivity measurements to absolute gallium concentrations was not possible accurately by the normal standardization methods because of uncertainties in stoichiometry, moisture content, etc., of the gallium oxide source. (It must be remembered that the source was prepared from  $\text{GaCl}_3$  solution, not by irradiation of  $\text{Ga}_2\text{O}_3$ .) In view of this the conversion was made by superimposing the tracer and electrically obtained gallium profiles in the tail region of the profile where concentrations were less than about  $10^{18}$   $\text{cm}^{-3}$ . At these concentrations the electrical parameters used are well substantiated and therefore it is a reasonable assumption that the electrical profile is correct. In the following results the term "electrical profile," for both gallium and phosphorus, refers to profiles obtained from electrical measurements and converted to total concentrations via Irvin's curves as detailed above. At high phosphorus concentrations ( $> 10^{20}$   $\text{cm}^{-3}$ ) the conversion parameters are not well substantiated and thus the form of the profile in this range is subject to uncertainty.

### Results

Experiments were performed to examine the effects of a high concentration phosphorus emitter diffusion on a previously diffused  $^{67}\text{Ga}$  base. Two emitter diffusion temperatures were used and in each case the entire pushed-out base profile was determined and compared with the nonpushed-out base.

**1050°C emitter diffusion.**—Two silicon wafers were diffused simultaneously with  $^{67}\text{Ga}$  for 15 min at  $1100^\circ\text{C}$ . The oxide was removed from one slice which was then given a  $3\frac{1}{2}$  min/ $1050^\circ\text{C}$  phosphorus diffusion, and finally both samples were profiled. The electrical phosphorus profile and the tracer and electrical gallium profiles are shown in Fig. 2. Conversion of tracer activity to gallium concentration was made by comparing the tracer and electrical profiles of the nonpushed-out base, as described above. The conversion factor is the same for both the pushed-out and nonpushed-out tracer profiles because the initial Ga diffusions were

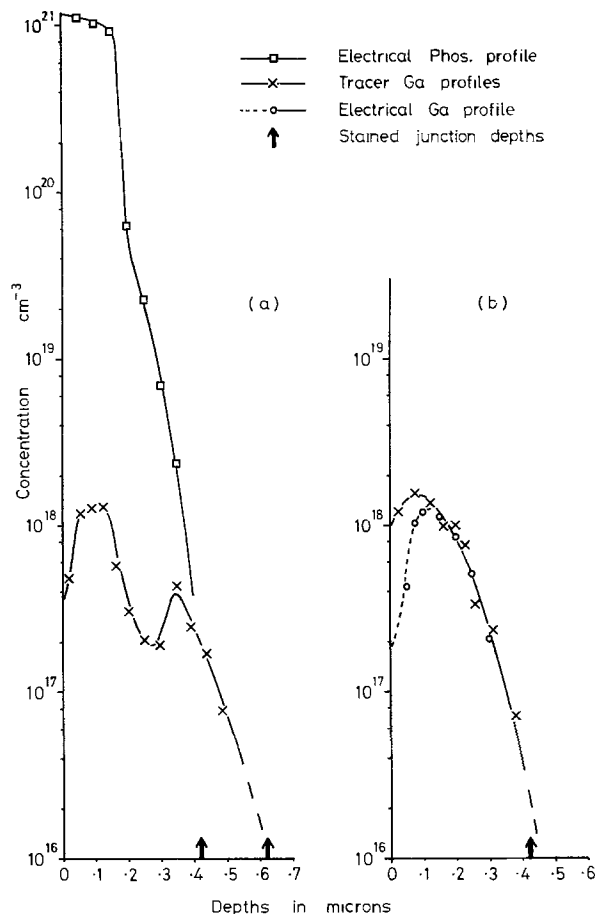


Fig. 2. Profiles before and after push-out: (a) 15 min/1100°C Ga diffusion followed by 3½ min/1050°C P diffusion, (b) 15 min/1100°C Ga diffusion only. —□— electrical P profile; —×— tracer Ga profiles; ---○— electrical Ga profile; ↑ stained junction depths.

performed simultaneously. Electrical measurements of the pushed-out base (beyond the emitter) proved to be impossible in this experiment because of the low concentration and narrowness of the base.

The junction depths by staining for this experiment were:  $a = 0.42 \mu\text{m}$ ,  $b = 0.42 \mu\text{m} \approx x_j$ ,  $c = 0.62 \mu\text{m}$ , so that the push-out was  $(c - b) = 0.20 \mu\text{m}$ . These depths are in good agreement with the junction depths inferred from the profiles although close to  $c$  tracer measurements were impracticable due to the low activity of the thin layers removed.

The gallium profile in Fig. 2(a) is the first determination of the complete base profile in a pushed-out transistor and it can be seen that the profile is not gaussian or erfc, but has a marked dip within the emitter at about  $0.28 \mu\text{m}$  from the surface.

A repeat experiment was performed, using as near as possible identical conditions, and the results are shown in Fig. 3. The shape of the pushed-out base is very close to that of the previous experiment showing that the profiles are highly reproducible.

**900°C emitter diffusion.**—Two wafers were diffused with  $^{67}\text{Ga}$  for 15 min at 1100°C and the oxide removed from one; both slices were then placed in the phosphorus-diffusion furnace for 30 min (900°C). In this way both slices received the same heat-treatment but phosphorus only diffused into one slice, the other being protected by its oxide. The resultant profiles are shown in Fig. 4. As with the previous experiments (1050°C emitter) a dip in the tracer gallium profile occurs within the emitter but the dip is now shallower, at  $0.23 \mu\text{m}$ , and closer to the emitter/base junction. The wider base width produced in this experiment allowed electrical profiling in the pushed-out base and close

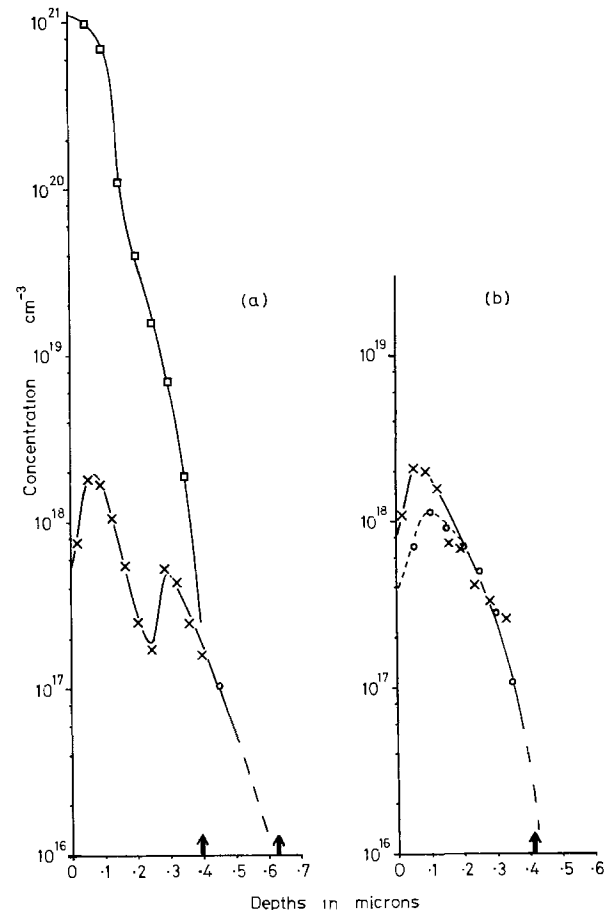


Fig. 3. Repeat experiment using the same conditions as Fig. 2. Symbols same as Fig. 2.

agreement is seen between tracer and electrical profiles except near the emitter/base junction where the electrical profile falls more steeply due to compensation by the tail of the phosphorus profile.

The junction depths by staining were:  $a = 0.28 \mu\text{m}$ ,  $b = 0.53 \mu\text{m}$ ,<sup>1</sup>  $c = 0.71 \mu\text{m}$ , hence the push-out was  $0.18 \mu\text{m}$ .

Some general remarks are appropriate as a result of the above experiments:

(i) In both experiments using the 1050°C emitter diffusion the pushed-out base was found, by integrating areas under the profiles, to contain approximately 18% less gallium atoms/cm<sup>2</sup> than the initial base, while in the 900°C emitter experiment the pushed-out base contained 2% more than the nonpushed-out base. The last result is the most significant because here both the pushed-out and nonpushed-out base received exactly the same heat-treatment and the negligible difference at 900°C indicates that the loss of gallium apparent in the 1050°C emitter experiments was simply due to the extra heat-treatment involved in the phosphorus diffusion and not connected with the presence of diffusing phosphorus. It is probable that this loss is an out-diffusion process similar to that thought to contribute to the original profile, see Part I (3).

(ii) In Fig. 2(b) and 3(b) there is evidence of non-electrically-active gallium (or compensation) in the high concentration surface regions of the nonpushed-out base whereas this does not apparently happen in Fig. 4(b) where the nonpushed-out base underwent the 900°C/30 min anneal following Ga diffusion.

(iii) The phosphorus emitter profiles are characteristic of shallow, high concentration phosphorus diffu-

<sup>1</sup>The deeper base in this experiment compared with the previous experiments was due to the use of a different gas composition during Ga diffusion which gave a higher initial Ga vapor pressure and faster source consumption.

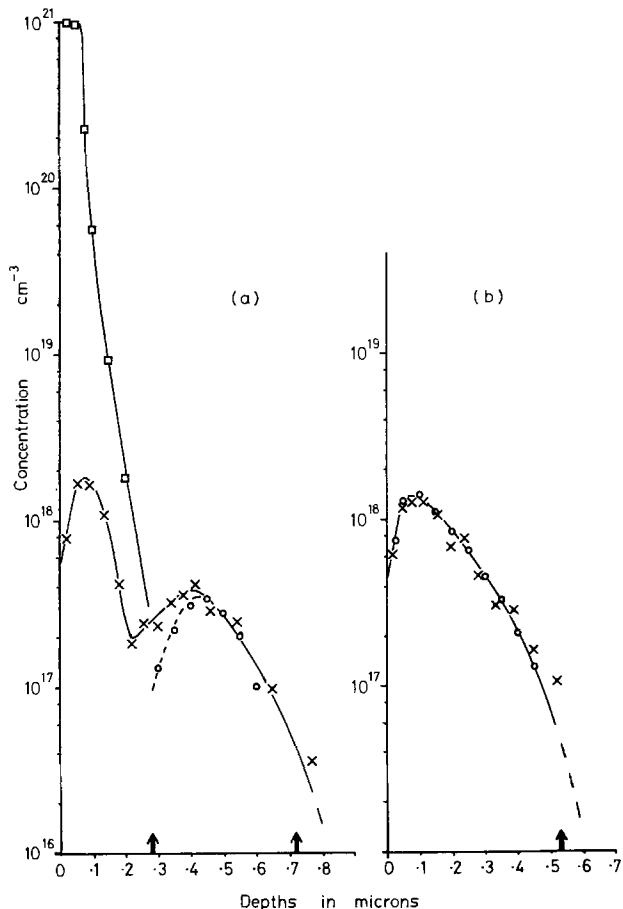


Fig. 4. (a) 15 min/1100°C Ga diffusion followed by 30 min/900°C P diffusion, (b) as (a) but protected from P diffusion by a covering oxide. Symbols same as Fig. 2.

sions below 1100°C (15) having a flat top and a kink. It can be seen that the kink occurs at a lower concentration for the lower diffusion temperature as found by Schwettmann and Kendall (16).

(iv) The tracer measurements show that push-out is caused wholly by a real inward movement of gallium atoms during the phosphorus diffusion rather than being partly due to some other process, such as conversion of the collector dopant to an electrically inactive form; a distinction which purely electrical measurements could not recognize.

(v) It should be noted that comparison of the pushed-out and nonpushed-out gallium profiles for a particular experiment can be made quite independently of standardization because the samples were diffused simultaneously from one tracer source.

(vi) The position of the dip in the pushed-out base relative to the emitter is given increased accuracy in these experiments because the emitter and base profiles were obtained using the same depth data. In other words errors in the depth measurements would not shift the gallium profile relative to the phosphorus profile: this is a considerable advantage over the technique used by Ziegler, Cole, and Baglin (17) to measure boron-base, arsenic emitter profiles.

The results reported above give, for the first time, concentration vs. depth distributions of all the impurities in a pushed-out, diffused transistor. Possible reasons for the anomalous shape found in the pushed-out base are discussed in the following section.

### Discussion

*Enhancement of the tail of the pushed-out base.*—The simplest model of push-out assumes that during the emitter diffusion the only effect the emitter has on

the base is to enhance the base diffusivity by an amount  $\chi$  which is constant with time and depth (3, 6, 8). Such a model has been applied to the tracer gallium profiles as follows.

First theoretical curves were fitted to the experimental initial base profiles [e.g., Fig. 2(b) and 4(b), strictly speaking Fig. 4(b) is not an initial base profile but the difference should be negligible for this purpose]. These experimental profiles are not erfc in shape because the very small Ga<sub>2</sub>O<sub>3</sub> source used in the tracer experiments could not maintain a constant gallium vapor pressure during the diffusion. It is possible, however, to fit gaussian curves over most of the experimental points and the initial base profile is then described by

$$N = N_0 \exp\left(\frac{-x^2}{4D_1t_1}\right) \quad [1]$$

where  $N$  = gallium concentration,  $N_0$  is the maximum value of  $N$ ,  $x$  = depth,  $D_1$  = effective base diffusivity,  $t_1$  = effective base diffusion period. Both  $N_0$  and the product  $D_1t_1$  are obtained by fitting. The final profile, after emitter diffusion is then given by

$$N = N_0 \left[ \frac{D_1t_1}{D_1t_1 + \chi D_2t_2} \right]^{1/2} \exp\left\{ \frac{-x^2}{4(D_1t_1 + \chi D_2t_2)} \right\} \quad [2]$$

where  $\chi$  = diffusion enhancement factor,  $D_2$  = normal gallium diffusivity at emitter diffusion temperature, and  $t_2$  = emitter diffusion period. The pre-exponential term in Eq. [2] arises from the assumption that the total number of gallium atoms is conserved. The only unknown in Eq. [2] is  $\chi D_2$ , the enhanced diffusivity, since  $t_2$  is known and both  $N_0$  and  $D_1t_1$  have been fixed by the fit to the initial profile. By adjusting the value of  $\chi D_2$ , Eq. [2] was fitted to the final profile at a concentration of  $N \approx 10^{17} \text{ cm}^{-3}$ . Two examples of this procedure are given in Fig. 5 and it is apparent

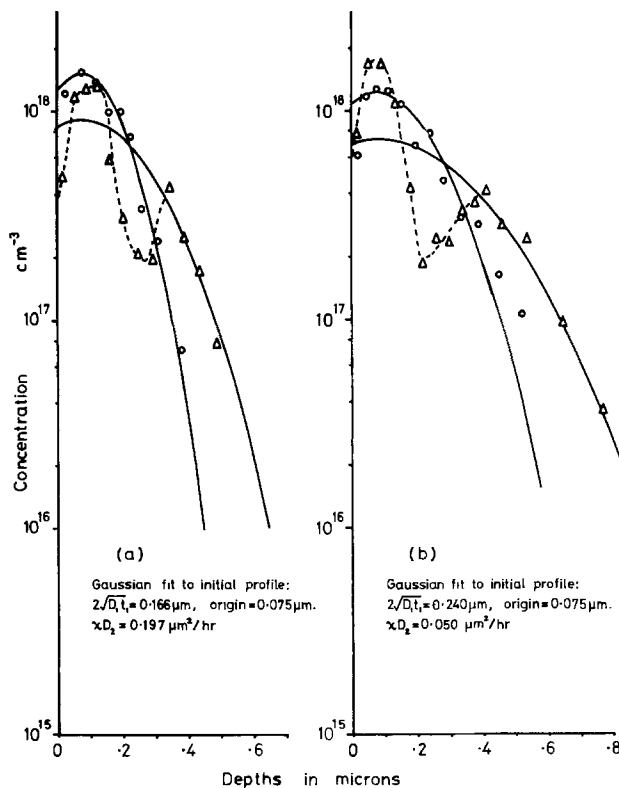


Fig. 5. Curve fitting to initial base, and tail of pushed-out base: (a) 1050°C emitter experiment of Fig. 2, (b) 900°C emitter experiment of Fig. 4. — Theory; ○ experiment before emitter; ---△--- experiment after emitter.

that a reasonable fit is obtained to the experimental profiles beyond the dip by using  $\chi D_2$  values of  $0.197 \mu\text{m}^2/\text{hr}$  at  $1050^\circ\text{C}$  and  $0.05 \mu\text{m}^2/\text{hr}$  at  $900^\circ\text{C}$ . The corresponding values for  $\chi$  are:  $\chi \approx 8$  at  $1050^\circ\text{C}$  and  $\chi \approx 100$  at  $900^\circ\text{C}$ ; these are only approximate since  $D_2$  is not known precisely. The  $\chi(1050^\circ\text{C})$  value of 8 is the same as that calculated from junction depths (using Eq. [2] in Part I), and assuming gaussian distributions, in the boron push-out work of Part I, thus providing additional evidence that gallium pushes out in the same way as boron.

The assumption, used above, that the base diffusivity is constant with depth during the emitter diffusion is probably incorrect. Experimentally Okamura (18) has found that uniform, heavy n-type doping retards gallium diffusion and the present work shows that there is no extra out-diffusion due to the phosphorus diffusion (see  $900^\circ\text{C}$  emitter results) which suggests that the base diffusivity is not enhanced near the surface. In order to estimate the importance of a varying diffusivity the situation was simplified as follows. Suppose  $D = D_2$  for  $0 < x < x_k$  and  $D = \chi D_2$  for  $x > x_k$ , where  $x_k$  defines an imaginary boundary between the two regions of different  $D$ . The boundary position was taken as the depth of the kink in the phosphorus profile and it was further assumed that  $x_k = ht^{1/2}$ , where  $h$  is a constant obtained from the final kink depth at time  $t_2$ . At the start of the emitter diffusion the whole of the base suffers an enhancement but as the diffusion proceeds the diffusivity in a growing surface region of depth  $x_k$  is not enhanced. This procedure has been applied to the experimental results of Fig. 2 and the final profile shape is shown in Fig. 6. A good fit is obtained in the tail region using the same  $\chi D_2$  product as for the uniform enhancement. The gallium profile has a kink and a higher concentration is retained near the surface than for the uniform enhancement model.

The above analysis demonstrates the point made by Hu and Yeh (6) and discussed fully in Part I (3) that the amount of push-out is determined by the base diffusivity beyond the emitter irrespective of how the diffusivity varies inside the emitter. Consequently, simple models assuming a uniform diffusivity of  $\chi D_2$  are able to predict amounts of push-out quite well although they are very much in error as regards the over-all profile shape.

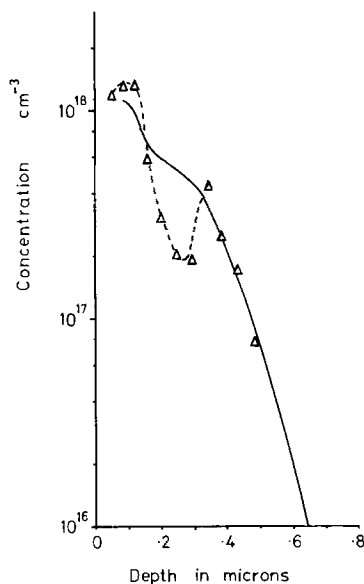


Fig. 6. Calculated profile for a step-function change in  $D$  with depth, based on experiment of Fig. 2, and compared with experimental profile. — Theory; --- $\Delta$ --- experiment. Gaussian initial profile as in Fig. 5(a).  $\chi D_2 = 0.197 \mu\text{m}^2/\text{hr}$ . Boundary reaching  $0.2 \mu\text{m}$  in 3.5 min.

*Formation of a dip in the pushed-out base.*—The simple diffusion enhancement theories described above cannot give rise to a dip in the pushed-out base profile but Hu and Schmidt (19) have shown theoretically that the emitter's electric field could cause a dip in the base profile. In 1972 a dip in a boron base following an arsenic emitter diffusion was measured experimentally by Ziegler, Cole, and Baglin (17) but their results did not prove conclusively that the dip was caused by the field effect (20). On the other hand more recent measurements on arsenic emitter/boron-base structures by Blanchard, Boris, De Brebisson, and Monnier (21) using the ion microprobe have tended to support Hu and Schmidt's prediction. The results described in this work show for the first time that a dip is also present when phosphorus is diffused after gallium and it is shown below that these results are consistent with an electric field model. The sequential diffusion equations deduced by Hu and Schmidt cannot be used directly in this case because the equations do not give the correct form for the phosphorus emitter profile.

When the only "driving forces" for diffusion are the concentration gradient and an electric field the flux of ionized base dopant atoms is given by

$$J_x = -D_2 \left( \frac{dN}{dx} \right) - s\mu N \mathcal{E} \quad [3]$$

where  $J_x$  = base impurity flux in the  $+x$  direction;  $s$  = charge state of the impurity;  $\mu$  = drift mobility of the impurity; and  $\mathcal{E}$  = electric field, defined as positive when the force on an electron is in the  $+x$  direction. The field term in Eq. [3],  $s\mu N \mathcal{E}$ , can either assist the concentration gradient or act against it depending on the direction of  $\mathcal{E}$ , and, if the field is sufficient, diffusion "up" the concentration gradient is possible. The way in which the field could produce a dip can be described qualitatively as follows. Suppose an impurity has been diffused from the surface to give the profile shown in Fig. 7(a) and an electric field is then applied such that the field is constant to a depth  $A$  and zero beyond this, see Fig. 7(b). Let the field have the direc-

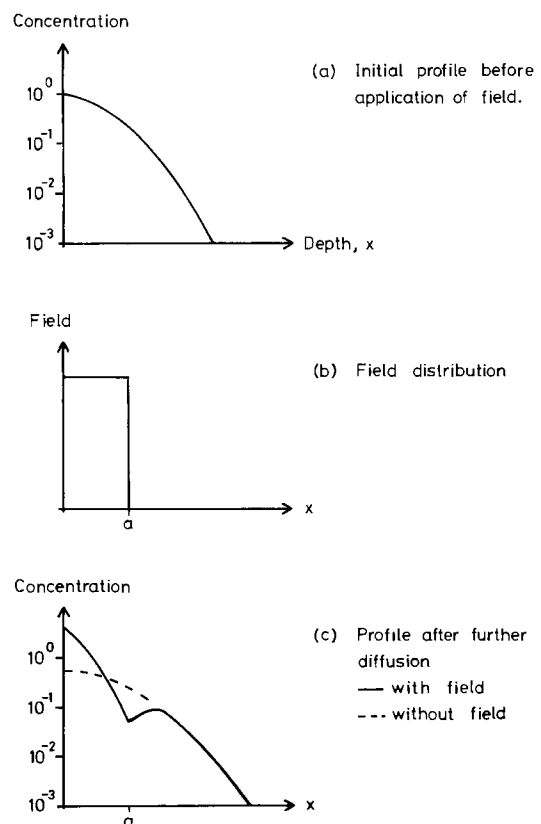


Fig. 7. Simple model of dip production by an electric field

tion and strength to overcome the concentration gradient so that the impurity flux is negative, that is toward the surface, for  $0 < x < A$ . If diffusion now continues, then as far as the impurities beyond  $A$  are concerned, the region  $0 < x < A$  appears as a sink since any impurity crossing  $x = A$  in the  $-x$  direction is swept toward the surface by the field which also prevents impurities crossing in the opposite direction. The profile is then depleted close to  $A$  and piled up near the surface. The result is a dip centered on  $x = A$  as shown in Fig. 7(c).

In order to see whether a situation such as that described above arises in practice, the magnitude and direction of the electric field created by phosphorus diffusion has to be calculated. Assuming electronic equilibrium is easily maintained during diffusion the Fermi level can be considered constant throughout the diffusing layers so the electric field is given by

$$\mathcal{E} = -\frac{1}{q} \frac{d(E_c - F)}{dx} \quad [4]$$

where  $q$  = electronic charge,  $E_c$  = conduction band edge, and  $F$  = Fermi level. Equation [4] can be used to calculate the field provided the variation of  $(E_c - F)$  with  $x$  is known. The dependence of  $(E_c - F)$  on donor doping concentration,  $N_D$ , at a particular temperature,  $T$ , was calculated using Fermi-Dirac statistics and assuming (i) that the phosphorus donor level is a discrete level 0.045 eV below  $E_c$  and (ii) that the bandgap is given by  $E_g(T) = [1.21 - 4.1 \times 10^{-4}T^2 \text{K}] \text{ eV}$  (22). This information was then used to determine  $(E_c - F)$  vs.  $x$  for the experimental  $N_D$  vs.  $x$  profiles. The method used to calculate Fermi levels is likely to be in error at high concentrations ( $>10^{20} \text{ cm}^{-3}$ ) due to heavy doping effects, but this is not significant at the levels important in this analysis. One of the band diagrams obtained is shown in Fig. 8 and beneath this is the field distribution calculated using Eq. [4] on the band diagram.

The field is in the right direction for dip formation, and to test whether it has sufficient strength the flux equation, Eq. [3], has been used with the gaussian fits to both the initial and pushed-out Ga profiles (Fig. 5). The flux equation is first rewritten using the Einstein relation,  $\mu = qD_2/kT$  (where  $k$  is Boltzmann's constant), and putting  $s = -1$  for Ga, and  $dN/dx = -xN/2Dt$  for gaussian profiles. Then

$$J_x = D_2N \left[ \frac{x}{2Dt} + \frac{q\mathcal{E}}{kT} \right] \quad [5]$$

For the 1050°C emitter experiment the gaussian profiles shown in Fig. 5(a) were used together with the field distribution of Fig. 8 to calculate  $J_x/D_2$  at various depths from Eq. [5]. Table I gives the results of these calculations which show that the field overcomes the concentration gradient and the impurity flux is toward the surface over a region with an upper limit 0.25  $\mu\text{m}$  from the surface and a lower limit which is approximately 0.15  $\mu\text{m}$  from the surface; the lower limit is uncertain due to heavy doping effects but it is the upper limit which is closely related to the dip. Using different assumptions the upper limit is calculated (see Table I) as 0.32  $\mu\text{m}$  and the lower limit as approximately 0.1  $\mu\text{m}$ . The position of the bottom of the dip expected on this

Table I.  $J_x/D$  calculations for experiment of Fig. 2

Depth, $x$ , $\mu\text{m}$	$J_x/D$ using initial gaussian $10^{22} \text{ cm}^{-4}$	$J_x/D$ using final gaussian $10^{22} \text{ cm}^{-4}$
0.10	+1.38	-0.18
0.15	-0.32	-3.12
0.20	-17.70	-19.65
0.25	-0.52	-5.47
0.30	+1.71	-1.44
0.35	+1.46	+0.95
0.40	+0.72	+1.69

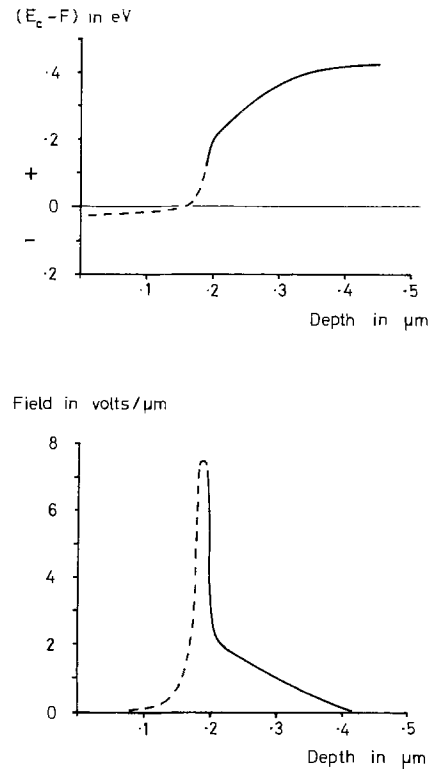


Fig. 8. Band diagram and field distribution at end of 1050°C emitter experiment (Fig. 2).

basis (and considering Fig. 7) is between 0.25 and 0.32  $\mu\text{m}$  which agrees well with the actual position of 0.28  $\mu\text{m}$ . Similar analysis for the 900°C emitter experiment predicts a dip in the region 0.22-0.25  $\mu\text{m}$  which again agrees well with the measured position of 0.23  $\mu\text{m}$ .

The above calculations can be summarized as follows: (a) the emitter's electric field is capable of producing a dip in the base profile, and (b) the predicted position of the dip agrees very well with the measured position.

*Possibility of predicting the complete base profile.*—In principle the above analysis could be developed to predict the entire base profile but before this can be accomplished the variation of the electric field,  $\mathcal{E}$ , and the base diffusivity,  $D$ , with both  $x$  and  $t$  must be established. As shown above,  $\mathcal{E}$  can be obtained from the phosphorus doping profile but the change of this with time is not well characterized because of the anomalous nature of high concentration phosphorus diffusion. For the purpose of calculating the base profile the cause of anomalous phosphorus diffusion need not be known, only the exact shape of the profile at any time, for which the analysis by Tsai (15) applies.

It has been shown above that beyond the emitter the base diffusivity can be considered constant at  $\chi D_2$  but inside the emitter there are three possible ways in which  $D$  could vary. These are:

(i) The push-out enhancement factor  $\chi$  may vary with depth inside the emitter. This will depend on the enhancement mechanism which, of course, is not yet established. Hu and Yeh's (6) vacancy generation by climbing dislocation mechanism leads to a  $\chi$  which from being unity at the surface increases with depth until it reaches a constant value for  $x \gtrsim 2\sqrt{D_3t_2}$  = the emitter diffusion length. Other models of diffusion enhancement (23, 24) have not been developed sufficiently to indicate how  $\chi$  varies with  $x$ .

(ii) The Fermi level may affect  $D_2$  via changes in the charged defect populations; assuming the base impurity diffuses by a defect mechanism. If acceptor impurities diffuse mainly via positively charged vacan-

cies, as suggested by Makris and Masters (25), the base diffusivity would be reduced inside the emitter because fewer vacancies could exist there in the positively charged state. The size of this effect depends on the relative importance of positively charged and neutral vacancies in the diffusion of an acceptor and on the position of the vacancy donor level at diffusion temperatures, both factors are uncertain at present. Hu and Schmidt (19) did not include this effect in their sequential diffusion theory (arsenic emitter) but Hu (26) accepts that it may be important.

(iii) Ion-pairing of emitter and base dopants prevents some of the base dopant from diffusing in the normal way. Reiss, Fuller, and Morin (27) have shown that ion pairing can be described in terms of a concentration-dependent diffusivity which is always smaller than the diffusivity in the absence of pairing. The extent to which pairing occurs at diffusion temperatures is not definitely known but Fair (28) has incorporated it into Hu and Schmidt's sequential diffusion theory for the arsenic emitter, boron-base structure and in his treatment it has a small but noticeable effect on the base profile within the emitter.

The combined influence of Fermi-level and ion-pairing effects can be determined experimentally using Okamura's approach (18, 40). He diffused low concentration radiotracer Ga into silicon uniformly doped n-type and found that at 1200°C Ga diffusivity was more than halved when the donor doping level reached  $10^{20} \text{ cm}^{-3}$ . Experiments at lower temperatures and higher donor concentrations are required to cover more emitter diffusion conditions.

From the foregoing discussion it will be realized that the prediction of a complete pushed-out base profile is not easy. However, now that experimental profiles are available for the first time the correctness of any model used can be checked.

In the absence of a complete mathematical description of base dopant redistribution during phosphorus emitter diffusions a few qualitative comments are worthwhile. Since the position of the dip in the base profile is primarily determined by the emitter's electric field then: (a) the steeper the emitter's diffusion front the closer the dip is to the emitter/base junction of the transistor, (b) for a very deep phosphorus emitter the field may become so small toward the end of the diffusion that the dip fills up again, and (c) lowering the diffusion temperature extends the field to lower doping concentration regions, that is, toward the emitter/base junction, so the dip will move closer to the junction. From the point of view of transistor operation it is probably desirable to have the dip entirely inside the emitter to avoid a retarding field for minority carriers crossing the base, but from the above comments it will be realized that this requirement may be incompatible with the shallow, low temperature diffusions commonly used in high frequency transistors. On the other hand phosphorus could be better than arsenic in this respect since arsenic diffusions apparently never exhibit tails and have very steep diffusion fronts which would always place the dip close to the emitter/base junction (19, 21).

*Possible causes of push-out.*—In the light of the new results presented here it is appropriate to summarize our present understanding of the push-out effect.

(i) The size of the base dopant atoms is not important in push-out, see Part I of this work.

(ii) The presence of phosphorus or boron in high concentration is required to produce push-out; oxidation without emitter dopant does not give rise to the large junction movements that occur in push-out [see Hill (30) and Gereth et al. (4)]; arsenic emitters give little or no push-out [see Parekh and Kolmann (39)].

(iii) Push-out can be attributed to a diffusion enhancement which is constant with time during the

emitter diffusion and with depth below the emitter [see this work, Hu and Yeh (6), and Nakamura *et al.* (8)].

(iv) The magnitude of enhancement is dependent on the emitter diffusion temperature varying from 8 times at 1050°C to 100 times at 900°C for the emitter diffusions used in this work (*i.e.*,  $\text{POCl}_3$  source and surface doped to solid solubility).

(v) The diffusion enhancement increases as the phosphorus emitter surface concentration increases [see Lee (7), and Nakamura *et al.* (8)].

(vi) The enhancement operates at least  $10 \mu\text{m}$  below the emitter as shown by the buried layer experiments of Lee and Willoughby (29). This suggests that enhanced diffusion could only be due to a point defect generated in the emitter region and capable of migrating considerable distances without being annihilated or trapped.

(vii) Diffusion enhancement occurs in all directions which means that a flux of point defects (32) is not primarily responsible [see Lee and Willoughby (29), Hill (30), and Adler (31)].

A mechanism is therefore required whereby a high concentration phosphorus (or boron) diffusion can introduce excess of a mobile point defect which can subsequently enhance the diffusion of any base dopant present. The point defects must be generated throughout the emitter diffusion period. The mechanism should explain the strong dependence on emitter surface concentration, the dependence on emitter diffusion temperature, and why phosphorus and boron produce much more push-out than arsenic.

The most highly developed theory of push-out is the vacancy generation by climbing dislocation model of Hu and Yeh (6). This theory fits the requirements detailed above but there are now several reports of push-out and anomalous phosphorus diffusion in the absence of dislocations (16, 30, 33-36).

Two mechanisms based on the break-up of *E*-centers (phosphorus-vacancy pairs) have been proposed. In both cases the *E*-center can be viewed as a means of transporting vacancies from the surface into the bulk where they are subsequently freed and can enhance the diffusion of any impurities present (provided these impurities diffuse by a vacancy mechanism). Peart and Newman (23) suggested that *E*-centers break up on changing from the negatively charged state, assumed to be stable, to the neutral state, assumed to be unstable. This change in charge state would occur as the *E*-center migrates out of the high concentration region where the Fermi level is above the *E*-center acceptor level into the lower concentration region where the Fermi level is below the acceptor level. The boundary between these two regions is located, in their model, at a phosphorus concentration equal to the kink concentration, thus vacancies would be released below the kink. Such a mechanism may be able to account for the enhancements observed provided most of the phosphorus flux is in *E*-center form and most of these *E*-centers break up after crossing the kink (37).

More recently Yoshida, Arai, Nakamura, and Terunuma (24) have proposed a mechanism in which *E*-center break-up occurs just beneath the silicon surface. The basis of their model is the assumption that phosphorus can only enter the silicon (at a surface) in the company of a vacancy. Once into the silicon these *E*-centers are in excess of the equilibrium requirement and so most of them immediately break up. Vacancy release would thus occur within a few hundred angstroms of the surface but it is not clear whether sufficient vacancies would diffuse deeper into the bulk to account for the observed enhancements. An important point raised by Yoshida *et al.*'s theory is that vacancy production in their model only occurs while phosphorus is entering the silicon at the surface,

therefore diffusion enhancement should stop on removal of the source. At first this prediction appears to be contradicted by an experiment reported by Yoshida *et al.* themselves [see region A of Fig. 6 in Ref. (33)] but it is not clear whether complete removal of the source was achieved in this experiment.

A variation on these *E*-center models is to assume that *E*-centers are breaking up throughout the diffusing phosphorus layer. Such a situation might occur if phosphorus only migrates as *E*-centers and some of these break up in order to try and maintain local equilibrium between *E*-centers and free phosphorus (37). It must be pointed out, however, that any *E*-center theory suffers from its inability to account for the observed difference between phosphorus and arsenic diffusions since an *E*-center type defect is known to exist for arsenic, at least at low temperatures (38).

### Conclusions

The first determination of the complete profile of a pushed-out base has been completed by radiotracer techniques. From these experimental results it is possible to conclude that:

(i) Push-out is entirely due to movement of the base dopant, and beyond the emitter this movement can be attributed to a simple diffusion enhancement which is constant with time during the emitter diffusion. The magnitude of enhancement is dependent on the emitter diffusion temperature, varying from 8 times at 1050°C to 100 times at 900°C for the emitter diffusions used in this work.

(ii) Localized interactions between a phosphorus emitter and a gallium base are complex and give rise to a dip in the gallium profile within the emitter. This dip can be explained by the electric field associated with the phosphorus, causing diffusion of gallium up its own concentration gradient.

It is felt that with the help of these experimental results theoretical prediction of the complete base profile should soon be possible and this would be of considerable assistance in the design and modeling of n-p-n diffused transistors. The cause of push-out is still uncertain but the *E*-center could provide a means of untransporting vacancies from the surface into the bulk where they are subsequently freed and can enhance diffusion of the base dopant.

### Acknowledgments

The authors wish to thank the Microelectronics Laboratory of Southampton University for providing phosphorus-diffusion facilities, Mr. J. M. Keen, of R. R. E. Malvern, M. L. Howlett of R. C. C. Amersham, and Mrs. M. Brown of Southampton University for useful discussions and suggestions, and Professor R. L. Bell for the provision of laboratory facilities. This work has been carried out with the support of Procurement Executive M.O.D. and sponsored by D.C.V.D.

Manuscript submitted March 31, 1976; revised manuscript received June 7, 1976.

Any discussion of this paper will appear in a Discussion Section to be published in the June 1977

JOURNAL. All discussions for the June 1977 Discussion Section should be submitted by Feb. 1, 1977.

### REFERENCES

1. A. F. W. Willoughby, *J. Mat. Sci.*, **3**, 89 (1968).
2. S. M. Hu, in "Atomic Diffusion in Semiconductors," D. Shaw, Editor, Plenum Press (1973).
3. C. L. Jones and A. F. W. Willoughby, *This Journal*, **122**, 1531 (1975).
4. R. Gereth, P. G. G. VanLoon, and V. Williams, *ibid.*, **112**, 323 (1965).
5. J. E. Lawrence, *J. Appl. Phys.*, **37**, 4106 (1966).
6. S. M. Hu and T. H. Yeh, *ibid.*, **40**, 4615 (1969).
7. D. B. Lee, *Philips Res. Rep. Supplements No. 5* (1974).
8. H. Nakamura, S. Ohyama, and C. Tadachi, *This Journal*, **121**, 1377 (1974).
9. K. H. Nicholas, *Solid State Electron.*, **9**, 35 (1966).
10. R. L. Kronquist, J. P. Soula, and M. E. Brillman, *ibid.*, **16**, 1159 (1973).
11. C. L. Jones and A. F. W. Willoughby, *Appl. Phys. Lett.*, **25**, 114 (1974).
12. C. J. Frosch and L. Derrick, *This Journal*, **105**, 695 (1958).
13. R. A. Evans and R. P. Donovan, *Solid State Electron.*, **10**, 155 (1967).
14. J. C. Irvin, *Bell Syst. Tech. J.*, **41**, 387 (1962).
15. J. C. C. Tsai, *Proc. IEEE*, **57**, 1499 (1969).
16. F. N. Schwettmann and D. L. Kendall, *Appl. Phys. Lett.*, **21**, 2 (1972).
17. J. F. Ziegler, G. W. Cole, and J. E. E. Baglin, *ibid.*, **21**, 177 (1972).
18. M. Okamura, *Jpn. J. Appl. Phys.*, **10**, 434 (1971).
19. S. M. Hu and S. Schmidt, *J. Appl. Phys.*, **39**, 4272 (1968).
20. R. B. Fair, *Appl. Phys. Lett.*, **22**, 186 (1973).
21. B. Blanchard, M. Boris, M. DeBrebisson, and J. Monnier, *Comptes Rendus de Colloque, Caracterisation des Materiaux et Technologies Semiconducteurs*, Grenoble (1972).
22. W. M. Bullis, *Solid State Electron.*, **9**, 143 (1966).
23. R. F. Peart and R. C. Newman, in "Radiation Damage and Defects in Semiconductors," I.O.P., London (1972).
24. M. Yoshida, E. Arai, H. Nakamura, and Y. Terunuma, *J. Appl. Phys.*, **45**, 1498 (1974).
25. J. S. Makris and B. J. Masters, *ibid.*, **42**, 3750 (1971).
26. S. M. Hu, in "Atomic Diffusion in Semiconductors," D. Shaw, Editor, p. 301, Plenum Press (1973).
27. H. Reiss, C. S. Fuller, and F. J. Morin, *Bell Syst. Tech. J.*, **35**, 535 (1956).
28. R. B. Fair, *J. Appl. Phys.*, **44**, 283 (1973).
29. D. B. Lee and A. F. W. Willoughby, *ibid.*, **43**, 245 (1972).
30. C. Hill, in "Radiation Damage and Defects in Semiconductors," p. 176, I.O.P., London (1972).
31. R. B. Adler, in "Atomic Diffusion in Semiconductors," D. Shaw, Editor, p. 328, Plenum Press (1973).
32. P. S. Dobson, *Phil. Mag.*, **24**, 567 (1971).
33. M. Yoshida and S. Kanamori, *Jpn. J. Appl. Phys.*, **9**, 338 (1970).
34. R. C. Booth, Ph.D. Thesis, Southampton University, (1974).
35. E. Biedermann and A. Bohg, *Appl. Phys. Lett.*, **17**, 457 (1970).
36. M. C. Duffy, F. Barson, J. M. Fairfield, and G. H. Schwuttke, *This Journal*, **115**, 84 (1968).
37. C. L. Jones, Ph. D. Thesis, Southampton University (1975).
38. E. L. Elkins and G. D. Watkins, *Phys. Rev.*, **174**, 881 (1968).
39. P. C. Parekh and K. Kolmann, *Solid State Electron.*, **17**, 395 (1974).
40. R. B. Fair and P. N. Pappas, *This Journal*, **122**, 1241 (1975).

# Silicon Nitride Film Thickness Dependence on Bipolar Transistor Characteristics

Hiroaki Mikoshiba

Nippon Electric Company, Limited, IC Division, 1753 Shimonumabe, Kawasaki, Japan

## ABSTRACT

The effect on device properties of the  $\text{Si}_3\text{N}_4$  film deposited on a thermally oxidized silicon wafer has been investigated. Oxide thickness used is mainly about 6000Å. It is shown that bipolar transistor characteristics, i.e., current gain, junction reverse current, and 1/f noise are improved with increasing  $\text{Si}_3\text{N}_4$  film thickness, except npn transistors at 2500Å of  $\text{Si}_3\text{N}_4$ . The minority carrier lifetime in the bulk silicon is also shown to be increased with increasing film thickness, based upon the fact that surface recombination velocity is not appreciably affected. Lattice strain measurements by Newton ring or x-ray rocking curve show that the lifetime increase is correlative with the reduction in the strain, which is a result of the thermal expansion rates difference. It is proposed that the lifetime be restored by the stress cancellation due to the combination of the  $\text{Si}_3\text{N}_4$  and the  $\text{SiO}_2$  on the silicon wafer. The film thickness dependence is also observed for  $\text{Al}_2\text{O}_3$  films.

$\text{Si}_3\text{N}_4$  films are widely used as an excellent passivation film against ionic contamination in bipolar IC's. However, very few things are known about the influence of these films on device characteristics. The fact that the npn transistor current gain is increased by depositing  $\text{Si}_3\text{N}_4$  films has only been empirically known among process engineers.

The current gain increase has been assumed to be attributed to surface recombination reduction. This assumption seems plausible, because these films often increase current gain at low collector current. However, it is difficult to believe that vapor-deposited  $\text{Si}_3\text{N}_4$  film on a relatively thick  $\text{SiO}_2$  layer reduces the number of trap centers at the  $\text{SiO}_2$ -Si interface or that positive charges at the  $\text{Si}_3\text{N}_4$ - $\text{SiO}_2$  interface are of benefit in reducing surface recombination. In addition, surface states are not sufficiently reduced by annealing in a hydrogen ambient at low temperatures, because of the existence of  $\text{Si}_3\text{N}_4$ , which prevents hydrogen from penetrating  $\text{SiO}_2$  (1-2).

During the  $\text{Si}_3\text{N}_4$  film sealed linear IC process development, the author found that the current gain depends on film thickness. This dependence was also found to be closely related to the stress which is induced in a silicon wafer due to mismatched thermal expansion rates (3).

Si and  $\text{SiO}_2$  thermal expansion rates are 2.5 and  $0.35 \times 10^{-6} \text{ deg}^{-1}$ , respectively. Therefore, a silicon wafer thermally oxidized at high temperature is stressed by the large difference in thermal contraction during the cooling period. It is known that stress magnitude is on the order of  $10^6$ - $10^7$  dyne/cm<sup>2</sup> at room temperature (4-5).

The thermal stress can be changed by depositing a dielectric film, such as  $\text{Si}_3\text{N}_4$  (6) or  $\text{Al}_2\text{O}_3$ , whose thermal expansion rate is larger than that of  $\text{SiO}_2$ , on the oxide layer under appropriate conditions. As shown in Fig. 1, a silicon wafer thermally oxidized at high temperature has lattice strain at room temperature due to the thermal stress. When the  $\text{SiO}_2$  on the back side of the wafer is etched away, the wafer warps, convexing the surface on which the  $\text{SiO}_2$  is left. However, when  $\text{Si}_3\text{N}_4$  film is deposited on  $\text{SiO}_2$  at relatively high temperature, the lattice strain, introduced in the course of cooling, is reduced and thus wafer warping is reduced at room temperature due to the large  $\text{Si}_3\text{N}_4$  thermal expansion rate. If  $\text{Si}_3\text{N}_4$  film is thin, the stress reduction effect is not con-

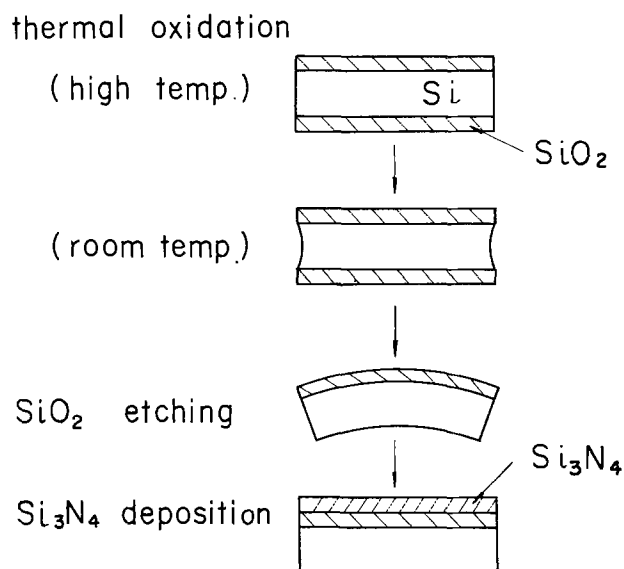


Fig. 1. Thermal stress due to thermal expansion rates difference

spicuous. If it is too thick, the stress inversely begins to increase, concaving the  $\text{Si}_3\text{N}_4$  deposited surface.

Table I lists the curvature radii and the stress in the silicon surface of a thermally oxidized silicon wafer on which  $\text{Si}_3\text{N}_4$  film was deposited at various thicknesses. The curvature radii were measured using the Newton ring method and stress was calculated from the curvature. These wafers underwent heat-treatments similar to the transistor process adopted in the present work. Oxide thickness was about 6000Å. Table I shows that the stress in silicon can be reduced by a factor of ten by depositing the  $\text{Si}_3\text{N}_4$  film.

Table I. Stress compensation by depositing  $\text{Si}_3\text{N}_4$  film. Wafers underwent a heat-treatment similar to that undergone by transistors shown in Fig. 2-9. Total oxide thickness was about 6000Å.

$\text{Si}_3\text{N}_4$ film thickness (Å)	Curvature radius ( $\times 10^6$ cm)	Stress ( $\times 10^6$ dyne/cm <sup>2</sup> )
0	1.3	17
300	2.1	11
600	2.3	9.8
1000	3.4	6.6
2000	12	2.0

Key words: silicon nitride, thermal stress, lattice strain, bipolar transistor.



The thermal stress is two or three orders of magnitude smaller than stress magnitude, at which the stress effect can be observed. In general, the stress effect is observed in silicon p-n junction devices under an anisotropic stress of more than  $10^9$  dyne/cm<sup>2</sup> (7-9). Increase and decrease in junction current and current gain is brought about by the change in carrier concentration due to stress-induced change in the energy gap. Although the thermal stress magnitude is small, it is characterized in that thermal stress rises at high temperature. Since silicon crystal is subjected to all sorts of defects at high temperature, it is expected that the thermal stress could affect the electrical properties of silicon devices (5).

Since the over-all stress is a result of the combination of Si<sub>3</sub>N<sub>4</sub> film and SiO<sub>2</sub> on the silicon wafer, oxide thickness and oxidation conditions are also important for the thermal stress. However, the present investigation has been carried out regarding only the effect of Si<sub>3</sub>N<sub>4</sub> films. The present work describes in detail the relation between Si<sub>3</sub>N<sub>4</sub> film thickness and electrical properties of various transistors, which are commonly used in linear IC's. The influence of stress change on the generation-recombination rates is investigated by separating the bulk from the surface effects. Transistor characteristics improvements, due to the vapor-deposited Si<sub>3</sub>N<sub>4</sub> film, are attributed to the increase in minority carrier lifetime in the silicon bulk. The possible mechanism for the generation-recombination centers reduction is discussed.

### Experimental

**Transistor fabrication.**—Si<sub>3</sub>N<sub>4</sub> sealed transistors, npn, lateral pnp, and collector-substrate pnp transistors, were fabricated in standard planar transistor process. The dimensions of each transistor are presented in Table II. 8 Ω·cm n-type (111) oriented silicon epitaxial wafers were used. Epitaxial layer and the substrate thickness are about 20 and 400 μm, respectively.

The isolation region was formed by usual boron diffusion. The npn transistor base and the pnp transistor emitter were formed by thermal diffusion of boron. The depth of these layers was about 2 μm. The npn transistor emitter was formed by phosphorus diffusion. In order to minimize thermal stress in a silicon wafer, both oxidation temperature and oxide thickness were reduced as much as possible. However, the oxide should be thick enough to have a masking effect for following diffusion steps. In this experiment, field oxide and oxide on base and emitter were about 6000 and 3000 Å thick, respectively.

Si<sub>3</sub>N<sub>4</sub> films were deposited at 780°C by SiH<sub>4</sub> and NH<sub>3</sub> decomposition. It is essential for the experiment that the deposition is the final high temperature treatment in wafer processing. In order to derive the full benefit of Si<sub>3</sub>N<sub>4</sub> passivation, the oxide section at contact windows was lapped over by Si<sub>3</sub>N<sub>4</sub>. Si<sub>3</sub>N<sub>4</sub> at contact windows was etched by hot phosphoric acid using vapor-deposited SiO<sub>2</sub> at 450°C as a mask.

In the experiment, a PSG layer was formed under Si<sub>3</sub>N<sub>4</sub>. Though PSG is not necessary, because of the perfection of Si<sub>3</sub>N<sub>4</sub> passivation, it was used in order to prevent any surface charge influence.

Similar experiments were carried out by depositing Al<sub>2</sub>O<sub>3</sub> instead of Si<sub>3</sub>N<sub>4</sub>, in order to confirm the same effect for Al<sub>2</sub>O<sub>3</sub> and to insure the effect of the thermal stress on transistor characteristics. Al<sub>2</sub>O<sub>3</sub> films were deposited at ca. 850°C by AlCl<sub>3</sub>-CO<sub>2</sub>-N<sub>2</sub> system hydrolysis.

Table II. Transistors dimensions

	Emitter area (μ)	Base width (μ)
npn	50 × 50	~0.3
Lateral pnp	25 × 25	17.5
Collect.-sub. pnp	70 × 30	~10

**Surface recombination velocity.**—In order to examine Si<sub>3</sub>N<sub>4</sub> film effect on surface properties, surface recombination velocity,  $S_0$ , was measured, using the gate-controlled diode. The p<sup>+</sup>-n diode was fabricated by boron diffusion into n-type 6 Ω·cm (111) oriented silicon wafers. Diffusions and oxidations conformed to the transistor process adopted in the present experiment. Oxide thicknesses on p<sup>+</sup> and n regions were about 3000 and 6000 Å, respectively.

**Minority carrier lifetime.**—To measure the minority carrier lifetime from the step response of a capacitance, the MNOS capacitor was made on n-type 6 Ω·cm (111) oriented silicon wafers 350 μm in thickness. To add the thermal stress to silicon wafer, thermal oxidation at 1140°C was repeated three times and the oxide on the back of a wafer was etched away every time oxidation was accomplished. Total oxide thickness was 5200 Å. The Si<sub>3</sub>N<sub>4</sub> film was deposited at 780°C by thermal decomposition of SiH<sub>4</sub> and NH<sub>3</sub>, in the same way as before. The gate electrode has a 2 × 2 mm area, so the surface recombination influence in the gate periphery space charge region can be reduced to a negligible amount (10). Capacitance-time response was measured on the wafer. 60V step voltages were applied to the gate to cause deep surface inversion. Capacitance step responses were measured at 1 MHz. Minority carrier lifetime was obtained by making a Zerbst plot from the capacitance-time response (11).

**Lattice strain.**—After the lifetime measurement, the aluminum gate was etched and lattice strain was measured by recording x-ray rocking curves which were obtained using a double crystal spectrometer. Two crystals were placed in the parallel (1, -1) position and diffraction was accomplished in (511)-(333) arrangement. The x-ray was obtained from the first copper K<sub>α</sub> radiation.

### Results

**Current gain.**—Forward voltage vs. collector current,  $I_C$ , and base current,  $I_B$ , characteristics are shown in Fig. 2 for various Si<sub>3</sub>N<sub>4</sub> film thicknesses. It is notable that  $I_C$  is not changed while  $I_B$  is changed. This means that the d-c common emitter current gain,  $h_{FE} = I_C/I_B$ , is changed. Figure 3 shows the relation between maximum current gain for  $I_C$   $h_{FE(max)}$  with its distribution and Si<sub>3</sub>N<sub>4</sub> film thickness.  $h_{FE(max)}$  is increased with increasing film thickness up to a certain value. However, degradation occurs at 2500 Å. As can be seen in Fig. 2, the slope of  $I_B$  at low current level approaches  $q/kT$  as film thickness increases. The normalized  $h_{FE}$  by  $h_{FE(max)}$  as a function of  $I_C$  is plotted in Fig. 4. It can be seen that the  $h_{FE}$  flatness for  $I_C$  is greatly improved by the Si<sub>3</sub>N<sub>4</sub>. Degradation at 2500 Å is also observed in the  $h_{FE}$  flatness.

Film thickness dependence was also found in pnp transistors. Figures 5 and 6 show  $h_{FE}$  vs.  $I_C$  characteristics of lateral and collector-substrate pnp transistors, respectively. pnp transistor  $h_{FE}$  is also increased with increasing Si<sub>3</sub>N<sub>4</sub> film thickness. However, degradation at 2500 Å does not occur in the case of pnp transistors.

**Junction reverse current.**—Figures 7 and 8 show the npn transistor emitter-junction and collector-junction reverse current for Si<sub>3</sub>N<sub>4</sub> film thickness, respectively. The reverse current properties of each pnp transistor junction were approximately equal to the collector-junction plots shown in Fig. 8. The reverse current is greatly dependent on film thickness, as well. As shown in Fig. 7, reverse current through the emitter-junction is increased at 2500 Å. This increase corresponds to the npn transistor  $h_{FE}$  degradation. On the other hand, at the collector-junction, which is equivalent to the pnp transistor emitter-junction, the reverse current is not increased at 2500 Å. This corresponds

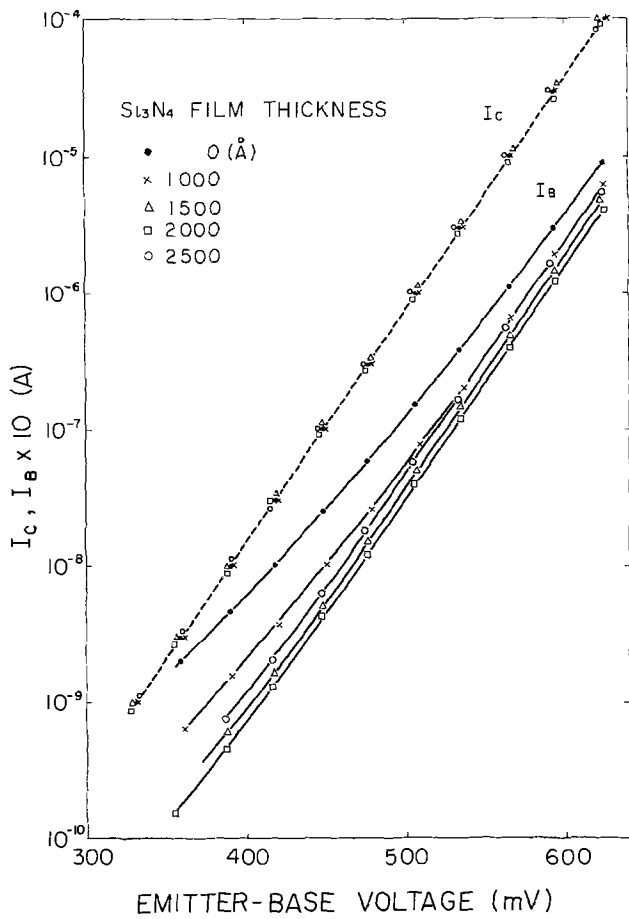


Fig. 2. Collector and base current vs. emitter-base voltage for  $\text{Si}_3\text{N}_4$  film thickness.

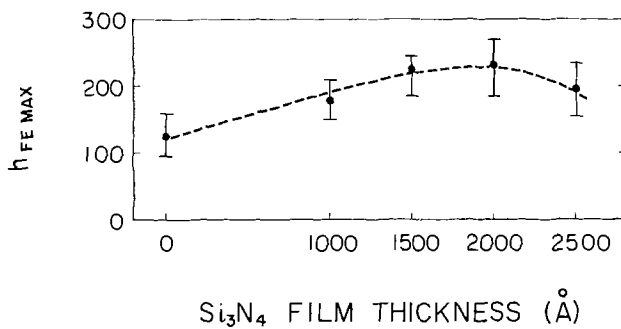


Fig. 3. Relation between  $h_{FE(\text{max})}$  and  $\text{Si}_3\text{N}_4$  film thickness

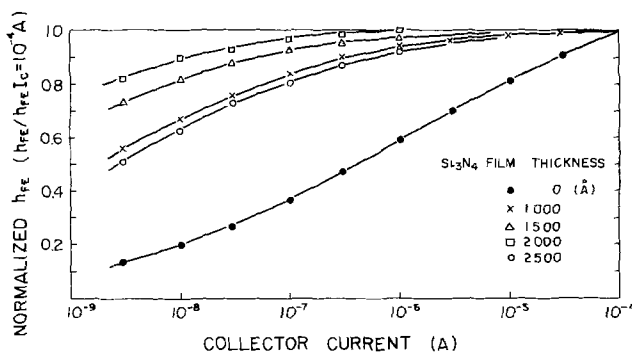


Fig. 4.  $h_{FE}$  normalized by  $h_{FE(\text{max})}$  vs. collector current with  $\text{Si}_3\text{N}_4$  film thickness as a parameter.

to the fact that  $h_{FE}$  is not decreased at 2500Å in a pnp transistor.

According to the fact that  $I_C$  is not affected by the  $\text{Si}_3\text{N}_4$  film, but both  $I_B$  and the reverse current depend on film thickness, it could be considered that the

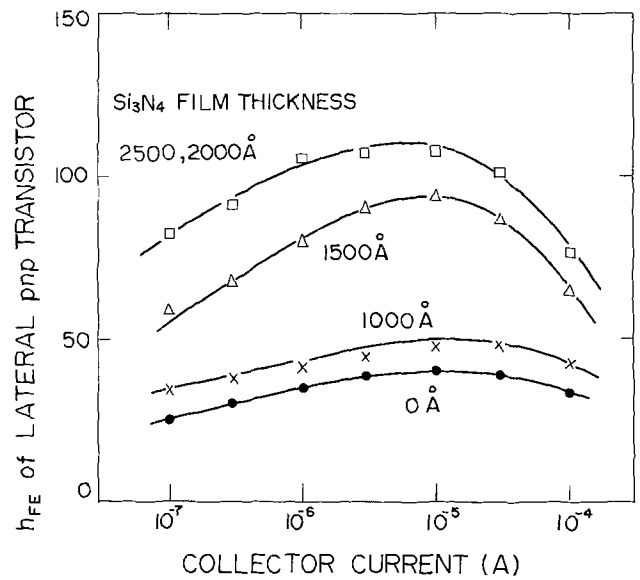


Fig. 5.  $h_{FE}$  of lateral pnp transistor vs. collector current with  $\text{Si}_3\text{N}_4$  film thickness as a parameter.

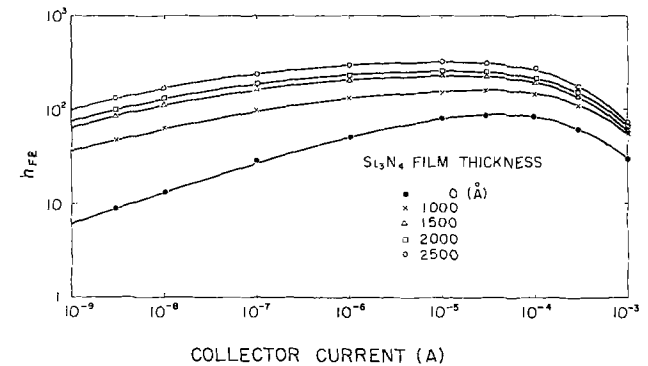


Fig. 6.  $h_{FE}$  of collector-substrate pnp transistor vs. collector current with  $\text{Si}_3\text{N}_4$  film thickness as a parameter.

generation-recombination rate in a space charge region is changed, but that carrier concentration is not changed. That is because  $I_C$  is primarily determined by the minority carrier concentration in the base region, while  $I_B$  and the reverse current result mainly from the carrier recombination and generation, respectively, in space charge regions.

**Noise characteristics.**—The npn transistor noise current spectrum is presented in Fig. 9 as a parameter of  $\text{Si}_3\text{N}_4$  film thickness. The drawing shows that 1/f noise is decreased as film thickness increases. The deterioration at 2500Å is also observed in noise current. It is interesting that noise vs. film thickness behavior is quite similar to that of low current  $h_{FE}$  and the reverse current. Considering that the 1/f noise results from recombination current fluctuation in emitter-junction space charge region (12), an assumption of a change in the generation-recombination rate seems agreeable. In addition, it is notable that burst noise was scarcely found in  $\text{Si}_3\text{N}_4$  film sealed transistors. If the burst noise is due to the modulation of carrier flow by trapped charge, as proposed by Hsu and Whittier (13), the burst noise decadence can be explained by the recombination current decrease.

**Deposited alumina film effect.**—The  $h_{FE}$  film thickness dependence was also observed in vapor-deposited  $\text{Al}_2\text{O}_3$  film. Figure 10 shows change in npn transistor  $h_{FE}$  for film thickness.  $h_{FE}$  is increased by the  $\text{Al}_2\text{O}_3$  film. It is significant that the film thickness dependence is not a special effect of  $\text{Si}_3\text{N}_4$ , but a phenomenon

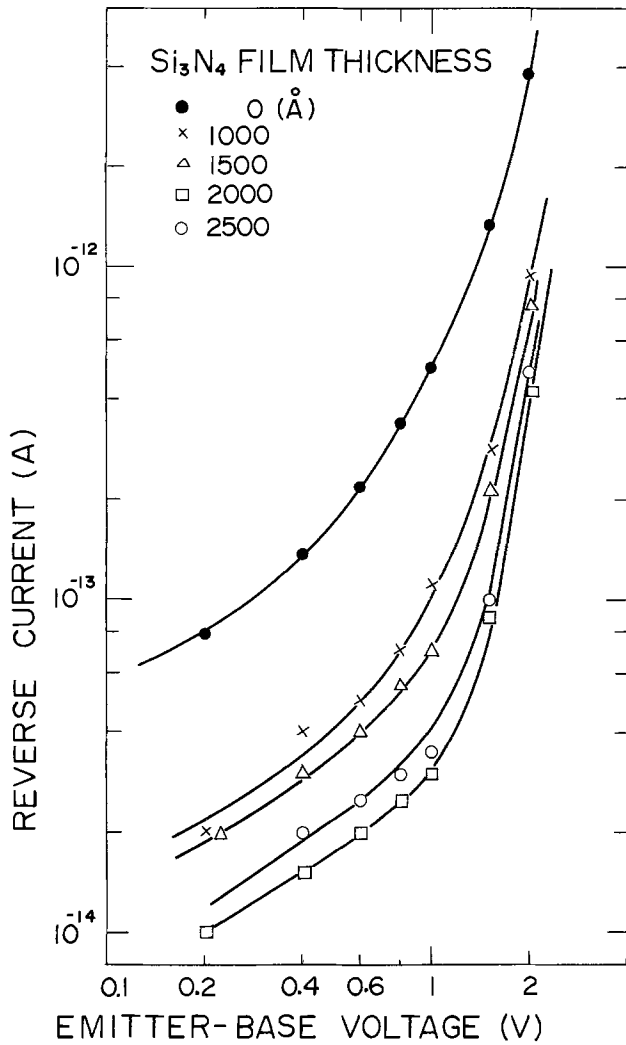


Fig. 7. npn transistor emitter-junction reverse current as a function of emitter-base voltage for Si<sub>3</sub>N<sub>4</sub> film thickness.

common to Si<sub>3</sub>N<sub>4</sub> and Al<sub>2</sub>O<sub>3</sub>. This substantiates thermal stress changing transistor characteristics, because the thermal expansion rate of both films is much larger than that of SiO<sub>2</sub>.

**Surface recombination velocity.**—Results obtained from gate-controlled diodes are listed in Table III. Only a slight increase in S<sub>0</sub> is shown to result from depositing Si<sub>3</sub>N<sub>4</sub> films. This indicates that the surface recombination is not appreciably affected. Therefore, it would be considered that the film thickness dependence is not caused in the silicon surface. This slight increase in S<sub>0</sub> seems to arise from the fact that surface state annealing is retarded by the presence of the Si<sub>3</sub>N<sub>4</sub> film (1-2).

**Minority carrier lifetime.**—Zerbst plots for various Si<sub>3</sub>N<sub>4</sub> film thicknesses are shown in Fig. 11. Table IV lists the effective lifetime, obtained from the linear portion of the Zerbst plot, the total time of c-t curve t<sub>r</sub>, and S<sub>0</sub> in the space charge region, calculated from

Table III. Surface recombination velocity obtained from gate-controlled diode. Oxide thicknesses on p<sup>+</sup> and n regions were about 3000 and 6000Å, respectively.

Si <sub>3</sub> N <sub>4</sub> film thickness (Å)	S <sub>0</sub> (cm/sec)
0	15
1000	26
1500	28
2000	34
2500	34

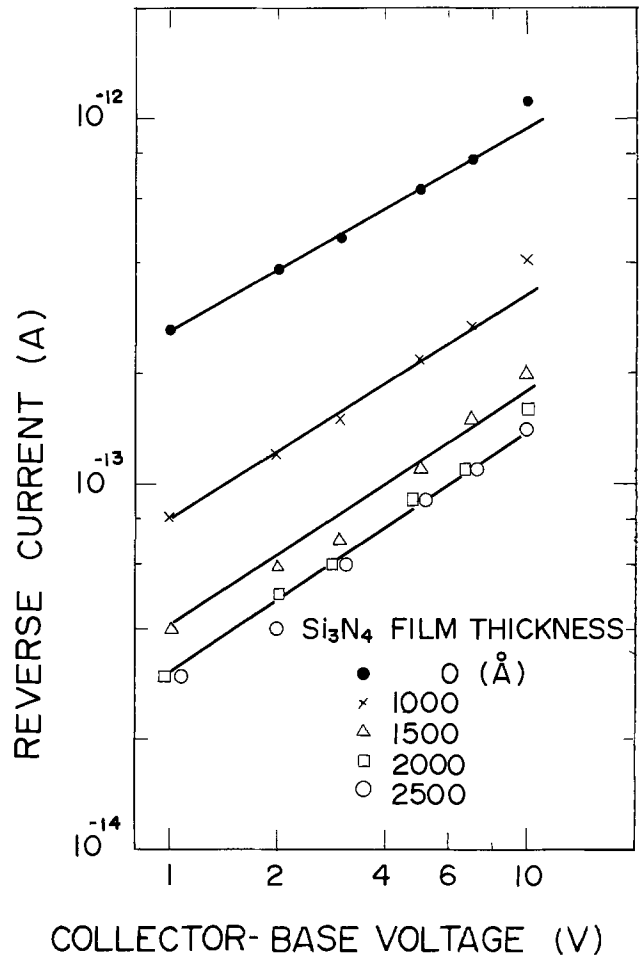


Fig. 8. npn transistor collector-junction reverse current as a function of collector-base voltage for Si<sub>3</sub>N<sub>4</sub> film thickness. These characteristics are equivalent to those of each pnp transistor junction.

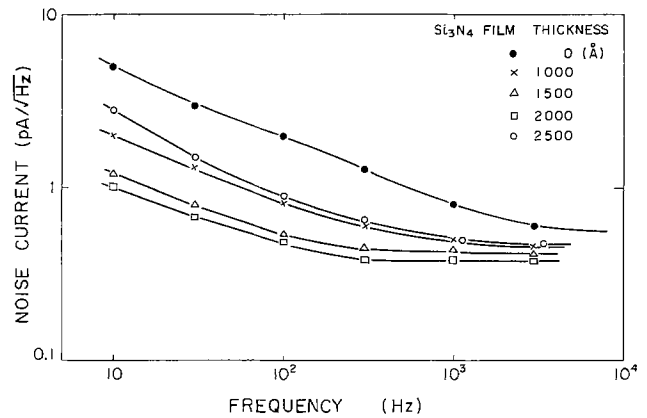


Fig. 9. npn transistor noise spectrum with Si<sub>3</sub>N<sub>4</sub> film thickness as a parameter.

c-t curves (14). The thus obtained S<sub>0</sub> value is in good agreement with the value obtained from the gate-controlled diode listed in Table III. Bulk lifetime, τ<sub>g</sub>, is related to effective lifetime, τ'<sub>g</sub>, by

$$1/\tau'_g = 1/\tau_g + PS_0/A_G$$

where P is gate periphery length and A<sub>G</sub> is gate area (10). Since A<sub>G</sub>, which is 2 × 2 mm, is large enough, lifetime surface component is only a few percent of τ<sub>g</sub>. Accordingly, τ'<sub>g</sub> can be considered as bulk dominated. From the fact that surface recombination is

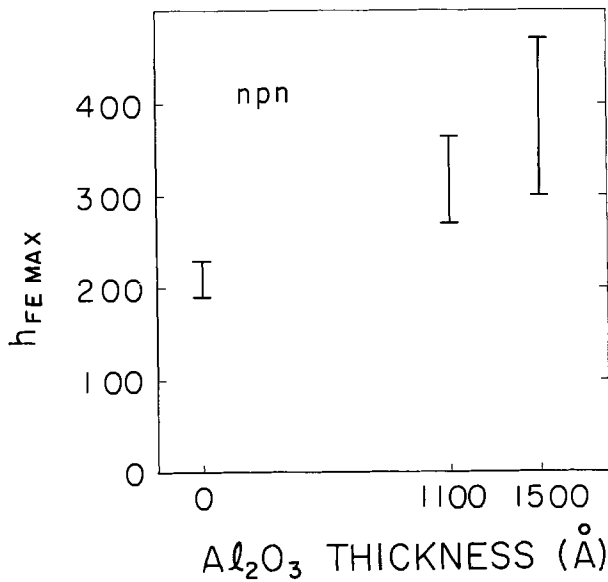


Fig. 10. Al<sub>2</sub>O<sub>3</sub> film deposition effect on npn transistor  $h_{FE}$ . Film thickness dependence is also observed in Al<sub>2</sub>O<sub>3</sub> film deposited transistors.

scarcely affected, it is concluded that the bulk lifetime is increased with increasing Si<sub>3</sub>N<sub>4</sub> film thickness.

**Lattice strain.**—Results of rocking curves, i.e., diffraction intensity and half-width, curvature radii of wafers, and stress in silicon surface calculated from curvature radii are given in Table IV. Curvature radii were obtained from the deviation of the peak of rocking curves at any two points on a wafer. As can be seen in Table IV, as Si<sub>3</sub>N<sub>4</sub> film becomes thick, the diffraction intensity increases and the half-width decreases. These values come up to those of a wafer which has had no thermal treatment. This tendency is in good agreement with the stress in silicon surface. These results show clearly that the lifetime increase is correlative with the strain reduction.

Figure 12 shows the transition of the lattice strain at each wafer processing step. When the Si<sub>3</sub>N<sub>4</sub> was etched, curvature radius and half-width became the same values as those of a wafer on which Si<sub>3</sub>N<sub>4</sub> had not been deposited. Therefore, it is known that the lattice strain due to deposited Si<sub>3</sub>N<sub>4</sub> film is within the elastic limit. However, as shown in Fig. 12, the residual strain is observed in a silicon wafer when the SiO<sub>2</sub> is removed. Therefore, it can be considered that the thermal stress exceeds the elastic limit of silicon during the thermal oxidation process because of high temperature.

**Discussion**

Both  $h_{FE(max)}$  and low current  $h_{FE}$  improvement, as well as decrease in reverse current, can be attributed to an increase in the bulk lifetime, as follows.  $h_{FE}$  of a npn transistor, whose base width,  $W_B$ , is much narrower than the electron diffusion length in the base region and whose emitter junction is deeper than the

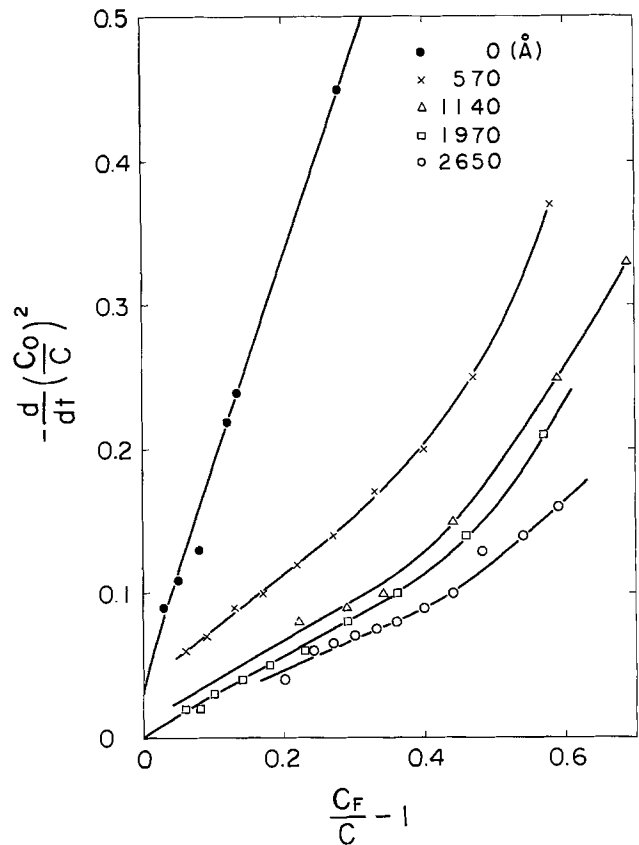


Fig. 11. Zerbst plots for MNOS capacitor c-t characteristics

hole diffusion length in the emitter region,  $L_{PE}$ , is described by the following expression (15)

$$\frac{1}{h_{FE}} = \frac{N_{AB} W_B D_{PE}}{N_{DE} L_{PE} D_{NB}} + \frac{N_{AB} W_B}{D_{NB}} \frac{W_{EB}/\tau_0 + S_0 A_s/A_J}{2n_i \exp[qV_{EB}/2kT]} \quad [1]$$

where  $N_{AB}$  is the acceptor concentration in the base,  $N_{DE}$  is the donor concentration in the emitter,  $D_{PE}$  is the diffusivity of holes in the emitter,  $D_{NB}$  is the diffusivity of electrons in the base,  $W_{EB}$  is the width of the space charge region of the emitter-junction,  $\tau_0$  is the effective lifetime within the space charge region,  $A_s$  is the depleted surface area, and  $A_J$  is the emitter-junction area. The first term of Eq. [1] represents  $h_{FE(max)}$ . The second term becomes dominant at low current level and determines low current  $h_{FE}$ . Since diffusion length  $L_{PE}$  is related to minority carrier lifetime  $\tau_{PE}$  in the emitter region by

$$L_{PE} = \sqrt{D_{PE} \tau_{PE}}$$

$h_{FE(max)}$  and low current  $h_{FE}$  of transistors with the same impurity profile are controlled by the minority carrier lifetime in the emitter neutral region and in the emitter-junction space charge region, respectively. Accordingly, the increment in lifetime results in in-

Table IV. Si<sub>3</sub>N<sub>4</sub> film deposition effect on lifetime and lattice strain. Silicon wafers were oxidized three times at 1140°C. Total oxide thickness was 5200Å.

Si <sub>3</sub> N <sub>4</sub> film thickness (Å)	S <sub>0</sub> (cm/sec)	t <sub>F</sub> (sec)	τ' (μsec)	Half-width (sec)	Diffraction intensity (%)	Curvature radius (cm)	Stress* (dyne/cm <sup>2</sup> )
0	12	13	28	7.5	24	1.9 × 10 <sup>3</sup>	+1.1 × 10 <sup>7</sup>
570	15	40	100	6.0	29	2.6 × 10 <sup>3</sup>	+7.4 × 10 <sup>6</sup>
1140	14	50	130	4.4	41	3.6 × 10 <sup>3</sup>	+5.7 × 10 <sup>6</sup>
1970	6	60	140	4.0	47	1.0 × 10 <sup>4</sup>	+1.9 × 10 <sup>6</sup>
2650	12	70	180	3.0	53	1.0 × 10 <sup>4</sup>	-1.9 × 10 <sup>6</sup>
Untreated wafer	—	—	—	2.4	61	∞	0

\* - = Compressive stress, + = tensile stress.

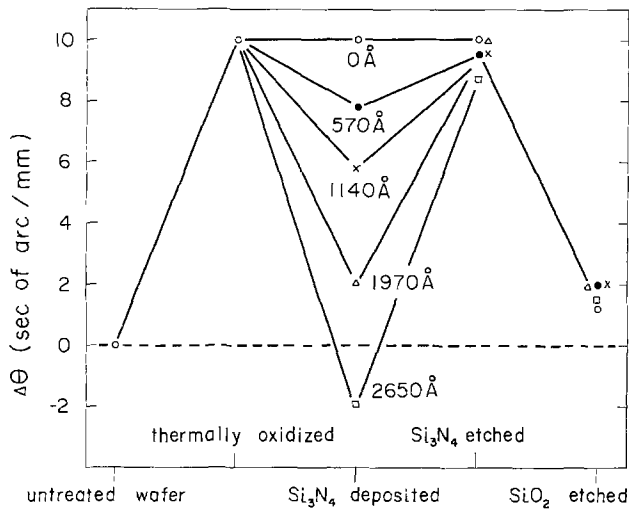


Fig. 12. Lattice strain transition at processing steps.  $\Delta\theta$  denotes rocking curve peak deviation at any two points in the distance of 1 mm on a wafer.  $\Delta\theta$  is proportional to the lattice strain.

creasing both  $h_{FE(max)}$  and low current  $h_{FE}$  at the same time.

As shown in Table III, surface recombination velocity  $S_0$  is scarcely changed by  $Si_3N_4$  film, but shows a tendency to slightly increase. This tendency is in an opposite direction for increment in  $h_{FE}$ . Consequently, the  $Si_3N_4$  film thickness dependence is not caused by the surface recombination, but is a result of the bulk recombination.

The same explanation is also applicable to a pnp transistor. However, because of relatively wide base, base transport factor

$$\frac{1}{2} \left( \frac{W_B}{L_{PB}} \right)^2$$

should be added to Eq. [1], where  $L_{PB}$  denotes the hole diffusion length in the base region. Since the base transport factor is inversely proportional to lifetime in a base neutral region, lifetime increase also produces additional  $h_{FE(max)}$  for a pnp transistor.

In the case of a silicon p-n junction, reverse current  $I_R$  is due to carrier generation in the space charge region and can be represented by

$$I_R = \frac{1}{2} q n_i A_J \frac{W_s}{\tau_0} \quad [2]$$

where  $W_s$  is the junction space charge region width (15). Reverse current is inversely proportional to the lifetime. As shown in Fig. 7-8, the reverse current is reduced to 1/3-1/8 by the deposited  $Si_3N_4$  film. That is, lifetime increases from 3 to 8 times, according to Eq. [2]. Converting the lifetime increase to change in  $h_{FE(max)}$ ,  $h_{FE(max)}$  increases to 1.7-2.8 times, because it is proportional to the square root of the lifetime value. This amount is in good agreement with the results illustrated in Fig. 3, 5, and 6. Thus, the film thickness dependence can consistently be explained by assuming the lifetime increment.

Another possible cause of the present effect is the energy gap change due to lattice strain. Since deviation in energy gap changes minority carrier density, p-n junction and transistor characteristics should be affected. However, the effect of the energy gap cannot be considered, for the following reasons.

(i) The thermal stress is on the order of  $10^6$ - $10^7$  dyne/cm<sup>2</sup>. According to the investigation reported by Monteith and Wortman (16), the change in the junction current due to energy gap change is only 0.1% for a stress in the order of  $10^8$  dyne/cm<sup>2</sup>. In order to change the stress magnitude in silicon, the back of

the wafer was etched down to about 100  $\mu$ m in thickness. However, no change in  $h_{FE}$  was observed. In addition, when the bending stress, which corresponds to the magnitude of the thermal stress, was applied to the silicon wafer scribed into strips,  $h_{FE}$  was not changed. For the stress of about  $2 \times 10^9$  dyne/cm<sup>2</sup>, only 10% increase in  $h_{FE}$  under compression stress and 5% decrease in  $h_{FE}$  under tension stress were observed. This change in  $h_{FE}$  would be due to the energy gap change, because the increase or decrease in  $h_{FE}$  is observed according to the direction of the stress.

(ii) The intrinsic carrier density is considered to be unchanged, because only reverse current depends on  $Si_3N_4$  film thickness and forward current, such as the collector current, does not.

(iii) As pointed out by Buhanan (17), the change of  $\Delta h_{FE(max)}$  in the maximum current gain due to the change of  $\Delta E_g$  in the energy gap is given by

$$\Delta h_{FE(max)} \propto \exp [-\Delta E_g/kT]$$

If  $h_{FE(max)}$  was increased by the change in the energy gap, temperature dependence should be affected by  $Si_3N_4$  film thickness. However, as shown in Fig. 13, the temperature coefficient of npn transistor is not appreciably influenced.

As mentioned before,  $h_{FE}$  is not affected at room temperature by stress which corresponds to thermal stress magnitude. Namely, lattice strain, which is equivalent to that due to thermal stress, has no effect at room temperature on the generation-recombination rate. Since the  $Si_3N_4$  film is deposited at a relatively high temperature of 780°C, heat-treatments seem to play an important role in addition to the reduction of the lattice strain. As shown in Fig. 12, residual lattice strain is observed in thermally oxidized silicon wafers. The existence of the irreversible lattice strain means that silicon wafers are plastically deformed, therefore lattice defects are introduced. Since no impurities are diffused into silicon, the plastic deformation would be caused by the thermal stress.

Lattice defects due to thermal stress could originate generation-recombination centers, therefore they could decrease the minority carrier lifetime. On the other

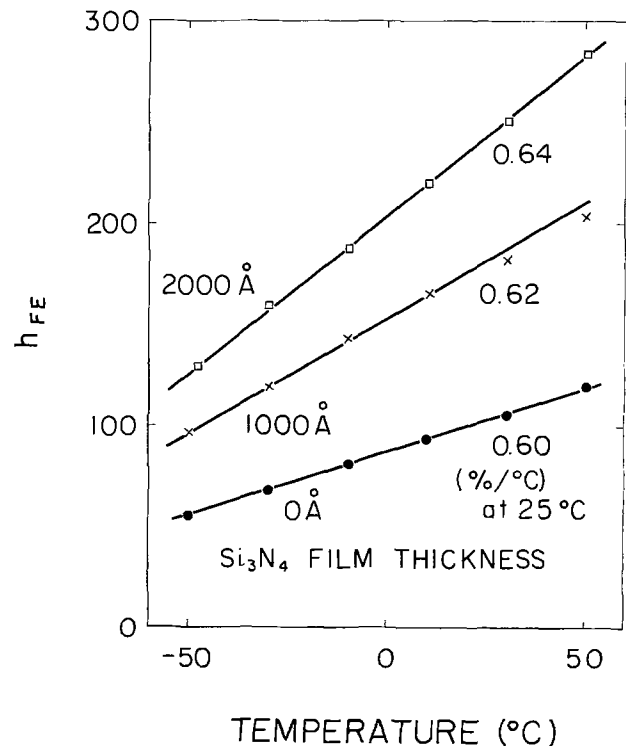


Fig. 13. Temperature dependence of npn transistor  $h_{FE(max)}$ . Temperature coefficient is not appreciably affected by  $Si_3N_4$  film.

hand, stress compensation by deposited  $\text{Si}_3\text{N}_4$  film could diminish the defects, because deposition is carried out at a relatively high temperature. As a result, the generation-recombination centers may be decreased and the minority carrier lifetime may be increased. The number of defects reduced by stress compensation would increase as  $\text{Si}_3\text{N}_4$  film becomes thick and stress in silicon is decreased.

For the degradation of npn transistor characteristics at 2500Å, this seems to result from the heavily doped phosphorus, which forms an emitter region. Because the phosphorus atomic radius is smaller than that of silicon, compressive lattice strain is already induced in the diffused layer (18). Vapor-deposited  $\text{Si}_3\text{N}_4$  on  $\text{SiO}_2$  gives compressive stress to silicon wafers. Therefore,  $\text{Si}_3\text{N}_4$  tends to increase the strain due to the phosphorus diffusion. As a result, it is considered that the degradation occurs in npn transistors.

### Conclusion

It has been found that both  $h_{FE(\max)}$  and low current  $h_{FE}$  increase and 1/f noise and reverse current decrease with increasing film thickness of  $\text{Si}_3\text{N}_4$  deposited on oxide layer, whose thicknesses are about 6000 and 3000Å on undiffused and diffused regions, respectively. However, these npn transistor characteristics begin to deteriorate when  $\text{Si}_3\text{N}_4$  film becomes thicker than a certain value, which is ca. 2500Å in the present experiment. Film thickness dependence results from lattice strain, which is induced into a silicon wafer by the difference in thermal expansion rates of  $\text{Si}_3\text{N}_4$ ,  $\text{SiO}_2$ , and Si. Lattice strain is reduced as  $\text{Si}_3\text{N}_4$  film becomes thick. However, it begins to increase in an opposite direction from the thickness which gives zero stress to a silicon wafer. The most improved transistor characteristics are achieved at about this thickness.

It has been verified by the lifetime measurement that transistor characteristics improvements are results of reduction in generation-recombination centers in the bulk due to the relaxation of the lattice strain. The surface recombination is not appreciably affected by deposited  $\text{Si}_3\text{N}_4$  film.

From the fact that residual lattice strain was observed in thermally oxidized silicon wafers, stress at high temperature seems to easily give rise to lattice defects as well as generation-recombination centers. Moreover, it seems to be essential for reducing generation-recombination centers that silicon lattice not be stressed at high temperature. It has also been found that  $\text{Al}_2\text{O}_3$  film has a similar effect on transistor characteristics as that of  $\text{Si}_3\text{N}_4$  film. Therefore, film thickness dependence is not an inherent  $\text{Si}_3\text{N}_4$  effect, but would be a common effect on films whose thermal expansion rate is larger than that of  $\text{SiO}_2$ .

Application of the developed process with the optimum  $\text{Si}_3\text{N}_4$  film thickness to a  $\mu\text{A}741$ -type operational amplifier has been proved to be effective in greatly

improving d-c and noise properties. That is, input offset voltage and current were successfully reduced down to 328  $\mu\text{V}$  and 1.2 nA in standard deviation, respectively. Input referred noise voltage from d.c. to 10 Hz of 0.25  $\mu\text{Vp-p}$  is achieved in typical value.

### Acknowledgments

The author wishes to thank Mr. Matsumura and Mr. Murase for the opportunity to study this problem and their encouragement, and Mr. Yoshimura for valuable suggestions and a critical reading of the manuscript. The author is also grateful to Mr. Hamada and Miss Yaguchi for their helpful assistance in the experiments. He is especially grateful to his many colleagues for their useful discussions.

Manuscript submitted Feb. 9, 1976; revised manuscript received May 3, 1976. This was Paper 146 presented at the Toronto, Canada, Meeting of the Society, May 11-16, 1975.

Any discussion of this paper will appear in a Discussion Section to be published in the June 1977 JOURNAL. All discussions for the June 1977 Discussion Section should be submitted by Feb. 1, 1977.

Publication costs of this article were assisted by Nippon Electric Company, Limited.

### REFERENCES

1. B. E. Deal, P. J. Fleming, and P. L. Castro, *This Journal*, **115**, 300 (1968).
2. B. E. Deal, E. L. Mackenna, and P. L. Castro, *ibid.*, **116**, 997 (1969).
3. H. Mikoshiba and K. Murase, Abstract 146, p. 346, The Electrochemical Society Extended Abstracts, Spring Meeting, Toronto, Canada, May 11-16, 1975.
4. S. D. Brotherton, T. G. Read, D. R. Lamb, and A. F. W. Willoughby, *Solid-State Electron.*, **16**, 1367 (1973).
5. T. Sugano and K. Kakemoto, *J. Inst. Electr. Commun. Eng. Jpn.*, **49**, 1887 (1966).
6. T. Tokuyama *et al.*, *Jpn. J. Appl. Phys.*, **6**, 1252 (1967).
7. W. Rindner, *J. Appl. Phys.*, **33**, 2479 (1962).
8. W. Rindner and I. Braun, *ibid.*, **34**, 1958 (1963).
9. J. J. Wortman, J. R. Hauser, and R. M. Burger, *ibid.*, **35**, 2122 (1964).
10. D. K. Schroder and H. C. Nathanson, *Solid-State Electron.*, **13**, 577 (1970).
11. M. Zerbst, *Z. Angew. Phys.*, **22**, 30 (1966).
12. A. Van Der Ziel, *Proc. IEEE*, **58**, 1178 (1970).
13. S. T. Hsu, R. J. Whittier, and C. A. Mead, *Solid-State Electron.*, **13**, 1055 (1970).
14. D. K. Schroder and J. Guldberg, *ibid.*, **14**, 1285 (1971).
15. A. S. Grove, "Physics and Technology of Semiconductor Devices," John Wiley & Sons, Inc., New York (1967).
16. L. K. Monteith and J. J. Wortman, *Solid-State Electron.*, **16**, 229 (1973).
17. D. Buhanan, *IEEE Trans. Electron Devices*, **ed-16**, 117 (1969).
18. B. G. Cohen, *Solid-State Electron.*, **10**, 33 (1967).

# Process for GaAs Monolithic Integration Applied to Gunn-Effect Logic Circuits

O. Wada, S. Yanagisawa, and H. Takanashi

Fujitsu Laboratories Ltd., 1015 Kamikodanaka, Nakahara-ku, Kawasaki, Japan

## ABSTRACT

A new technology based on the orientation dependent chemical etching of GaAs has been developed for simple and reproducible fabrication of monolithically integrated Gunn-effect circuits. By this technology, Schottky barrier gate Gunn-effect devices with fine structures and air-isolated cross-over interconnections can be produced. Using the lateral etching characteristics of  $\text{H}_2\text{SO}_4\text{-H}_2\text{O}_2\text{-H}_2\text{O}$  solution, design of the photomasks and the processing conditions are discussed and optimized. Experimental results including the application to a Gunn-effect shift register are demonstrated.

In recent years, several investigators have studied planar Gunn-effect logic devices with Schottky barrier gates to obtain rapid switching speeds (1-4). The AND/OR gates (5) and more complicated functional circuits using these gates have been already proposed (1, 6-8, 13). In order to make these proposals practical, a monolithic integration of Gunn-effect devices on one chip is required. One of the important techniques of fabricating integrated circuits concerns the delineation of fine patterns. The mesa etching technique is used in order to isolate devices. However, this conventional procedure has a disadvantage (9) in the generation of fine contact patterns over mesa steps due to the optical diffraction at the mask edge and its enhancement by the inhomogeneity of photoresist thickness around the mesa step which has a height as large as a few microns. Several remedies (8-12), including the two-plane projection method (8) and the proton bombardment technique (10, 11) have been proposed in order to overcome such a difficulty, but they require special equipment or complicate the whole fabrication process. Another important technique is that for interconnections, especially for cross-over interconnections. These have been achieved so far by the multilayer technique (13) where a dielectric layer such as silicon dioxide is used in order to isolate the upper conductive layer from the lower one, as has been frequently used in silicon technology. However, this technique may cause not only a difficulty in defining a small structure over the mesa step but a large parasitic capacitance between crossing conductive layers.

In this paper, we describe a newly developed technology for GaAs integrated circuits with small geometrical dimensions, which is simpler than those proposed so far and needs no special technique or equipment. In the present method, contacts and interconnections are defined on a flat surface of the substrate as has been done in the completely planar structure (9). The active area is then isolated by chemical etching. Lateral etching under the mask is used in this procedure. This chemical etching technique is also applied to realize a structure of multilevel conductive layers which are air-isolated from each other. In this fabricating method, conventional photolithographic processes can be used and the deposition of intermediate dielectric layers is not necessary. Adding to the simplicity of fabrication, the cross-over structure proposed here has an advantage of small parasitic capacitance between the crossing conductive layers.

In the next section, we describe method to fabricate an integrated circuit. The orientation dependence of chemical etching is described together with the experimental data. The application of this technology to fabricate experimental devices is discussed in the subsequent section.

**Key words:** Schottky barrier gate, pattern definition, cross-over interconnection, air isolation, parasitic capacitance.

## Method

In order to explain the concept of the present integration method, first the process for cross-over interconnections is presented. The process for Gunn-effect devices, which is presented later in this section, can be inserted in this process in the practical fabrication. Figure 1 shows the sequence of process steps for making an air-isolated multilayer structure.

(i) First, a metal layer having stripe geometry including windows is formed on a flat surface of GaAs with the (100) plane using conventional photolithographic process.

(ii) The epitaxial GaAs layer is removed by chemical etching with the use of the metal layer previously patterned as a protecting mask, thus a few "bridges" are formed. Step (i) and (ii) can be carried out together with the processes for Gunn-effect devices in the practical fabrication.

(iii) A photoresist layer is coated over the metal layer and a stripe window for the crossing metal layer is opened. In this procedure, a positive acting photoresist is used and it is overexposed to be removed under the bridges. Then the evaporation of the metal for the lower conductive layer is carried out using a directional evaporation technique. In this technique the evaporated metal beams are inclined from the substrate surface normal as schematically illustrated in Fig. 2. The angles can be optimized for values of the mesa height and the dimensions of the windows and the bridges of the upper layer.

(iv) By lifting off the metal layer deposited on the protecting photoresist layer, the structure of the cross-over interconnection is formed.

As has been suggested above, the lateral etching of GaAs plays an important role in the present technology. In order to use the crystallographic orientation dependence (14-16), the use of an etchant the rate of which is reaction limited is advantageous. Throughout our experiments,  $1\text{H}_2\text{SO}_4\text{-}8\text{H}_2\text{O}_2\text{-}1\text{H}_2\text{O}$  solution (16) is used at room temperature. This etchant does not attack Al and besides possesses a relatively fast and stable etch rate which is useful for our application where the epitaxial layer has a thickness as large as a few microns. Figure 3 shows the data of the etched distances *vs.* the etching time for various directions of the protecting masks made of  $\text{SiO}_2$  stripes. Insets in the figure illustrate the cross sections of the etched holes; the stripe is straight and along (A) the  $\langle 011 \rangle$  axis, (B) the  $\langle 001 \rangle$  axis and (C) the  $\langle 0\bar{1}1 \rangle$  axis, respectively. If the stripe width of the protecting mask is narrow and/or the etching time is long, a tunnel is formed under the stripe, as schematically shown in Fig. 4. In order to obtain appropriate geometries, the mask dimensions and the etching time should be designed using the results of Fig. 3. Examples of parameters for three

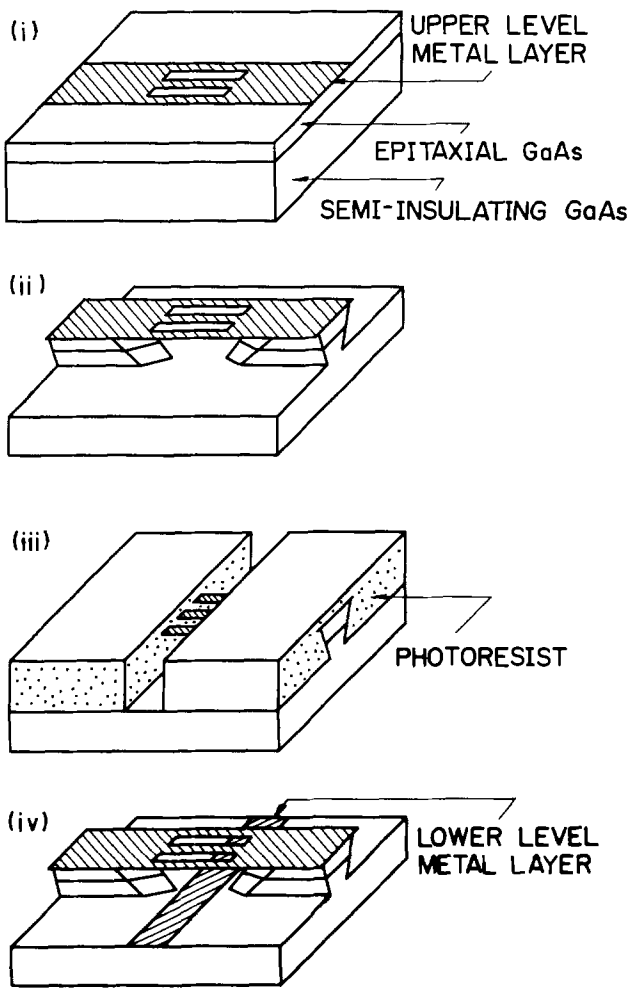


Fig. 1. Schematic illustration showing the process for fabrication of a crossover interconnection: (i) preparation of the upper level metal layer which has a few opening windows; (ii) isolation of the metal layer and formation of a tunnel under the metal layer using the chemical etching technique; (iii) coating of a positive acting photoresist followed by definition of the pattern for the lower level metal layer, and subsequent deposition of the metal using the directional evaporation technique; (iv) removal of the unwanted area of the metal layer by dipping the wafer into acetone. Thus, the structure of an air-isolated cross-over interconnection is formed.

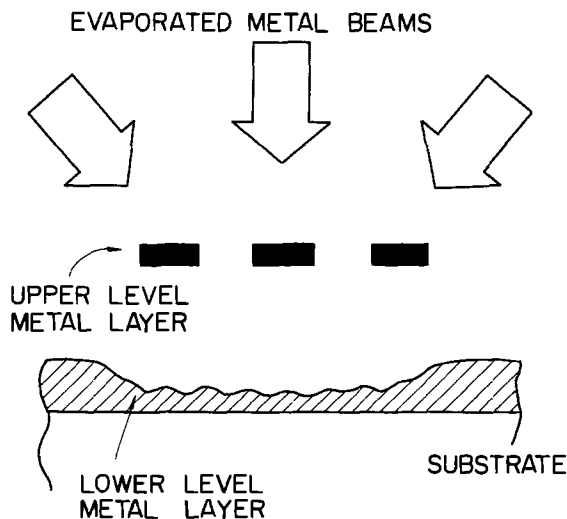


Fig. 2. Schematic representation of the formation of the lower level metal layer for a cross-over interconnection, using the directional evaporation technique. In order to avoid the shadowing effect caused by the upper level metal layer, the evaporated metal beams are inclined.

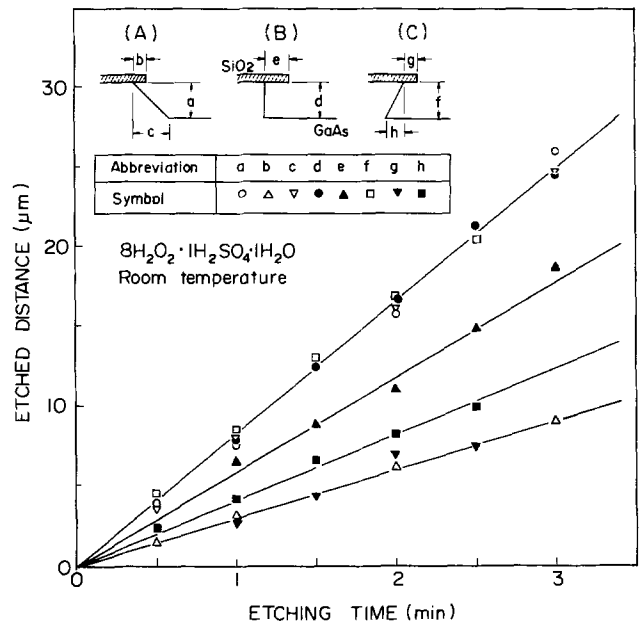


Fig. 3. Dependence of etched distance on the etching time for three directions of the mask edge. The orientation of the initial GaAs is (100). Inset (A) shows the cross section of the etched hole when the mask edge is set along the <011> axis, (B) for the <001>, and (C) for the <011>, respectively.

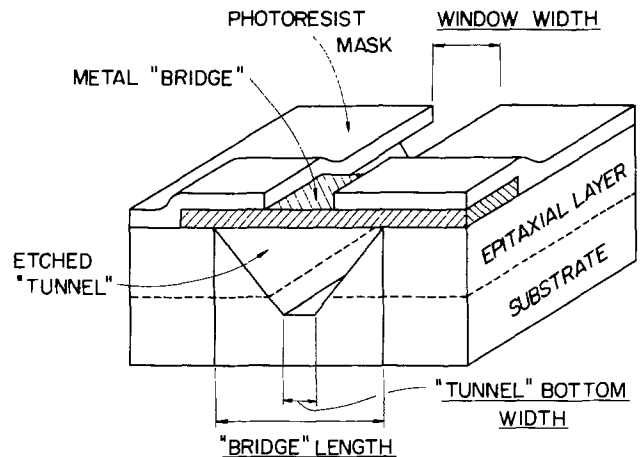


Fig. 4. Diagram showing the bridge structure formed by chemical etching of GaAs. The geometry of the etched tunnel and the bridge length depends on the mask dimensions and the orientation, as discussed in the text.

orientations are listed in Table I. Here, the thickness of the epitaxial layer and the width of the bridge have been assumed to be 5 and 2 μm, respectively. In the Gunn-effect device, as is described in the following, the gate bridge direction is perpendicular to the device current flow. The current flow directions have also been listed in the table for references.

Table I. Effect of crystal orientation on the window width, the etching time needed for the isolation of mesas, and the dimensions of resulted structure. The thickness of the epitaxial layer and the bridge width have been assumed to be 5 and 2 μm, respectively

Current flow direction	Bridge length direction	Min. window width (μm)	Min. etching time (sec)	Min. tunnel bottom width (μm)	Min. bridge length (μm)
<011>	<011>	>0	60	10.6	5.6
<010>	<001>	>0	40	7.2	7.2
<011>	<011>	6.4	40	>0	11



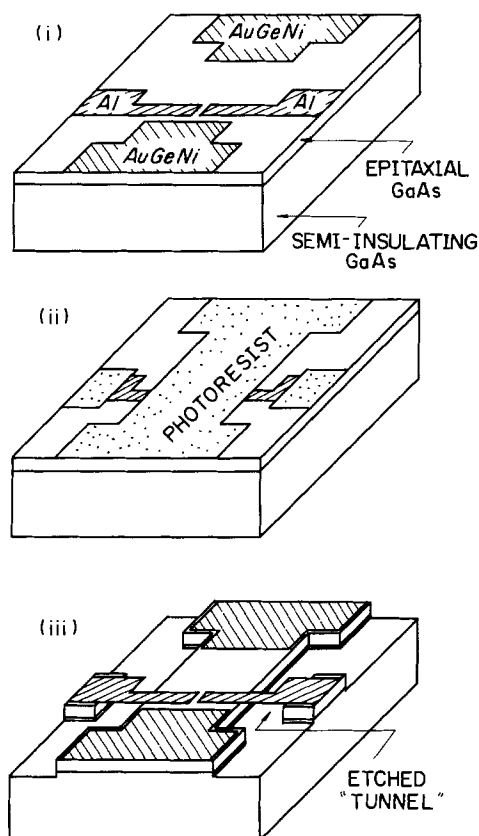


Fig. 5. Schematic illustration showing the process for fabrication of a dual Schottky barrier gate Gunn-effect device: (i) formation of the ohmic and the Schottky barrier contacts on a flat surface of epitaxial GaAs layer; (ii) preparation of the protecting mask for mesa etching using photoresist; (iii) mesa etching of the active area by the chemical etching technique. Thus the active area is isolated by the etched tunnels, and the gate contacts with bridge structures are formed.

Figure 5 separately illustrates the process for a dual-gate Gunn-effect device.

(i) The ohmic contacts are prepared by deposition of a 0.2-0.3  $\mu\text{m}$  thick Au-Ge-Ni film followed by delineation and subsequent alloying. The Schottky barrier gate contacts are formed by deposition of 0.4-0.5  $\mu\text{m}$  thick Al film and delineation. Fine patterns can be easily formed because the surface is flat.

(ii) The active area and the areas of bonding pads and contact leads excluding small portions of the Al stripes are coated with photoresist.

(iii) The uncoated areas of the epitaxial layer are removed by chemical etching. The tunnels produced under the Al bridges isolate the active area from the bonding pads and the contact leads. By removing the photoresist layer, the device structure is produced, in which the gate contacts are connected to the leads through the Al bridges.

These processes can be combined in the procedures (i) and (ii) of Fig. 1. Subsequent formation of lower conductive layer produces the whole circuit. The present integration technology makes use of the advantage of photolithographic delineation of small patterns on a flat substrate surface. The difficulty caused by the optical diffraction, which is deleterious for a thick photoresist layer particularly around the periphery of step on the substrate, can be avoided in the present method.

### Results and Discussion

We have examined fabricated devices using two of the current directions. Figure 6 shows the scanning electron micrographs of the fabricated devices. Figure 6(a) shows the scanning electron micrograph of a device structure the current direction of which is set

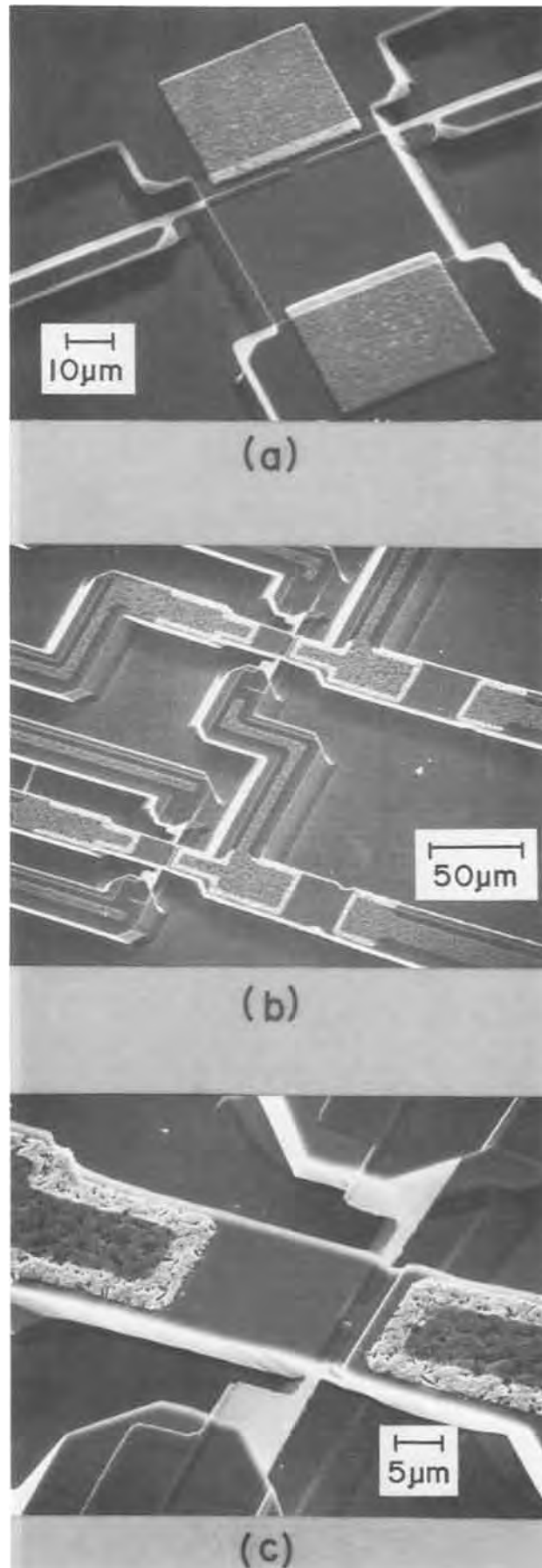


Fig. 6. Scanning electron micrographs showing a Gunn-effect unit device and an integrated circuit: (a) shows a unit device fabricated with the selection of the current flow direction along the  $\langle 011 \rangle$ ; (b) and (c) show a part of a Gunn-effect shift register circuit and a constituent unit device fabricated with the selection of the current flow direction along the  $\langle 0\bar{1}1 \rangle$ .

along the  $\langle 011 \rangle$  axis. It is worth noticing that a self-stopping effect (17) of etching may occur for this current flow direction. When the window width is excessively small, the appearance of (111) planes on the side walls makes the etched hole structure a V-shaped groove, because of the slowest etch rate of the (111) plane (16). This phenomenon drastically decreases the etch rate in the depth direction, and therefore it is difficult to remove the epitaxial layer completely at the groove bottom. In order to avoid this self-stopping effect, the window width has been designed to be larger than the minimum value as given in Table I. Fine geometry having gate contacts with bridge structures has been formed: the gate length is  $2 \mu\text{m}$  in this case. When the current direction is selected along the  $\langle 0\bar{1}1 \rangle$  axis, there is no restriction for the window width. With this orientation, the etching time should be longer than for other directions. However, the resulting structure has a small bridge length and a large tunnel bottom width. This results in a large mechanical strength and a good electrical isolation. We fabricated a 2 bit Gunn-effect dynamic shift register (18) composed of seven dual gate Gunn-effect devices and seven resistors. Figure 6(b) shows an example of the scanning electron micrograph of the shift register. Figure 6(c) shows the detail of a unit device. The thickness of the epitaxial layer is  $3.5 \mu\text{m}$ , the gate-anode separation is  $25 \mu\text{m}$ . A gate length of only  $2 \mu\text{m}$  has been obtained regardless of the large height of the mesa step.

Another advantage of the present fabrication method is that good electrical characteristics of the contacts can be obtained. It has been reported (19, 20) that a Schottky barrier with the metal deposited at room temperature sometimes shows a poor characteristic. In the case where Al is used, the characteristics can be improved by heating the substrate during or after the metal deposition (20). Taking account of the homogeneity of characteristics of the barriers over the wafer and the reproducibility, the heating during deposition is more useful. This procedure can easily be carried out in the present fabrication method, on the contrary it is prevented from being carried out when the lift off technique (21) is used. By making use of this advantage of the present method, we have made Schottky barrier gate contacts with ideality factors ( $n$ -values) better than 1.07. Concerning the dynamic characteristics of the circuits as shown in Fig. 6, we have succeeded in obtaining CW operations of dynamic shift registers with clock rates of 1.6 GHz and 2.7 GHz (18, 22). Figure 7 shows an example of the observed waveforms with the clock rate of 2.7 GHz; a two-bit shift of the signal is shown. The detailed discussions on performances and applications of the shift registers will be given shortly elsewhere.

Although we have not used the cross-over interconnections on the present level of the circuit integration, the integration of higher level inevitably needs these structures. To confirm the usefulness of the present technology, we have carried out experiments to realize cross-overs. The direction of the upper metal stripe is set parallel to  $\langle 0\bar{1}1 \rangle$  axis. With this orientation, a tunnel with a flat bottom surface is obtained by etching of the epitaxial layer as schematically shown in Fig. 1 (ii). In the subsequent photolithographic process to make a protecting mask for the deposition of the lower metal layer, the photoresist layer is removed completely even under the bridges, using the overexposure technique. In order to know how long the exposure time should be, measurements were made on the dimensions of the residual region of the photoresist (Shipley 1350J) after development, the data of which are shown in Fig. 8. The overexposure has been carried out with an intimately contacted photomask using a conventional exposure apparatus. As is observed in the figure, if the thickness of the photoresist is  $10 \mu\text{m}$  for example, 30 min exposure is necessary to wash out the photoresist under the bridge

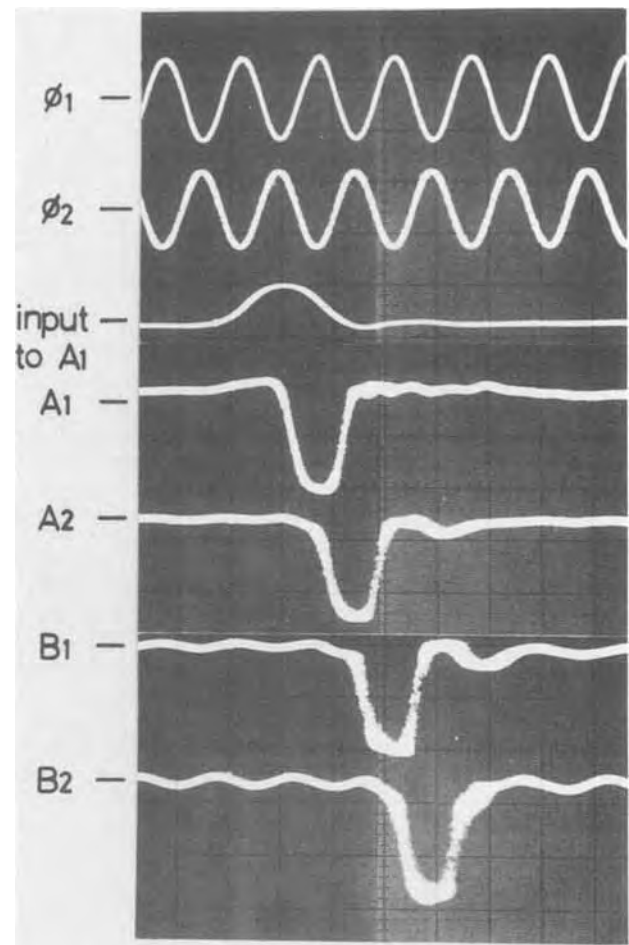


Fig. 7. Waveforms obtained by a shift register. Upper two traces ( $\phi_1$  and  $\phi_2$ ) are the clock pulses, the middle one is the input to the first device and the lower four ( $A_1$ - $B_2$ ) are the outputs of the following devices. A two-bit shift of the input signal synchronizing to the clock pulses is shown. The clock rate is 2.7 GHz and the constituent devices are biased by the subthreshold d-c voltages. Vertical scale is 2 mA/div., horizontal scale is 250 ps/div.

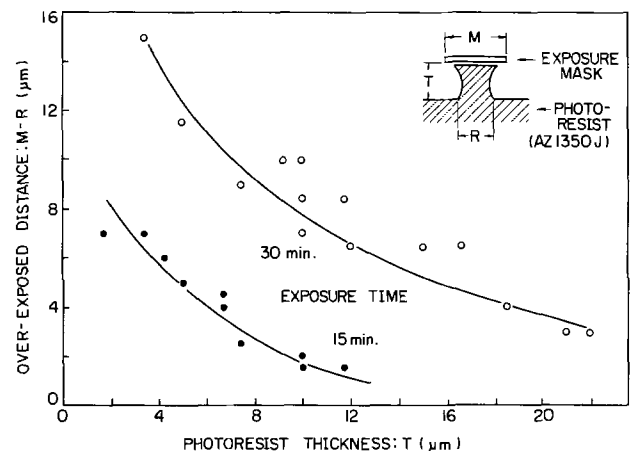


Fig. 8. Reduction of the width of the photoresist pattern after overexposure as a function of the photoresist thickness for two exposure times as parameters.

with  $8 \mu\text{m}$  width. The exposure time can be reduced down to 15 min when the bridge width is decreased down to  $2 \mu\text{m}$ . Relatively small bridge width is advantageous for the continuity of the lower conductive layer, as far as a sufficient mechanical strength is preserved. In our experiment, the bridge width has been fixed to be  $5 \mu\text{m}$ . Figure 9(a) shows an example of the

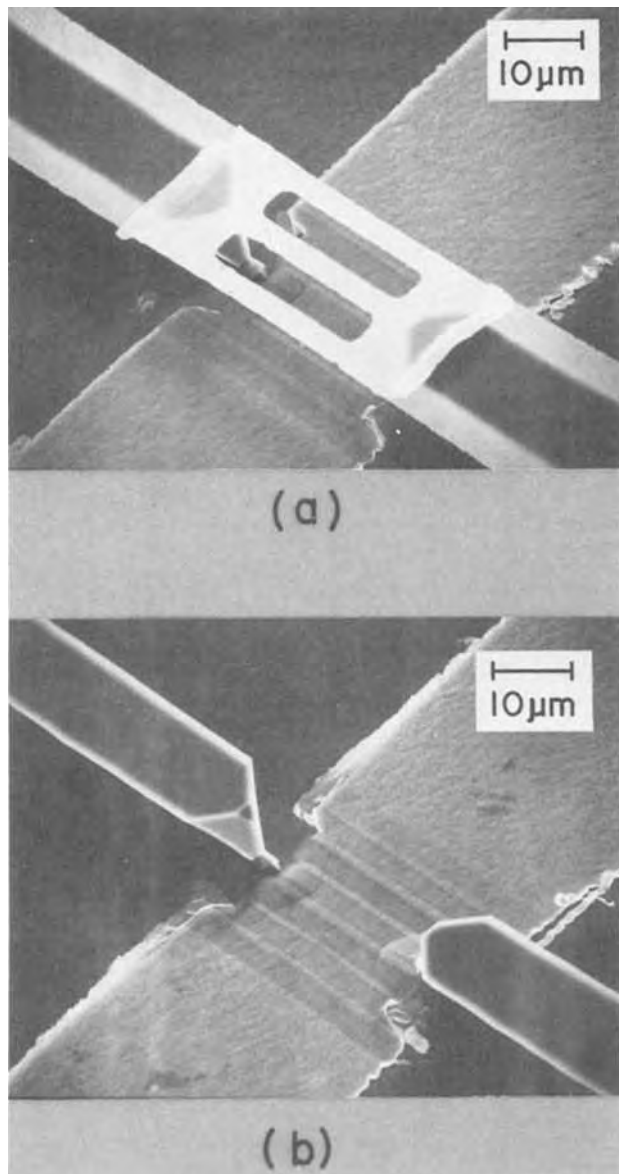


Fig. 9. Scanning electron micrographs showing an air-isolated cross-over interconnection; (a) the view of as-fabricated structure; (b) the view of structure after removal of the upper level metal layer. Note that the lower layer is continuous under the upper layer and isolated from the epitaxial layer.

produced structure. The mesa height is  $10\ \mu\text{m}$  and the widths of the upper and the lower conductive layer are  $25$  and  $50\ \mu\text{m}$ , respectively and the thicknesses of layers are about  $4000\text{\AA}$ . Figure 9(b) shows the structure after only the upper metal layer has been etched away, to demonstrate that the lower layer is continuous along the length and at the same time isolated from epitaxial layers. A complete isolation has also been confirmed by electrical measurement. Concerning the mechanical strength of the bridge structure, it has been observed that no sample having this structure is broken by the usual processing treatment, for example, ultrasonic bonding.

The elimination of depositing insulator films simplifies the process. Moreover, it is worth noticing that the resulting structure has a very small parasitic capacitance compared to the multiple layer structure with an insulator film. Only devices with negligible small parasitic capacitances can take full advantage of the fast response, which is one of the most important characteristics of Gunn-effect devices, and eliminate the possibility of cross-talk or other erroneous operations. For example, the parasitic ca-

pacitance of the structure shown in Fig. 9 is only  $0.001\ \text{pF}$ , which is about a hundred times smaller than that obtained by a multilayer structure having a  $5000\text{\AA}$  thick  $\text{SiO}_2$  layer and conductive layers with dimensions same as those in Fig. 9. This small value can be neglected compared with the gate input capacitance of the usual device of the order of  $0.01\ \text{pF}$ . The occurrence of resistive/capacitive losses due to the Schottky barrier capacitance between the upper conductive layer and the n-GaAs layer is also avoidable by using an intermediate ohmic contact layer, as has been carried out in Fig. 6(b).

Usually the lower conductive layer is connected at its end to one of the contacts of a unit device each of which lies on the upper level. For this purpose, the lower conductive layer should be transferred to the upper level across the mesa step. However, this procedure is carried out simultaneously in the last process step for the formation of lower conductive layers, and a high yield of the photolithographic process can be obtained due to relatively large widths of lower conductive layers.

### Conclusions

We have introduced a new technology of fabricating Schottky barrier gate Gunn-effect device and cross-over interconnection, both of which are important in a monolithically integrated Gunn-effect circuit. We can produce the unit Gunn-effect devices and the upper interconnections by first forming fine contact patterns on a flat surface of epitaxial layer and then isolating the active area by the chemical etching technique. Finally, the lower conductive layer is formed by the directional evaporation technique. The fabrication of monolithically integrated circuits with fine structures and good electrical characteristics can be achieved by the present technology. It has been confirmed experimentally that the present processes can easily be carried out with no sophisticated instrumentation as, for example, required by the proton bombardment technique. In the course of our work, we have succeeded in fabricating a Gunn-effect shift register with a clock rate of  $2.7\ \text{GHz}$  by applying this technology in forming unit devices. In addition, the small parasitic capacitance obtained by our method is considered to be useful for other semiconductor integrated circuits.

### Acknowledgments

The authors would like to thank T. Ogawa for assistance in the experiments, Y. Toyama, T. Nakamura and G. Goto for fruitful discussions, and Dr. T. Misugi and Y. Fukukawa for continual encouragement.

Manuscript submitted March 15, 1976; revised manuscript received June 1, 1976.

Any discussion of this paper will appear in a Discussion Section to be published in the June 1977 JOURNAL. All discussions for the June 1977 Discussion Section should be submitted by Feb. 1, 1977.

Publication costs of this article were assisted by Fujitsu Laboratories Limited.

### REFERENCES

1. T. Sugeta, H. Yanai, and K. Sekido, *Proc. IEEE*, **59**, 1629 (1971).
2. K. Mause, A. Schlachetzki, E. Hesse, and H. Salow, "Proceedings of the 4th Biennial Cornell Electrical Engineering Conference, 1972," p. 211 (1973).
3. M. Takeuchi, A. Higashisaka, and K. Sekido, *IEEE Trans. Electron Devices*, **ed-19**, 125 (1972).
4. K. Kurumada, T. Mizutani, and M. Fujimoto, *Electron. Lett.*, **10**, 161 (1975).
5. S. Kataoka, N. Hashizume, M. Kawashima, and Y. Komamiya, "Proceedings of the 4th Biennial Cornell Electrical Engineering Conference, 1972," p. 225 (1973).
6. H. L. Hartnagel, *Solid-State Electron.*, **12**, 19 (1969).
7. T. Nakamura, S. Hasuo, G. Goto, K. Kazetani, and T. Isobe, "ISSCC Digest of Technical Papers," p. 166 (1975).

8. K. Mause, A. Schlachetzki, E. Hesse, and H. Salow, *IEEE Trans. Commun.*, **com-22**, 1435 (1974).
9. K. H. Bachem, J. Engemann, and K. Heime, *Japan. J. Appl. Phys. Suppl.*, **43**, 222 (1974).
10. A. Schlachetzki and E. Hesse, *Solid-State Electron.*, **17**, 633 (1974).
11. L. C. Upadhyayula, S. Y. Narayan, and E. C. Douglas, *Electron. Lett.*, **11**, 201 (1975).
12. O. Wada, S. Yanagisawa, and H. Takanashi, *This Journal*, **123**, 420 (1976).
13. K. Mause, *Electron. Lett.*, **11**, 408 (1975).
14. S. Iida and K. Ito, *This Journal*, **118**, 768 (1971).
15. Y. Tarui, Y. Komiya, and Y. Harada, *ibid.*, **118**, 118 (1971).
16. J. J. Gannon and C. J. Nuese, *ibid.*, **121**, 1215 (1974).
17. M. J. Meclercq, L. Gerzberg, and J. D. Meindl, *ibid.*, **122**, 545 (1975).
18. S. Yanagisawa, O. Wada, and H. Takanashi, "International Electron Devices Meeting Technical Digest," p. 317 (1975).
19. B. L. Smith, *Solid-State Electron.*, **11**, 502 (1968).
20. O. Wada, S. Yanagisawa, and H. Takanashi, *Japan. J. Appl. Phys.*, **12**, 1814 (1973).
21. H. I. Smith, F. J. Bachner, and N. Efremow, *This Journal*, **118**, 821 (1971).
22. O. Wada, S. Yanagisawa, and H. Takanashi, *Proc. IEEE*, **64**, 566 (1976).

## The Nature of Defects in Silicon Dioxide

A. K. Zakzouk,<sup>1</sup> R. A. Stuart, and W. Eccleston

*Department of Electrical Engineering and Electronics, University of Liverpool, Liverpool L69 3BX, England*

### ABSTRACT

Localized conducting regions of silicon dioxide are a major source of failure of integrated circuits. By using liquid crystals in contact with the oxide, and simultaneously applying an electric field across such a sandwich structure, defective regions can be nondestructively identified. By examining the number of defects as a function of the polarity of the applied voltage, and time, it is possible to obtain information on the cause and nature of these localized regions of high conduction. Experiments of this type indicate that defects are frequently caused by imperfections in the silicon substrate and a model is proposed which accounts qualitatively for the results obtained with liquid crystal present.

Thin dielectric films are widely used in the electronics industry. One of the most important applications of such films is in planar technology. Silicon dioxide, silicon nitride, and alumina are the most widely used materials and each has its own set of advantages, particularly when used as an integral part of the gate dielectric of metal oxide semiconductor transistors (MOST). Silicon nitride and alumina are particularly impervious to the migration of sodium and proton ions, unlike silicon dioxide. These ions can give rise to instability in the threshold voltage of MOST devices. Silicon dioxide is still very widely used, however, because thin (1000Å) films can be produced by thermal oxidation of the silicon, providing a semiconductor-insulator interface which is relatively free from surface states. The thin films produced by thermal oxidation are dense and when free from "defects" pass negligibly small currents for the range of electric fields commonly found with MOS transistors. Oxide "defects" do occur in sufficient numbers, however, to cause unreliability in large scale integrated circuits. The failure of circuits may be due to either catastrophic breakdown, or high conduction in the dielectric. The problem is not restricted to conventional MOS circuits, but is also important in both charge coupled devices and bipolar transistor circuits.

Pinholes may be one possible cause of high conduction and are due in many cases to either contamination of the underlying silicon substrate or imperfections in photoengraving masks. High conduction is also found in the absence of pinholes and this is more difficult to explain. The study of defects of this type has been made more difficult, in the past, by the lack of availability of a nondestructive technique for locating them. Kern (1) has reviewed the currently available techniques. Keen (2) has shown that negative nematic crystals provide a good nondestructive method for locating defects in insulating layers. This technique has

been studied in more detail by the present authors (3) and is the subject of this publication. DiStefano (4) has used photoemission measurements to show that a highly localized reduction of the silicon-silicon dioxide barrier can occur, particularly after contamination of the oxide by impurity ions such as sodium. The barrier is lower after applying an electric field across the oxide which drives the impurity ions to the silicon surface. Williams *et al.* (5) have suggested that the cause of the localized barrier lowering is a condensation of sodium ions at particular points on the silicon surface. The potential energy of a particular ion is shown to be lower when it is situated near to a metallic-like surface. An accumulated silicon surface approximates such a surface and the positive sodium ions will induce such a surface condition. This effect promotes the condensation and would be expected to produce the highly localized barrier lowering described by DiStefano.

Raider (6) has demonstrated that sodium drift can be responsible for time-dependent breakdowns, presumably due to electron injection into the film at localized regions where the barrier is lowered. Chou and Eldridge (7) have studied the dependence of breakdown on processing parameters and this has been followed by a large amount of work on the effect of sodium on conduction and breakdown (8, 9), all of which must ultimately be fitted into any general theory of oxide conduction and breakdown.

Conduction has been studied in oxides with, presumably, minimal amounts of barrier lowering, by Lenzlinger and Snow (10). Their results, obtained on MOS capacitor structures, indicate that conduction is primarily limited by Fowler-Nordheim tunneling either from the metal or silicon into the oxide. Osburn and Weitzman (11) have arrived at similar conclusions, but also indicate the importance of mobile ions and trapping phenomena in the conduction process.

### The Liquid Crystal Technique

With this technique, the thermally oxidized slice is covered by a drop of liquid crystal which is then

<sup>1</sup> Present address: Department of Engineering, Alexandria University, Alexandria, Egypt.  
Key words: integrated circuit testing, liquid crystals, oxide defects density, field, thickness dependence.

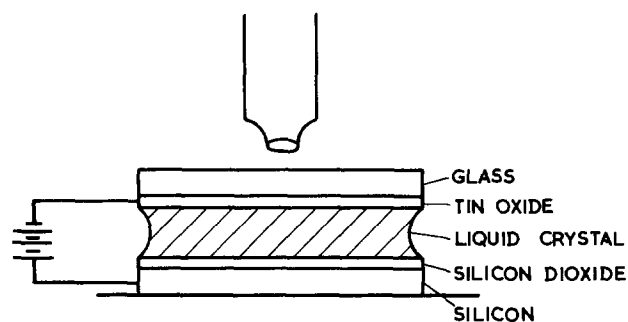


Fig. 1. The apparatus used for the study of oxide defects with liquid crystal. No spacers are necessary since the tin oxide coated glass plate is supported by the liquid crystal film.

placed beneath a tin oxide coated glass slide as shown in Fig. 1. The highly insulating nature of the silicon dioxide prevents the passage of large currents through the liquid crystal. Wherever the silicon dioxide is conducting, however, turbulence is seen in the liquid crystal. The thickness of the liquid crystal layer, under the weight of the glass slide, can be reduced to about  $10\ \mu\text{m}$  and this is the diameter of the area of turbulence seen through the microscope. The turbulence effect is known as dynamic scattering and has been discussed by Heilmeyer *et al.* (12) and DeGennes (13). The process by which it occurs is by no means certain. The following discussion would appear to represent a consensus view of the process and is the basis of our understanding of the effect when used for locating defects.

We consider an arrangement similar to that shown in Fig. 1, with the oxidized silicon slice replaced by a simple conducting electrode. The liquid crystal molecules, under the action of the applied field, align themselves parallel to the plates. This is due to the presence of a dipole, on each molecule, at right angles to the long axis of the molecule. The molecules, being neutral over-all, cannot provide a d-c current. If they absorb a water molecule, however, they can accept an electron from the negative electrode, move to the positive electrode under the action of the electric field, and there become discharged. A d-c current then passes through the liquid. As the molecule carrying the electron drifts through the liquid medium, molecules on either side rotate because of the electrostatic force on their dipoles. This turbulence causes a change of refractive index and can therefore be clearly seen through the microscope. If the negative electrode is providing electrons to the liquid crystal molecules uniformly over its area, the resultant torque on other molecules is zero and no turbulence is expected. Because of statistical variation in the rate of release of ions, no detailed balance in torque occurs and turbulence is seen.

When one of the electrodes has an insulating layer on its surface, conduction occurs in the liquid crystal in those places where high conduction in the insulating layer due to defects is present. The torque on the liquid crystal molecules in the region of the conducting defect is then particularly strong because of the large variation in the release of charged liquid crystal molecules at the defect compared with those regions of good insulator around it. The effect has been discussed by Keen (2), but has not been the subject of extensive quantitative study.

#### Fabrication of Samples

All the results described here, unless otherwise stated, were obtained on (111) n-type silicon. The silicon was initially degreased and was then boiled in nitric acid, followed by treatment in hydrofluoric acid, before washing in deionized water. The oxidation was carried out in dry oxygen at  $1000^\circ\text{C}$  for sufficient lengths of time to produce 1000 to 5000Å thick films.

The furnace was resistance heated and the silicon slices were contained on a quartz boat in a single wall quartz tube. All the oxidations were carried out with the slices horizontal, fully supported by the quartz boat. This minimizes the stress on the silicon during oxidation and cooling.

In many cases this procedure was preceded by steam oxidation of the silicon. Using conventional photolithography, small windows were etched in the "steam" oxide and the thin "dry" oxide was grown in the windows. This procedure was carried out to facilitate precise location of a particular region of oxide during the experiments and to simulate typical processing steps of MOS and charge coupled device oxides. The oxide was removed from the rear of the slice and this was placed in contact with an aluminum plate. A small amount of the nematic liquid crystal (p-methoxybenzylidene-p-n butyl-aniline) was then placed on the top of the oxidized surface of the slice, and the apparatus was set up as shown in Fig. 1.

#### Initial Experiments

Voltages of both polarity were applied to the tin oxide and the samples were observed for long periods of time. With negative bias on the tin oxide, very few turbulent regions were seen. The oxide itself showed faults in these regions when viewed without liquid crystal, and it is believed that these regions are pinholes presumably caused by contamination during the oxidation process. We shall, henceforth, refer to these as type I defects. Figure 2a shows a type I defect.

With positive bias applied to the tin oxide, many more defects were seen, although type I defects are still present. We shall refer to those defects occurring under positive bias only as type II defects. Figure 2b shows the appearance of a sample after applying positive bias to the tin oxide. Figure 2c shows the same region of oxide sometime later. Both Fig. 2a and b show the type I defect present in Fig. 2a. There is also, clearly, an increase in the number of type II defects with time.

Figure 3 shows the way in which the density of defects increases with time for two films of thickness 0.1 and  $0.19\ \mu\text{m}$ . In both cases (curves A and C), the number of defects saturates with time. If negative bias is applied to the top electrode, only type I defects are visible, but on subsequent positive biasing the number of type II defects is initially reduced. However, after a further time has elapsed the defect density rises above its earlier value and ultimately saturates (curves B and D).

On one sample, which had scratches in the silicon, lines of type II defects were seen along the scratches. In addition, defects occurred preferentially at the points of intersection of thick and thin oxide. At these points there is a ledge in the silicon due to silicon having been removed inside the window during the second oxidation process. This effect is clearly indicated in Fig. 4.

It was found also that the number of type II defects was not significantly affected by the presence of diffused p-type region in the surface of the silicon.

In general, type II defects are not visible as oxide flaws using optical microscopy.

#### Discussion of Initial Experiments

Three features of the initial results require explanation: the polarity and time dependence of the density of defects and the marked increase in density as a result of negative voltage on the tin oxide. It is conceivable that type II defects are submicroscopic pinholes. Their polarity dependence could then be due to a difference in the heights of the silicon-liquid crystal barrier and the tin oxide-liquid crystal barrier. This would appear not to be the case, however, since larger oxide pinhole defects are visible under both polarities. Measurements have been made on silicon slices of the variation of current with applied voltage, without an

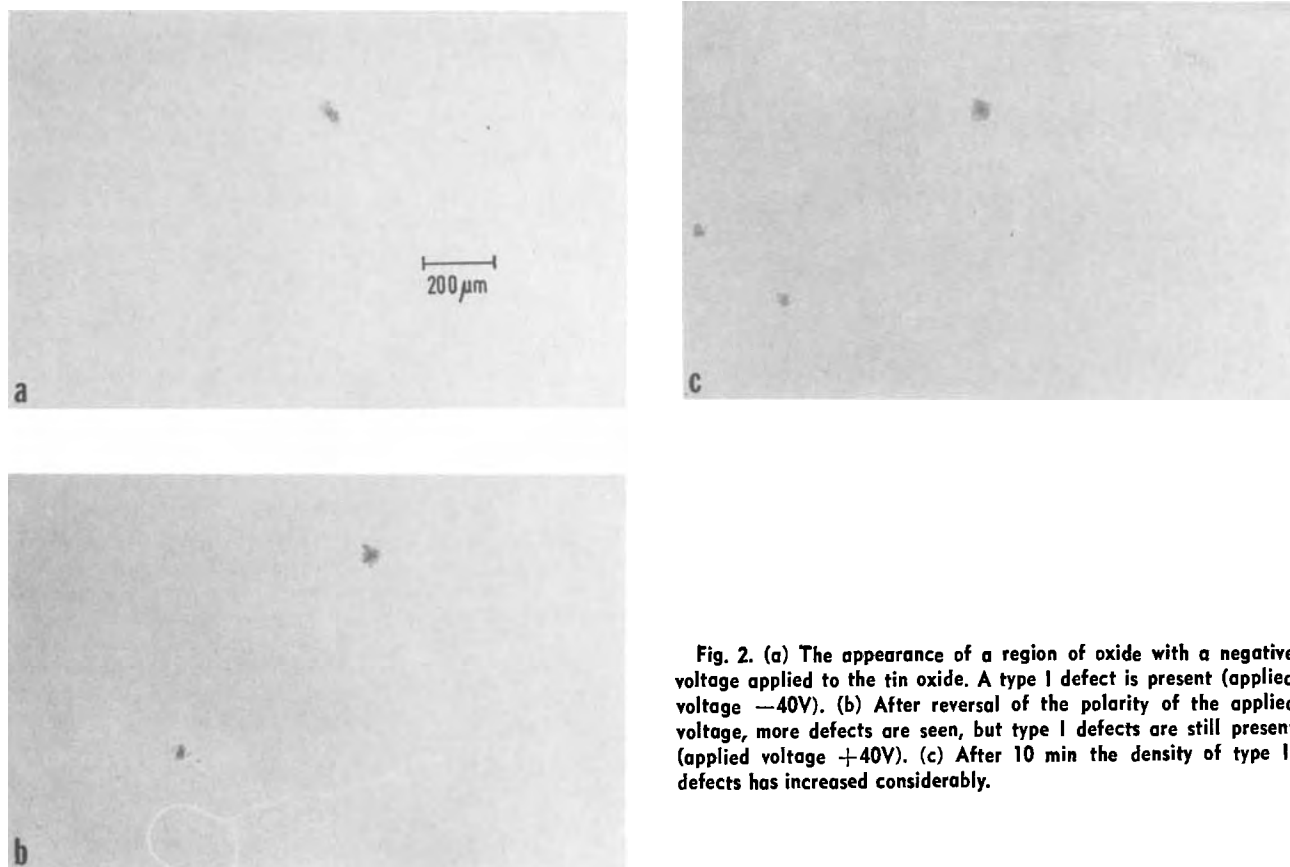


Fig. 2. (a) The appearance of a region of oxide with a negative voltage applied to the tin oxide. A type I defect is present (applied voltage  $-40V$ ). (b) After reversal of the polarity of the applied voltage, more defects are seen, but type I defects are still present (applied voltage  $+40V$ ). (c) After 10 min the density of type II defects has increased considerably.

oxide film, and no strong polarity dependence is seen. Figure 5 shows typical curves and can be compared with Fig. 6, for the situation where an oxide film is present, and a strong polarity dependence is present. It seems, therefore, that if type II defects are pinholes, then barrier height differences are not primarily responsible for their polarity dependence. This is in agreement with the earlier work of Heilmeier *et al.* for a wider variety of metal electrodes.

The tendency for type II defects to be distributed along ledges in the silicon indicates the importance of silicon imperfections in these phenomena. We suggest a simple model which would appear to account qualitatively for the initial results. Consider first the processes occurring in a typical oxide film free from defects when placed in the apparatus shown in Fig. 1. The charge motion is shown schematically in Fig. 7a. Electrons tunnel through the barrier from the conduction band of the silicon and then move through the oxide. At the outer surface of the oxide they attach themselves to liquid crystal molecules and are then transported to the positive anode where the molecules are discharged. During the application of the positive voltage any scratches or similar discontinuities act as points of field intensification and positive impurity ions in the film condense at these points. This, together with the field intensification due to the geometry of the irregularities, causes barrier lowering. Since the height of the barrier primarily controls the current, the current increases. Because of the relatively high mobility of electrons in the silicon dioxide, the barrier can be reduced by a large amount before the conduction becomes bulk limited. Presumably, the current ultimately becomes limited by some form of Poole-Frenkel conduction. As positive charge enters the regions of field intensification by diffusion from other parts of the film, one would expect the current and, hence, size of the turbulence to increase. Ultimately the total number of defects seen will saturate, either due to the number of available im-

purity ions becoming exhausted, or when all the available silicon sites are producing turbulence. Figure 3, curves A and C, would appear to indicate that saturation occurs after approximately 5 and 15 min, respectively. On applying negative voltage to the tin oxide, the positive ions are removed from the region of the silicon surface and geometrical effects cause the positive ions to spread out into the oxide. No turbulence is now present in the liquid crystal indicating that all the voltage is now falling across the oxide. It is well documented that such a high field causes the release, by tunneling, of electrons from traps in the oxide. The tunneling process involves no change of electron energy and the traps must therefore have energies coincident with the conduction band in the presence of the applied field for charge to transfer to the conduction band. Positive charge is created in the oxide. On returning to positive voltage on the tin oxide, the number of turbulences would be expected to be initially small. Impurity ions condense with the lapse of time and gradually the number of defects increases. The total positive charge is now due to not only impurity ions but also the ionized traps obtained through the previous application of negative bias to the tin oxide. It is not surprising that curves B and D of Fig. 3 show an increased number of turbulences since some smaller defects may now have sufficient positive charge surrounding them to produce large enough electron currents for them to become visible.

The model proposed would appear to be the simplest capable of explaining the present observations. If correct, it leads to further deductions about the behavior of oxides when viewed by this method. Since curves A and C show quite definite saturation, we are forced to deduce that we are primarily limited by the concentration of impurity ions in the oxide. Curves B and D indicate that more silicon imperfections are present in the sample than are shown in A and C. In view of the comparatively large amount



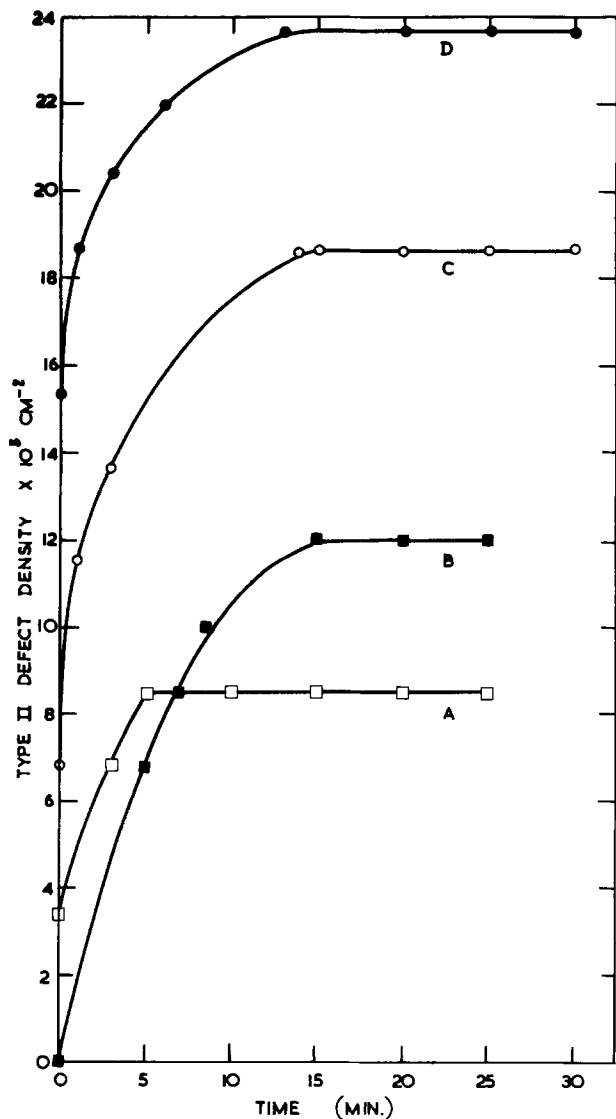


Fig. 3. Curve A shows the density of type II defects as a function of time. The tin oxide is positive and applied field is  $1.6 \text{ MV cm}^{-1}$ . The silicon oxide thickness is  $0.19 \mu\text{m}$ . Curve B was obtained on the same sample, but after biasing the tin oxide negatively for 35 min with a field of  $1.6 \text{ MV cm}^{-1}$ . Curve C was obtained in a similar way to Curve A for an oxide of  $0.1 \mu\text{m}$  thickness. Curve D was obtained in a similar way to curve B but is far the thinner oxide of curve C.

of liquid crystal in contact with the slice of silicon, it seems unlikely that the liquid is the source of impurity ions.

It has been suggested by a number of workers that imperfections could be due to crystalline regions of silicon dioxide. While the above model does not require crystallization, it does not preclude this as being a factor.

#### Further Experiments and Discussions

The above model depends primarily on the occurrence of field intensification at irregularities in the silicon. This is based on the fact that defects have been found to align on scratches on one sample and the higher concentration of turbulences seen at ledges in the silicon. It is clearly necessary to examine the region of a turbulence away from known irregularities in the substrate. Precise location of the center of a turbulent region is difficult, but in every case examined to date a turbulence has coincided with a silicon irregularity on scanning electron microscope pictures. It is not possible at present to give information on the cause of these irregularities since they

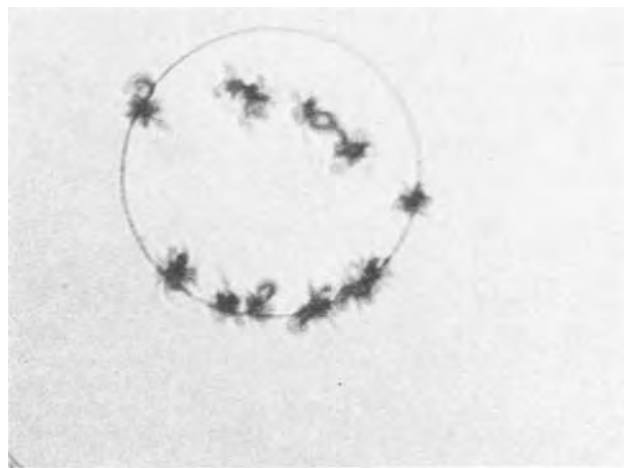


Fig. 4. After opening windows in the thick oxide, the dry oxide was grown. This thin oxide is contained within the circular area. It can be clearly seen that type II defects occur preferentially at the intersection of thin and thick oxides where a ledge in the silicon is situated (circle diameter =  $168 \mu\text{m}$ ).

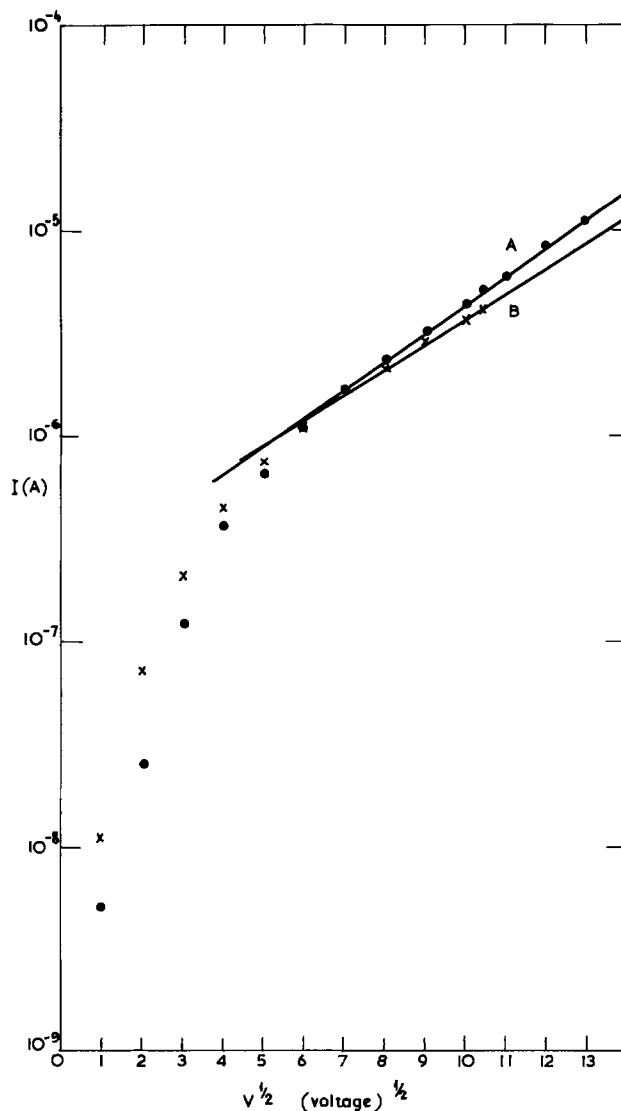


Fig. 5. Current-voltage characteristics of the cell with unoxidized silicon as one of the electrodes. Very little polarity dependence is seen. Curve A corresponds to the tin oxide positive, curve B with its negative. These results are in agreement with those given by Heilmeier *et al.* (12).

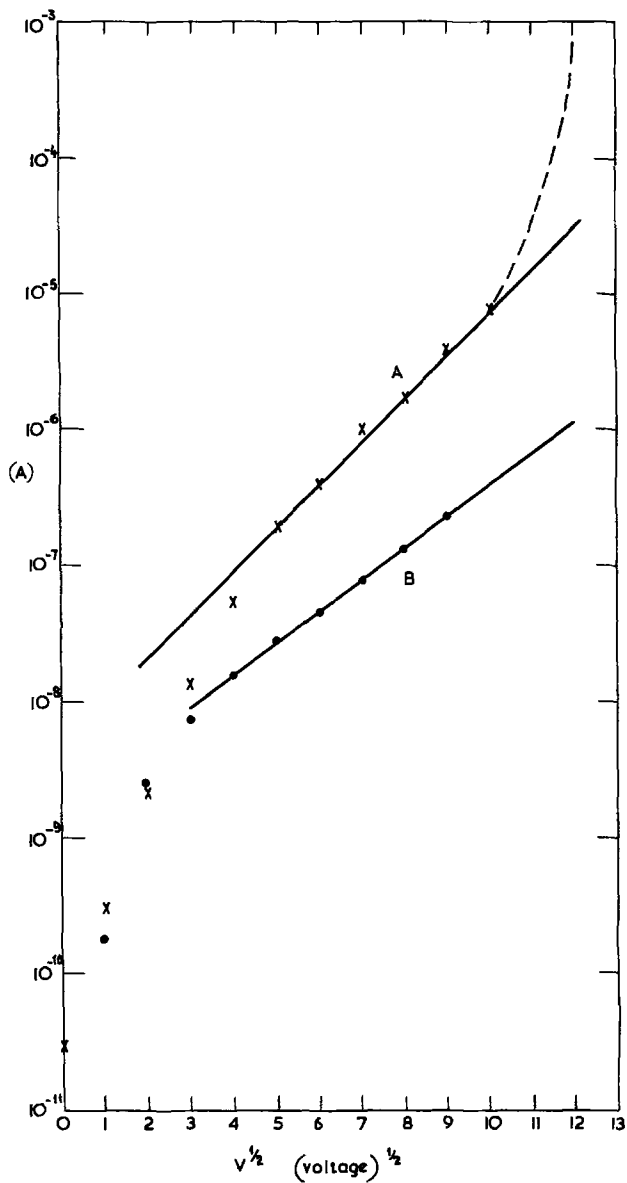


Fig. 6. Current-voltage characteristics of the cell with oxidized silicon and type II turbulences present. Curve A corresponds to the oxide positive, B to its negative. These results correspond to current densities approximately  $\times 10^{-3}$  less than those of Fig. 5.

can be of several forms, e.g., hillocks, etch pits, etc. In addition, when turbulence is seen on a silicon ledge as shown in Fig. 4, a very steep portion of the ledge is always present in the region of this turbulence.

A point of practical importance is the variation of defect density with oxide thickness and electric field. Figure 8 shows the variation of defect density as a function of oxide thickness for fields of 2 MV/cm, 3 MV/cm, and 4 MV/cm. Between 0.2 and 0.6  $\mu\text{m}$  the defect density  $D$  varies according to the expression

$$D = D_0 \exp\left(\frac{-x_0}{L}\right)$$

where  $D_0$  is a constant which is strongly dependent on the applied field.  $L$  is a constant which is field independent and has a value of almost exactly 0.1  $\mu\text{m}$ . At thickness less than 0.2  $\mu\text{m}$ , the defect density increases very rapidly.

We have noted that the current through a defect can depend on either the Fowler-Nordheim tunneling or, when the barrier is significantly reduced, on bulk conduction presumably by some form of Poole-Frenkel conduction. Neither of these phenomena would be expected to give a very strong dependence of density

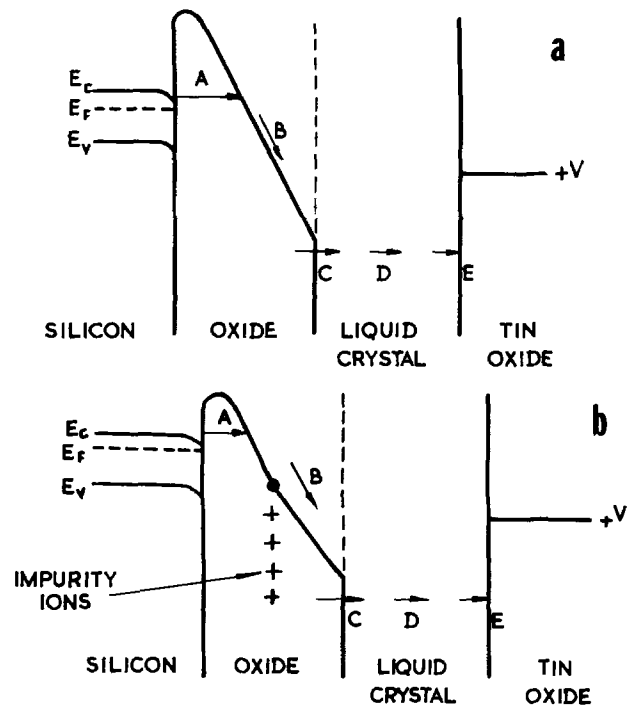


Fig. 7. (a) Diagram of the various conduction processes in the cell without impurities ions present. A is the Fowler-Nordheim process, B is presumed to be Poole-Frenkel bulk conduction, C is the transfer of electrons to liquid crystal molecules, D is the ionic conduction in the liquid crystal, and E the discharge at the positive tin oxide electrode. (b) Shows the same processes as A with additional barrier lowering due to field intensification and mobile impurity ions. In both (a) and (b) the conduction is probably limited by the barrier height (process A).

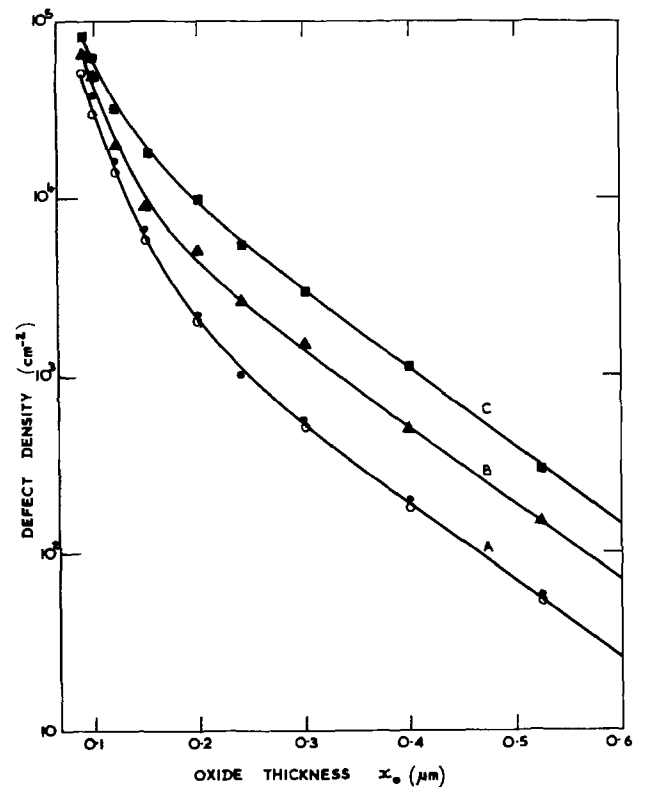


Fig. 8. The density of type II defects as a function of oxide thickness for various field values. Curves A, B, and C were obtained for field values of 2, 3, and 4  $\text{MV cm}^{-1}$ , respectively.

of turbulences on thickness for a given value of applied field. The field values quoted do not represent



the actual field experienced by the barrier since superimposed on the applied field is that due to the presence of positive charge in the oxide. This charge is, of course, accumulated very close to the silicon and under steady-state conditions its distribution is determined by the balance between the electric field at any point, which holds the charge near the silicon, and diffusion which counterbalances this effect. Calculations indicate that for a reasonable density of charge all the impurity ions are contained within a distance of a few angstroms from the silicon-silicon dioxide interface so that in the majority of the oxide the field is equal to the applied voltage divided by the oxide thickness. It is not possible without further measurements to explain the thickness dependence of defect density shown in Fig. 8. The result is presented here because of its practical importance in the design of MOS and CCD devices.

### Summary

Measurements have been performed on oxide conduction in thin layers of silicon dioxide grown in dry oxygen. The liquid crystal technique has been shown to be a valuable nondestructive technique for studying the behavior of oxide defects as a function of applied voltage and the polarity of this voltage. Two types of defect have been found. Type I defects are probably pinholes and have a very low density. Type II defects occur only under positive bias (on the tin oxide) and show a complex dependence of density on time. By cycling the voltage between positive and negative, it has been possible to suggest a simple qualitative model for the behavior of defects which would seem to be associated with physical irregularities in the silicon.

The model developed depends on the cooperative effects of impurity ions and slow trapping. It sug-

gests that devices will be subject to failure from oxide defects for either type of polarity.

### Acknowledgments

We would like to thank Professor J. H. Leck for the provision of facilities and Mr. N. M. St. J. Murphy for useful discussions. Thanks are also due to Mr. J. M. Keen of RRE Malvern for interesting us in the potentialities of the liquid crystal technique and for useful discussions.

Manuscript submitted Nov. 24, 1975; revised manuscript received May 24, 1976.

Any discussion of this paper will appear in a Discussion Section to be published in the June 1977 JOURNAL. All discussions for the June 1977 Discussion Section should be submitted by Feb. 1, 1977.

### REFERENCES

1. W. Kern, *RCA Rev.*, **34**, 655 (1973).
2. J. M. Keen, *Electron. Lett.*, **7**, 432 (1971).
3. A. K. Zakzouk, W. Eccleston, and R. A. Stuart, *Solid-State Electron.*, **19**, 133 (1976).
4. T. H. Distefano, *Appl. Phys. Lett.*, **23**, 34 (1973).
5. R. Williams and M. H. Woods, *ibid.*, **22**, 458 (1973).
6. S. I. Raider, *ibid.*, **23**, 34 (1973).
7. N. J. Chou and J. M. Eldridge, *This Journal*, **117**, 1287 (1970).
8. C. M. Osburn and S. I. Raider, *ibid.*, **120**, 1369 (1973).
9. C. M. Osburn and D. W. Ormond, *ibid.*, **121**, 1195 (1974).
10. M. Lenzlinger and E. H. Snow, *J. Appl. Phys.*, **46**, 278 (1969).
11. C. M. Osburn and E. J. Weitzman, *This Journal*, **119**, 603 (1972).
12. G. H. Heilmeyer, L. A. Zanon, and L. A. Barton, *IEEE Trans. Electron Devices*, **ed-17**, 22 (1970).
13. P. G. DeGennes, *Comments Solid State Phys.*, **2**, 35 (1970).

## A New Paint-On Diffusion Source

K. D. Beyer\*

IBM System Products Division, East Fishkill Facility, Hopewell Junction, New York 12533

### ABSTRACT

A new paint-on diffusion source has been developed utilizing chemically stable polymethylsiloxane resins, n-butylacetate as a solvent, and dopant compounds such as carborane polymers for boron, triphenylphosphate for phosphorus, and  $\text{As}[\text{O Si}(\text{C}_6\text{H}_5)_2\text{O}]_3\text{As}$  for arsenic. These paint-on diffusion sources were spun on silicon wafers by conventional photoresist spinners. Ozone was used at 200°C for the decomposition of paint-on diffusion sources into doped oxide films. Doped oxide densifications or diffusions were performed in the same furnace tube as the decomposition in order to prevent the moisture absorption of the undensified doped oxide. Doped oxide diffusions yielded average sheet resistances with standard deviations of 1.71% for boron and 1.65% for arsenic.

Paint-on diffusion sources offer an economic and simple method of introducing dopants into semiconductors (1-4). Previously, paint-on diffusion sources consisted of acyloxysilanes, monomeric dopant compounds, and solvents. Results of spin-on doped polymers were also reported (5), but composition and processing of such spin-on doped polymers were not disclosed. As acyloxysilanes easily decompose into  $\text{SiO}_2$  at low temperatures (3), the change from an organic acyloxysilane into  $\text{SiO}_2$  can be achieved by a low temperature heating step. However, the thermal instability of acyloxysilanes causes the difficulty of maintaining a sufficient long shelf-life for paint-on diffusion sources

consisting of acyloxysilanes. In the absence of any polymeric compounds, the surface tension of paint-on diffusion sources depends on the weight ratio of solvent, acyloxysilane, and dopant compound. Since the surface tension is low for monomeric solutions in comparison to polymeric solutions, it is difficult to obtain thick paint-on source film layers for monomeric solutions by using a single step spinning process on a conventional photoresist spinner.

In order to develop a paint-on diffusion source that would provide a liquid solution with a high chemical stability and a sufficient surface tension, solutions of silicone polymers such as polydialkylsiloxanes and polyalkyl resins were investigated. The siloxanes are known to be chemically stable and not humidity sensitive at room temperature (6). Only at elevated tem-

\* Electrochemical Society Active Member.

Key words: paint-on diffusion source, diffusion, diffusion source, densification, decomposition process.

temperatures above 250°C in the presence of O<sub>2</sub> does a change occur in the chemical composition of silicone polymers (7). Because of the high thermal stability of silicones in comparison to acyloxysilanes, a new processing technique had to be developed for paint-on diffusion sources containing silicones.

### Experimental

The complete removal of organic groups attached to silicone polymers can be accomplished by a heat-treatment in O<sub>2</sub> above 600°C (6, 7), by oxidation in ozone above 150°C, or in atomic oxygen at room temperature. After spinning of the paint-on diffusion source on silicon substrates, O<sub>2</sub> decomposition above 600°C caused slight pitting on the silicon surface; whereas during ozone and atomic oxygen decomposition, the silicon surface was not attacked. After ozone and atomic oxygen decomposition, the original paint-on diffusion source film changed from a polysiloxane into a porous SiO<sub>2</sub>. This porosity of SiO<sub>2</sub> is advantageous for the complete removal of organic groups. But this porosity imposes a problem because of the humidity sensitivity, unless the porous SiO<sub>2</sub> is immediately densified by a heat-treatment above 700°C (8). Since the atomic oxygen technique utilizes a photoresist ashing system operating only at low pressure conditions (9), the atomic oxygen decomposition technique cannot easily be combined with a high temperature diffusion furnace using diffusion ambients at atmospheric pressure. Therefore the ozone technique was adopted for the decomposition of the polysiloxane polymer into SiO<sub>2</sub>.

In order to prevent excessive shrinking of the polysiloxane film during the ozone decomposition, a polymethylsiloxane resin was chosen, which already contains 80 weight percent (w/o) SiO<sub>2</sub>. Such a polymethylsiloxane resin is commercially available under the trade name Type 650 Glass Resin of Owens-Illinois (10). The polymethylsiloxane resin was dissolved in an organic solvent together with the dopant compounds. The choice of a suitable solvent is important to obtain a uniform paint-on diffusion source film thickness over the entire wafer surface. The evaporation rate of the paint-on diffusion source solvent during the spinning operation on a photoresist spinner must be in the same order of magnitude as the spreading rate of the paint-on source solution during spinning. Using n-butylacetate as a solvent for polymethylsiloxane, a uniform paint-on source film was obtained except for an 8 mil wide rim of paint-on source material at the wafer edge.

Dopant compounds were selected in such a manner that they possessed a high chemical stability, low vapor pressure at room temperature, and low toxicity. Carborane polymers (11) were used as boron dopant compounds, which are produced by Olin Corporation under the trade name of Dexsil 202. Triphenylphosphate, (C<sub>6</sub>H<sub>5</sub>O)<sub>3</sub>PO, which has a melting point of 48.5°C (12), served as a phosphorus dopant compound. The arsenosiloxane compound As[OSi(C<sub>6</sub>H<sub>5</sub>)<sub>2</sub>O]<sub>3</sub>As, which exhibits a melting point of 195°C (13), was chosen as an arsenic dopant compound.

Paint-on diffusion sources were spun at 3000 rpm for 30 sec on a Headway Photoresist Spinner Model 1-EC 101 in a humidity-controlled hood (10% humidity). After spinning, the paint-on diffusion source film was decomposed in O<sub>3</sub> at temperatures between 150° and 250°C for a duration of 30 min. After decomposition in O<sub>3</sub>, the paint-on diffusion source was densified or diffused at temperatures above 700°C in oxygen, nitrogen, or argon.

The paint-on diffusion source processing tube is shown in Fig. 1. A rectangular tube (2¼ in. wide, 3½ in. high, and 68 in. long) is inserted into a 25 in. long furnace type Blue M Model OV-480A and into a 30 in. long diffusion furnace of the type Diffusitron Mark II. The ozone-decomposition furnace has an 8 in. long

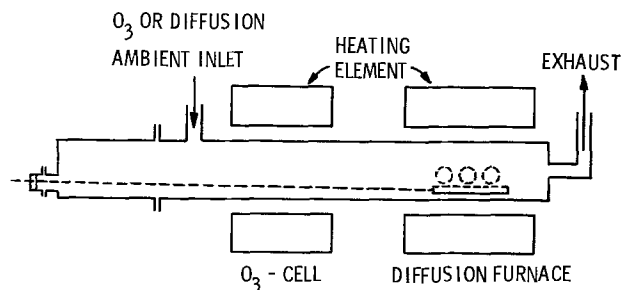


Fig. 1. Paint-on diffusion source processing tube

temperature plateau, which deviates less than 2°C from the mean temperature value. The diffusion furnace has a 12 in. long temperature plateau with a 1°C deviation from the mean value. In order to prevent time-consuming temperature profiling of the ozone-decomposition and diffusion furnace, the diffusion furnace was frequently operated as a densification furnace and the diffusion was carried out in a separate diffusion furnace. The gas inlet for ozone, oxygen, nitrogen, and argon is near the tube opening. All gases flow first through the O<sub>3</sub>-decomposition furnace and then enter the diffusion furnace before the gases are exhausted at the end of the tube. The ozone is generated by an ozone generator of the type Welsbach Model T-816. This ozone generator produces 16g ozone per hour in oxygen.

### Results of the Boron Paint-on Diffusion Source

A boron paint-on diffusion source consisting of 8g methylpolysiloxane glass resin, 40.0g n-butylacetate, and 0.8g carborane polymer was spun on an n-type 2¼ in. diam <100> 2 Ω-cm silicon substrate with 3000 rpm for 30 sec. After spinning, a paint-on diffusion source film thickness of 6000Å was measured. Five wafers were standing upright in each of the two rows of the quartz boat. First, the wafers, covered with paint-on source, were decomposed in ozone at 200°C for 30 min in the decomposition zone of the furnace tube. In the same furnace tube, the wafers were then densified at 700°C in N<sub>2</sub> for 30 min by pushing the wafer boat from the decomposition zone into the densification or diffusion zone. After densification, the original film thickness of the paint-on source film was decreased from 6000 to 3000Å. After densification, the wafers were diffused at 1050°C for 30 min in argon in a separate furnace of the type Electroglas Model 35.

In Table I, for five wafers in each row of the wafer boat, the average sheet resistance is given, taken from nine sheet resistance measurements on each wafer. A junction depth of 1.1 μm was observed by using the conventional bevel and stain technique. By applying Irvin's curves (14) to measured sheet resistance and junction depth values, a boron surface concentration of  $2.9 \times 10^{20}$  atom/cm<sup>3</sup> in silicon can be calculated. Total variations of less than 7% of the average sheet resistance value were obtained for our boron paint-on diffusion source. These percentile sheet resistance variations are comparable with sheet resistance variations of previous boron paint-on diffusion sources yielding total sheet resistance variations between 5 and 10% (2).

Table I. Sheet resistance uniformity for the boron paint-on diffusion source

	Row		
	1	2	1 and 2
Average sheet resistance (Ω/□) for 5 wafers in each row (9 data per wafer)	19.83	19.39	19.61
Standard deviation (%)	2.01	1.76	1.77

Different boron surface concentrations can be achieved by varying the amount of carborane present as a dopant compound in the boron paint-on diffusion source. In Fig. 2, the boron surface concentration in silicon is shown as a function of the carborane content in the boron paint-on diffusion source for a 1, 1½, and 4 hr diffusion at 1000°C in argon. According to Fig. 2, the boron surface concentration in silicon after diffusion increases with the amount of carborane dopant for all diffusion times. The decrease of boron surface concentration with diffusion time for the same carborane content, as shown in Fig. 2, can be attributed to the boron depletion at the interface of the 3000Å borosilicate layer and the silicon surface and to the boron out-diffusion (15).

The infrared absorption spectrum of the boron paint-on diffusion source utilized in the boron paint-on source uniformity study described above is shown in Fig. 3 for three conditions: (i) after spinning, (ii) after ozone decomposition at 700°C for 30 min, and (iii) after densification in N<sub>2</sub> at 200°C for 30 min. As seen from Fig. 3(a), the dominant infrared absorption after spinning of the paint-on source film is the Si-O stretching vibration located between 9 and 10 μm (16). This stretching vibration originates from the siloxane backbone of the polymethylsiloxane resin (16). The other absorptions at 7.8 and 13 μm, present in Fig. 3(a), are caused by the Si-CH<sub>3</sub> group, while the weak absorptions at 3 and 3.4 μm are due to the Si-OH and Si-O-CH<sub>3</sub> group, respectively (16). The weak absorption at 3.9 μm, according to Fig. 3(a) is caused by the stretching of the B-H bond (17). The Si-O, Si-CH<sub>3</sub>, and Si-OH groups identified in the infrared spectrum clearly indicate the presence of the methylpolysiloxane resin.

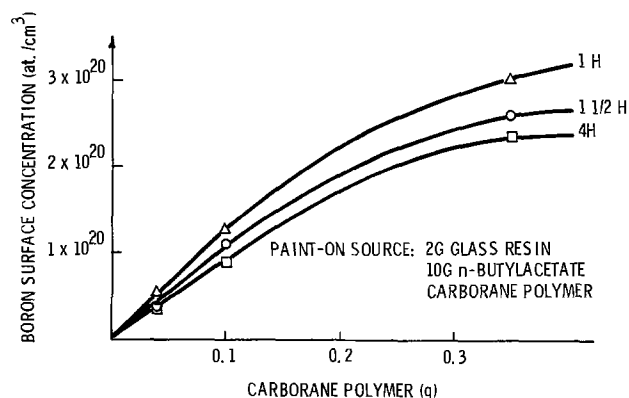


Fig. 2. Dependence of the boron surface concentration in silicon on the amount of carborane present in the boron paint-on diffusion source.

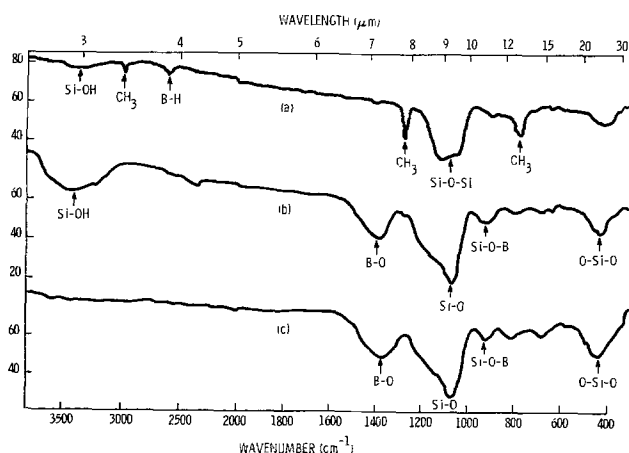


Fig. 3. Infrared spectrum of boron paint-on diffusion source after spinning (a), O<sub>3</sub> decomposition at 200°C for 30 min (b), and densification at 700°C for 30 min in argon (c).

The B-H infrared absorption can only be caused by the carborane polymer (17). Therefore, the infrared absorption spectrum of the paint-on diffusion source after spinning [3(a)] shows the solid components of the paint-on diffusion source.

After O<sub>3</sub> decomposition of the boron paint-on source, absorption bands are observed at 2.95, 7.2, 9.4, 10.8, and 23.5 μm, according to Fig. 3, trace (b). The infrared absorption spectrum of borosilicate glass has Si-O absorption peaks at 9.4 and 23 μm, a B-O absorption peak at 7.2 μm, and a Si-O-B absorption peak at 9.4 μm (8). Therefore except for the 2.95 μm absorption peak, the infrared absorption spectrum of the boron paint-on source after O<sub>3</sub> decomposition is in agreement with the infrared absorption spectrum of borosilicate glass. The absorption peak at 2.95 μm, found in the infrared absorption spectrum of the O<sub>3</sub> decomposed paint-on source, can be attributed to the presence of moisture absorbed from the laboratory environment by the porous borosilicate formed by the O<sub>3</sub> decomposition of the boron paint-on source (8). According to Fig. 3, trace (c), upon densification of the decomposed boron paint-on source film at 700°C, the H<sub>2</sub>O absorption peak at 2.95 μm disappears. Therefore the infrared absorption spectrum of the densified boron paint-on diffusion source is identical with the one of the borosilicate glass. In conclusion, the O<sub>3</sub> decomposition and the successive densification of the boron paint-on source transform the original organic polymer mixture into an inorganic borosilicate glass without any organic residues.

#### Results of the Phosphorus Paint-on Diffusion Source

A phosphorus paint-on diffusion source consisting of 2.0g glass resin, 10.0g n-butylacetate, and 0.16g triphenylphosphate was spun with 3000 rpm for 30 sec on 1¼ in. diameter <100> 10 Ω-cm p-type silicon wafers after 1, 5, 7, and 11 days past the date of the paint-on preparation. All phosphorus paint-on diffusion sources were decomposed in ozone at 225° for 30 min and diffused in argon at 1050°C for 105 min. After the removal of phosphosilicate in HF, sheet resistances and junction depths were measured in five sites of each wafer. Table II shows sheet resistances, sheet resistance variations, and junction depths as a function of the processing time after paint-on diffusion source preparation. According to Table II, the total percentile sheet resistance variations on the same wafer are less than 5%. An average sheet resistance value of 201 Ω/□ with a total variation of 10 Ω/□ can be calculated for all wafers shown in Table II. Therefore, the percentile sheet resistance variation is less than 5% from wafer to wafer for different processing times after source preparation. One may then assert that the phosphorus paint-on diffusion source has a sufficient chemical stability for producing uniform doping levels.

Figure 4 presents the phosphorus surface concentration in silicon as a function of triphenylphosphate dissolved in the paint-on source solution. As evident from Fig. 4, the phosphorus surface concentration increases with the amount of triphenylphosphate in the paint-on solution until a phosphorus surface concentration of approximately  $8 \times 10^{19}$  atom/cm<sup>3</sup> in silicon is reached. An explanation for the upper surface concentration limit for the phosphorus paint-on source may

Table II. Reproducibility of a phosphorus paint-on diffusion source as a function of the processing time after source preparation

Processing time after source preparation	Sheet- $\rho$ in $\Omega/\square$	Junction depth (in $\mu\text{m}$ )	Surface concentration atom/cm <sup>3</sup>
After 1 day	198 $\pm$ 4 $\Omega$	0.553	$2.34 \times 10^{19}$
After 5 days	207 $\pm$ 4 $\Omega$	0.633	$2.1 \times 10^{19}$
After 7 days	201 $\pm$ 10 $\Omega$	0.649	$2.04 \times 10^{19}$
After 11 days	198 $\pm$ 5 $\Omega$	0.574	$2.5 \times 10^{19}$

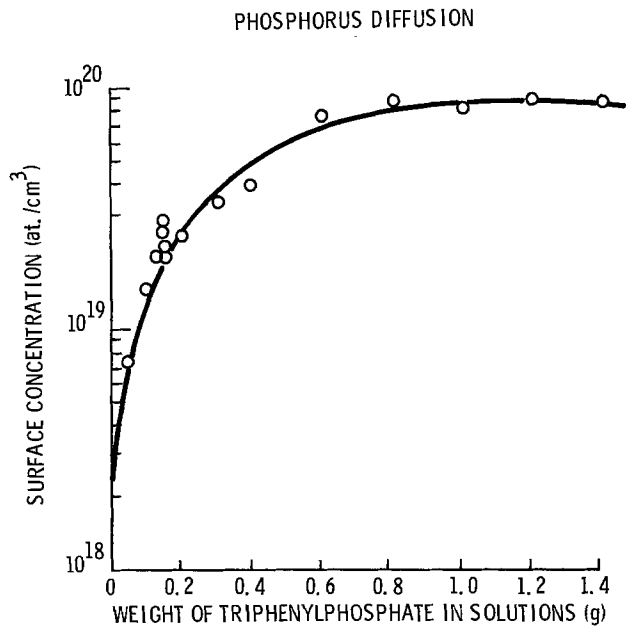


Fig. 4. Phosphorus surface concentration in silicon as a function of the amount of triphenylphosphate dissolved in the paint-on diffusion source solution.

be the separation of triphenylphosphate and glass resin during the spinning process. Precipitates of triphenylphosphate were actually observed after spinning on top of the paint-on source film for high triphenylphosphate concentrations.

#### Results of the Arsenic Paint-on Diffusion Source

An arsenic paint-on diffusion source solution consisting of 12.0g glass resin, 12.0g arsenosiloxane compound, and 100.0g n-butylacetate, designated as solution No. 33, was spun with 3000 rpm for 30 sec on nine  $\langle 100 \rangle$   $2\frac{1}{4}$  in. diameter 1-2  $\Omega$ -cm p-type silicon wafers. Three wafers were standing upright in each of the three rows of the quartz boat together with 28 wafers covered with an undoped polysiloxane resin film. After ozone decomposition at 181°C for 30 min and a diffusion at 1200°C for 15 min in  $O_2$  followed by a 55 min heat-treatment in  $N_2$ , the arsenic-doped oxide was removed by HF in order to measure the sheet resistance on nine sites of each of the nine wafers, which received the arsenic paint-on source diffusion.

The experiment was repeated under identical processing conditions for two different arsenic paint-on solutions containing different polymethylsiloxane resin batches, designated as solutions No. 35 and 38. Solutions No. 35 and 38 were applied for 8 and 2 silicon wafers, respectively. The sheet resistance results (highest, lowest, and mean sheet resistance including standard deviation) are given in Table III for all different paint-on source solutions. The junction depth measured by bevel and stain technique ranged between 2.1 and 2.4  $\mu$ m for all processed wafers. According to Table III, the

Table III. Sheet resistance uniformity for arsenic paint-on diffusion sources using different batches of polymethylsiloxane resin

	Solution		
	35 (9 samples)	35 (8 samples)	38 (2 samples)
Highest sheet resistance ( $\Omega/\square$ )	9.8	10.1	10.1
Lowest sheet resistance ( $\Omega/\square$ )	9.4	9.6	9.6
Mean sheet resistance ( $\Omega/\square$ )	9.6	9.8	9.8
Standard deviation ( $\Omega/\square$ )	0.10	0.14	0.16

Mean sheet resistance averaged over 3 runs:  $9.7 \pm 0.16 \Omega/\square$

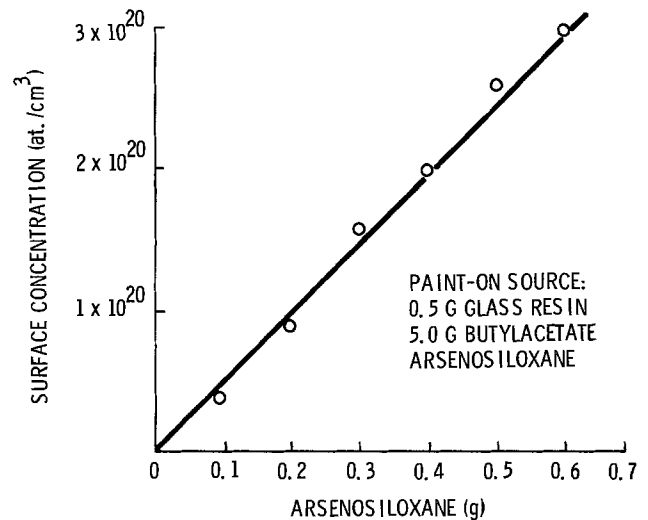


Fig. 5. Arsenic surface concentration in silicon as a function of the arsenosiloxane content in a paint-on diffusion source solution.

total sheet resistance variation from wafer to wafer and from run to run, using different resin batches, is less than 4.2% for a mean sheet resistance value of  $9.7 \Omega/\square$ . The percentile sheet resistance variations for the arsenic paint-on diffusion source are, therefore, smaller than for the phosphorus and boron paint-on diffusion sources, which have variations of 5 and 7%, respectively. As different batches of polymethylsiloxane resin were used for the solutions No. 33, 35, and 38 in the arsenic paint-on source study, the batch of the polymethylsiloxane resin has a negligible impact on the arsenic doping in silicon after the arsenic paint-on source diffusion because of the small sheet resistance variation of 4.2% for all arsenic paint-on source solutions.

In Fig. 5, the arsenic surface concentration, calculated from sheet resistance and junction depth values by using Irvin's curves (14), is shown as a function of the arsenosiloxane content in a 0.5g glass resin/5.0g n-butylacetate solution for a diffusion at 1150°C for 15 min in oxygen and for 75 min in argon. Figure 5 indicates the arsenic surface concentration in silicon increases linearly with the amount of arsenosiloxane dissolved in the glass resin solution. Therefore, different arsenic doping levels in silicon can be easily obtained by varying the amount of arsenosiloxane dissolved in the paint-on diffusion source solution.

#### Summary

A new paint-on diffusion technology has been developed for boron, phosphorus, and arsenic dopants. The uniformity of the new paint-on diffusion sources is equal to or better than the one of previous paint-on diffusion sources. The new paint-on diffusion source has a long shelf-life and is not humidity sensitive.

#### Acknowledgments

The author is grateful to R. F. Lever, H. S. Rupprecht, and T. H. Yeh for many technical discussions. Most of the measurements and evaluations were done with the technical assistance of M. Whitehill.

Manuscript submitted Feb. 19, 1976; revised manuscript received July 1, 1976.

Any discussion of this paper will appear in a Discussion Section to be published in the June 1977 JOURNAL. All discussions for the June 1977 Discussion Section should be submitted by Feb. 1, 1977.

Publication costs of this article were assisted by the IBM Corporation.

#### REFERENCES

1. K. Reindl, *Solid-State Electron.*, **16**, 181 (1973).
2. J. A. Becker, *ibid.*, **17**, 87 (1974).

3. M. Genser, U.S. Pat. 3,615,943.
4. M. Mar and R. Roo, Paper 435 RNP presented at The Electrochemical Society Meeting, Toronto, Canada, May 11-16, 1975.
5. M. L. Long, Kodak Microelectronics Seminar-Interface 1973, p. 38 (1974).
6. E. G. Rochow, *Chem. Eng. News*, **23**, 612 (1945).
7. K. A. Andrianov, "Metalorganic Polymers," p. 241, D. C. Bradley, Editor, Interscience Publishers, John Wiley & Sons, New York (1965).
8. W. A. Pliskin, in "Physical Measurement and Analysis of Thin Film," E. M. Must and W. G. Guldner, Editors, Plenum Press, New York (1969).
9. S. M. Irvin, Kodak Photoresist Seminar Proceedings, Vol. II, p. 26 (1968).
10. A. J. Burzynski, U. S. Pat. 3,460,980 (1965).
11. D. J. Mangold, *Appl. Polym. Symp.*, **11**, 157 (1969).
12. "Handbook of Chemistry and Physics," 48th ed., p. C-474, The Chemical Rubber Co., Cleveland, Ohio (1967).
13. B. L. Chamberland and A. G. McDiarmid, *J. Am. Chem. Soc.*, **82**, 4542 (1960).
14. T. C. Irvin, *Bell Syst. Tech. J.*, **41**, 387 (1962).
15. M. L. Barry and P. Olofsen, *This Journal*, **116**, 854 (1969).
16. A. L. Smith and T. A. McHard, *J. Anal. Chem.*, **31**, 1174 (1959).
17. H. A. Schroeder, T. L. Heying, and J. R. Reiner, *Inorg. Chem.*, **2**, 1092 (1963).

## The Redistribution of Gold during the Growth of an Oxide or of Phosphosilicate Glass on Contaminated Silicon Wafers

T. A. O'Shaughnessy and H. D. Barber\*

*Linear Technology Limited, Burlington, Ontario, Canada L7M 1T4*

and E. L. Heasell

*Department of Electrical Engineering, University of Waterloo, Waterloo, Ontario, Canada N2L 3G1*

### ABSTRACT

We have examined the redistribution between oxide, slice, and oxide surface of gold deposited from deliberately contaminated etching solutions onto silicon slices, during subsequent oxidation and phosphosilicate glass deposition. Results presented also show the distribution of gold throughout the oxide. The initial oxidizing or annealing conditions in the furnace are shown to have an important effect on the subsequent gold distribution.

During conventional device processing procedures, a silicon wafer is exposed to various etching, cleaning, and rinsing reagents. While the use of highly pure chemicals and rinse water is usual, it is difficult to completely eliminate the presence of residual heavy metal contaminants. Conventional cleaning procedures are not effective in removing such chemisorbed species from either silicon or SiO<sub>2</sub> (1-4) and, thus, they remain present during subsequent oxidation, diffusion, or other high temperature processes. It is of interest, then, to study the behavior of such surface contaminants during subsequent processing steps. Because we may assume it to be typical of a monovalent heavy metal, and because of its use in the control of lifetime in many devices we have chosen to study the redistribution of gold during the formation of either oxide, oxide-PSG, or PSG layers on silicon. From the latter studies we can also examine the gettering action, if any, of the composite and PSG layers.

### Experimental Methods and Results

Gold was deposited onto the freshly cleaned surface of polished silicon wafers by chemideposition from a 10% HF solution containing a carefully standardized concentration of neutron-activated gold. In the subsequent discussion reference to gold concentrations or contamination levels of 10, 1.0, or 0.1 ppm refers to the nominal concentration by weight of gold in the contaminated etch. Where the quoted experimental points do not coincide strictly with these concentrations, it indicates that surface absorption by the container and etching vessel walls has caused a decrease in

the gold concentration from the nominal values. The rate of deposition of gold onto silicon or SiO<sub>2</sub> was found to be temperature independent in the range 20°-50°C. Slices were immersed in the etch for ~15 min. For the concentration range 0.1-10 ppm, ancillary experiments showed that this period was sufficient for the surface gold concentration to approach equilibrium.

The oxidation of a contaminated wafer results in the redistribution of the gold between the slice, the oxide, and the oxide surface. The gold concentration in the slice is dependent upon both the conditions of contamination and of oxidation.

By selectively etching off first the gold at the air/oxide surface with hot aqua regia and then removing the oxide using buffered HF, it is possible to determine the net quantities of gold present at the surface of the oxide, dissolved in the oxide, and dissolved in the silicon slice. These observations are hampered by the tendency of the gold already taken into solution in the etch to redeposit upon the freshly exposed oxide or silicon (1-4). To eliminate the effects of such redeposition during the removal of the surface gold or the oxide and during the successive layering of the oxide, the samples were successively etched and rinsed several times in hot aqua regia and deionized water. Control experiments on both contaminated slices and oxides showed that this procedure was successful in removing replated gold, while leaving the oxide unaffected.

The quantities of gold present were determined at each stage by  $\beta$ -particle counting, making a direct comparison with standard samples of a similar counting geometry. The absorption coefficient for the  $\beta$ -particles,  $\lambda$ , was determined from the front-to-back count ratio

\* Electrochemical Society Active Member.  
Key words: silicon, gold, oxidation.

on a series of slices, between 0.004 and 0.016 in. thick, having gold on one surface only. The ratio was an accurately exponential function of slice thickness corresponding to an absorption coefficient of  $50.41 \text{ cm}^{-1}$ . Since the absorption of  $\beta$ -particles in this energy range is proportional to the specific gravity of the absorber (5), we can ignore the absorption of oxide layers when present.

If we consider the following counts:  $X_1$  = initial front surface count,  $Y_1$  = initial back surface count,  $X_2$  = front surface after removal of surface gold,  $Y_2$  = back surface after removal of surface gold,  $X_3$  = front surface after removal of oxide, and  $Y_3$  = back surface after removal of oxide, then we can determine the various net gold concentrations from their contribution to the total counts: front surface contribution,  $F_s = ((X_1 - X_2) - A(Y_1 - Y_2))/(1 - A^2)$  and back surface contribution,  $B_s = ((Y_1 - Y_2) - A(X_1 - X_2))/(1 - A^2)$ .

In a similar fashion, the concentration in the oxide is given as: front surface oxide contribution,  $F_o = ((X_2 - X_3) - A(Y_2 - Y_3))/(1 - A^2)$  and back surface oxide contribution,  $B_o = ((Y_2 - Y_3) - A(X_2 - X_3))/(1 - A^2)$ , where  $A = \exp(-\lambda t)$ , and  $t$  is the slice thickness. By comparison of  $F_s$ ,  $B_s$ ,  $F_o$ , and  $B_o$  with known standards, the corresponding net gold concentration was determined.

The determination of the gold concentration in the silicon slice is complicated by the effect of  $\beta$ -absorption. Generally, the profile of the dissolved gold is not known accurately. However, a comparison of the expected counts for a few extreme distributions shows that this is not a serious factor.

Calculation of the front and back counts,  $C_F$  and  $C_B$ , respectively, for gold distributions that are (i) all on one surface, (ii) equally divided between the surfaces, and (iii) uniform throughout the bulk for a range of slice thicknesses up to 9 mils shows that if we write  $N$  for the "correct" count and define the factor  $F$  so that  $N = F(C_F + C_B)$ , then  $F$  varies rather little with the gold distribution. Thus, for a slice of 8 mils thickness,  $0.736 \leq F \leq 0.799$ , a  $\pm 4\%$  variation for the three extreme distributions cited. If the profile is known only roughly, a more accurate correction factor can be estimated.

Boron-doped 10  $\Omega$ -cm silicon wafers, 0.008 in. thick,  $\langle 111 \rangle$  orientation, and mirror polished on both faces, were first chemically cleaned and then contaminated using etches containing known gold concentrations. The slices were placed quickly ( $< 30$  sec) into the hot zone of the oxidation furnace in an oxygen atmosphere and oxide grown for 60 min (700, 1000 and 1300Å at 1000°, 1050°, and 1100°C, respectively). After oxidation, the quantity of gold present at the surface of the oxide, dissolved in the oxide and dissolved in the slice, was measured.

The results of these studies are shown in Fig. 1-4. Similar experiments were carried out using composite  $\text{SiO}_2$ -PSG layers and PSG alone. The PSG layers were deposited at 1050°C for times between 20 and 120 min, from a mixture of 1%  $\text{PH}_3$  in argon, nitrogen, and oxygen in a ratio 3:50:50. Separate furnaces were used for oxidation and PSG deposition.

In the two-layer structures the slices were brought to the required temperature in a nitrogen atmosphere, oxidized for 1 hr, and then PSG layers of 600, 750, and 900Å were deposited at 1050°C. The experimental results for these samples are shown in Fig. 5 and 6.

The distribution of the gold through the  $\text{SiO}_2$  and  $\text{SiO}_2$ -PSG layers was examined in greater detail. By successive etching steps, using buffered HF and taking care at each step to remove any redeposited gold, a cumulative profile of the gold concentration was obtained. Oxide or oxide:PSG thicknesses were determined at each step by ellipsometer measurement. Etching times were chosen to give approximately 100Å steps. Counting times were selected to provide reason-

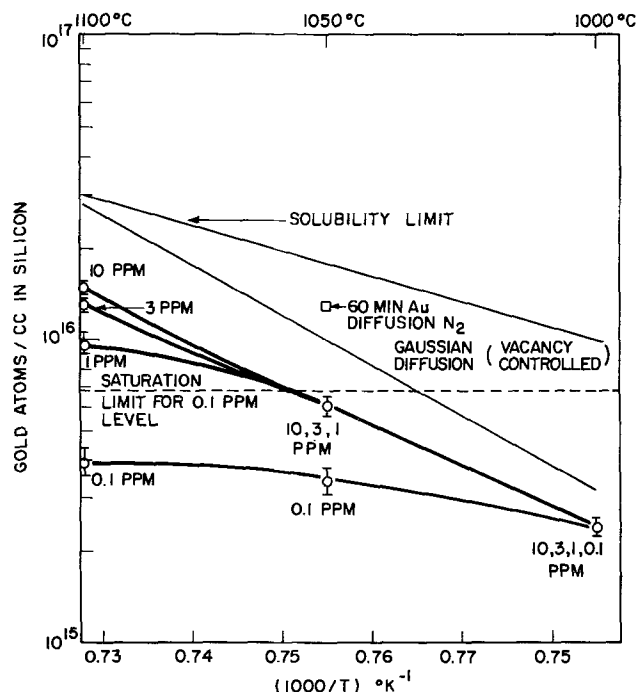


Fig. 1. Variation of the concentration of gold in solution in the silicon slice as a function of initial contamination level and temperature of oxide growth, for a growth time of 60 min.

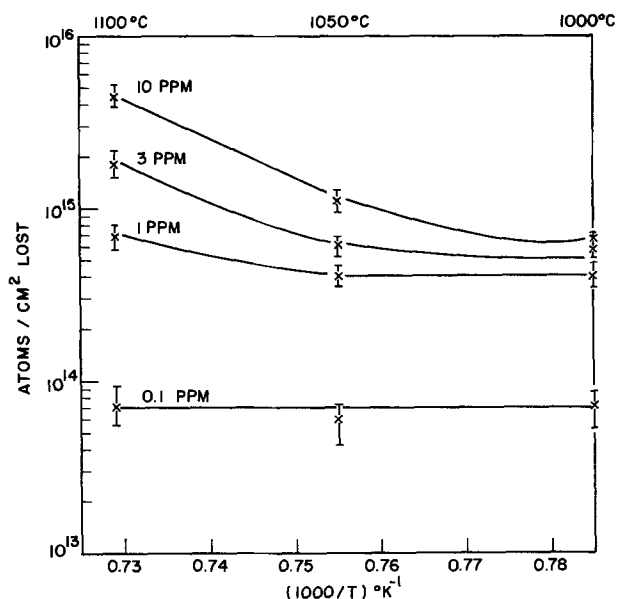


Fig. 2. Variation of the quantity of gold lost in the gas stream, as a function of initial contamination level and oxidation temperature during a 60 min oxidation.

able accuracy in the final profiles, e.g., the derivative of these results. Examples of such concentration profiles across the  $\text{SiO}_2$  and  $\text{SiO}_2$ -PSG layers are shown in Fig. 7 and 8. The profiles within 100Å of the interface are shown dotted since no measurements could be obtained within 50Å of the silicon surface. The lines drawn correspond to the net gold concentration measured at the penultimate layering operation, assuming a similar profile.

The profiling experiments were repeated using composite layers of 600Å of  $\text{SiO}_2$  and 600Å of PSG grown at 1050°C. Initial contamination levels of 10, 1.0 and 0.1 ppm were again employed. The corresponding profiles are shown in Fig. 8.

#### Discussion of Results

In Fig. 1, in addition to the experimental results, we indicate certain other physical data: (i) the solid

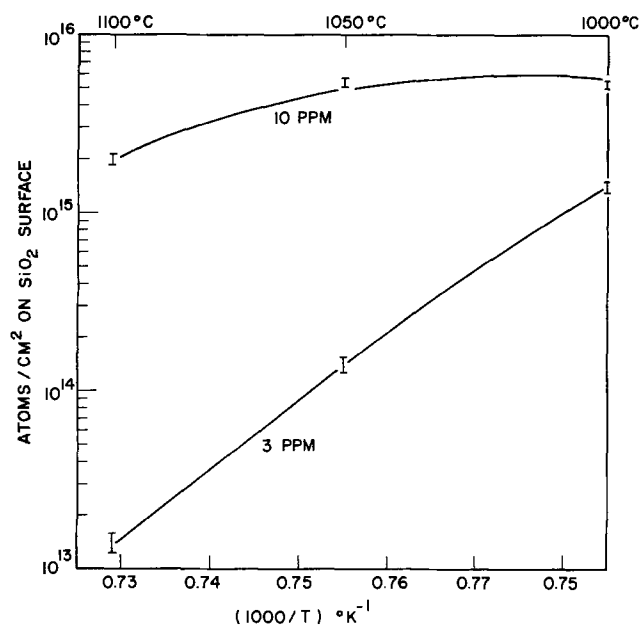


Fig. 3. Variation of the concentration of gold remaining on the surface of the grown oxide as a function of initial contamination level and oxidation temperature. Growth period 60 min.

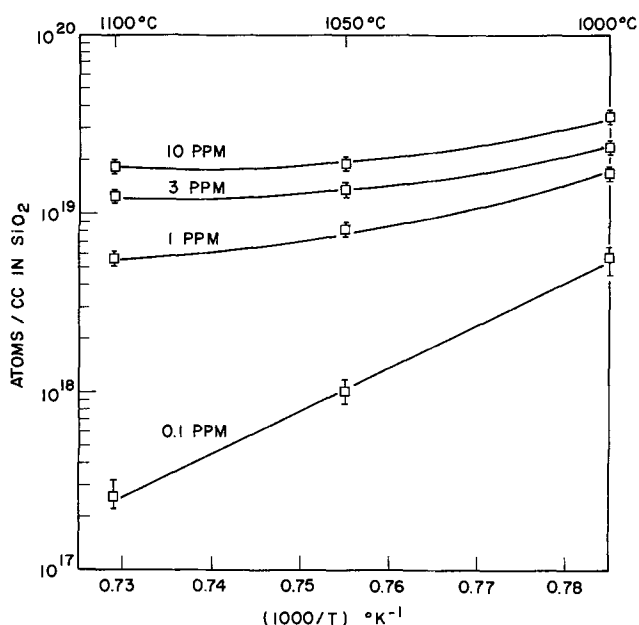


Fig. 4. The variation of net gold concentration in the grown oxide as a function of contamination and oxidation temperature. (See, however, discussion of Fig. 7 and 8.) Growth period 60 min.

solubility limit corresponding to the slice oxidation temperature; (ii) the net concentration that would be produced by a vacancy-controlled gaussian diffusion process from a saturated surface layer at that temperature; (iii) the gold concentration found after heating the sample in an inert nitrogen atmosphere for 60 min; and (iv) the uniform gold concentration that would result if all of the gold deposited onto the slice surface from 0.1 ppm etch were uniformly distributed through the slice.

The annealing experiment (iii) yields a concentration that is in reasonable agreement with that predicted from a simple diffusion process (ii). The results for the oxidized samples all show a significant decrease in the gold concentration remaining in the slice. At the lowest temperature (1000°C) the results for all contamination levels are approaching the diffusion-limited value.

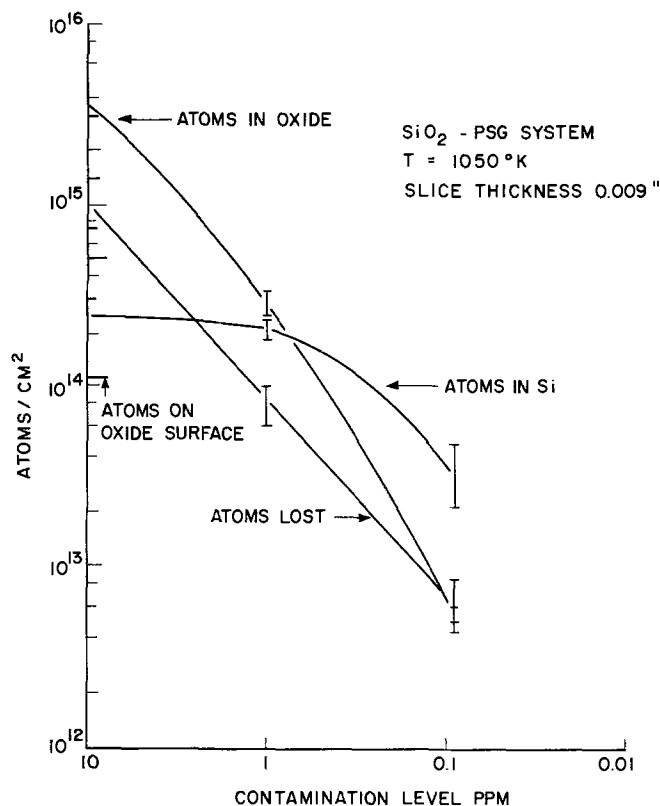


Fig. 5. The concentration of gold in the Si-SiO₂-PSG composite system, after growth at 1050°C, as a function of the initial contamination level.

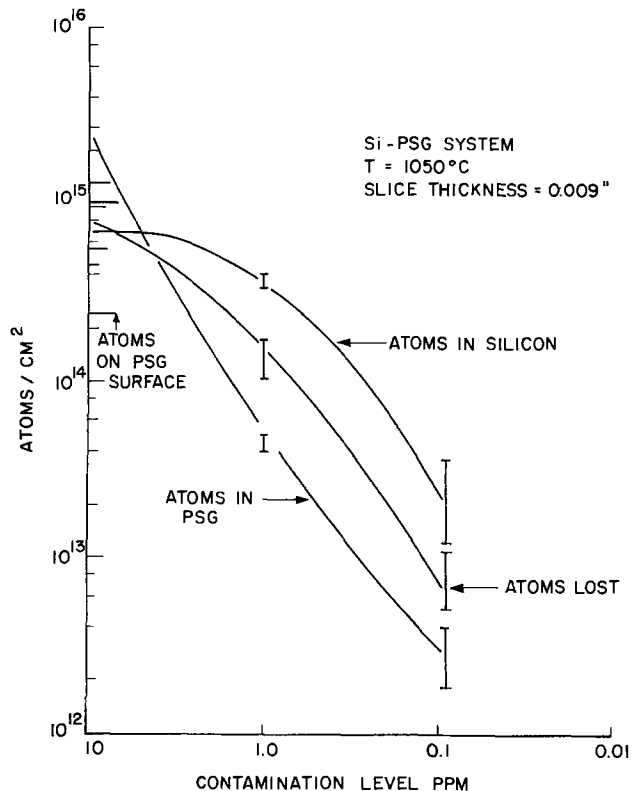


Fig. 6. The concentration of gold in the Si-PSG system, after growth at 1050°C, as a function of the initial contamination level.

Reference to Fig. 2 shows that gold is lost during the oxidation process, presumably by the evaporation of gold or of a high temperature oxide. However, in no case is this loss of gold large enough to completely

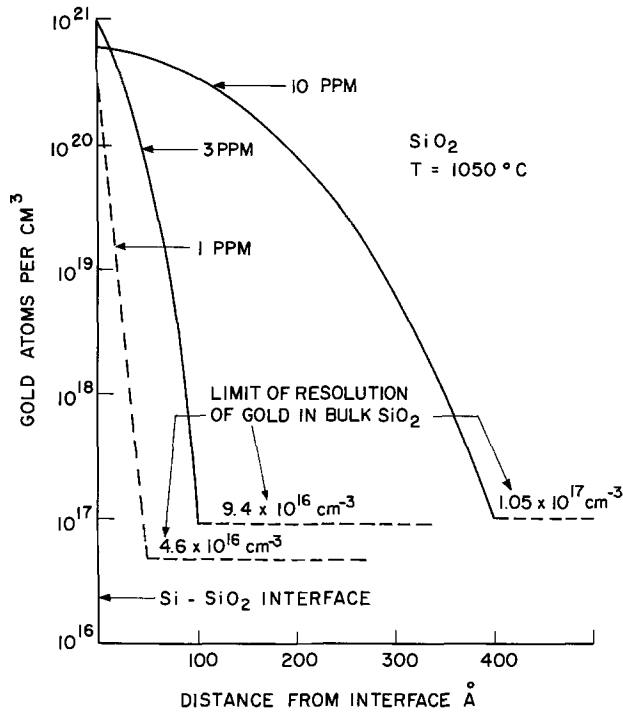


Fig. 7. The distribution of gold adjacent to the Si-SiO<sub>2</sub> interface for a range of initial contamination levels.

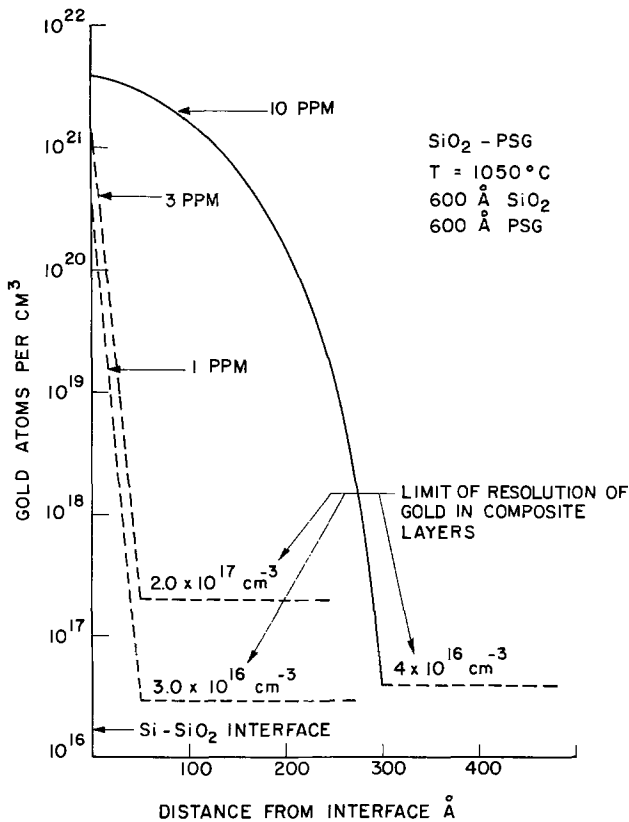


Fig. 8. The distribution of gold adjacent to the Si-SiO<sub>2</sub> interface after the growth of an SiO<sub>2</sub>-PSG composite layer.

account for the reduction in the amount of gold present in the silicon. Figure 3 shows that the amount of gold rejected to the surface of the oxide layer decreases with both increasing oxidation temperature and decreasing contamination level. For contamination levels below 3 ppm, no excess gold could be detected at the oxide surface. The very high net concentrations observed in the oxide layers (Fig. 4) will be considered later.

The reduction of the gold concentration in the slice after oxidation indicates that the transfer of gold from the surface of the oxide into the silicon slice is terminated at some point by the formation of the oxide layer. The presence of gold at the oxide/ambient surface indicates that, at some critical thickness, the oxide becomes relatively impermeable to further diffusion of gold. Table I shows, for the range of temperatures studied, the time that would be required for the measured quantity of gold to diffuse into the wafer, and the corresponding oxide thickness that would have formed at that time. It is evident that at all temperatures the formation of approximately 500Å of oxide has prevented the further diffusion of gold into the slice.

The standard deviation for the profiling measurements made on the 10 ppm oxides was  $1.05 \times 10^{12}$  atoms/cm<sup>2</sup>. If these atoms were gaussian distributed in the oxide, then using the smallest reported diffusion constant for gold in SiO<sub>2</sub> leads to an estimated surface concentration of  $1.5 \times 10^{17}$  atoms/cm<sup>2</sup>. Assuming that this concentration is maintained during the entire growth period, we may calculate the amount of gold that would have reached the slice (6-8). The calculated value is  $4.5 \times 10^{11}$  atoms/cm<sup>2</sup>, as compared to a measured value of  $2 \times 10^{14}$  atoms/cm<sup>2</sup>. Thus the gold present in the slice must have been incorporated before the growth of a substantial (~500Å) oxide layer.

The results shown in Fig. 1 and 3 may now be interpreted. In an oxidizing atmosphere, the gold initially saturates a very thin surface layer of the silicon, diffusion into the slice commences, and, at the same time oxide starts to form at the silicon surface (6), gold is rejected to the surface of this oxide. When the oxide thickness has reached about 500Å, it is effectively impermeable to further gold diffusion and the supply of gold to the slice is cut off. The gold that has already dissolved into the slice redistributes toward a uniform concentration while the gold at the oxide/ambient surface remains there and may be partially removed by oxidation/evaporation. If the initial surface concentration is low, effectively all of the gold available can diffuse into the slice during the initial oxidation.

Comparison experiments were made in which samples were brought to a temperature of 1050°C in an inert atmosphere and then oxidized for 60 min. At the 10 ppm contamination level the surface (oxide/gas) gold concentration fell to  $2 \times 10^{14}$  cm<sup>-2</sup> as compared with  $5 \times 10^{15}$  cm<sup>-2</sup> for a sample brought to temperature in an oxidizing atmosphere. No significant differences in the gold redistribution were found between composite SiO<sub>2</sub>-PSG layers and simple SiO<sub>2</sub> for the contamination levels 10, 1.0, and 0.1 ppm, although at the 10 ppm contamination level excess gold would have been rejected from the slice and oxide. There was no evidence of a significantly higher gold solubility either in the PSG layer or at the PSG-SiO<sub>2</sub> interface.

In experiments where PSG was grown directly on a slice, it was found that significantly more gold remained in the slice. Etching away the top 2μ of the slice reduced the amount of gold in the slice by almost 90% (Fig. 9). From this observation one can conclude that the enhanced gold concentration observed was entirely associated with the increased solubility of the gold in the regions of the slice that had been heavily doped n-type by contact with the glass layer. The enhancement shown in Fig. 9 for the

Table I

Temp (°C)	Contamination level (ppm)	Au atoms in Si, 60 min diff. with oxidation	Minutes to diffuse these atoms without oxidation	SiO <sub>2</sub> grown in this time (Å)
1000	10,3,1,0.1	$5 \times 10^{13}$	33	480
1050	10,3,1	$1.25 \times 10^{14}$	25	570
1100	10	$2.9 \times 10^{14}$	12	500



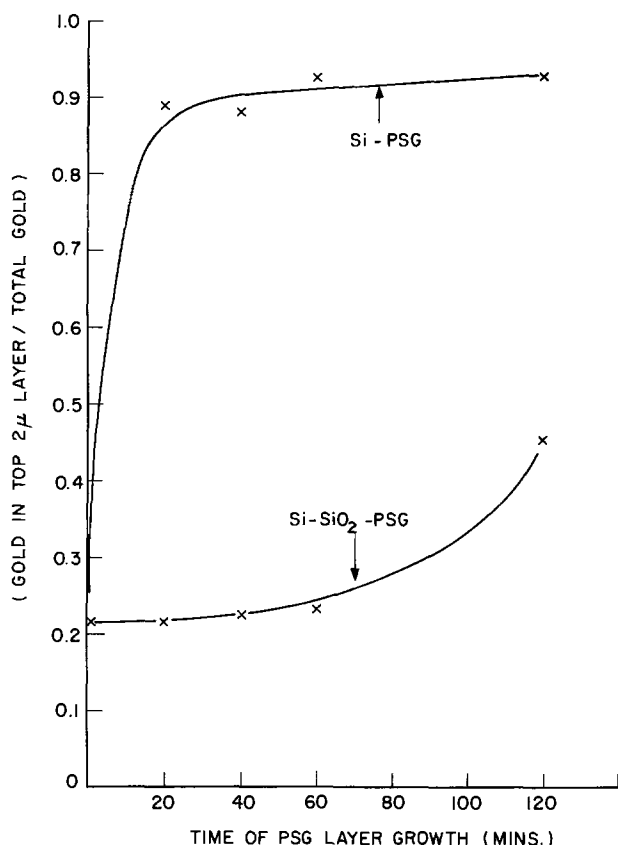


Fig. 9. A comparison of the ratio of the amount of gold in the top  $2\mu$  of the silicon slice, to the total amount in the slice after the growth of PSG and  $\text{SiO}_2$ -PSG composite layers.

composite  $\text{SiO}_2$ :PSG structures only occurred after prolonged deposition times and corresponded to the penetration of the  $\text{SiO}_2$  layer by the PSG.

The gold profile near to the Si-SiO<sub>2</sub> interface is approximately gaussian and for the 10 ppm contamination level the results would correspond to a diffusion constant of  $1.4 \times 10^{-16}$  cm<sup>2</sup>/sec. Previously reported values of the diffusion constant of gold in  $\text{SiO}_2$  range from  $9.0 \times 10^{-16}$  (9) to  $9.0 \times 10^{-15}$  cm<sup>2</sup>/sec (10) at 1050°C. However, no evidence of a similar profile was found at the  $\text{SiO}_2$ -ambient surface, even though there would have been a significant concentration of gold present at this surface for the higher contamination levels used.

The growth of  $\text{SiO}_2$  is endotaxial, all of the oxide grown has been formed from that region of the parent silicon slice that has the highest gold concentration. Thus the sharp decrease in the gold concentration in the first 50-300Å of oxide adjacent to the silicon implies a rejection process from the bulk oxide (or the failure of the gold to incorporate in the oxide). Otherwise we might expect a gold profile rising toward the oxide/ambient interface. This view is reinforced by the observation that when "excess" gold is rejected to the outer oxide surface, there is no detectable "diffusion" profile into the oxide in this region. Even at the highest temperatures and the lowest contamination levels, it appears (Fig. 4) that a substantial fraction of the chemi-deposited gold is rejected from the region where it could otherwise diffuse into the slice.

The enhanced solubility of impurities in the oxide phase and the corresponding depletion of the bulk dopant is well known. However, in the present case the concentration of the gold just inside the oxide at the oxide-silicon interface exceeds the concentration of gold just on the silicon side of the interface by a factor of more than  $10^5$ .

The implication of these observations is that the gold in the Si/SiO<sub>2</sub> interface region of the oxide is incorporated by some "chemical" bonding process characteristic of the nonstoichiometric nature of the oxide in that region. This gold is not available to participate in the normal diffusion process into either the slice or the oxide. The diffusionlike profile shown by the gold in this region is probably an artifact, associated with the process governing the oxide formation.

Thus the profiles displayed in Fig. 7, 8 should not be attributed to the normal processes of diffusion. It is well known that the growth and etching rates of the first few hundred angstroms of oxide adjacent to the parent slice are anomalous (11-14). This points to a significantly different oxide structure in the  $\text{SiO}_2$ -Si region from that found in the bulk oxide. The present observations of a substantial amount of dissolved gold close to the slice-oxide interface are further evidence of the different structural nature of the oxide in this region. The observation that the region of anomalously high gold concentration and the oxide thickness required to prevent transport between the gold at the oxide surface and the slice are both of the order 300-500Å further supports the view of a significantly different oxide structure in this region.

The detection limit in these observations was set by the masking effect of the residual  $\beta$ -radiation from the gold in solution in the slice itself. However, it is now possible to note that the net gold concentrations in the oxide observed earlier can be attributed entirely to the gold in the accumulation region occurring at the Si-SiO<sub>2</sub> interface. The interface concentrations of gold are somewhat higher in the PSG-SiO<sub>2</sub> system than in the simple  $\text{SiO}_2$  layers. However the composite layers are also thicker and more of the parent slice has been used to form the oxide and glass.

The experiments described could not determine the limiting solid solubility of gold in the  $\text{SiO}_2$  layer, since its activity was always masked by the residual activity of the gold piled up at the Si-SiO<sub>2</sub> interface. The lower limit of concentration indicated in Fig. 7 and 8 ( $9 \times 10^{16}$  cm<sup>-3</sup>) is set by the accuracy of the initial counting process ( $\pm 3\%$ ); it does not represent an estimate of the bulk solubility.

## Conclusions

The distribution of a model heavy metal contaminant, i.e., gold, during oxidation and/or the growth of PSG layers is dependent upon the previous thermal and ambient history of the slice. Under nonoxidizing conditions, gold will tend to be taken into solution in the silicon and its final concentration will be a function of temperature and initial doping. Excess gold left at the silicon surface will be rejected to the surface of any oxide which is then grown. If equilibrium with the slice is not reached during the initial heating/oxidation period, then further exchange of gold between the oxide/gas surface and the silicon slice will be terminated by the growth of approximately 500Å of oxide. After oxidation gold is found in solution in the slice, at the oxide surface, and dissolved in the oxide region adjacent to the silicon surface. The gold distributions are essentially unchanged by the growth of composite layers of  $\text{SiO}_2$  + PSG unless the PSG layer is in contact with the slice itself. In the latter case the enhancement of solubility observed at the slice surface is consistent with the Shockley-Moll model (15, 16) for Fermi level controlled solubility. No additional gettering action is observed either in the PSG layers or at the PSG-SiO<sub>2</sub> interface.

Manuscript submitted June 9, 1975; revised manuscript received April 30, 1976.

Any discussion of this paper will appear in a Discussion Section to be published in the June 1977

JOURNAL. All discussions for the June 1977 Discussion Section should be submitted by Feb. 1, 1977.

Publication costs of this article were assisted by the University of Waterloo.

#### REFERENCES

1. T. A. O'Shaughnessy, H. D. Barber, D. Thompson, and E. L. Heasell, in "Semiconductor Silicon 1973," H. R. Huff and R. R. Burgess, Editors, p. 683, The Electrochemical Society Softbound Symposium Series, Princeton, New Jersey (1973).
2. T. A. O'Shaughnessy, Ph.D. Thesis, University of Waterloo (1971).
3. J. W. Adamic, Jr. and J. E. McNamara, Paper 153 presented at The Electrochemical Society Meeting, Washington, D.C., Oct. 11-15, 1964.
4. G. Bemski and J. D. Struthers, *This Journal*, **105**, 583 (1958).
5. H. Frauenfelder and E. M. Henley, "Subatomic Physics," Prentice-Hall, Englewood Cliffs, New Jersey (1974).
6. J. R. Ligenza and W. G. Spitzer, *J. Phys. Chem. Solids*, **14**, 131 (1960).
7. P. J. Jorgensen, *J. Chem. Phys.*, **37**, 874 (1962).
8. W. A. Pliskin and R. P. Gnall, *This Journal*, **111**, 872 (1964).
9. D. R. Collins, D. K. Schroder, and C. T. Sah, *Appl. Phys. Lett.*, **8**, 323 (1966).
10. S. F. Cagnina and E. J. Snow, *This Journal*, **114**, 1165 (1967).
11. B. E. Deal and A. S. Grove, *J. Appl. Phys.*, **36**, 3770 (1965).
12. A. G. Revesz, K. H. Zainiger, and R. J. Evans, *J. Phys. Chem. Solids*, **28**, 197 (1967).
13. R. J. Jaccodine and W. A. Schlegler, *J. Appl. Phys.*, **37**, 2429 (1966).
14. M. E. Sproul and A. G. Nassibian, *Solid-State Electron.*, **17**, 577 (1974).
15. W. Shockley and J. L. Moll, *Phys. Rev.*, **119**, 1480 (1960).
16. T. A. O'Shaughnessy, H. D. Barber, D. A. Thompson, and E. L. Heasell, *This Journal*, **121**, 1356 (1974).

## A Solid Planar Source for Phosphorus Diffusion

N. Jones\*

Burroughs Corporation, San Diego, California 92127

and D. M. Metz, J. Stach,\* and R. E. Tressler\*

Departments of Material Sciences and Electrical Engineering,  
The Pennsylvania State University, University Park, Pennsylvania 16802

#### ABSTRACT

The sourcing lifetimes, microstructural stability, and diffusion performance of a new solid planar phosphorus source for silicon doping were investigated in the temperature range 900°-1100°C. The source wafers were highly porous ceramic wafers containing 25 weight percentage (w/o) SiP<sub>2</sub>O<sub>7</sub> as the "active" component in an inert refractory binder matrix. The microstructural stability and thermogravimetric analysis (TGA) results indicated the structural integrity and sourcing ability of this material at temperatures of at least 1050°C. Theoretical lifetimes of 260 and 3400 hr at 1000° and 900°C, respectively, have been predicted from the TGA results. Experimental data relating sheet resistance, junction depth, and diffusion coefficient for silicon wafers doped using these source wafers are presented. Special material handling procedures are also described.

The results of previous studies concerning the diffusion performance of boron nitride as a p-type dopant source for silicon technology have shown that planar sources offer several significant advantages over carrier gas diffusion systems using liquids and gases (1, 2). The benefits of planar diffusion sources have been previously reported by Goldsmith *et al.* (3), and it is towards this end that the development and evaluation of the new phosphorus source was aimed. In addition to the benefits presented by Goldsmith *et al.*, there is the added benefit of having a source material which has no toxic or corrosive by-products.

In using boron nitride as a source, the surface is oxidized (activated) to form B<sub>2</sub>O<sub>3</sub>, and the boron is vaporized and transported as an oxide to the silicon surface. An analogous refractory compound of phosphorus which can be fabricated into a ceramic wafer was not available to emulate the boron nitride technology. However, Murata (4) demonstrated that silicon pyrophosphate, SiP<sub>2</sub>O<sub>7</sub>, decomposes to SiO<sub>2</sub> and P<sub>2</sub>O<sub>5</sub> with the P<sub>2</sub>O<sub>5</sub> partial pressure being adequate to effectively dope silicon in the temperature range 850°-1100°C.

In this paper the discussion is confined to a wafer composition of 25 w/o SiP<sub>2</sub>O<sub>7</sub> in an inert matrix mate-

rial as manufactured by The Carborundum Company<sup>1</sup> and designated as Phosphorus Planar Diffusion Source Grade PH-1050.

#### Experimental

In order to establish that the SiP<sub>2</sub>O<sub>7</sub> phase was compatible (chemically inert) with the binder phase, the phases present after long-term annealing at temperatures encompassing the projected use temperatures were determined using standard x-ray diffraction techniques. The stability of the microstructure (retention of the fine grain, porous structure) was evaluated using scanning electron microscopic (SEM) analysis of similar samples.

To establish minimum sourcing lifetimes, the loss of P<sub>2</sub>O<sub>5</sub> was monitored as a function of time at projected use temperatures using a semimicro thermogravimetric analysis (TGA) apparatus. The samples were suspended in a fused silica tube in flowing nitrogen (0.21 SLPM) and heated rapidly from 350°C to the desired test temperature. The preheat at 350°C was necessitated by the reversible phase transition in the wafer discussed in more detail below.

All electrical measurements and diffusion experiments were performed with silicon wafers. The silicon wafers were 3.81 × 0.081 cm, boron-doped <111> ori-

\* Electrochemical Society Active Member.  
Key words: phosphosilicates, IC processing, n-type dopant, silicon.

<sup>1</sup>The Carborundum Company, Graphite Products Division, P.O. Box 577, Niagara Falls, New York 14302. Patent Application Number 500765.

ented substrates with resistivities of 0.005-0.010  $\Omega$ -cm, and boron-doped epitaxial layers 9.8-14.5 $\mu$  thick with resistivities of 1.5-4.5  $\Omega$ -cm. The phosphorus wafers were 3.81 cm in diameter and 0.089 cm thick. The resistivity data were obtained using a K&S Pacific Model 192 resistivity tester consisting of 0.001-10 mA  $\pm$  0.1% of full scale current source and 0-2V  $\pm$  0.5% of full scale digital voltmeter with an A&M Fell linear probe with 1.00 mm  $\pm$  0.01 spacing. Sheet resistance data,  $\rho_s$ , were measured by probing the silicon wafer in four quadrants plus the center and then averaging;  $\rho_s$  indicates the average of the five readings. The junction depth was measured using standard angle lapping and staining techniques with a 16 mm interferometer having a half-wavelength light source of 2935Å. The surface concentration of electrically active phosphorus was determined by use of incremental sheet resistance technique (5). All the diffusion experiments were done in an N<sub>2</sub> ambient with a spacing of 0.318 cm from source to silicon wafer (Fig. 1).

### Results and Discussion

The x-ray diffraction analyses showed that no new major phases were produced during the annealing treatments except for the SiO<sub>2</sub>-rich glass which resulted from the decomposition of SiP<sub>2</sub>O<sub>7</sub> to yield P<sub>2</sub>O<sub>5</sub> vapor. The persistence of a very small amount of the Si<sub>2</sub>P<sub>2</sub>O<sub>9</sub> phase until nearly all of the SiP<sub>2</sub>O<sub>7</sub> had decomposed indicates that the Si<sub>2</sub>P<sub>2</sub>O<sub>9</sub> phase is an intermediate reaction product in the decomposition of SiP<sub>2</sub>O<sub>7</sub>. However, no reactions between these SiO<sub>2</sub>-containing phases and the binder phase were observed.

Figure 2 demonstrates that after 48 hr at 1050°C (the maximum recommended use temperature) the fine grain, porous microstructure is retained which accounts for the dimensional stability and continued sourcing ability of these wafers.

The results of isothermal TGA experiments at 900° and 1000°C are presented in Fig. 3. In this figure the weight loss data are also plotted as percentage of available P<sub>2</sub>O<sub>5</sub>, the P<sub>2</sub>O<sub>5</sub> combined with SiO<sub>2</sub> to form SiP<sub>2</sub>O<sub>7</sub>. After an early nonparabolic period at both temperatures, the weight loss vs.  $\sqrt{\text{time}}$  curves become linear indicating, to a first approximation, a diffusion-controlled reaction in a stable microstructure.

The main value of these TGA results is in predicting the usefulness of the wafers as sources and, specifically, to predict minimum useful lifetimes. In Fig. 4 the TGA data for a period of 100 hr for the 25 w/o SiP<sub>2</sub>O<sub>7</sub> composition are presented. By fitting a straight line to the latter portion of this curve, the weight loss can be expressed as

$$W_D = 0.14t^{1/2}$$

where  $W_D$  is the percentage weight decrease in flowing N<sub>2</sub>, and  $t$  is time in minutes. By substituting the theoretically available P<sub>2</sub>O<sub>5</sub> percentage for  $W_D$ , one arrives at a minimum lifetime of  $\sim$ 260 hr, assuming no change in the rate constant. Doing the same exercise for the 900°C data yields a minimum lifetime of 3400 hr. It should be pointed out that these are mini-

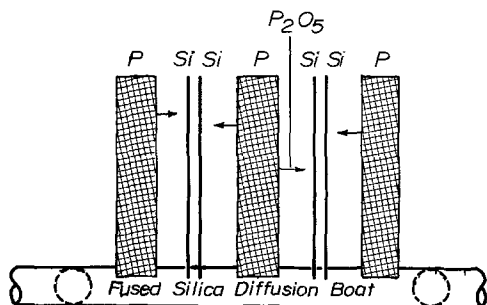


Fig. 1. Diffusion boat schematic with the solid phosphorus source

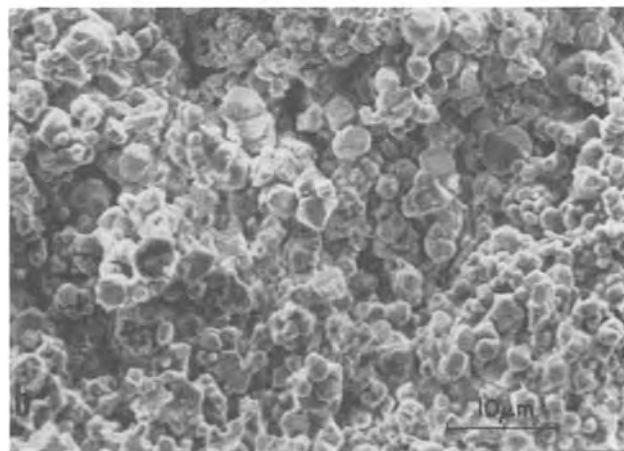
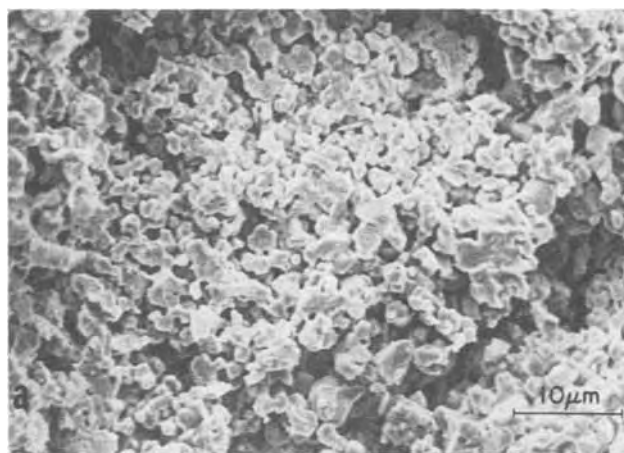


Fig. 2. Scanning electron micrographs of a fracture surface of PH-1050 wafer: (a) "as received," (b) after 48 hr at 1050°C.

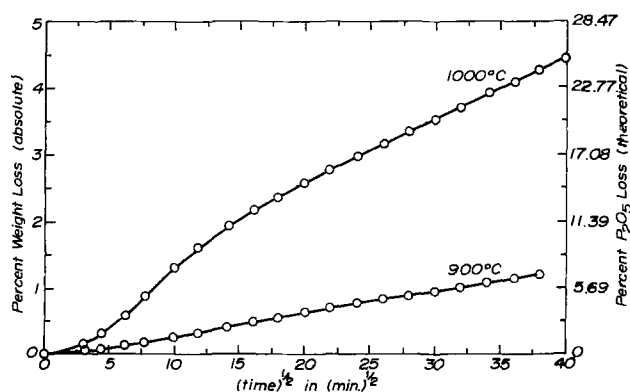


Fig. 3. Weight loss vs.  $\sqrt{\text{time}}$  for PH-1050 wafers at 900° and 1000°C.

imum lifetime estimates since they are based on TGA results in flowing nitrogen. They are probably low compared to those experienced in a typical diffusion environment. In a diffusion system the source wafer resides in a relatively stagnant vapor environment which has a P<sub>2</sub>O<sub>5</sub> partial pressure near the equilibrium P<sub>2</sub>O<sub>5</sub> partial pressure of the wafer, thus reducing the driving force for dissociation. In the TGA environment the evolved P<sub>2</sub>O<sub>5</sub> is continuously swept away resulting in a P<sub>2</sub>O<sub>5</sub>-poor vapor phase and a large driving force for dissociation. This effect has been experimentally verified by monitoring the amount of SiP<sub>2</sub>O<sub>7</sub> remaining in wafers subjected to long-term TGA experiments and long-term diffusion heat-treatments at the same temperature.

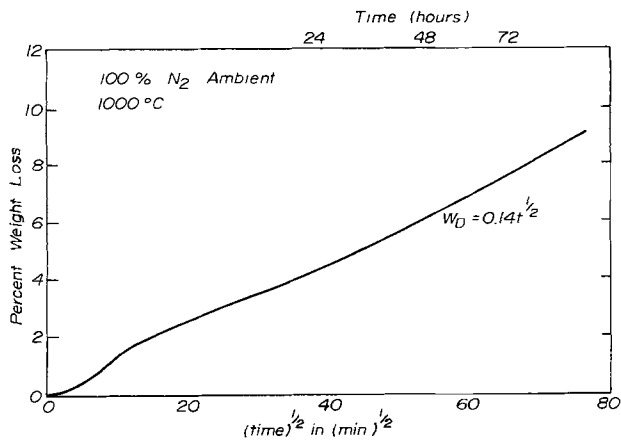


Fig. 4. Weight loss vs.  $\sqrt{\text{time}}$  for PH-1050 wafers at 1000°C to 100 hr.

The longest experiment to monitor sourcing effectiveness was for the 25 w/o SiP<sub>2</sub>O<sub>7</sub> composition at 1000°C which was still sourcing effectively after 216 hr of continuous usage.

The N<sub>2</sub> gas flow rate was found not to be a major factor in diffusion performance. The results of sheet resistance dependence on N<sub>2</sub> flow rate are shown in Fig. 5 for a 30 min diffusion at 1050°C. The sheet resistance tends to increase as flow rate increases which would seem to indicate that the dopant specie, P<sub>2</sub>O<sub>5</sub>, is being swept out by the N<sub>2</sub>. Under conditions of no N<sub>2</sub> flow, the sheet resistance is increased by nearly one order of magnitude. This was accompanied by an increase of phosphorus glass transfer and, consequently, could possibly be due to some Si-P surface phase (6), although no difficulty was experienced in glass removal.

Solmi *et al.* (7) have reported that in a POCl<sub>3</sub> system anomalous results have been observed when Si-P or SiO<sub>2</sub>-P<sub>2</sub>O<sub>5</sub> phases have been formed on or at the silicon interface. The change in sheet resistance accompanied by an increase in dopant glass suggests that Si-P or SiO<sub>2</sub>-P<sub>2</sub>O<sub>5</sub> phases have formed and are responsible for the observed anomalous behavior.

The sheet resistance data that were obtained for the range 950°-1100°C are shown in Fig. 6. The data compare favorably with other phosphorus sources such as POCl<sub>3</sub> (8) and PH<sub>3</sub> (9). Figure 7 shows sheet resistance as a function of  $\sqrt{t}$  at 1050°C. The graph is a straight line, as expected, and, hence,  $\rho_s \propto 1/\sqrt{t}$ , except at lower sheet resistance where  $\rho_s$  increases

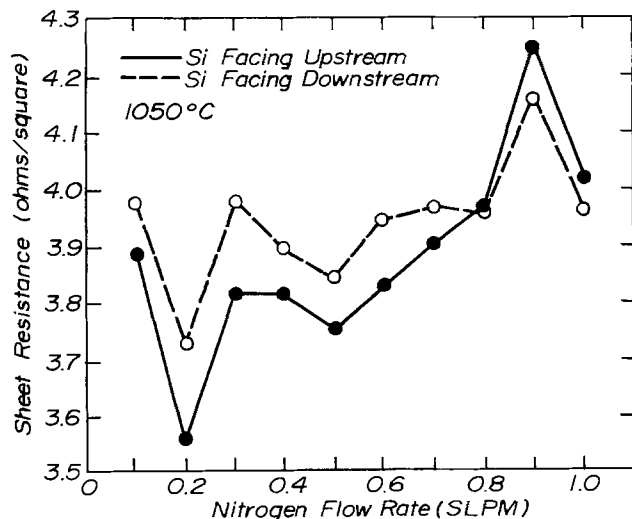


Fig. 5. Sheet resistance vs. flow rate

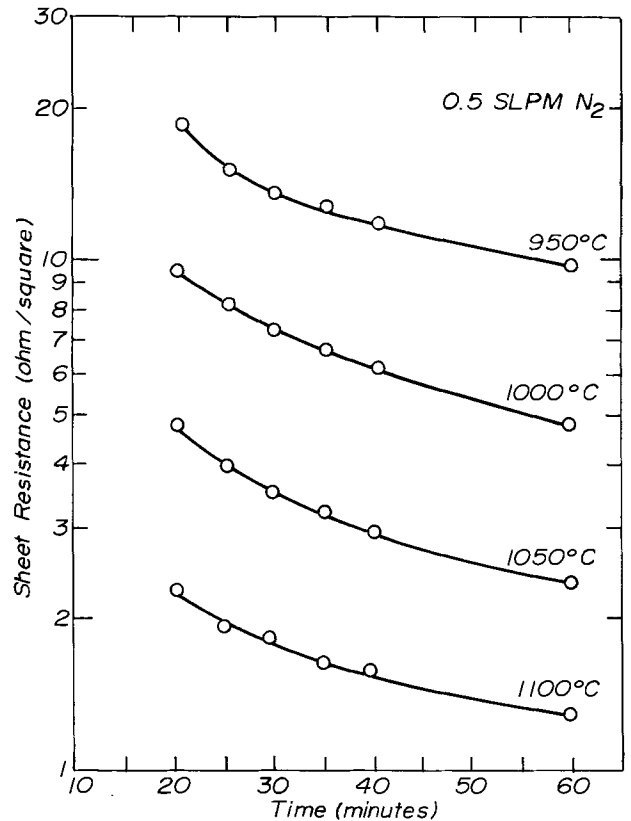


Fig. 6. Sheet resistance vs. time and temperature using 25/75 source.

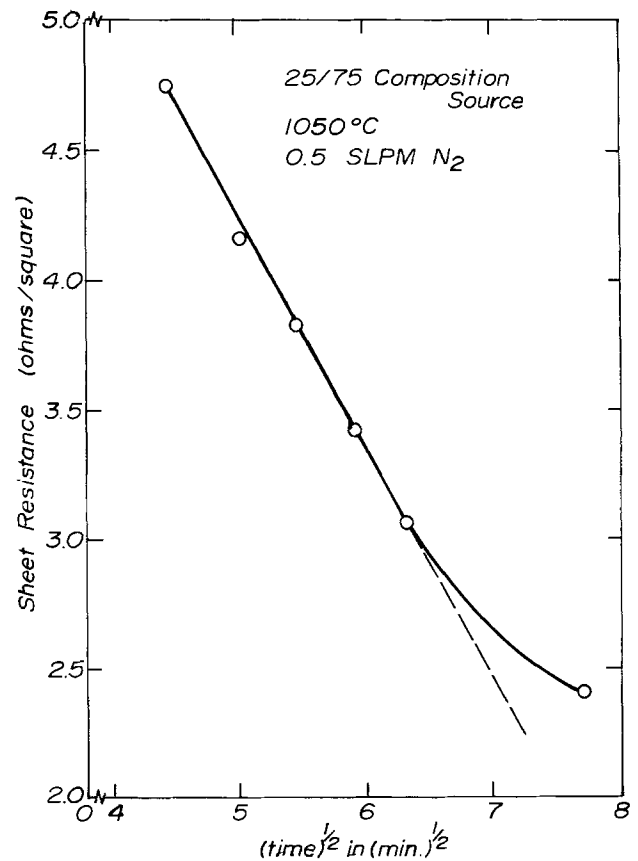


Fig. 7. Sheet resistance vs.  $\sqrt{\text{time}}$  for constant source diffusion

with  $\sqrt{t}$  which might be attributed to the Si-P phase formation. The junction depth,  $x_j$ , can be shown to be  $\sqrt{t}$  dependent for a one-step process

$$x_j = 2(Dt)^{1/2} \operatorname{erfc}^{-1} \left( \frac{C_B}{C_S} \right) \quad [1]$$

where  $D$  is the diffusion coefficient ( $\text{cm}^2/\text{sec}$ ),  $t$  is time (seconds),  $C_B$  is background concentration (atoms/ $\text{cm}^3$ ), and  $C_S$  is surface concentration (atoms/ $\text{cm}^3$ ). The graph of  $x_j$  vs.  $\sqrt{t}$  for  $1000^\circ\text{C}$  is shown in Fig. 8. The straight line relationship indicates that phosphorus obeys the complementary error function distribution. It is also possible to obtain information on the temperature dependence of  $x_j$  as well as the diffusion coefficient  $D$ . The diffusion coefficient,  $D$ , can be expressed in the Arrhenius form (10)

$$D = D_0 \exp - \frac{\Delta E_a}{kT} \quad [2]$$

where  $D_0$  is diffusion constant ( $T = \infty$ ) ( $\text{cm}^2/\text{sec}$ ),  $\Delta E_a$  is the activation energy (eV),  $k$  is Boltzmann's constant (eV/ $^\circ\text{K}$ ), and  $T$  is absolute temperature ( $^\circ\text{K}$ ). The substitution for  $D$  in Eq. [1] results in

$$x_j = 2(D_0 t)^{1/2} \operatorname{erfc}^{-1} \frac{C_B}{C_S} \exp - \frac{\Delta E_a}{2kT} \quad [3]$$

When  $D_0$ ,  $t$ ,  $C_B$ , and  $C_S$  are constant, Eq. [3] reduces to

$$x_j = K' \exp \frac{\Delta E_a}{2kT} \quad [4]$$

and its logarithm is

$$\log_{10} x_j = \log_{10} K' - \frac{\Delta E_a}{4.606k} \left( \frac{1}{T} \right) \quad [5]$$

Thus the logarithm of  $x_j$  is proportional to  $1/T$  and Fig. 9 shows  $\log x_j$  vs.  $1000/T^\circ\text{K}$  for a 60 min diffusion. It is also possible to obtain the diffusion constant,  $D_0$ , and the activation energy  $\Delta E_a$ . These data are of particular interest because most previous data for phosphorus diffusion were obtained in oxidizing ambients, and in some cases, with halogen vapor present, as is the case with  $\text{POCl}_3$  and  $\text{PBr}_3$  sources. In order to determine an effective diffusion coefficient, it is necessary to know the surface concentration, background concentration, and junction depth for various temperatures. The surface concentration was determined using the technique of incremental sheet resistance. Anodization was used to remove about  $525\text{\AA}$ . An average lamina resistivity was calculated to be  $3.08 \times 10^{-4} \Omega\text{-cm}$  which corresponds to a surface concentration of approximately  $7.5 \times 10^{20}$  atoms/ $\text{cm}^3$ . This result is in excellent agreement with the minimum resistivity,  $3 \times 10^{-4} \Omega\text{-cm}$ , associated with phosphorus-doped silicon reported by Kooi (6).

Using the junction depth data in Fig. 9 and a background concentration of  $6.1 \times 10^{15}$  atoms/ $\text{cm}^3$ , the effective diffusion coefficient for an erfc distribution was calculated for four temperatures and this is shown in the log-linear graph of Fig. 10. From this data the diffusion constant  $D_0$  was calculated to be

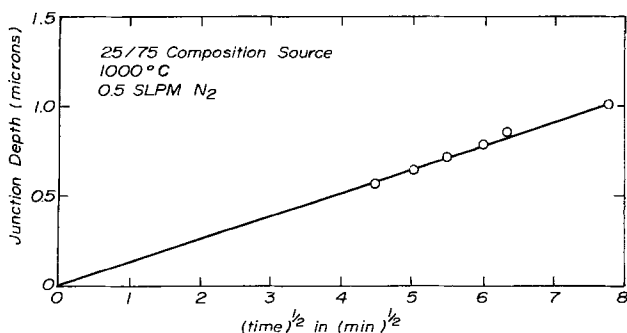


Fig. 8. Junction depth vs.  $\sqrt{\text{time}}$  for constant source diffusion

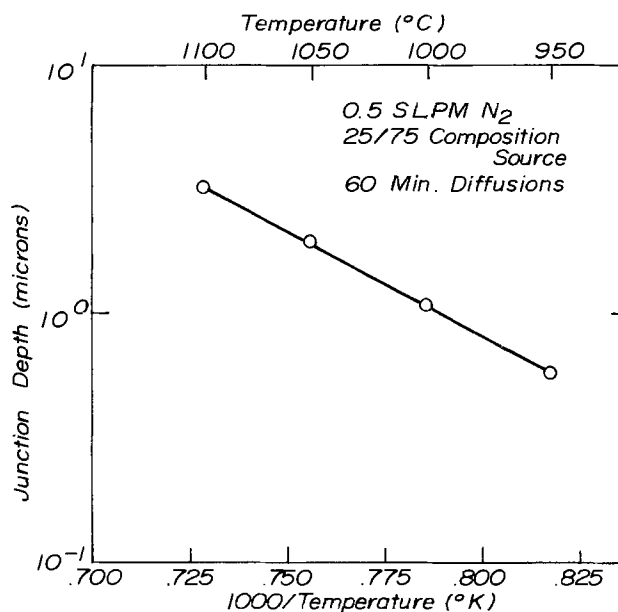


Fig. 9. Junction depth vs. reciprocal temperature for constant source diffusion.

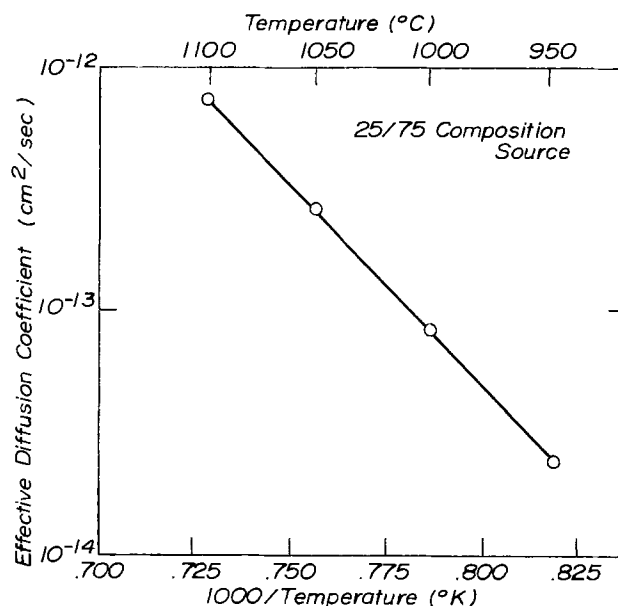


Fig. 10. Junction diffusion coefficient vs. reciprocal temperature for constant source diffusion.

$2.82 \text{ cm}^2/\text{sec}$  and  $\Delta E_a$  was found to be  $3.29 \text{ eV}$ . This is in good agreement with values considered to be most accurate by Kendall and DeVries (11), i.e.,  $\Delta E_a = 3.58 \text{ eV}$  and  $D_0 = 2.73 \text{ cm}^2/\text{sec}$ . The uncertainty in values is associated with the uncertainty of junction depth which probably accounts for the many published values. Also, Masetti *et al.* (12) have recently reported that activation energy also depends on diffusion ambient which accounts for the observed differences in inert and oxidizing ambient diffusions.

### Special Handling Procedures

One important aspect in the handling of the material is the effect of the reversible thermal expansion of this material, shown in Fig. 11. From this curve it can be seen that as the temperature of the PH-1050 wafers traverses the temperature range  $100^\circ\text{-}400^\circ\text{C}$ , the material undergoes a rapid phase transition of  $300^\circ\text{C}$  which is accompanied by a relatively large linear thermal expansion. If the temperature region from  $100^\circ$  to  $400^\circ\text{C}$  is traversed too rapidly, the source wafers break. The effect is more pronounced when

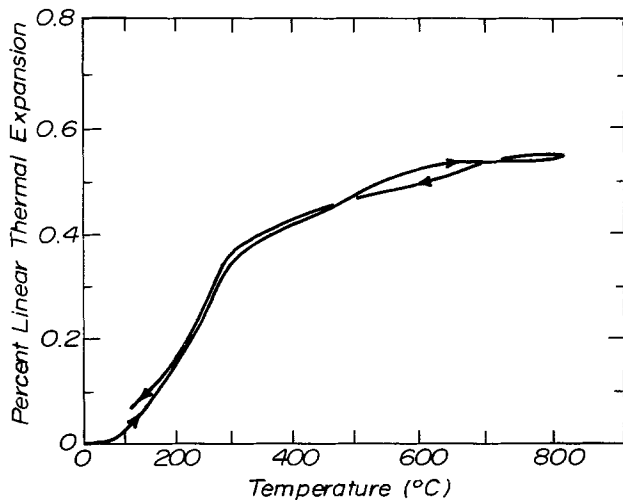


Fig. 11. Percentage linear thermal expansion vs. temperature for PH-1050 wafers.

the source wafers are utilized in the typical format shown in Fig. 1 due to the thermal gradient across the wafers upon insertion into the diffusion furnace. In order to overcome this problem, a preheat cycle has been developed. The function of the preheat cycle is to enable the source and silicon wafers to reach equilibrium at 350°C prior to insertion into the furnace. This can be accomplished by a preheated extension to the diffusion tube. Once the diffusion carrier reaches equilibrium, 350°C, the rate of insertion is not critical, so long as the temperature does not drop below 300°C, because the thermal expansion above 400°C is approximately that of fused silica.

#### Summary

The evaluation of a new solid planar source for phosphorus diffusion using  $\text{SiP}_2\text{O}_7$  as the "active"

Table I. PH-1050 preheat cycle

1. Insert diffusion carrier (boat) with phosphorus and silicon wafers into preheat zone at 350°C.
2. Allow the load to equilibrate at 350°C, time depends on mass and thermal capacity of heating tape.
3. Insert carrier into hot flat zone for desired sheet resistance.
4. Remove carrier from hot zone to preheat zone.
5. Pull carrier from preheat zone into a closed end "white elephant" and allow to cool.
6. Insert next load into preheat zone making sure that the temperature has been stabilized to 350°C.

compound in conjunction with an inert matrix phase has been described. From TGA results and assessment of the microstructural stability, the 25 w/o  $\text{SiP}_2\text{O}_7$  composition appears to fulfill structural and sourcing requirements for use to at least 1050°C. Lifetimes of ~260 and 3400 hr at 1000° and 900°C, respectively, have been predicted from the TGA results assuming all of the  $\text{P}_2\text{O}_5$  in  $\text{SiP}_2\text{O}_7$  can be vaporized. Sourcing effectiveness in diffusion runs has been verified for times as long as 216 hr at 1000°C.

The experimental in-service performance of the solid planar phosphorus diffusion source over the temperature range 950°-1100°C has been presented with data for sheet resistance and junction depth. The test results were achieved in a nitrogen ambient. Because the  $\text{P}_2\text{O}_5$  generated for the diffusion is the result of a solid-state chemical decomposition, there are no unspent gaseous by-products.

Manuscript submitted March 25, 1976; revised manuscript received June 11, 1976.

Any discussion of this paper will appear in a Discussion Section to be published in the June 1977 JOURNAL. All discussions for the June 1977 Discussion Section should be submitted by Feb. 1, 1977.

Publication costs of this article were assisted by The Pennsylvania State University.

#### REFERENCES

1. J. Stach and D. Rupprecht, *This Journal*, **120**, 1266 (1973).
2. J. Stach and A. Turley, *ibid.*, **121**, 722 (1974).
3. N. Goldsmith, J. Olmstead, and J. Scott, Jr., *RCA Rev.*, **28**, 344 (1967).
4. Y. Murata, Private communication.
5. J. C. Irvin, NBS Special Publication, 337, p. 101 (1970).
6. E. Kooi, *This Journal*, **111**, 1383 (1964).
7. S. Solmi, G. Celotti, D. Nobili, and P. Negrini, Abstract 172, p. 449, The Electrochemical Society Extended Abstracts, Fall Meeting, Dallas, Texas, October 5-10, 1975.
8. J. S. R. Heynes and J. T. Wilkerson, *Electrochem. Technol.*, **5**, 464 (1967).
9. J. S. Kesperis, *This Journal*, **117**, 554 (1970).
10. S. K. Ghandhi, "The Theory and Practice of Microelectronics," p. 67, John Wiley & Sons, Inc., New York (1968).
11. D. L. Kendall and D. B. DeVries, in "Semiconductor Silicon," R. R. Haberecht and E. L. Kern, Editors, p. 358, The Electrochemical Society Softbound Symposium Series, New York (1969).
12. G. Masetti, S. Solmi, and G. Soncini, *Solid-State Electron.*, **16**, 1419 (1973).

# Chemical Vapor Deposition of Tantalum Pentoxide Films for Metal-Insulator-Semiconductor Devices

E. Kaplan,<sup>1</sup> M. Balog,<sup>2</sup> and D. Frohman-Bentchkowsky

School of Applied Science and Technology, The Hebrew University of Jerusalem, Jerusalem, Israel

## ABSTRACT

Thin amorphous Ta<sub>2</sub>O<sub>5</sub> films were deposited by oxygen-assisted pyrolysis of tantalum dichloro-diethoxy-acetylacetonate. Index of refraction and the optical gap measurements of the films were in agreement with previous results. The d-c conduction mechanism appears to be bulk limited following the Poole-Frenkel mechanism with transition towards a space charge limited current at high current densities. The conduction level is high and breakdown voltage is low with respect to SiO<sub>2</sub> or Si<sub>3</sub>N<sub>4</sub>. The higher dielectric constant of Ta<sub>2</sub>O<sub>5</sub> films could make them attractive in double layer insulator MIS devices.

Tantalum pentoxide has been prepared and some of its properties were investigated previously (1-6). This work is concerned with chemical vapor deposition of Ta<sub>2</sub>O<sub>5</sub> films in order to investigate their properties with emphasis on their possible usage as part of the gate insulator in MIS devices.

## Film Deposition

Chemical vapor deposition (CVD) was used due to its advantage as a method of producing uniform and reproducible films with desired properties at low temperature (7). So far, TaCl<sub>5</sub> (3) and Ta alcoholates (4-6), especially Ta(OC<sub>2</sub>H<sub>5</sub>)<sub>5</sub> (4), had been tried as sources for deposition of Ta<sub>2</sub>O<sub>5</sub> films. The former requires high temperature (900°C) for the reaction, while the latter are very sensitive to oxygen, hydrolyze easily (8), and thus are inconvenient to work with and require special precautions. The use of organometallic compounds is advantageous since it enables the user to deposit films at lower temperature than others. Tantalum dichloro-diethoxy-acetylacetonate-TaCl<sub>2</sub>(OC<sub>2</sub>H<sub>5</sub>)<sub>2</sub>C<sub>5</sub>H<sub>7</sub>O<sub>2</sub>, first synthesized by Funk (9), proved to be a better source. It is stable, has a low melting point, and is easy to synthesize (9, 10).

The Ta<sub>2</sub>O<sub>5</sub> films were deposited by oxygen-assisted pyrolysis of the source on substrates of silicon and fused silica. The silicon substrates were n- and p-type 5-10 Ω-cm with (100), (110), and (111) orientations. The deposition apparatus is shown in Fig. 1. The source's vapor is carried in nitrogen, argon, or helium from the bubbler (e) through a heated line (o) to the oxygen-rich deposition chamber (f) where reaction yields Ta<sub>2</sub>O<sub>5</sub> and other volatile organic derivatives. Deposition conditions were optimized by varying the carrier gas flow rate, the source temperature, the substrate temperature, the geometry of the apparatus, and the diluting gas flow rate. Uniform good quality films are obtained under the following conditions

Carrier gas flow rate	~ 300 cm <sup>3</sup> /min
Diluting gas flow rate	~1500 cm <sup>3</sup> /min
Oxygen flow rate	~1500 cm <sup>3</sup> /min
Source temperature	150°C
Substrate temperature	300°-500°C

Unless otherwise specified, all film properties measurement work was carried out on samples obtained under these conditions.

## Film Properties

**General.**—The Ta<sub>2</sub>O<sub>5</sub> films deposited were up to 1 μm thick as evaluated by the Tolansky method (11).

<sup>1</sup> Present address: Tadiran Limited, Microelectronics Division, Tel-Aviv 61000, Israel.

<sup>2</sup> Present address: IBM Thomas J. Watson Research Center, Yorktown Heights, New York 10598.

Key words: tantalum pentoxide, chemical vapor deposition, MIS, insulator conduction mechanism.

The deposition conditions stated above resulted in uniform film deposited at a rate of ~70 Å/min. No dependence on substrate orientation was observed. The films could be easily etched in aqueous HF. In 1.5:1/48% HF:H<sub>2</sub>O, the etch rate was ~280 Å/min for films obtained at 500°C. Films deposited at lower temperatures had greater etch rates. The adhesion of the films to the substrates was good showing no evidence of cracking even on abrupt cooling by liquid air. Ta<sub>2</sub>O<sub>5</sub> films deposited at 300°C with a thickness greater than 1 μm tend to crack and peel off. Films deposited at 500°C did not show this phenomenon.

**Film structure.**—Metallurgical microscope and scanning electron microscope micrographs of the samples showed smooth film surfaces comparable with previous results (4). X-ray diffraction patterns showed that the films were amorphous. After annealing in an inert atmosphere at 800°C for 4 hr, the films became polycrystalline hexagonal δ-Ta<sub>2</sub>O<sub>5</sub> (12, 13) and not β-Ta<sub>2</sub>O<sub>5</sub> (14) as mentioned by Wang *et al.* (4).

**Optical properties.**—The index of refraction (*n*) of the films as determined by the Abeles method (15) varied between 1.96 and 2.30 for films obtained at 300° and 500°C, respectively (λ = 6328Å). This is in good agreement with values reported before (3-5).

The optical energy gap was evaluated from the absorption curve of films deposited at 500°C on fused silica disks measured on a Perkin Elmer 450 UV-VIS-NIR spectrophotometer. The absorption spectrum in the 2000-10,000Å region showed only one absorption

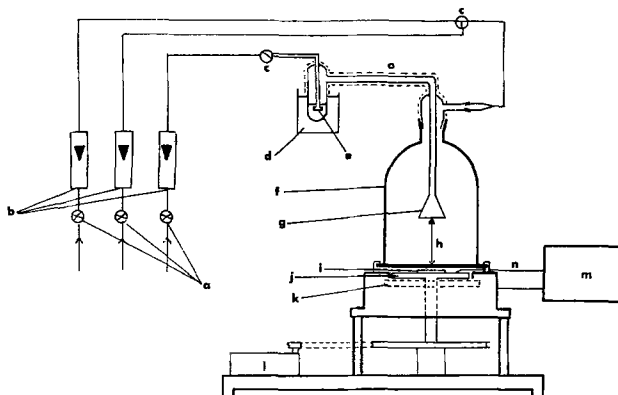


Fig. 1. Schematic representation of the deposition apparatus: a = needle valve, b = flowmeters, c = on-off valve, d = oil bath, e = bubbler, f = reaction chamber, g = funnel, h = distance between the funnel and the substrate, i = substrate, j = hot plate, k = resistance heater, l = motor, m = controller, n = thermocouple, o = heated line.

peak which was assumed to be due to the fundamental energy gap absorption. Plotting the square of the absorption coefficient as a function of the wavelength or the photon energy gives (16), by extrapolation to zero, the value of  $4.38 \pm 0.15$  eV for the optical bandgap (Fig. 2). This result is in agreement with values reported by Knausenberger *et al.* (3). It also agrees well with values calculated from the heat of formation (17).

**Electrical properties.**—The electrical properties were evaluated by measurements on MIS structures which were prepared by deposition of 900-2000Å Ta<sub>2</sub>O<sub>5</sub> films on 5-10 Ω-cm p- and n-type silicon wafers of (100) and (111) orientations. Aluminum dots of  $0.96 \times 10^{-3}$  cm<sup>2</sup> in area and 0.4 μm thick were EB evaporated to form the gate electrode. A film of Al was also evaporated as back contact. The samples were annealed in an inert atmosphere at 500°C for 5 min after evaporation.

**C-V measurements.**—The dielectric properties of the MIS structure incorporating the Ta<sub>2</sub>O<sub>5</sub> films as the gate dielectric were measured by the high frequency C-V technique (18). Figure 3 shows the C-V curve of a p-type specimen with (111) orientation. There was no difference among the three orientations of (100), (110), and (111). No hysteresis was observed at room temperature with the exception of films deposited at 300°C (Fig. 4) which gave irregular

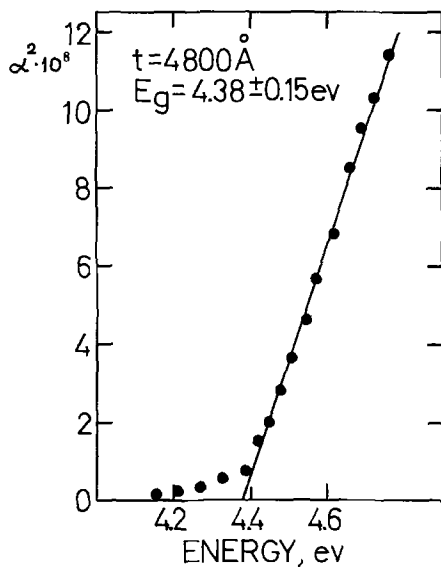


Fig. 2. (Absorption coefficient)<sup>2</sup> as a function of photon energy ( $h\nu$ ) for Ta<sub>2</sub>O<sub>5</sub>.

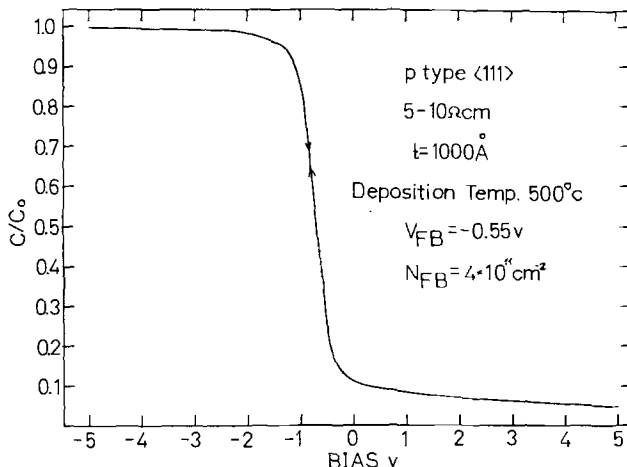


Fig. 3. Normalized C-V curve of a MIS structure with Ta<sub>2</sub>O<sub>5</sub> at 1 MHz.

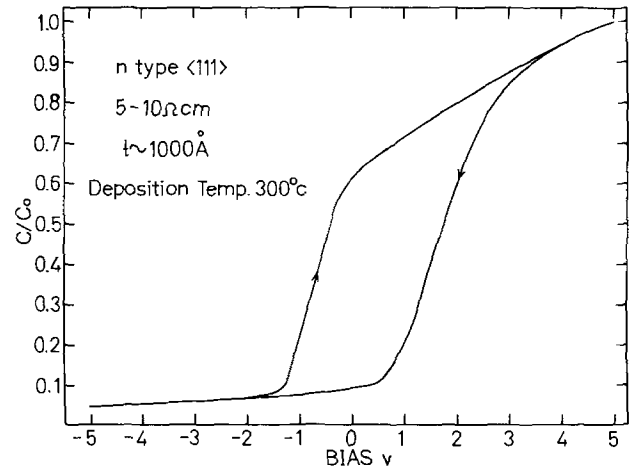


Fig. 4. Normalized C-V curve at 1 MHz for Ta<sub>2</sub>O<sub>5</sub> film deposited at 300°C.

results and thus were unreliable. Therefore, the rest of the electrical characterization was carried out on films deposited at 500°C. Flatband voltages ( $V_{FB}$ ) were determined according to Lehocvec (19). Their values were 0 to -0.35V and 0 to -0.6V for n- and p-type, respectively, for films in the thickness range of 900-1600Å. The effective surface state charge density ( $N_{FB}$ ) was calculated from

$$N_{FB} = (\phi_{ms} - V_{FB}) \frac{\epsilon\epsilon_0}{qt} \quad [1]$$

where  $\phi_{ms}$  is the work function difference between Al and Si (20),  $\epsilon$  is the relative dielectric constant of the Ta<sub>2</sub>O<sub>5</sub> films,  $\epsilon_0$  is the permittivity of free space, and  $t$  is the oxide thickness.  $N_{FB}$  values were less than  $5 \times 10^{11}$  cm<sup>-2</sup>. The turn-on voltage varied between 0 and -0.5V for different samples. The relative dielectric constant  $\epsilon$  was computed from capacitance measurements at 1 MHz and thickness measurements. It varied in the range of 22-25.

Bias-temperature (B-T) tests with +10V, -5V at 165°C (Fig. 5) do not indicate any substantial shifts in the C-V characteristics due to mobile ions such as sometimes found in SiO<sub>2</sub> (21, 22). The distortion in the C-V curve can be attributed to fast surface states (18).

**D-C conductivity.**—Current-voltage measurements were carried out using the Keithley 602 electrometer. The data are plotted (Fig. 6) in the form of a "Schottky plot" which applies both to the Schottky and to the Poole-Frenkel conduction mechanisms (23, 24).

The current density in the Schottky mechanism is given by

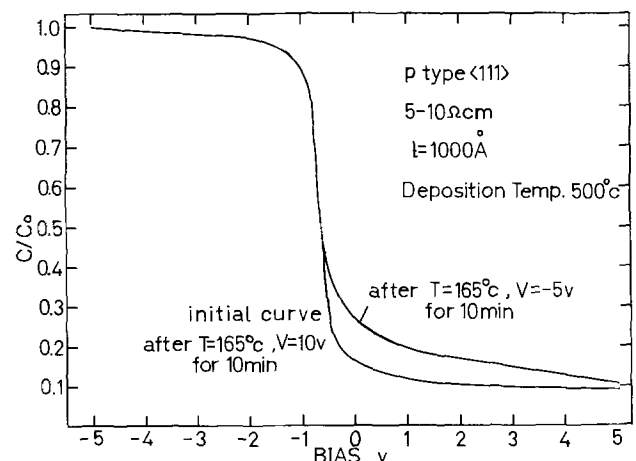
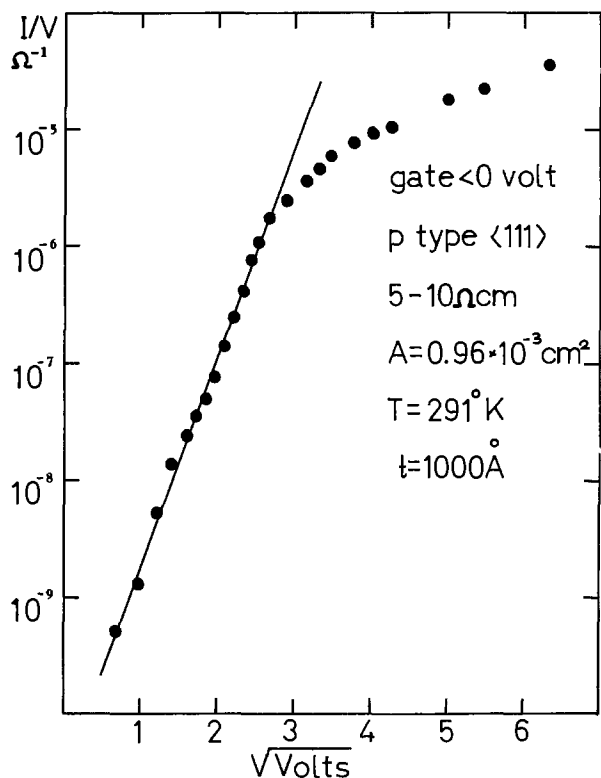


Fig. 5. Normalized C-V curve at 1 MHz of a bias-temperature test



Fig. 6. Log  $I/V$  vs.  $V^{1/2}$  for  $Ta_2O_5$  film on Si

$$J = AT^2 \exp \left\{ q \left[ \left( \frac{q}{4\pi\epsilon\epsilon_0 t} V \right)^{1/2} - \psi_s \right] / kT \right\} \quad [2]$$

where  $A$  is the Richardson constant,  $V$  is the voltage across the insulator, and  $\psi_s$  is the potential barrier between the metal and the insulator. In the Poole-Frenkel mechanism the current density is given by (25)

$$J = G_0 V \exp \left\{ q \left[ (qV/\pi\epsilon\epsilon_0 t)^{1/2} - \psi_{PF} \right] / kT \right\} \quad [3]$$

where  $G_0$  is a constant and  $\psi_{PF}$  is the potential barrier of the traps.

The slope of the linear region of Fig. 6 yields (Eq. [3]) a dielectric constant of 5.3 which fits the optical dielectric constant  $\epsilon = n^2 = 5.3$  (24). It appears that in the saturation region (Fig. 6 and 7) the current is space charge limited with a current-voltage relationship of  $J \propto V^{2.4}$  (26, 27).

The activation energy as measured from the slope of Fig. 8 is 0.45 eV which gives, after considering the Schottky effect, a barrier height of 0.55 eV. Similar values were found using the zero field current values plotted as a function of temperature (24). These values are in agreement with previous results (28). The low activation energy and the value of the dielectric constant evaluated from Fig. 6 suggest that the conduction in these  $Ta_2O_5$  films is bulk limited with a Poole-Frenkel mechanism at low current densities and a transition towards a space charge limited current at high current densities.

Figure 9 shows results of  $Ta_2O_5$  films in comparison with  $Si_3N_4$  and  $SiO_2$  obtained by Deal *et al.* (29). Note the high conductivity of  $Ta_2O_5$  with respect to the other films. The current saturation can also be noted on the vapor-deposited  $SiO_2$  film. Breakdown field of the  $Ta_2O_5$  films was  $\sim 4 \times 10^6$  V/cm.

### Conclusions

Properties such as good adhesion, ease of etching, large dielectric constant ( $\epsilon = 22-25$ ), and a possible good barrier against ionic contamination make  $Ta_2O_5$  films prepared by CVD of good potential for usage both as part of passive and active elements in in-

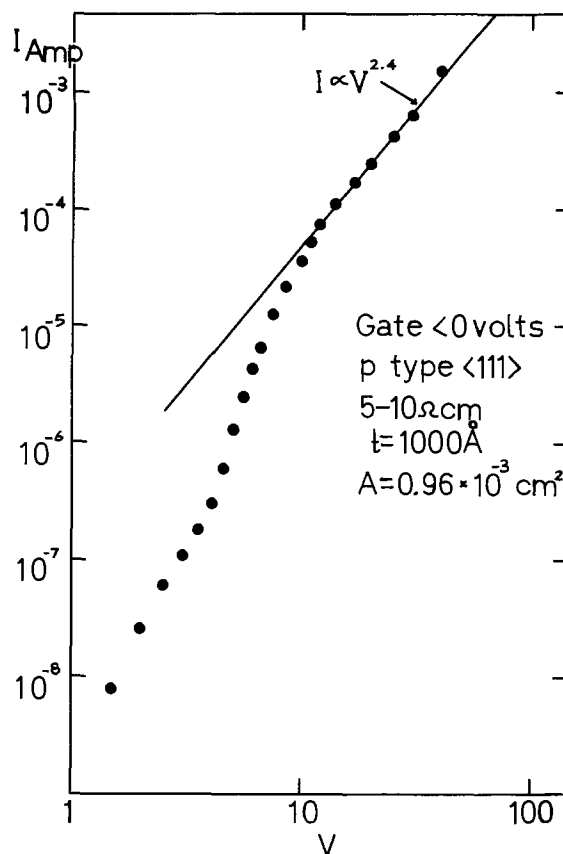
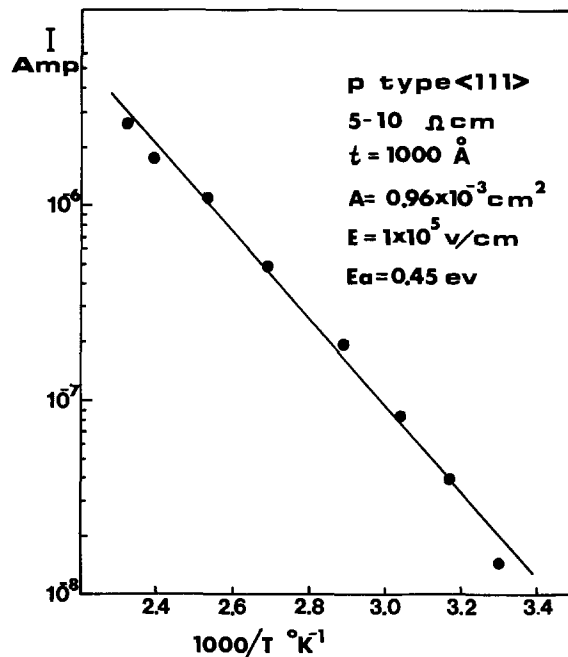
Fig. 7. Log  $I$  vs. log  $V$  curve of  $Ta_2O_5$  film on Si

Fig. 8. The current-temperature relationship at a constant electric field.

tegrated circuits. The high d-c conduction level and the low breakdown voltage relative to  $SiO_2$  and  $Si_3N_4$  make  $Ta_2O_5$  inferior to those films in MIS structures. However,  $Ta_2O_5$ 's other properties, as mentioned above, could make it useful as a second insulator layer to  $SiO_2$  in multilayer gate MIS devices (30).

### Acknowledgments

The authors wish to thank Professors S. Patai and M. Schieber for their valuable help in the course

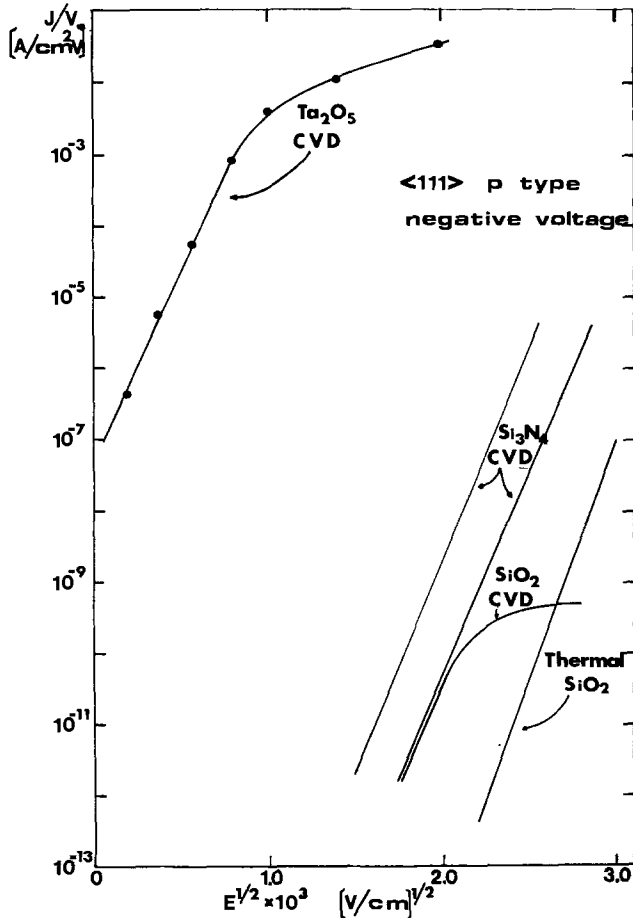


Fig. 9. Current-voltage relationships for 1000Å  $\text{Ta}_2\text{O}_5$  film (this work) and  $\text{SiO}_2$  and  $\text{Si}_3\text{N}_4$  films obtained by Deal et al. (29).

of this work and Mr. C. Assarf and the SEM Laboratory of the Hebrew University's staff for their technical assistance.

Manuscript submitted Jan. 5, 1976; revised manuscript received April 26, 1976.

Any discussion of this paper will appear in a Discussion Section to be published in the June 1977 JOURNAL. All discussions for the June 1977 Discussion Section should be submitted by Feb. 1, 1977.

## REFERENCES

1. D. A. McLean and W. H. Orr, *Bell Lab. Rec.*, **44**, 304 (1966).
2. M. Caulton, *Proc. IEEE*, **59**, 1481 (1971).
3. W. H. Knausenberger and R. N. Tauber, *This Journal*, **120**, 927 (1973).
4. C. C. Wang, K. H. Zaininger, and M. T. Duffy, *RCA Rev.*, **31**, 728 (1970).
5. S. Pakswar and P. Scoug, in "Chemical Vapor Deposition," Second International Conference, J. M. Blocher, Jr. and J. C. Withers, Editors, p. 619, The Electrochemical Society Softbound Symposium Series, New York (1970).
6. D. Peterson, "Non-Vacuum Deposition Techniques for Use in Fabricating Thin Film Circuits," Contract No. NObsr 91336 Final Report (Jan. 1967).
7. C. F. Powell, J. H. Oxley, and J. M. Blocher, Jr., Editors, "Vapor Deposition," John Wiley & Sons, Inc., New York (1966).
8. D. C. Bradley and W. Wardlaw, *J. Chem. Soc.*, 726 (1955).
9. H. Funk, *Chem. Ber.*, **67**, 1801 (1934).
10. C. Djordjevic and V. Katovic, *J. Inorg. Nucl. Chem.*, **25**, 1099 (1963).
11. G. R. Booker and C. E. Benjamin, *This Journal*, **109**, 1206 (1962).
12. X-Ray Diffraction File, ASTM Card No. 19-1299
13. N. Terao, *Jpn. J. Appl. Phys.*, **6**, 21 (1967).
14. X-Ray Diffraction File, ASTM Card No. 19-1298.
15. J. Raif, N. Ben-Yosef, and M. Oron, *J. Phys. E*, **6**, 48 (1973).
16. H. Y. Fan, *Rep. Prog. Phys.*, **19**, 107 (1956).
17. A. K. Vigh, *J. Phys. Chem. Solids*, **30**, 1999 (1969).
18. K. H. Zaininger and F. P. Heiman, *Solid State Technol.*, **13**, 49 (May 1970); *ibid.*, **13**, 46 (June 1970).
19. K. Lehovec, *Solid-State Electron.*, **11**, 135 (1968).
20. B. E. Deal, E. H. Snow, and C. A. Mead, *J. Phys. Chem. Solids*, **27**, 1873 (1966).
21. E. H. Snow, A. S. Grove, B. E. Deal, and C. T. Sah, *J. Appl. Phys.*, **36**, 1664 (1965).
22. S. R. Hofstein, *IEEE Trans. Electron Devices*, ed-14, 749 (1967).
23. J. R. Yeargan and H. L. Taylor, *J. Appl. Phys.*, **39**, 5600 (1968).
24. G. A. Brown, W. C. Robinette, and H. G. Carlson, *This Journal*, **115**, 948 (1968).
25. J. Frenkel, *Phys. Rev.*, **54**, 647 (1938).
26. J. G. Simons, *J. Phys. D.*, **4**, 613 (1971).
27. A. Rose, *Phys. Rev.*, **97**, 1538 (1955).
28. C. A. Mead, *ibid.*, **128**, 2088 (1962).
29. B. E. Deal, P. J. Fleming, and P. L. Castro, *This Journal*, **115**, 300 (1968).
30. D. Kahng and E. H. Nicollian, in "Applied Solid State Science," Vol. 3, p. 2, R. Wolfe, Editor, Academic Press, New York (1972).

# Technical Notes



## Phosphorous-Doped Polysilicon Growth

Z. Lieblich and A. Bar-Lev

Department of Electrical Engineering, Technion—Israel Institute of Technology, Haifa, Israel

Polysilicon is currently used in various technologies involving semiconductor devices: as mechanical support (3, 4), as resistive or field shaping layers (2, 5, 6), or as gates in MOS or CCD devices (1). These uses exploit its ease of deposition, the fact that it can

**Key words:** epitaxy, phosphorous, silane, doping, resistivity, mobility.

be deposited over silicon dioxide, and the fact that its deposition at relatively low temperatures does not appreciably affect underlying diffusions. They do not exploit its properties as a semiconductor which are relatively poor. This work is a study of polysilicon grown under conditions most favorable to its use as a semiconductor with the aim of forming a polysilicon

to silicon diode (7). The properties of polysilicon grown under these conditions are compared with those obtained by other workers of polysilicon grown under different conditions, generally chosen to emphasize some other properties particular to it.

### Experimental Procedure

**Gases.**—The layers were grown in a horizontal epitaxial reactor consisting of a water-cooled quartz tube through which the gases passed. The gas mixture consisted of 0.07%  $\text{SiH}_4$  in  $\text{H}_2$ . Phosphine was added to the mixture in concentrations varying from  $2 \times 10^{-5}$  to  $10^{-1}$  times that of the silane.

**Growth temperature.**—A SiC-coated carbon susceptor which supported the substrates was heated by rf induction. Substrate temperature during growth was  $800^\circ\text{C}$ , measured by an optical pyrometer and then confirmed by a thermocouple embedded in the susceptor. Silicon grown at less than  $600^\circ\text{C}$  is found to be amorphous (8). For increases in growth temperature up to  $750^\circ\text{C}$ , there is a progressive drop in resistivity of undoped layers (9), and, if the substrate is single crystalline silicon, the proportion of substrate-oriented grains increases until substrate orientation begins to dominate at  $800^\circ\text{C}$  (1). Above  $800^\circ\text{C}$ , grain size continues to increase without significant improvement in electrical properties, till above  $1050^\circ\text{C}$  when growth becomes epitaxial. Thus it can be seen that a growth temperature of  $800^\circ\text{C}$  is a good compromise for obtaining good electrical properties, while retaining the properties of a low temperature process.

**Preparation of samples.**—The substrates were  $\text{SiO}_2$ , thermally grown on single crystal silicon. After polysilicon growth,  $400 \times 400 \mu\text{m}$  square patterns were etched, and the circuit passivated with an  $\text{SiO}_2$  layer grown at  $350^\circ\text{C}$  by the Silox process. Windows were etched in the Silox for aluminum contacts. Resistivity ( $\rho$ ) and Hall mobility ( $\mu$ ) were measured by the Van der Pauw method. Active donor concentration was then obtained from the well-known relationship  $\rho = 1/q\mu N_d$ .

A separate wafer was grown in each run for measuring the thickness of the grown layers. Part of the polysilicon was etched down to the oxide substrate, and the height of the step measured with a Sloan Dektak surface profile tracer. Growth times were adjusted so that thickness would fall between 1.0 and  $1.5 \mu\text{m}$ .

### Results and Discussion

It was established that the growth of the polysilicon in this study is largely mass transfer limited. A check of growth rates at temperatures between  $700^\circ$  and  $800^\circ\text{C}$  revealed an activation energy at these temperatures of 0.26 eV. Since it is known (19) that activation energy in the surface reaction rate limited region is about 1.6 eV, it is apparent that we are operating in or near the mass transfer limited region, which is desirable for good thickness uniformity and control. This concurs with Eversteyn and Put (11), who found growth to be temperature independent above  $830^\circ\text{C}$ . Variation of thickness over the same wafer was found in our samples to be typically within  $\pm 3\%$ .

Figure 1 shows that the growth rate at  $800^\circ\text{C}$  is moderately dependent on the phosphine/silane ratio (P/Si) in the gas, and drops from  $1.0 \mu/\text{min} \% \text{Si}$  (%Si is the percentage of silane to hydrogen) for (P/Si) =  $10^{-5}$  to  $0.6 \mu/\text{min} \% \text{Si}$  for (P/Si) =  $10^{-1}$ . Eversteyn and Put (11) found a stronger dependence for their samples grown at  $680^\circ\text{C}$ , where growth rate drops from  $0.1 \mu/\text{min} \% \text{Si}$  for (P/Si) = 0 to  $0.04 \mu/\text{min} \% \text{Si}$  for (P/Si) =  $2.5 \times 10^{-3}$ . Two samples which they grew at  $800^\circ\text{C}$  are also shown in Fig. 1. A similarly strong inhibition of growth at  $680^\circ\text{C}$  has been found when doping with arsine (11), while at  $1200^\circ\text{C}$  the dependence is weakened (12).

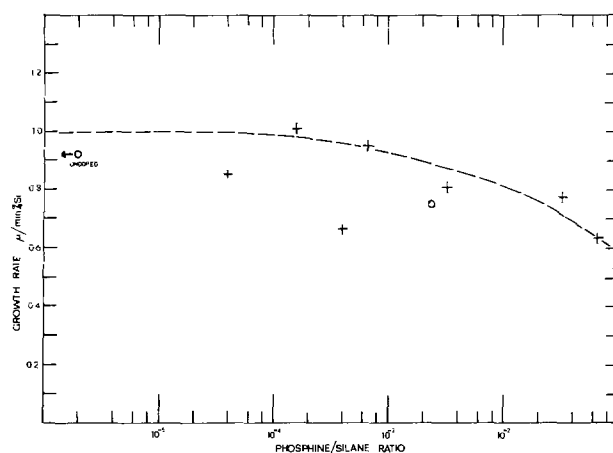


Fig. 1. Growth rate vs. phosphine-silane ratio in the gas phase: + =  $800^\circ\text{C}$ ,  $\text{SiH}_4\text{-PH}_3$  at  $0.07 \times 10^{-2}$  atm; O =  $800^\circ\text{C}$ ,  $\text{SiH}_4\text{-PH}_3$  at  $0.35 \times 10^{-2}$  atm, Ref. (11).

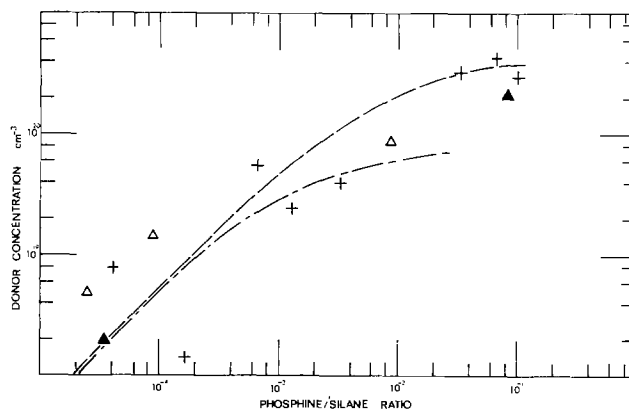


Fig. 2. Active donor concentration vs. phosphine-silane ratio in gas phase: + =  $800^\circ\text{C}$ ,  $\text{SiH}_4\text{-PH}_3$ ; ▲ =  $840^\circ\text{C}$ ,  $\text{SiBr}_4\text{-PH}_3$ , Ref. (13); Δ =  $650^\circ\text{C}$ ,  $\text{SiH}_4\text{-PH}_3$ , Ref. (13); --- phosphorus-doped single crystal silicon, Ref. (16).

In Fig. 2 it can be seen that for (P/Si) ranging from  $10^{-5}$  to  $10^{-2}$  the active donor concentration ( $N_d$ ) behaves according to the linear relationship

$$N_d \approx (\text{P/Si}) \cdot 5 \times 10^{22}$$

Cowher and Sedgwick (13) found that

$$N_d \approx (\text{P/Si}) \cdot 35 \times 10^{22}$$

for their samples grown at  $650^\circ\text{C}$ . Samples which they grew at  $840^\circ\text{C}$  from  $\text{SiBr}_4$  are also shown in Fig. 2. For (P/Si)  $\geq 10^{-2}$ ,  $N_d$  saturates at a value equal to the solid solubility of phosphorus in single crystal silicon at  $800^\circ\text{C}$  (14).

In Fig. 3 resistivity is shown as a function of  $N_d$ . This is compared with the curve for polysilicon grown at  $680^\circ\text{C}$  and doped with arsenic (12). It can be seen that resistivities below  $10^{-3} \Omega\text{-cm}$  can be attained.

Figure 4 compares mobility measurements of various workers with those obtained in this work. The most important feature seen is an increase in mobility as  $N_d$  increases above  $10^{18} \text{cm}^{-3}$ . This can be explained by either of two conduction theories:

(i) The "carrier trapping model" (15) which assumes that carriers are trapped in deep states at grain boundaries forming potential barriers and associated depletion regions which lower effective mobility. As  $N_d$  increases beyond the value at which the deep states are saturated, the height of the barriers, as seen by an electron in the conduction band, decreases and consequently increases mobility.

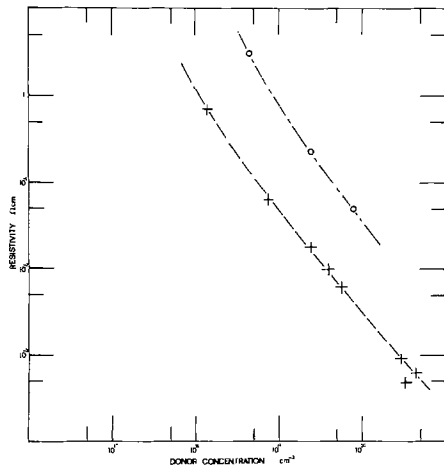


Fig. 3. Resistivity vs. active donor concentration: + = 800°C, SiH<sub>4</sub>-PH<sub>3</sub>; o = 680°C, SiH<sub>4</sub>-A<sub>3</sub>H<sub>3</sub>, Ref. (12).

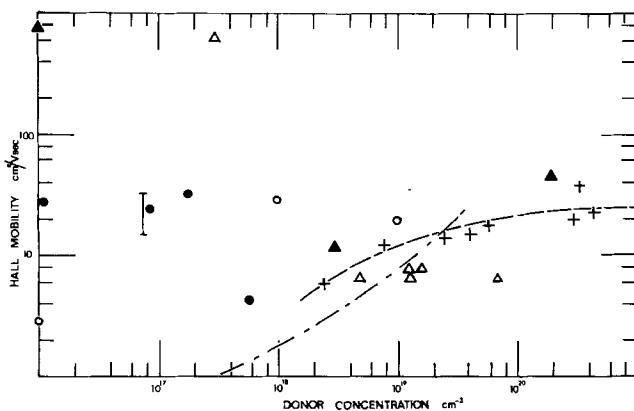


Fig. 4. Hall mobility vs. active donor concentration: + = 800°C, SiH<sub>4</sub>-PH<sub>3</sub>; ▲ = 840°C, SiBr<sub>4</sub>-PH<sub>3</sub>, Ref. (13); Δ = 650°C, SiH<sub>4</sub>-PH<sub>3</sub>, Ref. (13); ● = 1035°C, SiH<sub>4</sub>-PH<sub>3</sub>, Ref. (17); ○ = 1035°C, SiH<sub>4</sub>-PH<sub>3</sub>, Ref. (15); ⊥ = 1100°C, (CH<sub>3</sub>)SiHCl<sub>2</sub>-SiCl<sub>3</sub>-PCl<sub>3</sub>, Ref. (18); --- = 730°C; evaporation; dopant diffused; Ref. (2).

(ii) The "dopant segregation model" (13) assumes that at low dopant concentration the dopant atoms tend to segregate at the grain boundaries where they are not ionized and do not contribute free carriers. At concentrations of  $10^{18}$ - $10^{19}$  cm<sup>-3</sup>, the dopant atoms begin to enter the crystal grains and contribute carriers. The increase in mobility at these concentrations is attributed to the compensation of crystalline defects by the dopant atoms which effectively removes scattering centers.

### Summary

Polysilicon was grown in an epitaxial reactor at 800°C and doped during growth by adding phosphine to the gas mixture. It was found that phosphine doping

inhibits silicon growth at 800°C to a lesser degree than at lower temperatures, and that resistivities of less than  $10^{-3}$  Ω-cm can be achieved. The donor concentration ( $N_d$ ) in the layer is given by

$$N_d = (P/Si) \cdot 5 \times 10^{22}$$

where (P/Si) is the phosphine/silane molecular ratio.  $N_d$  saturates at a value of  $2 \times 10^{20}$  cm<sup>-3</sup>. Hall mobility in the polysilicon is 20-30 cm<sup>2</sup>/Vsec for  $N_d$  above  $10^{19}$  cm<sup>-3</sup>.

### Acknowledgments

Helpful discussions were held with Drs. S. Margalit and J. Shappir of the Microelectronics Laboratory, Technion. I. Rothstein and staff of the laboratory contributed to the technical work. The authors also wish to thank the Gledden Fund of the University of Western Australia for financial support.

Manuscript submitted March 4, 1976; revised manuscript received June 21, 1976.

Any discussion of this paper will appear in a Discussion Section to be published in the June 1977 JOURNAL. All discussions for the June 1977 Discussion Section should be submitted by Feb. 1, 1977.

### REFERENCES

1. F. Flaggin and T. Klein, *Solid-State Electron.*, **13**, 1125 (1970).
2. F. D. King *et al.*, *ibid.*, **16**, 701 (1973).
3. U. S. Davidson and F. Lee, *Proc. IEEE*, **57**, 1532 (1969).
4. Y. Sumitomo, K. Niwa, H. Sawazaki, and K. Sakai, in "Semiconductor Silicon 1973," H. R. Huff and R. R. Burgess, Editors, p. 893, The Electrochemical Society Softbound Symposium Series, Princeton, New Jersey (1973).
5. L. E. Clark and D. S. Zoroglu, *Solid-State Electron.*, **15**, 653 (1972).
6. C. K. Kim and E. H. Snow, *Appl. Phys. Lett.*, **20**, 514 (1972).
7. Z. Lieblch and A. Bar-Lev, To be published.
8. M. H. Brodsky, R. S. Title, K. Weiser, G. D. Pettit, *Phys. Rev.*, **B**, **1**, 2632 (1970).
9. J. D. Joseph and T. I. Kamins, *Solid-State Electron.*, **15**, 355 (1972).
10. T. I. Kamins and T. R. Cass, *Thin Solid Films*, **16**, 144 (1973).
11. J. C. Eversteyn and B. H. Put, *This Journal*, **120**, 106 (1973).
12. P. Rai-Choudhury and P. L. Hower, *ibid.*, **120**, 1761 (1973).
13. M. E. Cowher and T. O. Sedgwick, *ibid.*, **119**, 1565 (1972).
14. F. A. Trumbore, *Bell Syst. Tech. J.*, **39**, 205 (1960).
15. T. I. Kamins, *J. Appl. Phys.*, **42**, 4357 (1971).
16. E. Sirtl, in "Festkörper Probleme VI," D. Madelung, Editor, p. 27, Vieweg, Braunschweig, Germany (1967).
17. T. I. Kamins, *Solid-State Electron.*, **15**, 789 (1972).
18. E. Sirtl and H. Seiter, *This Journal*, **113**, 506 (1966).
19. T. I. Kamins, *IEEE Trans. Parts, Hybrids and Packaging*, **10**, 221 (1974).

## Light Emitting Patterns of Gallium Nitride Electroluminescence

A. Shintani and S. Minagawa\*

Hitachi, Limited, Central Research Laboratory, Kokubunji, Tokyo 185, Japan

The light production mechanism in GaN MIS light emitting diodes (LED's) is generally considered a radiative recombination of the minor carriers generated in a high electric field at the i-n junction. It

has been reported that the lights are emitted in the form of discrete spots around the electrode for a point contact (1) or at crystal subgrain boundaries for In metal contact over the i-layer surface (2, 3). However, the authors found the light occurrence at subgrain centers rather than at subgrain boundaries with respect to the i-n GaN LED's fabricated on

\* Electrochemical Society Active Member.  
Key words: light spot sites, dislocations, Zn concentration, growth hillocks.

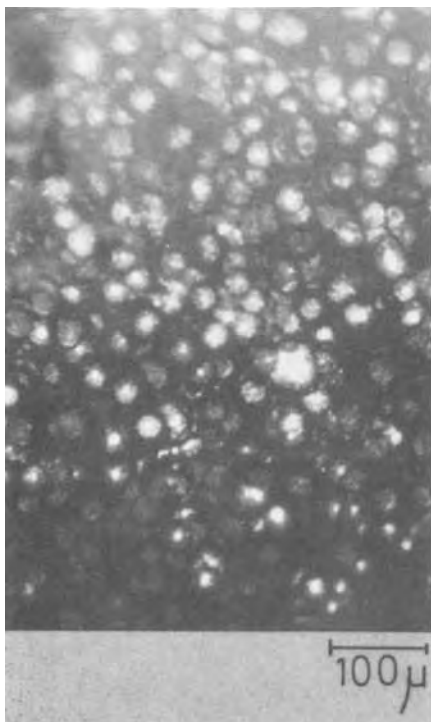


Fig. 1. Light spots observed from the substrate [(0001) orientation].

(0001) oriented sapphires (Fig. 1). In order to investigate the causes of these emissions at the centers, the study was performed by examining the correlation of the light spot sites with crystal growth morphology, Zn concentration, and etch patterns.

The GaN crystal growth method, phosphoric acid etching technique, and the fabrication process of the GaN:Zn LED's used in the study have been presented in detail elsewhere (4, 6). The Zn concentration distribution on the i-layer surfaces was measured by scanning electron microprobe analysis (EMA). The electron beam irradiated on the crystal surface is several microns in diameter, which is less than one-tenth of the crystal hillock diameter. To reduce measurement error due to surface roughness, the distribution condition of the Zn concentration was expressed by the  $K\alpha$ -ray intensity ratio of Zn to Ga, in which the Ga  $K\alpha$ -ray intensity was used as a reference level. Both  $K\alpha$ -rays were simultaneously measured. Optical microscopic studies on the electroluminescence (EL) and crystal morphology were carried out with an ordinal microscope which allowed focusing magnification up to  $400\times$ .

The Zn concentration tended to be higher at the peripheries than at the center regions of the growth hillocks by 1 ~ 25%. On the other hand, the etch patterns developed first on the peripheries of the growth hillocks and their distribution extended to the hillock faces as etching time increased. Moreover, a large etch pit developed at each apex of the growth hillock (Fig. 2). These etch patterns differ in form, development, and ascription from the hexagonal etch pits on the n-layer (4). The i-layer etch patterns are attributable to crystal defects or precipitates caused by doping with a large amount of Zn.

Thus, phosphoric acid etching of the i-layers indicates that the Zn doping process induces crystal defects including certain dislocations or precipitates within the i-layer growth hillock. The crystal growth mechanism of the i-layer is different from that of the n-layer with no hillock boundaries on both layers being superimposed on one another (4). The etch patterns on the peripheries and faces of the hexagonal

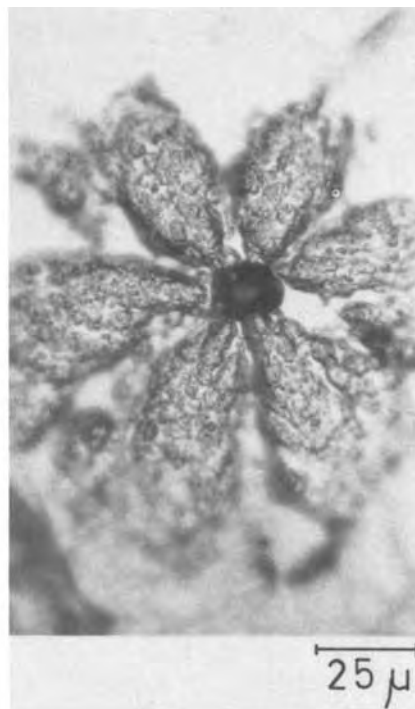


Fig. 2. Etch patterns on a large hillock of the i-layer. A large etch pit develops at the apex.

hillocks on the i-layer cannot be attributed to dislocations because they are not pitted, but prominent (4). To the contrary, the etch pit development at the apexes suggested that dislocations in the c axis direction can exist in the hillock centers. Therefore, other emission sites should be taken into account in addition to subgrain boundaries. Since the electrical characteristics of the dislocations can cause a channeling of carriers for occurrence of an avalanche breakdown (5), it is reasonable to assume that the light occurs at the hillock central dislocation. However, the etching technique gave no evidence that the dislocations passed through the i-n junction, because the etch pits at the hillock apexes on the lapped i-layer surface were difficult to distinguish from other etch patterns that were present in a high density condition.

The local nonuniformity of the diode internal electrical resistance due to the fluctuation of the Zn concentration distribution provides another reason for the EL occurrence at the growth hillock centers. The yellow LED's made in this work were estimated to have a Zn concentration twice or more that of the blue LED's. The internal resistance of the yellow LED's was found to be ten times or more that of the blue LED's. For example, the yellow LED emits light at 16.8V-1.9 mA and the blue LED at 3.5V-12.9 mA (6). Accordingly, the easier injection of electrons in the hillock center regions follows from the difference in Zn concentration between the two regions described previously. As a result, the light can occur more easily at the centers.

The In metal contact over the surface was employed for the above observations. When a probe was used as the electrode as in the first of Pankove's experiments (1), the lights occurred mostly around the probe without any relation to the growth hillocks. Also, lights sometimes occurred at diverse positions without any relation to the probe position. In the case of this point contact, it is difficult to extend the current over all the i-layer because of its high electrical resistance. This restriction of the current extension causes the light sites to be limited to the region around and under the probe. This light crea-

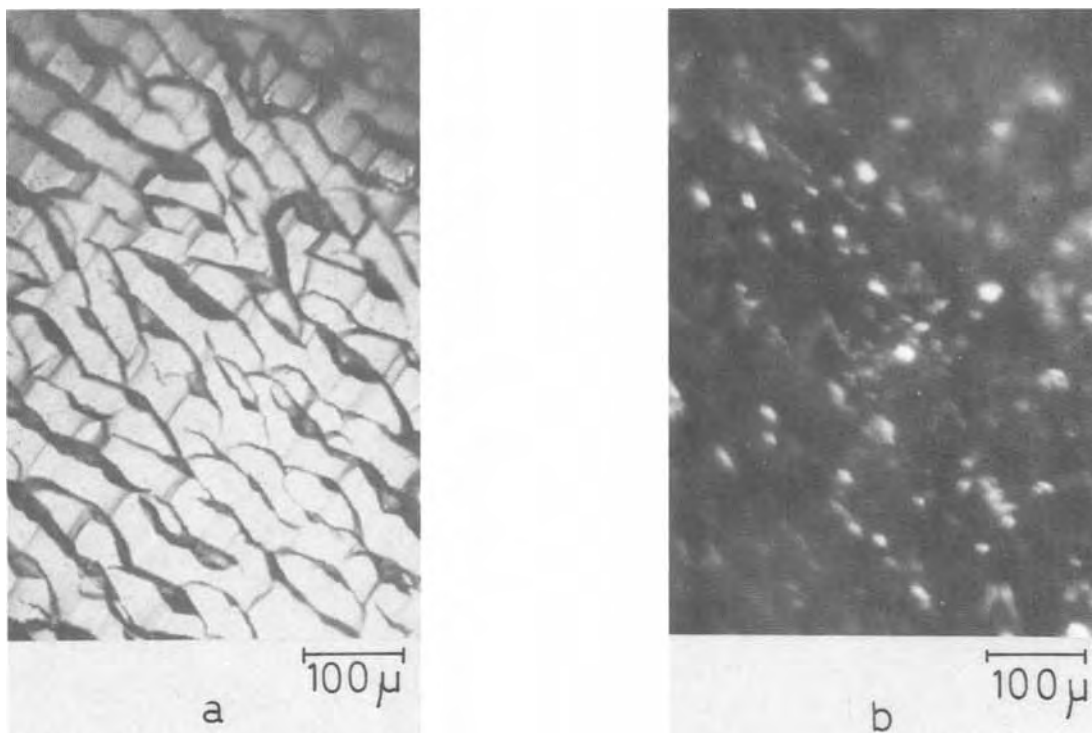


Fig. 3.  $\{11\bar{2}0\}$  GaN crystal surface (a) and light spots observed from the substrates (b)

tion does not reflect the nonuniformity of the crystal as well as the lights in the case of the In metal contacts.

The above description is concerned with  $\{0001\}$  crystals. On the other hand, crystals grown on  $(1\bar{1}02)$  substrates are oriented in  $\{11\bar{2}0\}$ , and their surfaces became more wavy [Fig. 3(a)]. The light spots with In metal contact over these surfaces were emitted along the ridges and/or valleys of the wavy surface. These positions disagreed with the observation made on GaN:Mg LED by Maruska *et al.* where the lights were produced with relation to crystal facets (3). The light form on the  $\{11\bar{2}0\}$  plane apparently differs from that on the  $\{0001\}$  plane, as seen in Fig. 3(b). Some of the lights seem to be a bar rather than a spot. The light spots on the  $\{11\bar{2}0\}$  crystal can be close to each other because there is no development of distinct growth hillocks as large as those on the  $\{0001\}$  crystal. As a result, the lights seem to be in a bar form. It was difficult to find whether or not crystal defects contributing to the emissions exist in the ridges and valleys because the etch patterns developed in a very high density condition on the  $\{11\bar{2}0\}$  plane. However, since one of the hexagonal crystal cleavage planes consists of a  $\{0001\}$  plane, it seems plausible that dislocations are formed in a direction perpendicular to the  $\{11\bar{2}0\}$  plane.

The lights themselves are actually created inside the devices on the two substrates with the emitting region being precisely at the i-n junction as shown in Fig. 4. This figure gives a more distinct light position than that given before on the GaN:Mg LED (3). The light positions differ from the GaN:Zn antistokes light position which is produced in the i-layer (7). The difference between these light positions in GaN:Zn LED is caused by reversing the electrical bias direction.

In summary, the EL lights in the case of the  $\{0001\}$  GaN crystals occur in the form of discrete spots at the growth hillock centers, but no light is emitted at hillock boundaries. These lights are concerned with certain dislocations at the hillock apexes and/or with Zn concentration nonuniformity within the hillocks. On the other hand, the EL lights in the case of



Fig. 4. Observation of the light occurrence (encircled) at the cleaved surface with a forward bias. The In contact over the i-layer surface is out of focus in the photograph.

the  $\{11\bar{2}0\}$  crystals are produced on the ridges or valleys of wavy surface. The lights seem to not always be in the discrete spot form.

#### Acknowledgments

The authors wish to express their thanks to Minoru Wada for fabricating the LED's used in this work.

Manuscript submitted March 10, 1976; revised manuscript received June 22, 1976.

Any discussion of this paper will appear in a Discussion Section to be published in the June 1977 JOURNAL. All discussions for the June 1977 Discussion Section should be submitted by Feb. 1, 1977.

Publication costs of this article were assisted by Hitachi, Limited.

#### REFERENCES

1. J. I. Pankove, E. A. Miller, D. Richman, and J. E. Berkeyheiser, *J. Lumin.*, **4**, 63 (1971).
2. H. P. Maruska and D. A. Stevenson, *Solid-State Electron.*, **17**, 1171 (1974).
3. H. P. Maruska, L. A. Anderson, and D. A. Stevenson, *This Journal*, **121**, 1202 (1974).
4. A. Shintani and S. Minagawa, *ibid.*, **123**, 706 (1976).

5. J. I. Pankove, "Optical Process in Semiconductors," p. 203, Prentice-Hall, Englewood Cliffs, New Jersey (1971).  
A. G. Chynoweth and G. L. Pearson, *J. Appl. Phys.*,

- 29, 1103 (1958).  
6. A. Shintani and S. Minagawa, To be published.  
7. J. I. Pankove, *Phys. Rev. Lett.*, **34**, 809 (1975);  
*IEEE Trans. Electron Devices*, ed-22, 721 (1975).

## Chemical Vapor Deposition of Silicon Nitride

J. J. Gebhardt, R. A. Tanzilli, and T. A. Harris

General Electric Company, Re-Entry & Environmental Systems Division and Space Sciences Laboratory, Space Division, Philadelphia, Pennsylvania 19101

Crystalline  $\alpha$ - $\text{Si}_3\text{N}_4$  is formed from the gas phase by the reaction of silane with ammonia or, somewhat less expensively and more conveniently, by reaction between a silicon tetrahalide and ammonia. Billy (1) has elucidated the chemistry of the silicon tetrachloride-ammonia and silicon tetrabromide-ammonia systems at lower temperatures ( $-78^\circ$ - $100^\circ\text{C}$ ), and has demonstrated that the silyl imide,  $\text{Si}(\text{NH})_2$ , and possibly polymers based on it are the principal precursors to silicon nitride. The precursors, on thermal decomposition to above ca.  $1000^\circ\text{C}$ , lead to only one product, identified as amorphous silicon nitride, which on further heat-treatment to about  $1450^\circ\text{C}$  yields  $\alpha$ - $\text{Si}_3\text{N}_4$ . Mazdiyasn and Cooke (2) have used the high purity, fine particle size powder obtained by this approach to form high density, fine-grained polycrystalline bodies by hot pressing, with magnesium nitride as a sintering aid. The formation, precipitation, and crystallization of the intermediate imides also appears to be the path by which dense, crystalline layers of  $\alpha$ -silicon nitride are formed by chemical vapor deposition under controlled conditions. Galasso, Kuntz, and Croft (3) have demonstrated that above about  $1100^\circ\text{C}$  and under suitable flow and concentration conditions, translucent deposits were formed and identified as  $\alpha$ - $\text{Si}_3\text{N}_4$ , of high purity and considerable preferred orientation. Similarly, Airey, Clarke, and Popper (4) deposited amorphous and crystalline silicon nitride from silane-ammonia and silicon tetrachloride-ammonia mixtures.

### Experimental Approach

Silicon nitride deposits were formed by reacting both silicon tetrachloride and silicon tetrafluoride with ammonia in a dynamic hot-wall reaction system, at low pressure (less than 5 Torr) and between  $1100^\circ$  and  $1550^\circ\text{C}$ . Silicon tetrachloride (Fisher Scientific Company, Technical Grade) was entrained in a nitrogen carrier gas, or alternatively, pumped directly into the furnace from a stainless steel reservoir through a metering valve. In the former case, the amount of tetrachloride fed was determined from the nitrogen flow and assuming liquid vapor equilibrium at the reservoir temperature. In the latter case, the metering valve was calibrated by determining the weight loss of the tetrachloride reservoir. Silicon tetrafluoride (Matheson Gas Products, 99.6% min.), a vapor at room temperature, was metered through a flowmeter, as was anhydrous ammonia gas (Matheson Gas Products 99.99%). All reagents were used as received, without further purification.

Deposits were prepared using a vertical, resistance-heated, graphite element vacuum furnace which contained a graphite reaction tube 1 in. in diameter by 8 in. long and made from Speer 580 graphite. Within this tube was fitted a graphite channel (Union Carbide Corporation, CS Grade),  $\frac{1}{2}$  in. square by 8 in. long, the inner surfaces of which were covered with a thin layer of Grafoil<sup>®</sup>,<sup>1</sup> which served as the actual deposi-

tion surface. Reagents were metered to the furnace as vapors through stainless steel lines and mixed within the furnace to prevent clogging of the lines by the solid adduct. Exhaust gases were pumped from the furnace through a liquid nitrogen trap and vented or passed through an alkaline scrubbing solution when silicon tetrafluoride was used. Solid by-products collected in cooler regions of the furnace as well as in the furnace exhaust lines in both the chloride and fluoride reactions, although in the latter case these deposits were slightly less voluminous. Accumulation of these solids constituted the limiting factor in the length of a given experiment due to closing off of the gas passages to the pump. Temperature was determined using a Leeds and Northrup disappearing filament pyrometer and sighting on the deposition surface through a window at the top of the deposition tube until the window became obscured with by-products. From this point, power settings were kept constant and thermal equilibrium was assumed. Prior to starting, the furnace was stabilized at deposition temperature for 30 min with a nitrogen flow equivalent in volume to the experimental flow.

The deposits were freed from the graphite channel by grinding away the bulk of the channel and heating the remainder in air for several hours at about  $650^\circ\text{C}$ , leaving the deposit as a free-standing, square cross-section tube. Portions of certain deposits were ground and polished for determination of optical properties; others were used for preliminary oxidation and creep studies. Most of the deposits were less than 0.5 mm (20 mils) thick.

### Discussion of Results

*Deposition process.*—Deposits obtained from the tetrachloride system ranged from white and glassy or vitreous at low temperatures to dark green around  $1500^\circ\text{C}$ . Under the conditions used, white or vitreous deposits were again obtained at  $1550^\circ\text{C}$ . Typical as-deposited surfaces are shown in Fig. 1. On the other hand, deposits made from the fluoride system were light tan in color at  $1500^\circ\text{C}$ . However, conditions leading to vitreous deposits were not used with the fluoride system as will be discussed shortly. The color difference between materials produced from the chloride vs. the fluoride system persisted through polishing, with the former yielding transparent yellow brown plates, while the latter materials were almost water white and clear.

Deposition stresses appeared to be greater at long residence times (8 msec) and cylindrical deposits appeared to contain residual compressive stresses around  $45$ - $70$  MN/m<sup>2</sup>, estimated from the change in radius on cutting a ring-shaped piece. At shorter residence times ( $\sim 1$  msec), the materials were of somewhat smaller grain size and presented no difficulty in cutting or machining for polishing. Residence times were estimated from the total gas volume fed, at deposition temperature and pressure, and the total reactor volume. Typical densities of polished specimens were around  $3.19$  g/cm<sup>3</sup>, close to the measured and calculated values of  $3.168$ - $3.169$  g/cm<sup>3</sup> of Wild *et al.* (5).

Key words: alpha-silicon nitride, vapor deposition, silicon tetrachloride-ammonia, silicon tetrafluoride-ammonia, spectral properties, oxidation of silicon nitride.

<sup>1</sup> Registered trademark, Union Carbide Corporation.



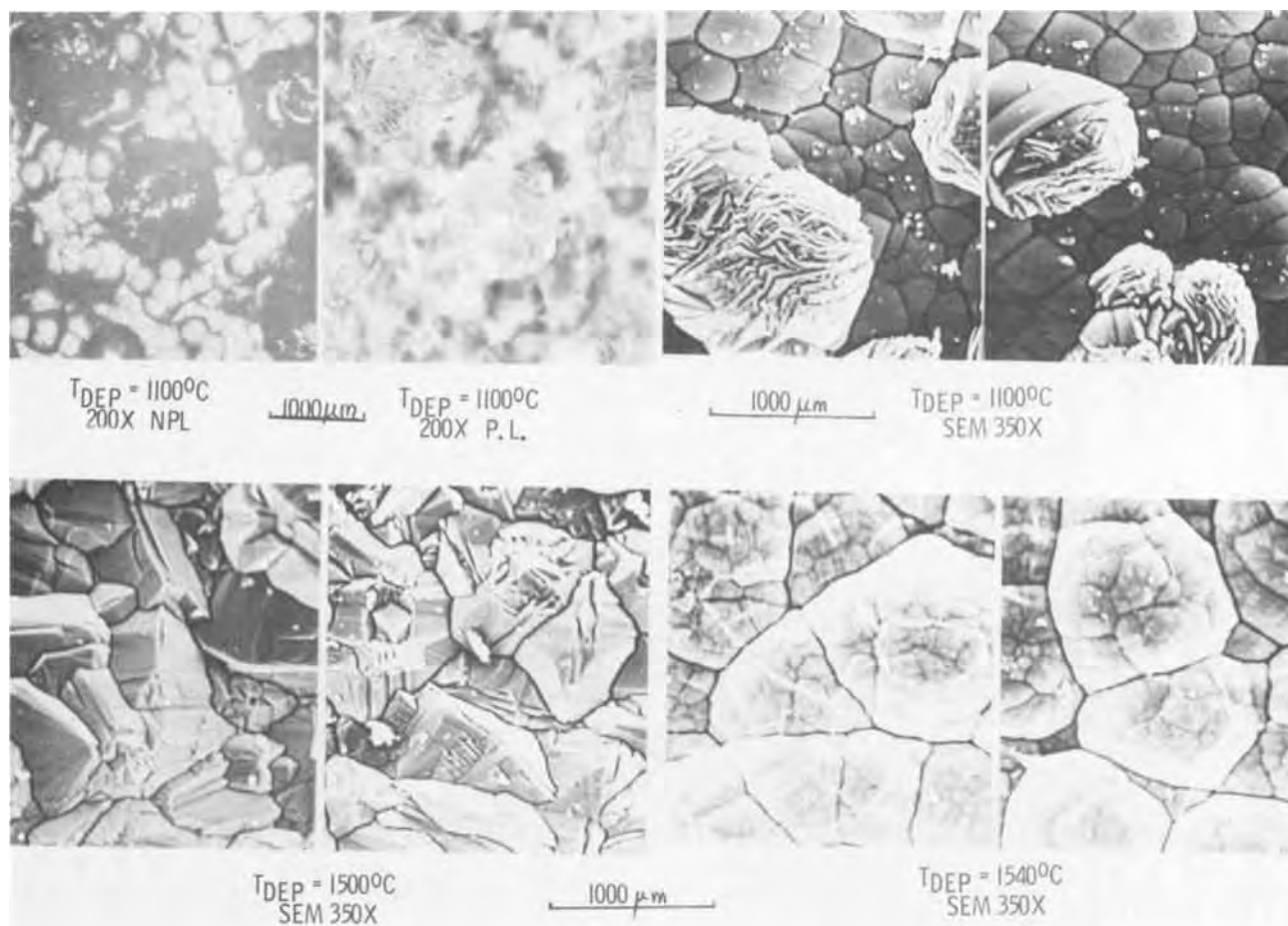


Fig. 1. Optical and scanning electron microscope views of as-deposited silicon nitride obtained from the chloride system. Adhering particles in upper right view appear to be precursors to crystalline material in lower left view.

The deposition of silicon nitride appears to differ in some respects from many other CVD processes in that solid deposition intermediates form immediately on mixing the reagents, rather than as a result of a gas phase reaction or decomposition which is controlled by chemical or diffusional kinetics. The situation is somewhat analogous to the deposition of boron nitride, but in that case, the last identifiable intermediate, B-trichloroborazole, is less stable and more volatile.

From the evidence presented in the literature (1,2), the stability of the silyl imide intermediate, at least up to about 1000°C, appears to be relatively high, while the crystallization rate is low, the formation of  $\alpha$ - $\text{Si}_3\text{N}_4$  requiring several hours to reach completion. Thus, unlike situations in which the deposition precursors are molecular species or fragments, silicon nitride is formed from precursor particles of considerably greater mass which require more time for complete decomposition and crystal formation. The latter can occur while the particles are still suspended in the gas phase, judging from the partially decomposed appearance of particles adhering to the surfaces of 1100°C deposits shown in Fig. 1. If intermediate concentrations are too high, the frequency with which they collide and grow in the gas phase, as well as the rate at which they strike and adhere to the substrate, may overbalance the rate at which particles attached previously can decompose and form crystalline material. Thus, despite temperature increases which tend to favor decomposition and crystallization, a vitreous material can be formed in the temperature range where crystalline deposits would otherwise be obtained.

Specimens of the by-products of both fluoride and chloride deposition experiments were collected from the furnace exhaust lines and examined briefly by means of infrared spectra, using the KBr pellet tech-

nique. In both cases, the specimens were somewhat contaminated with moisture during handling and had hydrolyzed to some extent. The respective ammonium halide salts were also present. The spectra showed the presence of ammonium ions and Si-O bonding as well as the respective ammonium halide ions. A sharp peak at about  $480\text{ cm}^{-1}$ , a frequency characteristic of Si-N stretching, may have been due to intermediates carried out of the furnace or to small silicon nitride particles already completely deaminated in the gas phase.

A specimen of the chloride system by-product was heated at 1450°C under flowing nitrogen (10 Torr) for 1 hr. This resulted in formation of elemental silicon, with no traces of  $\alpha$ - $\text{Si}_3\text{N}_4$ . Since traces of elemental silicon were occasionally found in x-ray diffraction patterns of crystalline deposits, it is possible that some disproportionation of the intermediate compound occurs during deposition of the nitride.

*X-ray studies.*—X-ray diffraction examination was carried out on powder specimens deposited at 1500°C from both chloride and fluoride mixtures. Both reaction systems yielded  $\alpha$ -silicon nitride. All experimentally determined d spacings and diffracted intensities compared favorably with the values listed in JCPDA tables (6) for  $\alpha$ -silicon nitride. There was no indication of noncrystalline or amorphous constituents in these deposits, in contrast to materials prepared at lower deposition temperatures (e. g., 1100°–1300°C).

X-ray diffractometry examination of thin (e. g., 0.8 mm) flat plates of both fluoride and chloride material showed some  $\alpha$ - $\text{Si}_3\text{N}_4$  reflections to be absent while others exhibited intensities greatly different from those obtained with randomly ordered powders of the same specimens. This is indicative of a degree of preferred orientation with respect to the



Table I. Principal lines and intensities of CVD  $\alpha$ -silicon nitride from chloride and fluoride deposition systems

$\alpha$ -Si <sub>3</sub> N <sub>4</sub> JCPDS (9-250)		I/h	Experimental (fluoride)		Experimental (chloride)	
d (Å)	hkl		d (Å)	I/h	d (Å)	I/h
6.690	100	8	—	—	—	—
4.320	101	50	4.33	100	4.33	100
3.880	110	30	3.88	100	3.90	2
3.370	200	30	3.37	9	3.36	9
2.893	201	85	2.89	48	2.89	70
2.823	002	5	—	—	2.82	32
2.599	102	75	2.59	35	2.59	80
2.547	210	100	2.54	28	2.54	29
2.320	211	60	2.31	25	2.32	20
2.283	112	8	2.27	5	2.28	8
2.244	300	5	—	—	—	—
2.158	202	30	2.16	65	2.16	28
2.083	301	55	2.08	38	2.08	13
1.937	220	2	—	—	—	—
1.884	212	8	1.88	44	1.84	8
1.864	310	8	1.86	5	—	—
1.806	103	12	—	—	1.81	15
1.771	311	25	1.77	22	1.77	5
1.751	302	2	—	—	—	—
1.637	203	8	1.63	3	1.64	5
1.596	222	35	1.60	26	1.60	24
1.552	312	2	—	—	—	—
1.542	320	5	—	—	—	—
1.507	213	8	1.51	5	1.51	6

deposition surface and has been noted by others (3). Table I lists the experimental relative peak intensities obtained with nickel-filtered copper radiation, for flat plates, parallel to the deposition substrate, and also includes the literature values for comparison. No corrections were made for polarization, absorption, etc. The data indicate that the (110) crystal planes of the fluoride deposits tend to be parallel to the substrate while the basal planes of the hexagonal unit cells (002) of the chloride deposits assume this orientation. It is not clear whether these orientations are the result of differences in the deposition chemistry of the two reaction systems, or if they are typical of all deposits obtained from these two processes.

**Optical properties.**—The region of transparency of polished crystalline  $\alpha$ -Si<sub>3</sub>N<sub>4</sub> was found to extend from 0.3 to 5.0  $\mu$ m, as shown by the transmittance data in Fig. 2 and 3. Other than visible color, little difference in optical transmittance characteristics was observed in deposits prepared using either silicon tetrachloride or tetrafluoride reactants in conjunction with ammonia. The polished deposits were translucent, although good imaging was obtained when the polished deposits were placed in contact with printed matter, as shown in Fig. 4. A quantitative measure of the degree of diffuse infrared scattering for specimens from the two reaction mixtures is given approximately by the differences in transmittance levels between the hemispherical and

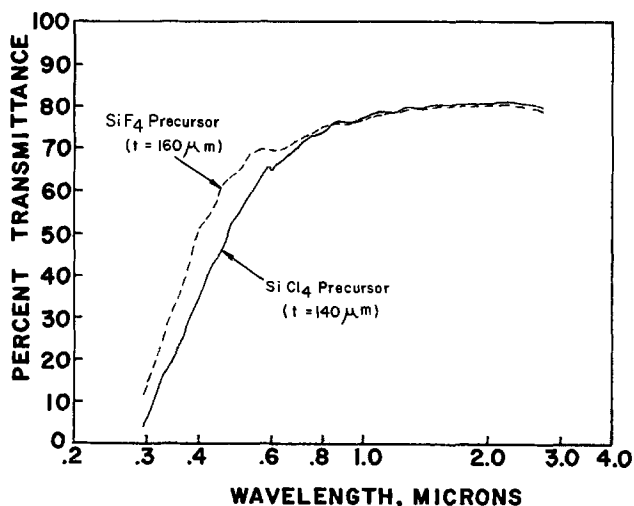


Fig. 2. Visible and near-infrared hemispherical transmission of polished silicon nitride deposits from both chloride and fluoride systems.

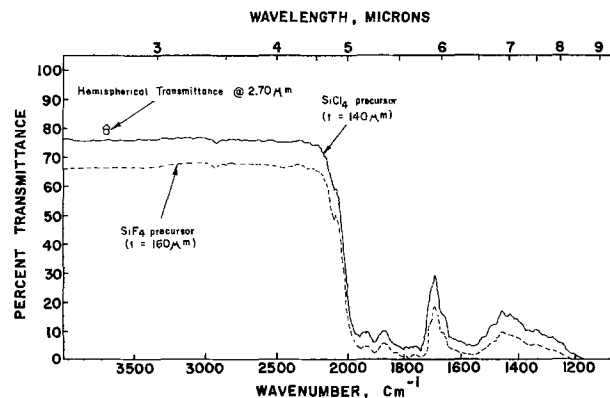


Fig. 3. Near-normal specular transmittance of polished silicon nitride deposits.

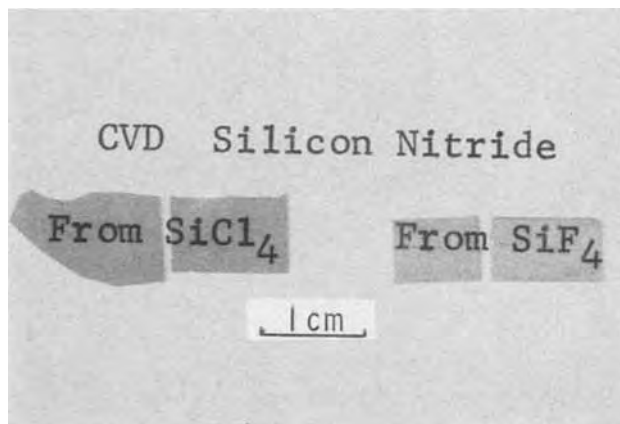


Fig. 4. Optically polished deposits from both fluoride and chloride systems; former is nearly water white transparent, latter is tan.

near normal specular data at 2.7  $\mu$ m, as shown in Fig. 3. A comparison of the specular reflectance spectra of the polished  $\alpha$ -Si<sub>3</sub>N<sub>4</sub> deposit (prepared from the chloride precursor) with that obtained from a polished specimen of hot-pressed  $\beta$ -Si<sub>3</sub>N<sub>4</sub> prepared by Norton Company (NC-132) is displayed in Fig. 5. Both modifications exhibit similar Reststrahlen peaks in the 9–12  $\mu$ m range. No attempt was made to analyze the detailed spectra, however; these differences are most likely related to crystallographic variations between the  $\alpha$ - and  $\beta$ -modifications of silicon nitride.

**Mechanical and oxidation tests.**—Preliminary oxidation and creep resistance data were obtained by

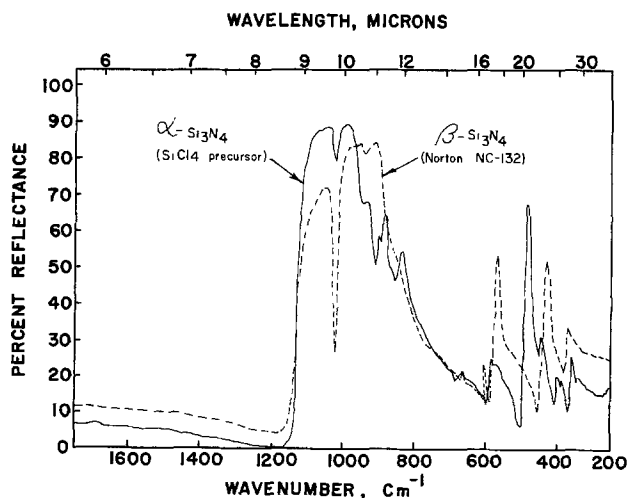


Fig. 5. Near-normal specular reflectance of CVD  $\alpha$ -Si<sub>3</sub>N<sub>4</sub> compared to hot-pressed  $\beta$ -Si<sub>3</sub>N<sub>4</sub>.

Rosolowski and Greskovich 7) using crystalline material prepared in this study from the chloride-ammonia system in the as-deposited condition. Creep at elevated temperatures was measured in air in three-point bending by supporting a piece of the silicon nitride, about  $2.5 \times 0.5$  cm, at its ends on silicon carbide knife edges, and suspending a weight across the center of the specimen on another knife edge. This apparatus was located in a furnace equipped with silica windows for temperature measurement as well as for photographic recording of beam deflections with time. Under the most severe conditions used, a  $69 \text{ MN/m}^2$  (10,000 psi) load at  $1560^\circ\text{C}$ , no measurable creep was observed after 198 hr at temperature. Assuming that a  $20 \mu\text{m}$  deflection had occurred, i.e., close to the minimum detectable movement, it was estimated that the upper limit of creep rate for this material was about  $1.6 \times 10^{-7} \text{ hr}^{-1}$ .

Preliminary estimates of oxidation resistance were made by maintaining as-deposited specimens at elevated temperatures in air with periodic removal from the furnace for weighing to determine the amount of silica formed (7). The specimens lay on a bed of silicon nitride powder during the experiments. The weight increase in each case was expressed in milligrams per square centimeter and the data plotted as a function of the square root of time in hours. Data obtained at  $1550^\circ\text{C}$  are shown in Fig. 6 and indicate a weight change of less than  $0.01 \text{ mg/cm}^2\text{-hr}^{-1/2}$ . Other specimens gave slightly higher rates at lower temperatures, probably because of greater surface roughness which made area calculations imprecise.

**Thermal stability.**—In order to evaluate the thermal stability of crystalline and vitreous deposits of silicon nitride under vacuum, as well as to assess qualitatively the degree of by-product entrapment, specimens were heated in a Knudsen cell between  $1400^\circ$  and  $2000^\circ\text{C}$  and the evolving gases analyzed by mass spectrometer. Crystalline materials, deposited from both fluoride and chloride systems at  $1500^\circ\text{C}$ , evolved only nitrogen, commencing ca.  $1450^\circ\text{-}1500^\circ\text{C}$  and ending ca  $1700^\circ\text{C}$ , probably through exhaustion of the specimen. A vitreous deposit prepared at  $1350^\circ\text{C}$  from the chloride system behaved similarly, although a much larger sample which evolved too much nitrogen to be measured also gave off relatively small amounts of both chlorine and silicon. By comparison to the latter case, vitreous boron nitride yielded considerably more ammonia, nitrogen, and chlorine as well as boron under similar circumstances (8). The silicon nitride deposits are evidently much "cleaner" than the respective boron nitride deposits despite the greater stability of its intermediate species.

A polished specimen of crystalline silicon nitride deposited at  $1500^\circ\text{C}$  showed evidence of intracrystal-

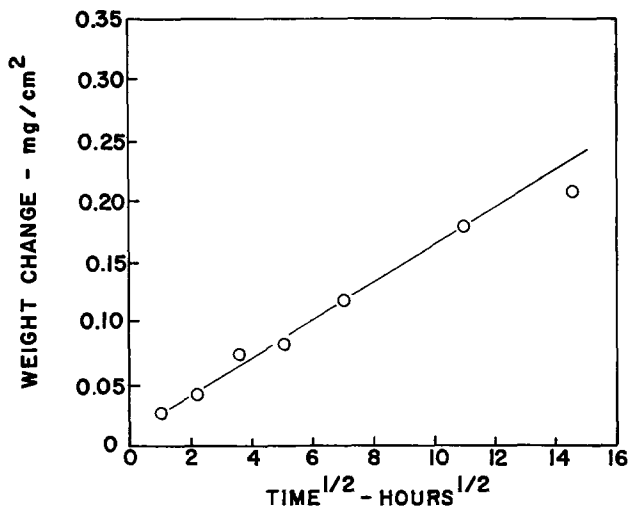


Fig. 6. Oxidation of CVD silicon nitride at  $1550^\circ\text{C}$  [Ref. (7)]

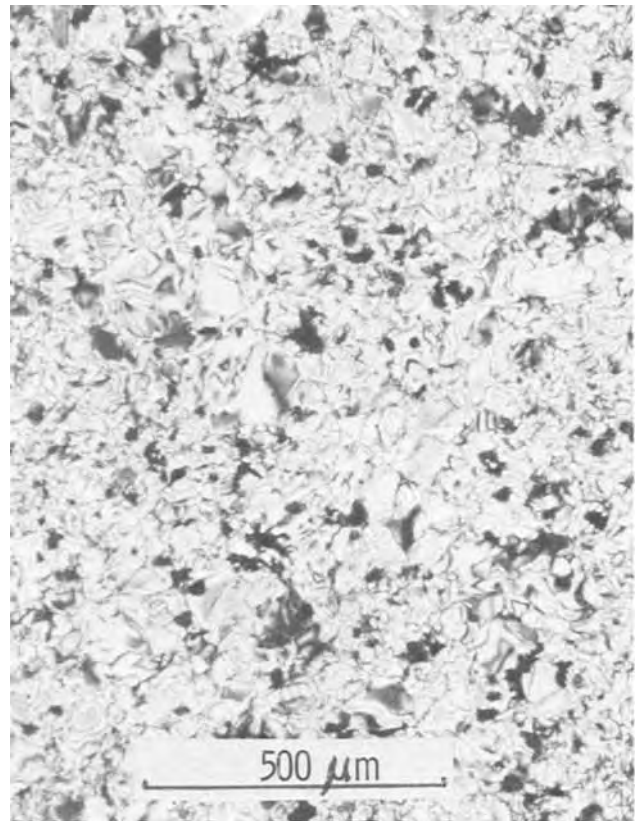


Fig. 7. Transmission microscope view of polished silicon nitride (PL).

line residual stresses in transmission micrographs as shown in Fig. 7. This heated specimen was placed on a silicon nitride platform and heated for 1 hr at  $1700^\circ\text{C}$  in a hydrogen-nitrogen mixture (1:5) at 1 atm. There was no change in the appearance of the specimen, nor any evidence of crystallographic transformation. A slight reduction in the  $1\text{-}5 \mu\text{m}$  region of the infrared transmittance spectrum was the only change produced. This is in agreement with other reports of the stability of very pure  $\alpha\text{-Si}_3\text{N}_4$  with respect to transformation to the beta-form (9). The vitreous material transformed to the alpha-form on heating at  $1600^\circ\text{C}$  and 10 Torr (nitrogen) but also decomposed sufficiently to produce strong  $\beta$ -silicon carbide lines as a result of reaction between the deposit or vaporizing species and the graphite substrate.

### Summary

Pure  $\alpha\text{-Si}_3\text{N}_4$  was deposited from mixtures of ammonia with silicon tetrachloride and tetrafluoride at reduced pressure and temperatures between  $1400^\circ$  and  $1500^\circ\text{C}$ . Vitreous or amorphous silicon nitride was obtained from the tetrachloride system below  $1400^\circ$  and above  $1500^\circ\text{C}$ , apparently as a result of excessive intermediate species formation and insufficient time for crystal formation.

Crystalline  $\alpha\text{-Si}_3\text{N}_4$  made by chemical vapor deposition is considerably more resistant to creep and oxidation in air than the hot-pressed materials which contain sintering additives.

Flat specimens from both reaction systems were able to be ground and polished to give transparent plates with relatively low intrinsic scatter. Optical properties were measured by transmission in the visible region and by both specular and hemispherical transmission and reflection in the infrared region. X-ray diffractometer measurements made on polished specimens indicated some degree of preferred orientation in both materials, although they differed regarding the direction of orientation.

### Acknowledgments

The authors gratefully acknowledge many helpful discussions with Dr. E. Feingold and Dr. M. J. Noone, as well as the experimental assistance of Mr. J. Yodsnuikis and Mr. N. Weiss.

Manuscript submitted Nov. 10, 1975; revised manuscript received June 7, 1976.

Any discussion of this paper will appear in a Discussion Section to be published in the June 1977 JOURNAL. All discussions for the June 1977 Discussion Section should be submitted by Feb. 1, 1977.

Publication costs of this article were assisted by General Electric Company.

### REFERENCES

1. M. Billy, *Ann. Chim. (Paris)*, **4**, 795 (1959); *C. R. Acad. Sci.*, **251**, 1639 (1960).
2. K. S. Mazdiyasi and C. M. Cooke, *J. Am. Ceram. Soc.*, **56**, 628 (1973).

3. F. Galasso, U. Kuntz, and W. J. Croft, *ibid.*, **55**, 431 (1972).
4. A. C. Airey, S. Clarke, and P. Popper, *Proc. Br. Ceram. Soc.*, **22**, 305 (1973).
5. S. Wild, P. Grieseson, and K. H. Jack, in "Special Ceramics," Vol. 5, P. Popper, Editor, pp. 385-395, British Ceramic Research Association, London (1972).
6. Powder Diffraction File, No. 9-250, Joint Committee on Powder Diffraction Standards, Swarthmore, Pennsylvania.
7. J. H. Rosolowski and C. D. Greskovich, "Ceramic Sintering," Semi-Annual Technical Report, ARPA Order No. 2698, Program No. 4D10, Advanced Research Projects Agency, Office of Naval Research, Arlington, Virginia (Oct. 1974).
8. J. J. Gebhardt, in "Chemical Vapor Deposition," Fourth International Conference, G. F. Wakefield and J. M. Blocher, Jr., Editors, pp. 460-472, The Electrochemical Society Softbound Symposium Series, Princeton, New Jersey (1973).
9. H. F. Priest, F. C. Burns, G. L. Priest, and E. C. Skaar, *J. Am. Ceram. Soc.*, **56**, 395 (1973).

## Metallurgical Structure of Be-Au and Si-Au Ohmic Contacts to GaP

W. A. Brantley,<sup>1</sup> V. G. Keramidis,\* B. Schwartz,\* M. H. Read, and P. M. Petroff

Bell Laboratories, Murray Hill, New Jersey 07974

Ohmic contacts to p- and n-type GaP can be obtained with Be-Au and Si-Au metallizations, respectively (1, 2). While satisfactory electrically for use in the fabrication of GaP LED's, little information is available regarding the metallurgical structure of these contacts. Recently, secondary ion mass spectrometry (SIMS) experiments have shown that extensive gallium migration and some phosphorous migration through the contact metallizations occur during the alloying<sup>2</sup> process; in addition, the presence of intermetallic compounds within the alloyed contacts was reported (3). In this note, the identification of these intermetallic compounds by transmission electron microscopy (TEM) and x-ray diffraction (XRD) is discussed in more detail, along with results from other experiments to elucidate the complex metallurgical structure of alloyed Be-Au and Si-Au contacts to GaP.

### Specimen Preparation

Metallizations were deposited by electron-gun evaporation over the full surfaces of GaP chips. The p-contact metallization consisted nominally of a 5000Å Be-Au layer evaporated from an alloy source having ~1 w/o Be in Au, followed by a 10,000Å gold film. These films were deposited on {111} P faces of p-type layers of GaP p/n junction material grown by liquid phase epitaxy (LPE) or p-type liquid encapsulated Czochralski (LEC) GaP, both having  $N_A - N_D \approx 5 \times 10^{17} \text{ cm}^{-3}$ . The n-contact metallizations consisted nominally of a 5000Å Si-Au layer evaporated from an alloy source having ~3 w/o Si in Au, followed by a 10,000Å gold film. These latter films were deposited on {111} Ga faces of n-type LEC GaP having  $N_D - N_A \approx 3 \times 10^{17} \text{ cm}^{-3}$ . Ohmic contacts were obtained by heating specimens at 600°C for 5 min in a N<sub>2</sub>-H<sub>2</sub> atmosphere.

\* Electrochemical Society Active Member.

<sup>1</sup> Present address: Department of Dental Materials, School of Dentistry, Marquette University, Milwaukee, Wisconsin 53233.

<sup>2</sup> The term "alloying" is used here to denote any heat-treatment for achieving ohmic contacts.

Key words: compound semiconductors, intermetallic compounds, ohmic contacts.

### Chemical Analyses of Film Compositions

The concentrations of beryllium and silicon in the as-deposited Be-Au and Si-Au layers were determined by atomic absorption spectrometry (AAS). For these analyses, Si-Au and Be-Au films, nominally 10,000Å thick, were deposited on sapphire substrates, and subsequently stripped from the substrates by aqua regia for examination. The AAS results indicated that the Be: Au ratio in the deposited film is approximately that of the starting alloy source. However, the Si: Au ratio for the film can be as much as an order of magnitude lower than in the alloy source, as a consequence of the higher vapor pressure of gold compared to silicon (4).

### Transmission Electron Microscopy Observations of Metallization-GaP Interfaces

The region near the metallization-GaP interface for the alloyed p- and n-contacts was examined by TEM to search for intermetallic compounds, as well as to investigate the structure of the metallization and the dislocation density in the GaP. For these specimens, the GaP substrates were mechanically polished using 0.3 μm Al<sub>2</sub>O<sub>3</sub> particles; subsequent thinning of both the GaP substrates and the alloyed films was accomplished by ion milling with 6 keV Ar<sup>+</sup> ions.

A bright-field electron micrograph for a region near the interface between the alloyed p-contact and GaP is illustrated in Fig. 1(a). Electron diffraction patterns, as shown in Fig. 1(b), indicate the presence of the β (~21 a/o Ga) and/or β' (~23 a/o Ga) phases (5) between gold and gallium, in addition to polycrystalline gold. Although β' is the room temperature equilibrium phase, β' and β have similar diffraction patterns (5) and both phases may be present. The satellite spots around some primary diffraction spots in Fig. 1(b) suggest (6) that the gold-gallium phase(s) initially form(s) an epitaxial layer with GaP, followed by a polycrystalline layer. These gold-gallium crystallites appear as bright spots in the dark-field electron micrograph of Fig. 1(c), corresponding to the indicated diffraction ring in Fig. 1(b). Similar micro-

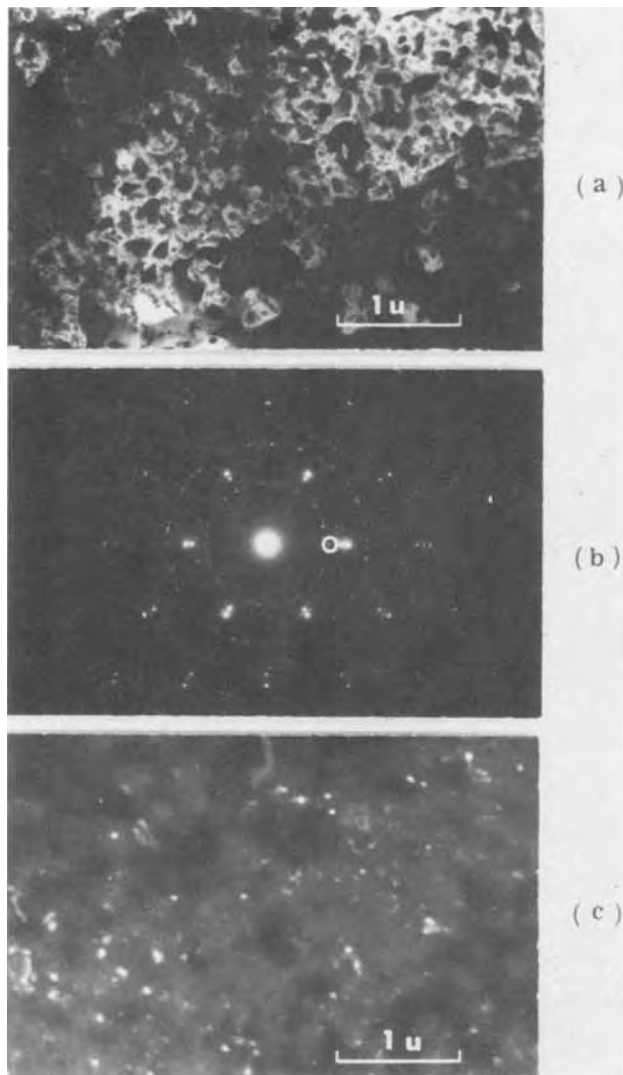


Fig. 1. (a) Bright-field electron micrograph of a region near the interface for the alloyed p-contact on GaP. (b) Electron diffraction pattern from the region of Fig. 1. (c) Dark-field electron micrograph corresponding to the first diffraction ring (indicated by the circle) in (b) for the  $\beta$  phase between gold and gallium.

structural results to those in Fig. 1 were observed by TEM for the alloyed n-contact; gold and the  $\beta$  and/or  $\beta'$  phase in the Au-Ga system again were the only phases near the metallization-GaP interface. The dislocation density detected by TEM in the GaP substrates near the interface was in the low  $10^4 \text{ cm}^{-2}$  range; thus, no interfacial region of high dislocation density is generated by the contact alloying process.

#### X-Ray Diffraction Studies

To complement the TEM analyses, alloyed contacts also were examined by XRD for the presence of intermetallic compounds. A wide film Debye-Scherrer technique was employed, utilizing Cu  $K\alpha$  radiation incident on the top surface of the metallization at an angle of  $\sim 16^\circ$  (7). In contrast to the TEM observations, no evidence of intermetallic compounds in the p- and n-contacts was detected by XRD, indicating that intermetallic compounds are not present in large concentrations near the surface. (The strongest lines for the  $\beta$  and  $\beta'$  Au-Ga phases coincide with weak gold diffraction lines from residual Cu  $K\beta$  radiation.)

In order to facilitate detection of intermetallic compounds, alloyed 5000Å thick Be-Au and Si-Au films on GaP also were investigated, where the 10,000Å gold overlay was omitted. For these specimens, a profusion of XRD lines due to intermetallic compounds was observed. Some preferred orientation for these phases was evident from the appearance (7) of the diffraction arcs. No significant differences for the XRD lines were noted when these latter films were alloyed for 30 min instead of 5 min. In all cases, the diffraction lines for gold were weak, indicating that the gold had principally formed intermetallic compounds.

For the Si-Au films alloyed with GaP, the strongest lines could generally be assigned to the  $\beta$  and/or  $\beta'$  Au-Ga phases. The positions of other lines suggested that the  $\alpha'$  ( $\sim 13$  a/o Ga) (5), AuGa, and AuGa<sub>2</sub> phases also might be present. [The interplanar spacings for the  $\gamma$  phase, which contains  $\sim 30$  a/o Ga, were not reported in Ref. (5).] No evidence for SiP<sub>2</sub> in these films was found.

The situation for the Be-Au films alloyed with GaP is more complicated than for the Si-Au films because beryllium and gold form a series of intermetallic compounds (8) whereas no intermediate phases exist between gold and silicon. The strongest XRD lines for these specimens could be assigned to Au<sub>3</sub>Be, while Au<sub>2</sub>Be also may be present; no evidence was found for AuBe and AuBe<sub>5</sub>. The presence of the Au-Be phases results in less certain identification for Au-Ga intermetallics because of similar line positions; the  $\beta$  and/or  $\beta'$  Au-Ga phases probably were present in these films. In addition, Be<sub>3</sub>P<sub>2</sub> also may form during alloying, but identification is difficult because of the very few relatively strong XRD lines for this compound.

SIMS experiments (3) could not provide support in interpreting the XRD results, such as whether or not Be<sub>3</sub>P<sub>2</sub> forms during the alloying process for p-contacts. At present, absolute concentrations for the various chemical species within the metallizations cannot be established by SIMS due to the lack of appropriate chemical standards for comparison and possible differential sputtering rates. (For example, beryllium can be in solid solution with gold, in intermetallic compounds, or segregated at grain boundaries in the films.) Attempts to obtain depth profiles for beryllium and silicon through alloyed p- and n-contacts using SIMS were unsuccessful because nonplanar sputtering fronts occur for deep "burns," due to gold globules lying on the film surfaces. Alternatively, accurate depth profiles could not be obtained by sputtering through the unmetallized back side of the GaP, because of uncertainties in the sputtering rate for the long duration burn required.

The formation of intermetallic compounds during alloying provides one potential source of stress in the semiconductor device and may adversely affect reliability. Using an x-ray diffraction lattice curvature measurement technique (9), an approximate value of  $\sim 3 \times 10^9 \text{ dyne/cm}^2$  was determined for the stress in a p-contact which had been alloyed with GaP at 600°C. The maximum value of the stress in the GaP at the interface with the contact (neglecting stress concentrations at the edges of the metallization) was  $\sim 7 \times 10^7 \text{ dyne/cm}^2$  ( $\sim 1 \times 10^3 \text{ psi}$ ), considerably lower than the stress in the contact because of the ratio of contact thickness to substrate thickness (10). No evidence of freshly generated dislocations in GaP was revealed near the periphery of alloyed p-contact dots by conventional (11) etching solutions. The stresses associated with ohmic n-contacts are expected to be of similar magnitudes.

It has not been possible from scanning electron microscopy and optical microscopy observations on numerous specimens to assess unambiguously the relative contributions of solid-state diffusion and/or formation of a liquid phase during the contact alloying. Efforts to delineate an alloyed region on a GaP cleavage face by

photoetching with HF:H<sub>2</sub>O<sub>2</sub> or prolonged chemical etching with aqua regia were unsuccessful. However, the absence of detectable (by XRD) amounts of intermetallic compounds in the outer portions of the alloyed n- and p-contacts suggests that dissolution of the metallizations during the alloying process may be principally confined to regions near the interface with GaP.

#### Acknowledgments

The authors are grateful to T. Y. Kometani for performing the atomic absorption spectrometry measurements, to T. T. Sheng for assistance with the transmission electron microscopy, to G. A. Rozgonyi for performing the x-ray diffraction stress measurement, and to G. W. Kammlott for performing the scanning electron microscopy. Special thanks are extended to C. R. Paola for helpful comments and extensive assistance regarding the deposition procedures.

Manuscript submitted Sept. 12, 1975; revised manuscript received June 12, 1976.

Any discussion of this paper will appear in a Discussion Section to be published in the June 1977 JOURNAL. All discussions for the June 1977 Discussion Section should be submitted by Feb. 1, 1977.

Publication costs of this article were assisted by Bell Laboratories.

#### REFERENCES

1. N. E. Schumaker and G. A. Rozgonyi, *This Journal*, **119**, 1233 (1972).
2. J. M. Ralston, *J. Appl. Phys.*, **44**, 2635 (1973).
3. W. A. Brantley, B. Schwartz, V. G. Keramidas, G. W. Kammlott, and A. K. Sinha, *This Journal*, **122**, 434 (1975).
4. See L. I. Maissel and R. Glang, Editors, "Handbook of Thin Film Technology," McGraw-Hill, New York (1970) and K. L. Chopra, "Thin Film Phenomena," McGraw-Hill, New York (1969).
5. C. J. Cooke and W. Hume-Rothery, *J. Less-Common Met.*, **10**, 42 (1966).
6. P. B. Hirsch, A. Howie, R. B. Nicholson, D. W. Pashley, and M. J. Whelan, "Electron Microscopy of Thin Crystals," Chap. 6, Butterworths, Washington (1965).
7. M. H. Read and D. H. Hensler, *Thin Solid Films*, **10**, 123 (1972).
8. M. Hansen and K. Anderko, "Constitution of Binary Alloys," p. 187, McGraw-Hill, New York (1958).
9. G. A. Rozgonyi and T. J. Ciesielka, *Rev. Sci. Instrum.*, **44**, 1053 (1973).
10. R. J. Jaccodine and W. A. Schlegel, *J. Appl. Phys.*, **37**, 2429 (1966).
11. R. H. Saul, *This Journal*, **115**, 1184 (1968).

## Brief Communications



### Defect Chemistry of BaTiO<sub>3</sub>

N.-H. Chan and D. M. Smyth\*

Materials Research Center, Lehigh University, Bethlehem, Pennsylvania 18015

We have been studying the defect chemistry of BaTiO<sub>3</sub> by measurement of the equilibrium electrical conductivity by a four-probe d-c technique as a function of temperature (600°-1000°C), oxygen pressure (10<sup>-24</sup>-1 atm), Ba/Ti ratio (0.9950-1.0000), and added impurities. The samples are polycrystalline bars, 98% dense, sintered from powders prepared by calcination of a homogeneous glassy solid obtained by polymerization of an organic solution in which the cationic constituents have been dissolved in precisely weighed amounts (1). The oxygen activities were obtained by precision-mixed Ar-O<sub>2</sub> (high pressure range), CO-CO<sub>2</sub> (low pressure range), and by means of an electrochemical oxygen pump and oxygen activity detector based on CaO-doped ZrO<sub>2</sub> for the midrange of pressures (2).

The results shown in Fig. 1 are typical of acceptor-doped and undoped material, and are very similar to previously reported results (3-5). This sample contained 134 ppm (atomic) of added aluminum as a Ti-site acceptor. We believe that all results reported to date have been dominated by acceptor impurities in the near-stoichiometric region, whether deliberately added or not. This reflects the greater natural abundance of acceptor-type impurities, e.g., alkali metals on Ba sites or Al, Mg, Fe on Ti sites, compared with donor-type impurities, e.g., rare earths or Th on Ba sites or Nb, Ta, W on Ti sites; and the very small con-

centration of intrinsic ionic disorder to be expected because of the highly unfavorable nature of such defects as Ba<sub>1</sub>·|O<sub>1</sub><sup>''</sup>, O<sub>1</sub><sup>''</sup>, and V<sub>Ti</sub><sup>'''</sup>.

The conductivity minima correspond to the completely compensated state, neglecting mobility differences, and their temperature dependence has been shown to correspond closely to the optical bandgap

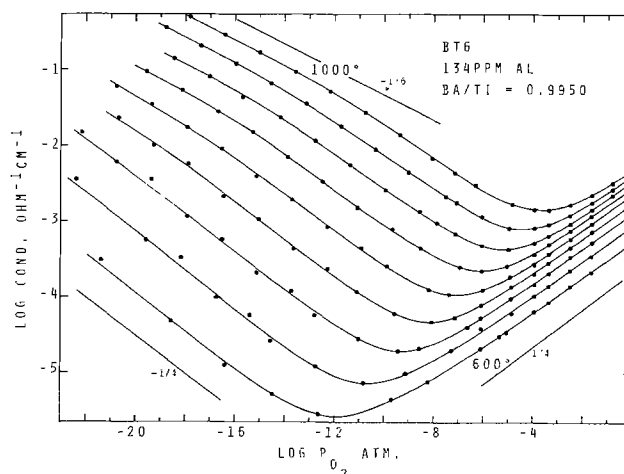
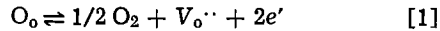


Fig. 1. Equilibrium conductivity of acceptor-doped BaTiO<sub>3</sub>. Temperatures at 50° intervals. Lines having ideal slopes are indicated for reference.

\* Electrochemical Society Active Member.  
Key words: barium titanate, stoichiometry, conductivity, donor-doped, acceptor-doped.

of BaTiO<sub>3</sub> (3-5). The results in the lower pressure range are in close accord with the reduction reaction



whose mass-action expression

$$[\text{V}_o^{\bullet\bullet}]n^2 = K_1 p_{\text{O}_2}^{-1/2} \quad [2]$$

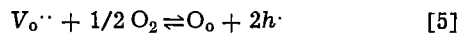
combined with the charge-neutrality condition

$$[A'] \approx 2[\text{V}_o^{\bullet\bullet}] \quad [3]$$

leads to  $\sigma \propto p_{\text{O}_2}^{-1/4}$  below the minima, where  $A'$  is an unknown or added acceptor impurity,  $\sigma$  is the electronic conductivity, and  $p_{\text{O}_2}$  the oxygen pressure. At the lowest  $p_{\text{O}_2}$  and highest temperature the pressure dependence changes to  $\sigma \propto p_{\text{O}_2}^{-1/6}$  as Eq. [1] becomes the dominant source of defects and the charge neutrality condition changes to

$$n \approx 2[\text{V}_o^{\bullet\bullet}] \quad [4]$$

At pressures above the conductivity minima, oxygen is easily added to the lattice by filling the impurity-related  $\text{V}_o^{\bullet\bullet}$



The mass-action expression for Eq. [5] combined with Eq. [3] gives  $\sigma \propto p_{\text{O}_2}^{1/4}$  as observed, as long as only a minor fraction of the impurity-related  $\text{V}_o^{\bullet\bullet}$  is filled. The ready availability of oxygen vacancies explains the unusual ease with which the material accepts a stoichiometric excess of oxygen, as indicated by the anomalously low temperature dependence of conductivity in the oxygen-excess region near 1 atm.

Compared with undoped samples, the acceptor-doped material with Ba/Ti = 0.9950 behaves as predicted by the combination of Eq. [2] and [3]. The conductivity is slightly higher above the conduction minima, and slightly lower below the minima, and the minima occur at lower  $p_{\text{O}_2}$ . The magnitude of these changes indicates that the net acceptor content of the doped sample is about twice that of the undoped sample. In the region where  $\sigma \propto p_{\text{O}_2}^{-1/6}$ , the conductivity is independent of impurity content, confirming that this region (and only this region) represents the intrinsic behavior of BaTiO<sub>3</sub>.

Samples prepared with Ba/Ti = 1.0000 rather than 0.9950 behave very similarly. It is concluded that the defects related to BaO deficiency, assumed to be  $\text{V}_{\text{Ba}}''$  and  $\text{V}_o^{\bullet\bullet}$ , must be almost entirely associated into defect complexes of the type  $(\text{V}_{\text{Ba}}''\text{V}_o^{\bullet\bullet})$ . Otherwise reaction [1] could not become the dominant source of  $\text{V}_o^{\bullet\bullet}$  at low pressures and the relationship  $\sigma \propto p_{\text{O}_2}^{-1/6}$  would not be observed.

The behavior of a donor-doped sample is shown in Fig. 2. Instead of a series of conductivity minima, there is an extensive region where the conductivity is nearly independent of temperature and  $p_{\text{O}_2}$ . We interpret this as indicating a region of impurity-controlled electron concentration

$$[\text{Nb}_{\text{Ti}}'] \approx n \quad [6]$$

where  $[\text{Nb}_{\text{Ti}}']$  represents the excess donor concentration. At very low pressures, the conductivity values and pressure dependence agree well with those of undoped and acceptor-doped samples, indicating a region of impurity-insensitive behavior.

The drop in conductivity as the oxygen pressure approaches 1 atm is attributed to a change from electronic compensation of the excess donor, as in Eq. [6], to compensation by an oxygen-excess ionic defect, most likely  $\text{V}_{\text{Ba}}''$

$$[\text{Nb}_{\text{Ti}}'] \approx 2[\text{V}_{\text{Ba}}''] \quad [7]$$

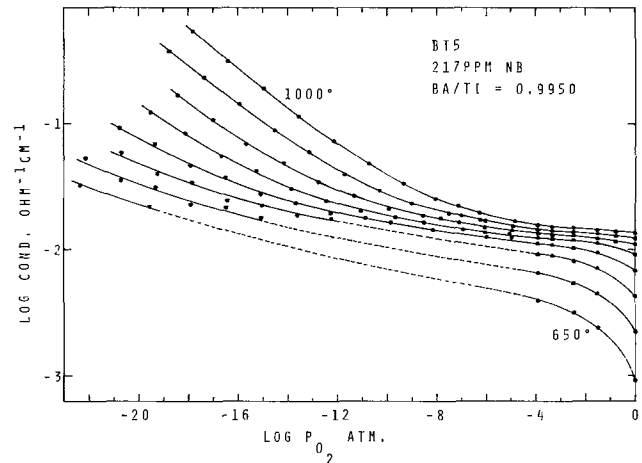
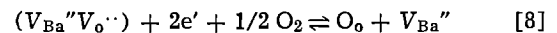


Fig. 2. Equilibrium conductivity of donor-doped BaTiO<sub>3</sub>. Temperatures at 50° intervals.

These could be generated by the filling of the  $\text{V}_o^{\bullet\bullet}$  part of the BaO-deficient defect complex



leading to the mass-action expression

$$\frac{[\text{V}_{\text{Ba}}'']}{[(\text{V}_{\text{Ba}}''\text{V}_o^{\bullet\bullet})]n^2} = K_3 p_{\text{O}_2}^{1/2} \quad [9]$$

As long as [6] is valid,  $[\text{V}_{\text{Ba}}'']$  will increase as  $p_{\text{O}_2}^{1/2}$ ; when [7] becomes valid,  $n$  will begin to decrease as  $p_{\text{O}_2}^{-1/4}$ , approximately as observed.

Over a considerable range of intermediate  $p_{\text{O}_2}$ , the donor-doped samples equilibrate with the ambient much more slowly than acceptor-doped or undoped samples, even when BaO deficient. Thus the BaO deficiency does not lead to mobile defects which can contribute to rapid changes in oxygen content. This is in accord with the hypothesis of association of the defects related to BaO deficiency. An association enthalpy of 2 eV would be adequate to provide the degree of defect association required by the above model. This does not seem unreasonable for doubly charged defects such as  $\text{V}_{\text{Ba}}''$  and  $\text{V}_o^{\bullet\bullet}$  on adjacent lattice sites, when it is recalled that the association enthalpies for singly charged defects in the alkali halides, such as  $(\text{Sr}_{\text{Na}}'\text{V}_{\text{Na}}')$  and  $(\text{V}_{\text{Na}}'\text{V}_{\text{Cl}}')$  are known to be about 0.5 and 1.0 eV, respectively. The latter defect involves adjacent lattice sites and is thus the closer analogue.

### Acknowledgments

This work was supported by NSF Grant DMR74-21095.

Manuscript submitted June 3, 1976; revised manuscript received June 22, 1976.

Any discussion of this paper will appear in a Discussion Section to be published in the June 1977 JOURNAL. All discussions for the June 1977 Discussion Section should be submitted by Feb. 1, 1977.

Publication costs of this article were assisted by Lehigh University.

### REFERENCES

1. M. Pechini, U.S. Pat. 3,330,697 (1967).
2. Y. K. Agrawal, D. W. Short, R. Gruenke, and R. A. Rapp, *This Journal*, **121**, 354 (1974).
3. S. A. Long and R. N. Blumenthal, *J. Am. Ceram. Soc.*, **54**, 515 (1971); *ibid.*, **54**, 577 (1971).
4. N. G. Eror and D. M. Smyth, Submitted to *ibid.*
5. A. M. J. H. Seuter, *Philips Res. Rep., Suppl.* **3** (1974).

# Structural Study of the Sunlight Absorber

S. Yamaguchi\*

National Institute for Researches in Inorganic Materials, Sakura-mura, Niihari-gun, Ibaraki-ken 300-31, Japan

A preliminary examination was conducted with a specimen of the sunlight absorber which is in practical use: a copper plate whose surface has been blackened by oxidation. The blackening of the surface was carried out by immersing it in an aqueous solution of sodium chlorite ( $\text{NaClO}_2$ ) at  $10^\circ\text{C}$  whose concentration was about 10% by weight. The black, mat surface produced in this way was investigated in terms of electron reflection. The diffraction pattern observed from the specimen is shown in Fig. 1. It can be noted in this figure that the reflections appear distinct which correspond to a uniform dispersion of  $\text{CuO}$  crystallites (see Table I). The mean particle size of the crystallites is estimated to be about  $500\text{\AA}$  from the half-value width of the reflections. It is of interest that this particle size is smaller than the wavelength of the sunlight. It can also be noticed in Fig. 1 that the (020) reflection from the  $\text{CuO}$  crystals shows a preferred orientation whose fibrous axis lies nearly perpendicular to the substrate face.

The appearance of the black surface in question was closely akin to that of platinum sponge, so far as the velvetlike matted darkness is concerned. It was, therefore, reasonable to reexamine a typical platinum black in terms of electron diffraction.

A porous spongy layer of platinum was prepared in the following way. The fine particles of platinum were deposited on a smooth metal surface by hydrothermally decomposing at  $130^\circ\text{C}$  an aqueous solution of  $\text{K}_2\text{PtCl}_4$  whose concentration was 0.1 mole/liter (2). The deposit obtained looked quite black and mat, which gave the electron reflection pattern shown in Fig. 2. This pattern corresponds to an evenly dispersed state of the platinum particles whose mean size is about  $500\text{\AA}$ . In Fig. 2 the reflections are relieved against the low background. This is due to the fact that the crystal particle size is not only uniform, but it is also suitable for a coherent penetration of the electrons applied. These observations are similar to those from the blacked copper specimen.

The black, mat surface of platinum could be distinguished from a lustrous mirror surface in terms of the electron reflection. Figure 3 was observed from the latter surface. In this figure, the reflections are blurred and the background is very high. These findings are characteristic of an amorphous and fluidal Beilby surface layer. Compare Fig. 2 with Fig. 3. From these experimental results one can infer the surface structure of the sunshine absorber as illustrated in Fig. 4.

\* Electrochemical Society Active Member.

Key words: sunlight absorber, cupric oxide, platinum sponge, blackbody, alumilite.



Fig. 1. Electron reflection pattern observed from the blacked surface of copper which is used practically as a sunshine absorber. The reflections correspond to those of monoclinic  $\text{CuO}$ . The (020) reflection shows a preferred orientation in relation to the substrate face. Wavelength of the electrons =  $0.0304\text{\AA}$ . Distance between the specimen and the screen = 50 cm.

Table I. Result of the analysis of Fig. 1

$d$ (Å)*	hkl	$I^{**}$
2.75	110	2
2.53	002, $\bar{1}11$	10
2.33	111, 200	10
1.94	112, 202	3
1.82	112	3
1.67	020	5
1.55	202	4
1.45	$\bar{1}13$	4
1.38	022, $\bar{3}11$	8
1.35	220	7

\* Interplanar spacings corresponding to the reflections in Fig. 1.

\*\* Reflection intensities in arbitrary unit.

These values measured agree with the known data of monoclinic  $\text{CuO}$  whose lattice constants are  $a_0 = 4.68$ ,  $b_0 = 3.43$ ,  $c_0 = 5.13\text{\AA}$ ,  $\beta = 99^\circ 28'$ ,  $C2/c$  (1).

Within the porous sponge there are found labyrinths for the incident sunlight (see Fig. 4). Since each particle situated at the sponge surface is smaller than the wavelength of the light, the incident rays are not reflected at the surface, but diffracted from there into the interior of the sponge.

In the following experiment, it is demonstrated by the aid of a physical specimen that the surface as composed of parts smaller than the wavelength of sunlight appears completely dark, labyrinths for the light being beneath the surface.

About 500 sewing needles, with pointed ends smaller than the light wavelength, were tied up tightly into a bundle. The dimensions of the needles employed are shown in Fig. 5. The surface of the prepared needle bundle is characterized by an extreme roughness. The sunlight falling nearly perpendicular to the surface of the bundle cannot be reflected there, but is diffracted into the interior of the bundle, insofar as the tips of the constituent needles are smaller than the light

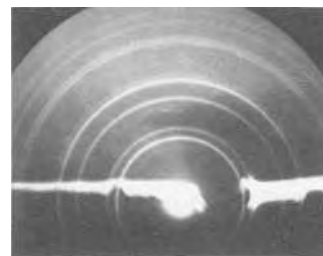


Fig. 2. Diffraction pattern from the platinum sponge. The reflections of Pt appear distinct, and the background is low. Electron wavelength =  $0.0380\text{\AA}$ .

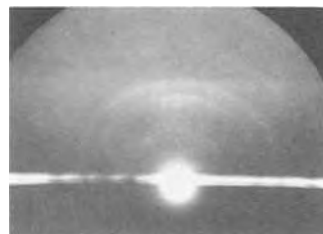


Fig. 3. Reflection pattern from a mirror surface of platinum. Reflections are blurred, and the background is high. Compare this figure with Fig. 2. Electron wavelength =  $0.0315\text{\AA}$ .



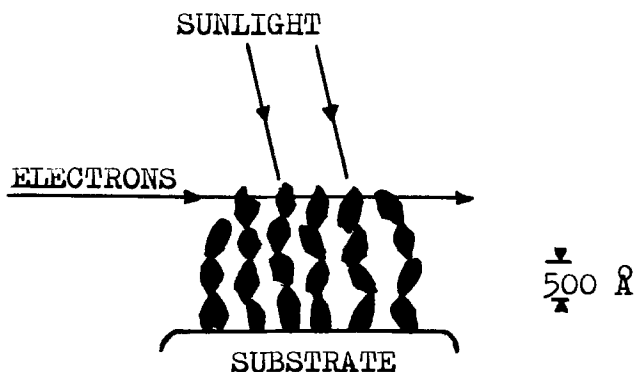


Fig. 4. Spongy state formed on the metal substrate, which serves as a sunlight absorber. The size of the particles constructing the sponge is about  $500\text{Å}$  so that it is smaller than the sunlight wavelength. The incident light is not reflected at the sponge face, but is diffracted there and then runs into the sponge interior. The electrons applied are able to coherently penetrate the crystallites of the  $500\text{Å}$  size.

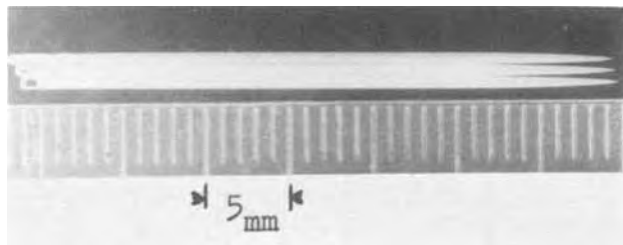


Fig. 5. The dimensions of the sewing needles employed for preparing the Planck's black body are seen here.

wavelength. The diffracted rays are repeatedly reflected at the lateral mirror faces of the needles, and finally they are completely absorbed into the bundle. It is of interest that the lateral faces of the needles are not transparent for the light. The behavior of the needle bundle, when exposed to the direct rays of the sun, is shown in Fig. 6 where it can be noticed that the surface of the bundle looks blacker than its shadow. The passages of the rays in the needle bundle are illustrated in Fig. 7 (3).

With the help of the needle bundle, this experiment amounts to a black-body simulation of the blacked copper plate and of the platinum black in the present study. The blacked copper plate is truly an able sunlight absorber, but it has been proved to weather in wet, polluted air. In fact, it has been found that

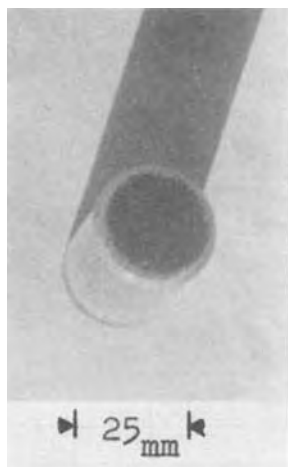


Fig. 6. A bundle of the sewing needles under the sun. The face of the bundle looks blacker than the shadow.

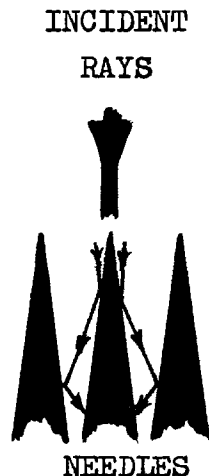


Fig. 7. Illustrating the diffraction of the light rays falling upon the face of the needle bundle.

verdigris is formed on the plate used over one year. In order to overcome this disadvantage, the corrosion-resisting surfaces with the prescribed geometric structure were produced on steel and aluminum plates.

A rolled plate of Cr-Mo-Ti steel (Cr: 18, Mo: 1, Ti: 0.4) was utilized as the material for sunshine absorber. The surface of the plate was oxidized in an acidic sodium dichromate solution ( $\text{Na}_2\text{Cr}_2\text{O}_7 \cdot 2\text{H}_2\text{O}$ : 200 g/liter,  $\text{H}_2\text{SO}_4$ : 600 g/liter) at  $100^\circ\text{C}$  for 20 min. The surface obtained in this way looked mat as well as black. According to the investigation by means of electron reflection, this surface was composed of the particles of the spinel type iron oxide which were regularly oriented against the substrate face and whose mean size was about  $500\text{Å}$ . These circumstances were analogous to those in the case of the blacked copper plate. The thermal efficiency of the blacked steel plate as a sunlight absorber was inferior to that of the copper plate, but the former plate was superior to the latter one in corrosion resistance. The surface of a plate of the eutectic aluminum alloy that contained silicon by 7 weight percent (w/o) was oxidized at  $10^\circ\text{C}$  by an anodic process with a current density of  $2\text{ A/dm}^2$ . The bath employed for the electrolysis consisted of oxalic acid and sulfuric acid whose concentrations were 2.4 and 0.14 w/o, respectively. After having experienced the anodic oxidation, the anode was treated with a boiling water in order to mask its surface with a stable böhmite film. The surface obtained in this way looked black, mat, and spongelike, similar to the platinum black. This alumilite plate could be utilized as a sunlight absorber, its thermal efficiency approaching that of the blacked copper. It should be underlined that aluminum is not only a cheaper and lighter material than copper, but it is also more plastic than steel.

#### Acknowledgments

The author thanks Dr. T. Yamauchi, Dr. H. Tagai who is the director of the Governmental Research Institute on Inorganic Materials in Japan, and Dr. Makishima (Tokyo University) for their assistance.

Manuscript submitted July 23, 1975; revised manuscript received March 9, 1976.

Any discussion of this paper will appear in a Discussion Section to be published in the June 1977 JOURNAL. All discussions for the June 1977 Discussion Section should be submitted by Feb. 1, 1977.

Publication costs of this article were assisted by the National Institute for Researches in Inorganic Materials.

#### REFERENCES

1. R. W. G. Wyckoff, "Crystal Structures," Vol. 1, p. 140, Wiley-Interscience, New York (1963).
2. S. Yamaguchi and T. Katsurai, *Sci. Papers Inst. Phys. Chem. Res. (Tokyo)*, **68**, 106 (1974).
3. M. Born, "Optik," p. 143, Springer-Verlag, Heidelberg (1965).



# An Abrupt Dopant Profile in GaAs Produced by Te Implantation

B. K. Shin

Systems Research Laboratories, Incorporated, Dayton, Ohio 45440

and Y. S. Park

Air Force Avionics Laboratory, Wright-Patterson Air Force Base, Ohio 45433

The recent advent of ion implantation technology in GaAs has generated much enthusiasm for the fabrication of optoelectronic and microwave devices as demonstrated by injection lasers (1), FET's (2, 3), TED's (4), and IMPATT diodes (5). Inasmuch as the fabrication of these devices requires a high degree of sophistication, the production of shallow layers having precisely controlled doping concentrations and a well-defined dopant profile is an important goal of ion implantation efforts.

In implantation doping usually a postimplantation heat-treatment at temperatures of 800°-900°C is required to remove radiation damage produced during implantation and to cause a substantial fraction of implanted ions to become electrically active. At these annealing temperatures, diffusion effects play an important role in the determination of the impurity distribution, even though other mechanisms such as enhanced diffusion effects or redistribution effects may also influence the profile. (In addition, decomposition and outdiffusion occur on these samples during annealing at these temperatures, and a careful selection of encapsulants must be made in order to protect the sample surface.) Therefore, knowledge of the diffusion coefficients of each impurity dopant becomes important in predicting implantation profiles.

In the present paper, the use of Te implantation in GaAs to achieve abrupt electrical profiles and the comparison of Te to other impurity dopants are presented and discussed briefly. Diffusion coefficients of Group II (Zn, Cd) p-type dopants and Group IV (Si, Sn) and Group VI (S, Se, Te) n-type dopants are considered at annealing temperatures of 900°C. It was found that the use of pyrolytically prepared  $\text{Si}_3\text{N}_4$  layer does not alter the electrical profile, predicted by diffusion properties, of either Cd- or Te-implanted GaAs.

## Experimental

The substrate material used was Cr-doped semi-insulating ( $\sim 10^9 \Omega\text{-cm}$ ) GaAs single crystal, oriented in the  $\langle 100 \rangle$  direction, obtained from the Laser Diode Laboratories. Prior to implantation, each sample was cleaned and etched in a freshly prepared  $5\text{H}_2\text{SO}_4:1\text{H}_2\text{O}_2:1\text{H}_2\text{O}$  solution, and then an  $\sim 300\text{\AA}$  layer of  $\text{Si}_3\text{N}_4$  was deposited on the sample at 720°C in a pyrolytic reactor (6). The implantation was carried out at an energy of 120 keV to a dose ( $\phi$ ) of  $10^{14}$  Te/cm<sup>2</sup> at an elevated temperature of 250°C. After implantation, each sample was annealed at  $T_A = 900^\circ\text{C}$  in flowing Ar-gas ambient. van der Pauw measurements, in conjunction with a chemical-etch-thin-layer-removal technique, were made at room temperature on the finished mesa structure. The details of such measurements are described elsewhere (7).

## Results and Discussion

Carrier concentration profiles measured on both Te- and Cd-implanted GaAs are displayed in Fig. 1 for  $T_A = 900^\circ\text{C}$ . The LSS distribution (8) for  $\phi = 10^{14}$  ions/cm<sup>2</sup> is also shown in the figure, and it can be seen that the actual profiles for Cd-implanted samples are

Key words: electrical profiles, ion implantation.

considerably broadened, closely following the profiles expected from the Cd-diffusion effect (9). In the case of Te implantation, a very abrupt profile similar to the LSS profile was obtained in the region where  $x > R_p$  ( $x \approx 600\text{\AA}$ ). The maximum electron concentration of  $\sim 2.6 \times 10^{18} \text{ cm}^{-3}$  was obtained near  $x = 600\text{\AA}$ ; the concentration is somewhat lower than the solubility limit of Te in GaAs (10, 11) ( $C_s = 5\text{-}8 \times 10^{18} \text{ cm}^{-3}$ ).

Table I shows the influence of diffusion effects upon the distribution of implanted impurities for various dopants of Group II, IV, and VI elements (9, 12-15). Here,  $R_p$  is the projected range,  $\Delta R_p$  is the mean range straggling,  $D$  is the diffusion coefficient of an impurity at  $T = 900^\circ\text{C}$ , and  $t$  is the diffusion time of 600 sec. An implantation energy of 120 keV is considered since an energy in the range of several hundred kiloelectron volts is required when an LSS profile of  $< 1 \mu\text{m}$  abrupt dopant distribution is desired for most of the n- and p-type dopants in GaAs. The ratio of the diffusion length to the mean range straggling,  $(Dt)^{1/2}/\Delta R_p$ , gives the indication of whether the broadening of the profile may be appreciable. The table indicates that the diffusion property affects the Group II p-type dopants sig-

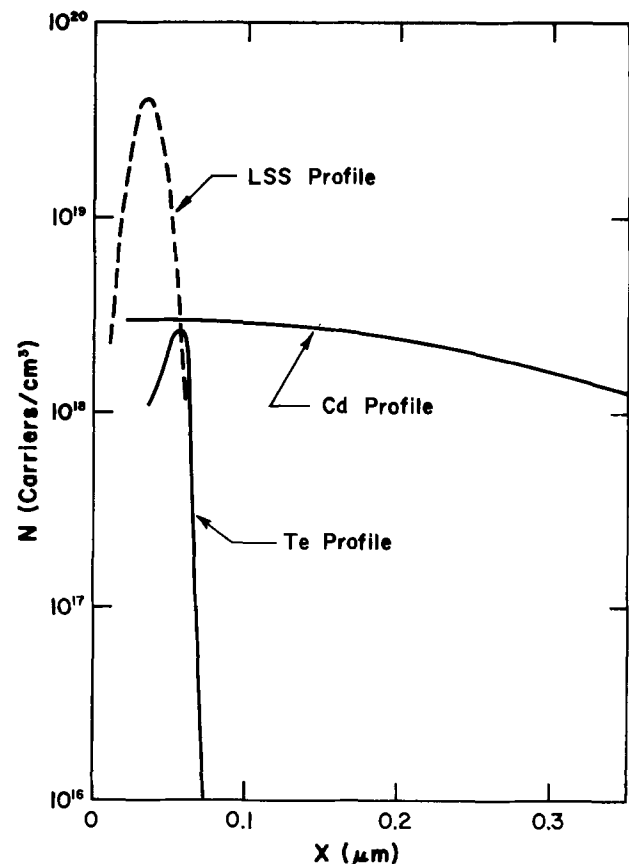


Fig. 1. Electrical profiles of Cd- and Te-implanted GaAs annealed at 900°C. The LSS profile is shown by the broken line for 120 keV,  $10^{14}$  ions/cm<sup>2</sup> implantation. (The LSS profiles for Cd and Te are almost identical.)

Table I. Comparison of diffusion coefficients with LSS ranges for various dopant impurities in GaAs

GROUP	ION	$R_p^*$ (Å)	$\Delta R_p^*$ (Å)	$D^†$ (cm <sup>2</sup> /sec)	$(Dt)^{\frac{1}{2}}$ (Å)	$\frac{(Dt)^{\frac{1}{2}}}{\Delta R_p}$	REF.‡
II	Zn	483	238	$3.0 \times 10^{-10}$	$4.24 \times 10^4$	178	12
	Cd	343	151	$4.6 \times 10^{-13}$	$1.66 \times 10^3$	11	9
VI	S	891	448	$1.8 \times 10^{-14}$	329	.73	12
	Se	435	206	$4.1 \times 10^{-15}$	157	.76	12
	Te	328	139	$1.4 \times 10^{-16}$	29	.21	13
IV	Si	1025	510	$1.4 \times 10^{-14}$	290	.57	14
	Sn	335	145	$1.1 \times 10^{-14}$	257	1.77	15

\* 120 keV (LSS Theory)

†  $T_A = 900^\circ\text{C}$ ,  $t = 600$  sec.

‡ References for diffusion coefficients.

nificantly, while it is less significant in the case of the Group IV and VI n-type dopants. In fact, implantation studies of Group II p-type dopants revealed considerable diffusion after annealing at  $800^\circ\text{--}900^\circ\text{C}$ . Diffusion effects in Group IV and VI impurities are not so clearly defined.

Recently, an abrupt profile was reported in Sn-implanted n-type GaAs (16) at an annealing temperature of  $700^\circ\text{C}$ . Implantation of other n-type impurities (17) such as S yielded a much deeper electrical profile than that expected from the diffusion table. In the present investigation, an abrupt profile resembling the LSS profile was obtained with implantation at 120 keV and annealing at  $900^\circ\text{C}$  with pyrolytic  $\text{Si}_3\text{N}_4$  encapsulation, and the diffusion was found to have little affect upon the final impurity distribution, as expected from the diffusion property of Te in GaAs.

In the profiles shown in Fig. 1, the absence of electrical activity in the region  $\lesssim 300\text{Å}$  represents the etched-away  $\text{Si}_3\text{N}_4$  layer after annealing. In analyzing the concentration profiles, it should be noted that since the range of Te is approximately equal to the thickness of the  $\text{Si}_3\text{N}_4$  layer (and the range of ions in GaAs and  $\text{Si}_3\text{N}_4$  is known to be almost identical), about one-half of the as-implanted Te ions would occupy the GaAs substrate region. (Since the value of range straggling is small and the thickness of the deposited  $\text{Si}_3\text{N}_4$  layer is not accurately known, it is difficult to predict the exact value of the Te ions implanted into the GaAs.) In the region  $300\text{Å} < x < 600\text{Å}$ , the Te concentration profile shows that the electrical activity is roughly one order of magnitude lower than the predicted LSS value. Furthermore, in this region, the electrical activity decreases with increasing Te ion concentration (with decreasing  $x$  toward  $R_p$ ), with the lowest doping efficiency being observed near  $R_p$ . Unlike Te implantation, a substantial amount of implanted Cd became electrically active after the  $900^\circ\text{C}$  anneal, which is consistent with the diffusion properties of Cd in GaAs shown in Table I. The low electrical activity observed in the Te implantation may arise from the electrical compensation of residual damages in the im-

planted region. The inverse relation of the LSS profile and the electrical profile near  $R_p$  supports the above statement since the damage profile might be expected to be closely related to the LSS profile. Further experiments are required to verify this.

### Acknowledgments

The authors wish to thank W. T. Lindley and R. McClelland of M.I.T. Lincoln Laboratory for allowing the pyrolytic  $\text{Si}_3\text{N}_4$  encapsulations to be performed in their facilities. We are also grateful to D. E. Johnson and J. E. Ehret of the Air Force Avionics Laboratory for technical assistance. Finally, thanks are due M. Whitaker for editorial assistance and preparation of the manuscript. This work was supported under U.S. Air Force Contract No. F33615-72-C-1099.

Manuscript submitted April 13, 1976; revised manuscript received June 11, 1976.

Any discussion of this paper will appear in a Discussion Section to be published in the June 1977 JOURNAL. All discussions for the June 1977 Discussion Section should be submitted by Feb. 1, 1977.

Publication costs of this article were assisted by Systems Research Laboratories, Incorporated.

### REFERENCES

1. M. K. Barnoski, R. G. Hunsperger, and A. Lee, *Appl. Phys. Lett.*, **24**, 627 (1974).
2. R. G. Hunsperger and N. Hirsch, *Solid-State Electron.*, **18**, 349 (1975).
3. B. M. Welch, F. H. Eisen, and J. A. Higgins, *J. Appl. Phys.*, **45**, 3685 (1974).
4. D. H. Lee, J. J. Berenz, and R. L. Bernick, *Electron. Lett.*, **11**, 189 (1975).
5. J. J. Berenz, R. S. Ying, and D. H. Lee, *ibid.*, **10**, 157 (1974).
6. The pyrolytic encapsulations were performed at Lincoln Laboratory, M.I.T., Cambridge, Massachusetts.
7. B. K. Shin, D. C. Look, Y. S. Park, and J. E. Ehret, *J. Appl. Phys.*, **47**, 1574 (1976).
8. J. Lindhard, M. Scharff, and H. E. Schiøtt, *K. Dan Vidensk. Selsk. Mat. Fys. Medd.*, **33**, 1 (1963); see also J. F. Gibbons, W. S. Johnson, and S. W. Mylroie, "Projected Range Statistics," Halsted Press, New York (1975).
9. M. Fujimoto, K. Kudo, and N. Hishinuma, *Jpn. J. Appl. Phys.*, **8**, 725 (1969).
10. G. M. Kuznetsov, O. V. Pelevin, A. D. Barsukov, V. V. Olenin, and I. A. Savel'eva, *Inorg. Mater.*, **9**, 759 (1973).
11. I. V. Mitchell, J. W. Mayer, J. K. Kung, and W. G. Spetzer, *J. Appl. Phys.*, **42**, 3982 (1971).
12. B. Goldstein, *Phys. Rev.*, **121**, 1305 (1961).
13. T. A. Karelina, T. T. Lavrishehev, G. L. Prikhod'ko, and S. S. Khludhov, *Inorg. Mater.*, **10**, 194 (1974).
14. T. Miyazaki and M. Tamura, in "Ion Implantation in Semiconductors, Science and Technology," p. 41, Plenum Press, New York (1975).
15. B. Goldstein and H. Keller, *J. Appl. Phys.*, **32**, 1180 (1961).
16. J. M. Woodcock, J. M. Shannon, and D. J. Clark, *Solid-State Electron.*, **18**, 267 (1975).
17. F. H. Eisen, in "Ion Implantation in Semiconductors, Science and Technology," p. 3, Plenum Press, New York (1975).



## Performance Characteristics of Solid Lithium-Aluminum Alloy Electrodes

Eddie C. Gay,\* Donald R. Vissers,\* Fredric J. Martino, and Karl E. Anderson

*Chemical Engineering Division, Argonne National Laboratory, Argonne, Illinois 60439*

### ABSTRACT

Lithium-aluminum alloy electrodes have shown a great deal of promise for meeting the performance requirements of negative electrodes in batteries for off-peak energy storage in utility networks and for vehicle propulsion. To develop negative electrodes that meet the cell performance goals, the effects of a number of variables on the lithium-aluminum electrode performance were determined. Investigations were conducted to determine the effects of volume fraction electrolyte in the electrode, electrode thickness, fabrication technique, lithium concentration in the Li-Al alloy, and current collector in the electrode. Electrochemically formed Li-Al electrodes that are 0.32 cm thick, have an electrolyte volume fraction of 0.2 in the charged state, and contain about 2 weight percent stainless steel wire current collector have demonstrated the performance goals for the negative electrodes in a Li-Al/FeS<sub>2</sub> electric automobile battery. For electrode thicknesses  $\geq 0.64$  cm, vibratorily loaded pyrometallurgical Li-Al electrodes with porous metallic current collectors have demonstrated the highest lithium utilization and capacity density over a wide range of discharge current densities and have met the performance goals for negative electrodes in a Li-Al/FeS<sub>2</sub> off-peak energy storage battery.

A lithium-aluminum alloy of approximately 50 atom percent (a/o) lithium has shown a great deal of promise for meeting the performance requirements of negative electrodes in lithium/metal sulfide batteries being developed at Argonne National Laboratory (ANL) (1-4). These batteries are being developed for use as energy storage devices for load leveling on electric utilities and as power sources for electric automobiles.

Lithium is attractive as a negative electrode material for high performance batteries (5-7) because of its low weight per unit of electricity delivered, low affinity for electrons, and high electrochemical reactivity. However, containment of liquid lithium in the negative electrode over a large number of cycles has proved to be a problem because, in time, uncontained lithium bridges to the positive electrode, forming electrical short circuits. Another problem with liquid lithium has been the high corrosion rates of ceramic separators and electrical feedthroughs. Our studies have indicated that these problems can be avoided by the use of solid Li-Al alloys. In previous work by other investigators, excellent electrochemical performance of electrochemically prepared lithium-aluminum alloy (composition range 17-62 a/o Li) in molten salt systems has been reported (8-10). The emf of a lithium-aluminum alloy electrode is constant, about 0.3V vs. Li reference, and independent of lithium concentration up to about 45 a/o Li in the alloy.

This paper describes a study to determine the effects of a number of variables on the performance of lithium-aluminum electrodes so that negative electrodes meeting the cell performance goals can be developed.

\* Electrochemical Society Active Member.

Key words: battery, rechargeable, sulfur, negative, electrolyte.

Investigations were conducted on the effects of volume fraction of electrolyte in the electrode, electrode thickness, fabrication technique, lithium concentration in the Li-Al alloy, and type of current collector in the electrode.

### Experimental

*Li-Al electrode fabrication.*—The solid lithium-aluminum electrodes were prepared by four processes:

1. Electrochemical formation in a substrate of compressed aluminum fibers. The initial porosities of the substrates were 40-80%, and the volume fraction electrolyte in the Li-Al electrodes in the fully charged state was 0.20-0.70.
2. Electrochemical preparation of the Li-Al electrode by direct contact with lithium. This was accomplished by placing a compressed aluminum-fiber disk in direct contact with stainless steel Feltmetal containing liquid lithium in electrolyte (LiCl-KCl).
3. Pyrometallurgical preparation of the Li-Al electrodes. In this procedure, the alloy was formed by heating lithium and aluminum to a temperature above the alloy melting point (720°C); the Li-Al alloy was cast and ground; the powder was then mixed with electrolyte; and the mixture was compacted (under pressure and above the melting point of the electrolyte) into disks of the desired thickness and diameter.
4. Vibratory loading of pyrometallurgically prepared Li-Al powder into a porous metallic structure. The structure also serves as the current collector.

A description of several of these electrodes is presented in Table I.

*Experimental cells.*—The electrodes were tested in cells with an electrolyte of LiCl-KCl eutectic (m.p. 352°C) and a counterelectrode of FeS<sub>2</sub>; the operating

Table I. Description of the negative electrodes used in cell S-69\*

Electrode designation	Symbol	Comp., a/o Li	Electrode type	Fabrication technique	Current collector	Volume fraction electrolyte	Volume fraction current collector	Thickness, cm	Theor. cap. density, A-hr/cm <sup>2</sup>	Theor. cap., A-hr
A-4	○	100	Liquid	—	SS Feltmetal	0.08	0.20	1.27	1.40	21.8
A-3	●	60	Pyromet.	Vibration loading	Ni Retimet†	0.46	0.042	1.62	1.55	24.2
A-2	□	51	Pyromet.	Vibration loading	Ni Retimet	0.46	0.042	0.80	0.73	11.3
A-1	■	50	Electrochem.	Direct contact	SS wire	~0.2	2‡	0.32	0.43	6.7
HP-2	△	51	Pyromet.	Hot-pressing	SS wire	0.23	3‡	0.47	0.53	8.2
HP-1	▲	51	Pyromet.	Hot-pressing	SS wire	0.20	3‡	0.32	0.72	11.2
B-1	◆	50	Electrochem.	—	SS wire	0.40	2‡	0.60	0.76	11.8

\* In cell S-69, a single FeS<sub>2</sub> positive electrode (capacity density, 0.92 A-hr/cm<sup>2</sup>) was used for all tests.

† Value is in weight percent.

‡ Manufactured by Dunlap, Ltd., England.

temperatures were between 390° and 450°C. An essential feature of the cells used in studying the performance of Li-Al electrodes is that the Li-Al electrode is the limiting electrode. The liquid lithium electrode would be an ideal electrode for the Li-Al characterization studies because of low polarization, even at high current densities, but this electrode has not been successfully operated in compact cell configurations. In order to obtain performance data in a practical cell configuration which could be used in a battery (negative and positive electrodes compressed against an electrode separator), most of the cells were operated with FeS<sub>2</sub> electrodes whose performance was well characterized. Reference electrodes were used in some cells to ensure that the Li-Al electrode was limiting. These results were compared to those of similar studies using liquid lithium counterelectrodes (11).

Two positive FeS<sub>2</sub> electrodes with housings of porous graphite were used to evaluate most of the Li-Al electrodes in this study. Zirconia cloth was attached to the housing for one of these electrodes (cell S-63) to retain the FeS<sub>2</sub> particulates. This electrode had a current collector of corrugated molybdenum mesh and an FeS<sub>2</sub> theoretical capacity density of 1.14 A-hr/cm<sup>2</sup>. The other electrode (cell S-69) utilized carbon fabric as the particulate retainer and vitreous carbon foam as the current collector, and had an FeS<sub>2</sub> theoretical capacity density of 0.92 A-hr/cm<sup>2</sup>. Boron nitride or yttria fabric was used as the electrode separator in both cells. The cell configuration for these electrodes is shown in Fig. 1. For cells that had a liquid lithium electrode, the lithium was contained in a Type 347 stainless steel porous metal structure, 20 cm<sup>2</sup> electrode area.

**Testing procedures.**—All of the experimental work that involved assembly of charged Li-Al electrodes, pyrometallurgical preparation of Li-Al alloy, electrochemical formation of Li-Al electrodes, and testing of cells was performed in a glove box containing a high purity (about 2 ppm each of O<sub>2</sub> and N<sub>2</sub> and <1 ppm H<sub>2</sub>O) helium atmosphere. Assembled cells were heated in a furnace well which was attached to the floor of the glove box and the temperature was maintained between 390° and 450°C. Current and voltage leads were connected to metering and recording equipment outside the glove box by means of hermetically sealed feed-throughs.

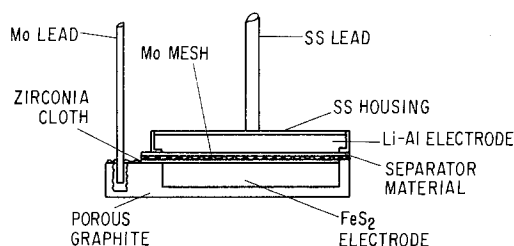


Fig. 1. Lithium-aluminum/iron sulfide cell configuration

Most of the discharge and charge operations were conducted at constant current with the aid of a regulated d-c power supply. The cells were connected to a meter relay that automatically reversed the polarity of the power supply when a cell reached the preset cutoff voltage for either charge or discharge. In this way, the cells could be automatically charged and discharged at selected (and often widely different) current densities. The total capacity (ampere-hour) for the charge and discharge half-cycles was determined electronically and was provided in a printout form. Since many of the cells were cycled for hundreds of cycles and hundreds of hours, variables such as cell voltage, current, charge and discharge time, and temperature were monitored by an automatic data acquisition system. The magnetic tapes could be fed to a computer to perform calculations and to produce performance curves.

## Results and Discussion

A summary of the performance of several negative electrodes used in cell S-69 is shown in Fig. 2. Descriptions of these electrodes were given in Table I and the designated symbols for the individual curves in Fig. 2 are keyed to the electrode descriptions in that table.

The ranges of variables in the negative electrodes were as follows: volume fraction electrolyte, 0.2-0.70;

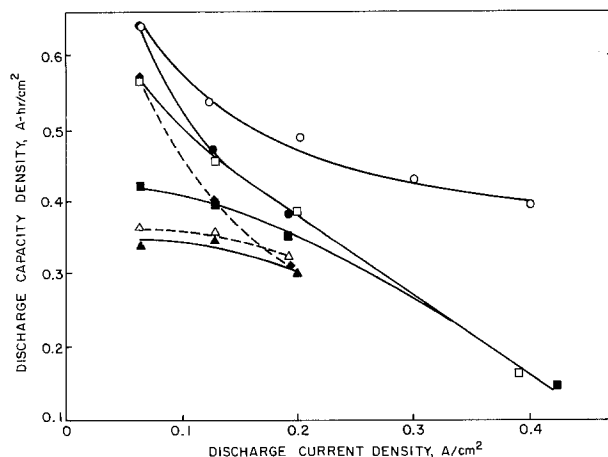


Fig. 2. Capacity density-current density curves for several negative electrodes.

Symbol	Electrode type	Fabrication technique	Volume fraction electrolyte	Thickness, cm
○	Liquid	—	0.08	1.27
●	Pyromet.	Vibration loading	0.46	1.62
□	Pyromet.	Vibration loading	0.46	0.80
■	Electrochem.	Direct contact	~0.2	0.32
△	Pyromet.	Hot-pressing	0.23	0.47
▲	Pyromet.	Hot-pressing	0.20	0.32
◆	Electrochem.	—	0.40	0.60

and thickness, 0.32-1.62 cm. The range of theoretical capacity density was 0.43-1.55 A-hr/cm<sup>2</sup>. Two of the negative electrodes had theoretical capacity densities greater than that of the FeS<sub>2</sub> electrode (0.92 A-hr/cm<sup>2</sup>); one was a liquid lithium electrode (1.40 A-hr/cm<sup>2</sup>) and the other was a pyrometallurgical Li-Al electrode (1.55 A-hr/cm<sup>2</sup>). These were operated primarily to serve as a basis for evaluating the FeS<sub>2</sub> electrode, but the liquid lithium electrode also served as a basis for certain evaluations of the Li-Al electrodes.

It is desirable to develop Li-Al electrodes having a low electrolyte content to increase the theoretical Li-Al capacity per unit electrode volume (ampere-hour/cubic centimeter). However, high utilization of the Li-Al electrode at discharge current densities greater than about 0.2 A/cm<sup>2</sup> is favored by a higher electrolyte content. Lithium-aluminum utilization is also strongly affected by electrode thickness. Therefore, investigations of these variables were necessary in order to optimize the performance for the two applications of interest. Several fabrication techniques were considered for the Li-Al electrodes in an attempt to determine the lowest cost electrode that appeared to be suitable for large quantity manufacture and that met the performance goals. Only the performance results are discussed in this paper.

The data presented in Fig. 2 and Tables I and II show the strong influence of current collector on the utilization of Li-Al electrodes. Significant improvement in Li-Al utilization results from improved current collection, at discharge current densities greater than 0.1 A/cm<sup>2</sup>, for vibratorily loaded Li-Al electrodes with porous metal structures and thicknesses greater than 0.6 cm. Electrode A-2 contained porous nickel current collector and showed much better Li-Al utilizations at the higher current densities than the electrochemically formed electrode B-1 which contained much less current collector.

The Li-Al electrode utilization as a function of current density is shown in Fig. 3, where the symbols are also keyed to the descriptions in Table I. The thinner Li-Al electrode designated A-1 (electrochemically formed, 0.32 cm thick) demonstrated the highest Li-Al utilization at high discharge rates.

The much higher performance at 0.4 A/cm<sup>2</sup> with the liquid lithium electrode (A-4) indicated that the best Li-Al electrode described in Fig. 2 and 3 and Table II was limiting at high discharge rates. The positive electrode, however, was capable of higher performance at the high discharge rates. These results were verified in tests in which reference electrodes were used to identify the limiting electrode.

The effects of electrolyte content (20, 46, and 70%) on the performance of thin, electrochemically formed Li-Al electrodes was determined in cell S-63. The Li-Al electrodes were electrochemically formed from aluminum wire disks; the electrodes were 0.32 cm thick and had an area of 15.6 cm<sup>2</sup>. The electrodes were charged at 0.064 A/cm<sup>2</sup> to a 2.27V (*IR*-included) cutoff. The cell resistance in each case was about 40 mΩ. The performance results for these electrodes are shown in

Table II. Performance of the negative electrodes used in cell S-69

Electrode designation	Electrode type	Volume fraction electrolyte	Thickness, cm	Current density, A/cm <sup>2</sup>	Capacity density, A-hr/cm <sup>2</sup>	Percentage theor. cap. density*
A-1	Electrochem.	0.2	0.32	0.13	0.40	93.0
				0.43	0.15	32.0
A-2	Pyromet.	0.46	0.80	0.064	0.57	78.0
				0.20	0.39	66.0
A-4	Liq. Li	0.08	1.27	0.064	0.65	71.0
				0.40	0.40	44.0
B-1	Electrochem.	0.40	0.60	0.064	0.52	70.0
				0.20	0.30	40.0

\* Percentage Li-Al theoretical capacity density except for A-4 where percentage FeS<sub>2</sub> theoretical capacity density is given.

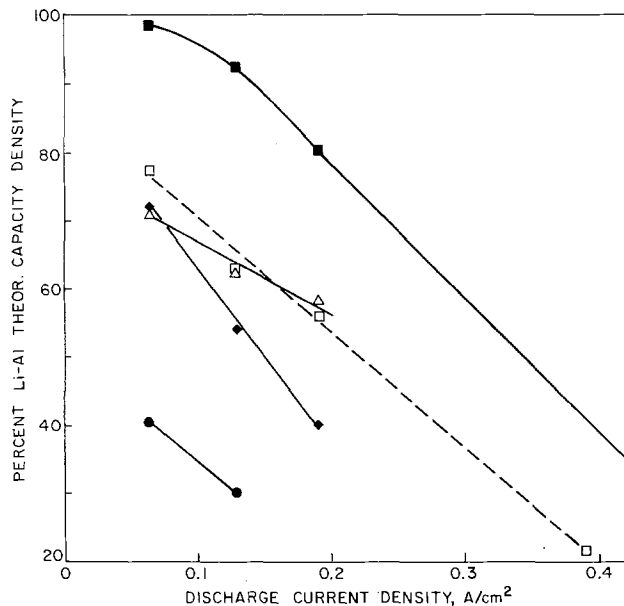


Fig. 3. Percentage utilization as a function of current density for several Li-Al electrodes.

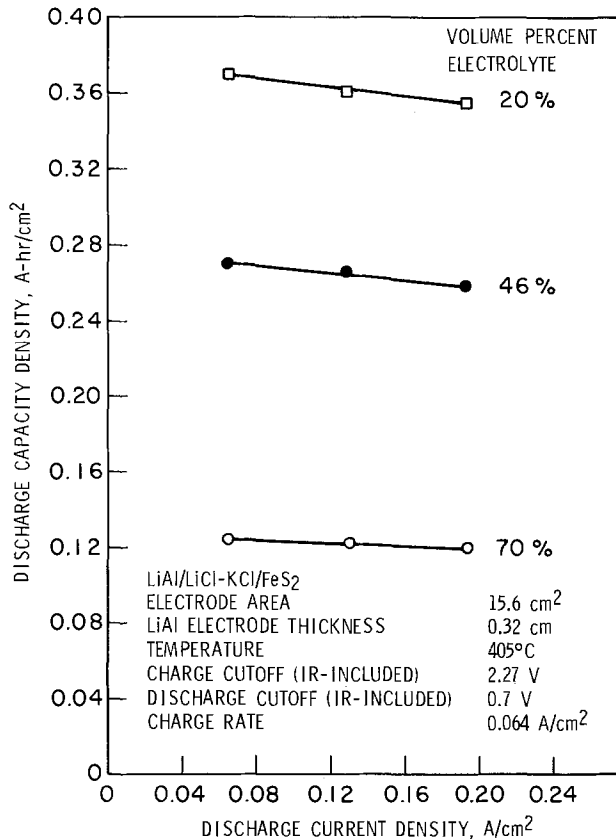


Fig. 4. Effect of electrolyte content on performance of Li-Al electrodes. LiAl/LiCl-KCl/FeS<sub>2</sub>; electrode area, 15.6 cm<sup>2</sup>; LiAl electrode thickness, 0.32 cm; temperature, 405°C; charge cutoff (*IR* included), 2.27V; discharge cutoff (*IR* included), 0.7V; charge rate, 0.064 A/cm<sup>2</sup>.

Fig. 4. As can be seen in the figure, the electrode containing 20 volume percent (v/o) electrolyte showed the best performance (86-83% of Li-Al theoretical capacity density) at current densities ranging from 0.064 to 0.19 A/cm<sup>2</sup>. The capacity densities for the electrode containing 46 v/o electrolyte were about 27% lower, and those for the electrode with 70 v/o electrolyte were 66.5% lower than the electrode with 20 v/o electrolyte. Thus, for thin (0.32 cm) electrodes and relatively low charge rates, the best results were obtained with 20 v/o electrolyte in the electrode.

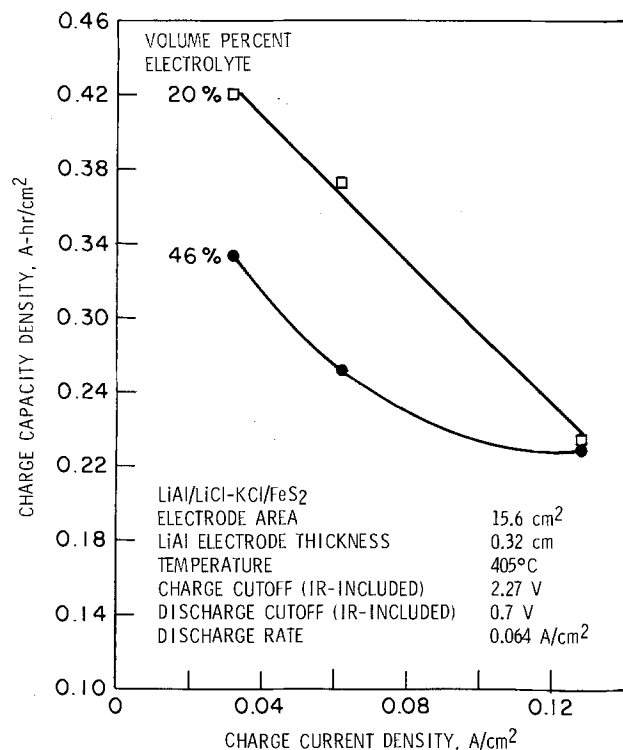


Fig. 5. Influence of electrolyte content on charge characteristics of Li-Al electrodes. LiAl/LiCl-KCl/FeS<sub>2</sub>; electrode area, 15.6 cm<sup>2</sup>; LiAl electrode thickness, 0.32 cm; temperature, 405°C; charge cutoff (IR included), 2.27V; discharge cutoff (IR included), 0.7V; discharge rate, 0.064 A/cm<sup>2</sup>.

The improvement in performance for the electrode with 20 v/o electrolyte was not nearly as great at high charge rates (see Fig. 5). At a charge current density of 0.128 A/cm<sup>2</sup>, the charge capacity densities were 0.234 and 0.228 A-hr/cm<sup>2</sup> (55 and 89% of theoretical) for the electrodes with 20 and 46 v/o electrolyte, respectively. With the charge conditions described above and a discharge rate of 0.192 A/cm<sup>2</sup>, discharge capacity densities of 0.223 A-hr/cm<sup>2</sup> (52.0% of the Li-Al theoretical capacity density) and 0.207 A-hr/cm<sup>2</sup> (69.2% theoretical), respectively, were measured for the electrodes with 20 and 46 v/o electrolyte. The capacity densities measured for these electrodes were nearly the same.

A plot of discharge capacity density vs. current density for a constant IR-included charge cutoff voltage is shown in Fig. 6. These results were obtained for the Li-Al electrode containing 20 v/o electrolyte, which demonstrated the highest performance. The IR-included charge cutoff voltage is significant in LiAl/FeS<sub>2</sub> cells because liquid lithium has been formed in some cells at high charge cutoff voltages and has, in some cases, bridged across the BN separator and caused electrical short circuits. The 2.27V charge cutoff used in the cells described in this paper was low enough to prevent liquid lithium formation. However, in attempts to charge the cells at high charge rates (0.13 A/cm<sup>2</sup>) to the same IR-free charge cutoffs as used at low charge rates (0.032 A/cm<sup>2</sup>), some shorting problems have been encountered. No reactions between the active materials or current collectors and the electrolyte have been observed at charge cutoffs below 2.27V. As shown in Fig. 6, over 90% of the Li-Al theoretical capacity density was obtained over a wide range of discharge rates for a charge rate of 0.032 A/cm<sup>2</sup>. However, at a charge rate of 0.13 A/cm<sup>2</sup>, the capacity density decreased to about 50% of theoretical.

The effects of charge rate and IR-free charge cutoff voltage on the performance of Li-Al electrodes were studied by other investigators at ANL in Li/Li-Al type cells (12). The electrical performance characteristics of a 0.32 cm thick Li-Al electrode with 20 v/o electrolyte were evaluated by cycling against a molten lithium

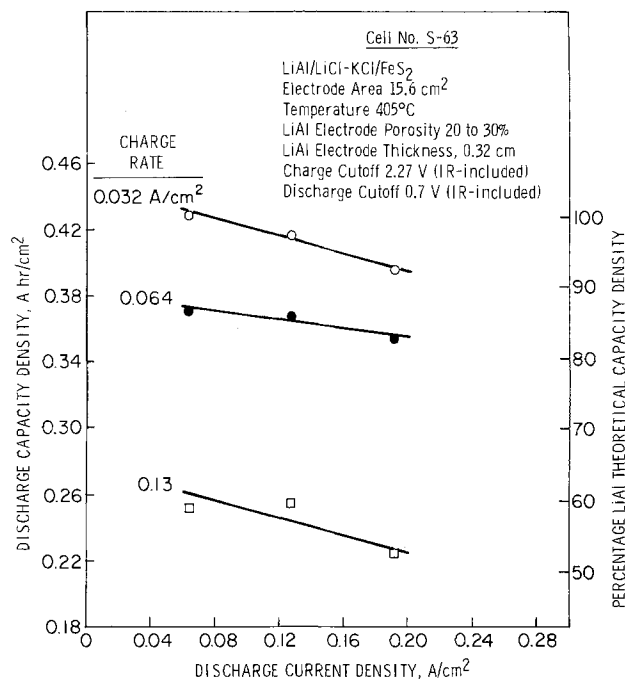


Fig. 6. Discharge capacity density vs. current density of cell No. S-63. LiAl/LiCl-KCl/FeS<sub>2</sub>; electrode area, 15.6 cm<sup>2</sup>; temperature, 405°C; LiAl electrode porosity 20 to 30%; LiAl electrode thickness, 0.32 cm; charge cutoff (IR included), 2.27V; discharge cutoff (IR included), 0.7V.

electrode. The capacity density was determined at charge rates of 0.05-0.10 A/cm<sup>2</sup> and discharge rates of 0.05-0.20 A/cm<sup>2</sup>. An IR-free cutoff potential vs. lithium of 0.15V was normally used during charge and 0.40V was used during discharge. At the 0.10 A/cm<sup>2</sup> charge rate, a cutoff potential vs. lithium of 0.04V was also used. At a charge and discharge rate of 0.05 A/cm<sup>2</sup>, greater than 90% of the Li-Al theoretical capacity density was achieved with a charge cutoff potential of 0.15V. At a charge and discharge rate of 0.2 A/cm<sup>2</sup>, the capacity density decreased to about 67.5% of the Li-Al theoretical capacity density. At a charge and discharge rate of 0.10 A/cm<sup>2</sup>, the lithium utilization is greater than 85% of the theoretical capacity density at the lower charge cutoff potential (0.04V). When the higher charge cutoff potential vs. lithium of 0.15V was used, the capacity density decreased to about 70% of theoretical.

The effects on electrode performance of fabrication technique, composition of the Li-Al alloy, and amounts of current collector were determined as follows. Lithium-aluminum alloys of 51 and 55 a/o Li were prepared by the pyrometallurgical process. This material was mixed with electrolyte and about 2 w/o stainless steel current collector and compressed at about 35.2 kg/cm<sup>2</sup> and 400°C to form two disks of approximately 20 v/o electrolyte and 0.32 cm thickness. These disks were placed in a stainless steel housing with a fine mesh screen for particulate retention in the electrode and the electrodes were operated against a FeS<sub>2</sub> electrode. The performance was then compared with that of an electrochemical Li-Al electrode with identical thickness and electrolyte content and which was operated against the same FeS<sub>2</sub> electrode.

A comparison of the capacity density-current density curves for these electrodes is shown in Fig. 7. For the electrochemically formed Li-Al electrode, capacity densities of 0.43-0.40 A-hr/cm<sup>2</sup> (greater than 90% of the Li-Al theoretical) were measured at discharge current densities of 0.05-0.20 A/cm<sup>2</sup>. The best performance with the pyrometallurgical Li-Al electrodes was achieved with the 55 a/o Li composition. However, this performance was about 15% lower than that measured for the electrochemical Li-Al electrode. These results

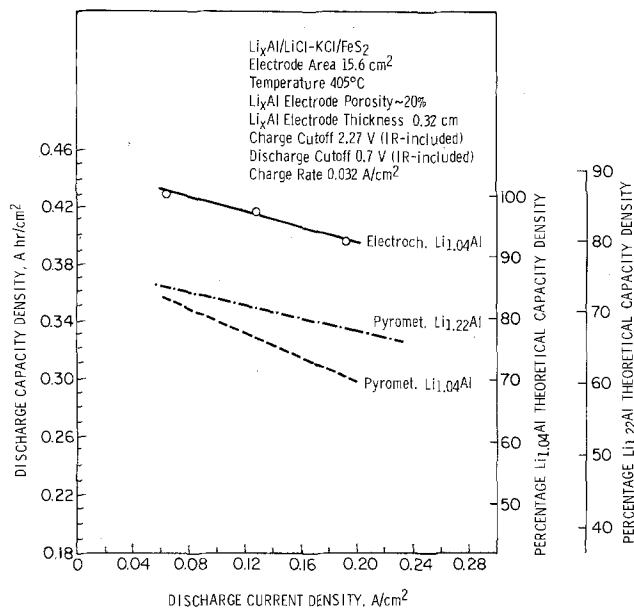


Fig. 7. Performance of thin Li-Al electrodes with small amounts of current collector.  $\text{Li}_x\text{Al}/\text{LiCl-KCl}/\text{FeS}_2$ ; electrode area,  $15.6 \text{ cm}^2$ ; temperature,  $405^\circ\text{C}$ ;  $\text{Li}_x\text{Al}$  electrode porosity,  $\sim 20\%$ ;  $\text{Li}_x\text{Al}$  electrode thickness,  $0.32 \text{ cm}$ ; charge cutoff (IR included),  $2.27\text{V}$ ; discharge cutoff (IR included),  $0.7\text{V}$ ; charge rate,  $0.032 \text{ A/cm}^2$ .

indicate that the electrochemical Li-Al electrode has the better performance for electrodes of 20 v/o electrolyte,  $0.32 \text{ cm}$  thickness, and small amounts of current collector ( $\sim 2 \text{ w/o}$ ).

Charge-discharge characteristics of cell S-63 (for the negative electrode A-1 described in Table I) are shown in Fig. 8. At charge and discharge current densities of  $0.032$  and  $0.064 \text{ A/cm}^2$ , respectively, no significant variation in the electrode polarization was observed. The resistance overvoltage on discharge showed little change with a value of  $0.01\text{V}$ . Similar observations were made at discharge current densities up to  $0.2 \text{ A/cm}^2$ .

Several of the Li-Al electrodes operated in these investigations meet our near-term performance goals for electrodes in the off-peak energy storage battery and the vehicle-propulsion battery. These goals are shown in Table III. Calculations to determine the performance requirements of electrodes for cells in electric vehicle batteries indicate that if the capacity density-current density behavior shown in Fig. 2 for the electrochemically formed Li-Al electrode of  $0.32 \text{ cm}$  thickness (A-1) can be maintained for larger diameter electrodes ( $\sim 15 \text{ cm}$  diameter), these electrodes would be suitable for this purpose. Similarly, the pyrometallurgical Li-Al

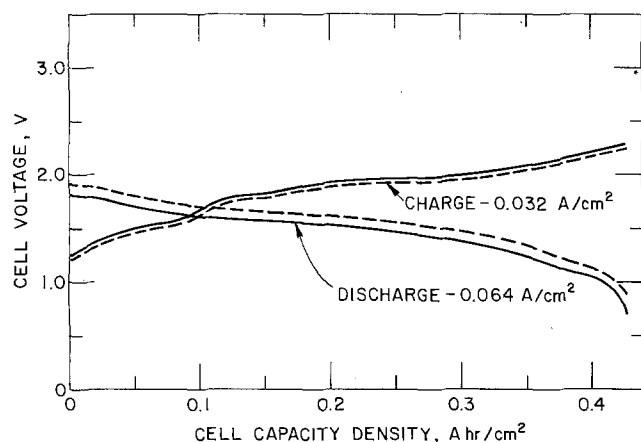


Fig. 8. Charge-discharge characteristics of cell S-63.  $\text{Li-Al}/\text{LiCl-KCl}/\text{FeS}_2$  (charged); positive electrode area  $15.6 \text{ cm}^2$ ; negative electrode area,  $15.6 \text{ cm}^2$ ; ---, IR-free voltage; —, IR-included voltage.

Table III. Tentative performance goals for electric automobile and off-peak energy storage battery cells

	Electric-vehicle propulsion	Off-peak energy storage
Normal discharge cycle, hr	2	10
Normal charge cycle, hr	4-6	4-8
Specific energy output, W-hr/kg	156	165
Cell specific power, W/kg	78	16.5
Cell current density, $\text{A/cm}^2$		
Peak	0.425*	0.3
Normal	0.139	0.074
Watt-hr efficiency, %	70	80
Cycle life	1000†	1500†
Cost of battery capacity, \$/kW-hr	20-30†	15-20†

\* Based upon power required to accelerate a  $1570\text{-kg}$  car  $0\text{-}80 \text{ mph}$  in 23 sec.

† Tentative; to be specified by systems and cost studies.

electrodes with the porous metal current collectors appear to be suitable for cells in off-peak energy storage batteries. Further improvements could be gained, however, by developing negative electrodes having higher performance at high current densities and by coupling these electrodes with a high performance positive electrode, such as the  $\text{FeS}_2$  electrode used in cell S-69 in these investigations.

### Conclusions

The following conclusions can be made from the studies described above:

1. Significant progress has been made in the development of Li-Al electrodes that meet the performance requirements of off-peak energy storage and electric vehicle propulsion batteries.
2. Increase in the  $\text{Li-Al}/\text{FeS}_2$  cell performance at high discharge rates ( $>0.2 \text{ A/cm}^2$ ) could be realized by the development of Li-Al electrodes with higher utilization under these operating conditions. The  $\text{FeS}_2$  electrode has demonstrated much greater utilization at high discharge rates.
3. Electrochemically formed Li-Al electrodes that are  $0.32 \text{ cm}$  thick, contain 20 v/o electrolyte in the charged state, and contain about 2 w/o stainless steel wire current collector, have demonstrated the performance goals of Table III for the negative electrodes in a  $\text{Li-Al}/\text{FeS}_2$  electric vehicle battery.
4. Capacity density measurements of  $0.32 \text{ cm}$  thick electrochemically formed Li-Al electrodes with 20, 46, and 70 v/o electrolyte indicated that the highest utilization was achieved with 20 v/o electrolyte.
5. Higher capacity density was achieved with electrochemically formed Li-Al electrodes of  $0.32 \text{ cm}$  thickness, 20 v/o electrolyte, and 2 w/o current collector, than with hot-pressed Li-Al electrodes fabricated from mixtures of pyrometallurgical Li-Al powder and electrolyte with the same thickness and electrolyte composition.
6. For electrode thicknesses  $\geq 0.64 \text{ cm}$ , vibratorily loaded, pyrometallurgical Li-Al electrodes with porous metallic current collectors have demonstrated the highest lithium utilization and capacity density over a discharge current densities range of  $0.05\text{-}0.4 \text{ A/cm}^2$ . These electrodes have demonstrated the performance goals for negative electrodes in a  $\text{Li-Al}/\text{FeS}_2$  off-peak energy storage battery shown in Table III.

### Acknowledgments

The authors are grateful to L. Burris, D. S. Webster, and P. A. Nelson for support and encouragement. The authors would also like to acknowledge the efforts of the Materials Group at ANL in preparation of the pyrometallurgical Li-Al powder. This work was performed under the auspices of the U. S. Energy Research and Development Administration.

Manuscript submitted Jan. 22, 1976; revised manuscript received June 23, 1976.

Any discussion of this paper will appear in a Discussion Section to be published in the June 1977 JOURNAL. All discussions for the June 1977 Discussion Section should be submitted by Feb. 1, 1977.

Publication costs of this article were assisted by Argonne National Laboratory.

## REFERENCES

1. P. A. Nelson *et al.*, Progress Report, July-December 1973, ANL-8057, Argonne National Laboratory (1974).
2. E. C. Gay *et al.*, Proc. 9th Intersociety Energy Conversion Engineering Conf., pp. 862-867, San Francisco, Calif., August 26-30, 1974.
3. P. A. Nelson *et al.*, Proc. 26th Annual Power Sources Conf., pp. 65-68, Atlantic City, April 29-30, 1974.
4. W. J. Walsh *et al.*, Proc. 9th Intersociety Energy Conversion Engineering Conf., pp. 911-915, San Francisco, Calif., August 26-30, 1974.
5. H. Shimotake *et al.*, Proc. 1st Int. Electric Vehicle Symp., Electric Vehicle Council, p. 392, New York (1969).
6. M. L. Kyle *et al.*, Proc. 6th Intersociety Energy Conversion Engineering Conf., SAE, p. 80, New York (1971).
7. E. C. Gay *et al.*, Proc. 8th Intersociety Energy Conversion Engineering Conf., AIAA, p. 96, New York (1973).
8. W. K. Behl *et al.*, U. S. Army Electronics Command, Ft. Monmouth, N.J., Report ECOM-3166, DA Task No. ITO 61102A 34A 00, Aug. 1969.
9. E. S. Buzzelli, U.S. Pat. 3,445,288 (1969).
10. N. P. Yao, L. A. Herédy, and R. C. Saunders, *This Journal*, **118**, 1039 (1971).
11. D. R. Vissers, and K. E. Anderson, Progress Report, July-December 1974, ANL-75-1, Argonne National Laboratory, pp. 78-87 (1975).
12. D. R. Vissers, M. F. Roche, and K. E. Anderson, Abstract 20, p. 56, The Electrochemical Society Extended Abstracts, Fall Meeting, Dallas, Texas, Oct. 5-10, 1975.

## Dental Amalgam Stabilization by Selective Interfacial Amalgamation

L. D. Zardiackas,\* G. E. Stoner,† and F. K. Smith

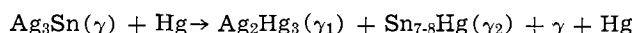
Department of Materials Science, University of Virginia, Charlottesville, Virginia 22901

## ABSTRACT

The purpose of this investigation was to explore the feasibility of enhancing the electrochemical stability of dental amalgam restorations by a process of "selective interfacial amalgamation." If dental amalgam restorations can be selectively alloyed at the tooth-amalgam interface, to a minor thickness as compared with the dimensions of the bulk amalgam, so as to present a more electrochemically stable phase than  $\gamma_2$  to the oral environment, corrosion will be reduced and desirable qualities of existing amalgams can be utilized.

Dental amalgam is the most successful of all bio-materials. In the United States alone, there are approximately  $1.6 \times 10^8$  amalgam restorations placed each year. Of these approximately 40% are for the replacement of amalgam restorations which have failed. Although the role that corrosion plays in this failure is not totally agreed upon, it is generally agreed that corrosion contributes to the failure of the amalgam and recurrent decay.

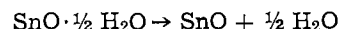
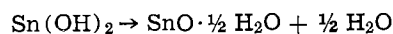
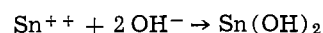
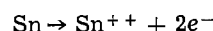
Dental amalgam is formed during a sintering reaction between an amalgam alloy, whose primary constituents are silver and tin, and mercury to form two new primary phases



These constituents upon trituration give a plastic mass which can be hand condensed into a prepared cavity and react to give a restoration with a tensile strength of the order of  $8 \times 10^3$  psi.

Corrosion of dental amalgam occurs due to the formation of an oxygen concentration cell. Thus dental amalgam corrodes at the tooth-amalgam interface below the external surface of the restoration. Wagner (1) in 1962 showed that the only phase which corrodes is the  $\text{Sn}_{7-8}\text{Hg}(\gamma_2)$  phase. Corrosion therefore occurs due to the anodic oxidation of tin and the cathodic reduction of oxygen. In addition, hydroxide precipitation and ingestion of food causes localized pH changes thereby initiating cathodic reduction of hydrogen. Subsequent to the work of Wagner, Jorgensen (2) showed that the  $\gamma_2$  phase formed a continuous network

throughout the amalgam and that excess mercury in the margins caused increased amounts of corrosion. The total reaction for the corrosion of dental amalgam *in vitro* have been suggested by Otani, Jesser, and Wilsdorf (3)



Mateer and Reitz (4) have identified the *in vivo* corrosion products as  $\beta$ - $\text{SnO}_2$   $\text{SnS}_3$ . There have been a number of attempts to reduce the corrosion of dental amalgam by alloying. Work done by Johnson and co-workers (5) has shown the elimination of the  $\gamma_2$  phase by the substitution of 10 weight percent (w/o) Au for Ag. This caused the formation of an  $\text{AuSn}_4$  intermetallic around the original alloy particles. Innes and Youdelis (6), in 1963, developed an alloy having a dispersant  $\text{Ag}_3\text{Cu}$  eutectic. Sarkar and Greener (7) confirmed the work of Dupéron, Nevile, and Kesloff (8) as to the superior corrosion resistance of Dispersalloy.<sup>1</sup> Mahler (9) reported the presence of a phase intermediate between the intermetallics of  $\text{Cu}_3\text{Sn}$  and  $\text{Cu}_6\text{Sn}_5$ , however work by Sarkar and Greener (7) has shown the presence of  $\gamma_2$  in Dispersalloy after 7 days. Work by Waterstratt (10) has shown the elimination of  $\gamma_2$  by alloying with manganese. Another attempt at reducing marginal corrosion has been through the use of organic cavity sealers. Both of

\* Electrochemical Society Student Member.

† Electrochemical Society Active Member.

Key words: dental amalgam, selective amalgamation, corrosion.

<sup>1</sup> Trade name manufactured by Johnson and Johnson.



these methods of electrochemical stabilization have shortcomings however.

Because of this, a new method from now on termed "selective interfacial amalgamation" has been developed. This method is diagrammatically shown in Fig. 1 and will be subsequently described. First the carious lesion is removed and the cavity prepared by ordinary clinical techniques. A silver suspension, emulsion, or the like, is painted onto the cavity surface using a camel's-hair brush. The suspension is air dried. A conventional dental amalgam is then hand condensed into the cavity using ordinary clinical technique. Mercury expressed from the amalgam bulk during hand condensing reacts with the silver in the suspension. This provides an interfacial region of the highly corrosion resistant  $\gamma_1$  phase at the tooth-amalgam interface.

### Experimental Procedure

Samples for differential aeration studies, scanning electron microscopy, and x-ray energy analysis were prepared using  $9 \times 5 \times 1$  mm Plexiglas molds. Lined samples were prepared by painting the mold cavity walls with suspensions ranging in composition from 40 to 92 volume percent (v/o) Ag and a methyl cellulose binder. Spherical amalgam containing a 50 w/o Hg admix was triturated for 20 sec then hand condensed into the mold cavity using conventional amalgam pluggers and a 2 kg balance apparatus to approximate clinical technique. Samples were allowed to react for 2 hr, then removed from the molds. Selectively amalgamated samples were then placed in petri dishes with the selectively alloyed side facing the bottom of the petri dish. The petri dish was then filled with 1.0 w/o NaCl, covered, and placed in an oven at  $37^\circ\text{C}$ . Controls were identically prepared and placed in an oven at  $37^\circ\text{C}$ . Periodic additions of distilled  $\text{H}_2\text{O}$  was necessary to maintain the 1.0 w/o NaCl concentration. Additional selectively amalgamated samples were prepared in the aforementioned manner for scanning microscopy and x-ray energy analysis. Samples were prepared for time lapse photography to determine reaction rates by hand condensing  $9 \times 5 \times 1$  mm amalgam samples onto a glass slide previously painted with silver suspension.

### Results

Preliminary screening of several silver suspensions showed that below 80 w/o silver in the suspension, there was insufficient bonding of the selectively amalgamated layer to the amalgam bulk to provide an integrated, electrochemically stable amalgam. Time lapse photography of the reaction as shown in Fig. 2 determined the reaction time of the amalgamated layer to be in the range of 1.5-2.0 hr. Scanning microscopy showed that this reaction was completed in all sam-

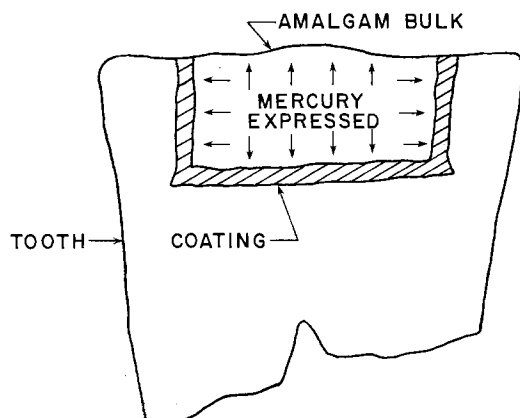


Fig. 1. Mercury expressed to cause selective interfacial amalgamation.

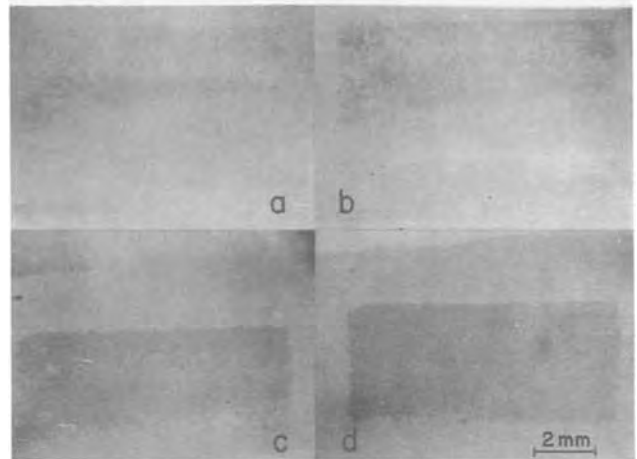


Fig. 2. Selective interfacial amalgamation formation

ples having initial unreacted silver layers ranging from 10 to  $500 \mu\text{m}$ . In addition scanning microscopy and x-ray energy analysis showed integrity of the selectively amalgamated layer, no tin present at the surface, and continuity of the  $\gamma_1$  phase into the amalgam bulk as shown in Fig. 3.

Corrosion testing results of spherical amalgam controls, high copper amalgam controls, and selectively amalgamated samples at 80 days are shown in Fig. 4. While the high copper alloy shows a significant improvement over the conventional alloy, both show corrosion while the selectively amalgamated sample shows none. The x-ray energy trace shown in Fig. 5 shows an absence of tin from the surface of the selectively amalgamated sample after corroding for 80 days while tin is present at the surface of the conventional alloy. At nine months the conventional alloy is essentially destroyed by the corrosion process while the selectively amalgamated sample shows good integrity. However at 9 months the alloyed layer is beginning to show dissolution not due to corrosion but due to the methyl cellulose binder of the original silver suspension.

### Conclusion

These results have shown that the process of selective interfacial amalgamation is indeed feasible. Samples prepared have shown no tin at the surface even though the solubility of tin in mercury is 1.1 w/o. This may be accounted for since up to 7 atoms of tin may be present in the  $\gamma_1$  lattice. In addition the  $\gamma_1$  layer becomes an integral part of the total amalgam with a continuity of the  $\gamma_1$  phase. Finally the amalgam system has been electrochemically stabilized showing a marked improvement of the corrosion characteristics



Fig. 3. Scanning electron micrograph of selectively amalgamated spherical alloy.

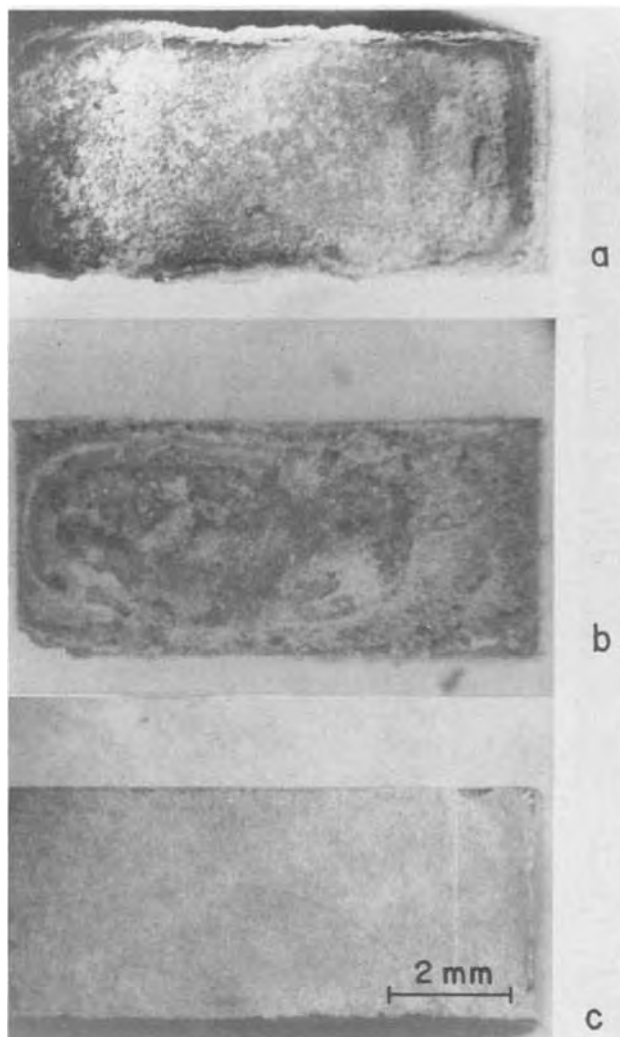


Fig. 4. Corrosion samples at 80 days in 1.0 w/o NaCl at 37°C. (a) Spherical alloy, (b) high Cu alloy, and (c) selective interfacially amalgamated sample.

of this system over both conventional and a high copper amalgam. Further work on this system is now in progress and results will be published in subsequent papers.

#### Acknowledgments

This investigation was supported in part by NIH Contract USPHS DE-02111 and NIDR Traineeship USPHS 5T0, DE00115.

Manuscript received June 9, 1976. This was Paper 30 presented at the Washington, D. C., Meeting of the Society, May 2-7, 1976.

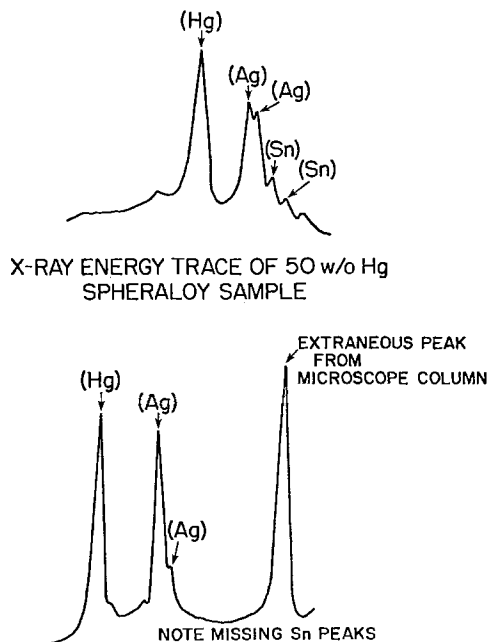


Fig. 5. X-ray energy trace of 50 w/o Hg silver coated spher alloy sample at 37°C for 80 days.

Any discussion of this paper will appear in a Discussion Section to be published in the June 1977 JOURNAL. All discussions for the June 1977 Discussion Section should be submitted by Feb. 1, 1977.

Publication costs of this article were assisted by the University of Virginia.

#### REFERENCES

1. E. Wagner, *Dtsch. Zahnärztl. Z.*, **17**, 99 (1962).
2. K. D. Jorgensen, *Acta Odontol. Scand.*, **23**, 347 (1965).
3. H. Otani, W. A. Jesser, and H. G. F. Wilsdorf, *J. Biomed. Mater. Res.*, **7**, 523 (1973).
4. R. S. Mateer and C. D. Reitz, *J. Dental Res.*, **49**, 399 (1970).
5. L. B. Johnson, K. R. Lawless, G. E. Stoner, J. Gardner, R. Young, T. R. Gerosky, S. Oppenheimer, S. T. Bender, and M. J. Neary, "Some Properties of Au-Containing Dental Amalgam," Unpublished, Univ. of Virginia (1971).
6. D. B. K. Innes and W. V. Youdelis, *J. Can. Dental Res.*, **29**, 587 (1963).
7. N. K. Sarkar and E. H. Greener, IADR 49th General Meeting, Chicago, March 1971.
8. D. F. Duperon, M. D. Neville, and Z. Kesloff, *J. Prosthet. Dent.*, **25**, 650 (1971).
9. D. G. Mahler, IADR 49th General Meeting, Chicago, March 1971.
10. R. M. Waterstrat, IADR, 54th General Meeting, Miami Beach, March 1976.

# Kinetics of the Extended Growth of Anodic Oxide Films at Platinum in H<sub>2</sub>SO<sub>4</sub> Solution

A. Ward,\* A. Damjanovic,<sup>1</sup> E. Gray, and M. O'Jea<sup>2</sup>

Xerox Corporation, Webster Research Center, Webster, New York 14580

## ABSTRACT

The kinetics of growth of anodic oxide films at platinum in 0.1N H<sub>2</sub>SO<sub>4</sub> solution have been studied by *in situ* chronoellipsometry both under constant potential and under constant current mode of polarization. Two regions of growth can now be distinguished. In the first, the kinetics of growth satisfy the formalism of the Cabrera-Mott model of high field assisted formation and migration of ions in the oxide phase, i.e.

$$i = i_0 \exp \left[ \frac{\alpha \Delta V_f}{d} \right]$$

where  $\Delta V_f$  is the potential difference across the oxide film and  $d$  is the film thickness. In the first region, oxide growth is the only reaction that occurs at the electrode. Following this initial growth, which is already completed at a thickness of 4-6Å depending on the rate of growth, oxygen starts to evolve but the oxide film continues to grow though now with a reduced rate. The kinetics of growth in the second region are described by an equation of the form

$$i = i_0 \exp \left[ \frac{-d(t)}{d_0} + \frac{\Delta V_f(t)}{V_0} \right]$$

This equation for the extended growth of platinum oxide films is diametrically different from that which describes the initial growth. The complex nature of oxide growth at platinum is discussed in relation to the oxygen evolution reaction.

It has been shown in a previous paper (1) that the frequently observed (2-6) linear charging curves associated with the initial galvanostatic growth of anodic films on Pt in acid solutions satisfy the formalism of the Cabrera-Mott model (7) for high field assisted ionic growth of oxide films. Starting from about 1.0V (*vs.* HE), electrode potential at any constant applied current density (*e.g.*, from 10<sup>-6</sup> to 10<sup>-2</sup> A·cm<sup>-2</sup>) initially increases linearly with time or charge,  $q$  (*cf.*, Fig. 1). No oxygen evolves in this linear  $V$ - $q$  region, hence  $q$  gives a measure of the anodic film thickness. The slopes  $(\partial V / \partial q)_i$  in this region are proportional (1) to  $\log i$ . Chronoellipsometric thickness-potential relationships closely follow the  $q$ - $V$  relationships. It follows then that the growth rate is represented by

$$i = i_0 \exp \left[ \frac{\alpha(V - V_0)}{d} \right] \quad [1]$$

where  $i_0$  is the exchange current density for oxide growth,  $\alpha$  is the transfer or field coefficient,  $d$  is the film thickness, and  $V_0$  ( $\approx 0.9V$ ) is the potential at  $d = 0$  so that  $(V - V_0)/d$  is the field within the oxide film. This equation has the same form as the Cabrera-Mott expression for high field assisted ionic growth of oxide films.

Following the linear  $V$ - $q$  or  $V$ - $d$  region, which ends at  $q = 0.8$  to  $1.3$  mC·cm<sup>-2</sup> depending on current density, oxygen begins to evolve and soon becomes the major reaction. After the knee in the  $V$ - $T$  curves (*cf.*, point N, Fig. 1), the electrode potential continues to increase with time but now only very slowly. Early work by Bockris and Huq (8) indicates that the increase in electrode potential is logarithmic. It has since been shown that this increase in potential under galvanostatic conditions is due to the effect

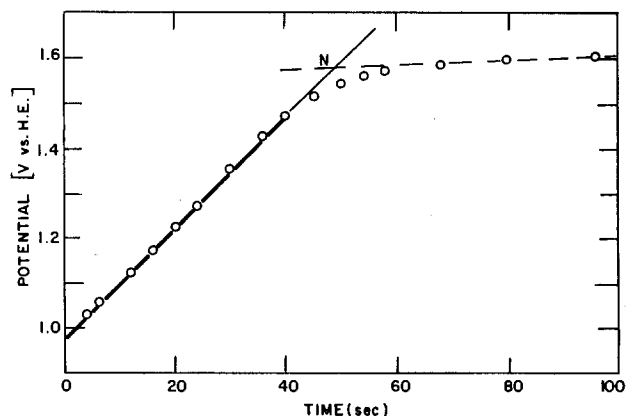


Fig. 1. Change of potential with time of polarization at constant current density  $i = 2 \cdot 10^{-5} \text{A} \cdot \text{cm}^{-2}$ .

of the very slow and extended growth of an insulating anodic oxide film on the catalysis of the oxygen evolution reaction. The relationship between anodic film thickness, electrode potential, and current density for oxygen evolution has been given by (9)

$$i_{O_2} = A \exp \left[ \frac{-\delta d}{2} \right] \exp \left[ \frac{\alpha F \Delta V}{RT} \right] \quad [2]$$

where  $\delta$  is independent of potential  $\Delta V$  ( $= V - V_{REV}$ ) or current density;  $A$  is a constant at a given pH and temperature; and  $\alpha$  is the transfer coefficient equal to about 0.5. Other symbols have their usual significance. Schultze and Vetter (10) have obtained a similar relationship but with  $\delta$  dependent on  $V$  and with  $\alpha \approx 0.62$ . Now, if potential increases with logarithm of time of polarization, as evident from Bockris and Huq's work, then from Eq. [2] it follows that the thickness,  $d$ , of the oxide film should increase logarithmically with time, i.e.

$$d(t) = a + b \log(t) \quad [3]$$

\* Electrochemical Society Active Member.

<sup>1</sup> Present address: Allied Chemical Corporation, Morristown, New Jersey 07960.

<sup>2</sup> Present address: Eastman Kodak Company, Rochester, New York 14650.

Key words: ellipsometry, growth mechanism, oxygen.

This dependence, which is known as the "direct logarithmic law of growth," has been observed for anodic film growth at platinum under constant potential conditions (11, 12).

For growth according to the Cabrera-Mott mechanism under conditions of constant potential difference across the oxide film, Eq. [1] can be integrated by parts and the dependence of thickness on time obtained (2). Writing  $\alpha V = d_0$  and assuming that all current is used for oxide growth, Eq. [1] reduces to

$$\frac{d_0}{d(t)} = \text{const.} = \log(t) \quad [4]$$

This equation is known as the "inverse logarithmic law of growth." It has recently been shown that under constant potential conditions the first anodic film on Pt grows according to this law (13).

Evidently, the extended growth of anodic oxides on platinum [and on gold (14)] under potentiostatic conditions either does not occur according to the Cabrera-Mott mechanism, or does not occur under conditions of constant potential difference across the oxide film.

In the present study, the long term growth of anodic oxides on platinum has been followed by chronoellipsometry under both galvanostatic and potentiostatic conditions with the objective of clarifying the growth kinetics and mechanism. There does not appear to have been any previous attempt to continuously monitor the time-dependence of oxide film thickness on Pt in the oxygen evolution region.<sup>3</sup>

In addition to this study of long term extended growth of anodic films, the behavior of the system has been examined during stepwise decreases of electrode potential following polarization at different constant potentials for a fixed time. The objective here was to confirm the validity of the oxygen evolution Eq. [2], derived previously on the basis of experiments under galvanostatic conditions, by examining the catalysis of the oxygen evolution reaction under potentiostatic conditions also.

### Experimental

An automatic recording ellipsometer was used to follow galvanostatic and potentiostatic anodic film growth on Pt as a function of time. The ellipsometric setup, cell, platinum disk electrode, and solution preparation (0.1N H<sub>2</sub>SO<sub>4</sub>) have been described previously (1). The azimuth,  $\alpha$ , and ellipticity,  $\epsilon$ , of the elliptically polarized light reflected from the Pt disk face were initially measured with the electrode held at +0.5V vs. HE (after first subjecting the electrode to several anodic and cathodic pulses, ending cathodic, and exchanging the electrolyte). A constant current density between 10<sup>-5</sup> and 3.10<sup>-3</sup> A-cm<sup>-2</sup> or constant potential between 1.5 and 1.8V was then applied to the disk and the ellipsometric parameters were monitored continuously at frequencies up to 54 sec<sup>-1</sup> for periods up to 10<sup>4</sup> sec. Potential or current was monitored synchronously.

It was first necessary to assess the effect of oxygen accumulation at the electrode on the ellipsometric parameters. This was done by comparing the azimuth and ellipticity monitored continuously with the same parameters monitored at intervals after vigorous purging of the electrode with a jet of oxygen directed at the reflecting surface. Except at the highest current densities ( $i > 10^{-3}$  A-cm<sup>-2</sup>) the discrepancy was surprisingly small and could be ignored. Upon close inspection the reason for this becomes clearer. Only that light which strikes the surface

clearly and is reflected without being intercepted by a bubble can remain within the acceptance angle of the detection system. Any light which encounters a bubble in its trajectory is scattered out of the regime of acceptance. Accordingly, the detector faithfully records azimuth and ellipticity as long as there is sufficient light to activate the system, i.e., as long as a significant portion of the electrode remains bubble free. Of course, it is no longer possible to monitor the relative intensity of the reflected light under these conditions so that a complete determination of the anodic film optical constants and thickness of the oxide film from ellipsometric parameters alone becomes inaccessible. However, in the case of the Pt/anodic oxide/aq. H<sub>2</sub>SO<sub>4</sub> system the optical characteristics have been well documented (16-19) so that a knowledge of the relative intensity variation is not required for an unambiguous determination of film thickness. In the work reported here the optical constants used in the analysis of the ellipsometric data have been taken from Kim, Paik, and Bockris (16) and the thickness calculations have been further simplified by the use of Drude's equations for thin non-absorbing films. The changes in  $\alpha$  and  $\epsilon$  associated with the changes in the electrode surface from the initial, freshly reduced film-free state (at +0.5V vs. HE) to the anodically oxidized state at some later time were used to calculate the change ( $\Delta_0 - \Delta$ ) in the relative phase retardation,  $\Delta$ , between components of the light polarized perpendicular and parallel to the plane of incidence, respectively. This change was used to calculate the mean film thickness,  $d$ , using Drude's approximation, i.e.

$$\tan \Delta = \frac{\tan 2\epsilon}{\sin 2\alpha} \quad [5]$$

$$(\Delta_0 - \Delta) = kd \quad [6]$$

where  $k$  depends on the refractive index of the film,  $n_1 = 2.80$ , the refractive index of the Pt substrate,  $n_2 = 1.94$ , and the absorption constant of the substrate,  $\kappa = 4.36$ , at the wavelength of light,  $\lambda = 5460\text{\AA}$ , and angle of incidence,  $\phi = 75^\circ$ , used in the experiments. Constant  $k$  is calculated as 0.263 deg·Å<sup>-1</sup>.

### Results

A typical relationship between potential and time (or thickness) for polarization at a constant current density is shown in Fig. 1. At this current density [corrected for roughness factor, see Ref. (1)] each increment of 0.1V in potential in the initial linear region of growth corresponds to an increase in mean thickness of the anodic film equivalent to 150 μC-cm<sup>-2</sup>. The growth at first is rapid and linear but levels off at a potential between 1.5 and 1.9V depending on applied current density [see Ref. (1)]. The point at which the linearity ceases (N in Fig. 1) is taken as the origin of a new time axis for extended galvanostatic growth. If potential at a constant current density is plotted on this new axis as a logarithmic function of time, a straight line results as shown in Fig. 2. A straight line also results when ellipsometric thickness is plotted in the same way (Fig. 3). Furthermore, the thickness-log-time relationships for different current densities are parallel and equally spaced for equal increments of log-current density.

It may be noted that only a small part of the current is used for oxide formation. For instance, at 10<sup>-3</sup> A-cm<sup>-2</sup> during the first 10<sup>3</sup> sec, less than 0.3% of the total charge goes for oxide formation, so oxygen evolution is the major reaction.

From Fig. 3 it is observed that

$$\left[ \frac{\partial d(t)}{\partial \ln t} \right]_{i_{02}} = \psi = 0.34\text{\AA} \quad \text{independent of } i_{02} \quad [7]$$

<sup>3</sup>Sirohi and Genshaw (15) have, however, used an intensity transient technique to monitor phase retardation,  $\Delta$ , on gold after potentiostatic polarization for various fixed times in aq. H<sub>2</sub>SO<sub>4</sub>. They found a logarithmic relationship between  $\Delta$  and time of polarization.

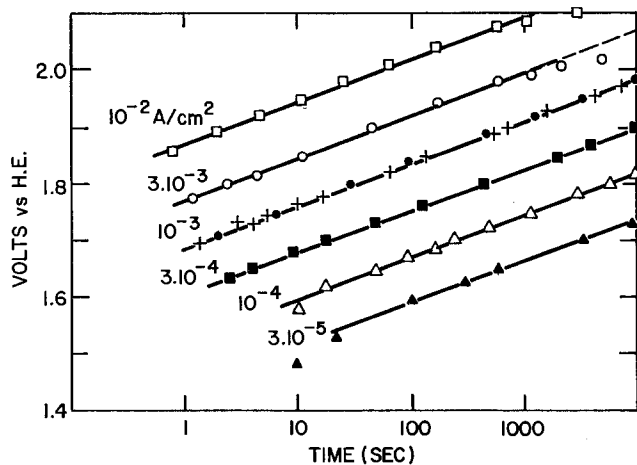


Fig. 2. Change of potential with time at various constant current densities,  $i_p$ .

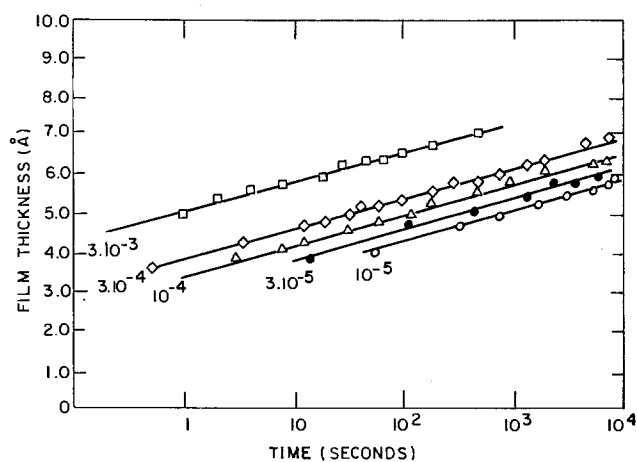


Fig. 3. Change of ellipsometric thickness with time of polarization at various constant current densities. The major reaction is  $O_2$  evolution.

Further, from the separation of the parallel  $d(t)$ - $\log t$  lines one obtains

$$\left[ \frac{\partial d(t)}{\partial \ln i_{O_2}} \right]_t = \epsilon = 0.38 \text{ \AA} \text{ independent of } (t) \quad [8]$$

as shown in Fig. 4.

At a constant potential too, the ellipsometric thickness of the oxide film increases logarithmically with time as shown in Fig. 5. Here, the initial growth is

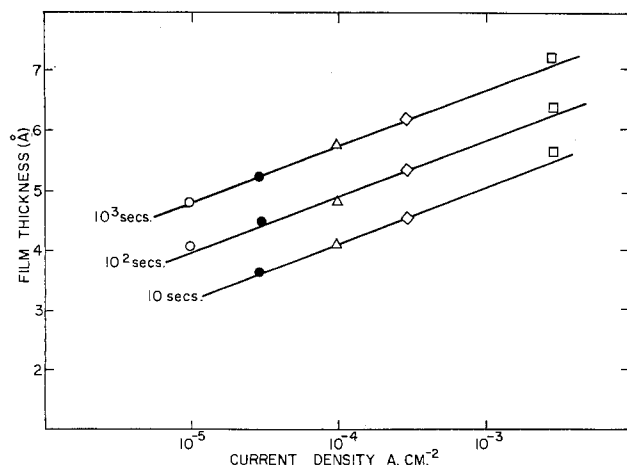


Fig. 4. Dependence of ellipsometric thickness on log current density of polarization for three fixed times of polarization.

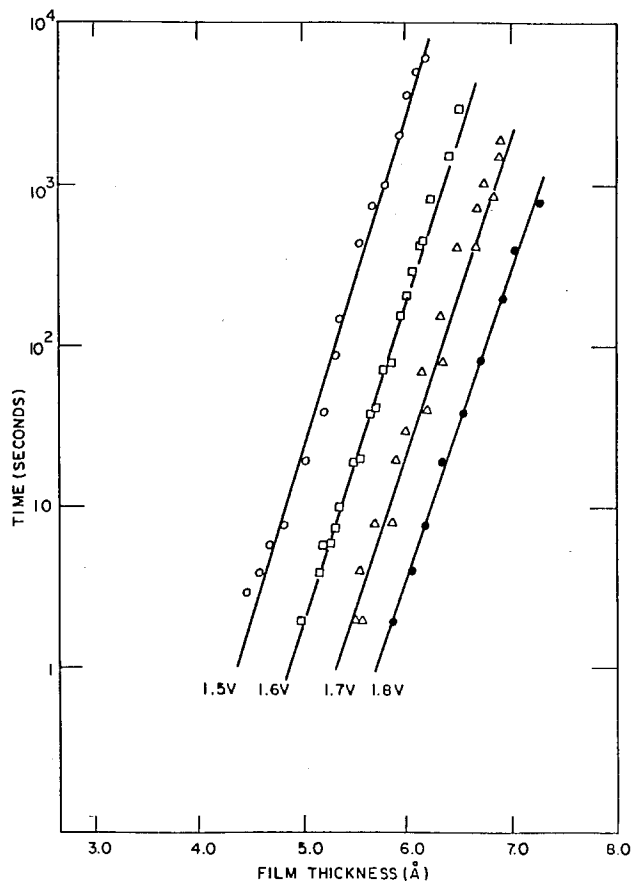


Fig. 5. Change of ellipsometric thickness with time of polarization at various constant potentials,  $V_p$ .

virtually instantaneous and the thickness-time relationship is evaluated from the onset of polarization, but see Ref. (13). Again, since the slopes of the lines for the different potentials are independent of other variables it follows that

$$\left[ \frac{\partial d(t)}{\partial \ln t} \right]_V = \omega = 0.23 \text{ \AA} \text{ independent of } V \quad [9]$$

Note, however, that  $\omega \neq \psi$ . Furthermore, the  $d$ - $\log t$  lines at different potentials are separated in such a way that

$$\left[ \frac{\partial d(t)}{\partial V} \right]_t = \sigma = 4.7 \text{ \AA } V^{-1} \text{ independent of } (t)$$

[10]

as shown in Fig. 6.

The effect on ellipsometric thickness and current density of polarizing at different constant potentials for fixed times of  $10^2$  and  $10^3$  sec is shown in Fig. 7 and 8, respectively. Also shown is the effect of making stepwise decreases of potential starting from the potential of the initial fixed-time polarization. The open circles in the left-hand side of Fig. 7 are the thicknesses obtained at a given potential,  $V_p$ , after 100 sec, starting from the initially oxide-free state. The open circles in the right-hand side of the same figure are current densities at various constant  $V_p$  for the same time of polarization. A linear dependence of both thickness and log current density on  $V_p$  is obtained under these conditions. The slope  $(\partial d / \partial V_p)$  is close to  $4.7 \text{ \AA } V^{-1}$  and  $(\partial V_p / \partial \log i)$  to  $170 \text{ mV/decade of current density}$ .

After an electrode has been kept at  $V_p$  for 10<sup>2</sup> sec and the potential decreased in steps, no change in thickness,  $d$ , is observed (open squares in the left-hand side of Fig. 7). In contrast to this, the current density,  $i$ , decreases as potential,  $V$ , is decreased (open squares in right-hand side of Fig. 7). The same be-

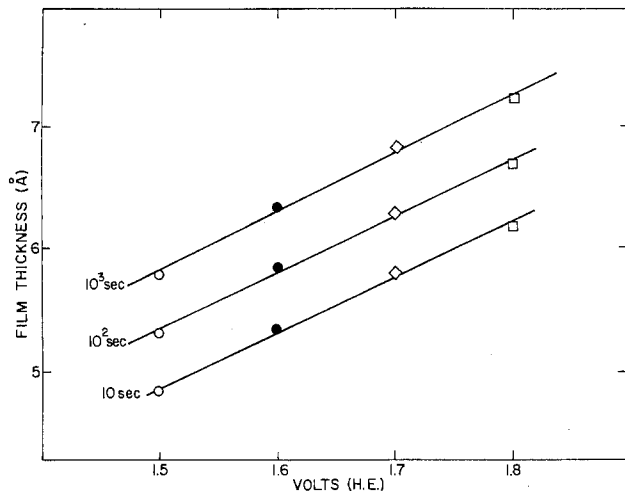


Fig. 6. Dependence of ellipsometric thickness on potential for three fixed times of polarization.

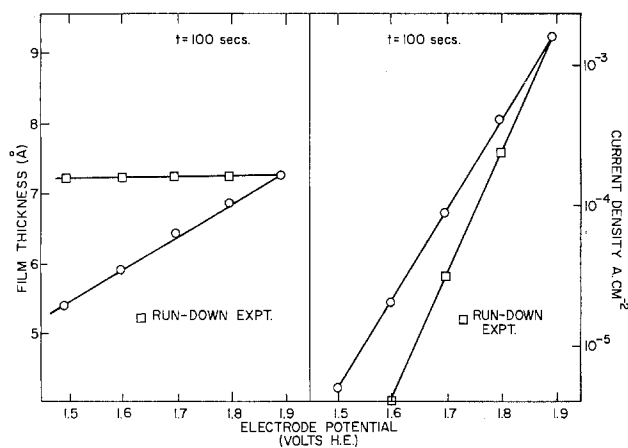


Fig. 7. Dependence of ellipsometric thickness and current density on electrode potential after potentiostatic polarization for 100 sec (open circles), and after subsequent stepwise decreases of potential (open squares).

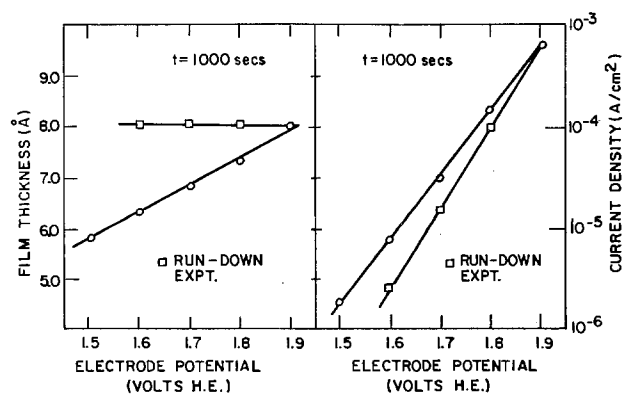


Fig. 8. Dependence of ellipsometric thickness and current density on electrode potential after potentiostatic polarization for 1000 sec (open circles), and after subsequent stepwise decreases of potential (open squares).

havior is observed for an electrode prepolarized at  $V_p$  for  $10^3$  sec as shown in Fig. 8. The slope ( $\partial V/\partial \log i$ ) is now close to 120 mV/decade of current density, i.e., close to  $2.3 (2RT/F)$ . No change is observed in any of the slopes when an electrode is polarized for a longer time. Note however, that for the shorter time of polarization the film thickness at any given potential is smaller and the current density is higher than that observed at longer times of polarization.

## Discussion

For any constant time of polarization at a constant potential,  $V_p$ , current density increases logarithmically with  $V_p$  at a rate close to  $(170 \text{ mV/decade})^{-1}$ . The same rate is obtained (9) when current density is held constant and potential is recorded after a fixed time of polarization. Film thickness achieved during potentiostatic polarization at  $V_p$  remains constant after potential is decreased to lower values. An analogous effect under galvanostatic conditions has already been reported (9). A "hysteresis" in surface coverage has been reported also in coulometric studies though in the potential region lower than that of the present work (20, 21).

A  $V$ - $\log i$  relationship which is linear over several decades of current density with slope  $dV/d \log i$  close to  $2.3 (2RT/F)$  is obtained therefore only under the condition of constant thickness of the oxide film, i.e.

$$\left[ \frac{\partial V}{\partial \ln i} \right] = \text{const.} = \frac{2RT}{F} \quad \text{independent of } V, d, i, t \quad [11]$$

The same result has been obtained in galvanostatic studies (9). It follows, as in the galvanostatic case, that a unique linear relationship exists between  $V$ ,  $\ln i$ , and  $d$ , i.e.

$$f(V, d, \ln i) = \text{const.} \quad [12]$$

This relationship can be obtained in the following way. First, from Fig. 7 and 8 one evaluates approximately  $(\partial \ln i/\partial d)$  at any  $V_p$  and then from<sup>4</sup>

$$d \ln i = \left[ \frac{\partial \ln i}{\partial V} \right]_d dV + \left[ \frac{\partial \ln i}{\partial d} \right]_V dd \quad [13]$$

obtains

$$\ln i = \frac{FV}{2RT} - \frac{\delta d}{2} + \text{const.} \quad [14]$$

Here,  $\delta = 2(\partial \ln i/\partial d) \approx 2.8 \text{ \AA}^{-1}$ . This equation is identical to Eq. [2]. As expected the same rate equation describes the oxygen evolution reaction regardless of the pretreatment of the electrode or mode of polarization. The observed changes in catalytic activity are due to changes in thickness of the anodic oxide film.<sup>5</sup>

Turning now to the long term growth of oxide films, inspection of Fig. 3 and 5, or integration of Eq. [7]-[10] gives the dependence of thickness on time during the extended growth

$$d(t) = \epsilon \ln i_{O_2} + \psi \ln \left[ \frac{t}{t_0} \right] + C' \quad [15]$$

for constant current, or

$$d(t) = \sigma V + \omega \ln \left[ \frac{t}{t_0} \right] + C'' \quad [16]$$

for constant potential mode of polarization. As shown above,  $\epsilon$ ,  $\sigma$ ,  $\psi$ , and  $\omega$  are constants independent of  $V_p$  or  $i_p$ . Equations [15] and [16] describe the "direct logarithmic law" of growth. A similar dependence has been deduced from coulometric thickness data by Feldberg, Enke, and Bricker (11) and by Vetter and Schultze (12). According to Vetter and Schultze, however, the  $(\partial q/\partial \ln t)_V$  slopes increase with increasing potential<sup>6</sup> so that  $\omega$  is not independent of  $V$ . Equation [16] for the extended growth of oxide films is diametrically different from Eq. [4] which describes the initial stages of growth of anodic films at constant potential.

From Eq. [15] combined with [2], which holds irrespective of the mode of polarization, one obtains

<sup>4</sup> Subscript  $p$  can now be dropped because of Eq. [12].

<sup>5</sup> A change in the film properties may also affect the rate at potentials higher than 2.0V as recently shown by Visscher and Bljlevens (22).

<sup>6</sup> However, in the potential range where oxygen evolution is the major reaction, e.g., from 1.6 to 1.9V, the  $q - \log t$  lines of Vetter and Schultze appear to be nearly parallel [cf. Fig. 5 in Ref. (12)].

$$\frac{2RTd}{F} \left[ \frac{1}{\epsilon} + \frac{\delta}{2} \right] = V + \frac{2RT\psi}{\epsilon F} \ln \frac{t}{t_0} + C''' \quad [17]$$

This equation can now be compared with [16]. The coefficient  $(2RT\psi/F\epsilon) \approx 0.044V$  is numerically nearly equal to  $\omega/\sigma (\approx 0.047V)$  of Eq. [16]. Further, with  $\delta$  evaluated from the constant potential data, the ratio ( $\approx 1.13$ ) of the coefficients for  $d$  in [16] and [17] is fairly close to 1. This comparison of coefficients suggests that these two equations are identical (excluding the constant terms), and that both equations are valid for either mode of polarization (with Eq. [2] providing the link between them). The apparent self-consistency of the experimental parameters leads to the conclusion that the mechanism of the extended growth is independent of the mode of polarization. Now one can obtain an equation for the rate of growth of the anodic oxide film in the extended growth regime. From Eq. [15], [16], and [2], differentiation and elimination yields

$$r \frac{dd}{dt} = i = i_0 \exp \left[ -\frac{d}{\omega} + \frac{\sigma}{\omega} \Delta V \right] \quad [18]$$

Here,  $r$  is a conversion factor ( $1.1 \cdot 10^{-4} \text{ CA}^{-1} \text{ cm}^{-2}$ ) and  $\Delta V$  refers here to any arbitrary zero. Again, this equation holds both for galvanostatic and for potentiostatic mode of polarization. Evidently, it is different from Eq. [1] which describes the initial stages of growth of anodic oxide films at platinum.

Constant potential mode of growth does not mean that the surface oxide film grows under the condition of constant potential difference across the oxide film itself,  $\Delta V_f$ . The major ongoing reaction is oxygen evolution and  $\Delta V_f$  will change with time to accommodate this reaction. It has recently been suggested that the current for oxygen evolution is given by (9)

$$i_{O_2} = X_0 \exp(-\delta d) \exp \left[ \frac{F\Delta V_f'}{RT} \right] \\ = A \exp \left[ -\frac{\delta d}{2} \right] \exp \left[ \frac{F\Delta V}{2RT} \right] \quad [19]$$

$\Delta V_f'$  is the change of potential across the oxide film from that at the reversible oxygen potential. It is taken that  $\Delta V_f' = \Delta V_f + \text{const.}$  From [19]  $\Delta V_f$  is given by

$$\Delta V_f' = \frac{RT}{2F} \delta d + \frac{\Delta V}{2} + \text{const.} \quad [20]$$

It follows that when  $V$  is constant the potential across the oxide film increases logarithmically with time.

The next step is to examine whether the apparent difference in the kinetics of the initial and extended growth is due to this logarithmic change of  $\Delta V_f$  with time rather than to a change in the mechanism of growth itself. The rate of growth can be obtained by differentiating [15], [16], and [20] with respect to time and eliminating  $dV/dt$  and  $d \ln i/dt$  with the help of [19]

$$i = i_0 \exp \left[ -\frac{1 + \epsilon\delta}{\psi} d(t) + \frac{F\Delta V_f'}{\psi RT} \right] \quad [21]$$

Equation [21], which holds for growth both under constant potential and constant current conditions, can now be compared with the rate equation [1] which, for a constant  $\Delta V_f = V - V_0$ , describes growth according to the "indirect logarithmic law". Clearly, the expressions are different. Furthermore, as shown in Fig. 9, plotting the experimental data for the extended growth in the form of  $1/d$  vs.  $\log t$  does not lead to the linear relationships predicted by Eq. [4]. The observed change in the kinetics of initial and extended growth is therefore due, not to a particular

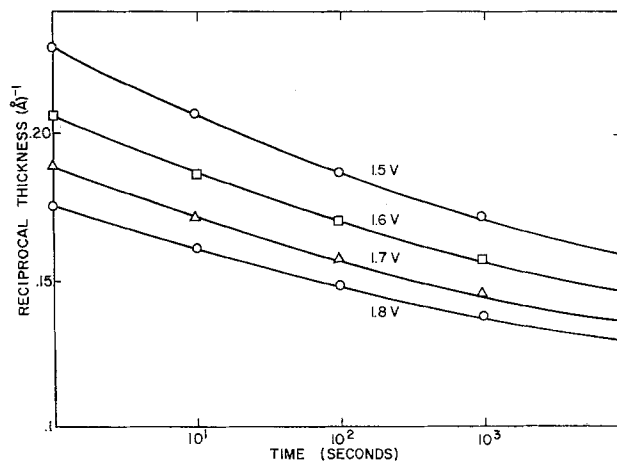


Fig. 9. Plot of the reciprocal of the ellipsometric thickness vs. time for polarization at various constant potentials. The plots are not linear.

change in  $\Delta V_f$ , but rather to a change in the mechanism of growth itself.

An equation identical in form to [18] is frequently observed for the growth of anodic oxide films at other metals, e.g., at iron with no evolution of oxygen, i.e., when the major reaction is the growth of the oxide film itself (23). At iron electrodes, the change of potential with time represents the change arising only from the increase in thickness of the oxide film (23-25). In contrast to this, at platinum electrodes, the change of potential with time represents the change due to the major ongoing reaction, the oxygen evolution reaction, and is only indirectly related to the thickness of the oxide film.

The change of growth mechanism from the initial growth that proceeds according to Eq. [1], to the extended growth, that proceeds according to Eq. [18] or [21], occurs after  $O_2$  starts to evolve or becomes the major reaction. It is not clear why the mechanism changes at this point or whether the change is related to the onset of an electronic current through the oxide film which in turn causes redistribution [cf. Ref. (26)] of the anode potential difference  $V$  between the potential difference across the oxide film,  $\Delta V_f$ , and that across the double layer,  $\Delta V_{dl}$ , in such a way that  $\Delta V_f$  is significantly reduced. If this were the case the mechanism of high field assisted diffusion and growth would cease to operate and an alternative mechanism, perhaps similar to that described by Sato and Cohen (23) for anodic oxidation of iron, would take over.

### Acknowledgments

The authors are grateful to Drs. M. L. Hair and L. B. Harris for valuable discussions. Thanks are due also to Ms. J. Hopkins for patient typing of the manuscript.

Manuscript submitted April 12, 1976; revised manuscript received June 10, 1976.

Any discussion of this paper will appear in a Discussion Section to be published in the June 1977 JOURNAL. All discussions for the June 1977 Discussion Section should be submitted by Feb. 1, 1977.

Publication costs of this article were assisted by Xerox Corporation.

### REFERENCES

1. A. Damjanovic, A. T. Ward, B. Ulrick, and M. O'Jea, *This Journal*, **122**, 471 (1975).
2. S. Schuldiner and T. B. Warner, *ibid.*, **112**, 212 (1965).
3. R. Thacker and J. P. Hoare, *J. Electroanal. Chem.*, **30**, 1 (1971).

4. J. L. Ord and F. C. Ho, *This Journal*, **118**, 46 (1971).
5. K. J. Vetter and J. W. Schultze, *J. Electroanal. Chem.*, **34**, 141 (1972).
6. A. Damjanovic and A. T. Ward, "International Review of Science, Physical Chemistry," Series II, p. 103, Butterworths, London (1976).
7. N. Cabrera and N. F. Mott, *Rep. Prog. Phys.*, **12**, 163 (1949).
8. J. O'M. Bockris and A.K.M.S. Huq, *Proc. Roy. Soc.*, **A237**, 271 (1956).
9. A. Damjanovic, A. T. Ward, and M. O'Jea, *This Journal*, **121**, 1186 (1974).
10. J. W. Schultze and K. J. Vetter, *Electrochim. Acta*, **18**, 889 (1973).
11. S. W. Feldberg, C. G. Enke, and C. E. Bricker, *This Journal*, **110**, 826 (1963).
12. K. J. Vetter and J. W. Schultze, *J. Electroanal. Chem.*, **34**, 131 (1972).
13. L. B. Harris and A. Damjanovic, *This Journal*, **122**, 593 (1975).
14. A. C. Makrides, *ibid.*, **113**, 1158 (1966).
15. R. W. Sirohi and M. A. Genshaw, *ibid.*, **116**, 910 (1969).
16. S. H. Kim, W. Paik, and J. O'M. Bockris, *Surf. Sci.*, **33**, 617 (1972).
17. A. K. N. Reddy, M. A. Genshaw, and J. O'M. Bockris, *J. Chem. Phys.*, **48**, 671 (1968).
18. W. Visscher, *Optic*, **26**, 407 (1967).
19. R. Parsons and W. Visscher, *J. Electroanal. Chem.*, **36**, 329 (1972).
20. H. A. Laitinen and C. G. Enke, *This Journal*, **107**, 773 (1960).
21. S. Gilman, *Electroanal. Chem.*, **2**, 111 (1967).
22. W. Visscher and M. Blijlevens, *Electrochim. Acta*, **19**, 387 (1974).
23. N. Sato and M. Cohen, *This Journal*, **111**, 512 (1964).
24. J. O'M. Bockris, M. Genshaw, V. Brusic, and H. Wroblowa, *Electrochim. Acta*, **16**, 1859 (1971).
25. H. Wroblowa, V. Brusic, and J. Bockris, *J. Phys. Chem.*, **75**, 2823 (1971).
26. A. Damjanovic and B. Jovanovic, *This Journal*, **123**, 374 (1976).

## Influence of Substrate Structure on Electroless Gold Deposition

R. Sard\* and B. C. Wonsiewicz

*Bell Laboratories, Murray Hill, New Jersey 07974*

### ABSTRACT

The electroless gold process invented by Okinaka is capable of producing high quality gold conductors by direct deposition onto catalytic regions of a substrate. This study shows that the crystallographic orientation of the metal substrates onto which electroless gold is plated may have a profound effect on the process kinetics and the structure of the deposits. On single crystal copper substrates, the initial plating rate can vary by an order of magnitude with  $\{111\} \gg \{100\} > \{110\}$ . TEM studies show that the initial growth is epitaxial and accompanied by profuse microtwinning. X-ray pole figure results clearly show that the transition from slow initial plating on  $\{100\}$  and  $\{110\}$  to a much faster rate equivalent to that of the  $\{111\}$  surfaces is due to the formation of a  $\langle 111 \rangle$  preferred orientation which occurs due to complex multiple twinning processes. Experiments with a variety of technologically relevant polycrystalline substrates are in general agreement with the single crystal results. The substrate effects identified in this work as being important for the electroless gold plating process are believed to be applicable to other catalytic systems for metal deposition.

In 1969, Okinaka discovered a plating process capable of autocatalytic gold deposition which is therefore called electroless gold (1, 2). It is suitable for a number of electronic applications and has recently been applied to the formation of beam leads on integrated circuits (3). These applications have utilized the unique attribute of selective gold deposition at catalytic regions of a substrate. Substrates capable of catalyzing the electroless gold reaction include Pd, Pt, Cu, and other noble metals (4). The gold is only applied where needed, therefore, raw materials are saved and gold does not have to be etched away. Moreover, process steps can be eliminated resulting in further economies.

The deposition conditions profoundly influence the structure of the plated film and the plating rate. In a study which examined a wide range of plating variables, Sard identified two distinct growth morphologies, a lateral or layer type and an outward or particle type (5). The more three dimensional morphology, outward growth, is favored by several factors which increase deposition rate; namely, decreasing gold concentration, increasing reducing agent concentration, and increasing temperature. Agitation is an exception; increasing agitation increases the deposition rate but favors lateral growth.

Sard also concluded that the orientation of the substrate was important in determining the orientation of the plated film. The initial stages of growth ( $\sim 10$  nm) on single crystal substrates were epitaxial; that is, the orientation of the film reproduced the orientation of the substrate. Preliminary observations indicated that the plating rate was greatest for  $\{111\}$  surfaces. When polycrystalline substrates were used, the orientation of thicker ( $1 \mu\text{m}$ ) films was similar to the substrate, as measured by the ratio of peak intensities in an x-ray diffractometer.

Oriented growth has been commonly observed in thin films (6), especially those grown by vacuum deposition or electroplating. Under special conditions epitaxial growth occurs; more generally, the deposit has a low index crystallographic direction (the fiber axis) oriented perpendicular to the plane of the sheet, but is rotationally symmetric in the plane of the sheet. Such textures are called fiber textures, by analogy with a bundle of fibers arranged with their axes all pointing in the same direction. Under certain conditions, the fiber axis in deposited films can be tipped away from the film normal, usually toward the direction of greatest mass flux.

In view of the link between substrate orientation, plating rate, and orientation for the electroless gold system, a more detailed investigation was carried out.

\* Electrochemical Society Active Member.

Key words: texture, structure, gold plating, catalysis.



A key improvement over previous studies was the use of x-ray pole figures to characterize the orientation distribution of the deposits. Pole figure determination is normally so tedious and time consuming as to rule it out for studying a large number of samples. However the use of a computer-aided system reduced the labor required to construct a pole figure from about 3 hr to 15 min (7).

The structure of films was studied at several stages of growth on single crystals and on several important polycrystalline substrates using the pole figure method. Additional data on the initial stages of growth were obtained by transmission electron microscopy (TEM), and scanning electron microscopy (SEM) was used to study the morphology of thick deposits. This approach has provided information relevant to some of the practical and fundamental aspects of electroless gold deposition. Some of our findings are undoubtedly applicable to other catalytic processes at solid/liquid interfaces.

### Experimental Details

**Single crystal substrates.**—A copper single crystal 1.5 cm in diameter was grown by the Bridgeman method. Several thin slices 1 mm thick were spark cut parallel to each of the low index planes: {111}, {100}, and {110}. The orientation of the cut surfaces was within about 1° of the true planes.

Surface damage was removed by mechanical polishing followed by a chemical bright dip in an aqueous solution of 40% H<sub>2</sub>SO<sub>4</sub>, 20% HNO<sub>3</sub>, and 0.1% HCl and electropolishing in 50% H<sub>3</sub>PO<sub>4</sub> solution. After gold plating and the completion of measurements, the crystals were recycled by dissolving the gold in an iodide solution (8), rinsing in methanol, and water, then repeating the bright dip and electropolish procedures. After about 4 such cycles the crystals showed signs of increased surface roughness and had to be repolished mechanically. This changing surface roughness was probably responsible for some minor variations noted in the plating rate and microstructure on different regions of the samples and from run to run; however these effects were judged to be of second order importance and are not considered further.

**Polycrystalline substrates.**—A number of experiments were conducted using polycrystalline samples of two different types: (i) evaporated noble metal films (Au and Pd) on titanium-coated sapphire and glass, and (ii) copper metal sheets. A more detailed description of these materials and their preparation history is given together with the results below.

**Electroless deposition.**—For most experiments, electroless deposition was carried out using the solution formulation which was previously found to give the layer-type growth: KAu(CN)<sub>2</sub>, 0.02M; KBH<sub>4</sub>, 0.4M; KOH, 0.2M; and KCN, 0.2M. Unless otherwise specified, experiments were performed at 75° ± 0.5°C using a PTFE holder to maintain the substrates in cylindrical geometry. The agitation conditions were changed by introducing a glass stirrer with flattened blade coupled to an external motor rotating at 3000 rpm. A few experiments were also performed using a carousel arrangement in which the substrates rotated at about 150 rpm on a 2 in. diameter PTFE wheel. An alternate solution, formulated with 0.005M KAu(CN)<sub>2</sub>, was also used for some experiments with forced agitation. This system was known to plate at a faster rate, due to its more negative deposition potential (9).

Film thicknesses were determined by the beta backscatter method using a promethium source and NBS calibration standards for the case of the bulk single crystal and polycrystalline Cu substrates. Although the absolute accuracy of these measurements is approximately ±5%, the results were checked against the weight gain method for sheet substrates and found to agree within 1-2%. The latter method was used for all thin film substrates. The plating rate was calculated by dividing the change in thickness averaged over the

sampling area by the plating time, based on the assumption of uniform deposits with the density of bulk gold.

**Structure determination.**—The crystallographic orientation distribution was determined by the standard pole figure technique (10) using Ni filtered Cu K<sub>α</sub> radiation and the (111) Bragg reflection. A block diagram of the system is shown in Fig. 1. An automatic pole figure goniometer (either Siemens or Norelco) was used to rotate the specimen along a predetermined scanning geometry. X-ray intensity was recorded on punched paper tape using an Ortec digital ratemeter and printout control and a Model 35 Teletype. Specimen identification and values for constructing the intensity contours were entered directly on the paper tape. The tape, together with a group of Fortran IV programs served as input to a Honeywell H-6000 computer which generated the final drawings on a Xerox LDX graphics device. The present computer charges are about three dollars for a finished pole figure. The programs are capable of making corrections for background and absorption and will smooth data if necessary. Generally, no corrections were necessary in this study. The experimental techniques used gave good results for gold deposits in excess of 0.2 μm thick.

Microstructure results were obtained using the standard methods of interference contrast (Normarski) optical microscopy and scanning and transmission electron microscopy.

### Results and Discussion

**Single crystal substrates.**—A typical set of results showing the effect of orientation on plating thickness as a function of time is illustrated in Fig. 2. The curves are drawn through averaged experimental points taken by removing the substrates periodically from a solution agitated with strong forced convection. The experimental points shown at the right edge of Fig. 2 were obtained by plating a similar set of substrates without forced convection. These data show clearly that the initial rate of gold plating, i.e., the initial slope, is highly orientation dependent with {111} > {100} > {110}, regardless of the transport conditions. By comparing the slopes over the interval 5-10 min and normalizing to {111}, one obtains relative rates for the three orientations of approximately 1 > 0.25 > 0.10. The interval from 0-5 min is complicated by the galvanic displacement effect which occurs in the first 10 nm of film growth. It is also evident from the curves that after 20 min, the rates are nearly the same

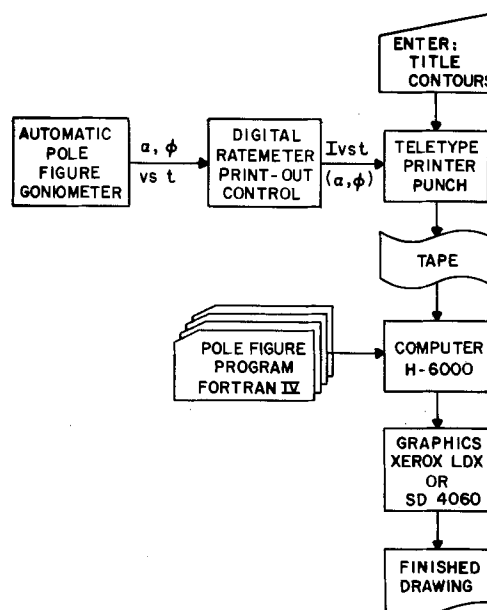


Fig. 1. Schematic of instrumentation used to obtain pole figures

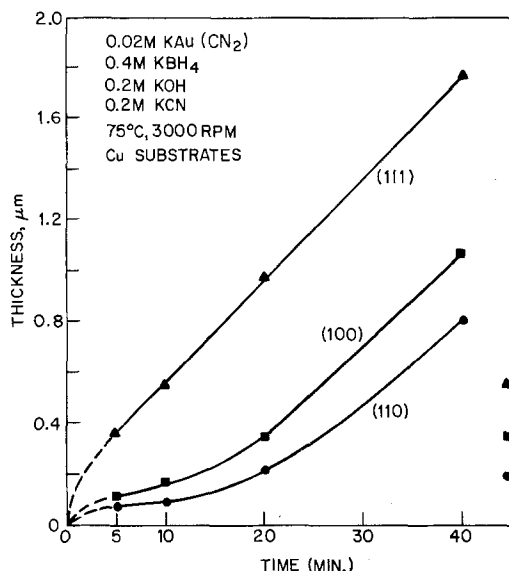


Fig. 2. Effect of orientation on electroless gold thickness vs. time of deposition.

on all three substrates, indicating a transition to steady-state conditions determined by the plating conditions. By following the changes in structure of such deposits, considerable insight was gained as to the physical aspects of the deposition mechanisms which govern this system.

The microstructures formed during the initial portion of the process, *i.e.*, the first 5 min or so, can be studied conveniently by transmission electron microscopy after chemical removal from the substrate (11). Figures 3a, 4a, and 5a illustrate the typical features evident in bright field images of Au deposits stripped from {111}, {100}, and {110} substrates, respectively, and their corresponding selected-area diffraction patterns are given in Fig. 3b, 4b, and 5b.

As the diffraction patterns show, the films at the earliest stages reproduce the substrate orientation, *i.e.*, the growth is epitaxial. This is apparently due to the displacement process as discussed previously (11). Small, parallel-sided features are visible in the micrographs; they are planar defects, small volumes of material which bear a twin orientation relationship with the matrix. In Fig. 3b, the six interior spots in hexagonal array are due to diffraction at the boundaries where twinning occurs. This result is similar to that for electroplated gold on copper (12). Similar microtwins have been observed in epitaxial evaporated films and the resulting twin-matrix structure is often called "double positioning" (13-15). The satellite reflections adjacent to the {100} reflections in Fig. 4b arise from double diffraction at the twin boundaries. This fact was confirmed by TEM dark field studies, *e.g.*, using the matrix and satellite spots encircled. The substructure evident in Fig. 3-5a is due primarily to the high density of twin faults which formed in the gold deposits.

The fact that these twins are due to deposition and not to deformation upon stripping the foils from the substrates was confirmed by the pole figures which were obtained with the deposits in place on the substrates.

Pole figures taken at the initial stages of film growth show quite clearly the epitaxial nature of the orientation as well as a weaker twin orientation. As the plating proceeds, the orientation distribution becomes more complex; the twin orientations with surface normals near  $\langle 111 \rangle$  grow in volume most quickly.

Pole figures corresponding to a later stage of plating show a very intricate structure. The simplest structure is found on the fast plating {111} substrate. In the pole figure, Fig. 6a, the solid triangles locate the {111} substrate orientation and the open triangles locate the

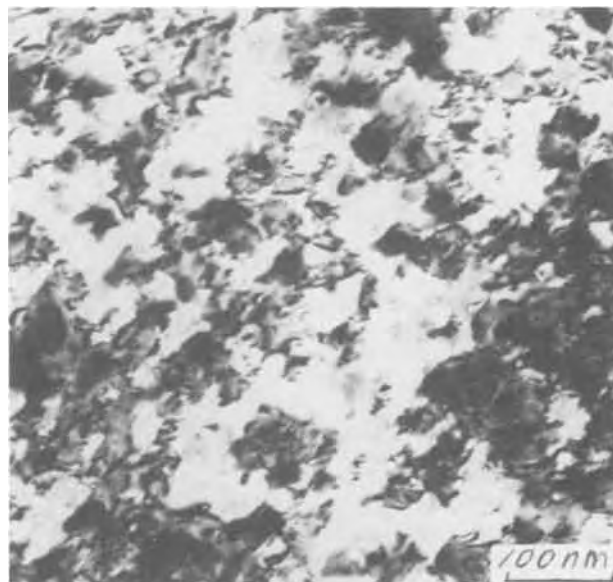


Fig. 3. TEM results for thin gold deposit on {111} substrate. (a, top) Bright-field image, original magnification 120,000 $\times$ . (b, bottom) Selected-area diffraction pattern.

twin orientation. The twinned material has mirror symmetry with the original matrix. This matrix-twin relationship is equivalent to the "double-positioning" structure evident in the early stages of film growth shown in Fig. 3.

The more complex structure evident in Fig. 6b is found in films plated on the {100} substrate. The pseudo-twelvefold symmetry apparent in the pole figure also arises from twinning. In the original epitaxial deposit, there are four  $\langle 111 \rangle$  poles symmetrically oriented as indicated by the four half-filled squares in Fig. 6b. Twinning on one of the {111} planes will produce the orientation shown as open squares labeled A(1) through A(4). Twinning on the other three original {111} planes produces the rest of the poles shown by open squares. Note that the twinning places four  $\langle 111 \rangle$  directions within 15.8° of the surface normal. Nevertheless the actual intensity recorded in Fig.

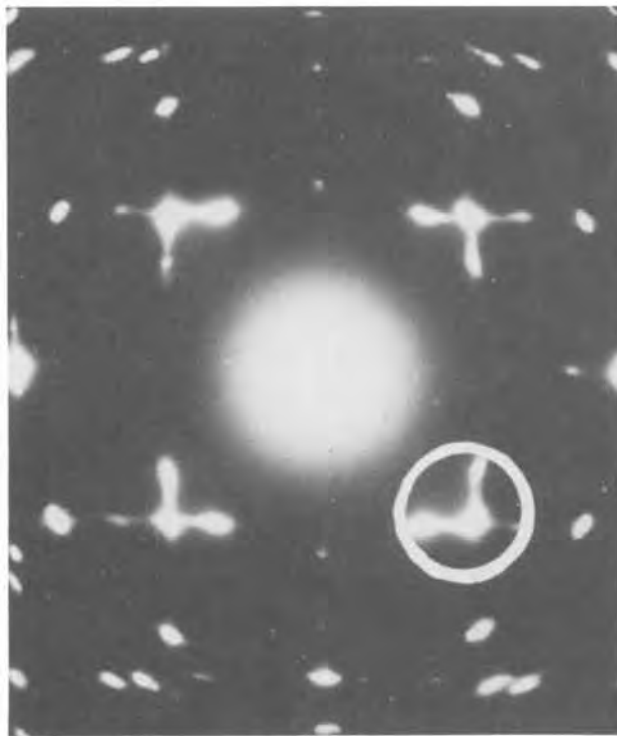
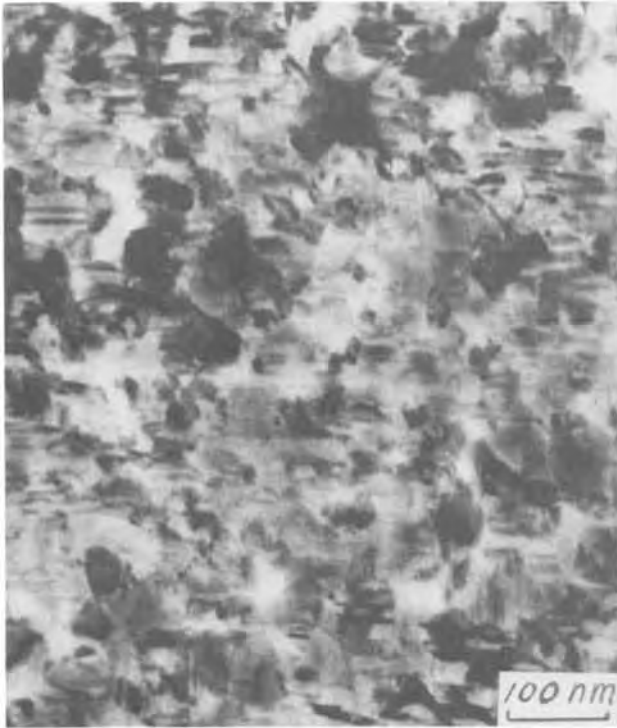


Fig. 4. TEM results for thin gold deposit on  $\{100\}$  substrate. (a, top) Bright-field image, original magnification  $110,000\times$ . (b, bottom) Selected-area diffraction pattern.

6a is greatest at the surface normal rather than  $15.8^\circ$  away. This indicates a rotation during growth to a final  $\{111\}$  film orientation. As can be seen in Fig. 6b, little intensity remains in the region of the original  $\{100\}$  orientation and the transition to the final  $\{111\}$  orientation is highly developed.

The films plated on the  $\{110\}$  copper substrate have a still more complex orientation. The original epitaxial orientation is indicated on the pole figure shown in Fig. 6c by the lens symbol. Note that there are twenty intensity maxima in addition to the two located by the original epitaxial orientation. All of them can be precisely located by twinning reorientations. The first

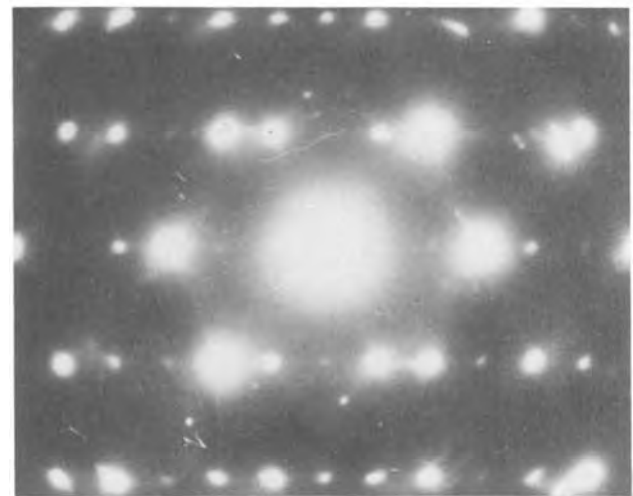
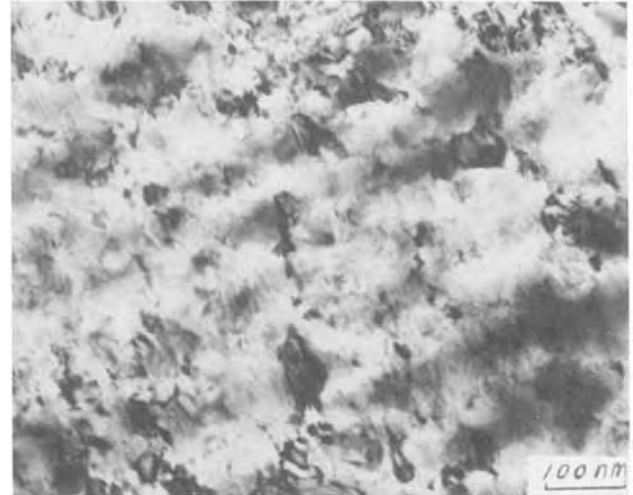


Fig. 5. TEM results for thin gold deposit on  $\{110\}$  substrate. (a, top) Bright-field image, original magnification  $120,000\times$ . (b, bottom) Selected-area diffraction pattern.

group of orientations indicated by the squares in Fig. 6c were produced by twinning on the two  $\{111\}$  planes visible in the pole figure; the new orientation locates the film normal about  $19.5^\circ$  away from  $[001]$ . The second group of orientations indicated by the triangles is obtained by retwinning of the previous orientation, the squares. The twin plane normal is designated by an overlapping square and triangle. After twinning first on the square and then on the triangle, the new orientation of the doubly twinned material is within  $5^\circ$  of the fast growing  $\{111\}$  orientation. The remaining group of orientations designated by the circles can be produced by twinning first on the triangles and then retwinning on the plane indicated by the overlapping circle and triangle. This doubly twinned volume is oriented about  $25^\circ$  from  $\langle 111 \rangle$ , midway between  $\langle 112 \rangle$  and  $\langle 113 \rangle$ . The combination of primary twinning followed by two different types of secondary twinning can explain all the maxima observed in Fig. 6c.

A generalization of the single crystal results is that the substrate orientation is reproduced in the film and that additional orientations are generated by  $\{111\}$  twinning. If the twinning or retwinning process places a  $\langle 111 \rangle$  direction in the vicinity of the film normal, a transition to a  $\{111\}$  film orientation begins. Agitation did little to modify these observations, except to produce slightly asymmetrical pole figures. When strong convection was present, orientations with  $\langle 111 \rangle$  directions inclined toward the direction of fluid flow were the most intense. This is in agreement with the observations of film growth from the vapor; namely

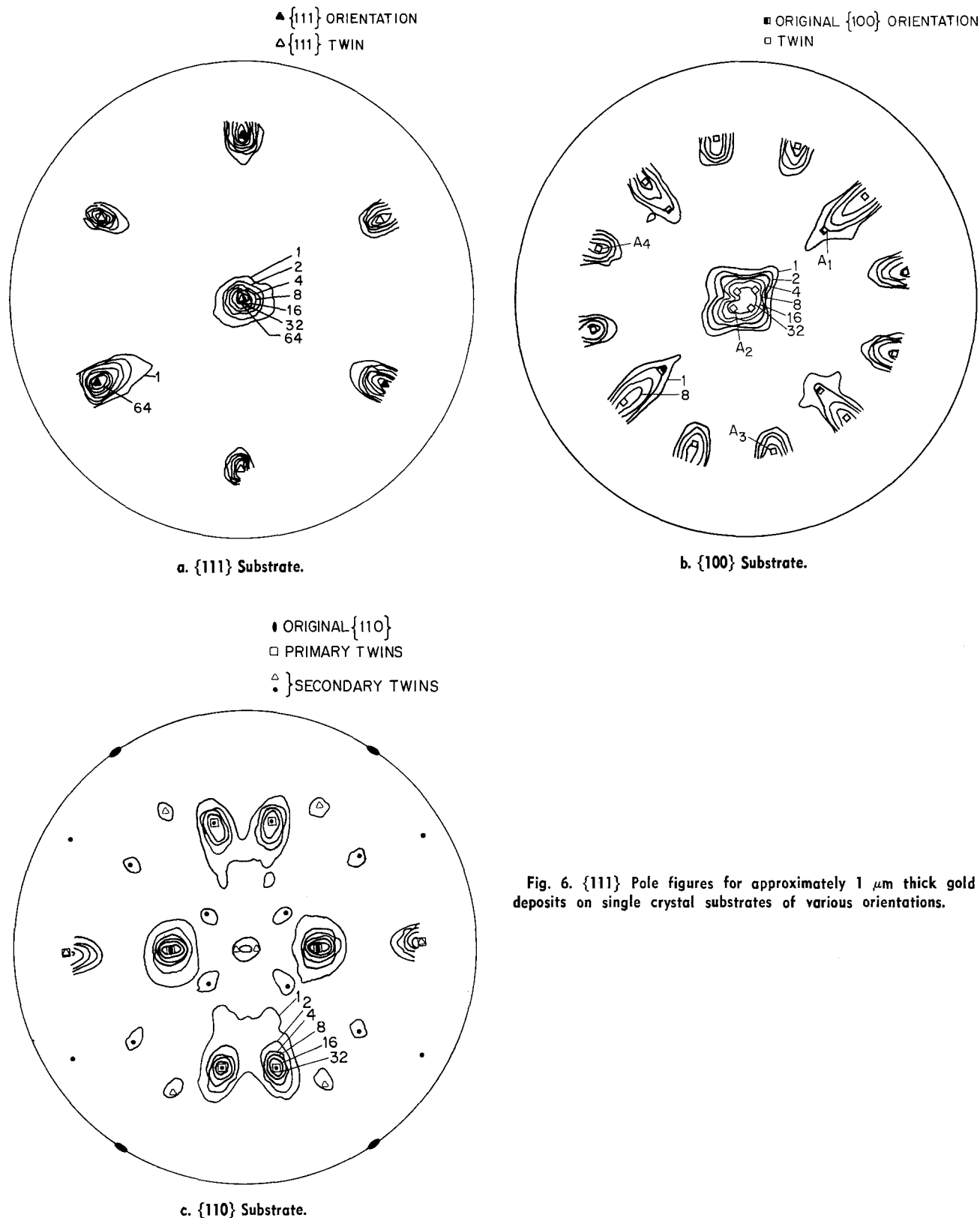


Fig. 6.  $\{111\}$  Pole figures for approximately  $1 \mu\text{m}$  thick gold deposits on single crystal substrates of various orientations.

that the  $\langle 111 \rangle$  direction is inclined toward the direction of greatest mass flux (6).

An interesting correlation exists between the change in plating rate, shown in Fig. 2, and the change in film orientation due to twinning. Once the various complex twinning mechanisms operative for the  $\{100\}$  and  $\{110\}$  substrates have taken place, the deposits all tend toward the  $\langle 111 \rangle$  preferred orientation and the rate of deposition becomes independent of substrate. At this point, the kinetics of the electroless gold reaction have reached steady state and are controlled by the deposition conditions and the mixed-electrode potential (9).

The catalysis literature contains numerous papers dealing with the effect of crystal orientation on the kinetics of gas phase reactions (16, 17), and the role of structural factors in electrocatalysis (18). Crystallographic orientation is the most important structural factor controlling the catalytic activity of platinum surfaces in studies of hydrogen evolution and the anodic oxidation of methanol (18). The rates of these reactions were greatest on the  $\{111\}$  face by up to an order of magnitude, as compared to other crystal faces with lower atomic packing density. Our results for the electroless gold system are in good agreement with these findings, as has been pointed out by Okinaka (9).

who noted that the chemisorption of reacting species is an important feature of catalytic processes. Other results from electrocrystallization studies have shown that exchange current densities for the electrodeposition of copper on copper single crystals increases by a factor of five on going from  $\{111\}$  to  $\{100\}$  to  $\{110\}$ . This means that the rate of deposition at constant overpotential increases in the order  $\{110\} > \{100\} > \{111\}$  (19). The electroless gold results (Fig. 2) are exactly opposite. Thus, from the standpoint of the deposition mechanism, the electroless gold has more in common with the electrocatalysis of platinum than the electrocrystallization of copper. One aspect of the electroless gold process not studied in this work but discussed elsewhere (9), is that the anodic reaction may be rate controlling.

Examination of the surfaces of the electroless gold deposits by optical microscopy and SEM also showed that the substrate orientation strongly affects the growth morphology, consistent with the established literature on electrocrystallization studies (20). Normarski optical microscopy revealed that the deposit on the  $\{111\}$  substrate consisted of 200-400  $\mu\text{m}$  features that were similar to previously reported structures for thick copper deposits on  $\{111\}$  (21). The other two substrate orientations yielded surfaces with much finer features that could not be resolved optically. Representative SEM results are shown in Fig. 7a-c for the  $\{111\}$ ,  $\{100\}$ , and  $\{110\}$  substrates, respectively. Because of the large features on the  $\{111\}$  surface, there is relatively little structure visible at high magnification unless one looks near the edges of the features as in Fig. 7a. The appearance of the surface on the  $\{100\}$  substrate (Fig. 7b) is quite similar to the smooth faceted structure which is commonly observed for technological deposits on polycrystalline substrates under these plating conditions (4). The deposits on the  $\{110\}$  substrate have an irregular microstructure with numerous fine features ( $\sim 0.2 \mu\text{m}$ ) as well as larger ones ( $> 2 \mu\text{m}$ ). These results suggest that the process of lateral growth occurs most readily on  $\{111\}$  substrates which is in agreement with recent findings for gold electrodeposits (22). Consideration of these data together with the plating rates (Fig. 2) and pole figures (Fig. 6) indicates that the twinning processes, the microstructure, and the nonuniform initial plating rates are interrelated.

**Polycrystalline substrates.—Evaporated films.**—Two sets of experiments were carried out using evaporated film substrates and the standard plating solution. In the first set, either Pd or Au films, 80 nm thick, were evaporated at 1.5 nm/sec using an e-beam system at  $2 \times 10^{-7}$  Torr onto a 30 nm thick layer of Ti which was freshly deposited onto clean, polished sapphire surfaces 9 mm  $\times$  2.0 cm in size. Three samples of each type of film were mounted in a PTFE holder and plated simultaneously either in still solutions or with vigorous stirring using a rod at 3000 rpm. The effects of agitation on plating rate have been discussed in detail elsewhere (4). The rate of deposition was 40% greater on the Au substrate than on the Pd substrate if the solution was agitated. Without agitation the difference was 20%. Since the difference in plating rate was suspected to be due to a difference in the structure of the substrates, the structure of both the substrates and deposits was studied in some detail. Pole figures for the deposits on the gold substrates showed a very strong  $\langle 111 \rangle$  fiber feature which was also quite strong in the substrate films; whereas, the gold deposits on Pd substrates showed a weaker  $\langle 111 \rangle$  fiber texture as did the substrates which were much more randomly oriented. Since the  $\langle 111 \rangle$  orientation is known to plate at a fast rate, Fig. 2, the difference in plating rate is probably due in part to the difference in orientation. Further examination of the substrates by TEM showed that the Pd films were uniformly fine grained ( $\sim 10$  nm) and the Au films

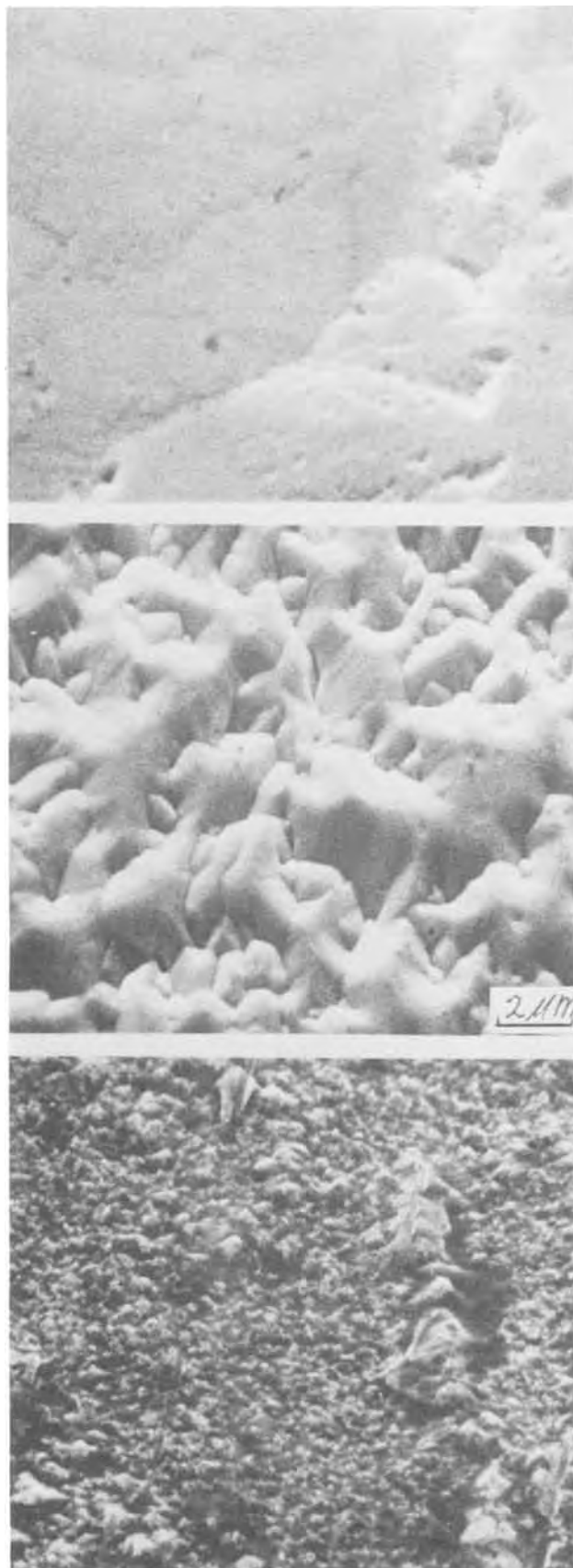


Fig. 7. SEM results showing surfaces of thick gold films on single crystal substrates, original magnification 5000 $\times$ . (a, top)  $\{111\}$  Substrate. (b, center)  $\{100\}$  Substrate. (c, bottom)  $\{110\}$  Substrate.

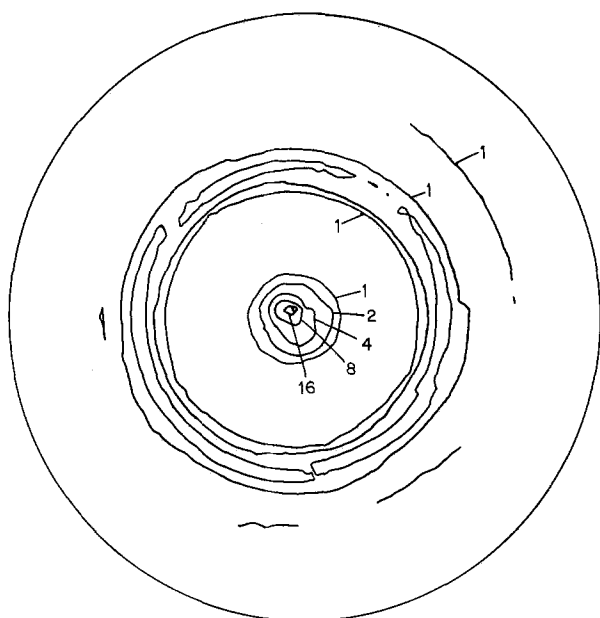
were more heterogeneous with many grains  $> 100$  nm in size.

In a second series of experiments Au/Ti/glass substrates were evaporated at higher pressure ( $\sim 2 \times 10^{-5}$  Torr). These substrates had a complex texture. The fiber axis was tilted away from the sheet normal toward the direction of mass flux during evaporation. The texture consisted of a strong  $\langle 111 \rangle$  component combined with a weaker  $\langle 100 \rangle$  component. The substrates were plated in the standard solution with different amounts of agitation. Figure 8a gives the pole figure for a 2  $\mu\text{m}$  thick deposit plated without agitation at the normal rate of 0.7  $\mu\text{m/hr}$ . The plated film reproduced the orientation of the substrate. The more complex pole figure in Fig. 8b corresponds to a deposit plated in the same bath to the same thickness but with carousel stirring at a velocity of 0.46 m/sec which produces a threefold increase in plating rate (4). These conditions yield a  $\langle 111 \rangle$  fiber texture with a strong  $\langle 311 \rangle$  component as seen in Fig. 8b.

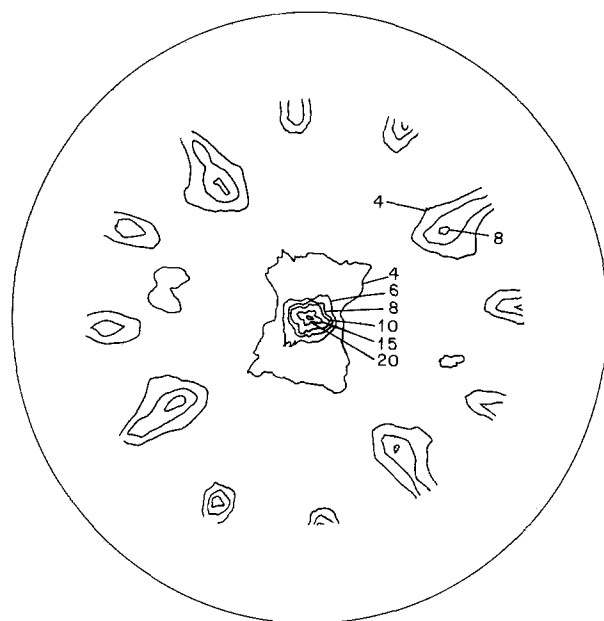
In both of these sets of experiments with evaporated noble metal film substrates it was found that the deposits were formed epitaxially and that the  $\langle 111 \rangle$

orientation of the substrates was maintained for deposits  $< 2 \mu\text{m}$  in thickness. Subtle but real effects due to substrate grain size and the strength or degree of the  $\langle 111 \rangle$  texture were observed.

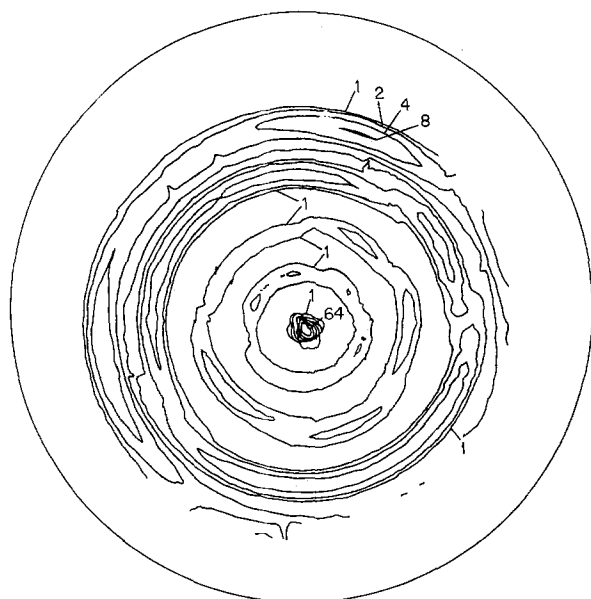
*Rolled sheet metal.*—In an initial set of experiments, two lots of nominally identical commercial copper foil plated at substantially different rates under the same conditions (23). One batch of material gave the normal plating rate (1.5  $\mu\text{m/hr}$ ) and the other showed a surprising twofold increase in rate which was maintained to a thickness of  $> 5 \mu\text{m}$ . Pole figures for both substrates showed them both to be qualitatively the same, with cube textures as expected. Figure 9a shows the pole figure for the deposit with the normal plating rate. Here we see the characteristic epitaxial growth of the cube texture and the transition to  $\{111\}$  by the multiple twinning mechanism which has already been discussed for the case of the  $\{100\}$  single crystal substrate, Fig. 6b. Figure 9b shows that the anomalously fast plating deposit remained in the cube orientation.



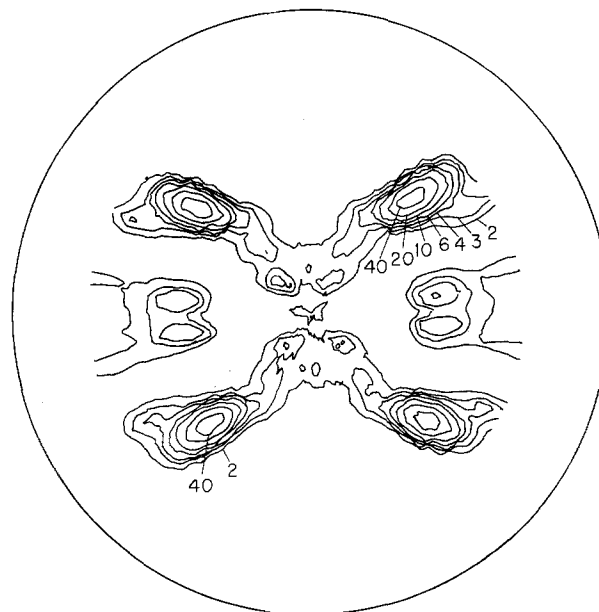
a. No agitation, plating rate 0.7  $\mu\text{m/hr}$ .



a. Normal plating rate 1.5  $\mu\text{m/hr}$ .



b. Agitation at 2750 cm/min, plating rate 2.1  $\mu\text{m/hr}$ .



b. Anomalous plating rate 3.0  $\mu\text{m/hr}$ .

Fig. 8.  $\{111\}$  Pole figures for 2  $\mu\text{m}$  thick gold deposits on evaporated gold thin film substrates.

Fig. 9.  $\{111\}$  Pole figures for thick gold deposits on copper sheet substrates of commercial material.



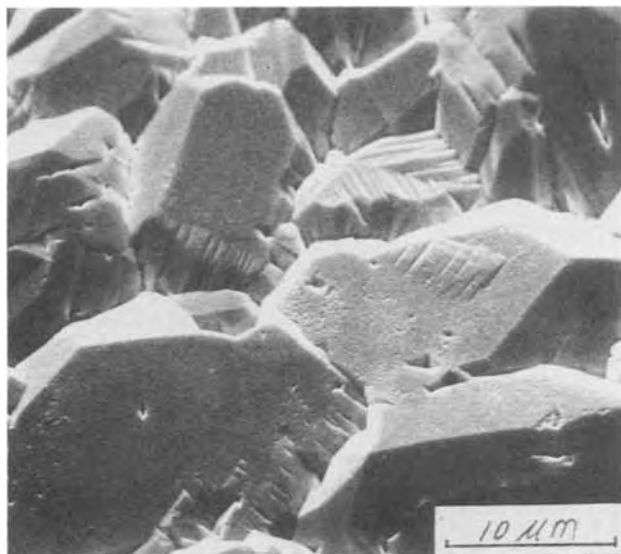


Fig. 10. Surface structure corresponding to Fig. 9b, original magnification  $2500\times$ .

The microstructure of this deposit observed in the SEM was also unusual and is shown in Fig. 10. Here we see a large, faceted grain structure with smooth features  $\sim 20\ \mu\text{m}$  across whereas the deposits plated at the normal rate showed a considerably finer microstructure with background features  $1\text{--}2\ \mu\text{m}$  in size and some larger, nodular features.

A SEM examination of etched samples of the two substrates indicated some qualitative differences such as the grain size and shape but did not permit us to explain the anomalously high plating rate. One possibility is that an impurity species, which may have dissolved from the surface region of the fast copper substrate during the initial displacement process, somehow altered the growth process by preventing the twinning mechanism from occurring. However, in this case we would expect the rate to be slow as one finds with  $\{100\}$  single crystals; but this is not the case for this material by at least an order of magnitude.

Additional experiments were conducted in an attempt to shed some light on the above result and see whether or not it could be reproduced using other copper sheet substrates. To do this, we started with bulk OFHC Cu and prepared sheet samples, 0.010 in. thick, by cold rolling to a 92% reduction. The pole figure in Fig. 11 indicates that this texture is copied by the electroless gold deposit, which in this case was  $1.5\ \mu\text{m}$  thick and plated at the normal rate. Deposits plated on annealed substrates from the same material ( $300^\circ\text{C}$ , 1 hr) showed a similar plating rate and the expected structure for the case of cube-texture substrates, i.e., identical to Fig. 9a. This set of experiments included other sheet substrates (Au and phosphor bronze) and plating runs at temperatures both  $10^\circ\text{C}$  above and below nominal. In no case were we able to find any increase in the plating rate, comparable to that observed with the "fast copper."

### Summary and Conclusions

The results of this study show that the structure of metal substrates onto which electroless gold deposits are plated may have a profound effect on the process kinetics and the structure of the deposits. On single crystal copper substrates, the initial plating rate can vary by an order of magnitude with  $\{111\} \gg \{100\} > \{110\}$ . In all three cases twinning is observed during the initial stages of growth ( $\sim 0.1\ \mu\text{m}$ ). The TEM results show twin fault densities  $> 10^{+11}/\text{cm}^2$ . X-Ray pole figures for thick deposits provide additional evidence for the importance of twinning in this deposition process. In particular, the pole figure results indicate that multiple twinning processes are responsible for

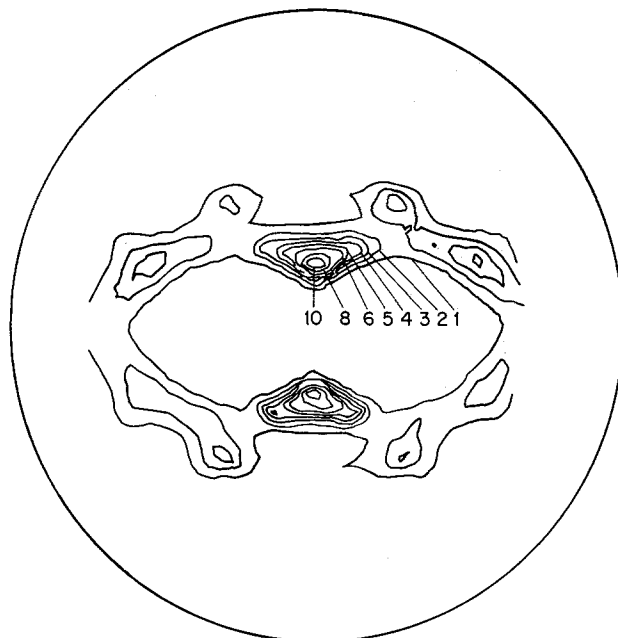


Fig. 11.  $\{111\}$  Pole figure of  $1.5\ \mu\text{m}$  thick gold deposit on cold-rolled OFHC copper sheet.

the transition from the slow initial plating rates on the  $\{100\}$  and  $\{110\}$  substrates to the faster rate typical of the  $\langle 111 \rangle$  preferred orientation.

Electroless gold deposits on evaporated noble metal film substrates exhibit a  $\langle 111 \rangle$  fiber axis which represents a continuation of the substrate texture. A somewhat lower rate of deposition is observed for Pd substrates relative to that on Au films. The magnitude of this effect is about 20% without forced convection and about 40% when the plating solution is stirred vigorously. The somewhat lower plating rate on Pd is apparently due to the fact that these substrate surfaces are comprised of much smaller grains ( $\sim 10\ \text{nm}$ ) that are more randomly oriented than the Au films.

Experiments with polycrystalline Cu sheet substrates are in general agreement with the single crystal results except for one particular batch of commercial material onto which deposits with an unusually large grained microstructure were formed at an anomalously fast plating rate. This result could not be reproduced with laboratory-prepared sheet substrates.

We conclude by noting that the substrate effects identified in this work as being important for the electroless gold plating process are likely to be applicable to other catalytic systems for metal deposition. This would appear therefore to be a fruitful area for further work.

### Acknowledgment

The authors wish to thank Y. Okinaka for his help and advice throughout this study.

Manuscript submitted Aug. 12, 1975; revised manuscript received May 20, 1976.

Any discussion of this paper will appear in a Discussion Section to be published in the June 1977 JOURNAL. All discussions for the June 1977 Discussion Section should be submitted by Feb. 1, 1977.

Publication costs of this article were assisted by Bell Laboratories.

### REFERENCES

1. Y. Okinaka, *Plating*, **57**, 914 (1970).
2. Y. Okinaka, in "Gold Plating Technology," F. H. Reid and W. Goldie, Editors, chap. 11, Electrochemical Publications, Ltd., Scotland (1974).
3. R. Sard, Y. Okinaka, and H. A. Waggener, *This Journal*, **121**, 62 (1974).
4. Y. Okinaka, R. Sard, W. H. Craft, and C. Wolowoduik, *ibid.*, **121**, 56 (1974).

5. R. Sard, Abstract 134, p. 220, The Electrochemical Society Extended Abstracts, Fall Meeting, Cleveland, Ohio, Oct. 3-7, 1971.
6. K. L. Chopra, "Thin Film Phenomena," p. 220, McGraw-Hill Book Co, New York (1969).
7. B. C. Wonsiewicz, "Rapid Computer Plotting of Pole Figures," Bell Laboratories, Murray Hill, New Jersey (1972).
8. Handbook of Thin Film Technology, L. I. Maissel and R. Glang, Editors, pp. 7-37, McGraw-Hill Book Co., New York (1970).
9. Y. Okinaka, *This Journal*, **120**, 739 (1973).
10. C. S. Barrett and T. B. Massalski, "Structure of Metals," 3rd ed., pp. 193-222, McGraw-Hill Book Co. New York (1966).
11. R. Sard, *This Journal*, **117**, 1156 (1970).
12. E. R. Thompson and K. R. Lawless, *Electrochim. Acta*, **14**, 269 (1969).
13. D. W. Pashley and M. J. Stowell, *Philos. Mag.*, **8**, 1605 (1963).
14. D. W. Pashley, *Adv. Phys.*, **14**, 327 (1965).
15. R. D. Burbank and R. L. Heidenreich, *Philos. Mag.*, **8**, 651 (1963).
16. A. T. Gwathmey and R. E. Cunningham, *Adv. Catal.*, **10**, 57 (1958).
17. H. Jaeger, *J. Catal.*, **9**, 237 (1967).
18. V. S. Bagotzky, Yu. B. Vassiliev, and I. I. Pyshnograeva, *Electrochim. Acta*, **16**, 2141 (1971).
19. J. O'M. Bockris and A. K. N. Reddy, "Modern Electrochemistry," Vol. 2, p. 1215, Plenum Press, New York (1970).
20. See, e. g., R. Piontelli, G. Poli, and G. Serravalle, "Transactions of the Symposium on Electrode Processes," E. Yeager, Editor, p. 67, John Wiley & Sons, New York (1961).
21. U. Bertocci and C. Bertocci, *This Journal*, **118**, 1287 (1971).
22. R. J. Morrissey and A. M. Weisberg, *Trans. Inst. Met. Finishing*, **53**, 9 (1975).
23. Y. Okinaka, Private communication.

## Electrodeposition of Cobalt Using an Insoluble Anode

G. R. Lakshminarayanan, E. S. Chen, J. C. Sadak, and F. K. Sautter

Benet Weapons Laboratory, Watervliet Arsenal, Watervliet, New York 12189

### ABSTRACT

A method has been developed which permits the use of an insoluble anode to electrodeposit cobalt by the addition of a sufficient amount of an electrochemically active substance such as vanadium pentoxide to the cobalt sulfate plating solution. In the absence of such additions, formation of  $\text{Co}^{3+}$  ions and cobalt oxide ( $\text{Co}_2\text{O}_3$ ) at the platinum anode results during plating. The effects of the addition of vanadium pentoxide on the electrode process during plating have been investigated through the analyses of various electrolysis products as a function of additive concentration and plating time. The results show that besides cobalt deposition, vanadium ions of lower oxidation state ( $\text{V}^{++}$ ,  $\text{V}^{+++}$ ,  $\text{VO}^{++}$ ) are formed at the cathode and these ions seem to be responsible for the reduction and suppression of  $\text{Co}^{3+}$  ions and the oxide at the platinum anode. It has also been observed that the concentration of the added electrochemically active substance changed very little, indicating no incorporation of vanadium with the deposit during plating. The mechanical properties of the deposits prepared using an insoluble anode are compared with those obtained using a soluble anode.

The electrodeposition of cobalt, dispersion-hardened cobalt, and cobalt-based alloys has been the subject of investigation (1-6) at this laboratory for many years because of the potential application as protective coatings to improve the wear and erosion characteristics of the substrates. In conventional cobalt plating, soluble anodes are used to replenish the metal deposited at the cathode. In plating the inside of small bore tubes such as small caliber gun tubes, however, it would be necessary and also highly advantageous to use an insoluble anode since the dimensions of the anode would not change. However, the use of an insoluble anode like platinum in cobalt plating solutions leads to the formation of undesirable black cobalt oxide particles at the anode. They appear at the anode as a strongly adherent black coating or remain as suspended particles in the plating solution. The codeposition of these particles with the deposits has a detrimental effect on the structure and properties of the deposits. In order to suppress the undesirable reactions leading to the formation of cobalt oxide, other electrochemically active substances were introduced in the plating solution. It was hypothesized that the oxide formation could be suppressed if other reducible agents were present in the electrolyte. The additive should be such that it does not interfere with the normal plating process and has no detrimental effect on the properties of the deposit. Vanadium pentoxide was found to be a very

effective and suitable chemical in this regard. By undergoing reduction at the cathode and oxidation at the anode without being codeposited, this substance provides electrochemically active species during plating which suppress the oxide formation. This investigation deals with a study of the effects of addition of vanadium pentoxide to the cobalt sulfate plating solution on the electrodeposition of cobalt using a soluble or an insoluble (platinum) anode.

### Experimental

*Plating solutions and plating procedure.*—All chemicals were of reagent grade quality and were used without further purification. A stock solution of cobalt sulfate (1.0M) was prepared and unless otherwise stated, 150 ml fresh solution was used for each experiment. Vanadium pentoxide (up to about 4.5 g/liter) was added to the plating solution. The dissolution of vanadium pentoxide was slow and it took up to 50-60 hr to dissolve 4.5 g/liter at 40°C and at pH 1.0. A regulated power supply was used as a power source. Cobalt or platinum anodes and stainless steel or brass cathodes (substrates) were used for plating. Cobalt plating was generally carried out at a current density of 5 A/dm<sup>2</sup>, a temperature of 40°C, and at an initial pH 1.00.<sup>1</sup>

Key words: insoluble anode, electrochemically active substances, electrode process.

<sup>1</sup> The low pH was used, in spite of reduced cathode efficiency, in order to obtain increased solubility of  $\text{V}_2\text{O}_5$  and reduced formation of black oxide particles.



**Analysis of solutions.**—The oxidation-reduction method of analysis (redox methods) was adopted to determine the concentration of the various electrode reaction products. Cerium (IV) sulfate and ferrous (II) sulfate solutions were prepared, standardized, and used for the analysis of the electrolysis products. A Beckman electroscan was used to monitor the variation of the potential during the titration of solutions. The cobalt oxide particles formed during the electrolysis were quantitatively determined by the gravimetric procedure (7) using millipore filters.

**Mechanical properties of the deposits.**—Cobalt was deposited on brass shim stock (0.003 in.) substrates from cobalt sulfate and cobalt sulfate-vanadium pentoxide plating solutions (1.8 liter). Both soluble and insoluble anodes were used to prepare the deposits. The brass substrate was anodically dissolved in a KOH-K<sub>2</sub>CO<sub>3</sub> solution. The deposits were cut into tensile specimens and the room temperature yield strength (0.2% offset), tensile strength, and elongation were obtained using an Instron tensile testing machine.

### Results and Discussion

**Electrolysis of cobalt sulfate solution.**—With a soluble cobalt anode, Co<sup>++</sup> ions are produced at the anode during plating and are reduced to Co at the cathode. When an anode such as platinum is used, no metal is dissolved at the anode during plating. The reaction which is essential for the passage of current from the anode to the electrolyte is one of oxidation of the components of the electrolyte at the anode-solution interface. Depending on the anode potential, several anode reactions may proceed simultaneously. In an acidic cobalt sulfate electrolyte, oxygen discharge takes place according to the reaction, 2H<sub>2</sub>O → 4H<sup>+</sup> + O<sub>2</sub> + 4e<sup>-</sup>. Simultaneously, Co<sup>2+</sup> ions are oxidized to Co<sup>3+</sup> ions leading to the formation of cobalt oxide (Co<sub>2</sub>O<sub>3</sub>) at the anode. The presence of Co<sup>3+</sup> ions in the plating solution can be quantitatively determined with ferrous sulfate solution according to the oxidation-reduction reaction Co<sup>3+</sup> + Fe<sup>2+</sup> ⇌ Co<sup>2+</sup> + Fe<sup>3+</sup>. The cobalt sulfate solution was electrolyzed for 3.5 hr at 5 A/dm<sup>2</sup> using an insoluble anode and a soluble anode separately and the solutions were analyzed for the Co<sup>3+</sup> ion content. The results of the analysis are shown in Fig. 1. Curve A shows the variation of potential with respect to saturated calomel electrode of the electrolyzed solution (with an insoluble anode) on titration with ferrous sulfate solution. Curves B and C represent the same data for the electrolyzed solution with a soluble anode and for the unelectrolyzed cobalt sulfate solution, respectively. It can be calculated from curve A that the electrolyzed solution contains Co<sup>3+</sup> ions corresponding to 4.03 × 10<sup>-3</sup> moles/liter. From curves B and C it can be concluded that these solutions contain no Co<sup>3+</sup> ions. It has been observed that the reaction between Fe<sup>2+</sup> and Co<sup>3+</sup> ions is relatively sluggish and attains steady potential values rather slowly. Co<sup>3+</sup> ions are relatively unstable; the concentration decreased in the above plating solution from 4.03 to 0.45 × 10<sup>-3</sup> moles/liter over a period of 21 hr on standing.

**Electrolysis of CoSO<sub>4</sub>-V<sub>2</sub>O<sub>5</sub> solutions.**—Vanadium, being a multivalent element, can exist in several oxidation states in solution. The species that form in aqueous solutions are V<sup>2+</sup>, V<sup>3+</sup>, VO<sup>++</sup>, and VO<sub>2</sub><sup>+</sup> ions and their formation depends on the potential and the solution pH. Vanadium pentoxide when added to the cobalt sulfate plating solution at pH 1.0 dissolves in it to form a VO<sub>2</sub><sup>+</sup> ion according to the reaction V<sub>2</sub>O<sub>5</sub> + 2H<sup>+</sup> → 2VO<sub>2</sub><sup>+</sup> + H<sub>2</sub>O. When this solution is electrolyzed, besides cobalt deposition at the cathode, other electrolysis products at cathode and anode are formed depending on whether a soluble or an insoluble anode is used.

When a cobalt anode is used, dissolution of the metal to Co<sup>++</sup> ions takes place and, at the cathode, in addi-

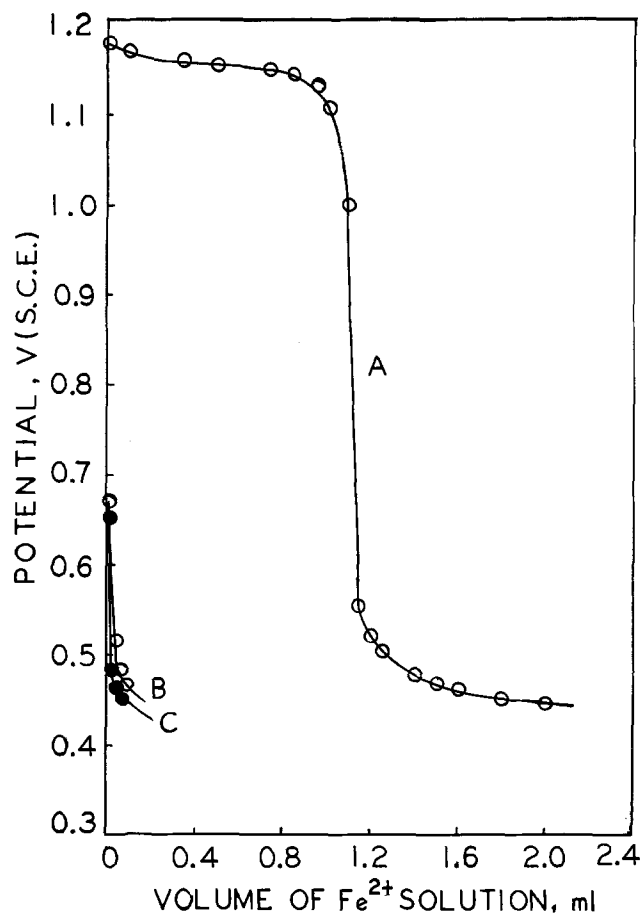
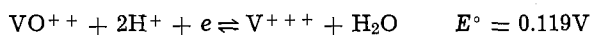
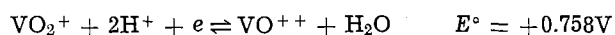


Fig. 1. Variation of potentials during titration of electrolyzed and unelectrolyzed CoSO<sub>4</sub> solutions (3.0 ml) with ferrous sulfate solution (0.0108M): A = electrolyzed CoSO<sub>4</sub> solution with an insoluble anode, B = electrolyzed CoSO<sub>4</sub> solution with a soluble anode, and C = unelectrolyzed CoSO<sub>4</sub> solution. Anode:cathode = 1:4, current density = 5 A/dm<sup>2</sup>, temperature = 40°C, pH (initial) = 1.00, and plating time = 3.5 hr.

tion to cobalt deposition, reduction of VO<sub>2</sub><sup>+</sup> ions occurs according to the reaction,



The potentials ( $E^\circ$ ) noted at which these reactions occur correspond to equilibrium potential values with respect to the saturated calomel electrode (8). A solution of CoSO<sub>4</sub>-V<sub>2</sub>O<sub>5</sub> (4.5 g/liter) was electrolyzed using a cobalt anode and the electrolysis products were analyzed using a standard cerium (IV) sulfate solution. The formation of various electrolysis products is shown as a function of plating time in Fig. 2. Prior to electrolysis vanadium ions exist as VO<sub>2</sub><sup>+</sup>. With electrolysis VO<sub>2</sub><sup>+</sup> ions are reduced to VO<sup>++</sup> and V<sup>3+</sup> ions initially and with further electrolysis V<sub>2</sub><sup>+</sup> ions are also formed. While all the VO<sub>2</sub><sup>+</sup> ions are reduced to lower oxidation states, the concentration of the lower oxidation species depends on the electrolysis time. These ions are not reoxidized to pentavalent (VO<sub>2</sub><sup>+</sup>) state and remain in solution as a mixture of two or three species depending on the length of plating time. This behavior is in contrast to the results obtained with an insoluble anode as is shown below.

When a CoSO<sub>4</sub>-V<sub>2</sub>O<sub>5</sub> solution is electrolyzed with an insoluble anode (platinum), one encounters a new situation. The electrolysis products at the cathode can be expected to be the same as with the soluble anode; however, at the anode, oxygen discharge, Co<sup>3+</sup> ion formation, and oxidation of vanadium ions (V<sup>2+</sup>, V<sup>3+</sup>,

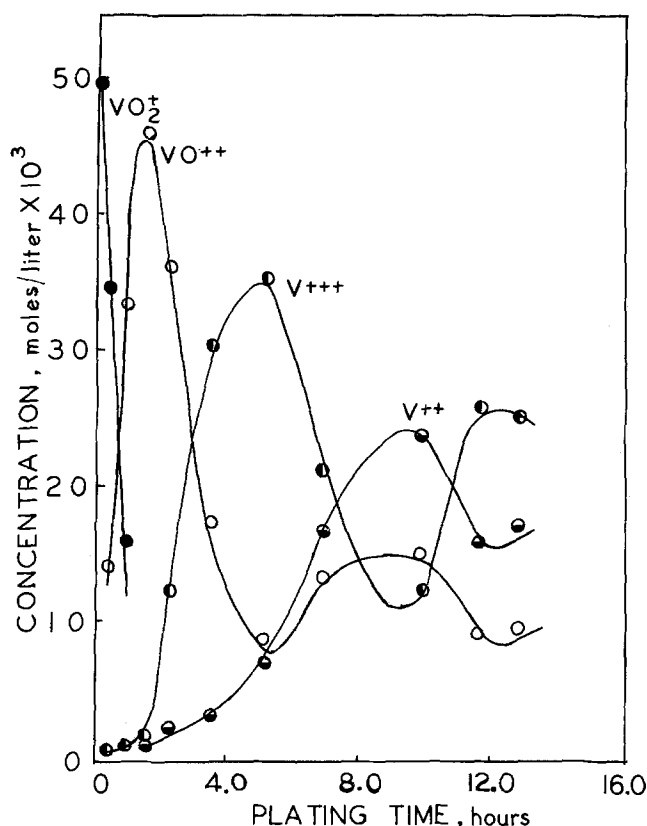


Fig. 2. Formation of vanadium ions of different oxidation state in  $\text{CoSO}_4\text{-V}_2\text{O}_5$  (4.5 g/liter) solution as a function of plating time. Soluble anode is used. Current density =  $5 \text{ A/dm}^2$ , temperature =  $40^\circ\text{C}$ ,  $\text{pH} = 1.00$ .

$\text{VO}^{++}$ ) to  $\text{VO}_2^+$  ion would take place. In addition, vanadium ions of a lower oxidation state could interact with  $\text{Co}^{3+}$  ions.

Figure 3 shows the results of an analysis of the electrolysis products when a cobalt sulfate- $\text{V}_2\text{O}_5$  (1.2 g/liter) plating solution is electrolyzed with an insoluble anode. Curves I and II represent the variation of potentials (with respect to saturated calomel electrode) of an electrolyzed and unelectrolyzed solution on titration with ferrous sulfate solution, respectively. The first equivalence point, A ( $1.67 \times 10^{-3}$  moles/liter), in curve I corresponds to the reduction of  $\text{Co}^{3+}$  to  $\text{Co}^{2+}$  and the second equivalence point, B ( $1.29 \times 10^{-2}$  moles/liter), corresponds to the reduction of  $\text{VO}_2^+$  to  $\text{VO}^{++}$ . The equivalence point C ( $1.28 \times 10^{-2}$  moles/liter) for the unelectrolyzed solution indicates the reduction of  $\text{VO}_2^+$  to  $\text{VO}^{++}$  only. It is interesting to note that the concentration of  $\text{VO}_2^+$  ions in the above plating solution before and after electrolysis changed very little. Similar analyses for various plating solutions were made and the results are summarized in Table I. A close agreement is seen in concentrations of vanadium (represented as  $\text{VO}_2^+$  moles/liter) before and after electrolysis, indicating that vanadium is not consumed or codeposited with cobalt during plating.

Table I. Analysis of plating solutions before and after electrolysis\*

Run	Before electrolysis		After electrolysis	
	$\text{VO}_2^+$ (moles/liter)	$\text{VO}_2^+$ (moles/liter)	$\text{VO}_2^+$ (moles/liter)	$\text{Co}^{3+}$ (moles/liter)
1**	$1.28 \times 10^{-2}$	$1.29 \times 10^{-2}$	$1.67 \times 10^{-3}$	
2***	$2.24 \times 10^{-2}$	$2.28 \times 10^{-2}$	$1.26 \times 10^{-3}$	
3***	$3.63 \times 10^{-2}$	$3.62 \times 10^{-2}$	$0.74 \times 10^{-3}$	
4***	$4.76 \times 10^{-2}$	$4.85 \times 10^{-2}$	$0.59 \times 10^{-3}$	

\* Vanadium concentration is represented as  $\text{VO}_2^+$  (moles/liter).

\*\* 3 hr plate,  $5 \text{ A/dm}^2$ ,  $40^\circ\text{C}$ , volume of plating solution = 75 ml, anode:cathode ratio = 1:4.

\*\*\* 3.5 hr plate,  $5 \text{ A/dm}^2$ ,  $40^\circ\text{C}$ , volume of plating solution = 150 ml, anode:cathode ratio = 1:1.

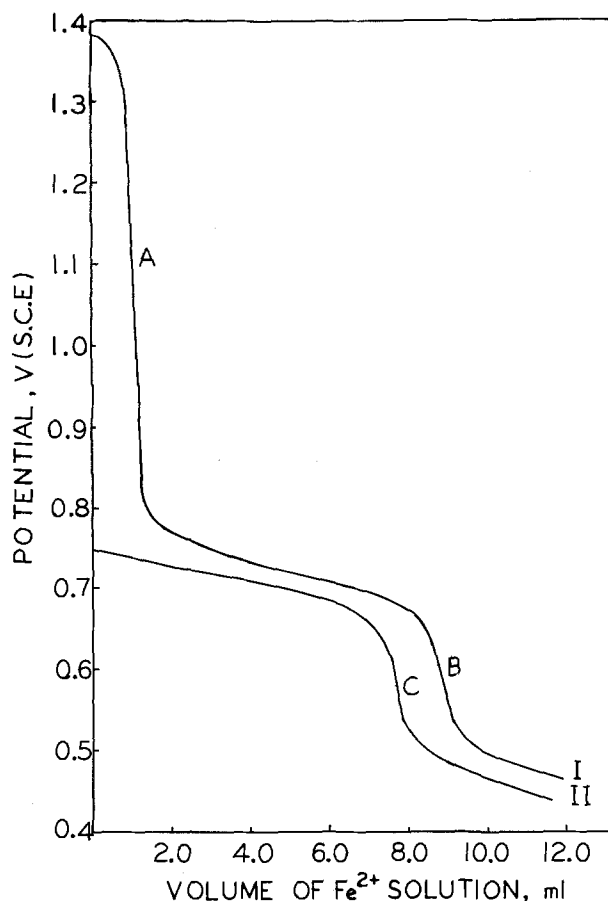


Fig. 3. Variation of potentials during titration of (I) electrolyzed and (II) unelectrolyzed  $\text{CoSO}_4\text{-V}_2\text{O}_5$  (1.2 g/liter) solution (3.0 ml) with ferrous sulfate solution (0.0054M). Volume of the solution used for plating = 75 ml, insoluble anode, anode:cathode = 1:4, current density =  $5 \text{ A/dm}^2$ , temperature =  $40^\circ\text{C}$ ,  $\text{pH}$  (initial) = 1.0, plating time = 3.0 hr.

Deposits were also analyzed for vanadium using an electron microprobe analyzer (Material Analysis Company). No vanadium was found up to the detection limit ( $\sim 0.05$  w/o) of the analyzer.

The effect of the concentration variation of vanadium pentoxide in the plating solution on the formation of  $\text{Co}^{3+}$  ions and the oxide is shown in Fig. 4. With the addition of vanadium pentoxide, the formation of  $\text{Co}^{3+}$  ions and the oxide is reduced. For example, in cobalt sulfate solution, after electrolysis with an insoluble anode, the concentration of  $\text{Co}^{3+}$  ions in solution is  $4.03 \times 10^{-3}$  moles/liter and the concentration of cobalt oxide formed is 0.32 g/liter. In the presence of 2.3 g/liter vanadium pentoxide, the concentration of  $\text{Co}^{3+}$  ions in solution is reduced to  $0.74 \times 10^{-3}$  moles/liter and the oxide is reduced to 0.025 g/liter. With the addition of 2.8 g/liter or more vanadium pentoxide, no oxide was formed during plating. The effect of electrolysis time on the formation of  $\text{Co}^{3+}$  ions in different  $\text{CoSO}_4\text{-V}_2\text{O}_5$  solutions is shown in Fig. 5. In a pure cobalt sulfate solution, the formation of  $\text{Co}^{3+}$  ions in solution increases from 1.2 to  $5.5 \times 10^{-3}$  moles/liter over a period of 0.5-5.5 hr and the oxide increases from 0.07 to 0.44 g/liter over the same period. With an addition of 2.3 g/liter vanadium pentoxide, the concentration of  $\text{Co}^{3+}$  ions is decreased; however, with time there is an increasing trend in the formation of  $\text{Co}^{3+}$  ions in solution, the concentration increase being  $0.56\text{-}1.04 \times 10^{-3}$  moles/liter over a period of 0.5-5.5 hr and the oxide increased from trace amounts to 0.025 g/liter. With 4.3 g/liter vanadium pentoxide in solution, no oxide is formed and a decreasing trend in  $\text{Co}^{3+}$  ion concentration was observed with an increase in plating time. In fact, when the solution is electrolyzed over

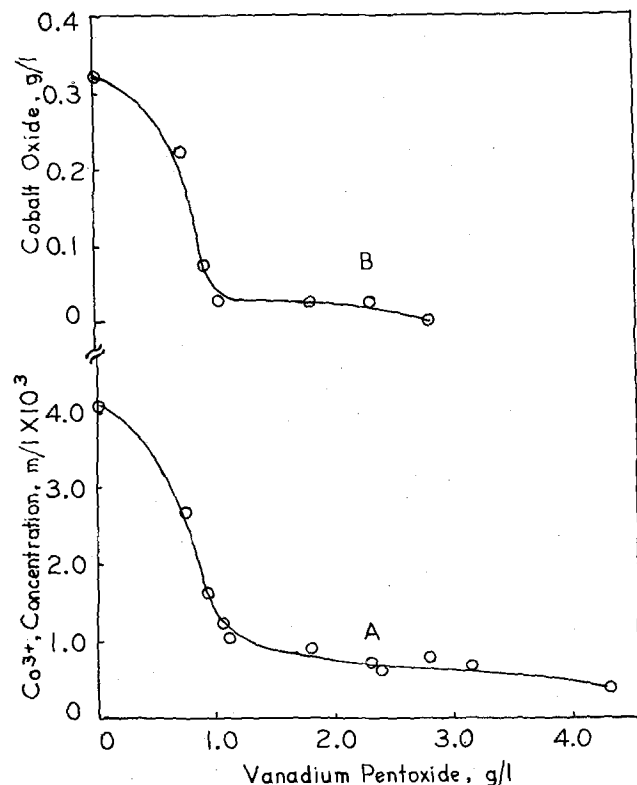


Fig. 4. Effect of  $V_2O_5$  concentration on the formation of (A)  $Co^{3+}$  ion in solution and (B) cobalt oxide in solution. Insoluble anode, anode:cathode = 1:4, current density = 5 A/dm<sup>2</sup>, temperature = 40°C, pH (initial) = 1.00, plating time = 3.5 hr.

a period of 8 hr, no  $Co^{3+}$  ion was found and the solution contained  $VO^{++}$  ions ( $1.9 \times 10^{-3}$  moles/liter). Another portion (300 ml) of  $CoSO_4-V_2O_5$  (4.3 g/liter) solution after 16 hr electrolysis was found to contain  $VO^{++}$  ( $5.6 \times 10^{-3}$  moles/liter) and no  $Co^{3+}$  ions. The results thus suggest that the formation of  $Co^{3+}$  ions in the plating solutions is reduced by vanadium ions of a lower oxidation state. The latter are produced at the cathode and are oxidized at the platinum anode.

*Mechanical properties of the deposits.*—The room temperature yield strength, ultimate tensile strength, and percent elongation of cobalt deposits prepared using both soluble and insoluble anodes are summarized in Table II. With a soluble anode, the pH of the bath increased somewhat (0.88 to 1.10) and with an insoluble anode it decreased (1.04 to 0.90). The rela-

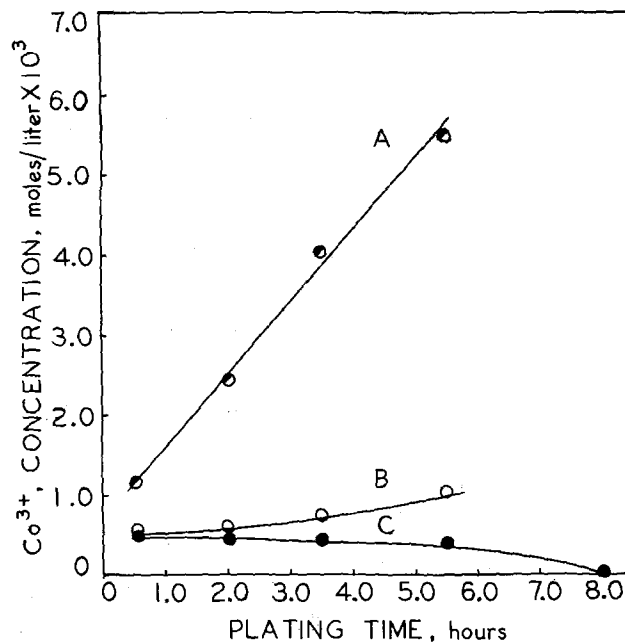


Fig. 5. Variation of  $Co^{3+}$  ion concentration with plating time: (A) in  $CoSO_4$  solution, (B) in  $CoSO_4-V_2O_5$  (2.3 g/liter) solution, (C) in  $CoSO_4-V_2O_5$  (4.3 g/liter) solution. Insoluble anode, anode:cathode = 1:4, current density = 5 A/dm<sup>2</sup>, temperature = 40°C, pH (initial) = 1.00.

tively low cathode efficiency is due to the lower pH conditions at which these deposits were prepared. With an insoluble anode, the efficiency was only 36% and this is partly due to the decrease in pH during plating. This can be improved and the pH of the bath can be maintained by adopting the method suggested by Sadak *et al.* (9) where a counterplating using a soluble cobalt anode is carried out in the same plating system. The deposits were silvery gray in appearance and relatively ductile. The addition of vanadium pentoxide to the cobalt sulfate bath does not affect the yield strength, ultimate tensile strength, and elongation values of the deposits. The results also show that the yield strength, tensile strength, and elongation for the deposits prepared with an insoluble anode are very similar to those obtained with a soluble anode. An examination of the microstructures (Fig. 6) shows no significant difference between the deposits prepared from cobalt sulfate solutions with and without vanadium pentoxide, respectively. The columnar structure, typical of electrodeposited cobalt, is seen in both cases.



Fig. 6. Microstructures of cobalt deposits prepared from (a)  $CoSO_4-V_2O_5$  plating solution, insoluble anode is used and (b)  $CoSO_4$  plating solution, soluble anode is used. Plating conditions are reported in Table II. 1000 $\times$  magnification.

Table II. Mechanical properties of cobalt deposits prepared from  $\text{CoSO}_4$  and  $\text{CoSO}_4\text{-V}_2\text{O}_5$  plating solutions

Plating solutions	Anodes	Room temperature strength data (psi)†		Elongation† (%)	Efficiency*** (%)
		Yield strength	Ultimate tensile strength		
$\text{CoSO}_4(1M)^*$	Soluble	89,000	144,000	12	47
$\text{CoSO}_4\text{-V}_2\text{O}_5^*$	Soluble	88,000	165,000	11	47
$\text{CoSO}_4\text{-V}_2\text{O}_5^{**}$	Insoluble (platinum)	90,000	146,000	15	36

Vanadium pentoxide, 4.3 g/liter, current density = 5 A/dm<sup>2</sup>, temperature = 40°C.

\* pH (0.88-1.10).

\*\* pH (1.04-0.90).

\*\*\* Efficiency based on 1.099 g/A-hr for cobalt baths (10).

† Values are the average of 3-4 tensile specimens (as-plated).

### Summary

It has been shown that during plating from a cobalt sulfate solution using an insoluble anode the formation of  $\text{Co}^{3+}$  ions and cobalt oxide ( $\text{Co}_2\text{O}_3$ ) results at the anode. The addition of a sufficient amount of an electrochemically active substance such as vanadium pentoxide to the plating solution has suppressed the formation of  $\text{Co}^{3+}$  ions and prevented the formation of cobalt oxide at the anode. The electrochemically active substance participates in the electrode reactions both at the cathode and anode but is not consumed or incorporated with the deposit. The mechanical properties of cobalt deposits obtained using an insoluble anode are comparable to those obtained using a soluble anode.

Manuscript submitted April 1, 1976; revised manuscript received May 17, 1976. This was Paper 255 presented at the Las Vegas, Nevada, Meeting of the Society, Oct. 17-22, 1976.

Any discussion of this paper will appear in a Discussion Section to be published in the June 1977 JOURNAL. All discussions for the June 1977 Discussion Section should be submitted by Feb. 1, 1977.

Publication costs of this article were assisted by Watervliet Arsenal.

### REFERENCES

1. G. R. Lakshminarayanan, E. S. Chen, and F. K. Sautter, *This Journal*, **122**, 1589 (1975).
2. E. S. Chen and F. K. Sautter, Submitted to *Plating*.
3. J. C. Sadak and F. K. Sautter, *Met. Eng. Q.*, **14**, 44 (1974).
4. J. C. Sadak and F. K. Sautter, *Plating*, **56**, 1041 (1969).
5. J. C. Sadak and F. K. Sautter, *ibid.*, **59**, 425 (1972).
6. J. C. Sadak and F. K. Sautter, *J. Vac. Sci. Technol.*, **11**, 771 (1974).
7. G. R. Lakshminarayanan and F. K. Sautter, Watervliet Arsenal Technical Report, WVT-7024 (1970).
8. R. B. Fischer and D. G. Peters, "Quantitative Chemical Analysis," p. 512, W. B. Saunders & Co., Philadelphia (1968).
9. J. C. Sadak, E. S. Chen, G. R. Lakshminarayanan, and F. K. Sautter, Paper presented at the International Conference of Metallurgical Coatings, San Francisco, California, April 1976.
10. E. Raub and K. Muller, "Fundamentals of Metal Deposition," p. 26, Elsevier Publish Company, New York (1967).

## Engineering Analysis of Shape Change in Zinc Secondary Electrodes

### I. Theoretical

King Wai Choi\* and Douglas N. Bennion\*\*

*Energy and Kinetics Department, School of Engineering and Applied Science, University of California, Los Angeles, California 90024*

and John Newman\*\*

*Materials and Molecular Research Division, Lawrence Berkeley Laboratory, and Department of Chemical Engineering, University of California, Berkeley, California 94720*

### ABSTRACT

Shape change, the redistribution of active material over the zinc electrode surface as a result of cell cycling, is hypothesized to be caused by convective flows driven primarily by membrane pumping. A mathematical model is formulated based on the convective flow hypothesis for the zinc-silver oxide secondary cell. The numerical solutions predict redistribution of zinc material over the zinc electrode, fluid flow rates, and variations of current distribution and cell potential with the number of cycles. These calculated results can be compared to experimental results. The results suggest that shape change can be eliminated if the convective flow in the zinc electrode compartment parallel to the electrode surface is stopped.

Zinc electrodes have been used as reducing agents in common primary cells like the Leclanché cell (dry cell) and the alkaline zinc-manganese dioxide cell. They have also been used as negative plates in secondary storage cells such as the zinc-silver oxide cell. The zinc electrode is attractive for use in secondary battery

systems because of its low cost, strong reducing potential, and low equivalent weight in comparison with other available negative electrodes. However, secondary cells using zinc negatives have a poor cycle life (100-400 cycles) (1). This is due mainly to the failure of the zinc electrodes (1, 2). If the cycle life of the zinc electrode can be extended, zinc-silver oxide cells would be much more valuable in aerospace and other applications where the high energy density justifies

\* Electrochemical Society Student Member.

\*\* Electrochemical Society Active Member.

Key words: battery, silver-silver oxide, electro-osmosis, osmosis, separators.

the costs. Also, an improved zinc electrode might stimulate development of the zinc-nickel oxide cell, which may yield a much lower cost and higher specific energy cell than the popular nickel-cadmium cell.

The failure of the zinc electrodes in zinc-silver oxide cells has been associated with several phenomena. Two causes of failure are migration of colloidal silver from the positive silver electrode to the negative zinc electrode and zinc dendrite growth through the separator causing short-circuiting inside the cell (1). These processes can be controlled successfully by the use of new membrane separator materials (2). It is currently widely believed that a main reason for the failure of zinc electrodes is "shape change." Shape change refers to the redistribution of zinc oxide material over the surface of the zinc electrode. Shape change in the zinc electrode has been demonstrated experimentally; for example, by Lander and Cooper (2), McBreen (3), and Choi *et al.* (4). In their cell designs, zinc oxide material was shown to move from the region near the top toward the center and bottom of the zinc electrode. The accumulation of zinc oxide in one place and depletion in the other is believed to contribute to loss of capacity until the cell potential on discharge falls below acceptable values.

Even though the failure of zinc electrodes due to shape change has been identified, the basic causes of shape change in zinc electrodes have not previously been adequately defined. McBreen (3) has explained shape change in zinc electrodes in terms of nonuniform current distribution. His experimental results demonstrated a correlation between observed shape change in the zinc electrodes and nonuniform current density distribution. However, the contention that shape change is caused by nonuniform current distribution is not proven clearly, and no mechanism for net transport of zinc species is included in the discussion.

An analysis is presented here based on a hypothesis that convective flows driven by membrane separator transport are coupled with changes in the concentration of soluble zinc species to cause the movement of zinc across the electrode.

### Hypothesis for the Cause of Shape Change

Several factors contribute to fluid motion within the porous electrodes. In a conventional zinc-silver oxide cell, a membrane<sup>1</sup> between the zinc electrode and the silver electrode separates the cell into two compartments, both of which are filled with concentrated potassium hydroxide solution which is originally saturated with respect to zinc oxide. A volumetric flow across the membrane is directly induced by an electro-osmotic force which arises from the passage of electric current through the membrane. During cycling, a solute concentration difference between the two compartments builds up due to chemical and electrochemical reactions. The resulting osmotic force will also produce a volumetric flow across the membrane. The net flow across the membrane (modified by changes in the porosities of the electrodes due to electrochemical, chemical, and physical phase-change reactions) may be observed as a convective flow in both compartments parallel to the membrane.

The undesirable formation of gas bubbles within the porous electrodes will also influence the fluid motion. Natural convection within porous electrodes is certainly possible (27), but experimental evidence indicates that the direction of the gravitational field does not affect the shape change (2, 4, 26).

The movement of solutes in the direction parallel to the membrane will be determined by the combination of convection, diffusion, and migration transport processes. In this direction, convection is the dominant effect, and migration is assumed to be negligible. As discussed in the preceding paragraphs, the convective

flow has a periodic nature due to the cycling process. Simultaneously, the concentration of soluble zinc species varies periodically because the cathodic deposition of zinc depletes the solution and the anodic process temporarily supersaturates the solution before zinc oxide can precipitate. The periodic motion of the fluid, coupled with the periodic concentration of zinc species, will result in a net movement of zinc species parallel to the membrane, in one direction or the other, and extended cycling will eventually produce a significant relocation of zinc. This is zinc shape change.

Let us examine these processes in more detail.

During discharge, as current flows from the zinc electrode to the silver electrode (see Fig. 1), there will be a flow of potassium ions in the same direction through the membrane, since the membrane is a cation exchanger. It is expected that the electro-osmotic force will generate a volumetric flow in the same direction because the cations will tend to entrain water molecules.

At the same time, the KOH concentration will decrease in the zinc electrode compartment and increase in the silver electrode compartment, during discharging, because the anodic process consumes hydroxide, the cathodic process produces hydroxide, and the potassium ions are transported across the cation-exchange membrane. (The use of an anion-exchange membrane would reduce considerably the concentration difference of KOH.) The volumetric flow induced by the osmotic effect due to the KOH concentration difference will be in the same direction as that expected for the electro-osmotic flow, but it will not respond as rapidly to changes in the current because of the time required for the KOH concentration to change.

Also, the concentration of zinc species, assumed to be the zincate ion  $Zn(OH)_4^{2-}$ , will increase in the zinc compartment during discharging due to oxidation and dissolution of zinc. The osmotic flow induced by this concentration change will be in the opposite direction from those enumerated above, but the combination of all the osmotic and electro-osmotic effects is expected to produce a volumetric flow across the membrane from the zinc electrode toward the silver electrode during discharging. The flow would be predominantly in the opposite direction during charging. This means that there will be a downward convective flow in the zinc electrode compartment during discharging (see Fig. 1) and an upward flow during charging.

Now consider the varying zinc concentration and the convective movement of soluble zinc species. During discharging, the solution in the zinc compartment is supersaturated with zincate, and the direction of the volumetric flow is downward. A large amount of zinc is convected downward as soluble zinc species. As the flow is going up in the zinc electrode compartment during charging, the electrolytic solution will be undersaturated with zinc species due to the deposition of

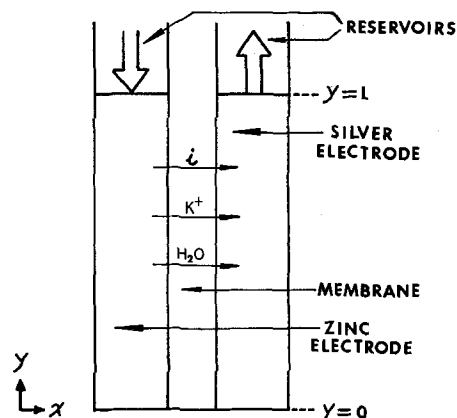


Fig. 1. Schematic cell cross section and flow pattern on discharge

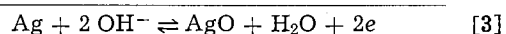
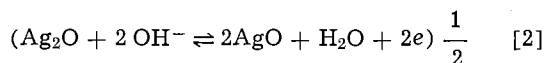
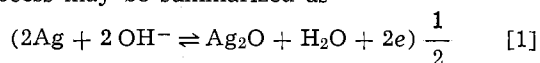
<sup>1</sup> In experimental studies by Lander and Cooper (2) and McBreen (3), RA1-P2291 cation-exchange membranes were used. A similar membrane was used in this study.

zinc. Less zinc moves up on charging than moves down on discharging, and there will be a net movement of zinc downward during a complete cycle. As the cycling process continues, the amount of zinc oxide in the region near the top of the zinc electrode will decrease, and the amount in the region near the center and bottom will increase due to the net transport resulting from low zincate concentration during upflow and high zincate concentration during downflow.

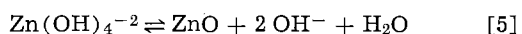
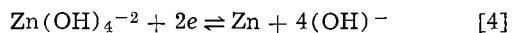
The hypothesis provides a theoretical basis for development of a mathematical model which formulates, with certain approximations, the physical behavior occurring in the cell during cycling into a set of non-linear, coupled, partial differential equations. These equations are solved by numerical techniques. The primary interest is in shape change in zinc secondary electrodes. A conventional zinc-silver oxide cell is chosen for analysis. As explained above, the convective flow is considered to be the main factor which causes redistribution of zinc oxide material over the zinc electrode. This convective flow is assumed to be driven only by osmotic and electro-osmotic forces, and to a minor extent by changes in the volume fractions of the solids due to chemical reaction. Therefore, shape change in the zinc electrode will be dependent on the resulting hydrodynamic behavior, but not on how the cell is positioned relative to the earth's gravitational field. Figure 1 shows a cross section of the cell. The  $x$  direction is parallel to the direction of the electric current, and the  $y$  direction is in the direction perpendicular to the electric current. One end of the electrode compartments at  $y = 0$  is closed, and the fluxes of species in the  $y$  direction are zero there. The other end of the electrodes at  $y = L$  is next to the reservoirs which allow fluid to flow into or out of the individual electrode compartments. If the convective flow moves in the positive  $y$  direction in the zinc electrode compartment on charge and in the negative  $y$  direction on discharge, then according to the hypothesis, the zinc oxide will be expected to move from the region near  $y = L$  to the region near  $y = 0$ .

### A Mathematical Model Based on the Convective Flow Hypothesis

*Reactions at the electrodes.*—The electrochemical reactions which occur at the silver electrode are believed to involve both monovalent and divalent silver oxides. Numerous studies (5-8) have confirmed that monovalent silver oxide forms first on the silver electrode surface in alkaline solution at the beginning of oxidation during charging, and divalent silver oxide forms later. The reverse process occurs during discharge. The process may be summarized as



A kinetic mechanism for zinc electrodes in alkaline media has been recently given by Bockris *et al.* (9) and Payne and Bard (10). Evidence shows that the behavior of zinc electrodes in alkaline solution is a dissolution-precipitation process (11, 12). The process occurring in the zinc electrode may be expressed as



*Species considered in the electrolytic solutions.*—In both the zinc and the silver electrode compartments, the electrolytic solution is initially concentrated KOH solution which is saturated with respect to ZnO. The solution phases contain the species  $\text{K}^+$ ,  $\text{OH}^-$ ,  $\text{H}_2\text{O}$ , and different complex forms of zinc ionic species. Generally,

these ionic zinc species include  $\text{Zn}^{+2}$ ,  $\text{Zn}(\text{OH})^+$ ,  $\text{Zn}(\text{OH})_2$ ,  $\text{Zn}(\text{OH})_3^-$ , and  $\text{Zn}(\text{OH})_4^{2-}$  which are thermodynamically interrelated by equilibrium constants. Among these zinc ionic species in alkaline solution, the species  $\text{Zn}(\text{OH})_4^{2-}$  is predominant (13-17). Since charge neutrality must hold in the bulk solution, the concentration of ionic species are not all independent. In the following,  $\text{K}^+$  species and zinc ion species are chosen as independent variables. The zinc ionic species are represented by the symbol  $\text{Zn}^{+2}$ . It is necessary to consider only the three independent fluxes of  $\text{Zn}^{+2}$ ,  $\text{K}^+$ , and  $\text{H}_2\text{O}$  along with current density in the  $x$  direction.

*Species transport across the membrane.*—If the pressure difference across the membrane is zero, then the fluxes of species  $\text{Zn}^{+2}$ ,  $\text{K}^+$ , and  $\text{H}_2\text{O}$  across the membrane in the  $x$  direction can be written as linear functions of three driving forces: the concentration differences of  $\text{Zn}^{+2}$  and  $\text{K}^+$  across the membrane and the electric current density through the membrane.

For the  $\text{Zn}^{+2}$  species

$$N_{\text{Zn},x}^m = L_{\text{zz}}(c_{\text{Zn}}^n - c_{\text{Zn}}^p) + L_{\text{zk}}(c_{\text{K}}^n - c_{\text{K}}^p) + \frac{t_{\text{Zn}}^m i}{2F} \quad [6]$$

For the  $\text{K}^+$  species

$$N_{\text{K},x}^m = L_{\text{kk}}(c_{\text{K}}^n - c_{\text{K}}^p) + L_{\text{kz}}(c_{\text{Zn}}^n - c_{\text{Zn}}^p) + \frac{t_{\text{K}}^m i}{F} \quad [7]$$

For the  $\text{H}_2\text{O}$

$$N_{\text{O},x}^m = -L_{\text{oz}}(c_{\text{Zn}}^n - c_{\text{Zn}}^p) - L_{\text{ok}}(c_{\text{K}}^n - c_{\text{K}}^p) + \frac{t_{\text{O}}^m i}{F} \quad [8]$$

where  $N_{\text{Zn},x}^m$ ,  $N_{\text{K},x}^m$ , and  $N_{\text{O},x}^m$  represent the fluxes of species  $\text{Zn}^{+2}$ ,  $\text{K}^+$ , and  $\text{H}_2\text{O}$ , respectively, across the membrane in the  $x$  direction,  $c_{\text{Zn}}^p$  and  $c_{\text{K}}^p$  represent the concentrations of  $\text{Zn}^{+2}$  and  $\text{K}^+$  in the silver electrode compartment, respectively, similarly  $c_{\text{Zn}}^n$  and  $c_{\text{K}}^n$  represent the concentrations of  $\text{Zn}^{+2}$  and  $\text{K}^+$  in the zinc electrode compartment. The symbol  $i$  represents the current density across the membrane in the  $x$  direction.

For the fluxes of species  $\text{Zn}^{+2}$  and  $\text{K}^+$ , only the primary concentration driving forces are considered, and the coupling effects are assumed negligible, that is,  $L_{\text{zk}}$  and  $L_{\text{kz}}$  are assumed to be zero. Then  $L_{\text{zz}}$  and  $L_{\text{kk}}$  can be regarded as equal to the diffusion coefficients of  $\text{Zn}^{+2}$  and  $\text{K}^+$  in the membrane divided by the thickness of the membrane. The symbols  $t_{\text{Zn}}^m$  and  $t_{\text{K}}^m$  represent the transference numbers of  $\text{Zn}^{+2}$  and  $\text{K}^+$  for the membrane, and they are assumed to be constant throughout the membrane. The flux of  $\text{H}_2\text{O}$  is written in terms of osmotic effects and an electro-osmotic effect. Therefore,  $L_{\text{ok}}$  and  $L_{\text{oz}}$  are interpreted to be the water transport coefficients across the membrane induced by the concentration differences of species  $\text{Zn}^{+2}$  and  $\text{K}^+$ . The symbol  $t_{\text{O}}^m$  is a proportionality constant for the water transport induced by the electro-osmotic effect and is called the electro-osmotic coefficient. These transport terms may be concentration dependent, but they are assumed to be constant.

*Conservation of species in the porous electrodes.*—Inside the porous zinc and silver electrodes, the local transfer current density, species concentration in the solution phase, porosity, conductance of the solid matrix, and the conductivity of the electrolytic solutions may have large ranges of variation. Numerous works have been published during the recent two decades on porous electrodes and their application to batteries. A review of porous electrodes in battery applications has been recently given by Newman and Tiedemann (18). Since the primary interest of this work is to investigate how the zinc oxide redistributes over the zinc electrode in the  $y$  direction after a certain number of cycles, it is for simplicity that the local current density, species concentrations, porosity, and conductivity of electrolyte are assumed not to vary in

the  $x$  direction inside the porous electrodes. Only the variations in the  $y$  direction are considered. This simplification allows the transformation of a two-dimensional problem into a one-dimensional problem which can be solved with much less cost. The transport of species across the membrane from one electrode compartment to the other will be treated as a source term in the species conservation equations in the electrode compartments.

The conservation equation for species in solution within a porous electrode can be written as follows

$$\frac{\partial \epsilon c_i}{\partial t} = - \frac{\partial N_{i,y}}{\partial y} + R_i \quad [9]$$

(Accumulation) = (Net input) + (Source)

where  $c_i$ ,  $\epsilon$ ,  $N_{i,y}$ , and  $R_i$  represent the concentration of species  $i$ , electrode porosity, flux of species  $i$  in  $y$  direction, and source term of species  $i$  respectively. If the dependence of the diffusion coefficient on tortuosity is not considered, then the flux of species  $i$  in the  $y$  direction can be written in the form

$$N_{i,y} = - D_{i\epsilon} \frac{\partial c_i}{\partial y} + c_i v_y \quad [10]$$

where  $D_i$  is the diffusion coefficient of species  $i$  and  $v_y$  is the superficial velocity in the  $y$  direction. The conservation equations for species  $Zn^{+2}$  and  $K^+$  in the electrode compartments can be expressed by substitution of Eq. [10] into Eq. [9]. In the silver electrode compartment

$$\frac{\partial c_{Zn^p} e^p}{\partial t} = - \frac{\partial}{\partial y} \left( -D_{Zn^p} e^p \frac{\partial c_{Zn^p}}{\partial y} + c_{Zn^p} v_y^p \right) + R_{Zn^p} \quad [11]$$

$$\frac{\partial c_{K^p} e^p}{\partial t} = - \frac{\partial}{\partial y} \left( -D_{K^p} e^p \frac{\partial c_{K^p}}{\partial y} + c_{K^p} v_y^p \right) + R_{K^p} \quad [12]$$

In the zinc electrode compartment

$$\frac{\partial c_{Zn^n} e^n}{\partial t} = - \frac{\partial}{\partial y} \left( -D_{Zn^n} e^n \frac{\partial c_{Zn^n}}{\partial y} + c_{Zn^n} v_y^n \right) + R_{Zn^n} \quad [13]$$

$$\frac{\partial c_{K^n} e^n}{\partial t} = - \frac{\partial}{\partial y} \left( -D_{K^n} e^n \frac{\partial c_{K^n}}{\partial y} + c_{K^n} v_y^n \right) + R_{K^n} \quad [14]$$

All the terms have meanings as defined previously. The superscripts  $p$  and  $n$  designate the quantities in the silver electrode compartment and the zinc electrode compartment, respectively.

Since the  $K^+$  species does not participate in any electrochemical or chemical reactions in both silver and zinc electrode compartments, the source terms of  $K^+$  in both compartments will be equal to the flux of  $K^+$  species across the membrane into the compartments. Then the source terms for  $K^+$  in the silver and the zinc electrode compartments can be expressed as

$$R_{K^p} = \frac{N_{K,x^m}}{w_p} \quad [15]$$

$$R_{K^n} = - \frac{N_{K,x^m}}{w_n} \quad [16]$$

where  $w_p$  and  $w_n$  are the thickness of the silver and the zinc compartments, respectively.

In the zinc electrode compartment, the  $Zn^{+2}$  species participates in the electrochemical reaction (oxidation or reduction of Zn) and the phase transformation reaction (dissolution or precipitation of ZnO). Therefore, the source term of  $Zn^{+2}$  in the zinc electrode compartment should include all these electrochemical and phase transformation reactions plus the transport of  $Zn^{+2}$  species across the membrane into the zinc electrode compartment. It is expressed as

$$R_{Zn^n} = - \frac{N_{Zn,x^m}}{w_n} + \frac{i}{2Fw_n} - ak(c_{Zn^n} - c_{Zn^{sn}}) \quad [17]$$

where the term  $i/2Fw_n$  represents the rate of the oxidation (or reduction) reaction of Zn due to the passage of current,  $ak(c_{Zn^n} - c_{Zn^{sn}})$  represents the rate of dissolution (or precipitation) reaction determined by the solubility of ZnO in KOH solution,  $c_{Zn^s}$  is the saturated concentration of  $Zn^{+2}$  species adjacent to the zinc oxide material surface in KOH solution,  $a$  is the available surface area for dissolution (or precipitation) of ZnO per unit volume of the electrode compartment, which will be a function of the porous solid matrix structure and the amount of ZnO, and  $k$  is the mass transfer coefficient for  $Zn^{+2}$  species transfer from the bulk solution to the sites of dissolution or precipitation of ZnO. The magnitude of  $k$  is affected by the hydrodynamic behavior occurring in the electrode compartment. It is assumed that the value of  $k$  increases with increasing convective flow during ZnO dissolution and decreases with increasing convective flow during ZnO precipitation.<sup>2</sup> The dependence of  $k$  on the convective flow is correlated by an empirical exponential term. The product of the two terms  $a$  and  $k$  can be expressed in an empirical form as follows.

During dissolution of ZnO

$$ak = R_d Q_{ZnO} \alpha e^{\beta a |v_y^n|} \quad [18]$$

During precipitation of ZnO

$$ak = R_p (1 + \xi Q_{ZnO} \alpha) e^{-\beta_p |v_y^n|} \quad [19]$$

where  $R_d$ ,  $R_p$ ,  $\alpha$ ,  $\xi$ ,  $\beta_d$ , and  $\beta_p$  are empirical constants,  $|v_y^n|$  is the absolute value of the velocity  $v_y^n$ , and  $Q_{ZnO}$  is the quantity of zinc oxide per unit area.

Equation [18] correlates the rate of dissolution of ZnO into the electrolytic solution with the amount of ZnO in the electrode compartment. As the amount of ZnO in the electrode compartment goes to zero, the dissolution rate of ZnO will go to zero. As the velocity of the convective flow goes to infinity, the rate of dissolution will also go to infinity. Equation [19] correlates the precipitation reaction of ZnO on the solid matrix surface plus the surface of ZnO material in the electrode compartment. As the convective flow goes to zero, the rate of precipitation of ZnO will be equal to the value at a stagnant state.

Similarly, the source term for  $Zn^{+2}$  species in the silver electrode compartment can be expressed by summing the net flux of  $Zn^{+2}$  species across the membrane and the effect due to precipitation or dissolution of ZnO in the silver electrode as follows

$$R_{Zn^p} = \frac{N_{Zn,x^m}}{w_p} - a^* k^* (c_{Zn^p} - c_{Zn^{sp}}) \quad [20]$$

where the term  $a^* k^*$  has the same terms for precipitation and dissolution of ZnO as shown in Eq. [18] and [19]. The empirical constants are specific for the silver electrode compartment.

For dissolution

$$a^* k^* = R_d^p Q_{ZnO} \alpha^p e^{\beta_d^p |v_y^p|} \quad [21]$$

For precipitation

$$a^* k^* = R_p^p (1 + \xi^p Q_{ZnO} \alpha^p) e^{-\beta_p^p |v_y^p|} \quad [22]$$

In a static solution or in an ideal convective flow (plug flow), the diffusion coefficient of species will be equal to the usual liquid phase diffusion coefficient. But in a more realistic fluid flow behavior in porous media, the diffusion coefficient for species in the solution phase should also include a dispersion contribution due to fingering and backmixing associated with

<sup>2</sup> In retrospect, the reasoning leading to this decreasing mass transfer coefficient on velocity, as manifested by the minus signs in Eq. [19] and [22], is fallacious. The effect on final numerical results is small. The cost of repeating the calculations was too large to justify making the correction.



flow through tortuous pores of varying size and the velocity profiles across the pores. Some correlations of data on dispersion in packed beds have been given recently by Sherwood *et al.* (19). The backmixing dispersion effect in porous electrodes has been discussed by Newman and Tiedemann (18). However, a correlation of data on the dispersion effect has not been obtained directly for porous electrodes. An empirical relationship to account for the dispersion effect in this study is expressed as

$$D_i = D_i^0(1 + \gamma|v_y|) \quad [23]$$

where  $D_i^0$  is the effective diffusion coefficient in a static solution within the porous electrode,  $v_y$  is the superficial velocity in the  $y$  direction, and  $\gamma$  is an empirical constant. As the velocity goes to zero, the dispersion effect will disappear, and the diffusion coefficient  $D_i$  becomes equal to  $D_i^0$ .

In a dilute electrolytic solution, the solvent concentration can usually be regarded as constant. But in a concentrated electrolytic solution, the solvent concentration will be affected by the change of solute concentration. For simplicity, the solvent (water species) concentration is assumed to be constant. Then the conservation equations for water species in the silver and zinc electrode compartments can be written as follows.

In the silver electrode compartment

$$c_o^p \frac{\partial e^p}{\partial t} = -c_o^p \frac{\partial v_y^p}{\partial y} + R_{H_2O^p} \quad [24]$$

In the zinc electrode compartment

$$c_o^n \frac{\partial e^n}{\partial t} = -c_o^n \frac{\partial v_y^n}{\partial y} + R_{H_2O^n} \quad [25]$$

where  $c_o^p$  and  $c_o^n$  are the water concentrations in the silver and the zinc electrode compartments, and  $R_{H_2O^p}$  and  $R_{H_2O^n}$  are the source terms for water in the silver and zinc electrode compartments, respectively. By summing the transport of water species across the membrane into the electrode compartment and the effects due to the electrochemical and phase transformation occurring in the electrode compartments, the source terms of water species in the silver and the zinc electrode compartments are expressed as

$$R_{H_2O^p} = \frac{N_{o,x^m}}{w_p} - \frac{i}{2Fw_p} + a^*k^*(c_{Zn^p} - c_{Zn^{sp}}) \quad [26]$$

$$R_{H_2O^n} = -\frac{N_{o,x^m}}{w_n} + ak(c_{Zn^n} - c_{Zn^{sn}}) \quad [27]$$

where the terms  $N_{o,x^m}/w_p$  and  $N_{o,x^m}/w_n$  represent the effect due to the transport of water species across the membrane, the term  $i/2Fw_p$  represents the effect due to the electrochemical reaction occurring in the silver electrode compartment according to Eq. [3], and the terms  $a^*k^*(c_{Zn^p} - c_{Zn^{sp}})$  and  $ak(c_{Zn^n} - c_{Zn^{sn}})$  represent the precipitation (or dissolution) reaction of ZnO in the silver and the zinc electrode compartments, respectively, which are due to the solubility of ZnO in KOH solution represented by Eq. [5].

The conversion of species in the porous electrodes from one solid phase to the other solid phase or from a solid phase to the liquid phase due to phase transition and electrochemical reactions occurring in the porous electrodes may cause changes in the porosities of the electrodes. For example, the transformation of solid silver oxide to solid silver in the silver electrode compartment, deposition of zinc ionic species as metallic zinc, and the dissolution of zinc oxide into the solution or the precipitation of zinc oxides from the solution to the electrode surfaces may change the electrode porosity.<sup>3</sup> Thus, the variations of the porosities with

<sup>3</sup>The treatment of such porosity changes in porous-electrode modeling occurs first in the work of Alkire *et al.* (28-31). It has subsequently been discussed by Dunning *et al.* (32, 33), Simonsson (34, 35), Micka and Rousar (36), and by Gidaspow and Baker (37, 38).

time in the silver electrode compartment and the zinc electrode compartment can be formulated according to Eq. [3], [4], and [5] as follows

$$\frac{\partial e^p}{\partial t} = (\bar{V}_{AgO} - \bar{V}_{Ag}) \frac{i}{2Fw_p} - \bar{V}_{ZnO} a^*k^*(c_{Zn^p} - c_{Zn^{sp}}) \quad [28]$$

$$\frac{\partial e^n}{\partial t} = \frac{\bar{V}_{Zn}}{2Fw_n} i - \bar{V}_{ZnO} ak(c_{Zn^n} - c_{Zn^{sn}}) \quad [29]$$

where  $\bar{V}_{Ag}$ ,  $\bar{V}_{AgO}$ ,  $\bar{V}_{ZnO}$ , and  $\bar{V}_{Zn}$  are the partial molar volumes of silver, silver oxide, zinc oxide, and zinc. The current density is defined to be positive on discharge and negative on charge. Equation [3] is assumed to be the main reaction in the silver electrode.

*Evaluation of the current density across the cell based on Ohm's law.*—Assuming the activation overpotential on the electrode surface to be negligible and the cell potential to be governed by the ohmic resistance of the electrolytic solutions in the porous electrodes and membrane, the current density can be written from Ohm's law as

$$i = -\kappa \frac{d\Phi}{dx} \quad [30]$$

where  $\kappa$  is the conductivity of the solution phase, which is a function of the bulk concentration and the porosity of the porous matrix. The over-all ohmic resistance across the cell includes the ohmic resistances of the silver electrode compartment, the membrane, and the zinc electrode compartment. After some algebraic manipulation, and making the approximate but convenient assumption that the transfer current density is constant across the electrodes, Eq. [30] can be rewritten in the form

$$i = -\frac{\Delta\Phi}{\frac{w_p}{\kappa_p} + \frac{w_n}{\kappa_n} + \int_0^{w_m} \frac{dx}{\kappa_m}} \quad [31]$$

where  $\Delta\Phi$  is the total ohmic potential drop across the cell, and  $\kappa_p$ ,  $\kappa_n$ , and  $\kappa_m$  are the effective conductivities of the electrolytic solutions in the silver electrode compartment, the zinc electrode compartment, and the membrane, respectively. By regarding the membrane as a porous medium and using a dependence of effective conductivity of solution on porosity suggested by Meredith and Tobias (20), the effective solution conductivities in the silver electrode compartment, the zinc electrode compartment, and the membrane are expressed as

$$\kappa_p = \kappa_p^0 (\epsilon^p)^{1.5} \quad [32]$$

$$\kappa_n = \kappa_n^0 (\epsilon^n)^{1.5} \quad [33]$$

$$\kappa_m = \kappa_m^0 (\epsilon^m)^{1.5} \quad [34]$$

where  $\kappa_p^0$ ,  $\kappa_n^0$ , and  $\kappa_m^0$  are the effective bulk solution conductivities in the silver electrode compartment, the zinc electrode compartment, and the membrane, respectively. In the membrane,  $\kappa_m^0$  is dependent on the local solution concentration which is treated as a linear function of the bulk solution concentrations in the silver electrode compartment and the zinc electrode compartment. The integral term in Eq. [31] can be approximated as follows

$$\int_m \frac{dx}{\kappa_m} = \frac{w_m}{M(\epsilon^m)^{1.5}} \sum_i^M \frac{1}{\kappa_{m,i}^0} \quad [35]$$

where  $w_m$  is the thickness of the membrane,  $M$  is the number of elements into which the membrane is theoretically sectioned,  $\epsilon^m$  is the membrane porosity, a constant, and  $\kappa_{m,i}^0$  is the local solution conductivity of the KOH solution in the  $i$ th element of the membrane assuming a linear concentration profile. Since the presence of zinc ions in KOH solution has been found not



to affect the conductivity appreciably (21), the conductivity of a pure KOH solution is employed here.

The ohmic potential drop in the collector screens in the  $y$  direction has been neglected. The system is designed so that the current density differs from one end of the electrodes to the other by only a few percent due to this effect. The nature of this effect does not change with cycling, and it has no major role in the shape-change process. The integration of current density across the electrode superficial area will be equal to the cell current

$$l \int_0^L i \, dy = I \quad [36]$$

where  $l$  is the width of the electrode,  $L$  is the length of the electrode, and  $I$  is the cell current. The total cell current is given as part of the problem statement.

*Current density distribution when limited by zincate depletion.*—As zinc oxide becomes redistributed, there eventually arise regions in which the zincate solution concentration begins to drop during charging due to insufficient solid zinc oxide being available to dissolve. These regions which are depleted in zinc oxide cannot accept the current density evaluated by Ohm's law alone. The current density in these regions becomes limited by the rate of supply of zincate to the reacting surfaces

$$i = \left\{ v_y^n \frac{\partial c_{Zn^n}}{\partial y} - \frac{\partial}{\partial y} \left( D_{Zn^n} \epsilon^n \frac{\partial c_{Zn^n}}{\partial y} \right) - \frac{L_{zz}}{w_n} c_{Zn^p} - ak c_{Zn^{sn}} \right\} \frac{w_n F}{(0.5 - t_{Zn^m})} \quad [37]$$

*Initial and boundary conditions.*—Equations [11], [12], [13], [14], [24], [25], [28], [29], and [31] or [37] form a set of nonlinear, coupled differential equations with nine unknowns  $c_{Zn^p}$ ,  $c_{Zn^n}$ ,  $c_{K^p}$ ,  $c_{K^n}$ ,  $v_y^p$ ,  $v_y^n$ ,  $\epsilon^n$ ,  $\epsilon^p$ , and  $i$ . These nine variables are functions of time  $t$  and position  $y$ . Equations [11] through [14] describe the concentrations of the solutes in the two electrode compartments while Eq. [24] and [25] relate how the velocity  $v_y$  changes with distance  $y$ , on the basis of material balances on the solvent. Equations [28] and [29] formulate the porosity variations of the positive and negative electrodes due to changes in the solid phases during cell operation. The last equation ([31] or [37]) is a description of the current density over the electrode.

The equations can be solved numerically with sufficient initial and boundary conditions. If the solutions can be obtained, then the distribution of ZnO material over the zinc electrode in the  $y$  direction may be calculated as

$$Q_{ZnO} = \frac{(1 - \epsilon^n) w_n - Q_{Zn} \bar{V}_{Zn} - \theta_B}{\bar{V}_{ZnO}} \quad [38]$$

where  $Q_{ZnO}$  is the amount of zinc oxide per unit area of the zinc electrode and  $Q_{Zn}$  is the amount of metallic zinc per unit area of the zinc electrode

$$Q_{Zn} = \int_0^t \frac{i}{2F} dt \quad [39]$$

and  $\theta_B$  is a constant term which corrects for the amount of inert material<sup>4</sup> in the zinc electrode.

Initially, before passing any current across the cell, the solution concentrations of species in both the silver and the zinc electrode compartments will be the same, the porosities of the silver electrode compartment and the zinc electrode compartment will be equal to their initial values, and both electrode compartments will be in a static situation. Immediately after the current is turned on, the flows begin and the initial conditions for time at zero plus are as follows

$$\begin{aligned} t = 0+, \text{ all } y & \quad I = I^0 \\ & \quad c_i^p = c_i^n = c_{i,0} \\ & \quad \epsilon^p = \epsilon_0^p \\ & \quad \epsilon^n = \epsilon_0^n \end{aligned} \quad [40]$$

At the boundary  $y = 0$  in both electrode compartments, the fluxes of species in the  $y$  direction are zero. Then the boundary conditions at  $y = 0$  can be written as follows

$$\begin{aligned} y = 0 & \quad \frac{\partial c_i^p}{\partial y} = 0 \\ & \quad \frac{\partial c_i^n}{\partial y} = 0 \\ & \quad v_y^n = 0 \\ & \quad v_y^p = 0 \end{aligned} \quad [41]$$

The subscript  $i$  implies either  $Zn^{+2}$  or  $K^+$ . At the other boundary,  $y = L$ , in both electrode compartments, solution may flow into or out of the electrode compartments by utilizing the reservoirs. The direction of flow changes during cycling. If it is assumed that the electrolytic solutions in the reservoirs are completely mixed whenever the fluids are flowing into or out of them, the changes of amount of species with time in the reservoirs will be equal to the fluxes of species across the boundary at  $y = L$  in both electrode compartments. Therefore, the boundary conditions at  $y = L$  are written as follows

$$\begin{aligned} y = L, \text{ in the silver electrode compartment} & \quad \frac{\partial c_i^p V_p}{\partial t} = N_{i,y^p} w_p l \end{aligned} \quad [42]$$

and in the zinc electrode compartment

$$\frac{\partial c_i^n V_n}{\partial t} = N_{i,y^n} w_n l \quad [43]$$

where  $V_p$  and  $V_n$  are the volumes of the reservoirs next to the silver electrode compartment and the zinc electrode compartment, respectively. The change of volumes of reservoirs with time are expressed as

$$\frac{\partial V_p}{\partial t} = v_y^p w_p l \quad [44]$$

$$\frac{\partial V_n}{\partial t} = v_y^n w_n l \quad [45]$$

where  $l$  is the width of the electrode.

*The computation procedure.*—There are nine principal equations (Eq. [11], [12], [13], [14], [24], [25], [28] [29], and [31] or [37]) to solve for the mathematical model subject to the initial conditions (Eq. [40]) and the boundary conditions (Eq. [41], [42], and [43]). The numerical solutions for the set of equations were carried out on an IBM digital computer 360/91 by use of a finite-difference numerical technique. The Crank-Nicolson implicit method (22) was used for Eq. [11], [12], [13], and [14]. Backward difference expressions were employed for Eq. [24] and [25]. Accuracy to order  $h^2$  was maintained by averaging quantities, other than derivatives with respect to  $y$ , between mesh points  $j$  and  $j-1$ . The time derivatives in Eq. [28] and [29] were expressed by a backward difference in  $\Delta t$ , and the other terms were averaged between the values of the previous and the present time steps. The accuracy of the numerical solutions was of the order  $h^2$  and  $(\Delta t)^2$ , where  $h$  and  $\Delta t$  are the grid sizes of distance and time. The equations were linearized about trial solutions and set in finite-difference forms. The resulting matrix was solved by use of the numerical method described by Newman (23-25). The convergence criterion was that the error of

<sup>4</sup>The inert material includes expanded silver grid, Teflon binder, and mercuric oxide.

two successive solutions for all the variables at all the mesh points be less than 0.001%. The details of the numerical calculation and procedure have been described by Choi (26). The values of the parameters for numerical calculations are summarized in the Appendix along with a table of the times for charging and discharging.

### Results

The hydrodynamic behavior occurring in the cell compartments during cell cycling is predicted by the model. The convective flow moves upward into the reservoir in the positive  $y$  direction in the zinc electrode compartment on charging and downward in the negative  $y$  direction on discharging. Since the convective flow is the main cause leading to the zinc material redistribution over the zinc electrode as a result of cycling, a comparison of the zinc movement through the solution phase upward on charging and downward on discharging gives a qualitative measure of how fast the zinc material redistributes over the zinc electrode. Numerical solutions for zinc movement through the solution midway along the zinc electrode for cycles 2, 5, and 8 are shown in Fig. 2, 3, and 4. These results (Fig. 2-4) indicate that the net movement of zinc material is from the upper region of the zinc electrode to the lower region of the zinc electrode as a result of cycling, using the midpoint of the electrode as reference. The net amount of zinc material moving per cycle down through the midpoint of the zinc electrode is initially about 0.21% of the total amount of zinc material in the electrode. It increased to 0.24% for cycle 5, and it remained almost constant (0.24%) for cycle 8. Figure 5 shows the redistribution of zinc material over the zinc electrode after 10, 20, 30, and 35 cycles due to the gradual downward movement of zinc material from the top to the bottom of the zinc electrode.

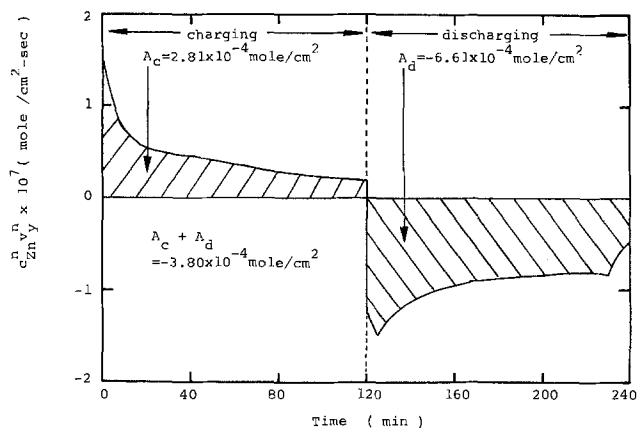


Fig. 2. Zinc movement midway along the zinc electrode during charging and discharging of cycle 2.

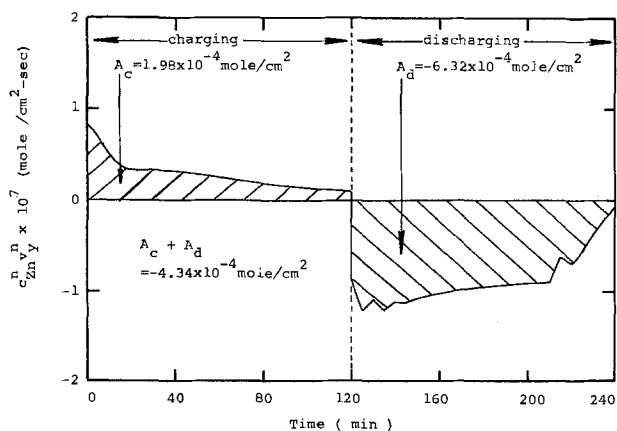


Fig. 3. Zinc movement midway along the zinc electrode during charging and discharging of cycle 5.

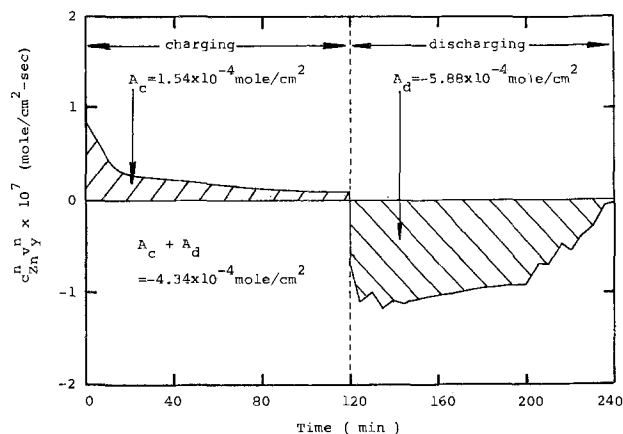


Fig. 4. Zinc movement midway along the zinc electrode during charging and discharging of cycle 8.

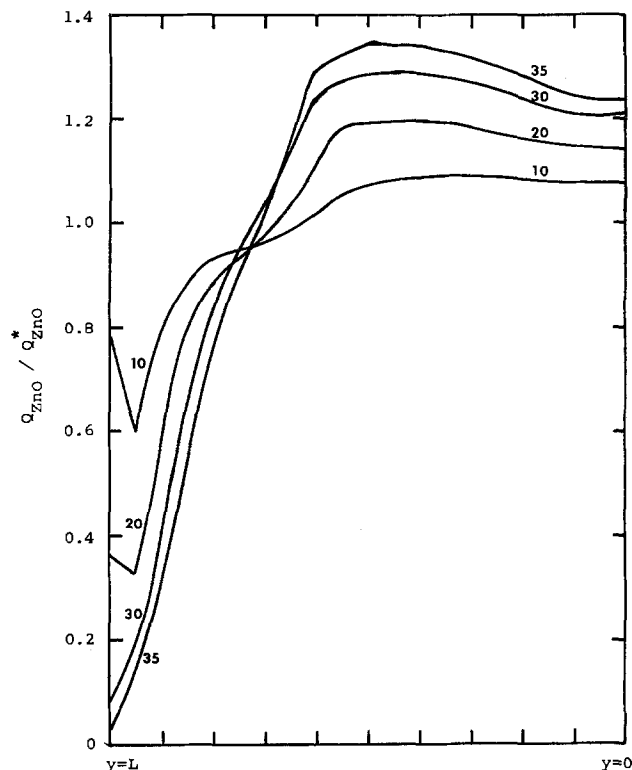


Fig. 5. Distribution of zinc material over the zinc electrode after 10, 20, 30, and 35 cycles.  $Q_{ZnO}^*$  is the quantity of ZnO initially present per unit area of the electrode.

The species concentrations in the electrode compartments also varied in the  $y$  direction due to the convective flow. Figures 6 and 7 show the variations of  $K^+$  and  $Zn^{+2}$  species concentrations at the end of discharge with number of cycles at three different locations of the zinc electrode. After cycles 8, 15, 22, and 28 the cell was allowed to stand for a long period of time until the species concentrations recovered to their initial values. Otherwise the cell was continuously cycled, while allowing only a 3 min rest period between successive half-cycles. These results show that there are large variations of species concentration in the  $y$  direction in the zinc electrode. The species concentrations near the bottom of the zinc electrode decreased with the number of cycles. The changes of species concentrations in the  $y$  direction and the changes of the porosity of the zinc electrode due to the redistribution of zinc material continuously affect the cell performance as cycling proceeds. Figure 8 shows the variation of cell performance in terms of the change in cell potential with the number of cycles. In

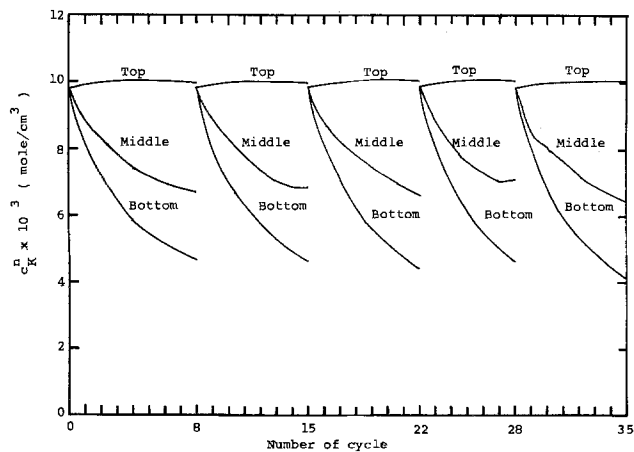


Fig. 6. Concentration profiles of KOH at the top, middle, and bottom of the zinc electrode as a function of the number of cycles. The values correspond to the end of the discharge half-cycle.

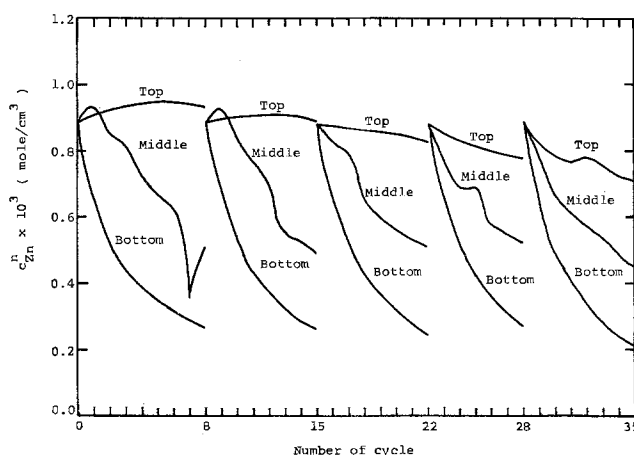


Fig. 7. Concentration profiles of dissolved zincate at the top, middle, and bottom of the zinc electrode as a function of the number of cycles. The values correspond to the end of the discharge half-cycle.

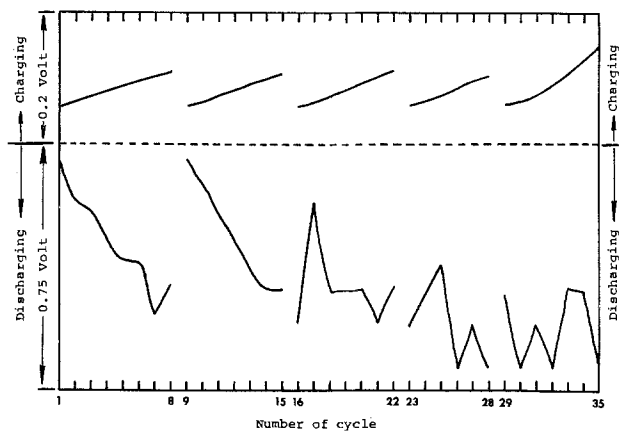


Fig. 8. Variation of cell potential at the end of charge and discharge as a function of the number of cycles

Fig. 8, it is shown that from cycles 1 through 8, the cell potential increases with the number of cycles on charging and decreases rapidly at the end of discharging.

If the cell is allowed to stand for a long period until the concentrations of species recover to their initial values, for example after cycle 8, the cell performance in cycle 9 behaves similarly to cycle 1. As cycling continues from cycle 9 through 15, the cell behavior is very similar to that for cycle 1 through 8 (Fig. 8). However, closer comparison of the cell behavior for

cycles 1 through 8 and for cycles 9 to 15 indicates that the cell performance has deteriorated since now a rest period is needed after seven cycles instead of eight. The cell potential at the end of charging and at the end of discharging of cycle 15 is the same as for cycle 8 (Fig. 8). Comparison of the continuous cycling processes for cycles 16 through 22, 23 through 28, and 29 through 35 also shows a steady decrease in cell potential at the end of discharging.

The change of cell performance with the number of cycles may also be reflected by the change in the distribution of metallic zinc and the current density distribution over the zinc electrode as a function of the number of cycles. Figures 9 and 10 show how the metallic zinc distribution varies with number of cycles at the end of charging and discharging. The area under the various curves is not constant because the amount of overcharging varied slightly from cycle to cycle. Zinc does not deposit in as great a quantity near  $y = 0$  compared to  $y = L/2$  during charging because water is pumped across the membrane, reducing the KOH concentration, increasing the electrical resistance, and decreasing the local current density. As the electrolytic solution flows up in the  $y$  direction, KOH is continually added to the solution, the electrical resistance decreases, current density increases, and the amount of zinc deposited increases. At 25°C, the electrical conductivity of KOH goes through a maximum at about 7.3M. Above 10M the conductivity falls rapidly with increasing concentration. Thus, near  $y = L$  the KOH concentration gets high enough during charging that it exceeds the conductivity maximum, the electrical resistance increases, current density decreases, and the amount of zinc deposited becomes less than near  $y = L/2$  as is shown in Fig. 9.

Figure 11 shows the variation of current distribution over the zinc electrode at the end of discharging with the number of cycles. These results show that metallic zinc distribution over the zinc electrode at the end of charging becomes more nonuniform as the number of cycles is increased (Fig. 9) which in turn affects the cell performance on discharging. At the end of discharging, Fig. 10 shows that there is no metallic zinc left near the regions close to the top and the bottom of the zinc electrode. Figure 10 also shows that as cycling continues, the area of the zinc electrode where there

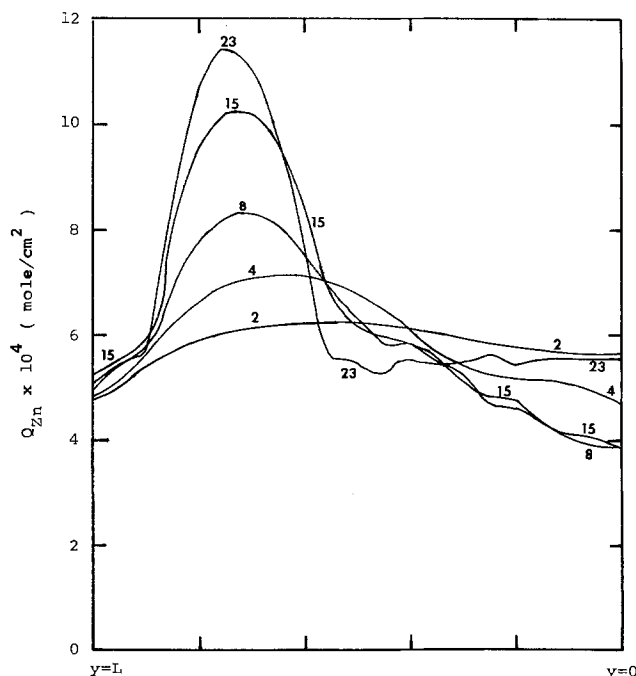


Fig. 9. Distribution of metallic zinc over the zinc electrode at the end of charging for cycles 2, 4, 8, 15, and 23.

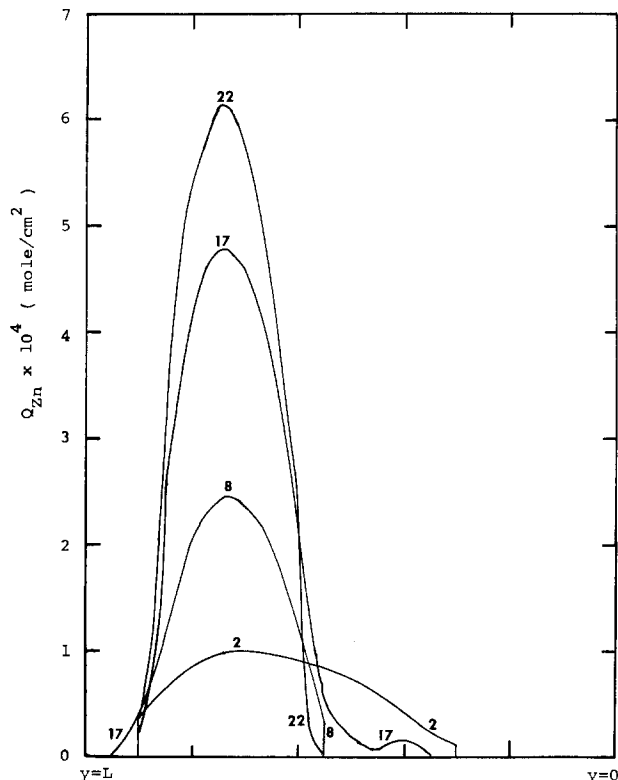


Fig. 10. Distribution of metallic zinc over the zinc electrode at the end of discharge of cycles 2, 8, 17, and 22.

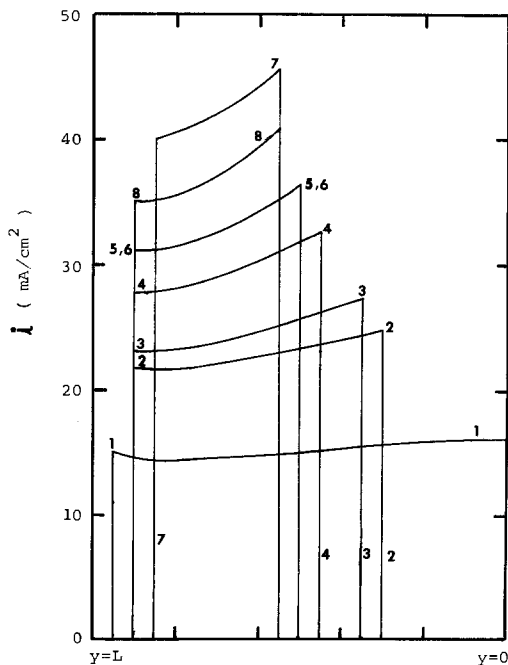


Fig. 11. Current distribution over the zinc electrode at the end of the discharge for cycles 1 to 8.

is metallic zinc left is getting smaller and more concentrated over a small area near the reservoir in the zinc electrode. This behavior can also be reflected by the current distribution over the zinc electrode at the end of discharging (Fig. 11). Figure 11 shows that at the end of discharging, most of the current is concentrated in a small area near the upper center portion of the electrode. This effective area becomes smaller with the number of cycles.

#### Discussion

*Movement of zinc.*—The movement of zinc material at the midpoint of the cell during cycles 2, 5, and 8,

reported in Fig. 2-4, is from the upper half of the zinc electrode to the lower half. This occurs because the convective flow of solution moving upward in the zinc electrode on charging is undersaturated with zincate because of deposition of zinc, and, as the convective flow of solution moves down in the zinc electrode on discharging, the solution in the zinc electrode is supersaturated with zincate species because of the dissolution of zinc. The amount of zinc material being carried upward in the zinc electrode on charging is less than the amount of zinc material being carried down on discharging because of the difference in zincate concentrations on charging and on discharging. This causes a net amount of zinc material to move downward from the upper region to the lower region in the zinc electrode for each cycle.

The data shown in Fig. 2 and 4 provide a measure of the percentage of the total amount of zinc material moving downward for each cycle. The rate of redistribution of zinc material over the zinc electrode may be estimated by comparison of these figures. Based on these results it can be projected that all of the zinc material in the top half of the cell will be transported to the bottom half after 208 cycles, the maximum possible cycles will, therefore, be less than 208 cycles for the cell being modeled.

Because of the gradual movement of zinc material from the top to the bottom in the zinc electrode, the zinc material near the center and bottom of the zinc electrode increases as cycling proceeds, see Fig. 5. The curves in Fig. 5 also indicate that the location of the maximum amount of zinc material gradually shifts to the center from the lower part of the zinc electrode. This is due to interrelationships between the variation of species concentration (KOH and zincate), convective flow behavior, and the current distribution.

During discharging, when the convective flow is in the downward direction in the zinc electrode, the rate of downward movement of zinc material at the midpoint of the cell slows near the end of the discharge cycle, see Fig. 2-4. At the same time, most of the cell current becomes concentrated near the center of the zinc electrode (Fig. 11) due to zinc metal depletion at the ends. This reduced current near  $y = 0$  is one cause of the reduced downward flow rate of solution. The higher current density near  $y = L/2$  causes a rapid increase in supersaturation of zinc species there. In addition, the KOH concentration near the middle of the zinc electrode becomes smaller (Fig. 6), decreasing the solubility of zinc oxide. The decreased flushing action of the convection, the increase in local zinc species concentration, and the decreased zinc oxide solubility all combine to increase the rate of zinc oxide precipitation in the upper middle portion of the zinc electrode near the end of a discharge period. As cycling proceeds, these effects are cumulative, and the zinc oxide collects more and more toward the lower middle portion of the zinc electrode.

As the zinc material near the top region of the zinc electrode moves down to the center and bottom of the zinc electrode, the zinc material right on the top boundary of the zinc electrode ( $y = L$ ) does not decrease as rapidly as the region next to it during the first 10 to 20 cycles because there is a large reservoir next to it. The existence of the reservoir, initially assumed to be saturated with zincate, provides a source for zinc and slows down the decrease of zincate concentration at the boundary, which in turn slows down the dissolution of zinc oxide at the boundary. But as cycling proceeds, the zincate concentration of the reservoir in the zinc electrode compartment becomes smaller, and the dissolution rate of the zinc oxide is no longer retarded. The amount of zinc oxide material at the boundary ( $y = L$ ) then shifts down to the minimum (see curve for 30 cycles, Fig. 5).

Since the zinc material movement is due to the convective flow in the zinc electrode, the shape change

behavior may be slowed if the convective flow in the zinc electrode is made smaller. If a neutral membrane (which has negligible electro-osmotic effects and smaller osmotic effects) is used as the separator, shape change behavior in the zinc electrode should not be as severe. It appears possible to eliminate shape change in zinc electrodes if the convective flow in the zinc electrode can be stopped. However there are beneficial effects of the convective flow which would also be eliminated. Some of these tradeoffs are discussed briefly in a later paper (4).

*Movement of KOH.*—As a result of the convective flow and cell reaction, there is a wide range of KOH concentration in the  $y$  direction in the cell. The variation of KOH in the  $y$  direction in the zinc electrode with number of cycles is shown in Fig. 6. The variation of KOH concentration directly and indirectly affects the cell performance and the redistribution of the zinc material over the zinc electrode during cycling. As the concentration of KOH is changing in the electrode, the conductivities of the electrolytic solution and the membrane are also changing. This, in turn, affects the current distribution over the zinc electrode. Also, a change of KOH concentration in the zinc electrode causes a change in the solubility of ZnO in KOH solution so that the rate of dissolution and precipitation of ZnO also changes. These interrelated mechanisms may be seen from the variations of KOH concentration (Fig. 6), variation of cell potentials (Fig. 8), distribution of metallic zinc (Fig. 9 and 10), and distribution of current (Fig. 11) with the number of cycles. They are discussed in the following section.

*Cell performance.*—Generally, the performance of a battery is evaluated from the current-potential behavior on charging and on discharging, the length of charging period, the length of discharging period under a certain load, and variations with number of cycles. A reliable cell should have a long cell cycle life. Under a constant load or a constant cell current, it should be possible to cycle a cell many times without causing a significant increase of the cell potential on charging or a significant decrease of the cell potential on discharging while the duration of charging and of discharging is held constant. The numerical solutions in this study indicate that the performance of the Zn-AgO cell varies with number of cycles because of variations in species concentration in the cell, redistribution of zinc material over the zinc electrode, and variations in the current distribution over the zinc electrode. These interrelated mechanisms may be examined by comparing operation of a cell with relatively uniform zinc distribution to that after the zinc distribution becomes nonuniform.

Before shape change in the zinc electrode became severe, the cell performance was affected by the gradual decrease of species concentrations near the center and bottom of the electrode (Fig. 6 and 7). In the first continuous cycling process (cycles 1 through 8), the cell potential on charging was increasing with number of cycles (Fig. 8). This was due to the gradually created nonuniform distribution of KOH concentration in the cell, which caused the effective cell resistance to increase with the number of cycles. The variation of KOH concentration within the cell also caused a variation of current density over the zinc electrode on charging which was manifested by the metallic zinc distribution after charge for cycles 2, 4, and 8 (Fig. 9). These results indicate that during charging the current density became larger near the center and smaller near the bottom of the electrode. The situation became more pronounced as the number of cycles was increased (compare cycles 2, 4, and 8 in Fig. 9). This decrease in current density was apparently due to the continuous decrease in KOH concentration near the bottom.

Because of the nonuniform distribution of metallic zinc over the zinc electrode after charging and during discharging, part of the electrode area became inactive before the completion of a constant time period of discharging due to depletion of metallic zinc in those areas. Therefore, the cell potential decreased during the rest of the discharging period because most of the cell current was concentrated in a small area, thereby causing an increase in the apparent cell resistance (see Fig. 8). The current distribution and metallic zinc distribution over the zinc electrode at the end of discharge (Fig. 10 and 11) support this hypothesis. The condition became more severe as cycling continued. The potential drop at the end of the discharge portion of the 8th cycle was smaller than that of cycle 7 (see Fig. 8) because the current distribution at the end of discharging during cycle 8 was more uniform than that at the end of cycle 7 (Fig. 11). As cycling continued (from cycle 1 through 8), the numerical solutions indicated that the region near the bottom could not maintain the initial capacity on charging due to the gradual decrease (Fig. 6 and 7) in available zincate in the solution, which was due to reduced solubility of zinc oxide caused by the decreasing KOH concentration and convective removal of zincate.

With only a 3 min rest between half-cycles, the numerical procedures did not allow the cycling process to continue after cycle 8. Allowing the cell to rest for a longer period, for example, until the species concentrations recovered to their initial values, did allow cycling to go on. From cycles 9 through 15, the cell performance was very similar to cycles 1 through 8. After the 15th cycle, the cell was refreshed again by allowing solution concentrations to return to initial values. Comparison of cycles 1 through 8 with cycles 9 through 15 indicates that the cell performance was decreased as the number of cycles increased because within the first cycling period (cycles 1 through 8) 8 continuous cycles were completed before refreshing was necessary, but only 7 continuous cycles were completed for the second cycling period (cycles 9 through 15).

As the loss of zinc oxide material from the region near the top of the zinc electrode became severe, after about 25 cycles, the numerical solution showed that the cause of the failure of the zinc electrode was due to the loss of zinc oxide material near the top of the zinc electrode. In the 28th cycle after 115 min of charging, the numerical solution indicated that the zincate concentration in the zinc electrode near the reservoir became completely depleted due to previous loss of zinc oxide in that region (Fig. 5). The cell was refreshed (all concentrations set at their initial values) and operation continued, as before, for three more cycles of 120 min charging and 120 min discharging with no additional zincate depletion at any point on the zinc electrode.

In the 32nd cycle, after 105 min of charging, the zinc electrode again became depleted of zincate in the region next to the zinc electrode reservoir. In later cycles, zincate depletion began as follows: after 97 min of charging in the 33rd cycle, after 85 min in the 34th cycle, and after 73 min in the 35th cycle. After zincate depletion began, continued charging (in order to maintain a constant charging time at the 1A rate for cycles 32, 33, 34, and 35) caused a significant rise in cell potential at and near the end of charging as shown in Fig. 8. In a real cell, this increased potential would be expected eventually to lead to an increase in hydrogen gas evolution at the zinc electrode (not accounted for in the theoretical model). Practically speaking, it would finally be impossible to continue the 2 hr charging period without reducing the charging current. The model indicates that this situation would become worse if cycling proceeded. A very uneven metallic zinc distribution over the zinc electrode would also result, causing a premature decrease in the cell potential dur-

ing discharge. Eventually, these combined effects would lead to unacceptable cell performance, and the cell would fail.

The region next to the reservoir in the zinc electrode would lose all of the zinc oxide material that was originally there if the cycling process proceeded far enough, as one can infer from the trend of shape change behavior which occurred in the zinc electrode as a result of cycling (see Fig. 5). When that occurs, the region next to the reservoir in the zinc electrode would lose all charge storage capacity. Then the current densities over that region would go to zero during continued cycling. Zero current densities over the region on the top of the zinc electrode have been observed experimentally by McBreen (3) in the later stage of cycling.

### Acknowledgments

Financial support for this work has been provided by the U.S. Air Force, Air Force Systems Command, and the University of California.

Manuscript submitted Feb. 18, 1976; revised manuscript received June 22, 1976. This was Paper 52 presented at the Dallas, Texas, Meeting of the Society, Oct. 5-9, 1975.

Any discussion of this paper will appear in a Discussion Section to be published in the June 1977 JOURNAL. All discussions for the June 1977 Discussion Section should be submitted by Feb. 1, 1977.

Publication costs of this article were assisted by the University of California, Los Angeles.

### APPENDIX

#### Numerical Values of Parameters Used in Numerical Calculations

$B_a^p$	$= 1.0 \times 10^3 \text{ sec/cm}$
$B_p^p$	$= 4.0 \times 10^3 \text{ sec/cm}$
$B_a^n$	$= 1.0 \times 10^3 \text{ sec/cm}$
$B_p^n$	$= 2.0 \times 10^4 \text{ sec/cm}$
$c_{K^{po}}$	$= 9.8487 \times 10^{-3} \text{ mole/cm}^3$
$c_{K^{no}}$	$= 9.8487 \times 10^{-3} \text{ mole/cm}^3$
$c_{Zn^{po}}$	$= 8.804463 \times 10^{-4} \text{ mole/cm}^3$
$c_{Zn^{no}}$	$= 8.804463 \times 10^{-4} \text{ mole/cm}^3$
$c_o^n$	$= 0.0465967 \text{ mole/cm}^3$
$c_o^p$	$= 0.0465967 \text{ mole/cm}^3$
$D_{Zn^o}$	$= 7.1 \times 10^{-5} \text{ cm}^2/\text{sec}$
$D_{K^o}$	$= 2.0 \times 10^{-4} \text{ cm}^2/\text{sec}$
$I$	$= 1.0 \text{ A}$
$L_{kk}$	$= 1.0 \times 10^{-5} \text{ cm/sec}$
$L_{zz}$	$= 1.0 \times 10^{-6} \text{ cm/sec}$
$L_{ok}$	$= 2.0 \times 10^{-5} \text{ cm/sec}$
$L_{oz}$	$= 1.4 \times 10^{-4} \text{ cm/sec}$
$L$	$= 10.2 \text{ cm}$
$l$	$= 6.6 \text{ cm}$
$M$	$= 11$
$Q_{Zn^o}$	$= 3.3747 \times 10^{-3} \text{ mole/cm}^2$
$R_d^p$	$= 2.0 \times 10^{-2} \text{ sec}^{-1}$
$R_p^p$	$= 3.0 \times 10^{-5} \text{ sec}^{-1}$
$R_d^n$	$= 3.0 \times 10^{-5} \text{ sec}^{-1}$
$R_p^n$	$= 6.0 \times 10^{-3} \text{ sec}^{-1}$
$t_K^m$	$= 0.5$
$t_{Zn}^m$	$= 0.0$
$t_o^m$	$= 1.6$
$\bar{V}_{Ag}$	$= 10.27 \text{ cm}^3/\text{mole}$
$\bar{V}_{AgO}$	$= 16.65 \text{ cm}^3/\text{mole}$
$\bar{V}_{Zn}$	$= 9.15 \text{ cm}^3/\text{mole}$
$\bar{V}_{ZnO}$	$= 14.51 \text{ cm}^3/\text{mole}$
$w_p$	$= 0.0381 \text{ cm}$
$w_n$	$= 0.1905 \text{ cm}$
$w_m$	$= 0.00762 \text{ cm}$
$\alpha^p$	$= 1$
$\alpha^n$	$= 1$
$\gamma^p$	$= 1.5 \times 10^4 \text{ sec/cm}$
$\gamma^n$	$= 1.0 \times 10^4 \text{ sec/cm}$
$\epsilon_p^o$	$= 0.3254$
$\epsilon_n^o$	$= 0.49274$
$\epsilon_m$	$= 0.01$
$\xi^p$	$= 300.0 \text{ cm}^2/\text{mole}$
$\xi^n$	$= 300.0 \text{ cm}^2/\text{mole}$
$\theta_B$	$= 0.047666$

### The Charging and Discharging Periods in the Numerical Calculation

Number of cycle	Charging (sec)	Discharging (sec)
1	7650	7200
2	7200	7200
3	7350	7200
4-9	7200	7200
10	7350	7200
11	7350	7350
12	7200	7200
13	7200	7350
14-16	7200	7200
17	7350	7200
18-19	7200	7200
20	7350	7200
21	7200	7200
22	7350	7200
23-26	7200	7200
27	7350	7200
28	6900	6900
29-33	7200	7200
34	7200	7100
35	7300	7200

### LIST OF SYMBOLS

$a$	available surface area per unit volume of zinc electrode for dissolution or precipitation of zinc oxide ( $\text{cm}^2/\text{cm}^3$ )
$a^*$	available surface area per unit volume of silver electrode for dissolution or precipitation of zinc oxide ( $\text{cm}^2/\text{cm}^3$ )
$B_d$	empirical constant in the expression for the dependence of rate of dissolution of zinc oxide material on velocity ( $\text{sec/cm}$ )
$B_p$	empirical constant in the expression for the dependence of rate of precipitation of zinc oxide on velocity ( $\text{sec/cm}$ )
$c_i$	concentration of species $i$ ( $\text{mole/cm}^3$ )
$D_i$	diffusion coefficient of species $i$ ( $\text{cm}^2/\text{sec}$ )
$F$	Faraday constant (96,479 C/equiv.)
$i$	current density ( $\text{A/cm}^2$ )
$I$	total cell current (A)
$k$	mass transfer coefficient for $\text{Zn}^{+2}$ species transfer from the bulk solution to the sites of dissolution or precipitation of zinc oxide in the zinc electrode ( $\text{cm/sec}$ )
$k^*$	mass transfer coefficient for $\text{Zn}^{+2}$ species transfer from the bulk solution to the sites of dissolution or precipitation of zinc oxide in silver electrode ( $\text{cm/sec}$ )
$l$	width of the electrode (cm)
$L$	length of the electrode (cm)
$L_{ij}$	transport coefficients describing the interaction of species $i$ and $j$ within the membrane ( $\text{cm/sec}$ )
$M$	number of sections in the membrane
$N_{i,x}$	flux of species $i$ in $x$ direction across the membrane ( $\text{mole/cm}^2\text{-sec}$ )
$N_{i,y}$	flux of species $i$ in $y$ direction in the electrode compartments ( $\text{mole/cm}^2\text{-sec}$ )
$Q_{Zn^o}$	amount of zinc oxide material over unit area of the zinc electrode ( $\text{mole/cm}^2$ )
$R_d$	empirical constant for the rate of dissolution of zinc oxide ( $\text{sec}^{-1}$ )
$R_i$	source term of species $i$ ( $\text{mole/cm}^3\text{-sec}$ )
$R_p$	empirical constant for the rate of precipitation of zinc oxide ( $\text{sec}^{-1}$ )
$t_{Zn}^m$	transference number of $\text{Zn}^{+2}$ species in the membrane
$t_K^m$	transference number of $\text{K}^+$ species in the membrane
$t_o^m$	electro-osmotic coefficient of the membrane
$v_y$	solution velocity in $y$ direction ( $\text{cm/sec}$ )
$\bar{V}_i$	partial molar volume of species $i$ ( $\text{cm}^3/\text{mole}$ )
$V_p$	volume of the reservoir in the silver electrode compartment ( $\text{cm}^3$ )
$V_n$	volume of the reservoir in the zinc electrode compartment ( $\text{cm}^3$ )
$w_n$	thickness of the zinc electrode (cm)
$w_p$	thickness of the silver electrode (cm)
$w_m$	thickness of the membrane (cm)

$\alpha$	empirical constant
$\gamma$	convective term for the dispersion coefficient
$\epsilon$	porosity
$\theta_B$	constant term to correct for the amount of inert material in the zinc electrode
$\kappa$	electrical conductivity of electrolytic solution (mho/cm)
$\xi$	empirical constant

## Subscripts

i	any arbitrary species
j	any arbitrary species
o	solvent

## Superscripts

n	zinc electrode compartment
p	silver electrode compartment
m	membrane

## REFERENCES

- J. J. Lander, in "Zinc-Silver Oxide Batteries," A. Fleischer and J. J. Lander, Editors, pp. 457-469, John Wiley & Sons, Inc., New York (1971).
- J. J. Lander and J. E. Cooper, Air Force Aero Propulsion Laboratory, Wright-Patterson Air Force Base, Technical Report AFAPL-TR-71-32 (Oct. 1971).
- J. McBreen, *This Journal*, **119**, 1620 (1972).
- K. W. Choi, D. Hamby, D. N. Bennion, and J. Newman, *ibid.*, **123**, 1628 (1976).
- C. P. Wales and J. Burbank, *ibid.*, **106**, 885 (1959).
- T. P. Dirkse, *ibid.*, **106**, 920 (1959).
- S. Yoshizawa and Z. Tokehara, *J. Electrochem. Soc. Jpn.*, **31**, No. 3, 91 (1963).
- M. J. Dignam, H. M. Barrett, and G. D. Nagy, *Can. J. Chem.*, **47**, 4253 (1969).
- J. O'M. Bockris, Z. Nagy, and A. Damjanovic, *This Journal*, **119**, 285 (1972).
- D. A. Payne and A. J. Bard, *ibid.*, **119**, 1665 (1972).
- R. W. Powers and M. W. Breiter, *ibid.*, **116**, 719 (1969).
- T. P. Dirkse, L. A. Vander Lugt, and N. A. Hampson, *ibid.*, **118**, 1606 (1971).
- T. P. Dirkse, C. Postmus, Jr., and R. Vandenbosch, *J. Am. Chem. Soc.*, **76**, 6022 (1954).
- T. P. Dirkse, *This Journal*, **101**, 328 (1954).
- A. O. Gubeli and J. Ste-Marie, *Can. J. Chem.*, **45**, 827 (1967).
- W. Van Doorne and T. P. Dirkse, *This Journal*, **112**, 1 (1975).
- D. P. Boden, R. B. Wylie, and V. J. Spere, *ibid.*, **118**, 1298 (1971).
- J. Newman, and W. Tiedemann, *AIChE J.*, **21**, 25 (1975).
- T. K. Sherwood, R. L. Pigford, and C. R. Wilke, "Mass Transfer," McGraw-Hill Book Co., New York (1975).
- R. E. Meredith and C. W. Tobias, *Adv. Electrochem. Electrochem. Eng.*, **2**, 15 (1962).
- C. T. Baker and I. Trachtenberg, *This Journal*, **114**, 1045 (1967).
- J. Crank and P. Nicolson, *Proc. Cambridge Phil. Soc.*, **43**, 50 (1947).
- J. Newman, UCRL-17739, Lawrence Radiation Laboratory, University of California, Berkeley (Aug. 1967).
- J. Newman, *Ind. Eng. Chem. Fundam.*, **7**, 514 (1968).
- J. Newman "Electrochemical Systems" pp. 414-425, Prentice-Hall, Inc., Englewood Cliffs, N.J. (1973).
- K. W. Choi, PhD Dissertation, School of Engineering, University of California, Los Angeles (Dec. 1975).
- R. Alkire and R. Plichta, *This Journal*, **120**, 1060 (1973).
- R. C. Alkire, Dissertation, University of California, Berkeley (1968).
- R. C. Alkire, E. A. Grens, and C. W. Tobias, Paper 366 presented at The Electrochemical Society Meeting, Montreal, Canada, Oct. 6-11, 1968.
- R. C. Alkire, E. A. Grens II, and C. W. Tobias, *This Journal*, **116**, 809 (1969).
- R. C. Alkire, E. A. Grens II, and C. W. Tobias, *ibid.*, **116**, 1328 (1969).
- J. S. Dunning, Dissertation, University of California, Los Angeles (1971).
- J. S. Dunning, D. N. Bennion, and J. Newman, *This Journal*, **120**, 906 (1973).
- D. Simonsson, Dissertation, Inst. kemisk teknologi, Kungl. Tekniska Högskolan, Stockholm (1973).
- D. Simonsson, *J. Appl. Electrochem.*, **3**, 261 (1973).
- K. Micka, and I. Rousar, *Electrochim. Acta*, **18**, 629 (1973).
- D. Gidaspow and B. S. Baker, Paper 18 presented at The Electrochemical Society Meeting, Miami Beach, Florida, Oct. 8-13, 1972.
- D. Gidaspow and B. S. Baker, *This Journal*, **120**, 1005 (1973).

# Engineering Analysis of Shape Change in Zinc Secondary Electrodes

## II. Experimental

King Wai Choi,\* Drannan Hamby,\*\*<sup>1</sup> and Douglas N. Bennion\*\*

*Energy and Kinetics Department, School of Engineering and Applied Science,  
University of California, Los Angeles, California 90024*

and John Newman\*\*

*Materials and Molecular Research Division, Lawrence Berkeley Laboratory  
and Department of Chemical Engineering, University of California, Berkeley, California 94720*

### ABSTRACT

Experimental data on zinc-silver oxide secondary cells were used to evaluate the convective flow hypothesis on the cause of shape change of zinc electrodes. A cell with flooded, vented electrodes designed to allow "normal" convective flow was studied. Zinc electrodes cycled in this cell showed extensive material redistribution in accord with predictions based on the hypothesis. Measured volume average fluid flow rates for this cell were also in agreement with predicted values. Zinc electrodes cycled in a second cell, designed to minimize convective flow in the zinc electrode compartment, showed virtually no active material redistribution.

Shape change of the zinc electrode is commonly accepted as a primary limiting factor in the life of zinc-silver oxide secondary cells which utilize grafted polyethylene films as separator materials. The phenomenon develops progressively during cell cycling and involves gross redistribution and densification of active material over the surface of the electrode and loss of cell capacity (1). Suggested causes of and methods for alleviation of shape change have been discussed by Oswin and Blurton (2) and by Dalin (3). Lander and Cooper provide a series of photographs which illustrate the progressive development of shape change in their report on active material migration in zinc electrodes (4). McBreen has summarized correlations between shape change and operating and construction parameters of cells and has published extensive data on the distribution of current and potential over the surface of a sectioned zinc electrode during cycling (5). He has offered a theory of shape change based on nonuniform current distribution as a cause.

Recently, a model has been developed for the zinc-silver oxide cell based on the hypothesis that the principal cause of active material redistribution over the zinc electrode is zincate concentration changes coupled with convective flow, parallel to the apparent electrode surface, driven primarily by membrane pumping effects (6, 7). When flow is toward the vent or reservoir location, the electrolytic solution within the porous zinc electrode is undersaturated with zincate. When flow is away from the vent location, the electrolytic solution is supersaturated with zincate. The net effect is a pumping of zinc away from the vent toward the center of the electrode. The model has been used to predict a number of measurable physical quantities as functions of time, including volume average fluid flow rates in the cell and zinc oxide distribution over the zinc electrode. The model has also provided a basis for the discussion of how changes in these and other quantities affect cell performance. The results suggest that material redistribution can be controlled by controlling convective flow in the zinc electrode compartment.

Experiments to test the validity of the basic hypothesis as well as predictions based on the model have been carried out. Fluid flow rates were measured in a flooded, vented zinc-silver oxide cell with "normal" convection.<sup>2</sup> These rates are compared with those predicted from the model. The discharged zinc electrodes from these experiments were sectioned and analyzed, and the ZnO distributions are compared to that on unused zinc electrodes to determine the extent of ZnO redistribution as a result of cell cycling. The observed redistribution of material is also compared with predictions based on the model. In a second cell, flooded, nonvented zinc electrodes have been cycled under conditions intended to minimize convective flow. Discharged electrodes from this cell have also been sectioned and analyzed. ZnO distributions are compared both with that on unused electrodes and those on electrodes cycled in the cell with normal convective flow. The variation of pressure in the zinc electrode compartment as a function of time has also been measured in a modified version of the second cell.

### Equipment and Procedures

**Electrical equipment.**—All cell cycling experiments were carried out at constant current. Power sources were commercially available galvanostats. Potential differences across the cell terminals were recorded continuously to  $\pm 0.025\text{V}$  with a recording voltmeter. A second recording voltmeter was used in conjunction with a power resistor in series with the cell to monitor cell current to  $\pm 25\text{ mA}$ . A Flexopulse HG 108A6, repeat cycle timer<sup>3</sup> was used as a reversing switch which allowed continuous variation in cell charge and discharge times. The switch also allowed for brief intervals of a few minutes duration with no cell current between half-cycles.

Signal output from the pressure transducer was measured to  $\pm 0.01\text{ mV}$  with a Hewlett Packard, Model 3440 A, digital voltmeter with digital print out. Sensitivity of the transducer was determined to be  $3.6\text{ mV/bar}$ .

**Electrodes.**—All electrodes used in this work were furnished by AFAPL (Air Force Aero Propulsion

\* Electrochemical Society Student Member.

\*\* Electrochemical Society Active Member.

<sup>1</sup> Present address: Linfield College, McMinnville, Oregon 97128.

Key words: battery, silver-silver oxide, electro-osmosis, osmosis, separators.

<sup>2</sup> Convection similar to that in commercial cells.

<sup>3</sup> Eagle Signal, 736 Federal Street, Davenport, Iowa 52803.



Laboratory, Wright Patterson Air Force Base, Ohio). The zinc electrodes came in the discharged state wrapped in Viskon (cellulose rayon) paper and consisted of pressed, blended ZnO, HgO, and Teflon binder on expanded silver screen ( $3.23 \times 10^{-2}$  g of Ag/cm<sup>2</sup>). These electrodes were prepared according to the procedure described by Keralla (8). They were 10.3 cm long, 6.4 cm wide, and 0.2 cm thick. Different batches of electrodes were found to vary slightly in composition, and different electrodes with the same batch differed in total weight by as much as 8%. During the analysis of both used and unused electrodes, a layered structure in the active material was observed. By color, it appeared that the layer near the collector screen was rich in HgO. This layer also appeared finer grained, more coherent, and more firmly bound together than the material which covered it. The quantity of ZnO present on each electrode was adequate to yield a theoretical capacity, at 100% utilization, of approximately 12 A-hr. HgO content in the electrodes was 33 mg HgO/g ZnO as determined using an atomic absorption spectrophotometer in this laboratory. The silver electrodes also came in the discharged state. They had approximately the same apparent surface area, 66 cm<sup>2</sup>, were 0.4 mm thick, and consisted of porous sintered silver (1% palladium) on expanded silver screen. They were prepared according to the procedure of Falk and Fleischer (9). Estimated theoretical capacity of these electrodes at 100% utilization is 6.5 A-hr.

*Cell designs.*—Two cells were used in the experiments; they are designated cell A and cell B.

Design and operating parameters for cell A (Fig. 1) were chosen to test directly the basic hypothesis that material redistribution over the zinc electrode is caused by convective flows driven by membrane pumping effects. Thus, the cell was designed to minimize convective flow in the zinc electrode compartment during cell operation. The zinc and silver oxide electrodes faced each other across a separator which consisted of three layers of 0.001 in. thick RAI P2291 (40/20) membrane<sup>4</sup> and one layer of 0.005 in. thick

<sup>4</sup> RAI Corporation, 225 Marcus Boulevard, Hauppauge, New York 11787.

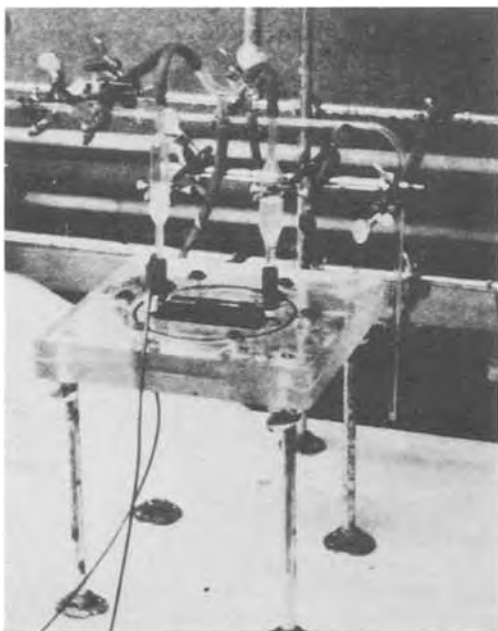


Fig. 1. Photograph of cell A. The cell is operated horizontally as shown with the zinc electrode located below the silver electrode. The silver electrode is flooded and vented.

Dynel<sup>5</sup> (Webril nonwoven fabric, 1418) which was placed on the silver electrode side of the separator. The RAI material is a beta radiation cross-linked low density polyethylene film which has been gamma radiation grafted with methacrylic acid. The Dynel is a porous, nonwoven acrylonitrile which is resistant to oxidation in the cell environment. The electrodes were recessed in rectangular chambers machined in flat, 3/4 in. thick, acrylic sheets. The zinc electrode chamber was just large enough to contain the electrode. No space was allowed, within machining tolerances, to provide reservoir space outside the porous electrode structure. The silver electrode chamber was deeper than necessary to contain the electrode. The additional space was filled with either an inert, non-absorbent material, latex sheet, or an absorbent material, for example, Dynel sheet, to provide additional electrolytic solution storage volume. A large O ring, laid in a rectangular groove surrounding the electrodes, sealed the cell when the acrylic sheets were bolted together with six 1/4 in. bolts. Sealed electrical contacts were made to the electrodes through the cell walls. Provision was made for evacuation of the electrode chambers through four ports which were subsequently used for filling the entire free cell volume with solution. The two evacuation and filling ports on the zinc side were normally sealed after the filling operation was complete. The silver electrode compartment could be sealed and the whole cell operated flooded and nonvented without head space, or the compartment ports could be left unsealed allowing the silver electrode to be operated flooded but vented as shown in Fig. 1. Under these circumstances, convection parallel to the long axis of the silver electrode occurred as fluid exchanged convectively between the silver compartment and the reservoirs above the filling ports during cell operation. Some fluid flow in the zinc electrode chamber parallel to the electrical current flux across the membrane was expected due to changes in volume of solids associated with the electrode reactions and straining of the container wall. This latter flow should not, according to the basic hypothesis, cause material redistribution as long as the effects are uniform over the whole electrode. All final seals were O ring seals.

In a modified version of cell A, designated cell AP, provision was made for sealing a Model 2201, pressure transducer<sup>6</sup> to the cell near the center of the zinc test electrode. Communication between the electrolytic solution filled stainless steel chamber of the transducer and the zinc test electrode compartment was through a 1/8 in. hole in the acrylic wall. The volume of the pressure chamber of the transducer was approximately 3.3 cm<sup>3</sup>. In cell AP, the silver electrode was replaced with a second zinc electrode which was precharged to 7.5 A-hr against silver electrodes at approximately 4 mA/cm<sup>2</sup>. The zinc counterelectrode was operated flooded and vented with the cell positioned horizontally, as in Fig. 1, with the test electrode below the counterelectrode.

The design and operating parameters for cell B were chosen to allow normal convective flow along the long axis of the electrodes. Experiments with this cell were carried out to collect data on flow rates and material redistributions which could be quantitatively compared with predictions based on the mathematical model. Thus, the design of cell B, shown schematically in Fig. 2, was similar to that of cell A, but it had some additional features. The separator system used with this cell consisted of two layers of RAI P2291 (40/20) with a 0.001 in. Dynel sheet between the silver electrode and the RAI material. The silver compartment was just deep enough to house the elec-

<sup>5</sup> The Kendall Company, Fiber Products Division, Walpole, Massachusetts 02081.

<sup>6</sup> Teledyne Tabor, 455 Bryant Street, North Tonawanda, New York 14120.

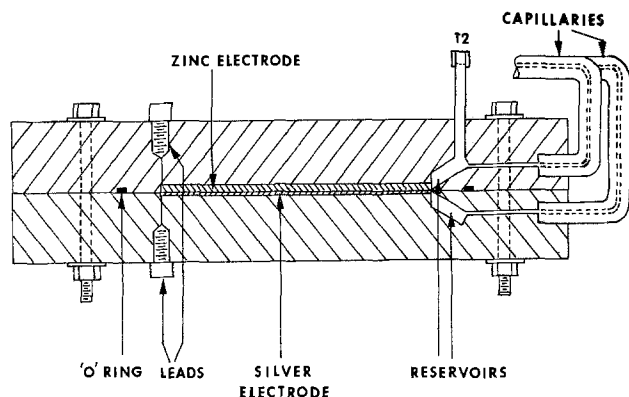


Fig. 2. Schematic drawing of cell B

trode, 0.46 mm. Small reservoirs were machined in the cell walls at one end of each electrode compartment. The two reservoirs were separated by solid, nonconducting acrylic walls. Glass capillaries (0.1 in. diameter), used to monitor fluid flows, exited the cell at the reservoir end. They were bent in such a manner that the flows in the capillaries were horizontal, that is parallel with the earth's surface and, consequently, hydrostatic pressure differences did not arise between the compartments. The cell could be operated with the electrodes oriented horizontally, as shown in Fig. 2, or vertically with respect to the earth's surface; these two configurations will be distinguished below by referring to cell BH and cell BV, respectively. Thus, cell B was operated in all cases with both electrodes flooded and vented, the reservoirs were always filled completely, and fluid partially filled the available lengths of the capillaries.

An additional feature of cell B was the second exit tube from the zinc compartment reservoir, labeled T2 in Fig. 2. This exit tube is used to determine the gas evolution rate from the zinc electrode as explained below.

**Electrolytic solution.**—The solution used for filling the cells was prepared from doubly distilled water and reagent grade chemicals. KOH was first dissolved in water to prepare a concentrated solution. This solution was diluted to a specific gravity of 1.40 at 20°C. Fine grained ZnO was then added in excess of the amount required to saturate the solution, and magnetic stirring continued for several hours. The solution with excess crystalline ZnO was stored in tightly capped polyethylene bottles.

**Cell filling.**—Filling of the cell was carried out with the electrodes positioned vertically with respect to the earth's surface. The filling procedure in all cases involved evacuation of the cell and rubber filling lines by mechanical pumping followed by slow, simultaneous vacuum filling of the compartments with solution from a common reservoir. Following return of pressure in the filled cell to atmospheric, the cell was normally left to soak for at least 24 hr before the appropriate ports were plugged and cycling was begun.

**Flow rate measurements.**—During selected periods of operation of cells BV and BH, the positions of the fluid menisci in the capillaries were observed with a precision cathetometer ( $\pm 0.005$  cm) to establish fluid flow rates in the cells. Average flow rates were calculated by dividing the volume of fluid flowing into or away from the reservoir by the time interval between observations. The uncertainty in the reported values is estimated to be  $\pm 10\%$  based on dimensional tolerance of the capillary, precision capability of the cathetometer, and uncertainty in the time interval measurements. Greater error could have been incurred by undetected gassing or dimensional changes

in the compartments, for example, membrane movement. The convention was adopted that positive flow rates indicated that fluid was flowing from the electrode compartment into the reservoir and hence into the capillary; a negative flow rate corresponded to fluid flowing from the reservoir into the compartment, that is, emptying the capillary.

**Gas evolution.**—During preliminary tests with cell BV, gas evolution at both electrodes was found to interfere with the fluid flow measurements. It was learned that little or no gassing at the positive electrode was detected as long as the charging rate was small (for example, 1.0A), and charging time was 2 hr or less. It was later learned that oxygen evolution at the silver electrode at higher rates of charge could be adequately suppressed by properly preforming the electrode at low current density (10). Hydrogen evolution was found to occur at the zinc electrode throughout a charge-discharge cycle including the no current rest period.

In order to correct observed flow rate data, the rates of hydrogen evolution were measured. The following procedure was used. A tube, T2 (see Fig. 2), which extends vertically upward from the zinc electrode reservoir was added to the cell. After filling the cell, the liquid level in tube T2 was initially the same as the liquid level in the capillary which extends from the zinc electrode reservoir. While current was passed through the cell at 1.0A, the top of tube T2 was closed. After a measured quantity of charge had passed through the circuit, gas bubbles in the zinc compartment were maneuvered into the tube T2. The position of the fluid in the capillary was then noted, the current terminated, and tube T2 opened to allow accumulated gas to escape. From the distance of movement of the meniscus in the capillary, the rate of hydrogen evolution was computed. The average volume rates of H<sub>2</sub> evolution, calculated for room temperature (22°C) and 1 atm pressure, were  $0.17 \times 10^{-4}$  cm<sup>3</sup>/sec during charge,  $0.15 \times 10^{-4}$  cm<sup>3</sup>/sec during discharge, and  $0.09 \times 10^{-4}$  cm<sup>3</sup>/sec during rest periods of no current flow. The volumetric data presented below have been corrected for the effects of H<sub>2</sub> evolution.

**Analytical procedures.**—Analytical procedures were required to obtain data which would allow quantitative comparisons of material distributions on used and unused zinc electrodes. The unused electrodes consisted of mixtures of ZnO, HgO, and inert binder on expanded silver screen. It was anticipated that used electrodes might contain, in addition to the substances listed above, metallic zinc and mercury and possibly various amalgams of zinc and silver.

In preliminary experiments with bulk reagents, it was found that ZnO could be separated from zinc and HgO by dissolution in concentrated aqueous KOH solution. Therefore, in later experiments ZnO was determined gravimetrically with adequate precision by treatment with concentrated KOH solution, with a specific gravity of 1.40. The fractions of HgO and granular metallic zinc which were lost during dissolution of the ZnO were less than 2%, which was considered negligible. A mixture 1M in NH<sub>4</sub>OH and 1M in NH<sub>4</sub>Cl was found to be equally effective in separating ZnO and Zn, and, from the standpoint of avoiding gravimetric errors, offered advantages over concentrated KOH as a separating agent; however, it was also found to dissolve HgO at an undesirably high rate. Therefore, in initial experiments the KOH solution was used. It was subsequently found that after 30 to 40 cycles of operation there was no detectable HgO (that is, less than 1 mg of HgO per sample for a sample size of approximately one gram) in the zinc electrode, and, therefore, the NH<sub>4</sub>OH-NH<sub>4</sub>Cl mixture could be used for ZnO dissolution without difficulty.

A Perkin Elmer Model 303 atomic absorption spectrophotometer was calibrated with standards prepared in this laboratory for determination of potassium, mercury, and zinc. This instrument was used in several cases to check the results of gravimetric measurements.

The procedures used in electrode analyses may be summarized as follows: The electrodes were sectioned into samples with scissors, and each sample was placed in a clean, preweighed and labeled 30 ml medium frit filtering crucible. Care was taken to record the position which the sample occupied on the electrode with respect to the electrode lead. Each sample was thoroughly rinsed with distilled water and then oven dried at approximately 120°C for at least 2 hr (11). After cooling in a desiccator, the samples were weighed. The samples were then repetitively treated with 20 ml portions of concentrated aqueous KOH, specific gravity 1.40, or the NH<sub>4</sub>OH-NH<sub>4</sub>Cl mixture followed by thorough rinsing with distilled water, drying, and weighing until weight losses caused by the last treatment were judged to be negligible (that is, less than 0.2% of accumulated weight loss). The sample weight losses from this treatment were attributed to ZnO dissolution.

Subsequently, the samples were similarly treated with 6N HCl. In the case of used electrodes this was done to determine the quantity of metallic zinc present; in the case of unused electrodes, to determine HgO. In selected cases, the HCl wash and rinse liquids were collected, made up with water to known volume, and tested for zinc, potassium, and mercury by atomic absorption spectrophotometry (AA). Also, in selected cases the metallic screens were separated from the residues after HCl treatment, and the residues and screens were subjected separately to treatment with warm concentrated HNO<sub>3</sub>. These liquids were then tested with AA for mercury.

In one case a used silver electrode (from cell A) was repetitively leached in 6N HCl, and the leach liquid made to volume and tested with AA for zinc.

*Treatment of data.*—In these experiments, emphasis was placed on the determination of the distribution of total zinc as ZnO over the used and unused electrodes. The used electrodes were, therefore, completely discharged before removal from the cell, and only residual quantities of metallic zinc were found; in no case more than 3% of the active material reported. In treating the analytical data, these small quantities of metallic zinc found on the used electrodes have been reported as ZnO. Because it was difficult to measure accurately the dimensions of the samples and because of total weight differences between different electrodes, the collector screen material was used to normalize the data. The normalization ratio used for each sample is

$$\frac{Q_{ZnO}}{Q_{ZnO}^*} = \left[ \frac{W_{ZnO}^i / (W_{es}^i \cdot 66.0 \text{ cm}^2)}{\left[ \sum_i W_{es}^i \right]} \right] \left[ \sum_i W_{ZnO}^i / 66.0 \text{ cm}^2 \right] \quad [1]$$

where  $W_{ZnO}^i$  = weight of ZnO, sample  $i$ , and  $W_{es}^i$  = weight of collector screen, sample  $i$ . Assuming that the weight per unit area of the collector was uniform, the numerator of the normalization ratio,  $Q_{ZnO}$ , is the weight of ZnO per unit area of sample. Similarly, the denominator,  $Q_{ZnO}^*$ , is the average weight of ZnO per unit area for the whole electrode. The ratio,  $Q_{ZnO}/Q_{ZnO}^*$ , compares the ZnO per unit area at a particular position on the electrode with the average value for the electrode as a whole.

Uncertainty in the reported values of  $W_{ZnO}^i$  is estimated to be no greater than  $\pm 3\%$ . Comparisons of samples from used electrodes with samples from unused electrodes on the basis of the normalized data

involves the assumption of uniformity of weight/area for the used collector screens.

*Preliminary experiment.*—Several preliminary experiments were carried out with cell A and cell AP to determine the most appropriate modes of cell operation in later tests. Certain interesting observations were made, especially with respect to the ability of the cells to accept charge under different conditions, which should be relevant to suggestions for improving the performance of zinc-silver oxide cells.

In one preliminary experiment, cell A was cycled with both electrodes flooded and neither electrode vented. With no preforming of the electrodes, the freshly filled cell would accept approximately 0.8 A-hr of charge at 2.0A before the terminal potential difference (TPD) rose rapidly above 2.3V. It was established that cells of this type would accept a greater initial charge to the 2.3V cutoff when charged at a lower rate, for example, 1.0 A-hr at 0.5A. However, it became apparent that cell behavior was strongly dependent on cell history since filling. Continued charging beyond the onset of rapid increase in polarization led to drastic initial polarization on discharge and to large decreases in charge acceptance on subsequent cycles, for example, from 0.8 to 0.2 A-hr at 2.0A.

It was found that cell capacity at the 2.0A rate,  $Q_2$ , based on a 2.3V cutoff, could, in the initial stages of operation, be increased to approximately 1.6 A-hr by operating the cell with the silver electrode flooded and vented as shown in Fig. 1. Further increase in  $Q_2$ , to approximately 2.0 A-hr, was achieved by providing some reservoir space in the silver electrode compartment by replacement of a 0.010 in. latex filler sheet with Dynel. Additional increase in the chamber size produced no significant increase in capacity. With the cell operated with the silver electrode flooded but vented, it was found that volumetric flows between the silver electrode compartment and the reservoirs above the compartment could be correlated with both the onset of rapid gas evolution at the positive and with the rapid increase in TPD near the end of charging. Fluid flows to and from the reservoirs above the silver electrode were observed to be reversible provided charging did not extend into the region of heavy gassing at the positive. A reversible flexing of the acrylic cell wall on the zinc side of the cell was also observed during these experiments. A mechanical strain gauge (least count = 0.001 in.) was used to measure deflections, and values as large as 0.0015 in. were observed during cycling. If copious gassing was allowed to occur at the positive, solution was driven into the reservoirs, and the silver electrode chamber would not refill spontaneously; apparent capacity,  $Q_2$ , dropped. Capacity could be partially regained by injecting electrolytic solution into the silver compartment by syringe; however, better results were achieved by vacuum refilling the cell.

To provide a clear test of the convective flow hypothesis, it was deemed desirable to cycle a zinc electrode to as great a depth as possible under conditions of minimized convective flow parallel to the membrane surface. Since operation of cell A with the silver vented allowed deeper cycling while maintaining the limited convection condition on the zinc side, this mode of operation was adopted for subsequent experiments.

During a preliminary experiment with cell AP, it was found that this cell also was subject to severe increases in rate of change of TPD after charging

$$Q_2 = 2.0 \int_{t_1}^{t_2} dt \quad [2]$$

where  $t_1$  = time at which charging begins with the cell initially in the completely discharged state, and  $t_2$  = time at which TPD reaches 2.3V at the 2.0A charging rate.

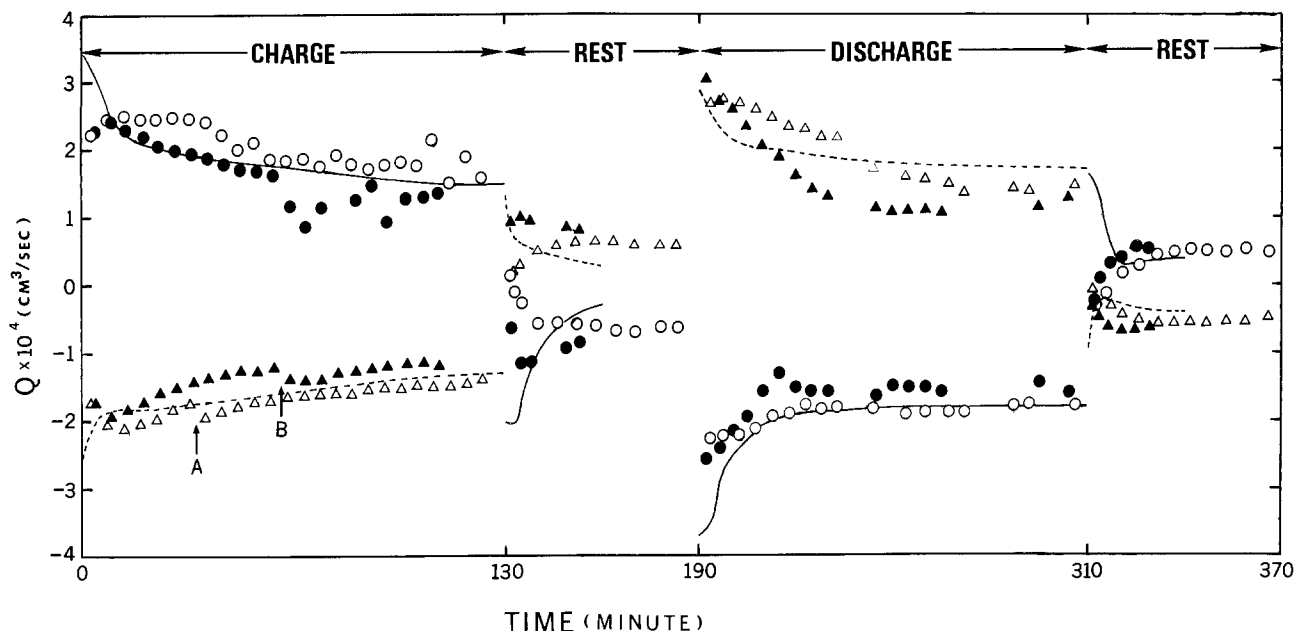


Fig. 3. Volumetric flow rate data for cells BV (cycle 6) and BH (cycle 2).  $\circ$ , Cell BV, zinc compartment;  $\bullet$ , cell BH, zinc compartment;  $\triangle$ , cell BV, silver compartment;  $\blacktriangle$ , cell BH, silver compartment. —, Predicted flow rate, zinc compartment; - - - - -, predicted flow rate silver compartment. Each cycle consisted of 2 hr of charge and 2 hr of discharge at 1.0A. A and B show points where cell potential indicated change from monovalent to divalent silver electrode reaction. A positive flow rate corresponds to flow of liquid out of that compartment through the vent, due to combined effect of an increase in the volume of solid and a flow of liquid through the separator into the compartment.

or discharging the test electrode in excess of 1 hr at 2.0A. Decreasing the cell current to 1.0A allowed several cycles to 2.5 A-hr without onset of severe polarization; however, after a few cycles at this rate a severe increase in rate of polarization again was observed to set in at about 2.0 A-hr.

### Results

**Cell BV.**—The electrodes were subjected to 36 cycles, 2 hr charge and 2 hr discharge, at a constant current of 1.0A, that is, an apparent current density of 15 mA/cm<sup>2</sup>. There was no preforming of either electrode. Irregular time gaps, varying from several minutes to several hours, occurred between half-cycles. TPD of the cell during charging rose gradually as cycling continued but did not reach a level at which noticeable gassing occurred. During the first six cycles, flow rate data were recorded. In Fig. 3, volumetric flow rate data, corrected for H<sub>2</sub> evolution at the zinc electrode, are shown for cycle 6. The data for the other cycles are similar in essential features and are presented elsewhere (7).

After 36 cycles, the zinc electrode was removed from the cell in the completely discharged state (the electrodes were discharged at the normal rate and then shorted for several hours). It was then cut perpendicular to the long axis of the electrode into ten sections of approximately equal area and analyzed for ZnO and Zn as described above. The results are shown in Fig. 4. Also shown in Fig. 4 for comparison are analytical data presented in the same manner for an unused electrode.

**Cell BH.**—The electrodes of the cell were subjected initially to three low current density forming cycles (2 A-hr at 0.01–0.10A cell current) and then to 43 cycles, 2 hr charge and 2 hr discharge, at 1.0A. Irregular time intervals occurred between half-cycles as with cell BV. Again, TPD on charge gradually increased with cycling. Flow rate data were taken during cycles 2, 23, and 38. Data for cycle 2 are included in Fig. 3. The data for cycles 23 and 38 are similar in essential features and are presented elsewhere (7). After the 43rd cycle, the zinc electrode was removed from the cell in the completely discharged state and

treated in the same manner as the zinc electrode from cell BV. Analytical data for the electrode are included in Fig. 4.

**Cell A.**—Cell A was cycled with the silver electrode flooded and vented as shown in Fig. 1. Initial cycling was at the 2.0A rate; there was no preforming of either electrode. Table I summarizes the types, numbers, and duration of all cycles. Irregular time intervals occurred between half-cycles as with cell BV. As operation proceeded, current densities and cycle

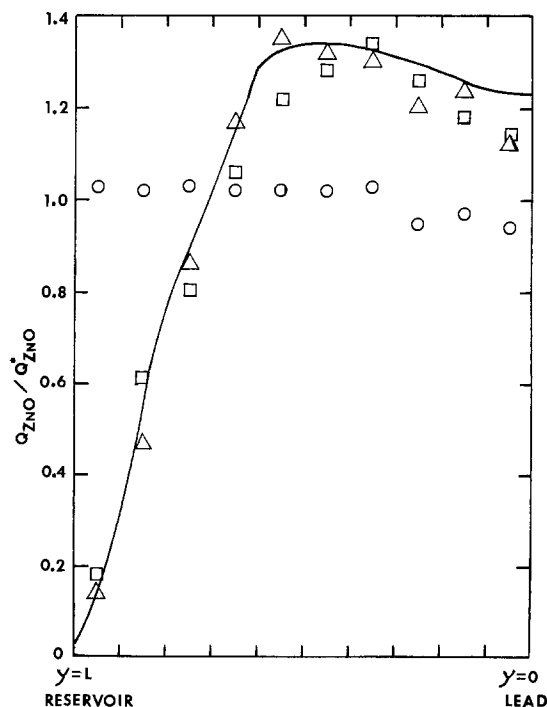


Fig. 4. Normalized ZnO distribution.  $\circ$ , Unused electrode;  $\square$ , used electrode after 43 cycles from cell BH;  $\triangle$ , used electrode after 36 cycles from cell BV. —, Predicted ZnO distribution after 35 cycles.

Table I. Cycle history for cell A

Cycle type	Number of cycles	Approximate duration of charge (hr)	Constant cell current (A)	Charge (A-hr)
A	10	1.0	2.0	20
B	12	0.5	2.0	12
C	9	2.0	1.0	18
D	30	1.5	1.0	45
E	77	1.0	1.0	77
F	17	0.75	1.0	13
G	4	0.5	1.0	2
H	34	1.5	0.5	26
I	12	1.0	0.5	6
	<u>205</u>			<u>219</u>

depths were altered as cell capacity changed. Capacity,  $Q_2$ , was measured initially and at selected times as shown in Fig. 5. After accumulating about 125 A-hr of charging, the cell was vacuum refilled, resulting in a substantial recovery of capacity; however, continued cycling resulted in rapid loss of capacity as shown. In total, the electrodes of this cell were subjected to over 200 constant current cycles of operation. Total charge delivered to the cell was approximately 219 A-hr.

The zinc electrode was removed from the cell in the completely discharged state. A photograph of the electrode is shown in Fig. 6. The electrode was then cut into 15 sections of approximately equal area for analysis (4 cuts perpendicular to the long axis and 2 cuts perpendicular to the short axis). A summary of the analytical results is shown in Fig. 7. Also shown in Fig. 7 are data for an unused zinc electrode. These data may also be stated in terms of average deviations and outlying results (furthest from the average) for the 15 samples. For the unused electrode the result is  $1.00 \pm 0.04$  with an outlying result of 1.07. For the used electrode the result is  $1.00 \pm 0.12$  with an outlying result of 0.78.

The HCl wash and rinse liquids from the analyses were tested by AA for mercury. No mercury was detected, indicating that negligible quantities of HgO were present at the end of cycling. Residues and collector screens of 5 samples were leached and dissolved, respectively, with warm concentrated nitric acid, and these fluids were tested for mercury. Mercury as determined by AA was found in approximately

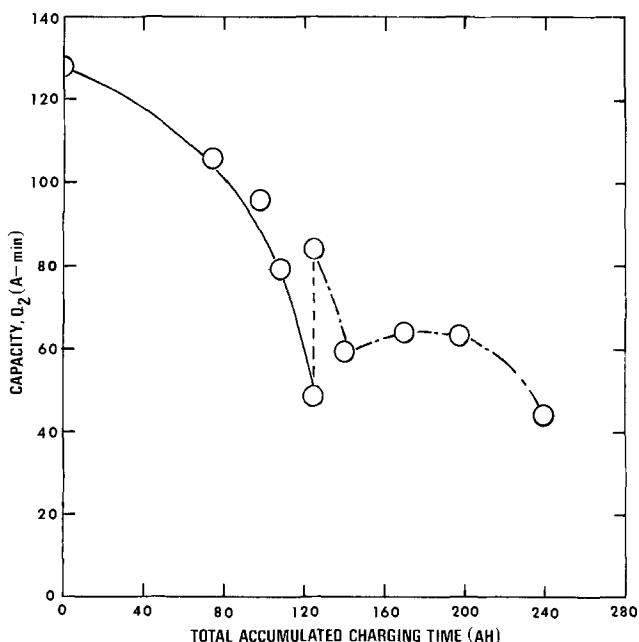


Fig. 5. Capacity,  $Q_2$ , for cell A as a function of accumulated charging time. The vertical dashed line denotes the improvement of capacity when the cell was vacuum refilled.



Fig. 6. Photograph of used zinc electrode from cell A. The electrode was discharged before removal from the cell. Total charge delivered to the electrode during cell operation was approximately 219 A-hr. The distribution of unconsumed, metallic zinc appears as dark, rough appearing areas.

equal quantities in the collector screens and residues. However, total mercury found by AA in the 5 samples tested was only about 60% of that anticipated on the basis of analysis of unused zinc electrodes.

The silver electrode from the cell was leached with stirring with two portions of 6N HCl for a total of

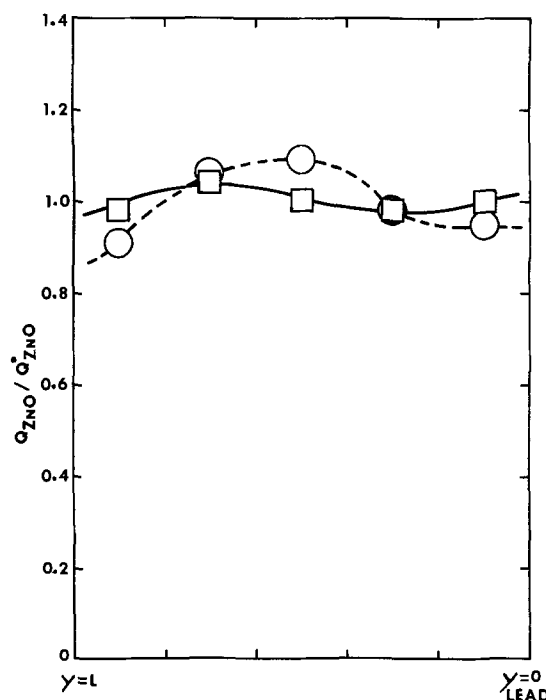


Fig. 7. Normalized ZnO distribution.  $\square$ , Unused electrode;  $\circ$ , used electrode from cell A. Each point is an average over three sections taken at the indicated value of y.

approximately 48 hr. The leach liquid was made to volume, and zinc determined by AA. The quantity 0.45g of zinc was found, or, reported as ZnO, 0.56g.

The data reported above for cell A are the results from the second experiment of this type which was carried out. In the first experiment the electrode arrangement differed only in that a single 0.001 in. Dynel interseparator was used rather than the 0.005 in. material. Approximately half as much total cell operating time was accumulated, 110 A-hr of charging at approximately 30 mA/cm<sup>2</sup>. Very similar ZnO distribution results were obtained. Problems with the first experiment, involving minor leakage around seals and greater uncertainty in analytical results, dictated that the work be repeated.

**Cell AP.**—The cell was cycled at 1.0A, 2 hr charge and 2 hr discharge. Observed values of TPD and pressure changes as functions of time are shown for three cycles of operation in Fig. 8.

**Membrane evaluation.**—Hundreds of hours of operation of several different cells produced only one case of shorting of a cell by zinc dendrites. It was determined that this case involved a prior mechanical puncture of the membrane incurred during cell assembly. Membranes were commonly darkened in color (dark brown to black) in the cell environment; the membrane layers nearest the silver electrode showed the greatest coloration.

### Discussion

**Basic hypothesis.**—According to the basic hypothesis, the principal cause of material redistribution over the zinc electrode is convective flow parallel to the apparent electrode surface. The direction of the flow alternates on cycling and couples with changes in the concentration of soluble zinc species (due also to cycling) to produce a net movement of zinc. After enough cycles, even a small movement of zinc per cycle will lead to a gross redistribution and battery failure. Practitioners of the art have observed convective flows in these cells, but little significance was attached to them.

In the present case, in cells BV and BH, one oriented vertically and one oriented horizontally, the convective flow patterns (Fig. 3) simulate those in commercial silver-zinc storage batteries, and a drastic redistribution of ZnO is observed after 36 or 43 cycles, 72 and 86 A-hr of charging, respectively (see Fig. 4).

In a different experiment in cell A designed to minimize convection parallel to the electrode, substantially less redistribution of ZnO was observed after a total charging of 219 A-hr. The data support the

basic hypothesis and also rule out gravity as an influence of redistribution.

**Convective flow.**—Several observations can be made with respect to the experimental volumetric flow rate curves, shown in Fig. 3: (a) The abruptness with which the flows are established initially, the rapid changes in the direction of the flows at the end of charge and discharge, and the abrupt increases in the flow rates at the beginning of discharge suggest that electro-osmotic pumping by the membrane is the main driving force for convective flow during charge and discharge. (b) When the cell current is terminated, the electro-osmotic effect is expected to decrease rapidly. Osmotic driving forces, if present, should also relax, but less rapidly. At the end of charge, the flow rates are observed to drop rapidly to zero, change sign, and then increase again to maximum values before beginning a very gradual relaxation to equilibrium. Consideration of the electrode reactions suggest that the osmotic force which tends to drive water from the zinc compartment into the silver compartment during this period of time is caused by a difference in zincate concentration across the membrane. The time necessary for the complete relaxation of this latter effect is approximately 16 hr, indicating a relatively low diffusion coefficient for zincate in this membrane. (c) An osmotic effect due to differences in potassium concentration across the membrane should also be expected. During and after charge this effect should tend to drive solvent across the membrane in the same direction as the electro-osmotic effect. The experimental flow rate data for the period after charge suggests that the difference in potassium ion concentration relaxes within minutes, much more rapidly than the difference in zincate concentration. These considerations are also reflected in the initial stages of charging. The flow into the zinc compartment builds up rapidly under the electro-osmotic force and an osmotic force due to a combination of potassium ion and zincate concentration differences. As charging continues, a maximum is observed because of the differences in transport rates of potassium and zincate ions across the membrane.

The membrane used in these studies is a weak cation exchange membrane characterized by particular values of transport coefficients. Evidently, the coefficient for electro-osmotic transport is large and leads to large convective flows in the electrode compartments of the cell with normal convection and, therefore, to rapid material redistribution. The desirability of being able to optimize membrane properties, including transport parameters, seems apparent.

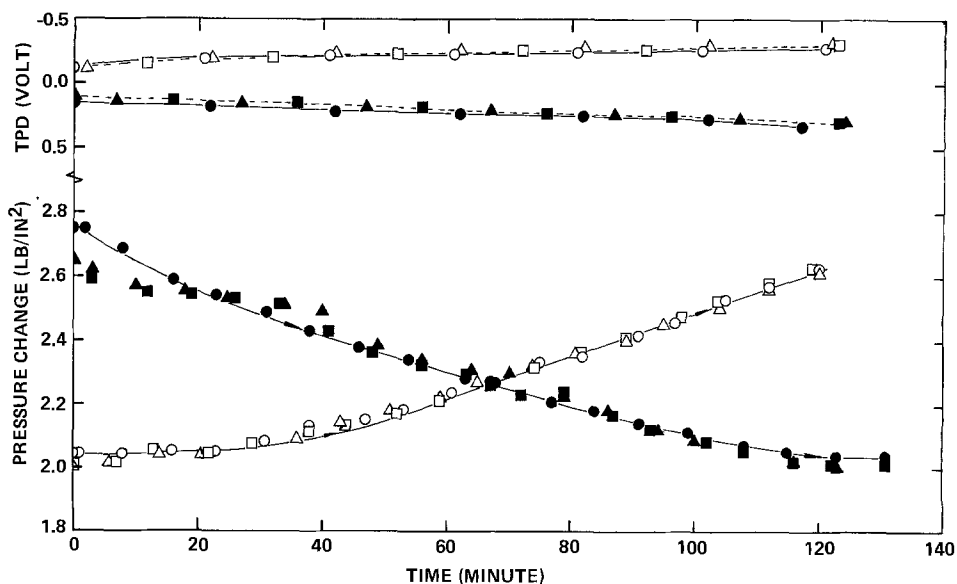


Fig. 8. Cell terminal potential difference (TPD), test electrode, counterelectrode, and pressure corresponding in the zinc test electrode compartment for cell AP as functions of time. ●, Cycle 6, discharge; ○, cycle 6, charge; ■, cycle 7, discharge; □, cycle 7, charge; ▲, cycle 8, discharge; △, cycle 8, charge.

*Cell capacity.*—During preliminary experiments with cell A when the cell was operated with both electrodes flooded and neither electrode vented, it was established that the freshly filled cell had a reproducible capacity,  $Q_2$ . The capacity was found to increase slightly when charging was carried out at a lower rate. Venting of the positive electrode compartment, which allowed both the escape of gas when generated and convective flow between the silver compartment and the reservoirs, led to a significant increase in  $Q_2$ . In addition, a correlation was noted between the rates of convective flow and both the onset of gassing and the rapid increase in TPD. Provision of additional reservoir space in the silver compartment also increased  $Q_2$  slightly. These observations indicated that  $Q_2$  was primarily limited by the development of concentration polarization at the positive electrode (hydroxyl ion starved) which led to gas evolution if charging was carried too far. Improvement in capacity through venting could be attributed to enhanced stirring due to the convective action or simply to maintenance of adequate solution volume in the electrode, that is, solution tended to flow from the positive to the negative electrode on charge due to osmotic and electro-osmotic effects, and the positive can be left in a "fluid starved" condition if fluid is not replaced. It is possible that the main effect of increased storage volume in the positive compartment was simply to facilitate convective flow into and through the compartment. In any event, observed capacity,  $Q_2$ , was at best only about 30% of the theoretical limiting value of 6.5 A-hr. One other possibility which has been suggested by other studies is a "choking" of the porous silver electrode, that is, the pores of the electrode are choked with product near the surface and only a small fraction of the total porous mass is utilized (12). Some experimental evidence has been presented in the results section which indicates an irreversible accumulation of precipitated ZnO in the positive electrode, which might also contribute to such an effect.

When cell A was repetitively cycled over a long period of time, capacity,  $Q_2$ , was observed to decrease with time as shown in Fig. 5. Only partial recovery of cell capacity, to 65% of initial, was achieved by vacuum refilling the cell, indicating that simple accumulation of gas in the electrode chambers was not the only reason for capacity decrease. Subsequent analysis of the zinc electrode revealed only slight material redistribution over the surface of the electrode.

Cell AP was operated with a zinc test electrode and a second zinc electrode replacing the silver electrode. It was initially hoped that greater depth of charge and discharge of the test electrode would be possible with this arrangement. In initial experiments, however, it was determined that this cell also was subject to similar severe increases in polarization after charging or discharging the test electrode in excess of 2 A-hr at the 2.0A rate. Decreasing the cell current again led to increased capacity, but with continued cycling the capacity decreased. Since no reference electrodes were utilized in this experiment, a determination of the distribution of the observed total polarization between the electrodes is impossible. It is clear, however, that polarization effects in cell A are not necessarily linked exclusively to the silver electrode.

*Pressure variations, cell AP.*—No theoretical analysis of pressure variations in the zinc electrode compartment of cell AP during operation was attempted. Reproducible values of pressure changes have been measured and presented in Fig. 8. One might have expected to observe more rapid changes in pressure reflecting the abrupt changes in electro-osmotic flow rate discussed above. In addition, based on simple

thermodynamic osmotic pressure calculations, much larger pressure differences would be expected. Several possible reasons why the observed changes are small and gradual rather than large and abrupt are offered: (a) The design of the cell and placement of the pressure sensing chamber may be a factor, that is, the electrodes are tightly packed in the cell, and the mouth to the pressure chamber is effectively plugged by the porous electrode; (b) flexing of the acrylic wall (which was actually observed); (c) gas bubbles in the electrode; (d) delayed changes in volumes of solids and liquids in the chamber due to the cell reaction, for example, such as might occur due to conversion of zincate to zinc followed by slow dissolution of ZnO; (e) movement of the membrane during cell operation.

*Model.*—The mathematical model for a cell with normal convection has been developed on the basis of the convective flow hypothesis. It is a one dimensional model which consists of a set of nonlinear, coupled differential equations with time and position parallel to the membrane surface as independent variables. Those factors have been included which are believed to be significant in governing the redistribution of material over the surface of the electrode. Such factors include: osmotic and electro-osmotic transport of ions and water across the membrane separator, transport of dissolved ions and water in the y direction (parallel to the electrode face) due to convection and diffusion, chemical species source and sink terms due to chemical reactions and precipitation-dissolution phase changes including the dependence of zincate solubility on KOH concentration, and provisions for quantitatively determining changing electrode porosity and local concentration changes with time and position y. Explicit details concerning the model and solution of the differential equations are presented elsewhere (6, 7).

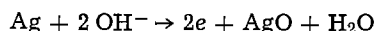
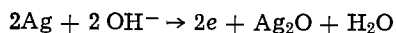
In Fig. 4, experimental ZnO distribution data are presented for the used electrodes from cells BV and BH and for an unused electrode. Also shown in the figure is a predicted ZnO distribution for an electrode which has been operated through 35 cycles at 1.0A for 2 hr charge and 2 hr discharge. Intervals between half-cycles were set at 3 min for the simulation. The computation was interrupted after the 8th, 15th, 22nd, and 28th cycles, and concentration differences which had developed were relaxed to their initial values before continued cycling. The reason for the interruption and relaxation may be explained briefly as follows: Numerical calculations indicated that at the 1.0A rate the normal cell reaction could not be sustained after seven or eight cycles because of variations in KOH and zincate concentrations in the cell, non-uniform distribution of zinc over the zinc electrode, and associated changes in current distribution. Redistributing the KOH and zincate (equivalent to a long rest period) allowed the cell to operate normally again and the theoretical cycling to continue. Experimentally this effect was manifested by increased cell polarization with cycling.

It was originally intended to carry the theoretical cycling to 40 cycles to produce a better comparison to experiment. However, in the 32nd charge cycle of the theoretical calculations, the zinc oxide became completely depleted for the first time near the reservoir end of the electrode. The computer program could handle this situation, but convergence became slow and computer calculation costs went up. Because of the increased cost, theoretical cycling was stopped after 35 cycles. Only one predicted ZnO distribution is shown in Fig. 4 for comparison with the two sets of experimental data because orientation of the cell with respect to the earth's gravitational field is neglected in the model. The agreement between the predicted and observed distributions is excellent



considering the variation of bases, 35 theoretical cycles, and 36 and 43 cycles for the two experimental runs.

In addition to redistribution of total zinc, the model can be used to predict a number of other cell variables as functions of position and time, for example, zinc metal, electrode porosities, ion concentrations, current densities, and volumetric flow rates, as well as their relevance to cell performance. In the experiments being described, only total zinc as ZnO redistributions and volumetric flow rates were measured quantitatively for comparison with predictions based on the model. In Fig. 3 one complete cycle of experimental volumetric flow rate data is plotted for cell BV and one complete cycle for cell BH. Also included in Fig. 3 are lines which represent the predicted flow rates. It is apparent that the model as it is currently constituted can yield flow rate curves which reproduce some of the main features of the experimentally determined curves and are in reasonable quantitative agreement with the observed rates over most of the complete cycle. There are interesting features of the experimental curves which are not reflected by the predicted curves, for example: (a) The result of the transition from production of monovalent to divalent silver oxide, marked A and B in Fig. 3, is clearly discernible in the flow rate data for the silver compartment during charging of both cells. This minor effect is not included in the model, that is, the cell charging reaction is modeled in terms of silver going to divalent silver oxide. It is interesting to note that the observed change in flow rate is in reasonable agreement with a change calculated on the basis of the two half-reactions



The difference involved in volume changes is  $5.5 \text{ cm}^3$  per two Faradays of charge; at 1.0A this volume change should produce a difference in flow rates of  $0.29 \times 10^{-4} \text{ cm}^3/\text{sec}$ . (b) During the adjustment times after abrupt changes in cell current, the experimental data reflect the relationships between the electro-osmotic and osmotic effects, for example, at the beginning of the charging period, the flow rate into the zinc compartment rises abruptly due to the electro-osmotic effect, continues to rise because of a rapidly developing osmotic effect due to potassium ion imbalance, and then drops slowly because of a developing opposite osmotic effect due to imbalance of zincate. Although the predicted curves do not currently reflect these changes, it is believed that they could be made to do so by proper adjustment of the appropriate membrane transport parameters.

There are several physical constants involved in the model, and definite values of these constants must be used in order to obtain numerical predictions from the model. In all cases where reliable data were available from the literature, these values were used in calculations. In other cases data simply were not available, and estimates have been made by the authors. The values used in calculations are presented elsewhere (6, 7). No systematic parametric study of the effects of the values of the constants on the predicted ZnO distribution or flow rates has been carried out at this time.

The one dimensional analysis is demonstrably successful in that one can use it to predict correctly ZnO redistribution at the zinc electrode in a cell with normal convection. It is probable that there are other physical processes which take place within the porous zinc electrode which are not adequately treated by the current model. These processes may take on greater importance under other circumstances. For instance, in cells such as cell A in which the zinc electrode is operated with limited convection, the data presented above indicate that mass transport in the

zinc electrode in the direction perpendicular to the membrane may be rate limiting.

### Conclusions

1. The data in Fig. 4 and 7 demonstrate that material redistribution over the zinc electrode in zinc-silver oxide cells is governed primarily by convective flow through the zinc electrode parallel to the apparent surface of the electrode. Furthermore, the data indicate that orientation of the electrode with respect to the earth's gravitational field has little impact on the material redistribution. Limitation of such parallel convective flow through the zinc electrode significantly decreases the rate of material redistribution.

2. The fluid flow rate data, samples of which are illustrated in Fig. 3, demonstrate that the average volumetric flows are in the directions which one would predict on the basis of osmotic and electro-osmotic pressure considerations. The data indicate that with the separator being used in this case, the primary driving force for convective flow during charge or discharge is electro-osmotic. The choice of the membrane material is important in the regulation of convective flow. Membranes with large electro-osmotic coefficients can be expected to yield large material redistribution effects in cells which allow normal convection; however, such membranes may be required to prevent zinc dendrites from reaching the positive electrode.

3. The one dimensional model for the cell with normal convection, based on the convective flow hypothesis, has been used successfully to predict ZnO redistributions and fluid flow rates. Good agreement between experimental observations and predicted values for these variables is strong evidence that the physically important phenomena in redistribution on the zinc electrode have been properly incorporated into the model.

4. The work done to date and reported above is strongly supportive of the basic convective flow hypothesis; however, much remains to be done in determining how this new knowledge might be used in the design of improved secondary cells. For instance, it appears that one can control the rate of development of shape change by controlling convective flow; however, evidence has also been obtained which indicates that the convective flow is important in determining utilization or capacity of the cell and, furthermore, it is believed that the convective flow also is important in determining the high rate capability of the cell. Gas evolution is frequently a problem in secondary cells; in a porous zinc electrode designed to minimize convection, the control of gas evolution will be critical to its successful operation. Membrane transport as well as chemical properties play important roles in determining cell performance. Continuing improvements in membrane science and technology which will permit detailed specification of membrane properties to optimize battery performance should be sought.

### Acknowledgments

Financial support for this work has been provided by the U.S. Air Force Systems Command and the University of California.

Manuscript submitted Feb. 18, 1976; revised manuscript received June 22, 1976. This was Paper 53 presented at the Dallas, Texas, Meeting of the Society, Oct. 5-9, 1975.

Any discussion of this paper will appear in a Discussion Section to be published in the June 1977 JOURNAL. All discussions for the June 1977 Discussion Section should be submitted by Feb. 1, 1977.

Publication costs of this article were assisted by the University of California, Los Angeles.

### REFERENCES

1. J. J. Lander, in "Zinc-Silver Oxide Batteries," A. Fleischer and J. J. Lander, Editors, pp. 457-



- 469, John Wiley & Sons, Inc., New York (1971).
2. H. G. Oswin and K. F. Blurton, *ibid.*, pp. 63-86.
3. G. A. Dalin, *ibid.*, pp. 87-95.
4. J. J. Lander and J. E. Cooper, Technical Report, AFAPL-TR-71-32, 39 pp. (Oct. 1971).
5. J. McBreen, *This Journal*, **119**, 1620 (1972).
6. K. W. Choi, D. N. Bennion, and J. Newman, *ibid.*, **123**, 1616 (1976).
7. K. W. Choi, Ph.D. Dissertation, School of Engineering, University of California, Los Angeles (1975).

8. J. A. Keralla, in "Zinc-Silver Oxide Batteries," A. Fleischer and J. J. Lander, Editors, pp. 183-198, John Wiley & Sons, Inc., New York (1971).
9. S. U. Falk and A. Fleischer, *ibid.*, pp. 199-208.
10. D. Pickett, Personal communication.
11. R. Giovanoli, H. R. Oswald, and W. Feitknecht, *Helv. Chim. Acta*, **49**, 1971 (1966).
12. J. S. Dunning, D. N. Bennion, and J. Newman, *This Journal*, **120**, 906 (1973).

## Anodic Oxidation of DDT, Methoxychlor, and Related Compounds

Richard R. Keenan<sup>1</sup> and James D. Stuart\*

Department of Chemistry, University of Connecticut, Storrs, Connecticut 06268

### ABSTRACT

DDT, DDE, methoxychlor, and the ethylene of methoxychlor (MeCe) were oxidized in a 5% aqueous acetonitrile solution at a platinum electrode containing tetraethylammonium perchlorate or tetraethylammonium perfluoroborate as supporting electrolytes. The major electrolysis products were those which resulted from the hydrolysis of the electron-deficient intermediates and included alcohols, ketones, benzoquinones, and acids. 1,1-Bis-(*p*-methoxyphenyl) 2,2,2-trichloroethanol, not previously reported as a metabolic degradation product of methoxychlor, was readily isolated as a major electrochemical oxidation product of both methoxychlor and MeCe.

No other man-made chemical has had more impact on the health of the human race or on the environment as has DDT. More than two million metric tons of DDT have been used for insect control since 1940. It has been estimated that DDT has saved fifty million human lives and spared one billion humans from such plagues as malaria, typhus, and yellow fever (1). DDT is considered to be the single major controllable factor that has led to the population explosion in underdeveloped nations of the world. Yet, due to its persistence in the environment, its ability to be "biologically magnified," and its ability to be rendered harmless by many strains of DDT-resistant insects, DDT has become the symbol of man's reckless environmental pollution (1). DDT or DDE, its more persistent degradation product, is found in virtually every environmental sample. DDT levels of from 1 to 10 ppm are generally observed in man. DDE has recently been recognized as the most abundant organochlorine pollutant in the environment.

In preliminary findings cited by Maugh (2), Moilanen and Crosby have shown that DDT undergoes rapid, vapor phase, sunlight degradation in air to DDE. DDE is in turn photodegraded much more slowly to at least eight other products, among them 4,4'-dichlorobenzophenone (DBP) and possibly to polychlorinated biphenyls (PCB's). Figure 1 shows the metabolic and photochemical degradation pathways of DDT involving oxidations. [A paper on the anodic oxidations of PCB's follows this paper (3)].

Effective on January 1, 1973, all use of DDT in the United States has been banned by the Environmental Protection Agency. Yet many agree that no single DDT substitute will be as inexpensive and as universally effective as was DDT. Methoxychlor, the methoxy analogue of DDT, has replaced DDT in certain commercial preparations as it has been found to be a persistent yet biodegradable insecticide. Metcalf has claimed that methoxychlor is one of the safest of all

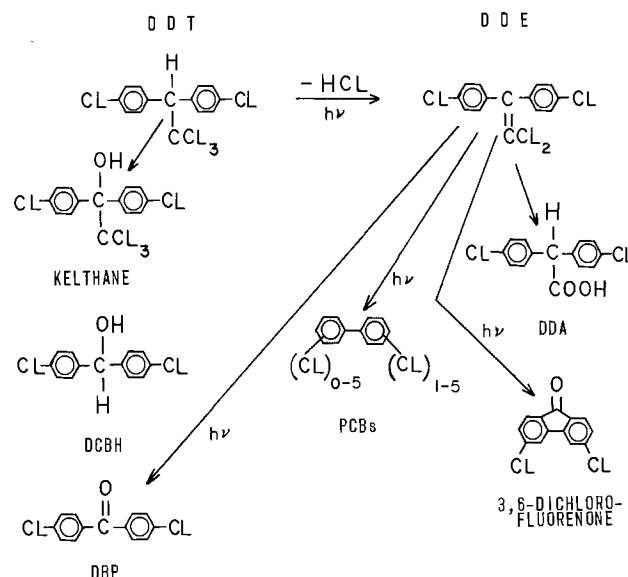


Fig. 1. Natural degradation pathways of DDT involving oxidations.  $h\nu$  denotes the proposed photochemical pathways in sunlight.

insecticides to higher animals (1). Figure 2 shows the known metabolic degradation pathways of methoxychlor (MeC) involving oxidations. Methoxychlor is metabolized through O-dealkylation to mono- and bisphenols, which are rapidly conjugated and excreted in higher animals or dehydrochlorinated to the corresponding ethylene (MeCe). Methoxychlor is more effective against DDT-resistant insects, such as the housefly, as the enzymatic-induced rate of dehydrochlorination of methoxychlor to the ethylene of methoxychlor (MeCe) is substantially reduced by the electron-donating properties of the *p*-methoxy groups in comparison to the over-all electron-withdrawing properties of the *p*-chloro groups of DDT.

It must be emphasized that the oxidative pathways occurring in this present report on the electrochemical

\* Electrochemical Society Active Member.

<sup>1</sup> Present address: Environmental Health Laboratory, United States Steel Corporation, Monroeville, Pennsylvania 15146.

Key words: hydroxylation, DDT, methoxychlor, pesticide.

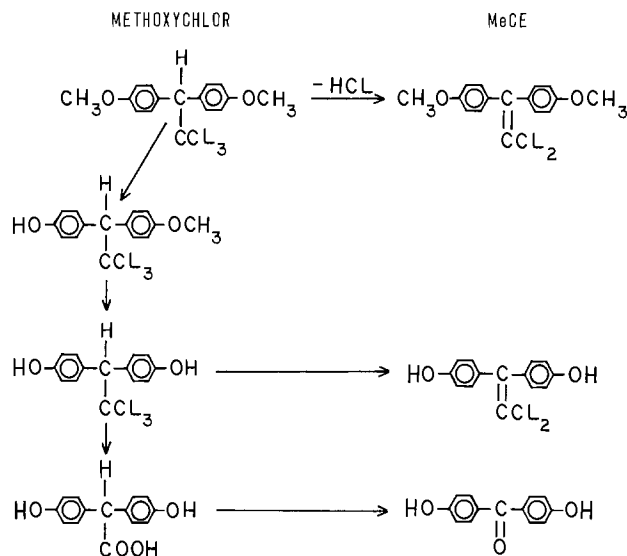


Fig. 2. Degradation pathways of methoxychlor involving oxidations.

oxidation of DDT, methoxychlor, and related compounds are no doubt different than the enzyme-assisted, natural degradation routes of these same chemicals. It is interesting that 1,1-bis-(*p*-methoxyphenyl)-2,2,2-trichloroethanol, never before reported as a metabolic product of methoxychlor, is readily isolated as a major electrolysis product from the electrochemical oxidation of methoxychlor (MeC). All previous electrochemical studies of DDT and related compounds have been concerned with their electrochemical reduction (4-7). Lund has reported the electrochemical oxidation of 4,4'-dichlorobenzhydrol (DCBH) at +2.07V vs. SCE in acetonitrile solvent to the ketone, 4,4'-dichlorobenzophenone (DBP) (8).

### Experimental

**Chemicals.**—The following chemicals were used as received after their purity had been checked by thin-layer or gas-liquid chromatography: 1,1,1-trichloro-2,2-bis-(*p*-chlorophenyl)ethane (DDT); 1,1-dichloro-2,2-bis-(*p*-chlorophenyl)ethylene (DDE); 1,1-bis-(*p*-chlorophenyl)-2,2,2-trichloroethanol (Kelthane); 4,4'-dichlorobenzophenone (DBP); 4,4'-dimethoxybenzophenone (DMBP); 1,1-dichloro-2,2-bis-(*p*-methoxyphenyl)ethylene (MeCe). 1,1,1-Trichloro-2,2-bis-(*p*-methoxyphenyl)ethane or methoxychlor (MeC) both purified and technical grade was kindly provided by the Biochemicals Department, E. I. du Pont de Nemours & Company, Wilmington, Delaware. The technical grade was easily purified by recrystallization from ethanol. The following compounds were chemically prepared following published procedures: 4,4'-dichlorobenzilic acid (DBA) (9); 4,4'-dimethoxybenzilic acid or anisilic acid (DMBA) (10).

The following three compounds were isolated as major electrolysis products: 1,1-bis-(*p*-methoxyphenyl)-2,2,2-trichloroethanol or dimethoxykelthane (DMK) was isolated from the large-scale electrolyses of methoxychlor (MeC) and the ethylene of methoxychlor (MeCe); 1,1,1-trichloro-2-(*p*-methoxyphenyl)-2-(3-chloro-4-methoxyphenyl)ethane (3-Cl-MeC) was isolated from the electrolysis of methoxychlor only in anhydrous MeCN (0.1F LiClO<sub>4</sub>) saturated with Na<sub>2</sub>CO<sub>3</sub>; 1,1,1-trichloro-2-(*p*-chlorophenyl)-2-(4-chloro-2,5-benzoquinone)ethane (DDT-Q) was isolated from the electrolysis of DDT, being the major product of the electrolysis of DDT in the flow-through cell. The physical as well as the spectroscopic data of these three new compounds have been reported elsewhere (11).

The acetonitrile solvent (MeCN) was purified by distillation from P<sub>2</sub>O<sub>5</sub> and then CaH<sub>2</sub>, the middle 80% fraction being retained. Tetraethylammonium perchlo-

rate (Et<sub>4</sub>NClO<sub>4</sub>), used as the supporting electrolyte, was recrystallized twice from distilled water, dried on top of an oven and in an evacuated drying pistol at 100°C with P<sub>2</sub>O<sub>5</sub> as dessicant. Tetraethylammonium fluoroborate (Et<sub>4</sub>NBF<sub>4</sub>) was prepared by reacting Et<sub>4</sub>NBr with HBF<sub>4</sub>, followed by a washing with ether, two recrystallizations with ethanol and then one with distilled water. This supporting electrolyte was also dried on top of an oven and in an evacuated drying pistol. Due to the hazards of working with perchlorates, especially in the presence of heavy metals, the use of fluoroborate salts as supporting electrolytes was preferred in the latter portions of this work. Perhaps because all work was done in 5% aqueous acetonitrile there appeared to be little difference in the types or amounts of the products when Et<sub>4</sub>NBF<sub>4</sub> was used instead of Et<sub>4</sub>NClO<sub>4</sub>.

Conventional electrochemical equipment was used for the cyclic voltammetry (12, 13) and for the controlled potential electrolyses (Amel Model 557 potentiostat-galvanostat). Controlled potential coulometry was accomplished either by the deposit of silver onto a silver wire cathode (auxiliary electrode) or through a graphic integration of the current-time curve. For cyclic voltammetry, the electrolysis cell was a 4 oz glass jar; the working electrode was a stationary platinum disk (Beckman 39273); the auxiliary electrode was a platinum electrode placed coaxially around the working electrode; the reference electrode was an aqueous SCE isolated from the electrolysis by a two-compartment salt bridge to prevent contamination of the electrolysis cell by chloride. For controlled potential electrolyses, the electrolysis cell was a 250 ml beaker or a glass flow-through cell. With the beaker, the working electrode was a cylindrical platinum mesh electrode; the auxiliary electrode, isolated by a medium porosity glass frit, was either a coiled silver wire in a solution of 0.1F AgClO<sub>4</sub>-0.1F Et<sub>4</sub>NClO<sub>4</sub> or Et<sub>4</sub>NBF<sub>4</sub> in MeCN or a cylindrical platinum mesh electrode in 0.1F of the same supporting electrolyte as the working compartment; the reference electrode was a Ag/0.1F AgClO<sub>4</sub> in MeCN electrode. All potentials are given vs. the aqueous saturated calomel electrode (SCE); those measured against the Ag/AgClO<sub>4</sub> reference electrode were converted to the SCE reference electrode by adding +0.30V to the measured value (14).

In order to isolate a greater proportion of the primary hydroxylated product before it could be further oxidized at the electrode, a single-pass flow-through electrolysis cell was used; its construction out of glass being diagramed in Fig. 3. While the over-all product yield was between 10 to 30%, there were significantly fewer products with this flow-through cell. In addition, the unreacted 70-90% of the starting material was used over again in subsequent single-pass electrolyses. In general, while there might be ten or more products detected by thin-layer or high pressure liquid chromatography from a conventional electrolysis, usually only one to three products were observed when the same compound was electrolyzed in the single-pass flow-through cell. It was not possible to make an exact mass balance as it was impossible to isolate in pure form nor to make satisfactory structure assignments to the many minor electrolysis products. As will be noted later, the product yields are low as they are based on the amount of pure isolated product after separation and purification. In most cases the electrolyses were run, exposed to the air, at the lowest controlled potential which produced significant current. The electrolysis was terminated when the current had reached a constant minimum value or when thin-layer chromatography indicated that all of the starting material had been consumed or interesting products were present. The solvent was removed by a rotary evaporator at temperatures below 50°C to minimize thermal degradation of unstable products. Procedures used for the isolation of various oxidation products were as follows: several extractions to isolate the neutral organic mate-

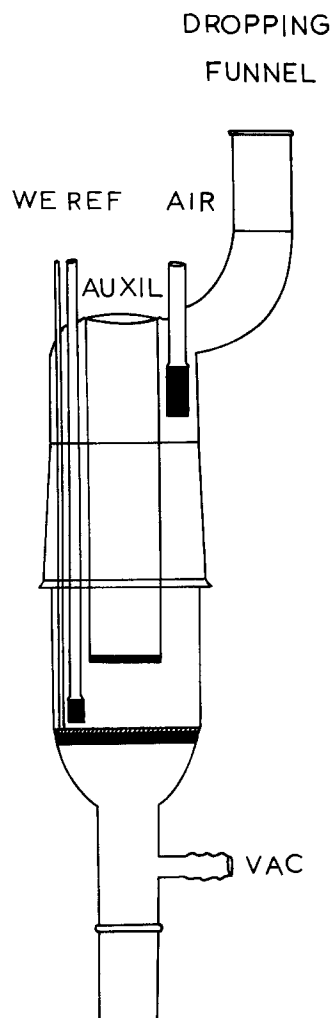


Fig. 3. Single-pass, flow-through electrolysis cell. Of all glass construction, cell height 40 cm by 7.0 cm in maximum diameter. Made out of a 150 ml Filter funnel having a medium porosity glass frit, 5.5 cm in diameter (Corning 36060). WE, Pt = working electrode, 100 mesh platinum, 5.5 cm in diameter, wire diameter 0.0076 cm; REF, SCE = reference electrode probe, ultra fine porosity, 0.5 cm in diameter located 1 cm above the working electrode; AUXIL = auxiliary compartment made of a medium porosity glass frit, 3.0 cm in diameter; CE, Pt = counterelectrode, 52 mesh platinum, 4.0 cm in height by 1.5 cm in diameter (not shown in the figure); AIR = coarse glass sparger to create a positive air pressure at the top of the cell, 1.5 cm in diameter; Dropping Funnel = dropping funnel, 100 ml graduated, ending in a 24/40 joint; VAC = provision to attach vacuum if needed to increase the flow rate.

rials from the acidic or phenol products, initial screening by thin-layer chromatography, open column chromatography to remove unwanted or long-eluting products, followed by either preparative thick-layer chromatography or semipreparative, high pressure, liquid chromatography. All of the chromatography was performed on the appropriate type of silica while the high pressure liquid chromatography was performed on 6-12 ft by 7 mm ID packed columns of 37-75 $\mu$  porous silica using a Waters ALC-201 chromatograph in the recycle mode with an all purpose refractive index detector. Visualization of products on TLC plates was accomplished by ultraviolet radiation or by one of the following spray reagents: concentrated sulfuric acid for DBA and many of the analogues of methoxychlor; diphenylamine-zinc chloride for Kelthane and dimethoxykelthane, 2,4-dinitrophenylhydrazine for the ketones and benzoquinones.

Product identifications were based on melting points compared to authentic samples, elemental analysis, infrared, nuclear magnetic resonance, and mass spectral

data (11). Mass spectra were obtained on an AEI MS-902 mass spectrometer with a resolution of 100,000.

### Results and Discussion

Cyclic voltammetry was initially used to determine the approximate potential at which to run the ensuing controlled electrolyses. Table I shows the anodic peak potentials for DDT, methoxychlor, and their related compounds. The diagnostic criteria of Nicholson and Shain (15, 16) were used to aid in suggesting the over-all major voltammetric anodic pathway of DDT, DDE, methoxychlor, and the ethylene of methoxychlor.

No signs of an electrochemical reversible couple (up to scan rates of 200 V/sec) were evident for any of the compounds listed in Table I except for a quasi-reversible peak for the ethylene of methoxychlor (MeCE) at scan rates greater than 1.0 V/sec. In general, the primary oxidation peak for DDT, DDE, MeC, and MeCE tended to shift to higher anodic potentials and the current function tended to decrease as the sweep rate was increased over four decades (0.01-100 V/sec). These behavior patterns are suggestive of an electron transfer followed by a fast irreversible chemical reaction [case VI of Ref. (15)] or an ECE pathway [either case I-I or I-R of Ref. (16)] with the second electron transfer being at the same or lower potential than the first electron transfer.

Referring to Table I, the presence of additional peaks at higher anodic potentials were due to the subsequent oxidation of the major electrolysis product, the corresponding benzophenone. Thus, the anodic peak at +2.65V for dichlorobenzophenone (DBP) is readily apparent in the anodic voltammograms of DDT, DDE, Kelthane, and DBA. Similarly the two anodic peaks of DMBP at +1.94 and +2.60V are observed in the anodic voltammograms of MeCE and DMBA and partially in the voltammograms of MeC and DMK.

As the controlled potential electrolyses of DDT and its related compounds proceeded very slowly in anhydrous MeCN, and in an effort to more nearly match natural oxidative degradation conditions, all electrolyses were run with water added to the acetonitrile solvent in an atmosphere of air. The weight of the AgCl precipitated in the anode compartment during the course of an oxidation indicated that an irreproducible amount of chloride was being lost from the  $\alpha$ -chloromethyl group of each compound. Chromatographies indicated a multitude of electrolysis products, often between ten to twenty; some of them being heat or light sensitive. Hence the isolation and characterization of only the more abundant electrolysis products was possible. The reported product yields are low as they are based on the amount of pure isolated product obtained after separation and purification remembering in certain cases that incomplete controlled potential electrolyses were carried out in the single-pass flow-through cell or in order to isolate the initial electrolysis product.

*Electrochemical oxidation of DDE.*—When DDE was electrochemically oxidized in 5% aqueous acetonitrile

Table I. Summary of anodic peak potentials of DDT, methoxychlor, and related compounds at 100 mV/sec vs. aqueous SCE

Compound	$E_p$ , V vs. SCE
DBP	+2.65
DMBP	+1.94, +2.60
DBA	+2.21, +2.6
DMBA	+1.57, +1.94, +2.60
Kelthane	+2.34, +2.66
DMK	+1.72, +1.88
DDE	+1.98, +2.75, (+2.15 to +2.30)*
MeCE	+1.54, +1.92, +2.60, (+1.57)*
DDT	+2.32, +2.6
MeC	+1.73, +2.6

\* An additional wave appearing only at scan rates of 2.5 V/sec or higher.

at +1.74V on a platinum electrode, the major products isolated were DBA in 10-60% yield and DBP in 30-80% yield. The variable yield of DBA can, in part, be explained by the fact that DBA itself is slowly oxidized at +1.74V to DBP. At +2.00V in 5% aqueous MeCN, DDE, in about  $10^{-2}$  F, is electrochemically oxidized to DBP in greater than 95% yield in 3-5 hr as opposed to an average electrolysis time of 20 hr at +1.74V. At the higher controlled voltage of 2.00V, any DBA that may have been initially formed upon electrolysis of DDE, is itself quantitatively oxidized to DBP.

The isolation of DBA from the electrolysis of DDE, along with the cyclic voltammetric data, suggests that DDE may be electrochemically oxidized in an ECE pathway proceeding through an unstable vicinal-glycol (I); this very unstable intermediate would undergo rapid hydrolysis and dehydrochlorination to DBA, or could undergo the loss of the good leaving group, dichloromethylene ( $\text{CCl}_2$ ), to produce the benzophenone DBP. This oxidation of the vicinal-glycol (I) is analogous to the oxidation of benzopinacol to benzophenone (17).

The fact that DBA at 1.74V is oxidized after 20 hr to DBP in only 20% yield (the remaining 80% being the starting material) and the highly irreproducible yields of DBP obtained in the oxidation of DDE at +1.74V, yet the consistent controlled potential coulometry indicating an over-all two-electron oxidation of DDE, suggest a branching pathway to the formation of DBP. Figure 4 depicts such a branching mechanism whereby the hydroxylated cationic species (II) or the vicinal-glycol (I) undergo a purely chemical breakdown to DBP. Such a purely chemical pathway must be a significant alternative, as the oxidation of DDE through DBA to DBP requires the loss of four electrons, not the two that is consistently observed in the coulometry.

An additional anodic voltammetric wave for DDE at approximately +2.2V is apparent at scan rates of 2.5 V/sec or higher. This suggests that a branching reactions sequence occurs that is dependent on the rate of the voltage scan. At slow voltammetric scan rates, an initial over-all two-electron oxidation occurs as depicted by the top line of Fig. 4, while at faster scan rates a stepwise EEC sequence occurs as shown on the left-hand part of Fig. 4. This branching sequence is suggested by a significant increase (within bounds) of the current for the new peak at +2.15V with increasing scan rate.

**Electrochemical oxidation of 1,1-dichloro-2,2-bis-(p-methoxyphenyl)-ethylene.**—When MeCe was electrochemically oxidized in 5% aqueous MeCN at +1.40V on a platinum electrode, the major products were DMBP in 32-43% yield and the unexpected DMK in 25% yield.

While DBA was a major product of the electrochemical oxidation of DDE at lower controlled potential, thin-layer chromatography indicated that no 4,4-dimethoxybenzilic acid (DMBA) was obtained in the electrochemical oxidation of MeCE. The closeness in the anodic peak potentials between MeCE and DMBA, within 0.03V (Table I), indicates that a significant accumulation of DMBA is not to be expected in the controlled potential electrolysis of MeCE. This is in sharp contrast to the 0.23V difference in anodic peak potentials between DDE and DBA, which permitted DBA to be isolated in significant amounts from the large-scale controlled potential electrolysis of DDE.

The isolation of DMK in 25% yield from the electrolysis of MeCE indicated that free chloride in the solution is capable of nucleophilic attack on the deficient intermediates to yield a tri-chloromethyl moiety. As MeCE exhibited cyclic voltammetric behavior similar to DDE, including the appearance of an additional anodic wave at +1.57V at faster scan rates, a branching mechanism similar to that proposed for DDE is proposed for MeCE and is depicted in Fig. 5.

**Electrochemical oxidation of DDT.**—When DDT was electrochemically oxidized in 5% aqueous MeCN at +2.10V on a platinum electrode, the products identified were DBP in an approximate yield of 25% and 1,1,1-trichloro-2-(p-chlorophenyl)-2-(4-chloro-2,5-benzoquinone)ethane (DDT-Q) in 10% yield and Kelthane (indicated by thin-layer chromatography and spray tests); however the isolation of the Kelthane was not possible due to the extremely small amount present. The isolation of a significant amount of Kelthane from the large-scale, conventional anodic oxidation of DDT was not expected as the oxidation peak of Kelthane occurs within 0.02V of the one for DDT (Table I). The use of a flow-through cell designed to enable the initial hydroxylated product to be swept away from the electrode before it could suffer further oxidation failed to produce Kelthane. Instead the sole product isolated from the flow-through electrolysis of DDT was DDT-Q.

Cyclic voltammetric data at all scan rates indicated that DDT is oxidized irreversibly followed at higher anodic potential by the prominent oxidation peak for DBP. While a stepwise ECE reaction sequences could be written, a more general over-all two-electron branching scheme is depicted in Fig. 6 to account for the formation of the major products. Thus a nucleophilic attack by water on the dicarbonium ion (III) at the central  $\alpha$ -carbon would result in the formation of Kelthane and DBP while a nucleophilic attack by water on the electron-deficient aromatic ring would lead to DDT-Q.

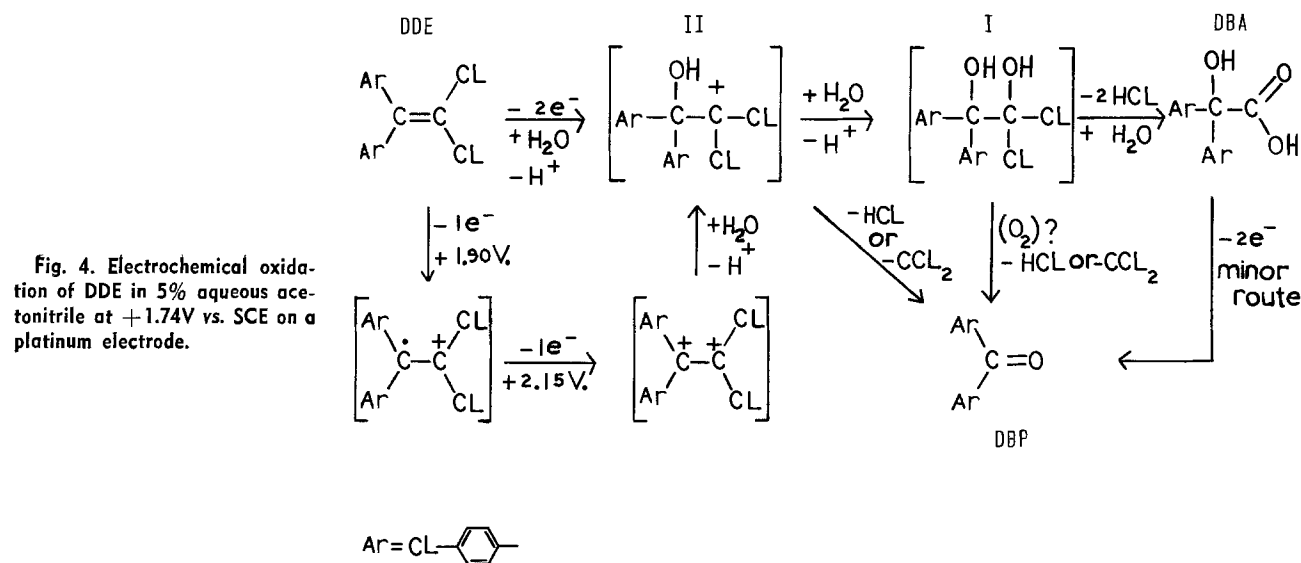


Fig. 4. Electrochemical oxidation of DDE in 5% aqueous acetonitrile at +1.74V vs. SCE on a platinum electrode.

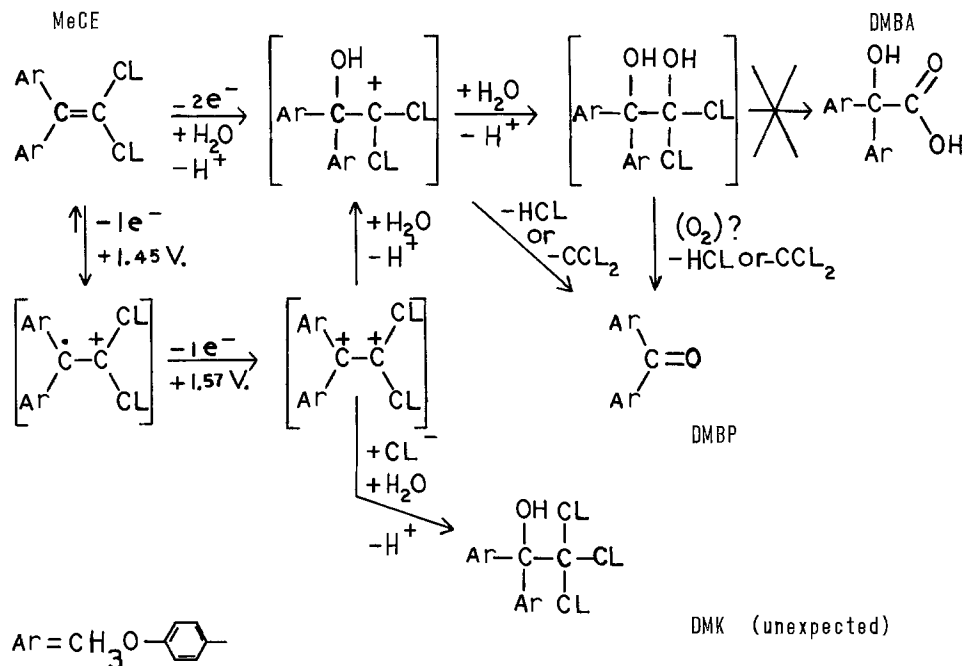


Fig. 5. Electrochemical oxidation of 1,1-dichloro-2,2-bis-(*p*-methoxyphenyl)-ethylene (MeCe) in 5% aqueous acetonitrile at +1.40V vs. SCE on a platinum electrode.

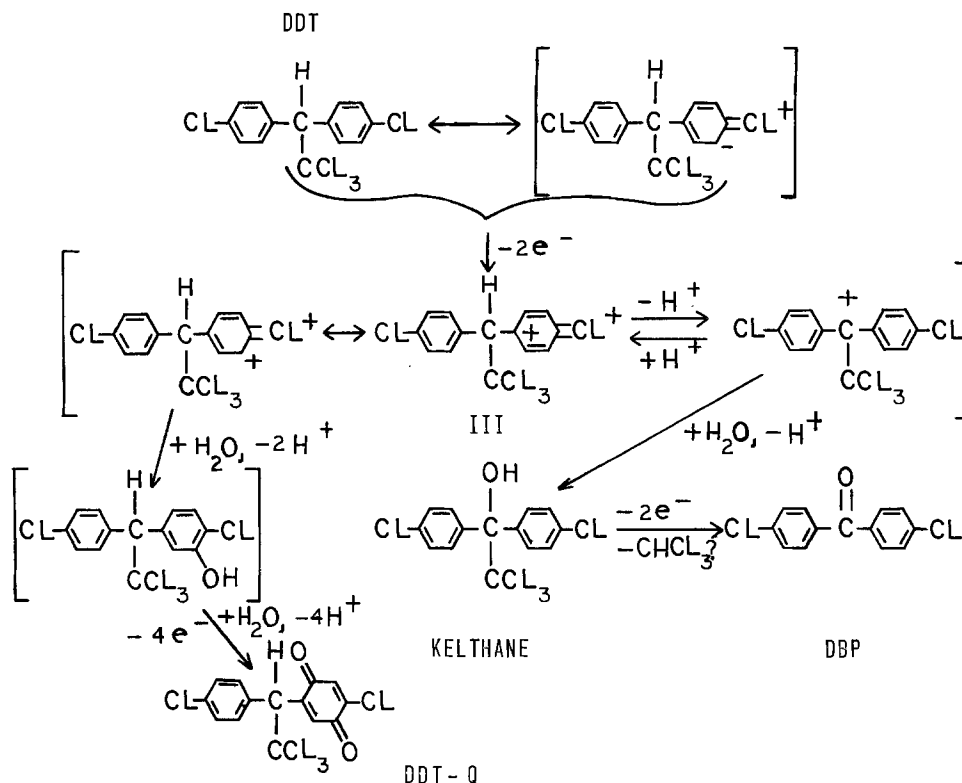


Fig. 6. Electrochemical oxidation of DDT in 5% aqueous acetonitrile at +2.10V vs. SCE on a platinum electrode.

**Electrochemical oxidation of methoxychlor.**—When methoxychlor (MeC) was electrochemically oxidized in 5% aqueous MeCN at +1.50V on a platinum electrode, the products identified were DMBP in an approximate yield of 35% and dimethoxykelthane (DMK) in 5–30% yield. This is the first report of the isolation and identification of DMK as a degradation product of MeC.

In dry MeCN (0.1F LiClO<sub>4</sub> as supporting electrolyte) saturated with Na<sub>2</sub>CO<sub>3</sub>, the major electrolysis product of MeC was found to be 1,1,1-trichloro-2-(*p*-methoxyphenyl)-2-(3-chloro-4-methoxyphenyl)ethane (3-Cl-MeC) in 20% yield. The production of this chloro-adduct must occur as a result of the nucleophilic attack by chloride ion which is produced by the previous degradation of a trichloromethyl group of another methoxychlor molecule. 3-Cl-MeC was not observed by thin-layer chromatography if the electrochemical oxidation

of methoxychlor was carried out in 5% aqueous acetonitrile.

The cyclic voltammetric data and product isolation suggest that methoxychlor is oxidized in a general over-all two-electron scheme in aqueous MeCN as shown in Fig. 7. There was no significant evidence for the production of phenols or of their subsequent oxidation products, the benzoquinones. These products would indicate that a nucleophilic attack by water on the electron-deficient aromatic rings does not significantly occur in electrochemical oxidation. O-dealkylation of the methoxy groups to yield *mono*- or *bis*-phenols are the major, known natural degradation pathways of methoxychlor (Fig. 2). Electrochemical oxidation of either 2- or 4-methoxyphenol involving the hydrolysis of the carbonium ion and the loss of methanol to yield the benzoquinone has been reported (18, 19). Apparently, ring hydrolysis to form a phenol or a benzo-

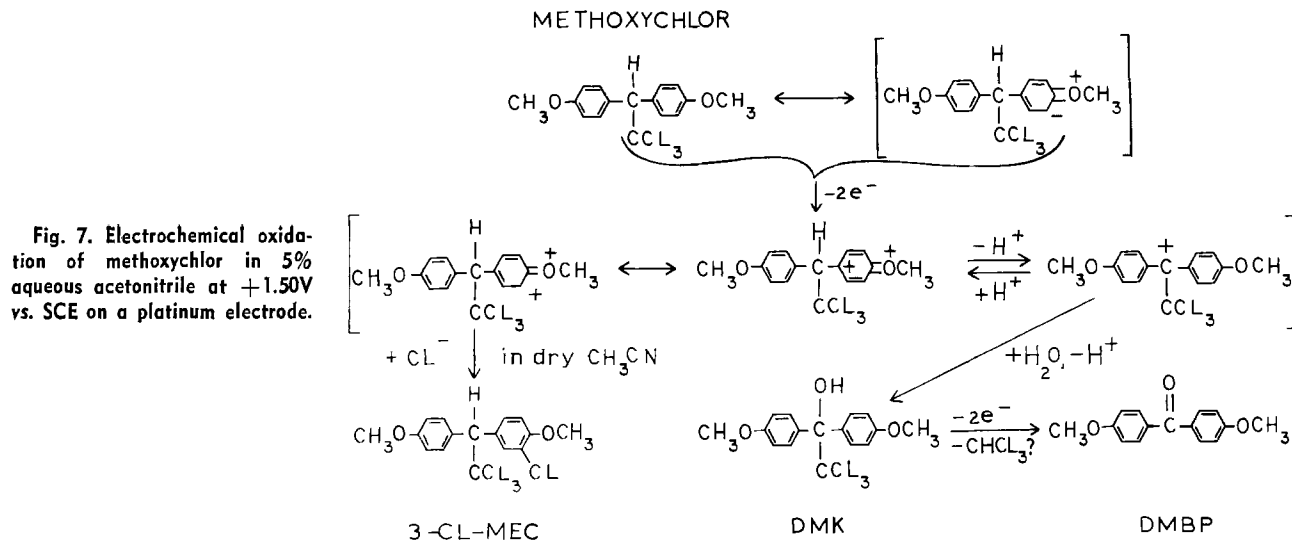


Fig. 7. Electrochemical oxidation of methoxychlor in 5% aqueous acetonitrile at +1.50V vs. SCE on a platinum electrode.

quinone with dealkylation is not a significant electrochemical oxidation pathway for methoxychlor in 5% aqueous acetonitrile at +1.50V.

### Summary

The major electrolysis products identified from the controlled potential electrolyses of DDT, DDE, methoxychlor, and the ethylene of methoxychlor in 5% aqueous acetonitrile solution were hydrolysis products. These products were either alcohols, ketones, benzoquinones, or acids that suggested that nucleophilic attack by water occurred mostly at the electron-deficient carbon located at the central  $\alpha$ -carbon of each compound studied. The appearance at higher oxidation potential of a voltammetric wave of the benzophenone for each compound studied attests to this fact. DBA is obtained in good yield from the electrochemical oxidation of DDE, and the never-before reported DMK is obtained in good yield from the electrochemical oxidation of methoxychlor and the ethylene of methoxychlor, MeCe. However, nucleophilic attack by water on the electron-deficient aromatic ring did occur in certain cases as a significant amount of DDT-Q was isolated from the electrochemical oxidation of DDT. In an anhydrous media, a nucleophilic attack by chloride ion onto the electron deficient aromatic ring of methoxychlor was evident.

### Acknowledgment

Initial support of this research by The University of Connecticut Research Foundation is gratefully acknowledged. Later portions of the investigation were supported by the National Institutes of Health Research Grant No. ES-01056 from the Environmental Health Science Group. Financial support for the mass spectrometer was made available through NSF Grant No. GP-18332. One of us (R. R. K.) acknowledges an NSF Graduate traineeship made available to the Graduate School, The University of Connecticut 1969-1973. This paper is based in part on a thesis of one of us (R. R. K.)

submitted in partial fulfillment of the requirements for a Ph.D. degree to the University of Connecticut.

Manuscript received May 6, 1976. This was Paper 175 presented at the Chicago, Illinois, Meeting of the Society, May 13-18, 1973.

Any discussion of this paper will appear in a Discussion Section to appear in June 1977 JOURNAL. All discussions for the June 1977 Discussion Section should be submitted by Feb. 1, 1977.

Publication costs of this paper were assisted by the University of Connecticut.

### REFERENCES

- R. L. Metcalf, *Crit. Rev. Environ. Contr.*, **3**, 25 (1972).
- T. H. Maugh II, *Science*, **180**, 578 (1973).
- R. J. Fenn, K. W. Krantz, and J. D. Stuart, *This Journal*, **123**, 1643 (1976).
- H. Sato, *Chem. Abstr.*, **62**, 14182c (1965).
- H. Keller, M. Hochweber, and H. V. Holban, *Helv. Chim. Acta*, **29**, 761 (1946).
- S. Yamamoto, *Chem. Abstr.*, **48**, 14087i (1954).
- I. Rosenthal and R. J. Lacoste, *J. Am. Chem. Soc.*, **81**, 3268 (1959).
- H. Lund, *Acta Chem. Scand.*, **11**, 491 (1957).
- P. J. Montagne, *Rec. Trav. Chim.*, **21**, 21 (1902).
- M. Bösler, *Chem. Ber.*, **14**, 327 (1881).
- R. R. Keenan and J. D. Stuart, *Arch. Environ. Contam. Toxicol.*, In press.
- E. R. Brown, T. G. McCord, D. E. Smith, and D. D. DeFord, *Anal. Chem.*, **38**, 1119 (1966).
- C. J. Neilsen and J. D. Stuart, *ibid.*, **44**, 1713 (1972).
- C. K. Mann, in "Electroanalytical Chemistry," Vol. 3, A. J. Bard, Editor, p. 64, Marcel Dekker, New York (1969).
- R. S. Nicholson and I. Shain, *Anal. Chem.*, **36**, 706 (1964).
- R. S. Nicholson and I. Shain, *ibid.*, **37**, 178 (1965).
- W. Kemula, Z. R. Grabowski, and M. K. Kalinowski, *Coll. Czech. Chem. Commun.*, **25**, 3306 (1960).
- L. Papouchado, J. Bacon, and R. N. Adams, *J. Electroanal. Chem.*, **24**, App. 1-5 (1970).
- D. Hawley and R. N. Adams, *ibid.*, **8**, 163 (1964).

# Anodic Oxidation of Two Polychlorinated Biphenyls

Robert J. Fenn,<sup>1</sup> Karl W. Krantz,<sup>2</sup> and James D. Stuart\*

Department of Chemistry, University of Connecticut, Storrs, Connecticut 06268

## ABSTRACT

Although very resistant to environmental oxidative degradation reactions, two specific polychlorinated biphenyls (PCB's) and typical commercial mixtures of PCB's are oxidized at very high anodic potentials at a platinum electrode in a medium of aqueous acetonitrile and tetraethylammonium fluoborate. Isolation of the chlorobiphenylols (or hydroxychlorobiphenyls) formed by initial oxidative hydroxylation reactions and the corresponding benzoquinones, in addition to cyclic voltammetric data, indicate an over-all ECE reaction scheme. Certain of the identified oxidation products of the PCB's studied have never been reported, while others are similar to their known metabolic or photochemical degradation products. This indicates that electrochemistry is a convenient method to study the degradation of these very persistent environmental pollutants, as well as a convenient synthetic route for certain of their key degradation products.

Mixtures of polychlorinated biphenyls (PCB's) have been commercially available since 1929, yet their first identification in environmental samples occurred in 1966. Only in the past few years have their long term persistence and wide dispersal in the environment been recognized. An informative text on the analysis, chemistry, and occurrence of PCB's is now available (1).

PCB's are a class of chemically inert, chlorinated hydrocarbons. PCB mixtures have had widespread commercial use as a result of their following favorable properties: high dielectric constant, high thermal and chemical stability, low vapor pressure, low water solubility, low flammability, and high miscibility with most organic solvents, polymers, and paints (2, 3). Different PCB mixtures, with varying degrees of viscosity and density, have been available in many industrial countries of the world. In the United States, PCB mixtures have been manufactured exclusively by the Monsanto Company and sold under the trade name Aroclor®. Their manufacture involves the large scale chlorination of biphenyl with chlorine gas using Fe or FeCl<sub>3</sub> as catalyst. The commercial products are a complex mixture of a large number of PCB isomers. While 209 isomers are theoretically possible, 102 isomers have been separated by gas-liquid chromatography in an Aroclor® mixture (1, 2). In September of 1970, Monsanto placed a voluntary reduction of sales on Aroclors®, and on July 6, 1973 the United States government restricted the use of PCB mixtures in commercial products to only those products that could eventually be disposed of in an efficient manner that would not contribute to the environmental contamination (4). No cheap, practical, safe, or as efficient substitute has been found for PCB mixtures in many commercial applications (5).

In the United States, in the record high year of 1970 in which 43 thousand metric tons of Aroclor® were produced, the most important use of PCB mixtures was as capacitor dielectric materials, commonly called Askarel®. It had been estimated that in past years more than 90% of all capacitors sold (80 million annually) contained Aroclor® mixtures. In addition, PCB mixtures had been widely used as insulation and heat transfer fluids, as hydraulic fluids and lubricants, and as components in plasticizers of paints, sealants, and varnish. Their high thermal stability allows them to be vaporized into the atmosphere in inefficient incinera-

tors thus facilitating their global distribution. It has been estimated that at least one million metric tons of PCB materials have reached the world environment from all sources, domestic and foreign (2).

PCB's had attracted little environmental concern, having often been detected but not identified as extraneous gas chromatographic peaks amongst chloro-organic pesticides, until a series of incidents drew attention to their chronic toxic effects in birds, fish, poultry, mammals, and man (1, 3, 6). In comparison to DDT and its principal degradation product DDE, PCB's are believed to be more resistant to enzymatic and photochemical degradation. This, along with their high lipid solubility, accounts for the "biological magnification," of PCB levels in going up the food chain (2).

Toxicological evidence has suggested that certain of the deleterious effects of foreign commercial PCB mixtures (I) may be due to the presence, in part per millions, of chlorodibenzofurans (III) and chlorodibenzo-*p*-dioxins V (7). The origin of (III) and (V), not only in foreign PCB mixtures but also in domestic commercial chlorophenol mixtures (IV), may be due to poorly developed, commercial purification procedures. For example, it had been reported that certain foreign PCB mixtures had been purified by the addition of lime or potassium hydroxide to neutralize the hydrochloric acid byproduct, or by blowing air over the heated crude, commercial mixture followed by distillation under reduced pressure (7, 8). Figure 1 shows PCB's (I), chlorobiphenylols or hydroxychlorobiphenyls (II), chlorophenols (IV) with their postulated alteration routes to the very toxic chlorodibenzofurans (III) and chlorodibenzo-*p*-dioxins (V).

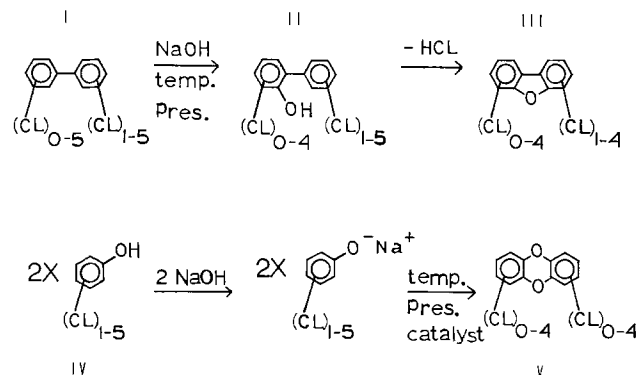


Fig. 1. PCB's, hydroxychlorobiphenyls, and possible transformation routes to chlorinated dibenzofurans and chlorinated dibenzo-*p*-dioxins.

\* Electrochemical Society Active Member.

<sup>1</sup> Present address: Department of Chemistry, University of Massachusetts, Amherst, Massachusetts 01002.

<sup>2</sup> Present address: Flow-Solv, Incorporated, Schenectady, New York 12309.

Key words: chlorobiphenylol, hydroxychlorobiphenyl, hydroxylation, PCB's.

Recent efforts have focused on identifying the principal metabolites of PCB's. It has been shown that hydroxychlorobiphenyls (II) are the most prominent metabolites in animals, microorganisms, and plants (1). Thus from rabbits, the principal urinary metabolites of 2,5,2',5'-tetrachlorobiphenyl, a predominant compound in a commercial PCB mixture, is the 3-OH and the 4-OH isomer as well as a 3,4-dihydroxy-3,4-dihydro-compound, suggesting that enzymatic hydroxylation occurs through an arene oxide intermediate with an oxygen attachment at both the open 3- and 4-positions (9).

It is the 3-hydroxy-2,5,2',5'-tetrachlorobiphenyl that is isolated as the major hydroxychlorobiphenyl product from the electrochemical oxidation of 2,5,2',5'-tetrachlorobiphenyl. Thus electrochemistry is a convenient method for the synthesis of the hydroxychlorobiphenyls, as few of these metabolic products are available. In addition, there are few good, organic synthetic methods available that lead to a single hydroxy-isomer in good yield (10). But it must be emphasized that our synthetic method is far different than the enzyme-assisted, natural alteration of the same PCB starting material.

Beland *et al.* have recently reported that a stepwise loss of chloride from a specific PCB by reductive voltammetry is characteristic enough to provide analytical identification of a specific pure PCB isomer (11, 12).

### Experimental

**Chemicals.**—The following chemicals were used as received after their purity had been checked by thin-layer or gas-liquid chromatography or they were purified as described below. 4,4'-Dichlorobiphenyl (DCB) from Aldrich Chemical Company, about 97% pure, was purified by vacuum sublimation, m.p. 146°–148°C [Lit. 146°, 148° (1)]; 2,5,2',5'-tetrachlorobiphenyl (TCB) was prepared in very high yield through the highly toxic 2,5,2',5'-tetrachlorobenzidine (11) and in much lower yield by the Ullman coupling reaction (13), m.p. 84.5°–85.5°C [Lit. 86°–87°C (1)]; decachlorobiphenyl, 99%, commercially available from Analabs Incorporated, North Haven, Connecticut; 2,3,7,8-tetrachlorodibenzo-*p*-dioxin kindly provided by E. H. Blair, Dow Chemical U.S.A., Midland, Michigan; perchlorination kit (Analabs PCR-A) used to fully chlorinate biphenyl, dibenzofuran, and dibenzo-*p*-dioxin; commercial Aroclor® mixtures were kindly provided by W. B. Papageorge, Monsanto Company, St. Louis Missouri.

The following compounds were prepared by organic synthetic methods as authentic samples to which the electrolysis products were compared. 4,4'-dichloro-2-biphenylol (or 2-hydroxy-4,4'-dichlorobiphenyl) prepared by making the diazonium salt of 2-methoxy-4-chloroaniline with isoamyl nitrite followed by a free radical coupling reaction with chlorobenzene (10). After washing and a vacuum distillation, the fraction containing the chloromethoxybiphenyls was demethylated with boron tribromide (13). The various hydroxychlorobiphenyl isomers were isolated first by open column chromatography from silica with toluene as eluent then by semipreparative, high pressure liquid chromatography on porous silica 37–75 $\mu$ , in columns 10 ft by 7 mm ID, with toluene as solvent in certain cases using the Waters 201 liquid chromatograph in the recycle mode. Careful evaluation of their infrared spectra (Perkin Elmer 337) using 0.2 mm thick NaCl liquid cells with carbon tetrachloride and carbon disulfide as solvents showed the first eluted isomer to be the 2,4'-dichloro-4-biphenylol, then the 2',4'-dichloro-2-biphenylol, followed by the desired 4,4'-dichloro-2-biphenylol.

As 2,5,2',5'-tetrachlorobiphenyl is a more symmetrical compound, a similar organic synthesis reaction of 2,5-dichloroaniline with 2,5-dichloroanisole yielded after demethylation (13) and similar chromatographic

separation by semipreparative liquid chromatography, then infrared spectroscopy for structure elucidation, in order of elution with toluene, 2,5,2',5'-tetrachloro-6-biphenylol, followed by 2,5,2',5'-tetrachloro-3-biphenylol, then 2,5,2',5'-tetrachloro-4-biphenylol. In addition, the structure of the major hydroxylated product from the electrochemical oxidation of 2,5,2',5'-tetrachlorobiphenyl was confirmed by comparing its chromatographic and infrared absorption spectra to that of an authentic sample of 3-hydroxy-2,5,2',5'-tetrachlorobiphenyl kindly provided by Gardner (9). He has identified the 3- and the 4-isomers as those being eluted in the urine of rabbits, as well as performing the organic synthesis and structure elucidation of each of the isomers. He has reported a convenient thin-layer chromatographic separation of the three isomers compared to 2,5-dichlorophenol as an internal standard (9).

The following compounds were isolated as major electrolysis products from the large-scale controlled potential electrolyses of pure PCB isomers. Those marked by an asterisk have previously not been reported in the available literature. Each compound had infrared, nuclear magnetic resonance and mass spectral data consistent with the assigned structure (14). 2-Chloro-5-(*p*-chlorophenyl)-1,4-benzoquinone (VI) (15, 16); 2-(*p*-chlorophenyl)-1,4-benzoquinone (VII) (16, 17). Both (VI) and (VII) were compared to authentic samples kindly provided by Bagli (16); 2,5-dichloro-3-(2,5-dichlorophenyl)-1,4-benzoquinone (IX)\*; bis-2,5-dichloro-1,4-benzoquinone (X)\*; 2-chloro-3-(2,5-dichlorophenyl)-1,4-benzoquinone (XI)\*; 2-chloro-6-(2,5-dichlorophenyl)-1,4-benzoquinone (XII)\*.

Tetraethylammonium fluoborate, Et<sub>4</sub>NBF<sub>4</sub>, was prepared by reacting Et<sub>4</sub>NBr and HBF<sub>4</sub> in distilled water (18) followed by washings with ether, two recrystallizations with ethanol and one with distilled water, and drying on top of an oven and in an evacuated drying pistol at 100° with P<sub>2</sub>O<sub>5</sub> as desiccant for 24 hr. This supporting electrolyte gave a low residual current to at least +3.5V vs. SCE. Upon the addition of progressive amounts of water to 0.1F Et<sub>4</sub>NBF<sub>4</sub> in MeCN solvent, an irreversible wave first appeared with a peak at +2.6V followed by an electrolyte breakdown at around +2.9V; the breakdown progressively shifted to lower anodic potentials as additional amounts of water were added (19).

All instrumentation, procedures, and reagents including the use of the single-pass, flow-through electrolysis cell were as described in the previous paper (20) except for what follows. Because of the high anodic potentials required to cause the electrochemical oxidation of PCB's, tetraethylammonium fluoborate, Et<sub>4</sub>NBF<sub>4</sub>, was used as the supporting electrolyte in the MeCN solution for the cyclic voltammetric studies. The use of dual cells and potentiostats were required to electronically subtract the appreciable residual current from the compound's faradaic current (21). All controlled potential electrolyses were carried out in a medium of 2–5% aqueous MeCN, with 0.1F Et<sub>4</sub>NBF<sub>4</sub> and 1–2% in 0.2F AgClO<sub>4</sub>. The AgClO<sub>4</sub> was added to remove the irreproducible amount of chloride ions eliminated during the electrolysis of each PCB isomer and made the formation of more highly chlorinated biphenyls less likely, thereby reducing the number of electrolysis products. Visualization of the products separated by thin-layer chromatography was accomplished by ultraviolet light for the PCB's, by 2,4,7-trinitro-9-fluorenone for the chlorobiphenyls (22), and by 2,4-dinitrophenylhydrazine for the benzoquinones. To determine whether oxidative electrochemical conditions used in this study converted the PCB isomers (DCB, TCB and decachlorobiphenyl) to the very highly toxic chlorodibenzofurans (III) or chlorodibenzo-*p*-dioxins (V), a gas-liquid chromatographic analysis was performed. Following the method of Williams and Blanchfield (23), the impure mixture



of an electrolysis product was fully chlorinated using the chlorination kit (Analabs); the relative retention times of the separated perchlorinated products were then compared with authentic retention times of octachlorodibenzofuran or octachlorodibenzo-*p*-dioxin. No conversion of the three PCB isomers studied to the more toxic compounds was evident by gas-liquid chromatography. It is estimated that as little as 0.1% conversion would have been detected.

### Results

Cyclic voltammetry was initially used to determine the approximate potential at which to run the ensuing controlled potential electrolyses. Table I shows the anodic half-peak potentials for several of the commercial Aroclor® mixtures. (The last two digits in the Aroclor® number indicates the average chlorine percentage by weight.) A general trend toward higher anodic potential with increasing percentage of chlorine is evident. This trend is to be expected, based on the electron-withdrawing effect of the chlorine substituents. The significant prewaves observed in the voltammograms are thought to be due to the oxidation of the lower chlorinated PCB fractions in the mixture; each mixture has been reported to contain between 40 to 80 different isomers (1).

Table II lists the half-peak potentials of those pure PCB isomers studied, along with those of benzene, biphenyl, and 4,4'-dimethoxybiphenyl for comparison. For the pure chlorinated biphenyl isomers, a similar trend toward higher oxidation potentials with increasing chlorine content is evident. Table III shows the relatively low oxidation potential of several commercially available chlorophenols and hydroxybiphenyls; this table illustrates that any hydroxychlorobiphenyl (II) formed in the large-scale electrolysis of PCB isomers would be further oxidized at the controlled potentials used for the oxidation of the PCB.

The diagnostic criteria of Nicholson and Shain were used to aid in suggesting the over-all major electrochemical pathway of the three pure PCB isomers in

Table I. Voltammetry of Aroclors®\*

Aroclor®	$E_{pk_{a/2}}$
1232	2.23 (prewave)
1242	2.39 (prewave)
1254	2.42 (prewave)
1260	2.43 (no prewave)

\* All are anodic potentials measured vs. aqueous SCE

Table II. Voltammetry of biphenyls\*

Biphenyls	$E_{pk_{a/2}}$
(Benzene)	(2.32)
Biphenyl	1.82
4,4'-Dimethoxybiphenyl	1.18
4,4'-Dichlorobiphenyl	1.88
2,5,2',5'-Tetrachlorobiphenyl	2.38
Decachlorobiphenyl	2.63

\* All are anodic potentials measured vs. aqueous SCE

Table III. Voltammetry of phenols\*

Phenols	$E_{pk_{a/2}}$
2-Chlorophenol	0.63
3-Chlorophenol	0.73
2,4-Dichlorophenol	0.65
2-Hydroxybiphenyl	1.27
3-Hydroxybiphenyl	1.47
4-Hydroxybiphenyl	1.24
3-Chloro,4-hydroxybiphenyl	1.30

\* All are anodic potentials measured vs. aqueous SCE

Table II. For each PCB isomer only one irreversible anodic wave is evident; its location tended to shift to higher anodic potentials, while its current function tended to decrease, as the sweep rate was increased over three decades of sweep rate (0.1-100 V/sec). These behavior patterns are suggestive of an electron transfer followed by a fast, irreversible chemical reaction [case VI of Ref. (24)] or an ECE pathway [either case I-I or I-R of Ref. (25)]. Adding increasing amounts of water to the solution caused the half-peak potentials at a scan rate of 0.1 V/sec to shift to a less anodic potential and the current function to double. This behavior is in agreement with a proposed ECE mechanism whereby the increasing amounts of water, acting as a nucleophile, caused the rate of the intervening chemical reaction to be significantly increased, and increased the likelihood of the second charge transfer occurring at lower anodic potential.

As expected, the fully chlorinated decachlorobiphenyl showed the appearance of a chlorine/trichloride redox system at +1.1 and +1.7V vs. SCE on the second and third cyclic voltammetric scans (26). The final electrolysis solution smelled strongly of HCl, and the thin-layer chromatography and infrared spectroscopy indicated the presence of several benzoquinones; all indicating that a significant loss of chloride ion from the decachlorobiphenyl had occurred. No attempt was made to further identify the electrolysis products due to the small amount of decachlorobiphenyl that was available for electrolysis.

In an effort to more nearly match natural oxidative degradation conditions, all electrolyses were run with water added to the acetonitrile solvent. The weight of the AgCl precipitated in the anode compartment during the course of an oxidation indicated that an irreproducible amount of chloride was being lost from the PCB compound. The reported product yields are low as they are based on the amount of pure isolated product obtained after separation and purification from incomplete controlled potential electrolyses.

**Electrochemical oxidation of 4,4'-dichlorobiphenyl.**—When 4,4'-dichlorobiphenyl (DCB) was electrochemically oxidized in 2.5% aqueous MeCN between +1.9 to +2.1V vs. SCE on a platinum electrode, with  $Et_4NBF_4$  and  $AgClO_4$  added, the major electrolysis products isolated were: 2-chloro-5-(*p*-chlorophenyl)-1,4-benzoquinone (VI) in 25-30% yield; 2-(*p*-chlorophenyl)-1,4-benzoquinone (VII) in 4-6% yield; a 4,4'-dichloro-2-biphenylol (VIII) in 4-6% yield; and a trichlorobiphenyl in 2% yield. Figure 2 shows the general electrochemical oxidation scheme of 4,4'-dichlorobiphenyl. [Hutzinger has shown that 4,4'-dichloro-3-biphenylol is the metabolic product of 4,4'-dichlorobiphenyl in rats and goats (1, 10, 27).]

**Electrochemical oxidation of 2,5,2',5'-tetrachlorobiphenyl.**—When 2,5,2',5'-tetrachlorobiphenyl (TCB) was electrochemically oxidized in 2.5% aqueous MeCN be-

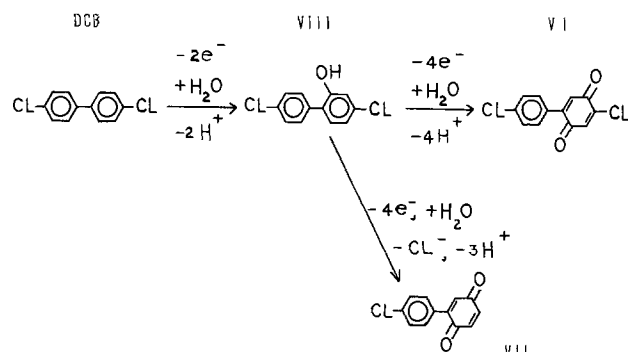


Fig. 2. General electrochemical oxidation scheme of 4,4'-dichlorobiphenyl in 2.5% acetonitrile at +1.9 to +2.1V vs. SCE on a platinum electrode.

tween +2.0 to +2.7V vs. SCE on a platinum electrode with  $\text{Et}_4\text{NBF}_4$  and  $\text{AgClO}_4$  added, the major electrolysis products isolated were: 2,5-dichloro-3-(2,5-dichlorophenyl)-1,4-benzoquinone (IX) in 13-17% yield, bis-2,5-dichloro-1,4-benzoquinone (X) in 4% yield, 2-chloro-3-(2,5-dichlorophenyl)-1,4-benzoquinone (XI) in 2% yield, 2-chloro-6-(2,5-dichlorophenyl)-1,4-benzoquinone (XII) in 2% yield, and 3-hydroxy-2,5,2',5'-tetrachlorobiphenyl (XIII) in from 1 to 6% yield. Figure 3 shows the general electrochemical oxidation scheme of 2,5,2',5'-tetrachlorobiphenyl. [Gardner has shown that the 3-hydroxy- and the 4-hydroxy-2,5,2',5'-tetrachlorobiphenyl are the metabolic products from the rabbits (9).]

### Discussion

The formation of *p*-quinones as the major electrolysis products from the electrolytic oxidation of aromatic hydrocarbons is well known. The quinones can be shown to be formed by further oxidation of their hydroxy intermediates. Several studies on the oxidation of phenols confirm this pathway (28-31). In this present study, the isolation of the hydroxychlorobiphenyls (VIII) and (XIII) constitute strong evidence for the general electrochemical oxidation schemes of 4,4'-dichlorobiphenyl and 2,5,2',5'-tetrachlorobiphenyl shown in Fig. 2 and 3. As seen by the voltammetric half-peak potentials in Table III, hydroxychlorobiphenyls are oxidized about 1.0V less anodic than the chlorobiphenyls and would be further electrochemically oxidized at the controlled potentials employed to oxidize the PCB's. Thus the isolation of hydroxychlorobiphenyls in exhaustive electrolyses is quite fortuitous.

In the single-pass flow-through cell, wherein the initial hydroxylated product is more effectively flushed and kept-away from the working electrode, higher yields (up to 10%) of the hydroxychlorobiphenyl was obtained. In the case of the 2,5,2',5'-tetrachlorobiphenyl about 80% of this PCB was recovered and could be recycled through the flow cell. Although the yields may not appear to be impressive, the ability to be able to prepare in a short time the hydroxy-adducts of such slow-to-degrade chemicals warrants more use of flow-through cells in small scale electroorganic synthesis.

As a result of product isolation and the cyclic voltammetric data, a general ECE oxidation scheme appears most reasonable for the electrochemical oxidation of 4,4'-dichlorobiphenyl and 2,5,2',5'-tetrachlorobiphenyl in aqueous MeCN solution. Thus an initial two-electron oxidation followed by hydrolysis would result in the formation of a hydroxychlorobiphenyl (a chlorophenyl phenol). At the controlled working electrode potential, the hydroxychlorobiphenyl would be rapidly further oxidized to the corresponding *p*-benzoquinone. The identification of various benzoquinones and the appearance of numerous minor electrolysis products, seen on the thin-layer chromatographic plate,

attest to the complexity of the electrochemical oxidation processes. Elimination of the chloro group, as measured by the weight of AgCl precipitate collected from the anode compartment, occurred to a variable extent.

While most biologically significant hydroxylations involve the reaction with molecular oxygen (32), with oxygen-transition metal complexes (33), or with hydroxyl or perhydroxyl radicals (34), nucleophilic addition of water to electron deficient centers cannot be excluded and, in fact, has been proven by showing that the  $\text{O}^{18}$  labeled water is added in an enzyme hydroxylation reaction to nicotinic acid (35). The "awkward hydroxylation of aromatic rings" (34) induced by enzymatic, photochemical, and now electrochemical methods is an important oxidative degradation route of environmentally persistent chemicals. But, it must be emphasized that the high anodic pathways used in this present study of the electrochemical oxidation of PCB isomers, are no doubt different than the enzyme-assisted, natural degradation route of these same chemicals.

### Acknowledgment

Financial support was provided by the National Institutes of Health Research Grant No. ES-01056 from the Environmental Health Science Group. Initial support by the University of Connecticut Research Foundation is gratefully acknowledged. Financial support for the mass spectrometer was made available through N.S.F. Grant No. GP-18332. We acknowledge the contribution of J. L. Wolk and A. Merrick for the organic synthesis; E. F. Knight for the semipreparative, liquid chromatographic separation. The authors wish to thank Drs. F. A. Beland, M. Bolgar, F. E. Guthrie, O. Hutzinger, J. D. McKinney, and I. H. Pomerantz for their valuable and timely suggestions, also J. F. Bagli, E. H. Blair, M. Bolgar, A. M. Gardner, O. Hutzinger, and W. B. Papageorge for providing authentic samples. A portion of this work was presented at the National Meeting of the American Chemical Society, New York, August 29, 1972.

Manuscript submitted May 6, 1976; revised manuscript received June 21, 1976. This was Paper 175 presented at the Chicago, Illinois, Meeting of the Society, May 13-18, 1973.

Any discussion of this paper will appear in a Discussion Section to be published in the June 1977 JOURNAL. All discussions for the June 1977 Discussion Section should be submitted by Feb. 1, 1977.

Publication costs of this article were assisted by the University of Connecticut.

### REFERENCES

- O. Hutzinger, S. Safe, and V. Zitko, "The Chemistry of PCB's," CRC Press, Cleveland, Ohio (1974).
- N. Nelson, *Environ. Res.*, **5**, 253 (1972).
- "Polychlorinated Biphenyls and the Environment," Interdepartmental Task Force on PCBs, COM-72-10419, National Technical Information Service, U.S. Department of Commerce, Springfield, Va. (1972).
- Anonymous, *Chem. Eng. News*, p. 10 (July 16, 1973).
- M. G. Broadhurst, *Environ. Health Persp.*, **2**, 81 (1972).
- G. Umeda, *Ambio*, **1**, 132 (1972).
- J. G. Vos, *Environ. Health Persp.*, **1**, 105 (1972) and references therein.
- D. Firestone, J. Ress, N. L. Brown, R. P. Barron, and J. N. Damico, *J. Assoc. Off. Anal. Chem.*, **55**, 85 (1972).
- A. M. Gardner, J. T. Chen, J. A. G. Roach, and E. P. Ragelis, *Biochem. Biophys. Res. Commun.*, **55**, 1377 (1973).
- O. Hutzinger, S. Safe, and V. Zitko, *J. Assoc. Off. Anal. Chem.*, **57**, 1061 (1974).
- S. O. Farwell, F. A. Beland, and R. D. Geer, *Anal. Chem.*, **47**, 895 (1975).
- S. O. Farwell, F. A. Beland, and R. D. Geer, *J. Electroanal. Chem.*, **61**, 315 (1975).

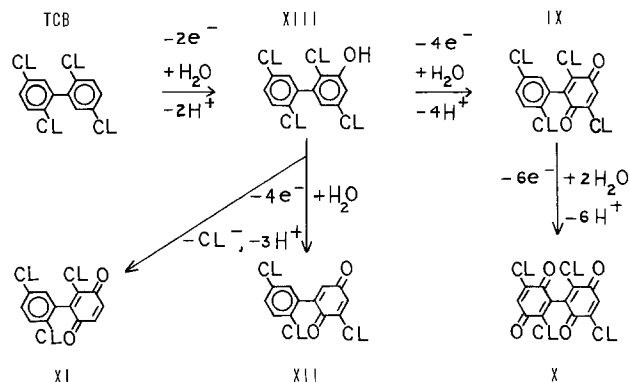


Fig. 3. General electrochemical oxidation scheme of 2,5,2',5'-tetrachlorobiphenyl in 2.5% aqueous acetonitrile at +2.0 to +2.7V vs. SCE on a platinum electrode.

13. O. Hutzinger, S. Safe, and V. Zitko, *Bull. Environ. Contam. Toxicol.*, **6**, 209 (1971).
14. R. J. Fenn, M. S. Thesis, University of Connecticut, Storrs (1973).
15. P. Brassard and P. L. L'Ecuyer, *Can. J. Chem.*, **39**, 1037 (1961).
16. J. F. Bagli, *J. Am. Chem. Soc.*, **84**, 177 (1962).
17. P. Brassard and P. L. L'Ecuyer, *Can. J. Chem.*, **36**, 700 (1958).
18. N. S. Moe, *Acta Chem. Scand.*, **19**, 1023 (1965).
19. L. C. Portis, J. C. Roberson, and C. K. Mann, *Anal. Chem.*, **44**, 294 (1972).
20. R. R. Keenan and J. D. Stuart, *This Journal*, **123**, 1637 (1976).
21. E. R. Brown, T. G. McCord, D. E. Smith, and D. D. DeFord, *Anal. Chem.*, **38**, 1119 (1966).
22. O. Hutzinger, W. D. Jamieson, J. D. MacNeil, and R. W. Frei, *J. Assoc. Off. Anal. Chem.*, **54**, 1100 (1971).
23. D. T. Williams and B. J. Blanchfield, *ibid.*, **55**, 93 (1972).
24. R. S. Nicholson and I. Shain, *Anal. Chem.*, **36**, 706 (1964).
25. R. S. Nicholson and I. Shain, *ibid.*, **37**, 178 (1965).
26. I. M. Kolthoff and J. F. Coetzee, *J. Am. Chem. Soc.*, **79**, 1852 (1957).
27. S. Safe, N. Platonow, and O. Hutzinger, *J. Agric. Food Chem.*, **23**, 259 (1975).
28. F. Fichter and E. Brunner, *Bull. Soc. Chim. Fr.*, **19**, 281 (1916).
29. N. L. Weinberg and H. R. Weinberg, *Chem. Rev.*, **68**, 486 (1968).
30. D. Hawley and R. N. Adams, *J. Electroanal. Chem.*, **8**, 163 (1964).
31. L. Papouchado, J. Bacon, and R. N. Adams, *ibid.*, **24**, App. 1-5 (1970).
32. G. Guroff, J. W. Daly, D. M. Jerina, J. Renson, B. Witkop, and S. Udenfriend, *Science*, **157**, 1524 (1967).
33. G. A. Hamilton, *Adv. Enzymol.*, **32**, 55 (1968).
34. R. L. Metcalf, in "The Enzymatic Oxidation of Toxicants," E. Hodgson, Editor, Chap. 7, Proceedings of a Conference held at North Carolina State University in 1967, available through Dr. F. E. Guthrie, Dept. of Entomology, North Carolina State Univ., Raleigh, N. C.
35. A. L. Hunt, D. E. Hughes, and H. M. Lowenstein, *Biochem. J.*, **66**, 2p (1957).

## Chronoamperometric Studies of Flash Photoemission at a Mercury Electrode

R. P. Baldwin<sup>1</sup> and S. P. Perone

*Department of Chemistry, Purdue University, West Lafayette, Indiana 47907*

### ABSTRACT

Flash irradiation and high speed potentiostatic monitoring have been utilized to study the electrochemical processes associated with the photoemission of electrons from a mercury electrode into various electrolyte solutions. Conditions in which no efficient hydrated electron scavenging species was present, as well as conditions employing  $10^{-3}M$  concentrations of  $NO_2^-$ ,  $H_3O^+$ ,  $NO_3^-$ , and acetophenone, were examined. The magnitudes of the resulting flash photocurrents and their variation with electrode potential agreed qualitatively with results obtained previously using continuous radiation or coulometric monitoring techniques. The temporal behavior of the currents showed that they were capacitive in nature, resulting from double layer recharging in response to the electron pulse caused by the extremely rapid electron emission and scavenging reactions. The charging current model appears valid for the wide variety of scavenging situations considered in this work.

The photoemission of electrons from a mercury electrode into a concentrated electrolyte solution, and the subsequent chemical and physical processes that accompany it, have in recent years been the subject of extensive experimental and theoretical investigations (1-6). The detailed succession of events which occurs upon electron emission has now been determined for a large number of chemical systems by means of a variety of experimental techniques. Specifically, the photoemission phenomenon has been shown to entail, sequentially, electron emission, thermalization, and hydration, followed by the competing processes of chemical scavenging and electrochemical oxidation.

In general, the instrumental approaches employed to generate large-scale photoemission and monitor the resulting events can be placed into one of two classifications. In the first, continuous or long-term electrode illumination is utilized to produce steady-state photocurrents (1,7-13). Measurements are made by mechanically chopping or electrically modulating the light source to provide both a photoemission and a reference signal, and monitoring the corresponding currents with a potentiostatic or polarographic system. Such methods are well suited for the observation of

the net currents associated with continuous electron emission, but are of little use for the direct study of transient photoemission processes.

The alternate experimental approach entails the use of a very short duration flash, or pulsed light, source to generate transient electron emission which can be followed directly to provide kinetic and mechanistic information (3, 14-17). Because of the large amount of noise pickup resulting from the flash discharge and the concomitant difficulties in maintaining adequate potential control at short times, potentiostatic chronoamperometric measurements have not been very useful previously. Rather, the monitoring of subsequent potential changes induced at the emitting electrode under coulometric conditions has been employed (3, 17). The difficulties inherent in the coulometric approach include the extremely low signal levels and the sometimes indirect nature of the measurements involved.

Thus, the development of high speed potentiostatic techniques suitable for the investigation of the photoemission process, and subsequent hydrated electron ( $e_{aq}^-$ ) chemistry, is certainly desirable. Furthermore, previous work in this laboratory has involved the photoelectrochemical study of rapid photolytic processes initiated by flash irradiation (18-21). Since these studies have entailed the potentiostatic monitoring of faradaic currents occurring at short times following the flash, an understanding of the direct effects of

<sup>1</sup>Present address: Department of Chemistry, University of Louisville, Louisville, Kentucky 40208.

Key words: photoelectrochemistry, photoemission, photopolarography.

photoemission in a potentiostatic system is imperative. Accordingly, the objectives of the work reported here were to develop flash photoelectrochemical instrumentation capable of observing photoemission currents potentiostatically, and to construct a working model capable of accounting for these observations in terms of the specific chemical and physical processes known to occur during and after the photoemission event. This required the optimization of the flash irradiation and potentiostatic monitoring systems and the analysis of photoemission results obtained experimentally under a wide range of chemical and electrochemical conditions.

### Experimental

**Flash radiation.**—The flash system employed was essentially the same as has been previously reported (21). The principal difference was that a spherical mirror was used in place of the linear parabolic reflector to permit more efficient collection and transmission of the flash irradiation to the hanging mercury drop electrode, as is shown in Fig. 1. Additional electromagnetic shielding was provided by enclosing the flash lamp, trigger circuit, and all the associated electronics in a separate, grounded faraday cage constructed from copper screening.

The lamp used was a Suntron-6C xenon flash lamp (Xenon Corporation, Medford, Massachusetts). It is a high intensity, fast-extinguishing micropulse flashtube capable of dissipating a maximum energy of 100j with a pulse duration of approximately 10  $\mu$ sec. The capacitor bank discharged during the flash consisted of a total of 4  $\mu$ f charged to a limit of 7000V (LK100-405YND, Plastic Capacitors, Incorporated, Chicago). Since it was especially important to know with certainty the precise flash shape and duration associated with this specific setup, the flash output was monitored directly with a Raytheon 929 vacuum photodiode; the results indicated that the flash possessed a width at half-maximum of 8  $\mu$ sec and exhibited no significant tailing effects.

A further factor often complicating the study of faradaic photocurrents due to electron emission is the occurrence of nonfaradaic currents caused by the irradiation of the electrode/solution interface and related to changes in interfacial temperature and consequent structural changes of the electrical double layer (22). Therefore, it was normally found useful to remove all high wavelength radiation from the flash output and allow only the lower wavelength components to reach the electrochemical cell. Accordingly, a u.v.-transmitting, visible-absorbing Corning 7-54 glass filter was routinely inserted into the flash path to prevent transmission of light of wavelengths longer than 410 nm. This precaution served to attenuate the so-called "thermal" photocurrents (22) to a degree, but did not eliminate them entirely.

**Instrumentation.**—The cell, electrodes, potentiostat, and general operating procedures were all similar to

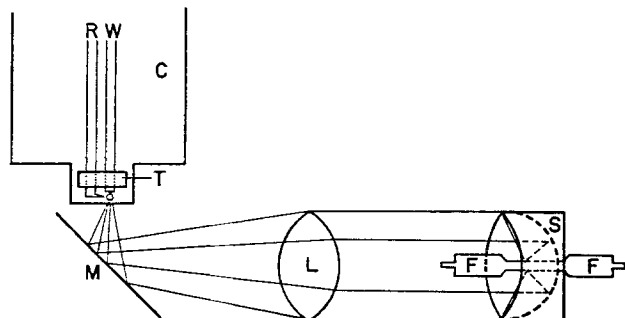


Fig. 1. Flash optics. R, Reference electrode probe; W, working electrode (HMDE); C, electrochemical cell; T, Teflon electrode positioner; M, reflecting mirror; L, quartz lens; S, spherical reflector; F, xenon flash lamp.

those described earlier (21). All experimental current-time measurements were made using a Hewlett-Packard (Palo Alto, California) Model 141A oscilloscope with a Model 1421A time-base generator and a Model 1402 dual-trace amplifier. Oscilloscope traces were recorded on a Hewlett-Packard Model 197A Polaroid camera. Oscilloscope triggering was synchronized with the initiation of the flash by means of a photo-transistor (PT-100, Fairchild Semiconductor, Mountain View, California) to ensure that the initial times for all measurements corresponded to the beginning of the flash itself.

A typical example of a constant potential chronoamperometric photoemission experiment is shown in Fig. 2. Each experiment consisted of two separate runs: a "blank" or noise run generated by placing an opaque shutter between the flash lamp and the emitting electrode, and a "flash" trace generated by removing the shutter and allowing photoemission to occur. Any current present in the blank trace corresponded only to flash-induced noise, while the flash signal contained the same noise effects superimposed on the photoemission-related currents. Consequently, it was the difference between the flash and blank traces that was used as a measure of the photoemission current of interest. Because of the finite width of the flash and the substantial amount of rf noise pickup still present upon flash discharge, transient current measurements were never considered at times earlier than 15  $\mu$ sec after the start of the flash.

**Reagents.**—All chemicals used were reagent grade. Water was deionized by passage through a mixed-bed ion-exchange column and doubly distilled. Solvent-saturated, deoxygenated high purity nitrogen was used to deaerate all solutions prior to irradiation and was allowed to flow continuously over the solution surface during all experimentation.

### Results and Discussion

**General.**—The over-all sequence of events known to occur upon electron photoemission is summarized in Fig. 3. When light of sufficiently low wavelength is incident on a mercury surface that is held at a suitably cathodic potential, electrons are emitted and undergo very rapid thermalization and hydration.<sup>2</sup> Once hydrated, the electrons are free either to react chemically with any electron-accepting scavenger (S) present in

<sup>2</sup> The occurrence of "dry" (nonhydrated) electron reactions is a possibility which may be significant at high scavenger concentrations (>1 mole/liter). In the experiments described here, the scavenger concentration never exceeded  $10^{-3}M$ ; hence all electrons are considered to undergo hydration prior to any scavenging or return to the electrode.

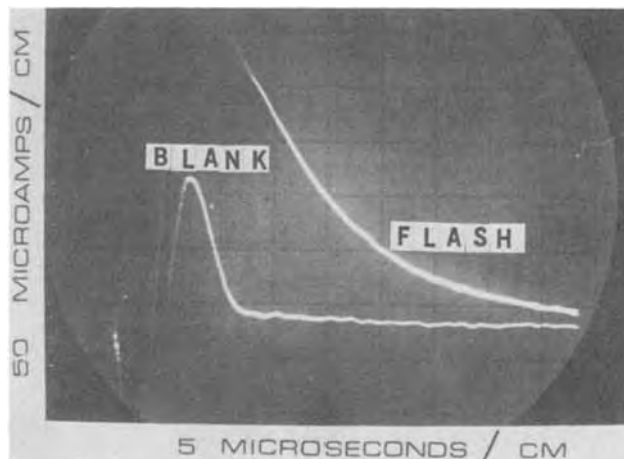


Fig. 2. Continuous potentiostatic analysis following flash irradiation. Analysis of  $\text{NaNO}_2$  solution ( $1.0 \times 10^{-3}M$ ,  $1.0M$  KCl) at  $-1.700V$  vs. SCE. Upper trace corresponds to flash current observed with irradiation, and the lower trace illustrates the blank signal with flash, shutter closed.

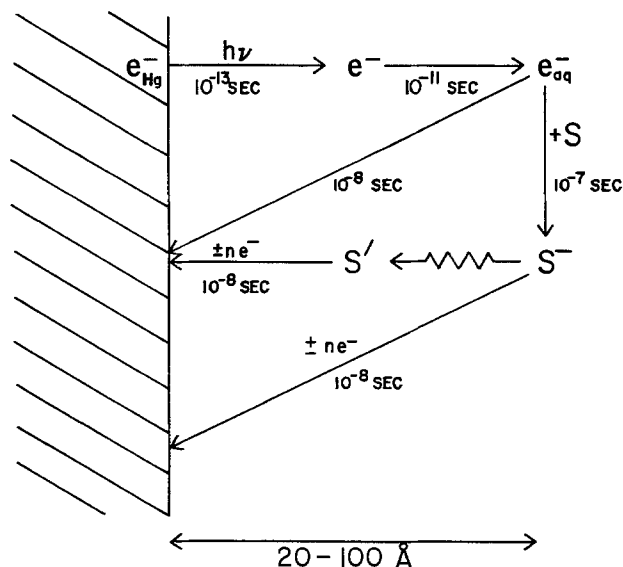


Fig. 3. Processes occurring upon electron photoemission

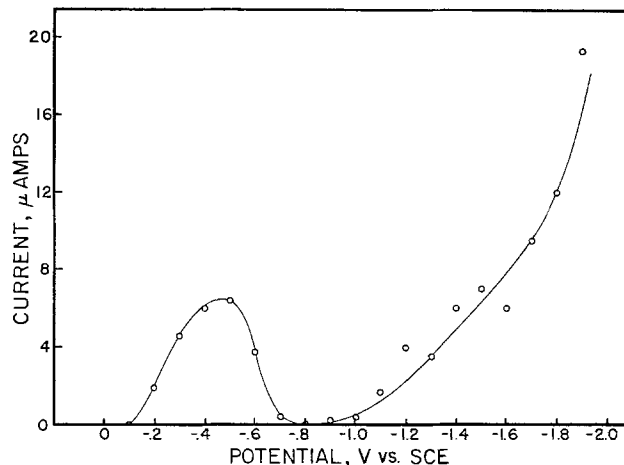
solution near the electrode surface or to diffuse back to the electrode surface and return through an electrochemical oxidation process. Similarly, the primary scavenging product ( $S^-$ ) may undergo further chemical reaction or may participate, along with any secondary scavenging products ( $S'$ ), in possible redox processes at the electrode. All of these phenomena take place in solution either at or very near the mercury surface and occur at relatively rapid rates compared to the time scale of the flash and the time-constant of the electrochemical cell.

The net effect of all of these phenomena depends heavily on the presence or absence of an efficient scavenging species in solution, its scavenging rate constant, its concentration, and the identity and stability of its primary and secondary scavenging products. When no adequate hydrated electron-accepting species is present, or when the scavenging products are themselves oxidizable, nearly all of the photoemitted electrons ultimately return to the electrode; and there is very little net electron loss. But when scavengers which form products that can be electrochemically reduced are present, there is a net loss of at least two electrons for every one that is emitted and scavenged. Furthermore, the temporal characteristics observed for the photoemission processes are directly dependent on the rates of formation and decay of the scavenging products involved. Accordingly, the experimental approach taken in this work consisted principally of observing and interpreting the photoemission currents resulting from the presence of a number of different scavengers and scavenging conditions.

Fortunately, the products and mechanisms of several scavenging species have previously been determined (23). A list of the scavengers employed in this work and some of their relevant characteristics is provided in Table I. Each scavenger and the flash photocurrents observed with each will be discussed in turn.

Table I. Characteristics of important hydrated electron scavengers

Scavenger	$k_{e^-_{aq}}$ ( $M^{-1} \text{ sec}^{-1}$ )	Products	Product electroactive?
Electrolyte	$< 10^{10}$		
$\text{NO}_2^-$	$4.6 \times 10^9$	NO	Yes; reducible ( $n = 1$ )
$\text{H}_3\text{O}^+$	$2.2 \times 10^{10}$	H	Yes; reducible ( $n = 1$ )
$\text{NO}_3^-$	$8.5 \times 10^9$	$\text{NO}_2$ , OH	Yes; reducible ( $n = 1$ )
Acetophenone	$10^9 - 10^{10}$	$\text{CH}_3-\overset{\text{O}}{\parallel}{\text{C}}-\text{C}_6\text{H}_5$	Yes; oxidizable ( $n = 1$ )

Fig. 4. Current-voltage profile from continuous potentiostatic analysis. 1.0M KCl solution. Currents represent values measured at 15  $\mu\text{sec}$  after initiation of the flash.

*No scavenger.*—The simplest and most straightforward photoemission scheme occurs, of course, when no efficient hydrated electron scavenger is present and the solution contains only "inert" electrolyte (such as KCl, NaCl, or  $\text{Na}_2\text{SO}_4$ ). In such situations, no scavenging should take place; and all or most of the electrons emitted should return to the electrode via an electrochemical oxidation step.

When such solutions were flashed, only very small photocurrents were observed experimentally. These currents were cathodic in direction, indicating a net loss of electrons from the hanging mercury drop electrode. Furthermore, their magnitude was found to be dependent on the electrode potential, with the observed currents becoming gradually larger at increasingly cathodic potentials.<sup>3</sup> A corresponding current-voltage profile is shown in Fig. 4.

This behavior is all well accounted for on the basis of the photoemission model described thus far. Since most of the electrons, once photoemitted, are thought to return immediately to the electrode, the net currents expected should be relatively small in magnitude. The fact that even a small number of electrons do indeed fail to return can be explained by the possible slow reaction of  $e_{aq}^-$  with a trace electron-scavenging impurity, with the electrolyte species, with water molecules, or perhaps with another  $e_{aq}^-$  (1, 17). In addition, the observed potential dependence is analogous to that previously noted for photoemission phenomena in both flash and continuous radiation experiments (4, 5), and is due to the lowered work function and, therefore, higher probability for electron emission at higher cathodic potentials.

*Scavengers present.—Nitrite and hydrogen ions.*—Both  $\text{NO}_2^-$  and  $\text{H}_3\text{O}^+$  have two important scavenging properties that allow them to be grouped together: They both react with  $e_{aq}^-$  at nearly diffusion-controlled rates, and on reaction they both rapidly form products that undergo a diffusion-controlled one-electron reduction process within the relevant potential range. Upon scavenging,  $\text{NO}_2^-$  rapidly decomposes ( $t_{1/2} < 2 \mu\text{sec}$ ) to yield NO, which is known to be reduced at potentials more cathodic than  $-1.1\text{V vs. SCE}$  (24). Similarly, the immediate scavenging product of  $\text{H}_3\text{O}^+$  is thought to be the hydrogen atom which itself is reduced more cathodic than  $-0.8\text{V vs. SCE}$  (11).

When solutions containing these ions were flashed, extremely large cathodic currents were observed (as shown in Fig. 2). The potential dependences, however, were approximately the same as that previously ob-

<sup>3</sup> The photocurrents referred to here are those occurring at potentials more negative than  $-0.8\text{V}$ . The small cathodic currents occurring between  $-0.1$  and  $-0.7\text{V}$  correspond to the "thermal" currents referred to earlier. They do not appear to be related to photoemission at all (22).

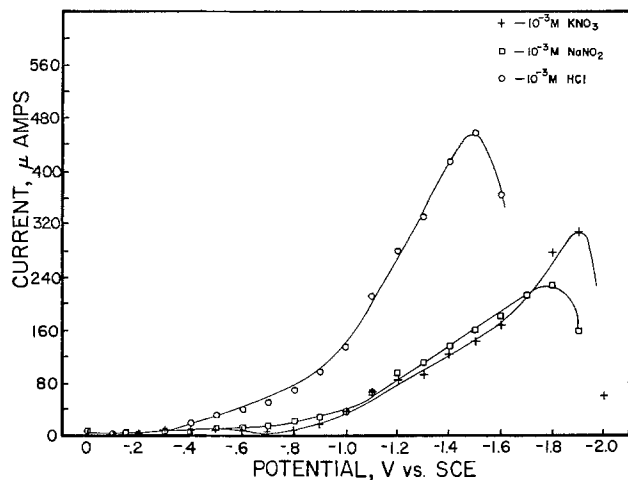


Fig. 5. Current-voltage profiles from continuous potentiostatic analysis.  $1.0 \times 10^{-3}M$  solutions of various scavengers (1.0M KCl). Currents represent values measured at 15  $\mu$ sec after initiation of the flash.

served with no scavenger in solution, as can be seen from the current-voltage profiles represented in Fig. 5.

The most interesting and unexpected property of the  $\text{NO}_2^-$  and  $\text{H}_3\text{O}^+$  photocurrents was their similar time dependence. Upon observing lifetimes and decay rates of the currents generated for both scavengers under a wide range of solution conditions, it became apparent that their temporal behavior was determined directly by the magnitude of the electrochemical cell time-constant ( $\tau$ ) prevailing for the particular experimental conditions. At low cell time-constant values, the photocurrents were short-lived; but as  $\tau$  was lengthened, the photocurrent lifetimes increased accordingly. Similar results were obtained independently of the method used to control the value of  $\tau$ . It was of no consequence whether  $\tau$  was manipulated chemically, by changing the electrolyte concentration, or electronically, by externally increasing the magnitude of the uncompensated resistance.

Such cell time-constant time dependence represents behavior that is typically characteristic of the charging current generated in routine potential-step experiments. In fact, the customary method employed in the determination of  $\tau$  values consists of applying a small amplitude potential step to the potentiostat input, measuring the subsequent charging current that flows, and plotting the logarithm of that current as a function of time. The resulting plot should be linear, and the reciprocal of its slope is related to the value of the cell time-constant. Such a cell time-constant plot of current resulting from the input of a 20 mV potential step to a nitrite-containing solution is shown in Fig. 6. When the same log plot was made of the photoemission current that occurred upon flashing an identical  $\text{NO}_2^-$  solution under constant potential conditions, a nearly identical graph was obtained. The plot was linear; and, when a "photocurrent time-constant" ( $S$ ) was calculated from the reciprocal of its slope, a value extremely close to  $\tau$  was obtained. Such a plot is also shown in Fig. 6.

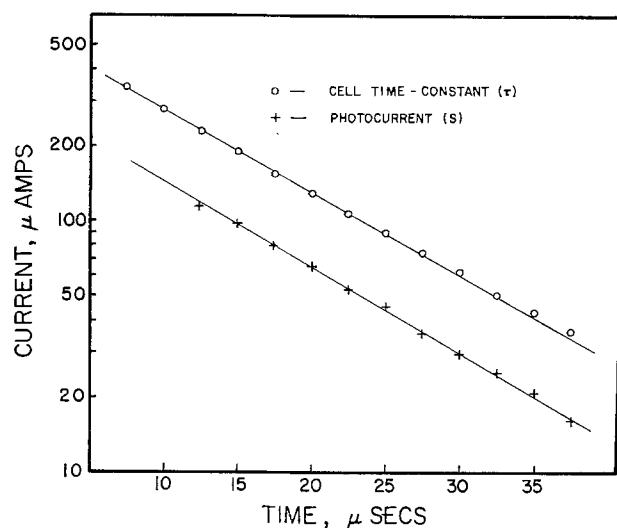


Fig. 6. Log current vs. time plots for both potential step and photoemission currents.  $1.0 \times 10^{-3}M$   $\text{NaNO}_2$  solution (1.0M KCl) at  $-1.700V$  vs. SCE. The upper trace represents the charging current resulting from a 20 mV potential step input, and the lower trace corresponds to the flash photocurrent resulting under constant potential conditions.

Similar plots were made at several potentials for  $\text{NO}_2^-$  and  $\text{H}_3\text{O}^+$  solutions containing electrolyte concentrations ranging from 1.0M to 0.01M and proved to be linear in every case. Further, the  $S$  values, reflecting the photocurrent lifetime calculated from log plots, without exception conformed closely to the  $\tau$  values measured for the identical solution under identical instrumental conditions. These results are summarized in Table II. Furthermore, linear log plots and clear correlation of  $S$  and  $\tau$  values were also found when the uncompensated resistance, and hence the cell time-constant, was artificially increased by inserting an external resistance between the working electrode and ground. For example, when an external resistance of  $66.5\Omega$  was employed, values of 39.9 and 40.2  $\mu$ sec were determined for  $\tau$  and  $S$ , respectively.

To all outward appearances, then, the photoemission currents monitored at constant potential following flash irradiation behaved as the classical charging currents that are generated routinely in potential-step experiments. The most convenient explanation is that the observed "photocurrents" themselves are primarily charging currents. There is no other apparent reason for them to decay according to an exponential time dependence in such close conformity to the prevailing cell time-constants. The key to explaining how the sequence of photoemission processes, known to occur as described in Fig. 3, is translated into charging current lies in the rapid rates at which the processes take place. When  $\text{NO}_2^-$  or  $\text{H}_3\text{O}^+$  solutions are flashed, electron emission, scavenging, and scavenging product reduction all occur within a time span of less than 2  $\mu$ sec, certainly at a much faster rate than the instrument can respond, even with a cell time-constant of 10  $\mu$ sec. As a result, all the photoemission and subsequent events are virtually coincident with the flash

Table II. Photocurrent and cell time-constant correlation

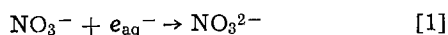
	1.0M KCl				0.2M KCl				0.01M KCl			
	-1400 mV		-1700 mV		-1400 mV		-1700 mV		-1400 mV		-1700 mV	
10 <sup>-3</sup> M NaNO <sub>2</sub>	$\tau$	$S$	$\tau$	$S$	$\tau$	$S$	$\tau$	$S$	$\tau$	$S$	$\tau$	$S$
	10.5	11.5	10.7	10.8	37.4	32.2	40.8	36.0	555	518	575	569
	-900 mV		-1400 mV		-900 mV		-1400 mV		-900 mV		-1200 mV	
10 <sup>-3</sup> M HCl	$\tau$	$S$	$\tau$	$S$	$\tau$	$S$	$\tau$	$S$	$\tau$	$S$	$\tau$	$S$
	5.8	6.9	8.1	7.2	23.1	24.2	26.1	20.8	114	104	138	117

$\tau$  and  $S$  values are in units of microseconds.

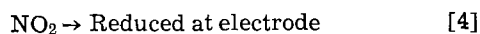
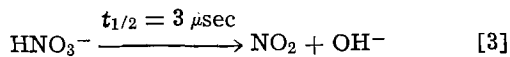
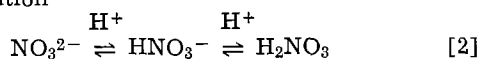
and have the net effect of depositing a large number of electrons into solution at the electrode surface. The immediate effect on the cell of such an "instantaneous" charge pulse is a rapid discharge of the double layer. The subsequent double layer recharging, provided by the potentiostat and limited by the cell time-constant, actually constitutes the long term "photocurrent" observed experimentally.

According to this model, the currents that we have termed photoemission currents (since they have their origin in actual photoemission processes) are capacitive in nature; and the time dependence that such photoemission currents are expected to exhibit should be close to that determined by the cell time-constant. Thus, the fact that several  $S$  values listed in Table II, especially those for  $\text{H}_3\text{O}^+$  and those measured at the lower electrolyte concentrations, are somewhat faster than the corresponding values of  $\tau$  calls for explanation. A possible rationalization is that the  $\tau$  values measured under nonflash conditions (as explained earlier) may not accurately reflect the actual cell time-constant that exists during and shortly after the flash, while photoemission and scavenging are taking place. Conceivably, the deposition of a large number of electrons near the electrode surface and the subsequent processes that occur cause a temporary variation in either the uncompensated solution resistance or in the capacitance of the double layer. Such an explanation is supported, qualitatively at least, by the following experimental observations: the discrepancies between  $S$  and  $\tau$  seem to be less significant at higher electrolyte concentrations, where the scavenging species itself plays only a minor role in determining  $\tau$ ; the discrepancies are more significant for  $\text{H}_3\text{O}^+$ , where its special mobility and conductivity allow it to play a larger role in determining  $\tau$ ; and there are no discrepancies in cases where an external resistance is employed to fix  $\tau$  artificially.

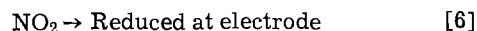
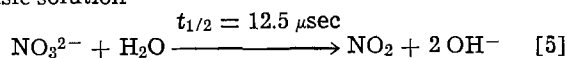
**Nitrate ion.**—The  $\text{NO}_3^-$  ion is similar to  $\text{NO}_2^-$  and  $\text{H}_3\text{O}^+$  in that it too is a nearly diffusion-controlled hydrated electron scavenger and that the final product of its scavenging also can undergo reduction throughout the appropriate potential range. The specific mechanism by which  $\text{NO}_3^-$  scavenging takes place has been clarified recently by Grätzel *et al.* (25) using pulse radiolytic techniques, and is summarized by the following series of reactions



In acidic solution



In basic solution



The most interesting features of this mechanism are its pH dependence and the differing time dependences of its two possible pathways. In acidic solution, the rapid protonation reaction [2] allows the final reducible scavenging product  $\text{NO}_2$  to be formed at a rate ( $t_{1/2} = 3 \mu\text{sec}$ ) that is relatively fast compared to the prevailing flash width and cell time-constant of 10–15  $\mu\text{sec}$ . As a result, the photoemission currents and their lifetimes observed for an acidic  $\text{NO}_3^-$  solution should be completely analogous to those previously observed with  $\text{NO}_2^-$  and  $\text{H}_3\text{O}^+$ . However, under alkaline conditions where reaction [2] is inhibited,  $\text{NO}_2$  can only be formed directly from the unprotonated  $\text{NO}_3^{2-}$  species at a slower rate ( $t_{1/2} = 12.5 \mu\text{sec}$ ) that is comparable to a cell time-constant of 10  $\mu\text{sec}$ . Ac-

Table III.  $\text{NO}_3^-$  pH dependence

pH	$\tau$	$S$	$S - \tau$
4.40	12.3	12.1	-0.2
6.09	11.1	10.8	-0.3
6.62	12.7	11.8	-0.9
7.11	11.9	12.0	+0.1
7.80	11.8	12.6	+0.8
8.72	11.4	13.0	+1.6
9.58	11.5	15.3	+3.8

$\tau$  and  $S$  values are in units of microseconds. Solution contained  $10^{-3}\text{M}$   $\text{KNO}_3$ ,  $7 \times 10^{-3}\text{M}$   $\text{KH}_2\text{PO}_4$ , 1.0M  $\text{KCl}$ , and  $\text{NaOH}$ .

cordingly, by utilizing basic conditions, the rate of  $\text{NO}_2$  formation, and hence of electron discharge into the double layer, should be decreased, perhaps sufficiently to affect directly the time dependence of the observed photoemission current.

When solutions containing  $\text{NO}_3^-$  were flashed, large cathodic currents possessing the expected photoemission potential dependence were obtained regardless of solution pH. A current-voltage profile so obtained is shown in Fig. 5.

In order to observe the temporal behavior of the nitrate photocurrents as a function of pH and duplicate Grätzel's experiments (25) as faithfully as possible, solutions containing  $10^{-3}\text{M}$   $\text{KNO}_3$ , 1.0M  $\text{KCl}$ , and  $7 \times 10^{-3}\text{M}$   $\text{KH}_2\text{PO}_4$  were adjusted to the desired pH by the addition of  $\text{NaOH}$ . The photoemission currents generated upon flashing were analyzed by means of log current *vs.* time plots, and the corresponding  $S$  and  $\tau$  values were calculated. Table III shows the results obtained for a series of solutions ranging in pH from 4.40 to 9.58.

At low pH values, there was excellent agreement between the cell time-constants and photocurrent time-constants measured for each solution. As the pH was gradually increased and made alkaline, however, the time dependence of the photoemission currents, as reflected in the  $S$  values, increased correspondingly and no longer seemed to be governed solely by the cell time-constant. This behavior is exactly as should be predicted on the basis of the  $\text{NO}_3^-$  scavenging mechanism: Under acidic conditions, where the scavenging products are formed rapidly, the photoemission currents are fundamentally charging currents and are entirely dependent on the cell time-constant, while in basic solution, where the secondary scavenging reactions are slower, the photoemission currents decay more slowly than would be predicted by the cell time-constant alone.

The same data is illustrated graphically in Fig. 7 along with Grätzel's estimates for the  $t_{1/2}$  of the  $\text{NO}_3^{2-}$

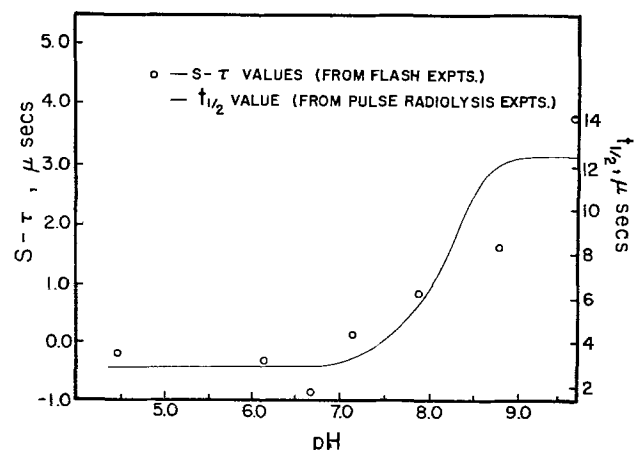


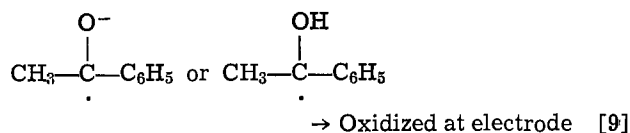
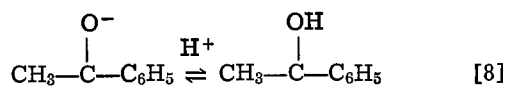
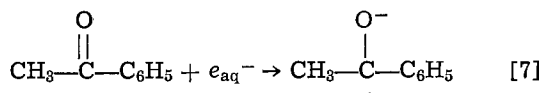
Fig. 7. Temporal behavior of  $\text{NO}_3^-$  photocurrent as a function of pH at  $E = -1.4\text{V}$  vs. SCE. The solid line represents the pH dependence of  $t_{1/2}$  for the decay of  $\text{NO}_3^{2-}$  as determined by Grätzel *et al.* (25). The circles correspond to  $(S - \tau)$  values calculated directly from flash experiments (Table III).



species. The quantity used as indication of the photoemission current lifetime is the difference ( $S - \tau$ ) between the measured photocurrent and cell time-constant. This quantity should reflect, qualitatively at least, the increasing half-life for the production of  $\text{NO}_2$  at higher pH values. The general agreement between the two methods is evident.

**Acetophenone.**—In general, the aromatic ketones represent a class of compounds that are known to be nearly diffusion-controlled  $e_{\text{aq}}^-$  scavengers (23). Their immediate scavenging product is a ketyl radical anion which, depending on the pH, may be in equilibrium with the corresponding ketyl radical (23, 26-28). Furthermore, the radicals and radical anions so produced are usually subject to a rapid one-electron oxidation throughout a wide potential range (29).

For acetophenone in particular, the scavenging mechanism can be summarized as follows



The most important feature of this sequence consists of the fact that every electron that is emitted and scavenged by acetophenone is ultimately returned to the electrode by means of the oxidation of the scavenging product. Hence, even though large-scale photoemission and scavenging should occur, there will be no net electron loss by the electrode.

Experimental observations made of the photoemission currents associated with acetophenone scavenging were complicated by two unavoidable factors. First of all, acetophenone (similarly to other aromatic ketones) absorbs ultraviolet and visible radiation of wavelengths less than 360 nm and undergoes photolysis (30). The products of the photolysis are the same ketyl radicals and radical anions produced by  $e_{\text{aq}}^-$  scavenging and are likewise readily oxidized electrochemically. Thus, any photoemission currents present are bound to be superimposed on a background of anodic photolysis current. Secondly, in the ethanol-water solvent system chosen for use with acetophenone, the value of the cell time-constant was found to be extremely potential dependent, increasing rapidly in magnitude in the range from  $-1.0$  to  $-1.6$  V vs. SCE as is shown in Fig. 8. For the interpretation of current-time and current-voltage information, such changes must certainly be taken into consideration.

The current-voltage profiles obtained when 1.0M KCl ethanol-water solutions, with and without  $10^{-3}$ M acetophenone, were flashed are shown in Fig. 9. For the background solution containing no  $e_{\text{aq}}^-$  scavenger, the behavior was similar to that observed earlier in non-ethanolic solutions containing no scavenging species (Fig. 4). The apparently distorted potential dependence exhibited between  $-1.2$  and  $-1.6$  V occurs in the same region where the cell time-constant most rapidly changes value. Because each point on the current-voltage profile corresponds to measurements made at the same point in time, and because the drastically slower cell response at more negative potentials results in a more drawn-out current-time curve, the measured currents are larger at the less negative potentials.

The current-voltage profile that was obtained when acetophenone was present differed from the back-

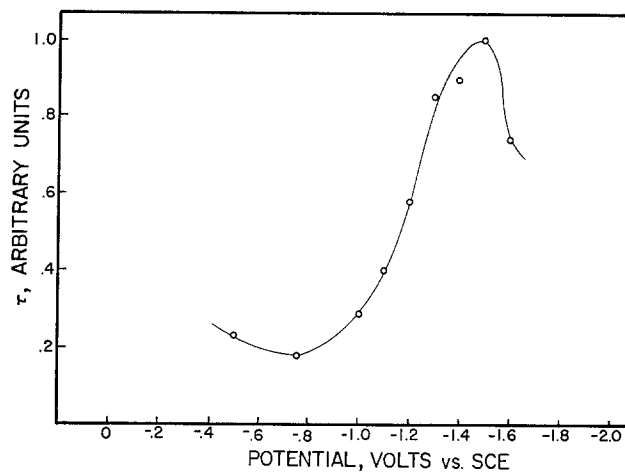


Fig. 8. Cell time-constant variation with potential for 1.0M KCl, 30% ethanol-water solution. Absolute  $\tau$  values measured for this system typically range from approximately  $5 \mu\text{sec}$  ( $E = -0.75$  V) to  $30 \mu\text{sec}$  ( $E = -1.5$  V).

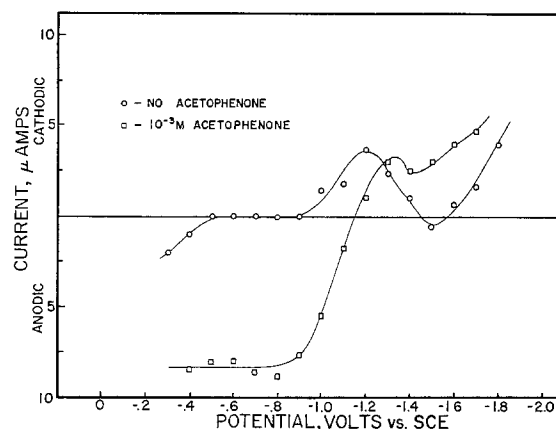


Fig. 9. Current-voltage profile from continuous potentiostatic analysis. With and without acetophenone in 1.0M KCl, 30% ethanol-water solution. Currents represent values measured at  $15 \mu\text{sec}$  after initiation of the flash.

ground profile by the addition of anodic photolysis current due to the oxidation of acetophenone ketyl radical species formed photochemically. The photolysis current gradually declined at the more negative potentials where acetophenone itself is reduced, and the profile resembled the background. When the variation of cell time-constant with potential was taken into account, the only major discrepancy between the photocurrents observed with and without acetophenone was the presence of the expected photolysis currents.

Thus, no noticeable contribution to the measured currents due to the photoemission process was detected, despite the presence of an excellent  $e_{\text{aq}}^-$  scavenger. In fact, no photocurrents even remotely comparable in magnitude to those seen with the previously studied scavengers were in evidence with acetophenone at any potential. (In contrast, the photoemission current observed, under identical conditions, for the analogous  $\text{NO}_2^-$ -containing ethanol-water solution was in excess of  $30 \mu\text{A}$  at  $E = -1.4$  V.) The absence of any comparable currents with acetophenone can only be due to the fact that, even though a large number of electrons are still photoemitted and scavenged, they are all returned to the electrode by the virtually instantaneous oxidation of the scavenger product; otherwise, the occurrence of some large-scale current (either anodic, cathodic, or mixed) would *a priori* be required. This fact allows meaningful electrochemical measurement of acetophenone photolysis occurring in solution and supports the validity of previous flash photoelectro-



chemical studies of aromatic ketones (18, 19, 21, 31, 32).

### Conclusions

Through the use of flash irradiation and high speed potentiostatic monitoring, currents clearly related to electron photoemission have been observed. Although the expected dependences on electrode potential and scavenger presence were obtained, the time dependence of the observed flash photocurrents was found to be governed primarily by the prevailing electrochemical cell time-constant to such a large degree that they can only be explained as capacitive charging currents in response to a virtually instantaneous flash-induced electron injection into the double layer.

The charging current model for the photoemission-initiated currents, and the experimental results on which it is based, are consistent with the known chemical and physical processes that actually occur for a wide range of scavenging situations. Furthermore, for certain specialized cases (e.g.,  $\text{NO}_3^-$ ) in which the secondary scavenging reactions proceed sufficiently slowly, the time dependence of flash photocurrents can be related directly to the reaction rates of scavenging intermediates. In these cases, useful chemical information concerning  $e_{\text{aq}}^-$  chemistry and scavenging reactions can be obtained.

### Acknowledgment

This work was supported by Public Health Service Grant No. CA-07773 from the National Cancer Institute and the National Science Foundation.

Manuscript received Aug. 29, 1975. This was Paper 350 presented at the Toronto, Canada, Meeting of the Society, May 11-16, 1975.

Any discussion of this paper will appear in a Discussion Section to be published in the June 1977 JOURNAL. All discussions for the June 1977 Discussion Section should be submitted by Feb. 1, 1977.

Publication costs of this article were assisted by Purdue University.

### REFERENCES

- G. C. Barker, A. W. Gardner, and D. C. Sammon, *This Journal*, **113**, 1182 (1966).
- A. M. Brodsky and Yu. Ya. Gurevich, *Electrochim. Acta*, **13**, 1245 (1968).
- G. C. Barker, *Ber. Bunsenges. Phys. Chem.*, **75**, 728 (1971).
- A. M. Brodsky and Yu. V. Pleskov, *Prog. Surf. Sci.*, **2**, 1 (1972).
- Yu. V. Pleskov and Z. A. Rotenberg, *Khim. Vys. Energ.*, **8**, 99 (1974).
- D. B. Mathews and S. U. M. Khan, *Aust. J. Chem.*, **28**, 253 (1975).
- G. C. Barker, *Electrochim. Acta*, **13**, 1221 (1968).
- Yu. V. Pleskov and Z. A. Rotenberg, *J. Electroanal. Chem.*, **20**, 1 (1969).
- R. de Levie and J. C. Kreuser, *ibid.*, **21**, 221 (1969).
- G. Bomchil, D. J. Schiffrin, and J. T. D'Alessio, *ibid.*, **25**, 107 (1970).
- Z. A. Rotenberg, V. I. Lakomov, and Yu. V. Pleskov, *ibid.*, **27**, 403 (1970).
- G. C. Barker and V. Concialini, *ibid.*, **45**, 320 (1973).
- V. Concialini, O. Tubertini, and G. C. Barker, *ibid.*, **57**, 413 (1974).
- P. Delahay and V. S. Srinivasan, *J. Phys. Chem.*, **70**, 420 (1966).
- V. P. Sharma, P. Delahay, G. G. Susbielles, and G. Tessari, *J. Electroanal. Chem.*, **16**, 285 (1968).
- G. C. Barker, G. Bottura, G. Cloke, A. W. Gardner, and M. J. Williams, *ibid.*, **50**, 323 (1974).
- G. C. Barker, B. Stringer, and M. J. Williams, *ibid.*, **51**, 305 (1974).
- J. R. Birk and S. P. Perone, *Anal. Chem.*, **40**, 496 (1968).
- H. E. Stapelfeldt and S. P. Perone, *ibid.*, **41**, 628 (1969).
- J. I. H. Patterson and S. P. Perone, *J. Phys. Chem.*, **77**, 2437 (1973).
- G. L. Kirschner and S. P. Perone, *Anal. Chem.*, **44**, 443 (1972).
- G. C. Barker and G. Cloke, *J. Electroanal. Chem.*, **52**, 468 (1974).
- E. J. Hart and M. Anbar, "The Hydrated Electron," Wiley-Interscience, New York (1970).
- G. C. Barker, P. Fowles, and B. Stringer, *Trans. Faraday Soc.*, **66**, 1509 (1970).
- M. Grätzel, A. Henglein, and S. Taniguchi, *Ber. Bunsenges. Phys. Chem.*, **74**, 292 (1970).
- G. E. Adams, J. H. Baxendale, and J. W. Boag, *Proc. R. Soc. London, Ser. A*, **277**, 549 (1964).
- G. E. Adams, B. D. Michael, and J. T. Richards, *Nature*, **215**, 1248 (1967).
- G. E. Adams, B. D. Michael, and R. L. Willson, *ACS Adv. Chem.*, **81**, 289 (1968).
- W. Kemula, Z. Grabowski, and M. Kalinowski, *Naturwiss.*, **47**, 514 (1960).
- J. M. Coxon and B. Holton, "Organic Photochemistry," Cambridge University Press, London (1974).
- S. P. Perone and J. R. Birk, *Anal. Chem.*, **38**, 1589 (1966).
- J. I. H. Patterson and S. P. Perone, *ibid.*, **44**, 1978 (1972).

## Hemoglobin Reactions as Interfacial Phenomena

Martin Blank\*

Department of Physiology, Columbia University, New York, New York 10032

### ABSTRACT

The reactions of hemoglobin with various ligands lead to conformational changes in the macromolecule. The free energy of these changes can be estimated in terms of the surface free energy of a microemulsion droplet of the same size and surface charge as the hemoglobin molecule. Calculations on the basis of this model yield an equilibrium constant that varies with pH, as in the acid and alkaline Bohr effects, and with the ionic strength. The model also provides a physical meaning for the empirical constant in the oxygen binding equation, as well as some insight into the dissociation equilibrium of the hemoglobin tetramers. This approach to equilibria involving globular proteins should be useful for estimating the effects of conformational changes and subunit interactions in other systems.

The study of macromolecules as interfacial systems, i.e., the chemistry of hydrophilic colloids, was the first

\* Electrochemical Society Active Member.

Key words: hemoglobin, ligands, macromolecule, globular protein.

approach used to characterize the properties of globular proteins. This study was followed by the development of the physical chemistry of macromolecules or polymers, including polyelectrolytes, which then merged into molecular biology. The techniques of mo-

lecular biology, especially those of the subfield x-ray crystallography, have given and continue to give a great amount of structural detail about proteins and other macromolecules.

With each new development for studying proteins, there has been a tendency to overlook the approach that was used during the earlier stage. Perhaps this is inevitable, since change has generally been accompanied by progress. But the recent increase in detailed geometric information is not without its drawbacks. Despite the wealth of structural data, it is difficult to calculate the interaction energies between the parts of a macromolecule, even with the aid of computers. In addition, one cannot perform the reverse calculation, *i.e.*, to define a structure in terms of the energy, because of the large number of conformations with approximately equal energies. It is in the realm of energy calculations that the older approaches to the study of proteins may be useful.

In this paper we shall consider the energy changes in hemoglobin using concepts that were developed for dealing with the electrochemistry of surfaces. We shall smooth out the structure of hemoglobin into a hydrophilic sphere of the same size and charge as the macromolecule, and assume that the known changes in the molecular shape and charge upon interaction can be calculated as changes in surface free energy. This will allow us to estimate the variation of the equilibrium constant as a function of pH and ionic strength in a relatively simple way. We shall also consider other consequences of this model such as a description of the empirical constant in the oxygen equilibrium equation in terms of a surface excess, and an analysis of the energetics of dissociation reactions.

### Estimating Changes in Conformational Energy Using Surface Electrochemistry

Hemoglobin, a macromolecule containing four protein chains with attached heme groups, can bind four oxygens (or several other ligands) per molecule (1). The oxygen binding curve is sigmoid in shape, indicating a change in the affinity with the degree of oxygenation. The curve also shifts with pH (the Bohr effect) and ionic strength, indicating a variation of the affinity with pH and salt concentration. These unusual aspects of hemoglobin reactions are generally assumed to be due to the conformational changes in the macromolecule, but the quantitative relation between the conformational changes and the change of affinity has been difficult to establish.

The hemoglobin molecule is approximately spherical and has a diameter of about 60Å, which is in the size range of colloidal systems. If hemoglobin is considered a colloid, the conformational changes that accompany a reaction can be estimated in terms of the surface free energy (2). Using a model system, a protein monolayer stabilizing a spherical hydrophobic droplet, it is possible to derive expressions for the changes in the surface free energy ( $\Delta G_s$ ) as a result of changes in the interfacial area ( $\Delta A$ ) at constant volume, and in the number of surface charges ( $\Delta N$ )

$$\Delta G_s = f(\Delta A, \Delta N) \quad [1]$$

Assuming changes in the model surface similar to those that accompany the oxygenation reaction, we can estimate  $\Delta G_s$  from the x-ray data showing conformational changes (3) and the differential titration data showing changes in surface charge (4). The variation of the equilibrium constant,  $K_e$ , can then be evaluated in terms of the change in surface free energy in units of  $k'$

$$\Delta \ln K_e = \frac{\Delta G_s}{RT} = \frac{k'}{2} \quad [2]$$

The results of the calculation are shown in Fig. 1 for the variation of  $K_e$  with pH, and similar agreement can

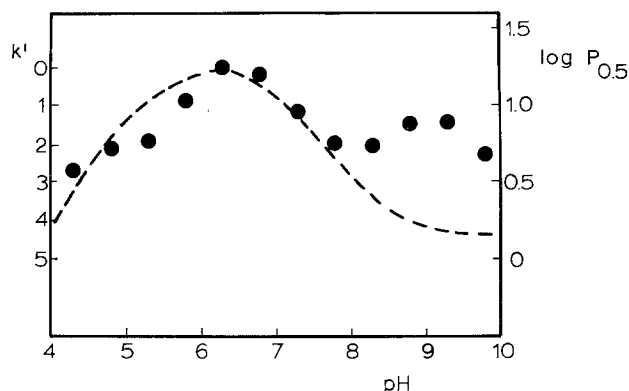


Fig. 1. Calculated values of  $K_e$  (●) in units of  $k'$ , superimposed on the dashed curve of observed values in units of  $\log p_{1/2}$  (the oxygen pressure for the half-saturation of hemoglobin).

be obtained for the variation of  $K_e$  with the ionic strength of the medium (5).

The model is able to account for basic aspects of the hemoglobin reactions with various ligands: (i) The sigmoid shape of the binding curve, which is characteristic of cooperative reactions, is present at all pH's as a result of the negative  $\Delta A$  during the conformational change. (ii)  $K_e$  shifts with pH even when  $\Delta N = 0$  due to the presence of a surface charge on the molecule. (iii) The calculated shift of  $K_e$  with pH and ionic strength can be of the right order of magnitude. (iv) The pH where the maximum in  $K_e$  occurs is below the IEP (the isoelectric point). (v) The Bohr effect should occur with all ligands that cause comparable changes in  $\Delta A$  and  $\Delta N$  upon interaction with hemoglobin.

The agreement of the calculations with the observations on the hemoglobin-oxygen system, suggests that changes in surface free energy can be used to evaluate the cooperative nature of the interaction and the variation of the equilibrium constant with pH and ionic strength. There are other aspects of the equilibrium which are not explained, since the system is more complicated than the model used and additional information is required (2). However, the approach outlined in this paper suggests a relatively simple way of relating the effects of conformational changes and cooperative interactions in globular proteins to changes in affinity.

### The Surface Excess and the Hill Coefficient

The interfacial model suggests a simple physical meaning for the Hill coefficient, the empirical constant used in equations governing binding equilibria that are cooperative. The usual binding equation considers that a concentration,  $C$ , of ligand reacts with a fraction,  $y$ , of available binding sites, and the equilibrium constant or affinity can be described as follows

$$K = \left( \frac{y}{1-y} \right) \frac{1}{C} \quad [3]$$

where  $y/(1-y)$  is the ratio of reacted to unreacted sites. A plot of  $y(C)$  gives the familiar rectangular hyperbola that is characteristic of the Langmuir adsorption equation, and that is observed when oxygen reacts with one of the monomers of hemoglobin. The affinity is related to  $\Delta G^\circ$ , the free energy change per mole when all substances are present at unit activity

$$K = \exp \left( - \frac{\Delta G^\circ}{RT} \right) \quad [4]$$

$\Delta G^\circ$  is due to the bonding reaction, but additional changes in free energy ( $\Delta G_s$ ) occur as a result of the conformational changes of hemoglobin.

The additional free energy change results in the displacement of the affinity to a new value

$$K' = \exp \left[ - \frac{\Delta G^\circ - \Delta G_s(y)}{RT} \right] \\ = K \exp \left[ - \frac{\Delta G_s(y)}{RT} \right] \quad [5]$$

From Eq. [5] it appears that when  $\Delta G_s < 0$ , the affinity increases, and since  $\Delta G_s$  varies with  $y$  there should be a gradual change in the equilibrium constant during a reaction. In practice, the affinity is assumed to remain constant at a new value,  $K_e$ , and the change in binding is usually considered in terms of a change in the dependence of  $y$  on  $C$ . This is done by raising the concentration to a power,  $n$ , as in the Hill equation for the combination of oxygen with hemoglobin

$$K_e = \left( \frac{y}{1-y} \right) \frac{1}{C^n} \quad [6]$$

where  $n > 1$  for  $\Delta G_s < 0$ . When  $n > 1$  the interaction is termed cooperative.

Using Eq. [3], [5], and [6], we can write two equivalent expressions for the effect of an additional free energy term on the fraction of sites bound

$$\Delta G^\circ + RT \ln \left( \frac{y}{1-y} \right) - nRT \ln C = 0 \quad [7]$$

$$\Delta G^\circ + \Delta G_s(y) + RT \ln \left( \frac{y}{1-y} \right) - RT \ln C = 0 \quad [8]$$

If we differentiate the two equations and subtract one from the other we see that

$$n - 1 = - \frac{d\Delta G_s(y)}{RT d \ln C} \quad [9]$$

Therefore  $(n - 1)$  has the form of the surface excess,  $\Gamma$ , in the Gibbs equation

$$\Gamma = - \frac{dG_s}{RT d \ln C} \quad [10]$$

where  $\Gamma$  is in mol/cm<sup>2</sup> if  $RT$  is in erg/mol and  $G_s$  is a surface free energy in erg/cm<sup>2</sup>. The empirical exponent  $n$  of Eq. [6] can therefore be interpreted rather simply in terms of surface excess. A plot of  $(n - 1)$  vs.  $C$  has the same form as graphs of surface excess in a classical interfacial system (6). (It should be noted that  $n$  is not constant, but varies with  $y$  and is equal to unity at the extremes of the range,  $y = 0$  and  $y = 1$ .)

### Subunit Dissociation Reactions as Colloidal Phenomena

The micro-emulsion droplet model of hemoglobin (where the relatively hydrophobic interior of the molecule is stabilized by a hydrophilic protein monolayer on the surface) suggests a simple qualitative explanation for the association-dissociation equilibria of hemoglobin solutions. We can describe the energetics of these equilibria in terms of the total surface free energy for the idealized model system

$$G = (\gamma_o - \pi)A \quad [11]$$

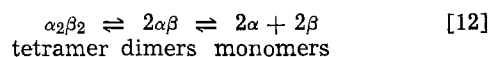
where  $\gamma_o$  = the interfacial free energy of the hydrophobic phase/water interface,  $\pi$  = the surface pressure of the hydrophilic film, and  $A$  = the total area. For example, with Eq. [11] we see that the unliganded form of hemoglobin has a lower tendency to dissociate than the various liganded forms. The decrease in  $A$  on oxygenation means that the surface free energy of the liganded form is lower than that of the free form. Therefore, the molecule is more stable with regard to dissociation into subunits.

Using the same qualitative reasoning we can describe the variation of the association-dissociation equilibria of hemoglobin with pH and ionic strength. The usual explanation for changes in the subunit interactions in proteins involves electrostatic factors. Thus an in-

crease in charge on either side of the IEP is believed to increase the electrostatic repulsion between the subunits and lead to dissociation. However, an increase in the ionic strength, which decreases the electrostatic interactions, also leads to dissociation. One can invoke the same explanation for the two observations only if one considers that at low net charge the electrostatic factors stabilize, but at higher charge they lead to dissociation. However, the logical inconsistency is reinforced by the knowledge that the tetramer is quite stable when the net charge is zero.

In the surface chemical model, electrostatic factors also come into play in the dissociation reactions, but not in the same way. On increasing the surface charge or decreasing the ionic strength there is an increase in  $\pi$  of Eq. [11], which leads to a lower  $G$ . However, as  $\pi$  approaches  $\gamma_o$ , the system becomes unstable and there is a tendency toward "phase inversion" or major conformational change. An "inversion" of the molecule requires a higher cost in free energy than the process of dissociation, which is therefore the preferred path.

If this is so, why do high salt concentrations (which decrease  $\pi$ ) also lead to dissociation of the hemoglobin tetramer into smaller subunits (*i.e.*, dimers and monomers)? The answer to this lies in another property of colloidal solutions, the large effect of ionic strength on the activity coefficient of a charged polymer. Consider the hemoglobin dissociation equilibria in terms of the following equation



For any set of conditions (*i.e.*, temperature, concentration, pH, ionic strength), there will be a distribution of the various forms in solution. If we add salt to the solution the activity coefficients of the different protein forms will change, *i.e.*, their solubilities will change. The effects of ionic strength on activity are generally larger for larger molecules (7), so at higher salt concentrations the large proteins will tend to be salted out of solution. Under these circumstances one would expect the equilibrium to shift in the direction of the smaller molecular weight forms. Thus one observes greater dissociation with an increase in the salt concentration, even though the smaller effect on  $\pi$  tends to stabilize association. (The variation of the activity coefficients with concentration of the protein molecules should also cause the dissociation reaction to vary.)

The dissociation reaction in an ideal constant volume system (going from a spherical tetramer to two spherical dimers) leads to an increase of 26% in the total  $A$ . If the number of charges remains constant but is spread over the larger area, there is a decrease in the surface charge density, and therefore in  $\pi$ . It is apparent that the  $A$  and  $\pi$  changes on dissociation both lead to a  $\Delta G_s > 0$ , and that under ordinary circumstances all of the factors oppose dissociation.

In making these qualitative statements we have considered that  $\gamma_o$  is constant upon dissociation. However, for droplets in the size range of hemoglobin, Gibbs (8) pointed out that there is a significant variation of the interfacial free energy with the curvature. The free energy increases with concavity and decreases with convexity when the droplet radii are smaller than  $10^{-6}$  cm (100Å). The variation of interfacial free energy,  $\gamma$ , with the radius,  $r$  is (9)

$$\frac{\gamma}{\gamma_\infty} = \left[ 1 + \frac{2\delta}{r} \right]^{-1} \quad [13]$$

where  $\gamma_\infty$  is the interfacial free energy when  $r = \infty$ , and  $\delta$  is a length on the order of the molecular diameter of the molecules in the liquid droplet. (It is difficult to estimate the characteristic length of a macromolecule like hemoglobin but one can probably consider it to be on the order of the diameter of the  $\alpha$  helix.) Therefore, there should be a decrease in the

value of  $\gamma_0$  as a result of dissociation, and the magnitude of the effect should be significant (on the order of 5-10%) in this size range. This would mean that the free energy change upon dissociation is not quite as large as expected.

The above qualitative discussion suggests that some of the ideas of colloid and surface chemistry are apt to be useful in understanding the energetics of globular proteins that are composed of several subunits. Recently, a related approach to the general problem of protein structure, which considers such factors as accessible surface areas, hydrogen bonds, and residue volumes, has apparently been successful in describing the structures of 15 proteins (10).

### Conclusion

By considering the hemoglobin molecule as a colloidal particle, it has been possible to obtain a number of insights into the energetics of reactions involving changes in conformation, surface area, and surface charge. Colloid chemistry has proved quite useful in the past in explaining phenomena where the dispersed phase was of the size of many globular proteins, and the ideas should continue to help us deal with the physical properties of protein solutions. Traditionally colloid chemistry has been devoted to the study of phenomena where the properties of interfaces play an essential role in determining the behavior of the sys-

tem. It is therefore appropriate for this subject to serve as an interface between the detailed structural information that has become available from molecular biology and the physical chemistry of the same substances in solution.

Manuscript received June 30, 1975. This was Paper 380 presented at the Toronto, Canada, Meeting of the Society, May 11-16, 1975.

Any discussion of this paper will appear in a Discussion Section to be published in the June 1977 JOURNAL. All discussions for the June 1977 Discussion Section should be submitted by Feb. 1, 1977.

### REFERENCES

1. E. Antonini and M. Brunori, "Hemoglobin and Myoglobin in Their Reactions with Ligands," North Holland, Amsterdam (1971).
2. M. Blank, *J. Colloid Interface Sci.*, **43**, 557 (1973).
3. H. Muirhead, J. Cox, L. Mazzarella, and M. Perutz, *J. Mol. Biol.*, **28**, 117 (1967).
4. B. German and J. Wyman, *J. Biol. Chem.*, **117**, 533 (1937).
5. M. Blank, *J. Theor. Biol.*, **51**, 127 (1975).
6. M. Blank, *J. Colloid Interface Sci.*, **41**, 97 (1972).
7. J. T. Edsall and J. Wyman, "Biophysical Chemistry," p. 277, Academic Press, New York (1958).
8. J. W. Gibbs, "Collected Works," Vol. I, p. 219 ff, Longmans Green, New York (1928).
9. R. C. Tolman, *J. Chem. Phys.*, **17**, 333 (1949).
10. C. Chothia, *Nature*, **254**, 304 (1975).

## A Thin Layer Spectroelectrochemical Study of Cob(I)alamin to Cob(III)alamin Oxidation Processes

Thomas M. Kenyhercz\*<sup>1</sup> and Harry B. Mark, Jr.\*\*

Department of Chemistry, University of Cincinnati, Cincinnati, Ohio 45221

### ABSTRACT

The air, electrochemical, and autooxidation of cob(I)alamin and also cob(I)inimide under various conditions have been studied. The time-resolved and potential-resolved spectra indicate that in the absence of cyanide ion or cyanide present in equivalent concentrations the reoxidation to aquocob(III)-alamin (vitamin B<sub>12a</sub>) and cyanocob(III)alamin (vitamin B<sub>12</sub>) exhibits two cob(II)alamin intermediates. It is speculated that the two intermediates represent "base-on" and "base-off" forms with respect to the coordination of the side chain benzimidazole group in the Y axial position. Experiments on the reoxidation of cob(I)alamin in presence of excess cyanide and on cob(I)-inimide support this conclusion.

A recent cyclic voltammetric study of vitamin B<sub>12</sub> type compounds has suggested that electrochemical and spectroscopic techniques be combined to elucidate the redox behavior of cobalamin compounds (1). The resultant spectropotentiostatic studies (2,3) of cobalamins have revealed a previously unobserved sequence of intermediates and steps are involved in the reoxidation mechanism of the cob(I)alamins in this biologically significant reaction (4-10). Optically transparent thin layer electrode (OTTLE) cells (11,12) have been used in conjunction with a Harrick rapid scanning spectrophotometer to study the reoxidation mechanism of cob(I)alamins (2). The reoxidation sequence of cob(I)alamins investigated by spectropotentiostatic and autooxidation techniques has yielded consistent results. The results apparently indicate the formation of two cob(II)alamin reoxidation inter-

mediates which have been interpreted as corresponding to "base-on" and "base-off" forms with respect to the coordination of the 5,6-dimethylbenzimidazole group at the Y axial site. Furthermore, attempts have been made to correlate cobalamin cyclic voltammetric behavior at a mercury-coated nickel minigrad electrode (Hg-Ni OTTLE) with the spectroelectrochemical evidence.

### Experimental

The recently developed mercury-coated nickel minigrad electrode (11) was used in a thin layer configuration during cyclic voltammetric experiments and as a thin layer electrolysis cell for spectroelectrochemical studies (2,3,13). The OTTLE which served as the working electrode was constructed according to established procedures (2,11). There was some concern that diffusion of unreacted material from the reservoir cup and the edges of the OTTLE cell could affect the mechanism and kinetics of the reoxidation. To check this, an OTTLE cell, in which the minigrad was in contact with the total solution volume (mini-

\* Electrochemical Society Student Member.

\*\* Electrochemical Society Active Member.

<sup>1</sup> Present address: Department of Chemistry, Purdue University, West Lafayette, Indiana 47907.

Key words: cobalamin, spectroelectrochemistry, optically transparent thin layer electrode (OTTLE), oxidation.

grid area was exactly equal to that of the solution area) and had no reservoir cup, was constructed. We did not note any measurable difference in experimental results for either OTTLE cell design. The mini-grid thin layer cell was assembled using a nickel minigrad (333 lines/in., 60% transmittance, Buckbee Mears Company, St. Paul, Minnesota), microscope slides (1 × 3 in.) and 2 mil Fluorofilm DF-1200 tape (Dilectrix Corporation, Farmingdale, New York). The preparation of Hg-Ni OTTLE used in this investigation has been described elsewhere (11). The exact thickness of the OTTLE cell was determined spectrophotometrically using a standard solution of dicyanocobalamin. The three-electrode system also employed a platinum wire as the auxiliary electrode while a miniature saturated calomel electrode (SCE) served as the reference electrode. The Hg-Ni OTTLE cell was mounted in a computerized Harrick rapid scanning dual beam spectrophotometer (RSS) (2, 14). Experimental procedures interface design, electrochemical instrumentation, computer programming including data acquisition, processing, and reduction has been described previously (15). Crystalline cyanocobalamin, vitamin B<sub>12</sub> (Sigma Chemical Company, St. Louis, Missouri) was used without further purification and was also employed in the synthesis of aquocobalamin (B<sub>12a</sub>) (16) and dicyanocobalamin (B<sub>12-CN</sub>). All solutions (except that noted in Fig. 3) were 1 mM in cobalamin and 1.0M in Na<sub>2</sub>SO<sub>4</sub> as the supporting electrolyte (1); the solutions for the B<sub>12-CN</sub> experiments were also 0.1M in KCN. All cobalamin solutions were deaerated with high purity argon. Unless noted an inert atmosphere of argon was maintained in the RSS. The deaerated cobalamin solutions were introduced into the OTTLE cell with the cobalt of the cobalamin in the +3 valence state. The 1 mM cobalamin solutions were then potentiostated at -1.0V vs. SCE until the spectra changed completely to that of the cob(I)alamin (see the first spectrum of Fig. 9) and remained constant for approximately one-half hour. The cob(I)alamin solutions were reoxidized by electrochemical means or by autooxidation in either the presence of air diffusing into the OTTLE cell or under an inert argon atmosphere. The potentiostat was disconnected from the OTTLE cell assembly during the autocatalysis experiments (2). The electrochemical electroreoxidation process involved a stepwise (25 mV increment) potentiostatic polarization (potentiostated at each potential value until the spectra ceased changing, approximately 2 min) under an inert argon atmosphere (2).

### Results and Discussion

**Thin layer cell cyclic voltammograms.**—Typical cyclic voltammograms for cyano- and dicyanocobalamin at a Hg-Ni OTTLE are shown in curves A and B, respectively, of Fig. 1 (3). These cyclic voltammograms appear quite complex and nonideal with respect to peak shape. The irreversibility appears to arise from a combination of slow electron transfer, associated chemical steps in the redox process, and strong adsorption of both reactants and products. Based on a previous study it is possible to at least quantitatively assign peaks to certain redox processes (3, 10, 17, 18). In curve A of Fig. 1 (B<sub>12</sub> at a Hg-Ni OTTLE), the reduction process occurring in the region of -0.95V vs. SCE represents a two-electron reduction corresponding to B<sub>12</sub> + 2e → B<sub>12s</sub> [Co(III) + 2e → Co(I)] (1, 3, 10, 17, 18). The reoxidation occurring at -0.85V vs. SCE is attributable to the process B<sub>12s</sub> - 1e → B<sub>12r</sub> [Co(I) - 1e → Co(II)] (1, 10, 17, 18). A cyclic voltammetric study of the supporting electrolyte (1.0M Na<sub>2</sub>SO<sub>4</sub>) containing millimolar amounts of cyanide has shown that anodic peaks in the region of -0.3 to 0.0V vs. SCE correspond to formation of mercury cyanide complexes (19, 20). The prominence of the mercury cyanide peaks is particularly evident in the B<sub>12-CN</sub> cyclic voltammo-

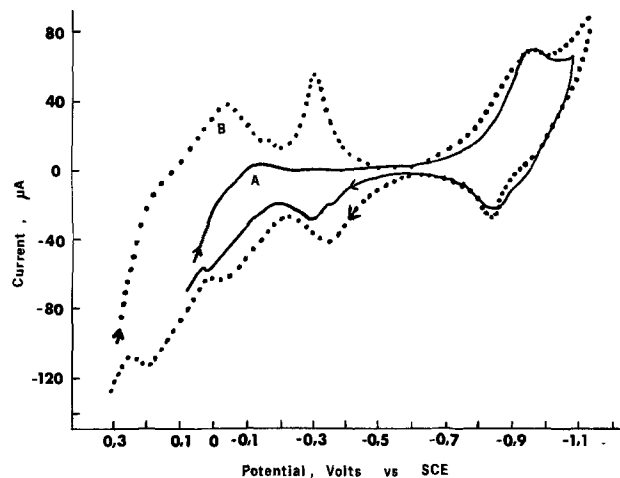


Fig. 1. Thin layer cyclic voltammograms of 1 mM solutions of cyanocobalamin, B<sub>12</sub> (curve A) and dicyanocobalamin (curve B) at a Hg-Ni minigrad electrode. Scan rate = 2 mV-sec<sup>-1</sup>. Initial scan cathodic. Curve A, B<sub>12</sub>: 1.0M Na<sub>2</sub>SO<sub>4</sub>, 0.1M NaNO<sub>3</sub>, pH = 7.0. Curve B, B<sub>23-CN</sub>: 1.0M Na<sub>2</sub>SO<sub>4</sub>, 0.1M KCN, pH = 10.4.

grams (Fig. 1, curve B). Though not shown in curve A of Fig. 1, a small peak does occur in the region of 0.2V vs. SCE which appears to correspond to the reaction B<sub>12r</sub> - 1e → B<sub>12</sub> [Co(II) - 1e → Co(III)] (1, 3). All successive cathodic scans of B<sub>12</sub> show the presence of a cathodic peak around -0.3V similar to those exhibited by B<sub>12-CN</sub> which correspond to the reduction of mercury cyanide complexes. The cyclic voltammetric behavior of dicyanocobalamin is illustrated in curve B of Fig. 1 (3). Thus, a comparison of curves A and B shows that electron transfer characteristics for B<sub>12-CN</sub> (curve B) are essentially the same as that of B<sub>12</sub> (curve A). The additional peaks in the B<sub>12-CN</sub> cyclic voltammogram are the same as those observed for supporting electrolyte solutions containing 1.0M Na<sub>2</sub>SO<sub>4</sub> supporting electrolyte and 2 mM KCN. The cyclic voltammetric behavior of aquocobalamin, vitamin B<sub>12a</sub> at a Hg-Ni OTTLE is given in Fig. 2 (3). Again, it is possible to assign the reduction peak occurring at about -0.95V vs. SCE to the process B<sub>12a</sub> + 2e → B<sub>12s</sub> or [Co(III) + 2e → Co(I)]. The reoxidation peak occurring in the region of -0.8V appears to correspond to the reaction of B<sub>12s</sub> - 1e → B<sub>12r</sub> while the peak in the region of 0.15V corresponds to the reaction B<sub>12r</sub> - 1e → B<sub>12a</sub>. The reduction peak at 0.2V is characteristic of the supporting electrolyte (1.0M Na<sub>2</sub>SO<sub>4</sub>) at the

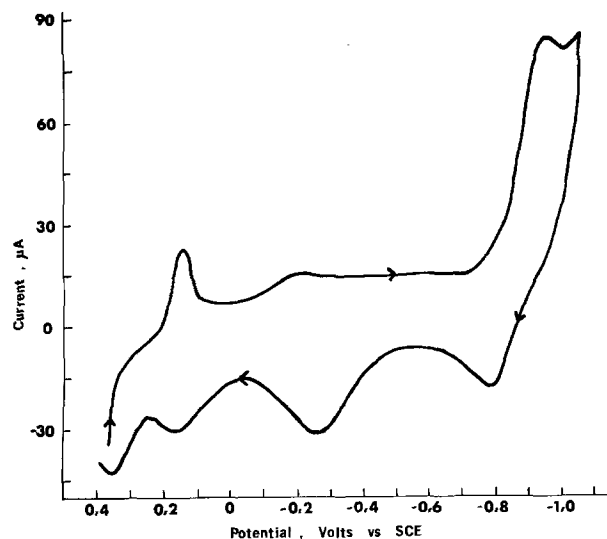


Fig. 2. Thin layer cyclic voltammogram of 0.9 mM solution of aquocobalamin, B<sub>12a</sub>, at a Hg-Ni minigrad electrode. Scan rate = 2 mV-sec<sup>-1</sup>. Initial scan cathodic 1.0M Na<sub>2</sub>SO<sub>4</sub>, 0.1M NaNO<sub>3</sub>, pH = 7.0.

Hg-Ni OTTLE, though the identity of the  $-0.25\text{V}$  anodic peak is uncertain. The potential range of this anodic peak is similar to the mercury cyanide anodic peak observed for  $B_{12}$ . As the  $B_{12a}$  was synthesized from  $B_{12}$  (6), one might suspect that some  $B_{12}$  remains as an impurity. However, no cyanide is thought to be present in the  $B_{12a}$  for several reasons. First of all, the second cathodic of the  $B_{12a}$  solution failed to produce the mercury (II) cyanide reduction peak observed for  $B_{12}$  and  $B_{12}\text{-CN}$ . Also the occurrence of this  $-0.25\text{V}$  reduction peak was investigated at a Hg-Ni OTTLE for  $B_{12a}$  samples that had been prepared under diverse conditions (3) (chemically, electrochemically synthesis from  $B_{12}$  or biological by microbial action). In all cases the  $B_{12a}$  solutions produced a  $-0.25\text{V}$  reoxidation peak at the mercury-coated nickel minigrad. Thus, it seems unlikely that a "common" cyanide impurity could exist for such diversified batch preparations of aquocobalamin. A further cyclic voltammetric examination of the  $B_{12a}$  at a hanging mercury drop electrode (HMDE, surface area =  $0.0293\text{ cm}^2$ ) was carried out (1, 3) which showed that this aquocobalamin did not exhibit a reoxidation peak in the region of  $-0.25\text{V}$  ( $\pm 50\text{ mV}$ ) (1). This leads one to speculate that some unique redox process may be occurring between a base-off cob(II)alamin and the Hg-Ni surface. Such an interaction for base-off forms with transition metals and transition metal complexes is not new and is well documented in the literature (21, 22). In general, with the exception given above, it appears as though the cobalamins exhibit the same electrochemical behavior at a Hg-Ni minigrad that they do at a HMDE. Thus, the mercury-coated nickel minigrad in an optically transparent thin layer electrode configuration has been used to study the spectroelectrochemical reoxidation mechanism (2, 3).

**Cob(I)alamin reoxidation studies.**—Curve A of Fig. 3 represents a typical spectrum of a partially air reoxidized solution of the cob(I)alamin,  $B_{12s}$ . The peaks occurring in the region of 380 and 560 nm are characteristic of a cob(I)alamin (23). The peaks at 475 and 410 nm have been previously observed in the spectrum of the cob(II)alamin,  $B_{12r}$  (23). The peak at 525 nm is assigned the final oxidation product  $B_{12a}$  (28) (see curve B, Fig. 3). Thus, the spectrum of curve A, Fig. 3, is that of a mixture of cob(I)-, cob(II)-, and cob(III)-alamins and the peaks of interest here, which we suggest correspond to cob(II)alamin intermediates in the oxidation sequence, occur at 410 and 475 nm. During the large scale preparations of  $B_{12a}$  (16), it was previously observed that the relative ratio of the 410 and 475 nm peaks varied markedly, depending on the rate at which oxygen was introduced into the cob(I)alamin,  $B_{12s}$ , solution. This is illustrated by comparing curve A of Fig. 6 to the first curve of Fig. 8. Curve A of Fig.

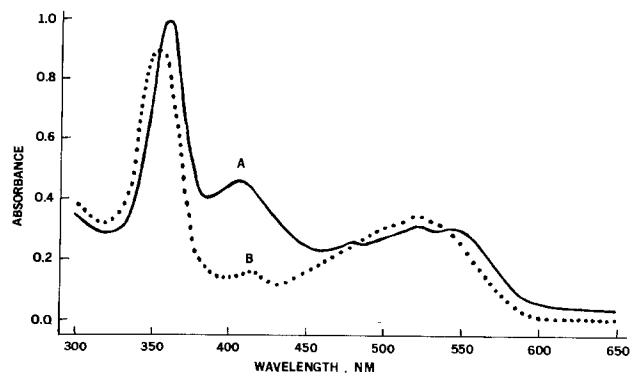


Fig. 3. Spectra of air reoxidized products formed following the exhaustive reduction of cyanocob(III)alamin in  $0.1\text{M NaNO}_3$ . Curve A represents a partially reoxidized solution of cob(I)alamin. Curve B represents the totally reoxidized cob(III)alamin, aquocobalamin.

3 was obtained on bubbling oxygen through a rapidly stirred solution of  $B_{12s}$ . Under these conditions the 410 nm peak is much larger than the 475 nm peak. In the curves shown in Fig. 4-11 the 475 nm peak is always much larger than the 410 nm peak. In the latter cases, oxygen was admitted to the system slowly (Fig. 4-8) (by diffusion into the  $B_{12s}$  solution from the edges of the OTTLE cell), or was excluded from the system by employing an argon atmosphere in the RSS, Fig. 9-11. Based on these results it is felt that the 410 and 475 nm peaks represent two different cob(II)alamin species, though past investigations have reported both of these peaks as being characteristic of a single species,  $B_{12r}$ .

The spectra obtained following the exhaustive reduction of  $B_{12}$ ,  $B_{12a}$ , and  $B_{12}\text{-CN}$  at  $-1.0\text{V vs. SCE}$  were characteristic of an identical cob(I)alamin species, as can be seen by comparing the initial curves in Fig. 9-11. This is the cob(I)alamin species designated as  $B_{12s}$ . Though the exact coordination geometry for the cob(I)alamin is unknown (27), it has been suggested that the coordinated axial benzimidazole is protonated in a base-off configuration with water molecules occupying each of the axial positions (24).

It was found that the time-resolved cobalamin spectral sequences and rates of peak changes were virtually the same in the absence of air and when air was allowed to diffuse into the OTTLE cell from the edges. This indicates that the mechanism for reoxidation under these conditions involves the reaction of cob(I)alamin with some other oxidant is faster than the rate of diffusion of oxygen into the OTTLE cell. The time-resolved spectra for the "autooxidation" of a cob(I)alamin solution (OTTLE cell in an argon atmosphere) obtained by the exhaustive reduction of cyanocob(III)alamin at  $-1.0\text{V}$  is shown in Fig. 4 and 5. Figure 4 shows that the cob(I)alamin, as monitored by the 385 nm peak is completely reoxidized to a cob(II)alamin (as seen by the development of the 475 nm peak) in the first 100 sec. The peak which develops at 475 nm corresponding to a cob(II)alamin species, grows to a maximum in the first 400 sec. The 475 nm peak then slowly decreases, finally vanishing at about  $5 \times 10^4$  sec. The cyanocob(III)alamin peak at 360 nm begins to develop at  $10^4$  sec and the  $B_{12}$  is completely regenerated by  $10^5$  sec. The time-resolved spectra for this regeneration of  $B_{12}$  can be seen in Fig. 5. The identical reoxidation experiment was performed using aquocob(III)alamin ( $B_{12a}$ ) following potentiostating at  $-1.0\text{V vs. SCE}$  to produce the cob(I)alamin. The time-resolved oxidation spectra for  $B_{12a}$  are shown in Fig. 6 and 7. The reoxidation sequence of a cob(I)alamin to  $B_{12a}$  is very similar to the cob(I)alamin autooxidation

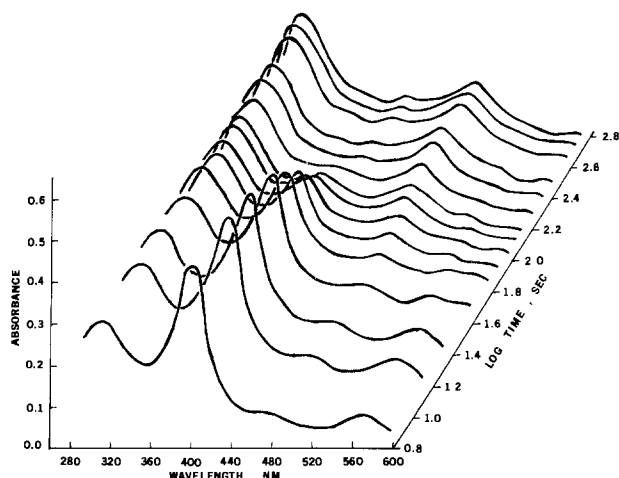


Fig. 4. Time-resolved spectra for the reoxidation of cob(I)alamin (from  $1.0\text{ mM}$  cyanocobalamin) to cob(II)alamin, in a  $1.0\text{M Na}_2\text{SO}_4$ ,  $0.1\text{M NaNO}_3$  solution;  $\text{pH} = 7.0$  initially. Time span =  $0\text{-}630$  sec, at a Hg-Ni OTTLE. Cell thickness =  $0.017\text{ cm}$ .

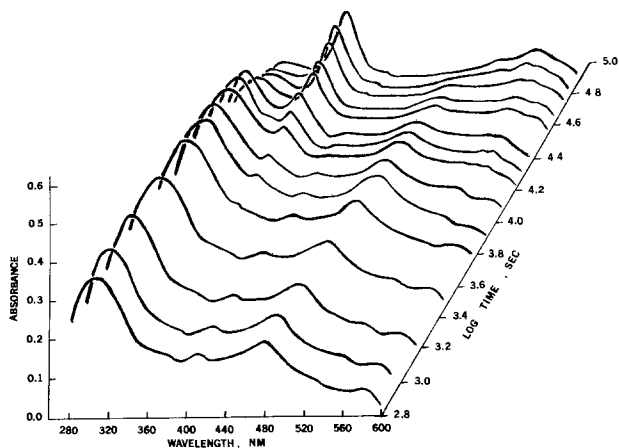


Fig. 5. Time-resolved spectra for the reoxidation of cob(II)alamin to a cob(III)alamin,  $B_{12r}$ , in a 1.0M  $Na_2SO_4$ , 0.1M  $NaNO_3$  solution. Time span = 630-70,000 sec at a Hg-Ni OTTLE. Cell thickness = 0.017 cm.

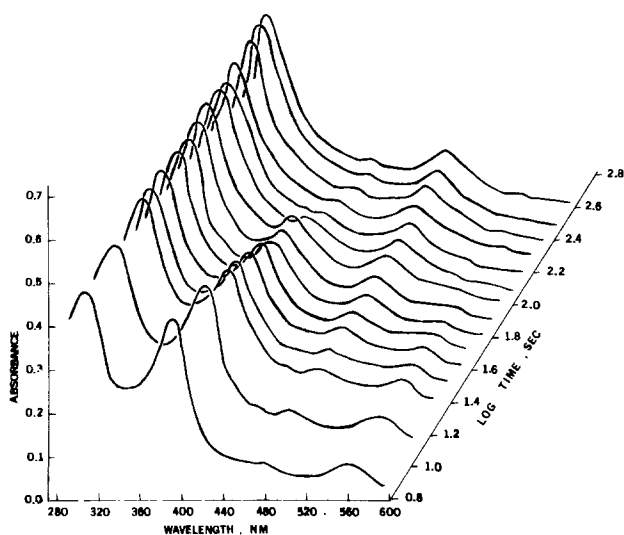


Fig. 6. Time-resolved spectra for the reoxidation of cob(I)alamin (from 0.9 mM aquocobalamin) to a cob(II)alamin, in a 1.0M  $Na_2SO_4$ , 0.1M  $NaNO_3$  solution; pH = 7.0 initially. Time span = 0-400 sec, at a Hg-Ni OTTLE. Cell thickness = 0.017 cm.

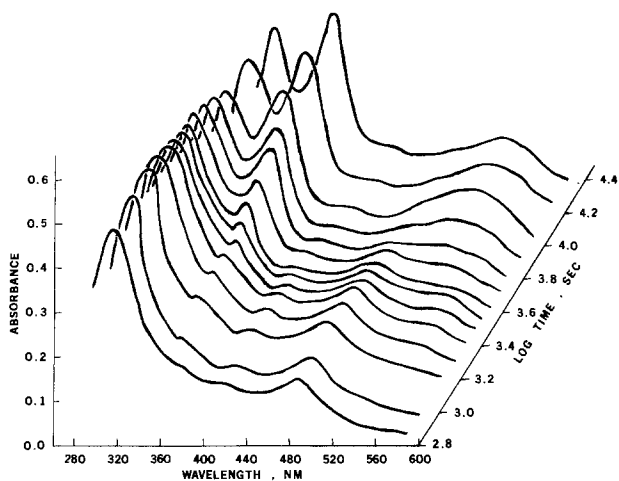


Fig. 7. Time-resolved spectra for the reoxidation of cob(II)alamin to a cob(III)alamin,  $B_{12a}$ , in a 1.0M  $Na_2SO_4$ , 0.1M  $NaNO_3$  solution. Time span = 630-25,000 sec at a Hg-Ni OTTLE. Cell thickness = 0.017 cm.

in the presence of equimolar  $CN^-$  to  $B_{12}$ . For all auto-oxidation studies involving both  $B_{12}$  and  $B_{12a}$ , the

spectra exhibits a 410 nm peak, which occurs in the same qualitative time period but not necessarily coincident with the absorbance-time values of the characteristic 475 nm cob(II)alamin peak. It appears within 200 sec, has reached a maximum by  $5 \times 10^3$  sec, and has disappeared by about  $2 \times 10^4$  sec. Furthermore, there are no peaks in the region of 370 nm which could identify either a Co(I) or Co(III) species during the time interval from 200 to 5000 sec. It is, therefore, felt that the 410 nm peak indicates a second different cob(II)-alamin intermediate which will be identified as  $B_{12r}'$ . These two cob(II)alamin species could correspond to base-on and base-off benzimidazole forms, although the possibility exists that some reversible alteration of the corrin ring could also be responsible for this behavior. It is felt that, as the peaks in this region have previously been associated with changes in the axial ligand configuration, this postulation that the two species are base-on and base-off forms is reasonable (25). From the spectra presented in Fig. 4 through 7 it is seen that the  $B_{12}$  and  $B_{12a}$  formation appears more concomitant with the disappearance of  $B_{12r}'$  than  $B_{12r}$ . The studies described below with  $B_{12}$ -CN and cob(III)inimide have been employed to test this base-on and base-off theory.

The time-resolved spectra for the autooxidation of cob(I)alamin,  $B_{12s}$ , obtained by the exhaustive reduction of dicyanocob(III)alamin (formed by adding a 100-fold excess of cyanide to  $B_{12}$ ) as shown in Fig. 8 is found to be quite different from those obtained of  $B_{12}$  and  $B_{12a}$ . From Fig. 8 it can be seen that dicyanocob(III)alamin is totally regenerated in less than 400 sec. The time dependency of the increase/decrease in the 290 nm band, the rise and fall of the 475 nm cob(II)alamin peak, the final development of the 368 nm peak plus the total absence of a 410 nm peak all strongly suggest that the reoxidation of  $B_{12s}$  in the presence of excess cyanide goes through only a  $B_{12r}$  type intermediate. The lack of a 410 nm intermediate in this case is consistent with the suggestion that this intermediate is a different axial ligand configuration rather than a ring alteration which would be consistent for the three cobalamins which were investigated. It is also reasonable that both the X and Y axial positions are occupied by  $CN^-$  in the case of a 100-fold excess  $CN^-$  in the solution and the base-on  $B_{12r}'$  does not form.

The electrochemical reoxidation sequence of the cob(I)alamins formed by the exhaustive reduction of  $B_{12}$ ,  $B_{12a}$ , and  $B_{12}$ -CN are shown in Fig. 9 through 11,

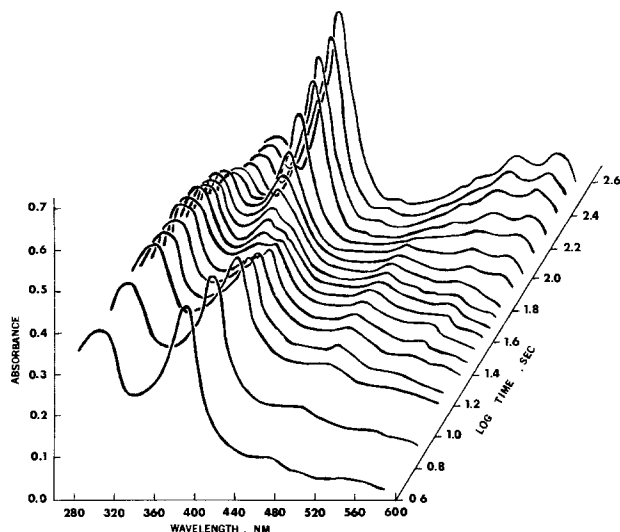


Fig. 8. Time-resolved spectra for the reoxidation of cob(I)alamin (from 1 mM dicyanocobalamin) to dicyanocob(III)alamin, in a 1.0M  $Na_2SO_4$ , 0.1M KCN solution; pH = 11.0. Time span = 0-410 sec at a Hg-Ni OTTLE. Cell thickness = 0.017 cm.



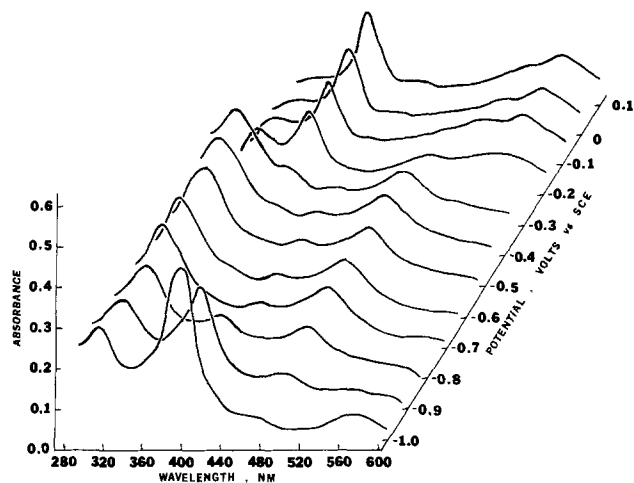


Fig. 9. Spectropotentiostatic curves for the reoxidation of cob(I)alamin (from 1 mM cyanocobalamin) to cyanocob(III)alamin,  $B_{12}$ , in 1.0M  $Na_2SO_4$ , 0.1M  $NaNO_3$ ; pH = 7.0 initially. Potential range =  $-1.0$  to  $+0.1V$  vs. SCE at a Hg-Ni OTTLE. Cell thickness = 0.017 cm.

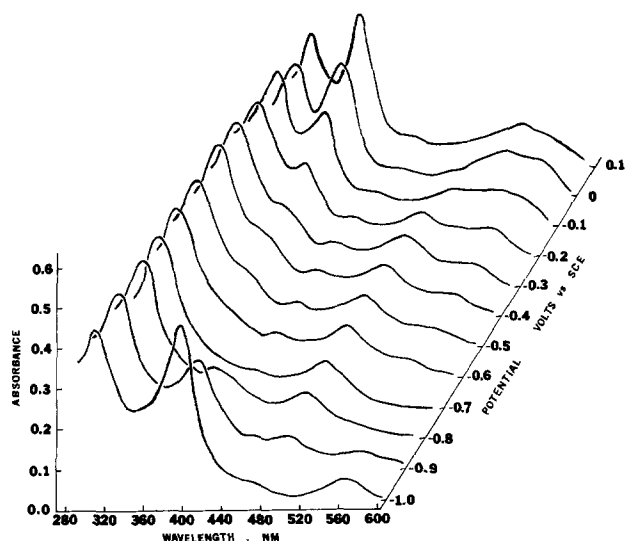


Fig. 10. Spectropotentiostatic curves for the reoxidation of cob(I)alamin (from 0.9 mM aquocobalamin) to aquocob(III)alamin,  $B_{12a}$ , in 1.0M  $Na_2SO_4$ , 0.1M  $NaNO_3$ ; pH = 7.0 initially. Potential range =  $-1.0$  to  $+0.1V$  vs. SCE at a Hg-Ni OTTLE. Cell thickness = 0.017 cm.

respectively. The spectroelectrochemical reoxidation sequence for cob(I)alamin prepared from electroreduced cyanocobalamin is illustrated in Fig. 9. The formation of the 475 nm cob(II)alamin peak becomes markedly evident as the potential is decreased below  $-0.9V$  vs. SCE (3). The 475 nm peak appears to reach a maximum in absorbance between  $-0.8$  and  $-0.7V$  SCE. A previous spectroelectrochemical study of  $B_{12}$  at 475 nm has shown that the reoxidation plateau region extends from  $-0.30$  to  $-0.77V$  vs. SCE (3). This fact is well substantiated by the spectropotentiostatic curves of Fig. 9. It can be seen from Fig. 9 that the development of the 410 nm peak is not coincident with the 475 nm peak, but appears to reach a maximum in the region of  $-0.5V$  vs. SCE, and then decreases. The development of the 360 nm peak characteristic of  $B_{12}$  begins in the potential region where the 475 nm peak begins to decline. The cyanocob(III)alamin species appear to have been regenerated in the potential region between 0.00 and 0.10V vs. SCE, which again agrees with the previous spectropotentiostatic investigation. The spectropotentiostatic reoxidation of aquocob(III)alamin ( $B_{12a}$ ) from cob(I)alamin ( $B_{12s}$ ) is shown in Fig. 10. In general the spectropotentiostatic reoxidation

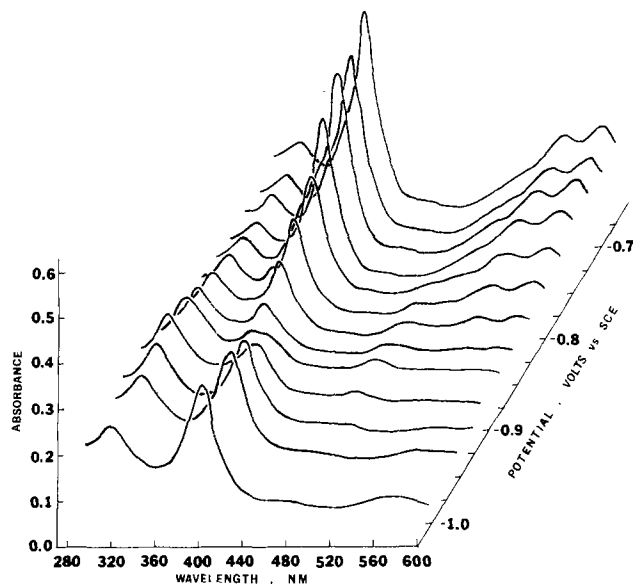


Fig. 11. Spectropotentiostatic curves for the reoxidation of cob(I)alamin (from 1 mM dicyanocobalamin) to dicyanocob(III)alamin,  $B_{12-CN}$ , in 1.0M  $Na_2SO_4$ , 0.1M  $NaNO_3$ ; pH = 11.0 initially. Potential range =  $-1.0$  to  $-0.67V$  vs. SCE at a Hg-Ni OTTLE. Cell thickness = 0.017 cm.

of  $B_{12a}$  corresponds almost identically with that of  $B_{12}$ . It should however be restated that the development of the 475 nm peak is noncoincident with that of the 410 nm peak. Figure 11 illustrates the spectropotentiostatic reoxidation curves for cob(I)alamin formed by the exhaustive reduction of dicyanocob(III)alamin ( $B_{12-CN}$ ). Several features of Fig. 11 are worth noting: (a) the potential region over which  $B_{12-CN}$  is reoxidized is drastically reduced when compared to  $B_{12}$  and  $B_{12a}$ , and (b) the total absence of a 410 nm absorbance peak during the electrochemical reoxidation sequence. The fact that the dicyanocobalamin reoxidation potential region is much narrower than that of either cyano- or aquocobalamin indicates much more reversible heterogeneous electron transfer kinetics which correlates with the homogeneous autooxidation rate curves shown in Fig. 4 through 8. The total absence of the 410 nm peak in the  $B_{12-CN}$  electrochemical reoxidation sequence is consistent also with the homogeneous autooxidation results.

In order to further examine the postulation that the 410 nm peak corresponds to a base-on cob(II)alamin,  $B_{12r}$ , the time-resolved autooxidation spectra of a cob(I)inimide (29) (no benzimidazole moiety on the corrin ring system) was examined. The absorbance-potential reduction characteristics of the cyanoaquocob(III)inimide (30) starting material and the rate of autooxidation parallel to those of vitamin  $B_{12}$  itself indicating that the lack of the benzimidazole moiety has not appreciably altered the redox properties of the central cobalt ion. However, the time-resolved autooxidation spectra of the cob(I)inimide do not exhibit a 410 nm peak as can be seen in Fig. 12 and 13. Thus, the  $B_{12-CN}$  and cob(I)inimide autooxidation spectra are consistent with the suggestion that the  $B_{12r}$  (410 nm peak) is a base-on intermediate in the  $B_{12}$  and  $B_{12a}$  mechanism.

Electrochemical reoxidation of cob(I)alamin, obtained by the electroreduction of  $B_{12}$  under an argon atmosphere, goes through both the  $B_{12r}$  (475 nm) and  $B_{12r'}$  (410 nm) intermediates in the potential region from  $-0.60$  to  $-0.01V$  vs. SCE yielding  $B_{12}$  at  $+0.10V$  vs. SCE. The conditions of the electrochemical reoxidation experiments indicate that the 410 nm peak is not indicative of an oxygen adduct type of cobalamin species.



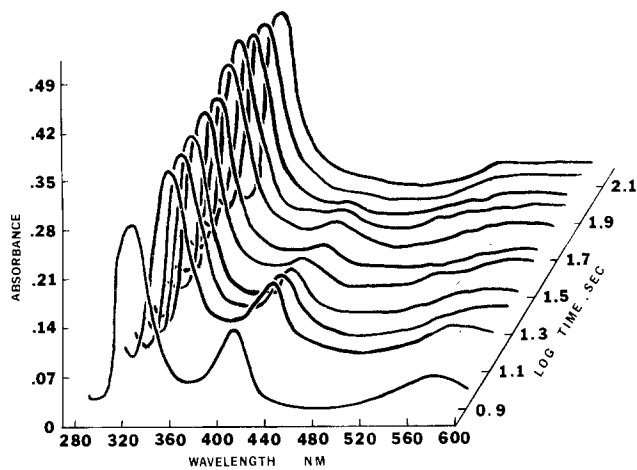


Fig. 12. Time-resolved spectra for the reoxidation of cob(I)inimide (from 1.0 mM aquocyanocob(III)inimide) to a cob(II)inimide in a 1.0M  $\text{Na}_2\text{SO}_4$  solution; pH = 7 initially. Time span = 0-400 sec at a Hg-Ni OTTLE. Cell thickness = 0.017 cm.

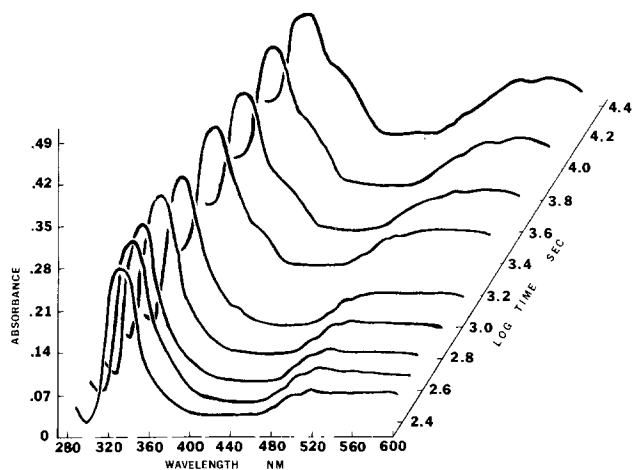
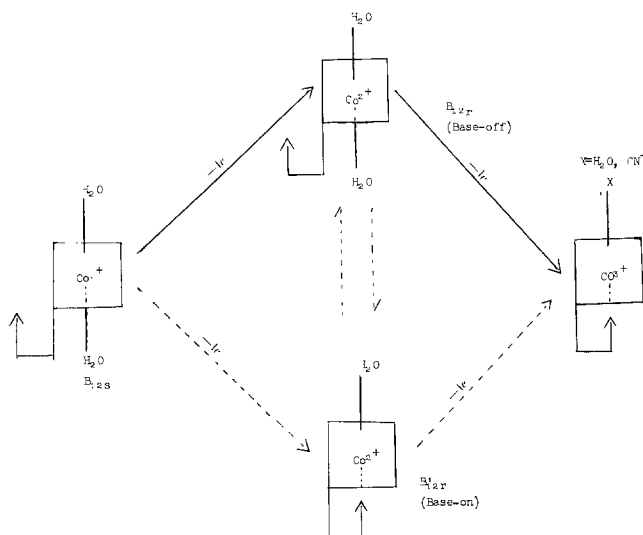


Fig. 13. Time-resolved spectra for the reoxidation of a cob(II)inimide to a cob(III)inimide in a 1.0M  $\text{Na}_2\text{SO}_4$  solution; pH = 7 initially. Time span = 630-70,000 sec at an Hg-Ni OTTLE. Cell thickness = 0.017 cm.

Qualitatively, the time-resolved spectra indicate that the reoxidation of cob(I)alamin in the presence of stoichiometric or less amounts of  $\text{CN}^-$  follows the reaction scheme illustrated below.



As previously mentioned, the presence of excess cyanide ion affects the reoxidation scheme such that either the  $B_{12r}$  (base-on) species is not formed or that

the oxidation of the  $B_{12r}$  (base-off) species is kinetically favored. It has been postulated by others (5-10) that cob(I)alamin autooxidizes to a cob(II)alamin with the evolution of hydrogen. This process would certainly explain the reoxidation of  $B_{12s}$  to  $B_{12r}$  where under existing conditions the hydrogen would be soluble in solution and bubbles not observed in the OTTLE cell. Furthermore, the postulation that the cob(II)alamin can disproportionate to form a cob(I) and a cob(III)alamin species (5-10) cannot be directly observed by this study. The identical time-resolved spectral data would be observed for either (i) a direct sequential two-step oxidation where the first step is fast and the second is slow or (ii) a fast initial one-electron transfer to  $B_{12r}$  followed by a slow disproportionation to  $B_{12s}$  and  $B_{12}$ . The work of Birke *et al.* (10) estimated that the thermodynamic and kinetic parameters for such a disproportionation are very unfavorable. It has not been possible to calculate meaningful kinetic parameters from the time and potential resolved spectra as no quantitative diffusion model has been postulated. Moreover, we cannot really tell if the  $B_{12s}$  oxidizes directly to both  $B_{12r}$  and  $B_{12r}'$  at different rates or that if  $B_{12r}'$  results simply from a rapid equilibrium with  $B_{12r}$  as shown in the proposed mechanism. [Cobalt (II) complexes of this type are generally labile (26).] This same argument applies to the interpretation of  $B_{12r}$  and  $B_{12r}'$  oxidizing to cob(III)alamin(s). However, it does appear that the reoxidation of  $B_{12r}$  to dicyanocob(III)alamin occurs much more rapidly than the reoxidation of either  $B_{12r}$  or  $B_{12r}'$ . This can be seen by comparing the time scale of Fig. 5 and 7 to that of Fig. 8. Quantitative kinetic studies will be carried out in the near future.

#### Acknowledgments

This research was supported by National Science Foundation Grant GP-35979. One of us wishes to acknowledge partial financial assistance received through the Lowenstein-Schubert-Twitchell Fellowship Fund. The authors gratefully acknowledge helpful discussions with Dr. E. A. Deutsch and Dr. W. R. Heineman. One of us (T.M.K.) gratefully acknowledges the Office of the University Dean for travel support to present this paper at the Society's Toronto Meeting.

Manuscript received Sept. 25, 1975. This was Paper 349 presented at the Toronto, Canada, Meeting of the Society, May 11-16, 1975.

Any discussion of this paper will appear in a Discussion Section to be published in the June 1977 JOURNAL. All discussions for the June 1977 Discussion Section should be submitted by Feb. 1, 1977.

Publication costs of this article were assisted by the University of Cincinnati.

#### REFERENCES

1. T. M. Kenyhercz and H. B. Mark, Jr., Submitted to *J. Phys. Chem.*
2. T. M. Kenyhercz, A. M. Yacynych, and H. B. Mark, Jr., Submitted to *J. Am. Chem. Soc.*
3. T. M. Kenyhercz, T. P. DeAngelis, B. J. Norris, W. R. Heineman, and H. B. Mark, Jr., Submitted to *J. Am. Chem. Soc.*
4. F. M. Huennekens, in "Biological Oxidations," Thomas P. Singer, Editor, pp. 482-502, Interscience Publishers, New York (1968).
5. S. L. Tackett, J. W. Collat, and J. C. Abbott, *Biochem.*, **2**, 919 (1963).
6. J. W. Collat and J. C. Abbott, *J. Am. Chem. Soc.*, **86**, 2308 (1964).
7. G. N. Schrauzer, E. A. Deutsch, and R. J. Windgasen, *ibid.*, **90**, 2441 (1968).
8. R. Yamada, S. Shimizu, and S. Fukui, *Biochem.*, **2**, 1713 (1968).
9. H. Rudiger, *Eur. J. Biochem.*, **21**, 264 (1971).
10. R. L. Birke, G. A. Brydon, and M. F. Boyle, *J. Electroanal. Chem.*, **52**, 237 (1974).
11. W. R. Heineman, T. P. DeAngelis, and J. F. Goelz, *Anal. Chem.*, *In press*.
12. W. R. Heineman, B. J. Norris, and J. F. Goelz, *ibid.*, **47**, 79 (1975).

13. However, experiments were performed with the minigrad electrode area increased to cover the entire cell volume (maxigrad cell). This was done to determine if edge effects from the diffusion of unreduced cob(III)alamin from the bulk of solution which was not in contact with the grid surface affected the time-resolved spectra. No difference between the spectra obtained using the maxigrad and minigrad electrode cells was observed.
14. J. W. Strojek, G. A. Gruver, and T. Kuwana, *Anal. Chem.*, **41**, 481 (1969).
15. H. B. Mark, Jr., et al., in "Computer Assisted Chemical Research Design," S. Fujiwara and H. B. Mark, Jr., Editors, University of Tokyo Press, Tokyo, Japan (1975). In press.
16. T. M. Kenyhercz and H. B. Mark, Jr., *Anal. Lett.*, **7**, 1 (1974).
17. S. L. Tackett and J. W. Ide, *J. Electroanal. Chem.*, **30**, 510 (1971).
18. P. G. Swetik and D. G. Brown, *ibid.*, **51**, 433 (1974).
19. J. Heyrovsky' and J. Kuta, "Principles of Polarography," p. 168, Academic Press, New York (1966).
20. J. Heyrovsky' and J. Kuta, *ibid.*, pp. 175-176.
21. J. M. Pratt, "Inorganic Chemistry of Vitamin B<sub>12</sub>," p. 162, and references therein, Academic Press, New York (1972).
22. W. M. Scovell, *J. Am. Chem. Soc.*, **9**, 3451 (1974).
23. G. H. Beaven and E. A. Johnson, *Nature*, **176**, 1264 (1955).
24. J. M. Pratt, "Inorganic Chemistry of Vitamin B<sub>12</sub>," p. 184, Academic Press, New York (1972).
25. J. M. Pratt, *ibid.*, p. 55.
26. F. Basolo and R. G. Pearson, "Mechanisms of Inorganic Reactions," p. 144, John Wiley & Sons, Inc., New York (1967).
27. J. M. Pratt, "Inorganic Chemistry of Vitamin B<sub>12</sub>," p. 109, Academic Press, New York (1972).
28. E. Kaczka, D. E. Wolf, and K. Folkers, *J. Am. Chem. Soc.*, **71**, 1515 (1959).
29. J. M. Pratt, "Inorganic Chemistry of Vitamin B<sub>12</sub>," p. 20-27, Academic Press, New York (1972).
30. The cyanoaquocob(III)inimide was prepared by a previously described method: Ref. 21, p. 294.

## Corrosion and Thrombogenesis of Cardiovascular Prostheses

N. Ramasamy,\* B. R. Weiss, B. Stanczewski, and P. N. Sawyer

*Electrochemical and Biophysical Laboratories and the Vascular Surgical Services,  
Departments of Surgery and Surgical Research, State University of New York,  
Downstate Medical Center, Brooklyn, New York 11203*

and G. W. Kammlott

*Bell Telephone Laboratories, Murray Hill, New Jersey 07974*

### ABSTRACT

*In vitro* methods have been developed over the last several years to predict the implantation behavior of cardiovascular prostheses. With metals and alloys, their spontaneous potentials in blood or physiological saline, the corrosion behavior in sodium chloride, and surface cleanliness are factors that determine the *in vivo* patency in animals and humans. The materials used for cardiac valves have a wide passivation region. *In vivo* monitoring of cardiac prostheses indicates an anodic shift of their rest potentials. Surface contamination appears to cause premature thrombosis and occlusion of cardiac valves.

### Blood and Biocompatibility of Prosthetic Materials

Substitution or replacement of living tissues by artificial materials brings in its wake the problem of biocompatibility. Biocompatibility comprises a broad area covering a number of different types of prosthetic materials; dental, orthopedic, and cardiovascular (Table I). The mechanical, biochemical, and physicochemical requirements of prosthetic materials differ widely for these applications. While noninteraction with the surrounding tissue or body fluids is a primary condition for any implant, the requirements become far more stringent when it comes to cardiovascular prostheses. In this review we plan to cover the problems met with, and progress made in, the use of metallic prosthetic materials in the cardiovascular systems of animals and man.

Cardiovascular applications are varied and cover a very wide range, from *in vitro* and *ex vivo* devices such as cardiopulmonary bypasses and dialyzers, to *in vivo* prosthetic shunts, bypass grafts, and cardiac valves (Table I). Prosthetic materials that are used in any of these applications must satisfy some basic criteria of blood compatibility (Table II) (1). The material foreign to the body must have minimal effects on (i) denaturation of plasma proteins, (ii) red cell destruction due to toxicity of the material, (iii) platelet adhesion, release, and aggregation, and (iv) destruction or activation of blood coagulation factors resulting in

thrombogenesis. If the prosthetic material is of biologic origin, such as porcine or bovine heterografts, the antigenic property also becomes an important parameter in determining its acceptance.

### Polymeric Materials as Prostheses

The choice of the material depends on the end use. For bypass grafts and shunts (Table I), porosity and

Table I.

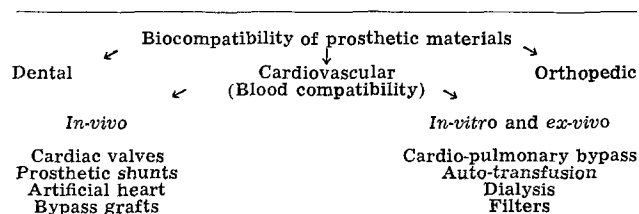
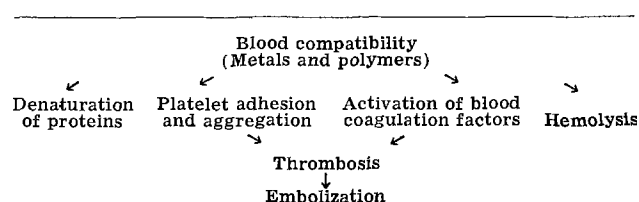


Table II.



\* Electrochemical Society Active Member.

Key words: thrombogenesis, prostheses, corrosion, metals.

flexibility are very important for *in vivo* patency. Dacron velours, expanded polytetrafluoroethylene, knitted dacron tubes and heterografts are normally used extensively for these applications.

Because of the various uses for polymers as blood compatible materials in the cardiovascular system, extensive studies have been carried out on (i) interactions of polymer surfaces with blood cells (2) and blood proteins (3), (ii) modification of surfaces of polymers by chemically binding with anticoagulants (4) and fibrinolytic agents (5), (iii) alteration of the constituent ionic groups (6) or use of chemical building blocks of desired structures (7) to synthesize suitable polymers, (iv) devising methods to increase the distribution of pores and regulation of pore size (8), (v) increasing the hydrophilic character (9), and (vi) modification of surfaces using the electret effect (10). These studies have led to the development of blood compatible polymers of better durability.

A few theoretical criteria have been developed to predict the *in vivo* patency of a polymeric material. As animal experimentations are expensive, a preliminary screening by *in vitro* techniques such as adsorption of platelets from whole blood (11), critical surface tension (12), and net surface charge (13) have been helpful in selection of materials. A number of basic studies concerning interactions of blood proteins at the molecular level have been carried out. As the purpose of this communication is to describe the work relating to the use of metals and alloys as cardiovascular prostheses, these aspects are not elaborated.

### Metallic Prostheses

Metals and alloys are mainly used in cardiac valves, as, the positioning of the valve in the heart, ease of implantation, and flow conditions require sufficient mechanical strength of the material. The *in vitro* and *in vivo* methods of evaluation of a metallic prosthesis are described in Table III. Very low corrosion, low toxicity and blood destruction, nondenatured adsorption of blood proteins, low degree of platelet aggregation or adhesion are all necessary conditions for satisfactory function of a prosthesis in the vascular tree. However, factors like flow through the valve, stasis, turbulence pockets, and contamination can lead to premature failure of an otherwise satisfactory material or device. In the subsequent sections are described: (a) the *in vitro* tests, (b) an analysis of the factors contributory to thrombogenesis of metallic prostheses, (c) *in vivo* dysfunction, and (d) a few typical results of implantation of materials to illustrate how these factors contribute to proper function of the valves.

#### *In Vitro* Methods of Evaluation

**Corrosion studies.**—*Determination of open-circuit potentials.*—It has long been recognized that thrombosis is an interfacial reaction. In metals and alloys, their spontaneous potentials in blood or physiologic saline (0.9% NaCl) give an indication of thrombogenicity (14). It was observed that noble metals developing highly positive spontaneous potentials *vs.* NHE in blood or physiologic saline are invariably thrombogenic. Base metals like aluminum, on the other hand, tend to be nonthrombogenic (14). With metals and alloys, it is felt that a factor that determines interactions with blood is the point of zero charge (pzc)

of the component metals (15) and how anodic the rest potential of the alloy is to the pzc of these component metals. It has been generally observed that *in vivo* implantation of the material results in a progressive anodic shift in rest potentials (16). Prosthetic cardiac valves and experimental tubes of the same material have been known to show wide variation in their rest potentials due to storage and accumulation of corrosion products (17). It has been recently observed that commercially available cardiac valves that have welded portions show different potentials at different points of the strut (17). An inhomogeneous potential difference between parts of the same valve can be contributory to thrombosis. Thus the determination of rest potential of the metallic prosthesis gives a first indication of its prospective use in the cardiovascular system.

An extensive electrochemical study of materials for surgical implants in chloride media has been carried out (18). Iron, nickel, cobalt, and titanium based alloys were used for the investigation. Current-potential and potential-time curves were determined in NaCl and Hank's solution. The schematic of open-circuit potential-time curves (*E-t*) is shown in Fig. 1. Alloys which are potentially useful as implantable materials should have an intact passive film as shown by the *E-t* curve in Fig. 1 (curve c). Vitallium, titanium, and some of its alloys, exhibit this type of potential-time behavior (18). Open-circuit potential-time studies were carried out in Hank's solution using mechanical and electropolished titanium alloys (19). The effects of including amino acids such as tryptophan, cysteine, glycine, cystine, and uric acid (the building blocks of most physiological proteins) on the *E-t* curves were also studied (19). It is observed that addition of these acids to the solution brings about an anodic shift in open-circuit potentials. These findings are similar to our observation of anodic shift in rest potential of implanted materials *in vivo* (16).

**Polarization studies.**—*In vitro* and *in vivo* galvanostatic, potentiostatic, and linear polarization studies have been carried out for a number of metals and alloys used as surgical implants over the last several years (18-28).

The effects of aeration of solution, cold-working, and annealing of some stainless steels have been studied using steady-state potentiostatic current-potential (*i-E*) determinations (20). Aeration has a marked effect on the shape of *i-E* curves of stainless steel 316 in Ringer's solution. Saturation of solution with oxygen shifts the passive breakdown potential relative to the deaerated solution by +350 mV *vs.* NHE. The oxygen capacity of human blood is reported to be 20 ml oxygen/100 ml (29) and plasma oxygen pressure in the human artery is 85 mm Hg (30). Thus it is very important to know the alteration in corrosion behavior of metals and al-

Table III.

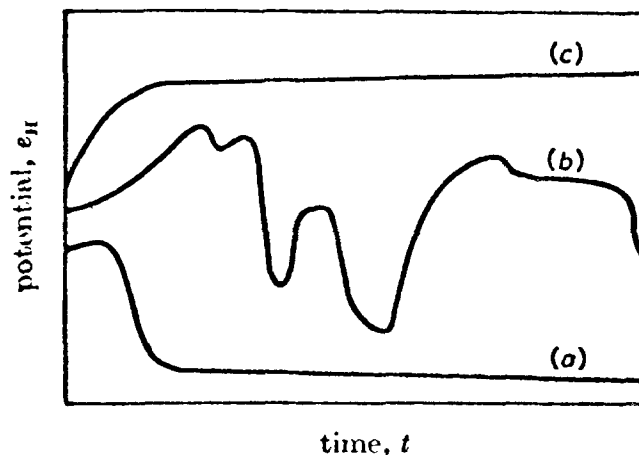
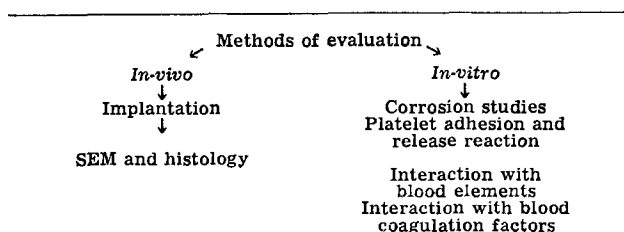


Fig. 1. Schematic potential-time curves (a) general corrosion, (b) pitting corrosion, and (c) film remains intact.

loys due to oxygenation. Metallurgical processes like cold-working and annealing have distinct effects on passivation region, transpassive current-potential behavior, and breakdown potential for stainless steel 316. A comparative evaluation of titanium, Vitallium, and stainless steel clearly shows the remarkable passivity of titanium. Polarization studies show that pure titanium remains passive in the potential range  $-0.05$  to  $+1.15\text{V vs. NHE}$  (20). Figure 2 shows the striking passivity of titanium compared to annealed 316 stainless steel and cast Vitallium. Even Vitallium, which shows marked resistance to pitting attack, does not exhibit the polarization characteristics and passivity of pure titanium (20).

This group has done some studies with Haynes-25 to determine the polarization behavior of the alloy in deaerated physiologic saline. (21). Figure 3 shows the steady-state potentiostatic current-potential curve

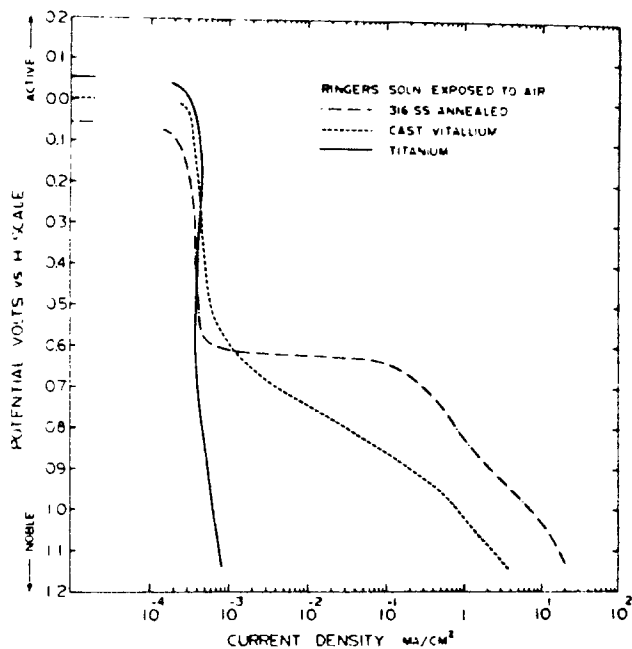


Fig. 2. Polarization behavior of annealed 316 stainless steel, cast Vitallium, and titanium in Ringer's solution.

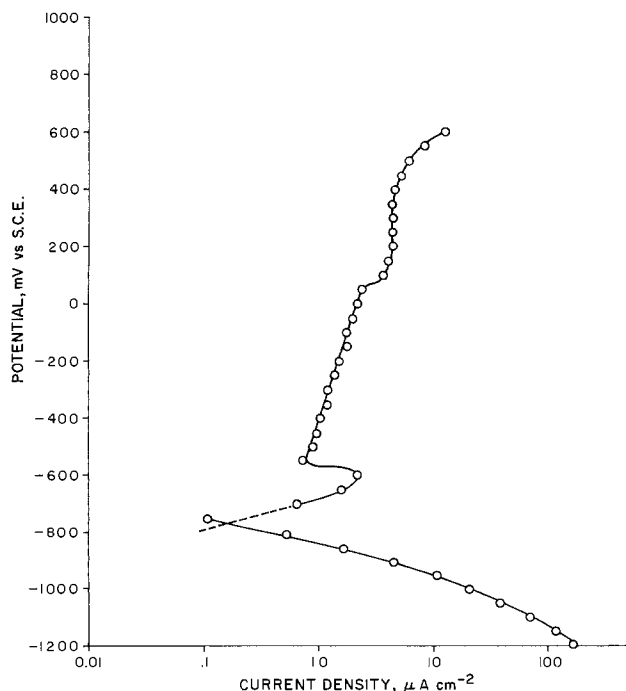


Fig. 3. Polarization behavior of Haynes-25 alloy in 0.9% NaCl

(log  $i-E$ ) for Haynes-25 alloy in normal saline. The alloy has an extensive passive region ( $-600$  to  $+400$  mV SCE) and low corrosion ( $0.1 \mu\text{A cm}^{-2}$ ) and passivation ( $1.2 \mu\text{A cm}^{-2}$ ) current densities. These characteristics make the alloy relatively passive in a chloride ion environment.

Corrosion characteristics of various anode materials used in implantable power sources were determined using *in vitro* and *in vivo* polarization studies (22). *In vitro* anodic linear polarization studies in 0.9% NaCl showed corrosion rates of zinc and magnesium alloy AZ31B to be two to three orders of magnitude greater than that of aluminum under no load conditions. A significant decrease in corrosion currents for each of the metals following autoclave sterilization was observed. Loading of the anode at  $25 \mu\text{A cm}^{-2}$  (equivalent to that used for powering presently available commercial pacemakers) increases the corrosion current for both zinc and aluminum metals, although, more so for the latter (22). These *in vitro* and *in vivo* corrosion studies showed the desirability of aluminum as an implantable anode to power pacemakers.

*Effect of surface treatment on corrosion and passivity.*—Aside from the base material used, surface preparation is of great importance in the incidence and rate of corrosion. This broad heading includes electrochemical and mechanical cleaning and polishing as well as sterilization techniques. The effect of chemical cleaning of Ti-6Al-4V with conc HCl on current-potential curve is seen in Fig. 4 (23). Since the HCl-treated sample has slightly higher passivation and corrosion currents, it is possible that the HCl treatment de-passivates the surface.

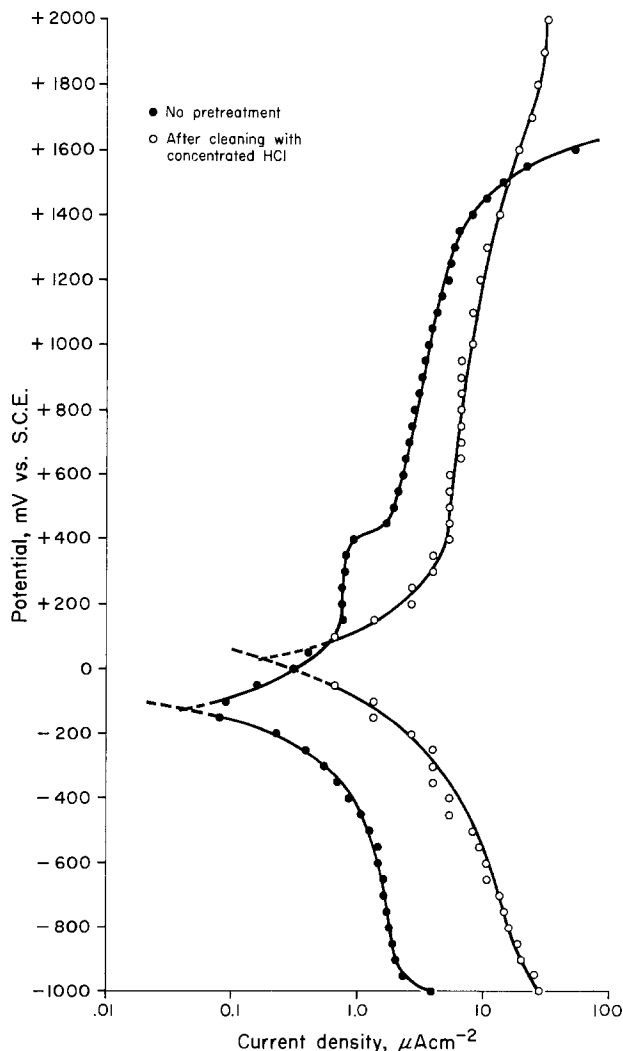


Fig. 4. Polarization behavior of Ti-6Al-4V alloy in 0.9% NaCl

The effects of surface roughness, prepassivation, and sterilization on the corrosion behavior of titanium, Vitallium, and stainless steel 304 and 316 were determined (24, 25). As could be expected, surfaces which were sandblasted, rough and fine mechanically polished and electrochemically polished (stainless steel 316 samples) showed a wide variation in passivation currents ( $i_{pass}$ ). There was a difference of an order of magnitude in  $i_{pass}$  between sandblasted and electropolished samples. Prepassivation of surfaces tends to reduce the  $i_{pass}$  of stainless steel and Vitallium though the effects on titanium are less marked (24). Our implantation studies with aluminum and Stellite surfaces show that proper surface treatment has a definite effect in prolonging the patency of the material in the animal (26, 27).

The effect of sterilization, a procedure carried out prior to implantation, on subsequent corrosion behavior has also been studied (19, 25, 28). Electron diffraction studies of surfaces of some titanium alloys which were steam sterilized after electropolishing show the presence of oxides of titanium on the surface formed due to sterilization (19). It is believed that these can provide better initial protection for the implant. Steam sterilization has only minimal effect on  $i_{pass}$  of titanium, but leads to a marked reduction in  $i_{pass}$  of stainless steel (25). The *in vivo*  $i_{pass}$  is also reported to be decreased due to sterilization of some stainless steels (28).

As a final note, it should be pointed out that although sterilization tends to decrease corrosion, it appears to enhance surface thrombogenicity due to extraneous contamination. This effect of sterilization is dealt with later in the section on contamination and valvular dysfunction.

#### Platelet Adhesion and Release Reaction

A thrombus is formed *in vivo* by the following stages. Platelets from circulating blood stream adhere to a foreign surface or to the site of vascular injury. The adhesion of platelets leads to platelet release reaction, a process in which they exude a number of biochemical agents including adenosine tri, di, and monophosphates (ATP, ADP, and AMP) and glucose-6-phosphate (G-6-P) (31). Release of ADP in turn leads to sticking together of more platelets. This process is called platelet aggregation. The aggregated platelet plug is the first line of defense in preventing excessive blood loss due to injury. After this primary hemostasis, a permanent process of activation of blood coagulation proteins takes place resulting in polymerization of fibrinogen to fibrin (31). The fibrin strands trap further cellular elements to form a firm clot called a thrombus. This necessary defense reaction of the body, when triggered on a prosthetic material, leads to thrombosis and obstruction of function of the prosthesis.

From the foregoing, it is clear that the study of platelet adhesion and release reaction *in vitro* provides a valuable method in predicting the *in vivo* interactions. Platelet adsorption from whole blood has been used in the evaluation of blood compatibility of polymeric materials (11).

Cell precipitation or potential dependent adhesion of red cells and platelets has been studied using platinum electrode (32). It is observed that at potentials more anodic than +200 mV NHE, there is increased cell adhesion. Drugs that are well-known anticoagulants, those that affect platelet aggregation, and membrane poisons reduce the cell adhesion to platinum at all potentials (33), (Fig. 5). Metals and alloys that are presently used as prosthetic materials are now being studied using this test system to determine the extent of platelet adhesion.

Effect of some metals and alloys on platelet release reaction was investigated using rat platelets (34). Platinum, silver, copper, nickel, zinc, aluminum, and stainless steel powders were incubated with washed rat platelets and the release of adenine nucleotides

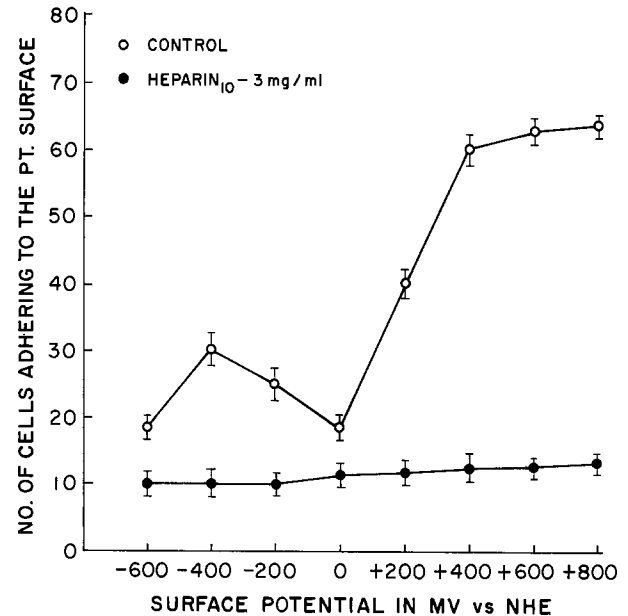


Fig. 5. Effect of heparin on potential dependent adhesion of platelets to platinum.

ATP, ADP, and AMP and G-6-P were determined. The results show (Fig. 6) that the highly corrodible metals like Mg, Zn, and Fe and readily complexed Cu cause extensive cellular destruction. Aluminum, nickel, and stainless steel do not cause either destruction of platelets or significant release of adenine nucleotides. Metals like Ag and Pt cause release of adenine nucleotides from platelets. As the release reaction results in platelet aggregation, it appears that those noble metals that show positive potentials in blood can cause platelet aggregation and subsequent thrombosis. These findings essentially agree with the earlier observations relating rest potentials of metals to thrombogenesis (14).

#### Interaction with Blood Elements

Circulating blood contains, in addition to platelets, red cells, leukocytes, lymphocytes, and blood coagulation proteins. Destruction of platelets leading to the release reaction has been discussed. Recent studies have shown that leukocytes are possibly involved in occlusion of prosthetic devices used *in vitro* and *in vivo*. The evidence is essentially circumstantial and one of the initial events taking place when a foreign surface, (e.g., kidney dialyzer) comes in contact with blood is entrapment of leukocytes (35). Some animal studies also have shown that leukocytes are implicated in the pathogenesis of thrombosis (36). But detailed investigation as to interactions of foreign surfaces with leukocytes is lacking.

Red cell destruction is another important parameter. This is otherwise called hemolysis. A few tests reveal the occurrence of hemolysis due to implanted materials (37). A lowering of hematocrit is a direct indication of hemolysis. A few other indicators are plasma hemo-

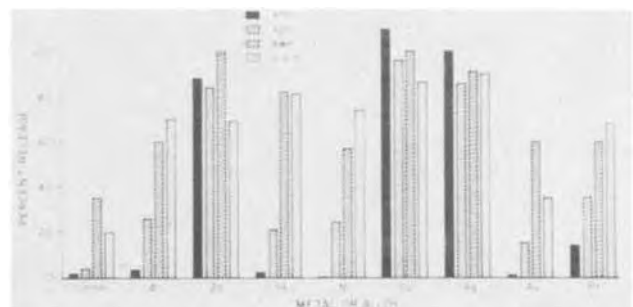


Fig. 6. Effect of some metal powders on the release of adenine nucleotides from platelets.

Table IV. Destructive and thrombotic effects of some metal powders on canine blood

Metal	pH change*	% Red cell destruction	% White cell destruction	% Change clotting time
Magnesium	+2.8	99	94	+51
Aluminum	+0.1	25	29	+45
Zinc	+0.9	51	35	+40
Stainless steel 304	+0.1	20	28	+33
Cobalt	+1.5	29	50	+33
Nickel	+0.2	21	47	-47
Copper	+0.1	39	36	-36
Platinum	+0.1	41	36	-36
Gold	+0.2	31	37	-37

Concentration of metal powder 50 mg/ml.

\* (+) Increase. (-) Decrease.

Table V. Effect of metal powders on coagulation of fibrinogen

Metal	Solution	$\Delta$ pH	Thrombin time (sec)	
			Control	Treated
Aluminum	Phosphate (pH 7.4)	+0.2	33.5 $\pm$ 1.8	29.9 $\pm$ 3.1
Copper	0.9% NaCl (pH 7.2) (restored to 8.4)	+3.2	19.4 $\pm$ 0.6	>2000 >1000
Silver	Tris (pH 7.3)	—	15.9 $\pm$ 0.3	15.8 $\pm$ 0.4
Gold	Tris (pH 7.3)	+0.05	15.9 $\pm$ 0.3	15.3 $\pm$ 0.3
Stainless steel 304	Tris (pH 7.4)	+0.5	21.0 $\pm$ 0.4	19.1 $\pm$ 0.9

globin, serum iron, red cell survival, serum hepatoglobin, urine hemoglobin, and urine iron.

The *in vitro* cell destruction has been determined for many metals and alloys. Using canine erythrocytes (red cells) and metal powders (Mg, Al, Zn, Cu, Ag, and Pt) the red cell destruction has been determined (38). The results show that metals like copper, platinum, zinc, and magnesium are highly toxic and lead to significant red and white cell destruction (Table IV). The importance of minimal red cell destruction can be understood from the fact that even a very mild red cell destruction of 0.08% in 24 hr due to a practical cardiac valve results in an increased production load on the bone marrow of 10% to prevent occurrence of hemolytic anemia (39).

#### Interaction with Blood Coagulation Factors

The interfacial reactions of blood coagulation proteins at metallic surfaces have been investigated extensively at the basic level using many electrochemical techniques (40-46). The adsorption and charge transfer reactions of purified blood proteins have been studied at platinum, mercury, and gold-solution interfaces (40-45). In general, highly cathodic potentials lead to desorption of blood proteins at the interface while anodic potentials show an increase in adsorption. Fibrinogen seems to be "electropolymerized" to fibrin-like material at anodic potentials (45). Fibrinogen is readily adsorbed on to the metallic surfaces. The strong adsorption of fibrinogen may be due to the number of tryptophan residues in the molecules (44).

The effect of certain metal powders on whole blood clotting times (38), fibrinogen polymerization time, and thrombin recalcification time for plasma were determined (47). Some of the typical results are shown in Tables IV-VI. It is observed that copper is readily

complexed by blood proteins and hence results in abnormally long clotting times. The effects of aluminum, gold, and platinum on plasma and fibrinogen clotting times appear to be minimal, especially if fibrinogen solutions are well buffered. Copper is complexed by blood proteins as can be seen by the development of blue color and incoagulability of fibrinogen and plasma.

The importance of extension of such studies to practical prosthetic materials that are presently used in cardiac valves need not be overemphasized. Adsorption and activation of blood proteins at surfaces can serve as a trigger mechanism for the blood coagulation cascade resulting in conversion of fibrinogen to fibrin (48). Fibrin is the essential constituent of all formed thrombi *in vivo*. A basic understanding of adsorption of blood coagulation proteins at these metal (alloy)-solution interfaces is necessary for proper choice of blood compatible materials. The studies carried out using Pt, Hg, and Au show that anodic potentials favor adsorption (40-45). An *in vivo* follow up of potentials of implanted prostheses show an anodic shift with time (16). Thus the study of potential dependent adsorption of proteins and consequent transformation or denaturation will be highly fruitful. With practical prostheses, however, such studies have not been reported.

Recently adsorption of fibrinogen on Stellite-21 has been studied using radioactively labeled fibrinogen (49). The results are of particular relevance in the design and manufacture of cardiac valves. It was observed that adsorption of fibrinogen is (i) less on polished glass compared to polished Stellite-21, (ii) the amount of fibrinogen adsorbed on to polished Stellite-21 is dependent on polishing characteristics of the surfaces, and (iii) Teflon-coated Stellite-21 surfaces adsorb more fibrinogen (Fig. 7) (49).

#### In Vivo Evaluation

The *in vivo* evaluation of a material which has satisfactory *in vitro* interactions could be carried out in a number of ways. Polymeric tubes and materials have been tested on an *ex vivo* system by extra-corporeal shunting of the artery of experimental animals through the prostheses (50). This is a fast and inexpensive short-term study where one can examine the thrombi deposited in short periods of time. A more stringent preliminary method of evaluation is to implant the prosthesis in the form of a Gott ring (51) or Sawyer tube (52) in the thoracic inferior vena cava or descending thoracic aorta of an experimental animal for varying periods of time. On removal, the implant is visually examined for junctional thrombus and the nature of thrombus deposited is studied by histologic and electron microscopic techniques.

#### Thrombogenic Propensity of Metallic Prostheses: Alteration by Artificial Means

A potentially highly thrombogenic metallic prosthesis can be made virtually thrombus-free *in vivo* by artificial means. As described earlier, metals and alloys that show highly negative spontaneous potentials in blood or physiologic saline are nonthrombogenic (14). If materials that develop positive spontaneous potentials are maintained at cathodic potentials by passing a cathodic current (53) or galvanic coupling (54), the *in vivo* patency can be radically improved. The re-

Table VI. Effect of metal powders on coagulation of plasma

Metal	TRT* (sec)		APTT** (sec)		RCT† (sec)	
	Control	Treated	Control	Treated	Control	Treated
Copper	15.0 $\pm$ 0.1	>500	44.0 $\pm$ 2.0	>500	105.2 $\pm$ 0.8	>1000
Stainless steel 304	8.5 $\pm$ 0.5	6.9 $\pm$ 0.4	35.8 $\pm$ 2.4	25.8 $\pm$ 1.3	143.8 $\pm$ 3.0	130.2 $\pm$ 4.0
Gold	9.3 $\pm$ 0.4	9.1 $\pm$ 0.3	36.5 $\pm$ 3.3	38.0 $\pm$ 2.0	102.9 $\pm$ 0.7	108.0 $\pm$ 2.3

\* TRT = Thrombin recalcification time.

\*\* APTT = Activated partial thromboplastin time.

† = Recalcification time.

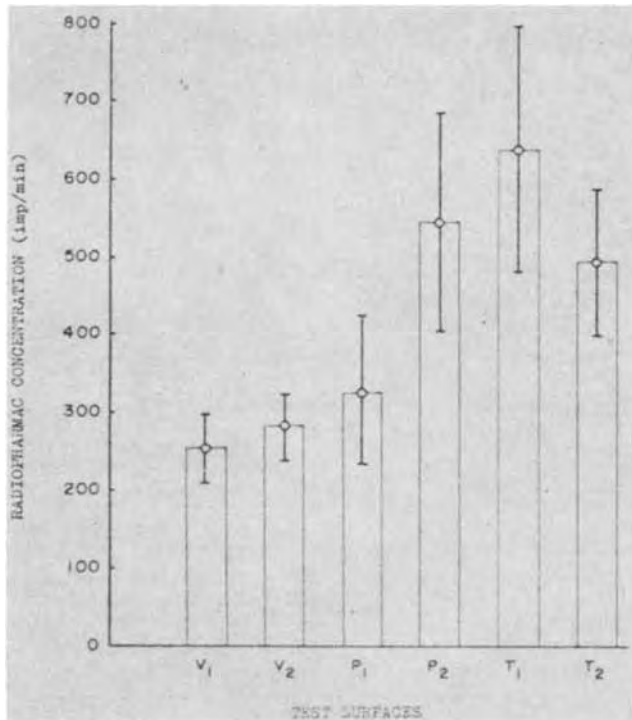


Fig. 7. Adsorption of  $^{125}\text{I}$  labeled fibrinogen to (a) polished glass ( $V_1$  and  $V_2$ ); (b) polished Stellite-21 ( $P_1$  and  $P_2$ ); and (c) Teflon-coated Stellite-21 ( $T_1$  and  $T_2$ ) surfaces.

sults of such studies clearly show the importance of negative potentials in maintaining *in vivo* patency of a metallic implant in the cardiovascular system. Two typical examples of prosthetic materials illustrate this point.

Copper is highly thrombogenic, toxic to blood, complexed by body proteins, and occludes completely in a few hours when implanted as a cardiac valve or as a tube (in canine thoracic inferior vena cava) (53). A thrombosed copper prosthesis is shown in Fig. 8. When the copper tube is maintained at a negative potential either by passing a cathodic current (Fig. 9) (53), or high frequency (100 Hz) alternating current (Fig. 10) (55), no thrombus is deposited in the tube for as long as the circuits are operational. It is clear from Table VII that both the techniques result in development and maintenance of a negative potential on the prostheses in the blood stream. Histologic evaluation of the thin deposit on the tubes that have been polarized by a.c. reveals randomly scattered green, brown, and red specks throughout the protenacious matter indicating leaching of Cu as Cu(II) that gets later precipitated

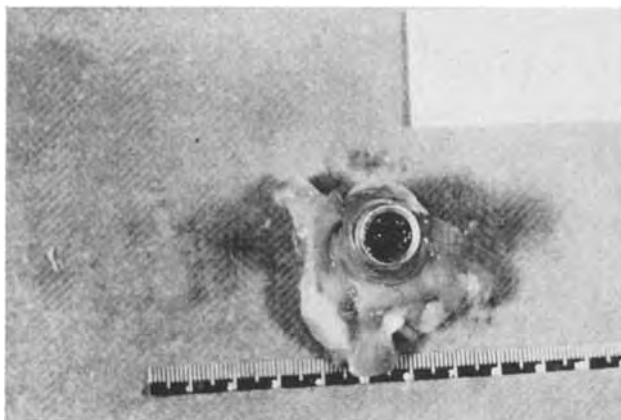


Fig. 8. A fully thrombosed copper tube implanted for a day in the thoracic inferior vena cava of a dog.

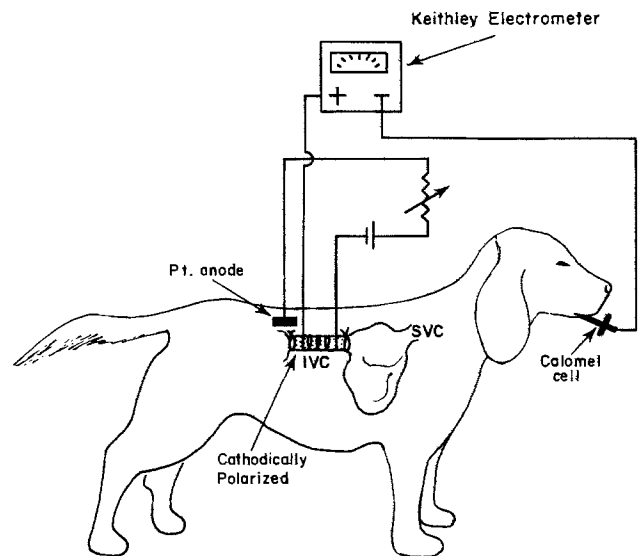


Fig. 9. Cathodically polarized copper tube in a dog, schematic including method for determination of *in vivo* rest potential.

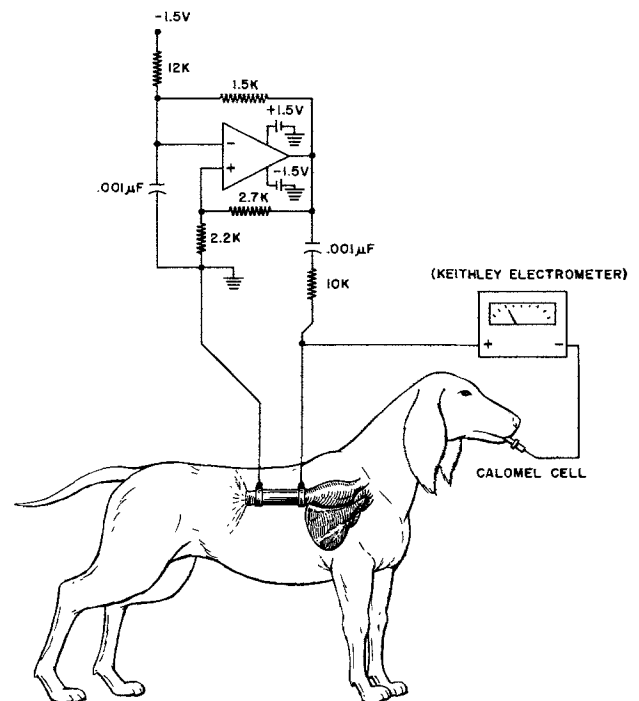


Fig. 10. Copper tube with 100 kHz a-c polarization, schematic

probably as basic copper oxides (55). Thus the inherent reactivity of copper is still observable though the thrombotic problems are virtually eliminated.

Another equally interesting case investigated is a titanium alloy (Ti-6Al-4V). Corrosion studies with this alloy have been carried out (Fig. 4) (23). The *i-E* curve shows a large passive region with low corrosion and passivation currents. But the rest potentials are positive vs. NHE (Table VIII). Tubes of the alloy, irrespective of the mode of pretreatment, occlude completely in the animal and the longest survivor lasted only for 135 min (Table VIII). The same material was galvanically coupled with aluminum and one could see from Table IX the improvement in *in vivo* patency. As could be expected, wrapping aluminum foil on the outside of the tube shifts the rest potential to highly cathodic values and tubes are thrombus-free.

#### Factors Resulting in Dysfunction of Cardiac Valves

*Choice of material and design of the valve.*—Metallic heart valves in major use today, are the Starr-Ed-

Table VII. Results of implantation of copper tubes in canine T.I.V.C.\*

Group	Potential of the tube (mV vs. NHE)			Duration of implantation H (hr) D (days)	Condition of tube at sacrifice
	Before implantation	After implantation	Postmortem		
I Control copper	+80	+10	+40	2 H	90% Occlusion
	+110	+10	+90	6 H	90% Occlusion
	+10	-100	+100	24 H	90% Occlusion
II Cathodically polarized -380 $\mu$ A -190 $\mu$ A -190 $\mu$ A	+60	-160	+40	6 D	Minimal junctional thrombi
	+60	-60	+20	8 D	Minimal junctional thrombi
	+60	-60	+40	14 D	Minimal junctional thrombi
III A-C polarized 100 kHz, 200 mV† 10 $\mu$ A 10 $\mu$ A 10 $\mu$ A 10 $\mu$ A	+90	-60	-110	2 H	No visible thrombi
	+40	-100	-90	6 H	No visible thrombi
	+40	-110	-100	1 D	No visible thrombi
	+40	-110	-80	1 D	No visible thrombi
	+40	-110	-80	42 D	No visible thrombi

\* = Thoracic inferior vena cava.

† = Peak to peak.

wards, Lillehei-Kaster, Bjork-Shiley and Smelloff-Cutter valves. Only titanium and cobalt base alloys are used for the manufacture of these valves; Stellite-21 (Starr-Edwards series), titanium (Smelloff-Cutter, Lillehei-Kaster), and Haynes-25 (Bjork-Shiley). The compositions of the two alloys are given in Table X (56, 57). Based on open-circuit potential-time measurements, and *in vitro* and *in vivo* corrosion studies, it was felt that the best materials for surgical implants are titanium and cobalt based alloys (18). All these metals are passive in chloride medium, take a good mechanical polish, are mechanically strong, and have minimal blood cell and blood protein interactions. The disk or

ball used in these valves are made of either Stellite, silastic or pyrolytic graphite. These are also nontoxic and nonreactive. A successful cardiac valve must be designed in such a way as to lower blood trauma, possess long durability, develop low pressure gradient, and result in minimal regurgitation (39). These additional problems, caused by blood flowing through a valve that has impaired flow characteristics, and imperfect closing, can lead to serious valvular dysfunction.

Despite proper choice of materials, design and standardized methods of manufacture, packing and storage, varying degrees of success in long-term function of the valve have been achieved at different centers. The factors that are contributory to this unpredictable dysfunction are indicated in Table XI. The problems related to stasis of blood and hemolysis are tackled purely by better designs which result in (i) exposure of minimal areas for blood stasis, and (ii) reduced areas of overlap between the disk or ball and the seat, which lessens trauma to cellular elements in blood and hence lowers hemolysis. Another clinically relevant factor, though of not much interest from the electrochemical standpoint, is poor healing of the sutured valve, resulting in fibroblastic invasion, proliferation of collagen, total trapping of the disk or ball, and consequent failure. This problem has been virtually eliminated in our laboratory animal implantations by the autogenous venous ring technique (58).

**Contamination.**—This is one of the factors contributory to serious thrombosis and embolization. Only recently this aspect of valvular dysfunction has been recognized and studied in detail (26, 27, 59). Sources of surface contamination can occur (i) during manufacture, (e.g., polishing waxes), (ii) during storage, due to accumulation of corrosion products, (iii) during autoclaving prior to implantation, and (iv) during actual

Table VIII. Results of implantation of Ti 6-4 Eli Cutter Laboratories tubes in canine T.I.V.C.

Code Number SUNY	Cutter Labs	Rest Potential mV NHE			Time of Implanta- tion	Condition of Tube	Comments
		before cleaning	After HCl cleaning	After implanta- tion			
P-17-73	15	+60	-360	-30	1 Min		Sacrificed
P-14-73	23	-100	-	+200	15 Min		Sacrificed Junc. & laminar thrombus
P-13-73	22	+40	-660	0	15 Min		Sacrificed Junc. thrombus
P-12-73	16	+90	-240	+150	30 Min		Sacrificed Laminar throm- bus
P-11-73	25	+60	-70	-60	115 Min		Dead 100% occlusion
P-10-73	14	-100	-250	+90	135 Min		Dead 90% occlusion
P-15-73	19 *	-110	-360	+40	105 Min		Dead Junc. & laminar thrombus
P-16-73	30 *	+30	-340	+50	85 Min		Dead laminar throm.

\* Cathodically cleaned.

\*\* No HCl cleaning.

Table IX. Ti 6-4 Eli tubes galvanically coupled with aluminum. Results of implantation in canine T.I.V.C.

Code Number SUNY	Cutter Labs	Pre- treatment	Potential after galvanic coupling mV/NHE		Time of Implanta- tion	Condition of tube	Comments
			before	after			
P-20-74	17	-	-	-	1 Min.		Sacrificed clean
P-21-74	17	-	-	-	120 Min.		Sacrificed Junctional thrombus
P-22-74	18	-	-	-	120 Min.		Sacrificed Partially thrombosed
P-23-74	18	HCl	-510	-	120 Min.		Sacrificed clean
P-27-74	27	HCl	-510	-	120 Min.		Sacrificed Junctional thrombus
2-24-74	26	HCl	-510	-	120 Min.		Sacrificed Clean
2-25-74	21	HCl	-510	-	240 Min.		Dead Junctional thrombus
2-26-74	27	cathodic cleaning	-510	-	180 Min.		Dead Junctional thrombus

Table X. Composition of some alloys used as cardiac valves

Alloy	Percentage of elements							C	Co
	Cr	Mn	Fe	W	Ni	Mo	Si		
Stellite-21	27.0	1.0	3.0	—	2.5	5.5	1.00	0.25	Bal.
Haynes-25	20.0	1.5	3.0	15.0	10.0	—	1.00	0.15	Bal.

Table XI.

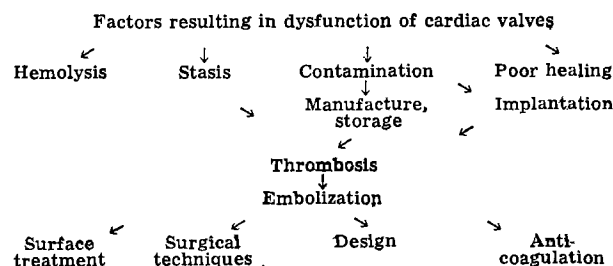






Fig. 11. Scanning electron microscopic (SEM) examination of a Stellite-21 Starr-Edwards heart valve showing the bare and contaminated surfaces.

implantation as a result of talc and foreign materials from gloves.

A systematic study of the influence of these factors has been made in our laboratories during the last five years. Scanning electron microscopy coupled with x-ray spectroscopy is a highly useful technique for "screening" and identification of surface contamination on cardiac valves. Figures 11 and 12 show the surface of a Starr-Edwards Stellite-21 valve subjected to different types of pretreatment and autoclaving. The incorporation of extraneous ions due to steam autoclaving could be seen clearly in the x-ray spectroscopic photographs (Fig. 12). In some of the cardiac valves removed due to failure, one could see fingerprints on the valve "preserved" by thrombi formed on these sites.

It thus appears extremely important to maintain care during pretreatment and implantation of these valves if reproducible long-term patency is to be achieved.

The contamination problem raises the question of the best method of pretreatment. We have obtained excellent results in animal implantation studies using electropolished or electrocleaned valves (26, 27). Figure 13 shows an electropolished aluminum valve implanted for 82 days. It is clear that even the striations on the strut surface, formed due to gas evolution during electropolishing, do not serve as foci for thrombus deposit.

The effect of the factors described above on the long-term survival of cardiac valves and tubes in experimental animals is seen clearly in Fig. 14 and 15. The function of aluminum and one of the commercially used cardiac valves are compared. One can see that thrombogenesis and long-term survival are critically dependent on type of surface treatment employed, the care with which implant was handled during surgery, and proper healing of the valve seat in the heart.

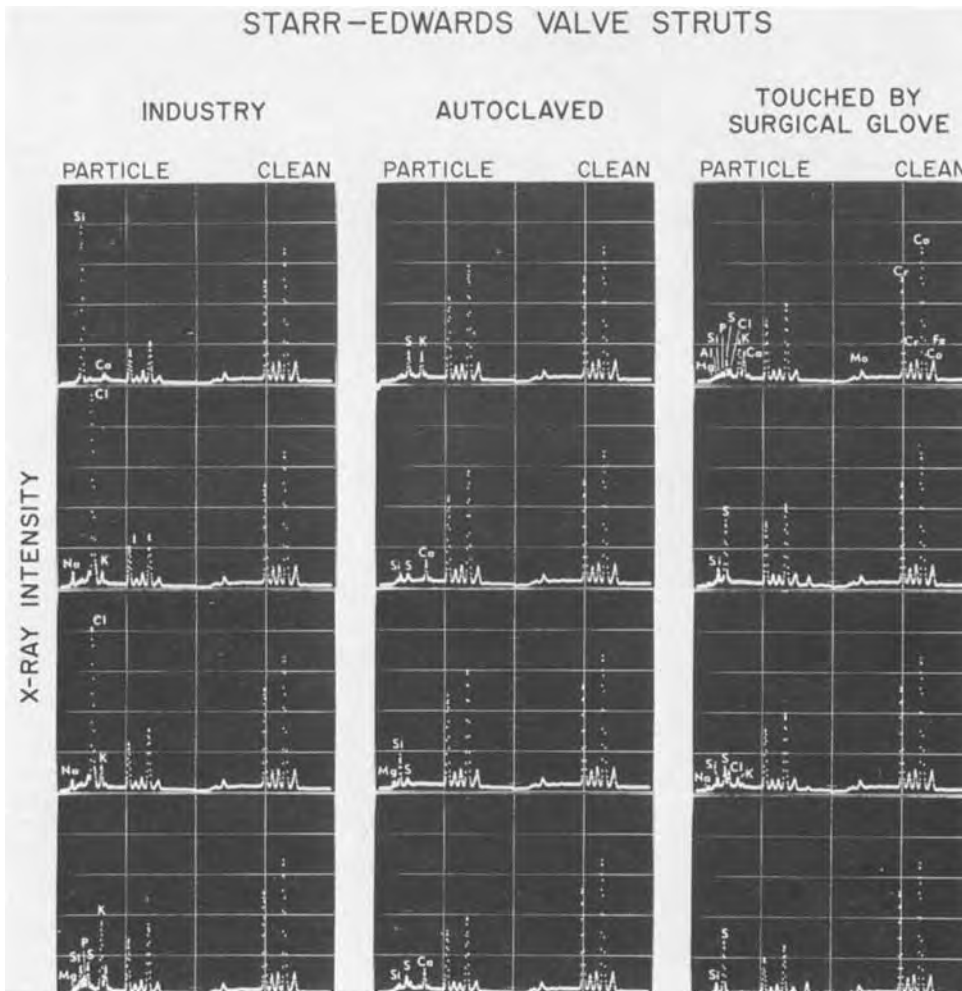


Fig. 12. Characterization of surface contamination using x-ray spectroscopy. The peaks on the left side marked "particle" of the three columns represent areas on Fig. 11 where one could see particulate matter. X-ray peaks on the right side of the three columns, marked "clean" represent the particle free areas of Fig. 11.

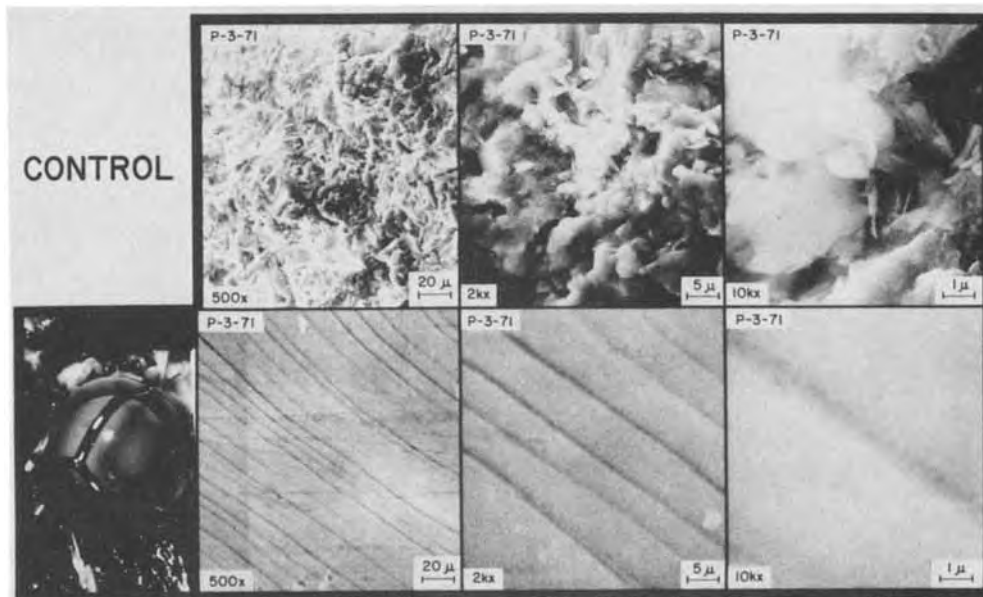


Fig. 13. Electropolished aluminum valve implanted for 82 days, on SEM study.

**Embolization.**—Despite the precautions taken during implantation, embolization is still a problem in humans. When a formed thrombus breaks loose and is carried away by the blood stream, the small thrombi, called emboli can cause death if they manage to occlude blood vessels in the brain or lung. Thus most humans with prosthetic heart valves are on some form of anticoagu-

lant therapy for the rest of their lives. Cases of fatality are reported due to insufficient anticoagulation (39).

**Conclusion**

A metal or an alloy that could be used as a cardiovascular prosthesis has to satisfy the following criteria: (a) the material must be passive or have very low corrosion rate in physiologic medium, (b) it should have low toxicity to blood cells, (c) the platelet adhesion and release must be minimal, and (d) it must not react or activate the blood coagulation proteins.

The spontaneous potential of the material appears to predict the *in vivo* function if it is clean. Thus metals showing high negative potentials (*vs.* NHE) are non-thrombogenic. In practical prostheses, additional factors, including design of the valve, contamination, and poor healing, can contribute to valvular dysfunction. *In vitro* corrosion studies and measurement of rest potentials give an indication of the suitability of a metal as a candidate for cardiovascular prosthesis. Electrochemical cleaning and polishing techniques appear to be effective in improving the long-term patency of many metallic cardiac implants.

Manuscript received June 30, 1975. This was Paper 370 presented at the Toronto, Canada, Meeting of the Society, May 11-16, 1975.

Any discussion of this paper will appear in a Discussion Section to be published in the June 1977 JOURNAL. All discussions for the June 1977 Discussion Section should be submitted by Feb. 1, 1977.

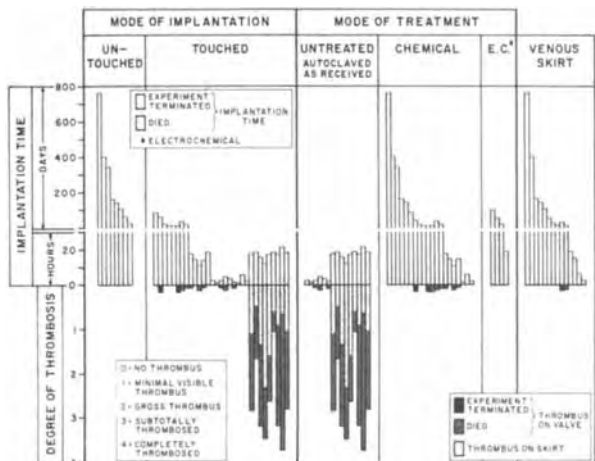


Fig. 14. Surface contamination and thrombogenicity of aluminum heart valves.

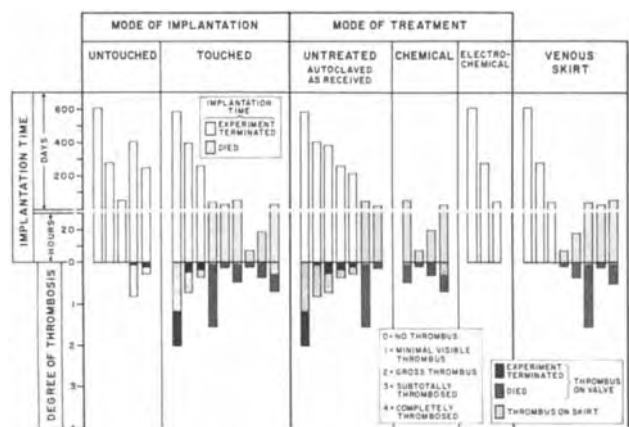


Fig. 15. Surface contamination and thrombogenicity of Starr-Edwards Stellite-21 heart valves.

**REFERENCES**

1. S. D. Bruck, *Biomat. Med. Dev. Art. Org.*, **1**, 79 (1973).
2. R. G. Mason, in "Progress in Hemostasis and Thrombosis," T. H. Spaet, Editor, Vol. 1, Grune and Stratton, New York (1972).
3. D. E. Scarborough, *Curr. Top. Path.*, **54**, 95 (1971).
4. L. S. Hersh, H. H. Weetall, and I. W. Brown, Jr., *J. Biomed. Mater. Res. Symposium*, **1**, 99 (1971).
5. B. K. Kusserow, R. Larrow, and J. Nichols, *Trans. Am. Artif. Int. Organs*, **17**, 1 (1971).
6. M. C. Musolf, V. D. Hulce, D. R. Bennett, and M. Ramos, *ibid.*, **15**, 18 (1969).
7. A. Renbaum, S. P. S. Yen, R. F. Landel, and M. Shen, in "Biomedical Polymers," A. Renbaum, and M. Shen, Editors, Marcel Dekker Inc., New York (1971).
8. C. D. Campbell, D. Goldfarb, D. D. Detton, R. Roe, K. Goldsmith, and E. B. Diethrich, *Trans. Am. Soc. Artif. Int. Organs*, **20**, 86 (1974).
9. O. Wichterle and D. Lim, *Nature*, **185**, 117 (1960).
10. R. J. Gable and R. A. Wallace, *J. Biomed. Mater. Res.*, **8**, 91 (1974).
11. D. J. Lyman, J. L. Brash, and K. G. Klein, in *Arti-*

- ificial Heart Program Conference Proceedings, June 1969, p. 113, Washington, D. C. U.S. Dept. of Health, Education and Welfare, U.S. Govt. Printing Office, Washington, D. C.
12. R. E. Baier and R. C. Dutton, *J. Biomed. Mater. Res.*, **3**, 191 (1969).
  13. P. N. Sawyer and S. Srinivasan, *Am. J. Surg.*, **113**, 42 (1967).
  14. P. S. Chopra, S. Srinivasan, T. Lucas, and P. N. Sawyer, *Nature*, **215**, 1494 (1967).
  15. P. N. Sawyer, J. C. Ogoniak, and P. J. Boddy, *Surg.*, **61**, 484 (1967).
  16. S. Srinivasan, N. Ramasamy, B. Stanczewski, and P. N. Sawyer, in "Cardiovascular Physics of Medical Procedures and Devices," D. N. Ghista, V. E. Vollenhoven, and W. J. Yang, Editors, Delft University Press, Holland, In press.
  17. B. Stanczewski, N. Ramasamy, and P. N. Sawyer, Unpublished results.
  18. T. P. Hoar and D. C. Mears, *Proc. R. Soc. London, Ser. A*, **294**, 486 (1966).
  19. A. C. Fraker, A. W. Ruff, and M. P. Yeager, in "Titanium Science and Technology," R. I. Jaffee and H. M. Burte, Editors, Vol. 4, Plenum Press, New York (1973).
  20. H. J. Mueller and E. H. Greener, *J. Biomed. Mater. Res.*, **4**, 29 (1970).
  21. B. R. Weiss, N. Ramasamy, and P. N. Sawyer, Unpublished results.
  22. R. B. Beard, H. M. Carim, S. E. Dubin, and J. F. DeRosa, *This Journal*, **121**, 1129 (1974).
  23. P. N. Sawyer, L. Lucas, L. Chapa, B. Stanczewski, N. Ramasamy, G. W. Kammlott, and S. H. Goodenough, Paper presented at the Biomaterials Symposium, San Diego, Calif., February 1975.
  24. R. W. Revie and N. D. Greene, *Corros. Sci.*, **9**, 763 (1969).
  25. R. W. Revie and N. D. Greene, *ibid.*, **9**, 755 (1969).
  26. P. N. Sawyer, B. Stanczewski, N. Ramasamy, G. W. Kammlott, J. G. Stempak, and S. Srinivasan, *Trans. Am. Soc. Artif. Int. Organs*, **19**, 195 (1973).
  27. P. N. Sawyer, B. Stanczewski, S. Srinivasan, J. G. Stempak, and G. W. Kammlott, *J. Thorac. Cardiovasc. Surg.*, **67**, 571 (1974).
  28. R. W. Revie and N. D. Greene, *J. Biomed. Mater. Res.*, **3**, 465 (1969).
  29. Biology Data Book, II ed., P. L. Altman, and D. S. Ditmer, Editors, Vol. 3, p. 1863, Federation of American Societies for Experimental Biology, Bethesda, Maryland (1974).
  30. *Ibid.*, p. 1947.
  31. H. I. Horowitz and A. R. Spielvogel, in "Thrombosis and Bleeding Disorders, Theory and Methods," N. U. Bang, F. K. Beller, E. Deutsch, and E. F. Mammen, Editors, Chap. 9, Academic Press, New York (1971).
  32. P. N. Sawyer, K. T. Wu, S. A. Wesolowski, W. H. Brattain, and P. J. Boddy, *Proc. Nat. Acad. Sci.*, **53**, 294 (1965).
  33. T. R. Lucas, F. Bonavita, N. Ramasamy, and P. N. Sawyer, To be published.
  34. R. V. Zivkovic, S. Srinivasan, and P. N. Sawyer, Abstract 140, III Congress of the International Society on Thrombosis and Hemostasis, (1972).
  35. L. Vroman, Private communication.
  36. R. G. Lerner, R. Goldstein, and G. Cunnings, Paper presented at the 15th Annual Seminar on Hemostasis, New York, February 1975.
  37. S. Nitter-Hauge, S. C. Sommerfelt, K. V. Hall, T. Froysaker, and L. Efskind, *Brit. Heart J.*, **36**, 781 (1974).
  38. P. N. Sawyer and S. Srinivasan, in "Medical Engineering," C. D. Ray, Editor, Year Book of Medical Publishers, Inc., Chicago (1974).
  39. V. O. Bjork, A. Henze, and A. Holmgren, *J. Thorac. Cardiovas. Surg.*, **68**, 393 (1974).
  40. N. Ramasamy, S. Srinivasan, and P. N. Sawyer, *Electrochim. Acta*, **19**, 137 (1974).
  41. L. Duic, S. Srinivasan, and P. N. Sawyer, *This Journal*, **120**, 348 (1973).
  42. N. Ramasamy, M. Ranganathan, L. Duic, S. Srinivasan, and P. N. Sawyer, *ibid.*, **120**, 354 (1973).
  43. G. E. Stoner and S. Srinivasan, *J. Phys. Chem.*, **74**, 1088 (1970).
  44. G. E. Stoner, *J. Biomed. Mater. Res.*, **3**, 655 (1969).
  45. G. E. Stoner and L. Walker, *ibid.*, **3**, 645 (1969).
  46. B. W. Morrissey, L. E. Smith, C. A. Fenstermaker, and R. R. Stromberg, Abstract 383, p. 870, The Electrochemical Society Extended Abstracts Spring Meeting, Toronto, Canada, May 11-16, 1975.
  47. L. Lucas, W. Sutro, J. S. Keates, N. Ramasamy, S. Srinivasan, and P. N. Sawyer, To be published.
  48. Y. Nemerson and F. A. Pitlick, in "Progress in Hemostasis and Thrombosis," Vol. I, T. H. Spaet, Editor, Ch. 1, Grune and Stratton, New York (1972).
  49. P. C. P. Lemos, E. M. C. Tolosa, E. E. Camargo, J. G. Maksoud, B. Langer, N. A. G. Stolf, T. M. Barreto, A. Nasser, and E. V. Zerbini, *J. Thorac. Cardiovasc. Surg.*, **68**, 405 (1974).
  50. P. D. Didisheim, in "Progress in Hemostasis and Thrombosis," Vol. I, T. H. Spaet, Editor, p. 199, Grune and Stratton, Inc., New York (1972).
  51. V. L. Gott, M. D. Ramos, F. S. Najjar, J. L. Allen, and K. E. Becker, in Artificial Heart Program Conference Proceedings, June 1969, Washington, D. C., p. 181, U.S. Govt. Printing Office, Washington, D. C. (1969).
  52. P. N. Sawyer, K. T. Wu, S. A. Wesolowski, W. Brattain, and P. J. Boddy, *Arch. Surg.*, **91**, 735 (1965).
  53. E. Gileadi, B. Stanczewski, A. Parmiggiani, T. R. Lucas, M. Ranganathan, S. Srinivasan, and P. N. Sawyer, *J. Biomed. Mater. Res.*, **6**, 489 (1972).
  54. P. N. Sawyer, N. Ramasamy, B. Stanczewski, R. Stillman, W. Wrezlewicz, and S. H. Goodenough, Submitted for presentation at the 28th ACEMB Meeting, New Orleans, October 1975.
  55. T. R. Lucas, B. Stanczewski, N. Ramasamy, S. Srinivasan, G. W. Kammlott, and P. N. Sawyer, *Biomater. Med. Dev. Art. Organs*, In press.
  56. Haynes Alloy No. 25, A ductile cobalt base alloy for high temperature service; Technical Brochure, p. 3, Stellite Division of Cabot Corporation, Kokomo, Indiana.
  57. A Guide to Investment Casting, p. 25, Technical Brochure, Arwood Corporation, New York.
  58. M. J. Kaplitt, R. Rubin, and P. N. Sawyer, *Cur. Top. Surg. Res.*, **2**, 477 (1970).
  59. J. W. Pate, *Am. J. Surg.*, **108**, 436 (1964).

# Studies in Photoelectrochemistry

## III. Theory for Induced Charging Currents in Potentiostatic Chronoamperometry Involving Competing Chemical Reactions

S. S. Fratoni, Jr.<sup>1</sup> and S. P. Perone

Department of Chemistry, Purdue University, West Lafayette, Indiana 47907

### ABSTRACT

The first paper in this series (1) developed a theoretical model for characterizing the charging currents induced by changing faradaic currents measured under potentiostatic conditions. This paper describes application of the theoretical model to measurements involving electrolysis mechanisms complicated by competing reactions. The model is particularly relevant for flash photoelectrochemical studies. The mechanisms considered here include first order and second order decay of electroactive photoproducts. The dependence of measured currents on various experimental and chemical parameters—including the cell time-constant, photoproduct concentrations, and rate constants—is described for a wide range of conditions. Theoretical relationships can be used to predict total measured currents, or to tabulate correction factors to extract purely faradaic currents from measured currents. In addition, an alternative derivative-correction method for extracting faradaic signals from combined currents is described.

The concept of "induced" charging currents in potentiostatic chronoamperometric experiments has been described previously (1). Even under applied potentiostatic conditions, such as in flash photoelectrochemical studies (2,3), changing faradaic current causes a change in potential across the double layer and consequently induces charging current to flow. Because these induced currents depend on the nature of the faradaic current time dependence, an experimental "blank" cannot be obtained. Thus, a theoretical model was developed (1) to characterize this effect. The model was then applied to the specific case involving diffusion-limited faradaic current (1), and the predicted relationships were verified experimentally (4).

This paper considers the extension of the theoretical model to potentiostatic chronoamperometric measurements of systems involving chemical complications. Specifically, the induced charging current effects are characterized for systems in which the electroactive species is also involved in a chemical reaction. First and second order competing reactions are considered, assuming instantaneous generations of transient electroactive species, such as in flash photolysis experiments.

### Theory

The same model and method of analysis as presented previously (1) is used here. The basic procedure consists first of defining an electrical equivalent representation of the electrochemical cell and potentiostat (Fig. 1). Standard electrical circuit analysis (5) is then performed to determine the relationships between

<sup>1</sup> Present address: Physical Sciences Division, Stanford Research Institute, Menlo Park, California 94025.

Key words: photoelectrochemistry, photopolarography, chronoamperometry.

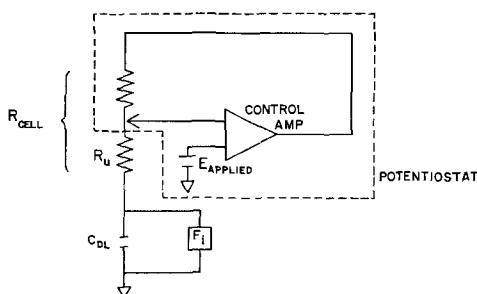


Fig. 1. Simplified model of electrochemical cell

the current terms. The first step in this analysis involves transformation of the equivalent circuit into its Laplace domain representation (Fig. 2). This allows analysis of the circuit based on fundamental electrical laws to find the Laplacian expression for the total current. The time domain function can then be obtained by taking the inverse transform. Following this procedure, as demonstrated in (1), the following Laplace domain expression is obtained

$$I_T(s) = \frac{1}{R} \cdot \left[ \frac{E_f}{s} - \frac{\frac{E_f}{sR} + E_i C - I_F(s)}{\frac{1}{R} + sC} \right] \quad [1]$$

where  $I_T(s)$  = Laplace transform of total current,  $R$  = effective uncompensated resistance (assumed to be constant),  $s$  = Laplace variable,  $E_f$  = reference electrode potential during experiment,  $E_i$  = reference electrode potential immediately before experiment,  $C$  = double layer capacitance (assumed to be constant),  $I_F(s)$  = Laplace transform of faradaic current. This general expression is next modified to represent the specific conditions present during the measurement. For this work, potentiostatic conditions are assumed. This is accomplished by letting  $E_f = E_i = E$ , where  $E$  is the applied potential. Substituting into Eq. [1] and rearranging gives

$$I_T(s) = \frac{1}{RC} \left[ \frac{I_F(s)}{s + \frac{1}{RC}} \right] \quad [2]$$

This expression will hold for any electrolysis mechanism under potentiostatic conditions.

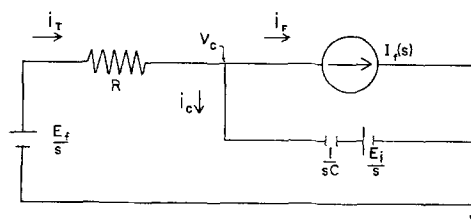


Fig. 2. Laplace domain equivalent circuit representation of electrochemical cell (arrows indicate direction of anodic current).

For this work, flash-initiated electrolysis currents will be assumed, with a typical example of the electrode process



Previously (1, 4), the specific case where R was a stable species, and reaction [4] produced diffusion-limited faradaic currents described by the Cottrell equation, was considered. The results indicated that, rather than following the expected Cottrell behavior, the measured current should reflect both charging and faradaic contributions, as described by Eq. [5]

$$i_T(t) = \frac{2K}{\sqrt{\pi RC}} e^{-t/RC} \int_0^{\sqrt{t/RC}} e^{\lambda^2} d\lambda \quad [5]$$

Here,  $t$  = time after the flash and  $K = nFAD^{1/2}C^0$ , with the various symbols having their usual electrochemical meaning.

This paper is concerned with the case where the electrode process involves a chemical reaction, parallel to [4] above, involving species R. The nature of this competing reaction must be considered in order to determine  $I_F(s)$ . The specific cases of a first and second order competing reaction will be given below.

It is important to note here that the only assumptions made thus far specify potentiostatic conditions, constant electrolysis mechanism, and constant  $R_u$  and  $C_{DL}$ . Therefore, the derivation is not limited to photolysis-initiated processes. The expressions are equally valid for other electrochemical experiments, such as potential step, with the addition of the standard charging current term to compensate for the applied potential change (1). However, regardless of how the chemical process is initiated, such as with a potential step, the form of the faradaic current expression,  $I_F(s)$ , must be known to derive the total current. The derivations below are, for convenience, described in photopolarographic terms.

**First order case.**—If the photolyzed species produced by the flash decays by a first order process in addition to being oxidized at the monitoring electrode, the reactions involved would be



Assuming an infinitesimally short flash, homogeneous production of R around the electrode, Z is not electrochemically active, and the electrode potential is always on the diffusion plateau, then the faradaic current measured should be described by (2)

$$i_F(t) = \frac{K}{\sqrt{\pi t}} e^{-k_1 t} \quad [9]$$

where  $K = nFAD^{1/2}C^0$ ,  $k_1$  = first order rate constant,  $t$  = time after flash,  $C^0$  is the initial concentration of species R, and the other terms have their usual meaning.  $I_F(s)$  is then found simply by taking the Laplace transform of Eq. [9]

$$I_F(s) = \frac{K}{\sqrt{s + k_1}} \quad [10]$$

Substituting this into Eq. [2] above gives

$$I_T(s) = \frac{K}{RC} \cdot \left[ \frac{1}{\sqrt{s + k_1} (s + 1/RC)} \right] \quad [11]$$

The inverse transform of Eq. [11] will then give the time domain expression for the total current

$$i_T(t) = \frac{K}{RC\sqrt{k_1 - 1/RC}} e^{-t/RC} \text{erf} [\sqrt{(k_1 - 1/RC)t}] \quad [12]$$

This expression can be simplified by making the following substitutions

$$\tau = t/RC \quad [13]$$

$$\beta = \frac{k_1}{1/RC} = k_1 RC \quad [14]$$

$$\text{erf}(x) = \frac{2}{\sqrt{\pi}} \int_0^x e^{-u^2} du \quad [15]$$

$$K' = \frac{K}{\sqrt{\pi RC}} \quad [16]$$

The resulting equation is

$$i_T(\tau) = \frac{2K'e^{-\tau}}{\sqrt{\beta - 1}} \int_0^{\sqrt{(\beta - 1)\tau}} e^{-u^2} du \quad [17]$$

This expression can only be evaluated for  $\beta > 1$ , ( $k_1 > 1/RC$ ). Equivalent expressions can be derived in order to determine the magnitude of the total current for the case of  $\beta = 1$  (by taking the limit of Eq. [17] as  $\beta \rightarrow 1$ ), and  $\beta < 1$  (by factoring out a  $\sqrt{-1}$  from  $(\beta - 1)$  terms in Eq. [17]). The resulting expressions are: for  $\beta = 1$ , (or  $k_1 = 1/RC$ )

$$i_T(\tau) = 2K'\sqrt{\tau} e^{-\tau} \quad [18]$$

for  $\beta < 1$ , (or  $k_1 < 1/RC$ )

$$i_T(\tau) = \frac{2K'}{\sqrt{1 - \beta}} e^{-\tau} \int_0^{\sqrt{(1 - \beta)\tau}} e^{u^2} du \quad [19]$$

Figure 3 gives plots of total current as a function of time (in terms of  $\tau$ ) and  $\beta$ . From these curves, it is evident that as  $\beta$  increases, the peak maximum is less, it occurs at shorter times, and the current decays to zero faster. Interpretation of these observations is simplified by referring to Eq. [14].  $\beta$  is a dimensionless parameter that represents the ratio of the "time constants" of the chemical and capacitive process. Increasing  $\beta$  corresponds to increasing the rate of reaction [8] compared to the electrolysis reaction [7]. A composite plot of the total, faradaic, and charging currents vs. time for  $\beta = 1$  is given in Fig. 4. Because the ratio between  $i_F$  and  $i_T$  is dependent on both RC and  $k_1$ , the time at which the induced charging current can be considered negligible cannot be described

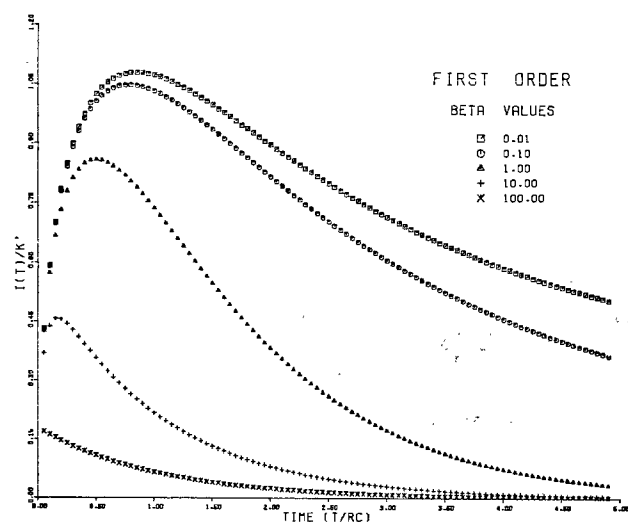


Fig. 3. Total current vs.  $t$  with  $\beta = 0.01, 0.1, 1.0, 10.0,$  and  $100.0$ , for potentiostatic/first order case ( $\tau = 0.0-5.0$ ).

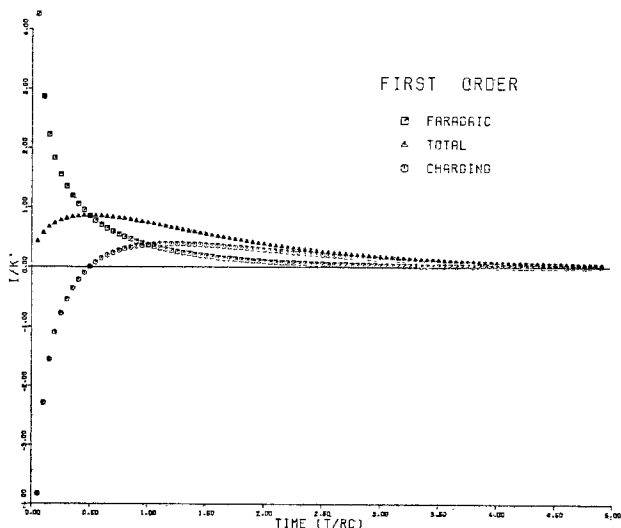


Fig. 4. Composite plot of predicted  $I(T)/K'$ ,  $I(C)/K'$ , and  $I(F)/K'$  vs.  $\tau$  with  $\beta = 1.0$  for potentiostatic/first order case ( $\tau = 0.0-5.0$ ).

solely in terms of the cell time-constant as was the case for diffusion-controlled faradaic currents (1).

**Second order case.**—A more common occurrence in photopolarographic experiments involves a second-order competing reaction and a corresponding mechanism as given below.



Again it is assumed that R is produced homogeneously around the electrode by an instantaneous flash, that Z is electrochemically inactive, and that the electrode potential is always on the diffusion plateau. The faradaic current expected in this case would be (2, 6)

$$i_F(t) = \frac{K}{0.73k_2C^0\sqrt{\pi}} \cdot \left[ \frac{1}{\sqrt{t}(t + 1/0.73k_2C^0)} \right] \quad [23]$$

where  $k_2$  = second order rate constant,  $C^0$  = initial concentration of electroactive species, and other terms as defined previously. Transforming this into the Laplace domain gives

$$I_F(s) = \frac{K\sqrt{\pi}}{\sqrt{0.73k_2C^0}} e^{s/0.73k_2C^0} \operatorname{erfc} [\sqrt{s/0.73k_2C^0}] \quad [24]$$

In order to find the total current expression, Eq. [24] is substituted into Eq. [2]

$$I_T(s) = \frac{K\sqrt{\pi}}{RC\sqrt{0.73k_2C^0}} \left[ \frac{e^{s/0.73k_2C^0} \operatorname{erfc} \sqrt{s/0.73k_2C^0}}{s + 1/RC} \right] \quad [25]$$

The time domain expression for the total current is found next by taking the inverse transform of Eq. [25]. However, in this case the inverse transform cannot be taken directly by reference to available tables. In this case, the convolution integral (7) was used

$$\mathcal{L}^{-1} F_1(s) F_2(s) = \int_0^t f_1(\lambda) f_2(t - \lambda) d\lambda \quad [26]$$

where  $\mathcal{L}$  is the Laplacian operator,  $\mathcal{L}^{-1}$  is the inverse operation, and  $F_x = \mathcal{L}(f_x)$ . Equation [25] can be broken down by letting

$$F_1(s) = e^{s/0.73k_2C^0} \operatorname{erfc} \sqrt{s/0.73k_2C^0} \quad [27]$$

$$\text{and } f_1(\lambda) = \frac{\sqrt{1/0.73k_2C^0}}{\pi\sqrt{\lambda}(\lambda + 1/0.73k_2C^0)} \quad [28]$$

$$F_2(s) = \frac{1}{s + 1/RC} \quad [29]$$

$$\text{and } f_2(t - \lambda) = e^{-(t-\lambda)/RC} \quad [30]$$

Substituting these expressions into Eq. [25] results in

$$i_T(t) = \frac{K}{RC\sqrt{\pi}} e^{-t/RC} \int_0^t \frac{e^{\lambda/RC}}{\sqrt{\lambda}(0.73k_2C^0\lambda + 1)} d\lambda \quad [31]$$

This integral cannot be evaluated in its present form because the integrand is undefined at  $\lambda = 0$ , even though the over-all integral should be continuous. This problem is resolved by defining a new variable  $z$  such that

$$z = \sqrt{\lambda/RC} \quad [32]$$

In addition, the equation can be generalized by defining a dimensionless parameter  $\alpha$  such that

$$\alpha = \frac{0.73k_2C^0}{1/RC} = 0.73k_2C^0RC \quad [33]$$

$\alpha$  is the ratio of the time constants for the chemical and capacitive processes. The final expression for the total or measured current, after making the above substitution in addition to those given in Eq. [13] and [16] gives

$$i_T(\tau) = 2K'e^{-\tau} \int_0^{\sqrt{\tau}} \frac{e^{z^2}}{1 + \alpha z^2} dz \quad [34]$$

A plot of the resulting current terms (total, faradaic, and charging) vs. time for  $\alpha = 1$  is given in Fig. 5. The effect of  $\alpha$  on the total current is shown in Fig. 6. The change in the total current with increasing  $\alpha$  is very similar to the first order case where  $\beta$  is varied. Obviously, the significance of the induced charging current at any time will be dependent on the values of the second order rate constant ( $k_2$ ) and initial concentration of electroactive species ( $C^0$ ), as well as the cell time-constant ( $RC$ ).

## Discussion

**Known electrolysis mechanism.**—The two expressions for the total current derived above for the first and second order cases (Eq. [17] and [34]) should approach the diffusion-limited case as  $\alpha$  or  $\beta$  go to zero. This would correspond to the competing reactions, [8]

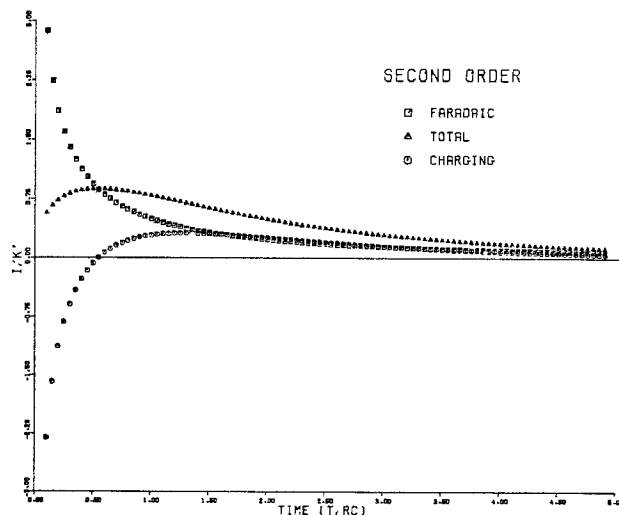


Fig. 5. Composite plot of predicted  $I(T)/K'$ ,  $I(C)/K'$ , and  $I(F)/K'$  vs.  $\tau$  with  $\alpha = 1.0$  for potentiostatic/second order case ( $\tau = 0.0-5.0$ ).

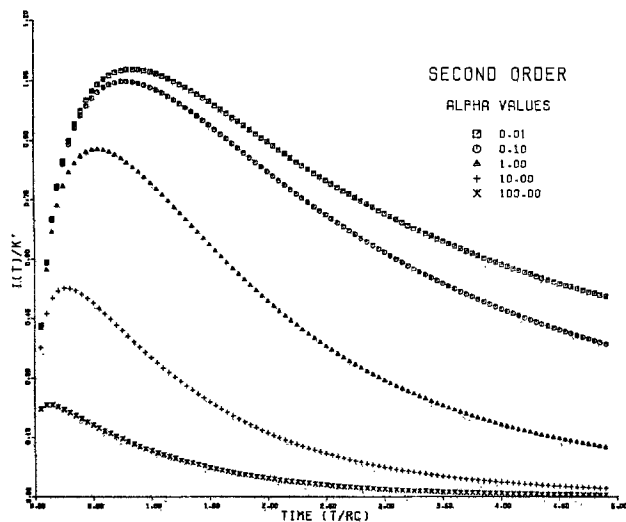


Fig. 6. Total current vs.  $\tau$  with  $\alpha = 0.01, 0.1, 1.0, 10.0,$  and  $100.0$ , for potentiostatic/second order case ( $\tau = 0.0-5.0$ ).

or [22], becoming negligible. It is obvious for the first order case (Eq. [19]), as  $\beta \rightarrow 0$ , and for the second order case (Eq. [34]) as  $\alpha \rightarrow 0$ , that the diffusion-limited expression (Eq. [5]) is obtained. As a further indication that both Eq. [34] and [19] do approach the diffusion-limited case, the value of  $\tau$  at which the maximum total current occurs was calculated vs.  $\beta$  (Table I) and  $\alpha$  (Table II). As is evident from these tables, the peak maximum for both the first and second order total currents approach, with decreased  $\alpha$  or  $\beta$ , the diffusion-limited value (1) of  $\tau_{IT(\max)} = 0.85$ . These results support the validity of the derivations given here.

Application of these expressions for experimental correction should follow the approach used previously. A correction factor composed of the predicted ratio  $i_F(\tau)/i_T(\tau)$  based on the measured time is first calculated. The measured current at each point is then multiplied by its corresponding factor. For these cases, however, the value of  $\alpha$  or  $\beta$  must be known in addition to the cell time-constant ( $RC$ ). For the diffusion-limited case, only the cell time-constant had to be known, in addition to the measured time, to evaluate the correction factor. The time constant can be measured in a separate experiment, or, as was demonstrated for the diffusion-limited cases (4), found directly from the measured current-time curves (for longer cell time constants). For the two cases presented here, the time constant does not appear to be directly determinable from the total current. Tables I and II,

Table I. Dependence of  $\tau$  at  $I_T(\max)$  on  $\beta$  for first order case

$\beta$	$\tau I_T(\max)$
0.001	0.85
0.05	0.81
0.10	0.78
0.5	0.61
1.0	0.50
10.0	0.16
100.0	0.04

Table II. Dependence of  $\tau$  at  $I_T(\max)$  on  $\alpha$  for second order case

$\alpha$	$\tau I_T(\max)$
0.001	0.85
0.05	0.81
0.10	0.78
0.5	0.63
1.0	0.54
10.0	0.26
100.0	0.12

however, indicate that the peak current time ( $\tau_{IT(\max)}$ ) may be indicative of the value of  $\alpha$  or  $\beta$ .

As is evident from the two cases presented above, the theoretical model (1) is adaptable to any form of electrolysis mechanism. The procedure demonstrated above should be the general approach used to find the explicit mathematical expression for the total current when the time dependence of the faradaic current is mathematically defined.

Derivation of the time domain representation of the total current can be shortened in future work, however, by application of the convolution integral directly to Eq. [2]. This eliminates determination of the Laplace transform of the faradaic time function (which may be extremely difficult for complex electrolysis mechanisms), as in Eq. [24], and inverse transformation of the Laplace expression for the total current, as in Eq. [25].

Equation [2], which will hold for any electrolysis mechanism under applied potentiostatic conditions, can be rewritten as the product of two terms

$$I_T(s) = [I_F(s)] \cdot \left[ \frac{1}{RC} \cdot \frac{1}{s + 1/RC} \right] \quad [2]$$

The convolution integral (refer to Eq. [26]) can be applied directly to this product to obtain a time domain expression of the total current without first obtaining a Laplace domain expression for  $i_F$ . The first term ( $f_1$ ) will be the time-dependent expression for the faradaic current with the  $t$ 's replaced by  $\lambda$ 's. The second term ( $f_2$ ) of the resulting integral will be

$$\frac{1}{RC} e^{-(t-\lambda)/RC} \quad [35]$$

as given above. By this method, true Laplace domain analysis can be accomplished without requiring intermediate transformations.

*Unknown electrolysis mechanism.*—The work presented here and previously (1) has employed a theoretical model based on prior knowledge of the electrolysis mechanism. This knowledge is necessary if the total current expression is to be derived. However, many instances may occur when the mechanism is not known. Under these conditions it is possible to correct observed currents for induced charging current by following an alternative procedure described below.

The induced charging current can be computed directly from observed total currents, under potentiostatic conditions, as long as  $RC$  is known. The general relationship is given by (1)

$$i_T = i_F + i_{ch} \quad [36]$$

Assuming constant double layer capacitance

$$i_{ch} = C \frac{dE_{DL}}{dt} \quad [37]$$

where  $E_{DL}$  is the potential across the double layer,  $R = R_u$ , and  $C = C_{DL}$ . Also

$$E_{DL} = E_p - i_T R \quad [38]$$

where  $E_p$  is the applied cell potential. Combining these and rearranging, Eq. [39] is obtained, which allows for direct calculation of corrected faradaic current

$$i_F = i_T + RC \frac{di_T}{dt} \quad [39]$$

Although experimental difficulties exist in obtaining the necessary derivative in Eq. [39], principally due to noisy signals, the corrected currents should be much closer to the "true" value than the measured total current. Subsequent evaluation of the faradaic current behavior should lead to a possible mechanism for the chemical system. Once this preliminary analysis is per-



formed, it is still advantageous to use the method demonstrated above to obtain a rigorous mathematical expression for the total current. Such an expression will indicate the effect of all experimental factors on the signal being measured in order to optimize the measured current for the data acquisition system. Experimental information may also be directly obtainable from the total current, e.g.,  $RC$  in the diffusion-limited case (1) and  $\alpha$  or  $\beta$  as shown above, which cannot be determined directly from the faradaic current. The explicit expression for  $i_T$  also allows for inclusion of current terms other than just the faradaic and induced charging currents as was assumed in Eq. [36].

### Conclusion

The implications of this work are twofold. The specific expressions derived for reactions involving first and second order competing steps are directly applicable to chronoamperometric measurements in general, and specifically to photoelectrochemistry. Application of correction factors obtainable from these expressions allows for meaningful faradaic current measurements at times short compared with the cell time constant. The magnitude of this improvement is expected to be comparable to that reported previously (4) for diffusion-controlled currents. The explicit expressions obtained from this model also allow for more comprehensive characterization of the total currents involved; consequently additional information (e.g., determination of  $\alpha$  or  $\beta$  directly from the measured current) may be obtained.

Another important aspect of this work is the development of a general procedure for applying the theoretical model to other systems. The procedures and suggestions presented here should allow for application of this model to more complicated electrolysis mechanisms and photoelectrochemical processes. Experimental studies have been completed which provide a verification of the expressions derived above. These data are presented elsewhere (8).

An important extension of the concepts discussed here and earlier (1) is the compounding effect of induced potential change. The induced charging current described above arises from a potential change across the double layer as the result of changing faradaic current and a finite, uncompensated resistance. This potential shift was briefly noted by Booman and Holbrook (9), in a derivation similar to ours (1), in their description of various sources of inaccuracy in con-

trolled potential electrolysis. Our studies [including, Ref. (1), (4), and (8)], have been limited to faradaic processes that are potential independent, and therefore involve a constant electrolysis mechanism even with changing potential (e.g., where the double layer potential remains on the redox plateau). Although the effect of induced charging current is significant under these limited conditions (4), it is expected to be a much more important factor when potential-dependent faradaic currents are involved. Work is presently underway in this laboratory to employ this model under these conditions and characterize the effect on relevant controlled-potential, electrochemical methods.

### Acknowledgments

This work was supported by Public Health Service Grant No. CA-07773 from the National Cancer Institute and by the Office of Naval Research Contract N00014-75-C-0874. One of the authors, S. S. Fratoni, Jr., also received the Edward Weston Fellowship, awarded by The Electrochemical Society, for the summer of 1974.

The authors would like to thank S. W. Feldberg and A. A. Pilla for helpful discussions regarding this work.

Manuscript submitted Sept. 29, 1975; revised manuscript received Feb. 20, 1976. This was Paper 351 presented at the Toronto, Canada, Meeting of the Society, May 11-16, 1975.

Any discussion of this paper will appear in a Discussion Section to be published in the June 1977 JOURNAL. All discussions for the June 1977 Discussion Section should be submitted by Feb. 1, 1977.

### REFERENCES

1. S. S. Fratoni, Jr. and S. P. Perone, *Anal. Chem.*, **48**, 287 (1976).
2. J. R. Birk and S. P. Perone, *ibid.*, **40**, 496 (1968).
3. J. I. H. Patterson and S. P. Perone, *J. Phys. Chem.*, **77**, 2437 (1973).
4. K. F. Dahnke, S. S. Fratoni, Jr., and S. P. Perone, *Anal. Chem.*, **48**, 296 (1976).
5. M. E. Van Valkenburg, "Network Analysis," Prentice-Hall, Englewood Cliffs, New Jersey (1964).
6. D. Britz and B. Kastening, *Electroanal. Chem. Interfac. Electrochem.*, **56**, 73 (1974).
7. F. E. Nixon, "Handbook of Laplace Transformation," Prentice-Hall, Englewood Cliffs, New Jersey (1965).
8. K. F. Dahnke and S. P. Perone, *This Journal*, **123**, 1677 (1976).
9. G. L. Booman and W. B. Holbrook, *Anal. Chem.*, **37**, 795 (1965).



# Studies in Photoelectrochemistry

## IV. Flash Photolysis Studies of pH Dependence of Benzophenone Photodimerization

K. F. Dahnke<sup>1</sup> and S. P. Perone

Department of Chemistry, Purdue University, West Lafayette, Indiana 47907

### ABSTRACT

A chronoamperometric study of the pH dependence of flash photodimerization of benzophenone in H<sub>2</sub>O/ethanol solution is presented. Measured potentiostatic currents have been corrected for induced charging currents prior to kinetic analysis. Either a curve-fitting technique or a derivative correction method was used to obtain purely faradaic currents. Rate constants for the photodimerization reaction in acidic solution are reported here for the first time. Three methods were used for the extraction of kinetic information from current-time data: (i) approximate chronoamperometric theory, (ii) rigorous chronoamperometric theory, and (iii) digital simulation. The latter two techniques produce nearly identical rate constants for a given data set. This suggests that both are valid; also, it demonstrates that the digital simulation approach may be applied successfully to other coupled kinetic-diffusion problems where rigorous mathematical solutions do not exist. The pH study presented here was used to obtain individual rate constants for the radical-radical, radical-radical anion, and radical anion-radical anion reactions. The values reported are  $2.5 \times 10^8 \text{ M}^{-1} \text{ sec}^{-1}$ ,  $1.1 \times 10^9 \text{ M}^{-1} \text{ sec}^{-1}$ , and  $\leq 7.8 \times 10^4 \text{ M}^{-1} \text{ sec}^{-1}$ , respectively.

Flash photoelectrochemistry has been used with varying degrees of success to study photochemical reactions (1-9). The electrochemical methods, while inherently sensitive and specific, have suffered because they perturb the measured system due to electrolysis. As a result, the interpretation of chronoamperometric signals is not always straightforward. For example, in previous photoelectrochemical studies, measured potentiostatic currents were considered to be totally faradaic in nature, ignoring any charging current contribution that may have been present. Also, rigorous solutions of kinetic-diffusion equations, allowing useful kinetic data to be extracted, did not exist for other than the first order case (10).

An approximate solution to the second order case was reported by Birk and Perone (2), and has been used in several kinetic studies, including flash photoelectrochemistry (2-4) and pulse radiolytic polarography (11). However, a more rigorous, generally useful theoretical approach is needed to allow the study of a wide variety of photoelectrochemical processes. A digital simulation technique, developed by Feldberg (12) for complex kinetic-diffusion equations, has been applied here to the second order kinetic case in flash photoelectrochemistry.

Britz and Kastening (13) have recently reported a rigorous mathematical solution to the coupled second order kinetic-diffusion problem for flash photopolarography at stationary planar or spherical electrodes. Their results indicate that the second order rate constant obtained using the Birk-Perone approximation (2) is about 27% too low, although the initial intermediate concentration obtained from their expression is correct.

In this paper, results have been compared for the Britz-Kastening (13), Birk-Perone (2), and digital simulation data interpretation methods for the benzophenone photodimerization reaction (2, 14). Also, the measured currents have been corrected for induced charging currents, using the approaches described by Fratoni and Perone (15, 16), prior to kinetic analysis by any of the above methods. Because of the theoretical refinements mentioned above, it was possible

to conduct a study of the pH dependence of the second order photodimerization reaction of the benzophenone ketyl radical and/or radical anion (2, 14) over a wider range than had previously been attainable (2). Rate constants obtained using each of the above three methods have been compared. Also, rate constants for the three individual reactions (radical-radical, radical-radical anion, radical anion-radical anion) have been calculated from the pH study.

### Experimental

**Instrumentation.**—All of the instrumentation used in this work has been extensively reported elsewhere (16). No modifications of the electrode and cell design, potentiostat, flash, or measurement devices have been made. The system utilizes a 200J 15  $\mu\text{sec}$  xenon flash; the monitoring electrode is a hanging mercury drop (HMDE); the potentiostat has a 0.16  $\mu\text{sec}$  transient response time; and the minicomputer data acquisition system uses a 50 kHz maximum data rate. Cell time constant measurements were made as described previously (16).

**Data handling.**—*Second order curve-fitting method.*—A computer program was used to extract second order rate constants and initial radical concentrations from the measured chronoamperometric data using the Fratoni-Perone curve-fitting method (15). A second order data handling program (SODH) allowed for correction of current-time data for induced charging current, while calculating values for  $k_d$  and  $C^0$  using the Birk-Perone second order plot technique (2). The program carries out an iterative calculation starting with an initial estimate of  $\alpha$ , ( $k_d C^0 R_u C_{DL}$ ), from the raw data and the measured cell time constant (15); finding the appropriate  $i_F/i_T$  values; multiplying the measured currents ( $i_T$ ) by these factors to obtain  $i_F$ ; calculating  $1/i\sqrt{t}$  vs. time; and calculating a new  $k_2 C^0$  for the corrected data. The whole procedure is repeated until  $\alpha$  converges to within preset limits. Final values of  $k_d$ ,  $C^0$ ,  $i$ , and  $1/i\sqrt{t}$  are printed out. ( $R_u$  is the uncompensated cell resistance and  $C_{DL}$  is the double layer capacitance. Their product is the cell time constant.)

*Derivative correction method.*—Another computer program was written to extract purely faradaic currents based on the following method. If the electrochemical cell is represented schematically as shown in Fig. 1,

<sup>1</sup> Present address: Phillips Petroleum Company, Phillips Research Center, 238RB-1, Bartlesville, Oklahoma 74004.

Key words: photoelectrochemistry, photopolarography, flash photolysis.

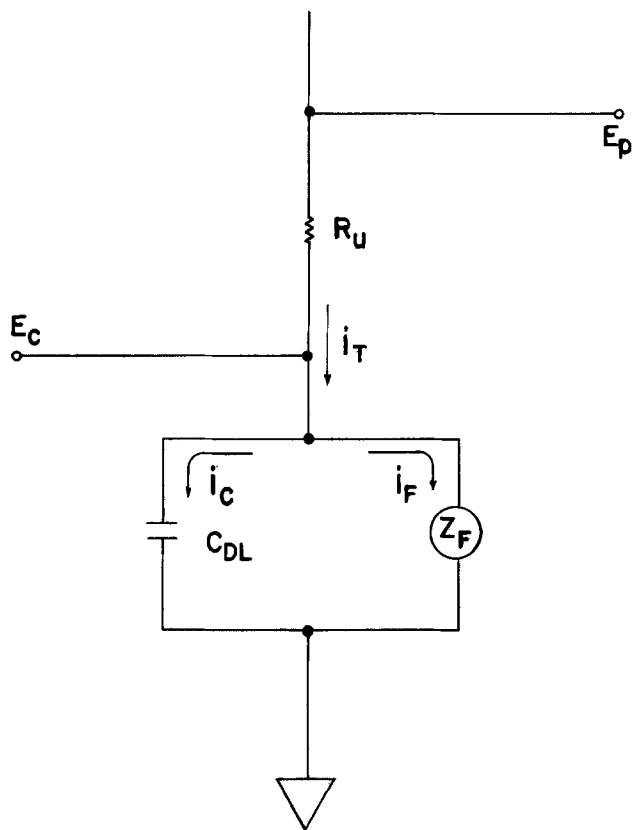


Fig. 1. Electrochemical cell model, induced charging currents:  $E_P$  = applied potential from potentiostat,  $E_C$  = actual working electrode potential,  $R_U$  = uncompensated resistance,  $C_{DL}$  = capacitance of electrode double layer,  $Z_F$  = faradaic resistive element,  $i_T$  = total current,  $i_F$  = faradaic current,  $i_C$  = faradaic-induced charging current.

the total current,  $i_T$ , flowing through the cell at any time may be expressed as

$$i_T = i_F + i_C \quad [1]$$

where  $i_F$  = the faradaic current and  $i_C$  = charging current. But, the charging current is defined as follows

$$i_C = C_{DL} \left( \frac{dE_C}{dt} \right) \quad [2]$$

Since

$$E_C = E_P - i_T R_U \quad [3]$$

and

$$\frac{dE_C}{dt} = -R_U \frac{di_T}{dt} \quad [4]$$

Under potentiostatic conditions, the applied potential  $E_P$  is constant; therefore the following expression should be valid

$$i_F = i_T + R_U C_{DL} \left( \frac{di_T}{dt} \right) \quad [5]$$

Hence, if  $di_T/dt$ , the derivative of the measured current-time curve, is obtained, and if the cell time constant is known, purely faradaic current values may be extracted. The computer program calculates the derivative of a current-time curve at each point as  $(i_2 - i_1)/(t_2 - t_1)$  and calculates  $i_F$ . A smoothing routine using the Savitsky-Golay seven-point or nine-point method (17) may be elected to reduce the noise introduced to the  $i_F$ - $t$  curve due to the derivative processing technique.  $k_d$  and  $C^\circ$  values are then calculated using the Birk-Perone second order plot method (2) from the  $i_F$ -time values. Figure 2 shows a comparison of a typical current-time curve that was uncorrected corrected using the curve-fitting SODH program, and corrected by the derivative technique.

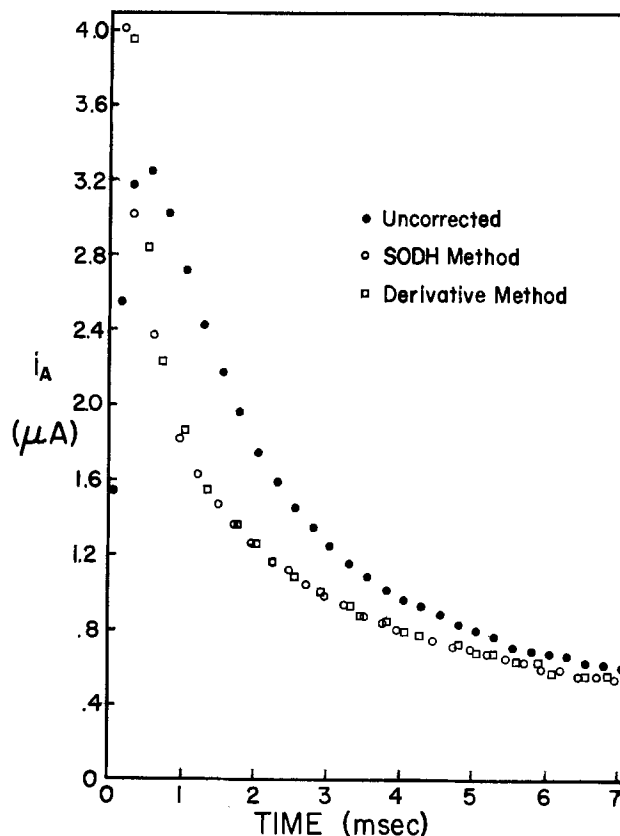


Fig. 2. Current-time curves, correction method comparison:  $5 \times 10^{-4}M$  benzophenone, 0.01M NaOH, 0.25M KCl, 50% ethanol/ $H_2O$ ,  $RC = 568 \mu\text{sec}$ .

*Other computer programs.*—A program was written to provide calculation of the digital simulation (12) working curve for the coupled second order kinetic-diffusion problem. Calculation of  $k_d$  from corrected experimental data was done manually from this curve.

Other programs allow calculation of charging-current-free current-voltage profiles by either of the above techniques. All programs were written in Hewlett-Packard BASIC with BASIO subroutine overlay (16), modified to allow 50 kHz data acquisition.

*Experimental procedures.*—The following procedures were used to obtain current-voltage profiles. At all potentials positive of the start of the benzophenone reduction wave, potentiostatic current measurements were made. For potentials more negative than the foot of the wave, a potential step was applied, simultaneously with the flash, to the monitoring potential of interest, from a potential where benzophenone is not reduced.

There are two kinds of background signals for which various chronoamperometric experiments must be corrected. One of these pertains only to potential-step experiments, and this is due to potential-step charging current. This background was measured as described above for potential-step experiments, except the solution contained only the background electrolyte. This blank was then subtracted off-line from the potential-step currents measured with benzophenone present.

The other type of background signal pertains to all chronoamperometric experiments, including the potential-step blank runs. This is the combined background due to electronic disturbances related to the flash discharge and any amplifier drift or offset. A measure of this background is obtained prior to every flash experiment by initiating the flash discharge and measuring the resulting current-time curve while preventing the light from reaching the cell with a movable shutter. This background signal is then subtracted on-line from a subsequent current-time curve, obtained

either potentiostatically or with potential step, with the shutter open or closed. Further off-line data processing (extraction of faradaic currents and kinetic plots) proceeded only on data corrected for background signals. At least two experimental curves were averaged at each potential.

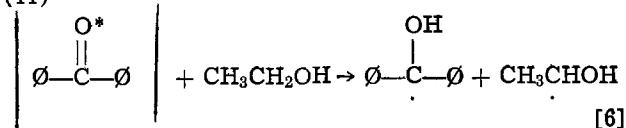
Electrode positioning and optical alignment were maintained throughout the entire current-voltage profile and blank measurement processes. At least 1 ml of solution was removed from the immediate vicinity of the mercury drop after every flash, and nitrogen was bubbled throughout for 10-15 sec to insure homogeneity in solution for the next flash experiment. No noticeable change in the total concentration of benzophenone present was observed after many flashes of the same solution, as long as the minimum volume was not allowed to fall below 20 ml from the initial 90 ml.

Individual current-time curves used for the kinetic study were obtained potentiostatically using the above procedures. At least 10  $i-t$  curves were averaged together, however, for these data sets.

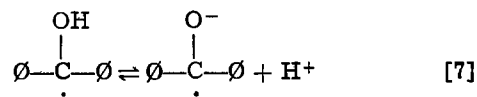
**Reagents.**—All studies were conducted in 50% ethanol/water solutions. Buffers down to pH 9 were prepared using  $\text{CO}_2$ -free water from KCl-NaOH- $\text{NaHCO}_3$  solutions. For kinetic studies the ionic strength was maintained at 0.25, except for the 0.5M NaOH solution. The pH 5.5 solution was prepared using an 0.25M acetate buffer. The pH 7 solution was prepared from a 0.01M phosphate buffer, adjusted to pH 7.0 with NaOH; because of the limited solubility of this buffer in the ethanol/water solvent, the ionic strength was adjusted to 0.25 with KCl. pH measurements were made with a Corning Model 110 expanded scale pH meter (Corning Laboratory Products, Corning New York). All chemicals were analytical reagent grade.

### Results and Discussion

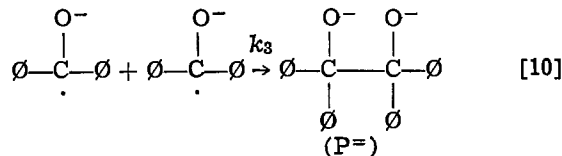
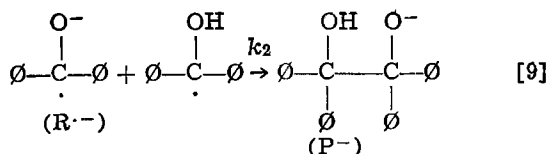
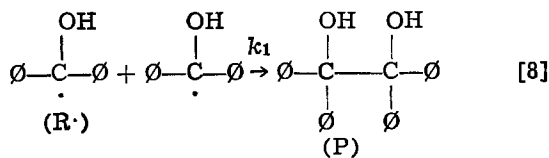
Benzophenone in 50% ethanol/ $\text{H}_2\text{O}$  was studied at various pH values. The mechanism for the photochemical reduction of benzophenone in solvents like ethanol has been reported elsewhere (2, 14, 18). Benzophenone absorbs radiant energy below about 390 nm and undergoes efficient intersystem crossing to form its excited triplet state, which then can abstract an  $\alpha$ -hydrogen from a solvent like ethanol. This produces a ketyl radical plus a very short-lived ethanol radical (11)



The ketyl radical is in rapid equilibrium with its radical anion



The ketyl radical or radical anion species can then react by three possible paths, all second order



Each reaction forms the benzopinacol product. In basic solution, the pinacol dissociates slowly to benzhydrol and benzophenone. The over-all second order rate process has been studied electrochemically (1-4, 19-21). The total amount of ketyl radical plus ketyl radical anion can be monitored electrochemically, since both species are oxidized at any potential positive of the benzophenone reduction potential. However, if the reaction is studied over a pH range where all three reactions occur significantly, the second order rate constant for each of the three above reactions may be obtained.

The flash photoelectrochemical behavior of benzophenone in very alkaline solution is shown in the charging-current-free current-voltage profiles in Fig. 3 and 4. Region I represents current due to a 2-electron reduction of benzophenone (20) before and after the flash. Region II shows current due to a 1-electron oxidation of the ketyl radical/radical-anion intermediate. Region III shows current due to the 2-electron oxidation of the benzopinacol product. No benzopinacol oxidation is noted in Fig. 3 because of the very "slow" kinetics relative to 2 msec after the flash. Except for changes in half-wave potentials, similar profiles for the benzophenone system are obtained at every pH studied here. However, the time scale must be modified to accommodate kinetic changes with pH.

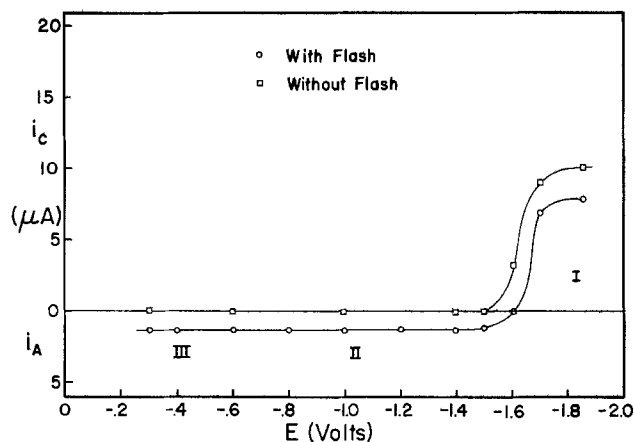


Fig. 3. Current-voltage profile:  $5 \times 10^{-4}\text{M}$  benzophenone, 0.25M NaOH, 50% ethanol/ $\text{H}_2\text{O}$ ,  $t = 2$  msec after start of experiment (with or without flash).

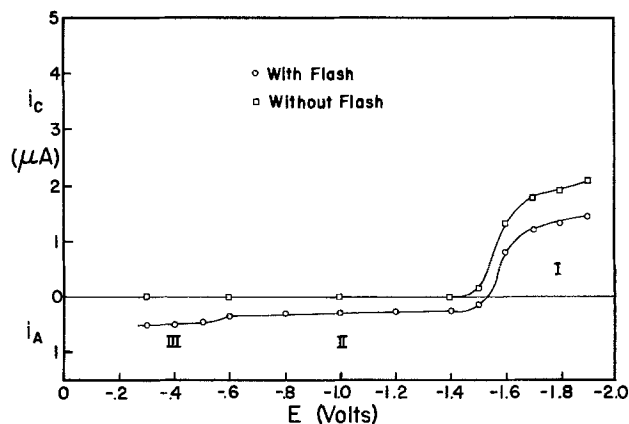
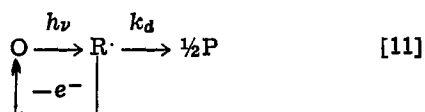


Fig. 4. Current-voltage profile:  $5 \times 10^{-4}\text{M}$  benzophenone, 0.25M NaOH, 50% ethanol/ $\text{H}_2\text{O}$ ,  $t = 50$  msec after start of experiment (with or without flash).

If a potential on the oxidation plateau of the radical species is applied, one can monitor currents related to the total concentration of the ketyl radical/radical anion present at any time after the flash. Only currents corrected for faradaic-induced charging current have been used in the kinetic studies reported below; no previously reported photoelectrochemical studies of this reaction (1-4, 8-9) have considered the significance of the induced charging current, and the comparison between results reported here and previously will be discussed.

**Theory.**—Assuming the following photodimerization-electrochemical model



Birk and Perone (2) applied Eq. [12] to the analysis of chronoamperometric data for the oxidation of the radical intermediate

$$\frac{1}{it^{1/2}} = \left[ \frac{\pi^{1/2}}{nFAD^{1/2}} \right] \left[ \frac{1}{C^0} + k_d t \right] \quad [12]$$

$C^0$  is the initial concentration of the radical plus radical anion,  $k_d$  is the second order rate constant for the disappearance of total R, and the other symbols have the usual electrochemical meanings (22). Thus, a plot of  $1/it^{1/2}$  vs. time should be linear, having a slope proportional to  $k_d$  and intercept related to  $C^0$ . However, because Eq. [12] represents only an approximate solution to the kinetic-diffusion equation (2), it was felt that a more generally applicable method would be desirable.

A digital simulation of the coupled second order kinetic-diffusion process defined in Eq. [11] was formulated here, using the method of Feldberg (12), which is an explicit approach to the solution of partial differential equations by finite differences. The fundamental expression which relates the change of concentration of species R ( $\Delta C_R$ , change in total ketyl radical plus radical anion) in discrete volume elements  $X$  units away from a planar electrode, as a function of time, is as follows

$$\Delta C_R = \frac{(\Delta t) D_R}{(\Delta X)^2} \cdot (C_{RX-1} - 2C_{RX} + C_{RX+1}) - k_d C_{RX}^2 (\Delta t) \quad [13]$$

This expression is a restatement of Fick's second law of diffusion for the second order kinetic case, defined in Eq. [11], in terms of discrete values for distance,  $X$ , time,  $t$ , and concentration,  $C_R$ . The term  $D_R$  is analogous to the diffusion coefficient of the intermediate. A computer program was written to calculate  $\Delta C_R$  in Eq. [13] for up to 1000 volume and time elements. The program calculates the change of concentration of the intermediate at the electrode surface for a given time element and then calculates the flux, or current per unit electrode area, as a function of time. This information is most appropriately represented as a plot of two dimensionless parameters,  $[(\text{flux})t^{1/2}]/(C^0 D^{1/2})$  and  $k_d C^0 t$ . Such a plot is shown in Fig. 5 for the second order kinetic-diffusion case, and, since it is independent of the  $k_d$ ,  $C^0$ , or  $D_R$  values, it can be used as a working curve for kinetic studies. From experimental flash chronoamperometric data, the value of the function  $(it^{1/2})/(nFAD^{1/2}C^0)$  can be determined, assuming all of the denominator terms are known. This expression corresponds to the Y-axis parameter for the simulator plot. Thus, the second order rate constant,  $k_d$ , can be found from the corresponding value of the X parameter on the simulator working curve. The  $k_d$  values obtained for different times from a single current-time curve should be the same within experimental error ( $\pm 10$ -15%). If this is not the case, the kinetic model

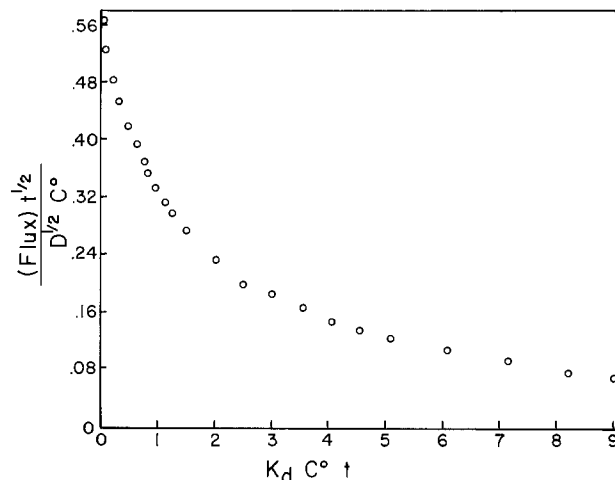


Fig. 5. Digital simulator working curve, coupled second order kinetic-diffusion problem.

is probably not correct for the real data. A serious complication, of course, is that the initial concentration,  $C^0$ , must be known from independent data.

Very recently, a rigorous mathematical solution to the coupled second order kinetic-diffusion problem has been presented by Britz and Kastening (13), without any experimental verification. Their results for a planar electrode were as follows

$$\frac{1}{it^{1/2}} = \frac{\pi^{1/2}}{nFAD^{1/2}} \cdot (1/C^0 + 0.7268k_d t) \quad [14]$$

This expression is totally analogous to the Birk-Perone approximation (2) (Eq. [12]), except for the factor 0.7268, which indicates that the  $k_d$  value obtained from the slope of the Birk-Perone second order plot will be less than the "true"  $k_d$  by about 27%. This difference is attributed to the fact that the Birk-Perone derivation neglects the nonhomogeneous decay rate profile in the diffusion layer for the second order process. The intercept for either expression gives the same initial intermediate concentration. Britz and Kastening (13) extended their derivation to the spherical electrode case. That expression reduces to the form of Eq. [14], however, on the time scales used to make the measurements reported in this work. All three methods require that the diffusion coefficient,  $D$ , either be known from independent measurements or be estimated accurately (20). Also, as mentioned previously, regardless of the theoretical treatment, purely faradaic currents are assumed. Thus, experimental data must be corrected for induced charging currents, as pointed out by Fratoni and Perone (15). Figure 6 demonstrates the results obtained for kinetic analysis of ketyl intermediate oxidation currents for flash photolysis of benzophenone at pH 12. The SODH program described earlier was used, and the improvement is obvious. The derivative method gives very similar results. The initial intermediate concentration calculated from the intercept of the corrected data second order plot agrees very well with that obtained by performing the same experiment at higher pH (13.5) where the dimerization reaction is slow, and making measurements at very short times where diffusion-limited currents are obtained.

**Faradaic current extraction methods comparison.**—Both methods used here to extract faradaic current from the total measured current have inherent advantages and disadvantages. The curve-fitting method, based on the technique proposed by Fratoni and Perone (15), uses the SODH program which was discussed earlier. Faradaic currents will be extracted correctly only if the proper kinetic mechanism is known beforehand for the given data set. Also, the alpha value which is used ( $k_d C^0 RC$ ) must be such that the limits of the

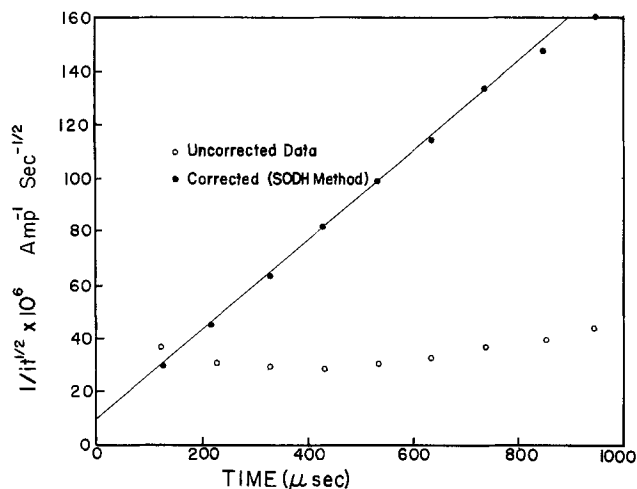


Fig. 6. Second order kinetic plot (Birk-Perone method):  $5 \times 10^{-4}M$  benzophenone,  $0.1M$  NaOH,  $0.15M$  KCl, 50% ethanol/ $H_2O$ .

computer's accuracy are not exceeded. Thus, for our computer system,  $\alpha$  must be  $>10^{-2}$ . For example, if  $t_{1/2} = 100$  msec, the cell time constant must be  $> 1$  msec or convergence will not occur. (If necessary, an external resistance may be inserted between the working electrode and ground to attain a longer cell time constant and an appropriate value for  $\alpha$ . This does not diminish the effectiveness of data interpretation so long as the cell time constant is not too long compared to the reaction half-life.) The SODH program can be rather time consuming, however, depending upon how many points are used and how long it takes the curve-fitting program to converge to the desired accuracy in  $\alpha$ .

The derivative approach is a much more general method which can be used for any data set. No experi-

mental limitations need be imposed during data acquisition. Any data may be used, even if the mechanism of the kinetic process is not known beforehand. However, considerable noise can be injected into the data by the derivative procedure, and even the digital smoothing methods used (17) usually cannot diminish noise to the level of the SODH results. In addition, these smoothing and derivative methods cause data points to be lost at the beginning and end of the data set. It has been found also that it is far better to take the derivative of the raw data first, correct the data to get  $i_F$ , and then apply digital smoothing, rather than in the inverse order.

In this work, current-time data at each pH were processed using both correction methods, and the kinetic data obtained agreed within the experimental precision ( $\pm 10$ -15%). Data reported in Tables I and II reflect average values for at least 10 runs processed both ways.

*pH dependence of photodimerization rate constant.—Alkaline solution.*—A kinetic study of the radical dimerization reaction was carried out by a series of flash photolysis experiments at various pH's. The current-time data were corrected as described above.

In Table I our results are used to compare the kinetic data obtained with the three different data handling techniques. Using our experimental data, the Birk-Perone approximate theory results are in column 1 (2), the digital simulation results in column 2, and the Britz-Kastening rigorous theory results (column 1 plus 27%) in column 3. [As discussed previously (2) the experimental limitation on kinetic accuracy is about  $\pm 25\%$ . Experimental precision, however, is about  $\pm 10\%$ .] The significant point is that the results in columns 2 and 3 agree very closely at all pH values. This indicates that the digital simulation and the rigorous theory expression both provide valid solutions to the same kinetic-diffusion problem. All subsequent kinetic studies reported here use one of these methods of analysis.

Table I. Comparison of kinetic data for benzophenone photodimerization using three different data processing methods\*

pH	1 Approximate theory (2)	2 Digital simulation	3 Rigorous theory (13)
0.5M NaOH	$5.4 \times 10^4 M^{-1} \text{ sec}^{-1}$	$7.8 \times 10^4 M^{-1} \text{ sec}^{-1}$	$7.6 \times 10^4 M^{-1} \text{ sec}^{-1}$
0.25M NaOH	$7.2 \times 10^4$	$9.2 \times 10^4$	$9.3 \times 10^4$
13.0	$1.4 \times 10^6$	$1.6 \times 10^6$	$1.7 \times 10^6$
12.5	$4.7 \times 10^6$	$6.2 \times 10^6$	$5.9 \times 10^6$
12.0	$1.3 \times 10^7$	$1.7 \times 10^7$	$1.7 \times 10^7$
11.2	$7.5 \times 10^7$	$10.5 \times 10^7$	$9.5 \times 10^7$
10.0	$1.6 \times 10^8$	$2.2 \times 10^8$	$2.0 \times 10^8$
9.0	$2.0 \times 10^8$	$2.5 \times 10^8$	$2.5 \times 10^8$
7.0	$(5.9 \times 10^7)^{**}$	$(9.3 \times 10^7)^{**}$	$(7.5 \times 10^7)^{**}$
5.5	$2.0 \times 10^8$	$2.6 \times 10^8$	$2.5 \times 10^8$

\* The same raw data were used for each method. All current-time curves were corrected for induced charging currents. All values  $\pm 20$ -25%.

\*\* Because of limited buffer capacity at this pH (see experimental section) this value of  $k_d$  may be in error.

Table II. Comparison of kinetic data for benzophenone photodimerization obtained from three different studies

pH	Birk-Perone*	Beckett-Porter**	Dahnke-Perone***
0.5M NaOH	$3.6 \times 10^4 M^{-1} \text{ sec}^{-1}$	$3.6 \times 10^4 M^{-1} \text{ sec}^{-1}$	$7.8 \times 10^4 M^{-1} \text{ sec}^{-1}$
0.25M NaOH	$5.3 \times 10^4$	$7.1 \times 10^4$	$9.2 \times 10^4$
13.0	$1.4 \times 10^6$	$1.8 \times 10^6$	$1.6 \times 10^6$
12.5	—	—	$6.2 \times 10^6$
12.0	$1.6 \times 10^6$	$1.8 \times 10^6$	$1.7 \times 10^7$
11.2	$1.1 \times 10^7$	$1.6 \times 10^7$	$10.5 \times 10^7$
10.0	$0.9 \times 10^8$	$1.8 \times 10^8$	$2.2 \times 10^8$
9.0	—	—	$2.5 \times 10^8$
7.0	—	—	$(7.5 \times 10^7)^\dagger$
5.5	—	—	$2.6 \times 10^8$

\* Taken from Ref. (2); flash photoelectrochemistry.

\*\* Taken from Ref. (14); flash photolysis-kinetic photometry. Second order decay of radical anion.

\*\*\* Data obtained in this work using digital simulation method; currents corrected for induced charging current. All values  $\pm 20$ -25%.

† Because of limited buffer capacity at this pH (see experimental section) this value of  $k_d$  may be in error.

Table II compares previous and current electrochemical results with each other and with Beckett and Porter's (14) spectroscopic results. Our results agree quite well with the others at the very highest (>13) and very lowest (<11) pH values, but the intermediate results vary. The discrepancy in the electrochemical kinetic results is not surprising, as the earlier work (2) utilized approximate theory and also neglected effects of induced charging currents. Thus, at high pH, where the reaction half-life ( $t_{1/2} = 1/k_d C^0$ ) is long compared to the cell time-constant, the effect of induced charging current is small and the kinetic data disagree only slightly. At lower pH, these effects cannot be ignored and large errors in the earlier kinetic data are obvious. The disagreement with Beckett and Porter's results (14) is probably because, spectroscopically, they were monitoring the rate of disappearance of the radical anion, whereas electrochemically we cannot differentiate the two radical species and are always monitoring the sum of the two. Hence, in the pH range where the radical-radical anion reaction predominates (pH 11-13), it is not surprising that our results disagree significantly with Beckett and Porter's.

**Acid solution.**—At pH <10, the benzophenone photodimerization reaction becomes very rapid, approaching the diffusion-controlled rate. Because the reaction is so fast, it has not been studied previously in this pH region. To apply either the SODH or derivative correction methods, the value of the cell time-constant must be known very accurately, as it is close to  $t_{1/2}$  of the reaction. When an external resistance is added between the working electrode and ground, the effective cell time-constant is much less dependent upon variations in the electrochemical cell conditions, and hence it may be measured more accurately. Experimental data at pH 9, 7, and 5.5 were obtained with a 1 kohm resistance between the working electrode and ground. The kinetic results are given in Tables I and II, and show that the reaction rate constant levels off below pH 10, indicating that radical dimerization is probably the dominant reaction. A current-voltage profile of the system obtain at pH 5.5, 490  $\mu$ sec after the flash, appears in Fig. 7. These corrected faradaic currents were obtained using the derivative program method, with a Savitsky-Golay nine-point smooth (17) applied to each corrected current-time curve. The profile is qualitatively similar to those at higher pH, except that the oxidation  $E_{1/2}$  of benzopinacol is about  $-0.15V$ , and the reduction  $E_{1/2}$  of benzophenone is about  $-1.20V$  vs. SCE. The lack of any additional oxidation or reduction waves suggests that other short-lived oxidizable or reducible species are not present on this time scale.

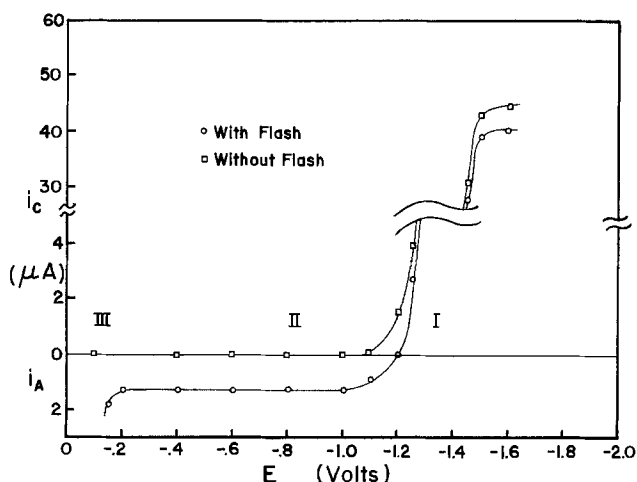


Fig. 7. Current-voltage profile:  $5 \times 10^{-4}M$  benzophenone, 0.50M acetate buffer, 50% ethanol/ $H_2O$ , pH = 5.5,  $t = 490 \mu$ sec after flash.

**Calculation of individual rate constants.**—The pH study allows calculation of the three second-order rate constants for Eq. [8]-[10]. Because  $R\cdot$  and  $R\cdot^-$  are indistinguishable electrochemically, an over-all rate expression may be written

$$\frac{dP}{dt} = \frac{1}{2} \left[ \frac{dC_T}{dt} \right] \quad [15]$$

where  $P$  = product benzopinacol, and  $C_T = C_{R\cdot} + C_{R\cdot^-}$ . From this and Eq. [8]-[10] it follows

$$\frac{dC_T}{dt} = \frac{dC_{R\cdot}}{dt} + \frac{dC_{R\cdot^-}}{dt} \quad [16]$$

$$\frac{dC_{R\cdot}}{dt} = - [k_1(C_{R\cdot})^2 + k_2 C_{R\cdot} C_{R\cdot^-}] \quad [17]$$

$$\frac{dC_{R\cdot^-}}{dt} = - [k_3(C_{R\cdot^-})^2 + k_2 C_{R\cdot} C_{R\cdot^-}] \quad [18]$$

$$\frac{dC_T}{dt} = - [k_1(C_{R\cdot})^2 + 2k_2 C_{R\cdot} C_{R\cdot^-} + k_3(C_{R\cdot^-})^2] \quad [19]$$

$$\frac{dC_T}{dt} = - k_d(C_T)^2 \quad [20]$$

Where  $k_d$  = second order rate constant measured electrochemically. Rearranging this expression in terms of the equilibrium constant (23) between ketyl radical and radical anion ( $K_{eq} = 10^{9.2} = 1/K_A$ )

$$k_d = \frac{k_1 K_{eq}^2 (H^+)^2 + 2k_2 K_{eq} (H^+) + k_3}{[1 + K_{eq} (H^+)]^2} \quad [21]$$

Inserting the values for  $k_d$  (digital simulation method) and  $(H^+)$  from Table I into Eq. [21], one obtains 10 equations with 3 unknowns. When these are solved as discussed below, one obtains the results in Table III for  $k_1$ ,  $k_2$ , and  $k_3$ . Hence, these three rate constants can be measured even though the individual processes cannot be monitored directly. Values which were measured spectroscopically for disappearance of the radical anion in isopropanol/water solution by Beckett and Porter (14) are also shown in Table III for comparison.

The values obtained for these rate constants are subject to experimental limitations. For example, at no pH does the  $R\cdot^-$  dimerization reaction (Eq. [10]) dominate. Even at pH 13.6, the radical-radical anion reaction still is significant because it is so fast. Hence, the value given for  $k_3$  in Table III is the upper limit for that process;  $k_3$  cannot be faster than  $7.8 \times 10^4 M^{-1} sec^{-1}$ . On the other end of the pH scale however, this problem does not exist. At pH 5.5, the reaction which is measured is due almost completely to the radical dimerization. Hence, the  $k_d$  value measured is  $k_1$  directly. The value of  $k_2$  given is the average value calculated from Eq. [21] with the intermediate pH data, using the above values for  $k_1$  and  $k_3$ .

### Conclusions

The studies reported here have served several purposes. One of these was to demonstrate the validity of the theoretical expressions for combined faradaic and induced charging currents presented previously (15). The evaluation of two approaches for extracting faradaic currents from experimental measurements showed that the derivative method is more generally useful, but suffers from some practical limitations in implementation. The experimental verification of the

Table III. Individual radical reaction rate constants

Reaction	$k$	Beckett-Porter (14)
$(k_1) R\cdot + R\cdot$	$2.5 \times 10^8 M^{-1} sec^{-1}$	$5.9 \times 10^7 M^{-1} sec^{-1}$
$(k_2) R\cdot + R\cdot^-$	$1.1 \times 10^9$	$1.1 \times 10^9$
$(k_3) R\cdot^- + R\cdot^-$	$\leq 7.8 \times 10^4$	$\leq 1.8 \times 10^5$

Britz-Kastening (13) and digital simulation theoretical expressions for photodimerization kinetic studies resolves a long-standing question in photoelectrochemistry. The availability of valid kinetic-diffusion theory and accurate corrections for induced charging currents has allowed the extension of benzophenone photoreduction studies into the acid pH range for the first time. Finally, it has been shown here that the quantitative interpretation of current-voltage-time relationships is now possible because of more accurate extraction of faradaic currents.

#### Acknowledgments

The authors wish to thank Sam Fratoni, Jr. for help with the SODH program and second order faradaic current extraction method, Nancy Stanford Davis for her digital simulation programming, Betty Hall for obtaining some of the kinetic data, and S. W. Feldberg for his helpful comments about the derivative  $I_F$  extraction technique. This work was supported by Public Health Service Grant No. CA-07773 from the National Cancer Institute and by a grant from the National Science Foundation.

Manuscript submitted Sept. 29, 1975; revised manuscript received June 8, 1976. This was Paper 352 presented at the Toronto, Canada, Meeting of the Society, May 11-16, 1975.

Any discussion of this paper will appear in a Discussion Section to be published in the June 1977 JOURNAL. All discussions for the June 1977 Discussion Section should be submitted by Feb. 1, 1977.

#### REFERENCES

1. S. P. Perone and J. R. Birk, *Anal. Chem.*, **38**, 1589 (1966).
2. J. R. Birk and S. P. Perone, *ibid.*, **40**, 496 (1968).
3. G. L. Kirschner and S. P. Perone, *ibid.*, **44**, 443 (1972).
4. J. I. H. Patterson and S. P. Perone, *ibid.*, **44**, 1978 (1972).
5. S. P. Perone and H. D. Drew, in "Analytical Photochemistry and Photochemical Analysis," J. M. Fitzgerald, Editor, chap. 7, Marcel Dekker, Inc., New York (1971).
6. J. I. H. Patterson and S. P. Perone, *J. Phys. Chem.*, **77**, 2437 (1973).
7. R. A. Jamieson and S. P. Perone, *ibid.*, **76**, 830 (1972).
8. H. Berg and H. Schweiss, *Electrochim. Acta*, **19**, 425 (1964).
9. H. Berg and H. Schweiss, *Z. Anal. Chem.*, **216**, 165 (1966).
10. K. E. Reinert and H. Berg, *Monatsber. Dtsch. Akad. Wiss. Berlin*, **4**, 26 (1962).
11. M. Grätzel, K. M. Bansal, and A. Henglein, *Ber. Bunsenges. Phys. Chem.*, **77**, 11 (1973).
12. S. W. Feldberg, in "Electroanalytical Chemistry," Vol. 3, A. J. Bard, Editor, pp. 199-295, Marcel Dekker, Inc., New York (1969).
13. D. Britz and B. Kastening, *Electroanal. Chem. Interfac. Electrochem.*, **56**, 73 (1974).
14. A. Beckett and G. Porter, *Trans. Faraday Soc.*, **59**, 2038 (1963).
15. S. S. Fratoni, Jr. and S. P. Perone, *This Journal*, **123**, 1672 (1976).
16. K. F. Dahnke, S. S. Fratoni, Jr., and S. P. Perone, *Anal. Chem.*, **48**, 296 (1976).
17. A. Savitsky and M. J. E. Golay, *ibid.*, **36**, 1627 (1964).
18. D. C. Neckers, "Mechanistic Organic Photochemistry," chap. 7, Reinhold, New York (1967).
19. W. Kemula, Z. R. Grabowski, and M. K. Kalinkowski, *Naturwissenschaften*, **22**, 514 (1960).
20. S. P. Perone, Ph.D. Thesis, University of Wisconsin, Madison (1963).
21. M. Suzuki and P. J. Elving, *J. Phys. Chem.*, **65**, 391 (1961).
22. H. E. Stapelfeldt and S. P. Perone, *Anal. Chem.*, **41**, 628 (1969).
23. G. Porter and F. Wilkinson, *Trans. Faraday Soc.*, **57**, 1686 (1961).

## Photo-oxidation of Water at Barium Titanate Electrodes

John H. Kennedy\* and Karl W. Frese, Jr.

Department of Chemistry, University of California, Santa Barbara, California 93106

#### ABSTRACT

Photoeffects at polycrystalline, semiconducting barium titanate were investigated. Photocurrent efficiencies were related to solid-state properties and agreement was found between donor densities calculated from efficiency-potential plots and those calculated from Mott-Schottky plots. The existence of a significant temperature effect on the photocurrent efficiency was demonstrated. The influence of pH on the flatband potential was also determined.

A number of studies (1-8) of photoeffects at polycrystalline semiconductor electrodes in electrochemical cells have been reported in the recent literature. However, measurement of photocurrent efficiencies and the distribution of potential in semiconducting BaTiO<sub>3</sub> have not been investigated. Also the effect of temperature on efficiency has been largely ignored for TiO<sub>2</sub> and titanates although Wrighton *et al.* (9) reported on temperature effects at SnO<sub>2</sub> electrodes.

In this study we have applied the standard techniques for studying single crystal electrodes to polycrystalline sintered BaTiO<sub>3</sub> and have demonstrated a temperature effect of the photocurrent efficiency. Our use of well-known semiconductor depletion layer theory allows a useful interpretation of our efficiency data in terms of solid-state properties.

\* Electrochemical Society Active Member.

Key words: barium titanate, photo-assisted electrolysis of water, photo-oxidation, semiconductor electrodes.

#### Experimental

*Electrode preparation.*—Barium titanate was prepared from Ba(NO<sub>3</sub>)<sub>2</sub> (reagent grade) and TiO<sub>2</sub> (99.9%). The materials were dry mixed for 24 hr in an alumina ball mill and then heated at 1000°C for 12 hr. After further grinding, the mixture was pressed into disks at 4000 psi and sintered in air at 1350°C for at least 2 hr. The conductivity of the BaTiO<sub>3</sub> was increased by heating the sintered material in a stream of H<sub>2</sub> at temperatures up to 1300°C for several hours. Resistivities were 10<sup>3</sup> Ω-cm and final densities were 5.2-5.5 g/cm<sup>3</sup>. The samples were cooled in N<sub>2</sub> from about 800°C and were found to have a black insulating layer presumably due to some reoxidation by O<sub>2</sub> in the N<sub>2</sub> stream. This layer was removed by light mechanical polishing with SiC paper and thorough ultrasonic washing in deionized water. The resulting material was dark blue, characteristic of Ti<sup>3+</sup> ions. Contact to the

electrode was made by applying Ag epoxy (Epoxy Technology) to which a copper wire was soldered. The electrode was then mounted in a glass tube and sealed with epoxy resin. Current-voltage curves for reduced BaTiO<sub>3</sub> with Ag epoxy electrodes were found to follow Ohm's law.

**Illumination.**—The BaTiO<sub>3</sub> electrodes were illuminated (quartz window) with a 150W Xe lamp using a Bausch and Lomb visible grating monochromator and collimating lens. The photon flux at 360 nm was determined using 0.006M ferrioxalate actinometry (10). The flux at 350 and 360 nm was determined from relative power density measurements using a YSI Model 65A radiometer. These intensities agreed well with those obtained from Reinecke actinometry (11) at 504 nm and radiometric measurements. Reflection losses from the cell window were accounted for by the actinometry procedures, however the light reflected from the electrode surface was ignored in the calculations.

**Electrochemical measurements.**—The cell arrangement consisted of a BaTiO<sub>3</sub> working electrode, platinized Pt counterelectrode and a SCE reference electrode. Buffer solutions were NBS standard buffers in 0.5M KCl or Mallinckrodt Standard "Buffer" solutions. Current-potential curves were obtained with a PAR Model 174 polarographic analyzer at a scan rate of 2 mV/sec. Solutions were deoxygenated with N<sub>2</sub> gas before all measurements and a N<sub>2</sub> atmosphere was maintained during the measurements.

**Capacitance measurements.**—Capacitance measurements of the cell BaTiO<sub>3</sub>/buffer solution/Pt were made with a General Radio Model 1650-A impedance bridge operating at 1000 Hz. The bridge was biased using a Harrison 6112A power supply. The BaTiO<sub>3</sub> electrode potential was measured vs. SCE with a Hewlett Packard Model 412 A VTVM.

## Results

**Flatband potentials.**—The flatband potential of sintered BaTiO<sub>3</sub> electrode was measured in the dark as a function of pH. The determination of the flatband potential,  $V_{FB}$ , for a wide gap semiconductor is based on the Mott-Schottky relation (12)

$$1/C_{sc}^2 = \frac{2}{q\epsilon_0 N_D} (V - V_{FB} - kT/q) \quad [1]$$

where  $C_{sc}$  is the space charge capacitance per unit area,  $q$  is the electronic charge,  $\epsilon$  is the dielectric constant of the space charge layer [1500 for polycrystalline BaTiO<sub>3</sub> (13)],  $\epsilon_0$  is the permittivity of vacuum,  $N_D$  is the donor density, and  $V$  is the BaTiO<sub>3</sub> electrode potential vs. a reference electrode. Typical Mott-Schottky plots are shown in Fig. 1. The donor concentration

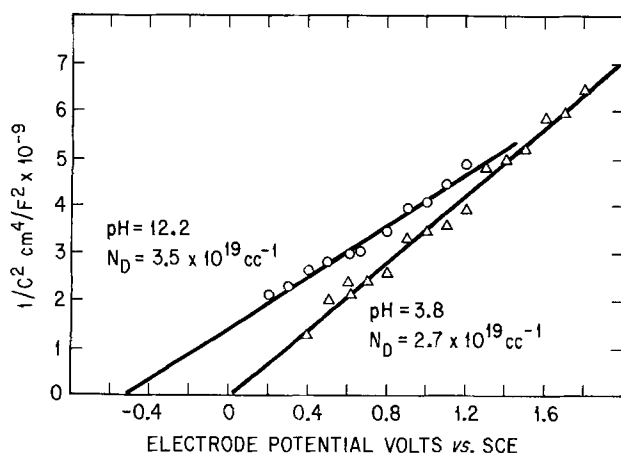


Fig. 1. Mott-Schottky plots for polycrystalline barium titanate. In dark,  $t = 23^\circ\text{C}$ .

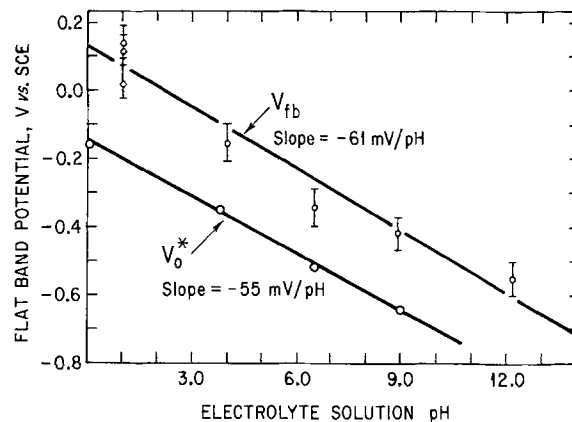
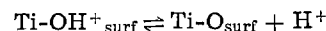


Fig. 2. Flatband potential and zero-efficiency potential of barium titanate vs. pH,  $t = 23^\circ\text{C}$ .

calculated from these slopes is  $\sim 3 \times 10^{19} \text{ cm}^{-3}$ . Similar linear plots were obtained for electrodes with donor densities as low as  $10^{16} \text{ cm}^{-3}$ . Figure 2 shows the effect of solution pH on the flatband potential. The slope of the  $V_{FB}$  vs. pH plot was found to be  $-61 \text{ mV/pH}$ . The usual interpretation (12) for this value is that a dissociative equilibrium exists between a protonated oxide ion on the surface of the lattice and the solvent. Thus the change of the Fermi level with pH at the electrode surface is determined by the free energy change for the reaction



It should be noted that these flatband potentials found for BaTiO<sub>3</sub> are approximately 0.75 and 0.35V more anodic than for single crystal SrTiO<sub>3</sub> (14, 15) and TiO<sub>2</sub> (16), respectively.

**Photocurrent efficiencies.**—Figure 3 shows typical photocurrent vs. electrode potential curves at 360 nm for various pH values. The equivalent photon current was  $48 \mu\text{A}$ . The photocurrent efficiency,  $\eta_p$ , was calculated from

$$\eta_p = \frac{i(\text{light}) - i(\text{dark})}{i(\text{photon})} \quad [2]$$

It can be seen that for a given overvoltage the efficiency was practically independent of pH. This result suggests that the rate-limiting step depends on processes occurring within the semiconductor. This point will be further discussed below. The effect of pH on the potential of zero efficiency  $V_o^*$  is shown in Fig. 2. The slope  $dV_o^*/dpH$  was found to be  $-55 \text{ mV/pH}$ .

The open-circuit voltage,  $V_{oc}$ , at pH 3.8 in 0.5M KCl was found to be  $-0.054\text{V}$  vs. SCE in the dark and  $-0.32\text{V}$  vs. SCE under illumination at 360 nm. The corresponding flatband potential in the dark was  $-0.10\text{V}$

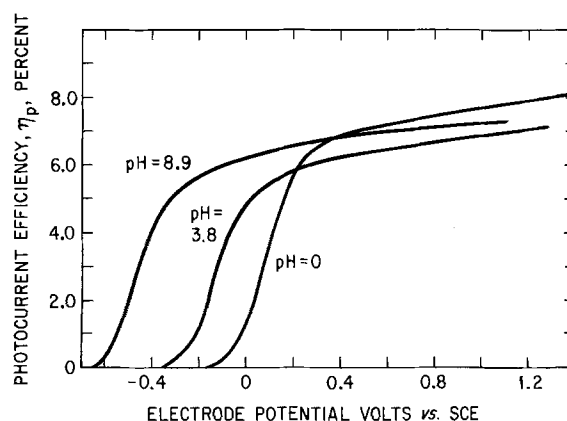


Fig. 3. Photocurrent efficiency of polycrystalline barium titanate.  $\lambda = 360 \text{ nm}$ ,  $t = 23^\circ\text{C}$ .



from Fig. 2. This result indicates that the bands were bent slightly upward in the dark at open circuit and that in the dark the open-circuit voltage and flatband potential are approximately equal. It follows from the agreement between  $V_{oc}$  and  $V_{FB}$  in the dark and  $V_{oc}^*$  and  $V_o^*$  ( $-0.32V$  vs.  $-0.35$ ) that  $V_o^*$  would measure approximately the flatband potential under illumination.

**Temperature effect.**—Figure 4 shows the effect of solution temperature on the photocurrent efficiency. At the two wavelengths shown, the rate of increase of  $\eta_p$  with temperature is almost identical at  $\sim 0.11\%/^{\circ}C$ . For  $BaTiO_3$  the efficiency can be doubled for a  $60^{\circ}C$  increase in temperature. Although the high temperature efficiencies are still low compared to  $TiO_2$ , the existence of a temperature effect could have important consequences for other higher efficiency semiconductors allowing some use of longer wavelength solar radiation. Similar increases of efficiency with temperature were found for polycrystalline  $TiO_2$  and  $SrTiO_3$ . In each case rate of increase was  $\sim 0.1\%/^{\circ}C$  at  $1.0V$  vs. SCE. Typical values of  $\eta_p$  at room temperature and  $340$  nm were 37 and 19% at  $1.0V$  vs. SCE for  $TiO_2$  and  $SrTiO_3$ , respectively. At elevated temperatures, typical values of  $\eta_p$  for  $TiO_2$  and  $SrTiO_3$  were 40% at  $55^{\circ}C$  and 21% at  $50^{\circ}C$ , respectively. It should be noted that efficiencies for polycrystalline  $SrTiO_3$  reported here are nearly the same as those reported by Watanabe *et al.* (14) for single crystal  $SrTiO_3$ . Although it is anticipated that single crystals may exhibit highest efficiencies, especially for anisotropic material which could be oriented for maximum efficiency, it is clear from these results that polycrystalline material can produce photocurrents comparable to single crystals.

**Discussion**

A reasonable interpretation of our efficiency results for  $BaTiO_3$  can be made by use of the theory of depletion-layer photoeffects as given by Gärtner (17) and discussed by Myamlin and Pleskov (18). The photocurrent efficiency  $\eta_p$  under anodic bias (bands bent up) for negligible recombination is given by

$$\eta_p = 1 - \frac{e^{-aL}}{1 + aL_p} \tag{3}$$

where  $a$  is the absorption coefficient,  $L$  is the effective width of the space charge region, and  $L_p$  is the mean diffusion length for holes outside the space charge region. The width of the space charge region is related to solid-state properties of the semiconductor and the overvoltage in the space charge region,  $\Delta\phi_s$ , by the relation (18)

$$L = \left( \frac{\epsilon\epsilon_0}{2qN_D} \right)^{1/2} \Delta\phi_s^{1/2} \tag{4}$$

Algebraic manipulation of Eq. [3] and [4] leads to

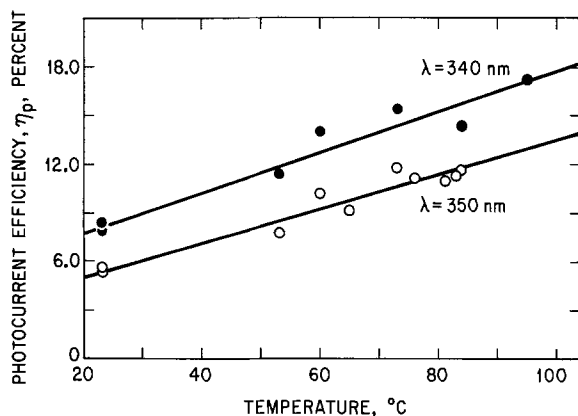


Fig. 4. Effect of temperature on photocurrent efficiency for polycrystalline barium titanate, pH = 7.0.

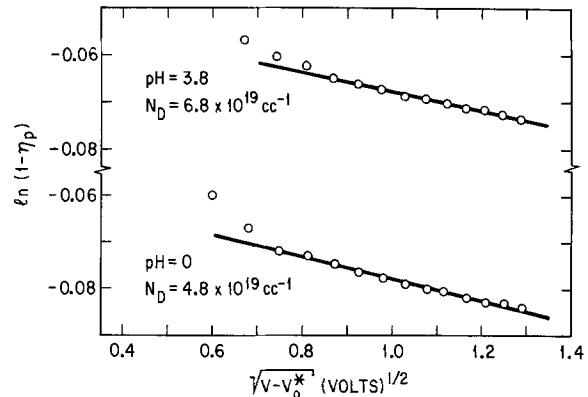


Fig. 5. Determination of  $N_D$  and  $L_p$  from photocurrent vs. potential for polycrystalline barium titanate.  $\lambda = 360$  nm.

Eq. [5]

$$\ln(1 - \eta_p) = -a \left( \frac{\epsilon\epsilon_0}{2qN_D} \right)^{1/2} \Delta\phi_s^{1/2} - \ln(1 + aL_p) \tag{5}$$

which shows that a plot of  $\ln(1 - \eta_p)$  vs.  $\Delta\phi_s^{1/2}$  should be linear with a slope of  $-a(\epsilon\epsilon_0/2qN_D)^{1/2}$  and an intercept of  $-\ln(1 + aL_p)$ . This relation is expected to hold for sufficiently large overvoltages so that recombination of holes and electrons generated by illumination in the space charge region is negligible. Thus Eq. [3] and [5] provide a basis for photocurrent potential curves under anodic bias. In addition to the linearity discussed above, a further test of the validity of Eq. [5] can be made by comparing values of  $N_D$  obtained from the efficiency-potential plots using known  $\epsilon$  and  $a$  with those obtained from Mott-Schottky slopes. Figure 5 shows some of our results for  $BaTiO_3$  at various values of pH where we have assumed that  $\Delta\phi_s$  can be approximated by  $V - V_o^*$ , i.e.,  $V_o^*$  measures the flatband potential under illumination and all the potential drop occurs across the space charge layer. Table I summarizes the results for  $BaTiO_3$  at room temperature and  $360$  nm where  $a \cong 8 \times 10^3$   $cm^{-1}$  (19-21). It can be seen that the two methods give fair agreement between  $N_D$  values and the diffusion lengths of about  $700\text{\AA}$  are independent of pH as expected.

Our data on the temperature effect of the photocurrent efficiency can be understood with the help of Eq. [3] and absorption coefficient data for  $BaTiO_3$  at various temperatures and energies. The absorption coefficient vs. temperature and photon energy has been studied by Wemple (19) in the wavelength region where  $\ln a$  is a linear function of energy at constant temperature. These data were used to calculate  $\eta_p$  at  $23^{\circ}$  and  $50^{\circ}C$  using Eq. [3]. Over this temperature range the dielectric constant is reasonably constant at  $1500$ . The only assumptions made were the validity of Eq. [3] and that  $L_p$  was independent of temperature. The values of  $N_D$  and  $L_p$  were averages of those given in Table I, and  $\Delta\phi_s$  was taken to be  $1.5V$  which corresponds to an electrode potential of  $1.0V$  vs. SCE at pH 7. The ratio,  $\eta_p^{50}/\eta_p^{23}$  was calculated to be 3.0, 2.5, and 1.8 at 3.0, 3.1, and 3.3 eV, respectively. The decrease in relative efficiency is due to the smaller effect of tem-

Table I. Comparison of  $N_D$  obtained from Mott-Schottky plots with  $N_D$  obtained from photocurrent efficiency ( $\lambda = 360$  nm,  $a \cong 8.0 \times 10^3$   $cm^{-1}$ )

pH	Mott-Schottky calc.		Photocurrent efficiency calc.	
	$N_D, cm^{-3}$	$L_p, cm$	$N_D, cm^{-3}$	$L_p, cm$
0	—	—	$4.8 \times 10^{19}$	$7.0 \times 10^{-6}$
3.8	$2.7 \times 10^{19}$	—	$6.8 \times 10^{19}$	$6.1 \times 10^{-6}$
6.5	$2.2 \times 10^{19}$	—	$7.0 \times 10^{19}$	$6.9 \times 10^{-6}$
8.4	$2.1 \times 10^{19}$	—	$6.6 \times 10^{19}$	$6.4 \times 10^{-6}$
12.2	$3.5 \times 10^{19}$	—	—	—

perature on the absorption coefficient as higher energies are approached. Therefore, we would expect the ratio to be  $< 1.8$  at 3.6 eV, the photon energy used for the data given in Fig. 4. The experimental value was 1.4 which is quite reasonable, and thus we conclude that temperature effects primarily reflect changes in absorption coefficient as the simple theory of depletion layer photoeffects predicts. It cannot be overlooked, however, that over large temperature ranges other factors such as  $L$ ,  $L_p$ , and  $\epsilon$  may also play an important role.

We are currently extending our measurements to higher temperatures with the aim of investigating the effect of the tetragonal  $\rightarrow$  cubic phase change at the ferroelectric Curie point ( $\sim 120^\circ\text{C}$ ). It is well established that an anomalous shift in the bandgap to lower energy occurs in the region of the phase transition. The bandgap values for ferroelectric materials such as  $\text{BaTiO}_3$ ,  $\text{SrTiO}_3$ , and  $\text{KTaO}_3$  must be defined at an arbitrary value of absorption coefficient because of the exponential decay of  $a$  vs. photon energy (Urbach edge). Therefore the quoted shifts in bandgap probably reflect changes in  $a$ .

Measurements of  $\eta_p$  in the wavelength region where  $\eta_p$  is small ( $\leq 0.10$ ) and  $aL_p \leq 0.10$  at constant electrode potential and temperature can provide an additional test for the applicability of the theory. Under the above conditions, Eq. [3] may be written after expansion of the logarithms as

$$\eta_p \cong a(L + L_p)$$

It can be seen that plotting  $\eta_p$  vs. absorption coefficient should be linear with a slope  $(L + L_p)$ . We have measured  $\eta_p$  at 10 nm intervals from 400 to 360 nm at 1.0V vs. SCE, pH 3.8,  $23^\circ\text{C}$  in 0.5M KCl. The slope,  $d\eta_p/da$ , was found to be  $8.6 \times 10^{-6}$  cm. From the value  $N_D = 6.3 \times 10^{19} \text{ cm}^{-3}$  given in Table I, and  $\Delta\phi_s = 1.35\text{V}$ ,  $L$  can be calculated from Eq. [4] giving  $3 \times 10^{-6}$  cm. Combining this result with  $d\eta_p/da$ , we calculate  $L_p$  to be  $5.6 \times 10^{-6}$  cm, in good agreement with  $6.6 \times 10^{-6}$  cm obtained from intercepts of plots using Eq. [5]. It can be concluded that our data and the theory of depletion layer photoeffects are consistent with respect to changes in  $\eta_p$  arising from changes in electrode potential, temperature, and absorption coefficient.

#### Acknowledgments

The authors acknowledge partial financial support of this project by the National Science Foundation, Grant

No. DMR73-07507 A02 and by the Committee on Research, University of California.

Manuscript submitted June 21, 1976; revised manuscript received July 22, 1976.

Any discussion of this paper will appear in a Discussion Section to be published in the June 1977 JOURNAL. All discussions for the June 1977 Discussion Section should be submitted by Feb. 1, 1977.

Publication costs of this article were assisted by the University of California, Santa Barbara.

#### REFERENCES

1. F. Möllers, H. J. Tolle, and R. Memming, *This Journal*, **121**, 1160 (1974).
2. K. L. Hardee and A. J. Bard, *ibid.*, **122**, 739 (1975).
3. J. G. Mavroides, D. J. Tchernev, J. A. Kafalas, and D. F. Kolesar, *Mater. Res. Bull.*, **10**, 1023 (1975).
4. F. Möllers and R. Memming, *Ber. Bunsenges. Phys. Chem.*, **76**, 469 (1972).
5. H. Kim and H. A. Laitinen, *This Journal*, **122**, 53 (1975).
6. W. Gissler, P. L. Lensi, and S. Pizzini, *J. Appl. Electrochem.*, **6**, 9 (1975).
7. J. Keeney, D. H. Weinstein, and G. M. Haas, *Nature*, **253**, 719 (1975).
8. M. Shiozawa, K. Narita, Y. Fujita, S. Kurita, M. Takata, and H. Yanagida, *Yogyo Kyokai Shi*, **83**, 61 (1975).
9. M. S. Wrighton, D. Morse, A. Ellis, D. Ginley, and H. Abrahamson, *J. Am. Chem. Soc.*, **98**, 44 (1976).
10. C. G. Hatchard and C. A. Parker, *Proc. R. Soc. London, Ser A*, **235**, 518 (1956).
11. E. Wegner and A. Adamson, *J. Am. Chem. Soc.*, **88**, 394 (1966).
12. H. Gerisher, in "Physical Chemistry," Vol. IXA H. Eyring, D. Henderson, and W. Jost, Editors, chap. 5, Academic Press, New York (1970).
13. F. Galasso, "Structure, Properties, and Preparation of Perovskite-Type Compounds," p. 82 Pergamon Press, Oxford (1969).
14. T. Watanabe, A. Fujishima, and K. Honda, *Bull. Chem. Soc. Japan*, **49**, 355 (1976).
15. M. S. Wrighton, A. Ellis, P. Wolczanski, D. Morse, H. Abrahamson, and D. Ginley, *J. Am. Chem. Soc.*, **98**, 2774 (1976).
16. T. Watanabe, A. Fujishima, and K. Honda, *Chem. Lett.*, 897 (1974).
17. W. W. Gärtner, *Phys. Rev.*, **116**, 84 (1959).
18. V. A. Myamlin and Y. V. Pleskov, "Electrochemistry of Semiconductors," Plenum Press, New York (1967).
19. S. H. Wemple, *Phys. Rev. B*, **2**, 2679 (1970).
20. C. Gähwiller, *Phys. Kondens. Mater.*, **6**, 269 (1967).
21. C. Gähwiller, *Solid-State Commun.*, **5**, 65 (1967).

# Mass Transfer to a Rotating Disk in Transition Flow

Charles M. Mohr, Jr.\* and John Newman\*\*

Inorganic Materials Research Division, Lawrence Berkeley Laboratory, and Department of Chemical Engineering,  
University of California, Berkeley, California 94720

## ABSTRACT

An experimental study of mass transfer to a rotating disk electrode has been employed to determine an empirical correlation for the mass transfer rate in the Reynolds number regime lying between simple laminar and turbulent flows. This domain, apparently characterized by a regular vortex pattern, was found to extend from a Reynolds number of  $2.0 \times 10^5$  to approximately  $3.0 \times 10^5$ . The resultant correlation for the average transfer rate, in terms of dimensionless Nusselt, Reynolds, and Schmidt numbers, is

$$\bar{Nu} = 0.89 \times 10^5 Re_o^{-1/2} Sc^{1/3} + 9.7 \times 10^{-15} Re_o^3 Sc^{1/3}$$

The result is strictly applicable to the case of a uniform surface concentration; that is, to the limiting-current condition.

The mass transfer behavior of the rotating disk electrode is of continuing interest. While the bulk of its uses are based upon the uniform-accessibility property described by Levich (1) for disks upon which simple laminar flow (2) prevails, for sufficiently high rotation speeds turbulence may be reached near the edge of the disk. The nonuniform (enhanced) mass transfer rate resulting from this turbulence may be a desirable feature for some studies. In particular, this behavior has been found useful for studies of corrosion, when the effect of a varying local rate of oxygen transport to the surface of the corroding metal is of interest (3-6).

An accurate description of the behavior of such an electrode requires knowledge of the local transfer rate for the full range of Reynolds numbers involved. The Reynolds number found appropriate for the disk is  $Re = r^2 \Omega / \nu$ , where  $r$  is the radial distance from the center of rotation,  $\Omega$  the angular rotation speed, and  $\nu$  the kinematic viscosity of the fluid in which the disk rotates. This behavior for simple laminar flow, as described by von Kármán (2), is well known, having been first described by Levich (1), who gave the mass transfer rate as

$$\bar{Nu}_{lam} = 0.6205 Re_o^{1/2} Sc^{1/3} \quad [1]$$

where the Nusselt number  $\bar{Nu} = \bar{i}r_o/nFD\Delta c$ , the Schmidt number  $Sc = \nu/D$ , and  $Re_o$  is the Reynolds number based upon the electrode radius  $r_o$ .  $\bar{i}$  is the average current density on the electrode,  $n$  the number of electrons transferred per ion reacting,  $F$  Faraday's constant,  $D$  the diffusion coefficient of the active species, and  $\Delta c$  is the concentration driving force for diffusion, bulk concentration minus concentration at the electrode surface.

The transfer rate for well-developed turbulent flow has been the subject of several studies (7-12), and accurate correlations have been proposed for its dependence upon the Reynolds number. The two most useful of these correlations are due to Ellison and Cornet (7) and Daguene (9), since both of these also include the Schmidt number influence upon the Nusselt number. Ellison and Cornet report that the mass transfer may be described as

$$\bar{Nu}_{turb} = 0.0117 Re_o^{0.896} Sc^{0.249} \quad [2]$$

while the result of Daguene is

$$\bar{Nu}_{turb} = 0.00725 Re_o^{0.9} Sc^{0.33} \quad [3]$$

We have chosen to use Daguene's equation for two reasons. First, the bulk of the data gathered by Ellison was for larger Reynolds numbers than are of interest here ( $Re_o > 10^6$ ), while Daguene thoroughly investigated the flow regime immediately adjacent to the transition region ( $3 \times 10^5 < Re_o < 10^6$ ). Second, in light of the many studies of turbulent transfer in different geometries, it seems that the exponent 1/3 is more realistic than 1/4 for the Schmidt number dependence. This conclusion is supported by the investigations of Donovan *et al.* for turbulent boundary layers (13), Hubbard and Lightfoot (14, 15), and Vielstich *et al.* (16). The influence of the structure of the turbulent flow upon this exponent is discussed by Levich (17). Also, Ellison and Cornet's data for  $Re_o < 10^6$  are quite scattered and may possibly be better fit by a  $Sc^{1/3}$  dependence.

However, we have refit Daguene's data, as shown in Fig. 1, according to the correlation

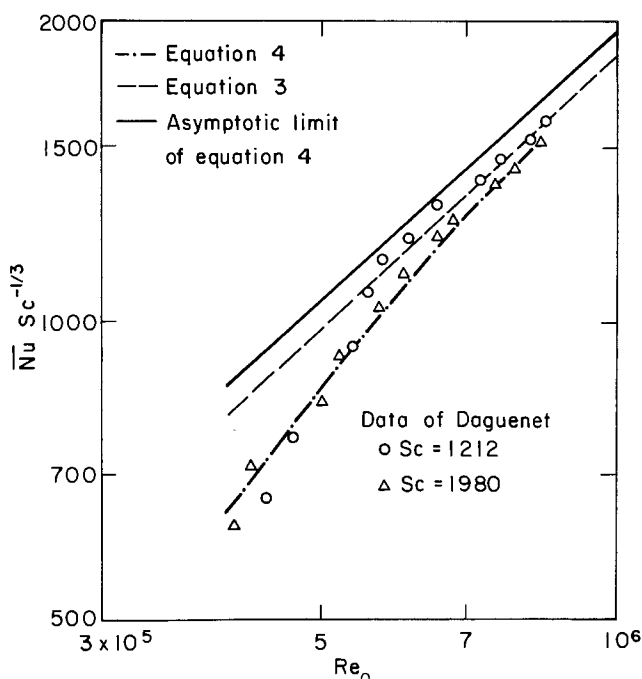


Fig. 1. Correlation of Daguene's data for turbulent mass transfer to a rotating disk.

\* Electrochemical Society Student Member.

\*\* Electrochemical Society Active Member.

Key words: limiting current, turbulence, fluid flow.

$$\overline{Nu} Sc^{-1/3} = 0.0078 Re_0^{0.9} - 1.38 \times 10^5 Re_0^{-1/2} \quad [4]$$

This form is based on the supposition that the local asymptotic transfer rate is proportional to  $Re_0^{0.9}$ , although over-all Nusselt numbers for  $Re_0 < 10^6$  are still significantly dependent upon transfer in the laminar and transition zones. The coefficient of the last term in Eq. [4] will thus be adjusted subsequently by integration of local rates in the laminar and transition zones, while the first term should depend only on the asymptotic behavior in the turbulent regime. This leads to the following correlation for the large Reynolds number asymptotic mass transfer behavior

$$\overline{Nu}_{turb} = 0.0078 Re_0^{0.9} Sc^{1/3} \quad [5]$$

The problem remains to describe the mass transfer behavior as a function of Reynolds number for the region in which the simple laminar flow becomes unstable and yields to turbulence. The range of Reynolds numbers over which this change takes place has been termed the "transition region," and the experimental determination of its mass transfer behavior is the purpose of this investigation.

The nature of this transition region was first described by Gregory, Stuart, and Walker (18) who demonstrated that the simple laminar flow found near the center of the disk becomes unstable at a Reynolds number equal to approximately  $1.8 \times 10^5$ , and that fully developed turbulence was not reached until  $Re \sim 3 \times 10^5$ . Stuart (18) also developed a nonlinear stability analysis which showed that stable periodic solutions to the Navier-Stokes equation could be expected for this range of Reynolds numbers. The experimental and theoretical results both point to the presence of a stable vortex pattern, rather than a predominantly random flow, in the transition region.

Subsequent work by others has served to reinforce the conclusions of Gregory *et al.* In particular, the work of Chin and Litt (19) has provided perhaps the most accurate determination of the critical Reynolds numbers bounding the transition region. These investigators embedded a small electrode in a disk at some distance from the center of rotation. By varying the rotation speed, the electrode was subjected to a range of Reynolds numbers. A spectral analysis of the current signal to the electrode was used to determine if a regularly varying mass transfer mode was present, indicating vortices moving across the electrode. Their results agreed well with Gregory *et al.* (18) for the lower bound of the transition region, their value being  $Re = 1.7 \times 10^5$ , but they found evidence that the vortices persist to a Reynolds number of about  $3.5 \times 10^5$ , well beyond the value reported by Gregory.

Various studies of mass transfer in the turbulent flow regime also include some data in the transition region. Kreith, Taylor, and Chong (11) report significant deviation from values predicted by the Levich analysis for laminar flow beginning at a Reynolds number of about  $2 \times 10^5$ . The rather scattered data of Cobb and Saunders (12) tend to agree with this. Dagenet (9) reported a lower bound of the transition region of approximately  $2.6 \times 10^5$ , but this value varied with the Schmidt number of the solution. An experimental study performed by Tien and Campbell (10) agreed more closely with Chin and Litt in that they reported enhanced mass transfer beginning at  $Re = 1.8 \times 10^5$ . Ellison and Cornet (7) have also performed an experimental (and theoretical) investigation of mass transfer in the turbulent regime. While their data for low ( $< 3 \times 10^5$ ) Reynolds numbers are somewhat scattered, they state that significant deviation from the Levich theory does not begin until  $Re = 3 \times 10^5$  is reached.

In view of the lack of agreement about the value of the Reynolds number at which the Levich theory becomes inappropriate and the lack of a correlation for mass transfer in the transition region, an experimental study of this problem was performed. It is hoped that a

more exact treatment of the dependence of the local transfer rate upon the Reynolds number, particularly in the transition region, will be found useful for such studies in which variation of the local mass transfer rate (as a function of position) is desired.

### Experimental Work

*Electrochemical systems of interest.*—Two reactions were chosen for study: the electrodeposition of copper from a cupric sulfate-sulfuric acid solution onto a rotating copper disk, and cathodic reduction of ferricyanide ions to ferrocyanide ions, also on a copper disk, from a potassium ferricyanide-potassium ferrocyanide-potassium hydroxide solution. Concentrations of the active species were approximately 0.005M, while 1.5M sulfuric acid and 0.85M potassium hydroxide were used as supporting electrolytes. For the ferricyanide reduction, an excess of ferrocyanide was used (conc  $\sim 0.007M$ ) to help insure that the limiting current was achieved on the cathode (disk) before excessive oxygen evolution occurred at the anode. Oxygen evolution at the anode of the ferricyanide system is not desirable since it reduces the amount of ferrocyanide oxidized, thus depleting the solution of ferricyanide. A counterelectrode of copper was used for the cupric acid system to provide the atomic copper for the anodic reaction. A nickel counterelectrode was used for the ferricyanide system anode.

*Experimental apparatus.*—A series of three PTFE slinger rings on the rotating shaft, each in its own compartment, was used to prevent loss of the solution at high rates of revolution and minimize aeration of the solution during the trials. The electrode consisted of a copper disk approximately  $2\frac{1}{4}$  in. in diameter soldered to a  $\frac{1}{4}$  in.-20 machine screw which provided electrical continuity to the shaft. The back and edge of the electrode were insulated with Shell epoxy casting resin which was extended  $\frac{1}{4}$  in. beyond the edge of the electrode to reduce the effect of the hydrodynamic disturbance due to the edge of the disk upon the flow field over the conducting area. A series of six baffles around the perimeter of the cell was used to minimize bulk rotation of the fluid.

The peripheral electronic equipment consisted of a galvanostat (with a built-in current ramp generator) which was built to order for high current applications. Continuous polarograms were recorded on a Hewlett-Packard Model 7044A X-Y plotter. Current measurements were made by placing a precision resistor (0.1495 $\Omega$ , 25W maximum power dissipation) in the lead to the counterelectrode, and the voltage drop across it measured directly using the X-Y plotter. The rotation speed of the electrode was determined with a "Strobotac" stroboscopic tachometer.

*Electrode preparation.*—The electrode was polished prior to each series of runs with 4/0 grit emery paper followed by buffing on a canvas polishing wheel coated with 6  $\mu$ m diamond paste to a mirror finish. Following both the polishing and buffing, the electrode was washed with Amway L.O.C. cleaning solution followed by rinsing with distilled water and ethanol and drying in a stream of hot air. Due to the low concentrations of  $Cu^{++}$  in the cupric sulfate solutions (approximately 0.005M) and the short duration of the trials, the surface remained quite smooth and mirrorlike even after a series of 15-20 trials. The trials involving the ferricyanide solutions were observed not to alter the surface detectably during the experiments, although the copper would apparently corrode if allowed to remain in contact with the KOH solution.

*Experimental procedure.*—For each series of trials, the cell was disassembled and cleaned, and the proper counter and reference electrodes were installed and polished with emery paper. Freshly prepared solution was introduced into the cell, with care being taken to exclude air bubbles. The solution level found to mini-

mize apparent aeration at high rotation speeds was reached when the surface was approximately at the same level as the middle slinger ring, which required about 1.6 liter of solution. The polarograms were recorded at various rotation speeds, noting the temperature of the solution at each trial. A series of 15 trials was found to increase the temperature about 1°C. Typical polarograms for a series of measurements are shown on Fig. 2. Viscosities of the solutions were determined for the range of temperatures encountered using a capillary viscometer. Diffusion coefficients were measured with the experimental electrode system operated at low revolution speeds using the Levich formula (1) for laminar flow to a rotating disk. For slight temperature variations, the Stokes-Einstein equation  $D\mu = CT$ , where  $T$  is degrees Kelvin and  $\mu =$  absolute viscosity, was used. During the run, measurements were made at low rotation speeds to monitor possible concentration variation, a problem which occurred in the ferricyanide system due to oxygen evolution at the anode.

### Results

The inflection point on the plateau of a polarogram in Fig. 2 corresponds, in essence, to the limiting current. The shape of the curve thus introduces some uncertainty into the values so obtained. The experimental results are presented on Fig. 3 as a graph of  $\overline{Nu} Sc^{-1/3}$  vs.  $Re_o$ . The data gathered for  $Re_o < 1.4 \times 10^5$ , used to determine the diffusivity of the reacting species and monitor concentration changes, are not shown on this figure. The departure from the predictions of the Levich formula, Eq. [1], are observed to begin at approximately  $Re_o = 2 \times 10^5$ , in agreement with previous studies. The approach to the values predicted by Eq. [5] is also shown.

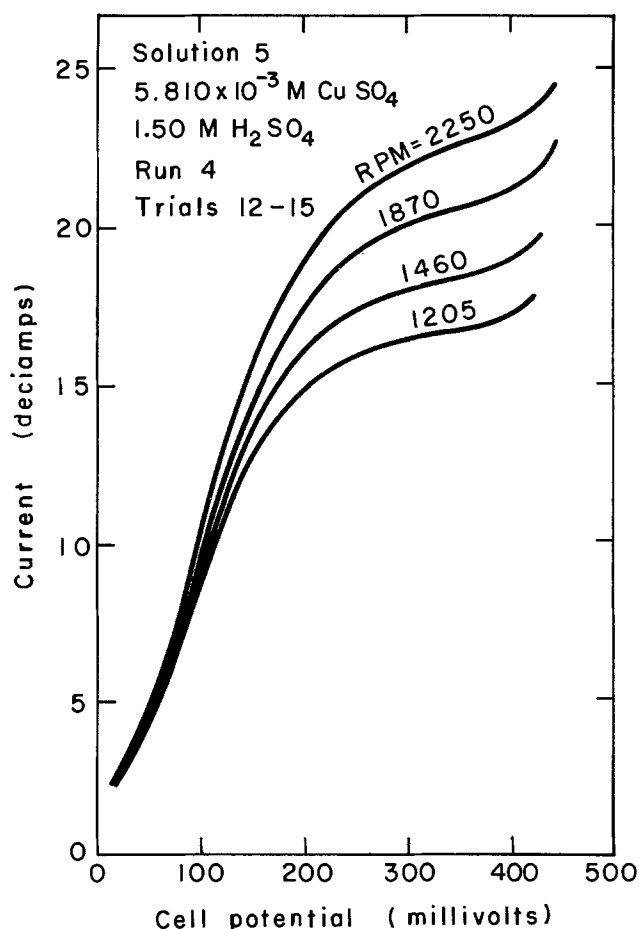


Fig. 2. Typical polarograms for mass transfer to a rotating disk

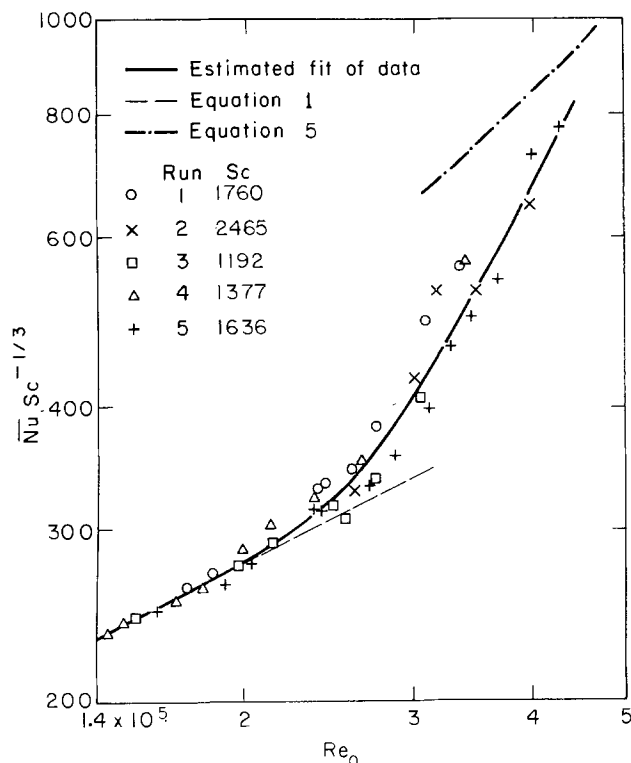


Fig. 3. Over-all mass transfer rate ( $\overline{Nu} Sc^{-1/3}$ ) vs. Reynolds number for laminar, transition, and turbulent regimes. Standard deviations for the Schmidt numbers are 31, 41, 26, 38, and 57 for runs 1 to 5. Runs 3 and 4 involve deposition of copper; the others are reduction of ferricyanide.

To determine the local mass transfer rate as a function of Reynolds number from the experimental data and Eq. [1]-[5], one may use the expression (4, 5)<sup>1</sup>

$$Nu_{loc} = \frac{i_{loc} r}{\pi F D \Delta c} = \frac{1}{2} \frac{d}{d(Re_o^{1/2})} [\overline{Nu} Re_o^{1/2}] \quad [6]$$

$\overline{Nu} Sc^{-1/3} Re_o^{1/2}$  is shown on Fig. 4 as a function of the square root of the Reynolds number. While the scatter in the data detracts from the accuracy of the derivatives determined from the curve fit, the results should still be useful in providing an estimate of the local transfer rates which lie within the data scatter. It should provide an improvement over previous work (4, 5) in which the local transfer rate for the laminar region was spliced (with considerable discontinuity) directly to the local transfer rate predicted from the work of Ellison and Cornet, Eq. [2].

The local Nusselt number derived from Eq. [1] (using Eq. [6]) is

$$Nu_{lam} = 0.6205 Re_o^{1/2} Sc^{1/3} \quad [7]$$

In a similar manner, Eq. [4] or [5] yields

$$Nu_{turb} = 0.01092 Re_o^{0.9} Sc^{1/3} \quad [8]$$

These equations, along with the local Nusselt numbers for the transition region determined by differentiation of the curve fit given in Fig. 4, are given in Fig. 5. A straight-line fit of the data for the transition region seems reasonable; the one shown dotted in Fig. 5 leads to a correlation for the local Nusselt number

<sup>1</sup> This equation may be derived by transforming the variable  $r$  to  $\sqrt{\frac{r}{\Omega}}$  in the integral identity defining the average current density

$$\overline{ir} = \int_0^{r_o} 2\pi r i dr$$

and differentiating with respect to  $Re_o^{1/2}$ , recalling that  $r$  and  $i$  are both independent of  $Re_o$ .

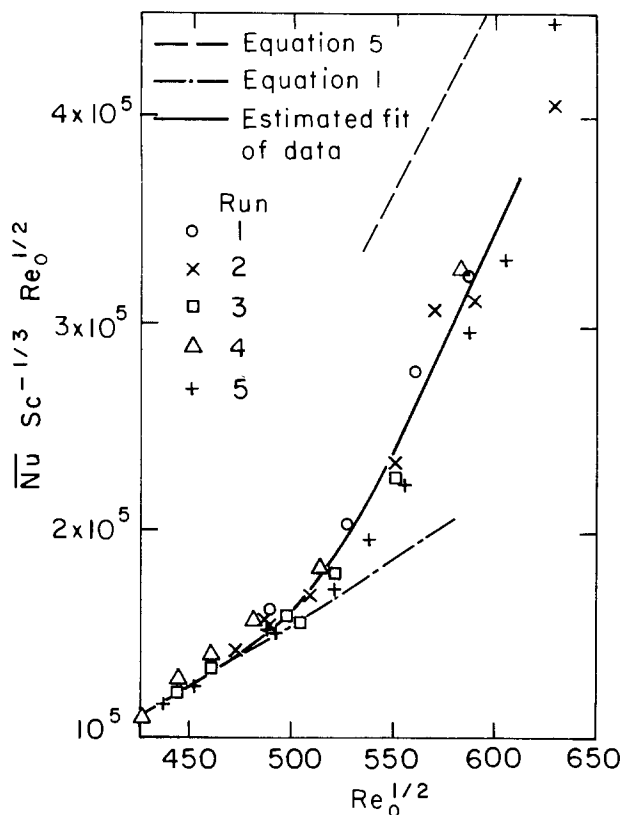


Fig. 4. Over-all mass transfer rate vs. square root of the Reynolds number.

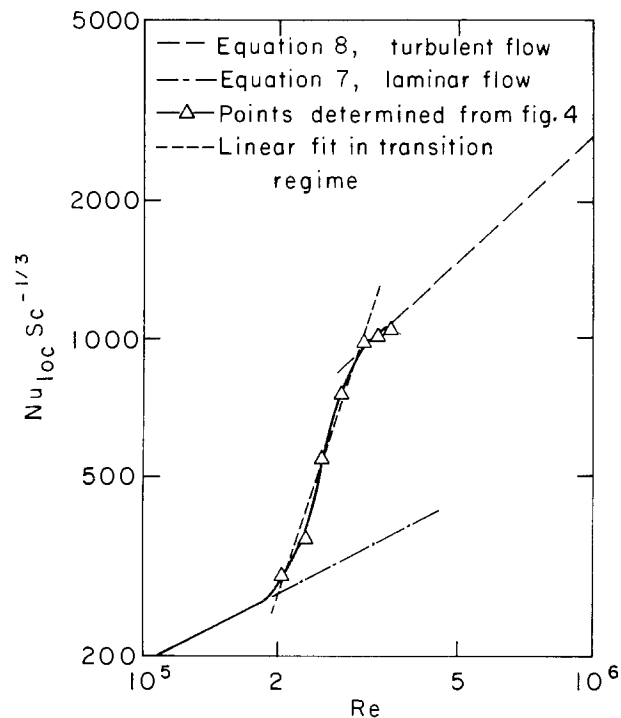


Fig. 5. Local mass transfer rate vs. Reynolds number for transition, laminar, and turbulent regimes.

$$Nu_{trans} = 3.4 \times 10^{-14} Re^3 \quad [9]$$

for Reynolds numbers between  $2.0 \times 10^5$  and  $3.0 \times 10^5$  and is continuous with the laminar and turbulent Eq. [7] and [8] at these values of  $Re$ . A rigorous statistical curve fit of the data was not attempted, since a pre-

ferred form for the curve was not determined. While this could have been done once the linear approximation was adopted for the local transfer rate (Eq. [9]), the readily apparent limits of the transition region forced the straight-line fit through these points, with reasonable agreement in the intervening region.

Given these results for the local transfer rate in the three regions, we can reconstruct the over-all transfer rate behavior by integrating Eq. [6]. For the laminar region, Eq. [1] is unchanged. In the transition region,  $2 \times 10^5 < Re_0 < 3 \times 10^5$ , integration of Eq. [9] leads to

$$\begin{aligned} \overline{Nu}_{trans} Re_0^{1/2} &= 2 \int_0^{\sqrt{2 \times 10^5}} Nu_{lam} d(Re^{1/2}) \\ &+ 2 \int_{\sqrt{2 \times 10^5}}^{\sqrt{Re_0}} Nu_{trans} d(Re^{1/2}) = (0.89 \times 10^5 \\ &+ 9.7 \times 10^{-15} Re_0^{3.5}) Sc^{1/3} \quad [10] \end{aligned}$$

For the turbulent region,  $Re_0 > 3 \times 10^5$

$$\begin{aligned} \overline{Nu}_{turb} Re_0^{1/2} &= 2 \int_0^{\sqrt{2 \times 10^5}} Nu_{lam} d(Re^{1/2}) \\ &+ 2 \int_{\sqrt{2 \times 10^5}}^{\sqrt{3 \times 10^5}} Nu_{trans} d(Re^{1/2}) \\ &+ 2 \int_{\sqrt{3 \times 10^5}}^{\sqrt{Re_0}} Nu_{turb} d(Re^{1/2}) \\ &= (0.0078 Re_0^{1.4} - 1.30 \times 10^5) Sc^{1/3} \quad [11] \end{aligned}$$

when the appropriate expressions are substituted for  $Nu_{lam}$ ,  $Nu_{trans}$ , and  $Nu_{turb}$ .

The over-all Nusselt numbers given by Eq. [1], [10], and [11] are shown on Fig. 6 as a function of Reynolds number. The curve representing the fitted experimental data is also shown, along with the modified correlation of Dagenet for the turbulent region. The graph supports the statement by Ellison and Cornet (7) that for  $Re > 10^6$  only the contribution to the over-all mass transfer due to the turbulent region is of consequence. At  $Re = 10^6$ , the difference between the correlation of Dagenet, Eq. [5], and the results which include the contribution of the laminar and transition regions, Eq. [11], is less than 7%. This is within the range of the maximum deviation of the data from the fitting curve. The estimated local Nusselt numbers in the transition region differ from the experimentally determined val-

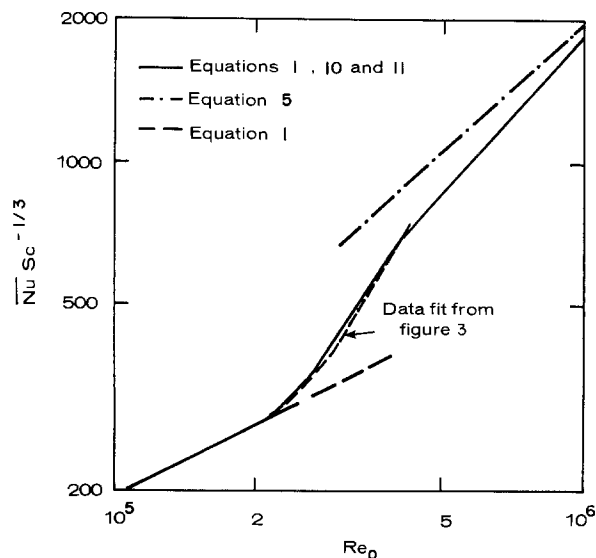


Fig. 6. Over-all mass transfer rate as predicted by correlations for the transition and turbulent flow regimes.

ues, shown on Fig. 5 by at most 10% near  $Re = 3.5 \times 10^5$ ; the fit is improved for larger Reynolds numbers.

### Acknowledgment

This work was supported by the U.S. Energy Research and Development Administration.

Manuscript submitted Nov. 6, 1975; revised manuscript received May 25, 1976.

Any discussion of this paper will appear in a Discussion Section to be published in the June 1977 JOURNAL. All discussions for the June 1977 Discussion Section should be submitted by Feb. 1, 1977.

Publication costs of this article were assisted by the University of California, Berkeley.

### LIST OF SYMBOLS

$\Delta c$	concentration difference between bulk and surface, mole/cm <sup>3</sup>
$D$	diffusion coefficient of limiting solute, cm <sup>2</sup> /sec
$F$	Faraday's constant, 96,487 C/equiv.
$\bar{i}$	average current density, A/cm <sup>2</sup>
$n$	number of electrons transferred per ion or molecule reacting
$Nu_{loc}$	local Nusselt number
$Nu$	average Nusselt number
$r$	distance from axis of rotation, cm
$r_0$	electrode radius
$Re$	Reynolds number
$Sc$	Schmidt number
$T$	absolute temperature, °K
$\mu$	viscosity of solution, g/cm-sec
$\nu$	kinematic viscosity of solution, cm <sup>2</sup> /sec
$\Omega$	rotation speed, sec <sup>-1</sup>

### REFERENCES

1. B. Levich, *Acta Physicochim. URSS*, **17**, 257 (1942).
2. T. von Kármán, *Z. Angew. Math. Mech.*, **1**, 233 (1921).
3. F. L. LaQue, *Corrosion*, **13**, 303 (1957).
4. N. Vahdat and J. Newman, *This Journal*, **120**, 1682 (1973).
5. N. Vahdat, M.S. Thesis, University of California, Berkeley (1972).
6. I. Cornet and U. Kaloo, Paper 213 presented at the Third International Congress on Metallic Corrosion, 1966.
7. B. T. Ellison and I. Cornet, *This Journal*, **118**, 68 (1971).
8. B. T. Ellison, Ph.D. Dissertation, University of California, Berkeley (1969).
9. M. Daguenet, *Int. J. Heat Mass Transfer*, **11**, 1581 (1968).
10. C. L. Tien and D. T. Campbell, *J. Fluid Mech.*, **17**, 105 (1963).
11. F. Kreith, J. H. Taylor, and J. P. Chong, *J. Heat Transfer*, **81**, 95 (1959).
12. E. C. Cobb and O. A. Saunders, *Proc. R. Soc. London, Ser. A*, **236**, 343 (1956).
13. L. F. Donovan, O. T. Hanna, and S. Yerazunis, *Chem. Eng. Sci.*, **22**, 595 (1967).
14. D. W. Hubbard, Ph.D. Dissertation, University of Wisconsin, Madison (1964).
15. D. W. Hubbard and E. N. Lightfoot, *Ind. Eng. Chem. Fundam.*, **5**, 370 (1966).
16. W. Vielstich, A. Inocencio, and J. Heitbaum, *Ber. Bunsenges. Phys. Chem.*, **78**, 1252 (1974).
17. V. Levich, "Physicochemical Hydrodynamics," Prentice-Hall, Inc., Englewood Cliffs, New Jersey (1962).
18. N. Gregory, J. T. Stuart, and W. S. Walker, *Philos. Trans. R. Soc. London, Ser. A*, **248**, 155 (1956).
19. D. T. Chin and M. Litt, *J. Fluid Mech.*, **54**, 613 (1972).

## SEM Studies of Discharge Products from Alkaline Iron Electrodes

Lars Öjefors<sup>1</sup>

Department of Chemical Technology, Royal Institute of Technology, S-100 44 Stockholm 70, Sweden

### ABSTRACT

Anodic oxidation products in 5N KOH of both planar and porous iron electrodes have been investigated with SEM techniques. On the first discharge level well-defined crystallites of Fe(OH)<sub>2</sub> are formed, while on continued discharge the products become sludge formed, probably consisting of hydrated FeOOH. The morphologies support the dissolution-precipitation mechanism during the first discharge step. The second anodic level proceeds probably via migration of ions and electrons in the solid phase. The crystallite size increases with temperature which depends on that the relative supersaturation decreases.

The anodic discharge process of a charged iron electrode occurs at two distinct voltage levels  $-0.85$  and  $-0.65$  V vs. Hg/HgO in alkaline media. The reaction mechanisms and the nature of the products formed during these steps have been investigated by several workers (1-19) with various results.

Foerster (1) found that metallic iron was converted to Fe(OH)<sub>2</sub> during the first and to Fe(OH)<sub>3</sub> during the second discharge level. Faust (2) was of the opinion that at discharge a Fe-H compound was formed which during the second step was converted to metallic iron. In (3) Foerster and Herold explain the second step as mainly representing the conversion of Fe(OH)<sub>2</sub>

to Fe(III) oxide, which runs parallel to the oxidation of metallic iron. The latter process is supposed to depend on uncovering of Fe by a break up of the Fe(OH)<sub>2</sub> layer. Kabanov and Leikis (4) found from theoretical considerations a topochemical reaction to be impossible because of the thick oxide layer produced. They proposed a dissolution-precipitation process where HFeO<sub>2</sub><sup>-</sup> and FeO<sub>2</sub><sup>-</sup> are intermediate species during the first and second steps, respectively.

By studying the increase in weight of an iron electrode during discharge Winkler found FeO to be the product of the first level instead of Fe(OH)<sub>2</sub>. He also found that the length of the first discharge step increased with cycling at the expense of the second. Addition of HgO or S<sup>2-</sup> to the electrodes had a stabilizing effect on the processes.

<sup>1</sup> Present address: Swedish National Development Company, Fack, S-103 40 Stockholm 40, Sweden.

Key words: iron anode, discharge products, scanning electron microscopy.

Schwarz and Simon (7) studied the behavior of carbonyl and ingot iron in 4N KOH at 90°C. During anodic polarization they found that iron dissolves into  $\text{FeO}_2^{2-}$  which due to its low solubility precipitates to a layer of  $\text{Fe}(\text{OH})_2$ . They also determined the corrosion current in this media to  $2 \cdot 10^{-6}$  A/cm<sup>2</sup> at 90°C which is a low value when compared to self-discharge measurements.

Salkind, Venuto, and Falk (8) studied the discharge products for iron active material from ESB Incorporated and NIFE Jungner with x-ray diffraction techniques. The patterns were obtained by *in situ* measurements on electrodes cycled in sealed polyethylene bags, as well as with washed and dried active materials. From the first plateau only patterns of  $\text{Fe}(\text{OH})_2$  and  $\alpha$ -Fe were observed with the *in situ* technique. On continuation of discharge patterns of  $\alpha$ -Fe,  $\text{Fe}(\text{OH})_2$ , and  $\text{Fe}_3\text{O}_4$  were observed although very weak for the latter two products. For the material washed with distilled water and dried,  $\text{Fe}_3\text{O}_4$  was also found during the first discharge step.

Flerov *et al.* (9) studied iron powder electrodes in order to determine the reaction mechanism for the second anodic step. They found that temperature is a very important factor for this discharge level, since this is at 20°C of 50% extent of the first anodic phase, while the two potential steps are of similar extension at 60°C. Changes in electrolyte concentration and addition of LiOH had no noticeable effect on the second step. The investigators propose that this potential step occurs without intermediate ionization and the process continues into the active particles by migration of electrons and ions in the solid phase.  $\text{FeOOH}$  is found to be the most probable product. A voltammetric study by Flerov and Pavlova (10) shows that the discharge reactions go over the dissolved forms of the divalent and three-valent hydroxides ( $\text{HFeO}_2^-$  and  $\text{FeO}_2^-$ ) which are supposed to be responsible for the slow rate of the electrochemical processes. This study by Flerov consequently contradicts his former study on iron powder electrodes.

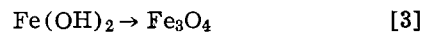
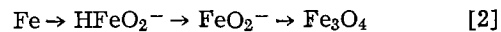
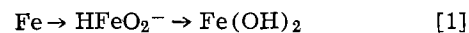
From potential-time studies on planar electrodes at constant currents Sherstobikova *et al.* (11) verified Flerov's theory that  $\text{FeOOH}$  was the product of the second discharge plateau. The same authors have studied (12) the mechanism of solution and passivation of iron in alkali as well as the velocity ratio of these two processes by an impedance measurement method. They found that the solution process of the first stage is divided into two steps where the first is the transition  $\text{Fe} \rightarrow \text{Fe}(\text{I})$  with the loss of one electron, which leads to the intermediate complex  $\text{Fe}(\text{OH})_{\text{ads}}$ . The second step is represented by the conversion of  $\text{Fe}(\text{OH})_{\text{ads}}$  to  $\text{HFeO}_2^-$ , which is rate determining. Parallel to this step oxides with valencies exceeding two are formed which are supposed to have a passivating effect.

Silver and Lekas (13) identified the following phases in a porous carbonyl iron electrode at different discharge states with x-ray diffraction. At the end of the first plateau they found  $\alpha$ -Fe and  $\text{Fe}(\text{OH})_2$ , and at the end of the second plateau  $\alpha$ -Fe and  $\text{FeOOH}$  after the first cycle. On subsequent cycling a gradual conversion to  $\text{Fe}_3\text{O}_4$  was observed at the end of the second anodic potential step. For an electrode cycled in 30% KOH saturated with LiOH only  $\alpha$ -Fe and  $\text{Fe}_3\text{O}_4$  were detected at this plateau. These results were confirmed by Labat, Jarrousseau, and Laurent who quantitatively studied the discharge products of industrial iron electrodes from SAFT with x-ray diffraction. They found, apart from  $\alpha$ -Fe, mainly  $\text{Fe}(\text{OH})_2$  formed during the first discharge level with some traces of  $\text{FeOOH}$  at the end of it. The discharge products of the second plateau after three cycles consisted mainly of  $\text{FeOOH}$  with less than 5%  $\text{Fe}_3\text{O}_4$ .

Armstrong and Baurhoo (15,16) studied the discharge and charge reactions of the alkaline iron electrode by using a ring-disk system in order to get in-

formation on the soluble intermediates. The results clearly indicate that, above room temperature and in more concentrated KOH solutions,  $\text{Fe}(\text{II})$  species, probably  $\text{HFeO}_2^-$  or  $\text{Fe}(\text{OH})_3^-$ , are produced as intermediates. At moderate overpotentials,  $-0.86\text{V}$  vs.  $\text{Hg}/\text{HgO}$ , the intermediate precipitates to  $\text{Fe}(\text{OH})_2$  while at higher potentials  $\text{Fe}(\text{II})$  is easily oxidized to  $\text{Fe}(\text{III})$  which precipitates to  $\text{FeOOH}$  or  $\text{Fe}_3\text{O}_4$ .

Chnoblach *et al.* (19) studied the different reactions of iron powder on a magnetic electrode by scanning it slowly (2 V/min) in the region  $-1.1$  to  $-0.4\text{V}$  vs.  $\text{Hg}/\text{HgO}$  in 6N KOH. In full agreement with (14) three separate peaks appeared apart from the one representing oxidation of hydrogen produced during the charge process. During anodic scan (from  $-1.1$  to  $-0.4\text{V}$ ) the peaks were found to represent the following reactions



When scanning the electrode back in the same interval identical reactions appear but naturally in opposite order and direction. The investigators opinion that  $\text{Fe}_3\text{O}_4$  is the product of second discharge level is based on (8,13), and not on the result of any qualitative analysis.

The behavior of iron in LiOH solutions has been studied by (16,17) and seems not to differ considerably from that in KOH. The reaction products from the second anodic potential level were found to be  $\text{Fe}_2\text{O}_3$  or  $\text{Fe}(\text{OH})_3$ .

The present study has been undertaken to define the discharge products for both planar and porous iron electrodes with scanning electron microscope (SEM) technique. This method is also of interest to study the decrease in porosity during discharge which depends on the high volume of the oxidation products.

## Experimental

Planar and porous iron electrodes were discharged galvanostatically in 5N KOH solution at room temperature and at 50°C. The morphology of the discharge products were examined with scanning electron microscope (JSM-U2, JEOLCO, Japan). The basic concept of the test cell and other equipment used is presented in (20) where also the manufacturing process of the porous electrodes is described.

For the planar electrode, a piece ( $10 \times 10 \times 3$  mm) of highly pure electrolytic iron was used on which all sides but one was covered with polymer material. The open face ( $10 \times 10$  mm) was before insertion in the cell mechanically polished with silicon carbide paper, then with powder of the same material. After assembling the cell it was deaerated with nitrogen. A constant current (1 mA/cm<sup>2</sup> calculated on the geometrical area) was applied and the electrode cycled twice down to  $-0.5\text{V}$  vs.  $\text{Hg}/\text{HgO}$ . Thereafter the electrode was discharged down to the potential to be studied with the same current density. It is notable that capacity increased during these three cycles.

The porous electrodes studied were 1.2 mm thick, 9.5 mm in diameter, and weighing 0.2g. Average pore diameter was 7  $\mu\text{m}$  and Hg-porosimetry curve is given in Fig. 1. No nets were incorporated in order to increase mechanical stability. After assembling and deaerating the cell, the electrode was cycled twice with 20 mA.

After galvanostatic discharge down to the potential level to be studied, the electrodes were immediately taken out of the cell, washed with distilled water, and dried under nitrogen atmosphere. The top surface of the planar electrode and the interior of the porous plaques after breaking them along their diameters were studied. No gold or other current-conducting material was vaporized on the specimen.



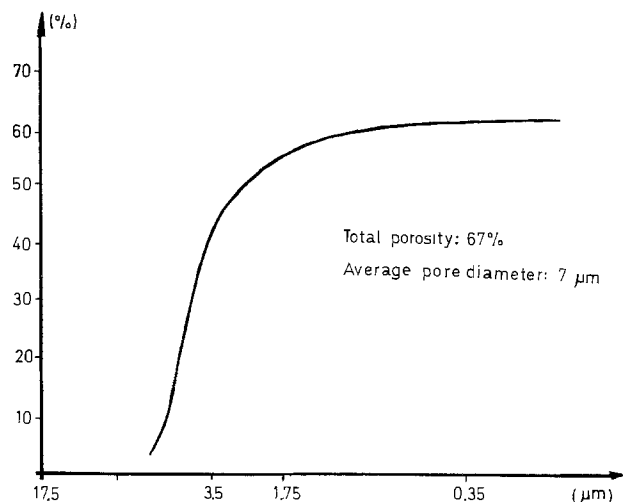


Fig. 1. Hg-porosimetry curve of the electrodes tested

**Results**

Figure 2 shows the variation in potential at room temperature for the planar electrode and also the potential levels for Fig. 3.1 and 3.2. At the end of first plateau the  $Fe(OH)_2$  crystallites appear distinctly. On continuation of discharge (Fig. 3.2) the structure becomes covered with a gelatinous precipitation, probably hydrated  $FeOOH$ , which can be written  $Fe_2O_3 \cdot nH_2O$ , in accordance with Table I which gives crystal structures of possible oxidation products. The distinct morphological features of the first anodic step, together with the observed looseness of the crystallites on the surface, give support to the dissolution-precipitation mechanism during discharge.

Figure 5 shows a micrograph of a porous iron electrode before any electrochemical treatment and in Fig. 6 and 7 the same structure in discharged state. A similar pattern to the planar electrodes is shown for both levels. The micrographs show that nucleation and growth of  $Fe(OH)_2$  play the dominant role at the early part of the first discharge step. During the later part crystal growth predominates with a possible secondary growth due to dissolution of smaller crystallites and increase of larger ones. Also these facts support the precipitation-dissolution mechanism.

On continuation of discharge the same sludge-formed precipitation as on planar electrodes appears. The form of the oxidation products indicates that this process goes over migration of ions and electrons in the solid phase. No opening up process can be noted when comparing Fig. 6.2 and 6.3. This means that the volume density of the oxidation products of both levels must be of the same magnitude and that hydrated  $FeOOH$  is the product of the second anodic step.

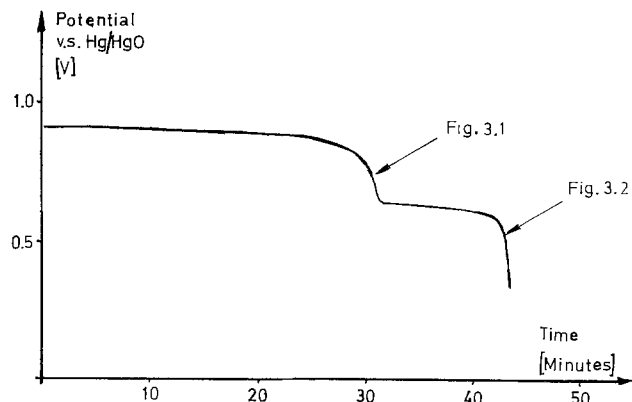
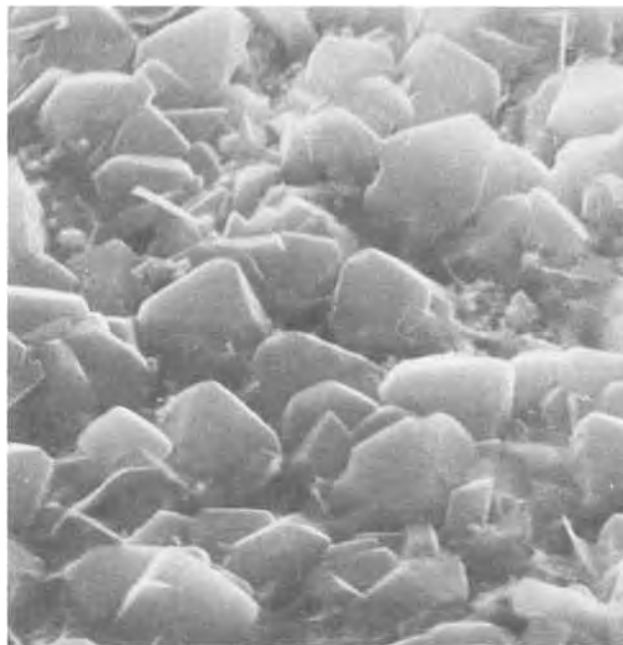
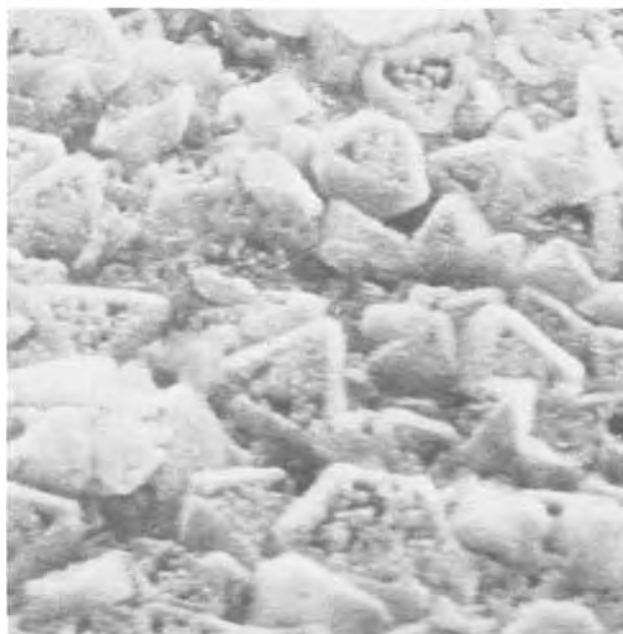


Fig. 2. Potential of planar electrodes during discharge (1 mA/cm<sup>2</sup>, 25°C).



3.1



3.2

Fig. 3. Micrographs of planar electrode at two different discharge states.

The micrographs shown in Fig. 7.1 to 7.4, from 50°C, show crystallite size 2-3 times larger compared to room temperature, even at beginning of discharge. The nucleation process seems not that important at this temperature level and current density. This depends on that the relative supersaturation is lower since the solubility of the intermediate  $HFeO_2^-$  increases with

Table I. Crystal structures of possible oxidation products of iron (23)

Name	Formula	Crystal structure	Density (kg/liter)
Iron (II) hydroxide	$Fe(OH)_2$	Hexagonal	3.4
Iron (III) oxyhydrate	$Fe_2O_3 \cdot nH_2O$	Gelatinous	2.44-3.60
Iron oxide	$Fe_3O_4$	Cubic	5.18

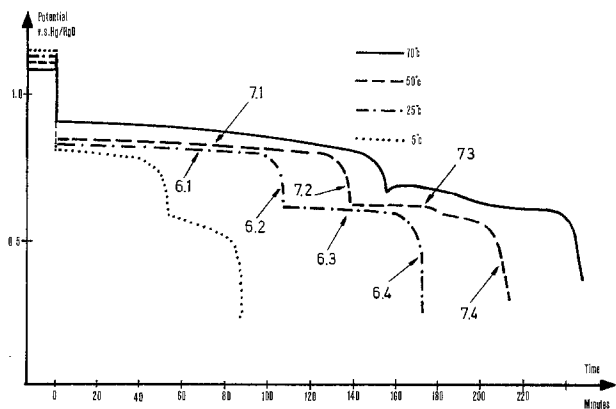


Fig. 4. Potential of porous iron electrodes during discharge at different temperatures (100 mA/g active material).

temperature (21, 22). Also the diffusion rate increases naturally with temperature. When increasing the current density the morphology of the products become similar to those of lower temperature. At continuation of discharge at 50°C the same sludge-formed precipitation appears as in Fig. 3 and 5. Toward the end of the second anodic plateau small crystallites of prob-

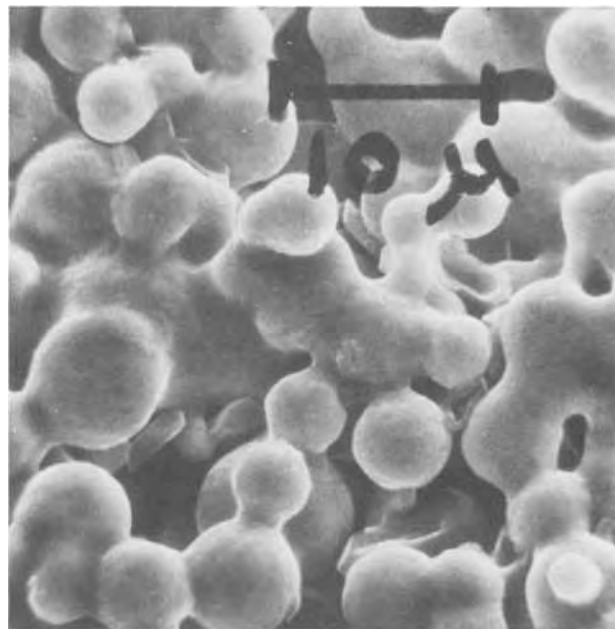
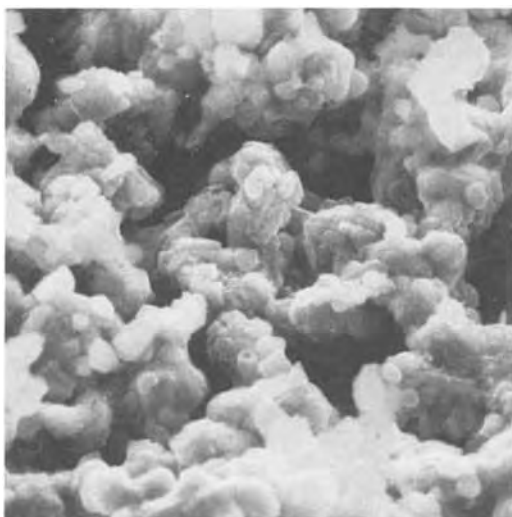
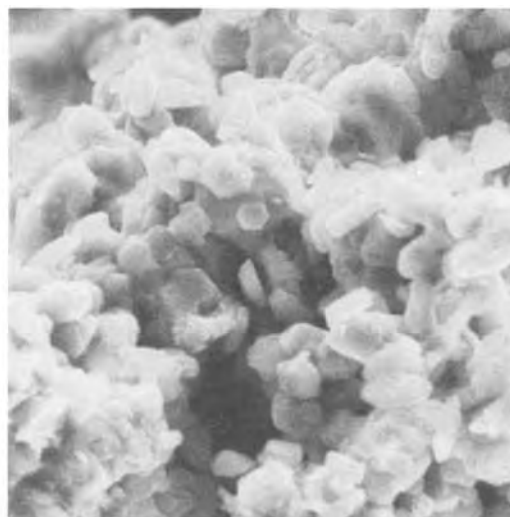


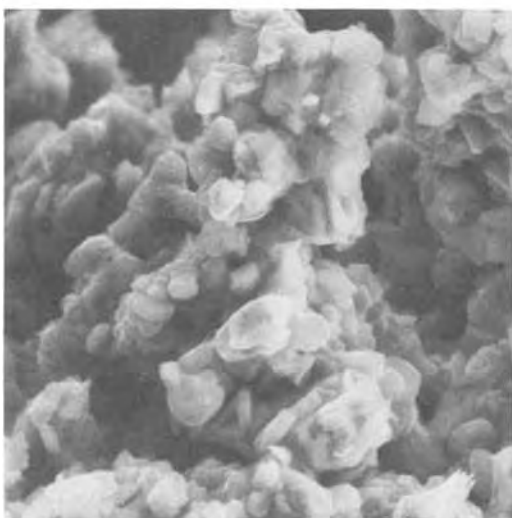
Fig. 5. Micrograph of porous iron electrode before discharge



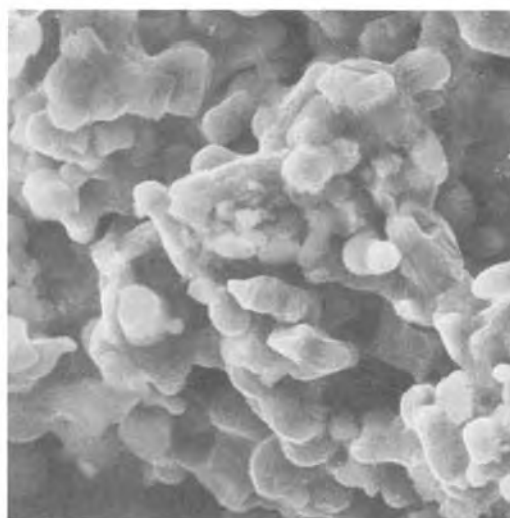
6.1



6.2

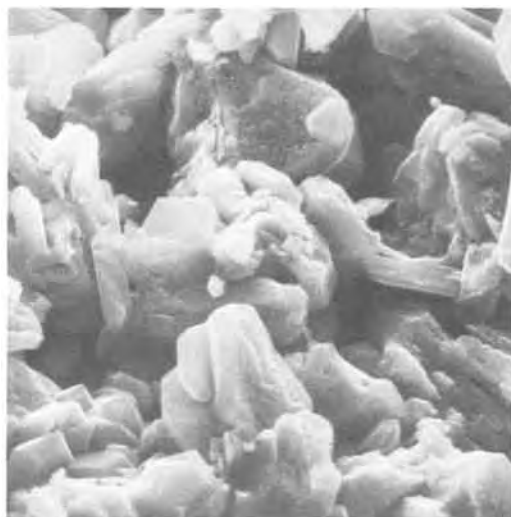


6.3

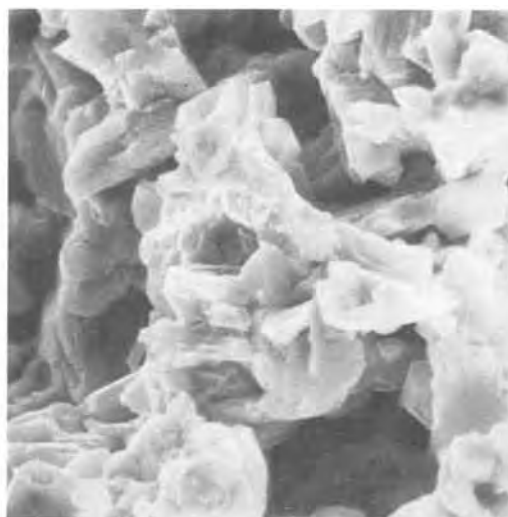


6.4

Fig. 6. Micrographs of porous iron electrode at different discharge stages (25°C)



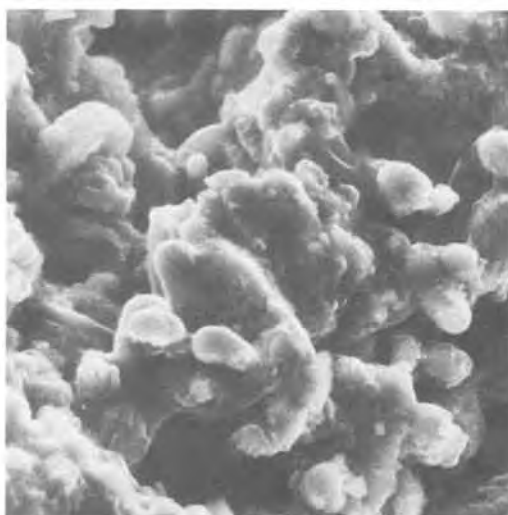
7.1



7.2



7.3



7.4

Fig. 7. Micrographs of porous iron electrode at different discharge stages (50°C)

ably  $\text{Fe}_3\text{O}_4$  appear, the formation of which is favored by higher temperatures in accordance with the Schikorr reaction.

#### Discussion

The results obtained support the dissolution-precipitation theory presented by Flerov and Pavlova (10), which also has been suggested by Armstrong and Baurhoo (16, 17) from experimental data obtained with ring-disk technique. The products found on second discharge level are in full accordance with the results of (13) and (14) where  $\text{FeOOH}$  was found during the first cycles.

It is quite evident that a possible change in composition of the discharge products may occur during the washing procedure. This treatment is however more lenient to the products than the cleaning and milling procedure preceding most x-ray studies here discussed.

Manuscript submitted Jan. 28, 1976; revised manuscript received May 11, 1976.

Any discussion of this paper will appear in a Discussion Section to be published in the June 1977 JOURNAL. All discussions for the June 1977 Discussion Section should be submitted by Feb. 1, 1977.

Publication costs of this article were assisted by the Swedish National Development Company.

#### REFERENCES

1. F. Foerster, *Z. Elektrochem.*, **11**, 948 (1905).
2. O. Faust, *ibid.*, **13**, 161 (1907).
3. F. Foerster and V. Herold, *ibid.*, **16**, 461 (1907).
4. B. N. Kabanov and D. I. Leikis, *Acta Physiochim. USSR*, **21**, 769 (1946).
5. H. Winkler, *Elektrotechnik*, **6** (8), 355 (1952).
6. H. Winkler, *Electrochim. Acta*, **3**, 123 (1960).
7. W. Schwartz and W. Simon, *Ber. Bunsenges.*, **67**, 108 (1963).
8. A. J. Salkind, C. J. Venuto, and S. U. Falk, *This Journal*, **111**, 493 (1964).
9. V. N. Flerov, L. I. Pavlova, and L. V. Uzingier, *Zh. Prikl. Khim.*, **38**, 569 (1965).
10. V. N. Flerov and L. I. Pavlova, *Elektrokhimiya*, **3**, 621 (1967).
11. I. N. Sherstobikova, B. N. Kabanov, and D. I. Leikis, *ibid.*, **4**, 1228 (1968).
12. I. N. Sherstobikova, D. I. Leikis, and B. N. Kabanov, *ibid.*, **5**, 461 (1969).
13. H. G. Silver and E. Lekas, *This Journal*, **117**, 5 (1970).
14. J. Labat, J. C. Jarrousseau, and J. F. Laurent, *Power Sources 3*, Brighton (1970).
15. R. D. Armstrong and I. Baurhoo, *J. Electroanal. Chem.*, **34**, 41 (1972).

16. R. D. Armstrong and I. Baurhoo, *ibid.*, **40**, 325 (1972).  
 17. D. D. MacDonald and D. Owen, *This Journal*, **120**, 317 (1973).  
 18. N. A. Hampson *et al.*, *J. Appl. Chem.*, **3**, 61 (1973).  
 19. H. Chnoblach *et al.*, *Chem. Ing. Tech.*, **45** (4), 203 (1973).  
 20. B. Andersson and L. Öjefors, *This Journal*, **123**, 824 (1976).  
 21. O. Lindström, *Power Sources* 5, Brighton (1974).  
 22. L. Öjefors, *This Journal*, **123**, 1139 (1976).  
 23. *Handbook of Chemistry and Physics*, New York (1970).

# Technical Notes



## Aluminum Perchlorate in Aluminum-MnO<sub>2</sub> Dry Cells

Brooke Schumm, Jr.\*

Union Carbide Corporation, Battery Products Division, Cleveland, Ohio 44101

Aluminum appears to be an attractive substitute for zinc in dry cells. It is higher than zinc in the electromotive series, higher in coulombic yield per unit weight, is more abundant in nature, and inexpensive (see Table I). As a possible anode material, however, it does not behave as well as zinc (1). In neutral pH solutions passive surface oxide layers tend to form creating an ineffective electrode surface. In common acid or alkaline salt solutions aluminum is an active anode (2-4), but when not on load corrodes rapidly with evolution of hydrogen. These difficulties must be overcome for aluminum to be commercially useful in dry cells.

The success of aqueous perchlorate electrolyte in magnesium or zinc cells (5, 6) suggests that similar opportunities exist in other metal anode-manganese dioxide systems. Aluminum perchlorate was studied to find if alone in aqueous solution or in combination with other agents in aluminum-manganese dioxide "dry" cells it would allow the following characteristics: (i) a balance between anode activity and passivity during cell storage, (ii) low internal cell resistance, and (iii) adequate chemical activity and ion diffusion in the electrolyte during discharge.

Observation of the corrosion rate and manner of corrosion attack of aluminum perchlorate solutions on aluminum metal could be expected to guide the choice of concentration of salt and any addition agents which would be needed. For the best electrochemical performance, the anode surface should be corroding very slowly without the formation of pits in the anode metal (7). This state allows cell current generation on demand without undesirable waiting periods for electrodes to reach full activity. Experience with corrosion rates in commercial Leclanché cells indicates that up to 0.05 mg/cm<sup>2</sup>/day of aluminum could be lost in storage and be acceptable. Usually a small amount of inhibitors and carefully chosen salt concentrations give the necessary balance of anode activity and corrosion resistance (8, 9).

For the cathode mix, the proper percentages of conductive phase (usually carbon) manganese dioxide and of salt and solution are necessary to have low internal cell resistance. The choice of separator material is also important. The optimized combination of materials

Table I. Anode potential, capacity, and price of some common metals

Metal	Theoretical potential	Capacity (A-hr/g)	Price (cents/lb)
Magnesium	-2.34	2.20	92
Aluminum	-1.67	2.98	41
Zinc	-0.76	0.82	38
(Hydrogen)	(0.00)	(26.6)	—

also allows the necessary chemical activity and diffusion in the electrolyte during discharge. Often less than optimum composition for one aspect is more than compensated by improvement in other factors.

If the aluminum alloy (10-13), separator, and cathode mixture combination is found which will fulfill the stated objectives, then performance matching that of other commercial dry cells should be achieved.

### Experimental

The solution pH was expected to have a major effect since aluminum corrodes rapidly in extremely acid solutions which are typical of aluminum salts such as aluminum chloride. The results of measurement of the pH of aluminum perchlorate solutions are given in Table II.

Aluminum coupons prepared from commercially (99.5%) pure aluminum were cut, 2.54 × 10.16 cm, and immersed 2.54 cm into the test solution. Since the pH is so low at even small salt concentrations and the observed corrosion rates so high (Table III), the effect of the addition of small amounts of sodium hydroxide on the pH of the solutions was studied. The corrosion rate tests were repeated for solutions which might be sufficiently buffered to be less corrosive yet low enough in pH to be an active electrolyte. In the encouraging

Table II. pH of aluminum perchlorate solutions

Concentration of aluminum perchlorate (g/liter)	pH of solution
32	1.2
300	-0.42
600	-1.27
900	-1.75
1200	-2.32

\* Electrochemical Society Active Member.

Key words: aluminum dry cell, manganese dioxide cell, aluminum anode, aluminum perchlorate, electrolyte.

**Table III. Corrosion weight loss of aluminum coupons in buffered and unbuffered aluminum perchlorate solutions, mg/cm<sup>2</sup>/day (pH of solutions in parentheses)**

Sodium hydroxide (g/liter)	Aluminum perchlorate (g/liter)			
	366	759	937	1200
0		0.240 (-1.5)	0.643 (-1.8)	5.84 (-2.32)
6	0.103 (0 ± 0.2)			
34		0.043 (0 ± 0.2)		
40			0.025 (0 ± 0.2)	
70				0.032 (0.13)

results three of the values observed of corrosion loss (in Table III) were better than the maximum acceptable rate of 0.05 mg/cm<sup>2</sup>/day. In a nearly sealed cell the corrosion could be expected to be even lower.

**Cell Assembly**

Aluminum perchlorate and sodium hydroxide concentrations were chosen for cell cathode mix from the lower ranges of the region which showed acceptable rates of attack on aluminum. This was to allow for the addition of aluminum and hydroxyl ions to the solution of the cells during discharge which would move the anolyte composition to the higher buffered aluminum concentrations of Table III. The chosen electrolyte mixture (Table IV) was added to a dry blend of seven parts of natural African manganese dioxide (79% MnO<sub>2</sub>) and one part acetylene black. 60g of this cathode mix were packed into D-size aluminum (0.6% zinc) alloy cans (12) with an alpha-cellulose uncoated paper liner and a Kraft bottom cup. The usual porous, wet-proofed carbon electrode was driven into the mix as a collector. The cell was sealed with a poured asphalt layer on a cardboard washer as shown in Fig. 1.

**Cell Test Results**

*Initial cell properties and fresh tests.*—The cells exhibited an open-circuit voltage of 1.52-1.55V and a short-circuit current of 3-4A which the cells could support for several minutes. On 2 1/4Ω continuous drain three cells averaged an excellent voltage vs. time discharge for a paper-lined cell (Fig. 2). Similarly, attractive performance was found on 2 1/4Ω LIF test (4 min/hr, 8 hr/day) both on cells tested after 1 month of aging at room temperature and on other cells tested after an additional month at 45°C (Fig. 3). Cell to cell variation was high, however, and discharge voltage readings less predictable after the elevated temperature storage.

The cells had a slight starting delay, as magnesium cells do (5), but the shape of the initial voltage curve was interesting (Fig. 4). The sample voltage delay shown occurred at the start of the sixth 4 min test cycle on the second day (fourteenth cycle after 52 min on load). Note that the voltage never went more than 0.30V below the final closed-circuit value and recovered to within 0.05V of the final value in 0.45 sec. A magnesium cell often would drop much farther below the final loaded voltage level.

*Cell efficiency and effects on continuous load.*—The cells achieved an average anode efficiency of 70% and a cathode efficiency of 40% to 0.65V on 2 1/4Ω continuous drain. The rest of the anode consumption represented

**Table IV. Cathode mix composition**

African manganese dioxide (79% MnO <sub>2</sub> )	47%
Acetylene black	6.7%
Aluminum perchlorate	16.5% (478 g/liter)
Sodium hydroxide	1.1% (32 g/liter)
Water	28.7%
pH mixture = 3.0	

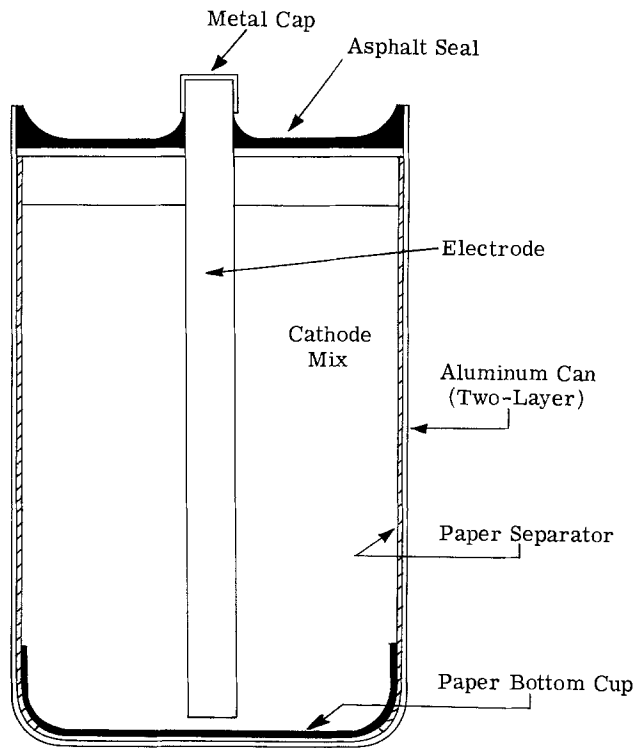


**Fig. 1. Aluminum paper-lined cell**

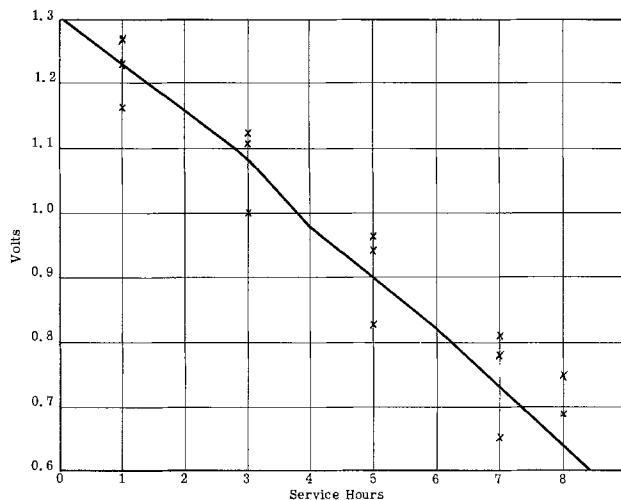


**Fig. 2. Aluminum cells with perchlorate electrolyte on 2 1/4Ω continuous test.**

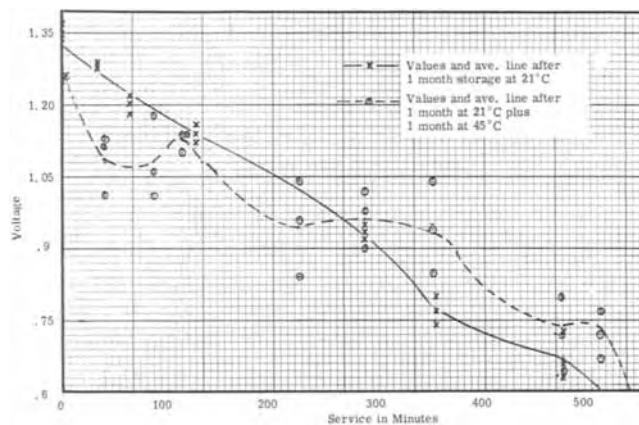


**Fig. 3. Aluminum cells with perchlorate electrolyte on 2 1/4Ω LIF test.**

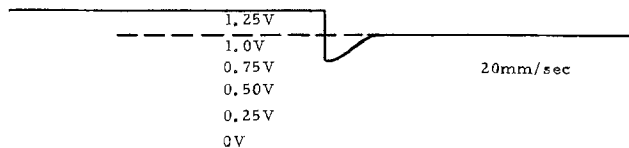


Fig. 4. Starting delay on 2 1/4Ω LIF test, 14th cycle

corrosion loss accompanied by generation of substantial amounts of hydrogen gas. This gas forced open the seals and contributed to the advent of cell leakage shortly after the end of useful cell life.

**Cell leakage.**—These aluminum cells exhibited electrolyte movement similar to that seen in paper separator Leclanché cells. Electrolyte movement on heavy loads such as 2 1/4Ω continuous associated with hydrogen generation makes containment of the electrolyte very difficult. Special constructions and gas-venting mechanisms would be necessary to achieve reasonable cell leakage resistance.

### Discussion of Results

The open-circuit and initial closed-circuit voltage of these aluminum-perchlorate electrolyte-manganese dioxide cells was much lower than expected considering the place of aluminum in the electromotive series. A cell could have shown as high as 2.59V (open circuit) if the theoretical half-cell voltage of aluminum were exhibited when the manganese dioxide contributes approximately 0.92V (*vs.* hydrogen) as in a Leclanché cell. The actual half-cell manganese dioxide contribution is more nearly 1.03V (14) considering the electrolyte pH. Thus the aluminum is not operating at full theoretical voltage. A complete study and discussion of this phenomenon is beyond the scope of this paper.

If the cell electrolyte pH rises on discharge as observed in Leclanché cells, hydrated aluminum hydroxide will precipitate (15). This rapid removal of water from the system by the precipitation of hydrated aluminum hydroxide should eventually severely limit necessary diffusion in the cathode because of loss of the ion carrier medium. Nonetheless the performance on heavy service tests was good when compared to commercial Leclanché cells with similar natural manganese dioxide.

Of particular interest was the surprisingly good service maintenance after 1 month at 45°C even though no strong inhibitors were included in the cell chemicals. With the small initial delay it can be concluded that the desirable balance between a tendency for the aluminum anode to corrode and to passivate on-shelf had been achieved. The irregular form of the curve, however, indicates probable anode surface change from partially passivated (due to oxide film and possibly being too dry) to moist with the oxide film dissolved during discharge.

The cell initial internal resistance was rather high. At the same manganese ore to carbon ratio a Leclanché D cell would exhibit 7-10A short-circuit current as compared to the 3-4A found with these aluminum cells. Although short-circuit current is only an approximate measure, the internal resistance of the experimental cells is thus at least twice that of similar Leclanché cells.

With such a high internal resistance the encouraging performance on heavy drains indicates that the concentration polarization and activation polarization of the Al-aluminum perchlorate-MnO<sub>2</sub> cell must be low. These latter factors are evidently sufficient to override the resistance losses and water consumption and allow adequate cell service.

Other systems such as in magnesium-manganese dioxide cells and zinc-manganese dioxide cells with zinc chloride electrolyte usually show little or no electrolyte movement on abusive discharge. The different action here observed probably is caused by precipitation of aluminum hydroxide which interferes with the diffusion of ions near the separator. Ion concentration imbalances then build up in the aluminum cell. Water moves in the cell to bring about concentration equilibrium causing the appearance of exudate and cell leakage next to the aluminum anode. This action is aggravated by the pumping action of the hydrogen gas released during rapid discharge.

### Conclusions

Attractive service performance can be obtained from aluminum manganese dioxide cells with an aqueous aluminum perchlorate electrolyte. Corrosion resistance of aluminum has been good in the presence of a cell electrolyte buffered to a pH of 0-4 with sodium hydroxide. Internal resistance of such cells is higher than that of Leclanché cells, but the low concentration polarization and activation polarization in the over-all system appear to compensate for the internal resistance losses. The amount of gaseous corrosion by-product observed on discharge combined with undesirable electrolyte movements makes the cells difficult to seal and be simultaneously safe against leakage or swelling.

Manuscript submitted Feb. 9, 1976; revised manuscript received June 1, 1976. This was Paper 50 presented at the Dallas, Texas, Meeting of the Society, Oct. 5-9, 1975.

Any discussion of this paper will appear in a Discussion Section to be published in the June 1977 JOURNAL. All discussions for the June 1977 Discussion Section should be submitted by Feb. 1, 1977.

Publication costs of this article were assisted by Union Carbide Corporation.

### REFERENCES

1. A. Smits, *Z. Elektrochem.*, **30**, 423 (1924).
2. R. Muller, H. Kumpfmüller, and H. Bauer, *Z. Anorg. Allg. Chem.*, **156**, 65 (1926).
3. L. Brull, *Am. Chem. Applicata*, **28**, 547 (1938).
4. D. E. Sargent, U.S. Pat. 2,554,447 (1951).
5. A. J. Legath and D. B. Wood, "Proceedings at the 23rd Annual Power Sources Conference," pp. 86-90, PSC Publication Committee, New Jersey (1969).
6. J. Augustynski, F. Dalard, and J. Y. Machat, *J. Appl. Electrochem.*, **2**, 91 (1972).
7. N. D. Tomashov and V. N. Modestova, *Tr. Inst. Fiz. Khim., Akad. Nauk SSSR.*, **5**; *Issledovan, Korroz. Metal.* **4**, 75 (1955).
8. S. Zaromb, *This Journal*, **109**, 1125 (1962).
9. Y. Yokota, *Denki Kagaku*, **28**, 518 (1960).
10. J. Kerti, *Magy. Kem. Foly.* **70**, 305 (1964).
11. S. Ruben, U.S. Pat. 2,638,489 (1953).
12. J. J. Stokes, Jr., U.S. Pat. 2,796,456 (1957).
13. T. Sakano and K. Toda, *Jpn. Pat.* 2003 (1959).
14. N. C. Cahoon, *This Journal*, **99**, 343 (1952).
15. D. Belitskus, *ibid.*, **119**, 295 (1972).

# Effect of Surface Dissolution on Plastic Deformation of Iron and Steel

Herbert H. Uhlig\*

Woods Hole Oceanographic Institution, Woods Hole, Massachusetts 02543

The slow plastic deformation of a metal subject to an applied stress, usually at a value below the elastic limit, is called creep. Our previous results on the mechanism of corrosion fatigue (1, 2) suggested that a metal deforms plastically much more readily when it is actively corroding. According to this viewpoint a corroding metal should also exhibit accelerated creep. This expectation was confirmed for brass and for pure copper by Revie and Uhlig (3, 4). The effect was large: A corrosion rate for 0.027 cm diam Cu wire corresponding to 0.9 mA/cm<sup>2</sup> accounted for a 600% increase in extension over its corresponding extension in air, independent of any thinning caused by the corrosion process. A characteristic delay in change of creep rate was observed on either starting or stopping corrosion. Reversed polarity (cathodic protection) had little or no effect on the creep rate of fine grained copper, but did accelerate creep of large grained copper. It was proposed that the latter effect was caused by reduction of surface energy and consequent ease of slip step

\* Electrochemical Society Active Member.  
Key words: corrosion, creep, anodic polarization.

formation occurring in the large outer grains that influence the creep rate. On the other hand, it was suggested that anodic dissolution generates surface divacancies which readily diffuse into the metal, whether small or large grained, to interact with piled-up dislocations below the surface causing dislocation climb followed by increased plastic deformation. Accordingly the time for divacancies to reach the dislocation arrays is equated to the observed delay in creep response with change in corrosion rate. The effect of corrosion to similarly accelerate plastic deformation of iron and steel is presently reported.

## Experimental

Experiments were carried out on cold-rolled Armco iron strip, 1.6 mm wide, 0.065 mm thick, and on high strength 0.77% C steel wire 0.71 mm (28 mils) diam. The latter was supplied courtesy of The United States Steel Corporation and was used in the heat-treated and cold-drawn state as received. For some tests, the cold-rolled strip was annealed in a N<sub>2</sub> atmosphere; this was accomplished by passing an electric current through the strip to red heat and gradually reducing the current over a period of ½ min. Stress was applied by weighting a pan attached by a lever arm to the chuck holding the wire or strip. Displacement of the lever arm was measured by a Sanborn DC LVDT transducer connected to a chart recorder. Linear sensitivity of the transducer as measured at the chuck holding the iron specimen was  $1.42 \times 10^{-4}$  cm/mV. A glass cylinder 3½ cm diam fitted with a cylindrical Pt electrode surrounded the lower portion of the test specimen. The specimen made a water-tight seal when pressed between a Teflon insert in a rubber stopper at the bottom opening of the glass cylinder (Fig. 1). The electrolyte was either 3% NaCl or 3% NaCl + 3% Na acetate solution.

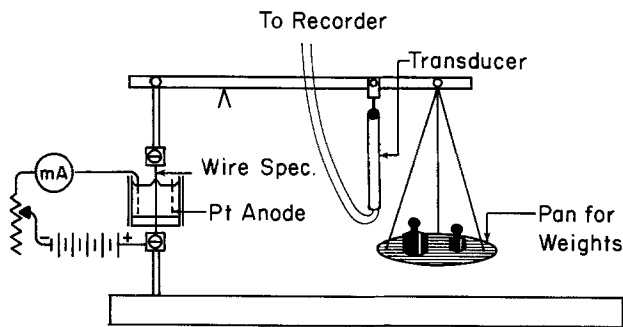


Fig. 1. Schematic sketch of creep apparatus

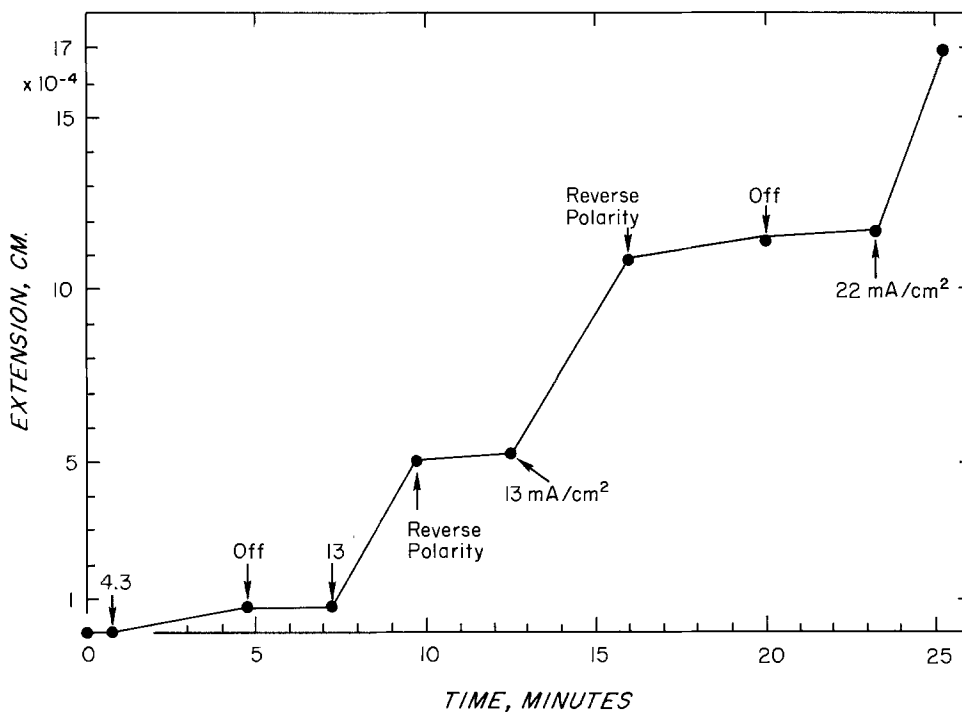


Fig. 2. Effect of anodic dissolution and cathodic protection on creep extension of cold-rolled Armco iron strip in 3% NaCl, 3% Na acetate solution, 55.5 kg/mm<sup>2</sup> (79,000 psi), room temp.



The effect of applied anodic polarization current densities, on creep extension of the cold-rolled Armco iron strip is illustrated in Fig. 2. This is measured in correspondence to a variety of controlled corrosion rates. The indicated points are arbitrary references taken directly from the continuous chart record. It is observed that accelerated creep or extension of the strip increases with current density, and that reversed polarity (cathodic protection) in common with no current at all has no effect. Since the iron strip (as well as the steel wire) is fine grained, no effect of cathodic protection is expected. Accelerated creep also occurs when corrosion is caused by a corrosive solution, such as  $\text{FeCl}_3 + \text{HCl}$ , in absence of anodic polarization. On the other hand, anodic polarization of the strip in dilute  $\text{Na}_2\text{SO}_4$  solution to within the passive region fails to accelerate creep because the anodic corrosion rate is negligible. In contrast to the effects for copper, the response of the cold-rolled strip to changes in corrosion rate show no appreciable delay time. The annealed strip, as described later, behaves differently.

Taking slopes of extension *vs.* time for a given applied anodic current density, the effect of current density on creep rate is shown in Fig. 3. These results, as well as those presented later, are for short-time tests in the order of 3-10 min at each current density. The increase in creep rate at 10 mA/cm<sup>2</sup>, corresponding to a corrosion rate of 25,000 mg/dm<sup>2</sup>/day, over that in air is approximately 650%. Thinning of the strip by corrosion is not a factor, as is shown by the low observed creep rate at zero current measured at the termination of all the runs. Calculation applying Faraday's law confirms that the total corrosion during any series of tests does not significantly reduce cross-sectional area of the strip.

The effect of applied stress on the creep rate of cold-drawn Armco iron strip at various current densities is shown in Fig. 4. The usual semilogarithmic relation between stress and creep rate holds at each current density. This relation does not hold at low applied stresses in view of extrapolated positive creep rates at zero stress. Data of Fig. 3 and 4 are consistent

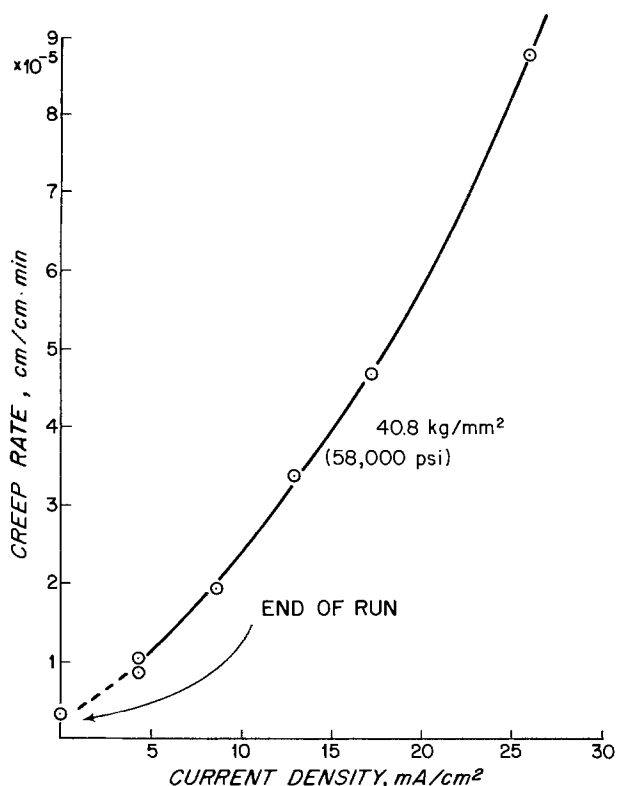


Fig. 3. Effect of anodic current density on creep rate of cold-rolled Armco iron strip in 3% NaCl, 3% Na acetate solution, room temp.

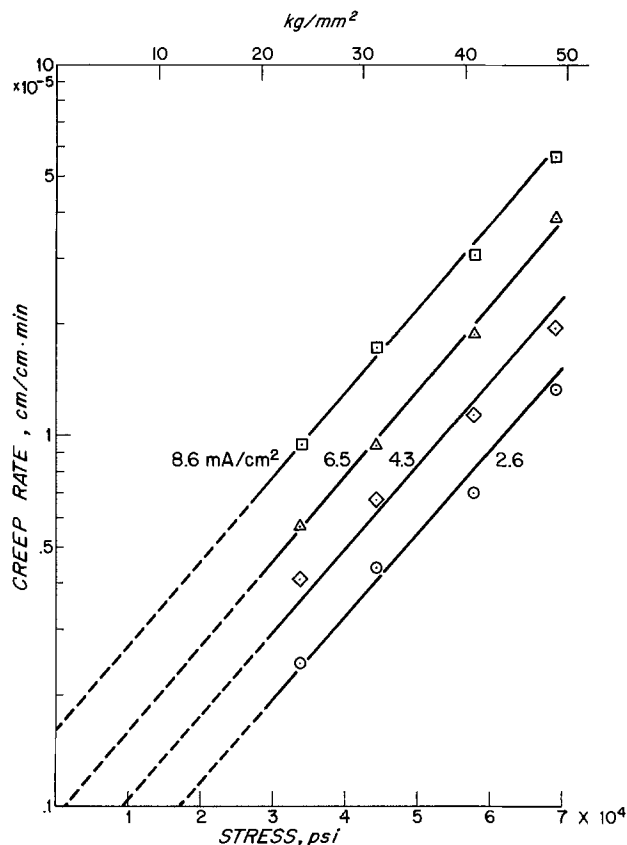


Fig. 4. Effect of applied stress on creep rate of cold-rolled Armco iron strip at various anodic current densities in 3% NaCl, 3% Na acetate solution, room temp.

within the presently observed experimental variations of creep rate for different strip specimens.

The effect of annealing the strip is shown in Fig. 5. The creep rate at a given applied stress is much larger than for cold-rolled material (Fig. 2) and anodic corrosion again exerts a large accelerating effect. The accelerating effect at low current densities, or low corrosion rates, is more pronounced at an applied stress of 11.7 kg/mm<sup>2</sup> (16,600 psi) compared to 10.3 kg/mm<sup>2</sup> (14,700 psi). Another characteristic is a longer time required to achieve a linear extension *vs.* time compared to that for cold-rolled strip, and also a longer time to regain the normal creep rate upon shutting off the current or reversing polarity.

The effect of anodic current density on the creep rate of high strength carbon steel wire is shown in Fig. 6. The creep rate at a given applied stress is considerably less than for the cold-rolled strip but the percentage acceleration induced by a given corrosion rate is comparable. Again, there is no effect on creep for reversed polarity corresponding to cathodic protection of the wire. The shape of the creep *vs.* current density for this high strength differs from that for the lower strength wires, but the reasons are unknown.

As previously suggested for copper (4), the cause of accelerated creep is plausibly related to the formation of divacancies generated by the corrosion reaction. The divacancies, in turn, diffuse into the metal at room temperature across grain boundaries to interact with dislocations piled up below the metal surface. The diminished delay time or its absence for cold-rolled strip and high strength wire indicates that either piled-up dislocations are located nearer the surface compared to the situation for copper, or that divacancies diffuse at a higher rate in the present ferrous materials. Similar to copper, there is no evidence that a hard debris layer forms at the surface of a plastically deformed iron, the dissolution of which supposedly accounts for increased creep. This was demonstrated by corroding a previously loaded cold-rolled strip for sev-



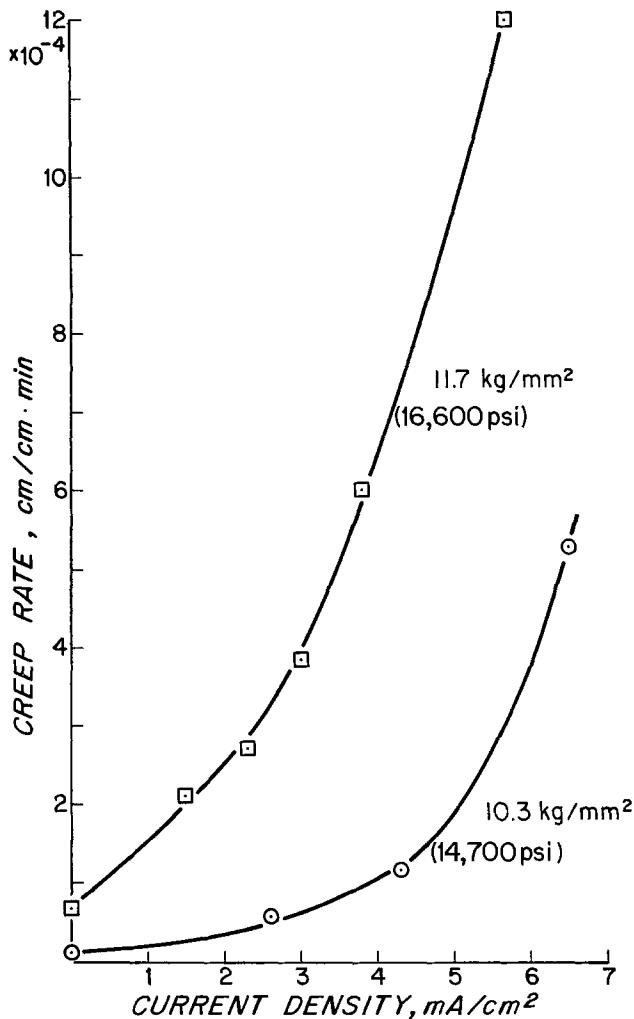


Fig. 5. Effect of anodic current density on creep rate of annealed Armco iron strip in 3% NaCl solution, room temp.

eral minutes at zero stress, then applying the normal stress at zero current and noting no change of creep rate. Had the debris layer been present, an increased creep rate would be expected. Further arguments on this matter by Kramer (5) and by Revie and Uhlig (6) have been published.

The effect of corrosion on creep acceleration probably applies generally to all metals, not only to copper and iron. This is in view of the fact that corrosion usually reduces observed fatigue life of metals.

However, the effect of corrosion on creep acceleration, unlike its effect on fatigue, is limited to shapes corresponding to a large surface to volume ratio, *i.e.*,

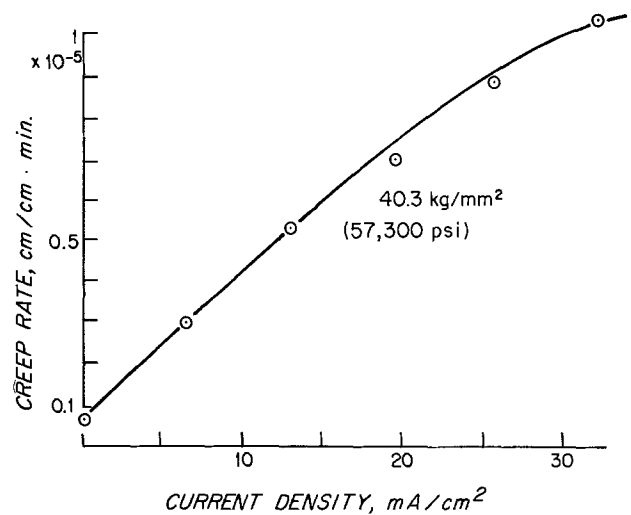


Fig. 6. Effect of anodic current density on creep rate of high strength 0.77% C steel wire, 0.71 mm diam, in 3% NaCl, 3% Na acetate solution, room temp.

wire or strip. The large effect of the present high strength steel wire (0.71 mm in diameter) on creep brings current observations into the area of relevancy since many present practical applications for wire include this diameter. These results also lend additional support to the previously proposed mechanism of corrosion fatigue based on the effect of corrosion to accelerate plastic deformation of stressed metals.

### Conclusions

1. Creep of stressed Armco iron strip or high strength 0.77% C steel wire is appreciably accelerated by surface dissolution, independent of any thinning caused by the corrosion process.
2. The results lend additional support to the previously proposed mechanism of corrosion fatigue based on the effect of corrosion to accelerate plastic deformation of stressed metals.

Manuscript submitted March 11, 1976; revised manuscript received June 7, 1976.

Any discussion of this paper will appear in a Discussion Section to be published in the June 1977 JOURNAL. All discussions for the June 1977 Discussion Section should be submitted by Feb. 1, 1977.

### REFERENCES

1. D. Duquette and H. Uhlig, *Trans. Am. Soc. Metals*, **61**, 449 (1968); **62**, 839 (1969).
2. H. Lee and H. Uhlig, *Metall. Trans.*, **3**, 2949 (1972).
3. R. Revie and H. Uhlig, *Corrosion Sci.*, **12**, 669 (1972).
4. R. Revie and H. Uhlig, *Acta Metall.*, **22**, 619 (1974).
5. I. R. Kramer, *Scr. Metall.*, **8**, 1231 (1974).
6. I. R. Kramer, *ibid.*, **8**, 1235 (1974).

## Holographic Study of Electropolishing

R. J. Schaefer and J. A. Blodgett

Naval Research Laboratory, Washington, D.C. 20375

Electropolishing can produce bright, specular surfaces on metals, but these surfaces often have poor flatness because the local rate of dissolution of the metal is influenced by convection or other inhomogeneous processes. Although these effects can often be mitigated, for example by careful selection of an electrolyte or by controlled flow patterns, they usually cannot be entirely eliminated, especially if the object be-

Key words: interferometry, convection, copper.

ing polished is large or complex in shape. Therefore it is important to understand the effects which lead to locally inhomogeneous rates of dissolution.

We have previously reported on the use of holography to study crystal growth of transparent materials, using transmitted light (1, 2). We describe here a holographic study of the electropolishing of copper, using light reflected from the surface of copper specimens. Double-exposure and real-time holography (3) have

enabled us to measure interferometrically the development of convection-related inhomogeneities in the polishing rate.

### Experimental

Flat copper specimens were illuminated at normal incidence by a collimated beam of light from an argon or krypton ion laser. The reflected light was directed by a beam-splitter to a film or plate which was simultaneously illuminated by a coherent reference beam to form the hologram. All components of the apparatus were rigidly mounted on a vibration isolation table.

The electropolishing specimens were prepared as strips of annealed copper sheet 1.5 cm wide which were first polished mechanically to 3/0 grade polishing paper and then electropolished to give a uniform bright surface. This surface was then masked by a transparent insulating lacquer everywhere except for a small "window" where the metal was left bare for the subsequent electropolishing experiments. The polishing windows had several different shapes with typical over-all dimensions of 5-10 mm. The strips were mounted vertically in a glass polishing chamber with two copper cathodes. The electrolyte was 70%  $H_3PO_4$  and polishing was carried out at a constant applied voltage of 1.5V. The current density at the anode polishing window reached a steady-state value of approximately 35 mA/cm<sup>2</sup> within 90 sec of the start of polishing, after the decay of an initial transient pulse of about ten times the steady-state current density.

Double-exposure holograms were made by recording two exposures in sequence without moving either the specimen or the photographic plate. The reconstructed double-exposure holograms showed interference fringes indicating changes in the specimen in the time interval between the two exposures. Real-time holography was accomplished by recording a single-exposure hologram of the copper anode in position in the polishing cell before the start of polishing. This hologram was then removed from its holder, processed, and replaced exactly in its original position. The virtual

image reconstructed by the hologram was thus superimposed on the specimen itself, and changes in the specimen, in the form of moving fringes, could be seen as they occurred.

Holographic interferometry was found to work well only on specimens which already had smooth, bright surfaces; hence the initial polishing of the copper strips before coating with the insulating lacquer. However, the quality of the initial surface required was much less than the fraction of a wavelength surface which would be required if performing the experiment by means of conventional interferometry. An etching or microscopic roughening of the specimen surface, in either its initial or final state, caused an unresolvable jumble of contorted fringes which obliterated the fringes due to larger scale events.

The fringes in the reconstructed holograms are due to changes in the optical path length of the laser light. These changes are caused both by changes in the geometrical path length, as metal is removed from the copper surface, and by changes in refractive index of the electrolyte, as its composition changes during polishing. These two effects cannot in general be separated, except that it can be shown that the electrolyte composition eventually reaches a quasi-steady state so that further optical path length changes are due entirely to increases in the geometrical path length.

### Results

Figure 1(a) shows an image reconstructed from a double-exposure hologram of an electropolishing specimen. The first exposure was recorded before the start of polishing and the second exposure was recorded after 2 min of polishing. The fringes visible within the square polishing area result from the combined effects of the geometrical path length increase due to metal removal, and the refractive index change due to compositional variation of the electrolyte. The fringes visible in the masked area below the polishing window are due entirely to the downward convection of the dense,

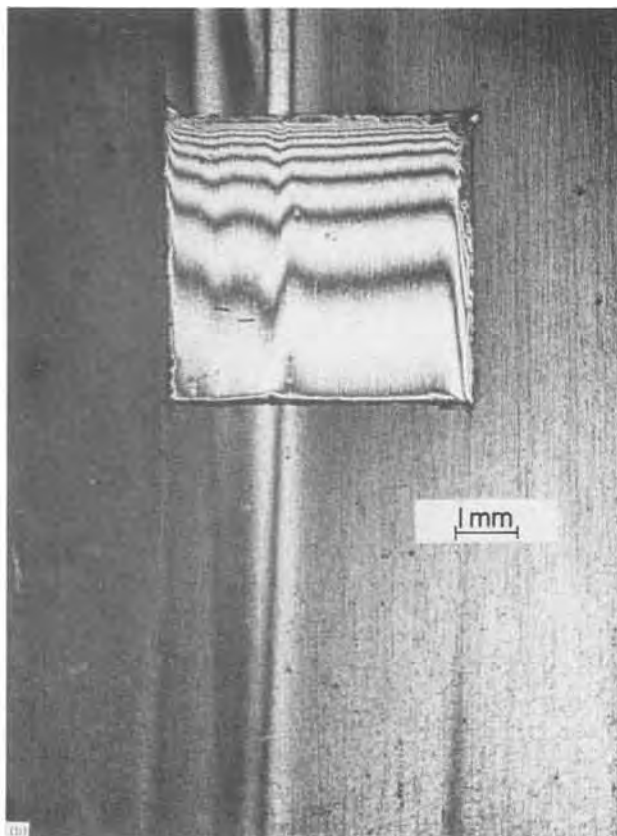
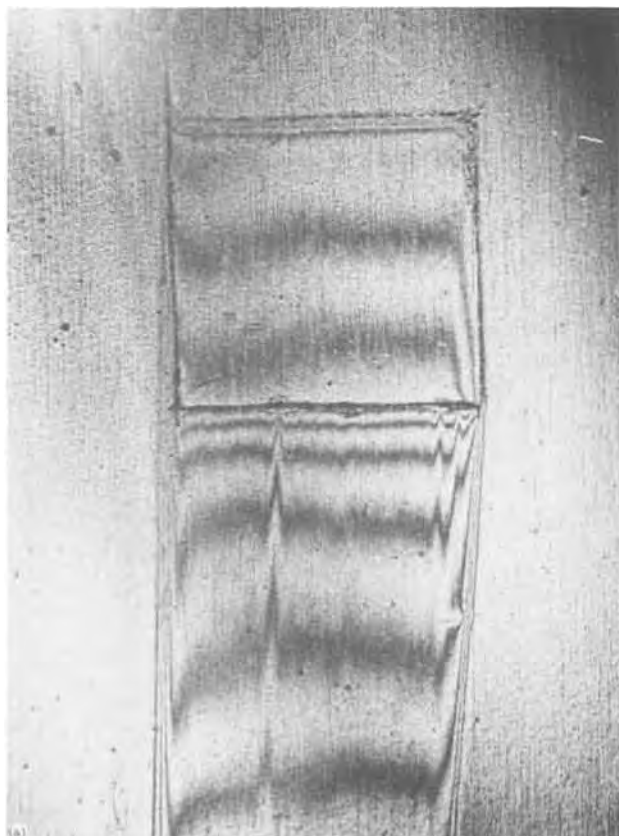


Fig. 1. Double-exposure holograms of copper specimen electropolishing in  $H_3PO_4$  solution: (a) exposures at  $t = 0$  and  $t = 2$  min, (b) exposures at  $t = 8$  min and  $t = 10$  min.

copper-rich electrolyte. Figure 1(b) shows a reconstructed double-exposure hologram of the same specimen, the two exposures in this case having been recorded 8 and 10 min after the start of polishing. No fringes are now seen in the masked region below the polishing window, indicating that the downward-streaming electrolyte has reached a steady-state condition. It is reasonable to assume that the electrolyte composition in the region of the polishing window has also reached a steady-state condition and that the fringes in the polishing region are thus due solely to the geometrical path length increase resulting from metal removal. The fringes indicate that the metal removal rate changes rapidly as the top edge of the polishing window is approached.

Each fringe in this case corresponds to a change in surface elevation of  $\lambda/2n$ , where  $\lambda$  is the wavelength in air (514.5 nm) and  $n$  is the refractive index of the electrolyte (1.424). In this system the fringe interval is thus 0.18  $\mu\text{m}$ . Analysis of the fringes of Fig. 1(b) indicates that over most of the specimen area the inhomogeneous part of the metal removal rate can be described by the equation

$$\frac{dh}{dt} = \frac{0.66}{z^{0.34}} - 0.3 \quad 0.2 \text{ mm} < z < 5 \text{ mm} \quad [1]$$

where  $dh/dt$  is the rate of metal removal in micrometers per minute, and  $z$  is the distance in millimeters from the top edge of the polishing window. One can of course expect this equation to apply only under the specific conditions of electrolyte composition and applied voltage that were used in these experiments.

To determine whether the fringes near the top of the polishing window represent increasing or decreasing metal removal rate, a small angular offset of the beam illuminating the specimen was introduced between the two exposures of the hologram. A series of vertical fringes was thereby produced in the reconstructed hologram, and the direction of fringe displacement corresponding to increasing path length was known. The fringes within the polishing area then showed clearly that the polishing rate decreases as one moves downward from the top of the polishing window. This decrease can be attributed to the buildup of the down-

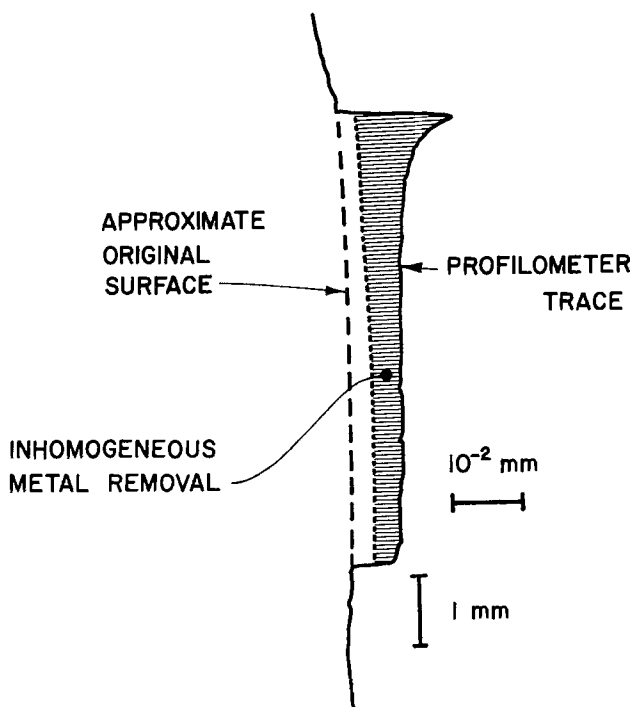


Fig. 2. Surface relief of electropolished copper specimen as measured by profilometer. The shaded region represents the inhomogeneity in metal removal rate associated with the top edge of the polishing window, as given by Eq. [1].

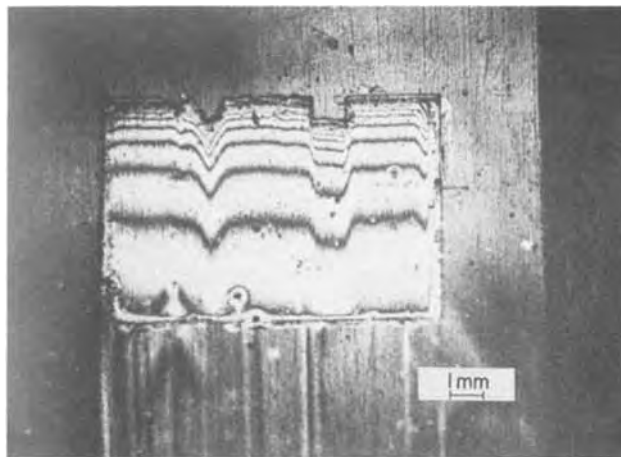


Fig. 3. Double-exposure hologram of a copper specimen with irregularities in the top edge of the polishing window. The fringes show the inhomogeneous rate of metal removal under steady-state polishing conditions.

ward-streaming, copper-rich laminar layer adjacent to the metal surface.

Confirmation of the interpretation of the fringes was obtained by electropolishing an initially flat specimen for 10 min and then measuring the depth of metal removed from the surface by means of a Dektak profilometer. Figure 2 shows the specimen profile with the much greater depth of metal removed near the top edge of the polishing window. Using Eq. [1] to subtract out the inhomogeneous part of the metal removal rate from the profile of Fig. 2, we obtain the dotted line, closely paralleling the original specimen surface and thus confirming the validity of Eq. [1].

The sensitivity of the local polishing rate to the proximity of the top edge of the polishing area can be dramatically shown by introducing irregularities in the shape of the top edge. Figure 3 shows a specimen in which small triangular and rectangular irregulari-

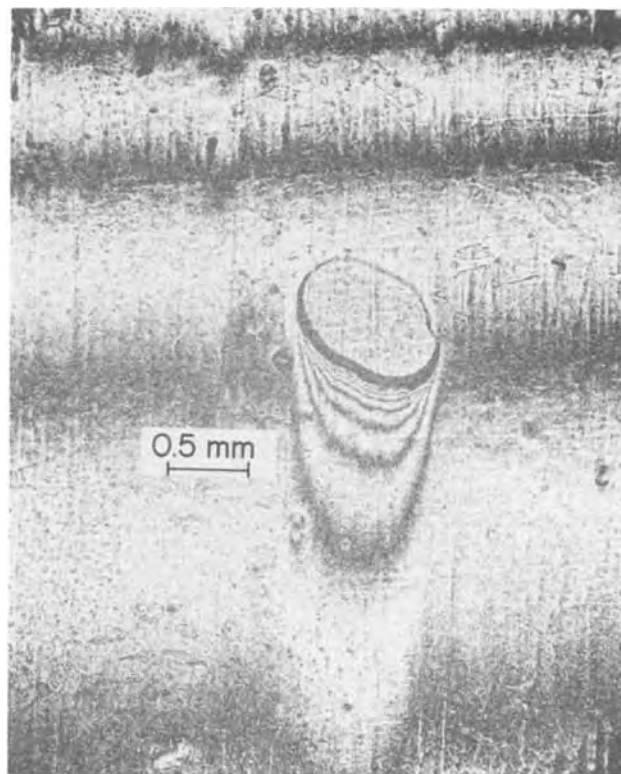


Fig. 4. Inhomogeneous metal removal rate in the vicinity of a small spot of insulating lacquer on the copper surface.

ties have thus been introduced. The shape of the irregularities is faithfully reproduced in each of the fringes in this reconstructed double-exposure hologram, indicating that there is little lateral spreading of the downward-flowing electrolyte.

When a small spot of insulating lacquer is placed in the middle of the polishing window (Fig. 4), it is seen that the metal removal rate is considerably greater immediately below the spot than at the sides or top of the spot. This experiment demonstrates that the metal removal rate at a point on the surface is not simply a function of the total amount of copper per unit area in the laminar layer covering that point, which may be expressed as

$$C(y,z) = \int_0^{\infty} c(x,y,z) dx \quad [2]$$

where  $c(x,y,z)$  is the local concentration of copper,  $x$  is the distance from the copper surface, and  $y$  and  $z$  are the other two Cartesian coordinates. Because of the laminar nature of the surface layer,  $C(y,z)$  below the insulated spot cannot be significantly less than  $C(y,z)$  immediately above the spot, yet the metal removal rate is much greater below the spot than above it. We can therefore conclude that the metal removal rate is not a function of  $C(y,z)$  but rather is related to the concentration  $c(x=0,y,z)$  directly at the metal surface, which could differ significantly above and below the insulated spot. Unfortunately, while  $C(y,z)$  can be measured holographically through its influence on the

optical path length,  $c(x=0,y,z)$  cannot be measured holographically.

The double-exposure technique suffers from the disadvantage that it is not possible to measure the absolute local rates of metal removal, but only the inhomogeneities in the rate. An absolute measurement would require an enumeration of the order of the individual fringes since it is impossible to trace the individual fringes across the sharp step at the edges of the polishing area.

With real-time holography one can measure the rate at which fringes sweep across the surface of the specimen and thereby determine the absolute rate of metal removal, once the electrolyte has reached its steady-state composition distribution. One can also observe transient phenomena during the initial stages of polishing. The moving fringes in our real-time holograms were recorded on motion picture film for later analysis. Real-time holography is much more demanding than double-exposure holography with respect to experimental requirements such as vibration isolation and equality of object and reference path length, and the fringes in real-time holograms were often faint and difficult to follow.

The real-time holograms compare the specimen's current condition to its condition before the start of polishing. Thus, within the polishing area, the change in path length is due to both electrolyte composition changes and metal removal. The holograms show, however, that convection of the electrolyte does not become

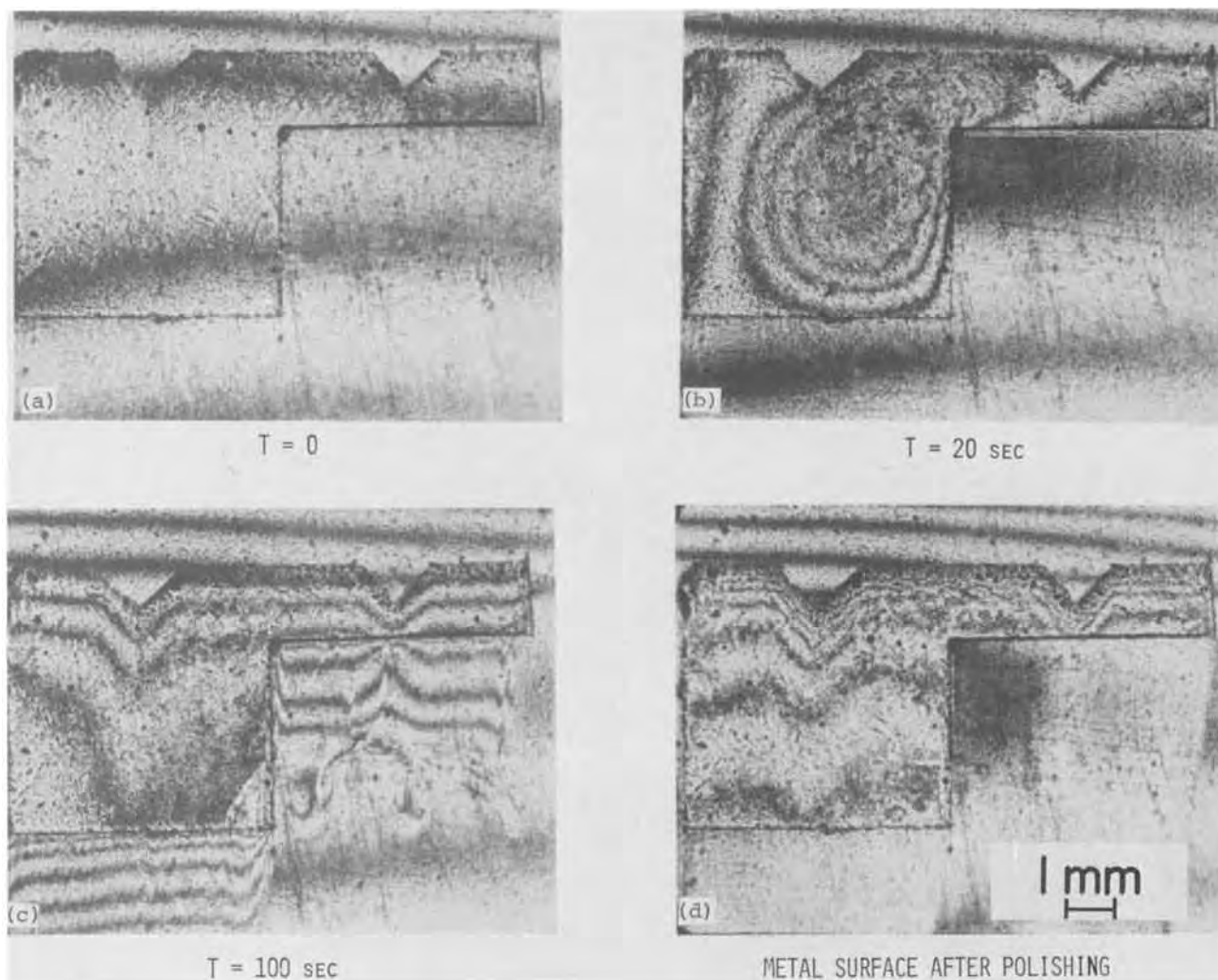


Fig. 5. Real time holography showing: (a) the initial appearance of the specimen with the superimposed holographic reconstruction, (b) the appearance during the initial transient period of polishing with current highest at the corners and edges, (c) the appearance after the start of convective flow, and, (d) the appearance after polishing is stopped and the copper-enriched electrolyte has been allowed to dissipate.

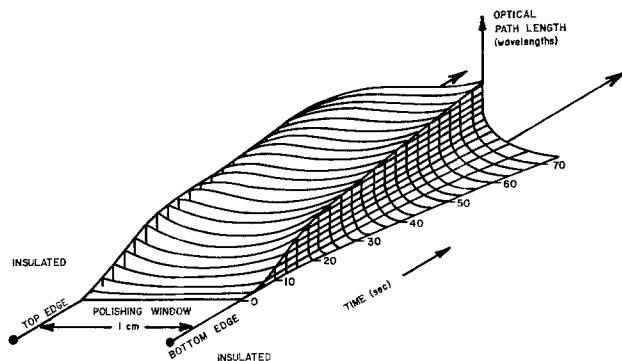


Fig. 6. Optical path length increase as a function of time, along a vertical line through the center of a 1 cm square polishing window.

significant until about 25 sec after the start of polishing. Therefore we can expect that during the first 25 sec the electrolyte composition change at any point is proportional to the metal removed from the surface at that point, and the increase in optical path length at that point is thus related in a linear manner to the amount of metal removed.

The real-time holograms in Fig. 5 show that initially the rate of removal is highest at the edges and corners of the polishing window [Fig. 5(b)], i.e., in those areas where the current would be largest if the current is limited by the ohmic resistance of the electrolyte. As the electrolyte composition at the interface changes, however, the flow of current is retarded locally, thus tending to make the current distribution more uniform. Later, as convection sweeps the copper-rich electrolyte downward, the current density and metal removal rate are highest near the top edge of the polishing area, where fresh electrolyte is sweeping in [Fig. 5(c)].

The inhomogeneities in the total amount of metal removed during an electropolishing experiment were revealed by observing the specimen a few minutes after the applied voltage had been removed. This time interval allowed dissipation of the inhomogeneous boundary layer and the fringes then revealed the shape of the metal surface [Fig. 5(d)].

Figure 6 shows the increase in optical path length, as a function of time, along a vertical line through the center of a 1 cm square polishing area. Initially, metal removal is fastest at the top and bottom edges. After convection starts, copper-rich electrolyte spills over

the bottom edge of the polishing area, and the optical path length within the polishing area can no longer be interpreted as the sum of two terms which are directly proportional to one another.

During the first few seconds of electropolishing, the polishing rate showed a small sensitivity to crystallographic orientation, and the corresponding offset of the fringe pattern produced optical contrast, rendering the grain structure of the copper visible. The difference in the amount of metal removed from adjacent grains corresponded to no more than about one-half of a fringe (roughly  $0.1 \mu\text{m}$ ), and at later times the contrast between grains disappeared, indicating that the effects of the nonuniform removal rate had been eliminated.

### Summary

Holographic interferometry can be used to observe changes occurring at a metal surface during electropolishing. When it can be demonstrated that the refractive index of the electrolyte is in a steady-state condition, variations in the local rate of metal removal can be measured.

During the electropolishing of small vertical areas of copper in a quiescent phosphoric acid electrolyte, the current is initially greatest near the edges and corners of the polishing area. Later, the layer of copper-rich electrolyte accumulating adjacent to the metal surface flows downward in a laminar manner, and the local metal removal rate is greatest near the top edge, where the copper-rich layer is thinnest. Irregularities in the upper perimeter of the polishing area result in grooves or ridges in the metal surface, extending downward from the irregularities.

Manuscript submitted April 19, 1976; revised manuscript received July 31, 1976.

Any discussion of this paper will appear in a Discussion Section to be published in the June 1977 JOURNAL. All discussions for the June 1977 Discussion Section should be submitted by Feb. 1, 1977.

Publication costs of this article were assisted by the Naval Research Laboratory.

### REFERENCES

1. M. E. Glicksman, R. J. Schaefer, and J. A. Blodgett, *J. Cryst. Growth*, **13/14**, 68 (1972).
2. J. A. Blodgett, R. J. Schaefer, and M. E. Glicksman, *Metallography*, **7**, 453 (1974).
3. Robert K. Erf, Editor, "Holographic Nondestructive Testing," Academic Press, Incorporated, New York (1974).

## A Multilayer Iron-Thionine Photogalvanic Cell

D. E. Hall and J. A. Eckert

*Exxon Research and Engineering Company, Solar Energy Conversion Unit, Linden, New Jersey 07036*

and N. N. Lichtin and P. D. Wildes

*Department of Chemistry, Boston University, Boston, Massachusetts 02215*

Recent interest in the conversion of solar energy directly to electricity has resulted in several publications concerning the iron-thionine photogalvanic system (1-5). This communication reports our most recent progress in this area. A novel photogalvanic cell, with two transparent semiconductor electrodes, has been designed and evaluated. The use of two transparent electrodes has made possible the construction of multilayer photogalvanic devices, in which there are several layers of photogalvanically active iron-thionine solution. An increased efficiency has been obtained with these devices.

Key words: photogalvanic, solar, thionine.

A multilayer photogalvanic device is shown in Fig. 1. Each layer is an individual photogalvanic cell, containing a tin oxide anode and an indium tin oxide cathode. Tin oxide was obtained from Corning Glass Works as thin films on low alkali glass substrates. Cathodes were prepared by sputtering indium tin oxide on glass, or were obtained from PPG. Sheet resistances, measured with a four-point probe, were about  $30 \Omega/\text{sq}$  for  $\text{SnO}_2$  and about  $10 \Omega/\text{sq}$  for sputtered indium tin oxide. Both electrodes were quite transparent (80-90%T) at 600 nm. Sputtered platinum films were used as cathodes in single layer cells, and as the rear element in some multilayer cells.

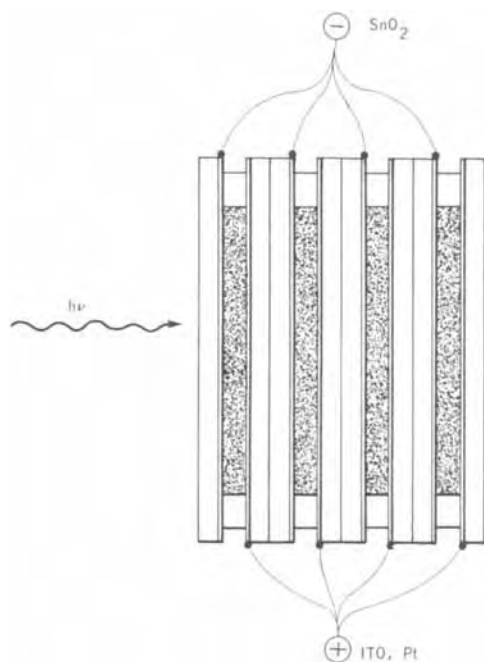


Fig. 1. Four-layer cell, top view

Electrodes making up each element were separated by strips of inert spacing material, usually 80  $\mu\text{m}$  thick Teflon. Spacers used in some single layer cells were made of 25  $\mu\text{m}$  thick Celgard 2400. Cell elements were filled with solution by capillarity.

Photogalvanic solutions typically contained  $10^{-2}M$   $\text{H}_2\text{SO}_4$  in acetonitrile/water (50/50, v/v) as solvent,  $10^{-2}M$   $\text{FeSO}_4$ , and saturated ( $\sim 1$  mM) thionine, added as the free base. Ferric ion was present as impurity from ferrous sulfate, at  $\sim 5 \times 10^{-4}M$ .

Cells were illuminated by light from a 650W tungsten spot heater. The light was focused into a 2-in. beam and passed through a water tank and infrared filter. The resultant light incident on the cell produced the same power output as 35  $\text{mW}\cdot\text{cm}^{-2}$  sunlight. This value was used in calculating efficiencies.

Table I shows the output measured from a four-layer cell, wired in parallel. The outputs for each separate layer are also shown. These outputs were measured in the assembled multilayer device. The drop in short-circuit current ( $I_{sc}$ ) from the front to the rear element is caused by the increased screening experienced by a given element as the number of layers of dye solution between it and the light source increases. Open-circuit voltages ( $V_{oc}$ ) show the same behavior, but also reflect variations due to slight differences in the electrode materials.

The efficiency of the multilayer device is estimated in the following way. The effective illuminated area of individual layers varied, and could not be determined exactly. Therefore, an opaque mask with a  $1 \times 2$  cm slit was inserted between the light source and cell to provide a common area of illumination. The power output of the device per square centimeter is

$$\text{Power} = \frac{V_{oc} \times I_{sc} \times ff}{\text{Area}} = \frac{0.134\text{V} \times 1.0 \times 10^{-3}\text{A} \times 0.33}{2 \text{ cm}^2} = 2.2 \times 10^{-5} \text{ W}\cdot\text{cm}^{-2}$$

The fill factor,  $ff$ , is the ratio of the product of current and voltage at maximum power to the product of  $I_{sc} \times V_{oc}$ . The value 0.33 was found to be representative for the photogalvanic device in several determinations. Using the value of 35  $\text{mW}\cdot\text{cm}^{-2}$  for incident light intensity gives

Table I. Output of four-layer cell

Layer	$V_{oc}$ , V	$I_{sc}$ , mA*
1-4	0.134	1.60
1 (Front)	0.137	0.55
2	0.142	0.47
3	0.132	0.35
4 (Rear)	0.128	0.23

\*  $I_{sc}$  from 2.0  $\text{cm}^2$  area = 1.0 mA.

$$\text{Efficiency} = \frac{2.2 \times 10^{-5}\text{W}}{3.5 \times 10^{-2}\text{W}} = 0.063\%$$

This represents the efficiency of converting incident light directly to electrical power and has been termed the sunlight engineering efficiency (SEE) (1).

A totally illuminated cell is possible because the  $\text{SnO}_2$  electrode exhibits selectivity in its response. In the dark, both electrodes are governed at equilibrium by the  $\text{Fe}^{+2}/\text{Fe}^{+3}$  couple. The dye is essentially all in the oxidized form. Under illumination, photoreduction of thionine to leucothionine causes a substantial amount of each form to exist at steady state. The dye couple reacts readily at  $\text{SnO}_2$  (5). However, the reactions of the  $\text{Fe}^{+2}/\text{Fe}^{+3}$  couple at  $\text{SnO}_2$  are suppressed through a large potential range (5). The redox potential of  $\text{Fe}^{+2}/\text{Fe}^{+3}$  is considerably more anodic than the flat-band potential ( $E_{fb}$ ) of  $\text{SnO}_2$  in the photogalvanic cell. This, together with the large rearrangement energy (6) of  $\text{Fe}^{+2}/\text{Fe}^{+3}$ , makes it difficult for  $\text{Fe}^{+2}$  oxidation to occur even though the  $\text{SnO}_2$  is anodically polarized with respect to  $E_{fb}$ . The reduction of  $\text{Fe}^{+3}$  is also suppressed due to the lack of electrons available in the depletion region and the relatively high energy levels of  $\text{Fe}^{+3}$  in solution resulting from the large rearrangement energy. The behavior of  $\text{Fe}^{+2}/\text{Fe}^{+3}$  at  $\text{SnO}_2$  electrodes is discussed in more detail elsewhere (6, 7).

Under illumination, the potential of the  $\text{SnO}_2$  electrode is thus determined mainly by the thionine/leucothionine couple (Table II). Its redox potential is closer to  $E_{fb}$ , and in addition, the lower rearrangement energy characteristic of quinone-type system (8) is probably effective in creating a much greater degree of overlap of redox energy levels with the lower edge of the conduction band. The platinum electrode shows only a slight potential shift under illumination thus responding primarily to the  $\text{Fe}^{+2}/\text{Fe}^{+3}$  couple. The dye couple does have some effect on the potential of the platinum electrode, however. Upon illumination, the concentration ratio of  $\text{Fe}^{+3}$  to  $\text{Fe}^{+2}$  increases. Thus, the potential of the platinum electrode would shift anodically in the absence of any dye couple effects. The observed slight cathodic shift represents an efficiency loss. A selective electrode, at which only the iron couple could react (i.e., at which the dye couple has a very low  $i_0$ ), would be desirable as a cathode.

The degenerate indium tin oxide (ITO) electrode used as a cathode material in the multilayer cell exhibits nearly metallic behavior toward the  $\text{Fe}^{+2}/\text{Fe}^{+3}$  couple, as shown in Fig. 2. The redox reactions are slightly less reversible at ITO than at platinum. Short-circuit currents from single layer cells containing ITO rather than Pt are about 30% lower, while open-circuit voltages are about the same or slightly lower.

Monochromatic quantum efficiencies (MQE) for single layer photogalvanic cells were measured using a

Table II. Photogalvanic electrode potentials (vs. SCE)

Electrode	Condition	$E$ vs. SCE, V
$\text{SnO}_2$	Light	0.210
	Dark	0.385
Pt	Light	0.385
	Dark	0.395

$V_{oc}$  measured in the light = 0.175V.



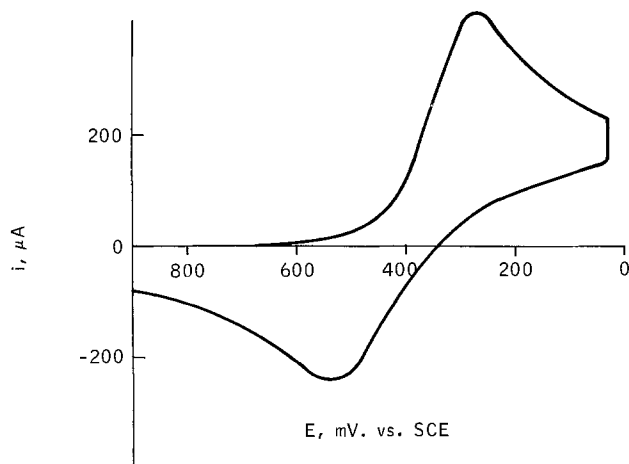


Fig. 2. Cyclic voltammetry of  $10^{-3}M$   $Fe^{+2}$  and  $10^{-3}M$   $Fe^{+3}$  in  $0.12M$   $H_2SO_4$  at an indium tin oxide thin film electrode. Scan rate =  $100$   $mV\text{-sec}^{-1}$ .

semitransparent ( $135\text{\AA}$  thick) platinum cathode, so that light absorption could be measured by an Eppley thermopile placed directly behind the cell. Band pass filters of 578, 589, and 620 nm were placed in the incident light beam to provide monochromatic illumination. Results of MQE measurements of  $80\ \mu m$  thick cells are shown in Table IIIA. The quantity calculated is defined as the short-circuit current flow in electrons  $sec^{-1}$  divided by the absorbed light in photons  $sec^{-1}$ . There is some scatter in the data, but there appears to be no significant dependence of quantum efficiency on the wavelength of incident light.

MQE was also measured as a function of the solution thickness. As shown in Table IIIB, decreasing the cell thickness by a factor of 3 causes only about a 10% drop in short-circuit current, using the tungsten light source. Correspondingly, MQE is about twice as high for  $25\ \mu m$  thick cells as for  $80\ \mu m$  thick cells. These results indicate that the collection of electroactive species from the first  $25\ \mu m$  of solution occurs more efficiently than from the extra volume contained in the  $80\ \mu m$  cell.

Kinetic data make the above interpretation reasonable. An analysis of reaction rates in solution gives an estimated lifetime for leucothionine of  $\sim 1.1$  sec. If one assumes that the movement of electroactive leuco-

Table IIIA. Monochromatic quantum efficiency at selected wavelengths of incident light

$\lambda$ , $\mu m$	Intensity, $mW\text{-cm}^{-2}$	MQE, %
578	0.61	7
589	0.53	5-9
620	0.77	8

Table IIIB. Monochromatic quantum efficiency vs. cell thickness (intensities as in Table IIIA)

Thickness, $\mu m$	$\lambda$ , $\mu m$	MQE, %
25	578	13
80	578	7
25	589	18
80	589	5-9

Table IIIC.  $V_{oc}$  and  $I_{sc}$  vs. cell thickness (tungsten illumination,  $35$   $mW\text{-cm}^{-2}$ )

Thickness, $\mu m$	$V_{oc}$ , V	$I_{sc}$ , mA
25	0.135	0.60
80	0.143	0.64

Cell area  $\sim 6$   $cm^2$ .

Table IV. Two-layer two-dye cell (tungsten illumination,  $35$   $mW\text{-cm}^{-2}$ )

Layer 1: $SnO_2$ anode, ITO cathode, $\sim 1$ $mM$ thionine. Layer 2: $SnO_2$ anode, Pt cathode, $\sim 4$ $mM$ methylene blue.		
Layer	$V_{oc}$ , V	$I_{sc}$ , mA
1 + 2	0.135	0.82
1	0.155	0.64
2	0.115	0.27

Cell area  $\sim 5.5$   $cm^2$ .

thionine in the solution is solely due to diffusion, the average distance traveled by a leucothionine molecule during its lifetime can be estimated by the relation  $l = (2Dt)^{1/2}$ , which applies to one-dimensional motion between two planes. Taking  $D$  as  $7.6 \times 10^{-6}$   $cm^2\text{-sec}^{-1}$ , the value reported (9) for methylene blue, a similar molecule, in water solution, the calculated value of  $l$  is  $41\ \mu m$ , indicating that the collection of leucothionine generated in the  $25\ \mu m$  of solution nearest the anode should proceed quite efficiently. The fraction of leucothionine reaching the anode from the remaining  $55\ \mu m$  of solution in the  $80\ \mu m$  cell would be substantially lower.

The monochromatic quantum efficiency results, together with the above calculation, indicate that a multilayer cell with  $25\ \mu m$  solution layers rather than  $80\ \mu m$  layers should be more efficient in converting absorbed light to electricity.

Several thiazine dyes other than thionine show substantial photogalvanic activity. These include methylene blue, Azure A, Azure B, and Toluidine Blue O. Combinations of photogalvanically active thiazines have been used in the multilayer device to broaden the spectral response of the photogalvanic cell. This approach was suggested in a recent publication (3). Results obtained with a two-layer cell containing one layer of thionine solution and one layer of methylene blue solution are shown in Table IV.

The development of a photogalvanic device using two transparent thin film electrodes has permitted the construction of multilayer devices. These devices can be used to increase the conversion efficiency of light at a given wavelength by increasing the number of active solution layers. In addition, the spectral response of the photogalvanic device can be broadened by using successive solution layers of photogalvanically active dyes which absorb light at different wavelengths.

### Acknowledgment

This research was performed under Grant No. SE/AER/72-03579 of the National Science Foundation's Research Applied to National Needs Program.

Manuscript submitted May 28, 1976; revised manuscript received July 5, 1976.

Any discussion of this paper will appear in a Discussion Section to be published in the June 1977 JOURNAL. All discussions for the June 1977 Discussion Section should be submitted by Feb. 1, 1977.

Publication costs of this article were assisted by Exxon Research and Engineering Company.

### REFERENCES

- W. D. K. Clark and J. A. Eckert, *Solar Energy*, **17**, 147 (1975).
- R. A. Hann, et al., *Nature*, **244**, 126 (1973).
- R. Gomer, *Electrochim. Acta*, **20**, 13 (1975).
- D. A. Fine and A. N. Fletcher, Naval Weapons Center Report NWC TP 5813, February 1976.
- D. E. Hall, W. D. K. Clark, J. A. Eckert, N. N. Lichten, and P. D. Wildes, Submitted for publication.
- R. Memming and F. Möllers, *Ber. Bunsenges. Physik. Chem.*, **76**, 475 (1972).
- F. Möllers and R. Memming, *ibid.*, **76**, 469 (1972).
- R. Memming and F. Möllers, *ibid.*, **76**, 609 (1972).
- K. J. Vetter and J. Bardeleben, *Z. Elektrochem.*, **61**, 135 (1957).

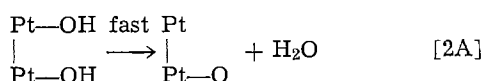
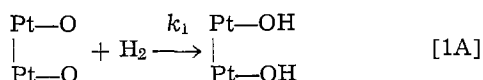
# A Kinetic Model for the Reduction of Transiently Formed Oxide Film on Smooth Platinum Electrodes with Hydrogen under Open-Circuit Conditions

C. G. Rader and B. V. Tilak

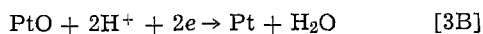
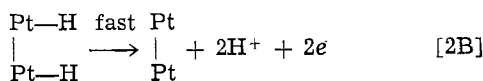
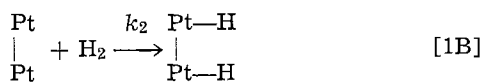
Hooker Chemicals & Plastics Corporation, Research Center, Grand Island, New York 14072

It has been well established (1)<sup>1</sup> that the rate at which PtO is reduced by H<sub>2</sub> under open-circuit conditions increases with time. Shibata and Sumino (1) carried out thorough investigations on the kinetics of reduction of thin films of PtO formed on smooth Pt electrodes by hydrogen, in an attempt to elucidate the nature of oxide films deposited under steady-state and transient conditions, and made the suggestion, following Breiter (2), that the observed variation in the reduction rate with surface coverage could be explained by considering the following reaction scheme

scheme A (chemical reaction)



scheme B (electrochemical sequence)



At high surface coverages, step [1A] was assumed to be rate determining; in the low coverage region, dissociation of molecular H<sub>2</sub> on the "free" Pt sites (step [1B]) was considered to be the rate-controlling step. [See Ref. (11) for a discussion of the kinetics of the oxidation of H<sub>2</sub> on the Pt electrodes in aqueous H<sub>2</sub>SO<sub>4</sub>.]

In the present communication, the kinetics of transiently formed platinum oxide (TFO) reduction are re-examined in an attempt to provide a unified theory for the mechanism of TFO reduction over the entire coverage range, and evaluate the kinetic parameters which are consistent with the data reported by Shibata and Sumino (1). Shibata and Sumino's reaction scheme and alternate reaction sequences are considered. Kinetic behavior of the reduction of platinum oxide films formed under steady-state conditions was not dealt with here because of the ambiguity regarding the formation of more than a monolayer of PtO, and the likelihood of further oxidation of PtO to PtO<sub>2</sub>, especially when polarized beyond ~1.5V (4, 9).

## Shibata and Sumino's Model

One possible reaction scheme for the reduction of transiently formed oxide layers by hydrogen under open-circuit conditions is the one considered by Shibata and Sumino which assumes parallel rate-controlling pathways involving steps [1A] and [1B].

The variation of the fractional coverage of the electrode surface by Pt-O,  $\theta$ , with time,  $t$ , may be ex-

pressed, taking into account the interaction effects between the adsorbed species, as

$$-\frac{d\theta}{dt} = k_1 p_{\text{H}_2} \theta^2 \exp(2g_1\theta) + k_2 p_{\text{H}_2} (1 - \theta)^2 \exp(2g_2\theta) \quad [1]$$

where  $k_1$  and  $k_2$ , respectively, refer to the rate constants of steps [1A] and [1B], and  $g_1$  and  $g_2$  to the change in the free energy of adsorption (in units of  $RT$ ) with coverage under Temkin conditions of nonactivated adsorption (3).

The first term on the right-hand side of Eq. [1]<sup>2</sup> represents the contribution from the initial step of the chemical reaction (scheme A) and the second term arises from the slow dissociative chemisorption of H<sub>2</sub> on Pt (step [1B]). Induced heterogeneity factors are invoked in the present treatment since we are dealing with a highly interacting system: a surface covered with several chemical and/or structurally dissimilar adsorbed species, *viz.*, PtOH, PtO, H<sup>+</sup>, PtH, H<sub>2</sub>.

An analytical solution for the coverage-time relationship may be found by neglecting the interaction parameters in Eq. [1], *i.e.*,  $g_1 = g_2 = 0$ , and integrating between the limits  $\theta_1$ , at time 0, and  $\theta$ , at time  $t$ ; the resulting expression appears as

$$t = -\frac{1}{k_1 p_{\text{H}_2} \sqrt{A}} \left\{ \tan^{-1} \left[ \frac{(1+A)\theta - A}{\sqrt{A}} \right] - \tan^{-1} \left[ \frac{(1+A)\theta_1 - A}{\sqrt{A}} \right] \right\} \quad [2]$$

where  $A = k_2/k_1$ .

The time dependence of surface coverage when  $g_1 \neq g_2 \neq 0$  can readily be solved by numerical integration of Eq. [1] between the limits of  $\theta_1$  and  $\theta$ . It is instructive at this point to examine the influence of the rate constants  $k_1$  and  $k_2$  and the interaction parameters  $g_1$  and  $g_2$  on the surface coverage-time relationship which is shown in Fig. 1 for some values of  $k_1$  and  $k_2$ . In the absence of the electrochemical step, *i.e.*, when  $k_2 = 0$ , the time required for complete reduction of the surface oxide decreases as the chemical reaction rate constant  $k_1$  is increased (cf. curve 2 *vs.* curve 1 in Fig. 1). On the other hand, when  $k_1 = 0$  and the electrochemical rate is the rate-controlling step, the  $\theta$ -log  $t$  curve is characterized by a long induction period followed by an abrupt decrease in the surface coverage (curve 4 of Fig. 1). If repulsive interactions were to prevail, inclusion of the  $g$  term in the expression for  $d\theta/dt$  would lead to a profound influence on the rate at which PtO reduction takes place, as it tends to accelerate the overall process (see curve 3 in Fig. 1). It should be noted that in all the above analyses the hydrogen partial pressure ( $p_{\text{H}_2}$ ) was taken to be constant, at a value of 1 atm.

Figure 2 illustrates the effect of the interaction term for constant (and arbitrary) values of the chemical re-

<sup>1</sup>A review of the pertinent literature is also given in Ref. (1).  
Key words: chemical reduction, hydrogen ionization, coupled reactions.

<sup>2</sup>A detailed discussion of the second order dependence on surface coverage of the chemical reaction rate and the "electrochemical reaction" rate may be found in Ref. (1).



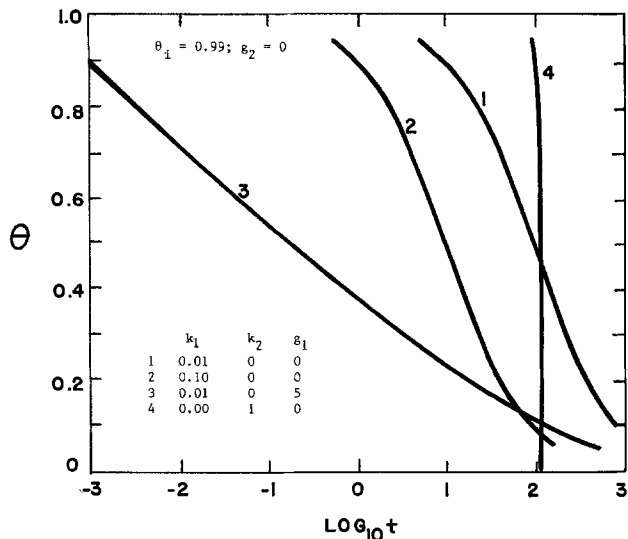


Fig. 1. Coverage variation with  $\log_{10} [t \text{ (in sec)}]$  calculated using Eq. [1] for various values of  $k_1$ ,  $k_2$ , and  $g_1$ , when  $\theta_i = 0.99$  and  $g_2 = 0$ .

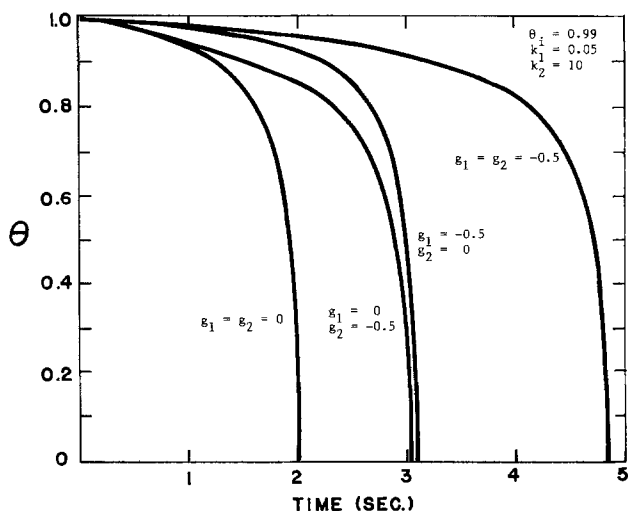


Fig. 2. Coverage variation with time (in sec) calculated using Eq. [1] for various values of  $g_1$  and  $g_2$ , shown in the figure, when  $\theta_i = 0.99$ ,  $k_1 = 0.05 \text{ sec}^{-1}$ , and  $k_2 = 10 \text{ sec}^{-1}$ .

action rate constant ( $k_1 = 0.05 \text{ sec}^{-1}$ ) and electrochemical reaction rate constant ( $k_2 = 10 \text{ sec}^{-1}$ ). Negative  $g$  values (representing attractive forces between the oxide species on the surface) tend to increase the time required for complete reduction of the surface oxide. On the other hand, when  $g$  is positive, the reduction process is accelerated, since increasing  $g$  would indirectly imply an increase in the rate constants  $k_1$  and  $k_2$ .

The analytical solution for the combined chemical/electrochemical reduction of TFO may now be used to determine the time required for complete reduction of the surface oxide. Thus for  $\theta = 0$ , the total reduction time ( $\tau$ ) may be expressed

$$\tau = -\frac{1}{k_1 p_{H_2} \sqrt{A}} \left\{ \tan^{-1} (-\sqrt{A}) - \tan^{-1} \left( \frac{(1+A)\theta_i - A}{\sqrt{A}} \right) \right\} \quad [3]$$

From Eq. [3] it can be seen that if the reaction rate constants  $k_1$  and  $k_2$  are known, the time required for reduction of a transiently formed platinum oxide surface covered by any site fraction of PtO (up to  $\theta_i = 1$ ) can be computed.

The initial premise in the present treatment stated that pure chemical reaction is rate controlling at high surface coverage (i.e.,  $\theta_i \rightarrow 1$ ) and that electrochemical PtO reduction is rate controlling at lower surface oxide fractions. It is proposed to utilize these physical arguments to provide first order estimates of the reaction rate constants from the kinetic rate data reported by Shibata and Sumino (1).

Equation [3] may be rewritten in the following form

$$\frac{\tau + D}{C} = \tan^{-1} \chi \quad [4]$$

where

$$C \equiv \frac{1}{k_1 p_{H_2} \sqrt{A}}$$

$$D \equiv C[\tan^{-1} (-\sqrt{A})]$$

and

$$\chi \equiv \frac{(1+A)}{\sqrt{A}} \theta_i - \sqrt{A}$$

Limiting case I ( $\chi^2 < 1$ ).—For  $\chi^2 < 1$ ,  $\tan^{-1} \chi \approx \chi$ . Under this restriction, Eq. [4] becomes

$$\tau \approx \frac{(1+A)}{k_1 p_{H_2} A} \theta_i - \left[ \frac{1}{k_1 p_{H_2}} + \frac{\tan^{-1} (-\sqrt{A})}{k_1 p_{H_2} \sqrt{A}} \right] \quad [5]$$

When  $A \gg 1$ , Eq. [5] further reduces to the following

$$\tau \approx \frac{1}{k_1 p_{H_2}} \theta_i - \left[ \frac{1}{k_1 p_{H_2}} + \frac{\tan^{-1} (-\sqrt{A})}{k_1 p_{H_2} \sqrt{A}} \right] \quad [6]$$

Thus, for  $\chi^2 < 1$  (corresponding to  $\theta_i \approx 1$ ) a plot of  $\tau$  vs.  $\theta_i$  should yield a straight line of slope  $1/k_1 p_{H_2}$ . This limiting case provides a means for estimating the chemical reaction rate constant  $k_1$ . Figure 3 illustrates this analysis applied to the Shibata and Sumino data. From Fig. 3 the chemical reaction rate constant is estimated to be  $0.41 \text{ sec}^{-1}$ .

Limiting case II, ( $\chi^2 > 1$ ).—For  $\chi^2 > 1$ ,  $\tan^{-1} \chi \approx \pi/2 - 1/\chi$ . For these conditions Eq. [4] yields the following expression for  $\tau$

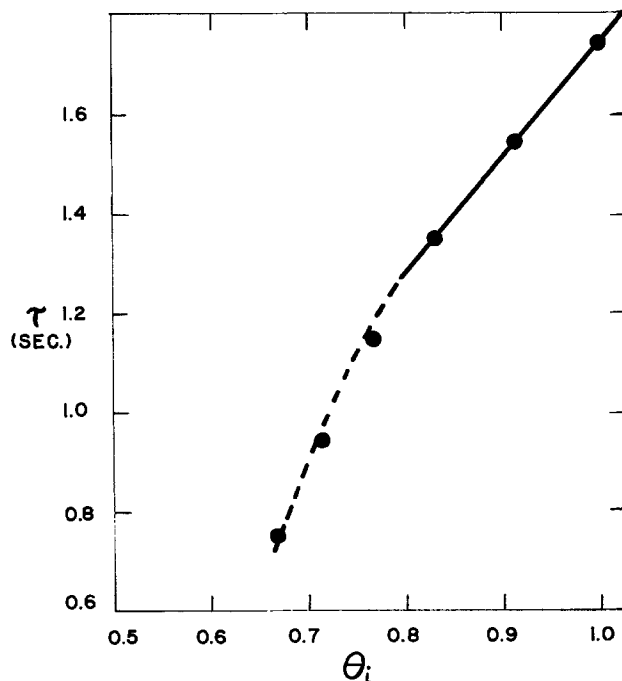


Fig. 3. Dependence of  $\tau$  (in sec) on the initial value of surface coverage using the data from Ref. (1).

$$\tau \approx \left[ \frac{C\pi}{2} - D \right] - \frac{1}{k_1 p_{H_2} (1 + A)} \left[ \frac{1}{\theta_1 - \frac{A}{(1 + A)}} \right] \quad [7]$$

Again for the case where  $A \gg 1$

$$\tau \approx \left[ \frac{C\pi}{2} - D \right] + \frac{1}{k_2 p_{H_2}} \left[ \frac{1}{1 - \theta_1} \right] \quad [8]$$

From Eq. [8] it is apparent that a plot of  $\tau$  vs.  $1/1 - \theta_1$  should yield a straight line of slope  $1/k_2 p_{H_2}$ . Figure 4 again depicts the data of Shibata and Sumino (1) subjected to the present analysis. From the data presented in Fig. 4, the electrochemical reaction rate constant is estimated to be  $2.47 \text{ sec}^{-1}$ .

The reaction rate constants for the reduction by hydrogen of transiently formed PtO were estimated to be  $k_1 = 0.41 \text{ sec}^{-1}$  and  $k_2 = 2.47 \text{ sec}^{-1}$ . Using these values of  $k_1$  and  $k_2$ , the total reduction time  $\tau$  can be directly computed as a function of initial surface coverage  $\theta_1$  according to Eq. [3]. This  $\tau$  vs.  $\theta_1$  function is plotted in Fig. 5, along with the experimental data reported by Shibata and Sumino (1). Also included in Fig. 5 is the complete numerical solution of Eq. [1] for total reduction time  $\tau$ , for  $k_1 = 0.41 \text{ sec}^{-1}$ ,  $k_2 = 2.47 \text{ sec}^{-1}$ ,  $g_1 = -0.25$ , and  $g_2 = 0$ . The inclusion of the interaction parameter  $g_1$  tends to provide slightly better agreement between theory and experiment. It is important to note that the choice of  $g_1 = -0.25$  is completely empirical and inclusion of this factor is difficult to justify solely on the basis of improved correlation between theory and experiment. The present results may be compared with Shibata and Sumino's estimates of  $k_1 = 0.49 \text{ sec}^{-1}$ ,  $k_2 = 7.2 \text{ sec}^{-1}$ , and  $\tau$  (for  $\theta_1 = 1$ ) =  $0.7 \text{ sec}$ , deduced from an alternate solution of Eq. [1].

#### Modified Reaction Scheme for the Reduction of TFO by $H_2$

Thermodynamic considerations suggest that the corrosion mechanism represented by the electrochemical

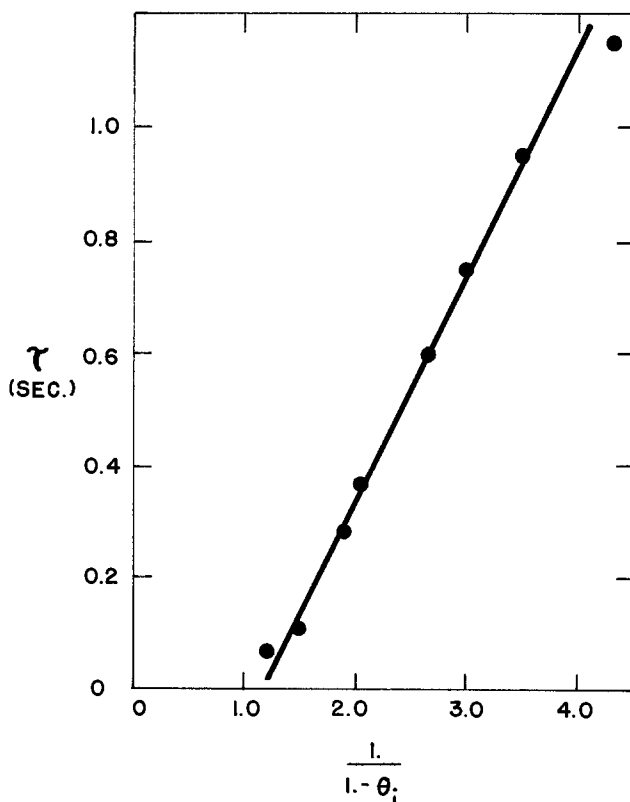


Fig. 4. Variation of  $\tau$  (in sec) with  $1/1 - \theta_1$  employing the data from Ref. (1).

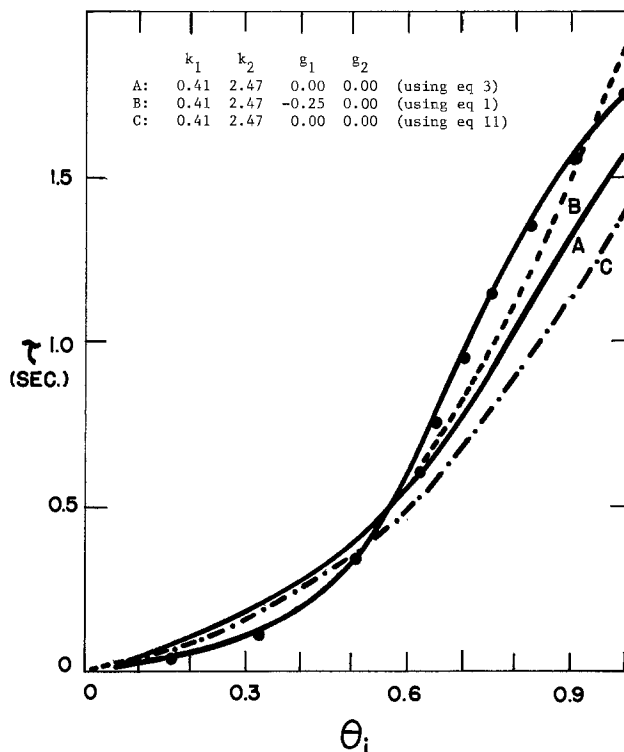
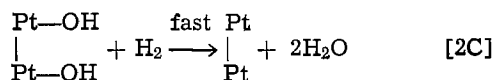
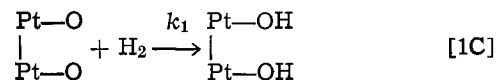


Fig. 5. Comparison of the experimental values of  $\tau$  (in sec) [from the data in Fig. 5 and 12 of Ref. (1)] with the calculated values for  $k_1 = 0.41 \text{ sec}^{-1}$  and  $k_2 = 2.47 \text{ sec}^{-1}$ , using Eq. [3] when  $g_1 = g_2 = 0$  (curve A);  $g_1 = -0.25$ ,  $g_2 = 0$  (curve B). Line C refers to values calculated using Eq. [10] with  $k_1 = 0.41 \text{ sec}^{-1}$ ,  $k_2 = 2.47 \text{ sec}^{-1}$ , and  $g_1 = g_2 = 0$ .

route (scheme B) will be operative under the conditions where PtO is reduced by  $H_2$  on open circuit. However, it is difficult to rationalize (4) the chemical reaction sequence (scheme A), especially the dehydration step [1B] which implies generation of "free Pt" sites at potentials where the oxidation of Pt readily takes place (4, 9). This dilemma may be resolved by considering two alternate reaction sequences instead of reaction scheme A. In the first instance, the following steps for the chemical reduction of PtO by  $H_2$  may be considered

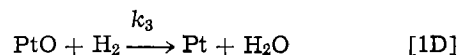
scheme A1



For this reaction scheme, the expression for the reduction of PtO would be identical to that proposed by Shibata and Sumino, and the treatment presented in the previous section (along with the  $k_1$  and  $k_2$  values) would describe the kinetics of TFO reduction by hydrogen.

Instead of postulating the various elementary steps for the chemical reduction schemes A and A1, the over-all chemical reaction may be regarded as one of the rate-controlling steps in the coupled chemical-electrochemical route

scheme A2



when the over-all process of TFO reduction by  $H_2$  proceeds via schemes A2 and B, the coverage variation can be expressed as

$$\frac{d\theta}{dt} = -k_3 p_{H_2} \theta \exp(g_3 \theta) - k_2 p_{H_2} (1 - \theta)^2 \exp(2g_2 \theta) \quad [9]$$

where  $g_3$  refers to the interaction parameter described earlier. Setting  $g_3 = g_2 = 0$ , Eq. [9] may be integrated between the limits  $\theta_1$  (at time = 0) and  $\theta$ , at time  $t$ . The coverage variation with time appears as

$$t = -\frac{2}{k_3 p_{H_2} \sqrt{4a - 1}} \left\{ \tan^{-1} \left( \frac{(2a(\theta - 1) + 1)}{\sqrt{4a - 1}} \right) - \tan^{-1} \left( \frac{(2a(\theta_1 - 1) + 1)}{\sqrt{4a - 1}} \right) \right\} \quad [10]$$

where  $a \equiv k_2/k_3$ . The time for the complete reduction of the oxide,  $\tau$ , corresponding to  $\theta = 0$ , would then be equal to

$$\tau = -\frac{2}{k_3 p_{H_2} \sqrt{4a - 1}} \left\{ \tan^{-1} \left( \frac{1 - 2a}{\sqrt{4a - 1}} \right) - \tan^{-1} \left( \frac{(2a(\theta_1 - 1) + 1)}{\sqrt{4a - 1}} \right) \right\} \quad [11]$$

Denoting  $\delta = \frac{(2a(\theta_1 - 1) + 1)}{(\sqrt{4a - 1})}$ , one may examine the limiting conditions when  $\theta_1 \rightarrow 0$  or 1, following the procedure in the previous section.

*Limiting case I* ( $\delta^2 < 1$ ).—When  $\delta^2 < 1$ ,  $\tan^{-1} \delta \approx \delta$  and Eq. [11] becomes

$$\tau \approx \left\{ \frac{(4a(\theta_1 - 1) + 2)}{k_3 p_{H_2} (4a - 1)} - \frac{2}{k_3 p_{H_2} \sqrt{4a - 1}} \tan^{-1} \left( \frac{1 - 2a}{\sqrt{4a - 1}} \right) \right\} \quad [12]$$

For  $4a \gg 1$ , Eq. [12] further reduces to

$$\tau \approx \frac{1}{k_3 p_{H_2}} \left\{ \theta_1 + \left( \frac{1 - 2a}{2a} \right) - \frac{2}{\sqrt{4a - 1}} \tan^{-1} \left( \frac{1 - 2a}{\sqrt{4a - 1}} \right) \right\} \quad [13]$$

Thus, for  $\delta^2 < 1$  (when  $\theta_1 \sim 1$ ), a plot of  $\tau$  vs.  $\theta_1$  should again result in a straight line with a slope equal to  $1/k_3 p_{H_2}$ . This is illustrated in Fig. 3, from which  $k_3$  is estimated to be  $0.41 \text{ sec}^{-1}$ .

*Limiting case II* ( $\delta^2 > 1$ ).—When  $\delta^2 > 1$ ,  $\tan^{-1} \delta \approx \pi/2 - 1/\delta$  and

$$\tau \approx \frac{1}{k_3 p_{H_2}} \left\{ \frac{1}{\sqrt{4a - 1}} \left( \pi - 2 \tan^{-1} \left( \frac{1 - 2a}{\sqrt{4a - 1}} \right) - \left( \frac{2}{(2a(\theta_1 - 1) + 1)} \right) \right) \right\} \quad [14]$$

For  $2a(\theta_1 - 1) \gg 1$

$$\tau \approx \left\{ \frac{1}{k_3 p_{H_2} \sqrt{4a - 1}} \left[ \pi - 2 \tan^{-1} \left( \frac{1 - 2a}{\sqrt{4a - 1}} \right) \right] + \left( \frac{1}{k_2 p_{H_2} (1 - \theta_1)} \right) \right\} \quad [15]$$

It is seen from Eq. [15] that  $k_2$  can again be estimated from a plot of  $\tau$  vs.  $1/(1 - \theta_1)$  as depicted in Fig. 4.

### Conclusions

The present work has illustrated, for the three reaction schemes presented for PtO reduction by hydrogen, that the calculation procedure for estimating the reaction rate constants is the same. The final equations representing the total oxide reduction time as a function of initial surface coverage are identical for reaction scheme A and scheme A1; the analogous expres-

sion for reaction scheme A2 is similar in form to the other solutions.

Figure 5 depicts all of the  $\tau$  vs.  $\theta_1$  functions derived in the present note, along with the data reported by Shibata and Sumino. It is interesting to note that all of the proposed mechanisms for the coupled chemical-electrochemical reduction of transiently formed PtO provide reasonable agreement with Shibata and Sumino's experimental data. For reasons already discussed, it is unlikely that scheme A is a realistic representation of the chemical reduction of PtO at high surface coverage. The most reasonable mechanism for the purely chemical PtO reduction appears to be scheme A1, in which the rate-determining step is taken to be the chemical reaction of  $H_2$  with two PtO surface sites. The concept of an over-all rate-determining chemical reaction (i.e., scheme A2) does not seem likely, in view of the work reported earlier [cf., Ref. (5-11)] regarding the existence of PtOH as an intermediate in the surface oxidation of platinum.

Following the suggestion of Shibata and Sumino that the reduction by hydrogen of transiently formed PtO proceeds via a coupled chemical-electrochemical reaction mechanism, the present communication has extended the previous analysis theoretically, by accounting for molecular interaction, and procedurally, by providing an internally consistent means for estimating the kinetic rate constants of the coupled process. Assuming that reaction scheme A1 is operative at high surface coverages, and that the dissociation of  $H_2$  to form H on Pt applies at lower coverages, the present analysis provides good agreement with the experimental data reported by Shibata and Sumino over the entire range of  $\theta_1$ . In view of these encouraging results, despite the approximations involved in the estimation of the kinetic rate constants, a finer distinction of PtO and PtOH in normal and rearranged states as proposed (4, 9) during the reduction of surface oxides on platinum under potentiodynamic conditions was not made in this communication.

The work reported by Shibata and Sumino also involved application of the coupled chemical-electrochemical theory to the seemingly more complex case of steady-state formed oxides of platinum. However, the present analysis was not extended to this situation, in view of the physical complexities stated earlier.

### Acknowledgments

The authors wish to thank Professor B. E. Conway and Dr. H. Angerstein-Kozłowska for helpful discussions and useful suggestions during the course of this work. We also wish to thank Hooker Chemicals & Plastics Corporation for permission to publish this note.

Manuscript submitted May 24, 1976; revised manuscript received Aug. 5, 1976.

Any discussion of this paper will appear in a Discussion Section to be published in the June 1977 JOURNAL. All discussions for the June 1977 Discussion Section should be submitted by Feb. 1, 1977.

Publication costs of this article were assisted by Hooker Chemicals & Plastics Corporation.

### REFERENCES

1. S. Shibata and M. P. Sumino, *Electrochim. Acta*, **20**, 739 (1975).
2. M. W. Breiter, *This Journal*, **109**, 425 (1962).
3. E. Gileadi and B. E. Conway, in "Modern Aspects of Electrochemistry," Vol. 3, J. O'M. Bockris and B. E. Conway, Editors, Butterworths, Washington (1964).
4. B. V. Tilak, B. E. Conway, and H. Angerstein-Kozłowska, *J. Electroanal. Chem.*, **48**, 1 (1973).
5. F. G. Will and C. A. Knorr, *Z. Electrochem.*, **64**, 258 (1960).
6. M. Breiter, H. Kammermaier, and C. A. Knorr, *ibid.*, **60**, 37 and 119 (1956).
7. W. Böld and M. W. Breiter, *Electrochim. Acta*, **5**, 145 (1961).
8. P. Stonehart, H. Angerstein-Kozłowska, and B. E.

- Conway, *Proc. R. Soc. London, Ser. A*, **310**, 541 (1969).
9. H. Angerstein-Kozłowska, B. E. Conway, and W. B. A. Sharp, *J. Electroanal. Chem.*, **43**, 9 (1973).
10. D. Gilroy and B. E. Conway, *Can. J. Chem.*, **46**, 875 (1968).
11. K. J. Vetter, "Electrochemical Kinetics," pp. 549-554, Academic Press, New York (1967).



## Electrical Conduction in CaO-Doped Thoria Electrolytes

H. S. Maiti<sup>1</sup> and E. C. Subbarao

Department of Metallurgical Engineering, Indian Institute of Technology, Kanpur 208016, India

### ABSTRACT

The electrical conductivity of sintered specimens of nominally pure thoria and thoria doped with 1-15 mole percent (m/o) CaO was measured between 600° and 1400°C in the  $p_{O_2}$  range of  $1-10^{-25}$  atm. The measured conductivity decreases initially with decreasing  $p_{O_2}$  (mixed conduction region where electron holes and oxygen ions contribute), until it becomes independent of  $p_{O_2}$  (ionic conduction region). The  $p_{O_2}$  corresponding to the transition between these regions is a function of temperature and composition. The variation of conductivity with temperature gives rise to three regions: the high temperature region where the conductivity is attributed to dissociated vacancies, an intermediate temperature range where associated vacancy-impurity complexes dominate, and a low temperature region where grain boundary effects appear to become significant. The activation energy for electrical conduction is a function of composition and  $p_{O_2}$ .

Zirconia-based electrolytes are useful in high temperature galvanic cells, fuel cells, oxygen gauges, oxygen pumps, etc. Detailed investigations (1-4) on the defect structure and the electrolytic properties of "pure" and yttria-doped thoria electrolytes have demonstrated that these electrolytes behave as mixed conductors with a predominant electron hole conduction near 1 atm of oxygen pressure and become exclusively oxygen ion conductors in the lower partial pressure range, down to a much lower oxygen partial pressure than zirconia-base electrolytes.

When thoria is doped with CaO, it has been suggested that the electrical neutrality is maintained by the introduction of oxygen vacancies. The observed internal friction and dielectric loss peaks in  $ThO_2-1.5$  o/o CaO have been explained with a model where  $Ca^{2+}$  ions are associated with oxygen vacancies (5). Kiukola and Wagner (6) in their pioneering work on solid-state galvanic cell measurements did not use  $ThO_2-CaO$  electrolytes since they were found to be less conductive than either  $ZrO_2-CaO$  or  $ThO_2-Y_2O_3$  electrolytes. Based on their limited conductivity measurements, Steele and Alcock (7) also concluded that the conductivity of  $ThO_2-CaO$  electrolytes was lower than that of the corresponding  $ThO_2-Y_2O_3$  compositions and the hole contribution is higher at a given oxygen partial pressure in the mixed conduction region. On the other hand, a preliminary investigation on  $ThO_2-CaO$  solid solutions made earlier by the present investigators (8) showed that the conductivity values in air are not too low compared to those of  $ThO_2-YO_{1.5}$  solid solutions measured by Lasker and Rapp. A detailed measurement of electrical conductivity under various experimental conditions of temperature, oxygen partial pressure, and composition was, therefore, undertaken in order to ascertain the electrolytic behavior as well as the defect structure of CaO-doped  $ThO_2$  electrolytes.

<sup>1</sup> Present address: Materials Science Centre, Indian Institute of Technology, Kharagpur 721302, India.

Key words: electrical conduction, ionic conductivity, defect structure, thoria, doped thoria, solid electrolytes.

### Experimental Procedure

CaO-doped  $ThO_2$  specimens were prepared from reactor grade thorium oxide (impurities in excess of 10 ppm are Ca 2000, sulfate 120, Fe 90, phosphate 25, Cr 10) and analytical grade anhydrous calcium carbonate, as per procedures described earlier (8). The sintered pellets were about 10 mm in diameter and 2-3 mm thick and possessed more than 95% of the theoretical density except that "pure"  $ThO_2$  had only 89% of the theoretical density. For electrical measurements, the flat surfaces of the specimens were painted with unfluxed platinum paste (Engelhard No. 6926) and were heated to around 900°C. The a-c electrical conductivity at a frequency of 1000 Hz was measured over a temperature range of 600°-1400°C and oxygen partial pressure range of  $1-10^{-25}$  atm. The desired oxygen partial pressures were generated by using an electrochemical oxygen pump, similar to that of Kröger *et al.* (9-11) and Agrawal *et al.* (12) and is described elsewhere (13). The oxygen partial pressure of the gas was measured through a zirconia tube oxygen probe. It was difficult to control the  $p_{O_2}$  in the range of  $10^{-8}$ - $10^{-18}$  atm with the help of oxygen pump and therefore the ionic conductivity of a few of the samples was checked by using metal-metal oxide pellets. The temperature of the specimens was measured with a Pt-Pt 10% Rh thermocouple, the tip of which was placed within 2-3 mm of the specimens. The a-c conductance of the specimens was measured either with a two-probe bridge method (in lower temperature range) or by a four-lead *I-V* technique which has been described earlier (8). At each temperature and oxygen partial pressure, sufficient time was allowed for equilibration. Equilibrium was assumed to have been attained when two conductance readings at an interval of 1 hr remained unchanged.

### Results

The a-c total conductivity of "pure"  $ThO_2$  and  $ThO_2-CaO$  solid solutions with CaO contents ranging from 1 to 15 m/o was measured initially in air in the tempera-

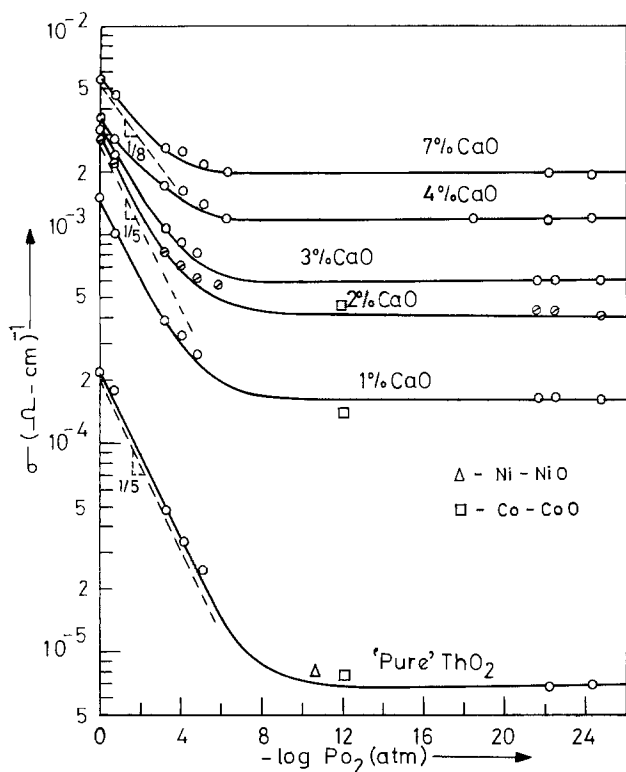


Fig. 1. Electrical conductivity of  $\text{ThO}_2$ -CaO solid solutions as a function of oxygen partial pressure at  $1000^\circ\text{C}$ .

ture range of  $600^\circ$ - $1400^\circ\text{C}$ . At each temperature, the conductivity increases sharply for small additions of CaO ( $< 2$  m/o CaO) and goes through a flat maximum around 10 m/o CaO. It should be mentioned here that the conductivity values reported earlier [Ref. (8)] for 8 m/o specimen were later found to be for 4 m/o specimen. Samples containing more than 7 m/o CaO were excluded from the rest of the present measurements because the effect of dopant on conductivity in this range is rather insignificant and also due to possible existence of a second phase. The conductivities of "pure" and CaO-doped thoria specimens were also measured in the  $p_{\text{O}_2}$  range of  $1$ - $10^{-25}$  atm and at temperatures between  $600^\circ$  and  $1200^\circ\text{C}$ . Figure 1 shows the typical plots of conductivity vs.  $\log p_{\text{O}_2}$  for "pure" and CaO-doped  $\text{ThO}_2$  specimens at  $1000^\circ\text{C}$ . There are clearly two regions: (i) the conductivity decreases with decreasing  $p_{\text{O}_2}$  with a slope of  $1/5$  for "pure" and slightly doped samples, the slope decreasing to  $1/8$  for more impure ones and (ii) the conductivity is independent of  $p_{\text{O}_2}$  at low values of  $p_{\text{O}_2}$ . The  $p_{\text{O}_2}$  value corresponding to the onset of region (ii) is a function of impurity content and temperature. For example, for "pure"  $\text{ThO}_2$  the plateau is reached at  $10^{-8}$  atm at  $800^\circ\text{C}$  and the value decreases to  $10^{-10}$  atm at  $1200^\circ\text{C}$ , while in a 7 m/o CaO specimen the corresponding values are  $10^{-7}$  and  $10^{-5}$  atm, respectively. The conductivity value at any  $p_{\text{O}_2}$  increases steadily with temperature as well as with impurity content.

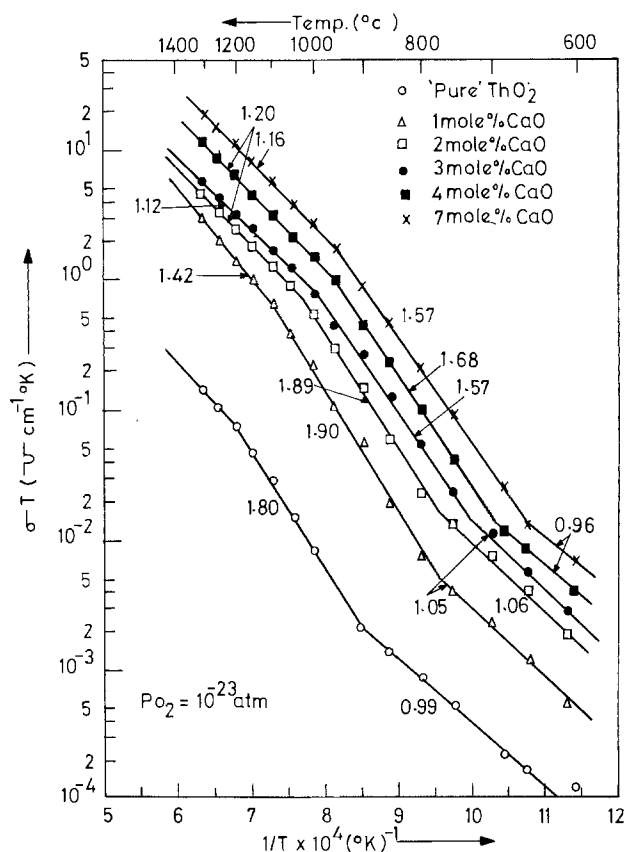


Fig. 2. Electrical conductivity of  $\text{ThO}_2$ -CaO solid solutions as a function of temperature at an oxygen partial pressure of  $10^{-23}$  atm.

The conductivity of "pure" and CaO-doped thoria specimens has been measured as a function of temperature between  $600^\circ$  and  $1400^\circ\text{C}$  under fixed oxygen partial pressures of  $10^{-23}$ ,  $10^{-5}$ ,  $10^{-0.7}$  (air), and  $10^0$  atm (oxygen). Typical results at  $p_{\text{O}_2} = 10^{-23}$  atm and in oxygen atmosphere are shown in Fig. 2 and 3, respectively. In the plots of  $\log \sigma T$  vs.  $1/T$ , straight lines with different slopes are obtained in the different temperature regions. In each region, the activation energy was calculated from the slope of the straight line which has been fitted to the experimental points by a least squares method. Table I gives the complete list of observed activation energies under different experimental conditions.

At a very low oxygen partial pressure ( $10^{-23}$  atm) where all the specimens may be considered as exclusive ionic conductors, three distinctly different temperature ranges having different activation energies are evident (Fig. 2). The activation energy is highest in the intermediate temperature range while it is lower both in the low and high temperature regions. The activation energy in the low temperature range is of the order of 1.0 eV and does not change significantly with the CaO content. However, in the intermediate temperature range, the activation energies for highly doped

Table I. Activation energy for conduction in  $\text{ThO}_2$ -CaO under various experimental conditions

Comp.	$p_{\text{O}_2}$	Low temperature			Intermediate temperature				High temperature				
		$10^0$	$10^{-0.7}$	$10^{-5}$	$10^{-23}$	$10^0$	$10^{-0.7}$	$10^{-5}$	$10^{-23}$	$10^0$	$10^{-0.7}$	$10^{-5}$	$10^{-23}$
"Pure" $\text{ThO}_2$		1.52	1.50	1.00	0.99	1.34	1.30 (1.32)*	1.40	1.80	0.98	0.97 (0.955)**	1.40	1.28
1 m/o CaO		1.58	1.65	1.52	1.05	1.30	1.38 (1.31)*	1.52	1.91	1.13	1.20 (1.26)**	1.36	1.42
2 m/o CaO		1.51	1.20	1.35	1.06	1.24	1.20 (1.18)*	1.39	1.89	1.13	1.03 (1.08)**	1.13	1.20
3 m/o CaO		1.18	1.23	1.39	1.06	1.18	1.23 (1.21)*	1.39	1.57	1.13	1.03 (1.06)**	1.10	1.12
4 m/o CaO		1.18	1.23	1.37	0.96	1.18	1.23 (1.17)*	1.37	1.68	0.92	1.09 (1.06)**	1.10	1.20
7 m/o CaO		1.20	1.20	1.37	0.96	1.20	1.20 (1.19)*	1.37	1.57	0.92	1.13 (1.09)**	1.07	1.16

\* Data from Ref. (8) at temperatures below  $1100^\circ\text{C}$  in air.

\*\* Data from Ref. (8) at temperatures above  $1100^\circ\text{C}$  in air.

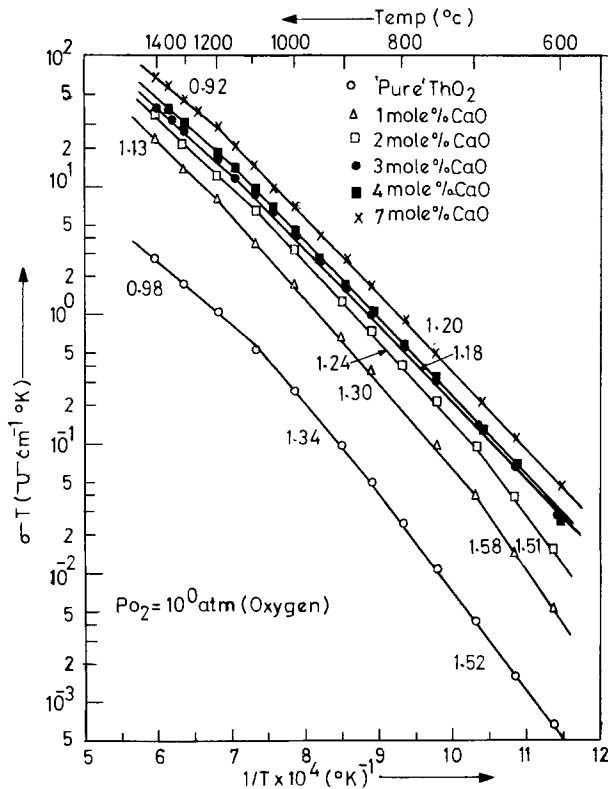


Fig. 3. Electrical conductivity of ThO<sub>2</sub>-CaO solid solutions as a function of temperature in oxygen atmosphere.

specimens (3-7 m/o CaO) are lower (~ 1.60 eV) than that of "pure" ThO<sub>2</sub> (1.80 eV) as well as those with lower dopant concentration (1-2 m/o CaO). The activation energy in the high temperature region varies between 1.12 and 1.42 eV but does not follow any definite trend with the variation of CaO.

The transition temperatures corresponding to the breaks in the conductivity curve (Fig. 2) in the low-intermediate-high temperature ranges decreases with increasing CaO content. For example, in "pure" ThO<sub>2</sub> the breaks occur at 900° and 1200°C whereas in a specimen containing 7 m/o CaO the corresponding temperatures are 650° and 950°C.

It may be noted that the activation energy in the different temperature ranges varies in different ways with oxygen partial pressure and, therefore, the overall shape of the log  $\sigma_T$  vs.  $1/T$  plots also changes with oxygen partial pressure. The activation energy increases with decreasing  $p_{O_2}$  in the intermediate temperature range whereas it decreases markedly with decreasing  $p_{O_2}$  in the low temperature range. As a consequence, at low oxygen partial pressures (Fig. 2), the low temperature activation energy is lower than that in the intermediate temperature range but with increasing oxygen partial pressure (Fig. 3), the trend is reversed especially in specimens having a lower percentage of CaO. The high temperature activation energy, on the other hand, is always lower than that in the intermediate temperature range.

**Discussion**

*Defect structure.*—In a ThO<sub>2</sub>-CaO solid solution, substitution of Th<sup>4+</sup> ions by Ca<sup>2+</sup> ions results in an overall charge of -2 per each impurity cation site (Ca<sub>Th</sub>'') and therefore the neutrality condition may be written using Kröger-Vink type notations as

$$[h\cdot] + 2[V_{O\cdot\cdot}] = [e'] + 2[O_i''] + 2[Ca_{Th}''] \quad [1]$$

Even with a small amount of impurities, the concentration of oxygen vacancies in a CaO-doped ThO<sub>2</sub> lattice will far exceed that of oxygen interstitials i.e.

$$[V_{O\cdot\cdot}] \gg [O_i'']$$

and therefore the defect concentration will be chiefly determined by the concentration of the impurity ions. In the intermediate  $p_{O_2}$  range where ionic defect compensation takes place

$$[V_{O\cdot\cdot}] = [Ca_{Th}''] = [CaO] \quad [2]$$

and

$$[h\cdot] = \left\{ \frac{K_2[CaO]}{K_1} \right\}^{1/2} p_{O_2}^{1/4} \quad [3]$$

where  $K_1$  and  $K_2$  are the equilibrium constants for the anti-Frenkel and oxygen interstitial defect formation reactions, respectively.

It may be noted that in the mixed conduction region the hole concentration in a doped oxide is proportional to  $p_{O_2}^{1/4}$ . Therefore, it is expected that a plot of log  $\sigma_h$  vs. log  $p_{O_2}$  will yield a slope of  $1/4$ . This becomes evident when one plots log  $(\sigma_T - \sigma_{ion})$  vs. log  $p_{O_2}$  (Fig. 4), assuming  $\sigma_{ion}$  to be independent of  $p_{O_2}$  even in the mixed conduction region and the value equals that obtained at lower partial pressures (1). However, in Fig. 1 the plots of  $\sigma_T$  vs. log  $p_{O_2}$  indicate lower slopes (1/5 to 1/8) since the oxygen partial pressures in this range are very much within the transition zone between  $p_{O_2}$  independent ionic conduction and characteristic mixed conduction regions. In this connection, Bransky and Tallan (2) have earlier pointed out that the predicted  $1/4$  pressure dependence in the impurity-controlled mixed conduction region may not be observed in plots of log  $\sigma_T$  vs. log  $p_{O_2}$  unless  $\sigma_T/\sigma_{ion} \geq 10$ .

*Transference number.*—The ionic transference number of ThO<sub>2</sub>-CaO electrolytes in the mixed conduction region may be expressed as

$$t_{ion} = \frac{1}{1 + 1/2\beta_h(K_2/K_1)^{1/2}p_{O_2}^{1/4}[CaO]^{-1/2}} \quad [4]$$

in which  $\beta_h$  is the ratio of mobilities of electron hole ( $\mu_h$ ) and that of oxygen vacancy ( $\mu_v$ ). Ionic transference numbers for "pure" and doped specimens have been calculated from the conductivity isotherms (Fig. 1) at different oxygen partial pressures following the procedure adopted by Lasker and Rapp (1) in which it is assumed that the ionic contribution remains constant in the mixed conduction region and is given by the pressure independent conductivity value in the lower partial pressure range. The results of the calculation are shown in Fig. 5 for two different temperatures (800° and 1000°C). As predicted from the con-

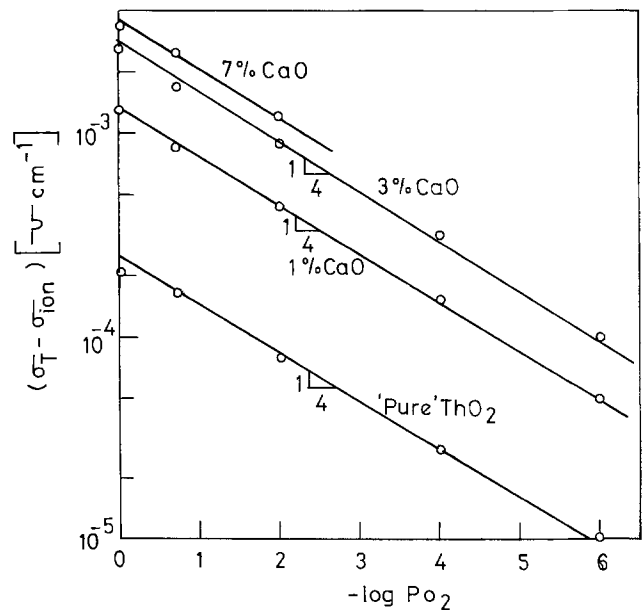


Fig. 4. Plots of  $(\sigma_T - \sigma_{ion})$  vs. log  $p_{O_2}$  for ThO<sub>2</sub>-CaO electrolytes at 1000°C.

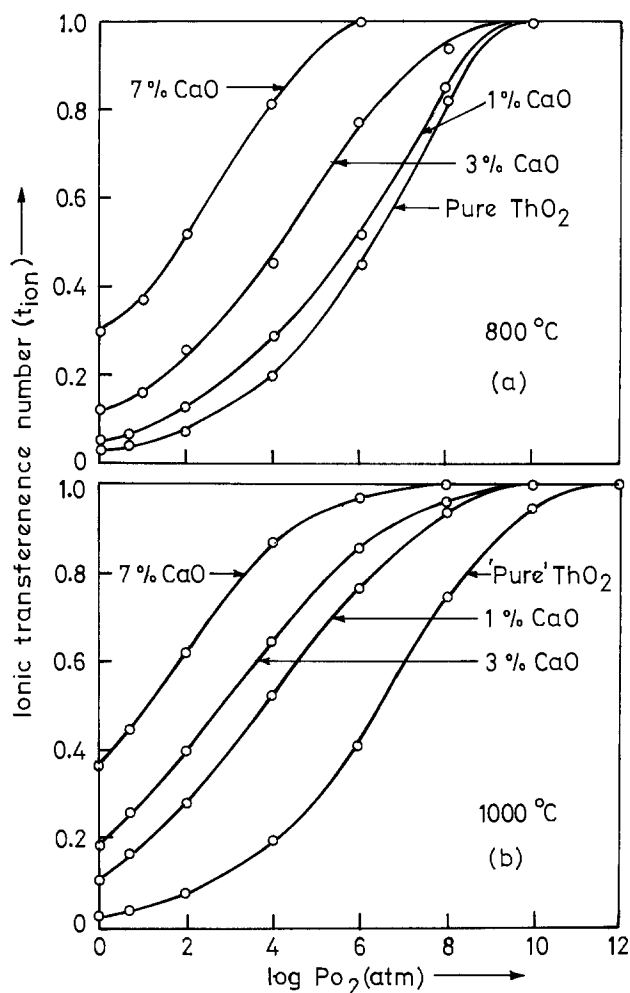


Fig. 5. Ionic transference numbers of ThO<sub>2</sub>-CaO solid solutions as a function of oxygen partial pressure at 800°C (a) and 1000°C (b).

ductivity curves, the value of  $t_{ion}$  increases with decreasing  $p_{O_2}$  and it becomes unity when the conductivity becomes independent of  $p_{O_2}$ .

As expected from Eq. [4], addition of CaO increases the ionic transference number at each  $p_{O_2}$  and therefore improves the electrolytic behavior of the solid solution. By addition of 7 m/o CaO, the conductivity of the solid solution becomes fully ionic below about  $10^{-6}$ - $10^{-8}$  atm, depending on temperature, and may be considered as a useful solid electrolyte below this partial pressure range. It may be pointed out that yttria-doped thoria electrolytes are also useful in the same partial pressure range.

**Ionic conductivity.**—Assuming that the mobility is independent of the defect concentration, the ionic conductivity of ThO<sub>2</sub>-CaO solid solution is expressed as

$$\begin{aligned}\sigma_{ion} &= 2 |e| \mu_v [VO^{\cdot\cdot}] \\ &= 2 |e| \mu_v [CaO]\end{aligned}\quad [5]$$

which shows that  $\sigma_{ion}$  is proportional to [CaO]. In Fig. 6, log ionic conductivity of ThO<sub>2</sub>-CaO electrolytes has been plotted vs. percent anion vacancy as well as mole percent impurity concentration, along with that of ThO<sub>2</sub>-YO<sub>1.5</sub> electrolytes obtained by different investigators (1, 3, 7). As expected the conductivity increases with increasing CaO content. The ionic conductivity of pure thoria obtained in the present investigation is lower than that obtained by the earlier investigators. A lower conductivity may be expected in a purer sample, but it is not the case in the present study. The variation is, however, within the scatter in conductivity values measured by various investigators. On the other hand,

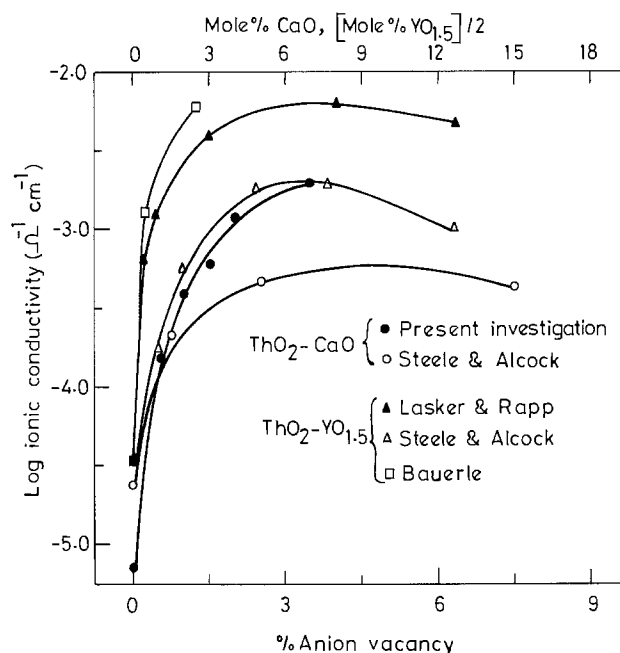


Fig. 6. Ionic conductivity of ThO<sub>2</sub>-base electrolytes as a function of mole percent anion vacancy at 1000°C.

the conductivities of the ThO<sub>2</sub>-CaO solid solutions are higher than the corresponding values obtained by Steele and Alcock (7) and are very close to those of ThO<sub>2</sub>-YO<sub>1.5</sub> electrolytes measured by the same investigators. However, the conductivity values of ThO<sub>2</sub>-YO<sub>1.5</sub> electrolytes measured by Bauerle (3) are much higher than those measured by either Lasker and Rapp (1) or Steele and Alcock (7). In the present investigation, the ionic conductivities were not determined beyond 7 m/o CaO content. However, from the conductivity values obtained in air, it is expected that a slightly higher ionic conductivity may be obtained at around 10 m/o CaO. At higher concentrations the lowering of conductivity in both the systems may be attributed to the decreased mobility of the defects mainly due to impurity defect interactions.

**Activation energy in the low temperature region.**—

It has been observed in the present investigation that the activation energy for ionic conduction in both "pure" and CaO-doped thoria specimens decreases in the low temperature region relative to that in the intermediate temperature region (Fig. 2 and Table I). A plausible explanation for this may be advanced on the basis of the effect of grain boundaries at low temperatures. However, this explanation needs verification by varying grain size systematically.

In a polycrystalline material, grain boundaries are crystallographically disordered regions. Further, the grain boundaries contain a larger concentration of solute atoms (15), giving rise to a higher defect concentration. These factors lead to enhanced diffusion and ionic conductivity in the grain boundaries relative to the bulk. Enhanced oxygen diffusion along grain boundaries or dislocations has been observed in a number of oxide systems such as Al<sub>2</sub>O<sub>3</sub> (16), MgO (17, 18), Fe<sub>2</sub>O<sub>3</sub> (19), CoO (20), SrTiO<sub>3</sub> (21), etc. The activation energy for diffusion through the grain boundaries is lower compared to that for bulk diffusion. However, since the volume of the grain boundary region is much smaller than the bulk volume, the grain boundary contribution becomes significant only at lower temperatures where the bulk diffusion is not large. Similarly, higher electrical conductivity along the grain boundaries has been observed in ionic conductors like alkali halides (22) and CaO-stabilized zirconia specimens (23). The observed activation energy for grain boundary conduction of  $1.0 \pm 0.05$  eV in the present investi-



gation is very close to that of 0.96 eV obtained in calcia-stabilized zirconia specimens (23). It may be noticed in Fig. 2 that the effect of grain boundaries becomes observable at lower temperatures as the CaO content of the specimen is increased. The addition of CaO increases the defect concentration (and consequently the ionic conductivity) of the bulk more sharply than that of the grain boundaries which are already grossly defective and disordered to start with. Therefore, the transition from the low temperature region where the grain boundary effects are predominant to the intermediate temperature range where the bulk diffusion is more important should occur at lower temperatures as the CaO content increases, which in fact was observed (Fig. 2).

While the activation energy for ionic conduction is less in the low temperature range due to the effect of grain boundaries, it is not so at higher oxygen pressures where the samples are predominantly electron hole conductors. Between  $p_{O_2} = 1$  and  $10^{-5}$  atm, samples with lower dopant concentration show larger activation energies at low temperatures compared to those in the intermediate temperature range. The difference in activation energies becomes distinct when  $\log \sigma_h$  instead of  $\log \sigma_T$  is plotted against  $1/T$  (Fig. 7). A similar behavior has been observed in pure  $ZrO_2$  by Kumar *et al.* (24) who plotted electronic conductivity against  $1/T$  and obtained an activation energy of 3.74 eV below 700°C compared to 1.33 eV above this temperature. The reason for such a break is not very clear. However a possible explanation may be that the activation energy for movement of electrons or electron holes through the grain boundaries is expected to be higher than that through the bulk because the grain boundaries can act as effective scattering centers for the free electrons, due to their highly disordered nature. The effect of grain boundaries is predominant at low temperatures and, therefore, it increases the activation energy for conduction in this temperature

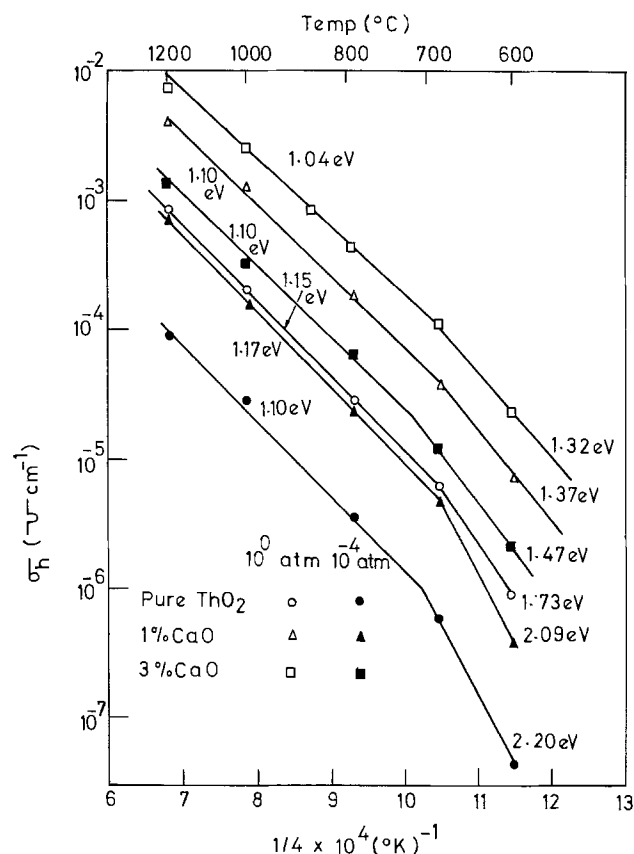


Fig. 7. Plots of electron hole conductivity vs. inverse of temperature for  $ThO_2$ -CaO electrolytes.

range. On the other hand, no difference in the activation energy could be detected between the intermediate and low temperature regions in case of samples having higher percentages of CaO (Table I). This may be due to the higher total conductivity and the larger ionic transference number for these samples. The activation energy for hole conduction above 700°C is found to be of the order of 1.10 eV and is nearly independent of either  $p_{O_2}$  or composition compared to a value of 0.85 eV measured by Hammou and Deportes (4) in "pure"  $ThO_2$ .

*Activation energy in the high and intermediate temperature regions.*—The activation energy in the high temperature region is observed to be lower than that in the intermediate temperature range for each of the oxygen partial pressures and compositions studied (Fig. 2 and 3 and Table I). [Data from Ref. (8) is also included in Table I and is seen to compare well.] The change in activation energy is comparatively more distinct at the lowest  $p_{O_2}$  value where the samples may be considered as exclusive ionic conductors. Earlier studies on "pure"  $ThO_2$  (2), pure  $HfO_2$  (25), and yttria-doped thoria (26) showed similar behavior at high oxygen partial pressures. However, Ullmann (27) has observed a higher activation energy at temperatures greater than 1100°C than that at lower temperatures for  $ThO_2$  and CaO- $ThO_2$  samples measured in air. Further, Bransky and Tallan (2) have observed that at low  $p_{O_2}$  (ionic conduction region) the activation energy in the high temperature range is higher than that at intermediate temperatures.

The activation energy for ionic conduction in "pure"  $ThO_2$  obtained in the intermediate temperature range in the present study (1.80 eV) compares well with the most recent data of Choudhury and Patterson (28), *viz.*, 1.93 and 1.81 eV for two different samples for  $ThO_2$ . However, these values are considerably higher than the activation energy of about 1.5 eV of Bransky and Tallan (2). While it is tempting to associate the higher activation energies with the intrinsic behavior and higher purity of the samples, it is not considered a plausible explanation, at least in the case of the present samples. Alternately, the larger activation energy may include migration energy and dissociation energy for defect complexes. The latter explanation appears more appropriate for  $ThO_2$  samples of the present study, since the activation energy for ionic conduction in the high temperature range is lower (1.28 eV) compared to that in the intermediate temperature range. This value is in reasonable agreement with the 1.17 eV obtained by Bransky and Tallan (2) in the same temperature region.

In the  $ThO_2$ -CaO specimens, the activation energies in air for different compositions are 0.97-1.20 eV at high temperatures and 1.20-1.38 eV in the intermediate temperature range (Table I). For the same system the activation energy values of 1.1 and 0.9 eV were obtained in air by Valchenkova and Palguez (29) and Ullmann (27), respectively. The results of the present investigation are thus in reasonable agreement with the published results in air atmosphere. No earlier results, however, are available at lower partial pressures to compare with the present data on these solid solutions.

The activation energies observed for the  $ThO_2$ -CaO compositions may also be compared with those reported in the  $ThO_2$ - $YO_{1.5}$  system for which the observed activation energies are 1.12-1.38 (30) in air, 1.2 (1), 1.09 (7), and 0.85-1.1 eV (26) for ionic transport. These values are close to those observed on CaO-doped  $ThO_2$  specimens measured in air over a wide temperature range, but are lower than the values observed in the ionic conduction region at intermediate temperatures.

The high values of activation energy in the intermediate temperature region compared to those at high temperatures may be explained if one considers that

the oxygen vacancies are associated with the impurity cations in this temperature range. The formation of such defect complexes is favored in a  $\text{ThO}_2$ -CaO lattice due to a favorable charge distribution between the oxygen vacancies and the  $\text{Ca}^{2+}$  ions. Dielectric and mechanical relaxation experiments have earlier indicated the presence of such defect complexes in CaO-doped  $\text{ThO}_2$  specimens (5). The high value of activation energy (1.80 eV) in the intermediate temperature range in pure thoria of the present investigation compared to that of other investigators (1, 2) may be attributed to the presence of a significant quantity ( $< 2000$  ppm) of Ca in the starting material compared to total impurity content of  $< 90$  ppm in their samples.

It may also be noticed in Table I that the activation energy for ionic conduction (i.e., at  $p_{\text{O}_2} = 10^{-23}$  atm) remains high and nearly constant (1.80-1.90 eV) in the intermediate temperature region up to 2 m/o CaO and decreases thereafter (Fig. 2). These results may be interpreted as follows: The introduction of increasing amounts of CaO in  $\text{ThO}_2$  lattice tends to increase the concentration of defect complexes referred to above which in turn leads to an increase in activation energy for defect migration. However, at higher CaO contents the lattice becomes more open with a larger number of vacancies and consequently the activation energy for conduction is reduced.

By increasing oxygen partial pressure, the contribution from the hole conductivity is increased and therefore the observed activation energy is less representative of the motion of defect complexes.

In the high temperature region, the activation energies are much closer to those observed earlier in pure  $\text{ThO}_2$  and  $\text{ThO}_2$ - $\text{YO}_{1.5}$  solid solutions and it may be expected that the defects are in the dissociated state at these high temperatures. The difference between the activation energies in the high and intermediate temperature ranges, in that case, gives the binding energy for the defect complex and is found to vary between 0.4 and 0.7 eV for different CaO-doped  $\text{ThO}_2$  specimens. The dissociation energy of the vacancy defect has been observed to be 0.22 eV in the internal friction and dielectric loss measurements (5), compared to a calculated value of 0.71 eV. The present values are closer to the theoretical value. Possible existence of impurity cation-oxygen vacancy interaction in "pure"  $\text{ThO}_2$  has also been pointed out by Hammou and Deportes (4). These values may be compared with those of 0.3-0.4 eV (31) obtained for alkali halides with divalent impurities. For oxide systems, a higher binding energy is expected due to the higher charges associated with the defects.

### Conclusions

Like all other  $\text{ThO}_2$ -base electrolytes,  $\text{ThO}_2$ -CaO solid solutions are predominantly electron hole conductors in the high oxygen partial pressure range and become fully ionic below  $10^{-6}$ - $10^{-10}$  atm, the exact value being dependent upon the composition and temperature. The ionic conductivities of these solid solutions are quite comparable to those of  $\text{ThO}_2$ - $\text{Y}_2\text{O}_3$  electrolytes and may be considered useful in the same  $p_{\text{O}_2}$  range as that of the latter. Both ionic conductivity and the transference number increase with increasing CaO content at least up to 10 m/o of CaO.

The variation of conductivity with reciprocal temperature led to three temperature regions with different activation energies. The activation energy for ionic conduction in the low temperature range is lower while that of hole conduction is higher than that in the intermediate temperature range and appears to be the effect of grain boundaries. The activation energy for ionic conduction is higher than that for hole con-

duction and is a function of composition. A defect complex formation appears to be operative in the intermediate temperature range while the conductivity at the highest temperatures represents the behavior due to dissociated defects.

### Acknowledgments

This paper is based on a thesis submitted by H. S. Maiti in partial fulfillment of the requirements of the Ph.D. degree at the Indian Institute of Technology, Kanpur, India, in 1975. The financial support, in part, of the Aerospace Research Laboratories under contract AFOSR 71-2136 is gratefully acknowledged. The authors are thankful to C. B. Choudhary for helpful discussions.

Manuscript submitted Feb. 3, 1976; revised manuscript received June 17, 1976. This was Paper 47 presented at the Toronto, Canada, Meeting of the Society, May 11-16, 1975.

Any discussion of this paper will appear in a Discussion Section to be published in the June 1977 JOURNAL. All discussions for the June 1977 Discussion Section should be submitted by Feb. 1, 1977.

### REFERENCES

1. M. F. Lasker and R. A. Rapp, *Z. Phys. Chem. (N.F.)*, **49**, 198 (1966).
2. I. Bransky and N. M. Tallan, *J. Am. Ceram. Soc.*, **53**, 625 (1970).
3. J. E. Bauerle, *J. Chem. Phys.*, **45**, 4162 (1966).
4. A. Hammou and C. Deportes, *J. Chim. Phys.*, **71**, 1071 (1974).
5. J. B. Wachtman, Jr., *Phys. Rev.*, **131**, 517 (1963).
6. K. Kiukola and C. Wagner, *This Journal*, **104**, 379 (1957).
7. B. C. H. Steele and C. B. Alcock, *Trans. Met. Soc. AIME*, **233**, 1359 (1965).
8. A. K. Mehrotra, H. S. Maiti, and E. C. Subbarao, *Mater. Res. Bull.*, **8**, 899 (1973).
9. D. Yuan and F. A. Kröger, *This Journal*, **116**, 594 (1969).
10. H. Yanagida, R. J. Brook, and F. A. Kröger, *ibid.*, **117**, 593 (1970).
11. R. J. Brook, W. L. Pelzmann, and F. A. Kröger, *ibid.*, **118**, 185 (1971).
12. Y. K. Agrawal, D. W. Short, R. Guenke, and R. A. Rapp, *ibid.*, **121**, 357 (1974).
13. C. B. Choudhary, H. S. Maiti, and E. C. Subbarao, To be published.
14. F. A. Kröger and H. J. Vink, in "Solid State Physics," Vol. 3, F. Seitz and D. Turnbull, Editors, p. 307, Academic Press, New York (1956).
15. W. D. Kingery, *J. Am. Ceram. Soc.*, **57**, 74 (1974).
16. Y. Oishi and W. D. Kingery, *J. Chem. Phys.*, **33**, 480 (1960).
17. Y. Oishi and W. D. Kingery, *ibid.*, **33**, 905 (1960).
18. H. Hashimoto and M. Hama, *J. Appl. Phys.*, **43**, 4828 (1972).
19. W. D. Kingery, D. C. Hill, and R. P. Nelson, *J. Am. Ceram. Soc.*, **43**, 473 (1960).
20. J. B. Holt, *Proc. Br. Ceram. Soc.*, **9**, 157 (1967).
21. A. E. Paladino, L. G. Rubin, and J. S. Waugh, *J. Phys. Chem. Solids*, **26**, 391 (1965).
22. J. F. Lauront and J. Banard, *ibid.*, **7**, 218 (1958).
23. T. Y. Tien, *J. Appl. Phys.*, **35**, 122 (1964).
24. A. Kumar, D. Rajdev, and D. L. Douglass, *J. Am. Ceram. Soc.*, **55**, 439 (1972).
25. N. M. Tallan, W. C. Tripp, and R. W. Vest, *ibid.*, **50**, 279 (1967).
26. J. M. Wimmer, L. R. Bidwell, and N. M. Tallan, *ibid.*, **50**, 198 (1967).
27. H. Ullmann, *Z. Chem.*, **9**, 39 (1969).
28. N. S. Choudhury and J. W. Patterson, *J. Am. Ceram. Soc.*, **57**, 90 (1974).
29. Z. S. Valchenkova and S. P. Palguyev, *Trans. Inst. Electrochem.*, **1**, 104 (1961).
30. E. C. Subbarao, P. H. Sutter, and J. Hrizo, *J. Am. Ceram. Soc.*, **48**, 443 (1965).
31. A. J. Dekker, "Solid State Physics," p. 175, Prentice-Hall, Englewood Cliffs, N. J. (1957).

# The Crystallographic Site of Cosputtered Eu in RF-Sputtered SnO<sub>2</sub> Films

Takao Tohda, Kiyotaka Wasa, and Shigeru Hayakawa

Matsushita Electric Industrial Company, Limited, Materials Research Laboratories, Kadoma, Osaka, 571 Japan

## ABSTRACT

Polycrystalline SnO<sub>2</sub> films doped with various amounts of Eu were prepared on glass substrates by a cosputtering process in an rf-sputtering system. The site of the cosputtered Eu in the SnO<sub>2</sub> films was investigated by cathodoluminescence studies. It has been found that the films with a 1 atomic percent (a/o) Eu concentration show sharp emission lines due to a magnetic dipole transition  ${}^5D_0-{}^7F_1$ , while the films with a 14 a/o Eu concentration show strong emission lines due to an electric dipole transition  ${}^5D_0-{}^7F_2$ . In the former the films have a good crystallinity and the cosputtered Eu has been substituted for Sn in the SnO<sub>2</sub> crystal matrix, while in the latter the cosputtered Eu inhibits the SnO<sub>2</sub> crystal grain growth and is possibly incorporated into regions with large disorder near the grain boundaries.

A cosputtering process using a multicomponent target or multitargets is available for controlling the structural and electrical properties of resultant sputtered films. In an earlier paper (1) dealing with the influence of cosputtered Al and Cu on the structural and electrical properties of sputtered ZnO films, it has been shown that, as one would expect, the addition of Al lowers the resistivity of the ZnO films, whereas the addition of Cu increases it. Furthermore, the addition of Al inhibits the growth of the c-axis orientation, whereas Cu favors it. Very few studies of the location of cosputtered minor constituents in the host crystal films have been reported. Recently we have made Eu-doped SnO<sub>2</sub> films on glass substrates by cosputtering Eu with SnO<sub>2</sub> in an rf-sputtering system. In SnO<sub>2</sub> single crystals, Crabtree (2) suggested that Eu could be doped as much as 8 mole percent (m/o) by heating the crystals with EuCl<sub>3</sub>. This paper describes a cathodoluminescence study of the cosputtered Eu in the SnO<sub>2</sub> films.

## Experimental

A planar electrode rf-sputtering system with an ultrahigh-vacuum diffusion pump was used for the cosputtering process. The background pressure before sputtering was  $2 \times 10^{-5}$  Torr. Electrode construction is shown in Fig. 1. The distances from the target to the anode and substrates were 13 and 18 mm, respectively. The anode was perforated and the substrates were placed behind it. Cosputtering of Eu with SnO<sub>2</sub> was achieved by using sintered SnO<sub>2</sub> disk targets with various amounts of Eu. The diameter and thickness of the targets were 20 and 3 mm, respectively. They were prepared by pressing 99.9% pure SnO<sub>2</sub> powder mixed with 99.9% pure Eu<sub>2</sub>O<sub>3</sub> powder at 1000 kg/cm<sup>2</sup> and successively firing at 1000°C for 5 hr in air. The concentration of Eu was varied from 1 to 14 a/o. Corning 7059 glass plates were used as the substrates, since their thermal expansion coefficient was close to that of SnO<sub>2</sub>. The substrates were cleaned in boiling trichloroethylene.

The sputtering was carried out at  $2 \times 10^{-2}$  Torr of Ar and O<sub>2</sub> with an oxygen concentration of 50%. The cathode current density and potential were 2 mA/cm<sup>2</sup> and -1100V, respectively. The substrate temperature was 70°C. Before the deposition of SnO<sub>2</sub>, presputtering was done for 30 min. Films of 1 ~ 2 μm thickness were deposited on the substrates in 1 hr. These sputtered films were annealed at 500°C for 1 hr in air.

The cathodoluminescent properties of the SnO<sub>2</sub> films were examined by bombarding them with 2 keV electrons at a current density of 50 μA/cm<sup>2</sup>. The emitted

Key words: cathodoluminescence, thin films, rf sputtering.

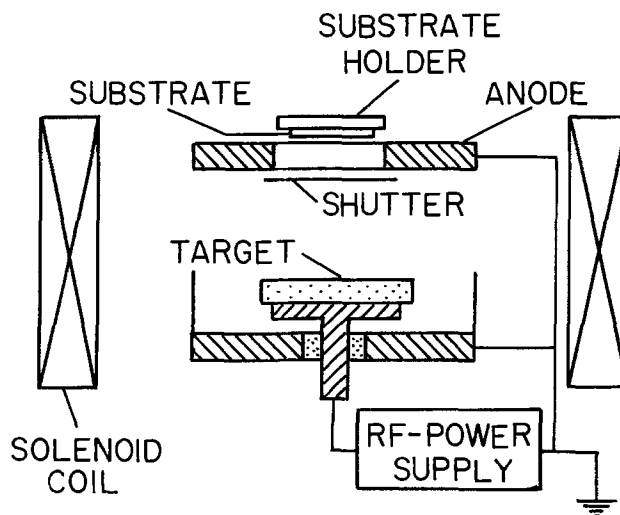


Fig. 1. Electrode construction of an rf-sputtering system

light was focused on the entrance slit of an Ebert grating monochromator (Nippon Jarrell-Ash) and detected by a photomultiplier (HTV, R446). The resolution of the monochromator during these experiments was 5 Å.

## Results and Discussion

Figure 2 shows the emission spectrum obtained from the SnO<sub>2</sub> target with an Eu concentration of 5 a/o. The spectrum is quite similar to that of the single crystal SnO<sub>2</sub> doped with Eu (2); a strong magnetic dipole emission  ${}^5D_0-{}^7F_1$  and weak electric dipole emissions

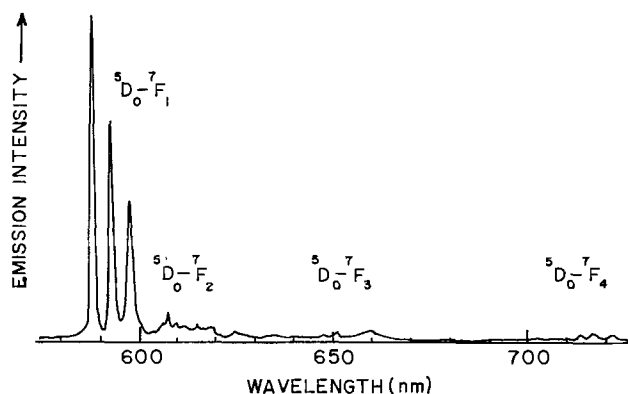


Fig. 2. Emission spectrum from SnO<sub>2</sub>:Eu (5 a/o) target

${}^5D_0-{}^7F_{2,3,4}$  suggest that most of the  $\text{Eu}^{3+}$  ions are incorporated into the Sn site of the  $\text{SnO}_2$  crystal matrix. Similar emission spectra were also observed from the targets with Eu concentrations of 1 and 14 a/o. The annealed  $\text{SnO}_2$  films exhibited, however, different emission spectra. They vary with the amount of Eu, as shown in Fig. 3. Spectrum (a) was measured from 1 a/o Eu-doped films. The spectrum is similar to that of the single crystal  $\text{SnO}_2$ . This indicates that the crystal field around the  $\text{Eu}^{3+}$  ions in the films is similar to that in the single crystal. Spectrum (b) was measured from 5 a/o Eu-doped films. A broad electric dipole emission  ${}^5D_0-{}^7F_2$  is superposed on the magnetic dipole emission  ${}^5D_0-{}^7F_1$ . This indicates that some of the  $\text{Eu}^{3+}$  ions stay at the center of symmetry of the  $\text{SnO}_2$  crystal, while the rest stays at a site with no inversion symmetry (3). In 14 a/o Eu-doped films, the electric dipole emission is strongly enhanced and the magnetic dipole emission is reduced, as seen in spectrum (c). This indicates that most of the  $\text{Eu}^{3+}$  ions stay at sites with no inversion symmetry. The crystal field around the  $\text{Eu}^{3+}$  ions which emanate the electric dipole emission varies from ion to ion, since the spectrum shows broad emission bands.

X-ray diffraction measurements showed that the films crystallized to a rutilelike polycrystalline structure with the (110) plane parallel to the substrate

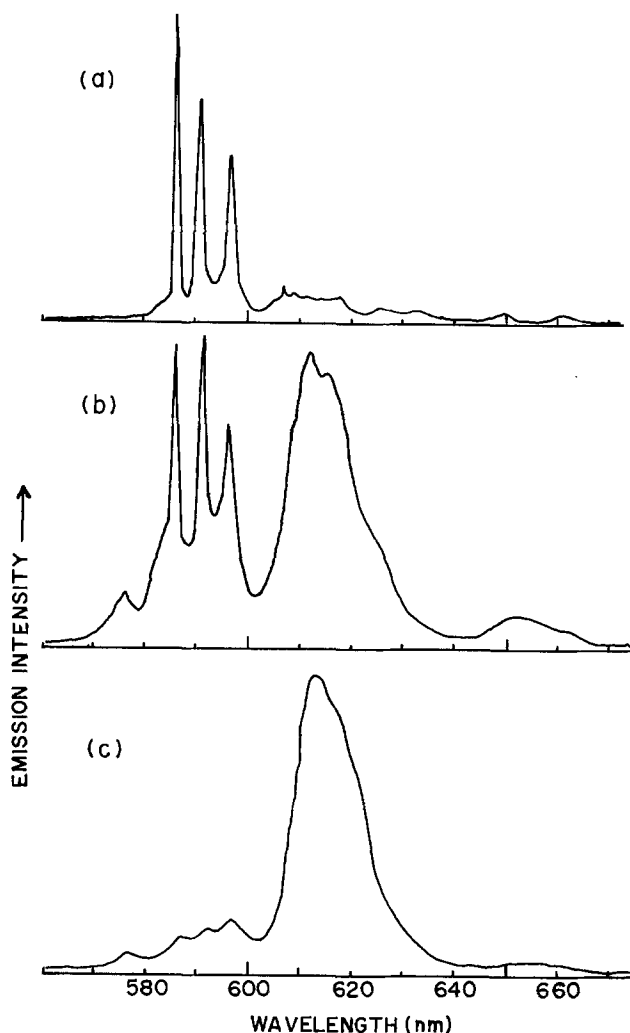


Fig. 3. Emission spectra from annealed  $\text{SnO}_2$  films of 4000Å thickness doped with 1 a/o Eu (a), 5 a/o Eu (b), and 14 a/o Eu (c).

Table I. (110) line half-widths of undoped  $\text{SnO}_2$  crystal and annealed films (x-ray diffraction measurements)

Sample	Line half-width ( $2\theta$ deg)
Undoped $\text{SnO}_2$ crystal	0.2
1 a/o Eu-doped film	0.3
5 a/o Eu-doped film	0.4
14 a/o Eu-doped film	1.5

surface. Table I compares the (110) diffraction line half-widths of the annealed  $\text{SnO}_2$  films with that of an undoped  $\text{SnO}_2$  crystal. It is seen that in the annealed films with a low Eu concentration, the half-width is nearly equal to that of the undoped  $\text{SnO}_2$  crystal. This indicates that the films have good crystallinity and that Eu is quite possibly substituted for Sn. At high Eu concentration, the cosputtered Eu inhibits  $\text{SnO}_2$  crystal grain growth and reduces the grain size. This consideration is supported by the fact that the highly Eu-doped films show a broad x-ray diffraction line. The grain size calculated from the half-width of the (110) diffraction line is found to be as small as 50Å. It is speculated that the Eu may be incorporated mostly into regions with large disorder near the grain boundaries. This may cause the enhanced electric dipole emission. These crystal structures in the highly Eu-doped films are unusual ones in thermally Eu-doped  $\text{SnO}_2$  crystals in which the enhanced electric dipole emission is scarcely observed. In the sputtering process, the films grow under nonthermal equilibrium conditions. The cosputtered Eu may strongly affect the film growth process and the unusual crystal structures may easily be quenched, as is observed in Ge-doped  $\text{Bi}_2\text{O}_3$  prepared by the cosputtering process (4).

The present annealing process may not essentially affect the crystallographic site of the cosputtered Eu since the cathodoluminescent spectra from as-sputtered Eu-doped  $\text{SnO}_2$  films are similar to those of the annealed ones, although they are much less intense.

### Conclusion

The crystallographic site of cosputtered Eu in  $\text{SnO}_2$  films can be determined by studying their cathodoluminescent spectra. The results are as follows.

(i) The sputtered films with a low Eu concentration show a sharp magnetic dipole emission. This indicates that the cosputtered Eu is substituted for Sn in the  $\text{SnO}_2$  crystal matrix.

(ii) The sputtered films with a high Eu concentration show a strong electric dipole emission. In this case, the cosputtered Eu inhibits  $\text{SnO}_2$  crystal grain growth and reduces the grain size. It is speculated that the Eu may mostly be incorporated into regions with large disorder near the grain boundaries.

Manuscript submitted June 1, 1976; revised manuscript received July 12, 1976.

Any discussion of this paper will appear in a Discussion Section to be published in the June 1977 JOURNAL. All discussions for the June 1977 Discussion Section should be submitted by Feb. 1, 1977.

Publication costs of this article were assisted by Matsushita Electric Company, Limited.

### REFERENCES

1. T. Hada, K. Wasa, and S. Hayakawa, *Thin Solid Films*, **7**, 135 (1971).
2. D. F. Crabtree, *J. Phys. D*, **8**, 107 (1975).
3. G. Blasse and A. Bril, *Philips Tech. Rev.*, **31**, 304 (1970).
4. T. Mitsuyu, K. Wasa, and S. Hayakawa, *This Journal*, **123**, 94 (1976).

# Structure and Properties of Boron Nitride Films Grown by High Temperature Reactive Plasma Deposition

S. B. Hyder\* and T. O. Yep

Varian Associates, Corporate Solid State Laboratory, Palo Alto, California 94303

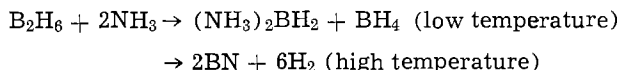
## ABSTRACT

Thin films of boron nitride were grown by reactive plasma deposition using the ammonia-diborane reaction. The crystalline growth on substrates of silicon, compression-annealed pyrolytic graphite, and compression-annealed pyrolytic BN was investigated by electron microscopy, and composition of the deposited material was determined by electron microprobe analysis. The effect of gas ratio and substrate temperature on growth rate was also investigated. Some crystalline order was observed; the largest single crystal BN grains were obtained on compression-annealed pyrolytic graphite. Resistivities of the order of  $2 \times 10^9 \Omega\text{-cm}$  were measured with dielectric constant varying from 2.7 to 7.7 for growth with different gas ratios. Efforts to determine the drift velocity of carriers in thin films of BN were not successful.

The interest in BN stems from the fact that it is a high resistivity III-V compound with a large bandgap (3.8 to 7.58 eV) (1, 2) and if crystalline thin films could be obtained with large carrier drift velocity, it could be a promising material for certain microwave devices. This communication describes the results of the study undertaken to obtain crystalline thin films of BN by reactive plasma deposition (RPD) using the reaction of  $\text{NH}_3$  with  $\text{B}_2\text{H}_6$ .

## Experimental

Thin films of BN were grown on Si substrates by chemical vapor deposition (CVD) by Rand and Roberts (1) using the reaction between  $\text{NH}_3$  and  $\text{B}_2\text{H}_6$  in hydrogen. The reaction proceeded as follows



with the free energy equal to  $-165$  and  $-177$  kcal/mole at  $900^\circ$  and  $1100^\circ\text{K}$ , respectively. Alexander, Joyce, and Sterling (3) have also grown BN by reactive plasma deposition at room temperature.

The present work describes the results of the growth of BN using the reaction of  $\text{NH}_3$  with  $\text{B}_2\text{H}_6$  in  $\text{H}_2$  at a high substrate temperature ( $> 1000^\circ\text{K}$ ) together with an rf plasma on graphite, Si, and BN substrates. The deposited material was smooth and transparent and was found to have better crystalline quality than the material obtained by  $\text{NH}_3:\text{B}_2\text{H}_6$  CVD at high temperature alone.

Figure 1 shows a schematic of the reactive plasma deposition system. The  $\text{NH}_3$  and 1.96%  $\text{B}_2\text{H}_6$  diluted in  $\text{H}_2$  gases are metered by their respective Tylan mass flow controllers and are mixed in the heated mixing chamber. The 13.5 MHz rf excitation is coupled into the plasma within the radiant furnace hot zone by a capacitive coupler consisting of a platinum grid electrode placed outside a 3 in. diameter furnace tube and the grounded graphite susceptor inside the furnace tube. The input and reflected rf power were measured by a Thruline wattmeter manufactured by Bird Electronic Corporation. Typically 4W of rf power was absorbed by the plasma. The substrates and graphite susceptor are heated to the deposition temperatures by a 14 kW parabolic clamshell radiant heater furnace manufactured by Research, Incorporated. The temperature is monitored by a Chromel-Alumel thermocouple imbedded in the graphite susceptor close to the substrate. Six 40 liter Varian Vacorb pumps are used to

maintain the plasma at a pressure of 39-133 Pa (300-1000  $\mu\text{m}$ ).

In a typical run, the reactor tube is evacuated to ca. 0.66-1.33 Pa (5-10  $\mu\text{m}$ ) pressure using the Vacorb pumps. The substrates are then heated until a steady temperature is recorded by the thermocouple. After the desired substrate temperature is reached,  $\text{NH}_3$  and  $\text{B}_2\text{H}_6$  are let into the mixing chamber at the desired ratio, but with a flow rate about a tenth of the normal flow rate during deposition. The slow initial growth rate promotes better nucleation and consequently a better crystalline structure. The plasma is ignited with a Tesla coil as the gases enter the hot zone. The pressure in the reactor tube stabilizes to ca. 39-66.5 Pa (300-500  $\mu\text{m}$ ). After the nucleation period, the reactive gases are introduced at full flow which ranges from 26 to 120  $\text{cm}^3/\text{min}$  for  $\text{NH}_3$  and 480 to 575  $\text{cm}^3/\text{min}$  for  $\text{B}_2\text{H}_6$ , depending upon the gas ratio being used. The pressure in the reactor tube increases with deposition duration and is adjusted by increasing the pumping rate to sustain a vacuum less than 133 Pa (1000  $\mu\text{m}$ ) in order to maintain the plasma.

Different gas ratios and substrate temperatures were examined. Substrates used were: (111)Si, compression-annealed graphite (CAPG) from Union Carbide and Pfizer, and compression-annealed pyrolytic BN (CAPB) from Union Carbide. The growth rate generally increased with increasing temperature and decreased with increasing  $\text{NH}_3:\text{B}_2\text{H}_6$  ratio but was practically independent of the substrate and its orientation. The growth rate was also highest upstream where the gases enter the hot zone. Table I shows the growth rate for different substrate temperatures and gas ratios for some of the reactive plasma chemical vapor depositions made.

## Results

**Material.**—The RPD material deposited at high temperatures had better crystalline quality than the material deposited by high temperature  $\text{NH}_3:\text{B}_2\text{H}_6$  CVD

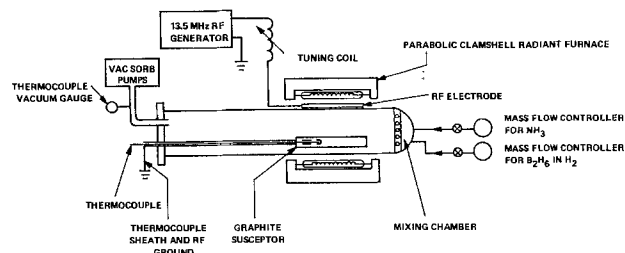


Fig. 1. Reactive plasma deposition system for BN

\* Electrochemical Society Active Member.

Key words: crystalline growth, dielectric constant, drift velocity, electron diffraction.

Table I. Growth parameters for BN deposition

Run No.	NH <sub>3</sub> :B <sub>2</sub> H <sub>6</sub> ratio	Substrate temp (°C)	Growth rate (μm/min)
3-27	19.2	757	0.30
3-24	13.6	950	0.57
4-1	11.6	800	0.42
4-3	8.1	770	0.16
4-22	8.1	850	0.44
5-15	8.1	1000	0.72
5-27	4.5	750	0.57
5-1	4.5	800	0.62
5-16	4.5	1000	0.82
6-5	2.2	750	0.72

alone. A typical example of the improvement in grain size with high temperature RPD over CVD is observed in the electron diffraction patterns shown in Fig. 2 (a) and (b) for material grown by CVD and RPD, respectively. In both cases the material was grown under the same conditions of gas ratio (NH<sub>3</sub>:B<sub>2</sub>H<sub>6</sub> 8:1) and substrate temperature (770°C) on graphite substrates obtained from the Supertemp Corporation.

Compression-annealed pyrolytic graphite (CAPG) from Pfizer and Union Carbide was examined with the 100 keV electron microscope for the degree of single crystallinity. The reflection electron diffraction patterns of the CAPG material from Pfizer and Union Carbide are shown in Fig. 3(a) and 4(a), respectively. Diffraction patterns from the Union Carbide CAPG substrate indicates coarse grained crystalline material. The Pfizer graphite on the other hand consists of fine grain randomly oriented polycrystalline material, as evidence by the series of sharp circular rings in the diffraction pattern. Figures 3(b) and 4(b) are transmission electron diffraction micrographs of BN films on



Fig. 2. (a) Reflection electron diffraction pattern of CVD BN deposited on Supertemp graphite substrate. (b) Reflection electron diffraction pattern of high temperature reactive plasma BN deposited on Supertemp graphite substrate.



Fig. 3. (a) Reflection electron diffraction pattern of Pfizer compression-annealed pyrolytic graphite. (b) Transmission electron diffraction pattern of reactive plasma BN deposited on Pfizer compression-annealed pyrolytic graphite.

graphite substrates from Pfizer and Union Carbide, respectively. The BN layers that separated from the substrate due to differences in thermal expansion were thinned in hot phosphoric acid for the transmission microscopy. The diffraction micrograph for the BN layer deposited at 770°C with a NH<sub>3</sub>:B<sub>2</sub>H<sub>6</sub> gas ratio of 8:1 on the Union Carbide CAPG shows rather markedly that this BN layer has larger single crystallites than the BN films deposited on the other substrate, and the single crystals are large enough so that there are but a few single crystal grains within the 50 μm objective aperture of the microscope.

A comparison of the electron diffraction patterns of the RPD BN layers in Fig. 3(b) and 4(b) with their respective CAPG substrates in Fig. 3(a) and 4(a) show that the single grain size in the deposited BN is larger than that in the substrate.

Figure 5 shows the diffraction pattern that is typically obtained in BN deposited on CAPG material from Union Carbide. After indexing the diffraction spots, two grains with zone axes along (01 $\bar{1}$ 0) and ( $\bar{1}$ 5 $\bar{4}$ 1) could be identified in the multigrain structure.

BN films were also deposited on (111) Si substrates with some degree of single crystallinity. Figure 6 is a transmission electron diffraction pattern of a BN film grown again with a gas ratio of 8:1 at a temperature of 770°C on a (111) Si substrate. The Si substrate was etched off the BN for the transmission electron microscopy. In addition to the diffraction spots, Kikuchi lines were also observed, indicating fairly large grain crystalline material.

Chemically vapor deposited hexagonal BN from Union Carbide that had been compression annealed for improved ordering of the crystalline structure was also

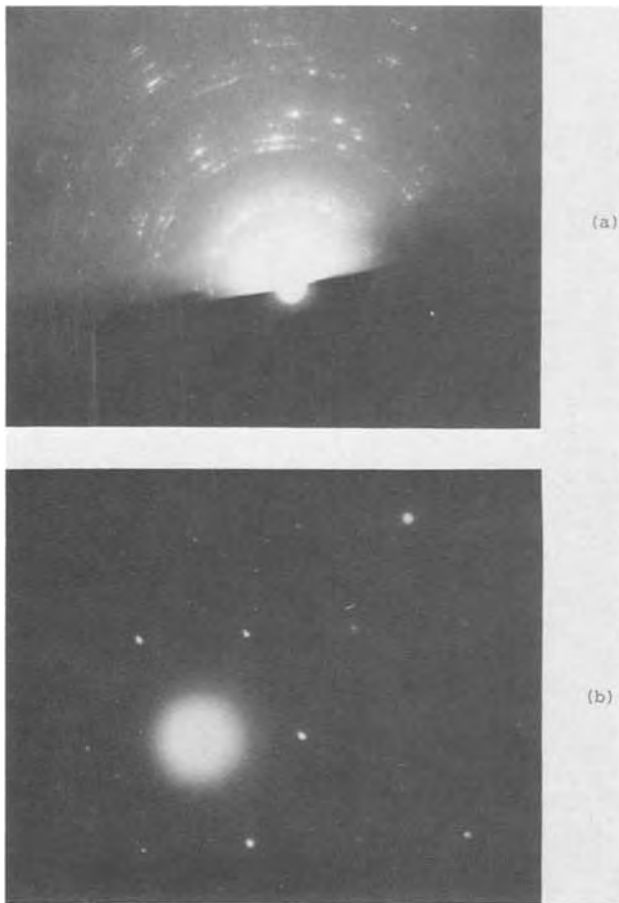


Fig. 4. (a) Reflection electron diffraction pattern of Union Carbide compression-annealed pyrolytic graphite. (b) Transmission electron diffraction pattern of reactive plasma BN deposited on Union Carbide compression-annealed pyrolytic graphite.

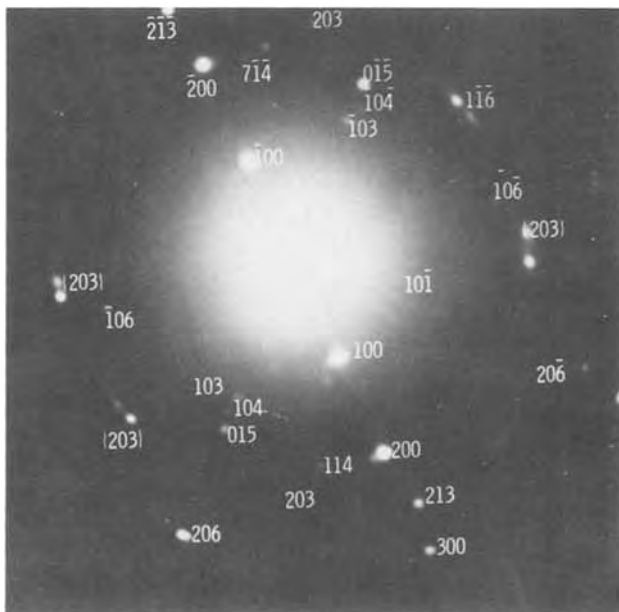


Fig. 5. Typical electron diffraction pattern of multigrain BN film deposited on compression-annealed graphite from Union Carbide.

used as substrate material. Figure 7(a) is a transmission electron diffraction micrograph of some of this substrate material, which indicates that the material consists of preferentially oriented crystallites. Figure



Fig. 6. Transmission electron diffraction pattern of reactive plasma BN deposited on (111) Si substrate.

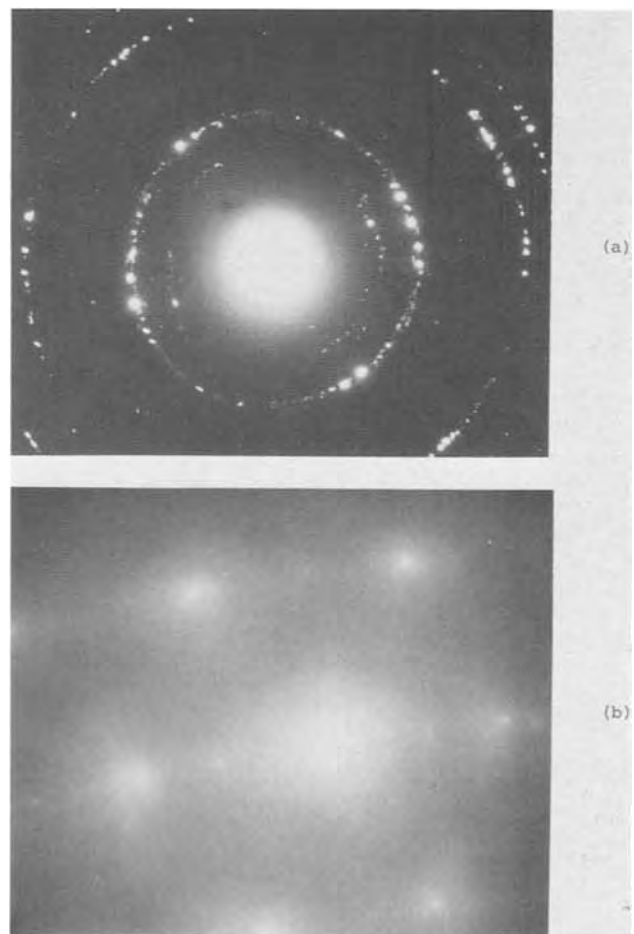


Fig. 7. (a) Transmission electron diffraction pattern of compression-annealed pyrolytic BN from Union Carbide. (b) Transmission electron diffraction pattern of reactive plasma BN deposited on Union Carbide compression-annealed pyrolytic BN.

7(b) shows a transmission electron diffraction of the BN film grown by reactive plasma that peeled away from the substrate. The hexagonal symmetry of the multiple grain is evident from the diffraction pattern.



Table II. B-N composition EMP analysis

Specimen	B (%)	N (%)	NH <sub>3</sub> :B <sub>2</sub> H <sub>6</sub> ratio	Temp (°C)
4-14	49.25	50.75	4.5:1	1000
4-8	55.40	44.60	4.5:1	930
5-15	41.67	58.33	8.1:1	1000
Allied Chemical	46.32	53.68	—	—
Boralloy (U.C.)	45.29	54.71	—	—
Theoretical	43.56	56.44	—	—

The effect of varying the NH<sub>3</sub>:B<sub>2</sub>H<sub>6</sub> ratio from 4.5:1 to 19.2:1 was also examined, and the substrate growth temperature was varied from 750° to 1000°C. The most ordered single crystals of deposited BN were obtained for a NH<sub>3</sub>:B<sub>2</sub>H<sub>6</sub> ratio of 8:1 with a growth temperature range of 770°–1000°C.

A Kevex energy-dispersive electron microprobe analysis was made on some compression-annealed BN "Boralloy" from Union Carbide, a vapor-liquid solution-grown BN specimen obtained from R. Kirk of Allied Chemical, and our reactive plasma BN films. Table II contains a summary of the compositional analysis. When compared to the theoretical composition for stoichiometric BN, all of the BN specimens tested were B rich except sample No. 5-15, which was N rich and had been deposited with the largest NH<sub>3</sub>:B<sub>2</sub>H<sub>6</sub> ratio. This would indicate that a stoichiometric BN composition could be obtained from a reactive plasma BN deposition at 1000°C using a NH<sub>3</sub>:B<sub>2</sub>H<sub>6</sub> gas ratio of 7.1:1.

**Measurements.**—Infrared absorption measurements were made on our reactive plasma BN films with a Model 457 Perkin-Elmer infrared spectrometer over the wavelength range of 2.5–40 μm. The typical spectrum observed on our depositions is shown in Fig. 8. The BN optical phonon absorption peak occurs at 7.1 μm and a possible B-N-B resonance is at 12.5 μm. This is the standard spectrum also observed in commercially available BN.

A four-point probe measurement utilizing a Tektronix 576 curve tracer as the constant current source and a Keithley 602 electrometer to measure the voltage determined that the room temperature electrical resistivity of our BN films was typically  $2 \times 10^9 \Omega\text{-cm}$ .

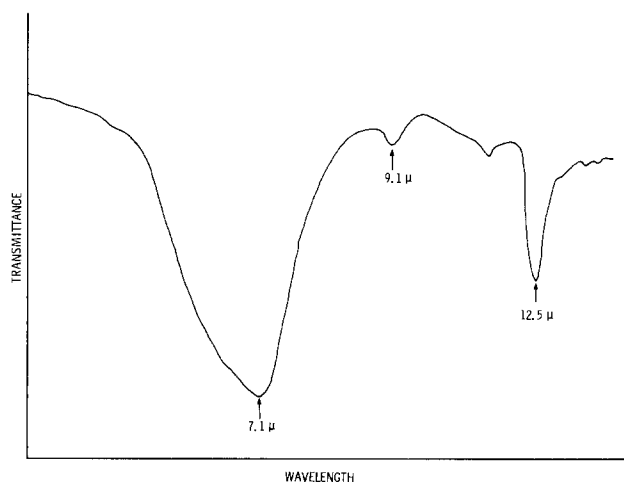


Fig. 8. Typical infrared absorption spectrum of reactive plasma BN.

The I-V characteristics were essentially linear to a field of  $10^4$  V/cm at which the resistivity was measured.

A General Radio 1615A capacitance bridge was used to determine the dielectric constants at 100 kHz of BN films deposited with different NH<sub>3</sub>:B<sub>2</sub>H<sub>6</sub> ratios by measuring the capacitance of BN capacitors of known area and thickness. Evaporated Al electrodes 3 mm in diameter were used. For a ratio of NH<sub>3</sub>:B<sub>2</sub>H<sub>6</sub> of 4.5:1 and substrate temperature of 1000°C, the dielectric constant was 2.7. For a ratio of NH<sub>3</sub>:B<sub>2</sub>H<sub>6</sub> of 11.6:1 and substrate temperature of 800°C, the dielectric constant varied from 5.3 to 7.7 from sample to sample.

An attempt was made to measure the carrier drift velocity by the method of Ruch and Kino (3), but no meaningful electrical response on the sampling scope could be detected from the incident 15 keV electron beam current on all our BN material. BN thicknesses from 10 to 75 μm were used. Electric fields up to  $10^6$  V/cm were applied across the BN specimens. Evidently the density of recombination centers is too high to permit any measurable carrier transit current to be observed.

### Conclusions

Thin films of BN were grown by high temperature reactive plasma deposition using the reaction of ammonia and diborane. The crystalline growth on substrates of Si, pyrolytic graphite, and compression-annealed pyrolytic BN was investigated by transmission and reflection electron microscopy. The highest crystalline order with the largest single crystal grains was observed to occur for deposits on Union Carbide compression-annealed pyrolytic graphite grown with an ammonia/diborane ratio of 8:1 at temperatures between 770° and 1000°C. Energy dispersive electron microprobe analysis of the BN films indicated that stoichiometric BN should be obtained by growths at 1000°C with an ammonia/diborane ratio of 7.1:1. The electrical measurements indicated the BN films had room temperature resistivities of  $2 \times 10^9 \Omega\text{-cm}$  and 100 kHz dielectric constants of 2.7–7.7 depending on the growth conditions. No drift velocity values for carriers in BN could be obtained.

### Acknowledgments

This work was supported by the Office of Naval Research, Arlington, Virginia, under Contract NOO14-75-C-0020.

Manuscript submitted April 23, 1976; revised manuscript received June 29, 1976.

Any discussion of this paper will appear in a Discussion Section to be published in the June 1977 JOURNAL. All discussions for the June 1977 Discussion Section should be submitted by Feb. 1, 1977.

Publication costs of this article were assisted by Varian Associates.

### REFERENCES

1. M. J. Rand and J. F. Roberts, *This Journal*, **115**, 423 (1968).
2. P. S. Schaffer, Final Report on Contract AF19-628-1616, 62P, AD 610-496, Lexington Laboratories, Incorporated, Lexington, Kentucky (1964).
3. J. H. Alexander, R. J. Joyce, and H. F. Sterling, Abstract 462, p. 343, The Electrochemical Society Extended Abstracts, Fall Meeting, Montreal, Canada, October 6-11, 1968.
4. J. G. Ruch and G. S. Kino, *Phys. Rev.*, **174**, 921 (1968).



# Optical Properties of GaN Light Emitting Diodes

Akira Shintani\* and Shigekazu Minagawa\*

Hitachi, Limited, Central Research Laboratory, Kokubunji, Tokyo 185, Japan

## ABSTRACT

Gallium nitride light emitting diodes (LED's) fabricated on  $\{1\bar{1}02\}$  oriented sapphire substrates are found to emit only green light independent of Zn concentration during the i-layer growth of i-n structures, while LED's on  $\{0001\}$  substrates are found to be able to emit blue to yellow light by controlling the Zn concentration. In investigating the temperature dependence of electroluminescence and photoluminescence spectra, it was found that the spectra consist of two components: blue emission and yellow or green emission. The relative intensity of the blue emission increased with the decrease in temperature. On the other hand, the yellow and green emissions were found to increase in their relative intensities when the temperature was raised to room temperature. These results imply that two kinds of acceptors are formed by doping with Zn into a GaN crystal. The acceptor contributing to the blue emission is located at 0.4 eV above the valence band. The other acceptor responsible for the yellow and green emissions is an impurity band situated at a position higher than 0.8 eV above the valence band.

Since gallium nitride light emitting diodes (LED's) composed of the i (Zn- or Mg-doped layer)-n (undoped layer) junction were reported by Pankove and his co-workers (1, 2), various GaN LED's with blue (3), yellow (4), red (5), and violet color emission (6, 7) have been fabricated. However, the mechanism by which GaN LED's emit at various wavelengths throughout the visible spectrum has remained unclear, though luminescence centers contributing to the various emissions have been found to extend from 0.6 to 1.1 eV above the valence band (4).

This paper reports that there are some differences in the color of the emission between the LED's fabricated on  $\{0001\}$  and  $\{1\bar{1}02\}$  oriented sapphire substrates. The LED fabricated on  $\{1\bar{1}02\}$  substrate was found to emit green light almost independent of the Zn concentration during the i-layer growth, though the emission from the LED on  $\{0001\}$  substrate was found to vary in color by controlling the Zn concentration. The LED's on  $\{0001\}$  substrates produced blue to yellow color emissions. In this work, it was also found that there is a different temperature dependence in the relative intensity and spectrum shift between the blue emission and the other emissions. A peak energy difference between the spectra of photoluminescence (PL) and electroluminescence (EL) was observed at room temperature for the blue LED, but not for the yellow and green LED's.

## Experimental

*Crystal growth and LED fabrication.*—The GaN crystals used in this work were grown according to the Maruska and Tietjen method (8). Substrates used were  $\{0001\}$  and  $\{1\bar{1}02\}$  oriented sapphires grown by the Czochralski method. These substrates were annealed in air at 1000°C for 5 hr in order to reduce any strain in the crystals. The surfaces were etched off in  $H_3PO_4$  at 320°C to remove lapping scratches. First an undoped n-type conducting layer was grown on these substrates and then a Zn-doped layer was grown. Thus, an i-n junction was formed during crystal growth. The reactor employed had three horizontal inlet nozzles, which were used to introduce HCl,  $NH_3$ , and Zn vapor. The quartz boat for Zn was movable by magnet from up to down stream in the gas flow. This boat permitted evaporation of Zn at high temperatures during the i-layer growth time after the n-layer deposition. A Zn source temperature of about 600°C was required to

compensate native donors. The n-layers obtained were  $3 \times 10^{18} \sim 7 \times 10^{19} \text{ cm}^{-3}$  in carrier concentration by the van der Pauw method and were 50 ~ 80  $\mu\text{m}$  thick. The i-layers were about 10  $\mu\text{m}$  thick. Their carrier concentrations were unknown because of their semi-insulating characteristics.

The wafers were cut into 3 to 5 mm square disks. An indium contact was soldered onto the whole surface of the i-layer, while the other contact was attached to the n-layer exposed on the chip side. Electroluminescence could be obtained with a forward bias of 3.5-20V (9) with respect to the i-layer surface. Emission was observed through the substrate at the back. The reverse bias generated almost no light. This phenomenon is contrary to what has already been reported (4).

*Zinc concentration distribution in the i-layer.*—The Zn concentration distribution in the i-layer surface was semiquantitatively analyzed by scanning electron microprobe analysis (EMA). The electron beam incident on the crystal surface was several microns in diameter. This is less than one-tenth the crystal growth hillock diameter. To reduce the error in the measurement due to surface roughness, the relative Zn concentration was expressed by the  $K_{\alpha}$ -ray intensity ratio of Zn to Ga,  $(Zn/Ga)_i$ , in which the Ga  $K_{\alpha}$ -ray intensity was used as an internal criterion. The Zn and Ga  $K_{\alpha}$ -rays were simultaneously measured. The ratios,  $(Zn/Ga)_i$ , were also employed to compare the Zn concentration between samples.

*EL and PL measurements.*—The devices fabricated in this way were mounted on the cold finger of a liquid nitrogen cryostat. Then, their EL spectra at room (RT) and liquid nitrogen temperatures (LNT) were measured by a Spex-II spectrometer and an RCA 7625 photomultiplier.

The specimens used for the PL measurements were prepared from the same sample used for the EL measurements. For these measurements, Kr laser light (3509A) was irradiated on the i-layer surface through a lens system. The measurements were carried out at RT and liquid helium temperature (LHeT) using a Perkin Elmer El spectrometer and an HTV-592 photomultiplier.

## Results

*Case of  $\{0001\}$  substrates.*—In this case, the crystals in the  $\{0001\}$  orientation are grown. The EL color of a diode fabricated on  $\{0001\}$  substrate (hereafter referred to as  $\{0001\}$  diode) depended on the Zn concentration in the i-layer, i.e., the color of the emission shifted to the longer wavelengths with the increase in

\* Electrochemical Society Active Member.

Key words: substrate orientation, electroluminescence photoluminescence temperature dependence, luminescence centers.

Zn concentration. This result agrees qualitatively with Pankove's experiment (3). However, there has been no report clarifying the quantitative correlation of Zn concentration during i-layer growth [supplied amount ratio of Zn to Ga,  $(\text{Zn}/\text{Ga})_g$ ] with that in the i-layer  $[(\text{Zn}/\text{Ga})_i]$  and the color of the emission. Investigating the relationship between the two kinds of Zn concentrations, i.e.,  $(\text{Zn}/\text{Ga})_g$  and  $(\text{Zn}/\text{Ga})_i$ ,  $(\text{Zn}/\text{Ga})_i$  was found to increase steeply with  $(\text{Zn}/\text{Ga})_g$  when  $(\text{Zn}/\text{Ga})_g$  was in the narrow range below 0.1 (Fig. 1). The  $(\text{Zn}/\text{Ga})_i$  increased gradually with  $(\text{Zn}/\text{Ga})_g$  in the range above 0.1. When  $(\text{Zn}/\text{Ga})_g$  was above 0.5, i.e., i-layer Zn concentration was high, yellow LED's were usually obtained. Orange to red lights were sometimes produced; when  $(\text{Zn}/\text{Ga})_g$  was below 0.2, blue light emission was apt to occur. Then Zn concentration in the i-layer of the yellow LED was two or more times that of the blue one (Fig. 1). The steep increase of  $(\text{Zn}/\text{Ga})_i$  in the near zero range of  $(\text{Zn}/\text{Ga})_g$  may be caused by complete incorporation of the Zn supplied into the GaN crystal. As a result,  $(\text{Zn}/\text{Ga})_i$  fluctuated widely with small fluctuations in the amount of Zn supplied when the  $(\text{Zn}/\text{Ga})_g$  was below 0.2. For this reason, blue LED's are difficult to obtain with good reproducibility. On the contrary, yellow LED's doped with a high concentration of Zn could be fabricated with good reproducibility.

The EL spectra of the blue LED and yellow LED measured at RT [Fig. 2(a)] consisted of a single band peaking at 450 nm (2.76 eV) and 585 nm (2.12 eV), respectively. The EL spectrum of the blue LED at RT is analogous in the peak position and half-width to that reported already (3). On the other hand, the EL spectrum of the yellow LED fabricated in this work differs from the EL spectrum observed by Pankove *et al.* (4) in a broad orange contribution peaking at 1.7 eV. No shoulder band is observed in Fig. 2(a). When the yellow LED made in this work was cooled to LNT, a subband corresponding to the emission peak of the blue LED was apparent [Fig. 2(b)]. No side band developed in the EL spectrum of the blue LED at LNT, although the peak position was found to shift to higher energy, i.e., blue shift. However, in the EL spectrum of the yellow LED no shift of the main band peak position occurred. The blue shift of the GaN EL is known to

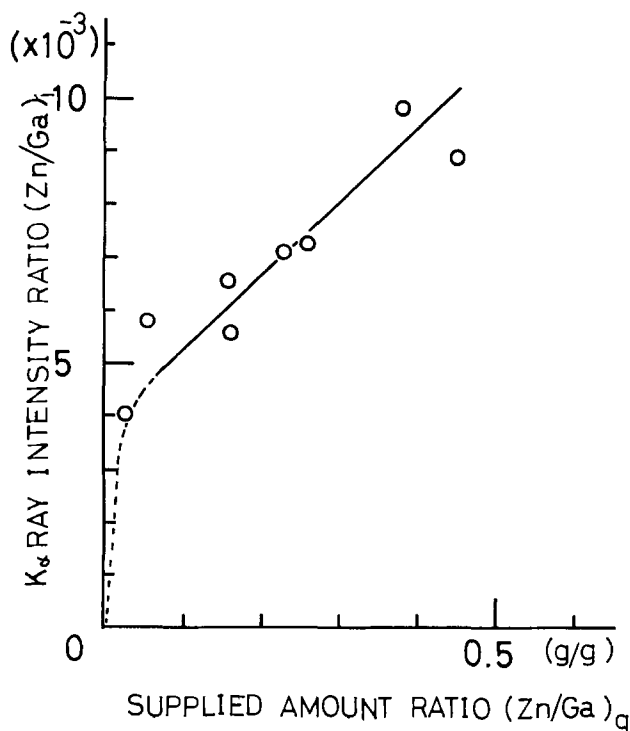


Fig. 1. The relationship between relative Zn concentrations in the i-layers,  $(\text{Zn}/\text{Ga})_i$ , and the supplied  $(\text{Zn}/\text{Ga})_g$  ratio.

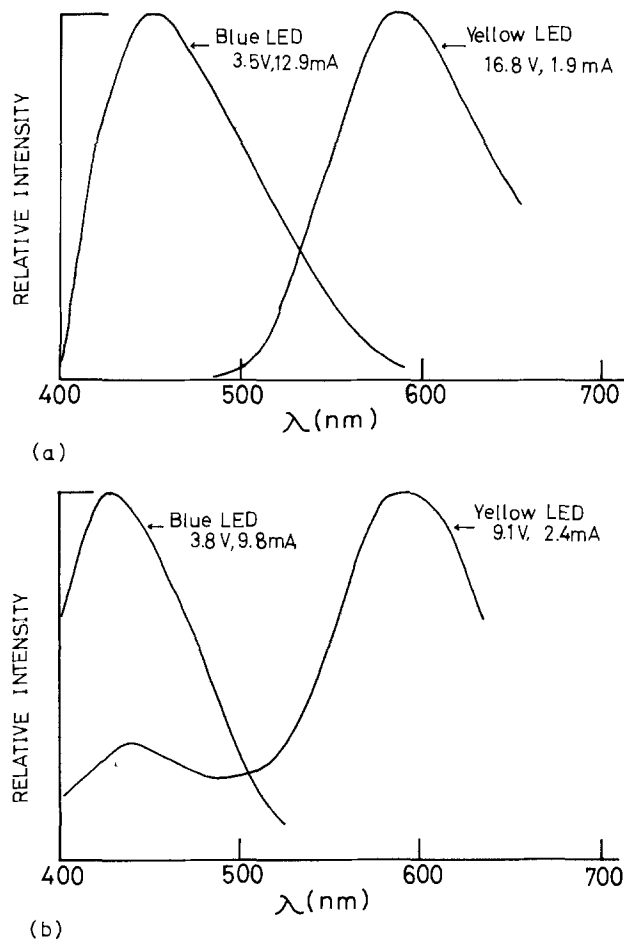


Fig. 2. Electroluminescence spectra of blue and yellow LED's at RT (a) and at LNT (b). The values in the spectra show the applied voltages and current through the diodes.

occur with the increase in current through the diode (7, 9). The peak shift observed here was not caused by the current increase, since the current through the blue LED in Fig. 2 was less at LNT than at RT.

As opposed to the EL spectrum differences between the blue and yellow LED's mentioned above, no large peak energy difference was observed in the PL spectra between the blue and yellow LED's [Fig. 3(a)]; the peak energies were located around 560 ~ 580 nm (2.12 ~ 2.14 eV). In comparing the spectrum peak energy difference between the PL and EL at RT, however, there was some difference between the blue LED and yellow LED. The peak energy of the EL spectrum was found to be higher than that of the PL spectrum by 0.5 eV in the blue LED, whereas no peak energy difference was found in the yellow LED. When temperature was decreased to LHeT, the PL spectrum of the yellow LED occurred at the same peak position as that of the blue one [Fig. 3(b)]. The peak was located at 445 nm (2.79 eV), and this peak position is nearly in agreement with that of the blue component of the EL spectra at LNT [see Fig. 2(b)]. The spectrum shown in Fig. 3(b) was almost entirely in agreement with the low temperature PL spectra reported already.

*Case of  $\{1\bar{1}02\}$  substrates.*—The epitaxial layers of GaN crystals of  $\{1\bar{1}20\}$  oriented surface were grown on  $\{1\bar{1}02\}$  surfaces of sapphire substrates. The LED's made on  $\{1\bar{1}02\}$  sapphires (hereafter referred to as  $\{1\bar{1}20\}$  LED) differed from  $\{0001\}$  LED's in the Zn concentration dependence of the EL. That is, the peak energy for the EL spectrum of the  $\{1\bar{1}20\}$  LED was almost independent of  $(\text{Zn}/\text{Ga})_g$ . Even when  $(\text{Zn}/\text{Ga})_g$  values were varied in the range from 0.4 to 1.1,  $\{1\bar{1}20\}$  LED's generated only green light, although  $\{0001\}$  LED's

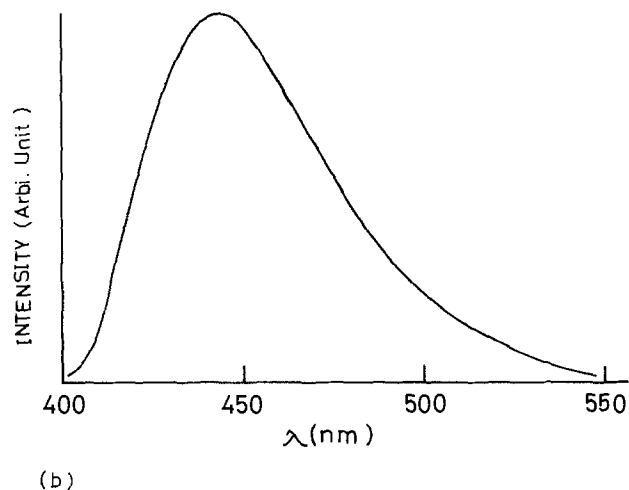
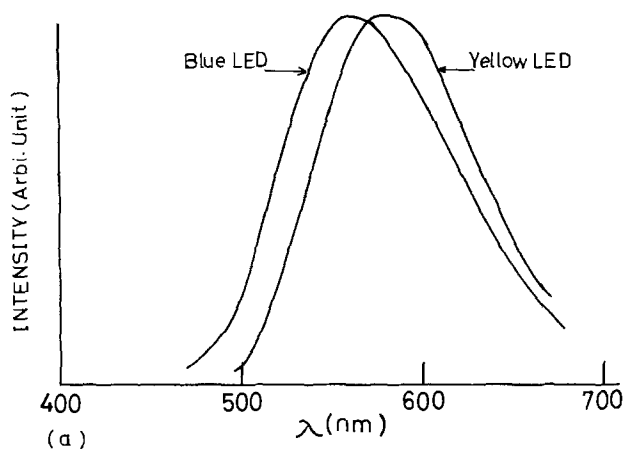


Fig. 3. Photoluminescence spectra of the i-layers of blue and yellow LED's at RT (a) and at LHeT (b). At LHeT, the two spectra are completely superimposed on one another.

under similar conditions produced yellow to red light. The  $\{11\bar{2}0\}$  green LED's were apt to be lower in  $(\text{Zn}/\text{Ga})_i$ , measured in EMA, than the  $\{0001\}$  yellow LED's, though there were some exceptions. The  $\{11\bar{2}0\}$  green LED's were midway between blue and yellow  $\{0001\}$  LED's with regard to electric resistance. These results imply that the Zn concentration in the green LED is intermediate between the blue and yellow LED's. In the case of Zn supplying conditions such as used when fabricating the blue LED on  $\{0001\}$  substrate, the GaN crystals grown on  $\{11\bar{2}0\}$  substrate did not become a semi-insulator. It was therefore found that there is a limit to the amount of Zn incorporated into  $\{11\bar{2}0\}$  oriented GaN crystal.

The EL spectrum of the  $\{11\bar{2}0\}$  green LED consisted of a single band peaking at 520 nm (2.38 eV) (Fig. 4). No large peak position difference was observed between the spectra at RT and LNT, similarly to the case of the yellow LED. However, no blue side band such as seen in the EL spectrum of the yellow LED was observed even at low temperature.

With regard to the peak position correspondence between the PL and EL spectra, the green LED resembled the yellow one. That is, the PL spectrum at RT of the  $\{11\bar{2}0\}$  green LED agreed in its peak energy (515 nm, 2.4 eV) with the EL spectrum as seen in Fig. 4 and 5. When temperature was decreased, the peak position of the PL spectrum of the green LED shifted to 450 nm (2.76 eV) (LHeT) which is nearly in agreement in peak energy with those of the blue and yellow  $\{0001\}$  LED's. The PL spectrum of the green LED at LHeT was broader than the others (Fig. 3 and 5).

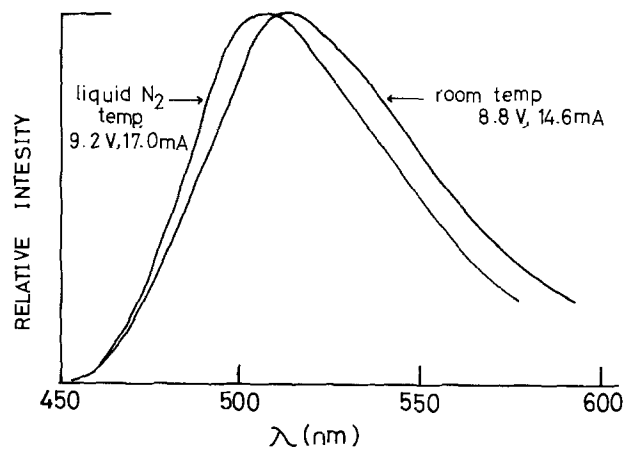


Fig. 4. Electroluminescence spectra of green LED at RT and at LNT.

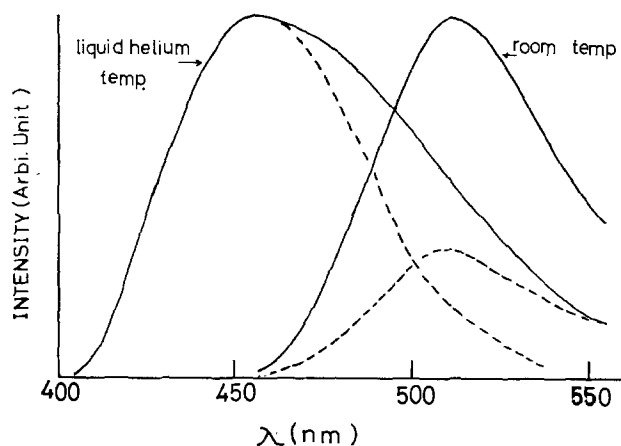


Fig. 5. Photoluminescence spectra of green LED's i-layer at RT and at LHeT. The PL spectrum at LHeT consists of two components (broken lines).

## Discussion

**Luminescence of  $\{0001\}$  LED's.**—The luminescence center responsible for the blue and yellow emissions from GaN:Zn, such as shown in Fig. 2, has been generally considered to be one kind of energy band in the forbidden gap described previously (4). This model cannot interpret the fact that the side band contributing to a blue emission develops in the EL spectrum of the yellow LED at low temperature [Fig. 2(b)]. It is also incapable of interpreting that there is a peak position shift (0.5 eV) over the bandgap reduction [0.07 eV (11)] with the temperature difference, which was observed in the PL spectra of the blue LED in the temperature range RT-LHeT [Fig. 3(a) and (b)]. Furthermore, a subband sometimes accompanied the main yellow band at 580 nm (2.14 eV) in the PL spectra at RT of i-layers used for fabricating yellow LED's. The intensity of this blue side band increased relative to the yellow band as temperature was lowered, so that the spectrum changed into a single blue band at LHeT. Thus, there exist two emission components in the spectra of both EL from the i-n junction and PL from the i-layer. These two components are different in their temperature dependence; the temperature dependence of each component does not change in PL and EL. These facts do not indicate that the color variation of the emission light described above is caused by a broad luminescence center such as explained previously. They clearly imply that two kinds of luminescence centers generated by doping with Zn atoms into GaN crystal are responsible for the emission color variation. It was already reported that the blue PL increases in intensity as temperature is lowered (10,

12). However, there has been no report on the observation of the two bands in the EL spectrum from one GaN LED or in the PL spectrum from one GaN semi-insulating layer. In addition, no study on temperature dependences of the two bands has been carried out. The reason that these two components have not been observed is that the samples used for that observation may be lower in Zn concentration than the samples used in this work. A model of the two luminescence centers is presented below.

The large difference between the EL and PL spectra of the blue LED at RT in the spectrum peak energy is presumed to be caused by the Zn concentration gradient near the i-n junction along the crystal growth direction. The electric potential distributions across the junction measured by Pankove (13) and Maruska *et al.* (14) change near the i-n junction, but not abruptly. This potential distribution indicates that the Zn concentration near the junction increases along the crystal growth direction. The EL occurs precisely at the junction (14, 15), *i.e.*, at the interface of the n- and i-layers. Accordingly, these facts suggest that the EL is generated at the lowest Zn concentration region of the i-layer. On the other hand, the PL emissions reflect properties of the i-layer near the surface where the Zn concentration is high. The reason that no peak energy difference between the EL and PL of the yellow LED's is observed is assumed to be that the  $(\text{Zn}/\text{Ga})_g$  is so high that the yellow luminescence center formed exists at the junction.

**Luminescence of  $\{1\bar{1}20\}$  LED's.**—The broader PL spectrum of the green LED, as opposed to those of the blue and yellow LED's, can be divided into two components. One of these is responsible for the blue emission, while the other contributes to the green emission (Fig. 5). At LHeT this blue component is higher in emission intensity than the green component. At RT the blue component vanished, while the other component survived. The green emission is analogous in the temperature variation of its intensity to the yellow emission; the green emission intensity is higher at RT than at lower temperatures. At lower temperatures the blue component intensity increases. Accordingly, there exist two kinds of luminescence centers, the properties of which differ, as in the case of the yellow LED.

Easier fabrication of the green LED on  $\{1\bar{1}02\}$  than  $\{0001\}$  substrate is assumed to be related to dependence of the Zn incorporation on the crystal surface orientation.

**Luminescence center model.**—There have been some discussions on blue emission peaking at 2.8 eV, *i.e.*, whether this emission is based on a conduction-band-to-acceptor transition (10) or a complex center (12). As previously described, the emission bands located in the range 445 nm (2.79 eV) to 580 nm (2.14 eV) (Fig. 2, 3, 4, and 5) are clearly influenced by Zn dopant; and it is generally thought that Zn atoms incorporated in a GaN crystal compensate native donors and form acceptors because the crystal becomes semi-insulating. Accordingly, the two luminescence centers mentioned previously are assumed to be two kinds of acceptors formed by Zn doping. One of these acceptors contributing to blue emission (acceptor I) is situated at 0.4 eV above the valence band. The other, responsible for green and yellow emissions (acceptor II), is located at a position higher than 0.8 eV above the valence band. This energy estimation is based on the bandgap (3.22 eV) of Zn-doped GaN at RT (17). The electrons at these acceptors are raised to the conduction band by photoexcitation or collisions with hot electrons (18). As a result, the holes arise at the acceptors. The radiative recombinations of these holes occur with electrons at donors or the conduction band. The holes at the acceptors are thermally excited to the valence band with increasing temperature. The density of the hole excited from acceptor I,

which has an energy level lower than acceptor II with respect to the valence band, increases relatively with the decrease in temperature. Thus, the hole density at the acceptors varies according to temperature, thereby causing the electron transition probabilities from the conduction band or the donor states to the acceptors to vary. Because of this probability variation, the blue emission as a result of the transition to acceptor I is relatively higher at LNT or LHeT than RT.

The acceptors are formed in the following way. Zinc atoms in GaN crystals are first substituted for Ga, thus forming acceptor I. If the number of Zn atoms introduced to the crystal is increased, Zn atoms can occupy N-vacancy sites (16). They can also be incorporated into interstitial sites because of the crystal lattice expansion due to the large atomic radii of Zn at N-vacancies and Ga sites. Therefore, these Zn dopants are assumed to form a broad impurity band (acceptor II) in the forbidden gap. The impurity levels may be associated with other impurities, such as Cu and Fe. In our samples, Al and Si of concentrations less than 0.005 w/o were detected by spectrochemical analysis. Lower concentrations of Mg, Cu and Fe were also detected.

It is known that the EL emission peak shifts to the short wavelength side with the increase in current through the diode (7, 9). The increase in the current density induces enhancement of electron density excited from the acceptors by impact ionization. The excited electrons fill up energy states of the conduction band tail. Consequently, if all the blue, green, and yellow EL emissions are generated by electron transitions from the conduction band to acceptors I and II, the blue shift of the EL emission with the current can be explained.

### Summary

In summary, the wavelength of the light emitted from the GaN LED can be controlled by varying the Zn dopant density. In the case of  $\{0001\}$  GaN crystals, the Zn concentration is two or more times higher for yellow LED's than for blue LED's. On the other hand, green LED's are easier to fabricate for  $\{1\bar{1}20\}$  GaN crystals than for  $\{0001\}$  GaN crystals. The blue emission, when compared with the green and yellow emissions, is found to be higher in relative intensity at lower temperatures than RT. All these emissions are produced by electron transitions from the conduction band to the two kinds of acceptors; one responsible for the blue emission is located 0.4 eV above the valence band, while the other contributing to the green to yellow emissions is situated at positions higher than 0.8 eV above the valence band.

### Acknowledgments

The authors wish to thank Mr. Minoru Wada for his expert technical assistance. Thanks are also due to Drs. Toshikazu Shimada and Yasuhiro Shiraki for their valuable assistance in PL measurements, and to Prof. Shigeo Shionoya of the University of Tokyo for his critical reading of the manuscript.

Manuscript submitted April 3, 1976; revised manuscript received July 23, 1976.

Any discussion of this paper will appear in a Discussion Section to be published in the June 1977 JOURNAL. All discussions for the June 1977 Discussion Section should be submitted by Feb. 1, 1977.

Publication costs of this article are assisted by Hitachi, Limited.

### REFERENCES

1. J. I. Pankove, E. A. Miller, and J. E. Berkeyheiser, *RCA Rev.*, **32**, 383 (1971).
2. J. I. Pankove, E. A. Miller, D. Richman, and J. E. Berkeyheiser, *J. Lumin.*, **4**, 63 (1971).
3. J. I. Pankove, E. A. Miller, and J. E. Berkeyheiser, *ibid.*, **5**, 84 (1972).
4. J. I. Pankove, E. A. Miller, and J. E. Berkeyheiser, *ibid.*, **6**, 54 (1973).
5. J. I. Pankove, *ibid.*, **7**, 114 (1973).

6. H. P. Maruska, W. C. Rhiness, and D. A. Stevenson, *Mater. Res. Bull.*, **7**, 777 (1972).
7. H. P. Maruska and D. A. Stevenson, *Appl. Phys. Lett.*, **22**, 303 (1973).
8. H. P. Maruska and J. J. Tietjen, *ibid.*, **15**, 327 (1969); A. Shintani and S. Minagawa, *J. Cryst. Growth*, **21**, 1 (1974).
9. A. Shintani and S. Minagawa, *J. Appl. Phys.*, To be published.
10. J. I. Pankove, J. E. Berkeyheiser, and E. A. Miller, *ibid.*, **45**, 1280 (1974).
11. B. Monemar, *Phys. Rev. B*, **10**, 676 (1974).
12. M. Ilegems, R. D. Dingle, and R. A. Logan, *J. Appl. Phys.*, **43**, 3797 (1972).
13. J. I. Pankove and M. A. Lampert, *Phys. Rev. Lett.*, **33**, 361 (1974).
14. H. P. Maruska, L. J. Anderson, and D. A. Stevenson, *This Journal*, **121**, 1202 (1974).
15. A. Shintani and S. Minagawa, *ibid.*, **123**, 1575 (1976).
16. J. I. Pankove and J. E. Berkeyheiser, *J. Appl. Phys.*, **45**, 3892 (1974).
17. The energy gap of Zn-doped GaN at RT was estimated at 3.22 eV from the plots of (optical density)<sup>2</sup> vs. absorption photon energy measured in this work.
18. H. P. Maruska and D. A. Stevenson, *Solid-State Electron.*, **17**, 1171 (1974).

## Topology of Silicon Structures with Recessed SiO<sub>2</sub>

E. Bassous,\* H. N. Yu, and V. Maniscalco

IBM Thomas J. Watson Research Center, Yorktown Heights, New York 10598

### ABSTRACT

The performance and packing density of silicon integrated circuits can be increased by the use of thermally grown silicon dioxide for the dielectric isolation of the active components of the circuit and by employing fabrication procedures which yield devices with flat surfaces. Using Si<sub>3</sub>N<sub>4</sub> masking, anisotropic etching of the silicon substrate, and thermal oxidation, structures were fabricated in which the SiO<sub>2</sub> was recessed below the original surface. Because of the lateral oxidation under the edge of the Si<sub>3</sub>N<sub>4</sub> mask, a so-called bird's beak shaped structure is formed at the Si-SiO<sub>2</sub> and SiO<sub>2</sub>-Si<sub>3</sub>N<sub>4</sub> interfaces. Factors which influence the surface planarity due to the bird's beak formation have been studied experimentally. This investigation studies the minimization of the bird's beak by using a combination of a thick Si<sub>3</sub>N<sub>4</sub> film, a thin SiO<sub>2</sub> pad, and a suitable thickness of recessed oxide (ROX). Uniform anisotropic etching and parallel alignment to <110> are also required to maintain dimensional control.

The use of silicon dioxide for the isolation of the active components of silicon integrated circuits offers the potential for the fabrication of circuits with increased performance and high packing density (1). The enhanced performance can be achieved by reducing the capacitance between the active regions of the circuit, while the increased packing density can be obtained by the use of high resolution lithography to reduce the spacing between circuit elements. To define patterns in the micrometer or submicrometer range, it is preferred to have the oxide used for isolation recessed into the silicon substrate to form a recessed oxide (ROX) structure whose surface is substantially coplanar with the silicon surface.

In the fabrication of MOS and bipolar devices with thermally grown recessed SiO<sub>2</sub> (2-10), Si<sub>3</sub>N<sub>4</sub> is commonly used as the oxidation barrier. The surface of a wafer is protected in selected regions with a thin film of Si<sub>3</sub>N<sub>4</sub> and the recessed oxide layer is thermally grown in the exposed areas. The volume of the thermally grown SiO<sub>2</sub> is about twice the volume of silicon consumed in forming the oxide. The SiO<sub>2</sub> film thickness is thus divided approximately equally above and below the original silicon surface, more exactly 55.7 and 44.3%, respectively, to yield a semirecessed oxide (SEMIROX) structure. To obtain a planar surface with a fully recessed oxide, part of the exposed silicon is removed prior to thermal oxidation as shown in Fig. 1.

The ideal profiles shown in Fig. 1 are not obtained in practice due to the diffusion of oxygen and the growth of SiO<sub>2</sub> under the edge of the Si<sub>3</sub>N<sub>4</sub> film during thermal oxidation. A ridge of thermal oxide which protrudes above the ROX surface is formed around the perimeter of the Si<sub>3</sub>N<sub>4</sub> mask. The profile of the oxide ridge in

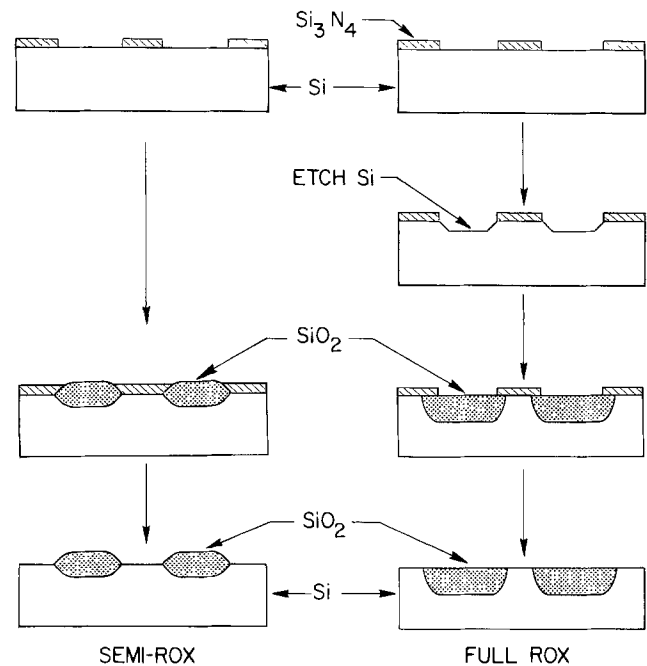


Fig. 1. Formation of semirecessed oxide (SEMIROX) and fully recessed oxide (FULL ROX) silicon structures using Si<sub>3</sub>N<sub>4</sub> as an oxidation mask. Ideal profiles are shown.

cross section appears as a bird's head with a prominent crest and "beak" as shown in Fig. 2. Such ridges or bumps on an otherwise planar surface which result from this dielectric isolation process are undesirable. They create abrupt topographic features on the surface

\* Electrochemical Society Active Member.

Key words: oxide isolation, recessed oxide, Si<sub>3</sub>N<sub>4</sub>, Si<sub>3</sub>N<sub>4</sub> oxidation mask, MOSFET fabrication.

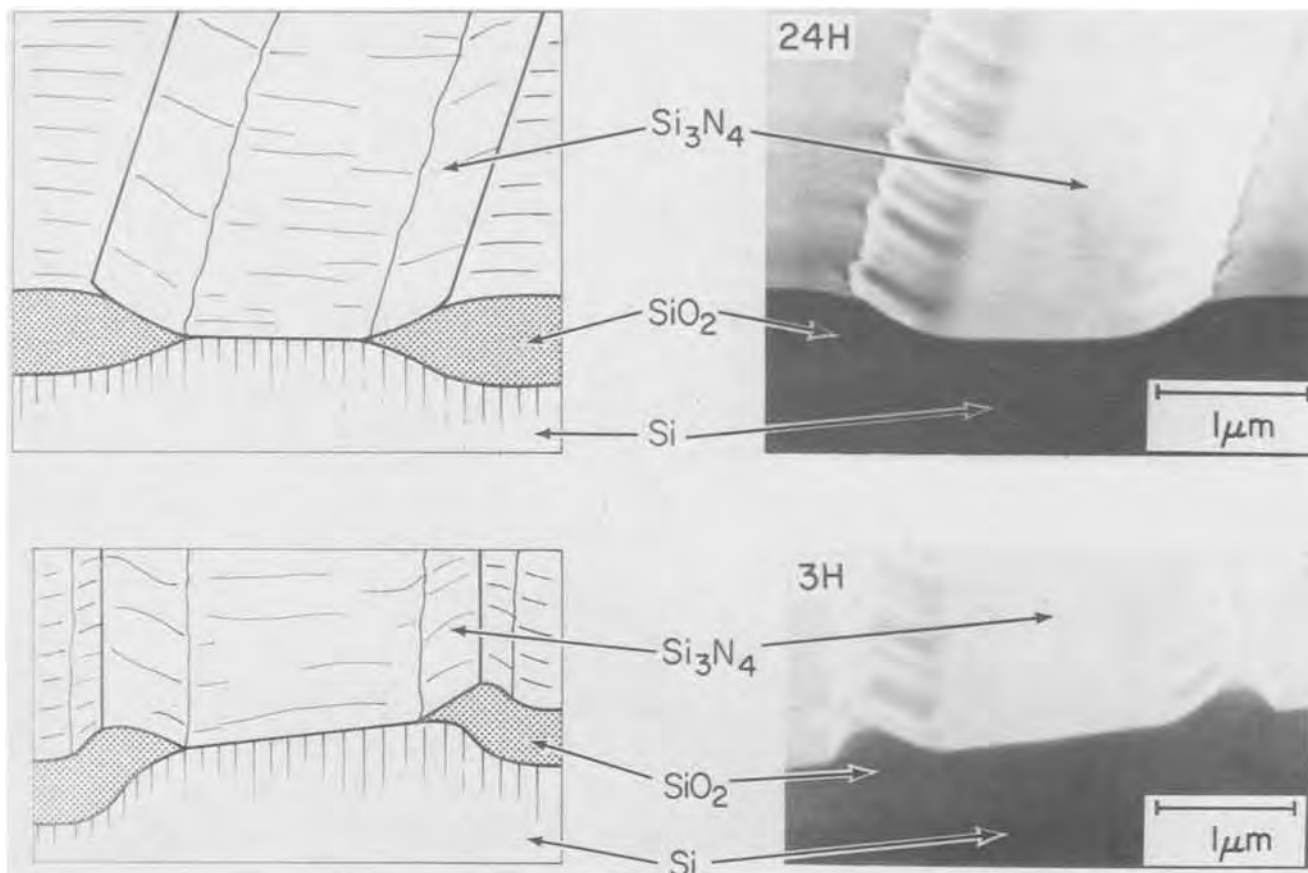


Fig. 2. Cross sections through experimental silicon structures showing SEMIROX (top) and full ROX (bottom) profiles

which can cause breaks or discontinuities in thin films covering the steps. The bird's beak is also undesirable because it reduces the available active surface area and thus detracts from the packing density of the integrated circuit. This experimental study was therefore undertaken to determine the conditions required to fabricate fully recessed oxide structures with a high degree of surface planarity suitable for the fabrication of very high density n-channel FET memory circuits.

### Experimental

For convenience of fabrication and examination of the bird's beak, silicon test structures were fabricated consisting of sets of parallel lines of thermal  $\text{SiO}_2$  recessed into the silicon substrate. The width of the oxide lines and silicon mesa lines varied between 2 and 30  $\mu\text{m}$ . The sequence of steps in the fabrication process is shown in Fig. 3 and involves a single masking step using processing conditions which are compatible with the fabrication of high density FET circuits.

**Fabrication steps.**—As shown in Fig. 3(a), an oxidation mask consisting of a thin film of thermal  $\text{SiO}_2$  and a film of CVD  $\text{Si}_3\text{N}_4$  is deposited on the surface of a (100) oriented silicon wafer, 2  $\Omega\text{-cm}$  p-type, 1.25 in. diameter. A third layer of CVD  $\text{SiO}_2$  is also deposited to serve as an etching mask for the underlying  $\text{Si}_3\text{N}_4$  film.

After the wafer is coated with photoresist, sets of parallel lines oriented along the  $\langle 110 \rangle$  direction are defined and etched in the CVD  $\text{SiO}_2$  film using buffered HF. The photoresist is removed and the  $\text{Si}_3\text{N}_4$  film is now etched in boiling  $\text{H}_3\text{PO}_4$  at 180°C. The oxide pad between  $\text{Si}_3\text{N}_4$  and the Si substrate is dip etched in buffered HF to yield a structure as shown in Fig. 3(b).

The exposed silicon substrate is etched to a predetermined depth in an anisotropic etching solution containing KOH, water, and isopropanol to form sets of parallel trenches of varying width. A cross section of a single silicon mesa line is shown in Fig. 3(c).

The silicon wafer is then thermally oxidized in steam at 1000°C to form the recessed oxide (ROX) in the etched trenches as shown in Fig. 3(d).

The wafer is scribed and cleaved across the sets of parallel lines and examined by SEM.

**Processing conditions.**—**Oxidation mask.**—A single layer of  $\text{Si}_3\text{N}_4$  deposited directly on silicon serves as an excellent oxidation mask. If the  $\text{Si}_3\text{N}_4$  film is sufficiently thick, it gives rise to only a small bird's beak. It was experimentally determined, however, that the silicon surface becomes heavily doped with n-type impurities due to the etching of the  $\text{Si}_3\text{N}_4$  film in  $\text{H}_3\text{PO}_4$  at 180°C. Furthermore, oxides grown on a silicon surface which had been coated with  $\text{Si}_3\text{N}_4$  and subjected to annealing in steam exhibited poor dielectric breakdown characteristics. Figure 4 shows C-V curves of MOS capacitors fabricated on Si wafers 10  $\Omega\text{-cm}$ , n-type, which were immersed in  $\text{H}_3\text{PO}_4$  at 180°C prior to oxidation. From the change in capacitance under strong inversion, it appears that the average surface doping caused by  $\text{H}_3\text{PO}_4$  is about  $1 \times 10^{18} \text{ cm}^{-3}$ . The doping layer introduced by  $\text{H}_3\text{PO}_4$  can be substantially eliminated by etching in buffered HF prior to oxidation. The doping and degradation of the silicon surface can be minimized if a thin layer of  $\text{SiO}_2$  (oxide pad) is introduced between the  $\text{Si}_3\text{N}_4$  film and the silicon surface.

TEM examination of silicon surfaces as shown in Fig. 5(a) and (b) clearly shows damage caused by  $\text{Si}_3\text{N}_4$  deposition which increases with the thickness of the film. The damage is reduced significantly if a thin  $\text{SiO}_2$  layer is introduced at the  $\text{Si}_3\text{N}_4$ -Si interface.

The  $\text{SiO}_2$  pad is thermally grown in dry oxygen at temperatures varying between 700° and 1000°C, depending on the thickness required. The  $\text{Si}_3\text{N}_4$  film is deposited at 800°C using a ratio of  $\text{NH}_3:\text{SiH}_4$  of 150:1 by volume, with  $\text{N}_2$  as a carrier gas. The deposition rate is 180  $\text{\AA}/\text{min}$ , the refractive index of the  $\text{Si}_3\text{N}_4$  film is 2.0, and the etch rate in  $\text{H}_3\text{PO}_4$  at 180°C is about

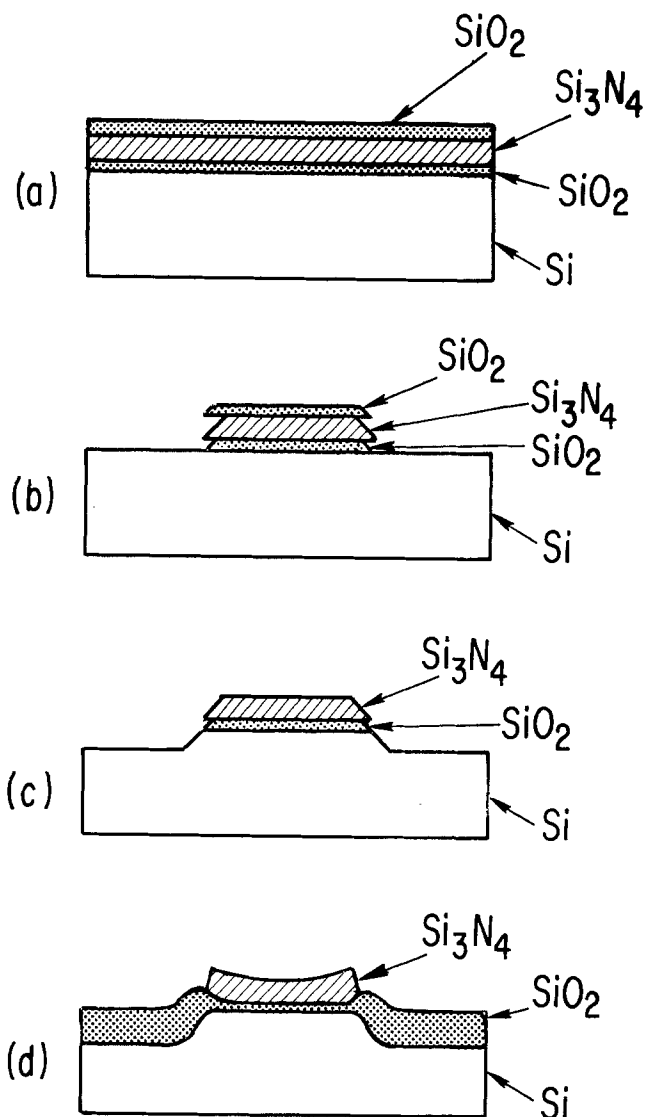


Fig. 3. Sequence of steps in the fabrication of experimental silicon recessed oxide structures.

100 Å/min. The CVD  $\text{SiO}_2$  which serves as an etching mask for  $\text{Si}_3\text{N}_4$  is deposited *in situ* immediately following the nitride deposition. The deposition rate is 160 Å/min at 800°C using  $\text{SiH}_4$  and  $\text{N}_2\text{O}$  with  $\text{N}_2$  carrier gas.

**Anisotropic etching.**—Anisotropic etching of (100) oriented silicon wafers followed by thermal oxidation has been proposed (11) as a method to fabricate densely packed and dielectrically isolated silicon integrated circuits. The characteristic feature of anisotropic etchants such as KOH and other strongly alkaline solutions (12-20) is that the etch rate varies widely depending on the crystallographic orientation of the silicon substrate. For the three low index crystal planes of silicon, the etch rate decreases in the order (100), (110), and (111). If holes are etched in (100) silicon with an anisotropic etching solution, the cavities formed are pyramidal in shape, bounded on four sides by the slowest etching (111) crystal planes which form an angle of 54.7° with the (100) surface plane. Rectangular openings whose sides are aligned parallel to the <110> direction, *i.e.*, parallel or perpendicular to the (110) flat of a (100) wafer, yield trenches with (111) sloping side walls and no significant undercutting. Because the profile of the cavities is highly predictable and the depth can be accurately controlled, the ROX line density can be greatly increased. Isotropic etchants, on the other hand, are not crystallographically preferential, cause excessive undercutting,

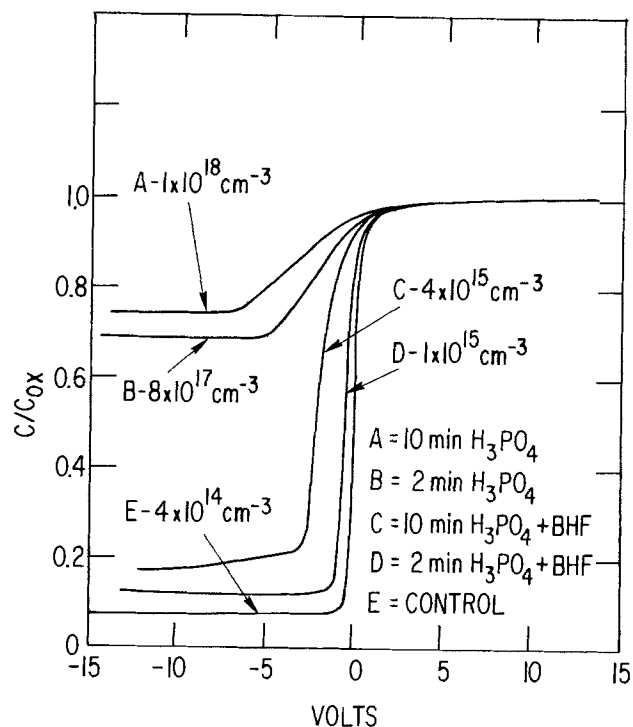


Fig. 4. Normalized capacitance-voltage characteristics of  $\text{SiO}_2$  grown on 10-20  $\Omega$ -cm n-type Si. Wafers A and B were subjected to boiling  $\text{H}_3\text{PO}_4$  at 180°C prior to oxidation, wafers C and D were also etched in buffered HF for 15 sec prior to oxidation. The average donor concentration at the surface shown for each curve is calculated from the ideal MOS minimum capacitance curves of A. [Ref. (23).]

and thus are not as useful in the fabrication of high density circuits using ROX technology.

The etching solution used in these experiments is a mixture of 100 ml 2M aqueous KOH and 25 ml isopropanol at 44°-45°C. The etch rate of (100) oriented silicon is about 10 Å/sec and is uniform over extended etching times.

### Results and Discussion

The shape of the bird's beak and crest at the transition between the  $\text{Si}_3\text{N}_4$  masked area and the recessed oxide region depends on the following factors: (i) the thickness of the  $\text{SiO}_2$  pad between the  $\text{Si}_3\text{N}_4$  film and the Si surface; (ii) the thickness of the  $\text{Si}_3\text{N}_4$  film used as the oxidation mask; (iii) the thickness of silicon etched from the substrate to form the trench and the extent of the undercutting of the oxide pad which tends to decrease the width of the silicon mesa lines; (iv) the uniformity of the etching of the Si substrate, the profile of the etched trench, and the degree of misalignment of line patterns relative to the <110> direction of a (100) oriented wafer; and (v) the thickness of the thermally grown recessed oxide.

The relative size of the bird's beak and the prominence of the bird's crest are illustrated in Fig. 6. As silicon is removed by etching to enable the oxide to be recessed deeper into the substrate, the beak tends to increase in length and the crest tends to be more pronounced. In SEMIROX structures, which are formed without etching the silicon substrate, the oxide thickness is approximately equally divided above and below the original silicon surface. A step appears at the ROX-Si boundary but no crest is apparent. The absence of a protruding crest is a distinguishing feature of a SEMIROX structure as compared to a full ROX structure.

The thicknesses of the nitride layer and of the oxide pad have opposing effects on the size of the bird's beak and crest. As the nitride thickness is increased, the growth of bird's beak and crest are more effectively suppressed due to the increasing rigidity of the nitride



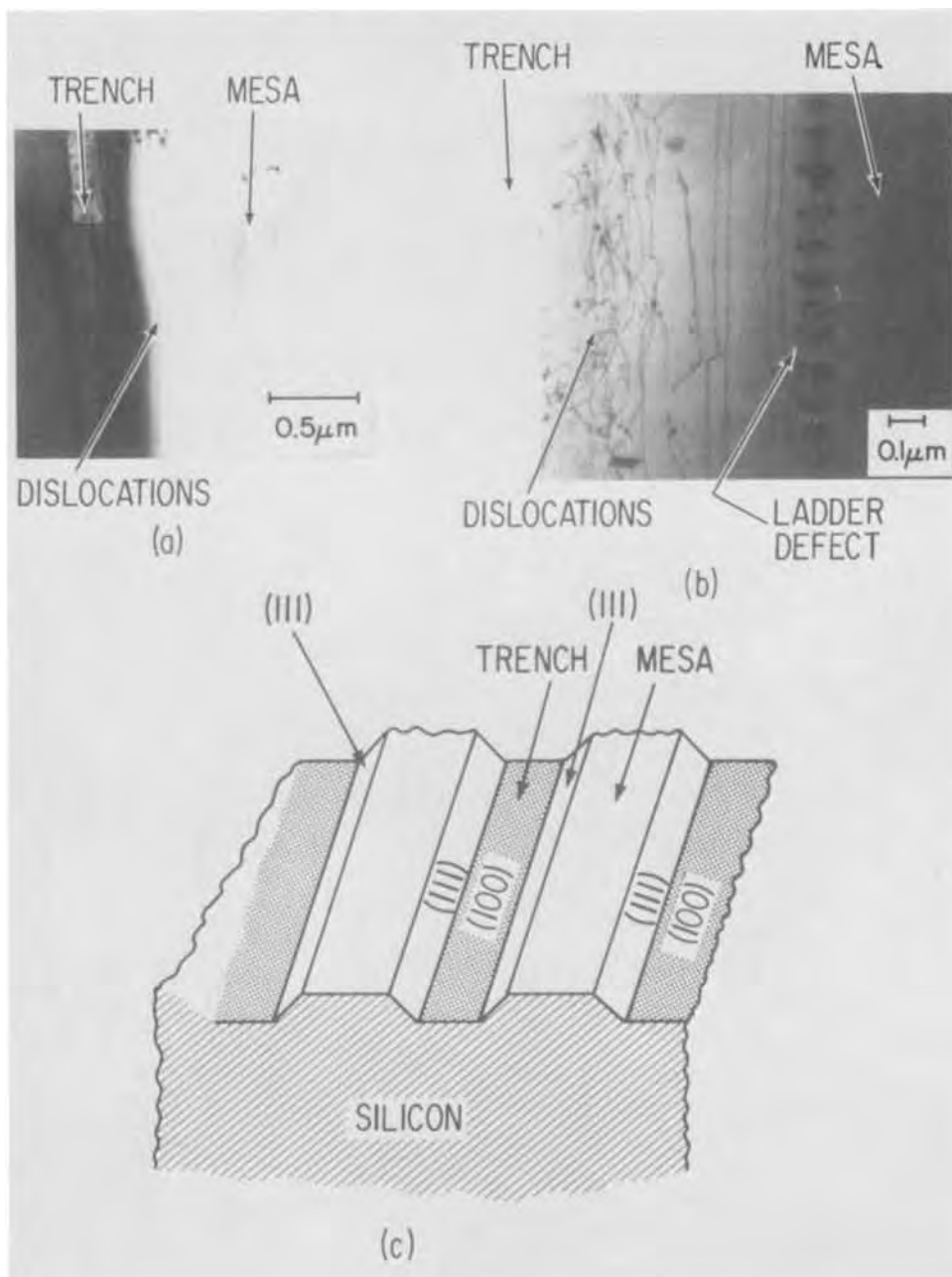


**Fig. 5. Transmission electron micrographs of ROX structures showing dislocations and damage in the silicon mesa lines and (111) sidewalls. The trenches etched in silicon are 2000Å deep, and the ROX grown is 4500Å thick, SiO<sub>2</sub> pad 50Å under Si<sub>3</sub>N<sub>4</sub>. (a) Si<sub>3</sub>N<sub>4</sub> 2000Å, (b) Si<sub>3</sub>N<sub>4</sub> 4500Å.**

film. Figure 7 shows SEM photomicrographs of ROX structures prepared under similar conditions with nitride films ranging between 300 and 4500Å in thickness. After the growth of the recessed oxide, the nitride film is strained and tends to bend. The curvature of the strained nitride film is apparent for thicknesses less than 2000Å. With a nitride film 300Å in thickness, it shows considerable curvature as evident in the semicylindrical shape of the 2 μm wide line in sample 3H of Fig. 7.

Although suppression of the bird's beak and crest is desirable for device fabrication, thick nitride films tend to damage the silicon and to degrade the dielectric properties of the oxide subsequently grown on it. A film of Si<sub>3</sub>N<sub>4</sub> 4500Å in thickness suppresses the bird's beak; however, the stress in the film is so large that it causes a visible distortion of a 0.2 mm thick wafer. Thin nitride films, on the other hand, tend to curl, giving rise to a large beak and crest after the ROX growth. Selection of parameters for a trade-off between a complete suppression of the bird's beak and

the avoidance of damage to the silicon surface is necessary in the fabrication of ROX device structures.

The oxide pad thickness determines the ease of oxidation between the nitride film and the silicon substrate. As expected, the bird's beak tends to increase as the pad thickness increases, as is evident in Fig. 8 which shows SEM photomicrographs of cross sections of SEMIROX structures prepared without anisotropic etching of the silicon substrate. A similar but more pronounced increase in the bird's beak is also observed as the thickness of the recessed oxide is increased as shown in the SEM photomicrographs of Fig. 9.

Quantitative measurements of the bird's beak and crest were made from SEM photomicrographs of cross sections of ROX device samples. The results are plotted as a function of various film thicknesses in Fig. 10, 11, and 12.

In Fig. 10 the magnitude of the bird's beak and crest are plotted as a function of the thickness of silicon which is anisotropically etched from the substrate to form the recessed oxide structures. All the data points



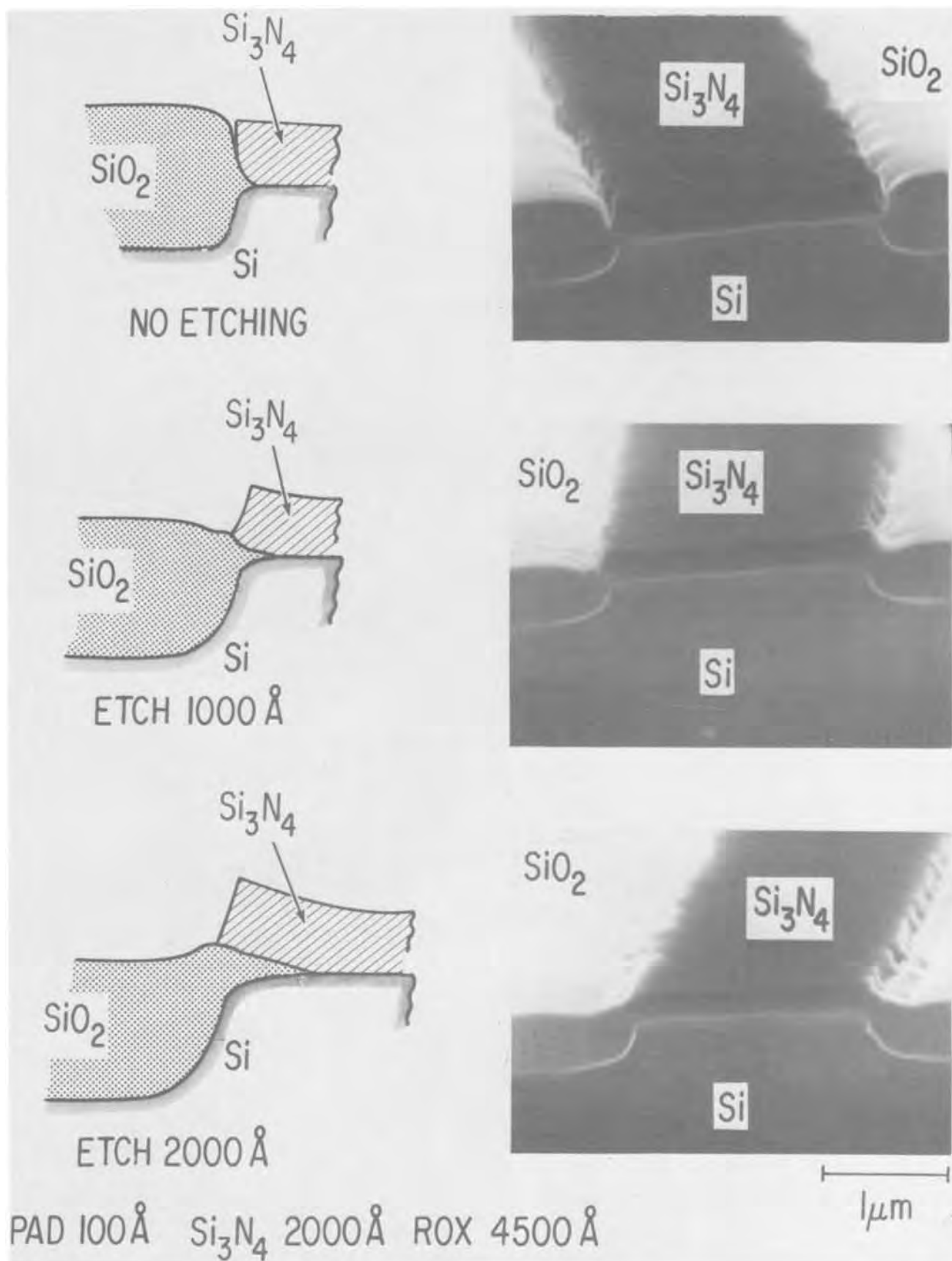


Fig. 6. Cross sections of recessed oxide structures showing the change in the shape of the bird's crest and beak as silicon is anisotropically etched from the substrate. Top: no etching of Si substrate prior to thermal oxidation to form the SEMIROX structure. Note absence of crest. Middle: 1000Å of Si etched from the substrate prior to growing the recessed oxide. Bottom: 2000Å Si etched from the substrate prior to growing the full ROX structure. Note prominence of bird's beak and crest.

shown in Fig. 10 are for samples prepared with 50Å  $\text{SiO}_2$  pad, 1000Å  $\text{Si}_3\text{N}_4$ , and 4500Å of recessed oxide. The beak appears to be relatively insensitive to the

thickness of silicon etched from the substrate in the range 0-2000Å provided there is no undercutting. The crest, however, is initially unaffected but then shows a

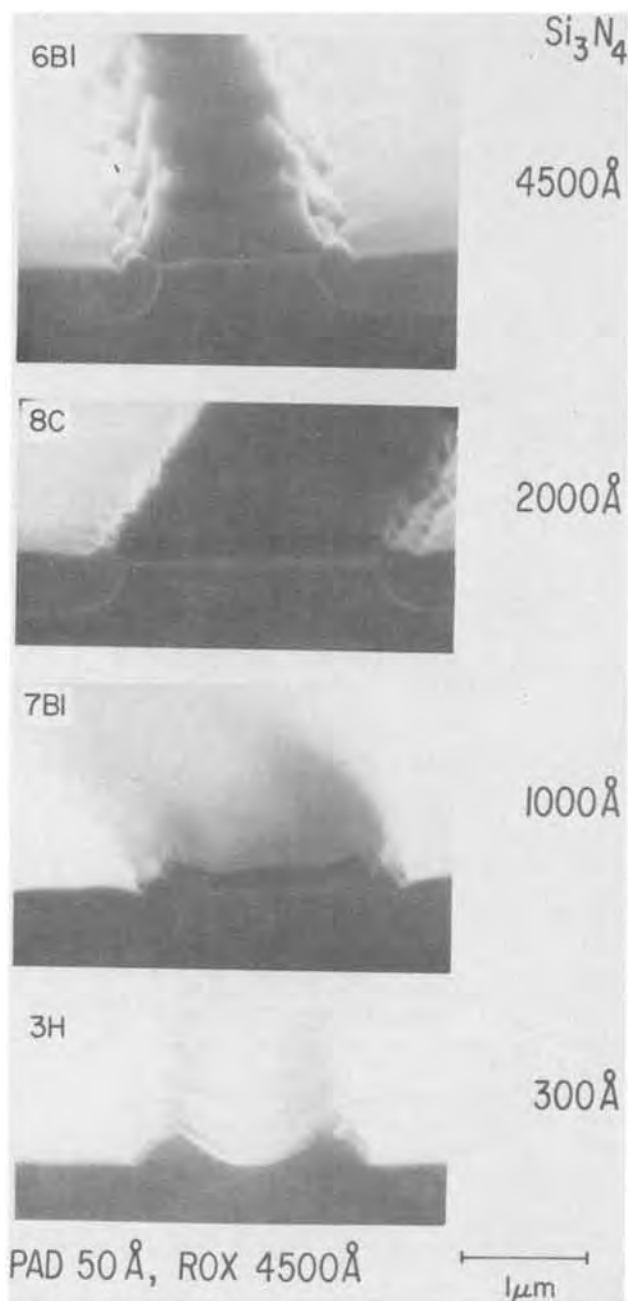


Fig. 7. SEM photomicrographs of ROX structures fabricated with different thicknesses of  $\text{Si}_3\text{N}_4$ .  $\text{Si}_3\text{N}_4$  4500 Å thick is rigid and gives rise to a minimum crest and no beak, whereas a film 300 Å thick shows a large curvature, with a pronounced crest and a long beak (sample 3H).

sharp increase between 1000 and 2000 Å of etched silicon. The sample formed by etching 2000 Å of Si is a fully recessed oxide structure whose surface is essentially coplanar with the surface of the substrate with the crest appearing as a raised ridge above the wafer surface. The samples prepared with less than 2000 Å of etched silicon have partially recessed oxides showing little or no protruding ridges but exhibit a step with a gradual sloping sidewall where the ROX surface is raised relative to the surface of the Si substrate. Surface ridges or steps exist in both fully recessed and partially recessed oxide structures, but they differ in geometry and magnitude depending on processing conditions.

The effect of the thickness of the  $\text{Si}_3\text{N}_4$  film on fully recessed oxide structures prepared by anisotropic etching of 2000 Å of silicon followed by growing 4500 Å of ROX to form a quasi-planar surface is shown in Fig.

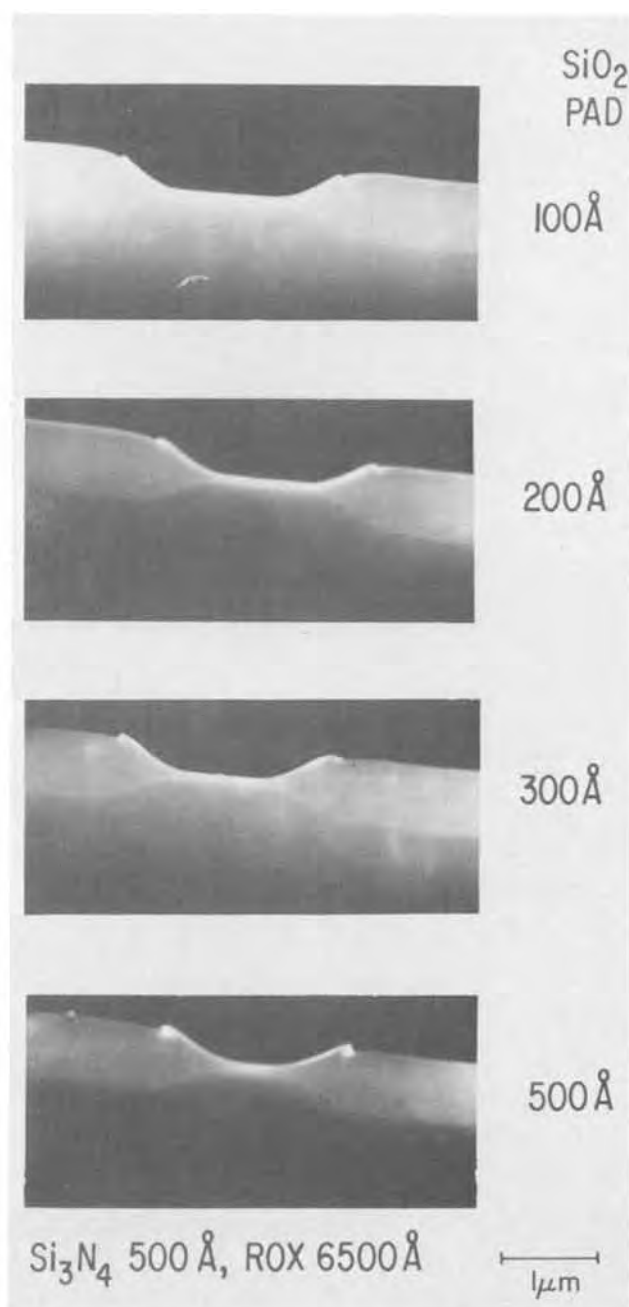


Fig. 8. SEM photomicrographs of cross sections of SEMIROX structures showing the increase in the bird's beak as the  $\text{SiO}_2$  pad thickness is increased. The  $\text{SiO}_2$  pad is between the Si substrate and the  $\text{Si}_3\text{N}_4$  oxidation mask.

11. The bird's head is diminished in proportion to the thickness of  $\text{Si}_3\text{N}_4$  film used, whereas the opposite result is observed if the oxide pad is increased from 50 to 100 Å. The bird's beak and crest are also equally sensitive to processing conditions particularly in regard to the extent of undercutting of the oxide pad during the fabrication of ROX structures. As shown in Fig. 4, the CVD  $\text{SiO}_2$  used as an etching mask for  $\text{Si}_3\text{N}_4$  is etched off prior to anisotropic etching, causing undercutting of the oxide pad by 50-100% of the thickness of the CVD  $\text{SiO}_2$  film. To minimize the bird's beak, the CVD  $\text{SiO}_2$  film should either be as thin as possible or be removed after the recessed oxide is formed to avoid any undercutting. Undercutting will also take place in the anisotropic etching of silicon if the line pattern is misaligned relative to the  $\langle 110 \rangle$  directions which are parallel to and perpendicular to the (110) "flat" on a (100) oriented silicon wafer. The

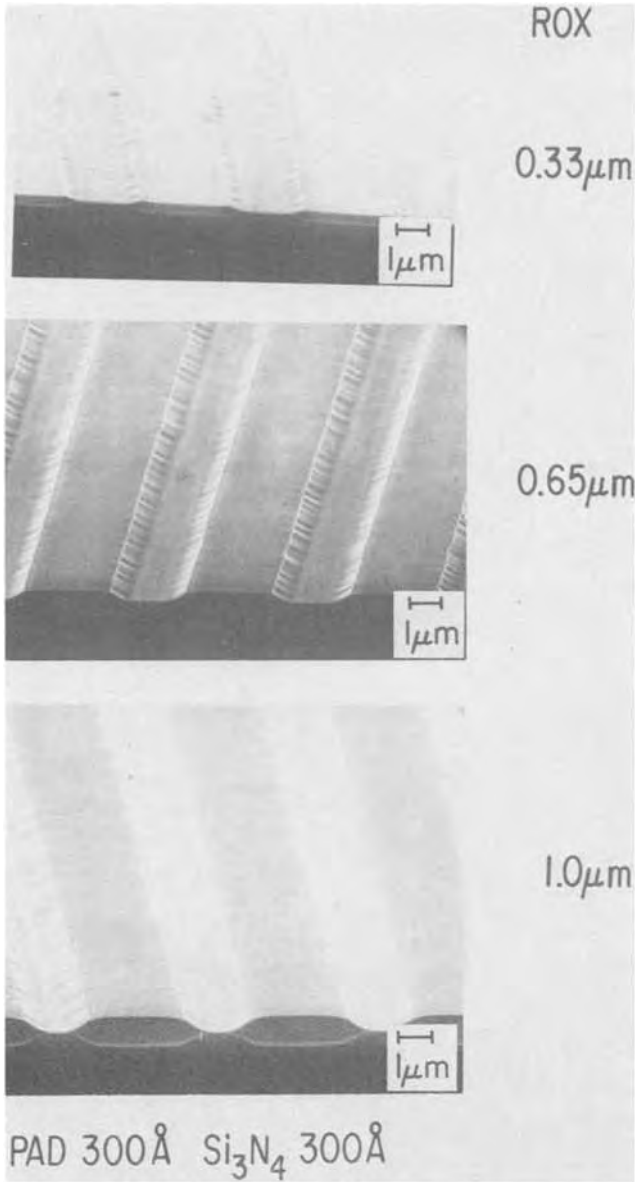


Fig. 9. SEM photomicrographs of SEMIROX structures showing the increase in the bird's beak as the thickness of the recessed oxide in the field is increased.

degree of undercutting is a maximum when the line pattern makes an angle of  $45^\circ$  with the  $\langle 110 \rangle$  direction and is a minimum when this angle is  $0^\circ$ .

The corresponding curves for semirecessed oxide structures prepared with no anisotropic etching of the substrate are shown in Fig. 12. The oxide pad thickness has little effect on the curvature of the  $\text{Si}_3\text{N}_4$  film after growing the recessed oxide, but has some influence on the bird's beak. The data points in Fig. 12 for samples prepared with  $500\text{\AA}$   $\text{Si}_3\text{N}_4$  were measured from the SEM photomicrographs shown in Fig. 8. The  $500\text{\AA}$  CVD  $\text{SiO}_2$  film used as an etch mask for the  $\text{Si}_3\text{N}_4$  film was etched off prior to the oxidation of these samples.

Most of the experimental ROX structures were fabricated on (100) oriented silicon with trenches etched anisotropically to form a profile with (111) sidewalls slanting at an angle of  $55^\circ$  with the horizontal. In order to find out how a trench with vertical sidewalls affects the geometry of ROX structures (21), trenches in (110) oriented wafers were etched by aligning them parallel to one set of the (111) planes which intersect the (110) surface plane vertically. As shown in Fig. 13, properly aligned and etched trenches can be obtained with vertical sidewalls and no observable undercutting. They yield a recessed oxide whose topography displays

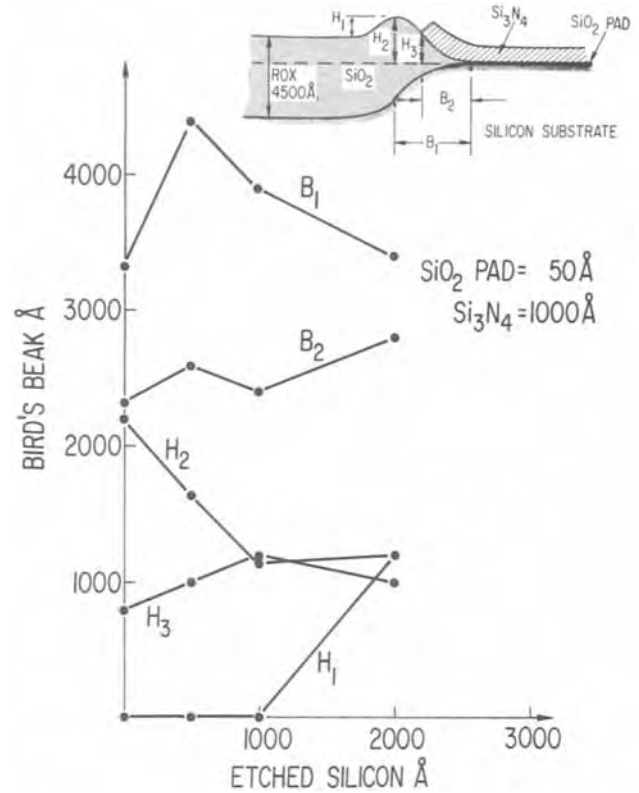


Fig. 10. Selected features of the bird's beak and crest plotted as the ordinate vs. the thickness of silicon removed from the substrate by anisotropic etching prior to thermally growing  $4500\text{\AA}$  of recessed oxide.

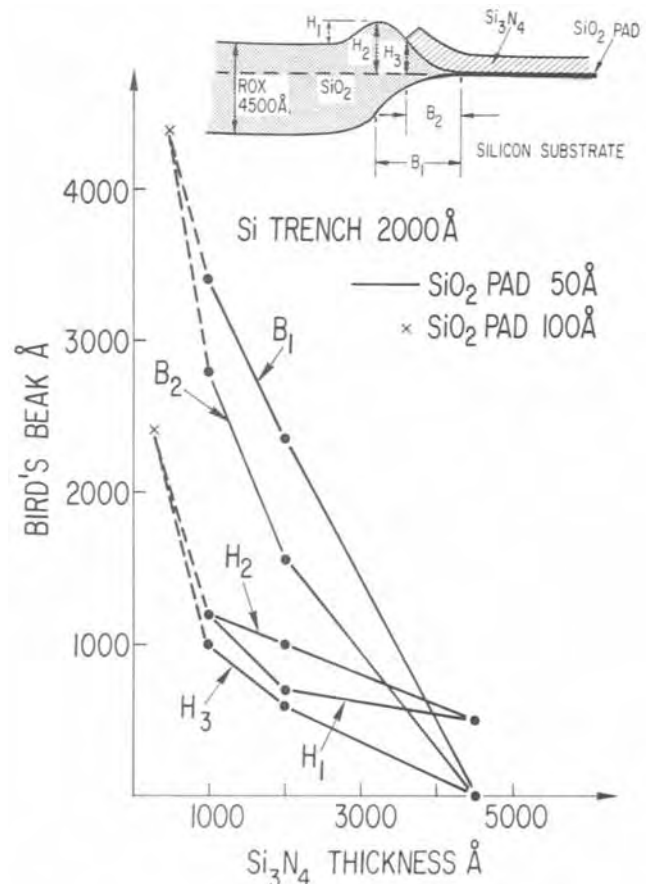


Fig. 11. Selected features of the bird's beak and crest of full ROX structures plotted as the ordinate vs. the thickness of  $\text{Si}_3\text{N}_4$  used as the oxidation mask. The thickness of silicon etched anisotropically from the substrate was  $2000\text{\AA}$  prior to thermally growing  $4500\text{\AA}$  of recessed oxide.

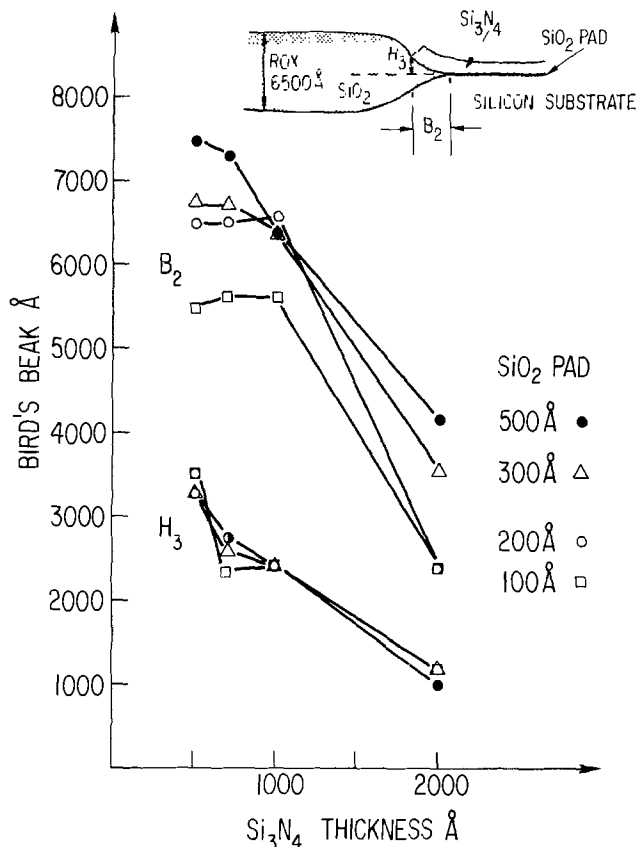


Fig. 12. Selected features of the bird's beak of SEMIROX structures plotted as the ordinate vs. the thickness of  $\text{Si}_3\text{N}_4$  used as the oxidation mask, for different thicknesses of  $\text{SiO}_2$  pad. The semirecessed oxide  $6500\text{\AA}$  thick is the same for all the samples.

a prominent crest and beak conforming with the profile of the etched trench configuration. The surface planarity in this case shows no improvement over the ROX structures formed in (100) wafers.

An optimum surface planarity with minimum bird's beak was obtained using  $50\text{\AA}$   $\text{SiO}_2$  pad, an oxidation mask of  $\text{Si}_3\text{N}_4$   $2000\text{\AA}$  thick, anisotropic etching of the silicon substrate to form trenches  $2000\text{\AA}$  deep, and a fully recessed field oxide  $4500\text{\AA}$  thick. These processing conditions have been successfully applied to the fabrication of an experimental 8K bit MOSFET memory chip  $1.1 \times 1.6 \text{ mm}^2$  with  $1.25 \mu\text{m}$  minimum linewidth with a fully recessed field oxide (22).

### Conclusions

Silicon structures with recessed oxide which are fabricated using  $\text{Si}_3\text{N}_4$  as the oxidation mask, anisotropic etching of the silicon, and thermal oxidation deviate from surface planarity due to lateral oxidation at the edge of the  $\text{Si}_3\text{N}_4$ -masked region. The protruded structure on the surface of the wafer appears as a bird's head whose size can be predicted from the processing conditions used to fabricate the structures. The suppression of the bird's beak and crest which is highly desirable for IC fabrication can be achieved by increasing the thickness of the  $\text{Si}_3\text{N}_4$  oxidation mask, decreasing the thickness of the  $\text{SiO}_2$  pad between the Si substrate and the  $\text{Si}_3\text{N}_4$  layer, and by minimizing the ROX thickness. Too thick a layer of  $\text{Si}_3\text{N}_4$  will degrade or damage the Si surface. A compromise of  $50\text{\AA}$   $\text{SiO}_2$ ,  $2000\text{\AA}$   $\text{Si}_3\text{N}_4$ , and ROX  $4500\text{\AA}$  grown in an anisotropically etched substrate  $2000\text{\AA}$  deep was found to be satisfactory in the fabrication of a high density 8K bit MOSFET memory chip with  $1.25 \mu\text{m}$  minimum linewidth.

### Acknowledgments

We wish to express our thanks to S. Mader for the TEM analysis and to R. Dennard, V. L. Rideout, and

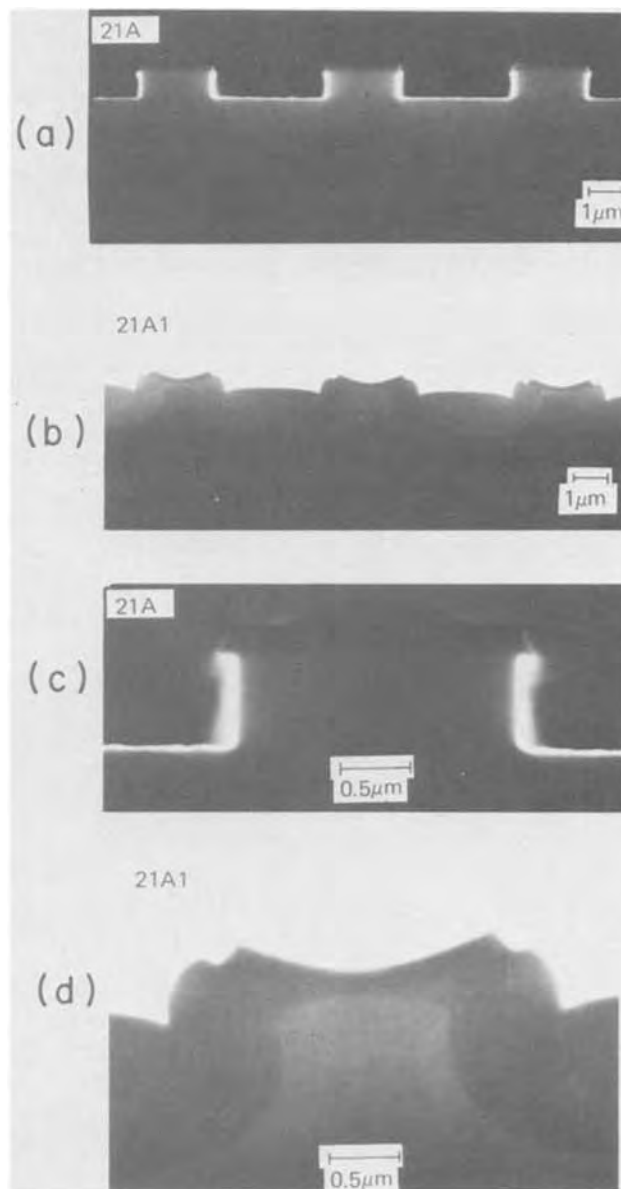


Fig. 13. SEM photomicrographs of cross sections through silicon mesa lines and ROX structures fabricated by anisotropic etching of (110) oriented Si wafers: (a) 3 mesa lines with vertical sidewalls; (b) ROX structures formed after thermal oxidation of sample (a); (c) single mesa line, showing minimum undercutting; (d) ROX structure formed after thermal oxidation of sample (c).

C. M. Osburn for many helpful discussions. The technical assistance of J. Kucza, M. Smyth, A. Cramer, H. Lazzari, J. Kuran, and E. Petrillo is gratefully acknowledged.

Manuscript submitted April 9, 1976; revised manuscript received July 15, 1976.

Any discussion of this paper will appear in a Discussion Section to be published in the June 1977 JOURNAL. All discussions for the June 1977 Discussion Section should be submitted by Feb. 1, 1977.

Publication costs of this article were assisted by IBM Corporation.

### REFERENCES

1. K. E. Bean and W. R. Runyan, Paper 138 presented at The Electrochemical Society Meeting, New York, New York, Oct. 13-17, 1974.
2. F. Morandi, IEEE International Electron Devices Meeting, Session 18, Oct. 1969.
3. E. Kooi and J. A. Appels, in "Semiconductor Silicon 1973," H. R. Huff and R. R. Burgess, Editors, p. 860, The Electrochemical Society Softbound

Symposium Series, Princeton (1973).

4. D. Peltzer and B. Herndon, *Electronics*, **44**, 52 (1971).
5. D. L. Peltzer, U.S. Pat. 3,648,125 (1972).
6. W. J. Evans, A. R. Tretola, R. S. Payne, M. L. Olmstead, and D. V. Speeney, *IEEE J. Solid-State Circuits*, **sc-8**, 373 (1973).
7. R. Edwards, R. S. Payne, C. F. Gibbon, M. L. Olmstead, R. A. Moline, D. L. Kushler, G. R. Weber, and R. T. Kraetsch, in "Semiconductor Silicon 1973," H. R. Huff and R. R. Burgess, Editors, p. 905, The Electrochemical Society Softbound Symposium Series, Princeton (1973).
8. I. E. Magdo and S. Magdo, U.S. Pat. 3,855,609 (1974).
9. I. E. Magdo and S. Magdo, U.S. Pat. 3,859,231 (1974).
10. E. Bassous, H. N. Yu, and V. Maniscalco, Paper 175, presented at The Electrochemical Society Meeting, Dallas, Texas, Oct. 5-9, 1975.
11. R. Dennard, V. L. Rideout, and E. J. Walker, U.S. Pat. 3,899,363 (1975).
12. A. I. Stoller, *RCA Rev.*, **31**, 271 (1970).
13. R. M. Finn and D. L. Klein, *This Journal*, **114**, 965 (1967).
14. D. B. Lee, *J. Appl. Phys.*, **40**, 4569 (1969).
15. R. C. Rosenfeld and K. E. Bean, Proceedings of the IEEE Ultrasonics Symposium, p. 186 (1972).
16. T. O. Sedgwick, A. N. Broers, and B. J. Agule, *This Journal*, **120**, 1769 (1972).
17. J. B. Price, in "Semiconductor Silicon 1973," H. R. Huff and R. R. Burgess, Editors, p. 339, The Electrochemical Society Softbound Symposium Series, Princeton (1973).
18. K. E. Bean and J. R. Lawson, *IEEE J. Solid-State Circuits*, **sc-9**, 111 (1974).
19. D. L. Kendall, *App. Phys. Lett.*, **26**, 195 (1975).
20. M. J. Declercq, L. Gerzberg, and J. D. Meindl, *This Journal*, **122**, 545 (1975).
21. P. Tsang, Private communication.
22. H. N. Yu, R. H. Dennard, T. H. P. Chang, C. M. Osburn, V. Dilonardo, and H. E. Luhn, *J. Vac. Sci. Technol.*, **12**, 1297 (1975).
23. A. Goetzberger, *Bell Syst. Tech. J.*, **45**, 1097 (1966).

## High Surface Concentration Zn Diffusion in GaAs

K. K. Shih\*

IBM Thomas J. Watson Research Center, Yorktown Heights, New York 10598

### ABSTRACT

A high surface concentration layer is essential for obtaining good ohmic contact on GaAs devices. Zn diffusion in GaAs using  $Zn_3As_2$ ,  $ZnAs_2$ ,  $Zn_3As_2 + ZnAs_2$ , and  $ZnAs_2 + As$  as diffusion sources at low temperatures (600°-730°C) has been studied. The resulting surfaces were reproducible and undamaged, and the surface concentrations were in the  $10^{20} \text{ cm}^{-3}$  range.

The use of Zn as a diffusion source to obtain a high surface concentration layer for the purpose of reducing the contact resistance of p-type GaAs has been applied to many devices, especially the GaAs- $Al_xGa_{1-x}As$  double heterojunction lasers. Most of the Zn diffusions were carried out under excess As pressure, using Zn and As compounds as diffusion sources at low temperatures to obtain thin, high surface concentration layers (1-3). In this paper, a systematic study of the diffusion processes using  $Zn_3As_2$ ,  $ZnAs_2$ ,  $Zn_3As_2 + ZnAs_2$ , and  $ZnAs_2 + As$  as diffusion sources at low temperatures (600°-730°C) was made. The resulting diffused layers had high surface concentrations ( $\sim 10^{20} \text{ cm}^{-3}$ ) with undamaged surfaces, and reproducible results were obtained.

### Phase Diagram Consideration

The diffusion of Zn in GaAs is affected by the Ga vacancy concentration, which in turn is governed by the As pressure. Hence, in order to understand the diffusion results, it is necessary to determine the phase relationship between the constituents. Under the conditions of our experiments, it is expected that the gaseous and liquid phases and the surface of the GaAs will be in mutual equilibrium. It is therefore permissible to use the equilibrium phase diagram in discussing these parts of the system (4, 5).

From a study of the Ga-As-Zn phase diagram, it was found that at low temperatures, say between 600° and 730°C, all the liquid and solid phases in the phase diagram have nearly the same boundaries at all temperatures within this range. Figure 1 is a 700°C isothermal section of the ternary phase diagram using the data of Panish (6). At this temperature there is a large region where no liquid phase exists.

Diffusion of Zn in GaAs is limited to regions that have solid GaAs in equilibrium with other phases. These are regions I-VI in Fig. 1 where regions III and V are grossly exaggerated. Since region I contains a series of liquid phases and II contains liquid phase A, the surface of GaAs may deteriorate if diffusion is held in one of these two regions. Hence, only regions III-VI where there are no liquid phases in these regions are to be considered.

The consequences for diffusion in regions III-VI can be best understood in terms of the number of degrees of freedom  $F$ . For an isothermal ternary system in

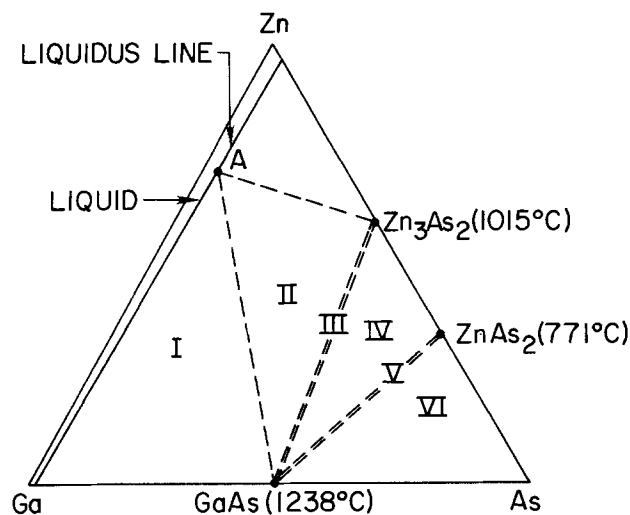


Fig. 1. The 700°C Ga-As-Zn ternary isotherm. Regions I-VI have solid GaAs in equilibrium with other phases.

\* Electrochemical Society Active Member.

Key words: Zn diffusion,  $ZnAs_2$ ,  $Zn_3As_2$ , GaAs.

contact with the vapor, the phase rule (7) specifies that  $F = 3 - P$  where  $P$  is the number of condensed phases.

(i) Region III is a narrow region separating regions II and IV. There is no liquid phase, but there are two solid phases, GaAs and  $Zn_3As_2$ , so that  $F = 1$ . Hence one parameter such as the As pressure can specify the system. This is the region to be considered when  $Zn_3As_2$  is used as a diffusion source for Zn diffusion in GaAs. The As pressure in this region can vary from the As pressure in region II to that in region IV depending on the weights of source and GaAs samples and the volume of the diffusion ampul. Therefore the control of weight and volume is required for a reproducible junction depth.

(ii) In region IV, there are three solid phases, GaAs,  $Zn_3As_2$ , and  $ZnAs_2$ , so that  $F = 0$ . This means that everything is fixed in this region, including the As pressure. There is a large area where there is no liquid phase. This is the region of interest when  $Zn_3As_2 + ZnAs_2$  is used as a diffusion source. In this region, the result of Zn diffusion is independent of the weights of the source and GaAs samples and volume of the ampul and depends only on temperature, because a small change in the amount of material placed in the ampul will have no effect on the Zn and As vapor pressure if diffusion is done in this region. It is in this region where reproducible results with undamaged surfaces can be obtained.

(iii) Region V is also a narrow region similar to region III. This is the region to be considered when  $ZnAs_2$  is used as a diffusion source. The As pressure can be varied from that in region IV to that in region VI, depending on the weights of the source and GaAs samples and the volume of the ampul. Therefore the control of weight and volume is also required for a reproducible junction depth.

(iv) Region VI can be discussed in the same manner as that of region IV. Same as region IV, reproducible results with undamaged surface can be obtained if diffusion is held in this region. This is the region of interest when  $ZnAs_2 + As$  is used as a diffusion source. The As pressure in this region is not only fixed but it is also the highest among all the regions.

### Experimental

The diffusion sources  $Zn_3As_2$  and  $ZnAs_2$  of 6-9's quality were obtained from the Cerac Company. Three (100) oriented GaAs single crystals, which, respectively, were Sn-doped with electron concentration about  $2 \times 10^{17} \text{ cm}^{-3}$ , Si-doped with electron concentration about  $2 \times 10^{18} \text{ cm}^{-3}$ , and Zn-doped with hole concentration about  $3 \times 10^{18} \text{ cm}^{-3}$ , were used as samples in each diffusion experiment. The surfaces were chemically polished to provide a damage-free surface. Cleaning prior to sealing consisted of degreasing and washing in solvents and deionized water. All three GaAs samples, each approximately  $\frac{1}{4}$  in. square and about 25 mil thick, were sealed in a fused-silica ampul along with 1-4 mg of the source materials. This amount of source is in excess in order to maintain a solid phase during the diffusion. Source and samples were separated by slightly necking down the 10 mm ID silica tubing near the end to form a bubble shape. The ampul was evacuated to a pressure of about  $10^{-7}$  Torr and sealed at a length of 3 in. Numerous diffusions were made between 600° and 730°C for times ranging from 10 min to 4 hr. After diffusion, the source end of the tube was withdrawn first and cooled rapidly to prevent deposition of the vapor on sample surfaces.

The sheet resistance of each sample was then measured using the four-point probe method. The junction depth was measured after the samples were cleaved and stained in 1:1:10 HF:H<sub>2</sub>O<sub>2</sub>:H<sub>2</sub>O solution under illumination.

### Results and Discussion

The smooth and shiny appearance of the wafer surfaces was retained after three diffusions. After exam-

ining the junction depth,  $x_j$ , of all three samples from the same diffusion, it was found that the values were very close to each other, indicating that the diffusion profiles are very steep. These results are consistent with that reported previously for the diffusion of Zn into GaAs under excess As pressure (4, 5). In order to demonstrate the reproducibility of these diffusion processes, some of the diffusions have been repeated several times and the same junction depth has been obtained. The junction depth vs. the square root of time for various diffusions using  $Zn_3As_2$ ,  $ZnAs_2$  or  $Zn_3As_2 + ZnAs_2$ , and  $ZnAs_2 + As$  as diffusion sources is plotted in Fig. 2, 3, and 4, respectively. The straight line relationship indicates that Fick's law (8) is obeyed.

By comparing Fig. 2, 3, and 4, it was found that at the same temperature, the junction depth was the greatest when  $Zn_3As_2$  was used as a diffusion while the junction depth was the smallest when  $ZnAs_2 + As$  was used as a diffusion source. These results were expected because the As pressure was the lowest when  $Zn_3As_2$  was used as a diffusion source and the highest when  $ZnAs_2 + As$  was used as a diffusion source. These results are consistent with that reported in Ref. (4) where the junction depth decreases with increasing As pressure.

It was also noted that at a given temperature the junction depth for diffusions using either  $ZnAs_2$  or  $Zn_3As_2 + ZnAs_2$  as diffusion sources was exactly the same. This suggests that the As pressure in the ampul for both sources was the same during our diffusion studies. From the discussion of the phase diagram in Fig. 1, it was concluded that the As pressure in the region containing  $Zn_3As_2 + ZnAs_2$  is fixed at a given

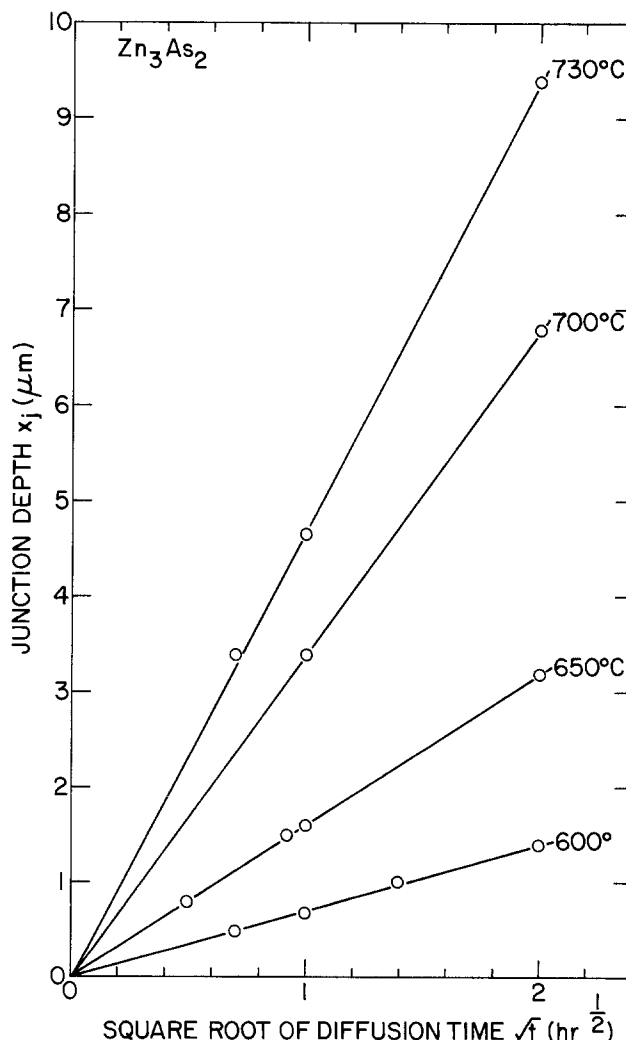


Fig. 2. The junction depth vs. square root of time at different temperatures (diffusion source  $Zn_3As_2$ ).

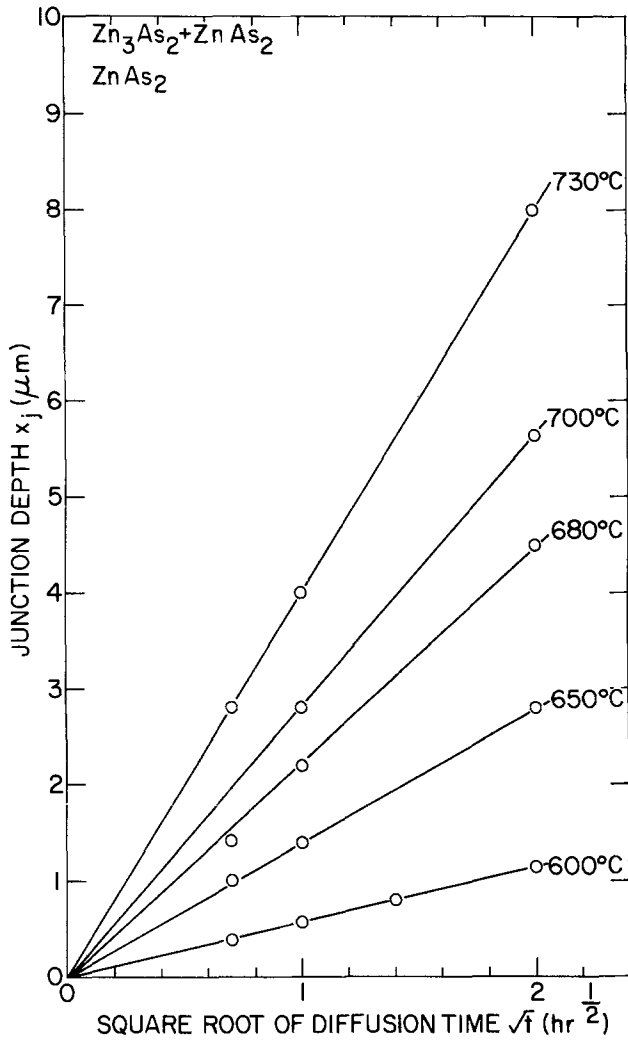


Fig. 3. The junction depth vs. square root of time at different temperatures (diffusion source  $\text{ZnAs}_2$  or  $\text{Zn}_3\text{As}_2 + \text{ZnAs}_2$ ).

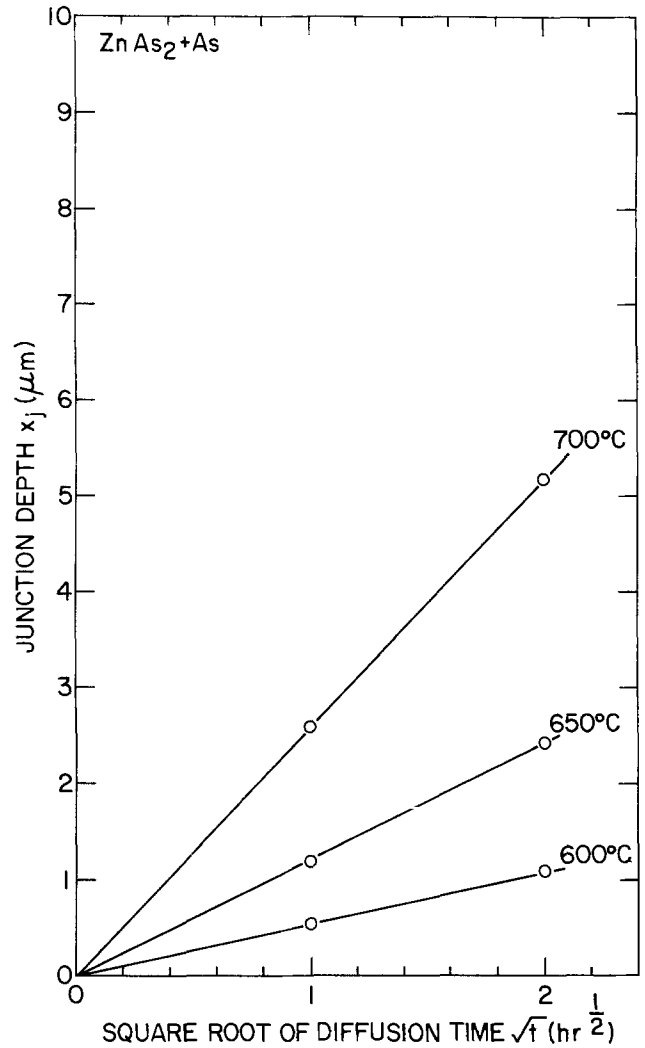


Fig. 4. The junction depth vs. square root of time at different temperatures (diffusion source  $\text{ZnAs}_2 + \text{As}$ ).

temperature, while the As pressure in the region containing  $\text{ZnAs}_2$  can be varied from that in the region containing  $\text{Zn}_3\text{As}_2 + \text{ZnAs}_2$  to higher values. Since the weight of the  $\text{ZnAs}_2$  source, which was about 1 mg in our diffusion case, was small in comparison with the weight of the GaAs samples, which was over 100 mg, with no extra As added in the system, the As pressure using  $\text{ZnAs}_2$  as a diffusion source in our studies was always on the low side and therefore closer to the As pressure using  $\text{Zn}_3\text{As}_2 + \text{ZnAs}_2$  as a diffusion source. This also applies to the  $\text{Zn}_3\text{As}_2$  case, where the As pressure using  $\text{Zn}_3\text{As}_2$  as a source in our diffusion studies was also on the low side and closer to the As pressure in region II.

The variation of junction depth vs. temperature at a given time using  $\text{ZnAs}_2$  or  $\text{Zn}_3\text{As}_2 + \text{ZnAs}_2$  as diffusion sources was deduced from Fig. 3 and the results are plotted in Fig. 5. The information presented in Fig. 5 is useful in predetermining the junction depth at various temperatures. The same kind of information can be deduced from Fig. 2 and 4 for the other two sources.

The sheet resistance,  $\rho_s$ , of the diffusion layers has been measured by the four-point probe method. In Fig. 6, the resistivity  $\rho$  which is the product of sheet resistance  $\rho_s$  and junction depth  $x_j$  is plotted as a function of temperature for different diffusion sources. The average conductivity  $\bar{\sigma}$  of a diffused layer can be expressed as (9)

$$\bar{\sigma} = \frac{1}{\rho} = \frac{1}{\rho_s x_j} = q\mu N \quad [1]$$

where  $q$  is the electron charge,  $\mu$  is the average carrier

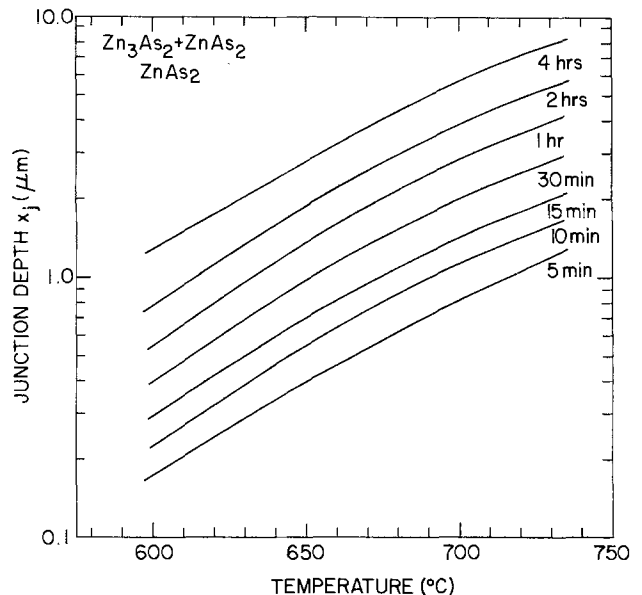


Fig. 5. The variation of junction depth with temperature at different time (diffusion source  $\text{ZnAs}_2$  or  $\text{Zn}_3\text{As}_2 + \text{ZnAs}_2$ ).

mobility, and  $N$  is the density of carriers. For high Zn diffusion with excess As pressure, the diffusion profiles are very steep so that we can assume that  $N \cong \bar{C} \cong C_0$  where  $\bar{C}$  is the average concentration of the diffused

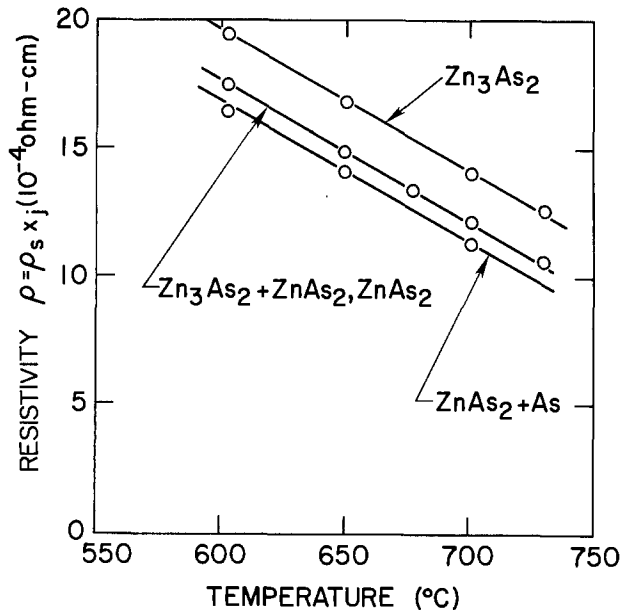


Fig. 6. Resistivity vs. temperature for different diffusion sources

layer and  $C_0$  is the surface carrier concentration. From Eq. [1],  $C_0$  can be approximately expressed as

$$C_0 \cong \frac{1}{q\mu\rho} \quad [2]$$

For example, at 700°C with  $Zn_3As_2 + ZnAs_2$  source,  $\rho = 12 \times 10^{-4} \Omega\text{-cm}$  (from Fig. 6),  $q = 1.6 \times 10^{-19} \text{C}$ , and if  $\mu$  is assumed to be  $25 \text{ cm}^2/\text{Vsec}$  from Ref (10), then  $C_0 \cong 2.1 \times 10^{20} \text{ cm}^{-3}$  which is close to the experimental value of  $2.5 \times 10^{20} \text{ cm}^{-3}$  from Ref. (5).

The results in Fig. 6 also indicate that slightly higher surface concentrations can be obtained using  $ZnAs_2 + As$  as the diffusion source because of the lower resistivity values that can be obtained. At temperatures as low as 600°C,  $C_0$  in the  $10^{20} \text{ cm}^{-3}$  range can be easily obtained using any one of the four sources. Since the doping level for most devices is in the range be-

tween  $10^{17}$  and  $10^{18} \text{ cm}^{-3}$ , the contact resistance can be reduced by orders of magnitude using these diffusions (11).

In summary, Zn diffusion in GaAs between 600° and 730°C to obtain high surface concentrations has been studied using different diffusion sources. The junction depth at different temperature and time has been determined and the surface carrier concentration can be approximately determined. This information is valuable for choosing optimum diffusion conditions not only for making good contact but also for making devices with diffusion techniques.

#### Acknowledgments

The author acknowledges the technical assistance of J. F. Degelormo and helpful discussions with A. E. Blakeslee.

Manuscript submitted June 15, 1976; revised manuscript received Aug. 2, 1976.

Any discussion of this paper will appear in a Discussion Section to be published in the June 1977 JOURNAL. All discussions for the June 1977 Discussion Section should be submitted by Feb. 1, 1977.

Publication costs of this article were assisted by IBM Corporation.

#### REFERENCES

1. I. Hayashi, M. B. Panish, and F. K. Reinhart, *J. Appl. Phys.*, **42**, 1929 (1971).
2. R. L. Hartman, J. C. Dymant, C. J. Hwang, and M. Kuhn, *Appl. Phys. Lett.*, **23**, 181 (1973).
3. L. A. D'Asaro, *J. Lumin.*, **7**, 310 (1973).
4. K. K. Shih, J. W. Allen, and G. L. Pearson, *J. Phys. Chem. Solids*, **29**, 379 (1968).
5. H. C. Casey and M. B. Panish, *Trans. AIME*, **242**, 406 (1968).
6. M. B. Panish, *J. Phys. Chem. Solids*, **27**, 291 (1966); *This Journal*, **113**, 861 (1966).
7. L. S. Darken and R. W. Gurry, "Physical Chemistry of Metals," McGraw-Hill Book Company, New York (1953).
8. P. G. Shewmon, "Diffusion in Solids," McGraw-Hill Book Company, New York (1963).
9. J. C. Irvin, *Bell Syst. Tech. J.*, **41**, 387 (1962).
10. S. M. Sze and J. C. Irvin, *Solid-State Electron.*, **11**, 599 (1968).
11. K. L. Kohn and L. Wandering, *This Journal*, **116**, 507 (1969).



# CdS-Cu<sub>2</sub>S Solar Cells Fabricated on Cd<sub>2</sub>SnO<sub>4</sub>-Silica Substrates

L. C. Burton,\* T. Hench, and G. Storti

*Institute of Energy Conversion, University of Delaware, Newark, Delaware 19711*

and G. Haacke

*American Cyanamid Company, Chemical Research Division, Stamford, Connecticut 06904*

## ABSTRACT

Cadmium stannate (Cd<sub>2</sub>SnO<sub>4</sub>) films of 1Ω per square sheet resistance and 85% average transmissivity (500-650 nm) have been grown by means of rf sputtering onto silica substrates. CdS-Cu<sub>2</sub>S thin film solar cells with conversion efficiencies greater than 5% for front and rear illumination have been fabricated. The reflection of transmitted light back through the cell has increased the light generated current. Fabrication techniques are described and current-voltage and spectral response measurements are presented for front-wall and backwall modes of operation.

Solar cells fabricated on transparent substrates allow the backwall mode of operation to be utilized, whereby light is incident on the p-n junction interface through the wide gap material and absorbed in the narrow gap layer (see Fig. 1). In this investigation, the wide gap material is CdS (n-type, 2.4 eV bandgap) and the narrow gap material is Cu<sub>2</sub>S (p-type, 1.2 eV gap). For the CdS-Cu<sub>2</sub>S cell, a possible advantage of the back-wall mode of operation is that more light is absorbed near the heterojunction than near the Cu<sub>2</sub>S surface. If the Cu<sub>2</sub>S layer is on the order of a minority carrier diffusion length thick, one anticipates that the back-wall collection efficiency would exceed that of the frontwall mode since a larger fraction of the minority carriers are created near the junction (of course, absorption of light in the back electrode and the CdS must also be taken into account). In addition, the back-wall mode could be less dependent upon the thickness and other physical characteristics of the Cu<sub>2</sub>S layer. Instead of applying a grid pattern to the Cu<sub>2</sub>S surface to act as the anode, as must be done for the frontwall cell, a continuous metallic layer could be used. This would have practical advantages, as well as providing a reflecting surface on the front of the cell which would increase the backwall response.

We would like to describe the fabrication of CdS-Cu<sub>2</sub>S cells on Cd<sub>2</sub>SnO<sub>4</sub>-silica substrates, and measurements of the front and rear modes of operation. The major phases of research that we report here deal with the following:

(i) Construction of a transparent, conducting, and stable film of Cd<sub>2</sub>SnO<sub>4</sub> (cadmium stannate) on a transparent substrate (silica).

(ii) Deposition of an adherent and pinhole-free film of CdS onto the Cd<sub>2</sub>SnO<sub>4</sub>.

(iii) Formation of a CdS-Cu<sub>2</sub>S heterojunction resulting in a photovoltaic cell.

(iv) Cell electrical characterization, including diode analysis and spectral response in frontwall and backwall modes of operation

A general diagram of the cell that is to be discussed is shown in Fig. 1. The items outlined above are described below.

### The Cd<sub>2</sub>SnO<sub>4</sub>-Silica Substrate

The transparent cadmium stannate electrodes were coated onto silica substrates (1 × 1 in. or 1 × ½ in.) by rf sputtering from a hot-pressed Cd<sub>2</sub>SnO<sub>4</sub> target.

\* Electrochemical Society Active Member.

Key words: solar energy, photovoltaics, energy conversion, thin film.

During deposition the substrate surface temperature should exceed 400°C to achieve film crystallization. Polycrystalline films have the required high electrical conductivities (1); the conductivities of amorphous cadmium stannate (2) are too low for solar cell applications. Heating of the substrate surface is conveniently done by utilizing the energy of the rf plasma so that an auxiliary heater is not required.

Sputtering can be carried out either in an oxygen or argon/oxygen plasma. Best results are obtained with pure oxygen. The sputtered films are n-type semiconductors with an apparent energy gap of 2 eV. Their free electron concentration is of the order of 10<sup>19</sup> cm<sup>-3</sup> and the Hall mobilities reach 10 cm<sup>2</sup>/Vsec. The x-ray spectra of these films indicate the presence of a small concentration of cadmium oxide.

The transparent electrode properties of the sputtered cadmium stannate films improve substantially if they are subjected to a short heat-treatment. After a 10 min exposure to an argon/cadmium sulfide atmosphere at 600°-700°C, the optical absorption edge shifts to 2.9 eV and the cadmium oxide phase disappears from the x-ray spectra. Simultaneously, the free electron concentrations increase to 10<sup>21</sup> cm<sup>-3</sup> and the Hall mobilities to approximately 30 cm<sup>2</sup>/Vsec resulting in electrical conductivities of 6000 Ω<sup>-1</sup> cm<sup>-1</sup> and higher.

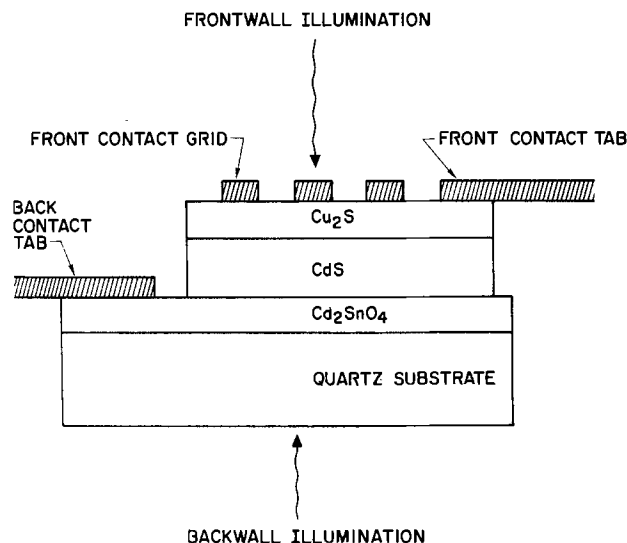


Fig. 1. Simplified cross section of cell. The cell is placed on an absorbing or reflecting surface for those modes of operation.

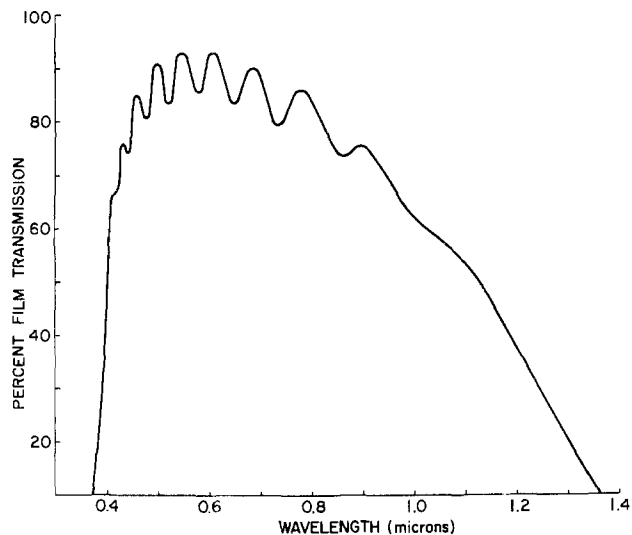


Fig. 2. Optical transmission of a sputter-coated cadmium stannate film with  $1.4 \Omega/\text{square}$  sheet resistance.

A typical example of the transparent electrode properties, which can be achieved with cadmium stannate films, is given in Fig. 2. This figure shows the optical transmission as a function of wavelength for a coating with approximately  $1 \Omega/\text{square}$  sheet resistance. Maximum film transmission occurs in a wavelength range in which the solar spectrum also has its highest intensity. The short wavelength cutoff at  $350 \text{ nm}$  is considerably below that of CdS. The backwall response of the CdS/Cu<sub>2</sub>S cell, therefore, is not limited by the short-wavelength transmission characteristics of the cadmium stannate electrode.

### Cell Fabrication

Cadmium sulfide layers (n-type,  $\sim 1 \Omega\text{-cm}$  resistivity) of  $20\text{-}30 \mu\text{m}$  thickness are deposited onto the Cd<sub>2</sub>SnO<sub>4</sub>-silica substrates using conventional thermal evaporation techniques. A graphite crucible for the CdS is used, and the deposition rate is about  $2 \mu\text{m}/\text{min}$ . The substrate temperature is maintained nominally at  $160^\circ\text{C}$  during the deposition by means of a radiation heater, the temperature being monitored by means of a thermocouple placed against the Cd<sub>2</sub>SnO<sub>4</sub> surface.

Adherence of the CdS to the Cd<sub>2</sub>SnO<sub>4</sub> has proven to be excellent, with no cracking or peeling evident. The ohmic nature of the CdS-Cd<sub>2</sub>SnO<sub>4</sub> contact and the bulk resistivity of CdS layers have been determined using the technique illustrated in Fig. 3. The central part of the Cd<sub>2</sub>SnO<sub>4</sub> is etched away, providing a space for the CdS "resistor" deposited onto the substrate. The current-voltage characteristics are linear, with bulk resistivities of about  $1 \Omega\text{-cm}$ . In addition, bulk resistivity measurements were made using indium as the contact to the CdS (3). The bulk resistivity values found using these two techniques agree to within experimental error. The ohmic nature of the CdS-Cd<sub>2</sub>SnO<sub>4</sub> contact is also verified by examination of the resulting cell current-voltage characteristics.

CdS films were examined by means of optical and scanning electron microscopes. SEM pictures of the CdS surface are shown in Fig. 4 (magnification = 3000). A grain size of about  $5\text{-}10 \mu\text{m}$  is evident for the as-deposited CdS.

X-ray diffraction scans verify that the CdS film is highly ordered in the c-direction in comparison to CdS films deposited under similar conditions onto metal substrates. It is not evident that this order has any major effect on the quality of the resulting cell.

The CdS is typically etched in HCl (55%,  $40^\circ\text{C}$ , 3 sec) prior to formation of the Cu<sub>2</sub>S layer. As shown in Fig. 4, the etched surface is extremely rough, due in part to preferential etching along grain boundaries. It has been found that the etch substantially reduces the

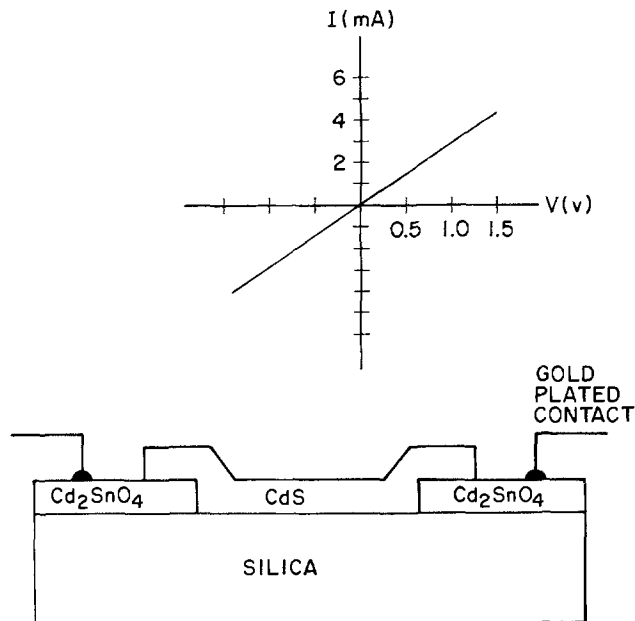


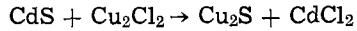
Fig. 3. Geometry used to measure CdS resistivity and to verify ohmic nature of CdS-Cd<sub>2</sub>SnO<sub>4</sub> contact.



Fig. 4. SEM pictures of CdS on Cd<sub>2</sub>SnO<sub>4</sub>/silica substrate. Lower: as deposited. Upper: after 5 sec etch in 55% HCl solution at  $40^\circ\text{C}$ . Width of field =  $35 \mu\text{m}$ .

average reflectivity of the cell surface, with the resulting light generated current being increased by about 15% due to this effect.

The copper sulfide (Cu<sub>2</sub>S) layer is formed by means of a well-known ion exchange reaction (4)



resulting from immersion of the CdS and substrate in a hot (95°C) cuprous chloride solution for several seconds.

The Cu<sub>2</sub>S thickness is 0.2-0.3 μm (depending on reaction time) as measured by Auger spectrometry accompanied by argon ion milling, by Rutherford backscattering and electrolytically. The stoichiometry factor  $x$  (in Cu <sub>$x$</sub> S) has been electrolytically measured to be  $1.997 \pm 0.002$ . This is consistent with the Cu<sub>2</sub>S resistivity values of about 0.1 Ω-cm measured on these samples (5, 6).

After formation of the Cu<sub>2</sub>S layer, a gold-plated copper contact grid (10 × 60 lines per inch) is laminated onto the Cu<sub>2</sub>S surface by means of epoxy under a 0.0005 in. Mylar cover. Lamination conditions are: temperature = 190°C, pressure = 100 lb/in.<sup>2</sup>, time = 20 min.

### Cell Electrical Characteristics

Immediately following the attachment of the grid onto the Cu<sub>2</sub>S surface, cell current-voltage characteristics are measured. The solar simulator supplies tungsten illumination filtered by a 0.12% Cu<sub>2</sub>SO<sub>4</sub> solution, and is calibrated to AM1 equivalent illumination by adjusting the short-circuit current of a CdS standard cell supplied by NASA. [Due to the fact that the filtered tungsten radiation has a larger fraction of its total power in the most spectrally sensitive region of the cell than does natural insulation, AM1 equivalent conditions correspond to an incident power density of about 58 mW/cm<sup>2</sup> (7).]

As is the case for CdS-Cu<sub>2</sub>S cells made on metal substrates (4-8), the current-voltage characteristics significantly improve after a 16 hr heat-treatment at 130°C, at a pressure of about 400 μm. Current-voltage characteristics for a heat-treated cell are shown in Fig. 5.

Due to partial transparency of the Cu<sub>2</sub>S layer, light can be reflected back through the cell for a second pass by means of a front surface mirror, thus enhancing response in both the front and rear modes of operation. A detailed analysis of this effect as applied to

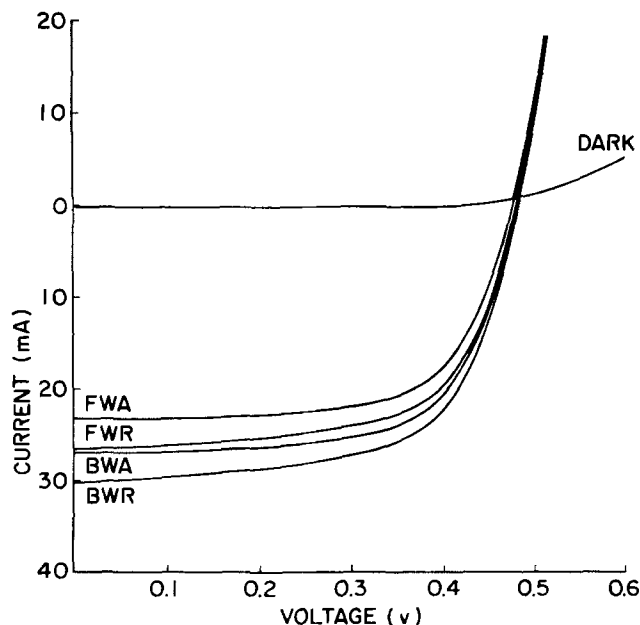


Fig. 5. Current-voltage characteristics for the four modes of cell operation.

this type of cell was reported elsewhere (9). Short-circuit current values have been improved by up to 35% for some cells, although 10-15% is more typical.

The characteristics seen in Fig. 5 thus represent the four possible modes of operation in the light: front-wall and backwall with the cell located either on an absorbing or reflecting surface. The current density dependence on voltage under illumination can be approximated by the diode relation (for unit area)

$$J = -J_L + J_0 \left[ \exp \frac{q}{nkT} (V - JR_s) - 1 \right] - \frac{V - JR_s}{R_{sh}}$$

where  $J_L$  is the light generated current density,  $R_s$  and  $R_{sh}$  are the series and shunt resistances, and  $n$  is a diode parameter. The preexponential factor  $J_0$  is described by

$$J_0 = J_{00} \exp \left[ \frac{-\phi_B}{kT} \right]$$

where  $J_{00}$  is the available reverse saturation current density. Salient parameters for a 5% efficient cell are listed in Table I.

The cell series resistance, for the current densities presently obtainable (14-18 mA/cm<sup>2</sup>), is not a serious problem. The rather low fill factors of 60-65% are due to a rounding of the  $I$ - $V$  characteristic in the fourth quadrant believed to be due to a nonohmic grid contact resistance and not to high series or low shunt resistance values. From geometrical considerations, the 1.0Ω series resistance measured in far forward bias can be attributed to the Cd<sub>2</sub>SnO<sub>4</sub> (about 0.3Ω for 1 Ω/square sheet resistance) and the CdS (the remaining 0.7Ω). A detailed analysis has been performed of the dependence of cell efficiency upon Cd<sub>2</sub>SnO<sub>4</sub> thickness, for parameters pertaining to the CdS-Cu<sub>2</sub>S cell (10). In this regard, a tradeoff must be made between series resistance (thick Cd<sub>2</sub>SnO<sub>4</sub> layer desirable) and light absorption in the backwall and backwall reflection modes (thin Cd<sub>2</sub>SnO<sub>4</sub> film desirable). It was found in this analysis that for cell parameters such as those listed in Table I an optimum Cd<sub>2</sub>SnO<sub>4</sub> thickness is 1.0-1.3 μm, depending on exact cell parameters used, and on the Cd<sub>2</sub>SnO<sub>4</sub> absorption coefficient and sheet resistance. Cd<sub>2</sub>SnO<sub>4</sub> thicknesses in this range were used for the cells herein reported.

CdS-Cu<sub>2</sub>S cells on metal substrates, made under otherwise identical conditions, exhibited efficiencies in the 5.5-6.0% range when measured under tungsten illumination (8). This was due mainly to larger fill factors (68-71%) for those cells.  $V_{oc}$  and  $J_{sc}$  values typically measured for metal and glass substrate cells are not significantly different. It should also be noted that for the 10 × 60 lpi contact grids, roughly 17% of the incident light is lost due to shading.

### Spectral Response Measurements

Collection efficiencies were computed over the spectrally sensitive region of a given cell from measurements of short-circuit current and incident light flux. Samples were illuminated with wide band (~40 nm) light from a Bausch and Lomb monochromator, with the beam collimated to an area of approximately 0.5

Table I. Summary of key cell parameters (cell 132A)\*

Mode**	$V_{oc}$	$J_{sc}$	$\eta$	FF
FWA	0.475V	14.2 mA/cm <sup>2</sup>	4.40%	65.2%
FWR	0.485	16.6	5.17	64.0
BWA	0.475	15.4	4.66	63.6
BWR	0.480	17.1	5.20	63.4

\*  $R_s = 1.0\Omega$ ,  $R_{sh} = 1500\Omega$ ,  $\phi = 0.88$  eV,  $n = 1.0$ ,  $J_0$  (25°C) =  $4.20 \times 10^{-8}$  mA/cm<sup>2</sup>,  $J_{00} = 8.15 \times 10^7$  mA/cm<sup>2</sup>, cell area = 1.7 cm<sup>2</sup>.

\*\* Key: FWA = frontwall absorbing, FWR = frontwall with reflection, BWA = backwall absorbing, BWR = backwall with reflection,  $V_{oc}$  = open-circuit voltage,  $J_{sc}$  = short-circuit current,  $\eta$  = efficiency, FF = fill factor.

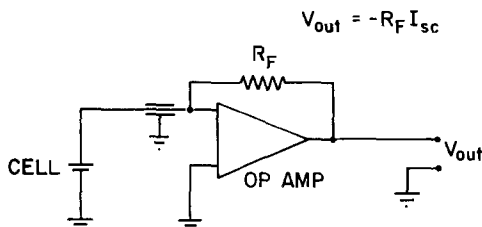


Fig. 6. Electrical circuit used for spectral response measurements

cm<sup>2</sup>. The current-measuring circuit is shown in Fig. 6. Light intensity was measured by means of a Tektronix Model J16 digital photometer. The cell holder had provisions for sliding an absorbing or reflecting surface immediately behind the sample.

Figure 7 shows the spectral dependence of collection efficiency for cell 132A in the four modes of operation. Salient features of the curves are (i) the significant response for  $\lambda \leq 500$  nm in the FW modes, (ii) the cutoff at  $\lambda \sim 500$  nm for BW modes, and (iii) the sharp decrease in response beyond  $\lambda = 650$  nm for all modes. Similar results were obtained for a number of cells prepared as described above.

In the FW modes, light response for  $\lambda \leq 500$  nm results from minority carrier generation in and collection from both the Cu<sub>2</sub>S and the CdS. [This is in contrast to the behavior seen in this spectral region for other thin film CdS cells. For example, Brandhorst *et al.* (11) report little spectral sensitivity for  $\lambda \leq 500$  nm. These differences will be the subject of a separate communication.]

No response is detected for  $\lambda \leq 500$  nm in the BW modes because of the complete absorption of light in the CdS. The decrease in response for  $\lambda \geq 650$  nm is due to a quenching phenomenon that has been previously reported (11-14), whereby illumination of the CdS space charge region decreases the current collected from the Cu<sub>2</sub>S. These effects can be removed by simultaneous illumination with shorter wavelength light, or by white light (11-14). Consequently, the collection efficiency improves considerably.

The maximum collection efficiency measured was about 0.52 at 625 nm. There are several sources of current loss that may result in this value. These include interface reflections, absorption in the Cd<sub>2</sub>SnO<sub>4</sub> and CdS, and losses due to electronic processes in the cell. Examples of the latter include surface and interface recombination, and bulk recombination in the Cu<sub>2</sub>S.

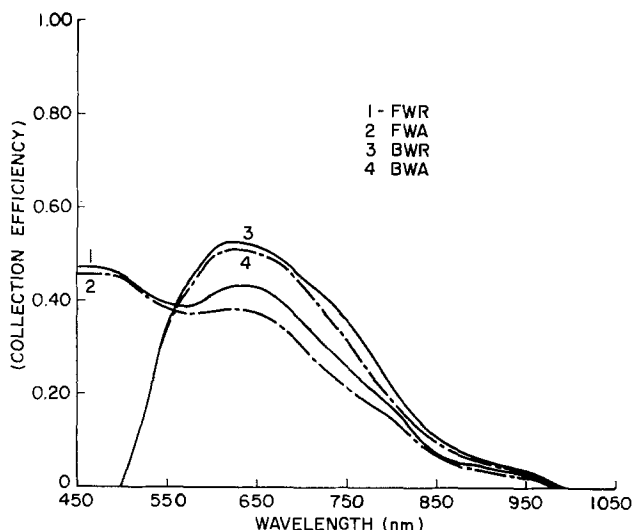


Fig. 7. Spectral dependence of collection efficiency for the four modes of cell operation.

## Conclusions

We have verified that Cd<sub>2</sub>SnO<sub>4</sub> films are suitable for a performance standpoint for CdS-Cu<sub>2</sub>S solar cells operating in the backwall mode. Even though this mode does show a higher collection efficiency than the frontwall, total response is somewhat reduced due to absorption in the CdS. On the other hand, a reflecting surface was used to increase the response, due to incomplete light absorption in the Cu<sub>2</sub>S. The use of Cd<sub>2</sub>SnO<sub>4</sub> films as solar cell electrodes, and of a reflecting surface to pass transmitted light back through the cell, should also be applicable to other types of photovoltaic devices.

## Acknowledgments

We would like to acknowledge the National Science Foundation for supporting this work under Grant AER73-07957. Thanks are extended to Dr. B. Baron for measuring the Cu<sub>2</sub>S stoichiometry and to Dr. A. Rothwarf for helpful discussions related to cell operation.

Manuscript submitted May 18, 1976; revised manuscript received July 28, 1976. This was Paper 255 presented at the New York, New York, Meeting of the Society, Oct. 13-17, 1974 and Paper 237 presented at the Washington, D.C., Meeting of the Society, May 2-7, 1976.

Any discussion of this paper will appear in a Discussion Section to be published in the June 1977 JOURNAL. All discussions for the June 1977 Discussion Section should be submitted by Feb. 1, 1977.

Publication costs of this article were supported by the University of Delaware.

## REFERENCES

1. G. Haacke, *Appl. Phys. Lett.*, **28**, 622 (1976).
2. A. J. Nozik, *Phys. Rev. B*, **6**, 453 (1972).
3. K. W. Böer and R. B. Hall, *J. Appl. Phys.*, **37**, 4739 (1966).
4. L. R. Shiozawa, F. Augustine, G. A. Sullivan, J. M. Smith III, and W. R. Cook, Final Report ARL 69-0155, Cleveite Corporation, Cleveland, Ohio (1969).
5. F. Guastavino, H. Luquet, and J. Bougnot, International Congress on the Sun in the Service of Mankind, Proceedings of Photovoltaic Power and its Applications in Space and on Earth, Paris (1973).
6. L. Burton and V. Ricca, Technical Report, NSF/RANN/AER72-03478 A04/TR75/7 Institute of Energy Conversion, University of Delaware, Newark, Delaware (1975).
7. A. Rothwarf and H. C. Hadley, Jr., Technical Report NSF/RANN/AER 72-03478 A03/TR 75/2, University of Delaware, Newark, Delaware (1975).
8. L. Burton, Proceedings of the International Workshop on Cadmium Sulfide Solar Cells and Other Abrupt Heterojunctions, p. 305, University of Delaware, Newark, Delaware (1975).
9. A. Rothwarf, L. C. Burton, H. C. Hadley, Jr., and G. M. Storti, Proceedings of the 11th IEEE Photovoltaic Specialists Conference, p. 476, Scottsdale, Arizona (1975).
10. L. C. Burton, T. Hench, and G. Haacke, Abstract 237, p. 582, The Electrochemical Society Extended Abstracts, Spring Meeting, Washington, D.C., May 2-7, 1976.
11. H. W. Brandhorst, Jr., R. L. Schalla, A. E. Potter, and L. Rosenblum, NASA TND-5521, NASA Lewis Research Center, Cleveland, Ohio (1970).
12. L. R. Shiozawa, G. A. Sullivan, and F. Augustine, Seventh IEEE Photovoltaic Specialists Conference (1968).
13. G. Lindmayer and A. G. Revesz, *Solid-State Electron.*, **14**, 647 (1971).
14. W. D. Gill and R. H. Bube, *J. Appl. Phys.*, **41**, 3731 (1970).

# Four-Point Probe Correction Factors for Use in Measuring Large Diameter Doped Semiconductor Wafers

David S. Perloff

Signetics Corporation, Research and Development Laboratory, Sunnyvale, California 94086

## ABSTRACT

Conformal mapping techniques are employed to determine geometrical correction factors for the general case of an in-line four-point probe positioned on a thin circular sample. Simplified expressions are also obtained which relate the correction factor to a single dimensionless quantity when the probe separation distance is a small fraction ( $\lesssim 10\%$ ) of the wafer radius. Experimental results are presented which confirm the validity of the theoretical correction factors and demonstrate the importance of accounting for geometric effects when presenting data in the form of iso-sheet resistance contour maps.

The homogeneity of doped semiconductor wafers is commonly determined by measuring the sheet resistance  $\rho_s$  at a number of points on the wafer using the in-line four-point probe (FPP) described by Valdes (1). If the probe separation is at least twice the thickness of the doped layer,  $\rho_s$  will be given by the expression

$$\rho_s = k \frac{\Delta V}{I} = kR \ (\Omega/\square) \quad [1]$$

where  $k$  is a correction factor which in general depends on the location of the FPP and the shape of the sample,  $I$  is a current through two of the probes,  $\Delta V$  is the potential difference measured between the remaining two probes, and the resistance  $R$  is defined as  $\Delta V/I$  (2). Ordinarily, the outer probes are chosen to carry current and the inner probes to measure voltage since, for an FPP having equal separations between the probe needles, this assignment results in the largest value of  $\Delta V$  (3).

Logan (4) has shown that a circular sample doped on both sides should behave as if its front surface were part of a continuous infinite sheet for which the correction factor is a constant value, independent of the location of the FPP. (For an in-line FPP having equal separations between the probe needles,  $k = \pi/\ln 2 = 4.532$ .) If however, the sample is doped on one side only, as for example in the case of ion implanted wafers, one must take into account the orientation and position of the probe array when employing Eq. [1] (5, 6).

The most common orientation of the probe array on a circular sample is either perpendicular to or along the wafer radius. Correction factors for these particular cases were derived by Swartzendruber (7) and Logan (4) and tabulated by the National Bureau of Standards (8). In recent years, wafer probing equipment has become available which makes it possible to automate sheet resistance measurements, as described by Crossley and Ham (9). In order, however, to employ such equipment for FPP sheet resistance measurements, it is necessary to account for the varying orientation of the FPP with respect to the wafer radius. This paper provides a general solution for the in-line FPP on a thin circular sample and supplies experimental data which confirm its validity. Examples of iso-sheet resistance topographs are presented which illustrate the importance of accounting for geometric effects. For the case of manual wafer probing, in which the positioning of the FPP is generally imprecise, simplified expressions are derived which may be used to estimate correction factors when the probe separation is a small fraction ( $\lesssim 10\%$ ) of the wafer radius.

Key words: contour map, silicon, sheet resistance, wafer probing.

## Correction Factors for Thin Circular Samples

*General case.*—The general case of an in-line FPP oriented arbitrarily with respect to the radius of a thin circular sample [Fig. 1(a)] is treated in Appendix A using conformal mapping techniques. The cases dealt with by Logan (4) and Swartzendruber (7) correspond, respectively, to setting  $\theta = 0$  and  $\pi/2$ .

Frequently, one is concerned with the relative variation of  $\rho_s$  over the semiconductor wafer. For a uniformly doped wafer,  $k$  is a maximum (since  $\Delta V$  is a minimum) when the FPP is located at the center of the wafer. It is thus convenient to employ this location as a reference point. Smits (2) has shown that the correction factor for an FPP (probe separation  $s$ ) located

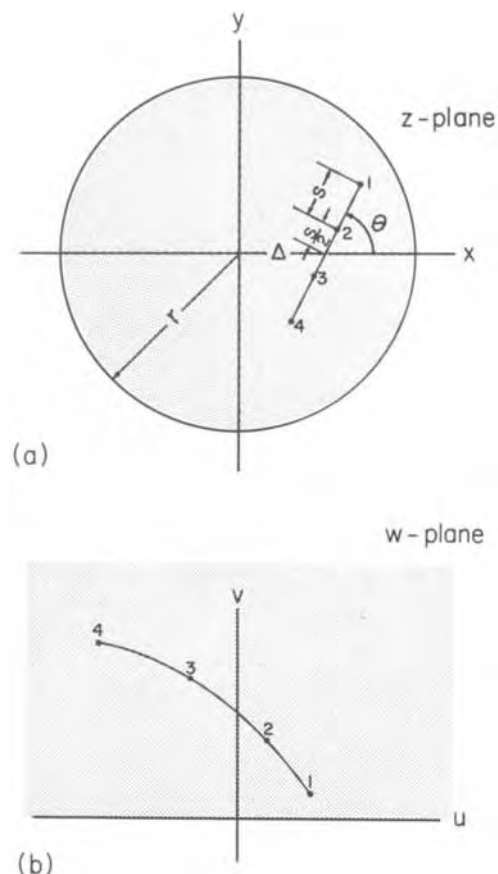


Fig. 1. Coordinate system for an in-line four-point probe array on a circular sample (a). The interior of the circle in the  $z$ -plane is conformally mapped into the upper half of the  $w$ -plane (b) to facilitate determination of the potential distribution.

at the center of a wafer of radius  $r$  is given by the expression

$$k^* = \frac{\pi}{\ln 2} \cdot \frac{1}{1 + \eta} \quad [2]$$

where

$$\eta = \frac{\ln \left[ \frac{1 + 3 \left( \frac{s}{2r} \right)^2}{1 - 3 \left( \frac{s}{2r} \right)^2} \right]}{\ln 2} \quad [3]$$

When the FPP is displaced a distance  $\Delta$  from the center of the wafer (or, equivalently, a distance  $a = r - \Delta$  from the edge of the wafer), the value of  $k$  will decrease by the fractional amount

$$\delta_k = \frac{k - k^*}{k^*} \quad [4]$$

The relationship between the dimensionless parameters  $a/r$  and  $s/r$  as a function of  $|\delta_k|$  is shown in Fig. 2 for the FPP positioned perpendicular to the wafer radius and in Fig. 3 for the FPP positioned along the wafer radius. The solid lines represent the exact solution, obtained by iteration of the general expressions of Appendix A. The broken lines represent the approximate solution for  $k$  discussed in the following section.

Figures 2 and 3 enable one to determine, for  $\theta = \pi/2$  and  $\theta = 0$ , the location of the FPP at which the measured resistance  $R(\pi/2)$  or  $R(0)$  exceeds the resistance at the center of the wafer  $R^*$  by some fixed percentage. As an example, consider the case of a 62.5 mil FPP used to measure the sheet resistance of a 3 in. diameter wafer ( $s/r = 0.0625/1.500 = 0.0417$ ) and suppose one wishes to determine the value of  $a$  for which  $R(\pi/2)/R^* = k^*/k(\pi/2) = 1.01$ . According to Fig. 2,  $k(\pi/2)$  is 1% lower in value than  $k^*$  (or, equivalently,  $R(\pi/2)$  is 1% greater in value than  $R^*$ ) when  $a/r \approx 0.3$ , i.e., when  $a \approx 0.45$  in. Examination of Fig. 2 and 3 shows that  $k$  decreases dramatically as the FPP approaches the edge of the wafer ( $a/r \rightarrow 0$ ), and that the magnitude of  $k(0)$  is always smaller than that of  $k(\pi/2)$ .

**Large wafer approximation.**—In the majority of practical applications involving silicon wafers,  $s/r \leq$

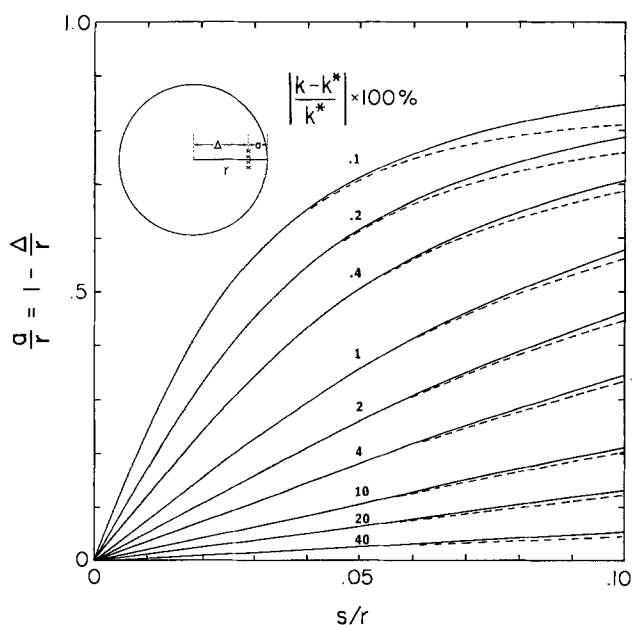


Fig. 2. Plot of  $a/r$  vs.  $s/r$  for an in-line four-point probe oriented perpendicular to the radius of a thin circular sample, for various values of the parameter  $|\delta_k|$ . The solid lines represent a solution of the exact equations of Appendix A, while the broken lines represent the approximate solution given in Eq. [7].

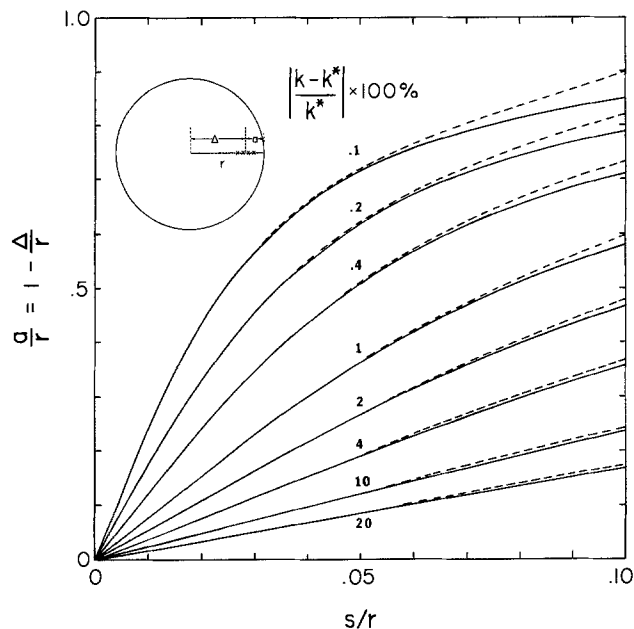


Fig. 3. Plot of  $a/r$  vs.  $s/r$  for an in-line four-point probe oriented along the radius of a thin circular sample, for various values of the parameter  $|\delta_k|$ . The solid lines represent a solution of the exact equations of Appendix A, while the broken lines represent the approximate solution given in Equation [8].

0.0625 (assuming  $s \leq 62.5$  mil and  $r \geq 1.0$  in.). When the probe separation is small compared to the radius of the sample, the expressions derived in Appendix A may be simplified considerably. The analysis of Appendix B shows that, for  $s/r \ll 1$ , an arbitrarily oriented FPP (probe separation  $s$ ) located a distance  $a$  from the nonconducting edge of a thin circular sample [Fig. 4(a)] will have the same correction factor as a similarly oriented FPP (probe separation  $s' = s/(1 - a/2r)$ ) located a distance  $a$  from the nonconducting edge of a thin semi-infinite sample [Fig. 4(b)]. When the FPP is oriented perpendicular to the wafer radius Eq. [B-11] reduces to the expression

$$k \left( \frac{\pi}{2} \right) \approx \frac{\pi}{\ln 2 + \frac{1}{2} \ln \left[ \frac{(a/s')^2 + 1}{(a/s')^2 + \frac{1}{4}} \right]} \quad [5]$$

Similarly, when the FPP is positioned along the wafer radius

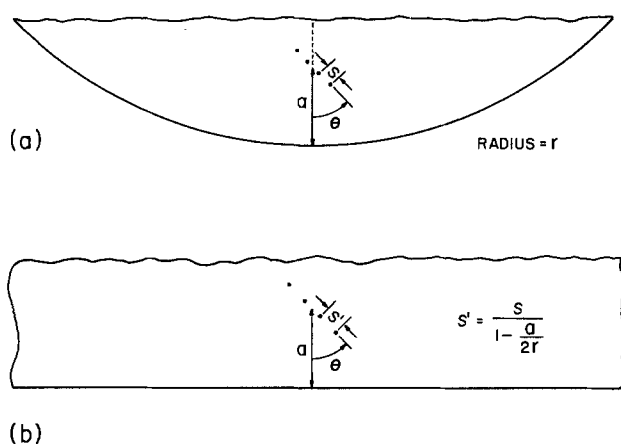


Fig. 4. An arbitrarily oriented four-point probe (probe separation  $s$ ) located a distance  $a$  from the nonconducting edge of a thin circular sample of radius  $r$  (a) is equivalent, in the limit  $s \ll r$ , to a similarly oriented four-point probe (probe separation  $s'$ ) located a distance  $a$  from the nonconducting edge of a thin semi-infinite sample (b).

$$k(0) \approx \frac{\pi}{\ln 2 + \frac{1}{2} \ln \left[ \frac{(a/s')^2 - \frac{1}{4}}{(a/s')^2 - 1} \right]} \quad [6]$$

Eq. [5] and [6] may be rearranged to yield closed expressions relating  $a/r$  and  $s/r$  when  $s \ll r$

$$\frac{a}{r} \approx 1 - \sqrt{1 - 2 \frac{s}{r} \sqrt{\frac{4^{\lambda-1} - 1}{1 - 4^\lambda}}} \quad \left( \theta = \frac{\pi}{2} \right) \quad [7]$$

and

$$\frac{a}{r} \approx 1 - \sqrt{1 - \frac{s}{r} \sqrt{\frac{1 - 4^{\lambda+1}}{1 - 4^\lambda}}} \quad (\theta = 0) \quad [8]$$

where

$$\lambda = \frac{\eta + |\delta_k|}{1 - |\delta_k|} \quad [9]$$

Equations [7] and [8] are represented by the broken lines in Fig. 2 and 3, respectively. The agreement with the exact solution (solid lines) is seen to be excellent for  $s/r \sim 0.05$  but still satisfactory for  $s/r \sim 0.10$ . As an example, again consider the case of a 62.5 mil FPP used to measure the sheet resistance of a 3 in. diameter wafer. Substituting  $s/r = 0.0417$  in Eq. [3], one has that  $\eta = 3.757 \times 10^{-3}$ . Taking  $|\delta_k(\pi/2)| = 0.01$ , one finds using Eq. [9] that  $\lambda = 0.01390$ . For these values of  $\lambda$  and  $s/r$ , Eq. [7] yields the result that  $a/r \approx 0.3041$ . This value compares favorably with the actual value of 0.3047, obtained by iterative solution of the expressions in Appendix A, and the value of 0.3 graphically determined in the preceding section from Fig. 2.

**Geometry independent case.**—Rymaszewski (3) has shown that the method employed by van der Pauw (10) for determining the sheet resistance of peripherally contacted, arbitrarily shaped laminar samples may be applied, under certain circumstances, to FPP measurements on the interior of such samples. For a circular geometry, the requirements specified by Rymaszewski are satisfied only for the case of an in-line FPP oriented along a sample radius. As in the case of van der Pauw patterns,  $\rho_s$  is determined by measuring the resistance associated with each of two independent current/voltage configurations. Employing the configurations defined in Table I, one has that

$$k'(0) = \frac{\rho_s}{R_a(0)} = \frac{\pi}{\ln 2} g(\xi) \quad [10]$$

where

$$\xi = R_a(0)/R_c(0) \quad [11]$$

$$g(\xi) = (1 + 1/\xi)f(\xi) \quad [12]$$

and the function  $f(\xi)$  satisfies the transcendental relation derived by van der Pauw

$$\frac{\xi - 1}{\xi + 1} = \frac{\cosh^{-1} \left\{ \frac{1}{2} \exp(\ln 2/f) \right\}}{\ln 2/f} \quad [13]$$

The symbol  $k'(0)$  has been introduced in Eq. [10] to identify the geometry- and sheet resistance-independent correction factor empirically determined by the method of Rymaszewski. The symbol  $k$  will continue to

Table I. Possible current/voltage configurations for an in-line four-point probe array. The probe numbering convention is shown in Fig. 1(a)

Configuration	Current (or voltage)	Voltage (or current)
A	(1,4)	(2,3)
B	(1,3)	(2,4)
C	(1,2)	(4,3)

be used to identify the correction factor calculated in terms of the geometric parameters  $r$ ,  $\theta$ , and  $\Delta$ .

Configurations A, B, and C are related through the expression

$$R_c = R_a - R_b \quad [14]$$

It may be shown that  $0.977 \leq R_a/R_b \leq 1.262$  for  $0 \leq s/r \leq 3/2$ , so that the resistances measured in configurations A and B are comparable in magnitude. In contrast,  $4.819 \leq R_a/R_c \leq 42.96$  for  $0 \leq s/r \leq 3/2$ . It may thus be convenient, when carrying out actual measurements, to determine  $R_c$  by measuring  $R_a$  and  $R_b$  and employ Eq. [14]. This approach is utilized in the example given in the following section.

### Experimental Results

**Position dependence.**—In order to verify the derivation of Appendix A, FPP measurements were carried out at a number of locations along the radius of a 3-in. diam boron-implanted ( $5 \times 10^{14}$  cm<sup>-2</sup>, 70 keV) 10  $\Omega$ -cm n-type silicon wafer annealed to full electrical activity (950°C, 30 min, dry N<sub>2</sub>). The measurement current  $I$  was provided by a Keithley 225 constant ( $\pm 0.005\%$  stability) current supply; the potential  $\Delta V$  was measured with a resolution of 10  $\mu$ V by a Nonlinear Systems Corporation Model MX-1 digital voltmeter. The polarity of the current supply was reversed and readings of  $\Delta V$  averaged to eliminate small offset voltages associated with thermoelectric effects. Table II shows results of measurements made along a radius of this wafer using a precision FPP (11) ( $s = 25$  mil) in conjunction with a conventional x-y wafer probing apparatus capable of stepping in 1-mil increments. With the FPP oriented along the wafer radius, the resistance was measured in configurations A and B (Table I) in order to obtain the values identified by  $R_a(0)$  and  $R_b(0)$  in Table II. Equations [10]-[14] were then employed to compute the geometry-independent correction factor  $k'(0)$ . After rotating the wafer 90° to orient the FPP perpendicular to the wafer radius, values of  $R_a(\pi/2)$  were measured and used to compute the correction factor from the formula

$$k''(\pi/2) = \frac{\rho_s}{R_a(\pi/2)} = k'(0) \frac{R_a(0)}{R_a(\pi/2)} \quad [15]$$

[The symbol  $k''(\pi/2)$  is intended to indicate that this correction factor is computed using results for  $\theta = 0$ .]

According to Table II, the values of  $k(0)$  and  $k(\pi/2)$  obtained from the expressions given in Appendix A are in excellent agreement with the empirically determined values  $k'(0)$  and  $k''(\pi/2)$ . Because the minimum practical distance of approach to the edge of the wafer was 0.04 in. for  $\theta = 0$ , the values of  $k''(\pi/2)$  for  $a \leq 0.03$ -in. are based on an estimate of  $\rho_s$  obtained from the average of the values measured at  $a = 0.04$  and 0.05 in. For this reason, and the fact that there may

Table II. Results of four-point probe measurements made along the radius of a 3 in. diameter doped silicon wafer. The correction factors  $k'$  and  $k''$  are determined empirically; the correction factor  $k$  is computed using the expressions derived in Appendix A ( $s = 0.025$  in,  $r = 1.50$  in.).

$a = r - \Delta$ (in.)	$R_a(0)$ ( $\Omega$ )	$R_b(0)$ ( $\Omega$ )	$k'(0)$	$k(0)$	$k''(\pi/2)$	$k(\pi/2)$
0.01	—	—	—	—	2.603*	2.574
0.02	—	—	—	—	3.156*	3.125
0.03	—	—	—	—	3.572*	3.563
0.04	58.78	52.66	3.543	3.518	3.840	3.853
0.05	53.41	46.11	3.882	3.889	4.034	4.040
0.06	50.90	42.92	4.080	4.086	4.151	4.163
0.08	46.59	39.99	4.266	4.279	4.287	4.305
0.10	47.49	38.58	4.361	4.368	4.358	4.379
0.20	46.32	37.05	4.468	4.488	4.450	4.489
0.50	45.78	36.40	4.501	4.524	4.490	4.524
1.00	46.20	36.72	4.513	4.529	4.521	4.529
1.50	46.77	37.09	4.527	4.530	4.521	4.530

\* Assuming  $\rho_s = 207.4 \Omega/\square$ .

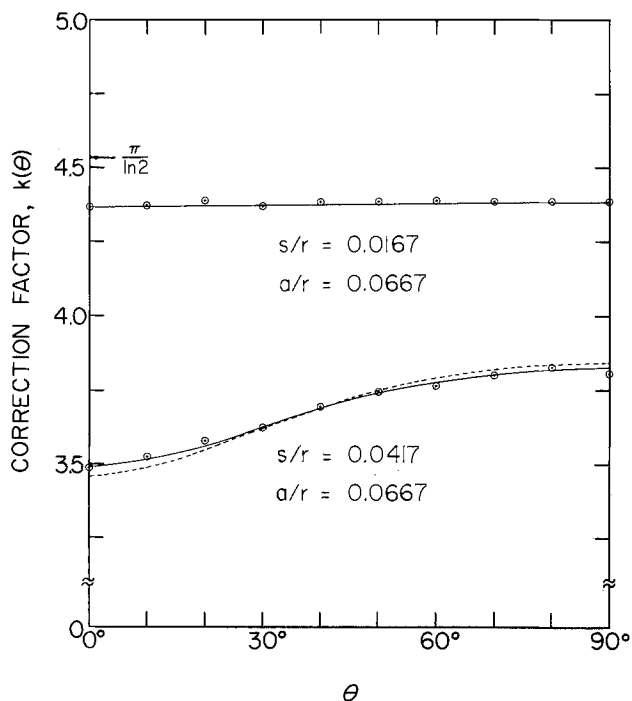


Fig. 5. Calculated (solid lines) and experimental values (open circles) for  $k$  as a function of angle of orientation with respect to the radius of a 3 in. diameter doped circular sample. The broken line represents an approximate solution which is appropriate in the limit  $s/r \ll 1$ .

have been small errors in specifying the location of the FPP, the agreement between  $k''(\pi/2)$  and  $k(\pi/2)$  is somewhat poorer for  $a \leq 0.02$  in. than for the larger values of  $a$  in Table II.

**Orientation dependence.**—The orientation dependence of the correction factor was examined with the FPP oriented at angles between 0 and 90°, in 10° increments, at a distance  $a = 0.100$  in. from the edge of the implanted wafer described in the previous section. Data are shown in Fig. 5 for  $s/r = 0.0167$  ( $s = 25$  mil) and  $s/r = 0.0417$  ( $s = 62.5$  mil). The experimental points were computed in the manner described above, according to the more general formula

$$k''(\theta) = \frac{\rho_s}{R_a(\theta)} = k'(0) \frac{R_a(0)}{R_a(\theta)} \quad [16]$$

In this case, a group of values  $R_a(0)$ ,  $R_b(0)$ , and  $R_a(\theta)$  was obtained at each of 10 different locations on the wafer, since the equipment employed permitted rotational movement of the wafer but not of the FPP as-

sembly. The solid curves of Fig. 5 represent the exact solution for  $k(\theta)$ , using the expressions derived in Appendix A. The broken line for  $s/r = 0.0417$  represents the approximate solution of Eq. [B-11]. (For  $s/r = 0.0167$ , the exact and approximate solutions are essentially identical.)

These results show the  $s = 25$  mil FPP is almost completely insensitive ( $k(\pi/2)/k(0) = 4.3794/4.3683 = 1.0025$ ) to angular variations within 0.1 in. of the edge of a 3 in. diameter wafer. In contrast, the correction factor for the 62.5 mil FPP is much more sensitive to angular variations ( $k(\pi/2)/k(0) = 3.8241/3.4948 = 1.0942$ ) at the same distance from the edge of the wafer.

The angular independence of the 25 mil FPP is an example of a limiting case for which the parameter  $(a/s')^2 \gg 1$ . Under these circumstances, it is easily shown that Eq. [B-11] reduces to

$$k \rightarrow \frac{\pi}{\ln 2 + \frac{1}{2} \ln \left\{ 1 + \frac{3}{4} \left( \frac{s'}{a} \right)^2 \right\}} \quad [17]$$

a result which is independent of  $\theta$ . For  $a = 0.100$  in.,  $s = 0.025$  in., and  $r = 1.5$  in.,  $a/s' = 4.14$  and hence  $(a/s')^2 = 17.1$ . From Eq. [17],  $k \rightarrow 4.3778$ , a value which is bracketed by the exact values  $k(\pi/2) = 4.3794$  and  $k(0) = 4.3683$ .

**Wafer mapping.**—Results are presented in this section for a boron-implanted ( $5 \times 10^{14}$  cm $^{-2}$ , 155 keV) 3 in. diameter n-type silicon wafer annealed to full electrical activity (950°C, 30 min, dry N $_2$ ) which demonstrates the importance of correction factors when using the FPP for automated wafer testing. Resistance measurements were carried out at 118 uniformly distributed test sites using the equipment and procedure described above. Data were automatically recorded and subsequently analyzed by means of a Digital Equipment Corporation PDP 11 computing system equipped with program and disk drives, tape reader, and terminal. An iso-sheet resistance contour map was generated for each of the conditions to be described below. This method of presenting data has been found to be a highly effective means of exhibiting the spatial homogeneity not only of impurity distributions but, for example, of the thickness of the various insulating layers used to fabricate devices in silicon wafers (12).

Figure 6 and 7 are computer-drawn iso-sheet resistance topographs for, respectively,  $s = 25$  mil and  $s = 62.5$  mil FPP assemblies (11). The heavy contour line represents the mean sheet resistance  $\bar{\rho}_s$ . The lighter contour lines represent values of  $\rho_s$  which differ from  $\bar{\rho}_s$  in increments of 1%. The symbol + (−) identifies the location of an experimental point whose value is

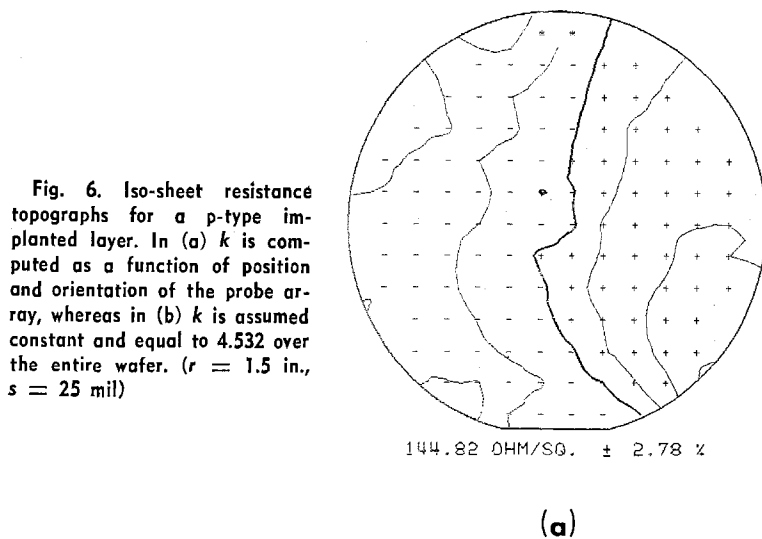
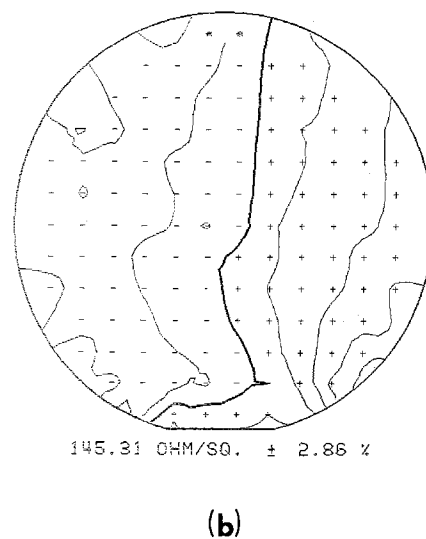


Fig. 6. Iso-sheet resistance topographs for a p-type implanted layer. In (a)  $k$  is computed as a function of position and orientation of the probe array, whereas in (b)  $k$  is assumed constant and equal to 4.532 over the entire wafer. ( $r = 1.5$  in.,  $s = 25$  mil)





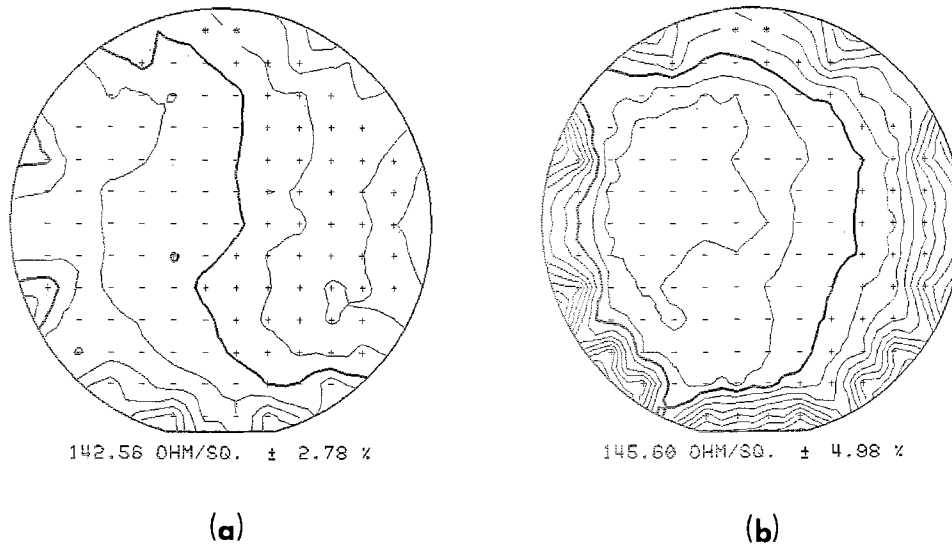


Fig. 7. Iso-sheet resistance topographs for the p-type implanted layer of Fig. 6, with  $s = 62.5$  mil. As in Fig. 6,  $k$  is computed as a function of the position and orientation of the probe array in (a), but assumed constant and equal to 4.532 in. (b).

greater(less) than  $\bar{\rho}_s$ . The uniformity is expressed as  $\pm 2\sigma/\bar{\rho}_s \times 100\%$ , where  $\sigma$  is the standard deviation. The symbol \* denotes an experimental point which falls beyond preassigned sorting limits.

Figure 6 represents data obtained using the  $s = 25$  mil probe assembly. In Fig. 6 (a) the data have been corrected for geometric effects using the results of Appendix A, whereas in (b) they have not. Both topographs reveal the presence of a distinctive left-to-right doping gradient which is characteristic of a wafer which has been tilted (about an axis perpendicular to the flat) relative to the ion beam in an electrostatically scanning implantation system (6). The corrected data are found to have a slightly smaller standard deviation and mean sheet resistance than the uncorrected data.

Figure 7 represents data obtained by probing the same wafer with an  $s = 62.5$  mil probe assembly. Again Fig. 7 (a) represents the data which have been corrected for geometric effects, whereas (b) represents data to which the appropriate correction factors have not been applied. In this case, the doping gradient cannot be identified in topograph (b), since the geometrical effects of the wafer boundary completely overwhelm the underlying pattern of doping. This behavior is a consequence of the greater sensitivity of the 62.5 mil probe array to the wafer edge, as may be ascertained by reference to Fig. 2 and 3.

The corrected data presented in Fig. 6 (a) and 7 (a), while in satisfactory quantitative and qualitative agreement, indicate that small errors in specifying the position of the FPP become significant when  $a \sim s$ . In particular, the topograph of Fig. 7 (a) exhibits various features along the wafer edge which are not present in Fig. 6 (a). This is especially evident near the wafer flat, where the assumption of a circular boundary is no longer valid. [Perloff *et al.* (6) have described an alternative approach which involves the use of photolithographically defined test patterns to maintain a constant value of  $k$ . This method, however, requires additional processing steps.]

### Conclusion

The homogeneity of doped semiconductor wafers may be determined by measuring the sheet resistance at a number of points using a conventional in-line four-point probe. Correction factors have been derived which take into account varying orientation of the probe array with respect to the wafer radius, making it possible to automate such measurements using standard x-y wafer probing equipment. Simplified expressions have also been obtained which relate the correction factor to a single dimensionless quantity for the case of the probe separation small ( $\lesssim 10\%$ ) in comparison with the wafer radius.

### Acknowledgment

The author wishes to acknowledge the contribution of Mr. F. E. Wahl who developed much of the computer software and wafer evaluation techniques, the assistance and support of Dr. J. Conragan in the area of data acquisition and analysis, and the interest and cooperation of Mr. J. Reimer and Ms. K. Dettenrieder of the Signetics Quality Control Laboratory.

Manuscript submitted Feb. 27, 1976; revised manuscript received June 1, 1976.

Any discussion of this paper will appear in a Discussion Section to be published in the JUNE 1977 JOURNAL. All discussions for the June 1977 Discussion Section should be submitted by Feb. 1, 1977.

Publication costs of this article were assisted by Signetics Corporation.

### APPENDIX A

Figure 1(a) illustrates the case of an in-line FPP oriented at an arbitrary angle with respect to the radius of a circular pattern. The coordinates of the probes are given by

$$x_1 = \Delta + \frac{3}{2}s \cos \theta$$

$$x_2 = \Delta + \frac{1}{2}s \cos \theta$$

$$x_3 = \Delta - \frac{1}{2}s \cos \theta$$

$$x_4 = \Delta - \frac{3}{2}s \cos \theta$$

$$y_1 = \frac{3}{2}s \sin \theta = -y_4$$

$$y_2 = \frac{1}{2}s \sin \theta = -y_3 \quad [\text{A-1}]$$

where  $\Delta$  is the distance of the center of the probe array from the center of the circle,  $\theta$  is the angle of inclination of the probe with respect to the radius, and  $s$  is the probe separation distance.

According to conformal mapping theory, a circle in the  $z$ -plane can be mapped into the upper half of the  $w$ -plane [Fig. 1(b)] using the transformation

$$w = i \frac{r - z}{r + z} \quad [\text{A-2}]$$

where  $i = \sqrt{-1}$ ,  $z = x + iy$ , and  $w = u + iv$ . Thus

$$u(x,y) = \frac{2ry}{(r+x)^2 + y^2}, \quad v(x,y) = \frac{r^2 - x^2 - y^2}{(r+x)^2 + y^2} \quad [\text{A-3}]$$

describes the location of points 1, 2, 3, and 4 in the  $w$ -plane. By introducing images of the current sources at  $(u_1, -v_1)$  and  $(u_4, -v_4)$  the problem reduces to that of determining the potential difference between points 2 and 3 due to the four current sources in the  $w$ -plane. Since a current source in an infinite sheet results in a logarithmic potential (2), the potential difference is

$$\Delta V = \frac{I\rho_s}{4\pi} \left[ \ln \frac{\alpha_1\alpha_2}{\alpha_3\alpha_4} + \ln \frac{\beta_1\beta_2}{\beta_3\beta_4} \right] \quad [\text{A-4}]$$

where

$$\alpha_1 = (v_2 - v_4)^2 + (u_2 - u_4)^2$$

$$\alpha_2 = (v_2 + v_4)^2 + (u_2 - u_4)^2$$

$$\alpha_3 = (v_2 - v_1)^2 + (u_2 - u_1)^2$$

$$\alpha_4 = (v_2 + v_1)^2 + (u_2 - u_1)^2$$

and

$$\beta_1 = (v_3 - v_1)^2 + (u_3 - u_1)^2$$

$$\beta_2 = (v_3 + v_1)^2 + (u_3 - u_1)^2$$

$$\beta_3 = (v_3 - v_4)^2 + (u_3 - u_4)^2$$

$$\beta_4 = (v_3 + v_4)^2 + (u_3 - u_4)^2 \quad [\text{A-5}]$$

The correction factor defined by Eq. [1] is thus

$$k = 4\pi \cdot \left[ \ln \frac{\alpha_1\alpha_2}{\alpha_3\alpha_4} + \ln \frac{\beta_1\beta_2}{\beta_3\beta_4} \right]^{-1} \quad [\text{A-6}]$$

for an FPP oriented at an arbitrary angle with respect to the radius of a thin circular pattern.

$$k(\theta) \approx \frac{\pi}{\ln 2 + \frac{1}{4} \ln \left\{ \frac{\left[ (a/s')^2 + \sin^2 \theta - \frac{1}{4} \cos^2 \theta \right]^2 + \cos^2 \theta \sin^2 \theta}{\left[ (a/s')^2 + \frac{1}{4} \sin^2 \theta - \cos^2 \theta \right]^2 + \cos^2 \theta \sin^2 \theta} \right\}} \quad [\text{B-11}]$$

#### APPENDIX B

According to Eq. [A-1] and [A-3]

$$u(x,y) = \frac{2ry}{(r+x)^2} \cdot \left[ 1 + \frac{y^2}{(r+x)^2} \right]^{-1} \approx \frac{2ry}{(r+x)^2} \quad [\text{B-1}]$$

and

$$v(x,y) = \left[ \frac{r-x}{r+x} - \frac{y^2}{(r+x)^2} \right] \cdot \left[ 1 + \frac{y^2}{(r+x)^2} \right]^{-1} \approx \frac{r-x}{r+x} \quad [\text{B-2}]$$

since  $y^2/(r+x)^2 \ll 1$  when  $s \ll r$ . Using Eq. [A-1], and defining  $u' = u \cdot (r+\Delta)$  and  $v' = v \cdot (r+\Delta)$ , the coordinates of probe location 1 may be written (again assuming  $s \ll r$ )

$$\begin{aligned} u_1' &= u_1 \cdot (r+\Delta) \\ &= \frac{2r}{r+\Delta} \cdot \frac{3}{2} s \sin \theta \left[ 1 + \frac{\frac{3}{2} s \cos \theta}{r+\Delta} \right]^{-2} \\ &\approx \frac{2r}{r+\Delta} \cdot \frac{3}{2} s \sin \theta \end{aligned} \quad [\text{B-3}]$$

and

$$\begin{aligned} v_1' &= v_1 \cdot (r+\Delta) \\ &= \left( r - \Delta - \frac{3}{2} s \cos \theta \right) \left[ 1 + \frac{\frac{3}{2} s \cos \theta}{r+\Delta} \right]^{-1} \end{aligned}$$

$$\approx r - \Delta - \frac{2r}{r+\Delta} \cdot \frac{3}{2} s \cos \theta \quad [\text{B-4}]$$

Introducing the effective probe separation distance

$$s' = \frac{2r}{r+\Delta} s = \frac{s}{1 - \frac{a}{2r}} \quad [\text{B-5}]$$

where

$$a = r - \Delta \quad [\text{B-6}]$$

is the distance to the edge of the wafer, one has that

$$u_1' \approx \frac{3}{2} s' \sin \theta, \quad v_1' \approx a - \frac{3}{2} s' \cos \theta \quad [\text{B-7}]$$

A similar treatment for the coordinates of probe locations 2, 3, and 4 leads to the expressions

$$u_2' \approx \frac{1}{2} s' \sin \theta, \quad v_2' \approx a - \frac{1}{2} s' \cos \theta \quad [\text{B-8}]$$

$$u_3' \approx -\frac{1}{2} s' \sin \theta, \quad v_3' \approx a + \frac{1}{2} s' \cos \theta \quad [\text{B-9}]$$

$$u_4' \approx -\frac{3}{2} s' \sin \theta, \quad v_4' \approx a + \frac{3}{2} s' \cos \theta \quad [\text{B-10}]$$

Equations [B-7]-[B-10] describe a probe array of separation  $s'$  oriented at an angle  $\theta$  with respect to a line drawn normal to the nonconducting edge of a semi-infinite sample [Fig. 4(b)]. Images of the current sources may be located at  $(u_1', -v_1')$  and  $(u_4', -v_4')$  and Eq. [A-5] and [A-6] used to compute the correction factor as was done for the general case described in Appendix A. The result is

subject to the requirement that

$$\left( 1 - \frac{a}{r} + \frac{3}{2} \frac{s}{r} \cos \theta \right)^2 + \left( \frac{3}{2} \frac{s}{r} \sin \theta \right)^2 \leq 1 \quad [\text{B-12}]$$

Equation [B-12] is a statement of the condition that all four probes must lie within the boundary of the circular sample. Uhlir (13) has previously treated the case of an FPP near the edge of a semi-infinite sample of finite thickness. The solution, however, was obtained in terms of functions related to the potential of a line of point charges.

#### REFERENCES

1. L. B. Valdes, *Proc. Inst. Radio Eng.*, **42**, 420 (1954).
2. F. M. Smits, *Bell Syst. Tech. J.*, **37**, 711 (1958).
3. R. Rymaszewski, *J. Sci. Instr.*, **2**, 170 (1969).
4. M. A. Logan, *Bell Syst. Tech. J.*, **40**, 885 (1961).
5. J. Stephen, B. J. Smith, and G. W. Hinder, *Proc. 4th Int. Conf. Ion Implantation in Semiconductors and Other Materials*, Osaka, 1974.
6. D. S. Perloff, F. E. Wahl, and J. T. Kerr, *Proc. 7th Int. Conf. Electron and Ion Beam Science and Technology*, Washington, D.C., 1976.
7. L. J. Swartzendruber, *Solid-State Electron.*, **7**, 413 (1964).
8. L. J. Swartzendruber, *Nat. Bur. Stand. Tech. Note* 199, U.S. Govt. Printing Office, Washington, D.C. (1964).
9. P. A. Crossley and W. E. Ham, *J. Electron. Mater.*, **2**, 465 (1973).
10. L. J. van der Pauw, *Philips Res. Rep.*, **13**, 1 (1958).
11. Manufactured by A. M. Fell Ltd., London, England.
12. D. S. Perloff, F. E. Wahl, and J. Reimer, To be published.
13. A. Uhlir, Jr., *Bell Syst. Tech. J.*, **34**, 105 (1955).

# Impurity Profiles within a Shallow p-n Junction by a New Differential Spreading Resistance Method

O. Kudoh, K. Uda, Y. Ikushima, and M. Kamoshida

Nippon Electric Company, Limited, IC Division, Kawasaki, 211 Japan

## ABSTRACT

A new simple model for profiling the impurities within a shallow p-n junction from spreading resistance data is proposed. Dickey's capacitance analogue method is extended to a "multilayer" geometry. Direct translation of the differential sheet conductance method to the spreading resistance method is performed. As examples of this approach, the cases of shallow boron ( $^{11}\text{B}^+$ )-, phosphorus ( $^{31}\text{P}^+$ )-, and arsenic (As)-doped layers in silicon are discussed.

Mechanical or technical problems involved in obtaining reliable spreading resistance data have been almost completely settled and automatic measuring equipment is commercially available.<sup>1</sup> However, the procedure for determining impurity profiles from spreading resistance data is still worthy of improvement. Many attempts have been made to determine accurate correction factors, which must be applied to the measured spreading resistance values in order to get the corrected resistivities (1-4). The simplest formula is the "unilayer" theory, which sometimes gives inaccurate information concerning impurity profiles, especially in the cases of profiles within shallow p-n junctions (1). As the correction factors of the "unilayer" theory depend only upon the distance between the probe tip and the p-n junction, only the concentrations averaged between the probe tip and the junction can be attainable from this theory.

The "multilayer" theory has been successfully adopted to determine accurate correction factors, by solving  $(2N + 2)$  matrix determinants, where  $N$  is the layer number (4). However, this procedure could not be employed without utilizing a computer on a large scale.

In this report, a new simple model for profiling impurities within a shallow p-n junction from spreading resistance data is proposed which does not require a direct determination of correction factors. Only hand calculation or, at most, calculation by a minicomputer is required with this new approach. As examples of this method, boron ( $^{11}\text{B}^+$ ) and phosphorus ( $^{31}\text{P}^+$ ) ion-implanted layers and arsenic (As)-diffused layers are considered.

## Analysis Procedure

In a shallow p-n junction, where the junction depth is smaller than the effective radius of the probe tip, current is forced to flow parallel to the surface, and the equipotential of the probe can be approximated as reaching the junction edge. Dickey calculated correction factors of the uniformly doped layer of this two-point geometry by using a capacitance analogue of the two-parallel-wire transmission line (5). Dickey's formula can be extended to the layer consisting of  $N$  thin layers of resistivity  $\rho_1, \rho_2, \dots, \rho_{N-1}, \rho_N$ , as shown in Fig. 1.

The spreading resistance,  $R_N$  is defined as

$$\frac{1}{R_N} = \sum_{I=1}^N \frac{\pi d}{2\rho_I \cdot \ln(D/a)} \quad [1]$$

where  $D$  is the probe spacing,  $a$  is the effective probe tip radius,  $d$  is the thickness of each thin layer, and  $\rho_I$  is the resistivity of the  $I$ -th thin layer (6).

Key words: profile measurement, spreading resistance calculation, ion implantation profile, arsenic diffusion profile.  
<sup>1</sup> The ASB-100 automatic spreading resistance probe, Solid State Measurements Incorporated, was used in this work.

Equation [1] permits the differential sheet conductance method to be applied to spreading resistance data taken along a beveled edge. Setting  $R_{N-1}$  as the spreading resistance of the layer, after removing the uppermost  $N$ -th thin layer from the layer shown in Fig. 1,  $\rho_N$  is given as

$$\rho_N = \frac{\pi d}{2 \ln(D/a)} \cdot \frac{R_{N-1} \cdot R_N}{R_{N-1} - R_N} \quad [2]$$

Accordingly, determining only two adjacent data values from among the measured spreading resistance data sequence is sufficient to determine accurate resistivity of each thin layer. The resistivity can be converted to net impurity concentration according to Irvin's curve (7).

However, in contrast to the differential sheet conductance method, the measured spreading resistance  $R_m$  contains a contribution  $R_B$ , the barrier resistance between the probe and the sample surface, in addition to the true spreading resistance  $R$

$$R_m = R_B + R \quad [3]$$

The barrier resistance  $R_B$  depends strongly upon surface layer resistivity and other complex factors (8). With the present state of knowledge,  $R_B$  can be best estimated for arbitrary resistivity  $\rho$  by using several uniformly doped wafers of known resistivity, as calibration specimens and employing the interpolation procedure, described by Mazur and Dickey (1). This estimate assumes that barrier resistance and contact potential are independent of current and voltage distribution under the probe tip.

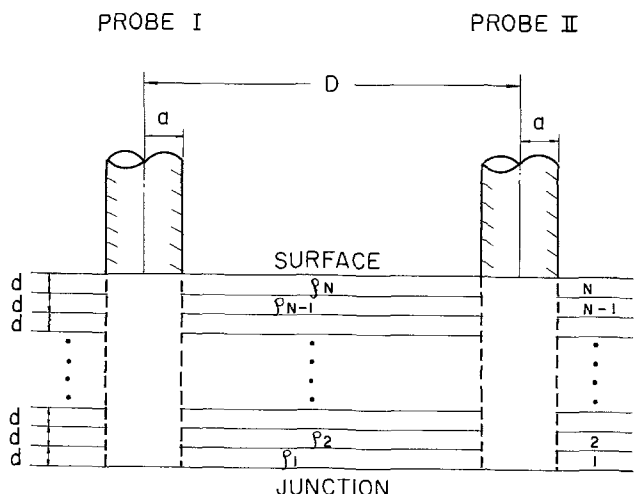


Fig. 1. Two point geometry for multilayer case between surface and junction.

To determine the impurity profile from measured spreading resistance data,  $R_{m1}$ ,  $R_{m2}$ , ...,  $R_{mN}$ , the following iteration procedure is necessary.

1. Set  $\rho'_I = 2a R_{mI}$
2. Compute  $R_B(\rho'_I)$
3. Set  $R_I = R_{mI} - R_B(\rho'_I)$

$$4. \text{ Compute } \rho_I = \frac{\pi d}{2 \ln(D/a)} \cdot \frac{R_{I-1} \cdot R_I}{R_{I-1} - R_I}$$

( $R_{I-1}$ ; known)

5. If  $|\rho'_I - \rho_I| > \rho'_I \cdot \epsilon$ , set  $\rho'_I = \rho_I$  and repeat step 2.
6. If  $|\rho'_I - \rho_I| < \rho'_I \cdot \epsilon$ , record  $R_I$  and set  $\rho_{I \text{ true}} = \rho_I$ .

Knowing  $\rho_I$ , resistivities of the whole layer can be subsequently obtained, beginning from the junction edge and continuing toward the surface, in the following sequence

$$\begin{array}{cccccccc} \rho_1 & \rho_2 & \dots & \rho_{I-1} & \rho_I & \dots & \rho_{N-1} & \rho_N \\ \downarrow \nearrow & \downarrow \nearrow & & \downarrow \nearrow & \downarrow \nearrow & & \downarrow \nearrow & \downarrow \nearrow \\ R_1 & R_2 & \dots & R_{I-1} & R_I & \dots & R_{N-1} & R_N \end{array}$$

For fast convergence of this calculation, the "skip" procedure is sometimes convenient for a small difference of  $R_{I-1}$  and  $R_I$ .

### Experimental Results and Discussions

Figure 2 shows profiles of a  $^{11}\text{B}^+$ -implanted layer, determined by the three different methods. The implant was performed at an energy of 150 keV and dose of  $4 \times 10^{14} \text{ cm}^{-2}$ . The sample was annealed at 900°C for 30 min in dry  $\text{N}_2$ . The squares and the triangles were obtained by the "no correction" method, which contains no geometrical correction, and the "unilayer" method of Dickey (5), respectively. These results are far from the profile predicted by the LSS theory (9) and empirical reports (10). The circles were obtained by the present method. The resultant profile seems to be reliable, considering the profile of the LSS theory (9) which is shown as the dashed-line curve in Fig. 2.

Figure 3 shows the same profiles as presented in Fig. 2, obtained by the present method, as a function of implant dose ( $4 \times 10^{13}$ - $2 \times 10^{15} \text{ cm}^{-2}$ ). Observed profiles are similar to a gaussian distribution, especially on the p-n junction side. However, they are not symmetrical and are widely spread on the surface side. Their peak concentration positions are slightly shallower than the projected range  $R_p$  of the LSS theory (9). Recently,  $^{11}\text{B}^+$  profiles in silicon shallower than those of Ref. (9) were published accounting for the new data on electronic cross sections (11). The LSS theory predicts an asymmetrical  $^{11}\text{B}^+$  profile in silicon, skewed toward the surface (12). Theoretical profiles incorporating these effects would be expected to explain the results shown in Fig. 2 and 3. As the integrated sum of each profile in Fig. 3 closely fits each implant dose, implanted  $^{11}\text{B}^+$  ions are fully electrically activated over the whole dose range considered here (13).

The measured peak concentrations shown in Fig. 3 are plotted vs. the implant dose in Fig. 4. Considering the redistribution during annealing, coincidences of measured values with LSS theoretical values are sufficient except for the low dose region. As the impurity concentration becomes lower, the difference between adjacent values of measured spreading resistance data becomes smaller. In these cases, the present method is not applicable. This situation is quite similar to the differential sheet conductance method.

Comparison between the differential sheet conductance method and the present method is shown in Fig. 5 for the case of  $^{11}\text{B}^+$  implanted layer at an energy of 50 keV and dose of  $1 \times 10^{14} \text{ cm}^{-2}$ . The open and closed

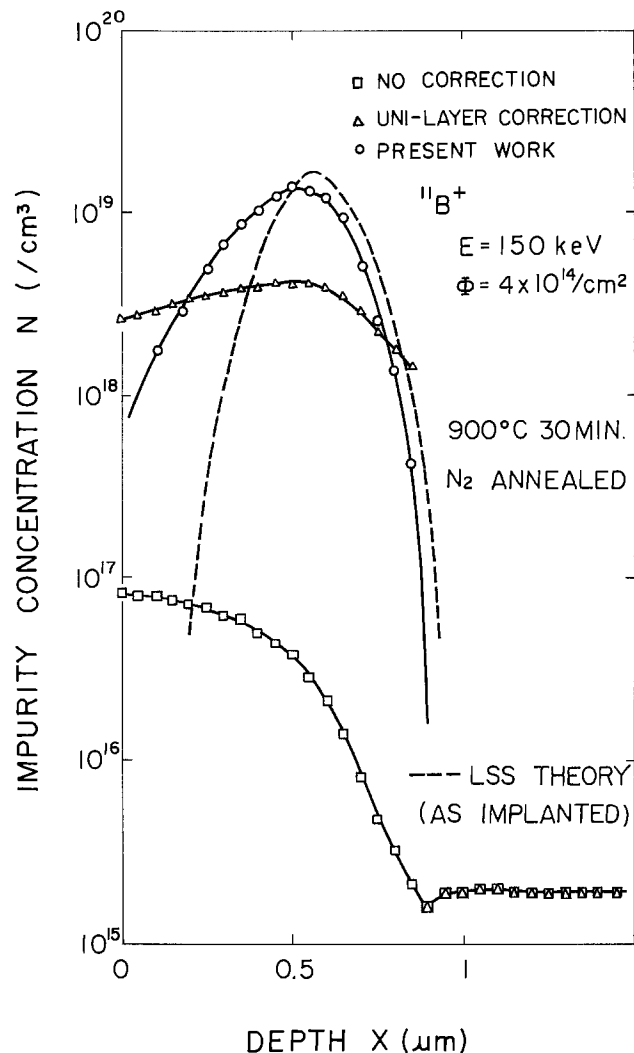


Fig. 2. Comparison of profiles obtained by three different methods for the case of a  $^{11}\text{B}^+$  layer implanted at an energy of 150 keV and dose of  $4 \times 10^{14} \text{ cm}^{-2}$ . Dashed-line curve shows LSS theoretical values.

circles were obtained by the four-point differential conductance method, employing a layer removal technique, and the present spreading resistance method, respectively. They coincide well within measuring error limits. This result confirms the reliability of the present method.

The second example of this method is the measurement of a  $^{31}\text{P}^+$  layer implanted at an energy of 100 keV and dose of  $1 \times 10^{16} \text{ cm}^{-2}$  into a bare silicon surface. Figure 6 shows annealing time dependences of  $^{31}\text{P}^+$  ion profiles for activation at 900°C in dry  $\text{N}_2$ . Measured profiles have much deeper junction depths than those of the LSS theory and have a "kink" at a concentration of nearly  $2 \times 10^{19} \text{ cm}^{-3}$ . One of the reasons for these results would be the ion-channeling effect during implantation (14). As the "kink" was also observed in the thermally diffused phosphorus case (15, 16), there remains some possibility that the inherent property of phosphorus in silicon is playing a role in determining the profiles shown in Fig. 6.

The third example is the arsenic profile shown in Fig. 7. Arsenic was diffused for 60 min at 1000°C from an As-doped polysilicon film, which was chemically deposited at 750°C in a mixed flow of  $\text{SiH}_4$  and  $\text{AsCl}_3$ . Again, good agreement is obtained for the two resultant As profiles, measured by the four-point differential sheet conductance method ( $\circ$ ) and the present spreading resistance method ( $\bullet$ ). Note that the data spacing of the spreading resistance method is 125Å and that the deviations of the measured concentrations are still

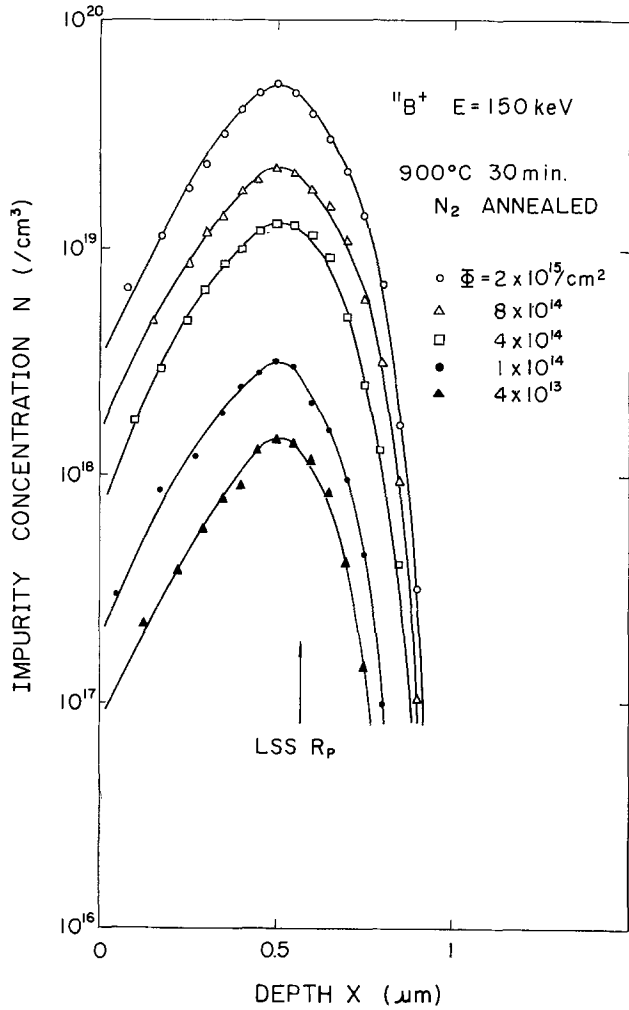


Fig. 3.  $^{11}\text{B}^+$  implanted profiles with implant dose as a parameter. Energy was 150 keV.

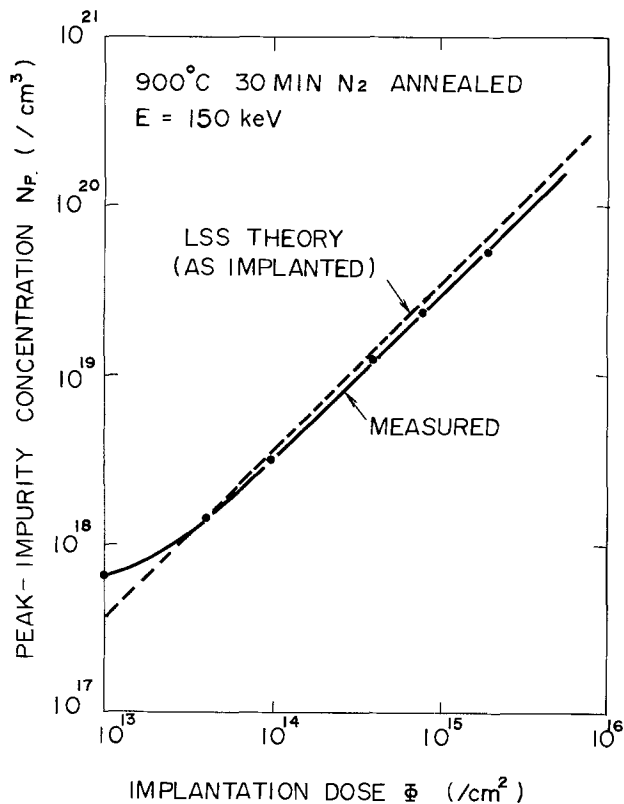


Fig. 4. Peak concentrations of  $^{11}\text{B}^+$  profiles as a function of implant dose, obtained from Fig. 3. Dashed line corresponds to LSS theoretical peak concentrations.

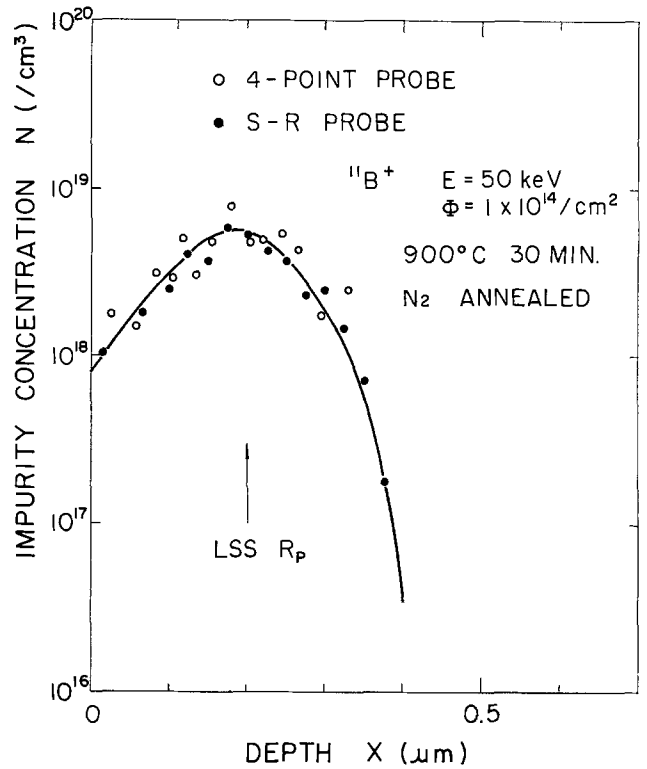


Fig. 5. Comparison of  $^{11}\text{B}^+$  implanted profiles obtained from the four-point differential sheet conductance method and the present spreading resistance method.

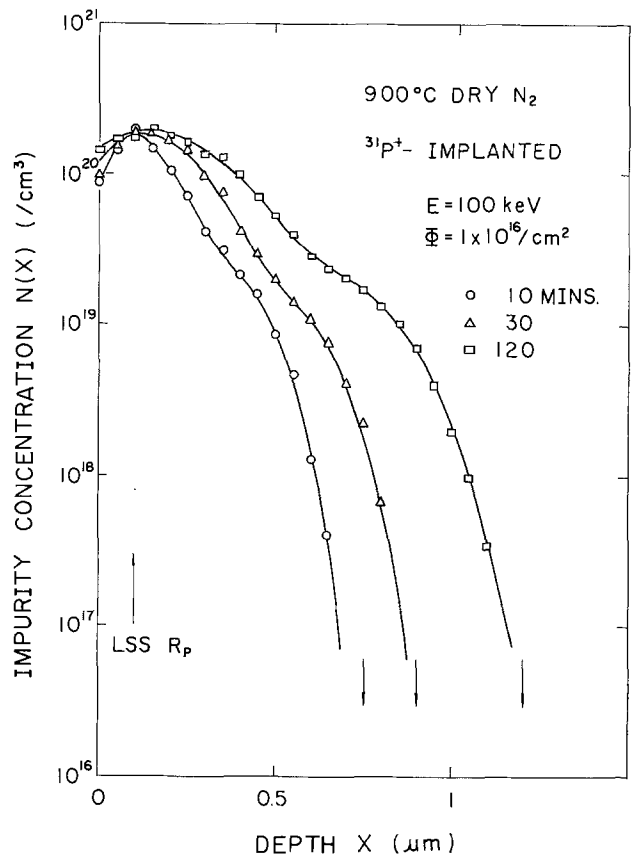


Fig. 6.  $^{31}\text{P}^+$  implanted profiles at an energy of 100 keV and dose of  $1 \times 10^{16} \text{ cm}^{-2}$  with annealing time as a parameter at  $900^\circ\text{C}$ .

small. The sample was lapped at an angle of 17 min. If the sample preparation is good enough, the present method yields quite accurate information for impurity

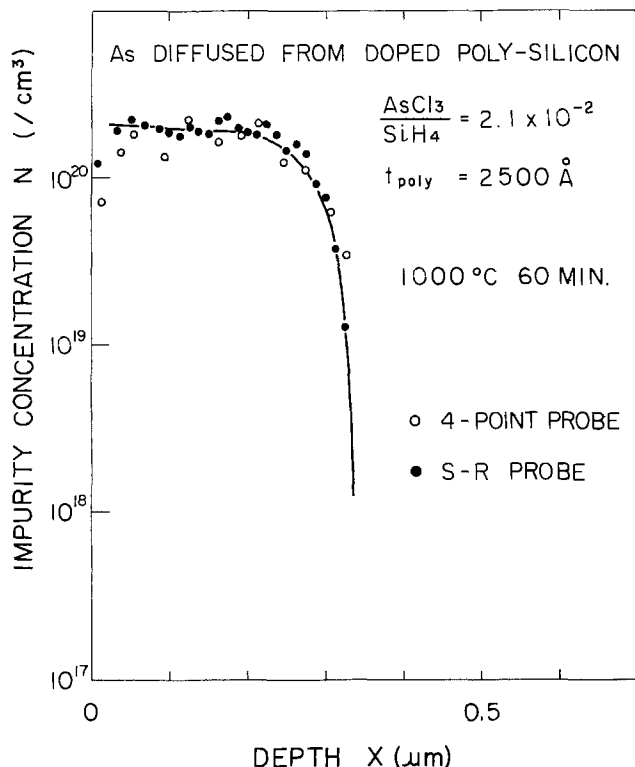


Fig. 7. Comparison of As profiles obtained from the four-point differential sheet conductance method and the present spreading resistance method. As was diffused from a doped polysilicon film for 60 min at 1000°C.

profiles in semiconductor devices, even for such a short data spacing.

#### Conclusion

The present new approach to the spreading resistance method has proved to be a reliable means of profiling impurities within shallow p-n junctions in silicon. Obtained profiles of implanted  $^{11}\text{B}^+$  and  $^{31}\text{P}^+$  ions and As diffused from a doped polysilicon film are consistent with those of LSS theory, the differential sheet conductance method, and the work performed previously by other authors.

#### Acknowledgment

The authors would like to express their thanks to Dr. T. Okada for his discussions and encouragement.

Manuscript submitted March 5, 1976; revised manuscript received July 12, 1976. A part of this report was presented at the Spring meeting of the Applied Physical Society of Japan, 1975, and the 8th Symposium on Semiconductors and Integrated Circuits Technology of the Electro-chemical Society of Japan, Tokyo, 1975.

Any discussion of this paper will appear in a Discussion Section to be published in the June 1977 JOURNAL. All discussions for the June 1977 Discussion Section should be submitted by Feb. 1, 1977.

Publication costs of this article were assisted by Nippon Electric Company, Limited.

#### REFERENCES

1. R. G. Mazur and D. H. Dickey, *This Journal*, **113**, 255 (1966).
2. P. A. Schumann, Jr. and E. E. Gardner, *Solid-State Electron.*, **12**, 371 (1969).
3. P. S. Schumann, Jr. and E. E. Gardner, *This Journal*, **116**, 87 (1969).
4. T. H. Yeh and K. H. Khokhani, *ibid.*, **116**, 1461 (1969).
5. D. H. Dickey, Abstract 57, p. 151, The Electrochemical Society Extended Abstracts, Spring Meeting, Pittsburgh, Pa., April 15-18, 1963; also see Appendix A of the ASR-100 Manual.
6. D. H. Dickey, Paper 250 RNP presented at The Electrochemical Society Meeting, Dallas, Texas, Oct. 5-9, 1975.
7. J. C. Irvin, *Bell Syst. Tech. J.*, **41**, 387 (1962).
8. S. J. Fonash, Proceedings of NBS Spreading Resistance Symposium, NBS Special Publication 400-10, Washington, D.C.
9. W. S. Johnson and J. F. Gibbons, "LSS Projected Range Statistics in Semiconductors," Stanford University Press, Stanford, California (1970).
10. T. E. Seidel, in "Proceedings of the Second International Conference on Ion Implantation in Semiconductors," I. Ruge and J. Graul, Editors, p. 41, Springer-Verlag, Berlin (1971).
11. J. F. Gibbons, W. S. Johnson, and S. W. Mylroie, "Projected Range Statistics in Semiconductors and Related Materials," 2nd ed., Halstead Press, New York (1975).
12. S. W. Mylroie and J. F. Gibbons, in "Proceedings of the Third International Conf. on Ion Implantation," W. Crowder, Editor, p. 243, Plenum Press, New York (1972).
13. F. N. Schwettman, *Appl. Phys. Lett.*, **45**, 1918 (1974).
14. P. Blood, G. Dearnaley, and M. A. Wilkins, *J. Appl. Phys.*, **45**, 5123 (1974).
15. J. C. C. Tsai, *Proc. IEEE*, **57**, 1499 (1969).
16. M. Yoshida, E. Arai, H. Nakamura, and Y. Terunuma, *J. Appl. Phys.*, **45**, 1498 (1974).

## Technical Notes



### Silicon Monoxide Thin Films

S. I. Raider\*

IBM Thomas J. Watson Research Center, Yorktown Heights, New York 10598

and R. Flitsch

IBM System Products Division, East Fishkill Facility, Hopewell Junction, New York 12533

The composition of thin, solid, silicon monoxide (SiO) films remains controversial despite numerous

\* Electrochemical Society Active Member.  
Key words: silicon oxide, dielectric, x-ray photoelectron spectroscopy, ESCA.

investigations (1-7). Structural studies of deposited films have led to conjecture as to whether SiO exists as a unique species in the solid state. Brewer and Greene (8) observed that an SiO condensate is metastable and

has no temperature range of thermodynamic stability. Evaporated SiO films have been described in terms of unique species, such as SiO, Si<sub>2</sub>O<sub>3</sub>, Si, and SiO<sub>2</sub>, and also as a continuous distribution of suboxide species, SiO<sub>x</sub>, centered about SiO<sub>1.0</sub>. In the gas phase, spectroscopic evidence (9, 10) indicates that a monomeric species, SiO, does exist and is similar in electronic structure to gaseous carbon monoxide (11). The variability in SiO thin film composition is determined by film deposition parameters which include the evaporation rate, the source temperature, the substrate temperature, and the pressure in the evaporating system (1, 4). SiO vapor condenses to form a solid product with an O:Si composition ratio equal to 1:1.

We have examined deposited SiO films using x-ray photoelectron spectroscopy, or ESCA (electron spectroscopy for chemical analysis), as part of a study of silicon-oxygen bonding in thin films. The O 1s and Si 2p photoelectron binding energies and the O 1s:Si 2p intensity ratio in SiO were compared with similar data from spectra of SiO<sub>2</sub> and Si. A model of chemical bonding near an SiO surface is described based on observed differences in Si 2p photoelectron binding energies, O 1s:Si 2p intensity ratios, and variations in photoelectron line half-widths (FWHM)<sup>1</sup> from SiO deposited at 24°C and from similar samples subsequently heated to 400°C.

### Experimental

SiO films, 800-4000Å thick, were prepared by SiO (Cerac/Pure Incorporated, 99.99% pure) evaporation at pressures of 6-8 × 10<sup>-6</sup> Torr, and by deposition onto cleaned Si substrates, at a substrate temperature of 24°C, at source temperatures of 1300°-1450°C, and at deposition rates of 7.5-30 Å/sec. An AEI-ES 100 electrostatic analyzer was used to measure the Si 2p, O 1s, C 1s, and Au 4f<sub>7/2</sub> photoelectron lines. Binding energy data were referenced to Si 2p lines in Si (99.3 eV) and in SiO<sub>2</sub> (103.7 eV) (12), Au 4f<sub>7/2</sub> (83.8 eV), and C 1s (284.9 eV). The binding energy of a reference gold film was measured. Binding energies were corrected for charging effects which increased with film thickness and varied between 0.1 and 0.6 eV. Distinct Si and SiO<sub>2</sub> impurity Si 2p lines with binding energies at 99.3 and 103.7 eV, respectively, and characteristic linewidths, were sometimes observed in SiO spectra and used as reference lines. Spectra were generally obtained with the sample at room temperature, although measurements were also made with the sample at 400°C in order to desorb surface impurities. Variations in spectrometer stability were less than ±0.1 eV. ESCA measurements were made after exposure of deposited SiO samples to air for periods of less than 1 hr to several days.

### Results

In Fig. 1, O 1s and Si 2p photoelectron spectra of a 1000Å SiO film are plotted as a function of binding energies corrected for charging effects. The initial spectra were obtained at 23°C about 1 hr after SiO deposition. The O 1s line has a binding energy of 532.5 ± 0.4 eV and a linewidth (FWHM) of 1.8 eV. The Si 2p line consists primarily of a single line at a binding energy of 101.5 ± 0.1<sub>5</sub> eV with a width (FWHM) of 2.4 eV. The Si 2p linewidth is sensitive to small changes in SiO deposition parameters and was generally found to be greater than 2.4 eV. A shoulder with a binding energy similar to that of free silicon (99.3 eV) is superimposed on the Si 2p line and comprises 2-4% of the total Si 2p intensity. On heating the SiO sample to 400°C for ½ hr in vacuum, the major Si 2p line shifts to a binding energy of 101.6 eV and increases in width to 2.5<sub>5</sub> eV. The intensity of the shoulder doubles in intensity but remains at a binding energy of 99.3 eV. The O 1s binding energy and linewidth remain constant after heating to 400°C. Photoelectron line intensity ratios, I(O 1s):I(Si 2p), for SiO were 1.3-1.45. No changes in ESCA spectra were observed after exposing a similar sample

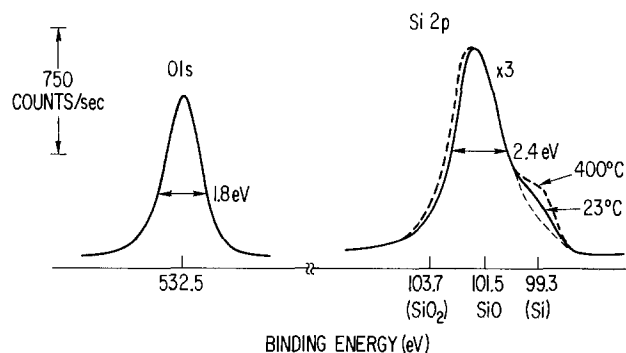


Fig. 1. ESCA O 1s and Si 2p spectra of a deposited SiO film

to air for one week at 23°C. ESCA data of Si, evaporated SiO, and SiO<sub>2</sub> are compared in Table I.

SiO films were also deposited at lower deposition rates and with higher evaporator background pressures. A broad Si 2p line with a binding energy characteristic of SiO was observed in all ESCA spectra. However, distinct additional Si 2p lines, asymmetric broadening of the SiO Si 2p spectrum, and consistent changes in the I(O 1s):I(Si 2p) ratio indicated that excess oxygen, excess silicon, or silicon dioxide and silicon were present as impurities in these SiO samples. Oxygen-rich components of an SiO film, present as impurities, were preferentially removed by chemical etching with diluted HF (1:10). Silicon and silicon-rich components, which increased in concentration with decreasing deposition rates, were often detected as the major impurity lines in spectra of SiO films. This may account for the detection of Si in deposited SiO films by diffraction techniques.

### Discussion

A photoelectron line intensity is proportional to the total number of emitting atoms in a homogeneous sample if the surface is representative of the bulk (13). With a noncontaminated surface, the O:Si composition ratio in SiO can be estimated by comparing ESCA intensity ratio data, i.e., I(O 1s):I(Si 2p), with intensity data from a reference compound such as SiO<sub>2</sub> (12). The presence of excess nonoxidized Si atoms located at the film surface, rather than excess oxidized Si atoms, indicates that oxygenated species adsorbed at an SiO surface have not altered the chemical composition of the film. Comparison of intensity ratios of SiO and SiO<sub>2</sub> samples exposed for several days to air leads to an SiO stoichiometry of SiO<sub>1.0 ± 0.1</sub>. These results for SiO are surprisingly good if we consider that, besides possible changes in surface chemistry, differences in adsorbed contaminants present on both surfaces will further modify an intensity ratio for elements with different mean escape depths.

The O 1s binding energy in SiO and SiO<sub>2</sub> (12) films is 532.5, which suggests that a similar chemical environment for oxygen exists in both materials. The siloxane linkage is characteristic of SiO<sub>2</sub>, of silicones, and is expected of other polymeric silicon-oxygen species (14). A high melting point and low vapor pressure of solid SiO indicate that SiO is not molecular but has a cross-linked polymeric structure (14). Furthermore, in infrared spectra of gaseous SiO isolated in Ar or N<sub>2</sub>

Table I. Relative photoelectron intensities, binding energies, and linewidths (FWHM) for Si, SiO, and SiO<sub>2</sub>

	I(O 1s): I(Si 2p)	O 1s (eV)	FWHM (eV)	Si 2p (eV)	FWHM (eV)
Si				99.3	1.3
SiO	1.3-1.45	532.5 ± 0.4	1.8	101.5 ± 0.1 <sup>*</sup>	2.3 <sup>*</sup>
SiO <sub>2</sub>	2.7	532.5	1.7	103.7	1.7

<sup>1</sup> FWHM: full width at half maximum.

<sup>\*</sup> Extrapolated value (see text).

matrixes at 20°K (15, 16) dimeric and trimeric units,  $\text{Si}_2\text{O}_2$  and  $\text{Si}_3\text{O}_3$  were observed together with monomer units of SiO. These polymeric species formed ring structures with siloxane bridges as the probable first step in the formation of condensed solid polymeric SiO.

The O 1s linewidth of 1.8 eV in SiO is greater than the O 1s linewidth in  $\text{SiO}_2$  (1.5 eV). No increase in O 1s linewidth was detected for SiO or  $\text{SiO}_2$  upon exposure to air for several days or after heating SiO at 400°C. SiO and  $\text{SiO}_2$  films are amorphous and have oxygen atoms in similar chemical environments. Second-order bonding about oxygen in SiO with distributions of species changing from  $\text{O}_3\text{-Si-O-Si-O}_3$  to  $\text{Si}_3\text{-Si-O-Si-Si}_3$  is a likely cause of this broadened line.

A change in binding energy of an element has been associated with first-order changes in bonding in a series of similar materials (13). The Si 2p binding energy in SiO is located at about half the binding energy difference between Si (99.3 eV) and  $\text{SiO}_2$  (103.7 eV), as is indicated in Fig. 2. A linear, or nearly linear, empirical relationship exists between changes in binding energy and changes in oxygen content of silicon oxide films. The tetrahedral configurations shown in Fig. 2 represent examples of the change in average composition about photoexcited Si atoms with change in binding energy, and provide a basis for determining oxide film composition (12, 17). During SiO evaporation, some SiO is dissociated and then deposited as nonoxidized Si atoms and O atoms. The O atoms presumably oxidize the partially oxidized Si atoms. This results in a small increase in the Si 2p binding energy and linewidth. Depositing the SiO onto a heated substrate may enhance this dissociation (1, 4). Heating the SiO sample, which was deposited at 24°C, to 400°C does not alter the O:Si ratio but does cause internal chemical changes in the film. More nonoxidized silicon is formed; the remainder of the film is more highly oxidized, which causes the Si 2p binding energy and linewidth to increase. An estimated SiO binding energy and linewidth of 101.5 and 2.3 eV, respectively, are obtained by extrapolation to form a Si 2p line free of nonoxidized Si atoms.

ESCA spectra of Si 2p photoelectron lines in SiO evaporated film (7) and SiO powders (18) have recently been described and may be compared with our results. The binding energy separation between the Si 2p lines in SiO and in Si (2.2 eV) obtained by Hollinger *et al.* (7) is in agreement with our data (2.2 eV). For the SiO powder (18), this separation in Si 2p binding energies (estimated from a published spectrum) is about 3.3 eV and suggests that the oxidized Si in the powder possesses an O:Si ratio significantly greater than 1:1. From analysis of Auger spectra of SiO evaporated onto substrates held at 200°C and ion sputtered for a short time, Johannessen *et al.* (19) proposed that

SiO is a mixture of Si and  $\text{SiO}_2$ . However, both deposition onto a heated substrate and ion sputtering of the SiO surface may alter the SiO composition by enhancing decomposition to Si and  $\text{SiO}_2$ .

Si atoms are generally tetravalently bonded, and multiple bonds involving Si atoms are unknown. Si atoms in SiO possess, on the average, tetrahedral Si atoms bonded to two oxygens and two silicons, i.e.,  $\text{Si-(O)}_2(\text{Si})_2$ , a configuration intermediate between tetrahedra in silicon,  $\text{Si-(Si)}_4$ , and in silicon dioxide,  $\text{Si-(O)}_4$ . The larger Si 2p linewidth value in SiO (2.3 eV) relative to the linewidth in a Si single crystal (1.3 eV) or in an amorphous  $\text{SiO}_2$  film (1.8 eV) is also consistent with the presence of a continuous distribution of oxidized tetrahedral Si species contributing to a Si 2p line in SiO. Furthermore, the decomposition of SiO at 400°C does not cause unique oxide compounds, such as  $\text{SiO}_2$ , to form, but rather extends the distribution of Si atoms already oxidized to include a greater number of more completely oxidized Si atoms (Fig. 1). A unique SiO species does not exist in the solid state. Rather, SiO has a composition  $\text{Si-(O)}_x(\text{Si})_y$ , where  $x + y = 4$ , with the most probable composition being  $x = y = 2$ . The absence of two distinct Si 2p lines at 99.3 and 103.7 eV, and the presence of a single line at 101.5 eV, is a direct indication that a properly evaporated SiO film is not composed of a mixture of Si and  $\text{SiO}_2$ . Similarly, no single unique  $\text{Si}_2\text{O}_3$  species was identified from ESCA SiO spectra. Properly prepared SiO contains Si, SiO,  $\text{Si}_2\text{O}_3$ ,  $\text{SiO}_2$ , etc., only as components of a normal distribution of silicon oxide species whose average composition is  $\text{SiO}_{1.0}$ . This model of an SiO surface derived from ESCA data is in agreement with the previously reported conclusions of Philipp (6) for thick SiO films.

### Acknowledgments

We thank T. Hickmott and B. H. Vromen for their helpful criticisms of this manuscript. In addition, we are grateful to J. M. Brown, M. J. Palmer, and B. H. Vromen for providing SiO films.

Manuscript submitted June 23, 1976; revised manuscript received Aug. 3, 1976.

Any discussion of this paper will appear in a Discussion Section to be published in the June 1977 JOURNAL. All discussions for the June 1977 Discussion Section should be submitted by Feb. 1, 1977.

Publication costs of this article were assisted by IBM Corporation.

### REFERENCES

- G. Haas, *J. Am. Ceram. Soc.*, **33**, 353 (1950).
- E. F. White and R. Roy, *Solid State Commun.*, **2**, 151 (1964).
- M. V. Coleman and D. J. D. Thomas, *Phys. Status Solidi*, **22**, 593 (1967).
- W. A. Pliskin and H. S. Lehman, *This Journal*, **112**, 1013 (1965).
- S. C. H. Lin and M. Joshi, *This Journal*, **116**, 1740 (1965).
- H. R. Philipp, *J. Phys. Chem. Solids*, **32**, 1935 (1971).
- G. Hollinger, J. Tousset, and Tran Minh Duc, in "Tetrahedrally Bonded Amorphous Semiconductors," M. H. Brodsky, S. Kirkpatrick, and D. Weaire, Editors, p. 102, American Institute of Physics, New York (1974).
- L. Brewer and F. T. Greene, *J. Phys. Chem. Solids*, **2**, 286 (1957).
- K. F. Bonhoeffer, *Z. Phys. Chem. (Leipzig)*, **131**, 363 (1928).
- P. G. Saper, *Phys. Rev.*, **42**, 498 (1932).
- A. D. McLean and M. Yoshimura, *IBM J. Res. Dev.*, **12**, 206 (1968).
- R. Flitsch and S. I. Raider, *J. Vac. Sci. Technol.*, **12**, 305 (1975).
- K. Siegbahn, C. Nordling, A. Fehlgren, R. Norberg, K. Hamrin, J. Hedman, G. Johansson, T. Bergman, S.-E. Karlsson, and I. Lindberg, "ESCA-Atomic, Molecular and Solid State Structure Studied by Means of Electron Spectroscopy," Almqvist and Wiksells, Uppsala, Sweden (1967).

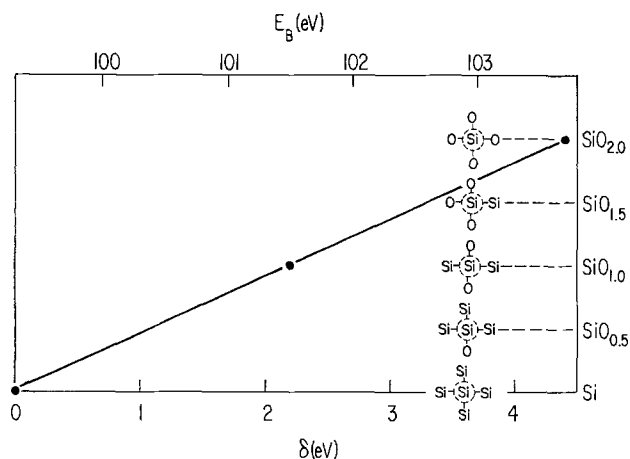


Fig. 2. Variation of Si 2p binding energy with average oxide film composition. Encircled Si atoms in tetrahedral configurations represent photoexcited atoms.



14. L. Spialter and J. S. Smith II, in "Decomposition of Organometallic Compounds to Refractory Ceramics and Metal Alloys." Proceedings of the 1967 International Symposium, K. S. Mazdeyasni, Chairman, p. 195, University of Dayton Press, Dayton, Ohio (1968).
15. J. H. Anderson and J. S. Ogden, *J. Chem. Phys.*, **51**, 4189 (1969).
16. J. W. Hastie, R. H. Hauge, and J. L. Margrave, *Inorg. Chim. Acta*, **3**, 601 (1969).
17. S. I. Raider and R. Flitsch, *J. Vac. Sci. Technol.*, **13**, 58 (1976).
18. R. A. Clarke, R. L. Tapping, M. A. Hopper, and L. Young, *This Journal*, **122**, 1347 (1975).
19. J. S. Johannessen, W. E. Spicer, and Y. E. Strausser, *Appl. Phys. Lett.*, **27**, 452 (1975).

## Electrophotographic Characteristics of ( $\text{HgI}_2$ :CdS) Binder Layers

P. K. C. Pillai, S. K. Agarwal, and R. C. Ahuja

*Department of Physics, Indian Institute of Technology, New Delhi 110029, India*

The combination of a photoconductor and insulating resin provides a photoconductive insulator capable of retaining a surface charge in dark and discharging in light. These combinations have some unique aspects: (i) The photoconductive material need not have high dark resistivity (which is required to retain charge) and this allows for a wide choice of materials. (ii) The independent characteristics of several photoconductors can be incorporated in one layer by dispersing these as powders in the resin binder. Several studies have been reported on the binder-type plates of Se (1), ZnO (2), anthracene (3), CdS (4), and their combinations (5-6).

The present investigations deal with the surface charge characteristics of  $\text{HgI}_2$ :CdS mixed system in polystyrene. Our earlier photoconductivity studies (6) have shown that the binder layers of CdS dispersed in polystyrene have  $I_{\text{photo}}/I_{\text{dark}} = 100$  and a low speed of response, while the binder layers of  $\text{HgI}_2$  have  $I_{\text{photo}}/I_{\text{dark}} = 150$  and a fast speed of response. This suggested that the binder layers of  $\text{HgI}_2$ :CdS mixed system might possess some characteristics more desirable for use in electrophotography. The experiments have shown that the layer containing  $\text{HgI}_2$  and CdS in the 60:40 ratio exhibits the maximum value of  $I_{\text{photo}}/I_{\text{dark}}$  ( $5 \times 10^3$  at 1750 lx). It was then felt worthwhile to study the surface charge characteristics.

The surface charge studies were made as follows: The photoconducting layers backed by NESAs coated glass plates were charged by using a scorotron unit and the resulting surface charge was measured in terms of surface potential by a vibrating condenser unit. A 100W tungsten filament lamp was used to discharge the layers.

Figure 1 shows typical dark and light decay curves of the  $\text{HgI}_2$ , CdS, and  $\text{HgI}_2$ :CdS layers. It is seen that (i) maximum surface potential is retained by the  $\text{HgI}_2$  layers, (ii) dark and light decay are fastest in  $\text{HgI}_2$  layers, and (iii)  $\text{HgI}_2$ :CdS layers show slow dark and fast light decay rates.

The effect of binder percentage on the dark and light decay rates of the  $\text{HgI}_2$ :CdS layers is shown in Fig. 2. It is seen that as the percentage of binder is increased, the dark and light decay rates slow down, and that the surface potential retained by the layer increases. From these characteristics it is evident that the binder layers containing  $\text{HgI}_2$ :CdS in the 60:40 composition dispersed in 60% by weight of polystyrene show the optimum characteristics for use in electrophotography. For this layer, the surface potential decays only by 5% in a period of 5 sec in dark, while during the same period the light decay is about 70% for 100 lx white illumination. These values indicate that a good image contrast can be obtained, which could be further improved by exposing the layer to higher intensities of light.

Key words: xerography, surface charge, photoconductor.

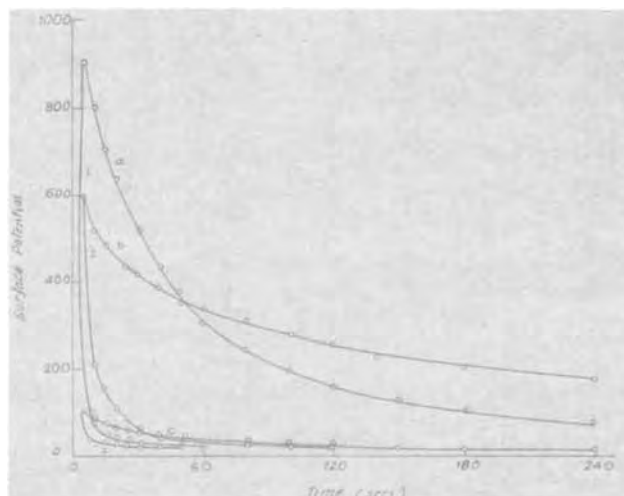


Fig. 1. Dark and light decay curves. Dark decay: (a) 100%  $\text{HgI}_2$ , (b) 60:40  $\text{HgI}_2$ :CdS, (c) 100% CdS. Light decay: (1) 100%  $\text{HgI}_2$ , (2) 60:40  $\text{HgI}_2$ :CdS, (3) 100% CdS. Binder percentage is 40 in all the samples.

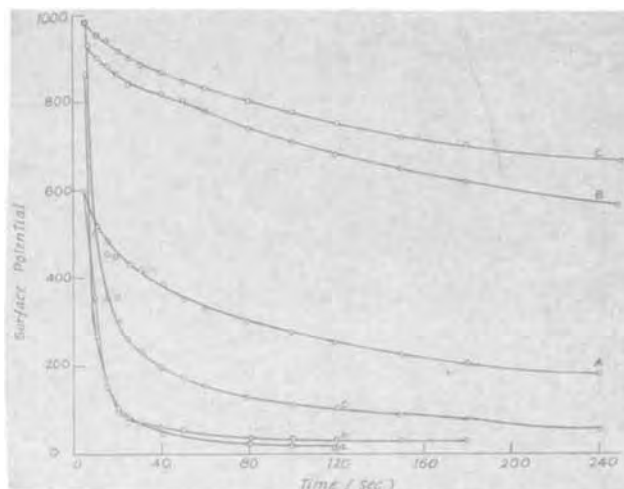


Fig. 2. Effect of binder percentage on the dark and light decay rates of the  $\text{HgI}_2$ :CdS layers. Dark decay: (A) binder percentage = 40, (B) binder percentage = 60, (C) binder percentage = 80. Light decay: (a) binder percentage = 40, (b) binder percentage = 60, (c) binder percentage = 80. Corona voltage = 5.5 kV, grid voltage = 1100V, charging time = 1 min.

Thus, ( $\text{HgI}_2$ :CdS) in polystyrene binder seems to offer good promise for use as a master plate in charge transfer electrophotography. The image contrast ob-

tainable with this plate appears to be comparable to that of commercially available plates.

Manuscript submitted Oct. 29, 1975; revised manuscript received Feb. 9, 1976.

Any discussion of this paper will appear in a Discussion Section to be published in the June 1977 JOURNAL. All discussions for the June 1977 Discussion Section should be submitted by Feb. 1, 1977.

## REFERENCES

1. P. H. Keck, *J. Opt. Soc. Am.*, **42**, 221 (1952).
2. R. B. Comizolli, *J. Appl. Phys.*, **41**, 4148 (1970).
3. J. H. Dessauer, G. R. Mott, and H. Bogdonoff, *Photogr. Eng.*, **6**, 250 (1955).
4. M. Smith and A. J. Behringer, *J. Appl. Phys.*, **36**, 3475 (1967).
5. D. W. Chapman and F. J. Styker, *Photogr. Sci. Eng.*, **11**, 22 (1967).
6. P. K. C. Pillai and R. C. Ahuja, *ibid.*, **18**, 544 (1974).

## Discontinuous Precipitation as a Mode of Internal Oxidation

D. J. Young,<sup>\*1</sup> J. S. Kirkaldy, and W. W. Smeltzer\*

Department of Metallurgy and Materials Science, McMaster University, Hamilton, Ontario, Canada L8S/M1

Discontinuous precipitation is the process whereby a supersaturated phase decomposes to a solute-depleted but structurally identical product and a precipitate phase ( $\alpha \rightarrow \alpha' + \beta$ ) by growth of parallel  $\alpha'$  and  $\beta$  lamellae into the parent  $\alpha$  phase (1, 2). It is emphasized that  $\alpha'$  and  $\alpha$  denote different compositions of the same phase. This mechanism often substitutes for or competes with the more common phenomenon of general precipitation, when reaction temperatures lead to very low volume diffusion rates. Discontinuous precipitation should be distinguished from a eutectoid reaction in which one phase decomposes into two new phases ( $\gamma \rightarrow \alpha + \beta$ ), although both reactions are controlled by segregation of alloy constituents at or near the interface between the parent phase and the products. Under usual conditions where the supersaturated phase ( $\alpha$ ) is produced by quenching to a fixed reaction temperature, the velocity,  $v$ , at which the interface advances is approximately constant. This does not imply that all discontinuous precipitation reactions proceed at a constant velocity. Indeed, approximately parabolic cellular reactions in multicomponent systems have been observed (3).

It was recently reported by the present authors (4) that a Ni-20 weight percent (w/o) Mo alloy exposed at 700°C to  $H_2S/H_2$  atmospheres adjusted to yield  $1 \times 10^{-10} \leq p_{S_2} \leq 4 \times 10^{-10}$  atm underwent internal sulfidation in such a way as to yield this cellular morphology. The purpose of the present communication is to present chemical and microstructural evidence that the mechanism of this internal sulfidation reaction is in fact that of discontinuous precipitation as defined above.

The general appearance of the reaction product is illustrated in Fig. 1. Phases were identified by energy dispersion analysis of the x-rays excited in a scanning electron microscope. The outer scale was found to be Ni sulfide plus Mo sulfide; the inner layer was Mo sulfide (dark region) plus nearly pure Ni metal (white region). The sulfide particles were too small to yield reliable analyses and so their stoichiometries were not established. The formation of the inner layer is described in chemical terms as internal sulfidation. As the equilibrium sulfur partial pressures at 700°C for the reactions  $4/3 Mo + S_2 = 2/3 Mo_2S_3$ ,  $2Mo_2S_3 + S_2 = 4 MoS_2$ , and  $(3-x)Ni + S_2 = Ni_{3-x}S_2(1)$  are respectively (5, 6),  $6.3 \times 10^{-12}$ ,  $3.1 \times 10^{-11}$ , and  $3.4 \times 10^{-10}$  atm, selective sulfidation is thermodynamically expected. In the present nomenclature, the reaction may be written as



Internal oxidation (or sulfidation) has long been known (7) and the kinetics have been described in detail by Wagner (8) on the supposition that step [1] is rate controlling. In step [2] the internally produced reaction product is assumed to nucleate and precipitate at random sites (*i.e.*, general precipitation) and thereafter play no role in the reaction. Wagner's theory supposes that step [1] is controlled by inward diffusion of the oxidizing species through the depleted matrix,  $\alpha'$ , to reach the as yet unreacted alloy and, therefore, that both the penetration depth of the precipitation zone and the weight gain follow parabolic kinetics. The situation where external scale growth is combined with internal oxidation is rather more complex and has been reviewed by Rapp (9). Under these circumstances a variety of reaction rate laws is possible, depending on the precise nature of the rate-controlling process.

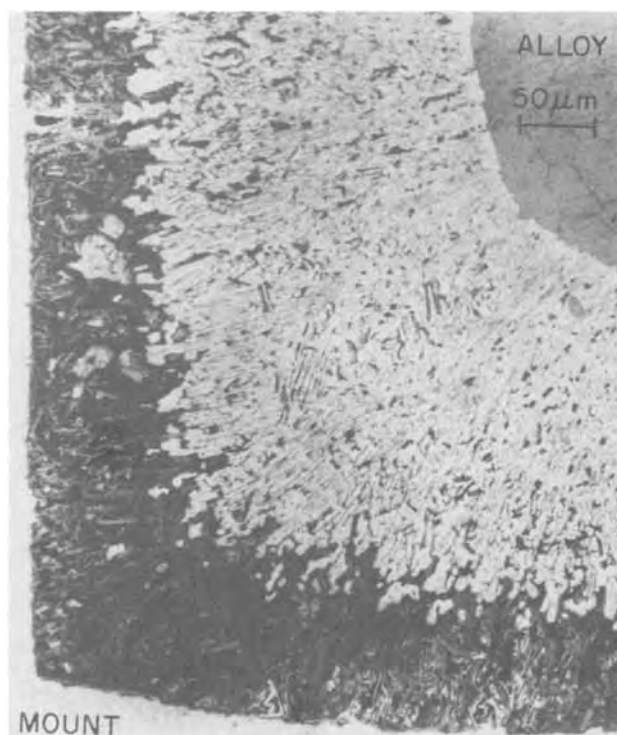


Fig. 1. Cross section of corner of Ni-20Mo sulfidized at  $p_{S_2} = 3.5 \times 10^{-10}$  atm for  $\sim 10$  hr. Etched in  $HNO_3$ -50 v/o  $CH_3COOH$ . Phases are identified in text.

\* Electrochemical Society Active Member.

<sup>1</sup> Present address: Division of Chemistry, National Research Council of Canada, Ottawa, Ontario, Canada K1A 0R9.

Key words: Ni-Mo-S system, internal oxidation, discontinuous precipitation.

In the present case the observed weight change kinetics are approximately linear (4). Results of metallographic studies of the precipitation zone penetration and the corresponding interlamellar spacing,  $\delta$ , are summarized in Fig. 2. Penetration has been measured as the distance between the precipitation front and the precipitation zone, external scale interface. The error involved in approximating the position of this latter interface to that of the original alloy surface is less than the experimental error of the measurement. It is seen that the data, with the exception of one deviant point of unknown origin, are described by linear kinetics ( $v \approx 5.5 \times 10^{-7}$  cm sec $^{-1}$ ) and constant lamellar spacing. It is therefore concluded that step [1] is not rate controlling in the present case.

To rationalize these results we note that data are available for the diffusion coefficient of S in Ni (10) and in the sulfides. At 700°C,  $D_{S^{Ni}} \approx 10^{-11}$  cm $^2$  sec $^{-1}$ , and for the diffusion of S through the Mo sulfides (11),  $D_S \approx 10^{-13}$  cm $^2$  sec $^{-1}$ . Clearly, neither of these processes can possibly supply S to the reaction front at a rate sufficient to support the observed velocity of that front, so the classical model of internal sulfidation via lattice diffusion of the sulfur is inapplicable. This point is further discussed below.

Morphologically, the present reaction has all the characteristics of discontinuous precipitation. Here it is found that the internal precipitates form as platelets approximately normal to the original alloy surface and to the reaction front (Fig. 1, 3), that these plates are arranged at a regular uniform spacing (Fig. 2, 4), that the orientation of the platelets is independent of the prior grain structure of the alloy (Fig. 1, 3), that the penetration depth of the platelets is uniform (Fig. 3), and that a sharply defined interface exists between the alloy,  $\alpha$ , and the depleted matrix,  $\alpha'$ . This last feature is seen in an optical micrograph (Fig. 1, 3) as a difference in etching characteristic, and in the scanning electron micrograph (Fig. 5) as a difference in back-scattered electron intensity. It was verified by x-ray energy dispersive analysis as being due to a compositional change: within the spatial resolution of this technique ( $\pm 1 \mu\text{m}$ ) it was found that a discontinuous change occurs from nearly pure Ni as depleted matrix to Ni-20 w/o Mo in the as yet unaffected alloy.

Lamellar precipitates have occasionally been noted in other internal oxidation reactions. As examples, internal oxidation of several copper alloys containing In, Zn, Al, or Si (7), and of Nb-Zr (12, 13) and U-Nb (14) alloys results in the formation of lamellar precipitates from oxygen diffusion as a rate-determining step. Also, cycling the reaction temperature (15) or oxidant pressure (16) can lead to platelike morphologies. In all of these examples oxygen diffusion is rate controlling and

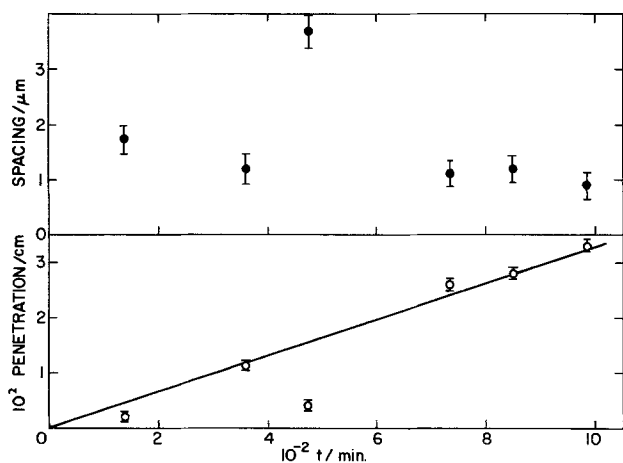


Fig. 2. Penetration depth of precipitate zone and lamellar spacing as a function of time for samples sulfidized at  $1 \times 10^{-10} \approx p_{S_2} \approx 4 \times 10^{-10}$  atm.

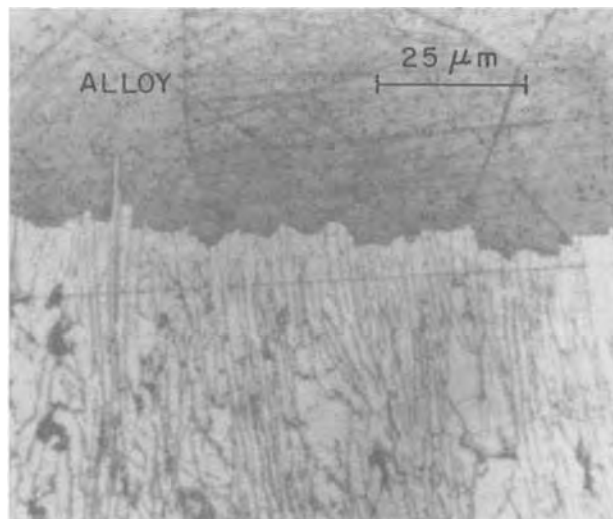


Fig. 3. Optical micrograph of etched cross section showing the precipitation front. Sulfide precipitates have etched black, the Ni matrix appears white, and the unreacted alloy is medium gray with grain boundaries revealed.

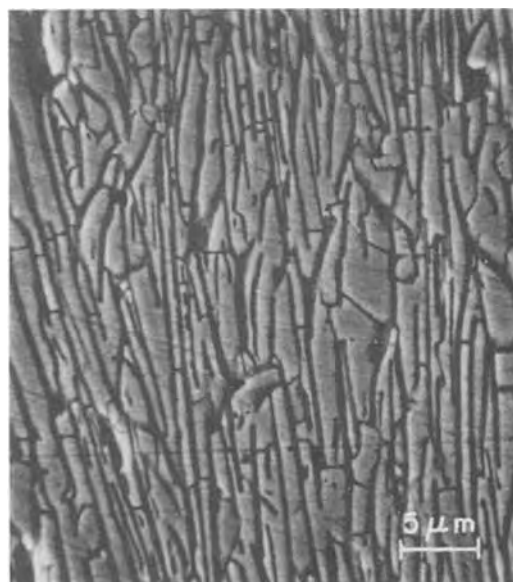


Fig. 4. Scanning electron micrograph of region in precipitation zone. Sulfide precipitate lamellae appear black.

parabolic kinetics are observed. The presently considered internal sulfidation reaction differs from the above examples in two key ways. Firstly, the kinetics are not parabolic. Secondly, a discontinuous change in concentration is found between the alloy,  $\alpha$ , and its solute-depleted form,  $\alpha'$ , the distance over which this change occurs being much less than the distance between precipitates. This novel pattern of behavior is rationalized in the following.

The existence of fine, closely spaced, lamellar precipitates running all the way from the outer metal surface to the reaction front provides a very large  $\alpha'/\beta$  interfacial area connecting the outer metal surface, the source of sulfur, to the reaction front. We therefore conjecture that S is delivered to the precipitation front by rapid diffusion along these precipitate-matrix boundaries, and that little over-all resistance to the reaction is thereby offered.

Both the morphology and kinetics can be accounted for by a mechanism involving alloy component segregation. If segregation is achieved by volume diffusion within  $\alpha$ , then the mechanism is morphologically ana-

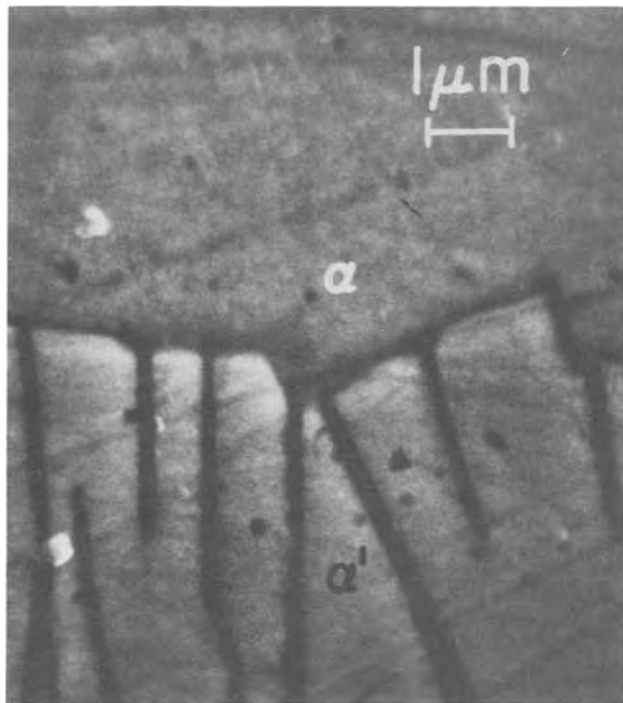


Fig. 5. Scanning electron micrograph of precipitation front. Back-scattered electron image of alloy is darker than that of Ni matrix lamellae.

logous to an isothermal eutectoid transformation in a homogeneous solid and  $v$  is related to the lamellar spacing,  $\delta$ , by

$$v \simeq \frac{D^A}{\delta} f \quad [3]$$

where  $D^A$  is the alloy diffusion coefficient and  $f$  is the relative supersaturation (1), which will be here estimated as 0.1. If segregation is achieved by boundary diffusion along the  $\alpha/\alpha'$  interface, then an approximate growth equation analogous to [3] is obtained by substituting  $D^B b/\delta$  for  $D^A$ , where  $D^B$  is the diffusion constant within the boundary of width  $b$ . To a first approximation then

$$v = 0.1 D^A/\delta \quad \text{volume diffusion} \quad [4]$$

$$v = 0.1 D^B b/\delta^2 \quad \text{boundary diffusion} \quad [5]$$

Substitution of the values of  $v$  and  $\delta$  reported in Fig. 2 into [4] and [5] assuming  $b = 10\text{\AA}$  yields  $D^A \sim 10^{-9} \text{ cm}^2 \text{ sec}^{-1}$  or  $D^B \sim 10^{-6} \text{ cm}^2 \text{ sec}^{-1}$ . Extrapolation of

high temperature results (17) for volume interdiffusion in the Ni-Mo solid solution yields, at  $700^\circ\text{C}$ ,  $D^A \sim 10^{-15} \text{ cm}^2 \text{ sec}^{-1}$ , indicating that segregation must be achieved by the second mechanism of diffusion along the advancing interface. This is almost universally the case with discontinuous precipitation.

It is concluded from the simultaneous observations of linear kinetics, uniform lamellar morphology, and a discontinuous change in concentration at the reaction front that the mechanism of internal sulfidation of Ni-20Mo is that of discontinuous precipitation. It is not possible, however, to conclude that the reaction rate is controlled entirely at the precipitation front. Since the kinetics of the over-all reaction are approximately linear, so too are those of external scale growth. Such behavior in an alloy exposed to  $\text{H}_2\text{S}/\text{H}_2$  atmospheres has frequently been ascribed to rate control by a process occurring at the solid-gas interface. If this is the case in the present instance, then the penetration velocity and interlamellar spacing of the internal precipitation zone may be partially determined by this external constraint.

Manuscript submitted March 15, 1976; revised manuscript received July 26, 1976.

Any discussion of this paper will appear in a Discussion Section to be published in the June 1977 JOURNAL. All discussions for the June 1977 Discussion Section should be submitted by Feb. 1, 1977.

Publication costs of this article were assisted by McMaster University.

#### REFERENCES

1. M. Hillert, "The Mechanism of Phase Transformations in Crystalline Solids," p. 231, Institute of Metals, London (1969).
2. E. Hornbogen, *Metall. Trans.*, **3**, 2717 (1972).
3. J. W. Cahn and W. C. Hagel, *Acta Metall.*, **11**, 561 (1963).
4. D. J. Young, W. W. Smeltzer, and J. S. Kirkaldy, *Oxid. Met.*, **7**, 149 (1973).
5. J. R. Stubbles and F. D. Richardson, *Trans. Faraday Soc.*, **56**, 1460 (1960).
6. T. Rosenquist, *J. Iron Steel Inst.*, **176**, 37 (1954).
7. F. N. Rhines, *Trans. AIME*, **137**, 246 (1940).
8. C. Wagner, *Z. Elektrochem.*, **63**, 772 (1959).
9. R. A. Rapp, *Corrosion*, **21**, 382 (1965).
10. J. A. Chitty and W. W. Smeltzer, *This Journal*, **120**, 1362 (1973).
11. J. Gerlach and H. J. Hamel, *Metall.*, **24**, 488 (1970).
12. R. A. Rapp and G. N. Goldberg, *Trans. AIME*, **236**, 1619 (1966).
13. V. F. Urbanic and W. W. Smeltzer, *This Journal*, **119**, 1527 (1972).
14. J. V. Cathcart, R. E. Pawel, and G. F. Peterson, *Oxid. Met.*, **3**, 497 (1971).
15. J. L. Meijering, *Z. Elektrochem.*, **63**, 824 (1959).
16. R. A. Rapp, *Acta Metall.*, **9**, 730 (1961).
17. C. P. Heijwegen and G. D. Rieck, *Acta Metall.*, **22**, 1269 (1974).

## Growth Texture of Polycrystalline Silicon Prepared by Chemical Vapor Deposition

Baruch Pratt,<sup>1</sup> Subhash Kulkarni, D. P. Pope, and C. D. Graham, Jr.

Departments of Electrical Engineering and Science, and Metallurgy and Materials Science, University of Pennsylvania, Philadelphia, Pennsylvania 19174

We are undertaking a study of the high temperature deformation of polycrystalline silicon as part of a program to find low cost methods of manufacturing silicon solar cells. The material used as samples in these deformation experiments was commercially available,

<sup>1</sup> Permanent address: The Technion, Haifa, Israel.

Key words: silicon, polycrystalline silicon, grain structure, texture, chemical vapor deposition, crystallographic orientation.

high purity semiconductor grade silicon. This is a polycrystalline material grown by chemical vapor deposition at about  $1150^\circ\text{C}$  by the decomposition of trichlorosilane. The silicon rod samples were prepared by Dow-Corning Company, and had a diameter of about 15 cm. Figure 1 shows the grain structure of a cross section of the silicon rod. Growth begins on a single crystal core,

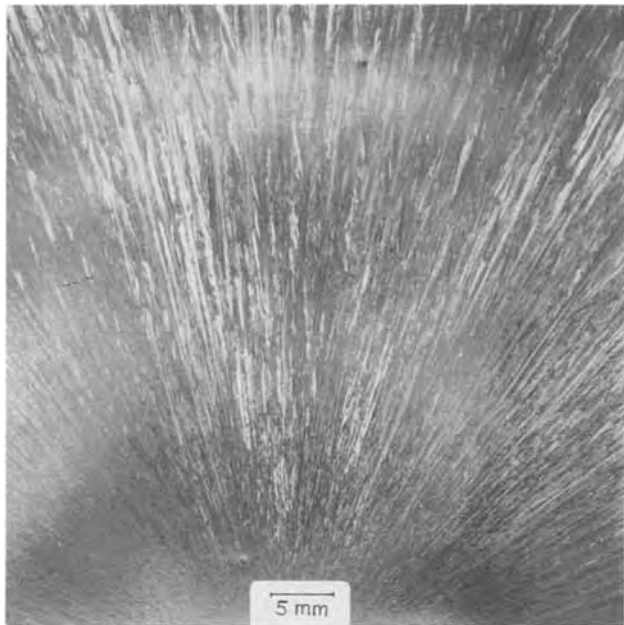


Fig. 1. Etched surface of 15 cm diameter silicon rod. Surface is perpendicular to log axis. Radial grains emanate from the slim rod.

the slim rod. Columnar grains elongated in the growth direction are clearly visible; many of the grains show a substructure of straight, parallel needles aligned with the growth direction. The appearance of these needles suggests the possibility of growth twins, but they have not been studied in detail. The over-all structure strongly suggests a preferred crystallographic texture in the as-deposited rod. Such a texture is of obvious importance in measurements of the mechanical properties, and since we were unable to find in the literature any determination of the texture, we undertook the study described here.

#### Experimental Procedure

A 2.5 cm thick slab was cut from the 15 cm diameter rod, perpendicular to the log axis. Samples for x-ray diffraction, each  $2.5 \times 2.5 \times 0.2$  cm, were cut in various orientations and from various parts of the rod, as shown in Fig. 2. The samples were cut with a diamond saw, mechanically polished, and finally etched heavily in a solution of  $5\text{HNO}_3:3\text{HF}:3\text{CH}_3\text{COOH}$ . Samples denoted  $\perp$  were cut with their large faces perpendicular to the rod axis. Samples denoted  $\parallel$  were cut with faces parallel to the log axis and perpendicular to a diameter. Those denoted  $\parallel\parallel$  were cut with faces parallel to the log axis and parallel to a diameter. Sample sets 1

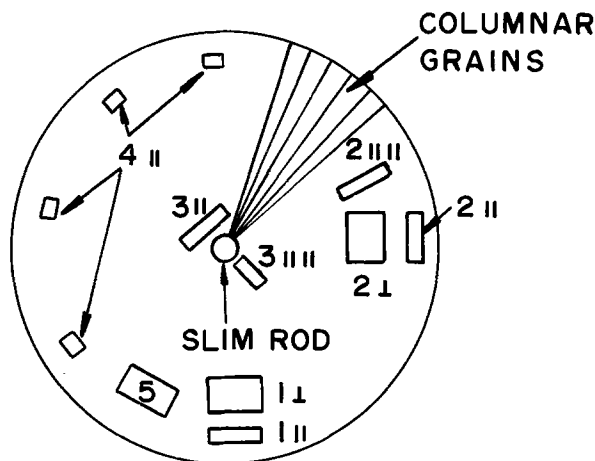


Fig. 2. Identification of samples cut from silicon rod. For explanation, see text.

and 2 were taken near the log surface, at two points  $90^\circ$  apart. Sample set 3 was taken as near the slim-rod core as possible, and sample set 4 consisted of four pieces, each  $0.6 \times 2.5 \times 0.2$  cm, and each cut with the  $0.6 \times 2.5$  cm surface perpendicular to a log diameter. These four pieces were assembled to make one x-ray sample; this was done to minimize the spread in orientation resulting from the fanlike growth of the columnar crystals. Sample 5 was cut with faces inclined at  $45^\circ$  to the log axis; it has an orientation halfway between the  $\perp$  and the  $\parallel$  samples, related to them by rotation of  $45^\circ$  about an axis parallel to a log diameter. A small sample was also cut from the slim rod itself. Textures were determined by the Schultz reflection method (1, 2).

Samples were mounted in a Siemens texture diffractometer and irradiated with  $\text{Cu K}\alpha$  radiation at 30 kV and 20 mA. Reflections from (111), (220), and (400) planes were recorded, and pole figures were plotted from the resulting strip charts. Diffracted intensities were recorded for a full  $\Psi = 360^\circ$  rotation about the normal to the surface of the samples in steps of  $\alpha = 2.5^\circ$  away from this normal out to  $80^\circ$ . The resolution of the technique was  $d\Psi = \pm 4^\circ$  and  $d\alpha = \pm 0.05^\circ$ . Intensities were compared to those of a random sample prepared from silicon powder held on a glass slide with petroleum jelly. The samples were aligned by eye so that the diameter of the log appeared as the vertical axis of the pole figures of the  $\perp$  and  $\parallel\parallel$  samples, and the log axis as the vertical axis of the pole figures in  $\parallel$  samples.

#### Results

The recorder chart traces of all samples with faces parallel to a log diameter (types  $\perp$  and  $\parallel\parallel$ ) consisted of a series of very narrow peaks of high intensity. The small width of the peaks, plus the irregularities in their outlines caused by the relatively large grain size of the samples, made the plotting of conventional contour lines on the pole figures impossible. Instead, the height of each peak was read and plotted as a corresponding point on the pole figure. Examples are shown in Fig. 3.

All the pole figures from samples of type  $\perp$  and  $\parallel\parallel$  were in agreement, and indicated clearly that the crystallographic texture of the silicon rod is a very sharp  $\langle 110 \rangle$  fiber texture with the  $\langle 110 \rangle$  axis parallel to the growth direction, and with no preferential orientation about this axis. Pole figures of samples of type  $\parallel$  unexpectedly showed almost random intensity instead of the circular symmetry about the midpoint expected for a fiber texture examined parallel to the fiber axis. Suspecting that this phenomenon might be associated with the spread in orientation of the fiber axis caused by the cylindrical growth geometry, we prepared the composite sample 4 as explained above; its (220) pole figure showed the expected form (Fig. 4) although with lower intensity than predicted.

As a final check, sample 5 was cut at  $45^\circ$  to the rod axis. The resulting (111) pole figure is shown in Fig. 5; it has the expected form of the (111) pole figure of Fig. 3a, rotated  $45^\circ$  about the equator.

The pole figures of sample set 3, cut near the central slim rod, were closely similar to those of sets 1 and 2. The slim rod itself was found to have a  $\langle 100 \rangle$  direction parallel to the rod axis.

#### Conclusions

The crystallographic texture of CVD polycrystalline silicon is found to be a very sharp  $\langle 110 \rangle$  fiber texture, with the  $\langle 110 \rangle$  direction parallel to the direction of growth, and with no preferred orientation about this axis. The texture does not appear to be influenced by the orientation of the rod from which growth starts. This  $\langle 110 \rangle$  growth texture has also been found in silicon films grown by similar methods on various substrates (3).

#### Acknowledgments

The authors are grateful to Fred Witt of the U.S. Army Frankford Arsenal for interest, advice, and help.

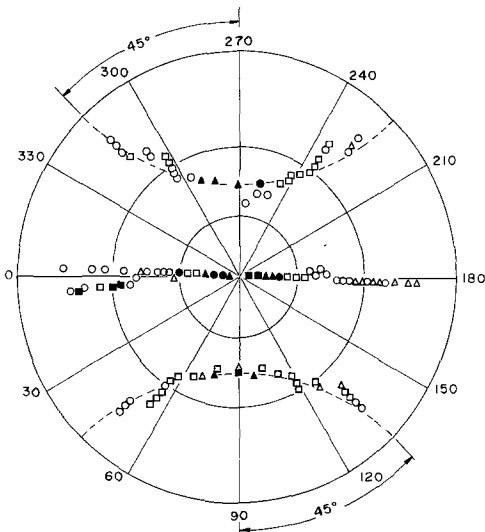
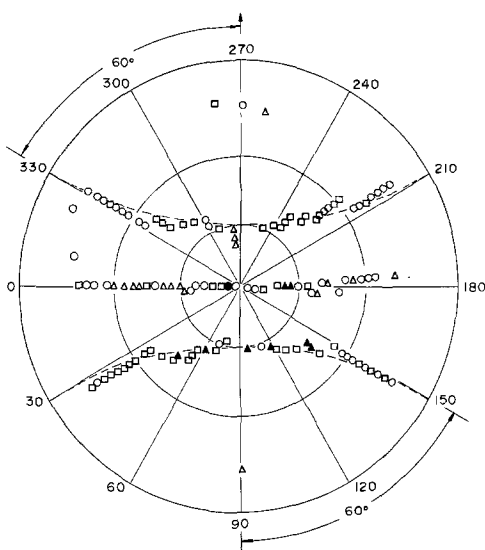
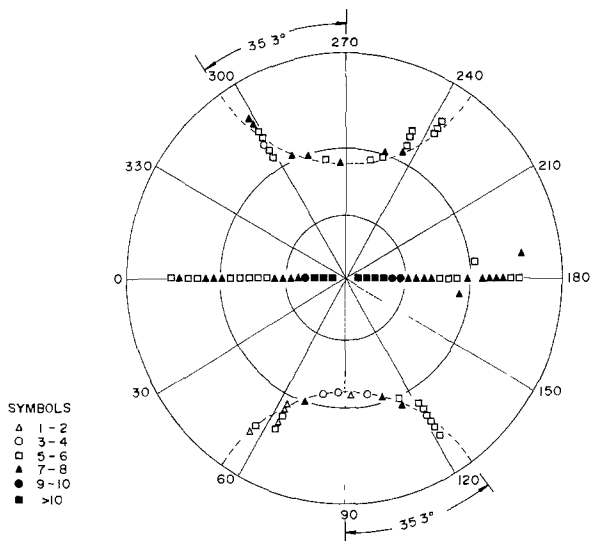


Fig. 3. Pole figures, (a, top) for (111), (b, middle) for (220), and (c, bottom) for (400) reflections plotted as multiples of the intensities observed on the random (powder) sample. For sample 2 || ||. Columnar grain axis along 90°-270° line in the figure.

They also thank the Department of Metallurgical Engineering of Drexel University for permission to use the

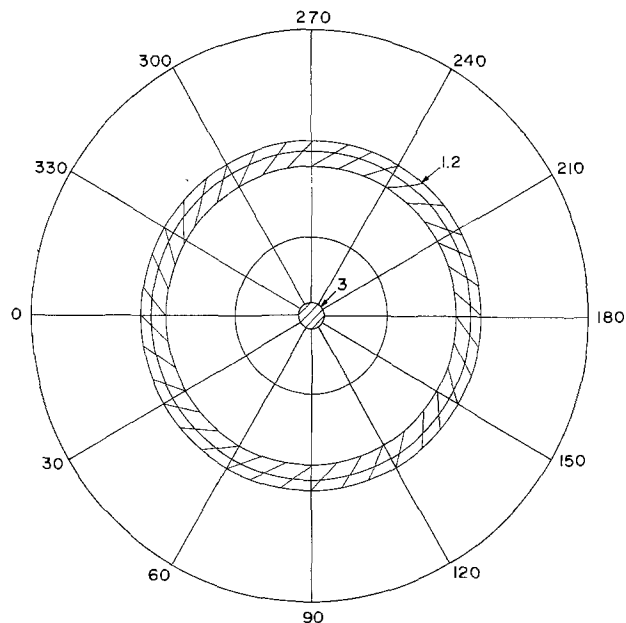


Fig. 4. Pole figure of composite sample 4 ||, for (220) reflection. Numbers indicate relative intensities as described in Fig. 3. Rod axis along 90°-270° line in the figure.

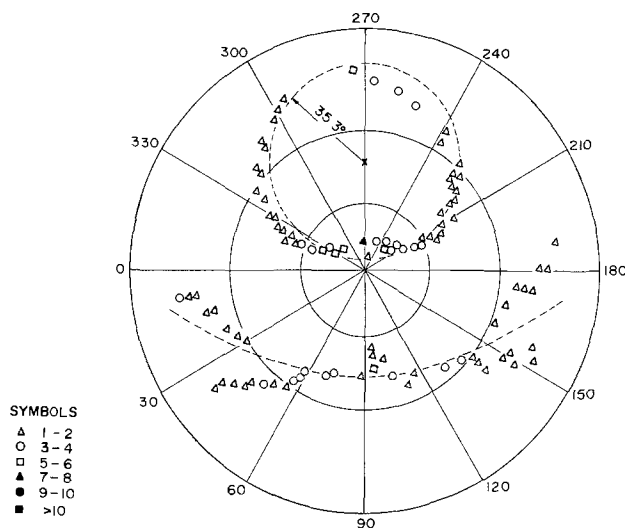


Fig. 5. Pole figure for (111) reflection of sample 5, cut at 45° to the rod axis. Intensities noted as in Fig. 3.

Siemens texture diffractometer, and Vishu Dosaj of Dow-Corning for providing the silicon. This work was partly supported by the Energy Research and Development Administration.

Manuscript submitted May 7, 1976; revised manuscript received July 27, 1976.

Any discussion of this paper will appear in a Discussion Section to be published in the June 1977 JOURNAL. All discussions for the June 1977 Discussion Section should be submitted by Feb. 1, 1977.

Publication costs of this article were assisted by the University of Pennsylvania.

REFERENCES

1. L. G. Schultz, *J. Appl. Phys.*, **20**, 1030 (1949).
2. B. D. Cullity, "X-Ray Diffraction," p. 290, Addison-Wesley, Reading, Massachusetts (1956).
3. P. Rai-Choudhury and P. L. Hower, *This Journal*, **120**, 1761 (1973).





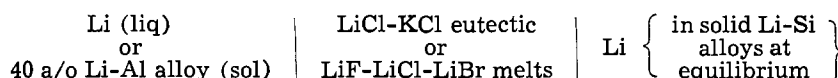
## Thermodynamic Properties of the Lithium-Silicon System

Ram A. Sharma\* and Randall N. Seefurth\*

General Motors Corporation, Electrochemistry Department, Research Laboratories, Warren, Michigan 48090

### ABSTRACT

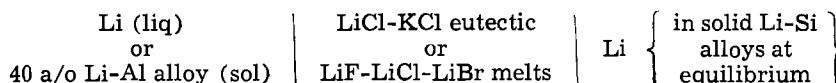
The feasibility of using silicon as an alloying agent for the negative electrode in Li/FeS<sub>2</sub> cells was determined by studying cells of the type



The Li-Si electrode was found reversible with respect to lithium between 650° and 725°K. The nonstoichiometry ranges of the respective Li-Si compounds and electromotive forces (emf's) in the two-phase regions of the Li-Si phase diagram between 650° and 750°K were measured. These studies indicated a new compound, Li<sub>21</sub>Si<sub>8</sub>, which was confirmed by x-ray diffraction, scanning electron microscope, and differential thermal analysis. The activities and relative partial molar properties of lithium and silicon in the two-phase regions of the phase diagram were calculated from the emf's in the temperature range 650°-750°K, and the standard free energy of formation for the compounds Li<sub>2</sub>Si, Li<sub>21</sub>Si<sub>8</sub>, Li<sub>15</sub>Si<sub>4</sub>, and Li<sub>22</sub>Si<sub>5</sub>, were also determined.

At present, two types of negative electrodes are used for developing Li/FeS<sub>2</sub> cells for secondary batteries of high specific energy and high specific power. One type is pure lithium entrapped in a metallic matrix (1,2) generally made of stainless steel or nickel. This electrode has a problem retaining lithium for a prolonged period of time during repeated charge-discharge cycles. Lithium also severely attacks the ceramic insulator and separator of the cell.

The second type of negative electrode is made of



solid Li-Al alloy (3,4). In this case, the lithium retention problem is solved, but the theoretical specific energy is reduced because of the additional inert weight of aluminum and decreased cell voltage compared to a cell using a pure lithium electrode. Current densities are also limited because of the difficulty of transport of active material in the solid alloy. However, the reduced activity of lithium decreases its tendency to corrode the ceramic parts.

Silicon, which is next to aluminum in the Periodic Table and forms a few compounds with lithium (5-8), appears to be a suitable alloying agent for the negative electrode. Like Li-Al alloy, Li-Si alloys will probably not have the problems of lithium retention and corrosion and, because of the higher lithium content of solid Li-Si alloys, the specific capacity of the electrode would be higher than that of the Li-Al alloy electrode.

The Li-Si phase diagram (5-8) indicates only two compounds, Li<sub>2</sub>Si and Li<sub>4</sub>Si, but compounds such as Li<sub>13</sub>Si<sub>7</sub>, Li<sub>7</sub>Si<sub>2</sub>, and Li<sub>22</sub>Si<sub>5</sub> are also reported in the

literature (9-11). Therefore, this investigation was conducted to determine the feasibility of using Li-Si alloys as negative electrodes in Li/FeS<sub>2</sub> cells, to determine the various phases of the Li-Si system, and to obtain the relevant thermodynamic data for the phases by emf measurements.

### Experimental

All preparatory procedures and cell studies were carried out in a helium atmosphere dry box. The cells used were of the type

Schematic diagrams of the cells are shown in Fig. 1. The typical cell assembly consisted of a quartz enclosure (70 mm diameter, 300 mm high) fitted with a cap which served to position the electrodes and thermocouple, and a stainless steel cup (50 mm diameter, 100 mm deep) to hold the electrolyte. All of the metallic parts were hydrogen-fired at 1375°K for 7.5 msec before use.

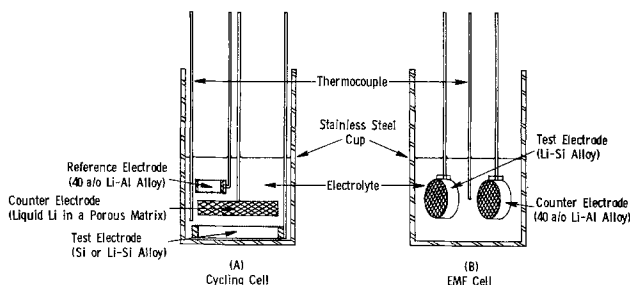


Fig. 1. Schematic representations of the lithium-silicon alloy test cells.

\* Electrochemical Society Active Member.  
 Key words: Li-Si phase diagram, emf's, thermodynamic properties.

**Negative or reference electrode.**—For the lithium electrode, a fibrous nickel block (80% porous), 12 mm diameter and 12 mm high, was attached to a nickel rod voltage lead, 3 mm diameter and 450 mm long. The block was loaded by immersing it in a pool of molten lithium (99.97% pure) at 975°K for 120 sec.

For the Li-Al alloy electrode, a chamber was made by heliarc-welding a 304 stainless steel nut onto the side of a 5 mm long piece of 304 stainless steel tubing (12 mm ID, 16 mm OD). A 304 stainless steel rod (3 mm diameter, 450 mm long) was threaded into the nut to serve as a voltage lead. After hydrogen-firing this compartment, the electrode was completed by inserting a few pieces of 40 atom percent (a/o) Li-Al alloy (4/20 mesh) and spot-welding two 150 mesh 304 stainless steel screen disks over the open sides.

**Lithium-silicon alloy positive electrodes.**—For the preparation of the alloys, a preweighed amount of clean lithium was placed in a nickel crucible and its temperature was raised to about 600°K. Powdered silicon (99.999% pure) was slowly added to the lithium, avoiding any violent reaction. After adding the calculated amount of silicon, the temperature was raised to 1025°K and maintained there until the melt became homogeneous. The melt was then cooled slowly to room temperature. A few pieces of solidified alloy were then used to prepare a positive electrode, using the method described for the Li-Al alloy electrode. Powdered silicon instead of Li-Si alloy was used for preparation of the pure silicon electrodes.

**Electrolyte.**—Two types of electrolyte, 57 mole percent (m/o) LiCl-43 m/o KCl eutectic (12) and 22 m/o LiF-31 m/o LiCl-47 m/o LiBr, were used. The LiCl-KCl electrolyte was prepared using LiCl of 99.6% purity and KCl of 99.9% purity. It was purified by bubbling chlorine through it at 725°K for 7 ksec, and subsequently scavenging the chlorine by bubbling helium for about 3.5 ksec (13). The reaction of KCl in the electrolyte with lithium in the electrodes (13) should not influence the emf measurements, as they were carried out in only the two-phase regions of the Li-Si system, where composition change should not have any effect. The rate of the reaction was further suppressed by the reduced activity of lithium in the Li-Al alloys used. In addition, any possible uncertainty in the measurements was removed by using LiF-LiCl-LiBr electrolyte. Lithium bromide of 99.0% purity and high purity optical grade LiF were used for the ternary electrolyte. Prior to adding the LiF, the LiCl-LiBr melt was also purified by bubbling chlorine through it at 850°K for 3.5 ksec subsequently removing the resultant bromine by bubbling helium for an additional 3.5 ksec.

**Apparatus.**—A tubular furnace (150 mm high, 75 mm diameter) was used in conjunction with a proportional band temperature controller to heat the cell. Chromel-Alumel thermocouples and a millivolt potentiometer were used for temperature measurements and another millivolt potentiometer for the emf measurement. The other electrical instruments included a d-c power supply, together with the necessary logic and switching circuitry to cycle the cell automatically according to a preset charge-discharge program, and a dual-channel recorder for measuring cell potential and current.

**Procedure.**—About 0.1 liter of the electrolyte was placed in the stainless steel container which, in turn, was placed inside the quartz enclosure in the furnace. The electrolyte was heated to a particular temperature and the electrodes were positioned in the melt.

After thermal equilibrium was attained, the emf measurement was carried out. Measurements were continued until the value became constant (less than  $\pm 0.1$  mV) at that temperature. The equilibrium period was observed to be about 1.8 ksec, but 110 ksec were given for some measurements to see if any fluctuation in the emf value would occur. The emf measurements were

made at several temperatures (by alternately raising and lowering the temperature) in each of the two-phase regions of the Li-Si system.

**Preparation of samples for analyses.**—A mixture of 72.4 a/o lithium and 27.6 a/o silicon was melted in a nickel container, cooled to room temperature, and ground to a fine powder. It was then annealed at 775°K for 600 ksec, cooled slowly to room temperature, and reground. A small portion of this powder was sealed in a fine silica capillary for x-ray diffraction analysis. Another portion (0.3g) for differential thermal analysis (DTA) was sealed in a small, specially designed nickel container which could be closed nearly gas-tight with a threaded cap. A second DTA run was carried out using a 60 a/o Li-Si mixture which was prepared in the same manner.

The sample for the scanning electron microscope was prepared by melting a 72.4 a/o Li-Si mixture in a nickel container, holding it at 925°K for 15 ksec, and then cooling slowly to room temperature.

## Results and Discussion

A series of charge-discharge cycles was carried out between a silicon electrode (0.5g/5 cm<sup>2</sup>) and a lithium electrode starting from a very low current density (2 mA/cm<sup>2</sup>) and increasing gradually. The silicon electrode was charged only to a composition of 80 a/o lithium. The charge-discharge cycles (a plot of a typical cycle at 40 mA/cm<sup>2</sup> and 680°K is shown in Fig. 2) proved that the Li-Si electrode is reversible with respect to lithium, and exhibits current efficiencies greater than 95%. The cycles also indicated three well-defined voltage plateaus up to 80% lithium composition. This type of observation was also made by other workers (14-17), but is in conflict with the Li-Si phase diagram (5-8), according to which two plateaus should appear; one from pure silicon to 66.66 a/o lithium, and the other between 66.66 and 80 a/o lithium.

The three voltage plateaus appearing before 80 a/o lithium were confirmed by an experiment in which a pure silicon electrode (0.2g/10 cm<sup>2</sup>) was charged at a very low current density (1 mA/cm<sup>2</sup>) using a lithium counterelectrode. The results presented in Fig. 3 as cell voltage vs. capacity, show three well-defined plateaus before 80 a/o lithium and two more plateaus

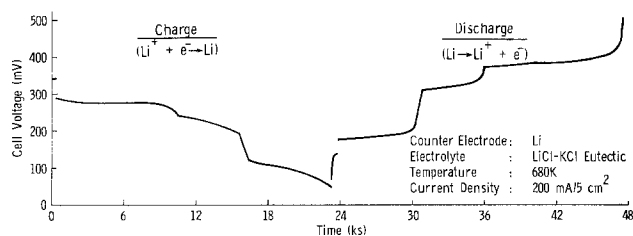


Fig. 2. Discharge-charge cycle for a Li/LiCl-KCl/Li-Si cell

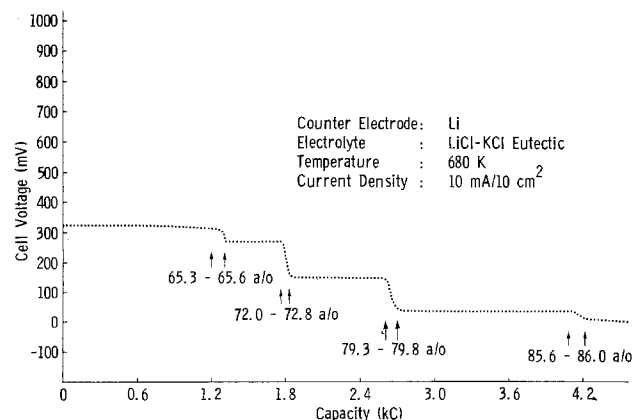


Fig. 3. Slow-rate charge of a silicon electrode



beyond 80 a/o lithium. The same number of plateaus at less than 80 a/o lithium were also observed when a counterelectrode of 40 a/o Li-Al alloy was used (Fig. 4), and when the experiment was repeated using LiF-LiCl-LiBr electrolyte and a 40 a/o Li-Al alloy counterelectrode, the results again showed five voltage plateaus (Fig. 5).

It was previously observed that lithium at its higher activities reacts with KCl in the LiCl-KCl electrolyte and produces volatile potassium which is lost from the cell (13). As a result of this reaction, the lithium concentration of a Li-Si compound calculated from coulometric data can be in error. This is indeed observed in the present case when the results presented in Fig. 5 are compared with those presented in Fig. 3 and 4. They show that the exchange reaction between lithium from the Li-Si alloy and KCl in the electrolyte caused a shift in composition at which the voltage moves to a new plateau value above 80 a/o lithium. This is clearly indicated in Fig. 3 by the transition in the voltage plateau at an approximate composition corresponding to the compound  $\text{Li}_6\text{Si}$  instead of  $\text{Li}_{22}\text{Si}_5$ . Evidently a certain amount of the lithium calculated from the coulometric data was lost by reacting with KCl and thus contributed an error in the composition of the compound. The exchange reaction apparently has no effect on the composition ranges covered by the plateaus before 80 a/o lithium, presumably due to lower lithium activity in the alloy.

These studies indicate four compounds are present in the Li-Si system:  $\text{Li}_2\text{Si}$ ,  $\text{Li}_{21}\text{Si}_8$ ,  $\text{Li}_{15}\text{Si}_4$ , and  $\text{Li}_{22}\text{Si}_5$ . The compounds  $\text{Li}_2\text{Si}$  and  $\text{Li}_4\text{Si}$  (in place of the  $\text{Li}_{15}\text{Si}_4$  found in this investigation) are reported by the Li-Si phase diagram (5-8). The compound  $\text{Li}_{15}\text{Si}_4$  has been reported by Böhm (5) and Klemm and Struck (18). The compound  $\text{Li}_{22}\text{Si}_5$  has also been reported in the literature (11) and its melting point was determined to be  $891^\circ \pm 3^\circ\text{K}$  in the present investigation. However, no information has been found about the compound

Table I. X-ray diffraction data of powdered  $\text{Li}_{21}\text{Si}_8$  taken by a 114.6 mm camera using  $\text{CuK}\alpha$ -radiation and a Ni filter

$2\theta$	I*	d (Å)	$2\theta$	I*	d (Å)
20.0	S	4.4357	48.8	M	1.8646
24.4	M	3.6449	51.6	S	1.7698
28.6	W	3.1185	56.0	S	1.6247
33.0	VS	2.7120	62.0	M	1.4955
35.8	S	2.5061	67.8	W	1.3810
39.8	W	2.2629	75.8	M	1.2539
42.6	W	2.1204	79.0	W	1.2109
44.0	M	2.0562	85.6	M	1.1337
46.6	S	1.9473	—	—	—

\* VS = very strong, S = strong, M = medium, and W = weak.

$\text{Li}_{21}\text{Si}_8$ , except the probability of its existence, which was reported in recent studies (14, 15, 17). The existence of this compound was confirmed by x-ray diffraction analysis. The data are given in Table I. In addition, its melting point was determined by DTA with heating and cooling rates from  $3^\circ$  to  $10^\circ\text{K}/\text{min}$ . The compound was observed to melt incongruently at  $976^\circ \pm 8^\circ\text{K}$ . However, it was also observed that once the compound had melted, it did not reform on cooling because of the probable slow peritectic reaction or supercooling of the melt. The scanning electron microscope photograph (Fig. 6) also indicates a single phase for this compound.

The maximum nonstoichiometric ranges of the Li-Si compounds were clearly indicated by plots such as one in Fig. 7, where a typical profile of voltage vs. time during a transition from one voltage plateau to another is shown. As observed in this figure, the voltage profile is curved at each end of the transition. The length of the transition may be influenced by the presence of a composition nonuniformity, giving rise to a mixed potential. The maximum range of nonstoichiometry for each compound was determined from the compositions given by the intersections of the extrapolated straight sections of the curves (Fig. 7). The nonstoichiometric ranges determined in this way are

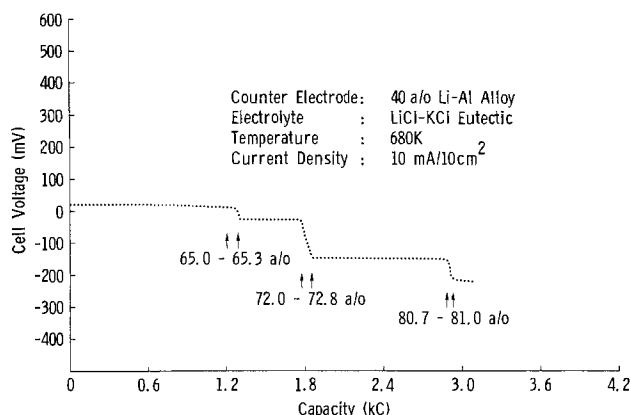


Fig. 4. Slow-rate charge of a silicon electrode

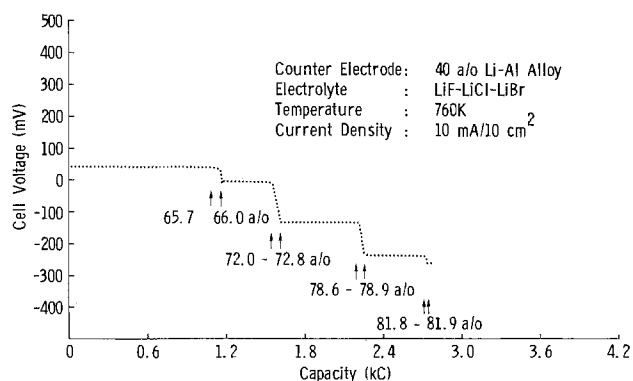
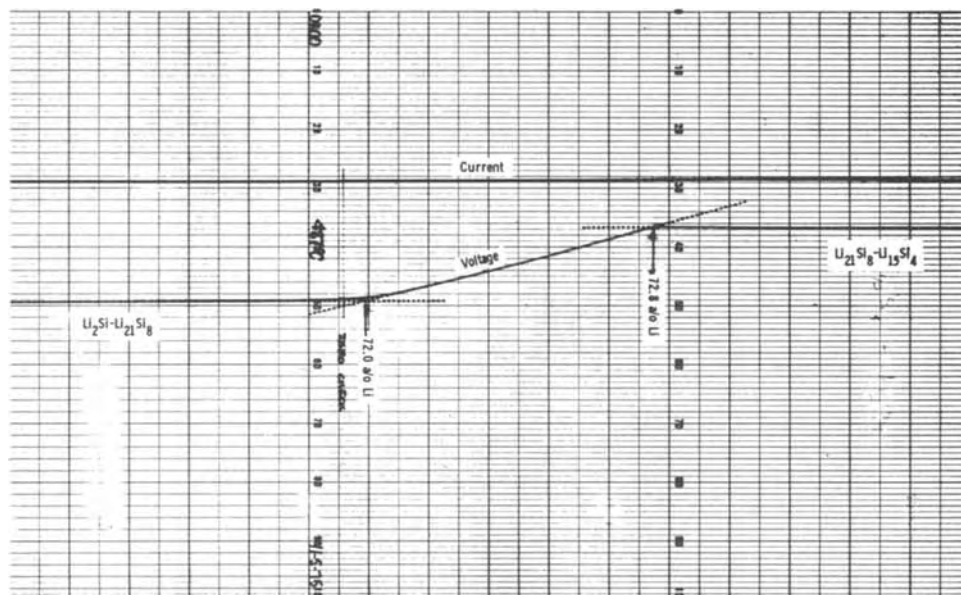


Fig. 5. Slow-rate charge of a silicon electrode



Fig. 6. Scanning electron microscope photograph of the solidified melt of 72.4 m/o Li-Si alloy after annealing at  $925^\circ\text{K}$  for 14.5 ksec showing a single phase of the compound  $\text{Li}_{21}\text{Si}_8$ .

Fig. 7. Typical profile of voltage vs. time through the composition range  $\text{Li}_{21}\text{Si}_8$ . (Electrolyte:  $\text{LiF-LiCl-LiBr}$  and counterelectrode: 40 a/o Li-Al alloy.)



shown by arrows in Fig. 3, 4, and 5. The stoichiometric lithium percentage was found to vary within 0.15 a/o for  $\text{Li}_2\text{Si}$ , within 0.4 a/o for  $\text{Li}_{21}\text{Si}_8$ , within 0.15 a/o for  $\text{Li}_{15}\text{Si}_4$ , and within 0.1 a/o for  $\text{Li}_{22}\text{Si}_{15}$ . Fedorov and Ioffe (6) reported the stoichiometric lithium percentage to vary within 0.475 a/o for  $\text{Li}_4\text{Si}$ . If this nonstoichiometry is taken for the compound  $\text{Li}_{15}\text{Si}_4$ , then it is higher than that of this investigation.

The revised Li-Si phase diagram, after incorporating the results of the present investigation and including the experimental literature data, is presented in Fig. 8. The eutectic temperature,  $908^\circ \pm 5^\circ\text{K}$ , reported by Böhm (5) appears to be correct as it was confirmed by a DTA run on a 60 a/o Li-Si mixture in this investigation. The melting point of the compound  $\text{Li}_4\text{Si}$  ( $\text{Li}_{15}\text{Si}_4$  observed in this investigation) was also found to be in agreement with that reported in the literature (5, 6). On the silicon side of the phase diagram, the liquidus reported by Böhm (5) appears to be correct as the reported melting point of pure silicon ( $1685^\circ\text{K}$ ) is in agreement with the literature value ( $1685^\circ \pm 3^\circ\text{K}$ ) (20), and the liquidus curve is of the pattern generated by using the heat of fusion of silicon and heat capacity data (20).

Further work was directed to emf measurements on compositions in the various two-phase regions of the Li-Si system at selected temperatures. These measurements were made against a 40 a/o Li-Al alloy electrode and are presented in Fig. 9.<sup>1</sup> In the temperature range of  $650^\circ\text{-}725^\circ\text{K}$ , they are also represented by the relations

$$E = -34.525 + 0.1056T \quad (0\text{-}66.3 \text{ a/o Li}) \quad [1]$$

$$E = -88.097 + 0.1122T \quad (66.6\text{-}72 \text{ a/o Li}) \quad [2]$$

$$E = -187.529 + 0.0731T \quad (72.8\text{-}78.8 \text{ a/o Li}) \quad [3]$$

$$E = -311.452 + 0.0954T \quad (79.1\text{-}81.4 \text{ a/o Li}) \quad [4]$$

$$E = -473.856 + 0.2632T \quad (81.6 \text{ a/o Li to Li [liq] equilibrium}) \quad [5]$$

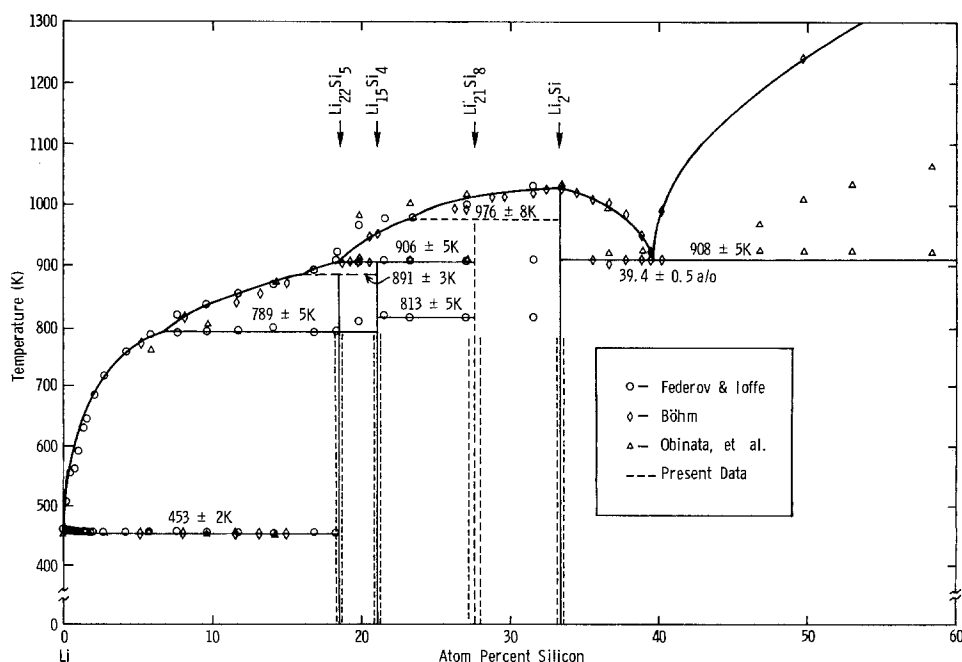
$$E = -464.438 + 0.2488T \quad (9\text{-}47 \text{ a/o Li in Li-Al alloy vs. Li [liq]}) \quad [6]$$

where  $E$  = emf (mV) and  $T$  = temperature ( $^\circ\text{K}$ ).

The lithium activities with reference to pure liquid lithium as the standard state were calculated by con-

<sup>1</sup> The curves in these figures are least squares fits to the data points.

Fig. 8. Lithium-silicon phase diagram.



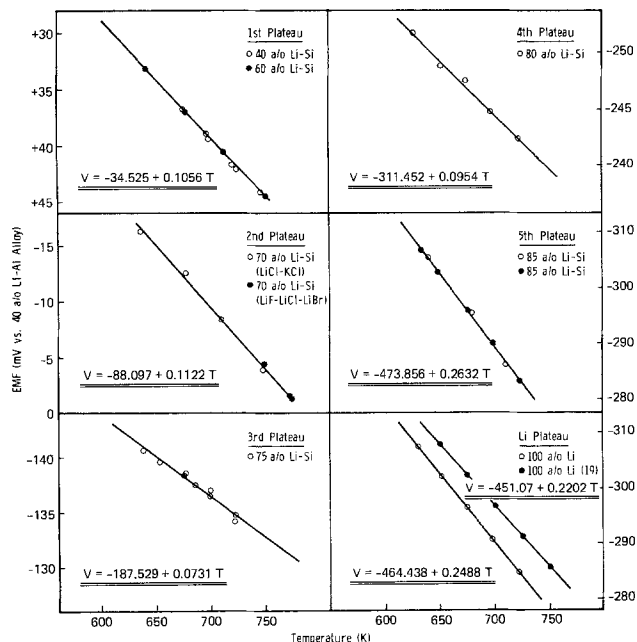
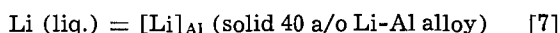


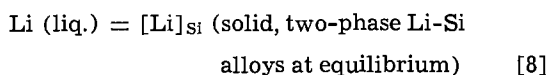
Fig. 9. Lithium-silicon alloy voltage plateaus

considering the following cell reactions



for which

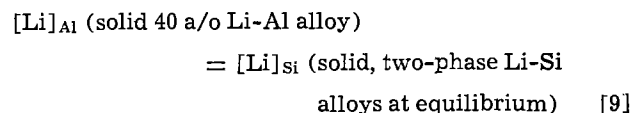
$$-nFE_{[7]} = \overline{\Delta G}_{\text{Li}} = RT \ln a'_{\text{Li}} \quad [7A]$$



for which

$$-nFE_{[8]} = \overline{\Delta G}_{\text{Li}} = RT \ln a_{\text{Li}} \quad [8A]$$

and



for which

$$-nFE_{[9]} = \overline{\Delta G}_{\text{Li}} - \overline{\Delta G}'_{\text{Li}} = RT \ln \frac{a_{\text{Li}}}{a'_{\text{Li}}} \quad [9A]$$

where  $R$  = gas constant,  $T$  = temperature  $^{\circ}\text{K}$ ,  $F$  = Faraday constant,  $n$  = number of electrons,  $a'_{\text{Li}}$  and  $a_{\text{Li}}$  = lithium activities in the Li-Al alloy and the Li-Si alloys, respectively, and  $\overline{\Delta G}'_{\text{Li}}$  and  $\overline{\Delta G}_{\text{Li}}$  = the relative partial molar free energies of Li in the Li-Al alloy and the Li-Si alloy, respectively.

Since reaction [8] is the sum of reactions [7] and [9] ( $E_{[8]} = E_{[7]} + E_{[9]}$ ), the relative partial molar-free energies  $\overline{\Delta G}_{\text{Li}}$  and activities,  $a_{\text{Li}}$ , of lithium were calculated from the measured values of  $E_{[7]}$  and  $E_{[9]}$  using relation [8A]. The results are given at various temperatures in Table II.

The relative partial molar entropies of lithium,  $\overline{\Delta S}_{\text{Li}}$ , were calculated from the relation

$$\overline{\Delta S}_{\text{Li}} = nF dE/dT \quad [10]$$

using the experimental values of  $dE/dT$  reported earlier in Eq. [1]-[6]. These results are reported in Table III.

The relative partial molar enthalpies of lithium,  $\overline{\Delta H}_{\text{Li}}$ , were calculated from the relation

$$\overline{\Delta H}_{\text{Li}} = -nFE + nFT dE/dT \quad [11]$$

and are also given in Table III. In addition,  $\overline{\Delta H}_{\text{Li}}$ , in

Table II. Thermodynamic properties of lithium and silicon in the two-phase regions of the Li-Si system at various temperatures

Temp (K)	EMF* (mV vs. Li)	$a_{\text{Li}}$	$-\overline{\Delta G}_{\text{Li}}$ (cal/g-atom)	$a_{\text{Si}}$	$-\overline{\Delta G}_{\text{Si}}$ (cal/g-atom)
In the region between Si and $\text{Li}_2\text{Si}$ at 40 and 60 a/o Li					
650	336.84	0.00244	7769.5	1	0
700	329.65	0.00422	7603.8	1	0
725	326.06	0.00540	7520.9	1	0
750	322.47	0.00680	7438.1	1	0
In the region between $\text{Li}_2\text{Si}$ and $\text{Li}_3\text{Si}_2$ at 70 a/o Li					
650	287.54	0.00589	6632.3	0.178	2,232.8
700	280.72	0.00951	6475.0	0.203	2,221.6
725	277.31	0.01179	6396.3	0.215	2,215.6
750	273.90	0.01441	6317.7	0.227	2,214.6
In the region between $\text{Li}_3\text{Si}_2$ and $\text{Li}_5\text{Si}_3$ at 75 a/o Li					
650	162.73	0.0547	3753.6	$5.06 \times 10^{-4}$	9,800.2
700	153.95	0.0778	3551.1	$8.01 \times 10^{-4}$	9,916.1
725	149.56	0.0912	3449.8	$9.84 \times 10^{-4}$	9,973.8
750	145.17	0.1057	3348.6	$11.93 \times 10^{-4}$	10,030.0
In the region between $\text{Li}_5\text{Si}_3$ and $\text{Li}_7\text{Si}_4$ at 80 a/o Li					
650	53.26	0.386	1228.5	$2.09 \times 10^{-7}$	19,865.3
700	45.63	0.469	1052.4	$7.52 \times 10^{-7}$	19,612.2
725	41.81	0.512	964.3	$10.02 \times 10^{-7}$	19,898.5
750	37.99	0.555	876.3	$15.99 \times 10^{-7}$	19,887.7
In the region between $\text{Li}_7\text{Si}_4$ and liquid Li-Si at 85 a/o Li					
650	0.400	0.993	9.2	$0.33 \times 10^{-8}$	25,215.3
700	0.678	0.989	15.6	$2.84 \times 10^{-8}$	24,166.5
725	1.036	0.984	23.9	$13.28 \times 10^{-8}$	24,023.7
750	1.393	0.979	32.1	$13.22 \times 10^{-8}$	23,602.3

\* Calculated from Eq. [1]-[6].

Table III. Relative partial molar enthalpies,  $\overline{\Delta H}$ , and relative partial molar entropies,  $\overline{\Delta S}$ , of lithium and silicon in the two-phase regions of the Li-Si system

Composition range (a/o Li)	$\overline{\Delta H}_{\text{Li}}$ (cal/g-atom)	$\overline{\Delta H}_{\text{Si}}$ (cal/g-atom)	$\overline{\Delta S}_{\text{Li}}$ (cal/deg/g-atom)	$\overline{\Delta S}_{\text{Si}}$ (cal/deg/g-atom)
0-66.3	-7769.5	0	-3.315	—
66.6-72.0	-8677.3	-2,358.0	-3.146	-0.194
72.8-78.8	-6386.4	-8,305.2	-4.050	-2.300
79.1-81.4	-3517.9	-19,540.2	-3.522	-0.486
81.6-liquid Li (equiv.)	215.3	-35,527.5	0.330	-16.00

the composition range 81.6 a/o Li to liquid lithium, was calculated using the equilibrium lithium mole fractions,  $X_{\text{Li}}^{\text{Sat}}$ , at various temperatures (given in the phase diagram) and assuming a lithium activity coefficient of unity. This assumption is not unreasonable at these high concentrations of lithium ( $X_{\text{Li}} > 0.95$ ) when the activity coefficient of lithium in Li-Al alloys at concentrations of greater than 80 a/o Li is observed to be unity (21). The value of  $\overline{\Delta H}_{\text{Li}}$  calculated by the relation

$$\overline{\Delta H}_{\text{Li}} = R \left[ \frac{\partial \ln X_{\text{Li}}^{\text{Sat}}}{\partial 1/T} \right] \quad [12]$$

was found to be 196.7 cal/g-atom, which was in good agreement with the value of 215.3 cal/g-atom determined from the emf data.

The silicon activities with reference to pure solid silicon as the standard state were calculated using a Gibbs-Duhem relation (22) of the type

$$\log \gamma_{\text{Si}} = - \left[ \frac{\log \gamma_{\text{Li}}}{(1 - X_{\text{Li}})^2} \right] X_{\text{Li}} X_{\text{Si}} - \int_{X'_{\text{Si}}}^{X_{\text{Si}}} \left[ \frac{\log \gamma_{\text{Li}}}{(1 - X_{\text{Li}})^2} \right] dX_{\text{Si}} - \int_{X_{\text{Si}}=1}^{X'_{\text{Si}}} \left[ \frac{\log \gamma_{\text{Li}}}{(1 - X_{\text{Li}})^2} \right] dX_{\text{Si}} \quad [13]$$

where  $\gamma$  = the activity coefficient of the designated component ( $\gamma = a/X$ ),  $X$  = the mole fraction of the

designated component, and  $X'_{Si}$  = the mole fraction of silicon with a known activity.

The calculated silicon activities,  $a_{Si}$ , and the relative partial molar free energies of silicon,  $\overline{\Delta G}_{Si}$ , obtained using the relation

$$\overline{\Delta G}_{Si} = RT \ln a_{Si} \quad [14]$$

are given at various temperatures in Table II.

The relative partial molar enthalpies of silicon,  $\overline{\Delta H}_{Si}$ , were calculated from plots of  $\log \gamma_{Si}$  vs.  $1/T$  and the relative partial molar entropies of silicon,  $\overline{\Delta S}_{Si}$ , were calculated from the relation

$$\overline{\Delta G}_{Si} = \overline{\Delta H}_{Si} - T \overline{\Delta S}_{Si} \quad [15]$$

The calculated values of  $\overline{\Delta H}_{Si}$  and  $\overline{\Delta S}_{Si}$  are given in Table III.

In addition the standard free energies of formation,  $\Delta G^\circ_f$ , for the compounds  $Li_2Si$ ,  $Li_{21}Si_8$ ,  $Li_{15}Si_4$ , and  $Li_{22}Si_5$  per gram atom of lithium at 650°, 700°, 725°, and 750°K were obtained from the relation

$$\Delta G^\circ_f = \overline{\Delta G}_{Li} + \frac{X_{Si}}{X_{Li}} \overline{\Delta G}_{Si} \quad [16]$$

and are given in Table IV.

### Summary

A series of charge-discharge cycles were carried out between silicon and lithium electrodes at various current densities at 680°K. These measurements indicated: (i) the Li-Si alloy electrode is reversible with respect to lithium and exhibits current efficiencies of greater than 95%, (ii) the existence of a new compound,  $Li_{21}Si_8$  in the Li-Si system, and (iii) the range of non-stoichiometry of the various Li-Si compounds.

The electromotive forces in the two-phase regions of the Li-Si system were measured in the temperature range of 650°-750°K and these values were used to calculate the activities and relative partial molar properties of lithium and silicon. In addition, the standard free energy of formation for  $Li_2Si$ ,  $Li_{21}Si_8$ ,  $Li_{15}Si_4$ , and  $Li_{22}Si_5$  were also determined over the specified temperature range.

### Acknowledgments

The authors are thankful to Messrs. David W. Buttram, Ernest J. Verrier, and Walter J. Wright for as-

sistance in the experimental work; Dr. Jack Johnson and Mr. A. C. Ottolini of the Analytical Chemistry Department for the x-ray diffraction and SEM analyses; Dr. Seymour Katz of the Metallurgy Department for the DTA; and Drs. Elton J. Cairns and John S. Dunning of the Electrochemistry Department for useful suggestions and discussions.

Manuscript submitted April 9, 1976; revised manuscript received June 28, 1976. This was Paper 36 presented at the Las Vegas, Nevada, Meeting of the Society, Oct. 17-22, 1976.

Any discussion of this paper will appear in a Discussion Section to be published in the June 1977 JOURNAL. All discussions for the June 1977 Discussion Section should be submitted by Feb. 1, 1977.

Publication costs of this article were assisted by General Motors Corporation.

### REFERENCES

1. T. G. Bradley and R. A. Sharma, *Proc. Ann. Power Sources Conf.*, **26**, 60 (1974).
2. P. A. Nelson *et al.*, USAEC Report ANL-8058, Argonne National Laboratory, Argonne, Ill. (1974).
3. R. A. Rightmire and A. L. Jones, *Proc. Ann. Power Sources Conf.*, **21**, 42 (1967).
4. P. A. Nelson *et al.*, USAEC Report ANL-75-1, Argonne National Laboratory, Argonne, Ill. (1975).
5. V. H. Böhm, *Z. Metallk.*, **50**, 44 (1959).
6. P. I. Fedorov and A. A. Ioffe, *Izv. Vyssh. Uchebn. Zaved., Tsvetn. Metall.*, **5**, (1), 127 (1962).
7. I. Obinata *et al.*, *Metall (Berlin)*, **19**, 21 (1965).
8. F. A. Shunk, "Constitution of Binary Alloys, Second Supplement," p. 480, McGraw-Hill Book Co., New York (1969).
9. H. Schaefer, H. Axel, and A. Weiss, *Z. Naturforsch., Teil B*, **20**, 1010 (1965).
10. H. Schaefer, H. Axel, and A. Weiss, *ibid*, **20**, 1302 (1965).
11. G. I. Oleksiv and P. I. Kripyakevich, *Kristallografiya*, **9**, (3), 338 (1964).
12. E. Elchardus and P. Laffit, *Bull. Soc. Chim. Fr.*, **51**, 1572 (1932).
13. R. N. Seefurth and R. A. Sharma, *This Journal*, **122**, 1049 (1975).
14. S. Sudar, L. R. McCoy, and L. A. Heredy, *Proc. 1975 IECEC*, **10**, 642 (1975).
15. S. Lai and L. R. McCoy, Paper 21 presented at The Electrochemical Society Meeting, Dallas, Texas, October 5-9, 1975.
16. P. A. Nelson *et al.*, USERDA Report ANL-75-36, Argonne National Laboratory, Argonne, Ill. (1975).
17. L. R. McCoy and S. Lai, "Proceedings of the Symposium and Workshop on Advanced Battery Research and Design," ANL-76-8, B-167 (March 1976).
18. W. Klemm and M. Struck, *Z. Anorg. Chem.*, **278**, 117 (1955).
19. N. P. Yao, L. A. Heredy, and R. C. Saunders, *This Journal*, **118**, 1039 (1971).
20. JANAF Thermochemical Tables, Second Edition, NSRDS-NBS 37 (June 1971).
21. S. P. Yatsenko and E. A. Saltykova, *Zh. Fiz. Khim.*, **48**, 2366 (1974).
22. L. S. Darken and R. W. Gurry, "Physical Chemistry of Metals," p. 264, McGraw-Hill Book Co., New York (1953).

Table IV. Standard free energies of formation,  $\Delta G^\circ_f$ , for the compounds of the Li-Si system at various temperatures\*

Temp (K)	- $\Delta G^\circ_f$ , cal per g-atom of Li, for the compounds			
	$Li_2Si$	$Li_{21}Si_8$	$Li_{15}Si_4$	$Li_{22}Si_5$
650	7770-7752	7484-7415	6367-6477	5743-5695
700	7604-7589	7322-7256	6195-6234	5510-5465
725	7521-7508	7241-7176	6110-6222	5487-5441
750	7438-7428	7162-7096	6023-6131	5396-5354

\* Range indicates the values for lithium-deficient to lithium-abundant compounds.

# Life Cycle Testing of SLI Batteries with Pb-Ca-Sn Grids Containing Various Amounts of Bismuth

John L. Devitt\*

Consulting Electrical Engineer, Denver, Colorado 80224

and Michael Myers

Central Research Laboratories, ASARCO Incorporated, South Plainfield, New Jersey 07080

## ABSTRACT

The effects on battery life of lead-calcium-tin grids (Pb + 0.07%Ca + 0.7%Sn) with bismuth content in the range 7-420 ppm have been studied. Full-sized batteries were cycled to failure using either modified SAE J240 or J537 procedures. The results showed that in the test designed to cause failure by corrosion (SAE J537), no ill effects due to bismuth were noted. In the tests designed to model automotive service (J240), cycle life tended to increase with increasing bismuth content of the grids.

The growing production of maintenance-free, lead-acid, SLI batteries has focused attention on the impurity elements in the lead used in alloying of the lead-calcium-tin grid metal. Bismuth is one of the most common impurities in both refined primary and secondary lead, and, because of its chemical similarity, it is excessively expensive to remove below 200 ppm. Some manufacturers imply that bismuth even at the 200 ppm level is deleterious to the performance of the grid alloy by specifying as little as 10 ppm maximum while others allow as much as 500 ppm.

The chemistry of the primary and secondary available lead is such that a bismuth content requirement for this application below 200 ppm would eliminate major sources of lead from use in lead-calcium-tin grid alloys. The importance of establishing the effects of bismuth at levels at or above 200 ppm is therefore obvious. Toward this end, research has been carried out by both primary and secondary producers. Sokolov and co-workers (3) have reported that bismuth up to 180 ppm has no effect on casting or mechanical properties of lead-calcium-tin grids or the gassing properties of the grids.

The investigation reported herein studied the effect on battery life of lead-calcium-tin grids with bismuth contents in the range 5-500 ppm using full-size batteries tested by modified SAE life cycle testing requirements.

These batteries were cycled to failure in two modes: one designed to cause failure by corrosion (Cycle A) and the other to closely model service in an automobile (Cycle B). It was intended to determine the influence of bismuth, if any, on battery cell overcharge current, gassing, grid corrosion, and active-material stability. Also, valuable insight into the characteristics of lead-calcium-tin MF batteries would be obtained.

## Experimental Procedures

**Battery construction.**—Twenty batteries were constructed in all, eighteen with lead-calcium-tin grids and two with antimonial grids. All of the lead-calcium-tin were of nominal composition Pb-0.07%Ca-0.7%Sn. Nominal bismuth contents were 5, 20, 200, and 500 ppm by weight. The actual composition of these alloys and of the standard antimonial lead composition employed are presented in Table I.

The lead-calcium-tin grids were cast in 600# lots at Wirtz Manufacturing Company, Port Huron, Michigan, on a commercial grid casting machine. In size they were nominally 4-7/8 in. × 5-11/16 in. × 0.062 in.

\* Electrochemical Society Active Member.

Key words: batteries, bismuth, cycling, grids, lead.

The only intentional variation in the batteries was in the bismuth content of their grids. A standard 12V, Group 24 design was used employing polypropylene containers with over-the-wall interconnections. All batteries were handmade and had the following features in common:

Nominal capacity: 50 A-hr, equivalent to approximately 70 min reserve capacity rating.

Plates per cell: Four positive, five negative.

Active material: Conventional formula employing commercially available lead oxide. Cube weight (density) of the pastes was controlled to 67-68 g/in<sup>3</sup> (Approx. 4.1 g/cm<sup>3</sup>).

Separators: Standard automotive Daramic, 0.065 in. over-all and 0.20 in. web. Separators were folded around each positive plate with ribs inward and the fold at the bottom.

Vent plugs: Standard Richardson gang-vent plugs.

Formation: In 1.120 sp gr acid. Four hours at 2A followed by 44 hr at 3.5A. At the latter rate battery voltage was limited to 16V maximum.

One important difference between these batteries and mass-produced batteries is that the thicknesses of the pasted positive and negative plates were approximately equal. In commercial batteries the amount of positive material is usually greater than the amount stoichiometrically needed for reaction with the negative plates, in order to prolong the life of the battery as the positive plates wear out. The test batteries, however, had approximately 25% less positive material than negative material, assuring capacity limiting by the positive plates throughout the duration of the test. Further, the use of only 9 plates per cell (as compared to at least 13 for commercial maintenance-free batteries) increased current density per plate, again reducing battery life. These design variations changed the rate of failure but not the mode.

**Test Cycle A.**—This test is based upon the overcharge-life test of SAE Standard J537. Each cycle has

Table I. Analysis of battery grids

Alloy No.	% Ca	% Sn	ppm Bi	Battery No.
1	0.055	0.77	7	1, 2, 9, 13, 14
2	0.071	0.66	25	3, 4, 10
3	0.072	0.76	190	5, 6, 11, 15, 16
4	0.055	0.68	420	7, 8, 12, 17, 18

Antimonials: Sb-4.80%, As-0.38% Sn-0.37%, Bi-200 ppm 19, 20

a duration of exactly one week, and is described as follows:

**Overcharge:** Place battery on constant current charge at 2A for a total of 110 hr.

**Stand:** Let battery rest on open circuit for 48 hr.

**Test discharge:** Apply 150A load to battery for 30 sec, or to a battery end-point voltage of 7.2V, whichever occurs first. Then return battery to overcharge step.

**Water:** Top up battery as required, weekly.

**Temperature:** All of the above steps are conducted at 75° or 120°F. At 75°F the battery is kept in controlled room ambient, to within 2°F. At 120°F the battery is in a water bath constructed per SAE J537 and controlled to within 1°F.

**Failure:** The battery is considered failed the first time it fails to remain above 7.2V for at least 30 sec in the test discharge step above.

The Cycle A current at 2A was selected by subjecting cells of the same design and materials used in the subsequent test to various constant overcharge currents (Table II), ranging from 0.3 to 4.5A (SAE standard current). At 2A (and 75°F) the battery voltage was 17.0V (2.83V/cell) with a positive plate potential of 1.42V vs. Hg/HgSO<sub>4</sub> reference. These conditions were sufficiently severe to produce a significant rate of corrosion without a totally unrealistic (regarding automotive service) battery voltage.

**Results Cycle A.**—Twelve batteries were subjected to Cycle A, two of each alloy at 75°F and one of each at 120°F. The batteries were cycled to failure as defined above. Battery lifetimes (cycles to failure) are listed in Table III. There is no trend, positive or negative, on cycle life due to bismuth.

While Test Cycle A was in progress, separate tests were run on the batteries to determine the characteristic overcharge current vs. battery voltage curves for each of the batteries. These curves were obtained as follows: After the weekly 110 hr overcharge period, the batteries were left on charge at 2A and voltage

Table II. Cell and positive-plate voltages vs. overcharge current-test cells

Over charge amperes	Avg. cell V (room temp.)	Reference electrode (room temp.)	Avg cell V (120°F)	Reference electrode
0.3	2.70	1.37	2.62	1.32
1.0	2.80	1.41	2.73	1.37
2.0	2.83	1.42	2.78	1.40
4.5	2.90	1.44	2.85	1.42

Note: Reference electrode measurements were made with a stabilized PbO<sub>2</sub> electrode, but expressed here vs. an Hg/Hg<sub>2</sub>SO<sub>4</sub> electrode for direct comparison to the literature.

Table III. Data from Test Cycle A

Battery No.	Alloy No.	Bismuth ppm	Test temperature	Weekly cycles to failure	Average life in alloy group
1	1	7	75°F (24°C)	28	27.0
2	1	7	75°F (24°C)	26	
3	2	25	75°F (24°C)	28	26.5
4	2	25	75°F (24°C)	25	
5	3	190	75°F (24°C)	29	28.5
6	3	190	75°F (24°C)	28	
7	4	420	75°F (24°C)	23	24.5
8	4	420	75°F (24°C)	26	
9	1	7	120°F (49°C)	20	
10	2	25	120°F (49°C)	19	
11	3	190	120°F (49°C)	19	
12	4	420	120°F (49°C)	19	

Additional data: There was no consistently observed difference in the water consumption patterns between any of the batteries. Toward the end of life there were sporadic reductions in water consumption owing to short circuits in the cells in the high temperature batteries. No shorting was observed in the lower temperature units.

measurements were made. Voltages of 3 cells per battery were measured, as were voltages from the positive plates to a PbO<sub>2</sub> reference electrode inserted into the electrolyte through the cell vent opening. These two sets of voltage readings represent very stable values because of the 110 hr period of constant current which had preceded the measurements. Then voltage measurements were taken, at lower constant-current settings. All potential measurements were made after waiting enough hours, per data point, for equilibrium to be reached. While the data are shown as being taken at the end of 11 weeks of cycling, similar runs were made at 8 and 15 weeks with essentially identical results.

The resulting curves are presented in Fig. 1 and 2. The significance of these curves is that the overcharge current at a given battery voltage does not vary with bismuth content of the grid. This means that bismuth, up to 420 ppm does not affect the gassing or corrosion rate of the batteries. This supports the data of Table III in that, although all batteries failed by corrosion, the time to failure was not a function of the bismuth content.

The appearance of the dismantled batteries showed that the principal mode of failure was certainly grid corrosion. The grids had corroded to such an extent that meaningful weight and dimensional measurements could not be obtained. The positive active material on the remaining portions of the grids appeared to be in good condition. Shedding losses of active material were estimated to be less than 10%.

During the course of Cycle A, no variation in the amount or rate of water loss was noted among the alloys.

**Test Cycle B.**—This test is based upon the life test described in SAE J240. Each cycle has a duration of exactly 1 week and is described as follows:

**Shallow cycles:** Each cycle consists of a discharge of 25A for 3.5 min, followed immediately (switching time allowed) by a charge at a voltage limited to 14.8V and a current limited to 25A. Charging time is 10 min. In practice the first portion of charge is current limited

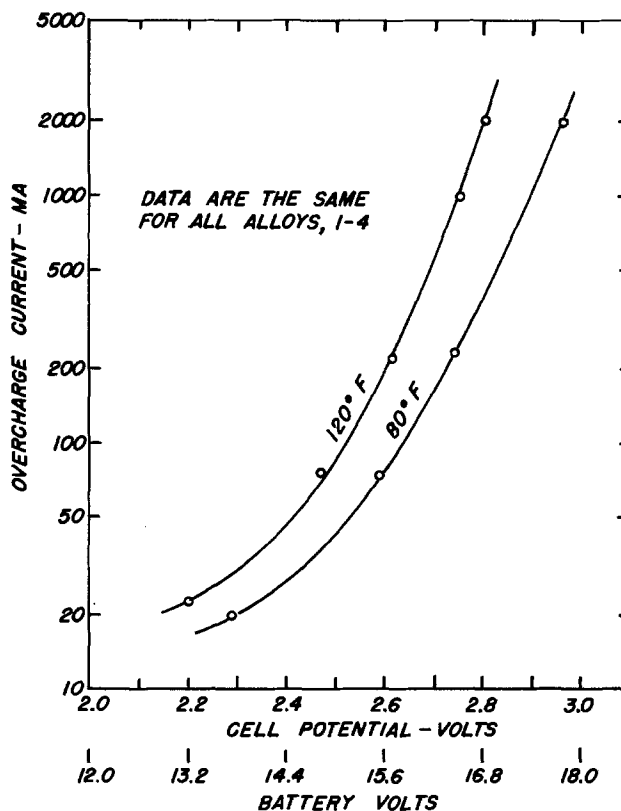


Fig. 1. Overcharge currents vs. cell potential

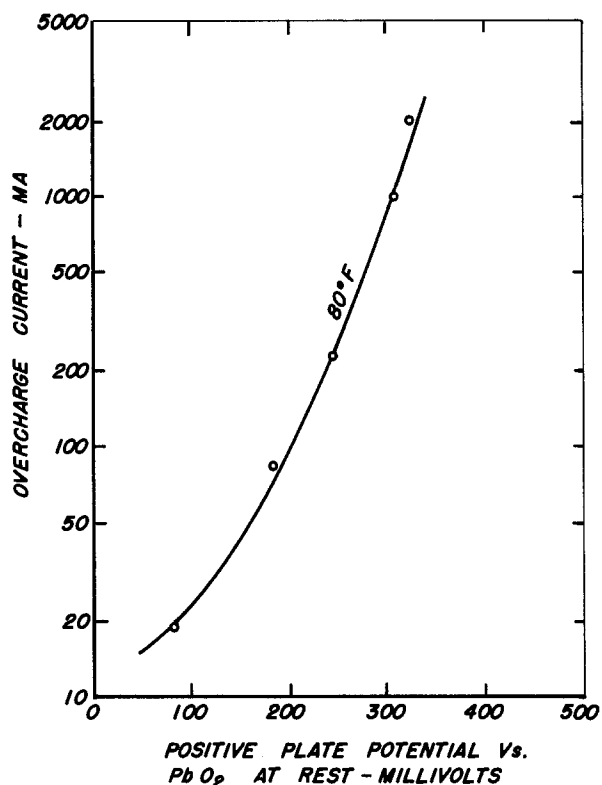


Fig. 2. Overcharge gassing currents, alloys 1 thru 4 (vs. positive plate potential).

and the latter portion is voltage limited. Following the charging period the battery is given a 30 sec rest on open circuit. This shallow cycling is repeated 429 times per week, for a total of 100 hr.

Stand: The battery is given a 60 hr rest on open circuit.

Test discharge: Same as in Test Cycle A except load current is 300A. This is equivalent to 1.48 A/in.<sup>2</sup> or 0.229 A/cm<sup>2</sup> of apparent total positive plate surface area. The battery is then returned to the shallow cycles without a separate charge.

Water: As in Test Cycle A.

Temperature: Maintained at 105°F.

Failure: Defined as in Test Cycle A.

Instead of the SAE J240 2 min shallow cycle discharge, a 3.5 min discharge time was used for Test Cycle B. It has been found that the mild 2 min discharge lengthens the test time to an unreasonable degree (years) if the test is applied to batteries made of lead-calcium-tin grids. This is because of the very low end-of-charge current and consequent low amount of grid corrosion as compared to standard antimonial grid batteries. There is also much less gassing to disrupt the active material in MF batteries. Therefore, a discharge time which nearly doubles the SAE recommended depth of discharge was used. The shallow cycle portion of this test cycle was automatically controlled by apparatus constructed expressly for this experiment.

**Results Cycle B.**—Eight batteries in all were subjected to Test Cycle B: six lead-calcium-tin and two antimonial. The results (cycles to failure) are presented in Table V. As in Cycle A there was no deleterious effect with increasing bismuth. On the contrary, cycle life increased as bismuth content increased.

Following failure, the positive grids from Cycle B batteries were removed from the cases, dried, and weighed with the active material intact. The active material was then removed in a solution of sodium hydroxide, mannitol, and hydrazine hydrochloride. The bare grids were reweighed. The resultant weight losses of active material and grid metal are included in Table IV. Corrosion of the antimonial grids was so severe that meaningful measurement could not be made.

Table IV. Data from Test Cycle B

Battery No.	Alloy No.	Bismuth ppm	No. of 14 min cycles to failure	Avg. per cent loss in positive grid weight	Avg. per cent loss in positive act. material weight
13	1	7	6006	—	—
14	1	7	6435	22%	13%
15	3	190	6435	25%	10%
16	3	190	7722	25%	13%
17	4	420	8151	22%	20%
18	4	420	8580	21%	20%
19	Sb	200	4290	—	—
20	Sb	200	4290	—	—

1. Battery 13 failed because of an apparent short circuit in a cell. The problem has not been located visually. Therefore, it was felt that its grid corrosion and active material loss data were not meaningful.

2. As noted in the test, the two antimonial batteries, at failure, contained such badly disintegrated positive grids that removal from the container was difficult and further weighing and other analysis was essentially impossible.

The mechanism of failure in Cycle B in the lead-calcium-tin batteries is not clear. Failure seems to have occurred due to a combination of factors: (i) surface shedding of positive-active material; (ii) loosening positive pellets of PbO<sub>2</sub> by a combination of grid corrosion and overcharge gassing, possibly concentrated at the grid-active material interface; and (iii) piling up of shedded PbO<sub>2</sub> within the lower portion of the folded separators which tended to "block off" a significant part of the positive plate. Grid growth was not noticeable in any of these batteries and definitely was not a cause of failure.

In the case of the antimonial batteries the failure mode was primarily severe grid corrosion. During the conduct of the test it was noted that the end-of-charge current, at 14.8V, ranged from 0.2-0.4A for lead-calcium-tin grid batteries, and 4-6A for the antimonial batteries. For the lead-calcium-tin batteries this current decreased as a function of life presumably because of the progressive drop in available capacity. In the antimonial batteries the end-of-charge current increased during life, owing to the familiar antimony poisoning phenomenon at the sponge lead surface. Thus, the current at end of life was 30 times higher for the antimonial type than the other. Therefore, one would expect the antimonial batteries to fail more by grid corrosion, and they did. Even in this case, however, no grid growth could be found.

### Summary

In an overcharge life test (based on SAE J537) designed to cause battery failure by grid corrosion, no ill effects due to bismuth were noted. Characteristic curves of overcharge amperage vs. battery voltage were virtually identical for lead-calcium-tin batteries containing 7-420 ppm bismuth.

In a cycle life test (based on SAE J240) designed to model automotive service, lead-calcium-tin batteries containing 7-420 ppm bismuth failed to show any ill effect due to bismuth. In fact, there was an unmistakable trend to increased cycle life with increasing bismuth.

### Acknowledgments

The authors wish to thank the Wirtz Manufacturing Company, Port Huron, Michigan, for their assistance in producing the battery grids employed in these experiments.

Manuscript received June 25, 1976. This was Paper 3 presented at the Las Vegas, Nevada, Meeting of the Society, Oct. 17-22, 1976.

Any discussion of this paper will appear in a Discussion Section to be published in the June 1977 JOURNAL. All discussions for the June 1977 Discussion Section should be submitted by Feb. 1, 1977.

Publication costs of this article were assisted by ASARCO Incorporated.

## REFERENCES

1. T. W. Caldwell and V. S. Sokolov, Paper 34 presented at Electrochemical Society Meeting, Boston, Massachusetts, Oct. 7-11, 1973.
2. M. Myers, H. R. Van Handle, and C. R. DiMartini, *This Journal*, **121**, 1526 (1974).
3. U. S. Sokolov and L. J. Crosby, Proceedings of the Battery Council International Convention, p. 145, Hollywood, Florida (1975).
4. M. Myers, *ibid.*, p. 135.

## A Solid-State Galvanic Cell with Fluoride-Conducting Electrolytes

J. Schoonman\*

*Solid State Department, Physical Laboratory, State University of Utrecht, Sorbonnelaan 4, Utrecht-De Uithof, The Netherlands*

## ABSTRACT

$\text{BiO}_{0.09}\text{F}_{2.82}$  and  $\beta\text{-PbF}_2\text{:AgF}$  are suitable fluoride conducting electrolytes for application in galvanic cells. A simple fabrication method for the cell  $\text{Pb}/\beta\text{-PbF}_2\text{:AgF}/\text{BiO}_{0.09}\text{F}_{2.82}/\text{Bi}$  is described. Open-circuit voltages are in accord with a theoretical value of 0.33V based on the cell reaction  $3\text{Pb} + 2\text{BiF}_3 \rightarrow 3\text{PbF}_2 + 2\text{Bi}$ . Cells were discharged in the temperature region  $298^\circ\text{-}375^\circ\text{K}$  with current densities of 12-63 mA/m<sup>2</sup>. Short-circuit currents range from 15.7 to 386 mA/m<sup>2</sup>. Relatively constant load-circuit voltages were attained over periods of days.

The electrical properties of fluoride conductors with fluorite or tysonite structure have received considerable interest in the recent literature (1-8). Some of these materials are presently used as solid electrolytes.

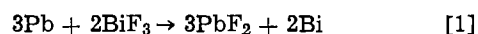
$\text{PbF}_2$  has been applied successfully as a solid electrolyte in a thin film galvanic cell (5). Thin film galvanic cells  $\text{Pb}/\text{PbF}_2/\text{CuF}_2(\text{PbF}_2)/\text{Cu}$  have been fabricated by vacuum evaporation (5).  $\text{CuF}_2$  is, however, a highly resistive material at room temperature. In order to improve the conductivity  $\text{CuF}_2$  was codeposited with  $\text{PbF}_2$ . This in turn leads to an open-circuit voltage (OCV) lower than the theoretical OCV of 0.70V. Both  $\text{CuF}_2$ , and especially  $\text{AgF}$  are reactive toward moisture in air. Special precautions are, therefore, needed to avoid blistering of thin films (5).

Kennedy and Miles (6) have tested potassium fluoride-doped  $\beta\text{-PbF}_2$  as an electrolyte in galvanic cells with  $\text{CuF}_2$  or  $\text{AgF}$  as cathode materials. Open-circuit voltages of 0.70 and 1.30V, respectively, were achieved, but the cell potentials fell rapidly when placed under load and current drawn. This poor performance could be due to the formation of an anode passivation layer consisting of low conductivity pure  $\alpha\text{-PbF}_2$  (6).

Recently, we have reported on solid electrolyte properties of tysonite-related  $\text{BiO}_x\text{F}_{3-2x}$  ( $x = 0.09 \sim 0.1$ ) (9). The conductivity is ionic and exceeds at ambient temperatures the conductivity of undoped  $\beta\text{-PbF}_2$ . When  $\beta\text{-PbF}_2$  is doped with monovalent cations the conductivity substantially increases. Mass transport then occurs via fluoride ion vacancies as in  $\text{BiO}_x\text{F}_{3-2x} \cdot \text{BiO}_x\text{F}_{3-2x}$ , as well as  $\beta\text{-PbF}_2$  doped with monovalent cations exhibit such conductivity values that extremely thin films are not required. Fabrication of galvanic cells by tedious vacuum evaporation techniques can therefore be avoided. Moreover, both fluorides are quite stable in air.

Solid-state galvanic cells  $\text{Pb}/\beta\text{-PbF}_2\text{:AgF}/\text{BiO}_x\text{F}_{3-2x}/\text{Bi}$  were fabricated using a very simple technique. Their discharge characteristics were studied in the temperature region  $290^\circ\text{-}375^\circ\text{K}$ .

The cathode-electrolyte  $\text{BiO}_x\text{F}_{3-2x}$  ( $x = 0.09 \sim 0.1$ ) can be considered as oxide-doped bismuth fluoride (9). The following cell reaction



should then lead to an OCV of 0.33V.

## Experimental Aspects

$\text{BiO}_x\text{F}_{3-2x}$  phases were obtained by heating mixtures of  $\text{Bi}_2\text{O}_3$  (Merck, p.a.) and excess  $\text{NH}_4\text{F}$  (Baker, AR). A heat-treatment at  $575^\circ\text{K}$  for a period of 2 hr yielded a phase, of which powder diffraction data revealed good agreement with data reported for the phase  $\text{BiO}_{0.09}\text{F}_{2.82}$  (10). Upon heating this phase in air for periods shorter than 1 hr at  $925^\circ\text{K}$  we obtained the approximate composition  $\text{BiO}_{0.1}\text{F}_{2.8}$  without the reported (11) fcc  $\beta$ -phase.

$\beta\text{-PbF}_2\text{:AgF}$  [0.5 mole percent (m/o)] was prepared by melting zone-refined lead fluoride (Merck, Optipur) with  $\text{AgF}$  (Merck). The melting procedure was carried out under dried, oxygen-free nitrogen in graphite crucibles (12). The solid electrolytes were ground in a ball mill. The resulting powders were wetted with the volatile ethyl acetate. Thin disks of Pb and Bi (thickness  $\sim 1 \times 10^{-3}\text{m}$ , area  $2.83 \times 10^{-5}$  or  $1.77 \times 10^{-4}\text{m}^2$ ) were painted with the  $\beta\text{-PbF}_2\text{:AgF}$ -ethyl acetate and  $\text{BiO}_x\text{F}_{3-2x}$ -ethyl acetate mixtures, respectively. After evaporation of the ethyl acetate each disk was covered with about  $1 \times 10^{-5}$  kg solid electrolyte. Galvanic cells  $\text{Pb}/\beta\text{-PbF}_2\text{:AgF}/\text{BiO}_x\text{F}_{3-2x}/\text{Bi}$  were then obtained by spring-loading the disks in the appropriate sequence between two flat platinum electrodes of a conventional conductivity cell. This cell was equipped with a furnace. The total thickness of the solid electrolytes was about  $1 \times 10^{-4}\text{m}$ .

OCV measurements were recorded from a Keithley Model 616 digital electrometer. Short-circuit currents were measured with a Keithley Model 445 digital picoammeter. Polarization currents through the cell  $(-)\text{Bi}/\text{BiO}_x\text{F}_{3-2x}/\text{Pt}(+)$  were measured with a Keithley Model 153 microvolt-ammeter, whereas applied potential differences across the cell were made using a Keithley Model 610 BR electrometer.

Alternating-current conductivities here referred to were measured with impedance bridges, details of which have been published before (4).

## Experimental Results

The galvanic cells exhibited room temperature OCV's of 0.330-0.335V. These values are in good agreement

\* Electrochemical Society Active Member.

Key words: galvanic cell, thin films, lead fluoride, bismuth oxide fluoride, discharge characteristics.



Table I. Frequency independent electrolyte resistances  $R_e$ , d-c resistances  $R_{dc}$ , and short-circuit currents  $I_{sc}$  of  $2.83 \times 10^{-5} \text{ m}^2$  area cells\*

$T$ ( $^{\circ}\text{K}$ )	$R_e$ ( $\Omega$ )	$R_{dc}$ ( $\Omega$ )	$R_L$ ( $\Omega$ )	$I_{sc}$ ( $\text{mA}/\text{m}^2$ )
300	$5.52 \times 10^5$	$5.70 \times 10^5$ $5.76 \times 10^5$	$1 \times 10^6$ $2 \times 10^5$	15.7
363	$3.66 \times 10^4$	$8.7 \times 10^4$	$2 \times 10^5$	386

\* Cathode material:  $\text{BiO}_{0.09}\text{F}_{2.82}$ .

with the theoretical OCV. These OCV's remain constant over periods of weeks. After such storage periods these cells and freshly prepared cells were used in discharge experiments. These were all performed in air.

Upon application of a constant load ( $R_L$ ) the load-circuit voltage (LCV) dropped within 5 min to a stable value. LCV's then remained nearly constant during discharge: at room temperature the LCV dropped from 0.15 to 0.13V over a period of 14 days, the load being 1 M $\Omega$ . At 363 $^{\circ}\text{K}$  and a load of 0.2 M $\Omega$  the LCV decreased from 0.23 to 0.22V in 2 days. After these periods discharges were terminated. After disconnecting a load theoretical OCV's were reached within 30 min.

The d-c resistances of cells were calculated using the usual expression

$$R_{dc} = \frac{\text{OCV} - \text{LCV}}{\text{LCV}} R_L \quad [2]$$

Discharge under a 1 M $\Omega$  and a 0.1 M $\Omega$  load revealed at room temperature d-c resistances in the range  $1.1 \times 10^5$ - $5.5 \times 10^5$  and  $0.58 \times 10^6$ - $1.23 \times 10^6 \Omega$  for  $1.77 \times 10^{-4}$  and  $2.83 \times 10^{-5} \text{ m}^2$  area cells, respectively. These resistances were obtained regardless of whether  $\text{BiO}_{0.09}\text{F}_{2.82}$  or  $\text{BiO}_{0.1}\text{F}_{2.8}$  was used as cathode material. For two galvanic cells ( $2.83 \times 10^{-5} \text{ m}^2$  area) frequency independent electrolyte resistances  $R_e$  and  $R_{dc}$  values are summarized in Table I. In addition to these data short-circuit currents are included.

These data are to be compared with a room temperature value of about  $1.8 \times 10^6 \Omega$ , which can be inferred for the d-c resistance of a  $1 \times 10^{-5} \text{ m}^2$  area thin film galvanic cell  $\text{Pb}/\text{PbF}_2/\text{CuF}_2(\text{PbF}_2)/\text{Cu}$  from the discharge curve under a 3.3 M $\Omega$  load. Discharge under a 0.3 M $\Omega$  load revealed for this type of cell for  $R_{dc}$  the value  $3.36 \times 10^5 \Omega$  (5).

Performance characteristics improved substantially at elevated temperatures. Figure 1 presents normalized

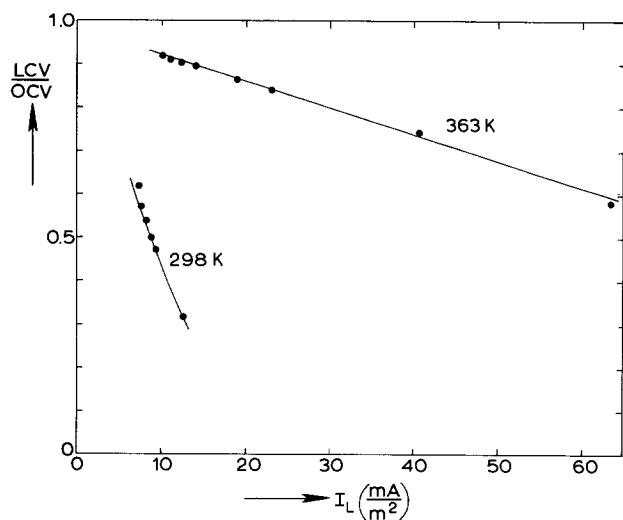


Fig. 1. Normalized load-circuit voltages (LCV/OCV) vs. load current densities for  $2.83 \times 10^{-5} \text{ m}^2$  area cells with  $\text{BiO}_{0.09}\text{F}_{2.82}$  as cathode material.  $T = 298^{\circ}\text{K}$ ,  $R_L = 0.3$ - $1.0 \text{ M}\Omega$ ;  $T = 363^{\circ}\text{K}$ ,  $R_L = 0.1$ - $0.9 \text{ M}\Omega$ .

Table II. Performance of  $2.83 \times 10^{-5} \text{ m}^2$  area cells\*

$T$ ( $^{\circ}\text{K}$ )	Capacity (C)**	Load (M $\Omega$ )	Discharge time (days)†
298	0.16	1	14
363	0.20	0.2	2

\* Cathode material:  $\text{BiO}_{0.09}\text{F}_{2.82}$ .

\*\* Measured from discharge.

† Discharge was terminated after these periods.

load-circuit voltages (LCV/OCV) vs. current densities at 298 $^{\circ}$  and 363 $^{\circ}\text{K}$ . Data on the performance of two galvanic cells at different temperatures are summarized in Table II.

In Fig. 2 the temperature dependence of  $R_{dc}$  is plotted vs. reciprocal temperature. An activation enthalpy of 0.30 eV was obtained for a freshly prepared cell, and a value of 0.41 eV for a cell which had been discharged for 2 weeks under a 1 M $\Omega$  load (cf. Table II).

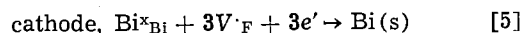
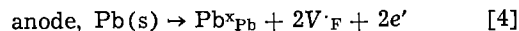
Cells of the type  $\text{Pt}/\text{Bi}/\text{BiO}_{0.09}\text{F}_{2.82}/\text{Pt}$  were prepared by spring loading a Bi disk, which had been covered with a thin layer of  $\text{BiO}_{0.09}\text{F}_{2.82}$  between two Pt electrodes of a conductivity cell. Cells were polarized with the Bi electrode negative. Steady-state currents exponentially increased on applied potential difference  $E$  (Fig. 3). The currents can be expressed by (1)

$$I = \frac{RT}{LF} \sigma_h [\exp(EF/RT) - 1] \quad [3]$$

where  $L$  denotes the cell constant (ratio of electrolyte thickness to electrode area), and  $\sigma_h$  the specific electron hole conductivity for  $\text{BiO}_{0.09}\text{F}_{2.82}$  in contact with Bi. Frequency independent conductances showed the electrolyte conductivity to be  $6.47 \times 10^{-4} \text{ Sm}^{-1}$ , (Siemens/m) while the polarization currents lead to the value  $1.24 \times 10^{-8} \text{ Sm}^{-1}$  for  $\sigma_h$ .

### Discussion

The experimental OCV's confirm the cell reaction to be reaction [1]. The electrode reactions may be considered in terms of the mobile majority ionic point defects



Polarization studies of the cell (-)Pb/ $\beta$ -PbF<sub>2</sub>/C(+) revealed (6, 13) that the interface Pb/ $\beta$ -PbF<sub>2</sub> behaves reversibly to both ionic and electronic species. Electrode reaction [4] was used to derive the quantitative

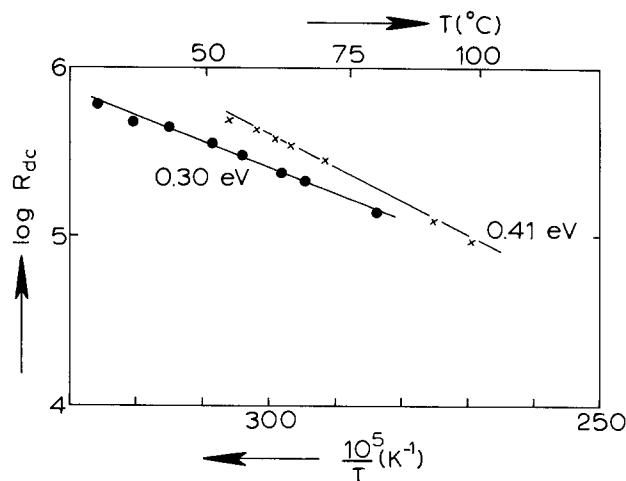


Fig. 2. Temperature dependence of  $R_{dc}$  plotted as  $\log R_{dc}$  vs.  $10^5/T$ .  $\bullet$ , Freshly prepared cell;  $\times$ , discharged under a 1 M $\Omega$  load for 2 weeks.

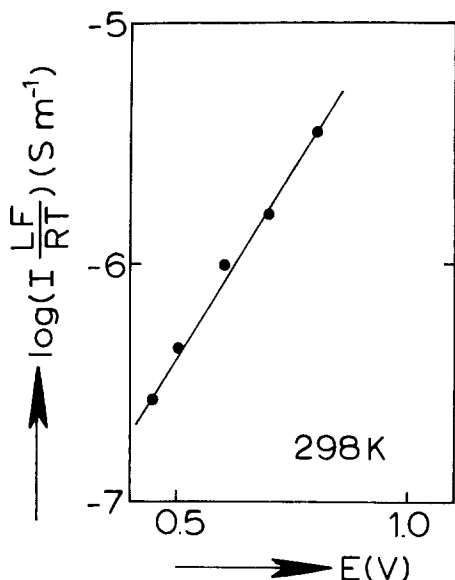


Fig. 3. Electronic conductivity in the cell (—)Bi/Bi<sub>0.09</sub>F<sub>2.82</sub>/Pt(+). Cell constant 10.6 m<sup>-1</sup>,  $\sigma_h = 1.24 \times 10^{-8} \text{Sm}^{-1}$ .

relations between the concentrations of electrons and ionic point defects  $F'_1$  and  $V_F$  in nominally pure and doped  $\beta\text{-PbF}_2$  (13). These expressions reveal that electron currents decrease upon increasing MF-concentrations. This has been confirmed by experimental observation (6). Electron currents will, therefore, be negligibly small in  $\beta\text{-PbF}_2\text{:AgF}$ .

A study of the frequency dispersion in the conductivity of BiO<sub>x</sub>F<sub>3-2x</sub> between ionically blocking electrodes already revealed negligible electronic conductivity (9). The data in Fig. 3 indicate that BiO<sub>0.09</sub>F<sub>2.82</sub> in contact with negatively polarized Bi exhibit very small electron hole currents. The slope of the  $\log [I(LF/RT)]$  vs.  $E$  curve is, however, smaller than the theoretical slope, a feature frequently observed for lead halides in contact with lead (1, 14, 15). Whether this behavior is caused by an inefficient blocking of the faradaic processes at the Pt/BiO<sub>0.09</sub>F<sub>2.82</sub> interface or a nonreversible behavior at the Bi/BiO<sub>0.09</sub>F<sub>2.82</sub> interface cannot be established from the present data.

Since both solid electrolytes exhibit negligible electronic conductivity, electronic leakage will not occur in the galvanic cells.

Plots of the normalized load-circuit voltages (LCV/OCV) vs. load current densities (Fig. 1) and data on  $R_e$  and  $R_{dc}$  (Table I) show that polarization occurs in the galvanic cells. The temperature dependence of  $R_{dc}$  revealed activation enthalpies of 0.30 eV for a freshly prepared cell, and 0.41 eV for a cell which has been discharged under a 1 M $\Omega$  load for 2 weeks. Both electrolytes have comparable conductivities at room temperature, the values being about  $6 \times 10^{-4} \text{Sm}^{-1}$  and about  $5 \times 10^{-4} \text{Sm}^{-1}$  for BiO<sub>0.09</sub>F<sub>2.82</sub> and  $\beta\text{-PbF}_2\text{:AgF}$  (0.5 m/o) (12), respectively. Conduction activation enthalpies of several relevant fluorides are summarized in Table III.

These activation enthalpies and the temperature dependence of  $R_{dc}$  indicate that the rate-determining step in the cell reaction involves the cathode electrolyte. In regard to the polarization studies on the electrolytes composing the galvanic cell it is also likely that cell

polarization partly originates at the Bi/Bi<sub>0.09</sub>F<sub>2.82</sub> interface.

The use of Pb/ $\beta\text{-PbF}_2\text{:AgF}$  could be limited by the formation of an anode passivation layer of  $\alpha\text{-PbF}_2$ . Kennedy and Miles (6) detected  $\alpha\text{-PbF}_2$  deposits at the anode interface Pb/ $\beta\text{-PbF}_2\text{:KF}$  after passage of 2 and 9C of charge through a cell Pb/ $\beta\text{-PbF}_2\text{:KF}$ /Pb. Such deposits were never higher than  $4 \times 10^{-5} \text{m}$ . At room temperature the measured discharge of a  $2.83 \times 10^{-5} \text{m}^2$  area cell was 0.16C (Table II). This could lead to a layer of  $\alpha\text{-PbF}_2$  of the order of  $10^{-6} \text{m}$ . The room temperature conductivity of  $\alpha\text{-PbF}_2$  is about  $4 \times 10^{-6} \text{Sm}^{-1}$  (1, 8). Such layers would then exhibit conductances of about  $1.1 \times 10^{-4} \text{S}$ . The conductance of the  $\beta\text{-PbF}_2\text{:AgF}$  layer having a thickness of about  $0.5 \times 10^{-4} \text{m}$  amounts to  $2.8 \times 10^{-4} \text{S}$ . At 363°K  $\alpha\text{-PbF}_2$  exhibits a specific conductivity which is lower than that of BiO<sub>0.09</sub>F<sub>2.82</sub> by about factor of 30, the difference with  $\beta\text{-PbF}_2\text{:AgF}$  being even smaller. The larger conduction activation enthalpy for  $\alpha\text{-PbF}_2$  (Table III) accounts for the reduction in the differences in the conductivities at increased temperatures. The thin film geometry is at this temperature again more in favor of  $\alpha\text{-PbF}_2$ . This in turn strongly supports the interpretation of the temperature dependence of  $R_{dc}$  and especially of the partly discharged cell.

Thin film cells of Kennedy and Hunter (5) with the CuF<sub>2</sub>(PbF<sub>2</sub>) cathode lead to maximum capacities of  $1 \times 10^{-2} \text{C}$  at 298°K ( $R_L = 3.3 \times 10^6 \Omega$ , discharge time 22 hr), and  $1.5 \times 10^{-2} \text{C}$  at 348°K ( $R_L = 0.3 \text{M}\Omega$ , discharge time 2 hr). At room temperature discharge times up to 30 hr were attained under a 4 M $\Omega$  load. In comparison with the thin film galvanic cells larger capacities are attained with the present cells (cf. Table II). These larger capacities are a direct consequence of the solid electrolyte properties of especially the cathode electrolyte BiO<sub>0.09</sub>F<sub>2.82</sub>. Extremely thin films are not required, which means that more cathode electrolyte is available in the present cells.

### Conclusions

The present study reveals that the solid electrolytes  $\beta\text{-PbF}_2\text{:AgF}$  and BiO<sub>0.09</sub>F<sub>2.82</sub> can be successfully used in a galvanic cell. Powders of these electrolytes are, when dispersed in ethyl acetate, particularly suitable for the fabrication of galvanic cells. The ethyl acetate quickly evaporates at room temperature. The solid electrolytes are stable in air. Their electronic conduction is practically negligible. Electronic leakage will, therefore, not occur in the galvanic cell.

Passivation of the anodes by  $\alpha\text{-PbF}_2$  will be a minor importance in the temperature region 298°-375°K and for capacities of 0.1-0.2C. In regard to the conductivity of  $\alpha\text{-PbF}_2$  at elevated temperatures the upper limit of the capacities to be attained can be set at  $\sim 1\text{C}$ , before anode passivation would seriously affect the operation of the cells.

### Acknowledgments

The author is indebted to Mr. G. J. Dirksen for the preparation of the electrolytes, and to Prof. Dr. G. Blasse for critically reading the manuscript.

Manuscript submitted April 19, 1976; revised manuscript received Aug. 9, 1976.

Any discussion of this paper will appear in a Discussion Section to be published in the June 1977 JOURNAL. All discussions for the June 1977 Discussion Section should be submitted by Feb. 1, 1977.

Publication costs of this article were assisted by the State University of Utrecht.

### REFERENCES

1. J. H. Kennedy, R. C. Miles, and J. Hunter, *This Journal*, **120**, 1441 (1973).
2. C. E. Derrington and M. O'Keefe, *Nature (London)*, *Phys. Sci.*, **246**, 44 (1973).
3. L. E. Nagel and M. O'Keefe, in "Fast Ion Transport in Solids," W. van Gool, Editor, p. 165, North Holland, Amsterdam-London (1973).

Table III. Activation enthalpies for conduction in the temperature region 300°-375°K

Electrolyte	$\Delta H$ (eV)	Reference
BiO <sub>0.09</sub> F <sub>2.82</sub>	0.39	(9)
$\beta\text{-PbF}_2\text{:AgF}$	0.20	(12)
$\alpha\text{-PbF}_2$	0.50, 0.51	(16)

4. R. W. Bonne and J. Schoonman, *Solid State Commun.*, **18**, 1005 (1976).
5. J. H. Kennedy and J. C. Hunter, *This Journal*, **123**, 10 (1976).
6. J. H. Kennedy and R. C. Miles, *ibid.*, **123**, 47 (1976).
7. C. Lucat, G. Campet, J. Claverie, J. Portier, J. M. Réau, and P. Hagenmuller, *Mat. Res. Bull.*, **11**, 167 (1976).
8. J. M. Réau, C. Lucat, G. Campet, J. Portier, and A. Hammon, *J. Solid State Chem.*, **17**, 123 (1976).
9. J. Schoonman, G. J. Dirksen, and R. W. Bonne, *Solid State Commun.*, **19**, 783 (1976).
10. B. Aurivillius and T. Lundqvist, *Acta Chem. Scand.*, **9**, 1209 (1955).
11. B. Aurivillius, *ibid.*, **9**, 1206 (1955).
12. R. W. Bonne and J. Schoonman, To be published.
13. J. Schoonman, G. A. Korteweg, and R. W. Bonne, *Solid State Commun.*, **16**, 9 (1975).
14. J. Schoonman and A. J. H. Macke, *J. Solid State Chem.*, **5**, 105 (1972).
15. A. V. Joshi and C. C. Liang, *J. Phys. Chem. Solids*, **36**, 927 (1975).
16. C. C. Liang and A. V. Joshi, *This Journal*, **122**, 466 (1975).

## Mechanism of Pit Initiation on Aluminum Alloy Type 7075

Steven Dallek\* and R. T. Foley\*\*

*Chemistry Department, The American University, Washington, D. C. 20016*

### ABSTRACT

The influence of anions on the initiation of pitting and the kinetics of pit growth on aluminum alloy Type 7075 has been investigated. The order of reaction (i.e., the number of anions per Al surface reaction site) and the energy of activation for pitting initiation have been measured in F<sup>-</sup>, Cl<sup>-</sup>, Br<sup>-</sup>, and I<sup>-</sup> solutions. The technique involved potentiostating the alloy in the range of anodic passivity, injecting a solution of halide ion, and recording the time,  $\tau$ , at which an exponential increase in corrosion current occurs. The slope of the plot of the logarithm of  $1/\tau$  vs. the logarithm of the concentration gives,  $n$ , the number of anions associated with an Al surface reaction site in the primary pitting initiation step. The value of  $n$  in 1N H<sub>2</sub>SO<sub>4</sub> varies with the anion as: for Cl<sup>-</sup>,  $n = 8$ ; for Br<sup>-</sup>,  $n = 4$ ; and for I<sup>-</sup>,  $n = 2$ . In an electrolyte of pH 5.8 the  $n$  value for Cl<sup>-</sup> is 2; for Br<sup>-</sup>, 2; and for F<sup>-</sup>, 3. The activation energies measured over the temperature range 5°-60°C in 1N H<sub>2</sub>SO<sub>4</sub> were: for Cl<sup>-</sup>,  $E_a = 18$  kcal mole<sup>-1</sup>; for Br<sup>-</sup>, 26 kcal mole<sup>-1</sup>; and for I<sup>-</sup>, 6.6 kcal mole<sup>-1</sup>. In an electrolyte of pH 5.8, the  $E_a$  is 12 kcal mole<sup>-1</sup> for Cl<sup>-</sup>; 10 kcal mole<sup>-1</sup> for Br<sup>-</sup>; and 4.6 kcal mole<sup>-1</sup> for F<sup>-</sup>. These results are interpreted in terms of the formation of transitory species akin to activated complexes, of specific composition, such as AlBr<sub>4</sub><sup>-</sup>.

The mechanism of the initiation of pitting of aluminum alloys is little understood but of vital concern, not only with respect to the corrosion of aluminum in various natural environments, but also in relation to special problems such as the stress corrosion cracking of high strength aluminum alloys. In the investigation reported here the influence of Cl<sup>-</sup>, Br<sup>-</sup>, I<sup>-</sup>, and F<sup>-</sup> ions on the initiation and kinetics of pitting of aluminum alloy Type 7075 is studied over a wide range of temperature and concentration.

Engell and Stolica (1), and later Hoar and Jacob (2), devised a technique to measure the kinetics of breakdown of passivity of iron and stainless steel by halide ions. This technique was applied to aluminum alloys by Bogar and Foley (3), and Foroulis and Thubrikar (4). In this technique the metal electrode is held potentiostatically in the passive range in an appropriate electrolyte, a specific concentration of chloride is injected, and the induction time,  $\tau$ , for a sharp rise in current is recorded. In the previous investigations the rise in current is correlated with the breakdown of passivity and initiation of pitting. Further, from this induction time it is possible to arrive at the order of reaction,  $n$ , the number of chloride ions associated with the dissolution of a single aluminum atom, and the energy of activation,  $E_a$ . The reasoning proceeds as follows. The reciprocal of the induction time,  $1/\tau$ , is taken as the rate of pit initiation, i.e., the number of events per unit time. The rate equation is then

$$\left(\frac{1}{\tau}\right) = k[\text{Al}]^m[\text{X}^-]^n \quad [1]$$

wherein  $k$  is the rate constant,  $[\text{Al}]$  is the aluminum atom concentration,  $[\text{X}^-]$  is the halide ion concentration, and  $m$  and  $n$  are the respective orders of reaction. The activity coefficients are included in  $k$ . The logarithm form of [1] is

$$\log\left(\frac{1}{\tau}\right) = \log k + m \log [\text{Al}] + n \log [\text{X}^-] \quad [2]$$

Thus, if  $k$  and  $[\text{Al}]$  are taken as constant, then the plot of  $\log(1/\tau)$  vs.  $\log[\text{X}^-]$  will give  $n$ , the order of reaction with respect to X<sup>-</sup> ions. We now have reason to think that the term  $m \log [\text{Al}]$  is only constant for a specific halide reaction and that  $m$  is equivalent to the number of atoms involved in a surface reaction site, i.e., the coordination number of the surface in the sense used by Laidler and others in their development of the theory of absolute rate of surface reactions (5). At constant halide concentration,  $(1/\tau)$  will be proportional to the rate constant and

$$\left(\frac{1}{\tau}\right) = A e^{-E_a/RT} \quad [3]$$

Thus a conventional Arrhenius plot of  $\log(1/\tau)$  vs. the reciprocal of the temperature will yield the apparent activation energy for the initiation process.

These studies have been made within the broad context of examination of the complex ion theory of cor-

\* Electrochemical Society Student Member.

\*\* Electrochemical Society Active Member.

Key words: corrosion pitting, aluminum, passivity, chlorides, bromides.

rosion (6). This theory postulates that the role of an anion in a corrosion process may be explained by the direct participation of the anion in the elemental process of metal dissolution. The anion reacts with the metallic ion and the chemical nature of the resultant complex dictates whether the metal will dissolve or achieve a passive state.

### Experimental

The experiments were conducted in an electrolytic cell containing a specially designed Teflon electrode holder, a Hg/Hg<sub>2</sub>SO<sub>4</sub> reference electrode, a Luggin capillary, and a counterelectrode which was separated from the rest of the cell by a fine porosity glass frit. Stirring was provided by a submersible water-powered magnetic stirrer. The cell was thermostated to  $\pm 0.1^\circ\text{C}$  with a refrigerated and heated water bath. Experiments were conducted over the range of  $5^\circ\text{--}60^\circ\text{C}$ .

The potential of the working electrode was controlled by an Anotrol Model 4100 research potential controller; a Keithley Model 600A electrometer was used for an accurate measurement of the potential of the working electrode. The current was recorded on a Sargent Model SRL recorder.

Samples of aluminum alloy Type 7075-T6 were cut into circular samples for electrodes with an area of 0.637 cm<sup>2</sup> when mounted in a special Teflon electrode mount (7). The samples were cleaned by conventional procedures and, following cleaning, were allowed to stand for 24 hr in a desiccator.

In a typical experiment, the sample was allowed to come to equilibrium at a preset temperature. The potential of the working electrode was then set at a value (usually +0.18V) in the passive anodic range as determined by a polarization study of the sample. From the polarization curve run on the alloy prior to the experiment, a point was taken midway in the flat portion (steady-state current) of the curve. Thus, the starting point of the pitting experiment was always the same distance from the open-circuit potential but well above the critical potential. After the resulting passive anodic dissolution current (usually in the microampere range) was recorded for a specific duration (6 min), a solution containing the aggressive anion of known concentration was rapidly injected into the cell with an all-glass syringe. The time required for a sharp continuous rise in current above the steady-state dissolution current was recorded as the induction time,  $\tau$ , for pit initiation.

Most workers in the field recognize the statistical nature of pitting initiation and agree that impurities, flaws, or defects in the oxide film may play a role in pit initiation. Videm (8), in his aluminum pitting studies, concluded that differences from specimen to specimen usually make it difficult to obtain satisfactory reproducibility of pit initiation studies. In order to improve the reproducibility, a technique similar to that used by Videm (8) was used for screening "unsuitable" samples. Thus, following a uniform surface treatment, the sample was held at the predetermined anodic potential, and the resulting passive anodic dissolution current was recorded for a specific duration of time. An unstable current was observed with those samples which possessed certain surface abnormalities and these samples were thus discarded. An abnormal "leakage" current, usually characterized by the generation of current pulses, a form of oscillatory behavior connected with pitting corrosion, was thus used to sort out abnormal samples.

### Results

Following the initiation of the pit, the current rises rapidly and the current is a measure of the faradaic reactions associated with pit growth. Three types of current-time curves have been observed. The first is a smooth curve wherein the current increases exponen-

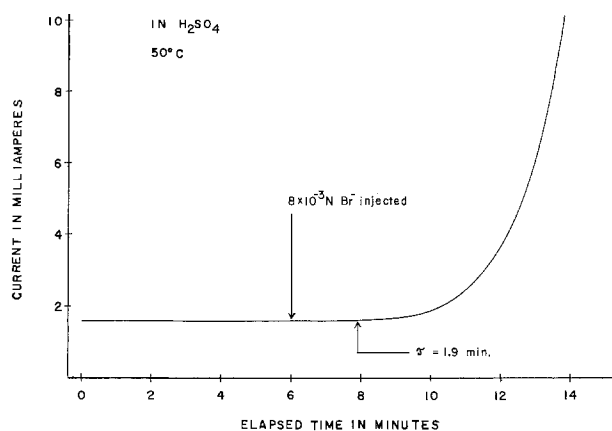


Fig. 1. Pitting initiation curve. Electrolyte, 1N H<sub>2</sub>SO<sub>4</sub>, 50°C,  $8 \times 10^{-3}\text{N Br}^-$  injected after 6 min.

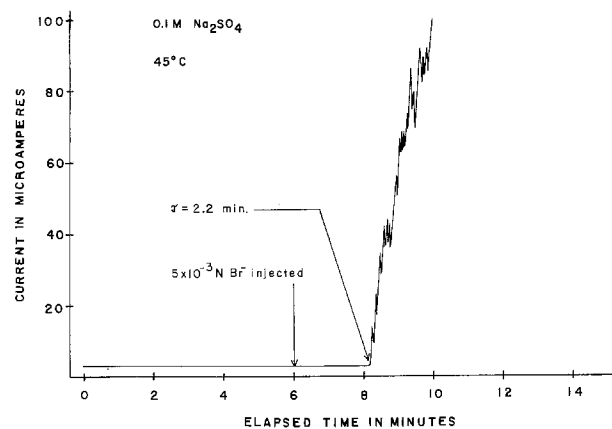


Fig. 2. Pitting initiation curve. Electrolyte, 0.1M Na<sub>2</sub>SO<sub>4</sub>, 45°C,  $5 \times 10^{-3}\text{N Br}^-$  injected after 6 min.

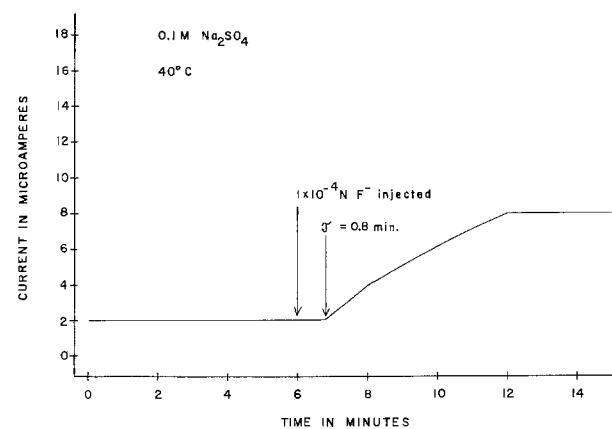


Fig. 3. Pitting initiation curve. Electrolyte, 0.1M Na<sub>2</sub>SO<sub>4</sub>, 40°C,  $1 \times 10^{-4}\text{N F}^-$  injected after 6 min.

tially, illustrated in Fig. 1<sup>1</sup> by the reaction of Br<sup>-</sup> ion in 1N H<sub>2</sub>SO<sub>4</sub> at 50°C. The second type of behavior is illustrated in Fig. 2 by the reaction of Br<sup>-</sup> ion in 0.1M Na<sub>2</sub>SO<sub>4</sub> (pH 5.80) at 45°C. This "ragged" curve is favored by the neutral solution and lower temperature, e.g., below 35°C. It is interpreted as resulting from a dynamic dissolution-repassivation process. The third type of behavior was shown by F<sup>-</sup> ion in 0.1M Na<sub>2</sub>SO<sub>4</sub> at 40°C (Fig. 3). The current instead of increasing ex-

<sup>1</sup> In this and similar figures, it is difficult to see the time at which the sharp rise in current occurs. However, on the original lined chart paper, it is quite obvious. Between 6 and 8 on the abscissa there are 20 divisions so that the rise in current can be set within a few seconds.

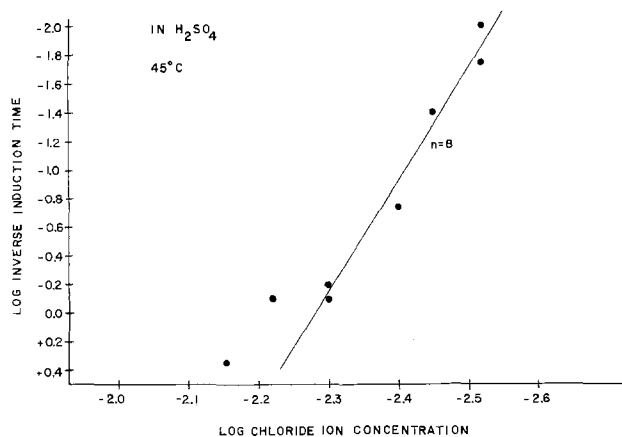


Fig. 4. Order of reaction plot. Electrolyte, 1N H<sub>2</sub>SO<sub>4</sub>, 45°C,  $n = 8$ .

ponentially reaches a plateau, and this is associated with the formation of a compound on the aluminum surface. It appears reasonable that the shape of the curve and the mathematical equation describing the current-time behavior is related to the geometric shape of the pits and this is now being pursued.

The slope of a plot of  $\log(1/\tau)$  vs.  $\log$  of the halide concentration yields  $n$ , the order of the reaction with respect to the halide ion concentration. In Fig. 4, a plot of the log of the inverse of the induction time in 1N H<sub>2</sub>SO<sub>4</sub> (pH 0.3) at 45°C vs.  $\log[\text{Cl}^-]$  yields an  $n$  value of 8. This approximates the value reported previously (3) for aluminum alloy Type 2024 in a 1.0N H<sub>2</sub>SO<sub>4</sub> electrolyte. A similar plot for the results in 0.1M Na<sub>2</sub>SO<sub>4</sub> (pH 5.80) yields an  $n$  value of 2, much lower than that observed in acid solution. This agrees reasonably well with the results reported by Foroulis and Thubrikar (4) who measured the induction time of a 99.99% aluminum sample at a pH of 5.9-6.1 and obtained an  $n$  of approximately 1.

A similar trend in reaction order was observed with Br<sup>-</sup> ion. In 1N H<sub>2</sub>SO<sub>4</sub> at 50°C,  $n = 4$ ; in 0.1M Na<sub>2</sub>SO<sub>4</sub> (pH 5.80) at 45°C,  $n = 2$ .

The reaction order for fluoride ion was only measured in 0.1M Na<sub>2</sub>SO<sub>4</sub>. From the plot at 50°C shown in Fig. 5, a value of  $n = 3$  was obtained, the reaction differing stoichiometrically from that of the Cl<sup>-</sup> and Br<sup>-</sup> ion.

The reaction order for I<sup>-</sup> is lower than that of the other halides. A plot from data at 23°C in 1N H<sub>2</sub>SO<sub>4</sub> yields an  $n$  value of about 2. These results coupled with the low activation energy, suggest a weaker type of binding.

The reaction orders are summarized for the different halides in Table I.

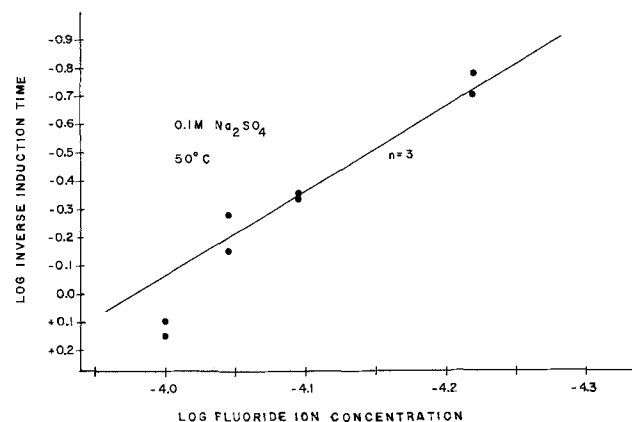


Fig. 5. Order of reaction plot. Electrolyte, 0.1M Na<sub>2</sub>SO<sub>4</sub>, 50°C,  $n = 3$ .

Table I. Order of reaction ( $n$ ) for halides with aluminum alloy Type 7075

Anion	$n$ pH of electrolyte	
	0.3	5.8
F <sup>-</sup>	—	3
Cl <sup>-</sup>	8	2
Br <sup>-</sup>	4	2
I <sup>-</sup>	2	—

The apparent energy of activation,  $E_a$ , may be calculated from the slope of the  $\log(1/\tau)$  vs.  $1/T$  plot if the halide concentration is held constant. Such Arrhenius-type plots are shown in Fig. 6 and 7 for constant [Cl<sup>-</sup>] in 1N H<sub>2</sub>SO<sub>4</sub> and 0.1M Na<sub>2</sub>SO<sub>4</sub>, respectively. The apparent energy of activation goes from 18 to 12 kcal in going from an acid to neutral solution. A similar trend was observed with Br<sup>-</sup> ion. The reaction in acid solution had a high  $E_a$ , 26 kcal, as compared with 10 kcal in the neutral solution. The activation energy for the I<sup>-</sup> ion reaction was low, 6.6 kcal, and the temperature-dependence plot showed considerable scatter. The temperature dependence of the F<sup>-</sup> ion reaction calculated from the corresponding Arrhenius-type plot contrasted with the other halides with a low activation energy,  $E_a = 4.6$  kcal.

The activation energies for the halide reactions are summarized in Table II.

A comparison of the induction times with the four halides allows for qualitative measure of the "aggressive" character of the halide. Thus the concentration of Br<sup>-</sup> required for a comparable induction time is about 2 times the Cl<sup>-</sup> concentration; the I<sup>-</sup>, 10 times; and the F<sup>-</sup> about 0.01 times.

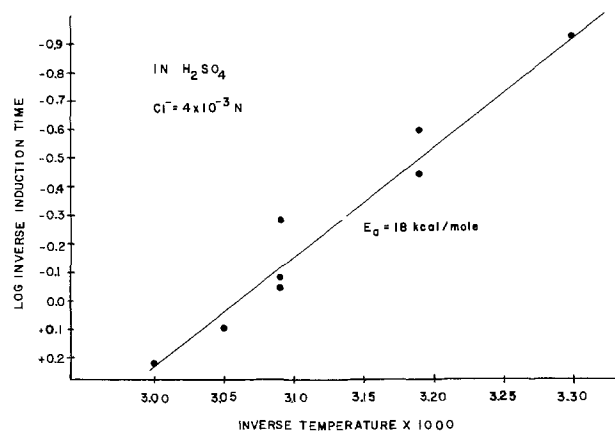


Fig. 6. Energy of activation plot. Electrolyte, 1N H<sub>2</sub>SO<sub>4</sub>, [Cl<sup>-</sup>] =  $4 \times 10^{-3}$ N;  $E_a = 18$  kcal.

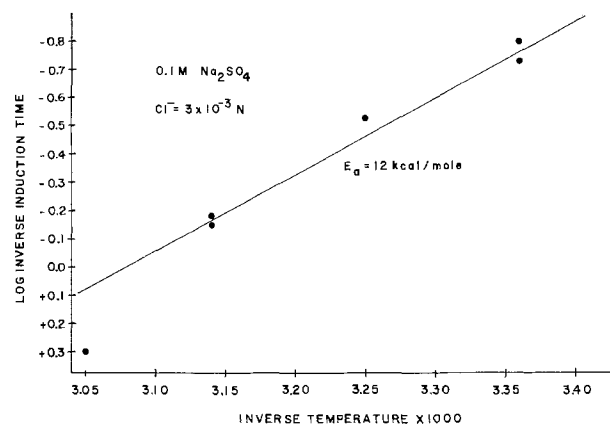


Fig. 7. Energy of activation plot. Electrolyte, 0.1M Na<sub>2</sub>SO<sub>4</sub>, [Cl<sup>-</sup>] =  $3 \times 10^{-3}$ N;  $E_a = 12$  kcal.

Table II. Activation energies for pitting initiation reaction of aluminum alloy Type 7075 with halides

Anion	$E_a$ (kcal mole <sup>-1</sup> )	
	pH 0.3	pH 5.8
F <sup>-</sup>	—	4.6
Cl <sup>-</sup>	18	12
Br <sup>-</sup>	26	10
I <sup>-</sup>	6.6	—

Following the pit initiation experiment, the specimens were examined microscopically. In general, the predominant shape of the pits was hemispherical. For aluminum alloy Type 7075, the pits produced in Cl<sup>-</sup> solutions were almost perfectly hemispherical, while those formed in Br<sup>-</sup> and I<sup>-</sup> solutions were more irregularly shaped. Pits produced in acid solution were more nearly hemispherical than those formed in near-neutral solution. For aluminum alloy Type 1199, on the other hand, both Cl<sup>-</sup> and Br<sup>-</sup> solutions produced perfectly hemispherical pits.

### Discussion

The contemporary thinking regarding the mechanism by which chloride ions break down passivity and initiate pitting has been recently summarized by Foroulis and Thubrikar (4). The prevalent explanations include the following: (i) penetration of the oxide film by Cl<sup>-</sup> ion; (ii) competitive adsorption of Cl<sup>-</sup> rather than OH<sup>-</sup> or O<sub>2</sub> on metal surface; (iii) migration of Cl<sup>-</sup> ions inward through the (passive) oxide lattice; (iv) peptization of the oxide film by adsorbed anions; (v) a dynamic breakdown-repair mechanism.

These authors pointed out that these concepts are inconsistent with their results on the kinetics of breakdown of passivity of preanodized aluminum by chloride ions and proposed the following two-step process. *Step 1.* Adsorption of Cl<sup>-</sup> on the oxide-solution interface under the influence of the electric field; the surface sites available for adsorption existing on the hydrated oxide surface rather than on the base metal surface. *Step 2.* Formation of a basic hydroxy chloride aluminum salt which is readily soluble.

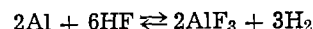
The results of the present study reaffirm the stoichiometric and chemical nature of the pitting initiation process as distinguished from continuous adsorption and oxide penetration processes traditionally associated with the breakdown of passivity. The technique used in the present investigation does not give information regarding the surface site at which pitting could be initiated, that is, the Al in Eq. [1] above could be in the aluminum alloy metallic lattice, or it could be an Al ion in the hydrated oxide lattice. Foroulis and Thubrikar (4) with their experiments with varying oxide thicknesses offer convincing evidence that the particular Al ion exists in the oxide lattice at the oxide-electrolyte interface.

The technique used here, on the other hand, does give definite information on the number of halide ions associated with the surface site and the energy of this reaction.

It is postulated that the initial step in the pitting of the Al alloy by Cl<sup>-</sup> ion in acid solution is the formation of the complex, Al<sub>2</sub>Cl<sub>8</sub><sup>=</sup>. Thus the reaction site involves two Al ions, and an activation energy of 18 kcal is commensurate with chemisorption or chemical reaction. In a similar fashion, a complex of AlBr<sub>4</sub><sup>-</sup> forms with Br<sup>-</sup> ion, also with a high activation energy. The large iodide ion is involved in a low energy process (6.6 kcal), very likely the physical adsorption of one or two I<sup>-</sup> ions per surface site. A consistent picture is drawn for the results in neutral solution wherein reaction orders of two were observed for the Br<sup>-</sup> ion and the Cl<sup>-</sup> ion. Complexes of the type Al(OH)<sub>2</sub>(Cl)<sub>2</sub><sup>-</sup> and Al(OH)<sub>2</sub>(Br)<sub>2</sub><sup>-</sup> are postulated, and, for such complexes, the activation energy is appreciably lower, in

agreement with previous reports wherein values of 12 kcal (3) and 6.7 kcal (4) were reported for pure Al at a pH of 6 in Cl<sup>-</sup> electrolytes. In nearly neutral solution, fluoride ion exhibits a reaction order of three, consistent with the formation of AlF<sub>3</sub> which has been reported as a stable species in aqueous solutions (9).

These results are consistent with observations on the complexing behavior of aluminum previously reported. The halides of aluminum (except F<sup>-</sup>) are dimeric in organic solvents such as benzene. Structures for the dimeric forms of Al<sub>2</sub>Cl<sub>6</sub> and Al<sub>2</sub>Br<sub>6</sub> are given by Durrant and Durrant (9). This dimeric formation has been attributed to the tendency of the aluminum atoms to complete their octets. Recently, Peled and Gileadi (10) reported the presence of the anions, Al<sub>2</sub>Br<sub>7</sub><sup>-</sup> and AlBr<sub>4</sub><sup>-</sup>, by measuring transference numbers of species formed by dissolving AlBr<sub>3</sub> and MBr (M = alkali metal or ammonium ion) in hydrocarbons. Morrey and Moore (11) reported the presence of the complex ions, AlCl<sub>4</sub><sup>-</sup> and Al<sub>2</sub>Cl<sub>7</sub><sup>-</sup>, in a KCl-AlCl<sub>3</sub> solvent (fused salt). All six fluoride species, i.e., AlF<sup>++</sup>, AlF<sub>2</sub><sup>+</sup>, AlF<sub>3</sub>, AlF<sub>4</sub><sup>-</sup>, AlF<sub>5</sub><sup>=</sup>, AlF<sub>6</sub><sup>=</sup>, have been reported to exist and their stability constants are given by Bjerrum (12). AlF<sub>3</sub> is reported as a stable species in aqueous solution (13). Katoh (14) has identified the products, AlF<sub>3</sub> · 3H<sub>2</sub>O and AlF<sub>3</sub> · H<sub>2</sub>O, by x-ray analysis of a sample corroded in NaF solution. Zotikov *et al.* (15) studied the corrosion of aluminum in hydrofluoric acid with varying water content and reported the formation of AlF<sub>3</sub> according to the reaction



The AlF<sub>3</sub> formed various hydrates such as AlF<sub>3</sub> · 3H<sub>2</sub>O.

Considering the relative concentrations of the ions, it would be expected that, except for the fluoride compound which forms an insoluble compound on the electrode, these complexes will be intermediates in a stepwise process that terminates eventually with the formation of the hydrated oxide film of aluminum. Thus, the halide ions operate as catalysts being regenerated by the hydrolysis of the hydroxy halide or halide complex. This accounts for the considerable pitting that occurs in dilute solutions, e.g., 10<sup>-3</sup>N.

These findings are consistent with the complex ion theory of corrosion (6). The anions function in a specific manner forming chemical species whose stabilities determine the subsequent behavior of the metal, be it accelerated dissolution or repassivation.

### Acknowledgments

The support of the Office of Naval Research under Contract N 00014-75-C-0799, NR 036-106 is gratefully acknowledged.

Manuscript submitted March 8, 1976; revised manuscript received Aug. 6, 1976.

Any discussion of this paper will appear in a Discussion Section to be published in the June 1977 JOURNAL. All discussions for the June 1977 Discussion Section should be submitted by Feb. 1, 1977.

Publication costs of this article were assisted by The American University.

### REFERENCES

- H. Engell and N. Stolica, *Z. Phys. Chem. (N.F.)*, **20**, 113 (1959).
- T. P. Hoar and W. R. Jacob, *Nature*, **216**, 1299 (1967).
- F. D. Bogar and R. T. Foley, *This Journal*, **119**, 462 (1972).
- Z. A. Foroulis and M. J. Thubrikar, *ibid.*, **122**, 1296 (1975).
- K. J. Laidler, "Chemical Kinetics," 2nd ed. p. 286, McGraw-Hill, New York (1965).
- R. T. Foley, *This Journal*, **122**, 1493 (1975).
- J. Myers, E. Gruenler, and L. Smulczenski, *Corrosion*, **24**, 352 (1968).
- K. Videm, "The Electrochemistry of Uniform Cor-

- rosion and Pitting of Aluminum," Kjeller Report-149, Kjeller, Norway (1974).
9. P. J. Durrant and B. Durrant, "Advanced Inorganic Chemistry," 2nd ed., Longman Group, Limited, London (1970).
  10. E. Peled and E. Gileadi, *This Journal*, **123**, 15 (1976).
  11. J. R. Morrey and R. H. Moore, *J. Phys. Chem.*, **67**, 748 (1963).
  12. J. Bjerrum, "Stability Constants," The Chemical Society, London (1958).
  13. F. A. Cotton and G. Wilkinson, "Advanced Inorganic Chemistry," p. 438, Interscience Publishers, New York (1967).
  14. M. Katoh, *Corros. Sci.*, **8**, 423 (1968).
  15. V. S. Zotikov, G. B. Bakhutova, N. A. Bocharova, and E. Ya. Semenyuk, *Zashch. Met.*, **10**, 164 (1974).

## Periodic Phenomena during Anodic Dissolution of $\text{Mo}_4\text{O}_{11}$ Single Crystals

R. M. Peekema\* and M. W. Shafer

IBM Thomas J. Watson Research Center, Yorktown Heights, New York 10598

### ABSTRACT

The electrochemical behavior of  $\text{Mo}_4\text{O}_{11}$  single crystals has been studied and periodic phenomena were observed during anodic dissolution in 1M  $\text{H}_2\text{SO}_4$ . These periodic effects were observed only on the (100) face, and are associated with a 12.3Å periodicity in the crystal structure along the [100] direction, where alternating layers of Mo(IV) and Mo(VI) species are found. A mechanism involving the slow chemical dissolution of Mo(VI) species and the rapid electrochemical dissolution of Mo(IV) species is offered, and is consistent with the experimental data. To the best of our knowledge, this is the first reported correlation of a periodic electrochemical effect with a periodicity in the crystal structure.

Periodic effects in electrochemical systems are not uncommon (1, 2) and usually are a result of a relaxation of a disturbed system toward an equilibrium or steady-state condition. While studying the electrochemical behavior of the molybdenum oxides, we observed periodic fluctuations in the dissolution current when the (100) face of a single crystal of  $\text{Mo}_4\text{O}_{11}$  was made anodic in acid solution. We have studied these oscillations in detail and in this paper we show that they are related to a periodicity in the crystal structure rather than to a relaxation phenomena.

### Experimental

The  $\text{Mo}_4\text{O}_{11}$  crystals were prepared at 800°C in sealed evacuated quartz tubes containing stoichiometric amounts of Mo and  $\text{MoO}_3$  powders, using small amounts of iodine as the transporting agent. Crystals with faces of 1-2  $\text{cm}^2$  have been grown by this method. A more detailed discussion of the preparative conditions and of the crystal properties is given elsewhere (3).

The electrochemical measurements were carried out using a Wenking potentiostat with a Wavetek function generator to obtain cyclic voltage sweeps, and an X-Y recorder to record the voltammograms. A Keithley digital electrometer was used to isolate the reference electrode from any voltage measuring or plotting circuitry, and a Keithley Picoammeter was placed in series with the working electrode to measure the currents. A Fluke constant current supply replaced the potentiostat when galvanostatic measurements were desired.

A three-compartment cell was used, with the working electrode, the reference electrode, and the counter-electrode each in a separate compartment. Most of the work was carried out in a cell where the three compartments were separated by 10 mm fine porosity (10F) fritted Pyrex disks. The working electrode compartment usually contained 5-15 ml of electrolyte, which was deaerated or agitated as necessary by ad-

mitting helium gas (without any pretreatment) through a 10F fritted Pyrex disk in the cell bottom. The crystal surface was mounted in a vertical position.

Reference electrodes were either mercury-mercurous sulfate in 1M  $\text{H}_2\text{SO}_4$  (MSE) or mercury-mercuric oxide in 1M KOH (MOE). All voltages are referenced to the normal hydrogen electrode (NHE). Solutions were made from reagent grade chemicals and deionized water, and were used without further purification or preelectrolysis. Crystal samples were usually mounted on gold disks, sometimes using indium solder to improve the electrical contact. Some samples were connected to gold wires by a silver-filled epoxy. The unwanted crystal faces and sample supporting areas were masked off with MICCROSTOP.<sup>1</sup> Specimen areas were measured graphically from a photomicrograph taken normal to the surface of a masked-off crystal face, using calibration factors obtained by photographing a rule at the same magnification.

### Results and Discussion

Periodic fluctuations in the anodic dissolution current for an  $\text{Mo}_4\text{O}_{11}$  crystal are shown in Fig. 1. This is a trace of a linear voltage sweep on the (100) face of a single crystal  $\text{Mo}_4\text{O}_{11}$  specimen in 1M  $\text{H}_2\text{SO}_4$ . Similar fluctuations occur in the voltage after a galvanostatic step, as shown in Fig. 2. A similar effect (not shown) is noted in the current after a potentiostatic step. The periodic effect in the voltammetry curve was observed to be dependent on scan rate and this is summarized in Table I.

The values for the period in Table I are given at a specified voltage (0.70V vs. NHE) because during the linear voltage sweep both the current and period change with potential. However, it is apparent from Table I that the period for the current fluctuations in the region of 0.7V is essentially constant at approximately 1 sec, over nearly an order of magnitude change in sweep rate. At higher sweep rates, one sees fewer peaks in the current over the same region of poten-

\* Electrochemical Society Active Member.

Key words: molybdenum oxide electrochemistry, dissolution, periodic phenomena,  $\text{Mo}_4\text{O}_{11}$  crystals.

<sup>1</sup>This is an electroplating mask-off material from Michigan Chrome and Chemical Company, Detroit, Michigan.

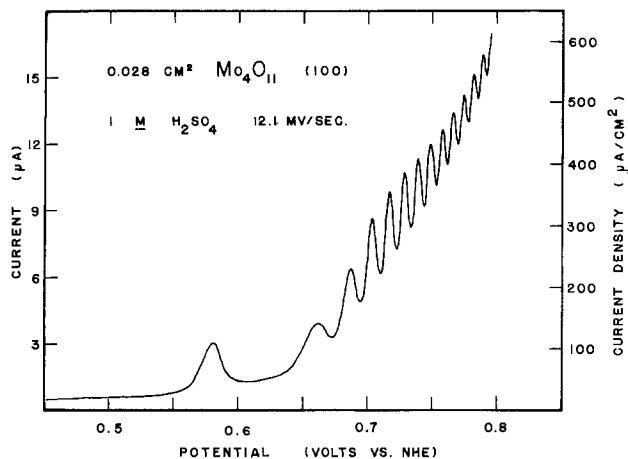


Fig. 1. Linear sweep voltammety of (100) face of  $\text{Mo}_4\text{O}_{11}$  single crystal.

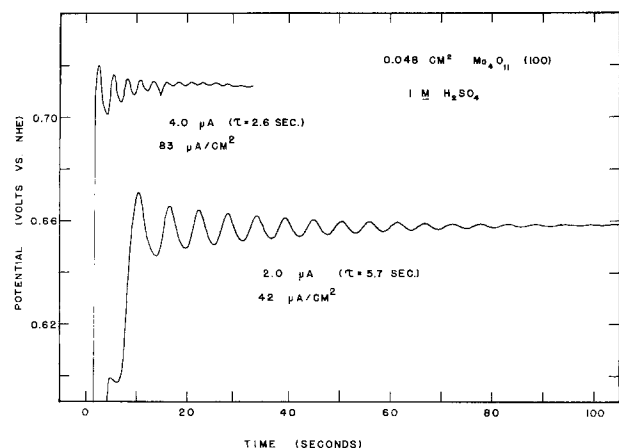


Fig. 2. Potential response to a current step of (100) face of  $\text{Mo}_4\text{O}_{11}$  single crystal.

tial, and in general the peaks are not as sharply defined. The conditions selected for Fig. 1, namely 12 mV/sec, were chosen because the magnitude of the current fluctuations is most effectively displayed and measured under those conditions. The constant current conditions in Fig. 2 show clearly that the period is nearly constant at a given current. Table II shows that  $Q$ , the charge density per period (the product of the current density and the period), is reasonably constant.

The magnitude of the periodic effects in general decreased with time and with cycling of the samples through the potential region of anodic dissolution. Table III summarizes the influence of other electrolytes on the periodic phenomena. As noted, the periodic effects in 1M perchloric acid disappeared after three

Table I. Effect of scan rate on periodic currents

Scan rate mV/sec	Peak separation mV (at 0.7V)	Period (at 0.7V) (sec)
65	~70	1.1
12.1	~12	1.0
7.7	~8	1.0

Table II. Galvanostatic periodic effects\*

$I$ ( $\mu\text{A}/\text{cm}^2$ )	$\tau$ (sec)	$Q$ ( $\mu\text{C}/\text{cm}^2$ )
83	2.6	217
42	5.7	238

\* See Fig. 2.

Table III. Anodic dissolution of  $\text{Mo}_4\text{O}_{11}$  (100) in various electrolytes

Electrolyte (1.0M)	Periodic effect?
$\text{H}_2\text{SO}_4$	Yes
$\text{HClO}_4$	Yes*
$\text{HCl}$	Yes
$\text{H}_3\text{PO}_4$	Yes
$\text{KOH}$	No

\* Disappears after three scans.

scans. The periodic effects did return on that same sample after it was returned to sulfuric acid and cycled several times. Further, no periodic effects were observed in 1M, KOH solution.

In order to explain the origin of these fluctuations it is necessary to consider the crystal structure of  $\text{Mo}_4\text{O}_{11}$ . This molybdenum oxide is one of five distinct oxide phases between  $\text{MoO}_2$  and  $\text{MoO}_3$  whose crystal structures have been determined by Magneli (4) and Kihlberg (5). They describe the structure of  $\text{Mo}_4\text{O}_{11}$  as being similar to the  $\text{ReO}_3$ -type structure. In this structure, shown in Fig. 3A, the  $\text{MoO}_6$  octahedra are linked exclusively at the corners. However,  $\text{Mo}_4\text{O}_{11}$  is oxygen deficient when compared to the pure  $\text{ReO}_3$ -type, and to allow for this deficiency a certain fraction of the molybdenums is tetrahedrally coordinated ( $\text{MoO}_4$ ). The arrangement of the  $\text{MoO}_6$  and  $\text{MoO}_4$  polyhedra is shown in Fig. 3B. It is seen that this structure is basically comprised of  $\text{ReO}_3$ -type slabs (the lightly shaded diamond-shaped polyhedra), which represent the  $\text{MoO}_6$  octahedra, joined together by black and heavily hatched triangles, representing the  $\text{MoO}_4$  tetrahedra at two levels. Since the slabs extend infinitely in the vertical direction and perpendicular to the plane of the

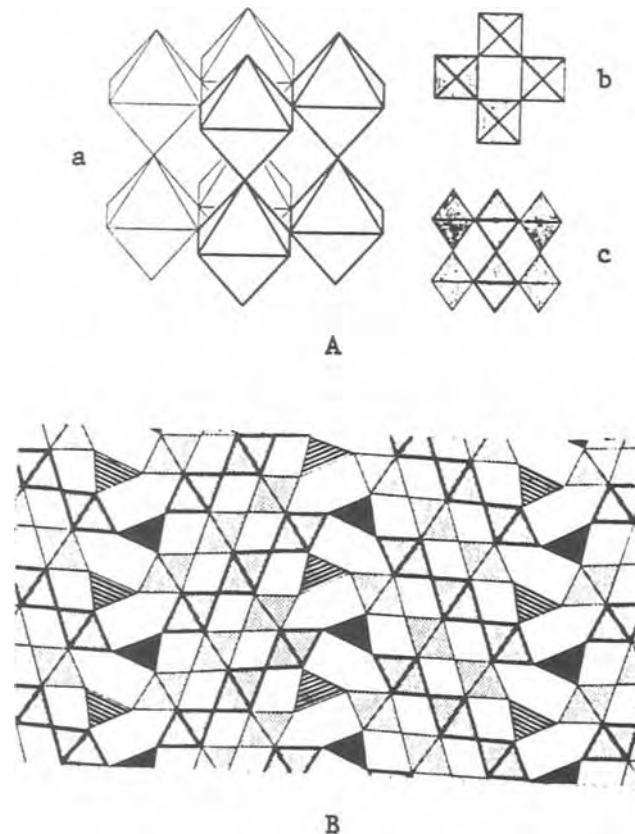


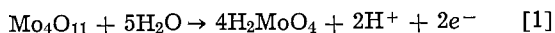
Fig. 3. (A) The octahedra arrangement in the  $\text{ReO}_3$ -type structure: (a) the octahedra arrangement as seen in perspective; (b) top view of (a); (c) side view of (a). (B) The crystal structure of  $\text{Mo}_4\text{O}_{11}$  viewed along the b axis. The relationship to the  $\text{ReO}_3$ -type structure is seen by comparing the linked octahedra to those shown in Fig. 3A (c).



paper, there is a distinct periodicity of the ReO<sub>3</sub> slabs normal to the [100]. The periodicity, *i.e.*, the distance between the interconnecting MoO<sub>4</sub> tetrahedra, is about 12.3Å, which is half of the *a*<sub>0</sub> dimension of the orthorhombic cell (*a*<sub>0</sub> = 24.49, *b* = 5.45, and *c* = 6.95). We have measured the electrical resistivity of Mo<sub>4</sub>O<sub>11</sub> by the four-probe method and find it to be  $2 \times 10^{-4} \Omega\text{-cm}$  at room temperature (3, 6). There was no evidence of anisotropy in the resistivity.

The observed current oscillations correlate well with the structural periodicity. Table IV shows the integrated charge associated with each of the current peaks shown in Fig. 1. A correction for charging current was made by extrapolating the base current in the region of 0.45-0.55V. As can be seen from Table IV, the charge associated with each peak is relatively constant, and amounts to some 260  $\mu\text{C}/\text{cm}^2$ . In addition, Table II shows a fairly constant charge per fluctuation, under constant current conditions, of approximately 230  $\mu\text{C}/\text{cm}^2$ . The charge per period of approximately 230  $\mu\text{C}/\text{cm}^2$  on that particular crystal is similar to the value shown in Table IV, obtained under potentiostatic conditions.

Based on the crystal density of 4.12  $\text{g}/\text{cm}^3$ , and complete oxidation of the oxide to Mo(VI) as given in Eq. [1]



we calculate the amount of charge consumed in oxidizing a 12.3Å layer to be 174  $\mu\text{C}/\text{cm}^2$ . This is some 50% less than the experimental values. To test the validity of Eq. [1] we measured the equivalent weight by observing the weight lost from a crystal during the passage of a known charge. Table V shows the observed equivalent weights for several different experiments, which are in excellent agreement with the expected value of 280  $\text{g}/\text{equiv}$ .

These equivalent weight results establish that the anodic dissolution of Mo<sub>4</sub>O<sub>11</sub> takes place according to Eq. [1], and that the charge associated with each 12.3Å layer is 174  $\mu\text{C}/\text{cm}^2$ . Observed values of charge per period range from 217 to 280  $\mu\text{C}/\text{cm}^2$ . We feel that this excess of charge is accounted for by undercutting of the mask-off and by nonuniform dissolution of the crystal face; both are effects which would increase the charge observed per period. Undercutting of the mask-off has been confirmed by surface profile measurements after mask-off removal, where observed surface discontinuities were less than one-third those expected from coulometric and weight loss calculations. Further,

Table IV. Charge associated with current peaks in Fig. 1

Peak No.	Q ( $\mu\text{C}/\text{cm}^2$ )
1	164
2	244
3	244
4	255
5	241
6	252
7	257
8	255
9	258
10	284
11	265
12	284
13	288
Average (2-13)	261 $\mu\text{C}/\text{cm}^2$

Table V. Equivalent weight by weight loss

Run No.	Wt loss ( $\mu\text{g}$ )	Anodic charge (mC)	Equiv. wt ( $\text{g}/\text{equiv}$ .)
1*	1320	450	283
2*	188	60	302
3**	266	90	285
4**	696	240	280

\* Runs 1 and 2 on multicrystal chunk.  
 \*\* Runs 3 and 4 on (100) face of single crystal.

subsequent microscopic examinations and surface profile measurements of crystal surfaces that had been covered by mask-off during the dissolution showed definite evidence of attack. One would expect relatively less undercutting at higher current densities, and the *Q* values in Table II are consistent with this view. Non-uniform dissolution was apparent in scanning electron microscope examination of surfaces exposed to anodic treatment, and by visual observation the smooth crystal facet was converted to a matte finish by extended dissolution.

The above evidence shows that the observed oscillations can be correlated with the periodic nature of the crystal structure. Further support of this conclusion is obtained by looking at the anodic dissolution of other crystal orientations of Mo<sub>4</sub>O<sub>11</sub> where there is no structural periodicity normal to the face being dissolved. The (111) is such a face and it is seen in Fig. 4 that there is no evidence of the oscillations seen in Fig. 1. We have examined a number of different crystals, looking at the (100) and (111) faces, and in all cases the oscillations are seen on the former and not the latter.

There is some evidence that not all the current need follow the reaction of Eq. [1]. We have observed the appearance of a deep blue solution and an EPR signal when Mo<sub>4</sub>O<sub>11</sub> is anodically dissolved at high current densities. Both these observations suggest the presence of some Mo(V) species, which is probably in solution. Since both EPR and colorimetric methods are highly sensitive for detecting the Mo(V) species it is likely that only a small fraction of the dissolution occurs via a reaction where the  $\text{Mo(IV)}_{\text{crystal}} \rightarrow \text{Mo(V)}_{\text{solution}}$ .

Let us now consider a dissolution mechanism which satisfactorily explains the above data. Assume that Mo<sub>4</sub>O<sub>11</sub> is a mixed oxide containing Mo(IV) and Mo(VI) in the ratio of 1:3.<sup>2</sup> We expect that all tetrahedral sites are occupied by Mo(VI) since it is a smaller ion than Mo(IV). Further, there is good evidence, from the Mo-O bond distances of the MoO<sub>6</sub> octahedra, that the Mo<sup>4+</sup> ions are found in the centers of the "ReO<sub>3</sub>-type" slabs rather than in those octahedra which connect to the tetrahedra. If the Mo-O distances (5) of the various types of octahedra are examined, it is seen that those octahedra which are on the "outer surfaces of the slabs" (Fig. 3B) are badly distorted, *i.e.*, their Mo-O distances vary by 0.45Å, while those in the center are more regular with variations of only 0.2Å. A comparison of the radius ratios,  $r_{\text{Mo(IV)}}/r_{\text{O}}$  and  $r_{\text{Mo(VI)}}/r_{\text{O}}$ , shows that the former (0.5) is more favor-

<sup>2</sup> Even though metallic type conductivity is seen in Mo<sub>4</sub>O<sub>11</sub> from which it could be inferred that the molybdenums would be completely nonlocalized, our ESCA measurements show very clearly that both Mo(IV) and Mo(VI) species are present, and in the 1:3 ratio.

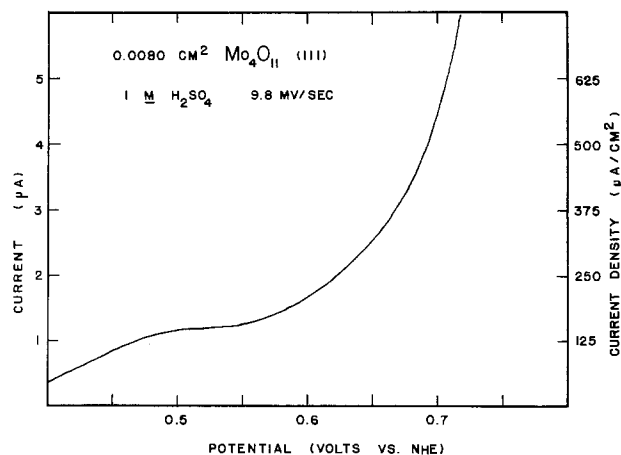


Fig. 4. Linear sweep voltammetry of (111) face of Mo<sub>4</sub>O<sub>11</sub> single crystal.

able for perfect octahedral coordination and should result in a less distorted octahedra. Since Mo(VI) is smaller, the  $r_{\text{Mo(VI)}}/r_{\text{O}}$  ratio (0.44) barely falls within the range defining octahedral coordination (0.44-0.732) and a more distorted octahedron is expected. From these data, it appears that the Mo(IV) ions are predominantly concentrated in the centers of the  $\text{ReO}_3$ -type slabs which run perpendicular to the [100] direction.<sup>3</sup> Thus if one looked at the (100) face of a  $\text{Mo}_4\text{O}_{11}$  crystal, one might expect to see predominantly one type of Mo species, either Mo(IV) or Mo(VI), depending on which layer of the crystal is exposed. Since the +4 state is thermodynamically unstable in aqueous solution (7), it is likely that only Mo(VI) species would be exposed on surfaces in contact with an aqueous solution, or even on a crystal exposed to normal atmospheric moisture and oxygen.

Using this model of the Mo ion distribution in the  $\text{Mo}_4\text{O}_{11}$  crystals, we propose the following mechanism, which offers a good explanation of the observed facts: (i) Mo(VI) type surfaces are slowly dissolved by the solution in chemical attack whose rate is governed by the pH, temperature, solution composition, etc.; (ii) Mo(IV) type surfaces are chemically insoluble, but are rapidly dissolved when made anodic. On  $\text{Mo}_4\text{O}_{11}$ , an Mo(VI) type surface could be considered equivalent to an  $\text{MoO}_3$  surface in terms of stoichiometry but not in terms of structure. These surfaces with the "MoO<sub>3</sub>-type" stoichiometry are more soluble than bulk crystalline  $\text{MoO}_3$ , which is relatively insoluble in acid solution. We feel that the reason for this increased solubility of the "MoO<sub>3</sub>" surface layer<sup>4</sup> is that it is less stable structurally than bulk  $\text{MoO}_3$ . This is because it represents either the exposed Mo(VI) plane perpendicular to the [100] or the oxidized Mo(IV) plane, which in both cases are likely to have their octahedra joined in a highly strained unstable arrangement which is likely to be more soluble.

An Mo(IV) type surface on  $\text{Mo}_4\text{O}_{11}$  is stoichiometrically equivalent to an  $\text{MoO}_2$  surface, and is chemically insoluble because of the instability of  $\text{Mo}^{+4}$  in aqueous solution. In order to dissolve chemically, Mo(IV) species would have to undergo disproportionation, which appears to be kinetically hindered. However, this kinetic limitation is avoided if the exposed Mo(IV) species are anodically oxidized to Mo(VI). Once the Mo(IV) species have been oxidized and dissolved, the surface is again comprised of Mo(VI) species which inhibit the further passage of current until that Mo(VI) layer chemically dissolves. This explains the periodic rise and fall of current as one anodically dissolves the (100) face. The absence of periodic effects in basic solution can be explained by the high solubility of Mo(VI) species in that medium (8).

Another observed phenomenon in need of explanation is the damping of the voltage fluctuations shown in Fig. 2. When the experiment is repeated after a brief period (seconds to minutes) at no current or very low currents, the fluctuations return almost identically. Why do these periodic oscillations damp out, only to return after a brief rest? Our explanation is that the dissolution processes, both chemical and anodic, do not proceed at exactly the same rate on all areas of the (100) surface, due to local inhomogeneities, proximity to other faces, concentrations of dislocations, etc. As one area gets out of step with another, i.e., one in chemical dissolution, another anodic, the over-all result is a continuous process with all the local periodic fluctuations averaged out. However, if one removes the applied current and allows a rest period, the chemical dissolution will then proceed on all exposed (100) faces until a layer of Mo(IV) species is uncovered. In other words, the chemical dissolution proceeds on each plateau of the (100) face to essen-

tially an equivalent point in the structure, and terminates there because of the blocking effect of Mo(IV) species. Then, when anodic dissolution is once again resumed, all the different plateaus of the (100) face begin their dissolution in phase, and the periodic phenomena appear with almost the same magnitude as before.

Finally, we believe that surface roughening accounts for the diminution of the periodic phenomena as a crystal is cycled many times in a potential region of anodic dissolution. Microscopic and scanning electron microscopic examination of such crystal surfaces confirms the etching and roughening effect of anodic dissolution. Since only (100) faces show periodic effects, a roughening of the (100) face would expose other crystal planes to anodic attack and thus diminish the periodic effect. This loss of the effect (not to be confused with the damping in Fig. 2) is generally not reversible, except possibly in the case of the perchloric acid medium.

### Summary and Conclusions

$\text{Mo}_4\text{O}_{11}$ , which exhibits metallic conduction, will dissolve anodically with periodic fluctuations in the dissolution currents.

Periodic effects are noted during the anodic dissolution of the (100) face of  $\text{Mo}_4\text{O}_{11}$  single crystals in acid solution, and occur under potentiostatic, galvanostatic, and voltage sweep conditions.

These effects are absent on other faces, and are related to a 12.3Å periodicity in the crystal structure along the [100] direction, where alternating layers of Mo(IV) and Mo(VI) species are found.

The slow chemical dissolution of Mo(VI) species and the rapid electrochemical dissolution of Mo(IV) species provide a mechanism to explain the observed results.

To the best of our knowledge, this is the first demonstration of a periodic electrochemical effect related to a periodicity in the crystal structure.

### Acknowledgments

We wish to thank R. A. Figat for the sample preparation, R. Title for the EPR measurements, T. Penney for resistivity measurements, and J. Horkans for helpful discussions.

Manuscript submitted May 18, 1976; revised manuscript received Aug. 4, 1976. This was Paper 59 presented at the Dallas, Texas, Meeting of the Society, Oct. 5-9, 1975.

Any discussion of this paper will appear in a Discussion Section to be published in the June 1977 JOURNAL. All discussions for the June 1977 Discussion Section should be submitted by Feb. 1, 1977.

Publication costs of this article were assisted by IBM Corporation.

### REFERENCES

1. J. Wojtowicz, in "Modern Aspects of Electrochemistry," Vol. 8, J. O'M. Bockris and B. E. Conway, Editors, pp. 47-120, Plenum Press, New York (1972).
2. J. F. Cooper, R. H. Muller, and C. W. Tobias, Paper 67 presented at The Electrochemical Society Meeting, Toronto, Canada, May 11-16, 1975.
3. M. W. Shafer, R. A. Figat, and T. Penney, To be published.
4. A. Magneli, *Acta Chem. Scand.*, **2**, 861 (1948).
5. L. Kihlberg, *Ark. Kemi.*, **21**, 365 (1964).
6. J. Horkans, M. W. Shafer, and R. Peekema, Proceedings of Workshop on Electrocatalysis on Nonmetallic Surfaces, NBS, Gaithersburg, Maryland (1975).
7. W. M. Latimer, "Oxidation Potentials," 2nd ed., p. 251, Prentice-Hall, Englewood Cliffs, New Jersey (1952).
8. M. Pourbaix, "Atlas of Electrochemical Equilibria in Aqueous Solutions," Pergamon Press, London (1966).

<sup>3</sup> It can also be concluded that there is a higher concentration of semilocalized electrons associated with the Mo(IV) so there is in fact a periodicity in the charge density along the [100].

<sup>4</sup> We assume a thickness of this layer to be approximately 8-15Å.

# Mechanism of the Anodic Oxidation of Nickel

B. MacDougall\* and M. Cohen\*

National Research Council of Canada, Ottawa, Ontario, Canada

## ABSTRACT

The electrochemical oxidation and subsequent reduction of nickel electrodes in acid sulfate solutions was studied with potentiodynamic and galvanostatic techniques in conjunction with potential step polarization. Surface activity measurements gave a relative measure of the extent of surface oxidation and stability of the oxide toward reduction and dissolution, but did not give independently the oxygen coverage. Cathodic galvanostatic charging curves of previously anodized nickel electrodes displayed an arrest structure which was dependent on the extent of anodization. While the arrest charge was related to the cathodic reduction of some oxygen species on nickel, parallel side reactions such as nonelectrochemical dissolution and hydrogen evolution affected substantially the reduction current efficiency. Under certain conditions, the arrest charge component arising from cathodic reduction of the oxygen species on nickel could be resolved and an attempt made at identifying the nature of this species. Initially, anodization resulted in oxygen chemisorption which reached a maximum coverage corresponding to one oxygen atom per surface nickel. Conversion to nickel oxide occurred very rapidly at the active surface sites but more slowly over the rest of the surface.

In a previous paper (1), the oxide film formed by steady-state anodization of nickel in the pH range 2.0-8.4 was studied. The film was composed of 9-12Å of nearly stoichiometric NiO (2, 3), its physical and chemical properties being independent of solution pH. The steady-state films were stable upon exposure to the atmosphere, allowing x-ray emission and electron diffraction techniques to be used for the oxide analysis. The present work extends the investigation at pH 2.8 to the initial stages of nickel oxidation. Electron-optical techniques could not be used to study these oxides since their thicknesses were less than that of the air-formed film (*i.e.*, 6-8Å) and the surfaces were therefore unstable to air exposure. *In situ* cathodic reduction techniques with monitoring of surface activity could, however, be used to study early oxide growth and the results may be interpreted in terms of an initial chemisorption of oxygen followed by conversion to NiO as the oxidation proceeds.

## Experimental

**Specimen preparation.**—Polycrystalline specimens, 1 × 2.5 cm, were prepared from zone-refined nickel sheet of 99.996% purity as described elsewhere (2). They were degreased with benzene, chemically polished (2), electropolished for 2 min at 23°C in a 57% sulfuric acid solution at 0.5 A-cm<sup>-2</sup>, and then annealed at 800°C in a vacuum of 10<sup>-8</sup> Torr. The specimens were electropolished again immediately before use in an experiment.

**Reference electrode.**—Potentials quoted in this paper are referred to the Hg<sub>2</sub>SO<sub>4</sub> electrode (+0.665V with respect to the standard reversible hydrogen electrode).

**Solution.**—Deaerated solutions of 0.15N Na<sub>2</sub>SO<sub>4</sub> had their pH adjusted to 2.8 (1). Experiments were conducted at 25°C.

**Apparatus.**—A Princeton Applied Research Model 175 universal programmer was used in conjunction with a Wenking fast-rise potentiostat to obtain potentiodynamic sweep profiles. These profiles and galvanostatic cathodic charging curves were recorded on a Hewlett-Packard Model 7004B X-Y recorder. A high speed Brush recorder was used to follow the initial rapid decrease of current after an anodic potential step treatment. Two types of electrochemical cell were used, one having the counter and recording electrodes

in the same compartment and the other having them in different compartments separated by a glass frit and stopcock. The former cell was used for potential step experiments since large, initial current surges were involved. Both cells contained 50 ml of electrolyte and gave similar potentiodynamic sweep and galvanostatic charging results.

**Electrochemical procedure.**—After electropolishing, the electrodes were immersed in a deaerated pH 2.8 Na<sub>2</sub>SO<sub>4</sub> solution under cathodic polarization sufficient to reduce the prior 6-8Å film of NiO. The procedures for subsequently anodizing and reducing the nickel electrodes were as described elsewhere (1).

With potentiodynamic sweep experiments, anodic cycling of the freshly reduced electropolished nickel initially resulted in a slight increase of the electrode surface area. Consequently, the multisweeps recorded in this paper are those which were obtained after the attainment of reproducibility, generally after 5 sweeps at 10 mV sec<sup>-1</sup>. Single sweeps were also recorded, especially when the effect of a specific cathodic treatment on a previously anodized electrode was under study.

Electrode surface activities were determined by either the potentiodynamic sweep or anodic potential step techniques. With the former, the surface activity of an electrode is given by the ratio of the charge under its anodic current peak (Fig. 1) to the corresponding (maximum) charge obtained when the electrode has an oxide-free starting surface. With the latter, surface activities were similarly obtained from the ratio of anodic charges passed during the first 2 sec after the potential was stepped to its anodization value, during which time the anodic current fell by about three orders of magnitude. Both techniques gave similar results. At pH 2.8, most of the measured anodic charge is due to nickel dissolution; therefore, the surface activity is a measure of the electrode's reactivity toward nickel dissolution. The surface activity of oxide-free nickel is by definition 100%.

## Results

**Kinetics of oxide formation and reduction.**—Figure 1 shows the potentiodynamic sweep profiles at 10 mV sec<sup>-1</sup> for a nickel electrode in an unstirred pH 2.8 Na<sub>2</sub>SO<sub>4</sub> solution. Along with the main anodic peak for nickel dissolution, two distinct cathodic peaks were observed with cycling in the range -1.5 to 0.0V. The cathodic peak at -1.4V was due to the deposition of nickel ions, Ni<sup>2+</sup>, from solution. The main cathodic

\* Electrochemical Society Active Member.  
Key words: nickel oxide, passivity, anodic oxidation, mechanism.

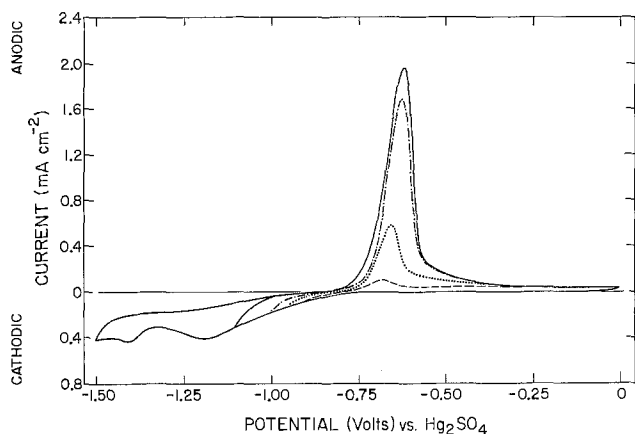


Fig. 1. Potentiodynamic current-potential profiles for a nickel electrode at  $10 \text{ mV sec}^{-1}$  in pH 2.8  $\text{Na}_2\text{SO}_4$  solution. The anodic reversal potential was  $0.0\text{V}$  while the cathodic reversal potential was: (—)  $-1.1\text{V}$  or  $-1.5\text{V}$ ; (---)  $-1.0\text{V}$ ; (···)  $-0.95\text{V}$ ; (-·-·)  $-0.9\text{V}$ ; i.e., at various stages of completion of oxide reduction. Sweep (—) was identical to that obtained on an oxide-free surface, i.e., cathodically reduced electropolished nickel.

peak at  $-1.2\text{V}$  was associated with oxide reduction and increased substantially with potential and time of anodization in the passive region. However, the charge under this peak gave anomalously high oxide thickness values, the calculated  $\text{NiO}$  thickness being  $40\text{--}50\text{\AA}$  after cycling to  $0.0\text{V}$  at  $10 \text{ mV sec}^{-1}$  (Fig. 1).

Figure 1 also shows the effect of cycling to different cathodic potentials (after a constant anodic treatment) on the nickel dissolution peak. The anodic treatment consisted of sweeping an oxide-free nickel surface to  $0.0\text{V}$ . The anodic current peak, and thus the surface activity, increased with increasing cathodic reversal potential until  $-1.1\text{V}$  with no further change upon cycling to more cathodic potentials. Similar results were obtained by reversing the direction of the anodic sweep at different potentials. Figure 2 shows the dependence of surface activity on anodic reversal potential with a constant cathodic reversal potential of  $-0.9\text{V}$ . The oxide formed by sweeping to more anodic potentials was increasingly difficult to remove.

Figure 3 shows the dependence of surface activity on cathodic reversal potential after prior cycling to  $0.0\text{V}$  (cf. Fig. 1) along with the effect of cathodic holding

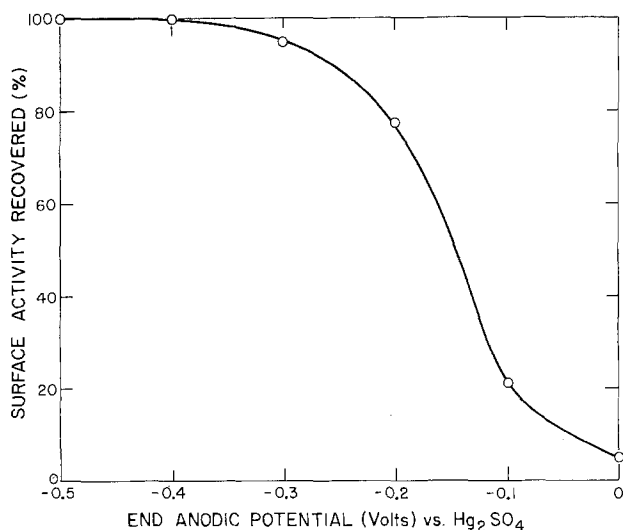


Fig. 2. Dependence of percentage surface activity, obtained during an anodic sweep, on the anodic reversal potential of the previous sweep. After cycling to the various anodic potentials shown, an intervening sweep to  $-0.9\text{V}$  provided the standard cathodic treatment. Sweep rate was  $10 \text{ mV sec}^{-1}$ .

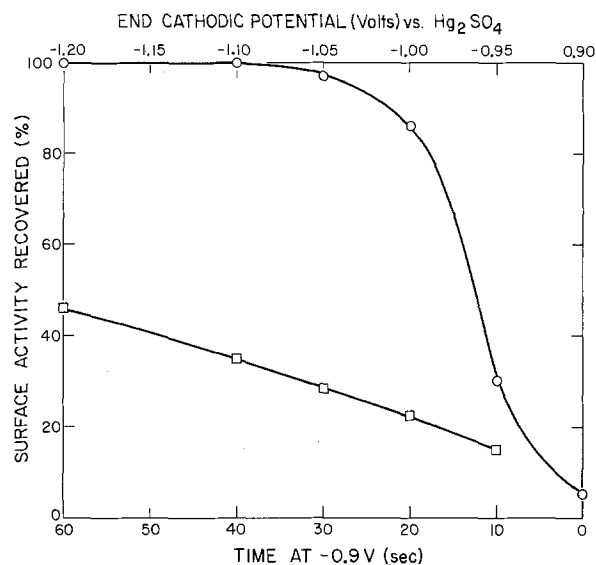


Fig. 3. (—○—) Variation of surface activity with cathodic reversal potential after prior cycling to  $0.0\text{V}$  at  $10 \text{ mV sec}^{-1}$ . (—□—) Effect of time of cathodic holding at  $-0.9\text{V}$  on surface activity of electrode previously cycled to  $0.0\text{V}$ . The holding period at each potential corresponds to the additional time spent in cycling to that potential from  $-0.9\text{V}$ . Sweep rate was  $10 \text{ mV sec}^{-1}$ .

at  $-0.9\text{V}$  for the extra time spent in the region of potentials more cathodic than  $-0.9\text{V}$ . The time in cycling to various potentials at the same sweep rate is seen to be important, and in order to study separately the role of time and potential, a potential step technique was used.

Figure 4 shows the effect of time at various cathodic step potentials on the activation of a surface which was initially anodized at  $0.0\text{V}$  for  $90 \text{ sec}$ . To obtain each data point the nickel surface was first given a complete reactivation followed by a potential step to  $0.0\text{V}$  for  $90 \text{ sec}$ , after which the potential was stepped to the cathodic value of interest for a certain period of time. The resulting activity of the surface was determined by stepping the potential back to  $0.0\text{V}$  and measuring the anodic charge transient.

The role of potential and time in the anodization of nickel was studied in relation to the cathodic reducibil-

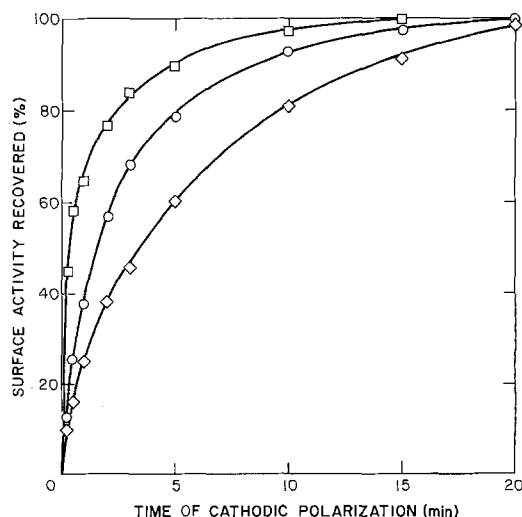


Fig. 4. Variation of surface activity with potential and time of cathodic treatment after anodization at  $0.0\text{V}$  for  $90 \text{ sec}$ . The potential step technique was used for both anodization and reduction, the cathodic potential of reduction being: (—□—)  $-0.95\text{V}$ ; (—○—)  $-0.9\text{V}$ ; (—◇—)  $-0.85\text{V}$ . To determine the surface activity, a potential step treatment back to  $0.0\text{V}$  was employed.

ity of the oxide formed. The change in surface activity recovered, using a constant cathodic treatment, was followed as a function of the condition of anodization. Figure 5 shows the decrease in surface activity with increasing extent of oxidation using a standard cathodic treatment of 30 sec at  $-0.85V$ . The differences in oxide reducibility for the different oxidation treatments may be due to changes in the amount and/or the type of oxide. Since an accurate measure of the oxide coverage was not possible with the sweep method, another electrochemical technique (galvanostatic charging) was used in an attempt to determine the oxide reduction charge component.

**Galvanostatic reduction of nickel oxide.**—Figure 6 shows the cathodic charging curves obtained with

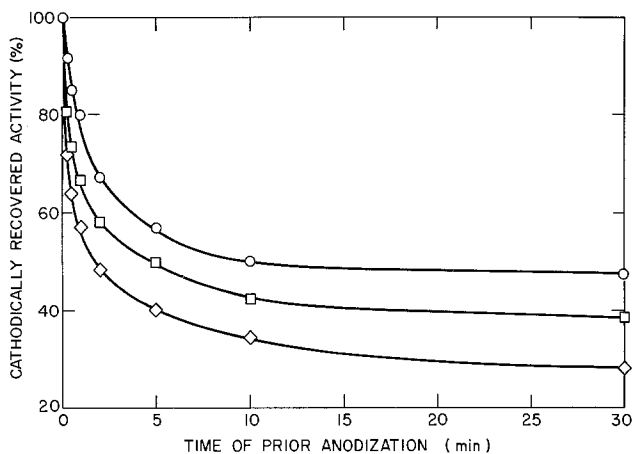


Fig. 5. Variation of surface activity with potential and time of anodic treatment using an intervening cathodic treatment of 30 sec at  $-0.85V$ . The potential step technique was used for both anodization and reduction, the potential of anodization being: (—○—)  $-0.4V$ ; (—□—)  $-0.3V$ ; (—◇—)  $-0.2V$ . A potential step back to  $0.0V$  was used to determine the surface activity.

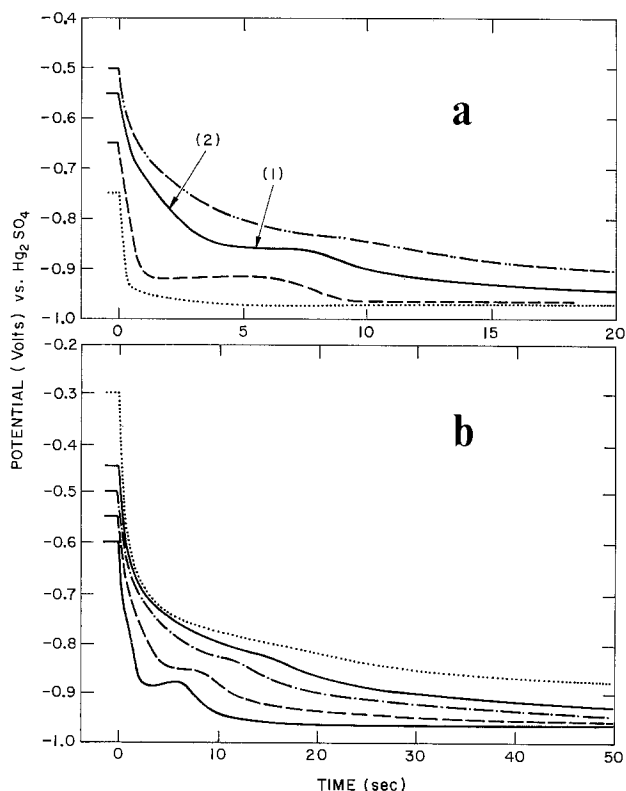


Fig. 6. Cathodic galvanostatic charging curves, at  $20 \mu A cm^{-2}$ , of nickel electrodes anodized for 90 sec at potentials in the range  $-0.75$  to  $-0.3V$ .

nickel electrodes which had previously been anodized at potentials in the range  $-0.75$  to  $-0.3V$  for 90 sec. After the milder anodic treatments, two distinct arrests were resolved and labeled arrest 1 and arrest 2. The shape and size of the arrests were independent of solution agitation by  $N_2$  bubbling during the cathodic treatment. Also the arrest structures did not significantly change on going from a solution  $Ni^{2+}$  content of  $0.2-100 \mu g ml^{-1}$ . With increasing anodic treatment the two arrests were replaced by a single arrest, and the time required to attain the potential corresponding to hydrogen evolution from an oxide-free surface increased. The development of the cathodic charging profile with time of anodization at  $-0.6V$  is given in Fig. 7.

Some general observations were made regarding the early stages of nickel oxidation at different anodic potentials. Anodization for a time period of  $< 5$  sec at  $-0.3V$  gave a cathodic charging profile similar to that obtained at less anodic potentials such as  $-0.6V$  for 90 sec (Fig. 6). In both cases, arrests 1 and 2 were initially well resolved with arrest 1 developing before 2. Also, the potential of the plateau associated with arrest 1 for short times at  $-0.3V$  corresponded with that for longer anodizations at  $-0.6V$ . Indeed, the whole spectrum of cathodic charging profiles associated with, e.g., 90 sec at  $-0.75$  to  $-0.3V$ , could be obtained with various times at  $-0.3V$ .

The dependence of the arrest charges on cathodic current was next investigated. After mild anodizations, e.g., 90 sec at  $-0.55V$ , the charge associated with both arrest 1 and 2 increased with increasing cathodic current density (Fig. 8). The measured arrest time decreased by less than one-half in going from a cathodic current of 4 to  $40 \mu A cm^{-2}$  rather than the expected factor of  $\approx 10$ . The fact that the duration of the arrest

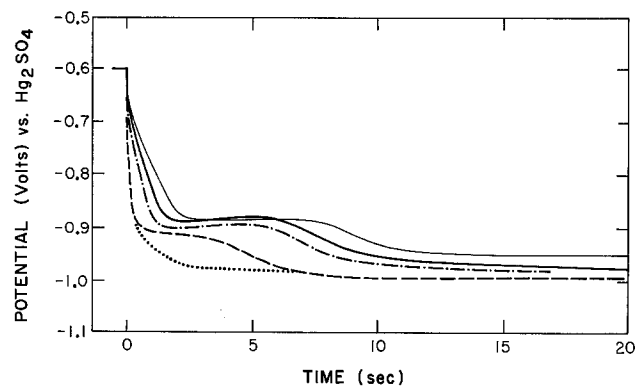


Fig. 7. Cathodic galvanostatic charging curves, at  $20 \mu A cm^{-2}$ , of a nickel electrode anodized at  $-0.6V$  for different times: (···) 1 sec; (---) 3 sec; (-·-) 20 sec; (—) 90 sec; (—) 10 min.

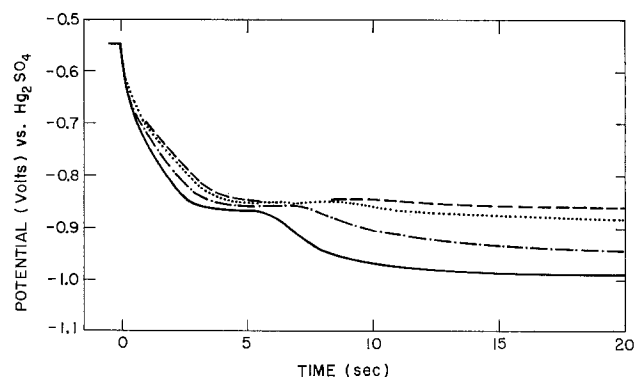


Fig. 8. Cathodic galvanostatic charging curves, for nickel electrodes anodized at  $-0.55V$  for 90 sec, at various charging currents: (---)  $4 \mu A cm^{-2}$ ; (···)  $10 \mu A cm^{-2}$ ; (-·-)  $20 \mu A cm^{-2}$ ; (—)  $40 \mu A cm^{-2}$ .

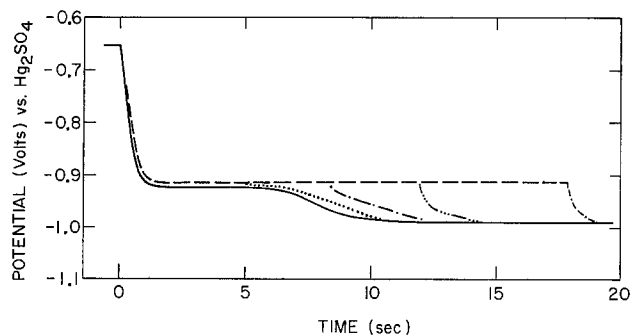


Fig. 9. Cathodic charging curves, at  $20 \mu\text{A cm}^{-2}$ , for electrodes anodized at  $-0.65\text{V}$  for 90 sec, with an intervening open-circuit treatment for various times: (—) 0 sec; (···) 5 sec; (- - -) 8 sec; (- · - ·) 12 sec; (- - - -) 18 sec. The open-circuit decay curve obtained after the anodic treatment and before initiation of the cathodic pulses is also shown (- - -).

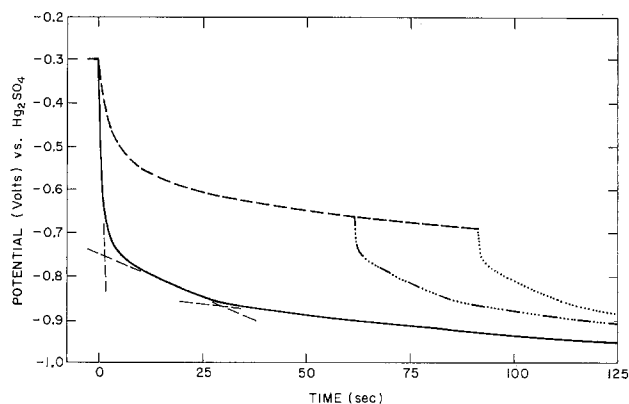


Fig. 10. As in Fig. 9 but with an anodization at  $-0.3\text{V}$  for 90 sec and with open-circuit times of 0 sec (—); 60 sec (- - -); and 90 sec (···). The open-circuit decay curve is given as (- - -). The standard method was used for determining the transition time of the cathodic arrest and is illustrated for the first charging profile. The points of intersection of the extrapolated lines for the various charging processes are taken as defining the beginning and end of the oxide reduction arrest.

was almost independent of the cathodic charging rate indicates that a nonelectrochemical process, probably oxide dissolution,<sup>1</sup> was playing a significant role. The cathodic faradaic reaction of hydrogen evolution from the oxidized nickel surface was responsible for charge consumption.

**Role of nonelectrochemical dissolution.**—Open-circuit experiments were performed to determine the stability of the initial oxide toward dissolution. With a previous mild anodization treatment, e.g.,  $V \leq -0.55\text{V}$  for 90 sec, a time-dependent fraction of the charge for arrests 1 and 2 disappeared on open circuit (Fig. 9). Indeed, with very thin films the initial portion of the open-circuit decay curve was almost coincident with the cathodic charging profile and the time on open circuit required to dissolve the oxide corresponded approximately with the time of arrest 1 and 2. The rate of open-circuit dissolution was found to decrease with increasing anodization treatment. With a previous anodization of 90 sec at  $-0.3\text{V}$ , the oxide arrest charge decreased by only 15% after 60 sec on open circuit (Fig. 10). (The points of intersection of the extrapolated lines for the various charging processes were taken as defining the beginning and the end of the oxide reduction arrest.) During cathodic charging at  $20 \mu\text{A cm}^{-2}$ , this 60 sec encompassed all the cathodic arrest. Figure 11 shows the decrease of arrest charge

<sup>1</sup> The term oxide dissolution as used here includes both physical undermining (1) and chemical dissolution (i.e.,  $\text{NiO} + 2\text{H}^+ = \text{Ni}^{2+} + \text{H}_2\text{O}$ ).

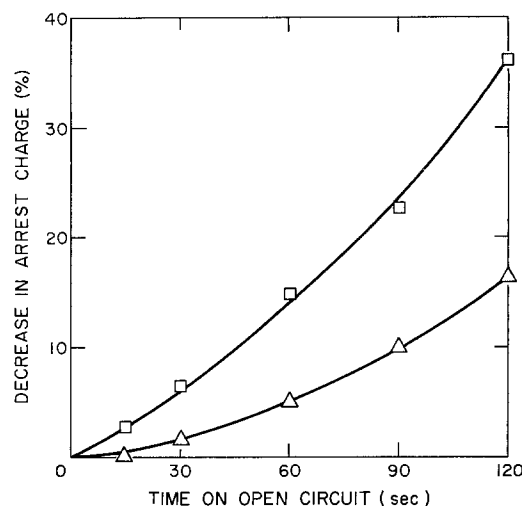


Fig. 11. Decrease of the oxide arrest charge with time on open circuit after previous anodizations at  $-0.3\text{V}$  (—□—) and  $-0.2\text{V}$  (—△—) for 90 sec. Cathodic charging current was  $20 \mu\text{A cm}^{-2}$ .

with time on open circuit after anodizations at  $-0.3$  and  $-0.2\text{V}$ .

**Determination of oxygen coverages.**—Figure 12 shows the dependence of the reduction arrest charge on the cathodic charging rate for 90 sec oxidations at  $-0.3$  and  $-0.2\text{V}$ . A linear dependence of arrest charge on cathodic current was obtained with all but the lowest charging rates. For those, the longer arrest times increased the probability that nonelectrochemical oxide dissolution was playing a role. The apparent contribution from oxide dissolution during cathodic charging was somewhat less than that predicted by open-circuit experiment (Fig. 11). This was probably due to cathodic protection of the underlying metal during charging and the subsequently diminished role of oxide undermining.

Extrapolation of the linear portion of the arrest charge profiles in Fig. 12 to  $i_{\text{cath}} = 0$  gives oxygen coverage values of 0.55 and  $0.46 \text{ mC cm}^{-2}$ . A surface roughness factor of 1.15 converts the former value to  $0.48 \text{ mC cm}^{-2}$ , which corresponds to one oxygen atom per surface nickel. To check on the extent of completion of cathodic reduction during the time of the arrest, the activity of the surface was determined at the end of the arrest. This was accomplished (1) by instantaneously stepping the potential back to either  $-0.3$  or  $-0.2\text{V}$ , after cathodic charging to the end of the arrest, measuring the resulting anodic charge and comparing it with that obtained on a previously oxide-

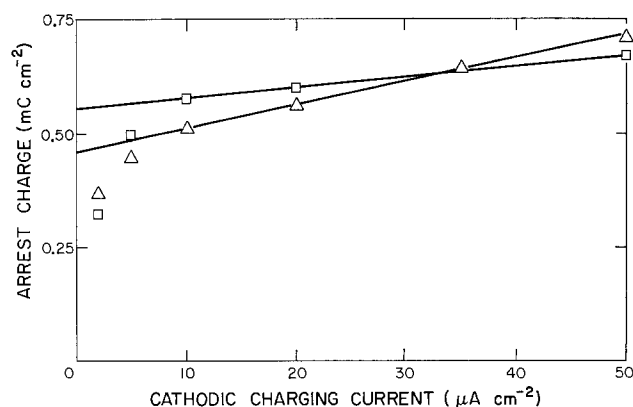


Fig. 12. Dependence of the observed oxide reduction arrest charge on cathodic charging current after prior 90 sec anodizations at  $-0.3\text{V}$  (—□—) and  $-0.2\text{V}$  (—△—).

Table I. Dependence of measured and corrected oxide reduction arrest charges and surface activity at end of arrest on previous anodization treatment

Potential, V	Anodization time	Measured arrest charge,* mC cm <sup>-2</sup>	Surface activity,** %	Corrected arrest charge, mC cm <sup>-2</sup>	Current efficiency, %
-0.5	90 sec	0.35	70		
-0.4	90 sec	0.52	52	0.49	94
-0.3	90 sec	0.60	39	0.55	92
-0.2	90 sec	0.56	27	0.46	82
-0.1	90 sec	0.52	13		
0.0	90 sec	0.35	6		
-0.3	17 min	0.45			
-0.5	10 min	0.47			

\* Measured at a cathodic charging current of 20  $\mu\text{A cm}^{-2}$ .

\*\* Measured at the end of the arrest.

free nickel surface. With the 90 sec anodization at  $-0.3\text{V}$ , the activity at the end of the cathodic arrest was 39%, i.e., the other 61% of activity would be recovered during the slow shift of cathodic potential to the value associated with hydrogen evolution on oxide-free nickel. For 90 sec at  $-0.2\text{V}$ , the activity at the end of the arrest had decreased to 27%. The 39 and 27% activity values were independent of cathodic charging rate, indicating that the linear increase in the arrest charge with  $i_c$  (Fig. 12) was not due to cathodic reduction of more of the oxygen on the surface. Table I gives the surface activity at the end of the arrest for oxidations in the range  $-0.5$  to  $0\text{V}$ . As may be observed, there was a substantial decrease in the percentage surface activity recovered at the end of the arrest with increasing potential and time of anodization. Also included in Table I are the arrest charges measured at a cathodic current of  $20 \mu\text{A cm}^{-2}$  (Fig. 6). The arrest charge reached a maximum after 90 sec at  $-0.3\text{V}$  and then began to decrease. Corrected arrest charge values, obtained by extrapolation to  $i_c = 0$  (as in Fig. 12), are given in the table and the current efficiency is the ratio of the corrected charge to the total arrest charge measured at  $20 \mu\text{A cm}^{-2}$ .

Figure 13 shows the change in surface activity as a function of cathodic charge passed during galvanostatic charging after previous 90 sec anodizations at  $-0.4$ ,  $-0.3$ , and  $-0.2\text{V}$ . It is to be noted that the surface activity values, within the time of the charge arrest, fall on fairly good straight lines. The deviation from linearity occurs at those points which mark the end of

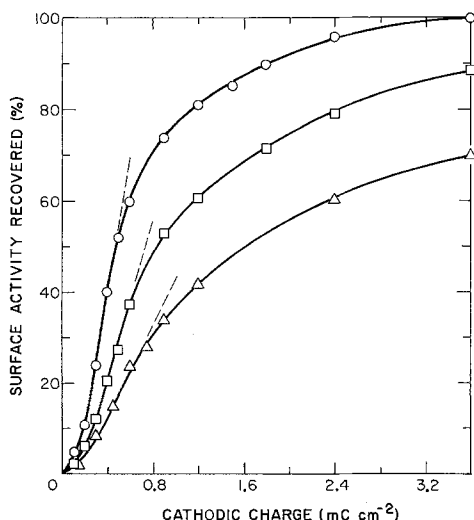


Fig. 13. Increase in surface activity with cathodic charge passed ( $i_c = 20 \mu\text{A cm}^{-2}$ ) after prior 90 sec anodizations at  $-0.4\text{V}$  ( $\circ$ — $\circ$ );  $-0.3\text{V}$  ( $\square$ — $\square$ ); and  $-0.2\text{V}$  ( $\triangle$ — $\triangle$ ). The initial linear increase of activity with charge passed is extended (---) to give an indication of the cutoff points.

the arrest, and the surface activity subsequently increases more slowly.

## Discussion

It has previously been shown that the steady-state oxide on anodized nickel (9-12Å of almost stoichiometric NiO) could be reduced with a moderate cathodic treatment at  $\text{pH } 2.8$ . The present results indicate that this is also true for the thinner, nonsteady-state films formed by transient anodization in  $\text{pH } 2.8$ . *In situ* cathodic reduction techniques, together with surface activity measurements, were consequently used to gain an understanding of the initial oxidation processes.

The potentiodynamic sweep experiments showed that the electrode activity is highly dependent on the anodic and cathodic reversal potentials (Fig. 1-3). However, the surface activity data provide only a qualitative measure of the degree of oxidation of the nickel surface, and independent oxide thickness determinations are required. The potentiodynamic sweep technique is not quantitative since the calculated NiO thicknesses, from the oxide reduction peak charge, are anomalously high (e.g., 40-50Å from Fig. 1). This result can be explained in terms of another cathodic reaction, most probably hydrogen evolution on NiO (1, 2), contributing to the charge under the current peak and thereby decreasing the current efficiency for oxide removal.

The effect of potential and time can be separated by using the potential step technique (Fig. 4 and 5). The surface activity recovered after cathodic polarization is decreased by increasing either the time or potential of previous anodic polarization and increased by increasing the time and potential of cathodic polarization.

Galvanostatic charging techniques were also used to reduce the film on anodized nickel. The cathodic charging curves of previously oxidized electrodes display a definite arrest structure, not associated with  $\text{Ni}^{2+}$  reduction, which varies with potential and time of anodization (Fig. 6 and 7). Other workers have observed a less well defined arrest (4-6); however, little useful information was obtained. In the present work, the very initial oxygen coverages cannot be determined by cathodic charging techniques because of dissolution (Fig. 8 and 9). The significance of oxide dissolution decreases with increasing extent of oxidation (Fig. 10 and 11), but continues to play an important role at the lowest cathodic charging rates, i.e.,  $< 10 \mu\text{A cm}^{-2}$  (Fig. 12). At the higher charging currents the contribution of dissolution becomes negligible, probably because of increased cathodic protection of the nickel surface and/or shorter times for oxide reduction, and oxygen coverage determinations are possible. The observed linear increase in apparent oxide reduction arrest charge with  $i_c$  above  $5 \mu\text{A cm}^{-2}$  (Fig. 12) is due to parallel evolution of molecular hydrogen. The contribution from hydrogen evolution increases with cathodic charging rate since reduction of the oxygen species on nickel is a slow surface process. Extrapolation to  $i_c = 0$  therefore gives corrected arrest charges, i.e., without the hydrogen evolution contribution.

The corrected arrest charges do not represent reduction of all of the oxide formed during anodization because the surface activities at the end of the arrests are less than 100%. A certain proportion of oxide is removed after the distinct arrest, and this proportion increases with extent of oxidation. Figure 13 shows that during the time of the arrest, there is a direct proportionality between cathodic charge passed and surface activity recovered. Since the current efficiency for removal of the oxygen species is very high during the arrest (Table I), a direct relationship exists between the oxygen coverage and recovered surface activity over a wide coverage range. The surface activity increases more slowly with cathodic charge passed in the region after the arrest, indicating a fundamental change in the type of oxygen species undergoing reduction.



From the above results it would appear that the anodic formation of an oxide film on nickel takes place in a sequence of steps which depends on both the anodic formation potential and time of polarization. At the very lowest coverages, the oxygen species are unstable with respect to nonelectrochemical dissolution (Fig. 8 and 9) and, although an arrest structure is evident, oxygen coverages cannot be accurately determined. With further anodization, the stability of the oxygen species increases and permits the detection of both chemisorbed oxygen and nucleated oxide at less than one monolayer coverage of the former, *i.e.*, still in the early stages of oxidation. Reduction of the chemisorbed oxygen gives the single, distinct cathodic arrest with the current efficiency for its removal approaching 100%. However, some oxygen remains on the surface even after removal of the chemisorbed oxygen as indicated by the less than 100% recovery of surface activity after the arrest. This oxygen is probably present as nucleated oxide on active sites. Further oxidation gives a maximum corrected arrest charge corresponding to a monolayer of chemisorbed oxygen. At the same time, there is enough nickel oxide on the surface to lower the activity by 60%, *i.e.*, this oxide must have formed on active surface sites since a very small amount has a large effect on activity. Reduction of the nickel oxide after the arrest is an inefficient process and a prolonged cathodic reduction is required to restore complete surface activity.

On anodic polarization for longer times and at higher potentials the chemisorbed monolayer is converted to bulk NiO. This oxide probably grows from the nuclei already present on the active sites. As the oxide thickens the cathodic wave associated with the reduction of chemisorbed oxygen decreases and disappears and the current efficiency for cathodic reduction of the oxide gradually decreases due to the simultaneous production of hydrogen. The oxide is also much more stable on open circuit than either the full or partial monolayer of chemisorbed oxygen.

This sequence of steps for the formation of oxide is quite similar to that proposed for the uptake of oxygen on nickel under ultra-high vacuum conditions (7-9). In this case the oxygen uptake can be measured by x-ray emission or Auger electron spectroscopy and structure changes followed by electron diffraction. The major change from a chemisorbed oxygen structure to an oxide structure takes place at about one monolayer coverage, but some nuclei of nickel oxide are present on the surface before this. The growth rate of the film is consistent with the concept of expanding circles of oxide from a constant number of nuclei present from the beginning.

The cathodic behavior of the oxide with regard to the character of the cathodic waves, the potentials of the waves, and the final reduction potential is also consistent with the proposed mechanism for the formation of the oxide. The initial chemisorbed layer cathodically reduces at a less negative potential than the final bulk oxide. Because the potential for reduction is less negative there is less contribution from hydrogen evolution as a secondary cathodic reaction and, as indicated in Fig. 12 and 13, it is possible to reduce the chemisorbed layer with close to 100% current efficiency. A second factor affecting the reducibility of the layer is the difference in hydrogen overvoltage on the oxide and the metal. In previous work it was shown that hydrogen overvoltage on clean nickel is much higher than on the anodically formed oxide. Hence the contribution of hydrogen evolution to the cathodic current is much less on a partially bare surface, such as one having less than a monolayer of adsorbed oxygen plus some oxide nuclei, than on a surface fully covered with nickel oxide.

The early presence of nucleated oxide is also indicated by the cathodic reduction curves. After oxidation at anodic potentials and times which give only partial

monolayer oxygen coverage (*e.g.*,  $-0.5V$  and 90 sec) the potential after cathodic reduction of the chemisorbed oxide layer corresponds to the hydrogen overpotential on oxide. The presence of oxide is confirmed by the less than 100% surface activity after reduction of chemisorbed oxygen. The involvement of active sites as nucleation centers for nickel oxide follows from its coexistence with a monolayer of chemisorbed oxygen. The active sites could be surface defects, previously reported to be preferential centers for oxide nucleation (10-12).

The partial monolayers formed at short times and low anodic potentials are easily removed by either chemical dissolution or cathodic reduction. At close to the monolayer coverage observed at higher potentials the adsorbed film is more stable toward chemical dissolution. This may be due to either a decrease in free nickel surface area leading to a decrease in undermining of the oxygen-containing film or a change in the character of the layer. The latter could result from a place exchange transformation (13-15) with alternate oxygen atoms exchanging with the nickel atoms.

Little information can be obtained by cathodic reduction about the thickness and/or coverage of the initially formed oxide due to the significant contribution of parallel oxide dissolution and hydrogen evolution. With further oxidation the amount and stability of the nickel oxide increased. After the corrected arrest charge had reached a maximum value corresponding to approximately a monolayer of  $NiO_{ads}$ , the increase in area of oxide coverage should be obtainable from the decrease in the arrest charge. However, caution must be used since the thickness of the oxide nuclei may be changing during oxidation (*i.e.*, 9-12Å oxide nuclei may not be present from the beginning). Also, the slow increase in cathodic potential observed after fairly strong anodic treatments will give distinct cathodic arrest structures if the time scale is sufficiently insensitive. Such a situation arose in a previous paper (1) after both 15 and 60 sec at 0.0V. However, the arrest charges corresponded to more than ten times the maximum measured coverage with nickel oxide (1-3), *i.e.*, the current efficiency for cathodic reduction was very low during the so-called arrest. Under such circumstances, the observed cathodic arrest will have little significance with regard to oxygen coverages and the nature of oxygen species on the anodized surface. It is therefore important to have information about the current efficiency for oxygen reduction during the arrest before drawing conclusions about the significance of the arrest.

The present results allow nickel oxidation to be roughly divided into three regions according to oxygen coverage: (i) very thin, *i.e.*, substantially less than one oxygen atom per surface nickel; (ii) intermediate, *i.e.*, *ca.* one oxygen atom per surface nickel; and (iii) thick, *i.e.*, up to the 3 to 4 oxygen atoms per surface nickel found in the steady state. Initially, both chemisorbed oxygen and oxide are formed on the surface but the amount of oxide is only substantial after a monolayer of  $NiO_{ads}$  has formed. With continued oxidation, the  $NiO_{ads}$  is converted to NiO with the eventual formation of the 9-12Å oxide film. As indicated by the structure in the cathodic charging curves, this general mechanism of oxidation is the same over the wide range of anodic potentials studied.

### Summary

1. Surface activity measurements can give a relative measure of the degree of oxidation and/or reduction of nickel and the stability of the oxygen species present toward either reduction or dissolution, but not the amount of oxygen on the surface.

2. The course of oxidation of a nickel electrode can be followed with cathodic charging techniques, the oxide arrest structure varying with the extent of prior anodization.



3. The cathodic charging technique indicates that two distinct oxygen species, most probably chemisorbed oxygen and nickel oxide, are formed on the surface.

4. Chemisorbed oxygen is reduced with a current efficiency close to 100% and gives a distinct arrest structure. Oxygen coverages can be determined since the roles of nonelectrochemical dissolution and parallel hydrogen evolution can be separated out from the cathodic reduction reaction.

5. The current efficiency for reduction of nickel oxide is poor and oxide coverages cannot be determined directly.

6. Oxidation initially gives nickel oxide at the active sites with simultaneous formation of  $\text{NiO}_{\text{ads}}$ , over the rest of the surface, up to a monolayer coverage. Further oxidation converts the  $\text{NiO}_{\text{ads}}$  to nickel oxide.

Manuscript submitted June 3, 1976; revised manuscript received Aug. 4, 1976.

Any discussion of this paper will appear in a Discussion Section to be published in the June 1977 JOURNAL. All discussions for the June 1977 Discussion Section should be submitted by Feb. 1, 1977.

Publication costs of this article were assisted by the National Research Council of Canada.

## REFERENCES

1. B. MacDougall and M. Cohen, *This Journal*, **123**, 191 (1976).
2. B. MacDougall and M. Cohen, *ibid.*, **121**, 1152 (1974).
3. P. B. Sewell, B. MacDougall, D. F. Mitchell, and M. Cohen, Proceedings 6th International Congress on Metal Corrosion, Sydney, Australia (1975).
4. J. O'M Bockris, A.K.N. Reddy, and B. Rao, *This Journal*, **113**, 1113 (1966).
5. D. E. Davis and W. Barker, Proceedings 2nd International Congress on Metal Corrosion, New York, p. 551 (1963).
6. M. Okayama and S. Haruyama, *Corros. Sci.*, **14**, 1 (1974).
7. P. H. Holloway and J. B. Hudson, *Surf. Sci.*, **43**, 123 (1974); **43**, 141 (1974).
8. D. F. Mitchell, P. B. Sewell, and M. Cohen, *ibid.*, In press.
9. H. H. Uhlig, *Corros. Sci.*, **7**, 325 (1967).
10. C. R. Crowe and S. G. Fishman, *ibid.*, **13**, 569 (1973).
11. L. N. Yagupalskaya and B. A. Movchan, Proceedings 4th International Congress on Metal Corrosion, Amsterdam, p. 473 (1969).
12. R. M. Latanision and H. Opperhauser, *Corrosion (Houston)*, **27**, 509 (1971).
13. A. M. Laynon and B. M. W. Trapnell, *Proc. R. Soc. London, Ser. A*, **227**, 387 (1955).
14. N. Sato and M. Cohen, *This Journal*, **111**, 512 (1964).
15. H. A. Kozłowska, B. E. Conway, and W. B. A. Sharp, *J. Electroanal. Chem.*, **43**, 9 (1973).

## Charge Transfer Processes during Anodic Polarization of Aluminum

K. Y. Kim,\* R. D. Smith, and O. F. Devereux\*\*

*Institute of Materials Science and Department of Metallurgy, University of Connecticut, Storrs, Connecticut 06268*

## ABSTRACT

During prolonged anodizing of aluminum in aqueous 3 weight percent ammonium tartrate, ionic current components representing porous oxide development and aluminum dissolution were evaluated by gravimetry and optical absorbance, respectively, and compared to the total flow of charge measured in the external circuit. Electrolytes of pH 6.1 and 7 were studied. The dissolution of aluminum was markedly higher at pH 7, whereas the rate of porous oxide development was only slightly increased. In both cases an electronic current, obtained by difference, was evaluated, but it was very small at pH 7. At pH 7 a large nonelectrode dissolution of aluminum was seen at the onset of anodizing. These observations are discussed in terms of steady-state processes in the barrier oxide layer involving both ionic transport and oxide dissolution.

Recent work has shown that a steady-state current develops during prolonged anodizing of aluminum in aqueous solutions of ammonium tartrate that is characteristic of the applied potential difference (1). It has been further shown that anodic films formed in this electrolyte, although traditionally regarded as "barrier-type," are, in fact, analogous to films formed in the traditionally "pore-forming" electrolytes (e.g., sulfuric acid), both with respect to structure development and transient behavior of the anodic current at constant applied potential difference (2, 3). In attempting to understand both steady-state and transient aspects of the anodic current it is pertinent to know the nature of the charge transfer processes that occur at the anode. During development of a barrier oxide layer and, in pore-forming electrolytes, subsequent growth of a porous layer, the mode of charge transfer through the anodic oxide has been tacitly regarded as

ionic for good and obvious reason. O'Sullivan and Wood, in their excellent treatise, discuss possible ionic processes in detail (4). The actual mechanism of ionic charge transfer is not certain, however, relatively recent tracer studies having supported cationic flow (5), anionic flow (6), and migration by both anions and cations (7, 8). While cationic current must be primarily due to aluminic ion, there may be a small protonic contribution (9, 10), and anionic current may be attributed to hydroxyl ions (9-12), oxide ions (8, 12), and acid anions (13, 14). In contrast, interest in anodic aluminum oxide films formed in "barrier-forming" electrolytes has stemmed largely from their ability to rectify alternating current. Again for obvious reason, the charge transfer mechanism in this case has been tacitly regarded as electronic, prompting considerable study of the role of both electronic and structural defects (11, 15-24). Electronic defects may arise either by hole injection at the metal/oxide interface, or electron injection at the oxide/electrolyte interface occasioned by oxygen liberation from water,

\* Electrochemical Society Student Member.

\*\* Electrochemical Society Active Member.

Key words: aluminum oxide, anodic oxidation, polarization, charge transfer.

hydroxyl ion, or other oxyanions. Diggle *et al.* (25) have suggested that the charge transfer mechanism in barrier-type films is field dependent; at high fields, the film is growing and both electronic and ionic flow occur, whereas at low fields this is not the case, only electronic flow being seen. Clearly the growth of a porous oxide layer on prolonged anodizing even in barrier-forming electrolytes, cited above (2, 3) and previously noted by others (26-28), is indicative of ionic flow under steady-state conditions.

The present study was performed to distinguish between ionic and electronic currents passed during prolonged anodizing of aluminum in a barrier-forming electrolyte. This was accomplished by measuring (i) the total current, and (ii) the ionic current, the latter being represented by the appearance of aluminum in the oxide film and also dissolved in the electrolyte. The electronic current (iii) was then established as the difference between (i) and (ii) above.

### Experimental Procedures

Anodic oxide films were formed on cylindrical specimens, approximately 1 cm long and 1/2 cm in diameter, prepared from 1/4 in. diameter rod of 99.9995% or 99.999% purity (obtained from Materials Research Company and Leico Industries, Incorporated, respectively). The specimens were center drilled and tapped on one end for incorporation into a specimen assembly described by Greene (29), mechanically polished to 600 grit SiC paper, degreased with benzene followed by methanol, and finally rinsed with doubly distilled water. Some specimens were annealed at this stage of preparation for 1 hr at 80°C, but this was found to have no effect on the experimental results. Subsequently the specimens were chemically polished for 20 min in a solution of 3 parts nitric acid, 80 parts phosphoric acid, and 17 parts distilled water, rinsed with doubly distilled water, and dried with warm air.

Anodizing was conducted in a standard six hole Corning polarization cell, described by Greene (29). This incorporated two platinum counterelectrodes as well as the aluminum working electrode, a thermometer, and a gas inlet tube by which the electrolyte was continuously purged with nitrogen. Before each experiment all assemblies were meticulously cleaned with detergent, followed by concentrated hydrochloric acid, and thoroughly rinsed with doubly distilled water. All experiments were conducted at  $30^\circ \pm 0.5^\circ\text{C}$ . The anodizing electrolyte was a solution of 3 weight percent (w/o) reagent grade ammonium tartrate in doubly distilled water. In one portion of the work this solution was used as-prepared, having a pH value of 6.1; in other experiments it was titrated with dilute ammonium hydroxide to pH 7. The cases have been distinguished in reporting the results. In all experiments the anodic current was initially controlled at 1 mA/cm<sup>2</sup> until the anodizing potential reached 50V. This required approximately 5 min. Subsequent to this point in each experiment the potential was controlled at 50V. Experiments were terminated after intervals ranging from the point at which constant potential was imposed to 64 hr.

Several experiments were run for each anodizing time; except as noted all results are reported as averages determined from actual experimental values, with the data spread indicated where possible. For each experiment the following measurements were made:

(a) Total charge passed. Total charge passed after a given anodizing time was determined by integrating the as-recorded anodic current over time, using Simpson's rule. Values were normalized by division by individual, as-measured specimen areas.

(b) Oxide film weight. Two methods were used to determine the weight of oxide film formed during anodizing. In one technique the anodized specimens were carefully washed with doubly distilled water, then with methanol, and dried in a dessicator. The films were then removed by immersion of the speci-

mens in a saturated aqueous mercuric chloride solution. The films were rinsed in doubly distilled water and again in methanol. The lower surface tension of methanol as compared to that of water reduced the degree of distortion seen in the films on drying. The dried films were weighed with a Cahn RG electro-balance; repetitive measurements showed a reproducibility of 1  $\mu\text{g}$ . The films were not removed intact; in order to obtain the area represented by each weight measurement the films were photographed together with a scale and the areas of the resulting images were determined with a planimeter.

The other technique involved making three weight determinations for each specimen: (i) weight before anodizing, (ii) weight after anodizing, and (iii) weight after removal of the anodic film. Weight (ii) minus weight (iii) constituted the weight of the oxide film, while weight (i) minus weight (iii) represented the total aluminum reacted. Oxide film removal was accomplished by repeated brief immersions in a hot phosphoric-chromic acid solution (30), with degree of film removal being monitored by weight measurement.

The second of these methods provided an additional evaluation of the total amount of aluminum reacted, providing an internal check for each experiment, but was less sensitive than the first method due to the greater mass being weighed. Results using the two methods were in agreement.

(c) Aluminum dissolved in the electrolyte. Although this could be determined indirectly by the second gravimetric technique described above, it was measured directly for each experiment using an optical absorbance technique, ASTM Standard D857-69, Method C (31). This method was modified by omission of correction procedures for iron and fluoride, and by preparing standard solutions for calibration with fresh anodizing solution rather than with distilled water. A Cary spectrophotometer Model 14R was used.

In addition to the measurements described above selected films and substrates were examined using a Phillips EM300 transmission electron microscope and a Cambridge scanning electron microscope, respectively.

### Results

Typical anodic current *vs.* time curves are shown in Fig. 1 for pH 6.1 and 7. The behavior of anodizing current over extended periods of time is analogous to that previously reported (1, 2). A dependence of current on pH is evidenced, with current values being higher for pH 7 than for pH 6.1. The total charge passed is shown as a function of time in Fig. 2. Since the anodizing current is virtually constant after the first few hours, the charge passed is linear with time, with a nonzero intercept indicative of the relatively high current passed during the initial constant current region of anodizing. The slopes for pH 6.1 and 7 are 21.44 and 28.14  $\mu\text{A}/\text{cm}^2$ , respectively. The oxide film weight, shown *vs.* anodizing time in Fig. 3, exhibits a

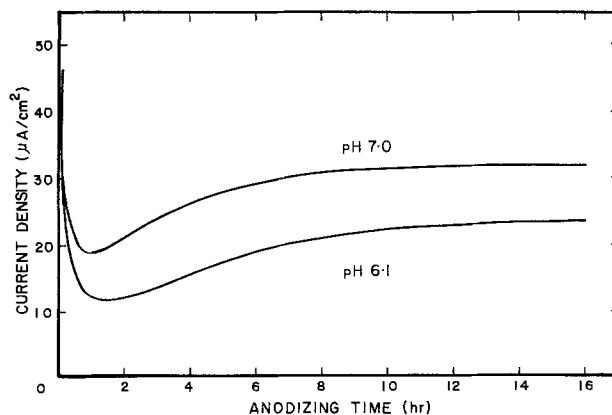


Fig. 1. Anodizing current *vs.* time

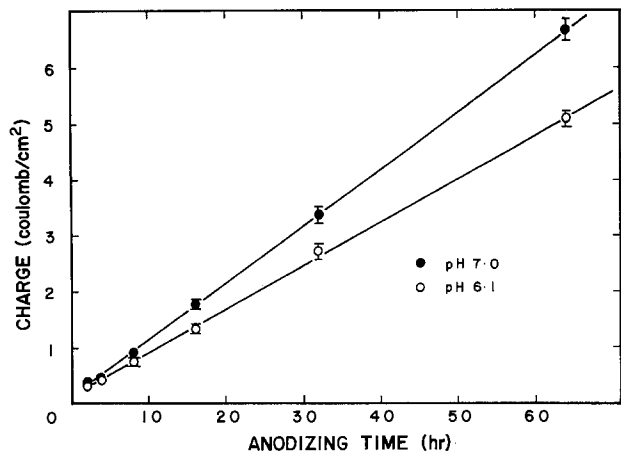


Fig. 2. Total charge passed per unit area vs. time

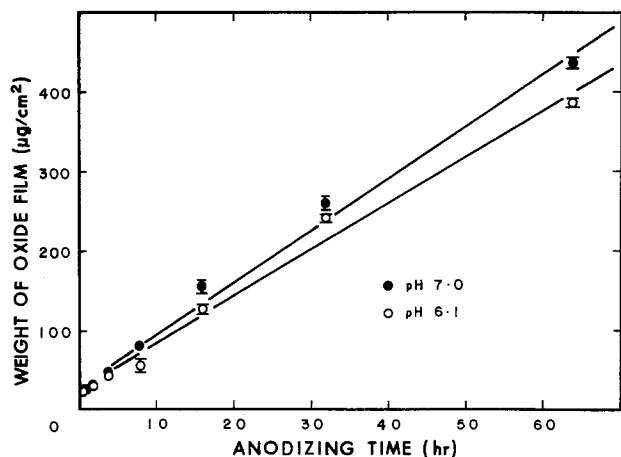


Fig. 3. Weight of anodic oxide per unit area vs. time

similar behavior, being approximately linear<sup>1</sup> with slopes of 5.84 and 6.57  $\mu\text{g}/\text{cm}^2\text{hr}$  at pH 6.1 and 7, respectively. Again, a nonzero intercept is seen, representative of rapid film formation under constant anodic current. The amount of aluminum dissolved in the anodizing electrolyte is shown in Fig. 4. Again, the behavior is approximately linear,<sup>1</sup> with a substantial dependence on pH, the slopes being 2.84 and 5.75  $\mu\text{g}/\text{cm}^2\text{hr}$  for pH 6.1 and 7, respectively. A near zero intercept and small

<sup>1</sup> Were the error brackets extended to the 95% confidence limits on the mean of each data set, the relationship would be linear. For convenience in the ensuing discussion, linearity is assumed.

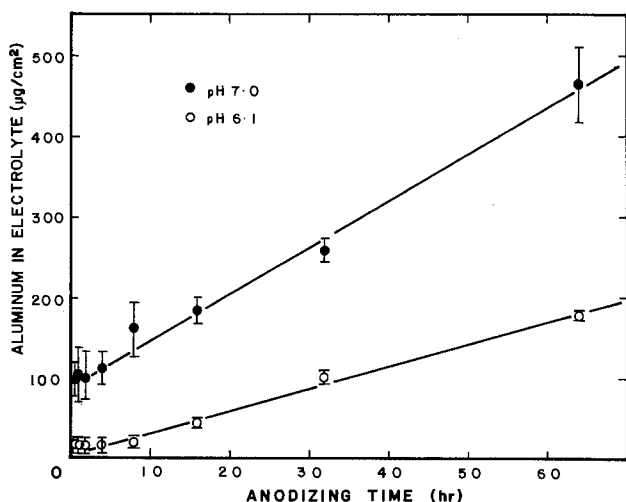


Fig. 4. Weight of aluminum in electrolyte per unit area vs. time

experimental scatter are seen at pH 6.1, while at pH 7 the intercept is approximately 90  $\mu\text{g}/\text{cm}^2$  and the scatter in analyses is substantial.

Transmission electron microscopy revealed pore development similar to that previously described (2), with pore initiation approximately coincident with the minimum in anodizing current shown in Fig. 1. With the use of stereo pairs (2), it was possible to directly measure the barrier layer thickness to be  $625 \pm 15 \text{ \AA}$ , corresponding to an anodizing constant of  $12.5 \pm 0.3 \text{ \AA}/\text{V}$ . SEM examination of the substrates revealed a substantial surface roughness, characteristic of chemical polishing.

Discussion

As noted in the preceding, a basic premise of this study was that the ionic current passed through the oxide could be accounted for by the appearance of aluminum as oxide and as aluminate ion dissolved in the electrolyte. It was further presumed that the difference between this value and the total current passed must represent electronic current. To facilitate comparison data from Fig. 3 and 4 were converted to equivalent charge, assuming that the oxide was stoichiometric  $\text{Al}_2\text{O}_3$  and that three equivalents of charge were passed for every gram atomic weight of aluminum oxidized. Figures 5 and 6 depict these comparisons for pH 6.1 and 7, respectively. The comparison for pH 6.1 is straightforward; the sum of the two ionic components of the charge passed, subtracted from the total charge passed, yields a net charge flow which must be attributable to electronic flow. This is not true at pH 7, where the sum of the ionic components is more than can be accounted for by the observed flow of charge through the external circuit.

This apparent discrepancy may be explained as follows. At pH 6.1 the charge representing dissolved aluminum has a zero intercept, indicating that the rate of dissolution essentially is constant in time. The total charge and the charge representing the oxide film have essentially identical positive intercepts, representing the initial high current period of anodizing. At pH 7, on the other hand, the charge flow due to dissolved aluminum, although linear, has a large positive intercept, representing a high dissolution rate at the onset of anodizing. This high rate is effective only for a brief period (results not shown in Fig. 6 suggest a period of less than 30 min of anodizing), beyond which the dissolution rate diminishes to a relatively small, constant value. The initial rapid dissolution of aluminum is clearly a nonelectrode process, inasmuch as there is insufficient charge flow in the external circuit to account for the oxidation of all of the aluminum by electrode processes. (As an example of such a nonelectrode process, we suggest reduction of one or both

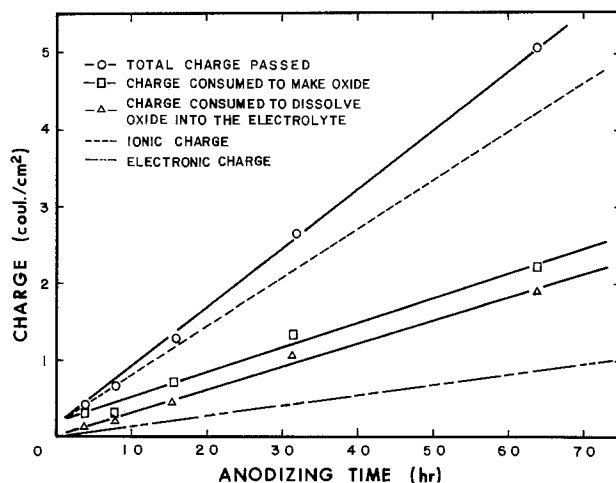


Fig. 5. Ionic and electronic contributions to total charge flow, pH 6.1.

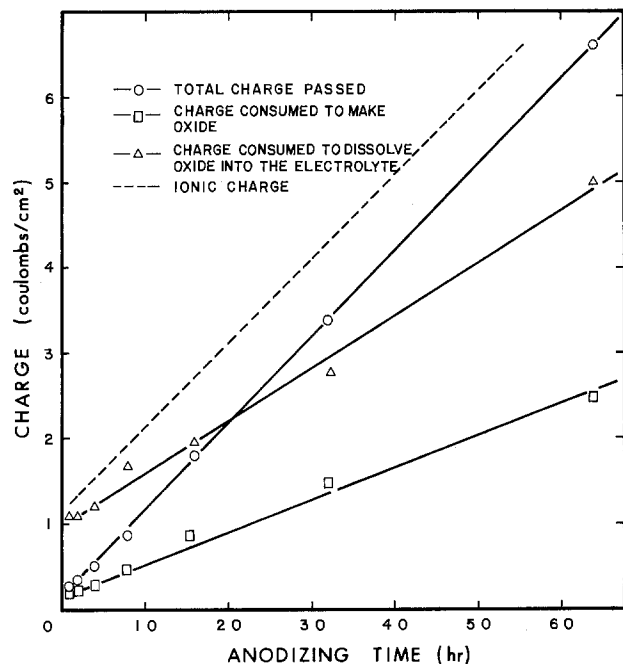
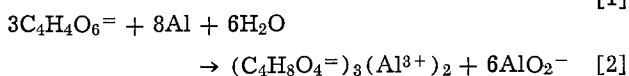
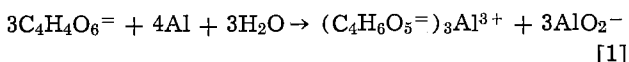


Fig. 6. Ionic contributions to total charge flow, pH 7

carboxyl groups on the tartrate ion by aluminum as more likely than evolution of hydrogen from hydroxyl ion or water due to the overwhelming tartrate concentration and the weaker nature of the carbon-oxygen bond as compared to the hydrogen-oxygen bond. These postulated reactions may be written, respectively



The reaction products are alcohols in which an ionic aluminum-oxygen bond has replaced a covalent hydrogen-oxygen bond.) Such a reaction will diminish markedly in rate as the anodic oxide develops; consequently, the nonelectrode dissolution is expected to be least significant in environments in which the anodic oxide is least soluble and therefore, develops most rapidly. In this regard it may be shown that anhydrous  $\alpha$ - $Al_2O_3$  exhibits minimum solubility in the vicinity of pH 5 (32). At higher pH, therefore, the solid oxide experiences a greater frequency of interaction with solvating hydroxyl ions via the reaction



so that the rate of dissolution as well as the equilibrium solubility must increase with increasing pH. Clearly, initial formation of the barrier oxide must progress more slowly at higher pH, allowing more time for nonelectrode dissolution in agreement with observation. (Although we recognize that there is considerable variation in the solubility data pertaining to the various morphological forms of aluminum oxide, and that the anodic oxide may be more properly regarded as a pseudo-amorphous  $\gamma$ - $Al_2O_3$  rather than  $\alpha$ - $Al_2O_3$  (33), we believe this argument to be qualitatively correct.)

Although the occurrence of a nonelectrode process precludes meaningful comparison of the components of the total charge passed at pH 7, it is clearly a discrete event pertaining only to the onset of anodizing and does not preclude comparison of components of the steady-state current developed after several hours of anodizing. Such currents, i.e., the slopes of the curves in Fig. 5 and 6, are listed in Table I. These values clearly indicate that the steady-state anodic current can be fully explained by electrochemical reactions involving both ionic and electronic currents.

Table I. Steady-state anodic current components

pH	Net current	Al as oxide	Dissolved Al	Total ionic current	Electronic current*
6.1	21.44**	9.21	8.46	17.67	3.77
7	28.14	10.64	17.13	27.77	0.37

\* By difference.

\*\* Current reported in  $\mu A/cm^2$ .

In discussing the values reported in Table I it is instructive to make use of the oxide growth/field-assisted dissolution model for porous oxide development (4, 9) depicted in Fig. 7. In this model a stable barrier oxide layer is presumed to exist, representing a steady-state balance of oxide growth due to field-assisted ionic transport on the one hand, and field-assisted dissolution of the oxide by the electrolyte on the other. A portion of the oxide dissolved by the electrolyte is presumed to precipitate to form a growing porous structure whose presence does not significantly affect the steady-state processes in the barrier layer. Recent dielectric studies have shown that the resistance of the film is dominated by the barrier layer even in the presence of a porous oxide layer orders of magnitude thicker (34). Components pertaining to barrier oxide development are plotted vs. field strength in the barrier oxide. To a first approximation, the rate of transport of ions through the oxide can be regarded as exponential with respect to the field (15), while a linear dependence of oxide dissolution on field has been previously assumed and found to be valid in describing the increase of pore diameter and depth with time (2). It is useful, but not essential, to regard the field strength as inversely proportional to barrier layer thickness, although it is clear that this represents an oversimplification (35). No significant dependence of ionic transport on pH is expected; however, as discussed above it may be assumed that the oxide dissolution rate will be higher at pH 7 than at pH 6.1, as illustrated. The dashed curves in Fig. 7 represent the net growth rate of the barrier layer, with the terminal or steady-state barrier layer being represented by zero growth rate.

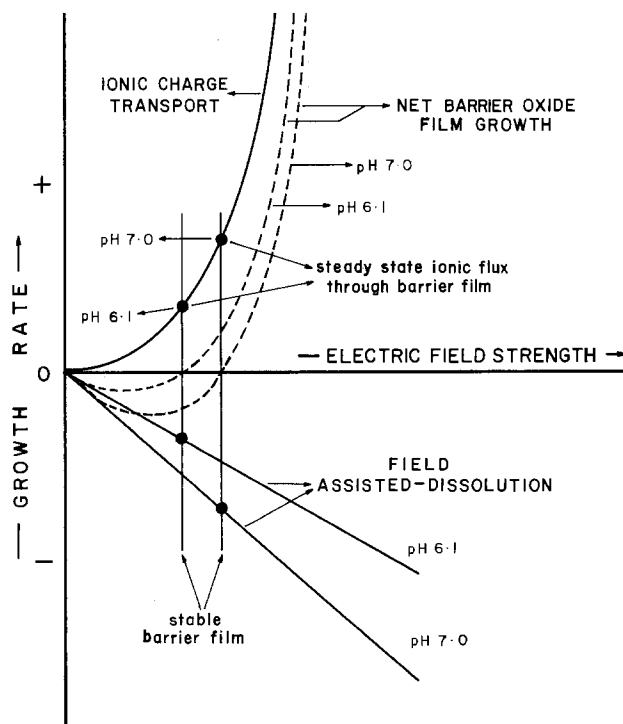


Fig. 7. Schematic representation of steady-state processes in the barrier layer.

The steady-state flux of ions through the oxide is clearly greater at pH 7 than at pH 6.1, reflecting the greater value of the field at steady state. This is in agreement with the values of total ionic flux reported in Table I. This model provides, however, no basis upon which to separate the total ionic flux into components representing growth of porous oxide and dissolution. Empirically, the growth rate is relatively insensitive to pH while, in agreement with the foregoing discussion, the dissolution rate is markedly enhanced by increase in pH in this range.

The observed dependence of electronic current on pH must be associated with a pH dependence of reducing agents at the oxide/electrolyte interface. Smith (22) has suggested electron injection by hydroxyl ions as the origin of the electronic current, although he and others later espoused a "weak spot" theory for conduction in anodic films (23, 15, 24). If electron injection by hydroxyl ion oxidation, in fact, occurs, the increased availability of hydroxyl ion at higher pH would suggest an increased electronic current. On the other hand, the data indicate a marked increase in the dissolution of oxide with increase in pH, effectively consuming near-surface hydroxyl ions by means of reaction (3). In other words, the higher flux of aluminum through the oxide/electrolyte interface may reduce the residence time of hydroxyl ions at the surface, thereby reducing the probability of an oxidation event. It is also possible to postulate oxidation of the tartrate hydroxyl groups as the electron injection mechanism, again with the increased instability of the surface oxide as the reason for reduced levels of injection at higher pH. Clearly further work involving other pH values is necessary in order to be definitive about this point.

In accord with the model of pore development, oxide film weights obtained prior to the appearance of the current minimum in Fig. 1 are representative of the barrier layer which, during the period of rapid current decay prior to the minimum, is growing only very slowly. Weights of films grown for 30 min in both pH 6.1 and 7 electrolytes are approximately equal, 27  $\mu\text{g}/\text{cm}^2$ . Using an oxide density of 3.2  $\text{g}/\text{cm}^3$  (36, 37) this observation corresponds to an anodizing constant of 16.9  $\text{A}/\text{V}$  in contrast to the directly observed value of 12.5  $\text{A}/\text{V}$ . Similarly, the steady-state current value of 28.14  $\mu\text{A}/\text{cm}^2$  measured at pH 7 is in contrast to the value of 17  $\mu\text{A}/\text{cm}^2$  obtained in the same environment on electropolished specimens (2). Both of these apparent discrepancies may be attributed to the significant surface roughness derived from the chemical polishing technique. Defining a surface roughness factor as the ratio of the true surface area to the macroscopic surface area, values of 1.35 and 1.65 are derived for the two observations, respectively, in qualitative agreement with SEM observations of the substrate.

### Conclusion

The steady-state leakage current observed on anodizing aluminum in a barrier-forming electrolyte, 3 w/o ammonium tartrate, may be regarded as the sum of three components: ionic currents leading to porous oxide formation and to dissolution of aluminum, and an electronic current observed as the difference between the net current and the ionic currents. The net current increases from pH 6.1 to 7, largely due to a doubling in the rate of aluminum dissolution, while the rate of porous oxide formation is relatively pH insensitive. The electronic current decreases with increase in pH, representing 17% of the total current at pH 6.1, but only 1.3% at pH 7. These observations are consistent with an established model of steady state in the barrier oxide layer with an increase in the rate of field-assisted dissolution at the higher pH. The decrease in electronic current with pH is attributed to instability of the oxide surface with a consequent decrease in the residence time of reducible species. A marked nonelectrode dissolution of aluminum is seen at pH 7, attributed to tartrate ion reduction.

### Acknowledgment

This work was sponsored by the National Science Foundation through grants GH 35580 and DMR 72-03201-A01, "Environment-Affected Properties of Oxide Films as Related to Defect Structure."

Manuscript submitted June 1, 1976; revised manuscript received Aug. 2, 1976.

Any discussion of this paper will appear in a Discussion Section to be published in the June 1977 JOURNAL. All discussions for the June 1977 Discussion Section should be submitted by Feb. 1, 1977.

Publication costs of this article were assisted by the University of Connecticut.

### REFERENCES

1. P. G. Anderson and O. F. Devereux, *This Journal*, **122**, 267 (1975).
2. Y. H. Choo and O. F. Devereux, *ibid.*, **122**, 1645 (1975).
3. T. A. Libsch and O. F. Devereux, *ibid.*, **122**, 1654 (1975).
4. J. P. O'Sullivan and G. C. Wood, *Proc. R. Soc. London, Ser. A*, **317**, 511 (1970).
5. J. E. Lewis and R. C. Plumb, *This Journal*, **105**, 496 (1958).
6. J. A. Davies, J. P. S. Pringle, R. L. Graham, and F. Brown, *ibid.*, **109**, 999 (1962).
7. J. A. Davies and B. Domeij, *ibid.*, **110**, 849 (1963).
8. J. A. Davies, B. Domeij, J. P. S. Pringle, and F. Brown, *ibid.*, **112**, 675 (1965).
9. T. P. Hoar and N. F. Mott, *J. Phys. Chem. Solids*, **9**, 97 (1959).
10. D. A. Vermilyea, *This Journal*, **110**, 345 (1963).
11. M. A. Heine and M. J. Pryor, *ibid.*, **110**, 1205 (1963).
12. A. J. Brock and G. C. Wood, *Electrochim. Acta*, **12**, 395 (1967).
13. T. P. Hoar, D. C. Mears, and G. P. Rothwell, *Corros. Sci.*, **5**, 279 (1965).
14. G. T. Rogers, P. H. G. Draper, and S. S. Wood, *Electrochim. Acta*, **13**, 251 (1968).
15. L. Young, "Anodic Oxide Films," Academic Press, New York (1961).
16. W. Ch. van Geel, *Physica*, **17**, 761 (1951).
17. W. Ch. van Geel, *Halbleiterprobleme*, **1**, 291 (1955).
18. R. L. Taylor and H. E. Haring, *This Journal*, **103**, 611 (1956).
19. Y. Sasaki, *J. Phys. Chem. Solids*, **13**, 177 (1960).
20. J. F. Dewald, in "Semiconductors," N. B. Hannay, Editor, p. 729, Reinhold, New York (1959).
21. A. K. Vijh, in "Oxides and Oxide Films," J. W. Diggle, Editor, Vol. 2, p. 1, Marcel Dekker, New York (1973).
22. A. C. Smith, *Can. J. Phys.*, **35**, 1151 (1957).
23. A. C. Smith, *ibid.*, **37**, 591 (1959).
24. D. A. Vermilyea, *J. Appl. Phys.*, **27**, 963 (1956).
25. J. W. Diggle, T. C. Downie, and C. W. Goulding, *Chem. Rev.*, **69**, 365 (1969).
26. T. P. Hoar and J. Yahalom, *This Journal*, **110**, 614 (1963).
27. M. S. Hunter and P. F. Towner, *ibid.*, **108**, 139 (1961).
28. J. S. Leach and P. Neufeld, *Corros. Sci.*, **9**, 413 (1969).
29. N. D. Greene, "Experimental Electrode Kinetics," Rensselaer Polytechnic Institute, Troy, N.Y. (1965).
30. ASTM Standard B 137-45, "The Weight of Coating on Anodically Coated Aluminum," *Annual Book of ASTM Standards Part 6*, p. 87, Amer. Soc. for Testing and Materials, Easton, Md. (1972).
31. *Annual Book of ASTM Standards*, Part 23, p. 70, Amer. Soc. for Testing and Materials, Easton, Md. (1972).
32. M. Pourbaix, "Atlas D'Equilibres Electrochimiques, Gauthier-Villars & Cie, Paris (1963).
33. D. J. Stirling and R. W. Bicknell, *This Journal*, **106**, 481 (1959).
34. T. A. Libsch and O. F. Devereux, *ibid.*, **123**, 864 (1976).
35. J. S. Enochs and O. F. Devereux, Unpublished.
36. G. Haas, *J. Opt. Soc. Am.*, **39**, 532 (1949).
37. R. C. Plumb, *This Journal*, **105**, 498 (1958).

# Studies of the Ag-Pt Interface Formed by Ag Deposition from Sulfolane Solutions on Thin Film Electrodes

Rod K. Quinn,\* M. L. Knotek,\* and N. R. Armstrong<sup>1</sup>

Sandia Laboratories, Albuquerque, New Mexico 87115

and N. E. Vanderborgh

Los Alamos Scientific Laboratory, Los Alamos, New Mexico 87545

## ABSTRACT

Vapor deposition, thin film fabrication techniques have been applied to the preparation of Pt electrodes of various topographies. Large variations were observed in the electrical resistivities of these electrodes as a function of porosities. The effect of these film preparation techniques on Ag electrodeposition from solutions of  $\text{AgClO}_4$  in sulfolane was examined. Roughness factors, obtained from differential capacitance measurements, varied from 1.0 to 32.8 over the range from bulk Pt to the most porous films. Analysis of cyclic voltammetric data and double potential step chronocoulometric results indicate silver deposition occurs without underpotential deposition in sulfolane in contrast to behavior found in aqueous medium. Little difference is noted in the diffusion-controlled Ag deposition currents as a function of active electrode surface area except at the shortest electrolysis times,  $\leq 5$  msec. Auger electron spectroscopy and argon ion sputter etching were used to examine the surface and depth profile of controlled potential-deposited thin layers of Ag. Porous films showed deep penetration of all monitored species (Ag, Pt, S, Cl). Detectable amounts of solvent and Ag are found throughout the film electrode. The degree of penetration decreases rapidly with increasing film density. The surface analysis results have been correlated to the electrochemical behavior and interpreted in terms of the extent of solvent, solute interaction prior to electrodeposition.

In recent years, the interest in using thin metal films for basic electrochemical studies has increased. High purity surfaces of various stoichiometries and topographies are routinely prepared using a variety of high vacuum techniques (1-7). Highly reproducible surfaces can be produced which need no additional pretreatment and are thus not subject to possible artifacts caused by polishing or other chemical treatment.

We have previously studied the variation in heterogeneous charge transfer rate of the ferrocene oxidation in the aprotic solvent sulfolane, at a variety of vapor deposited metal films (7). This present work describes the electrochemical deposition of silver using this solvent system. Studies in sulfolane are free from complicating electrode reactions, especially oxidation and reduction of the metallic surface (1,7). In addition, it is possible to measure the solvent interaction with the electrode using surface analysis techniques such as Auger electron spectroscopy (AES). This interaction may explain the abnormally low rates of heterogeneous charge transfer determined in this solvent (7).

Extensive studies of silver deposition in protic solvents have been reported for bulk metal, single crystal and vapor-deposited thin film electrodes (3, 6, 8-10). These data have led to the conclusion that the diffusion-controlled electrodeposition process is preceded by one or more monolayer depositions of the metal at potentials positive to the formal reduction potential (8). Direct plating then proceeds on this underpotential deposited layer.

This electrodeposition reaction represents the most direct type of electrode interaction. The deposition of silver was selected to demonstrate the extent of solvent and depolarizer interactions with several platinum film types. These processes were studied by comparing electrochemical behavior of thin films in the absence and presence of silver ion followed by surface analysis.

\* Electrochemical Society Active Member.

<sup>1</sup> Present address: Chemistry Department, Michigan State University, East Lansing, Michigan 48824.

Key words: thin film electrodes, surface capacitance, chronocoulometry, Auger electron spectroscopy, ion sputter etching.

Surface analysis techniques have been employed increasingly to study electrode surfaces in attempts to determine the type and extent of interaction with solution components (1,11) or to deduce stoichiometric changes where mixed metal or metal oxide electrodes are employed (12-15). The electrodeposition of silver from solution has served as a model for these studies, especially the Auger analysis of thin metallic films (1,16). Results reported here pertain to the study of the silver-platinum electrode system. Complete details of the surface analysis techniques and examination of possible experimental artifacts will be described elsewhere (16).

## Experimental

Chemical purification procedures for sulfolane (Shell Chemical) have been previously described (17). Tetrabutylammonium perchlorate (TBAP) and silver perchlorate, both obtained from Eastman Chemicals, were recrystallized from ethanol.

Platinum film electrodes, 20-30 nm thick, were prepared by vapor deposition sputtering. The details of this technique and a description of the resultant films can be found in Ref. (1) and (2). The density of the deposited metal was controlled by varying the argon pressure (20-80  $\mu\text{m}$ ) and by controlling the platinum target bias potential (1-4 kV). The highest density films were fabricated using electron beam evaporation of platinum under ultrahigh vacuum ( $\leq 10^{-9}$  Torr) conditions (16). These thin films were deposited onto either quartz (Esco Products) or sapphire (Adolph Mueller Company) substrates. Both surfaces were of good optical quality ( $\approx 25\text{\AA}$  rms roughness). The substrates were cleaned by (i) boiling in trichloroethylene, (ii) boiling in methanol, (iii) boiling in an Alconox solution, (iv) scrubbing with cotton using a hot Alconox solution, (v) boiling in distilled water, (vi) drying with a stream of dry nitrogen or argon, and (vii) repeating steps (iii)-(vi). The substrates were then clamped to a copper block secured on a flange to be mounted in the top of an ultrahigh vacuum system. The copper block had both

heaters and thermocouples affixed to it. A shutter mounted between the samples and the evaporator exposed one of three sample positions at a time so that three different types of films (e.g., thickness, substrate temperatures, evaporation rate, etc.) could be made on a given cycle of the vacuum system. The Pt metal (this technique is applicable to almost any material) was evaporated from a nickel-plated, water-cooled copper e-gun hearth (Varian Model 980-0001). The platinum used was at least 0.9999 pure and was formed into a button to fit into the hearth by arc melting high purity Pt wire in a He atmosphere. The thickness of the film was monitored using a Kronos FTT-300 quartz oscillator thickness monitor which was water cooled. The evaporation rate was less than 1 Å/sec for the films reported here. Before evaporation the substrates were heat cleaned at  $\approx 300^\circ\text{C}$  for 2-8 hr in ultrahigh vacuum (the entire vacuum system was prebaked at  $\approx 150^\circ\text{C}$ ). The substrates were held at  $\approx 250^\circ\text{C}$  during evaporation. The resulting films were of extremely high optical quality.

The Teflon electrochemical cell has been previously described (1, 7). The design is similar to that used for spectroelectrochemistry. Solution volume of this cell was approximately 2 cm<sup>3</sup>; an electrode of 0.108 cm<sup>2</sup> geometric area was used. The Ag reference electrode (AgRE) for this work was a silver wire previously anodized in a 0.1M TBAP solution. This electrode was positioned within 0.1 cm of the working electrode to minimize solution resistance. A large platinum flag positioned along the wall of the solution chamber served as the counterelectrode.

All solutions were deaerated with a purified argon stream for 1 hr immediately prior to use. Solutions were transferred to the electrochemical cell under an argon atmosphere and the electrochemical cell was sealed prior to measurement. Temperature was controlled at  $50.0 \pm 0.3^\circ\text{C}$  by means of an oil circulation system which flowed through the cell body; temperature could be varied from  $20^\circ$  to  $80^\circ\text{C}$ . Temperature was monitored using a thermistor probe which protruded directly into the solution. The thermistor was part of a bridge circuit which has been previously described (17).

Electrochemical measurements were made with techniques described previously (7, 17). The potentiostat was equipped with positive feedback compensation. Differential capacitances were determined using previously described methods (18). Usual cyclic voltammetric and double potential step experiments are described in the text. In certain experiments, the charge-time rather than current-time relationships were determined. Plating experiments were also conducted under conditions of diffusion control. Plating times ranged from 50 msec to 120 sec. After cathodic deposition, the potential on the electrode was stepped to a point where silver oxidation occurred.

Auger analysis of several electrodes was conducted following the electrochemical experiments. Small quantities of silver were deposited onto the electrodes. This was done either by controlled potential coulometry or by simply immersing the electrodes into a silver-containing solution. In some cases the silver was removed by anodic stripping. Following each electrode preparation, the materials were thoroughly washed with triply distilled ethanol, dried with high purity argon, and then introduced into the Auger spectrometer.

Auger measurements were made on an instrument constructed in these laboratories (19). This consisted of an all-metal, baked, ultrahigh vacuum system using an Auger spectrometer similar to that described by Gerlach and Tipping (20). The electron beam was controlled at 2 keV during an experiment and maintained a beam current of 10-20  $\mu\text{A}$ . The diameter of the incident electron beam was varied to control power density. The electron gun was coaxial to the analyzer.

After each Auger analysis, fractions of the electrode surface were removed by means of argon ion sputtering. The resulting surface was then reanalyzed. The ion beam was controlled at 1-2 keV with an argon background pressure of  $4 \times 10^{-5}$  Torr. This resulted in sputtering rates of 1.5-3.0 nm/min. Details of the calibration of sputtering rates are described elsewhere (16). This calibration was done by sputtering through measured thicknesses of platinum and silver films deposited on quartz substrates. Sputtering rates were the same for all types of platinum films.

## Results and Discussion

Electrode fabrication techniques resulted in four different types of electrode surfaces for study. Ion sputter deposition resulted in two quite different surfaces. Under conditions of relatively low target bias (2 keV) and high argon background pressure (80  $\mu\text{m Hg}$ ), a highly porous electrode was produced. Scanning electron microscopy (SEM) analysis indicated surface defects as large as  $\sim 100$  nm in width and 3000 nm in length for the 5000 nm thick films (1). High target bias voltages (4 keV) and low argon pressures (25  $\mu\text{m Hg}$ ) resulted in denser platinum films. This second type of film is subsequently referred to as medium porosity. SEM photographs at up to 10,000 $\times$  magnification showed little defect structure in these films. Conditions of high target bias and low background pressure allow appreciable surface diffusion before immobilization occurs. Alternate conditions of low target bias and high argon pressure cause immobilization of platinum into a dendritic type of film which leads to a porous structure (21). The densest film electrodes were prepared by electron beam evaporation onto heated substrates under ultrahigh vacuum (UHV). These UHV conditions permit maximum surface diffusion and result in the closest packed metal film (21). No surface structure could be observed by SEM at the highest possible magnification in this third thin film electrode type. The fourth electrode type (bulk Pt) was prepared by abrasively cleaning 10 mil Pt metal foil.

Film resistivities were determined using a four-probe technique that corrects for contact resistance (22). Measured values are listed in Table I. Increases in resistivity were observed as the porosity of the film increased. Resistivities for each film type also increased as the thickness of the deposit was decreased. These data are consistent with previously reported thin film resistance values (5, 21). Since the film thicknesses and the surface defect sizes approach the mean free path of the conduction electrons, these results seem reasonable (21).

Solution capacitance measurements (18) were made with each of these electrode types; results are also included in Table I. Measured capacitance-potential relationships for the different films are qualitatively similar although shifted in magnitude. Substantial increases in capacitance shown in Fig. 1, are observed for the porous electrodes. At 0.0V vs. the AgRE, the differential capacitance increased from 8.2 to 68  $\mu\text{F}/\text{cm}^2$  for the bulk platinum and porous films, respectively.

Table I. Physical and electrical properties of Pt bulk and film electrodes

Electrode	Thickness	$\rho$ ( $\mu\Omega\text{-cm}$ )	$C_{a,1}$ at 0.0V* ( $\mu\text{F}/\text{cm}^2$ )	Relative roughness factor**
Pt foil	0.13 mm	10	8.2	1.0
Pt (dense) on Al <sub>2</sub> O <sub>3</sub>	40 nm	20	9.9	1.45
Pt (med) on SiO <sub>2</sub>	45 nm	23	11.4	1.87
Pt (porous) on SiO <sub>2</sub>	50 nm	35	68	32.8

\* E (volts vs. AgRE).

\*\* Roughness factors were determined from slope of electrode charge vs. applied potential, ( $\Delta q/\Delta V$ ), at + 0.5V, cf. Fig. 2.



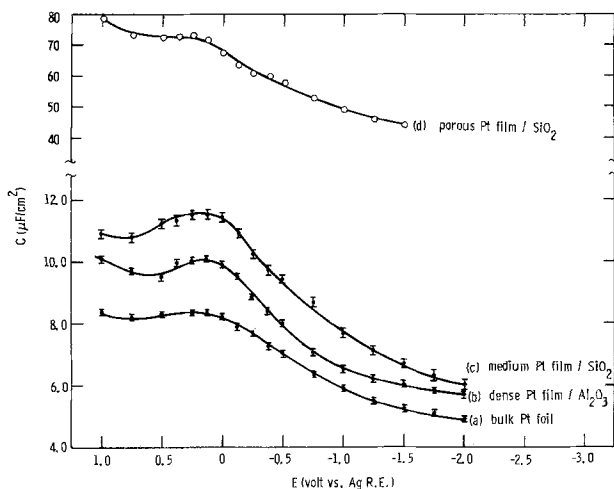


Fig. 1. Capacitance of four Pt electrode types measured as a function of applied potential ( $E$ ) vs. an Ag reference electrode. Measurements were made in 0.1M TBAP in sulfolane.

The charge-potential relationship was derived from the capacitance-potential plots and is shown graphically in Fig. 2. An electrode potential near the minima in the capacitance plot was arbitrarily chosen as the zero limit of electrode surface charge and electrode charges were computed from this point. From the slope of the charge-potential curves at the zero charge potential, relative roughness factors were evaluated for each electrode compared to the bulk metal (Table I). These slopes should be directly proportional to the electrochemically wettable electrode area (23). As expected, the relative roughness factor for the most porous film suggests appreciable void structure in this material.

Silver deposition from sulfolane solutions was measured on each electrode type. Figure 3 shows a cyclic voltammogram for this process from a 1 mM  $\text{AgClO}_4$ /0.1M TBAP solution using a platinum film electrode. Analysis of the current-voltage characteristics on the cathodic branch shows the  $\log(i_p - i)$  vs.  $E$  relationship is linear at the onset of the reduction. The silver reduction is slow in this medium. Separations in peak potentials exceeded 200 mV at scan rates greater than 20 mV/sec. For sweep rates of less than 20 mV/sec, integration of current as a function of time (for potential limits +0.325 to -0.350V vs. AgRE) indicates that the

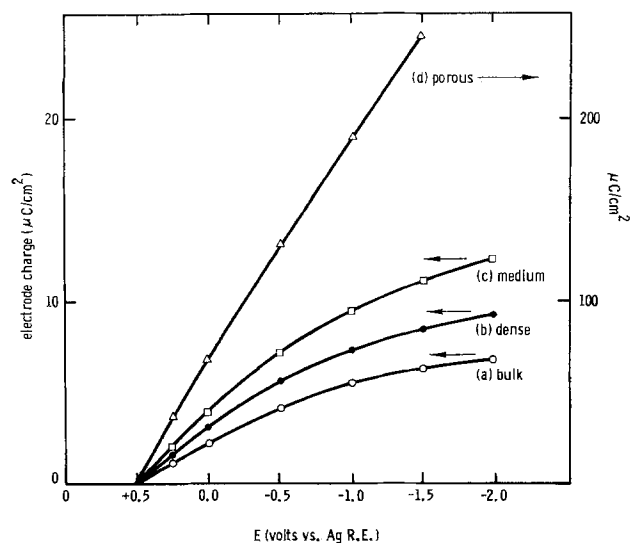


Fig. 2. The charge-potential relationship for each electrode type shown in Fig. 1. Results were derived from the capacitance-potential curves.

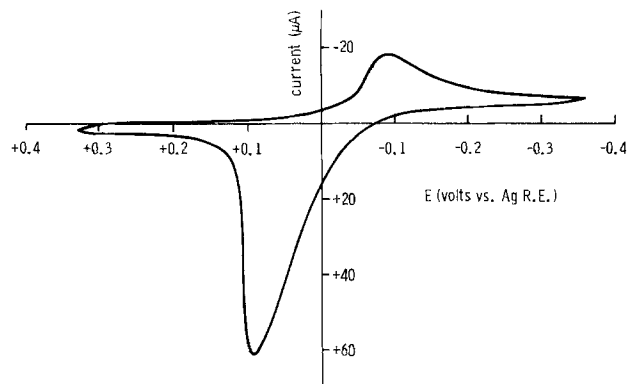


Fig. 3. Cyclic voltammogram scan of Ag plate and strip at a 20 nm Pt film of medium porosity on  $\text{SiO}_2$ . The electrolyte was 0.1 mM  $\text{AgClO}_4$ /0.1M TBAP/sulfolane solution. The scan rate was 20 mV/sec with a measured electrode area of 0.1  $\text{cm}^2$ .

charge passed on the reduction step,  $Q_r$ , is equal to that passed during the oxidation process,  $Q_b$ , i.e., that  $Q_r/Q_b = 1.00$ . There is no electrochemical evidence that residual silver is retained on the surface. Also, no underpotential deposition of silver was observed even when the silver concentration was increased by over an order of magnitude from that shown in Fig. 2. Potential scans were initiated at potentials more anodic than Fig. 3, yet no predeposition of silver was observed. This suggests that the solvation of silver ion by sulfolane competes favorably with solvation or neutralization of the ion by the metal surface. Silver deposition appears more straightforward in this solvent system compared to that found in aqueous media. Previous aqueous studies showed the necessity for the deposition of up to 2 monolayers of silver on the platinum surface prior to bulk deposition (6, 8, 10). The requirement for a reduced platinum surface for aqueous silver deposition has also been demonstrated (8). No oxidation or reduction of the platinum surface was observed electrochemically in these sulfolane experiments and surface oxides were not observed in the subsequent surface analysis experiments.

Double potential step chronocoulometric experiments were also made using these metallic films. Here the working electrode was stepped to a potential where diffusion-controlled reduction occurred and after a time,  $\tau$ , back to a potential corresponding to the oxidation of the deposited silver. Figure 4 shows a charge vs.  $(\text{time})^{1/2}$  plot for a  $\tau = 50$  msec experiment. The linear relationship suggests a diffusion-controlled reduction step. This result was found for all the electrodes investigated. This implies that the active electrochemical area of each electrode is approximately equal during this time frame. Similar current distributions should result if the size of the average surface defect is less than the diffusion layer thickness,  $2(Dt)^{1/2}$  (24). For electrolysis times of 5 msec and assuming a diffusion coefficient of  $10^{-6}$   $\text{cm}^2/\text{sec}$  (7,17), this thickness is 44  $\mu\text{m}$ , or more than an order of magnitude larger than the largest defect size measured by SEM. Variations in active electrode area at shorter electrolysis times were difficult to ascertain since the finite surface resistance of the platinum films caused a negative deviation in the charge vs.  $(\text{time})^{1/2}$  traces. At 5 msec and using a silver concentration of 1 millimolar, approximately 5% of an equivalent monolayer of silver was deposited.

The ratio of charge transferred on the oxidation step,  $Q_{b,2\tau}$  (at time =  $2\tau$ ), to charge measured on the reduction step,  $Q_{f,2\tau}$  (at time =  $\tau$ ), was computed. For every electrode, the ratio  $Q_{b,2\tau}/Q_{f,\tau}$  was determined as 0.5-0.6 at  $\tau = 50$  msec, 0.6-0.7 at  $\tau = 100$  msec, and increased to one as  $\tau$  approached 500 msec. The shape of the current-time traces for the reduction step is con-



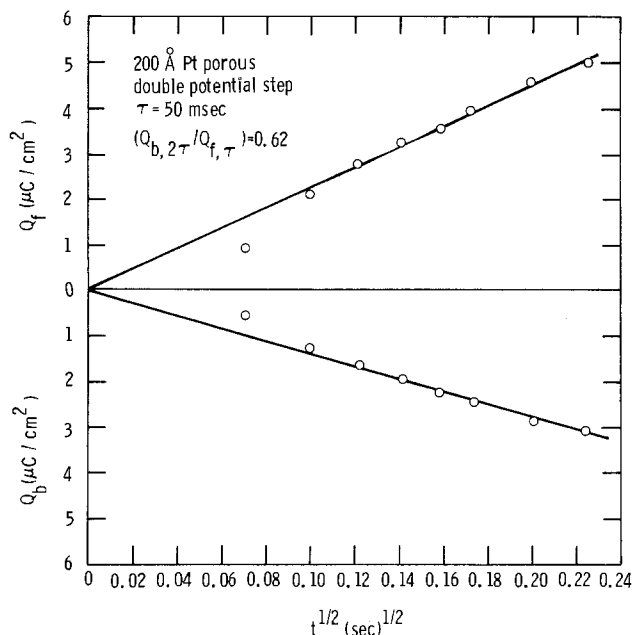


Fig. 4. Double potential step chronocoulometric results for a 50 msec plating ( $Q_f$ ) and stripping ( $Q_b$ ) experiment at a 20 nm porous Pt film. The plating solution was 0.1 mM  $\text{AgClO}_4/0.1\text{M}$  TBAP/sulfolane.

sistent with the type proposed by Thirsk and Harrison for progressive nucleation of silver on the electrode surface (25).

Experiments were conducted at much longer electrolysis times depositing larger amounts of silver (several hundred equivalent monolayers) followed by electrochemical stripping. The charge-time behavior was again observed. Specular reflectance studies show differences in the deposition reaction of silver between the first equivalent monolayer and subsequent reactions of silver deposition upon silver (6). Similar differences might be expected for the reactions reported here. Figure 5 shows a discontinuity in the normalized charge-time relationship when greater than 95% of the total silver has been removed from the electrode surface. This break may represent a change in the stripping mechanism from stripping of silver from silver to the removal of the last equivalent monolayers of silver from the platinum film. Slight differences were noted

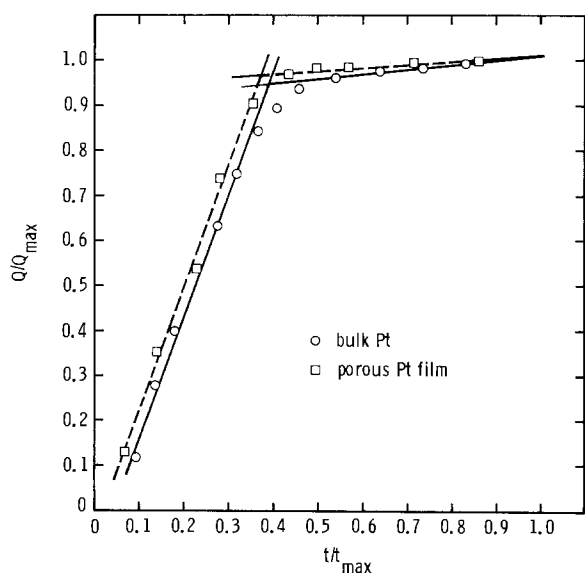


Fig. 5. Normalized charge-time relationship for anodic stripping of electrodeposited Ag at bulk Pt ( $\circ$ ) and 20 nm porous Pt film ( $\square$ ) electrodes.

between the several electrode studies. The position of this break in the charge-time plots always occurs at earlier dimensionless times for the more porous electrodes. The data suggest that these films expose a larger area of platinum available for deposition than does bulk metal.

The results of these stripping experiments can be compared with results obtained from Auger analysis of electrodes treated in a similar manner. Figure 6 shows several Auger spectra taken on a medium porosity, 20 nm Pt film, which had been previously electrodeposited with 50  $\mu\text{C}$  (approximately 14 equivalent monolayers) of silver from a 1 mM  $\text{AgClO}_4/0.1\text{M}$  TBAP/sulfolane solution. This amount of silver corresponds to a 2 nm thickness on the planar surface. The Auger energies are displayed from 0 to 500 eV. Auger analysis shows appreciable quantities of sulfur, chlorine, carbon, and silver. No signals are seen for the platinum substrate. Figures 6b, c, and d show spectra for the same electrode after various argon ion sputtering times. Sputtering rates (16) were 3 nm/min; thus these traces were run at depths of 3, 7.5, and 17.5 nm. Depth profiles for the elements of interest were constructed from these Auger spectra by measuring the peak-to-peak amplitude of each Auger transition at each sputtering depth. Typical results for two electrodes are shown in Fig. 7. The silver peak amplitude was computed using the 356 eV, MNN transition. The platinum peak was measured using the 237.5 eV signal, MMN transition, which did not interfere with other significant Auger signals. The sulfur and carbon levels were estimated from Auger transitions which overlapped slightly with signals from platinum and silver.

From these data it is apparent that silver is found well into the platinum matrix and this penetration is far greater than that of the solvent, represented by the carbon and sulfur signals. Data in Fig. 7 sug-

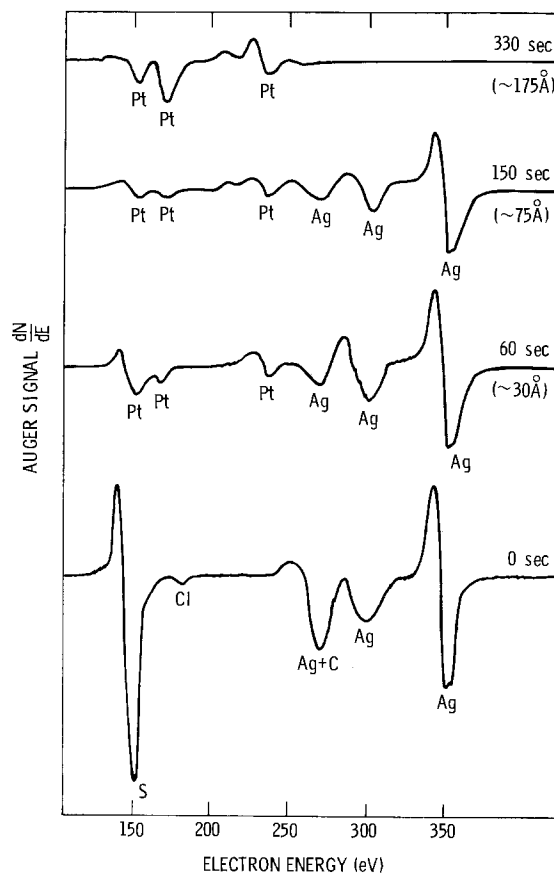


Fig. 6. Auger electron spectra over a limited energy range for a 20 nm, medium porosity Pt film with 500  $\mu\text{C}$  of electrodeposited Ag from 1 mM  $\text{AgClO}_4/0.1\text{M}$  TBAP/sulfolane. The times denote sputtering times with approximate depth after sputter in parentheses.

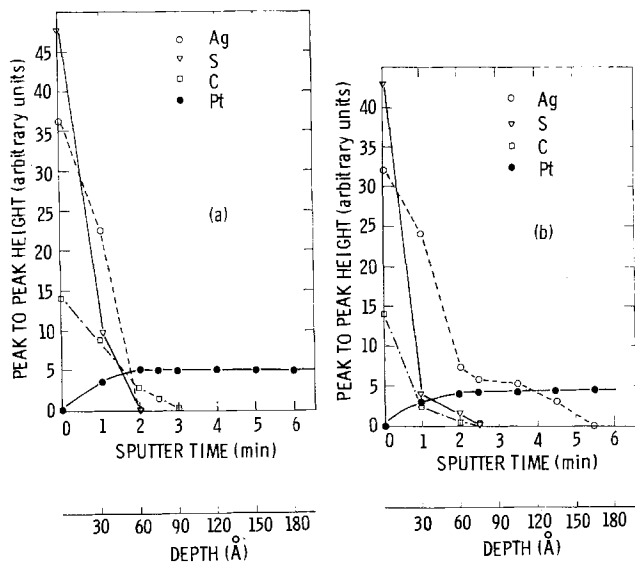


Fig. 7. Depth profiles for (a) medium dense and (b) porous Pt film electrodes plotted in peak-to-peak ratios of principal Auger electron peaks for Pt, Ag, C, and S. The depth is expressed both in sputter time and depth as estimated from the sputtering rate (17). In these experiments 500  $\mu\text{C}$  of Ag was electrodeposited from  $\text{AgClO}_4/\text{TBAP}/\text{sulfolane}$  solution onto 20 nm Pt film electrodes.

gest that extent of silver penetration correlates well with measured electrode porosities. Experiments done on the highest density platinum films as well as bulk metals show only a slight penetration of silver, *i.e.*, the Auger depth profiles show a sharp silver-platinum boundary. Figure 7a shows this boundary is broad for the medium dense platinum film while Fig. 7b shows silver may be in appreciable concentration throughout the entire porous platinum film thickness (20 nm). We assume our depth resolution for these experiments is sufficient to distinguish between cases Fig. 7a and 7b (16). We also assume that the escape depths of the Auger electrons from these films are approximately equal and that differential sputtering of individual atoms did not occur. This has shown to be the case in other experiments (16). No evidence for selective penetration or "knock on" of silver by the argon beam has been observed.

Figure 8 further emphasizes the extent of silver penetration during electrodeposition. The Auger signals from three platinum electrodes, normalized to the measured surface signal, are shown *vs.* sputtering depth. The extent of penetration of silver in a dense

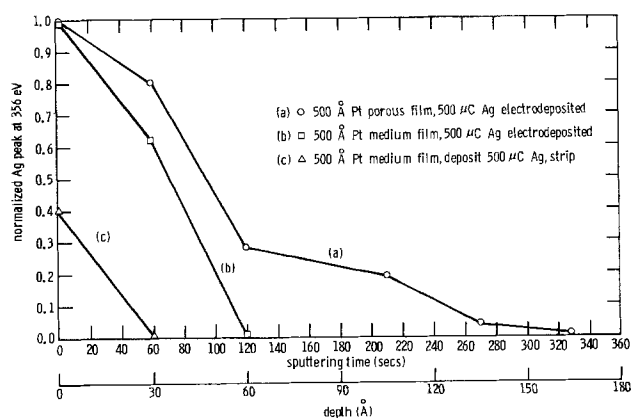


Fig. 8. Silver Auger electron peak at 356 eV (normalized to the measured surface signal) as a function of electrode depth for three platinum electrodes. All were treated in 0.1  $\text{mm}$   $\text{AgClO}_4/0.1\text{M}$   $\text{TBAP}/\text{sulfolane}$  solutions: (c) was plated with 5 nm of Ag then electrochemically stripped for a time equal to the plating time.

film which had been plated with approximately 5 nm of silver was studied in the following manner.

The electrode was electrochemically oxidized for a time sufficient to remove that same amount of silver. The absolute magnitude of the silver is lower and the penetration depth is appreciably less than that found for the fully deposited electrode. It is clear that the stripping step did not completely remove the silver deposit. We cannot rule out the possibility that this represents underpotential deposited silver, even though electrochemical experiments did not indicate its presence. Experiments where the electrodes were immersed in silver-containing solution with no electrolysis showed only minor levels of silver which were completely removed with less than 10 sec of argon sputtering, corresponding to a depth of less than 0.5 nm.

These sets of experiments provide interesting comparisons of the electrochemical behavior on several types of platinum surfaces. Vapor deposition techniques provide methods for producing high quality, reproducible surfaces not obtainable by chemical deposition or by polishing. Characterization of these materials both by resistivity and by capacitance measurements shows variations in active surface area and in defect structure. However, the differences in faradaic currents are not observed by usual measurements since the difference would be apparent only at short electrolysis times where defect structures are comparable in magnitude to the diffusion layer thickness (25). The similarity in faradaic response has been seen before with electrolysis data taken at similar electrodes studying the oxidation of ferrocene (1,7). As with the silver reduction, diffusion-controlled ferrocene oxidation appears independent of electrode type at electrolysis times greater than 5 msec.

This similarity in the faradaic silver deposition is contrasted by the differences in the charge-potential behavior and by the Auger analysis found for the various films. The Auger depth profiles suggest significant silver penetration well beyond that found for the solvent in the more porous materials. In fact electrochemical stripping does not completely remove silver deposited within the more porous electrodes. More dense electrodes showed that silver and solvent penetrate to smaller depths.

The absence of evidence for underpotential silver deposition prior to electrolysis in this system contrasts to aqueous systems where this process has been demonstrated (6, 8-10). Competition of the solvent for deposition sites may explain this observation. Appreciable energy would be necessary to overcome this solvent interaction which may contribute to the irreversible behavior of the silver reduction. Once electrodeposition begins silver appears to show appreciable mobility within the film. The solvent-platinum interactions may block surface sites forcing deeper penetration of the silver into the film.

Auger analyses of more porous films show deposition occurring deep in the metallic matrix. Moreover, silver levels are detected considerably deeper than those shown for the solvent. A specific chemical interaction, *e.g.*, alloying, between platinum and silver might contribute to the driving force for this penetration. That this penetration is a result of solvent interaction has been supported by other high vacuum experiments (16). Neutral and ionic silver were deposited onto similar platinum electrodes, within the vacuum apparatus. Auger analysis showed much sharper boundaries between the evaporated silver and the platinum substrates. Significantly less penetration of vacuum-deposited silver was noted on the porous electrodes compared to electrodes with electrochemically deposited silver.

In conclusion, good correlation has been observed between the wettable area of these electrodes, as measured by computing the surface charge, and the extent of penetration of an electrodeposited material such as

silver. Analysis, above, of faradaic currents does not indicate the defect structure of these electrodes. Surface analysis techniques are currently being applied to further study this type of interaction in other electrolyte-electrode systems.

#### Acknowledgments

The authors are grateful to D. M. Mattox and G. J. Kominiak for preparing the ion sputtered films. The excellent technical assistance of P. G. Neiswander and R. A. Jaramillo is acknowledged. This work was supported by the U.S. Energy Research and Development Administration.

Manuscript submitted Feb. 13, 1976; revised manuscript received July 24, 1976. This paper was presented in part as Paper 396 at the Electrochemical Society Meeting, Toronto, Canada, May 11-16, 1975.

Any discussion of this paper will appear in a Discussion Section to be published in the June 1977 JOURNAL. All discussions for the June 1977 Discussion Section should be submitted by Feb. 1, 1977.

Publication costs of this article were assisted by Sandia Laboratories.

#### REFERENCES

1. R. K. Quinn, N. R. Armstrong, and N. E. Vanderborgh, *J. Vac. Sci. Technol.*, **12**, 160 (1975).
2. D. M. Mattox and G. J. Kominiak, *ibid.*, **8**, 194 (1971).
3. J. D. E. McIntyre, *Surf. Sci.*, **37**, 658 (1973), and references therein.
4. W. von Benken and T. Kuwana, *Anal. Chem.*, **42**, 1114 (1970).
5. M. Fujihara and T. Kuwana, *Electrochim. Acta*, **21**, 565 (1975).
6. J. D. E. McIntyre and D. M. Kolb, *Symp. Faraday Soc.*, **4**, 99 (1970).
7. N. R. Armstrong, R. K. Quinn, and N. E. Vanderborgh, *This Journal*, **123**, 646 (1976); and N. R. Armstrong, Ph.D. Thesis, University of New Mexico (1974).
8. G. W. Tindall and S. Bruckenstein, *Electrochim. Acta*, **16**, 245 (1971).
9. A. K. Vijh, *Surf. Sci.*, **46**, 282 (1974).
10. W. J. Lorenz, H. D. Hermann, H. Wüthrich, and F. Hilbert, *This Journal*, **121**, 1167 (1974).
11. R. Adzic, E. Yeager, and B. D. Cahan, *ibid.*, **121**, 474 (1974).
12. N. R. Armstrong, A. W. C. Lin, M. Fujihara, and T. Kuwana, *Anal. Chem.*, **48**, 741 (1976).
13. G. C. Allen, P. M. Tucker, A. Capon, and R. Parsons, *J. Electroanal. Chem.*, **50**, 335 (1974).
14. K. S. Kim, N. Winograd, and R. E. Davis, *J. Am. Chem. Soc.*, **93**, 6296 (1971).
15. W. C. Johnson and L. A. Heldt, *This Journal*, **121**, 34 (1974).
16. M. L. Knotek, R. K. Quinn, N. R. Armstrong, and N. E. Vanderborgh, *J. Vac. Sci. Technol.*, Submitted for publication.
17. N. R. Armstrong, R. K. Quinn, and N. E. Vanderborgh, *Anal. Chem.*, **44**, 1759 (1974).
18. M. Babai, N. Tshernikovski, and E. Gileadi, *This Journal*, **119**, 1018 (1972).
19. M. L. Knotek, *J. Vac. Sci. Technol.*, **12**, 117 (1975).
20. R. L. Gerlach and D. W. Tipping, *Rev. Sci. Instrum.*, **42**, 151 (1971).
21. K. L. Chopra, "Thin Film Phenomena," McGraw Hill, New York (1969).
22. L. J. van der Pauw, *Philips Res. Rept.*, **13**, 1 (1958); *Philips Tech. Rev.*, **20**, 220 (1959).
23. D. Mohilner, in "Electroanalytical Chemistry," Vol. 1, A. J. Bard, Editor, p. 246, Marcel Dekker (1966).
24. R. deLevie, in "Advances in Electrochemistry and Electrochemical Engineering," Vol. 6, P. Delahey, Editor, p. 329, Interscience Publishers, New York (1967).
25. J. A. Harrison and H. R. Thirsk, in "Electroanalytical Chemistry," Vol. 5, A. J. Bard, Editor, p. 67, Marcel Dekker (1971).

# Electrodeposition of Gold

## Depolarization Effects Induced by Heavy Metal Ions

J. D. E. McIntyre\* and W. F. Peck, Jr.

Bell Laboratories, Murray Hill, New Jersey 07974

### ABSTRACT

Addition of trace quantities (ppm) of heavy metal ions such as Pb(II) or Tl(I) to soft gold electroplating baths induces a marked cathode depolarization that extends the current density range in which bright, fine-grained deposits can be obtained and produces uniform coverage of irregularly shaped substrates. In this study it is shown that the trace foreign metal additives which are most effective as depolarizers are those which tend to deposit uniformly on a gold surface to form an adsorbed monolayer at electrode potentials positive to those where their cathodic deposition as bulk metals begins, i.e., at underpotentials. Of the series of Group B elements (As, Bi, Cd, Cu, Ga, Hg, Pb, Sb, Sn, Tl, and Zn) investigated for depolarization action in alkaline phosphate solutions (pH 8, 70°C), only Pb, Tl, Bi, and Hg were found to induce significant effects. The latter two metals have not previously been reported to act as depolarizers in gold electrodeposition processes. The kinetics of the potential relaxation effects induced by these species under galvanostatic conditions were found to be strongly dependent on mass transport rate, gold deposition rate (i.e., plating current density), and temperature. In addition, it was found that Pb, Bi, Hg, and particularly Tl enhance the anodic dissolution of gold in cyanide-containing solutions. The ranges of underpotential deposition of the metals Pb, Tl, Bi, and Hg from very dilute ( $\sim 5 \mu\text{M}$ ) solutions of their ions in pure phosphate supporting electrolyte at 70°C were determined under steady-state mass transport conditions at a rotating gold disk electrode. By varying the disk rotational speed and the potential scan rate, it was shown that a significant amount of Pb(II) [the equivalent of  $\sim 20\%$  of a close-packed monolayer of Pb(0)] is specifically adsorbed in the ionic double layer at the gold surface and is not desorbed even at high anodic potentials. A similar phenomenon was observed for the Bi(III) species. The depolarization induced by the trace heavy metal ions is examined in terms of electrocrystallization and electrocatalytic mechanisms. From the magnitude of the potential relaxation ( $\sim 0.2\text{V}$ ), its temperature dependence, and the ability of Hg to alloy with Au, it is concluded that screw dislocation generation is not responsible for this effect. Failure of  $\text{Cs}^+$  ions to enhance the rate of electroreduction of  $\text{Au}(\text{CN})_2^-$  anions and also the ability of Pb(II) to catalyze the electroreduction of  $\text{O}_2$  indicates that electrostatic repulsion effects are of minor importance. It is concluded that the depolarization phenomenon is caused by an enhancement of nucleation rate produced by the strongly adsorbed foreign metal atoms. In addition, catalytic electrochemical displacement reactions are made possible by the fact that the exchange current densities of the various  $\text{M}^{z+}/\text{M}$  depolarizer couples are much greater than that of the  $\text{Au}(\text{CN})_2^-/\text{Au}$  couple and by the specific adsorption of the  $\text{M}^{z+}$  species. In the case of Hg, displacement is made thermodynamically possible by the complexation of  $\text{Hg}^{2+}$  by  $\text{CN}^-$  ions released during the electroreduction of  $\text{Au}(\text{CN})_2^-$ .

In electronic device manufacturing, soft gold coatings are extensively applied for corrosion protection, for conduction of electrical current, and to provide surfaces suitable for bonding (1). The addition of trace quantities (at the part per million level) of heavy metal ions such as thallium or lead to gold-plating baths has been found to yield consistently bright gold electrodeposits of suitable morphology, purity, and hardness, as well as uniform coverage of irregular pieces (2-8). Further, higher plating rates can be employed, underplating is reduced in integrated circuit fabrication, and the life of the bath before restoration becomes necessary is markedly extended.

As yet the mechanism of the marked cathode depolarization induced by these trace metal additives during the electrodeposition of gold has not been well understood. It was the purpose of the present study to examine kinetic and mechanistic aspects of the deposition process in order to reveal the origin of this electrocatalytic effect. It was also desired to determine whether species other than Tl(I) and Pb(II) additives could be used as depolarizers in gold-plating baths. For

this purpose, we have focused our attention on alkaline phosphate solutions (pH  $\sim 8$ ) where well-defined limiting currents for the reduction of potassium dicyanoaurate (I) [ $\text{KAu}(\text{CN})_2$ ] are observed and where the free cyanide concentration is very low. In contrast, no limiting current region is observed in citrate gold baths (pH 5) owing to the fact that hydrogen gas is evolved electrochemically in the same potential range where gold electrodeposition occurs (9).

This study revealed that the trace foreign metal additives which are most effective as depolarizers are those which tend to deposit uniformly on a gold surface to form an adsorbed monolayer at electrode potentials positive to those where their bulk metal deposition begins, i.e., at "underpotentials." [For a recent review of underpotential deposition phenomena, see Lorenz *et al.* (10).] Of the series of Group B elements (As, Bi, Cd, Cu, Ga, Hg, Pb, Sb, Sn, Tl, and Zn) investigated for possible depolarization action, only Hg, Tl, Pb, and Bi were found to induce significant effects. These four "super-B" metals follow Au in the third transition series and have atomic diameters from 9 to 22% greater than that of Au (2.88Å). Under galvanostatic conditions, the kinetics of the potential relaxation effects

\* Electrochemical Society Active Member.  
Key words: gold electrodeposition, depolarization, underpotential adsorption, electrocrystallization, electrocatalysis.

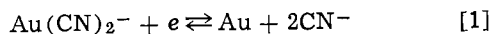
were found to be a function of mass transport rate, plating current density, and temperature.

It was also found that a high concentration of Cs<sup>+</sup> ions (>0.1M) in solution produced a slow depolarization effect. These large positive ions are only weakly hydrated and are able to contact adsorb on negatively charged metal electrodes such as mercury (11). Owing to a decrease in electrostatic repulsion at the electrode surface, the rate of electroreduction of a number of negatively charged anions, e.g., NO<sub>3</sub><sup>-</sup>, Fe(CN)<sub>6</sub><sup>3-</sup>, IO<sub>4</sub><sup>-</sup>, and S<sub>2</sub>O<sub>8</sub><sup>2-</sup> is accelerated [cf. Parsons (12), Frumkin *et al.* (13), Fawcett *et al.* (14), and references cited therein]. In the present case, however, the depolarization effect was found to be due to residual impurities in the electrolyte. Complementary oxygen reduction studies were also carried out in order to investigate the influence of electrostatic repulsion effects.

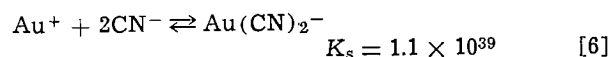
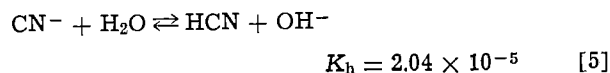
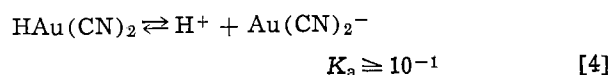
The results of these studies are examined in terms of the roles played by dislocation generation, nucleation, and electrocatalytic phenomena. It is shown that the depolarization effect can result from an enhancement of nucleation and crystal growth rate produced by foreign metal adatoms. In addition, electrochemical displacement reactions can occur in which trace heavy metals deposited on the surface in a zero-valent state reduce Au(CN)<sub>2</sub><sup>-</sup> anions at an enhanced rate. The oxidized depolarizer species do not leave the surface but remain adsorbed in the electrical double layer, where they can rapidly be reduced again electrochemically; the metal catalyst is thus regenerated. Finally, the physical and chemical characteristics of these "super-B" metals are examined in order to determine why these species are active as electrocatalysts not only for the reduction of Au(CN)<sub>2</sub><sup>-</sup> but also for other slow electrochemical reactions.

### Thermodynamics

The electrochemical oxidation and reduction of gold in cyanide-containing electrolytes is represented by

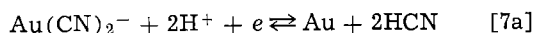


The standard electrode potential,  $E^\circ$ , of this reaction at  $\sim 19^\circ\text{C}$  was first determined by Bodländer (15) in 1903 to be  $-0.611\text{V}$  (Gibbs-Stockholm convention) with respect to the standard hydrogen electrode potential (SHE). More recently, Maja (16) has measured a value of  $-0.60\text{V}$  at  $25^\circ\text{C}$ . In practice, the equilibrium potential of the Au(CN)<sub>2</sub><sup>-</sup>/Au couple is affected by the reactions

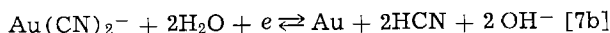


The equilibrium constants (17-19) are for a temperature of  $25^\circ\text{C}$ .

The  $pK_a$  values of HCN and HAu(CN)<sub>2</sub> at  $25^\circ\text{C}$  are 9.31 and  $\leq 1$ , respectively. Thus in alkaline phosphate solutions at  $pH \sim 7-8$ , the principal cyanide-containing species are Au(CN)<sub>2</sub><sup>-</sup> and HCN. The reversible electrode reaction [1] may be rewritten accordingly as



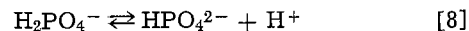
or



The standard potential of reaction [7] at  $25^\circ\text{C}$  is estimated to be  $+0.501\text{V}$  (SHE), or *ca.*  $+0.257\text{V}$  vs. a satu-

rated calomel electrode (SCE). In the phosphate gold solution employed in this work [ $0.0694\text{M}$  KAu(CN)<sub>2</sub>,  $pH$  8], the thermodynamic reversible potential of the Au(I)/Au couple at  $25^\circ\text{C}$  is *ca.*  $(-0.758 - 0.1183 \log [\text{HCN}])\text{V}$  (SCE). In gold-plating studies, the concentration of free HCN or CN<sup>-</sup> in solution increases continuously with the quantity of gold deposited (Eq. [1] and [7]). Further, the rest potential of a gold electrode may be affected by adsorbed CN<sup>-</sup> ions or a surface film of AuCN. Thus under actual operating conditions the true reversible potential is usually not well determined.

In well-buffered phosphate gold solutions, the  $pH$  is primarily controlled by the dissociation reaction



The  $pK_{a2}$  values at  $25^\circ$  and  $50^\circ\text{C}$  are 7.20 and 7.18, respectively; the temperature coefficient of dissociation is thus very low. In contrast, the dissociation of HCN has a much greater temperature dependence. At  $45^\circ\text{C}$  the  $pK_a$  of HCN is 8.78 (19) and at  $70^\circ\text{C}$  is estimated to be  $\sim 8.3$ . This implies that substantial quantities of free CN<sup>-</sup> will be released into a  $pH$  8 solution by the electroreduction of Au(CN)<sub>2</sub><sup>-</sup> at the high temperatures ( $50^\circ-80^\circ\text{C}$ ) usually employed in electroplating. In addition to the hydrolysis reaction (5), a number of other chemical side reactions can affect the concentrations of CN<sup>-</sup> and HCN at the electrode surface [cf. Reinheimer (20)] and hence alter the equilibrium potentials of reactions [1] and [7].

### Experimental

Experimental studies were conducted in the electrochemical cell illustrated schematically in Fig. 1. The small volume of this cell ( $\sim 100$  ml) minimizes consumption of gold salts. Rotating disk electrodes (RDE)

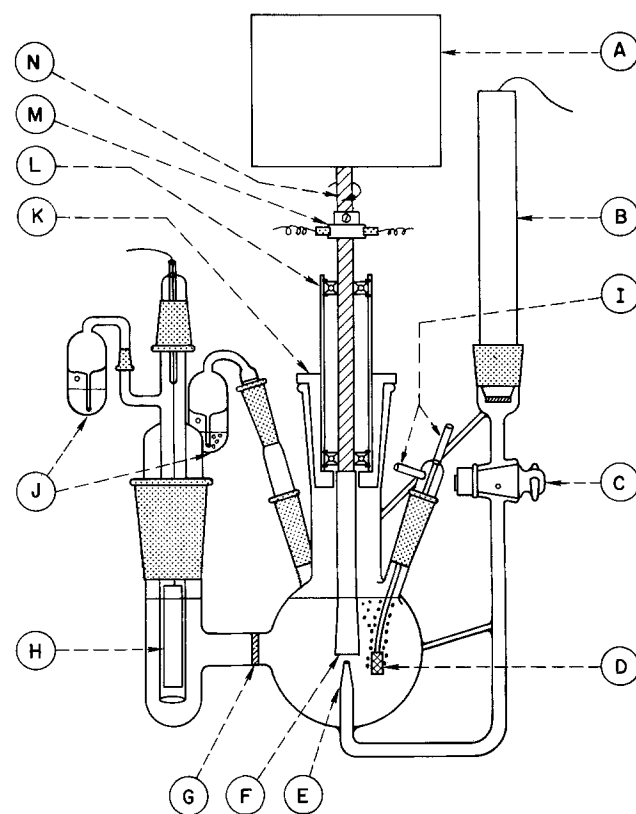


Fig. 1. Electrochemical cell with rotating disk electrode (RDE): A = d-c motor; B = saturated calomel reference electrode; C = Teflon stopcock; D = gas bubbler; E = Luggin capillary; F = RDE; G = fritted Pyrex disk; H = gold counterelectrode; I = gas inlets; J = gas outlets; K = Teflon gland; L = sealed ball bearing assembly; M = silver slip ring and graphite alloy brushes; N = stainless steel shafting.

were fabricated by silver soldering or mechanically joining platinum or gold disks to the ends of  $\frac{1}{4}$  in. diameter, precision-ground stainless steel shafting (PIC Design Corporation, Type A3). The lower RDE section around the joint was sealed in epoxy cement (21) (Union Carbide Corporation, ERL 3794 resin plus ERL 2807 curing agent, 5:1 by weight) to prevent leakage of electrolyte up the shaft. The upper, exposed section of the shaft was encased in dual-wall heat-shrinkable polyolefin tubing (Raychem Corporation, SCL Thermofit). After applying another overcoat of epoxy, the insulation was machined to a flared flat end on a lathe to expose the active electrode surface (Fig. 1). This surface was then metallographically polished to a mirror finish, using  $0.3 \mu\text{m}$  alumina (Linde A) for the final polish. RDE shafts press-fitted into Teflon rods were found not to be leak free at the higher temperatures used in this work.

In order to maintain an inert atmosphere over the electrolyte, the RDE shaft was passed into the cell through two precision gas-tight ball bearings [Barden Corporation, Type SR4FF(3) R21 G6]. Electrical contact to the shaft was made through two silver-graphite alloy brushes and a coin silver slip ring, (Graphite Metallizing Corporation, Types H9434 and 1165-8). The shaft rotational speed was accurately controlled over the range 100-10,000 rpm with a d-c motor (RAE Motor Corporation, Model M6) and programmable power supply (Kepco Incorporated, Model JQE 100-2.5M HS), using a d-c tachometer generator (Servo-Tek Products, Model SA-740A-7) in the feedback loop. An optical pickoff (General Radio Company, Type 1536A) and preset counter (Hewlett Packard, Model 5214L) were used to measure the exact angular velocity of the RDE.

Electrolyte solutions were prepared by dissolving ACS reagent grade salts in ultrapure conductivity water. The basic composition of the phosphate gold solution is

Salt	g/liter	Molarity
$\text{KAu}(\text{CN})_2$	20	0.0694
$\text{K}_2\text{HPO}_4 \cdot 3\text{H}_2\text{O}$	40	0.175
$\text{KH}_2\text{PO}_4$	10	0.0735

The pH of the electrolyte was adjusted to 8.0 with KOH. Depolarizing agents were introduced by adding small aliquots of stock solutions of the appropriate metal oxides or salts. For investigation of the underpotential deposition of the trace metal additives, it was found necessary to preelectrolyze the phosphate electrolyte extensively, using a gold gauze or mercury pool cathode to remove residual metallic impurities. Oxygen was purged from the cell by bubbling argon through the solution. This gas was prepurified by passage over a titanium getter in a furnace at  $800^\circ\text{C}$  (Centorr Associates, Incorporated, Model 2-B-20), in order to remove trace hydrocarbons, oxygen, and carbon dioxide, and was then presaturated with water vapor by passage through a bubbling tower filled with supporting electrolyte. The cell electrolyte was maintained at the desired temperature ( $25^\circ$ - $70^\circ\text{C}$ ) by immersing the electrochemical cell of Fig. 1 in a controlled-temperature water bath.

Electrode potentials and currents were controlled with a Princeton Applied Research Model 173 potentiostat and Model 175 universal programmer. All experimental potentials reported in this work are referred to a SCE at room temperature.

### Results and Discussion

A series of metallic and semimetallic ions from Groups IB, IIB, IIIB, IVB, and VB was added in trace quantities (ppm) to phosphate gold solutions and tested for their depolarizing action on the electrodeposition of gold. A number of these ions are known to adsorb at underpotentials on gold (10), but many are

only sparingly soluble in alkaline solution. Of the elements tested (Cu, Ag; Zn, Cd, Hg; Ga, In, Tl; Sn, Pb; As, Sb, Bi), only Hg, Tl, Bi, and Pb induced significant depolarization. In addition, concentrated solutions of  $\text{Cs}^+$  ions were found to produce a slow depolarization effect.

**Steady-state voltammetry.**—Figures 2 and 3 illustrate the form of the steady-state polarization curves measured for the cathodic reduction of  $\text{Au}(\text{CN})_2^-$  ions and the anodic dissolution of Au metal in a phosphate gold bath at  $70^\circ\text{C}$ . A platinum RDE was employed as substrate at the rotational speeds indicated and was stripped<sup>1</sup> after each run in order to prevent buildup of the active electrode area. The platinum disk is not attacked by the cyanide released during the cathodic reduction (Eq. [1] and [7]). After the first few monolayers of gold were deposited during each cathodic scan at  $10 \text{ mV/sec}$ , the electrode behaved effectively as a gold RDE.<sup>2</sup>

Consider first the cathodic current curves. The initial cathodic scan begins at  $0.0\text{V}$ . At a potential close to  $-0.8\text{V}$ , a small prewave is observed whose amplitude is independent of the stirring rate. This wave has been attributed to the reduction of specifically adsorbed  $\text{Au}(\text{CN})_2^-$  ions (12, 18). The integral charge passed in this wave in the present case, however, is ca.  $28 \text{ mC cm}^{-2}$ , corresponding to the deposition of  $\sim 125$  monolayer equivalents of gold on the disk surface, based on

<sup>1</sup> The gold deposit was chemically dissolved in a proprietary cyanide solution (Technic Incorporated, Techni Strip Au) at a temperature of  $60^\circ$ - $70^\circ\text{C}$ .

<sup>2</sup> At a current density of  $100 \mu\text{A cm}^{-2}$ , the equivalent of one close-packed monolayer of gold ( $\sim 1.4 \times 10^{16}$  atoms  $\text{cm}^{-2}$ ) is deposited in 2.2 sec.

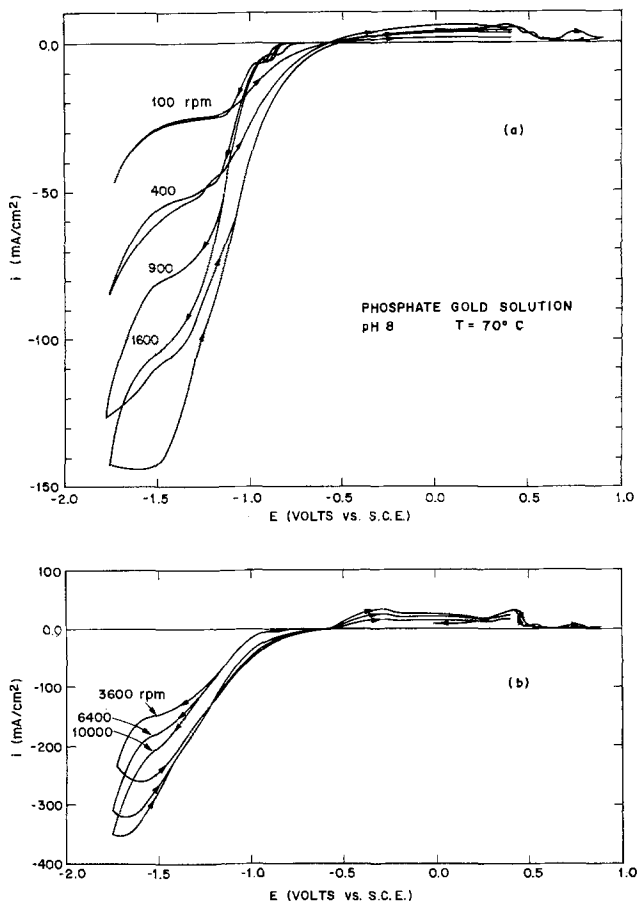


Fig. 2. Steady-state current-potential curves for the reduction and oxidation of gold at a rotating disk electrode in a phosphate buffered gold plating solution with no additives present.  $[\text{Au}(\text{CN})_2^-] = 0.0674\text{M}$ , pH 8,  $70^\circ\text{C}$ . Potential scan rate =  $10 \text{ mV sec}^{-1}$ . Rotational speed range: (a)  $m = 100$ - $1600$  rpm. (b)  $m = 3600$ - $10,000$  rpm.

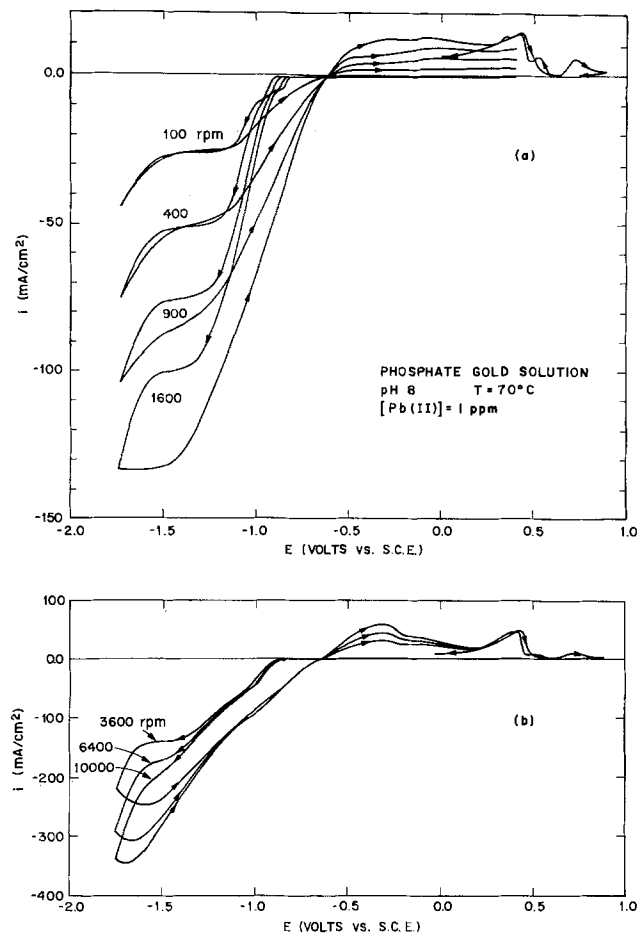


Fig. 3. Reduction and oxidation of gold in a phosphate gold plating solution containing 1 ppm Pb (II). Other conditions are the same as for Fig. 2.

its geometric area. This indicates either that adsorption of  $\text{Au}(\text{CN})_2^-$  on the surface is extremely rapid or, more probably, that this prewave is due to the reduction of an insoluble surface film such as  $\text{AuCN}$  or  $\text{Pt}(\text{CN})_2$  left by the stripping process. At more negative potentials, the current rises rapidly owing to the onset of reduction of  $\text{Au}(\text{CN})_2^-$  ions transported to the surface by convective diffusion. A well-defined limiting current region is observed at low rotational speeds, but at higher speeds the plateau region has a steeper slope. Finally, at potentials more negative than  $-1.5\text{V}$ ,  $\text{H}_2$  gas is evolved rapidly at the electrode surface. [The reversible potential of the hydrogen electrode reaction in this solution is  $\sim -0.7\text{V}$  (SCE).] During the reverse scan, appreciable hysteresis is observed at the higher rotational speeds. This is mainly due to the continuous increase in macroscopic surface area of the electrode with metal deposition time. In the limiting current region, the deposition rate is proportional to  $\sim m^{1/2}$ , where  $m$  is the disk rotational speed (rpm). The fact that the hysteresis becomes nearly constant at the higher speeds may indicate a change in the crystal growth form with increasing current density and decreasing diffusion layer thickness. Such morphological effects have been observed by Cheh and Sard (9). Evolution of hydrogen gas bubbles at the electrode produces turbulence in the diffusion layer, increasing the rate of mass transport of  $\text{Au}(\text{CN})_2^-$  to the surface and further accelerating the growth rate of the deposit.

As the current falls below the diffusion-limited value during the reverse scan, it is evident that the rate of metal deposition is markedly enhanced over that in the initial cathodic sweep. As kinetic control becomes dominant over mass transport control near the foot of the reduction wave, the magnitude of the current is determined by the total area of the microscopically

rough deposit rather than the projected area of the disk. Such deposits typically have surface asperities in the range  $0.1\text{--}1\ \mu\text{m}$  in diameter and hence high real surface areas (9). When dilute solutions of the gold salt (e.g., 1 mM) are employed, the hysteresis in the polarization curves is greatly reduced.

Anion desorption at the most cathodic potentials may also be effective in activating the surface. Anions such as  $\text{CN}^-$ ,  $\text{HPO}_4^-$ , and  $\text{OH}^-$  are strongly adsorbed on gold electrodes at potentials positive to the point of zero charge and their reabsorption is generally slow and kinetically limited (23). Since  $\text{CN}^-$  or  $\text{HCN}$  is continuously released during deposition (Eq. [1] and [7]), however, it is probable that this effect is of minor importance compared to the increase in area of the active surface.

As the electrode potential passes through the quasi-reversible potential at  $-0.62\text{V}$ , the current becomes anodic. The gold deposit on the surface begins to redissolve in the solution to form  $\text{Au}(\text{CN})_2^-$ , complexing with the cyanide ( $\text{CN}^-$  or  $\text{HCN}$ ) released during the cathodic scan (Eq. [1] and [7]). As the potential becomes more positive, the current rapidly becomes diffusion limited since the free cyanide concentration is very low. Two prominent peaks at  $0.43$  and  $0.73\text{V}$ , as well as smaller peaks at  $-0.05$  and  $-0.3\text{V}$ , indicate the possible formation or oxidation of gold cyanide or basic gold cyanide complexes. The nature of these products is not yet well established (22, 24). Between the two most anodic peaks, the surface is passivated by an  $\text{Au}_2\text{O}_3$  or  $\text{Au}(\text{OH})_3$  surface film, which begins to form at  $\sim 0.45\text{V}$ .

**Pb(II) additions.**—Figures 3a and b show the form of the steady-state polarization curves measured in the phosphate gold solution with 1 ppm Pb(II) added (as PbO). These runs were carried out in the same solution as that employed for the runs of Fig. 2a and b. Comparison of the cathodic branches of Fig. 2b and 3b reveals that in the limiting current region the  $i$ - $E$  curves are virtually identical, but in the kinetically controlled region above  $-1.2\text{V}$  there is a pronounced shift of the waves to less negative potentials in the case of the lead-containing solution. A marked depolarization effect is thus induced by only trace quantities of Pb(II) in the electrolyte. The magnitude of this potential shift increases with disk rotational speed since deposition of the lead depolarizer is controlled by its convection diffusion rate and a finite time is required for steady-state surface coverage and depolarization conditions to obtain (see below). It is this kinetically controlled region with high flow rates and current densities below  $30\ \text{mA}/\text{cm}^2$  which is usually of greatest interest for gold-plating applications (25).

In the anodic current region of Fig. 2b and 3b it is evident that there is an increase in the limiting current densities for the dissolution of  $\text{Au}(\text{O})$  in the lead-containing solution. This is simply due to the progressive accumulation of  $\text{OH}^-$  and  $\text{CN}^-$  in the solution with total cathodic charge passed. At  $\text{pH} \geq 8$ , the phosphate electrolyte is no longer well buffered. It should be noted that in each series of runs, the reversible potential is almost invariant, independent of the changing cyanide concentration in the solution. This suggests that the potential of the unpolarized gold electrode is determined by a cyanide surface layer, as mentioned above. In the lead-containing solutions, this potential is shifted negatively by  $\sim 60\ \text{mV}$ . This may imply that the anodic dissolution of gold is also accelerated by the presence of lead in the solution. Indeed, such effects have been observed for the dissolution of Au in more concentrated cyanide solutions (24, 26). The lead catalyst on the surface is thus bifunctional, accelerating both the cathodic deposition and anodic dissolution kinetics of gold.

**Tl(I) additions.**—The steady-state polarization curves for a phosphate gold solution with 1 ppm Tl(I) added (as  $\text{TlNO}_3$ ) are very similar to those obtained with

Pb(II) additions. Again, a significant depolarization effect is evident at the higher mass transport rates. In separate studies we have confirmed the finding of Cathro and Koch (24) that an addition of 10 ppm  $Tl^+$  to alkaline cyanide solution markedly enhances the anodic dissolution rate of gold. Thus thallium also acts as a bifunctional catalyst on gold surfaces.

**Galvanostatic transients.**—The nature of the depolarization effects induced by trace metal additives is more clearly revealed by polarization studies under conditions of forced convection and constant current, than by slow potential scanning, since time-dependent effects caused by surface area changes are minimized.

**Pb(I) additions.**—Figure 4 illustrates the potential transients observed during the electrodeposition of Au metal onto a gold RDE at a series of current densities in the presence and absence of Pb(II). In the lead-free solution, the absolute overpotential for metal deposition  $\eta = |E - E_r|$  ( $E_r$  is the reversible potential) rapidly attains an almost constant value which changes only slowly with time. Comparison with Fig. 2b reveals that at  $m = 3600$  rpm the deposition rate is solely under kinetic control. The slow potential relaxation at long deposition times probably results from an increase in surface area with deposit thickness, but may also be caused by a depolarization effect produced by deposition of residual impurities from the electrolyte.

In the solution containing 1 ppm Pb(II), an initial increase in  $\eta$  is followed by a decrease of 8–30 sec duration, as Pb(O) begins to accumulate on the Au surface. The difference in steady-state overpotential values, i.e., the depolarization, between the lead-free and lead-containing solutions is  $\sim 200$  mV. Now the reduction of  $Au(CN)_2^-$  has a Tafel slope,  $\partial\eta/\partial\log i$ , of 101 mV/decade (9). Hence at constant potential, the presence of 1 ppm Pb(II) in the phosphate gold solution would be expected to increase the reduction rate of  $Au(CN)_2^-$  ca. one hundredfold.

Figure 5 shows the potential transients observed during deposition of Au metal onto a platinum RDE. The initial large potential step is associated with the high activation overpotential required for the electroreduction of  $Au(CN)_2^-$  (see Fig. 2b). Superimposed on this step is a negative spike of 100–200 mV amplitude resulting from adion supersaturation during the initial formation of three-dimensional gold nuclei on the foreign substrate surface. As these nuclei grow, the surface area available for deposition expands and  $\eta$  rapidly decreases. Subsequently the growth centers coalesce and  $\eta$  rises to its final steady-state value. The time required for this to occur is inversely proportional to the deposition rate.

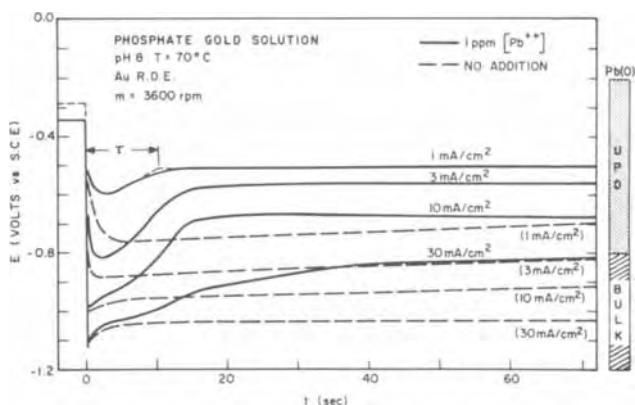


Fig. 4. Potential-time transients observed during the galvanostatic reduction of  $Au(CN)_2^-$  at a gold RDE in the presence and absence of 1 ppm Pb(II). The depolarization time,  $\tau$ , is calculated as shown. Also shown are the approximate potential ranges for underpotential and bulk metal deposition of Pb(O).

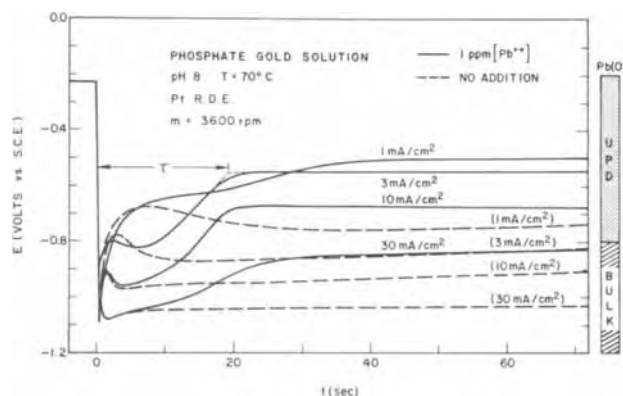


Fig. 5. Galvanostatic reduction of  $Au(CN)_2^-$  at a platinum RDE in the presence and absence of Pb(II).

The depolarization time,  $\tau$  (Fig. 4 and 5), is a function of the Pb(II) concentration in solution (27), its transport rate to the electrode surface, and the applied current density  $i$  (i.e., the gold deposition rate). Figure 6 shows the variation of  $\tau$  with  $i$  and  $m^{1/2}$ . Since the Pb(II) concentration is extremely low, its rate of deposition onto the surface is mass transport limited and inversely proportional to the convective diffusion layer thickness,  $\delta$ . At a RDE, the diffusion layer thickness for species  $j$  is

$$\delta_j = \frac{D_j}{L_j \omega^{1/2}} \quad [9]$$

where  $\omega = 2\pi m/60$  is the angular velocity of the disk

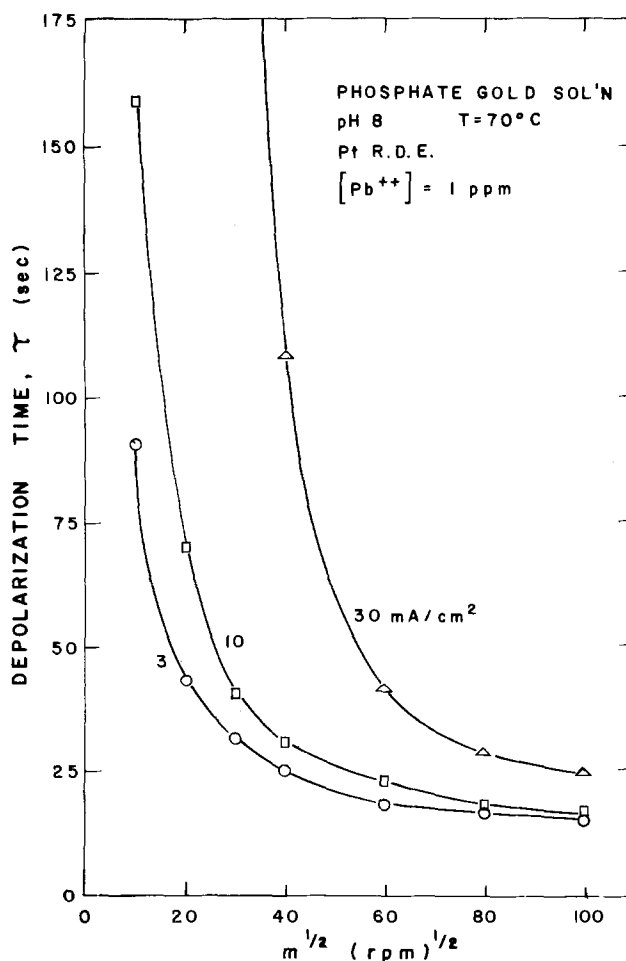


Fig. 6. Dependence of the depolarization time,  $\tau$ , on the applied current density and disk rotational speed during the galvanostatic reduction of  $Au(CN)_2^-$  at a platinum RDE.  $[Pb(II)] = 1$  ppm.



( $\text{rad sec}^{-1}$ ) and  $L_j$ , the Levich constant, is defined by (28)

$$L_j = \frac{0.62048 D_j^{2/3} \nu^{-1/6}}{1 + 0.2980(D_j/\nu) + 0.14514(D_j/\nu)^{2/3}} \quad [10]$$

Here  $D_j$  is the diffusion coefficient ( $\text{cm}^2 \text{sec}^{-1}$ ) of species  $j$ , and  $\nu$  is the kinematic viscosity ( $\text{cm}^2 \text{sec}^{-1}$ ) of the solution; the quantity  $\nu/D_j$  is the Schmidt number. The diffusion-limited flux of  $j$  to the surface is thus

$$J_j = L_j \omega^{1/2} C_j^0 \quad [11]$$

where  $C_j^0$  is the bulk solution concentration. For  $m = 3600 \text{ rpm}$  and  $[\text{Pb(II)}] = 1 \text{ ppm} = 4.8 \times 10^{-6} \text{ M}$ , the maximum rate of supply of Pb(II) to the electrode surface is  $9 \times 10^{-11} \text{ mole cm}^{-2} \text{sec}^{-1}$ , which is equivalent to the deposition of 0.057 close-packed monolayer of Pb(O) per second. Here we have assumed that the diffusion coefficient of Pb(II) is similar to that of  $\text{Au(CN)}_2^-$  in phosphate gold solutions ( $\sim 1.7 \times 10^{-5} \text{ cm}^2 \text{sec}^{-1}$  at  $70^\circ\text{C}$ ). Now at low rotational speeds, electroreduction of  $\text{Au(CN)}_2^-$  in 0.069M solution is under mixed kinetic and mass transport control (cf. Fig. 2 and 3), but for  $m \geq 3600 \text{ rpm}$  and  $i \leq 30 \text{ mA cm}^{-2}$  the gold deposition rate is limited solely by the kinetics of reaction [7]. A current density of  $1 \text{ mA cm}^{-2}$  corresponds to the deposition of 4.5 close-packed monolayer equivalents of Au(O) per second, which is greater than the maximum rate of deposition of Pb(O) by a factor of  $\sim 10^2$ . We might therefore expect that a large fraction of the discharged Pb atoms would be buried beneath the continuously plating Au metal and incorporated as impurities in the bulk deposit. The final Pb atom concentration in the bulk metal has been found to be proportional to the Pb(II) concentration in solution (4). However, the solubility of lead in gold is practically nil below  $500^\circ\text{C}$  (29). Thus there is a strong tendency for Pb atoms to segregate from the bulk to form an adsorbed layer on the surface, as has been observed in measurements of surface diffusivity at high temperatures (30). This segregation may occur by backdiffusion along grain boundaries. If it is assumed that the initial surface concentration of Pb adatoms is low, as evidenced by the rest potential, then the depolarization time  $\tau$  (Fig. 4 and 5) may be interpreted as the time required to establish a steady-state surface coverage of Pb(O). At low rotational speeds, long relaxation times are encountered because the rate of deposition of Au(O) (kinetically controlled) far exceeds that of Pb(O) (mass transport controlled). At high rotational speeds, steady-state conditions are established much more rapidly because of the faster Pb(II) transport rate. As yet the relative rates of supply of Pb(O) to the surface by electrochemical discharge of Pb(II) and backdiffusion of Pb(O) from the bulk deposit are not known.

It is important to note that for  $m = 3600 \text{ rpm}$  and  $[\text{Pb(II)}] = 1 \text{ ppm}$ , the values of  $\tau$  shown in Fig. 4 are  $\sim 20 \text{ sec}$ . It was shown above that under these conditions the flux of Pb(II) to the surface is equivalent to the deposition of  $\sim 0.057$  close-packed monolayer of Pb(O) per second. If the lead atoms are not buried by the overdepositing gold, one complete monolayer of Pb(O) would form in  $\sim 17.5 \text{ sec}$ . The close agreement of these values is remarkable and highly suggestive that the steady-state surface coverage by lead atoms during actual plating conditions is high. Preliminary x-ray photoemission spectroscopy (ESCA) measurements indicate that  $\sim 0.1$ - $0.2$  monolayer of lead is present on the surface of samples plated under similar conditions (31). We are also attempting to measure this surface coverage directly *in situ* using high speed chronocoulometry techniques.

**Tl(I) additions.**—Figure 7 illustrates the potential transients observed during the electrodeposition of Au metal onto a platinum RDE in a phosphate gold solution in the presence and absence of 1 ppm Tl(I). The

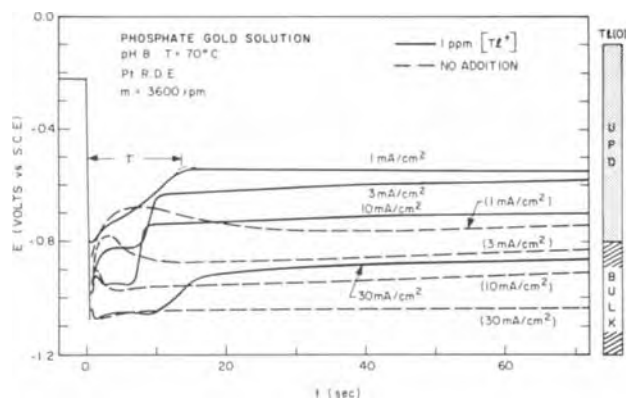


Fig. 7. Galvanostatic reduction of  $\text{Au(CN)}_2^-$  at a platinum RDE in the presence and absence of 1 ppm Tl(I).

depolarization curves are qualitatively similar to those observed with the Pb(II) additive (Fig. 5), but here the potential relaxations are more abrupt. The magnitudes of the depolarization are slightly smaller than those for lead.

Thallium salts are much more soluble than lead salts in alkaline solution because they do not hydrolyze appreciably (19). In phosphate gold solutions containing 10 ppm Tl(I), the depolarization times are approximately ten times less than in Fig. 7, as expected from Eq. [11]. Figure 8 shows the variation of  $\tau$  with  $i$ ,  $m^{1/2}$ , and  $C_{\text{Tl(I)}}^0$ . At the higher concentrations, the relaxation times become almost independent of  $m$  and  $i$ . This

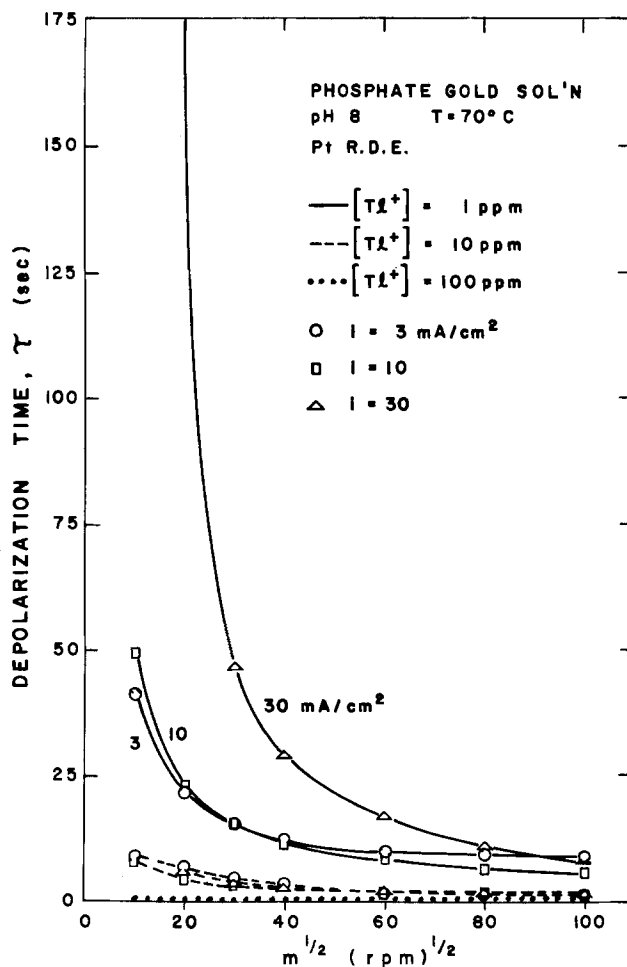


Fig. 8. Dependence of the depolarization time,  $\tau$ , on applied current density, disk rotational speed, and Tl(I) concentration during the galvanostatic reduction of  $\text{Au(CN)}_2^-$  at a platinum RDE.

is consistent with a report (3) that thallium does not codeposit from such solutions to form an Au-Tl alloy.

**Bi(III) additions.**—Marked depolarization effects are also observed when 1 ppm Bi(III) is added to the phosphate gold solution, as shown in Fig. 9. In this case, an initial depolarization is observed which is comparable to those observed for the Pb(II) and Tl(I) additives. But the depolarization times are longer for Bi(III) and, in addition,  $\eta$  increases again at longer deposition times. This might be attributed to the formation of a surface alloy. However, the solid solubility of Bi in Au at 25°C is virtually nil (29). Further, electrochemical studies of the deposition of Bi(O) on Au (32, 33) have revealed no evidence of alloy formation, contrary to the behavior observed for Bi(O) on Pt (34). In the present case, however, the large Bi atoms ( $d = 3.40\text{\AA}$ ) are codeposited with the smaller Au atoms ( $d = 2.88\text{\AA}$ ) and may form a supersaturated solid solution, as observed for electrodeposited Ag-Bi alloys (29). (Note that  $d_{\text{Ag}} = 2.88\text{\AA} = d_{\text{Au}}$ ). The increase in  $\eta$  may, therefore, result from a reconstruction of the deposit to relieve lattice strain. Alternatively, it may be caused by a growing together of three-dimensional crystallites with consequent decrease in electrode surface area. This phenomenon requires further investigation using electron microscopy techniques.

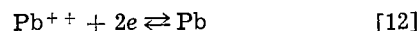
**Hg(II) additions.**—Owing to its smaller atomic radius ( $r_{\text{Hg}} = 1.57\text{\AA}$ ), mercury is able to alloy with gold and at 25°C has a solubility of 16 atom percent (a/o) (29). As shown in Fig. 10, significant depolarization effects are observed in phosphate gold solutions containing 1 ppm Hg(II). The potential relaxation times are five to ten times longer than those for the lead, thallium, or

bismuth additives. This is attributed to an amalgamation process which lowers the steady-state surface concentration of Hg adatoms.

**Cs<sup>+</sup> additions.**—Weakly hydrated Cs<sup>+</sup> ions, which are specifically adsorbed on negatively charged electrodes, are notable for their ability to enhance the electroreduction of negatively charged anions (12-14). This enhancement may occur through (i) a decrease in electrostatic repulsion (Frumkin  $\phi_2$  effect); (ii) ion-pair formation in the double layer, which also reduces electrostatic repulsion; (iii) ligand bridging with the adsorbed cation, which increases the charge transfer rate; (iv) a lowering of the activity coefficient of the activated complex; (v) discreteness-of-charge effects; (vi) ionic atmosphere and solvent reorganization effects. To test whether such effects could be responsible for the depolarization phenomena observed in the electroreduction of  $\text{Au}(\text{CN})_2^-$ , relaxation times were measured as a function of current density, disk rotational speed, and Cs<sup>+</sup> ion concentration. The depolarization times were found to be exceedingly long, comparable to those observed in phosphate supporting electrolytes which had not been preelectrolyzed. No enhanced depolarization effect was observed at low Cs<sup>+</sup> ion concentrations ( $[\text{Cs}^+] \leq 0.01\text{M}$ ). Further,  $\tau$  was found to decrease with increasing  $[\text{Cs}^+]$  and  $m$ . It is therefore concluded that Cs<sup>+</sup> ions *per se* are inactive in catalyzing the electroreduction of  $\text{Au}(\text{CN})_2^-$ . The depolarization effects observed in concentrated  $\text{CsNO}_3$  solutions are attributed to heavy metal ions introduced as impurities with the cesium salt.

**Underpotential deposition of heavy metals.**—The specific adsorption of metal ions on foreign substrates and their reduction at potentials anodic to the equilibrium potential for the metal ion/metal couple extends over a several hundred millivolt range. In order to correlate the catalytic effects of the Pb(II), Tl(I), Bi(III), and Hg(II) additives on the electroreduction of  $\text{Au}(\text{CN})_2^-$ , their underpotential deposition (upd) range on a gold RDE was measured in preelectrolyzed phosphate buffer solutions at 70°C. A more detailed interpretation of the upd phenomena will be given elsewhere. What we wish to establish here are the relative ranges of monolayer and bulk metal deposition and whether specific adsorption of the heavy metal ions occurs at the gold surface. For purposes of correlation, the approximate underpotential and bulk deposition ranges of the heavy metals investigated in this study have been indicated in Fig. 4, 5, 7, 9, and 10.

**Lead.**—The standard potential of the reaction



at 25°C is  $-0.126\text{V}$  (SHE). From temperature coefficient data (35) the standard potential at 70°C referred to an SHE at the same temperature is calculated to be  $-0.146\text{V}$ . In a 1 ppm  $\text{Pb}^{++}$  solution ( $4.8 \mu\text{M}$ ) at 70°C, the equilibrium potential of the  $\text{Pb}^{++}/\text{Pb}$  couple is therefore  $-0.327\text{V}$ . In alkaline phosphate solutions this potential is not realized because of the tendency of  $\text{Pb}^{++}$  ions to complex with hydroxyl and phosphate anions (19).

Figures 11a and b display the  $i$ - $E$  curves measured for the cathodic deposition and anodic stripping of Pb(O) at a gold RDE in preelectrolyzed phosphate supporting electrolyte (pH 8, 70°C) containing 1 ppm Pb(II). Since the bulk solution concentration of the lead additive is very low, a disk rotational speed of 4900 rpm was employed to maintain a rapid supply of this species to the electrode surface. Again assuming that the diffusion coefficient of Pb(II) is similar to that of  $\text{Au}(\text{CN})_2^-$ , we find from Eq. [11] that the limiting transport rate at  $m = 4900$  rpm is equivalent to the deposition of 0.067 close-packed monolayer of Pb(O) per second. Thus at a scan rate of 10 mV/sec the underpotential deposition of lead is essentially free from mass transport control; monolayer deposition is com-

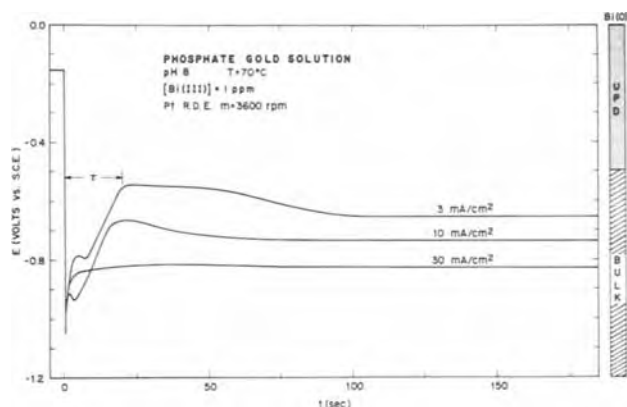


Fig. 9. Galvanostatic reduction of  $\text{Au}(\text{CN})_2^-$  at a platinum RDE in the presence of 1 ppm Bi(III).

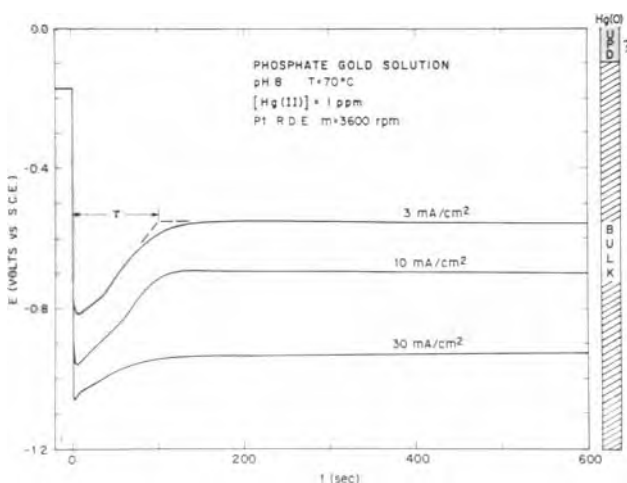


Fig. 10. Galvanostatic reduction of  $\text{Au}(\text{CN})_2^-$  at a platinum RDE in the presence of 1 ppm Hg(II).

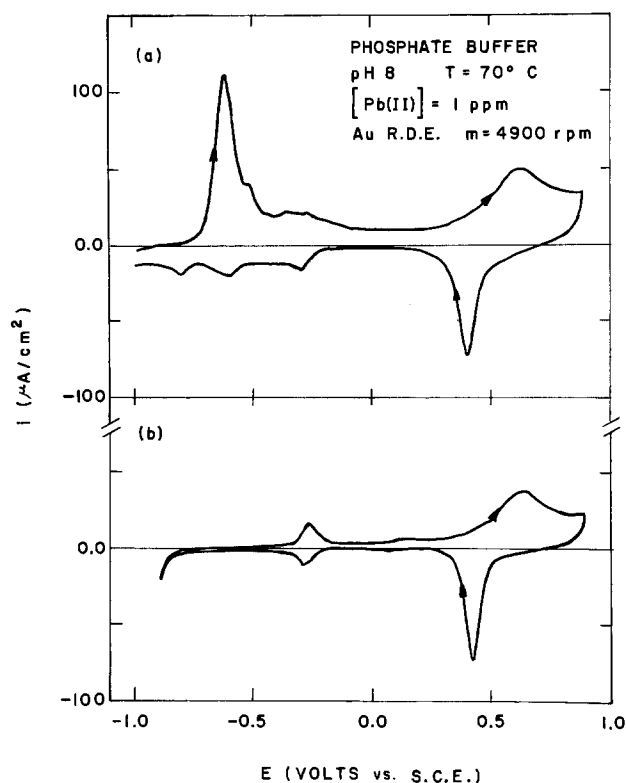


Fig. 11. Oxidation of Pb(O) and reduction of Pb(II) at a gold RDE in aqueous phosphate buffer solution (pH 8, 70°C).  $[Au(CN)_2^-] = 0$ ,  $[Pb(II)] = 1$  ppm. Potential scan rate =  $10 \text{ mV sec}^{-1}$ . (a) Disk held at  $-1.0\text{V}$  for 20 min before start of anodic scan. (b) Cyclic scans with no hold.

plete within the time required to scan through a voltage interval of 0.15V.

Prior to the commencement of the anodic sweep in Fig. 11a, the electrode was held for 20 min at  $-1.0\text{V}$  (SCE) in order to deposit bulk Pb metal. The large anodic current peak at  $-0.62\text{V}$  corresponds to the stripping of this phase. Current peaks due to the anodic oxidation of underpotential Pb(O) occur at  $-0.52$ ,  $-0.35$ , and  $-0.26\text{V}$ . In the cathodic scan, upd peaks are observed at  $-0.30$ ,  $-0.60$ , and  $-0.80\text{V}$ .

Figure 11b shows the  $i$ - $E$  curves measured during a cyclic voltammetric scan under the same conditions as Fig. 11a but with no cathodic hold. Only a single upd peak at  $-0.28\text{V}$  is observed in the cathodic scan. A conjugate peak of approximately equal amplitude appears in the anodic scan. The integral coulombic charge passed in the cathodic peak of width  $\sim 0.18\text{V}$  is  $\sim 100 \mu\text{C}/\text{cm}^2$ , based on the geometric surface area of the disk. For a surface roughness factor of 1.5-2, this charge is equivalent to the deposition of  $\sim 0.2$  close-packed monolayer of Pb(O) on the surface. To first order this charge is independent of the applied potential scan rate and disk rotational speed. This implies that the Pb(II) species is not removed from the surface during the cyclic scan but remains adsorbed in the double layer. This phenomenon is discussed in further detail in the analysis of underpotential bismuth deposition.

**Thallium.**—The standard potential of the reaction



at 25°C is  $-0.3363\text{V}$  (SHE). At 70°C the standard potential referred to a SHE at the same temperature is calculated to be  $-0.396\text{V}$ . In a 1 ppm Tl(I) solution ( $4.9 \mu\text{M}$ ) at 70°C, the equilibrium potential of the  $Tl^+/Tl$  couple is thus  $-0.758\text{V}$ . This thermodynamic reversible potential is closely approached in alkaline phosphate solutions because  $Tl^+$  ions are not strongly complexed (19).

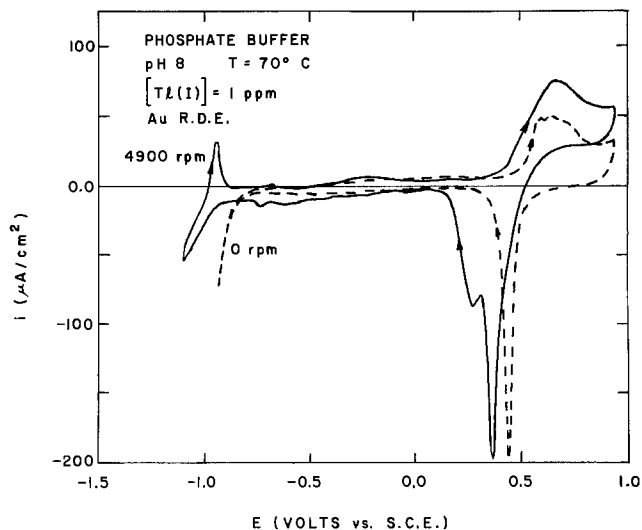


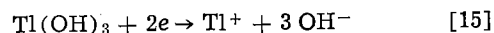
Fig. 12. Oxidation of Tl(O) and reduction of Tl(I) at a gold RDE in phosphate buffer solution. Scan rate =  $10 \text{ mV sec}^{-1}$ . ---  $[Tl(I)] = 0$ ,  $m = 0$  rpm. —  $[Tl(I)] = 1$  ppm,  $m = 4900$  rpm.

Figure 12 illustrates the  $i$ - $E$  curves measured for the cathodic deposition and anodic stripping of Tl(O) at a gold RDE ( $m = 4900$  rpm) in the phosphate buffer solution containing 1 ppm Tl(I). The cyclic voltammogram for the stationary disk in thallium-free solution is also shown for reference. In contrast to lead, bulk thallium metal readily deposits at a potential very close to its theoretical reversible potential in this solution [ $-1.00\text{V}$  (SCE)]. In the anodic scan at  $10 \text{ mV}/\text{sec}$ , this phase is rapidly stripped at  $-0.9\text{V}$ . A small, narrow current peak corresponding to the oxidation of underpotential Tl(O) appears at  $-0.7\text{V}$ . This is followed by a very broad oxidation peak with a maximum at  $-0.25\text{V}$ . Corresponding upd peaks are observed in the cathodic scan. Although not well resolved on this scale, additional cathodic underpotential peaks appear at  $-0.43$  and  $-0.60\text{V}$ . These are not distinguishable at higher sweep rates ( $\geq 30 \text{ mV}/\text{sec}$ ).

A remarkable effect occurs in the potential region of anodic oxide formation on the gold electrode in very dilute Tl(I) solutions. A steady-state anodic current of  $29 \mu\text{A}/\text{cm}^2$  is observed for a disk rotating at 4900 rpm (Fig. 12). This is attributed to the oxidation reaction



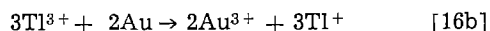
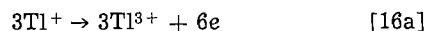
The standard potential of this reaction at 70°C is  $+1.29\text{V}$  (SHE) or  $\sim 1.05\text{V}$  (SCE), but this potential is shifted negatively by the formation of the sparingly soluble solid phase  $Tl(OH)_3$  (36). Comparison of the areas inside the oxide formation-reduction loops of the solid and dashed curves in Fig. 12 shows that the formation of an adsorbed O or anodic oxide layer on gold is only slightly inhibited by the presence of  $Tl^+$  ions. During the reverse cathodic scan from  $-0.95\text{V}$ , the gold oxide reduction peak is shifted to more negative potentials and broadened. On the trailing edge of this peak appears a secondary peak at  $-0.38\text{V}$ . The latter peak is attributed to the cathodic dissolution of  $Tl(OH)_3$ , viz.



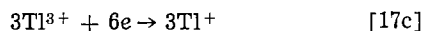
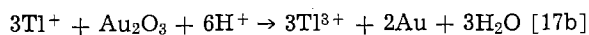
At higher sweep rates ( $\geq 30 \text{ mV}/\text{sec}$ ) this peak appears only as a small shoulder at the base of the gold oxide reduction peak because the rate of formation of the  $Tl(OH)_3$  surface film is controlled by the convective diffusion rate of  $Tl^+$  ions to the surface and the sweep rate. In more concentrated solutions of Tl(I), gold oxide formation is suppressed and gold dissolution enhanced.

It has been postulated (24, 26) that this increase in the gold corrosion rate is due to inhibition of the

formation of the passivating oxide layer by adsorbed thallium atoms. However, Tl(O) cannot exist on the surface at this high potential. An alternative catalytic mechanism which may explain the specificity of the dissolution process is

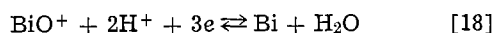


Conversely, since Tl(I) is a strong reducing agent, the adsorbed O or gold oxide layer may be reduced chemically as soon as it is formed electrochemically. In acid solution, for example



Removal of the oxide prevents the gold electrode from becoming passive and enhances its corrosion rate. Since in both of these mechanisms Tl(I) is continuously regenerated, only trace amounts are required to catalyze the gold dissolution process. Adsorption of the Tl(I) species is not required for either of these postulated mechanisms to be operative. Their applicability is currently under investigation.

**Bismuth.**—In the pH range 3.4–8.6, the reduction of Bi(III) to Bi(O) is formally represented as



At 25°C the standard potential of this reaction is +0.320V (SHE). Hence, at pH 8 the equilibrium potential of the BiO<sup>+</sup>/Bi couple in a 1 ppm Bi(III) solution (4.8 μM) is -0.109V. The temperature coefficient of *E*<sup>o</sup> has not been reported (35), and hence the equilibrium potential at 70°C cannot be calculated directly.

Figure 13 shows the *i*-*E* curves measured for the cathodic deposition and anodic stripping of Bi(O) at a gold RDE (*m* = 4900 rpm) in preelectrolyzed phosphate buffer solution (pH 8, 70°C) containing 1 ppm Bi(III). The potential scan rate was 10 mV/sec. Curves a, b, and c were measured after a potential hold at -0.9V (SCE) of 0, 1, and 2 min to reveal the bulk Bi(O) stripping peaks at -0.3V. The origin of the small anodic peaks at -0.24, -0.09, and +0.25 are attributed to the anodic oxidation of underpotential

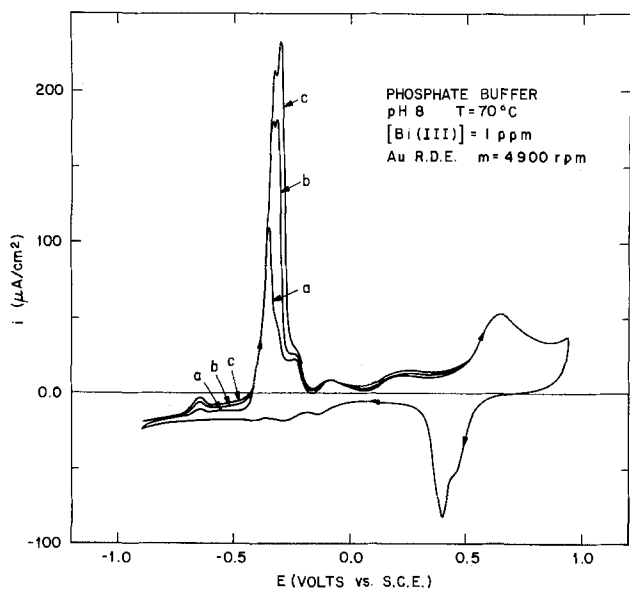


Fig. 13. Oxidation of Bi(O) and reduction of Bi(III) at a gold RDE in phosphate buffer solution. Scan rate = 10 mV sec<sup>-1</sup>. (a) Disk held at -0.9V for 0 min before anodic scan, (b) 1 min hold at -0.9V, (c) 2 min hold at -0.9V.

Bi(O), although the most positive peak has no apparent cathodic counterpart.

During the cathodic scan the gold oxide reduction peak at +0.4V is broadened and attenuated, possibly due to the adsorption of Bi(III) on the oxide surface (33) but more probably in the present case (pH 8), due to the reduction of higher valent bismuth oxides such as Bi<sub>4</sub>O<sub>7</sub>, Bi<sub>2</sub>O<sub>4</sub>, or Bi<sub>2</sub>O<sub>5</sub> which can be formed at potentials >0.6V (SCE) (36). At low scan rates (10 mV/sec) a shoulder appears on the leading edge of the gold oxide reduction peak. This shoulder is not observed at faster sweep rates (≥30 mV/sec).

On repetitively scanning over the potential range -1.0 to +1.0V at 30 mV/sec with a stationary disk (*m* = 0), only a single Bi(III) reduction peak at -0.15V and a conjugate anodic peak (a doublet) of equal amplitude at -0.10V are observed (Fig. 14a). The integral coulombic charge passed in each current peak is ~300 μC/cm<sup>2</sup>, based on the geometric surface area of the disk. Assuming a surface roughness factor of 1.5–2, this charge corresponds to the amount required to deposit or oxidize 0.3–0.4 close-packed monolayer of Bi(O) on the electrode surface. If *m* is increased to 3600 rpm at the same potential scan rate, a bulk stripping peak at -0.32V and the underpotential peak at -0.26V reappear (Fig. 14b), while the conjugate current peaks are shifted to -0.19V and their amplitude is halved. These results imply that the redox process associated with these current peaks is not diffusion controlled. At *m* = 3600 rpm the limiting rate of con-

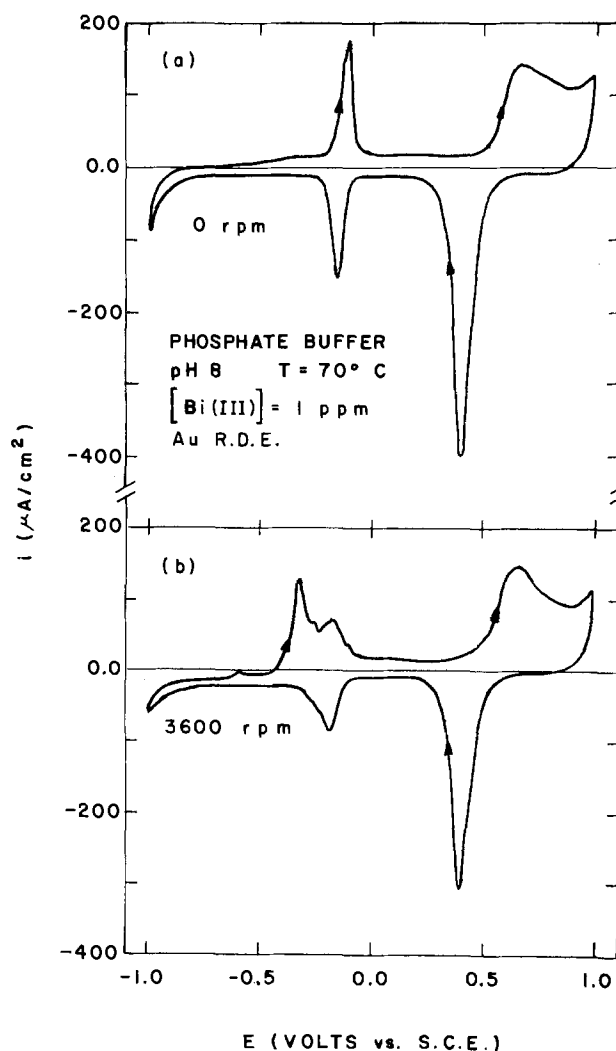
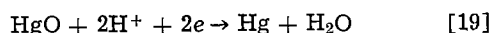


Fig. 14. Linear sweep voltammogram for the underpotential deposition and oxidation of Bi(O) at a gold disk electrode in phosphate buffer solution. Scan rate = 30 mV sec<sup>-1</sup>. (a) Stationary disk, *m* = 0 rpm. (b) Rotating disk, *m* = 3600 rpm.

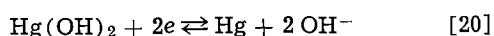
vective diffusion of Bi(III) to the surface in this very dilute solution corresponds to the deposition of  $\sim 0.06$  monolayer per second. However at  $m = 10$  rpm (a stirring rate greater than that due to natural convection at a stationary RDE), the maximum deposition rate is only  $3 \times 10^{-3}$  monolayer per second. At a scan rate of 30 mV/sec, the duration of the cathodic current peak is  $\sim 6$  sec, time for less than 0.02 monolayer of Bi(O) to deposit on the stationary disk. These results indicate clearly that a substantial fraction of the Bi(III) species does not diffuse away from the surface but remains adsorbed in the double layer. The kinetics of the charge redistribution among the various adsorption states of bismuth requires further investigation.

The conclusion that Bi(III) species remain adsorbed at the gold electrode is further confirmed by studies in more concentrated solutions. In a 10 ppm Bi(III) solution ( $4.8 \times 10^{-5}M$ ), the formation of the anodic gold oxide film is strongly inhibited and a steady-state limiting current is observed over the range  $-0.1$ - $1.0V$  which is presumed due to the anodic dissolution of gold. Similar results are observed in 1 ppm Bi(III) solutions after deposition of bulk Bi metal at  $-0.9V$  for 5-20 min.

**Mercury.**—In alkaline solutions, mercury metal is oxidized directly to the mercuric state with the formation of sparingly soluble HgO. The standard potential for the reaction



is  $+0.926V$  (SHE) at  $25^\circ\text{C}$ . At pH 8, the equilibrium potential of the Hg(II)/Hg(O) couple is  $+0.453$  (SHE) or  $\sim +0.209V$  (SCE). For the reduction of the sparingly soluble hydroxide



the standard potential is  $+1.034V$  (SHE). In a 1 ppm Hg(II) solution ( $5.0 \mu\text{M}$ ) at pH 8, the equilibrium potential of the Hg(II)/Hg(O) couple is  $+0.404V$  (SHE) or  $\sim +0.159V$  (SCE).

Figure 15 shows the  $i$ - $E$  curves measured for the cathodic deposition and anodic oxidation of Hg(O) at a gold RDE ( $m = 4900$  rpm) in preelectrolyzed phosphate solution (pH 8,  $70^\circ\text{C}$ ) with a scan rate of 10 mV/sec. In the cathodic scan a limiting current plateau is preceded by two small current peaks at  $0.0V$  (SCE) which may correspond to underpotential deposition. In

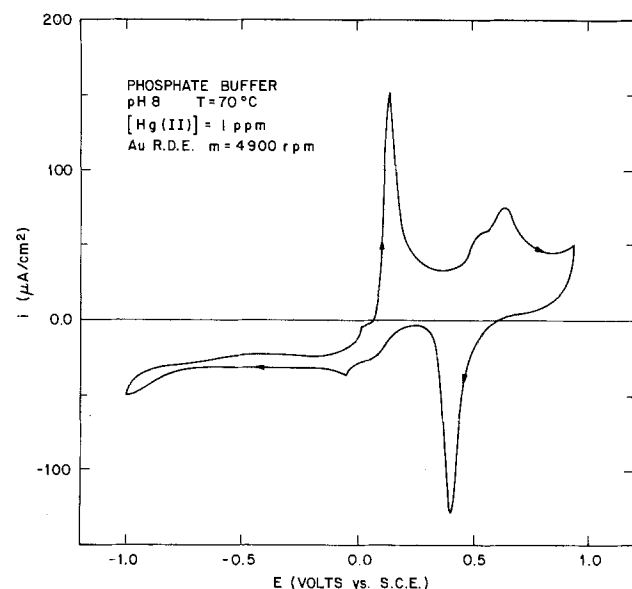


Fig. 15. Oxidation of Hg(O) and reduction of Hg(II) at a gold RDE in phosphate buffer solution.  $m = 4900$  rpm. Scan rate =  $10 \text{ mV sec}^{-1}$ .

the anodic scan, the peak at  $+0.14V$  corresponds to the oxidation of Hg(O) to Hg(OH)<sub>2</sub>. The tail on the anodic side of this peak is attributed to the slow back-diffusion of mercury to the surface of the amalgamated gold electrode. The anodic peak at  $+0.5V$  is thought to be due to the enhanced anodic dissolution of gold resulting from the inhibition of oxide layer formation. Since the gold RDE surface is extensively damaged by amalgamation, we have not studied these processes in further detail.

**Mechanism of the depolarization effect.**—Several physical and chemical mechanisms must be considered in attempting to account for the pronounced depolarization effects encountered in the electroreduction of  $\text{Au}(\text{CN})_2^-$  in the presence of trace quantities of heavy metal ions. Since these additives are present at extremely low concentration ( $\sim 5 \mu\text{M}$ ) in the bulk solution, it is evident that their rate of transport to the cathode surface is much too low (see above) for them to react directly with the  $\text{Au}(\text{CN})_2^-$  ions at or near the surface. Rather, the depolarizing species must initially be concentrated in some ionic or neutral adsorption state on the surface which enables them to increase the rate of one or more sequential steps in the electroreduction reaction. Alternatively, the depolarizer may cause the reduction of  $\text{Au}(\text{CN})_2^-$  to occur by a different mechanism.

The over-all reaction of metal deposition from an aqueous solution is represented by



This reaction comprises the following elementary steps: (i) transport of the hydrated metal ion,  $[\text{M}^{z+}(\text{H}_2\text{O})_n]_{\text{sol}}$ , from the bulk solution to a position at the outer Helmholtz plane in the ionic double layer; (ii) tunneling of an electron from the electrode to the ion in a suitably deformed solvation sheath; (iii) diffusion of the partially hydrated adion across the surface to a step site or crystal nucleus; (iv) migration of the particle to a fixed lattice position, e.g., a kink site or edge vacancy; and (v) final dehydration and discharge of the adion and incorporation of the metal atom into the lattice. It is clear that if the electrodeposition reaction is to be accelerated by an adsorbed depolarizer, then this species must either remain in its initial state on the surface or else be rapidly regenerated after each reduction event. On the other hand, if the depolarization is caused by incorporation of the large heavy metal atoms into the bulk lattice as the deposit grows, then the mechanism must operate through a long-range physical effect which propagates to the surface plane where reduction occurs. We now consider a number of mechanisms which can contribute to the depolarization phenomenon.

**Electrocrystallization effects.**—The trace foreign metal additives found most effective as depolarizers (Hg, Tl, Pb, Bi) in the electrodeposition of gold from alkaline phosphate solutions all have atomic radii substantially greater than that of gold ( $r_{\text{Au}} = 1.44\text{\AA}$ ;  $r_{\text{Hg}} = 1.57\text{\AA}$ ;  $r_{\text{Tl}} = 1.71\text{\AA}$ ;  $r_{\text{Pb}} = 1.75\text{\AA}$ ;  $r_{\text{Bi}} = 1.70\text{\AA}$ ). This suggests that the depolarization effect induced by these heavy metal atoms might result from their incorporation into the bulk gold lattice. In real metal crystals, screw dislocations originate at impurity sites or faults. Deposition or dissolution of metal at low overpotentials generally proceeds through these dislocations, with the growth site perpetuating itself (37, 38). Generation of an increased dislocation density in the interior of the crystal could produce, in turn, an increase in the concentration of step sites on the surface and hence a decrease in crystallization overpotential.

There are a number of arguments against this mechanism being the one responsible for the depolarization effect. Firstly, the magnitude of the depolarization ( $>0.2V$ ) is much larger than the crystallization overpotentials (37) observed for the deposition of a metal

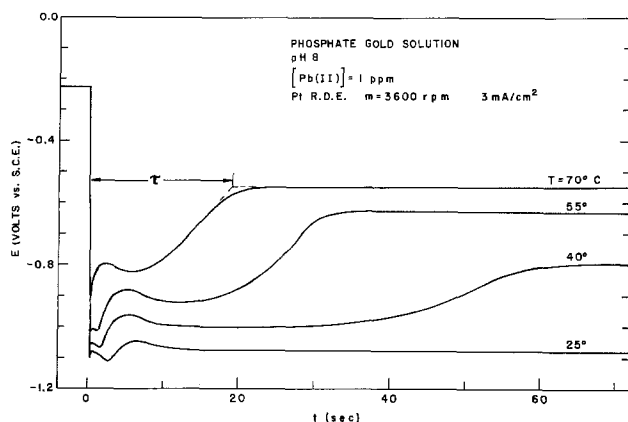


Fig. 16. Temperature dependence of the depolarization effect induced by 1 ppm Pb(II) in the galvanostatic reduction of  $\text{Au}(\text{CN})_2^-$  at a platinum RDE.  $m = 3600$  rpm,  $i = 3$  mA  $\text{cm}^{-2}$ .

onto a substrate of the same metal. Secondly, the depolarization effect has a strong temperature dependence. As shown in Fig. 16, the depolarization time in the phosphate gold solution containing 1 ppm Pb(II) increases as the temperature is lowered until at 25°C a depolarization is no longer observable. If the dislocation mechanism were operative, we would expect the opposite behavior, since higher temperatures should anneal the lattice strain more rapidly and also increase the rate of segregation of lead atoms to the surface or grain boundaries. Secondly, a pronounced depolarization effect is also observed for Hg(II) additives (Fig. 10). Mercury, however, is able to form a substitutional alloy with gold since the difference in their atomic radii is less than the Hume-Rothery limit of ~15%. Hence incorporation of adsorbed mercury atoms into the bulk deposit would not be expected to increase the dislocation density to the same extent as lead and the deposit should be relatively free of internal stress from this source. In contrast, gold deposits plated from a solution containing more than 2 ppm Pb(II) are found to be brittle (8). This may result from an impedance to the movement of dislocations in the bulk caused by the foreign metal atoms, or by their segregation to grain boundaries. Finally, according to classical electrocrystallization theory (37), the current density should be independent of the number of screw dislocations per unit area. From these considerations we conclude that generation of bulk dislocations is not the primary factor which induces the depolarization effect.

Another electrocrystallization effect that must be considered is the rate of two- or three-dimensional nucleus formation on the substrate surface. It is generally believed that polycrystalline metal deposits contain such a high concentration of defects and dislocations that nucleation cannot be a rate-determining step in the crystal growth process. However, in the presence of strongly adsorbing inhibitors it has been postulated (39) that the surface may act as though it were dislocation free since these inhibitors are preferentially adsorbed at defect sites on the surface. At low current densities, for example, copper deposits build up in layers with a preferred orientation as a result of two-dimensional nucleation and growth. At higher current densities and overpotentials, three-dimensional crystallization and growth is favored and a fine-grained deposit with no preferred orientation is formed. In the case of gold electrodeposition, a high concentration of potential inhibitors is generated continuously by the electroreduction process itself (Eq. [1] and [7]). Cyanide anions are strongly adsorbed on gold at potentials positive of the point of zero charge [ $\sim 0.0$  V (SCE)]. It is not yet known, however, whether they remain specifically adsorbed at the more negative po-

tentials required for electroreduction of  $\text{Au}(\text{CN})_2^-$ . The adsorption of foreign metal atoms such as Pb, Tl, Bi, or Hg may substantially modify the extent of  $\text{CN}^-$  adsorption. Note that the bulk metal phases of these elements have points of zero charge  $-0.4$  to  $-0.9$  V negative to that of gold (40).

High surface coverages by depolarizer metal adatoms may appreciably alter not only anion adsorption but also nucleation rate and the entire crystal growth mechanism. Recent theoretical calculations (41) have shown that impurity atoms which are strongly chemisorbed on the bulk metal surface can act as centers for two-dimensional nucleation. Thus gold adatoms diffusing across the surface may be trapped by lead atoms adsorbed at underpotentials, owing to the strong Pb-Au interaction energy. If the surface coverage by foreign metal adatoms is sufficiently high, then crystal growth will occur primarily at these sites rather than at step or kink sites on the bulk metal surface. This may increase the net reaction rate in several ways, e.g., by (i) decreasing the mean surface diffusion length of the gold adatoms, (ii) decreasing the size of the surface nucleus, (iii) increasing the total step edge length or the number of kink sites at existing steps, or (iv) reducing growth inhibition caused by impurity adsorption and step bunching. The foreign metal adatoms may also reduce the work of formation of two-dimensional nuclei on the surface and thus lower the crystallization overvoltage [cf. Pangarov (42-48)]. Preferential deposition of gold crystallites with low index planes parallel to the surface would then be expected, rather than the randomly oriented crystals formed at higher overpotentials. As yet the effect of depolarizers on the orientation of gold crystallites has not been studied experimentally and this postulate remains to be tested.

Finally, it should be noted that the magnitude of the depolarization produced by the foreign metal atoms is anomalously large compared to the crystallization overvoltages usually observed for two- or three-dimensional nucleation and growth [cf. Ref. (37)]. In addition to the enhanced nucleation and crystal growth rates, double layer and electrocatalytic effects may also contribute to the depolarization. The influence of these is discussed below.

**Electrostatic effects.**—As mentioned previously, cesium ions specifically adsorbed on negatively charged electrodes can enhance the electroreduction of negatively charged anions (12-14). Similar enhancement is observed for the electroreduction of cations in the presence of specifically adsorbed anions (12, 49-53). In the present work, however, we could find no evidence of an acceleration of the electroreduction of  $\text{Au}(\text{CN})_2^-$  anions by  $\text{Cs}^+$  ions, other than one attributable to impurities in the reagent salt. An alternative means of lowering the electrostatic repulsion between anions and the electrode may be provided by the underpotential deposition of metals. If the adsorbate layer has an electronegativity or work function less than that of the substrate, then a charge transfer will occur which leaves the atoms in this layer with a partial positive charge. Such may be the case for the adsorption of Pb, Tl, Bi, and Hg on Au ( $\chi_{\text{Au}} = 2.4$ ,  $\chi_{\text{Pb}} = 1.8$ ,  $\chi_{\text{Tl}} = 1.8$ ,  $\chi_{\text{Bi}} = 1.9$ ,  $\chi_{\text{Hg}} = 1.9$ ). While these metals all act as depolarizers in the electroreduction of  $\text{Au}(\text{CN})_2^-$  in alkaline solution, other additives such as Cu, Ag, Zn, Cd, In, Sn, and Sb do not. The latter all have electronegativities equal to or less than 1.9. Apparently the positive "electrosorption valency" of these adatoms has no specific electrocatalytic effect in this case.

Other evidence that electrostatic effects were not responsible for the depolarization phenomenon was provided by a study of the electroreduction of oxygen on gold in the phosphate supporting electrolyte. As shown in Fig. 17, the addition of 1 ppm Pb(II) to an  $\text{O}_2$ -saturated phosphate buffer electrolyte (pH 8,  $T = 70^\circ\text{C}$ ) markedly accelerates the rate of electroreduction of oxygen on gold in the potential region of partial ki-

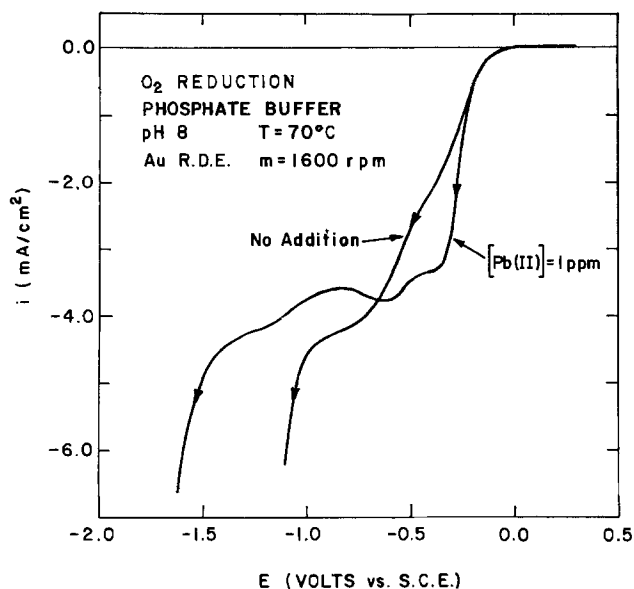


Fig. 17. Steady-state  $i$ - $E$  curves for the electroreduction of oxygen at a gold RDE in phosphate buffer solution (pH 8, 70°C) in the presence and absence of 1 ppm Pb(II).

netic control. Since the  $O_2$  molecule has no charge, electrostatic effects cannot be responsible for the enhancement of its reduction rate. In this case it is evident that the electrocatalytic effect arises from upd of Pb(O) on the Au electrode surface (cf. Fig. 11). Note, however, how the  $H_2$  evolution reaction is poisoned by Pb. Also of interest is the fact that when  $O_2$  is reduced galvanostatically at a low disk rotational speed (900 rpm), the electrode potential exhibits periods of growing and damped oscillation. The origin of this phenomenon is not yet known, but its occurrence suggests that the Pb(O) concentration on the surface fluctuates as a result of reaction with intermediate species (e.g., OH,  $HO_2$ ,  $H_2O_2$ ) generated during oxygen reduction.

**Electrochemical displacement.**—The ability of the heavy metal depolarizers to catalyze both the deposition and dissolution of gold leads us to consider also the possible occurrence of electrochemical displacement reactions. Owing to the high pH and the extremely low solution concentrations of the depolarizers, the equilibrium potentials of the metal ion/metal couples lie far negative of their standard potentials. In Table I the thermodynamic reversible potentials of these species at a solution concentration of 1 ppm are compared to that of the Au(I)/Au couple in a phosphate gold solution at 25°C and pH 8, with  $[Au(CN)_2^-] = 0.0694M$  and  $[HCN] = 10^{-4}M$ . The true reversible potentials of the Pb(II)/Pb and Bi(III)/Bi couples in this solution are probably more negative than the calculated values owing to complexation of the metal cations by  $OH^-$ ,  $CN^-$ , or  $HPO_4^{2-}$  anions. The monovalent Tl<sup>+</sup> ions are only weakly complexed by  $OH^-$  and not at all by  $CN^-$  (19). From these considerations it is evident that the bulk metals Pb, Tl, and Bi are thermodynamically capable of displacing gold from solution, e.g.

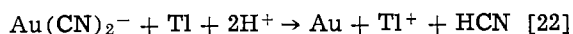
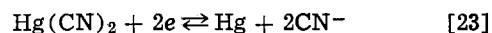


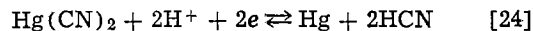
Table I. Thermodynamic reversible potentials at 25°C and pH 8

Couple	Solution concentrations	$E^{\circ}V$ (SHE)	$E_rV$ (SHE)
Au(I)/Au(O)	0.0694M $Au(CN)_2^-$ , $1.0 \times 10^{-4}M$ HCN	+0.501	-0.041
Pb(II)/Pb(O)	$4.83 \times 10^{-6}M$	-0.126	-0.283
Tl(I)/Tl(O)	$4.89 \times 10^{-6}M$	-0.336	-0.650
Bi(III)/Bi(O)	$4.79 \times 10^{-6}M$	+0.320	-0.109
Hg(II)/Hg(O)	$4.99 \times 10^{-6}M$	+1.034	+0.404

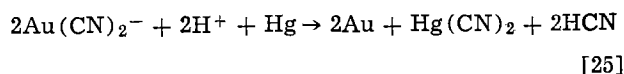
Now according to Table I, Hg(O) should not be able to reduce Au(I) since  $E_{Hg(II)/Hg} > E_{Au(I)/Au}$ . Recall, however, that the  $Hg^{2+}$  cation forms soluble, extremely stable complexes with  $CN^-$  which are not precipitated in alkaline solution. For example, the stability constant of  $Hg(CN)_2$  at 25°C is  $10^{35.3}$ , whereas that of  $Hg(CN)_4^{2-}$  is  $10^{41.5}$ . These complexes of  $Hg^{2+}$  are comparable in stability to  $Au(CN)_2^-$  ( $K_s = 10^{39.1}$ ). When the free cyanide concentration is very low ( $< 10^{-4}M$ ), the predominant complex is  $Hg(CN)_2$ . In alkaline solution (pH > 11) at 25°C, the standard potential of the reaction



is calculated to be -0.190V (SHE). For the corresponding reaction in acid or slightly alkaline solution (pH < 8)



the standard potential is +0.361V. [Recall that the analogous standard potentials for electroreduction of  $Au(CN)_2^-$  are -0.600 and +0.501V, respectively.] At pH 8, the equilibrium potential of the Hg(II)/Hg couple in a solution with  $[HCN] = 10^{-4}M$  and  $[Hg(II)] = 1$  ppm is -0.033V (SHE). This is very close to the value of -0.041V calculated for the Au(I)/Au couple in 0.0694M  $Au(CN)_2^-$  solution (Table I). At lower cyanide concentrations and also at lower pH,  $E_r(Hg(II)/Hg)$  lies negative of  $E_r(Au(I)/Au)$ , as shown in Fig. 18. Under these conditions, mercury metal is electropositive relative to gold and can act as a reducing agent, displacing Au(I) from solution by the reaction



The displacement is also favored by increasing  $Au(CN)_2^-$  concentration.

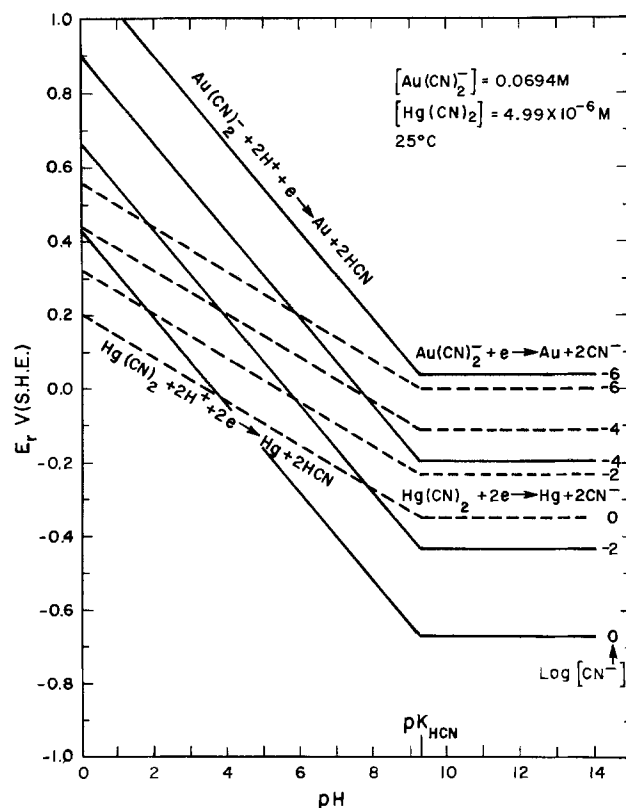
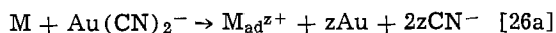


Fig. 18. Variation of the thermodynamic reversible potentials for the reduction of the complexes  $Au(CN)_2^-$  and  $Hg(CN)_2$  as a function of pH and free cyanide concentrations.  $[Au(CN)_2^-] = 0.0694M$ ,  $[Hg(CN)_2] = 1$  ppm =  $4.99 \times 10^{-6}M$ , 25°C.



The experimental observation of a pronounced depolarization effect in the electroreduction of  $\text{Au}(\text{CN})_2^-$  in the presence of 1 ppm  $\text{Hg}(\text{II})$ , which would not otherwise have been expected, strongly suggests that an electrochemical displacement reaction does in fact occur, although nucleation enhancement may also be responsible. The  $\text{Hg}(\text{O})$  species is rapidly regenerated by electroreduction in the negative potential range employed (Eq. [23]).

The over-all displacement and regeneration process for a depolarizer couple  $\text{M}^{z+}/\text{M}$  may be generally formulated as



Several criteria must be satisfied for such a mechanism to be operative. First, the thermodynamic reversible potential of the  $\text{M}^{z+}/\text{M}$  couple must be more negative than that of the  $\text{Au}(\text{CN})_2^-/\text{Au}$  couple in the gold plating solution employed. In the simplified treatment above we have considered only the difference in Nernst potentials of the metal ion/bulk metal couples, assuming the activity of the metal adatom layer to be near unity. This condition is approached near full monolayer coverage but at lower surface coverages the reversible potential of the  $\text{M}^{z+}/\text{M}$  couple is shifted anodically. A positive shift is also produced by specific adsorption of the  $\text{M}^{z+}$  species in the double layer. Second, the "oxidized" form of the catalyst must remain specifically adsorbed in the double layer since it cannot be replenished at a sufficiently rapid rate by mass transport. It is quite possible that this species is "contact adsorbed" and does not have the full formal charge of the ionic species  $\text{M}^{z+}$  in solution. Third, the exchange current density of the  $\text{M}^{z+}/\text{M}(\text{O})$  couple must be high in order for the zero-valent species to be regenerated rapidly. Recent studies (10) of the underpotential deposition of silver, lead, and thallium on gold have shown that the exchange current density in these systems is of the order of  $10 \text{ A cm}^{-2}$ . This implies that charge transfer polarization is negligible and that surface diffusion is the rate-determining step in the deposition process. In the galvanostatic reduction experiments (Fig. 4, 5, 7, 9, and 10), the final steady-state potentials are well clamped. This is consistent with the fact that the exchange current densities of the various  $\text{M}^{z+}/\text{M}$  couples are much greater than that of the  $\text{Au}(\text{CN})_2^-/\text{Au}$  couple. According to this mechanism, the final potential will be determined by the combined polarization curves of the  $\text{M}^{z+}/\text{M}$  and  $\text{Au}(\text{I})/\text{Au}$  couples, as illustrated schematically in Fig. 19. At

low current densities gold deposition will occur primarily through the displacement reaction mechanism (Eq. [26]), but at high current densities gold will be deposited mainly by the direct electroreduction mechanism (Eq. [1] and [7]). Finally, although underpotential deposition of a depolarizer is apparently not a prerequisite for catalytic reduction of  $\text{Au}(\text{CN})_2^-$  (cf. Fig. 4, 5, 7, 9, and 10), the formation of  $\text{M}(\text{O})$  adatoms on the surface enables other slow electrochemical reactions such as  $\text{O}_2$  reduction (Fig. 13) to be accelerated at potentials well positive of those where bulk deposition of  $\text{M}(\text{O})$  begins.

**Electroplating applications.**—On the basis of the mechanisms described above, it now becomes evident why the addition of trace heavy metal ions such as  $\text{Tl}(\text{I})$  to gold-plating solutions leads to uniformly distributed gold deposits on irregularly shaped small parts. According to the patent literature (2, 3), best results are obtained in the current density range of  $2\text{--}10 \text{ mA cm}^{-2}$ . Examination of Fig. 7 reveals that the corresponding overpotentials for gold deposition lie in the range of underpotential deposition of  $\text{Tl}(\text{O})$  on gold. Now underpotential deposition of a metal monolayer occurs uniformly on a foreign metal substrate, rather than in islandlike clusters, since its heat of adsorption is greater than the cohesive energy of its bulk form (33, 34, 54–57). As a result, the displacement reaction will also proceed uniformly on the substrate, thereby leading to good "throwing power" and reducing the amount of gold required to plate the part. Similarly, in selective plating of integrated circuits (6–8), adsorption of the depolarizer will occur preferentially on exposed bare metal surface (e.g., Pd) rather than on a metal surface covered by an oxide (e.g., Ti, Al). As a result, the gold deposition rate on beam leads is enhanced and bridging due to "underplating" on a surface inadequately protected by a photoresist mask is reduced.

**Electrocatalysis by heavy metal ions.**—Recent studies (58, 59) have shown that a number of slow electrochemical reactions are catalyzed by monolayers of metals (Pb, Tl, Bi) deposited at underpotentials on foreign metal substrates (Pt, Au). Examples include the  $\text{Fe}^{2+}/\text{Fe}^{3+}$  and  $\text{Ti}^{3+}/\text{Ti}^{4+}$  redox couples and the oxidation of formic acid. The catalytic effects have been attributed to the formation of new electronic surface states energetically more suitable for various stages of the oxidation-reduction reactions than the bare substrate. In the present study, however, we have seen that the electrocatalytic effects induced by trace quantities of heavy metal ions in the electroreduction of  $\text{Au}(\text{CN})_2^-$  are well accounted for on other grounds. Whether such mechanisms are generally applicable remains to be seen. Since upd layers of Pb, Tl, and Bi apparently catalyze a wide variety of electrochemical reactions, it is worthwhile to examine briefly their chemical and physical properties in order to ascertain the possible origin of their electrocatalytic activity. Here we point out only their essential features. A more detailed discussion will be given elsewhere.

Owing to the increase of nuclear charge across each of the transition series, the B metals have a much weaker tendency than the A metals to form ions or to form compounds with nonmetals (60). The B metal ions have high electron affinities and tend to seek out polarizable anions or ligands. The increasing polarizing power of the cations culminates in the final row of B metals: Au, Hg, Tl, Pb, Bi, and Po where the nuclear charge has been built up across the lanthanide as well as the third transition series. This increase in nuclear charge also leads to an increase in ionization potential. Oxidation from the  $(N-2)$  valence state  $N$  to the group-valence state  $N$  is particularly difficult in this last row owing to the inert-pair effect of the  $6s^2$  electrons.

Owing to its large size, ( $d = 2.88\text{\AA}$ ), the hydration energy of the monovalent  $\text{Tl}^+$  ion is expected to be

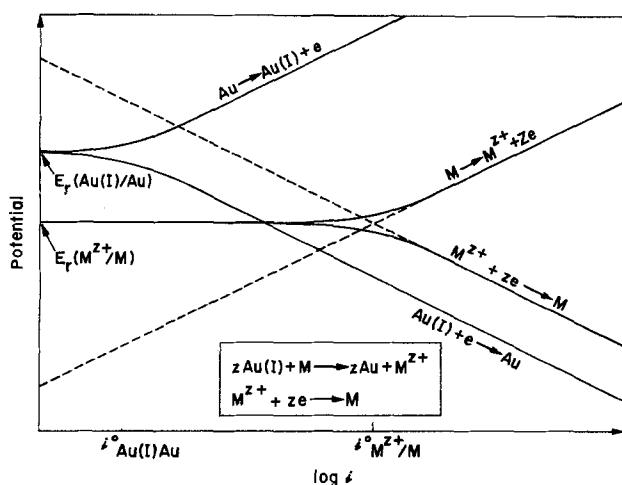


Fig. 19. Schematic representation of an electrochemical displacement reaction. The dashed lines show the variation of the individual anodic and cathodic components of the total current density for the oxidation and reduction of the depolarizer species.



weak. This is indeed the case. The hydration energy of the  $Tl^+$  ion is only  $-77$  kcal mole $^{-1}$ , which is comparable to the value of  $-61$  kcal mole $^{-1}$  found for the  $Cs^+$  ion. Thus contact adsorption of  $Tl^+$  on metal electrodes is favored and is observed experimentally. The large size and electronic polarizability of the  $Tl^+$  ion ( $\alpha = 3.9 \times 10^{-24}$  cm $^3$ ) also favors specific adsorption on the electrode surface through the action of London dispersion forces. Since the hydration energy of the  $Tl^+$  ion is low, the activation energy required to reorganize its solvation shell prior to charge transfer should be small and hence the exchange current density of this reaction should be high.

For the multivalent cations  $Hg^{2+}$ ,  $Pb^{2+}$ , and  $Bi^{3+}$ , the situation is more complex since these species have high hydration energies. Again their large size favors contact adsorption. Further, these ions tend to bond covalently to form extremely stable complexes such as  $Hg(CN)_2$ . The resulting negative shift in reduction potential enables these species to be effective as catalytic reducing agents.

### Conclusions

Underpotential adsorption of heavy metal atoms on gold produces a marked depolarization effect which extends the current density range in which bright, fine-grained electrodeposits can be obtained. Two mechanisms are proposed to be responsible for this effect: (i) the enhancement of nucleation rate by strongly adsorbed foreign metal atoms and (ii) the occurrence of electrochemical displacement reactions, made possible by the specific adsorption of heavy metal depolarizer ions. A later communication will report the results of depolarization studies in acidic gold electroplating solutions.

### Acknowledgments

It is a pleasure to acknowledge helpful discussions with K. J. Bachmann, W. R. Fawcett, G. H. Gilmer, B. Miller, S. Nakahara, D. K. Roe, and E. D. Winters during the course of this work. We also thank Caroline M. Newton for technical assistance.

Manuscript submitted Feb. 3, 1976; revised manuscript received Aug. 17, 1976. This was Paper 334 presented at the Washington, D. C., Meeting of the Society, May 2-7, 1976.

Any discussion of this paper will appear in a Discussion Section to be published in the June 1977 JOURNAL. All discussions for the June 1977 Discussion Section should be submitted by Feb. 1, 1977.

Publication costs of this article were assisted by Bell Laboratories.

### REFERENCES

- F. M. Reid and W. Goldie, "Gold Plating Technology," Electrochemical Publications Limited, Ayr, Scotland (1974).
- R. Duva and A. Simonian, U.S. Pat. 3,562,120 (1971).
- P. T. Smith and A. Fletcher, U.S. Pat. 3,644,184 (1972).
- H. A. Reinheimer, Personal communication.
- H. A. Reinheimer, U.S. Pat. 3,833,487 (1974).
- E. Winters and W. J. Corby, Personal communication.
- E. Winters, U.S. Pat. 3,873,428 (1975).
- C. C. Shiflett, Personal communication.
- H. Y. Cheh and R. Sard, *This Journal*, **118**, 1737 (1971).
- W. J. Lorenz, H. D. Hermann, N. Wüthrich, and F. Hilbert, *ibid.*, **121**, 1167 (1974).
- F. C. Anson, *Accounts of Chemical Research*, **8**, 400 (1975).
- R. Parsons, *J. Electroanal. Chem.*, **21**, 35 (1969).
- A. N. Frumkin, N. V. Nikolaeva-Fedorovich, N. P. Berezina, and Kh. E. Keis, *ibid.*, **58**, 189 (1975).
- B. G. Chauhan, W. R. Fawcett, and T. A. McCarrick, *ibid.*, **58**, 275 (1975).
- G. Bodländer, *Chem. Ber.*, **36**, 3933 (1903).
- M. Maja, *Atti Accad. Sci. Torino Cl. Sci. Fis. Mat. Nat.*, **99**, 1111 (1965).
- "Handbook of Chemistry and Physics," 53rd ed., Chemical Rubber Publishing Company, Cleveland (1972).
- B. Miller and S. Menezes Affonso, *This Journal*, **123**, 1006 (1976).
- L. G. Sillén, "Stability Constants of Metal-Ion Complexes," Section 1, Special Publication No. 17, The Chemical Society, London (1964).
- H. A. Reinheimer, *This Journal*, **121**, 490 (1974).
- B. Miller, *ibid.*, **118**, 1117 (1969).
- D. M. MacArthur, *ibid.*, **119**, 672 (1972).
- V. S. Bagotzky, Yu B. Vassilyev, J. Weber, and I. I. Pyshnograeva, *Electrochim. Acta*, **16**, 2141 (1971).
- K. J. Cathro and D. F. A. Koch, *This Journal*, **111**, 1416 (1964).
- H. J. Litsch, Personal communication.
- K. Cathro, *Proc. Australas. Inst. Min. Metall.*, **207**, 180 (1963).
- G. J. Plessl and E. D. Winters, Personal communication.
- J. Newman, *J. Phys. Chem.*, **70**, 1327 (1966).
- M. Hansen, "Constitution of Binary Alloys," 2nd ed, p. 222, McGraw-Hill, New York (1958).
- J. Henion and G. E. Rhead, in "Diffusion Processes," Proceedings of the Thomas Graham Memorial Symposium, Vol. 1, J. N. Sherwood, A. V. Chadwick, W. M. Muir, and F. L. Swinton, Editors, p. 381, Gordon and Breach, London (1971).
- J. D. E. McIntyre, G. K. Wertheim, and W. F. Peck, Jr., To be published.
- E. Schmidt, H. R. Gygax, and Y. Cramer, *Helv. Chim. Acta*, **53**, 649 (1970).
- S. H. Cadle and S. Bruckenstein, *This Journal*, **119**, 1166 (1972).
- S. H. Cadle and S. Bruckenstein, *Anal. Chem.*, **44**, 1993 (1972).
- A. J. de Bethune and N. A. Swendeman, Loud, "Standard Aqueous Electrode Potentials and Temperature Coefficients at 25°C," Clifford A. Hampel, Skokie, Illinois (1964).
- M. Pourbaix, "Atlas D'Equilibres Electrochimiques," Gauthier-Villars, Paris (1963).
- K. J. Vetter, "Electrochemical Kinetics," chap. 2D and 4B, Academic Press, New York (1967).
- J. O'M. Bockris and G. A. Razumney, "Fundamental Aspects of Electrocrystallization," Plenum Press, New York (1967).
- G. Eichkorn and H. Fischer, *Z. Phys. Chem.*, **53**, 29 (1967).
- R. S. Perkins and T. N. Andersen, in "Modern Aspects of Electrochemistry," Vol. 5, J. O'M. Bockris and B. E. Conway, Editors, chap. 3, p. 203, Plenum Press, New York (1969).
- G. H. Gilmer, Private communication.
- N. A. Pangarov, *Electrochim. Acta*, **7**, 139 (1962).
- N. A. Pangarov, *ibid.*, **9**, 721 (1964).
- N. A. Pangarov, *J. Electroanal. Chem.*, **9**, 70 (1965).
- N. A. Pangarov, and S. D. Vitkova, *Electrochim. Acta*, **11**, 1719 (1966).
- N. A. Pangarov and S. D. Vitkova, *ibid.*, **11**, 1733 (1966).
- N. A. Pangarov, S. D. Vitkova, and I. Uzonova, *ibid.*, **11**, 1747 (1966).
- N. A. Pangarov, S. D. Vitkova, and I. Uzonova, *ibid.*, **11**, 1753 (1966).
- B. Timmer, M. Sluyters-Rehbach, and J. H. Sluyters, *Surface Sci.*, **18**, 44 (1969).
- R. de Levie, *This Journal*, **118**, 185C (1971).
- R. Guidelli, *J. Electroanal. Chem.*, **53**, 205 (1974).
- M. L. Foresti and R. Guidelli, *ibid.*, **53**, 219 (1974).
- M. L. Foresti, D. Cozzi, and R. Guidelli, *ibid.*, **53**, 235 (1974).
- B. J. Bowles and T. E. Cranshaw, *Phys. Lett.*, **17**, 258 (1965).
- B. J. Bowles, *Nature*, **212**, 1456 (1966).
- S. H. Cadle and S. Bruckenstein, *Anal. Chem.*, **43**, 1858 (1971).
- S. H. Cadle and S. Bruckenstein, *ibid.*, **44**, 2225 (1972).
- R. R. Adžić and A. R. Despić, *J. Chem. Phys.*, **61**, 3482 (1974).
- R. R. Adžić, D. N. Simić, D. M. Dražić, and A. R. Despić, *J. Electroanal. Chem.*, **61**, 117 (1975).
- C. S. G. Phillips and R. J. P. Williams, "Inorganic Chemistry," Vol. 2, chap. 30-32, Oxford University Press, Oxford (1966).

# Transport Coefficients of Ions and Interdiffusivities in Multicomponent Ionic Solution of CaO-SiO<sub>2</sub>-Al<sub>2</sub>O<sub>3</sub> at 1500°C

K. Nagata<sup>1</sup> and K. S. Goto

Department of Metallurgy, Tokyo Institute of Technology, Tokyo, Japan

## ABSTRACT

The transport coefficients  $L_{ik}$ , defined by phenomenological equations for Ca<sup>2+</sup>, Al<sup>3+</sup>, Si<sup>4+</sup>, and O<sup>2-</sup> are evaluated for liquid solutions of CaO-SiO<sub>2</sub>-Al<sub>2</sub>O<sub>3</sub> at 1500°C. For the calculation, the authors have derived general relations between the transport coefficients and the measurable transport properties, e.g., tracer diffusivity, electric conductivity, etc. of the ionic melt, using an assumption of local thermodynamic equilibrium under isobaric and isothermal conditions. The diagonal terms calculated from the measurable properties in the literature were always positive values on the order of about 10<sup>-12</sup> mole<sup>2</sup>/cal cm sec and the cross terms were also of the same order but were sometimes negative. From the transport coefficients evaluated, the interdiffusivities have been calculated at 1500°C to be  $\tilde{D}_{11}^{30} = 1.9 \times 10^{-5}$ ,  $\tilde{D}_{12}^{30} = -9.9 \times 10^{-6}$ ,  $\tilde{D}_{21}^{30} = -5.3 \times 10^{-6}$ , and  $\tilde{D}_{22}^{30} = 2.2 \times 10^{-5}$  (in cm<sup>2</sup>/sec) for 40 w/o CaO-40 w/o SiO<sub>2</sub>-20 w/o Al<sub>2</sub>O<sub>3</sub> melt, where 1, 2, 3, and 0 mean Ca<sup>2+</sup>, Al<sup>3+</sup>, Si<sup>4+</sup>, and O<sup>2-</sup>, respectively. The interdiffusivities agreed fairly well with experimental results of other investigators.

In 1972, Varshneya and Cooper (1) experimentally determined the interdiffusivity matrix on ternary solid solutions of K<sub>2</sub>O-SrO-SiO<sub>2</sub> at 630°-810°C. This work greatly impressed the present authors because it was the first determination of the interdiffusivities in multicomponent oxide solutions. However, it raised other questions: is it possible to evaluate the transport coefficients of elementary ions in oxide solutions or, what is the relation between the transport coefficients and the interdiffusivities in the multicomponent oxide solutions? The present communication addresses those questions.

When the oxides of CaO, Al<sub>2</sub>O<sub>3</sub>, and SiO<sub>2</sub> are mixed and heated to 1500°C, they produce a homogeneous liquid solution in a relatively wide composition range. Though there is no direct experimental proof, it is generally believed that the solution is composed of ionic species of Ca<sup>2+</sup>, O<sup>2-</sup>, AlO<sub>2</sub><sup>-</sup>, Al<sub>2</sub>O<sub>5</sub><sup>4-</sup>, SiO<sub>4</sub><sup>4-</sup>, Si<sub>2</sub>O<sub>7</sub><sup>6-</sup>, etc. Therefore, the diffusion fluxes of these ionic species can be expressed by the linear relations with the gradients of electrochemical potential of these ions, which has been discussed by Onsager in 1931 (2) and in 1945 (3). The proportionality constants defined by the linear relation are called "transport coefficients of ions." However, the number of ionic species is clearly too large to apply Onsager's treatment to the oxide melt. Thus, in the present communication, the diffusion fluxes of ions are expressed in terms of the elementary ions of Ca<sup>2+</sup>, Al<sup>3+</sup>, Si<sup>4+</sup>, and O<sup>2-</sup>.

Transport coefficients of ions or their reciprocal coefficients called "friction coefficients" were determined by Miller (4) in 1966 on aqueous solutions of HCl, LiCl, or NaCl at 25°C. Between 1966 and 1973, Kawamura *et al.* (5-7) determined friction coefficients of ions at 300°-400°C in various fused nitrate solutions. In 1972, Richter (8) also determined friction coefficients at 290°C in other fused nitrate solutions.

These evaluations of the phenomenological coefficients in ionic solutions were preceded by the theoretical works of Klemm (9), Laity (10, 11), and Kirkaldy *et al.* (12, 13). However, the evaluation of the coefficients and the theoretical treatment have been limited

to the relatively simple solutions such as dilute solutions and quasi-binary solutions. Also, Cooper *et al.* (14, 15) have discussed some theoretical aspects of ionic solutions of multicomponents but they did not evaluate the transport coefficients on those melts. In a previous paper (16), the authors derived the relation between the transport coefficients and the measurable properties, such as electrical conductivity, tracer diffusivity, transference numbers, and interdiffusivities. However, the relations can be used only for ionic solutions containing single anionic species.

Therefore, in the present communication we attempt to derive very general relations between the phenomenological coefficients and the measurable properties of ionic solutions regardless of the number of cationic and anionic components. Further, the derived equations are used to evaluate the transport coefficients of the elementary ions in 40 w/o CaO-40 w/o SiO<sub>2</sub>-20 w/o Al<sub>2</sub>O<sub>3</sub> at 1500°C from the electrical conductivity, tracer diffusivities, and transference numbers in the literature. Once the transport coefficients are evaluated, it is also possible to estimate the interdiffusivity matrix. Thus, the penetration curves of interdiffusion have been estimated for the CaO-SiO<sub>2</sub>-Al<sub>2</sub>O<sub>3</sub> ternary system from the evaluated interdiffusivity matrix and then compared with the penetration curves measured by Oishi (17). Similar calculations were also made for CaO-45 w/o SiO<sub>2</sub> and CaO-50Al<sub>2</sub>O<sub>3</sub> at 1500°C.

For isothermal and isobaric conditions, the phenomenological equations express the fluxes  $j$  in  $n$ -component ionic systems in terms of linear functions of electrochemical potential gradients,  $\nabla\eta$ , as forces, if independent fluxes and independent forces exist in the system. Then, the following equation is obtained

$$j_i = - \sum_{k=1}^n L_{ik} \nabla \eta_k \quad (i = 1, 2, 3, \dots, n) \quad [1]$$

where  $L_{ik}$ <sup>2</sup> is a transport coefficient which is assumed to be a function of composition, temperature, and pressure but not a function of electrochemical potential gradients. On the other hand, the fluxes are expressed by  $j_i = C_i(v_i - v_o)$ , where  $C_i$  is the concentration of  $i$

<sup>2</sup> The relation between  $L_{ik}$  defined in this paper and  $L_{ik}'$  in the previous paper (16) is  $L_{ik} = L_{ik}' / |Z_i Z_k|$ .

<sup>1</sup> Present address: Centro de Ingenieria y Computacion, I.V.I.C., Caracas, Venezuela.

Key words: diffusion constant, ionic melt, blast furnace slag, electrical conductivity.

species,  $v_i$  is the local velocity of  $i$  species, and  $v_0$  is the local reference velocity. Thus, the transport coefficients take different values corresponding to choice of a reference frame. If the local reference velocity is given in the form of  $v_0 = \sum C_i v_i / \sum C_i$ , which is the average particle velocity and if the units of flux and concentration are, respectively, in mole/cm<sup>2</sup> sec and mole/cm<sup>3</sup>, the total flux always becomes zero, i.e.  $\sum j_i = 0$ . This means that the fluxes are dependent. Additionally, the forces are dependent because there is the Gibbs-Duhem relation, i.e.,  $\sum C_i \nabla \eta_i = 0$  on the assumption of local thermodynamic equilibrium. In this case, the transport coefficients are not uniquely defined and the Onsager reciprocal relations are not necessarily fulfilled. However, according to the treatment by De Groot and Mazur (18), dependent fluxes and dependent forces can be defined by a sensible set of  $(n-1)^2$  coefficients of  $L_{ik}$  ( $i, k = 1, 2, 3, \dots, n-1$ ). Other coefficients can

be defined by  $L_{in} = -\sum_k^{n-1} L_{ik}$ ,  $L_{ni} = -\sum_k^{n-1} L_{ki}$ , and

$L_{nn} = \sum_{i,k}^{n-1} L_{ik}$ , that is

$$\sum_{i \text{ or } k}^n L_{ik} = 0 \quad [2]$$

and the Onsager reciprocal relations can also be imposed

$$L_{ik} = L_{ki} \quad [3]$$

Additionally, according to the second law of thermodynamics, there are the following restrictions on  $L_{ik}$  (18)

$$L_{ii} \geq 0 \text{ and } L_{ij}L_{kk} \geq L_{ik}^2 \quad [4]$$

because the entropy production during diffusion must be positive.

As pointed out previously (16), only if these interrelations are valid, the number of independent transport coefficients is  $\frac{1}{2}n(n-1)$ , so that all of the  $L_{ik}$  can be determined by  $\frac{1}{2}n(n-1)$  independent physical properties.

### General Equations to Relate $L_{ik}$ to $\sigma$ , $Ht_i^r$ , $D_i^{tr}$ , and $\tilde{D}_{ik}^{AB}$

Let us assume that an ion has a fixed and immutable charge and that local thermodynamic equilibrium and local electrical neutrality prevail in the system. The electrochemical potential of  $i$ th ionic species can be defined (19) by

$$\eta_i = \mu_i + Z_i F \phi \quad [5]$$

where  $\mu_i$  is the chemical potential,  $\phi$  is the electrical potential,  $Z_i$  is the valence of  $i$ th ionic species, and  $F$  is the Faraday constant (96,500 C/equiv.).

*Relation between conductivity and  $L_{ik}$ .*—The total electric current density can be written (18)

$$I = \sum_i^n Z_i F j_i \quad [6]$$

under the condition of local electrical neutrality. The conductivity is usually defined as the ratio of the current per unit area to the electrical potential gradient, i.e.  $I/\nabla\phi$ . The chemical potential gradients of the species are zero during the conductivity measurement because concentration gradients do not occur. Thus, the conductivity ( $\Omega^{-1}\text{-cm}^{-1}$ ) can be expressed by

$$\sigma = F^2 S / 4.184 \quad [7]$$

where

$$S = \sum_i^n \sum_k^n Z_i Z_k L_{ik} \quad [8]$$

and 4.184 is the conversion factor.

*Relation between Hittorf transference number and  $L_{ik}$ .*—The definition of the Hittorf transference number (20),  $Ht_i^r$ , of  $i$ th ionic species relative to  $r$ th species as a reference component on passing  $1F$ , i.e.,  $Z_i F (j_i - j_r C_i / C_r) / I$ , gives

$$Ht_i^r = Z_i \sum_k^n Z_k (L_{ik} - L_{rk} C_i / C_r) / S \quad [9]$$

The external transference number,  $t_i^{\text{ex}}$ , which can be measured relative to the electrode or container of the cell as a reference frame, is related to the Hittorf transference number by the following equation

$$Ht_i^r = t_i^{\text{ex}} - t_r^{\text{ex}} Z_i C_i / Z_r C_r \quad [10]$$

*Relation between tracer diffusivity and  $L_{ik}$ .*—Let us consider the interdiffusion of an ionic species  $i$  and its tracer  $i^*$  in a multicomponent ionic solution with uniform concentration of other species. In this case the electrical potential gradient  $\nabla\phi$  is zero and the chemical potentials of the species, except  $i$  and  $i^*$ , are constant. If it is assumed that isotope effects are negligible, the cross terms  $L_{ii^*}$  and  $L_{i^*i}$  would be assumed to be zero. This assumption has not yet been experimentally proved but Laity (21) has also used this. From Eq. [1] and the above conditions,  $j_i = -L_{ii} \nabla\mu_i$  and  $j_{i^*} = -L_{i^*i^*} \nabla\mu_{i^*}$ . Noting that any reference velocity is zero and  $j_i + j_{i^*} = 0$ , one obtains the relation  $L_{ii} \nabla\mu_i + L_{i^*i^*} \nabla\mu_{i^*} = 0$ . Comparing the equation with the Gibbs-Duhem relation, i.e.,  $C_i \nabla\mu_i + C_{i^*} \nabla\mu_{i^*} = 0$ , one obtains  $L_{i^*i^*} = L_{ii} C_{i^*} / C_i$ . Then the flux of  $i^*$  species is written as  $j_{i^*} = -(RT/C_i) L_{ii} \nabla C_i$ . On the other hand, the flux of the isotope  $i^*$  is usually expressed by using tracer diffusivity  $D_i^{tr}$ , i.e.,  $j_{i^*} = -D_i^{tr} \nabla C_i$ . From the comparison of the above two expressions of the flux, the relation between the tracer diffusivity and the diagonal term of transport coefficient can be obtained as

$$D_i^{tr} = L_{ii} RT / C_i \quad [11]$$

The same equation is given by Laity (21) with different derivation.

*Relation between interdiffusion coefficient matrix and  $L_{ik}$ .*—Let us consider the one-directional diffusion, when two long rods with the different compositions are joined at a plane interface. When the two homogeneous ionic phases contact each other, the diffusion potential due to the composition difference can be observed. This diffusion potential can be related to the chemical potentials and the transport coefficients as follows (20). There is no net electric current passing through the system during the interdiffusion experiment, namely,  $I = 0$ . From Eq. [1], [5], and [6], the diffusion potential gradient can be expressed by

$$\nabla\phi = -(1/FS) \sum_i^n \sum_k^n Z_i L_{ik} \nabla\mu_k \quad [12]$$

Eliminating  $\nabla\phi$  from Eq. [1], the fluxes are represented only in terms of the chemical potential gradients, i.e.

$$j_i = -\sum_k^n T_{ik} \nabla\mu_k \quad [13]$$

where

$$T_{ik} = L_{ik} - (1/S) \sum_{k'}^n Z_{k'} L_{ik'} \sum_{i'}^n Z_{i'} L_{i'k} \quad [14]$$

The properties of  $T_{ik}$  are

$$T_{ik} = T_{ki} \quad [15]$$

$$\sum_k^n Z_k T_{ik} = 0 \quad [16]$$

The former can be derived from the reciprocal relation,  $L_{ik} = L_{ki}$  and the latter from Eq. [14].

Let us assume the relations between the chemical potentials of ions and salts according to Wagner (20) in order to express the flux in terms of the chemical potentials of electrically neutral components, because the chemical potentials of ions in the strictly thermodynamic sense are not measurable by any experiment

$$\mu_{\alpha}/Z_{\alpha} + \mu_{\beta}/|Z_{\beta}| = \mu_{\alpha\beta}/Z_{\alpha} \\ = \mu_{\alpha B}/Z_{\alpha} + \mu_{A\beta}/Z_{\alpha} - \mu_{AB}/Z_{\alpha} \quad [17a]$$

$$\mu_{\alpha}/Z_{\alpha} + \mu_e = \mu_{[\alpha]}/Z_{\alpha} \quad [17b]$$

$$\mu_{\beta}/|Z_{\beta}| + \mu_p = \mu_{[\beta]}/|Z_{\beta}| \quad [17c]$$

where  $\alpha\beta$ ,<sup>3</sup>  $[\alpha]$ , and  $[\beta]$  are electrically neutral combinations consisting of a cationic component  $\alpha$ , an anionic component  $\beta$ , electron  $e$ , and positive hole  $p$ . A and B are a master cation and a master anion, respectively, which are selected expediently. Equation [13] can be then rewritten as

$$j_i = - \sum_{\alpha} T_{i\alpha} \nabla \mu_{\alpha B} + \sum_{\alpha} (Z_{\alpha}/Z_A) T_{i\alpha} \nabla \mu_{AB} \\ - \sum_{\beta} (|Z_{\beta}|/Z_A) T_{i\beta} \nabla \mu_{A\beta} \quad [18]$$

The flux relative to external coordinates is expressed as

$$J_i = j_i + C_i v_o \quad [19]$$

The continuity equation is written as  $\partial C_i/\partial t + \nabla J_i = 0$ . Because the total moles of neutral components per unit volume is equal to the sum of the concentrations of

cations,  $C = \sum_{\alpha} C_{\alpha}$ , under the electroneutrality condition, the continuity equation is expressed as  $\partial C/\partial t =$

$-\nabla \left( \sum_{\alpha} j_{\alpha} + v_o C \right)$ . Assuming the constant molar volume, i.e.,  $\partial C/\partial t = 0$  [which has been assumed only to simplify the treatment by Darken (22) for the diffusion problem in a binary metallic system] and integrating under the condition that the reference velocity and the fluxes of components at a distance far from the initial interface of the diffusion couple are zero, one obtains

$$\sum_{\alpha} j_{\alpha} + v_o C = 0 \quad [20]$$

Eliminating  $v_o$  from Eq. [19], one obtains

$$J_i = j_i - (C_i/C) \sum_{\alpha} j_{\alpha} \quad [21]$$

From Eq. [18] and [21], the flux  $J_i$  is related to the chemical potential gradients of electrically neutral components which are experimentally measurable.

On the other hand, the flux  $J_i$  relative to external coordinates during interdiffusion experiments is expressed as a linear function of the concentration gradients of components. The number of independent concentration gradients is  $n - 2$  because of the electroneutrality condition and the Gibbs-Duhem relation,<sup>4</sup> while the number of independent fluxes  $J_i$  is also  $n - 2$  because of the relations of  $\sum J_i = 0$  derived from Eq. [20] and  $I = \sum Z_i J_i = 0$ .<sup>5</sup> Thus, one obtains

<sup>3</sup> Salt,  $\alpha\beta$ , is written as the stoichiometric number per unit cation, e.g.,  $AlO_{1.5}$  for alumina. Then the chemical potential per equivalent of the component  $MX_n$  can be expressed by  $\mu_{MX_n}/Z_M$  or  $\mu_{MX_n}/|Z_X|$ .

<sup>4</sup> The number of independent electrochemical potential gradients is  $n - 1$  from the condition of the Gibbs-Duhem relation on electrochemical potential, while the number of independent concentrations of ions is  $n - 2$  from the conditions of electroneutrality and the Gibbs-Duhem relation on chemical potential of ion. The latter conditions are included in the former one.

<sup>5</sup> This condition is true only in the case of the interdiffusion experiment.

$$J_i = - \sum_{k \neq A, B} \tilde{D}_{ik}^{AB} \nabla C_k \quad (i \neq A, B) \quad [22]$$

where  $\tilde{D}_{ik}^{AB}$  is the interdiffusion coefficient matrix which is experimentally determined by the Boltzmann-Matano method (23, 24).

Rewriting Eq. [22] in terms of the concentration gradients of the electrically neutral components under

the condition of electrical neutrality, i.e.,  $C_{\alpha} = \sum_{\beta} C_{\alpha\beta}$

and  $C_{\beta} = \sum_{\alpha} |Z_{\alpha}/Z_{\beta}| C_{\alpha\beta}$ , and comparing with Eq.

[21], the relation between the interdiffusion coefficient matrix and the transport coefficients can be obtained.

Let us consider the binary oxide system composed of oxides of 1O and 2O, where 1 and 2 are cations and O is oxygen anion. The flux  $J_i$  of cationic component 1 is expressed as follows by Eq. [18] and [21]

$$J_1 = - (RT/C) (T_{11} C_{2O}/C_{1O} - 2T_{12} + T_{22} C_{1O}/C_{2O}) \\ (1 + \partial \ln \gamma_{1O}/\partial \ln N_{1O}) \nabla C_{1O}$$

where the chemical potential gradient of oxide 2O is eliminated by the Gibbs-Duhem relation and the relation of  $\nabla \mu_{1O} = (RT/C_{1O}) (1 + \partial \ln \gamma_{1O}/\partial \ln N_{1O}) \nabla C_{1O}$  is used.  $\gamma_{1O}$  and  $N_{1O}$  are the activity coefficient and mole fraction of oxide 1O, respectively. The volumetric factor  $1 - \partial \ln V_m/\partial \ln N_{1O}$  is unity because of the assumption of constant molar volume. On the other hand, the flux of cation 1 is written from Eq. [22] as follows

$$J_1 = - \tilde{D}_{11}^{2O} \nabla C_{1O} \quad [22a]$$

where  $C_1$  is equal to  $C_{1O}$  because of electroneutrality. Comparing the above two equations, the following equation is obtained

$$\tilde{D}_{11}^{2O} = (RT/C) (T_{11} C_{2O}/C_{1O} - 2T_{12} + T_{22} C_{1O}/C_{2O}) \\ (1 + \partial \ln \gamma_{1O}/\partial \ln N_{1O}) \quad [23]$$

In the case of a ternary oxide system composed of 1O, 2O, and 3O, where 1, 2, and 3 are cations, the fluxes of cation 1 and cation 2 are expressed by

$$J_1 = - \tilde{D}_{11}^{3O} \nabla C_{1O} - \tilde{D}_{12}^{3O} \nabla C_{2O} \quad [22b]$$

$$J_2 = - \tilde{D}_{21}^{3O} \nabla C_{1O} - \tilde{D}_{22}^{3O} \nabla C_{2O}$$

From Eq. [18] and [21], the fluxes of cation 1 and cation 2 are expressed in terms of the chemical potential gradients of oxides. If the cross terms of  $G$  matrix (18) are assumed to be zero, the following equations are obtained

$$\tilde{D}_{11}^{3O} = \frac{RT}{C} \left[ \frac{C_2 + C_3}{C_1} T_{11} - T_{21} - T_{31} \right. \\ \left. - \frac{C_1}{C_3} \left( \frac{C_2 + C_3}{C_1} T_{13} - T_{23} - T_{33} \right) \right] \\ \left( 1 + \frac{\partial \ln \gamma_{1O}}{\partial \ln N_{1O}} \right) \frac{C_{2O}}{C_{3O}}$$

$$\tilde{D}_{12}^{3O} = \frac{RT}{C} \left[ \frac{C_1}{C_2} \left( \frac{C_2 + C_3}{C_1} T_{12} - T_{22} - T_{32} \right) \right. \\ \left. - \frac{C_1}{C_3} \left( \frac{C_2 + C_3}{C_1} T_{13} - T_{23} - T_{33} \right) \right] \\ \left( 1 + \frac{\partial \ln \gamma_{2O}}{\partial \ln N_{2O}} \right) \frac{C_{1O}}{C_{3O}}$$

$$\begin{aligned} \tilde{D}_{21}^{30} &= \frac{RT}{C} \left[ \frac{C_2}{C_1} \left( \frac{C_1 + C_3}{C_2} T_{21} - T_{11} - T_{31} \right) \right. \\ &\quad \left. - \frac{C_2}{C_3} \left( \frac{C_1 + C_3}{C_2} T_{23} - T_{13} - T_{33} \right) \right] \\ &\quad \left( 1 + \frac{\partial \ln \gamma_{10}}{\partial \ln N_{10}} \right) \frac{C_{20}}{C_{30}} \\ \tilde{D}_{22}^{30} &= \frac{RT}{C} \left[ \frac{C_1 + C_3}{C_2} T_{22} - T_{12} - T_{32} \right. \\ &\quad \left. - \frac{C_2}{C_3} \left( \frac{C_1 + C_3}{C_2} T_{23} - T_{13} - T_{33} \right) \right] \\ &\quad \left( 1 + \frac{\partial \ln \gamma_{20}}{\partial \ln N_{20}} \right) \frac{C_{10}}{C_{30}} \quad [24] \end{aligned}$$

The following restrictions are needed for a real solution of Ficks second law (25)

$$\begin{aligned} \tilde{D}_{11}^{30} + \tilde{D}_{22}^{30} &\geq 0 \\ \tilde{D}_{11}^{30} \tilde{D}_{22}^{30} - \tilde{D}_{12}^{30} \tilde{D}_{21}^{30} &\geq 0 \\ (\tilde{D}_{11}^{30} - \tilde{D}_{22}^{30})^2 + 4\tilde{D}_{12}^{30} \tilde{D}_{21}^{30} &\geq 0 \quad [25] \end{aligned}$$

#### Evaluation of Transport Coefficients of Liquid CaO-SiO<sub>2</sub>-Al<sub>2</sub>O<sub>3</sub> Slag at 1500°C

The transport coefficients of 40CaO-40SiO<sub>2</sub>-20Al<sub>2</sub>O<sub>3</sub> (in w/o) liquid oxide at 1500°C are evaluated here because its physical properties are well known from the viewpoint of its industrial importance as blast furnace slag for iron production. This slag system has sixteen coefficients but only six of them are independent, if Eq. [2] and [3] are valid. The physical properties measured in this melt are listed in Table I. The tracer diffusivities of calcium, aluminum, and silicon and the conductivity and the transference numbers of calcium ion and aluminum ion are judged more reliable than other properties.

The tracer diffusivity of calcium in this melt at 1500°C was measured at  $2.1 \times 10^{-6}$  cm<sup>2</sup>/sec by Towers and Chipman in 1957 (26). This value is in good agreement with the other values extrapolated to 1500°C from the measured values at lower temperature by other investigators (27-29). The tracer diffusivity of aluminum was measured at 1440°-1480°C by Henderson, Yang, and Derge in 1961 (30). The value at 1500°C is estimated to be  $6.3 \times 10^{-7}$  cm<sup>2</sup>/sec by extrapolating the measured values. The tracer diffusivity of silicon was measured at 1365°-1460°C by Towers and Chipman

in 1957 (27). The value at 1500°C is estimated to be  $2.3 \times 10^{-7}$  cm<sup>2</sup>/sec.

The conductivity in this melt was first measured at 1450°-1600°C by a Wheatstone bridge method by Martin and Derge in 1943 (31). The value at 1500°C is 0.144 Ω<sup>-1</sup> cm<sup>-1</sup>. Kammel and Winterhager (32) measured the conductivity at 1320°-1580°C by a Thomson bridge method in 1965. The value at 1500°C is 0.127 Ω<sup>-1</sup> cm<sup>-1</sup>. The latter value is considered to be more reliable and used for the following calculations because Kammel and Winterhager used inert platinum electrodes instead of graphite.

The transference numbers of calcium ion in the several melts with different compositions were measured by an isotope method at 1550°C by Esin and Kirianov (34) in 1955 and at 1530°C by Markin, Schwartzman, and Khokhlov (35) in 1958. From their reports the transference number of calcium ion in the 40CaO-40SiO<sub>2</sub>-20Al<sub>2</sub>O<sub>3</sub> melt is nearly unity at 1500°C though the latter report showed that it decreased with experimental time. For the following calculations a value of 0.95 is used. The transference number of aluminum ion has not been directly measured but has been estimated by Adachi and Ogino (36). They considered that aluminum ion contributes to the electrical conduction for compositions of large alumina content. Thus, the present authors estimated it to be 0.04 in the present composition. A value of 0.01 is used for silicon ion.

The transport coefficients in CaO-SiO<sub>2</sub>-Al<sub>2</sub>O<sub>3</sub> system can be calculated by the following equations which are derived from Eq. [2], [3], [7], [9], and [11]

$$\begin{aligned} L_{11} &= D_{1tr} C_1 / RT \\ L_{22} &= D_{2tr} C_2 / RT \\ L_{33} &= D_{3tr} C_3 / RT \\ L_{12} &= [-(6 + 10C_1/C_0 + 11C_2/C_0)A + 12(4 - C_2/C_0)B \\ &\quad + 12(5 + C_1/C_0)C] / 40(6 + 2C_1/C_0 + C_2/C_0) \\ L_{13} &= [(6 + 2C_1/C_0 + 11C_2/C_0)A + 20(C_2/C_0)B \\ &\quad - 20(3 + C_1/C_0)C] / 48(6 + 2C_1/C_0 + C_2/C_0) \\ L_{23} &= [(6 + 10C_1/C_0 + C_2/C_0)A - 8(6 + C_2/C_0)B \\ &\quad + 8(C_1/C_0)C] / 60(6 + 2C_1/C_0 + C_2/C_0) \\ L_{10} &= -L_{11} - L_{12} - L_{13} \\ L_{20} &= -L_{12} - L_{22} - L_{23} \\ L_{30} &= -L_{13} - L_{23} - L_{33} \\ L_{00} &= L_{11} + L_{22} + L_{33} + 2(L_{12} + L_{13} + L_{23}) \quad [26] \end{aligned}$$

where 1, 2, 3, and 0 mean, respectively, calcium, aluminum, silicon, and oxygen. Their valences, Z<sub>1</sub>, Z<sub>2</sub>, Z<sub>3</sub>, and Z<sub>0</sub>, are, respectively, +2, +3, +4, and -2. A, B, and C in the above equations are

Table I. Physical properties of 40 w/o CaO-40SiO<sub>2</sub>-20Al<sub>2</sub>O<sub>3</sub> melts reported in the literature

	Composition			Value at 1500°C	Range of temp (°C)	Method	Investigator	Year	Ref.
	CaO (w/o)	SiO <sub>2</sub> (w/o)	Al <sub>2</sub> O <sub>3</sub> (w/o)						
D <sub>Ca</sub> <sup>tr</sup>	40.32	40.06	19.15	$2.2 \times 10^{-6}$	1350-1450	Diffusion couple	Towers, Paris, Chipman	1953	(26)
	38.5	40.5	20.9	$2.1 \times 10^{-6}$	1350-1540	Capillary reservoir	Towers, Chipman	1957	(27)
	39.8	41.2	19.0	$2.1 \times 10^{-6}$	1350-1440	Diffusion couple	Saito, Maruya	1957	(28)
	40	40	20	$2.0 \times 10^{-6}$	1350-1450	Diffusion couple	Niwa	1957	(29)
D <sub>Al</sub> <sup>tr</sup>	38.6	41.3	20.1	$6.3 \times 10^{-7}$	1440-1480	Capillary reservoir	Henderson, Yang, Derge	1961	(30)
	38.5	40.5	20.9	$2.3 \times 10^{-7}$	1365-1460	Capillary reservoir	Towers, Chipman	1957	(27)
D <sub>Si</sub> <sup>tr</sup>	40.15	40.15	19.7	0.144	1450-1600	Wheatstone bridge	Martin, Derge	1943	(31)
				(Ω <sup>-1</sup> cm <sup>-1</sup> )					
σ	40	40	20	0.127	1320-1580	Thomson bridge	Kammel, Winterhager	1965	(32)
	38.7	38.9	22.4	0.35	1220-1480	Wien bridge	Kato, Minowa	1966	(33)
	37	45	18	0.89 at 1550°C		Tracer	Esin, Kirianov	1955	(34)
	38	42	20	1.0-0.85 at 1530°C		Tracer	Martin, Khokhlov, Schwartzman	1958	(35)
t <sub>Ca</sub>					Estimate	Adachi, Ogino	1962	(36)	
t <sub>Al</sub>	Larger ratio of Al <sub>2</sub> O <sub>3</sub> /CaO			1 - t <sub>Ca</sub>					
ρ	39	42	19	2.796	1400-1600	Max. bubble pressure	Thomas, Barrett	1956	(37)
	40	40	20	2.581	1350-1550	Archimedean	Kammel, Winterhager	1965	(32)

$$A = 4.184\sigma/F^2 - 16D_1^{tr}C_1/RT - 25D_2^{tr}C_2/RT - 36D_3^{tr}C_3/RT$$

$$B = 2.092Ht_1^0\sigma/F^2 - 4(1 + C_1/C_0)D_1^{tr}C_1/RT - 5(C_1/C_0)D_2^{tr}C_2/RT - 6(C_1/C_0)D_3^{tr}C_3/RT$$

$$C = 1.395Ht_2^0\sigma/F^2 - 4(C_2/C_0)D_1^{tr}C_1/RT - 5(1 + C_2/C_0)D_2^{tr}C_2/RT - 6(C_2/C_0)D_3^{tr}C_3/RT$$

The density used for calculation of the concentrations of ions<sup>6</sup> is 2.581 g/cm<sup>3</sup> in 40CaO-40SiO<sub>2</sub>-20Al<sub>2</sub>O<sub>3</sub> melt at 1500°C. This was measured by Kammel and Winterhager (32).

The results of the calculation are shown in Table II. The values of  $L_{ik}$  in the first column were calculated from the physical properties in the above-mentioned literature and satisfy the thermodynamic restrictions of Eq. [4]. In the second to sixth columns, the magnitudes of the errors of the evaluated  $L_{ik}$  arising from the original physical properties are shown. From the results it is shown that the cross terms of  $L_{ik}$  can take negative values and the magnitude of  $L_{ik}$  is on the order of 10<sup>-12</sup>. The signs of  $L_{ik}$  are constant within the errors of the physical properties.

From the evaluated values of  $L_{ik}$ , the interdiffusion coefficient matrix defined by Eq. [22b] can be calculated by Eq. [24].<sup>7</sup> The results are shown in the lower part of Table II. The thermodynamic factors in Eq. [24] are given as  $(1 + \partial \ln \gamma_{10}/\partial \ln N_{10})_{C_{20}/C_{30}} = 45.1$  and  $(1 + \partial \ln \gamma_{20}/\partial \ln N_{20})_{C_{10}/C_{30}} = 29.9$  from the data of activities of lime and alumina in CaO-SiO<sub>2</sub>-Al<sub>2</sub>O<sub>3</sub> melt which were measured by Fulton *et al.* (38).

The interdiffusion coefficient matrix has not yet been reported in the literature. However, Oishi (17) in 1972 reported the penetration curves of lime, silica, and alumina during the interdiffusion between two slags with the compositions 45CaO-35SiO<sub>2</sub>-20Al<sub>2</sub>O<sub>3</sub> and 35CaO-45SiO<sub>2</sub>-20Al<sub>2</sub>O<sub>3</sub> (in w/o) at 1500°C for 40 min. The analytical solution of Fick's second law of ternary diffusion with constant diffusion coefficients was given

<sup>6</sup>The concentrations of ions are calculated from the following equations:  $C_i = W_{i0}/100M_{i0}$  ( $i = 1, 2, \text{ and } 3$ ) and  $C_0 = [Z_1/Z_0]C_1 + [Z_2/Z_0]C_2 + [Z_3/Z_0]C_3$  where  $W_{i0}$  and  $M_{i0}$  are respectively the weight percent and the molecular weight of oxide  $iO$ .

<sup>7</sup>The following functions, which are derived from Eq. [8], [9], and [14], make it easy to calculate  $T_{ik}$ .

$$T_{ik} = L_{ik} - a_i a_k S \quad (i, k = 1, 2, \text{ and } 3)$$

where

$$a_1 = [(6 + C_2/C_0)Ht_1^0/2 - (C_1/C_0)Ht_2^0/3 - C_1/C_0] / (6 + 2C_1/C_0 + C_2/C_0)$$

$$a_2 = [-(C_2/C_0)Ht_1^0 + 2(3 + C_1/C_0)Ht_2^0/3 - C_2/C_0] / (6 + 2C_1/C_0 + C_2/C_0)$$

$$a_3 = [-(4 - C_2/C_0)Ht_1^0/2 - (5 - C_1/C_0)Ht_2^0/3 + (1 + C_1/C_0 + C_2/C_0)] / (6 + 2C_1/C_0 + C_2/C_0)$$

Table II. Calculated values of  $L_{ik}^*$  and  $\tilde{D}_{ik}^{30}$  for 40CaO-40SiO<sub>2</sub>-20Al<sub>2</sub>O<sub>3</sub> melt at 1500°C

	I	II	III	IV	V	VI	Unit
$D_{Ca}^{tr}$	$2.1 \times 10^{-6}$	$2.3 \times 10^{-6}$	←	←	←	←	(cm <sup>2</sup> /sec)
$D_{Al}^{tr}$	$6.3 \times 10^{-7}$	←	$7.6 \times 10^{-7}$	←	←	←	
$D_{Si}^{tr}$	$2.3 \times 10^{-7}$	←	←	$2.8 \times 10^{-7}$	←	←	
$\sigma$	0.127	←	←	←	0.121	←	(Ω <sup>-1</sup> cm <sup>-1</sup> )
$Ht_{Ca}^0$	0.95	←	←	←	←	1.00	(mole <sup>2</sup> / cal cm sec)
$Ht_{Al}^0$	0.04	←	←	←	←	0.00	
$L_{11}$	$1.1 \times 10^{-11}$	$1.2 \times 10^{-11}$	$1.1 \times 10^{-11}$	$1.1 \times 10^{-11}$	$1.1 \times 10^{-11}$	$1.1 \times 10^{-11}$	
$L_{22}$	$1.8 \times 10^{-12}$	$1.8 \times 10^{-12}$	$2.2 \times 10^{-12}$	$1.8 \times 10^{-12}$	$1.8 \times 10^{-12}$	$1.8 \times 10^{-12}$	
$L_{33}$	$1.1 \times 10^{-12}$	$1.1 \times 10^{-12}$	$1.1 \times 10^{-12}$	$1.4 \times 10^{-12}$	$1.1 \times 10^{-12}$	$1.1 \times 10^{-12}$	
$L_{12}$	$-1.9 \times 10^{-12}$	$-2.3 \times 10^{-12}$	$-2.1 \times 10^{-12}$	$-1.7 \times 10^{-12}$	$-2.0 \times 10^{-12}$	$-1.8 \times 10^{-12}$	
$L_{13}$	$-2.0 \times 10^{-12}$	$-2.4 \times 10^{-12}$	$-1.8 \times 10^{-12}$	$-2.2 \times 10^{-12}$	$-2.1 \times 10^{-12}$	$-1.9 \times 10^{-12}$	
$L_{23}$	$-5.5 \times 10^{-13}$	$-2.6 \times 10^{-13}$	$-7.1 \times 10^{-13}$	$-6.9 \times 10^{-13}$	$-4.6 \times 10^{-13}$	$-7.3 \times 10^{-13}$	
$L_{10}$	$-7.1 \times 10^{-12}$	$-7.4 \times 10^{-12}$	$-7.1 \times 10^{-12}$	$-7.2 \times 10^{-12}$	$-6.9 \times 10^{-12}$	$-7.4 \times 10^{-12}$	
$L_{20}$	$6.1 \times 10^{-13}$	$7.5 \times 10^{-13}$	$6.2 \times 10^{-13}$	$5.4 \times 10^{-13}$	$6.4 \times 10^{-13}$	$7.2 \times 10^{-13}$	
$L_{30}$	$1.5 \times 10^{-12}$	$1.5 \times 10^{-12}$	$1.4 \times 10^{-12}$	$1.6 \times 10^{-12}$	$1.4 \times 10^{-12}$	$1.5 \times 10^{-12}$	
$L_{00}$	$5.1 \times 10^{-12}$	$5.1 \times 10^{-12}$	$5.1 \times 10^{-12}$	$5.1 \times 10^{-12}$	$4.9 \times 10^{-12}$	$5.2 \times 10^{-12}$	
$\tilde{D}_{11}^{30}$	$1.9 \times 10^{-5}$	$3.1 \times 10^{-5}$	$1.8 \times 10^{-5}$	$2.0 \times 10^{-5}$	$2.4 \times 10^{-5}$	$7.5 \times 10^{-6}$	(cm <sup>2</sup> /sec)
$\tilde{D}_{12}^{30}$	$-9.9 \times 10^{-6}$	$-1.2 \times 10^{-5}$	$-1.3 \times 10^{-5}$	$-7.3 \times 10^{-6}$	$-1.1 \times 10^{-5}$	$-8.0 \times 10^{-6}$	
$\tilde{D}_{21}^{30}$	$-5.3 \times 10^{-6}$	$-1.3 \times 10^{-5}$	$-5.7 \times 10^{-6}$	$-2.6 \times 10^{-6}$	$-7.8 \times 10^{-6}$	$1.5 \times 10^{-6}$	
$\tilde{D}_{22}^{30}$	$2.2 \times 10^{-5}$	$2.1 \times 10^{-5}$	$2.7 \times 10^{-5}$	$2.3 \times 10^{-5}$	$2.2 \times 10^{-5}$	$2.3 \times 10^{-5}$	

\* All  $L_{ik}$  values satisfy the condition that entropy production is positive.

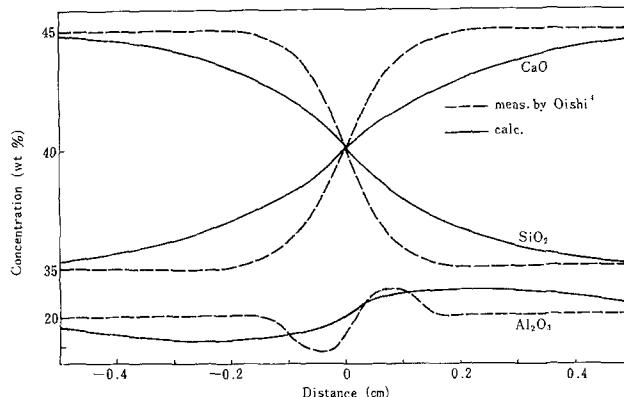


Fig. 1. Penetration curve of CaO, SiO<sub>2</sub>, and Al<sub>2</sub>O<sub>3</sub> calculated in 40CaO-40SiO<sub>2</sub>-20Al<sub>2</sub>O<sub>3</sub> slag at 1500°C for 40 min interdiffusion.

by Fujita and Gosting (25) in 1956. Thus, using the evaluated  $\tilde{D}_{ik}^{30}$ , the penetration curves for the same conditions as those by Oishi have been estimated and are shown in Fig. 1. The agreement between the estimated lines and the measured lines is not very good, but at present it is very difficult to judge which is close to the true one because of experimental errors involved in the original experiments. However, the estimated penetration curve of alumina shows up-hill diffusion and this tendency agrees with that observed in Oishi's experiment.

Similar calculations were made for CaO-SiO<sub>2</sub> and CaO-Al<sub>2</sub>O<sub>3</sub> melts, and all transport coefficients were obtained. The interdiffusivities were estimated to be  $6.16 \times 10^{-7}$  cm<sup>2</sup>/sec at 1500°C in CaO-50 w/o Al<sub>2</sub>O<sub>3</sub> melt and  $2.45 \times 10^{-6}$  cm<sup>2</sup>/sec at 1500°C in CaO-45SiO<sub>2</sub> melt. These are in relatively good agreement with other determinations (39).

### Estimation of Uncertainties Involved in the Evaluation of $L_{ik}$

The uncertainty of the transport coefficient can be estimated by the following equations which are derived from Eq. [26]

$$\Delta L_{ii} = a_{ii}^4 \Delta D_i^{tr} + a_{ii}^2 \Delta \rho \quad (i = 1, 2, \text{ and } 3)$$

$$\Delta L_{ik} = a_{ik}^4 \Delta L_{11} + a_{ik}^2 \Delta L_{22} + a_{ik}^3 \Delta L_{33} + a_{ik}^4 \Delta \sigma + a_{ik}^5 \Delta Ht_1^0 + a_{ik}^6 \Delta Ht_2^0 \quad (i \neq k)$$

where  $\Delta D_i^{tr}$ ,  $\Delta \rho$ ,  $\Delta \sigma$ ,  $\Delta Ht_1^0$ , and  $\Delta Ht_2^0$  are the uncertainties involved in the physical properties and  $\rho$  is density.

For the uncertainty of the interdiffusion coefficient matrix, the following equations are obtained from Eq. [24]

$$\tilde{\Delta D}_{ik}^{30} = b_{ik}^1 \Delta L_{11} + b_{ik}^2 \Delta L_{22} + b_{ik}^3 \Delta L_{33} + b_{ik}^4 \Delta \sigma + b_{ik}^5 \Delta_{Ht_1^0} + b_{ik}^6 \Delta_{Ht_2^0}$$

The factors  $a_{ik}^j$  and  $b_{ik}^j$  for the 40CaO-40SiO<sub>2</sub>-20Al<sub>2</sub>O<sub>3</sub> system are shown in Table III. In the second to sixth columns in Table II, the values of  $L_{ik}$  are obtained when the physical properties change by 5-20%. For example, the uncertainty of the conductivity of 5% produces uncertainties in  $L_{12}$ ,  $L_{13}$ ,  $L_{23}$ ,  $L_{10}$ ,  $L_{20}$ ,  $L_{30}$ , and  $L_{00}$  of, respectively, 7, 4, 18, 3, 5, 2, and 4%, and it also produces uncertainties in  $\tilde{D}_{11}^{30}$ ,  $\tilde{D}_{12}^{30}$ ,  $\tilde{D}_{21}^{30}$ , and  $\tilde{D}_{22}^{30}$  of, respectively, 23, 6, 47, and 2%.

Further, the results on  $\tilde{D}_{ik}$  include the errors due to neglect of the cross terms of the  $G$  matrix. Thus the disagreement in Fig. 1 may be due to these uncertainties.

**Conclusions**

The present authors have derived the general equations which relate the transport coefficients defined by the phenomenological equation to the measurable physical properties, e.g., electric conductivity, tracer diffusivities, transference numbers, and interdiffusion coefficient matrix on multicomponent ionic solutions. In this communication, the flux of an ionic species has been expressed as a linear function of electrochemical potential gradients of elementary ions but not as a function of realistic ionic species which has been proposed by other investigators (40). One of the reasons is that it is difficult to measure the electrochemical potentials of the complex ions. Another is that if an assumption of "local thermodynamic equilibrium" is true, the simplest but strict way to express the phenomenological equation is as a function of the electrochemical potential gradients of only elementary ions. The assumption of "local thermodynamic equilibrium" seems a very realistic assumption at high temperature.

The approximation of the constant molar volume of the melt was used, but the volumetric factor,  $(1 - \partial \ln V_m / \partial \ln N_{i0})$ , should be included in the relation between the interdiffusion coefficient matrix and the transport coefficients. However, this factor is usually very close to unity.

From the equations in this communication, one can derive many other useful relations, such as the Nernst-Einstein relation including the cross terms, and relations between the measurable properties and the tracer diffusivities which have no stable isotopes.

Finally, it can be stressed that this treatment of the flux in a multicomponent system can apply not only to ionic solutions but also to alloys when the electron is regarded as an ion.

**Acknowledgments**

The authors are grateful to Professor A. R. Cooper of Case Western Reserve University for his constructive criticism of the manuscript.

Manuscript submitted Oct. 21, 1975; revised manuscript received Aug. 17, 1976.

Any discussion of this paper will appear in a Discussion Section to be published in the June 1977 JOURNAL. All discussions for the June 1977 Discussion Section should be submitted by Feb. 1, 1977.

Publication costs of this article were assisted by Tokyo Institute of Technology.

**LIST OF SYMBOLS**

$L_{ik}$  transport coefficient (mole<sup>2</sup>/cal cm sec)  
 $J_i$  flux of  $i$  species relative to internal coordina-

**Table III. The factors  $a_{ik}^j$  and  $b_{ik}^j$  in the equations for the estimation of the uncertainties of  $L_{ik}$  and  $\tilde{D}_{ik}^{30}$  from the uncertainties of the physical properties on 40CaO-40SiO<sub>2</sub>-20Al<sub>2</sub>O<sub>3</sub>**

	The uncertainties of the physical properties					
	$\Delta D_{11}^{tr}$	$\Delta D_{21}^{tr}$	$\Delta D_{31}^{tr}$	$\Delta \rho$	$\Delta \sigma$	$\Delta_{Ht_1^0}$
$\Delta L_{11}$	$3.59 \times 10^{-3} \rho / T$	$1.97 \times 10^{-3} \rho / T$	$3.36 \times 10^{-3} \rho / T$	$3.59 \times 10^{-3} D_{11}^{tr} / T$	$(-1.8 + 3.9 Ht_1^0 + 3.6 Ht_2^0) \times 10^{-11}$	$3.86 \times 10^{-11} \sigma$
$\Delta L_{12}$	—	—	—	$1.97 \times 10^{-3} D_{12}^{tr} / T$	$(1.1 + 0.2 Ht_1^0 - 3.1 Ht_2^0) \times 10^{-11}$	$-3.06 \times 10^{-11} \sigma$
$\Delta L_{13}$	—	—	—	$3.36 \times 10^{-3} D_{13}^{tr} / T$	$(0.5 - 2.7 Ht_1^0 + 0.1 Ht_2^0) \times 10^{-11}$	$0.22 \times 10^{-11} \sigma$
$\Delta L_{21}$	—	—	—	—	$(0.6 - 4.1 Ht_1^0 - 0.5 Ht_2^0) \times 10^{-11}$	$-0.09 \times 10^{-11} \sigma$
$\Delta L_{22}$	—	—	—	—	$(1.3 - 1.1 Ht_1^0 - 3.6 Ht_2^0) \times 10^{-11}$	$-0.49 \times 10^{-11} \sigma$
$\Delta L_{23}$	—	—	—	—	$(-1.6 + 2.5 Ht_1^0 + 3.0 Ht_2^0) \times 10^{-11}$	$-3.64 \times 10^{-11} \sigma$
$\Delta L_{31}$	—	—	—	—	$(-0.3 + 2.7 Ht_1^0 + 1.2 Ht_2^0) \times 10^{-11}$	$2.52 \times 10^{-11} \sigma$
$\Delta L_{30}$	—	—	—	—	—	$1.17 \times 10^{-11} \sigma$
$\Delta L_{00}$	—	—	—	—	—	$-6.19 \times 10^{-6} \sigma T / \rho$
$\Delta D_{11}^{30}$	$1.53 \times 10^3 T / \rho$	$-5.89 \times 10^3 T / \rho$	$7.44 \times 10^3 T / \rho$	$-1.22 \times 10^6 - T / \rho$	$-2.79 \times 10^{-6} \sigma T / \rho$	$-4.80 \times 10^{-6} \sigma T / \rho$
$\Delta D_{12}^{30}$	$-2.52 \times 10^3 T / \rho$	$-1.32 \times 10^4 T / \rho$	$1.72 \times 10^4 T / \rho$	$2.55 \times 10^{-7} T / \rho$	$1.84 \times 10^{-7} \sigma T / \rho$	$-3.15 \times 10^{-7} \sigma T / \rho$
$\Delta D_{21}^{30}$	$-9.54 \times 10^3 T / \rho$	$-1.64 \times 10^4 T / \rho$	$1.79 \times 10^4 T / \rho$	$7.87 \times 10^{-7} T / \rho$	$1.39 \times 10^{-6} \sigma T / \rho$	$-3.10 \times 10^{-7} \sigma T / \rho$
$\Delta D_{22}^{30}$	$-2.06 \times 10^3 T / \rho$	$1.92 \times 10^4 T / \rho$	$2.65 \times 10^4 T / \rho$	$1.45 \times 10^{-7} T / \rho$	$2.77 \times 10^{-7} \sigma T / \rho$	$3.10 \times 10^{-7} \sigma T / \rho$

Note: The numbers in the factors are dependent only on composition and not on temperature. \* The values in these columns are calculated as  $Ht_1^0 = 0.95$  and  $Ht_2^0 = 0.04$ .

	tion (mole/cm <sup>2</sup> sec)
$J_i$	flux of <i>i</i> species relative to external coordination (mole/cm <sup>2</sup> sec)
$v_i$	local velocity of <i>i</i> species (cm/sec)
$v_0$	local velocity of reference frame (cm/sec)
$\eta_k$	electrochemical potential of <i>k</i> species (cal/mole)
$\mu_k$	chemical potential of <i>k</i> species (cal/mole)
$\phi$	electrical potential (V)
$\nabla$	gradient (liter/cm)
$Z_k$	valence of <i>k</i> ionic species
$C_i$	concentration of <i>i</i> species mole/cm <sup>3</sup>
$C$	total concentration (mole/cm <sup>3</sup> )
$I$	current density (A/cm <sup>2</sup> )
$\sigma$	conductivity ( $\Omega^{-1}$ cm <sup>-1</sup> )
$t_i^{\text{ex}}$	external transference number of <i>i</i> species
$h_i^{\text{tr}}$	Hittorf transference number of <i>i</i> species relative to <i>r</i> species
$F$	Faraday constant (96,500 C/equiv.)
$R$	gas constant (1.987 cal/mole deg)
$T$	absolute temperature (°K)
$D_i^{\text{tr}}$	tracer diffusivity of <i>i</i> species (cm <sup>2</sup> /sec)
$\tilde{D}_{ik}^{\text{AB}}$	interdiffusion coefficient matrix (cm <sup>2</sup> /sec)
$i^*$	tracer of <i>i</i> species
$\alpha$	cationic species
$\beta$	anionic species
$\alpha\beta$	electrically neutral combination consisted of $\alpha$ cation and $\beta$ anion
$A$	master cation
$B$	master anion
$e$	electron
$t$	time (sec)
$\gamma_{iO}$	activity coefficient of oxide <i>iO</i>
$V_m$	molar volume (cm <sup>3</sup> /mole)
$N_{iO}$	mole fraction of oxide <i>iO</i>
$\rho$	density (g/cm <sup>3</sup> )

## REFERENCES

1. A. K. Varshneya and A. R. Cooper, *J. Am. Ceram. Soc.*, **55**, 312 (1972).
2. L. Onsager, *Phys. Rev.*, **37**, 405 (1931); *ibid.*, **38**, 2265 (1931).
3. L. Onsager, *Ann. N.Y. Acad. Sci.*, **46**, 241 (1945).
4. D. G. Miller, *J. Phys. Chem.*, **70**, 2639 (1966).
5. K. Kawamura, *Trans. Nat. Res. Inst. Met.*, **12**, 181 (1966).
6. K. Kawamura, *Electrochim. Acta*, **12**, 1233 (1967).
7. K. Kawamura and T. Ando, *Trans. Jpn. Inst. Met.*, **14**, 457 (1973).
8. J. Richter, Thesis, Technical University, Aachen (1972).
9. A. Klemm, *Z. Naturforsch., Teil A*, **8**, 397 (1953).
10. R. W. Laity, *J. Phys. Chem.*, **63**, 80 (1959).
11. R. W. Laity, *ibid.*, **30**, 682 (1959).
12. J. S. Kirkaldy, G. R. Mason, and W. J. Slater, *Can. Inst. Min. Metall.*, **64**, 53 (1961).
13. J. S. Kirkaldy, Zia-Ul-Hak, and L. C. Brown, *Trans. Am. Soc. Met.*, **56**, 834 (1963).
14. A. R. Cooper, *Phys. Chem. Glasses*, **6**, 55 (1965).
15. T. O. Ziebold and A. R. Cooper, *Acta Metall.*, **13**, 465 (1965).
16. K. S. Goto, H. Schmalzried, and K. Nagata, *Tetsu To Hagane*, **61**, 2794 (1975).
17. Y. Oishi, Japan-U.S.A. Joint Symposium on Ceramics (1972).
18. S. R. De Groot and P. Mazur, "Non-Equilibrium Thermodynamics," North-Holland Publishing Company, Amsterdam and New York (1969).
19. E. A. Guggenheim, *J. Phys. Chem.*, **33**, 842 (1929).
20. C. Wagner, in "Advances in Electrochemistry and Electrochemical Engineering," Vol. 4, P. Delahay, Editor, pp. 1-46, Interscience Publishers, New York (1965).
21. R. W. Laity, "The Structure and Properties of Ionic Melts," The Aberdeen University Press, Limited, Aberdeen (1962).
22. L. S. Darken, *Trans. AIME*, **174**, 184 (1948).
23. L. Boltzmann, *Ann. Phys. (Leipzig)*, **53**, 959 (1894).
24. C. Matano, *Jpn. Phys.*, **8**, 109 (1933).
25. H. Fujita and L. J. Gosting, *J. Am. Chem. Soc.*, **78**, 1099 (1956).
26. H. Towers, M. Paris, and J. Chipman, *J. Met.* **5**, 1455 (1953).
27. H. Towers and J. Chipman, *ibid.*, **9**, 769 (1957).
28. T. Saito and K. Maruya, *Nippon Kinzoku Gakkaishi*, **21**, 728 (1957).
29. K. Niwa, *ibid.*, **21**, 304 (1957).
30. J. Henderson, L. Yang, and G. Derge, *Trans. Met. Soc. AIME*, **221**, 56 (1961).
31. A. E. Martin and G. Derge, *Trans. AIME*, **154**, 104 (1943).
32. R. Kammel and H. Winterhager, *Z. Erzbergbau Metallhuettenwes.*, **18**, 9 (1965).
33. M. Kato and S. Minowa, *Tetsu to Hagane*, **52**, 580 (1966).
34. O. A. Esin and A. K. Kirianov, *Izv. Akad. Nauk SSSR, Otd. Tekh. Nauk*, **12**, 28 (1955).
35. V. I. Markin, L. A. Schvartsman, and S. F. Khokhlov, "Metallugiya i Metallovedenie," p. 23, Izdatelystovo Akademiya Nauk SSSR, Moscow (1958).
36. A. Adachi and K. Ogino, *Yoyuen*, **5**, 1149 (1962).
37. A. G. Thomas and L. R. Barrett, *J. Soc. Glass Technol.*, **40**, 179T (1956).
38. J. C. Fulton, N. J. Grant, and J. Chipman, *Trans. AIME*, **197**, 185 (1953); J. C. Fulton and J. Chipman, *ibid.*, **200**, 1136 (1954); F. C. Langenberg and J. Chipman, *Trans. Met. Soc. AIME*, **215**, 958 (1959); these are compiled by J. F. Elliott, M. Gleiser, and V. Ramakrishna, "Thermochemistry for Steelmaking," Vol. 2, pp. 589-593, Pergamon Press, London (1963).
39. K. Nagata, M. Kawakami, and K. S. Goto, Proceedings of the Metal-Slag-Gas Reactions and Processes Symposium, American Electrochemical Society, pp. 183-198, Toronto, Canada (1975).
40. For example: J. O'M. Bockris and J. D. Mackenzie, *Rev. Met.*, **51**, 658 (1954) C. R. Masson, *Proc. R. Soc. London*, **287**, 201 (1965).



# On the Differential Thermal Analysis of the Platinum-Oxygen System

James P. Hoare,\* Robert F. Paluch, and Stuart G. Meibuhr\*

General Motors Corporation Electrochemistry Department, Research Laboratories, Warren, Michigan 48090

## ABSTRACT

Differential thermal analyses (DTA) curves were obtained on preanodized and HNO<sub>3</sub>-passivated platinum (Pt) samples. In both cases two kinds of adsorption states for oxygen on Pt were detected as well as oxygen dissolved in the interior of the Pt metal. The DTA results agree well with the cathodic stripping pulse data obtained earlier.

From x-ray diffraction analysis and vacuum fusion studies on samples of bright Pt passivated in air-saturated concentrated HNO<sub>3</sub>, it was concluded (1) that the Pt metal contained enough dissolved oxygen to be considered a Pt-O alloy. It was also found that oxygen could be made to diffuse through a thin Pt foil (2) under conditions of strong anodic polarization (6 mA/cm<sup>2</sup> at 2V) of the back side of the Pt diaphragm in solutions of H<sub>2</sub>SO<sub>4</sub> and that this anodization process can cause relatively large quantities of oxygen to be dissolved in the Pt lattice (3, 4). In these studies three kinds of sorbed oxygen were distinguished: surface adsorbed oxygen, dermasorbed oxygen dissolved in the first two or three metallic layers, and absorbed oxygen dissolved in the bulk of the metal. The properties of Pt-O alloys made by passivation in HNO<sub>3</sub> were somewhat different from those made by anodization (3, 5, 6). The HNO<sub>3</sub>-passivated Pt is much more stable than the Pt-O alloy obtained from anodization (6).

Babenkova *et al.* (7) investigated the forms of hydrogen sorbed by palladium by measuring the desorption of hydrogen during a linearly programmed temperature rise experiment. They were able to find two forms of adsorbed hydrogen on the surface as well as the hydrogen dissolved in the bulk Pd.

It seemed likely that a differential thermal analysis (DTA) of the platinum-oxygen system might enable one to observe the various forms of oxygen sorbed by Pt as well as to shed light on possible differences in the structure of Pt-O alloy formed by HNO<sub>3</sub> passivation or by anodization.

This report describes some DTA experiments made on Pt-O alloys.

## Experimental

All DTA curves were obtained with a furnace platform assembly with which analyses may be made on the sample in any controlled atmosphere at pressures ranging from  $1.3 \times 10^{-6}$  to 2 atm. The reference sample was Al<sub>2</sub>O<sub>3</sub> which is thermally inert in the temperature range of the scan, 0-1000°C.

The Pt-O alloy samples were made from small beads (0.11 cm in diameter) melted at the end of a Pt (99.99% pure) wire. These beads were cleaned by repeatedly heating to white heat in a H<sub>2</sub> jet followed by quenching in concentrated HNO<sub>3</sub>. Afterward, three beads were mounted in a Teflon cell filled with concentrated HNO<sub>3</sub> (70%) to soak for periods of time greater than 72 hr (6). Another set of three Pt beads were mounted in a Teflon cell filled with 2N H<sub>2</sub>SO<sub>4</sub> solution and were anodized at 6 mA/cm<sup>2</sup> ( $2.00 \pm 0.05V$ ) against a Pt gauze counterelectrode for periods of time greater than 24 hr. All Pt-O alloy samples were made at room temperature ( $24^\circ \pm 1^\circ C$ ).

After formation of the Pt-O alloy, a bead was cut off of the wire and weighed (~37 mg) in a small Pt dish of

known weight. In another small Pt dish, an amount of Al<sub>2</sub>O<sub>3</sub> powder was placed such that the weight (Pt dish + Pt bead) = weight (Pt dish + Al<sub>2</sub>O<sub>3</sub>). These dishes were mounted on the thermocouple elements of the furnace platform. After the entire DTA chamber was sealed from the atmosphere the chamber was evacuated and backfilled with N<sub>2</sub> three times before the first DTA run was made. Repeated runs were made in a N<sub>2</sub> atmosphere (inert) before the runs were made in a argon atmosphere containing 6% H<sub>2</sub> (reducing).<sup>1</sup> All DTA curves were obtained only during the increasing temperature sweep which was maintained at a constant rate of 10°C/min.

## Results

The DTA curves obtained on a bead which had been preanodized at 6 mA/cm<sup>2</sup> for 24 hr are shown in Fig. 1 and which had been preanodized for 5 days in Fig. 2. The upper traces in each figure were carried out in a N<sub>2</sub> atmosphere whereas the bottom trace was run in the 6% H<sub>2</sub> atmosphere. In Fig. 3, a family of DTA curves are plotted which were obtained on HNO<sub>3</sub> passivated beads, first in a N<sub>2</sub> atmosphere (Fig. 3, curve A) and then in a 6% H<sub>2</sub> atmosphere (Fig. 3, curves B-E). On a Pt bead which had been heated at 900°C in 6% H<sub>2</sub> for 6 hr, the DTA curve of Fig. 3, curve F is obtained.

## Discussion

A typical DTA curve obtained on a preanodized Pt bead in a N<sub>2</sub> atmosphere exhibits two broad peaks at about 100°C and at about 400°C as seen in Fig. 1, curve A. When a sample of Pt is anodized, the surface becomes covered with a layer of adsorbed oxygen (Pt-O)

<sup>1</sup>One of the reviewers requested that the DTA on pure gas-free Pt be made, but such a sample so far is not possible to obtain. To clean a Pt surface, it must be either heated in O<sub>2</sub> or anodized which produces oxides on the surface and oxygen dissolved in the Pt metal (2, 3). To remove the sorbed oxygen requires either heating in H<sub>2</sub> or cathodization which charges the Pt with dissolved hydrogen (25-27). The technique for exact H<sub>2</sub> or O<sub>2</sub> titration has eluded us so far.

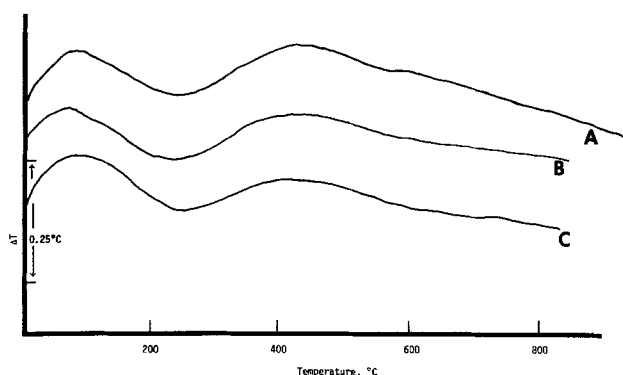


Fig. 1. DTA curves for a Pt bead anodized at 6 mA/cm<sup>2</sup> for 24 hr: curve A, 1st run in N<sub>2</sub>; curve B, 2nd run in N<sub>2</sub>; curve C, 1st run in 6% H<sub>2</sub>.

\* Electrochemical Society Active Member.

Key words: adsorbed oxygen on Pt, dermasorbed oxygen, absorbed oxygen in Pt, Pt-O alloys, adsorption sites on Pt.

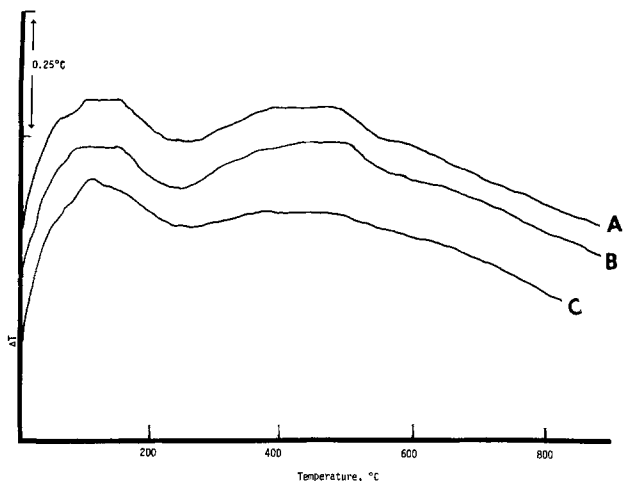


Fig. 2. DTA curves for a Pt bead anodized at 6 mA/cm<sup>2</sup> for 5 days: curve A, 1st run in N<sub>2</sub>; curve B, 2nd run in N<sub>2</sub>; curve C, 1st run in 6% H<sub>2</sub>.

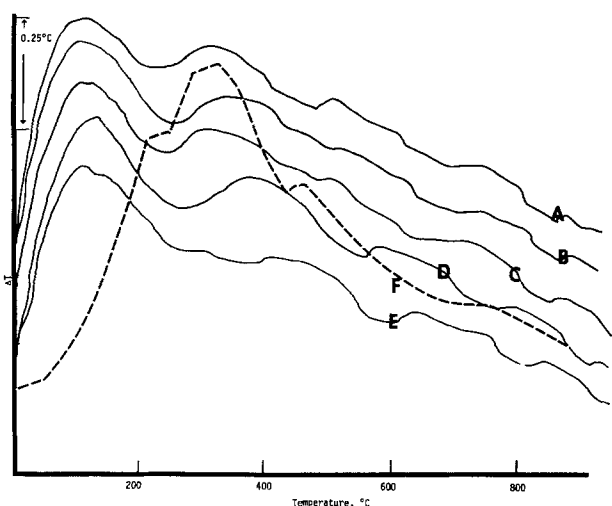


Fig. 3. DTA curves for a HNO<sub>3</sub> treated Pt bead: curve A, a run in N<sub>2</sub>; curve B, 1st run in 6% H<sub>2</sub>; curve C, 5th run in 6% H<sub>2</sub>; curve D, 7th run in 6% H<sub>2</sub>; curve E, 11th run in 6% H<sub>2</sub>; curve F, after holding the bead at 900°C for 6 hr in 6% H<sub>2</sub>.

before O<sub>2</sub> is evolved (3, 8, 9). Above 1.6V the Pt-O sites are converted to PtO<sub>2</sub> sites (3, 10-13). According to the literature (14-16), there are at least two kinds of surface Pt sites for the adsorption of hydrogen on Pt. Evidence for the existence of more than one kind of surface Pt site for the adsorption of oxygen has been presented recently (17-21). We associate the two peaks in Fig. 2, curve A with the decomposition of a thin layer of PtO<sub>2</sub> adsorbed on the two kinds of surface Pt sites (to be designated type I and type II). The decomposition at the more tightly binding sites (type II) produces the second peak at about 400°C whereas that at the weaker binding sites (type I) produces the first peak at about 100°C.

Because of the heterogeneous nature of the adsorption sites on a Pt surface, there is a distribution of binding energies between the surface Pt atoms and the adsorbed O atoms. Such a condition produces a broadening of the DTA peaks for the decomposition of the PtO<sub>2</sub> layers.

When a second temperature scan was made in the N<sub>2</sub> atmosphere, curve B, Fig. 2, was obtained showing two peaks in the same temperature range as those in Fig. 2, curve A. It has been shown (3, 22) that oxygen dissolved in the bulk metal by the anodization process can diffuse to the metal surface to replace the surface adsorbed oxygen which had been stripped away. Consequently, when the PtO<sub>2</sub> was removed from the Pt

surface by the temperature scan in Fig. 2, curve A, dissolved oxygen diffusing to the surface replaced the PtO<sub>2</sub> layer by a Pt-O layer which in turn produced the two peaks in Fig. 2, curve B during the second temperature scan. From an x-ray photoemission spectroscopic (XPS) analysis of the interaction of O<sub>2</sub> with Pt in the gas phase, Norton (17) also found that the temperatures at which oxygen was desorbed from the two adsorption states on Pt were separated by 300°C.

It is interesting that the binding energies in the PtO<sub>2</sub> layer (Fig. 2, curve A) occur in the same temperature region as those for the Pt-O layer (curve B). Such an observation is not expected. From electrochemical measurements on Pt anodes in acid solution, it was found (3, 23) that thin layers of PtO<sub>2</sub> in the presence of Pt are unstable below potentials of 1.5V and decompose to Pt-O species. Consequently, when the anodized sample was removed from the cell, washed, dried, and placed in the DTA chamber, the PtO<sub>2</sub> layer had decomposed to a Pt-O layer. Under these conditions, one would expect the DTA curves to be the same in Fig. 2, curves A and B. This necessary transfer of the electrochemically treated sample from the cell to the chamber of the surface analyzing apparatus raises a continuing serious problem for electrochemists. For example, it is doubtful that Dickinson and co-workers (24) were able to observe from an XPS study of anodized Pt a conversion of Pt-O layers to PtO<sub>2</sub> layers. More likely they observed the beginning of oxygen dermasorption (3) in the potential range 1-1.4V.

It appears from Fig. 2, curve A that the DTA curve does not return to the base line (intercept on the  $\Delta T$  ordinate) between the peaks and that a long tail exists at the high temperature end of the curve. It is suggested here that exothermic heat energy responsible for this behavior is due to the desorption of oxygen which is dissolved in the bulk Pt metal by the pre-anodization procedure (2, 3). This desorption takes place throughout the range of the temperature sweep providing a background  $\Delta T$  on which the peaks for the desorption of adsorbed oxygen ride.

When the DTA curve was obtained in the argon atmosphere containing 6% H<sub>2</sub>, the second peak was greatly diminished as noted in Fig. 1, curve C and Fig. 2, curve C. In the preparation for the run, the bead was in the presence of H<sub>2</sub> for 10-15 min before the DTA curve was taken. Under these conditions, most of the adsorbed oxygen was reduced by the H<sub>2</sub>. However, as the surface oxygen is removed by the H<sub>2</sub>, it is replaced by the dissolved oxygen diffusing from the bulk metal to the surface as adsorbed oxygen atoms (Pt-O).

When the adsorbed oxygen is removed by reacting with H<sub>2</sub> gas, water is formed; but, this water is formed in the presence of an adsorbed oxygen layer which is continually being renewed by oxygen diffusing from the bulk metal. Such water molecules are not strongly bound to the metal surface and are easily desorbed. From LEED and Auger (AES) studies of the removal of adsorbed oxygen from Pt by reaction with H<sub>2</sub>, the water was found (17, 26) to desorb at temperatures as low or lower than room temperature. It also appears (26) that there are two adsorption states for water on Pt. Any contributions to the DTA curve made by the desorption of H<sub>2</sub>O would be swamped out by the large contributions made by the desorption of adsorbed oxygen.

The shape of the DTA curve obtained in N<sub>2</sub> on a HNO<sub>3</sub>-passivated Pt bead (Fig. 3, curve A) is different from the one obtained on a preanodized Pt bead (Fig. 2, curve A). Although the peaks for adsorbed oxygen are present (peaks at 150° and at 350°C), additional diffuse peaks appear on the high temperature tail of the curve at 500°, 750°, and at 900°C. Also, the background  $\Delta T$  is greater in the HNO<sub>3</sub> passivated case indicating the presence of a much larger amount of dissolved oxygen in the bulk metal. We favor the notion that the adsorbed oxygen responsible for the two

peaks in Fig. 3, curve A exists as adsorbed atoms (Pt-O) and not PtO<sub>2</sub> species since the HNO<sub>3</sub> passivated Pt-O alloy had never been anodized and the quantity of charge associated with the cathodic stripping of this oxygen (6) is equivalent to a monolayer of atomic oxygen.

When the DTA curve was obtained in 6% H<sub>2</sub>, Fig. 3, curve B, the second peak at 350°C is significantly reduced, but the first peak as well as the large  $\Delta T$  background remain prominent. Even after 11 runs in 6% H<sub>2</sub>, Fig. 3, curve E, the two adsorbed oxygen peaks and the large  $\Delta T$  background with the diffuse peaks remain.

Guided by our earlier observations (3, 6) from constant current stripping studies obtained on Pt-O alloy beads, we suggested that the peaks on the high temperature tail of the DTA curve may be associated with a series of relatively stable dermasorbed oxygen layers in the Pt-O alloy lattice. The deeper these layers lie, the higher will be the temperature at which the dissociation peak will appear on the DTA curve.

The earlier studies (3, 6) indicated that the HNO<sub>3</sub>-passivated Pt-O alloy was very stable even under the extreme reducing conditions of strong cathodic polarization. The corresponding observation is found in the data of Fig. 3 where the Pt-O alloy structure is very evident, even after 11 runs in 6% H<sub>2</sub> (Fig. 3, curve E). After each run, the oxygen adsorption and dermasorption sites were occupied by oxygen diffusing from the metal interior.

It was also observed earlier (3, 6) that the Pt-O alloy structure could be destroyed by heating the sample white hot. In this case the sample was returned to the untreated Pt state. To simulate this condition in the DTA apparatus, the Pt-O alloy sample was heated at 900°C in 6% H<sub>2</sub> for 6 hr. After cooling in 6% H<sub>2</sub>, the DTA curve had the shape of Fig. 3, curve F. In this case, the Pt-O alloy structure is destroyed; and in its place, the curve exhibits one broad peak with two shoulders and a high temperature tail. This three-pronged peak may be interpreted in terms of the desorption of adsorbed hydrogen from two and possibly three kinds of adsorption sites known (14-16) to exist on the Pt surface. The large background  $\Delta T$  may be accounted for by the desorption of dermasorbed (25) and dissolved hydrogen (26, 27) in the bulk metal.

From x-ray diffraction studies of HNO<sub>3</sub> passivated Pt-O alloy samples (1), it was found that the Pt lattice had been expanded suggesting that the dissolved oxygen had entered the Pt lattice. In the case of anodized Pt-O alloy, oxygen diffusion studies (2, 4) indicate that oxygen migrates along the grain boundaries. Consequently, the dissolved oxygen in Pt may reside either in the grain boundaries or interstitially in the Pt lattice (most likely in the octahedral holes of the fcc lattice). Since the presence of stable dermasorbed layers are not detected on the DTA curves for anodized Pt-O alloy in Fig. 2, it is likely that much of the dissolved oxygen resides in the grain boundaries. The presence of stable dermasorbed layers are detected on the DTA curves for HNO<sub>3</sub> passivated Pt-O alloy in Fig. 3 and suggests that dissolved oxygen not only resides in the grain boundaries but also considerable amounts of dissolved oxygen are located interstitially in the Pt lattice.

It has been found from Auger (AES) studies (27) that both H<sub>2</sub> and O<sub>2</sub> are adsorbed on the low index planes of Pt such as the Pt (111) and Pt (100) planes with considerable difficulty. However, the adsorption of H<sub>2</sub> is greatly facilitated on stepped (28) surfaces which expose high index planes. On these stepped surfaces of Pt the dissolution of hydrogen into the metal interior is strongly promoted (27). From a study of the passivation of Pt in O<sub>2</sub>-free HNO<sub>3</sub> (6), it was found that the HNO<sub>3</sub> treatment seemed to give the Pt the properties of an oxygen sponge. We suggest that the soaking of polycrystalline samples of Pt in concentrated HNO<sub>3</sub> for periods of time greater than 72 hr etched the Pt sur-

face in such a way that certain high index planes are exposed. These high index planes greatly facilitate the penetration of adsorbed oxygen into the Pt lattice. Apparently, anodization either does not generate the required high index planes or at least not as efficiently as soaking in HNO<sub>3</sub>.

One possible physical picture of the two adsorption sites is as follows. One may associate the type I sites with adsorption of oxygen atoms at the edges of steps on the Pt surface whereas type II may be associated with corners along these steps somewhat similar to the diagrams drawn by Bockris and Conway (29) for adions on a metal surface. The two peaks in the DTA curves of Fig. 2 are separated by about 300°C corresponding to an energy difference of about 600 cal/mole or about 0.026 eV. This energy difference may represent the average difference in the binding energy of O atoms at edge sites and at kink or corner sites on the Pt surface.

Possible reasons for the lowering of the second peak in repeated DTA (Fig. 2, curve C, Fig. 3, curves B-E) runs are as follows. First, dissolved oxygen may diffuse to type I sites more easily than to the type II sites. Second, hydrogen may react with oxygen adsorbed at type II sites more rapidly than with that at type I sites. Third, the thermal treatment to which the sample is subjected during a standard DTA run may decrease the number of type II (kink) sites present on the sample surface. At this time, these data do not permit us to distinguish a preferred path from these suggested mechanisms.

In Fig. 3 the difference in energy between the two sites is less than in Fig. 2; and although the position of the first peak is unaffected, the second peak and the dermasorbed peaks are shifted to higher temperatures with each treatment in the hydrogen atmosphere. It appears that the nature of the kink sites is modified by the hydrogen treatment. Possibly the dermasorbed layers are related to the kink sites. Consequently, the nature of the HNO<sub>3</sub> passivated Pt surface is somewhat different than the anodized surface.

These data support the conclusions: that there are two different adsorption sites of oxygen on polycrystalline Pt; that thin layers of PtO<sub>2</sub> are unstable in the presence of Pt and decompose to Pt-O at potentials below 1.5V; that the HNO<sub>3</sub> treatment of Pt generates a more active surface for the dissolution of oxygen in the bulk Pt than anodization; that dissolved oxygen can reside in the grain boundaries or interstitially in the Pt lattice; that HNO<sub>3</sub> passivated Pt-O alloy is more stable and contains more dissolved oxygen than the anodized Pt-O alloy.

Manuscript submitted April 8, 1976; revised manuscript received June 21, 1976.

Any discussion of this paper will appear in a Discussion Section to be published in the June 1977 JOURNAL. All discussions for the June 1977 Discussion Section should be submitted by Feb. 1, 1977.

Publication costs of this article were assisted by General Motors Corporation.

#### REFERENCES

1. J. P. Hoare, S. G. Meibuhr, and R. Thacker, *This Journal*, **113**, 1078 (1966).
2. J. P. Hoare, *ibid.*, **116**, 612, 1390 (1969).
3. R. Thacker and J. P. Hoare, *J. Electroanal. Chem.*, **30**, 1 (1971).
4. J. P. Hoare, *This Journal*, **121**, 872 (1974).
5. J. P. Hoare, *ibid.*, **112**, 602, 849 (1965).
6. J. P. Hoare, R. Thacker, and C. R. Wiese, *J. Electroanal. Chem.*, **30**, 15 (1971).
7. L. V. Babenkova, N. M. Popova, D. V. Sokol'skii, and V. K. Solnyskhova, *Dokl. Akad. Nauk SSSR*, **210**, 888 (1973).
8. K. J. Vetter and D. Berndt, *J. Elektrochem.*, **62**, 378 (1958).
9. W. Bold and N. W. Breiter, *Electrochim. Acta*, **5**, 145 (1961).
10. T. Biegler, D. A. J. Rand, and R. Woods, *J. Electro-*

- anal. Chem.*, **29**, 269 (1971).
11. Yu. M. Tyurin *et al.*, *Elektrokhimiya*, **6**, 1854 (1970).
  12. R. Parsons and W. H. M. Visscher, *J. Electroanal. Chem.*, **36**, 329 (1972).
  13. P. R. Nadebaum and T. Z. Fahidy, *Electrochim. Acta*, **17**, 1659 (1972).
  14. T. C. Franklin and S. L. Cook, *This Journal*, **107**, 556 (1960).
  15. C. H. Presbrey and S. Schuldiner, *ibid.*, **108**, 985 (1961).
  16. F. G. Will, *ibid.*, **112**, 451 (1965).
  17. P. R. Norton, *J. Catal.*, **36**, 211 (1975).
  18. V. V. Gorodetskii and V. I. Savchenko, *Dokl. Akad. Nauk SSSR*, **215**, 366 (1974).
  19. J. Balej and O. Spalek, *Collect. Czech. Chem. Commun.*, **37**, 499 (1972); **38**, 29 (1973).
  20. V. I. Luk'yanycheva *et al.*, *Elektrokhimiya*, **10**, 485 (1974); **1**, 262 (1965).
  21. H. Angerstein-Kozłowska, B. F. Conway, and W. B. A. Sharp, *J. Electroanal. Chem.*, **43**, 9 (1973); D. Gilroy and B. E. Conway, *Can. J. Chem.*, **46**, 875 (1968).
  22. T. V. Kalish and R. Kh. Burshtein, *Dokl. Akad. Nauk SSSR*, **81**, 1093 (1951); **88**, 863 (1953).
  23. J. P. Hoare, *J. Electroanal. Chem.*, **12**, 260 (1966).
  24. T. Dickinson, A. F. Povey, and P. M. A. Sherwood, *J. Chem. Soc. Faraday Trans. I*, **71**, 298 (1975).
  25. S. Schuldiner and T. B. Warner, *This Journal*, **112**, 212 (1965).
  26. F. P. Netzer and G. Kneringer, *Surf. Sci.*, **57**, 1526 (1975).
  27. B. Lang, R. W. Joyner, and G. A. Somorjai, *ibid.*, **30**, 454 (1972).
  28. B. Lang, R. W. Joyner, and G. A. Somorjai, *ibid.*, **30**, 440 (1972).
  29. B. E. Conway and J. O'M. Bockris, *Electrochim. Acta*, **3**, 340 (1960).

## Electrochemistry of Mercuric Chloride in Molten Zinc Chloride-Potassium Chloride Eutectic

M. L. Deanhardt<sup>1</sup> and K. W. Hanck\*

*Department of Chemistry, North Carolina State University, Raleigh, North Carolina 27607*

### ABSTRACT

Chronopotentiometric and cyclic voltammetric studies indicate that the electroreduction of Hg(II) in an equimolar ZnCl<sub>2</sub>-KCl eutectic at 300°C proceeds by a reversible two-electron process to form Hg(O). A disproportionation reaction is observed when Hg(I) is added to the moderately acidic solvent. The formal potential of the Hg(II)/Hg(O) couple is estimated to be 0.800V vs. the Zn(II)/Zn(O) reference electrode. A diffusion coefficient of  $(2.17 \pm 0.07) \times 10^{-6}$  cm<sup>2</sup>/sec was observed for HgCl<sub>4</sub><sup>2-</sup> at 300°C. The presence of a pre-wave on the cyclic voltammograms of HgCl<sub>2</sub> indicates strong adsorption of Hg(O) on the Pt cathode. The system is further complicated by the chemical reaction of metallic mercury with the electrode to produce PtHg<sub>4</sub>. A mechanism consistent with the observed results is proposed.

The electrochemistry of mercury in molten halide solvents is highly dependent on solvent acidity. The reduction of mercuric chloride in molten LiCl-KCl, a basic solvent, was first studied by Laitinen, Liu, and Ferguson (1). They observed a single reduction wave for Hg(II) complicated by saw-tooth-like fluctuations which were attributed to discharge of gaseous mercury at the electrode surface. Mercury (I) was found to disproportionate in the melt at 450°C to Hg(II) and Hg(O).

A more extensive investigation of Hg(II) in molten LiCl-KCl was carried out by Hanck and Deanhardt (2). Based on chronopotentiometric, pulse polarographic, and cyclic voltammetric studies, a two-electron reversible reduction was observed for Hg(II). The electrode reaction was shown to follow a first-order EC mechanism in which the reduction product is sparingly soluble. The chemical step involved the reaction of metallic mercury with the platinum cathode to produce PtHg<sub>4</sub>.

Hames and Plambeck (3) investigated the electrochemistry of mercury in highly acidic molten AlCl<sub>3</sub>-NaCl-KCl at 150°C by potentiometric, voltammetric, and chronopotentiometric techniques. The results showed that Hg(II) is reduced in two steps to Hg(I) and Hg(O); however, the chronopotentiograms showed a long sloping region between the plateaus of the first and second steps and the expected ratio of  $\tau_2/\tau_1$  was not obtained.

Mamantov and co-workers (4, 5) observed three successive two-electron reduction steps for Hg(II) in acidic AlCl<sub>3</sub>-NaCl at 175°C. The first step produced Hg<sub>2</sub><sup>2+</sup>, the second produced a new ion, Hg<sub>3</sub><sup>2+</sup>, and the third yielded metallic mercury.

We have undertaken a study of the electrochemistry of mercury in an equimolar ZnCl<sub>2</sub>-KCl solvent at 300°C. The acidity of this solvent is less than that of the chloroaluminates but higher than that of LiCl-KCl.

### Experimental

Mercuric chloride was purified by sublimation of the reagent grade salt (J. T. Baker). Reagent grade mercurous chloride (J. T. Baker) was dried at 110°C for 1 hr and stored over magnesium perchlorate in a vacuum desiccator.

Preparation and purity of the ZnCl<sub>2</sub>-KCl eutectic, molten salt apparatus, and electrodes have been described previously (6).

Current-time and current-voltage curves were obtained with a Princeton Applied Research Corporation Model 173 potentiostat/galvanostat. A triangle wave generator constructed using the circuit of Bull and Bull (7) was interfaced with the Model 173 to obtain linear sweep voltammograms.

Data was digitized with an IBM system/7 data acquisition computer which was linked to the IBM 370/165 computer located at the Triangle Universities Computation Center. Interfacing of the laboratory instruments of the system/7 computer has been described in detail (8). In some cases data was collected with a

\* Electrochemical Society Active Member.

<sup>1</sup> Present address: Department of Chemistry, George Mason University, Fairfax, Virginia 22030.

Key words: adsorption, PtHg<sub>4</sub>, molten salt.

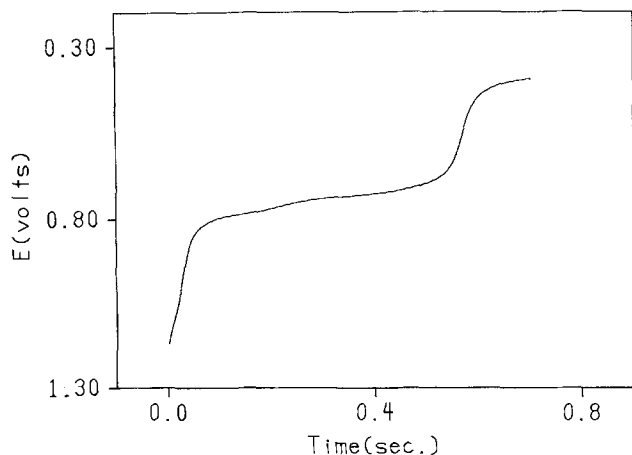


Fig. 1. Potential time curve for the chronopotentiometric reduction of  $\text{HgCl}_2$ . Current density =  $6.74 \text{ mA/cm}^2$ .  $[\text{HgCl}_2] = 24.24 \text{ mM}$ .

Tektronix 502-A oscilloscope equipped with a Model C-12 oscilloscope camera.

X-ray powder patterns were obtained with nickel-filtered copper radiation using a Rich. Seifert and Company debyeflex x-ray diffraction unit equipped with a 11.47 cm Debye-Scherrer camera.

### Results and Discussion

**Chronopotentiometry.**—Chronopotentiograms of  $\text{HgCl}_2$  were taken at several different concentrations and current densities. A typical chronopotentiogram is shown in Fig. 1. The analog data were digitized with the IBM system/7 computer and transition times were determined by the method of Noonan (9). Each chronopotentiogram gave a well-defined transition; however, a slight change in slope was observed in the horizontal portion of the curve. This is believed to be a prewave due to the adsorption of  $\text{Hg(O)}$  onto the platinum electrode and is discussed in a later section. Table I lists the range of concentrations and current densities used in the analysis. The reduction was found to obey the Sand equation; the regression analysis of Table II-A indicates a diffusion controlled process with  $I_0\tau^{1/2}/C$  equal to  $0.252 \pm 0.004 \text{ mA-sec}^{1/2}/\text{cm}^2\text{-mM}$ . From this slope  $nD_{\text{ox}}^{1/2}$  was calculated to be  $(2.95 \pm 0.05) \times 10^{-3} \text{ eq-cm/mole-sec}^{1/2}$ .

The reversibility of the electron transfer reaction was determined from the shape of the chronopotentiograms. Plots of  $E$  vs.  $\log(\tau^{1/2} - t^{1/2})/t^{1/2}$  were linear indicating a reversible electron transfer reaction. An example of such a plot is shown in Fig. 2; plots were

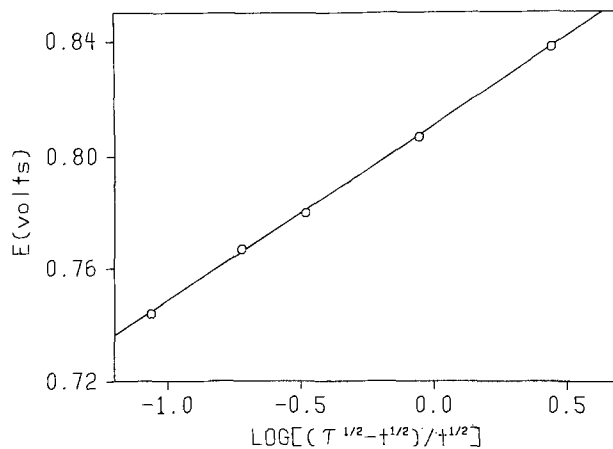


Fig. 2. Potential time analysis.  $[\text{HgCl}_2] = 14.88 \text{ mM}$ . Current density =  $3.84 \text{ mA/cm}^2$ .

made on 19 chronopotentiograms and the results are summarized in Table II-B. The theoretical slope for a reversible process at  $300^\circ\text{C}$  is  $113.7/n \text{ mV}$ . The experimental data predict a value of 1.98 for  $n$  indicating a two-electron reversible process. The diffusion coefficient of  $\text{Hg(II)}$  based on a two-electron process is  $(2.17 \pm 0.07) \times 10^{-6} \text{ cm}^2/\text{sec}$ . The quarter-wave potential,  $E_{\tau/4}$ , was found to be independent of current density and concentration over the range studied; the average value being  $800 \pm 10 \text{ mV}$  vs. the  $\text{Zn(II)/Zn(O)}$  reference electrode. The theoretical intercept for the reversible log plot should equal the quarter-wave potential; this was experimentally verified as shown in Table II-B. Prewaves on the chronopotentiograms were considered to be negligible and therefore were not subtracted from the data in Tables I and II.

Since a  $\text{Hg(I)}$  species is known to exist in molten salts (3-5), the reduction of mercurous chloride was also studied using chronopotentiometry. Mercurous chloride disproportionates upon dissolution in molten  $\text{ZnCl}_2\text{-KCl}$  yielding a black precipitate and a solution which yields well-defined chronopotentiograms. The slope of the chronopotentiograms were analyzed and the results are summarized in Table II-C. The average slope and intercept of the log plots are nearly identical to the values reported for mercuric chloride. This suggests that  $\text{Hg(I)}$  is not present in detectable concentration and that  $\text{Hg(I)}$  rapidly disproportionates to  $\text{Hg(II)}$  and  $\text{Hg(O)}$ . These results are similar to those observed in basic  $\text{LiCl-KCl}$  (2);  $\text{Hg(I)}$  is apparently stable only in strongly acidic melts such as the chloroaluminates.

**Cyclic voltammetry.**—Digitized cyclic voltammograms of  $\text{HgCl}_2$  were taken at several different sweep rates,  $\nu$ , from  $\sim 0.4$  to  $\sim 115 \text{ V/sec}$ ; the potential scan was from 1.3 to 0.5V vs. the  $\text{Zn(II)/Zn(O)}$  reference electrode. Effects of uncompensated solution resistance were minimized by using a low concentration of  $\text{HgCl}_2$  and positive  $IR$  compensation provided on the PAR 173 potentiostat. The voltammograms undergo a change in shape as a function of sweep rate as shown in Fig. 3. At slow sweep rates only two waves are observed (waves II and III, Fig. 3). Wave II has the shape of a reversible two-electron process with  $(E_{p/2} - E_p)_{\text{II}} = 55.2 \text{ mV}$ ; the theoretical value for a soluble two-electron process at  $300^\circ\text{C}$  is  $54.3 \text{ mV}$  (10). The peak potential occurs at 785 mV. The theoretical value of  $E_{1/2} - E_p$  is  $27.4 \text{ mV}$  for a two-electron process; therefore,  $E_{1/2}$  is calculated to be 812 mV which is in excellent agreement with the  $E_{1/2}$  value obtained from the chronopotentiometric data.

Wave III in Fig. 3A has a sharp, nearly symmetrical shape characteristic of the stripping of an insoluble deposit. The value of  $(E_p)_{\text{III}} - (E_p)_{\text{II}}$  is 138 mV, which is considerably larger than the theoretical value of 54.8 mV for a two-electron reversible process.

Table I. Chronopotentiometric data

$[\text{HgCl}_2]$ (mM)	$I_0\tau^{1/2}$ (mA-sec <sup>1/2</sup> /cm <sup>2</sup> )	Range of $I_0$ (mA/cm <sup>2</sup> )
8.83	2.24	2.42-5.01
14.88	3.80	3.84-7.34
28.42	7.17	4.91-10.90
62.60	16.00	15.70-20.00
117.10	29.50	34.40-42.60

Table II. Linear regression analysis of chronopotentiometric data\*

- A.  $I_0\tau^{1/2}$  (mA-sec<sup>1/2</sup>/cm<sup>2</sup>) vs.  $C$  (mM)  
Sample correlation coefficient = 0.9999  
Slope =  $0.252 \pm 0.004$   
Intercept =  $0.054 \pm 0.241$
- B.  $E$  (mV) vs.  $\log(\tau^{1/2} - t^{1/2})/t^{1/2}$   
Average slope =  $57.4 \pm 2.3$   
Average intercept =  $798 \pm 13$   
Average  $E_{\tau/4}$  =  $800 \pm 10$
- C.  $E$  (mV) vs.  $\log(\tau^{1/2} - t^{1/2})/t^{1/2}$  for  $\text{Hg}_2\text{Cl}_2$   
Average slope =  $63.7 \pm 3.5$   
Average intercept =  $800 \pm 10$   
Average  $E_{\tau/4}$  =  $799 \pm 11$

\* All uncertainties quoted in this paper are 95% confidence intervals.

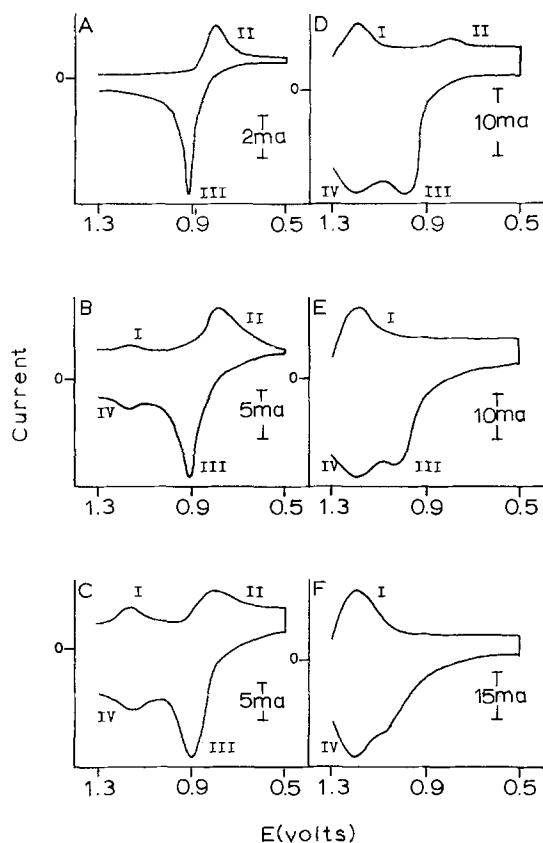


Fig. 3. Cyclic voltammograms of  $\text{HgCl}_2$  at various sweep rates.  $[\text{HgCl}_2] = 9.21 \text{ mM}$ . Beginning with curve A,  $\nu = 0.378, 3.69, 9.11, 21.4, 30.6,$  and  $45.8 \text{ V/sec}$ , respectively.

The formation of  $\text{PtHg}_4$  on the electrode surface has been confirmed by x-ray powder diffraction and is discussed in a later section. The oxidation of  $\text{PtHg}_4$  should occur at a more anodic potential than the oxidation of  $\text{Hg(O)}$  and therefore would account for the larger than theoretical value observed for  $(E_p)_{\text{III}} - (E_p)_{\text{II}}$ .

As the scan rate is increased  $(E_p)_{\text{II}}$  remains constant and the wave finally disappears with the formation of a prewave (wave I) at 1150 mV. Wave III shifts cathodic with scan rate and broadens approaching the shape expected for a reversible reoxidation of a soluble product; however, at very high sweep rates wave III also disappears with the formation of wave IV at 1150 mV.

The increase in wave I and decrease in wave II with scan rate indicates strong adsorption of the reaction product onto the electrode; waves I and IV represent the reduction of  $\text{Hg(II)}$  and the oxidation of adsorbed  $\text{Hg(O)}$ , respectively. Effects of adsorption of electroactive species in cyclic voltammetry have been discussed quantitatively by Wopschall and Shain (11). Quantitative measurements of the adsorption parameters of this system were not feasible due to the presence of a chemical reaction following charge transfer (i.e., formation of  $\text{PtHg}_4$ ).

**Current reversal chronopotentiometry.**—The mechanism for the reduction of  $\text{HgCl}_2$  was further characterized by current reversal chronopotentiometry. A typical reverse current chronopotentiogram is shown in Fig. 4. The difference between  $E_{0.250\tau}$  and  $E_{0.215\tau_r}$  is greater than that expected for a reversible process (12), due mainly to IR drop effects similar to those observed by Delahay and Mattax (13). The theoretical ratio of the reverse transition time to the forward time,  $\tau_r/t_f$  is equal to  $\theta^2/(2\theta + 1)$  for the formation of a soluble product where  $\theta$  equals the ratio of  $i_f$ , the forward current, to  $i_r$ , the reverse current. If the reduction product is insoluble and plates onto the electrode,  $\tau_r/t_f = \theta$ .

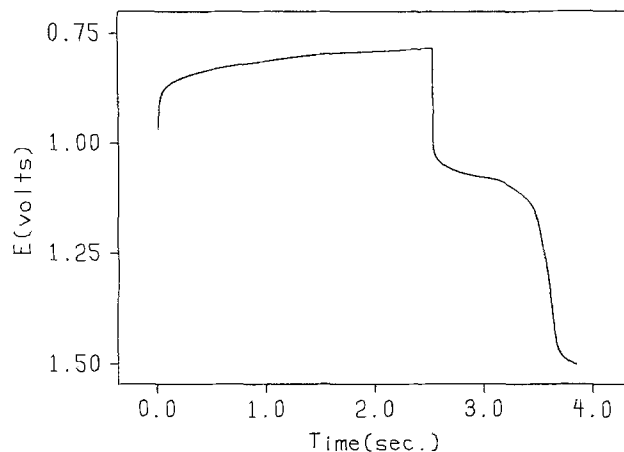


Fig. 4. Current reversal chronopotentiogram of  $\text{HgCl}_2$ .  $[\text{HgCl}_2] = 117.1 \text{ mM}$ .  $i_f = 7.53 \text{ mA/cm}^2$ .  $i_r = 7.53 \text{ mA/cm}^2$ .

A series of current reversal chronopotentiograms were performed in which the forward electrolysis time ( $t_f$ ) and  $i_f$  were chosen so that the forward charge was constant throughout a run but  $t_f$  varies from ca. 0.5 to 3.0 sec. Figure 5 shows the variation of  $\tau_r/t_f$  with  $t_f$  for some 30 current reversal chronopotentiograms at three different values of  $\theta$ . The concentration of  $\text{HgCl}_2$  was chosen to be very high in order to obtain a larger range of forward and reverse currents.

At large values of  $t_f$  (i.e., low values of  $i_f$ ),  $\tau_r/t_f$  approaches a value expected for the reoxidation of a soluble product; however at low values of  $t_f$  (i.e., large values of  $i_f$ ),  $\tau_r/t_f$  is greater than the value expected for the reoxidation of a soluble reduction product but less than that expected for the reoxidation of an insoluble reduction product. Cyclic voltammetric experiments indicate strong adsorption of the reduction product; Herman and Blount (14) observed an enhancement in the  $\tau_r/t_f$  ratio when the product was adsorbed on the electrode. Increasing  $i_f$  (decreasing  $t_f$ ), which is analogous to increasing the scan rate in cyclic voltammetry, should increase the value of  $\tau_r/t_f$  in the case of product adsorption. The data of Fig. 5 confirm the adsorption of the reduction product as suggested by the voltammetric data.

**X-ray powder diffraction analysis.**—The insoluble product indicated by the voltammetric experiments at slow scan rate was identified by x-ray powder diffraction patterns. A 2 cm length of 26 gauge Pt wire was electrolyzed in a  $\text{HgCl}_2$  solution at a controlled potential of 0.5V vs. the  $\text{Zn(II)/Zn(O)}$  reference electrode for 10 min. The wire was washed with deionized water, air dried, and mounted in an x-ray diffraction camera.

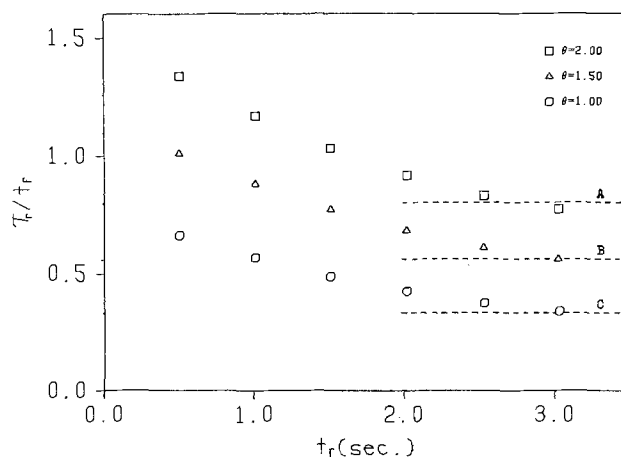
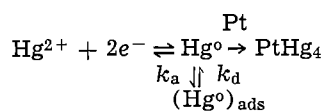


Fig. 5. Variation of  $\tau_r/t_f$  with  $t_f$ .  $[\text{HgCl}_2] = 117.1 \text{ mM}$ . Forward charge = 10.0 mC. A, B, and C indicate theoretical values of  $\tau_r/t_f$  for formation of a soluble product.

The sample was exposed to Ni-filtered  $\text{CuK}_\alpha$  radiation for 18 hr and a diffraction pattern identified as that of  $\text{PtHg}_4$  was observed. Robbins and Enke (15) found that  $\text{PtHg}_4$  is formed at room temperature when a Pt wire is allowed to stand in contact with metallic mercury. The reaction of  $\text{Hg(O)}$  with Pt to form  $\text{PtHg}_4$  was also observed in the reduction of  $\text{HgCl}_2$  in molten  $\text{LiCl-KCl}$  (2).

An additional experiment was performed in which  $\text{HgCl}_2$  was reduced on a Pt wire at a controlled potential of 0.5V for 5 min and then reoxidized at 1.3V for 5 min. The x-ray powder pattern for this sample was identical to the powder pattern of Pt metal which indicates that  $\text{PtHg}_4$  is oxidizable in the  $\text{ZnCl}_2\text{-KCl}$  solvent.

**Reduction mechanism.**—The electroreduction of  $\text{HgCl}_2$  proceeds by a reversible two-electron process to form  $\text{Hg(O)}$ ; no evidence was observed for the formation of  $\text{Hg(I)}$ . Based on our measurements of  $E_{1/2}$ , the formal potential of the  $\text{Hg(II)/Hg(O)}$  couple is 0.800V vs. the  $\text{Zn(II)/Zn(O)}$  reference electrode. A mechanism consistent with the observed results is



If the rate at which  $\text{Hg}^{2+}$  is electrolyzed is slow,  $\text{Hg(O)}$  is in contact with the Pt electrode for a longer period of time and  $\text{PtHg}_4$  is formed on the electrode surface. As the rate of electrolysis is increased, the formation of  $\text{PtHg}_4$  decreases as indicated by the broadening of peak III in Fig. 3. After the thickness of  $\text{PtHg}_4$  on the surface of the platinum reaches a certain value,  $\text{Hg(O)}$  is no longer in contact with metallic Pt and the influence of the chemical reaction diminishes. In the cyclic voltammetric experiments, the forward coulombs of the reduction are small (less than 1 mC) and the fraction of total  $\text{Hg(O)}$  reacting with the Pt electrode is large; however when the forward coulombs of the reduction are large as in the current reversal chronopotentiometric experiments (10 mC), the fraction of total  $\text{Hg(O)}$  reacting with the Pt electrode is small, and the system appears as a reversible process yielding a soluble product (see Fig. 5 at large values of  $t_f$ ).

The system is further complicated by the adsorption of  $\text{Hg(O)}$  onto the platinum electrode, which probably precedes the formation of  $\text{PtHg}_4$ . The absorption of a reduction product onto an electrode has been described by the Langmuir isotherm (11)

$$\Gamma_R = \Gamma_R^s C_R / (K_R + C_R) \quad [1]$$

where,  $\Gamma_R$  = surface concentration of adsorbed product (moles/cm<sup>2</sup>),  $\Gamma_R^s$  = surface concentration of adsorbed product at saturation (moles/cm<sup>2</sup>),  $C_R$  = concentration of product at electrode surface (moles/cm<sup>3</sup>), and  $K_R = k_d/k_a$ .

When  $C_R$  is small,  $\Gamma_R$  is directly proportional to  $C_R$ ; when  $C_R$  is large,  $\Gamma_R$  approaches  $\Gamma_R^s$ . The current for a process involving an adsorbed product is proportional

to  $\Gamma_R^s \nu^{1/2}$  while that for a process uncomplicated by adsorption is proportional to  $C^*_O \nu^{1/2}$  where  $C^*_O$  is the bulk concentration of the oxidized form of the couple. Both processes attempt to reduce the surface concentration of  $\text{Hg(II)}$ ; since the adsorption process occurs at a potential anodic of the diffusion process, an increase in the adsorption peak results in a decrease in the diffusion peak. In the case of mercury,  $\Gamma_{\text{Hg}^s}$  is much smaller than  $C^*_{\text{Hg(II)}}$ ; consequently at low values of  $\nu$  very little adsorption current is seen. As  $\nu$  is increased the adsorption current increases while the diffusion peak current decreases. At sweep rates above 45 V/sec all of the  $\text{Hg(O)}$  produced is adsorbed on the electrode. The fact that the diffusion peak completely disappears indicates that  $\Gamma_{\text{Hg}}$  has not reached  $\Gamma_{\text{Hg}^s}$ .

Chemical complications of the reversible charge transfer step could perhaps be eliminated by using some other working electrode other than platinum, for example, glassy carbon. This however would probably not add any other information concerning the electrochemistry of mercury in this solvent.

### Conclusions

The electroreduction of  $\text{HgCl}_2$  in an equimolar  $\text{ZnCl}_2\text{-KCl}$  solvent proceeds by a reversible two-electron process. The reduction mechanism includes two chemical complications, the adsorption of  $\text{Hg(O)}$  onto the Pt cathode and the chemical reaction of  $\text{Hg(O)}$  with the electrode to produce  $\text{PtHg}_4$ .

Manuscript submitted April 19, 1976; revised manuscript received July 19, 1976.

Any discussion of this paper will appear in a Discussion Section to be published in the June 1977 JOURNAL. All discussions for the June 1977 Discussion Section should be submitted by Feb. 1, 1977.

### REFERENCES

- H. A. Laitinen, C. H. Liu, and W. S. Ferguson, *Anal. Chem.*, **30**, 1266 (1958).
- K. W. Hanck and M. L. Deanhardt, *ibid.*, **45**, 176 (1973).
- D. A. Hames and J. A. Plambeck, *Can. J. Chem.*, **46**, 1727 (1968).
- G. Torsi and G. Mamantov, *Inorg. Nucl. Chem. Lett.*, **6**, 843 (1970).
- G. Torsi, K. W. Fung, G. M. Begun, and G. Mamantov, *Inorg. Chem.*, **10**, 2285 (1971).
- M. L. Deanhardt and K. W. Hanck, *This Journal*, **122**, 1627 (1975).
- R. H. Bull and G. C. Bull, *Anal. Chem.*, **43**, 1342 (1971).
- M. L. Deanhardt, Ph.D. Thesis, North Carolina State University, Raleigh, N. C. (1975).
- D. C. Noonan, Ph.D. Thesis, Columbia University, New York (1967).
- R. S. Nicholson and I. Shain, *Anal. Chem.*, **36**, 706 (1964).
- R. H. Wopshall and I. Shain, *ibid.*, **39**, 1514 (1967).
- W. E. Polke, C. D. Russell, and F. C. Anson, *ibid.*, **34**, 1171 (1962).
- P. Delahay and C. C. Mattax, *J. Am. Chem. Soc.*, **76**, 874 (1954).
- H. B. Herman and H. N. Blount, *J. Electroanal. Chem.*, **25**, 165 (1970).
- G. D. Robbins and C. G. Enke, *ibid.*, **23**, 343 (1969).



# Semiconductor Electrodes

## VII. Digital Simulation of Charge Injection and the Establishment of the Space Charge Region in the Absence and Presence of Surface States

Daniel Laser and Allen J. Bard\*

*Department of Chemistry, The University of Texas at Austin, Austin, Texas 78712*

### ABSTRACT

Transport of free carriers following charge injection to a semiconductor electrode is simulated. The relaxation of the free carrier results in the buildup of the space charge region whose properties are calculated. For an intrinsic semiconductor, the relaxation resembles that of the cations and anions in the diffuse double layer at a metal/electrolyte interface following charge injection to the metal. For an extrinsic semiconductor, some additional specific effects arise, which are discussed. The effect of surface states is considered and the interaction of a surface level with the semiconductor bands is simulated. This interaction results in trapping of charge from the space charge region and delivery of it to the surface. The properties of the space charge region in the presence of surface states are calculated, and their effect on the relaxation process demonstrated.

There has been much interest recently in semiconductor electrodes, and especially in photoeffects and photoelectrochemical experiments which may lead to devices of practical use, such as for solar energy utilization [see (1-3) and references therein]. Although the basic principles of the semiconductor electrode/electrolyte interface were formulated some time ago and have been reviewed extensively (4-8), the quantitative treatment of the behavior of semiconductor electrodes is quite complicated involving carrier diffusion and migration, thermal- and photogeneration, and recombination in the semiconductor itself in addition to the usual mass transfer and kinetic processes in the electrolyte phase and interphase charge transfer steps. Digital simulation methods (9, 10) have been very valuable in the treatment of complex kinetic or mass transfer problems in electrochemical systems. It is the aim of this paper and following ones in this series to apply digital simulation techniques to electrochemistry at semiconductor electrodes and the behavior of the semiconductor/electrolyte interface under illumination. In this paper we discuss the basic concepts of simulation of a semiconductor and the sequence of events following charge injection to a semiconductor electrode and leading to the formation of a space charge region. Following papers will describe the establishment of a photovoltage at an ideally polarized semiconductor electrode under steady illumination and the production of a photocurrent when charge transfer across the electrode/solution interface occurs.

### Digital Simulation Model of Formation of Space Charge Region

Although the carrier distribution and field in a semiconductor electrode can frequently be calculated by direct analytical methods (6-8), a digital simulation of it is convenient since these distributions provide the starting point for simulations of the photoeffects of interest. Moreover, simulations allow the investigation of the effect of surface states on the field and are useful in testing the digital model under conditions where some rigorous solutions are known. Consider a semiconductor electrode in contact with an electrolyte solution and at the flatband potential, *i.e.*, the point of zero charge. We now consider the events that occur following the coulostatic injection of charge into the semiconductor. As a dielectric the semiconductor electrode can sustain a charge and an electric field within its volume; however, because of the existence of mobile

carriers in the semiconductor, this charge is subject to redistribution and will ultimately accumulate at the semiconductor/electrolyte boundary in a region called the space charge region. Usually the charge distribution in a semiconductor electrode will be found somewhere between the two extreme cases of a metal electrode, where all the charge is essentially located at the surface, and a dilute electrolytic solution in contact with a charged metal electrode, in which the charge (ionic) distribution is very diffuse. The space charge region is of fundamental importance in describing the electrochemical properties of the semiconductor and it is the equilibrium distribution, rather than its mode of formation, that is usually of interest (5). The response of the semiconductor to charge injection is very similar to the relaxation of the diffuse double layer in solution following coulostatic charge injection to a metal electrode recently considered by Feldberg (10). The situation in a semiconductor differs from that for the usual electrolytic solution because of the much higher mobility of the carriers (holes and electrons) the presence of fixed charges (from acceptors or donors) in an extrinsic semiconductor, and the possible importance of dissociation and recombination processes in the semiconductor. The utilization of the basic concepts of electrostatics and mass transfer is very similar to that employed by Feldberg (10), however, so that only a brief outline of the simulation method will be given here. For those interested in utilizing this approach, the computer program is described briefly in the Appendix.

For the injection of positive charge with a charge density,  $Q$  ( $C/m^2$ ), the field at the semiconductor surface (*i.e.*, the semiconductor/solution interphase),  $E_s$  ( $V/m$ ), assuming planar geometry so that lines of force of the field are normal to the electrode surface, will be given by

$$E_s = Q/\epsilon_0\epsilon_r \quad [1]$$

where  $\epsilon_0$  is the permittivity of free space,  $8.85 \times 10^{-12} f m^{-1}$ , and  $\epsilon_r$  is the dielectric constant of the semiconductor relative to vacuum; for a positive charge,  $E_s$  is taken as positive pointing toward the solution. If charge is conserved in the semiconductor, the field at the surface ( $x = 0$ ) will always be given by Eq. [1]. In the interior of the semiconductor,  $E(x)$  will depend upon the charge distribution. At the instant of charge injection, the field everywhere in the semiconductor will be  $E_s$ . This field will cause holes ( $h^+$ ) to migrate toward the surface and electrons ( $e^-$ ) to migrate in the opposite direction. This migration is opposed by the diffusion of holes and electrons with the net flux of

\* Electrochemical Society Active Member.

Key words: semiconductors, digital simulation, space charge, surface states.



holes and electrons,  $f_+$  and  $f_-$ , respectively (with positive flux taken as toward the electrode surface), being governed by Eq. [2] and [3]

$$f_+ = (e/kT)E(x)D_p p + D_p \partial p / \partial x \quad [2]$$

$$f_- = -(e/kT)E(x)D_n n + D_n \partial n / \partial x \quad [3]$$

where  $D_p$  and  $D_n$  are the diffusion coefficients and  $p$  and  $n$  are the concentrations of holes and electrons, respectively. The net effect of this mass transfer is the transfer of positive charge to the electrode surface. This new charge distribution will modify  $E(x)$ . At equilibrium the space charge region is established with no charge remaining in the bulk semiconductor, so that the field there is zero, and with constant concentration profiles for holes and electrons maintained by the counterbalancing of the migrational flux caused by the equilibrium field distribution and the diffusional one. The surface potential,  $V_s$ , at all stages is given by Eq. [4], where  $E_b$  is the field in the bulk semiconductor

$$V_s = \int_0^\infty [E(x) - E_b] dx \quad [4]$$

### Results

**Intrinsic semiconductor in the absence of surface states.**—For an intrinsic semiconductor (e.g., intrinsic Ge), the response to charge injection and relaxation is quite analogous to diffuse double layer relaxation in solution given by Feldberg (10), with the holes replaced by cations and the electrons by anions (Fig. 1). The surface potential rises from zero to some maximum value and then relaxes to its new equilibrium value. The carriers which are attracted to the surface (e.g., holes) and which at equilibrium show a continuous drop in concentration with distance from surface towards the bulk, show a minimum in their concentration profile during the relaxation [as also observed in solution diffuse double layer formation (10)]. The relaxation processes occur in times  $10^4$ – $10^5$  smaller than for those in solution because of the higher  $D$  values of the carriers in the semiconductor (e.g.,  $95 \text{ cm}^2/\text{sec}$  for electrons and  $45 \text{ cm}^2/\text{sec}$  for holes in Ge) compared to those of ions in solution (ca.  $10^{-5} \text{ cm}^2/\text{sec}$ ). The space charge is essentially established within  $10^{-9}$  sec, a period during which double layer formation in solution will not yet have started. Thus space charge region effects probably can be differentiated from solution double layer ones according to the time window of the experiment.

**Extrinsic semiconductor in the absence of surface states.**—For a highly doped semiconductor (e.g., n-type Ge) the picture is different. Here, unless strong inversion prevails (e.g., at very positive potentials), the electrical state of the electrode will be mainly determined by the majority carrier distribution (electrons) and the dopant level (the donor atoms), while the minority carriers (holes) will adjust themselves to the field established by the donors and majority carriers. One must also consider the origin of the minority carriers (holes) arriving at the surface during relaxation, because positive charge injection at the metal/semiconductor ohmic contact of the n-type semiconductor occurs largely through electron extraction, rather than hole injection, and the total number of minority carriers originally existing in the bulk semiconductor may be insufficient to populate the space charge layer. A similar problem may apply to an intrinsic semiconductor as well. A typical simulation for n-Ge with a donor level,  $N_D$ , of  $2.5 \times 10^{16} \text{ cm}^{-3}$  is given in Fig. 2. The transport of the majority carriers is very fast and they are extracted nearly instantaneously from the surface (and arrive at the metallic contact to compensate for the electrons which were extracted from there by the charge injection). Because most of the charge distribution is associated with the electron distribution, the electric field and surface potential also quickly achieve

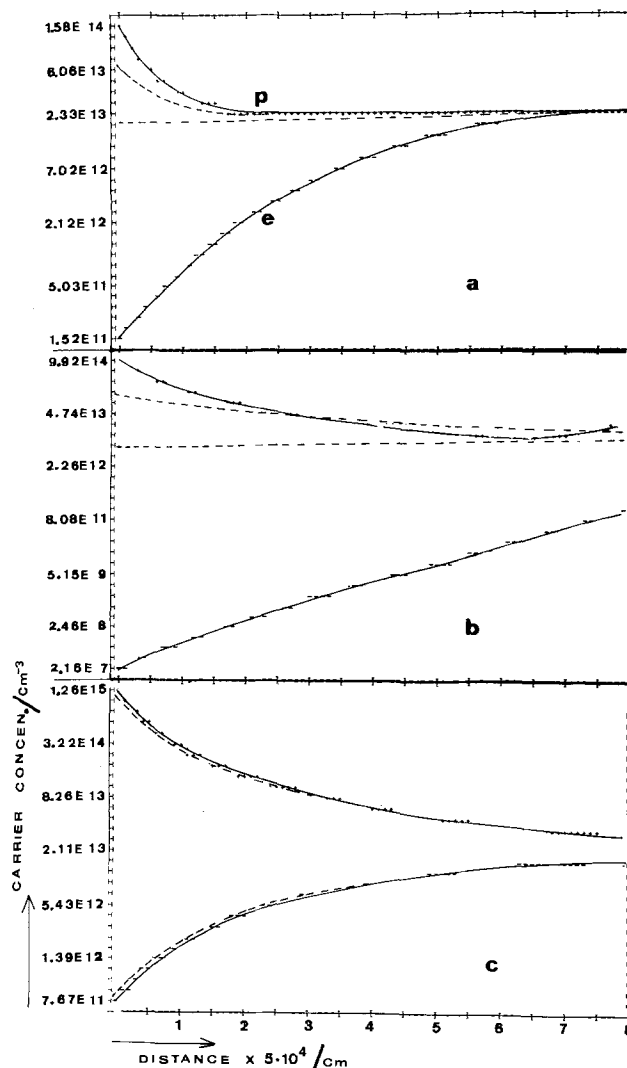
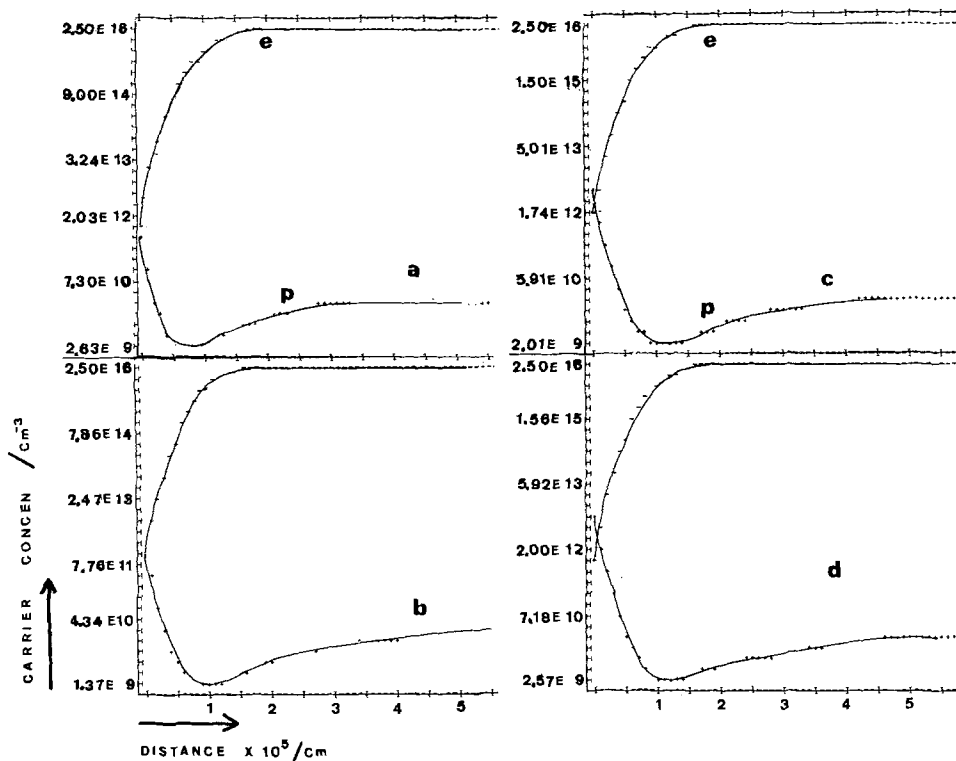


Fig. 1. Free carrier concentration for intrinsic Ge, with and without surface states.  $n^0 = p^0 = 2.5 \times 10^{13} \text{ cm}^{-3}$ ;  $\epsilon_r = 16$  esu,  $u_n$  and  $u_p$  are 3800 and 1800  $\text{cm}^2/\text{V}\cdot\text{sec}$ , respectively; charge injected =  $3.91 \times 10^{-7} \text{ C}/\text{cm}^2$ . Solid lines, without surface states; times after charge injection: (a)  $9.474 \times 10^{-12} \text{ sec}$  ( $V_s = 0.015\text{V}$ ,  $E_b = 2.37 \times 10^3 \text{ V}/\text{cm}$ ); (b)  $1.895 \times 10^{-10} \text{ sec}$  ( $V_s = 0.106\text{V}$ ,  $E_b = 7.03 \times 10^2 \text{ V}/\text{cm}$ ); (c)  $1.895 \times 10^{-9} \text{ sec}$  ( $V_s = 0.096\text{V}$ ,  $E_b = 2.8 \times 10^1 \text{ V}/\text{cm}$ ),  $V_s$  at equilibrium = 96 mV,  $E_s = 2.76 \times 10^3 \text{ V}/\text{cm}$  at all times. Dashed lines, with surface states for which  $N_t = 2.0 \times 10^{11} \text{ cm}^{-2}$ ,  $E_t = E_F^0$ ,  $k_e = 0.53 \times 10^{10} \text{ sec}^{-1}$ ;  $k_v = 2.63 \times 10^{-5} \text{ cm}^3 \cdot \text{sec}^{-1}$ . For the same times as in the absence of surface states, the results are: (a)  $V_s = 0.006\text{V}$ ,  $E_s = 2.757 \times 10^3 \text{ V}/\text{cm}$ ,  $\Delta Q_{SS} = 3.77 \times 10^{-10} \text{ C}$ ,  $E_b = 2.62 \times 10^3 \text{ V}/\text{cm}$ ; (b)  $V_s = 0.067\text{V}$ ,  $E_s = 2.71 \times 10^3 \text{ V}/\text{cm}$ ,  $\Delta Q_{SS} = 6.77 \times 10^{-7} \text{ C}$ ,  $E_b = 2.14 \times 10^3 \text{ V}/\text{cm}$ ; (c)  $V_s = 0.094\text{V}$ ,  $E_s = 2.65 \times 10^3 \text{ V}/\text{cm}$ ,  $\Delta Q_{SS} = 1.533 \times 10^{-8} \text{ C}$ ,  $E_b = 31 \text{ V}/\text{cm}$ .

their equilibrium value. Minority carriers show a relatively slow relaxation to their equilibrium value, because their low bulk concentrations can provide only small fluxes toward the surface. The holes are supplied to the surface and enter the space charge region (taken arbitrarily as the point where the electric field drops to  $10^{-4}$  times its surface value) mainly by diffusion. Thus, adjacent to the space charge region, which is the region of primary interest, a relatively wide diffusion layer [known as the "quasi-neutral region" (11)] will be formed. There the electrical field is nearly zero and minority carriers are transported across it by diffusion in a manner analogous to the diffusion of ions toward an electrode in solution in the presence of an excess of supporting electrolyte. In the experiment under consideration here, the quasi-neutral region will eventually disappear. In other kinds of experiments, however, e.g., those connected with a con-

Fig. 2. Free carrier concentration following charge injection to n-type Ge.  $n^0 = 2.5 \times 10^{16} \text{ cm}^{-3}$ ,  $p^0 = 2.5 \times 10^{10} \text{ cm}^{-3}$ ,  $\epsilon_r = 16 \text{ esu}$ ;  $u_n = 3800 \text{ cm}^2/\text{V-sec}$ ,  $u_p = 1800 \text{ cm}^2/\text{V-sec}$ ; injected charge  $= 4.96 \times 10^{-6} \text{ C/cm}^2$ . Time after charge injection: (a)  $2.37 \times 10^{-12} \text{ sec}$  ( $V_s = 250.5 \text{ mV}$ ); (b)  $4.74 \times 10^{-11} \text{ sec}$  ( $V_s = 251 \text{ mV}$ ); (c)  $2.37 \times 10^{-10} \text{ sec}$  ( $V_s = 251 \text{ mV}$ ); (d)  $4.74 \times 10^{-10} \text{ sec}$  ( $V_s = 251 \text{ mV}$ ).  $E_s = 3.50 \times 10^4 \text{ V/cm}$  and  $E_b < 2 \times 10^{-3} \text{ V/cm}$  for all times shown.



tinuous withdrawal of minority carriers from the electrode surface in a faradaic reaction, a steady-state quasi-neutral region will remain in which the gradient of minority carriers determines the limiting current. The diffusion layer width of the minority carriers is governed by the spontaneous thermal generation of carriers, which is not taken account of explicitly in the simulation. Within the time domain of the simulation (ca.  $10^{-9} \text{ sec}$ ) the number of holes generated thermally is negligibly small. For the n-type Ge ( $p^0 = 2.5 \times 10^{10} \text{ cm}^{-3}$ ) the value for the zero-th order generation rate constant is about  $10^{15} \text{ cm}^{-3} \text{ sec}^{-1}$ . This generation will terminate the diffusion layer of holes at some point when, at a given time, the flux divergence of holes will equal their net generation rate. For the sample under discussion, a wide and essentially linear diffusion layer for holes results, which in this relaxation mode gradually collapses. We cannot extend the simulation, which is concerned primarily with the thin space charge region, to such a distance from the electrode surface. Instead the thermal generation of minority carriers was considered indirectly by terminating the diffusion layer for the holes and arbitrarily assigning the hole concentration as the bulk value at some suitably large distance from the space charge region. Hence the simulated transport of holes to the electrode surface may be larger than the rate found for a more rigorous simulation, where the final relaxation of minority carriers would be determined by the thermal generation rate. Experimentally, it seems unlikely that the relaxation of minority carriers can be observed by purely electrochemical methods, since its influence on the electrode potential is negligibly small. Moreover, a current transient attributable to minority carrier relaxation which might probe their surface concentration would be complicated by the solution double layer relaxation effects. Some other technique, such as internal reflection spectroscopy at wavelengths which correspond to the absorption spectrum of holes and which is sensitive to their surface concentration (12, 13), might be useful.

**Effect of surface states.**—Surface states and their relevance to the electrochemistry of semiconductor electrodes have been widely discussed (8, 14). We shall confine ourselves here to a simple model and simulate

the interaction of a discrete surface level with the semiconductor bands at the surface in a charge injection experiment. In this case, charge is trapped by the surface level causing a simultaneous change in its occupancy. After relaxation, new surface concentrations and surface-state level occupancies will exist, such that the interaction between the level and the band again does not produce a net effect. The total injected charge will be distributed between the semiconductor surface and space charge region lowering the surface field and surface potential of the semiconductor compared to a situation without the surface states. The simulation assumes very fast (perhaps hypothetically fast) surface states which respond immediately to any perturbation in the equilibrium concentration of free carriers, thus modifying their surface concentrations during their relaxation. The final results should be valid for slower surface states as well. For slow surface states, the relaxation of free carriers can be considered complete before interaction between the space charge region and the surface level begins. Assume the existence of a discrete surface level with a concentration density of states  $N_t$ , located at an energy  $E_t$  with respect to the Fermi energy,  $E_F^0$ , and having an occupancy or filling function,  $f_t$  (representing the fraction of traps occupied by electrons). Figure 3 represents schematically this situation and the following expressions will be written for exchanging holes and electrons with the bands (6, 15)

$$R_e = k_e N_t f_t \quad [5]$$

$$R_c = k_c (1 - f_t) N_t n_s \quad [6]$$

$$R_v = k_v N_t f_t p_s \quad [7]$$

$$R_h = k_h N_t (1 - f_t) \quad [8]$$

The  $k$ 's are the corresponding rate constants for interaction of the surface level with the conduction and valence band, respectively;  $n_s$  and  $p_s$  are the surface concentrations of electrons and holes. Since the ratios  $k_e/k_c$  and  $k_h/k_v$  do not depend on the surface potential, their values determined at the flatband potential,  $V_{fb}$ , apply at other potentials, as well. At equilibrium at  $V_{fb}$ ,  $p_s = p^0$ ,  $n_s = n^0$ ,  $f_t = f_t^0$ ,  $R_e = R_c$ , and  $R_h = R_v$ . Then from Eq. [5]-[8]

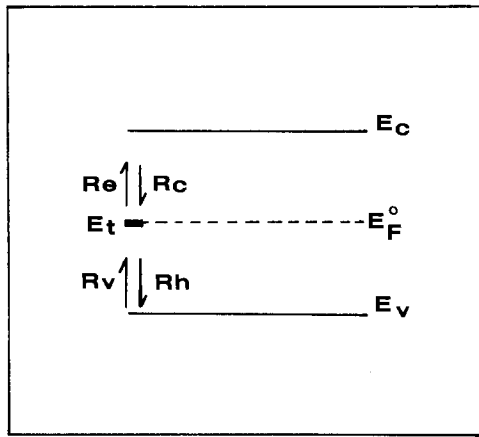


Fig. 3. Schematic model for interaction of a surface level with the semiconductor bands.  $R_e$  and  $R_c$  are the rates for exchange of electrons with conduction band;  $R_v$  and  $R_h$  are the rates for exchange of holes with the valence band.

$$k_c = k_e f_t^0 / (1 - f_t^0) n^0 \quad [9]$$

$$k_h = k_v p^0 f_t^0 / (1 - f_t^0) \quad [10]$$

Hence, for a given semiconductor,  $k_c/k_e$  and  $k_h/k_v$  depend only on  $f_t^0$ , i.e., on the relative position of  $E_t$  to  $E_F^0$ . If for any reason (e.g., because of charge injection)  $n_s$  and  $p_s$  are perturbed from their equilibrium values which have established a certain occupancy of the surface level, a net exchange of holes and electrons between the surface level and the conduction and valence bands will occur yielding

$$R_n = R_e - R_c = k_e N_t \left[ f_t - \left( \frac{f_t^0}{1 - f_t^0} \right) (1 - f_t) \frac{n_s}{n^0} \right] \quad [11]$$

$$R_p = R_v - R_h = k_v N_t \left[ p_s f_t - \left( \frac{f_t^0}{1 - f_t^0} \right) (1 - f_t) p^0 \right] \quad [12]$$

$R_n$  is the over-all rate at which electrons are transported from the surface level to the conduction band at the surface and  $R_p$  is the over-all rate at which holes from the valence band at the surface are transferred to the level. Both  $R_n$  and  $R_p$  have units of flux ( $\text{cm}^{-2} \text{sec}^{-1}$ ). The total rate at which the level loses electrons is  $R_n + R_p$ . This rate, when multiplied by the electronic charge, represents the rate at which the surface level collects positive charge from the space charge region (in  $\text{A}\cdot\text{cm}^{-2}$ ). The rate at which the field in the semiconductor at a point just inside the semiconductor/solution interface (where the surface states are presumably located) drops because of this loss of charge is  $e(R_n + R_p)/\epsilon_0 \epsilon_r$ . All of these effects were simulated along with the free carrier transport within the semiconductor phase described previously. When a new

position of equilibrium is established,  $R_p$  and  $R_n$  must vanish. Thus, both rates pass through a maximum when relaxing from one equilibrium situation to another and the values of the rate constants were chosen so that this effect could be observed within the simulation time domain. To obtain this situation we consider Eq. [11] and [12] in a somewhat more operational way. Assume that the semiconductor is initially at the flatband potential and  $f_t^0 = 1/2$  (i.e.,  $E_t = E_F^0$ ;  $f_t^0/(1 - f_t^0) = 1$ ). We call  $N_t f_t$  (the number of electrons in the level) SUR and  $N_t$  (the maximum number of electrons possible in this level) SURMAX. Then Eq. [11] and [12] can be rewritten as

$$R_n = k_e [\text{SUR} - (n_s/n^0) (\text{SURMAX} - \text{SUR})] \quad [13]$$

$$R_p = k_v [p_s \text{SUR} - p^0 (\text{SURMAX} - \text{SUR})] \quad [14]$$

Throughout the simulation  $n_s$ ,  $p_s$ , and SUR change. Before charge injection,  $p_s = p^0$ ,  $n_s = n^0$ , and  $\text{SUR} = \text{SURMAX}/2$ ; thus  $R_p = R_n = 0$ . Immediately after the charge injection (e.g., of positive charge),  $n_s$  becomes smaller than  $n^0$ ,  $p_s$  becomes larger than  $p^0$ , and at this instant SUR still is equal to  $\text{SURMAX}/2$ . As a result, both  $R_p$  and  $R_n$  become positive; the magnitude of SUR decreases as electrons are delivered to the edge of the conduction band and holes are collected from the edge of the valence band. As long as this mechanism is operative, concentration profiles in the space charge region will remain much more shallow than in the absence of surface states. This is shown in Fig. 1 for intrinsic Ge, where the charge injected was of such a size that the bands were bent in a way that the surface level was practically depopulated of electrons. At the new position of equilibrium, the value of SUR,  $p_s$ ,  $n_s$ , and  $\text{SURMAX} - \text{SUR}$  will cause the bracketed portions of Eq. [13] and [14] to be zero. A new concentration profile as well as a new surface level occupancy will result. Note that within the simulation negative values of  $R_p$  and  $R_n$  as calculated in Eq. [13] and [14] are possible. This occurrence results in an oscillatory behavior in which carriers move back and forth from the bands to the surface level. This behavior arose with large values of  $k_e$  and  $k_v$ , resulting in SUR becoming essentially zero within a few simulation steps. In the computer program such effects were prevented by stopping the interaction between the bands and the surface level (i.e., assigning  $R_p = R_n = 0$ ) whenever  $R_p$  and  $R_n$  were calculated to have a negative value. Table I summarizes the results of simulations and gives values of quantities of interest in the absence and presence of surface states (which are assumed to be at an energy,  $E_t = E_F^0$ ) with the initial condition taken as the flatband potential. Note that for the same total amount of charge injected the surface potential will be smaller in the presence of surface states than in their absence. Notice also that the total charge of the surface states and space charge region equals the injected charge and that the occupancy found for the surface level after the charge injection

Table I. Simulated properties of space charge region of Ge in absence and presence of surface states

Electrode	Without surface states				With surface states					
	Charge injected (C/cm <sup>2</sup> )	$E_s$ , surface field (V/cm)	$V_s$ , surface potential (mV)	$N_t$ ( $E_t = E_F^0$ ) (cm <sup>-2</sup> )	Charge trapped in ss (C/cm <sup>2</sup> )	$E_s$ , surface field (V/cm)	Calculated total charge* (C/cm <sup>2</sup> )	$V_s^{**}$ , surface potential (mV)	$f_t$ simulated**	$f_t$ calc***
Intrinsic Ge										
$n^0 = p^0 = 2.5 \times 10^{13}$	$3.91 \times 10^{-7}$	$2.76 \times 10^3$	96	$2 \times 10^{11}$	$1.53 \times 10^{-8}$	$2.65 \times 10^3$	$3.91 \times 10^{-7}$	94	0.022	0.023
$n^0 = p^0 = 2.5 \times 10^{13}$	$3.91 \times 10^{-7}$	$2.76 \times 10^3$	96	$4 \times 10^{11}$	$3.06 \times 10^{-8}$	$2.545 \times 10^3$	$3.91 \times 10^{-7}$	92	0.022	0.025
Extrinsic Ge										
$n^0 = 2.5 \times 10^{18}$	$1.42 \times 10^{-8}$	$1.0 \times 10^4$	40	$4 \times 10^{12}$	$1.7 \times 10^{-7}$	$8.80 \times 10^3$	$1.42 \times 10^{-6}$	33.5	0.23	0.21
$p^0 = 2.5 \times 10^{10}$	$2.56 \times 10^{-8}$	$1.80 \times 10^4$	86	$4 \times 10^{12}$	$2.76 \times 10^{-7}$	$1.60 \times 10^4$	$2.56 \times 10^{-6}$	73	0.068	0.051
$p^0 = 2.5 \times 10^{10}$	$4.96 \times 10^{-8}$	$3.50 \times 10^4$	251	$4 \times 10^{12}$	$3.2 \times 10^{-7}$	$3.27 \times 10^4$	$4.96 \times 10^{-6}$	223	$1.5 \times 10^{-4}$	$1.23 \times 10^{-4}$

\* Charge trapped in surface states plus charge equivalent to surface field; this total should equal charge injected.

\*\* Simulated surface level occupancy,  $f_t$ , at equilibrium after charge injection.

\*\*\* Surface level occupancy calculated using the function  $f_t = 1/[1 + \exp(eV^{**}/kT)]$ .

(initially 0.5 in all cases) agrees reasonably with that obtained from a thermodynamic or statistical expression (6).

### Acknowledgment

The support of this research by the National Science Foundation (MPS74-23210) is gratefully acknowledged.

Manuscript submitted Dec. 14, 1975; revised manuscript received Feb. 28, 1976.

Any discussion of this paper will appear in a Discussion Section to be published in the June 1977 JOURNAL. All discussions for the June 1977 Discussion Section should be submitted by Feb. 1, 1977.

Publication costs of this article were assisted by The University of Texas at Austin.

### APPENDIX

The desired region of interest is divided into space elements of width  $\Delta X$  (e.g., 25-100Å) which are assigned an index  $K$ , from  $K = 1$  (the surface element) to  $K = KMAX$ . The concentration of holes and electrons within each element ( $p_K, n_K$ ) is assumed constant and the electrical field between element  $K$  and  $K - 1$  is called  $E_K$ . The concentration at this boundary is assumed to have a concentration equal to the average value for the two elements on both sides of this boundary. Thus, e.g., for holes,

$$p_K = \frac{1}{2}(p_{K-1} + p_K) \quad [A-1]$$

According to the simulation technique, the change of carrier concentration in element  $K$ , due to the fluxes written in Eq. [2] and [3], within a time interval  $\Delta t$  can be expressed (e.g., for holes) as

$$\Delta p_K = DMP(p_{K-1} - 2p_K + p_{K+1}) + 0.5 UMP$$

$$\{E_{K+1}(p_K + p_{K+1}) - E_K(p_K + p_{K-1})\} \quad [A-2]$$

where  $DMP$  and  $UMP$  are simulation constants to be discussed later. Such an expression is written for all  $K$ 's, for holes as well as for electrons. The resulting changes in concentration are then added to the present ones. As a result a new concentration profile is established which is used to calculate the concentration changes for the next time interval. Changes in the electric field due to the concentration change will be written as

$$E_K = E_{K-1} - (e\Delta x/\epsilon_0\epsilon_r)(p_K - n_K + N_D - N_A) \quad [A-3]$$

where  $N_D$  and  $N_A$  are donor and acceptor concentrations, respectively. The initial conditions which follow the injection of charge  $q_{inj}$  are

$$p_K = p^0, n_K = n^0, E_K = q_{inj}/\epsilon_0\epsilon_r \quad (\text{at all } K) \quad [A-4]$$

The boundary conditions are

$$p_{KMAX} = p^0, n_{KMAX} = n^0, E_{K=1} = (q_{inj} - \Delta q_{ss})/\epsilon_0\epsilon_r \quad [A-5]$$

where  $\Delta q_{ss}$  is the charge trapped by the surface level.  $KMAX$  should be the value of  $K$  within the bulk of the electrode. However, unless a nonlinear space grid is employed, this  $KMAX$  will have too large a value for practical calculations for  $KMAX \cdot \Delta X$  to extend into the bulk semiconductor. Thus a smaller value of  $KMAX$  was used (which was still far outside the space charge region); this results in a somewhat steeper concentration profile for holes so that their flux toward the surface is slightly overestimated. The simulation constants are  $DMN$ ,  $DMP$ ,  $UMN$ , and  $UMP$ . They are defined (e.g., for electrons) as

$$DMN = D_n \Delta t / \Delta X^2 \quad [A-6]$$

$$UMN = U_n \cdot (\Delta t / \Delta X) = (e/kT) DMN \cdot \Delta X \quad [A-7]$$

with similar expressions for holes. As usual for simulations (9), both  $DMN$  and  $DMP$  must be less than 0.5. Similarly, the effect of migration requires that  $UMN \cdot E_{K=1}$  and  $UMP \cdot E_{K=1}$  both be smaller than 1 (where  $E_{K=1}$  is the maximum value of the electric field, at the surface). These conditions impose the following restriction on  $\Delta t$  and  $\Delta X$

$$\Delta t / \Delta X < 1/E_{K=1} U_N \quad [A-8]$$

Typical values which satisfy this requirement are  $U_n = 2000 \text{ cm}^2 \text{ sec}^{-1} \text{ V}^{-1}$ ,  $\Delta X = 5 \times 10^{-7} \text{ cm}$ ,  $DMN = 0.45$ , and  $E_{K=1} = 10^3\text{-}10^4 \text{ V/cm}$ .

### REFERENCES

1. A. Fujishima and K. Honda, *Nature*, **238**, 37 (1972).
2. M. D. Archer, *J. Appl. Electrochem.*, **5**, 17 (1975).
3. D. Laser and A. J. Bard, *Chem. Phys. Lett.*, **34**, 605 (1975).
4. P. J. Boddy, *J. Electroanal. Chem.*, **10**, 199 (1965).
5. H. Gerischer, in "Advances in Electrochemistry and Electrochemical Engineering," Vol. 1, P. Delahay and C. W. Tobias, Editors, Interscience Publishers, New York (1961).
6. V. A. Myamlin and Yu. V. Pleskov, "Electrochemistry of Semiconductors," Plenum Press, New York (1967).
7. P. J. Holmes, Editor, "The Electrochemistry of Semiconductors," Academic Press, New York (1962).
8. A. Many, Y. Goldstein, and N. B. Grover, "Semiconductor Surfaces," chap. 5, John Wiley & Sons, Inc., New York (1965).
9. S. W. Feldberg, in "Electroanalytical Chemistry," Vol. 3, A. J. Bard, Editor, chap. 4, Marcel Dekker, Inc., New York (1969).
10. S. W. Feldberg, *J. Phys. Chem.*, **74**, 87 (1970).
11. H. Gerischer, in "Advances in Electrochemistry and Electrochemical Engineering," Vol. 1, P. Delahay and C. W. Tobias, Editors, p. 182, Interscience Publishers, New York (1961).
12. K. H. Beckmann, *Angew. Chem. Int. Ed. Engl.*, **7**, 161 (1968).
13. D. Laser and M. Ariel, *Anal. Chem.*, **41**, 396 (1969).
14. E. O. Johnson, *Phys. Rev.*, **111**, 153 (1958).
15. W. Shockley and W. T. Read, *ibid.*, **87**, 835 (1954).

# Semiconductor Electrodes

## VIII. Digital Simulation of Open-Circuit Photopotentials

Daniel Laser and Allen J. Bard\*

Department of Chemistry, The University of Texas at Austin, Austin, Texas 78712

### ABSTRACT

A simulation technique is described for the calculation of semiconductor electrode properties at steady state, *e.g.*, at equilibrium in the dark or under constant illumination. Integration of the continuity equation with respect to distance at the steady state yields a relation between the light flux and free carriers, which can be used in a recursion relation to determine the free carrier concentrations and the electric field within the space charge region of the semiconductor electrode. The technique is used to calculate the Boltzmann distribution within the semiconductor electrode and to determine the photopotential in the absence of faradaic current and surface states.

In a previous paper in this series (1) we described a digital simulation method for semiconductor electrodes and the formation of the space charge region in a semiconductor electrode upon charge injection. The main motivation for these simulations has been the recent interest in semiconductor electrodes and their application to photoelectrochemical cells and devices (2). One characteristic of interest is the change in surface potential of a semiconductor/electrolyte interface under illumination, the photopotential. Although theoretical treatments of the photopotential have been given (3, 4), and its magnitude related to the semiconductor properties, surface potential, and light intensity, these treatments usually involve restrictive conditions, (*e.g.*, total light absorption in the space charge region, minority carrier diffusion length much larger than the size of the space charge region). We describe here the digital simulation of the steady-state photopotential which arises upon illumination of a semiconductor electrode previously brought to a given potential and now held at open circuit. Charge transfer reactions, *e.g.*, open-circuit corrosion, are assumed not to occur during this illumination.

### Physical Model

The general equation for the processes within a semiconductor electrode under illumination can be obtained by considering the creation of electron/hole pairs by light absorption, their mass transfer by diffusion and migration, and their recombination. Thus the change in concentration of holes,  $p$ , at a given location in the semiconductor is given (in one-dimensional form) by

$$\frac{\partial p}{\partial t} = \frac{\partial j_p(x)}{\partial x} + I_0 a e^{-ax} - R(x) \quad [1]$$

where  $I_0$  is the intensity of light incident on the semiconductor/electrolyte interface (taken as  $x = 0$ ),  $a$  is the coefficient of light absorption of the semiconductor,  $j_p(x)$  is the total flux of holes at  $x$ , and  $R(x)$  the rate of electron/hole recombination. We are concerned here with the steady-state photopotential. Thus with  $\partial p/\partial t = 0$ , integration of Eq. [1] yields

$$j_p(x) - j_p(0) = \int_0^x R(x) dx - I_0(1 - e^{-ax}) \quad [2]$$

where  $j_p(0)$  is the flux of holes crossing the interface, or the hole contribution to the faradaic current density,  $i_p$ . Thus

$$j_p(x) = i_p/e - I_0(1 - e^{-ax}) + \int_0^x R(x) dx \quad [3]$$

A similar expression can be written for electrons

$$j_n(x) = i_n/e + I_0(1 - e^{-ax}) - \int_0^x R(x) dx \quad [4]$$

where  $j_n(x)$  and  $i_n$  are the electron flux and the electron contribution to the faradaic current density, respectively. The light flux and electron flux are taken as positive going into the semiconductor from the solution and the hole flux is positive going out of the semiconductor to the solution. (A representation of the fluxes is shown in Fig. 1.) Equations [3] and [4] hold at all  $x$ , both within and outside of the space charge region. The net current density at any  $x$ ,  $i$ , is given by Eq. [5]

$$j_p(x) + j_n(x) = (i_p + i_n)/e = i \quad [5]$$

*i.e.*, at steady state a current (which may be zero) flows through the semiconductor phase. Equations [3] and [4] are employed in a digital or finite difference form in the simulation. The procedure follows the usual digital simulation approach (5). The semiconductor region of interest is divided into space elements of width  $\Delta x$  which are assigned an index  $K$ , from  $K = 1$  (surface element) to  $K = KMAX$  (Fig. 1). The carrier concentration within each element is assumed constant and represents the average value of  $p_K$  and  $n_K$  for holes and electrons, respectively, at that location. The electric field at the left boundary (the solution side) of element  $K$ , *i.e.*, between it and element  $K - 1$ , is denoted  $E_K$  and the carrier concentration at this

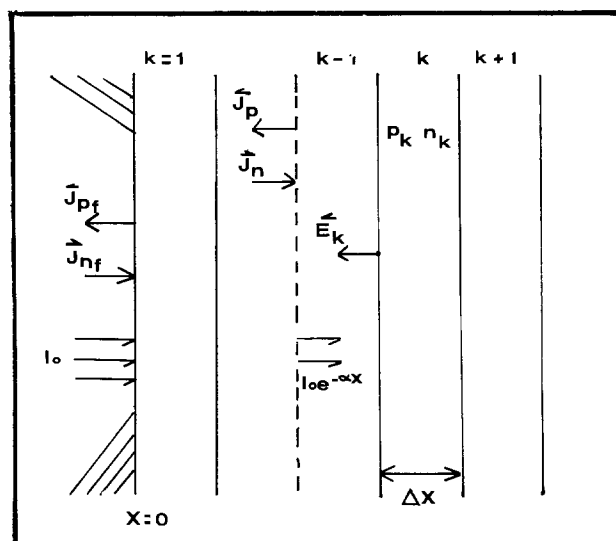


Fig. 1. Digital representation of the semiconductor phase and flux notation.

\* Electrochemical Society Active Member.  
Key words: semiconductors, digital simulation, photopotentials, photoeffects.

Table I. Comparison of differential and finite difference notation

Quantity	Differential notation	Finite difference notation
Distance, $x$		$(K - \frac{1}{2})\Delta x$
Migration flux of holes, $j_{p,m}$	$D_p \frac{\partial p}{\partial x}$	$\frac{1}{2} U_p E_K (p_K + p_{K-1})$
Diffusional flux of holes, $j_{p,d}$		$D_p (p_{K-1} - p_K)/\Delta x$
Electric field, $E$	$(1/\epsilon_0 \epsilon_r) \int_0^x Q(x) dx$	$(e\Delta x/\epsilon_0 \epsilon_r) \sum_{K=0}^{KMAX} (p_K - n_K + N_D - N_A)$
Recombination rate, $R(x)$ (e.g., for excess holes in an n-type semiconductor)*	$k_r n(x) (p(x) - p^{eq})$	$(n_K/\tau_p n_b) (p_K - p_K^{eq})$

\*  $\partial p(x)/\partial t = k_r n(x)p(x) - k_t$ , where  $k_r$  is the recombination rate constant given by  $1/\tau_p n_b$  and  $k_t$  is the formation constant, given by  $k_r n^{eq} p^{eq}$  (the superscript eq denotes the equilibrium concentrations in the n-type semiconductor). The equation in the table results when  $n^{eq} \approx n(x)$ .

boundary is taken as the average of that of the two adjacent elements [e.g.,  $\frac{1}{2}(p_K + p_{K-1})$ ]. A comparison of the differential and finite difference notation used in the simulation for expressing fluxes and other quantities of interest is given in Table I.

*Initial conditions. The Boltzmann distribution.*—The distribution of the carriers and the electric field in the semiconductor biased to a known potential (thus containing a known excess charge) and at equilibrium in the dark serves as the initial state preceding calculation of the photopotential. This equilibrium distribution is of fundamental importance in understanding and predicting the electrochemical behavior of semiconductor electrodes and is assumed to be essentially obeyed even in nonequilibrium situations (4-6). This distribution is usually obtained by using Fermi statistics for the occupancy of allowed energy states for which  $\exp[(E - E_F)/kT] \ll 1$  and which physically means that at low occupancy, spin requirements may be relaxed. In addition, the Poisson equation must be solved using charge density terms which are based on the equilibrium distribution of carriers as functions of a coordinate which is not yet explicitly known (7). In general, a closed-form explicit relation between the potential and its gradient cannot be obtained for a doped semiconductor (8). At equilibrium in the dark, there is no faradaic current and no excess free carriers to give nonequilibrium recombination effects. Thus Eq. [3] and [4] yield

$$j_p(x) = j_n(x) = 0 \quad (\text{for all } x) \quad [6]$$

and at the boundary of each element, the migrational flux is compensated by the diffusional one for both electrons and holes. Equating these fluxes using the digital-form equations in Table I and rearranging, we obtain

$$p_K = \frac{(D_p/\Delta x) - 0.5U_p E_K}{(D_p/\Delta x) + 0.5U_p E_K} p_{K-1} \quad [7]$$

$$n_K = \frac{(D_n/\Delta x) + 0.5U_n E_K}{(D_n/\Delta x) - 0.5U_n E_K} n_{K-1} \quad [8]$$

Equations [7] and [8] are used as recursion relations in an iterative computation beginning with the second element ( $K = 2$ ). For the first element (the semiconductor surface) the boundary conditions are (9)

$$p_1 = p^0 \exp(eV_s/kT) \quad [9a]$$

$$n_1 = n^0 \exp(-eV_s/kT) \quad [9b]$$

where  $V_s$  is the applied surface potential governing the distribution. The  $U$  and  $D$  values in Eq. [7] and [8] are related to each other via the Einstein relation

$$U (\text{cm}^2 \text{sec}^{-1} \text{V}^{-1}) = D/kT = 39D (\text{cm}^2 \text{sec}^{-1}) \quad [10]$$

at room temperature. A recursion relation for the electric field,  $E_K$ , which takes account of the semiconductor properties (dielectric constant, doping level) is obtained from Gauss' law

$$E_K = E_{K+1} + (e\Delta x/\epsilon_0 \epsilon_r) (p_K - n_K + N_D - N_A) \quad [11]$$

The boundary condition used with this relation is that in the bulk semiconductor ( $K \cong KMAX$ ),  $E_K = 0$ . The simulation proceeds by using the applied potential in the boundary condition, Eq. [9], and then calculating  $n_K$  and  $p_K$  ( $K = 1$  to  $KMAX$ ) assuming any arbitrary initial distribution (usually taken as a uniform one, i.e., a flatband condition). The  $E_K$  values are then calculated, using Eq. [11]. Alternate calculations of  $n_K$ ,  $p_K$ , and  $E_K$  are continued until the three arrays are constant with respect to further iterations. The resulting values, besides satisfying Eq. [7]-[11], also show the following features: (i) a numerical integration over the electric field from the bulk to the surface of the semiconductor yields the surface potential governing the distribution (which enters into the simulation only in assigning  $p_1$  and  $n_1$ ), thus demonstrating self-consistency in  $V_s$ ; (ii) the product  $p_K n_K$  is constant and equal to  $n_i^2$  (e.g., for Ge  $n_i^2 = 6.25 \times 10^{16} \text{cm}^{-6}$  at room temperature) for all  $K$ .

A problem arises in the selection of  $KMAX$ . If this value is too large, the simulation does not converge to a constant solution. Since the value of  $KMAX$ , representing the thickness of the space charge region, is not known in advance, an arbitrary value which will yield a solution is chosen and when a convergent solution is obtained,  $KMAX$  is increased. The calculation terminates with the highest value of  $KMAX$  which still gives a constant solution. Inspection of the result shows that only the very diffuse part of the space charge region, which contributes insignificantly (<1%) to the electrical state (fields, potentials) of the semiconductor cannot be displayed.

Note that in contrast to our previous simulation of space charge region formation in a semiconductor following charge injection which portrayed the time dependence of the fields and concentration profiles (1), the method employed here derives only the equilibrium properties at a given potential. The concept of time is omitted and the intermediate results have no physical meaning. Typical equilibrium concentration profiles of the mobile carriers in intrinsic and n-type Ge at several surface potentials obtained by the simulation are shown in Fig. 2-4. Figures 2 and 3 illustrate the final equilibrium situation under the same conditions as the relaxation results given previously (1). A comparison of the surface potential and space charge layer thickness (or Debye length) for a highly doped semiconductor obtained by the approximate "depletion layer" treatment, which underlies the Schottky-Mott plot (10), and our calculation is given in Table II. Note that the approximation becomes less applicable at low potentials when the concentration of the existing carriers in the space charge region cannot be neglected. Other related properties of the space charge at equilibrium, e.g., surface conductivity and capacitance, can be calculated as well using the simulation results. The space charge region capacitance is obtained as the additive contribution of the individual space charge elements connected in series, each having a capacitance of  $C_K = q_K/E_K \Delta x$  where  $q_K$  is the charge in element  $K$ . The surface conductivity may be deduced by considering

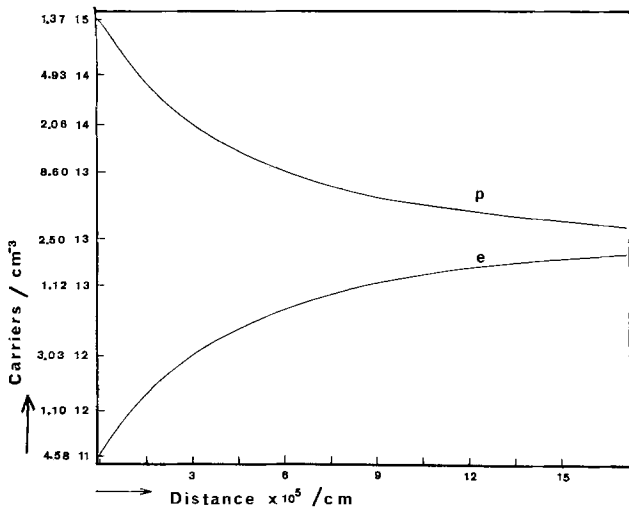


Fig. 2. Carrier concentration at equilibrium for intrinsic Ge.  $V_s = 100$  mV;  $p^0 = n^0 = 2.5 \times 10^{13}$  cm $^{-3}$ ;  $\epsilon_r = 16$  esu.

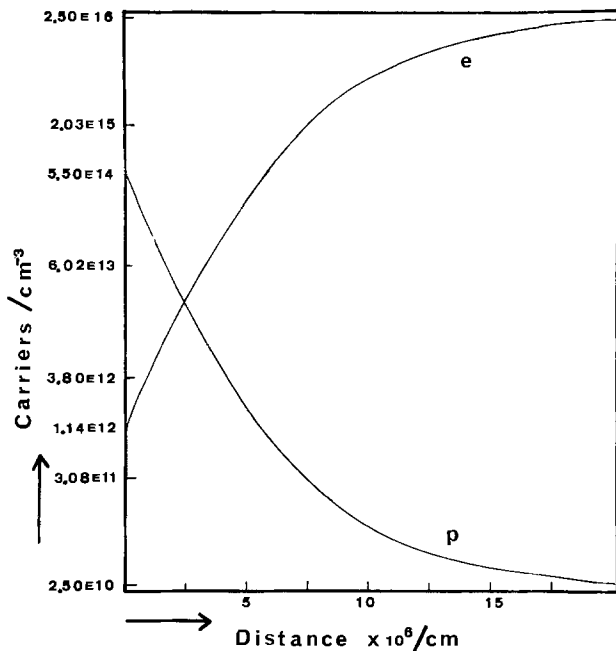


Fig. 3. Carrier concentration at equilibrium for n-type Ge.  $V_s = 250$  mV;  $n^0 = 2.5 \times 10^{16}$ ;  $p^0 = 2.5 \times 10^{10}$ ;  $\epsilon_r = 16$  esu.

the elements as representing resistors connected in parallel, each with a conductivity of  $e\Delta x(U_n n_K + U_p p_K)$ .

*The photopotential effect.*—Assume the initially biased semiconductor (now at open circuit) is illuminated with a constant light intensity. We now calculate the open-circuit, steady-state photopotential using an iterative procedure similar to that just described. A treatment of the time-dependent relaxation of carrier concentration, field, and surface potential under closed-circuit conditions is treated in the next paper in this series (11). The process at open circuit is a coulstatic one; charge in the semiconductor is conserved and the effect of light is simply to rearrange the concentration and field profiles within the semiconductor. (The same would hold true even when a faradaic current flows, if the number of holes crossing the interface is balanced by electrons extracted at the semiconductor ohmic contact or vice versa.) Consider an n-type semiconductor biased at a positive potential with respect to the solution. Under illumination the photogenerated holes will accumulate at the semiconductor surface and the electrons will move to the space charge region/semicon-

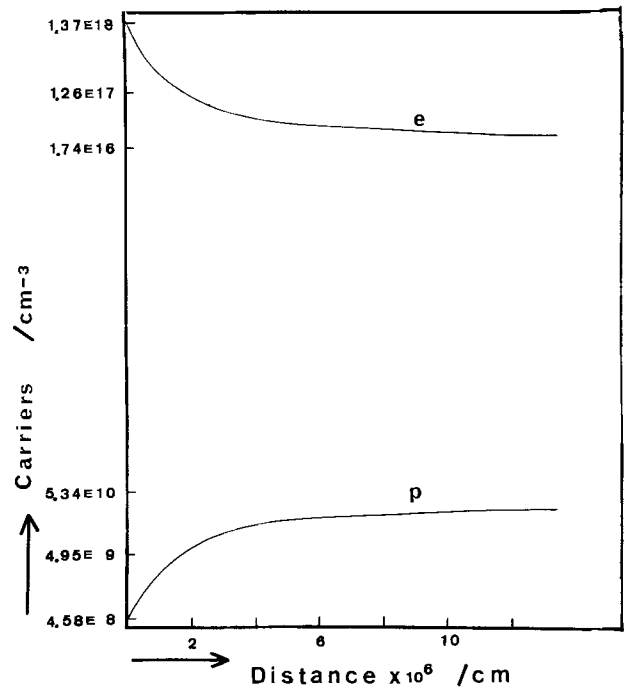


Fig. 4. Carrier concentration at equilibrium for n-type Ge (sample as in Fig. 2).  $V_s = -100$  mV.

ductor bulk boundary. The dimensions of the space charge region will change to accommodate these shifts in carrier concentration. The total charge, and hence the surface field, will remain constant, so that the semiconductor space charge region can be compared to a capacitor with a given charge which undergoes a decrease in its width resulting in an increase in capacitance and thus a decrease in the voltage drop across it under illumination. The steady state is characterized by the value of  $E_s$ , the surface field, known from the initial condition (Boltzmann distribution), and by the "minority injection level," here, the hole concentration immediately beyond the space charge region, which is directly proportional to illumination intensity. Analytical procedures exist for the rigorous determination of the injection level of minority carriers (here, holes) (12). For Ge, one can assume the existence of a diffusion layer,  $L_p$ , through which excess holes diffuse into the bulk (where  $L_p = \sqrt{D_p \tau_p}$ ).  $L_p$  is much wider than the space charge region thickness ( $L_1$ ) and if light is absorbed mainly in the space charge region, the expression obtained for the flux of holes at the space charge region/bulk boundary ( $x = L_1$ ) is (3)

$$j_p(L_1) = D_p(\partial(\Delta p)/\partial x)_{x=L_1} = D_p(p_{L_1} - p^0)/L_p \quad [12]$$

Table II. Comparison of the simulated electrical properties of a large bandgap semiconductor electrode (n-type TiO $_2$ ) and the electrostatic approximation of the depletion layer\*

$Q_s$ C/cm $^2$ ( $\times 10^7$ )	Simulated			Depletion layer approximation	
	$E_s$ , V/cm ( $\times 10^{-4}$ )	$L_1$ , cm ( $\times 10^6$ )	$V_s$ , V	$L_1^{**}$ , cm ( $\times 10^6$ )	$V_s^{***}$ , V
1.485	1.677	1.56	0.100	0.928	0.078
2.243	2.533	1.92	0.200	1.40	0.178
3.249	3.670	2.36	0.393	2.03	0.373
4.001	4.519	2.76	0.585	2.50	0.565
4.675	5.774	3.16	0.777	2.89	0.755
5.166	5.835	3.36	0.963	3.23	0.943
5.752	6.496	3.76	1.188	3.595	1.168
6.271	7.083	4.00	1.408	3.91	1.388

\* Assumed to consist of only immobile donors;  $N_D = 10^{17}$  cm $^{-3}$ ;  $\epsilon_r = 100$  esu.  
 \*\*  $L_1 = Q_s/l \cdot N_D$  (depletion layer width).  
 \*\*\*  $V_s = E_s/2L_1$  ( $E_s$ , surface field;  $V_s$ , surface potential).

From Eq. [3] this same flux is given by

$$j_p(L_1) = -I_0(1 - e^{-aL_1}) + \int_0^{L_1} R(x)dx \quad [13]$$

Equations [12] and [13] allow the assignment of an initial value to  $p_{L_1}$  (assuming at first no recombination in the space charge region) which is modified during the simulation due to the recombination term, using the given values of  $I_0$ ,  $a$ , and the semiconductor properties ( $D_p\tau_p$ ). The equivalent expression for the electrons is

$$n_{L_1} = n^0 + (p_{L_1} - p^0) \quad [14]$$

because in this region electroneutrality essentially holds (13). In more complicated cases, when  $L_p$  and  $L_1$  are comparable in magnitude, light is absorbed outside the space charge region as well and linearization of the diffusion layer is unjustified. In this case a simulation involving a fuller treatment of the diffusion layer can be undertaken to find the injection level.

$p_{L_1}$  and  $n_{L_1}$  serve as boundary conditions for the recursion formula between the elements, this time taken from the space charge region/semiconductor bulk boundary to the surface which at the steady state, according to Eq. [3] and [4] and Table I, is given by

$$p_K = \frac{L(K) - \Sigma R(K) + [0.5 U_p E_{K+1} + (D_p/\Delta x)] \cdot p_{K+1}}{(D_p/\Delta x) - 0.5 U_p E_{K+1}} \quad [15a]$$

$$n_K = \frac{L(K) - \Sigma R(K) - [0.5 U_n E_{K+1} - (D_n/\Delta x)] \cdot n_{K+1}}{(D_n/\Delta x) - 0.5 U_n E_{K+1}} \quad [15b]$$

where

$$L(K) = I_0(1 - e^{-a(K-\frac{1}{2})\Delta x}) \quad [\text{cm}^{-2}\text{sec}^{-1}] \quad [16]$$

$$\Sigma R(K) = \sum_{K=1}^K \left( \frac{p_K - p_K^{\text{eq}}}{\tau_p} \frac{n_K}{n^0} \Delta x \right) \quad [\text{cm}^{-2}\text{sec}^{-1}] \quad [17]$$

The electric fields are calculated with Eq. [11], this time proceeding from the surface to the bulk because the surface field is known.

Thus, starting with the semiconductor in the dark at a surface potential  $V_s$ , the condition under illumination is simulated by repetitively using Eq. [12]-[17] until three new constant arrays (holes, electrons, and electric field) are obtained. A numerical integration over the fields yields a new surface potential,  $V_s'$ , where the photopotential,  $\Delta V$ , is  $V_s - V_s'$ .

## Results

The simulated distribution of carriers with and without illumination is shown in Fig. 5; Fig. 6 compares the electric fields under these conditions. The dependence of the photopotential on the equilibrium surface potential which exists before illumination obtained by the simulation compared to the calculation method of Johnson (4) is given in Fig. 7 and the relation between the photopotential and the illumination intensity obtained by these two methods is shown in Fig. 8. Johnson's method of obtaining the photopotential usually uses the assumption that the Boltzmann distribution and the same analytical expression relating the potential and the field for the semiconductor holds both in the dark and as well as in the light (3, 4). This assumption was checked by the digital simulation and indeed we find that Eq. [18] and [19] hold

$$p_s' \simeq p_{L_1}' \exp(eV_s'/kT) \quad [18]$$

$$n_s' \simeq n^0 \exp(eV_s'/kT) \quad (n_{L_1}' \simeq n^0) \quad [19]$$

where the primed quantities denote values under illumination. This assumption applies, as has been pointed out previously (12), because there is fast trans-

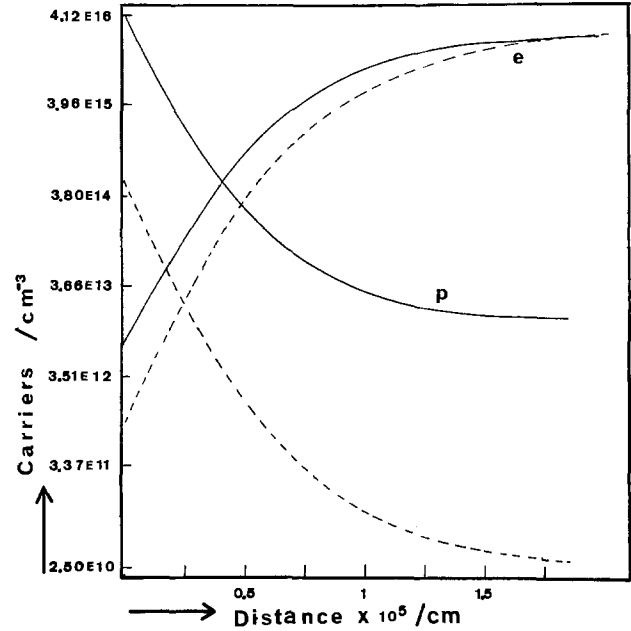


Fig. 5. Carrier concentration at steady state with constant illumination for n-type Ge (sample as in Fig. 3).  $I_0 = 10^{16}$  photons/cm<sup>2</sup>-sec,  $V_s$  (dark) = 250 mV. The dashed lines show the equilibrium concentration in the dark.

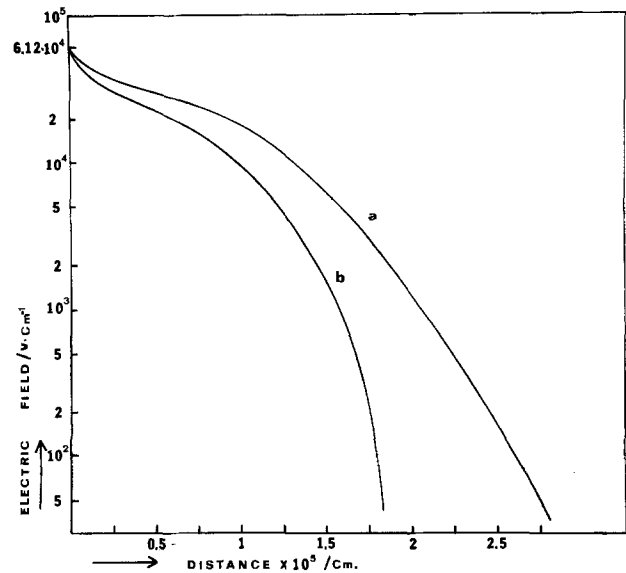


Fig. 6. Electric fields for n-type Ge (sample as in Fig. 3): (a) in the dark and (b) under constant illumination,  $I_0 = 10^{16}$  photons/cm<sup>2</sup>-sec.  $V_s$  (dark) = 400 mV.

port within the semiconductor phase. Thus only a very slight imbalance between the diffusional and the migrational fluxes (compared to their absolute magnitude) has to exist to provide the nonequilibrium flux which corresponds to moderate illumination. Hence, in practice, even under illumination, the carriers and electrical field will be distributed in such a way that  $u_i n_i E_i \simeq D_i (\partial n_i / \partial x)$ , which leads to the same functional relation as in the dark.

## Acknowledgment

The support of this research by the National Science Foundation (MPS74-23210) is gratefully acknowledged.

Manuscript submitted Feb. 3, 1976; revised manuscript received Feb. 7, 1976.

Any discussion of this paper will appear in a Discussion Section to be published in the June 1977 JOURNAL. All discussions for the June 1977 Discussion Section should be submitted by Feb. 1, 1977.



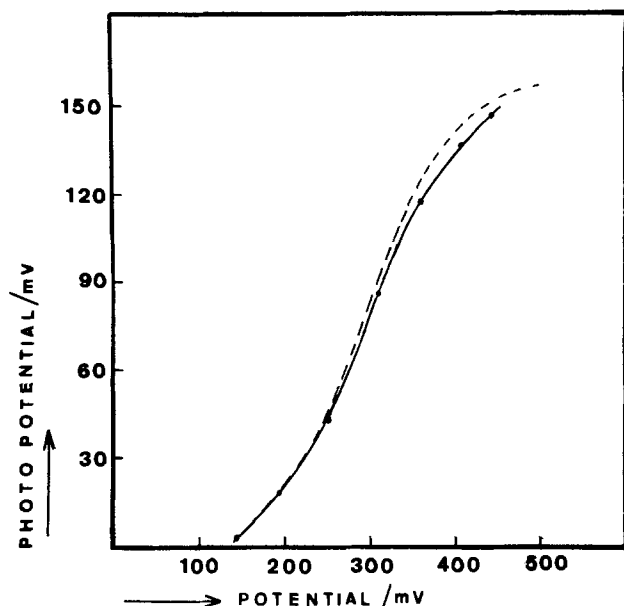


Fig. 7. The dependence of the photopotential for n-type Ge (sample as in Fig. 3) on dark surface potential  $V_s$ ;  $I_0 = 10^{16}$  photons/cm<sup>2</sup>-sec. Dashed line, calculated according to Johnson's method (4) assuming  $pL_1 = 1.3 \times 10^{13}$  cm<sup>-3</sup> (see text).

Publication costs of this article were assisted by The University of Texas at Austin.

#### REFERENCES

1. D. Laser and A. J. Bard, *This Journal*, **123**, 1828 (1976).
2. M. D. Archer, *J. Appl. Electrochem.*, **5**, 17 (1975).
3. C. G. B. Garrett and W. H. Brattain, *Phys. Rev.*, **99**, 376 (1955).
4. E. O. Johnson, *ibid.*, **111**, 153 (1958).
5. S. W. Feldberg, in "Electroanalytical Chemistry,"

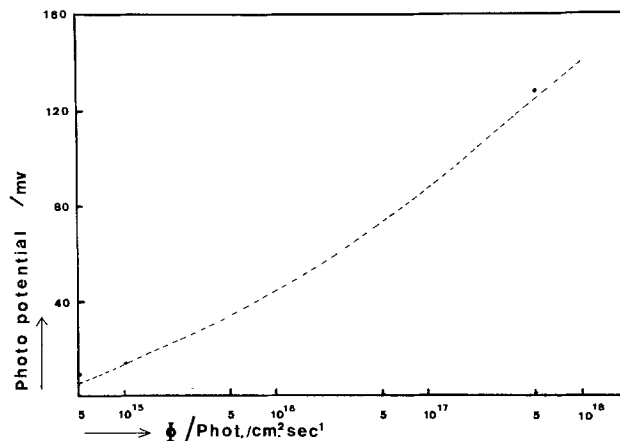


Fig. 8. Dependence of photopotential for n-type Ge (sample as in Fig. 2) on illumination intensity.  $V_s$  (dark) = 250 mV. Points are simulations and the dashed line was calculated by Johnson's method (4) assuming that the injection level was proportional to the light intensity and was  $1.3 \times 10^{13}$  cm<sup>-3</sup> at an illumination intensity of  $10^{16}$  photons/cm<sup>2</sup>-sec.

- Vol. 3, A. J. Bard, Editor, chap. 4, Marcel Dekker, Inc., New York (1969).
6. H. Gerischer, *This Journal*, **113**, 1174 (1966).
7. V. A. Myamlin and Yu. V. Pleskov, "Electrochemistry of Semiconductors," pp. 30-50, Plenum Press, New York (1967).
8. A. Many, Y. Goldstein, and N. B. Grover, "Semiconductor Surfaces," chap. 4, John Wiley & Sons, Inc., New York (1965).
9. V. A. Myamlin and Yu. V. Pleskov, *op. cit.*, p. 18.
10. *Ibid.*, p. 55.
11. D. Laser and A. J. Bard, *This Journal*, **123**, 1837 (1976).
12. A. Rothwarf and K. W. Böer, "Progress in Solid State Chemistry," Vol. 10, p. 71, Pergamon Press, Oxford (1975).
13. V. A. Myamlin and Yu. V. Pleskov, *op. cit.*, p. 182.

## Semiconductor Electrodes

### IX. Digital Simulation of the Relaxation of Photogenerated Free Carriers and Photocurrents

Daniel Laser and Allen J. Bard\*

Department of Chemistry, The University of Texas at Austin, Austin, Texas 78712

#### ABSTRACT

A digital simulation of the photoprocess at a semiconductor electrode is described. The simulation model accounts for photogeneration, recombination, and transport of excess free carriers within the semiconductor phase. The origin of the photopotential in the absence of faradaic current is elucidated. Quantitative current efficiency-potential curves for the photocurrents under a variety of conditions are calculated for n-type TiO<sub>2</sub> and these are compared to experimental results.

In previous papers in this series we have introduced the use of digital simulation methods for the treatment of semiconductor electrodes. In Ref. (1) the relaxation of free carriers following charge injection, with and without surface states, was described. In Ref. (2) a method of deriving the semiconductor electrode characteristics, equilibrium or steady state, at open circuit in the dark or under constant illumination, was presented. When a semiconductor electrode at equilibrium and in contact with solution is illuminated, a certain

time elapses before the photoeffects are observed. During this time a redistribution of free carriers and charges in the electric field in the space charge region occurs. [When the semiconductor electrode/solution interface is blocked to charge transfer, the new distribution of free carriers in the space charge region under illumination will cause a change in the potential of the electrode (the photopotential effect).] Frequently, illumination of the electrode is accompanied by charge transfer to solution species and this gives rise to a photocurrent. For example, irradiation of n-type TiO<sub>2</sub> with light of energy larger than the bandgap energy will result in the oxidation of water (3, 4), while

\* Electrochemical Society Active Member.

Key words: semiconductors, digital simulation, photoelectrochemistry, photogalvanic cells.

cathodic photocurrents arise at p-type semiconductor electrodes (5, 6). Numerous examples of photogalvanic effects and analytical treatments of these have been given (7, 8)

In this paper we treat the transient behavior of a semiconductor electrode following the onset of illumination and the photocurrents which are produced. The semiconductor electrode characteristics which affect the magnitude of the photocurrent are discussed and a comparison of the simulated light intensity-current and current-potential behavior with some experimental results given.

### Relaxation of Photogenerated Carriers in the Absence of Faradaic Current: Physical Model

The rate of change of the concentration of excess free carriers (e.g., holes, the minority carriers in an n-type semiconductor) during illumination is governed by their rate of generation by the adsorbed light, their recombination, and their transport

$$\partial \Delta p / \partial t = g(x) - (1/\tau_p) (n(x)/n_b) \Delta p + D_p (\partial^2 \Delta p / \partial x^2) + U_p \partial [\Delta(E \cdot p)] / \partial x \quad [1]$$

where  $\Delta p = p(x) - p(x)^{eq}$ ,  $\Delta E = E(x) - E(x)^{eq}$ . A similar expression can be written for excess electrons,  $\Delta n$ . The electrical field vector in the  $x$  direction is governed by Gauss' law

$$\frac{d\Delta E(x)}{dt} = \frac{e}{\epsilon_0 \epsilon_r} \int^x \left[ \frac{d}{dt} (p - n) \right] dx \quad [2]$$

Equations [1] and [2] were written in finite difference form by using the same space division and representation of fluxes given in Table I of Ref. (2); the actual expressions are given in the Appendix. The general notation and the terms in Eq. [1] and [2] are the same as those given in Ref. (1) and (2) and are discussed only briefly here. The generation function for free carriers by light,  $g(x)$ , can be written as

$$g(x) = I_0 a \exp(-ax) \quad [\text{cm}^{-3}\text{-sec}^{-1}] \quad [3]$$

$I_0$  is the incident light flux at the electrode surface ( $\text{cm}^{-2}\text{-sec}^{-1}$ ) and  $a$  is the absorptivity of the light [ $\text{cm}^{-1}$ ]. We assume here that all of the light absorbed leads to free carrier formation. The treatment is easily modified for less than unit efficiency of carrier formation by the introduction of a quantum efficiency factor. The term  $(1/\tau_p)\Delta p$  is the usual expression (9) for the recombination rate of excess minority free carriers in the semiconductor bulk, where the process is assumed to be pseudo-first order with respect to the excess minority carriers (i.e.,  $1/\tau_p = k_r n_b$ , where  $n_b$  is the bulk concentration of electrons and  $k_r$  is the second order recombination rate constant). The term  $n(x)/n_b$  is introduced to account for this effect inside the space charge region, where the concentration of electrons is not equal to the bulk value. The last two terms on the right-hand side of Eq. [1] are the divergence of the flux of excess free carriers by diffusion and migration. For a numerical calculation of the migration term, the properties of the semiconductor at equilibrium [ $p(x)^{eq}$ ,  $E(x)^{eq}$ ] have to be known. Similarly, calculation of the recombination term requires knowledge of  $n(x)^{eq}$ , in addition to  $\Delta n(x)$ . Thus, a simulation of the semiconductor electrode free carrier and electric field distribution in the dark at a given potential  $V_s$ , as given in Ref. (2), provides the initial conditions which precede simulation of the photoeffects. The usual simulation techniques were employed [see the Appendix and Ref. (10) and (11)]. Changes in  $\Delta p$  and  $\Delta n$  which occur during a short time interval,  $\Delta t$ , based on the carrier concentrations and fields from the previous time interval, were calculated. These changes are used to calculate new values of  $p(x)$  and  $n(x)$ , as well as a new field distribution  $E(x)$ , by Eq. [2]. These new values are then used for calculation of the values of

$\Delta p$  and  $\Delta n$  in the next time interval, etc. The distribution of excess free carriers and electric field are mutually dependent, since  $E(x)$  depends upon the charge and the migration of the free carriers depends upon the field.

### Results

The distributions of excess carriers for an n-type  $\text{TiO}_2$  electrode at two different times after the onset of illumination are shown in Fig. 1. In this example, the n- $\text{TiO}_2$  electrode at equilibrium in the dark was assumed to be initially biased positively ( $V_s = 0.8\text{V}$ ) to form a depletion layer. In the time interval considered, only very slight changes in electric field are observed. The changes in the charge density distribution, although noticeable, are still very small compared to the charge density at equilibrium or to the changes in charge density which exist at the steady state. Consider some aspects of the relaxation process which can be observed from the transient behavior. The generation function is an exponential one with respect to distance from the surface so that with the semilog axes of Fig. 1 it would be drawn as a straight line with a slope of  $-a$ . However, except for the very first instants following the onset of illumination, the shape of the perturbation (the light generation function) is not apparent. Because of the rapidity of the transport processes in the semiconductor phase, the distribution of excess free carriers reflects rather the momentary existing driving forces (electric fields and concentration gradients). Thus, the excess holes accumulate at the semiconductor surface (assuming no outlet to solution), while the electrons accumulate near the space charge region/bulk boundary. At this stage, some of the holes which are produced outside the space charge region and which escape recombination enter the space charge region by diffusion. Only at a later time, when the surface concentration of holes increases further, are they reflected back from the surface by diffusion, so that at the steady state [as in Ref. (2)] a flux of holes leaves the space charge region toward the bulk. At this time the concentration excess of holes outside the space charge region is about equal to the concentration excess of electrons ( $\Delta n = \Delta p$ ). This steady-state situation could not be achieved within the time domain of the transient simulation. The reason for this will be discussed in some detail, because it is directly related to the general problem of simulation of the photo-process. The steep concentration and field profiles which exist inside the space charge region require a

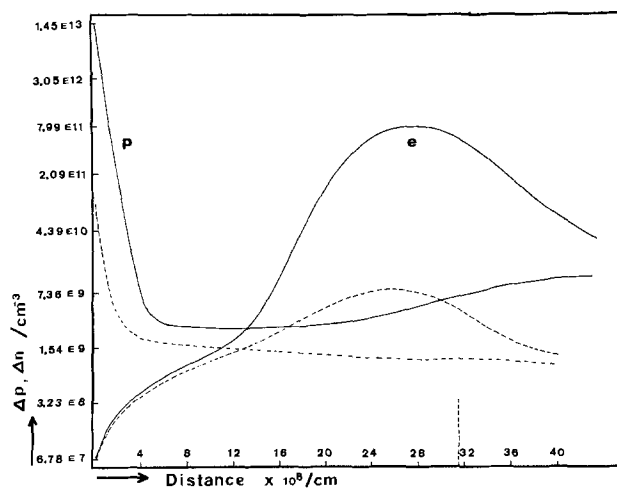


Fig. 1. Excess carrier concentrations in n-type  $\text{TiO}_2$  (dashed line)  $1.44 \times 10^{-11}$  sec and (solid line)  $1.16 \times 10^{-9}$  sec after turning on illumination ( $10^{16}$  photons  $\text{cm}^{-2}$   $\text{sec}^{-1}$ ).  $V_s = 0.8\text{V}$  (in dark);  $n^0 = 10^{17}$   $\text{cm}^{-3}$ ;  $p^0 = 0$ ;  $\epsilon_r = 100$  esu;  $U_n = 100$  and  $U_p = 50$   $\text{cm}^2\text{-sec}^{-4} \cdot \text{V}^{-1}$ ;  $a = 5 \times 10^4$   $\text{cm}^{-1}$ ;  $\tau_p = 10^{-9}$  sec. Vertical dashed line shows space charge region/bulk semiconductor boundary.

fine division of space elements ( $\Delta x \approx 20\text{-}50\text{\AA}$ ) to represent the quantities there to a sufficient accuracy in the digital simulation. Because of this, combined with the high value of the transport coefficients of the free carriers, a very short time interval must be used as a simulation time step (ca.  $10^{-14}$  sec) and the total simulated time is limited to the nanosecond range even after  $10^5$  simulation steps. For reasonable fluxes of light to be calculated (e.g.,  $10^{16}$  photons  $\text{cm}^{-2} \text{sec}^{-1}$ ), the excess of free carriers added to the space charge region within this time interval is far smaller than the amount which will be present there at the steady state to produce the photopotential. An attempt to overcome this problem by using higher light fluxes or slower transport coefficients (which, numerically, have the same effect) results in a distorted picture in which the generation of carriers is very exaggerated with respect to their transport. Thus the transport processes (migration and diffusion) dominate all others. The speed at which these driving forces, especially inside the space charge region, dissipate a large portion of any local perturbation (provided it is not too large) is what underlies the possibility of using the Boltzmann distribution in cases where actual equilibrium does not exist (7, 8). The simulated transient behavior allows us to deduce the sequence of events which leads to the steady state and causes the photopotential effect. This is shown schematically in Fig. 2. The charge density distributions at equilibrium in the dark and under illumination are given in Fig. 2a. Figure 2b shows the redistribution of the charge density caused by the changes  $\Delta p$  and  $\Delta n$  in the light. The total charge is conserved and so is the surface field, but its distribution shows an accumulation of positive charge at the surface and a loss of positive charge at the space charge region/bulk boundary (where the excess of electrons which accumulate there compensates for the

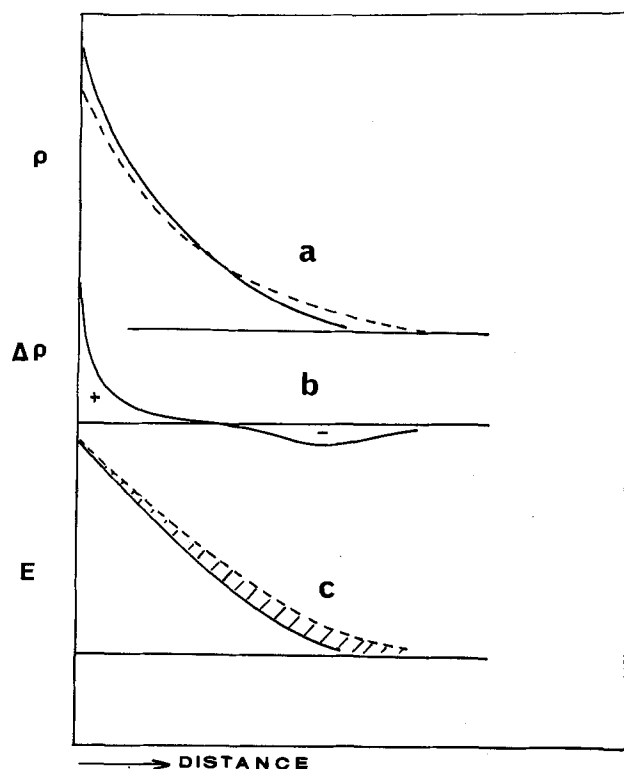


Fig. 2. Schematic representation of the production of the photopotential. (a) Charge density ( $\rho$ ) distribution in the space charge region (dashed line) in the dark; (solid line) under illumination. (b) Excess charge density distribution with illumination due to redistribution of excess carriers as shown in Fig. 1, ( $\Delta\rho^+ = \Delta\rho^-$ ). (c) Electrical field (dashed line) in the dark and (solid line) under illumination. The area between the curves represents the photopotential.

diffuse positive charge of the space charge region). The corresponding electric field distributions are shown in Fig. 2c. The area between the field curves, i.e., the integration of the difference in the electric field with respect to distance from the bulk semiconductor to the surface, is the decrease in surface potential due to illumination, the photopotential

### Photocurrent in the Absence of Kinetic Complications

If charge transfer across the semiconductor/solution boundary is possible, the situation differs from the open-circuit case described above. Two extreme cases can be considered. If the rate constant for charge transfer is infinitesimal, the open-circuit case, which is characterized by very small faradaic currents and the photopotential effect, is approached. At the other extreme, if the charge transfer to solution is limited only by the combined effect of generation/recombination and transport of carriers within the semiconductor phase, only a small accumulation of excess free carriers occurs leading to a smaller photopotential and larger faradaic currents. Thus, the rate constant for charge transfer to solution will have a key role in determining both the photocurrent and the electrical state of the semiconductor.

We simulate here the fast charge transfer case and calculate the photocurrent which is determined by the processes within the semiconductor phase. We use n-type  $\text{TiO}_2$ , a stable semiconductor electrode for which the photocurrent has been widely described (3, 4), as a model. The very low concentration of minority carriers (holes) in this sample somewhat simplifies the calculation because no oxidation current (hole injection to solution) exists in the dark.

The photocurrent density due to photogenerated holes within the semiconductor biased to positive potentials is expressed as the product of the charge transfer rate constant  $k_p$  ( $\text{cm}\cdot\text{sec}^{-1}$ ) and the hole concentration at the surface ( $x = 0$ ) (or in the simulation for space element,  $K = 1$ )

$$i_{p,t} = ek_p p(o) \quad [4]$$

The rate constants were chosen to be sufficiently large that the steady photocurrent calculated in the simulated time domain was independent of the value of  $k_p$ . The surface concentration of holes was found to be inversely proportional to  $k_p$ . The effect of the magnitude of  $k_p$  is shown in Fig. 3. The electron distribution is also affected by  $k_p$ , because for every hole which is injected into the solution, an electron is collected by the metallic contact to the semiconductor electrode

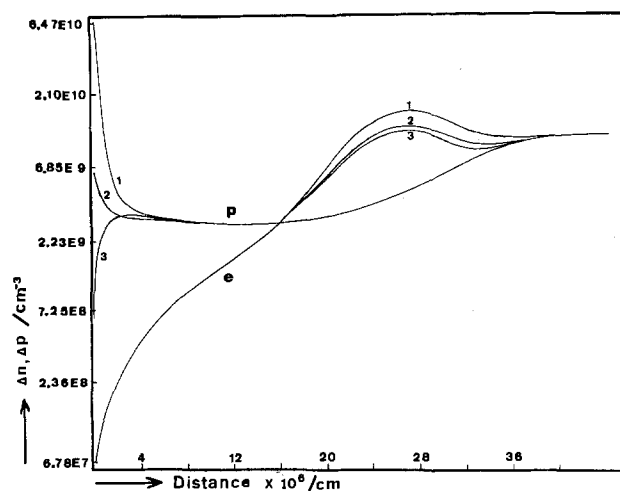


Fig. 3. Effect of  $k_p$  on the concentration profiles of excess free carriers. All conditions as in Fig. 1, except with holes transfer to solution with  $k_p$  values of (1)  $1.39 \times 10^5$ ; (2)  $1.39 \times 10^6$ ; (3)  $1.38 \times 10^7$  cm/sec. In all cases the calculated photocurrent,  $i_{p,t}$ , was 1.437 mA.

and is delivered to the counterelectrode. Although the effect of  $k_p$  is most prominent at the semiconductor surface, it also determines the whole level of excess holes inside the space charge region and hence the flux of holes which will enter this region. Under actual conditions the situation may be far more complex because  $k_p$  may depend upon the potential drop in the Helmholtz layer at the semiconductor/solution interface,  $\Delta\phi_H$ , e.g., it could be given by  $k_p^\circ \exp(\beta e \Delta\phi_H / kT)$  and where  $k_p^\circ$  may have a much smaller value than that used in the simulation. At the instant after illumination only a small photocurrent is expected, resulting in a pronounced accumulation of excess carriers in the space charge region, in a manner similar to that for the open-circuit case. This accumulation causes a photopotential to be built up gradually, which in a potentiostatic experiment will result in a gradual change in  $\Delta\phi_H$  and in an increase in  $k_p$ . At the steady state the charge transfer rate will be sufficiently fast to prevent any further accumulation of excess free carriers inside the space charge region. We did not simulate this suggested sequence of events which extends over two completely different time domains. Moreover,  $k_p$  could not be made too small because under these conditions, even after a lengthy computation, a steady state was not achieved. Therefore, we can only speculate that as long as migration is the predominant driving force (high fields and band bending) and  $k_p$  is not so small that a high accumulation of excess carriers is produced inside the space charge region thus changing considerably the fields there, only a minor dependence of photocurrent on  $k_p$  is expected. At low band bending, on the other hand (which would usually occur at the foot of the photocurrent-potential wave), diffusion may be the main transport process. The photocurrent will then strongly depend upon the diffusional flux of the holes inside the space charge region and towards the surface, which in turn will be determined by the concentration profile present and thus on  $k_p$ .

### Results

Photocurrent-potential curves assuming rapid charge transfer to solution under several different sets of conditions were simulated (Fig. 4). Curve a represents the steady-state currents for the electrode initially (in the dark) held at the indicated potential where all of the imposed potential is assumed to drop inside the semiconductor space charge region. No photopotential is observed. The dashed line a shows the calculated curve if electrons are allowed to cross the surface as well, to reduce the species just formed by the hole injection process, or to react with holes at the surface at a rate which is proportional to the absolute concentration of electrons at the surface. Both processes will have the same effect in reducing the net oxidation current. This back-reaction effect could be of importance, since the photosensitized oxidation at the semiconductor electrode frequently produces a species which is thermodynamically reducible at the electrode potential. For any value for the rate constant,  $k_n$ , chosen for this "back-reaction" effect, the observed photocurrent is found to rise very steeply (almost discontinuously) with potential. This steep rise is caused by the fact that the absolute electron concentration at the surface is an exponential function of potential. Such abrupt rises in photocurrent are not observed experimentally. A calculation in which the excess of electrons at the surface, rather than their absolute numbers, determines their contribution to the photocurrent is shown as curve a". A simple model for surface recombination, similar to that which was presented previously (1) results in the expression

$$i_f = e[k_p \Delta p(o) - k_n \Delta n(o)] \quad [5]$$

For the case under consideration, for holes,  $\Delta p \approx p$ , while for electrons,  $\Delta n = n - n^{eq}$ . This effect modifies somewhat the foot of the photocurrent-potential wave.

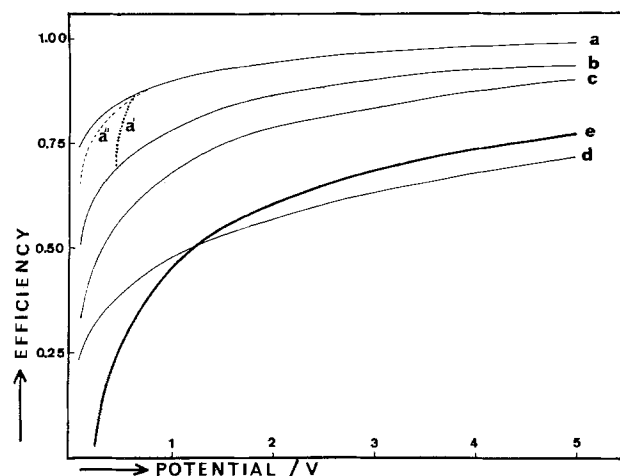


Fig. 4. Simulated photocurrent-potential curves for n-TiO<sub>2</sub>. Electrode as in Fig. 1,  $I_0 = 10^{16}$  photons  $\text{cm}^{-2}\text{sec}^{-1}$ ,  $k_p = 2.78 \times 10^6$   $\text{cm}^2/\text{sec}$ , except as noted below. Efficiency =  $i_{p,f}/I_0$ , with  $i_{p,f}$  given in holes per second. (a)  $\tau_p = 10^{-9}$  sec; (a') as in (a), assuming electrons cross to solution at a rate proportional to their absolute number at the surface, with a rate constant  $k_n = 1.39 \times 10^6$   $\text{cm}^2/\text{sec}$ ; (a'') as in (a) assuming electrons cross to solution at a rate proportional to their excess number at the surface,  $k_n = 1.39 \times 10^6$   $\text{cm}^2/\text{sec}$ ; (b) as in (a''),  $a = 3 \times 10^4$   $\text{cm}^{-1}$ ; (c) as in (b),  $\tau_p = 10^{-10}$  sec; (d)  $a = 3 \times 10^4$   $\text{cm}^{-1}$ ,  $\tau_p = 5 \times 10^{-11}$  sec,  $n^0 = 4 \times 10^{17}$   $\text{cm}^{-3}$ ; (e) experimental efficiency curve for a single crystal TiO<sub>2</sub> for water photo-oxidation (c axis normal to solution) measured at 375 nm; solution pH = 4.0; the potential axis in this case is the electrode potential vs. SCE.

At more positive potentials the excess of surface electrons is negligible (since they are repelled from the surface) compared to the excess of holes, and no "back-reaction" effect is noticed.

Two other factors govern the photocurrent and enter into the simulation. The first is the bulk recombination rate constant for the excess minority carriers ( $1/\tau_p$ ). This influences the number of holes which are generated outside the space charge region which will be collected by the space charge region and delivered to the surface. Photogenerated holes which are produced at a distance greater than  $\sqrt{\tau_p D_p}$  from the space charge region/bulk boundary are practically lost and will not contribute to the photocurrent. The effect is illustrated by Fig. 5. An extremely high bulk recombination rate constant can even reverse the direction of

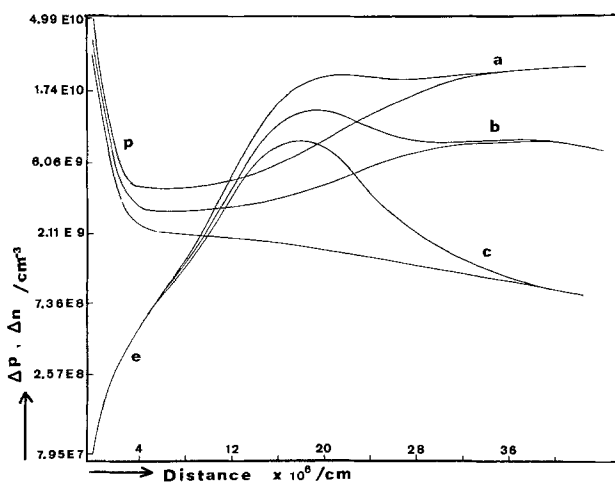


Fig. 5. Effect of bulk recombination rate constant for excess holes on the photocurrent and concentration profiles of excess free carriers. Electrode and illumination as in Fig. 1;  $V_s = 0.4V$ . (a)  $\tau_p = 10^{-9}$  sec,  $i_{p,f} = 1.096$  mA; (b)  $\tau_p = 10^{-10}$  sec,  $i_{p,f} = 0.8881$  mA; (c)  $\tau_p = 10^{-11}$  sec,  $i_{p,f} = 0.7186$  mA.

diffusion of holes, resulting in a hole flow from the space charge region to the bulk semiconductor. A second factor, directly related to the first, is the relative dimension of the space charge region to the light penetration depth. A more efficient photoprocess will be observed if practically all of the photogeneration process of free carriers occurs within the space charge region where the excess of holes suffer very little recombination and are delivered promptly to the surface by migration. The depletion layer thickness is determined by the potential imposed on the semiconductor electrode and its width can be taken as being proportional to the square root of the imposed potential (12). The upper quantum efficiency limit, which asymptotically approaches unity, represents the situation of a high surface potential resulting in an extended space charge region in which all of the light is absorbed. All of these simulated observations are consistent with Gartner's approximate treatment of the subject (12). Curves b, c, and d in Fig. 4 show the calculated results for variations in  $a$ ,  $\tau_p$ , and  $N_D$  (which influences the thickness of the space charge region). Curve e shows an experimental efficiency curve measured at a single crystal of  $\text{TiO}_2$  in a  $\text{pH} = 4.0$  solution with a monochromatic light of wavelength 375 nm. While the calculated saturation current can be adjusted to fit the experimental one, a larger discrepancy is revealed between the simulated and the experimental curve on the rising portion of the wave. A better fit to the experimental results will probably require consideration of the previously discussed kinetics of the charge transfer and other solution processes as well.

#### Acknowledgment

The support of this research by the National Science Foundation (MPS74-23210) is gratefully acknowledged.

Manuscript submitted Feb. 3, 1976; revised manuscript received Feb. 7, 1976.

Any discussion of this paper will appear in a Discussion Section to be published in the June 1977 JOURNAL. All discussions for the June 1977 Discussion Section should be submitted by Feb. 1, 1977.

Publication costs of this article were assisted by The University of Texas at Austin.

#### APPENDIX

Equation [1], the corresponding equation for electrons, and Eq. [2] were simulated according to the procedure shown in the Appendix of Ref. (1) and the space division and digital notation which were used in Table I of Ref. (2). For holes in the case of n- $\text{TiO}_2$ , with a bandgap of 3.0 eV, we can write

$$p^{\text{eq}}\Delta E \simeq 0 \quad \text{and} \quad \Delta p\Delta E \simeq 0 \quad [\text{A-1}]$$

$p^0 = p^{\text{eq}} \simeq 0$  across the whole semiconductor. The change of concentration of holes in element  $K$  within a time interval  $\Delta t$  is

$$\begin{aligned} \Delta p_K = & L_K - (\Delta t/\tau_p) \cdot (n_K/n_b) \cdot p_K \\ & + DMP(p_{K-1} - 2p_K + p_{K+1}) \\ & + 0.5 UMP \{E_{K+1}(p_K + p_{K+1}) - E_K(p_K + p_{K+1})\} \end{aligned} \quad [\text{A-2}]$$

For electrons, a more complicated expression arises because of the importance of the term  $U_n \partial \Delta(E \cdot n) / \partial x$

$$\Delta(E \cdot n) = E^{\text{eq}}\Delta n + n^{\text{eq}}\Delta E \quad [\text{A-3}]$$

where  $\Delta n = n - n^{\text{eq}}$  and  $\Delta E = E - E^{\text{eq}}$ . Here, the term  $n^{\text{eq}}\Delta E$  cannot be neglected, especially near the space charge region boundary. The resulting expression for electrons is

$$\begin{aligned} \Delta(\Delta n) = & L_K - (\Delta t/\tau_p) (n_K/n_b) p_K \\ & + DMN(\Delta n_{K-1} - 2\Delta n_K + \Delta n_{K+1}) \\ & + 0.5 UMN \{E_K^{\text{eq}}(\Delta n_K + \Delta n_{K-1}) \\ & - \Delta E_{K+1}^{\text{eq}}(\Delta n_K + \Delta n_{K+1}) + \Delta E_K(n_K^{\text{eq}} + n_{K-1}^{\text{eq}}) \\ & - \Delta E_{K+1}(n_K^{\text{eq}} + n_{K+1}^{\text{eq}})\} \end{aligned} \quad [\text{A-4}]$$

In Eq. [A-2] and [A-4] the following terms apply

$$\begin{aligned} L_K = & (I_0 a) \exp[-a(K - 1/2)\Delta x] \quad [\text{A-5}] \\ DMN = & D_n \Delta t / \Delta x^2 & DMP = D_p \Delta t / \Delta x^2 \\ UMN = & U_n \Delta t / \Delta x & UMP = U_p \Delta t / \Delta x \end{aligned}$$

The resulting change in the electric field caused by changes in  $\Delta p_K$  and  $\Delta n_K$  is

$$\Delta E_K = (e\Delta x / \epsilon_0 \epsilon_r) (\Delta p_K - \Delta n_K) + \Delta E_{K+1} \quad [\text{A-6}]$$

The following boundary conditions apply

$$\Delta p_{K \rightarrow \infty} = 0, \quad \Delta n_{K \rightarrow \infty} = 0, \quad E_{K \rightarrow \infty} = 0 \quad [\text{A-7}]$$

The calculation cannot be extended in reasonable simulation times to  $K$  values that rigorously will satisfy the conditions of Eq. [A-7]. Instead, the following boundary condition was chosen

$$\begin{aligned} \Delta p_{K\text{MAX}} = & \Delta p_{K\text{MAX}-1} \exp\{-\Delta x / (\tau_p D_p)^{1/2}\} \quad [\text{A-8}] \\ \Delta n_{K\text{MAX}} = & \Delta p_{K\text{MAX}} \quad \Delta E_{K\text{MAX}} = 0 \end{aligned}$$

where  $\Delta x \cdot K\text{MAX}$  is far outside the space charge region but still not in the bulk.

For the first element ( $K = 1$ ) (the semiconductor surface) within the semiconductor, only transport to the second element occurs. Charge transfer to solution is expressed, when desired, as the product of a rate constant  $k_p$  with the hole concentration in the first element. The initial conditions are the equilibrium distribution of carriers and electrical fields which are first obtained by the simulation procedure previously described (2).

#### LIST OF SYMBOLS

$a$	absorptivity of light
$D_p, D_n$	diffusion coefficients of holes, electrons
$E(x)$	electric field
$E(x)^{\text{eq}}$	electric field at equilibrium
$\Delta E(x)$	change in electric field with respect to equilibrium [ $E(x) - E(x)^{\text{eq}}$ ]
$g(x)$	generation function of light
$i_f$	total faradaic current
$i_{p,f}$	faradaic current due to holes
$I_0$	flux of light
$k_p, k_n$	charge transfer rate constants for holes, electrons
$k_r$	recombination rate constant
$K$	simulation distance index
$n(x)$	electron concentration
$n(x)^{\text{eq}}$	electron concentration at equilibrium
$n_b$	electron concentration in bulk semiconductor
$\Delta n$	excess concentration of electrons [ $n(x) - n(x)^{\text{eq}}$ ]
$p(x)$	hole concentration
$p(x)^{\text{eq}}$	hole concentration at equilibrium
$p_b$	hole concentration in bulk semiconductor
$\Delta p$	excess concentration of holes [ $p(x) - p(x)^{\text{eq}}$ ]
$\Delta t$	simulation time interval
$U_p, U_n$	mobility of hole, electron
$x$	distance from electrode surface
$\Delta x$	simulation space element thickness
$\beta$	transfer coefficient
$\Delta\phi_H$	potential drop in the Helmholtz layer
$\epsilon_0$	permittivity of free space (mks)
$\epsilon_r$	dielectric constant
$\tau_p$	average lifetime of excess minority carrier (hole) in bulk n-type semiconductor

#### REFERENCES

1. D. Laser and A. J. Bard, *This Journal*, **123**, 1828 (1976)
2. D. Laser and A. J. Bard, *ibid.*, **123**, 1833 (1976).
3. P. J. Boddy, *ibid.*, **115**, 199 (1968).

4. A. Fujishima and K. Honda, *Nature*, **238**, 37 (1972).
5. D. Laser and A. J. Bard, *J. Phys. Chem.*, **80**, 459 (1976).
6. H. Gerischer and I. Mattes, *Z. Phys. Chem. (Frankfurt)*, **49**, 112 (1966).
7. H. Gerischer, *This Journal*, **113**, 1174 (1966).
8. C. G. B. Garrett and W. H. Brattain, *Phys. Rev.*, **99**, 376 (1955).
9. A. Many, Y. Goldstein, and N. B. Grover, "Semiconductor Surfaces," chap. 2, John Wiley & Sons, Inc., New York (1965).
10. S. W. Feldberg, in "Electroanalytical Chemistry," Vol. 3, A. J. Bard, Editor, chap. 4, Marcel Dekker, Inc., New York (1969).
11. S. W. Feldberg, *J. Phys. Chem.*, **74**, 87 (1970).
12. W. W. Gärtner, *Phys. Rev.*, **116**, 84 (1959).

## Analysis of Multiple Reaction Sequences in Flow-Through Porous Electrodes

Richard Alkire\* and Ronald Gould\*\*

*Department of Chemical Engineering, University of Illinois, Urbana, Illinois 61801*

### ABSTRACT

The role of multiple reactions in flow-through porous electrodes has been investigated theoretically. The reaction sequences studied include simultaneous deposition of several metals, deposition of a metal in the presence of a redox system, and an ECE sequence which is characteristic of many electro-organic synthesis reactions. The model accounts for mass transport, multiple charge transfer reactions, homogeneous chemical reactions, ohmic and geometric parameters. Results are compiled in a series of graphs which elucidate electrode behavior over a wide region of parameter space.

One advantage of electrochemical processes is that a high level of selectivity for a desired reaction product can often be achieved through careful control of the potential under which reaction proceeds. On the other hand, the attainment of economically high volumetric reaction rates often requires optimizing around competing needs for large surface area, adequate mass transfer, and low ohmic resistance. Although flow-through porous electrodes are advantageous for achieving high reaction rates per unit volume, these devices often exhibit substantial potential variations over their interior surface so that the original electrochemical advantage of selectivity may thereby be lost. The purpose of this investigation is to develop theoretical methods for predicting the selectivity of flow-through porous electrodes in systems where multiple reactions occur, and to illustrate how such predictions can be compiled for use in engineering design.

### Literature Review

The use of fixed bed porous electrodes with a single electrode reaction has been recently reported for stripping copper (1), depositing antimony (2) and copper (3-5), carrying out redox reactions with iron (6) and ferricyanide couples (5, 7, 8), detecting dissolved gases (9-11), and for precipitating anionic species (12). Earlier work has been reviewed with emphasis on battery applications (13) for which a single electrode reaction is the preferred mode of operation. The extensive publications of Sioda, reviewed in Ref. (13), are especially noteworthy since they established many experimental procedures and theoretical methods of analysis. Many additional porous electrode studies are known which involve multiple electrochemical reactions in order to accomplish simultaneous removal of several metal ions from mixed solutions (14-21); separation of quinones (22), radioactive nuclides (23), and halide ions (24); and reduction of metal ions in the presence of competing reactions (25). Reaction schemes involving coupled electrochemical and homogeneous chemical steps have also been used in porous electrode cells for coulometric and preparative applications (12, 26-29), and for electro-organic synthesis applications

(30-36). It is abundantly clear that multiple reaction sequences are commonly encountered in many fixed bed porous electrode applications.

Theoretical considerations of multiple reaction effects in porous electrodes have led to the development of simple criteria for choosing the flow velocity and applied current such that (i) the potential distribution is sufficiently uniform that side reactions are avoided (8, 13, 37), or (ii) the residence time is convenient for maximizing the production of an intermediate species in a sequential reaction (27). In both cases, the approximate procedures are based on the need to attain a high degree of selectivity in the presence of multiple reactions. Therefore it seems appropriate to develop a more extensive theoretical basis for predicting the current and potential distribution behavior of porous electrodes in the presence of multiple homogeneous and heterogeneous reactions.

### Theoretical Formulation

The geometry of the porous electrode system under study is indicated in Fig. 1a. Electrolyte flows in the direction of the  $y$  coordinate; the electrode is of thickness  $l$ . The counterelectrode may be located either upstream or downstream from the porous electrode; in Fig. 1a, a downstream location is shown. Other details of cell construction are not shown since they are not included in the model equations. Electrolyte flows through the porous electrode, supplying reactants to the interior surface where electrochemical reaction occurs. The local reaction rate is a function of position since the potential and species concentrations vary along the reactor length owing to ohmic and transport limitations.

Figure 1b illustrates how the processes in the interior region of the porous electrode are envisioned by the model. The solid surface of the interior region, upon which electrochemical charge transfer occurs, is of arbitrary shape and is accounted for in the model only by a specific area term. The species concentration distributions at the solid surface,  $c_i^s(y)$ , are different from the species concentration distributions in the well-mixed core,  $c_i(y)$ , owing to the presence of a mass transfer diffusion layer between core and surface. The diffusion layer is assumed to occupy only a small fraction of the electrolyte volume so that (i) if homo-

\* Electrochemical Society Active Member.

\*\* Electrochemical Society Student Member.

Key words: porous electrode, mathematical model, multiple-metal deposition, metal-redox reactions, current distribution.

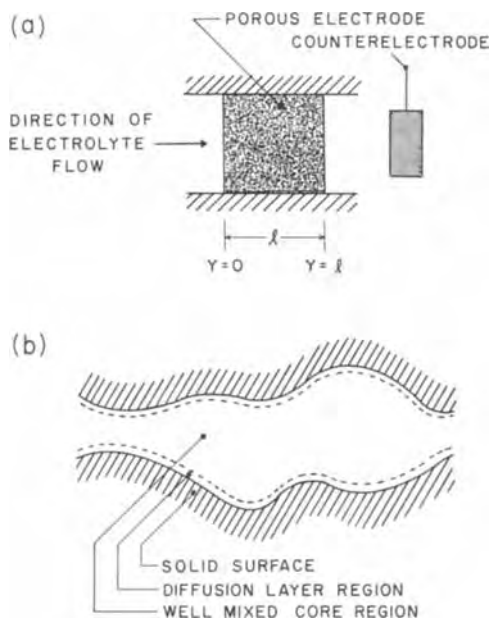


Fig. 1. (a) Configuration of electrode system. (b) Model of pore interior region.

geneous chemical reactions occur, they occur primarily in the well-mixed core region, and (ii) convection and axial diffusion effects occur only in the core region.

The equations representing the system are based on several assumptions: (i) isothermal operation takes place under steady-state conditions, (ii) the electrode is isopotential, its porosity is uniform, and the pore dimensions are large with respect to the double layer thickness, (iii) conduction in the electrolyte obeys Ohm's law, and migration effects are negligible, and (iv) convection through the porous electrode is by steady plug flow without channeling. These constraints allow the model equations to be written in one-dimensional form wherein both the heterogeneous electrode reactions and the homogeneous chemical reactions appear as pseudohomogeneous source terms.

In the electrolyte there are  $i$  reactive solute species which take part in a total of  $j$  reactions, which may be either heterogeneous or homogeneous. The stoichiometry of the reactions is defined by

$$\sum_i \nu_{ij} M_i^{+z_i} = n_j e^- \quad [1]$$

In addition to the  $i$  reactive solute species, there may be additional inert species which do not take part in the reactions and which are not taken into account in the analysis.

The steady-state one-dimensional species conservation equations are

$$D_i \frac{d^2}{dy^2} [c_i(y)] - v \frac{d}{dy} [c_i(y)] = \sum_j \nu_{ij} S_{ij} \quad [2]$$

Any particular reaction involving species  $i$  will be either heterogeneous (electrochemical) or homogeneous (chemical). Heterogeneous reactions take place on the interior surface and obey a rate equation in which the surface concentration appears

$$S_{ij} = \frac{a}{n_j F} f_j^e [c_i^s(y), \phi(y)] \quad [3]$$

Homogeneous reactions take place in the "core" of the flowing electrolyte within the porous electrode and obey rate equations in which the core concentrations appear

$$S_{ij} = f_j^h [c_i(y)] \quad [4]$$

The specific form of the rate equations  $f_j^e$  and  $f_j^h$  will

of course depend on the particular reactions as is illustrated below with several examples.

The local concentration difference between surface and core are related to the heterogeneous reaction rate through the mass transfer coefficient (5, 6, 13)

$$f_j^e [c_i^s(y), \phi(y)] = \nu_{ij} n_j k_i F [c_i^s(y) - c_i(y)] \quad [5]$$

The one-dimensional charge balance equation is

$$\frac{d^2}{dy^2} [\phi(y)] = \frac{a}{\kappa} \sum_j f_j^e [c_i^s(y), \phi(y)] \quad [6]$$

Equations [2], [5], and [6] comprise a set of  $(2i + 1)$  relations which are sufficient in number to determine the  $(2i + 1)$  unknown functions:  $c_i(y)$ ,  $c_i^s(y)$ , and  $\phi(y)$ . Whereas Eq. [5] is algebraic, [2] and [6] are differential equations and therefore require boundary conditions.

When the counterelectrode is upstream

at  $y = 0$

$$c_i = c_i^0$$

$$\phi = \phi^0$$

at  $y = l$

$$\frac{dc_i}{dy} = \frac{d\phi}{dy} = 0 \quad [7]$$

When the counterelectrode is downstream

at  $y = 0$

$$c = c_i^0$$

$$\frac{d\phi}{dy} = 0$$

at  $y = l$

$$\frac{dc_i}{dy} = 0$$

$$\phi = \phi^0 \quad [8]$$

Several different types of reaction sequences were investigated. For each particular system, the set of  $(2i+1)$  model equations was solved with use of a numerical procedure. The equations were first linearized about a trial solution and written in finite difference form. The resulting set of simultaneous tridiagonal matrices was then inverted with an IBM 360/75 computer (38). The solution of the nonlinear problem was gained by successive approximation until convergence to within 0.01% was obtained for all unknown functions. The number of iterations needed for convergence was dependent on the particular system under study, but was usually less than 15. The choice of 100 mesh points usually gave results which were accurate to within the line width used in graphical representation of the results.

## Results and Discussion

Three different example reactions have been investigated: cathodic deposition from electrolyte containing a mixture of metal ions, cathodic deposition of a metal from an electrolyte containing an aggressive redox couple, and a reaction sequence involving both electrochemical and homogeneous chemical reactions. In each example, the number of parameters is sufficiently large that it is not possible to compile simple rules of thumb which will adequately describe the electrochemical system. Conversely, the conduct of computer calculations over wide regions of parameter space have indicated qualitative trends which might not have been identified on the basis of intuition alone. These trends are discussed for each example reaction.

### Multiple Metal Deposition

Consider first the case where two metals are electro-deposited simultaneously from a mixture of their ions. Although more complicated rate equations could be used to suit special circumstances, let us assume that

the deposition of each metal proceeds independently of the other (that is,  $i = j$ ) with the reversible rate expression

$$f_i^e = i_{oi} \left\{ \exp \left[ \frac{\alpha_i n_i F}{RT} (\phi + \phi_{ri}) \right] - \frac{c_i^s}{c_i^o} \exp \left[ \frac{-\beta_i n_i F}{RT} (\phi + \phi_{ri}) \right] \right\} \quad [9]$$

In Eq. [9], the quantity  $\phi$  is the potential with respect to the rest potential of the ion of the most noble metal, while  $\phi_{ri}$  is the rest potential of the ion of the most noble metal with respect to species  $i$ . The rest potential difference is computed with use of ionic concentration of reactants as they enter the porous electrode.

The model equations can be made more compact by grouping the system parameters as follows

$$\begin{aligned} \Phi &= \frac{F\phi}{RT} & C_i &= \frac{c_i}{c_i^o} & Y &= \frac{y}{l} \\ \Phi_{ri} &= \frac{F\phi_{ri}}{RT} & \xi_i &= \frac{v l}{D_i} \\ \xi_i &= \frac{i_{oi} a l^2 F}{\kappa R T} & \chi_i &= \frac{i_{oi} a l^2}{n_i F D_i c_i^o} & \Gamma_i &= \frac{a k_i n_i F^2 l^2 c_i^o}{\kappa R T} \end{aligned} \quad [10]$$

By eliminating the surface concentration between Eq. [2] and [5], and by using the groupings of Eq. [10], the model equations become

$$\begin{aligned} C_i'' - \xi_i C_i' &= -\chi_i F_i \\ \Phi'' &= \sum_i \xi_i F_i \end{aligned} \quad [11]$$

where

$$F_i = \frac{e^{\alpha_i n_i (\Phi + \Phi_{ri})} - C_i e^{-\beta_i n_i (\Phi + \Phi_{ri})}}{1 + \frac{\xi_i}{\Gamma_i} e^{-\beta_i n_i (\Phi + \Phi_{ri})}}$$

Results will be given for the counterelectrode placed downstream from the porous electrode at  $Y = 0$

$$C_i = 1$$

$$\frac{d\Phi}{dY} = 0$$

at  $Y = 1$

$$\frac{dC_i}{dY} = 0$$

$$\Phi = \Phi^o$$

Were there only one metal ion undergoing reduction, the situation would be analogous to that investigated previously by Alkire and Gracon. The physical significance of the more important parameters in Eq. [10] is summarized in Table I. In addition to these, the quantity  $\Phi_{ri}$  represents the Nernstian rest potential under the upstream concentration conditions of reaction  $i$  with respect to a reference potential, usually chosen to be the rest potential of one of the reacting species.

Table II provides the range of parameter values for which calculations were carried out and reported below. In this study, interest centered primarily on the role of convective mass transport on reactor behavior

Table I. Physical significance of system parameters

$\xi_i$ :	Ratio of advection rate to axial dispersion rate in porous bed
$\Gamma_i$ :	Ratio of ohmic resistance to internal mass transfer resistance
$\xi_i$ :	Ratio of ohmic resistance to charge transfer resistance
$\chi_i$ :	Ratio of axial dispersion resistance to charge transfer resistance

Table II. Range of parameter values used in the calculations

	Parameters held constant	Parameters varied	Range of variation
1. Multiple metal deposition			
2 components	$\chi_1 = \chi = 10.0$ $\xi_1 = \xi = 0.5$ $\Phi_{r1} = 0.0$ $\Phi_{r2} = 7.0$	$\xi_1 = \xi$ $\Gamma_1 = \Gamma$	$-10^2$ to $-10^6$ $10^2$ to $10^6$
4 components	$\chi_1 = \chi = 10.0$ $\xi_1 = \xi = 0.4$ $\Phi_{r1} = 0.0$ $\Phi_{r2} = 5.0$ $\Phi_{r3} = 10.0$ $\Phi_{r4} = 15.0$	$\xi_1 = \xi$ $\Gamma_i = \Gamma$	$-10^2$ to $-10^6$ $10^2$ to $10^6$
2. Redox + metal deposition			
	$\chi_1 = \chi = 10.0$ $\xi_1 = \xi = 0.5$ $\lambda = 1.0$ $\Phi_r = 5.0$	$\xi_1 = \xi$ $\Gamma_i = \Gamma$	$-10^2$ to $-10^4$ $10^2$ to $10^6$
3. Coupled heterogeneous + homogeneous reactions			
	$\chi_1 = \chi_2 = 3 \times 10^3$ $\chi_4 = \chi_5 = 3 \times 10^5$ $\xi_1 = \xi = 10.0$ $\lambda_1 = 0.01$ $\lambda_2 = 1.0$ $\Phi_r = 1.0$	$\xi_1 = \xi$ $\Gamma_1 = \Gamma_2$ $\Gamma_4 = \Gamma_5$ $\Delta_1 = \Delta$	$10^1$ to $10^8$ $10^{-4}$ to $10^4$ $10^{-2}$ to $10^2$ $10^{-1}$ to $10^6$

near the limiting current. Therefore the parameters of greatest interest are the convective velocity ( $\xi_i$ ) and the mass transfer coefficient ( $\Gamma_i$ ). Under the conditions investigated, the role of kinetics and diffusion was purposely made negligible through judicious choice of parameters. In other words, the results below are essentially insensitive to the value of  $\xi_i$  and  $\chi_i$  used in the calculations. For still further simplification the same value of  $\xi_i$  was used for each species so that the subscript was deleted. Similarly, the same values were used for all  $\Gamma_i$  except as noted.

Figures 2 through 4 provide the current distributions predicted during the deposition of two metals, one of which (N) is more noble than the other (A). For each case studied, the electrode operated under the conditions of quantitative recovery of the ion of the more noble metal. The several curves in each figure correspond to different rest potentials between the two reactions. The current density given on the ordinate is defined by

$$\sum_i \int_0^1 J_i dY = 1 \quad [12]$$

That is, the integral of the total current over the entire electrode surface is normalized to the same value (unity) for each individual calculation.

Figure 2 shows the current distributions calculated for a high conductivity electrolyte with a slow flow rate for which both species were removed quantitatively from solution. The more noble metal is always deposited preferentially in the upstream regions. The less noble metal is deposited more uniformly to an extent which depends on the rest potential difference between the two reactions. These distributions indicate that while both metals may be deposited quantitatively, it may be difficult to recover the metals separately by postelectrolysis sectioning of the porous bed.

In comparison with Fig. 2, the distributions shown in Fig. 3 are for a higher flow rate but lower electrolyte conductivity. The more noble metal is deposited in upstream regions at the limiting current. Because of ohmic resistance effects, the less noble metal is deposited further downstream, nearer the counterelectrode; the current distribution exhibits a maximum owing to depletion of the ion of the less noble metal. If the rest potential difference is sufficiently large, the two metals can be made to deposit in distinctly different regions of the porous bed although the residence time for the less noble metal may be insufficient to allow its quantitative recovery. For the examples in Fig. 3, the percentage recovery of the ion of the less noble metal was 100, 99.5, and 90.6 for  $\Phi_r = 3, 5,$  and  $7$ , respectively. Figure 3 indicates that a properly



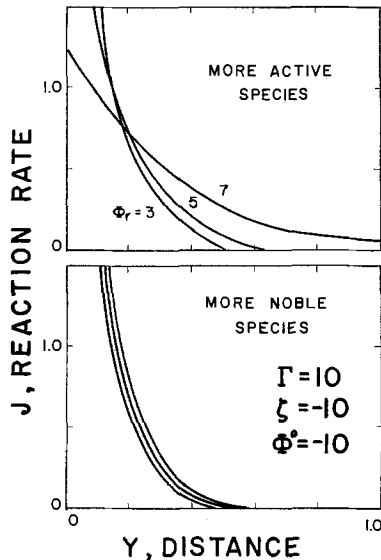


Fig. 2. Current distribution for deposition of two metals, low flow rate.

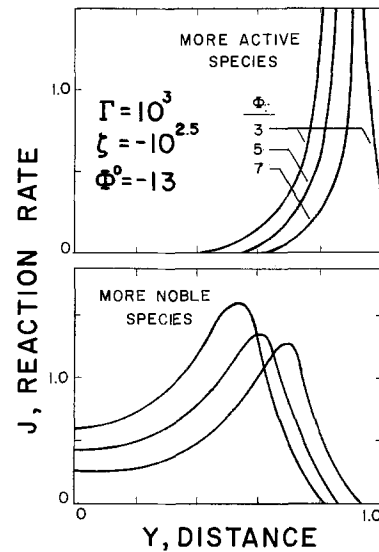


Fig. 4. Current distribution for deposition of two metals, high flow rate.

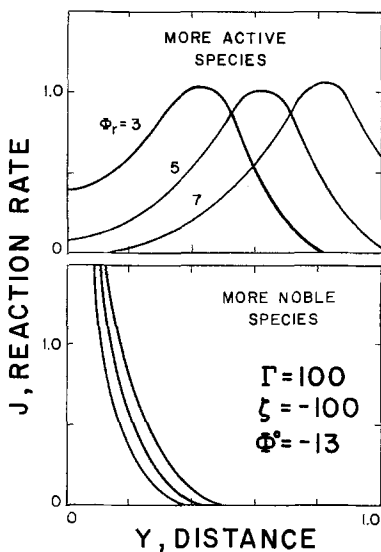


Fig. 3. Current distribution for deposition of two metals, medium flow rate.

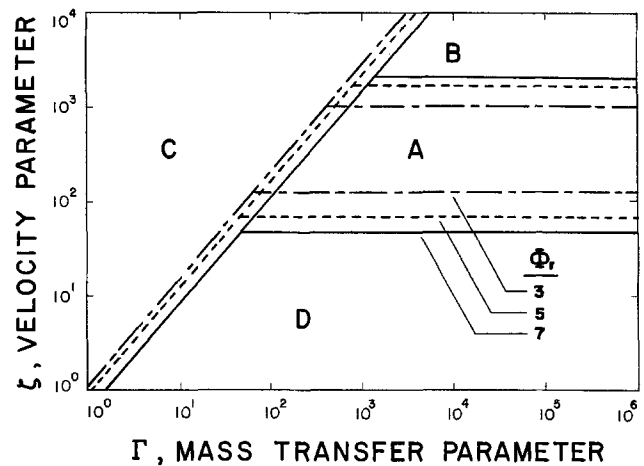


Fig. 5. Summary of deposit characteristics for two metals

designed electrode can remove metals quantitatively into different regions of the porous bed so that their subsequent recovery may be convenient.

The current distributions given in Fig. 4 are for a still higher flow rate and still lower electrolyte conductivity. The more noble metal is deposited in upstream regions, but not in the far upstream regions owing to ohmic limitations. The recovery of the less noble metal is in the exit region and may be very low if the rest potential difference is large. For the examples in Fig. 4, the percentage recovery of the less noble metal was 99.1, 86.2, and 41.2 for  $\Phi_r = 3, 5,$  and  $7$ , respectively. Figure 4 shows that while the two metals may be deposited in separate regions, it may not be possible to remove both of them quantitatively.

It is clearly evident from Fig. 2 through 4 that the quantitative recovery of two metals in separate regions of the porous bed can be achieved only through proper design of the electrolysis system. Figure 5 summarizes the regions of parameter space which determine the recovery and separability of the metals. The different line codes correspond to different rest potentials between the two reactions. Within region A, the two metals are deposited in distinctly separate regions of the porous bed, and the more noble metal is recovered quantitatively. In the region A, recovery of the less noble

metal varies from 100%, at the lower boundary, to essentially 0% at the upper boundary. In region B, the flow rate is so large that the residence time is insufficient to permit quantitative removal of the more noble metal; very little of the less noble metal is recovered in this region. With region C, the mass transfer coefficient is too small to allow quantitative recovery of the more noble metal. In region D, both metals are deposited quantitatively but the deposits overlap to an appreciable extent.

Figure 5 illustrates that, even under uniform electrolyte flow, the system behavior is quite sensitive to variations in the flow rate. It is often the case in practice, however, that channeling occurs owing to nonuniform flow distribution or bed packing. Therefore, it is of crucial importance that porous electrode systems be carefully designed so as to minimize undesirable hydrodynamic effects such as channeling.

The simultaneous deposition of more than two ionic species can also be modeled by the same procedure, although it is not convenient to present a graphical summary as was done with two metals. Figure 6 illustrates one example current distribution calculated for the simultaneous deposition of four species with rest potentials of 0, 5, 10, and 15 dimensionless units. The dashed lines correspond to the partial current distributions for each individual species; the solid line gives the total current distribution. It is seen that with a properly designed system, the four species can be deposited quantitatively in four distinctly different regions of the electrode.

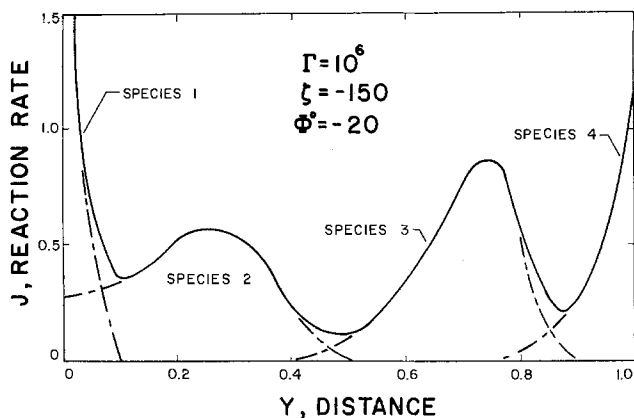
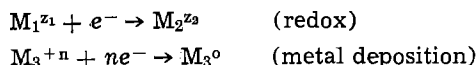


Fig. 6. Current distribution for deposition of four metals

#### Metal Deposition in the Presence of a Redox Couple

The reduction of a desired metal ion from a solution containing a more easily reduced species is encountered in several important industrial processes. If the more easily reduced species is the oxidized form of a redox couple, then a typical parallel reaction sequence is



For the calculations reported below, the redox rate expression had the form

$$j_{e, \text{redox}} = i_{o1} \left\{ \frac{c_2^s}{c_2^0} \exp \left[ \frac{\alpha_1 n_1 F \phi}{RT} \right] - \frac{c_1^s}{c_1^0} \exp \left[ \frac{-\beta_1 n_1 F \phi}{RT} \right] \right\} \quad [13]$$

while the metal deposition reaction had the form of Eq. [9].

By the same algebraic procedures described previously, the equations of the model are

$$\begin{aligned} C_1'' - \xi_1 C_1' &= -\chi_1 F_1 \\ C_2'' - \xi_2 C_2' &= \chi_2 F_2 \\ C_3'' - \xi_3 C_3' &= -\chi_3 F_3 \\ \Phi'' &= \xi_1 F_1 + \xi_3 F_3 \end{aligned} \quad [14]$$

where

$$\begin{aligned} F_1 = F_2 &= \frac{C_2 e^{\alpha_1 \Phi} - C_1 e^{-\beta_1 \Phi}}{1 + \frac{\xi_1}{\Gamma_1} [e^{\alpha_1 \Phi} + \lambda_1 e^{-\beta_1 \Phi}]} \\ F_3 &= \frac{e^{\alpha_2 n (\Phi + \Phi_r)} - C_3 e^{-\beta_2 n (\Phi + \Phi_r)}}{1 + \frac{\xi_3}{\Gamma_3} e^{-\beta_2 n (\Phi + \Phi_r)}} \end{aligned}$$

The boundary conditions for a downstream counter-electrode are

$$\begin{aligned} \text{at } Y = 0 & \\ C_1 &= 1 \\ \Phi' &= 0 \\ \text{at } Y = 1 & \\ C_1' &= 0 \\ \Phi &= \Phi^0 \end{aligned}$$

Were there only the redox reaction occurring, the situation would be analogous to that investigated previously by Alkire and Gracon. The physical significance of the important parameters in Eq. [14] is given in Table I. In addition to these, the quantity

$$\lambda_1 = \frac{c_2^0}{c_1^0} \quad [15]$$

represents the concentration ratio of the redox couple in the inlet stream.

Table II gives the values of the systems parameters used in the calculations reported here. The results calculated for the redox-metal sequence have indicated that the system behaves in many respects like the two-metal system described above. The current distribution for the metal deposition reaction is shown in Fig. 7 for four different operating conditions; the interpretation of these results is similar to that in Fig. 2-4 for the less noble metal. In Fig. 7, curve (a) shows the metal deposition distribution obtained under conditions of slow flow in a high conductivity solution. Deposition occurs in the upstream region and the metal is removed quantitatively; operation corresponds to region D of Fig. 6. By comparison, curve (b) corresponds to a more conductive solution moving at higher velocity. The ohmic resistance suppresses the large reaction rate at the upstream region and the reactive portion of the porous bed is thus too thin to capture all the reactants so that the metal recovery is less than 100%; operation is in region C of Fig. 6. Curve (c) corresponds to a desirable situation where the metal is deposited quantitatively in the interior regions of the bed. Reaction in upstream regions is suppressed by ohmic resistance limitations while the mass transfer coefficient is sufficiently high that quantitative removal of the metal is achieved further downstream; operation is on the lower boundary of region A in Fig. 6. In curve (d), the electrolyte conductivity is still lower and the velocity still higher so that the reaction zone is very near the downstream edge of the bed and the percentage metal recovery is low. Operation corresponds to the lower boundary of region B in Fig. 6; under such conditions, attempts to achieve high metal recovery efficiencies by mass transfer enhancement alone would be futile.

Figure 7 has shown that recovery of a metal from a redox containing system depends upon proper choice of the rate of reactant supply, the mass transfer rate, and the electrolyte conductivity. Figure 8 summarizes how the metal collection effectiveness depends upon  $\zeta$ ,  $\Gamma$ , and  $\Phi_r$ . The collection effectiveness decreases with flow velocity owing to the reduced residence time within the packed bed. The collection effectiveness improves with an increased mass transfer coefficient since the reactive pore surface is thereby made more accessible. The collection effectiveness is adversely affected by the presence of the redox agent to an extent which depends upon  $\Phi_r$ .

#### Coupled Heterogeneous and Homogeneous Reactions

Since the number of different sequences of coupled reactions which may be encountered is large, the purpose of presenting the following results is limited to (i) showing that, given sufficient experimental data,

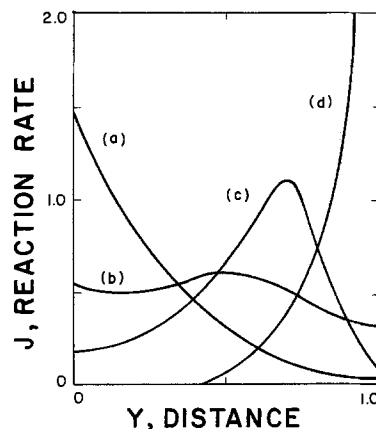


Fig. 7. Deposit distribution for deposition in presence of redox couple. (a)  $\zeta = -10$ ,  $\Gamma = 10$ ; (b)  $\zeta = -10^2$ ,  $\Gamma = 10$ ; (c)  $\zeta = -10^2$ ,  $\Gamma = 10^4$ ; (d)  $\zeta = -10^3$ ,  $\Gamma = 10^6$ .

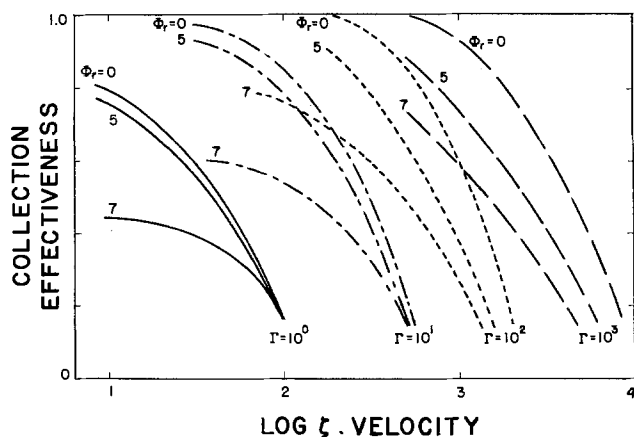
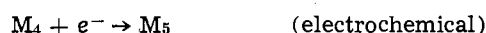


Fig. 8. Metal collection effectiveness for deposition in presence of redox couple.

any combination of reactions can be modeled to provide an engineering analysis of flow-through porous electrodes, and (ii) showing that, given a specific reaction sequence and design objective, a limited number of theoretical calculations can be compiled to provide design criteria for meeting those objectives.

For the sake of discussion, let us consider a mechanism of the form



in which the desired target molecule for production is species 4. Although any other rate equations could be used to suit special situations, let us assume that the two electrochemical reactions proceed with reversible Butler-Volmer kinetics as in Eq. [13], while the chemical reaction is irreversible and of first order

$$S_{22} = S_{32} = -S_{42} = -k_c c_2 c_3 \quad [16]$$

By following the manipulations described in previous examples, the equations for the model system are found to be

$$\begin{aligned} C_1'' - \zeta_1 C_1' &= -\chi_1 F_1 \\ C_2'' - \zeta_2 C_2' &= \chi_2 F_1 + \Lambda_1 C_2 C_3 \\ C_3'' - \zeta_3 C_3' &= \Lambda_2 C_2 C_3 \\ C_4'' - \zeta_4 C_4' &= -\chi_4 F_3 - \Lambda_3 C_2 C_3 \\ C_5'' - \zeta_5 C_5' &= \chi_5 F_3 \end{aligned} \quad [17]$$

$$\Phi'' = \xi_1 F_1 + \xi_4 F_3$$

where

$$\begin{aligned} F_1 &= \frac{C_2 e^{\alpha_1 n_1 \Phi} - C_1 e^{-\beta_1 n_1 \Phi}}{1 + \frac{\xi_1}{\Gamma_1} (e^{\alpha_1 n_1 \Phi} + \lambda_1 e^{-\beta_1 n_1 \Phi})} \\ F_3 &= \frac{C_5 e^{\alpha_3 n_3 (\Phi + \Phi_r)} - C_4 e^{-\beta_3 n_3 (\Phi + \Phi_r)}}{1 + \frac{\xi_4}{\Gamma_4} [e^{\alpha_3 n_3 (\Phi + \Phi_r)} + \lambda_2 e^{-\beta_3 n_3 (\Phi + \Phi_r)}]} \end{aligned}$$

The boundary conditions have been chosen for an upstream counterelectrode

at  $Y = 0$

$$C_i = 1$$

$$\Phi = \Phi^0$$

at  $Y = 1$

$$C_i' = 0$$

$$\Phi' = 0$$

In addition to the groups in Table I, the following dimensionless groups arise in this example

$$\begin{aligned} \Lambda_1 &= \frac{k_c l^2 c_3^0}{D_2} & \Lambda_2 &= \frac{k_c l^2 c_2^0}{D_3} \\ \Lambda_3 &= \frac{k_c l^2 c_2^0 c_3^0}{D_4 c_4^0} & \lambda_1 &= \frac{c_2^0}{c_1^0} \\ \lambda_2 &= \frac{c_5^0}{c_4^0} \end{aligned}$$

The calculations reported below were made with parameter values given in Table II. In the inlet stream, species 1 and 3 have the same concentration while species 2, 4, and 5 are 1% of  $C_1$  and  $C_3$ . The less interesting parameters were held constant for all calculations in order to focus attention on the more important parameters  $\zeta$ ,  $\Gamma$ , and  $\Lambda$ .

The calculations provide detailed predictions of the dependence of concentration, potential, and current distributions upon variation of system parameters. From these results, the efficiency for the production of species 4, the desired target molecule, was determined by

$$\begin{aligned} \text{Production efficiency} &= \frac{C_{4\text{outlet}} - C_4^0}{C_{4\text{max}} - C_4^0} \end{aligned} \quad [18]$$

$$C_{4\text{max}} = (C_1 + C_2 + C_4)_{\text{inlet}}$$

where  $C_{4\text{max}}$  is the maximum attainable concentration of species 4 if entering species are quantitatively converted to species 4.

Figure 9 illustrates how the production efficiency (PE) varies with  $\Gamma$  and  $\Lambda$  for one specific value of convective velocity,  $\zeta = +10$ . These data were calculated with sufficiently large applied potentials that behavior was controlled either by sluggish mass transfer processes or by sluggish homogeneous chemical kinetics. It is seen in Fig. 9 that the PE is always low when mass transfer limitations are severe (small  $\Gamma$ ) since the formation of  $C_2$  by the first electrochemical reaction is suppressed. Similarly, the PE can be low with excellent mass transfer (large  $\Gamma$ ) since the reaction proceeds past the target to yield high conversion to species 5. It is also seen that the PE is low when the homogeneous chemical reaction rate is slow (small  $\Lambda$ ), thereby suppressing the formation of species 4. High yields of the final product species can be obtained only when both the chemical reaction rate is sufficiently high and the mass transfer characteristics are carefully designed. For the case illustrated in Fig. 9, conditions necessary for product yields greater than 90% would be

$$0.1 < \Gamma < 1$$

$$\Lambda > 100$$

[19]

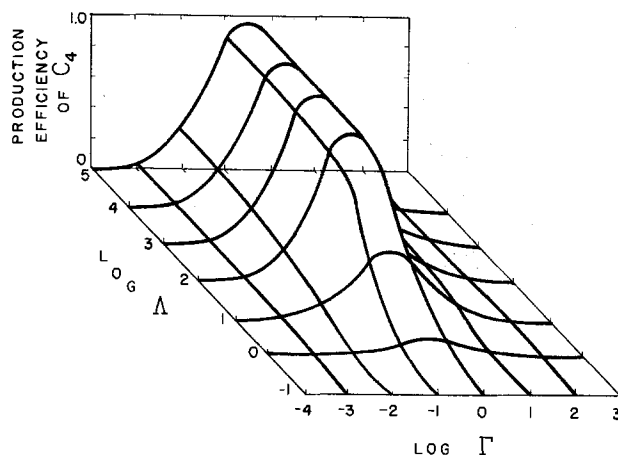


Fig. 9. Effect of  $\Lambda$  and  $\Gamma$  on production effectiveness for species 4 in ECE reaction sequence.

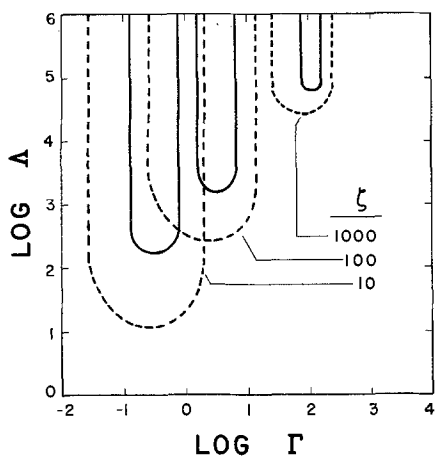


Fig. 10. Effect of system parameters on region of high production effectiveness for species 4 in ECE sequence.

For the system under consideration the design criteria cited in Eq. [19] are specific for the velocity used in Fig. 9. The dependence of these criteria upon flow rate is given by the solid lines in Fig. 10. For each velocity shown in Fig. 10, the solid lines enclose the "plateau" region seen in Fig. 9 over which the production efficiency is 90% or above. In a similar fashion, the dashed lines in Fig. 10 define the region within which the production efficiency is 50% or above. It is recognized that high flow rates lead to lower conversions since the residence time decreases linearly with velocity while the internal mass transfer coefficient increases only as the 1/3rd power of the flow rate. Optimum electrode performance is seen to be highly sensitive to the electrolyte flow rate.

By following similar procedures, the model could also be used to define regions of operation which would maximize yields of the other products in the reaction sequence such as  $C_2$  or  $C_5$ .

### Conclusions

Attempts to model complex porous electrode systems must rely on restrictive assumptions and perhaps artificial visions of physical reality in order to render the problem amenable to mathematical treatment. It is therefore of continued importance that controlled experimental studies be conducted on multiple reaction systems in order to test whether the assumptions used here betray physical reality beyond engineering tolerance. In particular, it would be important to test whether the diffusion layer is thin with respect to the pore size so that homogeneous chemical reactions would occur primarily in the "core" region of flowing electrolyte, as assumed.

The examples chosen here for theoretical discussion represent only a small number of possible reaction sequences found in the area of electrosynthesis. The model can incorporate many other types of sequences. In addition, the model could be applied to corrosion-type applications where there is no net current flowing in an external circuit (39, 40). That is, simultaneous anodic and cathodic reactions could occur within a bipolar porous flow-through electrode. Examples of applications would include cementation of Cu(II) during flow through a porous bed of iron, and leaching of Cu<sup>0</sup> from a porous bed with use of Fe(III) electrolyte.

Each example discussed above has illustrated that porous electrode behavior can be very sensitive to changes in convective flow rate. Therefore it is clearly important to avoid nonuniform flow effects which arise from localized channeling within the porous bed. Controlled experiments on channeling are suggested in order to improve understanding of the nature of channeling and its effect on electrode behavior.

The investigation has shown that while a high level of selectivity is possible in multiple reaction systems,

the rational engineering design of a porous electrode is critically important if the desired selectivity is to be realized. The model presented here should contribute toward the development of more efficient electrode systems.

### Acknowledgments

Portions of this study constituted partial fulfillment of requirements for a Master of Science degree in the Department of Chemical Engineering, University of Illinois, Urbana-Champaign. Fellowship support for Mr. Gould from the Atlantic Richfield Foundation and the Eastman Kodak Company is gratefully acknowledged. Research costs were supported by NSF Grant Eng 72-04168.

Manuscript submitted April 5, 1976; revised manuscript received July 26, 1976.

Any discussion of this paper will appear in a Discussion Section to be published in the June 1977 JOURNAL. All discussions for the June 1977 Discussion Section should be submitted by Feb. 1, 1977.

Publication costs of this article were assisted by the University of Illinois.

### LIST OF SYMBOLS

#### English characters

$a$	specific surface area, $m^2/m^3$ void
$c_i$	concentration of species $i$ , $mol/m^3$
$C_i$	concentration of species $i$ , dimensionless
$D_i$	diffusion coefficient of species $i$ , $m^2/sec$
$F$	Faraday's constant
$i_{0i}$	exchange current density of reaction $i$ , $A/m^2$
$J_i$	local electrochemical reaction rate, dimensionless
$k_i$	mass transfer coefficient of species $i$ , $m/sec$
$k_c$	rate constant of chemical reaction, $m^3 sec/mol$
$l$	electrode length, $m$
$M_i$	chemical symbol for species $i$
$n_j$	number of electrons taking part in reaction $j$
$v$	electrolyte velocity, $m/sec$
$y$	spatial variable, $m$
$Y$	spatial variable, dimensionless
$z_i$	valence of species $i$

#### Greek characters

$\alpha_i, \beta_i$	transfer coefficients for reaction $i$
$\Gamma_i$	mass transfer coefficient of species $i$ , dimensionless
$\xi_i$	flow velocity, dimensionless
$\kappa$	electrolyte conductivity, $(\Omega \cdot m)^{-1}$
$\lambda_i$	concentration ratio, dimensionless
$\Lambda$	chemical rate constant, dimensionless
$\nu_{ij}$	stoichiometric coefficient of species $i$ in reaction $j$
$\xi_i$	electrochemical rate constant, dimensionless
$\phi$	potential, $V$
$\phi_{r1}$	rest potential, $V$
$\Phi$	potential, dimensionless
$\Phi_{r1}$	rest potential, dimensionless
$\chi_i$	diffusion parameter, dimensionless

### REFERENCES

1. A. K. P. Chu and G. J. Hills, *J. Appl. Electrochem.*, **4**, 331 (1974).
2. A. T. Kuhn and R. W. Houghton, *ibid.*, **4**, 69, 173 (1974).
3. A. K. P. Chu, M. Fleischmann, and G. J. Hills, *ibid.*, **4**, 323 (1974).
4. J. M. Williams, U.S. Pat. 3,859,195 (1975).
5. R. C. Alkire and B. Gracon, *This Journal*, **122**, 1594 (1975).
6. G. B. Adams, R. P. Hollandsworth, and D. N. Bennion, *ibid.*, **122**, 1043 (1975).
7. F. Coeuret, *Electrochim. Acta*, **21**, 185, 195, 203 (1976).
8. R. Sioda, *Anal. Chem.*, **48**, 964 (1974).
9. E. L. Eckfeldt, *ibid.*, **31**, 1453 (1959).
10. E. L. Eckfeldt and E. W. Shaffer, *ibid.*, **36**, 2008 (1964).
11. R. E. Meyer, F. A. Posey, and P. M. Lantz, *Desalination*, **11**, 329 (1964).
12. R. E. Meyer and P. M. Lantz, *J. Electroanal. Chem. Interfacial Electrochem.*, **61**, 155 (1975).

13. J. S. Newman and W. Tiedemann, *AIChE J.*, **21**, 25 (1975).
14. J. Molnar, *Magy. Kem. Foly.*, **68**, 504 (1962).
15. T. Fujinaga, T. Nagai, C. Takagi, and S. Okazaki, *Nippon Kagaku Zasshi*, **84**, 941 (1963).
16. W. J. Blaedel and J. H. Strohl, *Anal. Chem.*, **36**, 1245 (1964).
17. D. K. Roe, *ibid.*, **36**, 2371 (1964).
18. T. Fujinaga, C. Takagi, and S. Okazaki, *Kogyo Kagaku Zasshi*, **67**, 1798 (1964).
19. T. Fujinaga, K. Izutsh, M. Koyama, S. Okazaki, and K. Tsuji, *Nippon Kagaku Zasshi*, **89**, 673 (1968).
20. T. Fujinaga, *Jap. Anal.*, **17**, 651 (1958).
21. G. A. Carlson and E. E. Estep, *This Journal*, **119**, 114C (1972); U.S. Pat. 3,459,646 (1969).
22. J. H. Strohl and K. L. Dunlap, *Anal. Chem.*, **44**, 2166 (1972).
23. T. Fujinaga, *Pure Appl. Chem.*, **25**, 709 (1971).
24. R. E. Meyer and F. A. Posey, *J. Electroanal. Chem. Interfacial Electrochem.*, **49**, 377 (1974).
25. P. R. Ammann, G. Cook, C. Portal, and W. Hadney, *This Journal*, **123**, 94C (1976).
26. J. A. Shropshire, *J. Electroanal. Chem. Interfacial Electrochem.*, **9**, 90 (1965).
27. R. E. Sioda, *Electrochim. Acta*, **19**, 57 (1974).
28. R. E. Sioda, *ibid.*, **20**, 457 (1975).
29. R. E. Sioda, *J. Electroanal. Chem. Interfacial Electrochem.*, **56**, 149 (1974).
30. S. Szpak, J. D. Elwin, and T. Katan, *Electrochim. Acta*, **11**, 934 (1966).
31. D. G. Braithwaite, U.S. Pat. 3,391,067 (1968).
32. A. F. MacClean and A. B. Stautzberger, U.S. Pat. 3,479,262 (1969).
33. R. E. Sioda, *Electrochim. Acta*, **13**, 375 (1968).
34. R. E. Sioda and W. Kemula, *J. Electroanal. Chem.*, **31**, 113 (1971).
35. R. E. Sioda and W. Kemula, *Electrochim. Acta*, **17**, 1171 (1972).
36. L. Ebersson and K. Nyberg, *Chem. Scr.*, **3**, 12 (1973).
37. D. J. Pickett and B. R. Stanmore, *J. Appl. Electrochem.*, **5**, 95 (1975).
38. J. S. Newman, *Ind. Eng. Chem., Fundamentals*, **7**, 514 (1968).
39. F. A. Posey and S. S. Misra, *This Journal*, **113**, 608 (1966).
40. R. C. Alkire, *ibid.*, **120**, 900 (1973).

## Microstructural Aspects of Grid Corrosion in the PbO<sub>2</sub> Electrode

Dennis Marshall and William Tiedemann\*

*Globe-Union, Incorporated, Corporate Applied Research Group, Milwaukee, Wisconsin 53201*

### ABSTRACT

A radical change in microstructure was examined for its effect on the mode of corrosive attack and corrosion rate for a 5 weight percent antimonial lead alloy. Metallography on as-cast microstructures indicates a transition from interdendritic to general attack with increasing overpotential. The potential region for general attack corresponds to a breakdown in the passivating abilities of PbO<sub>2</sub> and is marked by a sharp rise in the corrosion current. A simple heat-treatment, which alters the structure of the eutectic material, reduces interdendritic attack over the entire potential region studied.

Considerable research has been devoted to determining the merits of lead alloys for use as current collectors in the lead-acid battery (1). Because corrosion is a major mode of failure, much of this effort has been focused on the anodic behavior of lead and its alloys as they are used in the PbO<sub>2</sub> electrode.

Characterizing the corrosion of lead is complicated by the diversity of phases within the corrosion layer and experiments with pure lead (2-4) show the composition of the film varies with both time and potential. Below the equilibrium PbO<sub>2</sub>/PbSO<sub>4</sub> potential the corrosion layer contains numerous oxides and PbSO<sub>4</sub>; above this potential the  $\alpha$  and  $\beta$  phases of PbO<sub>2</sub> dominate.

In addition to imparting the physical strength required for present day automotive battery designs, alloying further complicates the corrosion process by introducing additional phases and increasing the number of microstructural variables. Most notable of these is the classical problem of localized attack of segregated materials such as the eutectic structure or intermetallic compounds. This effect has been well documented for the lead-acid system (6-11) and is particularly damaging not only for the effects on mechanical integrity but also for its contribution to internal resistance, a factor which limits battery performance. Moreover, other effects such as active mass to grid bonding, active mass morphology, and reduced overpotentials for gassing

have all been attributed to alloying, particularly antimony (1).

Partly because of the corrosion problem and primarily because of price, the antimony level in present battery grid alloys is dropping and, correspondingly, so is the strength. One of the possible solutions to the strength problem is heat-treatment, a process which is readily adaptable to antimonial leads. But in addition to the mechanical advantages, heat processing extensively alters the microstructure, raising questions as to its effect on subsequent corrosion life. Thus it was for the purpose of understanding the influence of heat-treatment on the corrosion behavior of antimonial alloys that this study was undertaken.

### Experimental Procedures

Corrosion samples were prepared by hand casting a commercial antimonial grid alloy into an aluminum mold. The nominal alloy composition is shown in Table I. Specimen geometry consisted of a sphere 1.44 cm in diameter with an integral wire, 0.65 cm long and 0.28

Table I. Composition of alloy used in this study

Element	Weight percent
Antimony	5.00 ± 0.25
Arsenic	0.45 ± 0.05
Tin	0.40 ± 0.05
Copper	0.035 ± 0.025
Sulfur	0.007 ± 0.003
Lead	Remainder

\* Electrochemical Society Active Member.

Key words: grid corrosion, lead dioxide electrode, heat-treatment, antimonial lead alloy microstructure.

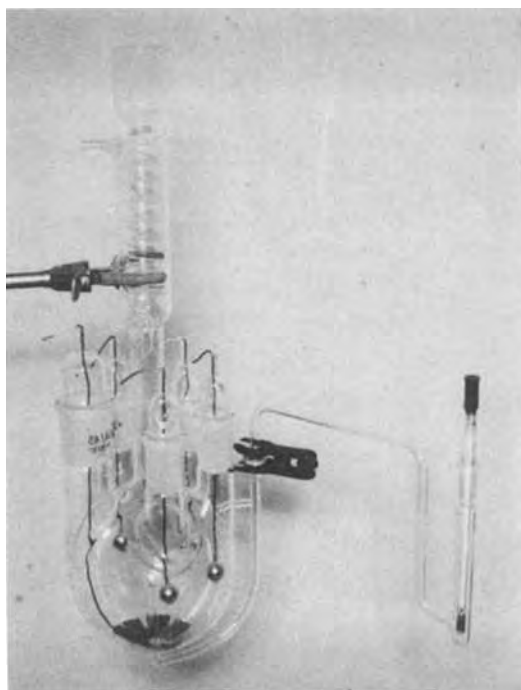


Fig. 1. The corrosion cell used in these experiments. A counter-electrode, fashioned from sheet lead, is shown at the bottom of the reservoir. Three samples are also visible located about the opening to the reference electrode shown at the right.

cm in diameter, attached. Total surface area, including a small protrusion corresponding to the mold gate, was  $7.1 \text{ cm}^2$ . Mold and pot temperatures were  $160^\circ \pm 0.5^\circ$  and  $324^\circ \pm 3^\circ\text{C}$ , respectively. Leads were attached to the integral wire with 63/37 solder and rosin flux followed by ultrasonic cleaning in acetone. Samples to be corroded in the heat-treated state were first heated at  $240^\circ\text{C}$  for 1-2 hr and quenched into room temperature water. Experiments with air-quenched and furnace-cooled samples were also carried out to examine the effects of precipitate formation within the primary lead phase. Leads were then attached as mentioned above.

The specimens were corroded in a refluxing-type apparatus pictured in Fig. 1. The reference electrode compartment was connected via an acid bridge, the end of which projected up through the bottom of the cell with its opening located at the center of the acid reservoir. Since changes in the corrosion layer are known to be time dependent, this construction permitted as many as four samples to be corroded simultaneously under nearly identical conditions, and then pulled for analysis at various time increments. The reservoir was filled with 900 ml of 1.27 sp gr sulfuric acid solution (4.61M). Temperatures were arbitrarily chosen at  $32^\circ$ ,  $49^\circ$ , and  $65.5^\circ\text{C}$  ( $90^\circ$ ,  $120^\circ$ , and  $150^\circ\text{F}$ ) and were maintained within  $\pm 0.5^\circ\text{C}$  in a water bath. However, as temperature only changed the degree and not the type of corrosion, only the results for  $49^\circ\text{C}$  are presented here.

Voltages for three separate cells were potentiostatically controlled using one Wenking and two custom-built potentiostats. In all cases potential variation held to  $\pm 1 \text{ mV}$  in the range from 1.170 to 1.500V with respect to  $\text{Hg}/\text{Hg}_2\text{SO}_4$  in 4.6M acid.

The extent of corrosion was measured both in terms of weight loss of lead and the electrochemical capacity of the corrosion layer. For the former, the lead wire was detached from the sample at the solder joint and the corrosion layer chemically stripped in a solution of the following composition:  $87 \text{ cm}^3 \text{ H}_2\text{O}$ , 10g NaOH, 2g mannitol, and 1g hydrazine dihydrochloride. Immersion time was limited to 30 min to preclude the deposi-

tion of lead from solution onto the sample. The lead content of the solution, in parts per million, was determined by atomic absorption and the result converted to milligrams of lead per square centimeter. Sample capacities were measured by constant current cathodic stripping in 1.27 sp gr  $\text{H}_2\text{SO}_4$ , using a Hewlett Packard 6181B d-c source. Only that portion of the sample up to the solder joint was immersed in the acid. Discharge potentials were monitored with a Keithley 616 digital electrometer and recorded on a Honeywell 194 strip chart recorder. Capacity was taken to a cutoff of 0.9V vs. an  $\text{Hg}/\text{Hg}_2\text{SO}_4$  reference electrode.

Samples for metallography were mounted in a room temperature curing epoxy and sectioned to approximately one-half their diameter. Rough grinding was done wet on silicon carbide paper using 240, 400, and 600 grits. Rough polishing was done on a wheel using 5.0 and then  $0.3\mu$  alumina and distilled water on billiard cloth. A Syntron vibratory polisher was used in conjunction with Leco Finish-Pol abrasive and microcloth for final polishing. The pH of the slurry was adjusted to reduce oxidation of the alloy during polishing.

This final polish technique was useful here since the microstructure and mode of attack were of interest; where the structure of the corrosion layer must be retained, this final polish method cannot be used due to localized discharge and friability of the layer.

## Results and Discussion

*Structural effect of heat-treatment.*—Figure 2 illustrates the radical effect heat-treatment has on the alloy microstructure. High temperatures, in this case only  $12^\circ\text{C}$  below the Pb-Sb eutectic temperature, effect some homogenization of the supersaturated grains and eutectic matrix. Thermodynamically, the grains can accept nearly 3.5% antimony at the heat-treating temperature, but 1-2 hr was not adequate to accomplish any significant solutioning of eutectic antimony in primary lead. A point count analysis (12) revealed no significant reduction in the volume percent eutectic antimony after heating. Instead, a reduction in surface energy was favored and diffusion along the surfaces of the antimony particles caused them to round off, reducing the continuity of the eutectic structure. This effect is general to lower antimonial alloys (13) and other alloy systems as well (14). The reduction in surface area would also tend to reduce any antimony flux into adjacent dendrites.

Unlike the antimony within the primary lead, eutectic Sb is exposed directly to corrosive attack and any change in its structure may be expected to alter corrosion even though there was no change in composition. As it relates to strength, the change in eutectic morphology is of secondary importance since low antimony alloys harden by precipitation. Since the solubility of antimony diminishes with temperature, precipitate distribution is readily controlled by quenching rate.

*Weight loss measurements.*—Figure 3 compares the weight loss data for samples corroded in the as-cast and heat-treated states at  $49^\circ\text{C}$ . The general magnitudes of these weight losses, as well as time trends in the data, are in excellent agreement with earlier findings by Lander (15, 16).

For equivalent times, weight losses at any potential are less for the heat-treated samples with the minimum in the curve shifting slightly to the right. Assuming the predominant lead species in the corrosion layer is  $\text{Pb}^{+4}$  (5), effective corrosion currents were calculated from weight loss differences between 24 and 48 hr and the result plotted as the upper set of curves in Fig. 4. A comparison of rates shows the greatest benefits of heat-treatment are obtained at higher potentials where  $\text{PbO}_2$  no longer provides a suitable barrier to corrosion. The sharp rise in corrosion is accompanied by profuse gassing which is at least partly responsible for the negative curvature between 1.35 and 1.47V. Earlier studies, involving the direct observation of

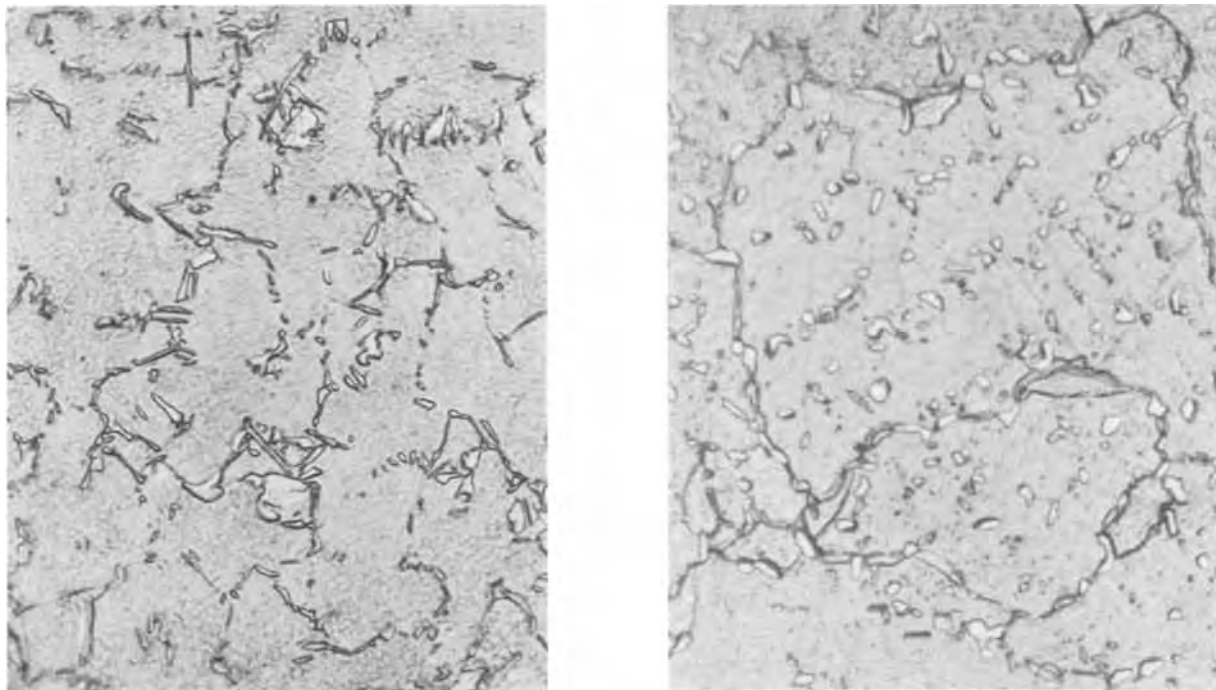


Fig. 2. Illustrates the microstructural changes associated with heat-treatment. Left, as cast (1500X); right, heat-treated (1500X)

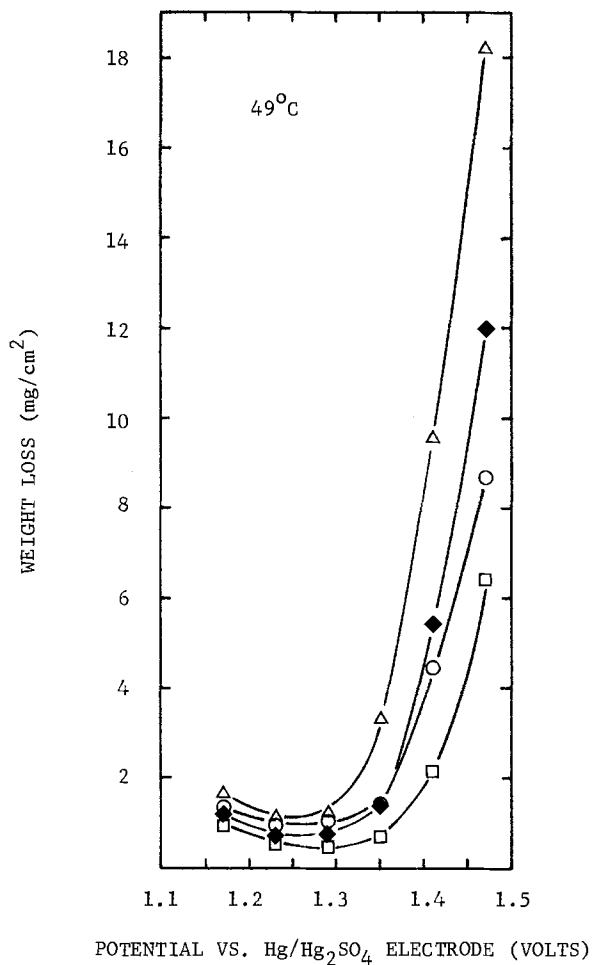


Fig. 3. Weight loss of lead from samples corroded at constant potential as determined by chemical stripping. ○, As cast, corroded 24 hr; △, as cast, corroded 48 hr; □, heat-treated, corroded 24 hr; ◆, heat-treated, corroded 48 hr.

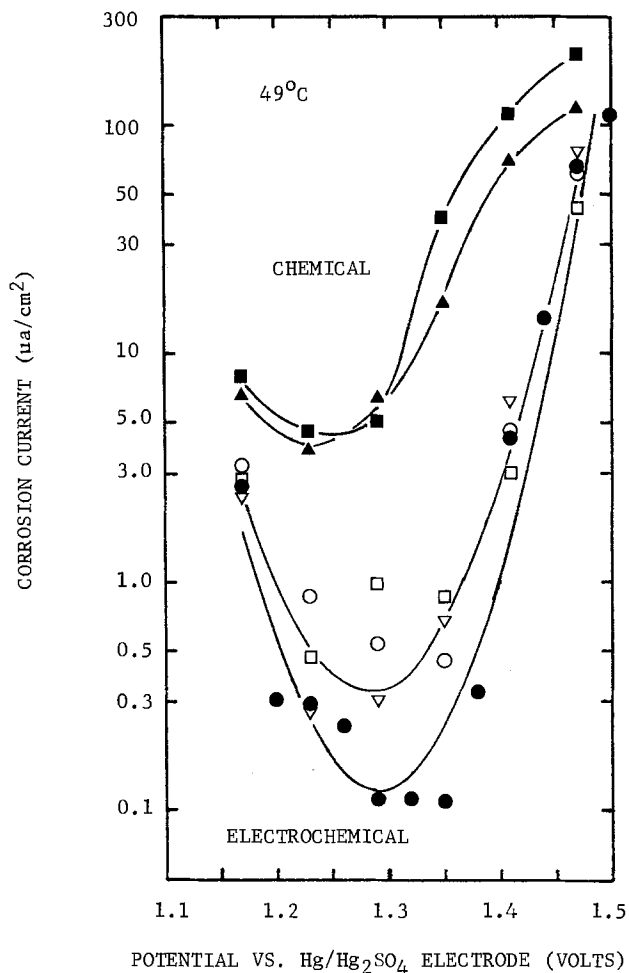


Fig. 4. A comparison of corrosion currents calculated from chemical and electrochemical data. ■, ●, As cast; ▲, □, heat-treated, water quenched; ▽, heat-treated, air quenched; ○, heat-treated, furnace cooled.



sample surfaces *in situ* with corrosion, showed vigorous gas evolution was capable of dislodging portions of the corrosion layer (17). This was verified qualitatively by analyzing the increasing amounts of  $\text{PbO}_2$  lying at the bottom of the reservoir at high potentials.

These findings are consistent with metallography on the corrosion interface shown in Fig. 5 and 6. For potentials up to about 1.29V, corrosion of the as-cast structure proceeds interdendritically. Since the dendrites are passivated by  $\text{PbO}_2$ , interdendritic attack will advance ahead of that on the primary lead until the surface area of the exposed dendrites increases sufficiently to offset the higher rate of eutectic attack. The relative rates will, of course, be altered by whatever potential drop and pH changes occur across the layer. This situation will be at its worst where abnormally long solidification times lead to larger dendritic arm spacings and the corresponding reduction in dendrite surface area.

From 1.35V and up the dendrite arms were consumed at an increasing rate until finally, at 1.47V, passivation was lost and dendrite attack caught up with the eutectic and corrosive penetration was relatively uniform.

Photomicrographs of heat-treated samples show that interdendritic attack was suppressed over the entire potential range, although the extent of the benefit is limited at lower potentials. But more importantly, a comparison of the metallography for both structures provides considerable insight into the significance and behavior of the eutectic material.

Beginning at 1.41V, heat-treated samples corrode intergranularly. Although morphological changes in the interdendritic and intergranular antimony resulting from heat-treatment are similar, rationalizing the differences in the corrosion of these two regions requires some consideration of what happens to the lead in the boundaries.

Since heating alters the shape of the eutectic antimony particles, antimony moving away from an old

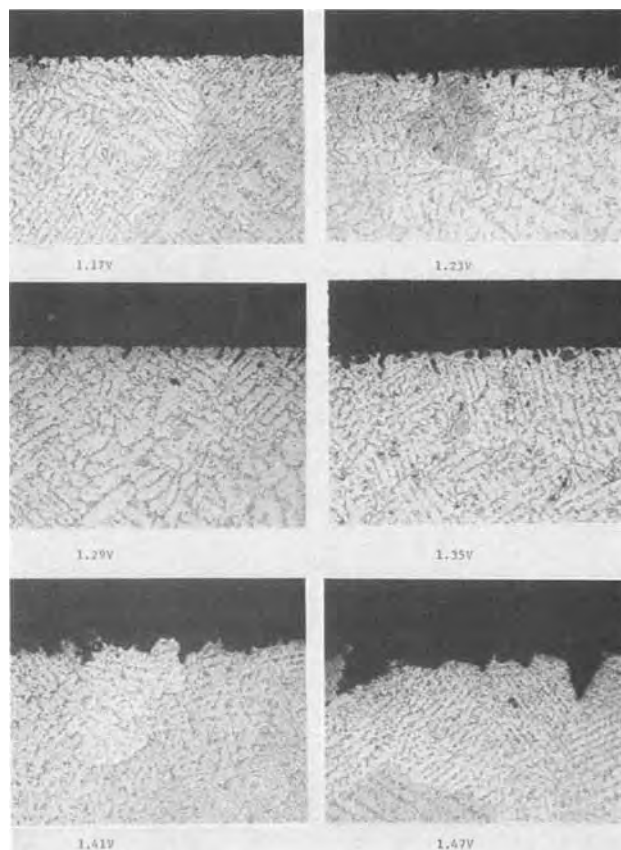


Fig. 6. Cross sections of corroded surfaces of heat-treated samples anodized at various overpotentials. (500 $\times$ ).

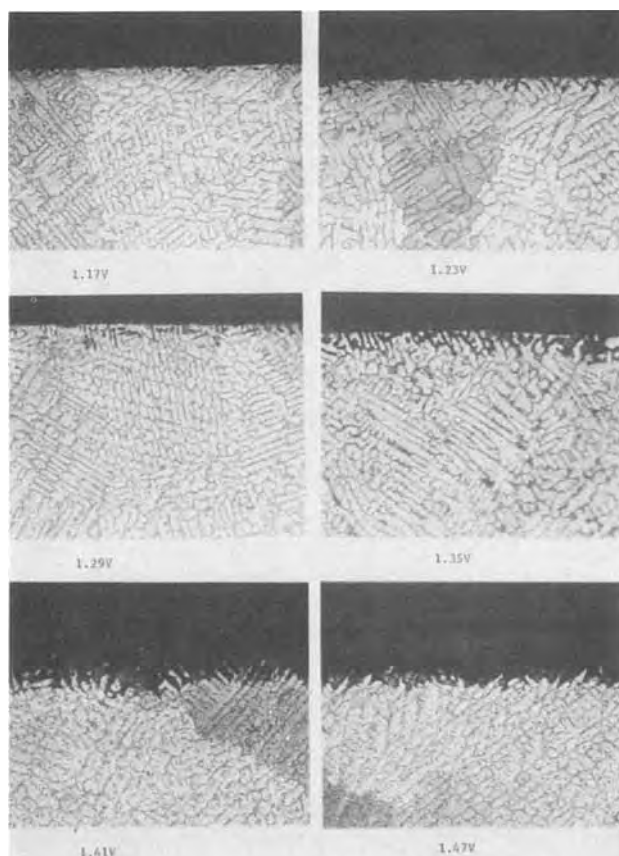


Fig. 5. Cross sections of corroded surfaces of as-cast samples anodized at various overpotentials. (500 $\times$ ).

site must be immediately replaced with lead. While this process is general to all boundaries, the resulting diffusion of lead leaves the interdendritic regions substantially changed when compared to the grain boundaries. Lead diffusing to old antimony sites may deposit epitaxially onto the primary lead on either side of a boundary. If it is a dendrite boundary there is no choice but to assume the crystallographic orientation of that grain whereas lead in the grain boundary may assume either orientation. The result is that lead dendrites within a grain grow together, closing in behind the receding eutectic antimony, while the grain boundary is essentially unchanged from this aspect. Corrosion, therefore, preferentially penetrates the grain boundary since any interdendritic attack will be stopped by a layer of passivated lead bridging between dendrites. In contrast, metallography on as-cast samples suggests that interdendritic and intergranular boundaries look relatively the same since there is no preferential attack.

These observations parallel the earlier work by Burbank and Simon (11) who observed a reduction in interdendritic penetration at reduced alloy content. At compositions equal to or less than about 0.5% Sb, there is a loss of eutectic continuity and they observed preferential intergranular penetration. Thus, heat-treatment accomplishes very much the same thing as a reduction in alloy content.

During the process of stripping corrosion films, small grayish residues were found in the bottom of the sample beakers. Upon investigation it was determined that the material was metallic lead, actually lead dendrites, which has been undercut and isolated in the corrosion layer. Since the stripping solution did not attack lead, dissolution of the corrosion layer released the lead particles which then settled to the bottom. This residue was collected from each sample corroded for 24 or 48 hr, dissolved in nitric acid, and quantified by atomic absorption. The results are plotted in Fig. 7.



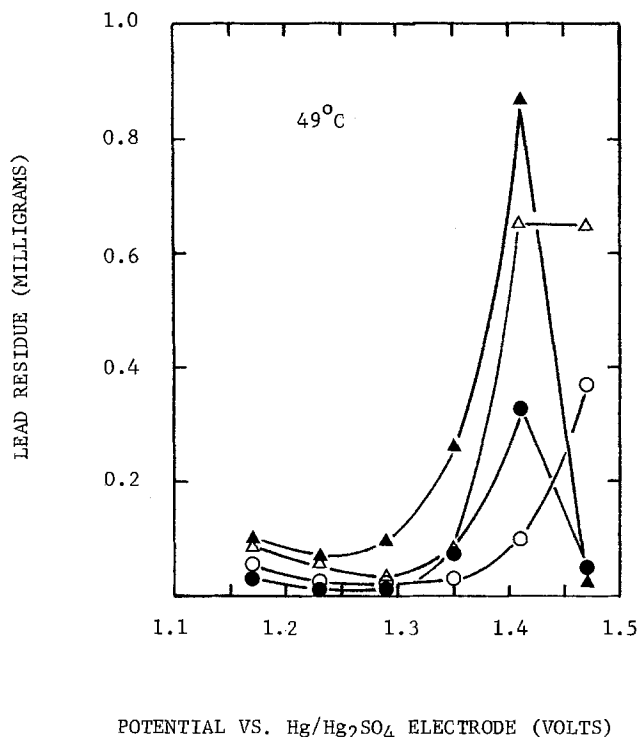


Fig. 7. Lead residue entrained in the corrosion layer. ●, 24 hr as cast; ▲, 48 hr as cast; ○, 24 hr heat-treated; △, 48 hr heat-treated.

As expected from the metallography, the difference in residue at low potentials is small. Of far greater significance is the change associated with the transition in corrosion mode. Between 1.29 and 1.41V, residues for heat-treated samples are smaller owing to the reduction in interdendritic attack. But, at 1.47V, lead is no longer passivated and the dendrites of the as-cast structure are consumed before they become isolated. Extensive metallography indicated that even where there were marked changes in dendrite arm spacing, corrosion was uniform at 1.47V.

Contrastingly, residues for heat-treated samples remain high at this potential as a result of intergranular attack in which much larger particles become isolated. Comparing the values for 24 and 48 hr at 1.41 and 1.47V the residue gain diminishes, probably because the grains are being consumed at an increasing rate.

**Cathodic stripping.**—The capacities of samples discharged at constant current were determined to a cut-off potential of 0.9V. For comparison's sake, these capacities were multiplied by two since those obtained chemically were calculated on the basis of a four-electron exchange.

Table II compares the amount of lead in milligrams per square centimeter involved in the discharge of as-cast samples with that incorporated in the entire layer as determined by chemical stripping. Only a portion of the corrosion layer is accessible during discharge; more material could have been reached using lower currents but this was precluded by self-discharge problems with the thin layers. Consequently, stripping currents were adjusted upward to the range 0.025-0.1 mA/cm<sup>2</sup> such that self-discharge would not significantly influ-

ence measured capacity. This in turn meant measured capacity was limited by polarization and that the percentage of material reached would be a function of the physical nature of the layer.

Referring again to Table II, the amount of material accessible during discharge varies with the corrosion potential. The fact that it reaches a low point in the middle potential region suggests there is something characteristically different about the layer which affords lead the maximum protection, e.g., differences in composition, density, or surface area.

From the capacities of samples corroded at different times but the same potential, corrosion currents were calculated as follows

$$i (\mu\text{A}/\text{cm}^2) = \frac{C_1 - C_0}{t_1 - t_0}$$

where  $C_0$  and  $t_0$  are the capacity and corrosion time for the first sample and  $C_1$  and  $t_1$  are the representative parameters for successive samples corroded under the same conditions.

These data were plotted as the lower set of curves in Fig. 4. Here again the measurements show a sensitivity to layer structure not seen by chemical means with the minimums in the curves being more depressed and shifted to the right. However, unlike the chemical data, differences between as-cast and heat-treated samples occur principally in the region of the minimum with the heat-treated specimens showing larger corrosion currents. This apparent reversal is attributed to certain structural changes occurring in the corrosion layer which are intimately linked to alloy microstructure. Referring to Fig. 8a, the as-cast dendrites are clearly outlined by holes in the layer resulting from the leaching of antimony and grain boundaries appear as jagged, deeply etched grooves, also resulting from antimony leaching. At higher magnifications, Fig. 8c, the holes appear as a nearly continuous network rimmed by closely spaced clusters of crystals. For heat-treated samples, the dendrites are distinguishable only at higher magnifications where the antimony holes can be resolved. In Fig. 8b, grain boundaries appear as slight ripples but have no other structural peculiarities compared to the remainder of the film.

Figures 8e and f reveal the extremely fine substructure which is credited for the differences in electrochemical behavior. The fact that this substructure is more uniform over the surface of the dendrites in the heat-treated sample suggests that solid solution antimony, now more homogeneously distributed, is influential in film formation. The as-cast dendrites also contain some of the substructure but are principally identified by a sparse growth of clusters containing larger crystals.

Quenching was also given some consideration for its possible influence on the corrosion of heat-treated samples. In addition to water quenching, specimens were both air and furnace cooled to room temperature from 240°C, all in an effort to modify antimony precipitation. Any possible effects arising from these treatments were not detectable by metallography nor were there any differences in the corrosion currents shown in Fig. 4.

These results indicate that changes in corrosion behavior are due to an alteration of the eutectic structure plus whatever homogenization occurs during heating,

Table II. A tabulation of selected data showing the amount of material involved in cathodic stripping compared with the total material present (chemical stripping) in the corrosion layer of as-cast samples

Overpotential	1.170	1.230	1.290	1.350	1.410	1.470						
Chemical stripping (mg/cm <sup>2</sup> )	1.3	1.7	0.9	1.1	1.0	1.3	1.4	3.3	4.4	9.5	8.7	18.2
Corrosion time (hr)	24.0	48.0	24.0	48.0	24.0	48.0	24.0	48.0	24.0	48.0	24.0	48.0
Cathodic stripping (mg/cm <sup>2</sup> )	0.32	0.54	0.046	0.060	0.062	0.074	0.070	0.088	0.13	2.4	5.6	—
Corrosion time (hr)	22.8	46.2	23.3	47	23.3	47.3	26.8	50.2	26.9	50.4	23.8	—

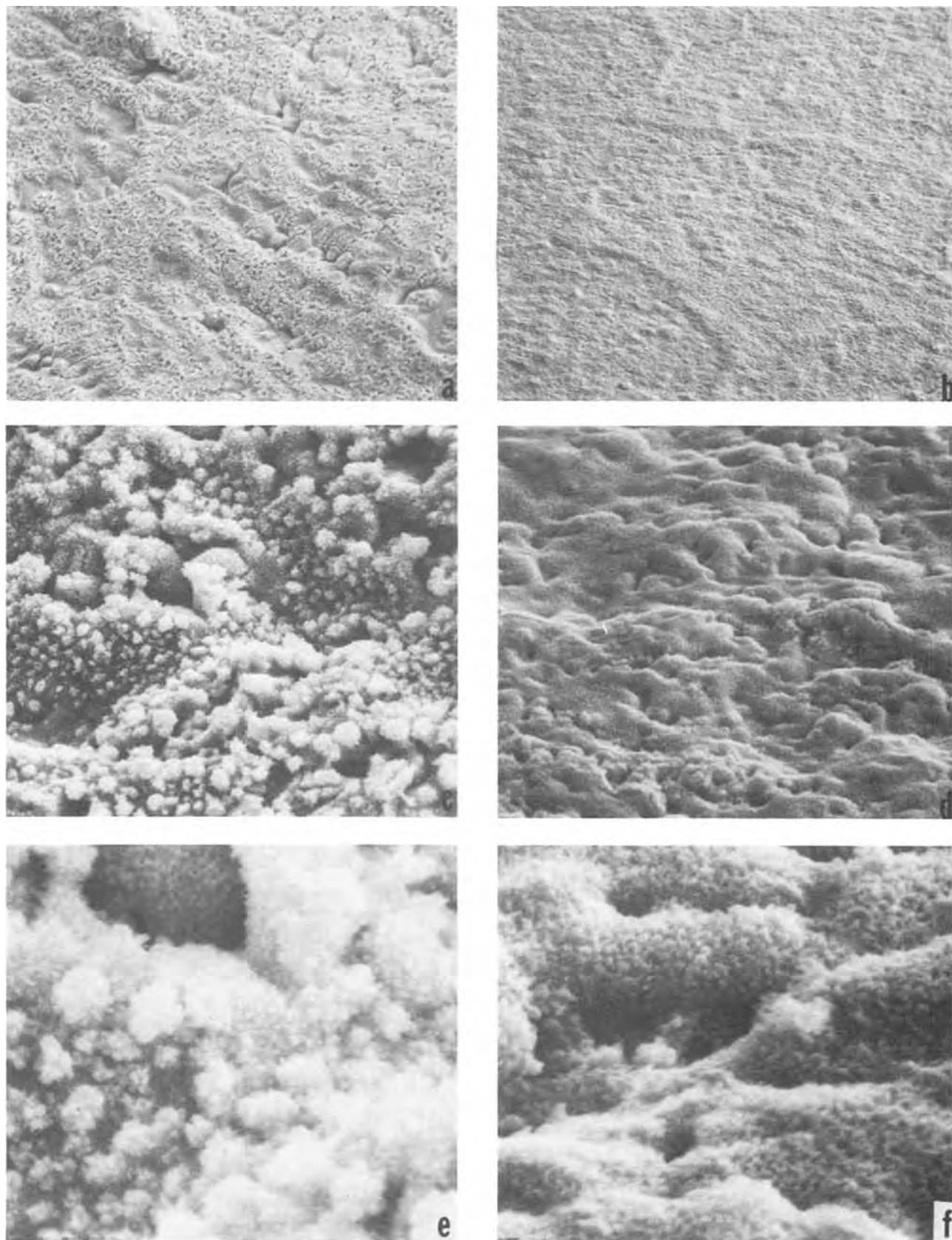


Fig. 8. SEM photomicrographs of the corrosion surfaces of samples anodized at 1.35V vs.  $\text{Hg}/\text{Hg}_2\text{SO}_4$ . a. As cast (300 $\times$ ). b. Heat-treated (300 $\times$ ). c. As cast (3000 $\times$ ). d. Heat-treated (3000 $\times$ ). e. As cast (10,000 $\times$ ). f. Heat-treated (10,000 $\times$ ).

while precipitate formation is relatively unimportant. This means the corrosion benefits of heat-treatment may be retained independent of the mechanical strength.

#### Conclusions

The corrosion of a nominal 5 weight percent antimonial grid alloy in the as-cast state was found to

change from interdendritic to a uniform mode of attack with increasing overpotential. A heat-treatment, consisting of a 1-2 hr soak at 240°C was effective in curtailing interdendritic attack especially at the higher potentials and also effected a reduction in the corrosion rate. However, heat-treated samples do corrode intergranularly at high potentials, a mode of attack not seen

in as-cast specimens. This difference is attributed to changes in the eutectic structure.

Results of an electrochemical and microstructural examination show the structure of the corrosion layer is sensitive to changes in both overpotential and alloy microstructure.

#### Acknowledgment

The authors wish to acknowledge the assistance of Mr. A. Matuszewski in the experimental work and Mr. A. Ortiguera for the metallography. Appreciation is also extended to Globe-Union, Incorporated for permission to publish these findings.

Manuscript submitted Dec. 15, 1975; revised manuscript received July 22, 1976.

Any discussion of this paper will appear in a Discussion Section to be published in the June 1977 JOURNAL. All discussions for the June 1977 Discussion Section should be submitted by Feb. 1, 1977.

Publication costs of this article were assisted by Globe-Union, Incorporated.

#### REFERENCES

1. J. Burbank, A. C. Simon, and E. Willihnganz, "Advances in Electrochemistry and Electrochemical Engineering," Vol. 8, C. Tobias, Editor, p. 157, Wiley-Interscience, New York (1971).
2. D. Pavlov, *Electrochim. Acta*, **13**, 2051 (1968).
3. D. Pavlov and N. Iordanov, *This Journal*, **117**, 1103 (1970).
4. D. Pavlov, C. N. Poulieff, E. Klaja, and N. Iordanov, *ibid.*, **116**, 316 (1969).
5. P. Ruetschi, *ibid.*, **120**, 331 (1973).
6. G. W. Mao, J. G. Larson, and P. Rao, *Metallography*, **1**(3-4), 399 (1969).
7. N. L. Parr, A. Muscott, and A. J. Crocker, *J. Inst. Metals*, **87**, 321 (1958).
8. G. W. Mao, J. G. Larson, and P. Rao, *This Journal*, **120**, 11 (1973).
9. G. W. Mao, T. L. Wilson, and J. G. Larson, *ibid.*, **117**, 1323 (1970).
10. A. C. Simon, *ibid.*, **114**, 1 (1967).
11. J. B. Burbank and A. C. Simon, *ibid.*, **100**, 11 (1953).
12. E. E. Underwood, "Quantitative Stereology," Morris Cohen, Consulting Editor, Addison-Wesley Publishers, Reading, Mass. (1970).
13. W. Hofmann, "Lead and Lead Alloys," English translation, G. Vibrans, Editor, Springer-Verlag, New York (1970).
14. H. L. Craig, Jr., ASTM Special Publication 516, p. 17, ASTM (1972).
15. J. J. Lander, *ibid.*, **98**, 213 (1951).
16. J. J. Lander, *ibid.*, **103**, 1 (1956).
17. D. Marshall and R. F. Amlie, Unpublished results.

## Technical Note



### Origin of Ridge Growth on a Copper Single Crystal (110) Face in Acid Copper Sulfate Bath

S. Nageswar

Department of Chemistry, Central College, Bangalore University, Bangalore, India

According to the screw dislocation theory of crystal growth of Burton, Cabrera, and Frank (1), pyramids are expected to grow on any plane in pure solution. Ridge-type growth is observed mainly on the (110) plane when deposited from a moderately pure solution (2-4). However, ridges are also observed on the surface of different orientations when the solution is not pure (5-7). Very careful experiments were carried out from highly purified solutions to study the pyramidal growth on the (110) single crystal plane of copper and attempts were made to explain the origin of ridge growth.

The experimental procedure has been described in detail elsewhere (6). All glass vessels were immersed in an acid mixture (HNO<sub>3</sub> + H<sub>2</sub>SO<sub>4</sub>, 1:1) overnight and then washed with distilled water followed by conductivity water. The solution was prepared using triple-distilled conductivity water, preelectrolyzed for 12 hr at 10 mA/cm<sup>2</sup>. The preelectrolyzed solution was then treated with activated charcoal and neutral alumina. H<sub>2</sub>SO<sub>4</sub> (AR grade) was redistilled separately and treated with activated carbon. A bath of 0.25M CuSO<sub>4</sub> + 0.1M H<sub>2</sub>SO<sub>4</sub> was then prepared.

The (110) plane was first mechanically polished on 3/0 and 4/0 emery paper using ethyl alcohol as a lubricant. Then the specimen was washed under running distilled water for 10 min and finally washed with conductivity water. To remove the damaged portion, the

Key words: rectangular pyramids, (110) plane, copper electrodeposits.

mechanically polished surface was subjected to electropolishing in 50% orthophosphoric acid bath at a constant cell potential of 1.2V (8).

#### Results and Conclusions

Ridges are noticed on the (110) plane of copper from moderately pure solution at all current densities (2, 5, 10, and 20 mA/cm<sup>2</sup>) as observed by earlier workers (2, 3). The direction of the ridge alignment is along [110] at 2 and 5 mA/cm<sup>2</sup>, as noticed by earlier workers (4). Furthermore, it has also been noticed that the ridges align in the [100] direction if the overpotential is below 100 mV and in the [110] direction above 100 mV (4).

In the present work, occasional rectangular pyramids were observed at a thickness corresponding to 2 C/cm<sup>2</sup> when copper was deposited from highly purified acid copper sulfate solution at 20 mA/cm<sup>2</sup> (Fig. 1). At a thickness corresponding to 4 C/cm<sup>2</sup>, the deposit consisted of a higher density of rectangular pyramids as shown in Fig. 2. When the thickness of the deposit was 6 C/cm<sup>2</sup>, there was a merging of rectangular pyramids (Fig. 3), the alignment of which was in the [110] direction. At a thickness of 8 C/cm<sup>2</sup>, there was a higher density of merging pyramids. Big ridges were observed at a thickness of 10 C/cm<sup>2</sup>. These ridges were also aligned along the [110] direction (Fig. 4).

The rate of formation of rectangular pyramidal growth depends upon the mean lifetime of an adion on the surface, the distance between the kinks, and the



Fig. 1. Formation of rectangular pyramids at 2 C/cm<sup>2</sup> at 20 mA/cm<sup>2</sup> on the (110) copper plane. 625 $\times$ .



Fig. 3. Merging of rectangular pyramids at 8 C/cm<sup>2</sup> at 20 mA/cm<sup>2</sup> on the (110) copper plane. 625 $\times$ .



Fig. 2. More number of rectangular pyramids at 4 C/cm<sup>2</sup> at 20 mA/cm<sup>2</sup> on the (110) copper plane. 625 $\times$ .



Fig. 4. Formation of ridge-type growth at 10 C/cm<sup>2</sup> at 20 mA/cm<sup>2</sup> on the (110) copper plane. 625 $\times$ . (10 C/cm<sup>2</sup> = 3.6  $\mu$ m).

exchange current density according to Vermilyea (9). In the case where the exchange current density is more than the current density applied, the dislocation step remains straight and does not form a pyramid through spiral formation. If the net current density is greater than  $i_0$ , pyramidal growth occurs on the surface. At low overpotentials the surface structure plays a decisive role in determining the rate of deposition. Furthermore, the incorporation of adions is easier along the [100] direction compared to the [110] direction as expected, since atomic density along the [100] is lower than along the [110] (10, 11). Hence, pyramids and ridges are aligned along the [100] direction at low overpotentials (2), and at high overpotentials they are aligned along the [110] direction.

#### Acknowledgments

The author wishes to express his grateful thanks to Dr. M. Shadaksharaswamy and Prof. T. D. Bhasker for their keen interest in the work and encouragement and to U.G.C., New Delhi, for financial support.

Manuscript submitted Jan. 19, 1976; revised manuscript received May 10, 1976.

Any discussion of this paper will appear in a Discussion Section to be published in the June 1977 JOURNAL. All discussions for the June 1977 Discussion Section should be submitted by Feb. 1, 1977.

#### REFERENCES

- Burton, Cabrera, and F. C. Frank, *Phil. Trans. R. Soc. London, Ser. A*, **123**, 299 (1951); *Nature*, **163**, 398 (1949).
- H. J. Pick and Wilcock, *Trans. Inst. Met. Finish.*, **35**, 298 (1958).
- G. G. Storey and Barnes, *ibid.*, **37**, 11 (1960).
- S. Nageswar and T. H. V. Setty, *Curr. Sci.*, **39**, 483 (1970).
- A. Damjanovic, T. H. V. Setty, and J. O'M. Bockris, *This Journal*, **113**, 429 (1966).
- S. Nageswar and T. H. V. Setty, *Proc. Indian Acad. Sci. Sect. A*, **73**, 178 (1968).
- S. Nageswar and T. H. V. Setty, *Trans. Soc. Adv. Electrochem. Sci.*, **7**, 129 (1972).
- Jackquet, *C. R. Acad. Sci. Paris*, **242** (1938).
- D. A. Vermilyea, *J. Chem. Phys.*, **25**, 1254 (1956).
- S. Nageswar, Ph.D. Thesis, Bangalore University (1971).
- N. Hackerman and Simpson, *Trans. Faraday Soc.*, **52**, 628 (1956).

# DISCUSSION SECTION



This Discussion Section includes discussion of papers appearing in the *Journal of The Electrochemical Society*, Vol. 123, No. 2 and 3; February and March 1976.

## Electrophoretic Mobilities of Cadmium Hydroxide, Nickel Hydroxide, and Silver Oxide in Ni-Cd and Ag-Zn Battery Electrolytes

S. W. Mayer (pp. 159-162, Vol. 123, No. 2)

**S. D. James:**<sup>1</sup> It gets increasingly hard to accurately measure electrokinetic effects at high salt concentrations. This difficulty arises because, in a dispersion, the measured electrical effect is always a combination of interfacial and bulk processes. Consider a solid dispersed in a salt solution. As salt concentration rises two things happen: first, the diffuse part of the electric double layer is compressed toward the solid, thus diminishing interfacial influence;<sup>2</sup> simultaneously, solution conductance rises, thus augmenting bulk solution influence. Eventually the interfacial contribution is lost in a much larger bulk solution effect. Apparently this usually occurs well below a salt concentration of 0.1*N* since electrokinetic effects have rarely, if ever, been reported above this value.<sup>3</sup> However, in the paper under discussion, unusually high electrophoretic mobilities are reported for battery oxides in 34 and 43 w/o KOH, i.e., at up to 10*N*. So if these data are valid, they represent a major advance in the electrokinetic literature. However, before this work can be accepted, the following questions must be answered.

1. How does the author calculate the tabulated mobilities? Using his raw data, I calculate that these mobilities and the derived zeta potentials should be about one thousand times higher than those he reports in Tables I-III. If my calculations are correct, the mobilities of the species range up to 2 cm/sec and their zeta potentials up to 1700V in 11*M* KOH (43 w/o). Since  $\zeta$  hardly ever exceeds a few hundred mV even in dilute solution and falls with increasing ionic strength,<sup>3</sup> such data seem highly questionable.

For the author's benefit I will itemize one of my calculations. I used his Eq. [2] in the form

$$m = W/t\sigma i f d$$

where  $m$  is electrophoretic mobility in (cm/sec<sup>-1</sup>)/(V cm<sup>-1</sup>),  $\sigma$  is specific resistance of suspension in  $\Omega$  cm,  $W$ , in grams, is observed change in mass of collection cell after the passage of  $i$  amp for  $t$  sec,  $f$  is product of volume fractions of solid and liquid, and  $d$ , in grams per cubic centimeter, is density difference between solid and liquid. This is the form in which the equation has been used by previous workers.<sup>4</sup> I will now calculate  $m$  and  $\zeta$  corresponding to the first data line of the author's Table I. This refers to electrolysis of a suspension, 13.9 w/o cadmium hydroxide in 34 w/o KOH which is also 0.8 w/o in potassium carbonate. From his figures of 13.9 and 6.4 for the weight percent and density (g/cm<sup>3</sup>) of cadmium hydroxide and using the density of 34 w/o KOH, 1.33 g/cm<sup>3</sup> as that of the liquid

phase,  $f$  is calculated as  $0.033 \times 0.97 = 0.032$ . Also,  $d = 6.4 - 1.3 = 5.1$  g/cm<sup>3</sup>;  $W = 0.031$ g;  $i = 0.005$ A;  $t = 360$  sec. As an approximation for  $\sigma$ , the specific resistance of the suspension, I used the value for pure, 34 w/o KOH at room temperature, viz., 1.9  $\Omega$  cm (2.5  $\Omega$  cm for 43 w/o KOH). Thus,  $m = 0.031/(360 \times 1.9 \times 0.005 \times 0.032 \times 5.1) = 0.056$  (cm sec<sup>-1</sup>)/(V cm<sup>-1</sup>). This mobility is 700 times greater than that tabulated by Mayer (viz., 0.00008).

A similar calculation made for the second data line of Table III produces  $m = 1.62$  (cm sec<sup>-1</sup>)/(V cm<sup>-1</sup>) for silver oxide in 43 w/o KOH, which is 960 times Mayer's tabulated figure. In calculating  $\zeta$  from  $m$ , Mayer evidently used  $\eta/D$  values of about 0.00045 poise in Tables I, II and 0.00079 in Table III. Using these values and applying his Eq. [3], I arrived at zeta potentials of 33 and 1660V for the two mobilities calculated above. [In checking the author's calculations of  $m$ , I assumed that the second column of his tables refers to his primary measurement, namely the observed increase in weight of the collection cell ( $=W_1$ ) rather than to the derived quantity which heads the column, "mg of suspension collected at anode (cathode)," ( $=W_2$ ). The two quantities are related by  $W_1/W_2 = d/(\text{solid density})$ . For the Ag, Cd, and Ni hydroxides, this ratio is 0.81, 0.80, and 0.68, respectively. Thus, even if my assumption is wrong, the biggest error involved is only 32%.]

2. How did the author avoid incurring serious errors from the electrolytic formation of gases at his stainless steel electrodes? At a steel cathode the passage of 0.005A for 360 sec should generate 0.228 cm<sup>3</sup> of hydrogen at 1 atm and 25°C. The resulting expulsion of 0.228 cm<sup>3</sup> of a 1.4 g/cm<sup>3</sup> suspension would lighten the collection cell by 0.319g, an amount greater than most of the author's tabulated  $W$ 's. (It is unlikely that reduction of suspended particles of metal oxide would significantly share the cathodic current.) At a stainless steel anode, this error would be smaller, first because not more than 0.114 cm<sup>3</sup> of oxygen could be evolved and second in proportion to the fraction of current carried by anodic dissolution of the steel. However, the resulting dissemination of heavy metal ions would seriously contaminate the suspension.

3. How did the author prevent his determination of  $W$  from including large errors caused by the settling of solid particles during the experiment? In my own experience with this type of measurement (using the Model 1202 apparatus of Micromeritics Instrument Corporation, Norcross, Georgia, spinning at 30 rpm) errors of up to 0.2g were common unless the suspension was very well dispersed. It seems unlikely that, up to 12*M* KOH (45 w/o), the author's suspensions were well enough dispersed to avoid settling errors since flocculation normally occurs at these high ionic strengths. (When I repeated the author's silver oxide suspension preparation, I obtained a very coarse and rapidly settling precipitate, quite unsuited for electrophoresis measurements.)

4. What were the exact details of the author's experimental arrangement? This is hard to visualize from the scant description in the article. He states that he used the method of Sennett and Olivier as modified by Long and Ross. However, in this modification the apparatus was (almost by necessity) stationary while the author's setup was rotated at 30 rpm.

<sup>1</sup> Naval Surface Weapons Center, White Oak Laboratory, Silver Spring, Maryland 20910.

<sup>2</sup> J. J. Bickerman, in "Encyclopedia of Electrochemistry," C. A. Hampel, Editor, p. 473, Reinhold, New York (1964).

<sup>3</sup> J. Th. G. Overbeek, in "Colloid Science," Vol. 1, H. R. Kruyt, Editor, Elsevier, Amsterdam (1952).

<sup>4</sup> J. P. Olivier and P. Sennett, Proceedings of the 15th Conference on Clays and Clay Minerals, p. 345, Pergamon Press, New York (1967).

## Effect of Temperature on Electrode Kinetic Parameters for Hydrogen and Oxygen Evolution Reactions on Nickel Electrodes in Alkaline Solutions

M. H. Miles, G. Kissel, P. W. T. Lu, and S. Srinivasan  
(pp. 332-336, Vol. 123, No. 3)

**B. Chatterjee:**<sup>5</sup> In the paper under discussion, the exchange current density  $i_0$  for the hydrogen evolution reaction (HER) is shown to compare closely with that for the oxygen evolution reaction (OER), except at 80°C. Since  $i_0$  is a major kinetic parameter in an electrochemical reaction, the above comparison, especially at low overpotential ( $\eta$ ), would suggest a similar rate of reaction and rate-controlling mechanism for HER and OER. This view is, however, not supported by the results of the paper under discussion where dissimilar activation energies for the two reactions are given. (For example, a higher activation energy for OER would imply a lower reaction rate than that for HER.) This apparent discrepancy can be resolved by estimating the chemical reaction rate constants at various temperatures. Such an approach is conceivable due to the similarity in the basic mechanism of chemical and electrochemical reactions in alkaline solution.<sup>6</sup> It is known that for cathodic reaction (HER) the relation between the chemical rate constant  $K_c$  and the potential  $V$  is given by

$$K_c = (i/nF) \exp(-\alpha VF/RT)$$

where  $i$  is the applied current density,  $n$  is the number of electrons involved in one set of reaction,  $\alpha$  the transfer coefficient,  $F$  the Faraday constant (96.5 kC mole<sup>-1</sup>),  $R$  the gas constant (8.317 J mole<sup>-1</sup> K<sup>-1</sup>), and  $T$  is the absolute temperature in °K. The corresponding equation for anodic reaction (OER) is

$$K_a = (i/nF) \exp[(1 - \alpha)VF/RT]$$

In the present calculation, the potential  $V$  at a particular temperature is obtained from the first slope of the dual Tafel regions of Fig. 3 in the paper under discussion, at a constant current density of 10 mA/cm<sup>2</sup>. Results in Table I are estimated by assuming a single electron transfer mechanism and using the  $\alpha$ -values as given by Miles *et al.* From Table I one can now get a better idea of the rate of HER relative to OER at a particular temperature. The Arrhenius plot of  $\log_{10}K$  against  $1/T$  is linear for HER, and the activation energies are about 6 and 11 kcal mole<sup>-1</sup> at low and high  $\eta$ , respectively. These values compare closely with those reported in the paper under discussion for the change of  $\log_{10}i_0$  with  $1/T$ . The linear Arrhenius plot for OER which includes data at 80°, 150°, and 208°C (at high  $\eta$ ) gives an activation energy (of about 11 kcal mole<sup>-1</sup>) similar to that for HER at high  $\eta$ . However, unlike HER, there is a sudden increase in the rate constant for OER as the temperature is raised from 208° to 264°C. Thus, except for anodic reaction at 264°C which will be discussed next, one would expect due to similar activation energy both HER (high  $\eta$ ) and OER being controlled by an identical rate-determining process, such as electrochemical desorption as

<sup>5</sup> The British Aluminium Company, Limited, Gerrards Cross, Buckinghamshire SL9 0QB, England.

<sup>6</sup> B. Chatterjee, *This Journal*, 123, 1920 (1976).

Table I. Estimated chemical rate constants ( $K$ ) at 10 A/cm<sup>2</sup> current density for the cathodic and the anodic reactions on polished nickel electrodes in 50 w/o KOH solutions

T (°C)	Cathodic reaction (HER)		Anodic reaction (OER)	
	$K_c$ (mole cm <sup>-2</sup> sec <sup>-1</sup> ) low $\eta$	high $\eta$	$K_a$ (mole cm <sup>-2</sup> sec <sup>-1</sup> ) low $\eta$	high $\eta$
80	—	$2.0 \times 10^{-9}$	—	$1.5 \times 10^{-13}$
150	$1.1 \times 10^{-8}$	$6.8 \times 10^{-9}$	—	$2.6 \times 10^{-13}$
208	$2.5 \times 10^{-8}$	$7.6 \times 10^{-9}$	$2.3 \times 10^{-9}$	$1.3 \times 10^{-11}$
264	$3.2 \times 10^{-8}$	$7.0 \times 10^{-9}$	—	$1.9 \times 10^{10}$

suggested in the paper under discussion. At low  $\eta$ , the Tafel slope of  $2RT/3F$  for HER which is lower than  $2RT/F$  at high  $\eta$  is associated with rate constants which give a lower activation energy of about 6 kcal mole<sup>-1</sup>. It seems probable that chemical desorption (Tafel recombination) is the rate-determining step for HER at low  $\eta$ .

The anodic Tafel slope of  $RT/3F$ , i.e.,  $\alpha = 3.3$  at 264°C is shown in the paper under discussion to be lower than the cathodic slope of  $2RT/3F$  at low  $\eta$ . However, despite the different  $\alpha$ -values the  $i_0$  values are reported nearly the same for anodic ( $1.0 \times 10^{-3}$  A/cm<sup>2</sup>) and cathodic ( $0.93 \times 10^{-3}$  A/cm<sup>2</sup>) reactions (Tables II and III of the paper under discussion). It is difficult to rationalize this apparent inconsistency of the experimental results in terms of the suggested magnetic change of the oxide which will be paramagnetic in all cases at 264°C. However, one can suggest that since  $\alpha$  is inversely proportional to the thickness of the double layer,<sup>7</sup> it is likely that during anodic polarization of nickel in alkaline solution the thickness of the double layer by certain mechanism is almost nonexistent at 264°C compared to that produced by the cathodic reaction. This can explain the abruptly high rate constant for OER at 264°C. Such a theory may be confirmed by experiments outlined elsewhere<sup>7</sup> on the effect of suitable additives on overpotential for both HER and OER in alkaline solution. The other suggestion to explain the above inconsistency of results would be to analyze them in terms of surface coverage by intermediates (oxide or peroxide).<sup>8</sup>

**M. H. Miles,<sup>9</sup> G. Kissel,<sup>10</sup> P. W. T. Lu,<sup>11</sup> and S. Srinivasan:**<sup>10</sup> We appreciate the interest shown by Dr. Chatterjee in our paper and believe that he raised an interesting question regarding the similar  $i_0$  values for the HER and OER at high temperatures. Unfortunately, however, his calculations of the chemical rate constants contain the following serious errors.

1. The use of the potential,  $V$ , *vs.* the dynamic hydrogen electrode (DHE) at 10 mA/cm<sup>2</sup> by Dr. Chatterjee rather than the overpotential,  $\eta$ , makes the numerical values of the chemical rate constants dependent on the choice of a reference electrode. The equations

$$\eta_a = V - E_{ROE}$$

$$\eta_c = V - |\eta_{DHE}|$$

can be used to calculate the necessary anodic and cathodic overpotentials by using the numerical values for  $E_{ROE}$  and  $|\eta_{DHE}|$  given in Table I of our paper. The equations given by Dr. Chatterjee for calculating the chemical rate constants also have sign errors in the exponential terms. However, he apparently compensated for this in his calculations.

2. Dr. Chatterjee's calculation of the anodic rate constant is incorrect. Our reported anodic transfer coefficient for the OER,  $\alpha_a$ , should be used directly in the exponential term rather than  $1 - \alpha$ . This error accounts for Dr. Chatterjee's unusually high anodic rate constant of  $1.9 \times 10^{10}$  mole cm<sup>-2</sup> sec<sup>-1</sup> at 264°C. Even for a diffusion-limited reaction, the rate constant should be less than about  $10^{-3}$  mole cm<sup>-2</sup> sec<sup>-1</sup> according to Fick's first law. The correct expression for calculating the anodic rate constant is

$$k_a = \frac{i_a}{nF} e^{-\alpha_a F \eta / RT} \quad [1]$$

and a value of  $3 \times 10^{-9}$  mole cm<sup>-2</sup> sec<sup>-1</sup> is obtained

<sup>7</sup> R. Parsons and J. O'M. Bockris, *Trans. Faraday Soc.*, 47, 914 (1951).

<sup>8</sup> A. Damjanovic, A. Dey, and J. O'M. Bockris, *This Journal*, 113, 739 (1966).

<sup>9</sup> Department of Chemistry, Middle Tennessee State University, Murfreesboro, Tennessee 37132.

<sup>10</sup> Department of Applied Science, Brookhaven National Laboratory, Upton, New York 11973.

<sup>11</sup> Department of Materials Science, State University of New York at Stony Brook, Stony Brook, New York 11794.

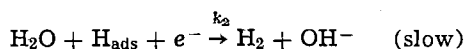
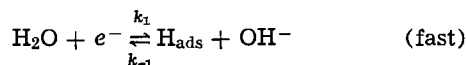


for the OER reaction at 264°C by using  $n = 4$  equiv./mole,  $\alpha_a = 3.3$ , and  $\eta = 0.03V$  at a current density of 0.010 A/cm.

Due to these errors, all of the chemical rate constants given by Dr. Chatterjee are incorrect and his comments based on these values are invalid. From Eq. [1],  $k_a = i_0/nF$  at zero overvoltage, hence the correct chemical rate constants are proportional to the exchange current densities, and their temperature dependencies would lead to the same activation energies as reported in our paper.

Several explanations can be offered for the similar  $i_0$  values observed for the HER and OER at high temperatures. The HER occurs on a bare nickel surface while the OER occurs on an oxide-covered surface. The roughness factor, therefore, may be considerably larger for the nickel anode surface than for the nickel cathode surface. This would tend to reduce the actual differences in  $i_0$  values for these two reactions. Also, increasing the temperature has a greater effect on the reaction of higher activation energy, hence the true differences in  $i_0$  values for HER and OER would diminish at higher temperatures.

Comparisons of  $i_0$  values are difficult due to the various parameters which affect the exchange current density. For the mechanism of the HER at high temperatures suggested in our paper



the exchange current density under Langmuirian conditions at low  $\eta$  is given by

$$i_0 = 2Fk_2 \frac{k_1}{k_{-1}} \frac{(a_{H_2O})^2}{a_{OH^-}} e^{-(1+\beta)F\Delta\phi_e/RT} \quad [2]$$

where  $\beta$  is the symmetry factor (usually about 0.5) and  $\Delta\phi_e$  is the absolute potential difference across the interface at equilibrium.<sup>12,13</sup> The ratio of rate constants,  $k_1/k_{-1}$ , is the equilibrium constant for the fast discharge step. According to LeChatelier's principle,  $k_1/k_{-1}$  will decrease with increasing temperature, hence this will tend to offset the normal increase of  $k_2$  with increasing temperature. This would account

<sup>12</sup> S. Srinivasan, Ph.D. Thesis, University of Pennsylvania, Philadelphia, Pennsylvania (1964).

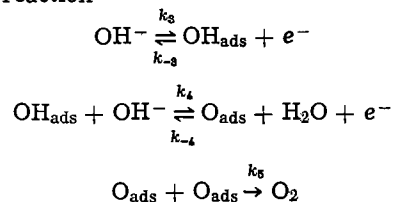
<sup>13</sup> J. O'M. Bockris and A. K. N. Reddy, "Modern Electrochemistry," Vol. 2, pp. 1238-1242, Plenum Press, New York (1971).

for the small increase in  $i_0$  for the HER at low  $\eta$  reported in our paper and explain the low  $\Delta H^\ddagger$  (8 kcal/mole) observed. For this same reaction mechanism at high  $\eta$ , the exchange current density

$$i_0 = 2Fk_2 a_{H_2O} e^{-\beta F\Delta\phi_e/RT} \quad [3]$$

is directly proportional to the rate constant,  $k_2$ , for the slow step. This would explain the larger  $\Delta H^\ddagger$  (14 kcal/mole) observed at high  $\eta$ .

Assuming the following mechanism for the oxygen evolution reaction



the exchange current density is given by

$$i_0 = 4Fk_3 (a_{OH^-}) e^{\beta F\Delta\phi_e/RT} \quad [4]$$

if the first electron transfer is the slow step. Since  $i_0$  is directly proportional to  $k_3$ , the observed  $\Delta H^\ddagger$  value of 18 kcal/mole could be related to the activation energy for this slow step. Since  $\Delta\phi_e$  may be quite different at the equilibrium potential for the OER as contrasted with the HER, it is difficult to relate the experimental differences in  $i_0$  found for these two reactions to the rates of the slow steps involved. Above 250°C where the nickel oxide becomes paramagnetic, the recombination of adsorbed oxygen atoms becomes the slow step, hence the expression for the exchange current density changes to

$$i_0 = 4Fk_5 \left(\frac{k_3}{k_{-3}}\right)^2 \left(\frac{k_4}{k_{-4}}\right)^2 \frac{(a_{OH^-})^4}{(a_{H_2O})^2} e^{4F\Delta\phi_e/RT} \quad [5]$$

For this mechanism,  $i_0$  no longer relates simply to the rate constant for the slow step. Equations 4 and 5 show that it is even difficult to compare  $i_0$  values for a given reaction if a change in the slow step occurs. For example, despite the significant rate increase observed for the OER between 208° and 264°C, the exchange current densities do not reflect this improvement in the kinetics.

In summary, the results presented in our paper are consistent with the above expressions, and, in fact, this theoretical analysis lends support to our original conclusions.



## A Rutherford Backscattering Analysis of Anodic Tantalum-Titanium Oxides

R. L. Ruth and N. Schwartz\*

Bell Laboratories, Murray Hill, New Jersey 07974

### ABSTRACT

Sputtered tantalum-titanium alloy thin films have been anodized in 0.01% aqueous citric acid, and the atom distribution, stoichiometry, and thickness determined by Rutherford backscattering analysis and stylus measurement. The anodic oxide film consists of a uniform amorphous mixture of  $Ta_2O_5$  and  $TiO_2$  with about 3% of the oxide at the electrolyte interface consisting of almost pure  $TiO_2$ . During anodization a small fraction of the titanium dissolves in the electrolyte. The apparent growth constant of the anodic oxide on  $Ta_{0.49}Ti_{0.51}$  films is  $1.88 \pm 0.02$  nm/V. The density of the oxide is determined as  $(5.9 \pm 0.2) \times 10^3$  kg/m<sup>3</sup>. From aqueous contact capacitance measurements, the dielectric constant of the alloy anodic oxide is  $24.7 \pm 0.9$ .

In an earlier paper (1), Schwartz and Peters investigated the suitability of tantalum-silicon alloys for use in tantalum thin-film component applications. Subsequently Silverman and Schwartz (2) related the properties of anodic oxide films formed on the tantalum-silicon alloy to their composition determined by Rutherford scattering. It has been found from this and other studies that alloying the tantalum with other metals generally increases the reliability of tantalum oxide thin-film capacitors. In cases investigated to date, however, this alloying has been accompanied by a decrease in the capacitance density of the film. It would be desirable to find a material which could maintain or improve the capacitance density characteristics while also increasing reliability.

Polycrystalline bulk titanium dioxide has a dielectric constant ranging from 48 to 110 depending upon phase (3), while in a recent review (4), the dielectric constants of anodic titanium oxides have reported values from 40 to 105, with some values as low as 21. These values are generally higher than those reported for anodic tantalum oxide of 26.7-27.6 (5, 6). The anodization of bulk Ta-Nb alloys (7) and bulk Ta-Ti alloy (8) have yielded oxide films with capacitance densities, and possibly dielectric constants, higher than that of tantalum alone, and it was anticipated that Ta-Ti anodized alloy films would have a higher capacitance density than comparable concentrations of silica (1) or alumina (5) in anodic tantalum pentoxide. To explore the possibility of Ta-Ti as a single material thin film system for passive integrated circuits, Peters and Schwartz (9) investigated tantalum-titanium for capacitor applications and its relation to the present tantalum thin-film technology. These results indicate that tantalum-titanium anodic oxide capacitors are superior to normal beta-tantalum based capacitors with respect to cathodic voltage life test stability. Oohashi and Yamanaka (10) had previously studied the resistive properties of tantalum-titanium alloy sputtered films.

This paper reports the results of a Rutherford backscattering analysis of approximately  $Ta_{0.5}Ti_{0.5}$  alloy samples and their anodic oxides as a function of anodizing voltage. Compositions of the films were determined before and after anodization, and a profile of the composition of oxides and unanodized films as a function of thickness were extracted from the spectra. Such information should yield insight into the mechanisms involved in the anodization process, and also complement the work done in earlier studies. For example, silicon and titanium can both have a bulk oxide valence of +4. If the mechanism of the two alloy anodizations were the same with respect to cation transport, then both silicon and titanium should have similar distributions in the anodic oxide. In the case of tantalum-silicon, anodization results in a duplex oxide, with an outer  $Ta_2O_5$  layer, and an inner layer consisting of a uniform mixture of  $Ta_2O_5$  and  $SiO_2$  (2). One purpose of this study was to determine whether the same distribution existed in tantalum-titanium anodized layers. Secondly, in order to understand the change in capacitance density with titanium additions, it is necessary to know the oxide film thickness. In a potentially complex oxide film, such as a duplex film, optical thickness determination techniques are difficult to interpret, and Rutherford scattering gives a direct result in terms of number of atoms per square centimeter, the atom distribution as a function of thickness, and stoichiometry.

### Experimental Procedure

*Sputtering, anodization, stylus measurement.*—The films used for this study were prepared in essentially the same way as described earlier (2).

The fused silica substrates used for the deposition were cleaned sequentially in: hot trichloroethylene vapor, ultrasonic agitation in detergent, boiling hydrogen peroxide, and overflow rinse in deionized water. The samples were dried in nitrogen at 110°C to remove bulk water and given a final half-hour bake at 550°C in air to remove traces of organic contaminants. After insertion into the vacuum station, the substrates were

\* Electrochemical Society Active Member.

Key words: alloys, sputtering, dielectric properties.



first heated at 500°C to remove gases adsorbed on the surface during exposure to air, and then cooled to 120°C. Deposition was accomplished by d-c diode sputtering of a composite cathode consisting of tantalum with titanium foil stretched across the surface. The sputtering was carried out in a glass bell jar pumped by a 6-in. oil diffusion pumping system with a liquid nitrogen trap. The atmosphere during deposition was argon at a pressure of  $20 \times 10^{-3}$  Torr (2.7 Pa). Sputtering from the 232 cm<sup>2</sup> cathode was done at a potential of 5 kV, a current density of 0.19 mA/cm<sup>2</sup>, and an interelectrode spacing of 7 cm. Following a 45 min pre-sputtering period during which the substrates were covered by a shutter, the films were deposited in 24 min. During the deposition, due to the energy of the discharge, the temperature rose from 120° to 180°C. The deposition rate varied from 0.8 to 1.2 nanometers/min depending on the relative areas of the tantalum and titanium at the cathode. For this study, the deposition resulted in films of approximately 50 atom per cent (a/o) Ti. The crystal structure was determined using a Read Camera (11), and found to be highly oriented single phase bcc with a cell constant of  $0.3307 \pm 0.0002$  nm.

For anodization, each  $2.5 \times 7.5$  cm slide was scribed and broken into six  $1.25 \times 2.5$  cm samples. On each sample, a thin piece of Minnesota Mining and Manufacturing electroplater's tape was used to mask the expected location of the electrolyte-air interface, and contact was made to the film with a small alligator clip. Anodization was performed in 0.01% citric acid using a tantalum cathode with an Electronic Measurements Incorporated constant current/constant voltage power supply. The current density during anodization was held at 1.5 mA/cm<sup>2</sup> until the desired voltage was reached, and then constant voltage was maintained for 20 min. The electroplater's tape was able to mask with a definition of 0.2 mm. All of the interference colors of the anodic oxide were bright and clear, indicating no obvious crystallization. Moreover, Read Camera x-ray analysis (11) indicated that all of the anodic oxides were amorphous with respect to Cu radiation.

For one sample, the thicknesses of the alloy film and the alloy anodic oxide were determined using a stylus method (12) after creating sharp steps using an electrochemical etching method in NH<sub>4</sub>Cl/absolute methanol solutions (13). This electrochemical etch completely undercuts the anodic oxide at the alloy-oxide interface leaving a transparent oxide which when dried is firmly adherent to the substrate allowing the stylus to traverse the step from the oxide-substrate very reproducibly.

The capacitance densities of the samples were determined on known areas of the samples in 8N sulfuric acid to minimize cell resistance, and on thin film capacitors with evaporated nichrome-gold counterelectrodes.

**Backscattering.**—Silverman and Schwartz describe the basic concepts behind the use of Rutherford backscattering in their work on the tantalum-silicon system (2). As in that study, the backscattering facility used was the Bell Laboratories van de Graaf accelerator. This apparatus, along with the equations used in analysis of the data, have been described in detail in an earlier paper (14).

In this study five anodized specimens were examined. All had been prepared from the same sputtered  $2.5 \times 7.5$  cm slide in order to provide a similar starting point for each case. Each sample was then anodized to a different final voltage: 46, 84, 134, 178, and 229V. In all cases the tantalum-titanium film was thick enough such that the alloy film was not consumed during anodization. Each specimen was analyzed in two different areas: (i) the original metal film, and (ii) the anodized film on top of the original metal film. Beam current was approximately 5 nA, and about 25 min was required to obtain counting statistics good to 1% for the titanium and oxygen regions of the spectra,

resulting in a total integrated beam charge of 6  $\mu$ C. The helium ion beam energy was  $1.90 \pm 0.01$  MeV. Energy resolution of the spectra was limited by the resolution of the silicon surface barrier detector to about 15 keV.

## Results

Figure 1 is the backscattered energy spectrum for the unanodized region of the sample subsequently anodized to 229V. The yields for the lower energy regions (titanium, argon, and substrate silicon-dioxide) have been magnified by a factor of 4 for clarity. Marks on the abscissa indicate the energies that detected particles would have if they were scattered by tantalum, titanium, argon, silicon, and oxygen atoms at the surface of a sample, calculated for the initial projectile energy of 1.90 MeV. The positions of the leading edges of the tantalum and titanium regions indicated on the figure show that both elements are present at the surface. Argon is trapped in the sputtered film during deposition, and one can see the trailing edge of the argon region on the left side of the titanium peak. The leading edge of the argon is hidden by overlap with the titanium peak.

Composition information can be extracted from data like Fig. 1 by comparing the yields of the various elements after removing the  $Z^2$  dependence of the scattering cross section. Determining the tantalum yield was straightforward since the background is less than 0.5% of the tantalum counts. The titanium and argon, however, presented a problem because of the overlap. Since other spectra indicated that argon is present up to the film surface, one could identify the leading and trailing edges of the argon region. In order to determine the magnitude of the argon yield, the assumption was made that argon is distributed uniformly throughout the film; this assumption is based on the results in the Ta-Si system, as well as the way the sputtering is done. One could then determine the argon yield from the height of the region to the left of the titanium plateau, and subtract an appropriate number of counts from that portion of the titanium plateau that overlaps the argon. Unlike the tantalum region, the background under the argon and titanium is significant and was subtracted from both totals.

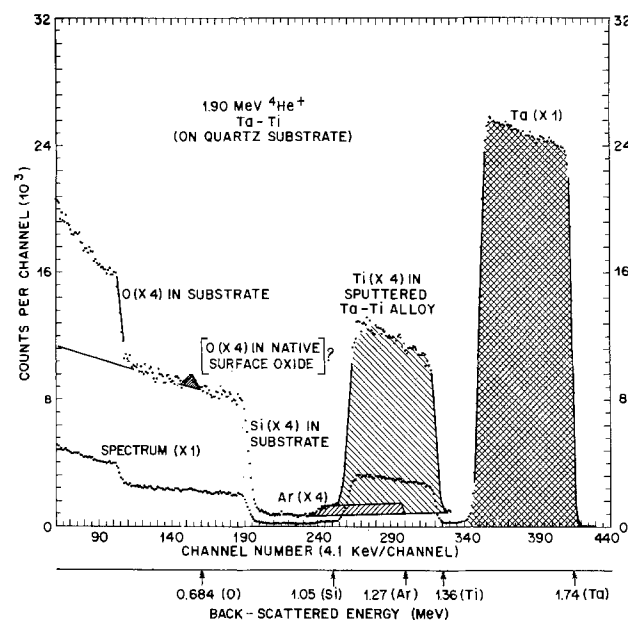


Fig. 1. Backscattered energy spectrum from a sputtered tantalum-titanium film about 260 nm thick, subsequently anodized to 229V. The yields for energies below those of the Ta region are shown magnified by a factor of 4. The energies marked on the abscissa are those of particles backscattered by the various elements (Ta, Ti, Ar, Si, O) at the surface of a film. The Ta, Ti, and Ar yields from the film are shaded and identified as are the Si and O yields from the fused silica substrate.

Table I. Film compositions of tantalum-titanium alloy films produced by d-c diode sputtering of a tantalum cathode with titanium foil stretched over the cathode surface

Sample No.	Identifying* anodization voltage, V	Composition
1	46	T <sub>20.47</sub> Ti <sub>10.49</sub> Ar <sub>0.038</sub>
2	89	T <sub>20.46</sub> Ti <sub>10.47</sub> Ar <sub>0.038</sub>
3	134	T <sub>20.45</sub> Ti <sub>10.48</sub> Ar <sub>0.038</sub>
4	178	T <sub>20.44</sub> Ti <sub>10.52</sub> Ar <sub>0.038</sub>
5	229	T <sub>20.45</sub> Ti <sub>10.51</sub> Ar <sub>0.038</sub>
Average		T <sub>20.47</sub> Ti <sub>10.49</sub> Ar <sub>0.038</sub>

\* This is the voltage to which the alloy film was subsequently anodized.

Table I shows the film composition determined for the unanodized samples. The argon level was  $\sim 4$  a/o, consistent with earlier findings (2). The metals were present in the ratio 49 a/o Ti/47 a/o Ta.

It is also possible to determine a profile of composition through the film using the raw data from a given spectrum. To do this, the yields from each element found at a given position in the film were considered. Backgrounds were subtracted from the yield of each element. Then each element's yield was adjusted to account for the scattering cross section dependence on atomic number. Peak widths of the lighter elements were increased to account for the decreasing width that accompanies a decrease in the atomic mass of the scattering species. Then a correction was made to account for the  $1/E^2$  scattering dependence so that scattering deep in the film, where projectile particles move with decreased energy, would be normalized to scattering near the surface. Finally, the yields were arbitrarily normalized. In order to generate this depth information, the stopping powers, initial ion energy, and energy width of the multichannel analyzer, along with the raw spectra, were used as input to a computer program that calculated the relative atomic concentrations of the individual elements as a function of depth. In this case there was no overlap of yields from the elements of interest. Brice (15) has published a rigorous treatment of the analysis problem that uses the stopping powers and reference spectra taken with the experimental setup used for the multiple element spectrum. Brice's treatment can also handle cases where there is partial overlap of the elemental yields.

The profile of Fig. 2 shows the result of such a procedure performed on the data of Fig. 1. In this figure, as well as Fig. 4, 5, and 6, the depth resolution is limited by the detector sensitivity which is equivalent to four channels, while the error in the relative atom concentrations is  $\pm 1\%$  for Ta,  $\pm 3.5\%$  for Ti, and  $\pm 5\%$  for O. Concentrations of tantalum and titanium through the alloy film shown in Fig. 2 are quite uniform. There is a slight decrease in the titanium concentration as the alloy film grows which is probably due to the Ti

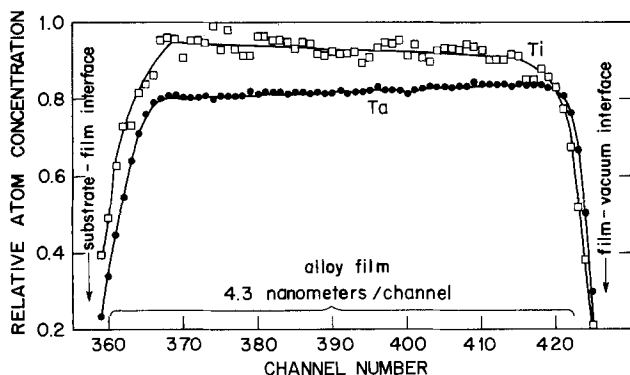


Fig. 2. Depth profile extracted from the spectrum of Fig. 1. Argon, which does not appear in the profile, was assumed to be uniformly distributed throughout the film in determining the Ti yield.

wires on the Ta cathode getting slightly coated with back-sputtered Ta and thus effectively decreasing the Ti sputtering area. Since argon is overlapped almost entirely by the titanium yield, it was assumed to be uniformly distributed throughout the film for this calculation.

The as-deposited samples were also used to determine the initial Ta-Ti alloy film thickness. When composition is known, one can use Bragg's rule to determine stopping powers for the mixtures, from

$$\frac{dE}{dx} \Big|^{AB} = (\text{wt. frac. A}) \frac{dE}{dx} \Big|^{A} + (\text{wt. frac. B}) \frac{dE}{dx} \Big|^{B} \quad [1]$$

where the stopping powers used by the authors are expressed in units of MeV/g/cm<sup>2</sup> (16). The stopping powers can then be used to calculate kinematic factors for the different elements

$$[s]_{A}^{AB} = k_A \frac{dE}{dx} \Big|_{in}^{AB} + \frac{dE}{dx} \Big|_{out}^{AB} \quad [2]$$

where

$$k_A = \left[ \frac{M_A - m_{He}}{M_A + m_{He}} \right]^2 \quad [3]$$

where  $M_A$  and  $m_{He}$  are the masses, respectively, of the scattering atom and helium. Using this kinetic factor,  $[s]$ , and the experimental energy width from the spectrum,  $\Delta E_x$ , one can calculate the alloy film mass surface density

$$d_s = \frac{\Delta E_x}{[s]_{x^{xy}}} \quad [4]$$

The above analysis yields an average  $d_s$  of  $(264 \pm 13) \times 10^{-5}$  kg/m<sup>2</sup>. The density of the alloy film can be evaluated from the lattice constant by

$$d = \frac{2[n_{Ta}A_{Ta} + n_{Ti}A_{Ti} + n_{Ar}A_{Ar}]}{N \times a^3} \quad [5]$$

where  $n_i$  = experimental atom fractions,  $N$  = Avogadro's number,  $a$  = experimental lattice constant, 0.3307 nm.

Use of Eq. [5] results in a density of  $10.2 \times 10^3$  kg/m<sup>3</sup>. This value is in agreement with the value calculated from the bulk lattice constant (0.32084 nm) (17) of  $10.7 \times 10^3$  when it is corrected by a factor of 0.964 to result in a value of  $10.3 \times 10^3$ . This factor of 0.964 is based on the ratio of the observed sputtered tantalum film density (18) to bulk tantalum density, and is caused by the incorporation of argon and other defects in sputtered films.

The density of  $10.2 \times 10^3$  kg/m<sup>3</sup> in combination with the determined surface density of  $(264 \pm 13) \times 10^{-5}$  kg/m<sup>2</sup> results in an average film thickness of  $259 \pm 13$  nm. This value is in excellent agreement with the stylus instrument value of  $262 \pm 5$  nm determined directly on an etched step.

Figure 3 is a spectrum taken from the sample anodized to 89V. The yield in the higher energy region due to scattering from tantalum and titanium is reduced due to the presence of oxygen which contributes to the energy loss of the helium ions and thus reduces the number of tantalum and titanium atoms per unit energy loss. In the low energy part of the spectrum one can see the oxygen yield in a position corresponding to oxygen at the surface and in the anodized part of the film.

The composition of the anodized region was determined for each of the five samples. Boundaries of the oxide plateaus in both the tantalum and titanium peaks were determined using a technique reported earlier by Mitchell *et al.* (19). The channel number of the plateau's low energy boundary (half-height) was taken to be the channel number of the midpoint between the oxide plateau and the as-deposited plateau. The oxy-

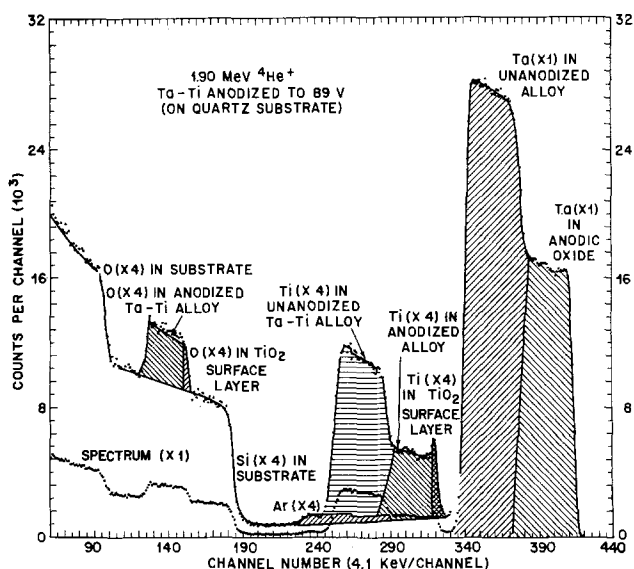


Fig. 3. Backscattered energy spectrum from a sputtered tantalum-titanium film anodized to 89V. The Ta and Ti regions are now each divided into two areas, anodized and unanodized as marked on the figure. Si and O in the substrate are shown as in Fig. 1, but now O yield from the oxide region appears superimposed on the substrate Si. The oxygen yield is consistent with the assumption that the oxides formed are Ta<sub>2</sub>O<sub>5</sub> and TiO<sub>2</sub>.

gen yield from the oxide was found by drawing a line along the silicon substrate yield and extending it under the oxygen yield. Determining the argon yield involved considerable uncertainty since the leading argon edge is under the titanium plateau. The assumption was made that the argon remained essentially stationary with respect to the original metal/air interface and so the amount in the anodized region could be estimated reasonably well.

Table II shows the results of a compositional analysis for oxide regions of the five samples. Average compositional ratios for Ta:Ti:O:Ar are 1.2:1:5.3:0.1, respectively. Table II suggests that the oxides are Ta<sub>2</sub>O<sub>5</sub> and TiO<sub>2</sub>, since the excess oxygen indicated in the table is within the previously stated  $\pm 5\%$  error for oxygen. In cases where the Ta and Ti spectra overlap, they can be separated because part of the Ti peak can be discerned as a partial projection above the Ta spectrum.

Figures 4 through 6 show depth profiles extracted from the spectra of the samples anodized to 46, 89, and 134V. (Meaningful profiles could not be extracted from the other two spectra because of overlap of tantalum and titanium dioxide yields.) Figures 5 and 6 plainly show a characteristic that can also be seen on the raw spectra: the appearance after anodization of a narrow peak at the high energy edge of the titanium dioxide region. Close examination of the leading edges of the tantalum spectra from the original and anodized samples shows that the tantalum region has moved to lower energy indicating that there is titanium, but not

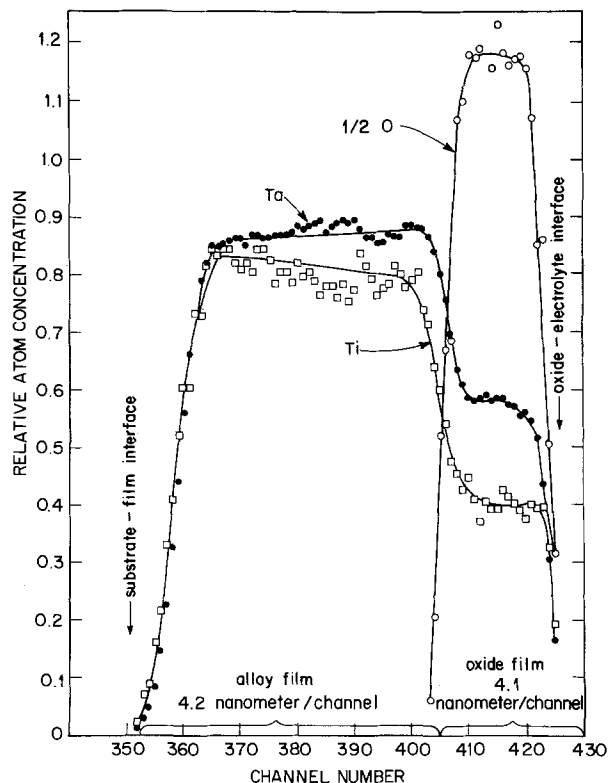


Fig. 4. Depth profile extracted from the spectrum of the 46V sample. Composition is relatively uniform in the as-deposited and anodized areas.

tantalum, present at the surface of the film. This shift is seen at the right edge of Fig. 6. One can see that the titanium is oxidized, because the yield from oxygen in the oxide begins at the surface energy; this surface oxide is assumed to be titanium dioxide. The spectra from samples anodized to 178 and 229V also indicate the presence of this titanium dioxide surface layer, but indirectly since overlap of the tantalum and titanium regions obliterate the titanium leading edge. In these cases one can observe only that the leading edge of the tantalum region has shifted to a lower energy and that oxygen remains at the surface. From the depth profiles and spectra, then, one finds that anodization can lead to the formation of an oxide surface layer that is very rich in titanium and ends up almost entirely as a titanium oxide. The layer is not apparent (either absent or unresolvable) at the lowest anodizing voltage investigated, but it appears for higher voltages with a thickness dependent on the magnitude of the voltage.

Oxide film surface densities were determined for the anodized films in a manner similar to that described above for the as-deposited samples. Results are plotted in Fig. 7 vs. the anodization voltage for each sample. The solid line is the least squares fit (20) for all points with an apparent anodization constant of  $(1.15 \pm 0.02) \times 10^{-5} \text{ kg}/(\text{m}^2\text{-V})$ .

Table II. Relative atomic concentrations of tantalum-titanium anodic oxides produced by anodization. In addition to the observed oxygen level for each sample, the expected oxygen level, assuming the presence of only Ta<sub>2</sub>O<sub>5</sub> and TiO<sub>2</sub>, is given.

Stoichiometries of anodized (Ta-Ti) oxides

Sample No.	Anodization voltage (V)	Observed Ta:Ti:O:Ar	Theoretical oxygen expected for Ta <sub>2</sub> O <sub>5</sub> , TiO <sub>2</sub>	Observed O / Expected O $\times 100\%$
1	46	1.26:1.0:5.78:0.10	5.15	112
2	89	1.55:1.0:5.98:0.12	5.88	102
3	134	1.10:1.0:4.84:0.09	4.75	102
4	178	1.05:1.0:4.73:0.08	4.63	102
5	229	1.09:1.0:5.35:0.09	5.00	107
Average				105

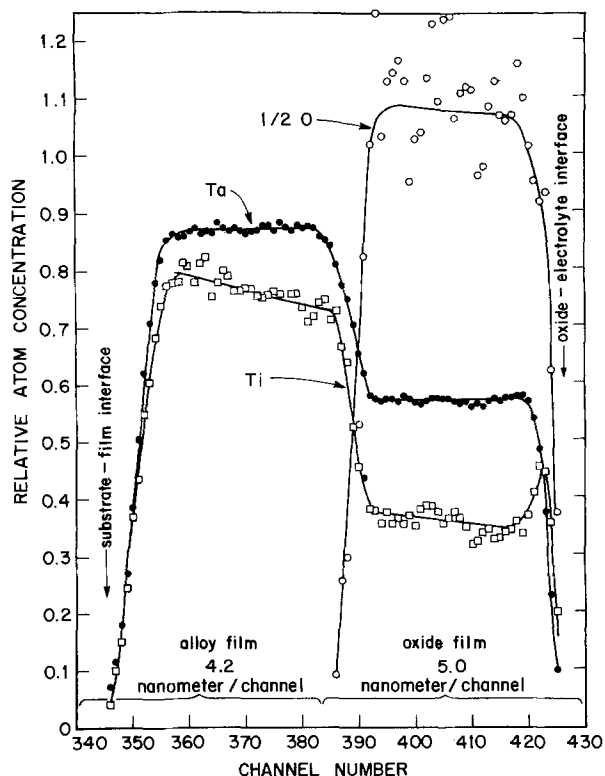


Fig. 5. Depth profile extracted from the spectrum of Fig. 3. Composition is relatively uniform in the different areas except near the surface where an increase in Ti concentration and a corresponding decrease in Ta occurs.

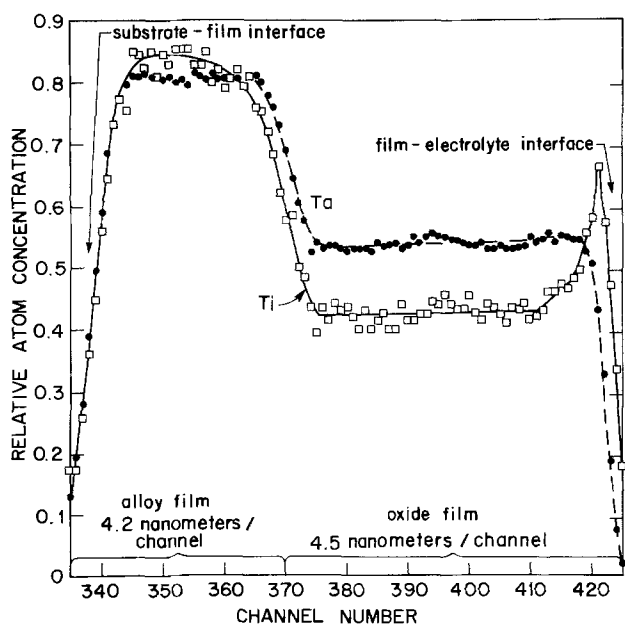


Fig. 6. Depth profile extracted from the spectrum of the 134V sample. Indicated results are similar to those of Fig. 5.

The density of the anodic oxide film was determined for one sample from the surface density (sample 3, Table III) of  $(157 \pm 4) \times 10^{-5} \text{ kg/m}^2$  and the stylus determined thickness of  $266 \pm 19 \text{ nm}$ , resulting in a value of  $(5.9 \pm 0.2) \times 10^3 \text{ kg/m}^3$ .

The determined density of the anodic oxide,  $(5.9 \pm 0.2) \times 10^3 \text{ kg/m}^3$ , can be compared to a value estimated from the densities of anodic tantalum oxide and "anodic" titanium dioxide. The value of the former is  $7930 \pm 3\%$  (6). The value of the latter is an average of the bulk values (21) of brookite and anatase decreased by a factor of 0.967 to account for the observed

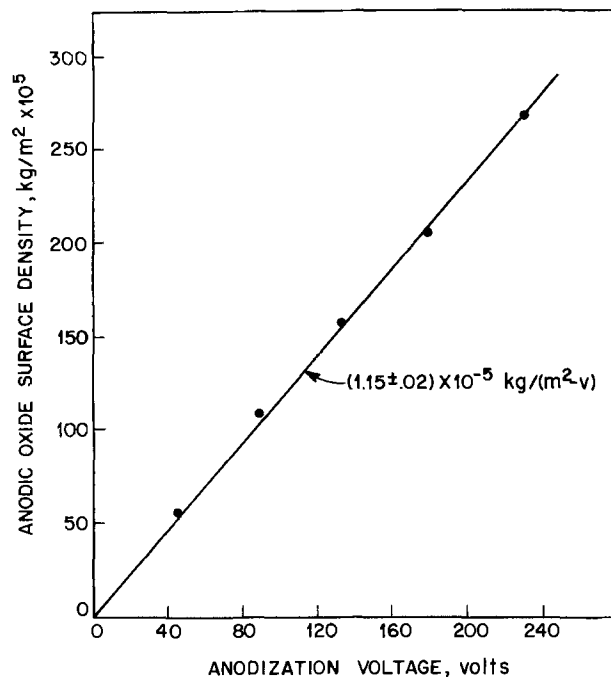


Fig. 7. Graph showing a plot of anodized film surface density determined from the Rutherford backscattering for the five samples vs. the anodizing voltage for each.

density ratio of anodic tantalum oxide/bulk tantalum oxide (i.e., 7930/8120). These estimates lead to a value of  $3870 \text{ kg/m}^3$  for anodic titanium dioxide. The density can then be calculated by a formula which seems to be quite accurate for determining bulk alloy densities

$$d_{\text{calc}} = \frac{\sum n_i A_i^0}{\sum n_i V_i^0} \quad [6]$$

$$V_i^0 = A_i^0 / d_i^0 \quad [7]$$

where  $n_i$  is the atom or mole fractions,  $A_i^0$  is the atomic or molecular weights,  $V_i^0$  is the atomic or molecular volumes, and  $d_i^0$  is the bulk densities. In these calculations,  $1780 \text{ kg/m}^3$  is used for argon (21). For sample 3, the density is calculated by

$$d_{\text{calc}} = 0.98 \frac{n_{\text{Ta}_2\text{O}_5} A_{\text{Ta}_2\text{O}_5} + n_{\text{TiO}_2} A_{\text{TiO}_2} + n_{\text{Ar}} A_{\text{Ar}}}{n_{\text{Ta}_2\text{O}_5} V_{\text{Ta}_2\text{O}_5} + n_{\text{TiO}_2} V_{\text{Ta}_2\text{O}_5} + n_{\text{Ar}} V_{\text{Ar}}} + 0.02 \frac{A_{\text{TiO}_2}}{V_{\text{TiO}_2}} = 6.08 \times 10^3 \text{ kg/m}^3$$

Table IIIA. Oxide film surface mass densities, volume densities, and thicknesses

Sample No.	Anodization voltage (V)	Surface density $\text{kg/m}^2 \times 10^5$	Volume density $\text{kg/m}^3$	Thickness nm
1	46	56	6240	90
2	89	109	6380	171
3	134	157	6080	258
4	178	205	6070	338
5	229	257	6070	423

Table IIIB. Approximate values for outer  $\text{TiO}_2$  layer determined from the shift of the leading tantalum edge, before and after anodization (Density  $\text{TiO}_2$ :  $3870 \text{ kg/m}^3$ )

Sample No.	Anodization voltage (V)	Surface density $\text{kg/m}^2 \times 10^5$	Approximate thickness nm
1	46	0	0
2	89	1.6	4
3	134	3.2	8
4	178	4.8	12
5	229	6.4	17

The second term in this equation accounts for the small  $\text{TiO}_2$  layer on the surface. A comparison of this value to the determined value of  $5.9 \times 10^3$  indicates that this method for anodic oxides is accurate to about 3%, and is within the probable error of the real value.

The density can also be calculated by another possible rule which sums the mole fraction times the bulk densities for each component

$$d_{\text{calc}}^2 = \sum n_i d_i^0 \quad [8]$$

which for sample 3 would be

$$d_{\text{calc}}^2 = 0.98 [n_{\text{Ta}_2\text{O}_5} d_{\text{Ta}_2\text{O}_5}^0 + n_{\text{TiO}_2} d_{\text{TiO}_2}^0 + n_{\text{Ar}} d_{\text{Ar}}^0] + 0.02 d_{\text{TiO}_2}^0 = 5.10 \times 10^3 \text{ kg/m}^3$$

This value when compared to the actual value of  $5.9 \times 10^3$  might indicate that there was about 14% porosity in the oxide. To evaluate the possibility of porosity, capacitance measurements were made in an aqueous electrolyte and metal counterelectrodes with the assumption that porosity of the order 14% would result in a considerably higher capacitance for the former.

Figure 8 shows the reciprocal capacitance/area ( $\text{m}^2/\text{F}$ ) as a function of anodization voltage in 8N sulfuric acid, as well as the reciprocal capacitance/area for nichrom-gold counterelectrodes for a sample anodized to 230V and a comparable figure for beta-tantalum based capacitors. At 230V, the capacitance for the wet electrolyte and metal counterelectrode differ by only 3%, indicating no high degree of porosity. Moreover the capacitance/area of the tantalum-titanium anodic oxide at 230V is 7% lower than that obtained for beta-tantalum capacitors. The least squares line in Fig. 8 gives a value for the slope equal to  $(8.6 \pm 0.3) \text{ m}^2/(\text{F}\cdot\text{V})$ .

The ability of Eq. [6] to calculate the true density for sample 3 was used to calculate variations in density for the other oxide films (see Table IIIA, column 4), due to composition variations because of loss of titanium (see below); these densities were used to calculate thicknesses (Table IIIA, column 5). The oxide thicknesses are plotted against anodization voltages in Fig. 9, and the solid line is the least squares fit to the points. The least squares evaluated slope is  $1.88 \pm 0.02 \text{ nm/V}$ . This anodization constant in combination with the value of  $(8.6 \pm 0.3) \text{ m}^2/(\text{F}\cdot\text{V})$  allows a calculation of the dielectric constant as  $24.7 \pm 0.9$ . All of these values are collected in Table IV.

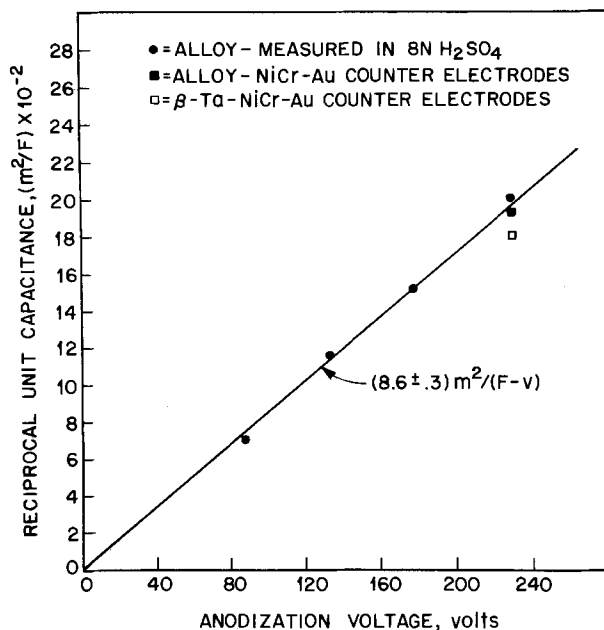


Fig. 8. Graph of reciprocal unit capacitance density against anodization voltage.

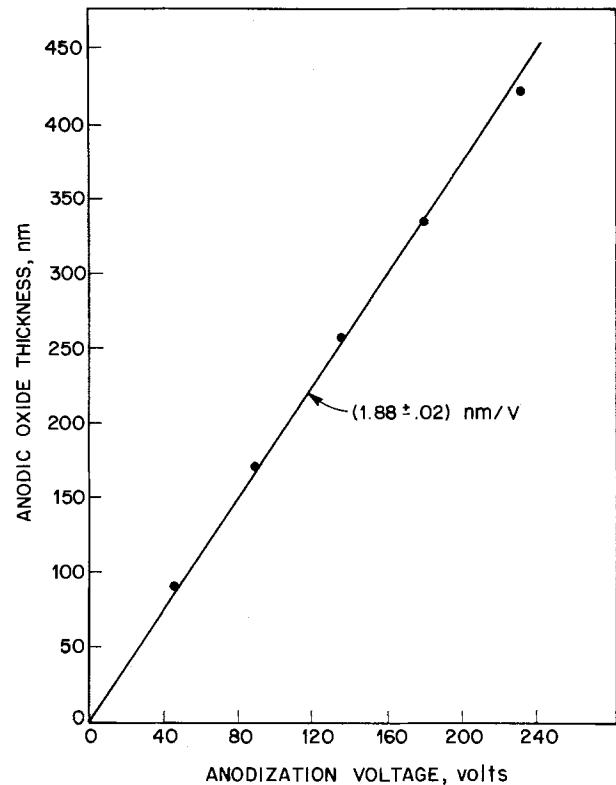


Fig. 9. Graph of thickness of anodic oxide against anodization voltage.

The profiles of Fig. 4-6 show that behind the surface titanium dioxide layer the oxide composition is relatively uniform. They do indicate, however, that the metal atom compositions in the anodized and unanodized regions are different, *i.e.*, that titanium may have been lost from the system during anodization. The possibility was checked by summing the titanium and tantalum yields in both the unanodized and anodized spectra for the sample anodized to 134V. The Ta:Ti ratio for the unanodized sample was 9.54:1. For the anodized sample, however, the ratio was 10.3:1, indicating a titanium loss of about 8%. Loss of titanium during anodization was finally confirmed by a chemical Coprex analysis (22) of the citric acid solution after anodization: titanium was detected in an amount indicating an 18% loss from the film. No test was made for tantalum in the solution, but anodization of tantalum alone in this electrolyte has never previously given any indication of tantalum dissolution. Table V gives the Ti:Ta ratios in the metal alloy and anodic oxide, as well as the percentage loss in Ti. There may

Table IV. Collected values of determined and calculated constants

A. Sputtered alloy film: $\text{Ta}_{0.47}\text{Ti}_{0.48}\text{Ar}_{0.04}$	
1. Lattice constant (bcc)	$= 0.3307 \pm 0.0002 \text{ nm}$
2. Density	$= (10.2 \pm 0.4) \times 10^3 \text{ kg/m}^3$
B. Anodic oxide: $\sim[(\text{Ta}_2\text{O}_5)_{0.85}(\text{TiO}_2)_{0.88}][\text{Ar}]_{0.05}$	
1. Density	$= (5.9 \pm 0.2) \times 10^3 \text{ kg/m}^3$
2. Anodization constant	$= (1.88 \pm 0.02) \text{ nm/V}$
3. Reciprocal charge storage	$= (8.6 \pm 0.3) \text{ m}^2/(\text{F}\cdot\text{V})$
4. Dielectric constant	$= 24.7 \pm 0.9$

Table V. Loss of titanium during anodization

Sample No.	Anodization voltage (V)	Ti/Ta ratio		Ti loss %
		Alloy	Oxide	
1	46	1.04	0.79	24
2	89	0.96	0.65	32
3	134	1.00	0.91	9
4	178	1.18	0.95	19
5	229	1.13	0.92	19
				21%

be a slight tendency for the Ti loss to be higher at lower anodization voltages.

### Discussion and Conclusions

In this study, anodic oxides were grown on sputtered tantalum-titanium thin films. Analysis of the as-deposited films indicated that the tantalum and titanium were distributed uniformly throughout the films by the sputtered process. Analysis after anodization revealed that a relatively uniform distribution of tantalum and titanium existed in the anodized region of the film in contrast to the duplex film in the anodized tantalum-silicon alloys. Three other growth effects were apparent:

1. In all but the 46V (low voltage) sample, a thin surface layer of titanium dioxide was formed during anodization. The thickness of the layer was directly dependent on the final anodization voltage; and most of the layer was essentially devoid of tantalum.

2. A change in the relative amounts of tantalum and titanium in the anodized region indicated a relative loss of titanium during anodization which was essentially confirmed by analysis of the solution for titanium after anodization.

3. The oxide growth constant of 1.88 nm/V is approximately equal to that of both tantalum (2) and titanium (4) alone, and also approximately equal to that of Ta-Si anodization (2).

As mentioned in the introduction, one reason for investigating Ta-Ti films was that the dielectric constant of titanium dioxide in bulk, and frequently in anodic oxides, is greater than that of Ta<sub>2</sub>O<sub>5</sub>. Because of this high bulk dielectric constant and the previous experimental results (7, 8), it was considered possible that addition of titanium to the tantalum would increase the capacitance density of the resulting oxide. The capacitor film studies (9) showed that the capacitance density decreases with increasing titanium dioxide content, but reaching only a 7% loss at about a Ta<sub>0.5</sub>Ti<sub>0.5</sub> alloy as indicated in Fig. 8; this decrease is less than that obtained with equivalent additions of Al<sub>2</sub>O<sub>3</sub> (5) or SiO<sub>2</sub> (1).

The present study shows that the anodization constant of 1.88 nm/V for this Ta<sub>2</sub>O<sub>5</sub>-TiO<sub>2</sub> combination is about equal to that for either Ta<sub>2</sub>O<sub>5</sub> or TiO<sub>2</sub> alone. The value of the dielectric constant, 24.7, is less than that of anodic tantalum oxide. There is no clear model for calculating the dielectric constants of solid solutions, but it is apparent that the addition of TiO<sub>2</sub> to anodic Ta<sub>2</sub>O<sub>5</sub> is not particularly efficient in raising the dielectric constant using these particular anodization conditions.

A further analysis of the previous tantalum-silicon data (2) is given below and indicates that during anodization of those films the tantalum cation transport mechanism is essentially the same as that for bulk tantalum alone, while the silicon remains relatively stationary. This mechanism leads in the tantalum-silicon case to the formation of a duplex oxide with an outer Ta<sub>2</sub>O<sub>5</sub> layer and an inner uniform mixture of Ta<sub>2</sub>O<sub>5</sub> and SiO<sub>2</sub>. The present study found that a duplex oxide is also formed but in this case with a very small amount of titanium dioxide at the surface while a uniform "amorphous" mixture of Ta<sub>2</sub>O<sub>5</sub> and TiO<sub>2</sub> composed the bulk of the oxide.

The data of the previous study (2) on the tantalum-silicon system can be interpreted in the following way. Examination of Fig. 4 in Ref. (2) indicates that the leading edge of the argon atom distribution is associated with the leading edge of the silicon atom distribution. Since the leading edge of the argon atom distribution was originally associated with the surface of the tantalum-silicon film at the electrolyte interface, it essentially acts as a transport marker if it does not move significantly during the anodization. Implanted argon has been used previously by Pringle (23) in bulk tantalum to determine the transport numbers of tantalum and oxygen to be 0.25 and 0.75, respectively.

He also demonstrated that the argon does not move significantly during the anodization, and it is reasonable to make the assumption in the present tantalum-silicon alloy case. With that assumption, it can be calculated that the tantalum cation transport is about 0.3, quite close to the pure bulk tantalum transport number; silicon cation transport is essentially zero, and it is oxidized by the migration of oxygen inward where the oxygen transport number is about 0.7.

A possible explanation for the feature that the tantalum cation moves in this system, while the silicon cation does not, is based on the fundamental equation of cation transport for anodic oxides

$$i_1^+ = i_1^0 e^{-\frac{(W - q_1 a E)}{kT}} \quad [9]$$

where  $i_1^+$  = fraction of current carried by cation 1;  $i_1^0$  = pre-exponential constant;  $W$  = activation energy separating two potential minima for a single cation jump;  $q_1 a E$  = decrease of the barrier height  $W$  due to the movement of a particle with effective charge,  $q_1$ , with half the jump distance,  $a$ , in a field,  $E$ ;  $k$  = Boltzmann constant;  $T$  = absolute temperature. If a second cation exists in an alloy system, then its transport equation is

$$i_2^+ = i_2^0 e^{-\frac{(W - q_2 a E)}{kT}} \quad [10]$$

where it is assumed that, because of the common environment,  $W$ ,  $a$ , and  $E$  are essentially equal for the two cationic species, while  $i_1^0$  and  $i_2^0$  are of the same order of magnitude. The ratio of the two currents then is

$$\log \frac{i_1^+}{i_2^+} = \frac{(q_1 - q_2) a E}{2.303 kT} \quad [11]$$

For  $q_1 - q_2$  equal to 1,  $a$  equal to about  $1.0 \times 10^{-8}$  cm, and  $E$  equal to  $5.5 \times 10^6$  V/cm, the ratio of

$$\frac{i_1^+}{i_2^+} = 8.5 \quad [12]$$

Thus for two cationic species differing by unit charge, one will essentially migrate, while the other will remain stationary. For the tantalum-silicon system the end point stoichiometry indicates that the oxide consists of a mixture of Ta<sub>2</sub>O<sub>5</sub> (Ta = +5) and SiO<sub>2</sub> (Si = +4). It is reasonable to assume that during transport, if the cations move at all, that their charge will differ by unity, and therefore, from the above equation, segregation will take place. This appears to be one possible explanation for the duplex film formed in the tantalum-silicon case.

The stoichiometry of the tantalum-titanium anodized film indicates a mixture of Ta<sub>2</sub>O<sub>5</sub> (Ta = +5) and TiO<sub>2</sub> (Ti = +4), and the above argument would require the formation of another duplex film. The appearance of a relatively uniform distribution in this case may be attributed to one of two possible mechanisms:

1. Since the argon leading edge is hidden by other peaks, it cannot be used as an internal transport marker. Therefore, it is quite possible that the entire cation transport mechanism has changed and its rate is essentially zero. On this basis, oxidation occurs by oxygen moving inward. This possibility may be compatible with some reports (4) that anodization of titanium takes place by oxygen migration. In this mechanism the small TiO<sub>2</sub> fraction at the surface would be due to a relatively small transport of titanium cations to the surface.

2. An alternative assumption can be made that the cation transport has not essentially changed from the pure tantalum or tantalum-silicon cases. This would imply that a major fraction of movement of the tantalum and titanium occurs by identical cation transport numbers with a very small fraction of the titanium moving by some faster mechanism. Rigo and Seijka (24) have proposed both a short and long range mech-

anism of niobium transport in the duplex structure of anodic oxides of tantalum films on bulk niobium. In the present tantalum-titanium alloys, a small amount of long range transport of titanium seems to exist to provide the small, pure,  $\text{TiO}_2$  film at the surface. An intriguing possibility for this long range fast transport is that it is due to the titanium ionizing to two different charge states. If this latter proposal is finally proven to be accurate, one can describe the effective charges of the various species as:  $\text{Si} = n - 1$ ;  $\text{Ta} = \text{Ti} = n$  (small amount of  $\text{Ti} = n + 1$ ).

Actually in order to make any concrete conclusions about relative effective ionic charges, detailed experiments are required with true transport markers and dilute concentration of the alloying element to ensure that the assumption of equal  $i_1^0$ ,  $i_2^0$ ,  $W$ ,  $a$ , and  $E$  holds for Eq. [9] and [10].

We have demonstrated in these studies that relatively minor changes in the nature of the chemical species, such as Si to Ti, causes a major change in the atom distribution. This sensitivity may lead to experiments which can probe in detail the fundamental mechanistic steps in anodic oxidation. In the past, arbitrary assumptions had to be made about the cation charge number, which led to unusually high values of " $a$ ", the half-jump distance. Further experiments of this sort may clear up this ambiguity.

#### Acknowledgments

The authors gratefully acknowledge valuable discussions and comments by C. D. Thurmond, W. Brown, R. P. Frankenthal, J. Poate, and A. English. Particularly, Ms. S. Vincent was responsible for the Coprex analysis, and F. G. Peters for the preparation of the Ta-Ti alloy films. We wish to thank the reviewers for very probing comments.

Manuscript submitted March 26, 1976; revised manuscript received Aug. 2, 1976.

Any discussion of this paper will appear in a Discussion Section to be published in the June 1977 JOURNAL. All discussions for the June 1977 Discussion Section should be submitted by Feb. 1, 1977.

Publication costs of this article were assisted by Bell Laboratories.

#### REFERENCES

1. N. Schwartz and F. G. Peters, Proc. Elec. Comp. Conf., p. 251, (1973).
2. P. J. Silverman and N. Schwartz, *This Journal*, **121**, 550 (1974).
3. Gmelin's "Handbook of Inorganic Chemistry," 8th ed., pp. 248-250, Verlag Chemie, Weinheim, Bergstrasse (1951).
4. A. Aladjem, *J. Mater. Sci.*, **8**, 688 (1973).
5. D. G. Muth, *J. Vac. Sci. Technol.*, **6**, 749 (1969).
6. L. Young, "Anodic Oxide Films," p. 82, Academic Press, London & New York (1961).
7. *Ibid.*, p. 192.
8. R. H. Lorenz and A. B. Michael, *Electrochem. Technol.*, **2**, 160 (1974).
9. F. G. Peters and N. Schwartz, To be submitted to *This Journal*.
10. T. Oohashi and S. Yamanaka, *Elec. and Comm. Japan.*, **55-C**, 59 (1972).
11. M. H. Read and D. Hensler, *Thin Solid Films*, **10**, 123 (1972).
12. N. Schwartz and R. Brown, *Trans. Am. Vac. Soc.*, **1961**, 836.
13. N. Schwartz and M. Gresh, *This Journal*, **112**, 295 (1965).
14. T. M. Buck, J. M. Poate, K. A. Pickar, and C. M. Hsieh, *Surface Sci.*, **35**, 362 (1973).
15. D. K. Brice, in "Proc. Int. Conf. on Ion Beam Surface Layer Analysis," J. W. Mayer and J. F. Ziegler, Editors, p. 121, Elsevier-Sequoia SA, Lausanne (1974).
16. J. F. Ziegler and W. K. Chu, *At. Data Nucl. Data Tables*, **13**, 463 (1974).
17. D. Sommers-Smith, *J. Inst. Metals*, **81**, 73 (1952-1973).
18. R. Brown, in "Measurement Techniques for Thin Films," B. Schwartz and N. Schwartz, Editors, pp. 178-190, The Electrochemical Society, Soft-bound Symposium Series, New York (1967).
19. I. V. Mitchell, M. Kamoshida, and J. W. Mayer, *J. Appl. Phys.*, **42**, 4378 (1971).
20. J. Topping, "Errors of Observation and Their Treatment," p. 102, 105, Reinhold Publishing Corp., New York (1960).
21. "Handbook of Chemistry and Physics," R. C. Weast, Editor, 56th ed., CRC Press (1975-1976).
22. C. L. Luke, *Anal. Chem. Acta*, **41**, 237 (1968).
23. J. P. S. Pringle, *This Journal*, **120**, 398 (1973).
24. S. Rigo and J. Seijka, *Solid State Commun.*, **15**, 259 (1974).

# Mechanical Failure of Anodic Films on Aluminum and Tantalum

Y. H. Choo\* and O. F. Devereux\*\*

Department of Metallurgy and Institute of Materials Science, University of Connecticut, Storrs, Connecticut 06268

## ABSTRACT

Anodized specimens of aluminum and tantalum were deformed in laboratory air; strain to failure and the failure characteristics of the oxide film were evaluated optically. Barrier-type anodic aluminum oxide films of thickness greater than  $\sim 400\text{\AA}$  failed at  $\sim 0.925\%$  strain normal to the tensile axis and apparently suppressed substrate slip emergence. Thinner anodic films on aluminum failed along substrate slip traces at  $\sim 1.12\%$  strain. These films did not suppress slip emergence, but were apparently stronger. The presence of a porous oxide superimposed on thin barrier-type films caused them to fail in the thick film mode; this was the only effect of a porous layer. Anodic films on mechanically polished tantalum failed at  $\sim 0.28\%$  strain, independent of thickness, but showed a failure mode dependence on thickness analogous to that of aluminum. Films on chemically polished tantalum substrates always failed in simple tension, but showed a thickness dependence, failing at  $\sim 0.14\%$  strain for thicknesses greater than  $\sim 680\text{\AA}$ , and  $\sim 0.20\%$  strain for thicknesses less than that value. Failure of these films was accompanied by separation of the films from the substrate.

Environment-sensitive failure processes such as stress corrosion cracking and corrosion fatigue involve a complex interplay of chemical and mechanical aggression and are far from well understood. Oxide film failure is seen by many investigators as a necessary prelude to the initiation and propagation of cracks in these processes (1-7). The literature dealing with the mechanical behavior of oxide films is not voluminous, and reported values of mechanical properties, e.g., Young's modulus, film strength, and film failure strain, exhibit large variations. Edeleanu and Law (8) strained thick porous anodic films on aluminum in tension and found them to be elastic, with failure occurring at 1-2% strain normal to the tensile axis. Bradhurst and Leach (9, 10) deformed aluminum specimens bearing barrier-type anodic films, detecting film failure by a variety of electrical methods to occur at 1-3% strain. For  $1500\text{\AA}$  films removed from the substrate, a failure strain of 2.48% and a Young's modulus of  $\sim 41 \times 10^3 \text{ MN/m}^2$  were determined. Also using electrical detection methods, Bubar and Vermilyea (11, 12) found thin anodic films on aluminum to exhibit some ductility, while thick films were brittle. They also observed a large ductility, as much as 50% elongation prior to fracture, in anodic tantalum oxide films tested in this wet manner, in marked contrast to the value of 0.83% reported by Eliezer and Brandon (13), who used a (dry) bulge test technique. In earlier work Young (14) had attributed this discrepancy to the presence of a surface film on chemically polished specimens. This film gave rise to poor adhesion of the anodic oxide, with consequent oxide detachment and brittle behavior, whereas removal of this "preanodic" film by leaching in boiling water resulted in a very adherent, ductile anodic oxide. Grosskreutz (15, 16) found anodic aluminum oxide films, both adherent to and separated from the substrate, to be elastic to fracture with the strain at failure being in the range of 0.1-0.3%. In adherent films fracture was seen both at slip steps and normal to the tensile axis. Humidity was found to have a significant effect on the oxide modulus with films displaying the bulk modulus under vacuum, but a value an order of magnitude lower at ambient humidity. In these studies fracture strain was seen to increase with humidity. Grosskreutz found a similar correlation between the water content of various environments and the density of cracks created

in anodic films on aluminum alloys by straining (17); as discussed later the crack density is directly related to the moduli of the film and substrate. Brandon *et al.* (18, 19) found a dependence of the failure strain and strength of barrier-type anodic aluminum oxide films on thickness. These parameters generally increased with thickness, although some results indicated a marked decrease in strength in films thicker than  $\sim 2000\text{\AA}$ . The elastic modulus in these studies was seen to decrease as film thickness increased to  $750\text{\AA}$ , beyond which it was constant.

Some observations have been made on the effect of an oxide film on the mechanical behavior of the substrate. Block *et al.* (20, 21) observed that thick anodic oxide films inhibited slip emergence at the surface of aluminum single crystals except where film cracking or buckling had occurred, and that the oxide/substrate interface was capable of withstanding significant shear strain. Although Block *et al.* reported some strengthening of the substrate by the anodic film, Leach *et al.* (22-24) reported a nearly 50% increase in the strength of a thin aluminum wire when coated with a  $2600\text{\AA}$  anodic film, provided the film remained intact. The effect vanished upon film failure at  $\sim 2\%$  strain. They also observed an increase in elongation in the presence of an anodic current, inferring that the oxide no longer strengthened the substrate but became ductile under the influence of an ionic flux. This they attributed to a field-activated diffusional mechanism for plastic deformation of the oxide, similar to the Herring-Nabarro model. Devereux *et al.* (25) have studied the failure strain of anodic films formed on an aluminum alloy as a function of the pH of an aqueous environment using electrical detection methods. A small, but significant pH dependence was seen with failure strain being maximum at pH 8, which was assumed to be the zero point of charge of the anodic film.

The following report deals primarily with the failure of anodic films on aluminum, with some observations on tantalum, these materials appearing to represent extremes of mechanical behavior in the aforesaid studies. The environment in all cases was laboratory air. Particular attention was devoted to the dependence between film failure and deformation of the substrate.

## Experimental Procedures

**Aluminum.**—A high purity aluminum ingot (99.99%) was sliced into plates 6.35 mm in thickness which were subsequently rolled into sheets of 0.254, 0.508, and 0.762 mm thickness. These sheets were cut into

\* Electrochemical Society Student Member.

\*\* Electrochemical Society Active Member.

Key words: anodic oxide, aluminum oxide, tantalum oxide.



rectangular specimens  $127 \times 12.7$  mm, from which were machined tensile specimens with a gauge length of 31.75 mm and a gauge width of 6.35 mm. Compression specimens of square cross section,  $5.08 \times 5.08 \times 15.24$  mm, were also prepared by slicing. All specimens were mechanically polished through 600 grit SiC paper to remove surface and edge irregularities, and were ultrasonically cleaned in benzene for 30 min. Following this preparation, the specimens were annealed, chemically polished, electropolished, and anodized according to the previously described procedures (26).

Deformation of both tensile and compression specimens was accomplished with a Hounsfield Type W tensometer fitted with a variable speed d-c drive motor. In this apparatus the applied load was measured by noting the movement of a mercury column caused by deflection of a calibrated spring beam. Strain was measured by means of an Instron extensometer of 25.4 mm gauge length clipped to the specimens. This was monitored with a Daytronic Model 300D transducer amplifier equipped with a Type 96 strain gauge input module. All tests were performed in laboratory air of nominal temperature  $\sim 23^\circ\text{C}$  and nominal relative humidity  $\sim 40\%$ . Strain rates were typically 0.03%/min. Specimens were deformed to predetermined values of strain while under observation with a low power ( $60\times$ ) binocular microscope. Deformed specimens were examined in detail with a high quality optical metallograph equipped with a Nomarski-type interference system. Films removed from deformed specimens were also examined by transmission electron microscopy.

Measurements of the Young's modulus of adherent oxide films on aluminum were made by performing flexure tests on small beams,  $57.15 \times 6.35 \times 0.0765$  mm. Deflection, before and after application of an anodic film of known thickness, was measured with a cathetometer under both end loading and center loading. Loads of 3 to 20 mg were used, and deflection was measured to 0.01 mm.

**Tantalum.**—Specimens were prepared from polycrystalline tantalum sheet of 99.9% purity and 0.254 mm thickness following, in essence, the above procedure. After ultrasonic cleaning, however, specimens were polished using one of two methods: chemical polishing for 20 sec in a solution of 5 parts by volume sulfuric acid (98%), 2 parts nitric acid (70%), and 2 parts hydrofluoric acid (48%) or mechanical polishing through  $0.05 \mu\text{m}$  alumina dust. Specimens were subsequently anodized in a solution of 1 weight percent (w/o) ammonium borate in double distilled water, using an anodizing potential in the range of 10-100V and an anodizing time of 3 hr. In order to study the morphology of such films, sample films were stripped using both cathodic polarization (14) and cellulose tape techniques. Mechanical testing was similar to that described for aluminum. The behavior of films formed on substrates subjected to leaching in boiling water was not studied.

## Results

**Aluminum oxide films.**—*Failure strain determination.*—To determine the effect of porous oxide growth on the failure strain of anodic aluminum oxide films, annealed and electropolished specimens were anodized at 50V for periods ranging from 45 min to 24 hr, corresponding to porous oxide layers from 0 to  $1550\text{\AA}$  in thickness superimposed on a barrier layer  $650\text{\AA}$  in thickness (26). Film failure was defined by the appearance of a distinct discontinuity in the film when viewed at  $1000\times$  subsequent to imposing a predetermined strain upon the specimen. Typical results are shown in Fig. 1, which indicates an apparent lack of failure strain dependence on porous layer thickness. A similar independence of anodizing time was seen for films formed at other potentials. Anodizing potential did effect failure strain, however, as shown in Fig. 2. The data shown represent the lowest strain

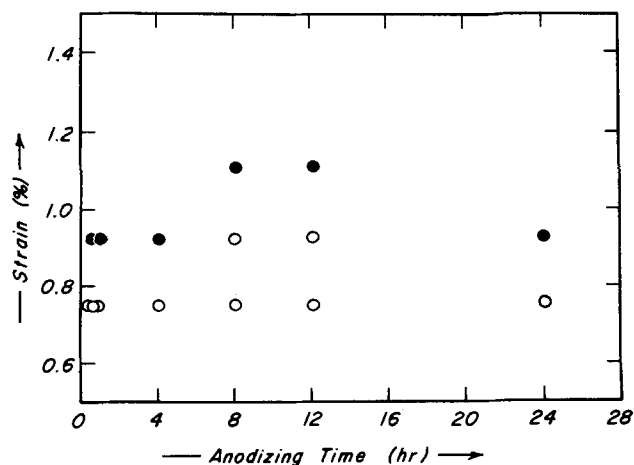


Fig. 1. Failure strain vs. anodizing time for anodic films formed on aluminum at 50V. Solid points denote failure; open points, unfailed specimens.

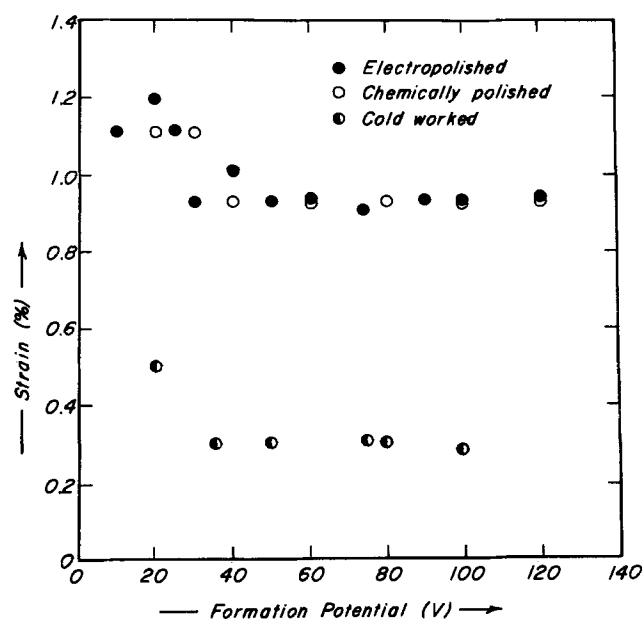


Fig. 2. Failure strain vs. formation potential for anodic films formed on aluminum.

value at which film failure was noted for a given anodizing potential. A distinct trend toward higher failure strains for films formed at potentials less than 30V is evident. Films formed on annealed and chemically polished substrates behaved in a similar manner, exhibiting no dependence of failure strain on anodizing time and the same dependence on anodizing potential, shown in Fig. 2, as did films formed on electropolished substrates. Also shown in Fig. 2 are data pertaining to films formed on substrates that were cold-worked prior to chemical or electropolishing. Although exhibiting a similar dependence on anodizing potential, these films failed at significantly lower strain values, indicating a dependence on the stress state of the substrate.

**Fracture behavior.**—In general two types of fracture were observed: (i) fracture along substrate slip steps at the failure strain of  $\sim 1.1\%$  seen in films at potentials of less than 30V, and (ii) fracture approximately normal to the tensile axis at the failure strain of  $\sim 0.9\%$  seen in films formed at potentials of 30V or more. In each case, as straining progressed failure in the other fracture mode occurred. That is, in films formed at less than 30V cracks were observed to form normal to the tensile axis at strains larger than required for the initial failure along slip steps, while in the thicker films which failed initially normal to the tensile axis further straining causes failure along

slip steps. Initial failure in fracture modes (i) and (ii), above, is shown in Fig. 3 and 4, respectively. A film formed at 35V, which initially showed fracture lines normal to the tensile axis when strained to 1.5%, is shown in Fig. 5 after straining to 10%. Displacement of the normal fracture lines by the subsequently occurring slip failure is evident.

In these studies, formation of substrate slip lines was clearly evident, especially in the case of electropolished

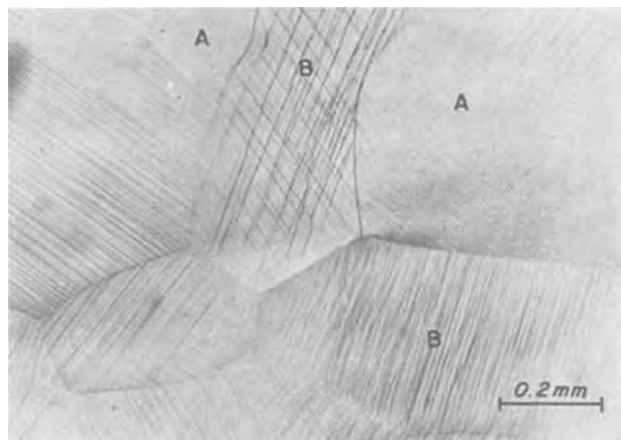


Fig. 3. 20V aluminum oxide film and substrate subsequent to 3% strain. Tensile axis is horizontal. Grains denoted A show substrate slip, but no film failure; grains denoted B show film failure along lines of substrate slip.



Fig. 4. 50V aluminum oxide film and substrate subsequent to 1.2% strain. Tensile axis is horizontal. Normal film fracture.



Fig. 5. 35V aluminum oxide film and substrate subsequent to 10% strain. Tensile axis is horizontal. Normal film failure followed by failure at substrate slip lines.

specimens, at strains as low as 0.5%. Careful optical examination did not reveal film fracture, however, at these low strain values. Removal of the films and examination by transmission electron microscopy substantiated this fact, *i.e.*, that the anodic oxide films were able to tolerate a considerable amount of substrate slip without failure. Although it is not clearly evident, Fig. 3 illustrates both substrate slip without film failure, in grains labeled A, and substrate slip with accompanying film fracture along the slip traces, in grains labeled B. Clearly, failure occurred first in those grains which suffered the greatest deformation, *i.e.*, those grains whose primary slip systems were most favorably oriented with respect to the maximum resolved shear stress,  $45^\circ$  to the tensile axis. In general, there is no indication of fracture initiation at grain boundaries, although the fractures seen in Fig. 3 clearly terminate with the slip traces at the boundaries. In the case of thicker films, *e.g.*, as shown in Fig. 4, normal fracture lines propagated independently of substrate slip traces and of grain boundaries. This case is clearly distinguishable from that illustrated in Fig. 5, where subsequent occurrence of fracture at slip traces caused displacement of the normal fracture lines. Similarly, in the case of thick films formed on chemically polished substrates, the normal fracture lines propagated unaffected by the marked hillock structure characteristic of chemical polishing, as shown in Fig. 6. In no case was deformation seen to have caused detachment of an aluminum oxide film from the substrate.

The mode of fracture of films formed at potentials less than 30V did exhibit a dependence on anodizing time, *i.e.*, on porous layer thickness. For example, a 25V film anodized for 45 min failed initially along substrate slip traces as described above, but a 25V film anodized for 8 hr failed in the normal fracture mode. Films formed at potentials of 30V or greater failed initially in the normal mode irrespective of anodizing time. Films formed on cold-worked substrates failed in the same manner as did those on annealed substrates, *i.e.*, normal fracture in thick films and fracture along substrate slip traces in thin films. Although film failure normal to the tensile axis was always seen as sharp, well-defined, continuous fracture lines, two types of fracture behavior were seen along substrate slip traces. In one, a sharp, well-defined, straight fracture along the slip trace was seen; in the other short fracture segments, each wholly or partially normal to the tensile axis, formed along each slip trace. The latter behavior is shown in Fig. 7.

In general, film fracture did not initially occur uniformly throughout the specimen gauge length, especially in the case of cold-worked substrates. Initial film failure occurred first in regions where there was a local concentration of shear deformation. In the

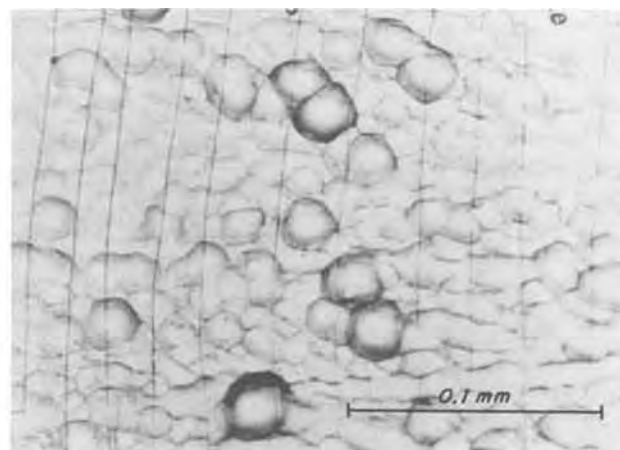


Fig. 6. 100V aluminum oxide film on chemically polished substrate with typical hillock structure subsequent to 1.2% strain. Tensile axis is horizontal.

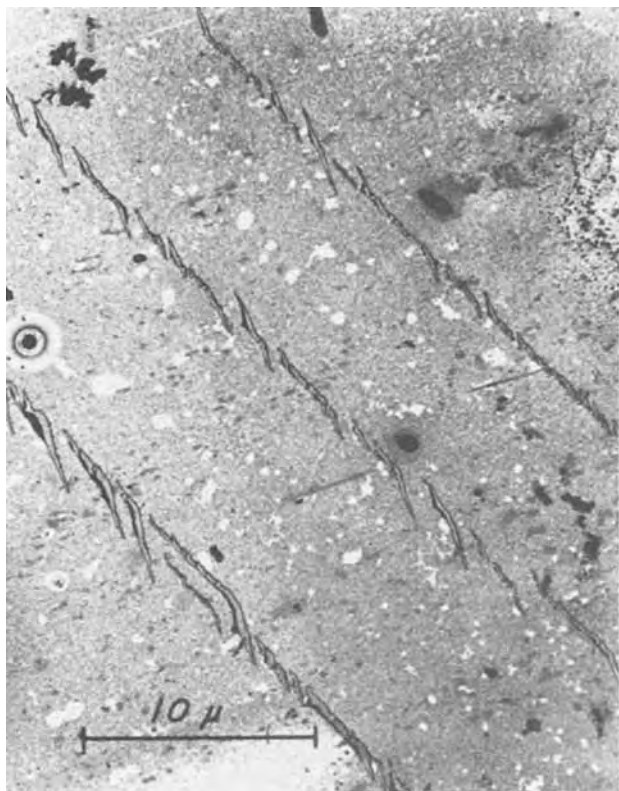


Fig. 7. Transmission electron micrograph of 20V aluminum oxide film strained to 3% showing discontinuous fracture along substrate slip lines. Substrate was reanodized after straining to patch cracked regions in film.

case of thick films, the region in which normal fracture lines were seen progressed along the specimens as did the region of substrate deformation, with fracture lines eventually becoming uniformly distributed throughout the gauge length of the specimen. On continued deformation, new fracture lines formed approximately midway between existing fractures. This process continued up to a certain strain level, beyond which no new cracks initiated. Accordingly, the average spacing between normal fracture lines is plotted in Fig. 8 as a

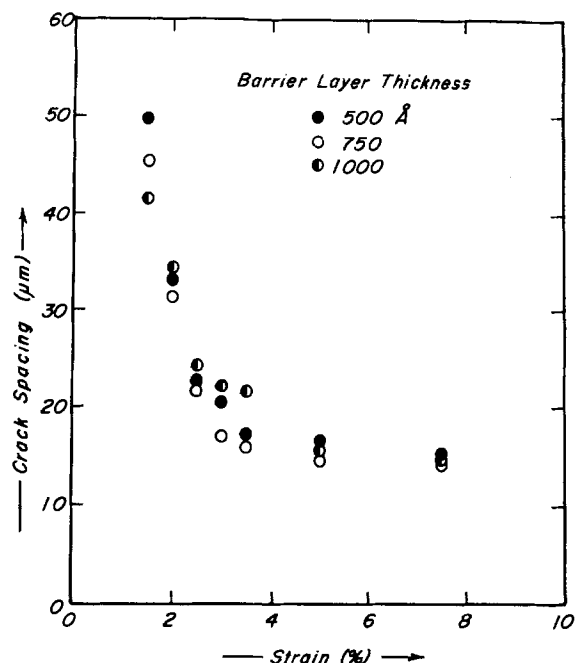


Fig. 8. Terminal crack spacing vs. strain for anodic aluminum oxide films of various (barrier-layer) thicknesses.

function of strain for several different film thickness values. These films were formed for 45 min only, and thus are simple barrier-type films. Using a stress relaxation analysis, Grosskreutz and McNeil (27) demonstrate that such data should follow

$$\ln(\epsilon/\epsilon_0) \approx (4g/d) [1 - (d/d_0)] \quad [1]$$

where  $d$  is crack spacing and  $\epsilon$  is strain, with  $(d_0, \epsilon_0)$  representing a convenient reference point. The significance of  $g$  was not established. As shown in Fig. 9 the present data follow Eq. [1] approximately until the crack spacing approaches the critical value of 15 μm beyond which further strain does not produce new cracks. It is not clear why the 1000 Å film deviates from the behavior exhibited by the 500 and 750 Å films.

Upon deforming compression specimens anodized in the range of 20-100V, film failure along substrate slip traces was seen in the strain range 1.4-1.7% as shown in Fig. 10. Upon further straining to 2.3-3.0% regularly spaced cracks were seen to form parallel to the compression axis, i.e., in the direction of substrate dilation. Assuming constant substrate volume, the compressive strain of 2.3% corresponds to a tensile strain of 1.15% in good agreement with the strain at which normal failure was seen in the tensile tests.

Young's modulus of adherent aluminum oxide.—An anodized aluminum beam may be regarded as a composite beam of two materials and may be analytically reduced to an equivalent beam of one

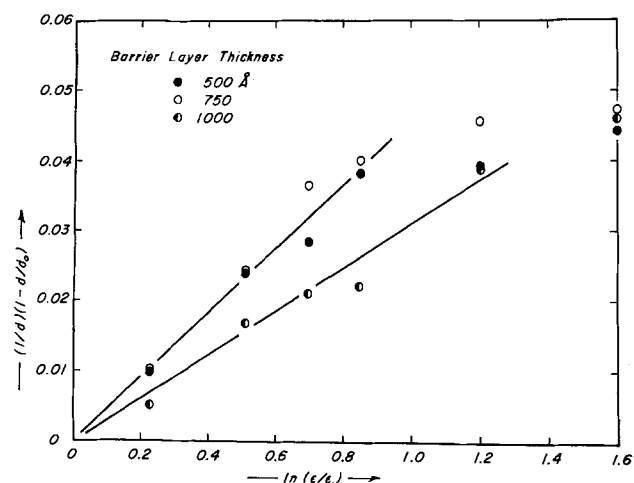


Fig. 9. Data of Fig. 8 plotted according to Eq. [1]

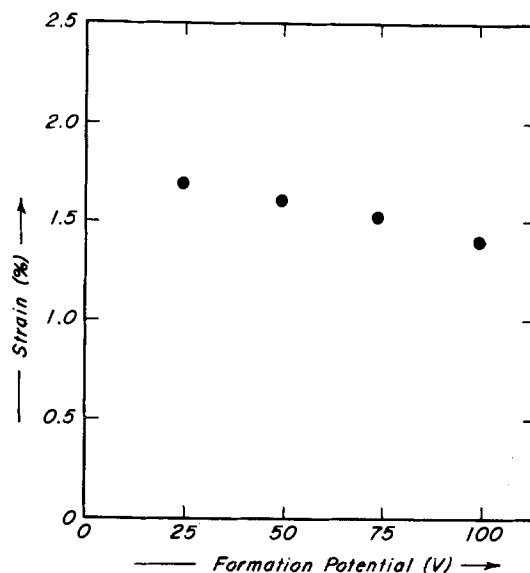


Fig. 10. Failure strain vs. formation potential for anodic aluminum oxide films on compression specimens.

material by transforming the dimensions of the beam section in accord with the ratio of the elastic moduli of the two materials. In doing so, we may express the flexure formula for a cantilever beam in end loading as

$$E_o = \frac{4Rl^3 - E_m X t_m^3}{2[4X t_o^3 + 3X t_m t_o (t_m + 2t_o)]} \quad [2]$$

where  $E_o$  and  $E_m$  are the moduli of the oxide and metal, respectively;  $R$ , the load/deflection ratio;  $l$ , the length of the beam;  $X$ , the width of the beam; and  $t_m$  and  $t_o$ , the thickness of the metal and of the oxide, respectively. The thickness of the oxide may, of course, be established by the anodizing ratio, and the thickness of the metal may be related to its thickness before anodizing,  $t_i$ , and the oxide thickness through the oxide density (28)

$$2t_o = 1.38(t_i - t_m) \quad [3]$$

Equation [2], thus contains on the right-hand side only measurable or calculable parameters and is valid for small deflections, corresponding roughly to the elastic range of the beam. In evaluating the load ratio,  $R$ , however, for a number of beams, it was found to be a function of the applied load as shown for a typical beam in Fig. 11, decreasing approximately linearly with increasing load before leveling off to an apparently constant value. This unexpected behavior was attributed to inaccuracy in measurement of the deflection, suggesting that the constant value of load ratio seen at higher loads was the true value. The modulus was estimated in this manner to be  $41.4 \times 10^3 \text{ MN/m}^2$  ( $6 \times 10^6 \text{ psi}$ ), in good agreement with values obtained by Bradhurst and Leach (9) and Grosskreutz (15).

**Tantalum.—Anodizing characteristics.**—In potentiostatic anodizing of high purity tantalum in aqueous ammonium borate, the anodic current decreases rapidly with time for the first 1/2 hr, followed by a slower continuous decrease, the anodic current being  $\sim 1 \mu\text{A/cm}^2$  after 3 hr and approaching  $0.1 \mu\text{A/cm}^2$  after several more hours. This is in contrast with the gradual increase in current with time seen in anodizing of aluminum coincident with pore formation and, indeed, there is no indication of pore formation in anodic tantalum oxide films. In comparison to chemically polished substrates, the leakage current on mechanically polished substrates was somewhat higher and took longer to stabilize. Although films formed on mechanically polished substrates were very adherent and could not be stripped, those on chemically polished

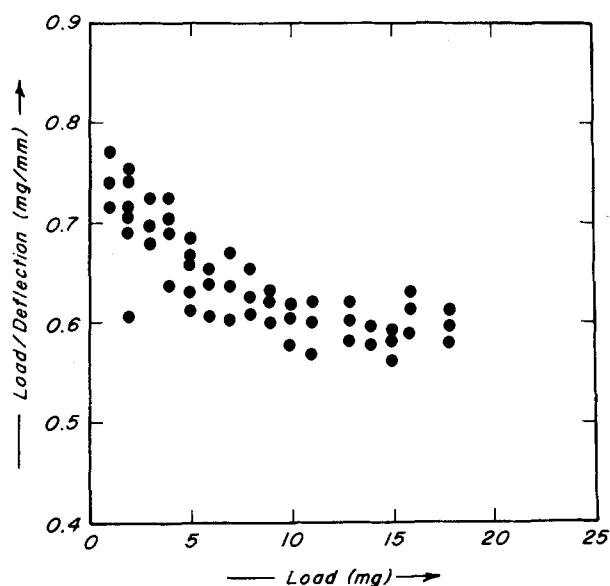


Fig. 11.  $R = \text{load/deflection}$  vs. load for composite aluminum/aluminum oxide beam.



Fig. 12. Transmission electron micrograph of anodic tantalum oxide film formed on chemically polished substrate at 50V for 3 hr.

substrates were only weakly adherent and easily removed by cathodic polarization or by cellulose tape. A transmission electron micrograph of such a film is shown in Fig. 12. Although electron diffraction by these films revealed an amorphous structure regardless of formation potential, crystallization was seen to occur in the microscope in localized areas due to electron beam heating. These areas had a diffraction pattern consistent with that of  $\beta\text{-Ta}_2\text{O}_5$ .

**Failure strain determination.**—For purposes of observing failure strain in anodic tantalum oxide, films were formed at potentials ranging from 20 to 100V, corresponding to thicknesses ranging from 340 to 1700Å based on the anodizing constant of 17 Å/V (11, 12). Failure strain is shown in Fig. 13 as a function of formation potential for both chemically polished and mechanically polished substrates. The behavior of films formed on chemically polished substrates is analogous to that of aluminum oxide films in that a discernable increase in failure strain is seen for films formed at potentials of 30V or lower, being  $\sim 0.14\%$  for the thicker films and increasing to  $\sim 0.2\%$  for thinner films. In contrast, films on mechanically polished substrates fail at a significantly higher strain,  $\sim 0.28\%$ , and exhibit no potential, i.e., thickness, dependence.

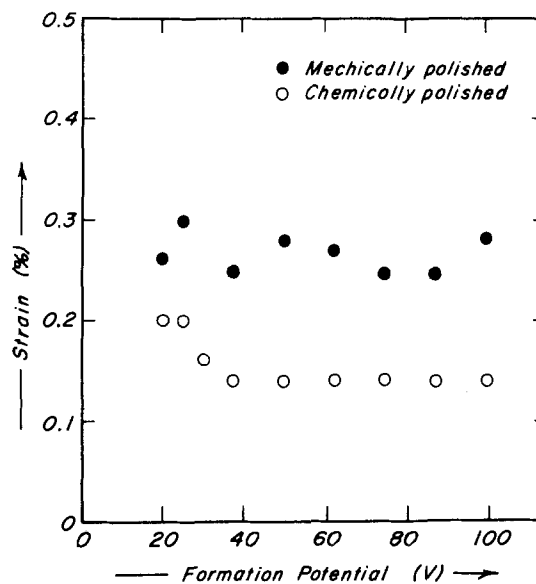


Fig. 13. Failure strain vs. formation potential for anodic films formed on tantalum.

**Fracture behavior.**—As mentioned above, film fracture was observed at strains as small as 0.14% in chemically polished specimens, coincident with substrate yield. No film detachment or film fracture was observed in the elastic strain region of the substrate; however, at the onset of yielding the film was seen to detach in localized areas, but only where substrate slip had occurred. Fracture initiation in the film appeared to be approximately coincident with film detachment. The localized regions of film detachment within areas of substrate yield initiated at substrate grain boundaries or triple junctions and propagated parallel to the tensile axis; film fracture appeared to be associated with the substrate grain boundaries, but propagated essentially normal to the tensile axis. These features are seen in Fig. 14, in which both film fractures and substrate grain boundaries can be distinguished. Detached areas of oxide film are evidenced by the optical interference patterns. Macroscopically, areas of film detachment were indicated by a marked change in interference color; for example, regions of substrate yield in 100V specimens were a vivid yellow in appearance in contrast to the normal blue of the unstrained film. This is due to an alteration of the interference condition occasioned by replacing the high index metal phase at the second reflecting interface by a low index air phase, thus altering the phase change upon reflection (14). Due to the very weak nature of the substrate-film bond, the stress relaxation mechanism of Grosskreutz and McNeil (27) did not appear to be operative, the normal film fracture lines displaying a somewhat random spacing as seen in Fig. 15.

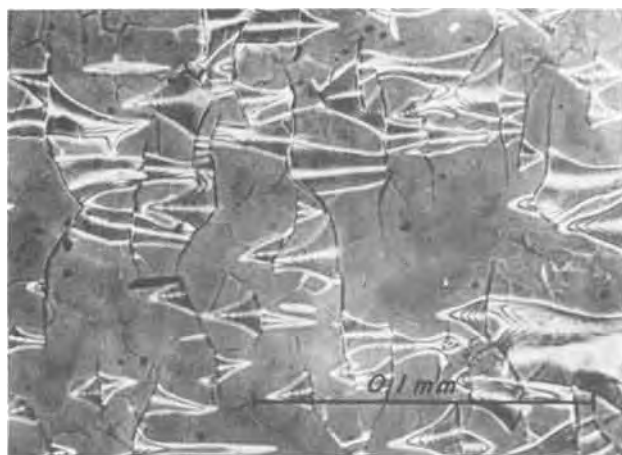


Fig. 14. 30V tantalum oxide film on chemically polished substrate subsequent to 3% strain. Tensile axis is horizontal. Film fracture and separation initiating at substrate grain boundaries.



Fig. 15. 100V tantalum oxide film on chemically polished substrate subsequent to 0.45% strain. Tensile axis is horizontal. Random spacing of normal fracture lines.

In contrast, films formed on mechanically polished substrates showed no indication of detachment, either by change in interference color or by the occurrence of interference fringes, upon straining of the substrate. Fracture lines tended to be short and irregular, appearing normal to the tensile axis in thicker films, Fig. 16, and following substrate slip in thinner films, Fig. 17, in analogy to the behavior seen in aluminum oxide films.

### Discussion

**Aluminum.**—*Failure parameters.*—As previously noted, other investigators (8, 9, 15) have found a considerable range in the failure strain of anodic aluminum oxide, bracketing the values found in this investigation. To a certain extent this may be attributed to differences in both forming and testing environments; however, it is also reasonable to suspect inaccuracies in fracture detection methods, especially indirect techniques relying upon electrical measurements. The optical technique used in this investigation appears to offer a definitive means of establishing a strain range within which film failure occurs, as established by subsequent transmission electron microscopy of detached films. Clearly the failure strain of anodic aluminum oxide films is independent of variations in substrate preparation, provided that the films remain adherent during testing, of porous layer thickness, and of barrier layer thickness beyond thicknesses of the order of 400Å. Bradhurst and Leach (9) observed a similar increase in fracture strain for thin anodic films on aluminum, although at higher strain values, and Beams *et al.* (29) observed an increase in

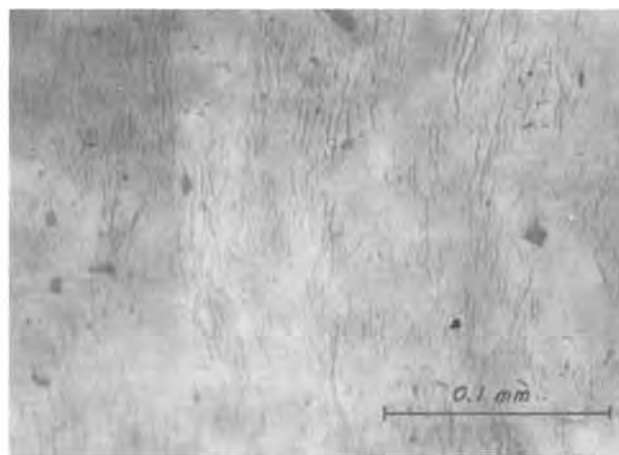


Fig. 16. 100V tantalum oxide film on mechanically polished substrate subsequent to 2% strain. Tensile axis is horizontal. Normal film fracture.

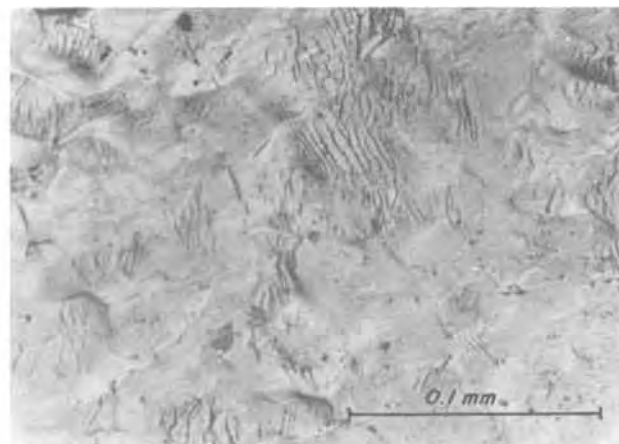


Fig. 17. 50V tantalum oxide film on mechanically polished substrate subsequent to 15% strain. Tensile axis is horizontal. Film fracture along slip traces.

the tensile strength of electrodeposited silver films with decrease in thickness.

Similarly, a range of values has been reported for the Young's modulus of anodic oxide films on aluminum. Grosskreutz studied this parameter as a function of humidity and found it to vary from  $20.7 \times 10^8$  MN/m<sup>2</sup> ( $3 \times 10^6$  psi) in saturated air to the bulk value,  $386 \times 10^8$  MN/m<sup>2</sup> ( $56 \times 10^6$  psi), in vacuum, with ambient humidity giving a value of the order of  $53 \times 10^8$  MN/m<sup>2</sup> (15). The modulus measurements of Bradhurst and Leach (9) in laboratory air are essentially in agreement with the present study, while the biaxial modulus value obtained by Eliezer and Brandon (13) corresponds to a Young's modulus of  $\sim 124 \times 10^8$  MN/m<sup>2</sup>. In the latter case, however, the film environment is ill-defined inasmuch as the test technique involved distending the film into an evacuated chamber by means of laboratory air pressure; therefore the effective film environment may be expected to have been somewhat less humid than ambient. Assuming validity of the value obtained in this study as representative of air at 40% relative humidity, the thicker films in this study failed at a stress of  $\sim 0.38 \times 10^8$  MN/m<sup>2</sup> (55,000 psi).

*Regular spacing of fracture lines.*—Once the continuity of a film on a substrate in tension has been interrupted by fracture, the film is no longer under axial loading and stress within the film must be applied by means of a shear stress at the film/substrate interface. Once the substrate deforms plastically, it is reasonable to regard this stress to have a uniform value of  $\tau$ , the shear flow stress of the substrate. Grosskreutz (17) has shown that the tensile stress in the film may then be written

$$\sigma = \frac{\tau}{t_0} x \quad [4]$$

where, again,  $t_0$  is the thickness of the film and  $x$  is a length parameter parallel to the tensile axis, measured from a film fracture line. The tensile stress in the film is maximum at the midpoint between fractures; hence as the stress level increases film segments are progressively halved until the crack spacing attains a minimum value,  $d_c$ , such that the maximum stress developed is inadequate for film fracture. Thus, the fracture stress of the film may be estimated from the observed minimum crack spacing by (17)

$$\sigma_f = \frac{\tau d_c}{2t_0} \quad [5]$$

Equation [5], however, shows a direct dependence of crack spacing on film thickness which was not observed in this study. It is reasonable to interpret this as implying an inverse dependence of film strength upon film thickness; however, this is not in agreement with the observations by Brandon and Eliezer (19). Using the observed yield stress of the substrate,  $\sigma_y = 10.34$  MN/m<sup>2</sup>, and the Tresca yield criterion,  $\tau$  may be estimated as 5.17 MN/m<sup>2</sup>. With the observed value of the critical crack spacing,  $d_c = 15 \mu\text{m}$ , the film fracture strength may be estimated as 517 MN/m<sup>2</sup> for a 750Å film, in rough agreement with the value estimated from the observed film modulus.

*Film fracture at slip steps.*—The effectiveness of a superficial film as a barrier to dislocation egress and consequent slip step development is dependent on the relative moduli of the film and substrate, the thickness of the film, and the strength of the film-substrate adhesion (16). The force exerted by a film on a dislocation in the substrate has been analyzed in detail (30-32); in general it may be stated that if the film modulus is lower than that of the substrate, dislocations are attracted to the interface, whereas if the film modulus is greater an energy well for the dislocation exists some distance from the interface, with the distance increasing as the ratio of the moduli increases. Hence as the film modulus increases above that of the

substrate, a greater suppression of surface plasticity in the substrate is predicted. This has not been borne out by studies of the effect of various metallic coatings on copper single crystals (33); however, Grosskreutz (16) observed entrapment of dislocations in anodized aluminum deformed in vacuum (high modulus film), but not in anodized aluminum deformed in air (low modulus film). In accord with this observation, Grosskreutz (34) found the fatigue life of anodized aluminum to be greater in vacuum than in humid air. Furthermore, increasing the thickness of the anodic film had a beneficial effect in vacuum, where the film modulus was greater than that of the substrate, but not in humid air, where the reverse was true. In studies of a somewhat different nature, Alden and Backofen (35) observed a beneficial effect of oxide films on the fatigue life of aluminum, provided that the film was repeatedly reformed.

In detailed analyses, Grosskreutz (15) and Grosskreutz and McNeil (27) interpreted the two fracture modes of anodic oxide in terms of interfacial adhesion stress and film strength; thick films having sufficient strength to withstand shear loading by slip steps on the substrate surface and, instead, separate from the substrate and fail normal to the tensile axis, while thin films failed by shear at slip steps without detachment. In the present investigation, however, the oxide was seen to exert considerable influence on plastic flow in the substrate in agreement with the observations of Block *et al.* (20, 21); with thin films, less than  $\sim 400\text{\AA}$  thick, distinct slip band formation and development of surface undulation were seen on deformation, but were absent when the anodic film was thicker. This influence can be manifested by the film offering a resistance to slip step emergence, thus altering the operative substrate slip systems as shown in Fig. 18. In Fig. 18 (a), two slip directions are shown operating on the same crystallographic plane. Even modest resistance to slip step emergence in one of these two directions, as by a surface film, however, will restrict slip to just one system, as shown in (b). Fracture along the slip steps generated in surface A in Fig. 18(b) is caused by shear loading normal to the plane of the film, whereas film fracture due to slip of the mode occurring on surface B is by shear loading parallel to the plane of the film. It is postulated that these different modes of film failure along lines of substrate slip are represented by the observed sharp, continuous fractures and by the discontinuous fractures as shown in Fig. 7, respectively. It must be noted that under ambient humidity the oxide film, being of lower modulus, should attract, rather than repel, dislocations suggesting that it would not offer resistance to slip step emergence. However, in order for a slip step to form at the surface, the film must rupture along the slip step or it must accommodate the step through deformation or through separation from the

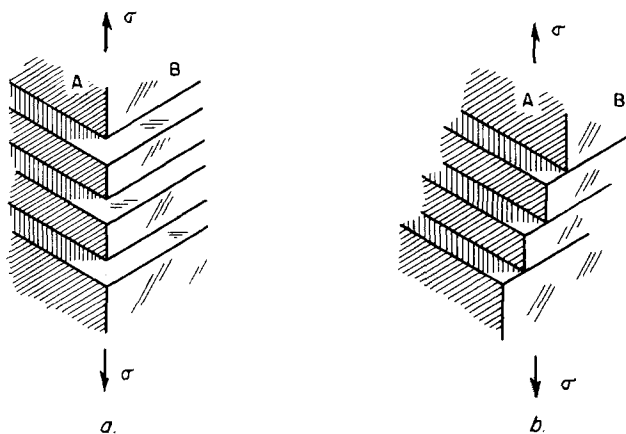


Fig. 18. Schematic representation of crystallographic substrate slip. (a) No film on surface A or B. (b) Film on surface B resisting slip step emergence.



substrate. These processes are governed by properties of the film and of the interface and are unrelated to substrate properties. Thus, even a weak or low modulus film must exert some effect on slip step emergence irrespective of its effect on dislocation movement.

Observations in this study clearly showed that sufficiently thin films could accommodate a certain degree of substrate slip without failure. The manner by which this may be accomplished has been subject to considerable speculation (15). Clearly simple deformation of the film around the contour of a sharply defined slip step is unrealistic due to the very high values of local strain that would be entailed. Film detachment is possible, but would still involve high local strain; there is, furthermore, no indication that such detachment does occur. The authors consider it feasible to postulate that the slip seen beneath intact oxide films is not, in fact, comprised of large, discrete steps, but of broad slip bands comprised of steps of atomic dimensions. This would permit film deformation along the substrate surface without necessitating inordinately high local strain values or local detachment of the film. Clearly, however, the strain in the film will be highest at such slip bands, thus film failure would necessarily occur along the bands. In the case of thicker films, where deformation of the substrate surface is suppressed, local regions of higher strain do not exist and the films simply fail normal to the applied loading. This analysis is clearly oversimplified, but appears to offer a viable rationale for the observed phenomena.

*Tantalum.*—The failure strain values reported in this study for anodic films on tantalum,  $\sim 0.14\%$ , are markedly different than those reported by Bubar and Vermilyea (11, 12), whose substrates were leached in HF following the chemical polishing procedure, and somewhat smaller than that of Eliezer and Brandon (13), whose value of  $0.83\%$  is reported as a "maximum" value, in general accord with the observations of Young (14). Analysis of the failure mode of anodic films on chemically polished tantalum substrates is simplified by the very weak adherence of such films. Clearly the films became detached by substrate deformation and their subsequent failure normal to the tensile axis was unaffected by the substrate surface. The films on mechanically polished substrates, however, were strongly bonded and behaved in a manner analogous to those on aluminum. It is interesting to note that a failure behavior intermediate between these cases could be obtained by lightly abrading chemically polished substrates prior to anodizing. The weak bonding on chemically polished substrates has been attributed to a superficial film associated with the polishing procedure (14, 36), possibly fluorine-rich (37), and to "flawed" regions (38). It is not clear why the mechanically polished specimens did not yield the ductile behavior previously observed in strongly adherent films.

### Conclusions

Anodic aluminum oxide films of thickness greater than a critical value of  $\sim 400\text{\AA}$  tested in ambient air fail at a strain of  $\sim 0.925\%$  independent of thickness. These films apparently suppress emergence of slip in the substrate and fail normal to the tensile axis (or, in the case of compressive loading, parallel to the compressive axis), forming regularly spaced cracks with a limiting, high strain spacing of  $\sim 15\ \mu\text{m}$ . The Young's modulus of these films was determined to be  $\sim 4 \times 10^4\ \text{MN/m}^2$ , implying a failure stress of the order of  $380\ \text{MN/m}^2$ . Films thinner than the critical thickness failed at a higher strain value of  $1.12\%$  along substrate slip traces, apparently due to their inability to suppress slip emergence and the consequent higher local strain at these sites. There is clearly an implication that film failure strain decreases with thickness. This behavior was unaffected by the manner of substrate surface preparation or by the

presence of a superimposed porous oxide layer except that a thick porous layer superimposed on a thin barrier layer caused it to behave as a "thick" film. No evidence of film detachment due to deformation was seen.

Anodic films on mechanically polished tantalum failed in a manner analogous to those on aluminum, at a strain of  $\sim 0.28\%$ . This value did not show a thickness dependence, however. Films on chemically polished tantalum substrates readily separated from the substrates on straining and failed in simple tension, normal to the tensile axis. Films thicker than  $\sim 680\text{\AA}$  failed at a strain of  $\sim 0.14\%$ , while thinner films failed at strains of  $0.2\%$ .

### Acknowledgments

The authors are pleased to acknowledge the support of NSF grants GH 35580 and DMR 72-03201-A01, "Environment-Affected Properties of Oxide Films as Related to Defect Structure."

Manuscript submitted June 16, 1976; revised manuscript received Aug. 1, 1976.

Any discussion of this paper will appear in a Discussion Section to be published in the June 1977 JOURNAL. All discussions for the June 1977 Discussion Section should be submitted by Feb. 1, 1977.

Publication costs of this article were assisted by the University of Connecticut.

### REFERENCES

1. A. J. McEvily and A. P. Bond, *This Journal*, **112**, 131 (1965).
2. A. J. Forty, in "Fundamental Aspects of Stress Corrosion Cracking," p. 64, NACE, Houston (1969).
3. A. J. Forty and P. Humble, *Phil. Mag.*, **8**, 247 (1965).
4. A. J. McEvily, Jr., in "Fundamental Aspects of Stress Corrosion Cracking," p. 72, NACE, Houston (1969).
5. H. H. Uhlig, *ibid.*, p. 86.
6. H. L. Logan, *J. Res. Nat. Bur. Stand.*, **48**, 99 (1952).
7. U. R. Evans, "Corrosion and Oxidation of Metals," p. 386, St. Martin Press, New York (1960).
8. C. Edeleanu and T. J. Law, *Phil. Mag.*, **7**, 573 (1962).
9. D. H. Bradhurst and J. S. L. Leach, *Trans. Br. Ceram. Soc.*, **114**, 793 (1963).
10. J. S. L. Leach, *Proc. Br. Ceram. Soc.*, **15**, 215 (1970).
11. S. F. Bubar and D. A. Vermilyea, *This Journal*, **113**, 892 (1966).
12. S. F. Bubar and D. A. Vermilyea, *ibid.*, **114**, 882 (1967).
13. D. Eliezer and D. G. Brandon, *Thin Solid Films*, **12**, 319 (1972).
14. L. Young, "Anodic Oxide Films," Academic Press, London (1961).
15. J. C. Grosskreutz, *This Journal*, **116**, 1232 (1969).
16. J. C. Grosskreutz, *Surface Sci.*, **8**, 173 (1967).
17. J. C. Grosskreutz, *This Journal*, **117**, 940 (1970).
18. D. G. Brandon and Z. Berger, *Israel. J. Tech.*, **8**, 247 (1970).
19. D. G. Brandon and D. Eliezer, *Mat. Res. Bull.*, **6**, 153 (1971).
20. N. J. Cochrane and R. J. Block, *This Journal*, **117**, 225 (1970).
21. P. Mehdi-zadeh and R. J. Block, *ibid.*, **119**, 1091 (1972).
22. D. H. Bradhurst and J. S. L. Leach, *ibid.*, **113**, 1245 (1966).
23. J. S. L. Leach and P. Neufeld, *Proc. Br. Ceram. Soc.*, **6**, 49 (1966).
24. J. S. L. Leach and P. Neufeld, *Corros. Sci.*, **9**, 225 (1969).
25. O. F. Devereux, T. A. Libsch, Y. H. Choo, and A. K. Bhambri, *ibid.*, **15**, 361 (1975).
26. Y. H. Choo and O. F. Devereux, *This Journal*, **122**, 1645 (1975).
27. J. C. Grosskreutz and M. B. McNeil, *J. Appl. Phys.*, **40**, 355 (1969).
28. G. Haas, *J. Opt. Soc. Am.*, **39**, 532 (1949).
29. J. W. Beams, J. B. Breazeale, and W. L. Bart, *Phys. Rev.*, **100**, 1657 (1955).
30. A. K. Head, *Phil. Mag.*, **44**, 92 (1953).

31. R. Weeks, J. Dundurs, and M. Stippes, *Int. J. Eng. Sci.*, **6**, 365 (1968).
32. Y. T. Chou, *Phys. Status Solidi*, **17**, 509 (1966).
33. R. M. Johnson and R. J. Block, *Acta Met.*, **16**, 831 (1968).
34. J. C. Grosskreutz, "Corrosion Fatigue: Chemistry, Mechanics, and Microstructures," p. 201, NACE, Houston (1972).
35. T. H. Alden and W. A. Backofen, *Acta Met.*, **9**, 352 (1961).
36. L. Young, *Trans. Faraday Soc.*, **53**, 841 (1957).
37. R. E. Pawel, J. P. Pemsler, and C. A. Evans, *This Journal*, **119**, 24 (1972).
38. D. A. Vermilyea, *ibid.*, **110**, 250 (1963).

## The Anodic Oxidation of Iron: Overpotential Analysis for a Two-Phase Film

J. L. Ord\* and D. J. De Smet\*<sup>1</sup>

Department of Physics, University of Waterloo, Waterloo, Ontario, Canada N2L 3G1

### ABSTRACT

The galvanostatic oxidation of iron in a neutral borate buffer of pH 8.4 has been studied using open-circuit transients to analyze the overpotential dependence of the optical and electrical properties of the process. A minicomputer which can control the current through the cell and read the potential of the electrode performed the experiments under program control, recording transients on magnetic tape at specified intervals, and recalling them later for least squares analysis. A self-nulling ellipsometer which is also linked to the computer is used to follow the process optically. Both the optical data and the Tafel slopes determined from transient analysis exhibit a structure characteristic of an oxide film composed of two distinct phases: an inner layer of  $\text{Fe}_3\text{O}_4$  and an outer layer of  $\text{Fe}_2\text{O}_3$ . The field in the inner  $\text{Fe}_3\text{O}_4$  layer appears to limit the process, and this field does not go to zero at the potential at which the protective outer layer of  $\text{Fe}_2\text{O}_3$  begins to reduce. The electrochemical behavior of the system appears to be in accord with the predictions of a field-controlled two-phase model of the process.

The extensive literature on the passivity of iron, from the original letters of Schoenbein (1) and Faraday (2, 3) through to the present time (4, 5), shows a continuing interest in the subject, but fails to present a comprehensive description of the phenomenon. This situation has come about because workers in the field have approached the problem with different viewpoints, chosen experimental conditions suited to their measurement technique, and ended up studying somewhat different phenomena. For example, studies of the anodic oxidation of iron which take care to avoid deposition of  $\text{FeOOH}$  from reaction products in the electrolyte give quite different results from studies in which  $\text{FeOOH}$  deposition occurs. One cannot say that one of these approaches is right and the other wrong, but a strong case can be made for studying anodic oxidation and electrodeposition separately rather than under conditions where both processes take place at the same time. Different results are also obtained depending on whether measurements are made under steady-growth or steady-state conditions. Steady growth is usually assumed to take place under galvanostatic oxidation across a restricted potential range, whereas a steady state is usually assumed to be reached after potentiostatic oxidation for an hour, although the system probably has no true steady state. Steady-growth conditions are usually chosen to study the kinetics of film growth, whereas steady-state conditions are more often chosen as the starting point for studies of the film itself. Our interest in this paper is in the oxidation process, and we make both our electrochemical measurements and our optical measurements under steady-growth conditions.

In recent years the most commonly used electrolyte for work on the passivity of iron has been the pH 8.4 boric acid-sodium borate buffer made popular by

Cohen and co-workers (6-9). This electrolyte, chosen initially by Cohen in order to obtain reliable cathodic reduction data, turns out to be ideal for optical work also. This is because an iron electrode can be passivated at a low enough current density to avoid roughening of the optical surface in the electrolyte and, in addition, the optical data return to their initial values after cathodic reduction. Some care must be taken when using the electrolyte because the behavior of iron in it is sensitive to both dissolved oxygen and ferrous ions. If the electrolyte contains appreciable dissolved oxygen, an iron electrode will spontaneously passivate with no current applied. If the electrolyte is free of dissolved oxygen, ferrous ions are stable in it and will deposit anodically to form a layer of  $\text{FeOOH}$  at all but the lowest potentials in the passive region.

The answer to the question of whether or not the borate buffer is a typical neutral electrolyte depends on the aspect of passivity in question. In one important respect the borate buffer is very special: the presence of dissolved oxygen in the electrolyte is not necessary for the passivation of iron. This is not true for sulfate or perchlorate electrolytes. This special property of the borate electrolyte appears related to the fact that  $\text{FeOOH}$  layers deposited in borate electrolyte contain boron and take on an amorphous structure rather than the crystalline structure they have when deposited in sulfate or perchlorate electrolyte (11-15). In an earlier paper from this laboratory (16), it was argued that passivation results from a reaction in which the surface of the layer  $\text{Fe}_3\text{O}_4$  formed in the active state is oxidized to  $\text{FeOOH}$ . It appears that boron involvement in this monolayer of  $\text{FeOOH}$  is necessary to render the electrode passive. Once passive, iron behaves the same way under further oxidation in borate and perchlorate electrolytes which are free of ferrous ions. Since our primary interest in this paper is in the mechanism of ionic conduction and film growth in the passive state, the borate buffer

\* Electrochemical Society Active Member.

<sup>1</sup> Present address: Department of Physics and Astronomy, The University of Alabama, University, Alabama 35486.

Key words: iron, oxidation, ellipsometry.



acts as a typical neutral electrolyte which happens to be convenient for this work.

Some time ago, a paper from this laboratory (17) argued on the basis of electrochemical evidence that the field in the oxide film limits conduction in the passive state, and that this field goes to zero at the Flade potential, the potential below which iron reverts to the active state. Since that time, two attempts have been made in this laboratory to test this argument by correlating the electrochemical measurements with optical measurements of film thickness made with an ellipsometer. In the first attempt (18), Tafel slopes from open-circuit transient analysis, proportional to film thickness in a field-limited model, were correlated with optical measurements of film thickness made with a manual ellipsometer. Although a linear dependence was found, the measured quantities were not proportional, and it was concluded that the layers formed in the active and passive states have quite different properties although no difference could be detected optically. In the second attempt (16), an automated self-nulling ellipsometer was used for the optical measurements, and the reciprocal capacitance from a-c impedance measurements was taken as an electrochemical measure of the film thickness. The greatly improved resolution of the optical measurements enabled two layers to be distinguished, but neither layer was found to have a thickness proportional to the reciprocal capacitance. Although the optical measurements presented a clear picture of a two-phase film, little progress could be made in clarifying the conduction mechanism.

In this paper we continue our study of the oxidation of passive iron using sensitive recording and analysis techniques to increase the resolution of our electrochemical measurements. The increase in resolution enables us to determine the electrochemical properties of the two phases detected optically, and a much simpler model of the conduction process emerges with a different significance given to the Flade potential.

### Experimental

The optical measurements were made with a self-nulling ellipsometer which has been described in detail elsewhere (19). The instrument has a resolution of  $0.01^\circ$  in the settings of its polarizing prisms, and nulls both polarizer and analyzer approximately twice each second under the optical conditions encountered in this experiment. The standard deviation in the null readings was less than the resolution of the instrument, therefore an increase in resolution was obtained by averaging the data if the properties of the film were not changing too rapidly. A helium-neon laser is used as the light source, and an angle of incidence of  $60^\circ$  is chosen to accommodate a cell made from an equilateral glass prism. The cell is fitted with standard taper joints for mounting the electrode holder, platinum counterelectrode, mercurous sulfate reference electrode, and gas dispersion tube. The cell has inlet and outlet connections enabling deaerated electrolyte to be added from a 2 liter reservoir, and electrolyte contaminated with ferrous ions to be pumped from the cell. The electrolyte, an equivolume mixture of 0.15N sodium borate and 0.15N boric acid of pH 8.4, was maintained at room temperature,  $23^\circ\text{C}$ . All potential values are relative to the mercurous sulfate reference electrode which uses a 0.1N  $\text{K}_2\text{SO}_4$  salt bridge.

The cylindrical single crystal sample of iron used as the working electrode is clamped between Teflon washers in a glass electrode holder. A flat on one side of the cylinder is used for the optical measurements. A surface area of approximately  $1.25\text{ cm}^2$  is exposed to the electrolyte in this configuration. The sample was chemically polished before being inserted into the cell. Subsequently, several oxidation-reduction cycles were run in order to reduce roughness and

stabilize the optical surface prior to beginning the experiment.

The laboratory computer, a Hewlett-Packard 2114B, was programmed to perform the experiments with little operator intervention and record the data on magnetic tape for later recall by analysis programs written in BASIC. The operating program was similar in many respects to one used earlier in a study of the anodic oxidation of platinum (20). Both the electrochemical control circuitry and the circuitry which operates the ellipsometer are built into multiplexed input-output interface of the computer. The computer reads the digital output from the ellipsometer, and uses digital-to-analog and analog-to-digital converters to control the current through the cell and read the electrode potential. A video terminal and an X-Y point plotter are used extensively for graphical display during the performance of the experiment and the analysis of the data.

Descriptions of the analysis of open-circuit transients appear in the literature (21, 22) and a current paper describes the digital techniques used in this laboratory (23). The basic equations governing open-circuit transients are obtained by writing the external current in the cell circuit,  $i_e$ , as the sum of the current charging the capacitance,  $i_c$ , and the faradaic current through an element in parallel with capacitance,  $i$

$$i_c + i = i_e \quad [1]$$

For an activation-controlled process, the exponential dependence of current density,  $i$ , on potential,  $V$ , can be written

$$i/i_0 = \exp((V - V^*)/V_0) \quad [2]$$

where  $V^*$  is the zero of overpotential,  $i_0$  is the exchange current density, and  $V_0$  is the Tafel slope expressed in natural logarithms. With  $i_e = 0$ ,  $i_c$  written as  $CdV/dt$ , and  $i$  given by Eq. [2], Eq. [1] becomes

$$CdV/dt + i_0 \exp((V - V^*)/V_0) = 0 \quad [3]$$

This equation can be integrated, assuming  $C$ ,  $i_0$ ,  $V_0$ , and  $V^*$  all constant, to give

$$V = V_1 - V_0 \ln(1 + t/T) \quad [4]$$

where the time constant  $T$  is defined by

$$T = CV_0/i_1 \quad [5]$$

and  $i_1$  and  $V_1$  are the values of  $i$  and  $V$  at  $t = 0$ . Transients are fitted by varying  $T$  in Eq. [4] until a linear  $V$  vs.  $\ln(1 + t/T)$  least squares analysis gives the minimum deviation in  $V$ .  $V_0$  is given directly by the slope of the fitted line.

The open-circuit data are recorded in a form well suited to this type of analysis. The potential is read at millisecond intervals, but data are stored at equal potential intervals rather than time intervals in order to produce a uniform point density along the least squares line. The 12 bit analog-to-digital converter has a 1/2 mV resolution and by summing eight successive readings taken over a 200  $\mu\text{sec}$  interval this resolution can be improved somewhat. The accuracy of the fitting procedure can be expressed in a variety of ways. The range over which the data are fitted is one for which  $dV/dt$  changes by a factor of ten. The standard deviation in  $V$  from the fitted least squares line is typically less than one least significant bit of the 12 bit converter for this fitting range. Expressed as a fraction of the potential range over which the transient is fitted, the deviation is on the order of 0.1%. The least squares analysis estimates the standard deviation in the  $V_0$  values to be on the order of 0.1%, but a complete replication of an experiment gives  $V_0$  values which differ by as much as 1%.

### Results

The experiments used to generate the data consist of a series of oxidation-reduction cycles with oxida-

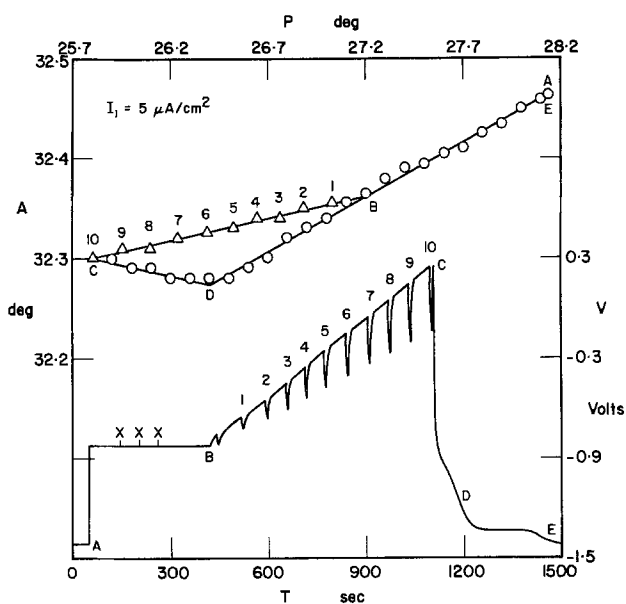


Fig. 1. Oxidation-reduction cycle with open-circuit transients for an iron electrode in deaerated borate buffer: oxidation at  $-0.825\text{V}$  (vs.  $\text{Hg}_2\text{SO}_4$ ) from A to B with electrolyte changes at X, oxidation at  $i_1 = 5 \mu\text{A}/\text{cm}^2$  from B to C with open-circuit transients applied at the points indicated, reduction at  $10 \mu\text{A}/\text{cm}^2$  from C to E.

tion current densities of  $5, 20, \text{ and } 80 \mu\text{A}/\text{cm}^2$  and a common reduction current density of  $10 \mu\text{A}/\text{cm}^2$ . The potential-time plot of a cycle with an oxidation current density of  $5 \mu\text{A}/\text{cm}^2$  is shown in the lower portion of Fig. 1. At point A the reduction segment of the previous cycle is complete, and the working electrode is passivated at a current density of  $1 \text{ mA}/\text{cm}^2$  until the potential reaches  $-0.825\text{V}$  where it is held until the current density drops to  $1 \mu\text{A}/\text{cm}^2$  (point B). At the three points labeled X, the circuit is opened briefly while the electrolyte is pumped from the cell and replaced by fresh, deaerated electrolyte which is free of ferrous ions. At point B the  $5 \mu\text{A}/\text{cm}^2$  oxidation current density is applied to the working electrode, and oxidation continues until the potential reaches  $0.25\text{V}$  at point C. During the oxidation, open-circuit transients are recorded at  $0.1\text{V}$  intervals from  $-0.75$  to  $0.25\text{V}$ . The open-circuit transient at  $-0.75\text{V}$  does not provide adequate data for analysis, but the other transients, labeled 1 through 10 in the figure, can all be analyzed to determine values for the Tafel slope,  $V_0$ , and reciprocal capacitance,  $1/C$ . Cathodic reduction at  $10 \mu\text{A}/\text{cm}^2$  begins at point C and continues through two potential arrests until the surface of the working electrode is free of oxide at point E.

Optical data consisting of the null settings of the polarizer, P, and the analyzer, A, are recorded at 1 sec intervals throughout the experiment except during changes of electrolyte. Representative optical data are plotted in the upper portion of Fig. 1. On a P vs. A plot, the optical data fall on four distinct line segments, A-B, B-C, C-D, and D-E. The points plotted during galvanostatic oxidation between B and C are the points labeled 1 through 10 at which analyzable open-circuit transients were recorded. The reduction data, plotted at  $0.1^\circ$  increments in P, fall on two distinct line segments, C-D and D-E, which correlate with the two potential arrests observed on reduction. The data obtained during passivation from A to B superimpose on the reduction data between these points. The line segments shown in the figure were fitted to the data using a least squares technique. Note that the A scale is expanded five times over the P scale in order to show the structure in the data.

Cycles with oxidation current densities of  $20$  and  $80 \mu\text{A}/\text{cm}^2$  differ little from the  $5 \mu\text{A}/\text{cm}^2$  cycle plotted in Fig. 1. The potential-time plots differ only in the

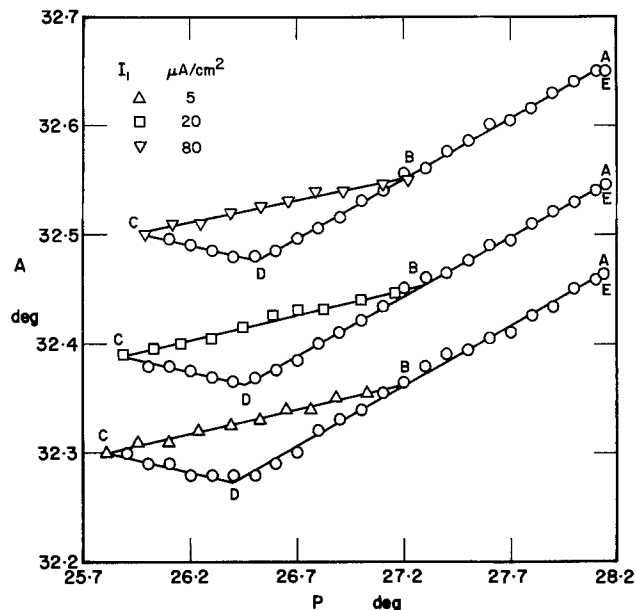


Fig. 2. Optical P-A plot for oxidation-reduction cycles with  $i_1 = 5, 20, \text{ and } 80 \mu\text{A}/\text{cm}^2$ . The cycle plotted at the bottom is the one from Fig. 1, and the upper two cycles are offset  $0.1^\circ$  and  $0.2^\circ$  in A to avoid overlap.

time scale between B and C, and the optical data show structure which differs only in the lengths of the various line segments. The optical data for all three current densities are plotted in Fig. 2 with the upper two cycles offset  $0.1^\circ$  and  $0.2^\circ$  in A to avoid overlap. As can be seen in the figure, the lengths of line segments B-C, C-D, and D-E all decrease somewhat with increasing oxidation current density. The expanded A scale enables some indication of the reproducibility of consecutive cycles to be seen in the figure. The cycles were performed in the sequence middle, top, bottom, and the uneven vertical spacing between cycles is the result of a drift in A of  $0.01^\circ$  over the course of the three cycles. Following the third cycle, the series of three cycles was repeated, and the optical data obtained agreed with the data plotted in Fig. 2 to within  $0.02^\circ$  in both P and A.

The optical data show an inflection during cathodic reduction on a P-t plot as well as on a P-A plot. In Fig. 3, P is plotted vs. time for the cathodic segments of the three cycles plotted in Fig. 2. In each case, the data show an inflection at the point labeled D' which

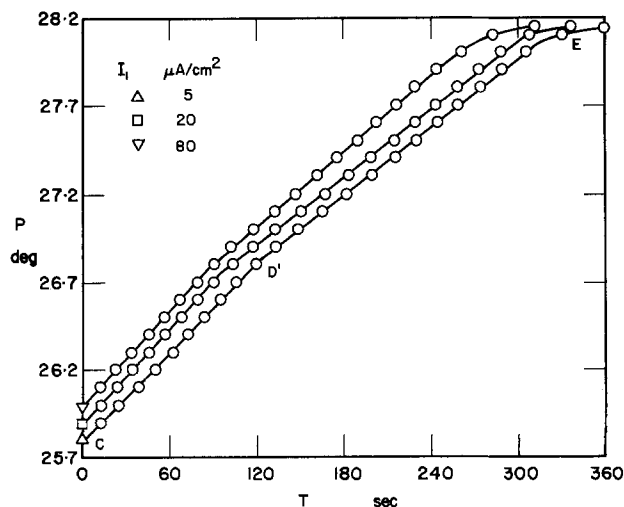


Fig. 3. Time dependence of the optical parameter P during reduction at  $10 \mu\text{A}/\text{cm}^2$  for the three cycles plotted in Fig. 2. The inflection at D' occurs later than the P-A inflection at D.

is reached somewhat later than point D, the  $P$ - $A$  inflection point which marks the end of the first reduction plateau.

Analysis of the open-circuit transients gives values for the Tafel slope,  $V_o$ , and the reciprocal capacitance,  $1/C$ , at ten values of the initial potential,  $V_1$ , and three values of the oxidation current density,  $i_1$ . These data, along with the corresponding thirty optical data points, form the data set on which subsequent analysis is based. Since the linear relation between  $P$  and  $A$  during galvanostatic oxidation does not depend on the oxidation current density, only one optical variable,  $P$ , is required to specify the optical data.

The first step in carrying the analysis further is to determine  $i_o$  and  $V^*$ , the remaining unknown parameters in Eq. [2]. If either one can be determined, the other can be calculated using Eq. [2]. Neither  $i_o$  nor  $V^*$  can be determined from the analysis of a single open-circuit transient, but common values for both can be determined for a set of transients with a common  $i_1$  provided  $V_o$  depends linearly on  $V_1$ . Two arguments may be advanced in support of constant values for  $i_o$  and  $V^*$ , one based on economy of parameters, the other on the physical significance of the parameters themselves. On thermodynamic grounds,  $V^*$ , the zero of overpotential, is expected to be independent of both  $i_1$  and  $V_1$ . On the other hand, the exchange current density,  $i_o$ , will be sensitive to any variation in the concentration of charge carriers at the activation barrier, and hence may depend somewhat on  $i_1$ , but should not depend on  $V_1$  for constant  $i_1$ .

The analysis to determine  $i_o$  and  $V^*$  from sets of  $V_o$  values can be displayed graphically on a plot of  $V_o$  vs.  $V_1$ . In Fig. 4,  $V_o$  values are plotted as a function of  $V_1$  for  $i_1$  equal to 5, 20, and 80  $\mu\text{A}/\text{cm}^2$ . For each of the three oxidation current densities, the upper six points with  $V_1$  values from  $-0.25$  to  $0.25\text{V}$  fall on a straight line. Graphically, the value of  $V^*$  common to all points on the line is given by the intercept of the line on the  $V_1$  axis, and  $\ln(i_1/i_o)$  is given by the reciprocal of the slope of the line. The intercepts of the least squares lines with  $i_1$  equal to 5, 20, and 80  $\mu\text{A}/\text{cm}^2$  give  $V^*$  values of  $-1.305$ ,  $-1.303$ , and  $-1.292\text{V}$ , respectively, and their slopes give corresponding values for  $i_o$  of 4.24, 8.25, and  $24.8 \times 10^{-5} \mu\text{A}/\text{cm}^2$ . The differences between the  $V^*$  values do not appear significant, particularly in view of the range of the extrapolation involved in their determination, and hence they can be averaged to give a value for  $V^*$  of  $-1.300\text{V}$  which applies to all open-circuit transient data with  $V_1$  equal to  $-0.25\text{V}$  or greater. The increase by a factor of six in  $i_o$  as  $i_1$

increases by a factor of sixteen is significant, consequently  $i_o$  cannot be considered to be independent of  $i_1$ . For  $V_1$  values less than  $-0.25\text{V}$ , either  $i_o$ ,  $V^*$ , or both differ from the values which apply in the linear region.

It should be emphasized that the dependence of  $V_o$  on  $V_1$  and  $i_1$ , and of  $i_o$  on  $i_1$  are dependences on the conditions which applied at the time the circuit was opened, and do not imply that the parameters  $V_o$  and  $i_o$  have explicit potential or current density dependence. This can be illustrated very simply in the case of the parameter  $V_o$  by plotting it as a function of  $P$  as is done in Fig. 5. The plotted line, fitted by least squares to the eighteen points for which  $V_1$  is  $-0.25\text{V}$  or greater, provides a reasonable fit to the data at all three oxidation current densities, thus  $V_o$  is solely a function of film thickness in this region.

Equation [5] enables a value of the capacitance to be calculated for each open-circuit transient once  $V_o$  and  $T$  have been determined. In Fig. 6, reciprocal capacitance values calculated using Eq. [5] are plotted as a function of  $V_1$  for each of the three values of  $i_1$ . As was the case for  $V_o$  in Fig. 4, the six points with  $V_1$  values of  $-0.25\text{V}$  or greater fall on straight lines. The two lines with  $i_1$  values of 20 and 80  $\mu\text{A}/\text{cm}^2$  cannot be distinguished in the figure, and intersect the  $V_1$

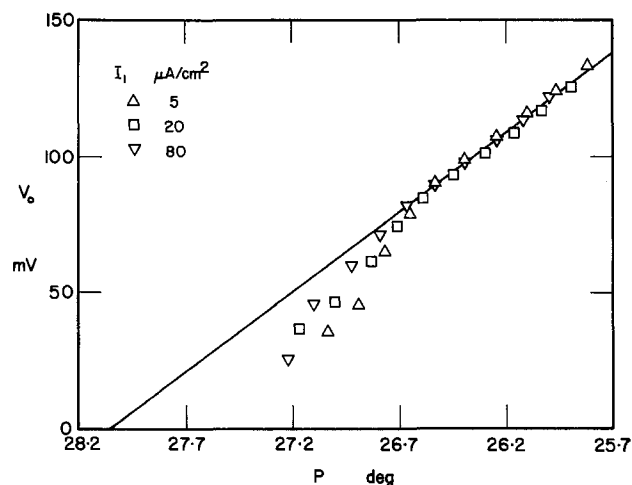


Fig. 5. Tafel slope from open-circuit transient analysis as a function of the optical parameter  $P$ . The line is fitted to the upper six points at each oxidation current density.

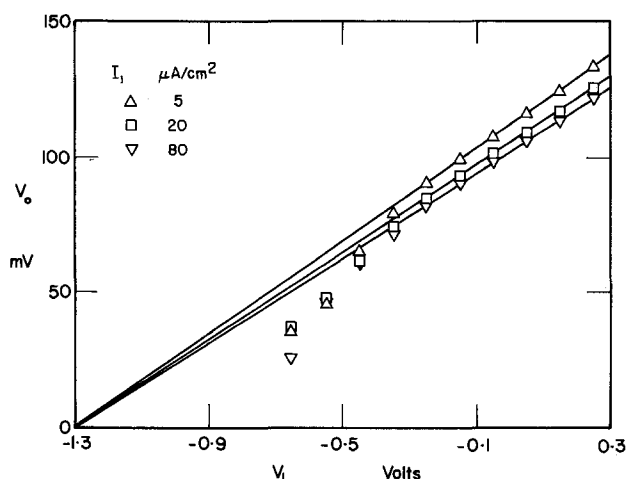


Fig. 4. Tafel slope from open-circuit transient analysis as a function of the initial potential. The lines are fitted to the upper six points at each oxidation current density.

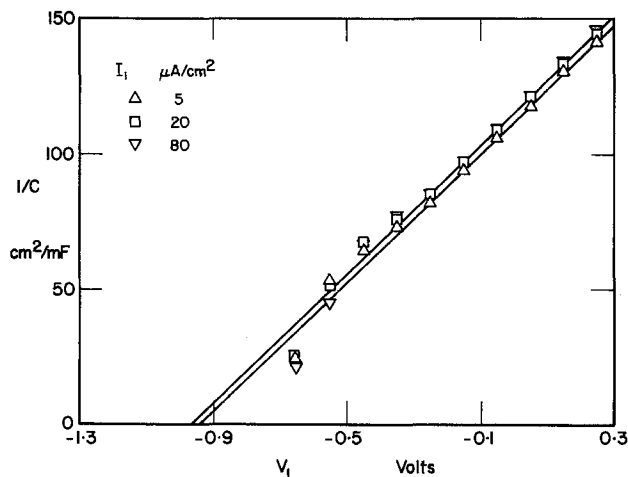


Fig. 6. Reciprocal capacitance from open-circuit transient analysis as a function of the initial potential. The lines are fitted to the upper six points at each oxidation current density.

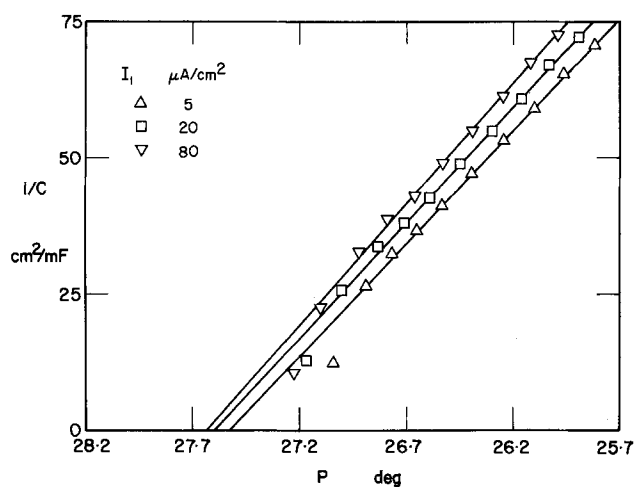


Fig. 7. Reciprocal capacitance from open-circuit transient analysis as a function of the optical parameter  $P$ . The lines are fitted to the upper six points at each oxidation current density.

axis at  $-0.965$  and  $-0.963$ V, respectively. The line with  $i_1$  equal to  $5 \mu\text{A}/\text{cm}^2$  intersects the  $V_1$  axis at  $-0.936$ V. These intercepts differ by more than  $1/3$ V from the  $V_o$  intercept which was identified as the zero of overpotential. The plot of reciprocal capacitance vs.  $P$  in Fig. 7 shows a linear dependence on film thickness at each value of  $i_1$ , but the lines at different values of  $i_1$  are distinct, and the reciprocal capacitance cannot be said to be solely a function of film thickness above  $-0.25$ V as was the case for the Tafel slope.

### Discussion

Although the evidence is indirect, ellipsometric measurements can be used to advantage in attempts to determine the structure of very thin films. The ellipsometric data reported here show the same structure exhibited by those we reported in an earlier paper in which we concluded that the oxide film is composed of a layer of  $\text{Fe}_3\text{O}_4$  covered by an outer layer of  $\text{Fe}_2\text{O}_3$ . This identification of the component layers agrees substantially with both the early (6-9) and recent (24) work of Cohen and co-workers, but disagrees with other recent work which identifies the oxide either as entirely  $\text{FeOOH}$  (4), or as  $\gamma\text{-Fe}_2\text{O}_3$  covered by  $\text{FeOOH}$  (25-28). The latter study (by Sato and co-workers) makes extensive use of ellipsometry to support the proposed model of the oxide film, and identifies  $\text{Fe}_3\text{O}_4$  as a product of cathodic reduction.

The question as to whether or not a layer of  $\text{FeOOH}$  is present on the surface is one which ellipsometry can answer directly. Although it is not possible to deduce refractive indexes uniquely from ellipsometric  $P$ - $A$  data for films which are very thin, the converse problem of detecting the growth of a film of known index can be dealt with directly.  $\text{FeOOH}$  films have been studied in detail in this laboratory (15), and their refractive indexes are known. The films grown in borate buffer are transparent amorphous films with a refractive index of 1.70 at  $\lambda = 6328\text{\AA}$ . On a  $P$ - $A$  plot with the scales used in Fig. 2, growth of a film of  $\text{FeOOH}$  displaces optical data upward to the left at approximately three times the slope of line segment C-D. Thus the data in Fig. 2 indicate that  $\text{FeOOH}$  is not a significant component of the anodic oxide under our experimental conditions. Optical data obtained under conditions where  $\text{FeOOH}$  is a significant component of the oxide film were included in a previous paper (16). Sato and co-workers (27), although lacking the instrumental resolution for direct detection of  $\text{FeOOH}$  deposition, found that the thickness of a potentiostatically grown oxide film depends on

the speed of passivation, and attributed this to the deposition of  $\text{FeOOH}$  from ferrous ions produced during active state dissolution. In their more recent work (28), they avoid the deposition of  $\text{FeOOH}$  by growing an initial  $25\text{\AA}$  of oxide using a pH 11.5 electrolyte in which iron has no active state. From this work they conclude that the oxide film grown in borate buffer has an outer layer of  $\text{FeOOH}$ , but their ellipsometric measurements still lack the resolution to detect two layers directly, and their optical analysis uses one common refractive index for the entire oxide film.

The question as to whether  $\text{Fe}_3\text{O}_4$  is present as a surface layer during anodic oxidation or is a product of cathodic reduction raises a very basic question concerning the interpretation of optical data. We have assumed that cathodic reduction simply planes away the surface of the film without producing bulk changes in it. This assumption is implicit in the statement that at point C the oxide film is composed of superimposed layers whose sequential removal displaces the optical data first from C to D, then from D to E. Alternate explanations of the structure in the optical data are certainly possible. Sato and co-workers (26) found an inflection in the time dependence of their optical data on the second reduction plateau, and concluded that prior to this point  $\text{Fe}_3\text{O}_4$  is a reaction product, and after this point  $\text{Fe}_3\text{O}_4$  is itself reduced. We observe an analogous inflection at point D', but find a smaller slope change at this point, presumably because our electrode has no  $\text{FeOOH}$  layer. Our optical data could be interpreted in terms of a model in which the film at point C composed of an inner  $\text{Fe}_3\text{O}_4$  layer (E-D') covered by an outer  $\text{Fe}_2\text{O}_3$  layer (D'-C) which reduces along C-D leaving a residual layer of  $\text{Fe}_3\text{O}_4$  (D'-D). We feel that we have insufficient evidence to choose between this model and our original model with an outer layer which leaves no  $\text{Fe}_3\text{O}_4$  behind on reduction. Our data are not consistent with a model in which most or all of the  $\text{Fe}_3\text{O}_4$  layer is a product of cathodic reduction. We conclude that both  $\text{Fe}_2\text{O}_3$  and  $\text{Fe}_3\text{O}_4$  are present as superimposed surface layers in the passive state.

The analysis of overpotential for the growth of a two-phase anodic oxide film is analogous in some ways to the treatment of corrosion processes by mixed potential theory. In corrosion processes two reactions take place at a common potential and the total current is the sum of the individual reaction currents, whereas for a two-phase oxide the current density is the same through each layer and the individual layer overpotentials appear in series. Although a detailed treatment of ionic transport through a two-phase film is not feasible in view of our limited understanding of ionic transport through single phase films, we can predict the general features of the dependence of current density on potential for this system. Since the electrochemical behavior of the system appears relatively insensitive to the thickness of the outer layer (16), we will assume that the field in the inner layer limits the process, and set up a two-phase model of this type for comparison with the experimental data. Each phase will have its own characteristic zero of overpotential, and the electrochemical behavior of the system will depend on both the position of the potential relative to these points and on the relation between current density and overpotential. The zero of overpotential of the layer in the higher oxidation state,  $V(\text{Fe}_2\text{O}_3)^*$ , will be higher than that of the layer in the lower oxidation state,  $V(\text{Fe}_3\text{O}_4)^*$ . The relation between current density and overpotential for a metal covered by a reducible oxide layer which can both support high fields and conduct electrons (by tunneling or other mechanisms) has some special characteristics. On the anodic side, oxidation requires ionic transport through the film, and this is usually a field-limited process. Electronic conduction is not involved because the electrolyte does not act as a source of electrons below the oxygen evolution potential. On the cathodic

side, reduction of the film does not require ionic transport, but does require conduction of electrons from the metal to the film-electrolyte interface.

At potentials well above both  $V(\text{Fe}_3\text{O}_4)^*$  and  $V(\text{Fe}_2\text{O}_3)^*$ , the field in the inner layer will control the process, and the Tafel slope, expressed in field units, will be constant. Since the Tafel slope is measured in potential units rather than in field units, it will vary linearly with potential under galvanostatic oxidation, extrapolating to zero at  $V(\text{Fe}_3\text{O}_4)^*$ . As the potential approaches  $V(\text{Fe}_2\text{O}_3)^*$ , the measured value for the Tafel slope will drop below the line for higher potentials, extrapolating to zero near  $V(\text{Fe}_2\text{O}_3)^*$ . This is due to the fact that an electronic current will begin to flow as the potential crosses  $V(\text{Fe}_2\text{O}_3)^*$ , and the remaining overpotential across the inner layer will not discharge until the outer layer has been reduced. In this model the system does not tend toward an equilibrium state under open-circuit conditions; the difference between  $V(\text{Fe}_2\text{O}_3)^*$  and  $V(\text{Fe}_3\text{O}_4)^*$  effectively acts as an overpotential driving an ionic current through the inner layer, and the electronic current which balances it reduces the outer layer.

The experimental results exhibit the general features predicted by the two-phase model. The plot of  $V_0$  vs.  $V_1$  is linear at high potentials as expected for a field-controlled process, and extrapolates to zero at  $V_1 = -1.360\text{V}$ . This is a reasonable value for  $V(\text{Fe}_3\text{O}_4)^*$ , lying as it does just above the second reduction plateau. At lower potentials, the  $V_0$  values inflect more sharply toward the axis, giving  $V(\text{Fe}_2\text{O}_3)^*$  a value of about  $-0.850\text{V}$ , just above the first reduction plateau, and below  $-0.825\text{V}$ , the potential used to passivate the electrode in these experiments. The passivation potential is just above the Flade potential, the lowest potential at which the electrode can be said to be truly passive. The position of  $V(\text{Fe}_2\text{O}_3)^*$  between the first reduction plateau and the passivation potential is exactly where the model requires it to be, but it has been argued that this potential is much too high for any known bulk oxide of iron. For this reason it would be tempting to identify the outer layer as  $\text{FeOOH}$  were it not for its refractive index. In our previous paper (16) we noted that the passivating layer of  $\text{FeOOH}$  became incorporated in the outer layer of  $\text{Fe}_2\text{O}_3$  on further oxidation, and concluded that the  $\text{Fe}_2\text{O}_3$  layer is partially hydrated, by which we mean that some of the  $\text{Fe}_2\text{O}_3$  has  $\text{FeOOH}$  bonding. It may well be that the characteristic potential of the oxide is very sensitive to this  $\text{FeOOH}$  bonding. It is certainly true that the first reduction plateau is not sharply defined under our experimental conditions, and is much sharper if the experiment is modified to include a potentiostatic region between the galvanostatic oxidation and reduction cycles. Under extended potentiostatic treatment, the first reduction plateau sharpens, and the outer portion of the  $\text{Fe}_2\text{O}_3$  layer begins to show an index closer to that of  $\text{FeOOH}$ .

The reciprocal of the slope of the  $V_0$  vs.  $V_1$  plot gives the value of the exponent in Eq. [2] at the oxidation current density in question. This is a convenient dimensionless parameter which can be used in the comparison of the anodic oxidation of different metals. At  $80 \mu\text{A}/\text{cm}^2$ ,  $V_1/V_0$  has the value 12.7 for iron, whereas it has the value 11.3 for tantalum and 7.9 for platinum at this current density. Elementary models of high field ionic conduction have this exponent proportional to the product of the valence of the mobile ion, the jump distance, and the field in the layer, but we feel that such models are not adequate to describe anodic oxidation, and we will not attempt to compare valences, jump distances, or fields. These elementary models also have a preexponential factor which is independent of oxidation current density, but this is not what we find experimentally for either iron or tantalum (29).

The plot of  $V_0$  vs.  $P$  demonstrates that the Tafel slope depends only on film thickness and reinforces the view that the process is field limited. Given a value for the ratio between layer thicknesses, we could use the  $P$  intercept from the  $V_0$ - $P$  plot to test the assumption that it is the field in the inner layer which limits the process. Both the lack of unique values for the refractive indexes of the layers and the possibility of some conversion of  $\text{Fe}_2\text{O}_3$  to  $\text{Fe}_3\text{O}_4$  during reduction make it impossible to determine the thickness ratio with sufficient accuracy to make such a quantitative test possible. On the basis of our results, we cannot rule out the possibility that a significant fraction of the overpotential may appear across the outer layer.

The conclusions reached in this study differ from those reached in our earlier work. We attempted essentially the same experiments reported here in our first optical work on iron (18), but we were using a manual ellipsometer at that time, and we recorded open-circuit transients on a strip-chart recorder. As a result, we missed the structure in both the optical and Tafel slope data. We concluded that the Flade potential was the zero of overpotential for passive state oxidation, and that no overpotential appeared across the layer formed in the active state. Later work with a self-nulling ellipsometer (16) correctly resolved the optical structure, but still identified the Flade potential as the zero of overpotential for passive state oxidation, and had to describe the inner layer as made up of two layers with differing electrochemical properties in order to fit the data. The main experimental advance in this study has been the improvement in our open-circuit transient technique which enabled us to detect the structure in the Tafel slope data. Although our data show a more complicated structure than did our earlier data, our conclusion is much simpler: the anodic oxide of iron behaves in exactly the manner one would predict for a two-phase film.

#### Acknowledgment

This work received partial support from the National Research Council of Canada under Grant No. A-1151.

Manuscript submitted May 21, 1976; revised manuscript received July 26, 1976.

Any discussion of this paper will appear in a Discussion Section to be published in the June 1977 JOURNAL. All discussions for the June 1977 Discussion Section should be submitted by Feb. 1, 1977.

Publication costs of this article were assisted by the University of Waterloo.

#### REFERENCES

1. C. T. Schoenbein, *London Edinburgh Philos. Mag. J. Sci.*, **9**, 53 (1836).
2. M. Faraday, *ibid.*, **9**, 57 (1836).
3. M. Faraday, *ibid.*, **9**, 122 (1836).
4. R. W. Revie, B. G. Baker, and J. O'M. Bockris, *This Journal*, **122**, 1460 (1975).
5. C. Lukac, J. B. Lumsden, S. Smialowska, and R. W. Staehle, *ibid.*, **122**, 1571 (1975).
6. M. Nagayama and M. Cohen, *ibid.*, **109**, 781 (1962).
7. M. Nagayama and M. Cohen, *ibid.*, **110**, 670 (1963).
8. N. Sato and M. Cohen, *ibid.*, **111**, 512 (1964).
9. N. Sato and M. Cohen, *ibid.*, **111**, 519 (1964).
10. D. B. Gibbs and M. Cohen, *ibid.*, **119**, 416 (1972).
11. V. Markovac and M. Cohen, *ibid.*, **114**, 674 (1967).
12. V. Markovac and M. Cohen, *ibid.*, **114**, 678 (1967).
13. J. L. Leibenguth and M. Cohen, *ibid.*, **119**, 987 (1972).
14. K. Hashimoto and M. Cohen, *ibid.*, **121**, 37 (1974).
15. J. L. Ord and D. J. De Smet, *ibid.*, **118**, 206 (1971).
16. F. C. Ho and J. L. Ord, *ibid.*, **119**, 139 (1972).
17. J. L. Ord, *ibid.*, **113**, 213 (1966).
18. J. L. Ord and D. J. De Smet, *ibid.*, **113**, 1258 (1966).
19. J. L. Ord, *Surf. Sci.*, **16**, 115 (1969).
20. J. L. Ord, D. J. De Smet, and M. A. Hopper, *This Journal*, **123**, 1352 (1976).
21. H. B. Morley and F. E. W. Wetmore, *Can. J. Chem.*, **34**, 359 (1956).
22. J. L. Ord, *This Journal*, **112**, 46 (1965).

23. J. L. Ord, J. C. Clayton, and W. P. Wang, *ibid.*, Submitted for publication.
24. M. Cohen and K. Hashimoto, *ibid.*, **121**, 42 (1974).
25. N. Sato and K. Kudo, *Electrochim. Acta*, **16**, 447 (1971).
26. N. Sato, K. Kudo, and T. Noda, *Corros. Sci.*, **10**, 785 (1970).
27. N. Sato, K. Kudo, and T. Noda, *Electrochim. Acta*, **16**, 1909 (1971).
28. N. Sato, T. Noda, and K. Kudo, *ibid.*, **19**, 471 (1974).
29. J. L. Ord and D. J. De Smet, *This Journal*, **116**, 762 (1969).

## Cathodoluminescence and Photoluminescence of Tb<sup>+3</sup> Activated LaAlO<sub>3</sub>

J. Loriers, R. Heindl,\* and F. Clerc

C.N.R.S., Laboratoire des Terres Rares, 92190 Meudon-Bellevue, France

and J. C. Bourcet

Laboratoire de Spectroscopie et de Luminescence, Université Claude Bernard, 69621 Villeurbanne, France

### ABSTRACT

Stable LaAlO<sub>3</sub> has been prepared and activated by Tb<sup>+3</sup>. The compounds show a strong cathodoluminescence. When excited by the appropriate wavelengths in the u.v., they show a strong photoluminescence, at least equal to LaPO<sub>4</sub>:Ce, Tb. The chromaticity coordinates, equivalent wavelengths, luminance, energetic yield, and the position of the phosphors in the chromaticity diagram have been determined. Strong <sup>5</sup>D<sub>3</sub>-<sup>7</sup>F<sub>J</sub> emission was found at low Tb concentrations with CR excitation, while at higher Tb concentrations the green <sup>5</sup>D<sub>4</sub>-<sup>7</sup>F<sub>5</sub> transition predominates.

In 1955, Terol and Ward (1) published their work on the luminescence, especially the cathodoluminescence, of rare earth activated LaAlO<sub>3</sub>. They said that only the Pr<sup>+3</sup>, Sm<sup>+3</sup>, and Eu<sup>+3</sup> activated compounds, obtained by firing of the coprecipitated raw material at 1150°C, give some effective cathodoluminescence, and only few samples were found to luminesce under 2537Å excitation. They mentioned also that Cr<sup>+3</sup> in LaAlO<sub>3</sub> shows no luminescence, although when this ion is dissolved in the perovskitelike structure of LaAlO<sub>3</sub> (which has a sixfold coordination towards the oxide ions, similar to ruby), it should fluoresce strongly.

Later, Forat, Jansen, and Trévaux (2) pulled Cr<sup>+3</sup> and Nd<sup>+3</sup> activated LaAlO<sub>3</sub> single crystals which showed strong luminescence. Because of these contradictory statements, we decided to reinvestigate LaAlO<sub>3</sub> as a host lattice for rare earth activators. In this paper we relate the synthesis of stable terbium-activated lanthanum aluminates La<sub>1-x</sub>Tb<sub>x</sub>AlO<sub>3</sub> with *x* ranging from 0.001 to 0.10 and give the results of the investigation of their optical characteristics.

### Experimental

**Sample preparation.**—Samples were prepared by coprecipitation of La<sup>+3</sup>, Tb<sup>+3</sup>, and Al<sup>+3</sup> by NH<sub>3</sub>. We used La<sub>2</sub>O<sub>3</sub> and Tb<sub>4</sub>O<sub>7</sub> (99.995%) from Péchiney and crystal grade AlNH<sub>4</sub>(SO<sub>4</sub>)<sub>2</sub> (Ugine). The dried hydroxides were fired twice at 1350°C for 24 hr in air. The body color of the undoped compound was white, that of the Tb-activated compounds was yellow brown. Firing them at 1000°C for 4 hr under forming gas gives a white material.

**X-Ray analysis.**—Powder diffraction patterns were taken in a 11.46 cm Debye-Scherrer camera with filtered Cu K $\alpha$  radiation from a Seiffert x-ray generator. Other diffraction diagrams were obtained from both a Seiffert and a GE XRD5 automatic x-ray recorder. Crystal parameters were calculated with the help of an

IBM 270 and a special program for refining parameters.

**Optical analysis.**—The emission spectra under 2250Å excitation were taken with a Cary 17, the excitation spectrum by monochromatic excitation from 850 to 4000Å, and by detecting the global-emitted radiation from <sup>5</sup>D<sub>3</sub> and <sup>5</sup>D<sub>4</sub> to the <sup>7</sup>F<sub>J</sub> states by 9558 EMI detector.

The emission spectra under electron excitation, luminance, efficiency, decay time, and chromaticity coordinates were obtained by depositing the phosphors under standard conditions on cathode-ray screens and exciting them with 15 kV, 4  $\mu$ A/cm<sup>2</sup>. The emitted radiation was analyzed by an automatic recording spectrometer fitted to a C.S.F. computer (St. Egreve, France).

### Results

**X-ray diffraction control.**—The synthesis of LaAlO<sub>3</sub> and La<sub>1-x</sub>Tb<sub>x</sub>AlO<sub>3</sub> was closely checked by x-ray diffraction. When the compounds were fired below 1300°C, and for shorter times, the reaction was not complete and the lines of unreacted La<sub>2</sub>O<sub>3</sub> were found in the x-ray diagram. Terol *et al.* (1), who fired the compounds at 1150°C, probably had no single phase material in their possession. They mentioned that LaAlO<sub>3</sub> would hydrolyze slowly in air, and then La(OH)<sub>3</sub> lines would be found in the diffraction pattern. We put LaAlO<sub>3</sub> prepared at 1350°C in contact with water for 5 days. After drying, no La<sub>2</sub>O<sub>3</sub> or La(OH)<sub>3</sub> lines were found in the x-ray diffraction diagram. Table I gives the crystal parameters of some of the compounds.

**Optical analysis.—Excitation by u.v. radiation.**—Only weak fluorescence is observed when LaAlO<sub>3</sub>:Tb is excited by short (2537Å) or long (3650Å) wave Hg lamps. These aluminates show only weak Tb<sup>+3</sup> absorption at these wavelengths. The main Tb<sup>+3</sup> absorption bands are situated at about 2225Å and between 3400 and 3900Å (excitation spectra, Fig. 1 and 2).

In contrast to other Tb-activated compounds, for example LaPO<sub>4</sub>:Tb, the absorption in the long u.v. wavelength range is stronger than in the short wavelength region. The absorption bands of the aluminates

\* Electrochemical Society Active Member.

Key words: cathodoluminescence, photoluminescence, terbium activated lanthanum-aluminates, fluorescence lifetimes, persistence, energetic yield.

Table I. Crystal parameters of some terbium activated lanthanum aluminates

Indexes	LaAlO <sub>3</sub> Geller (3), d <sub>o</sub>	LaAlO <sub>3</sub> Geller (3), d <sub>c</sub> ASTM	LaAlO <sub>3</sub> 1350°C	La <sub>0.98</sub> Tb <sub>0.02</sub> AlO <sub>3</sub>	La <sub>0.94</sub> Tb <sub>0.06</sub> AlO <sub>3</sub>	La <sub>0.90</sub> Tb <sub>0.10</sub> AlO <sub>3</sub>
0 1 2	3.797	3.791	3.795	3.7824	3.7652	3.748
1 0 4	2.657	2.678	2.680	2.6727	2.6673	2.6635
1 1 0						
0 0 6	2.188	2.190	2.188	2.1841	2.1805	2.1795
2 0 2						
0 2 4	1.896	1.895	1.894	1.892	1.884	1.8845
1 1 6	1.696	1.696	1.693	1.694	1.686	1.6894
2 1 4	1.548	1.548	1.546	1.544	1.541	1.540
3 0 0						
2 0 8	1.339	1.339	1.336		1.336	1.335
0 3 6	1.264	1.264	1.263		1.261	1.260
3 0 6						
1 3 4	1.199	1.199	1.198		1.196	1.193
a		5.365	5.368	5.359	5.348	5.344
c		13.11	13.12	13.105	13.083	13.077

are shifted by about 200Å toward longer wavelengths, from those found in LaPO<sub>4</sub>:Tb (4). Further, another group of Tb-absorption bands, similar to those found recently by Bourcet (4) in LaPO<sub>4</sub>:Tb, is observed between 3300 and 3900Å. The excitation peak at 2450Å

(for  $x = 0.002$ ), at 2425Å (for  $x = 0.012$ ), or 2380Å (for  $x = 0.06$ ) is certainly due to lattice absorption. Its shift, a function of the Tb concentration, is supposed to be due to the change, or perturbation, of the crystal field of LaAlO<sub>3</sub> by the introduction of the smaller Tb<sup>+3</sup> ions into it.

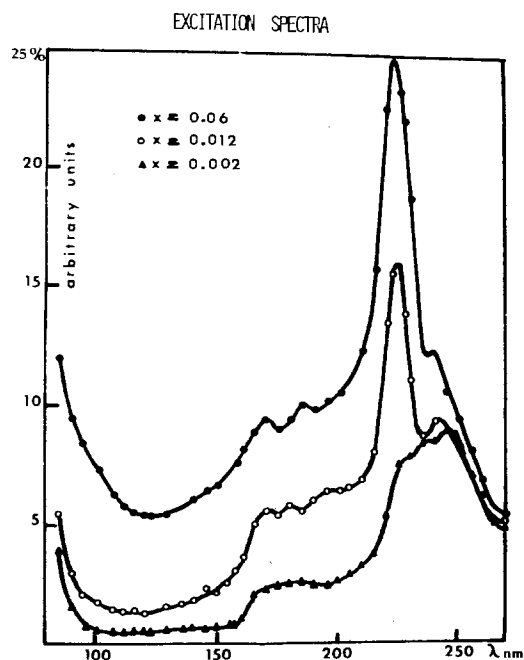


Fig. 1. Excitation spectra of La<sub>1-x</sub>Tb<sub>x</sub>AlO<sub>3</sub> for  $x = 0.06, 0.012, 0.002$ .

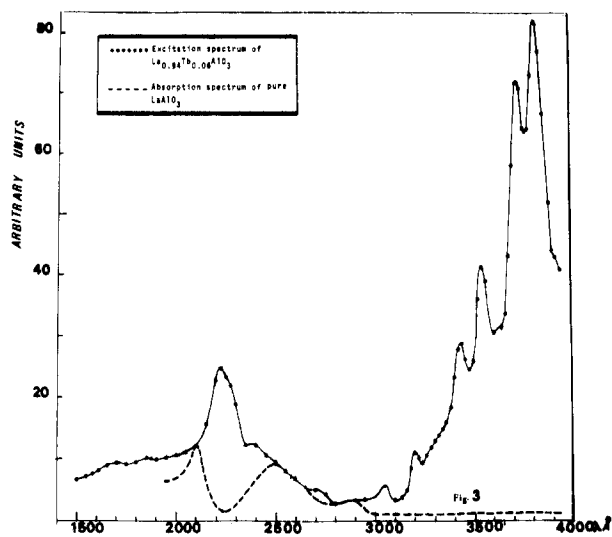


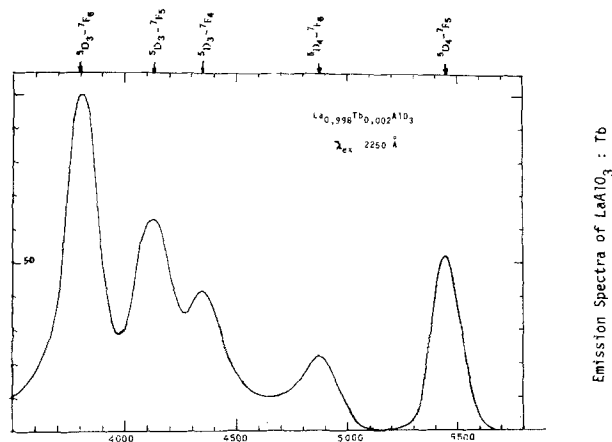
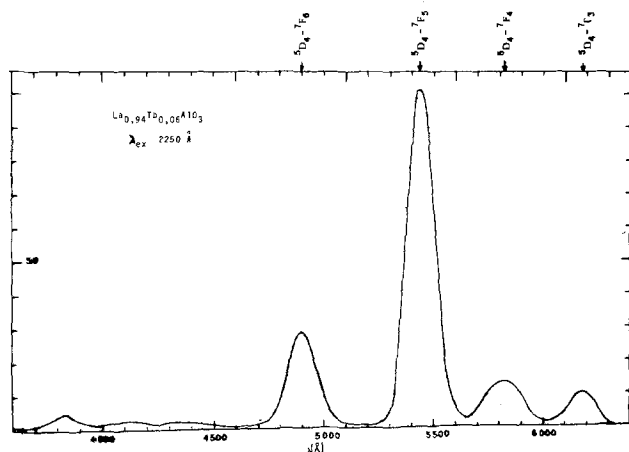
Fig. 2. Excitation spectrum LaAlO<sub>3</sub>:Tb compared to the absorption spectrum of pure LaAlO<sub>3</sub>.

Figure 3 shows the emission spectra of La<sub>0.998</sub>Tb<sub>0.002</sub>AlO<sub>3</sub> and La<sub>0.94</sub>Tb<sub>0.06</sub>AlO<sub>3</sub> under u.v. excitation. With low Tb concentration levels ( $x = 0.001-0.008$ ), the emission takes place mostly from the <sup>5</sup>D<sub>3</sub> level to the <sup>7</sup>F<sub>J</sub> manifold, as is usually observed 5-7, while at higher concentrations the main emission occurs from the <sup>5</sup>D<sub>4</sub> level, giving rise to a more or less saturated-green fluorescence. For excitation below 2000Å, strong transients are observed in the Tb emission intensity. Indeed, the emission intensity increases by a factor of two during the first 10 min of excitation. This is followed by a strong and long-lasting phosphorescence. The over-all emission of LaAlO<sub>3</sub>Tb is strong when excited with the appropriate wavelength, and compares favorably to LaPO<sub>4</sub>:Ce, Tb. Lifetime of the <sup>5</sup>D<sub>4</sub>-<sup>7</sup>F<sub>J</sub> transitions is about 400 μsec at 293°K, that of <sup>5</sup>D<sub>3</sub>-<sup>7</sup>F<sub>J</sub> (weak activator level) about 1 μsec.

CR excitation.—Lanthanum aluminates, La<sub>1-x</sub>Tb<sub>x</sub>AlO<sub>3</sub> with  $x = 0.001, 0.002, 0.005, 0.006, 0.007, 0.009, 0.010, 0.0011, 0.012, 0.016, 0.04, 0.06, 0.08, \text{ and } 0.10$  were excited by electrons. Figure 4 gives the emission spectra of La<sub>1-x</sub>Tb<sub>x</sub>AlO<sub>3</sub> with  $x = 0.002, 0.006, \text{ and } 0.10$ , which are similar to those under photon excitation. The increase of Tb emission observed after a long obtained u.v. excitation does not occur with a long-lasting (5-15 min) CR excitation. No phosphorescence is observed either. It seems to us that the CR excitation at 15 kV employed in this work may be compared to u.v. excitation at wavelengths longer than 1200Å. The persistence is given by Fig. 5. It is the same for all activator concentrations.

Table II gives chromaticity coordinates, equivalent wavelengths, luminance, and energetic yield. With  $x = 0.007$ , a first global emission maximum exists; a second is found at  $x = 0.06$  where the green emission peaks. Figure 6 shows the position of the emission of several samples in the chromaticity diagram.

We have found in these compounds, with CR excitation, the same resonant energy transfer from the Tb-<sup>5</sup>D<sub>3</sub> states to the Tb<sup>+3</sup> ground level at higher Tb concentrations, as found earlier with photon excitation (5, 6). At low Tb concentrations ( $x < 0.005$ ), the distances between the Tb<sup>+3</sup> ions are greater than the critical transfer distance and the possibility of energy transfer from an unexcited Tb<sup>+3</sup> ion in the <sup>5</sup>D<sub>3</sub> state to the ground level of an excited Tb<sup>+3</sup> ion in its vicinity is small. The emission then takes place simultaneously from the <sup>5</sup>D<sub>3</sub> and <sup>5</sup>D<sub>4</sub> states to the <sup>7</sup>F<sub>J</sub> manifold, with a somewhat greater probability for the <sup>5</sup>D<sub>3</sub>-<sup>7</sup>F<sub>J</sub> transitions. At higher Tb concentrations, an energy transfer from the <sup>5</sup>D<sub>3</sub> level to the <sup>7</sup>F<sub>6</sub> level of a Tb ion in the neighborhood takes place and the emission now occurs mainly from <sup>5</sup>D<sub>4</sub> to the <sup>7</sup>F<sub>J</sub> manifold.

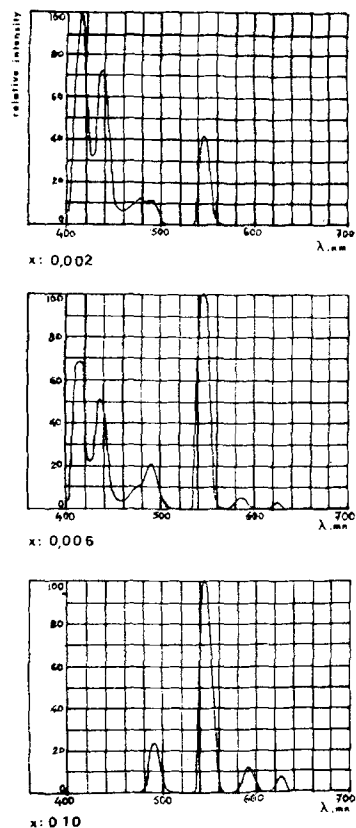
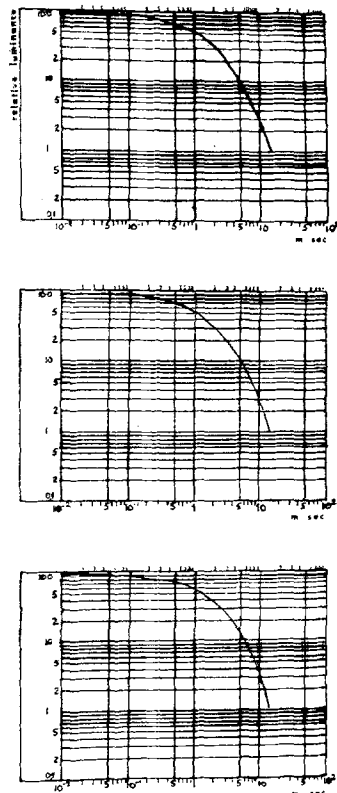
Fig. 3a. Emission spectrum of  $\text{La}_{0.998}\text{Tb}_{0.002}\text{AlO}_3$ Fig. 3b. Emission spectrum of  $\text{La}_{0.94}\text{Tb}_{0.06}\text{AlO}_3$ Fig. 3. Emission spectra of  $\text{La}_{1-x}\text{Tb}_x\text{AlO}_3$  under u.v. excitation

The corrected values of luminance (Table II) give an idea of the emission intensity of the  $^5\text{D}_3\text{-}^7\text{F}_J$  and  $^5\text{D}_4\text{-}^7\text{F}_J$  transitions. The luminance ( $\text{Cd}/\text{m}^2$ ) with  $x = 0.007$  is about 20 times higher as that for  $x = 0.001$ . At low concentrations,  $\text{Tb}^{+3}$  cannot collect the CR energy. At high concentrations,  $\text{Tb}^{+3}$  ( $^5\text{D}_3$ ) is depopulated by ion-ion exchange ( $^5\text{D}_3, ^7\text{F}_6 \rightarrow ^5\text{D}_4, ^7\text{F}_0$ ). Only at intermediate concentrations can CR energy be collected and can  $^5\text{D}_3 \rightarrow ^7\text{F}$  emissions compete against this interfering ion-ion energy exchange. The existence, even at strong u.v. or CR excitation, of a great number of nonexcited Tb ions in the lattice available for the energy transfer  $^5\text{D}_3\text{-}(\text{Tb}^{+3} \text{ excited}) \rightarrow ^7\text{F}_6$  ( $\text{Tb}^{+3}$  fundamental) means that the over-all excitation probability, this will say the absorption, is not very high in this Tb-activated compounds. A second intensity peak is found at  $x = 0.06$  where the green ( $^5\text{D}_4\text{-}^7\text{F}_5$ ) emission peaks. The energetic yield peaks at  $x = 0.007$ . Contrary to the results of Bourcet (4) and Denis (8) with photon excitation, we find that the  $^5\text{D}_4\text{-}^7\text{D}_6$  transition intensity (with CR excitation) is largely independent of the Tb content (Fig. 4).

### Discussion

The luminescence performance shown by these compounds under CR excitation is similar to that of the industrial P-1 phosphor. Table III gives the position of the main Tb emission lines in  $\text{La}_{1-x}\text{Tb}_x\text{AlO}_3$  with  $x = 0.002$  and 0.06 for comparison to those of  $\text{Ca}_{0.99}\text{Tb}_{0.01}\text{WO}_4$ .

Table IV gives lifetime values of the  $\text{Tb}^{+3}$  transitions measured by several authors with different  $\text{Tb}^{+3}$  activated lattices and by us with  $\text{LaAlO}_3\text{:Tb}$ . In accordance with theory, the lifetimes of the  $^5\text{D}_3\text{-}^7\text{F}_J$  transi-

Fig. 4. Emission spectra of  $\text{La}_{1-x}\text{Tb}_x\text{AlO}_3$  under CR excitation for  $x = 0.002, 0.006, 0.010$ .Fig. 5. Persistence of  $\text{LaAlO}_3\text{:Tb}$  under CR excitation

tions are always smaller than those of the  $^5\text{D}_4\text{-}^7\text{F}_J$ , except with  $\text{Sr}_{2.86}\text{Tb}_{0.08}(\text{PO}_4)_2$  where Brill (9) observed for both transitions the same high value of about 5 msec. Brandstadter, Reisfeld, and Larach (10) have observed a strong and long-lasting glow when a



Table II. Chromaticity coordinates, equivalent wavelengths, luminance, and energetic yield

$La_{1-x}Tb_xAlO_3$	Chromaticity coordinates		$\lambda_{equiv.}$ (nm)	Luminance (Cd/m <sup>2</sup> ) at 15 kV, 4 $\mu A/cm^2$	Energetic yield % Wrad/ Wexc	Color
	x	y				
$x = 0.001$	0.150	0.080	468	85.0	0.58	blue violet
0.002	0.156	0.153	477	180	0.903	blue
0.005	0.183	0.324	491	1050	2.63	blue green
0.006	0.184	0.328	441	1140.5	2.57	
0.007	0.190	0.344	492.7	1794	4.01	
0.008	0.198	0.346	492.7	1289	2.88	
0.009	0.205	0.441	503	1154	2.52	
0.010	0.208	0.424	501.2	1620	3.27	green (unsaturated)
0.011	0.230	0.475	510.8	1535	2.86	green (unsaturated)
0.012	0.244	0.476	514.5	1560	2.75	green (unsaturated)
0.040	0.288	0.647	546	2060	2.50	yellow green
0.060	0.251	0.660	539.5	2255	2.82	
0.080	0.262	0.657	542	1881	2.32	
0.100	0.279	0.629	544.5	1881	2.23	

Table III. Position of the emission peaks (in angstroms) of  $La_{1-x}Tb_xAlO_3$  ( $x = 0.002, 0.06$ ) and  $Ca_{0.99}Tb_{0.01}WO_4$  under u.v. excitation

Compound	$^5D_3 \rightarrow ^7F_6$	$^5D_3 \rightarrow ^7F_5$	$^5D_3 \rightarrow ^7F_4$	$^5D_4 \rightarrow ^7F_6$	$^5D_4 \rightarrow ^7F_5$	$^5D_4 \rightarrow ^7F_4$	$^5D_4 \rightarrow ^7F_3$
$La_{0.998}Tb_{0.002}AlO_3$	3795	4125	4350	4486	5450		
$La_{0.94}Tb_{0.06}AlO_3$	3840			4900	5430	5815	6185
$Ca_{0.99}Tb_{0.01}WO_4$		4150	4360	4900	5440	5900	6250

Tb-activated glass was bombarded by fast electrons. Crabtree (11) explains the high lifetime of  $^5D_4$  transitions of Tb in CR-excited  $SnO_2$  by the existence of trapped electrons which are slowly released and then excite the Tb  $^5D_4$  level. He gives no information on the behavior of the  $^5D_3$  levels. We found in CR-excited  $LaAlO_3:Tb^{+3}$ , with low or high Tb concentrations, a large emission duration of about 10 msec (Fig. 5), for both the  $^5D_3$  and  $^5D_4$  transitions. Creation of traps by

impinging electrons, as supposed by Crabtree, could be the reason. Recently, another mechanism has been proposed: the oxidation of the  $Tb^{+3}$  ions to  $Tb^{+4}$  occurs during excitation, their reduction to trivalency after excitation takes place via excited  $Tb^{+3}$  states which decay to the ground state by light emission [see also Ref. (13)]. However,  $Tb^{+4}$  ions present in  $LaAlO_3$  are not converted easily back into the trivalent state. Indeed  $LaAlO_3:Tb^{+4}$  must be heated in a reducing atmosphere in order to be converted to  $LaAlO_3:Tb^{+3}$ . When coprecipitated  $La_{1-x}Tb_x(OH)_3$  and  $Al(OH)_3$  are heated in air only a brownish compound is obtained, even with as little as 0.05 mole percent (m/o) of  $Tb^{+3}$ , probably a mixture of  $LaAlO_3$ ,  $Al_2O_3$ , and  $Tb_4O_7$ . No fluorescence nor any change of its brown body color into a white one ( $LaAlO_3:Tb^{+3}$ ) was observed when  $LaAlO_3:Tb^{+4}$ , left to itself, was exposed to u.v. radiation or cathode rays or was heated in air. From this it may be concluded that the  $Tb^{+4}$  reduction process does not occur in the present case. Creation of traps may also occur when  $LaAlO_3:Tb$  is excited by 1215Å radiation.

In Brill's compound [CR-excited  $Sr_{2.86}Tb_{0.08}(PO_4)_2$ ], cation vacancies exist. The long lifetime he found for both transitions (5 msec) makes us think he did not measure the lifetime of the Tb transitions but that of one of the above-mentioned energy-releasing processes. As the  $^5D_3$  emission remains strong even at high Tb concentration, we can assume that in this particular case the cation vacancies partially prevent the  $^5D_3 \rightarrow ^5D_4$  energy transfer, indicating that the spontaneous multiphonon cross-relaxation process ( $^5D_3 \rightarrow ^5D_4 \rightarrow ^7F_6 \rightarrow ^7F_0$ ) is hindered in this compound.

Manuscript submitted March 1, 1976; revised manuscript received June 14, 1976.

Any discussion of this paper will appear in a Discussion Section to be published in the June 1977 JOURNAL. All discussions for the June 1977 Discussion Section should be submitted by Feb. 1, 1977.

Publication costs of this article were assisted by C.N.R.S.

REFERENCES

1. S. Terol and R. Ward, *This Journal*, **102**, 524 (1955).
2. F. Forrat, R. Jansen, and P. Trévaux, *C.R.*, **4**, 1271 (1963).
3. S. Geller and V. B. Baba, *Acta Crystallogr.*, **21**, 1019 (1965).
4. J. C. Bourcet, Ph.D. Thesis, Université de Lyon (1974).

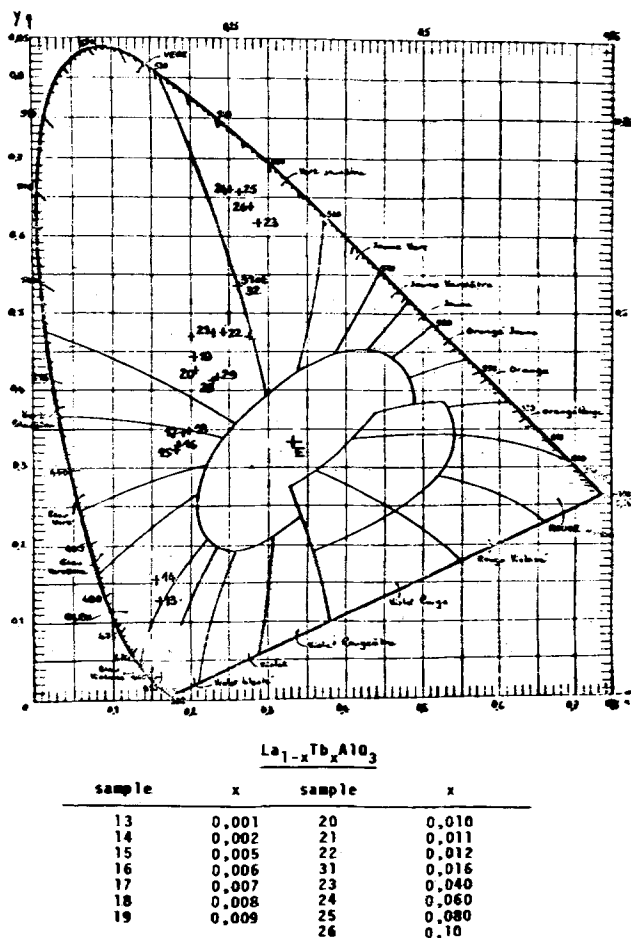


Fig. 6. Position of  $La_{1-x}Tb_xAlO_3$  in the chromaticity diagram

Table IV. Tb lifetimes collected from the literature and from this work

Author	Host	Transition	Lifetime	Temperature (°K)
Dike and Hall (1953)	TbCl <sub>3</sub> · 6H <sub>2</sub> O	<sup>5</sup> D <sub>4</sub> - <sup>7</sup> F <sub>6</sub> (u.v. excitation)	467 μsec	293
Peterson and Bridenbaugh (1963)	Tb hexa-antipyrene triiodide	<sup>5</sup> D <sub>4</sub> - <sup>7</sup> F <sub>6</sub> (u.v. excitation)	5000 μsec	293
<i>ibid</i>	SrMoO <sub>4</sub>	<sup>5</sup> D <sub>4</sub> - <sup>7</sup> F <sub>5</sub>	566 μsec	293
<i>ibid</i>	SrMoO <sub>4</sub> (low Tb conc.)	<sup>5</sup> D <sub>4</sub> - <sup>7</sup> F <sub>5</sub> (u.v. excitation)	189 μsec	293
Anderson et al. (1966)	ZnS (0.01-0.02 m/o Tb)	<sup>5</sup> D <sub>4</sub> - <sup>7</sup> F <sub>5</sub> (u.v. excitation)	200 μsec	77
Pearson et al. (1965)	Glass (1-10 m/o Tb)	<sup>5</sup> D <sub>4</sub> - <sup>7</sup> F <sub>5</sub> (u.v. excitation)	2700 to 1000 μsec	293
Van Uitert (1966)	Na <sub>0.5</sub> Y <sub>0.5-x</sub> Tb <sub>2x</sub> WO <sub>4</sub> (0.01 < x < 0.50)	<sup>5</sup> D <sub>4</sub> - <sup>7</sup> F <sub>5</sub> (u.v. excitation)	600 μsec	293
Bril et al. (1962)	Sr <sub>2-86x</sub> Tb <sub>0.08</sub> (PO <sub>4</sub> ) <sub>3</sub>	<sup>5</sup> D <sub>4</sub> - <sup>7</sup> F <sub>5</sub>	τ: 5 msec	
		<sup>5</sup> D <sub>3</sub> - <sup>7</sup> F (CR excitation)	5 msec	
Crabtree	SnO <sub>2</sub> (1 m/o Tb)	<sup>5</sup> D <sub>4</sub> - <sup>7</sup> F <sub>5</sub> (CR excitation)	2200 μsec	293
	SnO <sub>2</sub> (0.1 m/o Tb)	<sup>5</sup> D <sub>4</sub> - <sup>7</sup> F <sub>5</sub> (CR excitation)	640 μsec	293
This work	La <sub>0.92</sub> Tb <sub>0.08</sub> AlO <sub>3</sub>	<sup>5</sup> D <sub>4</sub> - <sup>7</sup> F <sub>5</sub> (u.v. excitation)	400 μsec	293
		<sup>5</sup> D <sub>3</sub> - <sup>7</sup> F <sub>5</sub> (u.v. excitation)	1 μsec	293
	La <sub>0.995</sub> Tb <sub>0.005</sub> AlO <sub>3</sub>	<sup>5</sup> D <sub>4</sub> - <sup>7</sup> F <sub>5</sub> (CR excitation)	10 msec (persistence)	293
		<sup>5</sup> D <sub>3</sub> - <sup>7</sup> F <sub>5</sub> (CR excitation)	10 msec (persistence)	293

5. Peterson and Bridenbaugh, *J. Opt. Soc. Am.*, **53**, 1129 (1963).
6. T. Hoshina, *Jpn. J. Appl. Phys.*, **6**, 1203 (1967).
7. G. Blasse and A. Bril, *Philips Res. Repts.*, **22**, 481 (1967).
8. J. P. Denis, Ph.D. Thesis, Université de Paris (1972).
9. A. Bril, L. Wanmaker, and J. W. ter Vrugt, *This*

- Journal*, **115**, 776 (1968).
10. I. J. Brandstadter, R. Reisfeld, and S. Larach, *Solid State Commun.*, **11**, 1235 (1972).
11. D. F. Crabtree, *J. Phys. D.*, **7**, 122 (1974).
12. Y. Tsusimoto, Y. Fukuda, S. Suagai, and M. Fukai, *J. Lumin.*, **9**, 475 (1975).
13. C. W. Struck and W. H. Fonger, *Phys. Rev. B*, **4**, 22 (1971).

## The Optical Anisotropy of the Anodic Oxide of Vanadium

J. C. Clayton<sup>1</sup> and D. J. De Smet\*

Department of Physics and Astronomy, The University of Alabama, University, Alabama 35486

### ABSTRACT

Ellipsometric measurements made during the anodic oxidation of vanadium can be most easily interpreted by assuming that the anodic oxide film is optically anisotropic with an optic axis parallel to the direction of film growth. This behavior is similar to that found by others for the anodic oxides of tantalum and niobium. The optical anisotropy of the vanadium oxide is found to depend on the applied electric field, but the dependence is not a simple power law since the anisotropy does not vanish when the electric field is removed from the film. This is in contrast to the behavior of tantalum and niobium. For these materials the anisotropy disappears when the electric field is removed.

Recent ellipsometric studies of the anodic oxidation of tantalum by Cornish and Young (1) and of the anodic oxidation of niobium by Yee and Young (2) demonstrate that these anodic oxides are optically anisotropic with an optic axis parallel to the direction of the film growth when the electric field strength in these films is large. Further, they conclude that when the electric field is removed these films become optically isotropic. These two works support and extend the work of Ord, Hopper, and Wang (3), who employed ellipsometry to demonstrate that changes in the applied electric field cause changes in both the thickness and the refractive index of the anodic oxides of tantalum, niobium, and tungsten. These authors interpreted their data in terms of an optically isotropic model of the film because they examined the film at thicknesses where ellipsometric measurements can most sensitively distinguish between changes in film thickness and changes in refractive index. As it turns out, at these thicknesses ellipsometry is quite insensitive to the optical anisotropy found by Young and co-workers. Nevertheless Ord had suggested that a

complete analysis of ellipsometric data for anodic oxides might show evidence of optical anisotropy (4).

Since the anodic oxides of both tantalum and niobium exhibit a field-dependent optical anisotropy it is pertinent to ask if such an anisotropy is a general property of anodic oxide films. The purpose of the present work is to demonstrate that the anodic oxide of vanadium, which is in many respects similar to other anodic oxides (5), shows an anisotropy similar to those of tantalum and niobium under high field conditions. We will also show that with vanadium, unlike tantalum and niobium, the anisotropy does not completely vanish when the electric field is removed from the film.

### Experimental

The instrumentation and sample preparation techniques used have been described adequately elsewhere (6). We state for the sake of clarity that the ellipsometric measurements presented here were made with the sample *in situ*, and that our ellipsometer has a quarter-wave plate between the polarizer and the sample, oriented so that its fast axis makes an angle of -45° with the plane of incidence. Two optical cells were used in this work. They were identical in construction but one of them appeared to have windows

\* Electrochemical Society Active Member.

<sup>1</sup> Present address: Department of Physics, University of Waterloo, Waterloo, Ontario, Canada N2L 3G1.

Key words: anisotropy, anodic oxide, vanadium, ellipsometry, index of refraction.

with lower birefringence than the other. Since we report our data directly as the measured polarizer and analyzer values at null and do not choose to make corrections to our data for cell window birefringence, we will make only qualitative statements concerning data obtained using the second, or poorer, cell. Since our automatic ellipsometer provides many more data points than can be effectively displayed, the figures show only representative data points.

The mathematics of interpreting ellipsometric data for a uniaxial film with its optic axis perpendicular to the film surface on an isotropic substrate is straightforward. Cornish and Young (1) give a brief outline of the necessary changes that must be made to the usual equations of ellipsometry and den Engelsen (7) and Dignam, Moskovits, and Stobie (8) have independently published complete solutions to this particular problem.

### Results

Before presenting the experimental data that demonstrate optical anisotropy in the vanadium oxide it is in order to recall the effects that optical anisotropy will have on ellipsometric measurements. Figure 1 shows the null settings of the polarizer and analyzer for the growth of the anodic oxide of vanadium under our experimental conditions. The null setting for zero thickness is marked "start" and the data trace out a curve in a clockwise direction as growth proceeds. After approximately 1500Å of film have been formed the experimental curve passes approximately through the starting point and almost retraces itself. We shall refer to each repetition of the data as a loop.

The effect of a uniaxial anisotropy with an optic axis parallel to the direction of film growth is to displace successive loops parallel to the  $P$  axis by an amount that depends on the size of the anisotropy and in a direction that depends on whether the film is uniaxial positive or uniaxial negative. For our particular configuration of the ellipsometer a uniaxial positive film ( $n_e > n_o$ ) will cause successive loops, to be displaced toward lower values of  $P$  whereas a uniaxial negative film ( $n_e < n_o$ ) will cause successive loops to be displaced toward higher values of  $P$ . Under these circumstances it is apparent that an anisotropy of this form will be most easily detected in the regions where  $P$  is either a minimum or a maximum.

Turning now to the experimental data, Fig. 2 shows the behavior of the null settings of the ellipsometer, plotted as open circles, for portions of three loops of the anodic growth curve for a film grown at a constant current density of  $394 \mu\text{A}/\text{cm}^2$ . Data taken in a region near the minimum value of the polarizer are shown in the left-hand portion of Fig. 2 and those near the maximum of the polarizer are shown in the right-hand portion of this figure. The data in this figure are

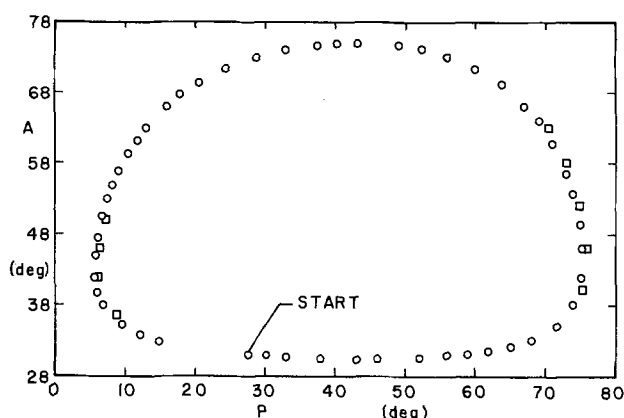


Fig. 1. Ellipsometer null settings for the growth of an anodic oxide film on vanadium at a current density of  $275 \mu\text{A}/\text{cm}^2$ . Circles, first loop; squares, second loop.

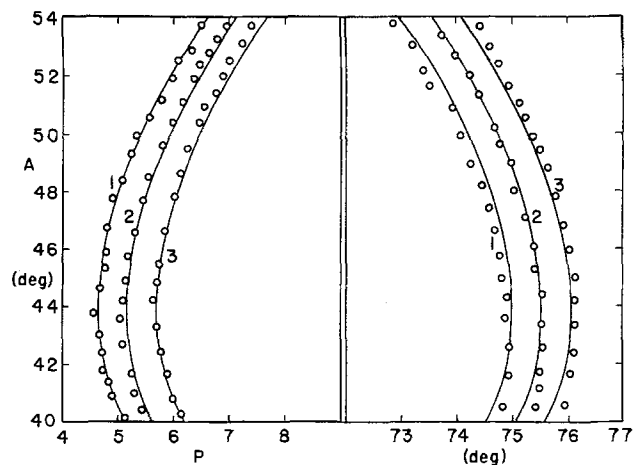


Fig. 2. Ellipsometer null settings in the regions of minimum and maximum  $P$  for the growth of an anodic oxide film on vanadium at a current density of  $394 \mu\text{A}/\text{cm}^2$ . Data points are represented by circles and the solid lines represent the calculated behavior for a uniaxial film with an optic axis normal to the surface of the film for which  $n_o = 2.349$  and  $n_e = 2.328$ . The refractive index of the substrate is assumed to be  $3.838 - 3.560i$ .

presented using expanded scales relative to Fig. 1. As is evident from this figure, successive loops are displaced toward increasing values of  $P$ . Thus we conclude that under constant current conditions the anodic oxide film on vanadium is a uniaxial negative material. This anisotropic behavior can also be seen by carefully examining Fig. 1. The squares in this figure, which represent data obtained for the second loop, are displaced slightly to the right of the circles.

Also shown in Fig. 2 are solid lines that represent the calculated behavior of the ellipsometer null settings assuming that we are dealing with a growing film with an ordinary refractive index of 2.349 and an extraordinary refractive index of 2.328 on a substrate of refractive index  $3.838 - 3.560i$ . The values of the optical parameters used in calculating these lines were estimated by making initial guesses of their values and then varying the value of each parameter in turn until a calculated curve was found that better approximated the experimental data in the sense that the root-mean-square deviation of the distance between the point and the curve was reduced. This procedure was repeated using reduced variations of the parameters until the RMS deviation ceased changing significantly. Therefore we have not actually calculated  $n_o$  and  $n_e$  from the experimental data, rather we have made reasonable estimates of the values of these parameters using a curve-fitting procedure. Nevertheless, these values of the optical parameters are in good agreement with the experimental data; therefore we assume that they closely approximate the true characteristics of the sample.

We must point out that there are other possible ways to interpret this data that cannot, *a priori*, be ruled out. First, since the anodic oxide of vanadium dissolves slowly in the electrolyte employed here we must determine whether a dissolution product adhering to the outer surface of the film can cause the observed ellipsometric behavior. Calculations have been performed using a model in which a second film is placed on top of the anodic oxide using a large range of thickness ratios for the two films and a number of values for the refractive index of the outer film. In no case were we able to generate curves that show the general characteristics of our experimental data for all three loops. Therefore, although we have not exhausted all possible combinations of numbers, it is very unlikely that this interpretation can apply to the results presented here.

Thus far we have only looked at the behavior of the film under constant current and hence constant field

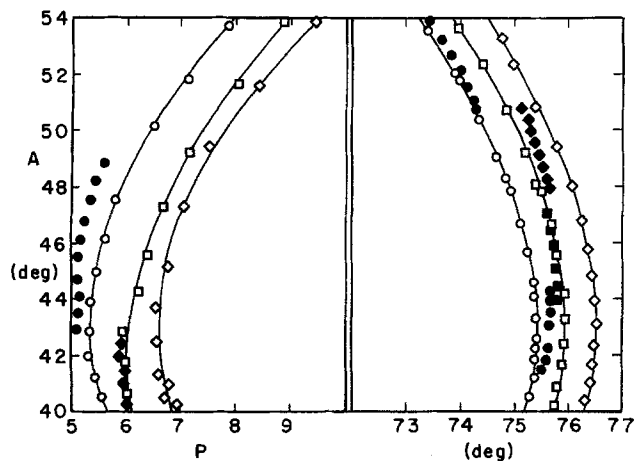


Fig. 3. Ellipsometer null settings (open symbols) in the regions of minimum and maximum  $P$  for the growth of an anodic oxide film on vanadium at a current density of  $394 \mu\text{A}/\text{cm}^2$ . The filled symbols represent data obtained under open-circuit conditions. Circles, first loop; squares, second loop; diamonds, third loop. The solid lines are drawn only as an aid in following the data.

conditions. Let us now examine the behavior of the optical data for a film for which the circuit is opened and the electric field is allowed to decay to zero. Figure 3 shows data for an experiment in which an anodic film was grown at an applied current density of  $394 \mu\text{A}/\text{cm}^2$ . At intervals during the growth of this film the circuit was opened and the electric field was allowed to decay to zero. The data shown in Fig. 3 were obtained using a poorer quality optical cell, therefore we will make only qualitative statements about the behavior of the film based on these data.

The open symbols in Fig. 3 are the  $P$ - $A$  points obtained with an applied anodic current. The open circles are for the first loop of the  $P$ - $A$  curve, the open squares are for the second loop, and the open diamonds are for the third loop. The solid lines through the open symbols in this figure do not represent a fit to the data but are added as an aid in following the shape of the curve. The filled symbols are the data points obtained when the circuit is opened and the field decays to zero. The closed circles are the open-circuit data points for the first loop of the  $P$ - $A$  growth curve, the closed squares are the open-circuit  $P$ - $A$  values obtained for the second loop of the growth curve, etc. After the circuit had been open for some time, the anodic current was again applied and growth of the film continued; the optical data returned to the growth curve.

The behavior of the optical data is not difficult to explain. Looking at the data near the minimum value of  $P$  for the first loop, as growth proceeds  $A$  increases. When the circuit is opened the  $P$ - $A$  values jump abruptly away from the growth curve and upward in  $A$ , indicating that the refractive indexes and perhaps the thickness of the film have changed. As open-circuit conditions are continued the optical data move downward in  $A$ , indicating that the film is decreasing in thickness. This is not unexpected since the film is slightly soluble in the electrolyte. When the anodic current is reapplied the ellipsometer null settings jump back to the growth curve (at a lower thickness since some of the film has dissolved) and then proceed again along the growth curve. A similar interpretation can be made for the data obtained near the maximum value of  $P$ .

The significant point to be made about the data shown in Fig. 3 is that the ellipsometric measurements made during the time that the circuit was opened do not lie on a single curve for all three loops of the data. That is, even under open-circuit conditions the data corresponding to the second loop lie to the right of the data taken for the first loop, and the data for the

third loop lie still further to the right. This indicates that the film is anisotropic even under open-circuit conditions. Since the circuit was open long enough (3-4 min) that the electric field decayed several orders of magnitude, if not actually to zero, we conclude that the anodic oxide of vanadium has a uniaxial negative optical anisotropy under conditions where there is no applied electric field.

It is also evident from Fig. 3 that the optical anisotropy diminishes when the electric field is removed from the film. For example, in the right-hand side of Fig. 3 it is apparent that for a given value of  $A$  the data taken under open-circuit conditions for the three loops have a smaller separation in  $P$  than the data taken with a current applied to the electrode. Thus part of the optical anisotropy is intrinsic to the film itself and part of it is caused by the applied electric field or current.

## Discussion

In the previous section we have shown that the optical properties of the anodic oxide of vanadium are similar to those of the anodic oxides of tantalum and niobium since each of these materials has an optical anisotropy with an optic axis parallel to the direction of film growth. Further, all of these films are uniaxial negative and the anisotropy depends on the applied current density or electric field, decreasing with decreasing field. Vanadium differs from tantalum and niobium only because it shows some optical anisotropy under zero field conditions.

It is interesting to compare the difference between the ordinary and extraordinary refractive indexes,  $\Delta n = n_o - n_e$ , and the steady-state electric fields for these three materials at comparable applied current densities. Assuming current densities in the range  $300$ - $400 \mu\text{A}/\text{cm}^2$ , for tantalum  $\Delta n = 0.0039$  at a field of  $6 \times 10^6 \text{ V}/\text{cm}$ , for niobium  $\Delta n = 0.0056$  at a field of  $4.3 \times 10^6 \text{ V}/\text{cm}$ , and for vanadium  $\Delta n = 0.021$  at a field of  $2.7 \times 10^6 \text{ V}/\text{cm}$ . (The values of  $\Delta n$  and the electric field for tantalum and niobium have been calculated using equations given in Ref. (2) in conjunction with current-field plots presented by Young and Zobel (10) and assuming a current density of about  $320 \mu\text{A}/\text{cm}^2$ .) Thus we note that for a given applied current density the material with the highest electric field has the lowest optical anisotropy and the material with the lowest electric field has the highest optical anisotropy.

The fact that the optical anisotropy of the vanadium oxide does not entirely disappear when the electric field is removed from the film may be due to a number of factors. First, it is possible that the amount of time required for the film to adjust changes if the electric field is greater than the amount of time for which the circuit was opened. However, Cornish and Young (1) found that upon suddenly applying a field to a film-covered tantalum electrode there is an exponential approach to the steady state with a time constant of about 10 sec and a similar behavior when the field is removed. We would expect approximately the same time constant with vanadium as Cornish and Young found for tantalum. Therefore, although we cannot entirely rule out this possibility, it is not a likely explanation since the 3-4 min that the circuit remained open ought to be more than enough time for any simple relaxation process to occur.

Another possible explanation of the residual anisotropy is that the film formed on vanadium, unlike those on tantalum and niobium, may be crystalline. Although we have not performed any measurements to determine this, Keil and Salomon (12), using x-ray diffraction, report that an anodic film formed on vanadium in this electrolyte is amorphous or only very slightly crystalline. Also, Arora and Kelly (13) concluded, on the basis of electron diffraction data, that only very thin anodic films on vanadium showed polycrystalline structure; films thicker than about  $200 \text{ \AA}$  were found to be amorphous.

Since it has been alleged that the anodic oxide film formed on vanadium may contain pores (9), we must examine the possibility that the anisotropy observed under zero electric field can be explained in terms of pores. If pores are present they would introduce a structural anisotropy that could cause an optical anisotropy or form birefringence. Let us assume that a porous structure can be modeled by an assembly of parallel cylindrical rods with an index of refraction  $n_1$  immersed in a medium with an index of refraction  $n_2$ . Such a structure will be optically anisotropic and the relation for the difference between the ordinary and extraordinary refractive indexes is given by (11)

$$n_e^2 - n_o^2 = \frac{f_1 f_2 (n_1^2 - n_2^2)^2}{(1 + f_1) n_2^2 + f_2 n_1^2} \quad [1]$$

Here  $f_1$  and  $f_2$  are the fractions of the total volume occupied by the rods and the medium, respectively, and the equation is valid for  $f_1 \ll 1$ . Whether we consider the index of refraction of the rods to be greater than that of the medium or less than that of the medium the values of  $n_e^2 - n_o^2$  will always be positive, indicating that this structure will be uniaxially positive. The anodic film on vanadium gave data that are consistent with a uniaxial negative material. Thus the observed optical anisotropy cannot be caused by pores. This does not exclude the possibility that pores exist, it merely indicates that they cannot be used to explain the experimental data.

One point that we have avoided until now is the functional dependence of the changes in the optical constants and the film thickness on the electric field. Young and co-workers (1, 2) found that for tantalum and niobium the changes in refractive index vary as the square of the electric field; that is,  $\Delta n_o = -aE^2$  and  $\Delta n_e = -bE^2$ , where  $\Delta n_o = n_o(E) - n(E=0)$  and  $\Delta n_e = n_e(E) - n(E=0)$ . Implicit in this statement of the electric field dependence of the optical constants is the fact that when the electric field is zero the film is isotropic. While the experimental data presented by Young and co-workers support this conclusion for tantalum and niobium, it is clearly not true for vanadium. Also, since the anodic oxide of vanadium shows a residual anisotropy when the electric field is zero, it would not be unreasonable to suspect that this residual anisotropy may depend on the value of the electric field at which the film was formed. This would preclude any analysis that assumes that the

state of the film at any time depends only on the conditions that prevail at that instant. We do not know whether this suspicion is justified, but until further evidence is available it would be improper to attempt an analysis of the dependence of the optical constants on the electric field for vanadium based on the present data.

The determination of the electric field dependence of the optical parameters and thickness for the anodic oxide of vanadium presents experimental difficulties. The fact that the film formed on vanadium is slightly soluble means that any changes in film thickness due to changes in the electric field will be superimposed on changes in thickness due to dissolution. In addition, with vanadium we cannot make measurements at different values of the electric field (the same in the sense that the film contains exactly the same amount of material) because of dissolution. Finally, the possibility that the field dependence may depend on the history of the film suggests that a number of very careful experiments must be conducted before any further conclusions can be drawn.

Manuscript submitted June 28, 1976; revised manuscript received Aug. 11, 1976.

Any discussion of this paper will appear in a Discussion Section to be published in the June 1977 JOURNAL. All discussions for the June 1977 Discussion Section should be submitted by Feb. 1, 1977.

#### REFERENCES

1. W. D. Cornish and L. Young, *Proc. R. Soc. London A*, **335**, 39 (1973).
2. K. K. Yee and L. Young, *Appl. Opt.*, **14**, 1316 (1975).
3. J. L. Ord, M. A. Hopper, and W. P. Wang, *This Journal*, **119**, 439 (1972).
4. J. L. Ord, Private communication (1967).
5. B. H. Ellis, M. A. Hopper, and D. J. De Smet, *This Journal*, **118**, 860 (1971).
6. J. C. Clayton and D. J. De Smet, *ibid.*, **123**, 174 (1976).
7. D. den Engelsen, *J. Opt. Soc. Am.*, **61**, 1460 (1971).
8. M. J. Dignam, M. Moskovits, and R. W. Stobie, *Trans. Faraday Soc.*, **67**, 3306 (1971).
9. R. G. Keil and K. Ludwig, *This Journal*, **118**, 864 (1971).
10. L. Young and F. G. R. Zobel, *ibid.*, **113**, 277 (1966).
11. M. Born and E. Wolf, "Principles of Optics," 3rd ed., p. 707, Pergamon Press, New York (1967).
12. R. G. Keil and R. E. Salomon, *This Journal*, **115**, 628 (1968).
13. M. R. Arora and R. Kelly, *ibid.*, **122**, 75C, Abstract No. 91 (1975).

## Effects of Additions to SnO<sub>2</sub> Thin Films

A. F. Carroll and L. H. Slack

Department of Materials Engineering,  
Virginia Polytechnic Institute and State University, Blacksburg, Virginia 24061

#### ABSTRACT

The effects of adding Sb and In to pyrolytic SnO<sub>2</sub> films were investigated. The large rise in resistivity for larger additions of Sb was studied using x-ray diffraction, effects of heat-treatment, determination of activation energy, and scanning electron microscopy. These results indicate that the rise is caused by a gradual loss of crystallinity and demonstrated the important effects of thermal history on the films' structure and electrical characteristics.

Undoped SnO<sub>2</sub> thin films formed by pyrolytic deposition have an appreciable conductivity in the range of  $10^2$ - $10^3$  ( $\Omega$ -cm)<sup>-1</sup> (1, 2, 4-7). Additions of a Group III element, In, cause the films resistivities to increase while additions of the Group V element, Sb, cause it to decrease (2-5). This doping effect on

Key words: antimony oxide additives, indium oxide additives, film crystallinity, heat-treatment, bonding.

resistivity is due to a controlled valency mechanism (3). It is interesting that large additions of Sb cause the films resistivity to increase, reversing the trend predicted by the controlled valency mechanism.

Conductivity of pure SnO<sub>2</sub> films has been attributed to a combination of chloride ions and oxygen vacancies which result from incomplete decomposition of SnCl<sub>4</sub> and incomplete oxidation of the film to

stoichiometric  $\text{SnO}_2$  (2, 3). These defects are considered to be electron donors. Nonstoichiometric  $\text{SnO}_2$  has been represented by  $\text{Sn}^{4+}_{1-\beta}\text{Sn}^{2+\beta}\text{O}^{2-(2-\beta)}$  (3) which contains  $\beta$  moles of oxygen vacancies which can donate  $2\beta$  moles of electrons for conduction.

Additions of only 3 mole percent (m/o) In caused resistivity to increase by  $10^4$ X (5). Small additions of Sb caused resistivity to decrease by approximately 10X to a minimum value. This minimum occurred at additions of 0.9 m/o (2), 0.6 m/o (4), and 3 m/o (5) Sb. Vincent (3) represented the composition of these films by:  $\text{Sn}^{4+}_{(1+\alpha)}\text{Sb}^{5+\alpha}\text{e}_\alpha\text{O}^{2-2}$ . This formula indicates the absence of  $\text{Sn}^{2+}$  ions and associated oxygen vacancies. Arai (2) believed that heat-treating of Sb-doped films did not alter resistivity, indicating that there were indeed no  $\text{Sn}^{2+}$  ions or associated oxygen vacancies. These low resistivity films have exhibited negligible temperature dependence of resistivity indicating that an impurity band overlaps the conduction band (6).

Since small additions of Sb are known to increase conduction electron concentration, one would expect larger additions to do the same. However, the unexpected rise in resistivity has been attributed to impurity scattering (2), atomic disorder (5), and precipitation of  $\text{Sb}_2\text{O}_5$  (4). A thermodynamic study of  $\text{Sb}_2\text{O}_3$  and  $\text{Sb}_2\text{O}_5$  stability has concluded that formation of  $\text{Sb}_2\text{O}_5$  in  $\text{SnO}_2$  films was not feasible (3).

The present study was undertaken to gain further insight into the effect of In and Sb additives on electrical conductivity in  $\text{SnO}_2$  films. Of particular interest was the rise in resistivity occurring at high levels of Sb. Causes for this rise were sought, using determinations of structure and activation energy, and heat-treatment studies.

### Procedure

$\text{SnO}_2$  films were formed pyrolytically by spraying a very finely dispersed 2.85  $\mu\text{m}$  solution of  $\text{SnCl}_4 \cdot 5\text{H}_2\text{O}^1$  dissolved in ethanol (8). Controlled additions of  $\text{SbCl}_3^1$  or  $\text{InCl}_3 \cdot 4\text{H}_2\text{O}^2$  were made to the spray solution to effect a change in Sb or In content of the films. The high degree of dispersion allowed deposition to be carried out at the relatively low temperature range of 300°-350°C.

All samples were examined by x-ray diffraction using filtered  $\text{CuK}_\alpha$  radiation.<sup>3</sup> The apparatus used a graphite crystal monochromator to increase the resolution of the diffracted signal. Attenuation of the glassy halo originating from the substrate was used to determine thickness of each film (9).

Electrical resistivity was measured by a four-terminal d-c method (10) in which Au-Nichrome thin film strips served as electrodes. For the heat-treated samples a four-point probe apparatus was used on uncoated  $\text{SnO}_2$  in order to avoid interaction of Au film with the  $\text{SnO}_2$  film during heating. An electrometer<sup>4</sup> was used for voltage measurement in this method facilitating conductivity measurements over a range of  $10^{10}$ . A hot-probe technique was used to determine sign of charge carriers.

Temperature dependence of electrical resistivity was measured by placing resistivity samples in a controlled temperature furnace capable of obtaining precise temperatures with negligible gradient. Activation energy of electrical conduction was calculated from slopes of graphs of log resistivity vs.  $10^3/T$  (°K).

Scanning electron microscopy (SEM)<sup>5</sup> was employed to examine film morphology. Energy dispersive an-

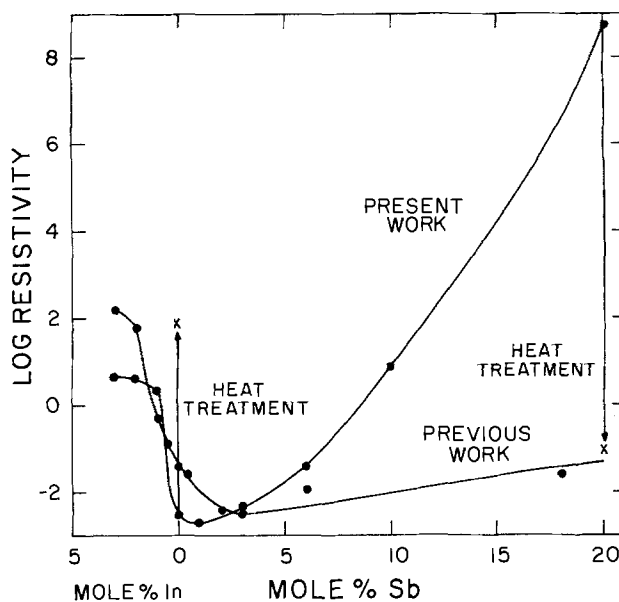


Fig. 1. Resistivity of  $\text{SnO}_2$  thin films as a function of additive concentration.

alysis by x-rays used with SEM identified the compositions of structural features in the films.

### Results

**Electrical characteristics.**—Logarithm of the films resistivities is plotted as a function of mole percent of antimony or indium in Fig. 1. One curve corresponds to films prepared in this work in which the glass substrates were held at 350°C during deposition and the second to films prepared at 600°C in a previous study (5). Small additions of antimony caused the film resistivity to decrease. For additions greater than 1 m/o the resistivity increased, with additions of 10 and 20 m/o of Sb causing very large increases in resistivity. However, these large additions of antimony in films prepared at 600°C caused only a small increase in resistivity. Small additions of indium caused increases in the film resistivity for both the low temperature and high temperature films. All films with resistivities below  $10^2 \Omega\text{-cm}$  were found to be n-type; the carrier sign of the more resistive film could not be measured.

Two of the films, one with no impurities and the other with 20 m/o antimony, were heat-treated. The changes in resistivity caused by 200 hr of heat-treatment at 600°C are indicated in Fig. 2. The variation in the films resistivities as a function of heat-treatment time is shown. The resistivity of the undoped tin oxide film increased by about three orders during the first 50 hr of heat-treatment, remained constant for the next 100 hr, and showed a rise at

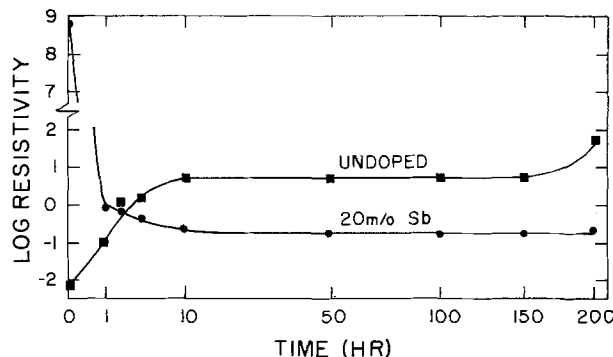


Fig. 2. Resistivity of thin film  $\text{SnO}_2$  as a function of heat-treatment duration at 600°C.

<sup>1</sup> Reagent Grade, J. T. Baker Company, Philipsburg, New Jersey.

<sup>2</sup> Ventron Corporation, Alfa Products, Beverly, Massachusetts.

<sup>3</sup> Norelco Diffractometer, North American Philips, Mount Vernon, New York.

<sup>4</sup> Keithley 610Br Electrometer, Keithley Electronics, Incorporated, Cleveland, Ohio.

<sup>5</sup> AMR 900, Advanced Metals Research Corporation, Bedford, Massachusetts.

Table I

Additive	Activation energy (eV)	X-ray diffraction peaks d(Å)	I/I <sub>0</sub>
None	Less than 10 <sup>-3</sup>	3.40	30
		2.644	100
		2.362	80
1 m/o Sb	Less than 10 <sup>-3</sup>	1.770	70
		3.37	40
		2.848	17*
		2.659	100
		2.374	50
3 m/o Sb	Less than 10 <sup>-3</sup>	1.771	100
		3.36	20
		2.858	20*
		2.659	90
		2.368	100
6 m/o Sb	2.0 × 10 <sup>-2</sup>	1.771	80
		3.36	60
		2.652	100
		2.374	10
		1.774	100
10 m/o Sb	8.2 × 10 <sup>-2</sup>	— Amorphous —	
20 m/o Sb	1.7 × 10 <sup>-1</sup>	— Amorphous —	
1 m/o In	2.6 × 10 <sup>-2</sup>	3.35	15
		2.644	100
		2.374	100
		1.768	15
		3.40	10
3 m/o In	1.5 × 10 <sup>-1</sup>	2.659	100
		2.386	20
		1.771	20
		3.36	10
		2.659	100
None, heat-treated at 600°C for 100 hr	1.2 × 10 <sup>-1</sup>	2.374	60
		1.771	60
		3.35	100**
		2.659	75
		2.380	10
20 m/o Sb, heat-treated at 600°C for 200 hr	3.0 × 10 <sup>-2</sup>	1.765	25

\* Sb<sub>2</sub>O<sub>3</sub>Cl<sub>2</sub>.

\*\* See Fig. 1.

200 hr of heat-treatment. The resistivity of the film containing 20 m/o Sb dropped approximately nine orders of magnitude during the first hour of heat-treatment at 600°C and dropped approximately one more order of magnitude during the following 50 hr of heat-treatment, after which it was constant. The films' activation energies for electrical conduction are listed in Table I. The activation energies varied in the same sense as did the films resistivities.

**Film structure.**—X-ray diffraction patterns of films containing 6 m/o antimony or less corresponded to the pattern of naturally occurring SnO<sub>2</sub>, cassiterite. Some differences in crystal orientation occurred with changing Sb content as indicated by changes in the relative intensity of the peaks (Table I) but the (101) peak was consistently strong. A very weak peak corresponding to a peak of Sb<sub>4</sub>O<sub>5</sub>Cl<sub>2</sub> was detected in samples with 1 and 3 m/o Sb. Films having additions of 10 or 20 m/o Sb had no x-ray diffraction peaks. The sample with 20 m/o Sb partially crystallized during the first hour of heat-treatment at 600°C. The diffraction patterns of this sample before and after 1 hr of heat-treatment are shown in Fig. 3. Continued heating to 200 hr brought no further change in the diffraction patterns. Samples with additions of 1 and 3 m/o In also exhibited the cassiterite structure with some variation in the crystal orientation.

Scanning electron micrographs of films containing 0 and 20 m/o Sb and the 20 m/o Sb after heat-treatment are shown in Fig. 4. Each of these films has varying amounts of spherically shaped crystals on the surface of an underlying film. The texture of this underlying film is seen to change with antimony content. The pure film had a coarser texture than did the one containing 20 m/o Sb, but the latter film acquired a coarser texture after the heat-treatment. EDAX detected small amounts of chlorine in these films.

### Discussion

Undoped tin oxide films have n-type extrinsic conduction. The Sn<sup>+2</sup> ions, associated with the oxygen

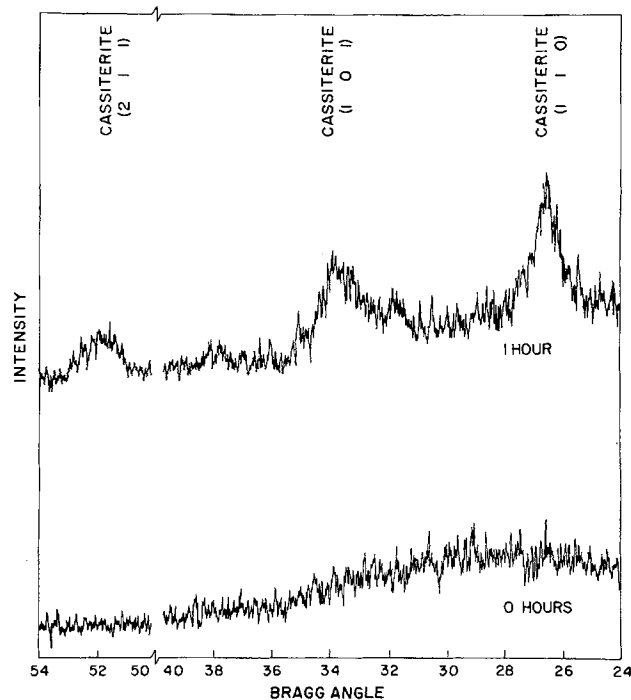


Fig. 3. X-ray diffraction of thin film SnO<sub>2</sub> with 20 m/o Sb before and after heat-treatment.

vacancies, and the residual Cl<sup>-</sup> ions are both capable of being electronic donors and probably both are responsible for this extrinsic conduction.

The rise in resistivity noted when the undoped film was heat-treated is most likely due to oxidation of the film which removed many of the oxygen vacancies. The chloride ions, substituting for oxygen ions, probably account for the remnant n-type conduction after prolonged heat-treatment.

The rise in resistivity seen when indium was added, and the decrease when antimony was added, can be accounted for by the controlled valency model proposed by Vincent (3). According to this model, the antimony would be considered to enter the cassiterite lattice as trivalent ions. Thermal energy could excite electrons from these ions into the crystal's conduction band. This excitation renders the antimony ions pentavalent. Likewise, the indium ions would enter the lattice as In<sup>+3</sup> but could accept electrons from the crystal's valence band, thereby becoming monovalent or divalent.

The controlled valence mechanism would apply to solids with ionic bonding. A consideration of the differences in electronegativities (14) of Sn and O shows the Sn—O bond to be equally ionic and covalent. A covalent model for semiconduction would consider In (Group III) and Sb (Group V) atoms to serve as acceptors and donors in tin (Group IV) oxide, as they do in covalently bonded Si and Ge (Group IV). The controlled valency and covalent models both qualitatively predict the observed resistivity vs. impurities behavior, and both mechanisms may be operative.

Since small additions of antimony cause the resistivity to drop by providing more donors, one would expect that large additions would cause the resistivity to drop further. The observed large rise is accompanied by a loss in crystallinity. This loss of crystallinity becomes progressively more pronounced as more antimony is added, causing the film to become more resistive. In the extreme case in which 20 m/o Sb is added, the film is noncrystalline and essentially insulating. This effect is too large to be accounted for by impurity scattering.



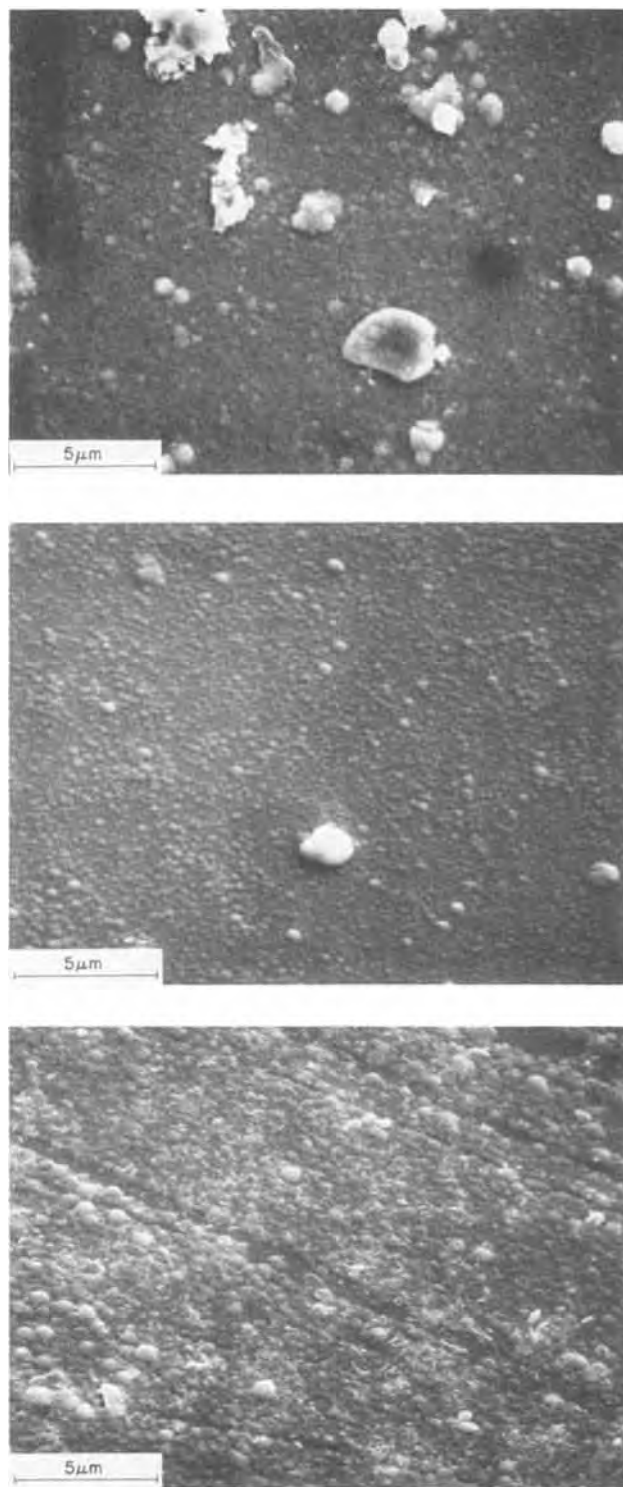


Fig. 4. Scanning electron micrographs of  $\text{SnO}_2$  films: (top) unannealed pure  $\text{SnO}_2$ , (middle) unannealed  $\text{SnO}_2$  with 20 m/o Sb, (bottom)  $\text{SnO}_2$  with 20 m/o after 200 hr heat-treatment.

Amorphous semiconductors (11, 12) behave as high resistivity intrinsic semiconductors whether they are pure or not. Impurities and other defects in the already defective structure of amorphous semiconductors do not act as donors or acceptors as they would in crystalline ones. One reason for this behavior is that the irregular structure of an amorphous semiconductor has atomic sites where impurities can reside without breaking covalent bonds. If no substitutions are made in the network of primary bonds, then the impurities will not be donors or acceptors.

When the 20 m/o Sb film was heat-treated, one would expect the film to become more stoichiometric and the resistivity to rise as it did for the pure film. However, the resistivity dropped by ten orders of magnitude. This drop was accompanied by the reappearance of a crystal structure and a coarsening of the texture as seen in the scanning electron microscope. In this case, the regaining of crystal structure had a stronger influence on resistivity than did the achievement of stoichiometry. If one would estimate that the removal of oxygen vacancies would cause the resistivity to rise by four orders of magnitude for the 20 m/o film as it did for the pure one, then the regaining of the crystal structure caused the resistivity to drop by fourteen orders of magnitude. The new equality of film resistivity after heat-treatment to that of a corresponding film of the previous study indicates that heat-treatment causes a similar crystal structure in both.

In the previous study in which the films were deposited at  $600^\circ\text{C}$ , the highly doped films had lower resistivities because they were more crystalline. However, even at this high temperature of deposition, crystallinity is partly destroyed by the large additions of antimony. This demonstrates the sensitivity of structure and resistivity to the thermal history of the film. Antimony oxide in the formation of bulk silicate glasses is known to be a glass former (13) and is acting as such in these  $\text{SnO}_2$  thin films.

The thermal history of the films governs both the oxygen vacancy concentration and the lack of crystallinity. It is, therefore, not surprising that the resistivity vs. Sb content varies so much from one investigator to another. When low deposition temperatures are used, higher degrees of amorphousness are obtained for the higher antimony contents giving rise to large resistances, and larger numbers of oxygen vacancies will be frozen into the structure causing resistivity to be lower especially at lower concentrations of Sb. This condition tends to make the minimum point occur at a very low level of antimony concentration. Conversely, as the temperature of deposition is increased, it will tend to make the resistivity rise at low Sb content because oxygen vacancies are being eliminated, and will cause the resistivity to drop at the higher concentrations because the films have a higher degree of crystallinity. These effects tend to move the minimum in the resistivity curve to larger Sb concentrations.

The films with low resistivities had very low activation energies for electrical conduction. This indicates that there were so many donors that a donor band forms which approached or overlapped the conduction band. As resistivity rises with In additions, the activation energy rises because a number of the donors have been compensated for by the In, thus decreasing the donor bandwidth. As resistivity rises as a result of Sb additions, the observed rise in activation energy is due to the elimination of donors again causing the width of the donor band to decrease, increasing the energy needed to excite electrons from the narrowed donor band to the conduction band.

### Conclusions

The ten order of magnitude rise in resistivity found when Sb concentration is increased in  $\text{SnO}_2$  films from 1 to 20 m/o is caused by a loss of crystallinity. These films behave as typical amorphous semiconductors in which impurities do not serve as electron donors or acceptors.

Heat-treatment caused resistivity of undoped  $\text{SnO}_2$  films to rise by four orders of magnitude due to film oxidation removing oxygen vacancies. Heat-treatment caused resistivity of the film with 20 m/o Sb to decrease by ten orders of magnitude because crystallinity was partially restored. These opposing effects



explain why the location of the resistivity minimum is sensitive to deposition conditions.

Manuscript submitted May 28, 1976; revised manuscript received July 12, 1976.

Any discussion of this paper will appear in a Discussion Section to be published in the June 1977 JOURNAL. All discussions for the June 1977 Discussion Section should be submitted by Feb. 1, 1977.

Publication costs of this article were assisted by the Virginia Polytechnic Institute and State University.

#### REFERENCES

1. V. K. Miloslavski, *Opt. Spectrosc.*, **7**, 154 (1959).
2. T. Arai, *J. Phys. Soc. Jpn.*, **15**, 916 (1960).
3. C. A. Vincent, *This Journal*, **119**, 515 (1972).
4. D. Elliot, D. L. Zellmer, and H. A. Laitinen, *ibid.*, **117**, 1343 (1970).

5. A. Rohatgi, T. R. Viverito, and L. H. Slack, *J. Am. Ceram. Soc.*, **57** (1974).
6. V. K. Miloslavski and A. P. Lyashenko, *Opt. Spectrosc.*, **8**, 455 (1960).
7. H. Kim and H. A. Laitinen, *J. Am. Ceram. Soc.*, **58**, 23 (1975).
8. T. R. Viverito, E. Rilee, and L. H. Slack, *Bull. Am. Ceram. Soc.*, **54** (1975).
9. D. L. Evans and G. R. Fischer, *ibid.*, **52**, 510 (1973).
10. L. B. Valdez, *Proc. IRE*, **42**, 420 (1954).
11. Ad Hoc Committee on the Fundamentals of Amorphous Semiconductors, "Fundamentals of Amorphous Semiconductors," National Academy of Sciences, Washington, D. C. (1972).
12. L. H. Slack and T. J. Gray, *J. Am. Ceram. Soc.*, **54**, 54 (1971).
13. W. D. Kingery, "Introduction to Ceramics," 2nd ed., John Wiley & Sons, Inc., New York (1976).
14. L. Pauling, "The Nature of the Chemical Bond," 3rd ed., Cornell University Press, Ithaca, New York (1959).

## Ion Beam Etching of Silicon Dioxide on Silicon

L. Mader and J. Hoepfner

Siemens AG, Research Laboratories, D-8000 München 70, Germany

#### ABSTRACT

An argon ion beam, 7.5 cm in diameter, with an energy of 0.6 keV and a current density of 0.5 mA/cm<sup>2</sup> is generated in an ion beam etching system using a Kaufman-type ion source (1), then neutralized by electrons. The principles of ion beam etching are outlined and SEM micrographs of ion etched grooves in thermally grown SiO<sub>2</sub> layers are shown. Grooves 1 μm wide and 0.4 μm deep were obtained using Shipley AZ 1350 H photoresist. The groove profiles are in good agreement with those predicted with the aid of an ion etching model. The slope angle of the sidewalls of the grooves is typically 65°. Redeposition effects reduce the effective ion etch rates for grooves of small linewidths. If the SiO<sub>2</sub> layer is ion etched down to the silicon substrate, a silicon surface layer of about 100 Å thickness will be damaged. This damage can be completely removed by wet chemical etching. The enhanced etch rate of ion-damaged SiO<sub>2</sub> surface layers in buffered hydrofluoric acid is used to taper steps in thermally grown SiO<sub>2</sub> in a controllable process.

Although chemical etching is still the most widely used method for the generation of patterns for semiconductor devices, physical etching methods such as rf sputter etching and ion beam etching are attracting growing interest because of certain inherent advantages (2-4).

In order to qualify an etching process, the following criteria have to be taken into account:

Are there dimensional changes as compared with the mask dimensions?

What type of contours do the sidewalls of the etched features have?

Is the etching process selective?

Is any contamination or damage introduced during the etching process?

Is the etching process effectively controllable?

The purpose of this paper is to discuss these criteria for ion beam etching. Our investigations are confined to the insulator layers of semiconductor devices.

#### Ion Beam Etching Apparatus

The principle of the ion beam etching apparatus<sup>1</sup> used for our experiments is shown schematically in Fig. 1. The system comprises two chambers. The ions generated in a plasma in the upper chamber are extracted from the plasma into the main vacuum

chamber by an extraction grid at ground potential. Electrons emitted from a heatable filament are allowed to drift into the ion beam to neutralize its space charge in order to avoid charge buildup on the insulator layers of the substrate. As a result, a neutralized and collimated monoenergetic beam of about 7.5 cm diameter impinges on the sample surface at the normal incidence angle. For our experiments we used argon ions with an energy of 600 eV; the current density was 0.5 mA/cm<sup>2</sup>. The distance between

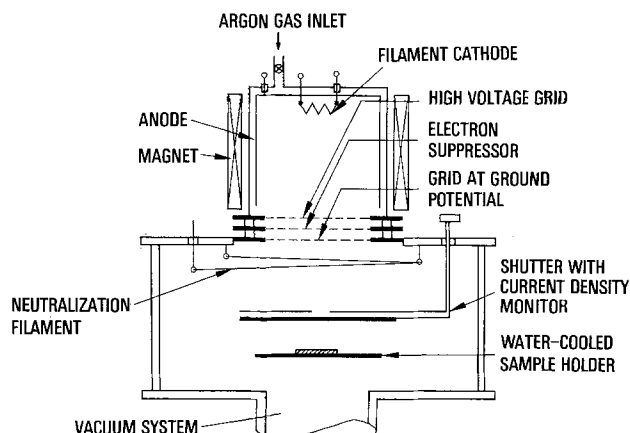


Fig. 1. Schematic cross section of the ion beam etching apparatus

Key words: ion beam etching, silicon dioxide film, MOS devices, etching model, photoresist mask, radiation damage, redeposition effect.

<sup>1</sup> VEECO Microetch System.

the grids and the shutter, where the current density is measured, is about 10 cm.

The 5 cm wafers were bonded onto a water-cooled target holder, using a vacuum oil<sup>2</sup> to assure thermal contact. The advantages over rf sputter etching are that, since the samples are etched in a field-free and plasma-free environment, there are no restrictions as to shape, size, and material of samples or the sample holder. The samples can be moved and tilted during etching in order to change the ion incidence angle and consequently the etch rate. The pressure in the main vacuum chamber is between one and two orders of magnitude below typical rf sputtering pressures.

### Principles of Ion Beam Etching

**Etch rate as a function of ion incidence angle.**—For the ion etching of silicon dioxide layers partially covered with photoresist (Fig. 2), the conditions at the photoresist sidewalls are of special importance. In these regions, the ion incidence is not normal to the photoresist surface; in Fig. 2 an angle is defined to denote the deviation from normal incidence. The etch rate for all materials increases as  $\alpha$  increases, reaches a maximum, and then falls off to zero at glancing incidence (5-8). Figure 3 shows our measurements of the ion etch rates in angstroms per minute for silicon, silicon dioxide, and photoresist AZ 1350 H as a function of the ion incidence angle. Unpatterned samples were used in the experiments. Tilting the samples changed the ion incidence angle relative to the surface of the substrate. The etch rates were determined by measuring the layer thickness after etching with a stylus apparatus. In the case of the monocrystalline silicon with a (100) surface orientation, the loss in weight of the wafers was measured. The curves in Fig. 3 show that the fastest etch rates are obtained at an incidence angle of about 60° even though the number of incident ions per square centimeter at 60° is only half that at normal incidence. The maximum etch rates are a factor of two to three higher than the etch rates at normal incidence. Silicon is etched at about the same rate as silicon dioxide, which means that etching does not stop at the silicon-silicon dioxide interface when silicon dioxide layers are etched. The etching process is nonselective.

**Ion beam etching profiles using photoresist masks.**—The simple diagrams in Fig. 4 illustrate schematically how the profiles of patterns change during ion beam etching as a function of the dependence of the etch rate on the ion incidence angle as shown in Fig. 3.

<sup>2</sup> Dow Corning 705 diffusion pump fluid. As the oil is only on the back of the wafers, it is not bombarded by ions and can therefore easily be removed by organic solvents.

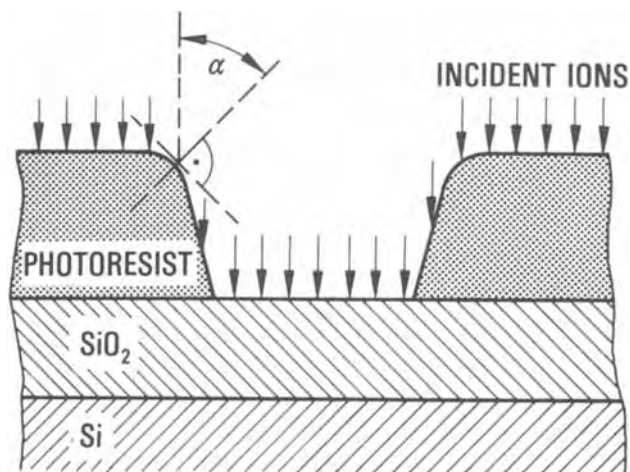


Fig. 2. Schematic diagram showing non-normal incidence of ions at photoresist sidewalls.

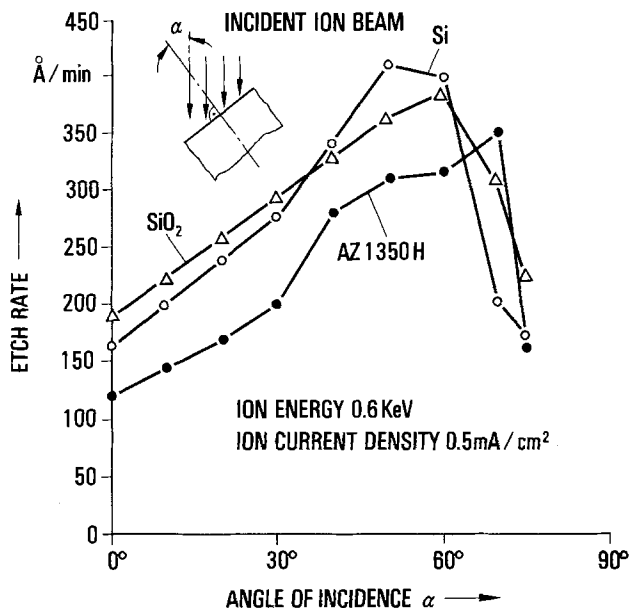


Fig. 3. Measured ion etch rates of silicon, silicon dioxide, and AZ 1350 H photoresist at different ion incidence angles.

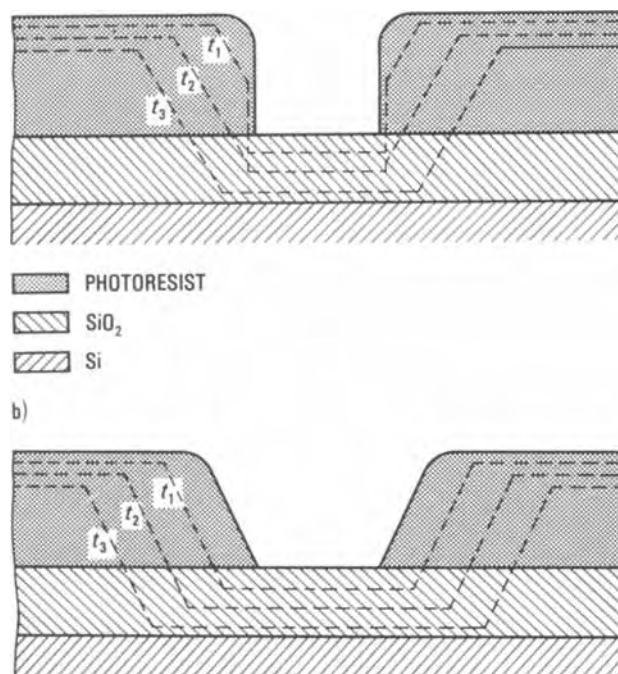


Fig. 4. Calculated profiles of a silicon dioxide film covered with a photoresist pattern during three different etch intervals  $t_1$ ,  $t_2$ , and  $t_3$  (dashed lines). The intervals  $t_1$ ,  $t_2 - t_1$ , and  $t_3 - t_2$  are equal. (a) Almost vertical photoresist sidewalls before ion etching; (b) 60° slope angle of sidewalls.

In Fig. 4(a) the photoresist sidewalls are assumed to be almost vertical, while in Fig. 4(b) a sidewall slope angle of 60° is assumed. The profiles (dashed lines) were determined using a step-by-step construction similar to that proposed by other authors (8-10). The procedure is as follows: first the initial photoresist contour is divided into small elements, the angle of each element relative to ion incidence is then determined, and the displacement of each element after a short etch interval,  $\Delta t$ , is read from the reference curves in Fig. 3. By this procedure the profile after time  $\Delta t$  was constructed. Starting with this profile, a new profile is obtained after the etch interval  $2\Delta t$ , and so on. Figure 4 shows the calculated

profiles after three different etch intervals  $t_1$ ,  $t_2$ ,  $t_3$ . The intervals  $t_1$ ,  $t_2 - t_1$ , and  $t_3 - t_2$  are equal.

Several conclusions can be drawn from the profiles in Fig. 4(a). As the ion etch rate of silicon dioxide is 1.5 times greater than that of photoresist in regions of normal ion incidence (Fig. 3), the photoresist should be at least two-thirds as thick as the silicon dioxide layer to be etched. In regions where the slope angle of the photoresist sidewalls is close to  $90^\circ$ , the etch rate is negligible. This means that these portions of the profile are not altered by ion etching. The largest alterations of the profile occur in those regions where the ions impinge at an angle of about  $60^\circ$ . This is the case along the upper edges of the photoresist sidewalls. A  $60^\circ$  facet is etched more rapidly than a plane normal or parallel to the ion beam and thus the facet grows in area. As a result, the vertical portion of the sidewalls gradually disappears until, by the end of the interval  $t_2$ , the walls exhibit a uniform slope angle of about  $60^\circ$ .<sup>3</sup>

Up to this time, no measurable broadening of the etched silicon dioxide geometry occurs at the bottom edge and the silicon dioxide linewidth corresponds to the initial photoresist linewidth. The etch depth in the silicon dioxide layer by the end of the interval  $t_2$  is about half the photoresist thickness. This means that, if the photoresist sidewalls are vertical or almost vertical, silicon dioxide layers thinner than half the photoresist thickness can be etched without any broadening in linewidth. Etching of thicker layers leads, however, to such broadening as illustrated in Fig. 4(a) by the profile recorded after the interval  $t_3$ . In the case shown in Fig. 4(b), where the photoresist sidewalls are assumed to have a slope angle of  $60^\circ$  just prior to etching, the silicon dioxide geometries start broadening right at the beginning of ion etching. The  $60^\circ$  angle remains throughout the entire etching period.

**Mask materials for ion beam etching.**—As noted above, photoresist can be suitably used as a mask for ion beam etching of  $\text{SiO}_2$ . However, the contours of the sidewalls of the etched  $\text{SiO}_2$  patterns depend on the thickness of the resist mask and the slope angle of the sidewalls of the mask.

If a resist mask (AZ 1350 H)  $1 \mu\text{m}$  thick with vertical slopes is used, a  $\text{SiO}_2$  layer of about  $0.2 \mu\text{m}$  can be etched with vertical sidewalls and without linewidth change [see Fig. 4(a)]. Further etching leads to a slope angle of about  $60^\circ$  at an etch depth of about  $0.4 \mu\text{m}$  [Fig. 4(a), interval  $t_2$ ]. If a thicker layer is etched with this mask, linewidth broadening will occur [Fig. 4(a), interval  $t_3$ ].

This broadening effect can be avoided, however, by choosing mask materials which exhibit a lower ion etch rate than photoresist, e.g., titanium, vanadium, or chromium (11, 12). The ion etch rate of these materials can be further reduced by injecting oxygen during etching (11, 12). We have made comparative studies of the effect of oxygen on the etch rate of titanium, aluminum, silicon dioxide, and photoresist. The etch rate depends critically on the partial pressure of the oxygen.<sup>4</sup> As shown in Fig. 5, the etch rates of titanium, aluminum, and silicon dioxide decrease, while that of photoresist (AZ 1350 H) increases. Drawbacks involved in using metal masks instead of photoresist masks are that more process steps are required and the edges of the metal geometries are often less smooth than the photoresist edges. Moreover, ion-etched geometries exhibit almost vertical sidewalls, which has an adverse effect on edge coverage in semiconductor device fabrication.

<sup>3</sup> Since the maxima of the etch rates of  $\text{SiO}_2$  and photoresist AZ 1350 H lie at the same angle within the measuring accuracy, a uniform slope angle can be expected.

<sup>4</sup> For these experiments a mixture of argon and oxygen is fed into the plasma chamber. The total pressure is kept constant ( $4 \cdot 10^{-4}$  Torr).

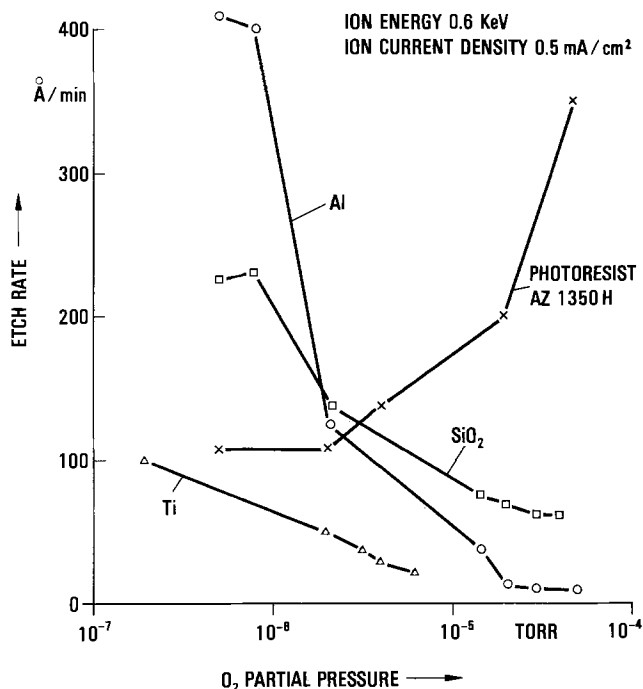


Fig. 5. Measured etch rates of AZ 1350 H photoresist, silicon dioxide, aluminum, and titanium as a function of partial pressure of the oxygen. The etch rates of silicon dioxide, aluminum, and titanium decrease, while that of the photoresist increases with increasing oxygen pressure.

### Experimental

**Sample preparation.**—Thermally oxidized silicon wafers with a diameter of 2 in. were used as substrates. The silicon dioxide thickness ranged between 0.06 and  $1 \mu\text{m}$ . After coating the wafers with AZ 1350 H photoresist about  $1 \mu\text{m}$  in thickness, patterns were generated by conventional contact-printing photolithography. Excessive heating of the samples during ion etching was prevented by bonding the wafers with vacuum oil to a water-cooled copper plate. After etching the photoresist was soaked in dimethylformamide and removed by ultrasonic agitation.

**Ion-etched silicon dioxide patterns.**—SEM micrographs of ion-etched silicon dioxide geometries in Fig. 6, 7, 8, and 9 confirm the validity of the described ion etching model.

The micrograph in Fig. 6(a) shows an AZ 1350 H photoresist line  $1 \mu\text{m}$  thick and  $7 \mu\text{m}$  wide deposited on a thermally grown silicon dioxide layer  $1 \mu\text{m}$  thick before ion etching. The photoresist sidewalls are almost vertical. The micrograph in Fig. 6(b) shows the silicon dioxide geometry after ion etching and the removal of the residual photoresist. The silicon dioxide is  $1 \mu\text{m}$  thick and its width, measured at the base, is  $6 \mu\text{m}$ . The reduction in linewidth from 7 to  $6 \mu\text{m}$  is readily explained from the etching model [Fig. 4(a)]. The edges of the silicon dioxide line are smooth and the slope angle, which can be determined from the SEM micrograph in Fig. 6(b) by simple geometrical inferences, is  $65^\circ$ .

Figure 7 shows a  $1 \mu\text{m}$  wide and  $0.4 \mu\text{m}$  deep ion-etched groove etched in a silicon dioxide layer. Compared to the photoresist geometry, which was  $1 \mu\text{m}$  thick and  $1 \mu\text{m}$  wide with almost vertical slopes similar to those shown in Fig. 6(a), no change in linewidth can be determined. This result corresponds to the case shown in Fig. 4(a) (dashed line denoted  $t_2$ ), where the vertical sidewalls assumed  $60^\circ$  slopes without dimensional change.

The SEM micrograph in Fig. 8(a) represents a chemically etched double layer structure consisting of a  $0.5 \mu\text{m}$  thick silicon dioxide layer and a  $0.1 \mu\text{m}$

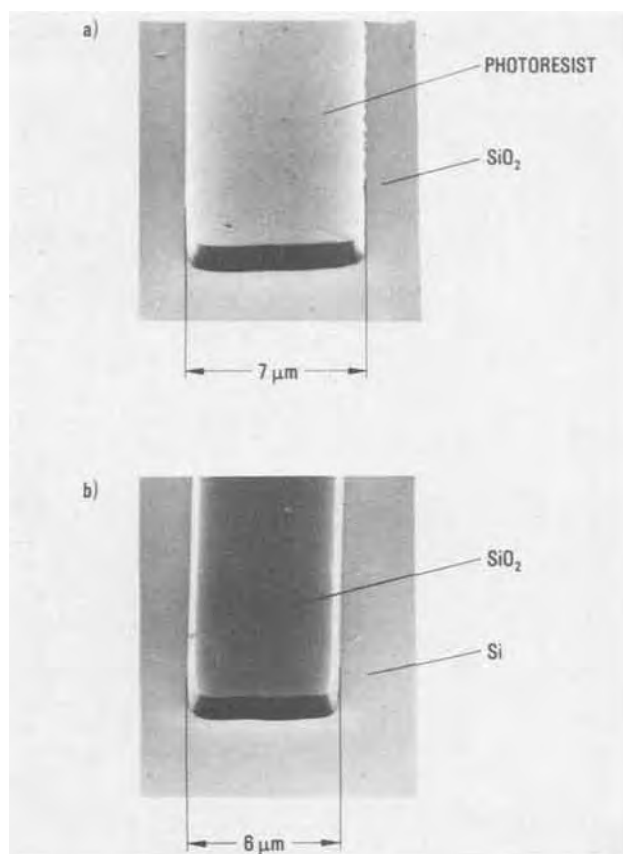


Fig. 6. (a) SEM micrograph (viewing angle  $70^\circ$ ) of an AZ 1350 H photoresist line  $1\ \mu\text{m}$  thick and  $7\ \mu\text{m}$  wide deposited on a thermally grown silicon dioxide layer. (b) Corresponding silicon dioxide geometry  $6\ \mu\text{m}$  wide and  $1\ \mu\text{m}$  thick after ion etching and removal of the residual photoresist. The reduction in linewidth from  $7$  to  $6\ \mu\text{m}$  is explained with the ion etching model shown in Fig. 4(a). The slope angle of the silicon dioxide sidewalls is  $65^\circ$ .

thick phosphorus silicate glass (PSG) layer with about 8 mole percent (m/o) of phosphorus pentoxide. Due to the fast etch rate of PSG in buffered hydrofluoric acid, the slope angle of the silicon dioxide layer is only  $18^\circ$ , the slope of the PSG layer is almost vertical. The SEM micrograph in Fig. 8(b) shows the geometry after ion etching of the same double layer. As the ion etch rates for PSG and for silicon dioxide are much the same, the slope angle is again uniformly  $65^\circ$ .

Similar results were obtained with silicon nitride/silicon dioxide and polycrystalline silicon/silicon dioxide double layer structures as well.

One specific geometrical effect must be taken into account if the geometries to be etched are to run over steps. Due to the faster etching of sloped regions (Fig. 3), these steps exhibit lateral shift. Figure 9(b) shows the ion-etched gate region of a MOSFET where the edges of the source and drain regions have been displaced by the distance  $\Delta x$ .

**Redeposition effect.**—The model discussed does not include the effect of the redeposition of sputtered material (13). Redeposition means that some of the sputtered particles leaving an etched groove become deposited on its sidewalls, from where they are resputtered and redeposited in the groove. If this effect is pronounced, grooves of different widths will be etched at different effective etch rates. Figure 10 shows ion-etched grooves in silicon dioxide with linewidths of 1.25, 2.5, 5, and  $10\ \mu\text{m}$ . A titanium pattern was used as a mask. The larger etch depths in the wider grooves are clearly visible. The area surround-

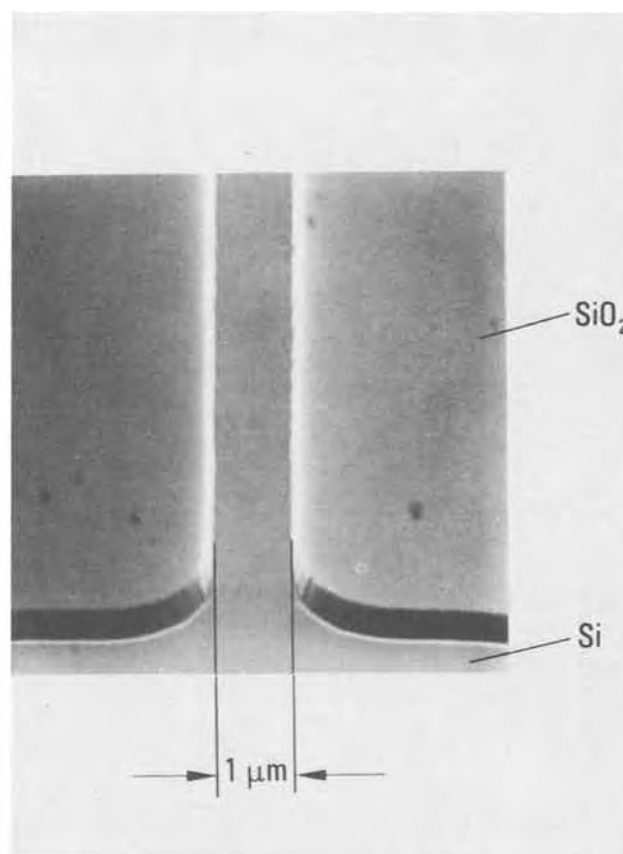


Fig. 7. SEM micrograph (viewing angle  $70^\circ$ ) of a  $1\ \mu\text{m}$  wide and  $0.4\ \mu\text{m}$  deep ion-etched groove in a silicon dioxide layer. No change in linewidth as compared to the original groove in the photoresist was observed. The slope angle of the silicon dioxide sidewalls is  $65^\circ$ .

ing the grooves is etched away as well. The  $0.8\ \mu\text{m}$  oxide step thus created is visible in the micrographs of Fig. 10.

In Fig. 11 the experimentally obtained etch rates are plotted as a function of linewidth for photoresist and titanium masking. Using a titanium mask, the effective etch rate remains constant for grooves with linewidths down to about  $10\ \mu\text{m}$ , but decreases by roughly 50% for linewidths of about  $1\ \mu\text{m}$ . If photoresist is used as the masking material, the corresponding decrease in etch rate is, however, only 25%.

**Surface damage caused by ion etching.**—We have observed from the ion backscatter as well as from MOS capacitance-voltage measurements that ion-etched surfaces suffer severe damage (14). If a silicon dioxide layer thermally grown on a single crystal silicon substrate is ion-etched down to the silicon substrate, a silicon surface layer about  $100\ \text{\AA}$  thick is damaged. An argon concentration of about  $10^{21}$  atoms/cm<sup>3</sup> can be measured for the ion energy and dose used. Furthermore, during ion etching particles are sputtered from metal parts inside the ion etching apparatus such as the tungsten neutralization filament, the molybdenum accelerating grids, and the copper ground plate. These particles contaminate the silicon surface and cause deep energy levels at the silicon-silicon dioxide interface (14). Their concentration is highly dependent on system parameters, specially on the extraction system of the grids (15). The contaminated and damaged surface layer can, however, be completely removed by wet chemical etching with a diluted HNO<sub>3</sub>/HF etchant.

We have observed that the damaged region near the surface of silicon dioxide layers exhibits a higher

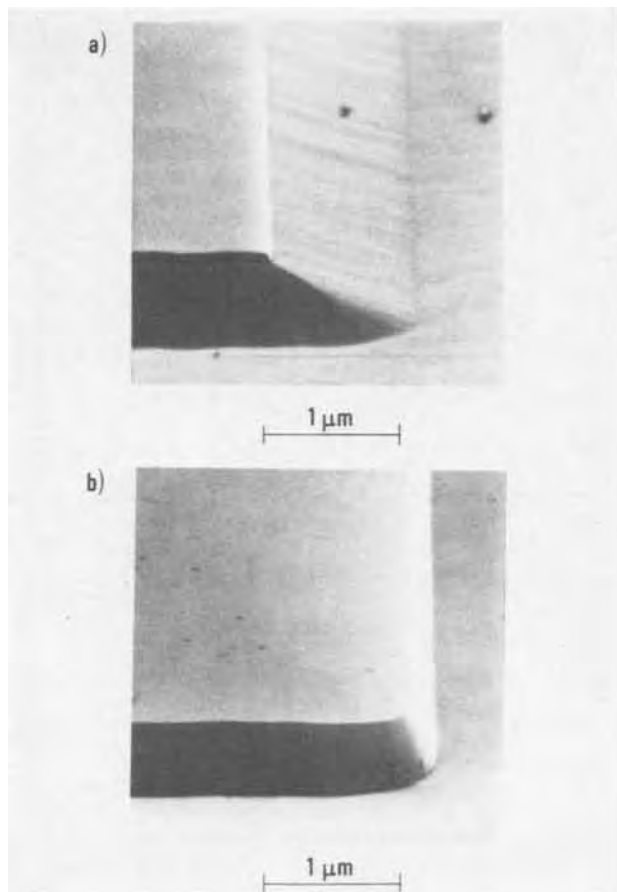


Fig. 8. (a) SEM micrograph (viewing angle  $70^\circ$ ) of a chemically etched double layer consisting of a  $0.5 \mu\text{m}$  thick silicon dioxide layer and a  $0.1 \mu\text{m}$  thick phosphorus silicate glass (PSG) layer. Due to the fast etch rate of PSG in buffered hydrofluoric acid, the slope angle of the silicon dioxide layer is only  $18^\circ$ , whereas the slope of the PSG layer is almost vertical. (b) SEM micrograph showing the corresponding step in the same double layer after ion etching. As the ion etch rates for PSG and for silicon dioxide are much the same, the slope angle is uniformly  $65^\circ$ .

etch rate in buffered hydrofluoric acid than undamaged silicon dioxide layers. This effect can be used to taper the edges of silicon dioxide patterns. A similar effect has been reported by Moline *et al.* (16) for ion-implanted silicon dioxide films. Figure 12 shows its mechanism. Prior to photoresist pattern generation, the silicon dioxide surface of the sample shown in Fig. 12(b) was exposed for only 10 sec to an ion beam with an energy of 0.6 keV and a beam current of  $0.5 \text{ mA/cm}^2$ . Then a photoresist pattern is created on top of the  $\text{SiO}_2$  layer. Due to the higher etching rate of the  $100\text{\AA}$  thick damaged part of the  $\text{SiO}_2$  layer, an etched  $\text{SiO}_2$  pattern with tapered edges is produced. Figure 12(b) shows the result. The slopes of the silicon dioxide lines are uniform; the slope angle is about  $25^\circ$ . Figure 10(a), in comparison, shows chemically etched  $\text{SiO}_2$  lines without ion bombardment prior to photoresist coating. This method can be used to taper steps in thermally grown  $\text{SiO}_2$  in a controllable manner (17).

### Summary

The ion beam etching process described is effectively controllable and yields reproducible results. Ion-etched grooves in silicon dioxide exhibit no significant dimensional change relative to photoresist geometries as long as the etching depth does not exceed half the resist thickness. The slopes of the sidewalls of the etched grooves are uniform. Typical slope angles are  $65^\circ$ . Adhesion between the mask and the sub-

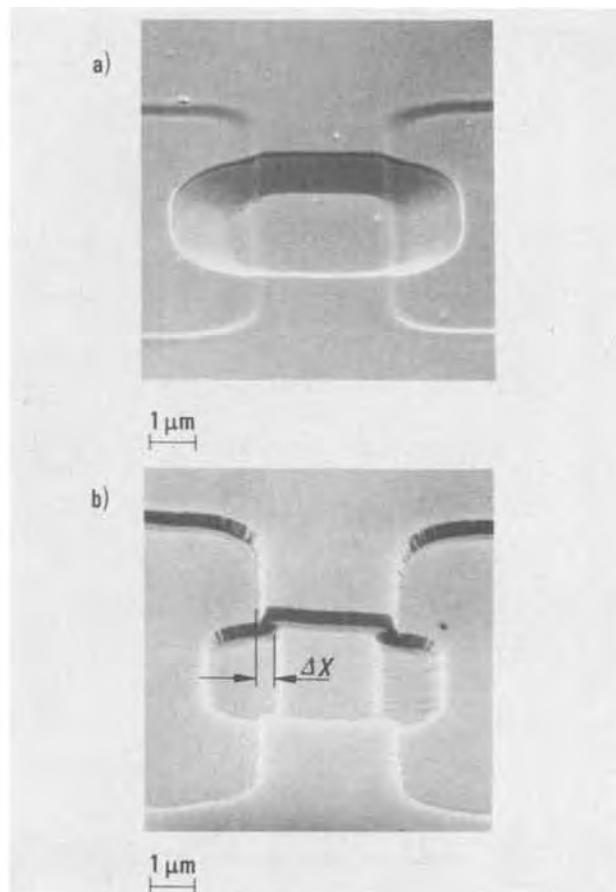


Fig. 9. (a) SEM micrograph (viewing angle  $70^\circ$ ) of a chemically etched gate region in a MOSFET. (b) SEM micrograph showing the same gate region after ion etching. The steps generated during reoxidation after the source and drain diffusion appear laterally displaced by the distance  $\Delta x$  due to the faster etching of sloped regions.

strate to be etched is without influence on the etch profile. As the ion etching process is nonselective, the silicon substrate can still be etched to a certain extent even if the silicon dioxide layer is etched down to the silicon surface. Redeposition effects reduce the effective ion etch rates for grooves of small linewidths. The damage suffered by the silicon surface layer due to ion bombardment can be completely removed by wet chemical etching. The enhanced etch rate of ion-damaged silicon dioxide surface layers in buffered hydrofluoric acid is used to taper steps in thermally grown silicon dioxide in a controllable manner.

### Acknowledgments

The authors wish to thank Drs. K.-U. Stein and M. Zerbst for suggesting the work, Mr. R. Sigusch for the preparation of the samples, Mrs. B. Nolte for the SEM micrographs, and Dr. D. Widmann for helpful discussions. This work has been supported under the technological program of the Federal Department of Research and Technology of the Federal Republic of Germany.

Manuscript submitted April 13, 1976; revised manuscript received Aug. 17, 1976. This was Paper 183 presented at the Toronto, Canada, Meeting of the Society, May 11-16, 1975.

Any discussion of this paper will appear in a Discussion Section to be published in the June 1977 JOURNAL. All discussions for the June 1977 Discussion Section should be submitted by Feb. 1, 1977.

Publication costs of this article were assisted by Siemens AG.

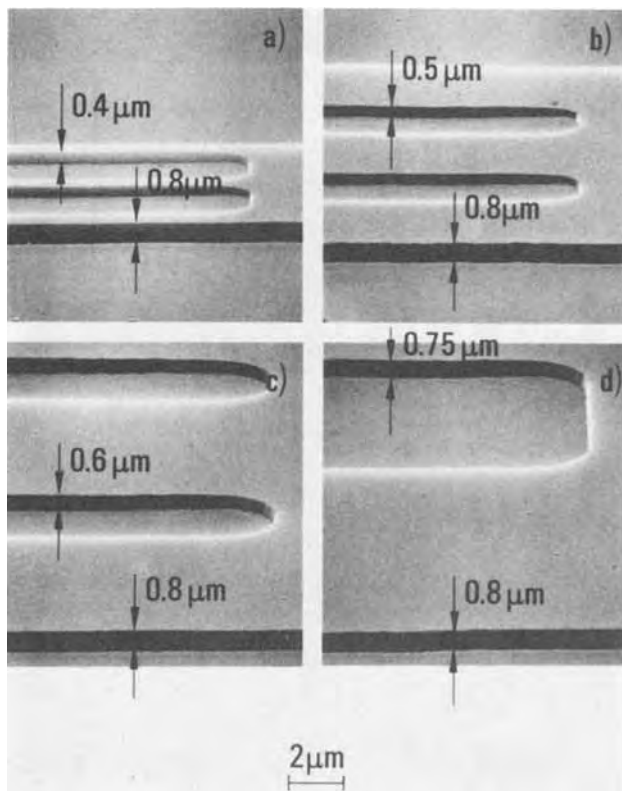


Fig. 10. SEM micrographs (viewing angle  $70^\circ$ ) of grooves in silicon dioxide ion etched under the same conditions. The widths of the grooves are (a)  $1.25 \mu\text{m}$ , (b)  $2.5 \mu\text{m}$ , (c)  $5 \mu\text{m}$ , and (d)  $10 \mu\text{m}$ . The masking material for ion beam etching was titanium. As the sidewalls of the etched grooves are almost vertical, the magnification ratio given for the horizontal direction of the SEM micrograph can also be used to calculate the step depths with good approximation. The calculated etch depths are denoted in (a)-(d).

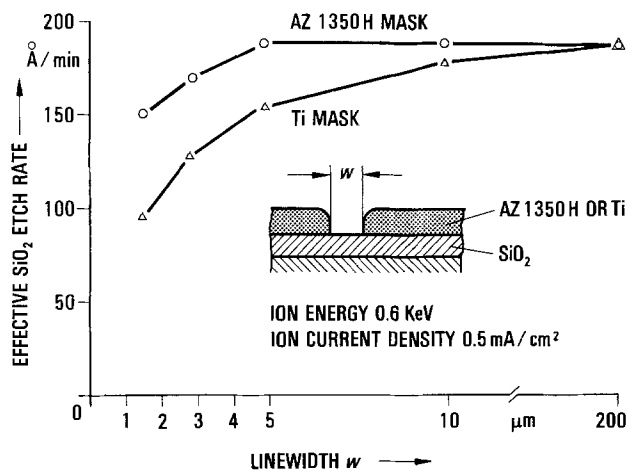


Fig. 11. Measured etch rates (see Fig. 10) vs. linewidth for photoresist and titanium masking. Using a titanium mask, the effective etch rate remains constant for grooves with linewidths down to about  $10 \mu\text{m}$ , but decreased by roughly 50% for linewidths of about  $1 \mu\text{m}$ . If a photoresist mask is used the corresponding decrease in the ion etch rate is only 25%.

#### REFERENCES

1. H. R. Kaufman, *Adv. Electron. Electron Phys.*, **36**, 265 (1974).

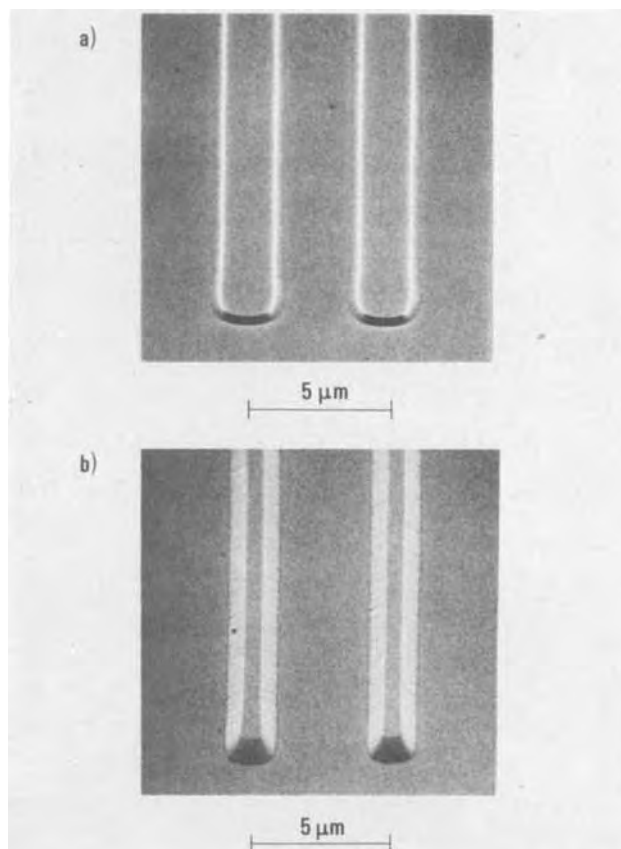


Fig. 12. SEM micrograph (viewing angle  $70^\circ$ ) of chemically etched silicon dioxide lines: (a) without ion bombardment prior to photoresist coating, (b) after ion pretreatment. Compared to the lines in (a), the lines in (b) exhibit straight and smooth sidewalls with tapered slopes at an angle of  $30^\circ$ . The silicon dioxide surface layer was bombarded for about 10 sec by argon ions with an energy of  $0.6 \text{ keV}$  and a beam current of  $0.5 \text{ mA/cm}^2$  prior to photoresist pattern generation.

2. R. T. C. Tsui, *Solid State Technol.*, **10**, 33 (1967).
3. P. G. Glöersen, *J. Vac. Sci. Technol.*, **12**, 28 (1975).
4. H. I. Smith, *Proc. IEEE*, **62**, 1361 (1974).
5. H. Oechsner, *Z. Phys.*, **261**, 37 (1973).
6. H. Bach, *J. Non-Cryst. Solids*, **3**, 1 (1970).
7. E. G. Spencer and P. H. Schmidt, *J. Vac. Sci. Technol.*, **8**, 52 (1971).
8. J. P. Ducommun, M. Cantagrel, and M. Marchal, *J. Mater. Sci.*, **9**, 725 (1974).
9. M. Cantagrel, *IEEE Trans. Electron Devices*, **ed-22**, 483 (1975).
10. A. D. G. Stewart and M. N. Thompson, *J. Mater. Sci.*, **4**, 56 (1969).
11. M. Cantagrel and M. Marchal, *ibid.*, **8**, 1711 (1973).
12. H. Dimigen and H. Lüthje, *Thin Solid Films*, **27**, 155 (1975).
13. A. R. Bayly, *J. Mater. Sci.*, **7**, 404 (1972).
14. H. R. Deppe, B. Hasler, and J. Hoepfner, To be published.
15. M. Cantagrel, Private communication.
16. R. A. Moline, R. R. Buckley, S. E. Haszko, and A. U. MacRae, *IEEE Trans. Electron. Devices*, **ed-20**, 840 (1973).
17. G. Bell and J. Hoepfner, in "Etching," H. G. Hughes, and M. J. Rand, Editors, p. 47, The Electrochemical Society Softbound Symposium Series, Princeton (1976).

# Annihilation of Stacking Faults in Silicon by Impurity Diffusion

H. Hashimoto, H. Shibayama, H. Masaki, and H. Ishikawa\*

Fujitsu Laboratories Limited, Nakahara-ku, Kawasaki, Japan

## ABSTRACT

The stacking faults grown into silicon during thermal oxidation were shrunk by high temperature heat-treatment in a nitrogen atmosphere. The activation energy for fault shrinkage was 5.2 eV, and nearly equal to that of silicon self-diffusion, 5.13 eV. The shrinkage phenomenon is due to the removal of silicon atoms, which form the stacking faults of extrinsic type, by diffusion via vacancies. Therefore the shrinkage rate depends on the vacancy concentration in silicon. The high concentration diffusion of boron, phosphorus, and arsenic in silicon generates the excess vacancies induced by donor doping, or by the stress due to solute lattice contraction of the impurity. The shrinkage of stacking faults by these excess vacancies was investigated. The faults shrank rapidly and disappeared for a short time in comparison with simple heat-treatment. The annihilation of stacking faults in silicon was also influenced by the coulomb interaction or the complex formation between the negatively charged vacancy and impurity.

Thermal oxidation is one of the important processes in the manufacture of silicon planar transistors and other devices. Crystallographic defects such as stacking faults are often introduced in silicon in this oxidation process (1-5). When stacking faults lie across a p-n junction, excess reverse leakage currents in the junction are increased (6). Therefore, it is necessary to suppress stacking fault generation. If a crystal free from mechanical damage and grown-in defects, which act as the nucleation, is used, stacking faults are not generated. However, it is difficult to obtain such a crystal. Accordingly, the suppression of stacking fault generation and shrinkage of the faults by HCl oxidation (7), or the preoxidation gettering of silicon wafers by misfit dislocations due to phosphorus diffusion (8), etc. have been carried out. Stacking faults also can be shrunk by high temperature heat-treatment (9).

In this study, the shrinkage of stacking faults was investigated first. It was found that the shrinkage related intimately to the vacancy concentration in silicon. The vacancy concentration depends not only on treatment temperature, but also on impurity doping. And so the relation between the annihilation of stacking faults and the excess vacancies which were induced during impurity diffusion into silicon was studied, and the mechanism of the annihilation is discussed.

## Experimental

The specimen wafers used in these experiments were 1-5  $\Omega$ -cm (100) oriented dislocation-free silicon crystals grown by the Czochralski method. They were doped with phosphorus for n-type and boron for p-type. The surface was mechanically polished and the thickness was about 250  $\mu$ m. After appropriate treatments, they were etched in a HF:HNO<sub>3</sub> = 1:5 solution for 2 min to remove the surface mechanical damage. The oxidation of silicon was carried out at 1200°C in dry oxygen for 210 min. This thermal oxidation grew a stacking fault in the silicon crystal about 40  $\mu$ m long, provided that the fault size was defined as the fault length on the silicon surface. After oxidation, the samples covered with grown oxide were treated at 1100°-1200°C in dry nitrogen to investigate the shrinkage process of stacking faults. In order to reveal the stacking faults, the samples were etched in a Sirtl solution (10) after dissolving the oxide layers in HF.

Furthermore, the annihilation behavior of stacking faults by impurity diffusion into silicon was examined.

Boron, phosphorus, and arsenic were diffused into silicon wafers having stacking faults. Impurities were diffused into silicon from doped oxide sources except for the diffusion of high arsenic concentration. The doped oxide sources were deposited onto silicon wafers by the reaction of silane, hydride of impurities, and oxygen. The reaction temperature was 350°C for the deposition of borosilicate and phosphosilicate glasses, and 450°C for arsenosilicate glasses. The diffusion was carried out at 1100°C in dry nitrogen. For the diffusion of high arsenic concentration, a capsule method was used, because the high arsenic diffused layers were not obtained by diffusion from the doped oxide source in the nitrogen atmosphere (11). The silicon wafers were placed in a quartz tube together with arsenic. The tube was then evacuated and sealed. The diffusion was also carried out at 1100°C. The surface concentration of diffused layers was determined using the anodic oxidation-resistivity technique (12) and Irvin's data (13).

## Results

*Shrinkage of stacking faults by heat-treatment.*—The shrinkage of stacking faults by heat-treatment in the nitrogen atmosphere was examined first. The silicon samples which had stacking faults about 40  $\mu$ m long were treated at 1100°-1200°C in dry nitrogen. The shrinkage rate of the stacking faults is shown in Fig. 1 as a function of treatment time. Stacking faults could be shrunk easily by high temperature heat-treatment. A linear relationship was found between fault length and heat-treatment time. The shrinkage rate vs. the

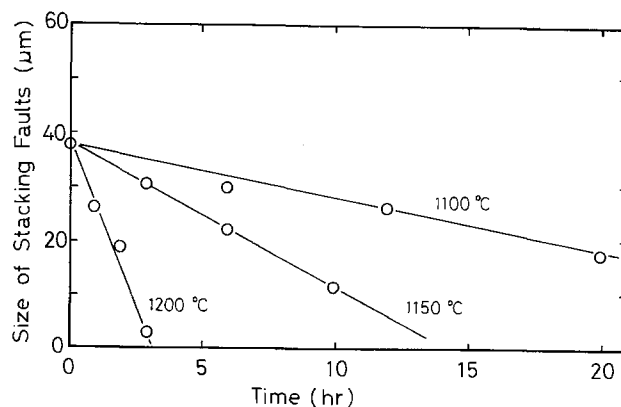


Fig. 1. Shrinkage of stacking faults after heat-treatment in nitrogen.

\* Electrochemical Society Active Member.  
Key words: silicon, stacking faults, diffusion.



reciprocal of treatment temperature is plotted in Fig. 2. The activation energy of shrinkage determined from this figure was 5.2 eV.

**Influence of boron diffusion on annihilation.**—Boron was diffused into silicon samples having about 40  $\mu\text{m}$  long stacking faults at 1100°C in dry nitrogen. The surface concentrations of diffused layers were  $4.3 \times 10^{19}$ – $2.7 \times 10^{20} \text{ cm}^{-3}$ , and their diffusion depths were 2.5–4.4  $\mu\text{m}$ . After boron diffusion, the samples were etched in a Sirtl solution for 10 sec. Typical photographs of the specimen surfaces are shown in Fig. 3. The stacking faults in the surface region disappeared in all samples during boron diffusion. When the surface concentration increased to more than  $1 \times 10^{20} \text{ cm}^{-3}$ , the slip dislocations due to solute lattice contraction of boron were generated (14).

In order to investigate the annihilation of stacking faults in the boron diffused layers and underneath them, another experiment was carried out. The samples were etched in a  $\text{HF}:\text{HNO}_3 = 1:5$  solution as shown in Fig. 4. Then the specimens were etched in a Sirtl solution. The results are shown in Table I. For the relatively low surface concentration,  $4.3 \times 10^{19} \text{ cm}^{-3}$ , the stacking faults still remained in the diffused layer near the diffusion front of the boron. Increasing the surface concentration, the stacking faults within the diffused layers disappeared. For the sample, of which the surface concentration was  $1.7 \times 10^{20} \text{ cm}^{-3}$ , the stacking faults underneath the boron diffused layer were annihilated. Moreover when the surface concentration was increased to  $2.7 \times 10^{20} \text{ cm}^{-3}$ , stacking faults remained and were not annihilated underneath the boron diffused layer.

**Influence of phosphorus diffusion on annihilation.**—The diffusion of phosphorus was identical with the boron diffusion described in the previous section. The phosphorus surface concentrations in diffused layers were  $5.3 \times 10^{19}$ – $3.6 \times 10^{20} \text{ cm}^{-3}$ , and their diffusion depths were 2.9–3.1  $\mu\text{m}$ . After phosphorus diffusion, the annihilation behavior of stacking faults was observed using the method illustrated in Fig. 4 and Sirtl etching. The results are shown in Table II. The stacking faults in the phosphorus diffused layers were annihilated during phosphorus diffusion in the concentration range of this experiment. However, the stacking faults underneath the diffused layers remained and were not annihilated. The slip dislocations which were observed for the diffusion of high boron concentration were not generated by the diffusion of high phosphorus concentration.

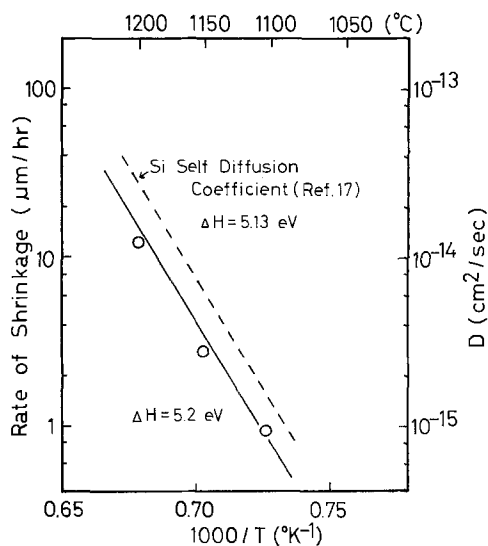


Fig. 2. Rate of shrinkage vs. reciprocal heat-treatment temperature, showing its relationship to the silicon self-diffusion coefficient.

**Influence of arsenic diffusion on annihilation.**—For the arsenic diffusion of comparatively low concentration, arsenic can be diffused in the nitrogen atmosphere using the doped oxide source method. In order to obtain diffused layers of high arsenic concentration by this method, arsenic must be diffused into silicon in oxygen. The treatment in the oxygen atmosphere grows stacking faults. Therefore a capsule method was used for the diffusion of high arsenic concentration. The surface concentrations of arsenic in diffused layers were  $2.2 \times 10^{19}$ – $3.0 \times 10^{20} \text{ cm}^{-3}$ . If arsenic diffuses in silicon to about 3  $\mu\text{m}$  in depth from the surface, a fairly long diffusion time is required because of the small diffusivity of arsenic in silicon (15). Stacking faults are considerably shrunk during such heat-treatment for long times. The diffusion depths of arsenic were limited to 0.6–1.2  $\mu\text{m}$ . Table III shows the results of stacking fault distribution in the specimens after arsenic diffusion. The stacking faults in the arsenic diffused layers disappeared for the diffusion of relatively low surface concentration. This is the same behavior as phosphorus. When the surface concentration increased more, the stacking faults remained even in the arsenic diffused layers. For the sample of which the surface concentration was  $3.0 \times 10^{20} \text{ cm}^{-3}$ , the faults near the silicon surface were hardly shrunk.

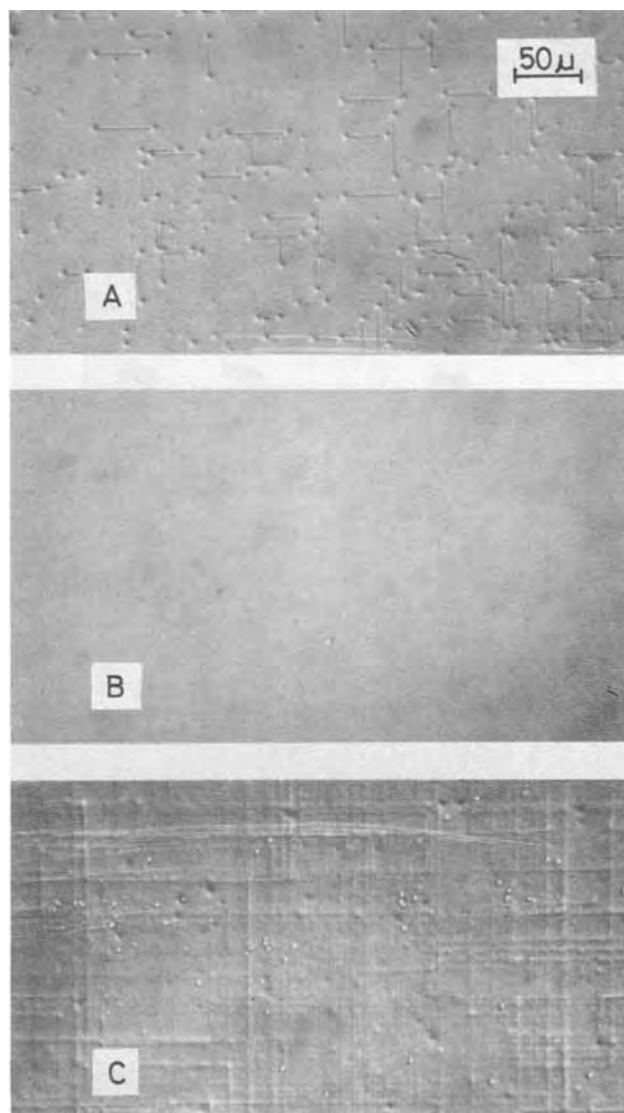


Fig. 3. Photographs of defects revealed by Sirtl etching. Etching time is 10 sec: (A) the sample oxidized at 1200°C in dry oxygen for 210 min; (B) and (C) the samples after boron diffusion into above oxidized silicon at 1100°C, their surface concentrations are  $4.3 \times 10^{19} \text{ cm}^{-3}$  and  $1.7 \times 10^{20}$ , respectively.



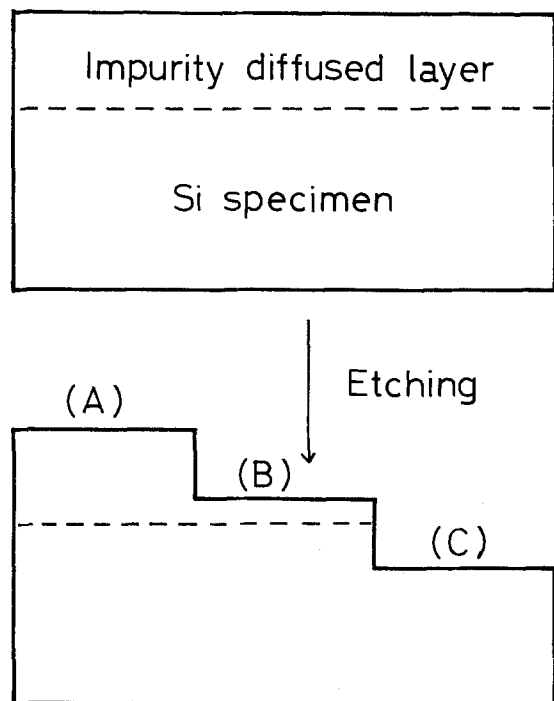


Fig. 4. Sample for investigating the distribution of stacking faults in silicon: region (A) the surface of the sample; (B) the impurity diffused layer near the diffusion front; (C) underneath the diffused layer.

### Discussion

The stacking faults are generated in silicon by heat-treatment in an oxidizing atmosphere. They can be shrunk by high temperature heat-treatment in an unoxidizing atmosphere. Sanders *et al.* (16) determined the activation energy for fault shrinkage to be 2.1 eV. This energy is smaller than the result of the present experiment, 5.2 eV. They made an annealing experiment using the ultrathin foils of silicon having stacking faults. The thermodynamics in such thin foils may be different from that of the bulk crystal. Therefore, the discrepancy of the activation energy probably came from the difference in the experimental conditions. The value in the present experiment, 5.2 eV, was nearly equal to the activation energy of silicon self-diffusion, 5.13 eV (17). In the shrinkage phenomenon it is considered that silicon atoms, which form the extra plane of the extrinsic-type stacking faults (3), are diffused outward via vacancies, and stacking faults are shrunk. Provided that this shrinkage mechanism is valid, the shrinkage of stacking faults depends strongly on the vacancy concentration in silicon. The vacancy concentration is influenced not only by treatment temperature, but also other factors. That is to say, the vacancies are increased with donor doping (18) or with the stress by solute lattice contraction of an impurity in silicon (19). These excessively induced vacancies are

Table I. Distribution of stacking faults in the samples after boron diffusion

Diffusion condition			Existence of stacking faults*		
Surface concentration (cm <sup>-3</sup> )	Time (min)	Depth (μm)	Region A	Region B	Region C
4.3 × 10 <sup>19</sup>	360	4.4	No	Yes	Yes
7.0 × 10 <sup>19</sup>	180	2.8	No	No	Yes
1.0 × 10 <sup>20</sup>	180	3.3	No	No	Yes
1.7 × 10 <sup>20</sup>	120	3.1	No	No	No
2.7 × 10 <sup>20</sup>	30	2.5	No	No	Yes

\* Yes = existence of stacking faults; No = no existence of stacking faults.

Table II. Distribution of stacking faults in the samples after phosphorus diffusion

Diffusion condition			Existence of stacking faults*		
Surface concentration (cm <sup>-3</sup> )	Time (min)	Depth (μm)	Region A	Region B	Region C
5.3 × 10 <sup>19</sup>	300	3.1	No	No	Yes
1.1 × 10 <sup>20</sup>	120	2.9	No	No	Yes
1.5 × 10 <sup>20</sup>	100	2.9	No	No	Yes
3.6 × 10 <sup>20</sup>	70	3.1	No	No	Yes

\* Yes = existence of stacking faults; No = no existence of stacking faults.

Table III. Distribution of stacking faults in the samples after arsenic diffusion

Diffusion condition			Existence of stacking faults*		
Surface concentration (cm <sup>-3</sup> )	Time (min)	Depth (μm)	Region A	Region B	Region C
2.2 × 10 <sup>19</sup>	600	1.2	No	No	Yes
6.0 × 10 <sup>19</sup>	180	0.9	No	Yes	Yes
2.0 × 10 <sup>20†</sup>	20	0.6	Yes	Yes	Yes

\* Yes = existence of stacking faults; No = no existence of stacking faults.

† A capsule method.

well known and are discussed as impurity diffusion in silicon (20). The excess vacancies cause the enhanced diffusion of the impurity.

If the vacancy in silicon acts as an acceptor (21), the vacancy concentration is changed by the shift, due to doping, of the Fermi level (18). The concentration of charged vacancies is given by

$$[V^-] = [V] / \{1 + \exp[(E_{VAC} - E_F)/kT]\} \quad [1]$$

where  $E_{VAC}$  and  $E_F$  are the vacancy and Fermi levels, respectively, and  $[V]$  is the total concentration of vacancies, which is the sum of charged and neutral vacancies. Assuming that the concentration of neutral vacancies is independent of impurity doping (22), and using Eq. [1], the ratio of the total vacancy concentration in extrinsic silicon doped with impurity,  $[V]_D$ , to intrinsic,  $[V]_I$  can be expressed by

$$\frac{[V]_D}{[V]_I} = \frac{1 + \exp[(E_{FD} - E_{VAC})/kT]}{1 + \exp[(E_{FI} - E_{VAC})/kT]} \quad [2]$$

where the suffixes, D and I, indicate the doped and intrinsic condition. The simple vacancy in silicon is known to be an acceptor having the energy level of 0.4 eV below the conduction band (21). Hence, in silicon heavily doped with a donor impurity, Eq. [2] becomes

$$\frac{[V]_D}{[V]_I} \cong \exp[(E_{FD} - E_{FI})/kT] = n/n_i \quad [3]$$

where  $n$  and  $n_i$  are the electron concentration in doped and intrinsic silicon, respectively. The vacancy concentration increases in silicon heavily doped with a donor-type impurity.

When phosphorus was diffused into silicon having stacking faults and its surface concentration exceeded the intrinsic carrier concentration, the stacking faults in the diffused layers were annihilated for a short time. The annihilation was probably enhanced by the donor-induced vacancies. Arsenic is the same type of donor as phosphorus, but the behavior differed somewhat from that of phosphorus. The annihilation effect of stacking faults in the arsenic diffused layers decreased as the surface concentration of arsenic increased. For the sample of which the surface concentration was  $3.0 \times 10^{20} \text{ cm}^{-3}$ , the faults almost entirely remained in

the arsenic diffused layer. Considering the discrepancy between total arsenic in silicon diffusion profiles obtained by Irvin's data and those determined by neutron activation analysis, and the dependence of the arsenic diffusion coefficient on concentration, Fair pointed out that ( $V_{Si}As_2$ ) complexes were formed and acted as vacancy sink (23, 24). The vacancy concentration probably became insufficient for the annihilation of stacking faults in the diffusion of high arsenic concentration.

The stacking faults were also rapidly annihilated by boron diffusion. For boron diffusion,  $[V]_D/[V]_I$  in Eq. [2] is unity, so that the same excess vacancies as donor doping are not induced. The covalent radius of boron is 0.89Å, which is smaller than that of silicon, 1.17Å. The stress due to solute lattice contraction is introduced in silicon doped heavily with boron. This stress causes the slip dislocations (14). When boron was diffused in silicon and its surface concentration exceeded about  $1 \times 10^{20} \text{ cm}^{-3}$ , the slip dislocations were observed as shown in Fig. 3. The excess vacancies might be emitted from these defects during their generation, and might have enhanced the annihilation of stacking faults. However, for the samples of which the surface concentration of boron exceeded  $1.7 \times 10^{20} \text{ cm}^{-3}$ , the annihilation effect decreased slightly. If the boron concentration approaches near to the solid-solubility limit, interstitial boron atoms probably increase. These interstitial atoms oppositely act as vacancy sink to occupy the lattice sites. And so, the annihilation effect by boron diffusion of extremely high concentration might be decreased.

Another remarkable phenomenon of boron diffusion was that the stacking faults underneath the boron diffused layer were annihilated under the adequate condition. This phenomenon is considered as follows. The negatively charged vacancies repulse with boron atoms, because boron is an acceptor. Then, the vacancies are able to diffuse deeply far from the diffusion front of boron. They possibly annihilate the stacking faults underneath the boron diffused layer. Therefore, this phenomenon was not observed for the diffusion of a donor impurity such as phosphorus and arsenic. In case of the diffusion of a donor impurity, the negatively charged vacancies are drawn to donors and remain mainly in the diffused layer. Because of this, the stacking faults underneath the diffused layer were not annihilated by diffusion of phosphorus and arsenic. This behavior differs remarkably from that of boron.

### Conclusions

The stacking faults generated in silicon during thermal oxidation are shrunk and annihilated by heat-treatment in a nitrogen atmosphere. This phenomenon is due to the removal of silicon atoms, which form the extrinsic-type stacking faults, by diffusion via vacancies. Therefore, the excess vacancies induced in silicon by the diffusion of donor-type impurities or by the stress due to solute lattice contraction of impurity, en-

hance the annihilation of stacking faults. This behavior is also influenced by the coulomb interaction between the negatively charged vacancy and impurity, or the complex formation between the vacancy and impurity.

From the results of these experiments, useful information for studying the various phenomena in other fields can be obtained. For instance, using the annihilation data, one can make clear the mechanism of anomalous diffusion of impurity in silicon, which is not sufficiently known.

### Acknowledgments

The authors wish to thank Dr. M. Maeda and Mr. S. Ohkawa for useful discussions,

Manuscript received May 3, 1976.

Any discussion of this paper will appear in a Discussion Section to be published in the June 1977 JOURNAL. All discussions for the June 1977 Discussion Section should be submitted by Feb. 1, 1977.

Publication costs of this article were assisted by Fujitsu Laboratories Limited.

### REFERENCES

1. D. J. D. Thomas, *Phys. Status Solidi*, **3**, 2261 (1963).
2. H. J. Queisser and P. G. Van Loon, *J. Appl. Phys.*, **35**, 3066 (1964).
3. G. R. Booker and W. J. Tunstall, *Phil. Mag.*, **13**, 71 (1966).
4. A. W. Fisher and J. A. Amick, *This Journal*, **113**, 1054 (1966).
5. J. E. Lawrence, *J. Appl. Phys.*, **40**, 360 (1969).
6. K. V. Ravi, C. J. Varker, and C. E. Volk, *This Journal*, **120**, 533 (1973).
7. H. Shiraki, *Jpn. J. Appl. Phys.*, **15**, 1 (1976).
8. G. A. Rozgonyi, P. M. Petroff, and M. H. Read, *This Journal*, **122**, 1725 (1975).
9. K. V. Ravi, *Phil. Mag.*, **30**, 1081 (1974).
10. V. E. Sirtl and A. M. Adler, *Z. Metallkd.*, **52**, 529 (1962).
11. T. Sakurai, H. Nishi, T. Furuya, H. Hashimoto, and H. Shibayama, *Appl. Phys. Lett.*, **22**, 219 (1973).
12. J. C. C. Tsai, *Proc. IEEE*, **57**, 1499 (1969).
13. J. C. Irvin, *Bell Syst. Tech. J.*, **41**, 387 (1962).
14. H. J. Queisser, *J. Appl. Phys.*, **32**, 1776 (1961).
15. C. S. Fuller and J. A. Ditzenberger, *J. Appl. Phys.*, **27**, 544 (1956).
16. I. R. Sanders and P. S. Dobson, *Phil. Mag.*, **20**, 881 (1969).
17. J. M. Fairfield and B. J. Masters, *J. Appl. Phys.*, **38**, 3148 (1967).
18. R. L. Longini and R. F. Greene, *Phys. Rev.*, **102**, 992 (1956).
19. S. M. Hu and T. H. Yeh, *J. Appl. Phys.*, **40**, 4615 (1969).
20. S. M. Hu and S. Schmidt, *ibid.*, **39**, 4272 (1968).
21. G. D. Watkins and J. W. Corbett, *Discuss. Faraday Soc.*, **31**, 86 (1961).
22. W. Shockley and J. L. Moll, *Phys. Rev.*, **119**, 1480 (1960).
23. R. B. Fair, *J. Appl. Phys.*, **44**, 283 (1973).
24. R. B. Fair, *Appl. Phys. Lett.*, **22**, 186 (1973).

# Chemical Etching of Silicon<sup>1</sup>

## IV. Etching Technology

B. Schwartz\*

*Bell Laboratories, Murray Hill, New Jersey 07974*

and H. Robbins\*

*Galamar Industries, Palo Alto, California 94304*

### ABSTRACT

The etching of silicon in HNO<sub>3</sub>-HF based systems proceeds by a sequential oxidation-followed-by-dissolution process. In those composition regions where the solution is very low in HNO<sub>3</sub> and rich in HF, the rate-limiting process is the oxidation step. Consequently, electron concentration, surface orientation, crystal defects, and catalysis by lower oxides of nitrogen play an important role. In those compositions where HF is in limited supply, dissolution of the formed oxide is the rate-controlling step and diffusion of the complexing fluoride species is the important factor. Therefore, crystal orientation and conductivity type independence as well as hydrodynamic control are the consequences. In order to meaningfully select an etching composition to solve a specific processing problem, it is necessary to understand this composition-mechanism interaction. Corollary with the mechanism understanding, sample geometry effects have been followed as a function of solution composition. The HF-HNO<sub>3</sub>-H<sub>2</sub>O solution composition plane has been characterized into various regions where the two basic mechanisms interact and specific processing utilization is shown. Similar results are shown for the system HF-HNO<sub>3</sub>-HC<sub>2</sub>H<sub>3</sub>O<sub>2</sub>. In addition, a number of particular etching problems are posed, and solutions offered, that make use of these composition characterizations, and show how one can use their information to solve other practical processing problems.

Most of the data on silicon etching that one can find in the literature involve studies of the mechanisms and kinetics of the dissolution process (1-4). There are a few examples of practical applications, but they deal primarily with crystallographic aspects of the etching, *e.g.*, defect delineation (5) or anisotropic crystal plane etching (6). Because of the sophistication of present-day silicon technology, it appears to be desirable to be able to control the geometrical aspects of a silicon slice, *e.g.*, from sharp, possibly peaked corners and edges to smooth and rounded edges and corners, merely by controlling the chemical etching environments. It would, therefore, seem appropriate to present some data on the geometrical effects observed on the etching of silicon rectangular parallelepipeds in solutions of HNO<sub>3</sub>, HF, and H<sub>2</sub>O with and without HC<sub>2</sub>H<sub>3</sub>O<sub>2</sub>. These observations were made at the same time as the previously published kinetics data were being obtained (1,2), but it is only recently that many requests for geometric information have made us aware of the usefulness of disseminating these configurational data.

In order to make the picture more complete, some of the original iso-etch-rate figures will also be included, for comparison purposes.

### Experimental Procedure

The technique used for the etching and thickness monitoring has been adequately described in previous publications (1-3). However, in order to make this paper useful, we will have to repeat some of the experimental detail, but will stress only the salient features of the sample and solution preparation methods and how the geometric aspects were followed.

The sample dice were rectangular parallelepipeds (0.125 × 0.125 × 0.025 in. on side) cut from n-type silicon slices with resistivities about 2 Ω-cm. The dice were cut so that the large-area surfaces were along the (111) plane while the remaining surfaces were

not controlled with respect to any particular crystal plane. Also, the dice were used as received, which means that the exposed surfaces contained saw damage.

All dice were etched three times, and each etch was performed in a fresh portion of the same solution. Since each etching period had been chosen to remove 4 to 6 mils from the specimen, it may be assumed that the work damage had been removed after the first etch. The third etch was performed with a few milligrams of NaNO<sub>2</sub> added to the solution for possible catalytic purposes (1). After each etching step, the sample was rinsed in distilled water, dried, and measured for dimensional changes with a micrometer to ± 0.05 mils, and then the geometry of the specimen was examined under a microscope.

Concentrated hydrofluoric acid, as normally supplied, may vary in concentration from 48 to 52 weight percent (w/o). Similarly, nitric acid may vary between the limits of 69 and 71%. In order to establish control over the composition of the etching solutions, it was necessary to standardize the stock acids from which the solutions were to be made. This was done by titrating samples of the acids against a standard sodium hydroxide solution. Potassium acid phthalate was used as the primary standard for the sodium hydroxide. The first bottle of hydrofluoric acid analyzed at 49.25%, and this concentration was accordingly selected as the standard HF reagent concentration. All subsequent bottles of hydrofluoric acid were adjusted to 49.25 ± 0.05% by the addition of 60% HF or water as dictated by the chemical analysis. In a similar manner, the value 69.51% HNO<sub>3</sub> was established as the standard nitric acid concentration and all subsequent stock bottles of nitric acid were adjusted to this value ± 0.05% by the appropriate addition of water or 90% HNO<sub>3</sub>. In a second series of experiments designed to cover a larger area of the composition range, 90.45 ± 0.05% HNO<sub>3</sub> and 59.75 ± 0.05% HF were the standard reagents used. In a third series of experiments, glacial acetic acid was used as a diluent, and the only water present was that found in the original HNO<sub>3</sub> or HF reagents.

\* Electrochemical Society Active Member.

<sup>1</sup> All of the data used in this paper were obtained while the authors were employed at Hughes Aircraft Company.

Key words: silicon, etching, geometry control.

The etching was done in a Teflon beaker 1 in. in diameter and 2½ in. deep. Agitation was provided by an electric stirrer equipped with a polyethylene paddle. The dice were etched one at a time in 10 cm<sup>3</sup> of solution, and duplicate results were obtained by repeating the entire experiment. To quench the reaction at the proper time, a large volume of water was poured into the beaker. The etching technique was later modified when the higher concentration reagents were used. Here the dice were etched two at a time, in 20 cm<sup>3</sup> of solution, while encased in a small perforated polyethylene basket. The basket and dice were agitated for the required time in the solution, then immersed in a beaker of cold water to quench the reaction. The agitating action consisted of approximately 150 vertical strokes per minute, with the etching jig rotated between the thumb and middle finger as rapidly as possible during the up and down strokes.

All etching was performed in a constant temperature bath regulated at 25.00° ± 0.02°C. Unfortunately, the heat transmission of polyethylene and Teflon is so poor that the temperature of the bath could not be realized in the etch solution, and even after long periods of equilibration the maximum initial etch temperature was only 24.70°C. As a further consequence of the poor heat transmission of the etching container, the more rapid etches were run under essentially adiabatic conditions.

It was realized early in the study that in some etch compositions the rate of attack on the die would be so high that if the specimen were left in the solution for one minute, either the sample would be etched away completely or it would be so thin that it would be very difficult to handle. For this reason an attempt was made to choose an etch time for each composition such that only 4 to 6 mils of material would be removed. The etch rate was then linearly extrapolated to obtain the 1 min value. The justification for the extrapolation is illustrated by Fig. 1 where the change in sample thickness is plotted as a function of time for two different etch compositions. It is quite possible that for compositions where the etch rate is very high, the linear relation between the amount of material removed and the time is not valid for the entire minute, since the reaction is known to be strongly exothermic and to proceed under adiabatic conditions. Nevertheless, it is believed that by limiting the etch time to minimize the effect of changes in experimental conditions, one could obtain numbers by linear extrapolation which are reasonably valid. The change in concentration of the etch system during the experiment was also considered an important factor. However, if one allows only about 0.005 in. of silicon to be etched away during the operation, this would correspond to reacting only about 0.4 mequiv. of silicon, and the change of concentration of the reagents due to reaction would be at most 1%, which is a negligible consideration.

Since the etching systems under study here were composed of three components (i.e., HF, HNO<sub>3</sub>, and H<sub>2</sub>O) with a fourth component present only when HC<sub>2</sub>H<sub>3</sub>O<sub>2</sub> was added, it was decided to represent the solution concentration field with a triangular coordinate system. The decision was also made to set two of the vertexes at 100 w/o of the concentrated HF or HNO<sub>3</sub> acids and to make the third vertex 100% added water or glacial acetic acid. This normalization of the axes to the concentrated acids results in data good only for the particular concentrations chosen as the basis for the study. The weight percent system, though, allows for ready conversion to other concentration units such as mole fraction and molality, and knowledge of the specific gravity of the solution<sup>2</sup> also enables one to calculate the molarity of the solution. By converting the concentrations to mole fractions, one can compare any concentration system with any other.

<sup>2</sup>The specific gravity of each solution was measured, but for brevity we will not discuss this point further.

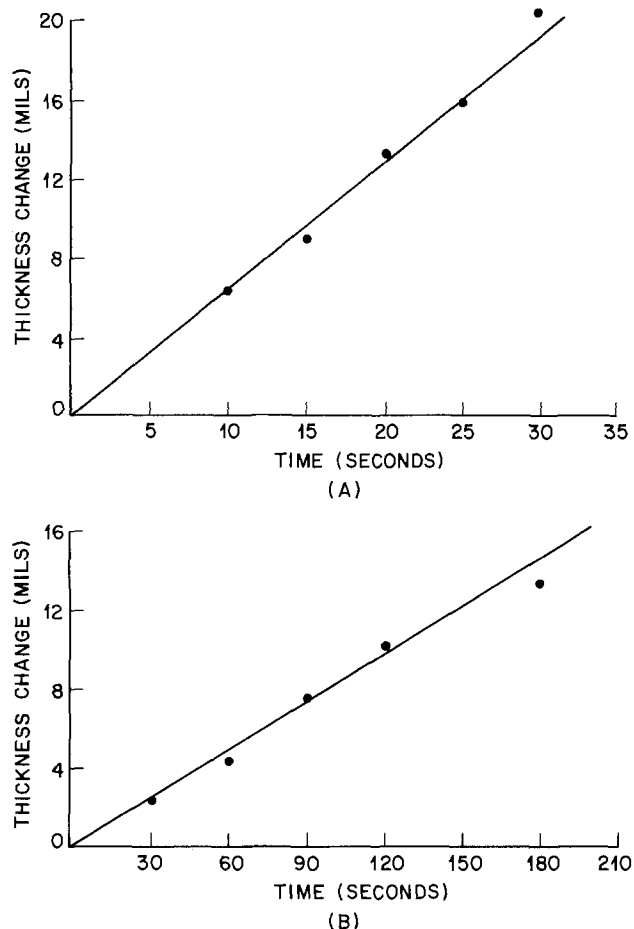


Fig. 1. Change of die thickness plotted as a function of die exposure time: (A) solution composed of 55% HF, 45% HNO<sub>3</sub>; (B) solution composed of 30% HF, 70% HNO<sub>3</sub>.

The solution composition field was subdivided into a number of evenly spaced points representing different compositions. The amounts of each reagent corresponding to each composition were then calculated, and the solutions were prepared by putting together the required amounts of reagents. The hydrofluoric acid was weighed out directly to ± 0.01g, but the weights of nitric acid and water were converted to volumes and measured out in a burette to ± 0.01 cm<sup>3</sup>.

### Experimental Results

Figures 2 and 3 represent the iso-etch-rate contours determined for the normal and high concentration

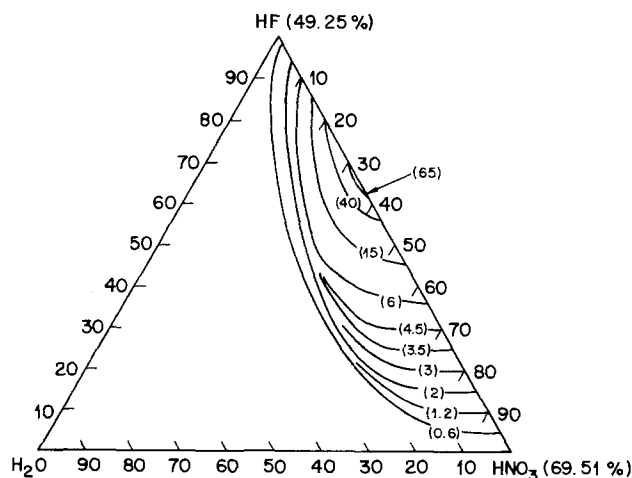


Fig. 2. Curves of constant rate of change of die thickness (mils per minute) as a function of etchant composition, in the 49% HF-70% HNO<sub>3</sub> system.

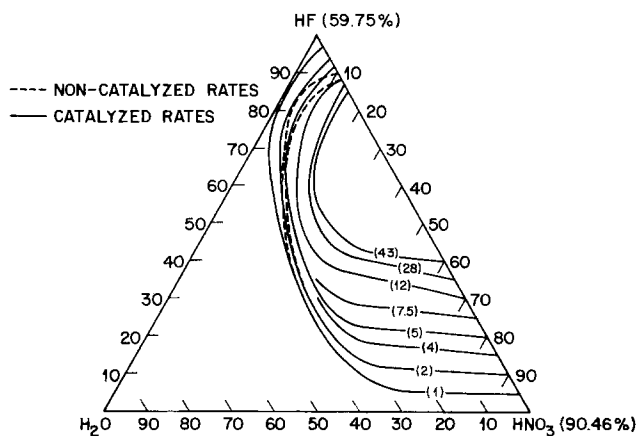


Fig. 3. Curves of constant rate of change of die thickness (mils per minute) as a function of etchant composition in the 60% HF-90% HNO<sub>3</sub> system; the effect of added catalyst (NaNO<sub>2</sub>) is shown as the dashed lines.

reagents [to obtain the etching rate on either of the (111) faces, divide the listed value by 2], with added water as the third vertex. Figures 4 and 5 are the same data, illustrating the shape of the etch-rate surface as a function of solution composition. The various regions and the mechanisms involved in the dissolution process were adequately covered previously (1-3). We shall just note that in the region around the HF vertex the reaction is primarily oxidation-reduction controlled, and in the region around the HNO<sub>3</sub> vertex, the reaction is primarily diffusion controlled. A consequence of the diffusion-governed kinetics is that different crystallographically oriented surfaces should all etch at the same rate. For two widely different etch compositions, the rate of attack on the (111) plane has been found to be identical to the rate of attack on the (110) plane. In preferential etch systems (e.g., NaOH), the (111) is the slowest etching plane and the (110) plane is one of the fastest etching planes.

Figures 6 and 7 are plots of the same solution composition fields, respectively, but in the latter two figures are shown the observed geometry effects on the initially rectangular parallelepipeds.<sup>3</sup> In these two figures it is seen that the geometry of the etched

<sup>3</sup> Although solid lines are drawn from which sharp discontinuities could be inferred, this is not the case. There are graded regions in going from one area to another, but this would make illustration well-nigh impossible.

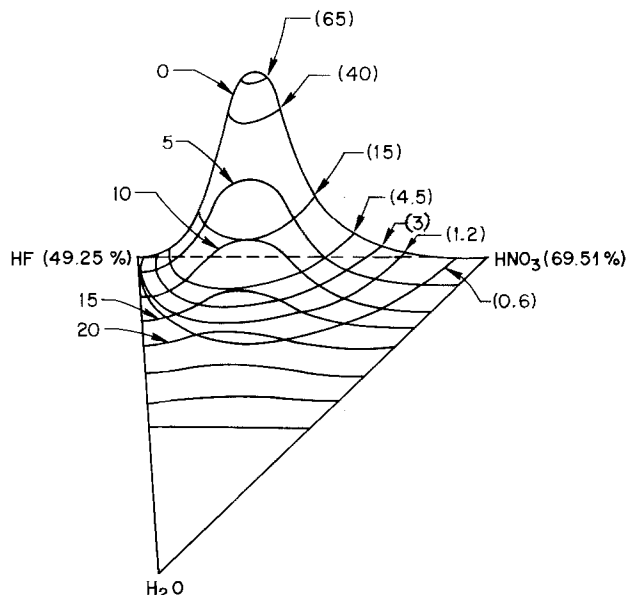


Fig. 4. Etch-rate surface as a function of etchant composition in the 48% HF-70% HNO<sub>3</sub> system.

specimen undergoes a gradual transition as the etching formula is changed along the HNO<sub>3</sub>-HF axis. In the high HF region the specimens have rough, pitted surfaces and sharply peaked corners and edges. At about

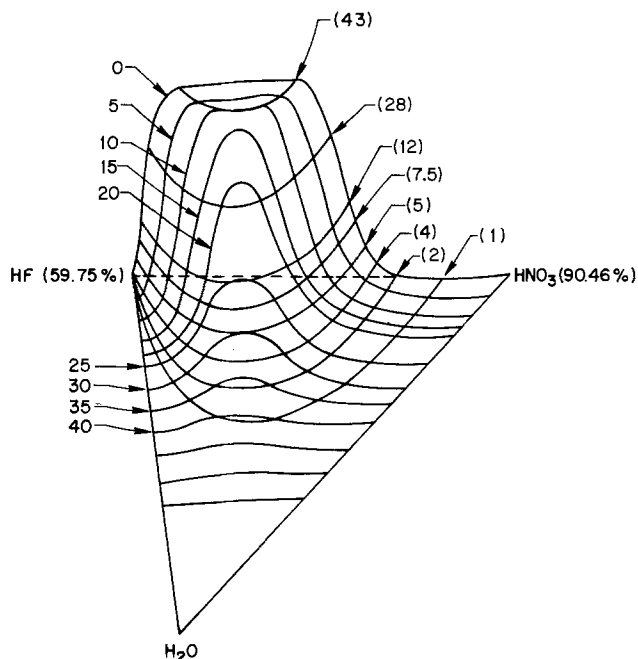


Fig. 5. Etch-rate surface as a function of etchant composition in the 60% HF-90% HNO<sub>3</sub> system.

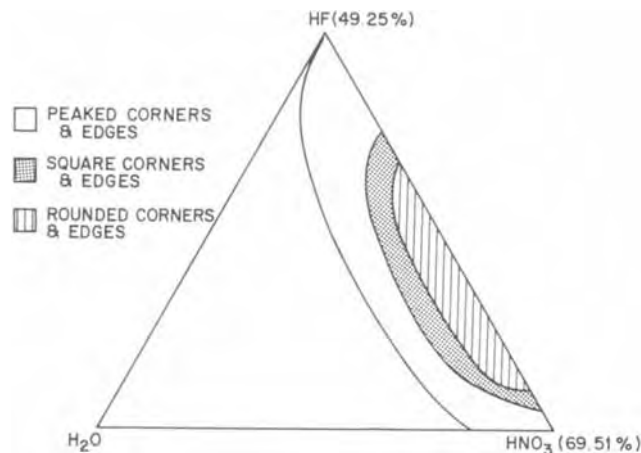


Fig. 6. Resultant geometry of the etched die as a function of the etchant composition in the 48% HF-70% HNO<sub>3</sub> system.

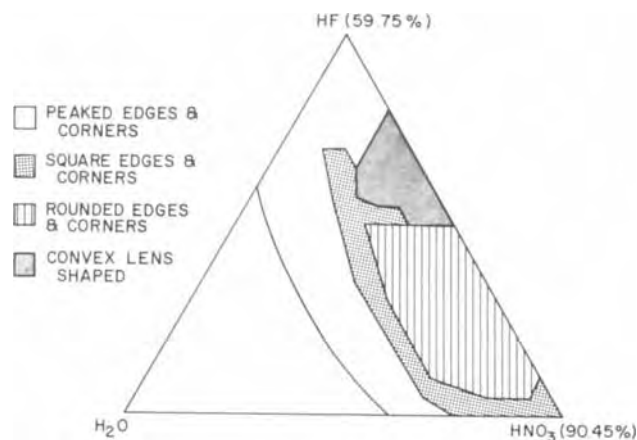


Fig. 7. Resultant geometry of the etched die as a function of the etchant composition in the 60% HF-90% HNO<sub>3</sub> system.

25% HNO<sub>3</sub> on this axis (Fig. 6), the geometry becomes square and the surface has a matte appearance. Further increase of HNO<sub>3</sub> above 35% is accompanied by progressive rounding of the corners and the development of a highly specular surface. The latter geometry and appearance prevail over the remainder of the composition range except that in the very high HNO<sub>3</sub> region the geometry again becomes peaked. A tendency toward peaking of corners is also observed as the composition is varied toward increasing water.

The natural tendency of a diffusion-controlled reaction is the development of rounded corners and edges, since the availability of reagent is greater at the corners and edges of the specimen than in the center. A factor must therefore exist that enhances the rate of attack of the reagent in the central portion of the specimen. This factor is the effect of catalysis on the reaction rate. We know that in some etching solutions, a work-damaged surface will etch readily while a preetched surface will be very difficult to etch. In the latter case, it has been observed that if the etching action can be started by any one of a number of means (e.g., seeding the solution with a die having a damaged surface), there is then no difficulty in sustaining the reaction. This phenomenon can be explained on the basis that one of the reaction products catalyzes the reaction. To verify this hypothesis, certain solutions were seeded with NaNO<sub>2</sub> in order to generate nitrogen oxides (1). The results are shown in Fig. 3; the enhancement of the etching rate by the addition of NaNO<sub>2</sub> in the high HF region and in the high H<sub>2</sub>O region is evidence of catalysis. The reaction is thought to be autocatalytic throughout the entire composition range, but the effect of added catalyst is negligible in those regions where the rate is sufficiently high so that any generated catalyst would far exceed the added amount. Since the reaction is autocatalytic, swirling dissipates the catalyst more rapidly from the corners and edges than from the central portion of the specimen. This might explain the high degree of attack in the central portion of the die relative to the attack on the edges and corners.

The rough surfaces of specimens etched in the high HF region can also be correlated with the autocatalytic mechanism. When the HNO<sub>3</sub> concentration is low, the reaction can begin only at low activation energy sites, such as crystal imperfections. From these sites, the reaction spreads to adjacent areas as the catalyst diffuses. If the reaction is slow, the catalyst is liberated slowly and there is a high probability that it will be dissipated before it can act to propagate the reaction. When the HNO<sub>3</sub> concentration is very low, the surface can be seen to be covered by isolated pits and craters. As the HNO<sub>3</sub> concentration increases, the density of pits and craters increases until they finally merge into a rough "orange peel" pattern. When the concentration of HNO<sub>3</sub> becomes sufficiently large, the entire surface becomes susceptible to attack, and as HF becomes the rate-limiting reagent, the surface becomes smooth and specular.

The ratio of the attack rate on the two (111) planes to that on the four unoriented surfaces is greater than unity in the high HF region, and much less than unity in the high HNO<sub>3</sub> region. This can also be correlated in the high HF region with the greater dependence of the rate on catalyst, and in the high HNO<sub>3</sub> region with the diffusion mechanism. Because of the greater availability of reagent at the edges, this region should show an enhanced etch rate with respect to the center. The fact that the edges etch more slowly than the center in the high HF region indicates that the dissipation of the catalyst is the predominating factor governing the behavior of etchants rich in HF. In the region of etch composition where the oxidation step ceases to be rate determining, the etch rate on the edges of the specimen is in accord with the expectation that these areas will etch faster.

Another observation lending itself to interpretation in terms of the autocatalytic nature of the reaction is

the peculiar dependence of the etching rates on the water concentration. In the lower region of Fig. 2 and 3, the contour lines run parallel with lines of constant HF for a considerable distance and then suddenly break upward. The rates at constant HF are independent of increasing water or decreasing HNO<sub>3</sub> up to a critical value. Around this critical point, the rates vary sharply with composition. It is reasonable to assume that as the concentration of nitric acid decreases, a point is reached where the rates become dependent on the nitric acid concentration, and thus on the coupling of the generated catalyst with the reacting system. The decrease in rate resulting from a decrease in the nitric acid concentration is amplified by the decreased coupling of the catalyst with the surface, so that as a result of this "positive feedback" effect the rates are strongly affected by relatively small changes in etch composition.

In the 60% HF-90% HNO<sub>3</sub> system there is a composition region (see Fig. 5 and 7) where the rate reaches a plateau value and the geometry is extremely rounded. This is a region of extremely rapid reaction rates, and the mechanism in this region is not very well understood; however, it is thought to involve the formation of a vapor barrier at the silicon surface owing to the high generation rate of SiF<sub>4</sub>.

Figures 8 and 9 are, respectively, the equivalent kinetic and geometry data for the acetic acid diluent system. A comparison of Fig. 2 and 8 clearly brings out the relationship between the two etching systems. The rates in the two systems obviously must converge to identical values along the HF-HNO<sub>3</sub> axis. In the

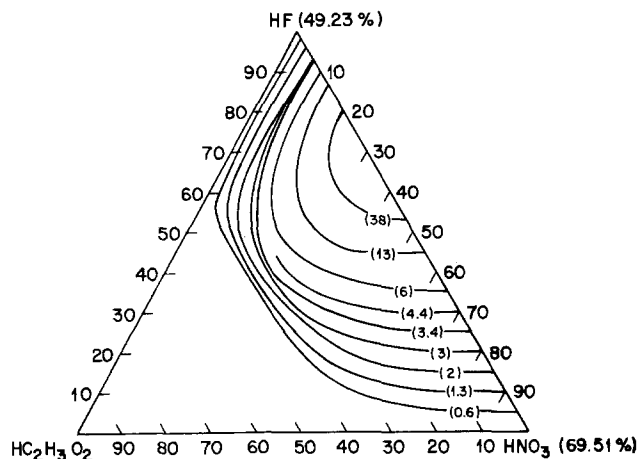


Fig. 8. Curves of constant rate of change of die thickness (mils per minute) as a function of etchant composition in the 48% HF-70% HNO<sub>3</sub>-HC<sub>2</sub>H<sub>3</sub>O<sub>2</sub> system.

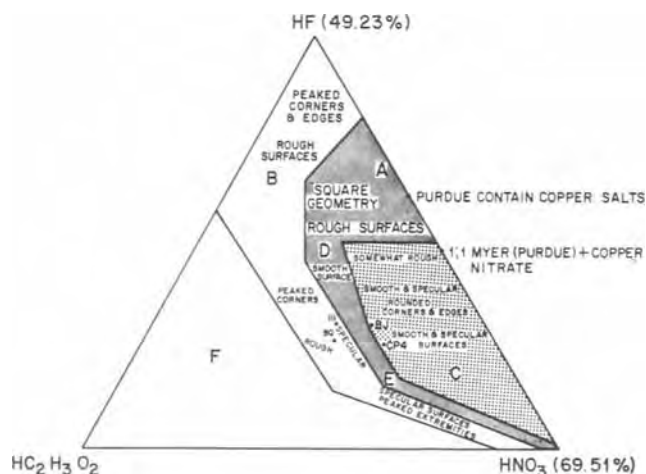


Fig. 9. Resultant geometry of the etched die as a function of the etchant composition in the 48% HF-70% HC<sub>2</sub>H<sub>3</sub>O<sub>2</sub> system.

lower portion of each plot, the constant etch-rate contours of both systems run identical courses over a considerable range of compositions. In the upper portion of each plot, however, the contours diverge immediately upon the addition of diluent. The noteworthy feature here is that the contours for the acetic acid system run parallel with lines of constant nitric acid concentration and the plot in general bears a striking resemblance to the high concentration acid system shown in Fig. 5. The equivalent etching systems  $\text{HF} + \text{HNO}_3 + \text{diluent}$  are seen to show a much greater tolerance for acetic acid than for water as the diluent.

Earlier in this section it was shown that in the high HF region the etch rates are affected by the oxidizing ability of the nitric acid and the reaction is critical with respect to the coupling of the generated catalyst. The tolerance of the system for acetic acid is thus in accord with the known enhanced oxidizing power of nitric acid in acetic acid over that of nitric acid in water (7,8). The addition of acetic acid does not reduce the oxidizing power of the nitric acid until a fairly large amount of the diluent has been added. Therefore, the rate contours remain parallel with lines of constant nitric acid over a considerable range of added diluent.

The same explanation is valid in the high  $\text{HNO}_3$  region. The sudden dependence of the etch rates on the amount of added diluent has been associated with a transition from an oxidation-independent mechanism to an oxidation-dependent mechanism. The effect of the acetic acid is primarily to defer the onset of the oxidation-dependent mechanism until a very large amount of this diluent has been added.

The striking similarity of the water diluted etching system and the acetic acid diluted system, coupled with the consistency of the etch rates irrespective of the nature of the diluent, provides an additional argument in favor of the diffusion-governed mechanism previously proposed. The fact that the etch rates are not affected by the enhanced reactivity of the nitric acid in acetic acid can only be explained on the basis that the rates are diffusion limited, not reactivity governed.

The acetic acid diluent etch composition plane may also be subdivided into general areas having different geometric etching characteristics (see Fig. 9). The principal difference between the two systems is that the areas in the acetic acid system are more extensive.

In Fig. 9, we have indicated several commonly used etches. The BJ etch and the CP4 etch are seen to be located in area C, and they should have similar properties. On the basis of our interpretation of the reaction mechanism in this area, we would venture that the bromine in the CP4 formula serves no useful function in the etching of silicon to obtain a specific geometry. The same comment may be made with respect to the copper in the Purdue etches. There may be factors, though, which we have not evaluated, such as resulting electrical properties of devices, etched with these solutions, that might show a need for the additive. From our point of view, however, the use of an additive in such compositions is pointless.

The 111 etch is interesting because it lies in a region where the resultant surfaces are specular, but where the corners tend to peak. It should produce better geometry retention than the BJ etch and it should be more reliable in the absence of added catalyst than its neighbor, the BQ etch. The latter is very critical, with respect to slight changes in composition, and with respect to the silicon surface. Infinitesimal composition changes such as the addition of one drop of acetic acid to 20 cm<sup>3</sup> of etchant, or the use of 48.5% HF instead of 48.9% HF to prepare the solution, have been observed to cause the second etch rate (*i.e.*, etching of a work-damage-free surface) to vanish. It has been observed that the etch rate in the BQ composition may have practically any value between zero and the diffusion-limited value for that composition. However, these disadvantages may possibly be overcome by the in-

troduction of a catalyst, and the BQ etch might prove to be quite useful in device work.

In summary, the behavior of the water diluted and acetic acid diluted etches based on HF and  $\text{HNO}_3$  is qualitatively very similar and is governed by the same considerations. The differences are primarily quantitative and reflect the greater tolerance of the system for acetic acid than for water. This does not mean that the acetic acid diluted system is less critical than the water diluted system, with respect to composition, but merely that a greater amount of diluent may be added before the system becomes critical with respect to diluent or composition. Except in the high HF region, both systems are initially indifferent to the addition of diluent, and the etching behavior is unaltered until the composition is reached where the direction of the contours begins to change. Then feedback mechanisms come into play and the behavior of the solution becomes erratic. It is significant that the etching characteristics reflect the critical dependence of the etch rate on the local catalyst concentration in this region, so that a favorable geometry is obtained at the expense of erratic or unpredictable behavior of the etchant. Any attempt to make the etchant noncritical, such as an increase in temperature or the excessive addition of catalyst, will simultaneously produce a change in the geometry of the specimen to that characteristic of a diffusion-limited mechanism.

In the high HF region, the solution is critical with respect to the addition of water, because the critical amount of diluent is already contained in the concentrated stock HF. The use of acetic acid in this region may serve some purpose in making the area less critical, and some useful sizing etches may be found here. It is surprising that the common etches containing acetic acid, such as CP4, were not formulated in this region, but in the region where the addition of acetic acid seems to serve no useful purpose. (The amount of acetic acid in CP4 is a little less than critical.)

It is often said that acetic acid moderates the reaction and slows the rate. This is not true in the high nitric acid region and in the high hydrofluoric acid region. However, in the vicinity of the maximum etch rate, the acetic acid does have the alleged effect.

It seems on the basis of the small amount of information we have presented that any etching behavior attainable with an acetic acid diluted etch can be duplicated with a water diluted etch. The choice of diluent is thus a matter of individual preference.

### Applications

A process specification for the fabrication of a semiconductor device usually includes one or more chemical etching steps. The etching operation is employed for the attainment of certain objectives such as the reduction of reverse current, machining to size, or the removal of unwanted material. The diversity of circumstances under which the etching is performed, coupled with the infinite variability of the etching formulas, has created a fertile field for the sorcerer and alchemist to practice their arts. It was inevitable that some excellent etching procedures should have been discovered in the course of time. However, these procedures were applicable only to the attainment of limited objectives with specific devices. Every situation became a separate problem which had to be coped with on a hit-or-miss basis, without the guidance of scientific principles. In such a state of affairs, a method for the selection of the optimum etch to accomplish a given objective appeared to be extremely valuable.

A key to the selection of an etch is an understanding of the etching characteristics of a solution as a function of the composition. The physical factors that influence the etching behavior have already been discussed. It may now be desirable to recapitulate some of the concepts developed above and show how they can be applied to the formulation of an etching solution having certain specific properties.



For convenience, the solution composition plane in Fig. 6 will be divided into six regions (see Fig. 10). The characteristics of each region will be discussed in relation to the basic physical processes that play important roles in these regions. When this foundation has been established, a few basic rules of thumb will be given for formulating etching solutions that can be applied to specific practical problems.

Let us first focus attention on area A in Fig. 10. As Fig. 6 shows, the rates in this region are very rapid. Control of the amount of etching in this area is very difficult, because of the extreme sensitivity of the rate to small fluctuations in composition. There are also very few desirable characteristics in this region to make etching in it worthwhile. For these reasons, no etching compositions in area A will be considered further.

Area B covers the largest range of compositions. The boundary between B and F is located where the etch rates become too low to be generally practical for device fabrication. The compositions in area F have not been investigated, and no further reference to this area will be made.

The behavior of region B is best understood if one considers the compositions in the upper portion of the field. It is also convenient here to refer to the contours represented in Fig. 3 because the greater range of compositions enables observation of the behavior of the system which can only be estimated by extrapolation from Fig. 2. On the other hand, the latter system is the most useful from the practical standpoint of application because of the ready availability of the materials, the decreased hazard to personnel, and the greater ease of handling, all of which are obtained at no sacrifice in versatility whatsoever.

In the high HF region, nitric acid and catalyst are both necessary for the reaction to proceed at a perceptible rate. In the absence of added catalyst, therefore, it is necessary to find a "spark" to kindle the reaction. Such a spark exists in the presence of crystal imperfections and high energy sites. Once these undergo attack, catalyst is generated and the reaction spreads to adjacent sites. The propagation of such a reaction is clearly dependent upon the experimental conditions. Vigorous stirring may dissipate the catalyst so rapidly that the reaction is quenched. Further reaction is then dependent upon the existence of additional sites at which it can be kindled anew. For this reason, a previously etched surface, from which all work damage can be presumed to have been removed, will not be attacked by certain etch compositions in this region. On the other hand, in the absence of stirring the reaction will proceed rapidly, as the

catalyst will be able to "couple" with the reacting system, thereby increasing the rate to the point where the limiting process of diffusion takes over. Once a reasonable etching rate has been established, the presence of the required catalyst becomes assured and the reaction will, from then on, proceed even under considerable agitation. Also, if the nitric acid concentration is increased, a greater number of reactive sites will be simultaneously attacked, so that the probability of coupling of catalyst with the reacting system is enhanced. When sufficient nitric acid is present to sustain a reasonable rate, the coupling of catalyst with the reaction becomes assured and the etchant will reetch a specimen even in the absence of added catalyst.

The reaction of nitric acid with silicon is, as described previously, an oxidation-reduction process. The essence of such a process is the transfer of electrons from the reducing agent to the oxidizing agent. It is now apparent that factors influencing the availability of electrons will affect the rate. The rates will therefore be subject to modification by the effect of galvanic couples or pn junctions. Etching compositions have been found that will not attack either p- or n-material alone but will, if a junction is present, etch the p-region preferentially.

In region C of Fig. 10, the rates are independent of the nitric acid concentration, and electron transfer processes have a minor effect on the geometry. One might say that the entire surface is covered with a sheath of  $\text{SiO}_2$ . The more reactive centers may begin to etch first, but they soon become covered with an oxide layer. The oxide protects the reactive center from excessive oxidation while the remainder of the surface "catches up." The net effect is that the hydrofluoric acid, which is the rate-limiting factor, acts on a uniform layer of oxide. The result is a smooth, specular surface with rounded corners and edges. The rounding of the geometry is also affected by the rate of the reaction. When the reaction is fast, the diffusion-governed mechanism produces considerable rounding. By decreasing the hydrofluoric acid concentration, it is possible to decrease the rate to such an extent that catalyst coupling again becomes important in spite of the high concentration of  $\text{HNO}_3$ . As a result, the geometry is observed to become square or slightly peaked in the extremely high  $\text{HNO}_3$  region.

The etching characteristics of region C in Fig. 10 may be summarized as nonselective, producing specular surfaces and rounded geometry. The surface quality is mediocre at the upper end of the region, but it improves considerably a short distance from region A. Any surface detail such as wavy lines can probably be attributed to a nonhomogeneous surface environment such as concentration or thermal differences, or perhaps major crystal defects.

Regions D and E of Fig. 10 correspond to compositions in Fig. 2 where the direction of the contour lines is changing. This indicates a transition of mechanism from an HF-limited process to an  $\text{HNO}_3$ -limited process. The geometry of specimens etched in regions D and E is square as the result of the transition to a catalyst coupling mechanism. The difference in the etching characteristics between regions D and E lies in the surface quality of the etched die. In area D the reaction is relatively more  $\text{HNO}_3$  dependent, and vestigial evidence of selective etching is apparent. The result is a somewhat rough surface. In area E, the reaction is more HF dependent, and highly lustrous, specular surfaces result.

Let us now consider a few practical etching problems. As the first example, let us look at the problem of a suitable sizing etch for thinning a silicon chip. It is desired to remove a rather large amount of material, control the resultant thickness within narrow tolerances, retain square edges and corners, and preferably end up with a smooth surface for the subsequent operation, which could be an evaporation step. Area B is not ideal for such an etch because of the catalyst coupling factor; the rates in this region are too erratic,

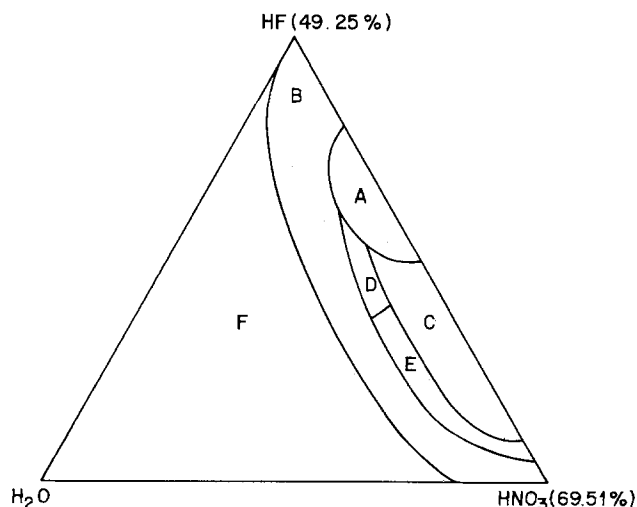


Fig. 10. Subdivision of the composition plane into general areas on the basis of the effect of the changing composition on the etching characteristics in the 48% HF-70%  $\text{HNO}_3$ - $\text{HC}_2\text{H}_3\text{O}_2$  system.



and they are also much too sensitive to small composition variations. The surfaces are also a bit too rough, although the geometry is favorable. In region C, the rates vary slowly with composition and the resulting surfaces are good, but the geometry is unfavorable. Possible solutions to the problem lie in the lower portion of area C, where the geometry turns square, or preferably in area E. If a large amount of material must be removed, then a two-stage process is possible where the etch may first be performed in a region of B where the rates are moderate but catalyst coupling is assured, and then finished up with a composition from regions C or E.

For the second example, let it be desired to remove the p-region from a large-area pn junction and to have the n-region relatively unaffected. A solution lies in choosing a "selective" etch, preferably near region F. The etch rate should be so low that the etching is essentially quenched by dissipation of the catalyst. Under these conditions, the attack will stop at the junction provided sufficient agitation is used, and provided that the volume of etch is sufficiently great that a negligible buildup of catalyst concentration occurs.

For the third example, consider the configuration shown in Fig. 11A. The problem is to remove a p-layer adjacent to an aluminum layer in order to contact the base n-type layer. One of the etches normally used gives a configuration such as is shown in Fig. 11B. Severe local etching in the vicinity of the aluminum plateau caused severance of the base area before any substantial portion of the p-region had been etched. The problem here was that a very selective etch was being influenced by the galvanic effects or catalytic effects of the aluminum layer to produce undesirable results. An answer to this problem lay in using a non-selective etch from area E of Fig. 10. An etch composed of 1HF:8HNO<sub>3</sub>:1H<sub>2</sub>O (by weight) was tried, and it gave the configuration illustrated in Fig. 11C.

There is a striking similarity between the problems of the second and third examples. In both instances it was desired to remove a p-layer and stop at a junction. In the former instance a selective etch did the job best because it had the built-in feature of stopping at the right time without danger of overetching. An alternative solution would be to use a nonselective etch, but this would require careful control of the time, temperature, and other factors governing the amount of etch, and also knowledge of the thickness of the p-layer. The presence of the aluminum and a second junction complicated the picture. The selective etching in the vicinity of the aluminum may have been caused by the trapping of generated catalyst first in the corner and later in the cavity. Under these circumstances it became necessary to sacrifice the automatic cutoff feature and use the alternative solution.

In the next example, consider the problem of bringing out the structural detail of a crystal by etching. The solution here also lies in a selective etch from region B or region F. A very slow etch must be chosen in order that catalyst coupling may be held to a minimum and mass action rather than diffusion may determine the mechanism, otherwise smudging of the structural detail might occur. The etch composition should therefore be in region F. Another solution might lie in selecting a nonautocatalytic etching system, in which diffusion is relatively unimportant, such as NaOH-H<sub>2</sub>O.

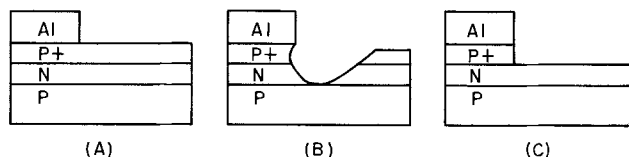


Fig. 11. The influence of solution composition on preferential etching: (A) initial configuration, (B) configuration after etching with 1HF:1HNO<sub>3</sub>:2HAc, (C) configuration after etching with 1HF:8HNO<sub>3</sub>:1H<sub>2</sub>O.

For a final example, examine the problem of junction etching for the improvement of the electrical properties and stability of a device. In the high HF region, etching will be localized at the junction, although all areas will be attacked to some extent. The tendency to attack attached leads made of copper, nickel, silver, etc. would be minimized because of the weakly oxidizing nature of the solution. The problem of lead attack is not merely one of weakening the structures, but also one of contamination of the etch by the reaction products. The localized etching in the desired portion of the device may allow for shorter time of exposure of the device to the etch. However, the roughness of the surface may provide a greater surface area for leakage and sharp points from which arcing may take place. Deep erosion of the junction also provides an overhanging roof to the device that is subject to mechanical damage and that constitutes a potential site for arcing. The possibility of severe local etching in the presence of metallic leads, aluminum layers, or crevices is also to be guarded against.

In the high HNO<sub>3</sub> region, the etched surfaces will be smooth. The junction will be visible as a fine line, but no major discontinuity in the surface will be noted. The tendency of the device to etch all over will be partly offset by the factor that the edges will etch faster than the (111) surfaces. The attack on metallic attachments will be somewhat greater than in the high HF region, but the chances of undercutting and local etching will be obviated. The minimized surface area may somewhat reduce surface leakage and the surface smoothness may possibly be conducive to better high voltage stability.

It is unfortunate that our knowledge of the surface, and of the factors contributing to high surface leakage and low breakdown voltage, is too meager to permit a statement of the problem in terms of etching objectives. In this instance, the method was to examine the etching characteristics of each region and make an educated guess as to which approach is the most promising. The answer will then probably be as valid as the premise that etching, and not some other unknown factor, holds the key to better electrical properties.

### Acknowledgments

The authors wish to express their gratitude to the many former colleagues at the Hughes Aircraft Company who contributed their helpful comments, suggestions and in some cases direct assistance. S. Pryor, P. Walker, F. Ludwig, and H. Winston are only a few of those who helped. Finally, we would like to thank the management of Bell Laboratories for allowing the time to prepare this paper for public dissemination.

Manuscript submitted May 27, 1976; revised manuscript received Aug. 18, 1976.

Any discussion of this paper will appear in a Discussion Section to be published in the June 1977 JOURNAL. All discussions for the June 1977 Discussion Section should be submitted by Feb. 1, 1977.

Publication costs of this article were assisted by Bell Laboratories.

### REFERENCES

1. H. Robbins and B. Schwartz, *This Journal*, **106**, 505 (1959).
2. H. Robbins and B. Schwartz, *ibid.*, **107**, 108 (1960).
3. B. Schwartz and H. Robbins, *ibid.*, **108**, 365 (1961).
4. B. A. Irving, in "The Electrochemistry of Semiconductors," P. J. Holmes, Editor, p. 256, Academic Press, New York (1962).
5. P. J. Holmes, in "The Electrochemistry of Semiconductors," P. J. Holmes, Editor, p. 329, Academic Press, New York (1962).
6. R. M. Finne and D. L. Klein, *This Journal*, **114**, 965 (1967).
7. E. Briner, *Helv. Chim. Acta*, **18**, 363 (1935).
8. E. Briner and P. Bolle, *ibid.*, **18**, 368 (1935).

# The Identification, Annihilation, and Suppression of Nucleation Sites Responsible for Silicon Epitaxial Stacking Faults

G. A. Rozgonyi\*

Bell Laboratories, Murray Hill, New Jersey 07974

R. P. Deysher\* and C. W. Pearce

Western Electric Company, Allentown, Pennsylvania 18103

## ABSTRACT

A study of the formation of epitaxial stacking faults in 2 in. diameter, dislocation-free (111) silicon wafers used in the fabrication of standard buried collector transistors has been made. The nucleation sites for the epitaxial faults are introduced during the initial oxidation of the wafer and are correlated with the presence of a high density of shallow, flat-bottomed, saucer-shaped etch pits. The saucer pits are selectively annihilated in the diffused or implanted regions during the fabrication of the Sb-doped buried collectors. For the ion-implanted process the annihilation of saucer pits extends laterally from 50 to 100  $\mu\text{m}$  beyond the boundaries of the collectors. Following epitaxial growth, epitaxial stacking faults, at a density of  $10^4 \text{ cm}^{-2}$ , are only found in those nonburied layer regions which have a saucer pit density of  $10^6$ - $10^7 \text{ cm}^{-2}$  before epitaxy. Therefore, epi stacking faults are not found in ion-implanted material with a separation between buried collectors of 100  $\mu\text{m}$  or less. Most 3 in. diameter, and the central regions of 2 in. diameter wafers do not have saucer pits or epi stacking faults. This is attributed to an *in situ* gettering of nucleation sites by  $\text{SiO}_2$  precipitates, which are known to form in wafers, or regions of wafers, with a high initial oxygen concentration. Additional procedures for deliberately suppressing or gettering the nucleation sites are presented. These include deliberate abrasion, deposition of strained  $\text{Si}_3\text{N}_4$  layers, introduction of misfit dislocations, and the use of an Sb ion implant, which are performed on the back side of wafers before the initial masking oxidation.

Following the recent wide scale introduction of dislocation-free wafers as starting material in the fabrication of silicon integrated circuits, defect-related problems have arisen which have either not occurred for some time, or may not have previously existed at all. We have found that when 2 in. diameter dislocation-free substrates were introduced into a processing line fabricating diffused buried collector epitaxial transistors, large increases in the density of epitaxial stacking faults,  $\text{SF}_{\text{epi}}$ , occurred. However, the use of 3 in. diameter wafers or a buried layer fabricated by ion implantation did not nucleate  $\text{SF}_{\text{epi}}$ . Also, the epitaxial stacking faults encountered in our diffused process were confined to those regions of the wafer which did not receive a buried layer diffusion before epitaxy. Figure 1 illustrates this phenomenon on a preferentially etched device chip after epitaxy. Note that the  $\text{SF}_{\text{epi}}$  density varies from zero in the buried layer areas to greater than  $10^4 \text{ cm}^{-2}$  in the nonburied layer regions.

It has previously been pointed out by Pomerantz (1) that wafers which are oxidized before epitaxy will have a high probability of nucleating stacking faults during epi growth. Pomerantz discovered that a characteristic saucer-shaped feature, called an S-pit, appeared after preferentially etching an oxidized wafer. The occurrence (or prevention) of the defect responsible for the S-pit was correlated with the presence (or absence) of stacking faults in the subsequently grown epi layer. Pomerantz also specified two gettering procedures, which, when applied to the back side of wafers prior to oxidation, would prevent the formation of S-pits and epi stacking faults.

We have recently rediscovered, while monitoring the defects introduced during epitaxy for standard buried collector transistor structures, the same connection between S-pits and  $\text{SF}_{\text{epi}}$ . In addition, we have found that the S-pits can be annihilated after oxidation, as well as gettered before oxidation by using an appropriate Sb ion implantation. Also, certain 2 in. and most 3 in. diameter wafers contain a built-in gettering ability which we believe to be re-

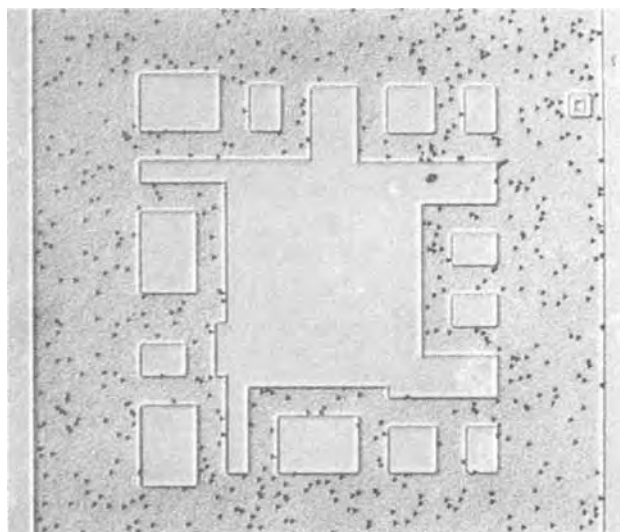


Fig. 1. Epitaxial stacking fault distribution revealed by 5 min Secco etch. The alignment square in the upper right-hand corner has an outside dimension of 50  $\mu\text{m}$ .

\* Electrochemical Society Active Member.

Key words: silicon defects, epitaxial stacking faults, gettering.

lated to the local oxygen concentration in the original crystal. In the present report we briefly review the observations common to Pomerantz's (1) work, and then describe how an understanding of the annihilation of the nuclei in the buried layer, lack of  $SF_{epi}$  in ion-implanted wafers, and the absence of nuclei in 3 in. diameter material led us to formulate several procedures for the suppression or gettering of the nuclei.

### Experimental Procedures

The starting material used in this study was from Czochralski crystals, (111) oriented, p-type, boron doped with a resistivity from 8 to 20  $\Omega$ -cm. The oxygen concentration in both 2 and 3 in. diameter wafers was examined by infrared transmission using a Perkin Elmer 457 spectrophotometer according to ASTM procedure F-121. In order to minimize the effects of slip-type dislocations all furnace operations above 900°C were ramped according to the schedule described by Moerschel (2). Defects were delineated using the preferential etch due to Secco D'Aragona (3) and observed in a Zeiss Ultraphot IV microscope using interference contrast objectives. The approach to the epi stacking fault problem was basically one of pulling wafers after each high temperature process and then microscopically examining them for defect etch features following a Secco etch. Once the defect nuclei were identified, defect interactions during subsequent high temperature treatments could be monitored. Since only three high temperature processes; oxidation, buried layer predeposition, and buried layer drive-in, were required before epitaxy, as listed in Table I, the epi fault problem was resolved in a rather direct way.

### Experimental Results

**Epitaxial layer growth.**—The initial observation of the  $SF_{epi}$  was made during the routine inspection of unetched epitaxial wafers using Nomarski interference contrast microscopy. As described above, the stacking faults only appeared in the nondiffused regions of 2 in. diameter wafers as shown in Fig. 1. It was also found that when 3 in. diameter wafers were run side by side with 2 in. diameter wafers on the same epi susceptor  $SF_{epi}$  only appeared in the 2 in. diameter material. The epitaxial deposition process was therefore ruled out as the source of  $SF_{epi}$  nuclei.

Since  $SF_{epi}$  are known to nucleate at the epi/substrate interface the amount of substrate material removed by gaseous HCl etching prior to epi growth was varied. Increasing the etch from the typical 0.5  $\mu$ m removed to greater than 1.5  $\mu$ m successfully eliminated the  $SF_{epi}$  nuclei. However, this extended etching was not compatible with the requirement of maintaining a buried layer sheet resistance of less than 25  $\Omega/\square$ . Further studies were therefore continued on substrate wafers before epitaxy.

**Diffused buried layer.**—Examination of an Sb diffused 2 in. diameter wafer Secco etched after the buried layer drive-in revealed S-pits, as predicted by Pomerantz (1) for oxidized (111) wafers before epitaxy. However, the distribution of S-pits corresponded to the buried layer pattern as shown in Fig. 2. The S-pit density in nonburied layer regions was on the order of  $10^6$   $cm^{-2}$  or greater, while it was

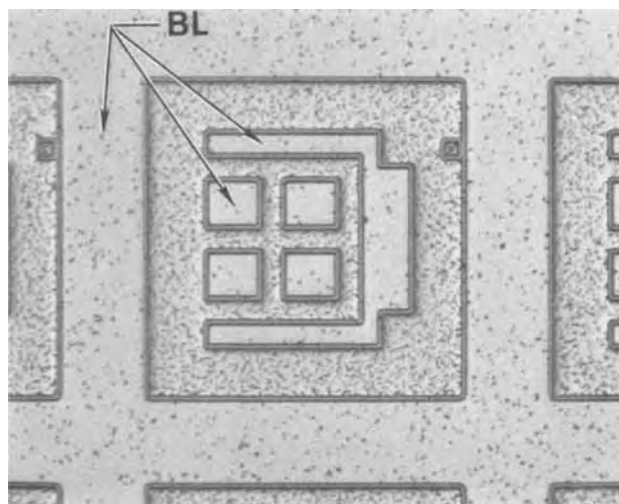


Fig. 2. Saucer pit distribution after buried layer drive-in

about  $10^4$   $cm^{-2}$  in the buried layer regions, as shown by the higher magnification micrographs in Fig. 3a and b. Note that the Secco etch produces a true saucer shape, i.e., the pits are round, whereas the Sirtl (4) etch used by Pomerantz (1) yields a faceted triangular pit. Wafers which were etched before the 2 hr 1250°C  $Sb_2O_3$  deposition had a uniform  $10^6$ - $10^7$   $cm^{-2}$  S-pit distribution over the entire wafer, indicating that the defect responsible for the formation of

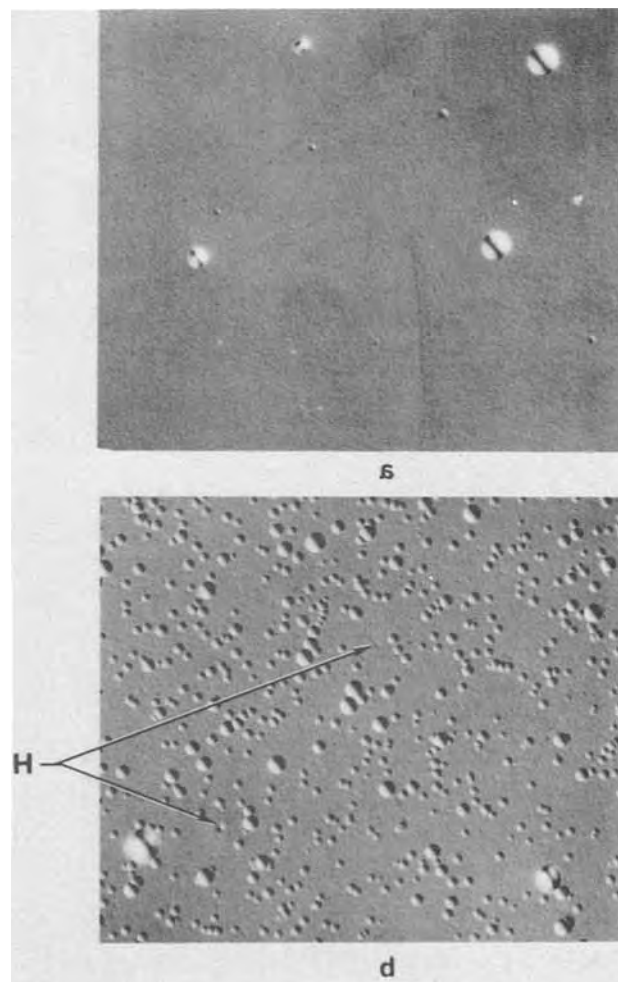


Fig. 3. Micrographs of S-pits at 690 $\times$  in (a) buried layer and (b) nonburied layer regions following Sb drive-in at 1250°C for 2 hr. Arrow H indicates raised hillock etch features.

Table I. High temperature processing data

Process	Temp, °C	Time (hr)	Miscellaneous
1. Steam oxidation	1100	1	6000-7000 Å
2. Photolithography			Pattern definition
3. Sb buried layer deposit			
(a) Diffusion	1250	2	$Sb_2O_3$ source
(b) Ion implant	300		$3.5 \times 10^{15}$ $cm^{-2}$ at 30 keV
4. Buried layer drive-in	1250	8	
5. Epi deposition	1200	10 min	8-10 $\mu$ m thick

S-pits was being annihilated in the diffused regions during the buried layer predeposition and drive in. Note that the density of  $SF_{epi}$  in Fig. 1 is two to three orders of magnitude lower than the S-pit density in Fig. 3b. Evidently only a very small percentage of the defects which give rise to an S-pit act as  $SF_{epi}$  nuclei during the growth of the epitaxial layer. In fact, none of the  $10^4$  S-pits observed in the buried layer regions, see Fig. 3a, nucleate epitaxial faults. Since the actual size of the pit seems less important than the total density, compare Fig. 3a and b, we can speculate that it may require a localized aggregate or colony of S-pit defects to nucleate one epitaxial stacking fault.

It is, of course, possible that there are other defects besides S-pit defects which are actually responsible for  $SF_{epi}$ . For example, several hillock-type etch features can be identified in a field of S-pits, see arrow H in Fig. 3b, whereas no hillocks are delineated in the buried layer region of Fig. 3a. It has previously been shown (5) in unoxidized (100) starting material that hillocks, and not saucers, will correlate on a one-to-one basis with the subsequent formation of oxidation-induced stacking faults (OSF). However, in this work the high density of S-pits precludes a reproducible differentiation between H-defects and S-pits, especially since some hillocks transform into saucers on further etching.

It should also be emphasized here that OSF are the primary defects delineated in oxidized (100) material while S-pits predominate in our (111) wafers. It is possible that the nuclei for the OSF in (100) wafers are in some way related to the source of  $SF_{epi}$  in (111) wafers. Perhaps it is a combination of a bulk defect, i.e., a hillock, with a surface-induced S-pit defect which gives rise to a small number of active or "super" S-pits which convert to  $SF_{epi}$ . Pomerantz (1) made a distinction between large and small saucers which we are not able to do because of the continuous size distribution revealed in both the diffused and nondiffused regions, see Fig. 3. The answer to these questions about specific active nucleation sites will require more sophisticated tools than the optical microscope. For example, a recent analysis of S-pit type defects using electron microscopy and micro x-ray fluorescence has been reported by Petroff and Katz (6). However, in terms of S-pit gettering, annihilation, etc. the more qualitative data provided by the optical microscope in the present paper has proved to be an extremely reliable measure of what to expect during epitaxial growth.

**Ion-implanted buried layers.**—A Secco etched 2 in. diameter Sb ion-implanted wafer before drive-in is shown in Fig. 4a. Note that the implanted buried layer region, see arrow I, has an S-pit density about one order of magnitude below that in the nonimplanted regions. An annihilation of S-pit defects also occurred during the deposition of the  $Sb_2O_3$  diffusion source layer, as noted above, but that process occurred at temperatures above  $1200^\circ\text{C}$  whereas the maximum temperature during implantation is  $300^\circ\text{C}$ . Attempts to grow epi on samples that were implanted, but not driven-in, were not successful because the implantation damage had not been annealed and this resulted in very poor epitaxy.

Those implanted samples which were Secco etched after drive-in revealed that it is possible to annihilate S-pits outside the boundaries of the buried layer, as shown in Fig. 4b. The arrow N points to a region completely denuded of S-pits. The range of the denuding action was found to be from 50 to  $100\ \mu\text{m}$ , which is larger than the average distance between buried layer contacts in an actual device pattern. The pattern in Fig. 4 is for a low packing density test chip which has a large field of nonimplanted material. The complete annihilation of S-pits in a high density device is shown in Fig. 5. Actually, there are often a few isolated  $SF_{epi}$  in the nonimplanted regions of the test chip wafer epi, but for all practical

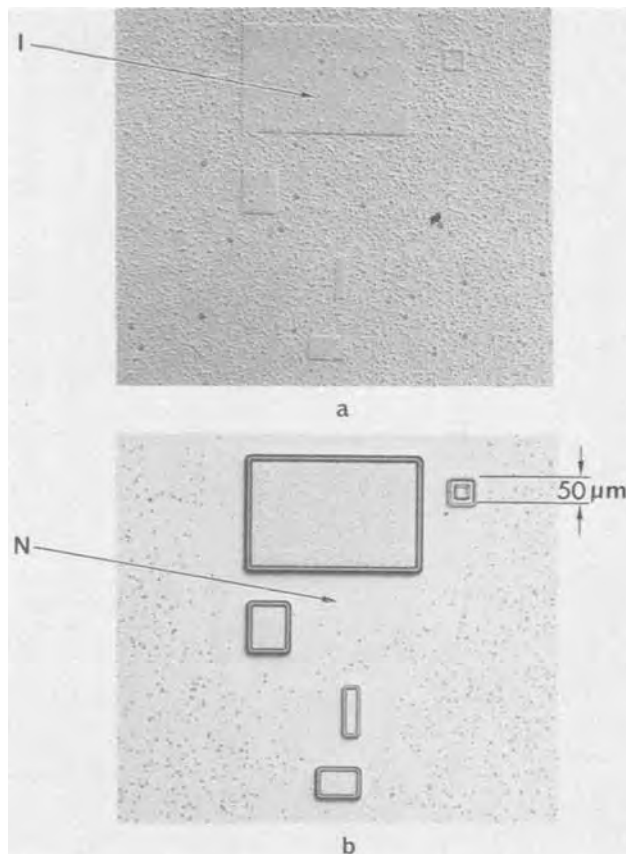


Fig. 4. Saucer pit distribution in ion-implanted wafer (a) before drive-in and (b) after drive-in at  $1250^\circ\text{C}$  for 8 hr. Arrow I indicates implanted area while arrow N is a nonburied layer region which is denuded of S-pits.

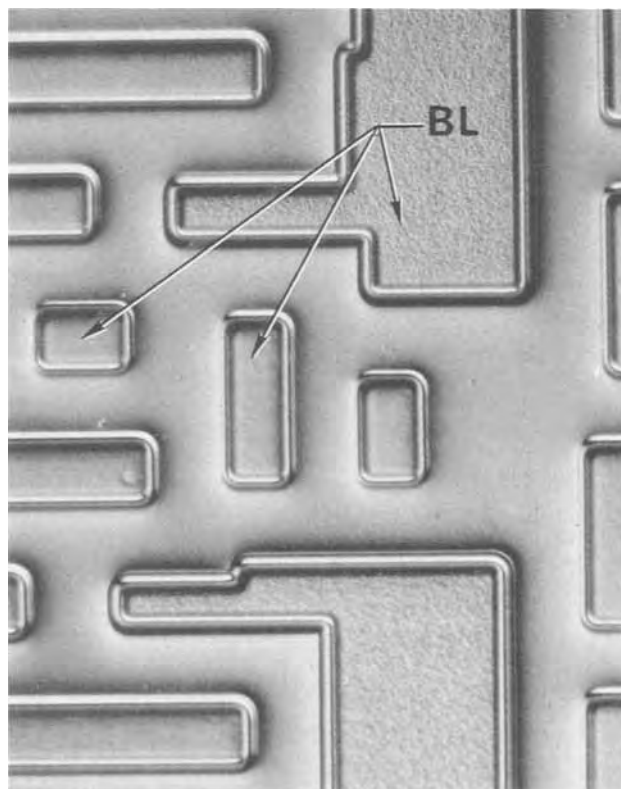


Fig. 5. Saucer pit-free region of ion-implanted device wafer

purposes the samples are free of  $SF_{epi}$ . The range of S-pit annihilation suggests that techniques for the

control of  $SF_{epi}$  by diffusion or interaction of nucleation sites is possible, *i.e.*, gettering, as discussed below in the section on crystal growth modifications.

We can conclude at this point that the absence of  $SF_{epi}$  in ion-implanted samples, or in the buried layer regions of diffused samples can be monitored by observing the presence or absence of S-pits. The process by which S-pit defects are introduced into wafers is discussed next.

**Oxidation-induced S-pits.**—Before oxidation (111) Secco etched wafers from Czochralski crystals pulled in our facility would not exhibit the high density of S-pits discussed above, nor did they show any growth related swirl patterns. However, wafers from outside suppliers would often contain  $10^6$ - $10^7$   $cm^{-2}$  S-pits and hillocks distributed in a swirled or coring pattern. The absence of swirl in our wafers may explain, in part, why we did not observe OSF in oxidized wafers. The swirl etch features are due to defects which are grown-in or native to the original crystal (5) and, in the case of float zone material, have been extensively studied by de Kock (7) and others (8-10). A simple way to distinguish between these native defect centers and process-induced S-pits, which are our main concern in this report, is to step-etch a wafer and see if the etch features are confined to the surface or distributed in depth.

Following this step-etch procedure on oxidized wafers we have found that the S-pits discussed in this report at a density of  $10^6$ - $10^7$   $cm^{-2}$  are all surface pits. In addition, by using a nonpreferential etch to remove approximately  $0.5$   $\mu m$  of silicon before Secco etching it is possible to reduce the S-pit concentration to less than  $10^4$   $cm^{-2}$ . Since it required an HCl etch of  $\sim 1.5$   $\mu m$  to eliminate the  $SF_{epi}$  nuclei just prior to epi growth we believe that the depth, or the size, of the S-pit defect increases from less than  $0.5$   $\mu m$  to greater than  $1.0$   $\mu m$  during the buried layer processing.

Another observation on S-pits in oxidized wafers is the presence of a denuded region in the center of many of the wafers. This is illustrated by the dark zigzag region in the center of the Secco etched 2 in. diameter wafer shown in Fig. 6. The absence of S-pits in these central regions is believed to be related to the radial distribution of oxygen in the original crystal. If the oxygen concentration is high enough, precipitation will occur during the various high temperature treatments (11) encountered during pre-epitaxial processing. When precipitation occurs the  $9$   $\mu m$  infrared absorption line (due to interstitial oxygen) decreases, as shown in Fig. 7, and the oxygen, although still present, is now in the form of  $SiO_2$

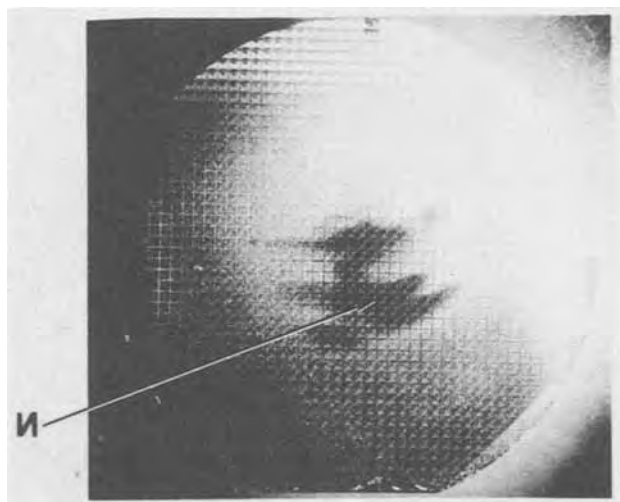


Fig. 6. Secco etched 2 in. diameter wafer with S-pit free region in center of wafer, see arrow N.

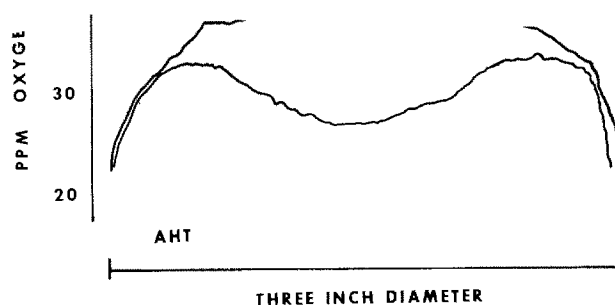


Fig. 7. Radial distribution of oxygen in a 3 in. diameter, 0.090 in. thick sample before (BHT) and after (AHT) a 3 hr precipitation treatment at  $900^{\circ}C$ .

precipitates. The process is reversible since an increase in the  $9$   $\mu m$  absorption line occurs if the material is reheated at temperatures greater than  $1300^{\circ}C$ . Since the oxygen content of 3 in. diameter wafers is, on the average, about 10 parts per million higher than 2 in. diameter wafers we believe that most 3 in. and the central regions, *i.e.*, high initial oxygen concentration, of certain 2 in. diameter wafers will be protected from S-pit nucleation during oxidation. This is accomplished by the gettering action of the  $SiO_2$  precipitates which act as sinks for S-pit defects giving rise to an *in situ* gettering, as shown by the localized denuded regions in the center of the wafer of Fig. 6. Further verification of the kinetics of oxygen incorporation as it relates to gettering are presented next.

**Crystal growth modifications.**—Based on the above analysis that an *in situ* gettering accompanies  $SiO_2$  precipitation, it was decided to adjust the crystal growth conditions of 2 in. diameter crystals so they would behave like 3 in. diameter material. This was easily accomplished by using higher seed rotation rates, 20 rpm instead of the typical 5 rpm, which increased the mixing conditions in the melt and enhanced the oxygen incorporation by an additional 5-10 ppm. Wafers processed through epi growth from these 2 in., grown like 3 in. wafers, showed a slight improvement in yield. However, the increase in wafers free of  $SF_{epi}$ , from 50 to 66%, was not considered significant enough to warrant changing the 2 in. diameter rotation rates. Additional work along these lines has recently been carried out by Katz and Hill (12) at rotation rates as high as 40 rpm. They have shown that the oxygen content in 2 in. diameter crystals could be maximized such that S-pits and  $SF_{epi}$  were suppressed, *i.e.*, the 2 in. wafers behaved like 3 in. wafers. The oxygen and S-pit data presented by Katz and Hill (12) are consistent with our model of an *in situ*  $SiO_2$  gettering mechanism.

It must be pointed out that high oxygen content crystals may, in certain cases, have a deleterious effect on the over-all defect density. That is, if the size of the  $SiO_2$  precipitate is large enough, then the kinetics of the stress relief in the vicinity of an individual precipitate may cause dislocation loops to be punched out. That is, the precipitates may act as a source of dislocations, rather than a sink for  $SF_{epi}$  nuclei. An example of this type of behavior is shown in Fig. 8a, which is a Secco etched oxidized 2 in. diameter wafer from an outside vendor whose material often has an oxygen concentration approaching 40 ppm. Note the extremely high (greater than  $10^6$   $cm^{-2}$ ) defect density in the center of the wafer and the presence of a concentric ring pattern of defects toward the outer perimeter. Higher magnification optical micrographs indicate both dislocation



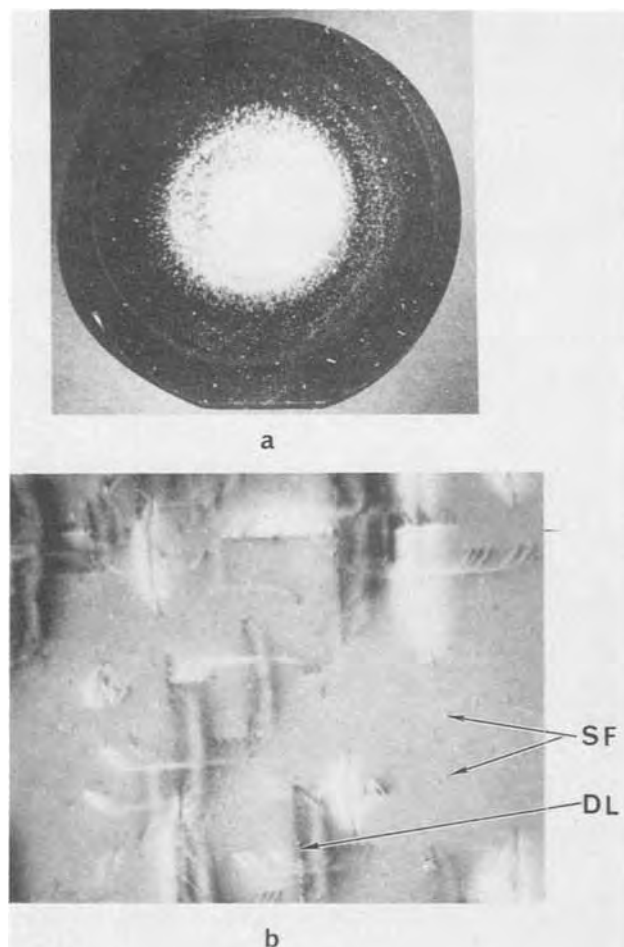


Fig. 8. (a) Macrophotograph of Secco etched 2 in. diameter wafer with excessively high initial oxygen concentration. (b) X-ray topograph of above wafer illustrating dislocation loops and oxidation-induced stacking faults.

etch pits and oxidation-induced stacking faults in the center, while the outer ring consists primarily of stacking faults. A transmission x-ray topograph is shown in Fig. 8b which gives the relative size and density of the dislocation loops (DL) and stacking faults (SF) in the center of the wafer in Fig. 8a. Although the topograph reveals a defect at the origin of the dislocation loops we cannot unequivocally state whether it is a precipitate or just another stacking fault. However, the loop generation in two orthogonal  $\{110\}$  directions is certainly consistent with stress relief around a single strained precipitate.

In addition to the higher rotation rate crystal growth experiments described above, it is possible to adjust the solidification rate of 2 in. diameter crystals to approach that of 3 in. material. Detailed work on the effects of adjustments to the crystal pull rate has been performed on float zone crystals by de Kock (7) and co-workers (13) in order to eliminate the swirl distribution of A and B cluster bulk defects. de Kock's modification was simply to increase the pull rate from about 3 to 5 mm/min. The resulting increase in the microscopic growth rate effected a favorable change in the concentration of native defects, thereby suppressing the formation of swirl defects. For the Czochralski crystals used in our studies, increasing the 2 in. crystal growth rate from 3 to 6 in./hr, which provided a volume solidification rate approximately that of 3 in. diameter crystals, also yielded wafers which were immune to the formation of S-pits and  $SF_{epi}$ . A complete understanding of these phenomena will require data on the native defect concentration which are not available to us at this time. However, it is clear that the oc-

currence of process-induced defects, such as S-pits and  $SF_{epi}$ , can be intimately related to the native defect density in the original crystal.

**Preoxidation gettering procedures.**—In addition to the crystal growth modifications presented above, a careful analysis of the data on the identification and annihilation of  $SF_{epi}$  nuclei already discussed led us to design a series of experiments which suppressed the formation of nuclei in individual wafers. These procedures are collectively known as POGO treatments, an acronym for preoxidation gettering of the other side, and are designed to remove potentially active nuclei from the front, i.e., device side, of a wafer and confine them to the back, nondevice, or other side of the wafer. Because of the high mobility of the nuclei, and/or their constituent elements, it was possible to achieve the desired gettering effect in a number of ways. These are reviewed in Table II which uses the POGO nomenclature introduced in a recent review (14). POGO I and IV, which use back side misfit dislocations and deliberate abrasion, respectively, were both effective in eliminating  $SF_{epi}$  nuclei, as expected from previous papers (1, 15). It was also found, as described by Petroff *et al.* (16), that depositing a layer of  $Si_3N_4$  with a stress of  $\sim 1 \times 10^{10}$  dynes-cm $^{-2}$  on the back of wafers, called POGO II, would also provide the desired gettering action. Although the high temperature POGO V procedures described by Hu (17) and Shiraki (18) for growing oxides free of OSF have not been examined in the context of S-pits and  $SF_{epi}$ , they were included in Table II for completeness. However, the POGO III process using Sb ion implantation was examined in detail and generated new data for the suppression or gettering of  $SF_{epi}$  nuclei.

Since an Sb implantation dose of  $3.5 \times 10^{15}$  ions cm $^{-2}$  at 30 keV had a range of 50-100  $\mu$ m for the annihilation of previously formed S-pit defects, a series of preoxidation implants were made into the back side of 2 in. diameter wafers with thicknesses varying from 0.015 to 0.035 in. in 0.005 in. increments. These wafers were then oxidized in steam at 1100°C for 1 hr. A complete suppression of S-pits was achieved for wafers 0.020 in. or less in thickness. For thicker wafers the POGO III treatment became progressively less effective, indicating a gettering range of about 500  $\mu$ m for the Sb implant used. This is consistent with previous work using misfit dislocations (15), POGO I in Table II, which showed that a 400  $\mu$ m range was possible for the suppression of OSF nuclei.

The oxidation temperature was varied between 700° and 1100°C for standard 2 in. diameter, 0.015 in. thick wafers to determine the lowest temperature for which Sb implant gettering was effective. After an oxidation as low as 800°C, S-pits were not observed. However, at 700°C the S-pits reappeared, indicating that the diffusion coefficient of the impurity and/or defect responsible for S-pit formation could be estimated. A simple calculation using a 375  $\mu$ m thick wafer for 60 min yields a diffusion coefficient of  $4 \times 10^{-7}$  cm $^2$  sec $^{-1}$ , which is typical of values for such commonly observed silicon impurities as copper and iron. Thus, the damage and associated strain introduced by the Sb implant could readily act as a back side sink for these front side or bulk impurities. It should be noted that, since the implant damage is annealed out during the oxida-

Table II. Preoxidation gettering designations

POGO	Requires	Produces
I	Misfit dislocations	Ordered array of line defects
II	$Si_3N_4$ layer	Strain from a deposited layer
III	Ion implantation	Strain and damage from an imbedded layer
IV	Abrasion	Disordered array of line defects
V	Anneal >1200°C. Add HCl	Dissolution of native defects, clean interface

tion, no gettering is observed during subsequent furnace operations. This is in contrast with misfit dislocation (15) and  $\text{Si}_3\text{N}_4$  (16), gettering which continue to provide a sink for nuclei.

### Conclusions

Based on the above study we have verified that the nucleation sites for epitaxial stacking faults are introduced during the initial oxidation of the wafer. The nuclei are readily correlated with the presence of a high ( $10^6$ - $10^7$   $\text{cm}^{-2}$ ) density of saucer-type pits after a preferential etch (19). The pits can be selectively annihilated during the fabrication of the Sb-doped buried collectors. Suppression or gettering of the nuclei for epitaxial stacking faults can be achieved by a variety of techniques. These include abrasion, deposition of a strained  $\text{Si}_3\text{N}_4$  layer, introduction of misfit dislocations, and the use of an Sb ion implant, all of which are performed on the back side of wafers before the initial masking oxidation. Additional *in situ* gettering is observed in material whose oxygen concentration is high enough to lead to  $\text{SiO}_2$  precipitation.

Manuscript submitted June 17, 1976; revised manuscript received July 27, 1976.

Any discussion of this paper will appear in a Discussion Section to be published in the June 1977 JOURNAL. All discussions for the June 1977 Discussion Section should be submitted by Feb. 1, 1977.

Publication costs of this article were assisted by Bell Laboratories.

### REFERENCES

1. D. I. Pomerantz, *J. Appl. Phys.*, **38**, 5020 (1967).
2. K. Moerschel, Unpublished data; also A. Wayne Fisher and G. L. Schnable, *This Journal*, **123**, 434 (1967).
3. F. Secco D'Aragona, *ibid.*, **119**, 948 (1972).
4. E. Sirtl and A. Adler, *Z. Metallkd.*, **52**, 529 (1961).
5. G. A. Rozgonyi, S. Mahajan, M. H. Read, and D. Brasen, *Appl Phys. Lett.*, **29**, 531 (1976).
6. P. M. Petroff and L. Katz, To be presented at Semiconductor Silicon Philadelphia, May 1977.
7. A. J. R. de Kock, *Philips Res. Repts, Suppl.* **1** (1973).
8. P. M. Petroff and A. J. R. de Kock, *J. Cryst. Growth*, **20**, 117 (1975).
9. H. Foll and B. O. Kolbesen, *Appl. Phys. (UK)*, **8**, 319 (1975).
10. K. Ravi and C. J. Varker, *J. Appl. Phys.*, **45**, 263 (1974).
11. H. J. Hrostowski and R. H. Kaiser, *Phys. Rev.*, **107**, 966 (1957).
12. L. E. Katz and D. W. Hill, Unpublished data.
13. A. J. R. de Kock, P. J. Roksnoer, and P. G. T. Boonen, "Semiconductor Silicon," H. Huff and R. R. Burgess, Editors, p. 83, The Electrochemical Society Softbound Symposium Series, Princeton, N.J. (1973).
14. G. A. Rozgonyi, Paper 59 presented at The Electrochemical Society Spring Meeting, Washington, D.C., May 2-7, 1976.
15. G. A. Rozgonyi, P. M. Petroff, and M. H. Read, *This Journal*, **122**, 1725 (1975).
16. P. M. Petroff, G. A. Rozgonyi, and T. T. Sheng, *ibid.*, **123**, 565 (1976).
17. S. M. Hu, *Appl. Phys. Lett.*, **27**, 165 (1975).
18. H. Shiraki, *Jpn. J. Appl. Phys.*, **15**, 1 (1976).
19. C. W. Pearce, *J. Vacuum Sci. Technol.*, To be published.

## Mössbauer Spectroscopy of $^{57}\text{Fe}^{2+}$ Impurities in $\text{LiNbO}_3$

U. Gonser

*Universität des Saarlandes, Fachbereich Angewandte Physik, D-6600 Saarbrücken, Germany*

H. Sakai

*Research Reactor Institute, Kyoto University, Osaka, Japan*

and W. Keune

*Labor für Angewandte Physik, Gesamthochschule Duisburg, D-4100 Duisburg, Germany*

### ABSTRACT

A  $\text{LiNbO}_3$   $^{57}\text{Co}$  single crystal Mössbauer source in the reduced state has been used in conjunction with a single crystal  $\text{FeCO}_3$  (siderite) absorber. From the angular dependence of the polarized  $\gamma$ -rays in a polarimeter arrangement, it could be shown that the principal axis of the EFG at the  $\text{Fe}^{2+}$  sites is colinear with the c axis of the  $\text{LiNbO}_3$  crystal which excludes charge-compensating nearest neighbor oxygen vacancies.

Iron-doped  $\text{LiNbO}_3$  has become of technological importance, mainly as a useful high resolution optical information storage material. Scientifically it is of interest to obtain information regarding the charge and defect state of the iron ions. In the past mostly macroscopic methods have been used in the investigations. In this communication we want to present results by a microscopic method: Mössbauer spectroscopy. Fortunately, the best and most easily handled Mössbauer resonance isotope is  $^{57}\text{Fe}$ . Particularly, the hyperfine interaction, that is, the quadrupole splitting, and isomer

Key words: Mössbauer spectroscopy,  $\text{LiNbO}_3$ , lattice defects.

shift are of interest here. By the latter the valence state can be easily distinguished. We restrict ourselves to  $\text{Co}^{2+}$  or  $\text{Fe}^{2+}$ , as parent or daughter isotope, respectively, and particularly to the question regarding the defect configuration. Some results on  $\text{Fe}^{3+}$  and  $\text{Fe}^{2+}$  have been published previously (1, 2).

$\text{LiNbO}_3$  single crystals were doped with  $^{57}\text{Co}$  or  $^{57}\text{Fe}$ , and an annealing treatment at  $800^\circ\text{C}$  for 24 hr in pure Ar atmosphere reduced the cobalt or iron entirely; at least, no trace of the trivalent state could be detected by Mössbauer spectroscopy. A conventional Mössbauer spectrum of a  $\text{LiNbO}_3$ : $^{57}\text{Co}$  source or  $\text{LiNbO}_3$ : $^{57}\text{Fe}$  ab-

sorber, obtained with a single line absorber or source, respectively, exhibits a two line quadrupole splitting ( $\Delta E_Q = 1.74 \pm 0.02$  mm/sec at room temperature) and a negative quadrupole coupling constant. The polarization or angular dependence of the quadrupole hyperfine interaction is reflected in the relative line intensities. Extreme line intensity ratios (3:1 and 3:5) are obtained in the cases of parallel or perpendicular arrangement of  $\gamma$ -ray propagation direction and principal axis of the electric field gradient (EFG) in the thin absorber approximation (no saturation effect) and lattice vibrational isotropy (no Goldanskii-Karyagin effect) and, in addition, under the condition that the resonance atom is in a local environment of axial symmetry (asymmetry parameter  $\eta = 0$ ). Our analysis of the relative intensities indicates that we are close to this situation.

A more precise determination regarding the orientation of the axis of the EFG can be obtained by polarization experiments where both source and absorber exhibit quadrupole splittings. In this case four resonance lines are expected. The number of lines is reduced to three if the magnitude of the quadrupole splitting in source and absorber is the same, i.e., degeneracy of the center line at zero velocity occurs. Furthermore, if a unique axis of all  $\text{Co}^{2+}$  and  $\text{Fe}^{2+}$  ions exists and the principal axis of the EFG is perpendicular to the  $\gamma$ -ray propagation direction, the emitted  $\gamma$ -rays corresponding to the  $\pm 3/2 \rightarrow \pm 1/2$  transition are linearly polarized. (The  $\gamma$ -rays corresponding to the  $\pm 1/2 \rightarrow \pm 1/2$  transitions are partially polarized.) Such linearly polarized  $\gamma$ -rays from the source (polarizer) will excite nuclear transitions with appropriate polarization in the absorber (analyzer), in analogy to an optical polarimeter (3). In such a polarimeter arrangement, we have placed a  $\text{LiNbO}_3:^{57}\text{Co}$  source in conjunction with a single crystal of siderite ( $\text{FeCO}_3$ ) absorber.

From crystal symmetry it is known that the  $\text{Fe}^{2+}$  ions in  $\text{FeCO}_3$  have axial symmetry,  $\eta = 0$ . The quadrupole splitting of  $\text{FeCO}_3$  ( $\Delta E_Q = 1.798 \pm 0.004$  mm/sec at room temperature) (4) is similar to the value of  $\text{LiNbO}_3:^{57}\text{Fe}$ , however, the quadrupole coupling constant is positive. The level diagrams of the nuclear resonance states are shown in Fig. 1, indicating the opposite sign of the quadrupole coupling constants in source and absorber. In Fig. 2 Mössbauer spectra are shown of a  $\text{LiNbO}_3:^{57}\text{Co}$  source and a  $\text{FeCO}_3$  (siderite) absorber with the c axes of the two crystals perpendicular to the  $\gamma$ -ray propagation direction.

The spectrum in Fig. 2(a) was obtained with the two c axes parallel and in Fig. 2(b) perpendicular to each other. The resonance line on the side of positive velocity is of interest because it results from the  $\pm 3/2 \rightleftharpoons \pm 1/2$  transitions in source and absorber. In the perpendicular arrangement, the  $\text{FeCO}_3$  absorber crystal is transparent for the polarized  $\gamma$ -ray from the source; only a small residual absorption contribution can be detected which is most likely due to imperfections in

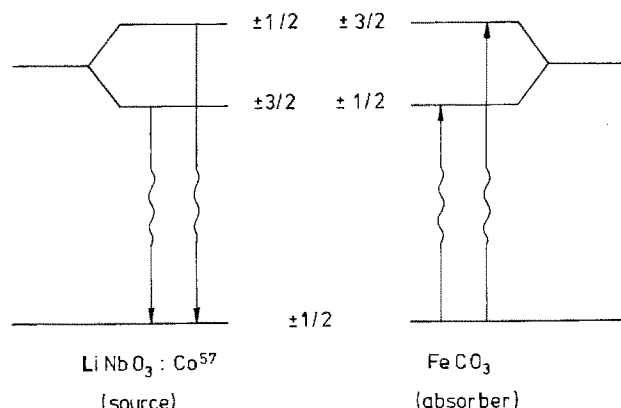


Fig. 1. Quadrupole splitting of the first excited state of  $^{57}\text{Fe}$

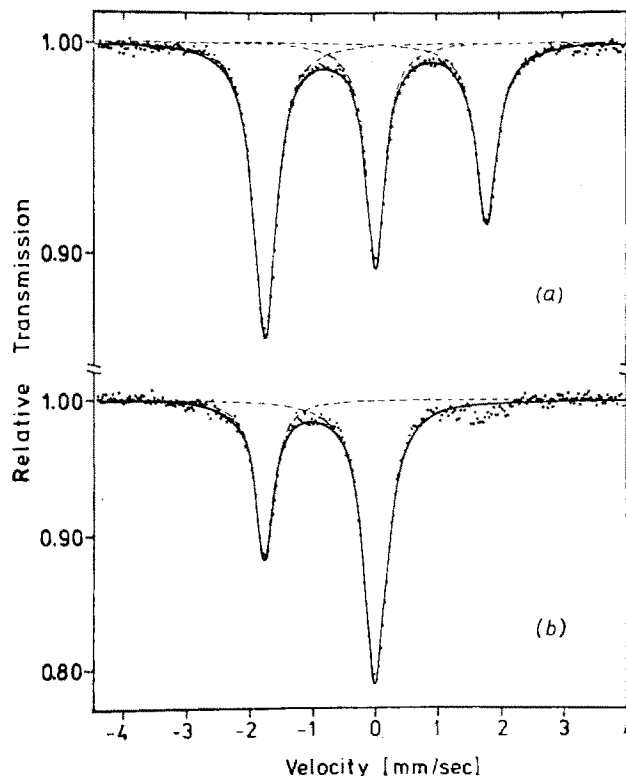


Fig. 2. Mössbauer spectra of a  $\text{LiNbO}_3:^{57}\text{Co}$  single crystal source and a single crystal  $\text{FeCO}_3$  (siderite) absorber at room temperature. Both crystals were oriented with their c axes perpendicular to the propagation direction of the  $\gamma$ -rays. In (a) the c axes in source and absorber were parallel and in (b) they were perpendicular to each other.

the mineral  $\text{FeCO}_3$  single crystal and also due to misalignment of the "polarimeter." The disappearance of the resonance line indicates, that the emitted  $\gamma$ -rays from the  $\text{LiNbO}_3:^{57}\text{Co}$  source are indeed linearly polarized to a high degree, and consequently, the principal axis of the EFG at the  $^{57}\text{Co}$  or  $^{57}\text{Fe}$  nuclear sites are oriented along the c axis and the asymmetry parameter is small or zero. Because the EFG is determined to a great extent by the nearest environment of the ions, any "defect" in the octahedral oxygen configuration would destroy the colinearity of the principal axis of EFG with the c axis and in addition would make  $\eta \neq 0$ . The conclusion can be drawn that most of the  $^{57}\text{Co}^{2+}$  or  $^{57}\text{Fe}^{2+}$  ions in  $\text{LiNbO}_3$  are not charge compensated by neighboring oxygen ion vacancies. This result does not necessarily contradict the model by Dischler *et al.* (5) because of the higher sensitivity of optical measurements.

#### Acknowledgment

This work was supported by the Deutsche Forschungsgemeinschaft, SFB 130.

Manuscript submitted July 6, 1976; revised manuscript received Aug. 16, 1976. This was Paper 433 presented at the Washington, D.C., Meeting of the Society, May 2-7, 1976.

Any discussion of this paper will appear in a Discussion Section to be published in the June 1977 JOURNAL. All discussions for the June 1977 Discussion Section should be submitted by Feb. 1, 1977.

Publication costs of this article were assisted by the Universität des Saarlandes.

#### REFERENCES

1. W. Keune, S. K. Date, I. Dezsai, and U. Gonser, *J. Appl. Phys.*, **46**, 3918 (1975).
2. W. Keune, S. K. Date, U. Gonser, and H. Bunzel, in Proceedings of European Meeting on Ferroelectricity, Zurich, Switzerland, in *Ferroelectrics*,



- 13, 443 (1976).  
 3. U. Gonser, in "Hyperfine Structure and Nuclear Radiation," p. 343, North-Holland Publishing Co., Amsterdam (1968).

4. D. L. Nagy, I. Dezsi, and U. Gonser, *N. Jb Miner. Mb.*, 101 (1975).  
 5. B. Dischler and A. Räuber, *Solid State Commun.*, 17, 953 (1975).

# Technical Note



## Electroluminescence in Rare Earth Doped $Y_2O_3$ , $La_2O_3$ , and $Y_2O_2S$ Powder Layers

Shosaku Tanaka, Youichi Maruyama, Hiroshi Kobayashi, and Hiroshi Sasakura

Department of Electronics, Tottori University, Tottori, Japan

Electroluminescent phosphors doped with trivalent rare earth ions give sharp line emissions which are characteristic of transitions in the  $(4f)^n$  electron configurations and cover the red to blue region. These phosphors are of interest because of the possibility of their application to flat-type color displays. Several investigations of electroluminescence have been reported in rare earth doped ZnS (1-3). However, ZnS is not the most suitable host for trivalent rare earth ions because of the low solubilities of rare earth ions in ZnS (4). In order to remove this disadvantage,  $Y_2O_3$  has been chosen as a suitable host; electroluminescence in this material has already been reported (5, 6). In order to find more suitable host materials, we have chosen  $Y_2O_3$ ,  $La_2O_3$ , and  $Y_2O_2S$  and investigated their electroluminescence.

$Y_2O_3:Ln$  phosphors were prepared by the following procedures.  $Y_2O_3$  and  $Ln_2O_3$  powders were dissolved in a 5% hot hydrochloric acid solution. Subsequently, oxalates were precipitated using ammonium oxalate as a precipitant. The oxalates were fired at 1100°C for 3 hr in air. The concentrations of rare earth ions were about 1 atom percent (a/o).  $La_2O_3:Ln$  phosphors were prepared by the same method as  $Y_2O_3:Ln$ .  $Y_2O_2S:Ln$  phosphors were prepared by firing the  $Y_2O_3:Ln$  powders in an  $H_2S$  atmosphere at 600°C for 3 hr. Either Eu (for red emission), Tb (for green emission), or Tm (for blue emission) was used as activators. Electroluminescence samples, fabricated from the phosphors, were about 50  $\mu m$  thick, and sandwiched between an Al plate and  $SnO_2$ -coated glass.

Electroluminescence spectra for  $Y_2O_3$ ,  $La_2O_3$ , and  $Y_2O_2S$  phosphors are shown in Fig. 1. The electroluminescence samples were excited with d-c voltage of 400 ~ 500V. The electroluminescence spectra show narrow lines caused by the transitions in the  $(4f)^n$  electron configurations of trivalent rare earth ions (7). The Eu-doped phosphors give rise to a red emission arising from the  $^5D_0 \rightarrow ^7F_2$  transition peaking at about 612 ~ 630 nm. The Tb-doped phosphors give rise to a green emission arising from the  $^5D_4 \rightarrow ^7F_5$  transition peaking at 544 nm and yield the brightest emission. The Tm-doped phosphors give rise to a blue emission arising from the  $^1G_4 \rightarrow ^3H_6$  transition peaking at 455 nm. In the electroluminescence spectra,

Key words: electroluminescence, rare earth doped phosphors, powder cells.

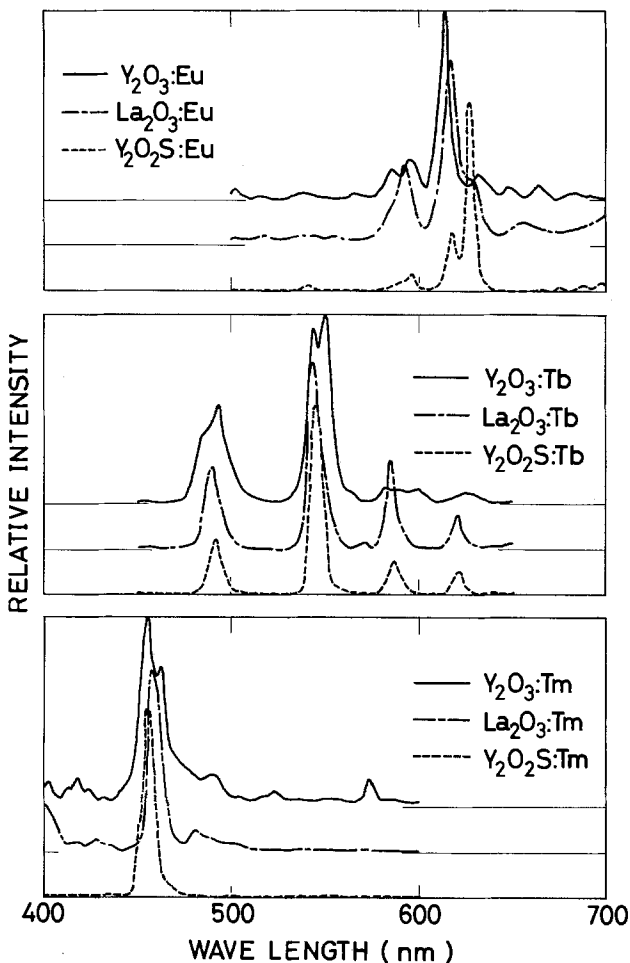


Fig. 1. Electroluminescence spectra for rare earth doped  $Y_2O_3$ ,  $La_2O_3$ , and  $Y_2O_2S$ .

no remarkable difference due to the host lattice has been observed.

In Fig. 2 are shown the voltage dependences of current density and brightness for the Tb-doped phosphors in electroluminescence, where the samples were excited by d-c voltage with the  $SnO_2$  electrode negatively biased. The current densities across the

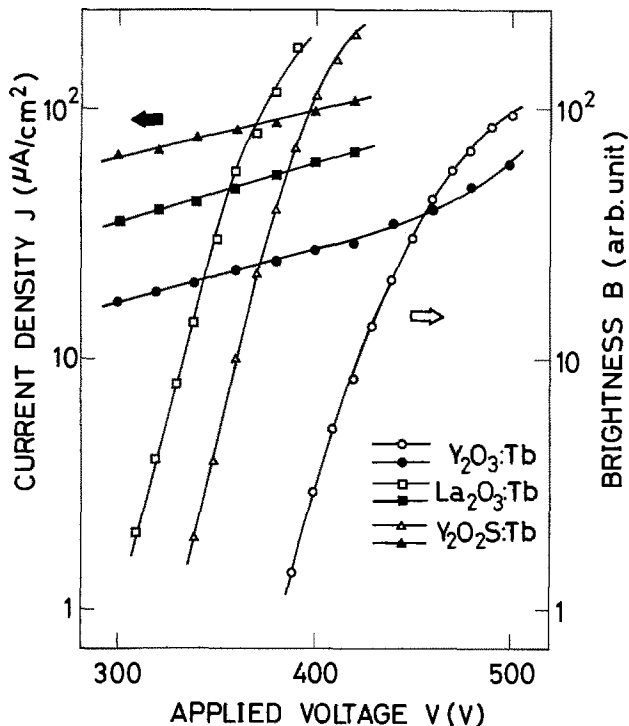


Fig. 2. Voltage dependences of current density and brightness for the Tb-doped phosphors.

samples increase exponentially with applied voltages, and are about 100, 60, and 25  $\mu\text{A}/\text{cm}^2$  for  $\text{Y}_2\text{O}_2\text{S}$ ,  $\text{La}_2\text{O}_3$ , and  $\text{Y}_2\text{O}_3$  phosphors, respectively, at 400V. These observations may probably be due to the difference in bandgaps of the hosts, but are not clearly understood yet. The emissions begin to occur at ap-

plied voltages of about 300, 330, and 380V for the  $\text{La}_2\text{O}_3$ ,  $\text{Y}_2\text{O}_2\text{S}$ , and  $\text{Y}_2\text{O}_3$  phosphors, respectively. These voltages correspond to an average electric field of about  $6 \sim 8 \times 10^4$  V/cm. The emissions increase exponentially with applied voltage. The  $\text{La}_2\text{O}_3:\text{Tb}$  phosphors show the brightest emission of about 10 f-L.

From these experimental results, we may conclude that a  $\text{La}_2\text{O}_3$  lattice is the most suitable host in order to obtain the brightest electroluminescence among the three phosphors studied. The excitation mechanisms of rare earth ions doped in these host materials are not clear yet and further experiments are now in progress.

Manuscript submitted July 13, 1976; revised manuscript received Aug. 16, 1976.

Any discussion of this paper will appear in a Discussion Section to be published in the June 1977 JOURNAL. All discussions for the June 1977 Discussion Section should be submitted by Feb. 1, 1977.

Publication costs of this article were assisted by Tottori University.

#### REFERENCES

1. E. W. Chase, R. T. Hepplewhite, D. C. Krupka, and D. Kahng, *J. Appl. Phys.*, **40**, 2512 (1969).
2. M. S. Waite and A. Vecht, *Appl. Phys. Lett.*, **19**, 471 (1971).
3. H. Kobayashi, S. Tanaka, H. Sasakura, and Y. Hamakawa, *Jpn. J. Appl. Phys.*, **13**, 264 (1974).
4. H. H. Woodbury, "Physics and Chemistry of II-VI Compounds," p. 230, North-Holland, Amsterdam (1967).
5. R. Nakano, *Jpn. J. Appl. Phys.*, **9**, 1003 (1970).
6. S. Tanaka, Y. Maruyama, H. Kobayashi, and H. Sasakura, "Proceedings of the 1975 International Conference on Luminescence," p. 911, North-Holland, Amsterdam (1976).
7. G. H. Dieke, "Spectra and Energy Levels of Rare Earth Ion in Crystals," John Wiley, New York (1968).

## Brief Communication



### The Influence of Etch Procedure on the Stability of Transit-Time Devices

D. de Cogan

Department of Electronic and Electrical Engineering, University of Birmingham, Birmingham, England B15 2TT

The performance of microwave devices such as Impatts, Trapatts, and Baritts is known to be extremely sensitive to surface conditions. Silicon-based  $p^+n$   $p^+$  microwave diodes produced by mesa etching with  $\text{HF}/\text{HNO}_3$  mixtures initially give an abrupt transition in the current-voltage characteristic, which is typical of punch-through. The sharpness of this transition is often found to be photosensitive. Upon exposure to the atmosphere, the dark characteristic deteriorates progressively and can be related to increasing hydrophilicity of the surface. Immersion in 49% HF makes the surface hydrophobic and temporarily restores the initial hard characteristic. For long term stability, methods of passivation using either thermal oxide or silox are used, but these in-

Key words: transit-time devices, stability, passivation, photosensitivity.

crease the complexity of processing and introduce resistive regions which lead to microwave losses. Accordingly, in order to achieve maximum efficiency of device operation, it is desirable to produce passive and stable surfaces without oxide layers.

Holmes (1) mentions that a tarnish develops on the surface of silicon etched in  $\text{HF}/\text{HNO}_3$  mixtures, if it is exposed to the air while etchant is still present. We have found that this tarnish is responsible for the surface instability and can be avoided by proper termination of the etch procedure. Further, it has been observed that the light sensitivity of the current-voltage characteristic can be used as an indicator of surface condition.

#### Experimental

Punch-through mesa diodes were made as follows. Masking layers of evaporated titanium/gold fol-

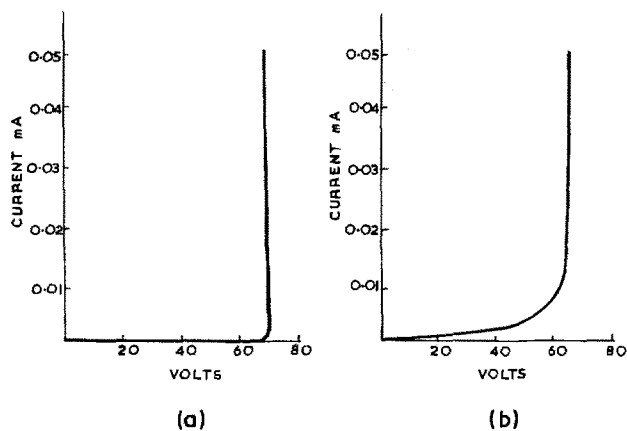


Fig. 1. Current-voltage characteristics of a device which was removed from the etch before rinsing: (a) dark, (b) illuminated.

lowed by plated gold ( $1 \mu\text{m}$ ) were placed on top of silicon double epilayer material ( $0.01 \Omega\text{-cm p}^+$  on  $8 \Omega\text{-cm n}$  on  $0.008 \Omega\text{-cm p}^+$  substrate).  $250 \mu\text{m}$  diameter dots were developed using Shipley positive resist and etched with  $\text{KI/I}_2$  to remove gold and  $\text{HF}$  to remove titanium. The slice was cut in half and one piece was etched in a mixture of 23%  $\text{HF}$ , 47%  $\text{HNO}_3$ , 30% acetic acid. At the end of 1 min, the slice, held in a Teflon basket, was removed from the etch and transferred to a beaker containing rinsing water. The slice was then examined using ellipsometry and the presence of a tarnish layer was confirmed.

The other portion was etched in an identical mixture, but at the end of 1 min the beaker containing the etch was flooded with a solution of 1:6  $\text{HF}$  in water. This was followed by pure water and only when the slice had been thoroughly rinsed was it moved into the air.

### Results

The results given below were typical over the whole slice and have been repeated over many slices. Figure 1(a) shows the current-voltage characteristic for a device which was removed from the etch before rinsing. The influence of illumination can be seen in

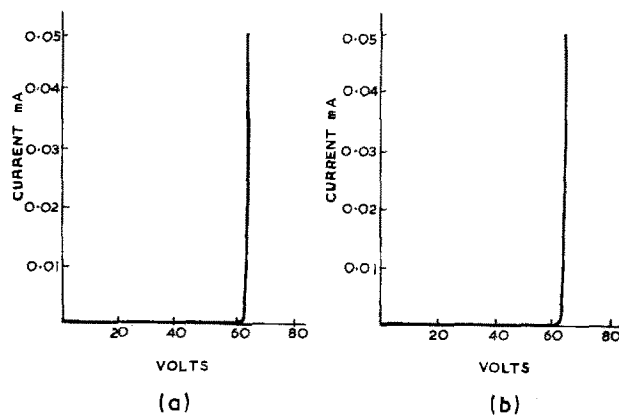


Fig. 2. Current-voltage characteristic of a device which was etched and rinsed before exposure to the atmosphere: (a) dark, (b) illuminated.

Fig. 1(b). The dark characteristic had completely deteriorated within 2 hr after etching. Figures 2(a) and 2(b) show the characteristic one month after etching of a device which was etched and rinsed without exposure to the atmosphere. It can be seen that illumination has no effect.

### Conclusion

It would appear that the effect of illumination on the current-voltage characteristics of punch-through devices indicates the presence of a contaminating surface layer. Devices with little or no light response seem to remain stable upon exposure to the atmosphere.

Manuscript received Aug. 9, 1976.

Any discussion of this paper will appear in a Discussion Section to be published in the June 1977 JOURNAL. All discussions for the June 1977 Discussion Section should be submitted by Feb. 1, 1977.

### REFERENCE

1. P. J. Holmes, "The Electrochemistry of Semiconductors," p. 346, Academic Press, New York (1962).

## DISCUSSION SECTION



This Discussion Section includes discussion of papers appearing in the *Journal of The Electrochemical Society*, Vol. 122, No. 11; November 1975; and Vol. 123, No. 1, 3, and 6; January, March, and June 1976.

### Simple Method for Separating Completed Diodes from Semiconductor Wafers

J. Klatskin and A. Rosen (pp. 1565-1566, Vol. 122, No. 11)

G. Greco and M. Tomassini:<sup>1</sup> The technological process described in the above-mentioned paper is very close to that developed in our laboratory since 1972 and now patented.<sup>2</sup> In addition, we wish to mention a paper<sup>3</sup> that reports a method for selectively plating heat sinks for microwave diode fabrication. We developed our process in a quite general way in order to be applicable to many different devices (IMPATT,

<sup>1</sup> Selenia S.p.A., Research Division, Rome, Italy.

<sup>2</sup> Italian Pat. 52366A/73 (1973); U.S. Pat. (1976).

<sup>3</sup> S. Umehachi, I. Kajihator, and T. Matsuda, *Nat. Tech. Rep.*, 20, 235 (1974).

GUNN, BARITT) and we have reported the results on Baritt diodes.<sup>4</sup>

We agree that this technique has many advantages over the more conventional sawing or dicing technique. In addition, we would like to point out that using this selectively plated heat sink method instead of the conventional continuous metal layer remarkably reduces the stresses induced by the metal into the semiconductor. In the case of avalanche diodes, this process has increased device yields due to the reduction of stress-induced microplasmas. As a result, it is possible to drive the diodes with current densities of about  $800 \text{ A/cm}^2$  without any particular care and to get an efficiency as high as 10% with a  $\text{p}^+\text{-n-n}^+$  silicon structure ( $f \approx 10 \text{ GHz}$ ).

Finally, we remark that for silicon devices silicon dioxide, thermally grown during the diffusion process,

<sup>4</sup> A. Chiabrera, G. Soncini, and M. Tomassini, *Proceedings of the Fourth European Microwave Conference, Montreux, Switzerland (1974)*.

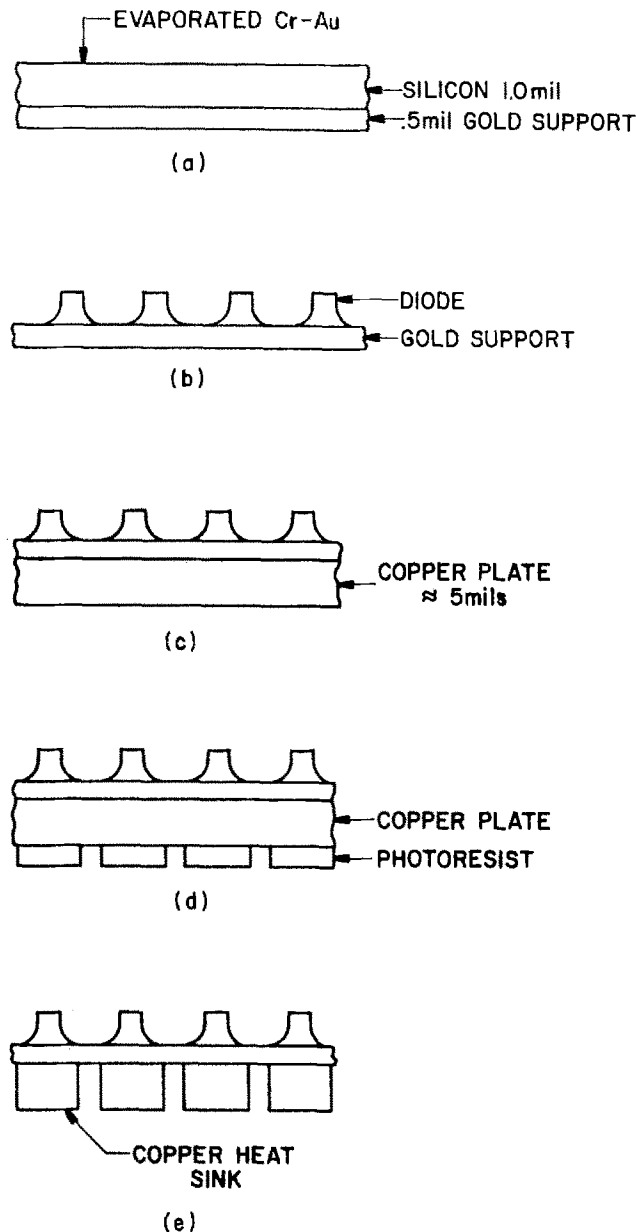


Figure 1

can be used instead of photoresist to get the heat sink patterns. This allows very thick metal layers to grow, thus avoiding the problems that normally arise with the photoresist.

**J. Klatskin and A. Rosen:**<sup>5</sup> We wish to thank Drs. Greco and Tomassini for bringing to our attention the details of their process. In this regard, it may be of interest to mention that we are currently using a somewhat different approach which tends to increase device yield. In this process a gold layer is plated on the  $n^+$  side of the wafer, Fig. 1a. The semiconductor material is then etched to form a plurality of devices on the previously evaporated and plated gold support, Fig. 1b. A copper heat sink is then formed, Fig. 1c. Note that the heat sink is always formed after completion of device structure (after etching) to reduce stress in the silicon wafer.<sup>6</sup> The diodes can then be separated as shown in Fig. 1d or as previously published in the paper under discussion.

<sup>5</sup> RCA Laboratories, David Sarnoff Research Center, Princeton, New Jersey 08540.

<sup>6</sup> A. Rosen, P. T. Ho, and J. B. Klatskin, *IEEE Trans. Electron Dev.*, To be published.

### Synthesis and Luminescence Properties of Europium-Activated Yttrium Oxy sulfide Phosphors

M. Koskenlinna, M. Leskelä, and L. Niinistö  
(pp. 75-78, Vol. 123, No. 1)

**G. W. Luckey:**<sup>7</sup> In their paper M. Koskenlinna, M. Leskelä, and L. Niinistö describe "a new method of preparing brightly emitting  $Y_2O_3:Eu$  phosphors" by reduction of yttrium sulfite. I believe that it is appropriate to call the authors' attention to Belgian Patent Application No. 777,915 which was published on January 31, 1972, and which describes the preparation of phosphors by the process in their article. Similar information is also given in U.S. Patent 3,705,858 which was issued on December 2, 1972.

**M. Koskenlinna, M. Leskelä, and L. Niinistö:**<sup>8</sup> We do regret that the patents of Dr. Luckey were missed and we thank him for kindly pointing this out. When comparing the details of U.S. Pat. 3,705,858 to our synthesis, we would like to mention that in examples 1-6 of the patent, sodium sulfite is suggested as the precipitating agent. The use of sodium sulfite probably leads, however, to double sulfite formation,<sup>9,10</sup> which increases the sodium concentrations of the phosphors. This can be avoided by using only sulfur dioxide and rare earth oxides as starting materials, as done in our synthesis.

### The Cathodic Corrosion of Aluminum

E. P. G. T. van de Ven and H. Koelmans  
(pp. 143-144, Vol. 123, No. 1)

**B. Chatterjee:**<sup>11</sup> The following comments may be of interest not only to those considering the valuable results in the paper under discussion, but to those interested in such reactions in general.

The Arrhenius plots in Fig. 2 of the paper under discussion show the slope for the cathodic corrosion rate of Al in neutral solution ( $5 \times 10^{-4}N$  NaCl) to be identical with that for the chemical dissolution in alkaline solution (0.1% NaOH). Although this would imply that the electrochemical and chemical dissolution behavior of Al is similar, it is not certain if this will apply to alkaline as well as acid solutions. However, results on the chemical dissolution of Al in both alkaline and acid solutions show similar slopes of the Arrhenius plots.<sup>12-15</sup> This indicates that the chemical dissolution of Al is not affected by the type of electrolyte used, namely alkaline or acid solutions. The same concept will apply to the electrochemical dissolution of Al due to its similarity with the chemical dissolution behavior as expressed earlier.

The activation energy for dissolution of Al in 0.4-5% NaOH<sup>12-16</sup> agrees with that reported in the paper under discussion using 0.1% NaOH. This suggests, as mentioned elsewhere,<sup>12</sup> that the alkaline etching of Al is controlled by a single rate-determining cathodic reduction common to all. The hydrogen evolution reaction (HER) is primarily involved in the cathodic reduction process and consists of an intermediate step of discharged hydrogen atoms adsorbed on the metal surface, followed by desorption.<sup>17</sup> An indication of the true

<sup>7</sup> Eastman Kodak Company, Research Laboratories, Rochester, New York 14650.

<sup>8</sup> Department of Chemistry, Helsinki University of Technology, SF-02150 Otaniemi, Finland.

<sup>9</sup> R. C. Vickery, *J. Chem. Soc.*, 51, 2360 (1955).

<sup>10</sup> O. Erametsa, L. Niinistö, and T. Korvela, *Suom. Kemistil. B*, 45, 394 (1972).

<sup>11</sup> The British Aluminium Company, Limited, Gerrards Cross, Buckinghamshire SL9 0QB, England.

<sup>12</sup> B. Chatterjee and R. W. Thomas, *Trans. Inst. Met. Finish.*, 54, 17 (1976).

<sup>13</sup> B. Chatterjee, To be published.

<sup>14</sup> J. Juhász-Kis, I. Lipovets, N. Lohoniati, and K. Sehter, *Period. Polytech. Chem. Eng.*, 17, 197 (1973).

<sup>15</sup> R. Bartonicek and J. Hron, *Werkst. Korros.*, 26, 764 (1975).

<sup>16</sup> M. A. Streicher, *Trans. Electrochem. Soc.*, 93, 285 (1948).

<sup>17</sup> J. O'M. Bockris and A. K. N. Reddy, "Modern Electrochemistry," Vol. 2, p. 1233, Plenum Press, New York (1971).

rate-determining step can be obtained by estimating the change of hydrogen overpotential on Al with applied current, *i.e.*, the Tafel slope.<sup>18</sup> From measurements on the potentiostatic cathodic polarization of Al (99.8% purity) in acids ( $H_2SO_4$  of sp gr 1.84 and  $H_3PO_4$  of sp gr 1.75) at a scan speed of 5 V/hr, the Tafel slopes at 25°C are estimated to be similar in all cases<sup>18</sup> and are comparable with the theoretical slope (0.12 V/decade) for proton discharge as the rate-controlling step. The theoretical slope is estimated by assuming a single electron transfer mechanism as expressed in the paper under discussion, and 0.5 as the symmetry factor.<sup>19</sup> Thus, a slow discharge, fast desorption process for HER is considered to be the likely mechanism during dissolution of Al in acids, and the same basic mechanism will apply to alkaline dissolution as well for reasons given earlier. One can, therefore, conclude that both the chemical and electrochemical dissolutions of Al are likely to be controlled by a slow discharge fast desorption HER, and are not affected by the electrolyte, namely alkaline and acid solutions.

Regarding the alkalization effect, it is probably due to the formation of basic oxy-acid complexes of  $Al^{20,21}$  on the solid surface which would tend to increase the pH of the adjacent solution. The formation of these complexes, hence the alkalization effect, is believed to be accentuated by water, and is thus more likely to occur in aqueous rather than in concentrated acids. Due to large hydration energy and primary hydration number of  $Al^{3+}$  ion,<sup>22,23</sup> a high degree of hydration of aluminum ion is expected during dissolution in aqueous acids. It seems<sup>20,21</sup> that a high degree of hydration will facilitate the formation and improve the stability of oxy-acid complexes.

The effect of anions on the dissolution of Al in the paper under discussion is in contradiction to the results given by others.<sup>24</sup> It is not clear if the mechanism suggested for chemical dissolution<sup>24</sup> will apply to the present results on electrochemical corrosion.

## H<sub>2</sub>-Induced B Diffusion in MOS Devices

D. M. Brown (pp. 412-415, Vol. 123, No. 3)

**L. M. Pecora and V. Srikrishnan:**<sup>25</sup> The author presents some interesting experimental results which show that at 1100°C and in the presence of hydrogen, boron (B) formed by reduction of  $B_2O_3$  diffuses through a molybdenum (Mo) gate in MOS devices. According to the author, although the chemical reaction  $3H_2 + B_2O_3 \rightarrow 2B + 3H_2O$  is unlikely in the bulk ( $\Delta G^\circ_{\text{reaction}} = 2.15$  eV/B atom), an entropy term arising from the dissolution of B atoms in Mo makes the reduction possible. The author claims that such interstitial dissolution provides the necessary driving force required for catalytic reaction (in this case  $B_2O_3$  reduction), which is otherwise energetically unfavorable. He further claims that this explains the high B diffusivity through the Mo gate, whenever  $H_2$  is present in the ambient.

We would like to point out that when Brown refers to enhanced diffusivity, he means enhanced B atom flux. The diffusion fluxes are determined by intrinsic diffusivities (*i.e.*, diffusion coefficients) and concentration gradients or more generally gradients of chemical potentials.<sup>26</sup> The mixing entropy term Brown refers to is nothing but a part of the chemical potential gradient

for diffusion and therefore has nothing to do with the diffusivities. The experimental evidence presented in the paper does not unequivocally show that the presence of hydrogen has any influence on the diffusivity. The enhancement in the diffusion fluxes could very well be a direct consequence of increased B concentration at the interface (or surface) in the presence of hydrogen.

The dissolution of B from the surface, we believe is only a B removal process from the site of the reaction. Brown's suggestion that "the free energy of a reaction can be lowered by the much larger entropy changes associated with the interstitial substrate dissolution of a product within the volume of the catalyst" is extremely misleading. The reaction to be considered then is no longer the original surface reaction alone but one that includes the dissolution (*i.e.*, the removal process) also. Hence, we are not lowering the free energy of a reaction, but actually changing the reaction to include a new process by which the product is removed. More realistically, the removal of the product does not influence the energetics of the reaction, but only perturbs the equilibrium concentration of the product, enabling the reaction to continue. For example, one can consider a catalytic reaction where the removal process is simply a desorption process. The desorption process cannot and does not influence the catalytic ability of the surface.

A possible explanation for the author's observations perhaps can be described as follows.  $H_2$  gets dissociatively chemisorbed on the surface. The reaction of interest is then  $6H + B_2O_3 \rightarrow 3H_2O + 2B$  which has a  $\Delta G^\circ \simeq -2.3$  eV/B atom. This is obviously much more favorable for producing B at local adsorbed sites than the one Brown has considered. Brown's reasoning that  $N_2$  atoms occupy interstitial sites in the solid and prevent the B atoms from dissolving yields unrealistic amounts of  $N_2$  in Mo interstitials. Since  $n \propto N$ , for a given  $\Delta g$ , where  $n$  is the number of B atoms dissolved and  $N$  is the number of interstitial sites available to B atoms, a reduction of 10% in  $n$  requires a reduction of 10% in interstitial sites, which means that approximately  $10^{21}$   $N_2$  atoms/cm<sup>3</sup> must be dissolved. The actual data show 50-100% decreases in  $n$  (of B) in the presence of  $H_2 + N_2$  mixture, requiring unrealistic amounts of  $N_2$  solution in Mo. A more straightforward explanation is that the surface reaction sites are reduced by the adsorption of  $N_2$  or N-H type molecules. This would result in lower H adsorbed sites, lower B surface concentrations, and hence low B diffusion fluxes.

We believe that the experimental observations are very interesting, but not conclusive on the effect of hydrogen on the diffusion of B into Mo. A good part of the problem, we feel, is firstly Brown's misinterpretation of the dissolution process and its role in changing free energies and secondly his overextension of a simple reaction-dissolution model to explain various phenomena which are not built into the model. The simpler explanations we have proposed seem to explain the observations adequately.

**D. M. Brown:**<sup>27</sup> Pecora and Srikrishnan contend that "the removal of the product does not influence the energetics of the reaction but only perturbs the equilibrium concentration of the product enabling the reaction to continue." That this statement is not of general validity can be seen by considering the disordering of a perfect crystalline solid. The formation of pairs of Frenkel defects consisting of vacant lattice sites and interstitial atoms is an endothermic process involving the absorption of an amount  $n\Delta h$  of energy where  $n$  is the number of defects and  $\Delta h$  is the formation enthalpy per defect. If the energetics of the equilibrium state were determined only by the enthalpy

<sup>18</sup> J. O'M. Bockris and D. Drazic, "Electrochemical Science," p. 115, Taylor and Francis, Ltd., London (1972).

<sup>19</sup> T. S. Lee, *This Journal*, **118**, 1278 (1971).

<sup>20</sup> A. Becerra and R. Darby, *Corrosion*, **30**, 153 (1974).

<sup>21</sup> D. E. C. Corbridge, in "Topics in Phosphorous Chemistry," Vol. 3, E. J. Griffith and M. Grayson, Editors, p. 172, Interscience Publishers, New York (1966).

<sup>22</sup> J. S. Muirhead-Gould and K. J. Laidler, *Trans. Faraday Soc.*, **62**, 944 (1966).

<sup>23</sup> E. Giueckauf, *ibid.*, **60**, 1637 (1964).

<sup>24</sup> K. F. Lorking and J. E. O. Mayne, *J. Appl. Chem.*, **11**, 170 (1961).

<sup>25</sup> Department of Chemical Engineering and Materials Science, Syracuse University, Syracuse, New York 13210.

<sup>26</sup> J. Bardeen and C. Herring, "Atom Movements," p. 87, American Society for Metals, Ohio (1951).

<sup>27</sup> General Electric Company, Research and Development Center, Schenectady, New York 12301.

and the vacancies and interstitials did not separate, the crystal could not be disordered. The equilibrium state is determined, however, not by the enthalpy but by the free energy  $\Delta G$  which involves an entropy term  $-T\Delta S$  arising from the distribution of the point defects over the available lattice and interlattice sites. The energetics of the disordering reaction are profoundly influenced by the entropy term which involves a random diffusion process.

A further example of a process for which their contention cannot be sustained is provided by the formation of a binary solid solution by the diffusion of atoms into a crystalline solid from the surface, for which the enthalpy of dissolution  $\Delta h$  has a positive value. The dissolution would not occur if the energetics of the equilibrium state of the system were determined only by the enthalpy  $\Delta h$  and not by the free energy  $\Delta G$  which involves an entropy term  $-T\Delta S$  and a random diffusion process. This process distributes the solute atoms over the available lattice sites and increases the entropy. The energetics of the reaction are again profoundly influenced by the entropy term.

An experimental observation which is of considerable importance in the fabrication of the MOSFET devices and which has to be explained is that a very thin layer of  $\text{SiO}_2$  under the Mo gate remains as an insulating oxide film when heated in the presence of hydrogen, whereas a thin layer of  $\text{B}_2\text{O}_3$  or  $\text{P}_2\text{O}_5$  in a borosilicate glass is reduced. This observation is adequately explained by the mechanism proposed in the paper. Use of the available thermodynamic data presented in the paper shows that the reduction mechanism for  $\text{B}_2\text{O}_3$  on the Mo surface proposed by Pecora and Srikrishnan which depends on the dissociative adsorption of hydrogen would be more effective in reducing  $\text{SiO}_2$  than  $\text{B}_2\text{O}_3$  so that, if this were the reaction mechanism, the thin insulating  $\text{SiO}_2$  layer could scarcely be expected to survive. In practice, the Mo is covered (i) with the borosilicate glass and (ii) there is probably a layer of adsorbed oxygen at the glass-Mo interface for which the heat of adsorption of 7.5 eV/molecule is considerably greater than that of hydrogen at 1.7 eV/molecule.<sup>28</sup> It appears that dissociative surface adsorption of hydrogen on Mo is unlikely to occur in these circumstances.

### Activities of SnO in the SnO-SiO<sub>2</sub> System

A. E. Grau and S. N. Flengas (pp. 852-856, Vol. 123, No. 6)

**Z. Kozuka:**<sup>29</sup> In the paper under discussion, Grau and Flengas emphasized that the "closed" cell was better than the "open" cell for emf measurement of the activities of SnO in SnO-SiO<sub>2</sub> liquid solutions. I acknowledge their statement, but I think the undesirable effect caused by the "open" cell was not so much due to the difference of oxygen potentials at the two electrodes because the difference was not so great. The authors'

<sup>28</sup> D. O. Hayward and B. M. W. Trapnell, "Chemisorption," pp. 203 and 205, Butterworths, Washington, D.C. (1964).

<sup>29</sup> Department of Metallurgical Engineering, Osaka University, Suita, Osaka, Japan.

Table I

	$\Delta G^\circ_{\text{SnO}}$	$\Delta G^\circ_{\text{SnO}}$ at 1300°K	$\Delta G^\circ_{\text{SnO}}$ at 1400°K
Kozuka <i>et al.</i>	-64,300 + 21.4T	-36,428	-34,340
Grau and Flengas	-66,242 + 22.940T	-36,420	-34,126

Table II

	$E^\circ$ (mV)	
	1300°K	1400°K
Kozuka <i>et al.</i>	156.9	154.9
Grau and Flengas	150.7	145.0

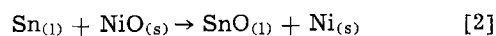
experimental results were in agreement with our results within about 10%, as shown in Table I. Therefore, I cannot understand why line (c) in Fig. 1 of the paper under discussion is in poor agreement with their results. Perhaps our paper was misquoted.

In our experiment, a Sn,SnO reference electrode was used and the solid electrolyte was attacked by the reference electrode. However, it was confirmed that the change of the cell's emf was negligibly small as black stains were not found on the external surface of the ZrO<sub>2</sub>-CaO tube. During our emf measurements, the undesirable effect due to any irreversible reaction was found to be negligibly small in spite of "open" cell characteristics; in our experiment the plots of emf vs. temperature were nearly linear even though the emf measurements were made at alternating temperature changes. In a recent separate experiment, it was found that the change of SnO-SiO<sub>2</sub> composition during emf measurement was negligibly small.

**A. E. Grau**<sup>30</sup> and **S. N. Flengas**:<sup>31</sup> The cells used by both Professor Kozuka and by us for the determination of the standard free energy of formation of liquid SnO are schematically described as



The corresponding cell reaction is



The emf vs. temperature relationship of Kozuka *et al.*<sup>32</sup> for this reaction may be obtained by dividing Eq. [7] in their paper by the quantity  $-2F$ ,  $F$  being the Faraday constant. The result of this calculation is

$$E^\circ = 183.2 - 0.0202T \text{ (mV)} \quad [3]$$

Our results, summarized in Eq. [6] of our paper, are

$$E^\circ = 225.5 - 0.0575T \text{ (mV)} \quad [4]$$

The disagreement between Eq. [3] and [4] is better seen in Table II. This is the disagreement we referred to in our paper. The good agreement for the formation potential of liquid SnO indicated by Professor Kozuka in this discussion is unfortunately fortuitous and probably due to the fact that the different data which we have used for the formation potential of NiO<sup>33,34</sup> compensates for the disagreement observed in Table II.

Despite the differences observed in the activity values of SnO reported by Kozuka *et al.*<sup>32</sup> and by us, it is interesting to observe that both sets of results indicate that SnO is one of the most acidic metal oxides with respect to SiO<sub>2</sub>. This is encouraging, particularly in view of the experimental difficulties which are inherent to the SnO-SiO<sub>2</sub> system.

<sup>30</sup> Quebec Iron and Titanium Corporation, Sorel, Quebec, Canada J3P 5P6.

<sup>31</sup> Department of Metallurgy, University of Toronto, Toronto, Ontario, Canada M5S 1A4.

<sup>32</sup> Z. Kozuka, O. P. Sahaan, and J. Morijama, *Trans. Jpn. Inst. Met.*, 9, 200 (1969).

<sup>33</sup> G. G. Charette and S. N. Flengas, *This Journal*, 115, 796 (1968).

<sup>34</sup> C. B. Alcock and T. N. Belford, *Trans. Faraday Soc.*, 60, 882 (1964).



# Physical Properties of SnO<sub>2</sub> Materials

## II. Electrical Properties

Z. M. Jarzebski

Centre for Interdisciplinary Studies in Chemical Physics, University of Western Ontario, London, Ontario, Canada

and J. P. Marton\*<sup>1</sup>

Welwyn Canada Limited, London, Ontario, Canada

### ABSTRACT

Stannic oxide in its pure form is an n-type wide-bandgap semiconductor. Its electrical conduction results from the existence of point defects (native and foreign atoms) which act as donors or acceptors. Some unique properties of SnO<sub>2</sub> make the material useful for many applications. Therefore, increasing attention is being paid to studies on this oxide, especially on the methods of preparation, and its electrical and optical properties. The purpose of this series is to provide a general up-to-date review of the investigations carried out and to help identify important areas for further studies. The first part<sup>2</sup> was concerned with the preparation and defect structure of single crystals, sintered polycrystalline samples, and thin films. In this part we review the electrical properties of these materials. The electrical properties of single crystals are well understood and the properties of sintered SnO<sub>2</sub> powder are similar to those of single crystals. However, those of SnO<sub>2</sub> films have not been explained satisfactorily up to the present time. They depend strongly on the manner of preparation and subsequent heat-treatments in various ambients. In the third part,<sup>3</sup> the optical properties of SnO<sub>2</sub> will be reviewed.

The methods of preparation of single crystals, sintered materials, and thin films of tin dioxide have been described in Part I. In this part, a review of the electrical properties of these materials is given. Research on the electrical properties of SnO<sub>2</sub> has been going on since 1910, mainly because of the variety of applications of this wide bandgap semiconductor of rutile structure. A great deal of experimental research has been conducted already, especially in recent years; therefore, it would seem proper to provide in this part a general up-to-date survey of the results obtained and make an attempt to find a more comprehensive and consistent interpretation. The data obtained on single crystals will be considered first as such systems are the most simple. The electrical properties of more complicated sintered powder materials of SnO<sub>2</sub> will be discussed in the second section, and in the third section the properties of the most complicated thin film materials will be described.

### Single Crystals

Some data on electrical properties of SnO<sub>2</sub> single crystals are presented in Table I. As can be seen from this table, the measurements have been carried out on the following three types of SnO<sub>2</sub> single crystals: (i) pure and intentionally doped crystals of good quality, (ii) pure crystals heat-treated at various temperatures and oxygen pressures, and (iii) impure single crystals containing various undesirable admixtures.

In this paper we will be concerned mostly with the data obtained from the first two types of crystals.

*Pure and intentionally doped crystals.*—One criterion for determining the purity of crystals is the charge carrier mobility at low temperatures: the higher this value, the higher the purity and the quality of the crystals. In Table II Hall mobility and carrier concentration data are listed for various samples. As can be seen from Table II, the measurements carried out by Nagasawa *et al.* (5) and Fonstad *et al.* (14) have been conducted on the best quality samples. Therefore, in this section the data obtained by these authors will be given the most consideration.

In Fig. 1 the results of conductivity measurements on SnO<sub>2</sub> obtained by Nagasawa and Shionoya (11) at temperatures of 4.2°–300°K are presented. The specimens had a conduction electron concentration of  $1.8 \times 10^{17} \text{ cm}^{-3}$  at 300°K. The curve shown in Fig. 1 consists of three different regions, namely: region I in a temperature range from 130° to 300°K, region II from 10° to 130°K, and region III from 4.2° to 10°K. The authors have given the values of the activation energies for the last two regions (cf. Table I), but it is difficult to find the physical meaning of these energies because the temperature dependence of resistivity  $\rho = 1/en\mu$  in the case of SnO<sub>2</sub> is governed greatly by temperature dependences either of conduction electron concentration,  $n$ , or charge carrier mobility  $\mu$  ( $e$  is the electronic charge). It is interesting, instead, that in the temperature range from 4.2° to about 130°K, the conductivity varies by nine orders of magnitude. Thus, pure SnO<sub>2</sub> crystals can be either a good insulator at very low temperatures (about 4.2°K) or a good conductor at a temperature of about 130°K.

\* Electrochemical Society Active Member.

<sup>1</sup> Present address: Department of Engineering Physics, McMaster University, Hamilton, Ontario, Canada.

<sup>2</sup> THIS JOURNAL, July 1976.

<sup>3</sup> To be published in THIS JOURNAL, October 1976.

Key words: electrical conductivity, Hall and Seebeck effects, mobility, point defects and impurities.

The authors assumed in their discussion that the temperature dependence of conductivity in region III results from point defect (impurity) level permutation

conduction with appropriate compensation by acceptors such as Fe and Ca (4). If wave functions of donors overlap sufficiently, a point defect band conduction

Table I. Electrical properties of SnO<sub>2</sub> single crystals found by various authors

Year	Author	Reference	Material	Property	Temperature range °K	Conclusions drawn by the author
1962	Kohnke	(2)	Natural cassiterite; a spectroscopic analysis showed Si, Al, and Fe to be most important impurities present with maximums of 0.5%	Conductivity Hall effect Hall mobility	100-500	Ionization energy of donors of 0.7 eV for samples with charge carrier concentration of $10^{14}$ - $10^{16}$ cm <sup>-3</sup> at 300°K. Hall mobility varies from 10 to 300 cm <sup>2</sup> /Vsec. Electron effective mass and donor concentration are about 0.8 $m_0$ and $10^{20}$ cm <sup>-3</sup> , respectively. Nature of donors is unknown. SnO <sub>2</sub> is a typical broad-band semiconductor.
1965	Marley and Dockerty	(3)	Single crystals, prepared by vapor-transport technique [cf. Ref. (1)]. Mass spectrographic analysis on undoped samples indicate the presence of Al and Fe in the range of 10-20 ppm. Samples were either heat-treated or antimony doped, and also as-grown	Conductivity Hall effect Hall mobility Seebeck effect	80-900 80-575 300	Donor ionization energy, $E_D$ , decrease with increasing donor concentration, $N_D$ . At infinite dilution $E_D = 0.15$ eV. Density-of-states effective mass $m^*$ obtained from Hall effect measurements amounts to 0.22 $m_0$ ; instead, the values of $m^*$ found from Seebeck effect measurements vary between 0.12 and 0.18 $m_0$ . Antimony-doped crystals with $N_D > 6.10^{18}$ cm <sup>-3</sup> are degenerate above 80°K. Above 300°K the polar optical mode scattering mechanism is assumed. At lower temperatures Hall mobility decreases with decreasing $N_D$ . The hypothesis of impurity-level transport is suggested in these temperatures.
1965	Nagasawa, Shionoya, and Makishima	(4)	Pure single crystals with concentrations of order of magnitude of $10^{17}$ cm <sup>-3</sup>	Conductivity Hall effect Hall mobility	77-300 300	The conductivity changes by the equation $\sigma = \text{const } T^{-2}$ above 250°K. At room temperature the crystals have the conductivity of a few (ohm-cm) <sup>-1</sup> and the mobility of about 200 cm <sup>2</sup> /Vsec.
1965	Nagasawa, Shionoya, and Makishima	(5)	Pure single crystals with concentrations of order of magnitude of $10^{17}$ cm <sup>-3</sup>	Conductivity Hall effect Hall mobility Seebeck effect	100-300 300	The ionization energy of donors is $(0.024 \pm 0.004)$ eV. The density-of-states effective mass obtained from Hall effect experiments is $(0.41 \pm 0.10) m_0$ , and from Seebeck effect measurement is 0.33 $m_0$ . Above 160°K the $T^{-2}$ dependence of Hall mobility has been found. The charge carriers are scattered mainly by acoustical phonons with contribution of scattering by optical phonons.
1966	Morgan and Wright	(6)	Crystals contained appreciable amounts of various impurities (7), e.g., 0.04-0.1% Si; Ca, Na $\leq$ 0.005%; Cr, Fe, Mg, and Al $\leq$ 0.01%. The samples investigated were doped with antimony	Conductivity Hall effect Hall mobility Seebeck effect	77-1100 77-600 300-1100	The values of electron effective mass varied from 0.10 to 0.17 $m_0$ . These values are obtained by combining Hall and Seebeck effects measurements. Optical mode lattice scattering is proposed above about 300°K, with an impurity scattering contribution below this temperature. The Hall coefficient was constant up to 600°K, which was the highest temperature of measurements.
1968	Wright	(8)	The same crystals as above, and also doped with chromium (about 80 ppm)	Conductivity Seebeck effect Hall effect	100-1100 100-600	In crystals having concentrations of antimony of $5 \times 10^{17}$ - $10^{19}$ cm <sup>-3</sup> the mobility is about 80 cm <sup>2</sup> /Vsec. The electron effective mass is about 0.16 $m_0$ along the a axis and may be a little lower along the c axis. The same conclusions as above concerning the scattering mechanisms apply.
1968	Nagasawa and Shionoya	(9)	Pure single crystals	Hall effect Hall mobility Magneto-resistance	77 and 300	The quasi-free electron scattering process at 77°K is dominantly due to acoustical phonons. At 300°K the resistivity, carrier concentration, and mobility are (0.11-0.33) ohm-cm, $(1.3-0.4) \times 10^{18}$ cm <sup>-3</sup> , and about 200 cm <sup>2</sup> /Vsec, respectively. Results of magnetoresistance measurements can be interpreted in terms of a single spheroidal energy valley model.
1968	Van Daal	(10)	Single crystals contained $3.6 \times 10^{19}$ and $1.8 \times 10^{20}$ cm <sup>-3</sup> of Al; and B, Fe, and Mg on order of magnitude of $10^{18}$ cm <sup>-3</sup>	Conductivity Hall effect Hall mobility	4.2-1600	Above 300°K polar optical mode scattering with an average characteristic temperature of 1050°K predominates. Below 300°K the electron mobility is determined mainly by impurity scattering.
1969	Crabtree Mehdi, and Wright	(7)	Crystals having electron concentrations between $10^{17}$ and $10^{18}$ cm <sup>-3</sup> , obtained by reduction in vacuum	Conductivity Hall effect Hall mobility	77-300	At 300°K the values of Hall mobility are between 200 and 250 cm <sup>2</sup> /Vsec. The highest value of the mobility at 77°K is 700 cm <sup>2</sup> /Vsec. At 300°K the quasi-free electrons are scattered by optical modes. Electron effective mass is 0.17 $m_0$ .
1971	Nagasawa and Shionoya	(11)	Crystals having charge carrier concentration of $1.8 \times 10^{17}$ cm <sup>-3</sup> at 300°K	Conductivity	4.2-300	Three different regions have been observed: region I (130°-300°K), region II (10°-130°K), and region III (4.2°-10°K). In the first region, the resistivity increases with increasing temperature while in the last two regions the resistivity decreases with increasing temperature with activation energies 0.0137 and 0.0034 eV, respectively.
1971	Nagasawa and Shionoya	(12)	Undoped SnO <sub>2</sub> single crystals heat-treated at temperature 1370°K and in vacuum of $10^{-8}$ Torr for 24 hr	Hall effect Hall mobility	77-300	Electrical properties of the reduced SnO <sub>2</sub> crystals are similar to those of Sb-doped tin oxide. They may be interpreted with the concept of degenerate semiconductor native defects resulting from nonstoichiometric composition from shallow donor centers.



Table I. Continued

Year	Author	Reference	Material	Property	Temperature range °K	Conclusions drawn by the author
1971	Nagasawa and Shionoya	(13)	Undoped SnO <sub>2</sub> crystals heat-treated at temperature 1570°K in oxygen of about 10 atm	Conductivity	300	The conductivity of the crystals decreases remarkably by the heat-treatment in high pressure oxygen. The conductivity is not uniform with a crystal. The surface layer has much lower conductivity than the interior.
1971	Fonstad and Rediker	(14)	Single crystals	Conductivity Hall effect Hall mobility Schottky barrier	20-625	Donor levels of 34 meV and 140 meV have been found. The first level is due to antimony, the second is due to oxygen vacancy. Above 250°K polar optical mode scattering with characteristics temperature of 1353°K predominates. Below 250°K acoustic deformation potential scattering dominates. Ionized point defect scattering is important at low temperatures.
1971	Button, Fonstad, and Dreybrodt	(15)	Pure single crystals	Hall effect Hall mobility Submillimeter cyclotron resonance	20-300	The samples show a charge carrier concentration of $7 \times 10^{15}$ cm <sup>-3</sup> and Hall mobility of 250 cm <sup>2</sup> /Vsec at 300°K. At 77°K the carrier concentration and mobility were $2 \times 10^{15}$ cm <sup>-3</sup> and 9000 cm <sup>2</sup> /Vsec, respectively. The first accurate measurement of the conduction-band effective-mass tensor components are $m^* = 0.299 m_0$ and $m^* = 0.234 m_0$ . The density-of-states effective mass is 0.275 $m_0$ .
1973	Samson and Fonstad	(16)	Pure single crystals	Conductivity	970-1620	In the temperature range of 1370°-1620°K and in partial oxygen pressure range of 10 <sup>-2</sup> - 1 atm dominant native defects in SiO <sub>2</sub> are doubly ionized oxygen vacancies. The donor levels related to these defects are: 30 meV and 150 meV. The hydrogen introduces a donor level of 50 meV.

will be formed, but if this overlapping is insufficient it will result in a point defect level permutation conduction (17). However, the nature of donors is unknown. It may be either oxygen vacancies or interstitial tin atoms (4) or other impurities.

The temperature dependence of resistivity, found by Nagasawa and Shinoya (11) in regions I and II is consistent with the more detailed results obtained at temperatures higher than 80°K by Fonstad and Rediker (14). The results are shown in Fig. 2. Their sample had a similar conduction electron concentration to the ones discussed above at 300°K. Specifications of three samples investigated by the latter authors are given in Table III. Fonstad and Rediker have also found that in the temperature range from 80° to about 130°K the conductivity  $\sigma$  of SnO<sub>2</sub> increases with increasing temperature, followed by a decreasing of  $\sigma$  with an increase of  $T$  at higher temperatures; this is similar to what was found by Nagasawa and Shinoya (11). Thus the complicated temperature dependence of conductivity in SnO<sub>2</sub> crystals is due mainly to the different temperature dependences of  $n$  and  $\mu$ .

Table II. Hall mobility and conduction electron concentration in SnO<sub>2</sub> single crystals at 77°K obtained by various authors

Mobility cm <sup>2</sup> /Vsec	Conduction electron concentration (cm <sup>-3</sup> )	Reference
ca. 10	—	(10)
96	$8.7 \times 10^{15}$	(6)
62	$8.0 \times 10^{15}$	(7)
700	ca. $10^{15}$	(5)
ca. 1000	—	(14)
8800	$1.99 \times 10^{15}$	

Table III. Values of charge carrier concentration and Hall mobilities at 77°K and 300°K for SnO<sub>2</sub> samples used in Fig. 2-4

Sample	77°K		300°K	
	$n$ (cm <sup>-3</sup> )	$\mu_H$ (cm <sup>2</sup> /Vsec)	$n$ (cm <sup>-3</sup> )	$\mu_H$ (cm <sup>2</sup> /Vsec)
A	$1.3 \times 10^{15}$	110	$2.2 \times 10^{15}$	150
B	$2.2 \times 10^{15}$	2200	$8.6 \times 10^{15}$	240
C	$1.9 \times 10^{15}$	8800	$8.5 \times 10^{15}$	260

Two other samples investigated by Fonstad and Rediker had carrier concentrations lower and higher than that discussed above. The temperature dependences of  $n$ ,  $\mu$ , and  $\sigma$  for these are shown in Fig. 3 and 4.

In analyzing the temperature dependence of charge carrier concentration for one of the samples (B) the well-known formula derived from nondegenerate statistics was used (18)

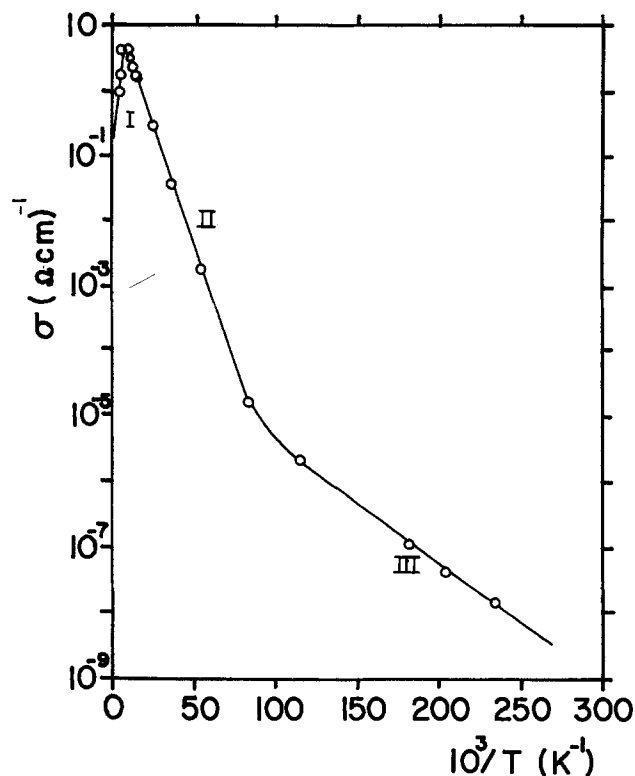


Fig. 1. The electrical conductivity  $\sigma$  of SnO<sub>2</sub> single crystals as a function of inverse temperature (11).

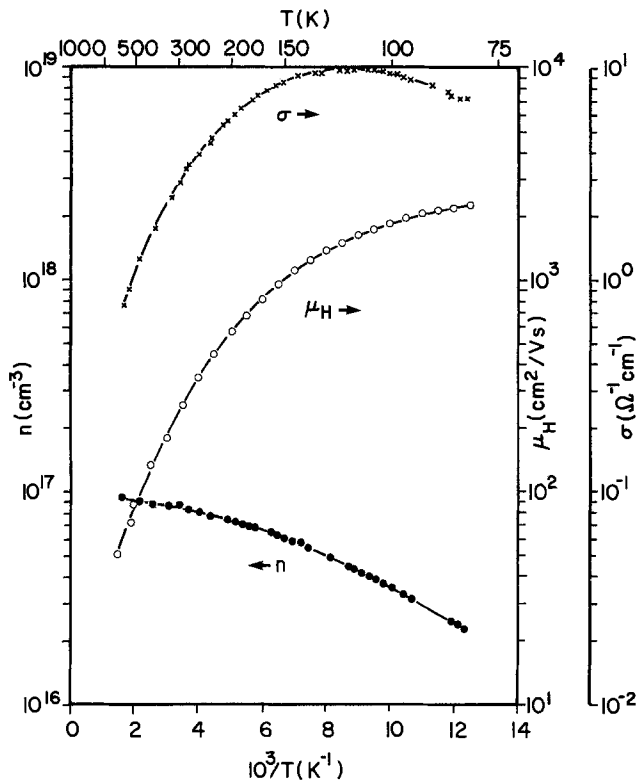


Fig. 2. Conductivity  $\sigma$ , Hall mobility  $\mu_H$ , and conduction electron concentration  $n$  in  $\text{SnO}_2$  single crystals (sample B) vs. inverse temperature (14).

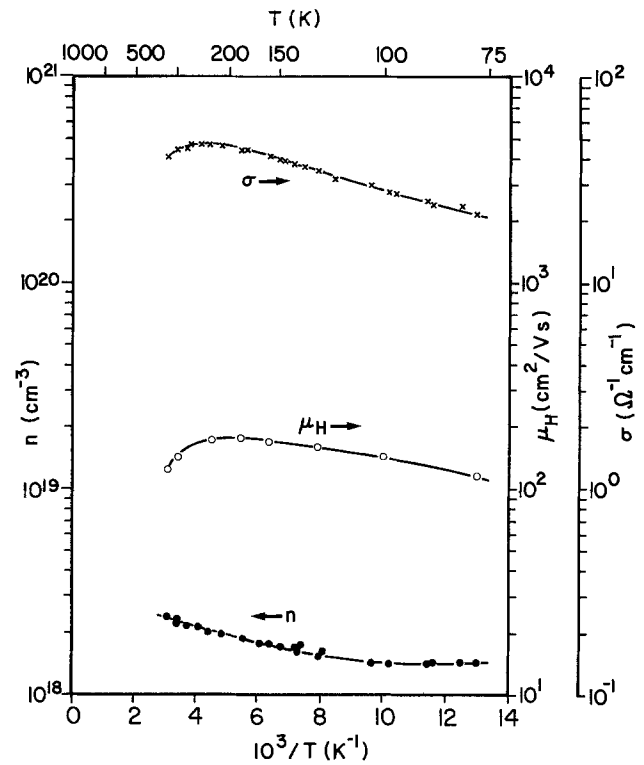


Fig. 4. Conductivity, Hall mobility, and charge carrier concentration in  $\text{SnO}_2$  single crystals (sample A) vs. inverse temperature (14).

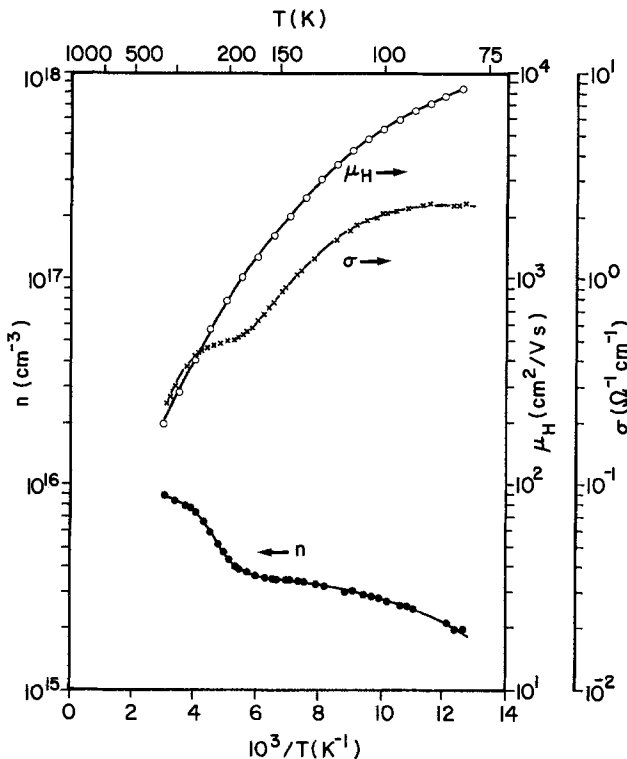


Fig. 3. Hall mobility, conductivity, and conduction electron concentration in  $\text{SiO}_2$  single crystals (sample C) as a function of inverse temperature (14).

$$\frac{n(n + N_A)}{(N_D - N_A - n)T^{3/2}} = \left( \frac{2\pi k m^*}{h^2} \right)^{3/2} \exp\left(-\frac{E_D}{kT}\right) \quad [1]$$

where:  $N_D$  is the concentration of donors,  $N_A$  is the

concentration of acceptors,  $E_D$  is the ionization energy of donors, and other symbols have the usual meanings. For this sample, it appears that only one donor level is active and the specimen is not degenerate. For sample C, it is seen that two donor levels are active, therefore, in this case, Fonstad and Rediker assumed the following more complicated formula

$$n = \frac{N_1}{1 + g_1 \exp[(E_1 - E_F)/kT]} + \frac{N_2}{1 + g_2 \exp[(E_2 - E_F)/kT]} \quad [2]$$

where  $g$  is the donor degeneracy factor and  $E_F$  is the Fermi level. The subscripts 1 and 2 refer to the shallower and deeper donor levels, respectively.

The Hutson method (19) was applied to find the net donor concentration ( $N_D - N_A$ ), donor ionization energy,  $E_D$ , and the carrier effective mass from Eq. [1] and [2]. As can be seen from Fig. 3, only the shallow donor is active below 150°K, and, in this case, the single donor level analysis used for sample B applies. For this reason, the authors assigned the value of  $g_1$  to be  $g_1 = 2$ , and assumed the second level to be the first ionized state of a double donor, with  $g_2 = 1/2$ . This combination gave the best fit for Eq. [2]. A density of states electron effective mass of  $0.39 m_0$  was also found for both samples B and C. Sample A, which had the highest concentration of charge carrier, has been found to be degenerate below 200°K, and the donor level has been estimated to lie between 10 and 15 meV from the slope of the curve  $\log n$  vs.  $1/T$  near room temperature. The net donor concentration ( $N_D - N_A$ ) and donor ionization energies,  $E_D$ , obtained by Fonstad and Rediker from the Hall effect experiments using Eq. [1] and [2] are shown in Table IV. In this table, the data of  $N_D - N_A$  found by the authors from the measurements of Schottky barrier capacitance vs. bias voltage (20) are also given.

Table IV. Net donor concentration,  $N_D - N_A$  in SnO<sub>2</sub> single crystals obtained from Hall effect and Schottky barrier measurements, as well as donor ionization energies,  $E_D$

Sample	$N_D - N_A$ (cm <sup>-3</sup> )		$E_D$ (meV)
	Hall effect	Schottky barrier	
A	$>2.2 \times 10^{18}$	$1.5 \times 10^{18}$	10-15
B	$9.4 \times 10^{18}$	$8.4 \times 10^{18}$	27.5
C	$9.2 \times 10^{18}$	$7.9 \times 10^{18}$	34, 140

The best data has been obtained from the formula

$$\frac{1}{C^2} = \frac{2(V_b - V_B)}{e\epsilon_s A} \cdot (N_D - N_A)^{-1} \quad [3]$$

where  $C$  is the small-signal barrier capacitance,  $V_b$  and  $V_B$  are the barrier voltage and the bias voltage, respectively,  $\epsilon_s$  is the static dielectric constant, and  $A$  is the barrier area. Thus, for uniformly doped samples, the value of  $N_D - N_A$  may be obtained from a slope of a plot of  $1/C^2$  vs.  $V_B$ , as this plot has been found to be a straight line. Table IV shows good agreement between the values of net donor concentrations found from the Hall effect and Schottky barrier experiments. It is also noteworthy that in the case of samples of similar charge carrier concentrations, the donor ionization energy found by Fonstad and Rediker for specimen B is almost the same as the one obtained by Nagasawa and Shionoya [27.5 meV vs.  $24 \pm 4$  meV (5)].

Fonstad and Rediker have assumed that the shallower donor can be related to antimony doping and that the deeper level may be due to oxygen vacancies. The last suggestion is consistent with the value of donor ionization energy (138 meV) found by Marley and Dockerty (3) in the case of SnO<sub>2</sub> samples heated at 1438°K at low oxygen pressure of 0.06 atm for 282 hr. Thus it is possible that in SnO<sub>2</sub> crystals which are heat-treated this way or which are not very pure, the native defects (e.g., oxygen vacancies) may be completely ionized. The deeper level may then be attributed to the second ionized level of the native point defects. Samson and Fonstad (16) recently came to the same conclusion and have assumed that in tin dioxide, oxygen vacancies predominate in a native disorder. Their results will be discussed in more detail below.

The decrease of the donor ionization energy with increasing donor concentration which is evidenced in Table IV is to be expected. This effect is commonly observed in both elemental and compound semiconductors and was explained by Pearson and Bardeen (21) on the basis of the hypothesis of an appreciable electrostatic attraction between electrons and ionized donors, which increases with increasing donor concentration. These authors have obtained the equation

$$E_D = E_0 - aN_D^{1/3} \quad [4]$$

from the investigations of boron-doped silicon, where  $E_0$  is the donor ionization energy at infinite dilution, and  $a$  is a constant.

Fonstad and Rediker's (14) limited data can also be written by an equation of this type, namely

$$E_D = 0.037 - 2 \times 10^{-5} N_D^{1/3} \text{ (eV)} \quad [5]$$

The general dependence expressed by Eq. [4] has also been observed by Marley and Dockerty (3) for SnO<sub>2</sub> crystals heat-treated in oxygen, but these authors found completely different values of  $E_0$  and  $a$ . The results obtained by Marley and Dockerty are shown in Fig. 5 and may be described by the equation

$$E_D = 0.15 - 8.7 \times 10^{-8} N_D^{1/3} \text{ (eV)} \quad [6]$$

At present, it is difficult to expand on this problem because of the lack of more detailed experimental data.

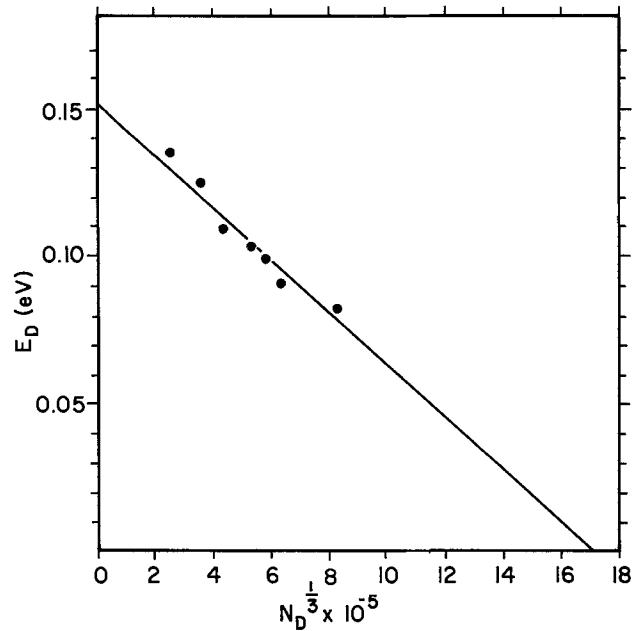


Fig. 5. Donor ionization energy in SnO<sub>2</sub> as a function of donor concentration (3).

The combined data of Hall mobility  $\mu_H$  vs.  $T$  for three samples, A, B, and C, investigated by Fonstad and Rediker (14) are shown in Fig. 6. The experimental curves are compared with those obtained from theoretical calculations, assuming either the polar optical scattering of quasi-free electrons or acoustic deformation potential scattering.

The calculations concerning the optical scattering have been carried out on the basis of the theoretical considerations of Eagles (22) and Low and Pines (23)

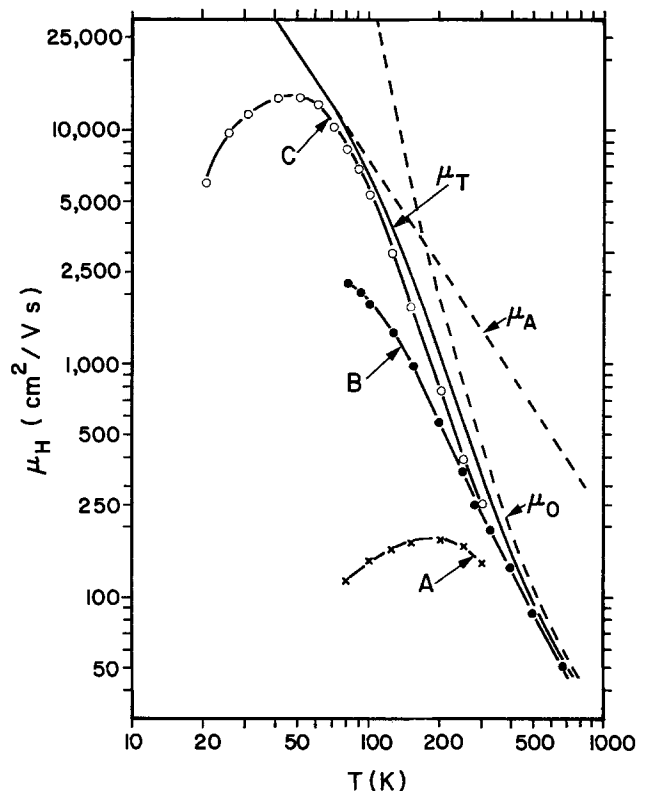


Fig. 6. Hall mobility in SnO<sub>2</sub> single crystals for samples A( $\times$ ), B( $\bullet$ ), C( $\circ$ ) as a function of temperature, and theoretical curves for acoustic deformation potential scattering mobility ( $\mu_A$ ), polar optical mode scattering mobility ( $\mu_O$ ), and total Hall mobility contribution of the two scattering mechanisms ( $\mu_T$ ).

using the values of frequencies of the longitudinal polar optical modes given by Van Daal (24) and Reddaway (25). The dashed curve labeled  $\mu_o$  in Fig. 6 is obtained from the equations

$$\mu_o = \frac{1}{\mu_{o1}} + \frac{1}{\mu_{o2}} + \frac{1}{\mu_{o3}} \quad [7]$$

where

$$\mu_{o1} = 1300 \left( \exp \frac{390}{T} - 1 \right) \frac{\text{cm}^2}{\text{Vsec}} \quad [8]$$

$$\mu_{o2} = 495 \left( \exp \frac{515}{T} - 1 \right) \frac{\text{cm}^2}{\text{Vsec}} \quad [9]$$

$$\mu_{o3} = 15.8 \left( \exp \frac{1080}{T} - 1 \right) \frac{\text{cm}^2}{\text{Vsec}} \quad [10]$$

The contribution to mobility from acoustic deformation potential scattering has been calculated on the basis of the theory of Bardeen and Shockley (26). The expression for  $\mu_A$  is

$$\mu_A = \frac{4.8 \times 10^8 \text{ cm}^2}{E^2 T^{3/2} \text{ Vsec}} \quad [11]$$

where  $E$  is the deformation potential in eV for dilating strain for the conduction band. The dashed curve labeled  $\mu_A$  in Fig. 6 is obtained if  $E$  is assumed to be 8.0 eV.

The total Hall mobility  $\mu_T$  represented by the solid curve in Fig. 6 is calculated from

$$\frac{1}{\mu_T} = \frac{1}{\mu_o} + \frac{1}{\mu_A} \quad [12]$$

It may be seen from Fig. 6 that the polar optical mode scattering  $\mu_o$  part predominates above 250°K. Below this temperature the acoustic deformation potential scattering and ionized point defect scattering mechanisms predominate. For the pure sample C with the lowest carrier concentration, the ionized point defect scattering is important except at temperatures below 50°K. Thus, in this case the acoustic deformation potential scattering predominates at temperatures between 50° and 250°K. Similar scattering behavior was also found in SnO<sub>2</sub> single crystals by Nagasawa and Shionoya (5, 9). For the doped sample A with the higher carrier concentration, the ionized point defect scattering already predominates below room temperature. Therefore, the acoustic deformation potential scattering is not observed. This type of scattering appears to be typical for doped SnO<sub>2</sub> crystals also with higher concentrations of impurities (3, 6, 7, 10, 12).

Anisotropies in the conductivity and Hall effect in SnO<sub>2</sub> crystals have been found to be small. At temperatures of 77° and 300°K, the ratio of  $\sigma_a/\sigma_c$  is 1.0 and 1.2, respectively, and the anisotropy ratio of the Hall scattering coefficient  $r_a^H/r_c^H$  is 1.00 and 1.01, respectively.

*Pure SnO<sub>2</sub> crystals heat-treated at various temperatures and oxygen pressures.*—The influence of heat-treatment at various oxygen pressures on the electrical properties of SnO<sub>2</sub> single crystals has been studied by Marley and Dockerty (3), Nagasawa and Shionoya (12, 13), and Samson and Fonstad (16). The results published by Marley and Dockerty are not discussed in this work because the crystals investigated contained considerable amounts of impurities.

Nagasawa and Shionoya (12) have measured the Hall coefficient and Hall mobility in SiO<sub>2</sub> single crystals as grown and heat-treated in a vacuum of 10<sup>-5</sup> Torr. The results are shown in Fig. 7 and 8. As can be seen in Fig. 7 for reduced tin oxide, the Hall coefficient is almost independent of temperature. This also holds true for Sb-doped SnO<sub>2</sub> crystals, investigated by Marley and Dockerty (3). Such experimental results may be interpreted satisfactorily in terms of degener-

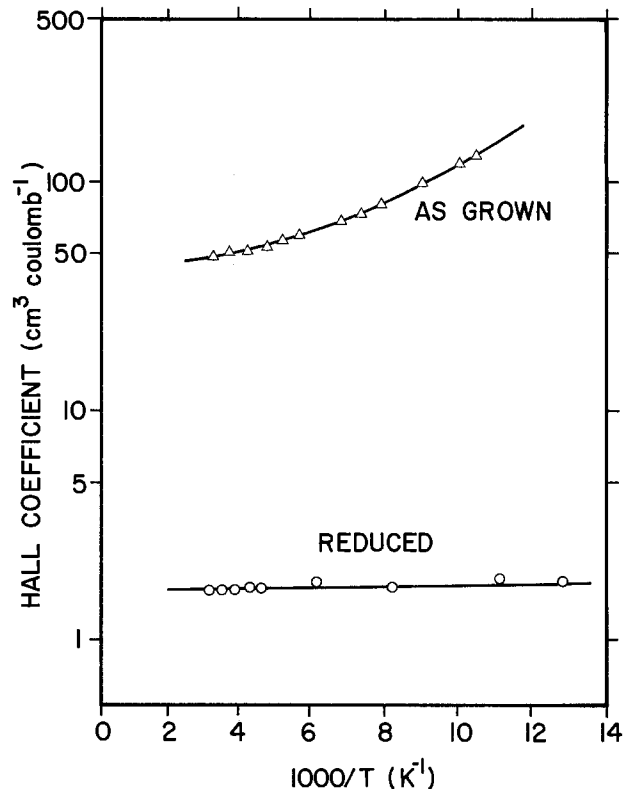


Fig. 7. Hall coefficient as a function of reciprocal temperature for as-grown and reduced SnO<sub>2</sub> single crystals (12).

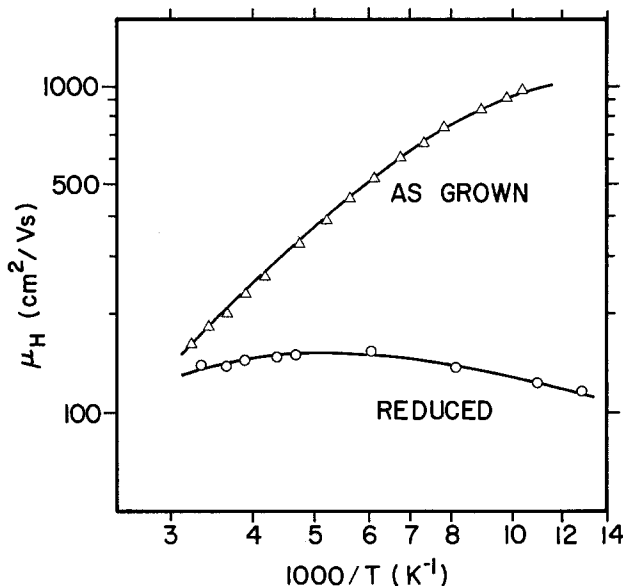


Fig. 8. Hall mobility as a function of reciprocal temperature for as-grown and reduced SnO<sub>2</sub> single crystals (12).

ate carrier concentrations in the semiconductor. Figure 8 shows the plots of Hall mobility vs. reciprocal temperature for as-grown and reduced SnO<sub>2</sub> single crystals. It is evident that in the temperature range considered, the mobility of conduction electrons in the reduced crystals is governed mainly by the ionized native point defect scattering. Nagasawa and Shionoya (13) have also measured the electrical conductivity in SnO<sub>2</sub> single crystals in high oxygen pressure up to 10 atm. They found that the conductivity decreased remarkably under these conditions. However, the conductivity was not uniform in the crystals. The surface layer was found to have a conductivity much lower than the interior, likely due to the decreased density of oxygen deficiency sites.

Extensive studies of the variation of the electrical properties of  $\text{SnO}_2$  with temperature and oxygen pressure have been carried out recently by Samson and Fonstad (16). The dependence of high temperature conductivity on oxygen pressure in equilibrium conditions found by these authors is shown in Fig. 9. Above  $1370^\circ\text{K}$  thermodynamic equilibrium was reached in 5-10 min. Reproducibility above this temperature was excellent. Below  $1370^\circ\text{K}$  the time necessary for equilibration was several hours. The curves  $\log \sigma$  vs.  $\log p_{\text{O}_2}$  have a slope of  $-1/6.5$ . Therefore, the authors assumed that doubly ionized oxygen vacancies predominate in  $\text{SnO}_2$  crystals. [Cf. Ref. (1) for the defect structure of  $\text{SnO}_2$  crystals.]

Figure 10 shows the results of the Hall effect measurement obtained by Samson and Fonstad in the temperature range from  $77^\circ$  to  $300^\circ\text{K}$  on five samples (C, D, E, F, and G) that were annealed at various oxygen pressures and high temperatures and then quenched.

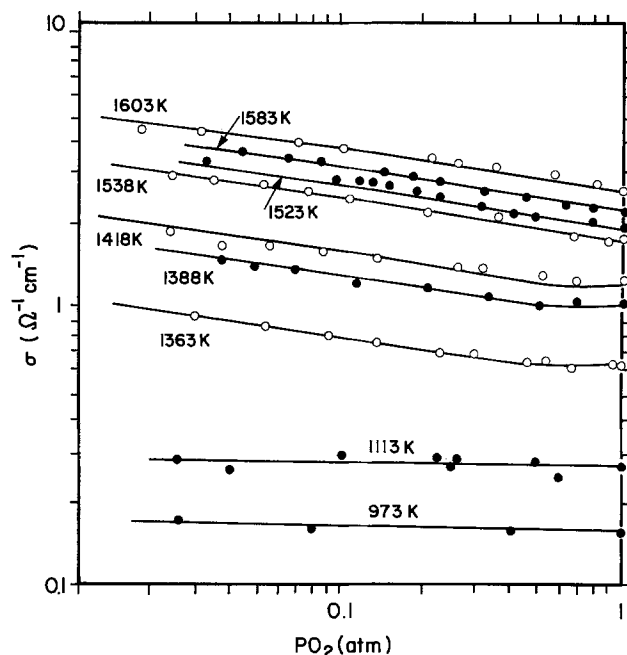


Fig. 9. Electrical conductivity of two  $\text{SnO}_2$  single crystals vs. oxygen pressure at high temperatures.

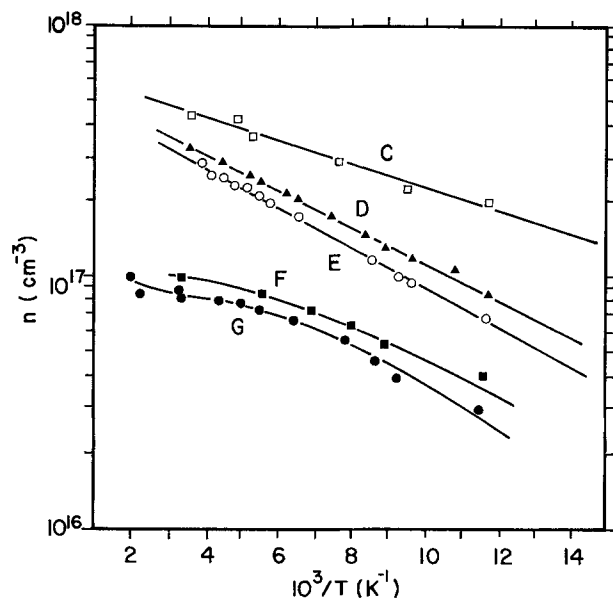


Fig. 10. Conduction electron concentration vs. reciprocal temperature for five samples of  $\text{SnO}_2$  heat-treated at various elevated temperatures and oxygen pressures and quenched.

Table V. Specifications of  $\text{SnO}_2$  single crystals investigated by Samson and Fonstad (16)

Sample	Annealing temperature ( $^\circ\text{K}$ )	Oxygen pressure (atm)	Time of annealing (hr)
C	1720	1	14
D	1620	1	14
E	1670	0.21	14
F	1548	1	20
G	1548	1	20

The annealing conditions are listed in Table V. On the basis of analysis of the temperature dependence of conductivity and Hall coefficient, the authors found two donor levels in  $\text{SnO}_2$ ; one at 30 meV and the other at 150 meV. The shallow level has been attributed to the first ionized state of the oxygen vacancy, and the deeper level has been attributed to the second ionized level of the oxygen vacancy.

Fonstad and Samson have found, as have Nagasawa and Shionoya (13), that the heat-treated crystals have high resistivity surface layers of  $10^5$  ohm-cm or more while the bulk resistivity is about 0.5 ohm-cm. Fonstad and Samson suggested that this high resistivity layer arises from doping by the various ceramic parts in the furnace. It is more likely, however, that this high resistivity surface layer is due to the near-perfect stoichiometry of the crystal in the surface region, which contains few native defects (i.e., oxygen vacancy).

Button and Fonstad (15) have studied submillimeter cyclotron resonance in  $\text{SnO}_2$  crystals. They found the conduction-band effective-mass tensor components to be  $m_{\perp}^* \simeq 0.299 m_0$  and  $m_{\parallel}^* \simeq 0.234 m_0$ . The density-of-states effective mass was found to be  $0.275 m_0$ .

The Seebeck effect in  $\text{SnO}_2$  crystals has also been measured by Marley and Dockerty (3) and by Morgan and Wright (6). The results obtained by Morgan and Wright for two samples, having different concentrations of conduction electrons, are shown in Fig. 11. The charge carrier concentrations for specimens 1 and 2 are  $8.8 \times 10^{19}$  and  $8.2 \times 10^{18} \text{ cm}^{-3}$ , respectively. However, the samples contain large amounts of impurities; therefore, the measurements cannot be interpreted satisfactorily.

### Sintered Materials

The electrical properties of sintered tin oxide have been investigated recently by Van Daal (10) and Matthews and Kohnke (27).

The measurement results obtained by Van Daal are presented in Fig. 12 and 13 and the specifications of the samples are given in Table VI. Measurements were performed in 1 atm of oxygen pressure (samples 3 and 6) and in argon with a partial oxygen pressure between  $10^{-6}$  and  $10^{-5}$  atm (samples 1, 2, 4, 5, I). At temperatures below  $50^\circ\text{K}$ , the temperature dependences of carrier concentration and conductivity indicate an impurity conduction mechanism. This may be seen from the plots in Fig. 12. The conclusion is also supported by the temperature dependence of Hall mobility (Fig. 13). In the intermediate temperature range between  $50^\circ$  and  $700^\circ\text{K}$ , it seems that conduction is due to partially compensated donors, probably originating from impurities. Van Daal found that the ionization energy of donors in this temperature range is at most

Table VI. Main impurity content in units of  $10^{17} \text{ cm}^{-3}$  for the  $\text{SnO}_2$  samples (10)

Sample	Al	B	Fe	Mg
1	2	<8	10	15
2	2	<8	1.5	7
3	5	<8	8	20
4	3	<8	15	20
5	50	<8	16	130
6	3	80	3	12
I	360	8	18	12

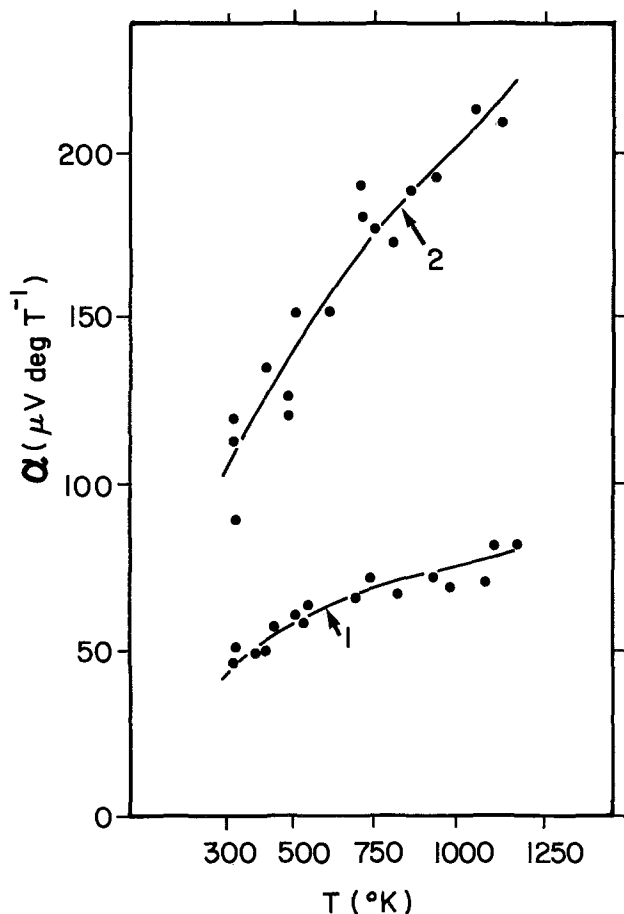


Fig. 11. Seebeck coefficient in  $\text{SnO}_2$  crystals as a function of temperature for two samples having different concentrations of conduction electrons: 1,  $8.8 \times 10^{19} \text{ cm}^{-3}$ ; 2,  $8.2 \times 10^{18} \text{ cm}^{-3}$  (6).

0.01 eV and that the compensation varies between about 90 and 99%. The impurities were found to be B and Fe. The author assumed that Mg probably gives rise to deep donor levels. Above  $700^{\circ}\text{K}$ , extra donors may be introduced in the tin oxide resulting from diffusion of impurity atoms from the surrounding into the sample. At high temperatures these donors presumably are native defects arising from the reduction of  $\text{SnO}_2$ . It seems that for sample 6, the conduction electron concentration is mainly due to native defects, which becomes highly compensated. The decrease of Hall mobility for sample 6 is probably due to a grain boundary effect (28).

The decrease of Hall mobility with increasing temperature starting at about  $100^{\circ}\text{K}$  in Fig. 13 is certainly due to lattice scattering, either polar optical modes or acoustic modes. The temperature dependence of mobility between  $600^{\circ}$  and  $1600^{\circ}\text{K}$  is in agreement with the weak coupling theory for polar scattering [broken curve (29)]. The characteristic temperature of  $1050^{\circ}\text{K}$  was used to calculate the broken curve.

Matthews and Kohnke (27) have investigated the influence of chemisorbed oxygen on the electrical conductivity of Zn-doped sintered stannic oxide. The samples were sintered at  $1730^{\circ}\text{K}$  for 6 hr. In Fig. 14 the temperature dependence of dark current conductivity in samples subjected to a variety of heat-treatment procedures is shown. The dark electrical conductivity has been measured as a function of temperature at fixed ambient gas pressures in surface equilibrium condition. The specifications of the samples and measurement conditions are listed in Table VII. The maximum temperature used in the fixing process was on the order of  $373^{\circ}\text{K}$  which made it unlikely that any bulk changes took place in the specimen.

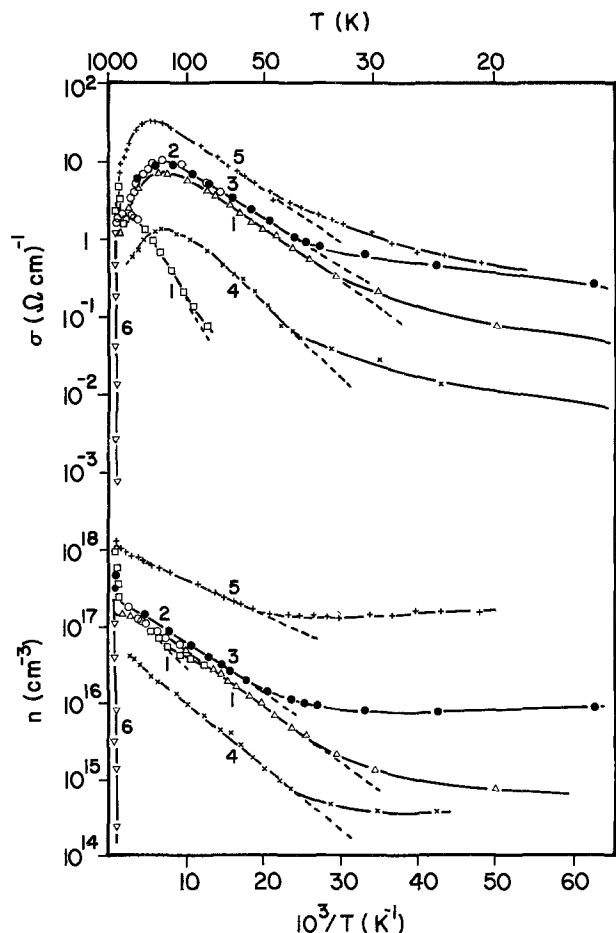


Fig. 12. Electrical conductivity  $\sigma$  and conduction electron concentration  $n$  as a function of reciprocal temperature for single crystal, 1, and polycrystalline, 1-6,  $\text{SnO}_2$  (cf. Table VI). Samples 1, 2, 4, 5, and 6 were measured in an argon atmosphere, and samples 3 and 6 in 1 atm pressure of oxygen (10).

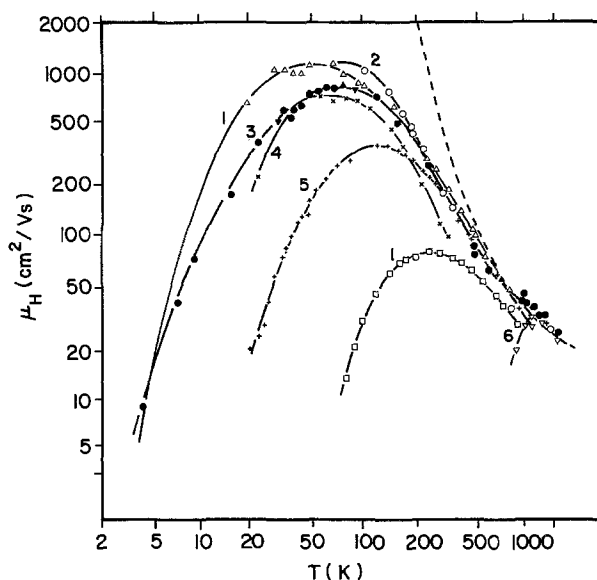


Fig. 13. Temperature dependence of Hall mobility for the same samples of  $\text{SnO}_2$  as in Fig. 12. The broken curve represents the temperature dependence of the drift mobility in the case of polar scattering of quasi-free electrons by longitudinal optical modes with the characteristic temperature of  $1050^{\circ}\text{K}$  (10).

Because the ionic sizes of  $\text{Zn}^{2+}$  and  $\text{Sn}^{4+}$  are nearly identical ( $0.74$  and  $0.71 \text{ \AA}$  for  $\text{Zn}^{2+}$  and  $\text{Sn}^{4+}$ , respectively), one can expect that during the sintering proce-

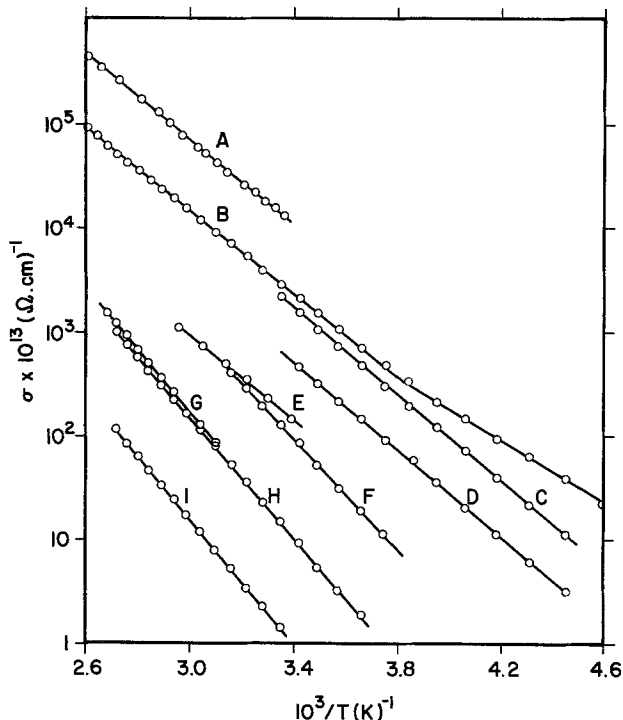


Fig. 14. Electrical conductivity of Zn-doped polycrystalline  $\text{SnO}_2$  as a function of the reciprocal temperature after various fixing procedures [cf. Table VII (27)].

ess  $\text{Zn}^{2+}$  are substituted in  $\text{Sn}^{4+}$  sites. This would give rise to a site imbalance which may be relieved either by the creation of oxygen vacancies or by the introduction of interstitial cations near the  $\text{Zn}_{\text{Sn}^{2+}}$  centers. Probably both processes took place in the experiments. The authors have assumed that Zn-doped  $\text{SnO}_2$  sintered samples are of n-type semiconductors with a high degree of bulk compensation and that variations in conductivity after different treatments are the result of additional compensation associated with changes in the surface concentration of chemisorbed oxygen atoms (30). Here again it is possible that the very low conductivities (samples D-I) were caused by rendering the material highly stoichiometric by heat-treatment in air.

### Films

The most useful form of  $\text{SnO}_2$  is in thick or thin film form. The material is suitable for transparent conductive coatings, electrical resistors, and other devices. The preparation and properties of such films are described in patents (31-51), technical literature (52-53), and in Part I of this review.

Comprehensive studies of  $\text{SnO}_2$  films have been carried out by Aitchison (54). He found that stoichiometric tin oxide films have a high resistivity (about  $10^8$  ohm-cm) at room temperature. The addition of atoms with

Table VII. Matthews and Kohnke, *J. Phys. Chem. Solids*, 29, 653 (1968)

Curve A:	Sample fixed at $10^{-6}$ Torr, 373°K for 10 min, measurements made while temperature decreased
Curve B:	Sample fixed at $2 \times 10^{-1}$ Torr, 367°K for 14 hr, measurements made while temperature increased
Curve C:	Sample fixed at $3 \times 10^{-1}$ Torr, 383°K for 80 hr, measurements made while temperature increased
Curve D:	Sample fixed at 1 atm dry air, 297°K for 12 hr, measurements made while temperature decreased
Curve E:	Sample fixed at 1 atm dry air, 297°K for 40 hr, measurements made while temperature increased
Curve F:	Sample fixed at 1 atm dry air, 297°K for 67 hr, measurements made while temperature increased
Curve G:	Sample fixed at 1 atm dry air, 374°K for 15 hr, measurements made while temperature decreased
Curve H:	Sample fixed at 1 atm dry air, 323°K for 67 hr, measurements made while temperature increased
Curve I:	Sample fixed at 1 atm dry air, 378°K for 66 hr, measurements made while temperature increased

a valence higher than four, e.g., Sb, has a similar effect to the reduction of  $\text{SnO}_2$  films and causes a significant increase in conductivity. Instead, the addition of trivalent atoms, e.g., In, has the opposite effect, i.e., it causes a decrease in conductivity.

Ishiguro *et al.* (55) have found that the conduction electron concentration in  $\text{SnO}_2$  transparent films is between  $10^{19}$  and  $10^{20}$   $\text{cm}^{-3}$  and the Hall mobility is about 30  $\text{cm}^2/\text{Vsec}$ . The authors assumed that coulomb scattering of quasi-free electrons by impurity ions was the predominant scattering mechanism in the transparent conducting films. Similar values of quasi-free electron concentrations were obtained by Arai (56).

Imai (57) studied the electrical properties of  $\text{SnO}_2$  films which were deposited on fused quartz plates. He measured electrical conductivity and the Hall effect in the temperature range between liquid nitrogen and room temperatures. In this temperature range the properties were found to be reproducible. Irreversible changes occur only when the temperature is raised above 470°K in vacuum. In Fig. 15 the results of conductivity  $\sigma$  and Hall coefficient  $R_H$  measurements are shown. As can be seen from the figure, both  $\sigma$  and  $R_H$  increase slightly with temperature, and therefore one can assume that the electrons in the  $\text{SnO}_2$  specimens are degenerate.

Kuznetsov (58) has obtained dielectric  $\text{SnO}_2$  by the hydrolysis of an ether-alcohol solution of  $\text{Sn}(\text{OC}_2\text{H}_5)_4$ , and he grew semiconducting films by the hydrolysis of  $\text{SnCl}_4$ , oxidation of metallic tin, and decomposition of  $\text{SnCl}_2$ . The electrical conductivity of dielectric  $\text{SnO}_2$  formed in this way was  $10^{-15}$   $\text{ohm}^{-1}\text{cm}^{-1}$  at room temperature. Kuznetsov found that the electrical conductivity of semiconducting  $\text{SnO}_2$  films obtained by hydrolysis of  $\text{SnCl}_4$  does not depend on film thickness

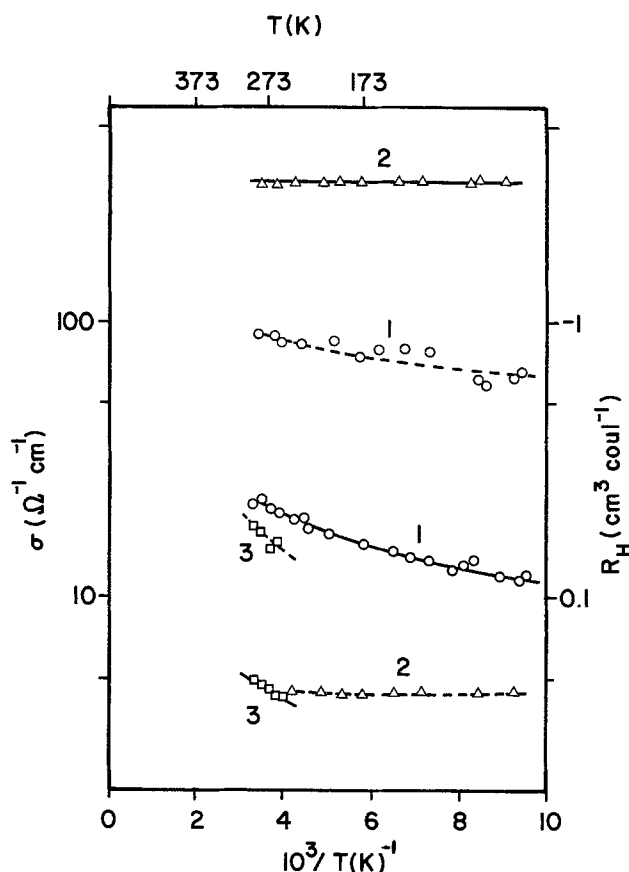


Fig. 15. Temperature dependence of conductivity (—) and Hall coefficient (---) in  $\text{SnO}_2$  films. Sample 1 was prepared by spraying an alcohol solution of pure  $\text{SnCl}_4$  on fused quartz substitute. Samples 2 and 3 were obtained by spraying the solution  $\text{SnCl}_4 + 1$  m/o  $\text{SbCl}_5$  and  $\text{SnCl}_4 + 3$  m/o  $\text{InCl}_3$ , respectively (57).

between 500 and 2500Å. He also measured the effect of heating his films in air. In Fig. 16 the dependence of conductivity on the time of heat-treatment is shown. At temperatures up to 500°K the conductivity remains unchanged, while at higher temperatures the conductivity was found to increase first and then to decrease drastically. The author has attempted but could not explain the observed changes satisfactorily. The introduction of Sb however, was found to improve the stability. This is shown in Fig. 17 for two samples at 1070°K.

In Fig. 18 the results of conductivity measurements carried out by Koch (59) are shown. He found that for pure SnO<sub>2</sub> films, with values of  $\sigma$  between 10<sup>-1</sup> to 3 × 10<sup>2</sup> (ohm cm)<sup>-1</sup> (electron concentration  $n$  between 10<sup>18</sup> to 2 × 10<sup>20</sup> cm<sup>-3</sup>) the conductivity at room temperature is proportional to  $n^{4/3}$ , namely

$$\sigma = \left( 0.35 \pm \begin{matrix} 0.15 \\ 0.08 \end{matrix} \right) \times 10^{-24} n^{4/3} \text{ (ohm-cm)}^{-1} \text{ [13]}$$

This is in accordance with the theory of Howarth and Sondheimer (29) for degenerate electron gas. Koch also found that at room temperature, the quasi-free electrons are scattered mainly by longitudinal optical modes.

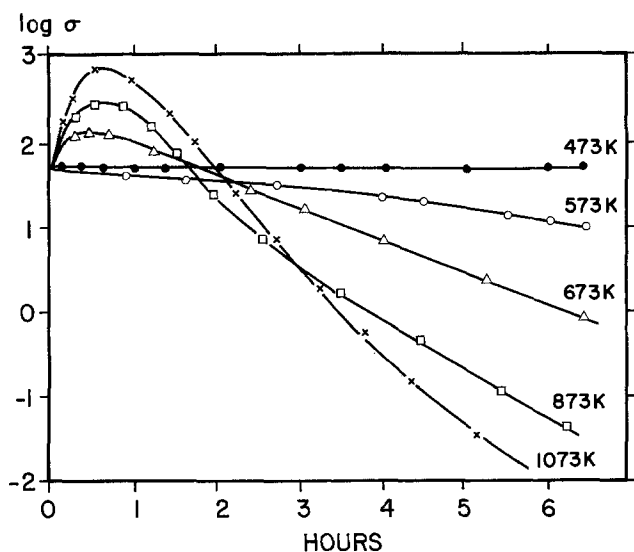


Fig. 16. The influence of heat-treatment in air on electrical conductivity of SnO<sub>2</sub> films (58).

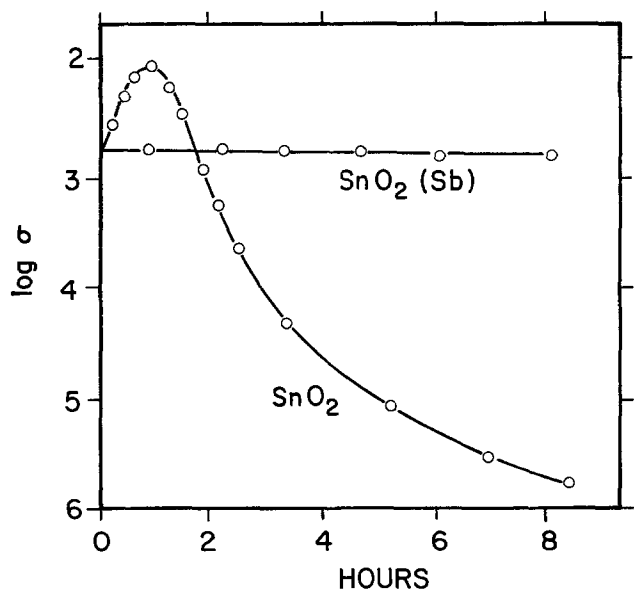


Fig. 17. Thermal stability in air and relation  $\sigma(T)$  for Sb-doped SnO<sub>2</sub> and for undoped SnO<sub>2</sub> films (58).

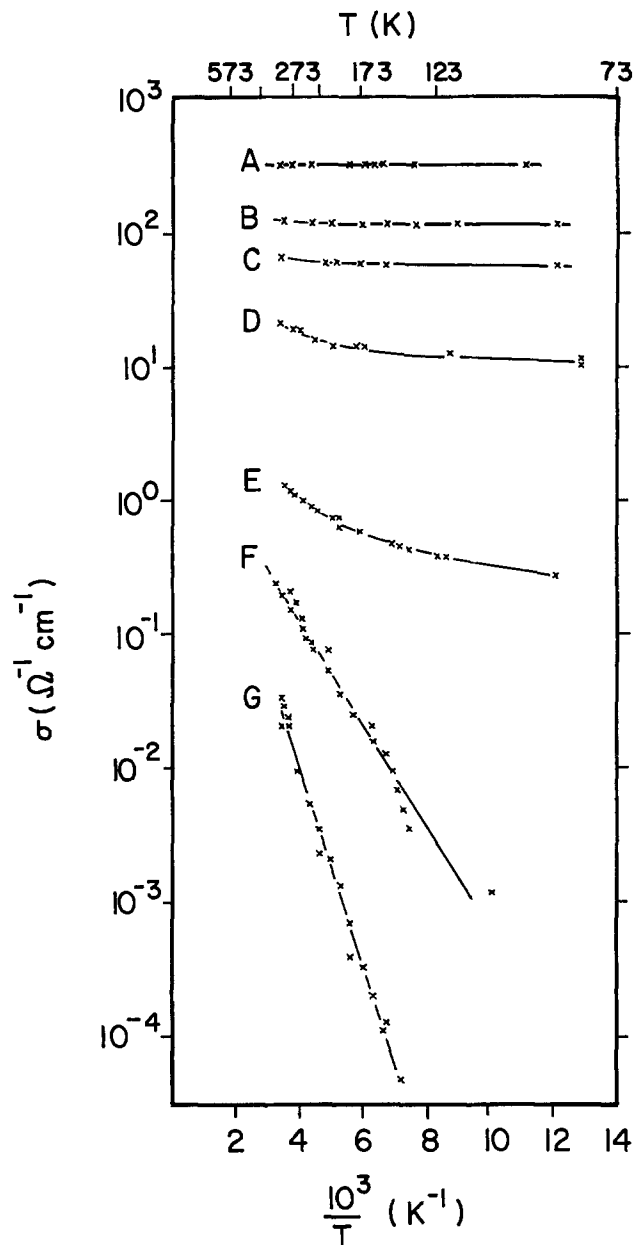
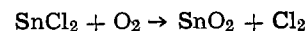


Fig. 18. Temperature dependence of conductivity for various SnO<sub>2</sub> films (59) with electron concentration  $n$  ranging from 10<sup>18</sup> (curve G) to 2 × 10<sup>20</sup> cm<sup>-3</sup> (curve A).

The temperature dependence of conductivity obtained by Inagaki *et al.* (60) for SnO<sub>2</sub> films with different amounts of antimony is presented in Fig. 19. The Sb concentration listed is the percentage of SbCl<sub>3</sub> (wt)/SnCl<sub>4</sub> · 5H<sub>2</sub>O (wt) in the solution used for film deposition. These authors have also measured films below 100°K and found the slope to be negative.

Bartholomew and Garfinkel (61) have investigated the electrical properties of stannic oxide films grown by the reaction



They observed that surface and volume resistivities of such films change slightly when heat-treated in the temperature range below 470°K. However these data have not been reproducible from sample to sample.

Nishino and Hamakawa (62) have studied the electrical properties of Si-SnO<sub>2</sub> heterojunctions. Tin oxide films were deposited by the evaporation of tin on a silicon substrate and the oxidation of tin films in a furnace. They found that such SnO<sub>2</sub> films show the properties of a degenerate n-type semiconductor. The current-voltage characteristics of Si-SnO<sub>2</sub> n-n hetero-



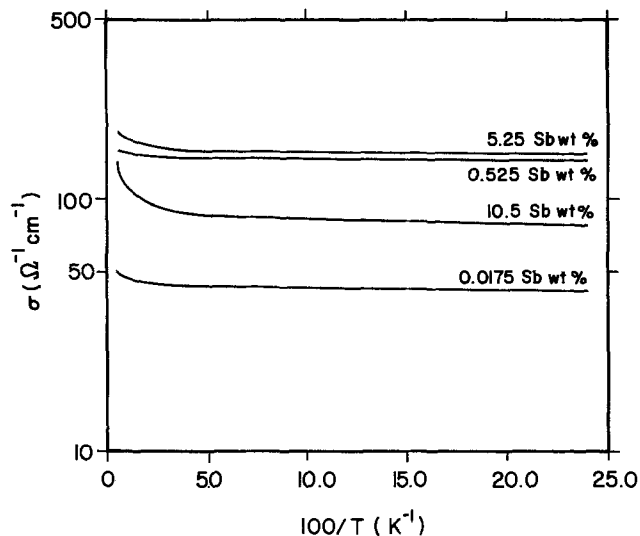


Fig. 19. Electrical conductivity of  $\text{SnO}_2$  films with different Sb contents as a function of reciprocal temperature (60).

junctions was found satisfactory for the purpose of rectification.

Elliott *et al.* (63) have measured the charge carrier concentration for a variety of  $\text{SnO}_2$ :Sb specimens as a function of donor concentration. They found disparities which they attributed to chlorine impurities in the samples.

Aboaf *et al.* (64) have measured the conductivity and Hall effect in  $\text{SnO}_2$  films deposited in various ambients at room and liquid nitrogen temperatures. All films were found to be of n-type, the charge carrier concentration being about  $10^{20} \text{ cm}^{-3}$ . The conductivity and charge carrier concentration was the same at the two temperatures indicating that impurity centers were almost completely ionized at 77°K. The conductivity of the films deposited in nitrogen was weakly dependent on the temperature of deposition. The conductivity of these films annealed in oxygen at 1233°K for 1.5 hr decreased by an order of magnitude. The authors ascertained that the changes in conductivity and charge concentration were due not only to variation of deviation from the stoichiometric composition but also to change in chlorine content.

Lepic (65) investigated  $\text{SnO}_2$  films doped with boron and antimony in the temperature range from 213° to 448°K. He found that electrical conductivity behavior is governed mainly by quasi-free electron scattering. In samples heavily doped with boron, the scattering by ionized point defects dominates, but generally the films exhibit a complicated interplay of acoustical and optical phonon scattering. It should be noted that the conductivity of pure  $\text{SnO}_2$  films may range over several decades (*e.g.*, Fig. 18) for a given temperature, as a function of sample preparation or postdeposition treatment. It is thought that this variation is due to the variability of stoichiometry of the film, similar to that found in the surface layer of single crystals and in sintered materials, and not due to impurities. This idea is based on the authors' work with  $\text{SnO}_2$  film, which showed large irreversible changes in conductivity when heated in oxygen gas at various pressures.

### Conclusions

Pure single crystals of  $\text{SnO}_2$  show two donor levels; a shallow one at 30 meV and a deeper one at 150 meV. These donor levels can be attributed to first and second ionization energy of oxygen vacancy (or interstitial tin ions). Donor ionization energy,  $E_D$  decreases with increasing donor concentration,  $N_D$ , according to the equation  $F_D = E_o - aN_D$ , where  $a$  is a constant. Degenerate crystals may be obtained either by heavily

doping with antimony or by heat-treating in vacuum on the order of  $10^{-5}$  Torr. Heat-treating in air or oxygen produces crystals with high resistivity surface layers of  $10^5 \text{ ohm-cm}$  or more while the bulk resistivity remains at about 0.5 ohm-cm.

Above room temperature the conduction electrons are scattered mainly by the polar optical mode. Below this temperature the electrons are scattered both by the acoustic deformation potential and ionized point defects (native and foreign atoms). For the pure crystals, the ionized point defect scattering is important at temperatures below 50°K. Thus, in this case, the acoustic deformation potential scattering dominates between 50°K and room temperature. For heavily doped or reduced crystals, only ionized point defect scattering dominates below room temperature.

The behavior of electrical conductivity, quasi-free electron concentration, and Hall mobility in sintered samples of  $\text{SnO}_2$  as a function of temperature is similar to that of impure single crystals. In-doped  $\text{SnO}_2$  sintered specimens are of n-type with a high degree of bulk compensation. Heat-treatment of such samples at temperatures up to 374°K causes variations in conductivity due to additional compensation associated with changes in the surface concentration of chemisorbed oxygen atoms.

The electrical properties of  $\text{SnO}_2$  films depend on the method of preparation and subsequent heat-treatment in various ambients at temperatures above 470°K. Below this temperature the specimens are rather stable.

Conducting transparent films have a quasi-free electron concentration of  $10^{18}$ - $10^{20} \text{ cm}^{-3}$ , and mobility about one order of magnitude smaller than in single crystals. The electrical properties of  $\text{SnO}_2$  films have not been characterized satisfactorily due to the variations caused by sample preparation and purity.

### Acknowledgments

Z. M. Jarzebski has been a visiting fellow during the course of this work at the Centre for Interdisciplinary Studies in Chemical Physics and is grateful for the support from the Centre.

Manuscript submitted Aug. 19, 1975; revised manuscript received Feb. 6, 1976.

Any discussion of this paper will appear in a Discussion Section to be published in the June 1977 JOURNAL. All discussions for the June 1977 Discussion Section should be submitted by Feb. 1, 1977.

Publication costs of this article were partially assisted by the Centre for Interdisciplinary Studies in Chemical Physics.

### REFERENCES

1. Z. M. Jarzebski and J. P. Marton, *This Journal*, **123**, 199C (1976).
2. E. E. Kohnke, *J. Phys. Chem. Solids*, **23**, 1557 (1962).
3. J. A. Marley and R. C. Dockerty, *Phys. Rev.*, **140A**, 304 (1965).
4. M. Nagasawa, S. Shionoya, and S. Makishima, *Japan. J. Appl. Phys.*, **4**, 19c (1965).
5. M. Nagasawa, S. Shionoya, and S. Makishima, *J. Phys. Soc. Japan*, **20**, 1093 (1965).
6. D. F. Morgan and D. A. Wright, *Brit. J. Appl. Phys.*, **17**, 337 (1966).
7. D. F. Crabtree, R. N. S. M. Mehdi, and D. A. Wright, *J. Phys. D.*, **2**, 1503 (1969).
8. D. A. Wright, *Proc. Brit. Ceram. Soc.*, **10**, 103 (1968).
9. M. Nagasawa and S. Shionoya, *J. Phys. Chem. Solids*, **29**, 1959 (1968).
10. H. J. Van Daal, *Solid State Commun.*, **6**, 5 (1968).
11. M. Nagasawa and S. Shionoya, *J. Phys. Soc. Japan*, **30**, 1213 (1971).
12. M. Nagasawa and S. Shionoya, *Japan J. Appl. Phys.*, **10**, 472 (1971).
13. M. Nagasawa and S. Shionoya, *ibid.*, **10**, 727 (1971).
14. C. G. Fonstad and R. H. Rediker, *J. Appl. Phys.*, **42**, 2911 (1971).
15. K. J. Button, C. G. Fonstad, and W. Dreybradt,

- Phys. Rev. B*, **4**, 4539 (1971).
16. S. Samson and C. G. Fonstad, *J. Appl. Phys.*, **44**, 4618 (1973).
  17. N. F. Mott, *Can. J. Phys.*, **34**, 1356 (1956).
  18. R. A. Smith, "Semiconductors," Cambridge University Press, London (1961).
  19. A. R. Hutson, "Semiconductors," N. B. Hannay, Editor, Reinhold, New York (1959).
  20. C. A. Mead, *Solid-State Electron.*, **9**, 1023 (1966).
  21. G. L. Pearson and J. Bardeen, *Phys. Rev.*, **75**, 865 (1949).
  22. D. M. Eagles, *J. Phys. Chem. Solids*, **25**, 1243 (1964).
  23. F. E. Low and D. Pines, *Phys. Rev.*, **98**, 414 (1955).
  24. H. J. Van Daal, *J. Appl. Phys.*, **39**, 4467 (1968).
  25. S. R. Reddaway, *Brit. J. Appl. Phys.*, **17**, 697 (1966).
  26. J. Bardeen and W. Shockley, *Phys. Rev.*, **80**, 72 (1950).
  27. H. E. Matthews and E. E. Kohnke, *J. Phys. Chem. Solids*, **29**, 653 (1968).
  28. H. J. Van Daal and A. J. Bosman, *Phys. Rev.*, **158**, 736 (1967).
  29. D. J. Howarth and E. H. Sondheimer, *Proc. Roy. Soc. (London)*, **A219**, 53 (1953).
  30. J. P. Low, *Chem. Rev.*, **60**, 267 (1960).
  31. J. K. Davis, U.S. Pat. 2,564,677 (1951).
  32. U.S. Pat. 2,567,331 (1951).
  33. U.S. Pat. 2,628,299 (1953).
  34. U.S. Pat. 2,648,754 (1953).
  35. U.S. Pat. 2,651,585 (1953).
  36. U.S. Pat. 2,667,428 (1954).
  37. U.S. Pat. 2,703,767 (1955).
  38. U.S. Pat. 2,857,294 (1958).
  39. Brit. Pat. 803,885 (1958).
  40. Brit. Pat. 806,189 (1958).
  41. Brit. Pat. 806,190 (1958).
  42. Brit. Pat. 814,674 (1959).
  43. U.S. Pat. 2,920,005 (1960).
  44. U.S. Pat. 2,959,499 (1960).
  45. Brit. Pat. 857,400 (1960).
  46. U.S. Pat. 3,108,019 (1963).
  47. Brit. Pat. 931,204 (1963).
  48. Brit. Pat. 995,972 (1965).
  49. Brit. Pat. 1,018,375 (1956).
  50. Brit. Pat. 1,052,959 (1966).
  51. U.S. Pat. 3,306,768 (1967).
  52. R. H. W. Burkett, *J. Brit. I.R.E.*, **21**, 1 (1961).
  53. R. H. W. Burkett, "The Properties of Tin Oxide Resistors," British Communications and Electronics, London (1963).
  54. R. E. Aitchison, *Australian J. Appl. Sci.*, **5**, 10 (1954).
  55. K. Ishiguro, T. Sasaki, T. Arai, and I. Imai, *J. Phys. Soc. Japan*, **13**, 296 (1958).
  56. T. Arai, *ibid.*, **15**, 916 (1960).
  57. I. Imai, *ibid.*, **75**, 937 (1960).
  58. A. Ya. Kuznetsov, *Sov. Phys.-Solid State*, **2**, 30 (1960).
  59. H. Koch, *Phys. Status Solidi*, **3**, 1059 (1963).
  60. T. Inagaki, Y. Nishimura, and H. Sasaki, *Japan. J. Appl. Phys.*, **8**, 625 (1969).
  61. R. F. Bartholomew and H. W. Garfinkel, *This Journal*, **116**, 1205 (1969).
  62. T. Nishino and Y. Hamakawa, *Japan. J. Appl. Phys.*, **9**, 1085 (1970).
  63. D. Elliott, D. L. Zellmer, and H. A. Laitinen, *This Journal*, **117**, 1343 (1970).
  64. J. A. Aboaf, V. C. Marcotte, and N. J. Chou, *ibid.*, **120**, 701 (1973).
  65. D. A. Lepic, M. Eng. Thesis, McMaster University (1974).

## Applications of Electrochemistry to Fabrication of Semiconductor Devices

G. L. Schnable\*

*RCA Laboratories, Princeton, New Jersey 08540*

and P. F. Schmidt\*

*Bell Laboratories, Allentown, Pennsylvania 18103*

### ABSTRACT

This paper reviews some of the principal applications of electrochemistry to fabrication of semiconductor devices. Some of the electrochemical techniques used in fabrication of early semiconductor devices, such as chemical polishing, plating of contacts, dislocation etches, and junction delineation techniques continue to be used in manufacturing of present-day devices. Principal newer uses of electrochemistry are in anisotropic etching of patterns in single crystal Si, in preferential etching of layers of a certain conductivity type or doping level without dissolution of an underlying (or adjacent) layer of Si of different type or doping level, in anodization of aluminum metallization on Si devices, and in Au plating for conductive layers in several types of silicon devices. A wide variety of other electrochemical techniques are being used in material and device characterization, and in fabrication of developmental-type devices.

Electrochemical techniques were extensively used in the 1950's to manufacture semiconductor devices. The technologies being used in 1975 continue to employ, in somewhat modified form, some of the principles and techniques developed in the 1950's. The purpose of this paper is to review briefly some of the principal types of electrochemical techniques which were used in early semiconductor device fabrication, and to then describe the types of electrochemical techniques presently being used in fabrication of semiconductor devices.

In the early 1950's, the most commonly manufactured semiconductor devices were diodes, rectifiers, and transistors (1-4). Small-signal transistors were most commonly pnp alloy-junction bipolar germanium (1, 3, 5). The chips used were chemically polished, alloyed, and then a chemical polish was used for clean-up etching (3). Subsequently, electrolytic clean-up etching in alkaline solutions was introduced; in this process the emitter and collector leads were biased positively and injection of minority carriers (holes) into the base resulted in electrolytic etching of a shallow moat around the periphery of the emitter and collector electrodes.

\* Electrochemical Society Active Member.  
Key words: integrated circuits, silicon devices, chemical etching, materials characterization.

In the early 1950's, the process of jet electrolytic etching for producing narrow-base devices was introduced (6). Acidic fluoride solutions were used, with intense light applied to generate the minority carriers required to etch n-type Ge. Emitter and collector contacts were formed by jet electroplating of In metal on Ge to form surface barrier-type contacts. Subsequent variations included In and Cd microalloyed types in Ge, and jet-etched Si transistors (7). Leads were attached by soldering of wires to which In or Sn solder alloys had been plated in molten form (8).

Electrochemical techniques were also extensively used in characterizing early semiconductor material and device structures. Examples included etching and staining techniques to reveal junction locations (9, 10), and etching techniques to delineate dislocations (11) and other crystallographic imperfections.

The introduction of vapor phase Ge homoepitaxy and improved Si technology led to substitution of batch (wafer) processing techniques for processes in which individual device chips were handled. As a result, many of the previously used electrochemical techniques were no longer required. The evolution of planar Si integrated circuits from relatively simple arrays to very complex circuits with requirements for vastly improved cost, performance, and reliability has led to the reintroduction of a number of electrochemical techniques. Principal newer uses are in anisotropic etching of patterns in single crystal Si, in preferential etching of layers of a certain conductivity type or doping level without dissolution of an underlying layer of Si of different type or doping level, in anodization of aluminum metallization on Si devices, and in Au plating for conductive layers in several types of silicon devices. A wide variety of other electrochemical techniques are being used in material and device characterization, and in fabrication of developmental-type devices.

The theory and principles of electrochemistry of semiconductors have been studied in detail since the early 1950's, and available information has been reviewed in a number of articles (12-15) and books (16-20).

### Chemical Polishing

Chemical polishes were extensively used in early semiconductor device fabrication, including removal of work damage from lapped slices, mesa etching, and clean-up etching of Ge and Si alloy-junction devices. Chemical polishes for Ge and Si generally contain an oxidizing agent plus a complexing agent to increase solubility of the reaction products. Commonly used solutions contain nitric acid and hydrofluoric acid, respectively, to accomplish these functions.

A number of years ago, silicon wafers were principally finished by chemical polishing or by mechanical polishing. More recently, a number of techniques for chemical-mechanical polishing (21-24) have been in widespread use. One process employs a solution containing copper ions plus fluoride ions (22, 25, 26). Another type of process employs a suspension of silica particles (21, 22, 27) in an aqueous solution adjusted to a suitable alkaline pH. Chemical-mechanical polishing processes to some extent combine the benefits of both mechanical and chemical polishing, providing relatively flat wafers similar to those obtained by mechanical polishing, with a relatively low level of mechanical damage. After chemical-mechanical polishing, silicon wafers are thermally oxidized prior to device fabrication (the thermal oxidation is generally performed to obtain the oxide mask which is then patterned for planar diffusion). The oxidation process results in conversion of approximately 0.5  $\mu\text{m}$  of the silicon surface to  $\text{SiO}_2$ , and thus serves as a final etching step. Chemical-mechanical polishing techniques have also been used with compound semiconductors (28, 29).

Methods, solutions, and applications for chemical polishing of germanium, silicon, and a wide variety of compound semiconductors such as GaAs (30, 31) have been described (32-36).

Chemical etchants continue to be used to prepare mesa-type geometries in high voltage devices. They are also used to remove mechanical damage in beveled high voltage structures.

### Anisotropic Etching of Silicon

Anisotropic (crystallographically preferential) etching of (100) orientation Si wafers is widely used to permit close control of lateral etching dimensions in silicon integrated circuits (37, 38). Etching solutions and conditions are employed which result in dissolution of the Si in (100) directions at a rate which is several orders of magnitude higher than the rate in the (111) directions. Anisotropic etching through a patterned  $\text{SiO}_2$  mask produces sharply defined V grooves, with the edges [(111) planes] at an angle of  $55^\circ$  from the (100) surface of the wafer, and the depth determined by the width of the opening in the oxide mask used to define the pattern (39). Typically, alkaline solutions containing alcohol are used (40, 41).

Anisotropic etching of the silicon is used to permit fabrication of high density integrated circuits, and to improve performance. Anisotropic etching has been used to manufacture a variety of Si devices (42), including V-groove isolation structures with Ti-Pt-Au metal lines crossing relatively shallow oxidized V grooves (43, 44), dielectric-isolated circuits in which edges of the oxide-isolated single crystal islands are delineated by anisotropic etching (45), air-isolated beam-lead circuits, Si-on-sapphire integrated circuits (46, 47), and beam-lead sealed-junction transistors and circuits in which the chip separation is accomplished by anisotropic etching. In high density oxide-isolated integrated circuits, (100) orientation silicon wafers are etched with a pattern of V grooves, followed by oxidation and subsequent deposition of a relatively thick layer of polycrystalline silicon. The wafers are then lapped and polished to provide single crystal regions of silicon, each surrounded by a wall of thermally grown silicon dioxide (44, 45, 48, 49).

Anisotropic etching has been used to produce a pyramidal-type surface texture on silicon solar cells, thus eliminating the need for an antireflection coating and improving cell efficiency (50, 51). Anisotropic etching of silicon has also been used to prepare thermal printers based on heating of transistor-resistor elements in silicon regions separated by V grooves (52), and to fabricate nonblooming vidicons (53). Developmental-type applications of anisotropic etching have included preparation of silicon diffraction gratings (54) and preparation of substrates of controlled topography for assessment of edge coverage of vapor-deposited films. Anisotropic etchants also have been used to produce etch figures which permit crystallographic orientation to be accomplished optically (55).

A considerable amount of information has been published on the effects of etchant composition, substrate doping level (41, 56), and etching conditions on rate of etching of various orientations of silicon (37, 40, 57-62). Anisotropic etching of germanium has also been described (63).

### Selective Etching

A number of new types of silicon integrated circuits are based on procedures which etch a layer of silicon of one conductivity type, but do not etch an underlying layer of a different conductivity type, or of a different dopant concentration. Both chemical (64, 65) and electrochemical techniques (66-74) have been used for this type of application.

One type of electrochemical technique which is being used to fabricate developmental structures is to perform electrochemical etching under conditions such that an  $n^+$  layer is dissolved but an underlying layer of n-type Si is not attacked. In this technique, electrolytic etching proceeds until all of the  $n^+$  material is dissolved, but does not etch the n-type layer if the donor level is less than approximately  $2 \times 10^{16}$  atoms/ $\text{cm}^3$ . Typical conditions would employ 5% aqueous HF

solution (66, 69), and total darkness. Substrates and conditions must be employed which do not result in localized avalanche breakdown in the n-type silicon (70, 75, 76).

An example of an application is the process for obtaining thin single crystal silicon layers on an insulating substrate (67, 72, 77). In one case, the final structure consists of a thin single crystal layer over an SiO<sub>2</sub> layer over a thick supporting layer of polycrystalline silicon (67, 72). Such structures would be used in some of the same applications as silicon on sapphire.

Several types of processes for controlled electrochemical etching of wafers have been described, including electrolytic etching to remove p-type layers from pn substrates, and to remove n<sup>+</sup> layers from n<sup>+</sup>n substrates. Another variation is to apply an external bias to a structure such that chemical etching of one type of layer occurs, but the process stops when the underlying layer is reached (68). Etch rate ratios for active *vs.* passive regions of greater than 200:1 have been obtained (68).

Alkali-alcohol-type etchants have been shown to etch only n-type silicon in samples containing pn junctions. Chemical etching techniques in which selected etchants dissolve Si of one doping level, with relatively little attack on an underlying (or adjacent) Si layer of different doping level, have also been used to prepare specialized device structures.

#### Diffusion, Anodization, and Passivation

The process of obtaining doped layers in silicon devices by diffusion from conventional sources, whether based on gas sources, solid wafer sources, doped oxide, or spin-on techniques, embodies essentially chemical or displacement plating, in that the silicon wafer at high temperatures reduces an oxide of the dopant at the oxide-silicon interface. Examples include borosilicate, phosphosilicate, and arsenosilicate glasses.

Anodization has been used to form capacitors in silicon linear integrated circuits. More commonly, thermal oxidation is used for that purpose at present. Much information has been published on anodization of Si (78-80).

Anodization of a number of III-V compounds has also been used to form overlying oxide layers. With indium antimonide detectors, for example, anodization has been used to improve surface-related electrical characteristics. With gallium arsenide, anodized layers have been used as a mask for subsequent diffusion (81). Anodization of GaP and Ga(AsP) has also been studied (82, 83). Properties of anodic oxides of InSb (84) and of GaAs (85-88) have been described. Anodic etching has been used to fabricate GaAs diodes (89).

Electrophoresis (deposition of charged, suspended particles from a liquid onto a surface of opposite polarity) is being used to selectively deposit glass particles on silicon power device surfaces, with the deposited glass subsequently fused to form a smooth, patterned layer of passivating glass in grooves or at the edge of etched mesas (90). For these applications the frit is generally a lead borosilicate-type glass, and the deposit, after fusion, may be 10-30 μm thick.

The process of anodization of silicon under conditions which result in a film of porous elemental silicon (91), followed by oxidation, has been used to obtain special patterned oxidized structures with absence of steep topographic steps (74, 92, 93). Anodization of silicon to form a thick porous oxide has also been used to obtain isolated integrated circuit elements (94).

#### Device Metallization and Processing

The electroless plating of nickel, which was used for electrodes in early transistor types, continues to be used for metallization of certain power silicon devices (90, 95). One technique employs chemical (galvanic) plating of noble metals on exposed silicon contact regions to attain catalyst films for initiation of electroless

Ni plating (95). Electroless plating has also been used to form ohmic contacts to certain III-V compounds (95).

Anodization of Al has been used to delineate patterns of metal in multilevel-metallized integrated circuit arrays (96-105). In one process the first level Al metallization is selectively anodized, with regions which are to remain Al metal masked by a photoresist pattern. The anodization process, while producing a volume of oxide somewhat larger than that of the aluminum metal from which it was formed, results in a surface topography which is free of steep steps, and is not difficult to cover with delineated lines in the second level metallization pattern. Anodization has also been used to delineate tungsten (106) and platinum (107) patterns, and to trim thin film resistors (108).

Anodization of aluminum metallization on silicon devices has been employed to form a thin anodic layer over Al conductors to attain beveled edges (109), and to decrease susceptibility of the aluminum to hillock formation (110) or to failure due to electromigration (current-induced mass transport) (111-113).

Gold plating is extensively used to deposit layers which are part of the metallization system in silicon devices, including both beam-lead-type devices (114) and other types of silicon devices with gold metallization systems (90, 115). Typically, the metal system is titanium-platinum (or titanium-palladium) deposited by vacuum techniques, followed by application of photoresist patterns and buildup, locally, of gold by electrodeposition in unmasked areas. Plating solutions and deposition conditions must be maintained to assure close control of lateral spreading of the resist-defined deposited gold layer (116) and of purity, hardness, and roughness of the gold (117-121). Jet plating techniques have been applied to permit use of higher current densities (122, 123). Electroless gold deposition techniques have also been shown to be feasible for fabrication of beam-lead devices (124, 125). Electroplating has also been used to form raised pads for flip chip or other wireless simultaneous bonding approaches (126, 127).

Electroplating is very widely used in preparation of lead frames, headers, studs, and other parts for assembly and packaging of semiconductor devices (95, 126). In preparation of lead frames for semiconductor devices, nozzles are sometimes used to direct the plating solution to those areas where a spot of electrodeposited gold is desired (128). While masking is sometimes used, it is possible to adjust conditions to achieve well-defined localized deposits without masking (128).

#### Electrochemical Techniques for Control of Semiconductor Device Manufacturing Processes

In addition to the direct use of electrochemical processes in fabrication of semiconductor devices, electrochemical processes are also extensively used in the characterization and evaluation of semiconductor materials and device structures, and in related processes. For example, several types of special etchants are widely used to define dislocations in silicon (129-132), germanium, gallium arsenide (133, 134), gallium arsenide-phosphide, indium antimonide, and other semiconductors (132). For silicon, Dash etch (11) was extensively used in early device fabrication. To a large extent Sirtl etch (135, 136) and a modified etch developed particularly for (100) silicon (137) have supplanted the earlier etchants (130, 131, 138).

One of the most widely used control methods for determining the depth of junctions in semiconductor device manufacturing today is based on angle lapping and staining techniques (138). While several refinements to the techniques have been made, the basic techniques are similar to that developed for early germanium and silicon transistors. Special etching solutions are also used to delineate high-low junctions in silicon, thus permitting determination of the depth of diffusion into substrates or determination of the thick-

ness of epitaxial layers (32). Etching techniques for revealing junctions in compound semiconductors such as PbS (139) have also been described. In general, junction delineation techniques depend on the difference in the electrochemical potential existing between p-type and n-type regions of the semiconductor under the illumination conditions employed. Somewhat similarly, the mechanism by which dislocation etchants define dislocations is based on the fact that localized, defective regions become anodic whereas more nearly perfect surrounding regions become cathodic in the etchant. Thus, in general, less perfect regions etch more rapidly than high quality crystalline regions. Etchants are also used to reveal resistivity striations (38, 140-142) and swirls in silicon and in other semiconductor materials. Copper displacement plating has been used to delineate imperfections in polished silicon substrates (143).

Reverse osmosis (application of pressure to an aqueous solution in contact with a semipermeable membrane) is being used in purification of water used in semiconductor device processing (144-146). The measurement of stability of thermally grown oxides to determine alkaline ion content is essentially an electrochemical process, with alkali ions moving in the amorphous silicon dioxide layer at temperatures such as 300°C in an electric field. Electrochemical processes (147), such as copper plating, electrophoretic decoration, electrolytic etching, and use of liquid crystal techniques (148) have also been used to assess the integrity of various types of dielectrics in semiconductor devices (149).

Electrolytic etching has been used to reveal dislocations in emitter and base regions of diffused silicon transistors (150). Anodic decoration techniques have also been used (151, 152) to reveal defects in devices.

One technique for profiling diffused layers in silicon is based on successive anodization followed by etching and measurement of sheet resistivity (153). This process is still being used in laboratory studies of profiles of diffused or ion-implanted structures. An electrochemical technique for automatic depth profiling of gallium arsenide has recently been described (154).

The prevention of corrosion of metallization materials in semiconductor devices constitutes a very important application of electrochemical principles. In the case of aluminum-metallized silicon devices, both cathodic and anodic corrosion have been shown to lead to electrical opens (155-159). With devices containing gold metallization, gold dendrites formed in humid atmospheres can produce shorts between conductors (118, 120, 158-163).

### Conclusions

Some of the early applications of electrochemistry for semiconductor device fabrication continue to be used, and in some cases almost in the same way as in the 1950's. In other cases, improvements and extensive modifications have been made. Some of the early applications, such as in germanium devices and in non-oxide-passivated silicon devices, have been supplanted by the use of other types of devices, primarily oxide-passivated silicon devices. Principal newer uses of electrochemistry are in anisotropic etching and preferential etching of certain layers of silicon, and in gold plating for conductive layers of metallization in several types of silicon devices.

Many of the early electrochemical techniques used for characterizing semiconductor materials and device structures, such as junction delineation techniques and dislocation etches, continue to be used in modified form in present-day silicon material assessment and process control.

### Acknowledgments

The authors would like to thank a number of people who contributed to the preparation of this review, including N. Feldstein, W. Kern, G. Lozier, and J. Vossen

for reading the manuscript and making helpful suggestions.

Manuscript submitted Oct. 14, 1975; revised manuscript received March 19, 1976. This was Paper 157 presented at the Dallas, Texas, Meeting of the Society, Oct. 5-9, 1975.

Any discussion of this paper will appear in a Discussion Section to be published in the June 1977 JOURNAL. All discussions for the June 1977 Discussion Section should be submitted by Feb. 1, 1977.

Publication costs of this article were assisted by RCA Laboratories.

### REFERENCES

1. A. Coblenz and H. L. Owens, "Transistors: Theory and Applications," McGraw-Hill Book Co., New York (1955).
2. "Transistors I," RCA Laboratories, Princeton, New Jersey (1956).
3. "Transistor Technology," Vol. 2 and 3, F. J. Biondi, Editor, D. Van Nostrand Co., Princeton, New Jersey (1958).
4. J. N. Shive, "Semiconductor Devices," D. Van Nostrand Co., Princeton, New Jersey (1959).
5. "Handbook of Semiconductor Electronics," 2nd ed., L. P. Hunter, Editor, McGraw-Hill Book Co., New York (1962).
6. W. E. Bradley *et al.*, *Proc. IRE*, **41**, 1702 (1953).
7. G. L. Schnable and W. M. Lilker, *Electrochem. Technol.*, **1**, 203 (1963).
8. G. L. Schnable, *This Journal*, **108**, 964 (1961).
9. D. R. Turner, *ibid.*, **106**, 701 (1959).
10. P. A. Iles and P. J. Coppen, *Brit. J. Appl. Phys.*, **11**, 177 (1960).
11. W. C. Dash, *J. Appl. Phys.*, **27**, 1193 (1956).
12. J. F. Dewald, in "Semiconductors," N. B. Hannay, Editor, pp. 727-752, Reinhold Publishing Corp., New York (1959).
13. P. J. Boddy, *J. Electroanal. Chem.*, **10**, 199 (1965).
14. H. Gerischer, in "Physical Chemistry," Vol. 9, Part A, W. Jost, Editor, pp. 463-542, Academic Press, New York (1970).
15. Y. V. Pleskov, in "Progress in Surface and Membrane Science," Vol. 7, J. F. Danielli, M. D. Rosenberg, and D. A. Cadenhead, Editors, pp. 57-93, Academic Press, New York (1973).
16. "The Surface Chemistry of Metals and Semiconductors," H. C. Gatos, Editor, John Wiley & Sons, Inc., New York (1960).
17. "The Electrochemistry of Semiconductors," P. J. Holmes, Editor, Academic Press, London (1962).
18. E. A. Efimov and I. G. Erusalimchik, "Electrochemistry of Germanium and Silicon," translation edited by A. Peiperl, Sigma Press, Washington, D.C. (1963).
19. V. A. Myamlin and Y. V. Pleskov, "Electrochemistry of Semiconductors," Plenum Press, New York (1967).
20. A. K. Vijh, "Electrochemistry of Metals and Semiconductors," Marcel Dekker, Inc., New York (1973).
21. T. M. Buck and R. L. Meek, in "Silicon Device Processing," C. P. Marsden, Editor, pp. 419-430, NBS Special Publication 337, Washington, D.C. (1970).
22. J. T. Law, *Solid State Technol.*, **14**, 25 (Jan. 1971).
23. J. V. Cesna, *ibid.*, **15**, 62 (March 1972).
24. J. J. Colacino and T. A. Bartush, *ibid.*, **16**, 30 (Aug. 1973).
25. E. Mendel and K. Yang, *Proc. IEEE*, **57**, 1476 (1969).
26. L. H. Blake and E. Mendel, *Solid State Technol.*, **13**, 42 (Jan. 1970).
27. J. H. Matlock, "Transactions of the Electronic Materials Conference," p. 1-1, Materials Research Corp., Orangeburg, New York (1973).
28. E. W. Jensen, *Solid State Technol.*, **16**, 49 (Aug. 1973).
29. E. Mendel and J. S. Basi, Abstract 167, p. 437, The Electrochemical Society Extended Abstracts, Fall Meeting, Dallas, Texas, Oct. 5-10, 1975.
30. C. D. Dobson, in "Gallium Arsenide Lasers," C. H. Gooch, Editor, pp. 193-222, Wiley-Interscience, London (1969).
31. V. L. Rideout, *This Journal*, **119**, 1778 (1972).
32. P. F. Kane and G. B. Larrabee, "Characterization of Semiconductor Materials," McGraw-Hill Book Co., New York (1970).

33. J. A. Copeland and S. Knight, in "Semiconductors and Semimetals," Vol. 7A, R. K. Willardson and A. C. Beer, Editors, pp. 3-72, Academic Press, New York (1971).
34. H. F. Wolf, "Semiconductors," pp. 130-136, Wiley-Interscience, New York (1971).
35. T. C. Harman and T. Melngailis, in "Applied Solid State Science," Vol. 4, R. Wolfe, Editor, pp. 1-94, Academic Press, New York (1974).
36. B. Tuck, *J. Mater. Sci.*, **10**, 321 (1975).
37. H. A. Waggener, R. C. Kragness, and A. L. Tyler, Abstract 11.1, p. 68, International Electron Devices Meeting Abstracts, October 1967.
38. W. J. Beyen and O. B. Cecil, in "Semiconductor Silicon 1973," H. R. Huff and R. R. Burgess, Editors, pp. 1-16, The Electrochemical Society Softbound Symposium Series, Princeton, New Jersey (1973).
39. K. E. Bean and P. S. Gleim, *Proc. IEEE*, **57**, 1469 (1969).
40. K. E. Bean, R. L. Yeakley, and T. K. Powell, Abstract 23, p. 68, The Electrochemical Society Extended Abstracts, Spring Meeting, San Francisco, Calif., May 12-17, 1974.
41. J. B. Price and W. C. Roman, Abstract 236, p. 584, The Electrochemical Society Extended Abstracts, Fall Meeting, Miami Beach, Florida, Oct. 8-13, 1972.
42. M. J. Declercq, *IEEE J. Solid-State Circ.*, **sc-10**, 191 (1975).
43. Staff article, *Electronics*, **44**, 35 (June 1971).
44. S. W. Fields, *ibid.*, **45**, 39 (July 1972).
45. K. E. Bean and W. R. Runyan, Abstract 138, p. 323, The Electrochemical Society Extended Abstracts, Fall Meeting, New York, N. Y., Oct. 13-17, 1974.
46. D. P. Clemens, Abstract 159, p. 407, The Electrochemical Society Extended Abstracts, Fall Meeting, Boston, Mass., Oct. 7-11, 1973.
47. C. Raetzl, S. Schild, and H. Schlötterer, Abstract 142, p. 336, The Electrochemical Society Extended Abstracts, Fall Meeting, New York, N.Y., Oct. 13-17, 1974.
48. Staff article, *Electronics*, **45**, 39 (July 1972).
49. W. R. Runyan, *Electronic Pkg. and Prod.*, **14**, 162 (July 1974).
50. R. A. Arndt, J. F. Allison, J. G. Haynos, and A. Meulenberg, Jr., Proceedings of the 11th IEEE Photovoltaic Spec. Conference, p. 40 (1975).
51. C. R. Baraona and H. W. Brandhorst, *ibid.*, p. 44 (1975).
52. T. R. Payne and H. R. Plumlee, *IEEE J. Solid-State Circuits*, **sc-8**, 71 (1973).
53. K. E. Bean and J. R. Lawson, *ibid.*, **sc-9**, 111 (1974).
54. W. Tsang and S. Wang, *J. Appl. Phys.*, **46**, 2164 (1975).
55. S. J. T. Owen and A. H. Watt, *Microelectronics*, **5**, No. 3, 37 (1974).
56. J. C. Greenwood, *This Journal*, **116**, 1325 (1969).
57. R. M. Finne and D. L. Klein, *ibid.*, **114**, 965 (1967).
58. W. K. Zwickler and S. K. Kurtz, in "Semiconductor Silicon 1973," H. R. Huff and R. R. Burgess, Editors, pp. 315-326, The Electrochemical Society Softbound Symposium Series, Princeton, New Jersey (1973).
59. J. B. Price, *ibid.*, pp. 339-353.
60. M. J. Declercq, L. Gerzberg, and J. D. Meindl, *This Journal*, **122**, 545 (1975).
61. D. F. Weirrauch, *J. Appl. Phys.*, **46**, 147 (1975).
62. M. J. Declercq, J. P. De Moor, and J. P. Lambert, Abstract 171, p. 446, The Electrochemical Society Extended Abstracts, Fall Meeting, Dallas, Texas, Oct. 5-10, 1975.
63. W. C. Erdman and P. F. Schmidt, U.S. Pat. 3,738,811 (1973).
64. G. L. Kuhn and C. J. Rhee, *This Journal*, **120**, 1563 (1973).
65. H. Muraoka, T. Ohhashi, and Y. Sumitomo, in "Semiconductor Silicon 1973," H. R. Huff and R. R. Burgess, Editors, pp. 327-338, The Electrochemical Society Softbound Symposium Series, Princeton, New Jersey (1973).
66. H. J. A. van Dijk and J. de Jonge, *This Journal*, **117**, 553 (1970).
67. M. J. J. Theunissen, J. A. Appels, and W. H. C. G. Verkuylen, *ibid.*, **117**, 959 (1970).
68. H. A. Waggener, *Bell Syst. Tech. J.*, **49**, 473 (1970).
69. R. L. Meek, *This Journal*, **118**, 437 (1971).
70. R. L. Meek, *ibid.*, **118**, 1240 (1971).
71. C. P. Wen and K. P. Weller, *ibid.*, **119**, 547 (1972).
72. T. I. Kamins, *Proc. IEEE*, **60**, 915 (1972).
73. H. A. Waggener and J. V. Dalton, Abstract 237, p. 587, The Electrochemical Society Extended Abstracts, Fall Meeting, Miami Beach, Fla., Oct. 8-13, 1972.
74. T. Yashiro, K. Saito, and T. Suzuki, Abstract 147, p. 351, The Electrochemical Society Extended Abstracts, Fall Meeting, New York, N.Y., Oct. 13-17, 1974.
75. M. J. J. Theunissen, *This Journal*, **119**, 351 (1972).
76. M. J. Hill, *ibid.*, **120**, 142 (1973).
77. C. J. Dell'Oca and H. G. Nonnenmacher, Abstract 146, p. 348, The Electrochemical Society Extended Abstracts, Fall Meeting, New York, N.Y., Oct. 13-17, 1974.
78. P. F. Schmidt and W. Michel, *This Journal*, **104**, 230 (1957).
79. E. F. Duffek, E. A. Benjamini, and C. Mylroie, *Electrochem. Technol.*, **3**, 75 (1965).
80. J. D. E. Beynon, G. G. Bloodworth, and I. M. McLeod, *Solid-State Electron.*, **16**, 309 (1973).
81. R. A. Logan, B. Schwartz, and W. J. Sundburg, *This Journal*, **120**, 1385 (1973).
82. F. Ermanis and B. Schwartz, *ibid.*, **121**, 1665 (1974).
83. C. S. Guenther, P. V. S. Rao, S. Thomas, and W. Paulson, Abstract 159, p. 420, The Electrochemical Society Extended Abstracts, Fall Meeting, Dallas, Texas, Oct. 5-10, 1975.
84. C. W. Wilmson, G. C. Vasbinder, and Y. K. Chan, *J. Vac. Sci. Technol.*, **12**, 56 (1975).
85. D. C. Rode, B. Schwartz, and J. V. DiLorenzo, *Solid-State Electron.*, **17**, 1119 (1974).
86. H. Hasegawa, K. E. Forward, and H. Hartnagel, *Electron. Lett.*, **11**, 53 (1975).
87. H. Hasegawa, K. E. Forward, and H. L. Hartnagel, *Appl. Phys. Lett.*, **26**, 567 (1975).
88. H. Hasegawa and H. L. Hartnagel, *This Journal*, **123**, 713 (1976).
89. W. C. Niehaus and B. Schwartz, *Solid-State Electron.*, **19**, 175 (1976).
90. G. L. Schnable, W. Kern, and R. B. Comizzoli, *This Journal*, **122**, 1092 (1975).
91. D. Turner, *ibid.*, **105**, 402 (1958).
92. K. Hamano, M. Sakamoto, and H. Yamanaka, *Jpn. J. Appl. Phys.*, **14**, 413 (1975).
93. Y. Watanabe, Y. Arita, T. Yokoyama, and Y. Igarashi, *This Journal*, **122**, 1351 (1975).
94. B. Cook, *Electronics*, **48**, 109 (Nov. 1975).
95. N. Feldstein, *Solid State Technol.*, **16**, 87 (Dec. 1973).
96. H. Tsunemitsu and H. Shiba, Abstract 18.4, p. 128, International Electron Devices Meeting Abstracts, IEEE (1969).
97. M. Crosset and N. Nouailles, *Rev. Tech. Thomson-CSF*, **2**, 497 (1970).
98. W. R. McMahon and B. G. Carbajal, Final Report to Naval Air Systems Command on Contract No. N00019-70-C-0487, Texas Instruments Inc., Dallas, Texas (1971).
99. D. R. Collins, S. R. Shortes, W. R. McMahon, R. C. Bracken, and T. C. Penn, *This Journal*, **120**, 521 (1973).
100. G. C. Schwartz, Abstract 3, p. 13, The Electrochemical Society Extended Abstracts, Spring Meeting, San Francisco, Calif., May 12-17, 1974.
101. G. C. Schwartz and V. Platter, *This Journal*, **123**, 34 (1976).
102. H. Tsunemitsu, Abstract 79, p. 179, The Electrochemical Society Extended Abstracts, Spring Meeting, Toronto, Canada, May 11-16, 1975.
103. H. D. Koritke, Abstract 82, p. 185, *ibid.*
104. G. C. Schwartz and V. Platter, *This Journal*, **123**, 300 (1976).
105. G. C. Schwartz and V. Platter, *ibid.*, **122**, 1508 (1975).
106. W. Kern and J. M. Shaw, *ibid.*, **118**, 1699 (1971).
107. R. P. Frankenthal and D. H. Eaton, *ibid.*, **123**, 703 (1976).
108. P. J. Dickerson, *West. Electr. Eng.*, **19**, 24 (Jan. 1975).
109. T. Agatsuma, A. Kikuchi, K. Nakada, and A. Tomozawa, *This Journal*, **122**, 825 (1975).
110. C. J. Dell'Oca and A. J. Learn, *Thin Solid Films*, **8**, R47 (1971).

111. C. J. Dell'Oca and M. L. Barry, *Solid-State Electron.*, **15**, 659 (1972).
112. T. Satake, K. Yokoyama, S. Shirakawa, and K. Sawaguchi, *Jpn. J. Appl. Phys.*, **12**, 518 (1973).
113. A. J. Learn, *J. Appl. Phys.*, **44**, 1251 (1973).
114. M. P. Lepselter, *Bell Syst. Tech. J.*, **45**, 233 (1966).
115. A. M. Tuxford and L. T. Ramankiw, Abstract 223, p. 551, The Electrochemical Society Extended Abstracts, Fall Meeting, New York, N.Y., Oct. 13-17, 1974.
116. K. R. Newby, "Fourth Plating in the Electronics Industry Symposium Proceedings," p. 225, American Electroplaters Society, East Orange, New Jersey (1973).
117. D. J. Huettner and R. C. Sanwald, *Plating*, **59**, 750 (1972).
118. J. J. Mazenko, "International Microelectronics Symposium Proceedings," ISHM, p. 450 (October 1974).
119. C. J. Raub, "Fifth Plating in the Electronics Industry Symposium Proceedings," p. 55, American Electroplaters Society, East Orange, New Jersey (1975).
120. J. J. Mazenko, "Proceedings of the 1975 Electronic Components Conference," IEEE, p. 65 (1975).
121. J. L. Jellison, *ibid.*, p. 271.
122. E. S. Figuli, *West. Electr. Eng.*, **18**, 18 (Jan. 1974).
123. E. S. Figuli, *Electron. Pkg. Prod.*, **14**, 49 (May 1974).
124. Y. Okinaka, R. Sard, C. Wolowodiuk, W. H. Craft, and T. F. Retajczyk, *This Journal*, **121**, 56 (1974).
125. R. Sard, Y. Okinaka, and H. A. Waggener, *ibid.*, **121**, 62 (1974).
126. E. F. Duffek, "Fourth Plating in the Electronics Industry Symposium Proceedings," p. 194, American Electroplaters Society, East Orange, New Jersey (1973).
127. H. Khajezadeh and A. S. Rose, 13th Ann. Proc. Reliab. Phys., p. 87 (1975).
128. G. R. Hower and D. C. Woerner, "Fifth Plating in the Electronics Industry Symposium Proceedings," p. 103, American Electroplaters Society, East Orange, New Jersey (1975).
129. A. Mayer, *Solid State Technol.*, **15**, 38 (April 1972).
130. S. Dash, in "Semiconductor Silicon 1973," H. R. Huff and R. R. Burgess, Editors, pp. 626-638, The Electrochemical Society Softbound Symposium Series, Princeton, New Jersey (1973).
131. D. G. Schimmel, Abstract 142, p. 336, The Electrochemical Society Extended Abstracts, Spring Meeting, Toronto, Canada, May 11-16, 1975.
132. W. R. Runyan, "Semiconductor Measurements and Instrumentation," pp. 21-63, 187-216, McGraw-Hill Book Co., New York (1975).
133. R. Glicksman, *Solid State Technol.*, **13**, 29 (Sept. 1970); *ibid.*, **13**, 39 (Oct. 1970).
134. D. J. Stirland and B. W. Straughan, *Thin Solid Films*, **31**, 139 (1976).
135. E. Sirtl and A. Adler, *Z. Metallkd.*, **52**, 529 (1961).
136. P. M. Garavaglia and H. W. Gutsche, *Solid State Technol.*, **15**, 39 (1972).
137. F. S. d'Aragona, *This Journal*, **119**, 948 (1972).
138. D. G. Schimmel, *ibid.*, **123**, 734 (1976).
139. H. Preier and H. Pfeiffer, *ibid.*, **121**, 595 (1974).
140. A. J. R. deKock and P. G. T. Boonen, *ibid.*, **119**, 1241 (1972).
141. K. V. Ravi and C. J. Varker, in "Semiconductor Silicon 1973," H. R. Huff and R. R. Burgess, Editors, pp. 136-149, The Electrochemical Society Softbound Symposium Series, Princeton, New Jersey (1973).
142. A. J. R. deKock, P. J. Severin, and P. J. Roksnor, *Phys. Status Solidi A*, **22**, 163 (1974).
143. M. J. Grieco, *This Journal*, **121**, 289 (1974).
144. A. R. Mills, *Solid State Technol.*, **13**, 41 (July 1970); *ibid.*, **13**, 71 (Aug. 1970).
145. C. K. Monzeglio, *ibid.*, **15**, 31 (Feb. 1972).
146. W. C. Savola and J. T. Wallace, *ibid.*, **16**, 47 (Nov. 1973).
147. L. B. Leder, *Surf. Technol.*, **4**, 31 (1976).
148. D. J. Channin, *IEEE Trans. Electron Devices*, **ed-21**, 650 (1974).
149. W. Kern, *RCA Rev.*, **34**, 655 (1973).
150. G. H. Plantinga, *IEEE Trans. Electron. Devices*, **ed-16**, 394 (1969).
151. W. K. Tice, R. C. Lange, and R. B. Shasteen, in "Semiconductor Silicon 1973," H. R. Huff and R. R. Burgess, Editors, pp. 639-650, The Electrochemical Society Softbound Symposium Series, Princeton, New Jersey (1973).
152. M. V. Kulkarni, P. J. Smith, G. A. A. James, and H. A. Troutman, *This Journal*, **121**, 280 (1974).
153. E. Tannenbaum, *Solid-State Electron.*, **2**, 123 (1961).
154. T. Ambridge and M. M. Faktor, in "Gallium Arsenide and Related Compounds, 1974," Inst. Phys. Conf. Ser., No. 24, p. 320, London (1975).
155. S. C. Kolesar, 12th Ann. Proc. Reliab. Phys., p. 155 (1974).
156. H. Koelmans, *ibid.*, p. 168.
157. W. M. Paulson and R. W. Kirk, *ibid.*, p. 172.
158. R. P. Frankenthal, in "Properties of Electrodeposits—Their Measurement and Significance," R. Sard, H. Leidheiser, Jr., and F. Ogburn, Editors, pp. 142-169, The Electrochemical Society Softbound Symposium Series, Princeton, New Jersey (1974).
159. E. P. G. T. van de Ven and H. Koelmans, *This Journal*, **123**, 143 (1976).
160. J. C. Wright, 11th Ann. Proc. Reliab. Phys., p. 224 (1973).
161. E. B. Hakim and J. R. Shappirio, *Solid State Technol.*, **18**, 66 (April 1975).
162. A. Shumka and R. R. Piety, 13th Ann. Proc. Reliab. Phys., pp. 93-98 (1975).
163. F. J. Grunthaler, T. W. Griswold, and P. J. Clendening, *ibid.*, pp. 99-106.





## Physical Properties of SnO<sub>2</sub> Materials

### III. Optical Properties

Z. M. Jarzebski

*Centre for Interdisciplinary Studies in Chemical Physics, University of Western Ontario, London, Ontario, Canada*

and J. P. Marton<sup>\*,1</sup>

*Welwyn Canada Limited, London, Ontario, Canada*

#### ABSTRACT

Stannic oxide in its pure form is an n-type wide-bandgap semiconductor. Its electrical conduction results from the existence of point defects (native and foreign atoms) which act as donors or acceptors. Some unique properties of SnO<sub>2</sub> make the material useful for many applications; therefore, increasing attention is being paid to studies on this oxide, especially on the methods of preparation, and its electrical and optical properties. The purpose of this series is to provide a general up-to-date review of the investigations carried out and to help identify important areas for further studies. The first part<sup>2</sup> was concerned with the preparation and defect structure of single crystals, sintered polycrystalline samples, and thin films, and in the second part<sup>3</sup> we reviewed the electrical properties of these materials. In this part we discuss the optical properties of SnO<sub>2</sub> single crystals and films. This concludes our review of the physical properties of SnO<sub>2</sub> materials.

The methods of preparation of single crystals, sintered materials, and thin films of tin dioxide and their defect structure have been described (1) in Part I of this series. In Part II the electrical properties of these materials in pure and doped forms have been reviewed (2). In this last part we discuss the optical properties of tin dioxide solids.

The optical properties of this material are unique in two respects. First, SnO<sub>2</sub> is one of the few electrical conductors that is optically transparent in the visible range of wavelengths in its undoped form, and second, it is the simplest oxide semiconductor of noncubic structure with nonorbital complications. The first feature is often applied to fabricate transparent conductive coatings on, e.g., glass, while the second provides a good medium to study symmetry effects in crystal potentials, etc. For these reasons the optical properties of various types of tin oxide materials have been studied extensively in the past.

In this paper we review the work done to date on the optical behavior of SnO<sub>2</sub> single crystals and films. A summary of major efforts is listed chronologically in Table I. It covers published results in the period 1954-1974.

#### Single Crystals

*Optical absorption.—Short wavelength properties.*—The first investigations of optical properties of SnO<sub>2</sub> single crystals were carried out in 1962 by Kohnke (8) on natural cassiterite. From the short wavelength cutoff, he found a fundamental optical energy gap,  $E_g$ , to be  $\geq 3.54$  eV with a thermal shift  $dE_g/dT$  of  $-6 \times 10^{-4}$  eV/°K measured in the temperature range from 80° to 415°K. The lower limit for the optical forbidden en-

ergy gap of 3.54 eV is in good agreement with the value of 3.44 eV obtained by Kohnke and Hurt (38) from the maximum of the conductivity spectral response curve. Kohnke also observed a sharp absorption of wavelength of 3.07  $\mu\text{m}$  which he attributed to the presence of O-H groups oriented in a plane perpendicular to the c axis of the crystal. He observed a long wavelength cutoff region at about 7.2  $\mu\text{m}$  with a slight transmission having a maximum at 7.55  $\mu\text{m}$ .

The first investigations of optical absorption in synthetic crystals of tin oxide were carried out by Summitt and Borrelli (9,10,15) and Summitt (18) on single crystals grown from the vapor phase by Marley and MacAvoy (1,39). They calculated the absorption coefficient,  $K$ , from the relation (40)

$$T = \frac{(1 - R^2) \exp(Kd)}{\exp(2Kd) - R^2} \quad [1]$$

and from tables (41). In the expression,  $T$  is the transmittance,  $R$  is the reflectivity, and  $d$  is the crystal thickness.

The ultraviolet absorption coefficient of SnO<sub>2</sub> as a function of photon energy was measured by Summitt, Marley, and Borrelli (9) and is shown in Fig. 1. As can be seen from the figure, pronounced dichroism exists in the u.v. region. The absorption edge for radiation polarized parallel and perpendicular to the c axis is separated by approximately 0.3 eV.

As it is well known (42), the absorption coefficient is related to photon energy for direct transitions as

$$K = K_0(h\nu - E_g)^{1/2} \quad [2]$$

where  $E_g$  is the vertical separation between valence and conduction bands, and  $K_0$  is a constant. By plotting the experimental values of  $K^2$  vs. photon energy and extrapolating to zero absorption, the width of the energy gap may be obtained. Using this method, the

\* Electrochemical Society Active Member.

<sup>1</sup> Present address: Department of Engineering Physics, McMaster University, Hamilton, Ontario, Canada.

<sup>2</sup> THIS JOURNAL, July 1976.

<sup>3</sup> THIS JOURNAL, September 1976.

Key words: single crystals, films, optical absorption, photoconductivity, luminescence, phosphorescence.



Table I. Optical properties of SnO<sub>2</sub> materials

Year	Author	Reference	Materials	Properties	Temperature range, °K	Conclusion drawn by author
1954	Aitchison	(3)	Films prepared by hydrolysis of SnCl <sub>4</sub>	Reflection Absorption	300	SnO <sub>2</sub> is transparent from 0.2 to 14 μm.
1958	Ishiguro, Sasaki, Arai, and Imai	(4)	Films prepared by hydrolysis of SnCl <sub>4</sub>	Transmission Reflection	300	Fundamental absorption gap is about 4 eV. Plasma frequency of the carriers lies in the near infrared region. Coulomb scattering of impurity ions is the predominant scattering mechanism in the transparent conducting films.
1958	Ishiguro, Sasaki, Arai, and Imai	(5)	As above	Refractive index	300	Lifetime of the plasma wave is about $2.6 \times 10^{-15}$ sec.
1959	Miloslavskii	(6)	Pyrolytic decomposition of SnCl <sub>2</sub> and SnCl <sub>4</sub>	Absorption Transmission	120-470	The absorption by impurity atoms was observed. Two bands were observed: a narrow band with a maximum at 16.4 μm and a wide band with maximum at $8.5 \pm 9$ μm. Both absorption bands increased with increasing conductivity.
1960	Arai	(7)	Conductive and non-conductive SnO <sub>2</sub> films and SnO films	Absorption Reflection Transmission	130-300	The absorption edge for conductive and nonconductive SnO <sub>2</sub> films is found to be $(3.82 \pm 0.030)$ and $(3.71 \pm 0.025)$ eV, respectively. The temperature change of absorption edge for both materials is $-2.0 \times 10^{-4}$ eV/°K.
1962	Kohnke	(8)	Natural single crystals	Absorption Transmission	80-415	Fundamental energy gap is 3.54 eV. $\frac{dE_g}{dT} = -6 \times 10^{-4} \frac{\text{eV}}{\text{K}}$ A sharp absorption observed at 3.07 μm is attributed to O-H groups.
1964	Summitt, Marley, and Borrelli	(9)	Single crystals grown by vapor transport technique	U.V. absorption	300	The u.v. absorption coefficients are as high as $10^3$ cm <sup>-1</sup> . The use of polarized light revealed a large dichroism, the absorption edges differing by about 0.3 eV for radiation polarized parallel and perpendicular to the c axis. Both edges represent intrinsic transitions with the direct energy gaps 3.93 and 3.57 eV for radiation polarized parallel and perpendicular, respectively. Thresholds for phonon coupled transitions occur approximately at 3.7 and 3.4 eV, but indirect transitions appear to involve several lattice vibrational frequencies.
1965	Summitt and Borrelli	(10)	As above	Infrared absorption	50-900	Near infrared absorption coefficient (0.5-0.6 μm) varies directly with the concentration of carriers over the range $n = 10^{17}$ to $2 \times 10^{16}$ cm <sup>-3</sup> , and the third power of wavelength.
1965	Reddaway and Wright	(11)	Single crystals grown by vapor reaction method	Absorption Refractive index	300	There are indirect transition edges at 2.55 and 2.45 eV and direct transition edges at 3.7 and 4.1 eV for polarization perpendicular to the c axis and parallel to this axis, respectively.
1965	Nagasawa Shionoya, and Miki-shima	(12)	Single crystals grown by hydrolysis of SnCl <sub>4</sub>	Transmission	300	Bandgap is estimated to be about 3.5 eV.
1965	Houston and Kohnke	(13)	Single crystals grown from cuprous flux	Photoconduction	80-400	Measurements of thermally stimulated current indicate the existence of trapping levels at 0.21, 0.52, and 0.60 eV. The results of intrinsic thermal quenching measurements indicate the existence of a compensated acceptor level lying 0.33 eV above the valence band.
1966	Houston and Kohnke	(14)	As above	Photoconduction	100-400	The optical quenching of photoconductivity is found in a single band extending from the fundamental optical gap at 4.0 eV down to a cutoff indicative of a 1.3 eV activation energy.
1966	Summitt and Borrelli	(15)	Single crystals grown by vapor transport technique	U.V. absorption	20-1300	Experimental results are fitted by the expression $E_g(T) = E_g^0 - c \left[ \exp\left(\frac{\theta}{T}\right) - 1 \right]^{-1}$ where $\theta = 196^\circ$ and $414^\circ\text{K}$ for radiation parallel and perpendicular to the c axis, respectively, and c is a constant.
1966	Nagasawa and Shionoya	(16)	Single crystals grown by hydrolysis of SnCl <sub>4</sub>	Absorption	1.3-300	Four main lines were observed in the absorption structure at 1.3°K. This structure is assumed to be originated from a direct forbidden exciton transition.
1967	Spence	(17)	Films obtained by evaporating and subsequently oxidizing tin	Absorption	300	The dependence of the absorption coefficient upon film resistivity is noted and an impurity peak at about 3.4 eV is observed. It is suggested that an indirect edge lies near 2.7 eV and a direct edge near 4.3 eV.
1968	Summitt	(18)	Single crystals grown by vapor transport technique	Infrared absorption	300	The infrared reflection spectrum has been observed and analyzed by the classical dispersion theory. For the cassiterite structure four lattice vibration modes may interact with infrared radiation, three with radiation polarized perpendicular to the c axis, and one with radiation polarized parallel to the c axis. Static dielectric constants have values of 9.58 and 13.5 for directions parallel and perpendicular to the c axis, respectively.
1968	Wright	(19)	Single crystals grown from gas phase	Absorption	77 and 300	The summary of the results published in Ref. (11) and (54).

Table I. (Continued)

Year	Author	Reference	Materials	Properties	Temperature range, °K	Conclusion drawn by author
1968	Van Daal	(20)	Single crystals grown from gas phase	Reflection	300	Polar optical modes with an average characteristic temperature of 1050°K dominate lattice scattering.
1968	Van Daal	(21)	Natural single crystals	Reflection	300	Static dielectric constants have values of $9.0 \pm 0.5$ and $14 \pm 2$ for directions parallel and perpendicular to the c axis, respectively.
1968	Nagasawa and Shionoya	(23)	Single crystals grown by hydrolysis of SnCl <sub>4</sub>	Zeeman effect	1.8	The exciton symmetries and possible band symmetries are obtained on the basis of group theory and appear to be consistent with the valence band of O 2p functions and the conduction band of Sn 5s functions
1969	Crabtree, Mehdi, and Wright	(24)	As above	Infrared absorption	300	For charge carrier concentrations $n_0$ from $6.5 \times 10^{16}$ to $8 \times 10^{17}$ cm <sup>-3</sup> , the absorption coefficient $K$ is proportional to $n_0$ . The log-log plot of $K$ against $\lambda$ gives a good straight line with slope 2.5-2.6. The results are in agreement with the theory of Visvanathan for optical mode scattering.
1969	Nagasawa and Shionoya	(25)	As above	Absorption	80-370	The absorption tails observed above 200°K are in agreement with Urbach's rule.
1969	Cunningham, Marton, and Schlesinger	(26)	As above	Photoconduction	300	Photoconductivity is found to have a peak response at 370 nm. Excitation spectrum for blue fluorescent emission is similar to that of photoconductivity.
1969	Cunningham, Marton, and Schlesinger	(27)	As above	Photoconduction	300	The rate of photoconductivity decay is found to depend on the crystal environment.
1970	Fillard, Gasiot, and deMurcia	(22)	Single crystals grown by vapor transport technique	Photoconduction	77-500	On the basis of thermally stimulated emission, 5 trap levels were found in the forbidden band: 0.22, 0.44, 0.47, 0.56, and 0.7 eV
1970	Nishino and Hamakawa	(28)	System Si-SnO <sub>2</sub> , films of SnO <sub>2</sub> grown by oxidation of evaporated tin on surface of Si single crystal	Transmission Photovoltage	83, 298	Si-SnO <sub>2</sub> n-n heterojunction has the photoresponse in the wide wavelength region from 400 to 1200 nm at room temperature.
1971	Nagasawa and Shionoya	(29)	Single crystals grown by hydrolysis of SnCl <sub>4</sub>	Absorption Transmission	300	The value of $p$ in the relation $K \sim \lambda^p$ increases with free electron concentration, which may be explained by influence of ionized point defect scattering.
1971	Nagasawa and Shionoya	(30)	As above	Absorption Transmission Photoconductivity	300	Absorption intensity is slightly lower for the oxidized crystal. Sufficiently oxidized crystals exhibit rather large photoconductivity when irradiated with u.v. light. Spectral dependence of photocurrent shows two peaks at 3.37 and at about 3.8 eV.
1971	Nagasawa and Shionoya	(31)	As above	Zeeman effect	1.3-80	The results of Zeeman effect measurements are consistent with group theoretical predictions based on a crystal field-split valence band of oxygen 2p functions and a crystal field-split conduction band of tin 5s functions both having their extrema at $k = 0$ . The effective Rydberg constant, the bandgap energy, and the anisotropic exciton-reduced-masses are estimated as 0.0345 and 3.5969 eV (at 1.8°K), and $\mu_x = 0.33 m_0$ , $\mu_z = 0.30 m_0$ , respectively.
1971	Nagasawa and Shionoya	(32)	As above	Absorption	7-350	At low temperatures, the spectrum for $\vec{E} \perp c$ begins with second class exciton transitions at $\Gamma$ point, while at temperatures above 200°K, the spectrum is interpreted in terms of Urbach's rule. For light $\vec{E} \parallel c$ , the relation $K^{2/7} \sim h\nu$ is found and a possible explanation is that the spectrum arises from fourth class direct transitions at $\Gamma$ point.
1972	Fillard, Gasiot, deMurcia, and Tran Trong Quynh	(33)	Single crystal grown by vapor transport technique	Phosphorescence Photoluminescence Photoconductivity	77 and 300	The active region is located near the surface and the blue light originates from nonconducting states probably located in the bulk.
1974	Crabtree	(34)	Single crystals grown by hydrolysis of SnCl <sub>4</sub> Doped with europium	Cathodoluminescence	300	The spectrum comprises the intrinsic emission band of the host lattice and bands due to the presence of the europium ion. The europium is incorporated in the host lattice as Eu <sup>2+</sup> .
1974	Crabtree	(35)	As above, doped with terbium	Cathodoluminescence	300	The spectra comprise the intrinsic emission band of the host lattice and bands due to the presence of the terbium ion. The terbium is incorporated in the host lattice as Tb <sup>3+</sup> .
1974	McRoberts and Fonstad	(36)	Single crystals grown using the reaction $\text{SnCl}_4 + 2\text{H}_2 + \text{O}_2 \rightleftharpoons \text{SnO}_2 + 4\text{HCl}$	Thermoabsorption	25-115	For light polarized perpendicularly to the c axis, a fine structure is observed which may be associated with the exciton-phonon quasi-bound state.
1975	Kim and Laitinen	(37)	Thin films obtained by hydrolysis of SnCl <sub>4</sub>	Photocurrent	300	Photocurrent in SnO <sub>2</sub> electrode is dependent on the intensity of the light, wavelength, and the applied potential. The photocurrent spectrum showed a sharp decrease near the bandgap energy.

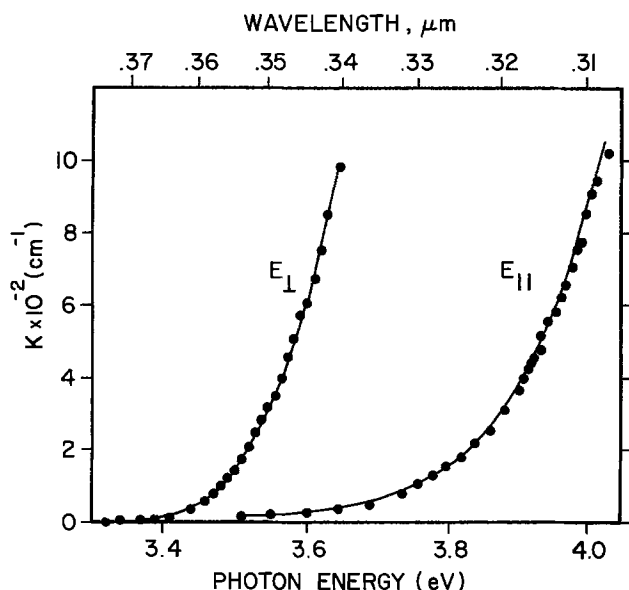


Fig. 1. U.V. absorption coefficient in  $\text{SnO}_2$  single crystals vs. photon energy for radiation polarized parallel and perpendicular to the  $c$  axis.

same authors obtained values of 3.93 and 3.57 eV for the parallel and perpendicular gaps, respectively. Summitt *et al.* assumed that the lower curved portion of  $K^2$  vs.  $h\nu$  dependence represents the allowed indirect phonon assisted transitions, which could vary as (42)

$$K = K_0' (h\nu - E_g' \pm E_p)^2 \quad [3]$$

where  $E_g'$  is the minimum forbidden energy gap and  $E_p$  is the phonon energy. When a single phonon frequency is involved, the plot of  $K^{1/2}$  vs. phonon energy should consist of two linear regions which extrapolate to  $E_g' + E_p$  and  $E_g' - E_p$ , from which one can obtain both  $E_g'$  and  $E_p$ . Extrapolating the linear portions to zero absorption, Summitt *et al.* obtained  $E_g' + E_p = 3.72$  and 3.42 eV for parallel and perpendicular gaps, respectively. Broadening occurred at the bottom of both edges, but it was found to be much larger at the parallel edge. Broadening of the perpendicular component suggests that several phonon frequencies participate in the absorption. Assuming  $E_p \leq 0.08$  eV (the highest optical lattice mode), the data obtained by Summitt *et al.* give estimates for the minimum energy gaps of  $E_g'$  (parallel)  $\leq 3.7$  eV and  $E_g'$  (perpendicular)  $\leq 3.4$  eV.

Differences in the shape of absorption curves at the two edges at low absorption were assumed to arise from forbidden transitions for light polarized parallel to the  $c$  axis. To account for these observations, oxygen 2p levels were assumed to split in the  $D_{4h}$  crystal lattice into two valence bands, with a difference between the upper edges of about 0.3 eV.

Summitt and Borrelli (15) investigated the temperature dependence of the u.v. absorption edges in  $\text{SnO}_2$  crystals in the range between 20° and 1300°K. Their results for parallel and perpendicular edges are shown in Fig. 2.

Above room temperatures both edges shifted linearly with temperature, where  $\Delta E_g/\Delta T = 1.2 \times 10^{-3}$  eV/°K. Between 20° and 300°K the shift in the parallel polarized edge was about 1.4 times larger than that in the perpendicular edge. Experimental results were fitted by the expression

$$E_g(T) = E_g^0 - c \left[ \exp\left(\frac{\theta}{T}\right) - 1 \right]^{-1} \quad [4]$$

where  $E_g^0$  corresponds to  $T = 0$  and  $c$  is a constant. The best fits were obtained when  $\theta = 196^\circ$  and  $414^\circ\text{K}$  for parallel and perpendicular edges, respectively.

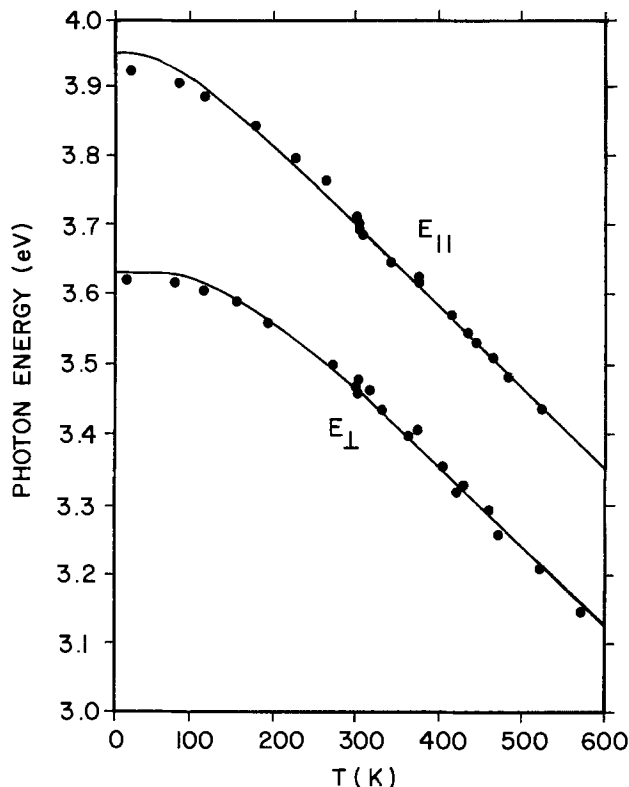


Fig. 2. Temperature dependence of the u.v. absorption edges in  $\text{SnO}_2$  single crystals at absorption coefficient  $\approx 75 \text{ cm}^{-1}$  for radiation polarized parallel and perpendicular to the  $c$  axis. Points are experimental values and curves are calculated from Eq. [4] where values of the parameters are:  $E_g^0 = 3.947$ ,  $c = 0.231$ ,  $\theta = 195.8$  for the parallel edge, and  $E_g^0 = 3.631$ ,  $c = 0.510$ ,  $\theta = 414.7$  for the perpendicular edge.

Equation [4] may be derived theoretically. For example, for isotropic crystals it has been shown (43, 44) that  $\Delta E_g(T)$  fulfilled the following equation

$$\Delta E_g(T) \sim \left[ \exp\left(\frac{h\omega_1}{kT}\right) - 1 \right]^{-1} \quad [5]$$

where  $\omega_1$  is the frequency of the longitudinal optical mode. Although theory has been developed in detail only for isotropic crystals having a single  $\omega_1$ , this proportionality is expected to apply generally to anisotropic polar crystals such as the tetragonal  $\text{SnO}_2$ .

These results show that the temperature shift of each edge may be determined by a single lattice frequency and that this frequency is different for the two edges. It also suggests that interaction with an electron in one of the two valence bands is dominated by one mode while a second mode controls interaction in the other valence band.

Wright *et al.* (11, 19, 24) have studied the optical properties of  $\text{SnO}_2$  crystals, obtained in their laboratory (1). Reddaway and Wright (11) studied the refractive index in the range from 0.35 to 10  $\mu\text{m}$ , and the absorption coefficient from 0.31 to 0.5  $\mu\text{m}$ . They reported direct absorption edges at 3.7 eV for polarization perpendicular to the  $c$  axis and near 4.1 eV for polarization parallel to it. As was mentioned above, Summitt, Marley, and Borrelli (9) in similar studies obtained the values as 3.6 and 3.9, respectively. For indirect absorption edges, Reddaway and Wright determined 2.55 eV for polarization perpendicular to the  $c$  axis and 2.45 eV for parallel polarization. The authors observed also a peak at 3.36 eV for parallel polarization, possibly with an excited state at 3.72 eV.

Extended investigations of optical properties of  $\text{SnO}_2$  single crystals of good quality (1) have been carried out by Nagasawa and Shionoya (12, 16, 23, 25, 29-32). Nagasawa, Shionoya, and Makishima (12) estimated

the optical bandgap to be about 3.5 eV. As it was mentioned previously, Kohnke observed a sharp absorption line at 3.07 μm in natural SnO<sub>2</sub> crystals, which he attributed to O-H groups. Since the crystals investigated by these authors were prepared using water as one of the starting materials, the existence of O-H groups is quite possible. However, no detectable absorption lines were observed. The crystals grown by this method were found to show the luminescence of a broad band with a maximum at 0.63 μm by the excitation of mercury light at room temperature.

To obtain information about the nature of the band extrema in SnO<sub>2</sub>, Nagasawa and Shionoya (25, 32) studied in detail the temperature dependence of the optical absorption edge in single crystals of this material. Absorption edge spectra for light polarized parallel and perpendicular to the c axis, obtained by Nagasawa and Shionoya at various temperatures, are shown in Fig. 3. As it is seen in this figure, large dichroism and shape difference between spectra for light polarized parallel ( $\vec{E} \parallel c$ ) and perpendicular ( $\vec{E} \perp c$ ) to the c axis are remarkable for the whole temperature range investigated (7°-370°K). This has been pointed out previously by Summitt *et al.* (9, 15). The spectra for  $\vec{E} \perp c$  become steeper with decreasing temperature while the spectra for  $\vec{E} \parallel c$  do not show any noticeable change in shape with temperature except for the movement of the entire curve with temperature.

As can be seen in Fig. 4, the energy and temperature dependences of the absorption coefficient in the spectra for  $\vec{E} \perp c$  above 200°K are well described by the empirical Urbach's rule (45) which is expressed by

$$K = K_0 \exp[\sigma_0(h\nu - E_0)/kT] \quad [6]$$

where  $K_0$  and  $E_0$  are material constants and  $\sigma_0$  is a constant on the order of unity. Equation [6] can also be written as

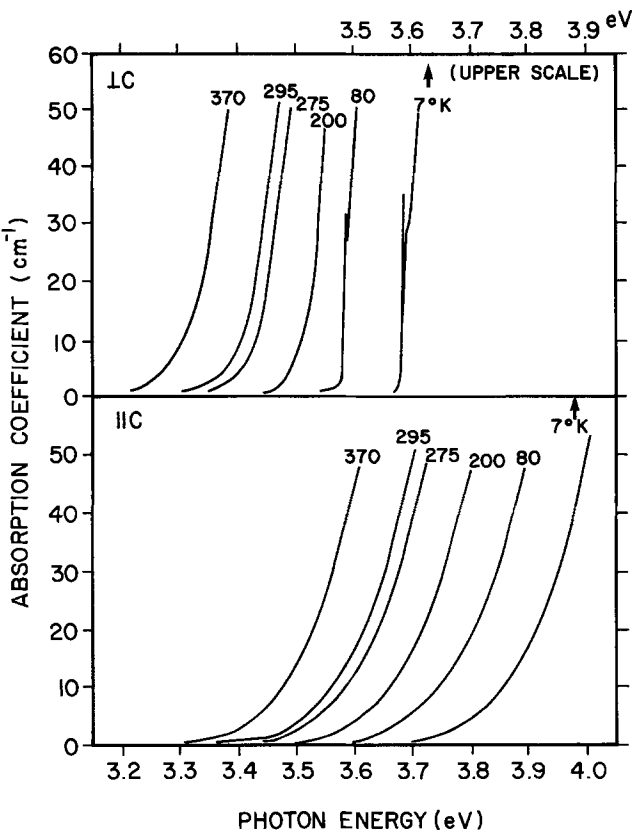


Fig. 3. The anisotropic fundamental absorption edge spectra in SnO<sub>2</sub> single crystals at various temperatures for light polarized perpendicular and parallel to the c axis. The spectra at 7°K are shifted in the energy scale to avoid overlap with those at 80°K.

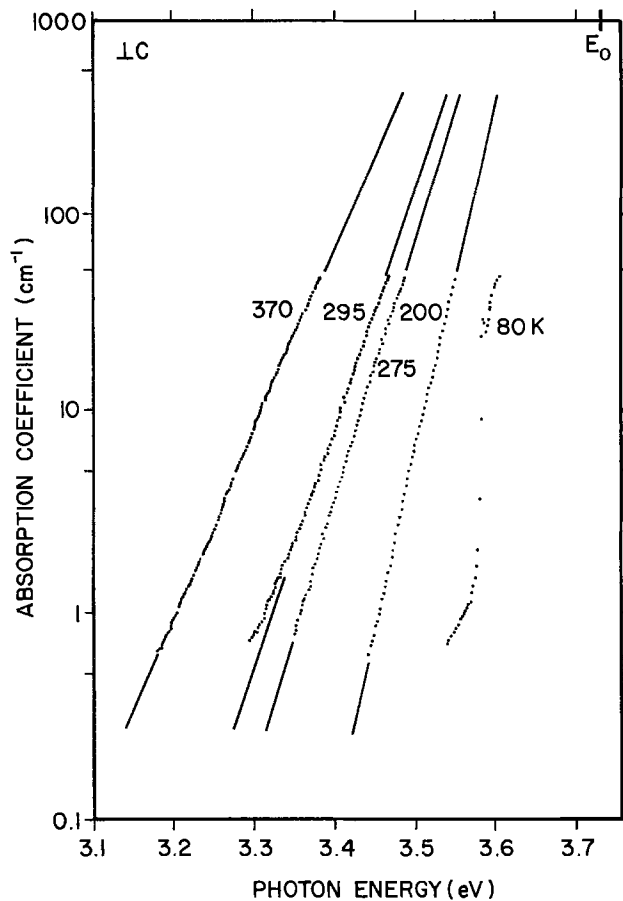


Fig. 4. Edge absorption spectra ( $E \perp c$ ) of SnO<sub>2</sub> single crystals at various temperatures. Points are experimental ones, while solid lines are calculated from Urbach's rule, where values of the parameters are  $K_0 = 1.5 \times 10^5 \text{ cm}^{-1}$ ,  $\sigma_0 = 0.70$ , and  $E_0 = 3.75 \text{ eV}$ .

$$(h\nu)_K = \ln(K/K_0) \cdot \frac{kT}{\sigma_0} + E_0 \quad [7]$$

where  $(h\nu)_K$  is the photon energy for which the crystal shows an absorption coefficient  $K$ . From Fig. 5 it is seen that the data obtained by Nagasawa and Shionoya above 200°K are also in agreement with Eq. [7]. It was assumed by these investigators that the Urbach tail is attributed to transitions from a  $\Gamma_5^-$  valence band (direct allowed for  $E \perp c$ ) about 0.15 eV below the top,  $\Gamma_3^+$ , valence band. Nagasawa and Shionoya, and also Agekyan (46, 47), have established the bottom conduction band and top valence band extrema symmetries as  $\Gamma_1^+$  and  $\Gamma_5^+$ , respectively. Urbach's empirical rule has been found to hold for a number of semiconductors and insulators (45); however, no satisfactory theory of this rule has appeared as yet.

*Long wavelength properties.*—Summitt and Borrelli (10) investigated the infrared properties of synthetic SnO<sub>2</sub> crystals and found that the absorption coefficient may be expressed in terms of the carrier concentration,  $n_e$  and wavelength,  $\lambda$ , as

$$K (\text{cm}^{-1}) = 1.72 n_e \lambda^3 \quad [8]$$

where  $n_e$  is given in  $10^{18} \text{ cm}^{-3}$  and  $\lambda$  in  $\mu\text{m}$ . Their experimental results are shown in Fig. 6. The investigations were carried out at a wavelength between 1 and 3 μm. The magnitude and wavelength dependence does not change over the range 50°-300°K, but the absorption increases slightly while the wavelength dependence decreases with increasing temperature between 300° and 900°K. Equation [8] suggests that this absorption is due to quasi-free electrons.

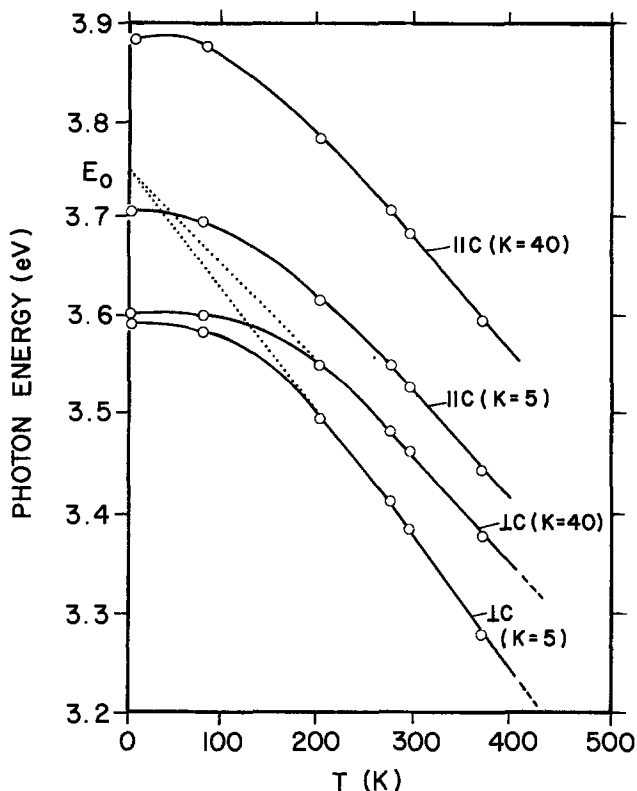


Fig. 5. Absorption curves near the fundamental absorption edge in  $\text{SnO}_2$  single crystals. Dotted lines are calculated from Eq. [7] with values of parameters  $K_0 = 1.5 \times 10^9 \text{ cm}^{-1}$ ,  $\sigma_0 = 0.70$ ,  $E_0 = 3.75 \text{ eV}$ .

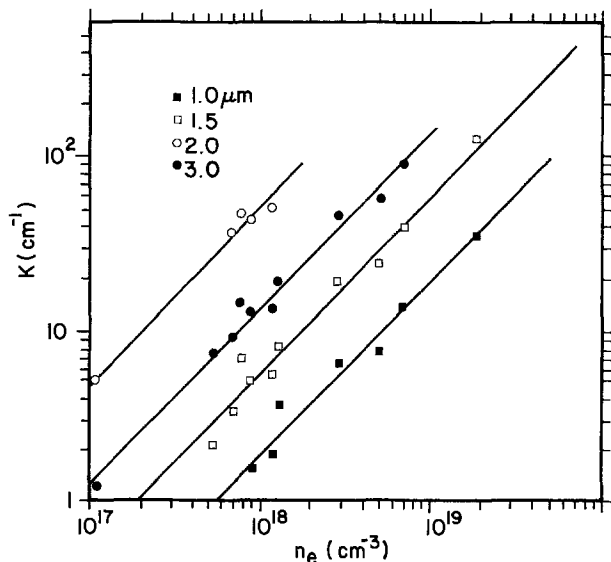


Fig. 6. Absorption coefficients  $K$  of  $\text{SnO}_2$  single crystals at constant wavelength vs. carrier concentrations.

In the case of absorption by free carriers, the absorption coefficient,  $K$ , is generally related to the wavelength,  $\lambda$ , in the form  $K \sim \lambda^p$ , where  $p$  is the numerical factor dependent on the charge carrier scattering process. For acoustic mode scattering (40, 48, 49), the free-carrier absorption coefficient is theoretically proportional to  $\lambda^2$  ( $p = 2$ ) and for optical phonon scattering (50),  $p = 2.5$ . The value of  $p$  is known to exceed 3 for ionized defect or impurity scattering (49-51). The dependence of the absorption coefficient on  $\lambda^3$  below  $300^\circ\text{K}$  obtained by Summitt and Borrelli suggests that acoustic phonon scattering is not dominant at  $300^\circ\text{K}$ . The linear variation of  $K$  with  $n_e$  suggests that scattering by ionized impurities is also unimportant at room temperature, because expressions for ionized impurity

scattering (49-51) indicate that the absorption coefficient varies with the product  $n_e N$ , where  $N$  is the concentration of ionized impurities and native point defects. Thus, the results obtained by these authors suggest that the major scattering in the range of temperatures investigated is by optical phonons. Summitt (18) investigated the infrared reflection spectrum of  $\text{SnO}_2$  single crystals at room temperature in the wavelength range  $10\text{-}50 \mu\text{m}$ . The experimental reflectance curves are shown in Fig. 7(a) and (b) for radiation polarized perpendicular and parallel to the  $c$  axis, respectively. The points are experimental, and the solid curves are computed from the classical dispersion oscillator theory (52, 53) using the parameters which gave the best fit to the experimental curves.

In the classical oscillator analysis of the reflection spectrum, it is assumed that the real and imaginary parts of the complex dielectric constants are related to a set of oscillator parameters by the equations (52)

$$\epsilon' = n^2 - k^2 = \epsilon_\infty + \sum_j \frac{4\pi\rho_j\nu_j^2(\nu_j^2 - \nu^2)}{(\nu_j^2 - \nu^2)^2 + \gamma_j^2\nu_j^2\nu^2} \quad [9]$$

$$\epsilon'' = 2nk = \sum_j \frac{4\pi\rho_j\nu_j^2\nu_j^2\gamma_j\nu}{(\nu_j^2 - \nu^2)^2 + \gamma_j^2\nu_j^2\nu^2} \quad [10]$$

where  $\epsilon_\infty$  is the high frequency dielectric constant,  $4\pi\rho_j$  the strength,  $\gamma_j$  the width, and  $\nu_j$  the frequency of the  $j$ th oscillator. The reflectivity,  $R$ , of radiation at normal incidence is related to the refractive index,  $n$ , and the extinction coefficient,  $k$ , by

$$R = [(n - 1)^2 + k^2] / [(n + 1)^2 + k^2] \quad [11]$$

The number of oscillators in the analysis should be the minimum number necessary for good agreement with the experimental data, but also should agree with the number deduced from group theoretical analysis of the crystal structure. The results of calculations by Summitt for the cassiterite structure agree well with the experiment if four lattice vibration modes interact with infrared radiation, namely three oscillators for

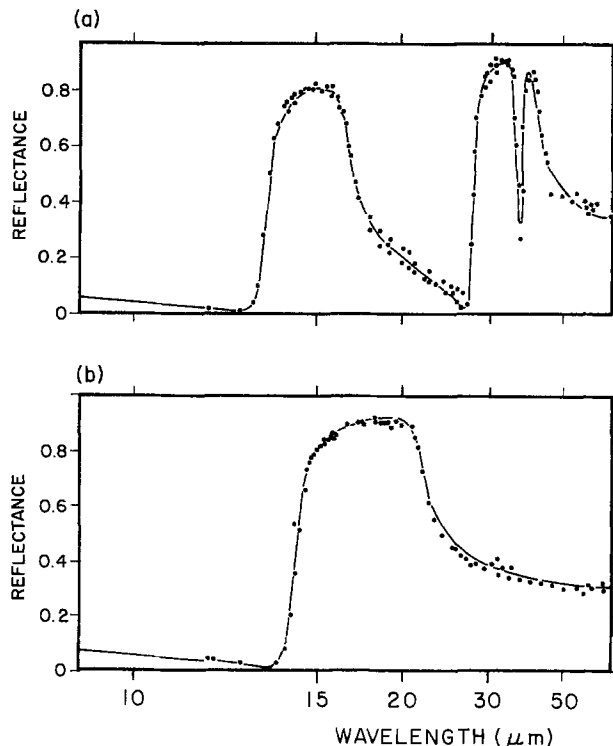


Fig. 7. Infrared reflectance spectrum of  $\text{SnO}_2$  single crystals. Points are experimental values and solid curves are computed from Eq. [9], [10], and [11] using the parameters of Table II; (a) radiation polarized perpendicular to the  $c$  axis. (b) radiation polarized parallel to the  $c$  axis.

Table II. Lattice-vibration parameters of stannic oxide from dispersion analysis of the infrared reflectance spectrum (18)

$E \perp c$					
Mode	Frequency, $\omega/2\pi$ (cm <sup>-1</sup> )	Absorption strength, $4\pi\rho$	Line-width, $\gamma$	Polarization, $p^2 \times 10^{-5}$	Fraction polarization
t1	243	5.80	0.032	0.687	0.328
t2	284	1.25	0.022	0.202	0.097
t3	605	1.64	0.034	1.204	0.575
l1	273			0.007	0.003
l2	368			0.278	0.131
l3	757			1.830	0.865
$E \parallel c$					
t	465	5.40	0.040		
l	704				

High frequency dielectric constants

$$\epsilon_{\infty \perp} = 3.785$$

$$\epsilon_{\infty \parallel} = 4.175$$

radiation polarized perpendicular to the  $c$  axis and a single oscillator for radiation parallel to the  $c$  axis. The oscillator parameters giving the best fit to the experimental curves are listed in Table II. The longitudinal oscillator frequencies found for the best fit to the experimental reflection curves are 243, 284, and 605 cm<sup>-1</sup> for radiation polarized perpendicular to the  $c$  axis and 465 cm<sup>-1</sup> for radiation polarized parallel to the axis. Low frequency dielectric constants were estimated from this analysis to be 13.5 and 9.58 for  $E \perp c$  and  $E \parallel c$ , respectively. The  $E \perp c$  value was confirmed directly in a substitution bridge measurement yielding  $15 \pm 1$  for the frequency range  $10^2$ - $10^6$  Hz. Reddaway (54) found the refractive index of crystals to be 2.0 at 0.53  $\mu\text{m}$  for polarization perpendicular to the  $c$  axis and 2.11 for polarization parallel to it. The absorption from 0.7 to 3  $\mu\text{m}$  in antimony-doped SnO<sub>2</sub> crystals was found by Reddaway to be approximately proportional to  $\lambda^3$ . This is in agreement with Summitt and Borrelli (10) and is reasonably consistent with optical mode polar scattering. As it was mentioned above, the theory of free-carrier absorption in this case was given by Visvanathan (50), and the measured absorption coefficient agrees approximately with this theory.

Crabtree, Mehdi, and Wright (24) studied the infrared absorption at room temperature for reduced crystals with different carrier concentrations,  $n$ , and confirmed that from  $6.5 \times 10^{16}$  to  $8 \times 10^{17}$  cm<sup>-3</sup> the absorption coefficient,  $K$ , is proportional to  $n_e$ , which is in agreement with the results obtained by Summitt and Borrelli (10). The dependence of  $\log K$  against  $\log \lambda$  is shown in Fig. 8 and gives a straight line with slope 2.5 for the lower values of  $n_e$  and 2.6 for the higher. These slopes are in excellent agreement with the theory of Visvanathan (50) for optical mode scattering and confirm that this is indeed the scattering process at room temperature. The higher slopes observed by Summitt and Borrelli (10) and Reddaway (55) are probably due to the influence of the presence of impurity scattering. On the basis of Visvanathan's (50) calculations and data shown in Fig. 8, Crabtree *et al.* found the electron effective mass to be 0.17  $m_0$ .

For the optical reflection in the Reststrahl region, Van Daal (20, 21) also concluded that polar optical modes with an average characteristic temperature of 1050°K dominate lattice scattering. He found that the static dielectric constant for directions parallel and perpendicular to the  $c$  axis has values of about  $9.0 \pm 0.5$  and  $14 \pm 2$ , respectively. These values are similar to those obtained by Summitt (18). This is in contradiction with the commonly accepted values of 24.0 and 23.4 found in the literature. The latter values are based on optical reflection data at room temperature for normal incidence of polarized light in the far infrared, obtained as early as 1919 by Liebisch and Rubens (56).

Nagasawa and Shionoya (29) studied optical transmission spectra of as-grown and reduced SnO<sub>2</sub> crystals.

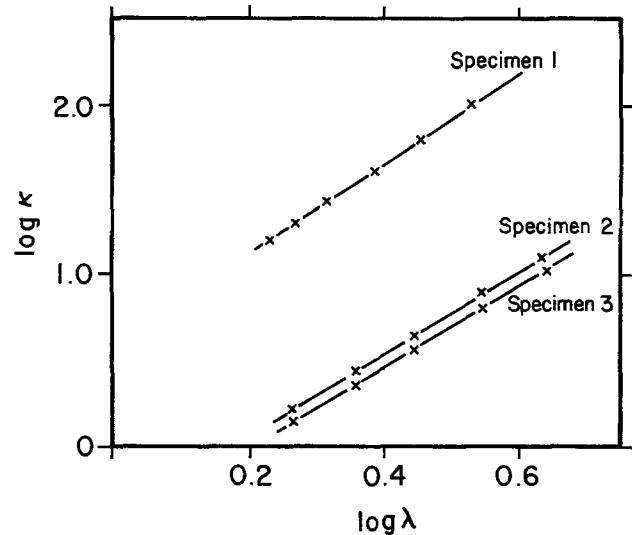


Fig. 8. Infrared optical absorption coefficients of SnO<sub>2</sub> single crystals as a function of wavelength. The charge carrier concentrations for specimens 1, 2, and 3 are  $8 \times 10^{17}$ ,  $10^{17}$ , and  $6.5 \times 10^{17}$  cm<sup>-3</sup>, respectively.

The results are shown in Fig. 9. Contrary to the results of Summitt and Borrelli (10), the data of Nagasawa and Shionoya show that the value of  $p$  in relation of  $K \sim \lambda^p$  increases with conduction electron concentration from  $p = 2.2$  and 2.5 for the as-grown crystals to  $p = 3.1$  for the reduced crystal. This may be due to the influence of ionized point defect scattering at room temperature. Nagasawa and Shionoya (30) also observed that absorption intensity is slightly lower for oxidized crystals which is caused by decreasing the amount of defect centers. Sufficiently oxidized crystals were found to exhibit rather large photoconductivity when irradiated with u.v. light.

**Exciton effects.**—Nagasawa and Shionoya (16) working with good quality (1) single crystals observed near the fundamental absorption edge a series of sharp lines having absorption coefficients less than 100 cm<sup>-1</sup>. Their results, obtained at 1.3°K, are shown in Fig. 10. It turned out that the photon energies of the main lines found satisfy the relation for hydrogenlike series, and that the line corresponding to the principal quantum number  $n = 1$  is missing. This experimental relation can be expressed by the following equation (16)

$$E_n = 3.5971 - 0.0330/n^2 \text{ (eV)} \quad [12]$$

or by (31)

$$E_n = 3.5969 - 0.0314/n^2 \text{ (eV)} \quad [13]$$

where the quantum number  $n = 2, 3, 4,$  and 5 represents the energy states corresponding to the first, second, third, and fourth line in the structure, respec-

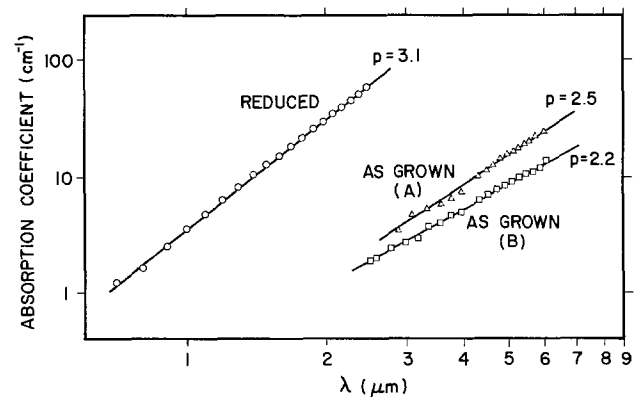


Fig. 9. Free-carrier absorption in as-grown and reduced SnO<sub>2</sub> crystals at room temperature. Straight lines present a relation  $K \sim \lambda^p$ .

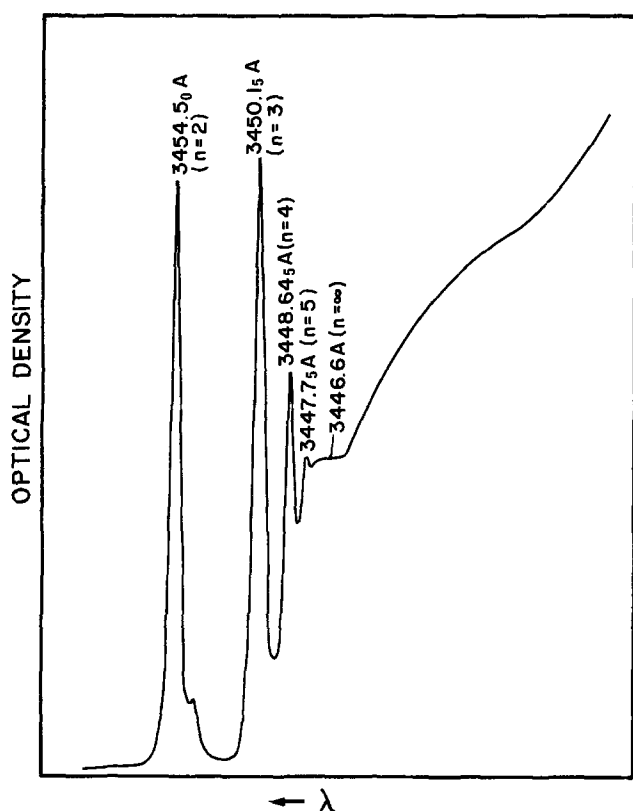


Fig. 10. Structure of the fundamental absorption edge of  $\text{SnO}_2$  single crystals at  $1.3^\circ\text{K}$ . Photon energies of the main lines fulfilled the relation for hydrogenlike series when the number  $n = 1$  is missing.

tively. Based on the fact that in the hydrogen series relation the line with  $n = 1$  is missing and also that the absorption coefficients of the lines are quite small, the authors concluded that the observed structure originates from a direct forbidden (second class) excitation transition (57).

To elucidate these spectra, Nagasawa and Shionoya (23) investigated the Zeeman effect of the exciton at  $1.8^\circ\text{K}$ . The magnetic field was perpendicular to the  $c$  axis and parallel to the wave vector of the exciting photon  $\vec{q}$ .

In the magnetic field new absorption lines appeared on the higher energy side of each zero-field line and their intensities increased with increasing magnetic field strength. With the magnetic field parallel to the  $c$  axis no new lines were found, but broadening and energy shifts of the zero-field lines were observed. From group theoretical predictions based on a crystal field-split conduction band of tin  $5s$  functions,

both having their extrema at  $k = 0$  ( $\Gamma$  point), Nagasawa and Shionoya concluded that zero-field lines are transitions from the crystal ground state to the hydrogenic  $nP_{\pm 1}$ . They also concluded that in a magnetic field perpendicular to the  $c$  axis of the crystal,  $P_{\pm 1}$  and  $P_0$  states will be mixed, and in accord with this,  $P_0$  increases in strength as the field is increased if the measurement is made in the geometry of  $\vec{H} \perp c$  and  $\vec{H} \parallel \vec{q}$ .

One may now assign the new lines as  $nP_0$ . In Fig. 11, peak positions of the  $nP_{\pm 1}$  and  $nP_0$  lines which were

observed with the geometry  $\vec{H} \perp c$  and  $\vec{H} \parallel \vec{q}$  are plotted against magnetic field strength. The energy shifts observed in the higher states are quadratic with respect to magnetic field strength, and hence may be due to the diamagnetic Zeeman effect, while those in  $n = 2$  states are mainly due to linear Zeeman effects.

An anisotropic-exciton-mass formalism has been derived by Hopfield and Thomas (58) and also by Wheeler and Dimmock (59), using the ellipsoidal effective-mass approximation. Wheeler and Dimmock (59)

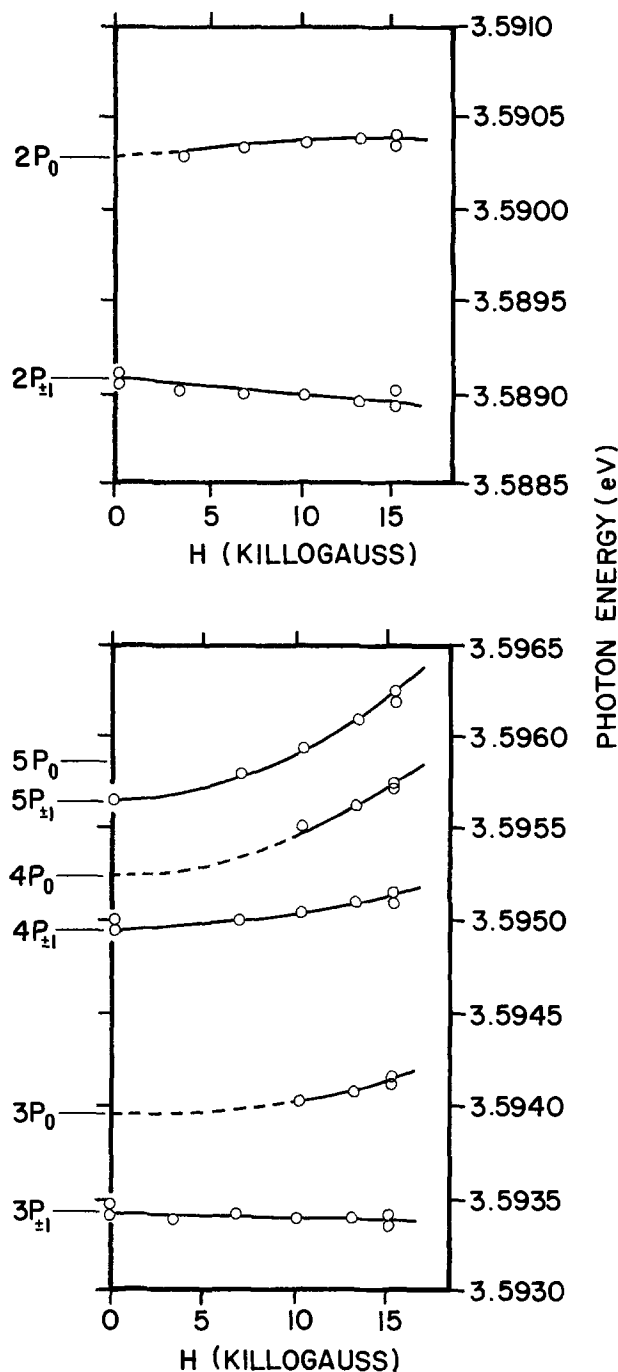


Fig. 11. The Zeeman effect of the exciton states in  $\text{SnO}_2$  single crystals at  $1.8^\circ\text{K}$  for  $H \perp c$  and  $H \parallel \vec{q}$ . On the left are shown the zero-field energies of the exciton states calculated semiempirically using the anisotropic-exciton-mass formalism.

calculated exciton state energies in the absence of an external magnetic field. The expressions obtained for exciton states  $nP_0$  and  $nP_{\pm 1}$  are, respectively

$$E_n = E_g - \frac{R_{\text{eff}}}{n^2} (1 + 3\alpha/5 + 9\alpha^2/28) \quad [14]$$

$$E_n = E_g - \frac{R_{\text{eff}}}{n^2} (1 + \alpha/5 + 9\alpha^2/140) \quad [15]$$

where  $E_g$  and  $R_{\text{eff}}$  are the bandgap energy and the effective Rydberg constant, respectively, and  $\alpha$  is an anisotropy parameter defined as

$$\alpha = 1 - \mu_x \epsilon_x / \mu_z \epsilon_z \quad [16]$$

where  $\mu$  and  $\epsilon$  are the exciton-reduced-mass and the

low-frequency dielectric constant, respectively. Using the expressions [14], [15], and [16], Nagasawa and Shionoya (23) calculated energies of  $nP_0$  and  $nP_{\pm 1}$  states (for  $n = 2, 3, 4$ , and 5). The values obtained are also shown in Fig. 11. Using the anisotropic-exciton-mass formalism, the authors also calculated the effective Rydberg constant, the bandgap energy, and the anisotropic exciton-reduced-masses at 1.8°K. These were found to be 0.0345 eV, 3.5969 eV and  $\mu_x = 0.33 m_0$ ,  $\mu_z = 0.39 m_0$ , respectively. The results of Zeeman effect measurements obtained by Nagasawa and Shionoya (23, 31) are consistent with group theoretical predictions assuming oxygen 2p valence band and tin 5s conduction band, both split by crystal field.

At low temperatures the spectra in SnO<sub>2</sub> crystals begin with second class exciton transitions at  $\Gamma$  point. The absorption spectra for light polarized parallel to the  $c$  axis do not show linearity in a  $\log K$  vs.  $T$  plot and hence do not fit Urbach's rule (45). It is possible that these spectra are due to phonon-assisted indirect transitions. Nagasawa and Shionoya (32) found that the best linearity between  $K$  and photon energy is obtained when  $K^{2/7}$  is plotted against  $h\nu$ . They suggested that the spectra for  $E \parallel c$  may arise from fourth class optical transitions, but this conclusion should be confirmed by other investigations. By extending the calculations of Elliott (60) on the first and second class transitions to the fourth class transition, Nagasawa and Shionoya found the following relation for energies far away from the edge

$$K = \frac{96\pi v e^2 x^3 N (2\mu)^{9/2}}{175 c \cdot \hbar^9} \cdot E^{7/2} \quad [17]$$

where  $e$  is the electron charge,  $x$  is a quantity which is of the order of the atomic radius,  $N$  is the number of unit cells in the crystal,  $\mu = m_e m_h / (m_e + m_h)$  is the excitation reduced mass, and  $E = h\nu - E_g$ . The experimental results of Nagasawa and Shionoya are qualitatively in agreement with Eq. [17]. The gradual onset of the  $E \parallel c$  edge is attributed to the fact that the  $\Gamma_3^+ \rightarrow \Gamma_1^+$  transition is triply forbidden for  $E \parallel c$ . It has been suggested by Nagasawa and Shionoya (30) that the lowest energy direct-allowed transitions to the conduction band for  $E \parallel c$  occur from a  $\Gamma_2^-$  valence band several tenths of an eV below the  $\Gamma_3^+$  and  $\Gamma_5^-$  bands.

McRoberts and Fonstad (36) studied the thermally modulated optical transmission (61) of SnO<sub>2</sub> crystals near the fundamental absorption edge, using polarized light, at temperatures 25°, 80°, and 115°K. Temperature modulation was accomplished by passing a pulsed heating current through the samples via ohmic contacts at the ends. The frequency of modulation was typically about 6 Hz. The transmitted signal was detected by a photomultiplier whose output was fed to two phase-sensitive synchronous amplifiers used in parallel to detect the 6 Hz signal, which was proportional to the change in transmitted intensity,  $\Delta I$ , and 210 Hz signal, which is proportional to the transmitted intensity,  $I$ . The ratio,  $\Delta I/I$ , was then recorded directly using an analog divider. Neglecting reflection and thermal expansion, the measured quantity  $\Delta I/I$ , is proportional to the  $dK/dT$  and to  $dK/d(\hbar\omega)$  or wavelength derivate of the spectrum.

The effect of temperature modulation is most evident by comparing the data taken at different temperatures. As can be seen from Fig. 12, 13, and 14, the primary change is the change in bandgap evidenced as the shift of the entire structure to lower energy with increasing temperature. One can also see the broadening of the exciton structure, observed first by Nagasawa and Shionoya, as the temperature is increased. At 115°K (Fig. 14) only the  $n = 2$  exciton line is distinct.

The structures A, B, C, and D in Fig. 12, 13, and 14 have not been reported previously. They do not appear for the light polarized parallel to the  $c$  axis. McRoberts and Fonstad have suggested that these structures may

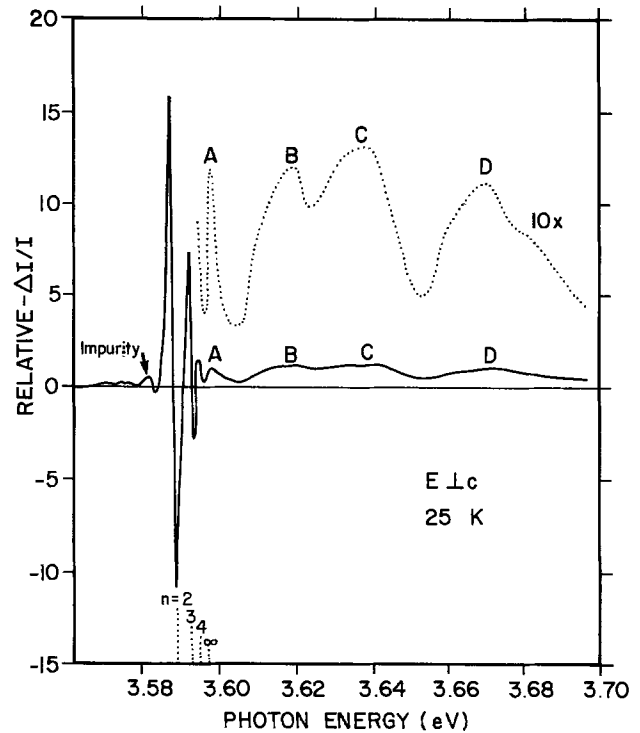


Fig. 12. Thermoabsorption,  $\Delta I/I$ , at 25°K in SnO<sub>2</sub> single crystals for light polarized perpendicular to the  $c$  axis. The temperature quoted refers to the sample temperature before application of the modulating signal. The positions marked on the horizontal axis are placed using the line spacings determined at 1.3°K by Nagasawa and Shionoya.

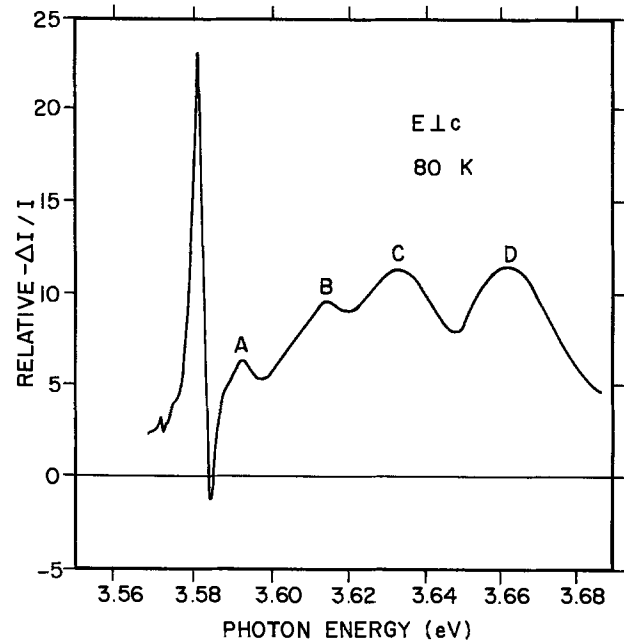


Fig. 13. Thermoabsorption,  $\Delta I/I$ , in SnO<sub>2</sub> single crystals at 80°K for light polarized perpendicular to the  $c$  axis.

be due to the exciton-phonon quasi-bound state (EPQBS) of Toyozawa (62). According to these authors, peak A may be associated with the EPQBS formed by the 1s exciton level and 46 meV LO phonon. Peak B can be associated with the 2s exciton level and 46 meV LO phonon; peak C with the 1s exciton level and 95 meV LO phonon. Finally, peak D may also involve the  $n > 1$  exciton states with the 95 meV LO phonon, with little EPQBS binding energy indicated. Fonstad and McRoberts have also suggested that peak



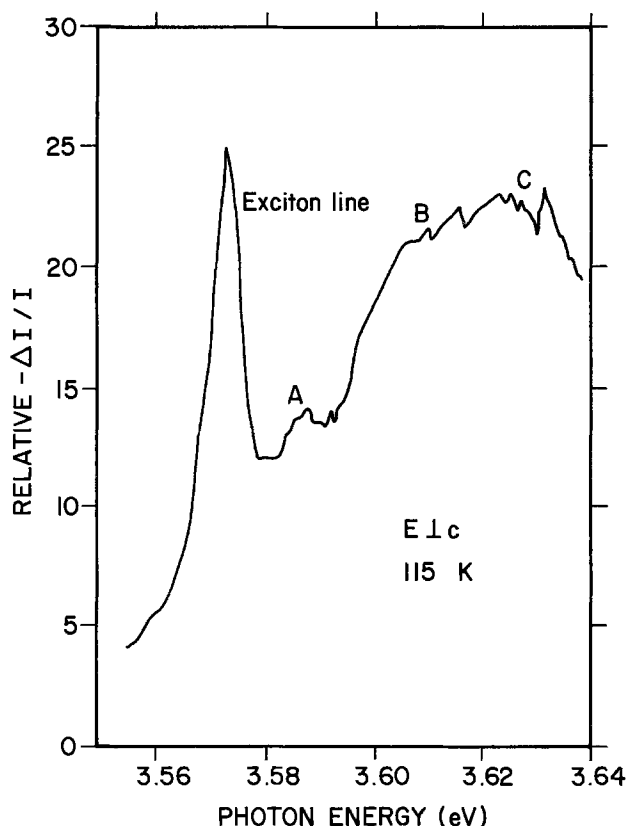


Fig. 14. Thermoabsorption,  $\Delta I/I$ , in  $\text{SnO}_2$  single crystals at  $115^\circ\text{K}$  for light polarized perpendicular to the  $c$  axis.

A is possibly attributable to a step in  $K$  produced by truncation of the EPQBS Lorentzian lineshape at the band edge (63). Since this step would occur over an energy interval of width  $kT$ , it is a quantitative reason for the decline in its derivative with increasing temperature, as well as for the general narrowness of peak A.

The results obtained by Fonstad and McRoberts for light parallel to the  $c$  axis indicate the onset of a direct-allowed transition around 0.4 eV higher than the  $E \perp c$  absorption edge.

Arlinghaus (64) calculated the energy band structure of  $\text{SnO}_2$  by a self-consistent augmented plane wave (APW) method. The calculation predicts  $\text{SnO}_2$  to be a semiconductor with an allowed direct bandgap of 3.68, corresponding to the transition  $\Gamma_5^+ \rightarrow \Gamma_1^+$  for light polarized perpendicularly to the  $c$  axis. The analogous optical direct gap for parallel polarized light corresponds to the  $\Gamma_1^- \rightarrow \Gamma_1^+$  transition at 4.07 eV. Forbidden direct transitions are predicted around 3.5 eV. Indirect transitions of somewhat lower energy are also predicted. The values obtained on the basis of theoretical calculations are consistent with the experimental data discussed above.

**Photoconduction.**—Houston and Kohnke (13) investigated photoconduction in  $\text{SnO}_2$  single crystals grown by a flux method from a cuprous oxide flux. The results of thermally stimulating current procedure indicated the existence of three trapping levels with average activation energies of 0.21, 0.52, and 0.60 eV. Comparison with dark conductivity data implied the 0.60 eV trap to be associated with the compensated portion of these donor states responsible for the normal  $n$ -type conductivity. The results of intrinsic thermal quenching measurements indicated the existence of a compensated acceptor level lying 0.33 eV above the valence band. The ratio of hole to electron capture cross sections for this level was found to be  $7 \times 10^2$ . The authors also found other semidiscrete levels (1.0, 1.3, and 1.8 eV below the conduction band). However,

it should be remembered that crystals grown by the flux technique may contain many uncontrolled impurities and therefore it is difficult to interpret the results obtained by Houston and Kohnke. In further measurements carried out on the same single crystals the same authors (14) found the optical quenching of photoconductivity in a single band extending from the fundamental optical gap at 4.0 eV down to a cut off indicative of a 1.3 eV activation energy, which is not in agreement with the value 0.33 eV obtained by these authors from above-mentioned thermal quenching measurements. Thermally stimulated emission in  $\text{SnO}_2$  single crystals grown by the Marley-MacAvoy technique (39) were studied by Fillard, Gasiot, and Murcia (22). They found 5 trap levels in the forbidden band at 0.22, 0.44, 0.47, 0.56, and 0.7 eV.

Cunningham, Marton, and Schlesinger (26, 27) investigated the photoconductivity in  $\text{SnO}_2$  single crystals grown by the hydrolysis of  $\text{SnCl}_4$ . Photoconductivity was observed only in samples with resistivity higher than  $10^4$  ohm-cm. The spectral dependence of photoconductivity and the optical transmission spectrum obtained by these authors are shown in Fig. 15. Photoconductivity was found to have a peak response at 370 nm corresponding to the absorption edge. Nagasawa and Shionoya (30) found two peaks at 37.37 and 3.8 eV in the spectral dependence of photocurrent in oxidized  $\text{SnO}_2$  single crystals grown by the same technique. Their results are shown in Fig. 16. The first peak was claimed to have a fairly good reproducibility from sample to sample, while the other showed a remarkable difference in sensitivity from sample to sample.

Cunningham, Marton, and Schlesinger (27) found the photoconductivity to be characterized by long rise and decay times. This is shown in Fig. 17. The rate of decay was found to depend on the crystal environment. As can be seen from the figure, in argon and nitrogen the curve was the same, and was independent of the gas pressure. The same decay curve was obtained in a vacuum of  $10^{-5}$  Torr. Introduction of air, oxygen, or water vapor to the measurement chamber during the experiments gave rise to a marked increase in the rate of decay. On the other hand, the introduction of hydrogen caused a slight increase in conductivity. The authors found that the magnitude of steady-state photoconductivity varied with oxygen pressure as it is shown in Fig. 18. They suggested that photoconductivity in the crystals investigated

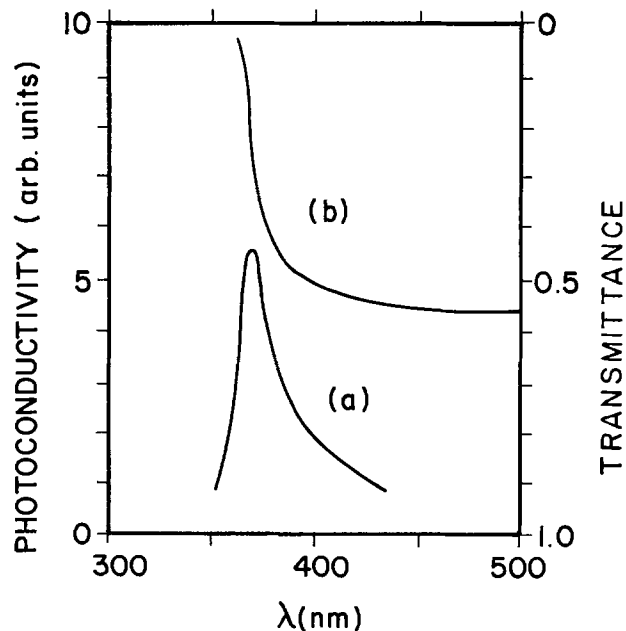


Fig. 15. Spectral dependence of photoconductivity (a) and transmittance (b) of  $\text{SnO}_2$  single crystals.

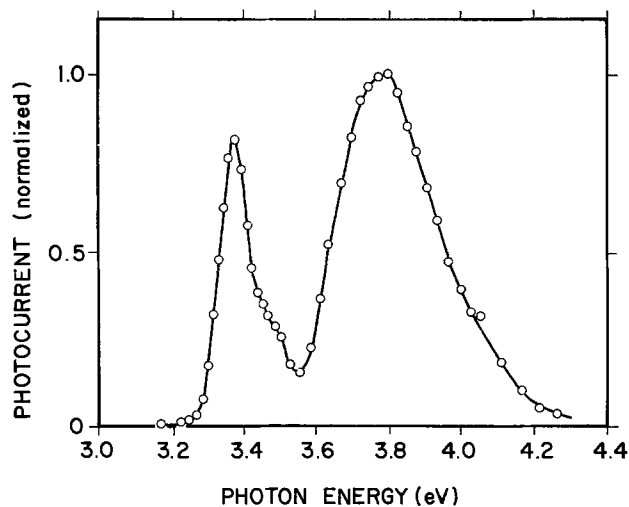


Fig. 16. Spectral dependence of photoconductivity of SnO<sub>2</sub> single crystals.

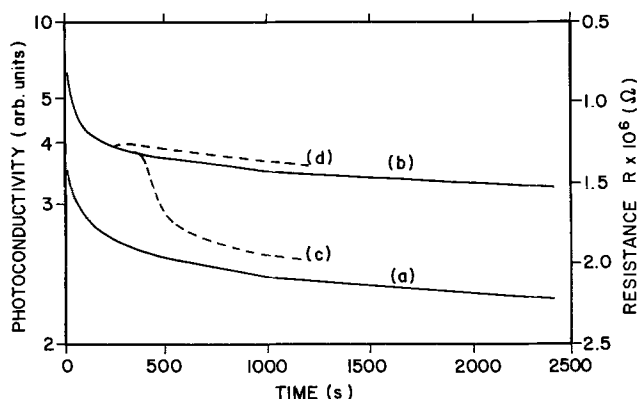


Fig. 17. Decay of photoconductivity in SnO<sub>2</sub> crystals in various atmospheres at room temperature: (a) in O<sub>2</sub> at 1 atm, (b) in N<sub>2</sub> or Ar at 1 atm, or N<sub>2</sub> and Ar at 2 Torr, or in vacuum (10<sup>-5</sup> Torr), (c) in N<sub>2</sub> at 2 Torr followed by introduction of O<sub>2</sub> at 1 atm after 400 sec, (d) in N<sub>2</sub> at 2 Torr followed by introduction of H<sub>2</sub> at 1 atm after 200 sec.

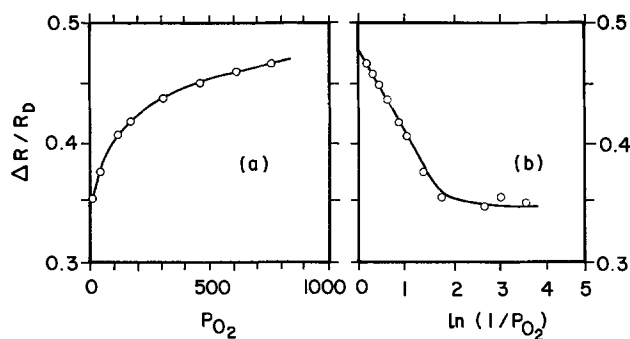


Fig. 18. Steady-state photoconductivity change in SnO<sub>2</sub> crystals, measured as resistance change  $\Delta R$  relative to dark resistance  $R_D$ , as a function of surrounding oxygen pressure at room temperature.

arose from photogeneration of electron hole pairs, hole trapping at O<sup>2-</sup> ions, and desorption of oxygen atoms. The decay of photoconductivity in an oxygen atmosphere was suggested to be caused by absorption of oxygen atoms and retrapping of electrons to give chemisorbed O<sup>-</sup> ions, while the decay in an inert gas atmosphere or in vacuum was suggested to proceed via trapping of electrons by intrinsic surface traps. The authors also assumed that the influence of water vapor on the photoconductivity decay is caused by OH<sup>-</sup> ions, which behave as surface acceptors as do chemisorbed O<sup>-</sup> ions. On the other hand, hydrogen may give rise

to a surface donor state, which would account for the observed increase in photoconductivity.

**Luminescence and phosphorescence.**—Luminescence of as-grown SnO<sub>2</sub> single crystals has received some attention (26, 33-35, 65). Cunningham, Marton, and Schlesinger (26) found that an excitation spectrum for blue fluorescent emission is similar to that of photoconductivity. They also observed thermoluminescence above room temperature after gamma irradiation, namely, two main glow peaks, both corresponding to a blue emission.

Phosphorescence emission from high resistivity SnO<sub>2</sub> single crystals using Hg bulb as the exciting source was investigated by Fillard *et al.* (33). The results are presented in Fig. 19. As can be seen from the figure, three emission bands exist centered at wavelengths 0.44, 0.56, and 0.64  $\mu\text{m}$ . The authors found that at 77°K the total emitted light shows a complex dependence on time, due to many kinds of levels involved; at room temperature the signal decreases exponentially with a time constant  $\tau = 2.25$  sec. The photoluminescence excitation spectrum has been found by these authors to be similar to that of the phosphorescence.

Crabtree (34, 35) investigated cathodoluminescence in SnO<sub>2</sub> crystals, as-grown and doped with europium and terbium. Luminescence was caused by bombarding the crystals with 10 keV electrons. The cathodoluminescence spectrum obtained by these authors for as-grown crystals is shown in Fig. 20. The broad featureless band obtained is like that found by Fillard *et al.* The emission spectrum of europium-doped SnO<sub>2</sub> shown in Fig. 21 seems to comprise the intrinsic emission band of the host lattice and bands due to the presence of the europium ions. In a rare earth ion, such bands are due to electronic transitions occurring among the inner, shielded 4f electrons. The orbits of the 4f electrons are so deeply buried within the electronic shell that the energy levels are only slightly perturbed when the ion is placed within a crystal. The spin-orbit splitting of the energy levels is about 1000 cm<sup>-1</sup>, while the

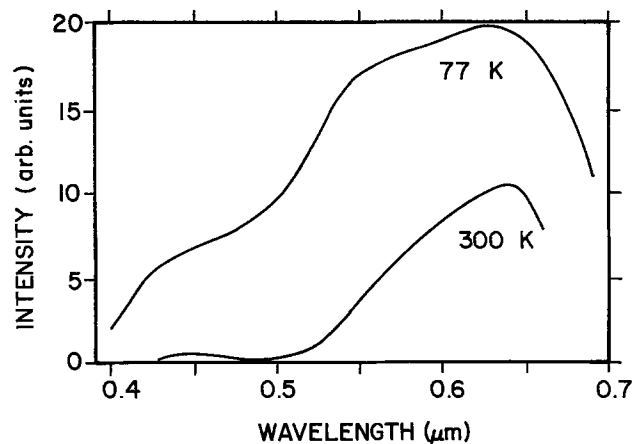


Fig. 19. Phosphorescence spectra in SnO<sub>2</sub> single crystals taken immediately after excitation at 77° and 300°K.

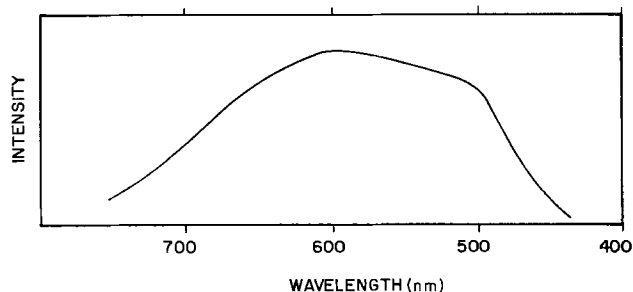


Fig. 20. Cathodoluminescence spectrum in SnO<sub>2</sub> crystals at room temperature.

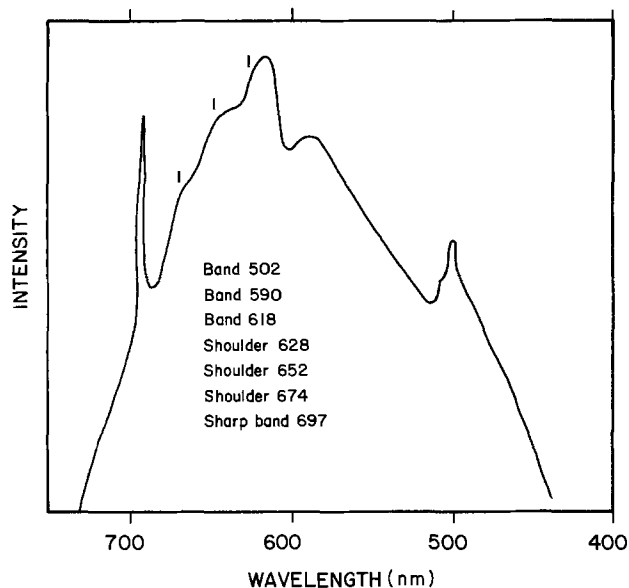


Fig. 21. Cathodoluminescence spectrum of  $\text{SnO}_2$  crystals doped with europium.

splitting of a given J level due to the crystalline field is about  $100 \text{ cm}^{-1}$ . Hence emission bands are relatively sharp and do not change much when a given rare earth ion is placed in different hosts. It seems that the europium ion is incorporated as  $\text{Eu}^{3+}$  in  $\text{SnO}_2$ . Similar results have been obtained in the case of  $\text{SnO}_2$  doped with terbium (35).

### Tin Oxide Films

The optical properties of tin oxide films were investigated by many authors [(3-7, 17, 28, 37) see Table I]. Tshiguro, Sasaki, and Arai (4) measured the transmission and reflection of highly conductive  $\text{SnO}_2$  films obtained by hydrolysis of  $\text{SnCl}_4$  on fused quartz or rock salt substrates. The conduction electron concentration in the samples was  $10^{19}$ - $10^{20} \text{ cm}^{-3}$ . These specimens were almost perfectly transparent in the visible region and the fundamental absorption began at about  $0.3 \mu\text{m}$  extending to a shorter wavelength. In the infrared region, the transmissivity decreased gradually whereas the reflectivity began to increase. The authors found that the fundamental absorption gap was at about 4 eV and the plasma frequency of carriers lay in the near infrared region. They also found that the carriers in transparent conducting films were scattered mainly by ionized impurities. The refractive index of  $\text{SnO}_2$  films obtained by Tshiguro *et al.* (5) was found to vary with the wavelength from 1.92 at  $\lambda = 0.5 \mu\text{m}$  to the minimum value 0.87 at about  $3.5 \mu\text{m}$  and 5.53 at  $30 \mu\text{m}$ .

Miloslavskii (6) investigated the optical properties of highly conductive ( $\sigma = 10^2$ - $10^3 \text{ ohm}^{-1} \text{ cm}^{-1}$ ) transparent  $\text{SnO}_2$  films prepared by spraying anhydrous  $\text{SnCl}_2$  and  $\text{SnCl}_4$  or alcohol solutions of these compounds on glass, and pyrolytic decomposition of these substances at  $770^\circ$ - $870^\circ\text{K}$  (66). The conduction electron concentration was  $10^{18}$ - $10^{20} \text{ cm}^{-3}$ . The observed index of refraction was  $n = 1.98 \pm 0.2$  for  $\lambda = 0.59 \mu\text{m}$ . Absorption was studied in  $\text{SnO}_2$  films deposited on thin plane-parallel plates of rock salt single crystal. Two absorption bands were observed, namely: a narrow band with a maximum at  $16.4 \mu\text{m}$  and a wide band with maximum at  $8.5$ - $9 \mu\text{m}$ . The intensity of both absorption bands increased with increasing conductivity. In the case of films with high conductivity, widening and overlapping of the absorption bands were also observed. As the temperature decreased from  $490^\circ$  to  $130^\circ\text{K}$ , a considerable increase of absorption coefficient of the two bands was observed. On the other hand, films of  $\text{SnO}_2$  obtained by oxidizing thin films of tin deposited by vaporization in vacuum had a considerably lower con-

ductivity (about  $1 \text{ ohm}^{-1} \text{ cm}^{-1}$ ) and were transparent throughout the measured range of the spectrum ( $1$ - $18 \mu\text{m}$ ). Miloslavskii assumed that the appearance of the absorption bands in the films obtained by pyrolytic decomposition of chlorides is related to the introduction of a large number of impurity atoms, and attributed it to electron transitions from the ground state of the impurity centers to higher energy levels. He suggested that the long wavelength band corresponds to a transition of an impurity atom to an excited energy state, while the short wavelength broad band is due to a transition to the  $\text{SnO}_2$  conduction band. This is indicated by the asymmetrical shape of the absorption band, i.e., a slow drop in absorption in the high energy range and a sharper drop in the long wavelength range. The increase of these bands as the temperature decreases is caused probably by an increase in the degree of occupancy by electrons in the ground state. It seems that the chlorine atoms are the impurity centers.

Miloslavskii also investigated the optical absorption and electrical conductivity of  $\text{SnO}_2$  films doped with antimony. The films were obtained by spraying  $\text{SnCl}_4$  containing a small amount (several percent) of  $\text{SbCl}_3$ . He found that increasing the concentration of  $\text{SbCl}_3$  caused increases in both the electrical conductivity and the absorption of these films. The films showed considerable absorption in the infrared region. The short wavelength end of the infrared absorption extends into the visible range, which imparts a blue color to the films and reduces transmissivity to 50-70%. The absorption observed was suggested to be due to free electrons, contributed by the Sb donors to the  $\text{SnO}_2$  conduction band.

The influence of free carriers on the optical absorption of conductive and nonconductive  $\text{SnO}_2$  films was investigated by Arai (7). Conductive  $\text{SnO}_2$  films were prepared by hydrolysis of  $\text{SnCl}_4$  and were also obtained by vacuum evaporation of chemically prepared  $\text{SnO}$  powder. Nonconductive  $\text{SnO}_2$  films were obtained from conductive  $\text{SnO}_2$  or  $\text{SnO}$  by heating them in air. Arai found that in the visible region of the spectrum, optical properties of conductive and nonconductive  $\text{SnO}_2$  films were similar. However, in the u.v. region there were some differences observed between the absorption behaviors of these materials. This is shown in Fig. 22. The absorption edge was found to be at  $3.82 \pm 0.030$  and  $3.71 \pm 0.025 \text{ eV}$  for conductive and nonconductive  $\text{SnO}_2$  films, respectively. The temperature change of absorption edge for both these materials was  $-2.0 \times 10^{-4} \text{ eV}/^\circ\text{K}$ . Differences in the transmissivity and reflectivity of conductive and nonconductive  $\text{SnO}_2$  films were observed also in the infrared region. It is likely due to the difference of the concentration of free electrons. Figure 23 shows the transmission and reflection curves of conductive  $\text{SnO}_2$  films doped with antimony, in the infrared region as measured by Arai.

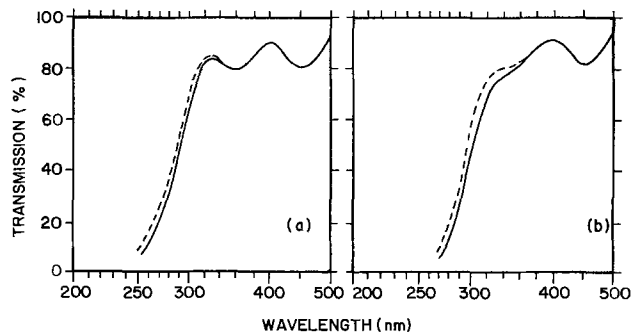


Fig. 22. Temperature change of transmission for  $\text{SnO}_2$  films; (a) conductive films. (b) nonconductive films. Full line at  $303^\circ\text{K}$ ; dotted line at  $128^\circ\text{K}$ .

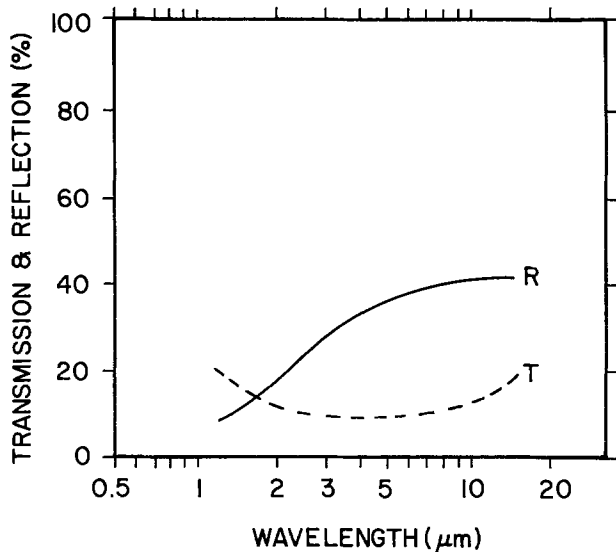


Fig. 23. Transmission and reflection curves of conductive SnO<sub>2</sub> films doped with 1% antimony.

Spence (17) measured the optical absorption edge of vacuum-evaporated films of SnO<sub>2</sub> at room temperature. The absorption coefficient was determined by the simple formula

$$K = (2.303/d) \log_{10} (1/T)$$

neglecting the reflectance; where  $d$  is the thickness in cm and  $T$  is the transmission in percent. From the dependences of  $K$ ,  $K^2$  and  $K^{1/2}$  vs. photon energy, and the extrapolation of linear portions of these curves to zero absorption, Spence found that the absorption edge occurs at about 3.7 eV, with direct transitions indicated at about 4.3 eV and indirect transitions at about 2.7 eV. The impurity peak reported at 3.36 eV was also observed. The value of the absorption edge is similar to that found by Arai, and the values of direct and indirect transitions are close to those measured by Reddaway and Wright (11) in SnO<sub>2</sub> single crystals.

The optical properties of Si-SnO<sub>2</sub> n-n heterojunctions were investigated by Nishino and Hamakawa (28). They carried out measurements of transmission over the wavelength region from 220 to 1400 nm. Transmission spectra for two samples at room temperature are shown in Fig. 24. The films have the ability to transmit about 90% and are almost transparent in the wavelength region above 350 nm. The absorption edge is seen near 350 nm as in the SnO<sub>2</sub> films investigated by Arai (7). This edge is not sharp because of a polycrystalline film. The photovoltage spectra for Si-SnO<sub>2</sub> n-n heterojunctions measured at

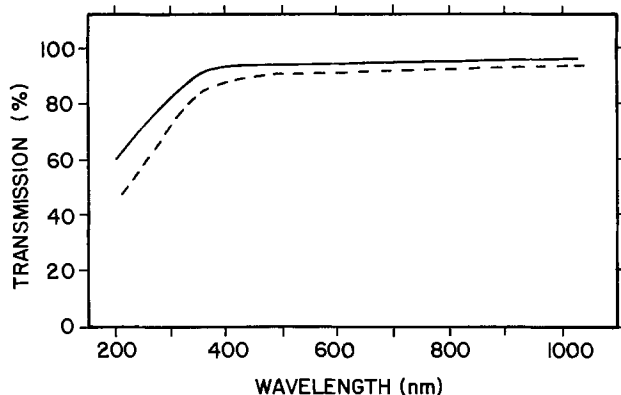


Fig. 24. Transmission spectra at room temperature for two conducting SnO<sub>2</sub> films deposited on quartz.

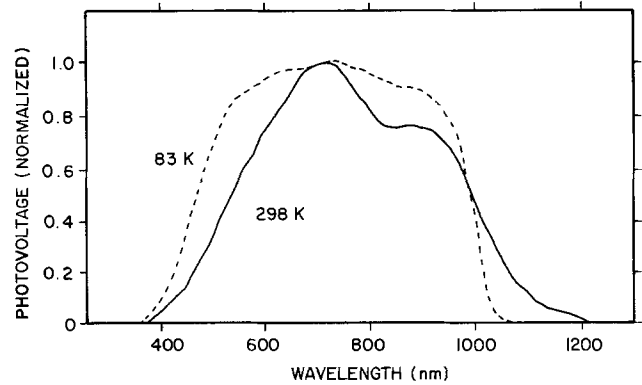


Fig. 25. Photovoltage spectra in Si-SnO<sub>2</sub> n-n heterojunction measured at two temperatures. Amplitude of photovoltage is normalized at the maximum value.

298° and 83°K are shown in Fig. 25. These relative spectra are normalized at the maximum values of photovoltage. The photovoltaic response is seen to spread in a wide wavelength range from 400 to 1200 nm. The wavelengths giving the maximum photovoltage are the same for both spectra at 710 nm. It is seen that the Si-SnO<sub>2</sub> photodiode would be applicable as a photosensor having the response in a wide wavelength region which is wider than a commercial silicon photodiode.

Kim and Laitinen (37) investigated the electrochemical behavior of thin film SnO<sub>2</sub> electrodes under sub-bandgap energy photoexcitation. They found that photocurrents were dependent on the intensity of the light, wavelength, and the applied voltage. The photocurrent spectrum showed a sharp decrease near the bandgap energy. The authors assumed that this photocurrent is due to the oxidation of water in the electrolyte by holes at the permitted energy levels in the bandgap region. These energy states may be formed by the presence of impurities.

### Conclusions

Allowed direct transitions in SnO<sub>2</sub> crystals were found at 3.57 eV (3.7 eV) and 3.93 eV (4.1 eV) for radiation polarized perpendicular and parallel, respectively. Indirect transitions were found at 3.42 and 3.72 eV for light polarized perpendicular and parallel to the  $c$  axis, respectively.

At low temperatures, the spectrum for  $E \parallel c$  begins with second class exciton transitions at the  $\Gamma$  point, while at temperatures higher than 200°K, the spectrum may be interpreted in terms of Urbach's rule. It was suggested that the spectrum for  $E \parallel c$  may arise from fourth class optical transitions. Studies of the thermally modulated optical transmission showed structures for  $E \parallel c$  which may be due to the exciton-phonon quasi-bound state of Toyozawa.

Static dielectric constants have been found to be 9 and 14 for radiation polarized parallel and perpendicular to the  $c$  axis, respectively. Investigations of infrared absorption showed optical polar scattering of carriers at room temperature. Electron effective mass was found to be  $0.17 m_0$ . Anisotropic exciton-reduced-masses have been estimated to be  $\mu_x = 0.33 m_0$  and  $\mu_z = 0.30 m_0$ .

Measurements of photocurrents in SnO<sub>2</sub> crystals showed many trapping levels of unknown origin. Photoconductivity was found to have a peak at 370 nm and to be characterized by long rise and decay times. The rate of decay was found to depend on the crystal environment.

The luminescence and phosphorescence spectra of SnO<sub>2</sub> crystals were also investigated but these phenomena are not elucidated yet. The optical properties of SnO<sub>2</sub> films are approximately similar to that of single crystals.

### Acknowledgments

Z. M. Jarzebski has been a visiting fellow during the course of this work at the Centre for Interdisciplinary Studies in Chemical Physics and is grateful for the support from the Centre.

Manuscript submitted Aug. 19, 1975; revised manuscript received March 5, 1976.

Any discussion of this paper will appear in a Discussion Section to be published in the June 1977 JOURNAL. All discussions for the June 1977 Discussion Section should be submitted by Feb. 1, 1977.

Publication costs of this article were partially assisted by the Centre for Interdisciplinary Studies in Chemical Physics.

### REFERENCES

- Z. M. Jarzebski and J. P. Marton, *This Journal*, **123**, 199C (1976).
- Z. M. Jarzebski and J. P. Marton, *ibid.*, **123**, 299C (1976).
- R. E. Aitchison, *Australian J. Appl. Sci.*, **5**, 10 (1954).
- K. Ishiguro, T. Sasaki, T. Arai, and I. Imai, *J. Phys. Soc. Japan*, **13**, 296 (1958).
- K. Ishiguro, T. Sasaki, T. Arai, and I. Imai, *ibid.*, **13**, 755 (1958).
- V. K. Miloslavskii, *Opt. Spectry.*, **7**, 154 (1959).
- T. Arai, *J. Phys. Soc. Japan*, **15**, 916 (1960).
- E. E. Kohnke, *J. Phys. Chem. Solids*, **23**, 1557 (1962).
- R. Summitt, J. A. Marley, and N. F. Borrelli, *ibid.*, **25**, 1465 (1964).
- R. Summitt and N. F. Borrelli, *ibid.*, **26**, 921 (1965).
- S. F. Reddaway and D. A. Wright, *Brit. J. Appl. Phys.*, **16**, 195 (1965).
- M. Nagasawa, S. Shionoya, and S. Makishima, *Japan J. Appl. Phys.*, **4**, 195 (1965).
- J. E. Houston and E. E. Kohnke, *J. Appl. Phys.*, **36**, 3931 (1965).
- J. E. Houston and E. E. Kohnke, *ibid.*, **37**, 3083 (1966).
- R. Summitt and N. F. Borrelli, *ibid.*, **37**, 2200 (1966).
- M. Nagasawa and S. Shionoya, *Phys. Letters*, **22**, 409 (1966).
- W. Spence, *J. Appl. Phys.*, **38**, 3767 (1967).
- R. Summitt, *ibid.*, **39**, 3762 (1968).
- D. A. Wright, *Proc. Brit. Ceram. Soc.*, **10**, 103 (1968).
- H. J. Van Daal, *Solid State Commun.*, **6**, 5 (1968).
- H. J. Van Daal, *J. Appl. Phys.*, **39**, 4467 (1968).
- J. P. Fillard, J. Gasiot, and M. deMurcia, *Phys. Status Solidi (a)*, **3**, 893 (1970).
- M. Nagasawa and S. Shionoya, *Phys. Rev. Letters*, **21**, 1070 (1968).
- D. F. Crabtree, R. N. S. M. Mehdi, and D. A. Wright, *J. Phys. D*, **2**, 1503 (1969).
- M. Nagasawa and S. Shionoya, *Solid State Commun.*, **7**, 1731 (1969).
- R. D. Cunningham, J. P. Marton, and M. Schlesinger, *Bull. Am. Phys. Soc.*, **14**, 310 (1969).
- R. D. Cunningham, J. P. Marton, and M. Schlesinger, *J. Appl. Phys.*, **40**, 4664 (1969).
- T. Nishino and Y. Hamakawa, *Japan. J. Appl. Phys.*, **9**, 1085 (1970).
- M. Nagasawa and S. Shionoya, *ibid.*, **10**, 472 (1971).
- M. Nagasawa and S. Shionoya, *ibid.*, **10**, 727 (1971).
- M. Nagasawa and S. Shionoya, *J. Phys. Soc. Japan*, **30**, 158 (1971).
- M. Nagasawa and S. Shionoya, *ibid.*, **30**, 1118 (1971).
- J. P. Fillard, J. Gasiot, M. deMurcia, and Tran Trong Quynh, *Phys. Status Solidi (a)*, **9**, K169 (1972).
- D. F. Crabtree, *J. Phys. D. Appl. Phys.*, **7**, L17 (1974).
- D. F. Crabtree, *ibid.*, **7**, L22 (1974).
- R. D. McRoberts and C. G. Fonstad, *Phys. Rev.*, **B15**, (1974).
- H. Kim and H. A. Laitinen, *This Journal*, **122**, 53 (1975).
- E. E. Kohnke and J. E. Hurt, *Bull. Am. Phys. Soc., Ser. II*, **4**, 428 (1959).
- J. A. Marley and T. C. MacAvoy, *J. Appl. Phys.*, **32**, 2504 (1961).
- H. Y. Fan, *Rept. Progr. Phys.*, **19**, 107 (1956).
- A. Kahan, *Appl. Opt.*, **3**, 314 (1964).
- R. A. Smith, "Semiconductors," Cambridge University Press, Cambridge (1961).
- A. Radkowsky, *Phys. Rev.*, **73**, 749 (1948).
- H. Y. Fan, *ibid.*, **82**, 900 (1951).
- R. S. Knox, "Theory of Excitons," Academic Press, New York (1963).
- V. T. Agekyon, *Opt. Spectry.*, **29**, 395 (1970).
- V. T. Agekyon, *ibid.*, **29**, 487 (1970).
- H. Y. Fan, W. Spitzer, and R. J. Collins, *Phys. Rev.*, **101**, 566 (1956).
- H. J. G. Meyer, *ibid.*, **112**, 298 (1958).
- S. Visvanathan, *ibid.*, **120**, 376, 379 (1960).
- E. Haga and H. Kimura, *J. Phys. Soc. Japan*, **19**, 658 (1964).
- W. G. Spitzer and D. A. Kleinman, *Phys. Rev.*, **121**, 1324 (1961).
- D. M. Eagles, *J. Phys. Chem. Solids*, **25**, 1243 (1964).
- S. F. Reddaway, *Brit. J. Appl. Phys.*, **17**, 697 (1966).
- S. F. Reddaway, Ph.D. Thesis, University of Durham (1968).
- T. Liebisch and R. Rubens, *Sitz ber. Preuss. Akad. Wiss.*, **2**, 876 (1919).
- R. J. Elliott, *Phys. Rev.*, **108**, 1384 (1957).
- J. J. Hopfield and D. G. Thomas, *ibid.*, **122**, 35 (1961).
- R. G. Wheeler and J. O. Dimmock, *ibid.*, **125**, 1805 (1962).
- R. J. Elliott, *ibid.*, **124**, 340 (1961).
- M. Cardona, in "Modulation Spectroscopy in Solid State Physics," Suppl. 11, F. Seitz, D. Turnbull, and H. Ehrenreich, Editors, Academic Press, New York (1969).
- Y. Toyozawa, "Proceedings of the Third International Conference on Photoconductivity," p. 151, Pergamon Press, Oxford (1971).
- J. C. Hermanson, *Phys. Rev.*, **B2**, 5043 (1970).
- F. J. Arlinghaus, *J. Phys. Chem. Solids*, **35**, 931 (1974).
- B. S. Kawasaki, B. K. Garside, and J. Shewchun, *Proc. IEEE*, **58**, 179 (1970).
- V. A. Riabov, O. V. Vorob'eva, and A. S. Egorova, *Steklo, Inform. Byul. Vses. Navchn. Issled. Inst. Steklo.*, **1**, (1957).



## Building a Better Electrochemical Mousetrap<sup>1</sup>

Robert Burns MacMullin



Robert B. MacMullin presents the Electrochemical Engineering and Technology Award Address.

Mr. President: This award, much appreciated by me, comes in the late November of my career. On this fine day in early May, it seems appropriate to return the cash part of the Award to the Society for reinvestment in the Fund, hopefully to encourage younger men to write and to publish the future chapters in electrochemical engineering science and technology.

Electrochemical engineering is not really a new discipline. There used to be a Course XIV by that name at MIT. I graduated as a chemical engineer, Course X, and drifted into electrochemistry from necessity. After all, the Mathieson Alkali Works Incorporated had been making chlorine and caustic soda at Niagara Falls since 1897. In 1920 I was to become familiar with acres and acres of Castner amalgam cells, the rocking variety, which then operated at about a thousand amperes. My first assignment was not electrochemical at all, just chemical: finding new uses for by-product chlorine. Up to that time, all the chlorine was converted to old-fashioned bleaching powder which was used, among other things, for the disinfection of outdoor toilets! As time went on, I became involved in devising better mercury cells, and even in making other commodities, such as metallic magnesium, in new types of electrolytic cells.

I stayed with Mathieson until 1945. Since then, as a consultant, I have been helping clients in their efforts

to make a wide variety of products by the electrochemical route. My field, then, is electrosynthesis, or if you prefer, electrowinning such things as metals, inorganic chemicals, and organics.

In the early days electrochemical engineering was, by and large, an art. In 1920, you flew by the seat of your pants. As time went on, theoretical electrochemistry became better understood. Young engineers learned some of the lingo, and began applying it on a scale of kiloamperes rather than milliamperes. This more scientific approach has come to be called electrochemical engineering. Even so, art still plays an important role. Innovation is an art, and you can't contribute much to electrochemical engineering without making innovations.

It is beyond my competence to describe the whole field, even if there were time. I have been personally involved in a number of unexpected and rather startling developments, and I propose to share a couple of these with you, to show what I mean by innovation. As a guideline, I will take as my theme, "Building a Better Electrochemical Mousetrap."

### YOU DREAM OF A BETTER MOUSETRAP

The world is waiting for it. Why not an electrochemical mousetrap?

### YOU START TO WORK ALONG CONVENTIONAL LINES

You design the mousetrap, making use of all available technology.

### YOU MAKE A DISCOVERY WHICH SEEMS TO VIOLATE ALL PRECONCEIVED NOTIONS

The mousetrap doesn't work the way you hoped it would, but strangely works better if you turn it upside down, or inside out, or if you leave out a part.

### YOU HASTEN TO UNRAVEL THE MYSTERY

You try everything in the book, including thermodynamics, kinetics, engineering, plus a little black art. You wind up with a new set of rules, including scale-up.

### YOU WAKE UP, YOU HAVE YOUR BETTER MOUSETRAP, BUT

It is ahead of its time, no market.

or, It's too costly to make, you can't sell it.

or, You may dream again of a still better mousetrap. Backers are scarce.

or, Everthing clicks. You build a plant and run into other problems.

or, Your dream is fulfilled, and eventually you get out of the red.

It so happens that both my chosen examples wound up in the same category: they were ahead of their times. They both follow the pattern for the better mousetrap. The inventions, of course, were adequately patented, but patents are poor media for describing the drama of innovation. The sophisticated electrochemical technology that was born still lies buried in corporate archives. Both examples deal with my long interest, bordering on passion, for electrochemistry in porous media. The first example concerns the electrowinning of titanium metal, and the second, the electrofluorination of hydrocarbons.

### Electrolytic Titanium

Right after World War II, there was considerable excitement over the possibility of using titanium metal in airframes and in gas turbines. Ti, a strong refractory metal with a density of only 4.5, became glamorous, and there was a scramble to develop viable, economic processes for its manufacture. (Fig. 1). The Kroll process led the way, using magnesium metal to reduce titanium tetrachloride. I'll call this "tickle 4" for short. The substitution of Na for Mg followed soon after. The Ti-Cl<sub>4</sub> was made by the reductive chlorination of rutile, a rather expensive titanium oxide ore. Only step 3 is electrolytic, and both Mg and Na were commercially available, and looking for new outlets.

In 1950 the New Jersey Zinc Company got the idea of building a better mousetrap, an electrochemical mousetrap (Fig. 2). They already had a stake in Quebec Iron and Titanium Limited which produced titanium slag high in TiO<sub>2</sub> from cheap Canadian ilmenite. More than eight years of effort and many millions of dollars were spent in perfecting this process and demonstrating it in a large pilot plant, using commercial prototype cells. Meantime, titanium lost its glamour when the Air Force canceled its plans for titanium aircraft. All hands then turned to the problem of finding other uses for the metal. The NJZ process was moth balled and rests in its cocoon to this day.

I propose to describe some of the electrochemical paradoxes that were encountered during this eight-year campaign to make a better mousetrap, and how a new technique in electrochemical engineering was developed to resolve the paradoxes.

A low melting eutectic of potassium, lithium, and sodium chlorides was chosen as supporting electrolyte, and cells were operated at about 550°C, 200° above the freezing point (Fig. 3). Now, TiCl<sub>4</sub> does not ionize, and has a very limited solubility in such a bath. The lower chlorides, however, are quite soluble, and ionize. The trick, then, was to carry out the process in stages, either sequentially, or in designated zones in the cell, as shown in Fig. 4.

How do you keep these zones separated? If you don't separate them, the lower chlorides would be rechlorinated at the anode, and the current efficiency would be essentially zero. Obviously a permeable diaphragm of some sort was needed. A variety of porous ceramics was tried, but they all failed in one way or another.

### KROLL TYPE PROCESSES

- 1)  $\text{TiO}_2 + \text{C} + 2\text{Cl}_2 = \text{TiCl}_4 + \text{CO}_2$   
rutile
- 2)  $\text{TiCl}_4 + 2\text{Mg} = \text{Ti} + 2\text{MgCl}_2$
- 3)  $2\text{MgCl}_2 \xrightarrow{\text{electrol.}} 2\text{Mg} + 2\text{Cl}_2$
- 2)  $\text{TiCl}_4 + 4\text{Na} = \text{Ti} + 4\text{NaCl}$
- 3)  $4\text{NaCl} \xrightarrow{\text{electrol.}} 4\text{Na} + 2\text{Cl}_2$

Figure 1

### NEW JERSEY ZINC CO'S DREAM

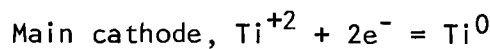
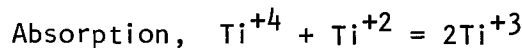
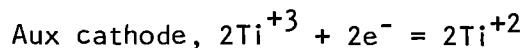
- 1)  $\text{TiO}_2 + \text{C} + 2\text{Cl}_2 = \text{TiCl}_4 + \text{CO}_2$   
slag
- 2)  $\text{TiCl}_4 \xrightarrow{\text{electrol.}} \text{Ti} + 2\text{Cl}_2$

Figure 2

- 1)  $2\text{TiCl}_3(\text{s}) \xrightarrow{2 \text{ Faradays}} 2\text{TiCl}_2(\text{s}) + \text{Cl}_2(\text{g})$
- 2)  $\text{TiCl}_4(\text{g}) + \text{TiCl}_2(\text{s}) = 2\text{TiCl}_3(\text{s})$   
chem reaction
- 3)  $\text{TiCl}_2(\text{s}) \xrightarrow{2 \text{ Faradays}} \text{Ti}(\text{c}) + \text{Cl}_2(\text{g})$
- $\Sigma \text{TiCl}_4(\text{g}) \xrightarrow{4 \text{ Faradays}} \text{Ti}(\text{c}) + 2\text{Cl}_2$

Figure 3

### CATHOLYTE ZONE



### ANOLYTE ZONE

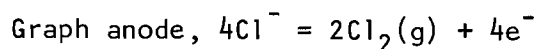


Figure 4

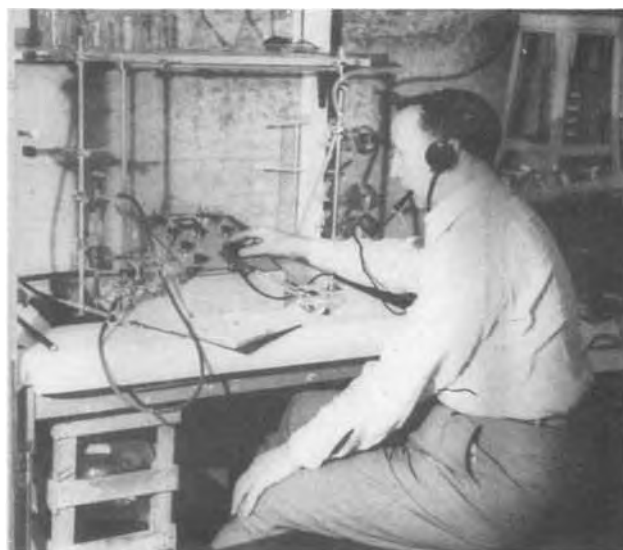


Figure 5

In 1955 I got the notion to do some research on my own, in my small cellar laboratory, on the characteristics of porous beds and structures (Fig. 5). I worked out the relation between permeability to viscous flow, and the electrical conductivity of such porous structures when saturated with electrolyte. The relation is shown in Fig. 6.

This equation is valid only if the solid matrix of the porous structure does not conduct. It is based on the notion that, in a porous insulator saturated with fluid electrolyte, the constraints to laminar fluid flow should be the same as the constraints to electrical current flow. In both cases, the flux is proportional to the gradient. The truth of this was easily demonstrated, using 1000 Hz a.c., and also using d.c.

$$\frac{m^2}{P} = k \frac{\rho}{\rho_0} \quad \text{MacMullin, Muccini 1956}$$

- m hydr. radius, sp. voids/sp. surf. cm
- P permeability, cm<sup>2</sup>
- $\rho$  sp. resist. porous body, sat'd with electrolyte
- $\rho_0$  sp. resist. electrolyte in pores
- k a universal constant = 3.67

Figure 6

If you switch to a porous matrix that conducts, such as porous metal or porous graphite, and use a.c., both the electrolyte in the pores and the matrix itself conduct, and the pathways for current flow are not the same as for fluid flow (Fig. 7).

On the other hand, if you use d.c., and take care that the potential between the electrolyte in the pores and the metallic matrix does not exceed the decomposition potential of the electrolyte, as in the center figure, no electrons are exchanged between the phases. The d.c. is constrained to the pores, and the analogy between fluid flow and electrical flow is restored.

Lastly, if the voltage drop across the conducting porous solid exceeds the decomposition voltage of the electrolyte, as in the lower figure, the matrix also conducts. The erstwhile porous diaphragm becomes a bipolar electrode, and its usefulness as a separator is destroyed.

Once these concepts were understood, let us see how the NJZ team made use of them. Why not use the dendritic, and therefore porous, deposit of titanium metal on the cathode as the diaphragm? The geometry is best seen on the drawing of a landmark patent by C. E. Barnett, U.S. Pat. 2908619 (Fig. 8).

Chlorine is evolved on the central graphite anode 11. The cathode is a cylindrical Inconel sheet 3, closed on the bottom 4, and the walls are punched out with round holes, or windows 5. TiCl<sub>4</sub> is introduced through pipe 13 dipping into the bath in the catholyte zone. A small concentration of TiCl<sub>3</sub> and TiCl<sub>2</sub> can be quickly built up by adding some off-grade Ti powder to this zone, since it will react with TiCl<sub>4</sub>. When the current is turned on, a dendritic deposit of Ti metal forms and quickly spreads over the holes. From then on, the anolyte and catholyte zones are separated.

What happens then? There are no soluble Ti ions in the anolyte, so Ti cannot deposit on the near (proximal) side of the cathode. However, the d.c. flows through the pores in the metal diaphragm to the other side where the soluble Ti ions are, and deposit Ti metal on the back (distal) side of the cathode. The way the deposit grows is shown in the next sequence of figures.

On the left in Fig. 9, an enlarged view of the holed cathode and anode. On the right, a cross section showing cathode and anode.

In Fig. 10, current paths are shown with solid lines, and the Ti deposit with dashed lines. Left, the current has been turned on and dendrites of Ti cover the holes. Right, the deposit starts to spread out over the cathode and the distal deposit becomes continuous.

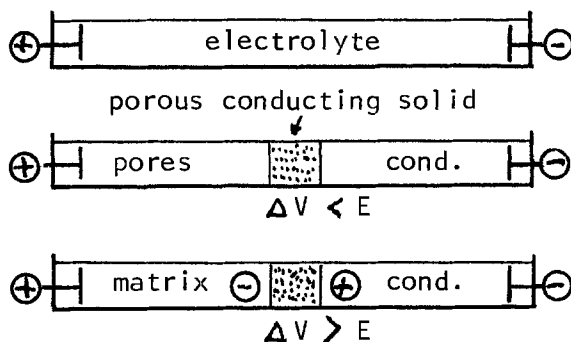
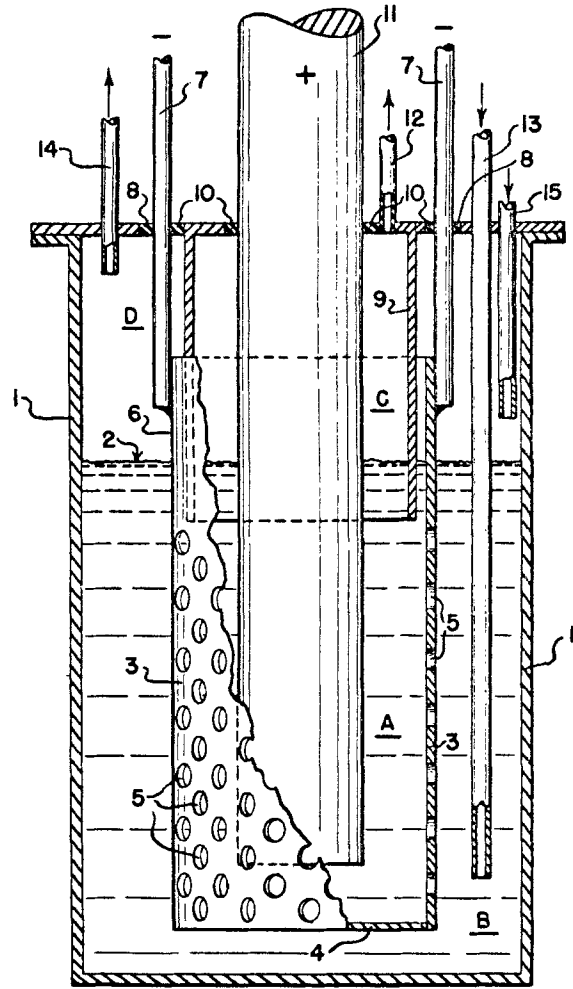


Figure 7



C. E. BARNETT US PAT. 2,908,619

Figure 8

Left in Fig. 11, a heavy deposit is built up at high current density. Right, last stage and prior to opening the cell, the soluble Ti chlorides are stripped from the catholyte at a lower current density. The fully developed deposit is several inches thick. Continuation would lead to deposition of Na on the proximal side. At this point the cathode is pulled from the cell and harvested.

Now let's look at the voltage distribution for the clue as to how thick the deposit may be before Na deposition ruins the current efficiency (Fig. 12).  $E_a$  is the equilibrium potential for Cl<sub>2</sub> evolution from the chloride melt, and  $\eta_a$  is the chlorine overvoltage. The slope of the IR drop in the bath is its resistivity. The slope is

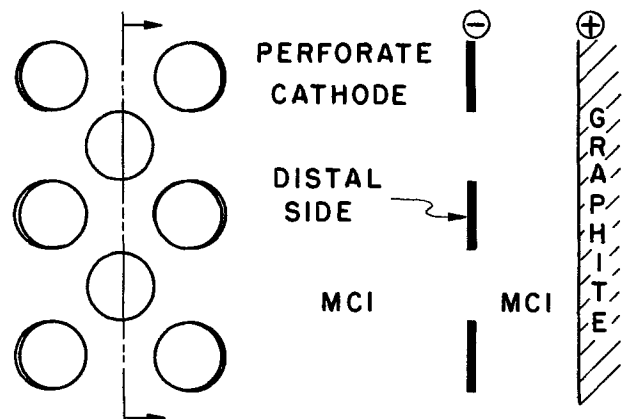


Figure 9



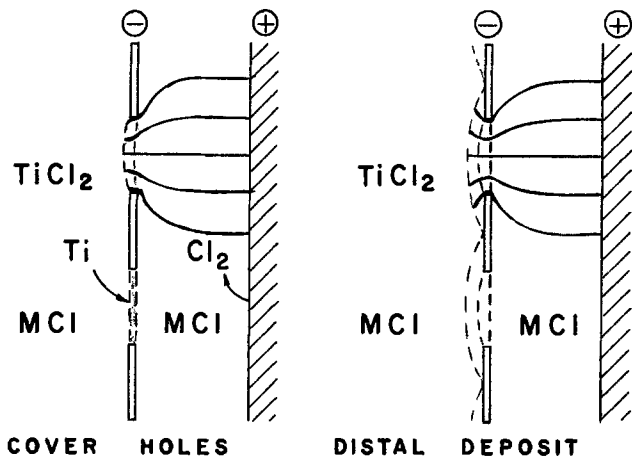


Figure 10

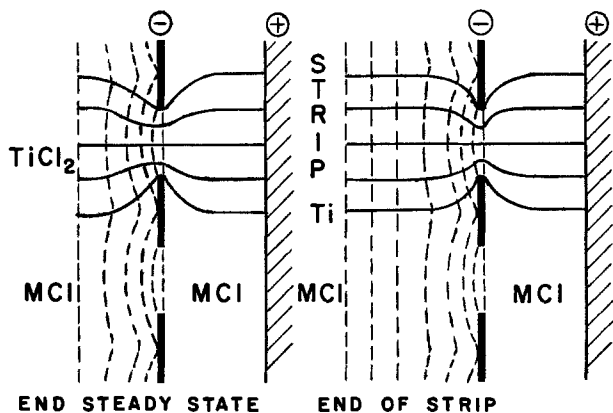


Figure 11

VOLTAGE DISTRIBUTION FOR DISTAL DEPOSITION

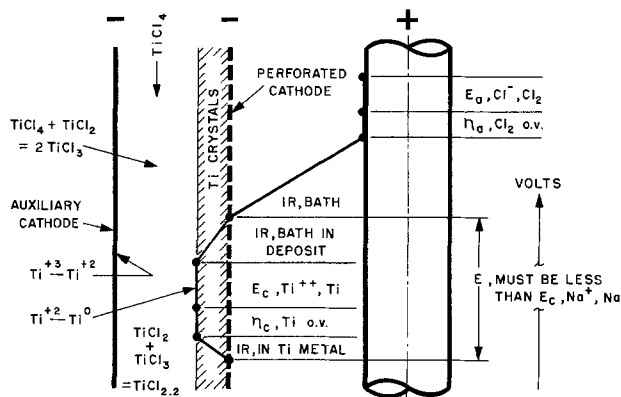


Figure 12

higher within the deposit because only the pores conduct.  $TiCl_4$  is fed between the two cathodes and reacts with the  $TiCl_2$  present to form  $TiCl_3$ . The  $TiCl_3$  is reduced to about  $TiCl_{2.2}$  at the auxiliary cathode, which may be the pot wall.

$E_c$  is the equilibrium potential for deposition of Ti metal, and  $\eta_c$  is the overvoltage, actually quite small. Electrons are given up by the Ti deposit at the bath interface, and there is a small IR drop as the current flows into the Inconel cathode.

Now the voltage drop marked  $E$  must be kept less than the alkali metal deposition potential, otherwise the alkali metal, Na in this case, will form on the proximal surface of the cathode. The sodium would back react with the chlorine, and this would be fatal to the current efficiency.

We are now ready to apply some electrochemical engineering to the unique and startling concept of metal deposition on the back side of a cathode!

EUTECTIC BATH

41.6% LiCl, 53.2% KCl, 5.2% NaCl  
 MP, 350°C Oper. temp., 550°C  
 Sp Gr bath, 1.66 metal, 4.50

TYPICAL DENDRITIC DEPOSIT

Ti content, 45 wt %  
 0.038 lb Ti / cu in  
 Vol. fraction occupied by bath,  
 $\epsilon = 0.768$

Figure 13

Figure 13 presents the salient facts about the bath and the deposit.

An easy way to measure the resistivity of the deposit as it builds up is to open the cell switch and measure the back emf (Fig. 14). The slope of the line is the resistivity. The slope, naturally, depends on the percent of Ti in the deposit, as this determines the void fraction  $\epsilon$  occupied by electrolyte.

At this point I will digress to explain, in a simple way, how current flows through the pores of several kinds of diaphragm.

Figure 15 shows a sheet made porous by punching out straight capillaries of uniform cross section, normal to the sheet. The pores are filled with electrolyte of resistivity  $\rho_0$ . The resistivity of the specimen is  $\rho$ , and it is easy to see that  $\rho$  is inversely proportional to the open area of the pores, which is identical to the void fraction  $\epsilon$  of the sheet. We will characterize the sheet resistivity by the dimensionless number  $N_r = \epsilon \cdot \rho / \rho_0$ . For this special kind of diaphragm,  $N_r = 1$ .

A more natural kind of porous body (Fig. 16) contains uniformly dispersed pores of irregular shape, these pores being interconnecting and isotropic. If we apply a voltage gradient along the x axis, only the pores lined up in this direction conduct. Those lined up in the y and z directions see no voltage gradient

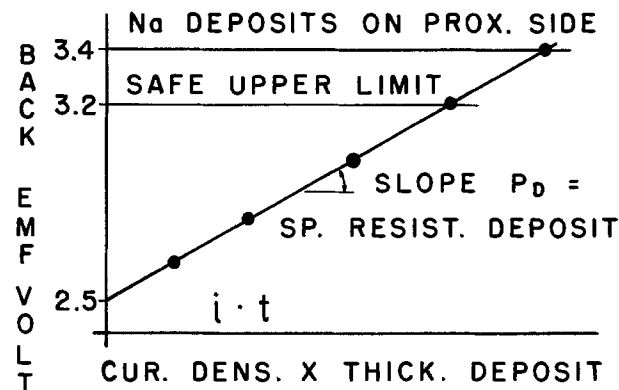


Figure 14

STRAIGHT CAPILLARIES  
 ⊥ TO SHEET



$\epsilon$  = void fraction

Ohm's Law applies  
 All capil. conduct

$\epsilon \cdot \rho / \rho_0 = 1$

Figure 15

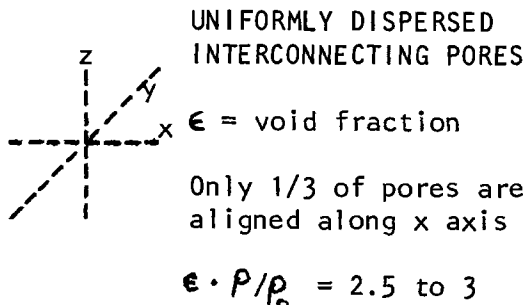


Figure 16

and do not conduct. For this kind of diaphragm we find that  $N_r = 2.5$  to  $3$ , approximately.

Figure 17 shows a dispersion of nonconducting spheres, such as glass beads or gas bubbles, in a conducting medium. The matrix, in this case, is the liquid medium, rather than the solid. According to Dr. Tobias, the resistivity ratio equals the void fraction to the minus 3/2 power. Therefore,  $N_r = \epsilon^{-0.5}$ .

If our diaphragm is made up of layered fibers (Fig. 18), as in sheet asbestos, or mats of metal, glass or carbon fibers, the resistivity ratio turns out to be surprisingly close to that given by the Tobias equation. From work done by Dr. Meredith,  $\rho/\rho_0 = \epsilon^{-1.54}$  over the range of interest. Therefore,  $N_r = \epsilon^{-0.54}$ .

How does the dendritic deposit of titanium behave? Does it resemble any of the diaphragms just shown? The dendrites are treed, and contain some spherical nodules as well.

Observe in Fig. 19 how the  $N_r$  changes with the density of the deposit. We can easily vary the percent of Ti in the deposit by adjusting the concentration of the soluble Ti in the catholyte, and also by varying the current density.

In Fig. 20 we have plotted the relative conductivity of the deposit against the volume fraction of salt in the deposit. See how the conductance of the deposit decreases as the weight percent Ti is increased. As indicated, one line shows, for comparison, what the curve should be for dispersed spheres, and another line, for

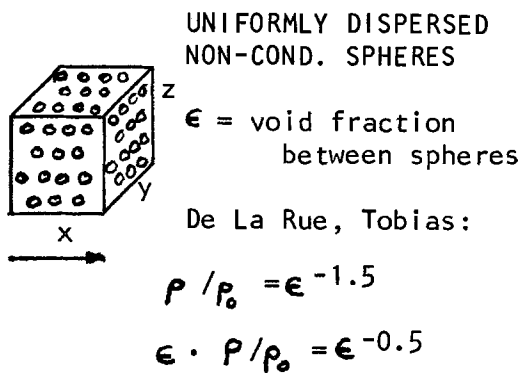


Figure 17

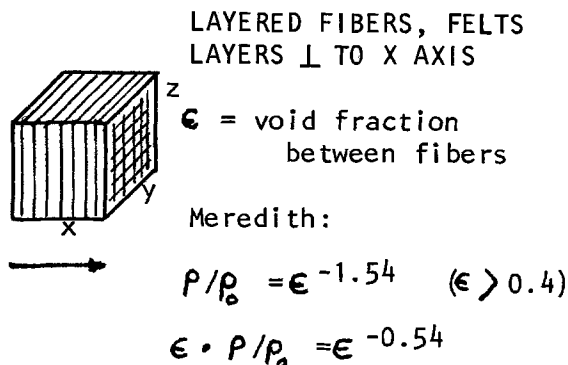


Figure 18

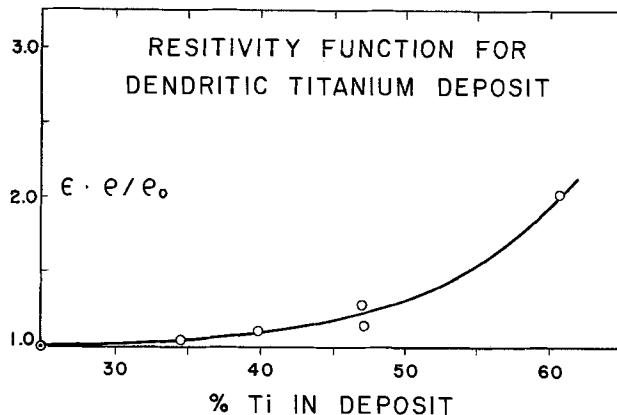


Figure 19

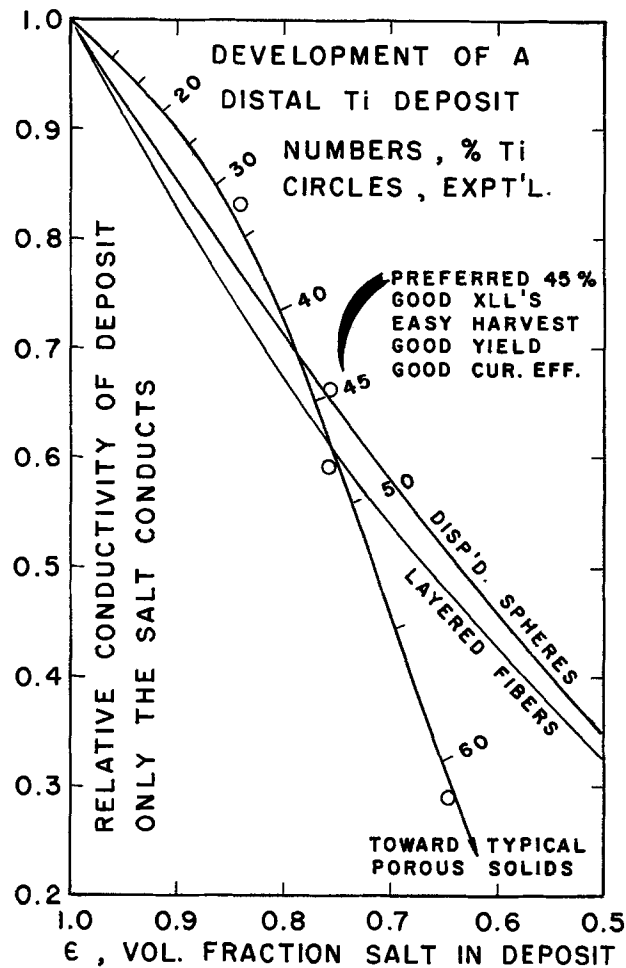


Figure 20

layers of fibers. The agreement is good at about 45% Ti. Beyond about 50% Ti the relative conductivity rapidly declines, and at 70%, approaches that of a typical porous solid with interconnecting pores, such as porous porcelain. The preferred deposit contains 45% Ti, which is easily achieved in actual operation.

For a safe back emf of 3.2V, Fig. 21 shows the allowable product of current density and thickness of deposit, as a function of the percent of Ti in the deposit.

Figure 22 shows that heavier deposits are obtained by sacrificing current density. In any case, the optimum kind of deposit would appear to contain 45% Ti. From here on, the engineering problem consists in evaluating the trade-offs between amount of metal harvested, and the time required to build the deposit. Optimization studies indicated the data shown in the next figure.

Harvesting the Ti from a cell is the last step of a four-step cyclic process (Fig. 23). The pilot plant cells, rated

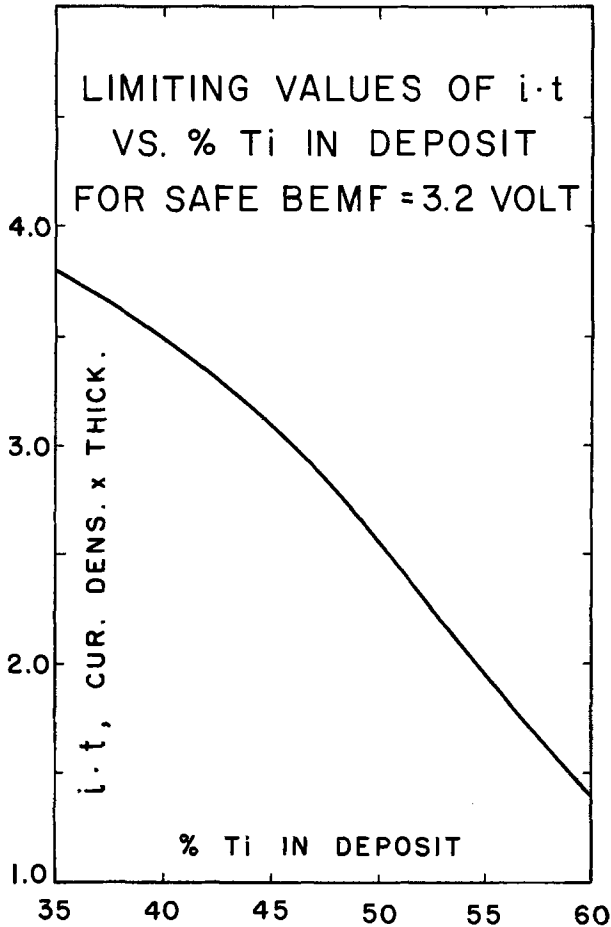


Figure 21

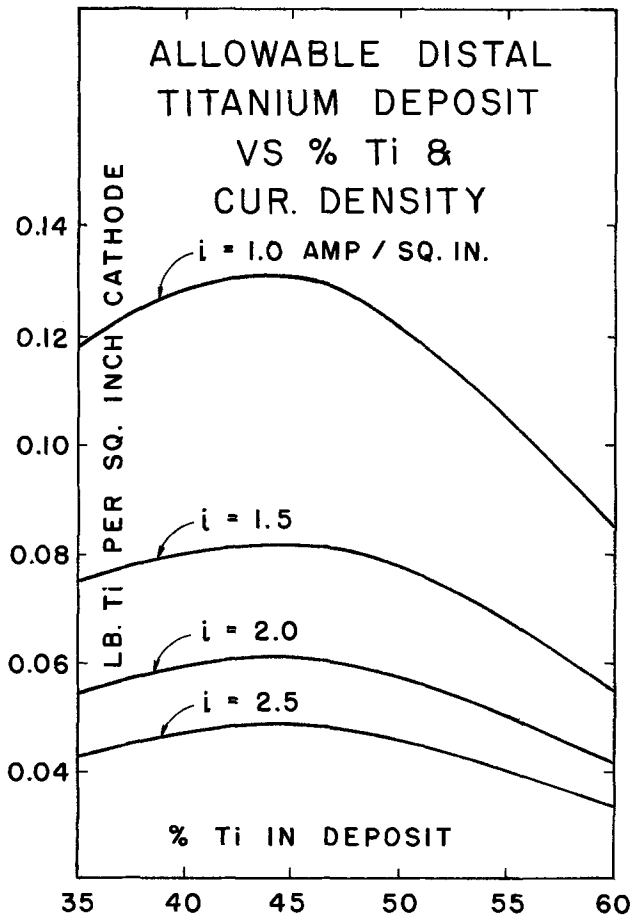


Figure 22

PILOT CELL CYCLE 7000 in<sup>2</sup> cathode

	Lb Ti	KAH	KA	HR
Buildup bath (194)		0	0	1
St'dy state	425	478	14	34
Strip bath	<u>184</u>	<u>114</u>	10	<u>11</u>
Harvest	609	592		46
On spec Ti	495, avg 250 lb/cell day			

Figure 23

at 14 to 18 kA, were thus able to produce 600 lb of metal, from which 500 lb of on-grade sponge was recovered. The harvesting of the Ti turned out to be absurdly simple. When the cathode is lifted out of the cell, the still-molten salts in the deposit protect it from oxidation in the air. If exposed, it is pyrophoric. If you drop the loaded cathode onto a hard surface before the salt freezes, the impact causes the whole deposit to slump off. The deposit is then allowed to freeze, and the frozen salt protects it from the atmosphere. Oxidation losses during further processing are minimal.

Figure 24 presents some key figures for a conceptual, semicommercial plant having a nominal capacity of 10 short tons of on-grade sponge per day. The average cell voltage is 8.2V, and the current efficiency is over 75%. About 80% of the harvested deposit can be recovered as on-spec Ti, and the off-spec Ti is recycled to the cells. The energy consumption is about 10 d-c kWhr per pound of on-spec metal.

Figure 25 is the conceptual flow diagram for making titanium ingots from titanium slag. There are three recycling operations. Chlorine from the cells, together with a small makeup, is used to make TiCl<sub>4</sub>. The salt in the deposit is leached out and recovered because of its valuable lithium content. Off-spec Ti fines, contain-

KEY FIGURES 10 ton/day Ti, BHN -100

Cathode, 42x52.5 in Deposit 2.3 in th  
 Cells on line, 78  
 Cells harvested, 41 per day  
 C.D. st'dy, 2 asi strip, 1.4 asi  
 Avg cell voltage, 8.16 volts  
 DC KAH/lb good metal, 1.2  
 DC KWH/lb good metal, about 10.  
 Yield good Ti from cath. sponge, +80%  
 Off grade Ti refined by recycling.

Figure 24

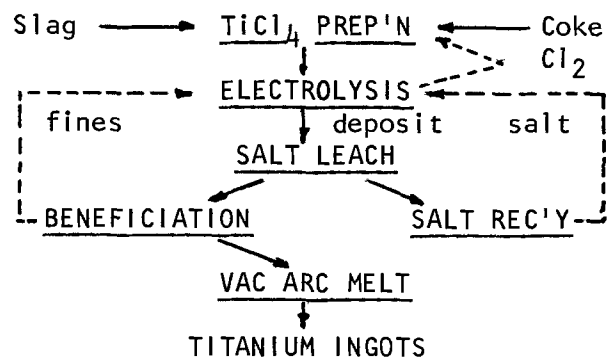


Figure 25

ing nonmetallic impurities, are recycled to the cells for the buildup step. There is a small charge for additional ampere hours as they are refined in subsequent steps. The on-spec sponge has a Brinell hardness less than 100, and is equal to the best metal made by the Kroll process.

Summarizing, I think this case history illustrates very well our theme about the better electrochemical mousetrap. The conventional approach didn't work because we couldn't find a suitable ceramic diaphragm. So we left out the diaphragm. We punched holes in the cathode to force deposition of metal onto the back side of the cathode, a truly revolutionary idea. The consequences of this mode of operation were fully explored and applied to the problem of scale-up. The better mousetrap worked very well on a large pilot scale. But: the better mousetrap was ahead of its time, the market wasn't there, and the dream of commercial rewards has remained unfulfilled to this day.

### Electrochemical Fluorination of Hydrocarbons

Prior to 1966, the only known method for electrochemical fluorination of organic compounds was by the technique invented by J. H. Simons (Fig. 26). The organic was dissolved in a bath of anhydrous HF containing some KF to make it conductive. Nickel electrodes were immersed in the bath, and fluorine gas was generated at the anodes, hydrogen gas at the cathodes. The  $F_2$  thus generated reacted with the H atoms in the organic, as shown. The heat generated exceeds that required to break the carbon-carbon bond, and scission of the carbon chain was frequently encountered.

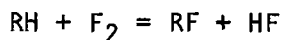
As reported in *This Journal* in 1964, researchers at Phillips Petroleum Company had successfully electrochlorinated liquid hydrocarbons at a porous, flow-through carbon anode, using aqueous hydrochloric acid as the electrolyte. It then occurred to them that it might be possible to electrofluorinate hydrocarbon gases or vapors in a conventional fluorine cell. The only change would be to use a porous carbon anode, so that the hydrocarbon feed could be forced through the anode. The electrolyte was anhydrous  $KF \cdot 2HF$ , the strength being maintained by adding HF as fast as it was depleted by electrolysis. They tried it, and it worked.

Curiously, there was no breakdown of the carbon chain. Why? As it turned out (Fig. 27), they weren't fluorinating with  $F_2$  gas, but with an intermediate addition product  $C \dots F_x$ . The voltage required to liberate free  $F_2$  from HF is about 2.9V, while that required to form the complex is only about 1.75V. From this information, the heat of the reaction shown in the figure is only about 60 kcal, not enough to break any carbon-carbon bonds.

Another curious thing was noted. The bath did not seep into a used porous anode. Why? The fluorinated surface of the carbon, inside and out, was hydrophobic to the electrolyte. To force the bath into the pores would require a hydrostatic pressure great enough to overcome the repulsion of the hydrophobic surface. For

### SIMONS' CELL

Nickel anodes



$$\Delta H = -106 \text{ to } -115 \text{ kcal}$$

C-C bond energy = 83 kcal

Result,  $R \rightarrow R_1 + R_2 + R_n$

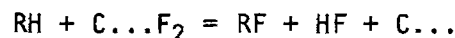
moieties of R

Figure 26

### PHILLIPS PETROLEUM CO'S CELL

Fox, Ruehlen & Childs, JECS 1971

Porous carbon anodes



$$\Delta H = \text{about } -60 \text{ kcal}$$

Result, no scission of R

Figure 27

a depth of immersion of 4 to 6 inches, the porous anode remained dry.

This led Messrs. Fox, Ruehlen, and Childs to the idea of introducing the feed gas into the open bottom of the porous anode (Fig. 28). The bath, pressing against the sidewalls of the immersed anode, sealed off the escape of gas, which then exited above the bath level. The feed gases rose through the dry porous anode like hot gases in a chimney. When the current was turned on, the  $C \dots F_x$  was formed at the anodic surface and, *mirabile dictu*, the hydrocarbon gas was fluorinated as it flowed by! Thus, the concept of the porous flow-by electrode was born. Up to 60 or more percent of the available hydrogen atoms in the feed could be replaced by fluorine in one pass up through the chimney! It looked like action, or rather reaction at a distance, something like Newton's concept of gravity. Radial gas diffusion seemed inadequate to explain the effect. Maybe the F atoms were hopping from site to site.

At this point the electrochemical engineers had a field day trying to model the actions and interactions. They asked for more data as fast as one theory after another went into the dustbin. They finally arrived at a

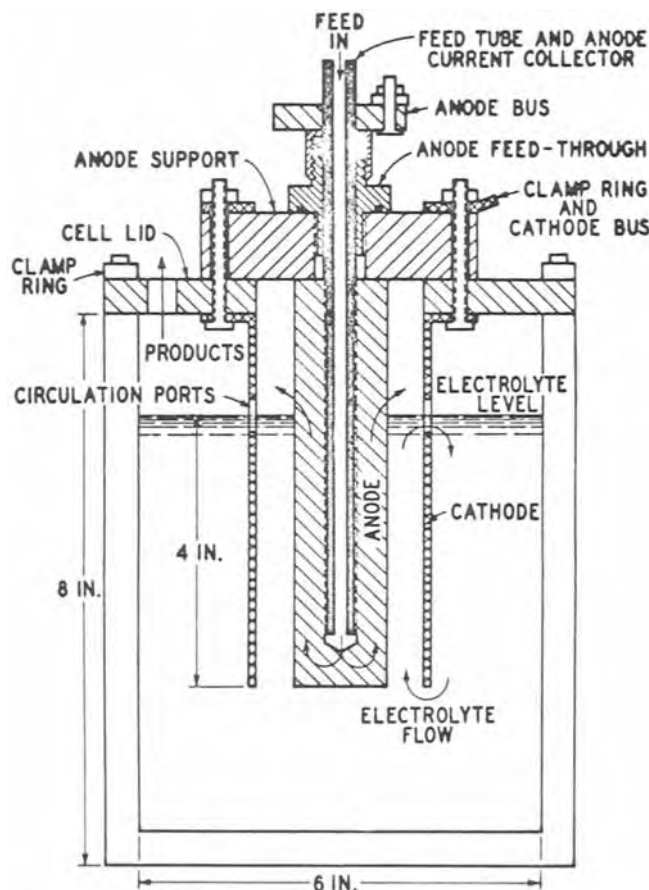


Figure 28

set of rules for scale-up to commercial sized prototypes. The field day lasted more than two years.

Consider the porous anode. We want the feed gas to rise through the anode without breaking out. If any breaks out, it can no longer be fluorinated. The gas pressure at any level equals the pressure where introduced, less the pressure drop in flowing up the anode up to that level. The pressure gradient at any level depends on the permeability of the porous structure, the gas flow rate, and the viscosity of the gases, as shown in Fig. 29. But, as the gas ascends, it reacts with the fluorine complex at a rate which depends on the current density at that level. Heat is generated, the temperature changes, and the volume of the gas changes. So does its composition and viscosity. All this information was processed in a computer program, and pressure and temperature profiles were printed out for just about any kind, size, and shape of anode we could imagine.

If the grain size of the porous carbon was too coarse, it had high permeability, and hence capacity, but was structurally weak. If too fine, it was nice and strong, but too low in capacity. We settled on a porous carbon having a permeability in the range of 20 to 30 API Darcies. We predicted that we could increase the immersion from 6 up to 12 inches, thus doubling the current rating of the anode. It worked. Anybody want to try for 24 inches? This worked, too, but there were complications. The bath did seep into the deep end, and seal off some of the pores, the bigger ones. We asked for a pressure and temperature traverse of a 24 inch deep anode in a working cell.

Figure 30 illustrates such a traverse made while fluorinating EDC to produce, eventually,  $C_2Cl_2F_4$ , or F-114. Note that the gas pressure  $p_g$  is less than the hydrostatic pressure  $p_h$  at all levels, proving that there was no gas breakout through the sidewalls.

Figure 31 is a similar traverse, same current, but with a much greater gas flow rate. Here also, no breakout. The temperature profiles were a surprise. A heat balance indicates that the bath seeping into the bottom of the anode percolates up along with the gas, and then exits higher up. This internal circulation of liquid not only tempers the reaction, but also dissolves HF from the gas phase and transfers it back to the main body of the bath, thus increasing the capacity by removing a reaction product. Furthermore, it explains in part the "reaction at a distance" paradox previously mentioned.

$$\frac{dp}{dx} = \frac{u n}{P g}$$

$$\text{press grad} = \frac{\text{veloc} \times \text{viscos}}{\text{permeability} \times g}$$

Figure 29

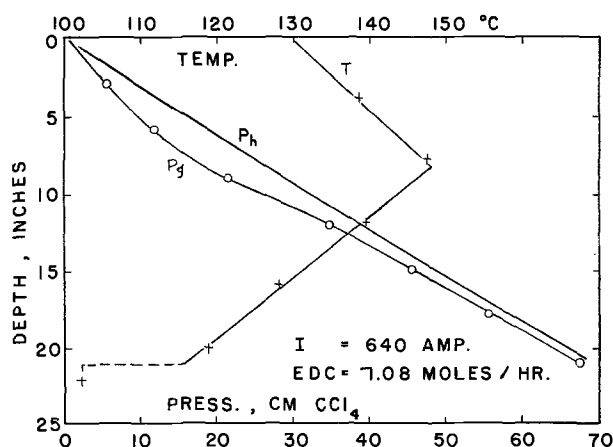


Figure 30

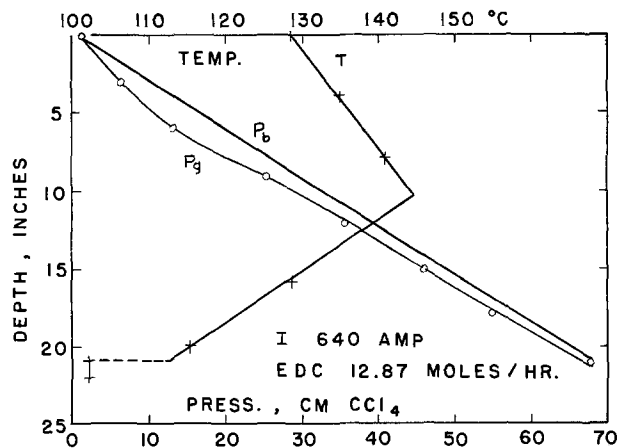


Figure 31

In order to use these data to estimate maximum permissible current densities and gas feed rates, we had to refine our mathematical model to allow for electrolyte invasion into the pores of the deep anodes. The first step was to measure the distribution of pore sizes in the porous carbon by means of a mercury porosimeter (Fig. 32).

We used the data to calculate the hydraulic radius  $m$  of the remaining porous structure as a function of the percentage of the pores invaded (Fig. 33). In a porous structure,  $m$  is simply the ratio of the specific volume of pores to the specific surface of the pores. It has the dimensions of length, shown as microns by the line labeled  $m$  in the figure.

Now, the permeability is proportional to  $m^2$ , and has the dimensions of area, or square microns, which is

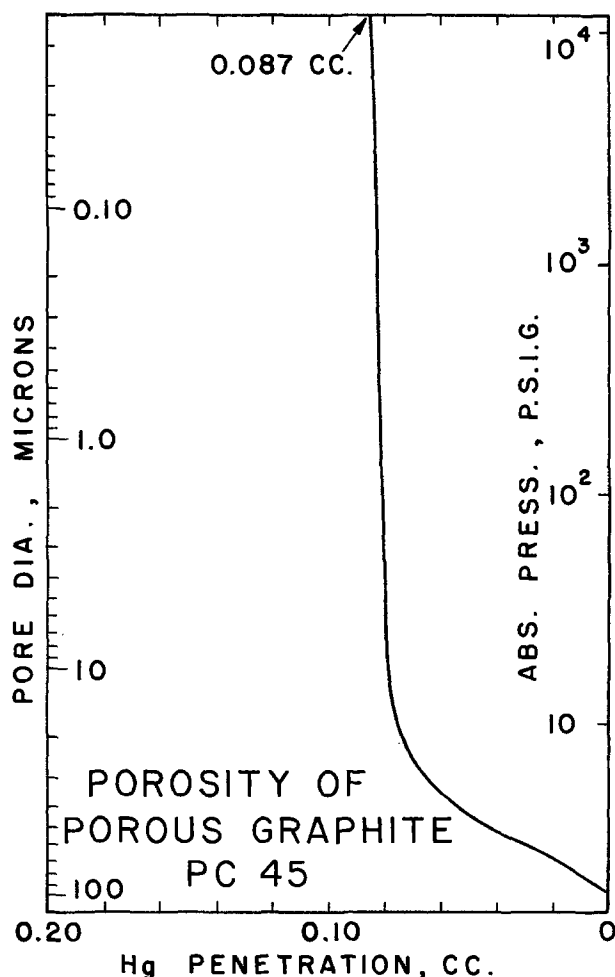


Figure 32

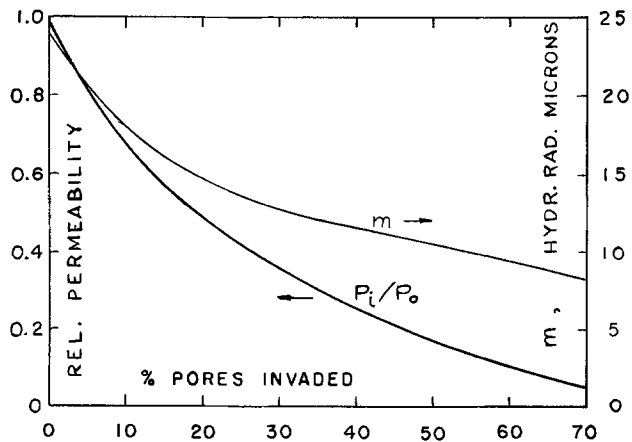


Figure 33

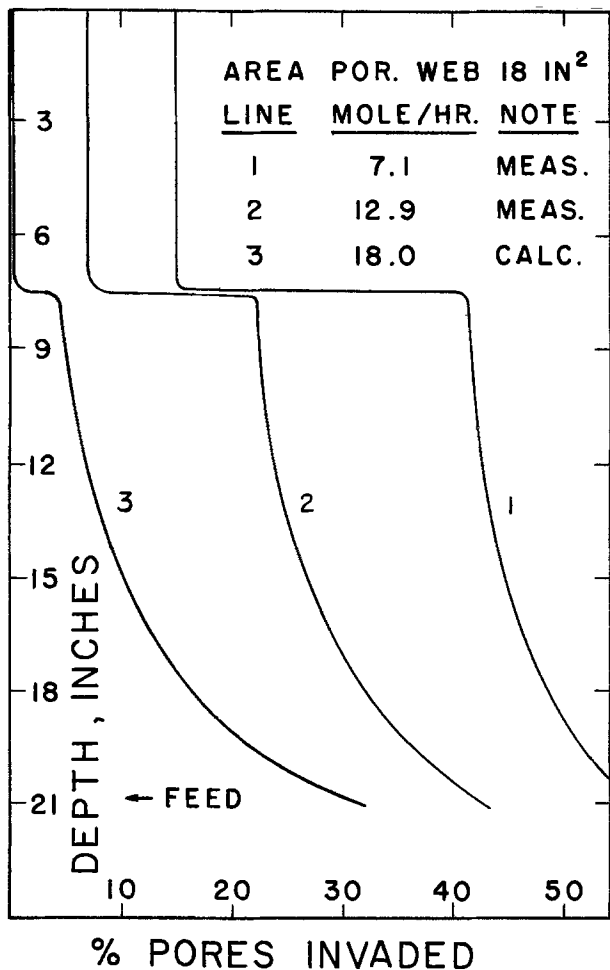


Figure 34

about the same as the conventional API Darcy unit. The lower curve shows the relative permeability of the anode as a function of the percentage of pores invaded. We can now crank this function into our computer program and arrive at the results shown in Fig. 34.

Curve 1 and curve 2 show the invasion profiles for the two traverses previously shown. Of the two, curve 2 is at the higher gas flow rate. Question: how much higher can we push the gas rate? The answer is shown in curve 3. The maximum permissible gas flow, without breakout, is about 18 gmole/hr.

One further result of our studies is the finding of an "invasion coefficient," defined as the product of the hydraulic radius and the differential pressure between electrolyte and gas, at any particular level (Fig. 35). That is,  $k_i = m (p_h - p_g)$ . This invasion coefficient appears to be a function of anode temperature. The in-

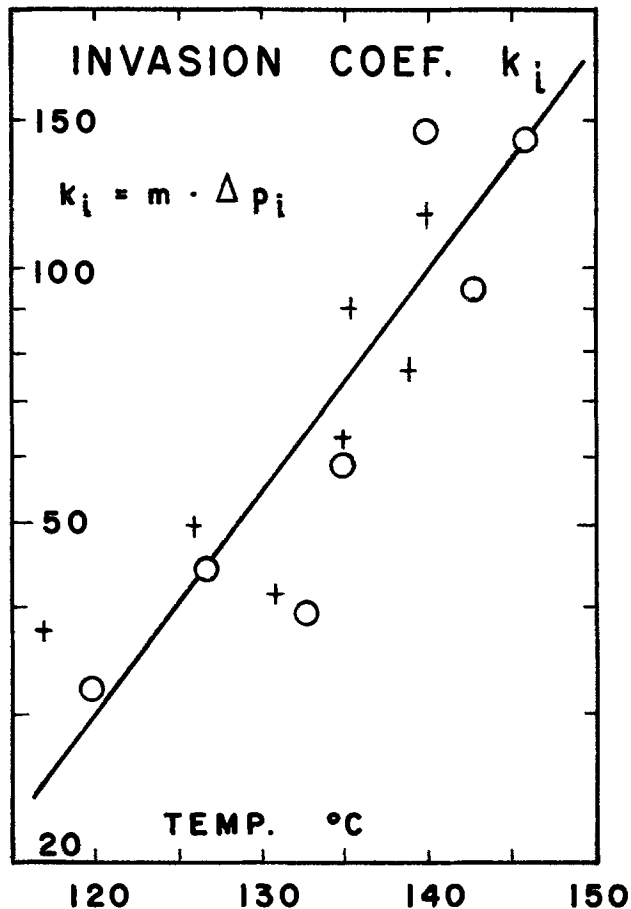


Figure 35

PART - E S U O M

Practical Electrochemical

Art of Society's

Reverse Un-

Thinking Orthodox

Mousetraps

Figure 36

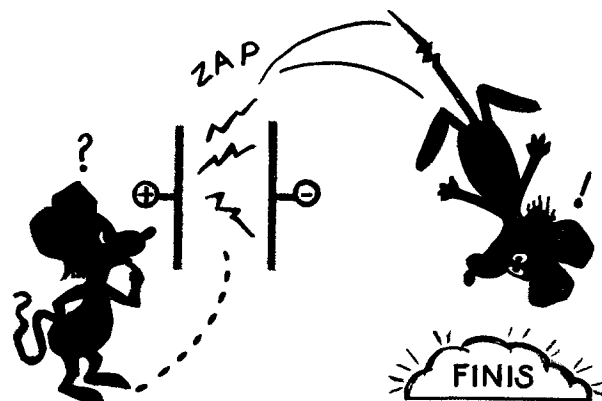


Figure 37

crease of  $K_i$  with temperature is undoubtedly related to changes in fluidity and surface tension of the electrolyte with temperature. The algorithm for the inva-

sion coefficient is a necessary subroutine for the computer program.

Summing up, it was necessary to unravel the paradoxes of the porous flow-by anode before proceeding with the design of a prototype commercial cell and the conceptual plant to go with it. There were other problems, to state it mildly, but these were all eventually solved. I think this bit of case history illustrates very well how electrochemical engineers are forced to innovate when confronted with problems for which there is no background technology whatever.

It further illustrates how the original concept of an electrochemical mousetrap never caught a mouse, and how the alert researchers redesigned the mousetrap to make it work very well indeed. As yet there is no large commercial plant, but you can purchase small lots of a new line of pure fluorocarbons from the Phillips people, prepared in this unique way.

Turning the mousetrap around (Fig. 36), we see that this stands for: Practical Art of Reverse Thinking—Electrochemical Society's Un-Orthodox Mousetraps.

That's all! (Figure 37.)